A publication of the American Pharmaceutical Association and the American Chemical Society

JOURNAL OF Pharmaceutical Sciences

January 1999
Volume 88, Number 1

MINIREVIEW

Pharmacokinetic Considerations in Obesity

ROBERT A. BLOUIN* AND GRAHAM W. WARREN

Contribution from *Division of Pharmaceutical Sciences, College of Pharmacy and Graduate Center for Toxicology, University of Kentucky, Lexington, Kentucky 40536-0082.*

Received April 22, 1998. Final revised manuscript received October 26, 1998.
Accepted for publication October 28, 1998.

Introduction

Obesity is a disease characterized as a condition resulting from the excess accumulation of body fat. In conjunction with increased stores of body fat, obesity has also been associated with increased mortality influenced by increased incidence of hypertension, atherosclerosis and coronary artery disease, diabetes, cancers of the breast, colon, prostate, endometrium, ovary, and cervix, and decreased overall survivability when compared with nonobese counterparts.[1−5] As a consequence, obese individuals generally require more therapeutic intervention earlier in life than nonobese individuals. A very important consideration for pharmacological treatment of obese individuals is the possible discrepancies between obese and nonobese individuals in pharmacokinetic and/or pharmacodynamic activities of a drug. Changes in pharmacokinetic parameters such as volume of distribution or clearance can significantly alter the pharmacologic impact of a drug; therefore, it is important to characterize the properties of drugs in obese individuals.

The direct causes of obesity are difficult to discern due to the plethora of physiological changes associated with obesity. Furthermore, characterizing metabolic and genetic differences between obese and nonobese individuals has proven complex resulting in broad scale attempts to study genetic and nutritional models of obesity in animals. These animal models can be used to help determine the possible causes and effects of obesity in humans resulting in possible agents to attenuate the causes and effects of obesity.

* Corresponding author: Tel: 606-257-5736. Fax: 606-257-7564. e-mail: rblou1@pop.uky.edu.

There have been several references reviewing the causes and pharmacological implications of obesity.[6−12] These show the effects of obesity on the pharmacokinetics of drugs in obese subjects; however, there have been considerable advances in the understanding of obesity, particularly in the genetic causes and changes in genetic expression asssociated with obesity. This article will attempt to comprehensively review current knowledge regarding obesity ranging from genetic and nutritional animal studies to pharmacokinetic studies of specific drugs in humans.

Obesity and Drug Absorption

The effects of obesity on absorption and overall bioavailability is poorly understood. In contrast to expected decreases in bioavailability associated with increased splanchnic blood flow in obesity,[23] the bioavailability of midazolam[13] and propanolol,[14] two compounds with moderate to high hepatic extraction, was shown not to be significantly different between obese and lean individuals. Body weight was shown to have no effect on the bioavailability of cyclosporine in renal transplant recipients.[15] No statistically significant difference in the bioavailability of dexfenfluramine could be established between obese and normalweight individuals.[16] Overall, studies indicate no significant difference in absorption between obese and lean subjects.

Obesity and Drug Distribution

The volume of distribution of a drug is dependent on a number of factors including tissue size, tissue permeability, plasma protein binding, and the affinity of drugs for a tissue compartment.[17] These factors can be affected by the

10.1021/js980173a CCC: $18.00
Published on Web 12/03/1998

physical and chemical properties of a drug in addition to the presence of many disease states. Obesity is a disease state associated with changes in plasma protein binding constituents[18,19] and increases in adipose tissue mass and lean body mass,[20] organ mass,[21,22] cardiac output,[23,24,25] cardiac size and blood volume,[23,24] and splanchnic blood flow[23] relative to normal-weight individuals.

A general trend has been observed for predicting changes in volume of distribution in obese subjects. Increasingly lipophilic substances, based upon the octanol/water lipid partitioning coefficients (LPC), are generally increasingly affected by obesity. Less lipophilic compounds, with lower LPCs, generally have little to no change in volume of distribution with obesity. There are exceptions to this generalization: cyclosporine, a highly lipophilic compound with a relatively large volume of distribution, has been shown in separate experiments to have comparable absolute volumes of distribution (V_{dss}) in both obese and normal-weight individuals.[15,26]

The effect of high lipid partition coefficients in barbiturates was demonstrated by Cheymol[8] when increasing LPC were correlated with increases in distribution into adipose tissue. Thiopental[27] and diazepam,[11,28] with corresponding LPC values of 676[29] and 309,[30] show significant increases in volume of distribution (V_{dss}) for obese individuals relative to normal-weight individuals. In both cases, the volume of distribution increased for both absolute volume of distribution and when normalized for total body weight. However, the absolute distribution (V_{dss}) of digoxin[31] and procainamide[32] has been shown to remain relatively consistent between obese and normal-weight individuals despite relatively high LPC values,[29,33] and the distribution of digoxin decreased in obese individuals when normalized to actual body weight.[31] Others have shown that digoxin does not have extensive distribution into adipose tissue.[34] These results are supportive of the explanation by Christoff et al.[32] that the high LPC values are too low to enhance distribution into adipose tissue. Ritschell and Kahl[33] have developed equations based upon several parameters (i.e., LPC, plasma protein binding, ionization, normal-weight volume of distribution, and body weight parameters) to help determine volume of distribution in obese individuals, but there has been little further experimental support of these equations.

Polar compounds have been shown to have several different relationships between body weight and volume of distribution. Theophylline, shown not to correlate well with ideal body weight (IBW) or total body weight (TBW),[35,36] was shown to adhere well to the following power equation suggested by Rizzo et al.:[37]

$$V_d \text{ (in liters)} = 1.29\text{TBW}^{0.74}$$

Several authors[38,39] agree that a better relationship between aminoglycoside volume of distribution and body weight is given in the following equation proposed by Bauer et al.:[40]

$$V_d \text{ (in liters)} = (0.26 \text{ L/kg})[\text{IBW} + (\text{CF} \times \text{AW})]$$

where CF is a correction factor between 0.2 and 0.5 and AW = TBW − IBW (adipose weight).

Neuromuscular agents are another group of generally polar compounds. The best method of calculating dosing strategies might be to base calculations on IBW. In one study, it was shown that the absolute volume of distribution (V_{dss}) of atracurium is unchanged in obese individuals.[41] At the same time, the volume of distribution corrected for TBW decreased. Some lipophilic substances, such as the β-adrenergic receptor blockers bisoprolol and nebivolol, also have volumes of distribution that decrease when corrected for TBW.[42,43] These decreased volumes of distribution when corrected for TBW indicate that these drugs distribute less into excess adipose tissue. Bisoprolol was shown to have an increased apparent volume of distribution but decreased volume when corrected for TBW. The authors concluded that these parameters indicated that bisoprolol distributed primarily into excess lean body mass relative to excess adipose tissue.

Plasma protein binding is an important determinant of a drugs pharmacokinetics. Changes in the concentrations of plasma binding proteins or alterations in the affinity of plasma proteins for substrate could affect the movement of drug into tissue compartments. The major plasma proteins are albumin, primarily responsible for binding acidic drugs, α_1-acid glycoprotein (AAG), primarily responsible for binding basic drugs, and lipoproteins. Studies have shown that drugs primarily bound by albumin (e.g., thiopental[27] and phenytoin[18,19,44]) show no significant changes in protein binding in obese individuals; however, the binding of drugs to AAG have been shown to increase and decrease in obesity. Benedek et al.[19] showed a significant increase in AAG concentrations in obese individuals with concomitant decreases in the free fractions of propanolol, principally bound by AAG. Cheymol et al.[45] showed no significant differences in AAG between obese and lean individuals; however, a decrease in volume of distribution of propanolol was observed which was more consistent with increased plasma protein binding. Derry et al.[46] also observed an increase in AAG with no change in the plasma free fraction of triazolam, a drug principally bound by AAG. These results indicate the possibility that plasma protein binding affinity may change in obesity without changes in protein concentrations. The plasma protein binding of verapamil, also associated with AAG binding, was unchanged between obese and nonobese individuals.[47] Due to higher triglyceride and cholesterol levels common in obesity, lipoprotein levels may be elevated in obese individuals; however the ramifications of elevated lipoprotein levels has been poorly studied and is not well understood to date.

The clearance of drugs can also be affected by obesity, though increases in clearance do not necessarily reflect changes in the half-life of a drug. The half-life of a drug can be related to both volume of distribution and clearance through the following relationship:

$$t_{1/2} = (V_d)(0.693)/\text{CL}$$

The half-life of a drug may increase without changes in clearance. Abernathy et al.[48] showed a significant increase in the plasma half-life of desmethyldiazepam without changes in clearance. Rather, the change in half-life was attributed to the increase in volume of distribution in obese individuals. LeJeunne et al.[42] demonstrated increased absolute volume of distribution (V_{dss}) and increased clearance of bisoprolol with no change in plasma half-life in obese versus nonobese individuals. These studies demonstrate the interrelationships between half-life, volume of distribution, and clearance as well as indicates the usefulness of volume of distribution and clearance over plasma half-life for a given drug.

Obesity and Drug Clearance

Changes in Metabolic Enzymes in Obese Humans—Measuring changes in hepatic metabolizing enzymes in humans is difficult due to the general lack of enzyme specific markers of metabolic activity. As a result, relationships are usually drawn between pharmacokinetic behavior

of a drug in humans and measured metabolic enzyme levels in animals. Important considerations are presented by the fact that fatty infiltration characterizes the livers of most individuals.[49] This fatty infiltration generally resembles mild alcoholic hepatitis in moderately obese individuals,[49] but morbidly obese individuals have markedly increased liver damage.[50] These factors could have a significant impact on the metabolic activity of the liver thereby dictating the importance of characterizing metabolism in obese individuals. There are some determinants of metabolic activity in humans that are generally considered as definitive markers for enzyme levels that have been used to show differences between obese and normal-weight individuals. These markers and the effects of obesity are discussed in the following paragraphs. Unless stated otherwise, clearance parameters are not normalized for body weight.

It was previously thought that hepatic oxidative metabolism was essentially unchanged in the obese individual when compared to a normal-weight individual. Caraco et al.[51] used obese and lean volunteers to evaluate the pharmacokinetics of antipyrine, a marker for hepatic oxidative metabolism. In the obese group, plasma half-life increased, apparent volume of distribution increased (but decreased when corrected for TBW), and the clearance remained unchanged. When volunteers were enrolled in a weight reduction program, obese individuals showed decreased half-life, decreased volume of distribution (increased when corrected for TBW), and a nonsignificant increase in clearance after losing weight. The nonsignificant changes in clearance indicate that the oxidative pathways employed by the liver for antipyrine metabolism remain unchanged between obese and normal-weight individuals; however, antipyrine undergoes extensive hepatic oxidative metabolism through multiple oxidative pathways, and a change in singular pathways would be difficult to assess.

Metabolism of chlorzoxazone to 6-hydroxychlorzoxazone has been used as a marker for hepatic cytochrome P450 (CYP) 2E1 activity in humans. O'Shea et al.[94] showed increased chlorzoxazone clearance in obese individuals as well as increased formation clearance of 6-hydroxychlorzoxazone from chlorzoxazone. The increase in chlorzoxazone clearance was attributed to increased CYP2E1 activity associated with obesity. The authors further stated that the increase in CYP2E1 activity may predispose obese individuals to CYP2E1-mediated toxicities associated with the production of toxic metabolites from environmental agents.

The formation of 6β-hydroxycortisol and *N*-methylerythromycin from cortisol and erythromycin has been shown to provide a general marker for cytochrome P450 3A activity in humans.[52,53] Hunt et al.[52] performed a study in volunteers to monitor the metabolism of cortisol and erythromycin to 6β-hydroxycortisol and *N*-methylerythromycin. Using these parameters as measures of CYP3A activity in humans, it was found that a negative correlation existed between percent IBW and *N*-methylerythromycin production. In contrast, cortisol metabolism showed no negative correlation between percent IBW and urinary 6β-hydroxycortisol/cortisol ratios. The authors thought that similar correlations should be drawn between percent IBW and *N*-methylerythromycin and percent IBW and 6β-hydroxycortisol/cortisol ratios. Another study by Hunt et al.[53] supported changes in CYP activity in humans by showing a negative correlation between erythromycin N-demethylation and percent IBW in elderly subjects. These contrasting studies demonstrate the difficulties associated with correlations between specific markers of drug metabolism and specific CYP isoform modulation.

Using drugs that are primarily transformed via Phase II conjugation pathways, glucuronidation and sulfation have been shown to increase in obese individuals. The clearance of oxazepam and lorazepam, benzodiazepines excreted primarily in the form of glucuronide conjugates, was shown to increase in obese individuals.[54] In another study, acetaminophen clearance was shown to increase with obesity,[55] though not as significantly as the increases shown with oxazepam and lorazepam.[54] It has been shown that acetaminophen is eliminated as both a glucuronide and sulfate conjugate in humans[56] whereas oxazepam and lorazepam are excreted primarily as glucuronide conjugates. It is likely that obesity affects different pathways through different mechanisms and levels: where glucuronidation might be significantly enhanced, sulfation may only be slightly to moderately enhanced due to obesity.

Other evidence supporting differential regulation of Phase II pathways are studies showing that the clearance of salicylate[57] and procainamide[32] is not significantly different between obese and lean individuals. Salicylate is conjugated to the glycine, phenolic, and acyl glucuronide, and procainamide is primarily acetylated. Together these results indicate that these pathways may not be significantly affected by obesity in humans.

Another interesting consideration in determining the metabolic activity of obese individuals is considering changes in metabolism in tissues other than the liver; specifically, due to the significant increase in adipose tissue in obese individuals, changes in metabolism within adipose tissue could be significant. Rafecas et al.,[58] using white adipose tissue from obese and lean patients, observed an increase in insulin cleavage in obese subjects relative to normal-weight subjects. In the absence of reduced glutathione, no insulin was cleaved, indicating that glutathione transhydrogenase, present in white adipose tissue, was likely the only enzyme responsible for insulin cleavage within white adipose tissue. The authors stated that hyperinsulinemia common in obesity may be offset by the substantial increase in adipose tissue possessing high intrinsic insulin cleaving activity. The results of this study point to the possibility that adipose tissue might play a significant role in energy regulation in obese individuals. Further evidence suggests that adipose tissue may play a role in the increased clearance of prednisolone in obese men.[59] The interconversion of prednisolone and prednisone is dependent on 11-hydroxysteroid dehydrogenase, an enzyme present in adipose tissue; therefore, the increase in adipose tissue may provide an alternative site of clearance for prednisolone.

In a series of studies, the pharmacokinetics of carbamazepine was evaluated in obese subjects before and after significant weight reduction[60] and in obese versus lean subjects.[61] In the first study, obese subjects were monitored to establish the pharmacokinetic parameters of carbamazepine, and then each subject was entered into a weight reduction program, regulating diet and exercise, after which the same pharmacokinetic parameters were assessed and compared for each individual. After significant weight reduction, the formerly obese individuals had a decreased plasma half-life, increased clearance, decreased absolute volume of distribution (Varea) with respect to bioavailability, and no significant change in Varea when normalized for total body weight. In the second study, relative to normal-weight individuals, obese individuals had increased absolute volume of distribution (Varea), increased plasma half-life, and unchanged clearance values. The disparity between changes in clearance remains unexplained, but it is important to note that obesity may be associated with changes in blood flow or metabolic activity. Further comparison between the two studies indicates that, for car-

bamazepine, the increased volume of distribution and half-life associated with obesity may involve reversible processes that may disappear following weight reduction.

Changes in Renal Function in Obese Humans

Elimination of a drug through the kidney can be accounted for by glomerular filtration, tubular secretion, and tubular reabsorption; however, there are several discrepancies regarding the influence of obesity on these functions. Davis et al.[62] and Stockholm et al.[63] have independently shown increases in glomerular filtration, measured using creatinine clearance, in obese women as compared to normal-weight women. Dionne et al.[64] has also shown increased creatinine clearance in obese subjects when compared to historical values of creatinine clearance; however, Ducharme et al.[65] showed decreased glomerular filtration via creatinine clearance in obese individuals from a patient population study of vancomycin pharmacokinetics. Reiss et al.[66] and Allard et al.[67] showed no significant difference between creatinine clearance in obese versus nonobese individuals. There are also discrepancies between studies of drug primarily excreted by glomerular filtration. Historical evidence has shown that the aminoglycoside antibiotics[68] including gentamicin[69,70] and vancomycin[71] are associated with increased clearance in obese individuals; however, recent evidence has shown that vancomycin clearance is unchanged in obese individuals greater than 1.3 times their IBW.[64] One possible explanation for these discrepancies might be due to the difference in extent of obesity and/or associated renal pathology.

Tubular function (i.e., tubular secretion and tubular reabsorption) in the kidney is often difficult to ascertain; thus, conclusions regarding tubular function are often indirect. Changes in tubular function have been indicated in several studies. The renal clearance of ciprofloxacin,[67] cimetidine,[72,73] procainamide,[32,45] and lithium[66] has been shown to increase in obese individuals. Since the renal excretion of ciprofloxacin,[92] cimetidine,[95] and procainamide[32] involves primarily glomerular filtration and tubular secretion, the increases in renal clearance of ciprofloxacin, cimetidine, and procainamide accompanied by a disproportionate increase in glomerular filtration supports increased tubular secretion in obese individuals. Renal clearance of lithium primarily involves glomerular filtration and tubular reabsorption;[93] consequently, the increase in the renal clearance of lithium with no increase in glomerular filtration[66] supports decreased tubular reabsorption in obese individuals.

Obesity and Drug Pharmacodynamics

A final but equally important consideration when developing a dosing strategy for an individual involves the consideration of drug efficacy. Obese subjects were shown to have increased sensitivity to triazolam as measured by a sedation score upon administration of a second dose.[46] The same dose of triazolam was used for both obese and nonobese individuals. Varin et al.[41] showed that even though obese individuals were exposed to significantly higher plasma concentrations of atracurium, no change was seen in the duration of neuromuscular blockade. The authors attributed this change in sensitivity to a combination of protein binding effects and desensitization of acetycholine receptors. Desensitization of acetylcholine receptors has been associated with chronic inactivity.[74,75] It is important to note that, with the plethora of probable genetic and nutritional changes associated with obesity, changes in receptor expression or affinity for ligand could be altered resulting in differential pharmacotherapeutic effects in obese individuals as compared to lean individuals.

Changes in Metabolic Enzymes in Obese Animals

The influence of pathophysiologic and morphologic changes associated with obesity on hepatic metabolism is not well understood. Before the late 1980s, studies correlating obesity-associated changes with either hepatic drug metabolizing enzymes (e.g., hepatic cytochrome P450) or drug markers (e.g., antipyrine) were nonexistent. In 1989, Corcoran et al.[12] showed no significant difference in CYP concentrations between obese and lean rats; however, total CYP increased per liver in the obese overfed rat. Beginning in the early 1990s, studies began showing changes in hepatic CYP resulting from obesity using both animal models and human markers. Studies dating as far back as the 1970s have indicated changes in Phase II metabolism pathways associated with obesity. The following paragraphs describe differences in Phase I and Phase II metabolism in obese animal models.

Research has been conducted to determine the effects of either genetically or nutritionally induced obesity in mice and rats. Irizar et al.[76] observed decreased total CYP expression in genetically obese (fa/fa) Zucker rats. When expressed as CYP activities per nmol of total CYP, CYP1A, CYP2B, CYP2E, CYP3A, and CYP4A were shown to increase in obese rats using specific substrates. Absolute CYP activities increased for CYP1A and CYP3A in obese rats whereas the increase in expression of other CYP isoforms resulted primarily due to the decrease in overall CYP levels. Anti-mouse CYP2D antibodies showed a decrease in apoprotein in obese rats when compared with normal rats. The investigators indicated the possibility that reduced growth hormone (reduced in obese male animals and shown to be partially responsible for the regulation of CYP3A expression) caused the increase in CYP3A activity. These results illustrate the possible ramifications of genetically induced obesity; however, parallels to humans are difficult to establish due to difficulty in characterizing the genetic causes of obesity in humans.

An alternative model of obesity uses nutritional modulation to induce obesity. Salazar et al.[79] previously reported an increase in CYP2E1 in obese overfed rats. Raucy et al.[77] used overfed Sprague Dawley rats to observe the effects of obesity on the expression of CYP2E1. Following 52 weeks of nutritional overfeeding, obese rats showed increased total CYP relative to control rats, unchanged CYP reductase and cytochrome b5, increased CYP2E1, and unchanged CYP2C11 and CYP3A. A strong correlation was also shown between CYP2E1 activity and CYP2E1 protein immunoblot staining thereby reducing the significance of posttranslational modifications common to CYP2E1. The authors further indicated that ketosis, often implicated as the mechanism by which CYP2E1 is increased, is likely not the primary mechanism of upregulation due to the fact that no significant increases were observed in CYP2B1 or CYP reductase activities also commonly associated with ketosis. Contrasting the genetic versus nutritional models, there appears to be a different mechanism of metabolic regulation influenced by either genetic expression or metabolic changes resulting in possible functional (i.e., enzymatic expression) and morphological (i.e., fatty infiltration in the liver associated with obesity) changes in obese rats. The importance of these factors could easily manifest itself by causing possible increases in toxicity following drug administration such as with the increased acetaminophen toxicity associated with obesity.[78]

Chaudhary et al.[80] provided evidence that glucuronidation increased and sulfation pathways were unaffected in

the genetically obese Zucker rat. Using acetaminophen as a substrate for glucuronidation and sulfation, the investigators observed no difference between urinary excretion of acetaminophen sulfate and increased urinary excretion of acetaminophen glucuronide in the genetically obese Zucker rat when compared to normal-weight rats. No change was observed for γ-glutamyl cysteine synthetase; however, total glutathione and UDPGT increased in obese rats relative to normal-weight rats. This is an important observation indicating that obese rats might have higher conjugation and detoxification pathways, but there is some discrepancy to this conclusion in that Barnett et al.[81] observed lower glutathione-S-transferase and total glutathione in genetically obese (ob/ob) mice indicating possibly higher susceptibility to toxicity in obese mice. The ob/ob mouse model associates noninsulin dependent diabetes with obesity which likely manifests differential enzymatic expression mechanisms than nondiabetes-associated obesity. Consequently, direct correlations between the two models is impossible, but the observation should be made that there are several presently unidentified mechanisms involved in obesity that could possibly result in the regulation and differential expression of many enzymes. An argument against the possibility that obese rats might have higher glutathione conjugation capacity is the fact that others have shown increased acetaminophen toxicity in obese rats indicative of depeted glutathione.[78]

Sastre et al.[82] used an overfed Wistar rat and Swiss mice model to demonstrate that overfed mice had lower levels of both reduced glutathione and oxidized glutathione than chow fed mice. This study seemed to parallel the study by Barnett et al.[81] using a genetically obese mouse model in that both models show a decreased propensity of obese mice for glutathione dependent conjugation and protection against cellular insult. The contrast mentioned before between obese Zucker rats and obese mice is also likely influenced by species specific differences in obesity, another complication in the elucidation and parallel application of obesity associated mechanisms involved in pharmacokinetic changes.

Contrasting the nutritional versus genetic models of obesity, differences can be seen between genetic obesity and nutritional obesity for both Phase I and Phase II enzymatic pathways. It should be noted that genetically induced obesity is targeted for a specific gene, but nutritional obesity can have effects on multiple genes that in turn can effect the expression of many other genes. Consequently, the pathways associated with nutritional obesity may be more variable and harder to elucidate. On the other hand, several current reviews[83–86] cover the genetic causes and effects of obesity should the reader be interested in broadening his/her knowledge of the genetic influences of obesity. Using genetic models, obesity has been linked to deficiencies in leptin, a hormone shown to be secreted by adipocytes[87] that reduces body weight and food intake in both obese and nonobese animals.[88] Research into the interactions of leptin with the body and the effects of obesity on leptin levels is generating volumes of new information into the molecular mechanisms of obesity and the possibilities that obesity might be under hormonal control. Several reviews[89,90] evaluate the current understanding of leptin and its relationship with the body.

Pharmacotherapeutic Toxicity in Obesity

The toxicity of substances can change with obesity. With possible increases in metabolism such as with the CYP system, drugs can be converted to toxic metabolites at higher rates; however, toxic drugs may also be converted to inactive metabolites at higher rates. Changes in the clearance, volume of distribution, bioavailability, or pharmacodynamics may affect the toxic potential of a drug. Additionally, changes in excretion mechanisms can alter the toxicity of a compound by either increasing exposure through decreased clearance or vice-versa. One study by Georgiadis et al.[91] observed the possible increases or decreases on the toxicity associated with the administration of a plethora of highly toxic chemotherapeutic agents to obese versus lean subjects with small-cell lung cancer. According to the study, no correlation could be established between obesity and increased toxicity for patients receiving cyclophosphamide, methotrexate, lomustine, etoposide, and cisplatin. Perhaps the most important conclusion to be drawn from the information presented in this article is that each drug behaves differently. Predicting toxicity associated with obesity is very difficult if not impossible. The best approach for pharmacotherapeutics in obese individuals is to use previous knowledge and be conservative. Careful monitoring of the obese patient is necessary when administering drugs with a small therapeutic index.

Summary

Using the parameters of volume of distribution and clearance, a therapeutic dosing strategy can be developed for a drug. Consequently, the effects of physiological disorders on these parameters is important for accurate pharmacotherapeutics. Regarding obesity, the volume of distribution has been shown to change in many situations. Generally, more lipophilic compounds are affected by obesity to a greater extent than hydrophilic compounds. More lipophilic compounds are associated with increases in volume of distribution in obesity; however, there are exceptions to this relationship. High LPC values did not correspond with markedly increased volumes of distribution for digoxin,[31] procainamide,[32] and cyclosporine.[15,26] Consequently, prior knowledge of the effects of obesity on specific drugs is essential for accurate dosing strategies based upon volume of distribution; generalizations among similar groups of drugs does not always result in proper physiologic responses between obese and lean individuals.

The clearance of a compound depends on the metabolic activity of characteristic enzymes that may be affected by obesity or diseases associated with obesity. Changes have been noted in both humans and animals for various CYP isozymes using either direct measurements (in animals) or through the use of metabolic markers (in humans) such as antipyrine or erythromycin. In addition, obesity has been associated with increased glucuronidation with questionable effects on sulfation. Changes between obese and lean subjects have also been observed for antioxidant systems including glutathione and catalase. It is important to note the variability in characterizing metabolic changes in obesity. Given the numerous possible genetic and environmental influences, predicting changes in metabolic activity can be difficult. Furthermore, there are possibilities that similar concentrations of a drug at its site of action may not elicit a similar response between obese and lean subjects, thereby making accurate therapeutic modifications more difficult for obese individuals.

Renal function, particularly glomerular filtration, has been shown to change with obesity. Increased glomerular filtration in some studies has been contradicted by decreases in glomerular filtration in other studies. These discrepancies illustrate the possible ramifications of different degrees of obesity, with morbidly obese individuals exhibiting different responses than moderately obese individuals. The effects of obesity on the toxicology of specific compounds is questionable depending upon not only the presence of enzymes that create toxic metabolites, but also

depending upon the presence of enzymes that remove toxic metabolites from the body. In conclusion, a safe therapeutic protocol for obese individuals should be based upon existing therapeutic information as well as careful monitoring of the patient during pharmacologic intervention.

References and Notes

1. Lew, E. A. Mortality and weight: Insured lives and the Americal Cancer Society studies. *Ann. Intern. Med.* **1985**, *103*, 1024−1029.
2. Pi-Sunyer, F. X. Medical hazards of obesity. *Ann. Intern. Med.* **1993**, *119*, 655−660.
3. Suissa, S.; Pollack, M.; Spitzer, W.; Margolese, R. Body size and breast cancer prognosis: a statistical explanation of the discrepancies. *Cancer Res.* **1989**, *49*, 3113−3116.
4. Seine, R. T.; Rosen, P. P.; Rhodes, P.; Lesser, M. L.; Kinne, D. W. Obesity at diagnosis of breast carcinoma influences duration of disease-free survival. *Ann. Intern. Med.* **1992**, *116*, 26−32.
5. Bastarrachea, J.; Hortobagyi, G. N.; Smith, T. L.; Kan, S. W.; Buzdar, A. U. Obesity as an adverse prognostic factor for patients receiving adjuvant chemotherapy for breast cancer. *Ann. Intern. Med.* **1994**, *119*, 18−25.
6. Cheymol, G. Clinical pharmacokinetics of drugs in obesity: an update. *Clin Pharmacokinet.* **1993**, *25*, 103−114.
7. Blouin, R. A.; Chandler, M. H. H. Special pharmacokinetic considerations in the obese. *Applied pharmacokinetics: principles of therapeutic drug monitoring, 3rd ed.*; Evans, W. E., Schentag, J. J., Jusko, W. J., Ed.; Applied Therapeutics: Vancouver, B.C., 1992; pp 11.3−11.20.
8. Cheymol, G. Drug pharmacokinetics in the obese. *Fundam. Clin. Pharmacol.* **1988**, *2*, 239−256.
9. Blouin, R. A.; Kolpek, J. H.; Mann, H. J. Influence of obesity on drug disposition. *Clin. Pharmacy* **1987**, *6*, 706−714.
10. Abernethy, D. R.; Greenblatt, D. J. Drug disposition in obese humans: an update. *Clin. Pharmacokinet.* **1986**, *11*, 199−213.
11. Abernethy, D. R.; Greenblatt, D. J.; Divoll, M.; Harmatz, J. S.; Shader, R. I. Alterations in drug distribution and clearance due to obesity. *J Pharmacol. Exp. Ther.* **1981**, *217*, 681−685.
12. Corcoran, G. B.; Salazar, D. E.; Sorge, C. L. Pharmacokinetic characteristics of the obese overfed rat model. *Int. J. Obes.* **1989**, *13*, 69−79.
13. Greenblatt, D. J.; Abernethy, D. R.; Locniskar, A.; Harmatz, J. S.; Limjuco, R. A.; Shader, R. I. Effect of age, gender, and obesity on midazolam kinetics. *Anesthesiology* **1984**, *61*, 27−35.
14. Bowman, S. L.; Hudson, S. A.; Simpson, G.; Munro, J. F.; Clements, J. A. A comparison of the pharmacokinetics of propanolol in obese and normal volunteers. *Br. J. Clin. Pharmacol.* **1986**, *21*, 529−532.
15. Flechner, S. M.; Kolbeinsson, M. E.; Tam, J.; Lum, B. The impact of body weight on cyclosporine pharmacokinetics in renal transplant recipients. *Transplantation* **1989**, *47*, 806−810.
16. Cheymol, G.; Weissenburger, J.; Poirier, J. M.; Gellee, C. The pharmacokinetics of dexfenfluramine in obese and nonobese subjects. *Br. J. Clin. Pharmacol.* **1995**, *39*, 684−687.
17. Rowland, M.; Tozer, T. N. *Clinical Pharmacokinetics: Concepts and Applications*, 2nd ed.; Lea and Febiger: Philadelphia, 1989; pp 131−137.
18. Benedek, I. H.; Fiske, W. D., III; Griffen, W. O.; Bell, R. M.; Blouin, R. A.; McNamara, P. J. Serum alpha$_1$-acid glycoprotein and the binding of drugs in obesity. *Br. J. Clin. Pharmacol.* **1983**, *16*, 751−754.
19. Benedek, I. H.; Blouin, R. A.; McNamara, P. J. Serum protein binding and the role of increased alpha$_1$-acid glycoprotein in moderately obese male subjects. *Br. J. Clin. Pharmacol.* **1984**, *18*, 941−946.
20. Kjellberg, J.; Reizenstein, P. Body composition in obesity. *Acta Med. Scand.* **1970**, *188*, 161−169.
21. Naeye, R. L.; Rode, P. The sizes and numbers of cells in visceral organs in human obesity. *Am. J. Clin. Pathol.* **1970**, *54*, 251−253.
22. Smith, H. L. The relation of the weight of the heart to the weight of the body and of the weight of the heart to age. *Am. Heart J.* **1928**, *4*, 79−93.
23. Alexander, J. K.; Dennis, E. W.; Smith, W. G.; Amad, K. H.; Duncan, W. C.; Austin, R. C. Blood volume, cardiac output, and disposition of systemic blood flow in extreme obesity. *Cardiovasc. Res. Cent. Bull.* **1962**−**1963**, *1*, 39−44.
24. Alexander, J. K. Obesity and cardiac performance. *Am. J. Cardiol.* **1964**, *14*, 860−865.
25. de Divitiis, O.; Fazio, S.; Petitto, M.; Maddalena, G.; Contaldo, F.; Mancini, M. Obesity and cardiac function. *Circulation* **1981**, *64*, 477−482.
26. Yee, G. C.; Lennon, T. P.; Gmur, D. J.; Cheney, C. L.; Oeser, D.; Deeg, H. J. Effect of obesity on CSA disposition. *Transplantation* **1988**, *45*, 649−651.
27. Jung, D.; Mayersohn, M.; Perrier, D.; Calkins, J.; Saunders: R. Thiopental disposition in lean and obese patients undergoing surgery. *Anesthesiology* **1982**, *56*, 269−274.
28. Abernethy, D. R.; Greenblatt, D. J.; Divoll, M.; Shader, R. I. Prolonged accumulation of diazepam in obesity. *J Clin Pharmacol* **1983**, *23*, 369−376.
29. Leo, A.; Hansch, C.; Elkin, D. Partition coefficients and their uses. *Chem. Rev.* **1971**, *71*, 525−616.
30. Arendt, R. M.; Greenblatt, D. J.; Divoll, M.; Abernethy, D. R.; Giles, H. G.; Sellers, E. M. Predicting *in vivo* benzodiazepine distribution based upon in vitro lipophilicity. *Clin. Pharmacol. Ther.* **1982**, *31*, 200−201.
31. Abernethy, D. R.; Greenblatt, D. J.; Smith, T. W. Digoxin disposition in obesity: clinical pharmacokinetic investigation. *Am. Heart J.* **1981**, *102*, 740−744.
32. Christoff, P. B.; Conti, D. R.; Naylor, C.; Jusko, W. J. Procainimide disposition in obesity. *Drug Intell. Clin. Pharm.* **1983**, *23*, 369−376.
33. Ritchel, W. A.; Kaul, S. Prediction of apparent volumes of distribution in obesity. *Methods Find Exp Clin Pharmacol* **1986**, *8*, 239−247.
34. Doherty, J. E.; Perkins, W. H.; Flanigan, W. J. The distribution and concentration of tritiated digoxin in human tissues. *Ann. Intern. Med.* **1967**, *66*, 116−124.
35. Rohrbaugh, T. M.; Danish, M.; Ragni, M. C.; Yaffe, S. J. The effect of obesity on apparent volume of distribution of theophylline. *Pediatr. Pharmacol.* **1982**, *2*, 75−83.
36. Gal, P.; Jusko, W. J.; Yurchak, A. M.; Franklin, B. A. Theophylline disposition in obesity. *Clin. Pharmacol. Ther.* **1978**, *23*, 438−444.
37. Rizzo, A.; Mirabella, A.; Bonanno, A. Effect of body weight on the volume of distribution of theophylline. *Lung* **1988**, *166*, 269−276.
38. Schwartz, S. N.; Pazin, G. J.; Lyon, J. A.; Ho, M.; Pasculle, A. W. A controlled investigation of the pharmacokinetics of gentamicin and tobramycin in obese subjects. *J Infect. Dis* **1978**, *138*, 499−505.
39. Blouin, R. A.; Mann, H. J.; Griffen, W. O., Jr; Bauer, L. A.; Record, K. E. Tobramycin pharmacokinetics in morbidly obese patients. *Clin. Pharmacol. Ther.* **1979**, *26*, 508−512.
40. Bauer, L. A.; Blouin, R. A.; Griffen, W. O., Jr; Bauer, L. A.; Record, K. E. Amikacin pharmacokinetics in morbidly obese patients. *Am. J. Hosp. Pharm.* **1980**, *3*, 519−522.
41. Varin, F.; Ducharme, J.; Theoret, Y.; Besner, J. G.; Bevan, D. R.; Donati, F. Influence of extreme obesity on the body disposition and neuromuscular blocking effect of atracurium. *Clin. Pharmacol. Ther.* **1990**, *48*, 18−25.
42. Le Jeunne, C. L.; Poirier, J. M.; Cheymol, G.; Ertzbischoff, O.; Engel, F.; Hugues, F. C. Pharmacokinetics of intravenous bisoprolol in obese and nonobese volunteers. *Eur. J. Clin. Pharmacol.* **1991**, *41*, 171−174.
43. Cheymol, G.; Woestenborghs, R.; Snoeck, E.; Ianucci, R.; Le Moing, J. P.; Naditch, L.; Levron, J. C.; Poirier, J. M. Pharmacokinetic study and cardiovascular monitoring of nebivolol in normal and obese subjects. *Eur. J. Clin. Pharmacol.* **1997**, *51*, 493−498.
44. Abernethy, D. R.; Greenblatt, D. J. Phenytoin disposition in obesity. *Arch. Neurol.* **1985**, *42*, 468−471.
45. Cheymol, G. Comparative pharmacokinetics of intravenous propanolol in obese and normal volunteers. *J. Clin. Pharmacol.* **1987**, *27*, 874−879.
46. Derry, C. L.; Kroboth, P. D.; Pittenger, A. L.; Kroboth, F. J.; Corey, S. E.; Smith, R. B. Pharmacokinetics and pharmacodynamics of triazolam after two intermittent doses in obese and normal-weight men. *J. Clin. Psychopharmacol.* **1995**, *15*, 197−205.
47. Abernethy, D. R.; Schwartz, J. B. Verapamil pharmacodynamics and disposition in obese hypertensives *J. Cardiovasc. Pharmacol.* **1988**, *11*, 209−215.
48. Abernethy, D. R.; Greenblatt, D. J.; Divoll, M.; Shader, R. I. Prolongation of drug half-life due to obesity: studies of desmethyldiazepam (clorazepate). *J. Pharm. Sci.* **1982**, *7*, 942−944.
49. Sherlock, S. *Diseases of the liver biliary system*, 7th ed.; Blackwell Scientific Publications: Boston, 1985, p 384.
50. Vaughan, R. W. Definitions and risks of obesity. In *Anesthesia and the Obese Patient*; Brown, B. R., Ed.; 1982; F. A. Davis Co.: Philadelphia, pp 1−8.
51. Caraco, Y.; Zylber-Katz, E.; Berry, E. M.; Levy, M. Antipyrine disposition in obesity: evidence for negligible effect of obesity on hepatic oxidative metabolism. *Eur. J. Clin. Pharmacol.* **1995**, *47*, 525−530.

52. Hunt, C. M.; Watkins, P. B.; Saenger, P.; Stave, G. M.; Barlascini, N.; Watlington, C. O.; Wright, J. T.; Guzelian, P. S. Heterogeneity of CYP3A isoforms metabolizing erythromycin and cortisol. *Clin. Pharmacol. Ther.* **1992**, *51*, 18−23.
53. Hunt, C. M.; Westerkam, W. R.; Stave, G. M.; Wilson, J. A. P. Hepatic cytochrome P-4503A (CYP3A) activity in the elderly. *Mech. Aging Dev.* **1992**, *64*, 189−199.
54. Abernethy, D. R.; Greenblatt, D. J.; Divoll, M.; Shader, R. I. Enhanced glucuronide conjugation of drugs in obesity: studies of lorazepam, oxazepam, and acetaminophen. *J. Lab. Clin. Med*. **1983**, *101*, 873−880.
55. Abernethy, D. R.; Divoll, M.; Greenblatt, D. J.; Ameer, B. Obesity, sex, and acetaminophen disposition. *Clin. Pharmacol. Ther.* **1982**, *31*, 783−790.
56. Cummins, A. J.; King, K. L.; Martin, B. K. A kinetic study of drug elimination: the excretion of paracetamol and its metabolites in man. *Br. J. Pharm. Chem.* **1967**, *29*, 150−157.
57. Greenblatt, D. J.; Abernethy, D. R.; Boxenbaum, H. G.; Matlis, R.; Ochs, H. R.; Harmatz, J. S.; Shader, R. I. Influence of age, gender, and obesity on salicylate kinetics following doses of aspirin. *Arthritis Rheum* **1986**, *29*, 971−980.
58. Rafecas, I.; Fernandez-Lopez, J. A.; Salinas, I.; Formiguera, X.; Remesar, X.; Foz, M.; Alemany, M. Insulin degradation by adipose tissue is increased in human obesity. *J. Clin. Endocr. Metab*. **1995**, *80*, 693−695.
59. Milsap, R. L.; Plaisance, K. I.; Jusko, W. J. Prednisolone disposition in obese men. *Clin. Pharmacol. Ther.* **1984**, *36*, 824−831.
60. Caraco, Y.; Zylber-Katz, E.; Berry, E. M.; Levy, M. Significant weight reduction in obese subjects enhances carbamazepine elimination. *Clin. Pharmacol. Ther.* **1992**, *51*, 501−506.
61. Caraco, Y.; Zylber-Katz, E.; Berry, E. M.; Levy, M. Carbamazepine pharmacokinetics in obese and lean subjects. *Ann. Pharmacother.* **1995**, *29*, 843−847.
62. Davis, R. L.; Quenzer, R. W.; Bozigian, H. P.; Warner, C. W. Pharmacokinetics of ranitidine in morbidly obese women. DICP *Ann. Pharmacother.* **1990**, *24*, 1040−1043.
63. Stokholm, K. H.; Brochner-Mortenson, J.; Hoilund-Carlsen, P. F. Glomerular filtration rate and adrenocortical function in obese women. *Int. J. Obes.* **1980**, *4*, 57−63.
64. Dionne, R. E.; Bauer, L. A.; Gibson, G. A.; Griffen, W. O., Jr; Blouin, R. A. Estimating creatinine clearance in morbidly obese patients. *Am. J. Hosp. Pharm.* **1981**, *38*, 841−844.
65. Ducharme, M. P.; Slaughter, R. L.; Edwards, D. J. Vancomycin pharmacokinetics in a patient population: effect of age, gender, and body weight. *Ther Drug Monit* **1994**, *16*, 513−518.
66. Reiss, R. A.; Haas, C. E.; Karki, S. D.; Gumbiner, B.; Welle, S. L.; Carson, S. W. Lithium pharmacokinetics in the obese. *Clin. Pharmacol. Ther.* **1994**, *55*, 392−398.
67. Allard, S.; Kinzig, M.; Boivin, G.; Sorgel, F.; LeBel, M. Intravenous ciprofloxacin disposition in obesity. *Clin. Pharmacol. Ther.* **1993**, *54*, 368−373.
68. Bauer, L. A.; Edwards, W. A.; Dellinger, E. P.; Simonowitz, D. A. Influence of weight on aminoglycoside pharmacokinetics in normal weight and morbidly obese patients. *Eur. J. Clin. Pharmacol.* **1983**, *24*, 643−647.
69. Korsager, S. Administration of gentamicin to obese patients. *Int. J. Clin. Pharmacol. Ther. Toxicol.* **1980**, *18*, 549−553.
70. Sketris, L.; Lesar, T.; Zaske, D. E.; Cipolle, R. J. Effect of obesity on gentamicin pharmacokinetics. *J. Clin. Pharmacol.* **1981**, *21*, 228−293.
71. Blouin, R. A.; Bauer, L. A.; Miller, D. D.; Record, K. E.; Griffen, W. O., Jr. Vancomycin pharmacokinetics in normal and morbidly obese subjects. *Antimocrob. Agents Chemother.* **1982**, *21*, 575−580.
72. Abernethy, D. R.; Greenblatt, D. J.; Matlis, R.; Gugler, R. Cimetidine disposition in obesity. *Am. J. Gastroenterol.* **1984**, *79*, 91−94.
73. Bauer, L. A.; Wareing-Tran, C.; Edwards, W. A.; Raisys, V.; Ferreri, L.; Jack, R.; Dellinger, E. P. Cimetidine clearance in the obese. *Clin. Pharmacol. Ther.* **1985**, *37*, 425−530.
74. Waud, B. E.; Waud, D. R. Turboaurarine sensitivity of the diaphragm after limb immobilizaiton. *Anesth. Analg.* **1986**, *65*, 493−495.
75. Gronert, G. A. Disuse atrophy with resistance to pancuronium. *Anesthesiology* **1981**, *55*, 547−549.
76. Irizar, A.; Barnett, C. R.; Flatt, P. R.; Ioannides, C. Defective expression of cytochrome P450 proteins in the liver of the genetically obese zucker rat. *Eur. J. Pharmacol. Environ. Toxicol. Pharmacol. Sect.* **1995**, *293*, 385−393.
77. Raucy, J. L.; Lasker, J. M.; Kraner, J. C.; Salazar, D. E.; Lieber, C. S.; Corcoran, G. B. Induction of cytochrome P450IIE1 in the obese overfed rat. *Mol. Pharmacol.* **1991**, *39*, 275−280.
78. Corcoran, G. B.; Wong, B. K. Obesity as a risk factor in drug-induced organ injury: increased liver and kidney damage by acetaminophen in the obese overfed rat. *J. Pharmacol. Exp. Ther.* **1987**, *241*, 921−927.
79. Salazar, D. E.; Sorge, C. L.; Corcoran, G. B. Obesity as a risk factor for drug-induced organ injury VI: increased hepatic P450 concentration and microsomal ethanol oxidizing activity in the obese overfed rat. *Biochem. Biophys. Res. Commun.* **1988**, *157*, 315−320.
80. Chaudhary, I. P.; Tuntaterdtum, S.; McNamara, P. J.; Robertson, L. W.; Blouin, R. A. Effect of genetic obesity and phenobarbitol treatment on the hepatic conjugation pathways. *J. Pharmacol. Exp. Ther.* **1993**, *265*, 1333−1338.
81. Barnett, C. R.; Abbott, R. A.; Bailey, C. J.; Flatt, P. R.; Ioannides, C. Cytochrome P450-dependent mixed-function oxidase and glutathione-S-transferase activities in spontaneous obesity diabetes. *Biochem. Pharmacol.* **1992**, *43*, 1868−1871.
82. Sastre, J.; Pallardo, F. V.; Llopis, J.; Furukawa, T.; Vina, J. R.; Vina, J. Glutathione depletion by hyperphagia-induced obesity. *Life Sci.* **1989**, *45*, 183−187.
83. Naggert, J.; Harris, T.; North, M. The genetics of obesity. *Curr. Opin. Genet. Dev.* **1997**, *7*, 398−404.
84. Pi-Sunyer, F. X. Energy balance: role of genetics and activity. *Ann. N.Y. Acad. Sci.* **1997**, *819*, 29−36.
85. Saladin, R.; Staels, B.; Auwerx, J.; Briggs, M. Regulation of ob gene expression in rodents and humans. *Horm. Metab. Res.* **1996**, *28*, 638−41.
86. Roberts, S. B.; Greenberg, A. S. The new obesity genes. *Nutr. Rev.* **1996**, *54*, 41−49.
87. Zhang, Y.; Proneca, R.; Maffei, M.; Barone, M.; Leopold, L.; Friedman, J. M. Positional cloning of the mouse obese gene and its human analogue. *Nature* **1994**, *372*, 425−432.
88. Campfield, L. A.; Smith, F. J.; Burn, P. The QB protein (leptin) pathway: a link between adipose tissue mass and central neural networks. *Horm. Metab. Res.* **1996**, *28*, 619−632.
89. Considine, R. V.; Caro, J. F. Leptin: genes, concepts, and clinical perspective. *Horm. Res.* **1996**, *46*, 249−256.
90. Caro, J. F.; Sinha, M. K.; Kolaczynski, J. W.; Zhang, P. L.; Considine, R. V. Leptin: the tale of an obesity gene. *Diabetes* **1996**, *45*, 1455−1462.
91. Georgiadis, M. S.; Steinberg, S. M.; Hankins, D. C.; Johnson, B. E. Obesity and therapy related toxicity in patients treated for small-cell lung cancer. *J. Nat. Cancer Inst.* **1995**, *87*, 361−366.
92. Vance-Bryan, K.; Guay, D. R.; Rotschafer, J. C. Clinical pharmacokinetics of ciprofloxacin. *Clin. Pharmacokinet.* **1990**, *19*, 434−461.
93. DePaulo, J. R.; Correa, E. I.; Sapir, D. G. Renal toxicity of lithium and its implications. *Johns Hopkins Med. J.* **1981**, *149*, 15−21.
94. O′Shea, D.; Davis, S. N.; Kim, R. B.; Wilkinson, G. R. Effect of fasting and obesity in humans on the 6-hydroxylation of chlorzoxazone: a putative probe of CYP2E1 activity. *Clin. Pharmacol. Ther.* **1994**, *56*, 359−367.
95. Drayer, D. E.; Romankiewicz, J.; Lorenzo, B.; Reidenberg, M. M. Age and renal clearance of cimetidine. *Clin. Pharmacol. Ther.* **1982**, *31*, 45−50.

Acknowledgments

G.W. was supported, in part, by an NIEHS Training Grant (ES07266).

JS980173A

Secondary Structure and Protein Deamidation

MINLI XIE AND RICHARD L. SCHOWEN*

Contribution from *Department of Pharmaceutical Chemistry, Simons Laboratories of the Higuchi Biosciences Center, University of Kansas, Lawrence, Kansas, 66047.*

Received June 16, 1998. Final revised manuscript received September 14, 1998.
Accepted for publication September 16, 1998.

Abstract □ The deamidation reactions of asparagine residues in α-helical and β-turn secondary structural environments of peptides and proteins are reviewed. Both kinds of secondary structure tend to stabilize asparagine residues against deamidation, although the effects are not large. The effect of β-sheet structures on asparagine stability is unclear, although simple considerations suggest a stabilization in this environment also.

Introduction

As peptides and proteins continue to enter the pharmaceutical marketplace, their stability becomes a pressing issue for the pharmaceutical sciences. One of the major routes of degradation of peptides and proteins that contain an asparagine (Asn) residue is the reaction illustrated in Figure 1, known as *deamidation*.[1] In deamidation, the NH center of the residue C-terminal to Asn attacks nucleophilically (with base catalysis) at the carbonyl center of the side-chain amide. Expulsion of ammonia produces a *cyclic imide* or *succinimide* derivative, which is activated toward hydrolysis. Hydrolysis occurs at both carbonyl centers, leading to a mixture of two products. Attack by water or water-derived species at the carbonyl center formed from the Asn side chain (the *β-carbonyl center*) produces a point-mutant peptide or protein in which Asn has been converted to aspartate (Asp), the *Asp product*. Attack at the carbonyl center derived from the backbone (the α-*carbonyl center*) produces a peptide or protein in which the un-natural amino acid iso-Asp has been incorporated into the backbone (the *iso-Asp product*). In some cases, the biological properties of the mutated proteins differ from those of the original material, and the degradation reaction is thus of pharmaceutical concern.

In the case of peptides or proteins that possess higher-order structure, the secondary, tertiary, or quaternary structural environment may affect the readiness with which deamidation can occur. Such an effect can arise in two different ways. First, the higher-order structure may place the Asn residue in spatial proximity to a functional group elsewhere in the primary sequence that is capable of accelerating or inhibiting the rate of deamidation. It is relatively difficult to generalize about effects of this kind, and they must be treated on a case-by-case basis. Second, the conformational properties of the Asn residue and the nearby peptide region containing it may be strongly conditioned by the nature of the structural environment that incorporates the residue. The work required to undergo the deamidation reaction, arising from such sources as strain energies that change on formation of the transition state(s) or vibrational entropy changes associated with the restriction of side-chain motions, may therefore vary substantially from one structural environment to another.

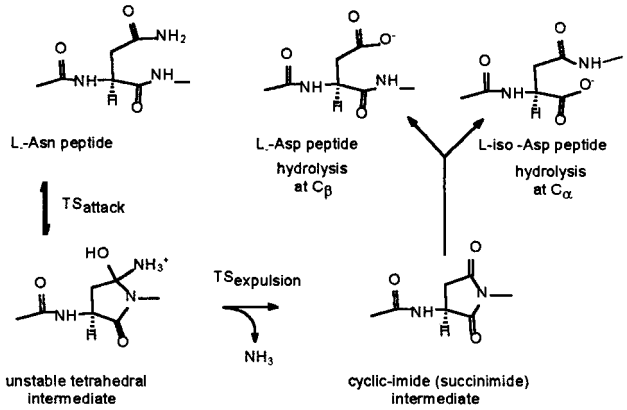

Figure 1—The mechanism of the Asn deamidation reaction at neutral and basic pH. The Asn-containing peptide (top left) undergoes base-catalyzed nucleophilic attack of the backbone NH center C-terminal to Asn on the side-chain amide carbonyl. This step, passing through the transition state TS_{attack}, leads to formation of the tetrahedral intermediate, an unstable species that never accumulates to observable concentrations. This unstable intermediate expels ammonia irreversibly in the transition state $TS_{expulsion}$ to generate the more stable cyclic imide intermediate at bottom right. This species accumulates to observable levels in the pH region 4–5, but decomposes as rapidly as it forms at higher pH. The cyclic imide undergoes hydrolytic attack at both carbonyl centers, leading to the Asp product and the iso-Asp product (upper right), the latter dominating in a ratio of 2:1 to 4:1. In addition to the reactions shown, racemization can occur by deprotonation of the chiral center in the ring, leading to racemized Asp product and iso-Asp product.

Examples of such effects have been provided by Kossiakoff,[2] who found that three of the 13 Asn residues of trypsin underwent relatively rapid deamidation. These residues (48, 95, 115) were characterized by a common conformation that favored the reaction and also by common hydrogen-bonding interactions with groups that could assist in the nucleophilic attack that occurs in deamidation. The conformation and the interactions were both results of the tertiary structure of trypsin.

In this minireview, we focus on secondary structural features and their role in governing deamidation rates. We further concentrate on experimental studies under highly defined conditions, omitting (with recognition of their great value) surveys of data collected under a range of conditions.[3,4]

Mechanism of Deamidation[5]

Figure 1 outlines the chief mechanistic features of the deamidation sequence as it occurs in the neutral and near-neutral pH regime (roughly pH 4−9). The cyclic imide intermediate is generated in a base-catalyzed reaction

* Author to whom correspondence should be sent. Telephone: 785-864-4080. Fax: 785-864-5349. E-mail: rschowen@ukans.edu.

10.1021/js9802493 CCC: $18.00
Published on Web 11/06/1998

involving deprotonation of the backbone NH center to generate a very small amount of the highly reactive conjugate base. Attack by this species at the side-chain amide function of Asn leads through the transition state labeled TS_{attack} to the tetrahedral intermediate shown. This species is very reactive and does not accumulate to observable levels. Instead, it decomposes either by return to reactant or by expulsion of ammonia to form the cyclic imide intermediate, the latter reaction occurring through the transition state labeled $TS_{expulsion}$. At the point when ammonia has been lost into the medium, return to the original reactant becomes very improbable, and the peptide or protein is committed to degradation.

Which of the two transition states is of higher free energy and thus governs the rate will depend on the pH and other factors, such as temperature and medium composition. The main form of the tetrahedral intermediate in the neutral region should be the cationic form because the pK_a of the ammonium-center is probably around 8.5 to 9. In this case, the choice of rate-limiting step is dictated by the relative ease of expulsion from the tetrahedral intermediate of the quite basic conjugate base of the backbone NH in competition with the less basic ammonia molecule. It is then likely that expulsion of ammonia is more rapid, and thus the rate-limiting transition state should be TS_{attack} for formation of the C−N bond.

The chemistry of decomposition of the cyclic imide intermediate to products is also mechanistically complex.[6] Unlike the tetrahedral intermediate, the cyclic imide accumulates to an observable extent under some conditions. Below and around pH 4, sizable concentrations of the cyclic intermediate may build up, and the material can often be isolated for independent study. At neutral and basic pH, base-catalyzed hydrolytic ring opening is rapid and precludes isolation or observation of the cyclic imide.

Hydrolytic attack occurs at both carbonyl centers of the cyclic imide, with attack at the (apparently) more sterically hindered C_α leading to the dominant iso-Asp product, and the less rapid attack at C_β leading to the Asp product. The ratio [iso-Asp]/[Asp] is quite generally around 4 in acidic solutions, tending toward 2.5−3 in more basic solutions. Very recent work[7] suggests that the determining feature in the regioselectivity is hydrogen bonding from the adjacent N-terminal NH, which promotes nucleophilic attack at C_α over that at C_β despite possible steric hindrance at C_α.

The roughly planar cyclic imide allows greater delocalization of electron density adjacent to C_α into the carbonyl group, rendering the C−H bond at the chiral center of the ring more acidic and more prone to removal by bases. Thus, conversion to a D-cyclic imide is possible. Hydrolysis of this species will lead to Asp and iso-Asp products of D configuration, and thus to partial or complete racemization.

Protein or peptide degradation becomes a certainty when formation of the cyclic imide intermediate, which is irreversible, is complete. The transition state TS_{attack} (Figure 1) is presumably rate-limiting in cylic-imide formation and it is therefore the effect of secondary protein structure on the free energy required to attain this transition state that determines how readily deamidation will occur in various protein or peptide secondary structural environments.

Structural Environment and Ring Formation

Prediction of the expected rate constant for deamidation under various circumstances remains a complex problem. The conversion of reactant state to TS_{attack}, as shown in eq 1, will require work equal to the free energy of activation ΔG^* and the rate constant will then be given by eq 2.

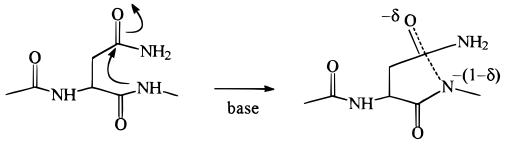

(1)

$$k = (kT/h)\exp\{-\Delta G^*/RT\} = (kT/h)\exp\{-\Delta H^*/RT + \Delta S^*/R\} \quad (2)$$

In eq 2, the free energy of activation (representing the total work of converting reactant state to transition state) is divided into its component parts ΔH^* and ΔS^*. The enthalpy of activation ΔH^*, measures such energetic quantities as the ring or conformational strain involved in formation of the new bond in eq 1, the energy requirement for partially breaking the amide carbonyl bond, the energy release for partial formation of the new C−N bond, the energy requirement for deprotonation of the backbone NH center, and any changes in solvation energies attendant upon conversion of reactant state to transition state. The entropy of activation ΔS^*, is a measure of the changes in molecular mobility or flexibility between reactant and transition states: loss of flexibility makes this quantity more negative, thus slowing the reaction, whereas increases of flexibility render the entropy of activation more positive, causing the reaction to proceed more rapidly. Clearly, the conformational flexibility of the molecule decreases on cyclization (loss of internal rotational entropy) but solvation changes, which will affect the translational mobility of the system, tend to be large and may contribute either positive or negative increments. The overall summation of effects contributing to ΔH^* and ΔS^* and thus to ΔG^*, thereby determining the rate constant of deamidation, is clearly a complicated matter about which generalization can be difficult.

Obviously, some of the features contributing to ΔH^* and ΔS^* will not be very sensitive to the secondary structural environment of an Asn residue in a peptide or protein. It is usually assumed that the energy changes associated with formation and fission of covalent bonds will be determined largely by the intrinsic chemistry of the nucleophilic reaction and will remain reasonably constant in various environments. On the other hand, the conformational contributions may be especially sensitive to the secondary structural environment.

Important Secondary Structural Elements

The complete enumeration of currently recognized elements of secondary structure in proteins and peptides would involve a large number of entries. A very useful summary has been given by Carter.[8] In this minireview, we will concentrate on the three most common secondary structural elements: the α-helix, the β-sheet, and the β-turn.

The α-helix consists of the right-handed coil in which every backbone carbonyl group is hydrogen-bonded to a backbone NH center of the fifth residue toward the C-terminus. All residues in an α-helix are conformationally equivalent in that their backbone dihedral angles are equal and all peptide bonds are in the trans configuration. Because all backbone NH centers of an α-helix are hydrogen-bonded, this factor alone might be expected to reduce the nucleophilic reactivity of the NH centers and thus the rate of deamidation of Asn residues in α-helices.

β-Sheets are structures obtained by alignment of fully extended peptide strands with all peptide bonds in the trans configuration so that all backbone carbonyl groups

of each strand are hydrogen-bonded to backbone NH centers in the adjacent strand, and vice-versa. The strands may be aligned either parallel to each other (C-terminus to C-terminus) or antiparallel (C-terminus to N-terminus). In either case, all NH centers are again hydrogen-bonded and will presumably exhibit reduced nucleophilic reactivity, and all residues are again conformationally equivalent.

The β-turns are present at points where strands of peptide reverse direction. Their defining feature is a hydrogen bond that unites the backbone carbonyl group of the first (N-terminal) residue of the turn to the backbone NH of the fourth residue (C-terminal) further on. The peptide bond between the second and third residues (the "middle peptide bond") defines a plane that is roughly perpendicular to the plane of the initial and final hydrogen-bonded peptide bonds. When the NH of the "middle peptide" is roughly trans to the side chain of the second residue, the β-turn is known as a Type I turn; when the configuration is roughly cis, the β-turn is known as a Type II turn. The simplest variants of these two types are Types I′ and II′ in which dihedral angles are reversed in sign while maintaining the other features unchanged. Other types of β-turns exist but are rare, and only Types I and II β-turns will be considered here. Each of the four residues involved in a β-turn is conformationally unique.

Clarke's Conjecture

Clarke[9] in 1987 noted that some generalizations about conformation and reactivity in deamidation are possible simply because, to react, the system must allow a juxtaposition of the nucleophilic backbone NH center and the electrophilic side-chain amide center of the Asn residue. The more difficult this juxtaposition, the slower deamidation should be, and the more readily the juxtaposition can be attained, the more rapid should deamidation become. Figure 2 illustrates this concept very schematically in terms of a *critical distance of approach* between nucleophile and electrophile for an Asn residue located in different secondary structural environments.

Clarke reasoned that secondary structural environments in which the conformation about the backbone bonds near an Asn residue favors a short critical distance of approach would be more likely to promote rapid deamidation than environments in which conformations favoring such an approach are not present. The side-chain conformation should also be important for deamidation but is unlikely to be affected systematically by the secondary structural environment. It is not certain how small the critical distance of approach actually must be at the deamidation transition state, but it is reasonable to expect that it is not greatly longer than the a typical C−N single bond (ca. 1.4−1.5 Å) because, according to Pauling's rule, a reduction in bond order by a factor of 2 corresponds to a lengthening of the bond by only 0.2 Å. Thus, a C−N bond of order 0.5 would be about 1.6−1.7 Å in length and a bond of order 0.25 would be about 1.8−1.9 Å in length. An Asn residue should, therefore, be protected with respect to deamidation in a structural environment that makes it hard to achieve critical distances of approach shorter than 2 Å.

In the most common types of secondary structure, the constraints imposed always predict a reduction in the rate of deamidation relative to the rate in a structurally unconstrained environment. Clarke's predictions suggest the following minimum critical distances of approach for different elements of secondary structure (see Figure 2 for schematic illustrations of these structures): α-helix, 2.5 Å; β-sheet (parallel or antiparallel), 3.5 Å; and β-turn (Type I or Type II), 3.1−3.3 Å. These distances are all so large as

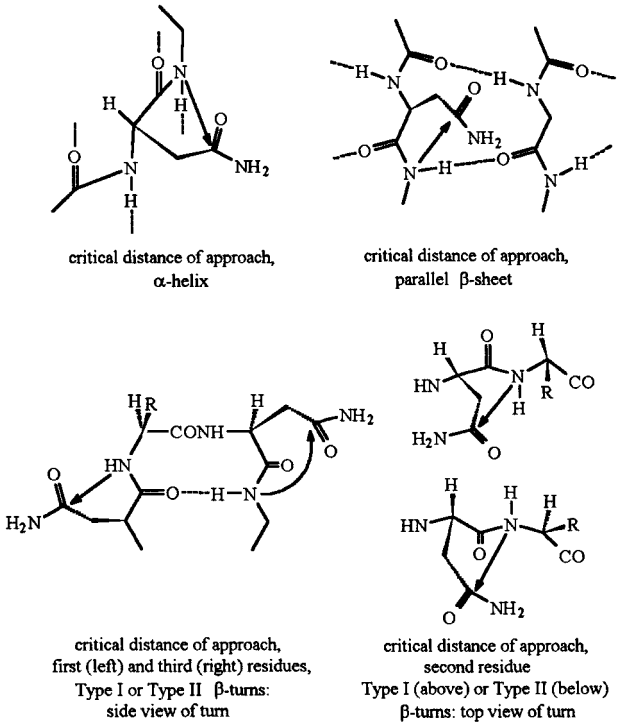

Figure 2—Schematic indications of the requisite directions of nucleophilic attack for Asn deamidation in various secondary structural environments. The arrows indicate the nucleophile–electrophile distance, which must be reduced to a critical value of less than about 2 Å to form the transition state TS_{attack}. Upper structures: α-helix (left) and β-sheet (right). The situation in the parallel β-sheet, which is shown, is not altered in the antiparallel sheet. Lower structures: β-turns. Left, first, and third residues of Type I or Type II β-turns, viewed from the side. Right, second residues of Type I (above) or Type II (below) β-turns.

to suggest that deamidation of Asn residues in any of these structural elements should occur less rapidly than for Asn residues in unstructured environments.

Clarke's estimates are based on the probability that the nucleophilic and electrophilic centers of an Asn residue in a particular secondary structural environment can reach the requisite critical distance of approach. It might be thought therefore that their origin should be in the entropy of activation ΔS^*. Despite the reasonable character of this idea, it is unlikely to be correct. Lightstone and Bruice[10] conducted an extensive investigation of the energetic factors involved in cyclic anhydride formation by intramolecular nucleophilic reaction of a carboxylate nucleophile with an ester electrophile. The conformation-dependent energetics of this reaction should be very similar to those in the deamidation reaction. Lightstone and Bruice showed that attainment of a "near-attack conformation," very similar to Clark's required critical distance between nucleophile and electrophile, requires both enthalpic and entropic contributions, and indeed the enthalpic components can be dominant. The same is almost surely true for deamidation.

Asparagine Deamidation in α-Helices

Asn is a somewhat infrequent residue in α-helices, being classified according to the Chou-Fasman rules[11,12] as a "weak helix-breaker." If the infrequency is caused by instability of Asn in the helical environment, the instability might suggest a more rapid rate of degradation. As already noted, the α-helical environment constrains the critical distance of approach to a quite long distance, which

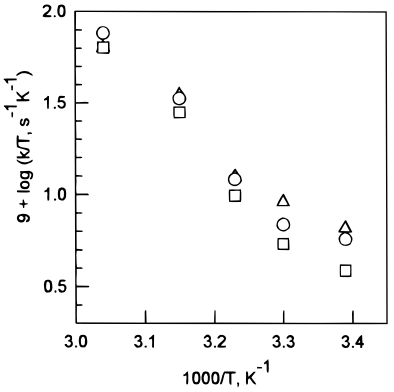

Figure 3—Eyring plot of deamidation rate constants determined by Bongers and co-workers[13] for deamidation at Asn-8 in the human growth-hormone releasing factor fragment hGRF(1–29) at pH 8 in aqueous solution at temperatures from 22 to 56 °C. The circles are for the wild-type (Thr-7 Gly-15), the triangles are for the Thr-7 Ala-15 mutant, and the squares are for the Pro-7 Gly-15 mutant.

suggests slow deamidation. Thus, from a general conceptual view, it is unclear what to expect.

Two experimental studies have been carried out in related model systems, and in fact have led to apparently contradictory results. Both make use of the structures derived from mammalian growth-hormone releasing factors (GRF), where Asn-8 is located in an α-helix. The helical region includes a glycine residue, Gly-15, which can be mutated to alanine (Ala), a helix enhancer, to increase the helical character or to proline (Pro), a helix breaker, to reduce the helical content. Alternatively, helical content may be reduced by mutation of threonine-7 to Pro.

Bongers and co-workers[13] obtained data that were interpreted as indicating that high helix content was associated with more rapid deamidation, and thus were contrary to the prediction of Clarke's conformational rule. They determined the deamidation rates at Asn-8 in aqueous buffers for the Ala-15 (high helix), Gly-15 (wild type), and Pro-7 (low helix) peptides (hGRF(1−29)NH_2) derived from human growth-hormone releasing factor, hGRF(1−44)NH_2. Data were obtained at five temperatures from 22 °C to 56 °C. Their findings are replotted as Eyring plots [log(k/T) versus (1/T)] in Figure 3.

The view of Bongers and co-workers is that the data for all three peptides fit a single temperature dependence at 37 °C and above. They attribute the roughly equal rates for the three to a proposed random-coil structure for all three peptides in this relatively high-temperature regime. The mutations at positions 7 and 15 were taken to have a minimal effect in the random-coil state on the deamidation of Asn-8. Bongers and co-workers then consider that the data disperse into three roughly parallel dependences in the low-temperature regime below 37 °C. The change in temperature dependences is postulated to be associated with a coil-to-α-helix transition occurring in the region around 37 °C.

In the low-temperature region, the Ala-15 peptide (assumed to have high helix content) reacts most rapidly, the Pro-7 peptide (assumed to have low helix content) reacts most slowly, and the Gly-15 peptide (assumed to have intermediate helix content) reacts at an intermediate rate. The structural assumptions were not confirmed by experiment. The low-temperature data thus, on this model, would indicate a fast reaction for the helix-enhancing mutant and a slow reaction for the helix-breaking mutant. This model suggests that presence in an α-helix renders an Asn residue *more labile*, rather than protecting it.

It is certainly clear that a single process is not at work throughout the temperature range represented in Figure 3: the plots for all three peptides are quite nonlinear. The *highest temperature* points suggest the following activation parameters for deamidation

$$\Delta H^* = \text{ca. } 10 \text{ kcal/mol (Ala-15)}$$
$$= \text{ca. } 14 \text{ kcal/mol (Gly-15 and Pro-7)}$$
$$\Delta S^* = \text{ca. } -50 \text{ eu (Ala-15)}$$
$$= \text{ca. } -35 \text{ eu (Gly-15 and Pro-7)}$$

The *lowest temperature* points suggest the following activation parameters

$$\Delta H^* = \text{ca. } 7.5 \text{ kcal/mol (Ala-15 and Pro-7)}$$
$$= \text{ca. } 4 \text{ kcal/mol (Gly-15)7}$$
$$\Delta S^* = \text{ca. } -60 \text{ eu (Ala-15 and Pro-7)}$$
$$= \text{ca. } -70 \text{ eu (Gly-15)}$$

Treated in this way, neither the high-temperature nor the low-temperature data support a systematic and simple interpretation: the similarities and differences in the rate constants (the largest range at any temperature is less than 2-fold) may arise from enthalpy−entropy compensation, although no credible claim in this direction is possible.

Some aspects of this study suggest that the break in the Eyring plots at around 37 °C may not arise from a thermal induction of helical structure. For example, the full-length GRF, hGRF(1−44)-NH_2, and the severely truncated peptide hGRF(1−29)-NH_2 exhibit equal rate constants for deamidation at the lowest temperature studied (22 °C, pH 8). This result is unexpected if helical character is present for the 29-mer but not for the 11-mer.

As Bongers and co-workers pointed out, the low-temperature data show a substantially lower enthalpy (or energy) of activation than is observed in many deamidation reactions. Further study must identify the anomaly that low temperatures are inducing in this particular case, although helical structure seems unlikely. One possibility is that aggregation of the peptides is occurring at the lower temperatures.

A later study gave results apparently in contrast to those of Bongers and co-workers, although the overlap between the two approaches is incomplete. Stevenson and co-workers[14] prepared the bovine GRF fragment [Leu^{27}]bGRF-(1−42)NH_2 with Gly, Ala, and Pro at position 15. Circular dichroism established that at 25 °C the overall helical content was 7.4% (Pro-15), 12.1% (Gly-15), and 17.7% (Ala-15). Addition of the helix-enhancing solvent methanol (MeOH) led to an increased helix content with preservation of the order seen in water: for 20% MeOH, the helical content was 16.3% (Pro-15), 28.6% (Gly-15), and 36.3% (Ala-15); and for 40% MeOH, the helical content reached 24.4% (Pro-15), 47.5% (Gly-15), and 52.5% (Ala-15).

For each of these circumstances, the deamidation rate constant for Asn-8 was determined at pH 10 in bicarbonate buffers (or the equivalent "pH" in aqueous methanol) at 37 °C. Figure 4 shows a plot in which the logarithm of the rate constant is related to the overall fractional helicity in the peptide. Although the errors are substantial, there is a discernible trend toward lower activity with greater helical character; the half-life times for deamidation increase from 6.9 h for the Pro-15 peptide in aqueous solution to 21.5 h for the Ala-15 peptide in 40% MeOH. Stevenson and co-workers therefore agree with the conclusion from Clarke's approach that presence in an α-helical environment protects Asn residues against deamidation, which stands in contrast to the interpretations put forward by Bongers and co-workers.

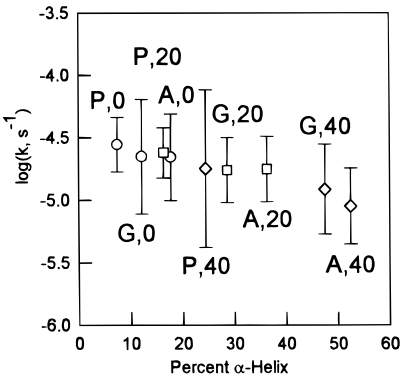

Figure 4—Plot of the logarithm of the rate constant determined by Stevenson and co-workers[14] for deamidation at Asn-8 in the bovine growth-hormone releasing fragment [Leu^{27}]bGRF(1–42)NH_2 at pH 10 in aqueous and aqueous–methanol solutions at 37 °C. Data are given for the wild-yype peptide Gly-15 (denoted by the letter G), for Ala-15 (denoted A), and for Pro-15 (denoted P). Each mutant was studied in three solvents: aqueous solution (circles; denoted by the number 0), 20% methanol/80% water (squares, denoted by 20), and 40% methanol/60% water (diamonds, denoted 40).

In neither of these studies are the rate effects attributed to α-helix incorporation large. Furthermore, in both studies, the methods used in attempting to control helix content may have given rise to other effects not connected with secondary structure. Bongers and co-workers introduced the presumed helix-breaking Pro at position 7, which is adjacent to Asn-8, the site of deamidation. This nearby structural change could have had effects on the rate not deriving from secondary structure. Stevenson and co-workers used methanol as a cosolvent to increase helix content. Brennan and Clarke,[15] however, have shown that the decreased dielectric constant in aqueous ethanol mixtures reduces the rate of deamidation; this effect will be at work in aqueous methanol solutions as well and will be superimposed on the conformational effect of the methanol. Bongers and co-workers attribute an acceleration of 1.8-fold in deamidation to the presence of Asn in an α-helix. In the work of Stevenson and co-workers, protection by a factor of 3 is attributed to presence of Asn in the α-helix. Thus without resolving the basis for the disagreement between these sets of results, one may tentatively conclude that deamidation rates are unlikely to vary by more than a factor of 10 on incorporation of an Asn residue into an α-helix.

Asparagine Deamidation in *β*-sheets

Clarke's approach indicates stabilization of Asn against deamidation when present in both parallel and antiparallel *β*-sheet structures, but no definitive study has yet been conducted to test this prediction experimentally.

One of the products of deamidation, the iso-Asp residue, does appear to induce *β*-sheet formation. The human *β*-amyloid protein undergoes deamidation at Asn-1 and Asn-7, giving rise in part to the iso-Asp residues at these positions.[16] Both polypeptides exhibit higher *β*-sheet content than does the native Asn polypeptide. This result suggests a lower free energy of the iso-Asp residue in the *β*-sheet than in other secondary structures, so that conversion of Asn to iso-Asp in *β*-sheet structures should be thermodynamically favored. For this thermodynamic effect to produce more rapid deamidation, the stabilization would have to be expressed in the deamidation transition state, which should occur only if this transition state resembled the iso-Asp structure. This effect is exceedingly unlikely because the rate-limiting transition state for deamidation must be one of those during irreversible formation of the cyclic imide intermediate, neither of which is related to the iso-Asp structure. Even in decomposition of the cyclic imide to the iso-Asp product, the transition state is more likely to resemble the ring structure than the open-chain structure. Thus the stabilization of the iso-Asp product by *β*-sheet structures is unlikely to be the cause of accelerated deamidation in *β*-sheets.

Asparagine Deamidation in *β*-Turns

Recent findings, described next, suggest that Asn located in any of the positions of a *β*-turn is stabilized against deamidation. This is also the prediction from the application of Clarke's conformational considerations (Figure 2). The same conclusion was reached for deamidation of Asn-12 in the HPr phosphocarrier protein,[17,18] a residue present in the third position of a Type I *β*-turn. This residue undergoes deamidation only under the very stringent condition of boiling water at basic pH. Furthermore, a number of proteins show faster deamidation in the unfolded form than in the native form for Asn residues located in *β*-turns of the native, folded structures or otherwise exhibit evidence of the stabilization of Asn or the related Asp residues in *β*-turn structures.[19–28]

In contrast, some crystallographic studies suggest that the transition state(s) for deamidation are stabilized in *β*-turns, and thus that deamidation should be accelerated in such structures. Capasso and co-workers[29] and Obrecht and co-workers[30] observed that structures containing a cyclic imide, such as Boc-L-Asu-Gly-OMe, exhibited a Type II′ *β*-turn in the crystal. The cyclic imide takes up the second position in the *β*-turn.

Because the cyclic imide structure is thus more stable when a *β*-turn is assumed, as shown by the preference for this structure in the solid state, it could be deduced that the presence of a *β*-turn would correspondingly favor conversion to a cyclic imide or to transition states resembling the cyclic imide. Because the transition state for deamidation is expected to resemble the cyclic imide, *β*-turns might well induce cyclization and deamidation. On the other hand, the adoption of the *β*-turn in the crystal structure might be conditioned by such features as crystal packing forces or the relatively nonaqueous environment of the crystal, and thus the conclusion derived from the crystal structure might not be accurate for proteins or peptides in solution.

In still unpublished work,[31] Asn-containing dipeptides were synthesized in cyclic forms, the N-terminus and C-terminus being united by the spacer, *ϵ*-aminocaproic acid. Such cyclic peptides assume a *β*-turn conformation, as was shown in these cases by nuclear magnetic resonance and circular dichroism spectroscopy. The deamidation rates of the cyclic *β*-turn mimics were compared with those of the open-chain analogues, which exhibited only random-coil structures. Universally, the *β*-turn structures showed slower deamidation rates than the random-coil structures. These results would suggest that *β*-turn structures indeed stabilize Asn residues against deamidation.

Summary

Two of the common forms of secondary structure (α-helices and *β*-turns) tend to stabilize Asn residues against deamidation. The effect is weak at best in α-helices, which may even destabilize Asn residues. Stabilization probably results at least in part from conformational restrictions, as deduced by Clarke, but may be additionally produced by the reduced nucleophilic reactivity of the backbone NH centers, which are hydrogen-bonded in α-helices and in all

except one position of the β-turns. Evidence is lacking for the third common form of secondary structure, β-sheets, but the prediction both from conformational considerations and from the reduced nucleophilicity of the backbone NH center is that stabilization would also be effected here.

References and Notes

1. *Deamidation and Isoaspartate Formation in Peptides and Proteins*; Aswad, D. W., Ed.; CRC: Boca Raton, FL, 1994.
2. Kossiakoff, A. A. Tertiary Structure is a Principal Determinant to Protein Deamidation. *Science* **1988**, *240*, 191−194.
3. Powell, M. F. A Compendium and Hydropathy/Flexibility Analysis of Common Reactive Sites in Proteins: Reactivity at Asn, Asp, Gln and Met Motifs in Neutral pH Solution. In *Formulation, Characterization and Stability of Protein Drugs*; Pearlman, R.; Wang, Y. J., Eds.; Plenum: New York, 1996; pp 1−134.
4. Wright, T. E. Sequence and Structure Determinants of the Nonenzymatic Deamidation of Asparagine and Glutamine Residues in Proteins. *Protein Engin.* **1991**, *4*, 283−294.
5. Capasso, S.; Mazzarella, L.; Sica, F.; Zagari, A.; Salvadori, S. Kinetics and Mechanism of Succinimide Ring Formation in the Deamidation Process of Asparagine Residues. *J. Chem. Soc., Perkin Trans. 2* **1993**, 679−682.
6. Xie, M.; Morton, M.; Vander Velde, D.; Borchardt, R. T.; Schowen, R. L. pH-Induced Change in Rate-Determining Step for the Hydrolysis of the Asp/Asn Derived Cyclic Imide Intermediate in Protein Degradation. *J. Am. Chem. Soc.* **1996**, *118*, 8955−8956.
7. Xie, M., unpublished results.
8. Carter, C. W., Jr. Protein Structure. In *Bioorganic Chemistry: Peptides and Proteins*; Hecht, S. M., Ed.; Oxford University: New York, 1998; pp 153−223.
9. Clarke, S. Propensity for Spontaneous Succinimide Formation from Aspartyl and Asparaginyl Residues in Cellular Proteins. *Int. J. Pept. Protein Res.* **1987**, *30*, 808−821.
10. Lightstone, F. C.; Bruice, T. C. Ground State Conformations and Enthalpic and Entropic Factors in the Efficiency of Intramolecular and Enzymatic Reactions. 1. Cyclic Anhydride Formation by Substituted Glutarates, Succinates, and 3,6-endoxo-Δ^4-tetrahydrophthalate. *J. Am. Chem. Soc.* **1996**, *118*, 2595−2605.
11. Chou, P. Y.; Fasman, G. D. Conformational Parameters for Amino Acids in Helical, β-Sheet and Random Coil Regions Calculated from Proteins. *Biochemistry* **1974**, *13*, 211−223.
12. Chou, P. Y.; Fasman, G. D. β-Turns in proteins. *J. Mol. Biol.* **1977**, *115*, 135−175.
13. Bongers, J.; Heimer, E. P.; Lambros, T.; Pan, Y.-C. E.; Campbell, R. M.; Felix, A. M. Degradation of Aspartic acid and Asparagine Residues in Human Growth Hormone-Releasing Factor. *Int. J. Pept. Protein Res.* **1992**, *39*, 364−374.
14. Stevenson, C. L.; Friedman, A. R.; Kubiak, T. M.; Donlan, M. E.; Borchardt, R. T. Effect of Secondary Structure on the Rate of Deamidation of Several Growth Hormone Releasing Factor Analogues. *Int. J. Pept. Protein Res.* **1993**, *42*, 497−503.
15. Brennan, T. V.; Clarke, S. Spontaneous degradation of polypeptides at aspartyl and asparaginyl residues: effects of the solvent dielectric, *Protein Sci.* **1993**, *2*, 331−338.
16. Fabian, H.; Szendrei, G. I.; Mantsch, H. H.; Greenberg, B. D.; Ötvös, L., Jr. Synthetic Posttranslationally Modified Human Aβ Peptide Exhibits a Markedly Increased Tendency to Form β-Pleated Sheets in vitro. *Eur. J. Biochem.* **1994**, *221*, 959−964.
17. Sharma, S.; Hammen, P. K.; Leung, A.; Georges, F.; Henstenberg, W.; Klevit, R. E.; Waygood, E. B. Deamidation of HPr, a Phosphocarrier Protein of the Phosphoenolpyruvate: Sugar Phosphotransferase System, Involves Asparagine 38 (HPr-1) and Asparagine 12 (HPr-2) in Isoaspartyl Acid Formation. *J. Biol. Chem.* **1993**, *268*, 17 695−17 704.
18. Brennan, T. V.; Anderson, J. W.; Jia, Z.; Waygood, E. B.; Clarke, S. Repair of Spontaneously Deamidated HPr Phosphocarrier Protein Catalyzed by the L-Isoaspartate (D-Aspartate) O-Methyltransferase. *J. Biol. Chem.* **1994**, *269*, 25 486−24 595.
19. Di Donato, A.; Ciardiello, M. A.; de Nigris, M.; Piccoli, R.; Mazzarella, L.; D'Alessio, G. Selective Deamidation of Ribonuclease A. *J. Biol. Chem.* **1993**, *268*, 4745−4751.
20. Thannhauser, T. W.; Scheraga, H. A. Reversible Blocking of Half-Cystine Residues of Proteins and an Irreversible Specific Deamidation of Asparagine-67 of S−Sulforibonuclease under Mild Conditions. *Biochemistry* **1985**, *24*, 7681−7688.
21. Stephenson, R. C.; Clarke, S. Succinimide Formation from Aspartyl and Asparaginyl Peptides as a Model for the Spontaneous Degradation of Proteins. *J. Biol. Chem.* **1989**, *264*, 6164−6170.
22. Wearne, S. J.; Creighton, T. E. Effect of Protein Conformation on Rate of Deamidation: Ribonuclease A. *Proteins: Struct. Funct. Genet.* **1989**, *5*, 8−12,153−223.
23. Capasso, S.; Di Donato, A.; Esposito, L.; Sica, F., Sorrentino, G.; Vitagliano, L.; Zagari, A.; Mazzarella, L. Deamidation in Proteins: the Crystal Structure of Bovine Pancreatic Ribonuclease with an Isoaspartyl Residue at Position 67. *J. Mol. Biol.* **1996**, *257*, 492−296.
24. Cacia, J.; Keck, R.; Presta, L. G.; Frenz, J. Isomerization of an Aspartic Acid Residue in the Complementarity-Determining Regions of a Recombinant Antibody to Human IgE: Identification and Effect on Binding Affinity. *Biochemistry* **1996**, *35*, 1897−1903.
25. Jia, Z.; Vandonselaar, M.; Quail, J. W.; Qelbaere, L. T. J. Active-center Torsion-angle Strain Revealed in 1.6 Å-Resolution Structure of Histidine-containing Phosphocarrier Protein. *Nature* **1993**, *361*, 95−97.
26. Bischoff, R.; Lepage, P.; Jaquinod, M.; Cauet, G.; Acker-Klein, M.; Clesse, D.; Laporte, M.; Bayol, A.; Van Dorsselaer, A.; Roitsch, C. Sequence Specific Deamidation: Isolation and Biochemical Characterization of Succinimide Intermediates of Recombinant Hirudin. *Biochemistry* **1993**, *32*, 725−734.
27. Szendrei, G. I.; Fabian, H.; Mantsch, H. H.; Lovas, S.; Nyeki, O.; Schon, I.; Ötvös, L. Aspartate-bond Isomerization Affects the Major Conformations of Synthetic Peptides. *Eur. J. Biochem.* **1994**, *226*, 917−924.
28. Chazin, W. J.; Kördel, J.; Thulin, E.; Hofmann, T.; Drakenberg, T.; Forsén, S. Identification of an Isoaspartyl Linkage Formed upon Deamidation of Bovine Calbindin D_{9k} and Structural Characterization by 2D ^{1}H NMR. *Biochemistry* **1989**, *28*, 8646−8653.
29. Capasso, S.; Mazzarella, L.; Sica, F.; Zagari, A. *tert*-Butyloxycarbonyl-L-aminosuccinyl-glycyl-L-alanine Methyl Ester (Boc-L-Asu-Gly-L-Ala-OMe). *Acta Crystallogr.* **1987**, *C43*, 1607−1610.
30. Obrecht, D.; Bohdal, U.; Daly, J.; Lehman, C.; Schönholzer, P.; Müller, K. A Novel Synthesis of (*R*)- and (*S*)-α-alkylated Aspartic and Glutamic Acids: α-Alkylated Aspartic Succinimides as New Type of β-Turn Type II and Type II' Mimics. *Tetrahedron* **1995**, *51*, 10 883−10 900.
31. Xie, M., unpublished work.

Acknowledgments

M.X. thanks the Pharmaceutical Research and Manufacturing Association for an advanced predoctoral fellowship. R.L.S. thanks the Alexander von Humboldt Foundation for support.

JS9802493

Pharmacokinetic and Metabolism Studies Using Microdialysis Sampling

DANNETTE K. HANSEN,[†] MALONNE I. DAVIES,[‡] SUSAN M. LUNTE,[*,§] AND CRAIG E. LUNTE[†]

Contribution from *the Departments of Chemistry and Pharmaceutical Chemistry and the Center for Bioanalytical Research, University of Kansas, Lawrence, Kansas 66047 and Bioanalytical Systems, Inc.–Kansas Research Laboratory, Lawrence, Kansas.*

Received March 31, 1998. Final revised manuscript received October 5, 1998. Accepted for publication October 6, 1998.

Introduction

ADME (adsorption, distribution, metabolism, elimination) studies on new drug entities, toxicological studies on environmental contaminants, and evaluation of chemicals in the workplace all involve gathering similar types of information. Such studies rely on a combination of in vitro, ex vivo, and in vivo techniques. Among the in vitro and ex vivo systems are isolated enzymes, microsomes, cell cultures, tissue homogenates, tissue slices, and isolated organs. Information about the role of specific enzymes and tissues, types of intermediates formed, and pathways for xenobiotic biotransformation are gained through these types of studies. However, because they represent parts rather than the whole physiological system, the types of information gained do not reflect the entire scheme of biotransformation within the intact organism.

Traditional in vivo techniques include sampling blood and other biological fluids, analysis of elimination products to determine final disposition of the parent compound and metabolites, and tissue sampling requiring one or more animals per time point. These studies provide general information about the metabolism and final disposition of a compound, but do not offer details about specific enzymes, intermediates, or in vivo metabolic pathways. An overall limitation to traditional approaches is that results obtained in vitro sometimes do not correlate with those found in vivo.

Microdialysis sampling has several characteristics that complement traditional in vitro and in vivo pharmacokinetic and metabolism techniques. This approach is accomplished by implanting a probe consisting of a hollow fiber dialysis membrane into the organ or biological matrix of interest. The short length of hollow fiber is affixed to pieces of narrow bore tubing that serve as inlet and oulet conduits for the probe. A solution, termed the perfusate, is pumped slowly through the probe. The perfusate is an aqueous solution that closely matches the ionic composition of the extracellular fluid (ECF). When the perfusate is correctly matched to the ECF, there should be no net exchange of water or ions across the membrane. Low molecular weight compounds can diffuse into or out of the probe lumen in response to concentration gradients and are pumped to the analysis system.

A diagram of the process is shown in Figure 1. For clarity, the diagram shows only one analyte (A), although several compounds are typically sampled at the same time in a microdialysis experiment. Large molecules such as proteins (P) and small molecules bound to proteins (P-A) are excluded by the membrane. Those molecules entering the lumen of the membrane are swept along by the perfusate and exit the probe. The solution leaving the probe, termed the dialysate, is collected for analysis. The probe can be thought of as an artificial blood vessel in that it can both deliver and remove compounds from the local area. Delivery of the parent compound via the probe permits study of local metabolism without systemic involvement. Figure 2 shows a basic diagram of a microdialysis system for sampling from an awake, freely moving animal.

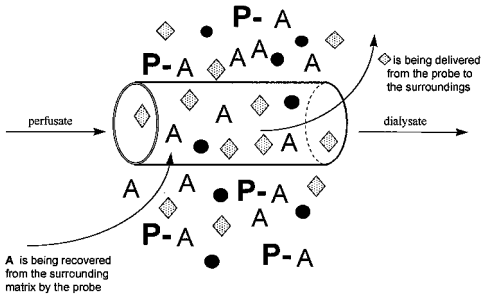

Figure 1—The microdialysis process.[37]

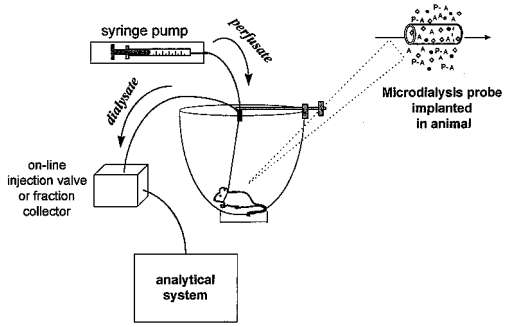

Figure 2—General diagram of microdialysis system for sampling from an awake, freely moving animal. The analysis may be performed on a variety of analytical systems, and coupling between the analytical and microdialysis systems may be on- or off-line.

Microdialysis is an established in vivo tool in the neurosciences and has been used in vitro and in peripheral tissues for a variety of applications of pharmacological and metabolic interest. Samples obtained by microdialysis represent a local profile of low molecular mass hydrophilic substances in the area surrounding the probe. For compounds of pharmaceutical interest, the dialysate reflects the free fraction of the compound of interest, which is the therapeutically active portion of the dose. Microdialysis sampling does not change the net fluid balance in the surrounding matrix or tissue, so higher temporal resolution can be achieved than with traditional techniques. Also, because there is no net fluid loss, samples can be collected continuously for hours or days from a single animal. Most importantly, each animal can serve as its own control, reducing the number of experimental animals needed.

Typically, sampling in vitro from various incubation mixtures or in vivo from blood or other fluids involves

* Author to whom correspondence should be addressed.
[†] Department of Chemistry and the Center for Bioanalytical Research.
[‡] Bioanalytical Systems, Inc.–Kansas Research Laboratory.
[§] Department of Pharmaceutical Chemistry and Center for Bioanalytical Research.

10.1021/js9801485 CCC: $18.00
Published on Web 12/11/1998

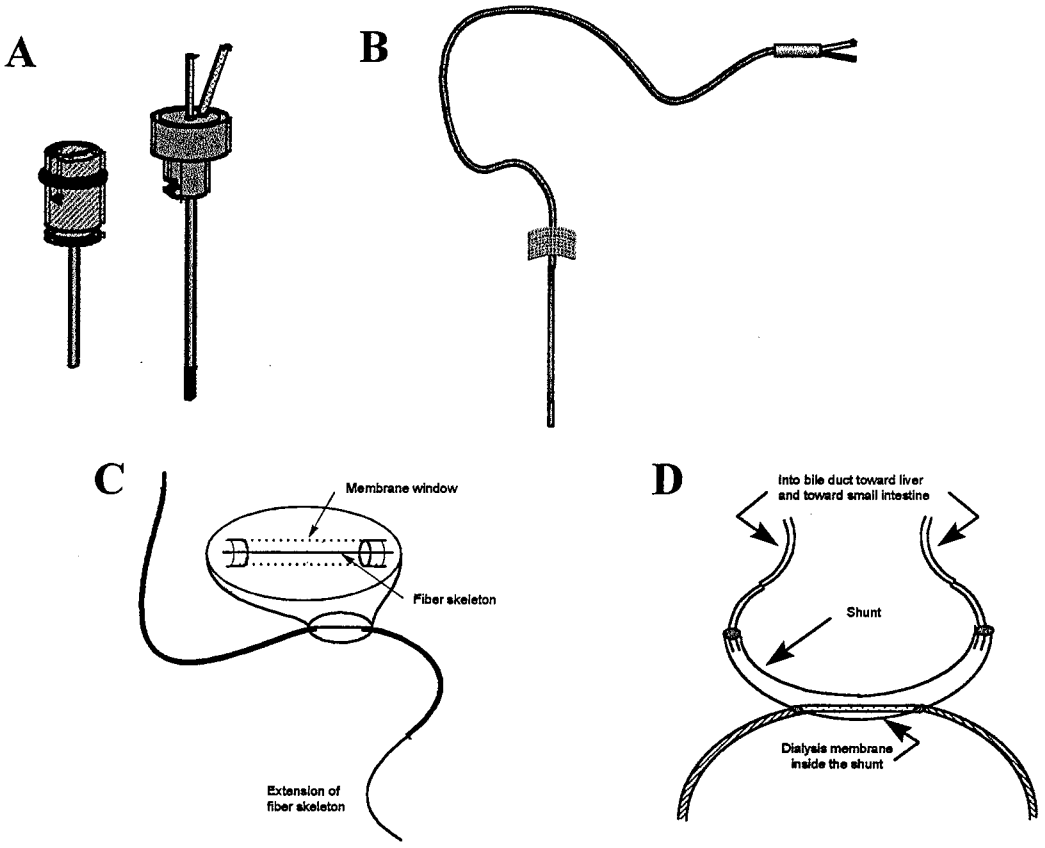

Figure 3—Microdialysis probe geometries (probes not drawn to scale). A. Intracerebral guide cannula and pin-style brain probe. B. Flexible probe for intravenous use. C. Linear probe for peripheral tissues. D. Shunt probe designed for sampling from bile duct of rat. (Used with permission of Bioanalytical Systems, Inc., West Lafayette, IN.)

manipulation of small volume samples and multiple step cleanup procedures, which produces poor temporal resolution relative to physiological or pharmacological events. Elimination products and tissue samples also require extensive sample cleanup prior to analysis. Because microdialysis sampling provides protein-free samples, loss of analyte during protein precipitation is avoided. Enzymes are also excluded from the dialysate sample; thus, there is no further enzymatic degradation of the sample.

Optimization of Microdialysis Sampling

Probe Design, Surgery, Tissue Response—The small size of the dialysis probe, nominally 300 μm o.d. with an active window in the range 4−10 mm in length, causes minimal perturbation to the tissue. Therefore, the technique can be used in awake, freely moving animals, and the integrity of tissues, organs, and systems is maintained. Several different probe geometries have been developed to facilitate in vivo sampling from various sites. Those commonly used are shown in Figure 3. The designs are of two general types: parallel and serial. Parallel perfusion probes are constructed of rigid or flexible cannula material and may have either a side-by-side or concentric arrangement. Probes with rigid cannulae are especially suited for intracerebral sampling, whereas those with flexible cannulae work well for venous sampling. Serial perfusion probes include linear and loop styles. They are typically used for sampling soft peripheral tissue such as skin, muscle, tumor, and liver. The shunt probe suspends a linear probe within a larger tube, allowing sampling from flowing fluids (such as bile or blood) without permanent diversion of the fluid.[1,2]

Several modified probe designs have also been reported, including a spinal loop dialysis catheter for use in sampling the spinal intrathecal space of unanesthetized rats[3,4] and a flexible intravenous probe for use with unanesthetized small animals.[5,6] In 1995, Kanthan et al.[7] described a method for microdialysis sampling in the human brain. This technique utilizes a Codman bolt kit, typically used to monitor intracranial pressures, and a custom-designed microdialysis probe with a probe sheath to accommodate variations in skull thickness. Using this system, five monoaminergic neurotransmitters[7] and glucose-induced decreases in glutamate levels[8] were monitored during acute focal ischemia.

Although the small size of the microdialysis probe causes minimal perturbation to the tissue, the surgery to implant the probe is invasive. Experimental animals are anesthetized during probe implantation, and the anatomical location of the target tissue dictates the duration of anesthesia and the severity of the surgical invasion. For example, probe implantation into the dermis or muscle is much less invasive to the animal than implantation in the liver or bile duct.

A few groups have examined tissue response to probe implantation and to indwelling probes. For intracerebral microdialysis, compromise of the blood−brain barrier (BBB) upon implantation of the guide cannula and/or probe must be considered. Benveniste and Hüttemeier[9] and deLange et al.[10] have reviewed the literature concerning BBB compromise and brain tissue response to probe implantation. One approach to evaluating the integrity of the BBB is to employ markers that do not normally cross the barrier. Several of these types of studies, which suggested that the BBB was generally intact within a short time after the surgery, are discussed in the reviews already mentioned. Other studies, however, have concluded that the BBB remains compromised for 24 h or longer after implantation takes place.[11−13] A second approach used to

assess changes in the BBB is to monitor alterations in the transport of a compound across the BBB after injection of compounds known to open the barrier. Again, conflicting results have been reported.[12,14] A study by Allen et al.[14] suggested that the rate of insertion of the probe into the tissue affects the amount of BBB damage and could account, to some extent, for the differing results.

Several publications from the laboratory of C. Lunte[15–17] have reported the responses of different tissues to the presence of a microdialysis probe over time. The tissues examined include dermis,[15] muscle and tumor,[16] and liver.[17] Dermis, muscle, and liver showed the expected acute inflammatory response, with the initial invasion of neutrophiles followed by macrophages. Tumor tissue showed little or no inflammatory response up to 72 h. Davies and Lunte[17] tested probes of various designs in liver tissue and found that using a 'needle' with a diameter smaller than that of the membrane minimized the extent of cell damage.

Quantitation Issues and Extraction Efficiency—Microdialysis sampling is not typically performed under equilibrium conditions, so the concentration of the analyte determined in the dialysate is some fraction of its actual concentration in the surrounding sample matrix. The relationship between the concentration of analyte in the dialysate and that of the sample matrix may be thought of as the extraction efficiency (EE) of the probe. Among the parameters that influence EE are temperature, perfusate flow rate, chemical and physical properties of the dialysis membrane, probe geometry, membrane surface area, and properties of the analyte. The diffusion rate of the analyte within the matrix also affects EE. In vivo uptake into cells, metabolic rate, extent of tissue vascularization, and blood flow will influence diffusion through the tissue.[18–20] Fortunately, under normal conditions of microdialysis sampling, these parameters remain constant; thus, a steady state is rapidly achieved although equilibrium is not established. Therefore, the EE of the probe for a given set of parameters is constant and the direction of net flux of the analyte across the membrane is determined by the concentration gradient of the analyte. In practice, the EE of the probe may be determined by recovery or delivery experiments.

Calibration of Microdialysis Probes—A major concern in the wider adoption of microdialysis sampling for pharmaceutical studies is the calibration of the microdialysis probes. Microdialysis is generally performed under nonequilibrium conditions where the recovery of a compound depends on many parameters. Recoveries ranging from <1% to >99% can be achieved. It is not always clear whether a high or low recovery is preferable. High recoveries are favored from the analytical perspective because higher concentrations are obtained. A high recovery also results in less depletion of the concentration around the probe because the situation is closer to equilibrium (i.e., the concentrations inside and outside the probe are the same). However, high recovery is typically achieved either using very slow perfusion rates or long dialysis membranes. Using a very slow perfusion rate leads to a loss of temporal resolution because of the relatively large sample volume requirement of most analytical methods. Higher recoveries can be obtained with large sampling windows; however, a loss of spatial resolution is the drawback. Low recoveries, on the other hand, result in less concentrated samples for analysis and a greater decrease in the analyte concentration around the microdialysis probe. However, these limitations may be offset by the fact that higher perfusion rates and shorter dialysis membranes can be used.

Although an in vitro determination of recovery provides a crude estimate of the behavior of a microdialysis probe with a given compound, extrapolating such a value to an in vivo experiment is impossible[21–24] because the nature of the tissue to be sampled and its interactions with the analyte affect the recovery. For many experiments, accurate calibration of the microdialysis probe is not necessary. For example, if the desired information is the relative change in concentration brought about by some experimental manipulation, only the concentration independence and stability of the recovery need be known. On the other hand, if a relative distribution of a compound to various sites is the information desired, then the behavior of each probe used must be normalized versus the other probes. Only when an absolute concentration is needed must each probe be calibrated for an accurate in vivo recovery. As this is often the most difficult step in a microdialysis experiment, careful experimental design should be practiced. If the desired information can be obtained from relative rather than absolute concentrations, the calibration issue is greatly simplified.

Calibration for Hydrodynamic Systems—Systems in which the sample is a flowing fluid, for example the blood and bile, present a special case for microdialysis sampling. Mass transfer in the sample is dominated by diffusion through the probe membrane rather than by diffusion through the surrounding tissue for such systems.[25] Diffusion must occur through a thin layer of stagnant fluid around the membrane. The thickness of this diffusion layer is a function of the velocity of the sample fluid. At low sample flow rates, the diffusion layer is thicker and diffusion through it is the rate-limiting step for microdialysis sampling. As the sample flow rate increases, the diffusion layer collapses and diffusion through the dialysis membrane begins to dominate. Eventually, diffusion through the dialysis membrane becomes the rate-limiting step, after which further increases in the sample flow rate do not affect the microdialysis process.

For hydrodynamic systems, an in vitro calibration can provide accurate recovery values if the perfusion flow rate and sample temperature are well controlled and the characteristics of the membrane do not change during the experiment. Because the membranes are hydrophilic and used in an aqueous environment, physical changes in the membrane are not likely. However, one must always be concerned that physiological responses to probe implantation may result in changes to the membrane environment. For example, there have been reports of the formation of clots around microdialysis probes implanted intravenously. Careful experimental design will usually prevent such problems, but one must always keep this possibility in mind.

Calibration in Tissues—A more difficult case is the use of microdialysis sampling in tissues, particularly those that are poorly perfused. It has been demonstrated that the recovery of a microdialysis probe depends on mass transport in three regions: the probe lumen, the dialysis membrane, and the sample medium.[18,23,24] The first two regions can be characterized in vitro and controlled. Mass transport in the probe lumen is limiting only when using very low perfusion rates, whereas transport through the dialysis fiber is limiting only when transport through the sample is rapid. Rapid transport through the sample occurs in most hydrodynamic systems as well as in highly perfused tissues. However, in most tissues, transport through the tissue determines the recovery of the microdialysis probes.[18,24] Under these conditions, calibration performed in vitro may not be valid in vivo. A number of approaches to the calibration of microdialysis probes in vivo have been described. The two most common methods involve (1) adding an internal standard to the perfusate, which is commonly known as "retrodialysis," or (2) estimating the equilibrium condition by adding varying concentrations of

analyte to the perfusate, which is known as the method of zero net flux. Alternatively, very slow perfusion rates can be employed, often circumventing the need for calibration.

Slow Perfusion—Justice et al.[26] have shown that at perfusion rates of <50 nL/min, recovery is >95% for compounds with molecular weights <500 Da. At such a slow perfusion rate, the error introduced by assuming 100% recovery is insignificant. One drawback to this approach is the difficulty in the collection and analysis of the dialysate sample. Off-line analysis generally requires at least 2 μL of sample. The use of on-line systems, such as microdialysis coupled to capillary electrophoresis or capillary liquid chromatography, makes it possible to analyze nanoliter volumes of sample.

Retrodialysis—In the retrodialysis method, an internal standard is added to the perfusate and the rate of delivery of this compound to the tissue is measured during microdialysis sampling.[27–30] The assumption is made that the recovery of the analyte is equal to the delivery of the internal standard. This method requires that the internal standard and the analyte behave in exactly the same manner. This requirement is usually met with regard to the diffusion coefficient of the two compounds, but is generally overlooked in terms of metabolism. Essentially, the internal standard and the analyte must be metabolized in an identical manner to provide a proper calibration of the probe. Of course, if this requirement were met, the internal standard could disrupt the experiment because it is being added to the system in relatively highly concentrations exactly at the site of sampling.

Method of Zero Net Flux—In the method of zero net flux, various concentrations of analyte are added successively to the perfusate.[31,32] The amount of analyte either lost or gained during dialysis is then determined. If the perfusion concentration is greater than the in vivo concentration, a loss has occurred; if the perfusate concentration is less than the in vivo concentration, there has been a gain. Only when the perfusate concentration and the in vivo concentration match has there been no net change in concentration because the system is at equilibrium. A plot of the change in concentration of dialysate versus the initial concentration of perfusate is made; this should result in a straight line. The slope of this line is the inverse of the concentration recovery and the y-intercept is the actual sample concentration. At this concentration, there is no net diffusion of the analyte into or out of the microdialysis probe, because the concentration in the sample and in the probe lumen is the same.

The method of zero net flux is more accurate than retrodialysis in that the actual compound of interest is used for calibration; however, it is a very time-consuming process. The precision of this method is highly dependent on the precision of the individual concentrations determined and the number of perfusion concentrations used. Several hours—up to 12 in some cases—are required to collect sufficient data at the various concentrations of standard added to the perfusate to provide an accurate estimate of the equilibrium state. During this time, the concentration of the analyte in the sample must remain constant. This requirement limits the use of the method to the determination of basal levels of endogenous compounds and steady-state concentrations of drugs during constant infusion experiments.

Delivery—Determining the delivery of the actual compound of interest is a variation of retrodialysis that overcomes the uncertainty introduced by using a standard to mimic the analyte.[15,33] First, the fact that the delivery is equal to the recovery is verified in vitro. This step serves to confirm the viability of the microdialysis probe. If the delivery and recovery are not equal for a given microdialysis probe, that probe is discarded. After the probe is implanted and the animal has recovered from surgery, the deliveries of the test compound and any other analytes of interest are determined prior to the start of the experiment. Finally, if possible, the deliveries are determined again after completion of the experiment. This procedure will verify any changes in the behavior of the probe during the course of the experiment. If the viability of the probe is tested prior to implantation, its behavior will not change during the course of the experiment within the constraints of tissue response, as was discussed previously. The shortcoming of this approach is that recovery changes resulting from the experiment are not detected. For example, administration of a vasodilator or constrictor can change recovery in a poorly perfused tissue by changing the blood flow. In general, changes in recovery as a result of experimental manipulation are more common when studying endogenous than exogenous compounds.

The various calibration methods are summarized in Table 1. Before undertaking in vivo calibration, the experimentalist should consider what information is desired from the microdialysis experiment. The need for in vivo calibration will generally fall into one of three categories. In the first, two states (such as basal versus excited or formulation A versus formulation B) are compared. In these cases, changes in analyte concentration usually provide sufficient information. Here, one does not need an exact EE value but, rather, a constant EE over the time course of the experiment. In this case, the behavior of the probe can be tracked using retrodialysis. In the second category, one needs to know only the order of magnitude of the analyte concentration in ECF. In other words, is the analyte present at 10 ng/mL or 100 ng/mL? In vitro calibration may be sufficient because it usually differs by not more than two or three times the in vivo value. If the EE is 60% in vitro and 30% in vivo, the concentration of analyte in the in vivo dialysate corrected for the in vitro EE will be within the order of magnitude of the analyte concentration in ECF. In the third category, where an accurate in vivo concentration is required, the in vivo EE must be determined for the analyte in the target tissue. The approaches that can be used to obtain this information include very low flow rates, zero net flux, and in vivo delivery of the analyte.

Analytical Considerations

Several features of microdialysis sampling are of considerable importance in the development of the analytical method. Because of the low flow rates employed, microdialysis typically results in small sample volumes of 1–10 μL. The process also inherently dilutes the samples as they are collected. Therefore, small volume samples, often with low analyte concentration (1 pM–1 μM), are typical and present a considerable challenge to the analyst.

From the analytical perspective, there are two primary considerations with respect to extraction efficiency. First, except in cases of local delivery via the probe, the dialysate concentration will be less than the actual tissue concentration of the analyte. Thus, the limit of detection must be less than the lowest in vivo concentration expected. Second, extraction efficiency increases as perfusion rate decreases. The slower the perfusion rate, the closer the dialysate concentration of the analyte will be to that in the sample matrix surrounding the probe.[34]

Increased temporal resolution is one of the advantages of microdialysis over blood sampling and traditional tissue sampling. For traditional blood sampling, the total fluid that can be withdrawn is limited, so the number of points that can be obtained is small. In traditional tissue sam-

Table 1—Approaches to In Vivo Calibration of Microdialysis Probes

method	description	considerations	reference
extrapolation to zero flow rate	An estimate of analyte concentration surrounding the probe is obtained by extrapolating to zero flow rate, where analyte concentration in the tissue and in the probe would presumably be in equilibrium.	Requires determining the recovery of the probe at several flow rates with the analyte at a steady-state concentration in the matrix throughout the determinations.	35
use of very low flow rate	This extension of the aforementioned method carries out microdialysis sampling at a flow rate (ca. 50 nL/min) where the probe recovery is >95% so that assuming 100% extraction efficiency introduces negligible error.	Practical considerations include long sampling intervals to collect sufficient volume for analysis and problems manipulating small-volume samples such as evaporation.	26
zero net flux	With the analyte at a steady-state concentration in the tissue, the probe is perfused with a succession of solutions containing known concentrations of the analyte. A plot of the change in perfusate concentration versus the initial perfusate concentration should be linear with the slope being the inverse of the probe recovery and the y-intercept being the point of zero net flux; that is, the concentration of the analyte in the tissue.	Tissue concentration of the analyte must remain at steady state, whereas the EE of the probe is determined for several different initial analyte concentrations in the perfusate.	31, 32
retrodialysis	Uses the in vivo delivery of an internal standard (usually an analog or mimic of the analyte) in the perfusate as the basis for probe calibration. The method assumes that the in vivo recovery of the analyte has a constant known relationship to the in vivo delivery of internal standard. In some cases that relationship is determined in vitro and assumed to hold in vivo.	The advantage of this method is convenience, especially in terms of time. The experimentalist should consider that, in a biologically active matrix, delivery of an internal standard that binds to receptors or is metabolized in the same way as the analyte will introduce unwanted perturbations in the tissue area being sampled.	27–30, 36
in vivo delivery of the analyte	A variation of retrodialysis that overcomes the uncertainty introduced when an analog is used as the internal standard. Essentially, the in vivo delivery of the analyte to the target tissue is determined before the actual experiment. If possible, the delivery is determined again after completion of the experiment to confirm that the probe behavior has not changed.	The method is simple, convenient, and has a minimal time requirement. This method assumes that the extraction efficiency of the probe in the tissue of interest is constant regardless of the direction of the concentration gradient of the analyte. The assumption should be validated for analytes and tissues of interest.	15, 37

pling, several animals must be sacrificed at each time point, and, thus, the frequency of time points is usually small to minimize the total number of animals used in each study. With microdialysis sampling, the same type of study can be conducted using only a few animals and, because there is no fluid loss or need to remove tissue, data can be collected continuously. The animal can also serve as its own control.

The temporal resolution of a microdialysis study is defined by the time interval at which the microdialysis samples are collected; it is dependent on the sensitivity and sample volume requirements of the analytical method as well as the recovery of the probe. Microdialysis provides a continuous flow of sample, whereas most analytical systems require discrete samples. Individual samples can be collected off-line with a fraction collector, but the sample volumes are very small due to the low perfusate flow rates used (typically 1 μL/min or less). If the analytical system requires a larger sample for injection or the method is not sensitive and requires a preconcentration step, larger volumes may be collected, albeit at the expense of temporal resolution. Overall, the analytical method with the lowest detection limit and smallest sample volume requirement affords the best temporal resolution for microdialysis experiments.

Another approach to overcoming problems associated with handling small volume samples is on-line coupling of the microdialysis system with the analytical system. This method minimizes the delay between sample collection and analysis and eliminates the problems of evaporation that can occur during any physical manipulation of small volume samples. Near real-time data on physiological events can be obtained, but the temporal resolution achieved by the coupled system will depend on the time needed for analysis (i.e., the analysis time must be less than the duration of the physiological event). Reviews of on-line coupling of microdialysis with LC and microseparation techniques are available.[38,39]

Three-Way Trade-Offs—When microdialysis sampling is applied in vivo, three previously independent systems become interlinked: the animal, the microdialysis sampling system, and the analytical system. The experimentalist must be aware that once these systems are linked, the conditions that were optimal for each element independently must now be considered in relation to the others. Frequently, the sample volume requirement of the analytical method necessitates increasing the microdialysis perfusion rate, which in turn lowers the extraction efficiency of the probe, thus providing samples with lower concentrations of analyte. Using a lower perfusion rate to increase probe efficiency and analyte concentration results in longer sampling times. Some degree of temporal resolution is lost through this compromise. In addition, the increased recovery may deplete compounds of low molecular mass in the tissue adjacent to the probe, in turn perturbing the biological system. The anatomical location and spatial resolution needed for obtaining the desired information influence the probe design and active window length. Although implantation of a microdialysis probe may cause little disruption of the target organ, the necessary anesthesia and extent of the surgical procedure also impact the biological system. The successful use of microdialysis sampling in vivo will depend on achieving a suitable balance among these systems.

The trade-offs among perfusate flow rate, concentration detection limit, and sample volume requirement will decide the temporal resolution that can be achieved for the experiment. A clear statement of the experimental question should dictate the balancing of the microdialysis sampling and analytical method parameters.

Analytical Methodologies

One of the main advantages of microdialysis sampling is that it can be used in conjunction with a wide range of analytical techniques. Non-separation-based methods can

be used to monitor one analyte at a time, and separation-based methods allow the detection of multiple analytes in each sample. This section will provide a brief overview of the considerations that must be heeded when coupling microdialysis sampling to various analytical techniques. Specific references will also be given in cases where the use of the analytical technique or the method of coupling to microdialysis sampling is novel.

Non-Separation-Based Sampling Approaches—In an attempt to further understand the complex nature of biological events, the idea of making real-time analytical measurements has attracted much attention. These types of measurements are achievable when using a continuous detection device, such as a biosensor. Microdialysis provides a possible alternative to implantable sensors. When on-line biosensors are used with microdialysis sampling, the apparatus typically consists of a syringe pump, a microdialysis probe, and a sensor or an enzyme reactor, followed by an electrochemical detector. The enzyme is present to provide specificity and to generate a redox-active species that can be detected electrochemically.

Although the response time of an on-line biosensor system coupled to microdialysis sampling is slower than that of an implantable modified microelectrode, the former is more quantitative and provides a higher conversion of analytes, a longer lifetime, and easier calibration. One disadvantage of biosensors is fouling of the electrode, usually by proteins. Coupling microdialysis sampling with a biosensor overcomes this problem because of the size-exclusion nature of the membrane. In vivo implantation of biosensors places size restraints on the dimensions of the electrode. Using a microdialysis probe in vivo reduces these restrictions on the biosensor.

One example of this methodology is the monitoring of extracellular L-glutamate with a microdialysis-based on-line biosensor subsequent to stimulation of cultured nerve cells.[40] A sensitivity of 24.3 nA/μM and a limit of detection of 7.2 nM for L-glutamate was reported with this system. In vivo levels of L-glutamate were also continuously monitored using microdialysis coupled to an enzyme-amperometric biosensor following cardiac arrest and K^+-induced local depolarization.[41] A limit of detection of 0.5 μmol/L was reported. In both of these examples, glutamate oxidase was employed to oxidize L-glutamate in the presence of oxygen, generating hydrogen peroxide, which was detected electrochemically. Similar sensors were applied to the real-time monitoring of lactate in the subcutaneous tissue of rabbits and humans through the use of microdialysis sampling and a lactate amperometric sensor;[42] glucose was monitored continuously with a glucose-oxidase-immobilized enzyme reactor.[43]

However, biosensors are not always used for continuous monitoring. Using injection valves, discrete microdialysis samples were injected into flow injection systems and analyzed with amperometric-based biosensors for L-lactate[44] and glucose.[45] A miniaturized flow injection thermal biosensor coupled with microdialysis sampling has been reported for the determination of glucose in subcutaneous fluid with a sampling rate of 42 samples/h.[46] Advantages of a flow injection analysis system are the ability to provide for on-line sample dilution, required when analyzing concentrated samples, and the capacity to periodically recalibrate the biosensor with standard solutions. Other non-separation-based methods without continuous monitoring have been reported, including immunoassays[47–49] and mass spectrometric analyses.[50,51] On-line interfacing of microdialysis and mass spectrometry (MS) has been reported for the analysis of tris(2-chloroethyl) phosphate in rat plasma,[52] along with the utilization of microdialysis for on-line sample cleanup of nucleic acid[53] and protein and peptide samples.[54]

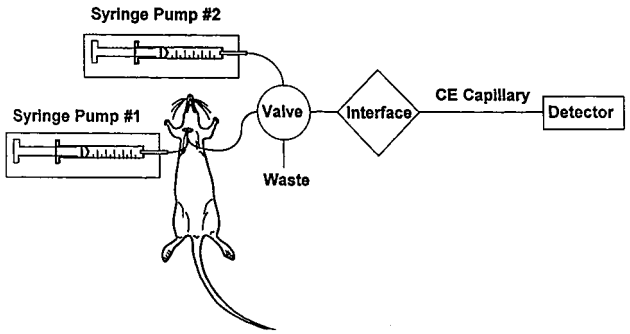

Figure 4—Schematic of the on-line microdialysis/capillary electrophoresis system used for the analysis of SR4233.[56]

Separation-Based Approaches—Microdialysates consist primarily of relatively small hydrophilic analytes in highly ionic aqueous samples. In general, these characteristics have made liquid chromatography (LC) the analytical method of choice to couple to microdialysis sampling. Reversed-phase or ion-exchange are the modes of liquid chromatography that are most compatible with direct injection of aqueous microdialysis samples. The mode of chromatography chosen for analysis is dependent on the physiochemical properties of the analyte. The type of column used (length, particle size, and internal diameter) is determined by the sampling interval desired and the required sensitivity. In a typical LC assay, 5–10 μL of sample are needed, which means that the temporal resolution is 5–10 min if a perfusion flow rate of 1 μL/min is employed. If lower microdialysate flow rates are used to increase recovery, temporal resolution is further decreased. Applications of on-line coupling of microdialysis with LC have been reviewed elsewhere.[38,39]

Capillary electrophoresis (CE) is another separation method that can be used for the analysis of microdialysis samples. The low sample volume requirement of CE is compatible with the small volumes generated by microdialysis sampling. Typical injection volumes in CE are 1–10 nL. However, 1–5-μL samples are generally required because of difficulties associated with the physical manipulation of submicroliter volumes, in particular, problems with surface tension and evaporation.

One disadvantage of CE is its incompatibility with high ionic strength samples. In CE the optimal procedure to achieve stacking, or compression of the injection zone, is to prepare the sample in an injection buffer that is 10-fold more dilute than the background electrolyte. The high ionic strength of the microdialysis sample causes anti-stacking and, therefore, lower detection sensitivity. In contrast, LC is amenable to high ionic strength samples.

There have been several reports of the on-line coupling of microdialysis and capillary electrophoresis with UV[55] and laser-induced fluorescence (LIF) detection.[56–58] The first reported coupling of microdialysis with CE and LIF detection involved the separation of an investigational antineoplastic, SR 4233, from its main metabolite, SR 4317.[55] Figure 4 shows a schematic of the on-line microdialysis/capillary electrophoresis system employed in this study. Resolution of the two compounds was achieved in <60 s, with an overall temporal resolution of 90 s. During the on-line study, a 4-mg/kg intravenous injection of SR 4233 was administered to the rat. A pharmacokinetic curve (Figure 5) was then constructed, and a 15.3 ± 1.0 min half-life of elimination and 1.1 ± 0.2 min half-life of distribution were determined for SR 4233. Another method of detection for use with the on-line coupling of microdialysis and CE that has been explored in our laboratory is electrochemical

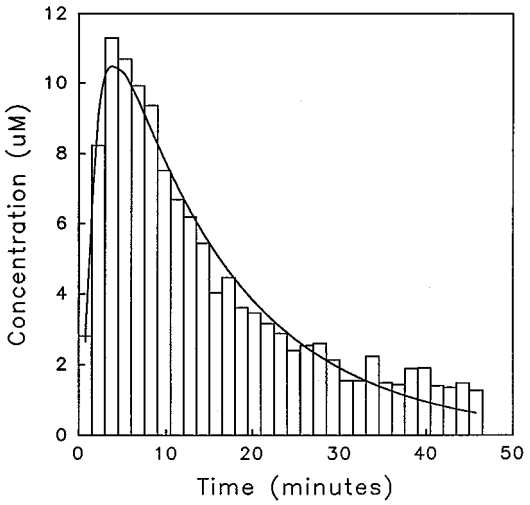

Figure 5—Pharmacokinetic curve following a 4-mg/kg ip dose of SR4233 obtained using an on-line microdialysis/capillary electrophoresis system.[56]

detection.[59] This detection system provides higher sensitivity than does ultraviolet (UV) detection and is comparable to LIF. Furthermore, the number of potential analytes that can be studied at high sensitivity is greatly increased because more compounds are electroactive than are naturally fluorescent.

Scope of Applications

As the number of research studies incorporating microdialysis sampling has continued to increase, secondary literature has appeared in the form of books[60] and review articles.[38,39,61–65] An exhaustive examination of the microdialysis literature is beyond the scope of this review. Many of these studies involve monitoring levels of endogenous compounds in response to the administration of drugs or other stimuli. Others report monitoring of the parent compound and/or metabolites in the dialysate. The small size and minimal invasiveness of microdialysis probes make the technique ideal for simultaneous monitoring in more than one organ or tissue. In the following overview of applications, we have focused on presenting a few examples to illustrate the breadth of possibilities for using microdialysis sampling in pharmacokinetic and metabolism studies.

In Vitro Studies

Microdialysis sampling does not change the net fluid balance of the surrounding sample matrix and provides clean samples in which analytes are separated from further enzymatic action. Thus, microdialysis is useful for in vitro drug development and evaluation applications. A series of reports on in vitro applications of microdialysis sampling has been published. These applications include tablet dissolution testing with both single and multiple vessel configurations,[66,67] erythrocyte membrane partitioning studies,[68] and enzyme kinetic studies.[69] Gunaratna and Kissinger[70] used microdialysis to follow metabolism kinetics in liver microsome incubations. In this application, an in vitro microdialysis system, shown in Figure 6, was used to monitor the metabolic profiles of three metabolites of diazepam following its incubation in liver microsomes (Figure 7). Several studies have been published in which microdialysis sampling was compared to traditional methods for determining drug binding to plasma proteins.[71–73] More recently, Yang and Elmquist[74] demonstrated the

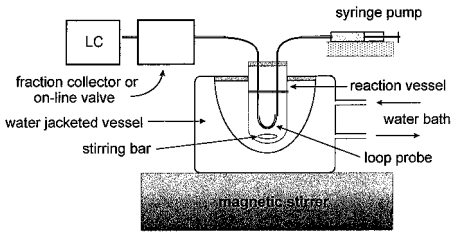

Figure 6—*In vitro* microdialysis sampling system for microsome or similar incubation process.[70]

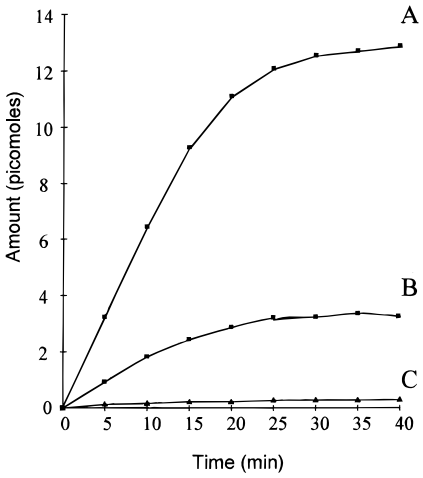

Figure 7—Metabolic profiles of diazapam metabolites sampled by microdialysis from liver microsome incubation mixture. Diazepam concentration was 145 M: (A) temazepam; (B) *N*-desmethyldiazepam; (C) oxazepam.[70]

feasibility of determining the plasma binding of a highly lipophilic drug, cyclosporin A, using microdialysis sampling.

Several researchers have employed in vitro microdialysis sampling to minimize sample preparation when monitoring fermentation and related bioprocesses. Mannino et al.[75] used an on-line microdialysis system to provide clean samples from milk products. They detected sugars amperometrically at a chemically modified electrode. Torto and co-workers[76] have demonstrated the utility of in situ microdialysis sampling for monitoring bioprocesses without perturbation of the process. Microdialysis sampling coupled on-line to LC with pulsed electrochemical detection was used to monitor an enzymatic hydrolysis that produced a mixture of oligosaccharides. Using the same system, Torto et al.[77] evaluated three microdialysis sampling modes with respect to their suitability for quantitative on-line monitoring of bioprocesses in small-volume (5 mL) bioreactors. They concluded that stopped-flow microdialysis modes were advantageous for small-volume reactors to avoid significant depletion of the analyte.

In Vivo Studies

Brain—Microdialysis sampling has been used to study a wide variety of endogenous and exogenous analytes in brain. The large number of papers published on this topic is beyond the scope of this review, so a brief overview of recent work from the laboratory of S. Lunte will be presented.

Tryptophan metabolism along the kynurenine pathway has been one area of interest in our research group. This pathway is responsible for approximately 90% of tryptophan metabolism in mammals and yields the formation of kynurenic acid, an endogenous glycine site NMDA receptor antagonist. Malone et al.[78] utilized CE with electrochemical detection for the determination of tryp-

tophan and kynurenine in brain microdialysates. In that study, an intraperitoneal injection of tryptophan was administered to an anaesthetized rat, and the levels of tryptophan and kynurenine in rat hippocampus were monitored for 6 h by microdialysis sampling. A three- to fourfold increase in dialysate tryptophan levels was observed, resulting in a maximum concentration of 2−3 μM tryptophan at approximately 90 min after ip administration. Sixty minutes after dosing, kynurenine was found to reach a maximum concentration of 1.3 μM. It was concluded that the high sensitivity and low volume requirements of CE with electrochemical detection allowed good temporal resolution and high recoveries to be realized. Kynurenic acid, however, cannot be effectively detected electrochemically; therefore, alternate methods for its determination were investigated. Capillary electrophoresis with LIF detection following zinc complexation was evaluated for monitoring the levels of kynurenic acid in brain microdialysis samples.[79] Kynurenic acid is essentially unable to penetrate the BBB; therefore, its presence in brain is dependent on its bioprecursor kynurenine, a major tryptophan metabolite. In this study, the increase in hippocampal kynurenic acid was monitored following a systemic injection of one of its bioprecursors, tryptophan or kynurenine. One of the greatest potential advantages of this methodology compared with those currently in use is its increased temporal resolution. Microdialysate samples could be analyzed every 10 min rather than the 30−60-min sampling intervals used with LC.

Another project involved the investigation of substance P metabolism in brain using microdialysis sampling followed by CE with postcolumn derivatization and laser-induced fluorescence detection.[80] A microdialysis probe implanted in the striatum of an anesthetized rat was perfused with substance P, and dialysate samples were analyzed for substance P and its metabolites. By introducing substance P into the brain via the microdialysis probe, metabolite formation in the immediate vicinity of the probe could be monitored.

Ocular—One of the major constraints in developing improved intraocular drug delivery systems has been the lack of information concerning the uptake, disposition, and elimination of drugs from the eye.[81] Ocular microdialysis is one technique that could provide such information; however, few studies using this method have been reported.

Continuous sampling of drugs in the vitreous humor of anesthetized rabbits has been reported.[81] This study involved the pharmacokinetic analysis of ganciclovir and acyclovir using a concentric microdialysis probe implanted in the vitreous humor. Ganciclovir is a purine nucleoside analog approved for the treatment of cytomegalovirus retinitis.

Ganciclovir or acyclovir was given as an intravitreal injection (100 mL) following implantation of the guide cannula. The microdialysis probe was then inserted into the guide cannula, and dialysates were collected every 20 min. It was found that the initial equilibration phase was over within the first 4 h, and that the microdialysis technique did not result in a breakdown of the blood−retinal barrier. The short vitreous half-lives of ganciclovir (2.62 ± 0.44 h) and acyclovir (2.98 ± 0.24 h) in albino rabbits suggest a transretinal mechanism of vitreous clearance for these compounds. In pigmented rabbits, however, the rate of elimination increased to 8.63 and 5.59 h for ganciclovir and acyclovir, respectively, as a result of binding to melanin. This research indicates that ocular microdialysis can be useful in assessing the vitreous concentrations of drugs and providing information on the uptake, disposition, and elimination of drugs from the eye.

Transdermal—Traditionally, transdermal drug delivery has been studied in vitro using isolated skin preparations; however, with the use of microdialysis sampling, in vivo studies can be performed.[15] In one such study, intradermal microdialysis was used to investigate the transdermal absorption of cyclosporin in rats.[82] Cyclosporin is an immunosuppressive agent that has been shown to be beneficial in treating several dermatological diseases. Due to the toxic effects found with systemic administration, topical application has been explored, but it is limited because of the poor ability of cyclosporin to penetrate the dermis. In this study, the use of an absorption enhancer, 1-[2-(decylthio)ethyl]azacyclopentan-2-one (HPE-101), and glycerin to increase the transdermal absorption of cyclosporin was evaluated. HPE-101 and glycerin were both found to significantly enhance the absorption of topically applied cyclosporin in rat skin. The authors concluded that utilizing an in vivo microdialysis method obviates the need for concern about hydration and microbial growth as with in vitro methods using excised skin.

Muscle—Two recent publications have focused on the use of microdialysis sampling correlated with traditional blood sampling to devise models for predicting the free concentration of drugs in muscle tissue from the plasma levels. Nolting and others[83] monitored piperacillin, a β-lactam antibiotic, in muscle tissue by microdialysis while collecting serial blood samples. They concluded that microdialysis sampling was suitable for determining concentrations of unbound drug in tissue. Kovar et al.[84] also used microdialysis sampling in muscle tissue to compare free tissue levels of ceftriazone, a highly bound drug, with free plasma levels determined from blood samples. Free levels were much higher in plasma than in muscle. To accurately predict free tissue levels of ceftriazone from plasma levels, the model required factors to account for nonlinear protein binding.

Adipose—Felländer and associates[85] examined the effect of α- and β-adrenoceptor blocking agents on lipolysis in human adipose tissue using microdialysis sampling during surgery. They found that in humans both α- and β-adrenogenic mechanisms modulated the response of adipose tissue to surgical trauma. In another study of lipolytic activity, Darimont et al.[86] used in vivo microdialysis sampling in rat adipose tissue. The effect of moxestrol, a potent estrogenic analog, on lipolysis was monitored by measuring extracellular glycerol in parametrial fat pads of estrus, diestrus, and ovariectomized animals.

Blood—The possibility of producing protein-free samples and conducting long-term continuous sampling without fluid loss is especially attractive for microdialysis sampling from blood vessels. In addition to commercially available venous probes, flexible probes for sampling from blood have been constructed by Telting-Diaz et al.[87] and Evrard et al.[5]

Nakashima and colleagues[88] applied microdialysis sampling to the study of in vivo plasma protein binding of valproate. Microdialysis probes were implanted in the femoral veins of rabbits prior to dosing the animals with valproate. Whole blood samples were collected simultaneously and prepared for analysis of the free fraction using ultrafiltration. No difference was found in the elimination half-lives determined from microdialysis and from blood sampling. Further, they found that in vivo dialysate concentrations could be corrected for probe efficiency using recovery values obtained from in vitro experiments performed in stirred rabbit plasma at 37 °C.

The monitoring of clinically relevant analytes in the blood of critically ill patients provides information vital to management and therapeutic decisions in their care. Rabenstein et al.[89] adapted the bile shunt probe introduced by Scott and Lunte[1] to obtain microdialysis samples from central vein catheters in greyhounds. The microdialysis

samples and blood samples were analyzed for glucose and lactate. In a related study, the same group used their probe system with a biosensor array to determine glucose and lactate.[2]

Tumor—The systemic concentration–time profile of a drug does not necessarily reflect its profile in the extracellular space of tissues. Antineoplastic drugs, because of their especially high cytotoxicity, and tumor tissue, being poorly perfused, are a case in point. A microdialysis probe implanted directly in tumor mass can monitor actual tissue levels of the drug and provide information concerning intumor metabolism, if any, of the drug. For example, Palsmeier and Lunte[16,33] applied microdialysis sampling to the investigation of the disposition and metabolism of SR-4233, a benzotriazine compound with preferential cytotoxicity for hypoxic tissue. They found that, using a systemic dose, much less drug reached the tumor than reached healthy muscle tissue. However, when the same amount of drug reached both tumor and muscle, which was accomplished by delivering the drug via a probe, the levels of reductive metabolites formed were significantly higher in tumor than in muscle.

Other oncological applications of microdialysis sampling include monitoring of carboplatin in cutaneous melanoma and in subcutaneous space to evaluate the portion of the dose reaching the cancerous tissue,[90] methotrexate transport in brain tumors,[91] and the influence of an angiogenesis inhibitor on the uptake of temozolomide.[92]

Transplacental—Ward and Pollack[93] used microdialysis sampling to monitor the effect of methanol on uteroplacental blood flow. The microdialysis probe was implanted through the uterine wall into the amniotic fluid of nearterm pregnant rats. Methanol was administered as an iv bolus dose or an iv infusion over several hours. In addition to producing data suggesting that maternal exposure to methanol may produce hypoxia in fetuses, their work demonstrated the value of microdialysis sampling as a tool for investigating the flux of compounds across placenta.

Bile—A shunt probe design introduced by Scott and Lunte[1] provides microdialysis samples from the bile duct of rats. Briefly, the microdialysis probe is suspended inside a tube that is implanted as a bile duct shunt. The shunt directs bile flow past the microdialysis membrane, then returns the bile to the duct prior to its entry into the small intestine. Because bile flow is maintained, continuous monitoring of compounds excreted into the bile is possible while maintaining enterohepatic circulation.

Scott and Lunte[1] monitored phenol and its metabolites in bile using the shunt probe. Hadwiger et al.[94] obtained pharmacokinetic profiles and parameters for tacrine and its hydroxylated metabolite in bile using the shunt probe design. Gunaratna and colleagues[95] demonstrated the use of this probe design in awake animals, choosing acetaminophen and its metabolites as the analytes.

Liver—Ischemia/reperfusion injury involves reactive oxidant species that are difficult to measure directly. Layton and colleagues[96] monitored two antioxidant species, uric acid and ascorbic acid, by microdialysis sampling in the liver of anesthetized rats during ischemia and reperfusion. As expected, the extracellular levels of both antioxidants decreased during and immediately following ischemia. High ascorbic acid levels were noted immediately after implantation of the microdialysis probe; however, this initially elevated level decreased to a stable basal level after 90 min.

Various drug delivery approaches are being evaluated for their ability to increase therapeutic effectiveness while reducing side effects associated with systemic doses. Sato et al.[97] found microdialysis sampling useful in evaluating microfibrous collagen sheets for local drug delivery. They studied the delivery of etoposide to liver tissues in rats in the presence and absence of cyclosporin A. Etoposide with or without cyclosporin A, a P-glycoprotein-mediated transport inhibitor, was incorporated in a microfibrous collagen sheet applied to the surface of the liver lobe over the site of the microdialysis probe. The microfibrous collagen sheet maintained drug concentrations in the liver with only low concentrations observed in plasma. Inclusion of cyclosporin A further prolonged the drug concentration in liver tissue.

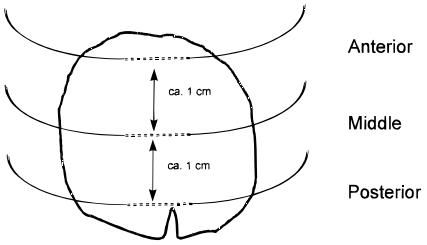

Figure 8—Placement of microdialysis probes implanted into the median lobe of the liver (viewed from the ventral surface) used to monitor phenol metabolism.[37]

Simultaneous Multiple-Probe Studies in the Same Organ—Malagié et al.[98] compared the effect of a combination treatment of WAY 100635 (a 5-HT_{1A} receptor antagonist) and fluoxetine (a 5-HT reuptake inhibitor) on two brain regions simultaneously. Microdialysis probes were implanted in the frontal cortex and ventral hippocampus prior to iv administration of either saline or WAY 100635, followed by ip administration of fluoxetine or saline. The 5-HT levels were monitored simultaneously in the cortex and hippocampus. Fluoxetine alone did not change the extracellular 5-HT levels in either region studied. When fluoxetine and WAY-100635 were coadministered, 5-HT levels in the frontal cortex but not the hippocampus increased by >200% compared with pre-dosing levels.

The spatial resolution of microdialysis sampling can provide information not readily accessible by other methods. Davies and Lunte[99] demonstrated this in a study of phenol metabolism in liver tissue. Three linear microdialysis probes placed in different regions (anterior, middle, and posterior) of the median lobe of rat livers revealed differences in metabolic profiles for the regions following iv administration of phenol (Figure 8). The levels of the conjugated metabolites phenol-glucuronide and glutathionyl-hydroquinone were significantly lower at the anterior position than at other positions, even though the levels of phenol reaching each region were the same (Figures 9 and 10).

Simultaneous Multiple-Probe Studies in Different Organs—Several studies have used simultaneous microdialysis sampling to study drug penetration of the BBB. Simultaneous microdialysis sampling from brain and blood was used by Malhortra et al.[100] to determine the penetration of an experimental NMDA antagonist into brain tissue. They found good agreement between the microdialysis-based pharmacokinetic parameters and those determined using conventional blood sampling. Nakashima et al.[101] evaluated simultaneous microdialysis sampling from blood and brain as a method for determining relative pharmacokinetics and metabolism of L-DOPA in the presence and absence of aromatic amino acid decarboxylase inhibitors. They found in vivo microdialysis to be a simple, reliable technique for the simultaneous determination of pharmacokinetics and metabolism in a target tissue and systemic circulation.

Other dual-site microdialysis sampling experiments have simultaneously examined L-DOPA in blood and muscle,[102,103] SDZ ICM 567 (a 5-HT_3 receptor antagonist) in blood and muscle,[104] lactate in muscle and adipose tissue in relation

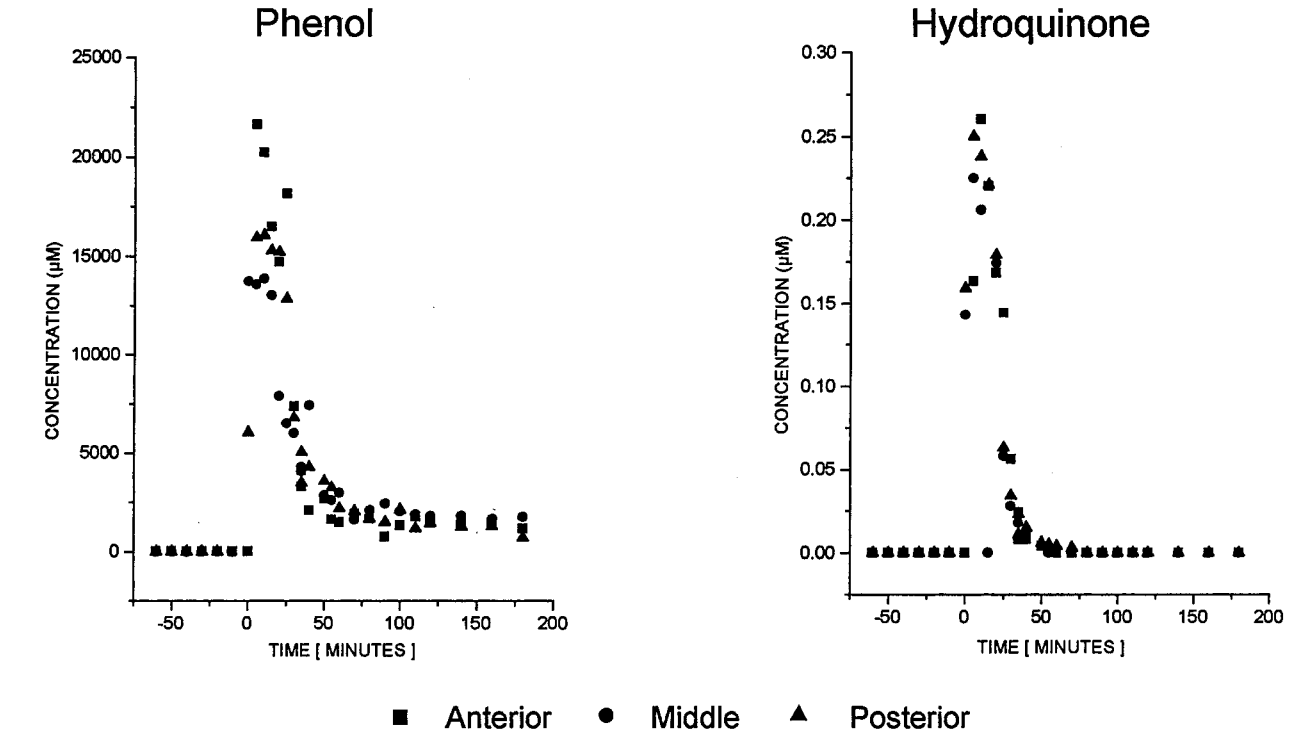

Figure 9—Typical concentration–time course for phenol (left) and hydroquinone (right) during and after a 20-min iv infusion of phenol (administration corresponding to 0–20 min).[37]

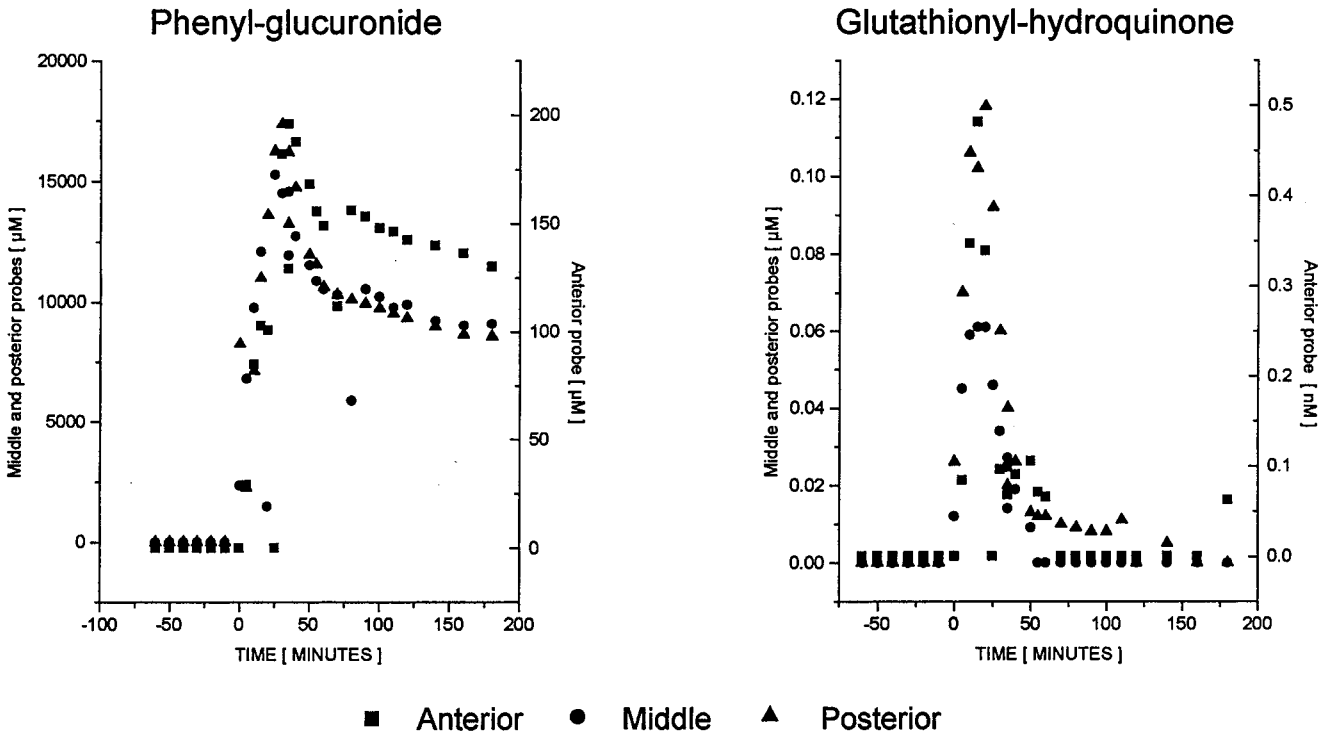

Figure 10—Typical concentration–time course for phenyl-glucuronide (left) and glutathionyl-hydroquinone (right) during and after a 20-min iv infusion of phenol (administration corresponding to 0–20 min). Note: scale for the anterior probe is the right-hand axis.[37]

to insulin action,[105] and antibiotics in human muscle and subcutaneous space.[106] Reports of simultaneous microdialysis sampling from three sites have also been published. These include disposition of phenol in bile, blood, and liver;[1] distribution kinetics of carbamazepine in brain, blood, and liver;[107] aluminum chelation by hydroxypyridinones in blood, liver, and brain;[108] methotrexate levels in kidney, liver, and muscle;[109,110] and lactate and xanthines in blood, liver, and small intestine during endotoxic shock.[111]

Multiple-site microdialysis sampling has proven useful in the investigation of pharmacokinetic drug–drug interactions.[112] Ekstrøm et al.[112] placed microdialysis probes in the blood, liver, and kidney of anesthetized rats to examine the interactions of methotrexate and the non-steroidal antiinflammatory drug (NSAID) naproxen. When animals were pretreated with naproxen, approximately a twofold increase in the areas under the curve (AUCs) of time versus concentration for methotrexate and 7-hydroxymethotrexate, the major metabolite, was found in all three tissues.

Conclusions

Quantitation or calibration of microdialysis probes and the challenge of analyzing the small volumes typical of microdialysis sampling are issues that must continue to be investigated. For microdialysis data to be quantitative, calibration of the probe is necessary. Approaches such as extrapolation to zero flow rates, the use of very low perfusion flow rates, and zero net flux tend to be time consuming. Retrodialysis and in vivo delivery are less time consuming; however, validation of these methods prior to initiation of the microdialysis study is necessary. In general, for applications where absolute tissue concentrations are required, the time involved in calibrating the probe can overshadow many of the other advantages of microdialysis sampling.

Another problem commonly encountered arises from the fact that the small sample volumes obtained from microdialysis sampling are usually less than that required for traditional analytical methodologies such as liquid chromatography. To obtain identical temporal resolution using standard separation methods, it is possible to increase the sample volume by increasing the microdialysis perfusion rate. However, this method decreases the concentration extraction efficiency of the probe. One solution to this problem has been the use of analytical systems with lower sample volume requirements, including microbore LC and capillary electrophoresis. Other approaches have employed preconcentration and stacking methods for LC and CE to overcome the problems of low concentration samples associated with using higher microdialysis perfusion flow rates.

Researchers have shown the feasibility of implanting microdialysis probes in a number of tissues; however, little has been published concerning the physiological response of the tissue to this probe implantation or the way in which tissue response may ultimately affect the pharmacokinetics or metabolic activity. Advances in probe design and dialysis membrane materials that result in less tissue damage as well as biocompatible materials for the construction of microdialysis probes continue to be of interest.

The simultaneous use of multiple probes is another area that has not yet been fully explored. This approach would permit investigations of tissue distribution in near real time while reducing the total number of animals necessary for a study in comparison with traditional methods. The challenge in multiple-probe experiments is preventing the tangling of numerous fluid lines. Multi-channel swivel systems exist for this purpose, but the channel volumes and resistance to turning increase with each additional channel. An alternative to multi-channel swivel systems is the use of a turntable to counter the animal's rotations.[113] These types of studies have become more practical with the commercial availability of swivel-free animal containment systems, such as the Raturn system from Bioanalytical Systems, Inc.

The capacity of microdialysis, performed in vivo, to provide continuous sampling over several days without detriment to the fluid volume of the animal, and the possibility of obtaining such samples simultaneously from multiple sites have the potential for significant reductions in the number of animals necessary for pharmacokinetic and distribution studies. When this technique is coupled on-line to a rapid LC or CE separation method, near real-time data can be obtained. Overall, the increasing application of microdialysis sampling to tissues other than brain, which has been demonstrated in the last decade, is likely to continue, especially as advances in analytical methods for small volume samples and suitable techniques for probe calibration are developed and refined.

Financial support from the National Institutes of Health (SBIR Grant R43-GM52272 with Bioanalytical Systems; RO1) is gratefully acknowledged. The authors thank Bioanalytical Systems, the Kansas Technology Enterprise Corporation, and the Center for Bioanalytical Research at the University of Kansas for their support, and also acknowledge the assistance of N. Harmony in editing and preparing the manuscript.

References and Notes

1. Scott, D. O.; Lunte, C. E. *In vivo* microdialysis sampling in the bile, blood, and liver of rats to study the disposition of phenol. *Pharm. Res.* **1993**, *10*, 335−342.
2. Dempsey, E.; Diamond, D.; Smyth, M. R.; Malone, M. A.; Rabenstein, K.; McShane, A.; McKenna, M.; Keaveny, T. V.; Freaney, R. *In vitro* optimisation of a microdialysis system with potential for on-line monitoring of lactate and glucose in biological samples. *Analyst* **1997**, *122*, 185−189.
3. Marsala, M.; Malmberg, A.; Yaksh, T. The spinal loop dialysis catheter: characterization of use in the unanesthetized rat. *J. Neurosci.* **1995**, *62*, 43−53.
4. Khan, I.; Marsala, M.; Printz, M.; Taylor, P.; Yaksh, T. Intrathecal nicotinic agonist-elicited release of excitatory amino acids as measured by *in vivo* spinal microdialysis in rats. *J. Pharm. Exp. Ther.* **1996**, *278*, 97−106.
5. Evrard, P. A.; Deridder, G.; Verbeeck, R. K. Intravenous microdialysis in the mouse and the rat: development and pharmacokinetic application of a new probe. *Pharm. Res.* **1996**, *13*, 12−17.
6. Evrard, P. A.; Deridder, G.; Verbeeck, R. K. Concentration-dependent plasma protein binding of flurbiprofen in the rat: an *in vivo* microdialysis study. *Pharm. Res.* **1996**, *13*, 18−22.
7. Kanthan, R.; Shuaib, A.; Goplen, G.; Miyashita, H. A new method of *in vivo* microdialysis of the human brain. *J. Neurosci. Meth.* **1995**, *60*, 151−155.
8. Kanthan, R.; Shuaib, A.; Greibel, R.; El-Alazounni, H.; Miyashita, H.; Kalra, J. Glucose-induced decrease in glutamate levels in ischemic human brain by *in vivo* microdialysis. *Neurosci. Lett.* **1996**, *209*, 207−209.
9. Benveniste, H.; Hüttemeier, P. C. Microdialysis-Theory and application. *Progr. Neurobiol.* **1990**, *35*, 195−215.
10. de Lange, E. C.; Danhof, M.; de Boer, A. G.; Breimer, D. D. Methodological considerations of intracerebral microdialysis in pharmacokinetic studies on drug transport across the blood-brain barrier. *Brain Res. Rev.* **1997**, *25*, 27−49.
11. Major, O.; Shdanova, T.; Duffek, L.; Nagy, Z. Continuous monitoring of blood-brain barrier opening to Cr51-EDTA by microdialysis following probe injury. *Acta Neurochir. Suppl. (Wien)* **1990**, *51*, 46−48.
12. Westergren, I.; Mystrom, B.; Hamberger, A.; Johansson, B. B. Intracerebral microdialysis and the blood-brain barrier. *J. Neurochem.* **1995**, *64*, 229−234.
13. Morgan, M. E.; Singhal, D.; Anderson, B. D. Quantitative assessment of blood-brain barrier damage during microdialysis. *J. Pharm. Exp. Ther.* **1996**, *277*, 1167−1176.
14. Allen, D. D.; Crooks, P. A.; Yokel, R. A. 4-Trimethylammonium antipyrine: a quaternary ammonium nonradionuclide marker for blood-brain barrier integrity during *in vivo* microdialysis *J. Pharmacol. Toxicol. Meth.* **1992**, *28*, 129−135.
15. Ault, J. M.; Riley, C. M.; Meltzer, N. M.; Lunte, C. E. Dermal microdialysis sampling *in vivo. Pharm. Res.* **1994**, *11*, 1631−1639.
16. Palsmeier, R. K.; Lunte, C. E. Microdialysis sampling of tumors for study of the metabolism of antineoplastic agents. *Cancer Bull.* **1994**, *46*, 58−66.
17. Davies, M. I.; Lunte, C. E. Microdialysis sampling for hepatic metabolism studies: Impact of microdialysis probe design and implantation technique on liver tissue. *Drug Metab. Dispos.* **1995**, *23*, 1072−1079.
18. Morrison, P. F.; Bungay, P. M.; Hsiao, J. K.; Ball, B. A.; Mefford, I. N.; Bedrick, R. L. Quantitative microdialysis: analysis of transients and application to pharmacokinetics in brain. *J. Neurochem.* **1991**, *57*, 103−119.
19. Smith, A. D.; Justice, J. B. The effect of inhibition of synthesis, release, metabolism and uptake on the microdialysis extraction fraction of dopamine. *J. Neurosci. Meth.* **1994**, *54*, 75−82.
20. Stenken, J. A.; Lunte, C. E.; Southard, M. Z.; Ståhle, L. Factors that influence microdialysis recovery. Comparison of experimental and theoretical microdialysis recoveries in rat liver. *J. Pharm. Sci.* **1997**, 86, 958−966.

21. Ståhle, L.; Segersvärd, S.; Ungerstedt, U. A comparison between three methods for estimation of extracellular concentrations of exogenous and endogenous compounds by microdialysis. *J. Pharmacol. Meth.* **1990**, *25*, 41−52.
22. Amberg, G.; Lindefors, N. Intracerebral microdialysis: II. Mathematical studies of diffusion kinetics. *J. Pharmacol. Meth.* **1989**, *22*, 157−183.
23. Benveniste, H.; Hansen, A. J.; Ottosen, N. S. Determination of brain interstitial concentrations by microdialysis. *J. Neurochem.* **1989**, *52*, 1741−1750.
24. Bungay, P. M.; Morrison, P. F.; Dedrick, R. L. Steady-state theory for quantitative microdialysis of solutes and water in vivo and in vitro. *Life Sci.* **1990**, *46* 105−119.
25. Stenken, J. A.; Topp, E. M.; Southard, M. Z.; Lunte, C. E. Examination of microdialysis sampling in a well-characterized hydrodynamic system. *Anal. Chem.* **1993**, *65*, 2324−2328.
26. Menacherry, S.; Hubert, W.; Justice, J. B., Jr. *In vivo* calibration of microdialysis probes for exogenous compounds. *Anal. Chem.* **1992**, *64*, 577−583.
27. Larsson, C. I. The use of an "internal standard" for control of the recovery in microdialysis. *Life Sci.* **1991**, *49*, PL73−PL78.
28. Wang, Y.; Wong, S. L.; Sawchuk, R. J. Microdialysis calibration using retrodialysis and zero-net flux: application to a study of the distribution of zidovudine to rabbit cerebrospinal fluid and thalamus. *Pharm. Res* **1993**, *10*, 1411−1419.
29. Wong, S. L.; Wang, Y.; Sawchuck, R. L. Analysis of zidovudine distribution to specific regions in rabbit brain using microdialysis. *Pharm. Res.* **1992**, *9*, 332−338.
30. Yokel, R. A.; Allen, D. D.; Burgio, D. E.; McNamara, P. J. Antipyrine as a dialyzable reference to correct differences in efficiency among and within sampling devices during *in vivo* microdialysis. *J. Pharmacol. Toxicol. Meth.* **1992**, *27*, 135−142.
31. Lönnroth, P.; Jansson, P.; Smith, U. A microdialysis method allowing characterization of intercellular water space in humans. *Am. J. Physiol.* **1987**, *253*, E228−E231.
32. Ståhle, L. Drug distribution studies with microdialysis: I. Tissue dependent difference in recovery between caffeine and theophylline. *Life Sci.* **1991**, *49*, 1835−1842.
33. Palsmeier, R. K.; Lunte, C. E. Microdialysis sampling in tumor and muscle: Study of the disposition of 3-amino-1,2,4-benzotriazine-1,4-di-*N*-oxide (SR 4233). *Life Sci.* **1994**, *55*, 815−825.
34. Lindefors, N.; Amberg, G.; Ungerstedt, U. Intracerebral microdialysis. I. Experimental studies of diffusion kinetics. *J. Pharmacol. Meth.* **1989**, *22*, 141−156.
35. Jacobson, I.; Sandberg, M.; Hamberger, A. Mass transfer in brain dialysis devices−a new method for the estimation of extracellular amino acid concentration. *J. Neurosci. Meth.* **1985**, *15*, 263−268.
36. Van Belle, K.; Dzeka, T.; Sarre, S.; Ebinger, G.; Michotte, Y. *In vitro* and *in vivo* microdialysis calibration for the measurement of carbamazepine and its metabolites in rat brain tissue using the internal reference technique. *J. Neurosci. Meth.* **1993**, *49*, 167−173.
37. Davies, M. I. Microdialysis Sampling for In Vivo Hepatic Metabolism Studies. Ph. D. Dissertation, The University of Kansas, Lawrence, Kansas, 1995.
38. Riley, C. M.; Ault, J. M.; Lunte, C. E. On-line microdialysis sampling. In *Pharmaceutical and Biomedical Applications of Liquid Chromatography*; Riley, C. M.; Lough, W. J.; Wainer, I. W., Eds.; Elsevier: Oxford, UK, 1994; pp 193−239.
39. Davies, M. I.; Lunte, C. E. Microdialysis sampling coupled on-line to microseparation techniques. *Chem. Soc. Rev.* **1997**, *26*, 215−222.
40. Niwa, O.; Torimitsu, K.; Morita, M.; Osbourne, P.; Yamamoto, K. Concentration of extracellular L-glutamate released from cultured nerve cells measured with a small-volume on-line sensor. *Anal. Chem.* **1996**, *68*, 1865−1870.
41. Zilkha, E.; Obrenovitch, T.; Koshy, A.; Kusakabe, H.; Bennetto, H. Extracellular glutamate: on-line monitoring using microdialysis coupled to enzyme-amperometric analysis. *J. Neurosci. Meth.* **1995**, *60*, 1−9.
42. Volpe, G.; Moscone, D.; Compagnone, D.; Palleschi, G. *In vivo* continuous monitoring of L-lactate coupling subcutaneous microdialysis and an electrochemical biocell. *Sensors Actuators B* **1995**, *24−25*, 138−141.
43. Yao, T.; Suzuki, S.; Nishino, H.; Nakahara, T. On-line ampoerometric assay of glucose, L-glutamate, and acetylcholine using microdialysis probes and immobilized enzyme reactors. *Electroanalysis* **1995**, *7*, 1114−1117.
44. Palmisano, F.; Centonze, D.; Quinto, M.; Zambonin, P. A microdialysis fiber based sampler for flow injection analysis: determination of L-lactate in biofluids by an electrochemically synthesized bilayer membrane based biosensor. *Biosens. Bioelectron.* **1996**, *11*, 419−425.
45. Csoregi, E.; Laurell, T.; Katakis, I.; Heller, A.; Gorton, L. On-line glucose monitoring by using microdialysis sampling and amperometric detection based on "wired" glucose oxidate in carbon paste. *Mikrochim. Acta* **1995**, *121*, 31−40.
46. Amine, A.; Digua, K.; Xie, B.; Danielsson, B. A microdialysis probe coupled with a miniaturized thermal glucose sensor for *in vivo* monitoring. *Anal. Lett.* **1995**, *28*, 2275−2286.
47. Muller, M.; v Osten, B.; Schmid, R.; Piegler, E.; Gerngross, I.; Buchegger, H.; Eichler, H. Theophylline kinetics in peripheral tissues *in vivo* in humans. *Naunyn-Schmeidebergs Arch. Pharmacol.* **1995**, *352*, 438−441.
48. Desrayaud, S.; Boschi, G.; Rips, R.; Schermann, J. Dose-dependent delivery of colchicine to the rat hippocampus by microdialysis. *Neurosci. Lett.* **1996**, *205*, 9−12.
49. Wagstaff, J.; Gibb, J.; Hanson, G. Dopamine D2-receptors regulate neurotensin release from nucleus accumbens and striatum as measured by *in vivo* microdialysis. *Brain Res. 721*, **1996**, 196−203.
50. Emmett, M.; Andren, P.; Caprioli, R. Specific molecular mass detection of endogenously released neuropeptides using *in vivo* microdialysis/mass spectrometry. *J. Neurosci. Meth.* **1995**, *62*, 141−147.
51. Boismenu, D.; Mamer, O.; Stemarie, L.; Vachon, L.; Montgomery, J. *In vivo* hydroxylation of the neurotoxin, 1-methyl-4-phenylpyridinium, and the effect of monoamine oxidase inhibitors: electrospray-MS analysis of intra-striatal microdialysates. *J. Mass Spectrom.* **1996**, *31*, 1101−1008.
52. Deterding, L. J.; Dix, K.; Burka, L. T.; Tomer, K. B. On-line coupling of in-vivo microdialysis with tandem mass spectrometry. *Anal. Chem.* **1992**, *64*, 2636−2641.
53. Liu, C.; Wu, Q.; Harms, A.; Smith, R. On-line microdialysis sample cleanup for electrospray ionization mass spectrometry of nucleic acid samples. *Anal. Chem.* **1996**, *68*, 3295−3299.
54. Wu, Q.; Liu, C.; Smith, R. On-line microdialysis desalting for electrospray ionization mass spectrometry of proteins and peptides. *Rapid Commun. Mass Spectrom.* **1996**, *10*, 835−840.
55. Lada, M. W.; Shaller, G.; Carriger, M. H.; Vickroy, T. W.; Kennedy, R. T. On-line interface between microdialysis and capillary zone electrophoresis. *Anal. Chim. Acta* **1995**, *307*, 217−225.
56. Hogan, B. L.; Lunte, S. M.; Stobaugh, J. F.; Lunte, C. E. On-line coupling of *in vivo* microdialysis sampling with capillary electrophoresis. *Anal. Chem.* **1994**, *66*, 596−602.
57. Zhou, S. Y.; Zuo, H.; Stobaugh, J. F.; Lunte, C. E.; Lunte, S. M. Continuous *in vivo* monitoring of amino acid neurotransmitters by microdialysis sampling with on-line derivatization and capillary electrophoresis separation. *Anal. Chem.* **1995**, *67*, 594−599.
58. Lada, M. W.; Kennedy, R. T. Quantitative *in vivo* monitoring of primary amines in rat caudate nucleus using microdialysis and capillary electrophoresis with laser-induced fluorescence detection. *Anal. Chem.* **1996**, *68*, 2790−2797.
59. Zhou, J.; Zuo, H.; Heckert, D. M.; Lunte, C. E.; Lunte, S. M. On-line coupling of *in vivo* microdialysis sampling with capillary electrophoresis/electrochemistry. *Anal. Chim. Acta*, in press.
60. *Microdialysis in the Neurosciences, Vol. 7, Techniques in the Behavioral and Neural Sciences*; Robinson, T. E.; Justice, J. B., Eds.; Elsevier, Amsterdam, 1991.
61. Westerink, B. H. Brain microdialysis and its application for the study of animal behaviour (review). *Behav. Brain Res.* **1995**, *70*, 103−124.
62. Lunte, C. E. Microdialysis and target organ exposure. In *Drug Toxicodynamics*; Johnson, D. E., Ed.; Marcel Dekker: New York, in press.
63. Fettweis, G.; Borlak, J. Topics in xenobiochemistry−application of microdialysis techniques in pharmacokinetic studies. *Xenobiotica* **1996**, *26*, 473−485.
64. Lunte, S. M.; Lunte, C. E. Microdialysis sampling for pharmacological studies: HPLC and CE analysis. In *Advances in Chromatography*; Grushka, E.; Brown, P., Eds.; Marcel Dekker: New York; 1996; pp 383−432.
65. Elmquist, W. F.; Sawchuk, R. J. Application of microdialysis in pharmacokinetic studies. *Pharm. Res.* **1997**, *14*, 267−288.
66. Shah, K. P.; Chang, M.; Riley, C. M. Automated analytical systems for drug development studies. II−A system for dissolution testing. *J. Pharm. Biomed. Anal.* **1994**, *12*, 1519−1527.
67. Shah, K. P.; Chang, M.; Riley, C. M. Automated analytical systems for drug development studies. 3. Multivessel dissolution testing system based on microdialysis sampling. *J. Pharm. Biomed. Anal.* **1995**, *13*, 1235−1241.
68. Knaub, S. R.; Chang, M. F.; Lunte, C. E.; Topp, E. M.; Riley, C. M. Automated analytical systems for drug development studies. Part IV. A microdialysis system to study the

partitioning of lomefloxacin across an erythrocyte membrane *in vitro*. *J. Pharm. Biomed. Anal.* **1995**, *14*, 121−129.
69. Zhou, J.; Shearer, E. C.; Hong, J.; Riley, C. M.; Schowen, R. Automated analytical systems for drug development studies. V. A system for enzyme kinetic studies. *J. Pharm. Biomed. Anal.* **1996**, *14*, 1691−1698.
70. Gunaratna, C.; Kissinger, P. T. Application of microdialysis to study the *in vitro* metabolism of drugs in liver microsomes. *J. Pharm. Biomed. Anal.* **1997**, *16*, 239−248.
71. Herrara, A. M.; Scott, D. O.; Lunte, C. E. Microdialysis sampling for determination of plasma protein binding of drugs. *Pharm. Res.* **1990**, *7*, 1077−1076.
72. Ekblom, M.; Hammarlund-Udenaes, M.; Lundqvist, T.; Sjöberg, P. Potential use of microdialysis sampling in pharmacokinetics: a protein binding study. *Pharm. Res.* **1992**, *9*, 155−158.
73. Sarre, S.; Van Belle, K.; Smolders, I.; Krieken, G.; Michotte, Y. The use of microdialysis for the determination of plasma protein binding of drugs. *J. Pharm. Biomed. Anal.* **1992**, *10*, 735−739.
74. Yang, H.; Elmquist, W. F. The binding of cyclosporin A to human plasma: An *in vitro* microdialysis study. *Pharm. Res.* **1996**, *13*, 622−627.
75. Mannino, S.; Cosio, M. S.; Zimei, P. Microdialysis sampling and high performance liquid chromatography with amperometric detection for sugar analysis in milk products. *Electroanalysis* **1996**, *8*, 353−355.
76. Torto, N.; Buttler, T.; Gorton, L.; Marko-Varga, G.; Stålbrand, H.; Tjerneld, F. Monitoring enzymatic hydrolysis of ivory nut mannan using on-line microdialysis sampling and anion-exchange chromatography with integrated pulsed electrochemical detection. *Anal. Chim. Acta* **1995**, *313*, 15−24.
77. Torto, N.; Marko-Varga, G.; Gorton, L.; Stålbrand, H.; Tjerneld, F. On-line quantitation of enzymatic mannan hydrolysates in small-volume bioreactors by microdialysis sampling and column liquid chromatography-integrated puled electrochemical detection. *J. Chromatogr. A* **1996**, *725*, 165−175.
78. Malone, M.; Zuo, H.; Lunte, S. M.; Smyth, M. Determination of tryptophan and kynurenine in brain microdialysis samples by capillary electrophoresis with electrochemical detection. *J. Chromatogr. A* **1995**, *700*, 73−80.
79. Hansen, D. K.; Lunte, S. M. Determination of kynurenic acid by capillary electrophoresis with laser-induced fluorescence detection. *J. Chromatogr. A* **1997**, *781*, 81−89.
80. Kostel, K. L.; Lunte, S. M. Evaluation of capillary electrophoresis with postcolumn derivatization and laser-induced fluorescence detection for the determination of substance P and its metabolites. *J. Chromatogr. B* **1997**, *695*, 27−38.
81. Hughes, P.; Krishnamoorthy, R.; Mitra, A. Vitreous disposition of two acycloguanosine antivirals in the albino and pigmented rabbit models: a novel ocular microdialysis technique. *J. Ocul. Pharmacol. Ther.* **1996**, *12*, 209−224.
82. Nakashima, M.; Zhao, M. F.; Ohya, H.; Sakuva, M.; Sasaki, H.; Matsuyama, K.; Ichikawa, M. Evaluation of *in-vivo* transdermal absorption of cyclosporin with absorption ehancer using intradermal microdialysis in rats. *J. Pharm. Pharmacol.* **1996**, *48*, 1143−1146.
83. Nolting, A.; Costa, T. D.; Vistelle, R.; Rand, K.; Derendorf, H. Determination of free extracellular concentrations of piperacillin by microdialysis. *J. Pharm. Sci.* **1996**, *85*, 369−372.
84. Kovar, A.; Costa, T. D.; Derendorf, H. Comparison of plasma and free tissue levels of ceftriazone in rats by microdialysis. *J. Pharm. Sci.* **1997**, *86*, 52−56.
85. Felländer, G.; Eleborg, L.; Bolinder, J.; Nordenström, J. Microdialysis of adipose tissue during surgery: effect of local alpha and beta-adrenoceptor blockade on blood flow and lipolysis. *J. Clin. Endocrinol. Metab.* **1996**, *81*, 2919−2924.
86. Darimont, C.; Delansorne, R.; Paris, J.; Ailhaud, G.; Negrel, R. Influences of estrogenic status on the lipolytic activity of parametrial adipose tissue *in vivo*: an *in situ* microdialysis study. *Endocrinology* **1997**, *138*, 1092−1096.
87. Telting-Diaz, M.; Scott, D. O.; Lunte, C. E. Intravenous microdialysis sampling in awake, freely moving rats. *Anal. Chem.* **1992**, *64*, 806−810.
88. Nakashima, M.; Takeuchi, N.; Hamada, M.; Matsuyama, K.; Ichikawa, M.; Goto, S. *In vivo* microdialysis for pharmacokinetics investigations: a plasma protein binding study of valproate in rabbits. *Biochem. Pharmacol. Bull.* **1994**, *17*, 1630−1634.
89. Rabenstein, K.; McShane, A.; McKenna, M.; Dempsey, E.; Keaveny, T. V.; Freaney, R. An intravascular microdialysis sampling system suitable for application in continuous biochemical monitoring of glucose and lactate. *Technol. Health Care* **1996**, *4*, 67−76.
90. Blöchl-Daum, B.; Müller, M.; Meisinger, V.; Eichler, H.; Fassolt, A.; Pehamberger, H. Measurement of extracellular fluid carboplatin kinetics in melanoma metastases with microdialysis. *Br. J. Cancer* **1996**, *73*, 920−924.
91. Devineni, D.; Klein-Szanto, A.; Gallo, J. M. *In vivo* microdialysis to characterize drug transport in brain tumors: analysis of methotrexate uptake in rat glioma-2 (RG-2)-bearing rats. *Cancer Chemother. Pharmacol.* **1996**, *38*, 499−507.
92. Devineni, D.; Klein-Szanto, A.; Gallo, J. M. Uptake of temozolomide in a rat glioma model in the presence and absence of the angiogenesis inhibitor TNP-470. *Cancer Res.* **1996**, *56*, 1983−1987.
93. Ward, K. W.; Pollack, G. M. Use of intrauterine microdialysis to investigate methanol-induced alteration in uteroplacental blood flow. *Toxicol. Appl. Pharmacol.* **1996**, *140*, 203−210.
94. Hadwiger, M. E.; Telting-Diaz, M.; Lunte, C. E. Liquid chromatographic determination of tacrine and its metabolites in rat bile microdialysates. *J. Chromatogr. B* **1994**, *655*, 235−241.
95. Gunaratna, C.; Lunte, S. M.; Zuo, H. Shunt probe: a new microdialysis probe design for *in vivo* drug metabolism studies. *Curr. Separations* **1994**, *13*, 80−83.
96. Layton, M. E.; Wood, J. G.; Yan, Z. Y.; Forster, J. Ischemia/reperfusion alters uric acid and ascorbic acid levels in liver. *J. Surg. Res.* **1996**, *64*, 1−5.
97. Sato, H.; Kitazawa, H.; Adachi, I.; Horikoshi, I. Microdialysis assessment of microfibrous collagen containing a P-glycoprotein-mediated transport inhibitor, cyclosporine A, for local delivery of the etoposide. *Pharm. Res.* **1996**, *13*, 1565−1569.
98. Malagié, I.; Trillant, A.; Douvier, E.; Anmella, M.; Dessalles, M.; Jancquot, C.; Gardier, A. M. Regional differences in the effect of the combined treatment of WAY 100635 and fluoxetine: An *in vivo* microdialysis study. *Naunyn-Schmeidebergs Arch. Pharmacol.* **1996**, *354*, 785−790.
99. Davies, M. I.; Lunte, C. E. Simultaneous microdialysis sampling from multiple sites in the liver for the study of phenol metabolism. *Life Sci.* **1996**, *59*, 1001−1013.
100. Malhotra, B.; Lemaire, M.; Brouillard, J.; Sawchuk, R. High-performance liquid chromatographic analysis of (*S*)-α-amino-5-phosphonomethyl[1,1′-biphenyl]-3-propanoic acid (EAB 5151) in brain and blood microdialysate (on-line) and in plasma ultrafiltrate of freely moving rats. *J. Chromatogr. B* **1996**, *679*, 167−176.
101. Nakashima, M.; Zhao, M. F.; Nakashima, M. N.; Sakurai, M.; Sasaki, H.; Matsuyama, K.; Ichikawa, M. *In vivo* microdialysis to determine the relative pharmacokinetics of drugs. *Biochem. Pharmacol. Bull.* **1996**, *19*, 988−994.
102. Deleu, D.; Sarre, S.; Michotte, Y.; Ebinger, G. Simultaneous *in vivo* microdialysis in plasma and skeletal muscle: a study of the pharmacokinetic properties of levodopa by noncompartmental analysis. *J. Pharm. Sci.* **1994**, *83*, 25−28.
103. Sarre, S.; Deleu, D.; Van Belle, K.; Ebinger, G.; Michotte, Y. Quantitative microdialysis for studying the *in vivo* L-DOPA kinetics in blood and skeletal muscle of the dog. *Pharm. Res.* **1995**, *12*, 746−750.
104. Van Amsterdam, C.; Boukhabza, A.; Ofner, B.; Pacha, W.; Lemaire, M. Measurement of free concentration of SDZ ICM 567 in blood and muscle using microdialysis sampling. *Biopharm. Drug Dispos.* **1995**, *16*, 521−527.
105. Yang, W. P.; Oshida, Y.; Wu, W.; Sato, J.; Ohsawa, I.; Sato, Y. Effect of daily voluntary running on *in vivo* insulin action in rat skeletal muscle and adipose tissue as determined by the microdialysis technique. *Int. J. Sports. Med.* **1995**, *16*, 99−104.
106. Müller, M.; Haag, O.; Burgdorff, T.; Georgopoulos, A.; Weninger, W.; Jansen, B.; Stanek, G.; Pehamberger, H.; Agneter, E.; Eichler, H. G. Characterization of peripheral-compartment kinetics of antibiotics by *in vivo* microdialysis in humans. *Antimicrob. Agents Chemother.* **1996**, *40*, 2703−2709.
107. Van Belle, K.; Sarre, S.; Ebinger, G.; Michotte, Y. Brain, liver and blood distribution kinetics of carbamazepine and its metabolic interaction with clomipramine in rats: A quantitative microdialysis study. *J. Pharmacol. Exp. Ther.* **1995**, *272*, 1217−1222.
108. Yokel, R. A. Aluminum chelation by 3-hydrozypyridin-4-ones in the rat demonstrated by microdialysis. *Biol. Trace Element Res.* **1996**, *53*, 193−203.
109. Ekstrøm, P. O.; Andersen, A.; Warren, D. J.; Giercksky, K. E.; Slørdal, L. Pharmacokinetics of different doses of methotrexate at steady state by in situ microdialysis in a rat model. *Cancer Chemother. Pharmacol.* **1995**, *36*, 283−289.
110. Ekstrøm, P. O.; Andersen, A.; Warren, D. J.; Giercksky, K. E.; Slørdal, L. Determination of extracellular methotrexate tissue levels by microdialysis in a rat model. *Cancer Chemother. Pharmacol.* **1996**, *37*, 394−400.

111. Oldner, A.; Goiny, M.; Ungerstedt, U.; Sollevi, A. Splanchnic homeostasis during endotoxin challenge in the pig as assessed by microdialysis and tonometry. *Shock* **1996**, *6*, 188−193.
112. Ekstrøm, P. O.; Giercksky, K. E.; Andersen, A.; Slørdal, L. Alterations in methotrexate pharmacokinetics by naproxen in the rat as measured by microdialysis. *Life Sci.* **1997**, *60*, PL359−364.
113. Molhotra, B. K.; Lemaire, M.; Sawchuk, R. J. Investigation of the distribution of EAB 515 to cortical ECF and CSF in freely moving rats utilizing microdialysis. *Pharm. Res.* **1997**, *11*, 1223−1232.

JS9801485

MDCK (Madin–Darby Canine Kidney) Cells: A Tool for Membrane Permeability Screening

JENNIFER D. IRVINE,* LORI TAKAHASHI, KAREN LOCKHART, JONATHAN CHEONG, JOHN W. TOLAN, H. E. SELICK, AND J. RUSSELL GROVE

Contribution from *Affymax Research Institute (a Glaxo Wellcome Company), Santa Clara, California 95051.*

Received August 5, 1998. Accepted for publication October 2, 1998.

Abstract □ The goal of this work was to investigate the use of MDCK (Madin–Darby canine kidney) cells as a possible tool for assessing the membrane permeability properties of early drug discovery compounds. Apparent permeability (P_{app}) values of 55 compounds with known human absorption values were determined using MDCK cell monolayers. For comparison, P_{app} values of the same compounds were also determined using Caco-2 cells, a well-characterized in vitro model of intestinal drug absorption. Monolayers were grown on 0.4-μm Transwell-COL membrane culture inserts. MDCK cells were seeded at high density and cultured for 3 days, and Caco-2 cells were cultured under standard conditions for 21 to 25 days. Compounds were tested using 100 μM donor solutions in transport medium (pH 7.4) containing 1% DMSO. The P_{app} values in MDCK cells correlated well with those in Caco-2 cells ($r^2 = 0.79$). Spearman's rank correlation coefficient for MDCK P_{app} and human absorption was 0.58 compared with 0.54 for Caco-2 P_{app} and human absorption. These results indicate that MDCK cells may be a useful tool for rapid membrane permeability screening.

Introduction

The rise of combinatorial chemistry and other drug discovery technologies has vastly increased the number of new compounds to be evaluated as potential drug candidates. Accordingly, new high-throughput strategies are required to evaluate compound properties beyond potency and selectivity. A major focus in the pharmaceutical industry is to develop new drugs with good oral bioavailability. One essential factor of oral bioavailability is the ability of a compound to be well absorbed in the small intestine. Because of its inherent simplicity compared to in vivo and in situ studies, there has been significant interest in the in vitro Caco-2 cell model of human intestinal drug absorption.

When cultured on semipermeable membranes, Caco-2 cells, derived from a human colon adenocarcinoma, differentiate into a highly functionalized epithelial barrier with remarkable morphological and biochemical similarity to small intestinal columnar epithelium.[1−3] Fully differentiated cell monolayers can be used to assess the membrane transport properties of novel compounds.[4,5] In addition, the apparent permeability (P_{app}) values obtained from Caco-2 transport studies have been shown to correlate to human intestinal absorption.[6,7] As a consequence, the Caco-2 cell monolayer model has proven extremely useful not only as a tool for mechanistic studies of drug absorption but also as an absorption screening assay for preclinical drug selection.[8−10]

Though well-characterized and time-proven, the Caco-2 assay remains a relatively low throughput method, due in part to the limitations of its 3-week growth period and regular maintenance feeding requirements. Proprietary culture conditions that greatly accelerate the Caco-2 monolayer differentiation rate, and hence reduce the required culture time, are commercially available, but at additional expense.[11] To reduce the tissue culture time, cost, and effort required for permeability testing, we chose to investigate whether a faster-growing cell line might be suitable for absorption screening.

MDCK (Madin−Darby canine kidney) cells are a common model for studying cell growth regulation, metabolism, and transport mechanisms in distal renal epithelia.[12−17] Like Caco-2 cells, MDCK cells have been shown to differentiate into columnar epithelium and to form tight junctions when cultured on semipermeable membranes.[18,19] The use of the MDCK cell line as a model cellular barrier for assessing intestinal epithelial drug transport was discussed by Cho et al.[20,21] Ranaldi et al. published P_{app} results from MDCK and Caco-2 testing of antimicrobial compounds, showing similar P_{app} values with both cell lines.[22,23] Others have pointed out that MDCK cells are a good candidate for modeling simple epithelia.[24] We chose to study a large number of compounds in both MDCK and Caco-2 assays to evaluate the suitability of MDCK cells as a possible tool for assessing membrane permeability.

Materials and Methods

Materials—Cell culture media and buffer components were purchased from Gibco BRL (Gaithersburg, MD). Fetal bovine serum (FBS) was heat-treated at 56 °C for 30 min prior to use. Caco-2 and MDCK cells were obtained from the ATCC (American Type Culture Collection, Rockville, MD). Transwell-COL tissue culture inserts (6.5 mm diameter, 0.4 μm pore size, collagen-coated PTFE (poly(ethylene terephthalate)) were purchased from Costar Corporation (Cambridge, MA). An EndOhm volt-ohm meter and electrode were purchased from World Precision Instruments (Sarasota, FL). Amoxicillin was from Fluka (Ronkonkoma, NY). Cephalexin monohydrate and loracarbef-D monohydrate were from USP (Rockville, MD). Practolol was from Tocris Cookson (St. Louis, MO). Zidovudine (AZT) was from Aldrich Chemical Company (Milwaukee, WI). Compound 0311C90, acrivastine, fluparoxan, lamotrigine, netivudine, ondansetron, sumatriptan succinate, and trimethoprim were received from Glaxo-Wellcome (Research Triangle Park, NC). Gabapentin was from Parke-Davis (Ann Arbor,

* Corresponding author. Telephone: (408) 522-5885. Fax: (408) 481-0393. E-mail: jennifer_irvine@affymax.com.

10.1021/js9803205 CCC: $18.00
Published on Web 12/05/1998

MI). Olsalazine disodium was a gift from Pharmacia & Upjohn (Kalamazoo, MI). Sotalol hydrochloride was a gift from Irotec Labs (Little Island, Cork, Ireland). All other chemicals were from Sigma Chemical Company (St. Louis, MO).

Cell Culture—Caco-2 cells were maintained in Dulbecco's Modified Eagle Medium (DMEM) containing 10% FBS, 1% nonessential amino acids, and 2 mM fresh L-glutamine. Cells were cultured at 37 °C in an atmosphere of 5% CO_2 and 95% relative humidity. Cells were passaged at 80−90% confluence (every 3−4 days) using Trypsin-EDTA solution (Gibco #25300−047). Culture inserts were preincubated with culture medium (1 h, 37 °C) and then seeded with 63 000 cells per cm^2 (0.33 cm^2 per insert). Caco-2 monolayers were fed with fresh medium 24 h after seeding and then 3 times per week. Caco-2 monolayers were cultured for 21−25 days before use. Caco-2 cells were used at passage number 31 to 42, after receipt at passage 18 from ATCC.

MDCK cells were maintained in Minimal Essential Medium (MEM) containing 10% FBS and 2 mM fresh L-glutamine. MDCK cells were cultured and passaged in the same manner as Caco-2 cells. Culture inserts were preincubated with culture medium (1 h, 37 °C) and then seeded with 664 000 cells per cm^2 (0.33 cm^2 per insert). MDCK monolayers were washed and fed with fresh medium 1 h post-seeding and again 24 h post-seeding. MDCK monolayers were cultured for 3 days before use. MDCK cells were used at passage number 59 to 80, after receipt at passage 51 from ATCC.

Transport Assays—*Monolayer Screening*—Cell monolayers were fed with the appropriate culture medium on the day of assay. Two hours after feeding, monolayers were washed with transport medium (Hanks' Balanced Salt Solution (HBSS, Gibco #14025−092) + 10 mM Hepes, pH 7.4). Monolayers were equilibrated in transport medium for 30 min at 37 °C, in 95% humidity. The electrical resistance of each monolayer was measured at 37 °C at three locations using an STX-2 "chopstick" electrode and volt-ohm meter. The resistance of bare filter inserts was subtracted from monolayer resistance values. Monolayer resistance values were multiplied by the membrane area (0.33 cm^2) and averaged to calculate transepithelial electrical resistance (TEER ($\Omega \cdot cm^2$)) values for each monolayer. TEER values indicate the degree of monolayer confluence and tight junction development.

MDCK cells consistently showed lower TEER values than Caco-2 cells. Caco-2 monolayers with TEER values less than approximately 230 $\Omega \cdot cm^2$ were not used. MDCK monolayers with TEER values <90 $\Omega \cdot cm^2$ were not used. These cutoff values were determined to be the lower limit of the usual TEER value observed for each cell line. Typically, 70−90% of both MDCK and Caco-2 monolayers were acceptable for testing using this pre-screen procedure.

Transport Assay—Transport assay donor solutions consisted of 100 μM test compound in transport medium containing 100 μM lucifer yellow and 1% DMSO (pH 7.4). All test compounds were evaluated for suitable solubility and stability under assay conditions and a detection limit of ≤ 1 μM prior to assay. DMSO (1%) was used to increase the solubility of more hydrophobic compounds and was previously found to have no effect on Caco-2 paracellular or transcellular permeability of five test compounds. Ethanol and methanol were found to be unacceptable cosolvents for Caco-2 transport assays (unpublished results). Lucifer yellow, a fluorescent marker for the paracellular pathway, was used as an internal control in every test to verify tight junction integrity during the assay.

Transport assays were conducted using 0.3 mL of apical (AP) donor solution and 1 mL of basolateral (BL) acceptor solution (transport medium, pH 7.4). All compounds were tested in six replicate monolayers. Monolayers were incubated with donor and acceptor solutions for 60 min at 37 °C, 95% humidity, with 30 rpm reciprocal shaking. BL compartments were sampled at 15, 30, and 60 min. AP compartments were sampled at 60 min. The quality control compound set (a pool of propranolol, salicylic acid, cephalexin, vinblastine, and lucifer yellow) was assayed as a pool under the same conditions as the test compounds, using a donor solution containing 100 μM of each compound in transport medium (pH 7.4). Under these assay conditions, PEPT 1 dipeptide transporter activity was assumed to be minimal, because this transporter requires a pH gradient.

Most compounds, including the quality control compound set, were quantified by HPLC (Hewlett-Packard 1050 system) using a C18 column (YMC J'Sphere H80), variable wavelength detection (HP1050−VWD), and an acetonitrile/0.02 M ammonium formate, pH 3.7, mobile phase. Gabapentin was quantified via derivitization with dansyl chloride followed by fluorescence detection (Jasco 920 HPLC fluorescence detector; Ex = 352 nm, Em = 510 nm) using a Nucleosil C18 column and an acetonitrile/0.05M Tris HCl, pH 7.5, mobile phase. Mannitol was quantified by ion-exchange chromatography (Carbo-Pac PA10) with pulsed amperometry detection (Dionex ED40) using a gold electrode and a mobile phase of 52 mM NaOH. Sumatriptan was quantified using DC amperometry (Dionex ED40) with a carbon electrode and a Zorbax Elipse XDB−C8 column with a mobile phase of methanol/0.075 M phosphate (30:70) at pH 7.0. Lucifer yellow was quantified using a fluorescence 96-well plate reader (CytoFluor II (Biosearch, a subsidiary of Millipore)), Ex = 485 nm, Em = 530 nm.

Calculations—P_{app} (apparent permeability) values were calculated according to the following equation:

$$P_{app} = \left(\frac{dQ}{dt}\right) \times \frac{1}{C_0} \times \frac{1}{A} \quad (1)$$

where dQ/dt is the permeability rate, C_0 is the initial concentration in the donor compartment, and A is the surface area of the filter. Permeability rates were calculated by plotting the percent of initial AP drug mass (peak area) found in the BL compartment versus time and determining the slope of the line. The P_{app} values for most compounds were calculated from 15 min data to ensure that <10% of initial compound was found in the acceptor compartment. In some cases, no compound was detected in 15-min samples, so later timepoints were used. Loracarbef was detected in 30-min samples from both cell lines. Gabapentin was detected in 60-min samples from both cell lines. Olsalazine was detected in 30-min samples from MDCK cells and in 60-min samples from Caco-2 cells. Amoxicillin was detected in 60-min samples from Caco-2 cells.

Lucifer yellow (LY) results were used as an internal control for each monolayer to verify tight junction integrity during the entire assay period. Variations in tight junctions can significantly affect permeability results for compounds using the paracellular transport route. Accordingly, LY P_{app} values were quantified from 60-min basolateral samples after background subtraction. The normal range for LY permeability in Caco-2 monolayers observed in our study was approximately 1 to 7 nm/sec (1 nm/s = 1×10^{-7} cm/s). Results from Caco-2 monolayers with LY $P_{app} > 10$ nm/s were not used in compound P_{app} calculations. LY permeability in MDCK monolayers was unknown at the start of this study, though it was expected to be somewhat higher than in Caco-2 cells because of the lower resistance values observed for MDCK monolayers. Initially, results from MDCK monolayers with LY $P_{app} > 30$ nm/s were not used. Later in the study, the MDCK LY cutoff was adjusted to 15 nm/s.

Spearman's rank correlation coefficient, a measure of association between two separate rankings of n items, was calculated as follows:

$$r_s = 1 - \frac{6\sum d^2}{n^3 - n} \quad (2)$$

where d equals the difference between the two ranks that each item received, and n equals the number of items.[25] The value r_s is always between −1 and +1. Greater r_s values indicate greater positive association. Lower r_s values indicate less association.

Calculated log water:octanol partition coefficient (CLogP) values were calculated using Pcmodelsx, a hydrophobicity and polarizability prediction from Daylight Chemical Information Systems, Inc. (Mission Viejo, CA).

Quality Control—As a quality control measure to monitor the consistency of the cells during this experiment, a standard set of six compounds was tested at the beginning and end of the study with both cell lines. The standard set was composed of passive transcellular and paracellular compounds (propranolol HCl and LY), one dipeptide transporter substrate (cephalexin), and one *p*-glycoprotein substrate (vinblastine sulfate). Salicylic acid and cimetidine were also included, though the transport mechanisms of these compounds are somewhat more complex. The standard set was tested as a pool containing 100 μM each of the six compounds. The P_{app} of each compound in the pool was previously determined to be equivalent to the P_{app} of each compound tested

individually. The LY and TEER values were also monitored to ensure monolayer consistency during the study.

Results

Compound Test Set Assembly—To perform this study, a set of test compounds with known human absorption values (% absorption) and a broad range of physicochemical properties was assembled from literature references and Glaxo Wellcome data (Table 1). [6,7,26–33] Great care was taken to verify human intestinal absorption values by identifying primary references wherever possible. Primary references for most of the compounds tested here have been cited individually elsewhere.[33] Bioavailability data were not used. It was a challenge to identify compounds with low to intermediate levels of absorption (10 to 70%) because most compounds with known human absorption data have been successful as oral formulations. Compounds were not otherwise pre-selected in any manner that should bias the results of this study.

Compounds transported by more complicated transport mechanisms than passive diffusion were purposely retained in this set. Both Caco-2 and MDCK cell lines are known to express *p*-glycoprotein (Pgp) and dipeptide transporters, important mechanisms in the intestinal and renal barriers that retain nutrients while exporting xenobiotics. We were particularly interested to see how results for these compounds would compare between the two cell lines. Six compounds tested (amoxicillin, cefatrizine, cephalexin, gabapentin, lisinopril, and loracarbef) were reported dipeptide transport substrates. Three of the compounds tested (dexamethasone, ranitidine, and sulfasalazine) were reported efflux substrates.

MDCK and Caco-2 Monolayers—The formation of confluent MDCK monolayers with functional tight junctions was confirmed by microscopy, TEER values, and LY permeability results. The use of optically clear semipermeable membranes for culture (Costar Transwell-COL) allowed for visual examinations by microscopy. The TEER values provided a simple quick estimate of tight junction formation, which was then assessed more thoroughly by examining LY permeability. Results from a growth study showed evidence of tight junction maturation as TEER values increased and LY permeability decreased with time from zero to 3 days (Table 2). The average MDCK TEER value during this study was 173 $\Omega \cdot cm^2$ ($\pm$ 51). The average MDCK LY P_{app} value was 6.3 nm/s ($\pm$ 6.1).

As for MDCK cells, Caco-2 monolayer confluence and tight junction integrity were assessed by microscopy, TEER values, and LY permeability values. The average Caco-2 TEER value during this study was 280 $\Omega \cdot cm^2$ ($\pm$ 50). The average Caco-2 LY P_{app} value was 3.1 nm/s ($\pm$ 2.8).

Monolayer Quality Control—Quality control results with the standard set of six compounds indicated that both Caco-2 and MDCK cell lines produced similar permeability values at the beginning and end of the study (Table 4). The differences between the beginning and ending values were similar to the normal day-to-day variability for permeability values observed with these compounds.

MDCK P_{app} versus Caco-2 P_{app}—MDCK and Caco-2 permeability results are shown in Table 1. Values are reported as the average of replicates $\pm$ the standard deviation (SD). Included in the table are the reported human intestinal absorption values for the same compounds. When MDCK and Caco-2 P_{app} values were plotted against each other, a clear relationship was observed (Figure 1). The calculated r^2 value was 0.79, denoting a high level of correlation. Data for the known dipeptide transport and *p*-glycoprotein efflux substrates fit the Caco-2/MDCK correlation well. Greater deviation from the linear trend was seen among low P_{app} compounds. Some departure from linearity was noted for very high permeability compounds, where P_{app} values tended to be slightly greater in MDCK cells than in Caco-2 cells. The significance of this observation has not been determined.

Table 1—Permeability Results with MDCK and Caco-2 Monolayers

compound	human % abs[a]	P_{app} (nm/s)[c] MDCK	P_{app} (nm/s)[c] Caco-2
0311C90	60[b]	11 ± 4.1	29 ± 6.6
acebutolol HCl	90	17 ± 4.0	38 ± 2.6
acetaminophen	80	350 ± 16	1000 ± 57
acetylsalicylic acid	100	74 ± 20	22 ± 2.0
acrivastine	88	22 ± 7.8	19 ± 9.9
acyclovir	16[b]	2.1 ± 1.6	not detected
alprenolol HCl	93	1600 ± 84	1700 ± 98
amoxicillin	94	2.4 ± 0.9	0.21 ± 0.1
antipyrine	100	1500 ± 100	1500 ± 120
atenolol	50	18 ± 9.2	33 ± 4.4
AZT (Zidovudine)	100	60 ± 12	280 ± 69
bretylium tosylate	18	14 ±4.4	11 ± 1.4
bupropion HCl	87	1300 ± 74	1500 ± 220
cefatrizine propylene glycol	76	25 ± 13	7.6 ± 1.3
cefuroxime sodium	5	1.6 ± 1.6	3.8 ± 3.2
cephalexin monohydrate	98	4.8 ± 2.4	2.7 ± 0.8
chlorothiazide	13	3.0 ± 0.8	3.2 ± 1.2
corticosterone	100	1400 ± 32	1200 ± 200
dexamethasone	100	200 ± 17	400 ± 38
fluparoxan	100[b]	2500 ± 180	2000 ± 190
furosemide	61	6.2 ± 4.3	1.4 ± 0.1
gabapentin	50	3.6 ± 1.9	0.10 ± 0.04
guanabenz	75	1900 ± 280	1000 ± 78
hydrochlorothiazide	67	10 ± 2.8	9.2 ± 4.0
hydrocortisone	91	310 ± 14	560 ± 63
ketoprofen	100	200 ± 20	930 ± 100
labetalol HCl	95	250 ± 23	760 ± 240
lamotrigine	70	880 ± 56	1100 ± 350
lisinopril dihydrate	25	1.8 ± 3.7	2.2 ± 4.1
loracarbef-D monohydrate	100	9.1 ± 0.9	2.4 ± 0.8
mannitol	15	not detected	5.7 ± 1.9
methylprednisolone	82	160 ± 90	250 ± 52
metoprolol tartrate	95	1500 ± 97	1400 ± 100
nadolol	34	14 ± 4.3	3.9 ± 3.4
netivudine (882C87)	28[b]	14 ± 5.7	6.8 ± 1.1
olsalazine disodium	2	0.48 ± 0.24	0.16 ± 0.06
ondansetron	100	1100 ± 20	1100 ± 140
oxyprenolol HCl	90	1300 ± 49	1600 ± 250
penicillin V	45	1.5 ± 0.13	1.7 ± 0.34
phenytoin	90	1200 ± 54	1600 ± 180
pindolol	90	590 ± 26	960 ± 79
practolol	100	13 ± 2.6	61 ± 17
progesterone	91	1600 ± 80	980 ± 60
propranolol HCl	90	1700 ± 65	1100 ± 130
propylthiouracil	75	410 ± 130	960 ± 87
ranitidine HCl	50	not detected	not detected
salicylic acid	100	100 ± 37	130 ± 11
sotalol HCl	95	47 ± 8.0	42 ± 13
sulfasalazine	65	4.8 ± 4.1	6.0 ± 11
sumatriptan succinate	75[b]	19 ± 3.1	not detected
terbutaline hemisulfate	60	10 ± 2.7	4.1 ± 1.6
testosterone	100	1400 ± 110	1000 ± 71
timolol maleate	90	550 ± 34	1000 ± 80
trimethoprim	97	520 ± 89	870 ± 130
warfarin sodium	98	440 ± 39	960 ± 210

[a] Human % oral absorption values were obtained from published values. [b] Human % oral absorption values were obtained from Glaxo-Wellcome. [c] P_{app} values are mean ± standard deviation.

P_{app} vs Human Intestinal Absorption—When MDCK and Caco-2 P_{app} values were plotted against percent human absorption, an approximately sigmoidal relationship was observed with both cell lines (Figure 2). Well-absorbed compounds showed generally high P_{app} values, and poorly

Table 2—MDCK Monolayer Development

growth time[a]	TEER[b]	LY P_{app}[c]
2	≤1	830 ± 130
24	30 ± 3	150 ± 60
72	100 ± 8	≤5

[a] Hours. [b] Average TEER ($\Omega \cdot cm^2$) of 4 replicates ± standard deviation. [c] Average P_{app} (nm/sec) of 4 replicates ± standard deviation.

Table 3—Spearman's Rank Correlation Coefficients (r_s)

comparison	r_s
Caco-2 P_{app} versus MDCK P_{app}	0.93
human absorption versus MDCK P_{app}	0.58
human absorption versus Caco-2 P_{app}	0.54
MDCK P_{app} versus cLogP	0.50
human absorption versus cLogP	0.25

Table 4—Quality Control Results for MDCK Validation Study[a]

cell	compound	start of study[a]	end of study[a]
Caco-2	cimetidine	15 ± 3.0	11 ± 2
	cephalexin	4.7 ± 1.0	1.9 ± 0.8
	salicylic acid	200 ± 7	120 ± 18
	propranolol HCl	600 ± 35	700 ± 35
	vinblastine SO_4	130 ± 10	120 ± 16
MDCK	cimetidine	15 ± 4	7.4 ± 3.1
	cephalexin	13 ± 9.8	5.9 ± 2.4
	salicylic acid	51 ± 5	37 ± 3
	propranolol HCl	1000 ± 81	830 ± 29
	vinblastine SO_4	72 ± 14	57 ± 5

[a] Average P_{app} (nm/s) ± standard deviation.

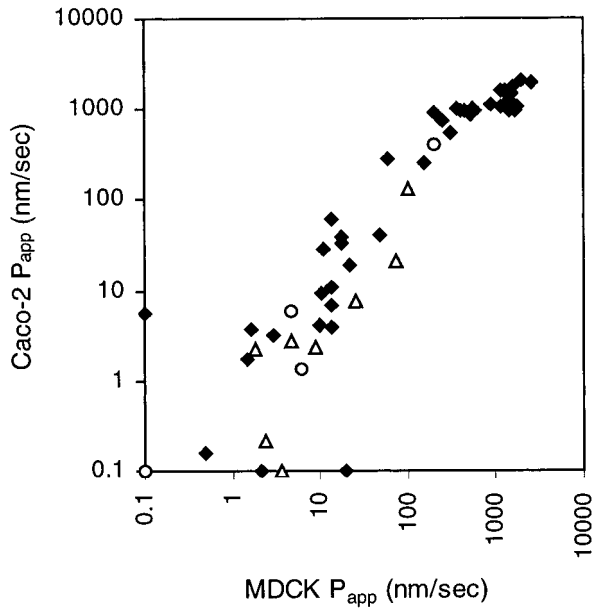

Figure 1—Correlation of MDCK and Caco-2 apparent permeability (P_{app}) values. P_{app} values plotted at 0.1 are actually ≤0.1, including zero for compounds not detected in the basolateral compartment. Key: (◆) = passive diffusion compounds; (△) active transport compounds; (○) efflux substrates.

absorbed compounds showed generally low P_{app} values. Some deviation from the sigmoidal trend was apparent with both cell lines, with somewhat greater deviation seen for Caco-2 data than for MDCK data. The compounds that fell out of the correlation were the same for both cell lines. Permeability values for amoxicillin, cephalexin, and loracarbef (three dipeptide transporter substrates) clearly underestimated their human absorption values of 94, 98, and 100%, respectively. Ranitidine (a *p*-glycoprotein efflux substrate) did not show detectable transport with either cell line, though it is reported to be 50% absorbed.

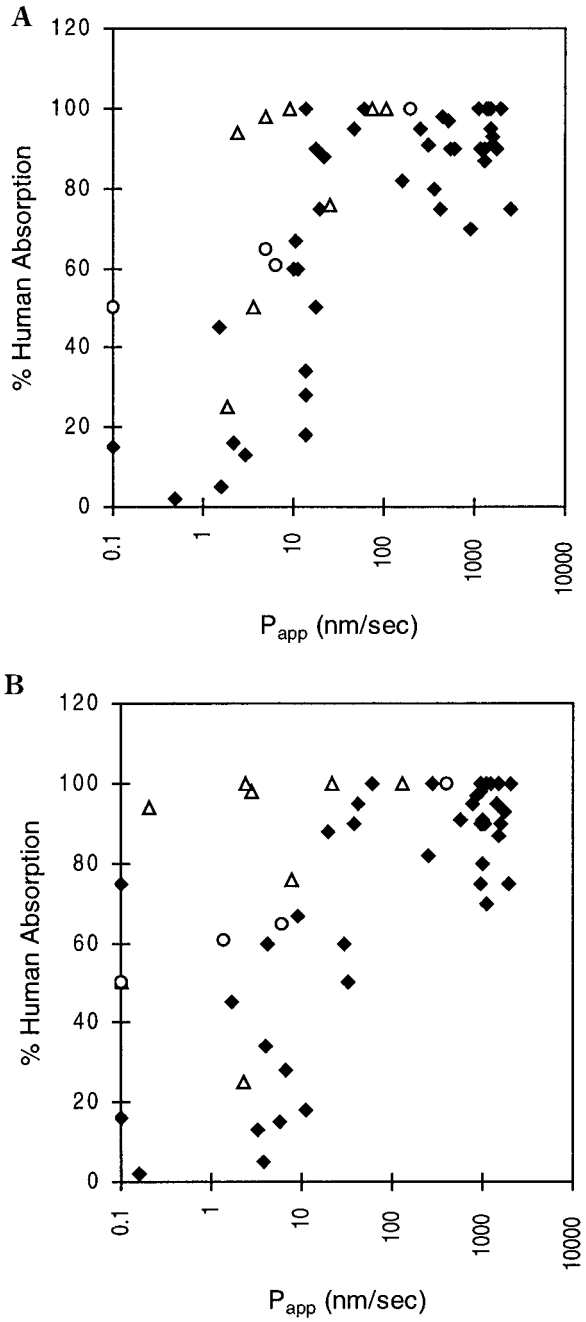

Figure 2—Correlation of apparent permeability (P_{app}) values and percent (%) human intestinal absorption. Figure 2A plots the relationship between MDCK P_{app} values and % absorption. Figure 2B plots the relationship between Caco-2 P_{app} values and % absorption. The P_{app} values plotted at 0.1 are actually ≤0.1, including zero for compounds not detected in the basolateral compartment. Key: (◆) passive diffusion compounds; (△) active transport compounds; (○) efflux substrates.

Rank Order—Because of the steep sigmoidal relationship between P_{app} values and human intestinal absorption and because of the variation in fit to the relationship, absolute absorption values are difficult to estimate from P_{app} data. In contrast, an estimate of rank order of absorption within a set of compounds, as measured by rank order of permeability, can be directly determined. Spearman's rank correlation coefficient was therefore calculated for MDCK and Caco-2 data to see how well either cell line modeled rank order of absorption (Table 3). The highest rank correlation was for MDCK P_{app} to Caco-2 P_{app} (0.93).

Rank correlations for MDCK P_{app} and Caco-2 P_{app} to human absorption were similar (0.58 and 0.54, respectively). In comparison, the rank correlation for cLogP to human absorption was 0.25. The rank correlation for human absorption to random number was calculated for perspective. For eight determinations, the average correlation was 0.0, however the value of one of the eight tests was 0.3.

Discussion

Although the MDCK cells are derived from dog kidney, whereas Caco-2 cells are derived from human colon, the two cell lines share many common epithelial cell characteristics.[15,17,34] That cells from such diverse origins could produce comparable transport results might seem surprising. Nonetheless, as a whole, we observed that permeability results from MDCK cells were similar to permeability results from Caco-2 cells. The r^2 value (0.79) for MDCK P_{app} versus Caco-2 P_{app} indicates the strength of that similarity, which is also visually evident in Figure 2. Because most of the compounds tested were passively absorbed, the good correlation between Caco-2 and MDCK P_{app} values suggests that the rules determining passive membrane permeability may be universal among cell types.

MDCK monolayers were seeded at a high density (664 000 cells/cm^2) to reduce tissue culture time. Similar high-density MDCK culture conditions have been reported by other labs.[14,34] MDCK TEER results in our studies (120−190 Ω·cm^2) were consistent with previously published data for cells seeded at a lower density and grown for 2−4 days.[20,24] Further studies in our lab have shown that the MDCK seeding density can be reduced by a factor of two or four without affecting assay performance (unpublished data). Caco-2 monolayers were seeded at a moderate density similar to those reported by other labs (63 000 cells/cm^2).[30,32] Caco-2 monolayers seeded at high density and assayed on day 3 showed high LY P_{app} values, which is evidence of poor tight junction integrity (unpublished results).

Permeability data from MDCK and Caco-2 monolayers correlated best for high P_{app} compounds. The weaker correlation observed for low P_{app} data may be partially due to greater variability in transport assay results for low permeability compounds and partially due to the magnification artifact of the log/log plot. We found permeability values of <10 tended to be poorly reproducible day to day. We therefore did not consider P_{app} results between 0.5 and 5.0 to be significantly different. Because of our interest in applying the permeation assay as a screening tool, that degree of error was tolerable.

Although most of the compounds tested here were absorbed by passive diffusion, to the best of our knowledge, some active transport compounds were included because oral absorption data was available. Caco-2 and MDCK P_{app} data for these active transport and efflux compounds appeared to correlate well. For the *p*-glycoprotein efflux substrates, the apical compound concentration may have been high enough to saturate the mechanism and negate any differences between the cells. For dipeptide transport substrates, both cell lines may have expressed roughly similar levels of transporters with roughly similar specificities. Caco-2 and MDCK permeability results for nonpassively absorbed compounds may not always correlate as well as observed here. This study was not designed to precisely examine and compare the permeability of active transport and efflux compounds in Caco-2 and MDCK cells. Although MDCK and Caco-2 cell lines have some active transport mechanisms in common, many transporters can affect drug permeability results.

The correlation between Caco-2 P_{app} values and human intestinal absorption that has been well-established by other laboratories was confirmed in these findings, and a similar correlation was observed for MDCK P_{app} values. In addition, both cell lines showed similar weaknesses with particular compounds. Thus, MDCK P_{app} values appear to function as well as Caco-2 cells when applied as a general absorption screen.

In conclusion, we have shown that drug permeability data from MDCK cells is similar to permeability data from Caco-2 cells, at least for passively absorbed compounds. We have found the fast-growing MDCK cell line can provide reliable results after only 3 days of culture, compared with the 21 days of culture required for Caco-2 testing. We suggest that it may be practical to use MDCK cells as a permeability screening tool to increase the throughput of membrane permeability screening in early drug discovery.

References and Notes

1. Pinto, M.; Robine-Leon, S.; Appay, M.-D.; Kedinger, M.; Triadou, N.; Dussaulx, E.; LaCroix, B.; Simon-Assmann, P.; Haffen, K.; Fogh, J.; Zweibaum, A. Enterocyte-like differentiation and polarization of the human colon carcinoma cell line Caco-2 in culture. *Biol. Cell* **1983**, *47*, 323−330.
2. Hidalgo, I. J.; Raub, T. J.; Borchardt, R. T. Characterization of the human colon carcinoma cell line (Caco-2) as a model system for intestinal epithelial permeability. *Gastroenterology* **1989**, *96*, 736−749.
3. Wilson, G.; Hassan, I. F.; Dix, C. J.; Williamson, I.; Shah, R.; Mackay, M. Transport and permeability properties of human Caco-2 cells: An *in vitro* model of the intestinal epithelial cell barrier. *J. Controlled Release* **1990**, *11*, 25−40.
4. Artursson, P. Epithelial transport of drugs in cell culture. I: A model for studying the passive diffusion of drugs over intestinal absorbtive (Caco-2) cells. *J. Pharm. Sci.* **1990**, *79*, 476−482.
5. Hilgers, A. R.; Conradi, R. A.; Burton, P. S. Caco-2 cell monolayers as a model for drug transport across the intestinal mucosa. *Pharm. Res.* **1990**, *7*, 902−910.
6. Artursson, P.; Karlsson, J. Correlation between oral drug absorption in humans and apparent drug permeability coefficients in human intestinal epithelial (Caco-2) cells. *Biochem. Biophys. Res. Comm.* **1991**, *175*, 880−885.
7. Stewart, B. H.; Chan, O. H.; Lu, R. H.; Reyner, E. L.; Schmid, H. L.; Hamilton, H. W.; Steinbaugh, B. A.; Taylor, M. D. Comparison of intestinal permeabilities determined in multiple in vitro and in situ models: relationship to absorption in humans. *Pharm. Res.* **1995**, *12*, 693−699.
8. Artursson, P.; Palm, K.; Luthman, K. Caco-2 monolayers in experimental and theoretical predictions of drug transport. *Adv. Drug Delivery Rev.* **1996**, *22*, 67−84.
9. Hidalgo, I. J. Cultured intestinal epithelial cell models. In *Models for Assessing Drug Absorption and Metabolism*; Borchardt, R. T., Smith, P. L., Wilson, G., Eds.; Plenum: New York, 1996; pp 35−50.
10. Delie, F.; Rubas, W. A human colonic cell line sharing similarities with enterocytes as a model to examine oral absorption: Advantages and limitations of the Caco-2 model. *Crit. Rev. Ther. Drug Carrier Syst.* **1997**, *14*, 221−286.
11. Chong, S. Evaluation of Biocoat intestinal epithelium differentiation environment as an absorption screening model with improved productivity. *Pharm. Res.* **1996**, *13*, S-240.
12. Horster, M.; Stopp, M. Transport and metabolic functions in cultured renal tubule cells. *Kidney Int.* **1986**, *29*, 46−53.
13. Horio, M.; Chin, K.-V.; Currier, S. J.; Goldenberg, S.; Williams, C.; Pastan, I.; Gottesman, M. M.; Handler, J. Transepithelial transport of drugs by the multidrug transporter in cultured Madin−Darby canine kidney cell epithelia. *J. Biol. Chem.* **1989**, *264*, 14880−14884.
14. Hunter, J.; Hirst, B. H.; Simmons, N. L. Transepithelial secretion, cellular accumulation and cytotoxicity of vinblastine in defined MDCK cell strains. *Biochim. Biophys. Acta* **1993**, *1179*, 1−10.
15. Hunter, J.; Jepson, M. A.; Tsuruo, T.; Simmons, N. L.; Hirst, B. H. Functional expression of *p*-glycoprotein in apical membranes of human intestinal Caco-2 cells. Kinetics of vinblastine secretion and interaction with modulators. *J. Biol. Chem.* **1993**, *268*, 14991−14997.
16. Brandsch, M.; Ganapathy, V.; Leibach, F. H. H+-peptide contransport in Madin−Darby canine kidney cells: expres-

sion and calmodulin-dependent regulation. *Am. J. Physiol.* **1995**, *268*, F391−F397.
17. Ganapathy, M. E.; Brandsch, M.; Prasad, P. D.; Ganapathy, V.; Leibach, F. H. Differential recognition of beta-lactam antibiotics by intestinal and renal peptide transporters, PEPT1 and PEPT2. *J. Biol. Chem.* **1995**, *270*, 25672−25677.
18. Misfeldt, D. S.; Hamamoto, S. T.; Pitelka, D. R. Transepitheleal transport in cell culture. *Proc. Natl. Acad. Sci. U.S.A.* **1976**, *73*, 1212−1216.
19. Cereijido, M.; Robbins, E. S.; Dolan, W. J.; Rotunno, C. A.; Sabatini, D. D. Polarized monolayers formed by epithelial cells on a permeable and translucent support. *J. Cell Biol.* **1978**, *77*, 853−880.
20. Cho, M. J.; Thompson, D. P.; Cramer, C. T.; Vidmar, T. J.; Scieszka, J. F. The Madin−Darby canine kidney (MDCK) epithelial cell monolayer as a model cellular transport barrier. *Pharm. Res.* **1989**, *6*, 71−77.
21. Cho, M. J.; Adson, A.; Kezdy, F. J. Transepithelial transport of aliphatic carboxylic acids studied in Madin-Darby canine kidney (MDCK) cell monolayers. *Pharm. Res.* **1990**, *7*, 325−331.
22. Ranaldi, G.; Islam, K.; Sambuy, Y. Epithelial cells in culture as a model for the intestinal transport of antimicrobial agents. *Antimicrob. Agents Chemother.* **1992**, *36*, 1374−1381.
23. Ranaldi, G.; Seneci, P.; Guba, W.; Islam, K.; Sambuy, Y. Transport of the antibacterial agent oxazolidin-2-one and derivatives across intestinal (Caco-2) and renal (MDCK) epithelial cell lines. *Antimicrob. Agents Chemother.* **1996**, *40*, 652−658.
24. Rothen-Rutishauser, B.; Kraemer, S. D.; Braun, A.; Guenthert, M.; Wunderli-Allenspach, H. MDCK cell cultures as an epithelial in vitro model: cytoskeleton and tight junctions as indicators for the definition of age-related stages by confocal microscopy. *Pharm. Res.* **1998**, *15*, 964−971.
25. Brown, B. W. Jr.; Hollander, M. *Statistics: A Biomedical Introduction*; John Wiley & Sons: New York, 1977.
26. Bryan, C. K.; Darby, M. H. Bretylium tosylate: A review. *Am. J. Pharm.* **1979**, *36*, 1189−1192.
27. Dressman, J. B.; Amidon, G. L.; Fleisher, D. Absorption potential: estimating the fraction absorbed for orally administered compounds. *J. Pharm. Sci.* **1985**, *74*, 588−589.
28. Amidon, G. L.; Sinko, P. J.; Fleisher, D. Estimating human oral fraction dose absorbed: a correlation using rat intestinal membrane permeability for passive and carrier-mediated compounds. *Pharm. Res.* **1988**, *5*, 651−654.
29. Gan, L.-S.; Hsyu, P. H.; Pritchard, J. F.; Thakker, D. Mechanism of Intestinal Absorption of Ranitidine and Ondansetron: Transport Across Caco-2 Cell Monolayers. *Pharm. Res.* **1993**, *10*, 1722−1725.
30. Rubas, W.; Jezyk, N.; Grass, G. Comparison of the permeability characteristics of a human colonic epithelial (Caco-2) cell line to colon of rabbit, monkey, and dog intestine and human drug absorption. *Pharm. Res.* **1993**, *10*, 113−118.
31. Hu, M.; Chen, J.; Zhu, Y.; Dantzig, A. H.; Stratford, R. E.; Kuhfeld, M. T. Mechanism and kinetics of transcellular transport of a new beta-lactam antibiotic loracarbef across an intestinal epithelial membrane model system (Caco-2). *Pharm. Res.* **1994**, *11*, 1405−1413.
32. Chong, S.; Dando, S. A.; Soucek, K. M.; Morrison, R. A. In Vitro permeability through Caco-2 cells is not quantitatively predictive of in vivo absorption for peptide-like drugs absorbed via the dipeptide transporter system. *Pharm. Res.* **1996**, *13*, 120−123.
33. Wessel, M. D.; Jurs, P. C.; Tolan, J. W.; Muskal, S. Prediction of human intestinal absorption of drug compounds from molecular structure. *J. Chem. Info. Comput. Sci.* **1998**, *38*, 726−735.
34. Thwaites, D. T.; Hirst, B. H.; Simmons, N. L. Passive transepithelial absorption of thyrotropin-releasing hormone (TRH) via a paracellular route in cultured intestinal and renal epithelial cell lines. *Pharm. Res.* **1993**, *10*, 674−681.

Acknowledgments

The authors express their appreciation for the skilled technical contributions of Rosana Datti, Aparna Malladi, Susan Olivan, Margrethe Schibig, Mengshu Zhao, and Francesca Zonin. The authors thank Dr. Anne Hersey for providing Glaxo Wellcome data. The authors thank Professor Ronald T. Borchardt for helping us establish the Caco-2 model at Affymax.

JS9803205

Preparation and In Vitro/In Vivo Evaluation of Luteinizing Hormone Releasing Hormone (LHRH)-Loaded Polyhedral and Spherical/Tubular Niosomes

PARINYA ARUNOTHAYANUN,[†] JOHN A. TURTON,[‡] IJEOMA F. UCHEGBU,[†,§] AND ALEXANDER T. FLORENCE*,[†]

Contribution from *Centre for Drug Delivery Research, The School of Pharmacy, University of London, 29-39 Brunswick Square, London WC1N 1AX, UK, and Centre for Toxicology, Department of Pharmacology, The School of Pharmacy, University of London, 29-39 Brunswick Square, London WC1N 1AX, UK.*

Received July 15, 1998. Accepted for publication October 6, 1998.

Abstract □ Niosomes are vesicles formed by the self-assembly of nonionic surfactants in aqueous dispersions. They can entrap drugs and have been used experimentally as sustained drug delivery systems. Apart from conventional spherical niosomes, various types of vesicle ultrastructures can be formed by varying the composition of the vesicle membrane. Hexadecyl diglycerol ether ($C_{16}G_2$), cholesterol, and poly-24-oxyethylene cholesteryl ether (Solulan C24) in the ratio 91:0:9 gave polyhedral niosomes, whereas spherical and tubular niosomes are produced at a composition ratio of 49:49:2. The mean size of both polyhedral and spherical/tubular niosomes were within the range of 6 to 9 μm. Both types of vesicle were visualized by cryo-scanning electron microscopy. The properties of the two forms of niosomes were studied using luteinizing hormone releasing hormone (LHRH) as a model peptide. Analysis by high-performance liquid chromatography demonstrated high entrapment of LHRH acetate in polyhedral niosomes when prepared by remote loading methods using pH or $(NH_4)_2SO_4$ gradients; in contrast, only low entrapment was achieved by passive loading methods (direct hydration at pH 7.4 or pH 3.0, dehydration–rehydration, and reversed-phase evaporation). In vitro studies demonstrated that both polyhedral and spherical/tubular niosomes were more stable in 5% rat skeletal muscle homogenate than in rat plasma. Also, polyhedral niosomes released more radiolabeled LHRH ([^{125}I]LHRH) than spherical/tubular niosomes in both muscle homogenate and plasma. In clearance experiments in the rat, following intramuscular injection, both polyhedral and spherical/tubular niosomes gradually released [^{125}I]LHRH into the blood, but some radioactivity remained at the injection site for 25 and 49 h, respectively. In contrast, [^{125}I]LHRH in phosphate buffered saline was completely cleared from the injection site at 2 h. The release of drug is sustained by both niosome formulations, but spherical/tubular niosomes possess more stable membranes than polyhedral niosomes due to the presence of cholesterol.

Introduction

Niosomes, analogues of liposomes, are nonphospholipid vesicles formed by the self-assembly of nonionic surfactants in aqueous dispersion and have been used experimentally as drug carriers.[1,2] Apart from conventional spherical vesicles, a range of niosome structures can be formed by varying the membrane composition of the vesicles. The properties of polyhedral, and spherical/tubular niosomes, formed by hexadecyl diglycerol ether ($C_{16}G_2$) cholesterol: poly-24-oxyethylene cholesteryl ether (Solulan C24) with molar ratios of 91:0:9 and 49:49:2, respectively, have been compared previously in relation to differences in ultrastructural morphology and membrane composition.[3,4] The irregular faceted shape of polyhedral niosomes results in a dispersion with a higher viscosity than that formed by their spherical/tubular counterparts.[3] Although polyhedral niosomes are less osmotically responsive in terms of size change in the presence of osmotic gradients, due to their rigid gel state membrane[5] and low curvature, they possess low cholesterol membranes that are very permeable to hydrophilic solutes such as carboxyfluorescein (CF).[4] However, we have found that the co-entrapment of sodium chloride with CF in polyhedral niosomes resulted in a very low CF release rate, regardless of the osmotic conditions.[4] It is believed that the dehydration of the polyoxyethylene chains of Solulan C24 in the membranes of polyhedral niosomes is responsible for this property.

In the present investigation we have studied the morphology of polyhedral and spherical/tubular niosomes using cryo-scanning electron microscopy. Luteinizing hormone releasing hormone (LHRH) was selected as a model peptide drug to investigate the possibility of using polyhedral and spherical/tubular niosomes and polyhedral niosomes prepared in the presence of NaCl as sustained drug delivery systems. A variety of preparation techniques were studied in an attempt to obtain a high level of LHRH entrapment in the vesicles.

Experimental Section

Materials—Hexadecyl diglycerol ether ($C_{16}G_2$) was a gift from L'Oreal (Paris, France), and poly-24-oxyethylene cholesteryl ether (Solulan C24) was donated by Ellis and Everald Anstead International (Essex, UK). Luteinizing hormone releasing hormone (LHRH) acetate salt, radiolabeled LHRH ([^{125}I]LHRH), and cholesterol were obtained from Sigma Chemical Company (Poole, UK). Sodium chloride, diethyl ether, and ammonium sulfate were supplied by BDH Laboratory Supplies (Poole, UK). Chloroform (HPLC grade) was purchased from Rathburn Chemicals (Walkerburn, UK). The water source was from an ultrahigh quality reverse osmosis water purifier (Elgastat UHQPS, Elga Ltd., Bucks, UK).

Methods—*Preparation of LHRH Acetate-Loaded Polyhedral Niosomes*—Six methods of preparation of LHRH loaded polyhedral niosomes, formed from $C_{16}G_2$:Solulan C24 (91:9) (60 μmol) and LHRH acetate (2 mg/mL), were investigated ($n = 3$).

Method A was direct hydration (hand-shaking) at pH 7.4. Dried surfactant film was hydrated with LHRH acetate prepared in pH 7.4 phosphate buffered saline (PBS) by mechanical shaking at 55 °C for 30 min.

Method B was direct hydration at pH 3.0. Dried surfactant film was hydrated with LHRH acetate prepared in pH 3.0 PBS at 55 °C for 30 min.

* To whom correspondence should be addressed. Telephone: 0171-753 5819. Fax: 0171-837 5092. E-mail: a.t.florence@ulsop.ac.uk
[†] Centre for Drug Delivery Research.
[‡] Centre for Toxicology.
[§] Present address: Department of Pharmaceutical Sciences, University of Strathclyde, Taylor Street, Glasgow G1, UK.

10.1021/js980286u CCC: $18.00
Published on Web 12/05/1998

Method C was dehydration−rehydration of vesicles (DRV). Surfactant film was hydrated with 5 mL of water at 55 °C for 30 min before adding of 1 mL of LHRH acetate in water. The niosome dispersion was then freeze-dried overnight and rehydrated with 1 mL of pH 7.4 PBS.

Method D was reversed-phase evaporation of vesicles (REV). Surfactants were dissolved in 10 mL of $CHCl_3$:diethyl ether (1:1). Then, 1 mL of LHRH acetate in pH 7.4 PBS was injected into the dispersion, which was then bath sonicated for 2 min. Finally, the organic solvents were vacuum evaporated.

Method E was remote loading by $(NH_4)_2SO_4$ gradient. Surfactant film was hydrated with 1 mL of 120 mM $(NH_4)_2SO_4$ at 55 °C for 15 min. The dispersion was ultracentrifuged at 4 °C, and the pellets were redispersed with LHRH acetate in pH 7.4 PBS and shaken gently at 60 °C for 15 min.

Method F was remote loading by pH gradient. Dried surfactant film was hydrated with 1 mL of pH 3.0 PBS at 55 °C for 30 min. The dispersion was ultracentrifuged at 4 °C, and the pellets were redispersed with LHRH acetate in pH 7.4 PBS and shaken gently at 60 °C for 15 min.

The dispersions were washed twice with PBS pH 7.4 (or at pH 3.0) by ultracentrifugation at 4 °C. The entrapped LHRH acetate was analyzed by reversed-phase HPLC (μBondapak C18, 3.9 × 150 mm; mobile phase: 0.03 M CH_3COONH_4 :ACN, 70:30, flow rate, 0.6 mL/min, detection wavelength, 279 nm).

For the in vitro/in vivo evaluation, polyhedral and spherical/tubular niosomes prepared from $C_{16}G_2$:cholesterol: Solulan C24 (91:0:9) and (49:49:2), respectively, were loaded with [^{125}I]LHRH (1.67 μCi/mL in pH 7.4 PBS) using the pH gradient method described in Method F. To study the effect of NaCl, phosphate buffer at pH 7.4 prepared in 2 M NaCl was used instead of pH 7.4 PBS, except when the washed niosomes were redispersed prior to injection. Niosomes were sized using a laser diffraction method (MasterSizer X, Malvern Instruments Ltd., Worcestershire, UK).

Cryo-scanning Electron Microscopy—Polyhedral and spherical/tubular niosomes, prepared in water, were plunge frozen in liquid nitrogen slush and transferred to a Philips XL20 scanning electron microscope (SEM), and the surface moisture was removed by sublimation (at −40 °C for 10 min). Samples were gold coated at −180 °C and photographed by SEM.

In Vitro Evaluation—*Animal Husbandry*—Male Wistar rats weighting 200 g (Bantin and Kingman Universal Ltd., Aldbrough, Hull, UK), were given diet (Rat and Mouse No. 1, SDS Ltd, Witham, Essex, UK) and drinking water ad libitum. A temperature of 20−22 °C was maintained with a relative humidity of 45 to 65% and a 12:12 h light:dark cycle (lights on at 07.00 h). Animals were acclimatized for at least 5 days before each experiment and were observed daily for clinical signs of illness.

Preparation of Plasma—Rats were killed by the intraperitoneal (ip) injection of pentobarbitone sodium (Sagatal, Rhône Mérieux Ltd., Harlow, Essex, UK). Blood was removed from the abdominal aorta and anticoagulated with lithium heparin, and the plasma was removed after centrifugation and stored at −30 °C.

Preparation of 5% Muscle Homogenate—Rats were sacrificed as already described. Skeletal muscles were removed from the posterior and anterior thighs, weighed, and homogenized with 19 parts of PBS, and aliquots were stored at −30 °C.

Evaluation of Niosomes In Vitro—A 0.1-mL sample of each niosome dispersion was mixed with 0.9 mL of rat plasma or 0.9 mL of 5% muscle homogenate in a glass vial, which was then incubated at 37 °C in a thermostated water bath (Grant Instruments, Cambridge Ltd., Cambridge, UK). Then, 0.1-mL aliquots were collected at 30 min, and 2, 5, and 9 h and mixed with 1.9 mL of PBS before being ultracentrifuged. Radioactivity in 1 mL of supernatant was counted (1275 Minigamma Gamma Counter, LKB Wallac, Turku, Finland), and the count/min in 2 mL was calculated as % LHRH released by comparison with the initial count/min of 0.01 mL of niosome dispersion.

In Vivo Evaluation—Male Wistar rats, 190 to 230 g, were injected intramuscularly (im; 25 GA 5/8 needle; right posterior thigh) with 0.1 mL of [^{125}I]LHRH prepared in pH 7.4 PBS, or spherical/tubular niosomes, polyhedral niosomes, or polyhedral niosomes prepared with a high concentration of NaCl. At 10 min, and 2, 7, 25, 32, and 49 h after injection, animals ($n = 2$) were weighed and killed by ip injection of pentobarbitone sodium, and blood was collected into lithium heparin. The radioactivity remaining at the injection site was determined by removing the injected leg and detaching the thigh muscles. The radioactivity in whole blood (2 mL) and muscle was counted using the gamma counter. The [^{125}I]LHRH in the total blood volume at each time point was calculated, based on the formula of total blood volume being 6 mL/100 g body weight in the mature male rat, and the count of radioactivity in 0.1 mL of [^{125}I]LHRH solution or niosome dispersion.

Results

Cryo-scanning Electron Microscopy—Cryo-scanning electron micrographs confirmed that niosomes formed by varying the amount of $C_{16}G_2$, cholesterol, and Solulan C24 resulted in a variety of vesicle structures (Figure 1). Polyhedral niosomes were formed in the absence of cholesterol whereas conventional spherical vesicles and also tubules were produced in the lipid/surfactant mixtures prepared with an equimolar level of cholesterol, confirming our previous findings.[3,4]

Effects of Preparation Methods on Entrapment Efficacy—Figure 2 shows that only a small amount of LHRH acetate could be entrapped into polyhedral niosomes using passive loading methods (i.e., direct hydration at pH 7.4 and 3.0, and DRV and REV) in comparison with higher levels of entrapment obtained by active loading methods [i.e., $(NH_4)_2SO_4$ gradient and pH gradient]. Calculated on the basis of available LHRH (2 mg), the entrapment levels obtained by passive loading methods were in the range 14−24%. The $(NH_4)_2SO_4$ gradient and pH gradient methods led to entrapments of 44% and 51%, respectively; these figures correspond to ratios of 12.4 and 14.5 nmol of entrapped LHRH/μmol of surfactants, respectively.

In Vitro Stability Study—As shown in Figure 3, polyhedral vesicles release more LHRH in both plasma and muscle homogenate than do spherical/tubular systems. Muscle homogenates are perhaps a better model for im formulations. Both formulations release less LHRH in these homogenates than in plasma.

In Vivo Clearance from Intramuscular Site—All niosomes used in vivo were unsonicated. The mean sizes were in the range of 6 to 9 μm, which was deemed most appropriate for im depot formulation. From Figure 4, it is seen that 99% of [^{125}I]LHRH in PBS was cleared from the site of injection in the first 2 h, whereas 14% and 70% of injected [^{125}I]LHRH prepared in polyhedral and spherical/tubular niosomes, respectively, was still present at the injection site. All the [^{125}I]LHRH in polyhedral niosomes was cleared from the injection site by 25 h, whereas some (8.5%) of the radioactivity in spherical/tubular niosomes could still be detected.

Figure 5 shows the level of [^{125}I]LHRH in the blood over the 49-h period after dosing. Unformulated [^{125}I]LHRH disappears from the injection site into the blood very rapidly, with a t_{max} of 12 min post dosing. Niosome preparations sustain the release of drug into the blood and prolong blood levels. Polyhedral niosomes exhibited a t_{max} of 2 h. Spherical/tubular niosomes provide a better sustained release system, with a t_{max} of 7 h post dosing. These results closely parallel the clearance data.

Co-entrapment of NaCl with [^{125}I]LHRH in polyhedral niosomes, which reduces the permeability of the bilayers,[4] was found not to change either the release pattern of the drug from the injection site (Figure 4), or the level of [^{125}I]-LHRH in the blood (Figure 5).

Discussion

We have previously reported the entrapment of hydrophilic solutes in $C_{16}G_2$ niosomes and described the morphology of these vesicle using fluorescence light microscopy and confocal laser scanning microscopy.[6,7] In this paper,

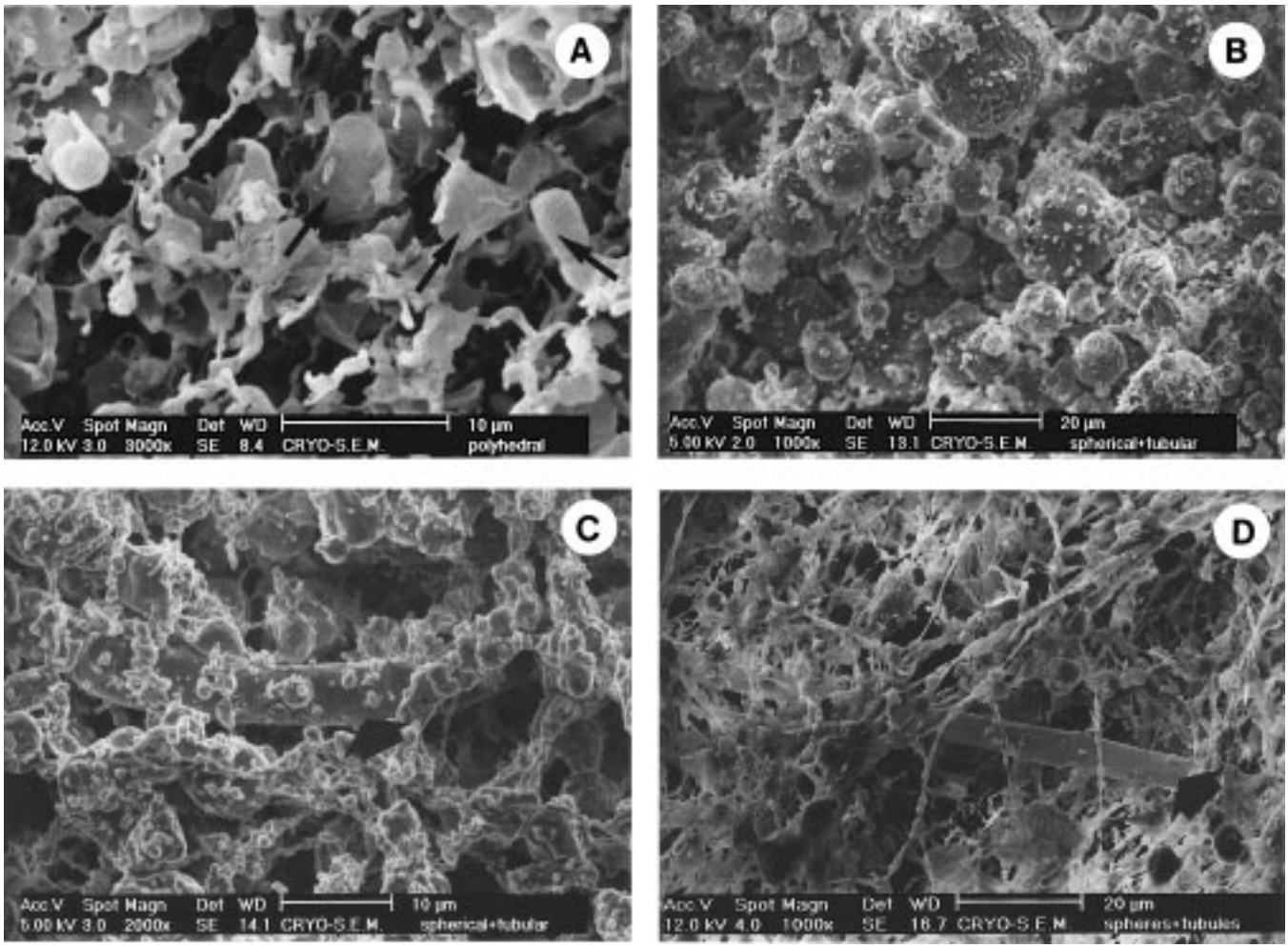

Figure 1—Cryo-scanning electron micrographs of (A) polyhedral niosomes (→) formed by $C_{16}G_2$:Solulan C24 (91:9), (B) spherical niosomes formed by $C_{16}G_2$:cholesterol:Solulan C24 (49:49:2), and (C) and (D) tubular structures (→) identified in the spherical niosome preparations of $C_{16}G_2$:cholesterol:Solulan C24 (49:49:2).

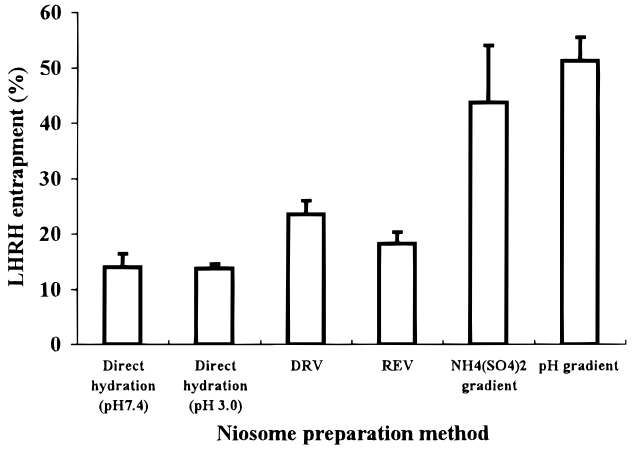

Figure 2—Percentage entrapment of LHRH acetate into polyhedral niosomes by six different preparation methods. Data are expressed as means and SD; $n = 3$, except for direct hydration at pH 3.0 and pH gradient entrapment, where $n = 2$ (DRV = dehydration–rehydration vesicles; REV = reversed-phase evaporation vesicles).

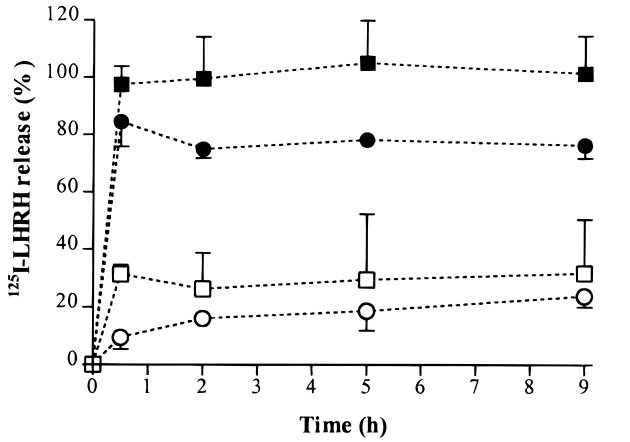

Figure 3—Release profile of [^{125}I]LHRH from polyhedral niosomes over a 9-h period in plasma (■) and in 5% muscle homogenate (□), and from spherical/tubular niosomes in plasma (●) and in 5% muscle homogenate (○). Data are expressed as means and SD; $n = 2$ for each niosome preparation at each time point.

the morphology of the vesicles has been examined using cryo-SEM. Polyhedral niosomes formed from $C_{16}G_2$ and Solulan C24 without cholesterol are asymmetric in nature, and different in their morphology from vesicles formed by these surfactants with 45 mol % cholesterol. The absence of cholesterol causes the membranes of $C_{16}G_2$ to form vesicle membranes with a lower curvature and fluidity.[4,7]

To study the possible use of such systems as sustained-release vehicles, LHRH acetate was selected as a model peptide. The binding of peptide to lipids can be enhanced by modifying the electrical charge or the hydrophobicity of the peptide.[8] However, LHRH is very hydrophilic and becomes a univalent cation at physiological pH. An increase in lipid–peptide interaction via electrostatic binding was

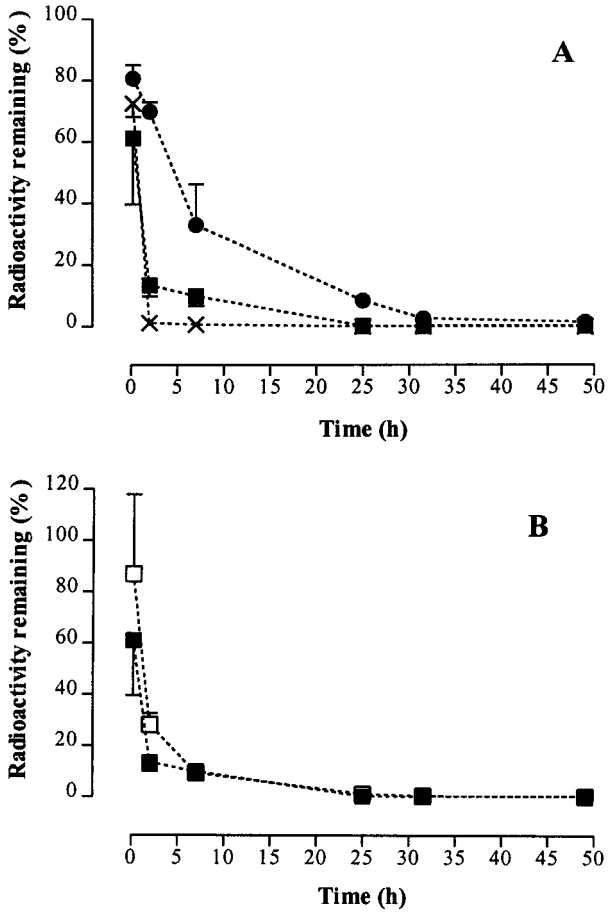

Figure 4—The amount of [^{125}I]LHRH as percent remaining at the injection site. (A) The [^{125}I]LHRH prepared in PBS at pH 7.4 (X), in polyhedral niosomes (■), and in spherical/tubular niosomes (●). (B) The [^{125}I]LHRH prepared in polyhedral niosomes (■), as presented in Figure 4A, and in polyhedral niosomes with NaCl (□). Data are expressed as means and SD; $n = 2$ for each niosome preparation at each time point.

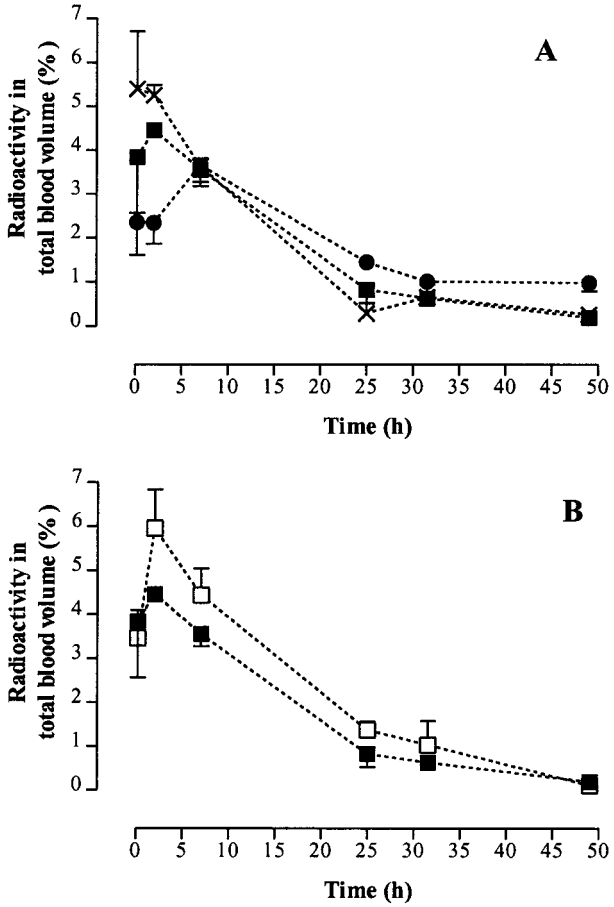

Figure 5—The amount of [^{125}I]LHRH as percent detected in blood after injection. The amount of radioactivity in the total blood volume was estimated and expressed as a percentage of the dose of radioactivity administered. (A) The [^{125}I]LHRH prepared in PBS at pH 7.4 (X), in polyhedral niosomes (■), and in spherical/tubular niosomes (●). (B) The [^{125}I]LHRH prepared in polyhedral niosomes (■), as presented in Figure 5A, and in polyhedral niosomes with NaCl (□). Data are expressed as means and SD; $n = 2$ for each niosome preparation at each time point.

described by Schäfer et al.[9] by the addition of phosphatidic acid, an anionic lipid, into the membranes of phosphatidyl choline vesicles. We obtained a very low entrapment of LHRH by passive loading methods (Figure 2), with the highest entrapment being achieved by the remote loading method (so-called "active" loading), which makes use of either the difference in pH, or in the amount of $(NH_4)_2SO_4$, between the inside and the outside of the vesicle. It is also of interest that LHRH (a decapeptide with a MW of 1182 Da) can be introduced through the vesicle membrane using a pH gradient[10] or an $(NH_4)_2SO_4$ gradient,[11] as has been demonstrated for other small molecules such as doxorubicin (MW of 543.5 Da). In our studies, the highest amount of drug to be entrapped using the pH gradient method was 14.5 nmol of LHRH/μmol of surfactants. This level appears low in comparison with values achieved for other drugs such as doxorubicin.[12] However we used a low concentration of LHRH (1 mM surfactants: 0.028 mM LHRH) and the amount of LHRH encapsulated was around 50% of the available drug.

The stability of parenteral drug delivery systems can be evaluated by measuring drug release during incubation in serum or plasma,[13,14] and muscle homogenate.[15] Both polyhedral and spherical vesicles are more stable in a 5% muscle homogenate than in plasma (Figure 3). Zuidema et al.[16] showed that plasma had a higher potential than muscle components to induce solute leakage from liposomes. Figure 3 also demonstrates that spherical/tubular niosomes released less [^{125}I]LHRH than polyhedral niosomes and these results compare with our earlier findings using CF as a marker.[4]

The mean size of both the polyhedral and the spherical/tubular niosomes were within the range of 6 to 9 μm. Zuidema et al. suggested that small liposomes (<200 nm) can be cleared from the im injection site by the lymphatic system,[16] whereas larger vesicles (4.9 μm) have been found to have a longer retention time at the site of injection.[17] It was thought that polyhedral niosomes, having a higher viscosity than spherical/tubular niosomes,[3] might remain at the site of injection for a longer period than spherical vesicles. However, probably due to differences in membrane permeability, this effect is masked as spherical/tubular vesicles were able to more effectively prolong the blood level of the peptide. These results compare therefore with the earlier in vitro stability studies.

Earlier we reported that the co-entrapment of NaCl with drug reduced the membrane permeability of polyhedral niosomes.[4] However, only a slight improvement in the release profile of LHRH-loaded polyhedral niosomes was observed in vivo (Figure 4B). Although liposomes may remain at the site of injection for <1 week,[18] their ability to retain the solute is an important factor in their use as a sustained-release system. Such an ability is related to the composition of the membranes, their lamellarity,[19] and the presence of cholesterol in the membranes.[14] Polyhedral niosomes formed without cholesterol, although being in the

gel phase, are therefore more leaky than their spherical/tubular counterparts.

LHRH is fairly stable in aqueous solution over a wide range of pH and temperature.[20] The blood levels of [^{125}I]-LHRH detected in this study were low, indicating that the peptide rapidly becomes accessible to protease enzymes on its release from the niosomes.

Conclusions

Niosomes can be used as sustained drug delivery systems that remain at the injection site over a period of around 48 h and slowly release drug into the blood. The shape of the vesicle, which gives a high viscosity to concentrated polyhedral niosome suspensions, is not as important as membrane permeability. Spherical/tubular niosomes that possess more stable membranes than polyhedral niosomes are more effective intramuscular depots.

References and Notes

1. Florence, A. T. Nonionic surfactant vesicles: preparation and characterization. In: *Liposome Technology*, Gregoriadis, G., Ed.; CRC: Boca Raton, FL, 1993; pp 157−176.
2. Uchegbu, I. F.; Florence, A. T. Nonionic surfactant vesicles (Niosomes): physical and pharmaceutical chemistry. *Adv. Colloid Interface Sci.* **1995**, *58*, 1−55.
3. Bernard, M.-S.; Arunothayanun, P.; Uchegbu, I. F.; Florence, A. T. Rheological and morphological study of polyhedral and spherical/tubular niosomes. 3rd UKCRS Symposium on Controlled Drug Delivery, University of Manchester, UK, January 1997; Abstract.
4. Arunothayanun, P.; Uchegbu, I. F.; Florence, A. T. Properties of polyhedral niosomes. *Pharm. Res.* **1996**, *13, Suppl.*, s-159.
5. Arunothayanun, P.; Craig, D. Q. M.; Uchegbu, I. F.; Florence, A. T. An investigation into the phase behaviour of polyhedral niosomes and high sensitivity differential scanning calorimetry. In *Proceed. 24th Intl. Symp. Control. Relat. Bioact. Mater.*, 1997; pp 977−978.
6. Uchegbu, I. F.; Schätzlein, A.; Vanlerberghe, G.; Morgatini, N.; Florence, A. T. Polyhedral nonionic surfactant vesicles. *J. Pharm. Pharmacol.* **1997**, *49*, 606−610.
7. Uchegbu, I. F.; McCarthy, D.; Schätzlein, A.; Florence, A. T. Phase transitions in aqueous dispersions of the hexadecyl diglycerol ether ($C_{16}G_2$) nonionic surfactant, cholesterol and cholesteryl poly-24-oxyethylene ether: vesicles, tubules, discomes and micelles. *S. T. P. Pharma Sci.* **1996**, *6*, 33−43.
8. Surewicz, W. K.; Epand, R. M. Role of peptide structure in lipid peptide interactions-high-sensitivity differential scanning calorimetry and electron-spin resonance studies of the structural-properties of dimyristoylphosphatidylcholine membranes interacting with pentagastrin-related pentapeptides. *Biochemistry* **1985**, *24*, 3135−3144.
9. Schäfer, H.; Schmidt, W.; Lachmann, U. Preparation and properties of GnRH-loaded multilamellar liposomes. *Pharmazie* **1987**, *42*, 674−677.
10. Mayer, L. D.; Madden, T. D.; Bally, M. B.; Cullis, P. R. pH Gradient-Mediated Drug Entrapment in Liposomes. In: *Liposome Technology: Entrapment of Drugs and Other Materials*, 2nd ed.; Gregoriadis, G., Ed.; CRC: Boca Raton, FL, 1992; pp 27−44.
11. Lasic, D. D.; Frederik, P. M.; Stuart, M. C. A.; Barenholz, Y.; McIntosh, T. J. Gelation of liposome interior. A novel method for drug encapsulation. *FEBS Lett.* **1992**, *312*, 255−258.
12. Madden, T. D.; Harrigan, P. R.; Tai, L. C. L.; Bally, M. B.; Mayer, L. D.; Redelmeier, T. E.; Loughrey, H. C.; Tilcock, C. P. S.; Reinish, L. W.; Cullis, P. R. The accumulation of drugs within large unilamellar vesicles exhibiting a proton gradient: a survey. *Chem. Phys. Lipids* **1990**, *53*, 37−46.
13. Guzmán, M.; Selles, E.; Abérturas, M. C. Effect of human plasma on the stability of large multilamellar liposomes with digitoxin. *Drug Dev. Ind. Pharm.* **1989**, *15*, 387−399.
14. Storm, G.; Van Bloois, L.; Steerenberg, P. A.; Van Etten, E.; De Groot, G.; Crommelin, D. J. A. Liposome encapsulation of doxorubicin: pharmaceutical and therapeutic aspects. *J. Controlled. Release.* **1989**, *9*, 215−229.
15. Arrowsmith, M.; Hadgraft, J.; Kellaway, I. W. The stability of a prodrug, liposome and a prodrug-liposome complex in simulated biological conditions. *Int. J. Pharm.* **1983**, *17*, 91−98.
16. Zuidema, J.; Kadir, F.; Titulaer, H. A. C.; Oussoren, C. Release and absorption rates of intramuscularly and subcutaneously injected pharmaceuticals (II). *Int. J. Pharm.* **1994**, *105*, 189−207.
17. Jackson, A. J. The effect of route of administration on the disposition of inulin encapsulated in multilamellar vesicles of defined particle size. *Res. Comm. Chem. Path. Pharm.* **1980**, *27*, 293−304.
18. Richards, R. L.; Hailey, J. R.; Egan, J. E.; Gordon, D. M.; Johnson, A. J.; Alving, C. R.; Wassef, N. M. Intramuscular fate and local effects of liposomes as carriers for drugs and vaccines. In *Liposomes in Biomedical Applications*, Shek, P. N., Ed.; Harwood Academic: Chur Switzerland, 1995; pp 167−178.
19. Schäfer, H.; Schmidt, W.; Berger, H.; Bergfeld, J. Pharmacokinetics of gonadotropin-releasing hormone and stimulation of luteinizing hormone secretion after single dose administration of GnRH incorporated into liposomes. *Pharmazie* **1987**, *42*, 689−693.
20. Powell, M. F.; Sanders, L. M.; Rogerson, A.; Si, V. Parenteral peptide formulations: chemical and physical properties of native luteinizing hormone-releasing hormone (LHRH) and hydrophobic analogues in aqueous solutions. *Pharm. Res.* **1991**, *8*, 1258−1263.

Acknowledgments

We thank L'Oreal, France, for providing $C_{16}G_2$. We appreciate the cooperation of Mr. David McCarthy, School of Pharmacy, for assistance with the cryo-SEM investigations. P.A. was supported by the Government Pharmaceutical Organization, Thailand.

JS980286U

Solubility and Mass and Nuclear Magnetic Resonance Spectroscopic Studies on Interaction of Cyclosporin A with Dimethyl-α- and -β-Cyclodextrins in Aqueous Solution

KOUZOU MIYAKE, FUMITOSHI HIRAYAMA, AND KANETO UEKAMA*

Contribution from *Faculty of Pharmaceutical Sciences, Kumamoto University, 5-1 Oe-honmachi, Kumamoto 862-0973, Japan.*

Received July 13, 1998. Accepted for publication October 27, 1998.

Abstract □ The interaction of cyclosporin A (CsA) with dimethyl-α- and -β-cyclodextrins (DM-α-CyD and DM-β-CyD) was investigated by the solubility method, electrospray ionization mass spectrometry (ESI-MS) and ^{1}H-nuclear magnetic resonance spectroscopy (^{1}H NMR). The extremely low solubility (1.9×10^{-5} M at 25 °C) of CsA in water was significantly improved by the complexation with DM-CyDs: for example, the solubility increased 87-fold in the presence of 5.0×10^{-2} M DM-β-CyD. The phase solubility diagram of CsA/DM-CyD systems showed an Ap type and the stability constants (1060 M^{-1} and 1050 M^{-1}, respectively) of the 1:1 CsA/DM-α-CyD and CsA/DM-β-CyD complexes were much higher than those of the 1:2 complexes (15 M^{-1} and 21 M^{-1}, respectively). In ESI-MS spectra of the CsA/DM-β-CyD system, a new signal emerged at 1268 which corresponds to the 1:1 adduct of the di-ionized guest molecule with the host molecule. This signal intensity was significantly decreased by the addition of chlorpromazine (CPZ) which has a large stability constant (8800 M^{-1}) of the DM-β-CyD complex, whereas the signal corresponding to the CPZ/DM-β-CyD complex was little affected by the addition of CsA, indicating a competitive inclusion of CPZ and CsA within the host cavity. CsA gave many new peaks in the ^{1}H NMR spectrum when the solvent was changed from chloroform to methanol/water, suggesting conformational diversity of CsA in polar solvents. Inspection of ^{1}H-chemical shift changes and the two-dimensional rotating frame nuclear Overhauser effect (ROESY) spectra of the CsA/DM-CyD system suggested that the side chains of amino acids in CsA molecule take part in the inclusion within DM-CyDs, although there is seemingly no preference of particular amino acid residues. All the data obtained here suggested that CsA forms inclusion complexes with DM-α- and -β-CyDs in an aqueous medium and side chains of CsA are mainly involved in the inclusion.

Introduction

Cyclodextrins (CyDs) are known to form inclusion complexes with various drug molecules in both solution and solid state, and their host/guest interaction has been investigated by using a number of chemical and physical techniques such as spectroscopies, potentiometric titration, kinetics, and the solubility method, etc.[1,2] For example, changes in ultraviolet (UV) and fluorescence spectra of a guest molecule due to the complexation are quantitatively analyzed to obtain the stability constant and stoichiometry of the complex and to gain insight into the inclusion structure in aqueous solution.[3] These physicochemical techniques are applicable on the interaction studies without difficulty when the guest or host is soluble in water and has some chromophores higher than about 210 nm. However, such application is limited when the guest is less soluble or insoluble in water and simultaneously has no chromophores in a molecule, because of difficulty in the preparation of the guest or host solution at suitable concentrations for UV or fluorescence measurements. Cyclosporin A (CsA) employed in this study falls under the category of drugs described above, i.e., the solubility in water being very low (1.9×10^{-5} M at 25 °C) and having no strong chromophore above 210 nm (Figure 1). Recently, mass spectrometry with the use of soft ionization techniques such as electrospray, ionspray, and fast atom bombardment has allowed the study of supramolecular complexes involving CyDs and crown ether,[4] etc., to go forward and has demonstrated capabilities for detecting intact noncovalent bound complexes including peptide/CyD complexes.[5−7] Furthermore, it is possible to use organic solvents such as methanol, acetonitrile, or glycerol as a matrix for solubilization of highly hydrophobic guest molecules.

CsA is an immunosuppressive drug and used in the treatment of autoimmune diseases and prevention of allograft rejection after organ transplantation. However, as has been pointed out, it is a drug exhibiting low oral bioavailability and quite large variability in absorption.[8,9] In a previous paper,[10] we reported that the low oral absorption and large variability of CsA is significantly improved by complexation with CyDs, particularly dimethyl-α- and -β-cyclodextrins (DM-α-CyD and DM-β-CyD, respectively) in rat model. In this continuing study, we investigated the complexation of CsA with DM-α-CyD and DM-β-CyD in water by means of the solubility method and electrospray mass spectrometry, both being useful for the interaction study of guests having low aqueous solubility. Furthermore, ^{1}H-nuclear magnetic resonance (NMR) spectroscopic studies of the CsA/CyD system were carried out in order to gain insight into the inclusion mode of CsA, using a mixed solvent of water/methanol.

Experimental Section

Materials—CsA was donated by Research Center of Shiseido Ltd. (Yokohama, Japan). DM-α-CyD and DM-β-CyD were supplied from Japan Maize Co. (Tokyo, Japan) and contained hexakis(2,6-di-*O*-methyl)- and heptakis(2,6-di-*O*-methyl)cyclodextrins (degrees of substitution of methyl group (DS) = 12 and 14, respectively) as a major component and the over-methylated homologue, 2,6-per-*O*-methyl-3^A-*O*-methyl-α- and -β-CyDs (DS = 13 and 15, respectively) as a minor component.[11] Because the separation of the minor component by recrystallization and column chromatography was significantly difficult, the DM-CyDs were used after recrystallization from methanol/water. The composition of the pure dimethyl derivative and the over-methylated homologue was determined to be 3:1 by fast atom bombardment mass spectrometry. All other chemicals and solvents were of analytical reagent grade, and deionized double-distilled water was used throughout the study.

* Corresponding author Tel and Fax: (+81-96)-371-4160; E-mail: uekama@gpo.kumamoto-u.ac. jp.

10.1021/js980284+ CCC: $18.00
Published on Web 12/05/1998

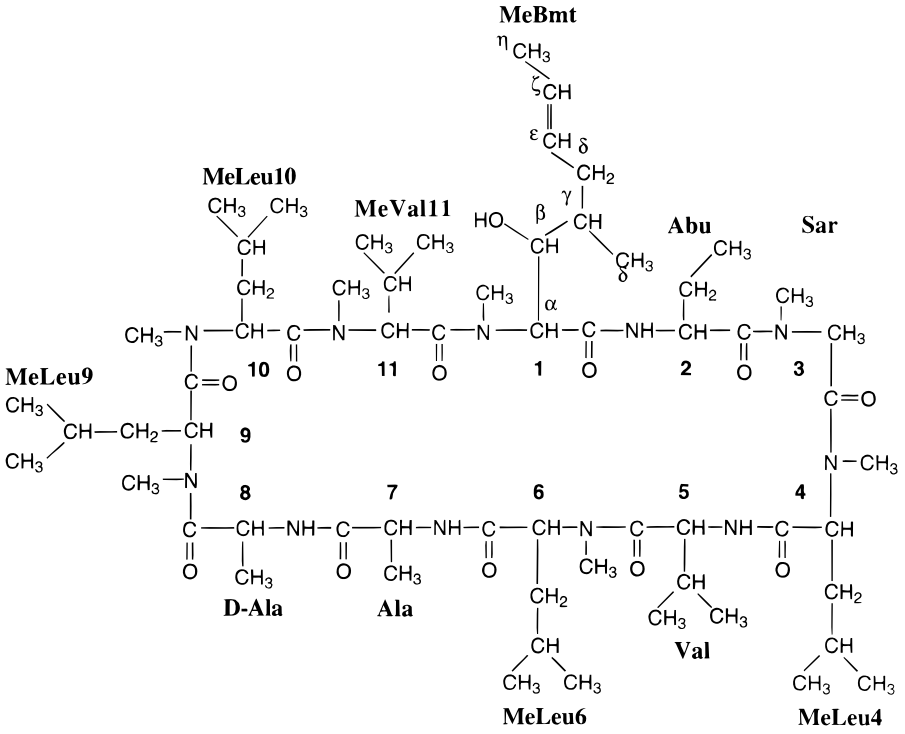

Figure 1—Structure of CsA.

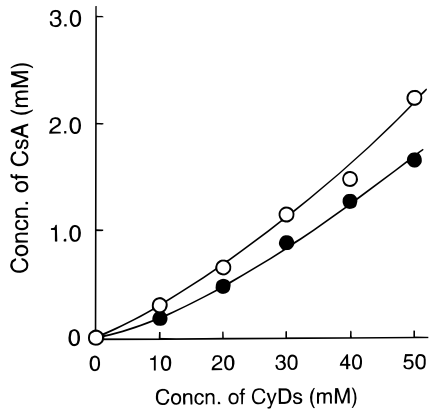

Figure 2—Phase solubility diagrams of CsA/DM-CyD systems in water at 25 °C. (○) DM-α-CyD, (●) DM-β-CyD.

Solubility Measurements—The solubility method was carried out according to the method of Higuchi and Connors.[12] The screw-capped vials containing CsA (5.0 mg) in excess amount in aqueous CyD solutions (5.0 mL) at various concentrations ($1.0-5.0 \times 10^{-2}$ M) were shaken at 25 °C. After equilibrium was attained (about 4 days), the solution was centrifuged at 800*g* force for 5 min, and the supernatant was filtered through a membrane filter (cellulose acetate membrane filter, ADVANTEC DISMIC 3CP045 (TOYO-Roshi), Tokyo, Japan) and analyzed for CsA by high-performance liquid chromatography (HPLC) under the following condition: a Hitachi L-6000 pump and an L-4000 UV detector (Tokyo, Japan) at 214 nm; a YMC ODS AM-312 column (6.0 mm × 150 mm i.d., Kyoto, Japan); a mobile phase of acetonitrile/methanol/water (60:30:10 v/v); a flow rate of 1.0 mL/min and a column temperature of 50 °C.

Mass Spectrometries—Electrospray ionization mass spectrometry (ESI-MS) was carried out on a Hitachi M-1200H LC/MS system (Tokyo, Japan) equipped with an electrospray ionization source. Ionization was achieved by applying 3.0 kV to the spray needle. The orifice potential was maintained at 70 V, and the spectra were recorded over a mass range of 300−2000 units in the positive-ion detection mode. Mass scale calibration was conducted using poly(ethylene glycol) 400, 600, and 1000, and agreement between observed and calculated *m/z* values was within 0.4. CsA or chlorpromazine (CPZ) was dissolved in water/methanol/acetic acid (47:47:6 v/v, pH ≈ 3) in the absence or presence of DM-CyDs. The final concentrations of CsA, CPZ, and DM-CyDs were 1.0×10^{-3} M, 1.0×10^{-3} M, and 2.0×10^{-3} M, respectively. An aliquot (2.0 μL) of the solution was injected into a flow (0.1 mL/min) of water/methanol/acetic acid (47:47:6 v/v) and transferred to the electrospray source.

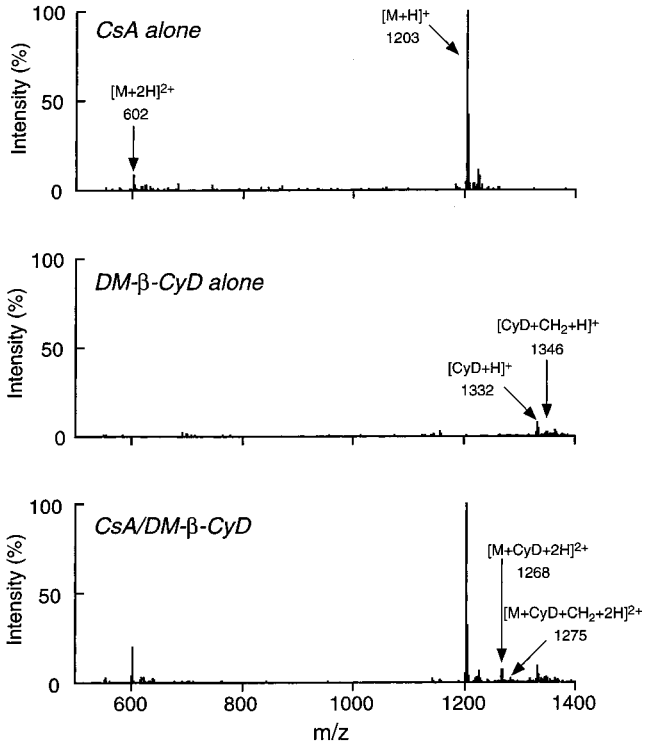

Figure 3—ESI mass spectra of CsA (1 mM) in positive ion mode in the absence and presence of DM-β-CyD (2 mM) in water/methanol/acetic acid (47/47/6 v/v).

^{1}H NMR Spectroscopies—^{1}H NMR spectra were obtained with a JEOL JNM-α 500 instrument (Tokyo, Japan) with a 5 mm inverse broad band probe, operating at 500 MHz and a sweep width of 10000 Hz, at 25 °C. Chemical shifts are given as parts

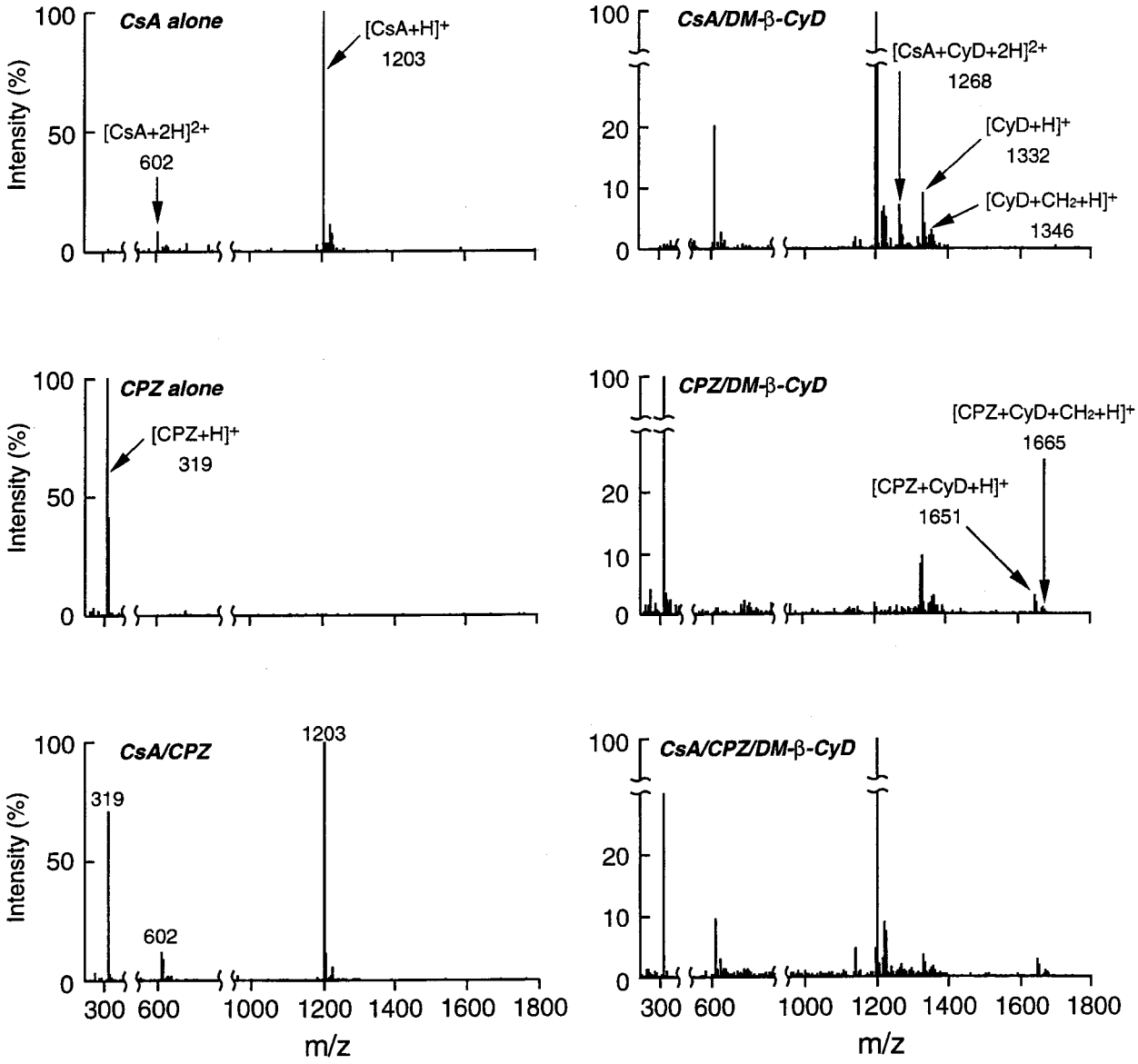

Figure 4—Effect of CPZ (1 mM) on ESI mass spectra of CsA (1 mM) in positive ion mode in the absence and presence of DM-β-CyD (2 mM) in water/methanol/acetic acid (47/47/6 v/v).

per million (ppm) downfield from that of tetramethylsilane, with an accuracy of 0.005 ppm. Phase-sensitive ROESY spectra were measured under the following conditions: sweep width, 5000 Hz; carrier frequency, 2.95 ppm; spin-lock field, 4 kHz; mixing time, 200 ms; 32 scans for each t_1 point with a pulse delay of 1.5 s; data matrix, 2 × 256 × 1K. CsA and DM-CyDs were dissolved at concentrations of 4.0×10^{-3} M and 3.0×10^{-2} M, respectively, in 50% v/v deuterated methanol (CD_3OD)/deuterium oxide (D_2O).

Results and Discussion

The solubility method is useful for investigating inclusion complexation of poorly water-soluble drugs with CyDs in water, because it gives not only the solubilizing ability of host molecules but also the stability constant of complexes by analyzing the solubility curve.[2] Figure 2 shows the phase solubility diagrams of CsA for the DM-α-CyD and DM-β-CyD complexes in water. The extremely low solubility (1.9×10^{-5} M at 25 °C) of CsA was markedly increased by the complexation with DM-CyDs: i.e., the solubility of CsA increased 87-fold in the presence of 5.0×10^{-2} M DM-β-CyD. The phase solubility diagrams showed an Ap type, as defined by Higuchi and Connors,[12] indicating the formation of high order complexes. Therefore, these upward curvatures were analyzed, by the method of Kristiansen and Higuchi using the iteration method,[13] to obtain the stability constants ($K_{1:1}$ and $K_{1:2}$) of 1:1 and 1:2 (guest:host) complexes. The $K_{1:1}$ and $K_{1:2}$ were determined to be 1060 M^{-1} and 15 M^{-1} for the DM-α-CyD complexes and 1050 M^{-1} and 21 M^{-1} for the DM-β-CyD complexes, respectively. The $K_{1:1}$ values were much higher than the $K_{1:2}$ values, suggesting that CsA forms predominantly the 1:1 complex with DM-CyDs in water.

As described in the Introduction section, the extremely low solubility of CsA together with the absence of chromophores above 210 nm in the molecule make it difficult to utilize UV, circular dichroism and fluorescence spectroscopic techniques for the investigation of CyD interaction with CsA in water. On the other hand, mass spectrometry has proved to be useful as one of the promising tools for detecting CyD complexes with peptides such as bradykinin (consisting of 9 amino acids),[5] synthetic Alzheimer amyloid (consisting of 40 amino acids),[6] and insulin (consisting of 51 amino acids),[7] etc. Therefore, the complexation of CsA (consisting of 11 amino acids) with DM-β-CyD was investigated by ESI-MS, using a water/organic solvent. Figure

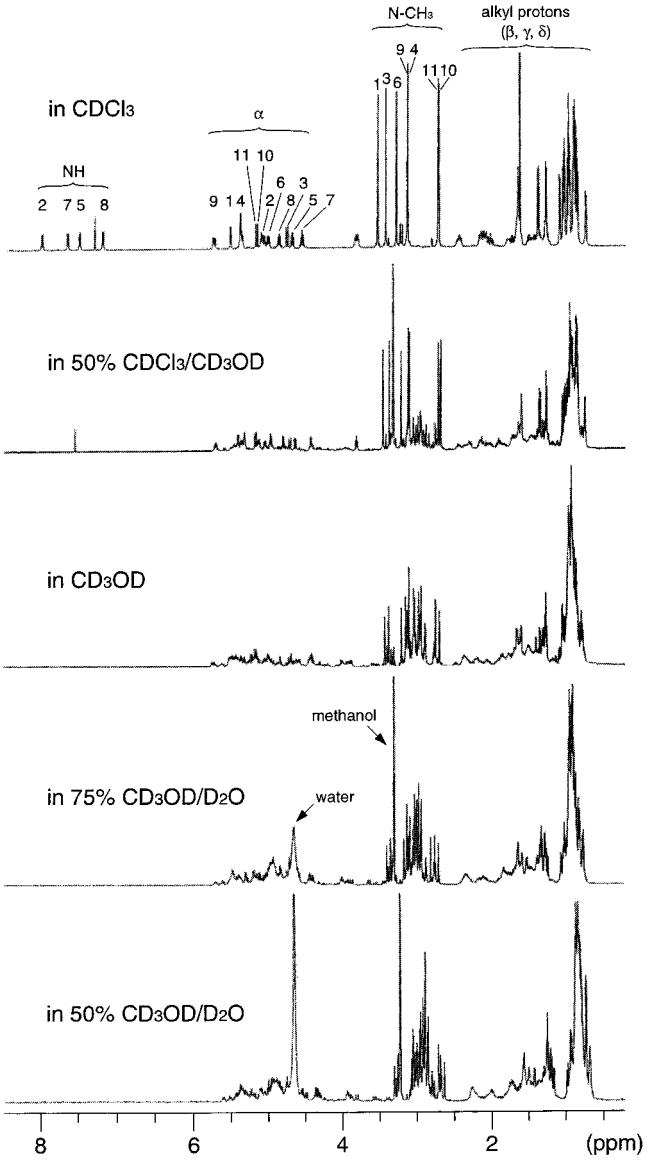

Figure 5—^{1}H NMR spectra of CsA (4 mM) in $CDCl_3/CD_3OD/D_2O$ solutions.

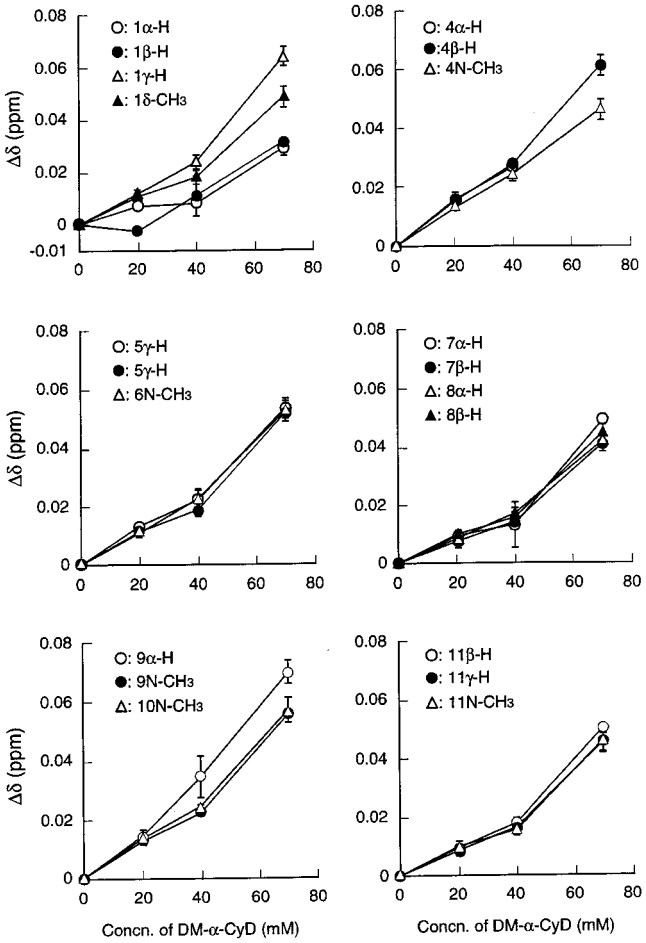

Figure 6—^{1}H NMR chemical shift displacements ($\Delta\delta$) of CsA (4 mM) as a function of DM-α-CyD concentrations in 50% v/v CD_3OD/D_2O. $\Delta\delta = \delta_{\text{in the presence of CyD}} - \delta_{\text{in the absence of CyD}}$.

3 shows ESI mass spectra of CsA alone, DM-β-CyD alone and the CsA/DM-β-CyD mixture in a molar ratio of 1:2 which were dissolved in water/methanol/acetic acid (47:47:6 v/v). CsA gave two signals at 1203 and 602 corresponding to $[M + H]^+$ and $[M + 2H]^{2+}$ ions and DM-β-CyD gave two signals at 1332 and 1346 corresponding to $[CyD + H]^+$ and $[CyD + CH_2 + H]^+$ of the pure DM-β-CyD and the over-methylated derivative, respectively, in a peak ratio of about 3:1. By the addition of DM-β-CyD (Figure 3), a new signal was observed at 1268 which corresponds to the 1:1 adduct of di-ionized CsA with DM-β-CyD, $[M + CyD + 2H]^{2+}$, whereas no signal corresponding to the adducts was observed by the addition of glucose and maltose. The peak of the 1:1 adduct of CsA with the over-methylated homologue was also observed at 1275, although its intensity was significantly weak and fell within a noise range. These results suggest that CsA interacts with DM-β-CyD, presumably involving hydrophobic groups of CsA amino acids in the interaction.

The inclusion of a guest molecule within the CyD cavity is inhibited by the addition of a second guest molecule, the extent of the inhibition being dependent on the stability constant of each complex. This competition is a characteristic feature of host/guest inclusion complexations involving CyDs and crown ethers, etc. Therefore, the competitive inclusion studies were conducted by ESI-MS in order to confirm the complexation of CsA with DM-β-CyD. CPZ was chosen as a competitive guest molecule because of the larger stability constant (8800 M^{-1}) of its DM-β-CyD complex,[14] compared with that (1050 M^{-1}) of the 1:1 CsA/DM-β-CyD complex. The relative magnitude of the constants was assumed not to change in the mixed solvent.[15] Figure 4 shows the effect of CPZ on the ESI mass spectra of CsA/DM-β-CyD complex. The CPZ alone gave a peak at 319 due to $[M + H]^+$, and the mass spectrum of the CsA/CPZ system was simply the superposition of each component, indicating no interaction between CsA and CPZ. The CPZ/DM-β-CyD system gave two new peaks at 1651 and 1665 corresponding to the 1:1 adducts of CPZ/DM-β-CyD, $[CPZ + CyD + H]^+$, and CPZ/the over-methylated homologue, $[CPZ + CyD + CH_2 + H]^+$, respectively, in a peak ratio of about 3:1. In the case of the ternary CsA/CPZ/DM-β-CyD system, the peak intensity of 1268 corresponding to the CsA/DM-β-CyD markedly decreased, whereas the intensity of the 1651 and 1665 peaks corresponding to CPZ/DM-β-CyD complex was almost constant. For example, the peak ratio of the CsA complex to the free drug ($I_{\text{complex}}/I_{\text{drug}}$) decreased from 0.064 (binary CsA/DM-β-CyD system) to 0.027 (ternary CsA/CPZ/DM-β-CyD system), whereas that of the CPZ complex was almost constant (0.039 and 0.040 for the binary and ternary systems, respectively). These results apparently indicate that CsA forms the complex with DM-β-CyD and the equilibrium is competitively inhibited by the addition of CPZ.

To gain insight into the inclusion mode of CsA with DM-CyDs, ^{1}H NMR spectroscopic studies were carried out.

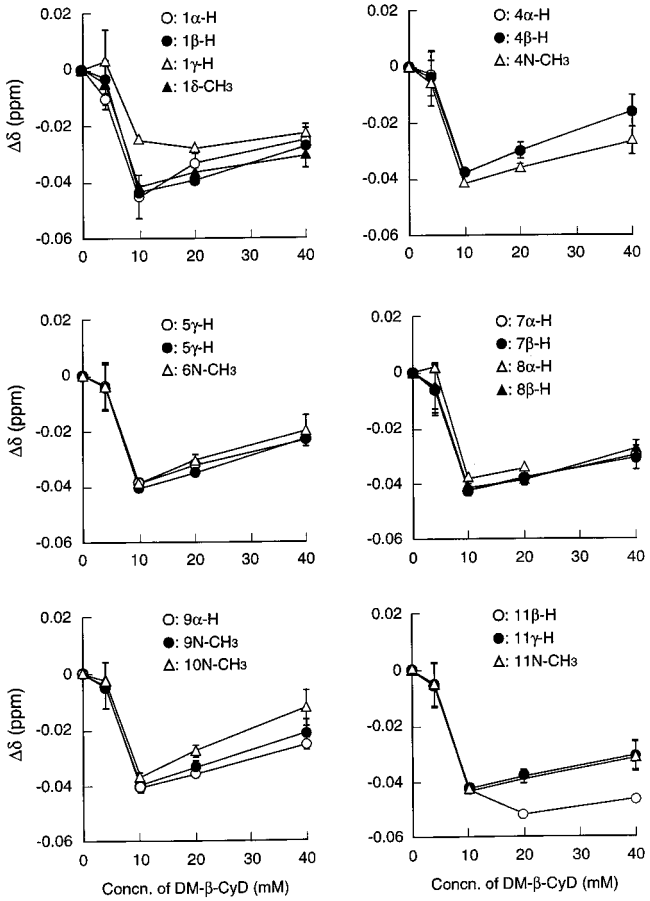

Figure 7—^{1}H NMR chemical shift displacements ($\Delta\delta$) of CsA (4 mM) as a function of DM-β-CyD concentrations in 50% v/v CD_3OD/D_2O. $\Delta\delta = \delta_{\text{in the presence of CyD}} - \delta_{\text{in the absence of CyD}}$.

Figure 5 shows ^{1}H NMR spectra of CsA in chloroform, 50% v/v methanol/chloroform, methanol, 75% v/v methanol/water, and 50% v/v methanol/water. It was difficult to obtain high-resolution spectra of CsA below 50% methanol concentration, because of precipitation of the substrate. The ^{1}H NMR signals of CsA in chloroform were successfully assigned according to the report of Kessler et al.[16] However, many new peaks appeared with severe splitting in methanol/chloroform solution, and this tendency became significant when polarity of solvents increased. For example, by changing the solvent from chloroform to 50% v/v methanol/water, the quintet (4.52 ppm) of the α proton of Ala7 (7α-H, Figure 1) changed to the multiplet (4.41 ppm), and the double-doublet (5.70 ppm) of the α proton of MeLeu9 (9α-H) changed to at least two double-doublets (5.60 and 5.52 ppm). Furthermore, the peak area of 5.60 ppm increased compared with that of 5.52 ppm. These results were in agreement of those reported by Kessler et al.,[16] Ko et al.[17] and Hasumi et al.,[18] suggesting that several conformational isomers of CsA may exist in polar solvents and they exchange slowly on the NMR time scale, whereas in chloroform CsA exists in one conformation. Because of the conformational diversity of CsA in polar solvents, it was difficult to assign unambiguously all ^{1}H-signals of CsA protons, but some of them in 50% v/v methanol/water solution could be assigned as follows: [1α-H (5.30 ppm), 1β-H (4.02 ppm), 1γ-H (2.33 ppm), and 1δ-CH_3 (0.76 ppm) for MeBmt], [4α-H (5.18 ppm), 4β-H (1.64 ppm), and 4N-CH_3 (3.08 ppm) for MeLeu4], [5γ-H (1.01 and 0.81 ppm) for Val5], [6N-CH_3 (3.15 ppm) for MeLeu6], [7α-H (4.41 ppm) and 7β-H (1.30 ppm) for Ala7], [8α-H (4.83 ppm) and 8β-H (1.28 ppm) for D-Ala8], [9α-H (5.60 ppm) and 9N-CH_3 (3.13 ppm) for MeLeu9], [10N-CH_3 (2.71 ppm) for MeLeu10]

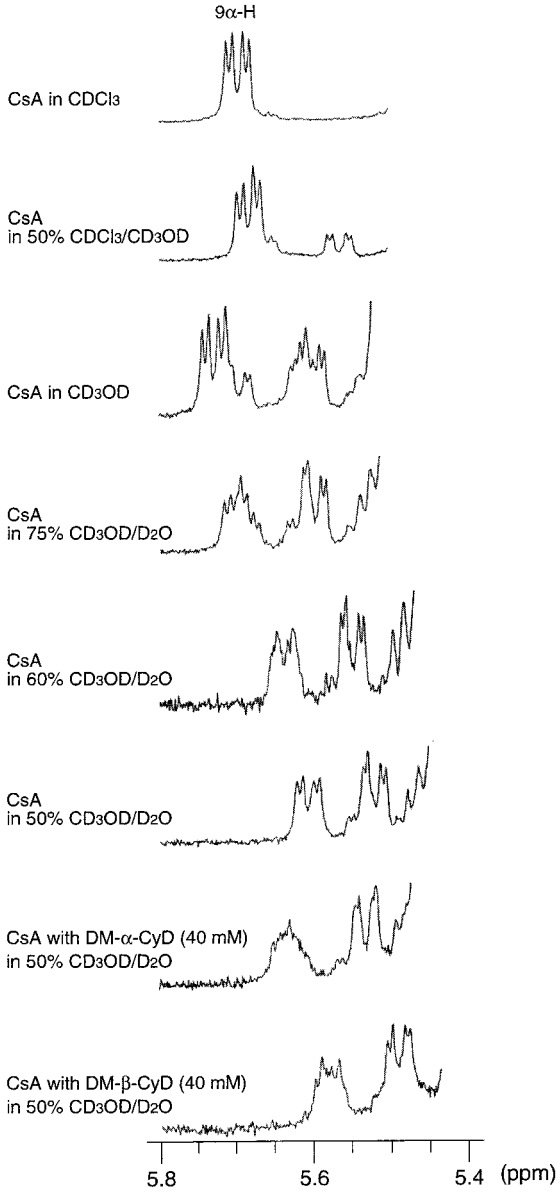

Figure 8—Changes of α proton peaks of MeLeu9 by the addition of DM-CyDs (40 mM) in 50% v/v CD_3OD/D_2O.

and [11β-H (2.11 ppm), 11γ-H (1.24 ppm) and 11N-CH_3 (2.76 ppm) for MeVal11].

Figures 6 and 7 show the effect of DM-α-CyD and DM-β-CyD, respectively, on the chemical shift of the assigned protons of CsA in 50% v/v methanol/water solution. The chemical shift of CsA protons shifted downfield by the addition of DM-α-CyD and magnitude of the change decreased generally in the order of (MeBmt ≈ MeLeu9 ≈ MeLeu10 ≈ MeLeu4) > (MeLeu6 ≈ Val5) > (MeVal11 ≈ Ala7 ≈ Ala8). These results suggest that DM-α-CyD includes preferably the hydrophobic side chains of amino acids such as the butenylthreonine and leucine, although there is seemingly no preference of the inclusion between MeBmt and four leucine residues in CsA molecule. On the other hand, DM-β-CyD system showed the upfield shift of CsA protons at lower concentrations of the host, while the shift was directed gradually toward downfield at higher concentrations, suggesting high order complexation. Similar biphasic change of ^{1}H NMR chemical shift was observed for the interaction of an antiulcer chalcone derivative with β-CyD.[19] The DM-β-CyD-induced shifts were uniform for all protons of CsA, indicating that the host having the larger cavity includes loosely a side chain of CsA without

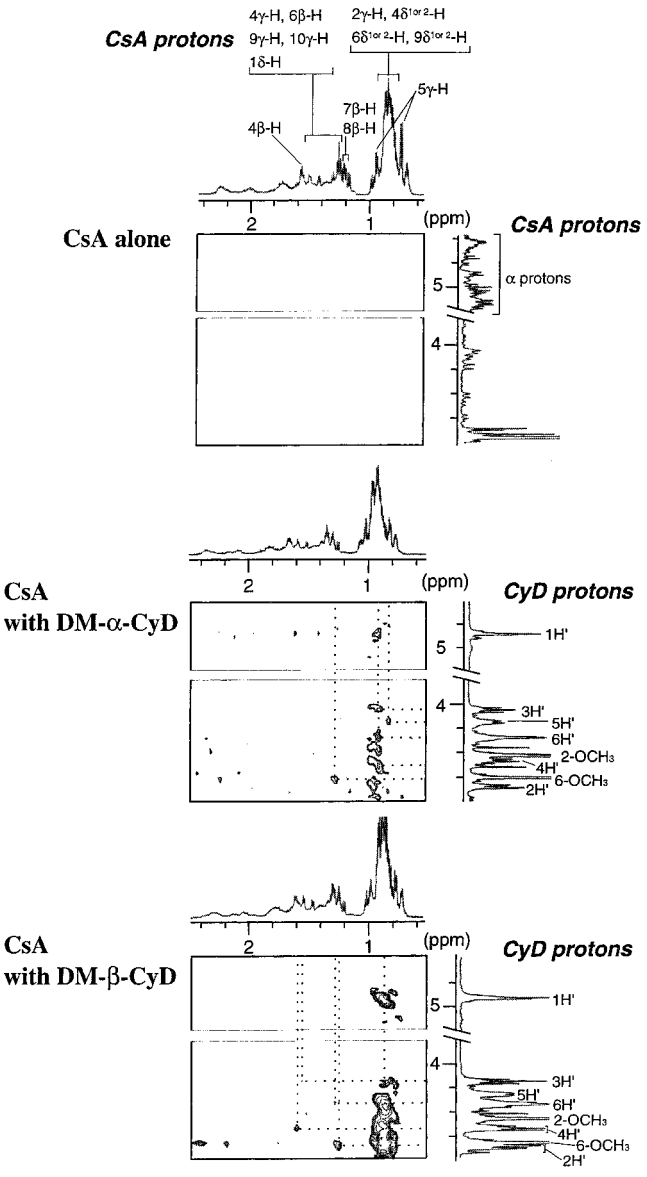

Figure 9—Partial contour plots of ROESY spectra of CsA (4 mM)/DM-CyDs (30 mM) systems in 50% v/v CD_3OD/D_2O.

a preferential inclusion of one particular amino acid. Figure 8 shows the changes of the α proton peaks of MeLeu9 (9α-H) due to the addition of DM-CyDs. As described above, the double-doublet (5.70 ppm) of 9α-H proton changed to at least two double-doublets (5.60 and 5.52 ppm), and the ratio of peak areas ($A_{5.52}/A_{5.60}$) at 5.60 and 5.52 ppm increased from 0 to 0.20, 0.69, 0.93, 0.95, and 1.00 by changing the solvent from chloroform to 50% v/v chloroform/methanol, methanol, and 75%, 60% and 50% v/v methanol/water solutions, respectively. The ratio of the peak area in 50% v/v methanol/water solution was insignificantly altered by the addition of DM-CyDs (0.91 and 1.06 in the presence of 4.0×10^{-2} M DM-α-CyD and 4.0×10^{-2} M DM-β-CyD, respectively). These results suggest that DM-CyDs do not interact so strongly with CsA as to alter the backbone structure of the guest, while they interact rather weakly with the side chains of CsA. The partial inclusion mode was further confirmed by ROESY spectra,[20,21] as described below. Figure 9 shows ROESY spectra of CsA in the absence and presence of DM-CyDs in 50% v/v methanol/water solution. DM-CyDs gave one ^{1}H-signal at 5.1 ppm and other signals between 3−4 ppm, and all signals were assigned according to the report of Chujo et al.[22] The signals of CsA can be generally classified to three groups, i.e., 4−6 ppm for α protons of amino acids, 2.5−3.5 ppm for *N*-methyl protons, and 0−2.4 ppm for protons of alkyl side chains. By the addition of DM-CyDs, new ROESY cross-peaks emerged between CyD protons and CsA alkyl side chain protons, whereas no cross-peaks were observed for *N*-methyl protons and α protons of CsA amino acids. These cross-peaks between DM-CyDs and the alkyl side chains were not observed in the absence of DM-CyDs. Furthermore, not only the inside protons of CyD (H3 and H5) but also the outside protons (H2 and H4) were involved in the cross-peaks. These results suggest that a hydrophobic side chain of CsA is included within the DM-CyD cavity, and other side chains interact with or fold on the outside of CyDs.

In conclusion, the data obtained from the solubility method and mass and NMR spectroscopic studies indicate that CsA interacts with DM-CyDs in aqueous solution, and the side chains of CsA may be involved in the inclusion. Furthermore, there is seemingly no preference of the inclusion of a particular side chain of CsA amino acid, but several complexes with different inclusion structures may exist simultaneously in solution, i.e., the so-called multimodal inclusion occurs in the interaction of CsA with DM-CyDs.

References and Notes

1. Bender, M. L., Komiyama, M., Eds. *Cyclodextrin Chemistry*; Springer-Verlag: Berlin, 1978.
2. Connors, K. A. The stability of cyclodextrin complexes in solution. *Chem. Rev.* **1997**, *97*, 1325−1357.
3. Hirayama, F.; Uekama, K. Methods of investigating and preparing inclusion compounds. In *Cyclodextrins and their industrial uses*; Duchêne, D., Ed.; Edition de Santê: Paris, 1987; pp 131−172.
4. Vincenti, M. Host−guest chemistry in the mass spectrometer. *J. Mass Spectrom.* **1995**, *30*, 925−939.
5. Camilleri, P.; Haskins, N. J.; New, A. P.; Saunders, M. R. Analysing the complexation of amino acids and peptides with β-cyclodextrin using electrospray ionization mass spectrometry. *Rapid Commun. Mass Spectrom.* **1993**, *7*, 949−952.
6. Camilleri, P.; Haskins, N. J.; Howlett, D. R. β-Cyclodextrin interacts with the Alzheimer amyloid β-A4 peptide. *FEBS Lett.* **1994**, *341*, 256−258.
7. Tokihiro, K.; Irie, T.; Hirayama, F.; Uekama, K. Mass spectroscopic evidence on inhibiting effect of maltosyl-β-cyclodextrin on insulin self-association. *Pharm. Sci.* **1996**, *2*, 519−522.
8. Fahr, A. Cyclosporin clinical pharmacokinetics. *Clin. Pharmacokinet.* **1993**, *24*, 472−495.
9. Lampen, A.; Christians, U.; Bader, A.; Hackbarth, I.; Sewing, K. F. Drug interaction and interindividual variability of ciclosporin metabolism in the small intestine. *Pharmacology* **1996**, *52*, 159−168.
10. Miyake, K.; Irie, T.; Hirayama, F.; Uekama, K. Improvements of gastrointestinal absorption and lymphatic transfer of cyclosporin A by various cyclodextrins. *Drug Delivery Syst.* **1998**, *13*, 369−375.
11. Spencer, C. M.; Stoddart, J. F.; Zarzycki, R. Structural mapping of an unsymmetrical chemically modified cyclodextrin by high-field nuclear magnetic resonance spectroscopy. *J. Chem. Soc., Perkin Trans. 2.* **1987**, 1323−1336.
12. Higuchi, T.; Connors, K. A. Phase-solubility techniques. *Adv. Anal. Chem. Instr.* **1965**, *4*, 117−212.
13. Higuchi, T.; Kristiansen, H. Binding specificity between small organic solutes in aqueous solution: classification of some solutes into two groups according to binding tendencies. *J. Pharm. Sci.* **1970**, *59*, 1601−1608.
14. Ishida, K.; Hoshino, T.; Irie, T.; Uekama, K. Alleviation of chlorpromazine-photosensitized contact dermatitis by β-cyclodextrin derivatives and their possible mechanisms. *Xenobiot. Metab. Dispos.* (in Japanese). **1988**, *3*, 377−386.
15. Shiotani, K.; Uehata, K.; Irie, T.; Hirayama, F.; Uekama, K. Characterization and the inclusion mode of β-cyclodextrin sulfate and its effect on the chlorpromazine-induced hemolysis of rabbit erythrocytes. *Chem. Pharm. Bull.* **1994**, *42*, 2332−2337.
16. Kessler, H.; Loosli, H. R.; Oschkinat, H. Assignment of the ^{1}H-, ^{13}C- and ^{15}N NMR spectra of cyclosproin A in $CDCl_3$

and C_6D_6 by a combination of homo- and heteronuclear two-dimensional techniques. *Helv. Chem. Acta* **1985**, *68*, 661−681.
17. Ko, S. Y.; Dalvit, C. Conformation of cyclosporin A in polar solvent. *Int. J. Pept. Protein Res.* **1992**, *40*, 380−382.
18. Hasumi, H.; Nishikawa, T.; Ohtani, H. Effect of temperature on molecular structure of cyclosporin A. *Biochem. Mol. Biol. Int.* **1994**, *32*, 505−511.
19. Utsuki, T.; Imamura, K.; Hirayama, F.; Uekama, K. Stoichiometry-dependent changes of solubility and photoreactivity of an antiulcer agent, 2′-carboxymethoxy-4,4′-bis(3-methyl-2-butenyloxy)chalcone, in cyclodextrin inclusion complexes. *Eur. J. Pharm. Sci.* **1993**, *1*, 81−87.
20. Saka, W.; Yamamoto, Y.; Inoue, Y.; Chûjô, R.; Takahashi, K.; Hattori, K. ^{1}H NMR study of conformation of formay-L-phenylalanyl-6-deoxy-6-amino-cyclomaltoheptaose that has excellent ability of chiral recognition. *Bull. Chem. Soc. Jpn.* **1990**, *63*, 3175−3180.
21. Owens, P. K.; Fell, A. F.; Coleman, M. W.; Kinns, M.; Berridge, J. C. Use of ^{1}H NMR spectroscopy to determine the enantioselective mechanism of neutral and anionic cyclodextrins in capillary electrophresis. *J. Pharm. Biomed. Anal.* **1997**, *15*, 1603−1619.
22. Onda, M.; Yamamoto, Y.; Inoue, Y.; Chûjô, R. ^{1}H NMR study of intramolecular hydrogen-bonding interaction in cyclodextrins and their di-*O*-methylated derivatives. *Bull. Chem. Soc. Jpn.* **1988**, *61*, 4015−4021.

JS980284+

Influence of Gender on Prednisolone Effects on Whole Blood T-Cell Deactivation and Trafficking in Rats

GUY M. L. MENO-TETANG,† JOGARAO V. S. GOBBURU,‡ AND WILLIAM J. JUSKO*§

Contribution from *Bioanalytical R & D, Wyeth-Ayerst Research, Pearl River, New York 10965, Center for Drug Development Science, Washington, D.C. 20007, and Department of Pharmaceutics, School of Pharmacy, State University of New York at Buffalo, 565 Hochstetter Hall, Buffalo, New York 14620.*

Received June 30, 1998. Final revised manuscript received September 29, 1998.
Accepted for publication October 2, 1998.

Abstract □ Prednisolone (5 mg/kg intravenous) was administered to adrenalectomized male and female Sprague-Dawley rats (250–350 g) to assess the effects of gender on disposition and pharmacoimmunodynamics. Plasma concentrations of prednisolone were determined by high-performance liquid chromatography. Incorporation of [^{3}H]thymidine (^{3}H-TDR) was used to determine whole blood T-cell (WBTC) trafficking and deactivation following stimulation with Concanavalin-A. Whole blood T-cell trafficking was determined indirectly by using the glucocorticoid receptor antagonist RU-40555 (250 ng/mL) added to ex vivo cultures of whole blood from animals dosed with prednisolone. Mean (± SD) prednisolone clearance values were 3.22 ± 0.88 and 3.46 ± 0.96 L/h/kg in males and females, respectively. After administration of prednisolone, relative T-cell counts decreased slowly with time to reach a nadir at 3–5 h and returned to baseline levels by 8 h. Fitting data using an indirect response model yielded mean prednisolone 50% inhibitory concentration for inhibition of WBTC trafficking (IC_{50T}) that was lower in males compared with females (0.14 ± 0.16 versus 1.03 ± 0.06 ng/mL; $p < 0.05$). In the absence of RU-40555, an immediate and complete inhibition of ^{3}H-TDR incorporation into WBTC was observed (deactivation) and baseline levels were recovered slowly as prednisolone was cleared from blood. The mean 50% inhibitory concentration for inhibition of WBTC deactivation (IC_{50D}) based on an inhibitory I_{max} model was similar in males and females (0.20 ± 0.24 versus 0.18 ± 0.12 ng/mL). Although male and female rats have similar exposure to prednisolone after 5-mg/kg doses, males are more sensitive to the inhibition of WBTC trafficking, whereas no gender effects on deactivation of WBTC exist.

Introduction

Glucocorticoids have a major role in the treatment of allograft rejection and several allergic, autoimmune, and malignant diseases in humans.[1] They profoundly suppress various nonspecific inflammatory responses and specific immunologic processes.[2] The mechanism by which they exert these actions is yet to be fully understood. However, lymphocytes mediate several glucocorticoid responses. The importance of trafficking of circulating lymphocytes and monocytes in mediating corticosteroid action has been documented.[3] In addition, corticosteroids profoundly inhibit T-cell activation (clonal expansion of antigen specific T-cells), cellular events that occur during an encounter with peptide antigens. Some of the current knowledge of cellular events in T-cell activation is based on in vitro experiments in which T-cells can be stimulated in a controlled manner with lectins, such as concanavalin-A (Con-A), and their proliferation can be measured by the incorporation of [^{3}H]-thymidine (^{3}H-TDR).[4]

Considering heart transplant recipients treated with prednisone and cyclosporine, female recipients have more rejection episodes at 3 and 12 months than do males. Also, early withdrawal of maintenance steroids is less often achievable in women as compared with men (17 versus 65%).[5] These differences may be explained by genetic differences between genders and/or by the interactions of sex hormones with glucocorticoids in the regulation of the immune system. Indeed, estrogens stimulate the production of corticosteroid binding globulin (CBG) in rats.[6] This stimulation may alter the kinetics of prednisolone.[7] The influence of female sex hormones on glucocorticoid receptor binding parameters has also been observed in some responsive organs.[8,9] Lew et al.[10] found a correlation between the logarithm of plasma estradiol-17β and sensitivity of women to methylprednisolone inhibition of basophil trafficking. Moreover, estradiol inhibits rat thymocyte proliferation, T-cell suppressor activity, and mixed lymphocyte reactions.[11−13]

Improved use of glucocorticoids as antiinflammatory or immunosuppressive agents may be achieved by an understanding of the influence of covariates, such as gender, in their pharmacokinetics (PK) and pharmacodynamics (PD). The objectives of this work were to assess the influence of gender on prednisolone pharmacokinetics in conjunction with gender influences on prednisolone effects on whole blood T-cell (WBTC) trafficking and deactivation in rats.

Experimental Section

Animals—Adrenalectomized Sprague-Dawley male and female rats weighing 250−350 g were purchased from Harlan Sprague-Dawley Inc. (Indianapolis, IN) and housed in a 12 h light/12 h dark cycle and constant temperature environment (22 °C). The rats had free access to rat chow (Agway RMH 1000) and normal saline (NaCl, 0.9%) prior to the experiments. A total of 8 rats (4 males and 4 females) were used in the study, which adhered to the principles of Laboratory Animal Care (NIH publication # 85-23, revised 1985). Female rats were taken at proestrus (phase of the ovarian cycle exhibiting high levels of sex hormones). The rat estrus cycle lasts 4−5 days and is identifiable by changes in the vaginal cytology. Each phase exhibits different levels of sex hormones.[14]

A silastic cannula was surgically implanted in the right jugular vein for drug administration and blood sampling 7 days prior to study day. The surgery was done aseptically under ketamine/xylazine anesthesia (50/10 mg/kg). Cannulas were flushed daily and kept patent with 200 U/mL of heparin.

Materials—Prednisolone hemisuccinate and betamethasone were purchased from Sigma (St. Louis, MO). A working solution of prednisolone hemisuccinate at 13.4 mg/mL (equivalent of 10 mg/mL prednisolone) was made in sterile saline to administer a total volume of 500 μL/kg to the animals. RU-40555 was obtained as a gift from Roussel Uclaf (Romainville, France). Tritiated thymidine (^{3}H-TDR; 6.7 Ci/mmol) was purchased from Amersham

* Corresponding author. E-mail: WJJusko@acsu.Buffalo.edu.

10.1021/js9802695 CCC: $18.00
Published on Web 12/08/1998

(Arlington Heights, IL). Concanavalin-A (Con-A) was obtained from ICN Biomedicals (Cleveland, OH).

Experimental Design—For assessment of incorporation of ^{3}H-TDR into WBTC (relative cell counts) as a function of time at baseline, 0.3 mL of blood were drawn with a heparinized syringe at 0, 3, 6, 9, and 12 h. Each blood sample was replaced with 0.3 mL of sterile normal saline. Because each phase of a 4-day estrus cycle lasts only 24 h, prednisolone was administered 4 days after baseline measurements. This delay allowed measurement of T-cell counts during baseline and prednisolone phases at the same stage of the estrus cycle of female rats. Prednisolone hemisuccinate (equivalent of 5 mg/kg of prednisolone) was administered as an intravenous (iv) bolus through the cannula, and then blood was sampled frequently over 12 h. After prednisolone administration, 0.4 mL of blood was withdrawn at 0.16, 0.33, 0.5, 0.75, 1, 2, 3, and 4 h and 0.2 mL at 0, 5, 6, 8, 9, and 12 h. Each blood sample was replaced with an equivalent volume of sterile normal saline. One hundred microliters of heparinized blood were used for ex vivo whole blood cultures. The remaining blood was centrifuged for 10 min at 5000 x *g*. The plasma was then aliquoted into Eppendorf tubes and stored at −20 °C for assay of prednisolone concentrations.

Assay Methodology—Whole Blood Cultures—The method of Fasanmade and Jusko[15] was used. Blood diluted 15-fold (145 μL) was dispensed into each well of 96-well flat-bottomed polystyrene multiple-well plate. Con-A (20 μL) was added to culture medium to give a final concentration of 10 ng/mL. Supplemented RPMI 1640 was added to give a total volume of 200 μL per well. Cells were incubated at 37 °C under a humidified atmosphere of 7% CO_2 for 96 h before adding ^{3}H-TDR (1 μCi per well). Cells were harvested with an automatic harvester (Skatron Instruments, Sterling, VA) at 20 h after the addition of ^{3}H-TDR. Cellularly incorporated radioactivity was assessed using a Packard Topcount microplate scintillation counter (Downers Grove, IL).

In Vitro Interaction of RU-40555 with Prednisolone in WBTC Deactivation—To determine the competitive inhibition of glucocorticoid receptors in vitro, whole blood from male rats was spiked with prednisolone to obtain final concentrations of 200, 1000, 2000, and 5000 ng/mL and incubated for 2 h at 37 °C prior to adding RU-40555 (250 ng/mL). The optimum concentration of RU-40555 was determined by Fasanmade and Jusko.[16] Whole blood was then diluted and stimulated with Con-A and cultured for an additional 96 h as described in the previous section. RU-40555 produces a complete inhibition of glucocorticoid receptor when the molar ratio RU-40555/glucocorticoids is 10 or greater. There is no difference between genders regarding the molar ratio for optimum inhibition (Dr. Gaillard-Kelly, personal communication, Roussel Uclaf).

High-Performance Liquid Chromatography (HPLC)—Prednisone was measured by the HPLC method of Rose and Jusko[17] as adapted for rats[18,19] using betamethasone as internal standard. The lower and upper limits of quantitation were 10 and 1500 ng/mL. The interday coefficient of variation (CV) for prednisolone was 7.03% at 25 ng/mL, 2.70% at 150 ng/mL, and 2.76% at 600 ng/mL.

Data Analysis—*Pharmacokinetics*—Prednisolone plasma concentrations (C_p) versus time (t) were described by:

$$C_p = Ae^{-\alpha t} + Be^{-\beta t} \quad (1)$$

The intercept coefficients (A and B) and slopes (α and β) were estimated by least-squares fitting using the ADAPT II.4 program (Biomedical Simulation Resource, Los Angeles, CA). The area under the prednisolone concentration−time curve (AUC = $A/\alpha + B/\beta$) and the area under the first-moment curve (AUMC = $A/\alpha^2 + B/\beta^2$) were then calculated. The mean residence time (MRT) was determined as the ratio of AUMC/AUC. Clearance (CL) was obtained as dose/AUC. The volume of distribution at steady-state was determined as $CL \cdot$MRT.

Pharmacodynamics—The model describing the time course of lymphocyte and ex vivo mitogen activation is depicted in Figure 1.

Lymphocyte Trafficking—Incorporation of ^{3}H-TDR into WBTC was used as an indirect measurement of WBTC counts. Because prednisolone inhibits lymphocyte trafficking, the incorporation of ^{3}H-TDR into WBTC varied with time following the pattern of a typical indirect response. Because blood samples from animals dosed with prednisolone contained the drug, complete deactivation of lymphocytes was observed after stimulation with Con-A causing inhibition of ^{3}H-TDR incorporation into WBTC. Thus, to assess the relative number of T-cells in 100 μL of diluted whole blood at each time point, samples of diluted blood from dosed animals were incubated with the glucocorticoid receptor antagonist RU-40555 (250 ng/mL). Complete blockade of prednisolone action then allowed the incorporation of ^{3}H-TDR into lymphocytes present in whole blood samples.

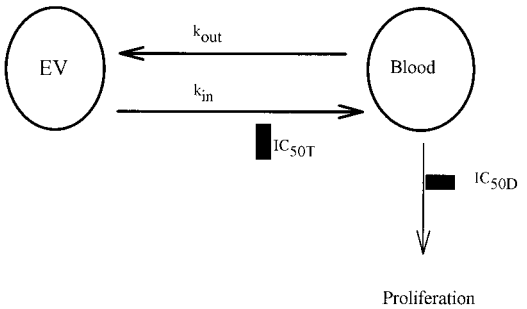

Figure 1—Pharmacodynamic model for the effects of prednisolone on whole blood T-cell trafficking and deactivation. Cells egress from blood to extravascular (EV) tissues with rate constant k_{out}, and the rate constant for return to blood is k_{in}. The IC_{50T} reflects prednisolone inhibition of k_{in} and IC_{50D} reflects the inhibition of mitogen-stimulated activation of whole blood T-cells.

Blood lymphocytes (L) circulate between the central and extravascular compartments. Corticosteroids inhibit the zero-order rate (k_{in}) of return of lymphocytes from the extravascular compartment without affecting their movement out of the central blood compartment (k_{out}). The scheme in Figure 1 and the following equation describe lymphocyte trafficking:[20]

$$\frac{dL}{dt} = k_{in} - k_{out}L \quad (2)$$

in which $L = L_0$ (cpm pre-dose) at $t = 0$. In the presence of prednisolone, the k_{in} is inhibited and the rate of change of lymphocyte counts with time is described by

$$\frac{dL}{dt} = k_{in}\left(1 - \frac{I_{max}C_p}{IC_{50T} + C_p}\right) - k_{out}L \quad (3)$$

where C_p is prednisolone plasma concentration, IC_{50T} is the concentration of prednisolone producing half-maximal inhibition (I_{max}) of k_{in}, and L is the observed cpm in ex vivo cultures treated with RU-40555.

Lymphocyte Deactivation—When whole blood samples drawn at various time points after prednisolone administration were cultured, an immediate and complete inhibition of ^{3}H-TDR incorporation into lymphocytes was observed and baseline levels recovered gradually. This inhibition was due to prednisolone concentrations present in blood samples. The level of ^{3}H-TDR observed was a function of the number of cells present in the blood at a given time (trafficking) and also a function of prednisolone plasma concentrations.

Lymphocyte deactivation by prednisolone is described as follows by the I_{max} model:

$$E = \left(1 - \frac{I_{max}C_p}{IC_{50D} + C_p}\right)L \quad (4)$$

where E is the observed cpm in cells from blood samples not treated with RU-40555 (intrinsic deactivation) and L is the observed cpm in cells treated with RU-40555, C_p is prednisolone plasma concentrations corrected for the dilution of blood, and IC_{50D} is prednisolone concentration producing half-maximal inhibition (I_{max}) of lymphocyte activation.

When both inhibition of cell trafficking and deactivation of lymphocytes occur, eqs 3 and 4 are fitted simultaneously.

To assess the net deactivation of WBTC following prednisolone administration, the area under lymphocyte trafficking (baseline for the deactivation process) and deactivation curves from 0 to 12 h were calculated using the Spline method.[21] These values were used to calculate the area between baseline and effect curves (ABEC) and the area suppression ratio (AUC_{SR}) determined by

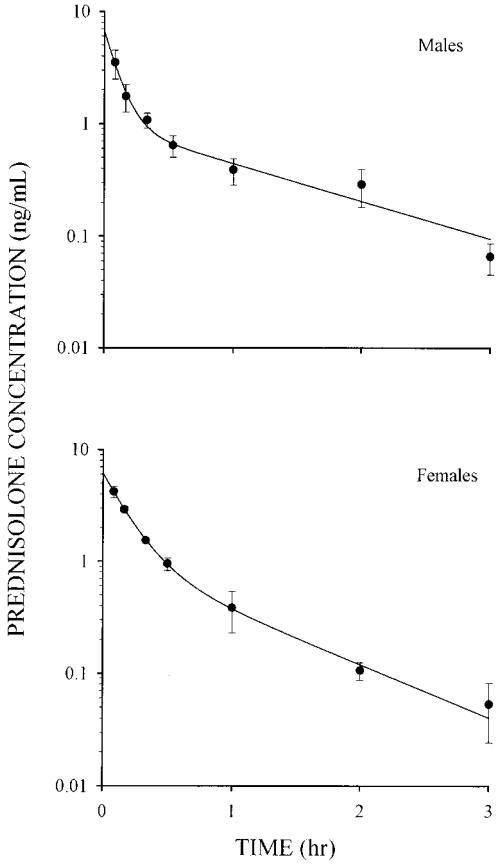

Figure 2—Mean (± SD) plasma concentration versus time profiles of prednisolone for males and females after iv administration of prednisolone 5 mg/kg. Symbols represent experimental data and lines are least-squares regression fittings.

eqs 5 and 6

$$\text{ABEC} = \text{AUC}^{12}_{0\ \text{BL}} - \text{AUC}^{12}_{0\ \text{E}} \quad (5)$$

$$\text{AUC}_{\text{SR}} = \frac{\text{AUC}^{12}_{0\ \text{E}}}{\text{AUC}^{12}_{0\ \text{BL}}} \quad (6)$$

where $AUC_0{}^{12}{}_E$ is the area under the deactivation curve from 0 to 12 h and $AUC_0{}^{12}{}_{BL}$ is the area under the trafficking curve from 0 to 12 h. Larger ABEC and smaller AUC_{SR} (which accounts for differing baselines) indicate greater net suppression.

The pharmacodynamic parameters for lymphocyte trafficking were determined by fitting cpm obtained with RU-40555 to eq 3, whereas pharmacodynamic parameters for lymphocyte deactivation were determined by simultaneously fitting cpm obtained with RU-40555 to eq 3 and cpm obtained without RU-40555 to eq 4. Prednisolone pharmacokinetic parameters were provided via eq 1. The ADAPT II.4 program (Biomedical Simulation Resource, Los Angeles, CA) was used for nonlinear regression fittings.

Statistical Aanalysis—The effects of gender on prednisolone CL, Vss, AUC_{SR}, ABEC, IC_{50T}, and IC_{50D} were assessed by an unpaired Student t-test, with statistical significance set at $p < 0.05$, using INSTAT (GraphPad Software, La Jolla, CA).

Results

Pharmacokinetics—Figure 2 shows mean plasma (± SD) concentrations versus time profiles of prednisolone in male and female rats. The disposition of prednisolone was biexponential, with a rapid initial phase followed by a slower elimination phase. Table 1 lists prednisolone pharmacokinetic parameters in the two groups. Mean (± SD) prednisolone clearance values were 3.22 ± 0.88 and 3.46 ± 0.96 L/hr/kg in males and females, respectively. Mean prednisolone $t_{1/2}$ values were 0.41 ± 0.12 h in males and 0.63 ± 0.40 h in females.

Table 1—Mean (± SD) Pharmacokinetic Parameters for Prednisolone in Male and Female Rats Following a Single iv Dose of 5 mg/kg (n = 4)

	males		females	
parameter	mean	SD	mean	SD
AUC (ng•h/mL)	1616	384	1526	436
MRT (h)	0.38	0.10	0.55	0.30
CL (L/h/kg)	3.22	0.88	3.46	0.96
Vd_{SS} (L/kg)	1.21	0.22	1.96	1.07
$t_{1/2}$ (h)	0.41	0.12	0.63	0.40

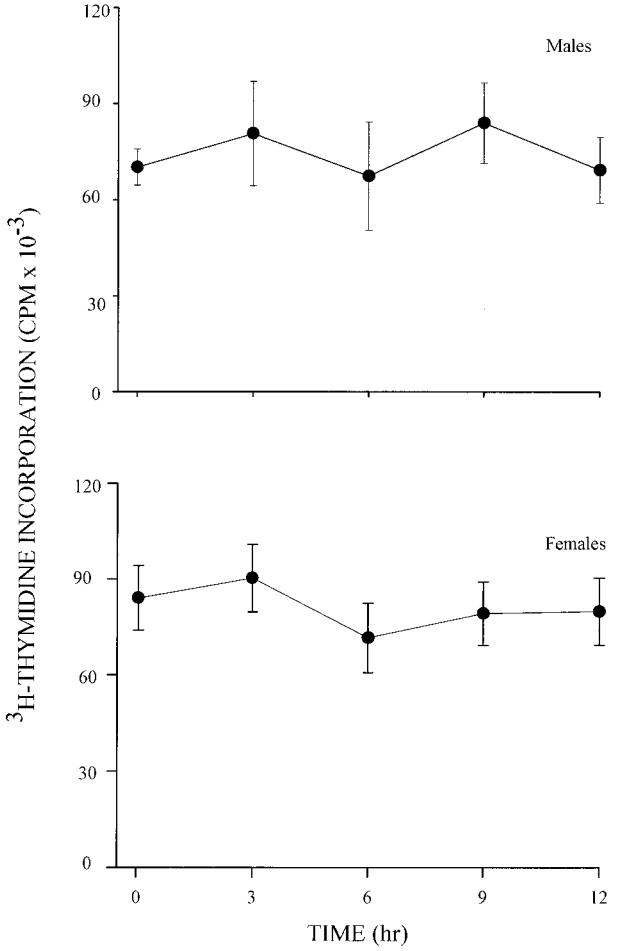

Figure 3—[^{3}H]Thymidine incorporation into whole blood T-cells as a function of time at baseline for male and females. Symbols represent mean (± SD) of data from four animals.

Pharmacodynamics—*Baseline ^{3}H-TDR Incorporation*—Figure 3 illustrates ^{3}H-TDR incorporation into WBTC (relative cell counts) as a function of time at baseline in male and female rats. No statistical differences were observed between time points, suggesting that baseline levels were steady over 12 h.

In Vitro Interaction of RU-40555 with Prednisolone in WBTC Deactivation—Figure 4 shows the influence of RU-40555 on prednisolone inhibition of lymphocyte proliferation in vitro (deactivation). This agent completely antagonized the effects of the steroid at all concentrations investigated. Additionally, RU-40555 did not produce any changes in WBTC from control values.

Lymphocyte Trafficking—Figure 5 depicts mean ± SD relative WBTC counts and T-cell deactivation as a function

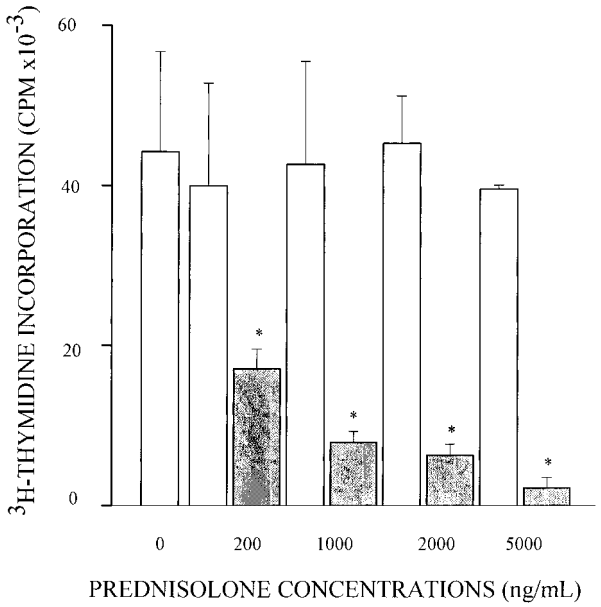

Figure 4—Joint effects of RU-40555 and prednisolone on whole blood T-cell deactivation in vitro. Key: (open bars) prednisolone + RU-40555 (250 mg/mL); (shaded bars) prednisolone alone; (*) $p < 0.05$ comparing single versus dual agents.

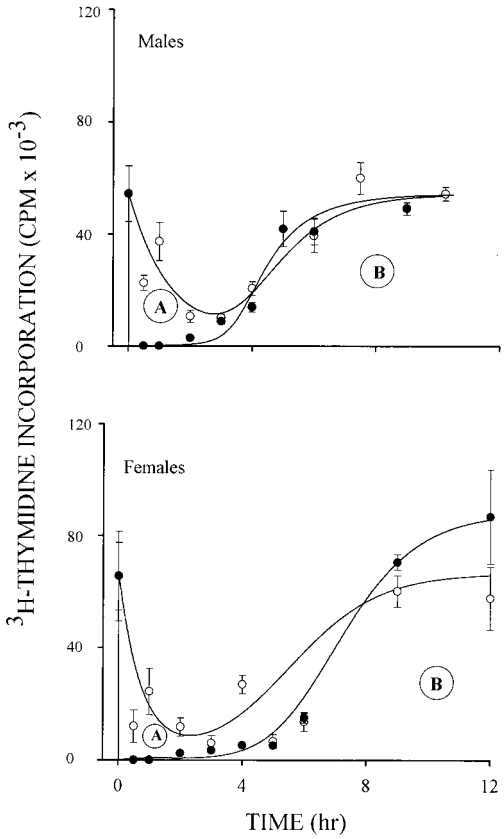

Figure 5—Mean (± SD) [^{3}H]thymidine incorporation into whole blood T-cells as a function of time in male and female rats after administration of prednisolone. Symbols are experimental data and lines represent fittings to the pharmacodynamic model. Key: (○) [^{3}H]thymidine incorporation in the presence of RU-40555 (trafficking); (●) [^{3}H]thymidine incorporation in absence of RU-40555 (deactivation). $AUC_{BL} = A + B$; $AUC_E = B$, and $AUC_{SR} = B/(A + B)$.

of time in male and female rats. After administration of prednisolone, the incorporation of ^{3}H-TDR into WBTC cultured with RU-40555 (relative WBTC counts) decreased slowly with time to reach a nadir at 3−5 h and returned to baseline levels by 8 h. Table 2 lists the pharmacodynamic parameters for trafficking and deactivation. Responses attained zero values and this complete inhibition allowed I_{max} to be set to 1. The mean (± SD) prednisolone IC_{50T} values for inhibition of WBTC trafficking was smaller in males compared with females (0.14 ± 0.16 versus 1.03 ± 0.06 ng/mL; $p < 0.05$). The net effect of prednisolone on lymphocyte trafficking (AUC_{SR}) could not be calculated because of the rebound effect observed in lymphocyte proliferation after the recovery of baseline in several animals (T-cell count rose above baseline levels).

Table 2—Mean (± SD)[a] Pharmacodynamic Parameters for Prednisolone Effects on Whole Blood T-Cell Trafficking and Deactivation in Male and Female Rats Following a Single iv Dose of 5 mg/kg

	trafficking				deactivation			
	males		females		males		females	
parameter	mean	SD	mean	SD	mean	SD	mean	SD
k_{in} (cpm/h) × 10^{-3}	44.0[b]	4.2	119	38	NA[c]	NA	NA	NA
k_{out} (h^{-1})	0.73[b]	0.18	1.35	0.44	NA	NA	NA	NA
IC_{50T} or IC_{50D} (ng/mL)	0.14[b]	0.16	1.03	0.06	0.20	0.24	0.18	0.12
ABEC (cpm·h) × 10^{-3}	NA	NA	NA	NA	130	80	232	208
AUC_{SR}	NA	NA	NA	NA	0.72	0.22	0.72	0.26

[a] All values represent the mean (± SD) of four individual animals. [b] $p < 0.05$ as compared with the respective value in females. [c] NA, Not applicable.

Lymphocyte Deactivation—Following prednisolone administration, an immediate and complete inhibition of ^{3}H-TDR incorporation into lymphocytes cultured without RU-40555 was observed and baseline levels recovered slowly as prednisolone was cleared from blood (Figure 5). This response also showed complete inhibition, allowing I_{max} to be set to 1.0. The mean (± SD) IC_{50D} values for WBTC deactivation were similar in males and females (0.20 ± 0.24 vs 0.18 ± 0.12 ng/mL). A reduced ^{3}H-TDR incorporation into lymphocytes was still observed after prednisolone concentrations declined below the limit of quantitation (3 h post dose). There were no statistically significant differences between males and females with respect to the net deactivation of WBTC as shown by the mean AUC_{SR} values (0.72 ± 0.22 in males and 0.72 ± 0.26 in females).

Discussion

To assess gender as a covariate in the optimization of glucocorticoid immunosuppressive therapy, we investigated WBTC trafficking and deactivation in male and female rats following a single dose of prednisolone. The pharmacokinetic parameters for prednisolone obtained in the present study were in the same range as those reported by Boudinot et al.[18] Although evidence exists supporting the role of sex steroid hormones in the regulation of transcortin (CBG), no statistical differences in prednisolone *CL* and steady-state volume of distribution (Vd_{ss}) between males and females were found (Table 1). These results may be explained by the relatively low dose used in this study (5 mg/kg). The binding of prednisolone to CBG is responsible for its dose-dependent disposition.[19] Unfortunately, we were unable to measure unbound prednisolone in this study.

Glucocorticoids exert some of their antiinflammatory actions by inhibiting the return of WBTC from the extravascular compartment to the blood compartment. In addition to such lymphocytopenia, these drugs deactivate T-cells to render them nonresponsive to peptide antigens. Glucocorticoids affect T-cell trafficking and deactivation via regulation of the secretion of cytokines, such as IL-2, and adhesion molecules.[22] Bloemena et al.[23] demonstrated that

decreased lymphocyte numbers in the peripheral blood are one of the determinant of the proliferative response of WBTC. Because proliferation of peripheral blood lymphocytes was measured in a standardized volume of blood (100 μL) at every time point, it was assumed that ^{3}H-TDR incorporation was determined by the proliferative capacity of individual lymphocytes as well as by the number of lymphocytes present in the peripheral blood. Thus the incorporation of ^{3}H-TDR into whole blood cultures was used to simultaneously determine the effects of prednisolone on WBTC trafficking and their intrinsic activation.

Relative WBTC number was determined by using the glucocorticoid receptor antagonist RU-40555 added to ex vivo cultures of whole blood from dosed animals.[24] This agent antagonizes prednisolone deactivation of WBTC in vitro (Figure 4) in the same concentration range as that obtained with a 5-mg/kg dose (Figure 2). The concentration of RU-40555 utilized did not affect WBTC (Figure 4). Therefore, the incorporation of ^{3}H-TDR into whole blood cultures measured in the presence of RU-40555 could be taken as the relative number of WBTC present at each time point. In normal humans, lymphocyte trafficking between blood and extravascular compartments parallels the circadian variation of endogenous cortisol (the number of lymphocytes shows a clear rhythmicity with high values at night and low values during the day).[25] In this study, we utilized adrenalectomized animals to suppress the effect of the latter because the adrenal gland is the main source of endogenous glucocorticoids. This objective was achieved because the incorporation of ^{3}H-TDR into whole blood cultures at baseline was stable over 12 h (Figure 3). Whole blood lymphocytes decreased after administration of prednisolone. This time profile (Figure 5) was similar to that obtained in humans. The maximum response was delayed with respect to prednisolone concentrations, showing that our method describes well the movement of cells between the blood and extravascular compartments. An innovative PK/PD model that incorporates features of indirect effects of prednisolone on cell trafficking as well as direct inhibition of ex vivo T-cell activation was used.[16] The model described well the experimental data, and pharmacodynamic parameters were obtained with relatively good precision (5−20% CV). Prednisolone had a significantly smaller IC_{50T} in males compared with females. This result show that male rats may be more sensitive than females to inhibition of WBTC trafficking by prednisolone. These observations may be due to gender differences in estrogen levels. Indeed, estrogen receptors are found on lymphoid cells.[26] Estradiol inhibition of polymorphonuclear leukocyte chemotaxis is mediated by estrogen receptors.[27] Also, estradiol down-regulates the expression of P-selectins, molecules involved in the regulation of cell trafficking.[28]

Following prednisolone administration, an immediate and complete inhibition of ^{3}H-TDR incorporation into lymphocytes was observed in whole blood without RU-40555. Baseline values were recovered slowly as prednisolone was cleared from blood. The diminished responsiveness of WBTC to stimulation with Con-A (intrinsic deactivation) appeared to be a direct effect of prednisolone because the degree of inhibition of ^{3}H-TDR incorporation paralleled that of prednisolone concentrations. This result required very small steroid concentrations. Indeed, considerable inhibition remained when the drug fell below the limit of quantitation. The sensitivity of WBTC to prednisolone deactivation was not affected by gender as no statistical differences were observed in the mean IC_{50D} and AUC_{SR} (net suppression) values between males and females. Ferron and Jusko[29] also recently found no gender differences in in vitro WBTC effects of prednisolone in adrenalectomized rats and in humans.

In conclusion, by using a glucocorticoid receptor antagonist, we were able to monitor simultaneously two major components of glucocorticoid immunosuppression (trafficking and deactivation). The use of RU-40555 allowed separation of these phenomena, permitting estimation of IC_{50} values for prednisolone effects on each component. Greater immunosuppression was achieved overall in male rats compared with females following a 5-mg/kg single dose of prednisolone. However, no gender differences were observed in either the exposure to the drug or WBTC deactivation.

Abbreviations

^{3}H-TDR	[^{3}H]thymidine
WBTC	whole blood T-cell
Con-A	concanavalin-A
IC_{50T}	concentration producing 50% inhibition of the zero-order rate constant (k_{in}) for return of blood T-cells from the extravascular compartment to the blood compartment
IC_{50D}	concentration producing 50% inhibition of whole blood T-cell activation
I_{max}	maximum inhibition of the zero-order rate constant (k_{in}) for return of blood T-cells from the extravascular compartment to the blood compartment or maximum inhibition of whole blood T-cell activation.
ABEC	area between baseline and effect curves
AUC_{SR}	ratio of the area between the effect curve and the area at baseline
cpm	counts per minute
k_{in}	zero-order rate for return of lymphocytes from the extravascular compartment to the blood compartment
k_{out}	first-order rate constant for exit of lymphocytes from the blood compartment
CL	Clearance
Vd_{ss}	apparent volume of distribution at steady state
$t_{1/2}$	terminal half-life
MRT	mean residence time
AUC	area under the plasma concentration−time curve
AUMC	area under the first moment curve

References and Notes

1. Boumpas, D. T.; Chousos, G. P.; Wilder, R. L.; Cupps, T. R.; Balow, J. E. Glucocorticoid therapy for immune-mediated diseases: Basic and clinical correlates. *Ann. Intern. Med.* **1993**, *119*, 1198−1208.
2. Barnes, P. J.; Adcok, I. Antiinflammatory actions of setroids: molecular mechanism. *TiPS* **1993**, *14*, 436−441.
3. Fauci, A. S.; Dale, D. C.; Balow, J. E. Glucocorticoid therapy: mechanisms of action and clinical considerations. *Ann. Intern. Med.* **1976**, *84*, 304−315.
4. Molecular basis of T-Cell antigen recognition and activation. In *Cellular and molecular immunology*, 2nd ed.; Abbas, A.; Lichman, A.; Pober, J., Eds.; W. B. Saunders: Philadelphia, 1994; p 158.
5. Crandall, B. G.; Renlund, D. G.; O′ Connell, J. B. Increased cardiac allograft rejection in female heart transplant recipients. *J. Heart. Transplant* 1988, *7*, 419−423.
6. Feldman, D.; Madon, C. E.; Herner, J. A. Glucocorticoids and estradiol regulation of corticosteroid binding globulin by rat liver. *Am. J. Physiol.* **1979**, *237*, E493−E499.
7. Ko, H. C.; Almon, R. R.; Jusko, W. J. Effect of corticosteroid binding globulin on the pharmacokinetics of prednisolone in rats. *Pharm. Res.* **1995**, *12*, 902−904.

8. Turner, B. B. Sex difference in glucocorticoid binding in rat pituitary is estrogen dependent. *Life Sci*. **1990**, *46*, 1399−1406.
9. Ferrini, M.; De Nicholas, A. F. Estrogen up-regulates Type I and Type II glucocorticoid receptors in brain regions from ovariectomized rats. *Life Sci*. **1991**, *48*, 2593−2601.
10. Lew, K. H.; Ludwig, E. A.; Milad, M. A.; Donovan, K.; Middleton, E., Jr.; Ferry, J. J.; Jusko, W. J. Gender-based effects on methylprednisolone pharmacokinetics and pharmacodynamics. *Clin. Pharmacol. Ther.* **1993**, *54*, 402−414.
11. Aboussaouira, T.; Marie, C.' Brugal, G.; Idelman, S. Inhibitory effect of 17-beta-estradiol on thymocyte proliferation and metabolic activity in young rats. *Thymus* **1991**, *17*, 167−180.
12. Paavonen, T.; Anderson, L. D.; Adlercreutz, O. Sex hormone regulation of in vitro immune response: estradiol enhances human B cell maturation via inhibition of suppressor T cells in pokeweed mitogen-stimulated cultures. *J. Exp. Med.* **1981**, *154*, 1935−1945.
13. Baral, E.; Kwok, S.; Berczi, I. The influence of estradiol and tamoxifen on the mixed lymphocyte reaction in rats. *Immunopharmacology* **1991**, *21*, 191−198.
14. Butcher, R. L.; Collins, W. E.; Fugo, N. W. Plasma concentration of LH, FSH, prolactin, progesterone and estradiol-17β throughout the 4-day estrus cycle of the rat. *Endocrinology* **1974**, *94*, 1704−1708.
15. Fasanmade, A. A.; Jusko, W. J. Optimizing whole blood lymphocyte proliferation in the rat. *J. Immunol. Methods* **1995**, *184*, 163−167.
16. Fasanmade, A. A.; Jusko, W. J. Pharmacokinetic/dynamic (PK/PD) model for methylprednisolone effects on whole blood T-cell deactivation and trafficking in the rat. *Pharm. Res.* **1995**, *12*, S-370.
17. Rose, J. Q.; Jusko, W. J. Corticosteroid analysis in biological fluids by high performance liquid chromatography. *J. Chromatogr.* **1979**, *162*, 273−280.
18. Boudinot, F. D.; Jusko, W. J. Fluid shifts and other factors affecting plasma protein binding of prednisolone by equilibrium dialysis. *J. Pharm. Sci.* **1984**, *73*, 774−780.
19. Boudinot, F. D.; Jusko, W. J. Dose-dependent pharmacokinetics of prednisolone in normal and adrenalectomized rats. *J. Pharmacokinet. Biopharm.* **1986**, *14*, 453−467.
20. Fisher, L. E.; Ludwig, E. A.; Jusko, W. J. Pharmacoimmunodynamics of methylprednisolone: trafficking of helper T-lymphocytes. *J. Pharmacokinet. Biopharm.* **1992**, *20*, 319−331.
21. Yeh, K. C.; Kwan, K. C. A comparison of numerical integrating algorithms by Trapezoidal, Lagrange, and Spline approximation. *J. Pharmacokinet. Biopharm.* **1978**, *6*, 69−98.
22. Gillis, S.; Crabtree, G. R.; Kendall, A. S. Glucocorticoid-induced inhibition of T cell growth factor production II. The effect on the in vivo generation of cytolytic cells. *J. Immunol.* **1979**, *123*, 1632−1638.
23. Bloemena, E.; Koopmans, R. P.; Weinreich, S.; Van Boxtel, C. J.; Schellekens, P. T. Pharmacodynamic modeling of lymphocytopenia and whole blood lymphocyte cultures in prednisolone-treated individuals. *Clin. Immunol. Immunopathol*. **1990**, *57*, 374−386.
24. Pearce, B. D.; Pariante, C. M.; Pisell, T. L.; Miller, A. H. Mechanism of action of the glucocorticoid receptor antagonist RU-40555. *Soc. Neur. Abs.* **1996**, *22*, 2013.
25. Milad, M. A.; Ludwig, E. A.; Anne, S.; Middleton, E., Jr. Pharmacodynamic model for joint exogenous and endogenous corticosteroid suppression of lymphocyte trafficking. *J. Pharmacokinet. Biopharm*. **1995**, *22*, 469−480.
26. Danel, L.; Souwein, G.; Monier, J. C.; Saez, S. Specific estrogen binding sites in human lymphoid cells and thymic cells. *J. Steroid Biochem*. **1983**, *18*, 559−563.
27. Ito, I.; Hayashi, T.; Yamada, K.; Kuzuya, M.; Naito, M.; Igushi, A. Physiological concentration of estradiol inhibits polymorphonuclear leukocyte chemotaxis via a receptor mediated system. *Life Sci*. **1995**, *56*, 2247−2253.
28. Jilma B.; Hilderbrandt, J.; Kapiotis, S.; Wagner, O. F.; Kitzweger, E.; Mullner, C.; Monitzer, B.; Krejcy, K.; Eichler, H. G. Effects of estradiol on circulating P-selectin. *J. Clin. Endocrinol. Metab.* **1996**, *81*, 2350−2355.
29. Ferron, G.M.; Jusko, W. J. Species- and gender-related differences in cyclosporine/prednisolone/sirolimus interactions in whole blood lymphocyte proliferation assays. *J. Pharmacol. Exp. Ther.* **1998**, *286*, 191−200.

Acknowledgments

This work was supported by NIH grant No. GM 24211 from the National Institute of General Medical Sciences. The authors thank Dr. A. Fasanmade for insightful comments on the manuscript.

JS9802695

In Vitro Regioselective Stability of β-1-*O*- and 2-*O*-Acyl Glucuronides of Naproxen and Their Covalent Binding to Human Serum Albumin

MASAHIRO IWAKI,* TARO OGISO, SHINAKO INAGAWA, AND KAZUAKI KAKEHI

Contribution from *Faculty of Pharmaceutical Sciences, Kinki University, 3-4-1 Kowakae, Higashi-Osaka, Osaka 577-8502, Japan.*

Received June 30, 1998. Final revised manuscript received September 15, 1998. Accepted for publication September 28, 1998.

Abstract □ β-1-*O*- (NAG) and 2-*O*-glucuronides (2-isomer) of (*S*)-naproxen (NA) were prepared to determine which positional isomer(s) of the acyl glucuronide of NA is responsible for forming covalent adducts with human serum albumin (HSA). Their comparative stability and covalent binding adduct formation with HSA were investigated at pH 7.4 and at 37 °C. NA and its acyl glucuronides were simultaneously determined by HPLC. Three positional isomers were formed successively after incubation of NAG in the buffer only. However, when NAG was incubated with HSA (30 mg/mL), isomers other than the 2-isomer were formed in little or negligible quantities. In HSA solution, NAG ($k_d = 2.08 \pm 0.08$ h^{-1}) was four times less stable than 2-isomer ($k_d = 0.51 \pm 0.02$ h^{-1}). NAG was degraded by hydrolysis ($k_{hyd} = 1.01 \pm 0.10$ h^{-1}) and isomerization ($k_{iso} = 1.07 \pm 0.07$ h^{-1}) to the same extent; however, hydrolysis was predominant for the 2-isomer ($k_d = 0.51 \pm 0.02$ h^{-1}). The incubation of both NAG and 2-isomer with HSA led to the formation of a covalent adduct; however, the adduct formation from the 2-isomer proceeded more slowly than that from NAG. The present results suggest that the covalent binding of NA to HSA via its acyl glucuronides proceeds through both transacylation (direct nucleophilic displacement) and glycation mechanisms; NAG rapidly forms an adduct that may be unstable, and the protein adduct from the 2-*O*-acyl glucuronide is as important for the covalent binding as those from the 1-*O*-acyl glucuronides.

Many acidic drugs with carboxylic acid functions are metabolized to reactive acyl glucuronides, which are susceptible to hydrolysis, isomerization (intramolecular acyl migration), and irreversible (covalent) binding to proteins under physiological conditions.[1,2] These reactions are considered to proceed through transacylations to the hydroxyl ion, to a different OH-group of the glucuronic acid moiety and to a nucleophilic group on the protein molecule, respectively, as suggested in an oxaprozin glucuronide study.[3] Formation of irreversible binding of carboxylic acid-containing drugs, such as nonsteroidal antiinflammatory drugs (NSAIDs), via their acyl glucuronide metabolites, is now well recognized and is a potential cause of hypersensitivity.[2,4,5] The exact mechanism underlying irreversible binding to proteins, however, has not yet been clarified due to the instability of acyl glucuronides. Two possible mechanisms can be considered: transacylation and glycation mechanisms.[6,7] Based on these proposed mechanisms, two different types of adduct can be formed: one is a transacylation adduct, where aglycon binds, via displacement of the glucuronic acid moiety from acyl glucuronide, directly to the protein NH_2, SH, or OH groups to yield an irreversibly bound adduct of aglycon linked to the protein by an amide, thioester, or ester linkage; the other is a rearrangement/glycation adduct, where acyl migration of the glucuronide has occurred, allowing the open chain form of the glucuronic acid moiety to react with an amino group to form an imine (Schiff's base). Subsequent Amadori rearrangement can then yield a more stable ketamine derivative.

The extent of covalent adduct formation via the acyl glucuronides varies from their parent NSAIDs. Benet et al.[6,8] showed that a striking correlation was observed between the extent of irreversible binding to protein and the degradation rate constant of acyl glucuronides. This strongly suggests that covalent adduct formation may reflect the reactivity of the corresponding acyl glucuronide. Although the degradation and covalent binding have been simultaneously investigated for some β-1-*O*-acyl glucuronides of NSAIDs,[9−11] it is not clear which ester(s) contributes to the formation of covalent binding to proteins. If the transacylation mechanism is predominant for the formation of irreversible binding to proteins, β-1-*O*-acyl glucuronide should relate mainly to the formation; if the Schiff's base mechanism is predominant, positional isomer(s) of β-1-*O*-glucuronide should contribute to the formation of covalent binding. In vitro stereoselective stability and binding properties of β-1-*O*-acyl glucuronides of (*S*)- and (*R*)-naproxen (NA) and in vivo stereoselective disposition of naproxen β-1-*O*-acyl glucuronide (NAG), using rats, have been reported by Benet et al.[8,12] However, the individual contributions of both hydrolysis and transacylation to the overall degradation of NAG, and the stability of positional isomers of NAG and their contribution to covalent protein binding, remain unclear.

In this study, we isolated the 2-*O*-acyl positional isomer (2-isomer) of (*S*)-NAG, in which the acyl-containing aglycon migrates from the glycosidic linkage at C-1 to a new ester linkage with a hydroxyl group at C-2 of the glucuronic acid moiety, and investigated its reactivity with human serum albumin (HSA) comparing it with that of (*S*)-NAG to test which possible mechanism is dominant for the formation of covalent binding. Our results show that (1) in the presence of HSA, NAG is subjected to both hydrolysis to NA and isomerization to the 2-isomer to the same extent, while further isomerization to the 3- and 4-*O*-acyl positional isomers is negligible, and (2) the covalent adduct of NA is formed mainly from 1-*O*-acyl- and 2-*O*-acyl glucuronides, not 3-*O*-acyl and 4-*O*-acyl glucuronides; the former may be unstable and act as an intermediate for HSA-catalyzed hydrolysis while the latter may be a stable adduct, which will be important for immunoreactive side-effects.

Experimental Section

Materials—(*S*)-NA (enantiomeric excess > 0.98), phenylmethylsulfonyl fluoride, and fatty acid free-HSA (fraction V) were purchased from Sigma Chemical Co. (St. Louis, MO). The molecular weight of HSA was assumed to be 69000.[13] Tryptophol [2-(3-

* Corresponding author. Tel: +81-6-721-2332 (ext. 3819). Fax: +81-6-730-1394. E-mail: masa_iwk@phar.kindai.ac.jp.

10.1021/js9802704 CCC: $18.00 *Published on Web 11/04/1998*

Table 1—List of the H-1 Chemical Shift of Naproxen Glucuronide and Their Related Compounds

compound	H-1	H-3	H-4	H-5	H-7	H-8	-CH_3	-CH-	-OCH_3	H-1′	H-2′	H-3′	H-4′	H-5′
(*S*)-NA	7.69 (m)	7.425 (dd, 2.0, 9.0)	7.69 (m)	7.13 (m)	7.13 (m)	7.69 (m)	1.583 (d, 6.7)	3.866 (q, 7.2)	3.905 (s)					
GlcA (α-isomer)										5.315 (d, 3.4)	3.63 (m)	3.784 (dd, 9.1)	3.63 (m)	4.060[a] (d, 9.9)
GlcA (β-isomer)										4.741 (d, 8.2)	3.343 (dd, 8.5)	3.578 (dd, 9.6)	3.63 (m)	4.383[a] (d, 10.0)
(*S*)-NAG	7.715 (d, 1.3)	7.425 (dd, 1.9, 8.0)	7.76 (bd, 8.9)	7.253 (d, 2.6)	7.140 (dd, 2.0, 9.0)	7.76 (bd, 8.9)	1.560 (d, 7.4)	4.036 (q, 6.9)	3.900 (s)	5.522 (d, 8.2)	3.432 (dd, 8.0, 9.4)	3.451 (dd, 9.4, 11.6)	3.520 (d, 8.8)	3.730 (d, 8.9)
S-2-Isomer	7.740 (d, 1.9)	7.456 (dd, 1.9, 8.5)	7.757 (d, 9.0)	7.246 (d, 2.4)	7.133 (dd, 2.4, 9.2)	7.757 (d, 9.0)	1.570 (d, 6.8)	4.003 (q, 7.0)	3.905 (s)	5.345 (d, 3.4)	4.652 (dd, 3.4, 9.9)	3.878 (d, 9.5)	3.556 (d, 9.6)	4.088 (d, 9.6)

[a] Signals are interchangeable.

indolyl)ethanol] was obtained from Tokyo Kasei Co. (Tokyo, Japan). Other chemicals used were of analytical or HPLC grade.

Preparation of Glucuronides of NA—(*S*)-NAG was extracted from human urine, which was collected following a 600 mg oral administration of (*S*)-NA (Naixan, Tanabe Pharmaceutical Co., Tokyo, Japan). Urine was collected over 24 h into a vessel containing phosphoric acid to stabilize the NAG by lowering the pH to 3−4. The urine was treated as described by Smith et al.,[14] with minor modifications. The extract was then separated by liquid-chromatography with a Cosmosil 75C18-OPN column (Nacalai Tesque Inc., Kyoto, Japan). NAG was eluted from the column with the stepwise gradient of acetonitrile/0.05 M acetic acid, 10:90, 20:80, and 30:70 (v/v). After the fractions containing NAG were evaporated with a rotary evaporator at 30 °C, the remaining aqueous solution was lyophilized. The 2-*O*-acyl positional isomer (2-isomer) of (*S*)-NAG was prepared after 6-h incubation of (*S*)-NAG in 0.1 M phosphate buffer at pH 7.4 and at 37 °C. 2-Isomer extracted from the solution was purified by Sephadex LH-20 using 50% methanol as an eluting solvent. The purity of the glucuronides obtained was determined by analytical HPLC and exhibited homogeneous properties (>98%) at a UV wavelength of 254 nm, with the remaining fraction represented by polar impurities that did not yield NA when treated with 1 M NaOH for 1 h. The structures of the glucuronides were confirmed by ^{1}H NMR and ^{1}H−^{1}H shift correlation NMR. NMR spectra were obtained on a JEOL GX-500 at 500 MHz using deuterated methanol, with tetramethylsilane as an external reference.

Analysis of NA and Its Glucuronides Using HPLC—Analyses of NA and NAGs were performed according to the method described by Bischer et al.[8] using a Shimadzu LC6AD solvent delivery system (Shimadzu Co., Kyoto, Japan), a Shimadzu RF-535 fluorescence monitor, a Shimadzu C−R4A Chromatopac integrator, and a Cosmosil 5C18-AR column (5 μm particle size, 4.6 × 250 mm, Nacalai Tesque Inc., Kyoto, Japan).

Stability Studies—NAG (35−40 μM) was incubated at 37 °C in 0.1 M sodium phosphate buffer (pH 7.4), and 50 μL aliquots were collected at timed intervals for analysis. Similar incubations using (*S*)-NAG (ca 35 and 135 μM) and *S*-2-isomer (ca. 30 μM) were also run in the presence of 30 mg/mL (435 μM) HSA. Aliquots were immediately mixed with 10 μL of 17% phosphoric acid and 50 μL of acetonitrile containing 4 μg/mL of tryptophol as an internal standard. The precipitated protein was removed by centrifugation, and a 3 μL-portion of the supernatant was analyzed by HPLC.

Determination of in Vitro Covalent Binding to HSA—NAG or 2-isomer was incubated at 37 °C for 30 h in 0.1 M phosphate buffer containing 30 mg/mL HSA, as described above. Aliquots (300 μL) of each reaction mixture were taken at different time points to assay the covalently bound drug. The binding yield for irreversible binding of the glucuronides was quantified using the method of Bischer et al.[8]

Data Analysis—The rate constants for hydrolysis and isomerization of the glucuronides were estimated using the model shown in Figure 1. The calculation for the kinetic parameters was performed with a nonlinear least-squares fitting program, WinNonlin (Scientific Consulting, Inc., Apex, NC).

Results

NMR Spectra of NAG and Its 2-*O*-Regioisomer—Identification of the purified acyl glucuronides was achieved using proton NMR analysis. Spectral features of NAG were similar to those reported by Wilson and Nicholson,[16] although confirmation of each proton signal was not performed. The results are summarized in Table 1, in which ^{1}H signals observed for GlcA in deuterated water and NA in deuterated methanol are also included as the reference compounds. A one-proton signal observed at 5.522 ppm as a doublet was easily assigned to H-1′ of the GlcA residue. The large coupling constant (J = 8.2 Hz) suggested that D-GlcA was bound to NA through a β-linkage. Due to lack of protons at the C-6 position, the proton signal (H-5′) attached to C-5 was also clearly observed as a doublet at a lower field (3.730 ppm). Starting from these characteristic signals of H-1′ and H-5′ of GlcA, all the proton signals were easily assigned by using the ^{1}H−^{1}H shift correlation spectra (data not shown).

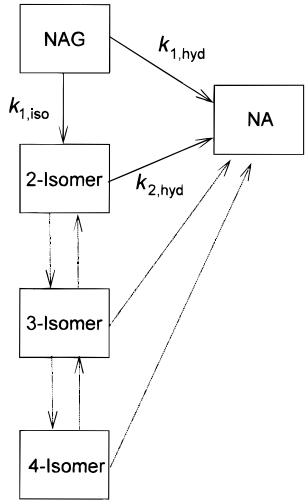

Figure 1—Kinetic model employed for the estimation of rate constants of hydrolysis and isomerization of NAG in HSA solution: $k_{1,hyd}$ and $k_{1,iso}$ are the first-order rate constants of hydrolysis to NA and isomerization to the 2-isomer from NAG, respectively. $k_{2,hyd}$ is the first-order rate constant of hydrolysis to NA from the 2-isomer.

The most abundant compound, 2-isomer, after 6-h incubation of NAG at pH 7.4 and at 37 °C was obtained in an almost pure state (>97% by HPLC). The ^{1}H−^{1}H shift correlation spectra of the 2-isomer is shown in Figure 2, which indicates the presence of a small amount of other isomers. Signals of GlcA moiety were assigned in Figure 2. The H-1′ signal of GlcA was observed at 5.345 ppm as a doublet with a small coupling constant (J = 3.4 Hz), indicating that the isomer was an α-isomer. The H-1′ signal of the corresponding β-isomer was not observed, probably due to overlap with a signal of HOD.[17] However, we were able to assign all of the signals from the ^{1}H−^{1}H shift correlation spectra. The H-2′ signal was observed at 4.652 ppm, which is 1.22 ppm lower than that of NAG. This

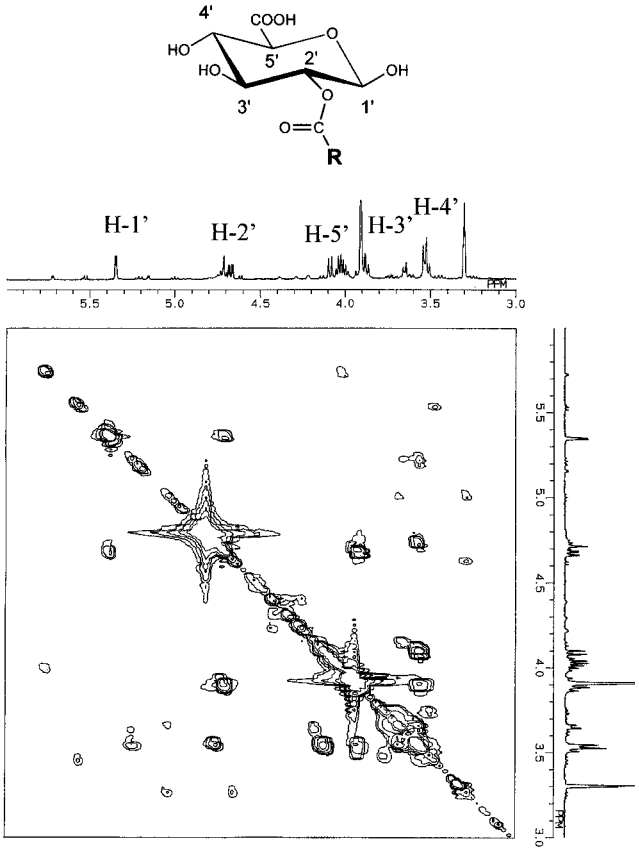

Figure 2—^{1}H–^{1}H shift correlation spectra of the *S*-2-isomer.

shift obviously indicated that the hydroxyl group attached at C-2 of GlcA was substituted with NA.

Degradation of NAG and Its Regioisomer—(*S*)-NAG was incubated at pH 7.4 and at 37 °C in 0.1 M phosphate buffer for 72 h. The HPLC chromatograms of the incubation medium of NAG are shown in Figure 3. The time dependence of the degradation of (*S*)-NAG and the appearance of its isomers and hydrolyzed NA is shown in Figure 4. As has been reported for several other 1-*O*-acyl glucuronides, (*S*)-NAG underwent nonenzymatic isomerization (acyl migration) and hydrolysis at pH 7.4. In HSA-free buffer, (*S*)-NAG was subjected predominantly to acyl migration resulting in a rapid appearance of the 2-*O*-acyl isomer (2-isomer) and then gradual formation of other isomers (at least three peaks detected by HPLC). Hydrolysis of 1-*O*-glucuronide and/or its isomers to NA was slow when compared with isomerization. After 72-h incubation, three regioisomers, including the 2-isomer, equilibrated to almost the same concentration; about half of the initial amount of NAG was hydrolyzed to NA. The apparent degradation rate constant ($k_{1,deg}$) for (*S*)-NAG was 0.343 ± 0.010 h^{-1} in HSA-free buffer.

The time dependence of degradation of the β-1-*O*- and 2-*O*-glucuronides of (*S*)-NA was investigated in the presence of 30 mg/mL of HSA. The results are shown in Figure 5, parts A and B, respectively. For comparison, the logarithmic plots for degradation of the glucuronides of NA in HSA solution are presented in Figure 6 as well as the result obtained in HSA-free buffer. As shown in Figure 6, the incubation of NAG with HSA at pH 7.4 resulted in a more rapid degradation when compared with the corresponding rate constant in HSA-free buffered solution, showing that HSA plays a major role in the degradation of NAG. In the presence of HSA, the contribution of hydrolysis to total degradation of NAG increased when compared with that in HSA-free buffer, as seen by the rapid

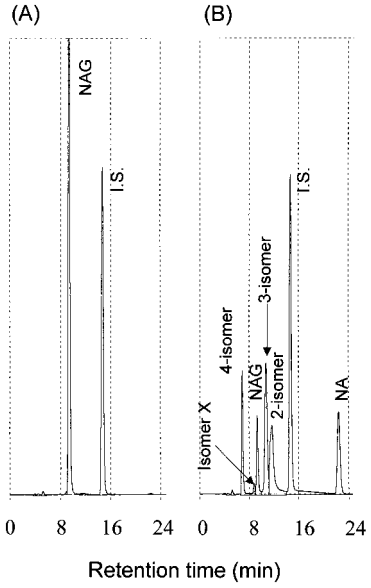

Figure 3—HPLC chromatograms of product mixtures from incubation of NAG after incubation in 0.1 M phosphate buffer (pH 7.4) at 37 °C for 30 s (A) and 6 h (B). Isomer X is an unidentified minor isomer which was hydrolyzed by 1 M NaOH but not β-glucuronidase. I.S. is tryptophol and was used as an internal standard. Retention times of NAG, 2-, 3-, 4-isomers, isomer X, and NA are 9.2, 11.6, 10.8, 7.0, 8.8 and 22.2 min, respectively.

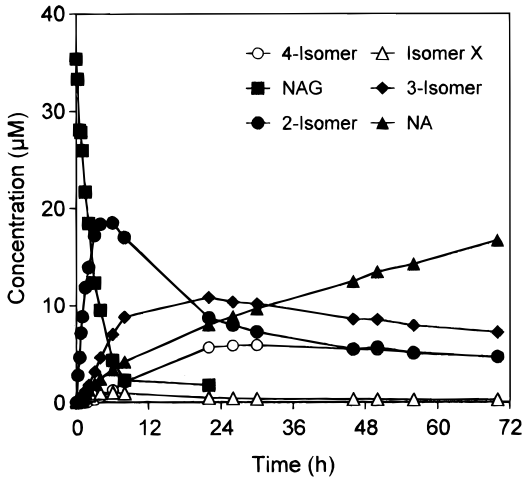

Figure 4—Time courses of rearrangement and hydrolysis of (*S*)-NAG in 0.1 M phosphate buffer (pH 7.4) at 37 °C. Only mean values (n = 3) are shown for the sake of visual clarity. Coefficients of variation for the data points ranged from 1 to 25%. Isomer X is an unidentified minor isomer which was hydrolyzed by 1 M NaOH but not β-glucuronidase.

appearance of NA. NAG was rapidly hydrolyzed to NA and isomerized to the 2-isomer, but no significant further acyl migration was observed in the buffer containing HSA (Figure 5A). This confirmed that further acyl migration of the 2-isomer to form the 3- and 4-isomers was negligible in the presence of HSA. The degradation rate constant ($k_{2,deg}$ = 0.514 ± 0.015 h^{-1}) was extremely slow for 2-isomer when compared with that for its β-1-*O*-acyl conjugates ($k_{1,deg}$ = 2.08 ± 0.08 h^{-1}), as shown in Figure 6. The 2-isomer was almost entirely hydrolyzed before further rearrangement, although only a small amount of the isomers was detected (Figure 5B). A higher initial concentration of (*S*)-NAG (mean 134 μM) resulted in a similar degradation pattern to the lower concentration experiments (data not shown).

The kinetic parameters of degradation reflecting both rearrangement and hydrolysis of each glucuronide were estimated based on the model shown in Figure 1. The

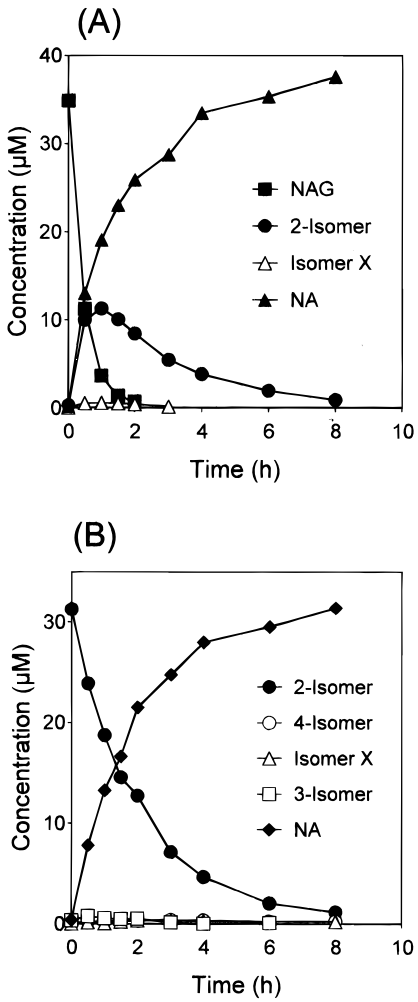

Figure 5—Time courses of rearrangement and hydrolysis of (*S*)-NAG (A) and *S*-2-Isomer (B) in 0.1 M phosphate buffer including 30 mg/mL of HSA (pH 7.4) at 37 °C. Only mean values ($n = 3$) are shown for the sake of visual clarity. Coefficients of variation for the data points ranged from 1 to 13%. Isomer X is an unidentified minor isomer which was hydrolyzed by 1 M NaOH but not β-glucuronidase.

parameters are shown in Table 2. The parameters were almost the same for the lower and higher initial concentrations, showing the linear kinetics in the degradation of β-1-glucuronides and its isomers under the conditions used. The contribution of hydrolysis of (*S*)-NAG to its total elimination was almost identical to the isomerization. The hydrolysis of the purified 2-isomer ($k_{2,hyd} = 0.514 \pm 0.015$ h^{-1}) occurred at approximately the same rate as for the 2-isomer formed in the (*S*)-NAG incubation experiment ($k_{2,hyd} = 0.446 \pm 0.043$ h^{-1}). The isomerization rate constant of (*S*)-NAG in the presence of HSA was also greater than its overall degradation rate constant in HSA-free solution, suggesting that HSA accelerated transacylation of (*S*)-NAG as well as its hydrolysis.

Irreversible Binding to HSA—The time dependence for irreversible binding formation of NA was investigated after incubation of NAG and 2-isomer at pH 7.4 and at 37 °C over 30 h. As shown in Figure 7, NAG rapidly produced a covalent adduct with HSA; the maximum yield was achieved after 1 h of incubation. The isomeric conjugate (2-isomer) also produced an irreversible binding adduct, although the maximum yield was achieved after ca. 8−10 h. The extent of irreversible binding yield from each of the glucuronides tested reached almost the same level, regardless of the differences in their stability. We calculated empirically the apparent first-order formation rate

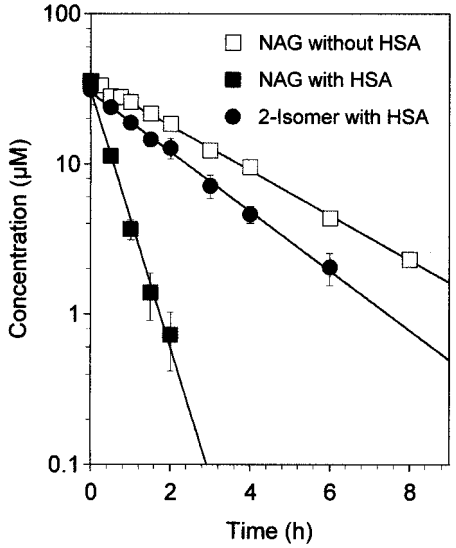

Figure 6—Logarithmic plots for degradation of NAG and 2-isomer without or with HSA. Each point and vertical bar represent the mean ± SD of three independent series. Error bar lines of NAG without HSA are within the outline of the symbol.

Table 2—Kinetic Parameters[a] for Hydrolysis and Isomerization of Glucuronides of NA in HSA Solution

	(*S*)-NAG		
parameter	lower (35 μM)[b]	higher (135 μM)	*S*-2-isomer (30 μM)
initial concentration (μM)	34.9 ± 0.3	134 ± 10	31.3 ± 6.4
$k_{1,hyd}$ (h^{-1})	1.01 ± 0.10	0.860 ± 0.199	
$k_{1,iso}$ (h^{-1})	1.07 ± 0.07	1.09 ± 0.02	
$k_{1,deg}$ (h^{-1})[c]	2.08 ± 0.08	2.05 ± 0.06	
$k_{2,hyd}$ (h^{-1})	0.446 ± 0.043	0.473 ± 0.012	0.514 ± 0.015

[a] Data are expressed as mean ± SD of three experiments. [b] Initial concentration. [c] $k_{1,deg} = k_{1,hyd} + k_{1,iso}$.

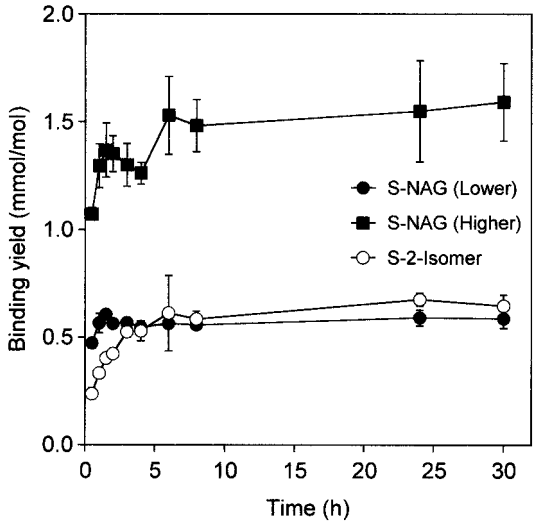

Figure 7—Time courses of irreversible binding of NA to HSA from acylglucuronides of NA in 0.1 M phosphate buffer (pH 7.4) at 37 °C. Each point and vertical bar represent the mean ± SD of three independent series.

constant of covalent binding using the following exponential equation: $BY = A(e^{-k_e t} - e^{-k_f t})$, where BY is the covalent binding yield, k_e and k_f being the apparent elimination and formation rate constants of the covalent adduct, respectively. The apparent formation rate constant ($k_f = 0.684 \pm 0.086$ h^{-1}) for irreversible binding from the

S-2-isomer was considerably smaller than that ($k_f = 3.55 \pm 0.39$ h^{-1}) from β-1-glucuronide, indicating that protein adduct formation from the 2-isomer occurred at a slower rate than that from NAG.

To test whether the extent of irreversible binding depended on the NAG concentration, a higher concentration of NAG was incubated under the same conditions. The increase in initial concentration of NAG to 134 μM from 35 μM for (*S*)-NAG produced a proportional increase in maximum adduct formation. However, interestingly, a secondary increase in adduct formation followed by a plateau level was observed. This phenomenon was not observed in the lower NAG concentration experiment.

Discussion

The stability and irreversible binding to protein of β-1-*O*-acyl glucuronides of many other carboxylic acid drugs have been reported. In this study, we compared the reactivities of a model acyl glucuronide, NAG, and its 2-*O*-positional isomer (2-isomer) in the presence of HSA, to gain an insight into the favored mechanism for irreversible binding. The present study clearly showed the regioselective differences of acyl glucuronides of NA in their stability and the formation of covalent binding to HSA.

To perform the study, we initially isolated a positional isomer (2-*O*-acyl derivative) of (*S*)-NAG and recorded its one-dimensional and two-dimensional proton NMR spectra when compared with (*S*)-NAG. The NMR data of some 1-*O*-acyl glucuronides[17,18] and the positional isomers of 1-*O*-acyl glucuronides[16,19,20] have been reported. In this study, all the proton signals of the positional isomer of NAG were confirmed. The regioisomers of β-1-acyl glucuronide can exist as α- and β-anomers. From a comparison with the NMR spectrum of GlcA, the 2-isomer exists mainly as α-anomer. The NMR spectrum of the mixture of isomers, which was obtained 6 h after incubation of (*S*)-NAG, was also analyzed (data not shown). Although other positional isomers (3- and 4-isomers), unfortunately, could not be obtained in a pure state, signals due to the H-1′ protons of the isomers were isolated from other ring protons of the GlcA residue. Hence, these signals in the anomeric region (around 5 ppm) may be good markers for determining the relative abundance of each isomer.

In the HSA-free buffer solution, at least four isomers of NAG were detected after incubation of NAG (Figure 3). Like diflunisal acyl glucuronide,[11,21] the 2-isomer was formed first followed by formation of other positional isomers. Finally, three abundant isomers reached an almost equivalent concentration. Since the 2-isomer was generally subject to further acyl migration,[11,21] these isomers, which appeared later, were probably 3- and 4-isomers. Acyl migration in the glucuronic acid residue is considered to proceed through an ortho ester-like intermediate.[22] Thus, we conclude that acyl migration occurs through the sequence β-1-glucuronide → 2-isomer, 2-isomer → 3-isomer and 3-isomer → 4-isomer. Therefore, the peaks of the isomers on the HPLC chromatogram are assigned here based on their order of appearance, as reported by Faed.[1] A similar result was reported for flufenamic acid and benoxaprofen.[18] The unidentified small amount of esters is probably their anomeric isomers.

In the buffer including HSA, the 2-isomer as well as NA was predominantly formed after incubation of NAG, and the formed 2-isomer was sequentially hydrolyzed before further rearrangement. Unlike the case in HSA-free buffer, the levels of regioisomers other than 2-isomer were near or below the detection limit. Additionally, the stability experiment of the purified 2-isomer (Figure 5B) in HSA solution showed that the rearrangement from the 2-isomer to the 3-isomer or 4-isomer was hardly observed. Although we cannot account clearly for the observation of no further acyl migration of the 2-isomer to form a 3- or 4-isomer in HSA solution, HSA may retard the formation of the ortho ester-like intermediate between the C-2 and C-3 positions of GlcA, resulting in predominant hydrolysis of the 2-isomer in its degradation pathway. In the case of β-1-acyl glucuronides of diflunisal,[11] tolmetin,[9] and salicylic acid,[26] it has been reported that HSA seems to stabilize the glucuronides.

On the basis of the calculation of the individual rate constants using the model shown in Figure 1, (*S*)-NAG was decomposed by hydrolysis and intramolecular rearrangement almost to the same extent (Table 2). Our preliminary experiment using *R*-NAG showed that *R*-NAG was preferentially isomerized (unpublished data), suggesting that the HSA-mediated hydrolysis was predominant for (*S*)-NAG. In many other acyl glucuronides,[3,23–25] including NAG,[8] the catalytic role of HSA in the degradation (hydrolysis and intramolecular rearrangement) has been reported. Our calculations of the individual rate constants of NAG in HSA solution clarified that both the hydrolysis and acyl transformation rate constants of NAG were greater than the overall degradation rate constant ($k_d = 0.343 \pm 0.010$ h^{-1}) in HSA-free solution, which should reflect acyl transformation and hydrolysis rate constants. This suggests the catalytic role of HSA not only in the hydrolysis of NAG but also in the isomerization of NAG. This may be due to the lowered free energy of ortho ester formation between the hydroxyl group at C-2 of the GlcA residue and the carboxyl group of NA by reversible binding to HSA, although we cannot explain exactly the enhancement effects of HSA on the isomerization of NAG.

We compared the stability and covalent binding formation of the 1-*O*- and 2-*O*-acyl glucuronides of (*S*)-NA. The 2-isomer, which was more stable than NAG, formed a protein adduct more slowly when compared with NAG. NAG, which forms the protein adduct most easily, achieved a maximum binding within 1 h of incubation. Although evidence exists for the two major mechanisms of covalent binding, it has not been clarified as to which of these is principally responsible.[28–32] If a covalent adduct is formed predominantly from the regioisomers of NAG, the formation rate of the adduct should be faster for the 2-isomer than for NAG, since no acyl migration time is required. Consequently, our results suggest that NAG can directly bind to the protein. Interestingly, the protein adduct formation temporarily declined, and a secondary increase in the formation was observed after incubation at a higher concentration of NAG. On the basis of comparison of the time dependence of degradation of NAG with the pattern of adduct formation, the covalent adduct in the earlier stage could be formed by β-1-acyl glucuronide, and the secondary peak of binding formation may arise from the formed 2-isomer. Additionally, in the case of NAG, 3-*O*- and 4-*O*-acyl glucuronides contribute little to the adduct formation under the conditions used. Finally, the covalent binding of NA to HSA seems to proceed via its acyl glucuronides in both the transacylation and glycation mechanisms. In the case of tolmetin, not only the β-1-isomer of tolmetin glucuronide but also other isomers can react with protein to give irreversibly linked products.[9] In this study, β-1-*O*- and 2-*O*-acyl glucuronides of NA clearly contribute the formation of protein adduct of NA. We quantified the regioselective difference in stability and covalent binding of acyl glucuronides of (*S*)-NA, although the stereoselective difference of *R*- and *S*-β-1-*O*-acyl glucuronides of NA in the protein adduct formation have been reported.[8]

Smith et al.[19] have reported that isomeric conjugates of zomepirac glucuronide occur via imine formation between

the free aldehyde of the open-chain GlcA and protein, followed by an Amadori rearrangement to the more stable adduct. The data suggest that although NAG can directly and rapidly form an adduct that is unstable and hydrolyzed almost as quickly as it is formed, intramolecular transacylation may well be a prerequisite for formation of a stable adduct. Presumably, the rapid complex formation of β-1-*O*-acyl glucuronide with HSA may assist in the HSA-mediated hydrolysis of NAG. We speculate that hydrolysis of acyl glucuronides may proceed through an acylated intermediate (acyl-HSA intermediate) such as an ester with a serin residue, thioester with a cysteine residue and/or acylimidazole with a histidine residue in HSA.[33] In the second step, the acyl-HSA intermediate is deacylated by hydrolysis. Thus, this transient adduct may be less important than the persistent one that arises from the 2-*O*-acyl glucuronide.

In conclusion, the present results indicate that covalent adduct formation proceeds via the proposed two kinds of mechanisms, transacylation and imine formation, according to the degree of formation of isomeric forms of the acyl glucuronide of NA.

References and Notes

1. Faed, E. M. Properties of acyl glucuronides: Implications for studies of the pharmacokinetics and metabolism of acidic drugs. *Drug Metab. Rev.* **1984**, *15*, 1213−1249.
2. Spahn-Langguth, H.; Benet, L. Z. Acyl glucuronides revisited: Is the glucuronidation process a toxification as well as a detoxification mechanism? *Drug Metab. Rev.* **1992**, *24*, 5−48.
3. Ruelius, H. W.; Kirkman, S. K.; Young, E. M.; Janssen, F. W. Reactions of oxaprozin-1-O-acyl glucuronide in solutions of human plasma and albumin. *Adv. Exp. Med. Biol.* **1986**, *197*, 431−441.
4. Park, B. K.; Kitteringham, N. R. Drug−protein conjugation and its immunological consequences. *Drug Metab. Rev.* **1990**, *22*, 87−144.
5. Worrall, S.; Dickinson, R. G. Rat serum albumin modified by diflunisal acyl glucuronide is immunogenic in rats. *Life Sci.* **1995**, *56*, 1921−1930.
6. Benet, L. Z.; Spahn-Langguth, H.; Iwakawa, S.; Volland, C.; Mizuma, T.; Mayer, S.; Mutschler, E.; Lin, E. T. Predictability of the covalent binding of acidic drugs in man. *Life Sci.* **1993**, *53*, 141−146.
7. Benet, L. Z.; Spahn, H. Acyl migration and covalent binding of drug glucuronides—potential toxicity mediators. In *Cellular and Molecular Aspects of Glucuronidation*, Proceedings of the Workshop, Montpellier France, 27−29 April 1988 Siest, G., Magdalou, J., Burchell, B., Eds.; John Libbey Eurotext Ltd.: Montrouge, France, 1988; Vol. 173, pp 261−269.
8. Bischer, A.; Zia-Amirhosseini, P.; Iwaki, M.; McDonagh, A. F.; Benet, L. Z. Stereoselective binding properties of naproxen glucuronide diastereomers to proteins. *J. Pharmacokinet. Biopharm.* **1995**, *23*, 379−395.
9. Munafo, A.; McDonagh, A. F., Smith, P. C.; Benet, L. Z. Irreversible binding of tolmetin glucuronic acid esters to albumin in vitro. *Pharm. Res.* **1990**, *7*, 21−27.
10. Grubb, N.; Weil, A.; Caldwell, J. Studies on the in vitro reactivity of clofibryl and fenofibryl glucuronides. Evidence for protein binding via a Schiff's base mechanism. *Biochem. Pharmacol.* **1993**, *46*, 357−364.
11. Williams, A. M.; Dickinson, R. G. Studies on the reactivity of acyl glucuronides—VI. Modulation of reversible and covalent interaction of diflunisal acyl glucuronide and its isomers with human plasma protein in vitro. *Biochem. Pharmacol.* **1994**, *47*, 457−467.
12. Ikeda, K.; Kurono, Y.; Ozeki, Y.; Yotsuyanagi, T. Effects of drug binding on esterase activity of human serum albumin. Dissociation constants of the complexes between the protein and drugs such as N-arylanthranilic acid, coumarin derivatives and prostaglandins. *Chem. Pharm. Bull.* **1979**, *27*, 7, 80−87.
13. Iwaki, M.; Bischer, A.; Nguyen, A. C., McDonagh, A. F.; Benet, L. Z. Stereoselective Disposition of Naproxen Glucuronide in the Rat. *Drug Metab. Dispos.* **1995**, *23*, 1099−1103.
14. Smith, P. C.; Song, W. Q.; Rodriguez, R. J. Covalent binding of etodolac acyl glucuronide to albumin in vitro. *Drug Metab. Dispos.* **1992**, *20*, 962−965.
15. Wilson, I. D.; Nicholson, J. K. Solid-phase extraction chromatography and NMR spectroscopy (SPEC NMR) for the rapid identification of drug metabolites in urine. *J. Pharm. Biomed. Anal.* **1988**, *6*, 151−165.
16. Sidelmann, U. G.; Gavaghan, C.; Carless, H. A. J.; Spraul, M.; Hofmann, M.; Lindon, J. C.; Wilson, I. D.; Nicholson, J. K. 750-MHz Directly coupled HPLC NMR: Application to the sequential characterization of the positional isomers and anomers of 2-, 3-, and 4-fluorobenzoic acid glucuronides in equilibrium mixtures. *Anal. Chem.* **1995**, *67*, 7, 4441−4445.
17. Bradow, G.; Kan, L.-S.; Fenselau, C. Studies of intramolecular rearrangement of acyl-linked glucuronides using salicylic acid, flufenamic acid, and (*S*)- and (*R*)-benoxaprofen and confirmation of isomerization in acyl-linked Δ9-11-carboxytetrahydrocannabinol glucuronide. *Chem. Res. Toxicol.* **1989**, *2*, 316−324.
18. McGurk, K. A.; Remmel, R. P.; Hosagrahara, V. P.; Tosh, D.; Burchell, B. Reactivity of mefenamic acid 1-*O*-acyl glucuronide with proteins in vitro and ex vivo. *Drug Metab. Dispos.* **1996**, *24*, 842−849.
19. Smith, P. C.; Benet, L. Z. Characterization of the isomeric esters of zomepirac glucuronide by proton NMR. *Drug Metab. Dispos.* **1986**, *14*, 503−505.
20. Sidelmann, U.; Hansen, S. H.; Gavaghan, C.; Nicholls, A. W.; Carless, H. A.; Lindon, J. C.; Wilson, I. D.; Nicholson, J. K. Development of a simple liquid chromatographic method for the separation of mixtures of positional isomers and anomers of synthetic 2-, 3- and 4-fluorobenzoic acid glucuronides formed via acyl migration reactions. *J Chromatogr. B Biomed. Appl.* **1996**, *685*, 113−122.
21. Dickinson, R. G.; King, A. R. Studies on the reactivity of acyl glucuronides- -II. Interaction of diflunisal acyl glucuronide and its isomers with human serum albumin in vitro. *Biochem. Pharmacol.* **1991**, *42*, 2301−2306.
22. Takiura, K.; Honda, S.; Endo, T.; Kakehi, K. Studies of oligosaccharides. IX. Synthesis of gentio-oligosaccharides by block condensation. *Chem. Pharm. Bull.* **1972**, *20*, 438−442.
23. Dubois, N.; Lapicque, F.; Maurice, M. H.; Pritchard, M., Gigleux, S. F.; Magdalou, J.; Abiteboul, M.; Siest, G.; Netter, P. In vitro irreversible binding of ketoprofen glucuronide to plasma proteins. *Drug Metab. Dispos.* **1993**, *21*, 617−623.
24. Hayball, P. J.; Nation, R. L.; Bochner, F. Stereoselective inteactions of ketoprofen glucuronides with hyman plasma protein and serum albumin. *Biochem. Pharmacol.* **1992**, *44*, 291−299.
25. Volland, C.; Sun, H.; Dammeyer, J.; Benet, L. Z. Stereoselective degradation of the fenoprofen acyl glucuronide enantiomers and irreversible binding to plasma protein. *Drug Metab. Dispos.* **1991**, *19*, 1080−1086.
26. Dickinson, R. G.; Baker, P. V.; King, A. R. Studies on the reactivity of acyl glucuronides—VII. Salicyl acyl glucuronide reactivity in vitro and covalent binding of salicylic acid to plasma protein of humans taking aspirin. *Biochem. Pharmacol.* **1994**, *47*, 469−476.
27. Rawn, J. Enzyme catalysis and enzyme kinetics. In *Biochemistry*; Neil Patterson Publishers: Burlington, NC, 1989; pp 158−165.
28. Smith, P. C.; McDonagh; A. F.; Benet, L. Z. Irreversible binding of zomepirac to plasma protein in vitro and in vivo. *J. Clin. Invest.* **1986**, *77*, 934−939.
29. Wells, D. S.; Janssen, F. W.; Ruelius, H. W. Interactions between oxaprozin glucuronide and human serum albumin. *Xenobiotica* **1987**, *17*, 1437−1449.
30. van Breemen, R. B.; Fenselau, C. Acylation of albumin by 1-O-acyl glucuronides. *Drug Metab. Dispos.* **1985**, *13*, 318−320.
31. Ding, A.; Ojingwa, J. C.; McDonagh, A. F.; Burlingame, A. L.; Benet, L. Z. Evidence for covalent binding of acyl glucuronides to serum albumin via an imine mechanism as revealed by tandem mass spectrometry. *Proc. Natl. Acad. Sci. U.S.A.* **1993**, *90*, 3797−3801.
32. Smith, P. C.; Liu, J. H. Covalent binding of suprofen acyl glucuronide to albumin in vitro. *Xenobiotica* **1993**, *23*, 337−348.
33. Kuchel, P.; Ralston, G. *Theory and problems of biochemistry* (Japanese edition); Ohmu Publisher: Tokyo, 1988; p 22.

Acknowledgments

We thank Dr Leslie Z. Benet for useful comments on this work and Ms Toshiye Minematsu for the NMR analysis.

JS9802704

Conformational Stability of Lyophilized PEGylated Proteins in a Phase-Separating System

MARTIN C. HELLER,[†] JOHN F. CARPENTER,[‡] AND THEODORE W. RANDOLPH*,[†]

Contribution from *Department of Chemical Engineering, University of Colorado at Boulder, Boulder, Colorado 80309-0424 and Department of Pharmaceutical Sciences, School of Pharmacy, University of Colorado Health Sciences Center, Denver, Colorado 80262.*

Received June 19, 1998. Final revised manuscript received September 17, 1998.
Accepted for publication September 21, 1998.

Abstract □ PEGylation of proteins is of great interest to the pharmaceutical industry as covalent attachment of poly(ethylene glycol) (PEG) molecules can increase protein sera half-lives and reduce antigenicity. Not surprisingly, PEGylation significantly alters the surface characteristics of a protein, and consequently, its conformational stability during freezing and drying. Freeze concentration-induced phase separation between excipients has been previously shown to cause degradation of the secondary structure in lyophilized hemoglobin. In this report we show how PEGylation of two proteins, hemoglobin- and brain-derived neurotrophic factor (BDNF), influences partitioning and protein secondary structure as determined by FTIR spectroscopy in a system prone to freezing-induced phase separation. PEGylation of hemoglobin reduces the loss of structure induced by lyophilization in a PEG/dextran system that phase separates during freezing, perhaps due to altered partitioning. The partition coefficient for native hemoglobin favors the dextran-rich phase (PEG/dextran partition coefficient = 0.3), while PEGylated hemoglobin favors the PEG phase (partition coefficient = 3.1). In addition, we demonstrate that PEGylation alters hemoglobin's stability during lyophilization in the absence of other excipients. In contrast, because native BDNF already partitions into the PEG-rich phase, PEGylation of BDNF has a less dramatic effect on both partition coefficients and conformational stability during lyophilization. This is the first report on the effects of PEGylation on protein structural stability during lyophilization and points out the need to consider modification of formulations in response to changing protein surface characteristics.

Introduction

The covalent attachment of poly(ethylene glycol) (PEG) to enzymes and proteins,[1] a process known as PEGylation, has received recent increased attention. PEGylation has created enzyme derivatives with improved solubility in organic solutes, making the process of interest to the field of nonaqueous enzymology.[2,3] Attachment to PEG has been used as a method of immobilizing enzymes.[4] Of greater interest to the pharmaceutical biotechnology arena, PEGylated proteins have demonstrated dramatically increased plasma half-lives and very low immunogenicity.[5] It is thought that PEGylation provides a biocompatible "protective coating" to proteins, reducing immune response. It also increases the effective molecular weight of the protein and thus reduces the rate of clearance through the kidney. These are both extremely attractive properties for proteins administered as therapeutic agents since clearance of such drugs from the bloodstream is often too rapid for a therapeutic response. In addition, PEGylated proteins generally remain biologically active. Reports of numerous PEGylated proteins exist in the literature, including superoxide dismutase,[6] horse cytochrome *c*,[7] hemoglobin,[8−10] recombinant human granulocyte-colony stimulating factor,[11] human growth hormone and growth hormone antagonist,[12] and brain-derived neurotrophic factor,[13] just to name a few. With the original patent covering PEGylation[1] expiring, many biotechnology companies are now considering PEGylated versions of protein products.

PEGylation affects a protein's immunogenicity and circulation half-life in part by altering the protein's surface characteristics. Clearly, PEGylation should also significantly alter a protein's partitioning in a PEG/dextran two-phase system. Similarly, we can expect that PEGylation may change the protein's storage stability and behavior in a given formulation. Considering PEG's incompatibility with a number of polymers and salts in aqueous solutions, phase separation of a PEGylated protein from other formulation components may be a potential instability pathway in lyophilization formulations.

Partitioning of proteins in an aqueous two-phase system depends on specific surface features of the protein, along with system conditions such as total composition, pH, ionic strength, etc. Numerous approaches to altering the partitioning behavior of a protein have been considered for improving selectivity of two-phase separation methods. These include immunoaffinity partitioning[14] and metal affinity partitioning,[15,16] to name a few. Metal affinity partitioning involves partially chelating a transition metal ion to a linear polymer such as poly(ethylene glycol) (PEG). Transition metals demonstrate strong affinity for electron-rich amino acid residues such as histidine and cysteine. Thus, the use of PEG-bound metal chelates in PEG/dextran two-phase systems can dramatically increase the partitioning of proteins with accessible surface histidines or cysteines to the PEG phase.

In this paper, we investigate the stability of PEGylated hemoglobin and BDNF lyophilized in PEG/dextran formulations. By altering the partitioning of protein in a PEG/dextran two-phase system through PEGylation, we provide additional information on the mechanisms responsible for protein damage during lyophilization. To our knowledge, this is also the first report on the conformational stability of PEGylated therapeutic proteins during freeze-drying and as such offers an introduction to possible concerns in formulating such products. We also consider a noncovalent attachment of PEG to hemoglobin via chelation using a PEG-copper complex.

* Corresponding author. Telephone: (303) 492-4776. Fax: (303) 492-4341. E-mail: randolph@pressure.colorado.edu.
[†] Department of Chemical Engineering.
[‡] Department of Pharmaceutical Sciences.

10.1021/js980257j CCC: $18.00
Published on Web 11/17/1998

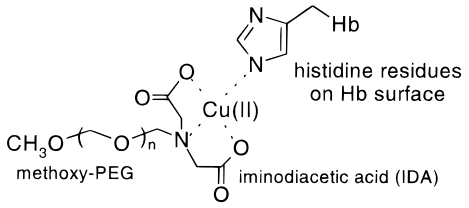

Figure 1—Structural representation of Cu(II)IDA-PEG. Copper partially coordinated with the IDA-modified PEG has a strong affinity for electron-rich surface amino acids. Adapted from Guinn.[16]

Materials and Methods

Materials—Recombinant human hemoglobin (Hb) was provided by Somatogen, Inc. (Boulder, CO). Poly(ethylene glycol) 3350 (PEG), average molecular weight 3350, was obtained from Sigma Chemical Co. and dextran T500, weight average molecular weight 519000, was obtained from Pharmacia Biotech. Polymers were dissolved in a stock solution at 20% (w/w) and combined to obtain solutions of 4% (w/w) PEG, 4% (w/w) dextran, and 10 mg/mL Hb (or PEG-Hb) with 5 mM potasssium phosphate buffered at pH 7.4 and 150 mM NaCl (or KCl). Cu(II)IDA-PEG 5000, a copper-chelated PEG derivative (average PEG molecular weight = 5000), was synthesized by Martin Guinn (lot no. MRG 5-105).[16] A structural representation of Cu(II)IDA-PEG is shown in Figure 1. For closer comparison to the 5000 molecular weight copper-chelated PEG, hemoglobin was also lyophilized in a solution of PEG 4600 (Aldrich) and dextran T500.

Human brain-derived neurotrophic factor (BDNF) and PEG-BDNF were supplied by AMGEN, Inc. (Thousand Oaks, CA). BDNF is a noncovalent homodimer with an approximate molecular weight of 27.8 kDa.[17] PEG-BDNF contains a PEG with average molecular weight of 20 kDa covalently attached to the N-terminal methionine of each BDNF monomer unit.[18] BDNF was received in 10 mM sodium phosphate/150 mM NaCl (pH 7.0). PEG-BDNF was received in 10 mM histidine/150 mM NaCl (pH 7.5), and transferred by dialysis to 10 mM sodium phosphate/150 mM NaCl (pH 7.0). All BDNF lyophilization solutions were made in this same sodium phosphate/NaCl buffer at a protein concentration of 1 mg/mL. It should be noted that, as defined in this report, mass concentrations of PEGylated proteins represent only the protein portion of the molecule. For example, a 1 mg/mL solution of BDNF and PEG-BDNF contains the same amount of protein.

PEGylation of Hemoglobin—Hb was PEGylated using a PEG–vinyl sulfone (molecular weight 5000)-activated PEG from Shearwater Polymers, Inc. (Huntsville, AL). At high pH (9–9.5), PEG–vinyl sulfone (PEG-VS) will react slowly with lysine groups:[19]

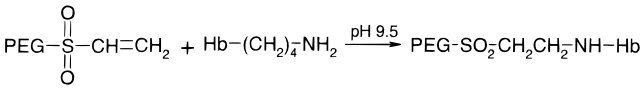

While more selective coupling with sulfhydryl groups occurs at lower pH (7–9), reaction with hemoglobin at lower pH was unsuccessful.

Hemoglobin in 5 mM potassium phosphate/150 mM NaCl was adjusted to pH 9.5 by careful addition of NaOH solution and a 2.4× molar excess of dry PEG-VS was dissolved in the solution. The reaction mixture was allowed to sit at 4 °C overnight. Half of the solution was dialyzed against 5 mM potassium phosphate/150 mM NaCl (pH 7.4) while the other half was dialyzed against 5 mM potassium phosphate/150 mM KCl (pH 7.4). Confirmation of PEGylation and fractionation of PEGylated and non-PEGylated hemoglobin was performed by FPLC size exclusion chromatography on a HiPrep 16/60 column containing Sephacryl S-200 resin (Pharmacia) with an elution buffer of 5 mM phosphate (pH 7.4)/150 mM NaCl at a flow rate of 0.7 mL/min. UV absorbance at 280 nm was used for detection. Hb and PEG-Hb concentrations were measured with a BCA total protein assay (Pierce).

Two-Phase Partitioning—The partitioning coefficient of each protein (concentration in the PEG phase divided by concentration in the dextran phase) was measured in a system of 7% PEG 3350/7% dextran/1 mg/mL protein. This system separates at room temperature. Samples were allowed to come to equilibrium over several hours, and the two phases were physically separated. Protein concentration in each phase was determined by UV absorbance at 280 nm for BDNF and PEG-BDNF and with a BCA total protein assay for Hb and PEG-Hb.

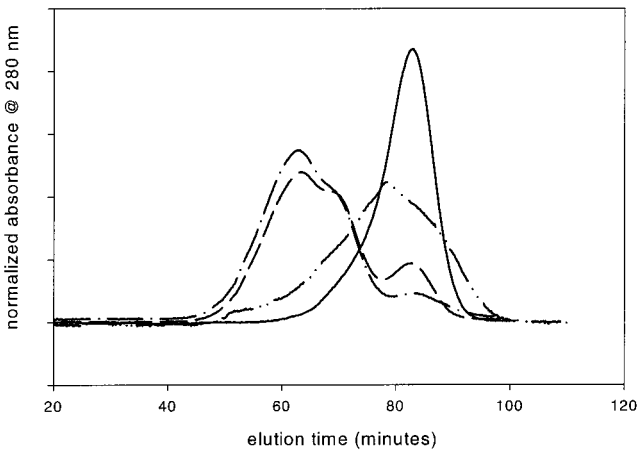

Figure 2—Normalized size exclusion chromatogram demonstrating PEGylation of hemoglobin. Solid trace: Hb; dashed trace: after PEGylation reaction; dash–dot trace: PEG-rich phase of 7% PEG/7% dextran/10 mg/mL PEG-Hb; dash–dot–dot trace: dextran-rich phase of 7% PEG/7% dextran/10 mg/mL PEG-Hb. All curves are normalized to the total area under peaks.

Lyophilization—Lyophilization was conducted in an FTS Systems microprocessor controlled tray dryer (Dura-Stop, Dura-Dry-MP). Samples were freeze-dried by the method previously described.[20] In short, samples for annealing experiments were quench frozen in a dry ice/acetone slurry and placed on the freeze-dryer shelf precooled to −7 °C. Samples were allowed to anneal at −7 °C for different lengths of time prior to drying. At "time zero", the samples were cooled to below −30 °C and held for 120 min. Primary drying proceeded at 60 mT vacuum with the shelf temperature set at −20 °C for 1000 min. Secondary drying consisted of 120 min at 0, 10, and 25 °C, while maintaining vacuum of 60 mT.

Infrared Spectroscopy—Protein secondary structure was monitored using Fourier transform infrared spectroscopy (FTIR). Spectral collection and processing were as previously described.[20,21]

IR Curve Fitting—Curve fitting of the second derivative IR spectra was used to determine the relative secondary structural content of BDNF in solution.[22,23] Normalized second derivative spectra were inverted by multiplying by −1 and then fitted with Gaussian band profiles using the Grams/386 (Galactic Enterprises) fitting routine. Component bands were assigned to secondary structural elements based on wavenumber according to the method of Dong and Caughey.[24]

Scanning Electron Microscopy—Lyophilized cake structures were examined using an ISI–SX-30 scanning electron microscope operating at an acceleration voltage of 30 kV. Dried samples were adhered with a graphite adhesive to SEM stubs and gold sputter coated.

Results and Discussion

Characterization of PEGylated rHb—PEGylation obviously increases the size and molecular weight of a protein; thus, size exclusion chromatography (SEC) can be used to evaluate the PEGylation reaction and offer some information on the extent of PEGylation. Figure 2 shows representative chromatograms of Hb before and after PEGylation. Clearly, PEGylation causes a gross shift to reduced elution times (and hence larger molecular weights), though it is also apparent that the entire Hb population was not PEGylated. Fractionation of PEG-Hb from non-PEGylated Hb was made between peaks at an elution time of approximately 75 min in Figure 2. A minimum of two peaks is identifiable in the PEGylated population, indicating that different degrees of PEGylation exist in the sample. Since PEG molecules (and therefore PEGylated

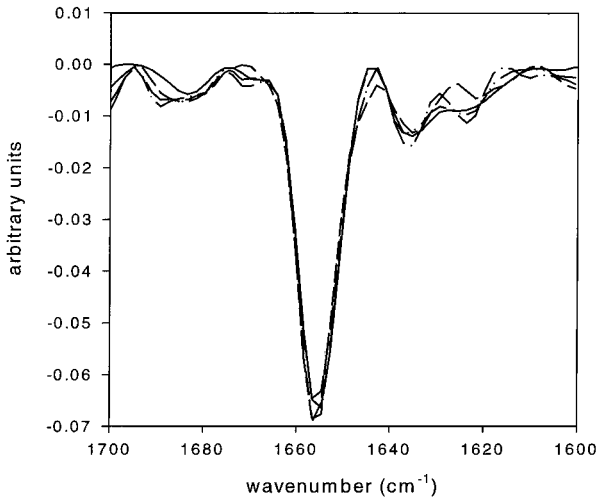

Figure 3—Second derivative IR spectra of hemoglobin controls in solution. Solid trace: Hb in buffer (pH 7.4); dashed trace: Hb in top phase of a 7% Cu(II)IDA-PEG/7% dextran system; dash–dot trace: Hb at PEGylation reaction conditions (pH 9.5); dash–dot–dot trace: PEG-Hb in buffer (pH 7.4).

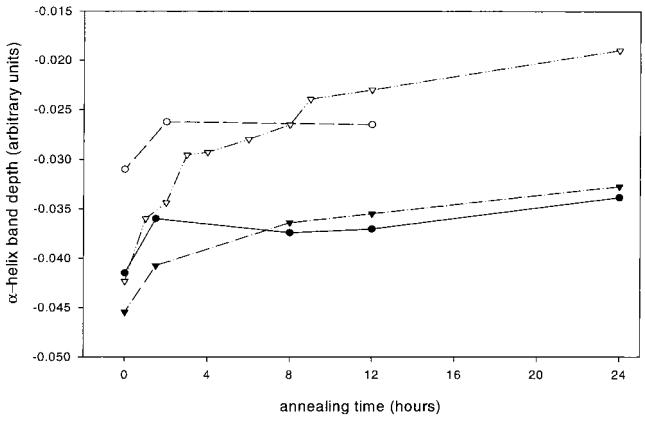

Figure 4—Effect of PEGylation on hemoglobin structure annealed in the PEG/dextran system. Depth of the α-helix band (ca. 1656 cm^{-1}) from second derivative infrared spectra of lyophilized Hb (open symbols) and PEG-Hb (filled symbols) as a function of sample annealing time at −7 °C prior to drying. Circles are for 10 mg/mL protein in 5 mM potassium phosphate/150 mM NaCl (pH 7.4). Triangles also contained 4% PEG 3350/4% dextran T500. Open triangles presented previously.[20,21]

proteins) "act" much larger in gel chromatography (as well as gel electrophoresis) than do proteins used for column calibration, it is difficult to assign quantitative information to the elution peaks corresponding to PEGylated proteins in Figure 2. However, based on the initial PEG-VS:HB stoichiometry and on SEC performed at different reaction times, the three main peaks observed by SEC can be tentatively assigned to un-PEGylated-, mono-PEGylated-, and di-PEGylated-Hb. PEGylation has no effect on the secondary structure of hemoglobin as seen by FTIR spectroscopy (Figure 3). However, partitioning of hemoglobin between the two phases of a system of 7% PEG 3350 and 7% dextran T500 is drastically effected by PEGylation. Hemoglobin partitions preferentially to the dextran phase with a partition coefficient (PEG phase/dextran phase) of about 0.3. PEGylated hemoglobin on the other hand has a partition coefficient of 3.1. In other words, while only about 30% of Hb is in the PEG phase, over 80% of the PEG-Hb sample is in the PEG phase.

Lyophilization of PEG-Hb—The formation of pure ice during freezing results in concentration of solutes. In protein formulations containing excipients, such concentration can cause solute−solute phase separation to become thermodynamically favored, albeit often with slow kinetics.[20,21,25] Annealing frozen solutions at subzero temperatures allows phase separations to proceed toward equilibrium and serves to magnify effects of such separations on protein stability. Annealing experiments that mimic those in the previous report[20] were conducted on PEG-Hb samples. In brief, samples were quench frozen and allowed to anneal for various lengths of time at −7 °C before freeze drying. After freeze-drying, hemoglobin structure in the dried solid was analyzed by IR spectroscopy as a function of annealing time. Figure 4 shows the depth of the α-helix band (ca. 1656 cm^{-1}) from second derivative IR spectra as a function of annealing time. The depth of the α-helix band is the primary indicator of "nativelike" structure in these hemoglobin studies (more negative values correspond to greater retention of nativelike structure; native hemoglobin has a α-helix band depth of ∼ −0.07 as can be seen in Figure 3). The first thing apparent in the data in Figure 4 is that PEG-Hb lyophilized in buffer alone retains more α-helix in the dried state than does Hb. This raises important questions regarding the possibility of covalently attached PEG acting as a stabilizer during freeze-drying. PEG is known to be an excellent protein stabilizer in frozen solutions.[26] However, studies in the literature have demonstrated the failure of PEG as a desiccoprotectant.[27] This is attributed to the tendency of PEG to crystallize during freeze-drying, making it unavailable to hydrogen bond with the protein[27] or form a "single phase glass".[25,28] It is likely, however, that covalent attachment to a protein surface will prevent, or at least greatly decrease, PEG crystallization. Whether one or two PEG molecules per protein would be sufficient to replace hydrogen bonds or form a protective glass is unknown.

Hb and PEG-Hb freeze-dried in 4% PEG/4% dextran also differ significantly in their native structural retention as seen in Figure 4. PEGylation appears to reduce the loss of nativelike structure with annealing. A number of explanations are possible. It may be that the added protection provided by PEGylation is also effective in reducing the damage in the phase-separating system. PEGylation also alters the surface properties of the protein, perhaps making it less active at the liquid−liquid interface created by the PEG/dextran phase separation. Since concentration and denaturation at this interface is a probable mechanism of damage,[20] removal of the protein from the interface by PEGylation could prevent this damage. Finally, if the loss of native structure of Hb with annealing is due to partitioning away from a stabilizer (PEG in this case), then reversing this partitioning would dampen the effect. Although dextran can form protective glasses and potentially replace some hydrogen bonds, its bulky size could make it less effective than PEG as a dessicoprotectant. This explanation seems unlikely, however, since Hb lyophilized in either 8% PEG or 8% dextran shows essentially equivalent levels of structural retention (data not shown).

PEG-Hb was also lyophilized in a 4% PEG/4% dextran solution with NaCl replaced with KCl. The results with PEG-Hb are the same as those seen with Hb: essentially no change in α-helix content occurs with annealing (Figure 5). We have previously shown[20] that switching to KCl prevents the phase separation from occurring. This is thought to be due to kinetic prevention of the PEG/dextran phase separation by the formation of a strong glass. Figure 5 also contains an anomalous result where an abrupt loss in structure occurs after 8 h of annealing. It is thought that this is the result of the thermodynamically unstable yet kinetically hindered phase separation relaxing sporadically. A corresponding radical change in cake structure is also seen in scanning electron microscopy images (not shown). The initiation of this relaxation is unknown. This

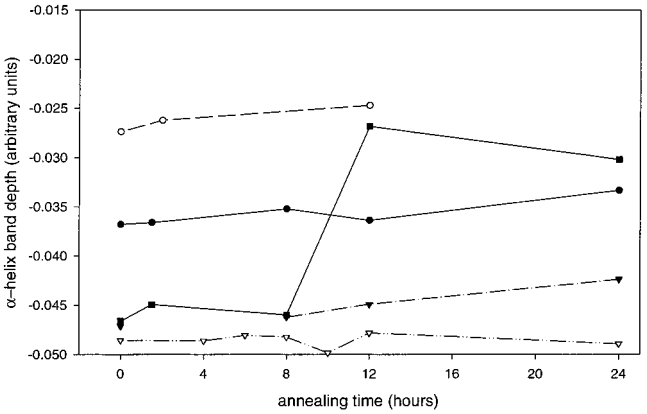

Figure 5—PEG-Hb lyophilized in KCl buffer. Depth of the α-helix band (ca. 1656 cm^{-1}) from second derivative infrared spectra of lyophilized Hb (open symbols) and PEG-Hb (filled symbols). Circles are for 10 mg/mL protein in 5 mM potassium phosphate/150 mM KCl (pH 7.4). Triangles also contain 4% PEG 3350/4% dextran T500. The square data points represent an anomalous example of a "relaxation" of the kinetically hindered phase separation (solutions same a triangles). Annealing is at –7 °C prior to drying. Open triangles presented previously.[20,21]

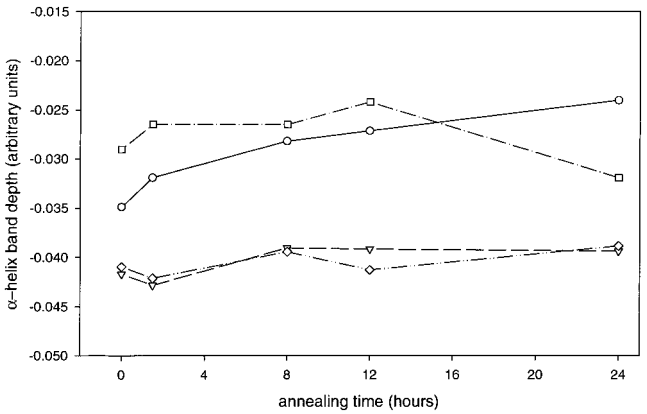

Figure 6—Hb lyophilized in Cu(II)IDA-PEG solutions. Circles, Hb in 3% PEG 4600/3% dextran T500; squares, Hb in 3% Cu(II)IDA-PEG; triangles, Hb in 3% Cu(II)IDA-PEG/3% dextran. All solutions contain 5 mM potassium phosphate/150 mM NaCl (pH 7.4).

is the only observed example of such sporadic behavior in kinetically hindered samples.

Lyophilization of Hb with Cu(II)IDA-PEG—Solutions of 4% Cu(II)IDA-PEG and 4% dextran T500 containing 10 mg/mL Hb form two phases at 0 °C. Thus, polymer concentrations were reduced to 3% Cu(II)IDA-PEG/3% dextran in freeze-drying studies to ensure single-phase solutions prior to freezing. Hb in a solution of 7% Cu(II)-IDA-PEG/7% dextran is entirely (within limits of detection) in the PEG-rich phase. While considerable copper-catalyzed oxidation of hemoglobin occurs in solutions of Cu-(II)IDA-PEG,[16] this is not a concern for the present study. Hb secondary structure is not affected by the presence of even high concentrations of Cu(II)IDA-PEG, as seen in Figure 3.

IR spectroscopy of Hb lyophilized in Cu(II)IDA-PEG-containing samples is summarized in Figure 6. There is not a significant change in α-helix content with annealing time in the system of 3% Cu(II)IDA-PEG/3% dextran. As in the case with PEG-Hb, the use of a metal affinity partitioning agent greatly increases the partitioning of hemoglobin to the PEG phase. The increased partitioning is even greater with the use of the metal-chelating ligand: essentially all of the hemoglobin is moved to the PEG phase at equilibrium. This increase in partitioning is larger than that caused by the covalent attachment of PEG-VS. This

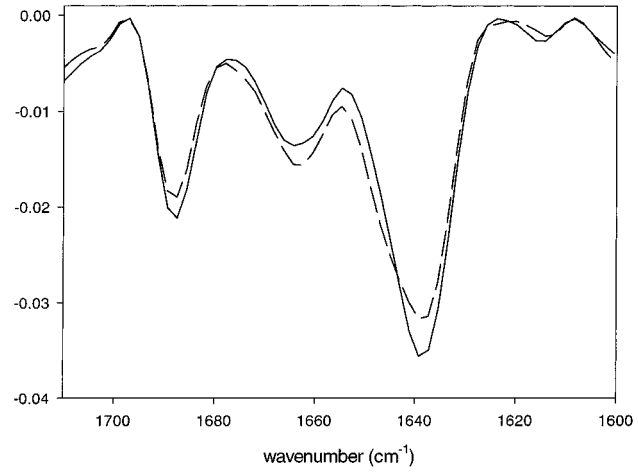

Figure 7—Amide I region of second derivative IR spectra of BDNF (solid trace) and PEG-BDNF (dashed trace) in solution (10 mM sodium phosphate (pH 7.0)/150 mM NaCl). Protein concentrations were >20 mg/mL.

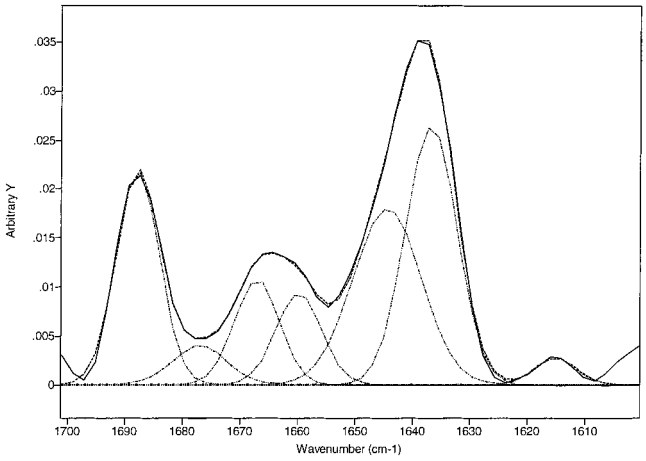

Figure 8—Curve-fitted inverted second derivative spectrum of BDNF in solution. Areas of fitted peaks are summarized in Table 1.

can be understood in terms of relative PEG attachment densities. Hb has 16 sites available for PEG attachment via Cu(II)IDA-PEG.[16] Although it is unlikely for steric reasons that all of the potential sites could ever be filled, there is almost certainly more PEG attached to Hb via Cu-(II)IDA-PEG chelation than by covalent attachment with PEG-VS. By increasing the affinity of the protein for the PEG phase, we are depleting the dextran phase of hemoglobin, but there is likely also a decreased concentration of protein at the liquid–liquid interface, due to the large difference in protein affinity of the two phases.

BDNF Solution Structure—FTIR spectroscopy of BDNF and PEG-BDNF in solution was first performed to gain information on the secondary structural content. Figure 7 shows the amide I region of second derivative IR spectra of BDNF and PEG-BDNF in 10 mM sodium phosphate/ 150 mM NaCl (pH 7.0). Quantitative analysis of BDNF secondary structure was obtained by curve fitting the second derivative spectra as seen in the example in Figure 8 and summarized in Table 1. This quantification is in fair agreement with reported structural assignments for BDNF (47% β-structure, 31% random coil, 22% reverse turns, no α-helix).[29] Table 1 shows that there is a slight increase in bands assignable to random structure and turns, and decreases in β sheet bands for the PEGylated protein, possibly indicating a less ordered structure.

Lyophilization of BDNF and PEG-BDNF—BDNF and PEG-BDNF were freeze-dried in the presence of 4%

Table 1—Band Positions, Relative Intensities, and Secondary Structural Assignment for the Amide I Region of Infrared Spectra of BDNF and PEG-BDNF

frequency (cm^{-1})	assignment	% area	
		BDNF	PEG-BDNF
1688	β-sheet	20.7	17.5
1677	turn	4.4	3.1
1667	turn	10.6	10.7
1660	turn	9.3	10.3
1644	random	26.9	35.1
1637	β-sheet	29.9	23.3

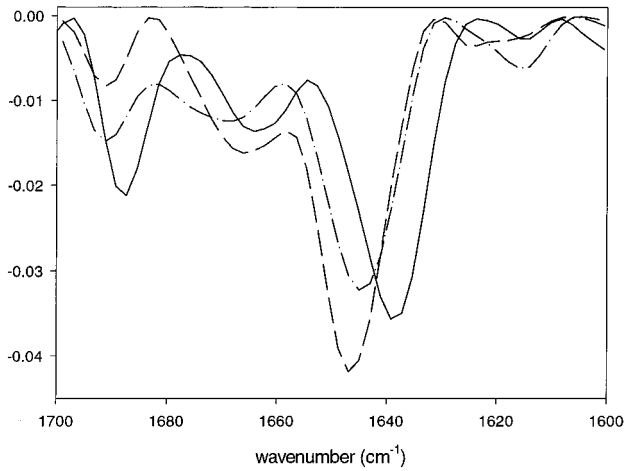

Figure 9—Second derivative IR spectra of BDNF (dashed trace) and PEG-BDNF (dash–dot trace) in the dried state, freeze-dried from buffer alone. The BDNF solution spectrum (solid trace) is shown for reference.

PEG/4% dextran, as well as in solutions containing only PEG or only dextran. Figure 9 shows the IR spectral changes seen with both BDNF and PEG-BDNF freeze-dried from buffer alone. In the dried state spectra, there is a considerable shift to higher wavenumbers for all of the structural bands. Frequency shifts in structural bands upon dehydration have been reported previously for β-sheet proteins.[23,30,31] Yet, it remains unresolved whether such a shift in band frequency reflects gross conformational changes in the protein upon dehydration or is simply due to a change in stretching vibration (and thus IR absorbance) in secondary structures due to the removal of hydrogen-bonded water. Allison et al.[30] report that shifts seen in the β-sheet bands upon lyophilization of chymotrypsinogen return to the frequencies of the solution state spectrum (before freeze drying) when the protein is freeze-dried in the presence of sucrose. This could be due to hydrogen bond replacement by the sugars.[32] In our studies with BDNF, all dried state spectra, regardless of excipient, have demonstrated the same shifting in resolved band frequencies. However, if the band frequencies and structural assignments for the solution spectra are fitted to the dried state spectra of BDNF, the result is a dramatic change in band area from the β-sheet band at 1637 cm^{-1} to the random structure band at 1644 cm^{-1} while maintaining the β-sheet band at 1688 cm^{-1}. This is an unlikely interpretation of the data: it seems unreasonable that one β-sheet vibrational mode would be nearly eliminated but not the other. Thus, for the sake of this study, we will interpret the shifting in band frequencies as a dehydration effect and not necessarily a secondary structural perturbation. In other words, the bands ca. 1645 and 1691 cm^{-1} in the dried solid will be considered to coincide with the 1637 and 1688 cm^{-1} β-sheet solution bands, respectively. The relative intensities of these bands, however, can be considered structural perturbations.

Table 2—Structural Retention of BDNF Freeze Dried in Various Excipient Combinations

excipient(s)	depth of band ca. 1690 cm^{-1} (arbitrary units)	β-sheet ratio[b]
solution (reference)	–0.0211	0.593
100 mM sucrose	–0.0174	0.544
8% PEG, 100 mM sucrose	–0.0149	0.682
8% PEG	–0.0145	0.442
8% PEG, 8 h[a]	–0.0132	0.411
8% PEG, 500 mM sucrose	–0.0118	0.304
4% PEG/4% dextran	–0.0101	0.285
500 mM sucrose	–0.0097	0.436
4% PEG/4% dextran, 8 h[a]	–0.0087	0.251
buffer alone	–0.0083	0.198
8% dextran, 500 mM sucrose	–0.0071	0.201
8% dextran, 100 mM sucrose	–0.0063	0.176
8% dextran, 8 h[a]	–0.0062	0.189
8% dextran	–0.0055	0.222

[a] Samples annealed for 8 h at –7 °C prior to drying (see Materials and Methods). [b] β-sheet ratio = (depth of band ca. 1690 cm^{-1})/(depth of band ca. 1640 cm^{-1}).

Table 3—Structural Retention of PEG-BDNF Freeze Dried in Various Excipient Combinations

excipient(s)	depth of band ca. 1690 cm^{-1} (arbitrary units)	β-sheet ratio[b]
solution (reference)	–0.0190	0.596
buffer alone	–0.0148	0.459
8% PEG	–0.0130	0.379
8% PEG, 100 mM sucrose	–0.0124	0.334
8% PEG, 8 h[a]	–0.0121	0.363
8% PEG, 500 mM sucrose	–0.0113	0.290
4% PEG/4% dextran, 8 h[a]	–0.0094	0.257
8% dextran, 8 h[a]	–0.0083	0.230
8% dextran, 500 mM sucrose	–0.0083	0.198
4% PEG/4% dextran	–0.0073	0.226
8% dextran, 100 mM sucrose	–0.0070	0.190
8% dextran	–0.0048	0.174

[a] Samples annealed for 8 h at –7 °C prior to drying (see materials and methods). [b] β-Sheet ratio = (depth of band ca. 1690 cm^{-1})/(depth of band ca. 1640 cm^{-1}).

The two β-sheet bands in BDNF presumably correspond to different types of β-sheet configurations. Monitoring the depth of the two β-sheet bands (as an indicator of band intensity) may be useful in resolving structural differences seen in different freeze-drying formulations. Table 2 reports the depth of the β-sheet band ca. 1690 cm^{-1} as well as the ratio of the band depth at 1640 cm^{-1} to that at 1690 cm^{-1} from second derivative IR spectra of BDNF in solution and freeze-dried in a number of formulations. Deviations in band depth from the solution spectrum are considered structural perturbations from the native structure. The formulations in Table 2 are ordered by the band depth at 1640 cm^{-1}. By this ordering, there is a clear segregation between samples containing PEG and those containing only dextran, with the PEG-containing samples retaining more nativelike structure. Unlike the hemoglobin results, little change in BDNF structure is seen with 8 h of annealing at −7 °C for the 4% PEG/4% dextran sample.

PEG-BDNF freeze-drying results are summarized in Table 3. While the order dictated by the β-sheet band at 1640 cm^{-1} is slightly different with PEG-BDNF than with BDNF, the general segregation between PEG and dextran samples remains. By this quantification, structural retention is better for PEG-BDNF lyophilized in buffer alone than in the presence of polymer. There may also be some

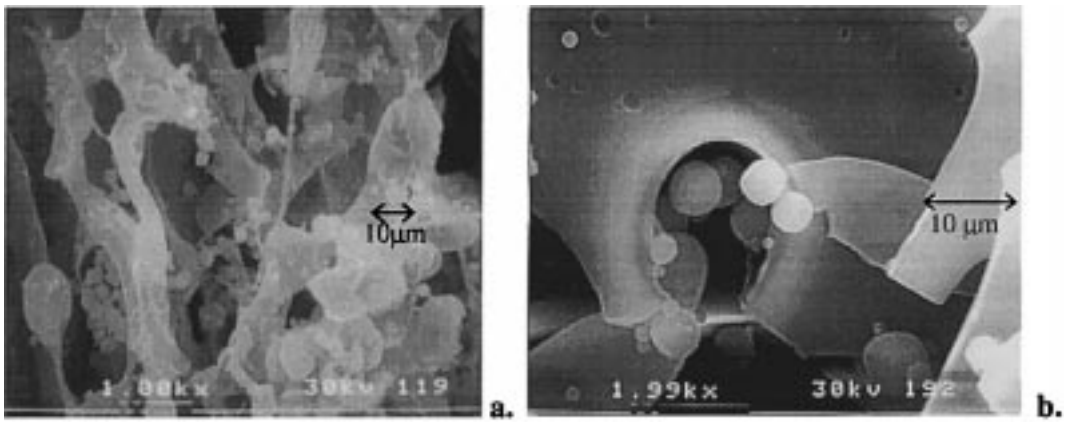

Figure 10—Scanning electron microscopy images showing potential polymer/protein phase separation. (a) BDNF freeze-dried in 8% dextran (1000× magnification) and (b) PEG-BDNF freeze-dried in 8% dextran (2000× magnification).

improvement in retention of secondary structure after annealing for PEGylated BDNF in the PEG/dextran system.

The detrimental effects of phase separation seen in hemoglobin studies (Figure 4) is not as apparent with BDNF or PEG-BDNF over the annealing times examined here, despite the fact that the PEG/dextran phase separation in the dried solid as seen by scanning electron microscopy looks similar (SEM not shown). The equilibrium partitioning of BDNF in a PEG/dextran two-phase system may be partly responsible for this result. While hemoglobin has a partition coefficient (concentration in the PEG phase divided by concentration in the dextran phase) of around 0.3 in a PEG/dextran two-phase system, BDNF's partition coefficient has been measured to be 2.4. This means that about 70% of hemoglobin partitions to the *dextran*-rich phase while about 78% of BDNF is in the *PEG*-rich phase. PEGylating hemoglobin causes the amount of protein in the PEG-rich phase to increase to over 80% while PEGylating BDNF causes the partition coefficient to increase to around 4.2 which means around 86% of the protein is in the PEG-rich phase. Thus, the change in partitioning as a result of PEGylation is considerably less for BDNF compared to hemoglobin. Therefore, unmodified BDNF may already receive the protective effect of a partitioning that favors the PEG-rich phase, namely removal from an interface and/or increased availability of PEG during drying. Alternatively, the differences in behavior between hemoglobin and BDNF may be intrinsic to the structural motifs of the two proteins. During lyophilization, secondary structural damage to hemoglobin is seen primarily as loss of α-helix. BDNF does not contain α-helical structure and therefore may not be sensitive to the same stresses.

Protein/Polymer Phase Separation—SEM images of the freeze-dried cake of BDNF and PEG-BDNF in dextran suggest a possible protein–polymer phase separation during lyophilization (Figure 10). A dispersed phase is present that is not typical of lyophilized dextran. Given BDNF's partitioning behavior in a PEG/dextran system, it may be reasonable to say that BDNF is more "PEG-like", which could lead to incompatibilities with dextran that result in a phase separation. Samples of PEG-BDNF-lyophilized in dextran show a similar separated phase. Phase separation in solutions of dextran and PEG-BDNF has been observed at room temperatures. Closer examination of BDNF structure when freeze-dried in dextran (Figure 11) suggests a structural change with annealing. The broad, flattened bands in the spectra of both BDNF and PEG-BDNF in dextran are typical of denatured proteins, representing a more disperse conformational population. These bands

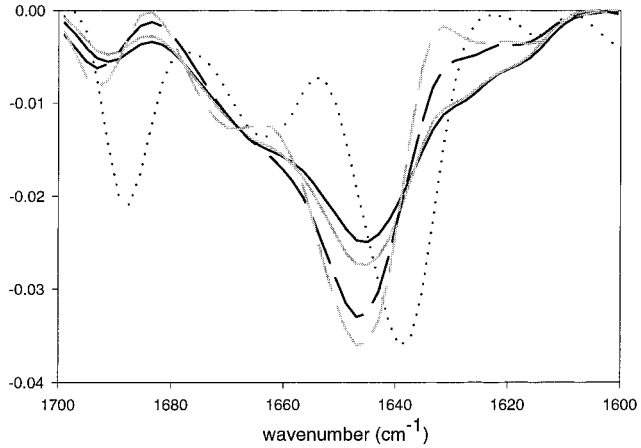

Figure 11—Second derivative IR spectra from BDNF (black lines) and PEG-BDNF (gray lines) lyophilized in 8% dextran. Broken lines were annealed at –7 °C for 8 h prior to drying while solid lines were not annealed. BDNF solution spectrum (dotted trace) is shown for reference.

narrow and deepen with annealing prior to drying, which could indicate added conformational stability. If a BDNF/dextran phase separation is occurring, more of the protein would be contained in a nondextran, high concentration protein phase with annealing. Protein self-association in a phase out of contact with dextran appears to provide BDNF with added stability in the dried state. This effect is greater with PEG-BDNF, emphasizing the greater separation driving force due to greater incompatibility with dextran.

Conclusions

Alteration of hemoglobin partitioning by PEGylation as well as by metal affinity ligands increases the structural integrity of the protein when lyophilized from a PEG/dextran system as well as from buffer alone. In contrast, both BDNF and PEGylated BDNF exhibit similar levels of damage during freeze-drying. This can in part be explained by the relative affinities of the various proteins and protein derivatives for PEG. Although PEG can be a potent stabilizing excipient, hemoglobin partitions away from a PEG-rich phase in PEG/dextran two-phase systems; this behavior is reversed upon PEGylation. On the other hand, unmodified BDNF favors the PEG-rich phase, and PEGylation only increases this tendency.

PEGylation of a protein can be expected to alter the protein's surface characteristics, and thus its interaction with other "surfaces", including interfaces and cosolutes.

Current theories of stabilizing mechanisms during lyophilization[27,28,33] all allude to the importance of compatibilities between the protein and a formulation's glass forming excipients. Addition of PEG to a protein surface changes the interactions between excipients and the protein. In this study, PEGylation actually improves hemoglobin structural retention in the dried state, and reduces BDNF structural loss during annealing in frozen solutions. However, caution is appropriate: therapeutic protein formulations optimized for the nonmodified protein may not generally provide adequate protection when formulating PEGylated derivatives.

References and Notes

1. Davis, F. F.; Es, T. V.; Palczuk, N. C. Nonimmunogenic polypeptides. United States patent no. 4179337, 1979.
2. Takahashi, K.; Ajima, A.; Yoshimoto, T.; Inada, Y. Polyethylene Glycol-Modified Catalase Exhibits Unexpectedly High Activity in Benzene. *Biochem. Biophys. Res. Commun.* **1984**, *125*, 761−766.
3. Klibanov, A. M. Enzymes that work in organic solvents. *Chemtech* **1986**, *16*, 354−359.
4. Bergstrom, K.; Holmberg, K. Protein Immobilization to Polystyrene via Long Poly(ethylene glycol) Chains. *Biotechnol. Bioeng.* **1991**, *38*, 952−955.
5. Zalipsky, S.; Lee, C.. In *PEG Chemistry: Biotechnical and Biomedical Applications*, Harris, J. M., Ed.; Plenum Press: New York, 1992; pp 347−370.
6. McGoff, P.; Baziotis, A. C.; Maskiewicz, R. Analysis of Polyethylene Glycol Modified Superoxide Dismutase by Chromatographic, electrophoretic, Light Scattering, Chemical and Enzymatic Methods. *Chem. Pharm. Bull.* **1988**, *36*, 3079−3091.
7. Mabrouk, P. A. Effect of Pegylation on the Structure and Function of Horse Cytochrome *c*. *Bioconjugate Chem.* **1994**, *5*, 236−241.
8. Labrude, P.; Mouelle, P.; Menu, P.; Vigneron, C.; Dellacherie, E.; Leonard, M.; Tayot, J. L. Hemoglobin solutions coupled with poly(ethylene glycol) 1900. *Int. J. Artif. Organs* **1988**, *11*, 393−402.
9. Ohno, H.; Yamaguchi, N. Redox Reaction of Poly(ethylene oxide)-Modified Hemoglobin in Poly(ethylene oxide) Oligomers at 120 °C. *Bioconjugate Chem.* **1994**, *5*, 379−381.
10. Nho, K.; Zalipsky, S.; Abuchowski, A.; Davis, F. F. PEG-Modified Hemoglobin as a Oxygen Carrier. In *Poly(Ethylene Glycol) Chemistry: Biotechnical and Biomedical Applications*; Harris, J. M., Ed.; Plenum Press: New York, 1992; pp 171−182.
11. Kinstler, O. B.; Brems, D. N.; Lauren, S. L.; Paige, A. G.; Hamburger, J. B.; Treuheit, M. J. Characterization and Stability of N-terminally PEGylated rhG-CSF. *Pharm. Res.* **1996**, *13*, 996−1002.
12. Olson, K.; Gehant, R.; Mukku, V.; O'Connell, K.; Tomlinson, B.; Totpal, K.; Winkler, M. Preparation and Characterization of Poly(ethylene glycol)ylated Human Growth Hormone Antagonist. In *Poly(ethylene glycol): Chemistry and Biological Applications*; Harris, J. M., Zalipsky, S., Eds.; American Chemical Society: Washington D. C., 1997; Vol. 680, pp 170−181.
13. Sakane, T.; Pardridge, W. M. Carboxyl-directed Pegylation of Brain-derived Neurotophic Factor Markedly Reduces Systemic Clearance with Minimal Loss of Biologic Activity. *Pharm. Res.* **1997**, *14*, 1085−1091.
14. Karr, L. J.; Donnelly, D. L.; Kozlowski, A.; Harris, J. M. Use of Poly(ethylene Glycol)-Modified Antibody in Cell Extraction. *Methods Enzymol.* **1994**, *228*, 377−389.
15. Wuenschell, G. E.; Naranjo, E.; Arnold, F. H. Aqueous two-phase metal affinity extraction of heme proteins. *Bioprocess Eng.* **1990**, *5*, 199−202.
16. Guinn, M. R. Isolation and Purification of Proteins by Single-stage Metal Affinity Partitioning in Aqueous Two-phase Systems and by Multi-stage Counter-current Distribution; Ph.D. Thesis; University of Colorado, Boulder, CO, 1996.
17. Leibrock, J.; Lottspeich, F.; Hohn, A.; Hofer, M.; Hengerer, B.; Masiakowski, P.; Thoenen, H.; Barde, Y.-A. Molecular Cloning and Expression of Brain-derived Neurotrophic Factor. *Nature* **1989**, *341*, 149−152.
18. Gaertner, H. F.; Offord, R. E. Site-Specific Attachment of Functionalized Poly(Ethylene Glycol) to the Amino Terminus of Proteins. *Bioconjugate Chem.* **1996**, *7*, 38−44.
19. Morpurgo, M.; Veronese, F. M.; Kachensky, D.; Harris, J. M. Preparation and Characterization of Poly(ethylene glycol) vinyl sulfone. *Bioconjugate Chem.* **1996**, *7*, 363−368.
20. Heller, M. C.; Carpenter, J. F.; Randolph, T. W. Manipulation of Lyophilization Induced Phase Separation: Implications for Pharmaceutical Proteins. *Biotechnol. Prog.* **1997**, *13*, 590−596.
21. Heller, M. C.; Carpenter, J. F.; Randolph, T. W. Effects of Phase Separating Systems on Lyophilized Hemoglobin. *J. Pharm. Sci.* **1996**, *85*, 1358−1362.
22. Dong, A.; Huang, P.; Caughey, W. S. Protein Secondary Structures in Water from Second-Derivative Amide I Infrared Spectra. *Biochemistry* **1990**, *29*, 3303−3308.
23. Dong, A.; Prestrelski, S. J.; Allison, S. D.; Carpenter, J. F. Infrared Spectroscopic Studies of Lyophilization- and Temperature-Induced Protein Aggregation. *J. Pharm. Sci.* **1995**, *84*, 415−424.
24. Dong, A.; Caughey, W. S. Infrared Methods for Study of Hemoglobin Reactions and Structures. *Methods Enzymol.* **1994**, *232*, 139−175.
25. Randolph, T. W. Phase Separation of Excipients during Lyophilization: Effects on Protein Stability. *J. Pharm. Sci.* **1997**, *86*, 1198−1203.
26. Carpenter, J. F.; Crowe, J. H. The mechanism of cryprotection of proteins by solutes. *Cryobiology* **1988**, *25*, 244−255.
27. Carpenter, J. F.; Prestrelski, S. J.; Arakawa, T. Separation of Freezing- and Drying-Induced Denaturation of Lyophilized Proteins Using Stress-Specific Stabilization I. Enzyme Activity and Calorimetric Studies. *Arch. Biochem. Biophys.* **1993**, *303*, 456−464.
28. Pikal, M. J. Freeze-drying of proteins. In *Stability, Formulation and Delivery of Peptides and Proteins*; Cleland, J. L., Langer, R., Eds.; ACS Symposium Series, American Chemical Society: Washington D. C., 1994; pp 120−133.
29. Narhi, L. O.; Rosenfeld, R.; Talvenheimo, J.; Prestrelski, S. J.; Arakawa, T.; Lary, J. W.; Kolvenbach, C. G.; Hecht, R.; Boone, T.; Miller, J. A.; Yphantis, D. A. Comparison of the Biophysical Characteristics of Human Brain-derived Neurotrophic Factor, Neurotrophin-3, and Nerve Growth Factor. *J. Biol. Chem.* **1993**, *268*, 13309−13317.
30. Allison, S. D.; Dong, A.; Carpenter, J. F. Counteracting Effects of Thiocyanate and Sucrose on Chymotrypsinogen Secondary Structure and Aggregation during Freezing, Drying and Rehydration. *Biophys. J.* **1996**, *71*, 2022−2032.
31. Prestrelski, S. J.; Tedeschi, N.; Arakawa, T.; Carpenter, J. F. Dehydration-induced Conformational Transitions in Proteins and Their Inhibitions by Stabilizers. *Biophys. J.* **1993**, *65*, 661−671.
32. Carpenter, J. F.; Crowe, J. H. An Infrared Spectroscopic Study of the Interactions of Carbohydrates with Dried Proteins. *Biochemistry* **1989**, *28*, 3916−3922.
33. Franks, F.; Hatley, R. H. M.; Mathias, S. F. Materials science and production of shelf-stable biologicals. *Biopharm (Jilove, Czech Repub.)* **1991**, *4*, 38−42.

Acknowledgments

This work was supported by grants from the Whitaker Foundation and the National Science Foundation (no. BES9505301).

JS980257J

A New Model Describing the Swelling and Drug Release Kinetics from Hydroxypropyl Methylcellulose Tablets

J. SIEPMANN,[†,*] K. PODUAL,[‡] M. SRIWONGJANYA,[†] N. A. PEPPAS,[‡] AND R. BODMEIER[†]

Contribution from *College of Pharmacy, Freie Universität Berlin, Kelchstr. 31, 12169 Berlin, Germany, and School of Chemical Engineering, Purdue University, West Lafayette, Indiana 47907*

Received May 28, 1998. Final revised manuscript received September 28, 1998.
Accepted for publication September 30, 1998.

Abstract □ A novel mathematical model for the water transport into and drug release from hydroxypropyl methylcellulose (HPMC) tablets is presented. Fick's second law of diffusion is used to describe the mass transfer processes in the three-component system drug/polymer/water. Numerical solutions of the respective set of partial differential equations are provided, considering axial and radial diffusion within cylindrical tablets. It is shown that the diffusion coefficients strongly depend on the water concentration (parameters quantifying this dependence have been determined). Swelling of the device is considered using moving boundary conditions, whereas dissolution processes are neglected. Experiments proved the applicability of the theory. The practical benefit of the new model is to calculate the required shape and dimensions of HPMC tablets to achieve a desired release profile.

Introduction

Hydroxypropyl methylcellulose (HPMC) is the dominant hydrophilic carrier material used for the preparation of oral controlled drug delivery systems.[1] One of its most important characteristics is the high swellability, which has a significant effect on the release kinetics of a drug. Upon contact with a dissolution medium, water or biological fluid diffuses into the tablet, resulting in polymer chain relaxation with volume expansion. Then, the drug diffuses out of the device.

Numerous studies have been reported in the literature to investigate the drug release kinetics from HPMC tablets.[2−4] The modification of the surface area of HPMC tablets in order to achieve a desirable release rate has been studied by Colombo et al.[5,6] Various techniques have been used to elucidate the physical processes involved in the release of drugs from HPMC tablets. For example, pulsed-field-gradient spin−echo NMR methods have been employed to measure the diffusivities of water and drugs in HPMC gels.[7] Recently, Fyfe and Blazek[8] investigated the hydrogel formation by NMR spectroscopy and NMR imaging techniques.

Yet, up to now there has not been any complete mathematical model that takes into account all the important phenomena occurring during drug release. Various simplifications have been made, e.g., neglect of the swelling process,[9] or assumption of constant diffusion coefficients.[11] Fu et al.[12] derived an analytical solution of Fick's second law, using cylindrical coordinates. The model is applicable to tablets that range from the shape of a flat disk (radius ≫ thickness) to that of a cylindrical rod (radius ≪ thickness), but they did not consider the volume expansion of the system and assumed constant diffusion coefficients.

A model for the prediction of the relative change in drug release rate as a function of formulation composition for HPMC tablets of adinazolam mesylate and alprazolam has been developed by Gao et al.[9] It is based on the equation derived by Higuchi[10] for the diffusional release of soluble drugs from polymeric matrixes, considering concentration dependent diffusivities. The swelling of the system is not taken into account, and the mathematical analysis reduced to one dimension. Cohen and Erneux[13,14] used free boundary problems to model swelling controlled release. Drug release is achieved by countercurrent diffusion through a penetrant solvent with the release rate being determined by the rate of diffusion of the solvent in the polymer.

Korsmeyer et al.[15] developed a model describing the diffusion of a penetrant and a solute in a swellable polymer slab and verified the model experimentally.[16] Concentration dependent diffusivities and dimensional changes in the system have been considered, but these theories[13−16] have been developed for thin films, not for cylindrical tablets.

The purpose of this study was to develop a new, physically realistic mathematical model, taking into account all the important processes including Fickian diffusion of water into and drug out of cylindrical tablets (in axial and radial direction, with concentration dependent diffusivities), as well as swelling. The model does not take into account dissolution processes. Thus, it is not valid for water-insoluble drugs whose release is governed by dissolution rather than by diffusion. To test the applicability of the new model, experiments were conducted with various drugs (chlorpheniramine maleate, diclofenac sodium, and propranolol hydrochloride) in different release media (0.1 M HCl, 0.1 M phosphate buffer (pH 7.4), and deionized water). The practical benefit of the new model is to optimize the shape and dimensions of HPMC tablets to achieve a desired release profile. For instance, the effect of the aspect ratio (radius/height) and size of the system on the release kinetics of a drug has been simulated.

Experimental Section

Materials—The following chemicals were obtained from commercial suppliers and used as received: chlorpheniramine maleate (Sigma Chemical Co., St. Louis, MO), diclofenac sodium (Lederle Arzneimittel GmbH, Wolfratshausen, Germany), propranolol hydrochloride (Sigma Chemical Co., St. Louis, MO), hydroxypropyl methylcellulose (Methocel K15M Premium Grade) (Colorcon, Nordmann Rassmann GmbH & Co., Hamburg, Germany).

Methods—The drug (20 mg) and HPMC were blended with a pestle in a porcelain mortar by geometric dilution. Tablets (200 mg, 13 mm diameter) were prepared by compressing the powder blend manually (Specac Hydraulic Press P/N 25.011, Specac Limited, Kent, UK; compaction force = 5 t, holding time = 15 s).

The USP XXIII rotating paddle method (37 °C, 50 rpm, 900 mL of deionized water, 0.1 M HCl or 0.1 M phosphate buffer (pH 7.4) USP XXIII) was used to study the drug release. The samples (2 mL, replaced with fresh medium) were withdrawn at predeter-

* Corresponding author. Phone: +49-30-77 000 446, fax: +49-30-77 000 492, e-mail: siepmann@zedat.fu-berlin.de.
[†] Freie Universität Berlin.
[‡] Purdue University.

10.1021/js9802291 CCC: $18.00 Published on Web 12/10/1998

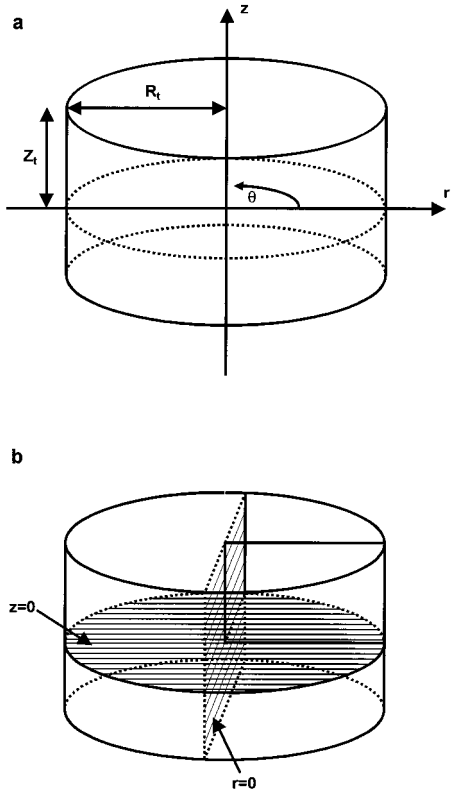

Figure 1—(a) Schematic of the tablet for mathematical analysis, with (b) symmetry planes in the axial and radial directions for the water and drug concentration profiles.

mined time intervals, filtered, and assayed spectrophotometrically (chlorpheniramine maleate, $\lambda = 264$ nm; diclofenac sodium, $\lambda = 276$ nm; propranolol hydrochloride, $\lambda = 290$ nm). All experiments have been conducted in triplicate.

Mathematical Modeling

A new model has been developed to describe water and drug transport in HPMC tablets. The following assumptions have been made: (i) Dissolution processes are neglected. (ii) Swelling is ideal, isotropic, and homogeneous throughout the device (including water-poor regions). The error resulting from this approximation only becomes significant in the case of extreme aspect ratios. The experimental results presented in this study and further results to be presented in a future paper prove the validity of this assumption for pharmaceutically common aspect ratios. (iii) The water concentration at the surface of the tablet is at its equilibrium value. (iv) Perfect sink conditions are maintained. (v) Water imbibing in axial/radial direction leads to a volume increase in axial/radial direction that is proportional to the relative surface area in this direction.

The mass transfer processes are based on Fick's second law of diffusion in cylindrical coordinates:[17]

$$\frac{\partial c_k}{\partial t} = \frac{1}{r}\left\{\frac{\partial}{\partial r}\left(rD_k\frac{\partial c_k}{\partial r}\right) + \frac{\partial}{\partial \theta}\left(\frac{D_k}{r}\frac{\partial c_k}{\partial \theta}\right) + \frac{\partial}{\partial z}\left(rD_k\frac{\partial c_k}{\partial z}\right)\right\} \qquad (1)$$

Here, c_k and D_k are the concentration and diffusion coefficient of the diffusing species ($k = 1$: water; $k = 2$: drug), respectively, and r denotes the radial coordinate, z the axial coordinate, θ the angle perpendicular to both axis, and t represents time. As there is no concentration gradient of any component with respect to θ [Figure 1a], this equation can be transformed into:

$$\frac{\partial c_k}{\partial t} = \frac{\partial}{\partial r}\left(D_k\frac{\partial c_k}{\partial r}\right) + \frac{D_k}{r}\frac{\partial c_k}{\partial r} + \frac{\partial}{\partial z}\left(D_k\frac{\partial c_k}{\partial z}\right) \qquad (2)$$

Two important features of diffusion in swellable polymer systems are considered in this mathematical model: (i) strong concentration dependence of diffusivities and (ii) volume changes due to water imbibition and drug release.

According to the free volume theory, a Fujita-type[18] exponential dependence of the diffusion coefficients for water and drug, D_1 and D_2, can be written as:

$$D_1 = D_{1eq}\exp\left(-\beta_1\left(1 - \frac{c_1}{c_{1eq}}\right)\right) \qquad (3)$$

$$D_2 = D_{2eq}\exp\left(-\beta_2\left(1 - \frac{c_1}{c_{1eq}}\right)\right) \qquad (4)$$

where β_1 and β_2 are dimensionless constants, characterizing this concentration dependence. Also c_{1eq} (762 mg/mL[20]) denotes the water concentration and D_{1eq} and D_{2eq} the respective diffusion coefficients of water and drug in the equilibrium swollen state of the system.

A schematic of the tablet for mathematical analysis is given in Figure 1, parts a and b. The tablet is allowed to swell in both axial and radial direction. The swelling is assumed to be ideal. Hence, the total volume of the tablet at any instant is given by the sum of the volumes of polymer, water, and drug. At $t = 0$ the tablet is dry and thus the water concentration at any position is equal to zero. The drug concentration within the tablet is uniform and equal to its initial concentration, c_{in}. This can be written for water as:

$$t = 0 \qquad c_1 = 0 \qquad 0 \le r \le R_0 \qquad 0 \le z \le Z_0 \qquad (5)$$

and for drug as:

$$t = 0 \qquad c_2 = c_{in} \qquad 0 \le r \le R_0 \qquad 0 \le z \le Z_0 \qquad (6)$$

where R_0 is the initial radius of the tablet, and Z_0 denotes the initial half-thickness of the cylindrical tablet.

At the surface of the tablet, the concentration of water is assumed to be at its equilibrium value, c_{1eq}, for $t > 0$. The respective boundary conditions are written as follows:

$$t > 0 \qquad c_1 = c_{1eq} \qquad 0 \le r \le R_t \qquad z = Z_t \qquad (7)$$

and

$$t > 0 \qquad c_1 = c_{1eq} \qquad 0 \le z \le Z_t \qquad r = R_t \qquad (8)$$

Here, R_t and Z_t represent the time dependent radius and half-height of the tablet. The drug concentration at the surface of the tablet is assumed to be equal to zero (perfect sink condition):

$$t > 0 \qquad c_2 = 0 \qquad 0 \le r \le R_t \qquad z = Z_t \qquad (9)$$

$$t > 0 \qquad c_2 = 0 \qquad 0 \le z \le Z_t \qquad r = R_t \qquad (10)$$

To minimize computation time, the origin of the coordinate system is placed at the center of the tablet (Figure 1a). As can be seen in Figure 1b, there are two symmetry planes for the drug and water concentration profiles. Thus, only the concentration profiles within a quarter of the cylindrical tablet have to be calculated. The mathematical treatment of this phenomenon is given by the following

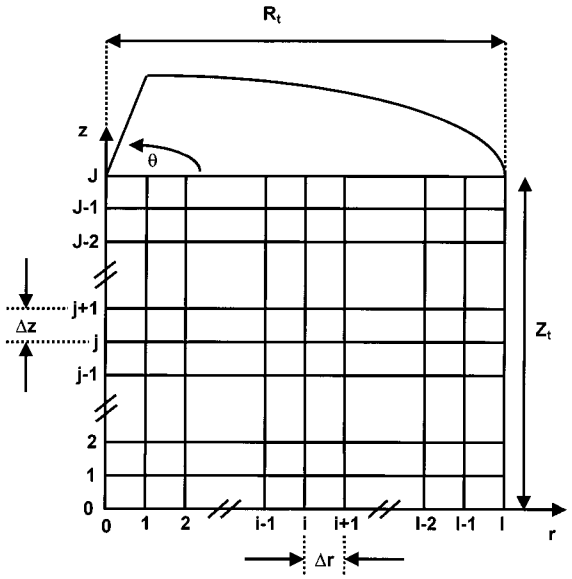

Figure 2—Schematic of the tablet for numerical analysis.

boundary conditions:

$$t > 0 \qquad \frac{\partial c_1}{\partial z} = 0 \qquad 0 \le r \le R_t \qquad z = 0 \qquad (11)$$

$$t > 0 \qquad \frac{\partial c_1}{\partial r} = 0 \qquad 0 \le z \le Z_t \qquad r = 0 \qquad (12)$$

for water, and

$$t > 0 \qquad \frac{\partial c_2}{\partial z} = 0 \qquad 0 \le r \le R_t \qquad z = 0 \qquad (13)$$

$$t > 0 \qquad \frac{\partial c_2}{\partial r} = 0 \qquad 0 \le z \le Z_t \qquad r = 0 \qquad (14)$$

for the drug.

Due to the concentration dependence of the diffusion coefficients, there is no analytical solution of this set of partial differential equations (eqs 2−14). Thus, they were solved numerically, using finite differences.

The principle of this method is illustrated in Figures 2 and 3. The time dependent radius, R_t, and half-height, Z_t, of the cylindrical tablets are divided into I and J space intervals, Δr and Δz, respectively, generating a grid of $(I + 1) \times (J + 1)$ grid points. The time is divided into g time intervals Δt (for most of the simulations we have chosen: $I = J = 50$ and $g = 500000$). Using eqs 2−4 and eqs 7−14, the concentration profiles of water and drug for a new time step ($t = t_0 + \Delta t$) can be calculated, when the concentration profile is known at the previous time step ($t = t_0$). The concentration at a certain inner grid point ($i \times \Delta r$, $j \times \Delta z$) for the new time step ($t = t_0 + \Delta t$) is calculated from the concentrations at the same grid point ($i \times \Delta r$, $j \times \Delta z$) and its four direct neighbors [$(i - 1) \times \Delta r$, $j \times \Delta z$; $i \times \Delta r$, $(j - 1) \times \Delta z$; $i \times \Delta r$, $(j + 1) \times \Delta z$; $(i + 1) \times \Delta r$, $j \times \Delta z$] at the previous time step ($t = t_0$). The concentrations at the outer grid points ($i = 0$ v $i = I$ v $j = 0$ v $j = J$) for the new time step ($t = t_0 + \Delta t$) are calculated using the boundary conditions (eqs 7−14). At time $t = 0$ the concentration profile of the drug and water are given by the initial conditions (eqs 5 and 6). Hence, the concentration profiles at $t = 0 + \Delta t$, $t = 0 + 2\Delta t$, $t = 0 + 3\Delta t$,..., $t = 0 + g\Delta t$ can be calculated sequentially.

In addition, the total amount of water and drug within the system is calculated at each time step (by integrating the respective concentrations with respect to r, z, and θ).

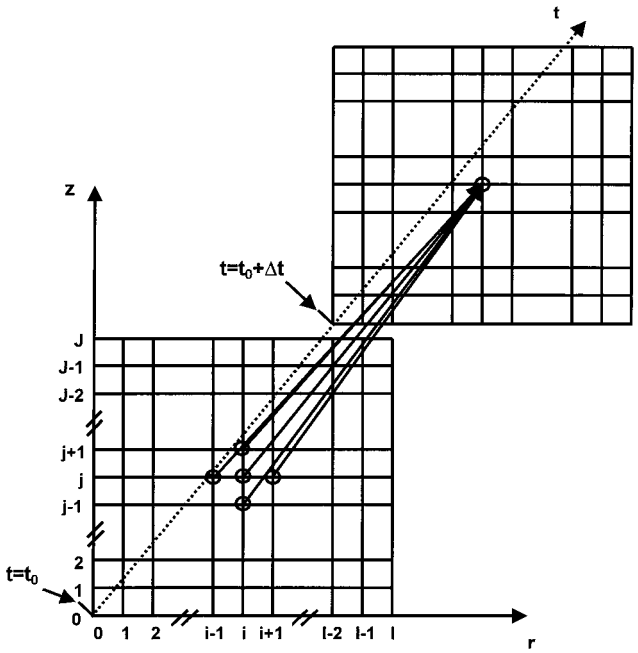

Figure 3—Principle of the numerical analysis: calculation of the concentration profile of a diffusing species at a new time step from the concentration profile at the previous time step.

Then, assuming ideal swelling, the new volume of the system is determined. With this knowledge, the new radius and height of the tablet are calculated. It is assumed that water imbibing in the axial direction leads to a volume increase in the axial direction, whereas water imbibing in the radial direction leads to a volume increase in the radial direction. The increase in volume in each direction is proportional to the surface area in this direction.

There are four unknown parameters in the presented model which have to be determined: β_1, β_2, D_{1eq}, and D_{2eq}. The constants β_1 and D_{1eq} are obtained by fitting eqs 2, 3, 5, 7, 8, 11, and 12 to experimental water uptake data of drug-free tablets ($c_{in} = 0$, thus, values for β_2 and D_{2eq} are not required) (least-squares method, combined with the Nelder−Mead method,[19] two-parameter fit), whereas the values for β_2 and D_{2eq} are subsequently determined by fitting the model (eqs 2−14) to experimental drug release data (two-parameter fit).

Results and Discussion

Water Uptake—Data for water uptake studies in HPMC were reported by Tahara.[20] Figure 4 shows the fit of the new model (to determine β_1 and D_{1eq}) to the experimentally determined relative amount of water taken up by HPMC tablets versus time. There is good agreement between theory and experiment (correlation coefficient = R^2 = 0.994). Thus, diffusion governs the water uptake into HPMC tablets. It was found that the diffusion coefficient of the diffusing species significantly depends on the water content of the system. The explanation for this phenomenon is based on the fact that the mobility of the polymer chains strongly depends on the water content of the tablet. Hence, the free volume available for diffusion is a function of the water concentration, resulting in concentration dependent diffusivities. The constant that characterizes this dependence, β_k, is specific for the diffusing molecules. For water, a value of $\beta_1 = 2.5$ was calculated. In addition, the diffusion coefficient of water within the fully swollen tablet was determined as $D_{1eq} = 5.6 \times 10^{-6}$ cm^2/s.

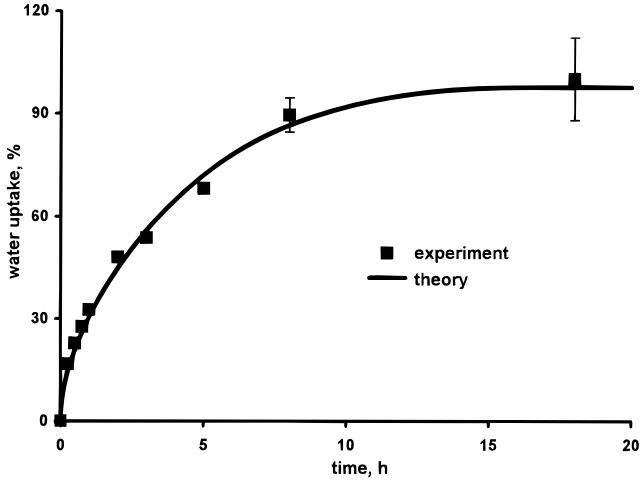

Figure 4—Fit of the model to the experimentally determined water uptake data.[20]

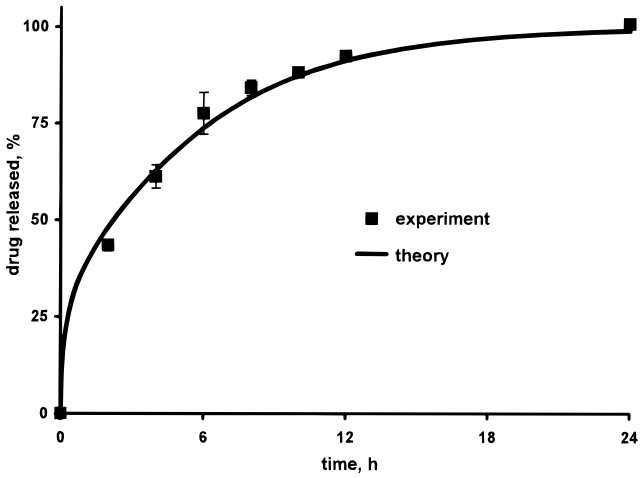

Figure 5—Fit of the model to the experimentally determined amount of propranolol hydrochloride released [release medium: phosphate buffer (pH 7.4)].

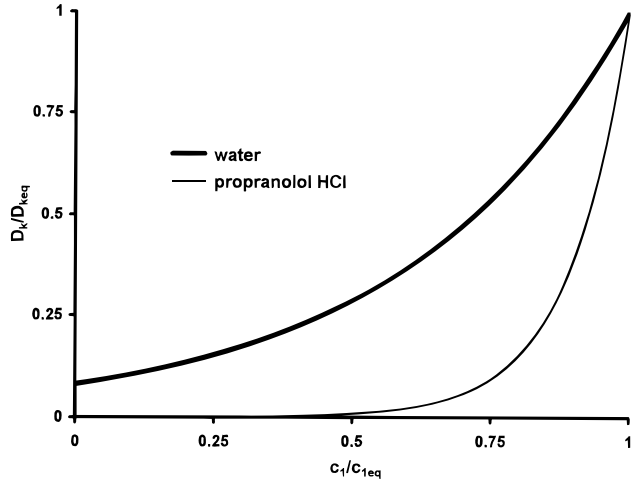

Figure 6—Normalized concentration dependencies (calculated) of the diffusion coefficients of water and propranolol hydrochloride on the water concentration in the system.

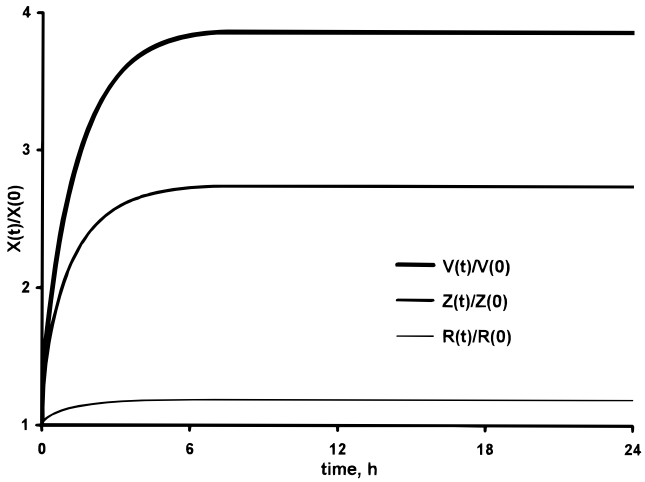

Figure 7—Swelling kinetics (calculated) of the HPMC tablets: increase in volume (*V*), half-height (*Z*), and radius (*R*).

Drug Release—The drug release kinetics of propranolol hydrochloride in 0.1 M phosphate buffer (pH 7.4) are shown in Figure 5 for tablet dimensions of $R_0 = 0.65$ cm, $Z_0 = 0.069$ cm. The new model was fitted to the experimentally determined relative amount of drug released versus time (correlation coefficient = $R^2 = 0.993$). Once more, diffusion governs the transfer kinetics, with concentration dependent diffusion coefficients. The two important parameters characterizing this process, the diffusion coefficient of the drug within the fully swollen tablet, D_{2eq}, and the constant β_2, characterizing the concentration dependence of D_2 on the water content, were determined as $D_{2eq} = 6.3 \times 10^{-7}$ cm^2/s, and $\beta_2 = 9.5$.

As expected from the free volume theory, D_{2eq} is less than D_{1eq}, and β_2 is greater than β_1. According to the theory, the size of the diffusing molecules significantly affects the transfer rate. The jump from one cavity to another for a given cavity size distribution is easier for smaller than for larger molecules. Hence, the diffusion coefficient of water in the fully swollen tablet is higher than the respective diffusion coefficient of propranolol hydrochloride.

Concerning the β-values, the relations are more complex. The dependence of the diffusivity on the water content of the system is a function of the molecular size of the diffusing species. The diffusion rate of small molecules within the polymer system is less affected by the mobility of polymer chains than is the diffusion rate of big molecules (above a certain minimum void size). For small diffusing molecules, much smaller than the average void size, diffusion occurs by localized activated jumps from one preexisting cavity to another; only a few monomer segments are involved. With larger diffusing species, preexisting cavities may be unable to accommodate the diffusing molecules. Therefore, larger numbers of monomer segments must be rearranged to allow the molecules to diffuse.[21] Thus, the relative increase of the diffusion coefficient of water with increasing water content is less steep than the respective increase of the diffusion coefficient of propranolol hydrochloride. These relations are illustrated for water and propranolol hydrochloride diffusivities in Figure 6, normalized to the equilibrium concentration of water and to the respective diffusion coefficients in the fully swollen tablet ($\beta_1 = 2.5$, $\beta_2 = 9.5$).

Swelling Kinetics—Swelling is associated with polymer chain relaxation with volume expansion. The increasing dimension of the system is considered in the new model by moving boundary conditions (eqs 7−14). It is assumed that the total volume of the system is equal to the sum of the volumes of the polymer, water, and drug. The increasing radius, R_t, half-height, Z_t, and volume, V_t, of the tablets can be calculated. Figure 7 shows the respective data of propranolol hydrochloride containing tablets ($R_0 = 0.65$ cm, $Z_0 = 0.069$ cm, release medium: phosphate buffer (pH 7.4), $\beta_1 = 2.5$, $D_{1eq} = 5.6 \times 10^{-6}$ cm^2/s), normalized to the

respective initial values at $t = 0$. It is shown that the swelling of the tablet is much faster than the release of the drug (Figure 5 shows the release profile of the same tablets). The water uptake is complete after approximately 6 h, whereas the drug is released over a period of approximately 24 h. This is due to the higher mobility of the water molecules in the system, resulting in higher diffusion coefficients in the fully swollen tablet. In addition, the β-value of water is much smaller than the β-value of propranolol hydrochloride.

The increase in radius and height is very high at the beginning and then declines with time. Interestingly, the relative increase in height is approximately 9-fold of the relative increase in radius. The reason for this phenomenon is the difference in the surface area of the tablet in both directions. In the axial direction the surface area is much greater than in the radial direction (2.65 cm^2, instead of 0.56 cm^2). Hence, more water can imbibe in the axial direction and cause the tablet to swell in this direction. The increase in volume of the tablet (by a factor equal to 4) is very important for the additional imbibition of water and for the drug release kinetics. As shown above, both processes are governed by diffusion. Increasing dimensions of the tablets lead to increasing diffusion pathways and thus to decreasing diffusion rates. The effect of the increasing diffusion pathways competes with the effect of the increasing diffusivities of the diffusing species, due to the increasing polymer mobility.

Water and Drug Concentration Profiles—With the new model, further insight into the mass transfer mechanisms is achieved. The concentration profiles of both species, water and drug, can be calculated at any instant. Figure 8 shows the water profiles within the tablets ($R_0 =$ 0.65 cm, $Z_0 = 0.069$ cm, release medium: phosphate buffer (pH 7.4), $\beta_1 = 2.5$, $D_{1eq} = 5.6 \times 10^{-6}$ cm^2/s) at 30 min (Figure 8a), and 3 h (Figure 8b). For reasons of clarity, the concentration profiles within only one-quarter of the tablet (as indicated in Figure 1b) are presented. Steep concentration gradients directed to the middle of the tablets are observed for small time periods. They are the driving force for additional water imbibition. The steepness of these curves declines with time; thus, the transfer rate declines with time. This effect overlaps with the two others, described above: the increasing diffusion pathways and the increasing diffusion coefficients. The respective concentration profiles of propranolol hydrochloride are presented in Figure 9 ($R_0 = 0.65$ cm, $Z_0 = 0.069$ cm, release medium: phosphate buffer (pH 7.4), $\beta_1 = 2.5$, $D_{1eq} = 5.6 \times 10^{-6}$ cm^2/s, $\beta_2 = 9.5$, $D_{2eq} = 6.3 \times 10^{-7}$ cm^2/s), at 30 min (Figure 9a), and 3 h (Figure 9b). Again, at the beginning there are steep concentration gradients, which are declining with time. The high driving force at the beginning, in combination with short diffusion pathways, leads to high release rates, as can be shown theoretically as well as experimentally (Figure 5).

Concentration Dependent Diffusivities—As described above, the diffusion coefficients of water and drug strongly depend on the water content of the tablet. Thus, they are functions of both time (t) and position (r, z, θ) within the system. With the new model, the diffusivities can be calculated at any time and position.

Figure 10 shows the diffusion coefficient of propranolol hydrochloride at three different positions as a function of time: (i) at the surface of the tablet, (ii) within the tablet ($r = R_t/2$, $z = Z_t/2$, θ), and (iii) at the center of the tablet. The following parameters have been used: $R_0 = 0.65$ cm, $Z_0 = 0.069$ cm, $\beta_1 = 2.5$, $D_{1eq} = 5.6 \times 10^{-6}$ cm^2/s, $\beta_2 = 9.5$, $D_{2eq} = 6.3 \times 10^{-7}$ cm^2/s (release medium: buffer pH 7.4). For reasons of clarity, the data are normalized to the respective diffusivities in the fully swollen system. The

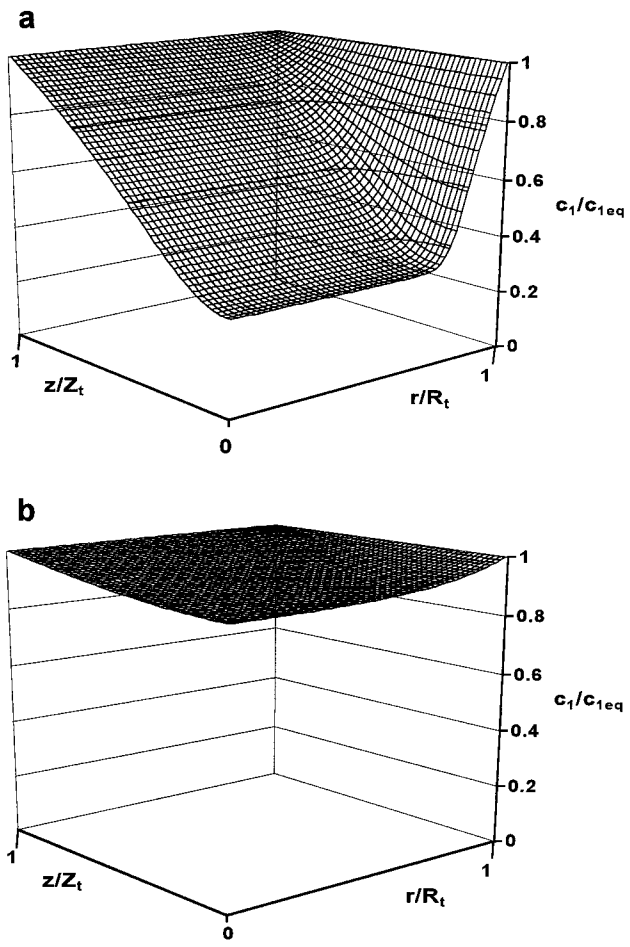

Figure 8—Concentration profile (calculated) of water within the tablets (containing propranolol hydrochloride): (a) $t = 30$ min, (b) $t = 3$ h [release medium: phosphate buffer (pH 7.4)].

diffusion coefficient levels off instantaneously to its equilibrium value at the surface of the tablet upon contact with the release medium. In contrast to this, the diffusivity within the tablet, as well as at the center, shows a sigmoidal behavior. First, it is very low and approximately constant. After a certain time period, it levels off and reaches its equilibrium value. The moment of leveling off is a function of the position (r, z, θ) within the tablet (Figure 10). The knowledge of these data is of great practical importance, when designing a new tablet with, e.g., nonuniform initial drug distribution, to achieve a desired release profile.

Influence of the Aspect Ratio of the Tablet on the Drug Release Kinetics—An easy tool to modify the release kinetics of a drug from a tablet is to vary its shape. The effect of the aspect ratio (radius/height) of the tablet on the drug release rate can be simulated with the new model. Figure 11 clearly shows the release kinetics of propranolol hydrochloride in phosphate buffer (pH 7.4) from three different types of tablet with the same volume (0.18 cm^3): (i) flat cylinders with $R_0/(2Z_0) = 20$, (ii) regular tablets with $R_0/(2Z_0) = 2$, and (iii) almost rod-shaped cylinders with $R_0/(2Z_0) = 0.2$ ($\beta_1 = 2.5$, $D_{1eq} = 5.6 \times 10^{-6}$ cm^2/s, $\beta_2 = 9.5$, $D_{2eq} = 6.3 \times 10^{-7}$ cm^2/s). It is shown that the release rate from the flat tablets is significantly higher than from the other two types: 90% of the drug is released within only 4.5 h, instead of 18.9 and 21.6 h, respectively. The reason for this phenomenon is the difference in the surface area of the tablets: 7.3 cm^2 in the case of flat tablets, 2.3 cm^2 and 1.9 cm^2 for the regular and "rodlike" tablets, respectively. Within a certain range, determined

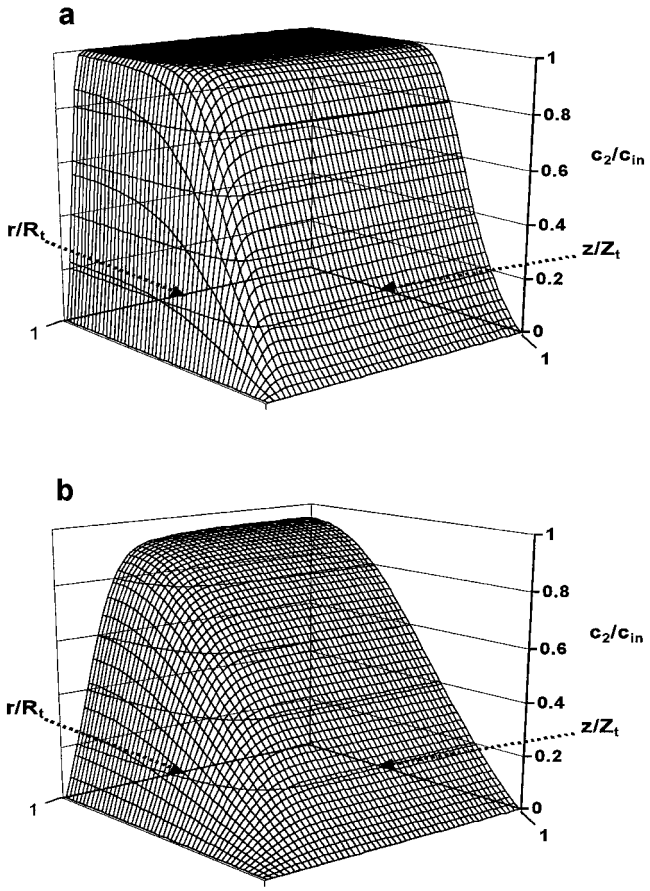

Figure 9—Concentration profile (calculated) of propranolol hydrochloride within the tablets: (a) $t = 30$ min, (b) $t = 3$ h [release medium: phosphate buffer (pH 7.4)].

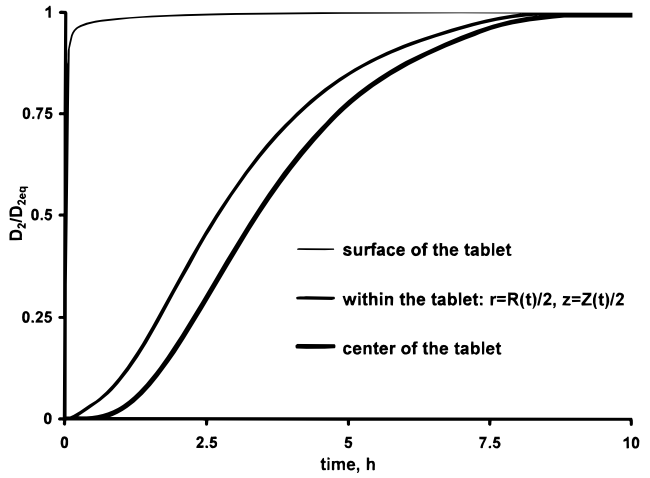

Figure 10—Diffusion coefficient (calculated) of propranolol hydrochloride at different positions within the tablet versus time [release medium: phosphate buffer (pH 7.4)].

by the applicability of the tablets, the variation of the aspect ratio (radius/height) is thus a very easy and effective tool to modify the release rate of the system. With the new model, the optimal shape can be calculated to achieve a desired release profile, without the need of experiments.

Influence of the Tablet Size on the Drug Release Kinetics—Another convenient method to achieve a desired release profile is to vary the size of the tablet. This effect is illustrated in Figure 12. Three types of propranolol hydrochloride tablets (with the same aspect ratio = radius/height = 1.25 and initial drug concentration $c_{in} = 109$ mg/

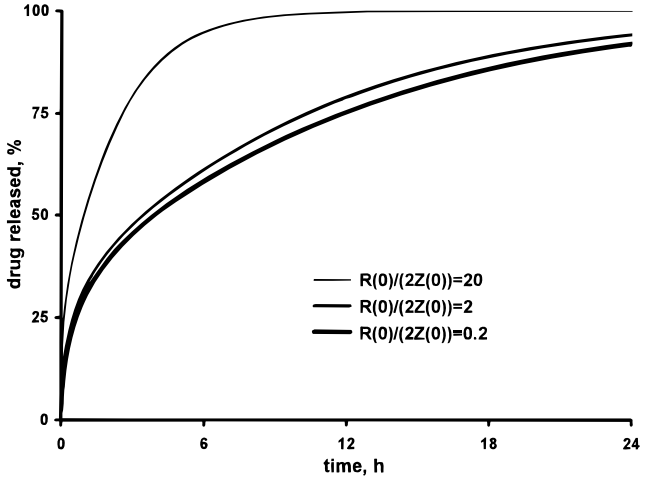

Figure 11—Influence of the aspect ratio (radius/height) of the tablet on the release kinetics (calculated) of propranolol hydrochloride [release medium: phosphate buffer (pH 7.4)].

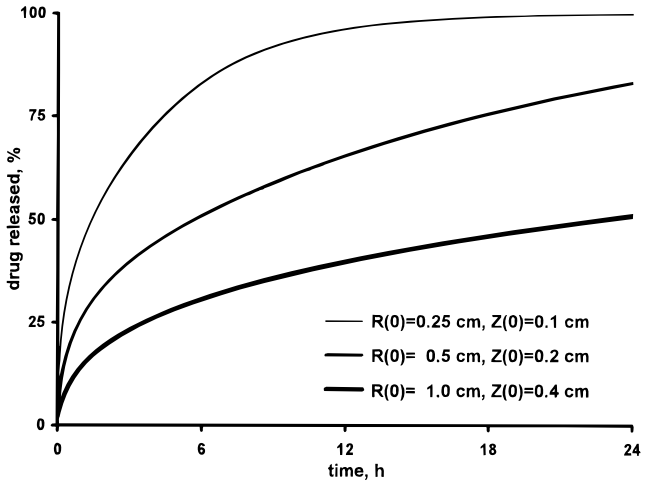

Figure 12—Effect of the size of the tablet on the release kinetics (calculated) of propranolol hydrochloride [release medium: phosphate buffer (pH 7.4)].

mL) have been investigated in phosphate buffer (pH 7.4): (i) small ones, with $R_0 = 0.25$ cm and $Z_0 = 0.1$ cm, (ii) medium-sized ones, with $R_0 = 0.5$ cm and $Z_0 = 0.2$ cm, and (iii) large ones, with $R_0 = 1.0$ cm and $Z_0 = 0.4$ cm ($\beta_1 = 2.5$, $D_{1eq} = 5.6 \times 10^{-6}$ cm^2/s, $\beta_2 = 9.5$, $D_{2eq} = 6.3 \times 10^{-7}$ cm^2/s). As expected, a very strong influence of the size of the tablet on the release rate is observed: Within 24 h, 99.8% of the drug has been released from the small, 83.1% from the medium-sized, and only 50.9% from the large tablets. The explanation for this phenomenon is obvious. Small tablets have a higher relative surface area (referred to the volume) than large tablets. In addition, the diffusion pathways are much longer in large tablets than in small ones. Thus, the relative amount of drug released versus time is much higher for small tablets. To release the same absolute amount of drug, more small tablets have to be administered than large ones. The variation of the size of the tablets is a very effective and easy tool to achieve a desired release rate. The new model can be used to simulate the drug release kinetics for different tablet sizes. Thus, the required dimensions to obtain a certain release profile can be predicted, avoiding time-consuming experiments.

Applicability of the Model—The release mechanism of a controlled drug delivery system can be affected by various parameters, e.g., type of drug and release medium. To prove the applicability of the presented model for

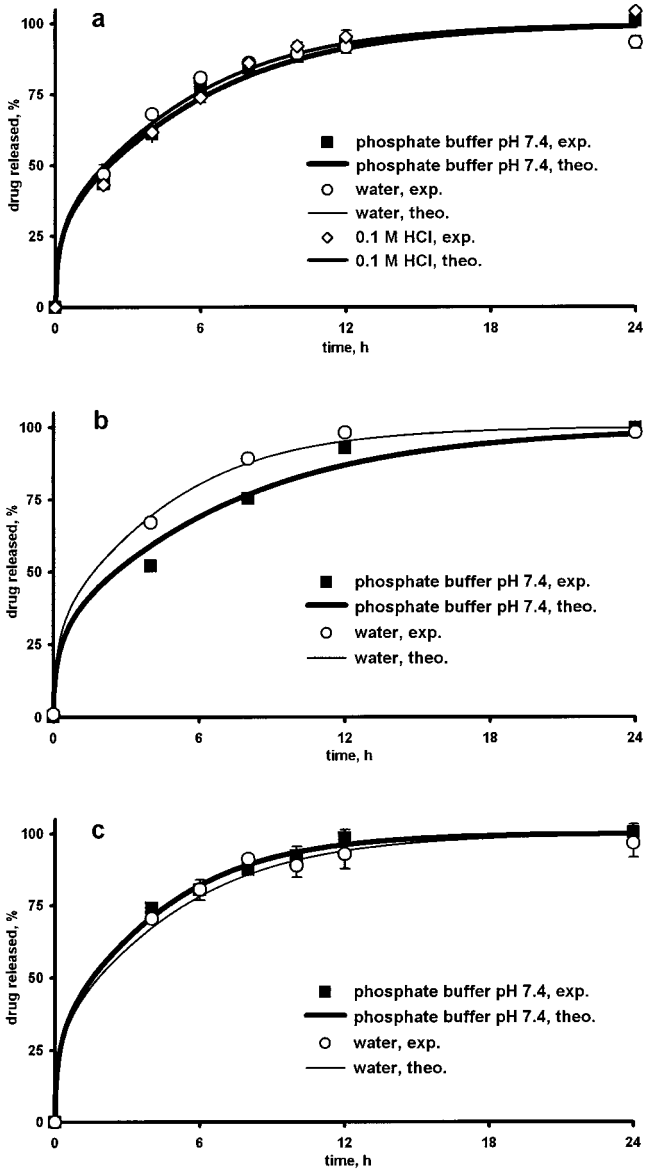

Figure 13—Applicability of the model for different drugs and release media: (a) propranolol hydrochloride, (b) diclofenac sodium, (c) chlorpheniramine maleate.

different drug-release media combinations, experiments have also been conducted with propranolol hydrochloride in 0.1 M HCl and deionized water, diclofenac sodium and chlorpheniramine maleate in deionized water and phosphate buffer (pH 7.4), respectively. Figure 13, parts a–c, show the theoretically ($\beta_1 = 2.5$, $D_{1eq} = 5.6 \times 10^{-6}$ cm^2/s, $R_0 = 0.65$ cm, $Z_0 = 0.069$ cm) and experimentally determined release kinetics. In each case, the experimentally determined data can be explained by the presented Fickian analysis considering concentration dependent diffusivities (correlation coefficient: $R^2 > 0.985$, Table 1). This is of great practical importance for the new model. It is not restricted to a certain drug-release medium combination. In addition, the respective diffusion coefficients in the fully swollen tablets, D_{2eq}, and the constants, characterizing the concentration dependence of the drug diffusivities on the water content of the tablet, β_2, have been determined (Table 1).

Influence of the Type of Release Medium on the Drug Release Kinetics—For propranolol hydrochloride, the calculated β_2-values in different release media (phosphate buffer (pH 7.4), deionized water, and 0.1 M HCl) are very similar: $\beta_2 = 9.5$, 9.4, and 9.4, respectively. This indicates the negligible effect of the type of release medium on the concentration dependence of the diffusivity. In addition, the diffusion coefficient of the drug within the fully swollen tablet varies only between 6.3×10^{-7} cm^2/s and 7.0×10^{-7} cm^2/s. Thus, the resulting release curves (Figure 13a) are very similar. For diclofenac sodium in phosphate buffer (pH 7.4) and deionized water, D_{2eq} was determined as 4.9×10^{-7} cm^2/s and 8.0×10^{-7} cm^2/s, respectively. The calculated β_2-values however, are approximately equal: $\beta_2 = 8.1$ and 8.3. As can be seen in Figure 13b, this results in a slightly different release rate of diclofenac sodium in phosphate buffer (pH 7.4) and deionized water. The explanation for this phenomenon is probably based on the different interactions of the phosphate buffer ions (K^+, Na^+, HPO_4^{2-}, $H_2PO_4^-$) with diclofenac sodium, HPMC, and water. The exact analysis of these interactions is beyond the scope of this study. For chlorpheniramine maleate, the following values have been calculated: D_{2eq}(buffer pH 7.4) $= 8.7 \times 10^{-7}$ cm^2/s, D_{2eq}(water) $= 7.3 \times 10^{-7}$ cm^2/s, β_2(buffer pH 7.4) $= 8.5$, and β_2(water) $= 8.4$. As in the case of propranolol hydrochloride, these values are approximately equal. The resulting release profiles are shown in Figure 13c, illustrating the negligible effect of the type of release medium on the liberation of chlorpheniramine maleate.

Table 1—Parameters Characterizing the Diffusion of Drugs within HPMC Tablets

drug	release medium	$D_{2eq} \times 10^7$ (cm^2/s)	β_2	R^2
propranolol hydrochloride	buffer pH 7.4	6.3	9.5	0.993
	deionized water	7.0	9.4	0.988
	0.1 M HCl	6.9	9.4	0.988
diclofenac	buffer pH 7.4	4.9	8.1	0.986
sodium	deionized water	8.0	8.3	0.997
chlorpheniramine	buffer pH 7.4	8.7	8.5	0.997
maleate	deionized water	7.3	8.4	0.991

Conclusions

The two major benefits of the presented model are: (i) the gain of further insight into the release mechanism of drugs from HPMC tablets and (ii) the ability to calculate the required shape and dimensions of HPMC tablets to achieve desired drug release profiles.

Notation

c	concentration within the tablet
c_{eq}	concentration in the equilibrium swollen state
c_{in}	initial concentration of the drug within the tablet
D	diffusion coefficient
D_{eq}	diffusion coefficient in the fully swollen tablet
g	number of time intervals for numerical analysis
i	integer for numerical analysis
I	number of space intervals along the radial axes for numerical analysis
k	subscript, indicating the diffusing species: $k =$ 1: water, $k = 2$: drug
j	integer for numerical analysis
J	number of space intervals along the axial axes for numerical analysis
r	radial coordinate
Δr	space interval along the radial axes for numerical analysis

R^2	correlation coefficient
R_0	initial radius of the tablet
R_t	radius of the tablet at time t
t	time
Δt	time interval for numerical analysis
V_t	volume of the tablet at time t
z	axial coordinate
Δz	space interval along the axial axes for numerical analysis
Z_0	initial half-height of the tablet
Z_t	half-height of the tablet at time t
β	constant, characterizing the dependence of the diffusion coefficient on the water concentration
θ	angle

References and Notes

1. Colombo, P. Swelling-controlled release in hydrogel matrixes for oral route. *Adv. Drug Del. Rev.* **1993**, *11*, 37−57.
2. Pham, A. T.; Lee, P. I. Probing the mechanisms of drug release from hydroxypropylmethyl cellulose matrixes. *Pharm. Res.* **1994**, *11*, 1379−84.
3. Colombo, P.; Bettini, R.; Massimo, G.; Catellani, P. L.; Santi, P.; Peppas, N. A. Drug diffusion front movement is important in drug release control from swellable matrix tablets. *J. Pharm. Sci.* **1995**, *84*, 991−7.
4. Liu, C.-H.; Kao, Y.-H.; Chen, S.-C.; Sokoloski, T. D.; Sheu, M.-T. In-vitro and in-vivo studies of the diclofenac sodium controlled-release matrix tablets. *J. Pharm. Pharmacol.* **1995**, *47*, 360−4.
5. Colombo, P.; La Manna, A.; Conte, U. System for the controlled release of active substances. U.S. Patent No. 4,-839,177, 1989.
6. Colombo, P.; Conte, U.; Gazzaniga, A.; Maggi, L.; Sangalli, M. E.; Peppas, N. A.; La Manna, A. Drug release modulation by physical restrictions of matrix swelling. *Int. J. Pharm.* **1990**, *63*, 43−8.
7. Gao, P.; Fagerness, P. E. Diffusion in HPMC gels. I. Determination of drug and water diffusivity by pulsed-field-gradient spin−echo NMR. *Pharm. Res.* **1995**, *12*, 955−64.
8. Fyfe, C. A.; Blazek, A. I. Investigation of hydrogel formation from hydroxypropylmethylcellulose (HPMC) by NMR spectroscopy and NMR imaging techniques. *Macromolecules* **1997**, *30*, 6230−7.
9. Gao, P.; Nixon, P. R.; Skoug, J. W. Diffusion in HPMC gels. II. Prediction of drug release rates from hydrophilic matrix extended-release dosage forms. *Pharm. Res.* **1995**, *12*, 965−71.
10. Higuchi, T. Mechanism of sustained action medication. Theoretical analysis of rate of release of solid drugs dispersed in solid matrices. *J. Pharm. Sci.* **1963**, *52*, 1145−9.
11. Hariharan, D.; Peppas, N. A.; Bettini, R.; Colombo, P. Mathematical analysis of drug delivery from swellable systems with partial physical restrictions or impermeable coatings. *Int. J. Pharm.* **1994**, *112*, 47−54.
12. Fu, J. C.; Hagemeir, C.; Moyer, D. L.; NG, E. W. A unified mathematical model for diffusion from drug-polymer composite tablets. *J. Biomed. Mater. Res.* **1976**, *10*, 743−58.
13. Cohen, D. S.; Erneux, T. Free boundary problems in controlled release pharmaceuticals. I: Diffusion in glassy polymers. *SIAM J. Appl. Math.* **1988**, *48*, 1451−65.
14. Cohen, D. S.; Erneux, T. Free boundary problems in controlled release pharmaceuticals. II: Swelling-controlled release. *SIAM J. Appl. Math.* **1988**, *48*, 1466−74.
15. Korsmeyer, R. W.; Lustig, S. R.; Peppas, N. A. Solute and penetrant diffusion in swellable polymers. I. Mathematical modeling. *J. Polym. Sci. Polym. Phys. Ed.* **1986**, *24*, 395−408.
16. Korsmeyer, R. W.; von Meerwall, E.; Peppas, N. A. Solute and penetrant diffusion in swellable polymers. II. Verification of theoretical models. *J. Polym. Sci. Polym. Phys. Ed.* **1986**, *24*, 409−34.
17. Crank, J. *The Mathematics of Diffusion*, 2nd ed.; Clarendon Press: Oxford, 1975; pp 4−5.
18. Fujita, H. Diffusion in polymer-diluent systems. *Fortschr. Hochpolym.-Forsch.* **1961**, *3*, 1−47.
19. Hoffmann, U.; Hofmann, H. *Einfuehrung in die Optimierung*, Verlag Chemie GmbH: Weinheim, Germany, 1971; pp 127−31.
20. Tahara, K.; Yamamoto, K.; Nishihata, T. Overall mechanism behind matrix sustained release (SR) tablets prepared with hydroxypropyl methylcellulose 2910. *J. Controlled Release* **1995**, *35*, 59−66.
21. Fan, L. T.; Singh, S. K. *Controlled release: a quantitative treatment*; Springer-Verlag: Berlin, 1989; pp 20−28.

Acknowledgments

This work was supported in part by the Deutscher Akademischer Austauschdienst, Bonn, Germany, and by a National Institutes of Health grant No. GM 43337.

JS9802291

Equilibrium and Kinetics of Rotamer Interconversion in Immunosuppressant Prodigiosin Derivatives in Solution

VINCENZO RIZZO,* AMEDEA MORELLI, VITTORIO PINCIROLI, DOMENICO SCIANGULA, AND ROBERTO D'ALESSIO

Contribution from *Pharmacia & Upjohn, viale Pasteur 10, I-20014 Nerviano, Italy.*

Received May 27, 1998. Final revised manuscript received September 2, 1998.
Accepted for publication September 8, 1998.

Abstract □ The equilibrium and relative rate of rotamer interconversion around the bond joining the 2,2′-bipyrrolyl and pyrromethene moieties in a synthetic analogue of immunosuppressant prodigiosin are investigated as a function of pHapp in a water/acetonitrile mixture (1/1 by volume). Two chromatographically separable isomeric forms are obtained in acid solutions (pHapp < 4), whereas rapid interconversion occurs above neutrality. Furthermore, pH modulates the conformational preference of the molecule according to nitrogen protonation on the three pyrrole rings system ($pK_a = 7.2$). At high pHapp (neutral form), the same conformer that is observed in pure acetonitrile prevails, whereas the other one is preferred by the protonated form. The nuclear magnetic resonance data indicate that the structures of the two conformers mainly differ in the value of the torsion angle around the aforementioned C–C bond. Kinetic and equilibrium data are quantitatively interpreted with a cyclic mechanism including two protonation ($pK_{a1} = 8.23 \pm 0.03$, $pK_{a2} = 5.4 \pm 0.2$) and two conformational rearrangement steps. A molecular interpretation of the observed behavior includes, for the preferred conformer at low pH, formation of a new hydrogen bond between the exocyclic oxygen and the neighboring pyrrole NH upon protonation of the three pyrrole rings system.

Introduction

Prodigiosins are a class of natural red pigments isolated from *Streptomyces Genus* that are endowed with potent antibacterial and cytotoxic properties.[1] More recently, immunosuppressive properties have been discovered for some members of this class,[2,3] and ascribed to a mechanism of action well distinguished from that exerted by cyclosporin A or other related drugs.[4] In a medicinal chemistry program devoted to the preparation of synthetic analogues of the natural prodigiosins,[5] PNU-156804 (Figure 1) emerged as a lead with very favorable pharmacological properties. These favorable properties prompted a detailed investigation of the solution properties of this analogue and the development of a specific analytical high-performance liquid chromatography (HPLC) method. Anomalous behavior (peak splitting, tailing, etc.) was immediately detected by reversed-phase HPLC under various conditions and attributed to geometrical isomerization in the time scale of chromatography. On the basis of this result, the equilibrium and kinetics of this geometrical transformation in solution were investigated with the aim of both optimizing conditions for chromatography and better understanding the molecular properties of this new class of compounds in water-containing solutions.

PNU-156804 contains the 2,2′-bipyrrolyl−pyrromethene chromophore whose structure is compatible with several

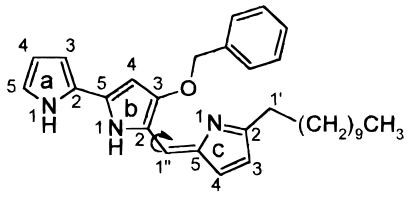

PNU-156804

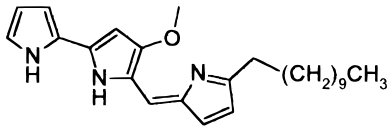

PNU-156737

Figure 1—Chemical structure of PNU-156804 and PNU-156737. The numeration system used in the presentation af results is shown for PNU-156804 together with the torsion angle that is involved in rotamer interconversion.

geometrical isomers arising from different equilibrium positions around the bonds connecting the three pyrrole rings. The extensive conjugation of this chromophoric system is apparent from the different mesomeric structures that can be written. As a consequence, rotation barriers lower than expected for ordinary double bonds may arise, and interconversion among geometrical isomers may become detectable at ordinary temperatures. In the present investigation we report data on both the equilibrium composition and the rate of interconversion for the two geometrical isomers that are chromatographically resolved at room temperature under acidic conditions. The compound is not soluble enough in pure water, but a study as a function of pHapp in solutions of water/acetonitrile (1/1) proved feasible. The study was carried out for solutions of various pHapp (glass electrode readings) as it was immediately clear that protonation of the molecule greatly affected the conformational equilibrium and the rate of interconversion. Finally, a structural model of the two conformers is proposed on the basis of two-dimensional nuclear magnetic resonance nuclear Overhauser enhancement spectroscopy (2D-NMR NOESY) data.

Materials and Methods

Materials—PNU-156804 (either as HCl or as CH_3SO_3H salt) and PNU-156737 were prepared as previously described.[5] The structure of both compounds has been verified with NMR and mass spectroscopy (MS) techniques. HPLC grade acetonitrile and methanol were Carlo Erba products. Methylene chloride RPE, trifluoroacetic acid RPE, and all chemicals for buffer preparation were purchased from Carlo Erba. Water was purified with a Milli-Q apparatus (Waters). Deuterated solvents were purchased from Merck.

Spectrophotometric Titrations and Kinetic Measurements—Data were collected on a Perkin-Elmer Lambda 4 instru-

* To whom future correspondence should be addressed.

10.1021/js980225w CCC: $18.00
Published on Web 11/14/1998

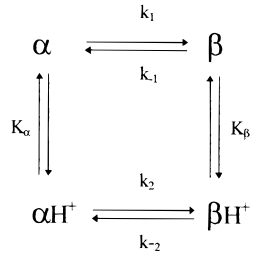

Scheme 1

ment connected to a Perkin-Elmer 7700 computer. The cuvette holder was thermostated at 25 °C with fluid circulation from a water bath (LTD-6, Grant). A fresh solution was prepared for each determination by adding 0.200 mL of a stock solution in acetonitrile (concentration (C) ≈ 0.04 mg/mL) to 2 mL of a titration solvent with pH near the desired value (the final concentration of PNU-156804 was around 0.004 mg/mL). The actual pHapp value (range 2−11) was determined in the cuvette immediately after the spectroscopic measurement (absorbance at 525 nm). The titration solvent was made out of a mixture containing 275 mL of aqueous phosphate 0.02 M, NaCl 0.1 M, and 225 mL of acetonitrile, whose pHapp was adjusted with small additions of 2 N HCl or NaOH to the desired value. The final solvent composition in the cuvette was 1/1 acetonitrile/aqueous phase by volume. Solutions for kinetic measurements were similarly prepared with both titration solvent and stock solution pre-thermostated at 25 °C, and the instrument was set in the time drive mode.

Kinetic Measurements: Stopped Flow—A High Tech SF51 instrument in the light absorption mode was used for fast kinetic measurements. The conformational change was induced by a change of pH and monitored by measuring light absorption at 500 nm at pH values between 3 and 7, and at 430 nm at pH values >7. In detail, the two syringes were filled with either a solution of PNU-156804 in acetonitrile/buffer at about pH 11 (1/1) when jumping from alkaline to neutral/acid region and at about pH 3 when jumping from the acid to the neutral/alkaline region or acetonitrile/buffer at the desired pH (0.02 M phosphate, NaCl 0.1 M). The pHapp of the final solution was determined after mixing equal volumes of the two solutions just mentioned in a test tube, and the final concentration of PNU-156804 in the observation chamber of the stopped flow was similar to that used for the spectrophotometric experiments (C ≅ 0.004 mg/mL).

HPLC Measurements—Chromatograms were collected with a Perkin-Elmer instrument with a LC-410 quaternary pumping system, a 235C diode-array detector, and a Turbochrom data station. Ordinary chromatograms were obtained with a Hipak C8 AB (250 × 4.6 mm, 5 μm) with a mobile phase (flow = 1 mL/min) of methanol/tetrahydrophuran/water (55/25/20 by volume) upon buffering the aqueous phase to the desired pH. Fast resolution was obtained with a C18 cartridge (3 × 3 CR, Perkin-Elmer) with a mixture of water/methanol/methylene chloride/acetonitrile/trifluoroacetic acid (300/400/150/150/1 by volume) as mobile phase at the flow rate of 2 mL/min. This procedure provided sufficient separation of the two isomeric forms in a short analysis time (8 min), which was needed to limit interconversion of the two conformers. Generally, 20 μL of an approximately 0.05 mg/mL solution were injected, and detection was obtained at 500 nm.

NMR Measurements—The ^{1}H NMR data were collected at 28 °C with a Varian Unity 600 instrument operating at 600 MHz. The standard Varian pulse sequences and processing software were used. Mixing times of 2.0 and 0.080 s were used in the 2D experiments NOESY and total correlation spectroscopy (TOCSY), respectively.

Equilibrium and Kinetic Model—Data interpretation was obtained with the following cyclic reaction model (Scheme 1), where α and β indicate the two conformers in neutral form and αH^+ and βH^+ indicate the corresponding protonated forms. No kinetic parameters are indicated for the two protonation steps, which are expected to be much faster than the other two conformational reorientations.

The four equilibrium parameters (two microscopic acidity constants, K_α and K_β, and two equilibrium constants, $K_1 = k_1 / k_{-1}$, $K_2 = k_2 / k_{-2}$) are not independent but are related through the cyclic equilibrium condition as follows:

$$K_\beta = K_\alpha \frac{K_1}{K_2} \tag{1}$$

The macroscopic equilibrium acidity constant, K_a, is consequently given by

$$K_a = K_\alpha \frac{1 + K_1}{1 + K_2} \tag{2}$$

With the assumption that both protonation reactions rapidly equilibrate and that only the two conformational isomerization steps contribute to the observable time dependence of the optical signal, only one reciprocal relaxation time, $k = 1/\tau$, is expected for the kinetic model just described. The derivation of the dependence of k on $[H^+]$ is shortly outlined here according to standard procedures.[6]

The rate equation for conformer α is

$$\frac{d(\alpha + \alpha H^+)}{dt} = -k_1\,\alpha - k_2 \alpha H^+ + k_{-1}\beta + k_{-2}\beta H^+ \tag{3}$$

Upon introducing the mass balance condition:

$$C_o = \alpha + \alpha H^+ + \beta + \beta H^+ \tag{4}$$

and the equilibrium condition for the two protonation steps

$$\alpha H^+ = \alpha [H^+]/K_\alpha \qquad \beta H^+ = \beta [H^+]/K_\beta \tag{5}$$

equation 3 transforms into

$$(1 + [H^+]/K_\alpha)\frac{d\alpha}{dt} = -\alpha\,(k_1 + k_2\,[H^+]/K_\alpha) - \alpha(k_{-1} + k_{-2}[H^+]/K_\beta)(1 + [H^+]/K_\alpha)/(1 + [H^+]/K_\beta) + C_o\,(k_{-1} + k_{-2}\,[H^+]/K_\beta) \tag{6}$$

which rearranges into a standard first-order rate equation:

$$d\alpha/dt = -k\alpha + \text{const} \tag{7}$$

with const = $C_o\,(k_{-1} + k_{-2}\,[H^+]/K_\beta)/(1 + [H^+]/K_\alpha)$ and the first-order rate

$$k = \frac{k_1 + k_2\,[H^+]/K_\alpha}{1 + [H^+]/K_\alpha} + \frac{k_{-1} + k_{-2}\,[H^+]/K_\beta}{1 + [H^+]/K_\beta} \tag{8}$$

At low pH values $k \approx k_2 + k_{-2}$, and the interconversion rate coincides with that of the protonated form; at high pH $k \approx k_1 + k_{-1}$, and the interconversion rate of the neutral form sets the pace.

Data Analysis—Best fit of experimental data to equations was obtained with the nonlinear regression procedure of the MATH menu within program SIGMAPLOT (Jandel). Analysis of first-order kinetics used the equation

$$y = A\,(1 - e^{-kt}) + \text{offset} \tag{9}$$

Spectrophotometric titration curves and pH dependence of HPLC peak areas and of the interconversion rate were analyzed with the following equation:

$$y = \frac{A + B\,10^{(pH - pK_a)}}{1 + 10^{(pH - pK_a)}} \tag{10}$$

where A is the limiting value of the observed property at low pH and B is that at high pH.

Analysis of pH dependence of kinetic data was accomplished with 8 (method 1) or with a combination of eqs 8 and 1 to reduce the number of free parameters (method 2) by means of a nonlinear

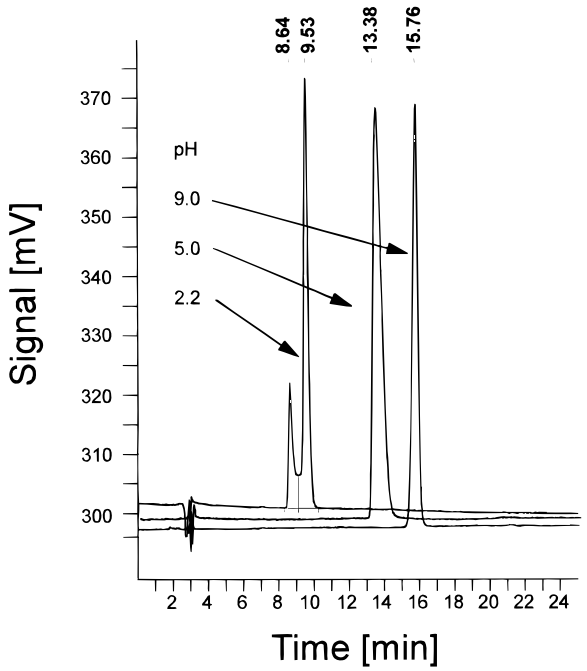

Figure 2—HPLC separation of PNU-156804 rotamers as a function of pH. Three chromatograms obtained with mobile phases buffered at different pH values are superimposed. Two peaks are obtained only with the most acidic mobile phase: the minor peak corresponds to β-rotamer in this case.

weighted least squares procedure (weights = $1/k$) written whithin the program SCIENTIST (Micro-Math).

Results

Spectrophotometric Titration—In the ultraviolet (UV)−visible spectrum of PNU-156804 dissolved in (1/1) water/acetonitrile, the long wavelength absorption band is observed at about 525 nm in acidic solution and, with reduced intensity, at about 460 nm in alkali conditions. This spectroscopic change is the basis for a spectrophotometric titration that leads to $pK_a = 7.20 \pm 0.04$ (average of two determinations: 7.16 and 7.25). This result is attributed to nitrogen protonation in the system of three conjugated pyrrole rings. Data were obtained with solutions equilibrated for at least 30 min at pHapp < 5 and for 10 min above this value, therefore, the pK_a value refers to the equilibrium mixture of two geometric isomers as discussed later.

Equilibrium and Rate of Conformational Change—The HPLC chromatograms of PNU-156804 are greatly affected by the pH of the mobile phase: above neutrality, a sharp peak is obtained that broadens at around pH 5 and splits into two peaks with an acid mobile phase (see Figure 2). Under these latter conditions, the interconversion rate is long in comparison with the chromatographic separation time (the retention times of the two peaks differ by about 1 min) and the relative peak areas approximately correspond to the population of the two conformers in the injected solution, which is a function of the pH and of the composition of this solution. Thus, conformational equilibrium composition of PNU-156804 in solution may be investigated by HPLC.

A pure acetonitrile solution produces a chromatogram similar to that obtained for water containing solutions at high pH (predominance of β-conformer). Preequilibrated solutions at low pH correspond to chromatograms with predominance of α-conformer. The pH dependence of relative peak area (Figure 3) nicely fits a titration curve corresponding to a pK_a of 7.16, which is in very good

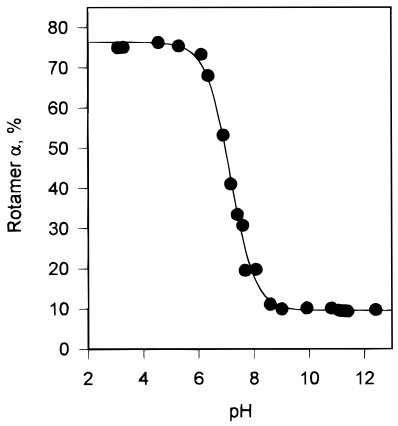

Figure 3—Equilibrium α-rotamer population as determined by HPLC using an acidic mobile phase. The pH dependence is well interpreted with a titration curve corresponding to $pK_a = 7.16$, which is in good agreement with spectroscopic titration data.

agreement with the value obtained from spectrophotometric titration. The limiting value of α-conformer population goes from about 75% at low pH down to 10% at high pH. Actually, high pH data are affected by partial reequilibration during chromatography in the acid mobile phase; thus, the effective limiting population of α-conformer can be much lower than 10%. Perturbation of the equilibrium during chromatographic separation is also likely at low pH, where conformer half-life is about 5 min and thus comparable with the separation time, and may depend on the composition of the mobile phase, which is not the 1/1 water/acetonitrile mixture used in all other experiments. Accordingly, the estimates of equilibrium constants ($K_2 \cong 0.3$ and $K_1 \geq 10$) as obtained with these data should be considered as approximate values.

The UV−visible absorption spectra of the two geometric isomers, as measured with diode array detection in HPLC, are similar but not identical, and the largest difference (about 10% of total absorbance) is observed at around 500 nm. The same spectroscopic change is seen when an acetonitrile solution of PNU-156804 is diluted to acetonitrile/acid buffer (1/1) and the spectrum measured soon after solution preparation is compared with that taken after 30 min. This difference is the basis for kinetic measurements that were made in an ordinary spectrophotometer at pHapp between 2 and 5, and with a stopped-flow apparatus at higher pHapp values by the pH-jump technique. At above pH 7, where the spectrum of the neutral form predominates, the best signal is obtained with detection at 430 nm. For acid solutions, where determination of rates was spectrophotometrically accessible, the two methods gave identical results. Data are analyzed with a first-order kinetic model (eq 4) that leads to determination of the reaction rate k. The dependence of this parameter on pHapp is shown in Figure 4 together with the results of model fitting obtained with eq 8 (method 1, 6 free parameters) and a combination of eq 8 and eq 1 (method 2, 5 free parameters). Values of the two acidity constants (see Table 1) are reasonably well determined and agree in both fitting methods. No error estimate is possible for the rate constants in method 1 because of strong parameter correlation; method 2 provides error estimates for all k values and also suggest a major indetermination for rate constants k_2 and k_{-2}, which are strongly method dependent. Not surprisingly, the estimated values of the equilibrium constants ($K_2 = 0.06$ and $K_1 = 30$, method 2) only qualitatively agree with results of the chromatographic investigation. Most likely as a consequence of the poor evaluation of the kinetic parameters, the estimate $pK_a =$

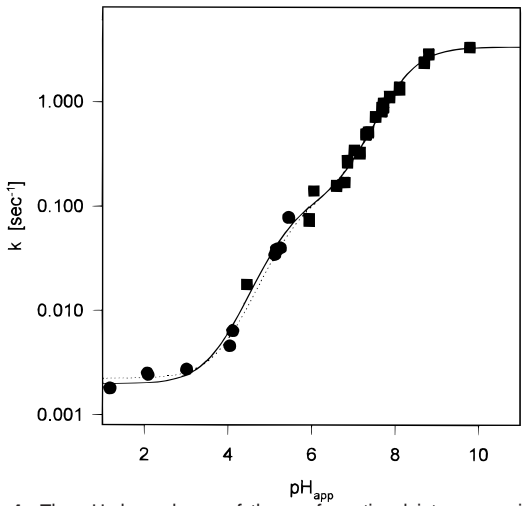

Figure 4—The pH dependence of the conformational interconversion rate constant *k*; the logarithmic scale is used to highlight the two-step behavior. Filled circles are results of spectrophotometric experiments, and squares are stopped-flow data. Fitting by method 1 (all parameters in eq 8 are allowed to vary) produced the solid line, a very similar result (dotted line) is obtained by method 2, where explicit use is made of the cyclic equilibrium condition, thus reducing the number of free parameters. Parameter values are reported in Table 1. The interconversion rate increases about 1000-fold for the unprotonated with respect to the protonated form of PNU-156804.

Table 1—Estimates of Kinetic Parameters from pH Dependence of Interconversion Rate

method[a]	k_1 [s^{-1}]	k_{-1} [s^{-1}]	k_2 [10^{-4} s^{-1}]	k_{-2} [10^{-3} s^{-1}]	pK_α	pK_β
1	3.3	0.1	5	1.5	8.23 ± 0.03	5.4 ± 0.2
2	3.26 ± 0.08	0.11 ± 0.02	1.3 ± 1.1	2.1 ± 1.6	8.23 ± 0.03	(5.5)

[a] Method 1 is nonlinear regression with eq 8 and 6 free parameters; method 2 makes explicit use of the cyclic equilibrium condition to reduce the free parameters to 5. In this latter case, pK_β is derived from the other 5 parameters according to eq 1.

6.7 according to eq 2 is significantly lower than the experimental value (7.2).

NMR Studies—The ^{1}H NMR spectra of PNU-156804, HCl salt, dissolved in $CDCl_3$ or in CD_3CN reveal the presence of only one conformer, which is β according to the notation just presented. Signals of the two conformers are well resolved in solvent mixtures containing H_2O or D_2O at low pH, such as CD_3CN/D_2O (1/1, pH 1.1), where conformer α and β coexist at about 2/1 ratio. This result is at variance with HPLC data (α/β ratio = 3/1). The higher concentration (~ 0.15 mg/mL) used in NMR work is not the cause of the observed discrepancy because no change of the conformer ratio was detected upon dilution of the NMR sample up to 8-fold. Most likely, the NMR data gave a correct measurement of the unperturbed conformer equilibrium in the 1/1 water/acetonitrile mixture, which is not the case of the HPLC data.

Rapid exchange of NH protons with water protons completely excludes (in D_2O) or greatly reduces (in H_2O) the detection of the corresponding signals and NOESY cross-peaks, which are of great structural significance. Fortunately, the $CH_3SO_3^-$ salt of PNU-156804 in $CDCl_3$ solution is found as a mixture of conformers (α/β = 1/2) in the presence of about 30% molar excess CH_3SO_3 H (see ^{1}H NMR spectrum in Figure 5), where a detailed structural identification of the two conformers is possible. Correspondence of conformers in different solvents is based on chemical shifts: CH_2-1′ protons resonate at 2.0−2.1 ppm in the α-conformer and at 2.6−3.0 ppm in the β-conformer and are highly diagnostic to this purpose. Other protons of the molecule display a definite chemical shift pattern: H-1″, OCH_2, H-4b, and the phenyl group (more deshielded in the α-conformer) or H-3c and NH-1c (more deshielded in the β-conformer). The NOESY data point out that the two conformers mainly differ for the C-2b−C-1″ torsion angle value and are thus rotamers; this angle is close to 0° for the β-rotamer and close to 180° for the α-rotamer (see Figure 6). Conformer α coincides with the reported crystal structure of a prodigiosin analogue[7] containing a sulfur atom in place of nitrogen at ring A (Figure 1). In this case, a hydrogen bond between the protonated nitrogen of the pyrromethene group and the exocyclic oxygen is apparently stabilizing the 180° rotamer. This result agrees

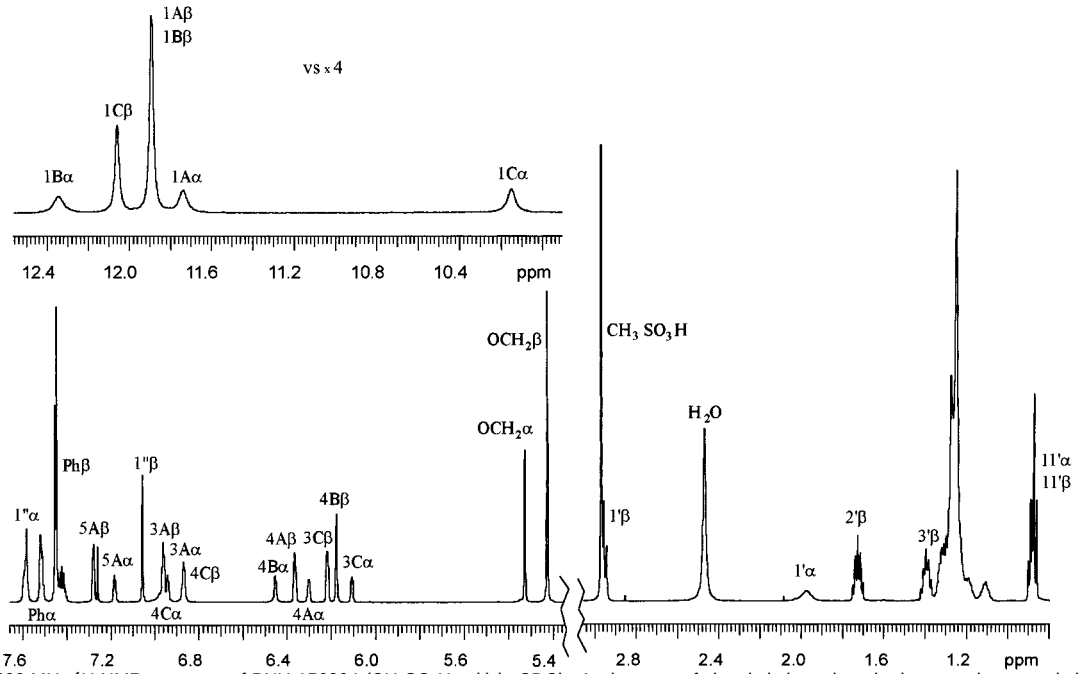

Figure 5—The 600 MHz ^{1}H NMR spectrum of PNU-156804 (CH_3SO_3H salt) in $CDCl_3$. Assignment of signals is based on the homonuclear correlation experiments TOCSY and NOESY. For proton numbering, see at Figure 1. Resonances of each pyrrole ring are recognized in the TOCSY spectrum from the different number of protons in each spin system (4, 2, and 3, respectively) and signal assignment is based on NOE effects with adjacent protons as detected in the NOESY spectrum (e.g., NH-1a/H-5a or CH_2-1′/H-3c).

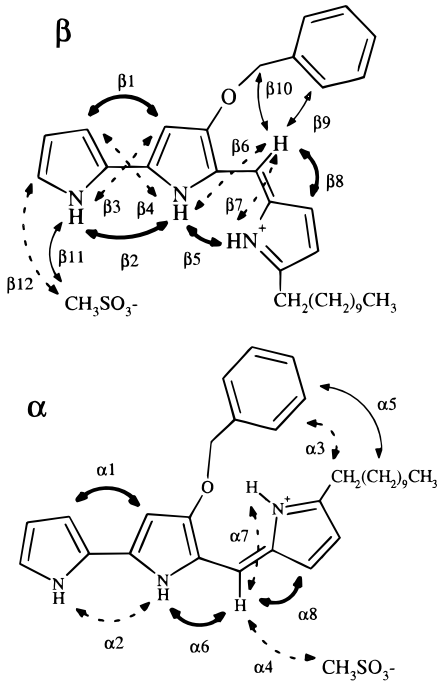

Figure 6—Structure of the α- and *β*-conformers as deduced from NOESY data on PNU-156804 in $CDCl_3$. The significant NOESY cross-peaks are indicated here with double arrows according to the following intensity-related code: heavy lines, strong, thin lines, moderate; and dashed lines, weak. Cross-peak *β*2 is not detected in this spectrum because of NH1a and NH1b signal overlapping. This NOE is detected in the NOESY spectrum of PNU-156804 (HCl salt) dissolved in $CDCl_3$, where only the *β*-conformer is present.

with the predominance of α-conformer at low pH values, as already observed.

Hindered rotation around (C-2a−C-5b) or (C-1″−C-5c) bonds can be excluded as a source of conformational diversity: the same nuclear Overhauser effects (NOEs) are detected for the two conformers in that part of the molecule (cross-peaks corresponding to *β*3 and *β*4 are not detected in the α-conformer because these NOEs are very weak and α is the minor isomer) and suggest a torsion angle close to 0° for both (C-2a−C-5b) and (C-1″−C-5c) bonds. This suggestion is consistent with the X-ray structure of the aforementioned prodigiosin analogue.[7] The most indicative NOEs that distiguish and characterize the two conformers are those labeled α6 (also present in *β* but very weak), α3 and α5 for the α-conformer, and *β*5, *β*9, and *β*10 for the *β*-conformer. The presence of NOEs between the methyl group of the methansulfonate and protons of the molecule (α4, *β*11, and *β*12) is probably due to ion-pairing with formation of hydrogen bonds between the counterion oxygens and NH protons. Chemical shift variation of CH_2-1′ in the two conformers (α, 1.98 ppm; *β*, 2.96 ppm) are simply rationalized in terms of a different C-2b−C-1" torsion angle value: when these protons are oriented toward the phenyl group (conformer α), its shielding cone causes an upfield shift. This interpretation is confimed by the ^{1}H NMR spectrum of PNU-156737 (the natural undecyl-prodigiosin that bears a methoxy group in place of the benzyloxy of PNU-156804, see at Figure 1), which shows no such chemical shift difference between the two conformers (α, 2.77 ppm; *β*, 2.86 ppm) as obtained in $CDCl_3$ solution in the presence of an excess CF_3COOH. Chemical shift changes of NH-1c (α, 10.15 ppm; *β*, 11.89 ppm) and H-1″ (α, 7.59 ppm; *β*, 7.06 ppm) must have a different origin because these are equally well observed for PNU-156737.

Conclusions

The conformational model of Figure 6 satisfactorily explains the results of the present investigation: the two geometrical isomers differ for the polar head structure (the conjugated system is expanded in α and compact in *β*) and for the solvent exposed hydrophobic surface (reduced in the α-conformer by the contact between phenyl and alkyl chain). This result explains the chromatographic separation on a reversed-phase HPLC column. In turn, this result is experimentally feasible only at low pH, where the interconversion rate of the two conformers is comparable or slower than analysis time. In 1/1 water/acetonitrile as solvent, the measured interconversion half-life is about 5 min for the protonated form, but this rate is probably slower in the HPLC mobile phase, which contains less water. Thus, the reasonably good quantitation of the two conformers by HPLC is understandable.

Both the rate of interconversion and the equilibrium distribution of the two conformers are greatly affected by nitrogen protonation. This influence can be attributed to hydrogen bonding between the protonated nitrogen and the exocyclic oxygen, as found in the crystal of a prodigiosin analogue,[7] but a general redistribution of the electron density in the system of three conjugated pyrrole rings after protonation may also play a role. In particular, our data indicate an increase of the rotational energy barrier around C-2b−C-1″ bond in the protonated form and the consequent freezing of the conformational equilibrium. On the basis of a rate-on comparison (k_1 and k_2), if we assume identical preexponential factor, a difference of 25 kJ/mol is estimated, which may be attributed to a strong hydrogen bond.

The different pK_a values of the two conformers, which drive the shift of the equilibrium position from preferred α-form at low pH to almost pure *β*-form at high pH (see eq 1), indicate that the α-conformer is much more easily protonated than the *β*-conformer. This observation is in keeping with the aforementioned extra hydrogen bond in the protonated α-rotamer. However, a clear intepretation of the observed experimental properties must clearly await a detailed theoretical study of the electronic properties of the 2,2′-bipyrrolyl−pyrromethene moiety, which appears well motivated by the important pharmacological effect of this group. In fact, the very limited conformational energy difference in play (few kilocalories, as inferred by the equilibrium constant values) suggests the possibility that equilibrium freezing may occur at the (yet unknown) biological receptor in either the pure α- or the pure *β*-form. In this regard, most intriguing is the analogy with the case of immunophilins, which are enzymes capable of catalyzing cis−trans amide bond isomerization in peptidyl-proline sequences[8] and are the primary target of the well-known immunosuppressant drugs cyclosporin A (cyclophilin) and FK506 (FK binding protein).

References and Notes

1. Williams, R. P.; Hearn, W. R. Prodigiosin. *Antibiotics* **1967**, *2*, 410−432.
2. Nakamura, A.; Nagai, K.; Ando, K.; Tamura G. Selective Suppression by Prodigiosin of the Mitogenic Response of Murine Splenocytes. *J. Antibiot.* **1985**, *39*, 1155−1159.
3. Tsuji, R. F.; Yamamoto, M.; Nakamura, A.; Kataoka, T.; Magae, J.; Nagai, K.; Jamasaky, M. Selective Immunosuppression of Prodigiosin 25-C and FK506 in the Murine Immune System. *Antibiotics* **1990**, *13*, 1293−1301.
4. Liu, J. FK506 and Cyclosporin, Molecular Probes for Studying Intracellular Signal Transduction. *Immunol. Today* **1993**, *14*, 290−295.
5. D'Alessio, R.; Rossi A. Short Synthesis of Undecylprodigiosin. A new Route to 2, 2′-Bipyrrolyl-pyrromethylene Systems. *Synlett* **1996**, 513−514.

6. Bernasconi, C. F. *Relaxation Kinetics*; Academic: New York, 1976; Chapter 4.
7. Blake, A. J.; Hunter, G. A.; McNab, H. A Short Synthesis of Prodigiosin Analogues. *J. Chem. Soc., Chem. Commun.* **1990**, 734−736.
8. Stamnes, M. A.; Rutherford, S. L.; Zucker, C. S. Cyclophilins: A New Family of Proteins Involved in Intracellular Folding. *Trends Cell. Biol.* **1992**, *2*, 272−276.

JS980225W

Acute and Long-Term Stability Studies of Deoxy Hemoglobin and Characterization of Ascorbate-Induced Modifications

BRUCE A. KERWIN,*,† MICHAEL J. AKERS,‡ IZYDOR APOSTOL,§ CAMILLE MOORE-EINSEL,§ JEFFREY E. ETTER,|| EDWARD HESS,§ JULIE LIPPINCOTT,§ JOSEPH LEVINE,§ ANTONY J. MATHEWS,§ PATRICIA REVILLA-SHARP,§ ROSS SCHUBERT,§ AND DOUGLAS L. LOOKER§

Contribution from *Amgen, One Amgen Center Drive, Mail Drop 8-1-C, Thousand Oaks, California 91320-1799, Eli Lilly and Company, Lilly Corporate Center, Indianapolis, Indiana 46285, Baxter Hemoglobin Therapeutics Inc., 2545 Central Avenue, Boulder, Colorado 80301, and RxKinetix, Inc., 1172 Century Drive, Suite 260, Louisville, Colorado 80027.*

Received May 26, 1998. Accepted for publication September 1, 1998.

Abstract □ The reaction of ascorbate with recombinant hemoglobin (rHb1.1) in the presence of differing partial pressures of oxygen was studied. In the presence of 15 000 ppm (1.5%) residual oxygen, ascorbate/oxygen-mediated reactions resulted in an increased rate of autoxidation, modification of the β-globin, increased oxygen affinity and decreased maximum Hill coefficient. One of the observed modifications to the β-globin was a 72 Da addition to its N-terminus. Detailed characterization indicates the modification was an imidazolidinone type structure. Thorough deoxygenation of the hemoglobin solution to <150 ppm of oxygen prior to addition of ascorbate was required to prevent these modifications. Addition of ascorbate to the deoxy hemoglobin (deoxyHb) at pH 8 induced aggregation, eventually leading to precipitation. No such precipitation was observed at pH 7. Long-term storage of the hemoglobin was carried out by addition of ascorbate to deoxyHb at pH 7. The level of methemoglobin remained at <2% for up to 1 year at 4 °C, with no detectable precipitation of the protein. Modifications similar to those observed by the acute studies were observed over the 1-year period and correlated with disappearance of the added ascorbate.

Introduction

Recombinant human hemoglobin (rHb1.1) is a pseudo-tetramer composed of two β-globins and genetically fused α-globins (di-α-globin). Each of the four subunits contains a heme prosthetic group. The Presbyterian mutation in the β-globin (Asn-108β→Lys) was introduced to decrease the oxygen affinity. Genetic fusion of the two α-globins prevents dissociation of the hemoglobin into αβ-dimers,[1] such that rHb1.1 can be used as an oxygen-carrying therapeutic. The ability to package and store this type of product as a ready-to-use large volume parenteral (LVP) liquid has many potential advantages during situations such as trauma and surgery when use of frozen formulations would not be as practical.

One of the major obstacles to long-term storage of hemoglobin is its propensity to autooxidize. Upon binding oxygen, the reduced form of the heme iron (ferrous, Fe^{2+}) can react with the oxygen to form ferric (Fe^{3+}) iron and superoxide:[2−4]

$$HbFe^{2+} + O_2 \leftrightarrow HbFe^{2+} - O_2 \rightarrow HbFe^{3+} + O_2^-$$

When the iron in heme is oxidized to the ferric form, oxygen can no longer bind to the heme iron and the hemoglobin is nonfunctional. Oxidation of the heme also leads to an approximately 1000-fold increase in the rate of heme loss,[5] which can result in denaturation and precipitation of the globin.[6] The activated oxygen species produced during the autoxidation reaction can damage the hemoglobin causing polymerization,[7,8] oxidation of the amino acid side chains,[9] and hemichrome formation.[10,11] These modifications can lead to changes in the tertiary and quaternary structure, resulting in decreased oxygen equilibrium binding parameters and eventually precipitation of the protein. In contrast, ferrous deoxy hemoglobin (deoxyHb) does not undergo autoxidation and is known to be intrinsically more stable than oxy hemoglobin (oxyHb) against thermal and chemical denaturation and precipitation of the protein.[12−14]

The nonenzymatic reduction of methemoglobin (metHb) has been achieved using reducing agents such as dithionite and ascorbate. In solution under deoxy conditions, dithionite ($S_2O_4^{2-}$) dissociates into $2SO_2^{\bullet-}$,[15] which can quickly react with MetHb, reducing it back to the ferrous form.[16,17] The byproduct of the reaction, bisulfite (HSO_3^-), can generate severe or fatal adverse reactions in humans,[18] making it unsuitable as a component of a LVP formulation. Ascorbate has been known since the 1940s to reduce deoxygenated metHb to the ferrous form[19,20] and can safely be given intravenously.[18] The literature indicates that ascorbate reduces metHb by first ionizing to the anionic form, ascorbate^{2-}, which reacts with the ferric iron to form ferrous hemoglobin and the anionic ascorbate radical, which eventually rearranges to form dehydroascorbate.[21]

To overcome the problems associated with storage of oxyHb solutions, we examined methods to store deoxygenated hemoglobin solutions at 4 °C. Ascorbate was added to reduce residual methemoglobin to the more stable ferrous form. Here we present studies that determined the effects of pH, oxygen tension, and ascorbate levels on rHb1.1 stability.

Materials and Methods

Materials—Recombinant hemoglobin (rHb1.1) was produced at Somatogen as previously described.[1] Ascorbic acid (sodium salt), sodium phosphate (monosodium and disodium salts), sodium chloride, ethylenediaminetetraacetic acid (EDTA, disodium salt), (*N*-[2-hydroxyethyl]piperazine-*N*′-[2-ethanesulfonic acid]) (HEPES), potassium cyanide, and tris(hydroxymethyl)aminomethane (Tris hydrochloride and sodium salt) were all purchased from Sigma Chemical Company (St. Louis, MO). Polysorbate 80 was purchased from either Calbiochem Corporation (San Diego, CA) or ICN Chemicals (Los Angeles, CA). Glass vials and gray butyl

* To whom correspondence should be addressed. Telephone: (805) 447−0712. Fax: (805) 498−8674. E-mail: bkerwin@amgen.com.
† Amgen.
‡ Eli Lilly and Company.
§ Baxter Hemoglobin Therapeutics Inc.
|| RxKinetix, Inc.

10.1021/js980221r CCC: $18.00
Published on Web 11/19/1998

rubber stoppers were purchased from Wheaton Corporation (Charlotte, NC). Stedim-5 bags were purchased from Stedim Corporation (Pleasant Hill, CA), aluminum foil overwraps were purchased from Kegan Corporation (Auburn, IN), and ZPT 100 "Ageless" oxygen scavengers were purchased from Mitubiabi Gas and Chemical Company (Japan).

Methods—*Dynamic Light Scattering*— Dynamic light scattering (DLS) was performed using a Nicomp 370 Submicron Particle Sizer equipped with a 40mW HeNe laser. Data were collected and averaged over 10 min and analyzed using the C370 v.12 software program provided by PSS (Particle Sizing Systems, Santa Barbara, CA).

Equilibrium Oxygen Binding—The parameters P_{50} and n_{max} were determined using a hemox analyzer as previously described[22] at 37 °C and pH 7.40 in 50 mM HEPES (free acid) and 150 mM NaCl.

Methemoglobin Concentration—Percent metHb was measured by determining the fractions of reduced and oxidized hemes using difference spectroscopy as described by Kerwin et al.[43]

Ascorbic Acid Analysis—Ascorbic acid analyses were performed by diluting samples 1:1 into 10 mM homocysteine (sparged with helium) to stabilize the ascorbate. The diluted samples were centrifuged in Centricon-30 microconcentrators (Amicon Inc., Beverly, MA), and the filtrate was analyzed by size exclusion chromatography (SEC) on a TosoHaas G2500W_{XL} (7.6 × 300 mm) column using an isocratic elution with 5 mM KH_2PO_4, pH 3, as the mobile phase. Flow rate was 1 mL/min. Analyte peaks were detected at 255 nm, and their concentration was determined by comparison with standards of known concentration.

Reversed-Phase HPLC (RP-HPLC)—Samples were prepared by precipitation with ice-cold acid/acetone[23] and solubilization of the pellet in 0.1% trifluoroacetic acid (TFA)/20% acetonitrile. The RP-HPLC analyses were performed using a Zorbax C3 analytical column (0.46 × 25 cm) mounted on an HP1090 HPLC system (Hewlett-Packard, Wilmington, DE). The oven temperature was maintained at 40 °C. Solvent A was 0.1% TFA in water and solvent B was 0.1% TFA in acetonitrile. The flow rate was 1 mL/min. The column was equilibrated in 65% solvent A/35% solvent B. Following sample injection, the column was maintained at the starting conditions for 5 min then ramped to 51% solvent A/49% solvent B over a period of 45 min.

Size Exclusion Chromatography—The molecular weight distribution of the hemoglobin was monitored by high-performance SEC (HPSEC) as described by Kerwin et al.[43]

Liquid Chromatography-Mass Spectrometry (LC-MS)—Mass spectrometry was performed using a Finnigan Mat LCQ as the end detector with an HP1090 HPLC on the front end to run reversed-phase separation. Analysis by MS/MS was performed as previously described by Lippincott et al.[24]

Tryptic Mapping—Tryptic mapping was performed as previously described by Lippincott et al.[24]

Sodium Dodecyl Sulfate Polyacrylamide Gel Electrophoresis (SDS-PAGE)—SDS-PAGE was performed based on the method of Laemmli.[25] Aliquots (5 μg) were diluted with 2 volumes of SDS sample buffer (Novex Corp., San Diego, CA) containing 0.1 M dithiothreitol (DTT) and heated at 65 °C for 5 min. Samples were electrophoresed on an 8−16% polyacrylamide gradient Tris-glycine gel for 2.5 h at 120 V. The gel was stained with Coomassie blue and then destained with a solution of 40% methanol, 10% glacial acetic acid, and 50% water. Destained gels were digitized using an IS-1000 digital imaging system (Alpha Innotech Corp., San Leandro, CA).

Pepsin Mapping of Multimeric rHb1.1—The multimeric fraction of rHb1.1 was isolated using SEC as previously described. The globins were precipitated with 20 volumes of cold 0.6% HCl in acetone, solubilized in 0.1% TFA, and separated by C3 RP-HPLC as previously described. Fractions containing β-globin and di-β-globin were collected, lyophilized, then resuspended in 8 M urea. Following resuspension, the samples were heated for 10 min at 60 °C, then diluted with 0.1% TFA to a final urea concentration of 2 M. The final globin concentration was 1 mg/mL. Pepsin (Pierce, Rockford, IL) was added to the sample at an enzyme: substrate ratio of 1:50 (w/w). After 2 h, the peptides were separated by RP-HPLC using a C18 column (Zorbax SB-300, 0.46 × 25 cm) on an HP1090 HPLC. Solvent A was 0.1% TFA(v/v) in water and solvent B was 0.1% TFA (v/v) in acetonitrile. The column was equilibrated in 5% solvent B at 1 mL/min. Following injection, the starting conditions were maintained for 5 min. The gradient was then developed by increasing to 70% solvent B over a period of 70 min. The absorbance was monitored at 215 nm.

Preparation of rHb1.1 Solutions Equilibrated with Headspace Oxygen Concentrations of 15 000 or 150 ppm—For oxygen and ascorbate modification experiments, solutions of rHb1.1 (50 mg/mL in 150 mM sodium chloride, 5 mM sodium phosphate, pH 7.2) were equilibrated with either a gas mixture of 15 000 ppm oxygen in nitrogen or purified nitrogen containing <10 ppm of oxygen. Equilibration was achieved by passing the gas mixture through water for humidification then over the hemoglobin solution, which was mixed using a Rotovap (Brinkman Instruments). The equilibration procedure was typically performed for 4−6 h, and the hemoglobin solution was maintained at ~10 °C in an ice-water bath. Following equilibration, the flask containing the hemoglobin solution was capped and transferred into a glovebag (Aldrich Chemical Company, Milwaukee, WI) along with all necessary equipment and solutions. The bag was sealed and equilibrated with either the gas mixture containing 15 000 ppm of oxygen or the mixture containing <10 ppm of oxygen. The oxygen content in the bag equilibrated with the <10 ppm oxygen mixture measured at 150 ppm of oxygen when monitored with a Mocon HS-750 analyzer (Modern Controls Inc.). Ascorbate (0.5 M in deoxygenated water) was added to aliquots of the hemoglobin solution to give final concentrations of 0.5, 1, 2, and 5 mM. Solutions were filtered through 0.2-μm syringe filters. Aliquots (0.5 mL) were transferred into 2-mL Wheaton glass vials, capped with gray butyl rubber stoppers, and sealed with crimp rings. All solutions were incubated at 4 °C. For pH-induced aggregation studies, hemoglobin solutions were diafiltered into buffer (150 mM sodium chloride, 5 mM sodium phosphate) at pH 7 or pH 8 at 4 °C. Solutions were equilibrated with nitrogen containing <10 ppm oxygen, reduced with 2 mM ascorbate, filtered through a 0.2-μm filter, and aliquoted into 2-mL glass vials as already described. The oxygen tension in the glovebag was maintained at ≪200 ppm oxygen.

Shaking-Induced Aggregation Studies—All manipulations of material were done in a nitrogen flushed glovebag (Aldrich) kept at <300 ppm of oxygen. Tween 80 was added to aliquots of deoxy-rHb1.1 (80 mg/mL in 150 mM sodium chloride, 5 mM sodium phosphate, pH 7.2, and <5 μM EDTA) to approximate final concentrations of 0, 0.025, 0.05, 0.075, and 0.1% (w/v). The solutions were then realiquoted (1.5 mL) into 3.5-mL Wheaton vials and sealed with gray butyl rubber stoppers, and the Tween 80 concentrations were measured as described below. The final Tween 80 concentrations were 0, 0.019, 0.045, 0.071, and 0.095%. All prepared samples were used within 1week of preparation. The deoxyHb aliquots (1.5 mL) were placed on their sides on a Hoeffer rotary shaker and shaken at either 100, 170, or 225 rpm for 1 h at room temperature. The samples were then assayed for protein aggregation by light obscuration.

Measurements of Protein Aggregates by Light Obscuration—Aggregates ≥2 μm were measured using a HIAC/Royco light particle counter equipped with a HIAC HRLD400HC sensor and a model 3000A sampler. Data were corrected for background counts and reported as the average from separate samples.

Measurement of Tween 80 Concentration in Hemoglobin Solutions—Samples were analyzed for Tween 80 in the following fashion: To a 1-mL aliquot of sample in a 15-mL polypropylene Falcon tube was added 1 mL of 6 M guanidine hydrochloride and 4 mL of dichloromethane. The mixture was then vortexed for 1 min to form a thick emulsion. The emulsion was separated by centrifugation at 4000 rpm for 20 min. The lower organic layer was isolated and placed into a clean 15-mL polypropylene Falcon tube. To that organic layer was added 1 mL of a cobalt ammonium thiocyanate test solution (250 g of ammonium thiocyanate, 110 g of cobalt nitrate, and 200 g of sodium chloride in 1 L of purified water). The mixture was then vortexed for 30 s and allowed to separate. The organic layer was then analyzed spectrophotometrically at 320 nm. The concentration of Tween 80 in the original sample, which is proportional to the absorption at 320 nm, was then calculated from a standard curve of know Tween 80 concentrations.

Preparation of deoxyrHb1.1 Solutions for Long-Term Stability Studies in Vials—Recombinant hemoglobin from our manufacturing plant (~50 mg/mL), in 150 mM sodium chloride, 5 mM sodium phosphate (pH 6.8−7.2), ~0.03% polysorbate 80, and <5 μM EDTA, was deoxygenated by stripping the oxyHb solution with nitrogen gas. Following deoxygenation, the hemoglobin was

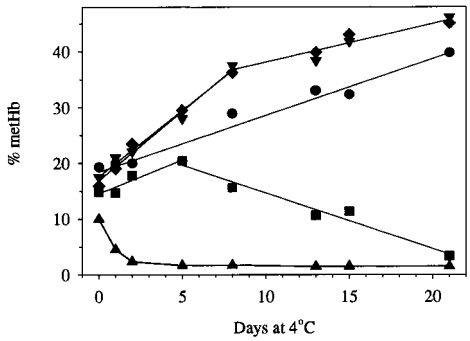

Figure 1—MetHb formation of rHb1.1-containing ascorbate in solution and equilibrated with 15 000 ppm of oxygen in the headspace. Recombinant hemoglobin (rHb1.1) was equilibrated with 15 000 ppm of oxygen and reacted with increasing concentrations of ascorbate. Symbols represent the following ascorbate concentrations in each sample: (circles) 0 mM ascorbate; (octagons) 0.5 mM ascorbate; (diamonds) 1 mM ascorbate; (squares) 2 mM ascorbate; (triangles) 5 mM ascorbate. Data from samples containing 0, 0.5, 1, and 2 mM ascorbate were fit using linear regression to generate rates of metHb formation.

concentrated to 80 mg/mL and ascorbate was added to a final concentration of 2 mM. The solution was then packaged into the glass vials as already described and incubated at 4 °C for up to 1 year.

Preparation of DeoxyrHb1.1 Solutions for Long-Term Stability Studies in Bags—Recombinant hemoglobin from our manufacturing plant (<50 mg/mL), in 150 mM sodium chloride, 5 mM sodium phosphate (pH 6.9−7.1), ~0.03% polysorbate 80, and <5 μM EDTA, was deoxygenated by stripping the oxyHb solution with nitrogen gas. Following deoxygenation, the hemoglobin was concentrated to 80 mg/mL and ascorbate was added to a final concentration of 2 mM. The solution was transferred to a nitrogen-purged glovebox and packaged as 30-mL aliquots in 60-mL flexible Stedim-5 containers then overwrapped with aluminum foil pouches. ZPT 100 "Ageless" oxygen scavengers were placed between the foil overwrap and the flexible containers prior to heat sealing the overwrap containers. The foil pouches were heat sealed and incubated at 4 °C for up to 1 year.

Results

Acute Studies—*Effects of Ascorbate and Oxygen Concentrations on Methemoglobin Formation*—The ability of ascorbate to reduce recombinant methemoglobin (met-rHb) in the presence of differing partial pressures of oxygen in the vial headspace was studied. Equilibration of the rHb solution with a gas mixture containing 15 000 ppm oxygen caused an increase in the rate of met-rHb formation above that observed for recombinant oxyhemoglobin (oxy-rHb) of 1% per day versus 0.7% per day, respectively (see Figure 1, oxy-rHb data not shown). Addition of ascorbate to 0.5 and 1 mM produced a two-stage autoxidation profile with an initial autoxidation rate of 2.4% per day through 8 days of storage, followed by a slower rate of 0.7% per day. Increasing the ascorbate concentration to 2 mM decreased the autoxidation rate to ~1.1% per day for the first 5 days, followed by a reduction in the met-rHb content at a rate of 1% per day for the remainder of the study period (15 days). In contrast, the hemoglobin solution containing 5 mM ascorbate demonstrated no overall increase in the level of met-rHb and showed a complete reduction by approximately 2 days following addition of the ascorbate. Hemoglobin equilibrated with 150 ppm of oxygen in the headspace oxidized at the rate of approximately 0.2% per day (see Figure 2). Addition of ascorbate (0.5−5 mM) decreased the concentration of met-rHb. The rate of reduction was dependent upon the concentration of ascorbate.

Effects of Ascorbate and Oxygen Concentrations on P_{50} and n_{max}—Recombinant hemoglobin typically has a P_{50} of

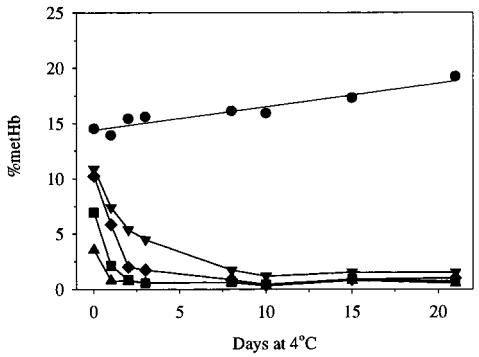

Figure 2—MetHb formation of rHb1.1-containing ascorbate in solution and equilibrated with 150 ppm of oxygen in the headspace. Recombinant hemoglobin (rHb1.1) was equilibrated with 150 ppm of oxygen and reacted with increasing concentrations of ascorbate. Symbols are the same as in Figure 1. The data for the sample containing 0 mM ascorbate were fit by linear regression to generate the rate of metHb formation.

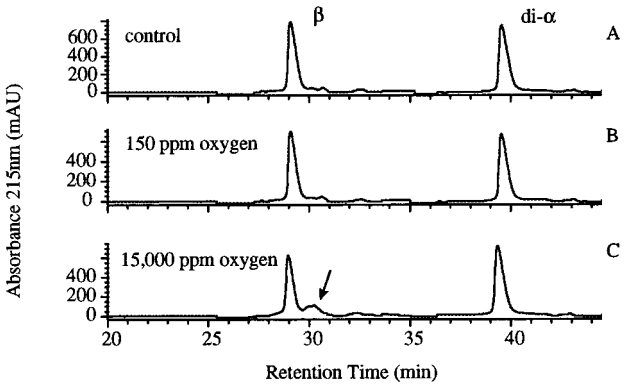

Figure 3—Reversed phase HPLC analysis of hemoglobin after incubation with 5 mM ascorbate at differing partial pressures of oxygen. Samples were the same as in Figure 1 and were analyzed following 15–16 days of storage at 4 °C. The control hemoglobin represents a sample of rHb incubated with 15 000 ppm of oxygen and 0 mM ascorbate. The arrow indicates the difference peak of the β-globin shoulder containing the M+72 addition.

32 mmHg and an n_{max} coefficient of 2.3. By 21 days, the hemoglobin sample equilibrated with 15 000 ppm of oxygen and containing 5 mM ascorbate demonstrated a P_{50} of 37.3 mmHg and an n_{max} coefficient of 1.5. The hemoglobin equilibrated with 150 ppm of oxygen and 5 mM ascorbate demonstrated a P_{50} of 33.8 mmHg and an n_{max} coefficient of 2.11 at 21 days.

Characterization of Ascorbate-Mediated Modification of Hemoglobin—Reversed-phase HPLC was used to evaluate potential ascorbate-mediated modifications of the globins. The sample equilibrated with 15 000 ppm oxygen and containing 5 mM ascorbate showed a decrease in the height of the β-globin peak compared with the control along with the appearance of an increased area on the trailing shoulder of the β-globin peak (Figure 3). In contrast, the chromatographic profile of the sample equilibrated with 150 ppm oxygen and containing 5 mM ascorbate was not significantly different from a control sample with no added ascorbate. The sample equilibrated with 15 000 ppm oxygen and 5 mM ascorbate was further analyzed by LC-MS. The analyses of the shoulders on the β-globin peak revealed the presence of three significant β-globin adducts with mass additions of 16, 42, and 72 Da. With the exception of the 42 Da mass gain on the β-globin, these mass additions were not observed in the hemoglobin solution prior to addition of the ascorbate. Tryptic mapping of the starting hemoglobin revealed a small peak assigned to acetylation of the N-terminus of the β chain with a characteristic 42 Da mass gain. Additionally, using single ion chromatograms, we searched for modifications on

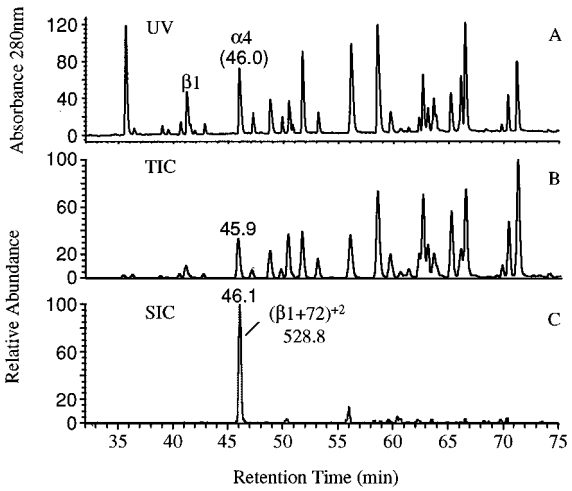

Figure 4—Tryptic map of ascorbate modified rHb1.1. Tryptic peptides of rHb1.1 incubated with 2 mM ascorbate were separated by C18 RP-HPLC and analyzed by mass spectrometry: panel A, UV trace at 280 nm; panel B, total ion chromatogram; panel C, specific ion chromatogram of the double-charged β1+72 ion.

tryptic peptides. Only one significant difference peak was found at 45 min; exhibiting a mass of 1055.4 amu and eluting as a trailing shoulder on the α4 peptide (see Figure 4). The peak was previously identified as the M+72 modification of the N-terminus of the β-globin affected by ascorbate and oxygen.[26] In agreement with the tryptic mapping, V8 mapping of this hemoglobin confirmed the existence of the M+72 at the N-terminus of the β-globin and did not show additional difference peaks.

The fraction containing the M+72 peptide from the tryptic map was isolated and infused into the LCQ mass spectrometer. The double-charged ion (528.8) was fragmented to elucidate the position and structure of the modification. MS/MS fragmenation spectra (see Figure 5) showed an unusual pattern of a neutral loss of 44 Da followed by an additional loss of 18 Da. These mass losses corresponded to mass gains of 28 and 10 Da on the unmodified peptide. The neutral loss of 44 and 18 Da is usually associated with decarboxylation and loss of water, respectively. The observed B ions, starting from B_2, showed gains of 10, 28, or 72 Da, confirming the presence of the modification within the first two residues. The series of Y ions was consistent with unmodified peptide, except the Y_7 and Y_8 ions. The Y_7+10 mapped a mass gain of 10 Da to His2 and the Y_8 ion mapped a mass gain of both 10 and 28 Da to the Met1 position. A mass gain corresponding to Y_7+28 was not found. The N-terminus was shown to be blocked to Edman sequencing.[26] Reduction with cyanoborohydride did not change either the elution position or the mass of the M+72 peptide. The data are consistent with an imidazolidinone structure for the modification.

Effects of pH on the Stability—The propensity of the deoxy-rHb in the presence of 2 mM ascorbate to aggregate and precipitate during 4 °C storage was studied at pH 7 and pH 8 by DLS. Comparison of the day 0 samples at pH 7 and pH 8 indicated that their size profiles are similar with no apparent aggregation (see Figure 6). Aggregates of ~100 and 500 nm were observed in the pH 8 sample after 2 weeks of incubation at 4 °C. Following an additional 2 weeks of storage, the size of the aggregates appeared to increase, and by 6 weeks a precipitate was visible in the bottoms of the vials. The pH 7 samples did not display any indications of aggregation or precipitation for up to 8 weeks of storage.

Effects of Tween 80 on Aggregation—The ability of Tween 80 to prevent protein aggregation of deoxy-rHb1.1 at a liquid surface interface was examined by shaking-induced aggregation. Samples not containing Tween 80 demonstrated an increase in the number of aggregates per milliliter at ≥2 μm with increasing shaking speed, resulting in an ~500-fold increase between 0 and 225 rpm (Figure 7A). Even greater increases were observed for aggregates ≥10 μm (Figure 7B) and ≥25 μm (Figure 7C), resulting in ~2000- and ~4000-fold increases, respectively. Addition of Tween 80 significantly decreased aggregation of the deoxyHb when shaken at speeds up to 170 rpm. At this speed, a slight increase in aggregates was observed compared with the 0 rpm sample, but no difference was seen between any of the Tween 80-containing solutions. Increasing the speed to 225 rpm produced a level of aggregation in the hemoglobin sample containing 0.019% Tween 80 similar to that observed without surfactant. In contrast, at 225 rpm, the samples containing 0.045−0.095% Tween 80 did not demonstrate an increase in aggregate levels above that observed for 170 rpm. Furthermore, these samples produced only an ~10-fold increase in counts for aggregates ≥2 μm (Figure 7A) and ≥10 μm (Figure 7B) and an ~5-fold increase for aggregates ≥25 μm (Figure 7C) compared with those observed prior to shaking.

Long-Term Storage in Vials—*Overall Stability of the Hemoglobin during Long-Term Incubation at 4 °C in Vials*—Based on the observations made during the acute stability studies, four sets of samples of rHb1.1 were prepared under deoxy conditions, defined as 150 ppm oxygen, followed by addition of 2.0 mM ascorbate. Polysorbate 80, 0.03%, was added to preclude aggregation of the protein during storage. The levels of ascorbate dropped steadily during the 12-month storage period from approximately 1.75 to 0.25 mM (see Figure 8, panel A). In accordance with the presence of ascorbate, the concentration of metHb remained at <2% (limit of quantitation) of the total protein during the course of the study (data not shown). Starting samples had a P_{50} value of approximately 32 mmHg and did not change for the first 6 months of storage (see Figure 8, panels B and C). Between 6 and 12 months, the P_{50} dropped slightly to 30 mmHg. The Hill Coefficient measured at n_{max} demonstrated a slight decrease between 0 and 6 months from an initial value of 2.2 to 2.0. A further change was observed at 12 months, with the n_{max} further decreasing to 1.8.

The propensity of the protein to aggregate during the incubation was measured by both SEC and DLS. We did not observe a change in the multimeric hemoglobin level (see Figure 8, panel D) or changes in the overall chromatographic HPSEC profile of the hemoglobin during the first 6 months of storage (data not shown). Between 6 and 9 months an increase in the level of multimer was observed which increased further between 9 and 12 months. Higher order aggregates (>2 μm) were not seen in the samples until 12 months incubation (see Figure 8, panel E). An initial apparent diameter of 6.2 nm was measured by DLS at the beginning of the study, with an apparent increase to 6.8 nm and the appearance of species with apparent diameters of 212, 240, and 306 nm at the end of 12 months. Precipitation was not observed on the vial walls during the study period (data not shown).

Characterization of the Multimeric Species—The multimer observed by SEC analysis was further characterized. Hemoglobin samples following 15 days and 1 year incubation at 4 °C were treated with 0.1 M DTT for 15 min and analyzed by SEC (Table 1). The DTT treatment of the 15-day sample resulted in reduction of 50% of the multimer, whereas only 25% of the multimer was reduced by DTT following a 1-year incubation. Prior to deoxygenation and addition of ascorbate, multimer present in the hemoglobin was completely reducible by DTT treatment (data not

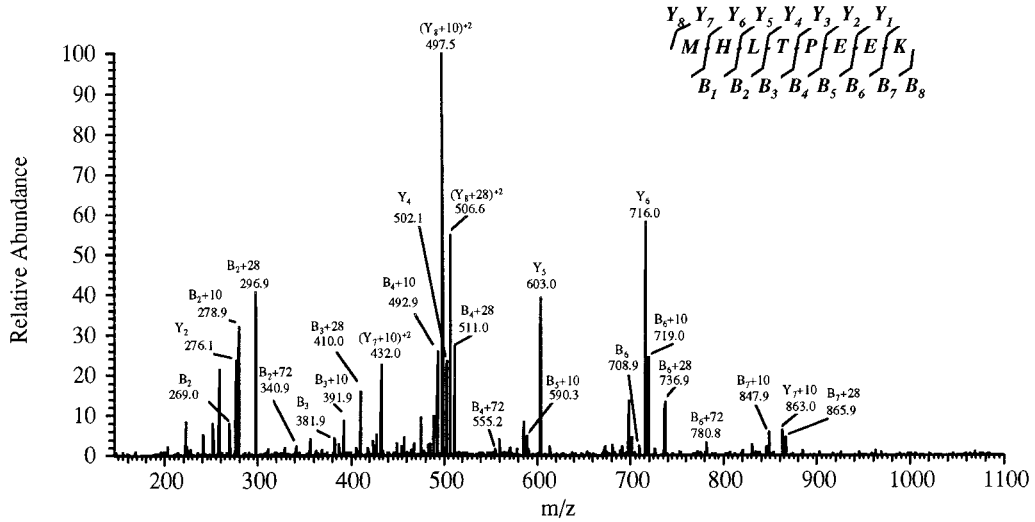

Figure 5—MS/MS fragmentation spectra of the M+72 difference peptide. The double-charged ion *m/z* 528.8 was chosen and fragmented. Due to the limits of the LCQ, the B_1 ion or its adducts were to small to detect. The B and Y ions were annotated according to the legend in the upper right of the figure.

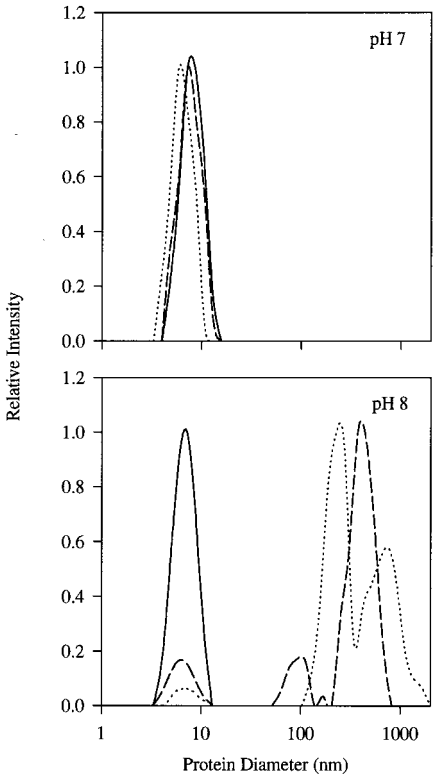

Figure 6—Dynamic light scattering analysis on the effect of pH during 4 °C storage: (solid line) starting material after equilibration at the indicated pH; (dashed line) after 4 °C incubation for 2 weeks; (dotted line) after 4 °C incubation for 4 weeks.

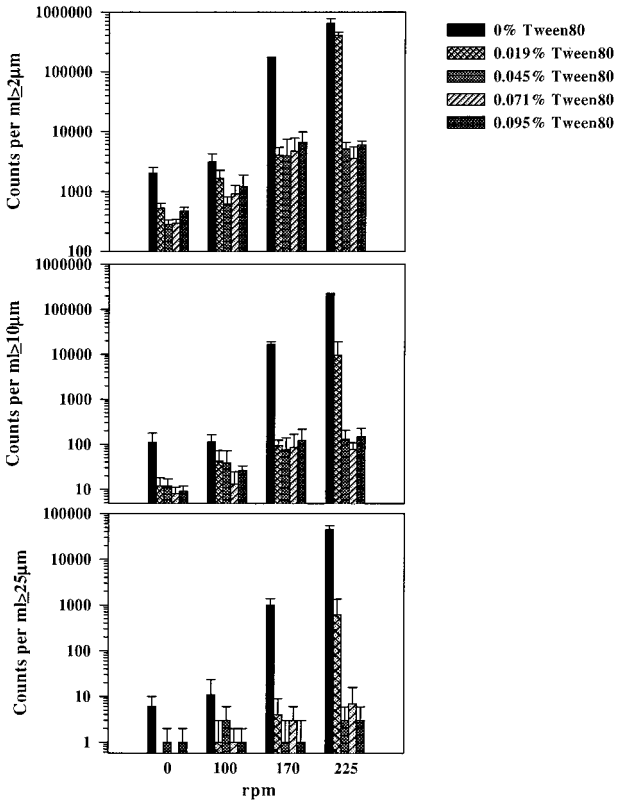

Figure 7—Effect of Tween 80 on protein aggregation of deoxy Optro during shaking in vials. Samples were prepared as described in *Materials and Methods* and shaken at the indicated speeds for 1 h at room temperature. Protein aggregation was measured using the Hiac/Royco particle counter. Triplicate vials were prepared for each Tween 80 concentration and analyzed separately. Values are reported as the average of values from the three vials ± standard deviation.

shown). Following treatment with DTT, the remaining multimer was isolated from the SEC column and analyzed by SDS-PAGE. As shown in Figure 9 (panel A), the isolated monomer peak only contained the β- and di-α-globin bands. A number of bands were present in the isolated non-DTT-reducible multimer peak with molecular weights ranging between 45 and 68 kDa. The origin of the cross-linked hemoglobins observed by SDS-PAGE was further investigated. Addition of ascorbate directly to oxyHb followed by overnight incubation at room temperature produced a cross-linking pattern similar to that observed for the 1-year samples (see Figure 9, panel B, lane 3). Saturation of the hemoglobin with carbon monoxide (lane 5) or deoxygenation (lane 8) prior to ascorbate addition prevented additional formation of the higher molecular weight bands. Addition of hydrogen peroxide to the CO-Hb sample (lane 6) produced a banding pattern similar to that observed with ascorbate and oxyHb. Deoxy-Hb incubated with ascorbate demonstrated a small increase in the intensity of the banding pattern over that seen in deoxyHb alone.

The DTT-reducible multimer was characterized by pepsin mapping. The SEC purified multimer from freshly prepared rHb1.1 was separated by C3 RP-HPLC and the

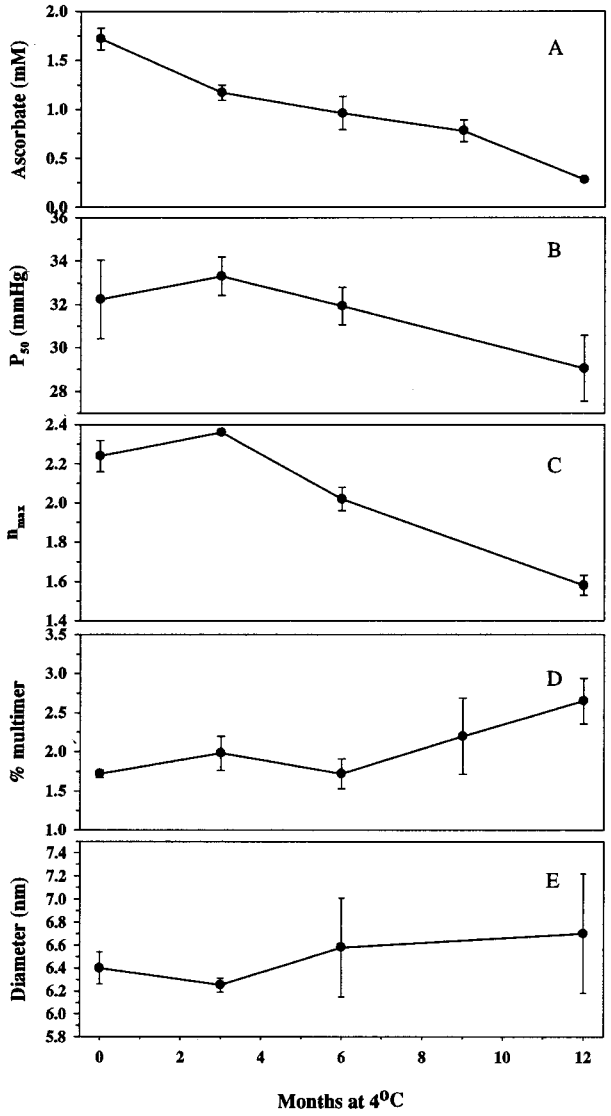

Figure 8—Change in ascorbate, P_{50}, n_{max}, percent multimer, and apparent diameter of samples of rHb during long-term storage in vials. All values are the average from four samples analyzed at the indicated time points. The value for ascorbate at 12 months is from a single sample. Data were analyzed for statistically relevant differences during the storage period using a one-way analysis of variance (ANOVA) and a Newman-Keuls post-hoc analysis. Panel A is the ascorbate concentration ($p < 0.05$ for 0 versus 3, 6, and 9 months; $p < 0.05$ for 3 versus 6 and 9 months; 6 and 9 months were not differerent). Panel B is the parameter P_{50} ($p < 0.05$ for 0, 3, and 6 versus 12 months; all others were not different). Panel C is the Hill coefficient, n_{max} ($p < 0.05$ for all samples versus each other). Panel D is the percent multimeric hemoglobin ($p < 0.05$ for 0, 3, 6, and 9 months versus 12 months). Panel E is the apparent diameter of the hemoglobin during incubation at 4 °C (samples were not statistically different from each other).

Table 1—Size Exclusion Chromatographic Analysis of Multimeric rHb Before and After Treatment with Dithiothreitol[a]

treatment	% multimer (–DTT)	% multimer (+DTT)	% change
15 days incubation at 4 °C	1.47	0.75	–50%
1 year incubation at 4 °C	2.84	2.05	–25%

[a] Analysis were performed on single samples.

β globin and di-β-globin were isolated and cleaved with pepsin. The pepsin-generated peptides were separated by C18 RP-HPLC, and a single difference peak in the di-β-globin map was found (see Figure 10, panel B). The same pepsin digest was incubated at pH 8.0 with 0.1 M DTT and

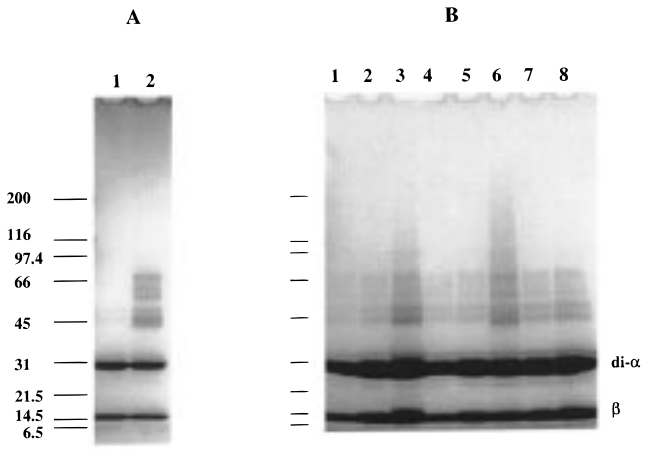

Figure 9—SDS–PAGE analysis of isolated monomer and multimer and reactions of rHb1.1 with ascorbate. Panel A: Hemoglobin (rHb1.1), incubated with 2 mM ascorbate for 1 year at 4 °C under reduced oxygen tension was reduced with DTT, and the nonreducible multimer was separated from the monomer by SEC and isolated: lane 1, isolated monomer; lane 2, isolated multimer. Panel B: Hemoglobin (rHb1.1) at 75 mg/mL, prepared as oxy, carbonmonoxy, or deoxy, was incubated overnight at room temperature with 2 mM ascorbate and then precipitated with acid acetone and resuspended in reducing buffer and analyzed: lane 1, rHb1.1 control; lane 2, oxy-rHb1.1 at room temperature overnight; lane 3, oxy-rHb1.1 + ascorbate; lane 4, CO-rHb1.1 at room temperature overnight; lane 5, CO-rHb1.1 + ascorbate; lane 6, CO-rHb1.1 + 4 mM hydrogen peroxide; lane 7, deoxy-rHb1.1 at room temperature; lane 8, deoxy-rHb1.1 + ascorbate.

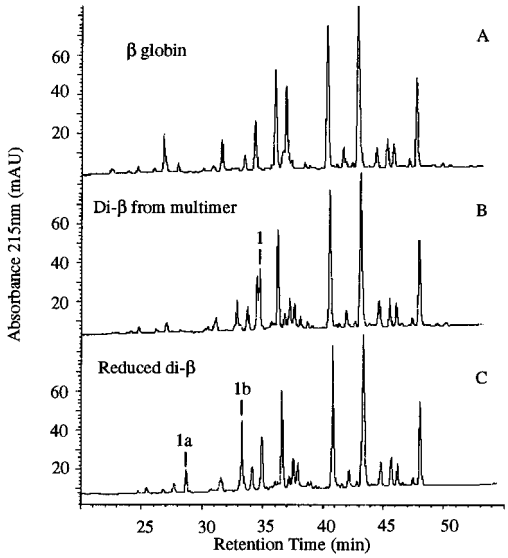

Figure 10—Pepsin maps of DTT-reducible cross-linked β-globin. Multimeric rHb1.1 was isolated by SEC and further separated by C3 RP-HPLC: panel A, pepsin-treated β globin isolated from RP-HPLC; panel B, pepsin-treated cross-linked β-globin from RP-HPLC (arrow denotes the difference peptide); panel C, isolated difference peptide from B after reduction with DTT.

rechromatographed. Two new difference peptides were generated, the first eluting at 28.7 min (1a, Panel C) and the second eluting at 32.6 min (1b, Panel C). Sequencing of the isolated peptides by Edman degradation identified the first peptide as β89−102 and the second as β86−102. Both of these peptides contain cysteine at position 93, suggesting the hemoglobin was cross-linked through Cys93 of the β-globins from separate monomeric hemoglobins.

Characterization of Globin Modification During One Year Incubation at 4 °C in vials—Modification of the hemoglobin primary structure was further examined by RP-HPLC analysis and in-line mass spectrometry (RP/LC-MS) to detect potential storage induced modification of the protein primary structure. Comparison of the control hemoglobin

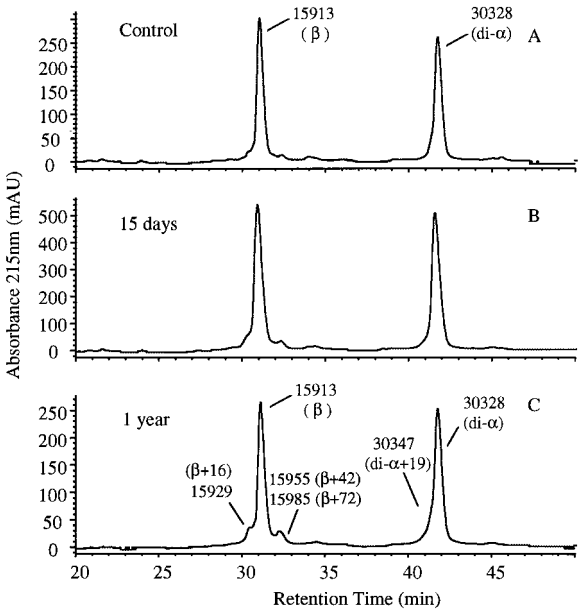

Figure 11—Reversed-phase HPLC analysis of rHb1.1 during 1 year of storage at 4 °C in vials. Samples were prepared and stored as already described. At the indicated period of time, samples were removed and aliquots were stored at –80 °C until analysis. Samples were prepared for analysis by acid/acetone precipitation immediately upon thawing and analyzed by RP-HPLC and RP/LC-MS as described in *Materials and Methods*.

with the samples stored in ascorbate for 1 year shows modification to both shoulders of the β-globin peak and the leading shoulder of the di-α-globin peak (see Figure 11). The main β globin peak showed a characteristic mass of 15 913 Da. The adduct eluting at 28.8 min in front of the main β peak had a mass increase of 16 Da, likely due to oxidation. The quantity of this adduct varied during the study period. Two β-globin adducts were observed in the peak eluting at 30.6 min and included mass additions of 42 and 72 Da. The peak eluting at that position increased from 2.2 to 4% during the study period. Cross-linked β globins were observed with masses of 31 825 and 31 908 Da. Only one modification was observed on the di-α-globin peak occurring on the leading shoulder with a mass increase of 19 Da compared to 30 328 Da observed for the main di-α peak. The main di-α peak is composed of the methylated (30 338 Da) and the unmethylated (30 324 Da) forms of the di-α-globin.[27]

Long-Term Storage in Bags—Studies of deoxy-rHb1.1 were also carried out with deoxyHb stored in oxygen-impermeable containers to prevent ascorbate degradation. Aggregation was not definitively observed with the long-term studies in vials, so polysorbate 80, 0.03%, was again included in the formulations to preclude aggregation of the protein during storage. The initial ascorbate levels present in each of the three lots were not significantly different from those present following 12 months incubation at 4 °C (Table 2). In accordance with the presence of ascorbate, the concentration of met-rHb remained at <2% (limit of quantitation) of the total protein during the course of the study. Changes were also not observed in the P_{50} and n_{max} measurements, with average values of 32 mmHg for the P_{50} and 2.17 for the n_{max} during the incubation period (Table 2). Additionally, we did not observe an increase in the multimer content (Table 2) or changes in the overall chromatographic HPSEC profile of the hemoglobin (data not shown).

Dynamic light scattering was used to ascertain the presence of higher order aggregates not detected by HPSEC. As seen in Figure 12, an initial diameter of 5.9–6.2 nm was measured by DLS at the beginning of the study, with

Table 2—Ascorbate, P_{50}, n_{max}, and Multimer Data for Deoxy-rHb1.1 Stored in Oxygen-Impermeable Bags[a]

lot	months at 4 °C	ascorbate (mM)	P_{50} (mmHg)	n_{max}	multimer (% of total Hb)
1	0	1.65 ± 0.03	32.5 ± 0.5	2.21 ± 0.03	2.7 ± 0.5
	12	1.67 ± 0.01	32.9 ± 0.2	2.21 ± 0.03	1.7 ± 0.1
2	0	1.42 ± 0.02	33.5	2.44	2.1 ± 0.3
	12	1.39 ± 0.01	33.4 ± 0.4	2.15 ± 0.04	2.1 ± 0.5
3	0	1.70 ± 0.02	32.0	2.01	1.3 ± 0.2
	12	1.64 ± 0.01	32.8 ± 0.1	2.22 ± 0.01	1.8 ± 0.4

[a] Three bags were analyzed at each time point, and the average ± standard deviation are reported. Samples without standard deviation are from analysis of a single analysis only.

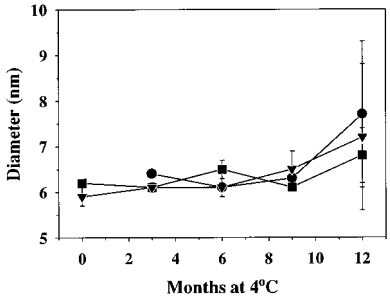

Figure 12—Dynamic light scattering analysis of rHb1.1 during 1 year of storage at 4 °C in bags. At the indicated periods of time, samples were removed and immediately analyzed for aggregates <0.2 μm by DLS as described in *Materials and Methods*. Three bags of each lot were analyzed at each time point, and the average ± standard deviation are reported.

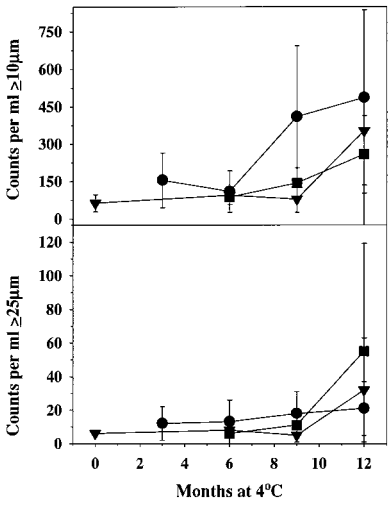

Figure 13—Light obscuration analysis of rHb1.1 during 1 year of storage at 4 °C in bags. At the indicated period of time, samples were removed and immediately analyzed for aggregates ≥10 and ≥25 μm by light obscuration as described in *Materials and Methods*. Three bags of each lot were analyzed at each time point and the average ± standard deviation are reported.

no discernible change through 9 months of storage. At 12 months, the mean diameter of the rHb in each of the lots increased to an average diameter of 7.2 nm, indicating the presence of aggregates. Distinct peaks were not differentiated by the instrument, rather the aggregation was detected as an overall increase in the size of the protein. Aggregates of 10 μm (Figure 13A) and 25 μm (Figure 13B) demonstrated a similar pattern with minimal changes through 9 months and a sharp increase between 9 and 12 months. Increases in the levels of aggregates were not associated with measurable precipitation of the protein because the soluble protein concentration did not decrease significantly during the course of the study (data not shown).

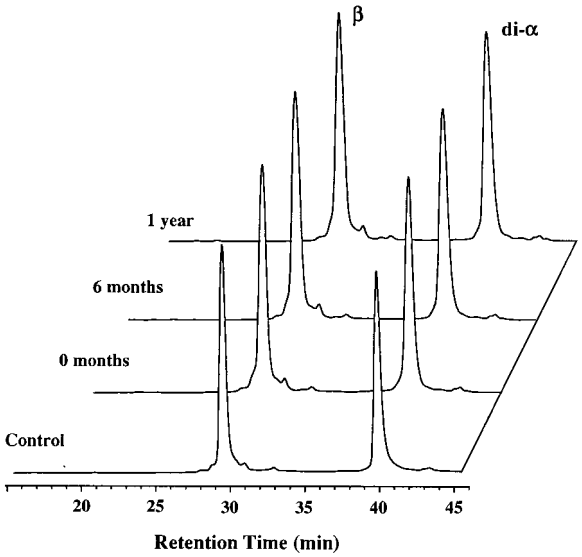

Figure 14—Reversed phase HPLC analysis of rHb1.1 during 1 year of storage at 4 °C in bags. At the indicated period of time, samples were removed and aliquots were stored at –80 °C until analysis. Samples were prepared for analysis by acid/acetone precipitation immediately upon thawing and analyzed by RP-HPLC and RP/LC-MS as described in *Materials and Methods*.

Modification of the hemoglobin primary structure was again examined by RP/LC-MS to detect potential storage-induced degradation of the protein primary structure. Comparison of the control hemoglobin with the hemoglobin formulated in ascorbate (Figure 14, compare panels A and B) shows modification to both the leading and lagging shoulders of the β-globin peak, with a corresponding decrease in the ratio of β- to di-α-globin peak heights from 1.14 to 1.07, respectively. Once the hemoglobin was formulated and put in storage conditions, RP-HPLC profiles did not reveal the presence of new peaks nor decreases in the height ratio of the β-globin-to-di-α-globin peaks. Ascorbate/oxygen-mediated modifications that were previously described were observed in the samples but did not appear to change qualitatively during the study period. We were unable to quantitate these adducts (in the hemoglobin) by RP/LC-MS due to a lack of mass resolution. The RP/LC-MS analysis of the β- and di-α-globin peaks demonstrated a consistent molecular weight for each of the globin chains during storage of 15 913 Da for the β globin and 30 330 for the di-α-globin.

Discussion

The purpose of this study was to investigate the effects of ascorbate, oxygen, and pH on the long-term stability of deoxyHb. Storage of deoxyHb has been investigated by other researchers.[28,29] Kramlova et al.[29] attempted to store stroma-free hemoglobin following bubbling of nitrogen through the solution. After 1 year at 4 °C, the metHb content increased from 5 to 41%. De Venuto[28] stored hemoglobin at 25 °C in sealed glass ampules following three cycles of gas evacuation and flushing with nitrogen. In those studies, the metHb content increased from 6.1 to 52.8% during the 8-week storage period. It is likely that the hemoglobin in those investigations oxidized due to incomplete deoxygenation of the solutions. Keilin[30] demonstrated that the rate of autoxidation increases dramatically if the hemoglobin is only partially deoxygenated. Investigations by Brantley et al.[2] using myoglobin confirmed these observations and demonstrated that under saturating oxygen conditions autoxidation occurs through a unimolecular dissociation of the neutral superoxide radical ($HOO^{\bullet}$) from the heme. At low oxygen concentrations, autoxidation may occur through the unimolecular reaction as well as a bimolecular reaction. The bimolecular reaction is facilitated by the structure of partially deoxygenated Mb, which allows a water molecule to coordinate with His64 and the ferrous iron of the deoxy heme. The water molecule is capable of stabilizing the ferric state of the oxidized heme, thereby facilitating the extraction of an electron from the ferrous iron by an approaching oxygen. When rHb1.1 was equilibrated with 15 000 ppm of oxygen in the headspace and stored at 4 °C, the autoxidation rate increased by approximately 50% over that normally observed for oxy-rHb1.1. Equilibrating the hemoglobin with 150 ppm of oxygen in the headspace of our containers did not completely prevent autoxidation, although it did decrease the rate by approximately 5-fold from that observed with 15 000 ppm of oxygen in the headspace (see Figures 1 and 2). Further reduction of autoxidation was accomplished by inclusion of the reducing agent, ascorbate. The ascorbate likely reacted with excess oxygen present in the solution and reduced any ferric hemoglobin back to the ferrous state.

Reaction of reducing agents such as ascorbate with oxygen can produce superoxide.[31] During our studies, inclusion of 0.5 and 1 mM ascorbate in formulations containing 15 000 ppm of oxygen in the headspace increased the autoxidation rate compared with the rate in solution without ascorbate (see Figure 1). The increased oxidation rate observed for the first 8 days was likely due to production of superoxide by ascorbate and oxygen until all the ascorbate in the solution was consumed. Superoxide quickly disproportionates to hydrogen peroxide, which can react with and oxidize ferrous Hb. In the sample of hemoglobin incubated with 2 mM ascorbate, it is likely that ascorbate consumed the oxygen and reduced the metHb. Both reactions conceivably occurred in competition, resulting in the slower rate of metHb reduction than that seen with 5 mM ascorbate.

The protein modifications observed during the long-term studies in vials (Figures 8–11) were similar to those observed during the acute studies and are likely related to the reaction of ascorbate with oxygen which produces superoxide.[31] Oxygen may have entered the reaction vials during the study period through the permeable butyl rubber stoppers. The protein cross-linking observed by SDS-PAGE (Figure 9) was likely related to formation of hydrogen peroxide from the superoxide anion because the cross-linking pattern in the presence of H_2O_2 was similar to that when the oxyHb was incubated with ascorbate. Additionally, a similar type of cross-linking pattern was observed when HbAo was incubated with hydrogen peroxide (data not shown), suggesting that the cross-linking was not due to a difference in susceptibility of the two hemoglobins to H_2O_2. The cross-linking of the protein would explain the decrease in the P_{50} and n_{max} observed during our long-term studies. A decrease in the oxygen binding parameters of recombinant hemoglobin has been observed after heterogeneous intramolecular cross-linking of the globins.[32]

Chemical modifications of the hemoglobin observed during the acute studies (see Figures 3 and 4) were also present in the material used for long-term stability following addition of ascorbate (see Figures 10 and 14), and increased during storage of the rHb1.1 in vials (see Figure 10). The modifications did not appear to increase when the hemoglobin was stored in an oxygen-impermeable storage system (Figure 14, compare panels B–D). Reduction of metHb by ascorbate produces dehydroascorbate, which could subsequently react with low levels of residual oxygen and produce other potentially highly reactive

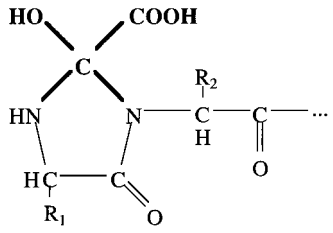

R_1 = Met
R_2 = His

Figure 15—Proposed structure of the M+72 addition to the N-terminal tryptic peptide of the β-globin. The section in boldtype represents the proposed +72 addition.

byproducts that could modify the protein.[33−36] A number of new modifications of hemoglobin were detected by C3 RP/LC-MS analysis. The most significant mass gains were 16 and 72 Da. Mass gains of 58 Da (carboxymethylation) and 130 Da (dehydroascorbate addition) could not be definitively assigned by LC-MS (data not shown). Only one difference peak was observed during peptide mapping and was assigned as a 72 Da addition to the N-terminus of the β chain. This result may indicate that other modifications are labile or heterogeneously distributed across β and di-α-globins. Heterogeneous modifications not detectable by tryptic mapping have also been observed.[32] The mass increase of 16 Da is likely due to oxidation of side chains of labile amino acids.[37,38] Amino acid analysis indicated the presence of a low level of labile oxo-histidine in the sample equilibrated with 15 000 ppm of oxygen and incubated with 5 mM ascorbate (data not shown).

Efforts were made to identify the M+72 modification at the N-terminus of the β-globin. The results from the MS/MS fragmentation together with the protein chemistry (blocked to Edman degradation and not reducible by borohydride) suggest that the modification is distributed between the Met1 and His2 residues, which is consistent with an imidazolidinone structure. Imidazolidinone structures have been postulated to form at the N-terminus of the β globin in reactions of human hemoglobin A_0 with aldehydes.[39−42] Our results also indicate that the modification is likely to contain labile carboxy and hydroxy groups, which is consistent with the observed neutral loss of 44Da- and 18 Da-derived fragments. The proposed structure for the modification is presented in Figure 15. The structure indicates a similarity to an oxalate-derived modification. However, incubation of hemoglobin with oxalate did not produce any trace of the M+72 modification (data not shown). Examination of the known ascorbate degradation pathway[34−36] did not indicate the presence of degradation byproducts that could directly derivatize the hemoglobin and result in a mass increase of 72 Da. A number of ascorbate degradation products containing carbonyl groups could initially form a Schiff's base with the N-terminus followed by rearrangement to the imidazolidinone structure and further degradation (i.e., oxidation) to produce the observed mass gain.

Surfactants may stabilize protein structure by binding to hydrophobic surfaces on proteins [44−46] or by competing with proteins for adsorption at liquid−surface interfaces.[47−49] Studies by Kerwin et al.[43] demonstrated that Tween 80 does not bind to the rHb1.1, suggesting that the decreased aggregation observed during the shaking studies (Figure 7) was due to competition of the surfactant with the liquid−surface interfaces. Therefore, because the hemoglobin would be stored for long periods of time while in contact with the ethyl vinyl acetate surface of the bag, Tween 80 was added to the hemoglobin solutions to circumvent possible aggregation during the study period. In contrast to the long-term study in vials in which little aggregation was observed by DLS, a variable degree of aggregation was observed by both DLS and light obscuration when the hemoglobin was stored in the bags. This difference may be due to differential affinities of the surfactant and the hemoglobin for either the glass or ethyl vinyl acetate surfaces. Work by Hlady and co-workers[49,50] has demonstrated that the interaction of proteins with surfaces is dependent on the surface chemistry. It is not likely that the aggregation was due to the initial modification of the hemoglobin following ascorbate addition (Figure 14) because similar observations were made during the long-term studies of deoxy-rHb in vials (Figure 11), which contained a much higher degree of protein modification at the end of the study period. The concentration of Tween 80 used in our formulation may have been too low to successfully prevent interaction of the hemoglobin with the ethylvinyl acetate bag surface, eventually leading to aggregation. It is also possible that the N-terminal methionine and the "glycine linker" between the α subunits, which are not present in HbAo, add to the instability of the protein, making it more prone to aggregation. However, we do not feel that this is the case because comparison of the α-carbons of the X-ray crystallographic structures of deoxy-rHb1.1 and HbAo have a root-mean-square (RMS) deviation of 0.187 with the met1-Cα and an RMS deviation of 0.170 without the met1-Cα (E. Brucker, personal communication).

The data presented here demonstrate a significant advance in our ability to successfully store hemoglobin-based oxygen-carrying therapeutics. To our knowledge this is the first evidence that a deoxygenated hemoglobin can be stored for an extended period of time in the presence of reducing agents without metHb formation or precipitation. Stability against met-rHb formation was increased >50-fold by deoxygenation and reduction of the protein with ascorbate. Storage of the deoxy-rHb in vials resulted in modification to the protein primary structure (Figure 11), decreased P_{50} and n_{max} values (Figure 8), and formation of cross-linked protein (Figure 9). These modifications were all likely related to the influx of oxygen through the vial stopper and were not observed following storage of the hemoglobin in the foil overwrapped containers.

References and Notes

1. Looker, D.; Abbott-Brown, D.; Cozart, P.; Durfee, S.; Hoffman, S.; Mathews, A. J.; Miller-Roehrich, J.; Shoemaker, S.; Trimble, S.; Fermi, G.; Komiyama, N. H.; Nagai, K.; Stetler, G. A human recombinant haemoglobin designed for use as a blood substitute. *Nature* **1992**, *356*, 258−260.
2. Brantley, R. E., Jr.; Smerdon, S. J.; Wilkinson, A. J., Singleton, E. W.; Olson, J. S. The mechanism of autoxidation of myoglobin. *J. Biol. Chem.* **1993**, *268*, 6995−7010.
3. Misra, H. P.; Fridovich, I. The generation of superoxide radical during the autoxidation of hemoglobin. *J. Biol. Chem.* **1972**, *247*, 6960−6962.
4. Wever, R.; Oudega, B.; Van Gelder, B. F. Generation of superoxide radicals during the autoxidation of mammalian oxyhemoglobin. *Biochim. Biophys. Acta* **1973**, *302*, 475−478.
5. Hargrove, M. S.; Whitaker, T.; Olson, J. S.; Vali, R. J.; Mathews, A. J. Quaternary structure regulates hemin dissociation from human hemoglobin. *J. Biol. Chem.* **1997**, *272*, 17385−17389.
6. Harvey, J. W.; Kaneko, J. J. Oxidation of human and animal haemoglobins with ascorbate, acetylphyenylhydrazine, nitrite and hydrogen peroxide. *Br. J. Haem.* **1976**, *32*, 193−203.
7. Sonaye, B.; Naik, A. A.; Yadav, S. D.; Chakrabarti S. Protein cross-linking during oxidative denaturation of methaemoglobin. *Ind. J. Med. Res.* **1995**, *101*, 75−80.
8. Thillet, J.; Michelson A. M. Oxidation and cross-linking of human hemoglobins by activated oxygen species. *Free Rad. Res. Comms.* **1985**, *1*, 89−100.

9. Steffek, R. P.; Thomas M. J. Hydrogen peroxide modification of human oxyhemoglobin. *Free Rad. Res. Comm.* **1991**, *12*−*13*, 489−497.
10. Rachmilewitz, E. A. Formation of hemichromes from oxidized subunits. *Ann. N. Y. Acad. Sci.* **1969**, ***165***, 171−184.
11. Rachmilewitz, E. A.; White J. M. Haemichrome formation during in-vitro oxidation of Hb Koln. *Nature (New Biol.)* **1973**, *241*, 115−117.
12. Cho, K. C.; Choy, C. L. Thermal stability of hemoglobin and myoglobin effect of spin states. *Biochim. Biophys. Acta* **1980**, *622*, 320−330.
13. Muller, R. G.; Schmid, K. Enthalpy of denaturation for human hemoglobin in the oxygenated and deoxygenated state. *Therm. Acta* **1983**, *69*, 115−125.
14. Reider, R. F. Hemoglobin stability: Observations on the denaturation of normal and abnormal hemoglobins by oxidant dyes, heat and alkali. *J. Clin. Inv.* **1970**, *49*, 2369−2376.
15. Lambeth, D. O.; Palmer G. The kinetics and mechanism of reduction of electron-transfer proteins and other compounds of biological interest by dithionite. *J. Biol. Chem.* **1973**, *248*, 6095−6103.
16. Dalziel, K.; O'Brien, J. R. P. Side reactions in the deoxygenation of dilute oxyhaemoglobin solutions by sodium dithionite. *Biochem. J.* **1957**, *67*, 119−124.
17. Dixon, H. B. F.; McIntosh R. Reduction of methaemoglobin in haemoglobin samples using gel filtration for continuous removal of reaction products. *Nature* **1967**, *213*, 399−400.
18. *Handbook of Pharmaceutical Excipients*; Wade, A.; Weller P. J., Eds.; The Pharmaceutical Press: London, 1994; pp 451−453.
19. Gibson, Q. H. The reduction of methaemoglobin by ascorbic acid. *Biochem. J.* **1943**, *37*, 615−618.
20. Vestling, C. S. The reduction of methemoglobin by ascorbic acid. *J. Biol. Chem.* **1942**, *143*, 439−446.
21. Al-Ayash, A. I.; Wilson, M. T. The mechanism of reduction of single-site redox proteins by ascorbic acid.. *Biochem. J.* **1979**, *177*, 641−648.
22. Hoffman, S. J.; Looker, D. L.; Roehrich, J. M.; Cozart, P. E.; Durfee, S. L.; Tedesco, J. L.; Stetler G. L. Expression of fully functional tetrameric human hemoglobin in *Escherichia coli*. *Proc. Natl. Acad. Sci. U.S.A.* **1990**, *8*, 8521.
23. Wikowska, H. E.; Bitsch, F.; Shackleton, C. H. Expediting rate variant hemoglobin characterization by combined HPLC/electrospray mass spectrometry. *Hemoglobin* **1993**, *17*, 227−242.
24. Lippincott, J.; Hess, E.; Apostol I. Mapping of recombinant hemoglobin using imobilized trypsin cartridges. *Anal. Biochem.* **1997**, *252*, 314−325.
25. Laemmli, U.K. Cleavage of structural proteins during the assembly of the head of bacteriophage T4. *Nature* **1970**, *227*, 680−685.
26. Kerwin, B. A.; Hess, E.; Lippincott, J.; Kaiser, R.; Apostol I. Oxygen and ascorbate mediated modification of a recombinant hemoglobin. In *Techniques in Protein Chemistry VIII*; Marshak D. R., Ed.; Academic: New York, 1997; pp 399−407.
27. Apostol, I.; Aitken, J.; Levine, J.; Lippinicott, J.; Davidson, J. S.; Abbott-Brown, D. Recombinant protein sequences can trigger methylation of N-terminal amino acids in *Escherichia coli*. *Protein Sci.* **1996**, *4*, 2616−2618.
28. DeVenuto, F. Stability of hemoglobin solution during extended storage. *J. Lab. Clin. Med.* **1978**, *92*, 946−952.
29. Kramlova, M.; Pristoupil, T. I.; Ulrych, S.; Hrkal, Z. Stroma-free haemoglobin solution for infusion: Changes during storage. *Haematologia* **1976**, *10*, 365−371.
30. Keilin, D. The oxidation of haemoglobin to methaemoglobin by oxygen. II. The relation between the rate of oxidation and the partial pressure of oxygen. *Proc. R. Soc. London, Ser. B.* **1935**, *118*, 560−577.
31. Stocker, R.; Frei B. Endogenous antioxidant defences in human blood plasma. In: *Oxidative Stress. Oxidants and antioxidants*; Sies H, Ed.; Academic: New York, 1991; pp 224−225.
32. Levine, J.; Weickert, M.; Pagratis, M.; Etter, J.; Mathews, A.; Fattor, T.; Lippincott, J.; Apostol, I. Identification of a nickel(II) binding site on hemoglobin which confers susceptibility to oxidative deamination and intramolecular cross-linking. *J. Biol. Chem.* **1998**, *273*, 13037−13046.
33. Kang, S.-O.; Snapper, H.; Lohman, W. The oxidative degradation of L-ascorbic acid via an α-keto aldehyde. *Z. Naturforsch* **1982**, *37*, 1064−1069.
34. Kimoto, E.; Tanaka, H.; Ohmoto, T.; Choami, M. Analysis of the transformation products of dehydro-L-ascorbic acid by ion-pairing high-performance liquid chromatography. *Anal. Biochem.* **1993**, *214*, 38−44.
35. Washko, P. W.; Welch, R. W.; Dhariwal, K. R.; Wang, Y.; Levine M. Ascorbic acid and dehyrdoascorbic acid analyses in biological samples. *Anal. Biochem.* **1992**, *204*, 1.
36. Kurata, T.; Sakurai Y. Degradation of L-ascorbic acid and mechanism of nonezymic browning reaction. *Agr. Biol. Chem.* **1967**, *31*, 177−184.
37. Davies, K. J. A.; Delsignore, M. E.; Lin S. W. Protein damage and degradation by oxygen radicals. II. Modification of amino acids. *J. Biol. Chem.* **1987**, *262*, 9902−9907.
38. Li, S.; Schoneich, C.; Wilson, G. S.; Borchardt, R. T. Chemical pathways of peptide degradation. V. Ascorbic acid promotes rather than inhibits the oxidation of methionine to methionine sulfoxide in small model peptides. *Pharm. Res.* **1993**, *10*, 1572−1579.
39. Braun, K. P.; Pavlovich, J. G.; Jones, D. R.; Peterson C. M. Stable acetaldehyde adducts: structural characterization of acetaldehyde adducts of human hemoglobin N-terminal β-globin chain peptides. *Alcohol Clin. Ex.p Res.* **1997**, *21*, 40−43.
40. San George, R. C.; Hoberman H. D. Reaction of acetaldehyde with hemoglobin. *J. Biol. Chem.* **1986**, *261*, 6811−6821.
41. Sillanaukee, P.; Hurme, L.; Tuominen, J.; Ranta, E.; Nikkara, S.; Seppa K. Structural characterisation of acetaldehyde adducts formed by a synthetic peptide mimicking the N-terminus of the hemoglobin β-chain under reducing and nonreducing conditions. *Eur. J. Biochem.* **1996**, *240*, 30−36.
42. Lin, R. C.; Smith, J. B.; Radtke, D. B.; Lumeng, L. Structural analysis of peptide-acetaldehyde adducts by mass spectrometry and production of antibodies directed against nonreduced protein-acetaldehyde adducts. *Alcohol. Clin. Exp. Res.* **1995**, *19*, 314−319.
43. Kerwin, B. A.; Heller, M. C.; Levin, S. H.; Randolph, T. W. Effects of Tween 80 and sucrose on acute short-term stability and long-term storage at −20 °C of a recombinant hemoglobin. *J. Pharm. Sci.* **1998**, *87*, 1062−1068.
44. Bam, N. B.; Randolph, T. W.; Cleland, J. L. Stability of protein formulations: investigation of surfactant effects by a novel EPR technique. *Pharm. Res.* **1995**, *12*, 2−11.
45. Sukow, W. W.; Sandberg, H. E.; Lewis, E. A.; Eatough, D. J.; Hansen, L. D. Binding of the Triton X-100 series of nonionic surfactants to bovine serum albumin. *Biochemistry* **1980**, *19*, 912−917.
46. Sukow, W. W.; Bailey, J. Characterization of the binding of Triton X-100 to equine and rabbit serum albumin. *Physiol. Chem. Phys.* **1981**, *13*, 455−459.
47. Claesson, P. M.; Blomberg, E.; Frogberg, J. C.; Nylander, T.; Arnebrandt, T. Protein interactions at solid interfaces. *Adv. Colloid. Interface Sci.* **1995**, *57*, 161−227.
48. Thurow, H.; Geisen, K. Stabilization of dissolved proteins against denaturation at hydrophobic interfaces. *Diabetologia* **1984**, *27*, 212−218.
49. Ho, C.-H.; Britt, D. W.; Hlady, V. Human LDL and HSA adsorption onto model surfaces studied by total internal reflection fluorescence and scanning force microscopy. *J. Mol. Recognit.* **1996**, *9*, 444−455.
50. Buijs, J.; Hlady, V. Adsorption kinetics, conformation and mobility of growth hormone and lysozyme on solid surfaces, studied with TIRF. *J. Colloid Interface Sci.* **1997**, *190*, 171−181.

Acknowledgments

We thank Dr. Richard Gorczinski and Dr. David Foster for critical reading of and helpful suggestions with the manuscript and Dr. Eric Brucker for analysis of the hemoglobin X-ray crystallographic structures. This work would not be possible without the support of a large group of Somatogen technical staff in manufacturing and assay services.

JS980221R

Ionization Constants and Distribution Coefficients of Phenothiazines and Calcium Channel Antagonists Determined by a pH-Metric Method and Correlation with Calculated Partition Coefficients

ULRICH FRANKE, ANGELA MUNK, AND MICHAEL WIESE*

Contribution from *Department of Pharmaceutical Chemistry, University of Halle and Wittenberg, Wolfgang-Langenbeck-Str. 4, D-06120 Halle, Germany*

Received May 13, 1998. Accepted for publication October 13, 1998.

Abstract □ The pH–metric technique was used to determine the ionization constants and distribution coefficients of 10 phenothiazines and five ionizable calcium channel antagonists. Because the studied compounds were poorly water soluble and quite lipophilic with partition coefficients in the range of 3.5 to 5.5, organic cosolvents had to be added for the determination of the ionization constants to avoid precipitation of the free bases. The effect of the cosolvents dioxane and methanol on the extrapolation to pure water was compared. For both cosolvents a very good agreement with accessible published ionization constants was obtained, however the slope of the regression line was much smaller for dioxane, yielding more reliable estimates according to the standard deviation of the extrapolated values. Thus, dioxane might be preferable to methanol as a cosolvent for the determination of ionization constants of sparingly water soluble bases. Also the *n*-octanol/water partition coefficients were determined and compared with published data and values calculated with the ClogP, ACD, and HINT programs. Although the obtained values were approximate in conformity with the published data, the calculated partition coefficients differed from the experimental ones considerably for the majority of the investigated compounds. Furthermore, the ion pair partitioning and the distribution coefficients at physiological pH 7.4 were determined. The pH-dependent distribution profiles showed the strong influence of the ionization constants and of the distribution of the ion pairs on the overall distribution. This result strongly suggests that greater use should be made of measured distribution coefficients in quantitative structure–activity relationship studies. The potentiometric method is a convenient way to determine the distribution properties of drug molecules at pH values relevant for the biological system under investigation.

Introduction

The knowledge of drug membrane interactions is important in the understanding of the biological action of many drugs.[1] Often the pharmacological behavior of drugs is related to their distribution or nonspecific binding in or to membranes.[2,3] *n*-Octanol/water is often used to model the distribution of a drug by measuring the partition coefficient in this system.[4] The partition coefficient, *P*, is most commonly defined for the uncharged form of an ionizable substance; in addition it can be also defined for the charged form of the substance. Often the neutral and charged forms of lipophilic molecules are able to partition into the organic phase in solvent/water mixtures.[5] The pH-dependent distribution profile enables the identification of the number of species present and is a powerful tool for comparing the properties of clusters of similar compounds.[6] Precisely and accurately determined values of the ionization constants, pK_a, and the partition coefficients of the neutral and charged species are necessary to obtain distribution coefficients. The conventional methods for measuring pK_a and/or log *P* values are UV spectroscopy, the shake-flask method,[7] HPLC,[8] and centrifugal partition chromatography,[9] respectively. A major drawback of these methods is that they are very time-consuming. An additional problem for these kinds of determination is often the very low solubility of pharmaceutical compounds. The acid−base titration in aqueous solution is an alternative for ionizable compounds.[10−15] To increase the solubility, a water-miscible cosolvent (methanol, dioxane, dimethyl sulfoxide) is added for the pK_a determination of sparingly water soluble compounds.

For phenothiazines used as neuroleptics, a good correlation between the determined log *P* values and a selected biological action has been reported.[16−20] Also, for calcium channel antagonists, the lipophilicity and interaction with membrane phospholipids seem to play a major role in their pharmacological activity.[2] In our efforts to characterize and better understand drug−membrane interactions and the distribution of membrane-active compounds, we first report in this paper the application of the pH−metric method to the determination of pK_a, log *P*, and log P_{ion} values for 10 structurely related phenothiazines and five calcium channel antagonists in *n*-octanol/water.

The aims of this work were severalfold: to validate the pH−metric method and to advance the exact analysis of pK_a values and the distribution in *n*-octanol/water of neutral and positively charged drugs; to study the influence of the cosolvents dioxane and methanol necessary in cases of poorly soluble compounds on the determined pK_a value; to compare experimental with calculated log *P* values to estimate the reliability of the latter ones; to establish the pH-dependent distribution profile of every sample; and to compare the application of either the log *P* values or apparent distribution coefficient (log *D*) values at physiological pH in quantitative structure−activity relationships (QSAR) studies (i.e., in attempting to predict the pharmaceutical potency or the in vivo absorption).

Experimental Section

Reagents—The pharmaceutical substances used are as follows: promethazine hydrochloride, chlorpromazine hydrochloride, triflupromazine hydrochloride, prochlorperazine dimaleate, trifluoperazine dihydrochloride, perphenazine, fendiline hydrochloride, and 1-octanol (HPLC grade) from Sigma Chemical Company, Germany; verapamil hydrochloride from Aldrich, Germany; methanol (HPLC grade) from Carl Roth GmbH, Karlsruhe, Germany; hydrochloric acid standardized ampules and potassium hydroxide

* Author to whom correspondence should be sent. Telephone: ++49 345 5525040. Fax: ++49 345 5527018. E-mail: wiese@pharmazie.uni-halle.de.

10.1021/js980206m CCC: $18.00 Published on Web 12/09/1998

standardized ampules from Riedel-de-Haen AG, Seelze, Germany; and potassium chloride (pro analysis) and dioxane from VEB Laborchemie, Apolda, GDR. The dioxane was distilled twice before use. The following drugs were generous gifts: levomepromazine hydrochloride from Bayer AG, Leverkusen, Germany; thioridazine hydrochloride and thiethylperazine dimaleate from Sandoz AG, Nürnberg, Germany; gallopamil hydrochloride from Knoll Deutschland GmbH, Ludwigshafen, Germany; amlodipine besylate from Pfizer GmbH, Karlsruhe, Germany; and nicardipine hydrochloride from Ciba-Geigy GmbH, Wehr, Germany. The water used was purified with an Elgastat Maxima, Elga Ltd., Bucks, UK.

Practical Part of pH−Metric Method—The pK_a and the log *P* values were determined by potentiometric titration using a PCA 101 instrument from Sirius Analytical Instruments Ltd., Forrest Row, UK, at 25.0 ± 0.2 °C at an adjusted ionic strength of the aqueous phase of 0.15 M potassium chloride. Details of the method have been previously published elsewhere.[10−15] The pK_a and log *P* measurements were done in separate experiments, and the concentration of the drug titrated was between 0.08 and 0.15 mM. The lower pK_a values of the diprotic phenothiazines were determined in triplicate in pure aqueous 0.15 M KCl. To avoid precipitation of the neutral bases, certain amounts of cosolvents were added in case of the higher pK_a values. The concentration of the dioxane cosolvent varied between 15 and 40 wt % and, for the phenothiazines, 20−50 wt % methanol cosolvent was used additionally. The apparent pK_a values (p$_s K_a$) were measured in at least five different cosolvent/water mixtures. The log *P* determinations were replicated at least three times with different volume ratios of *n*-octanol/water. Because of the high partitioning of all samples into the organic phase, a reasonable volume ratio of 0.005 to 0.05 was applied (0.1 to 1.0 mL octanol in 20 mL total volume). For the dimaleate counterion present in the prochlorperazine and thiethylperazine salts, a pK_a of 5.78 and a log *P* of −0.47 were determined in the pH range between pH 2.5 and 10.5, which is in close agreement with the literature (pK_a = 5.80; log *P* = −0.4).[21]

Theoretical Part of pH−Metric Method—An iterative least squares refinement procedure was used to calculate the final values. Typically, the values of the goodness of fit (GOF) weighting scheme used for all refinements were in the range from 0.6 to 1.4 for pK_a measurements without cosolvent, log *P* titrations, and multi-set refinements. A GOF value of 1 means that on average the observed and calculated curve differ not more than one internal standard deviation of the device. The Yasuda−Shedlovsky procedure extrapolates the real aqueous pK_a from the obtained p$_s K_a$ values by plotting the p$_s K_a$ value and the logarithm of the water concentration against the reciprocal of the dielectric constant, ϵ, for the mixtures according to eq 1:[13]

$$p_s K_a + \log [H_2O] = a + b/\epsilon \quad (1)$$

A negative slope of the regression line is characteristic for basic substances. To investigate the reliability of the electrode calibration factors supplied, comparative titrations in dioxane and methanol cosolvent mixtures were performed.

The partition coefficient, log *P*, of the neutral bases was calculated according to eq 2:

$$\log P = \log(10^{(pK_a - p_o K_a)} - 1) - \log(r) \quad (2)$$

If only the partitioning of the neutral species into *n*-octanol was assumed, the calculated partition coefficients decreased with increasing amounts of *n*-octanol, indicating a significant contribution of the monoprotonated form to partitioning. Therefore, the partitioning of the monoprotonated form was taken into account in the fitting process. For the monoprotic bases, the partition coefficient of the ion, log P_{ion}, was calculated iteratively, correcting the apparent log *P* value obtained in different *n*-octanol/water ratios to a constant value. According to this procedure, only the partitioning of the monoprotonated form accounted for the distribution for the investigated diprotic phenothiazine derivatives. To investigate the influence of the uncertainty in the pK_a determination on the log *P* measurement, the log *P* values were calculated again at ± one standard deviation of the determined pK_a value. Only in this manner, by taking into account the errors of measurements and extrapolations, can a realistic estimate of the reliability of the log *P* results be obtained. Finally, the pH-dependent apparent distribution coefficients, log *D*, were calculated as pH − log *P* − log P_{ion} profile by the analysis software.

Table 1—Comparison of Measured pK_a Values with Published Data

drug	measured pK_a in dioxane[a]	in methanol[b]	in water[c]	published pK_a
promethazine	8.86 ± 0.01[d]	9.07 ± 0.08		9.11,[29] 9.10[30]
promazine	9.00 ± 0.05[d]	8.92 ± 0.09		9.28,[29] 9.40[16]
chlorpromazine	9.15 ± 0.09[d]	9.22 ± 0.13		9.30,[29] 9.30[16]
triflupromazine	8.95 ± 0.03[d]	9.07 ± 0.19		9.20,[30] 9.20[16]
levomepromazine	9.03 ± 0.09[d]	9.07 ± 0.16		9.19[29]
thioridazine	9.19 ± 0.06[d]	9.25 ± 0.07		9.50[30]
prochlorperazine	3.77 ± 0.16	3.73 ± 0.04	3.79 ± 0.01[d]	3.73,[31] 3.78[30]
	8.21 ± 0.13[d]	7.96 ± 0.09		8.10[31]
trifluoperazine	3.70 ± 0.11	3.95 ± 0.35	3.91 ± 0.01[d]	3.60,[32] 3.90[5]
	8.11 ± 0.06[d]	8.38 ± 0.13		8.10,[32] 8.10[5]
thiethylperazine	3.65 ± 0.02	3.81 ± 0.27	3.80 ± 0.01[d]	
	8.00 ± 0.09[d]	8.06 ± 0.06		8.12[29]
perphenazine	3.97 ± 0.09	3.98 ± 0.05	3.59 ± 0.01[d]	3.70[31]
	7.90 ± 0.09[d]	7.82 ± 0.06		7.80[31]
verapamil	8.68 ± 0.09[d]			8.60,[33] 8.92[30]
gallopamil	8.57 ± 0.06[d]	8.42 ± 0.01		
fendiline	9.04 ± 0.03[d]			
amlodipine	9.31 ± 0.10[d]			9.02[34]
nicardipine	7.28 ± 0.10[d]			7.20,[35] 7.33[36]

[a] With cosolvent dioxane and Yasuda–Shedlovsky extrapolation. [b] With cosolvent methanol and Yasuda–Shedlovsky extrapolation. [c] In only aqueous solution. [d] pK_a value used for log *P* determination.

Calculation of log *P* Values—For comparative purposes, the partition coefficients in the *n*-octanol/water system were calculated with the programs ClogP,[22] ACD,[23] and HINT.[24] ClogP is based on the two-dimensional fragment method developed by Leo and Hansch[25] using fragment constants derived from differences in partition coefficient of substituted and unsubstituted compounds together with several correction terms that account for neighbor-group effects. The ACD program uses a similar algorithm, where the log *P* contribution values of atoms, fragments, and intramolecular interactions were derived from 3600 experimental log *P* values.[23] The calculated results are given with auxiliary certainty limits. HINT was developed as computational method for three-dimensional structures using hydrophobic atom constants. The lipophilicity contributions of hydrogens are constant and the lipophilicity values of the central atom(s) of a fragment are adjusted in a way that the sum of the atomic constants is equal to the fragment-constant value.[26] This program offers two methods for taking into account neighboring effects, either via bonds (e.g., according to the connectivity pattern) or through space, thus considering additionally the conformation of a molecule. The three-dimensional modeling was done with SYBYL.[27] The starting structures were extracted from the Cambridge Structural Database,[28] where entries for all compounds except gallopamil and nicardipine were found. The structures for these two compounds were built by modification of the X-ray structures of verapamil and amlodipine, respectively. The geometry optimization and the atom charge calculation of the neutral forms was performed with MOPAC 6 as implemented in SYBYL using the AM1 Hamiltonian and the keywords 'precise' and 'gnorm-0.2'. Both HINT log *P* values, with proximity effects via bonds, HINT-2D, and through space, HINT-3D, were calculated for the optimized structures.

Results and Discussion

The pK_a values measured in this study together with available published data are shown in Table 1. A very good agreement between potentiometrically measured and formerly reported pK_a values can be seen. The differences are mostly in the range of 0.1 to 0.2 units. This agreement can be regarded as very satisfactory because the published values have been determined in several laboratories and usually not all details about the conditions of the pK_a determination were given, so ionic strength and temperature might differ from our experimental conditions. The structures of all samples are shown in Figures 1 and 2.

Considering the statistics of the pK_a determinations, it can be concluded that the errors of pK_a values determined

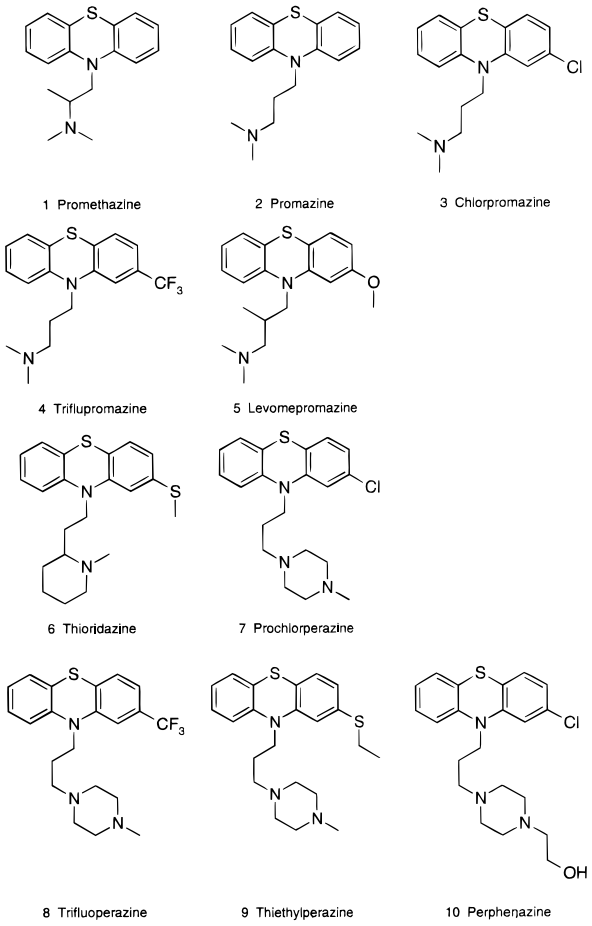

Figure 1—Structures of the phenothiazine derivatives investigated.

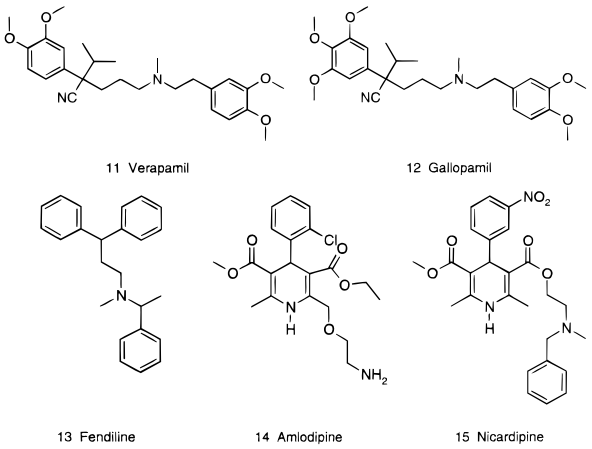

Figure 2—Structures of the calcium channel antagonists investigated.

in purely aqueous 0.15 M KCl seem to be negligible (standard deviations of about ±0.01). The quality of the Yasuda−Shedlovsky extrapolation depended on the number of titrations introduced, the amount and kind of cosolvent, and the quality of the electrode parameter validation at certain cosolvent concentrations. The comparison of the pK_a values obtained from either dioxane or methanol cosolvent mixtures showed generally good agreement, with differences in the range of <0.1 to 0.2 units. For all compounds, except promethazine, gallopamil, and the highest pK_a values of prochlorpromazine and trifluoperazine, the confidence intervals of the pK_a values overlap; therefore, they are statistically identical. The results obtained with dioxane seemed more reliable because lower concentrations were needed to keep the free bases in

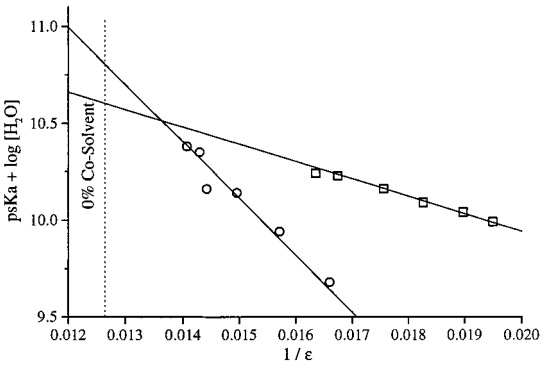

Figure 3—Yasuda–Shedlovsky extrapolation: cosolvent dioxane (□); pK_a of promethazine; extrapolation equation: $p_sK_a + \log [H_2O] = 11{,}745 - 89{,}6/\epsilon$; $pK_a = 8.86 \pm 0.01$ cosolvent methanol (○); pK_a of promethazine; extrapolation equation: $p_sK_a + \log [H_2O] = 14{,}528 - 291{,}9/\epsilon$; $pK_a = 9.07 \pm 0.08$.

Table 2—Comparison of Measured log *P* Values with Published Data

drug	measured log *P*	− limit[a]	+ limit[a]	GOF	published log *P*[b]
promethazine	4.51	4.47	4.55	1.15	4.30,[37] 4.75,[29] 4.81[30]
promazine	4.57	4.53	4.62	1.66	4.40,[37] 4.55,[30] 4.64[29]
chlorpromazine	5.10	5.02	5.21	1.03	5.00,[38] 5.16,[37] 5.35[30]
triflupromazine	5.17	5.14	5.25	1.02	5.03,[30] 5.19,[29] 5.30[37]
levomepromazine	4.89	4.84	5.02	0.71	4.40,[37] 4.86[29]
thioridazine	5.32	5.28	5.37	0.85	5.80,[37] 5.90[31]
prochlorperazine	4.79	4.66	4.91	0.78	3.00,[18] 4.60[30]
trifluoperazine	5.10	4.98	5.19	1.07	4.90,[37] 5.03,[30] 5.07[29]
thiethylperazine	4.82	4.70	4.90	0.75	4.60,[37] 5.18,[29] 5.41[30]
perphenazine	4.25	4.00	4.29	1.38	3.70,[18] 4.19,[37] 4.20[30]
verapamil	3.74	3.67	3.83	0.85	3.79,[30] 4.80[39]
gallopamil	3.71	3.65	3.77	0.68	
fendiline	4.89	4.84	4.91	0.93	
amlodipine	3.17	3.06	3.27	1.10	3.15,[40] 3.30[30]
nicardipine	4.65	4.53	4.74	0.60	3.82,[41] 4.96[30]

[a] The ± limits of log *P* based on ± one standard deviation of the corresponding pK_a values. [b] All published values were obtained by shake-flask method.

solution and the slope of this extrapolation line was less steep (Figure 3). In other words, the influence of the dielectric constant to the sum pK_a + log[H_2O] was less pronounced.

This result is also reflected in the lower standard deviations of pK_a values determined in dioxane/water compared with methanol/water mixtures. A comparison by linear regression yielded eq 3:

$$pK_a(\text{methanol}) = 0.14(\pm 0.14) + 0.99(\pm 0.02)\, pK_a(\text{dioxane}) \quad (3)$$

$$n = 15 \qquad SD = 0.15 \qquad r = 0.99 \qquad F = 3104.0$$

Intercept and slope of the regression line do not deviate significantly from their ideal values. Thus, the values obtained in both systems are comparable, confirming that the quality of the electrode parameter validation made by Sirius Analytical Instruments Ltd. is sufficient if the pK_a lies in the investigated pH range (3 to 10).

The log *P* results are shown in Table 2 together with estimated errors for the log *P* values. The given error estimations are based on the uncertainty in the pK_a determination and not on the much lower ones that result from the fitting procedure that assumes a perfect determination of pK_a. The range of the log *P* uncertainty reflected directly the limits of the pK_a determination.

For the investigated compounds, a good agreement with available experimental log *P* values from the literature was

Table 3—Comparison of Measured log *P* Values and Calculated Values with the ClogP, ACD, and HINT Software

no.	drug	PCA 101[a]	ClogP	ACD	HINT-2D[b]	HINT-3D[c]
1	promethazine	4.51 ± 0.04	4.73	4.69 ± 0.26	4.63	3.89
2	promazine	4.57 ± 0.05	4.55	4.63 ± 0.25	4.39	4.00
3	chlorpromazine	5.10 ± 0.11	5.29	5.36 ± 0.27	4.98	4.60
4	triflupromazine	5.17 ± 0.08	5.63	5.70 ± 0.37	4.79	4.40
5	levomepromazine	4.89 ± 0.13	4.81	5.05 ± 0.27	4.76	4.27
6	thioridazine	5.32 ± 0.05	6.95	6.13 ± 0.38	5.90	5.78
7	prochlorperazine	4.79 ± 0.13	6.16	4.76 ± 0.39	5.83	4.21
8	trifluoperazine	5.10 ± 0.12	6.49	5.11 ± 0.41	5.64	4.04
9	thiethylperazine	4.82 ± 0.12	6.31	5.05 ± 0.41	6.41	4.76
10	perphenazine	4.15 ± 0.15	5.58	4.49 ± 0.42	5.14	3.04
11	verapamil	3.74 ± 0.09	3.79	5.03 ± 0.39	5.29	4.88
12	gallopamil	3.71 ± 0.06	3.22	4.73 ± 0.40	5.59	4.93
13	fendiline	4.88 ± 0.04	6.10	6.55 ± 0.34	5.43	5.43
14	amlodipine	3.17 ± 0.10	2.78	3.72 ± 0.62	1.85	−1.14
15	nicardipine	4.65 ± 0.12	4.30	5.22 ± 0.62	3.53	0.86

[a] Values with the estimated error range. [b] Polar proximity 'via bond' and hydrogen treatment 'all'. [c] Polar proximity 'through space' and hydrogen treatment 'all'.

found. Two major exceptions are evident: in this study a log *P* value of 5.32 was determined for thioridazine in comparison with published values of 5.8 and 5.9. The source for this difference is not clear but it should be kept in mind that the determination of such high log *P* values by the shake-flask method is very difficult. This difficulty is also substantiated by the large variation of log *P* values reported in the literature for promethazine, levomepromazine, thiethylperazine, perphenazine, verapamil, and nicardipine (Table 2). For prochlorperazine, the log *P* value determined in this study was considerably higher than that published in ref 18. A comparison of this log *P* with values from other sources show that the values published in this article are much lower than expected and probably in error. This conclusion is also supported by comparison with log *P* values of other closely related phenothiazines, such as trifluoperazine.

As at least one of the reference values is in approximate agreement with the log *P* values determined by potentiometric titration, the applied two-step method for the determination of log *P* values of poorly water soluble compounds can be regarded as reliable.

The measured log *P* values were also compared with the values calculated by the ClogP, ACD, and HINT software (Table 3) to estimate the ability of the programs to predict log *P* values without experimental work.

Mannhold and Dross regarded a calculated partition coefficient as acceptable if the difference between experiment and calculation was lower than ±0.5 log *P* units.[42] In general, this wide range can be accepted in QSAR studies only if a large variance in log *P* among the compounds investigated exists. We used more stringent reliability measurements; first, the estimated error interval of the experimental values, and second, the range of ±0.3 units of the calculated values because this is the generally accepted error in log *P* values determined by the shake-flask method.

Visual comparison of experimental and calculated log *P* values showed that according to either of these criteria, none of the programs was able to calculate log *P* values accurately (Figure 4). The 'best' results were obtained with the ACD software where the standard errors given by the software overlapped with the experimental values in 10 cases. Comparing the calculated with experimental log *P* values, including their estimated error intervals, overlap was observed in only two cases for the ACD, three for the ClogP, one for HINT-2D, and in no case for the HINT-3D software. If the less stringent criterion of ±0.3 log *P*

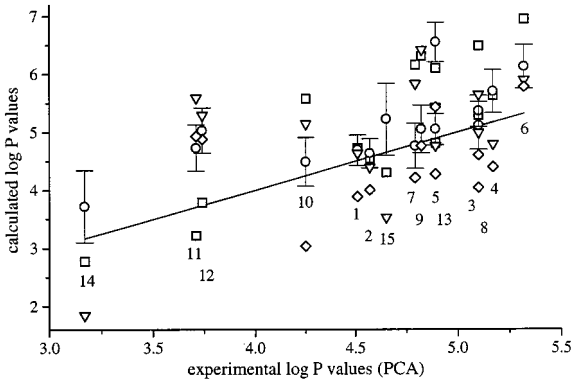

Figure 4—Prediction of measured log *P* values for the tested drugs; reference PCA (straight line), ClogP (□), ACD (○); (with error bars, values printed in Table 3), HINT-2D (▽), HINT-3D (◇).

deviation of the calculated values was applied, the success rate of the software did not increase much: seven coincidences in the case of ACD followed by five for ClogP, four for HINT-2D, and only one for HINT-3D.

For structurally related derivatives, the picture seemed to be less disappointing because all programs except HINT-3D predicted the log *P* values of promazine-type phenothiazines quite well. However, ClogP and HINT-2D highly overestimated the lipophilicity of the piperazine substituent (Table 3). The presence of a piperazine ring did not increase the partition coefficient very much compared with the corresponding promazine derivatives. Instead, the second polar nitrogen appeared to reduce the tendency of drug enrichment in *n*-octanol.[5]

A quantitative comparison of the quality of log *P* predictions was carried out by linear regression. Because we were interested in the calculation ability of the programs, the experimentally determined log *P* value was the dependent variable. This situation corresponds to the condition frequently encountered in a QSAR analysis; that is some log *P* values are known and one wants to calculate the missing ones. It also ensures that the standard deviations of estimation can be compared directly.

For all phenothiazines ($n = 10$) covering a log *P* range of about one log unit, the following results were obtained:

$$\log P_{\mathrm{PCA}} = 3.62 + 0.21 \log P_{\mathrm{ClogP}}$$
$$\mathrm{SD} = 0.30 \quad r = 0.53 \quad F = 3.5$$

$$\log P_{\mathrm{PCA}} = 1.84 + 0.59 \log P_{\mathrm{ACD}}$$
$$\mathrm{SD} = 0.15 \quad r = 0.91 \quad F = 29.1$$

$$\log P_{\mathrm{PCA}} = 4.02 + 0.16 \log P_{\mathrm{HINT.2D}}$$
$$\mathrm{SD} = 0.31 \quad r = 0.34 \quad F = 1.0$$

$$\log P_{\mathrm{PCA}} = 3.19 + 0.39 \log P_{\mathrm{HINT.3D}}$$
$$\mathrm{SD} = 0.21 \quad r = 0.81 \quad F = 14.8$$

As can be seen, only the equations using ACD or HINT-3D as the calculation method are significant at all. In all cases, the slopes are considerably lower than one and the intercepts are much higher than zero. According to these criteria and the statistical parameters, only the ACD program yielded reliable estimates. Inspection of the residuals showed, that in no case was an 'outlier' based on statistical reasoning present, meaning that the low correlations were due to the scatter in the calculated data. The exclusion of thioridazine from the regression, because our log *P* value differed by 0.5 from published data, even worsened the results (data not shown). Only for ACD were the statistics virtually unchanged; however, the intercept dropped to 1.17 and the slope increased slightly to 0.73.

To study the influence of the overestimation of the lipophilicity of the piperazine-containing compounds, the regressions for the two subsets of phenothiazines with alkyl amino or piperazine side chains were derived.

Phenothiazines with alkyl amino side chain ($n = 5$):

$$\log P_{PCA} = 1.79 + 0.61 \log P_{ClogP}$$
$$SD = 0.15 \quad r = 0.91 \quad F = 13.8$$

$$\log P_{PCA} = 1.58 + 0.64 \log P_{ACD}$$
$$SD = 0.09 \quad r = 0.97 \quad F = 45.1$$

$$\log P_{PCA} = -0.39 + 1.11 \log P_{HINT.2D}$$
$$SD = 0.20 \quad r = 0.81 \quad F = 5.7$$

$$\log P_{PCA} = 0.71 + 0.98 \log P_{HINT.3D}$$
$$SD = 0.11 \quad r = 0.94 \quad F = 24.6$$

Phenothiazines with piperazine ring ($n = 4$):

$$\log P_{PCA} = -0.73 + 0.89 \log P_{ClogP}$$
$$SD = 0.07 \quad r = 0.99 \quad F = 87.5$$

$$\log P_{PCA} = -0.83 + 1.15 \log P_{ACD}$$
$$SD = 0.17 \quad r = 0.92 \quad F = 11.6$$

$$\log P_{PCA} = 2.54 + 0.38 \log P_{HINT.2D}$$
$$SD = 0.36 \quad r = 0.57 \quad F = 0.9$$

$$\log P_{PCA} = 3.29 + 0.36 \log P_{HINT.3D}$$
$$SD = 0.30 \quad r = 0.73 \quad F = 2.2$$

It should be mentioned that the variance of log *P* in the subsets is only slightly lower than for all phenothiazines and that therefore the statistical parameters are comparable. The fit of the alkyl amino compounds was improved in all cases. The best results were obtained with the ACD program and especially with HINT-3D. A comparison of the slopes and intercepts of the equations shows that they differ considerably between the subsets. This difference clearly marks that even such small structural changes such as the replacement of an alkyl amino by a piperazine group are not well handled by the log *P* calculation programs. For the perazine-type phenothiazines, the best fit was obtained with ClogP.

The data for the investigated calcium channel antagonists ($n = 5$) comprised structurally diverse compounds and covered a slightly larger log *P* range of 1.7 units. For this subset, the following equations were obtained:

$$\log P_{PCA} = 1.99 + 0.51 \log P_{ClogP}$$
$$SD = 0.35 \quad r = 0.91 \quad F = 14.2$$

$$\log P_{PCA} = 0.81 + 0.64 \log P_{ACD}$$
$$SD = 0.35 \quad r = 0.91 \quad F = 14.0$$

$$\log P_{PCA} = 3.25 + 0.18 \log P_{HINT.2D}$$
$$SD = 0.75 \quad r = 0.41 \quad F = 0.6$$

$$\log P_{PCA} = 3.76 + 0.09 \log P_{HINT.3D}$$
$$SD = 0.77 \quad r = 0.37 \quad F = 0.5$$

As expected for a more diverse data set, the correlation decreased and the standard deviation increased. But again, no outliers were present so the regressions were not unduly influenced. As with the phenothiazines, high intercepts and low slopes were observed, pointing to a general overestimation of lipophilicity by the programs. Combining all investigated drugs ($n = 15$) yielded the following equations:

$$\log P_{PCA} = 2.40 + 0.43 \log P_{ClogP}$$
$$SD = 0.33 \quad r = 0.85 \quad F = 34.7$$

$$\log P_{PCA} = 1.33 + 0.64 \log P_{ACD}$$
$$SD = 0.45 \quad r = 0.71 \quad F = 13.2$$

$$\log P_{PCA} = 3.14 + 0.29 \log P_{HINT.2D}$$
$$SD = 0.54 \quad r = 0.52 \quad F = 5.1$$

$$\log P_{PCA} = 3.85 + 0.19 \log P_{HINT.3D}$$
$$SD = 0.53 \quad r = 0.55 \quad F = 5.5$$

Although the whole data set had a larger variance in log *P* (about 2.2 log units), the relationship between experimental and calculated log *P* values did not improve. It can be concluded that none of the programs used can calculate log *P* values for the investigated compounds with satisfying accuracy at all.

The ACD program performed best for phenothiazines, but did not yield satisfactory results for the other drugs investigated, and was followed next by the ClogP program. Phenothiazines with a piperazine or a piperidine ring in the side chain deviated the most; their lipophilicity was greatly overestimated by the programs. The HINT methodology, especially when taking into account the three-dimensional structure gave the least correlation between measured and calculated log *P* values for the studied derivatives. This result is mainly due to large errors for two calcium channel antagonists of the dihydropyridine type whose lipophilicity was greatly underestimated. HINT was also the only program that incorrectly assigned a chloro-substituent, which is a larger lipophilicity contribution in comparison with a trifluoromethyl group, at the same position in case of the phenothiazines (nos. 2 & 6 versus 3 & 7) and also overestimated the contribution of a 3,4,5-trimethoxyphenyl group compared with its 3,4-dimethoxyphenyl counterpart for the pair gallopamil and verapamil. These results emphasize the need for a further improvement in the accuracy of prediction of log *P* by calculation.

Additionally we focused our attention on the partition coefficients of the ions, log P_{ion}, and on the distribution coefficients at pH 7.4, log *D*, a quantity relevant for the distribution behavior of drugs under physiological conditions. Depending on the quality and quantity of the hydrophobic parts of a compound, a charged drug molecule can enter the organic phase. For example the ionized form of phenothiazines participated in hydrophobic interaction when its charge was suitably neutralized by appropriate anions.[5] Most of drugs analyzed were monoprotic bases that could be present as the neutral and ionic species in the organic phase. For phenothiazines with two basic nitrogens that were doubly protonated at low pH, only the neutral and the monoprotonated components were observed in the organic phase. Table 4 summarizes the partition and distribution coefficients together with published data.

A big advantage of the pH−metric method is that the distribution profile over the entire pH range can be obtained from the titration curves.[44] The calculated log *D* at pH 7.4 for promethazine, chlorpromazine, thioridazine, trifluoperazine, thiethylperazine, and perphenazine based on the measured log *P* and log P_{ion} corresponded excellently to values obtained earlier by the shake-flask method. On average, the distribution coefficients, log *D*, of bases containing two basic nitrogens were higher than those with only one basic nitrogen. This result was the opposite order in relation to the log *P* values. One reason for this discrepancy could be identified clearly; that is, because one

Table 4—Comparison of pH-dependent Distribution in *n*-Octanol/Water

drug	log *P*	log P_{ion}	log *D* pH 7.4	log D_{lit} pH 7.4
promethazine	4.51	1.38 ± 0.03	2.95	2.79,[37] 2.88[17]
promazine	4.57	2.08 ± 0.02	2.93	2.50,[37] 2,55[17]
chlorpromazine	5.10	1.52 ± 0.02	3.26	3.26,[16] 3.39[38]
triflupromazine	5.17	1.87 ± 0.03	3.52	3.39,[16] 3.70[37]
levomepromazine	4.89	1.76 ± 0.03	3.17	2.62[37]
thioridazine	5.32	2.08 ± 0.02	3.45	3.51[37]
prochlorperazine	4.79	1.47 ± 0.08	3.83	
trifluoperazine	5.10	2.26 ± 0.02	4.23	4.36[37]
thiethylperazine	4.82	1.92 ± 0.03	4.04	3.82[37]
perphenazine	4.25	1.50 ± 0.06	3.56	3.65[37]
verapamil	3.74	1.10 ± 0.09	2.37	1.83[43]
gallopamil	3.71	1.29 ± 0.06	2.45	
fendiline	4.89	2.14 ± 0.12	3.19	
amlodipine	3.17	1.06 ± 0.03	1.41	1.11[40]
nicardipine	4.65	1.39 ± 0.10	4.33	

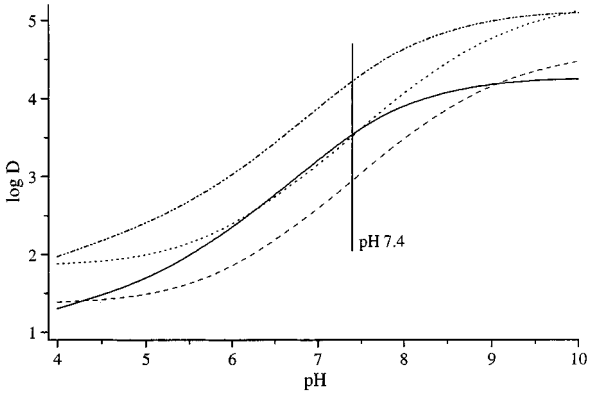

Figure 5—The pH-dependent distribution profile of four phenothiazines; promethazine (dashed line), triflupromazine (dotted line), trifluoperazine (dash/dotted line), and perphenazine (solid line).

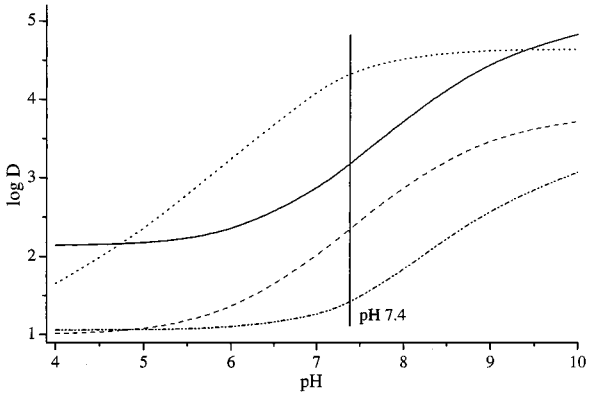

Figure 6—The pH-dependent distribution profile of four calcium channel antagonists; verapamil (dashed line), fendiline (solid line), amlodipine (dash/dotted line), nicardipine (dotted line).

pK_a value of the amino group of the piperazine ring is close to the physiological pH, the degree of protonation is relatively low compared with the monobasic drugs. The changes in lipophilicity of several drugs inspected that occurred during small changes in pH around 7.4 (Figures 5 and 6) were remarkable.

The pH-dependent distribution profiles of trifluoperazine and perphenazine shifted significantly to the curves of triflupromazine and promethazine (Figure 5). The order of the drugs (high to low values of log *P*) changed from triflupromazine = trifluoperazine > promethazine = perphenazine to trifluoperazine > perphenazine = triflupromazine > promethazine (high to low values of log *D* at pH 7.4). The phenothiazines containing a piperazine ring were more lipophilic at pH 7.4 than those with a dimethyl amino group. This result is in agreement with the pharmacological potency of the phenothiazine drugs because a replacement of the dimethyl amino group by a piperazine ring led to an increase of the neuroleptic power.

In Figure 6 the quite different pH-dependent distribution profiles of the structurally heterogeneous calcium channel antagonists verapamil, fendiline, amlodipine, and nicardipine are shown as a further example. The order of log *D* values at pH 7.4 (high to low values) was nicardipine > fendiline > verapamil > amlodipine. Fendiline and nicardipine had nearly the same log *P* values, but differed in their pK_a values. Therefore, the partitioning of nicardipine shifted to higher log *D* values over the whole pH range. As a consequence, the partitioning behavior became even more different at pH 7.4. This result illustrates that the choice of either of the partition or distribution coefficient can have a significant influence on the results of QSAR studies. The distribution coefficient should become more valuable than log *P* for many applications.

Conclusion

The pH−metric method is advantageous for the determination of pK_a values of ionizable compounds. The quality of the Yasuda−Shedlovsky extrapolation depends on the number of titrations performed and the concentrations and kind of cosolvent used. The pK_a values calculated from either dioxane or methanol cosolvent mixtures were in very good agreement in general, but the extrapolated pK_a was much less influenced by the cosolvent concentration in the case of dioxane. The log *P* measurements provided reliable and accurate partition coefficients of the neutral species and also of the corresponding ion. The pH-dependent partition profile can be obtained over the whole pH range investigated and should provide a better descriptor than log *P* for relationships between structure and distribution at physiological pH because it includes the contribution of the charged species to overall distribution. Although the studied data set is small, it can be concluded that the accuracy of log *P* calculation methods is not satisfactory for general use in QSAR analysis, because satisfying correlations were obtained only for selected subsets. None of the investigated programs showed a general superior performance. Therefore, calculation methods for log *P* without any experimental verification should be used with care.

A drawback of the popular *n*-octanol/water model system for the determination of the lipophilicity of drugs is, that it does not take into account specific ionic and hydrophobic interactions that can occur at an ordered interface like a membrane. Therefore, further studies to characterize and compare the distribution behavior in water/phospholipid systems are currently under way.

References and Notes

1. Pliska, V.; Testa, B.; Waterbeemd, H.v.d., Eds. Lipophilicity in Drug Action and Toxicology. In *Methods and Principles in Medicinal Chemistry*, Vol. 4; Mannhold. R.; Kubinyi, H.; Timmermann, H., Eds.; VCH: Weinheim, 1996.
2. Mason, R. P.; Gonye, G. E.; Chester, D. W.; Herbette, L. G. Partitioning and location of Bay K 8644, 1,4-dihydropyridine calcium channel agonist, in model and biological membranes. *Biophys. J.* **1989**, *55*, 769−778.
3. Seydel, J. K.; Velasco, M. A.; Coats, E. A.; Cordes, H. P.; Kunz, B.; Wiese, M. The importance of drug-membrane interaction in drug resaerch and development. *Quant. Struct.-Act. Relat.* **1992**, *11*, 205−210.
4. Collander, R. The partition of organic compounds between higher alcohols and water. *Acta Chem. Scand.* **1951**, *3*, 774−780.

5. Murthy, K. S.; Zografi, G. Oil−water partitioning of chlorpromazine and other phenothiazine derivatives using dodecane and *n*-octanol. *J. Pharm. Sci.* **1970**, *59*, 1281.
6. Le Petit, G. Die pH-abhaengige 'Lipidloeslichkeit' von Arzneistoffen. *Die Pharmazie* **1977**, *32*, 289−291.
7. Fujita, T.; Iwasa, J.; Hansch, C. A new substituent constant, π, derived from partition coefficient. *J. Am. Chem. Soc.* **1964**, *86*, 5175−5180.
8. Mirless, M. S.; Moulton, S. J.; Murphy, C. T.; Taylor, P. J. Direct measurement of octanol−water partition coefficients by high-pressure liquid chromatography. *J. Med. Chem.* **1976**, *19*, 615−619.
9. El Tayar, N.; Tsai, R.; Vallat, P.; Altomore, G.; Testa, B. Measurement of partition coefficients by various centrifugal partition chromatographic techniques. *J. Chromatogr.* **1991**, *536*, 181−194.
10. Avdeef, A.; Bucher, J. J. Accurate measurement of the concentration of hydrogen ions with a glass electrode: Calibration using the prideaux and other universal buffer solutions and a computer-controlled automatic titrator. *Anal. Chem.* **1978**, *50*, 2137−2142.
11. Avdeef, A. pH-Metric log P. 1. Difference plot for determining ion-pair octanol−water partition coefficients of multiprotic substances. *Quant. Struct.-Act. Relat.* **1992**, *11*, 510−517.
12. Avdeef, A. pH-Metric log P. 2. Refinement of partition coefficients and ionization constants of multiprotic substances. *J. Pharm. Sci.* **1993**, *82*, 183−190.
13. Avdeef, A.; Comer, J. E. A.; Thomson, S. J. pH-Metric log P. 3. Glass electrode calibration in methanol−water, applied to pK_a determination of water-insoluble substances. *Anal. Chem.* **1993**, *65*, 42−49.
14. Slater, B.; McCormack, A.; Avdeef, A.; Comer, J. E. A. pH-Metric log P. 4. Comparison of partition coefficients determined by shake-flask, HPLC and potentiometric methods. *J. Pharm. Sci.* **1993**, *83*, 1280−1283.
15. Takács-Novák, K.; Avdeef, A. pH-Metric log P. 9. Interlaboratory study of log P determination by shake-flask and potentiometric methods. *J. Pharm. Biomed. Anal.* **1996**, *14*, 1405−1413.
16. Glasser, H.; Krieglstein, J. Die Eiweissbindung einiger Psychopharmaka mit tricyclischem Ringsystem in Abhaengigkeit von ihrer chemische Konstitution. *Naunyn-Schmiedeb. Arch. Pharmak.* **1970**, *265*, 321−334.
17. Krieglstein, J.; Meiler, W.; Staab, J. Hydrophobic and ionic interactions of phenothiazine derivatives with bovine serum albumin. *Biochem. Pharmacol.* **1972**, *21*, 985−997.
18. Frisk-Holmberg, M.; v.d. Kleijn, E. The relationship between the lipophilic nature of tricyclic neuroleptics and antidepressants, and histamine release. *Eur. J. Pharmacol.* **1972**, *18*, 139−147.
19. Thoma, K.; Arning, M. Colloidal, partition and binding properties of phenothiazine derivatives, V: relationship between albumin binding and physical properties. *Archiv der Pharmazie* **1976**, *309*, 945−959.
20. Retzinger, G. S.; Cohen, L.; Lau, S. H.; Kézdy, F. J. Ionization and surface properties of verapamil and several verapamil analogues. *J. Pharm. Sci.* **1986**, *75*, 976−982 .
21. Sirius Analytical Instruments Ltd., In *Application and Theory Guide to pH-Metric pK_a and log P Determination*, Rev. 1.0; 1994; p 186.
22. ClogP Version 1.0.0 for Windows; BioByte Corp., 1995.
23. ACD Demo Version ACD/logP 1.0; Advanced Chemistry Development Inc., 1995.
24. HINT Version 2.20S for Sybyl 6.3; eduSoft LC, 1996.
25. Leo, A. J. Methods of Calculating Partition Coefficients. In *Comprehensive Medicinal Chemistry*, Vol. 4; Hansch, C.; Sammes, P. G.; Taylor, J. B., Eds.; Pergamon: Oxford, 1990; pp 295−319.
26. Kellog, G. E.; Semus, S. F.; Abraham, D. J. HINT: A new method of empirical hydrophobic field calculation for CoMFA. *J. Computer Aided Mol. Design* **1991**, *5*, 545−552.
27. SYBYL Version 6.3; Tripos Inc., 1996.
28. Cambridge Structural Database System, Version 2.3.7, 1995.
29. Mannhold, R.; Dross, K. P.; Rekker, R. F. Drug lipophilicity in QSAR practice: I. A comparison of experimental with calculative approaches. *Quant. Struct.-Act. Relat.* **1990**, *9*, 21−28.
30. Craig, P. N. Drug Compendium. In *Comprehensive Medicinal Chemistry*, Vol. 6; Hansch, C.; Sammes, P. G.; Taylor, J. B., Eds.; Pergamon: Oxford, 1990; pp 237−991.
31. Green, A. L. Ionization constants and water solubilities of some aminoalkylphenothiazine tranquilizers and related compounds. *J. Pharm. Pharmacol.* **1967**, *19*, 10−16.
32. Roth, H. J.; Eger, K.; Troschütz, R. In *Arzneistoffanalyse*; Roth, H. J.; Eger, K.; Troschütz, R., Eds.; Thieme Verlag: Stuttgart, 1990; p 737.
33. Schleinitz, H. Verapamilhydrochlorid. In *Hagers Handbuch der Pharmazeutischen Praxis*, Vol. 9; Bruchhausen, F.v.; Dannhardt, G.; Ebel, S.; Frahm, A. W.; Hackenthal, E.; Holzgrabe, U., Eds.; Springer-Verlag: Berlin, 1993; p 1167.
34. Mason, R. P.; Campbell, S. F.; Wang, S.-D.; Herbette, L. G. Comparison of location and binding for the positivly charged 1,4-dihydropyridine calcium channel antagonist amlodipine with uncharged drugs of this class in cardiac membranes. *Mol. Pharmacol.* **1989**, *86*, 634−640.
35. Lehmann, J. Nicardipin. In *Hagers Handbuch der Pharmazeutischen Praxis*, Vol. 8; Bruchhausen, F.v.; Ebel, S.; Frahm, A. W.; Hackenthal, E., Eds.; Springer-Verlag: Berlin, 1993; p 1141.
36. Kou, J. H.; Roy, S. D.; Du, J.; Fujiki, J. Effect of receiver fluid pH on in vitro skin flux of weakly ionizable drugs. *Pharm. Res.* **1993**, *10*, 986−990.
37. Limberg, J. Ph.D. Thesis, University of Münster, FRG, 1987.
38. Barton, P.; Davis, A. M.; McCarthy, D. J.; Webborn, P. J. H. Drug-phospholipid Interactions. 2. Predicting the sites of drug distribution using *n*-octanol/water and membrane/water distribution coefficients. *J. Pharm. Sci.* **1997**, *86*, 1034−1039.
39. Zamora, J. M.; Pearce, H. L.; Beck, W. T. Physical-chemical properties shared by compounds that modulate multidrug resistance in human leukemic cells. *Mol. Pharmacol.* **1988**, *33*, 454−462.
40. Austin, R. P.; Davis A. M.; Manners, C. N. Partitioning of ionizing molecules between aqueous buffers and phospholipid vesicles. *J. Pharm. Sci.* **1995**, *84*, 1180−1183.
41. Diez, I.; Colom, H.; Moreno, J.; Obach, R.; Peraire, C.; Domenech, J. A comparative study of transdermal absorption of a series of calcium channel antagonists. *J. Pharm. Sci.* **1991**, *80*, 931−934.
42. Mannhold, R.; Dross, K. Calculation procedures for molecular lipophilicity: A Comparative Study. *Quant. Struct.-Act. Relat.* **1996**, *15*, 403−409.
43. Rojratanakiat, W.; Hansch, C. The relative dependence of calcium antagonists and neuroleptics binding to brain and heart receptors on drug lipophilicity. *J. Pharm. Pharmacol.* **1990**, *42*, 599−600.
44. Avdeef, A. Assessment of Distribution-pH Profiles. In *Methods and Principles in Medicinal Chemistry*; Pliska, V.; Testa, B.; Waterbeemd, H.v.d., Eds. In *Lipophilicity in Drug Action and Toxicology*, Vol. 4; Mannhold, R.; Kubinyi, H.; Timmermann, H., Eds.; VCH: Weinheim, 1996; pp 109−139.

Acknowledgments

This work was supported by the Hans-Boeckler Foundation and in part by the Fonds der Chemischen Industrie. Karl J. Box (Sirius Analytical Instruments Ltd.) is gratefully acknowledged for helpful discussions.

JS980206M

Intravenous Pretreatment with Empty pH Gradient Liposomes Alters the Pharmacokinetics and Toxicity of Doxorubicin through In Vivo Active Drug Encapsulation

LAWRENCE D. MAYER,* JENNIFER REAMER, AND MARCEL B. BALLY

Contribution from *Advanced Therapeutics Department BC Cancer Agency 600 West 10th Avenue, Vancouver, B.C. V5Z 4E6, Canada.*

Received May 8, 1998. Final revised manuscript received October 20, 1998.
Accepted for publication October 21, 1998.

Abstract □ Liposomes have been used widely to improve the therapeutic activity of pharmaceutical agents. The traditional approach for such applications has been to formulate the pharmaceutical agent in liposomes prior to administration in vivo. In this report we demonstrate that liposomes exhibiting a transmembrane pH gradient injected intravenously (iv) can actively encapsulate doxorubicin in the circulation after iv administration of free drug. Small (110 nm) liposomes composed of phosphatidylcholine (PC)/cholesterol (Chol, 55:45 mol:mol) exhibiting a pH gradient (inside acidic) were administered iv 1 h prior to free doxorubicin, and plasma drug levels as well as toxicity and efficacy were evaluated. Predosing with egg PC/Chol pH gradient liposomes increased the plasma concentration of doxorubicin as much as 200-fold compared to free drug alone as well as to predosing with dipalmitoyl PC/Chol pH gradient liposomes or EPC/Chol liposomes without a pH gradient. The ability of the liposomes to alter the pharmacokinetics of doxorubicin was dependent on the presence of a transmembrane pH gradient and correlated with the extent of doxorubicin uptake into the liposomes at 37 °C in pH 7.5 buffer, indicating that doxorubicin was being actively accumulated in the circulating liposomes. This in vivo drug loading was achieved over a range of doxorubicin doses (5 mg/kg–40 mg/kg) and was dependent on the dose of EPC/Chol liposomes administered prior to free doxorubicin injection. The altered pharmacokinetic properties of doxorubicin associated with in vivo doxorubicin encapsulation were accompanied by a decrease in drug toxicity and maintained antitumor potency. These results suggest that pretreatment with empty liposomes exhibiting a pH gradient may provide a versatile and straightforward method for enhancing the pharmacological properties of many drugs that can accumulate into such vesicle systems at physiological temperatures.

Introduction

The developmental process for conventional liposomal anticancer drug formulations most typically includes studies where variations in the physical properties of the lipid carriers (size, lipid composition, and drug-to-lipid ratio) are evaluated in order to select the characteristics that provide optimized therapeutic and toxicity behavior. In addition, pharmaceutical criteria such as trapping efficiency, drug retention, and stability must be satisfied in order for these drug delivery systems to be considered clinically viable. The evolution of liposomal systems that could actively accumulate many lipophilic amine drugs in response to transmembrane ion gradients provided an avenue whereby these demands could be met (see refs 1−3 for review). The use of K^+, H^+, and $(NH_4)_2SO_4$ gradients resulted in liposomal anticancer drug formulations that could be loaded with trapping efficiencies approaching 100% at high drug-to-lipid ratios and for a wide variety of lipid compositions.[1−5] The most extensively studied drugs in this regard are the anthracycline anticancer agents doxorubicin and daunorubicin, both of which have obtained market approval in liposomal formulations.

Although transmembrane ion gradient liposomes have addressed many of the problems facing delivery vehicle-based drug formulations, maintaining the necessary physical and chemical stability properties for pharmaceutically relevant time periods (12−24 months) has still presented significant challenges. Retention of chemically intact drug inside the liposomes after the encapsulation procedure has remained the most problematic characteristic for liposomal formulations of doxorubicin and daunorubicin. This has resulted in formulations that either have a relatively limited shelf life,[6] utilize the transmembrane pH gradient to load the drug just prior to use at the hospital pharmacy[7] or have required extensive development of formulations with physical−chemical properties that will maintain the drug inside the liposomes for time periods beyond 1 year.[8] Clearly, any subsequent liposomal formulations of other drugs that use this encapsulation strategy will require significant characterization and development in this area prior to widespread clinical use.

Given that liposomes display low inherent toxicity and can remain intact in the blood stream over days post iv administration,[9−11] it may be postulated that vesicles with appropriate transmembrane ion gradients could accumulate drugs (those known to respond to these gradients in vitro) while circulating in the plasma compartment. If this could be accomplished, then one may predict that the in vivo loaded liposomes would engender pharmacological properties similar to those observed for drug encapsulated into liposomes prior to injection. This approach could significantly improve the versatility of liposome encapsulation applications, since a single formulation of empty ion gradient liposomes could be readily implemented in a variety of therapeutic applications once their inherent toxicity properties were established in initial Phase I clinical trials. In addition, information on the ability of empty ion gradient liposome to accumulate of drugs in vivo may be very useful in identifying potential interactions between systemic liposomal drug formulations and coadministered pharmaceutical agents.

For in vivo drug encapsulation to be pharmacologically effective, the liposomes would need to (1) retain their transmembrane ion gradient for extended times, (2) be constructed of lipid compositions that will allow membrane permeation and uptake of the drug at physiological tem-

* Corresponding author: Tel: (604) 877-6000, ext. 3153. Fax: (604) 877-6011. E-mail: lmayer@bccancer.bc.ca.

10.1021/js980202h CCC: $18.00 *Published on Web 11/25/1998*

peratures, (3) be present in the plasma at sufficient concentrations to completely sequester the subsequently administered drug without depleting the transmembrane ion gradient, and (4) rapidly accumulate drug in the plasma before distribution into tissues occurs upon iv drug injection. Data from previous studies suggest that small (approximately 100 nm diameter) egg phosphatidylcholine (EPC[1])/cholesterol (Chol) liposomes exhibiting a pH gradient (inside acidic, see references) may be well suited for such applications. Investigations have demonstrated that these liposomes can efficiently accumulate doxorubicin at physiological temperatures in vitro and, at appropriate doses, are retained for extended periods of time in the circulation.[2,9,12]

In the studies described here, we have evaluated the ability of EPC/Chol liposomes circulating in the plasma compartment to encapsulate doxorubicin administered iv in free form. The selection of doxorubicin for this investigation was based on its well characterized response to liposomes exhibiting a pH gradient as well as the extensive data available on the pharmacological properties of an EPC/Chol liposomal doxorubicin formulation in which the drug is encapsulated prior to in vivo administration.[2,9,12–14] These investigations demonstrate that empty pH gradient liposomes circulating in the central blood compartment can efficiently encapsulate subsequently injected free doxorubicin in a manner that provides improved in vivo activity comparable to that obtained for formulations where the drug is entrapped inside the liposomes prior to administration. The implications of this phenomenon with respect to its utility in favorably altering the pharmacology of drugs as well as potential drug–drug interactions that could arise from a wide range of therapeutic agents is discussed.

Materials and Methods

Materials—Egg PC and DPPC were purchased from Avanti Polar Lipids (Alabaster, AL) while cholesterol and all salts were obtained from Sigma Chemicals (St. Louis, MO). Adriamycin RDF was was obtained from Adria Laboratories (Mississauga, Ontario). Female DBA/2J mice were purchased from Jackson Laboratories (Bar Harbor, MA). Tritiated cholesteryl hexadecyl ether, a nonexchangeable, nonmetabolizable lipid used as a tracer for the liposomes, and ^{14}C-methylamine were purchased from NEN-Dupont (Mississauga, Ontario).

Production of Liposomes—Egg PC/Chol and DPPC/Chol liposomes were produced by lipid thin film hydration/extrusion methods described in detail previously.[15] Briefly, lipid mixtures consisting of EPC and cholesterol (55:45, mol %) were dissolved in $CHCl_3$ and subsequently concentrated to a homogeneous lipid film under a stream of nitrogen gas. The lipid film was placed under high vacuum for at least 4 h prior to hydration at room temperature (EPC/Chol) or 45 °C (DPPC/Chol) with 300 mM citrate buffer pH 4.0 to achieve a final lipid concentration of 100 mg/mL. The sample was frozen and thawed five times[16] before extruding 10 times through two stacked 100 nm pore size polycarbonate filters (Poretics) employing an extrusion device (Lipex Biomembranes, Inc., Vancouver, Canada). The resulting liposomes were sized by QELS using a Nicomp 270 submicron particle sizer operating at 632.8 nm. The liposomes exhibited a mean size distribution of approximately 110 nm. Transmembrane pH gradients were generated in the liposomal preparations prior to administration to mice by dialyzing the liposomes against 1000 volumes of 20 mM Hepes, 150 mM NaCl buffer overnight.

Plasma Clearance Studies—Female DBA/2J mice (18–22 g) were given a single bolus lateral tail vein injection of the indicated doses of liposomes. One hour later, free doxorubicin was injected via the tail vein at the indicated doses. At various times after free doxorubicin administration, mice (4 per group) were terminated by CO_2 asphyxiation. Blood was immediately removed by cardiac puncture and collected into an EDTA-coated microtainer tube. The sample was centrifuged at 500*g* in a clinical benchtop centrifuge for 10 min. Plasma was removed and placed into an eppendorf tube prior to analysis of lipid and/or doxorubicin.

Quantitation of Liposomal Lipid and Doxorubicin—Liposomal lipid was quantified by employing the nonexchangeable and nonmetabolizable lipid marker, ^{3}H-cholesteryl hexadecyl ether.[9] Upon animal termination plasma was assayed for lipid content. The samples (200 μL) were added directly to Pico-fluor 40, and radioactivity was determined by liquid scintillation counting.

Doxorubicin was quantified by a modified Bligh and Dyer based extraction assay as previously outlined.[9] Fifty μL of plasma was diluted to 0.8 mL with distilled H_2O. One hundred μL of 10% sodium dodecyl sulfate (SDS) and 100 μL H_2SO_4 (10 mM) were then added. Subsequently, doxorubicin was extracted into an organic phase following addition of 2 mL of chloroform/isopropyl alcohol (1:1, v/v). The mixture was vortexed vigorously and frozen at −20 °C overnight. After thawing and further vortexing, the samples were centrifuged at 1500*g* for 10 min at room temperature, and the organic phase was collected. The fluorescence of this phase was determined employing a Perkin-Elmer LS 50 B Luminescence Spectrometer with an excitation wavelength of 500 nm and emission wavelength of 550 nm. A standard doxorubicin curve was prepared in blank plasma employing an identical extraction procedure. Drug levels were estimated on the basis of doxorubicin fluorescent equivalents.

Sepharose CL4B gel filtration column separations were performed in order to confirm that doxorubicin, present in plasma containing pH gradient liposomes, was encapsulated inside these vesicles. This allowed for differentiation between free doxorubicin, doxorubicin associated with liposomes and doxorubicin associated with plasma proteins. A 1.5 cm × 18.5 cm Sepharose CL4B column was packed using 20 mM Hepes, 150 mM NaCl buffer, pH 7.5. The elution pattern of protein (plasma from untreated mice), free doxorubicin in plasma, doxorubicin encapsulated in EPC/Chol (55:45, mol/mol) liposomes, and liposomes containing doxorubicin was characterized by loading 200 μL of sample onto the column and collecting 0.6 mL fractions using a Gilson Micro Fractionator fraction collector. Protein content was determined using the Sigma Bicinchonic Acid Protein Assay. A protein standard curve was prepared from a stock bovine serum albumin solution. Two mL of protein determination reagent (4% copper(II) sulfate pentahydrate solution: bicinchoninic acid solution; 1:50, v/v) was added to both the standard curve samples and column fraction samples. Samples were incubated at 37 °C for 30 min, and absorbance was measured at 562 nm using a Beckman DU-64 spectrophotometer. Protein levels were determined by regression analysis of the standard curve. Lipid and doxorubicin were quantitated as described above. The gel filtration column was standardized for elution profiles of plasma (protein determination) and 100 nm liposomes as well as doxorubicin in buffer and plasma.

Once these elution patterns had been characterized, CD-1 mice (3/group) were given a 500 mg/kg bolus lateral tail vein injection of EPC/Chol (55:45, mol/mol) liposomes with or without a pH gradient. One hour later, free doxorubicin was injected via the tail vein at 20 mg/kg. One hour after free doxorubicin administration, the mice were terminated by CO_2 asphyxiation. Blood was removed and processed as previously above. Plasma samples from each group were pooled and run down the CL4B column. Fractions were collected and analyzed for lipid and doxorubicin as described above.

Determination of Transmembrane pH Gradient in Liposomes Recovered from Mouse Plasma—At various times after iv injection of pH gradient-bearing liposomes to DBA/2J mice, ^{14}C-methylamine was added to the collected plasma to achieve 0.1 μCi/mL. After 10 min incubations at room temperature, 150 μL samples were applied to 1 mL Sephadex G-50 spin columns[2] followed by 50 μL of Hepes/NaCl pH 7.5 buffer. The liposome-containing eluant fraction was collected, and aliquots from this fraction as well as the precolumn plasma samples were quantified for radioactivity by liquid scintillation counting. The transmembrane pH gradient was then determined by correlating the intravesicular and extravesicular methylamine concentration to transmembrane proton concentration gradients as described previously.[17]

Toxicity and Efficacy Studies—The toxicity of doxorubicin administered to mice injected 1 h previously with empty liposomes was assessed in dose range-finding studies using female DBA/2J mice. Mice were administered increasing doses of doxorubicin until either the weight loss nadir was greater than 20% or any mice died. Mice were monitored twice daily over 14 days for survival and signs of stress (ruffed coat, lethargy, impaired gait, etc.). The

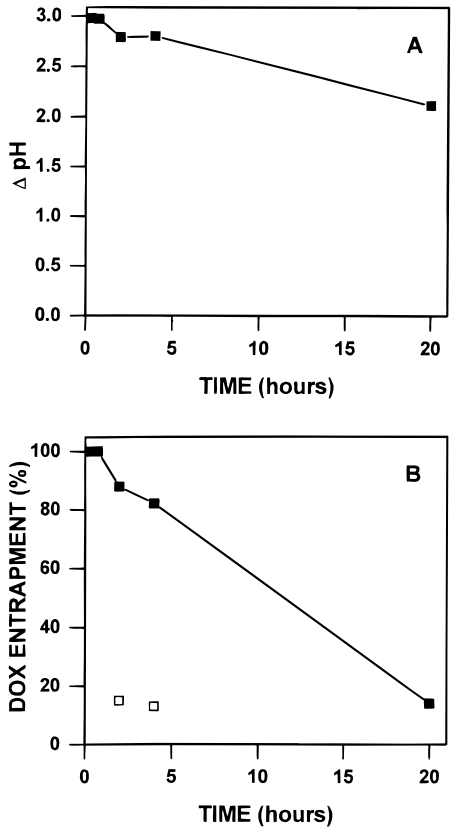

Figure 1—100 nm EPC/CHOL liposomes were administered IV to mice at a dose of 100 mg lipid/kg, and at the indicated times the liposomes recovered in the plasma were tested for residual pH gradient (panel A) and DOX trapping efficiency (panel B). Liposomes were administered exhibiting an internal pH of 3.0 (closed squares) or 7.5 (no pH gradient, open squares).

maximum tolerated dose of doxorubicin was defined as that where no deaths were observed and the body weight loss nadir was ≤15%. The L1210 ascites lymphocytic leukemia was utilized to determine the antitumor activity for the various treatment groups. In this model, 1×10^5 L1210 cells (maintained by serial passage in DBA/2J mice) were injected intraperitoneally in female DBA/2J mice (10/group) and iv doxorubicin treatment was initiated 24 h later (1 h after empty liposome iv injection, where indicated). Mice were then monitored twice daily for survival and weight loss/gain. The extent of antitumor activity was revealed as an increase in the survival time of treated mice relative to untreated mice (saline injections only). Comparisons were based on the percent increase in life span (%ILS) which was calculated as [(median survival time of treated mice ÷ median survival time of control mice) − 1] × 100. Statistical significance of differences between different groups was determined employing a two-tailed Wilcoxon ranking test.

Results

Initial experiments were designed to evaluate the ability of EPC/Chol liposomes to retain their transmembrane pH gradient in the blood compartment after iv injection and subsequently accumulate doxorubicin. These features are minimum criteria that must be met for the liposomes to be capable of altering the pharmacology of doxorubicin through in vivo drug encapsulation. Liposomes exhibiting a 3.5 unit pH gradient (pH 4.0 inside/7.5 outside) were injected iv at a dose of 100 mg total lipid/kg. At various times blood was harvested and the pH gradient of liposomes in the plasma was determined using ^{14}C-methylamine as described in Materials and Methods. As shown in Figure 1A, the EPC/Chol liposomes exhibited a pH gradient between 2.75 and 3.0 units over 4 h post administration. This pH gradient decreased to 2.0 units by 20 h.

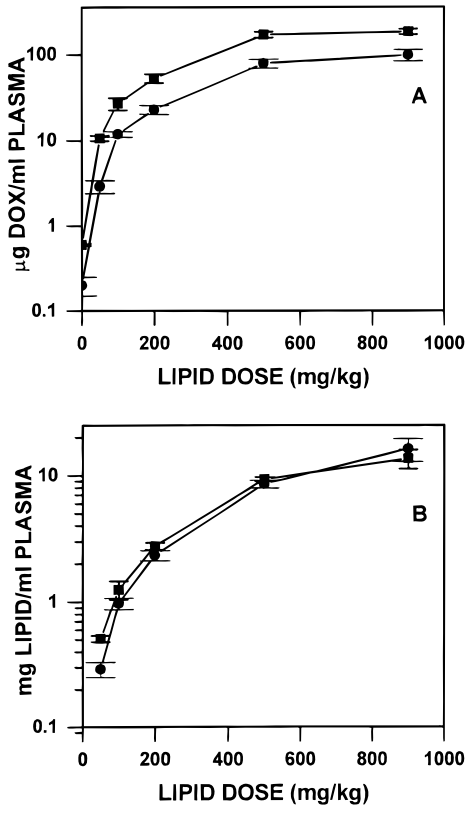

Figure 2—DOX (panel A) and lipid (panel B) concentrations in the plasma at 1 h (■) and 4 h (●) after administration of DOX at 20 mg/kg to mice pretreated with EPC/Chol pH gradient liposomes.

As a control, EPC/Chol liposomes exhibiting no pH gradient (pH 7.5 inside and outside) administered at 100 mg/kg yielded pH gradient measurements of approximately 0.5 units (data not shown). The basis of this small, nonspecific pH gradient appeared to reflect methylamine binding to either protein or lipoprotein components that coeluted with the liposomes during the gel filtration plasma processing step. Quantification of the liposomal lipid remaining in the plasma for pH gradient bearing liposomes at the dose of 100 mg/kg indicated that greater than 72%and 13% of the administered dose of liposomes remained in the circulation at 4 h and 20 h, respectively. Comparable lipid levels were observed for EPC/Chol liposomes in the absence of a pH gradient (data not shown).

Free doxorubicin was added to an aliquot of the liposome-containing plasma samples, and doxorubicin uptake into the vesicles was determined using the same gel filtration procedure as described for methylamine analysis. Liposomes obtained over the first hour after iv injection were able to encapsulate the doxorubicin with trapping efficiencies approaching 100% (Figure 1B). At the 2 h, 4 h, and 20 h timepoints, the efficiency of doxorubicin entrapment fell to 88%, 82%, and 14%, respectively. In contrast, EPC/Chol liposomes without a pH gradient provided doxorubicin entrapment levels that were approximately 10-fold lower than obtained for pH gradient bearing liposomal systems.

The data presented above suggest that optimal in vivo encapsulation of doxorubicin into EPC/Chol vesicles will be obtained when the doxorubicin is injected within 1 h of pH gradient-bearing liposome administration. Using this dosing schedule, the influence of liposome and doxorubicin dose was investigated in order to establish conditions that lead to optimized in vivo drug encapsulation and pharmacokinetic properties. In the first set of experiments, the dose of small (110 nm) EPC/Chol liposomes bearing a 3.5 unit pH gradient was varied from 50 mg/kg to 900 mg/kg. At 1

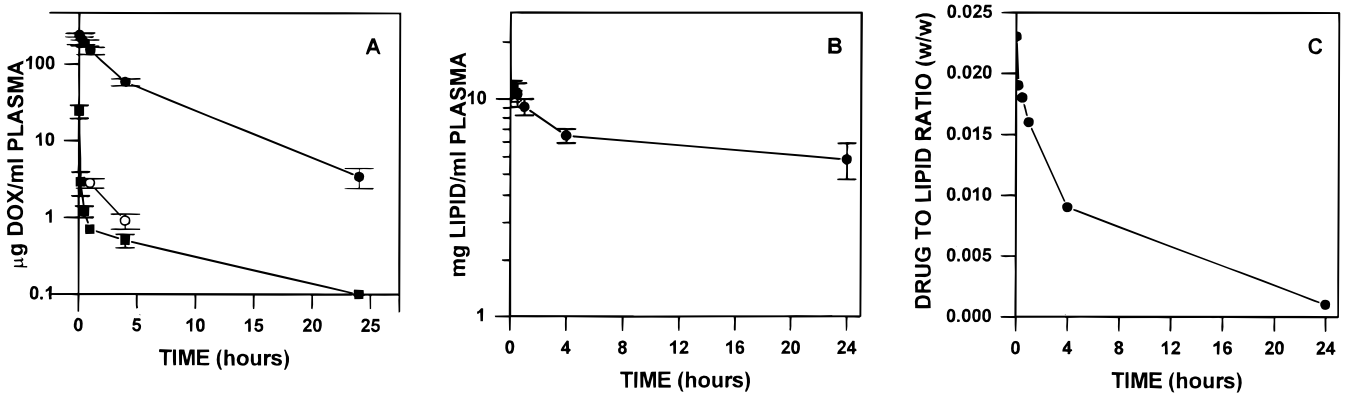

Figure 3—DOX (panel A) and liposomal lipid (panel B) plasma concentrations and circulating drug-to-lipid ratio (panel C) after administration of DOX in free form to mice in the absence (■) and presence (●) of a 500 mg/kg pretreatment dose of 100 nm EPC/CHOL liposomes.

h after iv liposome administration, doxorubicin was injected iv at a dose of 20 mg/kg. At a liposome dose of 50 mg/kg, the concentration of doxorubicin in the plasma was 17.6- and 14.5-fold higher than that observed for free doxorubicin injected in the absence of liposomes at 1 h and 4 h after drug administration, respectively (Figure 2A). Increases in the liposome dose led to increases in the concentration of circulating liposomes as well as the concentration of doxorubicin in plasma. Whereas the concentration of liposomes in the circulation increased proportional to the liposome dose between 50 and 1000 mg/kg for both 1 h and 4 h time points (Figure 2B), the concentration of doxorubicin in the plasma reached plateau levels at a liposome of 500 mg/kg (Figure 2A). At this dose of EPC/Chol pH gradient bearing liposomes, the circulating drug-to-lipid ratios (wt/wt) at 1 h and 4 h after 20 mg/kg doxorubicin injection were 0.02 and 0.01, respectively. Increasing the liposome dose further from 500 mg/kg to 1000 mg/kg resulted in a small increase in circulating doxorubicin concentrations from 170.9 +13.5 μg/mL to 184.8 ± 13.2 μg/mL.

A more detailed pharmacokinetic study was undertaken in order to characterize the effect of in vivo liposome encapsulation on the plasma elimination properties of doxorubicin. Mice were administered pH gradient-bearing EPC/Chol liposomes at a dose of 500 mg/kg 1 h prior to iv injection of 20 mg/kg doxorubicin. Mice were then sacrificed at various times postdrug injection, and their plasma was analyzed for doxorubicin and liposomal lipid as described in Materials and Methods. A comparison was made with doxorubicin injected iv at 20 mg/kg in the absence of any liposome pretreatment. As shown in Figure 3A, doxorubicin in the absence of liposomes is eliminated very rapidly from the circulation after iv injection, with a minimum of two distinct elimination phases. Within 2 min postinjection, >94% of the drug administered has been removed from the plasma and the level of drug eliminated increases to >99.7% within 30 min. In contrast, doxorubicin administered to mice pretreated with 500 mg/kg EPC/Chol pH gradient bearing liposomes is eliminated much more slowly, where <36% and <42% of the drug is removed from the plasma at 2 and 30 min after drug injection, respectively. The increases in doxorubicin concentration observed for mice pretreated with pH gradient liposomes compared to no pretreatment were 9.9-, 157.6-, 115.2-, and 35.0-fold at 2 min, 30 min, 4 h, and 24 h after doxorubicin administration, respectively. The corresponding 0−24 h trapezoidal area under the curve (AUC) values calculated using all time points were 5.5 μgh/mL for doxorubicin alone and 408.8 μgh/mL for doxorubicin in mice pretreated with 500 mg/kg EPC/Chol liposomes which reflected a 74.3-fold increase in total doxorubicin exposure in the plasma. Pretreatment with empty EPC/Chol liposomes prepared without a pH gradient (pH 7.5 inside and outside) at 500 mg/mL resulted in circulating doxorubicin levels that were comparable to those observed with free doxorubicin alone (Figure 3A). In addition, pretreatment with pH gradient-bearing liposomes composed of DPPC/Chol (55:45 mol %) provided circulating doxorubicin concentrations that were <10% of those obtained with EPC/Chol liposomes at 1 h and 4 h after drug administration (data not shown).

Although the plasma doxorubicin concentration in mice pretreated with EPC/Chol liposomes decreased from 237.4 ± 12.3 μg/mL at 2 min postinjection to 3.4 ± 1.5 μg/mL at 24 h (70-fold reduction), the circulating liposomal lipid levels over this time period decreased by only 2-fold from 10.4 ± 0.7 mg/mL to 5.3 ± 1.0 mg/mL (Figure 3B). As a result, the circulating drug-to-lipid ratio for this treatment group decreased from an initial (2 min) value of 0.023:1 (wt/wt) to a value of 0.0006:1 at 24 h (Figure 3C). This drug release (as defined by changes in the drug-to-lipid ratio) followed first-order kinetics and led to a reduction of the circulating drug-to-lipid ratio by 63% within 4 h and 97.4% within 24 h. These results suggest that the circulating liposomes initially accumulate the doxorubicin after it is injected iv and then slowly release the drug subsequently while remaining in the central blood compartment.

The fact that increased doxorubicin concentrations in plasma were obtained only when EPC/Chol liposomes exhibiting a pH gradient (inside acidic) were utilized as a pretreatment before free doxorubicin administration strongly suggested that doxorubicin was being actively sequestered inside the liposomes in response to the pH gradient. This was confirmed by chromatographing plasma from mice treated with EPC/Chol liposomes either with or without a pH gradient (500 mg/kg) and 20 mg/kg free doxorubicin on a Sepharose CL4B column (Figure 4). This resulted in the separation of liposomes (and entrapped doxorubicin) from plasma proteins and free drug. The column was first calibrated for elution profiles of empty liposomes, plasma protein content, and doxorubicin incubated in plasma. Liposomes were readily separated from plasma proteins and free doxorubicin, and it was observed that >90% of doxorubicin in plasma was recovered in the included volume of the column (Figure 4). When plasma obtained 1 h after doxorubicin injection to EPC/Chol liposome (with pH gradient) pretreated mice was applied to this column, >95% of the liposomal lipid and doxorubicin detected was recovered in the liposome fraction. Due to the very low doxorubicin concentrations in plasma after pretreatment with empty EPC/Chol liposomes without a pH gradient, doxorubicin could not be detected in any of the elution fractions (data not shown). It should be noted, however, that lipid concentrations for this treatment group were

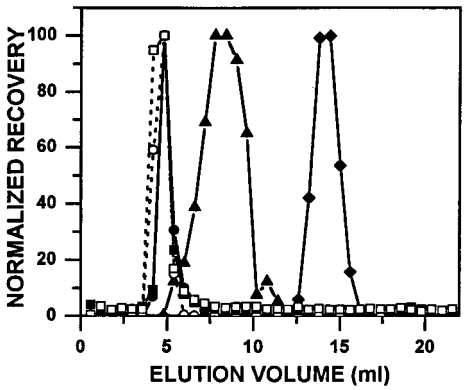

Figure 4—Sepharose CL4B elution profiles for liposomes and doxorubicin incubated in plasma (solid lines) or plasma from mice administered 500 mg/kg pH gradient-bearing EPC/Chol liposomes followed 1 h later by 20 mg/kg free doxorubicin (dashed lines). Elution fractions were analyzed for protein (▲), doxorubicin (◆), liposomal lipid for pre-encapsulated EPC/Chol doxorubicin (●), and doxorubicin pre-encapsulated in EPC/Chol pH gradient liposomes (■) to calibrate the elution positions of the various components. Doxorubicin (○) and liposomal lipid (□) were analyzed from mouse plasma following iv administration of 100 nm EPC/CHOL liposomes containing a pH gradient and free doxorubicin.

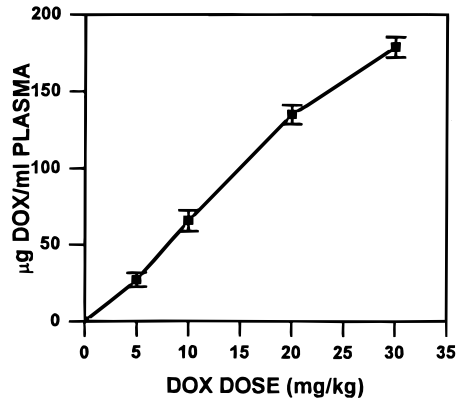

Figure 5—Pretreatment with 100 nm empty pH gradient EPC/CHOL liposomes was administered iv at 500 mg lipid/kg, and plasma DOX concentrations were determined at 4 h after free DOX administration iv at the indicated doses.

identical to those for pH gradient bearing liposomes and all of the liposomal lipid was recovered in the liposome elution volume.

In addition to altering the dose of pH gradient-bearing liposomes, the dose of doxorubicin administered after the liposome pretreatment was manipulated in order to determine the drug–dose dependence of the liposome induced pharmacokinetic changes. As shown in Figure 5, increasing the doxorubicin dose from 5 mg/kg to 30 mg/kg increased the plasma concentration of drug 4 h post iv injection from 27.1 ± 4.6 μg/mL to 178.8 ± 6.6 μg/mL. This increase was proportional to the doxorubicin dose where the percent administered doxorubicin recovered in the plasma at 4 h remained relatively constant (range of 29% to 35%) over a 6-fold range of drug dose. These results indicate that the doxorubicin pharmacokinetic alterations induced by pH gradient-bearing EPC/Chol liposomes are dose independent with respect to doxorubicin over the range studied here.

The biological activity evaluation of the in vivo drug encapsulation strategy described above was performed in order to correlate the changes in doxorubicin pharmacokinetics induced by pH gradient liposome pretreatment with toxicity and efficacy properties. These characteristics were also compared to treatment with free drug alone as well as doxorubicin administered in traditional liposomal formulations where the drug is encapsulated prior to use.

Table 1—Effect of In Vivo Liposomal Capture on Doxorubicin Toxicity[a]

group	DOX dose (mg/kg)	weight loss nadir (%)	toxicity-related mortality
free DOX	20	16	0/6
	25	26	2/6
	30	NA	6/6
preloaded	20	2	0/6
liposomal DOX	30	15	0/6
	40	NA	6/6
in vivo capture	20	5	0/6
liposomal DOX	30	16	0/6
	40	NA	6/6

[a] Preloaded liposomal DOX was prepared by entrapping DOX into 100 nm EPC/Chol liposomes exhibiting a 3.5 unit transmembrane pH gradient (inside acidic). In vivo capture DOX was performed by pretreating DBA-2J mice iv with empty pH gradient bearing EPC/Chol liposomes 1 h before iv injection of free DOX. NA: not applicable since animals died and nadirs cannot be accurately determined.

Table 2—Therapeutic Efficacy of Doxorubicin in Free Form, Preloaded Liposome Encapsulated Form and in Vivo Liposomal Capture Form against L1210 Murine Ascitic Leukemia Model[a]

group	dose (mg/kg) lipid	dose (mg/kg) DOX	median survival time (days)	60-day survival	%ILS
saline control	–	–	11.0	0/6	–
liposomes alone	500	0	10.5	0/6	–5
free DOX	0	10	18.5	1/12	68
	0	20	29.0	1/12	164
preloaded	50	10	19.5	0/6	77
liposomal DOX	100	20	31.0	1/6	182
in vivo capture	500	10	19.0	0/6	73
liposomal DOX	500	20	28.5	1/6	159

[a] Preloaded liposomal DOX was prepared by entrapping DOX into 100 nm EPC/Chol liposomes exhibiting a 3.5 unit transmembrane pH gradient (inside acidic). In vivo capture DOX was performed by pretreating tumor-bearing mice iv with empty pH gradient bearing EPC/Chol liposomes 1 h before iv injection of free DOX.

The results shown in Table 1 demonstrate that free doxorubicin administered iv to mice in the absence of a liposomes pretreatment exhibits signs of drug toxicity at doses of 20 mg/kg and higher. The occurrence of weight loss nadirs in excess of 20% as well as toxicity-related mortality at 25 mg/kg and above indicated a maximum tolerated dose of 20 mg/kg for this treatment group. In comparison, administration of free doxorubicin to mice pretreated with 500 mg/kg EPC/Chol pH gradient liposomes provided minimal weight loss at 20 mg drug/kg and a weight loss nadir of 16% with no mortality over 14 days was observed at 30 mg/kg (Table 1). However, increasing the doxorubicin dose to 40 mg/kg in pretreated mice resulted in 100% mortality. The dose response for doxorubicin toxicity (manifested by weight loss and mortality) observed in the group pretreated with empty pH gradient-bearing liposomes was very comparable to that obtained for doxorubicin entrapped inside 100 nm EPC/Chol liposomes using the pH gradient entrapment procedure just prior to in vivo administration (Table 1).

The antitumor activity of doxorubicin in mice pretreated with pH gradient-bearing EPC/Chol liposomes was evaluated in the murine L1210 ascites tumor model and compared with free doxorubicin alone as well as conventional liposomal doxorubicin encapsulated in pH gradient liposomes prior to injection. The results shown in Table 2 demonstrate that empty liposomes administered iv at a dose of 500 mg lipid/kg did not provide any antitumor activity compared to the saline treated control group. Free doxorubicin administered iv at 10 mg/kg and 20 mg/kg in

the absence of liposome pretreatment increased the median survival time to 18.5 days and 29.0 days, respectively. These survival times reflected increase in life span (ILS) values of 68% and 164% respectively, and one long-term survivor was observed in each treatment group. Administration of doxorubicin as either the EPC/Chol liposomal formulation (prepared prior to use) or as free drug in mice pretreated with EPC/Chol pH gradient-bearing liposomes provided equivalent antitumor activity as free doxorubicin alone. Median survival times for the conventional EPC/Chol liposomal doxorubicin formulation reflected ILS values of 77% and 182% at drug doses of 10 mg/kg and 20 mg/kg while the group receiving pretreatment with empty EPC/Chol pH gradient-bearing liposomes exhibited ILS values of 73% and 159% at 10 mg/kg and 20 mg/kg, respectively (Table 2). One long-term survivor was observed at the 20 mg/kg drug dose for both groups using liposomes. In all treatment groups, the 20 mg/kg drug dose levels were statistically more therapeutically active than 10 mg/kg ($p < 0.05$); however, no statistical significance could be established between groups treated with different formulations for a given doxorubicin dose.

Discussion

The use of liposomal carriers to improve the therapeutic activity of a variety of pharmacological agents in clinical settings has well established this technology as a viable and important approach in the design of pharmaceutical formulations. Early examples of the benefits of liposome encapsulation came primarily from their ability to decrease drug exposure to healthy, susceptible tissues which led to reductions in target organ toxicities.[2,12,18–21] Subsequently, it became apparent that liposomes also exhibit preferential accumulation into disease sites such as tumors and areas of infection/inflammation, thus providing increased selectivity for disease tissue and improved therapeutic index.[22–24] Various combinations of these properties have been utilized in clinically approved liposomal formulations for drugs such as doxorubicin, daunorubicin, and amphotericin B. For all of these liposomal formulations, a key feature that was important in obtaining regulatory approval was the reduced toxicity compared to their free (nonencapsulated) drug counterparts. This buffering of toxicity allows increased doses to be employed without compromising antitumor potency, thus improving the drug's therapeutic index. For the drugs cited above, many of the toxicities to healthy tissues have been associated with early stage drug distribution phases. Consequently, it is believed that the dramatic reduction of free drug exposed to susceptible tissues after administration of the liposomal formulations is largely responsible for the toxicity buffering effects.

The results presented here not only demonstrate that pH gradient bearing EPC/cholesterol liposomes are capable of encapsulating doxorubicin while circulating in the central blood compartment, but that this entrapment process is very efficient in sequestering free doxorubicin before the drug distributes into tissue compartments throughout the body. This is revealed by the fact that at a liposome pretreatment dose of 500 mg/kg, the amount of doxorubicin in the plasma reflects approximately 50% of the administered drug dose. This is comparable to the results observed previously for EPC/cholesterol liposome formulations with pre-encapsulated doxorubicin where approximately 50% of the entrapped drug is released from the liposomes over the first hour after iv injection.[2] It should be noted, however, that the lipid dose required to achieve this effect is 50-fold higher when pretreatment with empty pH gradient EPC/cholesterol liposomes is employed. Nonetheless, it is striking that the accumulation of doxorubicin into liposomes exhibiting a pH gradient can preempt the early phase distribution of free doxorubicin since >98% of free drug is eliminated from the plasma within 5 min of iv administration in the absence of any liposome pretreatment.

In vivo liposome entrapment of doxorubicin was shown here to be dependent on the presence of a transmembrane pH gradient (inside acidic) as well as low phase transition temperature phospholipid compositions. This indicates that the increased plasma doxorubicin concentrations observed in the presence of liposome pretreatment reflect drug that has been actively sequestered inside the liposomes in response to a pH gradient rather than simple passive partitioning of doxorubicin into the bilayer. Such conclusions are based on the fact that high doses of empty EPC/cholesterol liposomes exhibiting no pH gradient (pH 7.5 inside and outside) did not result in elevated plasma doxorubicin concentrations. In addition, the fact that minimal pharmacokinetic alterations were obtained with DPPC/cholesterol liposomes bearing a pH gradient suggests that doxorubicin uptake into such vesicles is relatively slow at 37 °C,[4] and free doxorubicin may be expected to distribute into tissue compartments prior to accumulation into the liposomes under these conditions. It should be pointed out that although the in vivo drug uptake phenomenon described here was accomplished using a pH gradient, alternate transmembrane ion gradients resulting in membrane potentials sufficient to drive drug accumulation could also provide similar effects.[1,4,5] Indeed, the presence of a transmembrane pH gradient in itself generates a membrane potential that would be expected to facilitate doxorubicin uptake.

Pretreatment with empty EPC/cholesterol liposomes that exhibit a pH gradient provides similar buffering of toxicity effects as EPC/cholesterol liposomes in which doxorubicin has been encapsulated prior to administration. This observation suggests that in vivo entrapment may represent a viable alternative to delivering doxorubicin in preencapsulated form. This approach would have clear advantages regarding problems related to chemical stability and liposome retention integrity that are experienced with traditional liposome entrapped formulations. Further, given that several other cancer chemotherapeutic agents such as other anthracyclines and vinca alkaloids[6,7,25–26] as well as drugs from a wide range of therapeutic classes can be efficiently loaded into liposomes displaying a pH gradient,[27] pretreatment with empty liposomes to improve therapeutic activity could be readily applied and evaluated in a variety of pharmaceutical applications. The pH gradient bearing liposomes may also be capable of favorably altering the pharmacokinetic and toxicity properties of combinations of drugs that can be sequestered into liposomes in response to a pH gradient. This is an important feature for many anticancer treatment regimens where combinations including anthracyclines and vinca alkaloids are often utilized. As such, these studies reveal the therapeutic potential of a novel application of pH gradient bearing liposomes.

A more direct and current application of the results obtained here concerns the potential for preloaded liposomes that exhibit transmembrane ion gradients (such as those employed for clinically used formulations of liposomal doxorubicin, daunorubicin, and vincristine) to sequester additional coadministered drugs in the circulation. This could have significant implications, either adverse or beneficial, on the pharmacology of the sequestered agents. Further, in vivo accumulation of additional agents into preloaded liposomes could affect the retention of the primary encapsulated drug (e.g. doxorubicin, daunorubicin, or vincristine) if the transmembrane ion gradient is altered.

This suggests that increased attention should be given to the pharmacology of relevant coadministered drugs when these types of liposome formulations are administered systemically.

Acknowledgments

This work was supported by a grant from the Canadian Medical Research Council (L.D.M. and M.B.B.).

References and Notes

1. Mayer, L. D.; Bally, M. B.; Madden, T. D.; Cullis, P. R. pH Gradient Mediated Drug Entrapment in Liposomes. In Liposome Technology; Gregoriadis, G., Ed.; CRC Press: Boca Raton, FL, 1992; Vol. II, pp 27−44.
2. Mayer, L. D.; Cullis, P. R.; Bally, M. B. The Use of Transmembrane pH Gradient-Driven Drug Encapsulation in the Pharmacodynamic Evaluation of Liposomal Doxorubicin. *J. Liposome Res.* **1994**, *4*, 529−553.
3. Barenholz, Y.; Crommelin, D.J.A. Liposomes as Pharmaceutical Dosage Forms. In *Encyclopedia of Pharmaceutical Technology*; Marcel Dekker: New York, 1994; pp 1−39.
4. Mayer, L. D.; Bally, M. B.; Hope, M. J.; Cullis, P. R. Uptake of Antineoplastic Agents into Large Unilamellar Vesicles in Response to Membrane Potentials. *Chem. Phys. Lipids* **1985**, *40*, 89−98.
5. Bolotin, E. M.; Cohen, R.; Bar, L. K.; Noam, E.; Ninio, S.; Lasic, D. D.; Barenholz, Y. Ammonium Sulfate Gradients for Efficient and Stable Remote Loading of Amphipathic Weak Bases into Liposomes and Ligandoliposomes. *J. Liposome Res.* **1994**, *4*, 455−479.
6. Girard, P. M.; Bouchaud, O.; Goetschel, A.; Mukawaya, G.; Eestermans, G.; Ross, M.; Rozenbaum, W.; Saimot, C. A. G. Phase II Study of Liposomal Encapsulated Daunorubicin in the treatment of AIDS-associated Mucocutaneous Kaposi's Sarcoma. *AIDS* **1996**, *10*, 753−757.
7. Janknegt, R. Liposomal Formulations of Cytotoxic Drugs. *Support. Care Cancer* **1996**, *4*, 298−304.
8. Lasic, D. D. Doxorubicin in Sterically Stabilized Liposomes. *Nature* **1996**, *380*, 561−562.
9. Bally, M. B.; Nayar, R.; Masin, D.; Hope, M. J.; Cullis, P. R.; Mayer, L. D. Liposomes with Entrapped Doxorubicin Exhibit Extended Blood Residence Times. *Biochim. Biophys. Acta* **1990**, *1023*, 133−139.
10. Allen, T. M. Long-circulating (sterically stabilized) liposomes for targeted drug delivery. *Trends Pharm. Sci.* **1994**, *15*, 215−220.
11. Woodle, Am. C.; Lasic, D. D. Sterically stabilized liposomes. *Biochim. Biophys. Acta* **1992**, *1113*, 171−199.
12. Mayer, L. D.; Tai, L. C. L.; Ko, D. S. C.; Masin, D.; Ginsberg, R. S.; Cullis, P. R.; Bally, M. B. Influence of Vesicle Size, Lipid Composition and Drug-to-Lipid Ratio on the Biological Activity of Liposomal Doxorubicin. *Cancer Res.* **1989**, *49*, 5922−5930.
13. Mayer, L. D.; Bally, M. B.; Cullis, P. R.; Wilson, S. L.; Emmerman, J. T. Comparison of Free and Liposome Encapsulated Doxorubicin Entrapped Tumour Drug Uptake and Antitumour Efficacy in the SC115 Murine Mammary Tumour. *Cancer Lett.* **1990**, *53*, 183−190.
14. Boman, N. L.; Cullis, P. R.; Bally, M. B.; Mayer, L. D. Preclinical and Clinical Activity of Liposomal Doxorubicin. In Liposomes in Biomedical Applications, Shek, P. N., Ed.; Academic Publishers: Perth, Australia, 1996; pp 85−103.
15. Mayer, L. D.; Hope, M. J.; Cullis, P. R. Vesicles of Variable Sizes Produced by a Rapid Extrusion Procedure. *Biochim. Biophys. Acta* **1986**, *858*, 161−168.
16. Mayer, L. D.; Hope, M. J.; Cullis, P. R.; Janoff, A. S. Solute Distributions and Trapping Efficiencies Observed in Freeze−thawed Multilamellar Vesicles. *Biochim. Biophys. Acta* **1985**, *817*, 193−196.
17. Mayer, L. D.; Tai, L. C. L.; Bally, M. B.; Mitilenes, G. N.; Ginsberg, R. S.; Cullis, P. R. Characterization of Liposomal Systems Containing Doxorubicin Entrapped in Response to pH Gradients. *Biochim. Biophys. Acta* **1990**, *1025*, 143−151.
18. Van Hossel, Q. G. C. M.; Steerenberg, P. A.; Crommelin, D. J. A.; van Dijk, A.; van Oost, W.; Klein, S.; Douze, J. M. C.; de Wildt, D. J.; Hillen, F. C. Reduced Cardiotoxicity and nephrotoxicity with preservation of antitumor activity of doxorubicin entrapped in stable liposomes in the LOU/M Wsl Rat. *Cancer Res.* **1984**, *44*, 3698−3705.
19. Rahman, A.; White, G.; Moore, N.; Schein, P. S. Pharmacological, toxicological and therapeutic evaluation in mice of doxorubicin entrapped in liposomes. *Cancer Res.* **1985**, *45*, 796−803.
20. Gabizon, A.; Dagan, A.; Goren, D.; Barenholz, Y.; Fuks, Z. Liposomes as in vivo carriers of adriamycin: reduced cardiac uptake and preserved antitumor activity in mice. *Cancer Res.* **1982**, *42*, 4734−4739.
21. Olson, F.; Mayhew, E.; Maslow, D.; Rustum, Y.; Szoka, F. Characterization, toxicity and therapeutic efficacy of adriamycin encapsulated in liposomes. *Eur. J. Cancer Clin. Oncol.* **1982**, *18*, 167−175.
22. Dvorak, H. F.; Detmar, M.; Claffey, K. P.; Nagy, J. A.; van de Water, L.; Senger, D. R. Vascular permeability factor/vascular endothelial growth factor: an important mediator of angiogenesis in malignancy and inflammation. *Int. Arch. Allergy Immunol.* **1995**, *107*, 233−235.
23. Wu, N. Z.; D. D.; Rudoll, T. L.; Needham, D.; Whorton, A. R.; Dewhirst, M. W. Increased microvascular permeability contributes to preferential accumulation of stealth liposomes in tumor tissue. *Cancer Res.* **1993**, *53*, 3765−3770.
24. Yuan, F.; Leunig, M.; Huang, S. K.; Berk, D. A.; Papahadjopoulos, D.; Jain, R. K. Microvascular permeability and interstitial penetration of sterically stabilized (Stealth) liposomes in a human tumor xenograft. *Cancer Res.* **1994**, *54*, 3352−3356.
25. Chang, C. W.; Barber, L.; Ouyang, C.; Masin, D.; Bally, M. B.; Madden, T. M. Comparison of the plasma clearance, biodistribution, and therapeutic properties of mitoxantrone encapsulated in conventional and sterically stabilized liposomes. *Br. J. Cancer* **1997**, *75*, 169−177.
26. Webb, M. S.; Harasym, T. O.; Masin, D.; Bally, M. B.; Mayer, L. D. Sphingomyelin-cholesterol liposomes significantly enhance the pharmacokinetic and therapeutic properties of vincristine in murine and human tumor models. *Br. J. Cancer* **1995**, *72*, 896−904.
27. Madden, T. D.; Harrigan, P. R.; Tai, L. C. L.; Bally, M. B.; Mayer, L. D.; Redelmeier, T. E.; Loughrey, H. C.; Tilcock, C. P. S.; Reinish, L. W.; Cullis, P. R. The Accumulation of Drugs Within Large Unilamellar Vesicles Exhibiting a Proton Gradient: A Survey. *Chem. Phys. Lipids* **1990**, *53*, 37−46.

JS980202H

Demonstration of the Terms Enantiotropy and Monotropy in Polymorphism Research Exemplified by Flurbiprofen

JAN-OLAV HENCK* AND MARIA KUHNERT-BRANDSTATTER

Contribution from *Institut für Pharmakognosie der Universität Innsbruck, Josef-Moeller-Haus, Innrain 52, A-6020 Innsbruck, Austria.*

Received May 5, 1998. Accepted for publication October 8, 1998.

Abstract □ The thermodynamic terms enantiotropy and monotropy are demonstrated by means of solid-state analytical results of polymorphous flurbiprofen (FBP). Vibrational spectra, differential scanning calorimetry (DSC), and thermomicroscopy investigations as well as X-ray powder patterns for three modifications of FBP are described. The melting points are mod. I 113–114 °C (enthalpy of fusion 27.9 ± 0.2 kJ mol^{-1}) for modification I (mod. I), 92 °C for mod. II, and 87 °C for mod. III. The true densities of mod. I (1.279 ± 0.001 g cm^{-3}) and mod. II (1.231 ± 0.002 g cm^{-3}) were measured at 25 °C. Modification I (commercial product) is the thermodynamically stable crystal form from absolute zero to its melting point. Modification II was crystallized on a gram scale from a warm saturated solution of FBP in *n*-heptane and rapid cooling of the solution to –18 °C. Modification I is monotropically related to mod. II and mod. III, due to application of the density rule and the entropy-of-fusion rule. The thermodynamic relationships between the three modifications are demonstrated by a semischematic energy/temperature diagram. Theoretical vapor pressure/temperature diagrams and energy/temperature diagrams are compared and briefly discussed.

Introduction

Compared with mineralogy and metallography, pharmacy was relatively slow to deal with the terms enantiotropy and monotropy, which are very important in crystal polymorphism research. Even today, some authors working in this area seem to have great trouble with these terms, as has been shown by recent publications in respected journals on chloramphenicol palmitate[1] and flurbiprofen.[2] Two pharmaceutically relevant modifications, mod. I (A) and mod. II (B), are of particular interest in the case of chloramphenicol palmitate. The lower melting form II is pharmacologically active and is used in suspensions, whereas form I is inactive as an antibiotic.[3] The reason for the loss of activity of suspensions of the drug substance is that mod. II is thermodynamically unstable under ambient conditions and, due to its better solubility, this crystal form slowly recrystallizes into mod. I in suspensions.

From the many papers about the polymorphism of chloramphenicol palmitate only the one published by Burger[4] will be mentioned here because it also contains a critical review of earlier contributions. Due to the differences in solubility (thermodynamically unstable modifications exhibit better solubility than the thermodynamically stable one at a given temperature) and the differences in the enthalpy of fusion (unstable modifications show a lower enthalpy of fusion than the stable one in a monotropically related system) it is obvious, that mod. II is thermodynamically unstable in relation to mod. I from absolute zero up to its melting point (mp); that is, mod. I and mod. II are monotropically related. This fact was denied by the cited authors[1] and they postulated enantiotropy in this case because they succeeded in obtaining mod. II by quenching and recrystallizing the melt of mod. I. This mistake obviously happened because these authors[1] are unaware of the fact that the terms enantiotropy and monotropy are related to the direct transition between two crystalline phases; that is, that solid−solid transitions occur and intervening melting processes are excluded. The term "enantiotropy" was chosen by Lehmann[5] because it refers to a reversible process in the solid state, whereas the converse "monotropy" implies that the transition can occur in one direction only. Furthermore, it seems that the authors[1] are not familiar with the fact that for more than 100 years, one of the most common methods to obtain polymorphic modifications is crystallization of supercooled melts. Of course, nature has used this method thousands of years ago to create polymorphic modifications of minerals and chemical elements. It is a matter of fact that the method of crystallizing mod. II out of the melt of mod. I using differential scanning calorimetry (DSC) has been successfully tested on numerous drugs.[6] Because the authors of the second paper[2] just mentioned were not quite sure whether the two modifications of flurbiprofen described by them are enantiotropic or monotropic ("probable enantiotropic transition of form II into form I"), we decided to check the polymorphism and found a third modification as well. With this new result it is possible to explain most of the apparent discrepancies.

It is a general question in pharmacy whether polymorphic modifications can transform reversibly (enantiotropy) or irreversibly (monotropy) at atmospheric pressure, because polymorphic crystal forms of a specific chemical compound have different physical properties caused by different arrangements of the molecules in the crystal lattice. These different characteristics often lead to considerable differences in grinding and compression behavior as well as in hygroscopicity, solubility, and bioavailability, etc. All these properties are of great importance for the production of pharmaceutical formulations. Using a thermodynamically unstable modification in the production of tablets, creams, suspensions, solutions, etc. is sometimes the reason why unwanted changes take place in such formulations after a time of storage, caused by transition into the room temperature, thermodynamically stable modification. In the worst case, as shown by the case of chloramphenicol palmitate, this transition may lead to a complete loss of activity of the drug substance. On the other hand it is possible, to apply thermodynamically unstable modifications intentionally, to take advantage of very special properties. There are thermodynamically unstable modifications known, which turned out to have a consider-

* Corresponding author. Telephone: 0043 512 5075306. Fax: 0043 512 5072939. E-mail: Jan-Olav.Henck@uibk.ac.at.

10.1021/js9801945 CCC: $18.00
Published on Web 12/05/1998

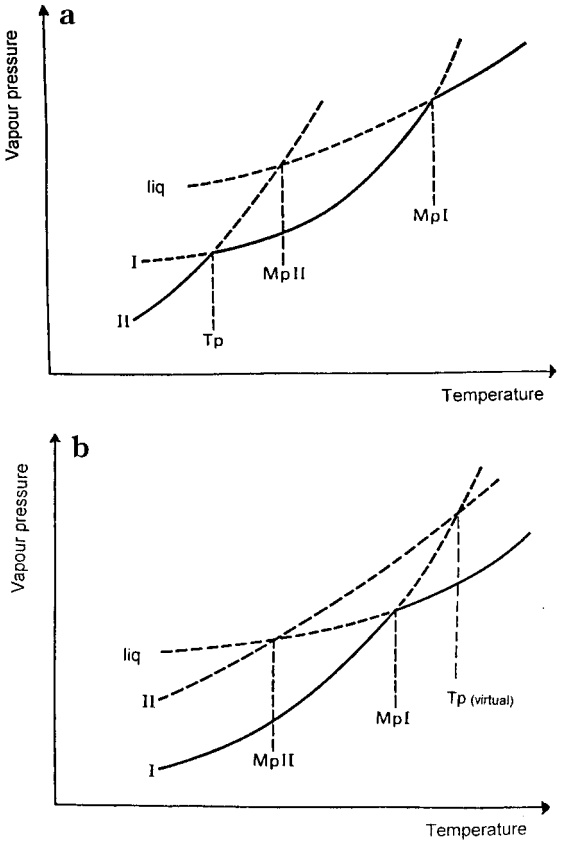

Figure 1—(a) Vapor pressure/temperature diagram: enantiotropy (*Mp*, melting point; *Tp*, thermodynamic transition point). (b) Vapor pressure/temperature diagram: monotropy (*Mp*, melting point; *Tp (virtual)*, thermodynamic transition point).

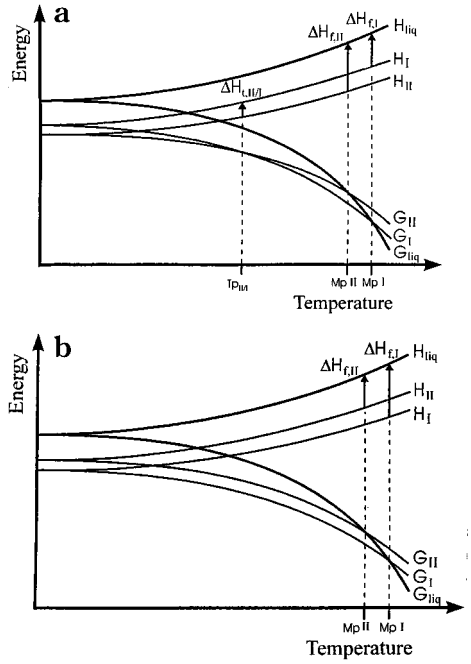

Figure 2—(a) Energy/temperature diagram: enantiotropy (*G*, free energy; *H*, enthalpy; ΔH_f, enthalpy of fusion; *liq*, melt; *Mp*, melting point; *Tp*, thermodynamic transition point; ΔH_t, enthalpy of transition). (b) Energy/temperature diagram: monotropy (*G*, free energy; *H*, enthalpy; ΔH_f, enthalpy of fusion; *liq*, melt; *Mp*, melting point).

able kinetic stability and show a very low transition tendency, if kept dry. Such modifications are called metastable and they may be enantiotropic or monotropic. One example is piracetam, where mod. II and mod. III appeared to show equivalent thermodynamic stability. Only after stirring a suspension of both forms in dioxane did the enantiotropic transition of the metastable and thermodynamically unstable mod. II into mod. III take place.[7]

Because of the increasing spread of generics, more drugs are appearing that exhibit different crystal forms. Often, their stability relationships need to be explained. One example should be mentioned here: 17 different samples of piroxicam supplied by eight pharmaceutical companies were investigated for polymorphism at the Instituto National de Medicamentos (Buenos Aires, Argentina). It was shown that some of the samples contained the pure β form (mod. I), some the 2 °C lower melting pure α form (mod. II), and some contained mainly the α or β form contaminated with the other polymorph.[8] The two forms are monotropically related.

The difference between enantiotropy and monotropy was defined by Ostwald[9] more than 100 years ago using a vapor pressure/temperature diagram, which was brought close to students for decades in standard textbooks of physical chemistry. The difference between enantiotropy and monotropy is defined by the position of the vapor pressure curves. In the case of enantiotropy, the vapor pressure curves intersect below the melting points, whereas in the case of monotropy, the intersection is above the melting points. The intersection point of two vapor pressure curves is the thermodynamic transition point (tp). Therefore the difference between enantiotropically and monotropically related modifications is based on the relative position of the melting points and tp. In an enantiotropic system, the two modifications of interest are in equilibrium at tp and the transition can take place in either direction depending on the temperature (Figure 1a). On the other hand, the tp is virtually in a monotropic system; therefore, the transition can only occur in one direction from the unstable to the stable form. (Figure 1b). The crystal form that shows the lowest vapor pressure at any temperature is the most thermodynamically stable one. The condition for validity of this rule is constant pressure (atmospheric pressure).

The semischematic energy/temperature diagram[10,11] (*E*/*T* diagram), which is based on the Gibbs function, offers more information than the vapor pressure/temperature diagram. For a detailed discussion on the construction and interpretation of *E*/*T* diagrams in general, refer to the literature.[10,11] To draw the *E*/*T* diagram, the isobars of the Gibbs free energy *G* and of the enthalpy *H* of (at least) two modifications, I and II, as well as of the melt *liq* are related to each other. At a given temperature, the thermodynamically stable modification has the lowest Gibbs free energy. Figure 2a represents a given enantiotropically related system of two modifications. Modification II shows the lowest Gibbs free energy until the tp is reached and is therefore thermodynamically stable from absolute zero up to tp. Beyond tp, the Gibbs free energy of mod. II is larger than for mod. I; therefore, this mod. II is thermodynamically unstable from tp up to its mp. At tp, mod. I and mod. II have equal Gibbs free energy and equal thermodynamic stability. The two modifications are enantiotropically related. ΔH_t represents the enthalpy of transition for the transformation II/I and ΔH_f the enthalpy of fusion for mod. II and mod. I, respectively.

Figure 2b describes the relations in a monotropic system. Modification II shows a larger Gibbs free energy than mod. I and is therefore thermodynamically unstable compared with mod. I from absolute zero up to its mp. There is no tp in this temperature region, but a transition in the solid state of mod. II into mod. I is possible; however, never the reverse transition.

Table 1—Flurbiprofen: Important Physicochemical Parameters of the Modifications

parameter	mod. I	mod. II	mod. III
preparation	crystallization from given solvent at 20 °C	crystallization from *n*-heptane, rapid cooling to –18 °C	crystal film
Mp [°C] DSC–onset	114.5	91[a]	—[e]
thermomicroscopy	113–114	92	87
enthalpy of fusion [kJ mol^{-1}]	27.9 ± 0.2[c]	—[e]	25[b]
enthalpy of transition [kJ mol^{-1}] to mod. I		—[e]	–2.9 ± 0.4
entropy of fusion [J mol^{-1} K^{-1}]	72.0[d]	—[e]	69.4[d]
measured density [g cm^{-3}]	1.279 ± 0.001[c]	1.231 ± 0.002[c]	—[e]

[a] Incongruent melting. [b] Calculated by heat-of-fusion rule:[10] $\Delta H_{f,III} = \Delta H_{f,I} + \Delta H_{t,III\rightarrow I}$. [c] ±95% CI. [d] Calculated by entropy-of-fusion rule:[11] $\Delta S_f = \Delta H_f/T_m$. [e] Not determined.

The heat physicists and mineralogists of the turn of this century were well aware of the fact that enantiotropic transition of the modification that is thermodynamically stable below tp into the higher temperature stable one is an endothermic process. On the other hand, the crystal form that is thermodynamically stable above tp shows an exothermic transition if cooled well below tp. Also it was very well-known that a monotropic transition is an exothermic process.[12] This knowledge, in connection with results using the DSC method, was laid down in modern literature as the **heat-of-transition rule**.[10]

Experimental Section

Materials and Solvents—The studies of flurbiprofen (FBP) INN [2-(2-fluorobiphenyl-4-yl) propionic acid; $C_{15}H_{13}FO_2$, M_r, 244.3] were carried out using the commercial product (mod. I) provided by Profarmaco Nobel (Italy). Modification II was obtained by rapid cooling of a warm saturated solution of FBP in *n*-heptane (analytical grade) to −18 °C. Modification III was obtained by quenching a melt film of flurbiprofen to 20 °C on a metal block. Afterward, heating the liquid amorphous material to 30 °C leads to crystallization of mod. III.

Thermoanalytical Methods—*Polarized thermomicroscopy*[13,14] was performed using a Kofler hot stage microscope (Thermovar, Reichert, Vienna, Austria). To prepare a crystal film, ca. 2 mg of FBP were heated between a microscope slide and a cover glass using a Kofler hot bench (Reichert, Vienna, Austria). The molten film was quenched to 20 °C using a metal block. To determine the melting points of mod. II and mod. III the hot stage was preheated to 85 °C. A crystal film preparation containing the two modifications was watched immediately after being placed onto the hot stage. The heating rate was 2 or 5 K min^{-1}. The *solubility test for stability relationships*[15] is made by carefully loosing the cover slip over a crystal film containing the three modifications and touching a drop of solvent to its edge so that the solvent flows in under the cover slip. The solvent must not be so good that the entire film is dissolved away. In the case of FBP, ethanol (70%) was used.

Differential scanning calorimetry (DSC) was carried out with a DSC-7 and Pyris software for Windows NT (Perkin-Elmer, Norwalk, CT) using perforated aluminum sample-pans (25 μL). Sample masses for quantitative analysis were 1−3 (±0.0005) mg (Ultramicroscales UM3, Mettler, CH-Greifensee, Switzerland). Nitrogen 99.990% (20 mL min^{-1}) was used as the purge gas. Calibration of the temperature axis was carried out with benzophenone (mp, 48.0 °C) and caffeine (mp, 236.2 °C). Enthalpy calibration of the DSC signal was performed with indium 99.999% (Perkin-Elmer, Norwalk, CT). The normal heating rate was 2 or 5 K min^{-1}.

Spectroscopic Methods—*Fourier transform infrared (FTIR) spectra* were recorded with a Bruker IFS 25 FTIR spectrometer (Bruker Analytische Meβtechnik GmbH, Karlsruhe, Germany) connected to a Bruker FTIR microscope (15 × Cassegrain-objective and visible polarization). Samples were scanned as potassium bromide pellets at an instrument resolution of 2 cm^{-1} (50 interferograms, internal mode). For recording microscope spectra,[16] small samples were rolled on a round zinc selenide window (13 mm diameter x 1 mm thickness) or a crystal film was made between two zinc selenide windows. The spectral resolution is 4 cm^{-1} (focus diameter 50 μm, 100 interferograms).

FT-Raman spectra were recorded with a Bruker RFS 100 FT-Raman spectrometer (Bruker Analytische Meβtechnik GmbH, Karlsruhe, Germany) equipped with a diode pumped 100 Nd:YAG Laser (1064 nm) as excitation source and a liquid nitrogen-cooled high-sensitivity detector (64 scans at 4 cm^{-1} instrument resolution).

X-ray powder diffraction patterns were obtained on a Siemens D-5000 X-ray diffractometer equipped with Θ/Θ-Goniometer (Siemens AG, Karlsruhe, Germany) using monochromatic Cu Kα radiation (tube voltage 40 kV, tube current 40 mA) from 2 to 40° 2Θ at a rate of 0.005° 2Θ s^{-1}. The diffractometer was fitted with a Göbel mirror and a scintillation counter. The single-crystal data for mod. I (data from Flippen and Gilardi[17]) were used to calculate the idealized X-ray powder pattern for a Cu Kα radiation with the program *PowderCell for Windows* (Kraus, W.; Nolze, G. PowderCell for Windows (V 1.0), *Program for manipulation of crystal structures and calculation of X-ray powder patterns*; Federal Institute for Materials Research and Testing: Berlin, Germany, 1997).

Density Measurements—The determination of the powder volumes were carried out with an air comparison pycnometer (Ultrapycnometer 1000, Quantachrome Corp., Syosset, NY) provided with a small sample cell at 25 °C. The samples (2−3 ± 0.0005 g) were purged with helium for 15 min. Calibration was carried out with a steel sphere.

Results

Thermomicroscopy—A melt film of FBP quenched on a metal cooling block (20 °C) and afterward heated (heating rate: 5 K min^{-1}) on the polarizing hot stage microscope leads to gray quadrangles and hexagons of mod. III (ca. 30 °C) and varicolored columnar aggregates and spherulites of mod. II (ca. 45 °C) and mod. I (ca. 45 °C). According to its morphology, mod. III differs considerably compared with the other crystal forms, whereas mod. I and mod. II are very similar. Continued heating leads to the transition of mod. III into mod. II and to the transition of mod. III into mod. I at about 50 to 60 °C at first, followed by the transition of mod. II into mod. I at about 75 °C. Transfer of a crystal film preparation that contains the three modifications to a preheated hot stage microscope allows the detection of the melting points (Table 1). After cooling the crystal film, the spherulites of mod. I show concentric shrinkage cracks, which are absent in mod. II. Modification II from *n*-heptane, consisting of fine needles, melts incongruently with separation of coarse prisms of mod. I.

The result of the *solubility test for stability relationships*[15] showed that the thermodynamically most unstable form (mod. III) dissolves immediately followed by mod. II after a few seconds. Because of the differences in solubility, crystals of the modification thermodynamically stable at room temperature (mod. I) grow in this solution.

Differential Scanning Calorimetry—Melting the commercial product in an aluminum pan using a hot bench and afterward quenching on a cooling block leads to a liquid amorphous phase, analogous to the melt film used for thermomicroscopy. Heating such a cooled melt in the DSC at a start temperature of 25 °C (heating rate: 2 K min^{-1})

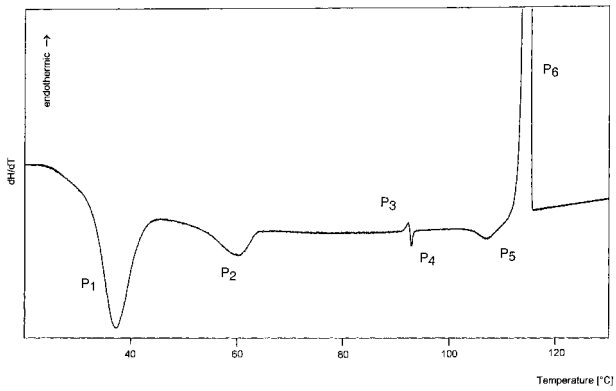

Figure 3—DSC curve of the quenched melt of flurbiprofen starting at 25 °C (heating rate: 2 K min^{-1}).

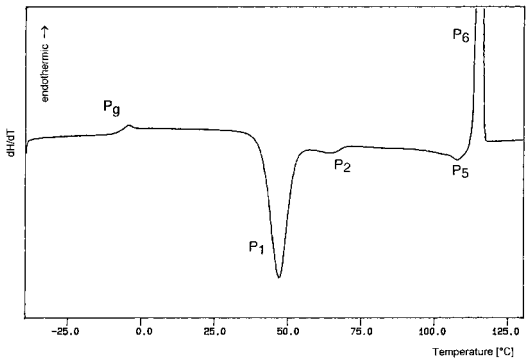

Figure 4—DSC curve of the quenched melt of flurbiprofen starting at −40 °C (heating rate: 5 K min^{-1}).

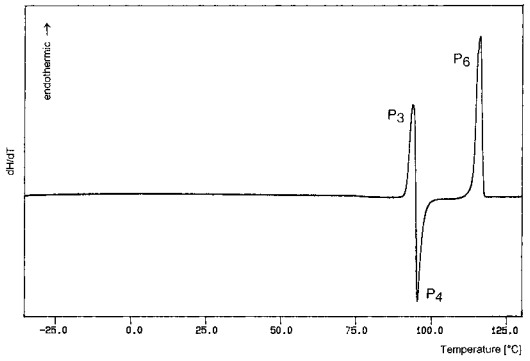

Figure 5—DSC curve of flurbiprofen starting with crystals of mod. II from *n*-heptane (heating rate: 5 K min^{-1}).

leads to crystallization of mod. III between 35 and 40 °C (P_1). The second exothermic peak (P_2) with a maximum at 60 °C represents the transition of mod. III to mod. I. In very few cases, small amounts of mod. II may also sometimes appear; these melt incongruently as indicated by P_3 and P_4. P_5 represents crystallization of remaining melt and P_6 marks the melting of mod. I (Figure 3). Cooling the melt to −40 °C leads to a solid amorphous phase. The DSC trace (Figure 4) of such a glass shows an endothermic peak (P_g), representing the glass transition at −8.5 °C, followed by an exothermic crystallization peak (P_1) and the transition peak (P_2). The DSC trace of pure mod. II (Figure 5) shows the incongruent melting (P_3), followed by the solidification of the melt to form mod. I (P_4) and the melting of mod. I (P_6).

DSC experiments where heating rates of up to 80 K min^{-1} were applied also show the incongruent melting of mod. II. Therefore it was not possible to measure the enthalpy of fusion for this crystal form. Also, attempts to determine the enthalpy of transition for the exothermic

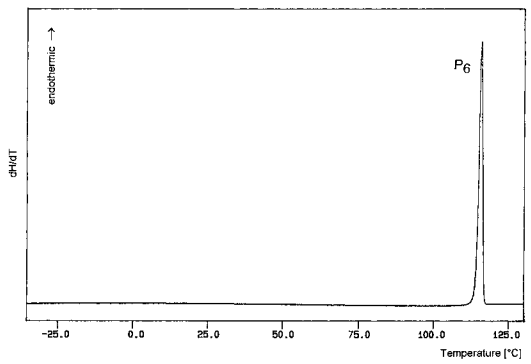

Figure 6—DSC curve of flurbiprofen starting with crystals of mod. I (commercial product, heating rate: 5 K min^{-1}).

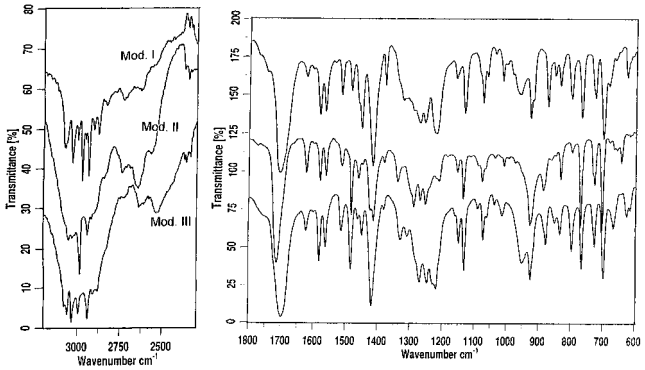

Figure 7—IR spectra of mod. I, mod. II, and mod. III of flurbiprofen recorded by FTIR microscopy.

transition of mod. II into I using a heating rate of 1 K min^{-1} were not successful. Thus, these two values are not given in Table 1. But the negative enthalpy of transition for mod. III into mod. I could be measured using preparations that contained this crystal form purely. The thermogram of mod. I shows one endothermic peak representing the melting of this crystal form (Figure 6).

FTIR Spectroscopy—The FTIR spectra of mod. I and mod. II were recorded using both the crystal powder (by means of KBr pellets) and using a crystal film on a zinc selenide window containing two kinds of spherulites representing the two crystal forms by FTIR microspectroscopy. Due to the two different methods of sampling, the spectra are identical except for small differences in the intensity of several absorption bands.[16] The spectrum of mod. III was only obtained by FTIR microscopy using a crystal film on zinc selenide. Because all three modifications show numerous shifts of significant absorption bands, they can easily be distinguished by their FTIR spectra (Figure 7). Good diagnostic value can be particularly attributed to the band representing the C═O (acid) functional group. The C═O stretching vibration appears to be located for mod. III at 1699 cm^{-1}, for mod. II at 1715 cm^{-1}, and for mod. I at 1705 cm^{-1}.

Raman Spectroscopy—FT-Raman spectra of mod. I and mod. II were also recorded. They show substantial differences in the region around 3000 cm^{-1} and between 300 and 50 cm^{-1} (Figure 8). Modification III could only be obtained as a crystal film, therefore a Raman spectrum of this crystal form could not be recorded.

X-ray Diffractometry—All three modifications were analyzed by X-ray powder diffractometry (Figure 9). A special method was used to prepare mod. III. The crystallization conditions were modified in such a way that in a melt film only this crystal form was created. The cover slip was removed from this preparation and the crystal film

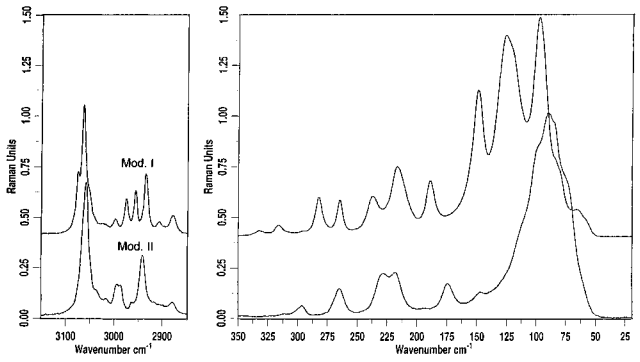

Figure 8—Raman spectra of mod. I and mod. II of flurbiprofen.

surface was used instead of the crystalline powder. The powder pattern calculated from the single-crystal structure data[17] is in very good agreement with the experimental pattern obtained for mod. I (Figure 9).

Density—The density is a very important parameter for determining which one of two modifications is the thermodynamically stable one at absolute zero. Therefore, the true densities of FBP mod. I (commercial product) and mod. II were determined. The result is that mod. I has the higher density than mod. II (Table 1). Because mod. III cannot be produced in macroscopic amounts, this value is missing in Table 1. According to the **density rule**[10] the modification with the lower density is thermodynamically unstable at absolute zero compared with the crystal form with the higher density. Therefore, mod. II is thermodynamically unstable from zero Kelvin up to its melting point compared with mod. I. More detailed remarks will be given in the Discussion.

Discussion

The measured and calculated physicochemical parameters for the three modifications of FBP are summarized in Table 1. The enthalpy of fusion could only be measured directly for mod. I. The enthalpy of fusion for mod. III was calculated by applying the heat-of-transition rule[10] using the enthalpy of transition for mod. III into mod. I measured by DSC. The enthalpy of fusion of mod. I is higher than that of mod. III. Therefore, it follows by means of the heat-of-fusion rule,[10] that these two crystal forms are monotropically related. The same is true for the entropy of fusion.[11] As already described, it was not possible to measure the enthalpy of fusion for mod. II because of its incongruent melting. The proof for the monotropic relation between mod. I and mod. II arises from the comparison of the density of these two crystal forms. Modification I shows higher density than mod. II and thus, according to the density rule,[10] monotropism is realized in this case. The *E*/*T* diagram[10,11] of FBP illustrates the thermodynamic relationships of the three modifications (Figure 10). Because the relevant physical parameters (Table 1) indicate monotropy between mod. III and mod. I (heat-of-transition rule[10]), as well as between mod. II and mod. I (density rule[10]), the diagram is in principle similar to the one given in Figure 2b. Modification I is the most stable crystal form of FBP. The result of the *solubility test for stability relationships* proves that mod. III is the most thermodynamically unstable crystal form at 20 °C and that mod. II is more stable than mod. III at ambient conditions because of its lower solubility. The thermoanalytical behavior of mod. III allows the assumption that monotropy is realized in relation to mod. II with high probability. In the case of FBP, this question is not of practical relevance. The FTIR spectra of the three modifications show significant differences. Compared with the IR spectra published by Lacoulonche et al.,[2] it is clear that our mod. I corresponds to their form I and our mod. II to their form II "recrystallized in heptane".[2] Comparison of the X-ray powder patterns of the different crystal forms clearly indicates that their form II[2] obtained by crystallization from the melt corresponds to our mod. III. This fact is also confirmed by the morphological description[2] of the crystals.

The results of our study on the polymorphism of FBP clearly show that three crystal forms can be obtained by crystallization from solution and the melt. Lacoulonche et al.[2] did not realize that they had obtained three modifications instead of two. Therefore, the physical properties of the modifications could not be assigned in a correct way and, hence, this led to the wrong conclusion on the thermodynamic relationships of this polymorphic system.

Modification III of FBP is only of analytical interest because this modification is not only thermodynamically unstable at 20 °C but also kinetically unstable. This crystal form can only be obtained in microscopic amounts. It transforms into mod. I at ambient conditions within a few minutes. Modification II is also thermodynamically un-

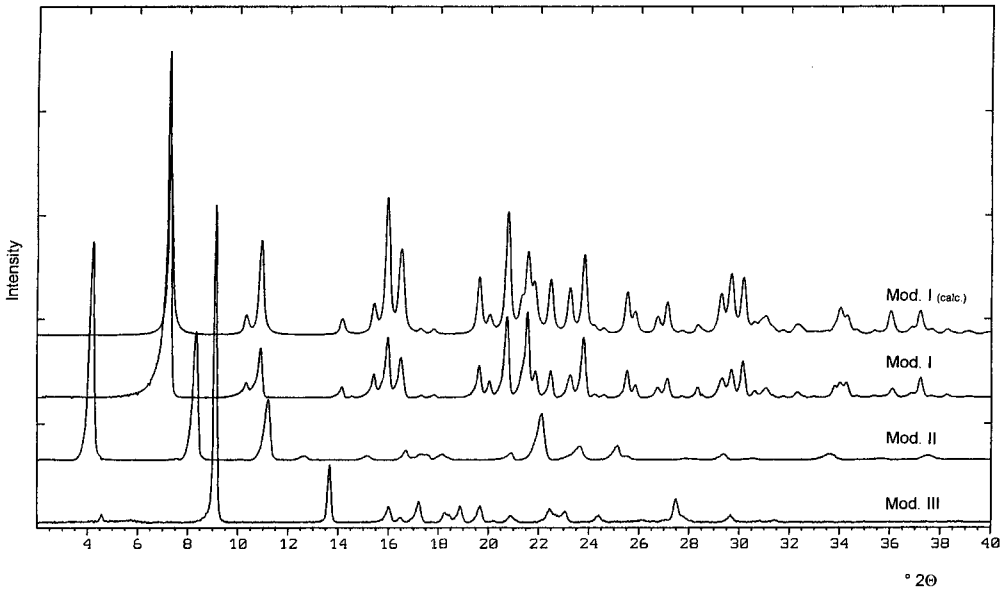

Figure 9—X-ray powder diffraction patterns of mod. I (also calculated from single-crystal data), mod. II, and mod. III of flurbiprofen.

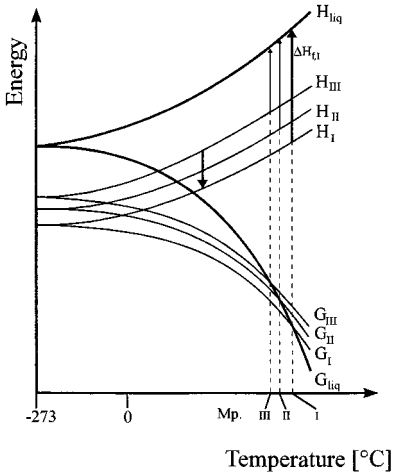

Figure 10—Energy/temperature diagram of the crystalline modifications of flurbiprofen and its melt: *G*, free energy; *H*, enthalpy; ΔH_t, enthalpy of fusion; *liq*, melt; *Mp*, melting point; measured enthalpy effects are drawn bold.

stable at 20 °C, but is durable for more than 6 months if kept under dry conditions. Also, grinding of mod. II with a mortar and pestle has not caused a transition into mod. I. Therefore this crystal form may have some practical implications. As has been shown on other polymorphic drug substances (e.g., paracetamol[18]), this marked kinetic stability could be suitable to perform direct compression experiments using this crystal form.

As a chiral substance, the modifications of FBP are in principle able to crystallize as conglomerates, racemic compounds, or solid solutions. Unfortunately, we did not have one pure enantiomer to investigate the phase diagram of this binary system and to answer this question on the nature of the three modifications.

References and Notes

1. Csakurda-Harmathy, Zs.; Konkoly Thege, I. Transformation of chloramphenicol palmitate from therapeutically inactive polymorph A to the active polymorph B. *J. Thermal Anal.* **1997**, *50*, 867−871.
2. Lacoulonche, F.; Chauvet, A.; Masse J. An investigation of flurbiprofen polymorphism by thermoanalytical and spectroscopic methods and a study of its interactions with poly(ethylene glycol) 6000 by differential scanning calorimetry and modelling. *Int. J. Pharm.* **1997**, *153*, 167−179.
3. Aguiar, A. J.; Krc Jr., J.; Kinkel, A. W.; Samyn, J. C. Effect of polymorphism on the absorption of chloramphenicol from chloramphenicol palmitate *J. Pharm. Sci.* **1967**, *56*, 847−853.
4. Burger, A. Neue Untersuchungsergebnisse zur Polymorphie von Chloramphenicolpalmitat. *Sci. Pharm.* **1977**, *45*, 269−281.
5. Lehmann, O. *Molekularphysik*; Engelmann: Leipzig, 1888; p 411.
6. Kuhnert-Brandstätter, M.; Riedmann, M. Thermal analytical and infrared spectroscopic investigations on polymorphic organic compounds. *Mikrochim. Acta* **1989**, *I*, 81−95.
7. Kuhnert-Brandstätter, M.; Burger, A.; Völlenklee, R. Stability behaviour of piracetam polymorphs. *Sci. Pharm.* **1994**, *62*, 307−316.
8. Pineyro de Castellano, L. L. A.; Ciura, J. M. E.; Chiale, C. Analisis cristalografico de polimorfos de piroxicam. *SAFYBI* (Revista De La Asociacion Argentina De Farmacia Y Bioquimica Industrial) **1996**, *35*, 17−31.
9. Ostwald, W. *Lehrbuch der allgemeinen Chemie II*; Engelmann: Leipzig 1885; p 440.
10. Burger, A.; Ramberger, R. On the polymorphism of pharmaceuticals and other organic molecular crystals. I: Theory of thermodynamic rules. *Mikrochim. Acta* **1979**, *II*, 259−271.
11. Grunenberg, A.; Henck, J.-O.; Siesler, H. W. Theoretical derivation and practical application of energy/temperature diagrams as an instrument in preformulation studies of polymorphic drug substances. *Int. J. Pharm.* **1995**, *118*, 11−21.
12. Doelter, C. Physikalisch-Chemische Mineralogie. In *Handbuch der Angewandten Physikalischen Chemie*; Vol. II.; Bredig, G., Ed.; J. A. Borth: Leipzig, 1905; pp 19−42.
13. Kuhnert-Brandstätter, M. *Thermomicroscopy in the Analysis of Pharmaceuticals*; Pergamon: Oxford 1971.
14. Kuhnert-Brandstätter, M. Thermomicroscopy of organic compounds. In *Wilson and Wilsons's Comprehensive Analytical Chemistry*; Vol. XVI; Svehla, G., Ed.; Elsevier: Amsterdam, 1982; pp 329−513.
15. Kuhnert-Brandstätter, M. Thermomicroscopy of organic compounds. In *Wilson and Wilsons's Comprehensive Analytical Chemistry*; Vol. XVI; Svehla, G., Ed.; Elsevier: Amsterdam, 1982; p 429.
16. Reffner, J. A. FTIR-Microspectrometry: Applications in Pharmaceutical Research. In *Infrared Microspectroscopy, Theory and Applications*; Messerschmidt, R. G.; Harthcock, M. A., Eds.; Marcel Dekker: New York, 1988; pp 179−196.
17. Flippen, J. L.; Gilardi, R. D. (±)-2-(2-Fluoro-4-biphenyl)-propionic Acid (Flurbiprofen). *Acta Crystallogr. B* **1975**, *31*, 926−928.
18. Di Martino, P.; Guyot-Hermann, A.-M.; Conflant, P.; Drache, M.; Guyot, J.-C. A new pure polymorph of paracetamol for direct compression: the orthorhombic form. *Int. J. Pharm.* **1996**, *128*, 1−8.

JS9801945

Estimation of Aqueous Solubility for Some Guanine Derivatives Using Partition Coefficient and Melting Temperature

ALBIN KRISTL

Contribution from *Faculty of Pharmacy, University of Ljubljana, Aškerčeva 7, 1000 Ljubljana, Slovenia*

Received April 28, 1998. Accepted for publication September 8, 1998

Abstract □ Aqueous solubilities for some guanine derivatives were estimated by semiempirical equations developed by Yalkowsky and Valvani[1] using the data for partition coefficient and melting temperature. It was shown that in the case of guanine derivatives examined in this study, the solubility values could not be estimated adequately by these equations.

Introduction

There exist several different methods of aqueous solubility estimation for organic compounds:[1] methods based directly on group contributions to measured aqueous activity coefficients; techniques based on experimental physicochemical properties such as partition coefficient, chromatographic retention, boiling point, and molecular volume; methods based on properties that cannot be experimentally determined but can be calculated from molecular structure (molecular surface area, molecular connectivity, and parachor); and techniques based on combinations of two or more parameters that can be experimentally measured, calculated, or generated empirically (solubility parameter, linear solvation energy relationship and others).

The first who recognized the relationship between aqueous solubility and *n*-octanol water partition coefficient (P) were Hansch et al.[2] One of the most well-known and popular equations for predicting the solubility of liquid and solid organic solutes using the *n*-octanol water partition coefficient was derived by Yalkowsky and Valvani:[1,3]

$$\log S_w \approx -1.00\log P - 1.11\frac{\Delta S_f(\mathrm{mp} - 25)}{1364} + 0.54 \quad (1)$$

where S_w is aqueous solubility in mol/L, mp is the solute melting point temperature in °C, and ΔS_f is the entropy of fusion. The parameter P is given as the concentration ratio in octanol and aqueous phases (C_o/C_w).

For rigid molecules, where ΔS_f was taken as 56.7 J/molK, one obtains

$$\log S_w \approx -1.05\log P - 0.012\mathrm{mp} + 0.87 \quad (2)$$

These semiempirical equations showed excellent correlation between the values for aqueous solubility and P for many nonelectrolytes, weak electrolytes, and even for acidic and basic substances.[1,3,4] They were used by many different researchers for aqueous solubility estimation of various substances, and good correlation between experimentally determined and calculated solubility values was shown.[5,6]

In this work we wanted to evaluate eqs 1 and 2 for predicting the aqueous solubility for some antivirus guanine derivatives, acyclovir (ACV) and deoxyacyclovir (DCV), and their acetyl derivatives.

Materials and Methods

The substances examined in this study, ACV (9-(2-hydroxyethoxymethyl)guanine) and DCV (2-amino-9-(2-hydroxyethoxymethyl)-9-*H*-purine) with their *O*-acetyl (OAcACV and OAcDCV), *N*-acetyl (NAcACV and NAcDCV), and *N*,*O*-diacetyl (diAcACV and diAcDCV) congeners were synthesized at the National Institute of Chemistry, Ljubljana, Slovenia.[7]

The melting temperatures (mp), entropies of fusion (ΔS_f) and corresponding activity coefficients (γ) as well as the values for aqueous solubility (S_w), partition coefficients, and different octanol/water solubility ratios at 22 ± 0.1 °C were determined previously[8] and are given in Table 1. Additionally, the thermal analysis measurements for all tested substances showed no enthalpy changes that would correspond to desolvation, except for ACV, which existed in hydrated form but after drying (T = 150 °C, air atmosphere), a stable anhydrous form was obtained.[9]

Experimentally determined values for partition coefficients[8] were used in eqs 1 and 2. The values for partition coefficients of tested guanine derivatives calculated by Rekker's fragmental approach differed significantly from those obtained by the experiment.[10]

Results and Discussion

Calculated values for aqueous solubility of tested substances, using eqs 1 and 2 are presented in Table 1. Equation 2, where the entropy value for the rigid molecules (56.5 J/mol K) is used, gives completely different results from the measured values, although tested substances are rigid and mostly do not have more than five nonhydrogen atoms in a flexible chain (the molecules with more than five units in the side chain are assumed to be partially flexible molecules).[1,3] These results were expected because all the experimentally determined values of ΔS_f for tested substances (Table 1) differ a lot from 56.5 J/mol K (except for ACV for which the ΔS_f value is close to 56.5 J/mol K).

Comparing the logarithmic values for aqueous solubility calculated by eq 1 (where the experimentally determined values for ΔS_f were used) with the measured ones reveals a rather large disagreement. The log P values determined for the same compound are acceptable if they do not differ by >0.2 log units[11] or even 0.3 log units,[12] which represent about two times higher/lower values in the nonlogarithmic scale. Using these estimations, one can say that calculated (by eq 1) and experimentally determined log S_w values are in good accordance for diAcACV and diAcDCV, are rather good for OAcACV and OAcDCV, and differ by large amounts in the case of the other tested substances.

Equations 1 and 2 were derived on the basis of the following rationales:[13]

(1) The solubility of nonpolar and semipolar solutes in octanol is approximately equal to the ideal solubility, γ_o = 1. Because $P = \gamma_w/\gamma_o$, it follows that log $\gamma_w \approx$ log P.

(2) The ideal solubility can be estimated from mp and ΔS_f of the solute.

(3) The ΔS_f of the solute is constant for rigid molecules.

10.1021/js980180z CCC: $18.00
Published on Web 11/21/1998

Table 1. Melting Temperatures (mp, in °C), Entropies of Fusion (ΔS_f, in J/Mol K), Activity Coefficients in Neat Water (γ_w) and in Neat Octanol (γ_o), and Logarithmic Values of Aqueous Solubilities

parameter	ACV	NAcACV	OAcACV	diAcACV	DCV	NAcDCV	OAcDCV	diAcDCV
T_m	255.0	217.0	242.0	204.0	189.0	181.0	135.0	134.0
ΔS_f	57.7	109.9	96.9	99.3	91.4	121.0	104.6	104.0
γ_w[a]	33.9	0.81	5.93	5.22	1.40	0.17	4.41	2.73
γ_o[a]	252.1	11.8	96.0	26.9	14.7	4.75	12.7	23.1
log S_w[b]	−053	−2.37	−2.58	−2.16	−1.38	−1.91	−1.17	−0.70
log S_w[c]	−0.54	−0.37	−0.91	−0.69	−0.26	0.09	−0.11	0.36
log S_w[d]	−2.14	−1.92	−2.70	−2.14	−1.08	−0.86	−0.97	−0.73
log P[d]	−1.57	−1.30	−1.07	−0.85	−1.08	−1.33	−0.61	−1.05
log S_o/S_w[d]	−1.82	−2.10	−2.15	−1.66	−1.96	−2.40	−1.40	−1.90
log S_{ow}/S_{wo}[d]	−1.60	−1.45	−1.16	−0.96	−1.26	−1.54	−0.72	−1.12

[a] Activity coefficients (γ) were calculated by the equation $\gamma = (f_2/f_2°)/S_2V_1$, where f_2 and $f_2°$ are the fugacities of the pure solid solute and of its subcooled liquid at the temperature of the solution, respectively, S_2 is the molar solubility of the solute and V_1 is the molar volume of the solvent.[8] [b] Calculated by eq 1 at T = 22 °C. [c] Calculated by eq 2 at T = 22 °C. [d] The logarithms of aqueous solubilities (log S_w), partition coefficients (log P), octanol/water solubility ratios (log S_o/S_w) and mutually saturated octanol/water solubility ratios (log S_{ow}/S_{wo}) for examined substances are also given (T = 22 ± 0.1 °C).[8]

(4) The ratio S_o/S_w is equivalent to P, that is, S_w is equal to S_o divided by P. These statements were additionally supported by recently published papers[14,15] where the authors confirmed the negligible effect of octanol/water mutual saturation on the partition coefficient. They stated that the octanol/water solubility ratio, S_o/S_w, can be used as the estimate for the partition coefficient and that there is negligible effect of octanol/water mutual saturation on the partition coefficient, although the average absolute estimation errors (when correlating log P with log(S_o/S_w) for 82 solutes) were >0.4 log units (which means >2.5-fold higher/lower values in the nonlogarithmic scale).[14] Additionally, the solubility of different organic compounds in octanol (using 124 solutes) was estimated by five methods (i.e.; ideal solubility, regular solution approach, UNIFAC approach, PS_w method, and OCTASOL), and the most reliable results were obtained by PS_w method (log S_o = log P + log S_w), where the average error of estimates is 0.29 log units (2-fold higher/lower value than the experimental one in nonlogarithmic scale).[15]

Regarding the observed discrepancies in calculated and experimentally determined values for aqueous solubilities of tested guanine derivatives one can assume that some of the aforementioned rationales could be invalid for predicting the aqueous solubility of these substances; although they represent semipolar solutes.[16] The values for γ_o of tested substances (Table 1) differ significantly from 1 in all cases, indicating that the solubility of these substances in *n*-octanol is not ideal. Despite these differences, the observed and calculated log S_w values (by the eq 1) are reasonably close in four out of the eight cases. This nonideal solubility in *n*-octanol also indicates that the activity coefficients of tested substances in water (γ_w) cannot be equal to P, expressed in mole fractions.

Additionally it was shown that in the case of tested guanine derivatives, ΔS_f of the solute is not constant for rigid molecules and cannot be taken as ΔS_f = 56.7 J/mol K.

We also found large differences in the solubility values determined in neat and mutually saturated solvents and consequently in the solubility ratios (Table 1), showing that mutual saturation plays an important role in partitioning and solubility not only of many highly lipophilic and hydrophilic solutes but also of semipolar substances such as the tested guanine derivatives.[8] It can be deduced that the values for partition coefficients (P) are not equivalent to the neat octanol/water solubility ratios (S_o/S_w) but more to the mutual saturated octanol/water solubility ratios (S_{ow}/S_{wo}; Table 1). These findings were also confirmed with the partition experiments performed with some higher alkanols (i.e., heptanol and nonanol).[17]

One can thus conclude that eqs 1 and 2 in the case of tested guanine derivatives do not give reasonable estimation of aqueous solubility.

References and Notes

1. Jalkowsky, S. H.; Banerjee, S. *Aqueous solubility (Methods of estimation for organic compounds)*; Marcel Dekker: New York, 1992.
2. Hansch, C.; Quinlan, J. E.; Lawrence, G. L. The linear free energy relationships between partition coefficients and the aqueous solubility of organic liquids. *J. Org. Chem.* **1968**, *33*, 347−350.
3. Yalkowsky, S. H.; Valvani, S. C. Solubility and partitioning I: Solubility of nonelectrolytes in water. *J. Pharm. Sci.* **1980**, *69*, 912−922.
4. Yalkowsky, S. H.; Pinal, R.; Banerjee, S. Water solubility: A critique of the solvatochromic approach. *J. Pharm. Sci.* **1988**, *77*, 74−77.
5. Mayer, J. M.; Rowland, M. Determination of aqueous solubilities of a series of 5-ethyl-5-alkylbarbituric acids and their correlation with log P and melting points. *Drug Dev. Ind. Pharm.* **1984**, *10*, 69−83.
6. Prankerd, R. J.; McKeown, R. H. Physicochemical properties of barbituric acid derivatives: IV. Solubilities of 5,5-disubstituted barbituric acids in water. *Int. J. Pharm.* **1994**, *112*, 1−15.
7. Štimac, A.; Muhič, D.; Kobe, J. A novel palladium-catalysed deoxygenation of guanine O^6-arene sulfonates. A practicable synthesis of 2-amino purine nucleosides and related analogues. *Nucleosides Nucleotides* **1994**, *13*, 625−636.
8. Kristl, A.; Vesnaver, G. Thermodynamic investigation of the effect of octanol−water mutual miscibility on the partitioning and solubility of some guanine derivatives. *J. Chem. Soc., Faraday Trans.* **1995**, *91*, 995−998.
9. Kristl, A.; Srčič, S.; Vrečer, F.; Šuštar, B.; Vojnovic, D. Polymorphism and pseudopolymorphism: influencing the dissolution properties of the guanine derivative acyclovir. *Int. J. Pharm.* **1996**, *139*, 231−235.
10. Kristl, A.; Pečar, S. Hydrolipophilic anomalies of some guanine derivatives. *Eur. J. Med. Chem.* **1997**, *32*, 3−8.
11. Rekker, R. F.; Mannhold, R. *Calculation of drug lipophilicity (The hydrophobic fragmental constant approach)*; VCH: Weinheim, New York, 1992.
12. Dearden, J. C.; Bresnen, G. M. The measurement of partition coefficients. *Quant. Struct. Act. Relat.* **1988**, *7*, 133−144.
13. Yalkowsky, S. H.; Valvani, S. C.; Roseman, T. J. Solubility and Partitioning VI: Octanol Solubility and Octanol−Water Partition Coefficients. *J. Pharm. Sci.* **1983**, *72*, 866−870.
14. Pinsuwan, S.; Li, A.; Yalkowsky, S. H. Correlation of Octanol/Water Solubility Ratio and the Partition Coefficients. *J. Chem. Eng. Data* **1995**, *40*, 623−626.
15. Li, A.; Pinsuwan, S.; Yalkowsky, S. H. Estimation of Solubility of Organic Compounds in 1-Octanol. *Ind. Eng. Chem. Res.* **1995**, *34*, 915−920.
16. Kristl, A.; Mrhar A.; Kozjek, F. The Ionization Properties of Acyclovir and Deoxyacyclovir. *Int. J. Pharm.* **1993**, *99*, 79−82.
17. Kristl, A. Thermodynamic Investigation of the Effect of the Mutual Miscibility of Some Higher Alkanols and Water on the Partitioning and Solubility of Some Guanine Derivatives. *J. Chem. Soc., Faraday Trans.* **1996**, *92*, 1721−1724.

JS980180Z

Importance of Tautomers in the Chemical Behavior of Tetracyclines†

HÉLIO A. DUARTE,‡ SANDRA CARVALHO,‡ EUCLER B. PANIAGO,‡,§ AND ALFREDO M. SIMAS*,||

Contribution from *Departamento de Química-ICEx, Universidade Federal de Minas Gerais, 31.270-901 Belo Horizonte-MG-Brazil, Departamento de Química Fundamental, Universidade Federal de Pernambuco, Recife-PE-Brazil, and Departamento de Química-ICEB, Universidade Federal de Ouro Preto, Ouro Preto-MG-Brazil.*

Received April 28, 1998. Final revised manuscript received July 21, 1998.
Accepted for publication September 8, 1998.

Abstract □ We advance the concept that tautomerism is crucial for the understanding of the chemical behavior of tetracycline. Indeed, considering four deprotonations, there are 64 different possible tautomers to be considered for tetracycline. Our results indicate that tetracycline is a very adaptive molecule, capable of easily modifying itself through tautomerism in response to various chemical environments. Indeed, its situation in solution can be more accurately pictured as an equilibrium among a diversity of tautomeric species–an equilibrium that can be easily displaced depending on the various possible chemical perturbations, such as varying the pH or the dielectric constant of the solvent. Moreover, we also show that tetracycline could undergo four deprotonations and predict for it a fourth pK_a of 13 and refer to our experimental determination of this parameter, which yielded the value of 12. We conclude that tautomerism is essential to the comprehension of the chemical behavior of tetracycline as determined by the semiempirical method AM1 as well as by the self-consistent reaction field method, which estimates the effects of the solvent on the tautomers. All tautomers in their different conformations have been fully optimized for each of the possible degrees of protonation of this molecule. Thus, the relative stabilities of the different tautomeric species have been computed.

1. Introduction

Tetracycline (TC, Figure 1) and its derivatives are widely used antibiotics.[1] The chemical−structural properties of tetracycline have been extensively studied.[2] TC has different acid groups in its chemical structure and the possibility to adopt different conformations. The different proton-donating groups of this molecule offer several possibilities of metal ions substitution. The complexation with metal ions increases the stability of the various TC derivatives.[3] In some cases, metal ion complexation reduces the availability of TC in the blood plasma[4] or eliminates its biological activity.[5] It is known that TC forms complexes in different positions with calcium and magnesium ions that are available in the blood plasma.[6,7] Undoubtedly TC is a complex molecule and, despite all effort, its mechanism of action is still not well understood.

The three acid dissociation constants normally observed in potentiometric experiments and the appropriate assignment of the various acid groups of TC to the respective dissociation constants are important to understand the chemical behavior in blood plasma and the biological

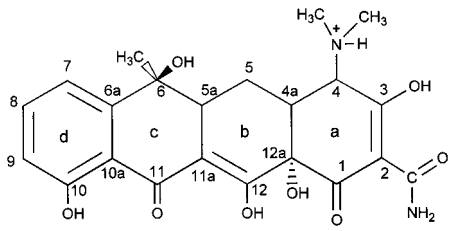

Figure 1—Chemical structure of TC.

activity of TC. The protonation scheme of TC has been the subject of controversy and intense study.[8−11] In 1956, Stephens et al.[8] proposed that pK_1 (= 3.30) is due to the protonation of the oxygen bonded to the C(3), pK_2 (= 7.68) is due to the protonation of the dimethylamino group, and pK_3 (= 9.69) is due to the protonation of the oxygen atoms bonded to the C(10) and C(12). Later, Leeson et al.[9] comparing the pK_as of different TC derivatives, suggested that pK_2 should be assigned to the protonation of the oxygen atoms bonded to the C(10) and C(12) and pK_3 to the protonation of the dimethylamino group. The effect of dielectric constant on the pK_a values of TC has been investigated by Garrett[12] studying TC in dimethylformamide−water mixtures. The observed decrease in pK_a values of uncharged acids with increasing dielectric constants supports the reversal in assignment of the 2nd and 3rd pK_as of TC. Rigler et al.,[10] using ^{1}H NMR, proposed a different protonation scheme. The chemical shifts of protons of the 4-dimethylamino group and the nonlabile protons of the phenolic group have been monitored as a function of pH. They assumed that the chemical shifts change depends exclusively on the respective protonation sites. Based on this assumption, they suggested that pK_2 and pK_3 have contributions from the dimethylamino and phenolic C(10) groups, respectively. The work of Asleson and Frank[11] using ^{13}C NMR supports the suggestion of Rigler et al.[10] and proposed that the protonation of the oxygen in C(12) is preferential with respect to the phenolic group C(10). They used the chemical shift of C(8) (see Figure 1) as a measure of protonation of the phenolic group C(10) and assumed that pK_1 is due to the tricarbonyl system of ring "a".

Another important aspect is the different conformations that this molecule can have depending on the medium. Mitcher et al.[13] have used circular dichroism (CD) to show that the conformation of TC in acid solution is different from the conformation it displays in neutral or basic solutions. Stezowski[14] showed that the hydrate crystals of TC are composed of zwitterionic structures. On the other hand, the anhydrous crystals of TC obtained by Stezowski and Jogun[15] have a different conformation. Stezowski et al.[16] studied the oxytetracycline in an ethanol/water solvent and showed evidence of the coexistence of zwitterionic and un-ionized forms of the free base in solution. They suggested that two conformations of TC are in equilibrium.

* Author to whom correspondence should be addressed. E-mail: ams@npd.ufpe.br.
† This work is based in part on the M.Sc. Dissertation of H. A. Duarte, UFMG, Belo Horizonte, MG, Brazil, 1993.
‡ Departamento de Química-ICEx.
§ Departamento de Química Fundamental.
|| Departamento de Química-ICEB.

10.1021/js980181r CCC: $18.00 Published on Web 12/11/1998

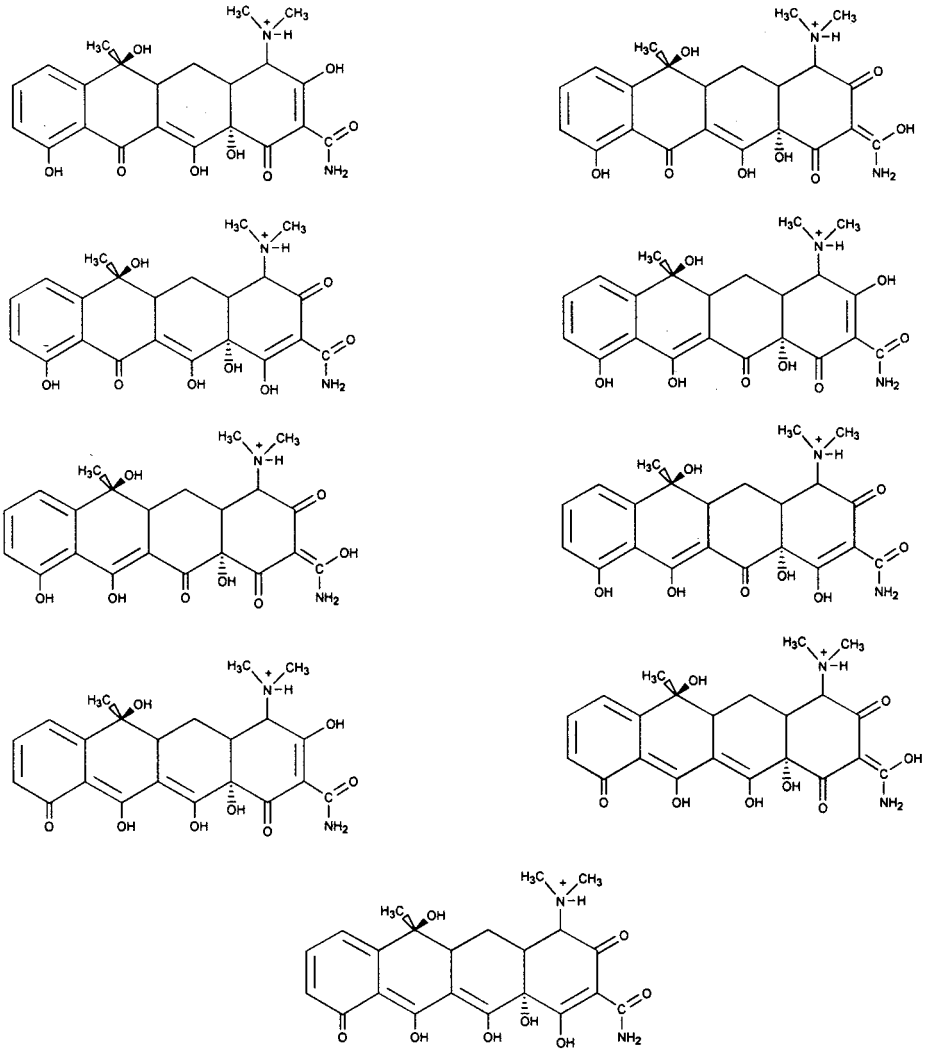

Figure 2—Possible tautomers of the completely protonated TC.

Metal ion coordination by TC has also received appreciable attention by researchers[6] due to the fact that some of the biological effects of TC and its derivatives arise from their interactions with metal ions.[17,18] TC has various possibilities for metal ion increasing the complexity of this system. Although some metallic complexes of TC in solid state have been isolated, most of them are studied in solutions. Complexes with Cr^{3+}, Nb^{2+}, Mn^{2+}, Fe^{2+}, Fe^{3+}, Co^{2+}, Ni^{2+}, Cu^{2+}, Zn^{2+}, Cd^{2+}, Hg^{2+}, Pb^{2+}, Al^{3+}, VO^{2+}, and VO_2^{2+} have been studied[6,7,19–22] and, according to different reports, the metal ions are either bonded to the O(1) or O(3) and to the oxygen of the amide group, or bonded to the acidic groups of the rings b, c, and d. Recently, anhydrotetracycline, a decomposition product of TC, has also received attention because of its importance to the understanding of the side effects and the mechanism of action of this drug.[23]

Despite all studies reported concerning the chemical and structural properties of TC, there are still several aspects that remain not well understood. Figure 1 shows the tautomer normally used to describe the structure of TC. However, this molecule has several other possibilities of tautomerism (see Figure 2). It is evident that different tautomeric species are present in the medium contributing to the macroscopic chemical behavior of TC. The relative ratio of different tautomers depends on the difference of free energy between two tautomeric species.

To our knowledge, the tautomerism of TC and its consequences for the understanding of chemical properties has not received attention, although it is of clear interest. In this paper we advance the concept that different tautomers of TC may be involved in its protonation scheme, in its metal ion complexation, in its chemical behavior in blood plasma, in its biological activity, etc. Moreover, we also show theoretical and experimental evidences that TC can undergo four deprotonations.

Recently, quantum mechanical semiempirical methods have been applied successfully to perform a conformational analysis of anhydrotetracycline[24] and to investigate its near ultraviolet (UV) and visible (VIS) electronic spectra.[25]

In the present work we have studied all possible tautomers of TC in different conformations and degrees of deprotonation using the semiempirical method AM1. The solvent effects have been included using the self-consistent reaction field (SCRF) method. Potentiometric and spectrophotometric experiments are also being presented showing evidences that TC undergoes a 4th deprotonation.

2. Computational Aspects

The semiempirical AM1 method (Austin Model 1)[26] implemented in the program MOPAC 6.0[27] was used to study the tautomerism of TC in its different degrees of deprotonation. The geometries were fully optimized and vibrational analysis was performed. All frequencies were positive, ensuring that true minima in the potential energy surface had been found. Finally, the solvent effect was

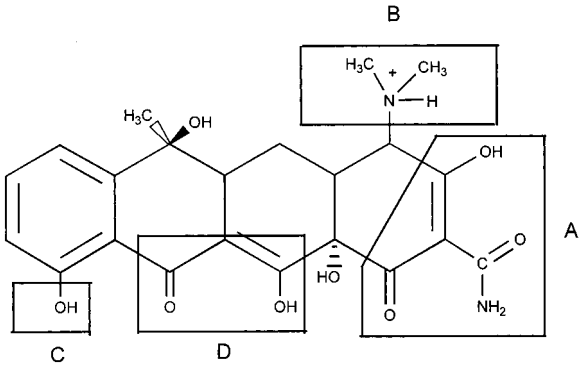

Figure 3—Possible sites of protonation of TC.

determined by the SCRF method, proposed by Tapia et al.,[28] merged with semiempirical methods of Zerner and co-workers.[29]

In this SCRF method, the solute lies inside a spherical cavity within a continuous dielectric medium representing the solvent. To determine the SCRF radius of the spherical cavity, rc, in which the tautomers are inserted, we used the method of Aguilar and Valle.[32] We chose this method because it is less arbitrary than most used to find the cavity radius. Indeed, it not only generates a single value per molecular structure but it is also based on a well-defined procedure for the adaptation of the molecular solute cavity size in a solvent that takes into account the charge distribution of the molecule.

The AM1/SCRF method is a reasonably good one to study this highly versatile and adaptive character of TC. This can be verified by examining the studies by Zerner et al.[29–31] on the tautomeric equilibria of the 5-nitroimidazole and 4-nitroimidazole, on the tautomeric equilibria of five-membered rings with two heteroatoms, and on 2-, 3-, and 4-substituted pyridines in aqueous solution.

3. Results and Discussion

3.1. Conformations and Protonation Sites of TC—The acid/base properties of TC are difficult to analyze because of its several protonation sites. Its deprotonation scheme has been subject of discussion and controversy.[8–11] Figure 3 shows the totally protonated TC and its four sites of protonation: $A^0B^+C^0D°$. According to this notation (and hereafter), A, B, C and D are protonation sites of TC. The superscripts −1 and 0 represent the ionic charge of the respective site. Therefore, superscripts + and − mean that this site has either received or lost one proton.

We have analyzed the two conformations that have been reported from X-ray experiments, the extended and folded conformations, by optimizing the zwitterionic form of TC, $A^{-1}B^+C^0D^0$ structure. The conformation we have obtained is similar to the one observed by Stezowski[14] when he analyzed hydrated crystals of TC; that is, the extended conformation. The difference between the experimental and calculated bond distances is <0.02 Å, which is in agreement with the expected accuracy of the calculated bond distances calculated by the AM1 method.[27] The dihedral angles are compared with the experimental data in Table 1. The differences for some dihedral angles can be explained if one takes into account that TC has been calculated in the gas phase without intermolecular interactions and the experimental geometry has been obtained from crystals.

The folded conformation of oxytetracycline has been observed in anhydrous crystals[14] in its nonionic form, $A^0B^0C^0D^0$ structure (according to the notation adopted in the present work). Because oxytetracycline and tetracycline are very similar,[14] the oxytetracycline is a suitable reference to compare with the calculated values of TC. The bond distances are <0.02 Å different from the available experimental data. The dihedral angles shown in Table 2 are in reasonable agreement with the experimental data.

Table 1—Calculated and Experimentally Determined Dihedral Angles of Extended Tetracycline

formula	angle, ° AM1[a]	angle, ° TC[b]	formula	angle, ° AM1[a]	angle, ° TC[b]
$C_{12}C_{12a}C_1C_2$	–147.2	–169.5	$C_{11}C_{11a}C_{5a}C_6$	46.0	41.6
$C_{12a}C_1C_2C_3$	4.5	5.4	$C_5C_{5a}C_6C_{6a}$	173.3	181.0
$C_1C_2C_3C_4$	–11.6	34.1	$C_{5a}C_6C_{6a}C_7$	–140.9	–146.6
$C_2C_3C_4C_{4a}$	36.6	–30.2	$C_6C_{6a}C_{10a}C_{11}$	–1.1	–3.2
$C_3C_4C_{4a}C_5$	65.6	110.5	$C_8C_9C_{10}C_{10a}$	–0.3	–1.0
$C_4C_{4a}C_{12a}C_1$	48.0	49.4	$C_9C_{10}C_{10a}C_{11}$	–178.9	–179.3
$C_{11}C_{11a}C_{12}C_{12a}$	174.4	179.7	$C_{10}C_{10a}C_{6a}C_7$	1.2	–0.3
$C_{11a}C_{12}C_{12a}C_1$	106.1	102.3	$C_6C_{6a}C_7C_8$	179.5	183.1
$C_{12}C_{12a}C_{4a}C_5$	48.6	47.7	$C_{6a}C_7C_8C_9$	0.6	–0.1
$C_4C_{4a}C_5C_{5a}$	172.7	173.3	$C_7C_8C_9C_{10}$	0.2	0.6
$C_{4a}C_5C_{5a}C_6$	166.7	171.5	C_1C_2C(amide)O(amide)	116.9	8.6
$C_5C_{5a}C_1C_{12}$	–9.0	–17.6	$C_2C_3C_4N$(amine)	–97.4	–163.3
$C_{10}C_{10a}C_{11}C_{11a}$	161.1	167.1	$C_3C_4N_4C$(amine A)	37.5	73.2
$C_{10a}C_{11}C_{11a}C_{12}$	174.7	177.8	$C_3C_4N_4C$(amine B)	172.4	201.0

[a] Calculated by the AM1 method. [b] From crystallographic data of the zwitterionic structure (Ref 14).

Table 2—Dihedral Angles of the Folded Tetracycline AM1: Calculated Geometry. OTC: Crystallographic Data of Oxytetracycline

angle	AM1[a]	OTC[b]	angle	AM1[a]	OTC[b]
$C_{12}C_{12a}C_1C_2$	–79.0	–72.7	$C_{11}C_{11a}C_{5a}C_6$	26.3	35.3
$C_{12a}C_1C_2C_3$	–11.5	–16.4	$C_5C_{5a}C_6C_{6a}$	–178.6	–171.8
$C_1C_2C_3C_4$	–3.3	–9.1	$C_{5a}C_6C_{6a}C_7$	–143.7	–159.9
$C_2C_3C_4C_{4a}$	–13.6	2.0	$C_6C_{6a}C_{10a}C_{11}$	–1.9	–6.1
$C_3C_4C_{4a}C_5$	167.1	153.8	$C_8C_9C_{10}C_{10a}$	–1.5	2.2
$C_4C_{4a}C_{12a}C_1$	–58.8	–53.2	$C_9C_{10}C_{10a}C_{11}$	–178.2	–175.7
$C_{11}C_{11a}C_{12}C_{12a}$	179.6	183.0	$C_{10}C_{10a}C_{6a}C_7$	–0.1	–0.4
$C_{11a}C_{12}C_{12a}C_1$	164.0	152.8	$C_6C_{6a}C_7C_8$	–179.7	–170.0
$C_{12}C_{12a}C_{4a}C_5$	–59.3	–58.3	$C_{6a}C_7C_8C_9$	1.2	–0.7
$C_4C_{4a}C_5C_{5a}$	–89.0	–79.0	$C_7C_8C_9C_{10}$	0.1	–3.2
$C_{4a}C_5C_{5a}C_6$	138.5	123.0	C_1C_2C(amide)O(amide)	160.9	182.7
$C_5C_{5a}C_1C_{12}$	–31.6	–22.8	$C_2C_3C_4N$(amine)	–142.2	–122.7
$C_{10}C_{10a}C_{11}C_{11a}$	156.0	180.3	$C_3C_4N_4C$(amine A)	–133.1	–84.1
$C_{10a}C_{11}C_{11a}C_{12}$	–164.6	–186.1	$C_3C_4N_4C$(amine B)	86.2	44.8

[a] Calculated geometry. [b] Crystallographic data of oxytetracycline.

The two conformations shown in Figure 4 have been used to generate all the tautomers studied in their different degrees of protonation.

3.2. Tautomerism and the Chemical Behavior of TC in Solution—It is important to analyze all possible tautomers of this molecule in their different degrees of protonation and conformation to understand the role of tautomerism in the chemical behavior of TC. We have optimized the structures of all 64 tautomers and calculated their heats of formation (ΔH_f^o). The use of heat of formation instead of the more correct Gibbs free energy is because it is difficult to evaluate the entropy factor for molecules in solution. Tests with totally protonated species in the gas phase showed that the entropy contribution to the relative stability is of about 0.1 kcal mol^{-1} and therefore much lower than the relative accuracy of AM1. This result has also been pointed out by Santos et al.[24] in their study of anhydrotetracycline, in which they used a thermodynamic cycle to justify the use of the entropy calculated in the gas phase as an estimate of the entropy contribution to the Gibbs free energy of species in solution.

There are different tautomers in equilibrium in each degree of protonation of TC. They have similar stabilities

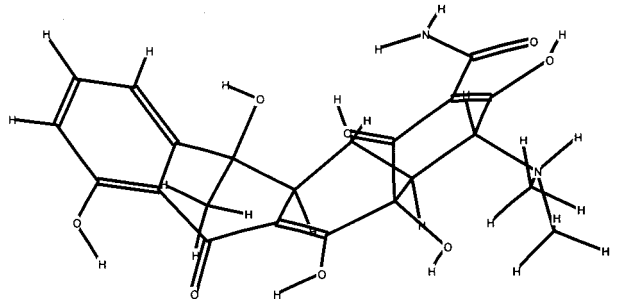

extended conformation

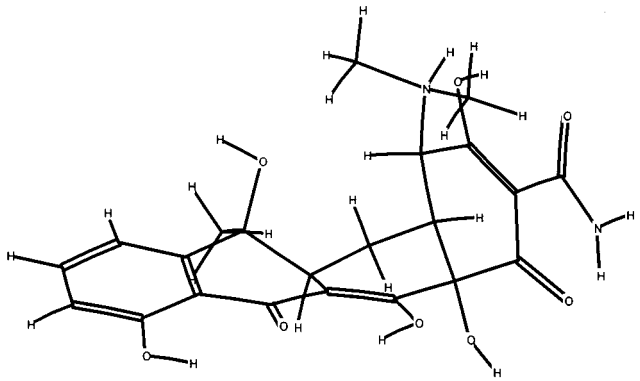

folded conformation

Figure 4—Two conformations of TC obtained from AM1 calculations.

and, therefore, they are present in considerable amount in the medium. The average error of the calculated heat of formation using AM1 is about 7 kcal mol^{-1} compared with experimental values.[26] This error should be much smaller when the relative stability of species is analyzed. Previous works showed that the relative stability of species calculated by the AM1 method is correctly predicted even for challenging systems.[29–31] However, the error bars of the calculated differences of enthalpies of different species are still too large to allow estimation of equilibrium constants.

It is important to observe that the interaction of those species with the solvent has been described by the SCRF method, which does not include specific interactions with the solvent. In the gas phase, the favored species are different, due to the lack of interaction with the solvent i.e. (with the dielectric constant of the medium). Therefore, one species that is favored in aqueous solution may not be favored in ethanol solution, due to the difference in the dielectric constant. These two species can have different conformations and different protonated sites. Stezowski,[16] for example, has shown that two species (zwitterionic and nonionized) are in equilibrium in ethanol/water mixtures. One could also argue that specific interactions (which are not taken into account in our model) of the tautomers with the solvent may also alter with a change of the medium. Thus, these specific interactions would modify the relative stabilities of different species. The chemical behavior of TC can therefore change depending on the conditions of the medium (solvent, ionic force, concentration, etc.) because different tautomers have different chemical properties.

Conformations, protonation sites and metal ion complexation sites of TC and its derivatives have been extensively studied in different solvents.[6–11,13–16,19–22] However, the difficulties and disagreements among researchers with respect to the interpretation of their experimental results and the assignment of metal ion complexation sites of TC, as a whole, constitute circumstancial evidence of the influence of the tautomers.

Now, we turn to the discussion of the tautomers in each one of the degrees of protonation of TC.

3.3. Degrees of Protonation of TC—*Totally Protonated Species*—The extended conformation is favored with respect to the folded one by about 2.8 kcal mol^{-1}. However, the most stable tautomer is the one with the proton of the site A on the amide group instead of the oxygen bonded to the C(3). It is important to notice that Stezowski[33] has already observed this type of tautomerism in solid state for a tetracycline derivative. Crystals of α-6-deoxyoxytetracycline have the amide oxygen of the site A protonated. The second most stable tautomer is 0.7 kcal mol^{-1} less stable than the first one. It is extended and has one proton on the oxygen bonded to the C(11) instead of the oxygen of the C(12). Figure 5 shows these two tautomers. Other tautomers lie at least 2.8 kcal mol^{-1} higher in energy than the most stable tautomer.

1st Deprotonation—Species resulting from the 1st deprotonation can be either in a neutral or zwitterionic form, in which case a positive charge is located on the amine group of the C(4) and a negative one on the site A (Figure 3). It has been experimentally shown that, in aqueous solution, TC attains the zwitterionic form. However, in the gas phase (or in a nonpolar solvent), it is expected that the neutral form of TC is favored. In solution, the separation of charge is stabilized by the polarization of the solvent around the TC. This stabilization depends on the value of the dielectric constant of the medium, this being the basic idea of the SCRF method used. However, the SCRF method has not been able to sufficiently stabilize the zwitterionic tautomers in order to invert its relative stability with respect to the neutral species. The results show that, despite the major stabilization of the zwitterionic species (because they have the largest dipole moments) with respect to the neutral ones, they are still not favored. It is important to observe that the SCRF method does not consider the specific interactions such as those arising from intermolecular hydrogen bonding and dipole–dipole interactions. These facts are important and should be kept in mind, because, the neutral species of TC are present in hydrophobic media like those found in biological systems.[16] Figure 6 shows the 10 most stable species. Folded conformation is favored, but the species still have the proton on the amide group.

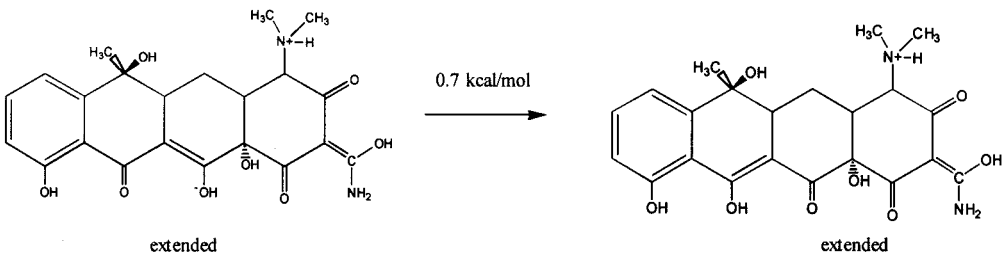

extended extended

Figure 5—Most stable completely protonated species according to AM1/SCRF calculations. The indicated value is $\Delta(\Delta H_f; r_c = 5.5$ Å).

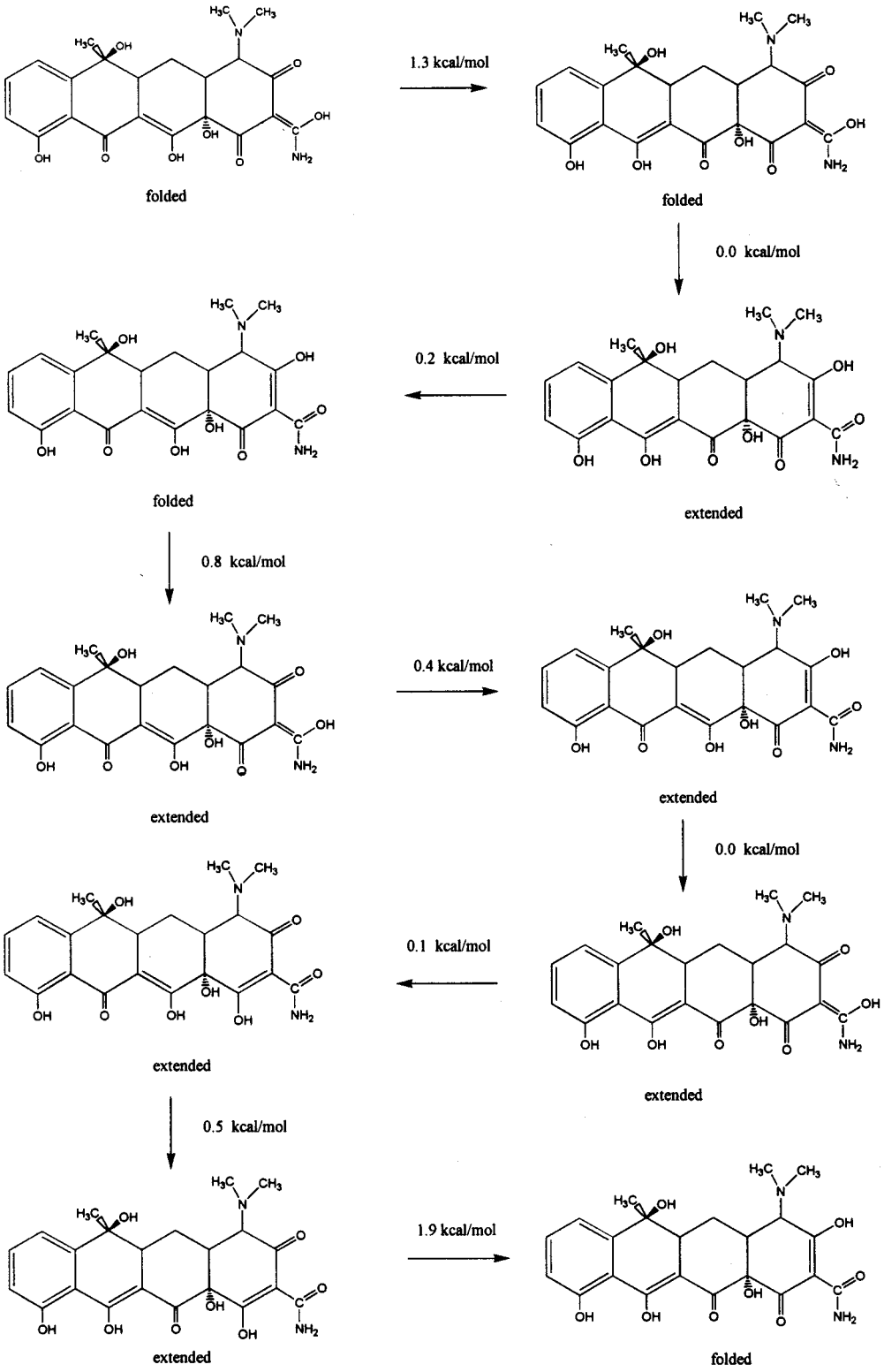

Figure 6—Most stable tautomers that arise from the 1st deprotonation according to AM1/SCRF calculations. The indicated values are $\Delta(\Delta H_f;\ r_c = 5.5$ Å).

2nd Deprotonation—It is accepted that the 2nd deprotonation lead to the formation of species of the form $A^{-1}B^0C^0D^0$ (i.e., species that have lost protons from sites A and B). Our results are in good agreement with these assumptions because the most stable tautomers present sites A and B deprotonated. The different tautomers arise from different conformations and from the exchange of protons between the oxygen bonded to C(11) and C(12). Figure 7 shows the most stable species.

3rd Deprotonation—The 3rd deprotonation occurs in the C and D sites. In fact, it is not possible to distinguish between these two sites. The most stable species have a proton bonded to one of the oxygens of either C(10), C(11), or C(12). Figure 8 shows the three most stable species. The most stable conformation is a folded one.

4th Deprotonation of TC—Even though only three acidic protons have been observed in potentiometric experiments with TC,[8–11] the analysis of its structure shows the pos-

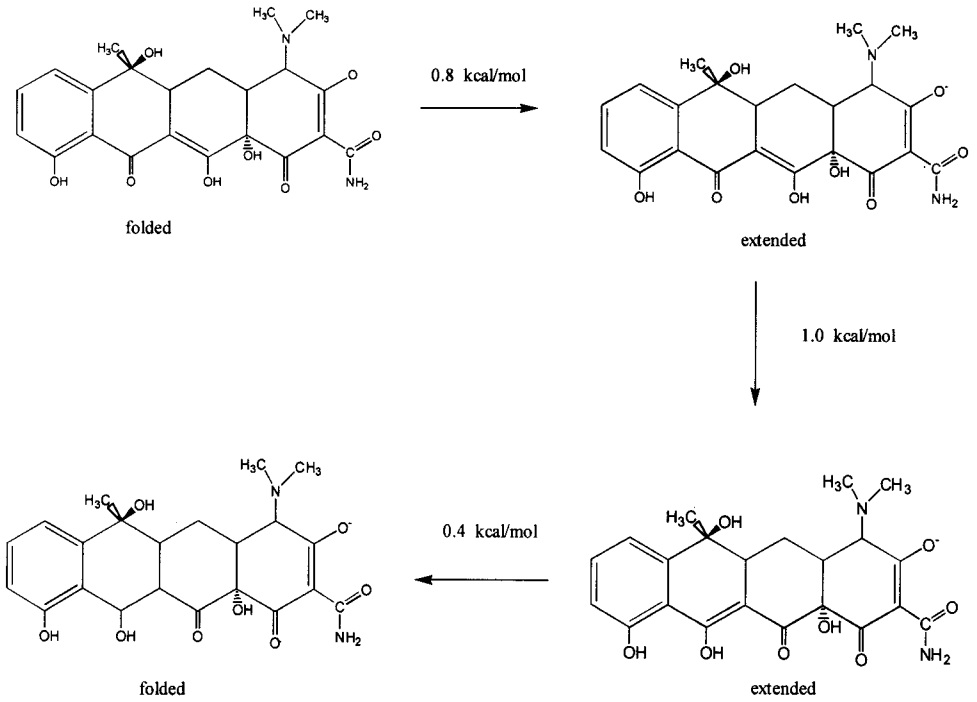

Figure 7—Most stable tautomers that arise from the 2nd deprotonation according to AM1/SCRF calculations. The indicated values are $\Delta(\Delta H_f;\ r_c = 5.5\ \text{Å})$.

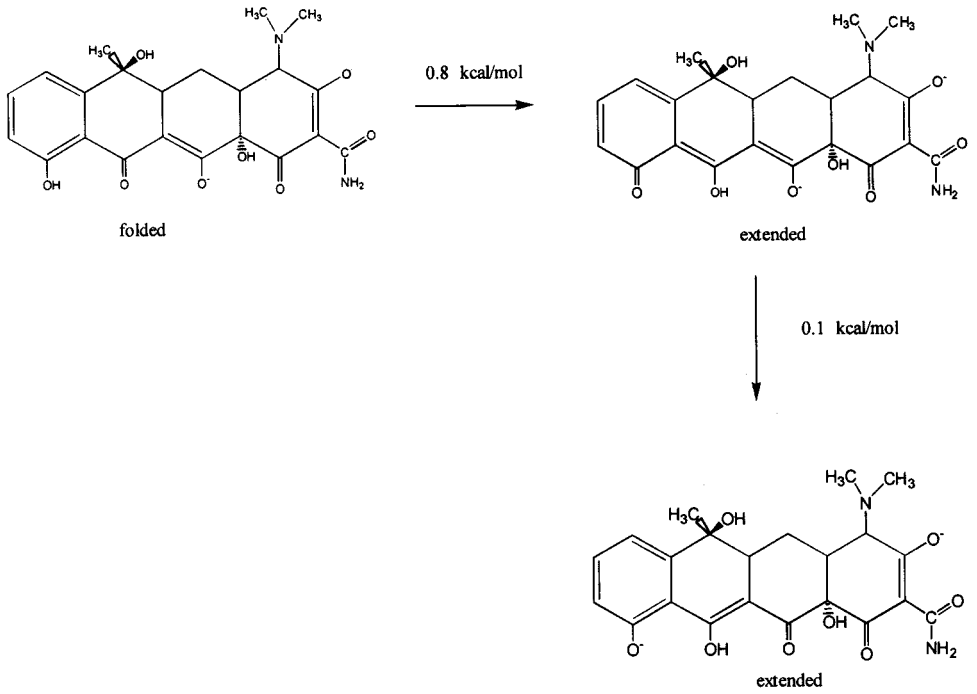

Figure 8—Most stable tautomers that arise from the 3rd deprotonation according to AM1/SCRF calculations. The indicated values are $\Delta(\Delta H_f;\ r_c = 5.5\ \text{Å})$.

sibility of a 4th deprotonation. Therefore, we have also analyzed the completely deprotonated species, aiming to contribute to the understanding of this so far unresolved problem. Our results indicate that the completely deprotonated species is a folded one and the extended conformation lies 4.4 kcal mol^{-1} higher in energy than the extended one.

Tetracycline methiodide possesses the equivalent of the TC acidic site B blocked by a methyl group. Therefore, Rigler et al.[10] had already suggested that the existence of three pK_as of tetracycline methiodide, the third equaling 10.67, should be construed as an evidence that TC itself should have a fourth acid group, which to date has seemingly not been accessible to potentiometric experiments.

One could suggest using the calculated heat of formations of the species to fit the known pK_a and to use this to estimate, by extrapolation, the rth dissociation constant of TC. This procedure is reasonable because a direct absolute calculation of pK_as would require computation of the proton solvation energy, which is very difficult to be evaluated theoretically with high accuracy.[34] Furthermore, the AM1 calculated values of Gibbs free energy[27] are in error of only about 7 kcal mol^{-1}, which is an additional argument in favor of the fit.

$$\Delta = A - B \ln K_n \qquad (1)$$

where

Table 3—Estimate of pK_4 According to Equations 1 and 2

n	Δ (kcal/mol)	-ln(K)[a]	pK_a[a]
4	–104.0	7.6 (8.2)	3.3 (3.6)
3	–87.1	17.5 (15.8)	7.6 (6.9)
2	–70.9	22.1 (23.2)	9.6 (10.1)
1	–54.0	(30.9)	(13.4)

[a] Estimated values in parentheses.

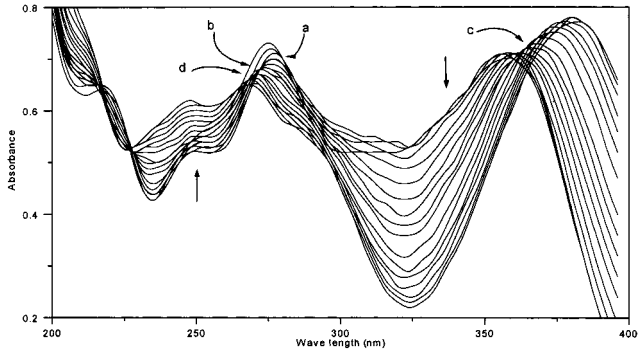

Figure 9—Spectra of a 0.5 mmol L-1 aqueous TC solution in the pH (–log(H^+)) range from 3.6 to 11.5 (as indicated by the arrows). Small letters correspond to isosbestic points. See text for details.

$$\Delta = \Delta H_{H_{n-1}L} - \Delta H_{H_nL} \qquad (2)$$

with n = 1, 2, 3, and 4 and H4L being the completely protonated TC. The values of A and B can be determined with the three experimental acid dissociation constants (3.3, 7.68, and 9.69) by least-squares fit. Accordingly, the estimated values of A and B are −121.8 and 2.19 kcal mol^{-1}, respectively, with correlation factor (**R**) of 0.98. Table 3 shows the experimental and estimated values of the pK_as using eq 1, together with the estimation of the pK_4 of about 13. Although these results are not conclusive, they are evidence that the discussions concerning a 4th deprotonation are meaningful.

If the possibility of a 4th deprotonation is accepted, then the value of pK_3 should be smaller. The determination of the dissociation constants from the experimental data neglecting the 4th deprotonation probably led to an overestimation of the pK_3 to compensate the lack of the 4th deprotonation.

3.4. Spectrochemical Evidence of the 4th deprotonation of TC—At the biological pH (about 7.4), the 4th deprotonation does not interfere in acid/base equilibria and can be neglected. However, in multiligand/multimetal systems, like blood plasma, considering the 4th dissociation constant of TC (hereafter the totally protonated tetracycline species is represented as H_4L^+) may have important consequences for the understanding of its chemical behavior. Therefore, we have carried out simultaneous potentiometric and spectrophotometric experiments (see *Appendix* for details of the experiments), searching for experimental evidences of the 4th deprotonation.

A series of spectra of a 0.5 mmol·L^{-1} TC aqueous solution in the pH range 3.5−11.5 is shown in Figure 9. Close inspection of these spectra reveal the existence of several isosbestic points, which prevail in limited pH ranges. Considering only the data >250 nm, four isosbestic points can be noticed. Below pH 5, a first one "a" can be seen at 280 nm and it can be related to the H_4L^+/H_3L equilibrium. In the pH interval from 5.5 to 7.5, two isosbestic points are seen at 272 "b" and 360 "c" nm, respectively, and they can be related to the H_3L/H_2L^- equilibrium. A fourth isosbestic point can be seen at 260 nm "d", limited to the pH range 9−10.5. This point can be related to the H_2L^-/HL^{2-} equilibrium. Its disappearance above pH 10.5 is clear evidence of a 4th deprotonation. Another piece of evidence is obtained when the absorbance at 380 nm is plotted against pH, as shown in Figure 10, together with a species distribution diagram. The absorbance at this wavelength increases up to pH 10 while the first three deprotonations occur, and absorbance starts to decrease when the 4th deprotonation starts to take place. A rapid acidification restored the spectrum of H_4L^+, ruling out the hypothesis of ligand degradation associated with the spectral modifications observed in high pH values. As mentioned before, the low concentration of L^{3-} in the pH range studied could explain the absence of the fourth dissociation constant in the literature.

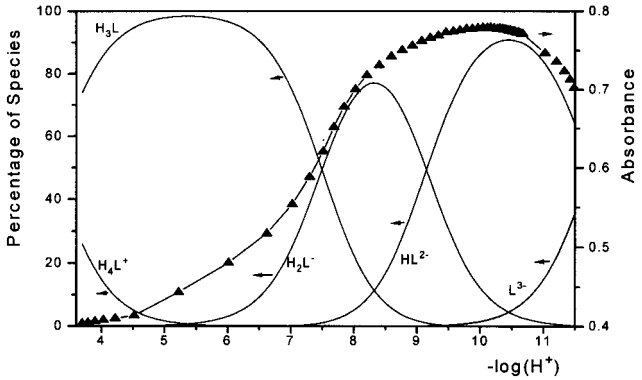

Figure 10—Distribution of TC species and the absorbance of TC in aqueous solution measured at 380 nm as functions of –log(H^+).

Table 4—Deprotonation Constants of Tetracycline at 25 °C (I = 0.1 mol/L, $NaClO_4$)

	measurements	
pK_n	potentiometric	spectrophotometric
1	3.24	3.36
2	7.49	7.33
3	9.15	8.97
4	11.75	11.81

Table 4 shows the estimated dissociation constants for TC obtained from potentiometric and spectrophotometric measurements. The different measurements have led to estimates of the dissociation constants that are in a good agreement with each other. With regard to the potentiometric data, we have observed that if the 4th deprotonation is neglected, pK_3 is estimated to be 10.7, one logarithmic unit larger than the value reported in the literature, which is 9.7. In addition, the statistical parameters C^2 and S, calculated by SUPERQUAD, decrease from 81.5 to 5.6 and from 12.24 to 0.86, respectively, when the 4th deprotonation is taken into account.

3.5. Importance of Tautomers in the Analysis of the Experimental Data—The tautomers of TC seem to have an important and so far unsuspected role in the actual behavior of TC, which explains a certain level of confusion present in the various interpretations of experimental results that appear in the scientific papers dealing with TC.

For example, the protonation scheme of TC and its derivatives has been a subject of discussions and disagreements between researchers about the interpretation of experimental results. Stezowski et al.[16] studied the behavior of free TC in ethanol/water solution using circular dichroism. According to them, two species are in equilibrium and are represented by (i) a zwitterionic species with extended conformation, which predominates in aqueous solution, and (ii) a neutral one with folded conformation,

which predominates in ethanol. It is important to note that our results are in agreement with this observation. Depending on the ethanol/water proportion, not only the conformation can be changed but also the tautomeric form of TC. However, our results do not support that the 1st deprotonation is due to site A. According to our results, the heat of solution of the zwitterionic species has to be >30 kcal mol^{-1} to invert the relative stability of the neutral form. This value is much larger than the expected error bar of the calculations performed in the present work. On the other hand, the solvent effects calculated by the SCRF method do not take into account the specific interactions (hydrogen bonding, dipole−dipole, etc.), and this could perhaps explain the discrepancies between calculated and the current interpretation of experimental results concerning the 1st deprotonation. The dimeric form of TC also has to be taken into account because it has been shown by Bogardus and Blackwood[35] that such species are also formed as a result of intermolecular hydrogen bonding of phenolic diketone system.

Stephens et al.[8] have eliminated some protonation sites of TC through reactions of etherification. The product dimethiloxytetracycline has the methoxy groups of the C(12) and C(1) and/or C(3) blocked for protonation. By means of potentiometric and UV spectra they determined two pK_as (7.5 and 9.4) and they concluded that the $pK_2 = 7.5$ should be assigned to site B. Therefore, the $pK_1 = 3.3$ of TC could not be assigned to site B because the electronegative inductive effect of the methoxy group could not increase the pK_1 from 3.3 to 7.5. It is necessary to consider that in the case of dimethiloxytetracycline, the $pK_2 = 7.5$ is related to a deprotonation of a positively charged species (because the site A is blocked by a methoxy) to a neutral one. In the case of TC, the situation is different. Supposing that $pK_a = 7.68$ is the deprotonation of site B, it would be related to a deprotonation of a neutral species to a negatively charged one. Thus, the two models are not so similar as to warrant straightforward conclusions.

Leeson et al.[9] have also compared values of three molecules derived from TC, however, these molecules have different total charges. Furthermore, different TC derivatives have different tautomers and conformations. Consequently, the chemical properties of the molecule can be completely changed. So, comparison between different molecules derived from TC, all probably also presenting a large degree of tautomerism, must be done with caution.

Rigler et al.[10] attributed the chemical shift of the dimethylamonium group exclusively to the protonation state of site B and the chemical shifts of the protons bonded to the phenolic ring to the protonation state of this group. They concluded that pK_2 and pK_3 should have contributions from sites B and C or D. According to Martin,[2] their supposition is not valid and the conclusions consequently not reasonable. For example, Martin mentioned the fact that after addition of 1 equivalent of base to the TC, the site A is 19% protonated, and after addition of 2 equivalents, 33% of site A remains protonated. It is known that chemical shifts are modified by the tautomeric forms and that has to be taken into account in the analysis by ^1H NMR. Deprotonation of site B modifies the electronic environment of the atoms around this site. However, if this deprotonation is followed by a change in the tautomeric form of site A, the chemical shifts of the protons of this site will also be changed. Eventually, unsuspected tautomerism can lead to wrong interpretations of the experimental data.

Asleeson and Frank,[11] from their ^{13}C NMR experiments, also concluded that the pK_2 and pK_3 have contributions from the B and C or D sites. They assumed that the 1st deprotonation is due exclusively to site A. Our results show that the site A proton is bonded to the oxygen of the amide group. After the 1st deprotonation, which our results indicate should occur on site B, the charge distribution on site A could, in turn, be completely modified because of changes in tautomeric forms that would change the ^1H and ^{13}C chemical shifts on site A.

Metal ions complexation by TC is also a field where there are disagreements among researchers. TC has several ways to complex metal ions. Depending on the solvents and conditions, different tautomeric species predominate in the medium and specific sites become more suitable for complexation of metal ions. This differentiation could explain the ability of TC to complex metal ions in different positions (see, for example, the Ca^{2+} and Mg^{2+} in the works of Caswell and Hutchison[7] and Lambs et al.[6]).

4. Conclusions—TC and its derivatives are a group of broad spectrum antibiotics that have been extensively studied in the last years. Their acid/base properties and chemical behavior in different mediums are extremely important to understand their mechanism of action and side-effects. However, tautomerism in these molecules has not received attention commensurate with its importance to the complete understanding of their chemical behavior in different mediums. We have explored all possibilities of tautomerism of TC by semiempirical calculations. We have shown that in solution, TC is in reality an equilibrium of different tautomers. This equilibrium can be displaced by varying the pH and the dielectric constant (solvent) of the system. We have also presented theoretical and experimental evidence that the discussion concerning the 4th deprotonation of TC is coherent. A theoretical estimation of the pK_4 of about 13 is in a good agreement with the potentiometric and spectrophotometric determinations of the pK_4 of about 12.

We conclude that TCycline seems to be a sort of a chameleon and highly adaptive molecule capable of modifying itself (its chemical bonds and of folding or extending itself) in a great diversity of manners in response to the environment in which it is immersed. And we extend this conclusion to the various TC derivatives with direct consequences to the understanding of their mechanisms of action.

6. Appendix

Potentiometric Measurements—Potentiometric titrations of 3 mmol L^{-1} aqueous solutions of TC HCl (Merck) were carried out with an automatic Methohm 670 apparatus coupled to a Metrohm Dosimat 665 autoburet. Experiments were carried out under nitrogen atmosphere and the temperature was kept constant at 25 °C. The ionic strength was maintained at 0.1 mol/L with sodium perchlorate. The electrode system was calibrated for $[H^+]$ before the measurements, by titration of $HClO_4$ with standardized NaOH, and vice versa, at an ionic strength of 0.10 mol L^{-1} with $NaClO_4$ solution. The symbol pH therefore represents $-\log[H^+]$ in this paper. TC stock solutions were prepared just before use to avoid ligand degradation caused by oxygen and light. The acidity constants were calculated from the potentiometric titration data with the SUPERQUAD[36] computer program, based on pH values ranging from 2.0 to 11.5.

Spectrophotometric Measurements—A typical spectrophotometric titration involved 25.0 mL of a 0.5 mmol L^{-1} TC HCl solution being titrated with 0.08 mol L^{-1} NaOH. This solution, while being potentiometrically titrated, was continuously circulated with a peristaltic pump through a 0.1-cm continuos flow quartz cuvette installed in a model 8451A Diode Array Hewlett-Packard spectro-

photometer. This setup allowed simultaneous measurements of the volume of titrant (NaOH) added, of the hydrogen ion concentration, and of the absorbance of the solution. This titration was performed with increments of volume and time intervals, both pre-fixed (known as monotonic titration), to obtain an absorbance spectrum and the hydrogen ion concentration after each addition of the titrating solution. Results are shown in Figure 9. The data were treated with the program SQUAD[37] to calculate both pK_as and molar absorptivities of each one of the species.

References and Notes

1. Duggar, B. M. Aureomycin: a product of the continued search for new antibiotics. *Ann. N. Y. Acad. Sci.* **1948**, *51*, 177−181. Finlay, A. C.; Hobby, S. Y.; Pan, S. Y.; Regna, P. P.; Routien, J. B.; Suley, D. B.; Shull, G. M.; Sobin, B. A.; Solomons, I. A.; Vinson, J. W.; e Kane, J. H. Terramycin, a New Antibiotic. *Science* **1950**, 111, 85. Putnam, L. E.; Hendricks, F. D.; Welch, H. Tetracycline, a New Antibiotic. *Antibiot. Annu.* **1953**−**1954**, 88. Bothe, J. H.; Morton, J.; Petisi, J. P.; Wilkinson, R. G.; Willians, J. H. Tetracycline. *J. Am. Chem. Soc.* **1953**, *75*, 4621.
2. Martin, R. B. Tetracyclines and Daunorubicin. In *Metal Ions in Biological Systems*, Siegel, H., Ed.; Marcel Dekker: New York, 1985; Vol. XIX, pp 19−51.
3. Sina, A.; Youssef, M. K.; Kassem, A. A.; Attia, I. A. Stability of Oxytetracycline in Solution and Injections. *Can. J. Pharm. Sci.* **1974**, *9*, 44−49. Benet, L. Z.; Goyan, J. E. Thermodynamics of Chelation by Tetracycline. *J. Pharm. Sci.* **1966**, *55*, 1184.
4. Albert, A.; Rees, C. W. Avidity of the Tetracyclines for the Cation of Metals. *Nature (London)* **1956**, *177*, 433.
5. Kakemi, K.; Sezaki, H.; Ogata, H.; Nadai, T. Absorption and Excretion of Drugs. XXVI. Effect of Calcium Ion on the Absorption of Tetracycline from the Small Intestine. 1. *Chem. Pharm. Bull.* **1968**, *16*, 2220−2225. Kakemi, K.; Sezaki, H.; Hayashi, M.; Nadai, T. Absorption and Excretion of Drugs. XXVIII. Effect of Calcium Ion on the Absorption of Tetracycline from the Small Intestine. 2. *Chem. Pharm. Bull.* **1968**, *16*, 2206−2212.
6. Mikulski, C. M.; Fleming, J.; Fleming, D. Chelates of Tetracycline with First Row Transition Metal Perchlorates. *Inorg. Chim. Acta* **1988**, *144*, 9−16. Mikulski, C. M.; Fleming, J.; Fleming, D. Tetracycline Adducts with 3d Metal Perchlorates. *Inorg. Chim. Acta* **1987**, *135*, L9-L11. Lambs, L.; Berthon, G. Metal Ion-Tetracycline Interactions in Biological Fluids. Part 7. Quantitative Investigation of Methacycline Complexes with Ca(II), Mg(II), Cu(II) and Zn(II) Ions and Assessment of their Biological Significance. *Inorg. Chim. Acta* **1988**, *151*, 33−43. Lambs, L.; Brion, M.; Berthon, G. Metal Ion-Tetracycline Interactions in Biological Fluids. Part 4. Potential Influence of Ca(II) and Mg(II) Ions on the Bioavailability of Chlortetracycline and Demethylchlortetracycline, as Expected from their Computer-Simulated Distributions in Blood Plasma. *Inorg. Chim. Acta* **1985**, *106*, 151−158. Brion, M.; Berthon, G.; Fourtillan, J−B. Metal Ion-Tetracyclines Interactions in Biological Fluids. Potentiometric Study of Calcium Complexes with Tetracycline, Oxytetracycline, Doxycycline and Minocycline and Simulation of Their Distribution under Physiological Conditions. *Inorg. Chim. Acta* **1981**, 55, 47−56. Stezowski, J. J.; Jogun, K. H. Chemical−Structural Properties of Tetracycline Derivatives. 2. Coordenation and Conformational Aspects of Oxytetracycline Metal Ion Complexation *J. Am. Chem. Soc.* **1976**, *98*, 6018−6026.
7. Caswell, A. H.; Hutchison, J. D. Selectivity of Cation Chelation to Tetracyclines: Evidence for Special Conformation of Calcium Chelate. *Biochem. Biophys. Rev. Commun.* **1971**, *46*, 625−630.
8. Stephens, C. R.; Murai, K.; Brunings, K. J.; e Woodward, R. B. Acidity Constants of the Tetracycline Antibiotics. *J. Am. Chem. Soc.* **1956**, *78*, 4155−4158.
9. Leeson, L. J.; Krueger, J. E.; e Nash, I. A. Concerning the Structural Assignment of the Second and Third Acidity Constants. *Tetrahedron Lett.* **1963**, *18*, 1155−1160.
10. Rigler, N. E.; Bag, S. P., Leyden, E. D.; Sudmeier, L. J.; Reilley, C. M. Determination of a Protonation Scheme of Tetracycline Using Nuclear Magnetic Resonance. *Anal. Chem.* **1965**, *37*, 872−875.
11. Asleson, G. L.; Frank, C. W. pH Dependence of Carbon-13 Nuclear Magnetic Resonance Shifts of Tetracycline Microscopic Dissociation Constants. *J. Am. Chem. Soc.* **1975**, *98*, 4745−4749.
12. Garrett, E. R. Variation of pK_a'-Values of Tetracyclines in Dimethylformamide-Water Solvents. *J. Pharm. Sci.* **1963**, *52*, 797−799.
13. Mitscher, L. A.; Bonacci, A. C.; and Sokolski, T. D. Circular Dichroism and Solution Conformation of the Tetracycline Antibiotics. *Tetrahedron Lett.* **1968**, *51*, 5361−5364. Mitscher, L. A.; Bonacci, A. C.; e Sokolski, T. D. Circular Dichroism and Solution Conformation of the Tetracycline Antibiotics. *Antimicrob. Agents Chemother.* **1968**, 78−86.
14. Stezowski, J. J. Chemical-Structural Properties of Tetracycline Derivatives. 1. Molecular Structure and Conformations of the Free Base Derivatives. *J. Am. Chem. Soc.* **1976**, *98*, 6012−6018.
15. Stezowski, J. J.; Prewo, R. Chemical−Structural Properties of Tetracycline Derivatives. 3. The Integrity of the Conformation of the Nonionized Free Base. *J. Am. Chem. Soc.* **1977**, *99*, 1117−1121.
16. Stezowski, J. J.; Hughes, L. J.; Hughes, R. F. Chemical−Structural Properties of Tetracycline Derivatives. 7. Evidence for Coexistence of the Zwitterionic and Nonionized Forms of the Free Base in Solution. *J. Am. Chem. Soc.* **1979**, *101*, 7655−7657.
17. Brion, M.; Lambs, L.; Berthon, G. Metal Ion-Tetracycline Interactions in Biological Fluids. Part 6. Formation of Copper(II) Complexes with Tetracycline and some of its Derivatives and Appraisal of their Biological Significance. *Inorg. Chim. Acta* **1986**, *123*, 61 and refs. therein.
18. Ginn, S. L.; Brown, M. H.; Skurray, R. A. Topology of the Metal-Tetracycline/H+ Antiporter TetA(K) frin Staphylococcus Aureus. *J. of Bacteriol.* **1997**, *179*, 3786. Someya, Y.; Niwa, A.; Yamaguchi, A. Site-Specificity of the Second-Site Suppressor Mutation of the Asp-285→Asn Mutant of Metal-Tetracycline/H+ Antiporter of *Escherichia coli* and the Effects of Amino Substitutions at the First and Second Sites. *Biochemistry* **1995**, *34*, 7. Yamaguchi, A.; Kimura, T.; Someya, Y. J. Metal-Tetracycline/H+ Antiporter of *Escherichia Coli* Encoded by Trasposon Tn10. *Biolog. Chem.* **1993**, *268*, 6496.
19. Ahmad, N.; Jamil, M. e Munir, C. Polynuclear Complexes of Bivalent Metal Ions with Antibiotic Tetracycline. *J. Chem. Soc. Pak.* **1990**, *12*, 168−173.
20. Jezowska-Bojczuk, M.; Lambs, L.; Kozlowski, H. Metal Ion-Tetracycline Interactions in Biological Fluids. 10. Structural Investigations on Copper (II) Complexes of Tetracycline, Oxytetracycline, Chlortetracycline, 4-(Dedimethylamnino)-tetracycline, and 6-Desocy-6-demethyltetracycline and Discussion of Their Binding Modes. *Inorg. Chem.* **1993**, *32*, 428.
21. Ohyama, T.; Cowan, J. A. Calorimetric Studies of Metal Binding to Tetracycline. Role of Solvent Structure in Defining the Selectivity of Metal Ion-Drug Interactions. *Inorg. Chem.* **1995**, *34*, 3083.
22. Ghandour, M. A.; Azab, H. A.; Hassan, A. Potentiometric Studies on the Complexes of Tetracycline (TC) and Oxytetracycline (OTC) with Some Metal Ions. *Monatshefte fur chemie* **1992**, *123*, 51.
23. Siqueira, M.; Carvalho, S.; Paniago, E. B.; Tosi L.; Beraldo, H. Metal Complexes of Anhydrotetracycline. 1. A Spectrophotometric Study of the Cu(II) and Ni(II) complexes. *J. Pharm. Sci.* **1994**, *83*, 291. Matos, S. V. M.; Beraldo, H. Metal Complexes of Anhydrotetracycline. 3. An Absorption and Circular Dichroism Study of the Ni(II), Cu(II), and Zn(II) Complexes in Aqueous Solution. *J. Braz. Chem. Soc.* **1995**, *6*, 405. Machado, F. C.; Demicheli, C.; Beraldo, H. Metal Complexes of Anhydrotetracycline. 2. Absorption and Complexes. Possible Influence of the Mg(II) Complex on the Toxic Side Effects of Tetracycline. *J. Inorg. Biochem.* **1995**, *60*, 163.
24. dos Santos, H. F.; de Almeida, W. B. and Zerner, M. C. Conformational Analysis of the Anhydrotetracycline Molecule: A Toxic Decomposition Product of Tetracycline. *J. Pharm. Sci.*, in press.
25. de Almeida, W. B.; Costa, L. R. A.; dos Santos, H. F.; Zerner, M. C. A Theoretical Investigation of the Near UV and VIS Electronic Spectra for the Fully Deprotonated Forms of Anhydrotetracycline. *J. Chem. Soc., Perkin Trans.* **1997**, *2*, 1335.
26. Dewar, M. J. S.; Zoebisch, E. G.; Heally; E. F.; Stewart, J. J. P. AM1: A New General Purpose Quantum Mechanical Molecular Model. *J. Am. Chem. Soc.* **1985**, *107*, 3902−3909.
27. Stewart, J. J. P. MOPAC−A Semiempirical Molecular Orbital Program. *J. Comput.-Aided Mol. Des.* **1990**, *4*, 1−105.
28. Tapia, O.; Goscinski, O. Self-Consistent-Reaction-Field Theory of Solvent Effects. *Mol. Phys.* **1975**, *29*, 1653−1661.
29. Zerner, M.; Karelson, M. M.; Tamm, T.; Katritsky, A. R.; Cato, S. J. M. O. Calculations Applicable to Condensed Phases: The Combination of Self-Consistent Reaction Field Theory with Semiempirical Quantum Chemical Methods. *Tetrahedron Comput. Methodol.* **1989**, *2*, 295−304.

30. Zerner, M. C.; Karelson, M. M.; Katritsky, A. R.; Szafran, M. A Theoretical Treatment of Solvent Effects on the Tautomeric Equilibria of Five-Membered Rings with Two Heteroatoms. *J. Chem. Soc., Perkin Trans 2* **1990**, 195−201.
31. Karelson, M. M.; Katritzky, A. R.; Szafram, M.; Zerner, M. C. Quantitative Predictions of Tautomeric Equilibria for 2, 3 and 4-substituted Pyridines in both the Gas Phase and Aqueous Solution: Combination of AM1 with Reaction Field Theory. *J. Org. Chem.* **1989**, *54*, 6030−6034.
32. Aguilar, M. A.; Olivares del Valle, F. J. Solute−Solvent Interactions. A Simple Procedure for Constructing the Solvent Cavity for Retaining a Molecular Solute. *Chem. Phys.* **1989**, *129*, 439−450.
33. Stezowski, J. J. Chemical−Structural Properties of Tetracycline Antibiotics 4. Ring A Tautomerism Involving the Protonated Amide Substituent as Observed in the Crystal Structure of ?-6-Deoxyoxytetracycline Hydrohalides. *J. Am. Chem. Soc.* **1977**, *99*, 1122−1129.
34. Li, G. S.; Ruiz-López, M. F.; Maigret, B. Ab Initio Study of 4(5)-Methylimidazole in Aqueous Solution. *J. Phys. Chem. A* **1997**, *101*, 7885−7892.
35. Bogardus, J. B.; Blackwood, R. K. Jr. Solubility of Doxycycline in Aqueous Solution *J. Pharm. Sci.* **1979**, *68*, 188−194.
36. Gans, P.; Sabatini, A.; Vacca, A. SUPERQUAD: An Improved General Program for Computation of Formation Constants from Potentiometric Data. *J. Chem. Soc., Dalton Trans.* **1985**, *6*, 1195−1200.
37. Kadish, K. M.; Legget, D. J.; Kelly, S. L.; Shine, L. R.; Wu, Y. T.; Chang, D. A Computational Approach to the Spectrophotometric Determination of Stability Constants-II Application to Metalloporphyrin-Axial Ligand Interactions in Nonaqueous Solvents *Talanta* **1983**, *8*, 579−586.

Acknowledgments

We thank Prof. Nivan Bezerra da Costa, Jr. for the suggestions and discussions during the development of this work. Financial support through grants from the Conselho Nacional de Desenvolvimento Científico e Tecnológico (CNPq), of Fundação de Amparo à Pesquisa de Minas Gerais (FAPEMIG), and Financiadora de Estudos e Projetos (FINEP) of Brazil are gratefully acknowledged.

JS980181R

Pharmacokinetics of Thalidomide in an Elderly Prostate Cancer Population

WILLIAM D. FIGG,* SANGEETA RAJE, KENNETH S. BAUER, ANNE TOMPKINS, DAVID VENZON, RAYMOND BERGAN, ALICE CHEN, MICHAEL HAMILTON, JAMES PLUDA, AND EDDIE REED

Contribution from *Medicine Branch, Division of Clinical Sciences, National Cancer Institute, National Institutes of Health, Building 10, Room 5A01, 9000 Rockville Pike, Bethesda, Maryland 20892.*

Received April 20, 1998. Final revised manuscript received July 23, 1998.
Accepted for publication July 31, 1998.

Abstract □ Thalidomide, a glutamic acid derivative, has recently been shown to inhibit in vitro angiogenesis, the process of formation of new blood vessels. This Phase II study examined the pharmacokinetics of thalidomide in patients with clinically progressive hormone-refractory prostate cancer. Patients (aged 55 to 80 years) were randomized to two different arms, low dose versus high dose. Patients in the low-dose group were given 200 mg of thalidomide and patients in the high-dose group received 200 mg of thalidomide, with subsequent dose escalations to 1200 mg. Serial serum or blood samples were obtained for pharmacokinetic assessment after administration of a single oral dose or multiple daily dosing of thalidomide and were assayed by reversed-phase HPLC. Pharmacokinetic parameters for both the single and multiple dosing were calculated with ADAPT II. A one-compartment model best fit the data. After single dosing, the oral clearance and apparent volume of distribution for the low-dose regimen ($n = 13$) were 7.41 ± 2.05 L/h and 66.93 ± 34.27 L, respectively, whereas for the high-dose regimen ($n = 11$), these values were 7.21 ± 2.89 L/h and 165.81 ± 84.18 L, respectively. The elimination half-lives for the low and high dose were 6.52 ± 3.81 and 18.25 ± 14.08 h, respectively. After the multiple dosing of thalidomide, the oral clearance and apparent volume of distribution for the low-dose group ($n = 10$) were 6.35 ± 1.64 L/h and 64.63 ± 23.20 L, respectively, whereas for the high-dose group ($n = 11$), these values were 7.73 ± 2.27 L/h and 167.85 ± 82.08 L, respectively. The elimination half-lives for the low and high dose were 7.08 ± 1.87 and 16.19 ± 9.57 h, respectively. For both the single and multiple dosing of thalidomide, the apparent volume of distribution and half-life were significantly higher for the high-dose group than those for the low-dose group. The higher apparent volume of distribution may be attributable to several factors, such as change in absorption, protein binding, etc. A dose-proportional increase in thalidomide steady-state concentrations was seen after multiple daily dosing of thalidomide.

Introduction

Prostate carcinoma is currently the most common cancer in American men. The initial therapy for metastatic prostate cancer is androgen deprivation; that is, medical or surgical castration with or without an androgen receptor antagonist. Once metastatic prostate cancer progresses in the face of hormonal therapy, it is classified as being hormone refractory. Therapeutic options for hormone-refractory prostate cancer are extremely limited, and cytotoxic chemotherapy has not been successful in prolongation of survival.

* Corresponding author. Telephone: 301-402-3622. Fax: 301-402-8606. E-mail: wdfigg@helix.nih.gov.

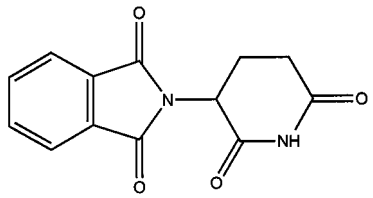

Figure 1—Structure of thalidomide.

Thalidomide (*N*-phthalidoglutarimide; $C_{13}H_9O_4N_2$; Figure 1) was initially introduced in 1954 as a sedative but was withdrawn from the market in the early 1960s because of its teratogenic effects. During the following years, this drug was found to be extremely effective in lepromatous leprosy and is currently being evaluated as an experimental drug in the treatment of a variety of diseases with an autoimmune character, including human immunodeficiency virus (HIV) infection and graft versus host disease.[1,2,3,8] Folkman and colleagues recently reported that thalidomide inhibited angiogenesis in the rabbit cornea micropocket assay.[4] Bauer et al. went on to show that a metabolite of thalidomide was responsible for the antiangiogenic properties.[5] Based on those data, four phase II clinical trials using thalidomide were initiated in solid tumors (Kaposi's sarcoma, glioblastoma, breast cancer, and prostate cancer). Herein, we characterize the pharmacokinetics of thalidomide from an open-labeled, phase II, randomized study (comparison of two dosing regimens) in an elderly population of men with hormone-refractory prostate cancer.

Patients and Methods

Patient Eligibility—Patients with clinically progressive hormone-refractory prostate cancer documented for at least 1 month and who had not undergone a radical prostatectomy or received radiation therapy, with a life expectancy of >3 months and an Eastern Cooperative Oncology Group performance status of 0 to 2, were eligible. Refractory disease was demonstrated after the withdrawal of the antiandrogen (i.e., flutamide). Patients were required to have a granulocyte count of >1000/mm^3, a platelet count of >75 000 mm^3, a measured creatinine clearance of >40 mL/min, and a total bilirubin of ≤1 mg/dL. At least 4 weeks must have elapsed from receipt of any form of anticancer therapy, and patients must have recovered from all toxicities related to the prior therapy.

Drug Administration—All eligible patients were randomized to two different arms, low dose or high dose. Patients on the low-dose arm were given 200 mg of oral thalidomide in the morning as the first dose and, thereafter, 200 mg of thalidomide orally every evening starting on day 2. Treatment was continued provided that there was no dose-limiting toxicity or progression of the disease. Patients on the high-dose arm were given 800 mg of oral thalidomide in the morning on day 1 and, thereafter, thalidomide was

10.1021/js980172i Not subject to U.S. copyright. *Published on Web 11/26/1998*

administered orally every evening starting at 200 mg/day on day 2 and increasing by 200 mg/day every 2 weeks to a maximum dose of 1200 mg/day. Dose increases were continued only if no side effects were noted. Treatment was continued provided there was no dose-limiting toxicity or disease progression. Patients took thalidomide at approximately the same time daily.

Pharmacokinetic Sampling—Blood samples were obtained from all patients for pharmacokinetic assessment. Samples (7 mL) were drawn in heparinized tubes immediately prior to the dose on day 1 (pre-level) and then at 0.5, 1, 1.5, 2, 3, 4, 5, and 7 h on day 1 and at 24, 27, and 31 h on day 2. Samples were also obtained in the morning at each clinic visit throughout the study. The instability of thalidomide requires that the plasma be harvested within 1 h of obtaining the blood samples.[6,7] After centrifuging the blood samples, the plasma was drawn off and stored at −70 °C until analysis. Plasma levels of thalidomide were determined using high-performance liquid chromatography (HPLC) with ultraviolet (UV) detection.

Analytical Method—A Hewlett-Packard 1090 Series II Liquid Chromatograph equipped with a photodiode-array detector was used for the chromatographic analysis of total thalidomide. A Waters Nova-Pak C-18 (3.9 × 300 mm) column was used, and a gradient mobile phase of water, acetonitrile, and a 0.5 M NaH_2PO_4 buffer (pH 3.0) was run at a flow rate of 1 mL/min. Thalidomide and phenacetin, the internal standard were isolated from the plasma by solid-phase extraction and detected at UV wavelengths of 220 and 248 nm, respectively, with a run time of 16 min. Ten percent H_2SO_4 was added to the plasma to prevent the nonenzymatic degradation of thalidomide (rate constant for degradation of thalidomide is ~0.175/h[8]). Standard curves were found to be linear in the range of 25 to 10 000 ng/mL, with the coefficient of determination (r^2) ≥0.995. The intraassay as well as inter-assay precision and accuracy errors were <10%.[6]

Pharmacokinetic Analysis—Plasma samples were obtained for pharmacokinetic assessment after administration of a single oral dose or multiple daily dosing of thalidomide. Pharmacokinetic parameters for both the single and multiple dosing of thalidomide were calculated by weighted nonlinear least-squares analysis fitting a one-compartment and two-compartment open linear model computed by ADAPT II (Biomedical Simulations Resource, University of Southern California, Los Angeles, CA). Model selection was determined based on Akaike's Information Criterion (AIC) and visual examination of the difference between the measured and fitted concentration. Pharmacokinetic parameters determined from single-dose studies were used as priors for determination of multiple-dosing parameters. In the present pharmacokinetic analysis, outlier points (points ≥2 standard deviations outside the fitted line) were not disregarded and all the data points were included in the fitting of the data. The r^2 values reported are the actual values and not the skewed values.

Statistical Analysis—The two-tailed Wilcoxon rank sum test was used for comparison of pharmacokinetic parameters.

Results

Pharmacokinetics—Data were obtained from 24 patients for the single dosing of thalidomide, out of which 13 patients received the low dose (200 mg) and 11 received the high dose (800 mg). Weighting with least-squares fitting as the estimator provided the best fit for 23 patients, whereas maximum likelihood gave the best fit in one patient. In addition, a one-compartment model fit the data best. Figure 2A shows a concentration versus time profile (mean ± SD) for patients on the low dose (200 mg), who received a single dose of oral thalidomide and Figure 2B shows a concentration versus time profile (mean ± SD) for patients on the high dose (800 mg), who received a single dose of oral thalidomide. Pharmacokinetic parameters obtained after the single dose are listed by dose level in Table 1. The t_{max} of thalidomide ranged between 2.01 and 7.09 h, with a median value of 3.32 h for the low-dose regimen (200 mg of thalidomide on day 1). For the high dose (800 mg of thalidomide on day 1), the t_{max} ranged from 1.35 to 7.12 h, with a median value of 4.40 h. Median C_{max} values of 1.97 μg/mL (range of 1.15 to 3.79) and 4.42 μg/mL (range of 2.41 to 8.41) were reported for the initial low-dose (200 mg) and the initial high-dose (800 mg) groups, respectively. The oral clearance and apparent volume of distribution for the low-dose regimen were 7.41 ± 2.05 L/h and 66.93 ± 34.27 L, respectively, whereas for the high-dose regimen, these values were 7.21± 2.89 L/h and 165.81 ± 84.18 L, respectively. The elimination half-lives for the low and high dose were 6.52 ± 3.81 and 18.25 ± 14.08 h, respectively (p = 0.0037). In general, an increase in the half-life of thalidomide was seen for the high-dose group. Also, there was a significant difference in the apparent volume of distribution between the low and the high-dose groups (p = 0.0039), with the high-dose group having a higher apparent volume of distribution.

Data were obtained from 21 patients for the multiple dosing of thalidomide. Ten patients received the low dose and 11 were randomized to the high-dose arm. In the low-dose arm, one patient was removed from the study because of unresolved grade 2 neuropathy. In the high-dose arm, 10 patients either had dose held for a period of time or

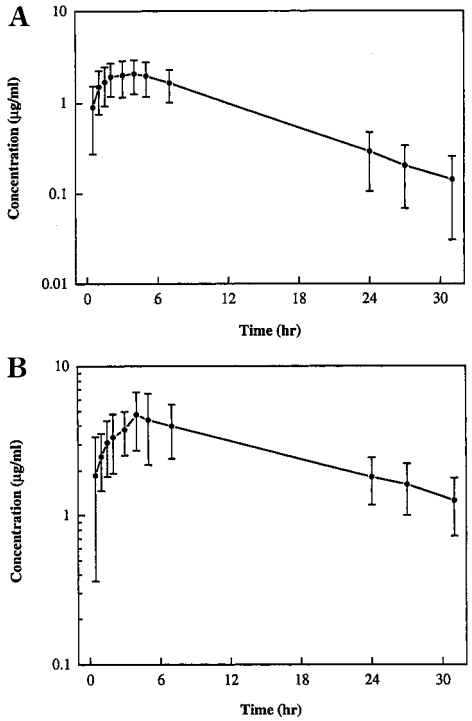

Figure 2—Plasma concentration versus time curves. (A) Plasma concentration versus time curve (mean ± SD) for patients in the low-dose group after a single oral dose of 200 mg of thalidomide. (B) Plasma concentration versus time curve (mean ± SD) for patients in the high-dose group after a single oral dose of 800 mg of thalidomide.

Table 1—Pharmacokinetic Parameters for the Low- and the High-Dose Level after a Single Oral Dose of Thalidomide

statistic	K_e (h^{-1})	Vd/F (L)	K_a (h^{-1})	CL/F (L/h)	$t_{1/2}$ (h)	r^2
			high dose (800 mg, n = 11)			
mean	0.0596	165.81	0.9075	7.21	18.25	0.835
SD	0.0431	84.18	0.8964	2.89	14.08	0.126
median	0.0561	155.10	0.7106	7.17	12.35	0.904
max	0.1410	284.60	3.345	13.43	55.44	0.945
min	0.0125	35.07	0.1405	3.49	4.91	0.625
			low dose (200 mg, n = 13)			
mean	0.1314	66.93	0.7148	7.41	6.52	0.897
SD	0.0679	34.27	0.4531	2.05	3.81	0.092
median	0.1242	62.64	0.6303	7.59	5.58	0.926
max	0.3359	158.80	1.5050	11.73	18.33	0.975
min	0.0378	24.89	0.1409	3.76	2.06	0.685

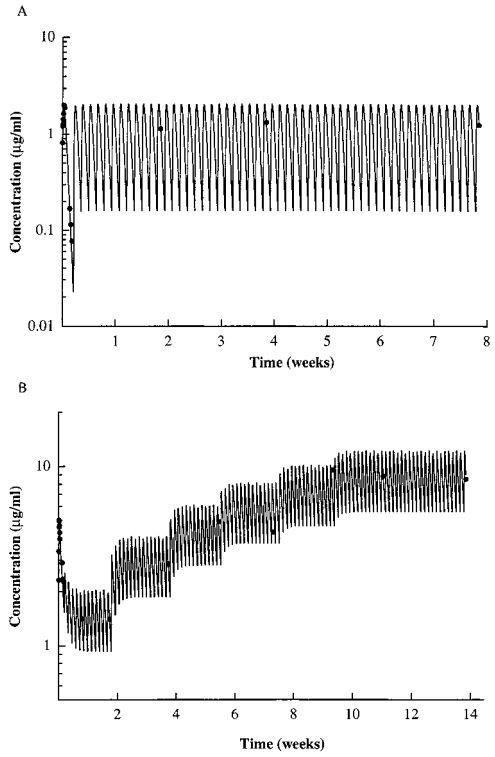

Figure 3—Plasma concentration versus time curves. (A) plasma concentration versus time curve for a patient in the low-dose group during daily oral dosing of 200 mg of thalidomide. (B) Plasma concentration versus time curve for a patient in the high-dose group during daily oral dosing of thalidomide with dose escalations after every 2 weeks.

received no dose escalations because of complications. The first patient had drug held for 24 days because of a pulmonary embolism, after which the dose was reduced to 200 mg of thalidomide followed by escalation every 2 weeks up to 1200 mg. The second patient had drug held for 7 days because of neutropenia and subsequently there was no dose escalation above 200 mg of thalidomide. The third patient had his dose held at 800 mg for 4 weeks because of shortness of breath, after which the dose was escalated to 1000 mg and subsequently to 1200 mg of thalidomide. The fourth patient had no dose escalation beyond 200 mg because of sedation, and the fifth patient had dose held at 400 mg for 5 weeks and subsequently there was no dose escalation beyond 600 mg. The sixth and seventh patients received no dose escalation beyond 800 mg of thalidomide, and thalidomide was discontinued after a dose of 200 mg for the eighth and ninth patients. The tenth patient had drug discontinued after a dose of 400 mg of thalidomide.

Figure 3A shows a representative concentration versus time profile for a patient on the low-dose arm (200 mg per day) who received multiple daily doses of oral thalidomide, and Figure 3B shows a representative concentration versus time profile for a patient on the high-dose arm (200 mg per day increasing by 200 mg every 2 weeks to a maximum of 1200 mg per day) who received multiple daily doses of oral thalidomide. Patients on the low-dose arm of the study were maintained on thalidomide for a mean of 67 days (median = 62 days), ranging from 55 to 123 days. Pharmacokinetic parameters and the average maximum concentrations at steady state ($C_{max\ ss}$) after the multiple dosing are listed by dose level in Tables 2and 3, respectively. The oral clearance and apparent volume of distribution for the low-dose regimen were 6.35 ± 1.64 L/h and 64.63 ± 23.20 L, respectively, whereas for the high-dose regimen, these values were 7.73 ± 2.27 L/h and 167.85 ± 82.08 L, respectively ($p = 0.31$ and 0.0028). The elimination half-lives for the low- and high dose groups were 7.08 ± 1.87 and 16.19 ± 9.57 h, respectively ($p = 0.013$). Similar to the single-dosing results, the apparent volume of distribution and half-life were significantly higher for the high-dose group than those for the low-dose group.

Table 2—Pharmacokinetic Parameters for the Low- and the High-Dose Level after Multiple Daily Dosing of Thalidomide

statistic	K_e (h^{-1})	*Vd/F* (*L*)	K_a (h^{-1})	*CL/F* (L/h)	$t_{1/2}$ (h)	r^2
			high dose[a]			
mean	0.0656	167.85	0.9462	7.74	16.19	0.809
SD	0.0538	82.08	0.8157	2.27	9.57	0.129
median	0.0492	153.70	0.7027	6.81	14.09	0.834
max	0.1756	281.70	3.0010	12.56	36.67	0.956
min	0.0189	38.13	0.1663	4.97	3.95	0.587
			low dose (200 mg, $n = 10$)			
mean	0.1044	64.63	0.7994	6.35	7.08	0.883
SD	0.0287	23.20	0.4542	1.64	1.87	0.058
median	0.1001	60.52	0.7102	6.44	6.94	0.890
max	0.1633	97.69	1.6090	8.27	10.07	0.963
min	0.0688	33.67	0.3046	3.73	4.24	0.762

[a] Dose (*n*): 200 (11); 400 (7); 600 (6); 800 (5); 1000 (3); 1200 (3), where *n* is the number of patients that reached the corresponding dose level in the high dose group.

Table 3—Maximum Steady-State Concentrations for the High Dose After Multiple Daily Dosing of Thalidomide

	concentration (μg/mL) at:					
statistic	200 mg ($n = 11$)	400 mg ($n = 7$)	600 mg ($n = 6$)	800 mg ($n = 5$)	1000 mg ($n = 3$)	1200 mg ($n = 3$)
mean	1.81	3.43	5.56	7.57	9.18	11.07
SD	0.81	0.73	1.77	1.83	1.95	2.47
median	1.57	3.15	5.23	8.05	10.10	12.17
max	4.02	4.28	8.50	9.90	10.50	12.80
min	0.98	2.61	3.90	5.55	6.94	8.24

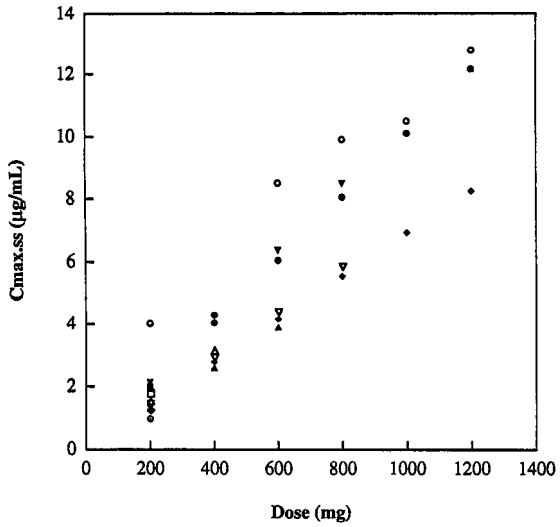

Figure 4—Maximum steady-state thalidomide concentrations as a function of dose after multiple daily dosing of oral thalidomide.

Figure 4 presents the model-predicted maximum steady-state concentrations of thalidomide as a function of dose. A dose-proportional increase in steady-state concentration of thalidomide was seen. Overall, the one-compartment linear model with first-order absorption fit the data well, as evidenced by the plot of observed versus fitted concentration for both single and multiple daily oral dosing of thalidomide (Figure 5A and B).

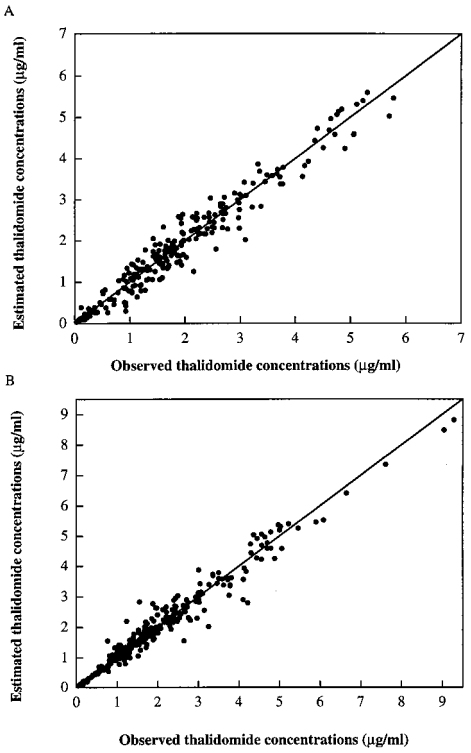

Figure 5—Estimated versus observed thalidomide concentrations. (A) Thalidomide concentrations estimated by a one-compartment model plotted against the observed thalidomide concentrations after a single oral dose. (B) Thalidomide concentrations estimated by a one-compartment model plotted against the observed thalidomide concentrations after multiple daily dosing.

Discussion

Thalidomide has been shown to inhibit tumor angiogenesis, the process of new blood vessel formation within a malignancy. Despite extensive clinical work with this compound for some 40 years, there are generally few data on the pharmacokinetics of thalidomide. Chen et al.[28] reported the pharmacokinetics of thalidomide after oral dosing in healthy male volunteers. The disposition of thalidomide in these patients was characterized by an elimination half-life of approximately 9 h, a clearance of 10 L/h, and an apparent volume of distribution of nearly 121 L. Piscitelli et al.[22] reported the pharmacokinetics of thalidomide in HIV-infected patients after a single oral dose. Thalidomide pharmacokinetics in these patients was characterized by slow absorption, with a mean t_{max} of 3.4 h, an elimination half-life of approximately 6 h, an oral clearance of approximately 8.5 L/h, and an apparent volume of distribution of approximately 85 L. For both the studies, the dose was no more than 300 mg. Our study reported nearly identical values for the low-dose arm (200 mg), but the apparent volume of distribution and the half-life were significantly different for the high-dose arm (800 mg test dose and then dose escalations every 2 weeks).

A one-compartment first-order oral absorption model provided the best fit for the data after single and multiple oral dosing of thalidomide in patients with hormone-refractory prostate cancer. In general, the model fit the data well, as evidenced by the plot of observed versus fitted concentrations. The oral clearance was comparable for the low- and the high-dose groups, but the apparent volume of distribution and half-life were significantly higher for the high-dose group. The higher volume of distribution may be attributable to several factors, such as change in absorption, protein binding, etc. Many drugs have been shown to have extended half-lives due to low aqueous solubility. The pH 7 solubility of thalidomide is 50 μg/mL.

Pharmacokinetic evaluation was reliable for 24 patients for the single dosing and 21 patients for the multiple dosing of thalidomide, (patients ranged in age from 55 to 80 years). No significant age dependency was observed in plasma clearance and elimination half-life. No dose-related changes in oral clearance were seen.

The pharmacokinetics of thalidomide have not been clearly characterized in men. Our study described the pharmacokinetic profile of thalidomide, after single as well as multiple oral dosing in an elderly population of men with cancer. Low- and high-dose groups were studied and pharmacokinetic parameters were determined for both. Patients in this study were diagnosed with hormone-refractory prostate cancer, but did not have active opportunistic infections or concomitant diseases. Additional studies are necessary to determine if age affects the clearance of thalidomide and whether the formation of the active metabolite of thalidomide that inhibits angiogenesis is altered by changes in clearance.

References and Notes

1. Kluken, N.; Wente, W. Indications for thalidomide therapy for leprosy. *Int. J. Dermatol.* **1974**, *13*, 20−25.
2. Sharpstone, D.; Rowbottom, A.; Nelson, M.; Gazzard, B. The treatment of microsporideal diarrhea with thalidomide. *AIDS* **1995**, *9*, 658−659.
3. Vincente, T.; Ortega, A.; Munoz, P.; Diaz, M.D.; Bouza, E. In vitro activity of thalidomdie against Mycobacterium avium complex. *Arch. Intern. Med.* **1993**, *153*, 534.
4. D'Amato, R. J.; Loughnan, M. S.; Flynn, E.; Folkman, J. Thalidomide is an inhibitor of angiogenesis. *Proc. Natl. Acad. Sci. U.S.A.* **1994**, *91*, 4082−4085.
5. Bauer, K. S.; Dixon, S. C.; Figg, W. D. Inhibition of angiogenesis by thalidomide requires metabolic activation, which is species-dependent. *Biochem Pharm.* **1998**, *55*, 1827−1834.
6. Simmons, B. R.; Lush, R. M.; Figg, W. D. A reversed-phase high performance liquid chromatography method using solid-phase extraction to quantitate thalidomide in human serum. *Anal. Chim. Acta* **1997**, *339*, 91−97.
7. Huupponen, R.; Pyykko, K. Stability of thalidomide in plasma. *Clin. Chem.* **1995**, *41*, 1199.
8. Eriksson, T.; Bjorkman, S.; Roth, B.; Fyge, A.; Hoglund, P. Stereospecific determination, chiral inversion in vitro and pharmacokinetics in humnas of the enantiomers of thalidomide. *Chirality* **1995**, *7 (1)*, 44−52.
9. Eriksson, T.; Bjorkman, S.; Roth, B.; Fyge, A.; Hoglund, P. Enatiomers of thalidomide: Blood distribution and the influence of serum albumin on chiral inversion and hydrolysis. *Chirality* **1998**, *10*, 223−228.
10. Heney, D.; Norfolk, D. R.; Wheeldon, J.; Bailey, C. C.; Lewis, I. J.; Barnard, D. L. Thalidomide treatment for chronic graft-versus-host disease. *Br. J. Haematol.* **1991**, *78*, 23−27.
11. Czejka, M. J.; Koch, H. P. Determination of thalidomide and its major metabolites by high-performance liquid chromatography. *J. Chromatogr.* **1987**, *413*, 181−187.
12. D'Argenio, D. Z.; Schumitsky, A. *ADAPT II User's Guide, Biomedical Simulations Resource*; University of Southern California: Los Angeles, CA.
13. Folkman, J. Tumor angiogenesis: therapeutic implications. *N. Engl. J. Med.* **1971**, *285*, 1182−1186.
14. Folkman, J. Angigenesis in cancer, vascular, rheumatoid and other diseases. *Natl. Med.* **1995**, *1*, 27−31.
15. Fabro, S.; Schumacher, H.; Smith, R. L.; Stagg, R. B. L.; Williams, R. T. The metabolism of thalidomide: some biological effects of thalidomide and it's metabolites. *Br. J. Pharmacol.* **1965**, *25*, 352−362.
16. Gibaldi, M.; Perrier, D. *Pharmacokinetics*, 2nd ed.; Marcel Dekker: New York.
17. Gordon, G. B.; Spielberg, S. P.; Blake, D. A.; Balasubramanian, V. Thalidomide teratogenesis: evidence for a toxic arene oxide metabolite. *Proc. Natl. Acad. Sci.; U.S.A.* **1981**, *78*, 2545−2548.
18. Jusko, W. J. Guidelines for collection and analysis of pharmacokinetic data. *In Applied pharmacokinetics: principles of therapeutic drug monitoring*, 3rd ed.; Evans, W. E.; Schentag, J. J.; Jusko, W. J., Eds.; Applied Therapeutics: Vancouver, WA.

19. Kenyon, B. M.; Browne, F.; D'Amato, R. J. Effects of thalidomdie and related metabolites in a mouse corneal model of neovascularization. *Exp. Eye Res.* **1997**, *64*, 971−978.
20. Moreira, A. L.; Sampaio, E. P.; Zmuidzinas, A.; Frindt, P.; Smith, K. A.; Kaplan, G. Thalidomide exerts its inhibitory action on tumor necrosis factor by enhancing mRNA degradation. *J. Exp. Med.* **1993**, *177*, 1675−1680.
21. Pollard, M. Thalidomide promotes metastasis of prostate adenocarcinoma cells (PA-III) in L−W rats. *Cancer Lett.* **1996**, *101*, 21−24.
22. Piscitelli, S. C.; Figg, W. D.; Hahn, B.; Kelly, G.; Thomas, S.; Walker, R. E. Single-dose pharmacokinetics of thalidomide in human immunodeficiency virus-infected patients. *Antimicrob. Agents Chemother.* **1997**, *41 (12)*, 2797−2799.
23. Schmahl, H. J.; Nau, H.; Neubert, D. The enantiomers of the teratogenic thalidomdie analogue EM 12: 1. Chiral inversion and plasma pharmacokinetics in the marmoset monkey. *Arch. Toxicol.* **1988**, *62*, 200−204.
24. Schumacher, H.; Blake, D. A.; Gillette, J. R. Disposition of thalidomide in rabbits and rats. *J. Pharmacol. Exp. Ther.* **1968**, *160*, 201−211.
25. Weidner, N.; Semple, J. P.; Welch, W. R.; Folkman, J. Tumor angiogenesis and metastasis-correlation in invasive breast carcinoma. *N. Engl. J. Med.* **1991**, *324*, 1−8.
26. Weidner, N.; Carroll, P. R.; Flax, J.; Blumenfeld, W.; Folkman, J.; Tumor angigenesis correlates with metastatsis in invasive prostate carcinoma. *Am. J. Pathol.* **1993**, *143*, 401−409.
27. Yamaoka, K.; Nakagawa, T.; Uno, T. Application of Akaike's information criterion in the evaluation of linear pharmacokinetic equations. *J. Pharmacokinet. Biopharm.* **1978**, *6*, 165−175.
28. Chen, T. L.; Vogelsang, G. B.; Petty, B. G.; Brundrett, R. B.; Noe, D. A.; Santos, G. W.; Colvin, O. M. Plasma pharmacokinetics and urinary excretion of thalidomide after oral dosing in healthy male volunteers. *Drug Metab. Dispos.* **1989**, *17*, 402−405.

Acknowledgments

We thank Valerie Dyer and Patricia Davis for their assistance with this study, as well as the NCI clinical associates and nursing staff. This research was funded by the U.S. Government.

JS980172I

PLGA Microspheres Containing Plasmid DNA: Preservation of Supercoiled DNA via Cryopreparation and Carbohydrate Stabilization

SHUICHI ANDO, DAVID PUTNAM, DANIEL W. PACK, AND ROBERT LANGER*

Contribution from *Massachusetts Institute of Technology, E25-342, 45 Carleton Street, Cambridge, Massachusetts 02139.*

Received April 17, 1998. Accepted for publication October 12, 1998.

Abstract □ Biodegradable microspheres containing plasmid DNA have potential uses as mediators of transfection in cells, particularly phagocytic cells such as macrophages. However, the hydrophilic nature and the structural instability of supercoiled DNA preclude its facile encapsulation in polymer matrixes such as poly(*d*,*l*-lactic-*co*-glycolic acid) (PLGA) by traditional methods. We initially studied the microencapsulation of plasmid DNA using the established water-in-oil-in-water double-emulsion solvent-evaporation method and found that (1) the encapsulation efficiency was low (about 20%), (2) the microencapsulation procedure nicked (degraded) the supercoiled DNA, and (3) lyophilization of the microsphere also nicked the DNA. We have therefore designed a new microsphere preparation method (called cryopreparation) to specifically address these concerns. Using the cryopreparation method, the aqueous phase of the primary emulsion containing the plasmid DNA is frozen and then subjected to homogenization. Because there is no shear stress inside a solid, we hypothesized that freezing the aqueous phase of the primary emulsion would help to preserve the supercoiled plasmid DNA during formation of the secondary emulsion. We also hypothesized that the formation of crystals from buffers within the primary emulsion was a causative factor for nicking during freezing or lyophilization, and that disruption of the crystal formation by the addition of saccharides into the primary emulsion would improve the supercoiled-DNA content of the spheres. Our results support the two hypotheses. Not only was the supercoiled-DNA content increased from 39% to over 85%, but the encapsulation efficiency was also elevated from 23% to over 85%.

Introduction

The importance of DNA therapeutics, in particular in gene therapy, has led to increased research and development in this area.[1−5] The use of such therapeutics can be problematic, however, because during delivery the DNA is subject to degradation. To maximize the power of these agents, it would be desirable to develop a mode of delivery in which the DNA-based therapeutic is protected from degradation. It is known that nano- or micro-encapsulation techniques can be used to protect sensitive bioactive agents, such as DNA, from degradation.[6−10]

Biodegradable microspheres, such as those based on PLGA, have the potential to act as mediators of DNA transfection targeted to phagocytic cells such as macrophages, and to protect against biological degradation by nucleases. Uptake of biodegradable microspheres by macrophages has been extensively studied,[11] and more recently Ciftci et al.[12] reported a method to introduce DNA into mammalian cells using a polymer-based gene-delivery system. Spheres in the range of 1−10 μm are too large to enter cells via endocytosis, and therefore "target" phagocytic cells such as macrophages by size exclusion. Because macrophages are antigen-presenting cells for the immune system, microencapsulated plasmid DNA is particularly useful for the rapidly developing field of DNA-based vaccines.[13]

One of the most common techniques for preparation of biodegradable polymer microspheres encapsulating hydrophilic molecules is the double-emulsion solvent-evaporation method. Using this technique, the molecule to be encapsulated is placed in aqueous solution while the polymer is dissolved in an organic phase commonly consisting of methylene chloride or ethyl acetate. The two phases (volume organic/volume aqueous = 3−20) are emulsified, typically by sonication or homogenization. This primary emulsion is then added to a second aqueous phase (20- to 100-fold larger volume) and again mixed by homogenization to form the (water-in-oil)-in-water double emulsion. Upon evaporation of the partially water-miscible solvent, the polymer-containing droplets harden to form microspheres which can then be isolated by filtration or centrifugation. Lyophilization removes water from the interior aqueous phase resulting in a dry suspension of the encapsulated material within the polymer matrix.

Our initial experiments using the standard double-emulsion microsphere formulation process demonstrated the tendency of plasmid DNA to be converted from its supercoiled state to a nicked or linear state. The preservation of the supercoiled DNA is important because it is known that supercoiled DNA retains the highest level of bioactivity.[14−16] Furthermore, the encapsulation efficiency of DNA into the hydrophobic matrix of PLGA was low, on the order of 20%. On the basis of these observations, we formulated hypotheses for the mechanisms of DNA degradation during the microsphere formulation process and then adopted a design approach to develop an encapsulation process that maximized both the supercoiled-DNA content in the microsphere and its overall encapsulation efficiency. Our hypotheses were as follows: (1) shear stress-induced plasmid DNA degradation occurred during homogenization and (2) buffer salt crystal formation induced plasmid DNA degradation during freezing or drying.

The first hypothesis led to the design and development of a new microencapsulation process for plasmid DNA called cryopreparation. Cryopreparation describes a process in which the temperature of the DNA-containing primary emulsion is lowered below the freezing point of the aqueous inner phase resulting in a solid particulate suspension prior to homogenization to form the secondary emulsion. Because the shear stress within a solid equals zero, the plasmid DNA frozen in the inner phase is exposed to minimum shear stress during homogenization, and the supercoiled state of the plasmid DNA should be preserved. Cryopreparation should also enhance the overall encapsulation efficiency by preventing diffusion of the plasmid DNA out of the microsphere during homogenization. Cryopreparation differs from other microsphere preparation methods that

* To whom correspondence should be addressed. Phone: (617) 253-3123. Fax: (617) 258-8827. E-mail: rlanger@mit.edu.

10.1021/js9801687 CCC: $18.00
Published on Web 12/01/1998

use temperature as a variable parameter in that cryopreparation involves selective freezing of the aqueous inner emulsion whereas other procedures freeze or gel the entire microsphere.[17,18] The second hypothesis led to the inclusion of saccharides in the primary emulsion to disrupt the formation of DNA-nicking crystals during homogenization and lyophilization.

Experimental Section

Materials—Plasmid DNA (pCMV-β-gal) was purified from *E. coli* (DH5α) using Plasmid Mega Kit column isolation (QIAGEN, CA), followed by ethanol precipitation. Poly(*d,l*-lactic-*co*-glycolic acid) (PLGA), with a comonomer ratio of 50:50 and an inherent viscosity $\eta = 0.4$ (Resomer RG503, MW 34 000) was purchased from Boehringer Ingelheim (Germany). The emulsifier, poly(vinyl alcohol) (PVA) (88 mol % hydrolyzed, MW 25 000), was purchased from Polysciences, Inc. (Warrington, PA). All other chemicals used were of the highest grade commercially available.

Cryopreparation—DNA-containing microspheres were prepared following the established water-in-oil-in-water double-emulsion solvent-evaporation method[19] except for specific steps noted below. The two phases, consisting of 250 μL of DNA solution (250 μg of DNA) and 7 mL of methylene chloride containing 200 mg of PLGA, were emulsified by sonication for 10 s (ultrasonic probe, Sonic & Materials Inc.) at room temperature. The primary emulsion temperature was then lowered below the freezing point of the aqueous inner phase by liquid nitrogen immersion, and 50 mL of a 5% PVA solution (4−7 °C) was added and homogenized at 5000−9000 rpm for 14 s (Silverson L4R homogenizer). After homogenization, the resulting emulsion was diluted in 100 mL of 1% PVA, and the system was stirred magnetically for 3 h to allow for evaporation of the organic solvent. Microspheres were finally collected by centrifugation and washed 3 times with water to remove excess PVA. Note that all PVA solutions were adjusted to the osmotic pressure of the inner aqueous phase using agents such as saccharides. The microspheres were resuspended in approximately 1 mL of water, frozen in liquid nitrogen, and lyophilized at room temperature for 24 h on a Labconco Freeze-Dryer 8.

Achieving DNA Stability against Lyophilization Using Excipients—The effect of lyophilization on DNA was studied by directly lyophilizing DNA samples (20 μg/mL). Aliquots (1 mL each) of the DNA solutions, with or without excipients, were frozen in 20-mL disposable scintillation vials by liquid nitrogen immersion and immediately lyophilized at room temperature for 15 h.

Optimized Microsphere Preparation—The two phases, consisting of 250 μL of DNA in water (750 μg of DNA) containing 1 mM EDTA and 300 mM lactose (pH 7.0) and 7 mL of methylene chloride containing 200 mg of PLGA, were emulsified by sonication as described above. After the primary emulsion was cryoprepared, 50 mL of 5% PVA solution containing 300 mM lactose was added to the solution and homogenized at 7000 rpm for 14 s. The resulting double emulsion was then diluted in 100 mL of 1% PVA solution with 300 mM lactose, and the system was stirred magnetically for 3 h to allow the evaporation of the organic solvent. Microspheres were finally collected by centrifugation, washed three times with distilled water, and then lyophilized at room temperature to obtain a powder.

Analysis of DNA Structure—The DNA structure was analyzed by agarose gel electrophoresis (1% agarose containing ethidium bromide, 110 V, 90 min) and compared to untreated stock DNA for semiquantitative determination of supercoiled-DNA content using a Bio Rad Gel Doc 1000 (Software, Molecular Analyst 2.1).

As shown in Figure 1, each DNA band was integrated as a volume. Supercoiled-DNA (SC DNA) content was defined as the volume integrated from the supercoiled DNA band over the total volume integrated from all bands. In other words, SC DNA content equals (SC DNA volume − background volume)/{SC DNA volume + linear DNA volume + nicked DNA volume − (3 × background volume)}. SC DNA content remaining after preparation was calculated as follows: SC DNA remaining (initial %) = 100 × (SC DNA content of sample DNA)/(SC DNA content of initial DNA).

Quantitation of DNA Content in Microsphere—The microsphere DNA content was determined using fluorescent reagent PicoGreen (Molecular Probes, Eugene, OR) which preferentially binds to double stranded DNA and to a lesser extent to single stranded DNA. Fluorescence (λ_{ex} = 480 nm, λ_{em} = 520 nm) of extracted DNA was compared to a standard curve, using plasmid DNA, which was linear from 1 to 50 ng/mL. The encapsulation efficiency was determined as the amount of DNA recovered from the microspheres relative to the initial amount of DNA used (encapsulation efficiency = 100 × (DNA recovered)/(initial DNA)).

Particle Size of Microsphere—Particle size distribution of microspheres was analyzed by a Coulter MultisizerII (Coulter Electronics Inc., Hialeah, FL), and the mean volume diameter distribution was determined.

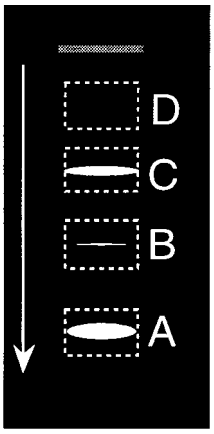

Figure 1—Schematic representation of agarose gel electrophoresis of DNA: (A) supercoiled DNA, (B) linear DNA, (C) nicked DNA, and (D) background.

Table 1—Effect of Homogenization Rate, Cryopreparation, and Addition of EDTA on Remaining Supercoiled DNA (SC DNA) ($N = 3$)

DNA solution	SC DNA remaining (initial% ± SD) at homogenization rate		
	5000 rpm	7000 rpm	9000 rpm
water without cryopreparation	36.9 ± 1.9	26.1 ± 3.6	20.1 ± 3.4
water with cryopreparation	54.4 ± 1.1	46.2 ± 0.7	37.3 ± 4.7
EDTA[a] without cryopreparation	68.4 ± 1.9	47.0 ± 2.6	40.6 ± 0.3
EDTAa with cryopreparation	92.2 ± 1.3	75.5 ± 2.1	64.7 ± 3.5

[a] 1 mM EDTA, pH 7.5.

Results and Discussion

Stability of DNA Structure against Shear Stress—In the cryopreparation method, the aqueous phase of the primary emulsion is frozen. Since the shear stress inside a solid equals zero, we hypothesized that cryopreparation would help to preserve the supercoiled DNA during homogenization. To test this hypothesis, the structure of the DNA after homogenization (and before lyophilization) was checked by agarose gel electrophoresis. Table 1 indicates that the supercoiled-DNA content decreases with an increase in homogenization rate, and that using the cryopreparation method preserves the supercoiled-DNA content. These results support our hypothesis that freezing the inner DNA solution protects the DNA from degradation by shear stress, and suggests that cryopreparation is a useful method to prevent supercoiled DNA from degrading during microsphere preparation. When ethylenediaminetetraacetic acid (EDTA) was added to the DNA solution, the supercoiled-DNA content of the resulting microspheres was significantly higher than in the absence of EDTA. EDTA is a chelator of divalent metal cations and inhibits the activity of DNase by this mechanism.[16] Therefore, it was possible that the DNA stability in the presence of EDTA was actually due to DNase inhibition. To examine the possibility of calcium-dependent DNase-mediated degradation, we also included a calcium ionophore (*N,N,N′,N′*-

Table 2—Effect of Excipients on Retaining Supercoiled DNA (SC DNA)[a]

DNA solution	SC DNA remaining (initial% ± SD)
water	46.2 ± 0.7
1 mM EDTA solution, pH 7.5	75.5 ± 2.1
1 mM calcium ionophore II	36.1 ± 0.8
10 mM Tris buffer, pH 7.5	40.5 ± 2.5
phosphate-buffered saline, pH 7.5	36.1 ± 3.5
300 mM lactose solution, pH 7.5	39.6 ± 2.7
1 mM EDTA/10 mM Tris buffer, pH 7.5	62.1 ± 2.7
1 mM EDTA/phosphate-buffered saline, pH 7.5	68.2 ± 5.2
300 mM lactose/1 mM EDTA solution, pH 7.5	94.5 ± 1.0
300 mM lactose/1 mM EDTA/10 mM Tris buffer, pH 7.5	86.2 ± 3.6

[a] Samples were prepared by cryopreparation; homogenization rate = 7000 rpm, 14 s (n = 3).

tetracyclohexyldiglycolic diamide: calcium ionophore II, log K_{Ca} = 10.1, μ = 0.1, 20 °C)[20] instead of EDTA (log K_{Ca} = 11.0, μ = 0.1, 20 °C).[21] As shown in Table 2, it is apparent that the calcium ionophore II did not act as a DNA stabilizer. Therefore, it is likely that the mechanism of DNA stabilization during cryopreparation is not a result of calcium-dependent DNase inhibition. However, DNase activity dependent on other divalent ions such as manganese and magnesium,[22] could not be eliminated. In addition, Table 2 indicates that DNA degradation during cryopreparation was not inhibited by the addition of PBS (1 mM K_2HPO_4, 10 mM Na_2HPO_4, 137 mM NaCl, 2.7 mM KCl, pH 7.0), Tris, or lactose to the DNA solution. In the case of addition of PBS or Tris to the DNA solution containing unbuffered EDTA, the supercoiled-DNA content was slightly lower than that in unbuffered EDTA solution, but we found that by adding lactose to the DNA/EDTA solution, the supercoiled-DNA content was increased from 75% to 95%. The exact mechanism of DNA stabilization is unknown. However, it is apparent that the presence of both lactose and EDTA in the DNA solution is important for the stabilization of supercoiled DNA against degradation during cryopreparation.

Regarding the analysis of the DNA structure by agarose gel electrophoresis, it is well-known that the intercalation efficiency of ethidium bromide to DNA is not the same among supercoiled, nicked, and linear DNA. In fact, the intercalation efficiency of ethidium bromide to supercoiled DNA is the lowest.[23] Thus we consider that the estimation of SC DNA ratio in our method is lower than the true value, and that this analytical method is a semiquantitative determination of the supercoiled-DNA content.

Predictably, the microsphere diameters are dependent on the homogenization rate.[24] The volume-mean diameters of microspheres formulated by cryopreparation were 10.2 (±2.4) μm at 5000 rpm, 4.6 (±0.3) μm at 7000 rpm, and 3.6 (±0.2) μm at 9000 rpm (N = 3). For optimum phagocytosis by macrophages, spheres with a size of approximately 5 μm or less are desired.[11] However, increasing the homogenization rate leads to increased DNA degradation. Therefore, homogenization at 7000 rpm was optimal for the cryopreparation method.

Stability of DNA Structure during Lyophilization—DNA samples were directly lyophilized to study the effect of lyophilization on DNA stability. Table 3 indicates that the DNA stability in 300 mM lactose and in 1 mM EDTA was the same as that of DNA in water. On the other hand, when Tris buffer or PBS was used in the DNA solution, DNA degradation was increased. Salts such as sodium phosphate are known to form crystals upon freezing,[25] and we speculated that DNA nicking was caused by the salt crystallization. (In the presence of 1 mM EDTA, however, the salt concentration might not be high enough to degrade DNA by its crystallization.) Saccharides are known cryoprotectants for proteins during lyophilization,[26,27] and we reasoned they may protect DNA in a similar fashion. Therefore, the effect of saccharides on DNA stability upon lyophilization from TE buffer was examined. Figure 2 indicates that the DNA degradation was decreased with an increase in the amount of saccharide. Other disaccharides such as maltose, trehalose, and cellobiose showed DNA stabilization similar to the effect of lactose (data not shown). The addition of saccharides in the inner aqueous phase of the primary emulsion improved the supercoiled-DNA content of the microspheres, as well (vide supra). Note that the concentrations of glucose are 100, 200, and 600 mM while those of sucrose and lactose are 50, 100, and 300 mM. This indicates that DNA stability depends on the total mass of saccharide and not the molar concentration of sugar.

Table 3—Effect of Lyophilization on Retaining Supercoiled DNA (SC DNA)[a]

DNA solution	SC DNA remaining (initial% ± SD)
water	97.9 ± 1.0
1 mM EDTA solution, pH 7.5	95.2 ± 0.6
10 mM Tris buffer, pH 7.5	70.1 ± 2.5
phosphate-buffered saline, pH 7.5	42.5 ± 3.8
300 mM lactose solution, pH 7.5	95.8 ± 0.4
1 mM EDTA/10 mM Tris buffer, pH 7.5	73.0 ± 0.8
1 mM EDTA/phosphate-buffered saline, pH 7.5	47.4 ± 2.6
300 mM lactose/1 mM EDTA solution, pH 7.5	95.6 ± 0.6

[a] DNA samples were directly lyophilized without the presence of plga or undergoing microsphere preparations.

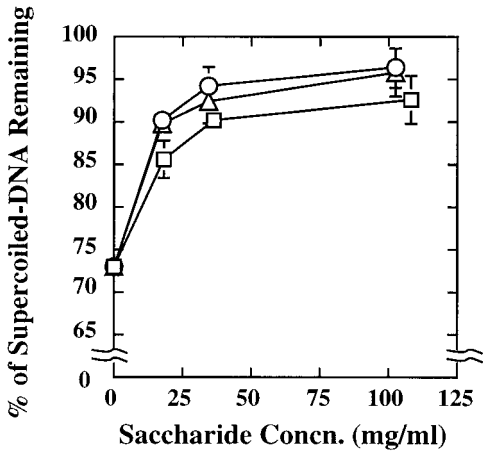

Figure 2—Effect of saccharides on DNA stability during lyophilization (DNA in TE buffer with increasing saccharide concentration). ○: Glucose, □: lactose, and △: sucrose.

Acidic pH is also known to damage DNA by depurination.[28] Freezing of sodium phosphate buffer, initially at pH 7.0, may result in pH as low as 4.0,[29] and this process could potentially contribute to the observed plasmid degradation. However, DNA which was incubated for up to 60 min at room temperature in PBS (Figure 3) or TE (10 mM Tris/1 mM EDTA; data not shown) showed no degradation at either pH 7.4 or pH 4.0. Thus, we believe any pH changes in the solution upon freezing have negligible effect on the DNA stability during microsphere preparation.

Characteristics of Microspheres Optimized for High Supercoiled-DNA Content—We have found that both (1) the addition of lactose and EDTA to the DNA solution and (2) the cryopreparation procedure were important to stabilize DNA against degradation during homogenization and lyophilization. We manufactured mi-

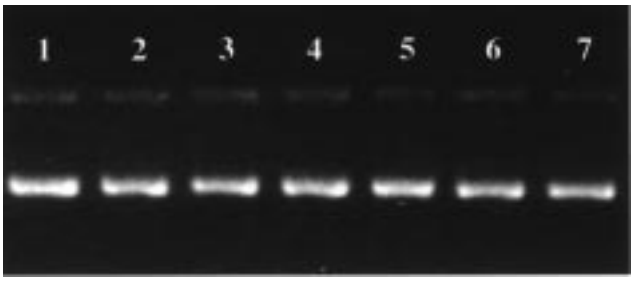

Figure 3—Agarose gel electrophoresis of DNA incubated at room temperature in PBS at pH 7.4 (lanes 1–4) and pH 4.0 (lanes 5–7) for 0 (lane 1), 10 (lanes 2, 5), 30 (lanes 3, 6), or 60 (lanes 4, 7) min.

Figure 4—Agarose gel electrophoresis of DNA in microspheres (MS) ($N = 3$). From left to right, lanes 1 and 11: 1 kb ladder; lanes 2–4: initial DNA; lanes 5–7: DNA in MS before lyophilization; lanes 8–10: DNA in MS after lyophilization.

Table 4—Effect of Excipients on Retaining Supercoiled DNA (SC DNA) under Microsphere Procedure Such as Homogenization and Lyophilization[a]

	SC DNA remaining (initial% ± SD)	
	before lyophilization	after lyophilization
water	42.3 ± 0.7	39.0 ± 4.2
1 mM EDTA solution, pH 7.5	78.2 ± 1.7	68.3 ± 3.6
phosphate-buffered saline, pH 7.5	49.1 ± 4.8	19.8 ± 0.4
300 mM lactose solution, pH 7.5	41.7 ± 2.4	20.8 ± 1.3
300 mM lactose/1 mM EDTA solution, pH 7.5	95.1 ± 0.7	88.6 ± 1.9

[a] Samples were prepared by cryopreparation, and the homogenization rate was 7000 rpm for 14 s ($n = 3$).

crospheres according to optimized conditions for the microsphere preparation described above to determine these combined effects. The characteristics of the microsphere such as particle size distribution, DNA conformation, and DNA encapsulation efficiency were determined.

Using the optimized conditions for microsphere preparation, the mean volume diameter of the microspheres was 4.8 μm, the remaining supercoiled DNA was 88% (Figure 4 and Table 4), and the DNA encapsulation efficiency was 89%. In comparison, using the standard double-emulsion preparation method (5000 rpm homogenization rate), the resulting microspheres had a mean volume diameter of 4.5 μm, a remaining supercoiled-DNA content of 39%, and a DNA encapsulation efficiency of 23%. It is apparent that cryopreparation prevents degradation of DNA and increases the encapsulation of DNA. These results suggest that the increase in DNA encapsulation efficiency is caused by preventing its diffusion out of the inner aqueous phase by freezing the primary emulsion. Furthermore, addition of DNA-nicking inhibitors to the DNA solution is important to prevent DNA degradation during this microsphere manufacturing process. Ninety-five percent of supercoiled DNA was retained before lyophilization, and 88% of supercoiled DNA was retained after lyophilization as shown in Figure 4. In addition, Table 4 compares the supercoiled-DNA content in microspheres using water, EDTA, PBS, or lactose in the DNA solution. The results also show the reproducibility of the DNA stability data as compared to the isolated homogenization and lyophilization experiments (Tables 2 and 3).

In conclusion, a method for the microencapsulation of plasmid DNA is presented. The method, cryopreparation, maximizes both the retention of supercoiled DNA and the overall DNA encapsulation efficiency. Cryopreparation is characterized by the freezing of the aqueous phase of the primary emulsion. DNA-nicking inhibitors such as lactose and EDTA significantly improve the supercoiled-DNA content in the final sphere preparation.

References and Notes

1. Friedmann, T. Progress Toward Human Gene Therapy. *Science* **1989**, *244*, 1275−1281.
2. Miller, A. D. Human Gene Therapy Comes of Age. *Nature* **1992**, *357*, 455−460.
3. Mulligan, R. C. The Basic Science of Gene Therapy. *Science* **1993**, *260*, 926−932.
4. Wilson, J. M. Vehicles for Gene Therapy. *Nature* **1993**, *365*, 691−692.
5. Crystal, R. G. The Gene as the Drug. *Nature Med.* **1995**, *1*, 15−17.
6. Langer, R. S. New Methods of Drug Delivery. *Science* **1990**, *249*, 1527−1533.
7. Kato, K.; Nakanishi, M.; Kaneda, Y.; Uchida, T.; Okada, Y. Expression of Hepatitis B Virus Surface Antigen in Adult Rat Liver. *J. Biol. Chem.* **1991**, *266*, 3361−3364.
8. Jong, Y. S.; Jacob, J. S.; Yip, K. P.; Gardner, G.; Seitelman, E.; Whitney, M.; Montgomery, S.; Mathiowitz, E. J. Controlled Release of Plasmid DNA. *J. Controlled Release* **1997**, *47*, 123−134.
9. Mathiowitz, E.; Jacob, J. S.; Jong, Y. S.; Carino, G. P.; Chickering, D. E.; Chaturvedi, P.; Santos, C. A.; Vijayaraghavan, K.; Montgomery, S.; Bassett, M.; Morrell, C. Biologically Erodable Microspheres as Potential Oral Drug Delivery Systems. *Nature* **1997**, *386*, 410−414.
10. Smith, T.; Zhang, Y.; Niven, R. Toward Development of a Non-Viral Gene Therapeutic. *Adv. Drug Del. Rev.* **1997**, *26*, 135−150.
11. Tabata, Y.; Ikada, Y. Phagocytosis of Polymer Microspheres by Macrophages. *Adv. Polym. Sci.* **1990**, *94*, 110−141.
12. Ciftci, K.; Kao, S.; Kumar, P.; Smiley, E.; Bonadio, J.; Levy, R. J. Polymer Based Gene Delivery Systems: An Effective Way to Introduce DNA into Mammalian Cells. *Pharm. Res.* **1997**, *14*, s639.
13. Hedley, M. L.; Curley, J.; Urban, R. Microspheres Containing Plasmid-Encoded Antigens Elicit Cytotoxic T-Cell Responses. *Nature Med.* **1998**, *4*, 365−368.
14. Xu, Y.; Szoka, F. C. Mechanism of DNA Release from Cationic Liposome/DNA Complexes Used in Cell Transfection. *Biochem.* **1996**, *35*, 5616−5623.
15. Yamaizumi, M.; Horwich, A. L.; Ruddle, F. H. Expression and Stabilization of Microinjected Plasmids Containing the Herpes Simplex Virus Thymidine Kinase Gene and Polyoma Virus DNA in Mouse Cell. *Mol. Cell Biol.* **1983**, *3*, 511−522.
16. Middaugh, C. R.; Evans, R. K.; Montgomery, D. L.; Casimiro, D. R. Analysis of Plasmid DNA from a Pharmaceutical Perspective. *J. Pharm. Sci.* **1998**, *87*, 130−146.
17. Sefton, M. V.; Brown, L. R.; Langer, R. S. Ethylene-Vinyl Acetate Copolymer Microspheres for Controlled Release of Macromolecules. *J. Pharm. Sci.* **1984**, *73*, 1859−1861.
18. Johnson, O. L.; Cleland, J. L.; Lee, H. J.; Charnis, M.; Duenas, E.; Jaworowicz, W.; Shepard, D.; Shahzamani, A.; Hones, A. J. S.; Putney, S. D. A Month-Long Effect from a Single Injection of Microencapsulated Human Growth Hormone. *Nature Med.* **1996**, *2*, 795−799.
19. Alonso, M. J.; Cohen, S.; Park, T. G.; Gupta, R. K.; Siber, G. R.; Langer, R. S. Determination of Release Rate of Tetanus Vaccine from Polyester Microspheres. *Pharm. Res.* **1993**, *10*, 945−953.

20. Schefer, U.; Ammann, D.; Pretsch, E.; Oesch, U.; Simon, W. Neutral Carrier Based Calcium-Selective Electrode with Detection limit in the Sub-Nanomolar Range. *Anal. Chem.* **1986**, *58*, 2282−2885.
21. Bell, C. F. *Principles and Applications of Metal Chelation*; Clarendon Press: Oxford, U.K., 1977; pp 75−91.
22. Price, P. A. Characterization of Ca and Mg Binding to Bovine Pancreatic Deoxyribonuclease A. *J. Biol. Chem.* **1972**, *247*, 2895−2899.
23. Brown, T. A. In *Gene Cloning*; T. A. Brown, Ed.; Chapman and Hall: New York, 1990; pp 30−46.
24. Hanes, J. Polymer Microspheres for Vaccine Delivery. Ph.D., Massachusetts Institute of Technology, 1996.
25. Murase, N.; Franks, F. Salt Precipitation During the Freeze-Concentration of Phosphate Buffer Solutions. *Biophys. Chem.* **1989**, *34*, 293−300.
26. Carpenter, J. F.; Prestrelski, S. J.; Anchordoguy, T. J.; Arakawa, T. Interactions of Stabilizers with Proteins During Freezing and Drying. *ACS Symp. Ser.* **1994**, *567*, 134−147.
27. Suzuki, T.; Imamura, K.; Yamamoto, K.; Satoh, T.; Okazaki, M. Thermal Stabilization of Freeze-Dried Enzymes by Sugars. *J. Chem. Eng. Jpn.* **1997**, *30*, 609−613.
28. Suzuki, T.; Ohsumi, S.; Makino, K. Mechanistic Studies on Depurination and Apurinic Site Chain Breakage in Oligodeoxyribonucleotides. *Nucleic Acids Res.* **1994**, *22*, 4997−5003.
29. Szkudlarek, B. A.; Anchordoquy, T. J.; Garcia, G. A.; Pikal, M. J.; Carpenter, J. F. pH Changes of Phosphate Buffer Solutions During Freezing and Their Influence on the Stability of a Model Protein, Lactate-Dehydrogenase. *Abstr. Pap. Am. Chem. Soc.* **1996**, *211*, 138-BIOT.

Acknowledgments

The authors are grateful to Ms. S. Hirosue for many helpful discussions. The authors are indebted to Dr. R. C. Mulligan for the use of the Bio Rad Gel Doc 1000, and to Dr. J. Gray for gel analytical experiments.

JS9801687

Effective Administration Route for the Deleted Form of Hepatocyte Growth Factor To Exert Its Pharmacological Effects

YASUHIRO UEMATSU,* NOBUAKI FUJISE, KAZUHIRO KOHSAKA, HIROAKI MASUNAGA, AND KANJI HIGASHIO

Contribution from *Research Institute of Life Science, Snow Brand Milk Products Co., Ltd., 519 Shimoishibashi, Ishibashi-machi, Shimotsuga-gun, Tochigi 329-0512, Japan.*

Received January 28, 1998. Final revised manuscript received June 23, 1998.
Accepted for publication September 17, 1998.

Abstract □ The pharmacokinetics and the pharmacological effects of the deleted form of hepatocyte growth factor (dHGF) after intravenous (iv), subcutaneous (sc), or intramuscular (im) administration (0.25 and 2.5 mg/kg) were studied in rats. After single iv administration (2.5 mg/kg), dHGF in serum rapidly decreased (α- and β-phase half-life: 3.2 and 26.5 min, respectively). Two to four hours after single sc or im administration (2.5 mg/kg), the serum level of dHGF reached a maximum and then gradually declined (half-life: 2.7 h). The serum levels were not changed by repetitive iv administration, but were dramatically decreased by repetitive sc or im administration. Liver weight and serum levels of total protein, albumin, and HDL-cholesterol were significantly increased by iv administration of dHGF (twice daily for 4 days at 0.25 mg/kg). Sc or im administration of dHGF did not increase these parameters at the same dose, but did significantly at 2.5 mg/kg. These observations suggest that iv administration is the most effective in exerting the pharmacological effects of dHGF among three administration routes. dHGF after iv administration was distributed mainly and rapidly into liver (53.6% of the injected dHGF within 5 min) and was sustained at a higher level in the liver than in plasma. In infusion (0.5 mg/kg/3 h), dHGF level in plasma and liver reached a steady-state 15 and 60 min after starting the infusion, respectively. The steady-state level of dHGF was 7- to 9-fold higher in liver than in plasma, and the higher level in liver was sustained beyond the steady-state.

Human hepatocyte growth factor (HGF) was purified and characterized as a mitogen for adult rat hepatocytes.[1,2] Two different complementary DNAs (cDNAs) encoding human HGF were cloned from human liver[3] and placenta[4] cDNA libraries. A major variant of HGF, the deleted form of HGF (dHGF), has been purified from conditioned medium of human fibroblasts.[5] dHGF cDNA, which lacks 15 nucleotides encoding a five-amino acid residue in the first kringle domain of HGF, has been isolated from human fibroblast cDNA library.[6] Like HGF, dHGF is a heparin-binding basic protein with an apparent molecular mass (M_r) of 76−80 kD and is a heterodimer composed of a large α-chain with a M_r of 52−56 kD and a small β-chain with a M_r of 30−34 kD.[6] dHGF is more mitogenic than HGF for adult rat hepatocytes[6−8] and epithelial cells.[7] HGF and dHGF are distinguishable in their target cell specificity in growth stimulation and in their tertiary structure.[7] Serum HGF or dHGF levels in patients with liver diseases are higher than those in healthy subjects.[9,10] These observations suggest that dHGF acts on hepatocytes and plays an important role in liver regeneration.

To determine the most suitable administration route of dHGF, we investigated pharmacokinetics of dHGF after intravenous (iv), subcutaneous (sc), or intramuscular (im) administration and compared the effects of dHGF on hepatic protein synthesis, hepatic cholesterol metabolism, and liver weight among three routes of administration. dHGF exerted the most potent accelerating effect on liver functions and on increase of liver weight after iv administration. We also examined distribution of dHGF into the liver after iv administration. Exogenous dHGF was distributed mainly and rapidly into the liver and was sustained at higher concentrations in the liver than in plasma.

Experimental Section

Animals—Male Wistar rats were obtained from Charles River Japan (Kanagawa, Japan). The animals were housed for at least 1 week before the study at 23 ± 2 °C under a 12 h light−dark cycle. Water and laboratory chow were provided ad libitum. All animals used were 7 weeks old and weighed between 185 and 245 g.

Reagents—dHGF was purified from the conditioned medium of Namalwa cells transfected with an expression plasmid comprising human dHGF cDNA.[7] The purified dHGF was diluted with sterile phosphate-buffered saline (PBS) containing 0.01% Tween 80. All other reagents were of analytical grade and were commercially available.

Preparation of Anti-dHGF IgG—Female Japanese White rabbits weighing about 2 kg received sc injections of dHGF (100 μg/rabbit) with complete Freund's adjuvant six times at intervals of 2 weeks, and blood was collected from the animals 1 week after the last injection. Anti-dHGF serum was subjected to protein A column (Nippon Bio-Rad Laboratories, Tokyo, Japan) chromatography, and the purified anti-dHGF IgG was stored at −20 °C. The concentration of anti-dHGF IgG was determined by the method of Lowry,[11] using bovine IgG as a standard protein.

Preparation of Anti-dHGF IgG-Peroxidase Conjugate—The anti-dHGF IgG was further purified by affinity chromatography on an Affigel 10 column (Nippon Bio-Rad Laboratories) coupled with dHGF. The purified anti-dHGF specific antibody (IgG) was conjugated to horseradish peroxidase using a ImmunoPure Maleimid Activated Horseradish Peroxidase kit (Pierce, Rockford, IL). The anti-dHGF IgG-peroxidase conjugate was supplemented with the same volume of glycerol and stored at −20 °C.

Collection of Serum Samples for Pharmacokinetic Study—In single administration, dHGF (0.25 or 2.5 mg/kg) was administered to rats through the tail vein (iv injection), dorsimesal subcutis (sc injection), or hind limb (im injection) of animals. In repetitive administration, dHGF (0.25 and 2.5 mg /kg/injection) was administered twice daily for 4 days to rats by iv, sc, or im injection as described above. Under ether anesthesia, blood was collected in a polypropylene tube through a glass capillary tube inserted into the orbital vein of the animals from 5 min to 24 h after iv injection and from 30 min to 24 h after sc or im injection. The blood samples were allowed to clot at room temperature and were centrifuged at 1300*g* for 10 min to separate serum. Each serum sample was transferred into a polypropylene microtube and was stored at −80 °C until used for dHGF assay.

Analysis of Liver Functions—dHGF (0.25 or 2.5 mg/kg) or vehicle was given to rats twice daily for 4 days by iv, sc, or im

* Corresponding author. Tel: +81 (0285) 52-1311, Fax: +81 (0285) 53-1314, e-mail: snowls0@mb.infoweb.ne.jp.

10.1021/js9800432 CCC: $18.00
Published on Web 11/06/1998

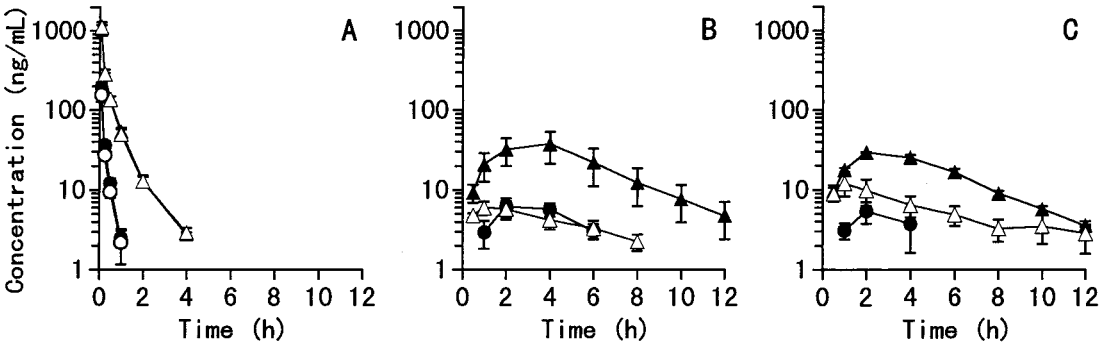

Figure 1—The concentration–time profiles of dHGF in serum after single and repetitive (A) iv, (B) sc and (C) im administrations of 0.25 and 2.5 mg/kg dHGF to rats. Key: single administration of 0.25 (●) and 2.5 (▲) mg/kg; repetitive administration of 0.25 (○) and 2.5 (△) mg/kg. Each point and bar represents the mean ± SD ($n = 3$). The concentrations of dHGF in serum after repetitive sc and im administrations of dHGF at a dose of 0.25 mg/kg were undetectable level (<1.25 ng/mL) in the greater part of the sampling time points.

injection. Under ether anesthesia 12 h after the last administration, blood was sampled from the inferior vena cava of the animals using a vacuum tube (Terumo, Tokyo, Japan). The blood sample was treated to separate serum as described above. The liver of each animal was excised for weighing at the same time. Serum samples were stored at −80 °C until used for assay. The concentrations of total protein, albumin, and HDL-cholesterol in serum were determined with a type 7150 automatic analyzer (Hitachi, Tokyo, Japan), using commercially available test reagents (Daiichi Pure Chemicals, Tokyo, Japan).

Collection of Plasma and Liver Samples for Distribution Study—The experiment on distribution of dHGF after iv bolus administration was carried out as follows. dHGF (0.5 mg/kg) was administered to rats through the tail vein. Under ether anesthesia, blood was collected from the inferior vena cava of the animals from 2 to 120 min after the administration using a vacuum tube containing EDTA. The liver was removed after perfusion with saline at the same time. The collected blood samples were centrifuged at 1300*g* for 10 min, and the obtained plasma samples were stored at −80 °C until used for dHGF assay. The removed liver was homogenized in 20 mM Tris-HCl (pH 7.5) containing 2 M NaCl, 0.1% Tween 80, 1 mM phenylmethylsulfonyl fluoride, and 1 mM EDTA with 4-fold volume of liver weight. The homogenate was centrifuged at 19000*g* for 30 min at 4 °C, and the resultant supernatant (liver extract) was collected and stored at −80 °C until used for dHGF assay. In addition, dHGF was administered to other rats at the same dose, and plasma and liver samples were collected up to 6 h after the administration as described above.

The experiment on distribution of dHGF after iv infusion was performed as follows. Under ether anesthesia, the right jugular vein was cannulated with polyethylene tubing (SP31, Natume, Tokyo, Japan). After recovery from anesthesia, iv infusion of dHGF solution through the tubing was performed at a flow rate of 2.1 μL/min (0.5 mg dHGF/kg/3 h) using a microsyringe pump (EP-60, Eicom, Kyoto, Japan). Under pentobarbital anesthesia, blood was collected and the liver was taken out from 15 min to 3 h after starting the infusion and from 15 min to 3 h after terminating the infusion, and these samples were treated and stored as described above.

Enzyme-Linked Immunosorbent Assay for dHGF—dHGF concentrations in serum, plasma, and liver extract were measured by a two-step sandwich enzyme-linked immunosorbent assay (ELISA) using rabbit anti-dHGF polyclonal antibody, which has no cross-reactivity to rat HGF.

ELISA for dHGF in serum or in plasma was performed as follows. Anti-dHGF IgG was diluted with 0.1 M $NaHCO_3$ to give a final concentration of 10 μg/mL. The diluted IgG solution (100 μL) was added to each well in 96-well immunoplates (MaxiSorp, InterMed, Roskilde, Denmark). The plates were allowed to stand at room temperature overnight. Subsequently, nonspecific binding sites of each well in the plates were blocked with 200 μL of Block Ace (Snow Brand Milk Products Co., Ltd., Tokyo, Japan) diluted 2-fold with water at room temperature for 1 h. After washing each well three times with PBS containing 0.1% Tween 20 (PBS-Tween), 50 μL of the first reaction buffer (50% Block Ace, 0.2 M NaCl, 0.1% Tween 20, 0.2% 3-[(3-cholamidopropyl)dimethylammonio]-1-propanesulfonate, 20 mM benzamidine hydrochloride, 10 mM EDTA in 0.2 M Tris-HCl, pH 7.3) was added to each well.

Table 1—Pharmacokinetic Parameters of dHGF after iv, sc, and im Administrations in Rats[a]

pharmacokinetic parameter	route of admin	single admin 0.25 mg/kg	single admin 2.5 mg/kg	repetitive admin 0.25 mg/kg	repetitive admin 2.5 mg/kg
AUC_{last}, ng·h/mL	iv	37.9 ± 3.4	302.5 ± 20.7	29.6 ± 3.4	309.9 ± 42.2
	sc	26.7 ± 6.2	230.9 ± 100.8	*b*	32.8 ± 7.0
	im	14.9 ± 4.7	177.8 ± 8.6	*b*	66.9 ± 20.4
F, %	sc	70.6	76.3	*b*	10.6
	im	39.3	58.8	*b*	21.6

[a] Each value is the mean ± SD of three animals. [b] Not calculated.

Then 50 μL of each serum (or plasma) sample or each dHGF standard prepared in normal rat serum (or plasma) was added to each well in the plates, and the plates were allowed to stand at 4 °C overnight. After washing each well three times with PBS-Tween, 100 μL of anti-dHGF IgG-peroxidase conjugate diluted 100-fold with the second reaction buffer (10% Block Ace, 0.15 M NaCl, 0.1% Tween 20 and 4% rat serum in 0.1 M phosphate buffer, pH 7.0) was added to each well, and the plates were incubated at 37 °C for 2 h. After washing each well six times with PBS-Tween, 100 μL of substrate solution (0.4 mg/mL of *o*-phenylenediamine dihydrochloride and 0.006% H_2O_2 in 0.1 M citrate−phosphate buffer, pH 4.5) was added to each well in the plates, and the plates were incubated at 37 °C for 30 min. The enzymatic reaction was terminated by addition of 50 μL of 6 N H_2SO_4. Absorbance at 492 nm was read using a microplate reader (MTP-32, Korona, Ibaragi, Japan).

To determine dHGF in liver extract, the ELISA system was modified slightly as follows. Here, 50 μL of liver extract in place of serum (or plasma) or 50 μL of dHGF standard prepared in liver extract derived from normal rats was added to each well containing 50 μL of the first reaction buffer. The plates were incubated at room temperature for 2 h. After washing the plates, 100 μL of anti-dHGF IgG-peroxidase conjugate diluted 200-fold with the second reaction buffer was added to each well in the plates, and the plates were incubated at room temperature for 2 h. After washing, bound peroxidase was assayed as described above.

Pharmacokinetic Analysis—The half-life in iv administration of dHGF (2.5 mg/kg) was calculated by fitting a biexponential equation using a nonlinear least-squares program of WinNonlin (Scientific Consulting Inc., Apex, NC). The terminal elimination half-lives in sc and im administrations (2.5 mg/kg), and the area under the concentration versus time curve up to the last measured time point (AUC_{last}) was calculated by using noncompartmental analysis program of WinNonlin. The bioavailability (*F*) was calculated by comparison of the AUC_{last} after sc or im administration with that after iv administration.

Statistical Analysis—The pharmacological data were analyzed by analysis of variance followed by Fisher's LSD test. Significance was established at $p < 0.05$ or $p < 0.01$. The values are expressed as the mean ± SD, unless otherwise noted.

Table 2—Effect of dHGF on Liver Weight and Serum Levels of Proteins and Cholesterol in Normal Rats[a]

route of admin	dose (mg/kg/injection)	liver weight (g/100 g body weight)	total protein (g/100 mL)	albumin (g/100 mL)	HDL-cholesterol (mg/100 mL)
iv	control	3.34 ± 0.04	5.6 ± 0.1	2.7 ± 0.0	38.8 ± 2.2
	0.25	3.71 ± 0.13[b]	6.4 ± 0.1[c]	3.1 ± 0.0[c]	72.0 ± 4.0[c]
	2.5	4.30 ± 0.17[c]	7.0 ± 0.1[c]	3.3 ± 0.1[c]	99.9 ± 6.9[c]
sc	control	3.44 ± 0.10	5.4 ± 0.0	2.6 ± 0.0	37.5 ± 2.0
	0.25	3.28 ± 0.09	5.6 ± 0.1	2.8 ± 0.1	44.6 ± 1.5
	2.5	4.33 ± 0.14[c]	6.9 ± 0.1[c]	3.4 ± 0.1[c]	99.4 ± 7.8[c]
im	control	3.34 ± 0.10	5.6 ± 0.1	2.7 ± 0.1	37.4 ± 1.0
	0.25	3.34 ± 0.06	5.7 ± 0.1	2.8 ± 0.0	39.8 ± 3.9
	2.5	4.08 ± 0.09[c]	6.8 ± 0.1[c]	3.3 ± 0.0[c]	83.1 ± 4.0[c]

[a] Measurements were made after eight administrations (twice daily for 4 days) of dHGF. Each value represents the mean ± SEM of five animals. [b] $p < 0.05$ vs control (solvent) of the same route. [c] $p < 0.01$ vs control (solvent) of the same route.

Results

Pharmacokinetics of dHGF—The concentrations of dHGF in serum decreased rapidly within 15 min and reached an undetectable level (<1.25 ng/mL) 2 to 8 h after a single iv administration of dHGF (0.25 and 2.5 mg/kg) to rats (Figure 1A). The profiles of dHGF level in serum after repetitive iv administration (twice daily for 4 days) of dHGF at the same doses were similar to the dHGF-elimination curves after single iv administration (Figure 1A). dHGF in serum after single and repetitive iv administrations (2.5 mg/kg) decreased biexponentially with a half-life of 3.2 min in the α-phase and with a half-life of 25.7 to 26.5 min in the β-phase. Single and repetitive iv administrations of dHGF at a dose of 2.5 mg/kg were about 10-fold larger in AUC_{last} value than those at a dose of 0.25 mg/kg (Table 1).

The concentration−time profiles of dHGF in serum after single sc and im administrations of dHGF (0.25 and 2.5 mg/kg) were similar (Figure 1, parts B and C). In both single administrations (2.5 mg/kg), the concentrations of dHGF in serum reached a maximum after protracted absorption, which continued at least for 2 to 4 h after the injections and then decreased with a half-life of 2.7 h. The maximum level of dHGF in serum after sc or im administration was lower than after iv administration. On the other hand, the concentrations of dHGF beyond 1 or 2 h after administration were sustained at higher levels for sc and im administrations than for iv administration (Figure 1, parts A−C). The bioavailabilities of dHGF after single sc and im administrations were 70.6−76.3% and 39.3−58.8%, respectively (Table 1).

The concentrations of dHGF in serum after repetitive sc and im administrations (twice daily for 4 days) at a dose of 0.25 mg/kg were undetectable level (<1.25 ng/mL) in the greater part of the sampling time points. The serum levels and the AUC_{last} values of dHGF in sc and im administrations of dHGF (2.5 mg/kg) were dramatically decreased by repeating their administrations (Figure 1, parts B and C, Table 1). The AUC_{last} values of dHGF in repetitive sc and im administrations at a dose of 2.5 mg/kg were decreased to 14.2 and 37.6% of those in single sc and im administrations at the same dose, respectively, and were almost comparable to those in single and repetitive iv administrations at a dose of 0.25 mg/kg.

Effect of Administration Routes of dHGF on Liver Weight and Functions—Rats were treated by repetitive iv, sc or im administration of dHGF (twice daily for 4 days at 0.25 and 2.5 mg/kg). Serum levels of total protein, albumin, HDL-cholesterol, and liver weight after the administration are shown in Table 2. These parameters were significantly increased by repetitive iv administration of dHGF at a dose of 0.25 mg/kg, but not by repetitive sc or im administration at the same dose. However, repetitive sc or im administration significantly increased these parameters at a dose of 2.5 mg/kg.

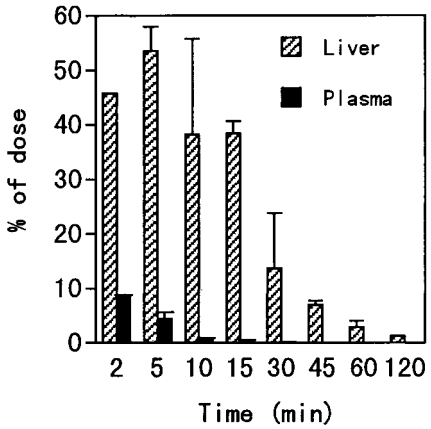

Figure 2—Distribution of dHGF in liver and plasma after iv bolus administration (0.5 mg/kg) to rats. Each value represents the mean ± SD (n = 2–3).

Distribution of dHGF into Liver—After iv bolus injection of dHGF (0.5 mg/kg) to rats, 53.6 ± 4.4% of the injected dHGF was distributed into liver within 5 min, and 1.2 ± 0.1% of the injected dHGF remained in liver up to 120 min (Figure 2). dHGF distributed in plasma 2 min after iv injection was only 8.8% of the injected dHGF (Figure 2). The concentration−time profiles of dHGF in plasma and liver up to 6 h after iv bolus injection (0.5 mg/kg) are shown in Figure 3A. The concentrations of dHGF decreased more slowly and were sustained at higher level in the liver than in plasma. The ratios of the dHGF level in liver to that in plasma after iv injection ranged from 4 to 166.

When dHGF was infused to rats at a rate of 0.5 mg/kg/3 h, the dHGF level in plasma reached a steady-state 15 min after starting the infusion and declined rapidly after terminating the infusion (Figure 3B). The steady-state level of dHGF in plasma ranged from 53.7 ± 10.0 to 76.0 ± 22.1 ng/mL. The dHGF level in the liver reached a steady-state 60 min after starting the infusion and declined more slowly than did that in plasma after terminating the infusion (Figure 3B). The steady-state level of dHGF in the liver was 7- to 9-fold higher than that in plasma and ranged from 486 ± 59 to 551 ± 51 ng/g liver.

Discussion

The concentrations of dHGF in serum after single iv administration of dHGF (2.5 mg/kg) decreased rapidly with an initial half-life ($t_{1/2}\alpha$) of 3.2 min. The initial half-life data reported here are consistent with the result on native dHGF purified from human embryonic fibroblasts[12] and with those on recombinant human HGF.[13−16]

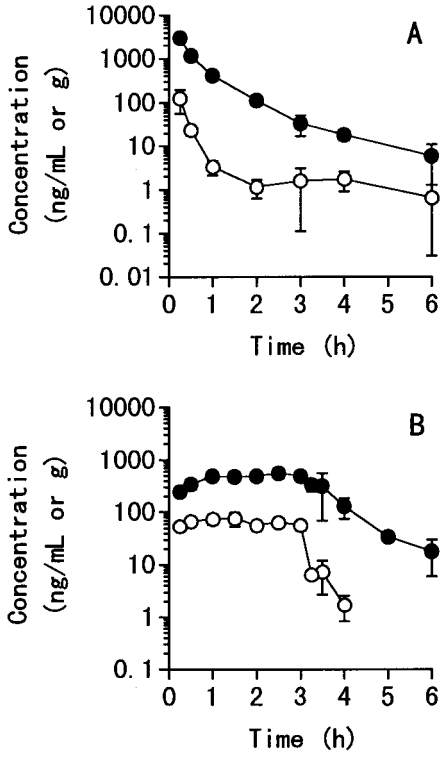

Figure 3—The concentration–time profiles of dHGF in plasma (○) and liver (●) after (A) iv bolus administration (0.5 mg/kg) and (B) iv infusion (0.5 mg/kg/3 h) to rats. Each point and bar represents the mean ± SD (n = 2–3).

The concentrations of dHGF in serum beyond 1 or 2 h after single sc and im administrations were sustained at a higher level than those in serum after single and repetitive iv administrations (Figure 1, parts A−C), indicating that dHGF was slowly released from injection sites into the systemic circulation. The concentration−time profiles of dHGF in serum after single sc and im administrations in rats were similar to those of other recombinant proteins such as human erythropoietin (EPO)[17] and human granulocyte colony-stimulating factor (G-CSF).[18] The values of terminal elimination half-life after single sc or im administration were larger than that after iv administration. The prolongation of half-life suggested that the absorption rate may be smaller than the elimination rate (i.e., "flip-flop") as found in G-CSF.[18]

dHGF has been found to ameliorate disorders of liver functions such as hepatic protein synthesis and cholesterol metabolism in various liver-injured rat models[19] and exert preventive effects against various liver injuries.[20] The prolongation of half-life in sc or im administration may be effective in enhancing the pharmacological effects of dHGF as found in EPO and G-CSF.[17,21]

We therefore compared the pharmacological effects of dHGF among iv, sc, and im administration. Serum levels of total protein, albumin, HDL-cholesterol, and liver weight were significantly increased by repetitive iv administration (twice daily for 4 days) of dHGF (0.25 mg/kg), but not by repetitive sc or im administration. However, repetitive sc or im administration of dHGF at 2.5 mg/kg significantly increased these parameters, indicating that repetitive sc or im administration was less effective in exerting the pharmacological effects of dHGF than repetitive iv administration. Although there was no difference in serum level and AUC_{last} value of dHGF between single and repetitive iv administrations (Figure 1A, Table 1), the serum level and the AUC_{last} values after sc or im administration of dHGF were dramatically decreased by repeating its administration (Figure 1, parts B and C, Table 1). Accordingly, the reduced pharmacological effects of dHGF in repetitive sc or im administration seemed to be due to the drastic decrease in serum level and AUC_{last} value of dHGF caused by repeating its administration. These findings suggested that a release of dHGF from injection sites into the systemic circulation declined. One of the mechanisms by which such a phenomenon occurs in repetitive sc or im administration may be due to altered absorption kinetics (related to dermal vascular changes, or other local and/or systemic processes). Such a phenomenon is also observed when recombinant human interlukin-3 (rhIL-3) has been administered by repetitive sc administration once daily for 4 days.[22] However, the decrease of AUC_{last} values of dHGF after repetitive sc administration was much greater than that of rhIL-3. The distinction between rhIL-3 and dHGF may be due to differences in the number of times of repetitive administration and/or in their physicochemical properties.

We next examined distribution of dHGF into liver after iv administration. A large amount of dHGF (53.6% of the injected dHGF) was distributed rapidly (5 min after iv injection) into liver. The high distribution of dHGF into liver may be due to its binding to extracellular matrix components such as heparan sulfate, because dHGF has a high affinity for heparin.[6] It has also been shown that HGF has a high affinity for heparin[2,23,24] and binds to heparin-like substances on the cell surface [25,26] and the extracellular matrix[27] in liver.

dHGF exerts maximal mitogenic activity for adult rat hepatocytes in a dose range of 10 to 500 ng/mL in vitro,[7] suggesting that a hepatic dHGF concentration of 10 ng/g of liver would be sufficient to exert a physiological function. The iv bolus injection of dHGF (0.5 mg/kg) sustained the effective hepatic level for more than 4 h (18.1 ± 4.9 ng/g) (Figure 3A). In addition, when dHGF (0.5 mg/kg/3 h) was administered by infusion, the effective level of dHGF in liver was sustained beyond the steady-state (for more than 6 h) (Figure 3B), suggesting that infusion would be more effective than iv bolus injection in enhancing the pharmacological effects of dHGF.

In conclusion, we demonstrated that dHGF in serum decreased more rapidly after iv injection than after sc and im injections, but that iv administration exerts the most potent pharmacological effect of dHGF among three administration routes. Further, we found that dHGF is distributed mainly and rapidly into liver and is sustained at a higher level in liver than in plasma.

References and Notes

1. Nakamura, T.; Nawa, K.; Ichihara, A.; Kaise, N.; Nishino, T. Purification and Subunit Structure of Hepatocyte Growth Factor from Rat Platelets. *FEBS Lett.* **1987**, *224*, 311−316.
2. Gohda, E.; Tsubouchi, H.; Nakayama, H.; Hirono, S.; Sakiyama, O.; Takahashi, K.; Miyazaki, H.; Hashimoto, S.; Daikuhara, Y. Purification and Partial Characterization of Hepatocyte Growth Factor from Plasma of a Patient with Fulminant Hepatic Failure. *J. Clin. Invest.* **1988**, *81*, 414−419.
3. Nakamura, T.; Nishizawa, T.; Hagiya, M.; Seki, T.; Shimonishi, M.; Sugimura, A.; Tashiro, K.; Shimizu, S. Molecular Cloning and Expression of Human Hepatocyte Growth Factor. *Nature* **1989**, *342*, 440−443.
4. Miyazawa, K.; Tsubouchi, H.; Naka, D.; Takahashi, K.; Okigaki, M.; Arakaki, N.; Nakayama, H.; Hirono, S.; Sakiyama, O.; Takahashi, K.; Gohda, E.; Daikuhara, Y.; Kitamura, N. Molecular Cloning and Sequence Analysis of cDNA for Human Hepatocyte Growth Factor. *Biochem. Biophys. Res. Commun.* **1989**, *163*, 967−973.
5. Higashio, K.; Shima, N.; Goto, M.; Itagaki, Y.; Nagao, M.; Yasuda, H.; Morinaga, T. Identity of a Tumor Cytotoxic Factor from Human Fibroblasts and Hepatocyte Growth Factor. *Biochem. Biophys. Res. Commun.* **1990**, *170*, 397−404.

6. Shima, N.; Nagao, M.; Ogaki, F.; Tsuda, E.; Murakami, A.; Higashio, K. Tumor Cytotoxic Factor/Hepatocyte Growth Factor from Human Fibroblasts: Cloning of Its cDNA, Purification and Characterization of Recombinant Protein. *Biochem. Biophys. Res. Commun.* **1991**, *180*, 1151−1158.
7. Shima, N.; Tsuda, E.; Goto, M.; Yano, K.; Hayasaka, H.; Ueda, M.; Higashio, K. Hepatocyte Growth Factor and Its Variant with a Deletion of Five Amino Acids are Distinguishable in Their Biological Activity and Tertiary Structure. *Biochem. Biophys. Res. Commun.* **1994**, *200*, 808−815.
8. Matsumoto, K.; Takehara, T.; Inoue, H.; Hagiya, M.; Shimizu, S.; Nakamura, T. Deletion of Kringle Domains or the N-Terminal Hairpin Structure in Hepatocyte Growth Factor Results in Marked Decreases in Related Biological Activities. *Biochem. Biophys. Res. Commun.* **1991**, *181*, 691−699.
9. Tsubouchi, H.; Niitani, Y.; Hirono, S.; Nakayama, H.; Gohda, E.; Arakaki, N.; Sakiyama, O.; Takahashi, K.; Kimoto, M.; Kawakami, S.; Setoguchi, M.; Tachikawa, T.; Shin, S.; Arima, T.; Daikuhara, Y. Levels of the Human Hepatocyte Growth Factor in Serum of Patients with Various Liver Diseases Determined by an Enzyme-Linked Immunosorbent Assay. *Hepatology* **1991**, *13*, 1−5.
10. Shima, N.; Higashio, K.; Ogaki, F.; Okabe, K. ELISA for F-TCF (Human Hepatocyte Growth Factor/hHGF)/Fibroblast-Derived Tumor Cytotoxic Factor Antigen Employing Monoclonal Antibodies and Its Application to Patients with Liver Diseases. *Gastroenterol. Jpn.* **1991**, *26*, 477−482.
11. Lowry, O. H.; Rosebrough, N. J.; Farr, A. L.; Randall, R. J. Protein Measurement with the Folin Phenol Reagent. *J. Biol. Chem.* **1951**, *193*, 265−275.
12. Fujiwara, K.; Nagoshi, S.; Ohno, A.; Hirata, K.; Ohta, Y.; Mochida, S.; Tomiya, T.; Higashio, K.; Kurokawa, K. Stimulation of Liver Growth by Exogenous Human Hepatocyte Growth Factor in Normal and Partially Hepatectomized Rats. *Hepatology* **1993**, *18*, 1443−1449.
13. Ishii, T.; Sato, M.; Sudo, K.; Suzuki, M.; Nakai, H.; Hishida, T.; Niwa, T.; Umezu, K.; Yuasa, S. Hepatocyte Growth Factor Stimulates Liver Regeneration and Elevates Blood Protein Level in Normal and Partially Hepatectomized Rats. *J. Biochem.* **1995**, *117*, 1105−1112.
14. Liu, K. X.; Kato, Y.; Narukawa, M.; Kim, D. C.; Hanano, M.; Higuchi, O.; Nakamura, T.; Sugiyama, Y. Importance of the Liver in Plasma Clearance of Hepatocyte Growth Factors in Rats. *Am. J. Physiol.* **1992**, *263 (Gastrointest. Liver Physiol. 26)*, G642−G649.
15. Appasamy, R.; Tanabe, M.; Murase, N.; Zarnegar, R.; Venkataramanan, R.; Van Thiel, D. H.; Michalopoulos, G. K. Hepatocyte Growth Factor, Blood Clearance, Organ Uptake, and Biliary Excretion in Normal and Partially Hepatectomized Rats. *Lab. Invest.* **1993**, *68*, 270−276.
16. Zioncheck, T. F.; Richardson, L.; DeGuzman, G. G.; Modi, N. B.; Hansen, S. E.; Godowski, P. J. The Pharmacokinetics, Tissue Localization, and Metabolic Processing of Recombinant Human Hepatocyte Growth Factor after Intravenous Administration in Rats. *Endocrinology* **1994**, *134*, 1879−1887.
17. McMahon, F. G.; Vargas, R.; Ryan, M.; Jain, A. K.; Abels, R. I.; Perry, B.; Smith, I. L. Pharmacokinetics and Effects of Recombinant Human Erythropoietin after Intravenous and Subcutaneous Injections in Healthy Volunteers. *Blood* **1990**, *76*, 1718−1722.
18. Tanaka, H.; Kaneko, T. Pharmacokinetics of Recombinant Human Granulocyte Colony-Stimulating Factor in the Rat: Single and Multiple Dosing Studies. *Drug Metab. Dispos.* **1991**, *19*, 200−204.
19. Masunaga, H.; Fujise, N.; Shiota, A.; Yamashita, Y.; Yasuda, H.; Higashio, K. Amelioration of Disordered Hepatic Protein Synthesis by the Deleted Form of Hepatocyte Growth Factor in Models of Liver Failure in Rats. *J. Pharm. Pharmacol.* **1996**, *48*, 876−879.
20. Masunaga, H.; Fujise, N.; Shiota, A.; Ogawa, H.; Sato, Y.; Imai, E.; Yasuda, H.; Higashio, K. Preventive Effects of the Deleted Form of Hepatocyte Growth Factor against Various Liver Injuries. *Eur. J. Pharmacol.* **1998**, *342*, 267−279.
21. Tanaka, H.; Okada, Y.; Kawagishi, M.; Tokiwa, T. Pharmacokinetics and Pharmacodynamics of Recombinant Human Granulocyte-Colony Stimulating Factor after Intravenous and Subcutaneous Administration in the Rat. *J. Pharmacol. Exp. Ther.* **1989**, *251*, 1199−1203.
22. Huhn, R. D.; Yurkow, E. J.; Kuhn, J. G.; Clarke, L.; Gunn, H.; Resta, D.; Shah, R.; Myers, L. A.; Seibold, J. R. Pharmacodynamics of Daily Subcutaneous Recombinant Human Interlukin-3 in Normal Volunteers. *Clin. Pharmacol. Ther.* **1995**, *57*, 32−41.
23. Nakamura, T.; Teramoto, H.; Ichihara, A. Purification and Characterization of a Growth Factor from Rat Platelets for Mature Parenchymal Hepatocytes in Primary Cultures. *Proc. Natl. Acad. Sci. U.S.A.* **1986**, *83*, 6489−6493.
24. Zarnegar, R.; Michalopoulos, G. Purification and Biological Characterization of Human Hepatopoietin A, a Polypeptide Growth Factor for Hepatocytes. *Cancer Res.* **1989**, *49*, 3314−3320.
25. Zarnegar, R.; DeFrances, M. C.; Oliver, L.; Michalopoulos, G. Identification and Partial Characterization of Receptor Binding Sites for HGF on Rat Hepatocytes. *Biochem. Biophys. Res. Commun.* **1990**, *173*, 1179−1185.
26. Naka, D.; Ishii, T.; Shimomura, T.; Hishida, T.; Hara, H. Heparin Modulates the Receptor-Binding and Mitogenic Activity of Hepatocyte Growth Factor on Hepatocytes. *Exp. Cell Res.* **1993**, *209*, 317−324.
27. Masumoto, A.; Yamamoto, N. Sequestration of a Hepatocyte Growth Factor in Extracellular Matrix in Normal Adult Rat Liver. *Biochem. Biophys. Res. Commun.* **1991**, *174*, 90−95.

JS9800432

Microparticles of Novel Branched Copolymers of Lactic Acid and Amino Acids: Preparation and Characterization

GIOVANNI CAPONETTI,[†,‡] JEFFREY S. HRKACH,[†] BURKHARD KRIWET,[†] MELISSA POH,[†] NOAH LOTAN,[§] PAOLO COLOMBO,[‡] AND ROBERT LANGER*[,†]

Contribution from *Massachusetts Institute of Technology, Department of Chemical Engineering, E25-342, Cambridge, Massachusetts 02139, Dipartimento Farmaceutico, Università degli Studi di Parma, Via delle Scienze, 43100 Parma, Italy, and Technion-Israel Institute of Technology, Department of Biomedical Engineering, Haifa, Israel 32000.*

Received December 2, 1997. Final revised manuscript received October 12, 1998. Accepted for publication October 14, 1998.

Abstract □ The preparation and characterization of microparticles produced from a new class of functionalized, biodegradable, comblike graft copolymers is presented. The copolymers are polyester–polyamino acid hybrids, composed of a poly(L-lactic acid–*co*-L-lysine) (PLAL) backbone, and poly(L-lysine), poly(D,L-alanine) or poly(L-aspartic acid) side chains extending from the lysine residues of PLAL. The microparticles have been characterized with regard to their surface properties, morphology, and size. Thus, electron spectroscopy for chemical analysis data and results of Zeta potential measurements suggest that the polyamino acid side chains tend to concentrate at the surface of the particles. Also, analyses by environmental scanning electron microscopy and confocal scanning laser microscopy indicate that particles carrying poly(lysine) chains have an unusual porous structure, most probably due to the combined effects of the amphiphilic, polyelectrolyte, and chemical nature of the composing copolymer, as well as of the particular preparation technique employed. The capabilities of the microparticles to serve as carriers in controlled drug release and delivery devices were demonstrated by encapsulation and release of rhodamine B, a low molecular weight drug model.

1. Introduction

The use of synthetic degradable polymers in drug delivery systems has dramatically expanded in the past decade. Several "old" drugs have gained renewed interest by improving their pharmacokinetic profile upon incorporation in polymer-based controlled-release systems.[1] Also, such systems, in the form of microcapsules, microparticles, and nanoparticles were found to be useful carriers for many low molecular weight compounds, peptides, and proteins, whose efficacy as drugs is highly dependent on the mode of their delivery to the body.[2−7]

One of the most advanced strategies in biopharmaceutics for the delivery of drugs and vaccines relies on the use of polymeric nano- and microparticles as carriers, mainly those composed of poly(lactic acid) (PLA) or poly(lactic acid−*co*-glycolic acid) (PLGA).[8] These degradable polyesters are nontoxic, well tolerated by living tissues, and degrade hydrolytically at controllable rates to yield naturally occurring metabolites. The procedure for incorporation of bioactive agents in these polymers is generally rather simple and reproducible. However, cases have been reported in which the conformational stability of incorporated proteins was impaired.[9,10]

The successful utilization of polymeric particles as drug carriers is highly dependent on their distribution in the body. Because of the surface characteristics of the particles, this distribution may not always be favorable. Thus, it has been extensively demonstrated that nanoparticles with a hydrophobic surface (e.g., PLA and PLGA) are rapidly taken up by the cells of the reticuloendothelial system (RES).[11−13] On the other hand, particles with a more hydrophilic surface can avoid this uptake to a greater extent, thus achieving a prolonged lifetime in the circulation and a better chance to efficiently deliver the therapeutic agent.[11−13] Toward this goal, such hydrophilic characteristics have been provided by modifying the surface of the otherwise hydrophobic particles with a hydrophilic polymer, either by chemical attachment or physical adsorption.[11−21]

These examples of modification of the preexisting PLGA copolymer represent an interesting approach for several applications. To advance this approach even further, it could be highly beneficial to prepare particles from an amphiphilic polymer that also possesses functional sites where chemical modifications can be carried out, and to utilize them for tailoring specific surface characteristics such as charge, hydrophilicity or targeting capabilities. For this purpose, we have prepared nanoparticles (data not presented) and microparticles from a new family of functional, degradable graft copolymers (PLAL-Lys, PLAL-Asp, and PLAL-Ala)[22,23] and from the linear copolymer PLAL.[24] The incorporation of poly(amino acid) side chains and PLA backbone in a hybrid copolymeric structure provides a unique opportunity to combine the attractive properties of these two classes of important biomedical polymers. PLAL-Lys and PLAL-Asp possess a large number of amino and carboxylic acid functional groups, respectively, and these may be utilized for further chemical modification (e.g., direct attachment of targeting moieties or drugs). At neutral pH, the poly(amino acid) side chains are positively charged (PLAL-Lys), negatively charged (PLAL-Asp), or neutral (PLAL-Ala). Here, we present the preparation of these microparticles and their characterization with regard to their surface properties (functionalization and charge), morphology, and size. In addition, incorporation in these particles of rhodamine B as a drug model and its release are also presented, and the data are considered for assessing the potential use of these particles as drug carriers. The use of PLAL-Lys microparticles as dry powder aerosols for pulmonary drug delivery has been investigated.[25,26]

2. Experimental Section

Materials—Poly(vinyl alcohol) (PVA; 88% hydrolyzed, MW 25 000) was obtained from Polysciences (Warrington, PA), rhodamine B base from Sigma (St. Louis, MO), and rhodamine B

* To whom correspondence should be addressed. Telephone: 617-253 3123. Fax: 617-258 8827. E-mail: rlanger@mit.edu.
[†] Massachusetts Institute of Technology.
[‡] Dipartimento Farmaceutico.
[§] Technion-Israel Institute of Technology.

10.1021/js970457f CCC: $18.00 *Published on Web 12/05/1998*

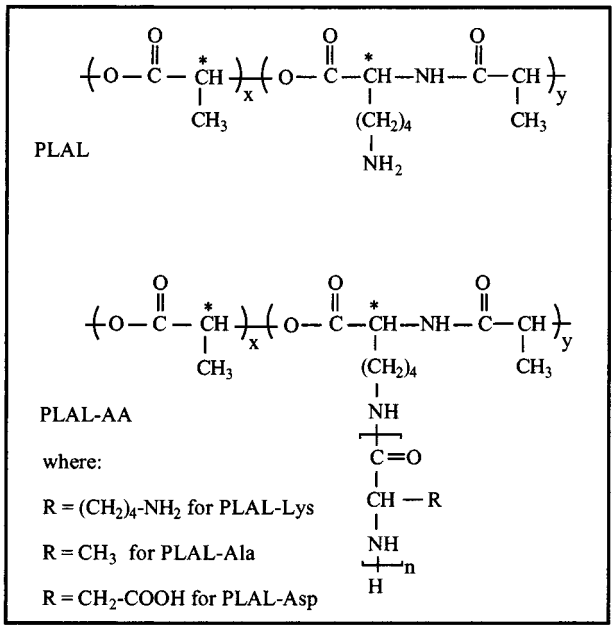

Scheme 1

isothiocyanate from Research Organics (Cleveland, OH). Phosphate buffered saline solution (PBS, 1 mM in KH_2PO_4, 10 mM in Na_2HPO_4, 137 mM in NaCl, 3 mM in KCl) was prepared with a pH of 7.4 unless otherwise noted.

Methods—*Synthesis of Copolymers*—PLAL was synthesized as described previously by Barrera et al.,[24] and PLAL-Lys, PLAL-Asp, and PLAL-Ala were synthesized as described by Hrkach et al.[22,23] The chemical structures of these copolymers are presented in Scheme 1. PLAL is a linear copolymer with approximately 2 mol % lysine randomly situated in a PLA backbone. The ϵ-amino groups of these lysine units are utilized as initiating sites for building poly(amino acid) chains from the PLAL backbone, thus leading to a comblike graft copolymer structure for PLAL-Lys, PLAL-Asp, and PLAL-Ala with total amino acid content of 15−20 mol %.

Preparation of Microparticles—Microparticles were prepared by the single emulsion/solvent evaporation method. One hundred milligrams of polymer were dissolved in 1 mL of dimethyl sulfoxide (DMSO) and subsequently mixed with 3 mL of methylene chloride. This solution was emulsified in 100 mL of PVA solution (5% w/v) for 60 s, using a homogenizer at 7500 rpm. The resulting emulsion was stirred continuously for 3 h in an open beaker to remove the organic solvents. The precipitated microparticles were centrifuged at 1000x *g* for 10 min, washed three times with distilled water, lyophilized, and stored under desiccation at room temperature.

For the preparation of particles incorporating rhodamine B, the same procedure was followed but 10 mg of rhodamine B were dissolved in CH_2Cl_2 before mixing with the polymer solution in DMSO.

Surface Modification—To investigate the structure of the PLAL-Lys and PLAL microparticles and their potential for attachment of targeting moieties or drugs, rhodamine B moieties were chemically attached to the lysine ϵ-amino groups on the surface of the microparticles. Two milligrams of microparticles were suspended in 1.5 mL of PBS and 0.5 mg of rhodamine B isothiocyanate (RITC) was added to the suspension. After stirring for 3 h, the suspension was centrifuged and washed three times with methanol to remove unreacted RITC. Microparticles were then suspended in water and analyzed by confocal microscopy (Biorad, MRC 600).

Characterization of Microparticles—*A. Size Distribution*—After lyophilization, a small amount of particles was resuspended in aqueous solution (Isoton solution) and the size distribution was measured using a Coulter Counter (Coulter Multisizer II, Coulter Electronics Ltd.). The average diameter was calculated as a mean value of the volume distribution.

B. Surface Charge—To evaluate the presence of electrostatic charges on the surface of the particles, the Zeta potential was determined by laser doppler anemometry (Zetasizer 3, Malvern Instruments, Malvern, UK) after suspending the particles in PBS at pH 7. The measurements were taken at 20 °C for 20 s, with an applied voltage of 150 V.

Table 1—Mean Diameters of Plain and Rhodamine-Loaded Particles

	plain particles	rhodamine-loaded particles	
constitutive polymer	average diameter (μm)	average diameter (μm)	dye loading (%w/w)
PLAL	4.9	6.1	2.2
PLAL-Lys	7.4	6.7	2.2
PLAL-Ala	6.2	8.5	18.7
PLAL-Asp	6.0	5.5	14.2

C. Surface Chemical Composition—For the chemical characterization of the particle surface, electron spectroscopy for chemical analysis (ESCA, also known as X-ray photoelectron spectroscopy, XPS, Model 5100, Perkin Elmer, with a magnesium anode as X-ray source at 15 kV and 300 W) was used. Aqueous suspensions of particles were mounted on metal stubs, and then the water was evaporated under vacuum over phosphorus pentoxide for at least 12 h. The angle between the sample surface and the analyzer was set to 45°. An elemental survey spectrum (0−1000 eV) was acquired for each sample.

D. Morphology—The morphology and structure of the microparticles were characterized using environmental scanning electron microscopy (ESEM, ElectroScan), and confocal scanning laser microscopy (MRC 600, BioRad Company, with rhodamine filter). For ESEM, samples were mounted with double-sided adhesive tape on metal stubs coated with gold−palladium to a thickness of 200−400 Å, and analyzed at 3−10 kV. For confocal microscopy, samples were first labeled with rhodamine isothiocyanate and suspended in water.

E. Incorporation and Release of Rhodamine B—To assess the incorporation efficiency and release characteristics of low molecular weight agents, rhodamine B base was used as a drug model. The incorporation efficiency was evaluated by measuring the fluorescence intensity (excitation: 554 nm; emission: 574 nm) of the solution obtained after complete degradation of 10 mg of particles in 0.1 M NaOH at 37 °C and by relating the results obtained to the fluorescence of a standard solution of rhodamine B in the same solvent. For these measurements a spectrofluorimeter (Photon Technology International) was used.

For the release studies, a known amount of dried microparticles were suspended in 5 mL of PBS in a plastic tube and incubated at 37 °C under continuous shaking. One milliliter of the supernatant from each tube was collected periodically after centrifugation and replaced each time with fresh PBS to mimic infinite sink conditions. The fluorescence intensity of the samples was measured as indicated for determination of loading and compared with a standard solution of rhodamine B base in the same solvent.

3. Results and Discussion

3.1. Particle Size Distribution—The size distribution of particles made of PLAL-Lys, PLAL-Asp, PLAL-Ala, or PLAL are presented in Figure 1. The PLAL microparticles show the narrowest size distribution and lowest mean diameter, whereas microparticles prepared from the graft copolymers exhibit a broader size distribution and a slightly larger average diameter. Nevertheless, it can be concluded that the commonly used single emulsion/solvent evaporation technique can be utilized effectively for the preparation of microparticles with relatively low average size ($<10\ \mu$m) from the new class of PLAL-amino acid graft copolymers. Table 1 summarizes the mean diameters of these particles, as well as of those in which rhodamine B base was incorporated. We note that, although different loading levels were achieved with various particles, incorporation of dye molecules had only a minimal effect on the average size of the particles.

3.2. Surface Chemical Composition—The presence of amino acid residues at the surface of the particles was confirmed by ESCA (Figure 2). The small nitrogen peak

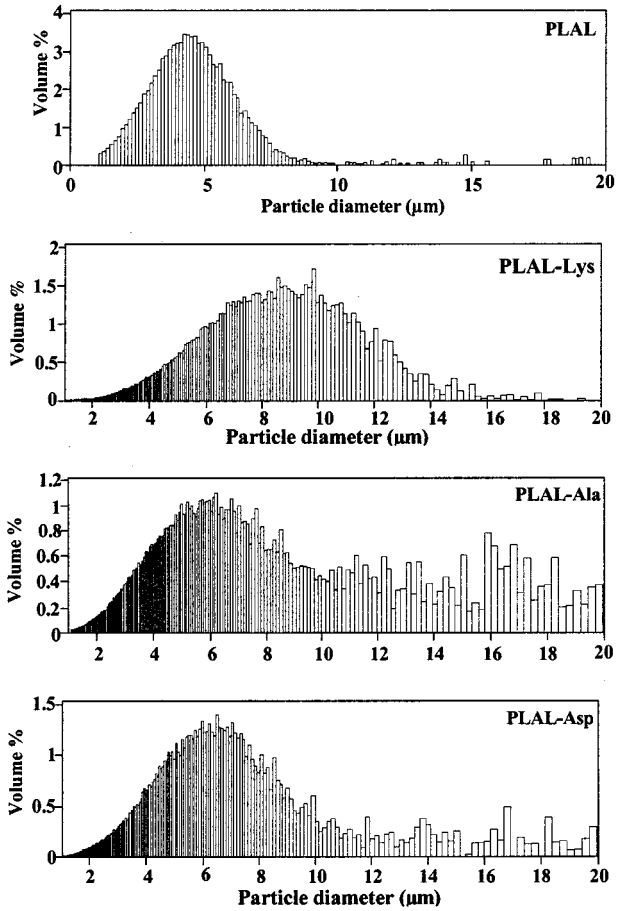

Figure 1—Size disributions of microparticles made of PLAL, PLAL-Lys, PLAL-Ala, and PLAL-Asp.

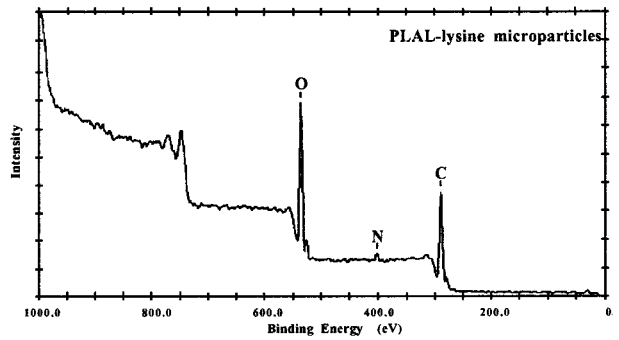

Figure 2—ESCA survey spectrum of PLAL-Lys microparticles.

at approximately 400 eV proves the presence of lysine residues at the outer layer of the particles, because these residues are the only nitrogen-containing ones in the copolymer. This result is in agreement with the hypothesis that the preparation procedure employed promotes orientation of the amino acid chains of the copolymer toward the outer layer of the particles. The relatively small size of the nitrogen peak in the ESCA spectrum is most likely due to the presence of PVA molecules in the outermost layer of the particles. As already stated, PVA was used as a surfactant to stabilize the microparticle structure during preparation. Thus, quantitative analysis of the nitrogen content, based on the ESCA spectrum, was not attempted.

ESCA spectra, similar to that of PLAL-Lys, were also obtained for PLAL-Asp and PLAL-Ala microparticles. However, for PLAL particles, the nitrogen peak was negligible due to the very low nitrogen content of their constitutive polymer (spectra not shown).

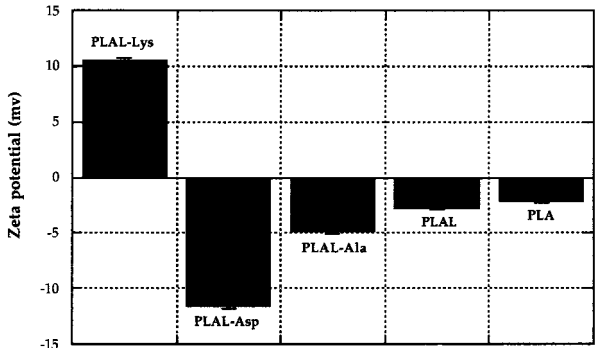

Figure 3—Zeta potential of microparticles made of PLAL, PLAL-Lys, PLAL-Ala, PLAL-Asp, and PLA.

3.3. Zeta Potential—Figure 3 shows the Zeta potentials of the microparticles in PBS at pH 7. The graph emphasizes the difference in surface charge among the microparticles studied. Thus, PLAL-Lys microparticles carry a positive charge, as expected from the presence of protonated ϵ-amino groups of the lysine residues at the particle surface. PLAL-Asp, PLAL-Ala and PLAL, on the other hand show negative charges. The large negative value for PLAL-Asp is attributed to the β- carboxylate groups of the aspartic acid residues. The apparently unexpected small negative charges exhibited by PLAL and PLAL-Ala particles are probably due to the terminal carboxylate groups of the backbone of their constitutive polymers. This view is supported by the fact that a similar, small negative charge is also exhibited by PLA particles. These results provide additional evidence for the presence of amino acid side chains on the surface of the particles, resulting from the extension of the hydrophilic portion of the comblike graft copolymer into the outer aqueous phase during preparation. More important, they demonstrate the versatility of this new class of materials. The ability to change the charge characteristics (type and strength) of the microparticles can be utilized to tailor their use for various drug delivery systems.

3.4. Particle Morphology and Surface Modification—ESEM and confocal microscopy were utilized to study the structure and morphology of the particles. As seen in Figure 4, ESEM reveals that PLAL particles show a smooth surface and a spherical structure, similar to what is observed with PLA or PLGA particles (data not shown). Apparently, the low amount of lysine (about 2 mol %) present in the PLAL chain does not significantly affect the particle morphology. On the other hand, PLAL-Ala and PLAL-Asp particles have a slightly corrugated surface. Most likely, the extension of the hydrophilic amino acids chains into the aqueous phase during particle preparation promotes the formation of the rougher surface exhibited by these particles, compared with that of PLAL, PLA, or PLGA particles prepared by the same technique. In strong contrast to the microparticles just mentioned, PLAL-Lys particles have an unusual shape and also a porous, spongelike structure. It is likely that the large amount of lysine in the copolymer structure, in the form of grafted poly(lysine) side chains, imparts specific characteristics to the polymer and to the resulting particles. The fact that only microparticles made of PLAL-Lys exhibit this structure is highly relevant. From these results it is possible to conclude that the porous structure does not stem solely from the presence of an amphiphilic or amino acid-based polymer in general, but specifically from the presence of lysine chains (and perhaps other poly-cationic chains).

The results of confocal microscopy analysis of PLAL-Lys and PLAL particles are shown in Figure 5. Covalent attachment of the fluorescent marker to the particles was

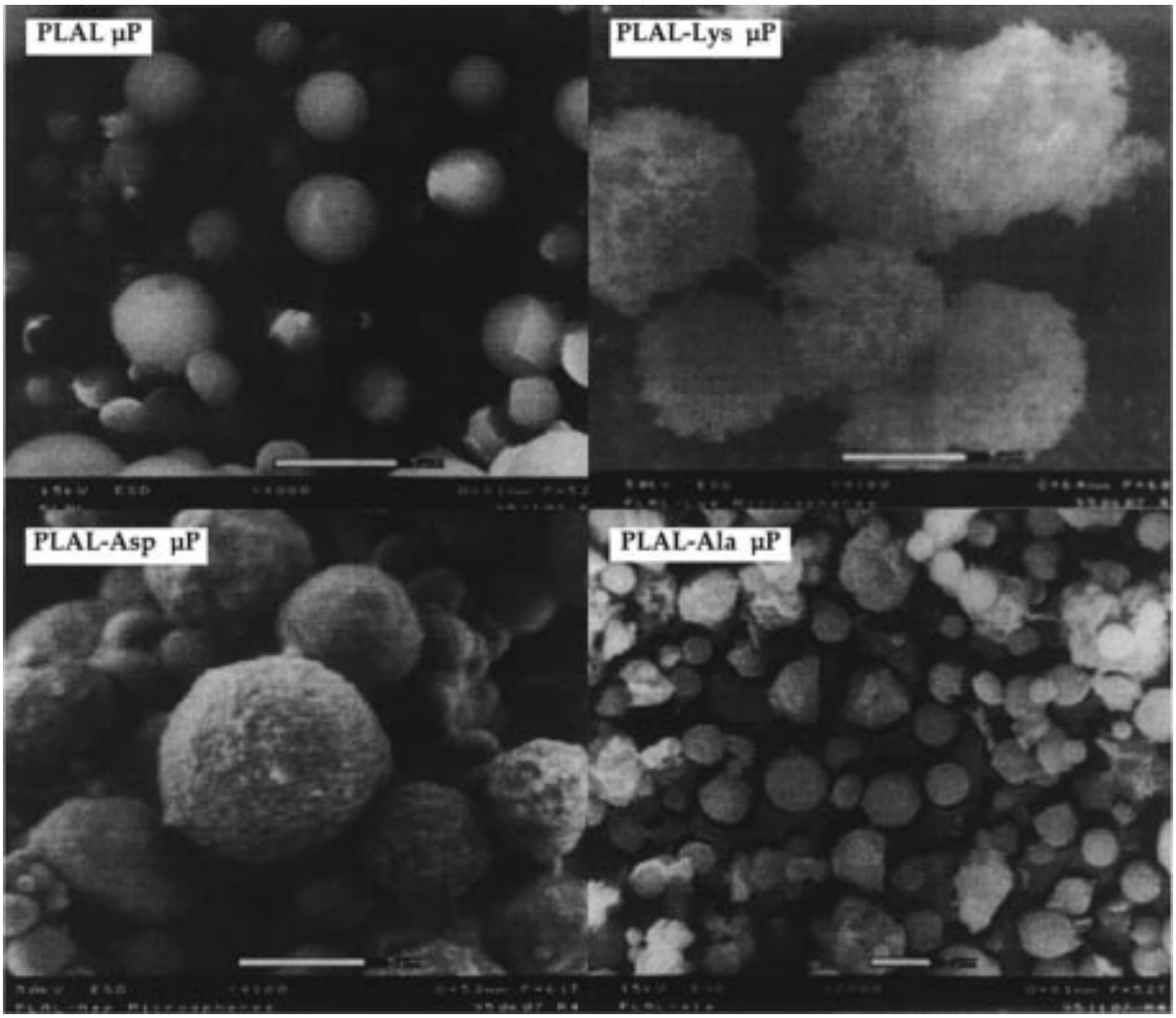

Figure 4—ESEM pictures of microparticles made of PLAL (magnification, ×4000), PLAL-Lys (x4100), PLAL-Ala (x2000), and PLAL-Asp (x4100). All scale bars = 5 μm.

accomplished through the reaction of rhodamine isothiocyanate with the lysine ϵ-amino groups on the surface of the particles. Under the same experimental conditions, PLA particles yield no fluorescent response (a completely dark field) confirming covalent attachment of rhodamine moieties at the surface amine groups of PLAL-Lys and PLAL and ruling out nonspecific adsorption of the dye to the particle surface. The successful coupling of rhodamine proves the availability of the surface amino groups for further chemical modification. This characteristic imparts great versatility to this new class of functional particles, and may be utilized to improve cellular targeting and uptake of peptides/proteins, anticancer drugs, and other therapeutic agents that require or could benefit from site-specific delivery.

The capacity of these particles for binding functional molecules onto their surface is very high indeed. For example, for PLAL-Asp particles with an aspartic acid content of 20 mol % and assuming that all the β-COOH groups of Asp residues are present at the surface, a capacity of 2.7 mmol-COOH/g is calculated. And if each carboxyl group would bind one molecule of dye of opposite charge and of molecular weight 440 (similar to that of rhodamine B base) a loading capacity of about 55% (w/w) dye could be accommodated. A similar calculation, when performed for PLAL-Lys particles contaning 20 mol % Lys residues, yields 2.4 mmol-NH_2/g and 50% (w/w) labeling capacity.

The structural characteristics of the PLAL-Lys particles have highly valuable implications in the area of pulmonary drug delivery as well. The flight characteristics of dry powders are crucial for the efficient delivery of therapeutic agents to the lungs, for either local or systemic therapy. In vitro aerosolization experiments carried out in our laboratory show that 57 ± 1.9% of the PLAL-Lys particles are in the respirable fraction, whereas only 9.3 ± 0.6% of the nonporous PLA or PLGA particles of the same size are respirable. Furthermore, in vivo studies in rats show that the pulmonary delivery of testosterone with PLAL-Lys particles results in prolonged release compared with nonporous particles.[25]

3.5. Incorporation Efficiency and Release Characteristics—In Table 1, data relating the average size of microparticles and their efficiency in incorporating rhodamine B are presented. We note that all the microparticles have essentially similar size distribution and mean diameter. However, their efficiency for loading this low molecular weight drug model seems to be significantly dependent on the chemical nature of the constitutive polymer and its interaction with the drug model molecule. Thus, the basic dye rhodamine B is efficiently incorporated (14.2%) in microparticles made of the acidic, negatively charged PLAL-Asp, but only very little dye (2.2%) is accommodated by particles made of the basic, positively charged PLAL-Lys. The highest incorporation efficiency (18.7%) was

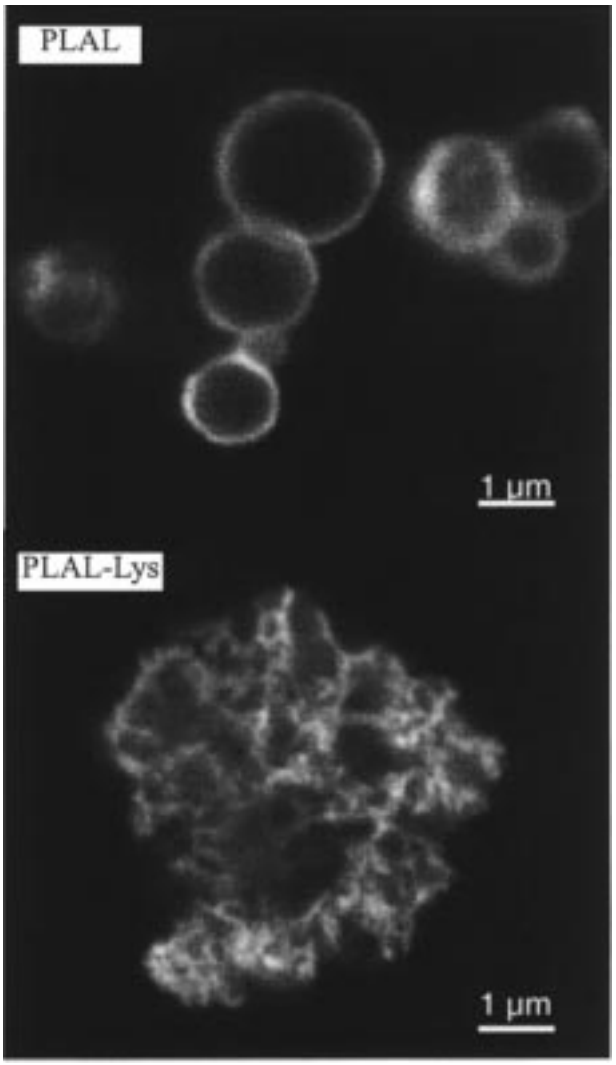

Figure 5—Confocal microscopy pictures of PLAL-Lys and PLAL microparticles, after labeling with rhodamine B isothiocyanate.

reached with the essentially neutral PLAL-Ala, whereas the similarly neutral PLAL particles exhibit very low efficiency (2.2%), similar to PLAL-Lys particles. These results indicate that, in addition to electrostatic interactions, dye incorporation efficiency is also to be related to other factors, such as hydrophobicity/hydrophilicity balance and dye partition characteristics.

The release profiles of rhodamine B from PLAL− and PLAL−poly (amino acid) microparticles over a period of 8 weeks are shown in Figure 6. All of the PLAL−poly(amino acid) microparticles exhibited a basically similar release behavior; namely, an initial burst in the first 2−3 days when some 35% of the incorporated dye is liberated, followed by a continuous much slower process, which was monitored only until day 56. Up to this point, only 45−50% of the dye is released and, obviously, the process continues further on. The release profile of rhodamine B from PLAL microparticles follows, in principle, the same time course as already described for the PLAL−poly(amino acid) microparticles. Yet it differs in the quantitative aspects of it: thus, only 6% dye is released during the initial burst of 1 day and only 25% of the dye is released by day 56, during the subsequent low rate process.

From these results it can be concluded that the very presence of poly(amino acid) side chains into a branched copolymer with PLA backbone may affect the drug loading capacity of these particles (see Table 1) yet may have a

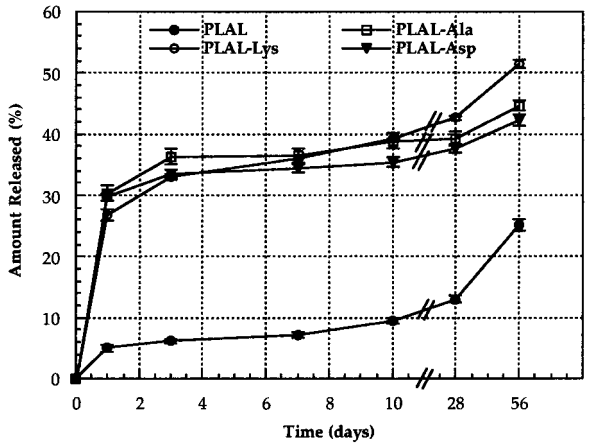

Figure 6—Release profile of rhodamine B from PLAL, PLAL-Lys, PLAL-Ala, and PLAL-Asp microparticles.

significant influence on the release of drugs from microparticles composed of these polymers. However, the specific properties of the various poly(amino acids) considered did not significantly affect the release process because the pertinent profiles for PLAL-Lys, PLAL-Ala, and PLAL-Asp microparticles are all similar. Obviously, depending on specific drug−polymer interactions, the release characteristics may be different when drug molecules of various structure, hydrophobicity, and charge are used.

Further studies focusing on the release of various drugs from these microparticles will be carried out to gain a better understanding of the role of the amino acid chains on the structure and properties of the microparticles and on the mechanism of drug release from them.

4. Conclusions

Microparticles made of PLAL, PLAL-Lys, PLAL-Ala, or PLAL-Asp were prepared and investigated. Due to their specific structure, this new class of copolymers imparts interesting surface (charge, external functional groups) and morphological (porosity) characteristics to the microparticles. The chemical attachment of molecular markers on the surface of PLAL and PLAL-Lys microparticles has also been accomplished. This attachment capability demonstrates the potential use of these particles for attaching various functional moieties, including targeting elements required for site specific controlled drug delivery.

References and Notes

1. *Biodegradable Polymers as Drug Delivery Systems*; Chasin, M., Langer, R., Eds.; Marcel Dekker: New York, Basel, Hong Kong, 1990; Vol. 45.
2. Heller, J. Polymers for controlled parenteral delivery of peptides and proteins. *Adv. Drug Del. Rev.* **1993**, *10*, 163−204.
3. Couvreur, P.; Puisieux, F. Nano- and microparticles for the delivery of polypeptides and proteins. *Adv. Drug Del. Rev.* **1993**, *10*, 141−162.
4. Couvreur, P.; Dubernet, C.; Puisieux, F. Controlled drug delivery with nanoparticles: current possibilities and future trends. *Eur. J. Pharm. Biopharm.* **1995**, *41*(*1*), 2−13.
5. Brannon Peppas, L. Recent advances on the use of biodegradable microparticles and nanoparticles in controlled drug delivery. *Int. J. Pharm.* **1995**, *116*, 1−9.
6. Davis, S. S.; Illum, L.; Moghimi, S. M.; Davies, M. C.; Porter, C. J.; Muir, I. S.; Brindley, A.; Christy, N. M.; Norman, M. E.; Williams, P.; Dunn, S. E. Microspheres for targeting drugs to specific body sites. *J. Controlled Release* **1993**, *24*, 157−163.

7. Cohen, S.; Yoshioka, T.; Lucarelli, M.; Hwang, L. H.; Langer, R. Controlled delivery systems for proteins based on poly-(lactic acid/glycolic acid) microspheres. *Pharm. Res.* **1991**, *8* (*6*), 713−720.
8. Alonso, M. J.; Cohen, S.; Park, T. J.; Gupta, R. K.; Siber, G. R.; Langer, R. Determinants of release rate of tetanus vaccine from polyester microspheres. *Pharm. Res.* **1993**, *10* (*7*), 945−953.
9. Schwendeman, S. P.; Cardamone M.; Klibanov A.; Langer R.; Brandon M. R. In *Microparticulate Systems for the Delivery of Proteins and Vaccines*; Cohen, S., Bernstein, H., Eds.; Marcel Dekker: New York, 1996; pp 1−49.
10. Iwata, M.; McGinity, J. W. Dissolution, stability and morphological properties of conventional and multiphase poly(D,L-lactic acid-*co*-glycolic acid) microspheres containing water soluble compounds. *Pharm. Res.* **1993**, *10*, 1219−1227.
11. Gref, R.; Minamitake, Y.; Peracchia, M. T.; Trubetskoy, V.; Torchilin, V.; Langer, R. Biodegradable long-circulating polymeric nanospheres. *Science* **1994**, *263*, 1600−1603.
12. Illum, L.; Davis, S. S. The organ uptake of intravenously administered colloidal particles can be altered using a nonionic surfactant (Poloxamer 338). *FEBS Lett.* **1984**, *167*, 79−82.
13. Illum, L.; Davis, S. S.; Muller, R. H.; Mak, E.; West, P. The organ distribution and circulation time of intravenously injected colloidal carriers sterically stabilised with block-copolymer poloxamine 908. *Life Sci.* **1987**, *40*, 367−374.
14. Stolnik, S.; Dunn, S. E.; Garnett, M. C.; Davies, M. C.; Coombres, A. G. A.; Taylor, D. C.; Irving, M. P.; Purkiss, S. C.; Tadros, T. F.; Davis, S. S.; Illum, L. Surface modification of poly(lactide-*co*-glycolide) nanospheres by biodegradable poly(lactide)-poly(ethylene glycol) copolymers. *Pharm. Res.* **1994**, *2*(*11*), 1800−1808.
15. Gref, R.; Domb, A.; Quellec, P.; Blunk, T.; Muller, R. H.; Verbavatz, J. M.; Langer, R. The controlled intravenous delivery of drugs using PEG-coated sterically stabilized nanospheres. *Adv. Drug Del. Rev.* **1995**, *16*, 215−233.
16. Stolnik, S.; Illum, L.; Davis, S. S. Long circulating microparticulate drug carriers. *Adv. Drug Del. Rev.* **1995**, *16*, 195−214.
17. Kwon, G. S.; Kataoka, K. Block copolymer micelles as long-circulating carriers for delivery of therapeutic and diagnostic agents. *Adv. Drug Del. Rev.* **1995**, *16*, 295−309.
18. Moghimi, S. M. Mechanisms regulating body distribution of nanospheres conditioned with pluronic and tetronic block-copolymers. *Adv. Drug Del. Rev.* **1995**, *16*, 183−193.
19. Torchilin, V. P.; Trubetskoy, V. S. Which polymers can make nanoparticulate drug carriers long-circulating? *Adv. Drug Del. Rev.* **1995**, *16*, 141−155.
20. Rooser, M.; Kissel, T. Surface-modified biodegradable albumin nano- and microspheres. I. Preparation and characterization. *Eur. J. Pharm. Biopharm.* **1993**, *39*(*1*), 8−12.
21. Hrkach, J. S.; Peracchia, M. T.; Domb, A.; Lotan, N.; Langer, R. Nanotechnology for biomaterials engineering: structural characterization of amphiphilic polymeric nanoparticles by ^{1}H NMR spectroscopy. *Biomaterials* **1997**, *18*, 27−30.
22. Hrkach, J. S.; Ou, J.; Lotan, N.; Langer, R. Synthesis of poly(L-lactic acid-*co*-L-lysine) graft copolymers. *Macromolecules* **1995**, *28*, 4736−4739.
23. Hrkach, J. S.; Ou, J.; Lotan, N.; Langer, R. Poly(L-lactic acid-*co*-amino acid) graft copolymers: A class of functional biodegradable biomaterials. In *Hydrogels and Biodegradable Polymers for Bioapplications*; Ottenbrite, R. M.; Huang, S. J., Park, K., Eds.; ACS Symposium Series No. 627; American Chemical Society: Washington, DC, 1996; Ch. 8, pp 93−102.
24. Barrera, D. A.; Zylstra, E.; Lansbury, P. T.; Langer, R. Synthesis and RGD peptide modification of a new biodegradable copolymer: Poly(lactic acid-*co*-lysine). *J. Am. Chem. Soc.* **1993**, *115*, 11010−11011.
25. Edwards, D. A.; Hanes, J.; Caponetti, G.; Hrkach, J. S.; Ben-Jebria, A.; Eskew, M. L.; Mintzes, J.; Deaver, D.; Lotan, N.; Langer, R. Large porous particles for pulmonary drug delivery. *Science* **1997**, *276*, 1868−1871.
26. Caponetti, G.; Hrkach, J. S.; Edwards, D. A.; De la Cruz, C. P.; Heidel, J. D.; Lotan, N.; Colombo, P.; Langer, R, manuscript in preparation.

Acknowledgments

The partial financial support by the National Institutes of Health grant GM 26698 is gratefully acknowledged.

JS970457F

Carrier-Mediated Absorption of Salicylic Acid from Hamster Cheek Pouch Mucosa

NAOKI UTOGUCHI,* YOSHITERU WATANABE, YUKA TAKASE, TAKAHISA SUZUKI, AND MITSUO MATSUMOTO

Contribution from *Department of Pharmaceutics, Showa College of Pharmaceutical Sciences, 3-3165 Higashi-Tamagawagakuen, Machida, Tokyo 194-8543, Japan.*

Received October 22, 1997. Final revised manuscript received October 6, 1998.
Accepted for publication October 7, 1998.

Abstract □ Previously, we found that monocarboxylic acids undergo carrier-mediated transport in primary cultures of oral mucosal epithelial cells.[1] In this study, we investigated whether carrier-mediated absorption of a monocarboxylic acid from the oral mucosa occurs in vivo. Salicylic acid was administered to hamster cheek pouch. At predetermined intervals, the concentration of salicylic acid in the fluid remaining in the cheek pouch lumen and the blood salicylic acid concentration were determined. The absorption of salicylic acid was saturable at high salicylic acid concentrations. Sodium azide, a metabolic inhibitor, and carbonylcyanide *p*-trifluoromethoxyphenylhydrazone (FCCP), a protonophore, significantly inhibited the absorption of salicylic acid but not the absorption of salicylamide from the oral mucosa. Various monocarboxylic acids inhibited the absorption of salicylic acid, whereas dicarboxylic acids had no such effect. Transfer of [^{14}C]salicylic acid from the cheek pouch mucosa to the systemic circulation was observed, and the blood [^{14}C]salicylic acid concentration in the case of coadministration with propionic acid was significantly lower than that in the case of no propionic acid coadministration. These results show that monocarboxylic acids undergo carrier-mediated absorption from the hamster cheek pouch mucosa.

Introduction

The oral mucosal route is advantageous for drug delivery into the systemic circulation because exposure of the administered drug to gastrointestinal juices and its hepatic first-pass elimination are prevented.[2] In general, the absorption of drugs from the oral mucosa can be explained in terms of the pH−partition hypothesis, which is well illustrated by passive diffusion mechanisms.[3] The hypothesis proposes that the rate of drug absorption depends on the percentage of drug molecules ionized and the lipid solubility of nonionized drug molecules. However, in vivo studies have revealed that some drugs undergo carrier-mediated absorption from the oral mucosa.[4,5] In previous studies, we demonstrated that a carrier-mediated transport system for monocarboxylic acids exists in rabbit oral mucosal epithelial cells in primary culture.[1] However, no data are currently available indicating that carrier-mediated monocarboxylic acid absorption occurs in vivo. In the present study, we investigated whether carrier-mediated drug absorption from hamster cheek pouch mucosa occurs in vivo.

Experimental Section

Materials—[^{14}C]Salicylic acid (55 Ci/mol) was obtained from American Radiolabeled Chemicals (St. Louis, MO). MCDB 153, an epidermal growth factor, and trypsin type III were obtained from Sigma Chemicals (St. Louis, MO). Fetal calf serum (FCS) was purchased from Biotech International Ltd. (Australia). Dispase II was obtained from Boehringer Mannheim (Germany). Tissue culture plates were purchased from Costar (Cambridge, MA). 2-Morpholinoethanesulfonic acid, monohydrate (MES) and *N*-[2-hydroxyethyl]piperazine-*N*′-[2-ethanesulfonic acid] (HEPES) were purchased from Dojin (Kumamoto, Japan). All other chemicals were of the highest available purity and analytical grade, and were purchased from Wako Pure Chemical Industries (Osaka, Japan)

Cell Culture—Oral mucosal epithelial cells were isolated from hamster cheek pouch mucosa and cultured by a previously described method[1] with slight modifications. Briefly, golden hamsters (body weight range, 180−220 g) were sacrificed by the administration of sodium pentobarbital, and their buccae were excised, washed with phosphate-buffered saline (PBS) containing antibiotics (penicillin G, 200 U/mL; streptomycin, 200 μg/mL; and gentamicin, 40 μg/mL), and then cut with a razor into small pieces (each about 3 × 6 mm in size). The tissue pieces were then incubated at 4 °C in Dispase II solution (2.4 U/mL) containing the antibiotics. After a 36-h incubation, the epithelial cell sheets were separated using forceps and centrifuged for 5 min at 200 x *g*. The cell pellets were suspended in a low Ca^{2+} medium, MCDB 153, supplemented with FCS (10%), insulin (5 μg/mL), transferrin (10 μg/mL), phosphorylethanolamine (14.1 μg/mL), penicillin G (100 U/mL), streptomycin (100 μg/mL), gentamicin (20 μg/mL), and epidermal growth factor (10 ng/mL). The resultant suspension was plated onto the wells in a collagen-coated 12-well tissue culture plates. After 24 h of cultivation at 37 °C in a 95% air:5% CO_2 humidified atmosphere, the cells were washed twice with PBS and fresh culture medium was added to each well. After 4 or 5 days of cultivation, drug uptake experiments were performed. The cell type was identified and the purity of the cell preparation was determined by indirect immunofluorescence staining of keratin.[6] More than 95% of the cells were positively stained for keratin (data not shown).

Uptake Experiments—The hamster oral mucosal epithelial cells (HOEpi) were washed twice with Hanks' balanced salt solution (HBSS; 136.7 mM NaCl, 0.385 mM Na_2HPO_4, 0.441 mM KH_2PO_4, 0.952 mM $CaCl_2$, 5.36 mM KCl, 0.812 mM $MgSO_4$, 25 mM D-glucose, and 10 mM MES for adjustment of pH to 5.0) before a test solution containing [^{14}C]salicylic acid was added. [^{14}C]-Salicylic acid (0.25 μCi/mL; 4.5 μM) was used as a marker for monocarboxylic acid carrier-mediated transport. The pH of the test solution was 5.0 except in pH-dependent uptake experiments. In pH-dependent experiments, the pH range of the incubation buffer was 5.0−7.5. The buffer solutions were prepared by adding MES (pH 5.0−6.5) or HEPES (pH 7.0−7.5) to HBSS. After 30 s, the test solution was aspirated and the cells were washed four times with ice-cold HBSS. For quantitation of [^{14}C]salicylic acid uptake, the cells were suspended in 0.5 N NaOH (300 μL) and the suspension was incubated at 37 °C for 12 h at which point 1.0 N HCl (150 μL) was added. The remaining radioactivity was quantified using a liquid scintillation counter (Aloka, LSC-5100). Cellular protein was quantified using a protein assay kit (Bio-Rad, CA), with bovine serum albumin as the standard. Details of the conditions for each experiment are given in the figure legends or table footnotes.

Data Analysis—The kinetic parameters of saturable uptake by HOEpi were determined using a nonlinear least squares

* Author to whom correspondence should be addressed. Telephone: +81-427-21-1556. Fax: +81-427-23-3585.

10.1021/js970412e CCC: $18.00
Published on Web 12/01/1998

regression analysis program, MULTI.[7] The uptake rate (J) was fitted to the following equation, which consists of both saturable and nonsaturable linear terms:

$$J = J_{max} \times C/(Kt + C) + k \times C \quad (1)$$

where J_{max} is the maximum uptake rate for a carrier-mediated process, C is the salicylic acid concentration, K_t is the half-saturation concentration (Michaelis constant), and k is a first-order rate constant.

In Vivo Absorption Experiments—The in vivo absorption experiments were performed using a slightly modified version of a method described previously.[3] Briefly, male golden hamsters (body weight range, 120−150 g) were anesthetized with urethane (1.5 g/kg, ip) and fastened onto a platform tilted at an angle of 55°. The cheek pouch was cleaned by multiple saline rinses. A vinyl tube (o.d., 1.2 mm; i.d., 0.8 mm; Natsume, Japan) was inserted into the cheek pouch to a depth of 50 mm. One milliliter of the drug solution (20 μM) dissolved in buffer was administered into the cheek pouch. In pH-dependent absorption experiments, the buffer pH ranged from 3.0 to 7.0. Buffer solutions of pH 6.0 were prepared by adding MES to HBSS, whereas for the pH 7.0 buffer solution, HEPES was added to HBSS. Citric acid−Na_2HPO_4 buffer was used for the pH 3.0−5.0 experiments. For other experiments also, citric acid−Na_2HPO_4 buffer (pH 5.0) was used. At predetermined time points after the drug administration, the fluid in the cheek pouch lumen was collected. The amount of the drug present in the fluid was determined by fluorescence (salicylic acid: Ex. 300 nm, Em. 430 nm) or UV (salicylamide: 235 nm) detectors. The reduction in concentration of the drug in the cheek pouch was used as a measure of the apparent absorption.

Plasma Concentration of Salicylic Acid—Under anesthesia, [^{14}C]salicylic acid solution (2.0 μCi/mL; 36 μM) was administered into the cheek pouch lumen. At predetermined time points after the administration, blood samples were collected from the ophthalmic vessels using a glass capillary coated with heparin (DURAN ringcaps, Germany). Each blood sample was placed in a scintillation vial to which 0.2 mL of perchloric acid solution was added. After vigorous shaking, 0.3 mL of hydrogen peroxide solution was added. After 30 min of incubation at 70 °C, scintillation cocktail (Clear-sol II, Nacalai Tesque, Japan) was added. Radioactivity was quantified using a liquid scintillation counter.

Statistical Analysis—All results were expressed as mean ± standard deviation (SD). One-way analysis of variance (ANOVA) was used for single and multiple comparisons. Values of p of 0.05 or less were considered to indicate statistical significance.

Results

Salicylic Acid Uptake by HOEpi—We reported previously on monocarboxylic acid transport across oral mucosal epithelial cells using cultured epithelial cells from rabbit oral mucosa.[1] The hamster is most widely used for studies of drug absorption from the oral mucosa. In the present study, we first determined whether a carrier-mediated monocarboxylic acid transport system exists in cultured hamster oral epithelial cells.

Concentration and Temperature Dependence of Salicylic Acid Uptake—The effect of incubation temperature on the rate of uptake of [^{14}C]salicylic acid by HOEpi was studied. The rate of uptake was much lower at 4 °C than at 37 °C, as shown in Figure 1. Figure 1 also shows the relationship between the initial rate of uptake of [^{14}C]-salicylic acid and its concentration in the incubation medium. The results indicate that the uptake of salicylic acid consists of two processes, a saturable process evident at low concentrations and an apparently nonsaturable process evident at high concentrations. The uptake processes were analyzed using eq 1. The kinetic parameters calculated for salicylic acid uptake were a J_{max} of 140 ± 16 nmol/30 s/mg protein, a K_t of 0.14 ± 0.03 mM, and a k of 33 ± 3 μL/30 s/mg protein.

Energy and Proton-Gradient Dependence of Salicylic Acid Uptake—The effect of a metabolic inhibitor on the uptake of [^{14}C]salicylic acid was studied to determine whether this uptake requires metabolic energy (Table 1). Sodium azide (10 mM), a metabolic inhibitor, inhibited the uptake of [^{14}C]salicylic acid by HOEpi. Carbonylcyanide *p*-trifluoromethoxyphenylhydrazone (FCCP; 50 μM), a protonophore, also significantly inhibited the uptake. These findings suggest that [^{14}C]salicylic acid uptake by HOEpi is energy- and proton-gradient-dependent.

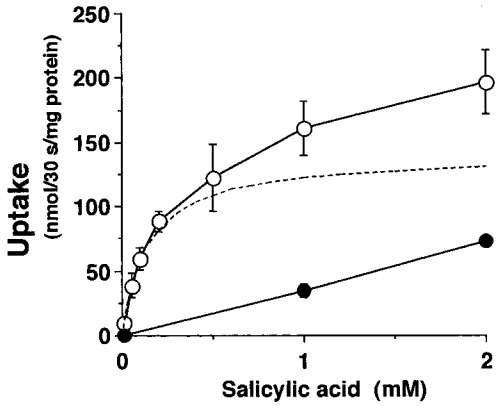

Figure 1—Concentration and temperature dependence of [^{14}C]salicylic acid uptake by HOEpi. The rate of uptake of [^{14}C]salicylic acid by HOEpi was measured at (○) 37 °C and (●) 4 °C. The dotted line represents the saturable component of the uptake of salicylic acid calculated from the kinetic parameters determined as described in the text. The vertical bar through each point represents the SD for four experiments.

Table 1—Effects of a Metabolic Inhibitor, a Protonophore, and Various Carboxylic Acids on [^{14}C]Salicylic Acid Uptake by HOEpi

variable type	compound	relative uptake (% of control)
metabolic inhibitor	sodium azide[a]	33.3 ± 8.7[b]
protonophore	FCCP[a]	15.9 ± 10.1[b]
monocarboxylic acid	*n*-butyric acid	8.0 ± 1.4[b]
	propionic acid	9.9 ± 3.0[b]
	valproic acid	12.2 ± 6.9[b]
	acetic acid	17.0 ± 8.2[b]
	lactic acid	46.6 ± 17.6[b]
	pyruvic acid	50.6 ± 4.6[b]
dicarboxylic acid	glutaric acid	95.4 ± 17.9
	fumaric acid	107.6 ± 37.5
	maleic acid	99.4 ± 24.0

[a] HOEpi were pretreated with sodium azide (10 mM) or FCCP (50 μM) for 15 min; all carboxylic acids were tested at 10 mM. [b] Significantly different from the control value ($p < 0.05$).

pH-Dependent Uptake—Figure 2 illustrates the effect of incubation buffer pH in the range of 5.0 to 7.5 on [^{14}C]-salicylic acid uptake by HOEpi. The rate of [^{14}C]salicylic acid uptake increased with decreasing pH from neutral to acidic. At pH 7.5, little salicylic acid uptake was observed. In the presence of 10 mM unlabeled salicylic acid, the uptake of [^{14}C]salicylic acid was significantly reduced and almost completely suppressed. The inhibitory effect of unlabeled salicylic acid increased with decreasing pH from neutral to acidic, suggesting that the passive diffusion route is a minor route and carrier-mediated transport is the major mechanism involved in the uptake of salicylic acid. Previous studies in our laboratory have shown the existence of pH-dependent, monocarboxylic acid transport in the rabbit oral mucosal epithelial cells.[1] In the present study, we also showed that FCCP inhibited the uptake of salicylic acid by HOEpi (Table 1). Our data suggest that carrier-mediated salicylic acid uptake by HOEpi is proton-gradient-dependent, implying that an acidic pH is suitable for the evaluation of monocarboxylic acid transport in HOEpi.

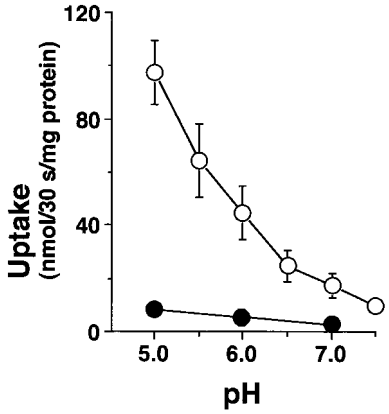

Figure 2—pH Dependence of [^{14}C]salicylic acid uptake by HOEpi. Uptake of [^{14}C]salicylic acid by HOEpi was measured at 37 °C in the (○) absence and (●) presence of 10 mM unlabeled salicylic acid. The vertical bar through each point represents the SD for four experiments.

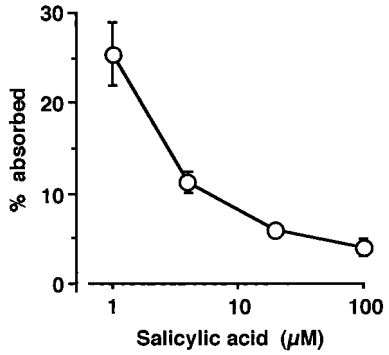

Figure 3—Concentration dependence of salicylic acid absorption. Salicylic acid (1–100 μM) was administered into a hamster cheek pouch. After 15 min, the fluid in the cheek pouch was collected and the amount of salicylic acid present in the fluid was measured. The reduction in concentration of the salicylic acid in the lumen of the cheek pouch was used as a measure of the apparent absorption. The vertical bar through each point represents the SD for four experiments.

Therefore, a pH 5.0 buffer was used for subsequent experiments.

Specificity of the Carrier—To investigate the properties of the carrier involved in [^{14}C]salicylic acid uptake by HOEpi, we studied the effects of various mono- and dicarboxylic acids on this uptake (Table 1). Each monocarboxylic acid significantly inhibited the uptake of [^{14}C]-salicylic acid, whereas none of the dicarboxylic acids had any significant effect. These results imply that the carrier that mediates monocarboxylic acid uptake by HOEpi is a nonspecific monocarboxylic acid carrier.

Salicylic Acid Absorption from the Oral Mucosa In Vivo—We determined whether a monocarboxylic acid transport system exists in hamster cheek pouch mucosa in vivo.

Concentration Dependence of Salicylic Acid Absorption—The effect of luminal concentration of salicylic acid in the hamster cheek pouch on its absorption from the cheek pouch was examined in the concentration range of 1.0 to 100 μM. The percentages of the apparent absorption at 15 min and pH 5.0 are shown in Figure 3. At high concentrations of salicylic acid, the apparent absorption was saturated.

Energy and Proton-Gradient Dependence of Salicylic Acid Absorption—The effects of a metabolic inhibitor and a protonophore on the absorption of salicylic acid were studied (Figure 4). Both sodium azide (10 mM) and FCCP (50 μM) significantly inhibited the apparent absorption of salicylic acid from the oral mucosa. However, neither

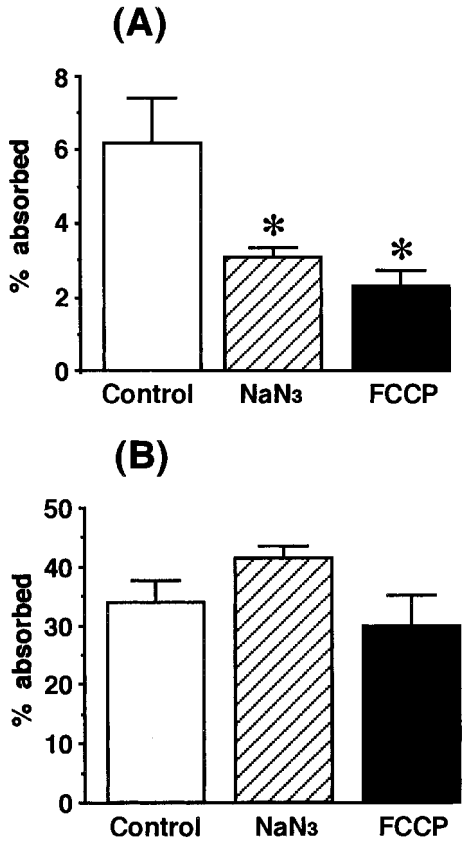

Figure 4—Effects of metabolic inhibitor and protonophore on (A) salicylic acid and (B) salicylamide absorption. A metabolic inhibitor (sodium azide, NaN_3, 10 mM) or a protonophore (FCCP, 50 μM) was administered into the hamster cheek pouch. After 15 min, salicylic acid (20 μM) or salicylamide (20 μM) was added. Then, 15 min later, the fluid in the cheek pouch was collected and the amount of salicylic acid or salicylamide present in the fluid was measured. The disappearance of salicylic acid and salicylamide from the lumen of the oral cavity was defined as the apparent absorption. The vertical bar through each point represents the SD for 3–5 experiments. The asterisk (*) indicates significantly different from the control ($p < 0.05$).

sodium azide nor FCCP affected the apparent absorption of salicylamide. These findings suggest that salicylic acid absorption from hamster oral mucosa is carrier-mediated and depends on the proton gradient and energy.

pH-Dependent Uptake—Figure 5 illustrates the effect of buffer pH in the range of 3.0 to 7.0 on salicylic acid absorption from hamster oral mucosa. The apparent absorption of salicylic acid increased with decreasing pH from neutral to acidic. In the present study, we also showed that FCCP inhibited the absorption of salicylic acid from hamster oral mucosa (Figure 4). These data suggest that salicylic acid absorption is proton-gradient-dependent, implying that an acidic pH is suitable for the evaluation of a monocarboxylic acid transport system in hamster oral mucosa. However, at very low values of pH (e.g., 3.0 or 4.0), most of the salicylic acid in solution exists in the nonionized form. An increase in the fraction of nonionized salicylic acid resulted in an increase in the passive diffusion of salicylic acid across the oral mucosa. Therefore, pH 5.0 buffer was used for subsequent absorption experiments.

Specificity of the Carrier—To investigate the properties of the carrier involved in salicylic acid absorption from hamster oral mucosa, we studied the effects of various mono- and dicarboxylic acids on this absorption (Table 2). Each monocarboxylic acid tested significantly inhibited the apparent absorption of salicylic acid, whereas none of the dicarboxylic acids had any significant effect. These results

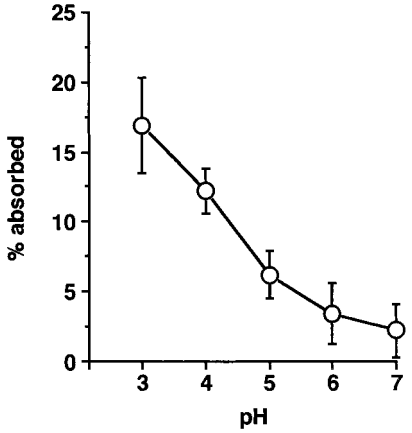

Figure 5—The pH dependence of salicylic acid absorption. Salicylic acid dissolved in various pH buffers (pH 3.0–7.0) was administered into the hamster cheek pouch. After 15 min, the fluid in the cheek pouch was collected and the amount of salicylic acid present in the fluid was measured. The disappearance of salicylic acid from the lumen of the oral cavity was defined as the apparent absorption. The vertical bar through each point represents the SD for four experiments.

Table 2—Effects of Various Carboxylic Acids on Salicylic Acid Absorption from Hamster Cheek Pouch Mucosa[a]

variable type	compound	relative absorption (% of control)
monocarboxylic acid	*n*-butyric acid	22.0 ± 15.3[b]
	propionic acid	7.3 ± 2.6[b]
	valproic acid	45.6 ± 1.5[b]
	acetic acid	14.4 ± 7.6[b]
dicarboxylic acid	glutaric acid	102.5 ± 17.8
	fumaric acid	78.0 ± 27.1
	maleic acid	93.2 ± 8.5

[a] All carboxylic acids were tested at 10 mM. [b] Significantly different from the control value ($p < 0.05$).

suggest that the carrier that mediates monocarboxylic acid absorption is a nonspecific monocarboxylic acid carrier.

Blood Concentration—We further examined whether the [^{14}C]salicylic acid that disappeared from the oral mucosal lumen was transferred to the systemic circulation. The blood concentration−time profiles of [^{14}C]salicylic acid following intracheek pouch administration in the presence and absence of propionic acid (10 mM) are shown in Figure 6. Transfer of [^{14}C]salicylic acid to the systemic circulation was detected. The blood concentration versus time curves demonstrate that propionic acid significantly inhibited the absorption of salicylic acid from the oral mucosa.

Discussion

In previous studies, we demonstrated that carrier-mediated monocarboxylic acid transport systems exist in rabbit oral mucosal epithelial cells in primary culture.[1] However, carrier-mediated absorption of monocarboxylic acids from the oral mucosa in vivo had not been previously described. In the present study, we demonstrated the existence of a carrier-mediated transport system for monocarboxylic acids in the oral mucosa in vivo.

Salicylic acid uptake by HOEpi is characterized as follows: (a) reduction of the incubation temperature from 37 to 4 °C markedly inhibited the uptake; (b) salicylic acid uptake was saturable at high concentrations; (c) a metabolic inhibitor and a protonophore significantly inhibited the uptake, indicating that this uptake process is energy- and proton-gradient-dependent; and (d) monocarboxylic acids significantly inhibited the uptake of salicylic acid.

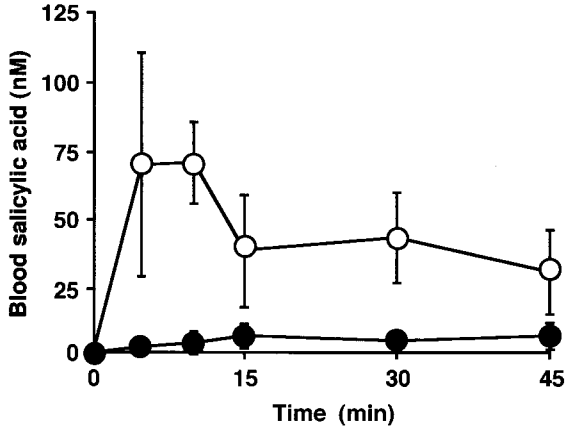

Figure 6—Blood concentration of [^{14}C]salicylic acid after intracheek pouch administration of [^{14}C]salicylic acid (●) with or (○) without 10 mM propionic acid. [^{14}C]Salicylic acid (2.0 μCi/mL; 36 μM) was administered into the hamster cheek pouch. Blood was collected from the ophthalmic vessels. The vertical bar through each point represents the SD for four experiments.

These characteristics of monocarboxylic acid uptake by HOEpi are similar to those observed in rabbit oral mucosal epithelial cells. These data demonstrate the existence of a carrier-mediated monocarboxylic acid transport system in HOEpi.

We also demonstrated carrier-mediated salicylic acid absorption from hamster cheek pouch mucosa. The apparent absorption of salicylic acid from the hamster cheek pouch mucosa in vivo is characterized as follows: (a) the apparent absorption of salicylic acid was saturable at a high initial concentration; (b) a metabolic inhibitor and a protonophore significantly inhibited salicylic acid apparent absorption, indicating that this apparent absorption is energy- and proton-gradient-dependent; and (c) monocarboxylic acids significantly inhibited the salicylic acid apparent absorption. These observations of monocarboxylic acid absorption in vivo are similar to those in vitro and strongly suggest the occurrence of carrier-mediated monocarboxylic acid transport in hamsters in vivo.

Moreover, the present study confirms the transfer of [^{14}C]-salicylic acid from the oral mucosa to the systemic circulation (Figure 6). These data demonstrate that salicylic acid that disappeared from the oral luminal cavity did not remain in the mucosal tissue but was transferred to the blood. Coadministration of propionic acid significantly reduced the blood concentration of [^{14}C]salicylic acid. Passive absorption of salicylic acid was not inhibited by coadministered propionic acid. Therefore, the coexistence of propionic acid with the absorbed salicylic acid indicates passive absorption. Figure 6 also shows that the rate of passive absorption of [^{14}C]salicylic acid from the oral luminal cavity is much lower than that of carrier-mediated absorption of [^{14}C]salicylic acid.

The surface of hamster cheek pouch mucosa is keratinized.[8] Therefore, no carrier-mediated transport occurs across this keratinized part because keratinized cell layers consist of differentiated dead cells. However, our data indicate that carrier-mediated absorption occurs in the hamster cheek pouch mucosa. This result may explain why the keratinized layer is not the main barrier to salicylic acid transport. Salicylic acid may be transported via a carrier-mediated system in the living epithelial cell layers that are located under the keratinized cell layers.

Figures 2 and 5 show pH-dependent uptake or absorption of salicylic acid. At neutral pH, little uptake was observed. However, the uptake of salicylic acid increases with a decrease of pH. Salicylic acid is an acidic compound; therefore, a decrease in pH increases the fraction of

nonionized salicylic acid. According to the pH−partition hypothesis, this increase in the fraction of nonionized form increases the passive absorption of salicylic acid across the oral mucosa. These data (Figures 2 and 5) alone are insufficient to conclude that the uptake of salicylic acid is proton-gradient-dependent. However, it is evident from Table 1 and Figure 4 that FCCP, a protonophore, inhibited the uptake of salicylic acid. These results strongly suggest that salicylic acid uptake is proton-gradient-dependent.

In in vitro experiments (Figure 1), the K_t of salicylic acid was 0.14 ± 0.03 mM. However, in in vivo experiments (Figure 3), the absorption of salicylic acid was saturated at 0.1 mM or less. We have no clear explanation as to why the saturation behavior is different between in vitro and in vivo conditions. There are some differences between in vivo and in vitro states. In vitro, salicylic acid transport was studied in terms of its uptake by cultured epithelial cell monolayers. This means that only the transport of salicylic acid from the apical side to intercellular spaces was evaluated. On the other hand, in vivo, the apparent absorption as determined by its disappearance from the hamster cheek pouch, by the oral mucosa which consists of multilayer epithelial cells was evaluated. The difference in results may be due to differences between cultured cells and cells in vivo, uptake and transport, and monolayer and multilayer.

Figure 4 shows that both sodium azide (10 mM) and FCCP (50 μM) significantly inhibit the apparent absorption of salicylic acid from the oral mucosa. However, neither sodium azide nor FCCP affected the apparent absorption of salicylamide. These findings suggest that salicylic acid absorption from hamster oral mucosa is carrier-mediated and depends on the proton gradient and energy. However, the absorption of salicylamide (the control) is six times higher than that of salicylic acid. The difference in the apparent absorption values between salicylamide and salicylic acid could be due to the differences in their lipophilicities. The apparent octanol−buffer (pH 5.0) distribution coefficient of salicylic acid at 37 °C is 0.45 ± 0.02, and that of salicylamide is 14.56 ± 0.09 (these results were obtained in our laboratory, although details of the experimental conditions are not shown). Salicylamide is 32 times more lipophilic than salicylic acid at pH 5.0, which may account for its higher apparent absorption.

The rate of absorption of a drug from the hamster cheek pouch mucosa is related to the lipophilicity of the drug.[3] A lipophilic index based on the results of reversed-phase HPLC has been used extensively as a measure of the lipophilicity of drugs.[9] Kurosaki et al. reported[3] that the lipophilic index of salicylic acid is the same as that of phenacetin. However, the absorption rate of salicylic acid from the hamster cheek pouch mucosa is about three times higher than that of phenacetin (48.6 ± 4.1 and 16.0 ± 0.6%, respectively, after 1 h). Kurosaki et al. did not discuss this finding in their report.[3] This higher percentage absorption of salicylic acid than that of phenacetin may be accounted for by carrier-mediated absorption of salicylic acid from the hamster cheek pouch mucosa.

Our present results suggest that drugs that have a monocarboxylic acid residue could potentially be delivered into the systemic circulation from the oral mucosa via carriers. This carrier-mediated oral mucosal absorption route may serve as a new approach for drug absorption from the oral mucosa.

References and Notes

1. Utoguchi, N.; Watanabe, Y.; Suzuki, T.; Maehara, J.; Matsumoto, Y.; Matsumoto, M. Carrier-mediated Transport of Monocarboxylic Acids in Primary Cultured Epithelial Cells from Rabbit Oral Mucosa. *Pharm. Res.* **1997**, *14*, 320−324.
2. de Vries, M. E.; Bodde, H. E.; Verhoef, J. C.; Junginger, H. E. Developments in Buccal Drug Delivery. *Crit. Rev. Ther. Drug Carrier Syst.* **1991**, *8*, 271−303.
3. Kurosaki, Y.; Aya, N.; Okada, Y.; Nakayama, T.; Kimura, T. Studies on Drug Absorption from Oral Cavity: Physicochemical Factors Affecting Absorption from Hamster Cheek Pouch. *J. Pharmacobio-Dyn.* **1986**, *9*, 287−296.
4. Hunjan, M. K.; Evered, D. F. Absorption of Glutathione from the Gastro-intestinal Tract. *Biochim. Biophy. Acta* **1985**, *815*, 184−188.
5. Evered, D. F.; Mallett, C. Thiamine Absorption across Human Buccal Mucosa In Vivo. *Life Sci.* **1983**, *32*, 1355−1358.
6. Claass, A.; Claus, S.; Hoft, J.; Prange, E. Long-Term Culture of Nasal Epithelial Cells. *Acta Histochem.* **1991**, *90*, 21−26.
7. Yamaoka, K.; Tanigawara, Y.; Nakagawa, T.; Uno, T. A Pharmacokinetic Analysis Proguram (MULTI) for Microcomputer. *J. Pharmacobio-Dyn.* **1981**, *4*, 879−885.
8. White, F. H.; Gohari, K. The Ultrastructural Morphology of Hamster Cheek Pouch Epithelium. *Arch. Oral Biol.* **1981**, *26*, 563−576.
9. Yamana, T.; Tsuji, A.; Miyamoto, E.; Kubo, O. Novel Method for Determination of Partition Coefficients of Penicillins and Cephalosporins by High-Pressure Liquid Chromatography. *J. Pharm. Sci.* **1977**, *66*, 747−749.

Acknowledgments

This work was supported by a Grant-in-Aid for Scientific Research from the Ministry of Education, Science, Sports and Culture, Japan.

JS970412E

Pharmacokinetics and Organ Distribution of Cationized Colchicine-Specific IgG and Fab Fragments in Rat

GUIYING HONG,* MARTINE I. BAZIN-REDUREAU, AND JEAN MICHEL G. SCHERRMANN

Contribution from *Inserm U26 and Department of Pharmacokinetics, University of Paris V, Hôpital Fernand Widal, Paris, France*

Received August 21, 1997. Final revised manuscript received June 10, 1998.
Accepted for publication September 2, 1998.

Abstract □ Pharmacokinetics of cationized goat colchicine-specific polyclonal immunoglobulin G (IgG) and antigen binding fragment (Fab) (cIgG and cFab, respectively) were studied in male adult Sprague–Dawley rats and compared with those of the native proteins (nIgG and nFab). All proteins were radioiodinated by the Iodogen method, and kinetics were investigated following trichloroacetic acid (TCA) precipitation or immunoprecipitation. Deiodination and catabolism were more pronounced with the cationized than the native proteins, especially for cFab. Both cIgG and cFab in plasma decreased more rapidly than nIgG and nFab. The elimination half-lives were 52.9 and 81.8 h for cIgG and nIgG, respectively. In addition, there was a 74-fold increase in the volume of distribution and a 114-fold increase in the systemic clearance of cIgG compared with nIgG. For cFab, the volume of distribution and systemic clearance were increased 6.4- and 3.5-fold, respectively. Organ uptake of cIgG and cFab was markedly increased compared with that of nIgG and nFab, especially in kidney, liver, spleen, and lung. Renal clearance of cIgG and cFab was also increased 30- and 10-fold compared with that of nIgG and nFab, respectively. The present data suggest that cationization of colchicine-specific IgG and Fab fragments increased the organ distribution and greatly altered their pharmacokinetics. Nevertheless, the smaller molecular size of Fab versus IgG did not enhance the distribution and clearance of cFab. These data pave the way for evaluating the biological efficacy of these more tissue-organ-interactive antibodies.

Introduction

Antibodies offer considerable potential for disease diagnosis and for treatments, such as the neutralization of bacteria, viruses, oncogenic proteins,[1] and toxins.[2] However, the diagnostic and pharmaceutical potential of antibodies is limited because these high molecular weight proteins [immunoglobulin G (IgG), 150 kDa] do not cross either capillary or cellular barriers.[3,4] Even trunctated forms of antibodies, such as antigen binding fragments (Fab, 50 kDa) or even sFv fragments (27 kDa), are too large to easily penetrate physiological membranes. Therefore, it is important to develop strategies for improving the delivery of antibodies to the site of action.

One of the recent developments in targeted delivery of proteins is their cationization,[5,6] in which the surface carboxyl groups of the protein are conjugated with primary amino groups resulting in an increase in the protein isoelectric point (pI). The positive charges of the cationized proteins so formed bind to negative charges on cellular surfaces and thus trigger absorptive-mediated endocytosis of the cationized proteins.[7] This interaction between cell membrane and cationized proteins can be evaluated by pharmacokinetic studies.

The first studies[5,8] concerning the pharmacokinetics of cationized IgG (cIgG) reported an enhanced organ uptake. However, the experimental protocols had a short sampling period and took little account of the influence of the different antibody size between cIgG and cationized Fab (cFab) fragments. In the present study, we report the plasma pharmacokinetics of cationized goat polyclonal colchicine-specific antibodies (IgG and Fab) and their organ distribution in the rat. In addition, their renal clearance and fecal elimination were also measured. This pilot study was conducted prior to assessing the potency of cationized colchicine-specific IgG and Fab for redistributing intracellular colchicine, a compound toxic to tubulin that either inhibits microtubule-dependent processes or disrupts the cytoskeleton.[9]

Materials and Methods

Materials—Goat IgG and Fab fragments of colchicine-specific polyclonal antibody were prepared as previously described.[10] IgG and Fab fragments were purified by gel chromatography to 97% and 92% for IgG and Fab fragments, respectively. Colchicine and thiocolchicine were obtained from Roussel Uclaf (Paris, France) and [^{3}H]colchicine (Ring C,^{3}H-methoxy, 66 Ci/mmol) was from New England Nuclear (Paris, France). Hexamethylenediamine (HMD), *N*-ethyl-*N*′-(3 (dimethylamino) propyl)carbodiimide (EDC), glycine, and others reagents for protein cationization were obtained from Sigma (St Quentin Fallavier, France). Affinity purified rabbit anti-goat IgG (H and L) antiserum (Rockland, PA) and protein A-agarose specific to rabbit polyclonal antibodies (Santa Cruz Biotechnology, Inc.) were purchased from Tebu (Paris, France).

Cationization of Colchicine Specific IgG and Fab—Native colchicine-specific IgG and Fab were cationized according to the method of Pardridge[11] with a small modification: 10 mg of both native IgG and Fab were slowly added to 4 mL of 2 M hexamethylenediamine (HMD, pH 6.2). To this mixture, 50 mg of fresh EDC was added, and the pH was adjusted to 6.2 with 6 M hydrochloric acid. The mixture was stirred for 3 h at room temperature, and the solution was kept on ice to avoid heating. The reaction was quenched by addition of 2 M glycine following by incubation for 60 min at room temperature. The mixture was then dialyzed overnight at 4 °C against 0.01 M Na_2HPO_4/0.15 M NaCl (PBS, pH 7.4). The precipitate was removed by centrifugation (1000 g, 10 min) and the solution was concentrated with polyethylene (6000 Da) at 4 °C. The solution was stored at −20 °C.

Characterization of Cationized IgG and Fab—The pI of cationized and native IgG and Fab were determined by isoelectric focusing (IEF).[6] Protein samples (30 μ) were dialyzed with 0.05% glycine overnight at 4 °C to eliminate excess ions and analyzed by isoelectric focusing (IEF) according to the manufacturer's instructions (Sigma, St Quentin Fallavier, France). After isoelectrophoresis, the gel was stained with Coomassie blue. The cationized antibodies were also subjected to sodium dodecyl

* Correspondence should be addressed to Guiying Hong at INSERM U26, Hôpital Fernand Widal, 200, Rue du Faubourg Saint-Denis, 75475 Paris, France. Tel: 33 01 40 05 43 46. Fax: 33 01 40 34 40 64.

10.1021/js970335n CCC: $18.00
Published on Web 12/12/1998

sulfate−polyacrylamide gel electrophoresis (SDS−PAGE) analysis in 8% or 12% acrylamide, using the Laemmli buffer system, to determine the molecular weight of the cationized and native antibodies.[12]

The affinity constant was determined by competitive radioimmunoassay (RIA) according to the method of Müller.[13] Specificity of the native and cationized antibodies was measured by the cross-reactivity of a colchicine analogue, thiocolchicine, using the RIA as previously described by Scherrmann et al.[2]

Radiolabeling of IgG and Fab—Antibodies were labeled using the Iodogen method.[14] One hundred micrograms of protein were incubated with 0.5 mCi of [^{125}I]Na (Amersham, Les Ulis, France) in Eppendorf tubes coated with 10 μg of Iodogen for 5 min at room temperature. Free iodine was removed by chromatography on a PD-10 Sephadex G-25 column (Pharmacia, Les Ulis, France). Specific activity ranged from 2 to 3 μCi/μg for native IgG (nIgG), 1−2 μCi/μg for cIgG, 1−2 μCi/μg for native Fab (nFab), and 0.6−1.5 μCi/μg for cFab. The radiochemical purity of cIgG, nIgG, cFab, and nFab was analyzed just after iodination and 24, 48, and 72 h and once a week up to 3 weeks after the iodination by SDS−PAGE autoradiography and immunoprecipitation (for procedure see: Comparison of Plasma Antibody Levels following TCA Precipitation and Immunoprecipitation). Finally, the percentage of antibody precipitable radioactivity was determined by trichloroacetic acid (TCA) precipitation.

Intravenous Administration of Cationized and Native IgG and Fab Fragments—Male Sprague−Dawley rats (250−300 g, Iffa Credo, Lyon, France) were given free access to food and water. Each rat was weighed and anesthetized with pentobarbital sodium (60 mg/mL, 60 mg/kg, ip). Body temperature was monitored using a rectal probe (Elba Thermometer model ET 3, Copenhagen, Denmark). During the experiment, each rat was housed in a metabolic cage for collection of urine and feces at the interval of 8 or 16 h. The femoral vein was cannulated with PE−10 tubing (Biotrol, Paris, France). Rats received a single bolus dose of 0.7 mg/kg of unlabeled antibody and 15 μCi of ^{125}I-labeled antibody dissolved in 0.9% NaCl via the cannulated femoral vein. Blood samples were collected in heparinized tubes from the tail at various times (0, 2, 15, 30, and 60 min, 2, 4, 8, and 24 h, and daily for 18 days for nIgG; 0, 1, 10, 20, and 30 min, and 1, 2, 4, 6, 8, 24, 30, 48, 54, 72, 96, and 120 h for cIgG; and 0, 1, 10, 20, and 30 min, and 1, 2, 4, 6, 8, 24, 28, 32, 48, 56, and 72 h for cFab and nFab). Aliquots of plasma were counted for total and TCA-precipitable radioactivity in a gamma counter (Minaxi gamma 5000, Packard Instruments, Rungis, France). Other aliquots were stored at −20 °C for SDS−PAGE followed by autoradiography. Urine and feces were collected throughout the experimental period for measurement of total excreted radioactivity. Free ^{125}I in urine was determined by precipitation with TCA.

Comparison of Plasma Antibody Levels following TCA Precipitation and Immunoprecipitation—To check whether the TCA-precipitable radioactivity corresponded to the intact native or cationized proteins, an immunoprecipitation methodology was applied in a satellite group of rats ($n = 3$). Blood samples (1 mL) were taken 0 and 5 min, and 2, 8, 24, and 48 h for cIgG and at nIgG; and 0 and 5 min, and 2, 4, 8, 24, and 48 h for cFab and nFab after intravenous administration, respectively. Two aliquots of plasma samples were counted for total and TCA-precipitable radioactivity in the gamma counter. Immunoprecipitation was performed as follows: to 200 μL of each plasma sample (or 10 μL of pure radiolabeled native or cationized IgG and Fab diluted in 200 μL rat plasma for the radiochemical purity determination), 100 μL of incubation buffer was added and the solution was incubated at 37 °C for 3 h, then at 4 °C for 1 h. The incubation buffer consisted of PBS (10 mM sodium phosphate, pH 7.4, with 0.14 M NaCl) and 30 μg/mL of rabbit polyclonal anti-goat IgG. Protein A-agarose (40 μL) was added to each tube. After overnight incubation at 4 °C, the immunoprecipitate was collected by centrifugation at 5000 rpm for 7 min at 4 °C, and the supernatant was aspirated and discarded carefully. The immunoprecipitate was washed with PBS (300 μL) and centrifuged as before. This step was repeated three times. After final washing, the immunoprecipitate fractions were counted for radioactivity. The nonspecific precipitation evaluated using normal rabbit plasma was <1%.

Distribution of Cationized and Native Antibodies in Organs—Distribution of antibodies in organs was studied at different times: 6, 72, 120, and 192 h for cIgG; 6, 72, 432, and 456 h for nIgG; and 2 h for both cFab and nFab. Kidneys, liver, spleen, heart, lung, brain, thyroid, and a portion of small intestine were removed, rapidly washed with saline, and blotted dry. Fragments of organs were weighed and solubilized in Soluene 50 according to Pardridge et al.[15] at 60 °C for 60 min and counted for radioactivity in gamma scintillation liquid. Distribution of antibodies in the organ was expressed as ng/g of tissue. Blood samples were taken just before rats were killed, and radioactivity was measured. As radioactivity remaining in the blood at the time of death was very different for native and cationized antibodies, total radioactivity in the organs was corrected according to levels found in the blood.[16]

SDS−PAGE and Autoradiography—Plasma (0.1 mL) containing native or cationized ^{125}I-labeled antibodies was analyzed by SDS−PAGE.[12] Radiolabeled antibodies and metabolites were autoradiographed using X-ray film (Amersham) and intensifying screens for several weeks. The migration zone of native ^{125}I-labeled antibodies or fragments was compared with protein markers of known molecular weights (Rainbow, Amersham, France); they are, myosin (205 kDa), β-galactosidase (116.5 kDa), bovine serum albumin (80 kDa), ovalbumin (49.5 kDa), and soybean trypsin inhibitor (27.5 kDa).

Detection of Rat Anti-goat Immune Response to the Cationized and Native IgG and Fab—An immunoradiometric assay (IRMA) was performed to detect anti-goat cIgG, nIgG, cFab, and nFab in rat plasma 1, 2, and 3 weeks after administration of a single dose (700 μg/kg) of each antibody. Microtitration plates (Falcon microtest III U50, Polylabo, Strasbourg, France) were coated with 200 μL of 100 mM sodium carbonate pH 9.6 containing 20 μg/mL of affinity-purified goat nIgG, nFab, cIgG, and cFab, respectively, by overnight incubation at 4 °C. The plates were washed three times with PBS containing 0.2% Tween-20 (PBS-Tween). Overcoating was achieved by a 1-h incubation at room temperature with 200 μL/well PBS containing 3% BSA to reduce nonspecific serum protein binding. Plates were then washed three times with PBS-Tween. Then, 100 μL of rat plasma samples, 100 μL of normal rat plasma containing 1 μg of rabbit anti-goat IgG (positive control), or 100 μL of normal rat plasma (nonspecific binding) were added to the sensitized plates and incubated for 2 h at room temperature. All assays were performed in triplicate. The plates were washed and incubated 1 h at room temperature with 100 μL of appropriate optimally diluted conjugate ([^{125}I]cIgG, [^{125}I]nIgG, [^{125}I]cFab, or [^{125}I]nFab, 70 000 cpm, respectively). Plates were washed three times with PBS-Tween and dried. Each well was cut out and placed in a 5-mL plastic tube. All tubes were capped and counted in a gamma counter. The radioactivity in each tube was expressed as % binding; that is, $(B - NS)/(T - NS) \times 100\%$, where B = bound, T = total radioactivity and N = the nonspecific binding of the tracer.

Pharmacokinetic and Statistical Analysis—Plasma cIgG, nIgG, cFab, and nFab TCA-precipitable concentrations were analyzed by model-independent techniques using the SIPHAR program (SIMED, Creteil, France). The terminal disposition rate constant (λ_d) was determined by linear regression analysis and the corresponding half-life ($t_{1/2}\lambda_d$) was calculated as $0.693/\lambda$. The area under the curve (AUC) of plasma ^{125}I-cationized or native IgG and Fab concentration versus time curve from zero to infinity was determined by linear trapezoidal estimation from zero to the last measured time with extrapolation to infinity by adding the value of the last measured plasma concentration divided by the terminal rate constant. Total body clearance (CL) and volume of distribution (Vd) were calculated using standard equations.[17]

Renal clearance was calculated by dividing the amount of protein in urine by the plasma AUC at the same time interval. Mean values for pharmacokinetic parameters were compared using one-way analysis of variance (ANOVA) followed by the Student-Newman-Keuls Multiple Comparisons Test (GraphPad software V 2.04 a). Significance was set at $p < 0.05$.

Results

Characteristics of Antibodies after Cationization and ^{125}I Radiolabeling—As measured by IEF, the pI of nIgG and nFab ranged from 5.85 to 9.0 and 8.65 to 9.3, respectively. The pI of cIgG and cFab were both raised and ranged from 8.65 to 10.3 and 9.5 to 11, respectively.

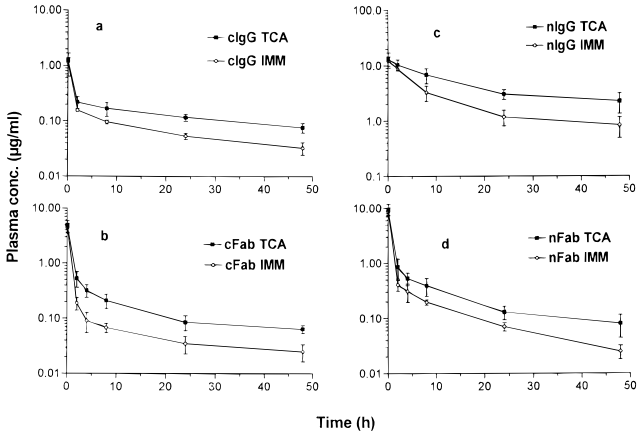

Figure 1—Time courses of plasma ^{125}I-labeled antibody concentrations precipitated by TCA and immunoprecipitation (IMM) in a satellite rat group. Graphs a, b, c, and d represent different antibodies. Data are mean ± SD (n = 3).

However, the process of cationization did not significantly change the affinity and specificity of IgG and Fab fragments. The affinity constants of cIgG and nIgG were 1.2 ± 0.13× 10^9 and 1.58 ± 0.2 × 10^9 M^{-1} (p > 0.05) respectively, and 1.08 ± 0.21 × 10^9 and 0.64 ± 0.18 × 10^9 M^{-1} (p > 0.05) for cFab and nFab, respectively. The cross-reactivity to thiocolchicine did not differ significantly between cationized and native forms. The percentages were 8.6 ± 1.13 and 8.9 ± 0.58% (p > 0.05) for cIgG and nIgG, respectively, and 25 ± 5.9 and 37 ± 8.67% (p > 0.05) for cFab and nFab, respectively. Furthermore, after cationization of IgG and Fab, high molecular weight aggregates were not detected by SDS−PAGE, and no alteration of the migration bands of the native and cationized antibodies were observed by autoradiography after iodination. Most (90−94%) of the total radioactivity of cationized and native antibodies was recovered by immunoprecipitation just after iodination or even 3 weeks later. The percentage of TCA-precipitable radioactivity of the native and cationized antibodies changed from 96−98% following iodination to 85 ± 5% at two weeks later. As a consequence, all pharmacokinetic studies were performed within 24 h after the radiolabeling of the native and cationized antibodies. Finally, we found that the cationized molecules bound nonspecifically to silicon and plastic tubing (nonspecific binding was 1.9 and 2.1%, respectively), we thus used glass tubing to avoid nonspecific binding (<1%).

Detection of Rat Anti-goat Immune Response to Cationized and Native IgG and Fab—The binding capacity of each antibody-treated (cIgG, cFab, nIgG, and nFab) rat plasma sample to its corresponding antigen accounted for <0.3% (but 46.12 ± 1.3% for the positive control) of the total radioactivity during the 3 weeks following the protein administration. This result indicates that no anti-goat immune response occurred during the experimental time period of the pharmacokinetic study after a single iv dose (700 µg/kg,) of the antibodies, not even for cationized IgG and Fab.

Comparison of Pharmacokinetics Following TCA Precipitation and Immunoprecipitation—Figure 1 shows the plasma concentration of cationized and native antibodies detected by TCA precipitation and immunoprecipitation in the satellite group of rats. Except at the earlier time of 5 min, the plasma concentration of each antibody detected by immunoprecipitation was lower than that detected by TCA precipitation, but plasma decline was parallel during terminal decay with both analytical methods. The ratios between immunoprecipitated and the TCA-precipitable AUC_{0-48h} were 0.53, 0.56, 0.41, and 0.39 for nIgG, cIgG, nFab, and cFab, respectively.

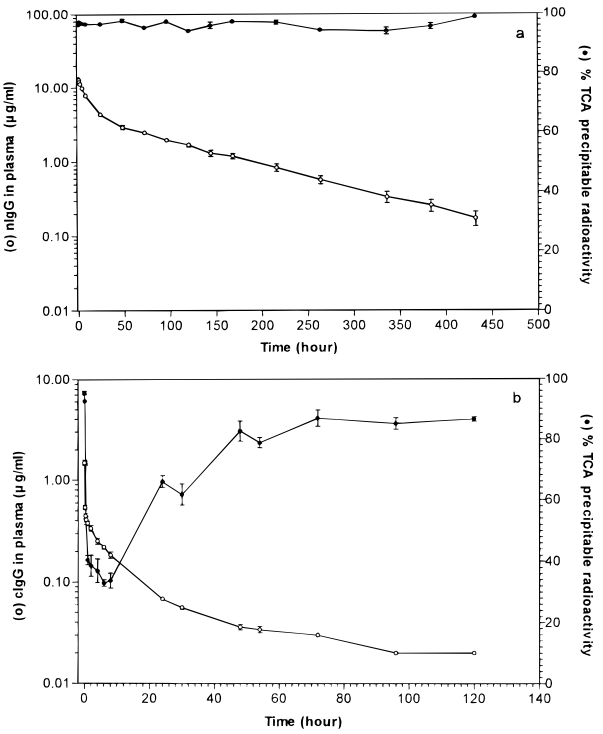

Figure 2—Plasma concentration of ^{125}I-nIgG and ^{125}I-cIgG. Plasma data were corrected for TCA precipitation. (a) The plasma concentration of ^{125}I-nIgG versus time and the percentage of TCA-precipitable plasma radioactivity for nIgG. (b) The plasma concentration of ^{125}I-cIgG versus time and the percentage of TCA-precipitable plasma radioactivity for cIgG. Data are mean ± SD (n = 5).

Pharmacokinetics of cIgG, nIgG, cFab, and nFab in Rat—Plasma TCA-precipitable cIgG and nIgG concentrations are shown in Figure 2. Plasma cIgG declined with a rapid distribution followed by a relatively slow elimination with a terminal half-life of 52.9 h. However, plasma nIgG declined slowly with a terminal half-life of 81.8 h. The $AUC_{0-\infty}$ of cIgG was 116-fold lower than for nIgG. In agreement with the reduction in AUC, the Vd and the total clearance of cIgG were 74 and 114 times higher compared with those of nIgG (Table 1).

Figure 3 shows the decline of TCA-precipitable cFab and nFab in plasma. Plasma cFab decreased more rapidly than plasma nFab in the early phase of decline. The terminal half-life of cFab (27.85 ± 6.75 h) was longer than that of nFab (18.23 ± 2.46 h; p > 0.5). However, the AUC of cFab was 4-fold lower than that of nFab. Systemic clearance of cFab (162.14 ± 32.2 mL/h/kg) was 3.5-fold higher than for nFab (46.85 ± 39.33 mL/h/kg), and Vd of cFab was increased nearly 6.4-fold compared to nFab (Table 1).

The percentage of plasma TCA-precipitable radioactivity for nIgG was >96% at all times (Figure 2a), whereas that of cIgG was about 95% at the beginning, then slowly decreased to 30% at 6 h after the iv injection, then gradually increased up to a plateau of about 88% at the end of the pharmacokinetic analysis (Figure 2b). The plasma TCA-precipitable percentage of cFab and nFab also changed with time, as shown in Figures 3a and 3b. It decreased to 12 and 45% for cFab and nFab, respectively, 6 h after iv injection, and then increased again to 63 and 81%, respectively, at the end of the pharmacokinetic experiment. Autoradiography of plasma samples showed a time-dependent decrease in the intensity of the protein bands of both cationized and native antibodies, and lower molecular weight products (29−35 kDa) were observed with cIgG and nIgG.

Table 1—Pharmacokinetic Parameters of Native and Cationized IgG and Fab[a]

parameter	cIgG	nIgG	cFab	nFab	p^b cIgG–nIgG	p^b cFab–nFab	p^b cIgG–cFab
$t_{1/2}\lambda_d$ (h)	52.92 ± 5.2	81.84 ± 12.3	27.85 ± 6.75	18.23 ± 2.46	>0.05	>0.05	>0.05
AUC (μg/mL h)	5.3 ± 0.17	620.29 ± 92.92	4.52 ± 0.88	18.05 ± 1.64	<0.001	<0.001	>0.05
CL_t (mL/h/kg)	131.6 ± 4.4	1.15 ± 0.16	162.14 ± 32.2	46.85 ± 39.33	<0.001	<0.05	>0.05
CL_r (mL/h/kg)	2.4 ± 0.9	0.08 ± 0.05	16.58 ± 1.58	1.62 ± 0.14	<0.001	<0.001	<0.001
Vd (mL/kg)	10042 ± 864	135.9 ± 5.13	6666 ± 2196	1048 ± 211	<0.05	<0.05	>0.05

[a] In all experiments, the dose was 0.7 mg kg^{-1}; data are mean ± SD (n = 5); $t_{1/2}\lambda_d$, elimination half-life; AUC, area under the plasma concentration–time curve; CL_t, total body clearance; CL_r, renal clearance; *Vd*, volume of distribution. [b] Values are given for comparison of cIgG versus nIgG, cFab versus nFab, and cIgG versus cFab.

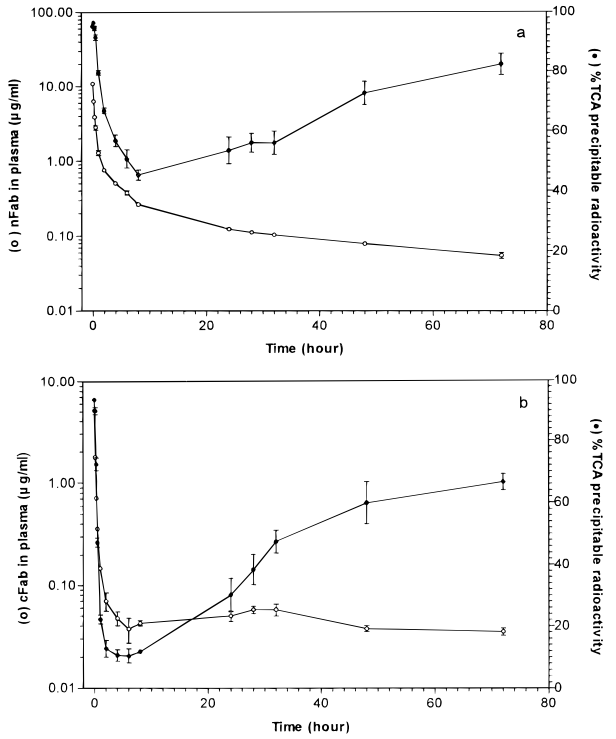

Figure 3—Plasma concentration of ^{125}I-nFab and ^{125}I-cFab. Plasma data were corrected for TCA precipitation. (a) The plasma concentration of ^{125}I-nFab versus time and the percentage of TCA-precipitable plasma radioactivity for nFab. (b) The plasma concentration of ^{125}I-cFab versus time and the percentage of TCA-precipitable plasma radioactivity for cFab. Data are mean ± SD (n = 5).

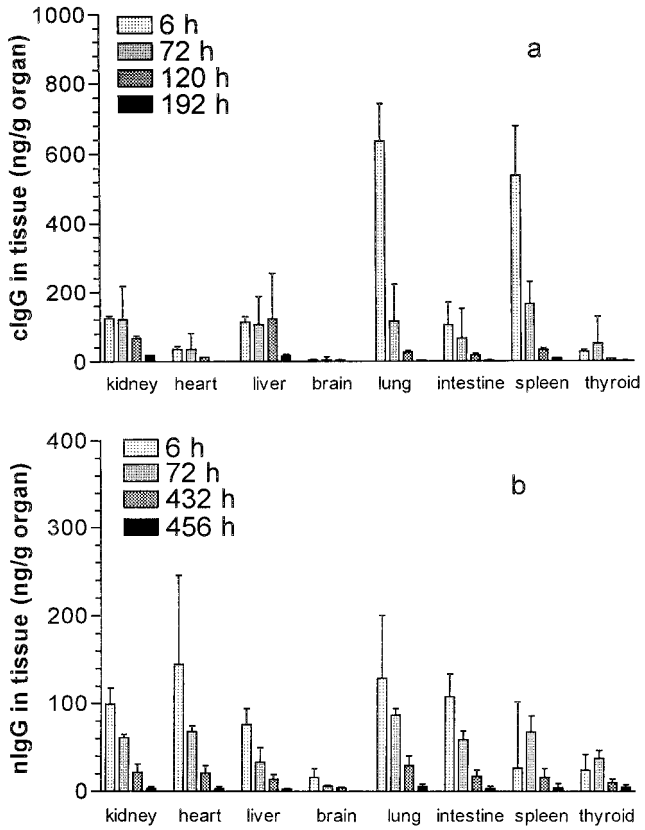

Figure 4—Biodistribution of ^{125}I-cIgG and ^{125}I-nIgG in several organs at different times after intravenous administration: (a) ^{125}I-cIgG; (b) ^{125}I-nIgG. Data are mean ± SD (n = 5).

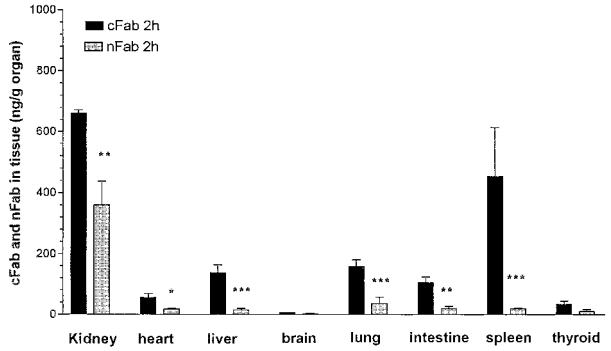

Figure 5—Biodistribution of ^{125}I-cFab and ^{125}I-nFab in several organs 2 h after iv administration. Data are mean ± SD (n = 5). Key: (*) $p < 0.05$; (**) $p < 0.01$; (***) $p < 0.001$.

Renal clearance of cIgG (2.4 ± 0.9 mL/h/kg) was only 1.8 ± 0.55% of total body clearance and 30-fold that of nIgG, which was 0.08 ± 0.05 mL/h/kg, representing 6.95 ± 4.0% of total body clearance. Renal elimination of cFab was the greatest (16.58 ± 1.58 mL/h/kg), which was 10-fold and 6.9-fold higher, respectively, than those values for nFab and cIgG (Table 1). The percentage ratios of renal clearance to the total body clearance of cFab, nFab, and cIgG were 10.2 ± 1.2, 3.46 ± 0.12, and 1.8 ± 0.8%, respectively.

The percentage of total radioactivity recovered in feces for cIgG (over 120 h), nIgG (over 456 h), cFab and nFab (both over 72 h) were 6.03 ± 0.83, 6.73 ± 0.95, 3.8 ± 0.6, and 12.08 ± 0.3%, respectively.

Organ Distribution of cIgG, nIgG, cFab and nFab in Rats—Figures 4 and 5 show the organ uptake of cIgG, nIgG, cFab, and nFab at different times following administration of antibodies. For both cationized antibodies, the organ distribution was much greater than for native antibodies. Nevertheless, this higher uptake of cationized antibodies varied between organs. Six hours after iv administration, uptake of cIgG was higher in lung and spleen (5- and 20-fold that of nIgG, respectively), whereas the uptake by kidney and liver was not so high and remained constant up to 120 h. Tissue uptake of cIgG by kidney, liver, and spleen was greatly superior to that of nIgG at all time points, whereas in lung, cIgG was

significantly increased only at 6 h ($p < 0.01$). There were no significant differences between heart, brain, intestine, or thyroid ($p > 0.05$). Tissue uptake of cIgG measured in lung, spleen, kidney, and liver at 6 h represented 0.43, 0.37, 0.08, and 0.08% of injected dose per gram of tissue, respectively. Compared with cIgG, cFab was more rapidly and extensively distributed to the organs. At 2 h, the uptake of cFab by kidney, spleen, lung, liver, intestine, and heart was greater than that of nFab, which accounted for 0.49, 0.32, 0.12, 0.10, 0.08, and 0.04% of injected dose per gram of tissue, respectively.

Discussion

One of the main problems to be solved to optimize in vivo use of antibodies is their delivery to the site of action, which can be located more deeply than the antibody distribution space. To overcome the physiological barriers limiting their diffusion, cationization based on absorptive-mediated transcytosis,[7] glycosylation,[18,19] hydrophobization,[20] and microinjection or cellular transfection[21] has been proposed for delivery of antibodies to target sites. Successful intracellular immunization of cationized anti-human immunodeficiency virus REV monoclonal antibody in human peripheral blood lymphocytes[11] and enhanced delivery of cationized immunoglobulin G across the blood-brain barrier[6] have already been described using cationized antibodies. These data encouraged us to apply the cationization concept to colchicine-specific IgG and Fab in the hope that they would be able to bind colchicine intracellularly and improve the level of detoxification already described by Chappey et al. with native colchicine-specific Fab.[9]

Following cationization, colchicine-specific IgG and Fab were resolvable into monomeric heavy and light chains with no detection of high molecular weight aggregates using SDS−PAGE. IEF confirmed that the pI of cIgG and cFab was increased to values ranging from 8.65 to 10.3 and 9.5 to 11, respectively. Moreover, there was no measurable alteration of the affinity and specificity of cIgG and cFab compared with those of nIgG and nFab. Surprisingly, we found higher cross reactivity of thiocolchicine with Fab than with either IgG. However, the cationization process cannot explain these differences because both native and cationized Fab had a similar cross reactivity. The cationized proteins were radiolabeled with ^{125}I, and the radiochemical purity and stability were similar to those of the native forms.

Radiolabeling by oxidative methods, such as the Iodogen method, could have two main drawbacks: first, the denaturation of the labeled protein and, second, the release of free iodine or smaller protein fragments labeled with iodine ^{125}I under the influence of catabolism. These drawbacks have been documented by Bauer et al.[22] who compared the pharmacokinetics of recombinant proteins with molecular weights ranging from 23 kDa to 80 kDa, which were either radiolabeled by iodine ^{125}I or quantified by specific immunoassay. This study revealed that the pharmacokinetics of proteins below about 60 kDa were different when assayed by radioactivity or immunoassay, but those proteins with a molecular weight of at least 80 kDa showed only minimal differences. A similar perturbation in the pharmacokinetics of epidermal growth factor, with a molecular weight of about 6 kDa, was attributed to molecular change in the protein configuration after radioiodination.[23] These findings had important implications for our study for at least two reasons: first, the molecular weight of Fab, about 50 kDa, is within the range of iodination side effects described by Bauer,[22] whereas IgG molecules are far above the side effects range, and, second, cationization could also have an influence on protein stability following radioiodination. For these reasons, cationized and native antibodies iodinated by the Iodogen method were measured in rat plasma by both TCA precipitation and immunoprecipitation in a satellite group of rats. More than 90% of the total radioactivity was detected by both TCA precipitation and immunoprecipitation for the four radiolabeled antibodies both before administration in the rat and in the early time in plasma (i.e., 5 min after antibody administration). These results indicate that both methods are almost equally efficient for the precipitation of radioactivity and that both radioiodinated cationized proteins can be kinetically investigated as well as radioiodinated native IgG and Fab. Nevertheless, the increased level of free ^{125}I following TCA precipitation in the distribution phase of the cIgG, cFab, and nFab kinetics suggests that the native and cationized antibodies were metabolized or deiodinated for these three compounds but not for the nIgG. The TCA-precipitable radioactivity markedly decreased and reached its lowest level at about 6−8 h after antibody administration and then increased versus time. This deiodination process could be caused by the sequestration of the native and cationized antibodies in the liver, lung, and spleen, which we have demonstrated to be the major organs of uptake (see Results section). This effect was more pronounced with the cationized than the native protein and more especially with cFab. Furthermore, urinary elimination of free iodine was maximal at 6 to 8 h after iv injection. Most of the urinary radioactivity observed with cIgG and cFab was free ^{125}I, which accounted for 98 ± 1 and 70 ± 1.7% of total radioactivity, respectively. A similar percentage of 98% of free iodine in the urinary excretion of cationized albumin has been reported by Bergmann et al.[24] However, although thyroid has a high affinity for free ^{125}I, we did not observe significant differences in iodine uptake by the thyroid for cIgG or cFab compared with nIgG and nFab. These data confirm the previous observation of Bauer[22] that high molecular weight radioiodinated proteins, such as IgG, are more stable than smaller proteins, such as Fab fragments. In addition, we also found that cationized IgG and Fab are more sensitive to deiodination than native antibodies, especially during the distribution phase. Though the TCA precipitation technique demonstrated the deiodination of the proteins, the immunoprecipitation technique showed a 2-fold decrease in the protein concentration that was similar for both cationized and native forms. This decrease could suggest that proteins were catabolized, which was not observed following SDS−PAGE autoradiography except with cIgG and nIgG for which a lower molecular weight band was observed. Nevertheless, the kinetic decline was parallel with the two techniques. These data demonstrate the analytical complexity of the analysis of radioiodinated proteins.

Another factor that could affect antibody pharmacokinetics is the immunogenicity of the native or cationized goat IgG and Fab in rats. The existence of a rat anti-goat immune response could modify antibody pharmacokinetics during the experiment. To check for such an immune response, an IRMA was used because it has been reported to be a reliable method for detection of trace amounts of protein as low as 0.013 μg/mL.[25] No rat anti-goat antibody immune response was detected following single-dose administration of either native or cationized IgG and Fab. This result can be explained by the fact that we administrated a single and relatively low dose of native and cationized antibodies. Data from the literature are variable. For example, Muckerheide et al.[26] reported that cationized bovine serum albumin (cBSA) exhibited a unique pattern of enhanced immunogenicity, and Apple et al.[27] showed that this enhanced immunogenicity was due to the increased uptake of cationized protein by antigen-present-

ing cells. In that study, the cationized antigens were administrated at high dose (100 μg/mouse) and emulsified in incomplete Freund's adjuvant. Pardridge et al.[28] reported that the repetitive administration of cationized rat albumin to rats (1 mg/kg/day for 8 weeks, sc) resulted in the development of a relatively low antibody response directed against the cationized rat albumin protein. In another study, Pardridge et al.[29] did not find any formation of antibodies directed against mouse IgG in mice treated with either native or cationized mouse IgG (7.5 mg/kg/day for 4 weeks, iv).

Taking into consideration all this methodological information, we have assessed whether the cationization process could offer significant advantages in terms of distribution and clearance between IgG or Fab. Because of the size difference between native IgG (150 kDa) and Fab (50 kDa), the volume of distribution and total clearance of native Fab are known to be higher than those of IgG because of their greater intercompartmental diffusion and glomerular filtration. Our pharmacokinetic parameters for both native molecules reflect these differences and are similar to those of previous studies,[30−32] with the exception that the terminal half-life and volume of distribution of nFab are slightly more elevated than the values most often reported. This effect could result from the persistence of a non-Fab specific radioactivity that is precipitable by TCA. In addition, our cationized antibody data clearly indicate that both cIgG and cFab were rapidly cleared from the plasma. The kinetic differences between the cationized and native forms reflect both phenomena: a marked increase in the volume of distribution, which was more pronounced for cIgG versus nIgG (ratio = 74) than for cFab versus nFab (ratio = 6.4), and in the total body clearance, which was also more pronounced for cIgG versus nIgG (ratio= 114) than for cFab versus nFab (ratio = 3.5). This higher reactivity of cIgG resulted in a volume of distribution and total body clearance that were similar to those of cFab despite its greater molecular size. The pharmacokinetic parameters of cationized and native IgG are consistent with those previously reported,[29,33,34] whereas no data were available for cFab. Based on comparison of the primary pharmacokinetic parameters, there are no marked pharmacokinetic differences between cIgG and cFab, except for the higher renal clearance of cFab (Table 1).

Even if increased transport to the extracellular fluid is in part responsible for the higher distribution and clearance of cIgG and cFab, it cannot be the only mechanism. The extracellular fluid volume in rat is approximately 240 mL/kg,[30] so the *Vd* values of cIgG and cFab are, respectively, 41- and 28-fold greater than the extracellular fluid volume, suggesting extensive tissue interactions and possible endocytosis. Thus, the rapid removal of cIgG and cFab from the plasma could be attributed to several mechanisms, such as increased escape to the extracellular space, binding to cells and basement membrane, intracellular uptake, and degradation or elimination in urine and feces. All these mechanisms are compatible with the observed increase in volume of distribution and total body clearance of cationized IgG and Fab.

The binding of cationized proteins to cells and basement membrane has already been demonstrated.[18,29] However, we have also observed enhanced intracellular uptake of colchicine-specific cIgG and cFab compared with nIgG and nFab by isolated parenchymal and nonparenchymal cells of the rat liver[35]and also in HL60 cells and human peripheral lymphocytes (results not given). Our data confirm the greater organ interaction of cIgG and cFab, although the distribution pattern was not exactly the same for cIgG and cFab. cIgG was predominantly taken up by lung and spleen, whereas kidney and spleen were more interactive with cFab; and, with both cationized compounds, liver uptake was also enhanced, whereas no or only moderate enhancement was observed in brain, thyroid, and intestine. This organ distribution profile is in agreement with previous studies,[7,29] except that we found a greater cIgG uptake in lung and spleen. These observations suggest that the transcapillary or transcellular passage of cationic proteins is an organ- and protein-specific process. The morphology of the vascular endothelium, which varies from organ to organ and from one location to another within the vasculature of the same organ,[33] could explain the differences in uptake of cationized proteins by different organs. Uptake of both cFab and cIgG was higher than that of the native forms in liver, which is to be expected because liver is an important interactive organ for cationic macromolecules.[36] Receptors for positively charged proteins have been identified on Kupffer cells as well as on endothelial cells.[24,37] In contrast to other organs in which the capillaries present a substantial barrier between vascular and interstitial spaces, the discontinuous endothelial capillaries of the liver favor the electrostatic interaction of cationic proteins with the negative charges of the liver cell surfaces.[36] A substance with a net cationic charge can reach a 4-fold higher intracellular concentration due to the inside negative membrane potential of the hepatocyte (−30 to 40 mV).[38] This effect might be the main explanation for the higher liver uptake of cIgG and cFab than of nIgG and nFab. In contrast, the poor enhancement of brain uptake of both cationized antibodies could be explained by the special anatomical features of the endothelial cells in brain capillaries. The tight junctions linking the endothelial cells of the cerebral vessels form a continuous endothelium that does not seem as favorable as fenestrated or discontinuous endothelium for the uptake of cationized antibodies.

In addition to these distribution properties, several clearance mechanisms can be observed with both cationized antibodies. First, renal clearance was enhanced for cationized proteins compared with native forms. The glomerular capillary wall functions as a barrier based on discrimination of molecular size and electric charge.[39] Normally, this wall restricts almost completely the passage of compounds with molecular weight >50 kDa[40] such as IgG. In contrast, the 50 kDa Fab is filtered and partially reabsorbed at the level of the proximal tubule,[41] and then undergoes extensive catabolism into peptides that recirculate in the blood. Little information is available concerning the influence of electric charge. Filtration of negatively charged dextran sulfate (64 kDa) is greatly restricted, whereas the positively charged diethylaminoethyldextran (DEAED, molecular weight 64 kDa) shows enhanced ability to cross the glomerular wall compared with neutral dextrans of similar size.[40] We found increased kidney distribution and renal clearance for both cIgG and cFab, in which renal clearance of cFab accounted for 10% of total body clearance.

Clearance could also be dependent on the degradation process affecting the protein itself and on iodine release. These last effects have been discussed by comparing the TCA and immunoprecipitation data.

In conclusion, this study demonstrates that cationization of both colchicine-specific polyclonal IgG and Fab fragments increased their organ distribution in vivo and markedly altered their plasma pharmacokinetics compared with the native compounds. These pharmacokinetic properties give new insights into the increased detoxification capability of these cationized antibodies. Colchicine has been reported to be ubiquitously distributed, with high accumulation in spleen, kidney, lung, liver, and heart.[42] Because cIgG and cFab also distribute within these tissues, cationized specific

IgG and Fab could be more effective at reversing colchicine toxicity because of their more extensive distribution to the intracellular colchicine action site within the tissues.

References and Notes

1. Waldmann, T. A. Monoclonal Antibodies in Diagnosis and Therapy, *Science* **1991**, *252*, 1657−1662.
2. Scherrmann, J. M.; Urtizberea, M.; Pierson; P.; Terrien, N. The Effect of Colchicine-Specific Active Immunization on Colchicine Toxicity and Disposition in the Rabbit. *Toxicology* **1989**, *56*, 213−222.
3. Brady, L. W.; Markoe, A. M.; Woo, D. V. Iodine-125-labeled Anti-epidermal Growth Factor Receptor-425 in the Treatment of Glioblastoma Multiforme. A Pilot Study. *Radiat. Ther. Oncol.* **1990**, *24*, 151−160.
4. Jain, R. K. Tumor Physiology and Antibody Delivery. *Radiat. Ther. Oncol.* **1990**, *24*, 32−46.
5. Pardridge, W. M. Absorptive-Mediated Transcytosis of Peptides Through the Blood-Brain Barrier. In *Peptide Drug Delivery to the Brain*; Raven: New York, 1991; pp 189−218.
6. Triguero, D.; Buciak, J. L.; Pardridge, W. M. Blood-Brain Barrier Transport of Cationized Immunoglobulin G. Enhanced Delivery Compared to Native Protein. *Proc. Natl. Acad. Sci., U.S.A.* **1989**, *86*, 4761−4765.
7. Triguero, D.; Buciak, J. L.; Pardridge, W. M. Cationization of Immunoglobulin G Results in Enhanced Organ Uptake of the Protein after Intravenous Administration in Rats and Primate. *J. Pharmacol. Exp. Ther.* **1991**, *225*, 186−192.
8. Pardridge, W. M. Transport of Small Molecules through the Blood-brain Barrier: Biology and Methology. *Adv. Drug Delivery Rev.* **1995**, *15*, 5−36.
9. Chappey, O. L.; Niel, E.; Debray, M.; Wautier, J. L.; Scherrmann, J. M. Efflux of Intracellular Colchicine in Lymphocytes with Colchicine-specific Fab Fragments. *J. Pharmacol. Exp. Ther.* **1995**, *274*, 1072−1076.
10. Sabouraud, A. E.; Urtizberea, M.; Benmoussa, K. Fab-bound Colchicine Appears to Adopt Fab Fragment Disposition in Rats. *J. Pharm. Pharmacol.* **1992**, *44*, 1015−1019.
11. Pardridge, W. M.; Bickel, U.; Buciak, J.; Yang, J.; Diagne, A.; Aepinus, C. Cationization of a Monoclonal Antibody to the Human Immunodeficiency Virus REV Protein Enhances Cellular Uptake but Does Not Impair Antigen Binding of the Antibody. *Immunol. Lett.* **1994**, *42*, 191−195.
12. Laemmli, U. K. Cleavage of Structural Proteins During the Assembly of the Head of Bacteriophage T_4 *Nature (London)* **1970**, *277*, 680−685.
13. Müller, R. Calculation of Average Antibody Affinity in Anti-Hapten Sera from Data Obtained by Competitive Radioimmunoassay. *J. Immunol. Meth.* **1980**, *34*, 345−352.
14. Fraker, P. J.; Speck, J. C. Protein and Cell Membrane Iodinations with a Sparingly Soluble Chloramide 1,3,4,6-Tetrachloro-3a, 6a-Diphenylglycoluril. *Biochem. Biophys. Res. Commun.* **1978**, *80*, 849−857.
15. Pardridge, W. M. Carrier-Mediated Transport of Thyroid Hormones Through the Blood-Brain Barrier. Primary Role of Albumin-Bound Hormone. *Endocrinology* **1979**, *105*, 605−612.
16. Ebling, W. F.; Wada, D. R.; Stanski, D. R. From Piecewise to Full Physiologic Pharmacokinetic Modeling: Applied to Thiopental Disposition in the Rat. *J. Pharmacokinet. Biopharm.* **1994**, *22* (*4*), 259−292.
17. Gibaldi, M.; Perrier, D. In *Pharmacokinetics*; Gibaldi, M.; Perrier, D.; Eds.; Dekker: New York, 1982.
18. Smith, K. R.; Borchardt, R. T. Permeability and Mechanism of Albumin, Cationized albumin, and Glycosylated Albumin Transcellular Transport Across Monolayers of Cultured Bovine Brain Capillary Endothelial cells. *Pharm. Res.* **1989**, *6*, 466−473.
19. Williams, S. K.; Devenny, J. J.; Bitensky, M. W. Micropinocytic Ingestion of Glycosylated Albumin by Isolated Microvessels: Possible Role in Pathogenesis of Diabetic Microangiopathy. *Proc. Natl. Aacad. Sci., U.S.A.* **1981**, *78*, 2393−2397.
20. Chekhonin, V. P.; Ryabukhin, I. A.; Zhirkov, Y. A. Transport of Hydrophobized Fragments of Antibodies through the Blood-Brain Barrier. *Neuroreport* **1995**, 129−132.
21. Mulcahy, L. S.; Smith, M. R.; Stacey, D. W. Requirement for Ras Proto-Oncogene Function during Serum-Stimulated Growth of NIH 3t3 Cells. *Nature* **1985**, *313*, 241−243.
22. Bauer, R. J.; Leigh, S. D.; Birr, C. A.; Bernhard, S. L. Alteration of the Pharmacokinetics of Small Proteins by Iodination. *Biopharm. Drug. Dispos.* **1996**, *17*, 761−774.
23. Kuo, B.; Nordblom, G. D.; Wright, D. S. Pertubration of Epidermal Growth Factor Clearance after Radioiodination and Its Implication. *J. Pharm. Sci.* **1997,** *86* (*13*), 290−296.
24. Bergmann, P.; Kacenelenbogen, R.; Vizet, A. Plasma Clearance, Tissue Distribution and Catabolism of Cationized Albumins with Increasing Isoelectric Points in the Rat. C*lin. Sci.* **1984**, *67*, 35−43.
25. Pepin, S.; Lutsch, C.; Grandgeorge, M.; Scherrmann, J. M. Snake F(ab′)2 Antivenom from Hyperimmunized Horse: Pharmacokinetics Following Intravenous and Intramuscular Administrations in Rabbits. *Pharm. Res.* **1995**, *12* (*10*), 1−4.
26. Muckerheide, A.; Domen, P. L.; Michael J. G. Cationisation of Protein Antigens. II. Alteration of regulatory properties. *J. Immunol.* **1987**, *138* (*9*), 2800−2804.
27. Apple, R. J.; Domen, P. L.; Muckerheide, A.; Michael J. G. Cationisation of Protein Antigens. III. Increased Antigen Uptake by Antigen-Presenting Cells. *J. Immunol.* **1988**, *140* (*10*), 3290−3295.
28. Pardridge, W. M.; Triguero, D.; Buciak, J. L.; Yang, J. Evaluation of Cationized Rat Albumin as a Potential Blood-Brain Barrier Drug Transport Vector. *J. Pharmacol. Exp. Ther.* **1990**, *255* (*2*), 893−899.
29. Pardridge, W. M.; Kang, Y.; Yang, J.; Buciak, J. L. Enhanced Cellular Uptake and in vivo Biodistribution of a Monoclonal Antibody Following Cationization. *J. Pharm. Sci.* **1995**, *84*, 943−948.
30. Pentel, P. K.; Keyler, D. E.; Gilbertson, D. G.; Ruth, G.; Pond, S. M. Pharmacokinetics and Toxicity of High Doses of Antibody Fab Fragments in Rats. *Drug Metab. Dispos.* **1988**, *16*, 141−145.
31. McClurkan, M. B.; Valentine, J. L.; Arnold, L., Owens; S. M. Disposition of Monoclonal Anti-phencyclidine Fab Fragments of Immunoglobulin G in Rats. *J. Pharmacol. Exp. Ther.* **1993**, *266***,** 1439−1445**.**
32. Bazin-Redureau, M. I.; Renard, C. B.; Scherrmann, J. M. G. Pharmacokinetics of Heterologous and Homologous Immunoglobulin G, F(ab′)2 and Fab after Intravenous Administration in the Rat. *J. Pharm. Pharmacol.* **1997**, *49*, 277−281.
33. Pardridge, W. M.; Buciak, J. L.; Friden, P. M. Selective Transport of an Anti-Transferrin Receptor Antibody through the Blood-Brain Barrier. *J. Pharmacol. Exp. Ther.* **1991**, *252*, 1247−1254.
34. Pardridge, W. M.; Kang, Y.; Diagne, A.; Zack, J. A. Cationized Hyperimmune Immunoglobulins: Pharmacokinetics, Toxicity Evalution and Treatment of Human Immunodeficiency Virus-Infected Human-Peripheral Blood Lymphocytes-Severe Combined Immune Deficiency Mice. *J. Pharmacol. Exp. Ther.* **1996**, *276*, 246−252.
35. Hong, G.; Bazin-Redureau, M. I.; Scherrmann, J. M. G. Hepatic Disposition and Toxicity of Cationized Goat Immunoglobulin G and Fab Fragments in Isolated Perfused Rat Liver. *Drug Metab. Dispos.*, in press.
36. Takakura, Y.; Fujita, T.; Hashida, M.; Sezaki, H. Disposition Characteristics of Macromolecules in Tumor-Bearing Mice. *Pharm. Res.* **1990**, *7*, 339−346.
37. Praaning-van Dalen, D. P.; Brouwer, A.; Knook, D. L. Clearance Capacity of Rat Liver Kupffer, Endothelial, and Parenchymal Cells. *Gastroenterology* **1981,** *81*(*6*), 1036−1044.
38. Meiger, D. K. F.; Mol, W. E. M.; Muller, M.; Kurz, G. Carrier-mediated Transport in the Hepatic Distribution and Elimination of Drugs, with Special Reference to the Category of Organic Cations. *J. Pharmacokinet.* **1990**, *18*, 35−70.
39. Taylor, A. E.; Granger, N. D. Exchange of Macromolecules Across the Microcirculation; In *Handbook of Physiology: the Cardiovascular System*, Section 2, Volume IV; Renkin, E. M.; Michel, C. C., Eds.; American Physiology Society: Bethesda, MD, 1984; pp 467−520.
40. Brenner, B. M.; Hostetter, T H.; Humes, H. D. Glomerular Permeselectivity: Barrier Function Based on Discrimination of Molecular Size and Charge. *Am. J. Physiol.* **1978**, *234*, 7455−7460.
41. Arend, W. P.; Silverblatt, F. J. Serum Disappearance and Catabolism of Homologous Immunoglobulin Fragments in Rats. *Clin. Exp. Immunol.* **1975**, *22* (*3*), 502−513.
42. Rochdi, M.; Sabouraud, A.; Baud, F. J.; Bismuth, C.; M., S. J. Toxicokinetics of Colchicine in Humans: Analysis of Tissue, Plasma and Urine Data in Ten Cases. *Hum. Exp. Toxicol.* **1992**, *11*, 510−516.

Acknowledgments

This work was supported by a grant from INSERM/Ministère de la Défense.

JS970335N

Artificial Neural Networks Applied to the In Vitro–In Vivo Correlation of an Extended-Release Formulation: Initial Trials and Experience

JAMES A. DOWELL,[†,‡] AJAZ HUSSAIN,[§] JOHN DEVANE,[†,||] AND DAVID YOUNG*[,†,‡]

Contribution from *In Vitro–In Vivo Relationship Cooperative Working Group, Pharmacokinetics-Biopharmaceutics Laboratory, Department of Pharmaceutical Sciences, University of Maryland at Baltimore, Baltimore, Maryland 21201, Food and Drug Administration, Rockville, Maryland 20855, and Elan Corporation plc, Athlone, Ireland.*

Received April 15, 1997. Final revised manuscript received March 9, 1998.
Accepted for publication September 8, 1998.

Abstract □ Artificial neural networks applied to in vitro–in vivo correlations (ANN–IVIVC) have the potential to be a reliable predictive tool that overcomes some of the difficulties associated with classical regression methods, principally, that of providing an a priori specification of the regression equation structure. A number of unique ANN configurations are presented, that have been evaluated for their ability to determine an IVIVC from different formulations of the same product. Configuration variables included a combination of architectural structures, learning algorithms, and input–output association structures. The initial training set consisted of two formulations and included the dissolution from each of the six cells in the dissolution bath as inputs, with associated outputs consisting of 1512 pharmacokinetic time points from nine patients enrolled in a crossover study. A third formulation IVIVC data set was used for predictive validation. Using these data, a total of 29 ANN configurations were evaluated. The ANN structures included the traditional feed forward, recurrent, jump connections, and general regression neural networks, with input–output association types consisting of the direct mapping of the dissolution profiles to the pharmacokinetic observations, mapping the individual dissolution points to the individual observations, and using a "memorative" input–output association. The ANNs were evaluated on the basis of their predictive performance, which was excellent for some of these ANN models. This work provides a basic foundation for ANN–IVIVC modeling and is the basis for continued modeling with other desirable inputs, such as formulation variables and subject demographics.

Introduction

It is often desirable to determine a good correlation between the in vitro dissolution data and the in vivo pharmacokinetics. This modeled relationship can then be used in product development or in establishing dissolution specifications. Many of the previous examples of defining an in vitro−in vivo correlation (IVIVC) in drug studies follow simple linear models, relating a parameter or a time point descriptive of the dissolution to a parameter or a time point descriptive of the pharmacokinetic absorption.[1−3] However, often a model is unsuccessful in completely describing the IVIVC and sometimes no relationship can be determined. The number of possible variables, the model being unable to account for some physiological rate determining process, and the possible amount of variability intrinsic to the parameters of these modeled relationships are some examples of these difficulties.[4−6]

It is an aim of the IVIVR Cooperative Working Group to extend the development of IVIVC using newer modeling tools, such as those in the field of artificial intelligence. The self-organizational properties of these methods and their ability to incorporate a large number of possible variables and relationships without a predefined model structure encourage the evaluation of artificial neural networks (ANN) in determining an IVIVC.

The term ANN refers to a group of algorithms used for pattern recognition and data modeling. As its name implies, ANN systems are loosely based on neural physiology, using the concept of a highly interconnected system of parallel processing units. It is not the intent of this paper to intensively cover ANN methodology; a review of the development of ANN can be found elsewhere,[7] as well as a complete description of the theory involved and tested in this research.[8−10]

The application of neural network concepts is relatively new to the field of pharmacokinetics and pharmacodynamics. An introduction to ANN as applied to the field of pharmacokinetics was given by Erb, who described the common back-propagation learning algorithm[11] and demonstrated its ability to be used as a bayesian classifier using simulated data.[12] The application of real pharmacokinetic data for the task of learning interspecies scaling, using different input−output data formats and neural network configurations, has been described by Hussain et al.[13] They also described the problem of the lack of a structured set of rules or guidelines in determining network configuration variables, such as the number of hidden nodes, the necessary number of training iterations, and the proper data format. Application of an ANN to predict drug behavior based on patient demographics and patient factors, and a comparison to a more traditional approach has also been described.[14] The implementation of ANNs in pharmacodynamics to predict the central nervous system activity due to the drug alfentanil has been examined.[15] ANNs have also been successfully implemented in problems very similar to IVIVC, such as product development[16] and quantitative structure−pharmacokinetic relationships,[17] again using a common back-propagation approach to ANN learning.

It is our eventual aim to develop a methodical approach to ANN−IVIVC, and the intent of this paper and current research is to show the feasibility of ANN−IVIVC by presenting the results from some common ANN configurations and data formats, using a relatively small set of IVIVC data for training and prediction. The results from a newer ANN, which does not use the back-propagation iterative learning paradigm, are also presented. It is not the intent of this paper to rigorously compare this method

* Author to whom correspondence should be addressed at: GloboMax LLC 7250 Parkway Dr., Suite 430 Hanover, MD 21076. Telephone: 410-712-9500. FAX: 410-712-0737. E-mail: youngd@globomax.com.
[†] In Vitro−In Vivo Relationship Cooperative Working Group.
[‡] Pharmacokinetics−Biopharmaceutics Laboratory.
[§] Food and Drug Administration.
[||] Elan Corporation plc.

10.1021/js970148p CCC: $18.00
Published on Web 11/19/1998

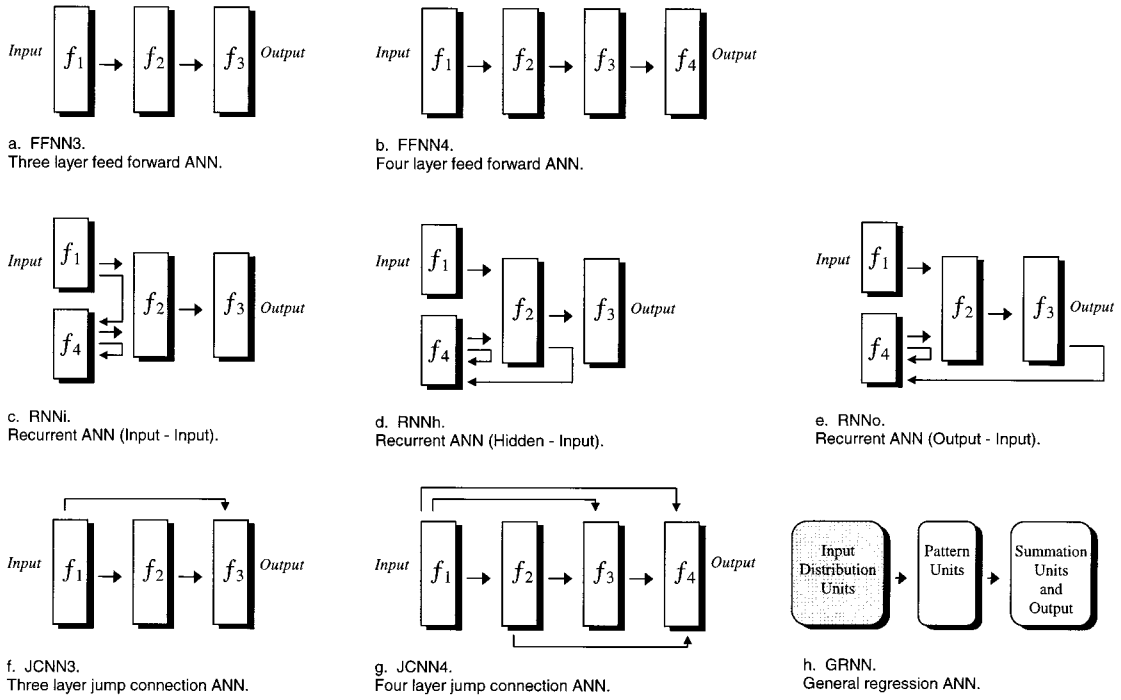

Figure 1—Block diagrams of the ANN architectures used in the study. Almost all of the architectures employ some type of back-propagation learning. The general regression neural network uses a statistical technique known as kernel regression.

with other available IVIVC methods, suggest this approach as appropriate for different situations, nor suggest that this method is a simpler means for correlating in vitro–in vivo data. Such comparisons and analyses, which are ongoing within our group, require numerous types of data and experimental design.

Methods

Description of Terms—There is a great deal of diversity in terminology within the ANN literature, and it is necessary to define some important terms that will be used throughout this paper. These defintions are not intended to be a glossary of terms in the area of artificial intelligence programming, but rather a necessary beginning in establishing a common foundation. Beginning with the format of data, each correlation between a set of input variable(s) and a set of output variable(s) is defined as an *input–output association* and all of the input–output associations collectively form a *pattern file.* ANNs learn using a pattern file known as a *training pattern file,* in which the individual input–output associations from this file are presented either randomly or in a defined order. A *validation pattern file,* which does not use data involved in training, is applied to the trained ANN to test the predictive capabilities of the trained ANN. *Memorization* of an ANN is a common problem referring to when an ANN has become over-trained and is mimicking the training pattern file. This is a situation where the ANN does not have the ability to predict well using inputs other than those found in the training pattern file. To avoid memorization and to establish a criteria to stop training, a *test pattern file* is constructed using associations from the training pattern file and applied periodically to the ANN during training. The input–output associations from the test pattern file are not used in the training, but as a measure of memorization and as a criteria to terminate training. The basic functional element of a neural network is defined as a *node,* which possesses a certain type of *transfer function.* The connections between nodes carry a weighting term, which is the element of an ANN that is continually adjusted during training. Nodes are arranged in layers: *input layer, hidden layer(s),* and *output layer.* It is necessary to define these terms prior to describing any methodology or discussing the results to prevent any confusion due to a lack of formalized vocabulary in artificial intelligence research.

Trial Data and Software—The data set reported in this study included in vitro inputs (% dissolved) and in vivo outputs (plasma concentrations). Inputs in the training pattern files consisted of the dissolution values from two extended-release formulations with seven dissolution time points each, at which six tablets were tested per formulation. Each formulation was administered to nine individuals in a crossover trial. Corresponding ANN outputs consisted of the drug plasma concentrations, sampled at 15 time points following oral tablet administration. A third extended release formulation, with the same experimental setup and part of the same crossover study, was used as a validation set. Success of the ANNs was based on the prediction of the validation profile.

The complete data set, consisting of the three separate formulations and correlated kinetics, was chosen because the pharmacokinetics for this drug was known to follow a "flip–flop" first-order absorption model, where the absorption of this drug was relatively slow compared with its elimination. This situation, as a trial for ANN–IVIVC, gave reasonable assurance that the dissolution kinetics could be considered a variable influential throughout the pharmacokinetic profile.

All ANN training and application were performed using Ward Systems' software package, NeuroShell 2.[18]

Choice of Neural Network Configurations—Part of the aim of these studies and the focus of this paper was to determine the best network configuration for this relatively small set of in vitro–in vivo data using a systematic approach. This determination was performed by initially selecting a set of common network architectures. Network configuration variables that are the focus here included the type of input–output association, network architecture, and for some architectures, the number of hidden layers.

Network Architectures—These trials involved four basic types of ANN architectures contained within the NeuroShell 2 software: traditional feed forward neural networks, recurrent neural networks, jump connection neural networks, and generalized regression neural networks. Diagrams of these network structures, with the nodes represented collectively as functional blocks, are shown in Figure 1. Including the type of network architecture and the number of hidden layers, we have tested a total of eight types of network architectures. A summary of each ANN architecture is given below and shown in Table 1.

Two of these ANN architectures are the common three and four layer feed forward neural networks (FFNN3 and FFNN4 shown in Figures 1a and 1b, respectively), which have one and two hidden layers, respectively. To give the network functional flexibility, a linear function ($f_1(x) = x$) was used for the nodes in the input

Table 1—Summary of the Eight Types of ANN Architectures Tested

type	architecture	data presentation	test set	node configuration (input-hidden-output)
FFNN3	feed forward 3 layers	random	≈10% randomly selected	linear–logistic–logistic
FFNN4	feed forward 4 layers	random	≈10% randomly selected	linear–logistic–logistic–logistic
RNNi	recurrent input–input	rotational	individual subject with single formulation with all 6 dissolution sets	linear–logistic–logistic
RNNh	recurrent hidden–input	rotational	individual subject with single formulation with all 6 dissolution sets	linear–logistic–logistic
RNNo	recurrent output–input	rotational	individual subject with single formulation with all 6 dissolution sets	linear–logistic–logistic
JCNN3	jump connections 3 layers	random	≈10% randomly selected	linear–logistic–logistic
JCNN4	jump connections 4 layers	random	≈10% randomly selected	linear–logistic–logistic–logistic
GRNN	general regression neural network	N/A	≈10% randomly selected to determine smoothing	N/A

Table 2—Pattern Files Constructed from the Different Input–Output Association Types[a]

#	association type	association input(s)	association output(s)	pattern structure	#associations/ formulation
1	functional	(7) dissolution set$_j$ (t_{DISS1}:t_{DISS7})	(15) PK$_i$ (t_{PK1}:t_{PK15})	subject$_{1-9}$ (dissolution set$_{1-6}$)	54
2	time series	(8) t_{PK}, dissolution set$_j$ (t_{DISS1}:t_{DISS7})	(1) PK$_i$ (t_{PK})	subject$_{1-9}$ (dissolution set$_{1-6}$($t_{PK\ 1-15}$))	810
3	time series	(2) $t_{DISS|PK}$, dissolution set$_j$ (t_{DISS})	(1) PK$_i$ (t_{PK}) only those outputs where $t_{PK} = t_{DISS}$	subject$_{1-9}$ (dissolution set$_{1-6}$($t_{DISS|PK\ 1-7}$))	378
4	time series memorative association	(1–8) t_{PK}, dissolution set$_j$ (if $t_{DISS} < t_{PK}$)	(1) PK$_i$ (t_{PK})	subject$_{1-9}$ (dissolution set$_{1-6}$($t_{PK\ 1-15}$))	810

[a] PK = Pharmacokinetic observations (in vivo); DISS = % dissolved (in vitro); i = subject number; j = tablet number; t_{PK} = pharmacokinetic time point; t_{DISS} = dissolution time point.

layer and a logistic function ($f_2(x)$, $f_3(x)$, $f_4(x) = 1/(1 + \exp(-x))$) was used for each node in the hidden and output layers.

The recurrent networks defined as RNNi, RNNh, and RNNo (Figures 1c, 1d, and 1e, respectively) had recurrent connections to the input, hidden, and output layers, respectively. Recurrent architectures do not have the input to output feed forward design; their recurrent design allows for a "long-term memory". This type of structure has the ability to learn sequences of input−output associations. Therefore, the setup of input−output data sequence presented in training and prediction becomes very important to these networks and their order must be considered, such as when the data is presented as a time series. The transfer function of each node in the hidden and output layers was set as a logistic function, whereas the input layer nodes were set to a linear function. The fourth layer can be called the network's "long-term memory", and has no node functionality. It contains the contents of the connected layer as it was in the previous training. These types of networks have been shown to work well with time series data that depend on history.[19]

The following two network architectures are a type of ANN known as jump connections. In this type of back-propagation network, every layer is connected in a feed forward manner. Three and four layer jump connection ANN architectures, designated JCNN3 and JCNN4 (Figures 1f and 1g), respectively, were used because they may be possible alternatives to the traditional feed forward structures, and were given the same node functions as FFNN3 and FFNN4.

Unlike the other ANNs, a general regression neural network (GRNN) is not an ANN that uses the back-propagation learning paradigm. The GRNN is an ANN system that involves a statistical technique known as kernel regression and requires the data to only be iterated once through the network during training.[10] Training of the GRNN was done using two options available in the NeuroShell 2 software. Patterns were compared based on their differences in distance using the vanilla or Euclidean distance metric, and smoothing was performed by using a genetic algorithm that selectively breeds a solution to the problem using a fitness function as a measure of survival. The mean squared error of the outputs in the test pattern file is used as the fitness function in the software. The NeuroShell 2 software manual contains descriptions of this terminology and these options with suggestions for their implementation.[18]

In all but the GRNN, training was performed by the software using a back-propagation scheme. Back-propagation is the most widely used learning algorithm employed in training neural networks. In its simplest form, it should be very familiar to those involved in data fitting and regression because it is an iterative gradient descent procedure that minimizes the error.[20]

Network Training Criteria—In all nonrecurrent networks, 10% of the training pattern file was randomly selected and placed aside as a test pattern file during training. Recurrent neural networks, however, rely on previous history, which required the data to be presented as a time series across input−output associations. This presentation also included the application of any test or validation pattern file. For this reason, the test pattern file applied to any recurrent architecture consisted of the associations from the ninth subject/second formulation, kept in time sequence.

The test pattern file was not included in the training, but was used as a periodic measure of the network's ability to successfully predict while being trained. The test pattern file was applied to the network after every 200 input−output associations (training events), using the NET-PERFECT feature in the NeuroShell 2 software. The prediction of the outputs in the test pattern file was used as a stop criterion. In each case, the network was directed to stop training after 20000 training events following a minimum error, and the weights corresponding to that minimum were saved as the trained ANN.

Associations and Pattern Files—Four different types of pattern files constructed from the same data were selected for evaluation. The pattern files, named ASSOCIATION 1 through 4, were unique because of different formatting of the input−output association. Each training pattern file had corresponding validation and test pattern files constructed with the same type of input−output association. A diagram of each type of input−output association is shown in Figure 2, indicating the structure of the relationship as well as using subscripts to show how the data are formatted across associations to create a pattern file. General descriptions of the input−output associations are given next, and a summary of the constructed pattern files is shown in Table 2.

ASSOCIATION 1—Initially the data were presented as the functional relationship shown in Figure 2a, with an input−output association that used all of the pharmacokinetic concentration values from an individual as an output set associated with an input set that consisted of the dissolution profile from an individual tablet. The pattern file then contained each pharmacokinetic observation set associated with each of the six tablet dissolution profiles. The dissolution mean was not used in this type of pattern file, or in either of the other three pattern files.

ASSOCIATION 2—Like ASSOCIATION 1, the input−output associations in this pattern file included the complete kinetic set of dissolution values for each tested tablet, but each was associated with a single respective pharmacokinetic output. Collectively, the input−output association lines of the pattern file formed a pharmacokinetic time sequence. The pharmacokinetic time point

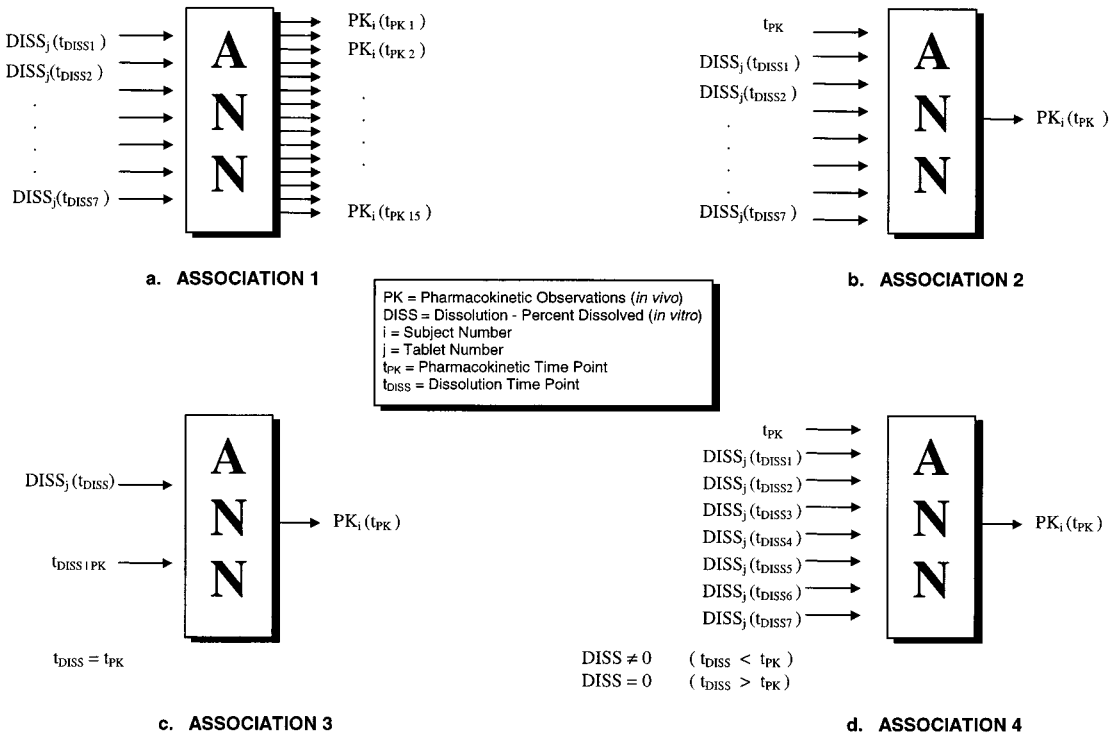

Figure 2—Diagrams of the input–output associations used in pattern files ASSOCIATION 1 through 4. The subscripts i and j are used to show the number of associations across association types.

was also included as an input. A diagram of this relationship is shown in Figure 2b.

ASSOCIATION 3—The input−output associations of this pattern file, shown in Figure 2c, consisted of each in vitro value as an input associated with each in vivo output. Pharmacokinetic observations with no directly associated dissolution observations were not used in the training. The time of the observation was also added as an input.

ASSOCIATION 4—This pattern file, shown in Figure 2d, attempted to unite some of the more desirable features of the previous pattern files that included presenting the entire dissolution profile per tested tablet as inputs (ASSOCIATIONS 1 and 2), presenting the data as a time sequence (ASSOCIATIONS 1, 2, and 3), and utilizing all of the in vitro data (ASSOCIATIONS 1, 2, and 4). Pattern file ASSOCIATION 4 was a sequential time series and included previous dissolution values as inputs. This type of pattern file can be termed a *memorative association* and was a type of time progressive synthesis neural network configuration described by Veng-Pedersen.[15] The output consisted of the pharmacokinetic concentration value, whereas the inputs were the pharmacokinetic time point and all the dissolution values that preceded that point in time. Dissolution values that occurred after that pharmacokinetic time point were set to zero in the pattern file and were interpreted as null inputs by the software.

Results and Discussion

A total of 29 network configurations, which included the eight different types of ANN architectures and four types of input−output associations, were tested. The three recurrent architectures were not used with ASSOCIATION 1, because this type of relationship did not have a sequential format across associations.

Each network was trained as described in the methodology, and the weights of each of the 29 trained ANNs were saved. Inputs from the training and validation pattern files were applied to the trained networks and these respective ANN outputs were compared to the actual observations. Shown in Table 3 are the results for both the training and validation pattern files for each ANN configuration, consisting of the correlation coefficient (R^2), mean prediction error (MPE), and mean absolute error (MAE). These values are defined as

$$R^2 = \frac{\sum(y - \hat{y})^2}{\sum(y - \bar{y})^2}$$

$$\text{MPE} = \frac{1}{N}\sum(\hat{y} - y)$$

$$\text{MAE} = \frac{1}{N}\sum|y - \hat{y}|$$

where y = actual observation, $\hat{y}$ = ANN prediction, $\bar{y}$ = average observation, and N = number of observations. Also shown is the ratio of R^2 between the predictions and training pattern files, as an indicator of possible network memorization.

Results from these trials, as summarized in Table 3, reflect the success of each ANN configuration with this particular set of IVIVC data. These results are measured by the precision and bias of the outputs from the training and validation pattern files. The ANNs attempted to determine a mean concentration curve based on the information contained in the dissolution kinetics, and in some configurations, attempted to account for the variability in the pharmacokinetics due to variability in the dissolution kinetics.

More than half of these ANN configurations could be considered successful in predicting the pharmacokinetic data from the dissolution kinetics. The better network architectures for this IVIVC data set seem to be the feed forward and the generalized regression architectures, based on their ability to give good model predictions with all four pattern files. The more successful pattern files included formatting the data as a functional relationship (ASSOCIATION 1) and as a memorative pattern file (ASSOCIATION 4). An example of a model prediction from one of these network configurations is shown in Figure 3 and Figure 4. In this example, the ASSOCIATION 4

Table 3—Statistical Results for the 29 Network Configurations Applied to ANN–IVIVC

network	training set R^2	training set MPE	training set MAE	validation set R^2	validation set MPE	validation set MAE	R^2 ratio (prediction/ training)
Association 1							
FFNN3	0.878	–0.229	3.110	0.803	–1.431	3.992	0.915
FFNN4	0.880	–0.196	3.109	0.790	–1.435	4.089	0.897
RNNi	N/A	N/A	N/A	N/A	N/A	N/A	N/A
RNNh	N/A	N/A	N/A	N/A	N/A	N/A	N/A
RNNo	N/A	N/A	N/A	N/A	N/A	N/A	N/A
JCNN3	0.875	0.454	3.207	0.819	–0.415	3.957	0.937
JCNN4	0.872	0.574	3.238	0.815	–0.526	4.007	0.935
GRNN	0.877	–0.001	3.180	0.800	–1.302	3.997	0.912
Association 2							
FFNN3	0.136	–1.371	9.486	0.142	–2.180	9.588	1.041
FFNN4	0.865	0.493	3.316	0.792	–0.910	4.179	0.915
RNNi	0.732	3.642	5.080	0.742	3.061	5.422	1.013
RNNh	0.728	4.351	5.101	0.692	3.731	5.749	0.950
RNNo	0.741	4.273	5.268	0.763	2.312	5.336	1.029
JCNN3	0.101	–2.234	9.520	0.114	–3.062	9.612	1.134
JCNN4	0.078	–1.365	9.653	0.149	–1.396	9.592	1.910
GRNN	0.878	–0.035	3.184	0.788	–1.357	4.178	0.897
Association 3							
FFNN3	0.749	–0.825	4.184	0.608	–2.931	5.352	0.812
FFNN4	0.752	–0.514	4.167	0.620	–2.623	5.296	0.824
RNNi	0.539	4.583	6.237	0.594	2.642	6.088	1.102
RNNh	0.420	6.089	7.171	0.559	3.493	6.381	1.333
RNNo	0.478	4.347	6.668	0.578	1.404	6.093	1.210
JCNN3	0.745	–0.073	4.267	0.614	–2.259	5.327	0.825
JCNN4	0.746	–0.235	4.238	0.617	–2.391	5.265	0.827
GRNN	0.769	0.031	3.998	0.634	–2.110	5.092	0.825
Association 4							
FFNN3	0.846	–0.076	3.540	0.771	–1.573	4.465	0.911
FFNN4	0.854	–0.538	3.389	0.770	–1.683	4.280	0.901
RNNi	0.658	4.650	5.626	0.571	5.540	7.196	0.868
RNNh	0.696	0.744	5.187	0.580	5.174	7.135	0.834
RNNo	0.596	1.252	6.111	0.628	3.404	6.303	1.054
JCNN3	0.841	–0.192	3.607	0.789	–0.798	4.230	0.938
JCNN4	0.856	–0.286	3.357	0.787	–1.618	4.098	0.919
GRNN	0.859	–0.015	3.303	0.773	–0.749	4.295	0.900

pattern file was used to train the GRNN. Following training, the dissolution values from the training pattern files were used as inputs to predict the pharmacokinetic data. Comparisons of the actual observations with these ANN outputs are shown in Figure 3. The dissolution values from the validation pattern file were then presented to this trained ANN, interpolating the pharmacokinetic predictions shown in a comparison with the actual pharmacokinetic observations in Figure 4. These figures are representative of those network configurations that did relatively well, with a MPE close to zero for both training and validation sets, an R^2 of >0.85 for the training set, and an R^2 of >0.77 for the validation set (R^2 ratio >0.9).

The common and relatively simple FFNN architectures (Figures 1a and 1b) worked well with this data set based on the predictions of the validation pattern file outputs, especially when the data were presented as a functional relationship (ASSOCIATION 1). For some IVIVC data, however, these types of architectures may not work as well as time series predictors. Some IVIVC tend to be nonlinear, requiring the ANN to incorporate past history. The feed forward structure cannot incorporate history, but this may be accounted for if the data is arranged as a memorative association (ASSOCIATION 4), which also proved successful with this IVIVC data. An interesting example of network performance as a function of configuration variables is seen in comparing the ASSOCIATION 2–FFNN3 trial with the ASSOCIATION 2–FFNN4 trial,

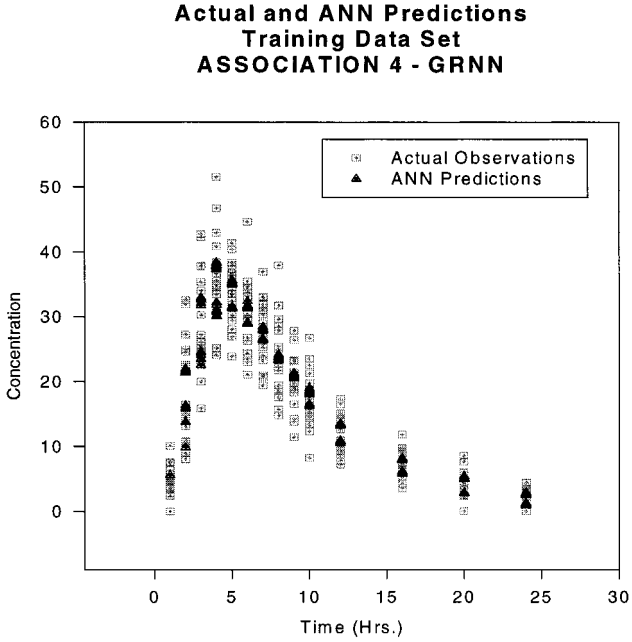

Figure 3—Actual pharmacokinetic observations from the training data set are compared with ANN pharmacokinetic predictions using in vitro inputs from the training data set. The GRNN was trained with the training pattern file ASSOCIATION 4.

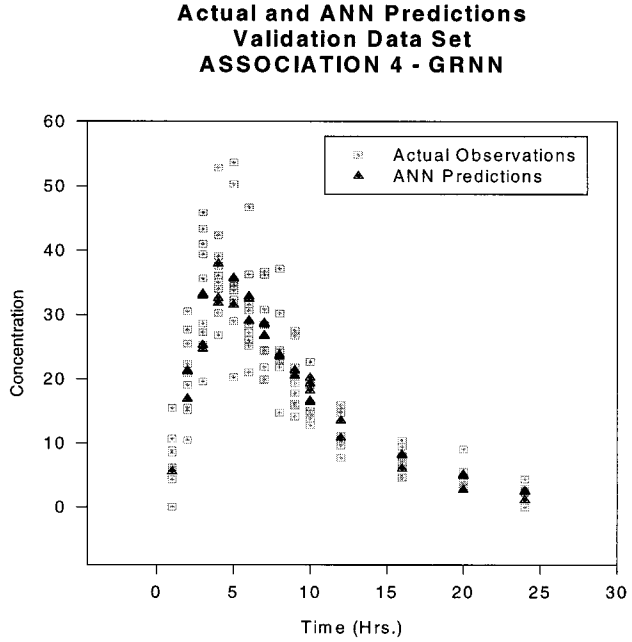

Figure 4—Actual pharmacokinetic observations from the validation data set are compared with ANN pharmacokinetic predictions using in vitro inputs from the validation data set. The GRNN was trained with the training pattern file ASSOCIATION 4.

where the additional hidden layer improved prediction dramatically. Practical ANN experience has shown that a majority of problems can be solved with a three-layered design, and that a four-layered ANN may be prone to fall into a local minima.[21] However, with this IVIVC data set formatted as the ASSOCIATION 2 pattern file, a four-layered feed forward structure predicted well, whereas the three-layered ANN failed to converge on a solution.

The JCNN architectures (Figures 1f and 1g), which are structurally very similar to the FFNN architectures, also compared well. The lack of any significant improvement in describing these data, however, suggests that the additional jump connections were not necessary.

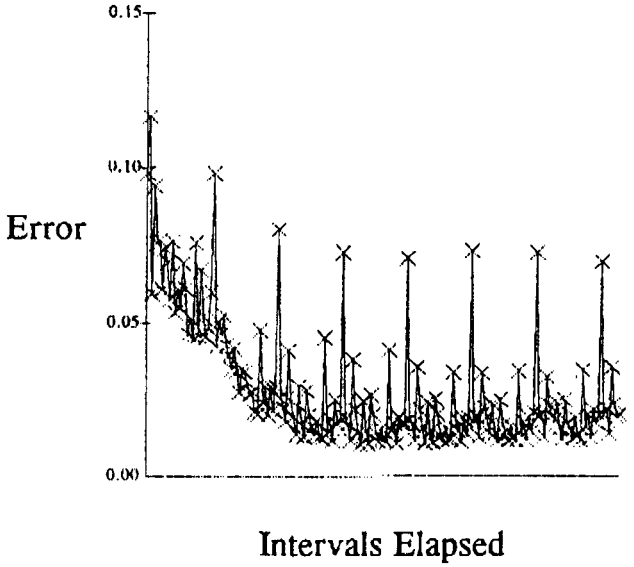

Figure 5—Error between actual observations and ANN predictions of the test pattern file during training of the recurrent network RNNo with ASSOCIATION 3 training pattern file. Each point (x) represents the error when the test pattern file is tested during network learning. The test pattern file was applied once after every 200 input–output associations of the training pattern file.

A thorough description of the theoretical development and implementation of the GRNN is too involved for this discussion, but can be referenced in the work by Specht.[10] This network structure requires only a single iteration to provide estimates of continuous variables and has a distinct advantage in that it can converge to a linear or nonlinear regression surface, even with relatively little data. This property as well as its success in these trials with all of the different types of pattern files encourage its use in this type of research.

A problem in implementing the recurrent network structures, as reflected in the results presented here, was the determination of a stopping criteria. As with all back-propagation network training performed in these trials, the test pattern file was applied periodically throughout training and was a measure used to indicate the completion of training before the onset of memorization. Because of the importance in keeping a sequential structure with recurrent networks, rather than the test set randomly constructed from the training data, the ninth subject receiving the second formulation was used as the selected test pattern file. This procedure proved to be a good measure that prevented memorization, but biased the trained network in the favor of this test set. A typical plot of the error as a function of the training intervals for a recurrent network is shown in Figure 5. Once a minimum is found, network training oscillates across subjects until training is stopped, the time of which is based on the number of iterations following a minimum in the test set. A trained network based on a minimum corresponding to the test pattern file is saved, biasing the results to the data used as the test set. So, although the recurrent ANN structures produced fair results, these results were biased to the selected test pattern file. Better results may be expected if a better "average" or unbiased test pattern can be found, the intersubject variability can be better described using additional inputs, or another method to protect against network memorization can be found.

In most ANN structures, the number of inputs and outputs dictate the number of input and output nodes, respectively. Hence, more inputs and outputs lead to a more complicated network structure. Although relatively successful here, the ASSOCIATION 1 pattern file had a total of 15 outputs, which must be considered in the evaluation of these types of input−output associations for ANN−IVIVC. When the level of complexity of the structure increases, the likelihood of obtaining a good solution decreases. As this research progresses, it is expected that the number of independent variables, or inputs, will be increased, adding to the complexity of the models and making input−output associations, like that found in ASSOCIATION 1, undesirable. The memorative type of input−output association used to construct the ASSOCIATION 4 pattern files worked well with all eight ANN architectures. This type of pattern file had the advantage of being a generalized format with a single output, which also allows the network to incorporate relationships from the previous inputs. A disadvantage of this pattern file is its inability to use information from dissolution values with a time of dissolution greater than the corresponding time of the pharmacokinetic observation. This pattern file may not predict well in data sets where the dissolution lags behind the pharmacokinetics.

The number of network configurations can be immense when considering some of the variables examined here, such as network architecture, data formats, and number of hidden layers, and considering some of the other possible network configuration variables not addressed; for examples, number of hidden nodes, additional network structures, learning algorithms, and the different types of node transfer functions. The number of hidden nodes in these trials were set to the software defaults, which were allowed to be conservatively large, because the periodic application of the test pattern file helps to prevent memorization. Some of the more common network architectures were examined in this study, but there were many more that may prove to be as good or better in ANN−IVIVC. Other possible structures that may prove to be applicable are the newer multilayer networks that include a lag in the data between the dependent and independent variables.[9] The node transfer functions were limited to the linear and logistic transfer functions in this study, but many other different types of functions, such as a limit, competitive, hyperbolic tangent, sine, or Gaussian may be used.

Conclusion

We have evaluated a number of possible network configurations, many of which successfully predicted a mean in vivo plasma concentration profile using dissolution kinetics. This work has demonstrated the feasibility of ANN−IVIVC by showing a number of potential ANN configurations that can be considered successful with this data set, but has illustrated a need for a methodical approach in applying ANN to problems. Additional input variables, including subject demographics, dissolution method variables, and formulation variables, are currently being introduced to attempt to account for the nonrandom error associated in the relationship. The ANN−IVIVC has the potential to establish complex relationships and may also possess the ability to interpolate pharmacokinetic parameters and profiles given formulation specifications. Also, algorithms and software currently exist to reverse map from the plasma concentration curve to the dissolution profile, possibly forecasting a range of dissolution profiles that will provide bioequivalent formulations.

References and Notes

1. Sullivan, T. J.; Sakmar, E.; Wagner, J. G. Comparative bioavailability: a new type of *in vitro-in vivo* correlation exemplified by prednisone. *J. Pharmacokinet. Biopharm.* **1976**, *4(2)*, 173−181.

2. Graffner, C.; Nicklasson, M.; J.-E. Lindgren, Correlations between in vitro dissolution rate and bioavailability of alaproclate tablets. *J. Pharmacokinet. Biopharm*. **1984**, *12(4)*, 367−380.
3. Caramella, C.; Ferrari, F.; Bonferoni, M. C.; Sangalli, M. E.; De Bernardi Di Valserra, M.; Feletti, F.; F., Galmozzi, M. R. In vitro/in vivo correlation of prolonged release dosage forms containing diltiazem HCl. *Biopharm. Drug Dispos.* **1993**, *14(2)*, 143−160.
4. Wood, R. W.; Martis, L.; Gillum, A. W.; Roseman, T. J.; Lin, L.; L.; Bernardo, P. In vitro dissolution and in vivo bioavailability of commercial levothyroxine sodium tablets in the hypothyroid dog model. *J. Pharm. Sci.* **1990**, *79(2)*, 124−127.
5. Barr, W. H.; Zola, E. M.; Candler, E. L.; S−M. Hwang, Tendolkar, A. V.; Shamburek, R.; Parker, B.; Hilty, M. D. Differential absorption of amoxicillin from the human small and large intestine. *Clin. Pharmacol. Ther.* **1994**, *56(3)*, 279−285.
6. Levy, G.; Hollister, L. E. Inter- and intra subject variations in drug absorption kinetics. *J. Pharm. Sci.* **1964**, *53(12)*, 1446−1452.
7. Anderson, J. A. *An introduction to neural networks*; The MIT Press: Cambridge, MA, 1995.
8. Gallant, S. I. *Neural Network Learning and Expert Systems*; The MIT Press, Cambridge, MA, 1993.
9. Hagan, M. T.; Demuth, H. B.; Beale, M. *Neural Network Design*; PWS Publishing: Boston, 1996.
10. Specht, D. F. A general regression neural network. *IEEE Trans. Neural Networks* **1991**, *2(6)*, 568−576.
11. Erb, R. Introduction to back-propagation neural network computation. *Pharm. Res.* **1993**, *10(1)*, 165−170.
12. Erb, R. The back-propagation neural network − A bayesian classifier. Introduction and applicability to pharmacokinetics. *Clin. Pharmacokinet.* **1995**, *29(2)*, 69−79.
13. Hussain, A. S.; Johnson, R. D.; Vachharajani, N. N.; Ritschel, W. A. Feasibility of developing a neural network for prediction of human pharmacokinetic parameters from animal data. *Pharm. Res.* **1993**, *10(3)*, 466−469.
14. Brier, M. E.; Zurada, J. M.; Aronoff, G. R. Neural network predicted peak and trough gentamicin concentrations. *Pharm. Res.*, **1995**, *12(3)*, 406−412.
15. Veng-Pedersen, P.; Modi, N. B. Application of neural networks to pharmacodynamics. *J. Pharm. Sci.*, **1993**, *82(9)*, 918−926.
16. Hussain, A. S.; Yu, X. Q.; Johnson, R. D. Application of neural computing in pharmaceutical product development. *Pharm. Res.* **1991**, *8(10)*, 1248−1252.
17. Gobburu, J. V. S.; Shelver, W. H. Quantitative structure-pharmacokinetic relationships (QPSR) of beta blockers derived using neural networks. *J. Pharm. Sci.* **1995**, *84(7)*, 862−865.
18. *NeuroShell 2 Manual Third Edition*; Ward Systems Group, Inc., Executive Park West, 5 Hillcrest Drive, Frederick, MD 21702, 1995.
19. Elman, J. L. Finding structure in time. *Cognitive Science* **1990**, *14(1)*, 179−211.
20. Haykin, S. *Neural networks: a comprehensive foundation*; Macmillan: New York, 1994.
21. De Villiers, J.; Barnard, E. Back-propagation neural nets with one and two hidden layers. *IEEE Trans. Neural Networks* **1992**, *4(1)*, 136−141.

Acknowledgments

The work reported in this manuscript and ongoing research in ANN-IVIVC is supported by the Elan Corporation, plc. as part of their overall sponsorship of the IVIVR Cooperative Working Group. The views expressed by Ajaz S. Hussain are his own and may not reflect the policies of the FDA. Figures are reproduced with the permission of Plenum Publishing from the book entitled *In Vitro-In Vivo Correlations*.

JS970148P

A publication of the American Pharmaceutical Association and the American Chemical Society

JOURNAL OF Pharmaceutical Sciences

February 1999
Volume 88, Number 2

RESEARCH ARTICLES

Use of Infrared Spectroscopy to Assess Secondary Structure of Human Growth Hormone within Biodegradable Microspheres

TZUNG-HORNG YANG,[†] AICHUN DONG,[‡] JEFF MEYER,[†] OLUFUNMI L. JOHNSON,[§] JEFFREY L. CLELAND,[||] AND JOHN F. CARPENTER*,[†]

Contribution from *School of Pharmacy, Box C238, University of Colorado Health Sciences Center, 4200 E. Ninth Avenue, Denver, Colorado 80262, Department of Chemistry and Biochemisty, University of Northern Colorado, Greeley, Colorado 80639, Formulations Department, Alkermes, Cambridge, Massachusetts 02139, and Pharmaceutical R & D, Genentech, S. San Francisco, California 94080.*

Received October 23, 1998. Accepted for publication November 2, 1998.

Abstract □ The purpose of this study was to test the utility of infrared (IR) spectroscopy to determine protein secondary structure in biodegradable microspheres. Encapsulation of proteins within biodegradable polymers, [e.g. poly(lactic-*co*-glycolic acid) (PLGA)] for controlled drug release has recently been the subject of intense research effort. The ability to assess protein integrity after microsphere production is necessary to successfully produce microspheres that release native proteins. We used IR spectroscopy, a noninvasive method—as opposed to conventional organic solvent extraction or in vitro release at elevated temperature—to assess the secondary structure of recombinant human growth hormone (rhGH) within dry and rehydrated microspheres. PLGA microspheres containing rhGH with different excipients were prepared by a conventional double-emulsion method. The protein IR spectra indicated that the encapsulation process could perturb the structure of rhGH and that excipients could inhibit this damage to varying degrees. A strong positive correlation was found between intensity of the dominant α-helical band in the spectra of rhGH in rehydrated microspheres and the percent monomer released from microspheres during incubation in buffer. We also studied microspheres prepared with zinc-precipitated rhGH. The addition of Zn^{2+} during microsphere processing partially inhibited protein unfolding and fostered complete refolding of rhGH upon rehydration. In conclusion, IR spectroscopy can serve as a valuable tool to assess protein structure within both dried and rehydrated microspheres.

Introduction

Over the past several years, there have been numerous reports of encapsulation of proteins within biodegradable microspheres (for a recent review, see ref 1), which are used for sustained release of therapeutic proteins. For these systems to be successful clinically it is essential that the encapsulated protein be released in a native, functional state. In addition, the structure of the protein in the dried microsphere product could greatly affect the storage stability of the encapsulated protein. However, the integrity of the encapsulated protein is difficult to assess. Organic solvents used in the fabrication process may be required to remove the protein from the microspheres for characterization, and this extraction process may itself cause degradation of the protein. Alternatively, the microspheres may be incubated in aqueous buffers at elevated temperatures (e.g., 37 °C) to facilitate erosion of the polymer matrix and release of the protein into the buffer. During this incubation period, the protein may undergo both physical and chemical degradation. Thus, protein degradation caused by the method of removing the protein from

* Author to whom correspondence should be sent. Telephone: 303-315-6075. Fax: 303-315-6281. E-mail: john.carpenter@UCHSC.edu.
[†] School of Pharmacy.
[‡] Department of Chemistry and Biochemistry.
[§] Formulations Department.
[||] Pharmaceutical R & D.

10.1021/js980423n CCC: $18.00
Published on Web 12/19/1998

the microspheres could prevent the accurate determination of protein integrity within microspheres.

Such assessment is necessary to ensure production of microspheres that release native proteins. For example, with a valid method, excipients may be screened for their ability to stabilize the protein during encapsulation and drying, and during rehydration under physiological conditions. The most valuable method is one that allows the encapsulated protein to be studied directly in the microspheres, without the need for extraction or dissolution steps. Infrared (IR) spectroscopy is one promising method because it can be used to study directly the secondary structure of proteins in any state, including dried solids, precipitates and, potentially, intact microspheres.[2−5] In this study, we investigated the utility of this method to determine the structure of recombinant human growth hormone (rhGH) in polylactic-*co*-glycolic acid (PLGA) microspheres. The secondary structure of rhGH in both dry and rehydrated, intact microspheres was compared with that for the native, aqueous soluble protein. Several different formulations of rhGH were screened for their ability to maintain the protein in its native state during a double-emulsion encapsulation process.[6] The degree of nativelike structure was compared with recoveries of native protein with the traditional in vitro release and organic solvent extraction methods.[7−9] Finally, the structure of rhGH was assessed in microspheres prepared by an alternative strategy, which employed protein that was precipitated with Zn^{2+} and spray-freeze-dried prior to encapsulation in PLGA.[7]

Experimental Section

Microsphere Preparation—Two different encapsulation processes were used to produce PLGA microspheres containing rhGH. PLGA polymer (RG502, RG752, and RG756) was purchased from Boehringer Ingelheim, and rhGH was supplied by Genentech Production Recovery Operations. The first encapsulation method was the conventional water-in-oil-in-water double emulsion process, which was performed as described previously.[6] To compare the results of secondary structural analysis obtained with IR spectroscopy to results obtained with dissolution and extraction procedures, microspheres prepared with rhGH containing various different excipients (e.g., mannitol, trehalose, carboxymethylcellulose, and dextran) were studied.[6] These different formulations had already been shown to provide a range of protein stabilities, as assessed by extraction of the native protein from the microspheres.[6] The same samples of these formulations were used here to determine if there would be a corresponding range in the degree of native secondary structure retention in the encapsulated rhGH.

With the second encapsulation method, rhGH was initially precipitated with Zn^{2+} and then spray-freeze-dried.[7] The protein powder was homogenized in methylene chloride containing PLGA and sprayed into liquid nitrogen and solid ethanol, as discussed previously.[7] For both methods, the final microspheres were stored as a dry powders at 2−8 °C prior to analysis.

Analysis of rhGH Release and Extraction from Microspheres Produced by the Double-Emulsion Procedure—To quantify the in vitro release of rhGH from PLGA, the microspheres were incubated in isotonic HEPES buffer, pH 7.4, at 37 °C for 1 h, using a previously described method.[8,9] The protein was extracted from a parallel set of microspheres by dissolution in methylene chloride, as previously described.[7] Protein released or extracted was analyzed by native size exclusion chromatography (SEC) to determine the amount of native monomeric rhGH.[8]

Analysis of Infrared Spectra—The IR spectra were obtained with a Nicolet Magna 550 spectrometer equipped with a DTGS KBr detector. For dry powder and microspheres samples, 0.5−1 mg of sample was mixed with 300 mg of KBr and annealed into disks. This process has previously been shown not to alter the IR spectra of dried proteins.[4] The aqueous protein or rehydrated microspheres samples were placed in a variable path length sample cell containing CaF_2 windows, which were separated by ca. 6 μm.

For each spectrum, 64 or 256 scans for dry or liquid sample, respectively, were collected in a single beam mode with a 4 cm^{-1} resolution. A reference spectrum was recorded under identical scan conditions with protein-free PLGA (placebo) or buffer, as needed. The protein spectra were obtained by subtraction of the reference spectra according to the criteria described in the *Results* section. Signals for liquid and gaseous water were digitally subtracted, as previously described.[10] Final spectra are presented as second derivatives in the conformationally sensitive amide I region. Seven-point smoothing using Omnic software (Nicloet) was performed to remove white noise. To compare spectra, the second-derivative spectra were imported into GRAMS/386 (Galactic) and the area of amide I region was normalized as described previously.[2,11] Finally, the relative degree of retention of native secondary structure was determined by calculating the depth of the dominant α-helix band, relative to that for native, aqueous rhGH.

To examine protein structure in rehydrated microspheres, the samples were incubated in H_2O for 4 h prior to the measurement. For microspheres rehydrated in D_2O, 2 mg of dry microspheres were incubated with 60 μL of D_2O for at least 20 h at room temperature. Prior to measurement, the supernatant was replaced with the same volume of D_2O. This treatment was used to ensure consistent deuterium−hydrogen exchange for each sample.

Results and Discussion

The Structure of rhGH in Dry PLGA Microspheres—For storage of the final product, protein encapsulated in microspheres must be stable in the dried state. There are no published studies defining the critical criteria for storage stability of proteins encapsulated in dried microspheres. However, it is well established for freeze-dried protein formulations that retention of native protein structure is one important factor for storage stability.[3] It seems reasonable to suggest that this factor may also be the case for long-term storage stability of encapsulated proteins. Thus, a noninvasive method, such as IR spectroscopy, to assess the effect of processing and/or formulations on protein structure within dry microspheres is essential to the ultimate development of products with sufficient shelf life.

To obtain a high quality IR spectrum of protein in microspheres, it is necessary to subtract out the contribution of PLGA from the amide I region, which is used for assessment of protein secondary structure. As shown in Figure 1A, the PLGA used in the current study had only minimal absorbance in the amide I region (1600−1700 cm^{-1}). There is a large absorbance of PLGA centered around 1750 cm^{-1}, but only a slight shoulder from this band extends into the region of 1680−1720 cm^{-1}. To ensure that this small contribution from PLGA was not affecting the final protein spectra, we digitally subtracted the absorbance of PLGA microspheres without protein from the spectrum of the microspheres containing rhGH (Figure 1). A successful subtraction was indicated by the presence of a flat region at about 1730−1710 cm^{-1}. We found this criterion provided reproducible results and consistent final protein spectra, even when different investigators performed the spectral subtractions.

Figure 2 shows examples of the resulting spectra of rhGH with different formulations in dry microspheres and the spectrum of native aqueous rhGH. The native protein is primarily α-helical in structure, and hence, its spectrum is dominated by a helix band at 1656 cm^{-1}. In the spectra of the dried microsphere samples, this band is greatly reduced in intensity, indicating a loss of native helix structure. This loss is compensated by an increase in β-sheet, as evidenced by the increase absorbance at ca. 1685 cm^{-1}. The greatest reduction in helix was seen for the microspheres prepared without excipient or with mannitol. There was a slight improvement in recovery of helix content with trehalose. However, in all cases (Figure 2), the helix content of rhGH in dried microspheres was less than that

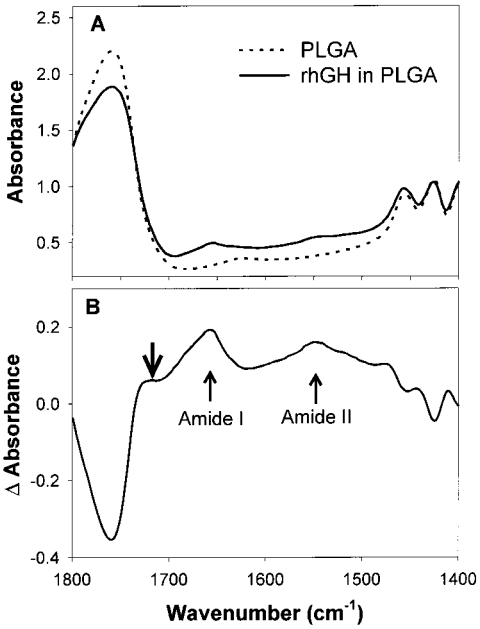

Figure 1—(A) Infrared spectra of dried rhGH in PLGA microspheres and PLGA microspheres alone. (B) The resulting spectrum of rhGH after the PLGA background was properly subtracted. The bold arrow indicates the criterion for the subtraction where a flat region should appear in the region between 1710 and 1730 cm^{-1}.

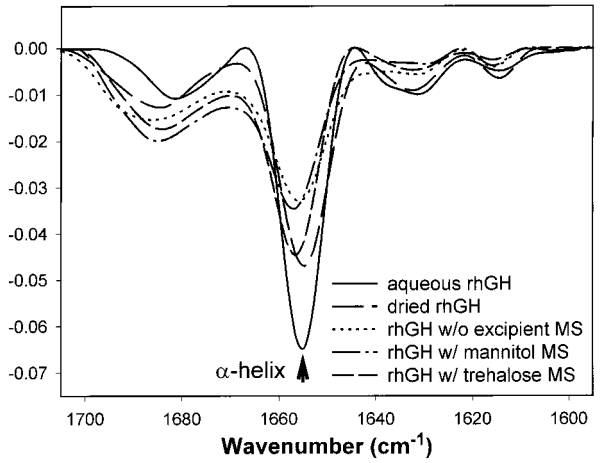

Figure 2—The second-derivative amide I spectra of dried rhGH powder and rhGH with different excipients within microspheres (MS). For comparison, the spectrum of aqueous, native rhGH in solution (measured at concentration of 20 mg/mL) is also shown. The major band at 1656 cm^{-1} is the α-helix, which is the main secondary structure of rhGH. The mannitol and trehalose formulations contained 1:1 and 0.25:1 mass ratios of excipient:rhGH, respectively, and 100 mM potassium phophate buffer, as described previously.[6]

for the protein in a lyophilized powder (prepared without excipient). This result indicates that in addition to the denaturation caused by the initial freeze-drying step, the protein structure could further be perturbed by the subsequent emulsion and encapsulation steps. Further research is needed to assess the relative effectiveness of excipients at inhibiting protein denaturation during the initial lyophilization and subsequent processing steps. This work will be necessary to obtain a final microsphere preparation with the optimal retention of native protein structure. With IR spectroscopy it should be straightforward to monitor the structure at each step.

The Structure of rhGH Microspheres rehydrated in H_2O—Although the structure of proteins in dried microspheres may be important for storage stability of the product, protein structure in rehydrated microspheres is

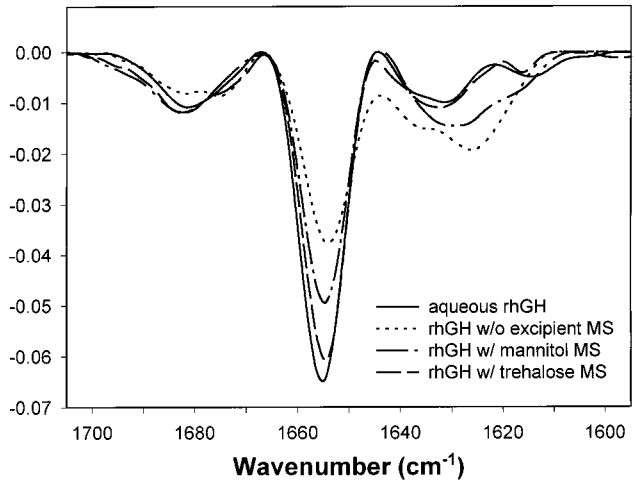

Figure 3—The second-derivative amide I spectra of H_2O-rehydrated rhGH microspheres (MS) and aqueous rhGH. The mannitol and trehalose formulations contained 1:1 and 0.25:1 mass ratios of excipient:rhGH, respectively, and 100 mM potassium phophate buffer, as described previously.[6]

most relevant to the performance of the product under physiological conditions. The structure of a dried protein is not necessarily predictive of that obtained after rehydration.[2–5,11] For example, with lyophilized protein formulations it has been found that unfolded protein molecules in the dried state may fully refold during rehydration.[2–5,11] Conversely, with some systems, it has been observed that not only is the native structure not recovered upon rehydration, but a substantial fraction of the protein population may form non-native aggregates.[2–5,11] These aggregates often have a large fraction of intermolecular beta sheet strucuture, which can be detected by specific bands in the amide I region of the IR spectrum.[2] The behavior of a given sample during rehydration depends on, at least, (1) the physicochemical properties of the protein itself, (2) the initial and final pH, (3) the effects of excipients on protein structure during the drying process and rehydration, and (4) the macroscopic properties of the dried material that dictate rates of rehydration and dissolution of protein molecules.[2–5,11] Clearly, it is not possible to predict how all of these parameters would affect the behavior of protein molecules during rehydration of microsphere formulations. Thus, direct examination of protein structure in the rehydrated microspheres is essential.

With rehydrated samples, we found that the PLGA used in the study had minimal absorbance in the amide I region. As is the case with all aqueous protein samples, the absorbance in this region was dominated by H_2O itself. We found that the well-established methods[10] for quantitatively subtracting this contribution from spectra of protein solutions also was appropriate for spectra of rhGH in rehydrated microspheres. The criterion for a successful subtraction was a flat baseline in the region 1800–2300 cm^{-1}, which has a strong absorbance from water but no signal from protein. This approach worked well for microspheres with a protein content >1% w/w (data not shown).

Figure 3 presents some examples of the second-derivative IR spectra in the amide I region of the rehydrated rhGH microspheres with different formulations. For the trehalose formulation, the α-helix band was almost identical to that for the native protein, indicating that the protein in the microspheres had refolded during rehydration (Figures 2 and 3). In contrast, the apparent extent of recovery of native α-helix was much less for the microspheres containing no excipients or for the mannitol formulation. Furthermore, the spectra for these samples had prominent absorbances in the 1620–1630 cm^{-1} region,

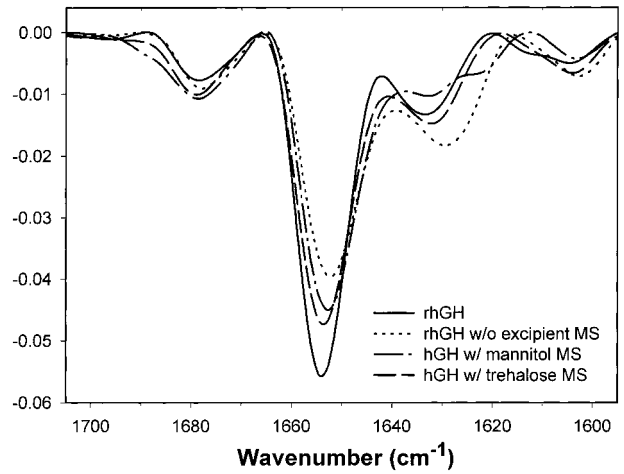

Figure 4—The second-derivative amide I spectra of D_2O-rehydrated rhGH microspheres (MS) and native rhGH in solution in D_2O. The mannitol and trehalose formulations contained 1:1 and 0.25:1 mass ratios of excipient:rhGH, respectively, and 100 mM potassium phophate buffer, as described previously.[6]

which are most likely due to the presence of intermolecular β-sheet.[2] This result indicates that a substantial fraction of the rhGH in these microsphere preparations formed aggregates during rehydration. These three examples clearly document that the behavior of proteins during rehydration of microspheres cannot necessarily be predicted from the structure of the protein in dried microspheres, as is the case for lyophilized protein formulations.

The Structure of rhGH Microspheres Rehydrated in D_2O and Its Correlation with Percent Monomer Released or Extracted from the Same Microspheres—When the protein content of microspheres was <1% wt/wt, we were not able to successfully subtract the contributions of water and PLGA from the spectrum of rhGH in microspheres (data not shown), which was, at least in part, because the concentration of protein relative to the total solution was relatively low. We have found that, even for protein solutions, the contributions of water to the amide I region cannot be subtracted quantitatively if the protein concentration is less than about 5 mg/mL (unpublished observation).

Because D_2O does not absorb strongly in the amide I region, we tested this solvent system for analyzing rehydrated microspheres. Contributions from solvent and PLGA were digitally subtracted from the spectrum for the protein in D_2O-rehydrated microspheres such that the region from 2100 to 2300 cm^{-1} was flat (data not shown).

As shown in Figure 4, the intensity of the α-helical band was again dependent on the formulation used, and we found the results were comparable overall and showed similar trends to those of H_2O-rehydrated microspheres (Figure 3). The most nativelike spectrum was seen for the trehalose formulation. The spectra for the sample prepared without excipients and that for the mannitol formulation had less intense α-helix bands and the presence of bands attributable to β-sheet at ca. 1630 and 1623 cm^{-1}, respectively.

Even microspheres with relatively low protein content could be studied in D_2O. Thus, we rehydrated all of the different formulations of rhGH in PLGA microspheres, which have previously been described,[6] in this solvent. Then, the depths of the α-helical band from the second-derivative spectra, relative to that for the native protein, were measured and used as indicators of degree of retention of native structure within the rehydrated microspheres. For each microsphere formulation, this parameter was plotted against the respective percentage of rhGH monomer recovered from either the 1-h in vitro release

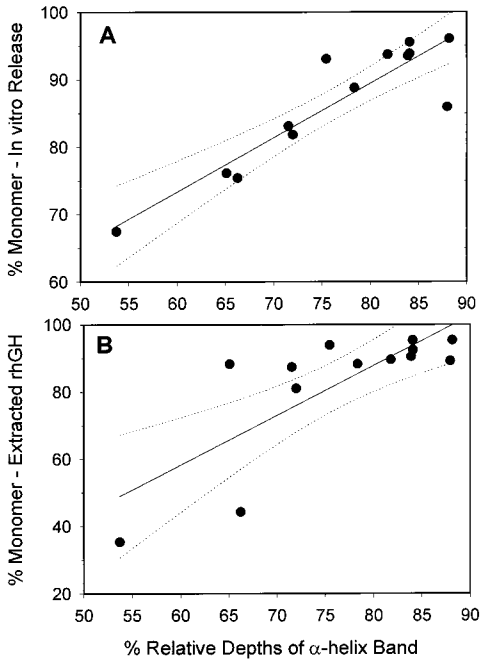

Figure 5—The linear regression analyses of the relative depth of α-helix band versus percent of recovery of rhGH monomers from either (A) 1-h in vitro release or (B) organic solvent extraction. The relations are $y = 25.1 + 0.8x$, $r^2 = 0.818$ and $y = -30.5 + 1.48x$, $r^2 = 0.618$ for A and B, respectively. The dotted lines indicate the 95% confidence intervals.

protocol or the organic solvent extraction of the microspheres (see *Methods*). As can be seen in Figure 5A, there is a strong positive correlation between the relative intensity of the α-helical band and the percent monomer obtained by the in vitro release protocol. The results of this analysis demonstrate that IR spectroscopy can not only be a valuable tool to assess the protein structure within microspheres but also may be useful to predict the integrity of protein initially released from microspheres.

Interestingly, there was a much weaker positive correlation between the relative intensity of the α-helix band and the percent of native rhGH monomer extracted from microspheres (Figure 5B). This result might reflect the fact that the organic solvent extraction of protein from microspheres could by itself furthur perturb protein structure.

The Structure of Zinc-Complexed rhGH within PLGA Microspheres—Recently, rhGH precipitated by Zn^{2+} and spray-freeze-dried has been used for the preparing PLGA encapsulated microspheres.[3] Figure 6 shows the spectra of dry rhGH prepared either from a zinc-free protein solution or from a zinc-induced precipitate (Zn-rhGH) and the spectra for dried microspheres prepared with either preparation. Both freeze-dried powders had similar spectra and almost identical loss in intensity of the α-helix band. Thus, the perturbation of rhGH secondary structure during freeze-drying was essentially the same for both preparations; zinc did not increase resistance to freeze-drying. For Zn-rhGH within microspheres, the reduction of α-helix was slightly greater than that for the freeze-dried powder, but was much less than that for microspheres prepared with non-zinc-treated rhGH. These results suggest that during the encapsulation in PLGA, the protein secondary structure could be further perturbed but that this damage is much less if the protein is initially freeze-dried as a Zn-hGH complex. More importantly, as shown in Figure 7, the Zn-rhGH within the microspheres completely refolded upon rehydration in H_2O. The spectrum for the rehydrated protein is essentially identical to that for the native, aqueous protein. Water was used in this rehydration experiment because the protein content

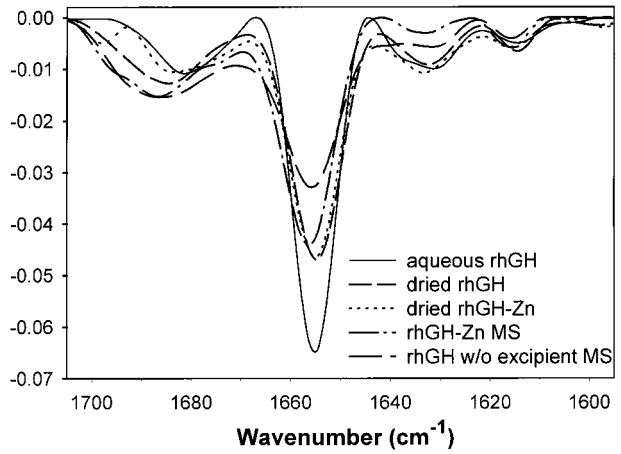

Figure 6—The second-derivative amide I spectra of dried rhGH, rhGH–Zn complex and their microspheres (MS). The spectrum of native, aqueous rhGH is also included for reference.

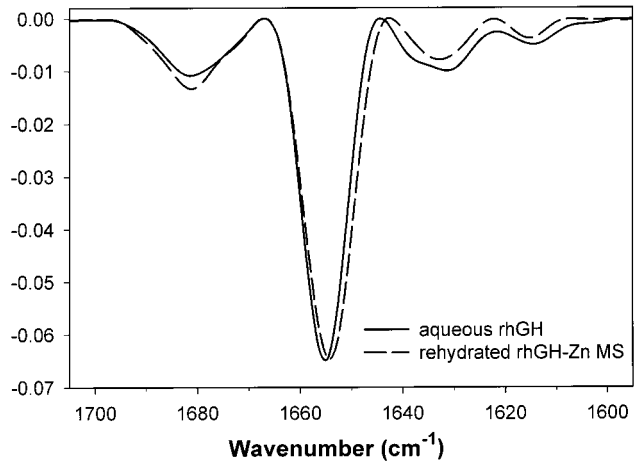

Figure 7—The second-derivative amide I spectra of H_2O-rehydrated rhGH–Zn microspheres and native, aqueous rhGH.

in these microspheres was 15% wt/wt. The refolding of the Zn-rhGH is in contrast to the aggregation of non-zinc-complexed protein during rehydration of microspheres prepared without excipients (Figures 3 and 7).

Conclusions

Noninvasive assessment of protein secondary structure in dried and rehydrated microspheres can be accomplished rapidly (e.g., <10 min is needed to acquire a high quality spectrum) with IR spectroscopy. The structure of the protein in dried microspheres may be predictive of storage stability of the protein, as is the case for lyophilized protein formulations.[3] However, more research on storage stability of proteins in dried microspheres is needed to test this suggestion. The secondary structure of protein in rehydrated microspheres is most relevant to the potential release of native, functional proteins under physiological conditions. With rhGH, the degree of retention of native secondary structure correlated directly with the percent of native monomer released during incubation in buffer. In addition, the relative effects of the method of microsphere preparation and excipients on the structure of rhGH were clearly discernible with IR spectroscopic determination of protein secondary structure. These results document that the method has utility for designing processing conditions and formulations that provide optimal retention of native protein structure in the microspheres. Finally, IR spectroscopic assessment of protein structure in microspheres could prove valuable for routine quality assurance testing of commercial lots.

References and Notes

1. Putney, S. D.; Burke, P. A. Improving protein therapeutics with sustained-release formulations. *Nature Biotech*. **1998**, *16*, 153−157.
2. Dong, A.; Prestrelski, S. J.; Allison, S. D.; Carpenter, J. F. Infrared spectroscopic studies of lyophilization- and temperature-induced protein aggregation. *J. Pharm. Sci.* **1995**, *84*, 415−424.
3. Carpenter, J. F.; Chang, B. S. Lyophilization of protein pharmaceuticals. In *Biotechnology and Biopharmaceutical Manufacturing, Processing and Preservation*; Avis, K. E.; Wu, V. L., Eds., Interpharm: Buffalo Grove, IL, 1996; pp 199−264.
4. Prestrelski, S. J.; Tedeschi, N.; Arakawa, T.; Carpenter, J. F. Dehydration-induced conformational changes in proteins and their inhibition by stabilizers. *Biophys. J.* **1993**, *65*, 661−671.
5. Allison, S. D.; Dong, A.; Carpenter, J. F. Counteracting effects of thiocyanate and sucrose on chymotrypsinogen secondary structure and aggregation during freezing, drying and rehydration. *Biophys. J.* **1996**, *71*, 2022−2032
6. Cleland, J. L.; Jones, A. J. S. Stable formulations of recombinant human growth hormone and interferon-γ for microencapsulation in biodegradable microspheres. *Pharm. Res.* **1996**, *13*, 1464−1475.
7. Johnson, O. L.; Cleland, J. L.; Lee, H. J.; Charnis, M.; Duenas, E.; Jaworowicz, W.; Shepard, D.; Shahzamani, A.; Jones, A. J. S.; Putney, S. D. A month-long effect from a single injection of microencapsulated human growth hormone. *Nature Med*. **1996**, *2*, 795−799.
8. Cleland, J. L.; Mac, A.; Boyd, B.; Yang, J.; Duenas, E. T.; Yeung, D.; Brooks, D.; Hsu, C.; Chu, H.; Mukku, V.; Jones, A. J. S. The stability of recombinant human growth hormone in poly(lactic-*co*-glycolic acid) (PLGA) microspheres. *Pharm. Res*. **1997**, *14*, 420−425.
9. Yang, J.; Cleland, J. L. Factors affecting the in vitro release of recombinant human interferon-g (rhIFN-r) from PLGA Microsphres. *J. Pharm. Sci*. **1997**, *86*, 908−914.
10. Dong, A.; Caughey, W. S. Infrared methods for study of hemoglobin reactions and structures. *Methods. Enzymol*. **1994**, *232*, 139−175.
11. Kendrick, B. S.; Dong, A.; Allison, S. D.; Manning, M. C.; Carpenter, J. F. Quantitation of the area of overlap between second-derivative amide I infrared spectra to determine the structural similarity of a protein in different states. *J. Pharm. Res*. **1996**, *85*, 155−158.

Acknowledgments

This work was supported by a grant from the National Science Foundation (BES9505301).

JS980423N

On the Structural Preservation of Recombinant Human Growth Hormone in a Dried Film of a Synthetic Biodegradable Polymer

KAREN G. CARRASQUILLO,[†] HENRY R. COSTANTINO,[‡,§] ROCIO A. CORDERO,[†] CHUNG C. HSU,[‡] AND KAI GRIEBENOW*,[†]

Contribution from *Department of Chemistry, University of Puerto Rico, Río Piedras Campus, P.O. Box 23346, San Juan, Puerto Rico 00931-3346 and Pharmaceutical Research and Development, Genentech, Inc., 1 DNA Way, South San Francisco, California 94080.*

Received July 6, 1998. Accepted for publication November 2, 1998.

Abstract □ In this work we describe the structural investigation of the model protein recombinant human growth hormone (rhGH) under conditions relevant to polymeric sustained-delivery depots, including the dried protein entrapped in a film of poly(DL-lactic-*co*-glycolic)acid. At each step of the procedure, dehydration of rhGH by lyophilization, suspension in methylene chloride, and drying from that suspension, the structure of rhGH was probed noninvasively using Fourier transform infrared (FTIR) spectroscopy. We found that the structure of rhGH was significantly changed by the dehydration process as indicated by a marked drop in the α-helix content and increase in the β-sheet content. Subsequent suspension of this powder in methylene chloride, drying from that suspension, and drying from a methylene chloride/PLGA solution introduced only minor additional structural changes when using appropriate conditions. This result is likely due to the limited molecular mobility of proteins in nonprotein-dissolving organic solvents. Finally, when rhGH was co-lyophilized with the lyoprotectant trehalose, which preserves the secondary structure, the rhGH entrapped in the PLGA matrix also had a nativelike secondary structure.

Introduction

Recent advances in biotechnology have facilitated the development of numerous biopharmaceuticals (peptides and proteins). The dozens of biopharmaceuticals already approved by the Federal Drug Administration (FDA),[1] in addition to hundreds of others in clinical trials,[2] will substantially aid in the prevention and management of disease.[1,3] However, drug delivery has been a major stumbling block. Because proteins are rapidly degraded in the gastrointestinal tract,[4] the oral route is impractical. Even when delivered by direct injection (e.g., insulin),[5] frequent administrations are often required. A promising approach is the sustained delivery of proteins from polymer matrixes,[6−8] which offers advantages such as targeting specific tissues and increasing patient compliance (and comfort). Poly(lactic-*co*-glycolic)acid (PLGA) is a good candidate for a protein encapsulation matrix.[9] PLGA, an FDA-approved material, has been intensively studied for its biocompatibility, toxicology, and degradation kinetics.[10−13] For this investigation we chose the model protein recombinant human growth hormone (rhGH) under a variety of conditions relevant to its encapsulation in PLGA as the model polymer.

Protein encapsulation in polymers is challenging because proteins are susceptible to deleterious chemical and structural modifications,[8,14−17] which may be induced by typical encapsulation procedures (e.g., the double-emulsion-solvent-evaporation-technique).[8,16] During such encapsulation procedures, protein structural perturbations may occur due to exposure to organic solvents,[18,19] mechanical stress,[20] creation of hydrophobic interfaces,[21] and dehydration.[22−25] Structural alterations caused by these factors may reverse upon release of protein from the polymeric device into the aqueous environment of body fluids. For example, lyophilization-induced structural changes are frequently reversible for small proteins.[25]

Even so, structural alteration is often the first step toward formation of irreversible aggregates when dehydrated proteins are exposed to moist environments in vitro, simulating the slow rehydration process occurring in a sustained-delivery device in vivo.[26−29] Dehydration-induced structural changes in rhGH are known to promote the formation of insoluble aggregates under accelerated storage conditions.[30] Aggregates may have lower activity (decreasing the efficiency of the expensive pharmaceutical protein) and increased immunogenicity, and thus must be avoided.[13] The simplest procedure to avoid such detrimental reactions would be to avoid any protein structural changes when processing. For rhGH, the addition of sugar excipients, such as trehalose, efficiently prevented storage-induced solid-state aggregation and conserved the protein structure upon lyophilization.[30]

It may be difficult to avoid such structural alterations when following the most common protocol of protein encapsulation in hydrophobic polymers, the double-emulsion-solvent-evaporation technique (also called the water-in-oil-in-water or w/o/w, technique).[16] In this approach, an aqueous protein solution is added to an organic solvent (typically methylene chloride) to form the first emulsion after probe sonication. Next, a second emulsion is formed by adding the first one to an aqueous solution containing an emulsifier followed by homogenization. Finally, microspheres are obtained after polymer hardening by solvent evaporation and dehydration of the particles, typically by lyophilization. A major difficulty is the exposure of the protein to denaturing conditions in aqueous solution. Under such conditions, proteins are relatively unstable and easy to denature, for example by organic solvents.[19] Structural investigations on the consequences of encapsulating the model proteins bovine serum albumin and lysozyme in PLGA microspheres by the w/o/w technique demonstrated substantial structural changes of both proteins.[31] Some of these changes could be prevented by adding the excipient trehalose to the aqueous protein solutions, but the proteins still were very much structurally perturbed in the micro-

* Corresponding author. Phone: 787-764-0000, ×7815. Fax: 787-756-8242. E-mail: griebeno@adam.uprr.pr.
[†] Department of Chemistry.
[‡] Pharmaceutical Research and Development.
[§] Current address: Alkermes Inc., 64 Sidney Street, Cambridge, MA 02139.

10.1021/js980272o CCC: $18.00
Published on Web 12/23/1998

spheres, as probed by Fourier transform infrared (FTIR) spectroscopy.[31]

Recently, Johnson et al.[13] reported the successful stabilization of a Zn-protein complex in PLGA for rhGH using a novel cryogenic, nonaqueous methodology (no emulsification). The encapsulated protein was delivered from PLGA with unaltered properties compared with rhGH before the procedure, although the protein structure in the polymer was not reported.[13] Herein, we employ a different (more general) nonaqueous approach, taking advantage of the increased rigidity of dehydrated proteins in organic solvents[19] and employing a sugar excipient to stabilize the protein structure. We have specifically focused on the protein secondary structure under various conditions related to processing in PLGA.

Recent developments of FTIR spectroscopy make this technique the method of choice to noninvasively probe the protein structure under all relevant conditions. Encapsulation in polymers involves steps during which the protein is in different physical states. All these conditions can be analyzed using FTIR spectroscopy; several recent works have utilized this technique to characterize the secondary structure of proteins in the amorphous solid state,[22,24,25,29] in powder suspension in organic solvents,[32,33] and also encapsulated in PLGA.[31] Utilizing FTIR spectroscopy as a noninvasive spectroscopic method, we demonstrate that rhGH can be encapsulated in PLGA with a nativelike secondary structure.

Materials and Methods

Protein—Recombinant human growth hormone (rhGH) was produced at Genentech, Inc. (South San Francisco, CA). The protein bulk containing 2 mg/mL of rhGH, 88 mM mannitol, and 5 mM sodium phosphate (pH 7.8) was buffer-exchanged into a 100 mM ammonium bicarbonate solution and lyophilized to obtain excipient-free protein.[34]

Chemicals—Trehalose and poly(DL-lactic-*co*-glycolic)acid (50:50; MW 40 000−75 000; lot no. 56H1176) were obtained from Sigma Chemical Company (St. Louis, MO) and used as supplied. All other chemicals were of analytical grade and from various suppliers.

Preparation of Lyophilized Excipient/rhGH Samples—Lyophilized excipient-free rhGH was reconstituted with deionized water to form a stock solution containing 2 mg/mL of protein, and trehalose was added at the required protein-to-trehalose ratio of 1:250 (mol:mol). Samples were lyophilized in a Labconco Freezone 6 unit at a chamber pressure of <100 μmHg and a shelf temperature of −42 °C for 48 h. The lyophilized material was used immediately or was sealed in glass vials and stored at 2−8 °C until use.

FTIR Spectroscopy—FTIR studies were conducted with a Nicolet Magna-IR System 560 optical bench as described previously.[19,25,30] A total of 256 scans at 2 cm^{-1} resolution using Happ-Ganzel apodization were averaged to obtain each spectrum. For all experiments involving aqueous solutions, a Spectra Tech liquid cell equipped with CaF_2 windows and 15-μm thick spacers was used. For all experiments involving suspensions in organic solvents, the same liquid cell was used with a 50-μm spacer. Samples of rhGH were dried in poly(lactic-*co*-glycolic)acid by casting (vide infra) and measured as thin films on a CaF_2 window.

Lyophilized protein powders were measured as KBr pellets (1 mg of protein per 200 mg of KBr).[19,25,33,35] It is important to note that the influence of the KBr pellet method on the vibrational spectrum of rhGH has been tested before.[35] In the current study, we have been careful to employ a KBr pellet method that has been shown previously not to induce any artifactual structural changes (i.e., same result as obtained with an IR microscope). It has also been reported that the KBr pellet method does not introduce spectral changes for various other proteins as well.[22] In addition, for recombinant human deoxyribonuclease, the sole protein reported to exhibit structural alterations due to IR sample preparation in KBr,[36] a recent study revealed that under judiciously mild conditions there were no structural changes that could be attributed to pressing the protein in a KBr pellet.[37]

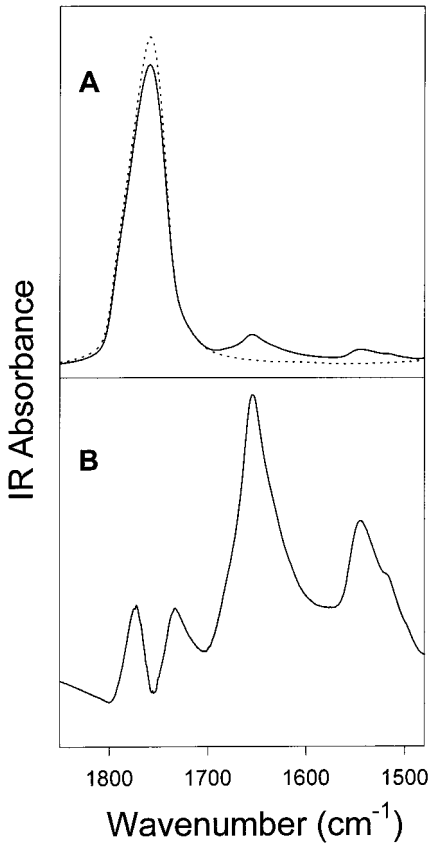

Figure 1—FTIR spectra of (A) rhGH encapsulated in PLGA (solid line) and of pure PLGA (dotted line) and (B) the rhGH spectrum after subtraction of the polymer background.

Each protein sample was measured at least four times. When necessary, spectra were corrected for the solvent background in an interactive manner using the Nicolet OMNIC 3.1 software[19,25,33] to obtain the protein vibrational spectra. We previously confirmed that this procedure is reliable for water background subtraction when using 15-μm thick spacers.[19]

RhGH was suspended in methylene chloride (25 mg protein/mL) using (1) a homogenizer (Virtishear Tempest 500W with an 18-mm shaft generator) for 2 min at the minimum speed setting of 1, (2) a probe sonicator (Branson Sonifier model 450) at 50 W at 50% duty cycle for 2 min, or (3) a sonication bath (Branson Sonication Bath model 2210) for 2 min. After suspension, the IR cell was immediately filled with the protein suspensions and the IR spectra were recorded. Encapsulation of lyophilized and co-lyophilized rhGH samples in poly(lactic-*co*-glycolic) acid (50:50) was carried out by suspending 10 mg of protein in a solution of 98 mg of PLGA in 1 mL of methylene chloride as already described. After suspension, samples were spread as thin films on a CaF_2 window and dried over a flow of dry N_2.

Spectra recorded for rhGH entrapped in PLGA were corrected for the polymer contribution. Although the polymer band with a maximum at ca. 1760 cm^{-1} is well separated from the amide I area (1700−1600 cm^{-1}), we were careful in excluding any artifactual influences of the subtraction procedure on the amide I spectrum. It can be seen from Figure 1A that the spectrum of PLGA was not identical in the absence and presence of the protein and could not be totally eliminated by the subtraction procedure. Thus, in principle, false subtraction could have led to the creation of some artifactual bands at ca. 1680−1700 cm^{-1}, where tailing of the peak into the amide I occurred. However, we were able to exclude such artifacts. To do so, the PLGA background was subtracted from lyophilized and co-lyophilized rhGH samples entrapped in PLGA employing different subtraction factors (e.g., 2.4133, 2.4737, and 2.5744 for the lyophilized protein and 0.9106, 0.9736, and 1.0456 for the co-lyophilizate), and no subtraction at all. For each of the spectra obtained, we calculated the secondary

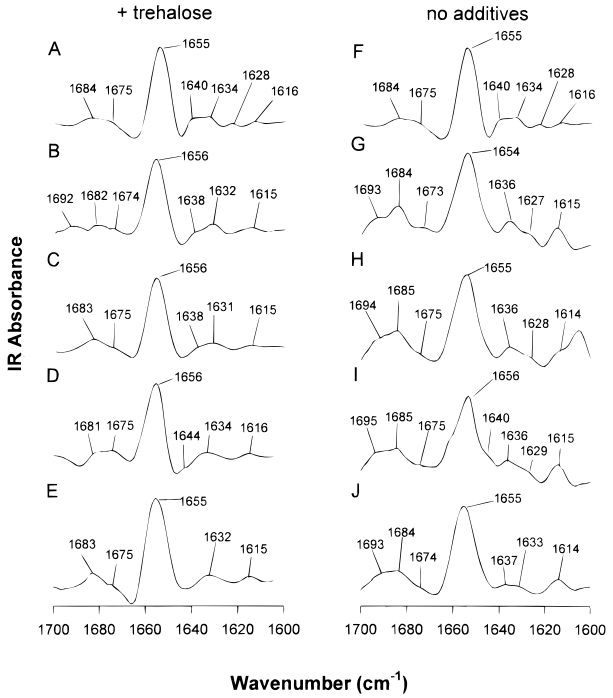

Figure 2—Second-derivative FTIR spectra of rhGH in the amide I region under various conditions. (A, F) rhGH in aqueous solution at pH 7.8; (B–E) rhGH co-lyophilized with trehalose at a 1:250 molar ratio from an aqueous solution at pH 7.8 under different conditions; [(B) co-lyophilized powder, (C) suspension in methylene chloride by homogenization, (D) dried powder after suspension in methylene chloride, and (E) entrapped in PLGA]; (G–J) rhGH powder lyophilized from pH 7.8 without additives under different conditions [(G) lyophilized powder, (H) suspension of the powder in methylene chloride by homogenization, (I) dried from suspension in methylene chloride, and (J) entrapped in PLGA].

structure by Gaussian curve-fitting. For the case of the lyophilized protein, the α-helix content determined was 39%, 35%, 37%, and 41% for four situations tested. For the case of the co-lyophilized protein, the α-helix content determined was 48%, 45%, 48%, and 46% for the four situations tested. The values were the same within the error of the method, excluding a significant influence of the PLGA background subtraction procedure on the amide I protein spectrum.

In addition, second-derivative spectra of rhGH entrapped in PLGA (Figure 2) were analyzed for any new components that could have been the result of the subtraction procedure. This analysis demonstrated no new components in these samples (Figures 2E and 2J) when compared with the spectrum of the lyophilized protein (Figures 2B and 2G). This result also excludes creation of artificial bands by the subtraction procedure.

FTIR Data Analysis—*Second Derivatization*—All spectra were analyzed by second derivatization in the amide I region for their component composition.[19,25,33,38,39] Second-derivative spectra were smoothed with an 11-point smoothing function (10.6 cm^{-1}).[19,25]

Fourier Self-Deconvolution (FSD)—FSD was applied to the unsmoothed spectra to enable quantification of the secondary structure in the amide I region by Gaussian curve-fitting[19,33,40,41] using the program OMNIC 3.1. The parameters chosen, a value of 24 for the full-width at half-maximum (fwhm) and $k = 2.4$ for the enhancement factor, are in the range of those published.[19,33,39,41–43] Note that FSD alters the band shapes but preserves the integrated band intensities when over-deconvolution is avoided.[38,42] The values chosen for FSD in our analyses were checked for the risk of such over-deconvolution (which could result in distorted band areas)[40,41] by the strategy outlined by Griebenow and Klibanov.[19]

Gaussian Curve-Fitting—The frequencies of the band centers found in the second-derivative spectra in the amide I region were used as starting parameters for the Gaussian curve-fitting (performed using the program GRAMS 386 from Galactic Industries, Inc.). The secondary structure contents were calculated from the areas of the individual assigned bands and their fraction of the total area in the amide I region.[19,33,39] Gaussian curve-fitting was performed in the amide I region after band-narrowing of the protein vibrational spectra by FSD.[39,41,43] In all cases, a linear baseline was fitted. The secondary structure content is reported as the averaged standard deviation of at least four measurements. To compare the structure of rhGH under different conditions, we performed a *t* test to determine within the confidence level of 95% whether the α-helix and β-sheet content were statistically significantly different. The null hypothesis used was that for both samples the values were the same within the error.

Band Assignments—The band assignment in the amide I region followed those in the literature[19,24,30,33,41] and is summarized for some typical samples in Table 1. For the aqueous solution, the main band at 1655 cm^{-1} was assigned to α-helices and a band at 1631 cm^{-1} to β-sheets. All other bands were assigned to other structural elements (β-turns, random coil, extended chains). The solution secondary structure content determined by Gaussian curve-fitting in the amide I region using these assignments was very similar to that determined previously [30,35] and to the X-ray crystal structure (60% α-helix).[44] The relatively high α-helix content of rhGH is advantageous when studying the influence of the encapsulation procedure on the structure of the protein under various conditions. For lyophilized or suspended proteins, the α-helix content is the most reliable criterion to describe their structural integrity when utilizing FTIR spectroscopy.[19,25,30]

Table 1—Infrared Band Positions, Areas, and Assignments for rhGH under Various Conditions[a]

	band position (cm^{-1})			
sample	SD[b]	Gaussian curve-fitting[c]	area (%)	assignment
aqueous solution (pH 7.8)	1684	1680	18 ± 3	other[d]
	1670	1670	7 ± 1	other
	1655	1655	57 ± 3	α-helix
	1641	1639	11 ± 3	other
	1628	1631	7 ± 3	β-sheet
co-lyophilized with trehalose[e]	1692	1693	5 ± 2	β-sheet
	1680	1681	9 ± 2	other
	1675	1671	15 ± 3	other
	1656	1656	52 ± 3	α-helix
	1639	1641	10 ± 1	other
	1632	1632	9 ± 2	β-sheet
co-lyophilizate entrapped in PLGA[e,f]	1683	1681	11 ± 1	other
	1674	1671	7 ± 1	other
	1656	1656	48 ± 1	α-helix
	1639	1642	23 ± 3	other
	1631	1630	11 ± 1	β-sheet

[a] Data are the average and standard deviation of four to five independent determinations. [b] Second derivative. [c] Gaussian curve-fitting was performed on Fourier self-deconvolved amide I spectra. [d] Other structures include random coil, extended chains, and turns. [e] rhGH co-lyophilized with 1:250 protein: trehalose (mol:mol) prior to encapsulation. [f] The rhGH:trehalose co-lyophilizate was homogenized in methylene chloride containing PLGA and the suspension was subsequently dried to entrap the protein.

Results and Discussion

Previously, we reported the use of FTIR spectroscopy as a tool to investigate the structural alteration of rhGH upon dehydration[35] and to develop strategies for solid-state stabilization.[30] Herein, we have further extended the use of FTIR spectroscopy to probe rhGH structure under a variety of conditions relevant to the encapsulation of the protein in sustained-release formulations.

The structural consequences of the different steps of a nonaqueous encapsulation procedure were probed. Lyophilization of rhGH in the absence of excipients induces significant structural changes, in particular a decrease in the α-helix and an increase in the β-sheet content.[30,35] Our FTIR spectroscopic data obtained for rhGH in aqueous solution at pH 7.8 (Figure 3A) and for the powder lyophilized from that pH value (Figure 3B) are in agreement

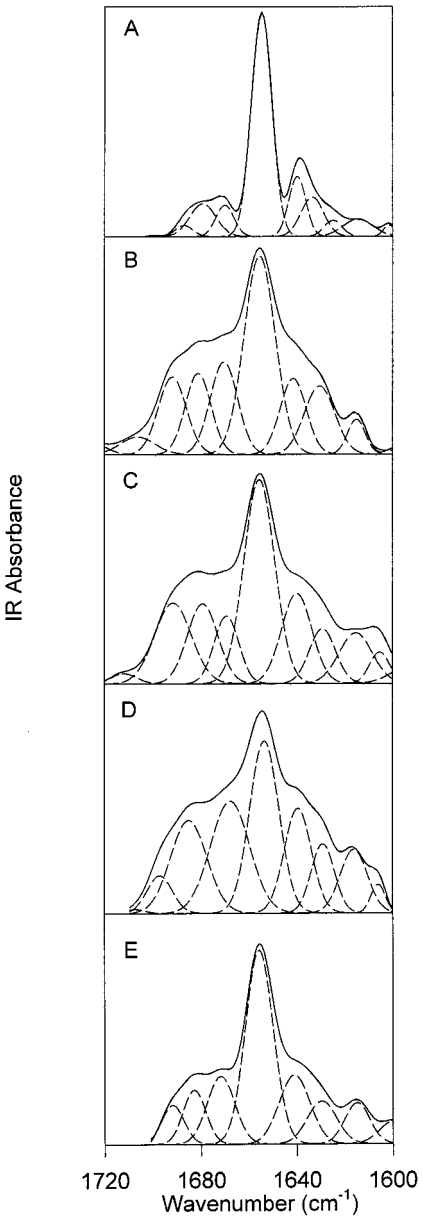

Figure 3—Fourier self-deconvolved FTIR spectra and Gaussian curve-fitting of rhGH without additives in the amide I spectral region under various conditions: (A) aqueous solution at pH 7.8, (B) lyophilized powder from that solution, (C) suspension of the powder in methylene chloride by homogenization, (D) dried from this suspension in methylene chloride, and (E) entrapped in PLGA. The solid lines represent the superimposed FSD and the curve-fit, and the dashed curves represent the individual Gaussian bands.

with these findings: the spectrum of rhGH in the amide I spectral region (1700−1600 cm^{-1}) showed pronounced changes. In particular, a broadening of the spectrum was observed for the lyophilized powder when compared with the aqueous spectrum. Such spectral changes are indicative of structural changes caused by the lyophilization process.[19,22,24,25,33,45] Quantitative analysis of the spectra by Gaussian curve-fitting (Table 2) revealed a statistically significant 20% decrease in the α-helix and 11% increase of the β-sheet content upon lyophilization, which is in agreement with results of previous investigations.[30,35]

When the excipient-free protein was suspended in methylene chloride using a homogenizer, the FTIR spectrum of this suspension (Figure 3C) was similar to the one of the lyophilized protein (Figure 3B). Quantitative analysis also revealed that there were no significant additional structural changes in the α-helix content and only a minor (but statistically significant) increase in the β-sheet content to 22% upon suspension of the protein in the organic solvent (Table 2).

Table 2—Secondary Structure of Excipient-Free rhGH under Various Conditions

sample	secondary structure content (%)[a] α-helix	β-sheet	other[b]
aqueous solution	57 ± 3	7 ± 3	36 ± 1
lyophilized powder	37 ± 4	18 ± 1	45 ± 3
powder suspension by probe sonication			
suspended in methylene chloride	23 ± 2	36 ± 2	41 ± 2
dried from methylene chloride	28 ± 3	33 ± 5	39 ± 4
powder suspension by homogenization			
suspended in methylene chloride	35 ± 2	22 ± 2	43 ± 2
dried from methylene chloride	29 ± 2	24 ± 1	47 ± 3
dried from methylene chloride/PLGA	39 ± 1	12 ± 3	49 ± 2

[a] The secondary structure of rhGH was calculated by Gaussian curve-fitting of the Fourier self-deconvolved amide I spectra. [b] Other structures include random coil, extended chains, and turns.

These data are in agreement with the hypothesis that dehydrated proteins have lower molecular mobility than in the aqueous state, which precludes them from being denatured by the organic solvent.[19,33] In contrast, another FTIR spectroscopic study found that suspension of the protein subtilisin in ethanol, hexane, and pyridine led to some structural rearrangements.[32] In that report, the exact details of the suspension conditions were not presented. Thus, to determine whether the suspension conditions used could affect the protein structure, we also suspended rhGH using probe sonication in methylene chloride. In this case, we found a significant additional reduction in the α-helix content to 23% and increase of the β-sheet content to 36% (Table 2). This additional structural instability may be related to the increased localized heating effect of suspensions achieved by probe sonication versus homogenization, which would promote increased molecular mobility.[46] Therefore, the means by which the suspension is obtained is important. FTIR spectroscopy may be useful as a tool to optimize the processing conditions with respect to structural preservation of pharmaceutical proteins.

We examined the effect of removing the organic solvent, which would be the next step in the preparation of an implantable or injectable depot. The spectra for rhGH suspended in methylene chloride with the homogenizer and of the dried powder obtained from that suspension (Figures 2C and 2D) were qualitatively quite similar. Quantitative analysis of the two spectra showed that some minor additional structural changes occurred upon drying of the suspension. There was a slight but statistically significant decrease in the α-helix content from 35% to 29% observed during this process, whereas the β-sheet content remained unchanged (Table 2).

A similar result was obtained when rhGH, suspended by probe sonication in methylene chloride, was dried from that solvent. The spectra were qualitatively very similar (data not shown) and the quantitative data (Table 2) were also similar. Thus, we conclude that removal of the organic solvent resulted in only minor additional structural alterations.

We also tested whether the presence of the polymer PLGA would have any influence on the structure of rhGH when following the same processing protocol. The protein was suspended in methylene chloride containing the polymer (98 mg/mL) using the homogenizer.[47] This suspension was directly applied to a FTIR window and a thin film produced by solvent evaporation under a stream of dry nitrogen gas. The structure of rhGH dried in the PLGA

film was essentially the same as in the lyophilized powder. The α-helix content was the same, but a small decrease in the β-sheet content was observed (Table 2). Thus, the structure of excipient-free rhGH dried in the presence of PLGA was not native. However, it was the freeze-drying process beforehand and not exposure to the organic solvent and/or PLGA that caused the structural perturbations.

Thus, to preserve the structure of rhGH in PLGA, the lyophilized formulation must first be optimized. It is well established from FTIR spectroscopic studies that lyophilization-induced structural changes can be prevented by addition of a co-lyophilized sugar or polyol.[22,24,25] For rhGH, several sugars proficient in stabilization against dehydration-induced structural changes (and also solid-state aggregation) have been identified; for example, trehalose.[30] Trehalose is an efficient lyoprotectant,[48] and has been shown to ameliorate the dehydration-induced structural alteration of various unrelated proteins, such as lysozyme[49,50] and bovine serum albumin.[51]

rhGH was co-lyophilized with trehalose at an excipient-to-protein ratio of 250:1 (mol:mol). At this ratio, the secondary structure of rhGH was largely preserved upon lyophilization. The second-derivative spectrum of the co-lyophilizate (Figure 2B) was very similar to that of the aqueous solution (Figure 2A). The main component was the band assigned to α-helices with a maximum at 1655 cm^{-1}. No significant changes in the frequencies or amplitudes of any component were noted in the second-derivative spectra. The quantitative analysis of the FTIR spectrum of the co-lyophilizate (Figure 4B) confirmed that the secondary structure was largely preserved by the lyoprotectant. The α-helix content for the sample was 52%, only slightly lower than in aqueous solution (57%, Table 3). An increase of 7% for the β-sheet was observed in the co-lyophilizate compared with the 11% increase for the excipient-free protein.

As the subsequent step, the rhGH:trehalose co-lyophilizate was suspended in methylene chloride using three different methods: probe sonication, homogenization, and a sonication bath. Probe sonication resulted in a statistically significant decrease in the α-helix content from 52% to 44%, indicating some pronounced structural changes by the method (Table 3). When we dried rhGH from this suspension, no further structural changes were noted (Table 3). These observations are in agreement with data for excipient-free protein as already discussed. Probe sonication in both cases caused some additional structural perturbation upon suspension in the organic solvent, and caution should be exercised when using this method.

A higher degree of structural preservation was achieved upon homogenization (Figures 2C and 4C) or suspension using the sonication bath (Table 3). The spectral changes upon suspension were very small in both cases. For example, the second-derivative spectrum of the rhGH:trehalose co-lyophilizate suspended by homogenization in methylene chloride (Figure 2C) was quite similar to that of the co-lyophilizate before suspension (Figure 2B). Quantitative analysis of the spectra by Gaussian curve-fitting did not indicate any statistically significant structural alterations upon suspension: the α-helix and β-sheet contents were, within the 95% confidence interval, the same as for the co-lyophilizate before suspension (Table 3).

The secondary structure was also determined for the protein in the co-lyophilizate dried from the organic solvent. Second-derivative spectra did not indicate any structural changes upon organic solvent removal. For the case of rhGH suspended by homogenization, the spectrum of the suspended protein and of the dried protein after suspension were very similar (Figures 2C and 2D). Furthermore, the second-derivative spectrum of the co-lyophilized protein

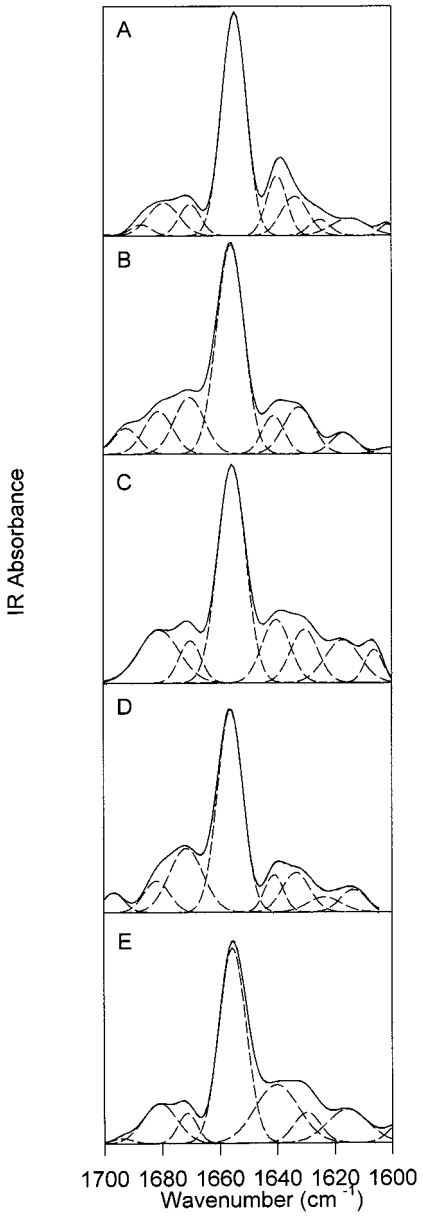

Figure 4—Fourier self-deconvolved FTIR spectra and Gaussian curve-fitting of rhGH in the amide I spectral region under various conditions: (A) aqueous solution at pH 7.8; (B) rhGH co-lyophilized with trehalose at pH 7.8; (C) suspension of the co-lyophilizate in methylene chloride by homogenization; (D) dried from this suspension in methylene chloride; and (E) entrapped in PLGA. The solid lines represent the superimposed FSD and the curve-fit, and the dashed curves represent the individual Gaussian bands.

dried after suspension in methylene chloride was comparable to that in aqueous solution.

Quantitative analysis of the spectra by Gaussian curve-fitting was in agreement with the qualitative observations (Figure 4D, Table 3). For the sample suspended by homogenization, the α-helix content (50%) and β-sheet content (13%) were the same, within the 95% confidence interval, as for the dried protein after suspension (48% and 14%, respectively). A slight but statistically significant decreases in α-helix (from 49% to 45%) and β-sheet content (from 16% to 13%) were noted for the sample suspended with the sonication bath upon drying (Table 3).

The trehalose-containing protein was then suspended in a solution of methylene chloride containing PLGA using the homogenizer and sonication bath because these methods were mild with respect to maintaining protein structure. The suspension was cast on a FTIR window and

Table 3—Secondary Structure of rhGH Co-Lyophilized with Trehalose under Various Conditions

sample	secondary structure content (%)[a]		
	α-helix	β-sheet	other[b]
aqueous solution[c]	57 ± 3	7 ± 3	36 ± 1
powder co-lyophilized with trehalose[d]	52 ± 3	14 ± 2	34 ± 1
powder suspension by probe sonication			
suspended in methylene chloride	44 ± 2	9 ± 2	47 ± 3
dried from methylene chloride	44 ± 1	12 ± 1	44 ± 3
powder suspension by homogenization			
suspended in methylene chloride	50 ± 2	13 ± 1	37 ± 1
dried from methylene chloride	48 ± 5	14 ± 3	38 ± 2
dried from methylene chloride/PLGA	48 ± 1	11 ± 1	41 ± 1
powder suspension by sonication bath			
suspended in methylene chloride	49 ± 2	16 ± 2	36 ± 3
dried from methylene chloride	45 ± 1	13 ± 2	42 ± 3
dried from methylene chloride/PLGA	51 ± 2	8 ± 3	41 ± 2

[a] The secondary structure of rhGH was calculated by Gaussian curve-fitting of the Fourier self-deconvolved amide I spectra. [b] Other structures include random coil, extended chains, and turns. [c] The aqueous solution did not contain trehalose. [d] The co-lyophilized powder was obtained using a protein-to-trehalose ratio of 1:250 (mol:mol).

evaporated under a stream of dry N_2 gas. The second-derivative spectra qualitatively revealed that the structure of rhGH was very similar to that in aqueous solution and to that of the co-lyophilizate. For example, for the sample obtained by homogenization, only minor differences were evident when comparing the spectrum of the aqueous solution (Figure 2A) and of the entrapped protein (Figure 2E). Quantitative data obtained by Gaussian curve-fitting were in agreement with this qualitative analysis. The spectra of rhGH co-lyophilized with trehalose dried in PLGA from a suspension that was homogenized (Figure 4E) or prepared using the sonication bath (data not shown) were similar to that of the aqueous solution (Figure 4A) and the co-lyophilizate (Figure 4B). Some minor differences were noted in both cases for bands representing unordered secondary structure (ca. 1640 cm^{-1}) and β-sheet structure (ca. 1631 cm^{-1}). Some changes in the area of these components indicate a minor structural rearrangement occurring under the different conditions.

For the protein co-lyophilized with trehalose and entrapped in PLGA, quantitative analysis of the spectra (Table 3) demonstrated that the processing conditions produced only very minor structural changes. The α-helix content of rhGH entrapped in PLGA by homogenization was 48% and thus only slightly lower than for the co-lyophilizate before encapsulation (52%). In addition, only small differences were found for the β-sheet content (11% and 14%, respectively). The same result was evident when employing the sonication bath. The α-helix content for rhGH entrapped in PLGA was 51%, the same (within the 95% confidence interval) as for the co-lyophilized powder (52%), and the β-sheet content was only slightly decreased (14% and 8%, respectively).

The data clearly demonstrate that a nonaqueous strategy can be employed to entrap rhGH in PLGA with a nativelike secondary structure. The key was to lyophilize the protein under conditions ensuring structural integrity and then employ processing conditions that are not detrimental to the structure. This finding is intriguing in light of the common wisdom that organic solvents, such as the one in our study, are known to denature proteins.[8] It should be noted that in the present study, following the lyophilization step, all processes were nonaqueous. A likely explanation is the proposed decreased molecular mobility of proteins in anhydrous organic milieu compared with the aqueous state.

Such increased rigidity of proteins in organic solvents was originally proposed as an explanation for kinetic observations when employing suspended dehydrated enzymes as catalysts in nonaqueous organic solvents. For instance, increased rigidity has been attributed to differences in the enzymatic activity in hydrophobic and hydrophilic organic solvents.[52−54] In addition, it has been hypothesized that the plunge in enzymatic activity when comparing aqueous and nonaqueous systems can in part be attributed to increased rigidity of enzymes in organic solvents.[54,55] Also, the phenomenon of so-called 'molecular imprinting' can only be explained when assuming an increased rigidity of enzymes in organic solvents.[56−58] Furthermore, proteins show an increased stability toward thermal denaturation in organic solvents.[59,60] A few spectroscopic investigations have directly addressed the issue of protein rigidity in organic solvents. Nuclear magnetic resonance experiments on the tyrosyl ring motion in α-lytic protease,[61] electron spin resonance spectroscopic studies,[62,63] time-resolved fluorescence anisotropy measurements,[64] and recently FTIR spectroscopic experiments[19] support the view that proteins have restricted mobility in organic solvents when compared with aqueous systems. Theoretical works support this picture,[65,66] and it has also been pointed out that water serves as a molecular lubricant and promotes extremely fast conformational fluctuations.[67]

In summary, this report illustrates that FTIR spectroscopy can be used as a tool to probe protein structure under various conditions relevant to encapsulation in PLGA. This approach should be generally applicable to the structural stabilization of proteins during encapsulation in other polymeric depots.

References and Notes

1. Robinson, J. R. Controlled drug delivery. In *Controlled Drug Delivery. Challenges and Strategies*; Park, K., Ed.; American Chemical Society: Washington, DC, 1997; pp 1−7.
2. Pramik, M. J. Protein stability grows in importance as more biodrugs enter clinicals. *Chem. Eng. News* **1995**, March 15.
3. Cleland, J. L.; Langer, R. Formulations and Delivery of Proteins and Peptides: Design and Development Strategies. In *Formulation and delivery of proteins and peptides*; Cleland, J. L., Langer, R., Eds.; ACS Symposium Series, ACS Books; pp 1−19.
4. Mrsny, R. J. Site-specific drug delivery in the gastrointestinal tract. In *Controlled Drug Delivery. Challenges and Strategies*; Park, K., Ed.; American Chemical Society: Washington, DC, 1997; pp 107−123.
5. Costantino, H. R.; Liauw, S.; Mitragotri, S.; Langer, R.; Klibanov, A. M.; Sluzky, V. The pharmaceutical development of insulin. Historical perspectives and future directions. In *Therapeutic Protein and Peptide Formulation and Delivery*; Shahrokh, Z.; Sluzky, V., Cleland, J. L., Shire, S. J., Randolph, T. W., Eds.; American Chemical Society: Washington, DC, 1997; pp 29−66.
6. Langer, R. New methods of drug delivery. *Science* **1990**, *249*, 1527−1533.
7. Langer, R. Biomaterials and biomedical engineering. *Chem. Eng. Sci.* **1995**, *50*, 4109−4121.
8. Schwendeman, S. P.; Costantino, H. R.; Gupta, R. K.; Langer, R. Peptide, protein, and vaccine delivery from implantable polymeric systems. Progress and challenges. In *Controlled Drug Delivery. Challenges and Strategies*; Park. K., Ed.; American Chemical Society: Washington, DC, 1997; pp 229−267.
9. Other synthetic biodegradable polymers suggested for the encapsulation of proteins include polyanhydrides [e.g., poly-[1,3-bis(*p*-carboxyphenoxy)propane-*co*-sebacic acid]), poly(ortho esters), polyiminocarbonates, and polyphosphazenes; see Langer[7] and Schwendeman et al.[8]].
10. Göpferich, A.; Langer, R. Modeling monomer release from bioerodible polymers. *J. Controlled Release* **1995**, *33*, 55−69.
11. Batycky, R. P.; Hanes, J.; Langer, R.; Edwards, D. A. A theoretical model of erosion and macromolecular drug release from biodegrading microspheres. *J. Pharm. Sci.* **1997**, *86*, 1464−1477.

12. Scholes, P. D.; Coombes, A. G. A.; Davies, M. C.; Illum, L.; Davis, S. S. Particle engineering of biodegradable colloids for site-specific drug delivery. In *Controlled Drug Delivery. Challenges and Strategies*; Park, K., Ed.; American Chemical Society: Washington, DC, 1997; pp 73−106.
13. Johnson, O. L.; Jarorowicz, W.; Cleland, J. L.; Bailey, L.; Charnis, M.; Duenas, E.; Wu, C.; Shepard, D.; Magil, S.; Last, T.; Jones, A. J. S.; Putney, S. D. The stabilization and encapsulation of human growth hormone into biodegradable microspheres. *Pharm. Res.* **1997**, *14*, 730−735.
14. Manning, M. C.; Patel, K.; Borchardt, R. T. Stability of protein pharmaceuticals. *Pharm. Res.* **1989**, *6*, 903−918.
15. Volkin, D. B.; Klibanov, A. M. Minimizing protein inactivation. In *Protein Function: A Practical Approach*; Creighton, T., Ed.; Oxford University: New York, pp 1−24.
16. Schwendeman, S. P.; Cardamone, M.; Brandon, M. R.; Klibanov, A. M.; Langer, R. Stability of proteins and their delivery from biodegradable polymer microspheres. In *Microparticulate Systems for the Delivery of Proteins and Vaccines*; Cohen, S., Bernstein, H., Eds.; Marcel Dekker: New York, 1996; pp 1−49.
17. Schöneich, C.; Hageman, M. J.; Borchardt, R. T. Stability of peptides and proteins. In *Controlled Drug Delivery. Challenges and Strategies*; Park, K., Ed.; American Chemical Society: Washington, DC, 1997; pp 205−228.
18. Desai, U. R.; Klibanov, A. M. Assessing the structural integrity of a lyophilized protein in organic solvents. *J. Am. Chem. Soc.* **1995**, *117*, 3940−3945.
19. Griebenow, K.; Klibanov, A. M. On protein denaturation in aqueous−organic mixtures but not in pure organic solvents. *J. Am. Chem. Soc.* **1996**, *118*, 11695−11700.
20. Maa, Y.-F.; Hsu, C. C. Effect of high shear on proteins. *Biotechnol. Bioeng.* **1996**, *51*, 458−465.
21. Sluzky, V.; Tamada, J. A.; Klibanov, A. M.; Langer, R. Kinetics of insulin aggregation in aqueous solutions upon agitation in the presence of hydrophobic surfaces. *Proc. Natl. Acad. Sci. U.S.A.* **1991**, *88*, 9377−9381.
22. Prestrelski, S. J.; Tedischi, N.; Arakawa, T.; Carpenter, J. F. Dehydration-induced conformational transitions in proteins and their inhibition by stabilizers. *Biophys. J.* **1993**, *65*, 661−671.
23. Desai, U. R., Osterhout, J. J.; Klibanov, A. M. Protein structure in the lyophilized state: a hydrogen isotope exchange/NMR study with bovine pancreatic trypsin inhibitor. *J. Am. Chem. Soc.* **1994**, *116*, 9420−9422.
24. Dong, A.; Prestrelski, S. J.; Allison, S. D.; Carpenter, J. F. Infrared spectroscopic studies of lyophilization- and temperature-induced protein aggregation. *J. Pharm. Sci.* **1995**, *84*, 415−424.
25. Griebenow, K.; Klibanov, A. M. Lyophilization-induced changes in the secondary structure of proteins. *Proc. Natl. Acad. Sci. U.S.A.* **1995**, *92*, 10969−10976.
26. Liu, R.; Langer, R.; Klibanov, A. M. Moisture-induced aggregation of lyophilized proteins in the solid state. *Biotechnol. Bioeng.* **1991**, *37*, 177−184.
27. Costantino, H. R.; Langer, R.; Klibanov, A. M. Solid-phase aggregation of proteins under pharmaceutically relevant conditions. *J. Pharm. Sci.* **1994**, *83*, 1662−1669.
28. Costantino, H. R.; Schwendeman, S. P.; Griebenow, K.; Klibanov, A. M.; Langer, R. The secondary structure and aggregation of lyophilized tetanus toxoid. *J. Pharm. Sci.* **1996**, *85*, 1290−1293.
29. Costantino, H. R.; Griebenow, K.; Mishra, P.; Langer, R.; Klibanov, A. M. Fourier transform infrared (FTIR) spectroscopic investigation of protein stability in the lyophilized form. *Biochim. Biophys. Acta* **1995**, *253*, 69−74.
30. Costantino, H. R.; Carrasquillo, K. G.; Cordero, R. A.; Mumenthaler, M.; Hsu, C. C.; Griebenow K. G. The effect of excipients on the structure and stability of lyophilized recombinant human growth hormone (rhGH). *J. Pharm. Sci.* **1998**, *87*, 1412−1420.
31. Fu, K.; Griebenow, K.; Hsieh, L.; Klibanov, A. M.; Langer, R. FTIR characterization of the secondary structure of proteins encapsulated within PLGA microspheres. *J. Controlled Release*, in press.
32. Dong, A.; Meyer, J. D.; Kendrick, B. S.; Manning, M. C.; Carpenter, J. F. Effect of secondary structure on the activity of enzymes suspended in organic solvents. *Arch. Biochem. Biophys.* **1996**, *334*, 406−414.
33. Griebenow, K.; Klibanov, A. M. Can conformational changes be responsible for solvent and excipient effects on the catalytic behavior of subtilisin Carlsberg in organic solvents? *Biotechnol. Bioeng.* **1997**, *53*, 351−362.
34. Overcashier, D. E.; Brooks, D. A.; Costantino, H. R.; Hsu, C. C. Preparation of excipient-free recombinant human tissue-type plasminogen activator by lyophilization from ammonium bicarbonate solution. An investigation of the two-stage sublimation phenomenon. *J. Pharm. Sci.* **1997**, *86*, 455−459.
35. Costantino, H. R.; Nguyen, T. H.; Hsu, C. C. Fourier transform infrared spectroscopy demonstrates that lyophilization alters the secondary structure of recombinant human growth hormone. *Pharm. Sci.* **1996**, *2*, 229−232.
36. Chan, H.-K.; Ongpipattanakul, B.; Au−Yeung, J. Aggregation of rhDNase occurred during the compression of KBr pellets used for FTIR spectroscopy. *Pharm. Res.* **1996**, *13*, 238−242.
37. Costantino, H. R.; Chen, B.; Griebenow, K.; Hsu, C. C.; Shire, S. J. Fourier transform infrared spectroscopic investigation of the secondary structure of aqueous and dried recombinant human deoxyribonuclease I. *Pharm. Pharmacol. Commun.* **1998**, *4*, 391−395.
38. Mantsch, H. H.; Casal, H. L.; Jones, R. N. Resolution enhancement of infrared spectra of biological systems. In *Spectroscopy of Biological Systems*, Clark, R. J. H.; Hester, R. E., Eds.; Wiley: New York, 1986; pp 1−46.
39. Susi, H.; Byler, D. M. Resolution-enhanced Fourier transform infrared spectroscopy of enzymes. *Methods Enzymol.* **1986**, *130*, 290−311.
40. Byler, D. M.; Susi, H. Examination of the secondary structure on proteins by deconvoluted FTIR spectra. *Biopolymers* **1986**, *25*, 469−487.
41. Görne-Tschelnokow, U.; Naumann, D.; Weise, C.; Hucho, F. Secondary structure and temperature behavior of acetylcholinesterase. Studies by Fourier transform infrared spectroscopy. *Eur. J. Biochem.* **1993**, *213*, 1235−1242.
42. Casal, H. L.; Köhler, U.; Mantsch, H. H. Structural and conformational changes of β-lactoglobulin B. An infrared spectroscopic study of the effect of pH and temperature. *Biochim. Biophys. Acta* **1988**, *957*, 11−20.
43. Heimburg, T.; Marsh, D. Investigation of secondary and tertiary structural changes of cytochrome *c* in complexes with anionic lipids using amide hydrogen exchange measurements. An FTIR study. *Biophys. J.* **1993**, *65*, 2408−2417.
44. De Vos, A. M.; Ultsch, M.; Kossiakoff, A. A. Human growth hormone and extracellular domain of its receptor. Crystal structure of the complex. *Science* **1992**, *255*, 306−312.
45. Wellner, N.; Belton, P. S.; Tatham, A. S. Fourier transform IR spectroscopic study of hydration-induced structure changes in the solid state of ω-gliadins. *Biochem. J.* **1996**, *319*, 741−747.
46. Maa, Y.-F.; Hsu, C. C. Effect of primary emulsions on microsphere size and protein-loading in the double emulsion process. *J. Microencap.* **1997**, *14*, 225−241.
47. Note that the artificial creation of bands by inappropriate subtraction of the PLGA background is excluded by demonstrating that the amide I FTIR spectra of rhGH co-lyophilized with trehalose were practically identical when measured as KBr pellets or encapsulated in PLGA. Furthermore, the spectra were very similar to that in aqueous solution. See *Materials and Methods* for details of the method used to subtract the PLGA background.
48. Colaço, C.; Sen, S.; Thangavelu, M.; Pinder, S.; Roser, B. Extraordinary stability of enzymes dried in trehalose: simplified molecular biology. *Bio/Technology* **1992**, *10*, 1007−1011.
49. Carpenter, J. F.; Crowe, J. H. An infrared spectroscopic study of the interaction of carbohydrates with dried proteins. *Biochemistry* **1989**, *28*, 3916−3922.
50. Belton, P. S.; Gil, A. M. IR and Raman spectroscopic studies of the interaction of trehalose with hen egg white lysozyme. *Biopolymers* **1994**, *34*, 957−961.
51. Carrasquillo, K. G.; Cordero, R. A.; Ho, S.; Franquiz, J. M.; Griebenow, K. Structure-guided encapsulation of bovine serum albumin in poly(D,L-lactic-*co*-glycolic)acid. *Pharm. Pharmacol. Commun.* **1998**, *4*, 563−571.
52. Zaks, A.; Klibanov, A. M. Enzymatic catalysis in nonaqueous solvents. *J. Biol. Chem.* **1988**, *263*, 3194−3201.
53. Klibanov, A. M. Enzymatic catalysis in anhydrous organic solvents. *TIBS* **1989**, *14*, 141−144.
54. Klibanov, A. M. Why are enzymes less active in organic solvents than in water? *Trends Biotechnol.* **1997**, *15*, 97−101.
55. Schmidtke, J. L.; Wescott, C. R.; Klibanov, A. M. The mechanistic dissection of the plunge in enzymatic activity upon transition from water to anhydrous solvents. *J. Am. Chem. Soc.* **1996**, *118*, 3360−3365.
56. Klibanov, A. M. What is remembered and why? *Nature* **1995**, *374*, 596.
57. Mishra, P.; Griebenow, K.; Klibanov, A. M. Structural basis for the molecular memory of imprinted proteins in anhydrous media. *Biotechnol. Bioeng.* **1996**, *52*, 609−614.
58. Rich, J. O.; Dordick, J. S. Controlling subtilisin activity and selectivity in organic media by imprinting with nucleophilic substrates. *J. Am. Chem. Soc.* **1997**, *119*, 3245−3252.
59. Zaks, A.; Klibanov, A. M. Enzymatic catalysis in organic media at 100 °C. *Science* **1984**, *224*, 1249−1251.

60. Volkin, D. B.; Straubli, A.; Langer, R.; Klibanov, A. M. Enzyme thermo-inactivation in anhydrous organic solvents. *Biotechnol. Bioeng.* **1991**, *37*, 843−853.
61. Burke, P. A.; Griffin, R. G.; Klibanov, A. M. Solid-state nuclear magnetic resonance investigation of solvent dependence of tyrosyl ring motion in an enzyme. *Biotechnol. Bioeng.* **1993**, *42*, 87−94.
62. Guinn, R. M.; Skerker, P. S.; Kavanaugh, P.; Clark, D. S. Activity and flexibility of alcohol dehydrogenase in organic solvents. *Biotechnol. Bioeng.* **1991**, *37*, 303−308.
63. Affleck, R.; Xu, Z.-F.; Suzawa, V.; Focht, K.; Clark, D. S.; Dordick, J. S. Enzymatic catalysis and dynamics in low-water environments. *Proc. Natl. Acad. Sci. U.S.A.* **1992**, *89*, 1100−1104.
64. Broos, J.; Visser, A. J. W.; Engbersen, J. F. J.; Verboom, W.; van Hoek, A.; Reinhoudt, D. N. Flexibility of enzymes suspended in organic solvents probed by time-resolved fluorescence anisotropy. Evidence that enzyme activity and enantioselectivity are directly related to enzyme flexibility. *J. Am. Chem. Soc.* **1995**, *117*, 12657−12663.
65. Hartsough, D. S.; Merz, K. M. Jr. Protein dynamics and solvation in aqueous and nonaqueous environments. *J. Am. Chem. Soc.* **1993**, *115*, 6529−6537.
66. Toba, S.; Merz, K. M. Jr. The concept of solvent compatibility and its impact on protein stability and activity enhancement in nonaqueous solvents. *J. Am. Chem. Soc.* **1997**, *119*, 9939−9948.
67. Barron, L. D.; Hecht, L.; Wilson, G. The lubrication of life: a proposal that solvent water promotes extremely fast conformational fluctuations in mobile heteropolymer structure. *Biochemistry* **1997**, *36*, 13143−13147.

Acknowledgments

This work was supported by the NIH-MBRS (GM08102-26S1) and NSF-EPSCOR (OSR-9452893) program grants to K.G.

JS980272O

Pressure Susceptibility of Polymer Tablets as a Critical Property: A Modified Heckel Equation

MARTIN KUENTZ AND HANS LEUENBERGER*

Contribution from *School of Pharmacy, University of Basel, Switzerland.*

Received September 14, 1998. Accepted for publication November 24, 1998.

Abstract □ The pressure susceptibility (χ_p), which is defined as the decrease of porosity (ϵ) under pressure was investigated. Of special interest are compacts obtained at very low pressures, because of the transition between the state of a powder and the state of a tablet. This range was found to be critical in respect to a diverging pressure susceptibility. Above a critical porosity (ϵ_c) or below the corresponding relative density (ρ_c), no pressure susceptibility can be defined, because of no rigid structure exists. To take this into account, a simple function was proposed for the pressure susceptibility: $\chi_p \propto 1/(\epsilon_c - \epsilon)$. This proposal leads to a new porosity vs pressure relationship. The new model was compared to the Heckel equation that involves a constant pressure susceptibility. Various polymers were tested from "out of die" measurements, and the new relationship was found superior to the Heckel equation. As a conclusion, the pressure susceptibility exhibits a curvature that can be called critical at low relative densities. Consequently, a better understanding evolves as to why the Heckel equation is not valid at low pressures. The new model has proven to be adequate for polymer tablets but, so far it is not clear whether other substances exhibit the same performance. Especially tableting materials exhibiting brittle fracture will be of interest considering their importance in compaction technology.

Introduction

Porosity−Pressure Relationship—A tablet can be considered as a special type of dispersion. The solid fraction and the air in pores constitute two phases of the system. This heterogeneous character of such a particulate material leads to a very complex mechanical behavior. In case of low packing fractions, rheological properties can be found. Thus, individual particles are movable to some extent, enabling many possible configurations. This aspect of a disordered structure holds for an analogy to liquids, and even an entropy S_t can be attributed to a particle packing.[1] Yet, the individuality of particles gets lost in tablets compacted at higher pressures. Consequently, also the entropy of the diverse particle configurations vanishes. Such very dense compacts can approach a continuum of the solid fraction, and therefore mechanics of practically homogeneous solids will evolve.

As a result, the character of the system undergoes dramatic changes as a function of the relative density. Particle rearrangements, occurrence of plastic flow, and possible brittle fracture contribute to a vast complexity. Hence, there is a number of different mathematical models, which are mostly empirical or contain at least some *heuristic* elements.

* Address correspondence to Prof. Dr. H. Leuenberger, School of Pharmacy, University of Basel, Totengässlein 3, CH-4051 Basel, Switzerland. Fax: + 41-61-261 7907. E-mail: leuenberger@ubaclu.unibas.ch.

The most widespread models used in the field of pharmaceutical technology are the Kawakita equation,[2] the approach according to Cooper and Eaton,[3] and the Heckel equation.[4,5] The latter model is of special interest for the present study:

$$\ln\left(\frac{1}{1-\rho}\right) = K\sigma + A \qquad (1)$$

where ρ equals the relative density and σ is the compression pressure, whereas K and A are constants. It is known that tablets compressed at higher pressures fulfill the relationship properly.[6] In a plot of $\ln(1/(1-\rho))$ versus applied pressure, K is determined from the slope, and A from the intercept. The general limitations of Heckel plots have been analyzed rigorously by Rue and Rees.[7]

Recent Developments—The lacking adequacy of the classical compression equations stimulated efforts for current investigations. Yu and Hall[8] analyzed very porous particle packings, using a double-logarithmic form of the Heckel plot. The fit of the new model was better than the original Heckel equation. Yet, the empirical nature of this approach lacking any theoretical background can be considered as a drawback. The same also can be remarked for the *heuristic* equation proposed by Lordi et al.[9]

An interesting modification of the original Heckel equation was attained by Carstensen et al.[10] They assumed the final compact of a pharmaceutical powder to always possess some residual porosity. Accordingly, the void volume decreases exponentially toward a value different from zero. The resulting model seemed capable to also describe experimental data in the nonlinear part of the Heckel plot and can potentially be extended to more than a one-component system.

Confined compression of particle agglomerates is mainly focused by an approach of Adams et al.[11] The bed in the die was modeled as a series of parallel columns, where only processes of friction were allowed. Thus, any system where elastic energy also is stored is not covered by this theory. However, the assumptions lead to a result that took approximately the same form as the Kawakita equation and therefore enabled a physical interpretation of its parameters.

Coming finally to a microscopic theory, Duncan−Hewitt[12] attempted a model of the compression process, where compact properties were predicted by the characteristics of single crystals. The behavior of brittle particles was found to be substantially different from the one of more ductile crystals, and so two distinct models evolved. However, the main problem of any microscopic theory can be understood in the change of relevant binding points. The tablet is heterogeneous, built up by particles whose binding points are distributed randomly to some extent. Consequently, disorder has to be taken into account by any theoretical approach.

The aspect of disorder is most interesting in that some very different physical problems can be treated similarly

10.1021/js980369a CCC: $18.00
Published on Web 01/05/1999

from a theoretical point of view.[13] Modern physics of phase transitions and critical phenomena[14] provides interesting new concepts that can potentially be applied to many scientific fields. Yet, an analogy between relevant physical problems may not always be obvious at first, but similarities can be revealed by studying the *response functions* of a system. The present paper introduces such a function in the context of powder compaction.

Theoretical Section

Pressure Susceptibility—For particle systems, a pressure susceptibility can be defined as a function of the porosity and compression pressure as stated below:

$$\chi_p \equiv -\frac{1}{\epsilon}\frac{d\epsilon}{d\sigma} \tag{2}$$

The porosity can equally be expressed by the relative density:

$$\rho = 1 - \epsilon, \quad \text{or in differential form:} \quad d\rho = -d\epsilon \tag{3}$$

Hence, eq 2 reads:

$$\frac{d\rho}{d\sigma} = \chi_p(1-\rho) \tag{4}$$

In case of a constant χ_p, eq 4 just holds for the differential form of the Heckel equation where χ_p equals K. Thus, a constant pressure susceptibility is the base of the theoretical concept of Heckel. Physically, this can be motivated by thinking of uniformly shrinking pores in a solid continuum. However, at low relative densities and pressures, the compacts are essentially particle agglomerates rather than homogeneously dispersed holes in a solid matrix. Consequently, a very different physical behavior can be expected.

Critical Behavior of the Pressure Susceptibility—Especially in the initial stage of the compression process, particle rearrangements dominate in many cases. In addition, fine particle systems can exhibit very porous structures by arching and formation of very loose agglomerates. Such structures are highly unstable and can collapse if only a minimal force is applied. Thus, the susceptibility to an external pressure can theoretically take any high value. Yet, it needs to be highlighted that in the case of a total lack of mechanical rigidity between the punches, the possibility to define pressure susceptibility is not available. Accordingly, a threshold value of the porosity ϵ_c or corresponding relative density ρ_c can be introduced, where a rigidity starts to evolve. The property χ_p exists therefore only for porosities lower than ϵ_c or relative densities higher than ρ_c. Hence, from these characteristics of the pressure susceptibility, the range in vicinity of the threshold can be called *critical*.

In line with these considerations, the Heckel model, where χ_p equals a constant K, needs to be replaced by an alternative approach, taking better account of the characteristics of pressure susceptibility. A related conjecture is an equation describing a hyperbola:

$$\chi_p = \frac{C}{\epsilon_c - \epsilon} = \frac{C}{\rho - \rho_c} \tag{5}$$

Where, C holds for a constant. Considering eq 5, it is interesting to notice that very different physical systems exhibit similar critical behavior. For example, the van der Waals theory expresses the compressibility (χ_T) of a gas as being proportional to $(T - T_c)^{-1}$, where T is the temperature and T_c is the critical temperature. Another example is the Curie–Weiss law that states the same for the magnetic susceptibility (χ_m). Here the critical temperature (T_c) is known in textbooks as the Curie temperature. However, the latter cases both hold for thermal phase transitions, whereas for tablets the relative density holds for an *order parameter*,[14] describing a geometric phase transition. Yet, it should be mentioned that such simple functions for χ_T or χ_m are based on a so-called *mean field approach*.[14] This theoretical view implies a simple mean potential, approximating the molecular interaction. In the context of compaction, the mean field can correspond to a mean pressure. A mean field approximation usually provides a rather good model and is valid in a broad range.

It should further be mentioned that percolation theory[15–18] assumes a power law for modeling a critical property. Unfortunately, such a power law has an unknown range of validity in the critical range. Keeping in mind the goal to find a new relationship between pressure and relative density, we used eq 5 for the present model.

A Modified Heckel Equation—Combination of eqs 2 and 5 results in the differential equation given below:

$$-\frac{1}{\epsilon}\frac{d\epsilon}{d\sigma} = C\frac{1}{\epsilon_c - \epsilon} \tag{6}$$

after separation of variables, it reads:

$$-\frac{\epsilon_c - \epsilon}{\epsilon}d\epsilon = Cd\sigma \tag{7}$$

Integration can be performed starting from the critical porosity ϵ_c at a negligible resting pressure $\sigma_0 \cong 0$:

$$\int_{\epsilon_c}^{\epsilon}\frac{\epsilon - \epsilon_c}{\epsilon}d\epsilon = C\int_0^{\sigma}d\sigma \tag{8}$$

$$[\epsilon - \epsilon_c \ln(\epsilon)]_{\epsilon_c}^{\epsilon} = C\sigma \tag{9}$$

$$\epsilon - \epsilon_c \ln(\epsilon) - [\epsilon_c - \epsilon_c \ln(\epsilon_c)] = C\sigma \tag{10}$$

$$\epsilon - \epsilon_c + \epsilon_c[\ln(\epsilon_c) - \ln(\epsilon)] = \epsilon - \epsilon_c + \epsilon_c \ln\left(\frac{\epsilon_c}{\epsilon}\right) = C\sigma \tag{11}$$

$$\sigma = \frac{1}{C}\left[\epsilon - \epsilon_c - \epsilon_c \ln\left(\frac{\epsilon}{\epsilon_c}\right)\right] \tag{12}$$

Hence, replacing porosity ϵ with the relative density ρ, a modified Heckel equation results:

$$\sigma = \frac{1}{C}\left[\rho_c - \rho - (1-\rho_c)\ln\left(\frac{1-\rho}{1-\rho_c}\right)\right] \tag{13}$$

Materials and Methods

Tablets (round, flat, 11 mm diameter, 400 ± 1 mg weight) were manufactured with a Zwick 1478 Universal Testing Instrument (Zwick GmbH, Ulm, Germany). Different pharmaceutical polymers were chosen as model substances, because of their ability to form tablets in the interesting critical range at comparatively low relative densities (Table 1). True density was determined with an Beckman Air Comparison Pycnometer Model 930 and the particle size assayed using a Malvern Mastersizer X.

For each powder system, five tablets were compressed at different pressure levels ranging from 1.05 MPa up to 105.23 MPa at a relative humidity of 45% ± 10%. The compression speed was 10 mm/min and tablets' geometry was assessed 48 h after manufacture ("out of die" determination).

All data of different substances were used for statistical evaluation, except for Klucel, where only values to a pressure of

Table 1—Characterization of the Polymer Substances

substance	true density [g/cm^3]	relative bulk density	relative tapped density	mean particle size (Sauter)[μm]
Emcocel 50M[a]	1.57	0.207	0.250	54
Avicel PH101[a]	1.57	0.205	0.260	48
Avicel PH102[a]	1.56	0.213	0.258	81
Klucel[b]	1.20	0.358	0.388	307
Pharmacoat 606[c]	1.33	0.275	0.357	45
Ac-Di-Sol[d]	1.57	0.317	0.393	41
Kollidon K17[e]	1.19	0.405	0.436	73
Kollidon CL[e]	1.26	0.283	0.345	41
Kollidon K90F[e]	1.22	0.427	0.466	138
PEG 8000[f]	1.23	0.466	0.543	50
PEG 10000[f]	1.22	0.525	0.572	158
PEG 20000[f]	1.22	0.522	0.558	229

[a] Type of microcrystalline cellulose. [b] Type of hydroxypropyl cellulose. [c] Type of hydroxypropyl methylcellulose. [d] Type of croscarmellose sodium. [e] Type of poly(vinylpyrrolidone). [f] Type of poly(ethyleneglycol)s.

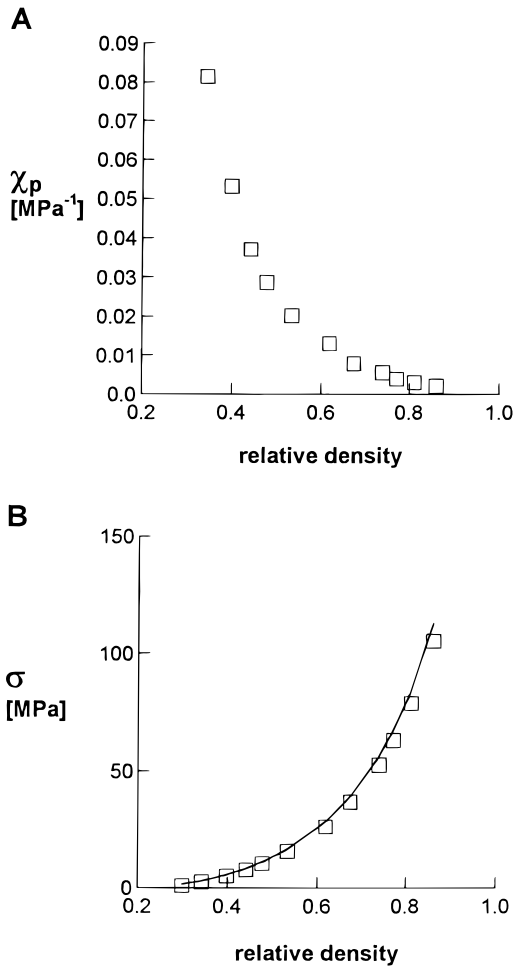

Figure 1—Avicel PH101: (A) Pressure susceptibility χ_p (MPa^{-1}) vs relative density (□). (B) Compression pressure σ (MPa) as a function of the relative density (□). The solid line represents the model according to eq 13.

36.8 MPa were evaluated. The program used for all calculations was SYSTAT for Windows Version 7.0 (SPSS Inc.).

Results and Discussion

The pressure susceptibility was calculated from experimental data according to eq 4 using finite differences for the differential quotient and plotted against ρ (see Figures1–4A). The graphs show that very high compressibility

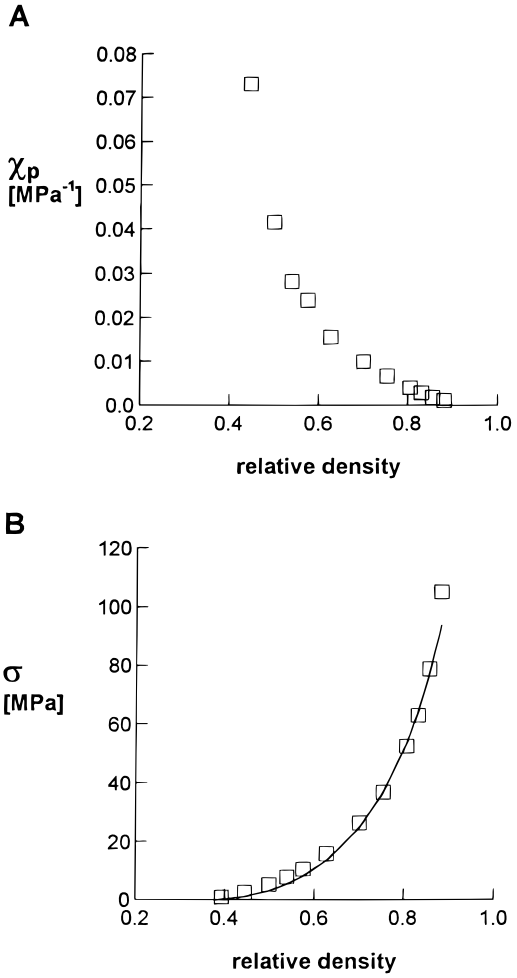

Figure 2—Pharmacoat 606: (A) Pressure susceptibility χ_p (MPa^{-1}) vs relative density (□). (B) Compression pressure σ (MPa) as a function of the relative density (□). The solid line represents the model according to eq 13.

decreases sharply with increasing relative densities. Thus, the assumption of Heckel to use a constant pressure susceptibility is only acceptable as a first approximation for comparatively dense compacts. Still, further changes of the property χ_p will take place, until a minimum is achieved at about zero porosity. Note that for the slight changes in this range, the experimental accuracy is a limiting factor. This is reflected by the scatter of the values for PEG 8000 (see Figure 4A).

Very porous tablets produce considerable porosity changes under strain. Such high compressibility can only be explained by particle displacement, i.e., particle rearrangements in the initial stages of compression. As long as a large extraparticulate void volume exists, a reduction of porosity can be achieved by a small pressure. The consequence is a high value of χ_p that was also observed in the experimental results (Figure 1–4A). Theoretically, the curve close to ρ_c can even extend to infinity but directly at the threshold and below the function χ_p vanishes. As a conclusion, the assumption of a hyperbola for χ_p eq 5 appears very suitable, whereas the approximation of a constant value for χ_p is clearly not correct for low-density tablets.

Focusing on the relationship between pressure and relative density,we compared the new model eq 13 and the Heckel eq 1, on the basis of "out of die" measurements (Table 2). A nonlinear fit was conducted with all substances using the new model equation (See Figure 1–4B). It shows that eq 13 is in good agreement with experimental results.

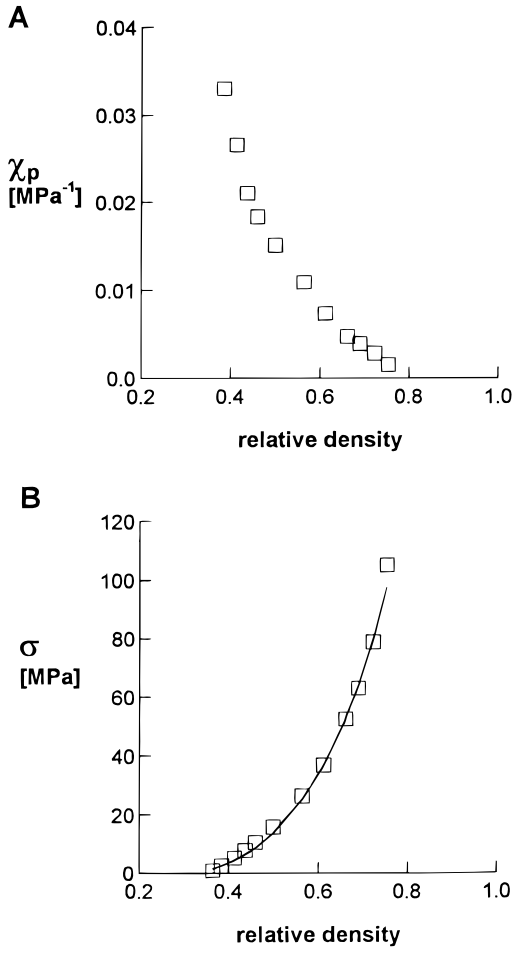

Figure 3—Kollidon CL: (A) Pressure susceptibility χ_p (MPa^{-1}) vs relative density (□). (B) Compression pressure σ (MPa) as a function of the relative density (□). The solid line represents the model according to eq 13.

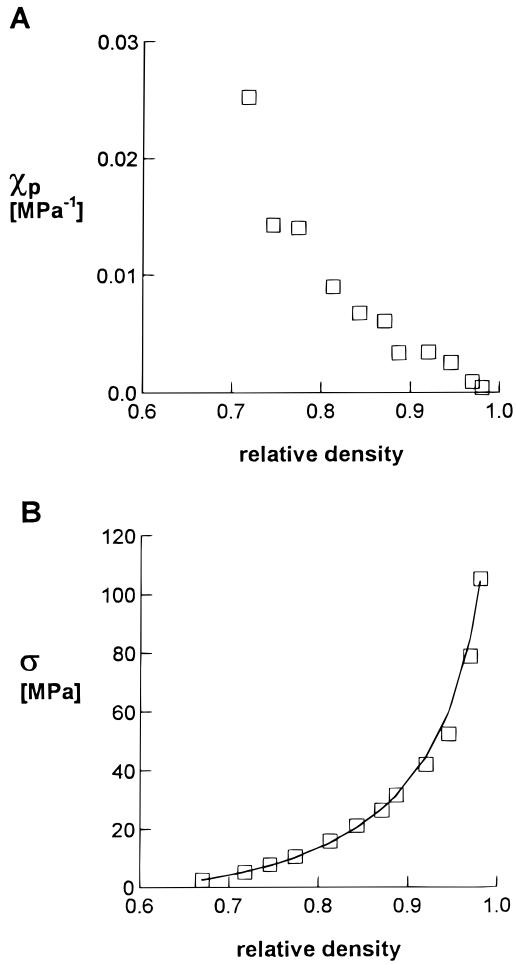

Figure 4—PEG 8000: (A) Pressure susceptibility χ_p (MPa^{-1}) vs relative density (□). (B) Compression pressure σ (MPa) as a function of the relative density (□). The solid line represents the model according to eq 13.

In addition, the comparison with the Heckel equation (Table 2) clearly showed a better goodness of fit of the new model. Yet, in some cases such as for Pharmacoat 606 (Figure 2) and Kollidon CL (Figure 3), the highest pressure did not properly match the new model.

It should be noticed that the number of parameters is the same for the Heckel equation and the new model. This low number of parameters, i.e., the simplicity of a model, is an important aspect. Yet, the complexity of the compression process is awesome, involving several physical phenomena of changing significance in different stages.[19,20] Thus, the proposal of a *power series* might be most adequate to describe the change of pressure susceptibility close to the threshold ρ_c. On the other hand, new parameters would be introduced and the problem of an a priori limited range of validity is still present. Therefore, a simple approximation on the average, as proposed by eq 5, is justified.

Comparing the constants C and K (Table 2), values for the new parameter C were all smaller than those of K by a factor of roughly between 2 and 4. Qualitatively it can be said that both parameters incorporate an experimental minimal susceptibility (χ_{pmin}) close to zero porosity. This parameter is independent of the tablet's pore structure because it is a characteristic of the solid continuum. The constant C is proportional to χ_{pmin} but further involves the threshold value ρ_c, which becomes apparent evaluating eq 5 at unity density. Thus, C depends on the initial structure of the particle packing.

Considering the parameter ρ_c, this value was defined in the theoretical section as a rigidity threshold. Thus, this critical value holds for the packing fraction, producing a negligible mechanical resistance between the punches. In a strictly geometric interpretation, this threshold ρ_c demonstrates the transition between dispersed solid in air and voids in a solid matrix. The coherent contact within the powder column will be already present only when the powder is poured in the die. Yet, it can be argued that contact between particles might not be enough for establishing a relevant rigidity.[21] Some initial particle rearrangements might require only minimal forces that can be

Table 2—Comparison between the Heckel Equation and the Proposed Modified Equation

	Heckel equation			Modified Heckel equation		
	K	*A*	$r^{2\,a}$	*C*	ρ_c	$r^{2\,a}$
Emcocel 50M	0.015	0.449	0.960	0.006	0.217	0.998
Avicel PH101	0.016	0.453	0.978	0.007	0.167	1.000
Avicel PH102	0.016	0.442	0.969	0.007	0.180	0.998
Klucel	0.044	0.682	0.934	0.014	0.379	0.986
Pharmacoat 606	0.017	0.638	0.952	0.006	0.356	0.993
Ac-Di-Sol	0.007	0.503	0.978	0.002	0.291	0.999
Kollidon K17	0.021	0.593	0.989	0.012	0.195	0.996
Kollidon CL	0.010	0.505	0.965	0.003	0.284	0.996
Kollidon K90F	0.011	0.621	0.986	0.003	0.323	0.998
PEG 8000	0.028	1.200	0.979	0.010	0.528	0.995
PEG10000	0.029	1.292	0.953	0.008	0.601	0.984
PEG 20000	0.028	1.127	0.933	0.009	0.560	0.971

[a] Corrected squared correlation coefficient.

neglected. Thus, the rigidity threshold ρ_c can be higher than the relative density needed for coherent contact.

The values for ρ_c (Table 2) according to eq 13 ranged for all substances close to the interval of the relative bulk density and tapped density (Table 1). It is interesting to notice that the different types of microcrystalline cellulose and poly(vinylpyrrolidone) displayed a trend for lower thresholds. This tendency seemed especially pronounced for Avicel PH102, Kollidon K17, and K90F, where values for ρ_c were even lower than the relative bulk density. The poly(ethylene)glycol)s showed reversed tendency, where critical rigidity was achieved close to the relative tapped density or slightly above as produced by PEG 10000 and PEG 20000. In line with these considerations, it can be concluded that the microstructure, being specific for a given substance, plays an important role for ρ_c.

The Heckel constant K in eq 1 can be used to characterize substances.[22] The question can therefore be asked if a similar information can also be acquired from the new parameters ρ_c and C. In line with the considerations so far, ρ_c appears to be a parameter being strongly affected by the microstructure of the powder system. Of further special interest is that particle systems can behave differently under compression or tension. The behavior under compression gives information on rigidity, whereas a behavior under tension is related to compact strength. Thus, the compressibility of a particle assembly can therefore be considered as a characteristic on its own apart from the binding capabilities. Yet again the situation is different for the dense compacts. If the applied pressure is high enough, plastic flow occurs at a compressive yield pressure (σ_Y). Accordingly, the value for χ_{pmin} can be expected to depend on σ_Y. This aspect can further be stressed by defining a compression modulus (G):

$$G \equiv \frac{1}{\chi_p} \tag{14}$$

The property G expresses the pressure needed to reduce porosity of a tablet. A maximal value (G_{max}) will therefore be limited by a compressive yield strength. Alternatively, it can be stated that the maximal compression modulus equals the maximal hardness (P_{max}) of the material if exclusive plastic flow occurs.

The inverse of the constant K can also be regarded as a compression modulus G. Its determination only from the linear part of the Heckel plot, results again in an estimate of compressibility at high pressures and therefore approximates G_{max}. Note that the constant K was assessed instead over the entire range of the relative density.

However, Heckel already conjectured that the inverse of the Heckel slope was proportional to the yield point of the particles with a proportionality factor equal to three.[5] This observation agrees with our considerations that maximal compressibility is limited by a compressive yield pressure. Furthermore, it should be mentioned that the yield point of a plastic material is known to equal one-third of the indentation hardness.[23] This again supports the view that for plastic substances, the inverse Heckel slope can also be regarded as a measure of maximal hardness. From these considerations it can be qualitatively concluded that G_{max} is a specific property of a substance and can potentially be used for characterization of a tableting material. Yet, it needs to be stressed that experimentally the zero porosity state can hardly be achieved even at highest pressures.[24] Therefore, arguments on G_{max} should be understood qualitatively first.

It is interesting to normalize the compression modulus G by its maximum G_{max}. This quotient only depends on the structure of the tablet. Using eq 5, one obtains:

$$\frac{G}{G_{max}} = \frac{\chi_p^{-1}}{\chi_{pmin}^{-1}} = \frac{(\rho - \rho_c)C}{(1 - \rho_c)C} = \frac{1}{1 - \rho_c}(\rho - \rho_c) \tag{15}$$

This result is consistent with the model of Leuenberger and Leu[25] based on the percolation theory. The eq 15 was previously pointed out to be consistent with a so-called *effective medium approximation*,[26–28] where a disordered medium is replaced on the average by a hypothetical homogeneous one.

Conclusions

It was shown that the pressure susceptibility exhibits very high values at comparatively low relative densities. The property χ_p was expected to be divergent in this range having a singularity at a critical relative density ρ_c. As a consequence, the Heckel equation, assuming a constant value for χ_p, is inadequate in this critical range. The proposal of a simple hyperbola function leads in the integrated form to a modified Heckel equation. This model has shown to be superior in describing different polymer tablets from "out of die" measurements. The understanding of the pressure susceptibility as a critical property links the process of compression to the theory of phase transitions. Thus, the present concept provides not only a new equation for the relationship between pressure and relative density, but contributes also to further insights in the complex nature of the compaction process.

Additional studies are needed for a complete evaluation of the proposed model equation. So far in this study, porosity was determined after manufacture and storage. Additional "in die" measurements would be of interest because no elastic recovery or other postcompressional changes are allowed under these conditions. Plus, brittle substances should be tested. This is especially of interest, regarding the importance of tableting material undergoing fragmentation during compaction.

Glossary

ϵ, ϵ_c	Porosity and critical porosity. The latter value is defined as the threshold porosity of a vanishing rigidity between the punches
ρ, ρ_c	Relative density and critical relative density. The threshold density corresponds to $1 - \epsilon_c$
σ	Applied pressure (MPa)
K, A	Constants of the Heckel equation, where K (MPa^{-1}) equals the slope, and A the intercept of the plot $\ln(1/(1 - \rho))$ with respect to σ
χ_p	Pressure susceptibility or compressibility, defined as $\chi_p \equiv -(1/\epsilon)(d\epsilon/d\sigma) = [1/(1 - \rho)](d\rho/d\sigma)(MPa^{-1})$
χ_{pmin}	Minimal value of the pressure susceptibility (MPa^{-1}) at zero porosity
C	Proportionality constant (MPa^{-1}) that links the porosity with the pressure susceptibility $\chi_p = C/(\epsilon_c - \epsilon) = C/(\rho - \rho_c)$. Hence, C can also be related to with the minimal pressure susceptibility at zero porosity: $C = \chi_{pmin}\epsilon_c = \chi_{pmin}(1 - \rho_c)$.
χ_T	Isothermal compressibility of a gas defined by a relation to the volume V (m^3), pressure P (Pa) and gas density ρ_g (kg m^{-3}): $\chi_T \equiv -(1/V)(dV/dP) = (1/\rho_g)/(d\rho_g/dP)$
χ_m	Magnetic susceptibility, defined over the relationship: $\chi_m \equiv (dM/dH)$, where M (A m^{-1}) is the magnetization and H (A m^{-1}) the magnetic field.

T, T_c Temperature and critical temperature. The threshold temperature can hold, for example, for the singularity at the end of the vapor vs pressure curve, or in case of magnetic systems, it marks the transition of ferromagnetism and paramagnetic behavior.

G Compression modulus (MPa) is by definition the reciprocal of χ_p.

G_{max} Maximal compression modulus (MPa) defined over the reciprocal of χ_{pmin}.

σ_N Compressive yield pressure (MPa).

P_{max} Maximal value of the deformation hardness (MPa).

References and Notes

1. Rivier, N. Order and disorder in packings and froths. In *Disorder and Granular media*; Bideau, D., Hansen, A., Eds.; Elsevier Publishers: North Holland, 1993; pp 93−95.
2. Lüdde, K. H.; Kawakita, K. Die Pulverkompression. *Pharmazie* **1966**, *21*, 393−403.
3. Cooper, A. R.; Eaton, L. E. Compaction behaviour of several ceramic powders. *J. Am. Ceram. Soc.* **1962**, *45*, 97−101.
4. Heckel, R. W. Density- pressure relationship in powder compaction. *Trans. Metall. Soc. AIME* **1961**, *221*, 671−675.
5. Heckel, R. W. An analysis of powder compaction phenomena. *Trans. Metall. Soc. AIME* **1961**, *221*, 1001−1008.
6. Ramberger, R.; Burger, A. On the application of the Heckel and Kawakita equation to powder compaction. *Powder Technol.* **1985**, *43*, 1−9.
7. Rue, J.; Rees, J. E. Limitations of the Heckel relation for predicting powder compaction mechanism. *J. Pharm. Pharmacol.* **1978**, *30*, 642−643.
8. Yu, A. B.; Hall, J. S. Packing of fine powders subjected to tapping. *Powder Technol.* **1994**, *78*, 247−256.
9. Lordi, N. G.; Cocolas, H.; Yamasaki, H. Analytical interpretation of powder compaction during the loading phase. *Powder Technol.* **1997**, *90*, 173−178.
10. Carstensen, J. T.; Geoffroy J.-M.; Dellamonica, C. Compression characteristics of binary mixtures. *Powder Technol.* **1990**, *62*, 119−124.
11. Adams, M. J.; Mullier, M. A.; Seville, J. P. K. Agglomerate strength measurement using a uniaxial confined compression test. *Powder Technol.* **1994**, *78*, 5−13.
12. Duncan-Hewitt, W. C. Uniaxial compaction modeled using the properties of single crystals. *Drug Dev. Ind. Pharm.* **1993**, *19*, 2197−2240.
13. Stanley, H. E. Fractals and Multifractals: The interplay of physics and geometry. In *Fractals and Disordered Systems*, 2nd ed.; Bunde, A., Havlin, S., Eds.; Springer: Berlin, 1996; pp 1−57.
14. Stanley, H. E. *Introduction to Phase Transitions and Critical Phenomena*; Oxford Sci. Pub.: Oxford, 1971; pp 76−93.
15. Flory, P. J. Molecular size distribution in three-dimensional polymers. *J. Am. Chem. Soc.* **1941**, *63*, 3083−3100.
16. Broadbent S. R.; Hammersley, J. M. Percolation process, I. Crystals and mazes. *Proc. Camb. Philos. Soc.* **1957**, *53*, 629−641.
17. Stauffer, D.; Aharony, A. *Introduction to Percolation Theory*, 2nd ed.; Taylor and Francis: London, 1992.
18. Leuenberger, H.; Rohera, B. D.; Haas, C. Percolation theory − A novel approach to solid dosage form design. *Int. J. Pharm.* **1987**, *38*, 109−115
19. Wray, P. E. The physics of tablet compaction revised. *Drug Dev. Ind. Pharm.* **1992**, *18*, 627−658.
20. Alderborn, G.; Nyström, C. *Pharmaceutical Powder Compaction Technology*; Marcel Decker, Inc.: New York, 1996.
21. Feng, S.; Sen, P. N. Percolation on elastic networks: New exponents and thresholds. *Phys. Rev. Lett.* **1984**, *52*, 216
22. Humbert-Droz, P. Analyse des caracteristiques de compression des substances medicamenteuses en relation avec le phenomene de dissolution Ph.D. Thesis, University of Geneva, 1982.
23. Rowe, R. C.; Roberts, R. J. Mechanical properties. In *Pharmaceutical Powder Compaction Technology*; Alderborn, G., Nyström, C., Eds.; Marcel Decker, Inc.: New York, 1996; pp 284
24. Carstensen, J. T.; Hou, X. P. The Athy-Heckel equation applied to granular agglomerates of basic tricalcium phosphate. *Powder Technol.* **1985**, *42*, 153−157.
25. Leuenberger, H.; Leu, R. The formation of a tablet: a site and bond percolation phenomenon. *J. Pharm. Sci.* **1992**, *81*, 976−982.
26. Landauer, R. The electrical resistance of binary metallic mixtures. *J. Appl. Phys.* **1952**, *23*(7) 779−784.
27. Kirkpatrick, S. Percolation and conduction. *Rev. Mod. Phys.* **1973**, *45*(4) 574−588.
28. Kuentz, M.; Leuenberger, H. Modified Young's modulus of microcrystalline cellulose tablets and the directed continuum percolation Model. *Pharm. Dev. Technol.* **1998**, *3*(1), 13−19.

Acknowledgments

We would like to acknowledge Swiss National Science Foundation (grant No.20-45592.95) for financial support.

JS980369A

Permeability Characteristics of Novel Mydriatic Agents Using an in Vitro Cell Culture Model That Utilizes Sirc Rabbit Corneal Cells

VENKAT R. GOSKONDA,[†] MANSOOR A. KHAN,[†] CHRISTINE M. HUTAK,[‡] AND INDRA K. REDDY*,[†]

Contribution from *Division of Basic Pharmaceutical Sciences, School of Pharmacy, Northeast Louisiana University, Monroe, Louisiana 71209, and New York College of Osteopathic Medicine of New York Institute of Technology, Department of Pharmacology, Toxicology, and Experimental Therapeutics, Old Westbury, New York 11568.*

Received September 2, 1998. Accepted for publication November 19, 1998.

Abstract □ The purpose of this study was to evaluate the permeability characteristics of a previously reported in vitro corneal model that utilizes SIRC rabbbit corneal cells and to investigate the permeability of three novel esters of phenylephrone chemical delivery systems (CDS) under different pH conditions using this in vitro model. The SIRC rabbit corneal cell line was grown on transwell polycarbonate membranes, and the barrier properties were assessed by measuring transepithelial electrical resistance (TEER) using a voltohmmeter. The permeabilities of esters of phenylephrone CDS across the SIRC cell layers were measured over a pH range 4.0–7.4. The esters tested include phenylacetyl (**1**), isovaleryl (**2**), and pivalyl (**3**). The SIRC rabbit corneal cell line, when grown on permeable filters, formed tight monolayers of high electrical resistance with TEER values increasing from 71.6 ± 20.8 Ω·cm^2 at day 3 in culture to 2233.42 ± 15.2 Ω·cm^2 at day 8 in culture and remained constant through day 14 in culture. The transepithelial permeability coefficients (P_{app}) at pH 7.4 ranged from 0.58×10^{-6} cm/s for the hydrophilic marker, mannitol, to 43.5×10^{-6} cm/s for the most lipophilic molecule, testosterone. The P_{app} at pH 7.4 for phenylephrine was 4.21×10^{-6} cm/s. The P_{app} values and the lag times of the three esters of phenylephrone were pH dependent. The P_{app} for **1**, **2**, and **3** at pH 7.4 were 14.76×10^{-6}, 13.19×10^{-6}, and 12.86×10^{-6} cm/s, respectively and the permeabilities decreased at conditions below pH 7.4. The lag times at pH 7.4 were 0.10, 0.17, and 0.12 h for **1**, **2**, and **3**, respectively, and the values increased at lower pH conditions. The TEER values of SIRC cell line observed at day 8 to day 14 in the present investigation are similar to the resistance value reported for rabbit cornea (2 kΩ·cm^2). All the esters showed significantly ($p < 0.05$) higher permeabilities than phenylephrine at pH 7.4. The rate and extent of transport of the drugs across the cell layers were influenced by the fraction of ionized and un-ionized species and the intrinsic partition coefficient of the drug. The results indicate that the permeability of ophthalmic drugs through ocular membranes may be predicted by measuring the permeability through the new in vitro cell culture model.

Introduction

Phenylephrine hydrochloride (HCl) is an α-adrenergic agonist and is commonly used in routine ophthalmic practice as a mydriatic and vasoconstrictor agent. Several cases of adverse systemic reactions after topical ocular application of phenylephrine HCl have been reported and include severe hypertension, subarachnoid hemorrhage, ventricular arrhythmia, and possible myocardial infarction.[1−6] Therefore, it would be most desirable to design a drug that could be delivered to the eye compartments with the least possible systemic absorption and/or no systemic side effects. Previous reports have shown that, after topical application to the eye, esters of adrenalone but not adrenalone itself can be converted via a reduction−hydrolysis sequence to deliver adrenaline (epinephrine) only at the iris−ciliary body, the site of action.[7,8] This suggested that lipophilic ketones can be reduced in the iris−ciliary body. Accordingly, phenylephrone chemical delivery systems (CDS) (Figure 1) were designed to release the active species phenylephrine, by a "reductive−hydrolytic activation" mechanism, selectively to iris−ciliary body, thus avoiding the various systemic side effects. We recently reported the physicochemical properties of the novel compounds as a part of preformulation study.[9]

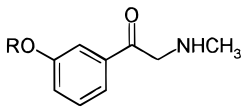

Phenylephrone CDS

1: R = -$COCH_2C_6H_5$ (phenylacetyl)
2: R = -$COCH_2CH(CH_3)_2$ (isovaleryl)
3: R = -$COC(CH_3)_3$ (pivalyl)

Figure 1—Structures of phenylephrone CDS.

Investigation of the absorption properties of a new drug moiety is also an important part in the preformulation process. The rate and extent of intraocular absorption and therapeutic effectiveness of topically applied drugs are dependent on the transport characteristics of ocular membranes, especially the cornea.[10−12] Characterization of the ocular penetration of drugs has been performed using hard-to-obtain ocular membranes from many animals. The establishment of a predictive method for the drug permeation using a cell culture model would be useful. In vitro cell culture models are of potential utility for some screening studies in which large quantities of corneas are needed. The SIRC rabbit cell line has been used by many researchers as a cellular model in studies of corneal physiology, immunology, and toxicology.[13−17] Hutak et al. recently developed an in vitro model for corneal permeability and reported that a single inoculation of SIRC rabbit corneal cells resulted in the formation of multiple epithelioid cell layers, with the number of layers increasing with culture time.[18] The objectives of the present study are to (a) evaluate the permeability characteristics of the SIRC rabbit corneal cell line system for potential use as an in vitro model for assessing drug permeability and (b) characterize the transport characteristics of three novel esters of the phenylephrone CDS using this model at varying pH conditions.

Materials and Methods

The SIRC cell line was obtained from American Type Culture Collection (ATCC no. CCL60; Rockville, MD). Earle's balanced salt solution (EBSS) without sodium bicarbonate, bovine calf serum,

* Corresponding author: Tel: (318) 342−1709. Fax: (318) 342-1606. E-mail: pyreddy@alpha.nlu.edu.

10.1021/js980362t CCC: $18.00
Published on Web 01/12/1999

lactalbumin hydrolysate, yeast extract, trypsin, and gentamycin sulfate were obtained from Gibco BRL, Grand Island, NY. All other chemicals were of tissue culture grade. Plastic filter units, cell culture flasks (75 cm^2), and transwell inserts were obtained from Fisher Scientific, Houston, TX. D-[1-^{14}C]mannitol (mol wt 182.2) with a specific activity of 50.0 mCi/mmol and a radiochemical purity of 98% was purchased from Sigma Chemical Co., St. Louis, MO. [4-^{14}C]testosterone, having a specific activity of 57.0 mCi/mmol and a radiochemical purity of 98.2%, was purchased from Nycomed Amersham, Arlington Heights, IL.

Cell Culture—SIRC cells were cultured as previously described by Hutak et al.[18] The cells were maintained at 37° C in EBSS containing 10% bovine calf serum, 1760 mg/L lactalbumin hydrolysate, 570 mg/L yeast extract, 860 mg/L sodium bicarbonate, and 50 mg/L gentamycin sulfate in an atmosphere of 5% CO_2 and 95% relative humidity. The cells grown in 75 cm^2 flasks were passaged every seventh day of culture at a split ratio of 1:2. The cells were rinsed with 0.1% EDTA (pH 7.4), suspended using trypsin–EDTA in EBSS (37° C, 5 min), and transferred to two new flasks containing fresh growth medium.

In the present investigations, 0.5 mL of growth medium was placed in each well of the microwell plates, and the tissue culture inserts were placed in the wells. The cells, grown for 7 days in culture, were suspended in 50 mL of growth medium. A 0.15 mL aliquot of culture medium was placed into each filter insert, followed by the addition of 0.1 mL cell suspension. The total volume of media and cell suspension was predetermined by the filter capacity specifications. The volume of cell suspension added to the inserts was determined by the relative surface area of the microwell insert to the culture flask. The cell layers were given fresh growth medium on every seventh day of growth. One milliliter of fresh growth medium was placed into a new well. Following removal of the old medium, the insert was placed into this new well, and 0.1 mL of fresh medium was added to each insert.

Electrical Resistance Measurements—The permeability of the cell monolayers was determined by electrical resistance measurements using a voltohmeter. The culture media (0.6 mL and 0.1 mL to the apical and basolateral chamber, respectively) were added prior to electrical measurements. Transepithelial electrical resistance (TEER) values, obtained in the absence of cells (caused by the electrical system and the collagen-coated polycarbonate membrane), were considered as background. For each experiment, total electrical resistance values were corrected for background, which ranged from 20 to 40 Ω·cm^2, to obtain the TEER values of the cell monolayers.

Transport Studies—SIRC cell monolayers grown on collagen-coated polycarbonate filters (Transwell) for 8–10 days were used for transport experiments. On the day of the transport experiment, the culture media (0.6 mL and 0.1 mL to the apical and basolateral chamber, respectively) was replaced with EBSS containing 25 mM glucose. The pH of the transport medium was adjusted with HCl or NaOH. After equilibration at 37 °C for 30 min, TEER values were obtained prior to transport study. The integrity of each batch of cells was further tested by measuring the flux of radiolabeled mannitol (0.01 mM) in representative cell monolayers ($n = 3$). The transport of the novel mydriatic agents (phenylephrone CDS) across SIRC cell monolayers at pH 4.0, 5.0, 6.0, and 7.4 was determined in triplicate. In apical (donor compartment) to basolateral (receiver compartment) transport studies, each well in the 24 well clusters received 0.6 mL of transport medium that had previously been equilibrated at 37 °C. Transport medium (0.1 mL) containing the drug [phenylephrine, 0.1 mM; phenylephrone CDS, 0.1 mM; testosterone, 0.01 mM] was applied to the apical side. Samples (100 μL) were removed from the basolateral side at various times up to 180 min and replaced with the same volume of fresh transport medium. Aliquots of 20 μL were taken from the apical side at the beginning and end of each experiment.

Assay Method—The esters of phenylephrone (phenylacetyl **1**, isovaleryl **2**, and pivalyl **3**) were analyzed by HPLC (Isco pump, Model 2350; Model 484, waters) using an electrochemical detector. The detection potential was 1.15 V. A μBondapak C18 column with a similar 6 cm guard column and a mobile phase (pH 3.6) consisting of acetonitrile:acetate buffer:triethylamine (25:75:0.05) with a flow rate of 1 mL/min were used for the resolution of the compounds. Calibration curves were obtained by plotting the peak area as a function of drug concentration. The radioactive materials were analyzed by using a Beckman LS-3801 liquid scintillation counter.

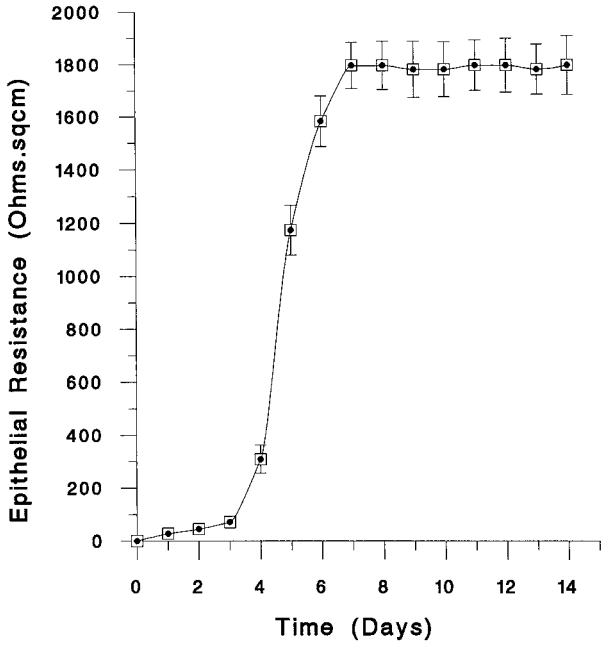

Figure 2—Transepithelial electrical resistance across SIRC cells grown on a polycarbonate membrane. Each value represents average (±SEM) of six experiments.

Data Analysis—Apparent permeability coefficients (P_{app}) of the three esters of phenylephrone and D-[1-^{14}C]mannitol and [4-^{14}C]testosterone were calculated using the following equation:

$$P_{app} = (1/AC_0)\,(dM/dt)$$

where dM/dt is the flux across the cell layers (μg/hr), A is the surface area of the membrane (0.33 cm^2), and C_0 is the initial drug concentration (μg/mL) in the donor compartment at $t = 0$. Flux per unit surface area ($1/A \times dM/dt$) was determined from the slope of linear portion of the cumulative amount permeated per unit surface area vs time plot. The lag time was also determined from this plot by extrapolating the linear portion to the abscissa. The results of experiments performed in triplicate are presented as mean ± SD. Statistical differences between the novel compounds in the amount permeated at each time point, and the means were determined by one-way analysis of variance (ANOVA). The criterion for statistical significance was $p < 0.05$.

Results and Discussion

Transepithelial Electrical Resistance Measurements—Measurement of electrical resistance across the cellular layers is a convenient and relatively sensitive measure of the integrity and permeability of the layer. These measurements reflect predominantly the resistance across the tight junctions and not the cell membranes.[19–23] The transcellular electrical resistance of the SIRC rabbit corneal cell layers increased with time up to the eighth day of culture with a resistance of 2233.42 ± 15.2 Ω·cm^2 and remained constant through the 14th day of culture (Figure 2). The electrical resistances shown by the SIRC cell line are slightly higher than the transepithelial resistances across the corneal membranes (2 kiloohms·cm^2).[24] However, methods used to derive resistance values from cell monolayers and excised tissue are different, and therefore comparisons should be considered with caution. The resistance values shown by the cell layers used in the flux experiments are slightly lower due to effects of media changes during washing. The TEER values were constant

Table 1—The Flux and P_{app} Values of D-[1-^{14}C]Mannitol and [4-^{14}C]Testosterone across SIRC Cell Layers at Different pH Conditions[a,b]

	pH 4.0	pH 5.0	pH 6.0	pH 7.4
		Mannitol		
flux (ng/cm^2 hr)	4.03 ± 0.08	3.87 ± 0.11	3.86 ± 0.21	3.80 ± 0.22
$P_{app} \times 10^6$ (cm/s)	0.62 ± 0.02	0.59 ± 0.01	0.59 ± 0.02	0.58 ± 0.02
		Testosterone		
flux (ng/cm^2 hr)	462.8 ± 12.6	459.3 ± 16.8	451.9 ± 14.7	456.5 ± 18.1
$P_{app} \times 10^6$ (cm/s)	44.1 ± 1.2	43.8 ± 1.6	43.1 ± 1.4	43.5 ± 1.8

[a] Values are means ± SEM of at least three experiments. [b] The values were obtained from the permeation studies performed up to 120 min at pH 4.0 and 5.0 and up to 150 min at pH 6.0 and 7.4.

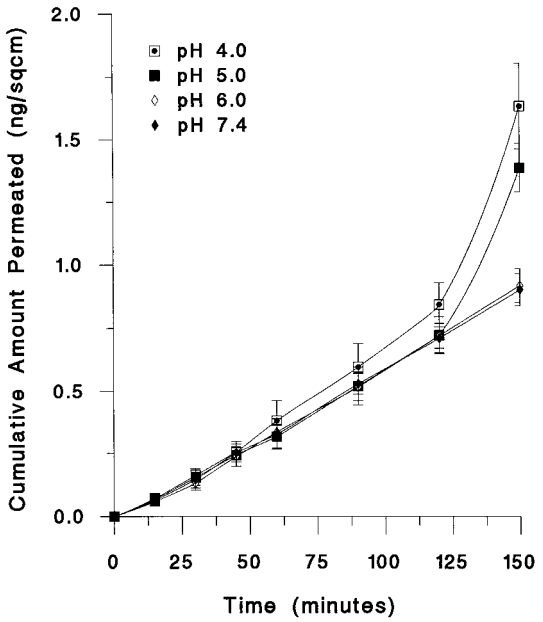

Figure 3—Apical to basolateral transport of mannitol across SIRC cell layers at different pH conditions. Each value represents average (±SEM) of at least three experiments.

throughout the transport studies at pH 6.0 and 7.4, but the values decreased when exposed to pH 4.0 and 5.0 after a period of 120 min.

Transport Studies—The permeability of the hydrophilic marker, D-[1-^{14}C]mannitol, was determined to further characterize the SIRC cell monolayers regarding its integrity as a molecular barrier. Mannitol, a molecule which is transported predominantly via the paracellular pathway, showed low permeabilities (0.58×10^{-6} cm/s) (Table 1) across the SIRC cell layers confirming that the cells formed tight junctions when grown on polycarbonate membranes. The permeability of mannitol across the SIRC cells was less when compared to the permeability across isolated corneal membranes.[25] Figure 3 shows the cumulative amount of mannitol permeated over time at different pH conditions. At pH 4.0, the mannitol permeability at 120 min was 0.62×10^{-6} cm/s and later increased to 2.1×10^{-6} cm/s. Similarly, the P_{app} values at pH 5.0 increased from 0.59×10^{-6} cm/s to 2.02×10^{-6} cm/s after 120 min. These differences in the permeabilities of the paracellular marker over time (and decrease in the resistance values) might be due to the damage caused to the surface layers of the SIRC cells when exposed to low pH conditions.

The gradual and reproducible development of resistance across the SIRC cells, when grown in culture medium, allowed study of the permeability characteristics of a group of novel mydriatic agents, esters of phenylephrone, and the lipophilic marker, testosterone. The highly lipophilic molecule, testosterone, is transported via the transcellular pathway. Testosterone exhibited a high permeability (43.5×10^{-6} cm/s) in the SIRC model at pH 7.4 (Table 1). Figure 4 illustrates the apical to basolateral transport of the phenylephrone esters, mannitol, phenylephrine, and testosterone across SIRC cell layers at pH 7.4.

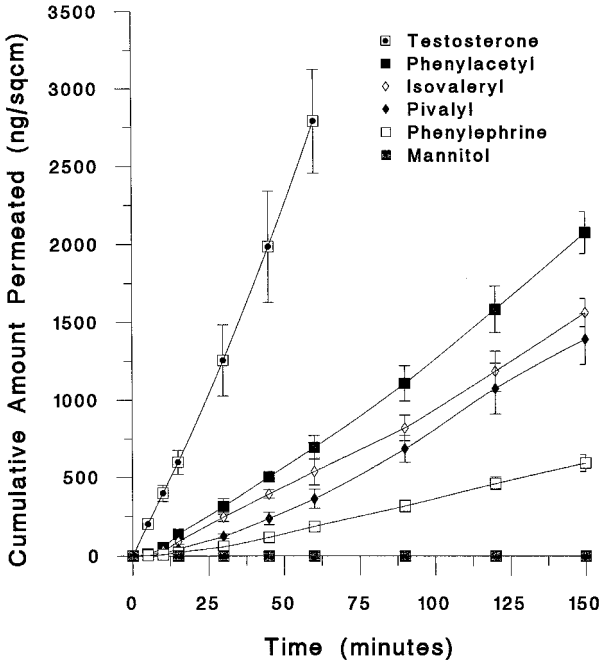

Figure 4—Apical to basolateral transport of testosterone, phenylephrone CDS, phenylephrine, and mannitol across SIRC cell layers at pH 7.4. Each value represents average (±SEM) of at least three experiments.

Table 2—The Flux, P_{app}, and Lag Time Values of Phenylephrone Esters across SIRC Cell Layers at Different pH Conditions[a,b]

	flux (μg/cm^2 h)	$P_{app} \times 10^6$ (cm/s)	lag time (h)
		Phenylephrine	
pH 4.0	0.33 ± 0.04	3.20 ± 0.08	0.51 ± 0.05
pH 5.0	0.35 ± 0.03	3.42 ± 0.10	0.49 ± 0.03
pH 6.0	0.40 ± 0.05	3.91 ± 0.26	0.31 ± 0.04
pH 7.4	0.43 ± 0.02	4.21 ± 0.34	0.28 ± 0.02
		Phenylacetyl Ester	
pH 4.0	1.18 ± 0.03	10.67 ± 0.28	0.39 ± 0.03
pH 5.0	1.22 ± 0.02	11.09 ± 0.31	0.30 ± 0.01
pH 6.0	1.41 ± 0.02	12.83 ± 0.21	0.19 ± 0.03
pH 7.4	1.62 ± 0.08	14.76 ± 0.61	0.10 ± 0.02
		Isovaleryl Ester	
pH 4.0	1.04 ± 0.02	10.08 ± 0.19	0.44 ± 0.02
pH 5.0	1.11 ± 0.02	10.77 ± 0.16	0.35 ± 0.02
pH 6.0	1.25 ± 0.03	12.17 ± 0.25	0.23 ± 0.03
pH 7.4	1.36 ± 0.05	13.19 ± 0.42	0.17 ± 0.01
		Pivalyl Ester	
pH 4.0	0.97 ± 0.01	9.51 ± 0.15	0.47 ± 0.03
pH 5.0	1.04 ± 0.02	10.14 ± 0.19	0.39 ± 0.01
pH 6.0	1.19 ± 0.01	11.65 ± 0.11	0.17 ± 0.02
pH 7.4	1.31 ± 0.04	12.86 ± 0.38	0.12 ± 0.02

[a] Values are means ± SEM of at least three experiments. [b] The values were obtained from the permeation studies performed up to 120 min at pH 4.0 and 5.0 and up to 150 min at pH 6.0 and 7.4.

The physicochemical properties of the diffusing solute and the physiologic function of the cell layer involved are the important factors affecting the transport rate. The phenylephrone esters had molecular weights 285.7−305.6, pK_a's 7.19−7.21, and log P values ranging from 1.92 to 2.35.[9] As shown in Table 2, the permeabilities of all the esters were significantly higher than that of mannitol ($p < 0.05$), indicating that the compounds might be permeat-

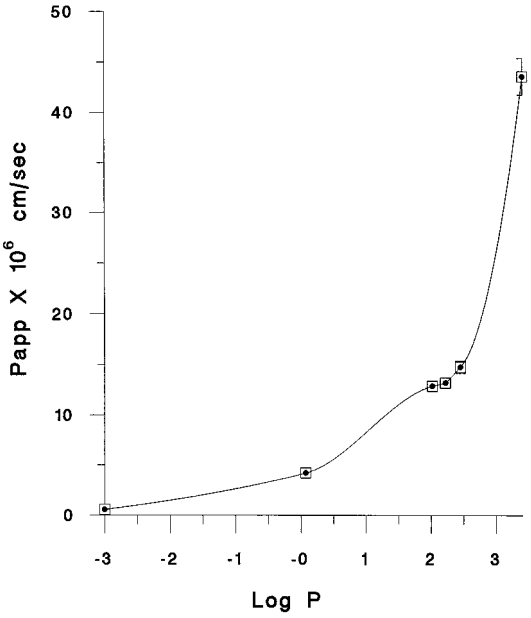

Figure 5—Relationship between apparent permeability coefficients of the various drugs and their respective log octanol–water partition coefficients at pH 7.4. From left to right, the compounds are mannitol, phenylephrine, pivalyl, isovaleryl, phenylacetyl esters of phenylephrone and testosterone. Each value represents average (±SEM) of at least three experiments.

ing via the transcellular pathway. Hamalainen et al. reported that molecules having a molecular weight less than 500 permeate through paracellular route.[26] Since all the compounds under investigation have low molecular weight, the paracellular route can also be considered as a pathway for permeation.

The permeabilities of the phenylpehrone CDS ranged from 12.86×10^{-6} cm/s to 14.76×10^{-6} cm/s at pH 7.4 and were found to be 3-fold higher compared to phenylephrine (4.21×10^{-6}). The rank order of permeation of the esters at any given pH was in accordance with their lipophilicities (**1** > **2** > **3**).[27] Phenylacetyl ester (**1**), which is the most lipophilic, exhibited a higher permeability compared to isovaleryl (**2**) and pivalyl (**3**) esters. Figure 5 illustrates the relationship between log octanol/water partition coefficients and transport rates of the compounds.

Permeability of all the three compounds was markedly dependent on the pH of the transport medium and also on the resistance of SIRC cell layers. The change in pH will affect the degree of ionization of the drug molecule if the drug has pK_a-value in that specific region. At pH 6.0 and pH 7.4, the esters showed significant differences in their permeation at all time points after 15 min ($p < 0.05$) but at pH 4.0 and pH 5.0 the differences in the amount permeated were found significant ($p < 0.05$) at time points after 45 min. At pH 6.0 and 7.4, the P_{app} value of phenylacetyl ester was significantly different from isovaleryl and pivalyl but at pH 4.0 and 5.0, only phenylacetyl and pivalyl esters showed significant difference in their P_{app} values. At higher pH conditions, the compounds under investigation predominantly exist in un-ionized form, causing an increase in diffusion through transcellular pathway resulting in higher permeabilities. The results showed decrease in permeabilities and increase in lag times of the compounds at lower pH conditions. One possible reason for the lag times might be due to the hydrolysis of the esters during the transport studies which are undetectable in the initial time points. Compound **2** showed higher lag time compared to **1** and **3** because of its higher rate of hydrolysis.[9] It is also possible that the lag times may be due to the hydrogen bonding between the compounds and the structures within the intercellular space that could impede molecular movement.[28]

The epithelia are negatively charged and are selective to positively charged solutes at physiological pH or pH above the isoelectric point (pI). Below the pI the reverse was observed.[29,30] Compounds used in this study are positively charged at low pH conditions and are excluded from absorption through aqueous paracellular pathway. This could be another possible explanation for the high lag times and low permeabilities of the phenylephrone esters at low pH conditions.

Conclusions

This paper reports the transport characteristics of the novel mydriatic agents and also the use of SIRC rabbit corneal cell line as an in vitro cell culture model for assessing corneal transport of drug molecules. The SIRC cell layers when grown on polycarbonate membranes exhibited high TEER and a low permeability to the hydrophilic marker, mannitol. This barrier property functionally characterizes these cell lines as "tight" ion transporting cell layers. Testosterone (a lipophilic molecule with a log *P* of 3.31), however, showed a high permeability across the SIRC cells. The results of this investigation suggest that the SIRC cell line, when grown on polycarbonate membranes, is a valid in vitro cell culture model for the study of corneal absorption and transepithelial transport of drugs. Studies on the permeability characteristics of novel mydriatic agents across the SIRC cell layers have shown that the esters of phenylephrone had higher transport rates compared to phenylephrine. The rate and extent of the transport of these compounds are influenced by the fraction of ionized and un-ionized species (which in turn depends on the pK_a of the drug and the pH of the solution) and the intrinsic partition coefficient of the drug. Studies are in progress to test the pharmacological activity and to assess the in vivo distribution and metabolism of the novel compounds in rabbits eyes.

References and Notes

1. McReynolds, W. U.; Havener, W. H.; Henderson, J. W. Hazards of the use of sympathomimetic drugs in ophthalmology. *Arch. Ophthalmol.* **1956**, *56*, 176−179.
2. Lansche, R. K. Systemic reactions: to topical epinephrine and phenylephrine. *Am. J. Ophthalmol.* **1966**, *61*, 95−98.
3. Solosko, D. Hypertension following 10% phenylephrine ophthalmic. *Anesthesiology* **1972**, *36*, 187−189.
4. Vaughan, R. W. Ventricular arrhythmias after topical vasoconstrictors. *Anesth. Analg.* **1973**, *52*, 161−165.
5. Wilensky, J. T.; Woodward, H. J. Acute systemic hypertension after conjunctival instillation of phenylephrine hydrochloride. *Am. J. Ophthalmol.* **1973**, *76*, 156−157.
6. Fraunfelder, F. T.; Scafidi, A. F. Possible adverse effects from topical ocular 10% phenylephrine. *Am. J. Ophthalmol.* **1978**, *85*, 447−453.
7. Bodor, N.; Visor, G. Formation of adrenaline in the iris−ciliary body from adrenalone diesters. *Exp. Eye Res.* **1984**, *38*, 621−626.
8. Bodor, N.; Kaminski, J. J.; Roller, R. G. Improved delivery through biological membranes VI. Potent sympathomimetic adrenalone derivatives. *Int. J. Pharm.* **1978**, *1*, 189−196.
9. Goskonda, V. R.; Khan, M. A.; Bodor, N. S.; Reddy, I. K. Chemical delivery systems: Evaluation of physicochemical properties and enzymatic stability of phenylephrone derivatives. *Pharm. Dev. Technol.* **1998**, in press.
10. Klyce, S. D.; Crosson, C. E. Transport process across the rabbit corneal epithelium: a review. *Curr. Eye Res.* **1985**, *4*, 323−331.
11. Ahmed, I.; Patton, T. F. Disposition of timolol and inulin in the rabbit eye following corneal versus noncorneal absorption. *Int. J. Pharm.* **1987**, *38*, 9−21.
12. Doane, M. G.; Jensen, A. D.; Dohlman, C. H. Penetration routes of topically applied eye medications. *Am. J. Ophthalmol.* **1978**, *85*, 383−386.

13. Niederkorn, J. Y.; Meyer, D. R.; Ubelaker, J. E.; Martin, J. H. Ultrastructural and immunohistological characterization of the SIRC corneal cell line. *In Vitro Cell. Dev. Biol.* **1990**, *26*, 923−930.
14. North-Root, H.; Yackovich, F.; Demetrulias, J.; Gacula, M.; Heinze, J. E. Evaluation of an in vitro cell toxicity test using rabbit corneal cells to predict the eye irritation potential of surfactants. *Toxicol. Lett.* **1982**, *14*, 207−212.
15. Jacaruso, R. B.; Barletta, M. A.; Carson, S.; Hardig, W. An in vitro method for assessing corneal opacification potential using a rabbit corneal cell line. *J. Toxicol.-Cut., Ocular Toxicol.* **1985**, *4*, 49−58.
16. Korbmacher, C.; Helbig, H.; Forster, C.; Wiederholt, M. Characterization of Na^+/H^+ exchange in a rabbit corneal epithelial cell line (SIRC). *Biochim. Biophys. Acta* **1988**, *943*, 405−410.
17. Jacaruso, R. B.; Carson, S.; Barletta, M. A. The use of cell lysis as an index of ocular irritation potential. *J. Toxicol.-Cut., Ocular Toxicol.* **1986**, *5*, 143−161.
18. Hutak, C. M.; Kavanagh, M. E.; Reddy, I. K.; Barletta, M. A. Growth pattern of SIRC rabbit corneal cells in microwell inserts. *J. Toxicol.-Cut., Ocular Toxicol.* **1997**, *16*, 145−156.
19. Hochman, J.; Artursson. P. Mechanisms of absorption enhancement and tight junction regulation. *J. Controlled Release* **1994**, *29*, 253−267.
20. Marshall, W. S.; Klyce, S. D. Cellular and paracellular pathway resistances in the "tight" Cl^--secreting epithelium of rabbit cornea. *J. Membrane Biol.* **1983**, *73*, 275−282.
21. Maurice, D. M. Epithelial potential of the cornea. *Exp. Eye Res.* **1967**, *6*, 138−140.
22. Klyce, S. D. Electrical profiles in the corneal epithelium. *J. Physiol.* **1972**, *226*, 407−429.
23. Rojanasakul, Y.; Robinson, J. R. Transport mechanisms of the cornea: Characterization of barrier permselectivity. *Int. J. Pharm.* **1989**, *55*, 237−246.
24. Morimoto, K.; Nakamura, T.; Morisaka, K. Effect of medium-chain fatty acid salts on penetration of a hydrophilic compound and a macromolecular compound across rabbit corneas. *Arch. Int. Pharmacodyn.* **1989**, *302*, 18−26.
25. Ahmed, M.; Gokhale, R. D.; Shah, M. V.; Patton, T. F. Physicochemical determinants of drug diffusion across the conjunctiva, sclera, and cornea. *J. Pharm. Sci.* **1987**, *76*, 583−586.
26. Hamalainen, K. M.; Kananen, K.; Auriola, S.; Kontturi, K.; Urtti, A. Characterization of paracellular and aqueous penetration routes in cornea, conjunctiva, and sclera. *Invest. Ophthalmol. Vis. Sci.* **1997**, *38*, 627−634.
27. Yoshida, F.; Topliss, J. G. Unified model for the corneal permeability of related and diverse compounds with respect to their physicochemical properties. *J. Pharm. Sci.* **1996**, *85*, 819−823.
28. Grass, G. M.; Robinson, J. R. Mechanisms of corneal drug penetration I: *In vivo* and *in vitro* kinetics. *J. Pharm. Sci.* **1988**, *77*, 3−14.
29. Rojanasakul, Y.; Wang, L. Y.; Bhat, M.; Glover, D. D.; Malanga, C. J.; Ma, J. K. H. The transport barrier of epithelia: A comparative study on membrane permeability and charge selectivity in the rabbit. *Pharm. Res.* **1992**, *9*, 1029−1034.
30. Liaw, J.; Rojanasakul, Y.; Robinson, J. R. The effect of drug charge type and charge density on corneal transport. *Int. J. Pharm.* **1992**, *88*, 111−124.

Acknowledgments

This study was supported in part by a grant from Research Council (Faculty Grants Program), Northeast Louisiana University.

JS980362T

Differences in the Lipoprotein Distribution of Halofantrine Are Regulated by Lipoprotein Apolar Lipid and Protein Concentration and Lipid Transfer Protein I Activity: In Vitro Studies in Normolipidemic and Dyslipidemic Human Plasmas

KISHOR M. WASAN,*,† MANISHA RAMASWAMY,† MICHELLE P. MCINTOSH,‡ CHRISTOPHER J. H. PORTER,‡ AND WILLIAM N. CHARMAN‡

Contribution from *Division of Pharmaceutics and Biopharmaceutics, Faculty of Pharmaceutical Sciences, The University of British Columbia, 2146 East Mall, Vancouver, British Columbia, Canada V6T 1Z3, and Victorian College of Pharmacy, Monash University, Parkville, Victoria, Australia, 3052.*

Received August 27, 1998. Final revised manuscript received November 4, 1998.
Accepted for publication November 9, 1998.

Abstract □ The purpose of these studies was to determine the distribution of a lipophilic antimalarial agent, halofantrine hydrochloride (Hf), in fasted plasma from hypo-, normo-, and hyperlipidemic patients that displayed differences in lipoprotein concentration and lipid transfer protein I (LTP I) activity. To assess the influence of modified lipoprotein concentrations and LTP I activity on the plasma distribution of Hf, Hf at a concentration of 1000 ng/mL was incubated in either hypo-, normo-, or hyperlipidemic human plasma for 1 h at 37 °C. Following incubation, the plasma samples were separated into their lipoprotein and lipoprotein-deficient plasma (LPDP) fractions by density gradient ultracentrifugation and assayed for Hf by high-pressure liquid chromatography. The activity of LTP I in the dyslipidemic plasma samples was determined in terms of its ability to transfer cholesteryl ester from low-density lipoproteins (LDL) to high-density lipoproteins (HDL). Total plasma and lipoprotein cholesterol (esterified and unesterified), triglyceride, and protein levels in the dyslipidemic plasma samples were determined by enzymatic assays. When Hf was incubated in normolipidemic plasma for 1 h at 37 °C, the majority of drug was found in the LPDP fraction. When Hf was incubated in human plasma of varying total lipid, lipoprotein lipid, and protein concentrations and LTP I activity, the following relationships were observed. As the triglyceride-rich lipoprotein (TRL) lipid and protein concentration increased from hypolipidemia through to hyperlipidemia, the proportion of Hf associated with TRL increased ($r > 0.90$). As the HDL lipid and protein concentration increased, the proportion of Hf associated with HDL decreased ($r > 0.70$). As the total and lipoprotein lipid levels increased, the LTP I activity of the plasma also proportionally increased ($r > 0.85$). Furthermore, with the increase in LTP I activity, the proportion of Hf associated with the TRL fraction increased ($r > 0.70$) and the proportion of Hf associated with the HDL fraction decreased ($r > 0.80$). In addition, a positive correlation between the proportion of apolar lipid and Hf recovered within each lipoprotein fraction was observed within hypo- ($r > 0.80$), normo- ($r = 0.70$), and hyperlipidemic ($r > 0.90$) plasmas. These findings suggest that changes in the HDL and TRL lipid and protein concentrations, LTP I activity, and the proportion of apolar lipid within each lipoprotein fraction may influence the plasma lipoprotein distribution of Hf in dyslipidemia.

Introduction

Lipoproteins are macromolecules of lipid and protein that transport lipids through the vascular and extravascular bodily fluids.[1] Great diversity in the composition and physical properties of lipoproteins are possible, particularly in disease states. However, it is becoming apparent that lipoproteins have a wider biological significance than simply in lipid transport. It has been demonstrated that the interaction of several compounds, including amphotericin B (AmpB)[2,3] and cyclosporine (CSA),[4] with plasma lipoproteins modifies the pharmacokinetics, tissue distribution, and pharmacologic activity of these compounds. In addition, recent studies have suggested that not only the relative levels of individual lipoproteins but also their lipid composition define the distribution of a number of hydrophobic compounds among plasma lipoproteins.[5−7]

Halofantrine (Hf), an effective agent in the treatment of malaria, has been shown to bind to lipoproteins upon incubation in human blood[8] and plasma.[9] Cenni et al.[8] have suggested that Hf interacts and binds mostly to low-density lipoproteins (LDL) and high-density lipoproteins (HDL) upon incubation in human blood from noninfected and malaria subjects. However two drawbacks of this work were that the Hf distribution experiments were not done at a physiologic temperature, but rather at 20 °C, and that the total Hf recovery from plasma was as low as 40%. Humberstone et al.[10] have demonstrated that the lipoprotein distribution of Hf within fasted and fed beagle plasma samples may be influenced by the relative pre- and postprandial lipoprotein profiles. Furthermore, McIntosh et al.[9] have recently concluded that these differences are regulated by the respective masses of core apolar lipoprotein lipid.

Recent studies have suggested that the binding of Hf to lipoproteins may also alter its pharmacokinetics and pharmacological effect. Humberstone et al.[10] have observed, following intravenous Hf administration to fasted and fed beagles, that a decrease in Hf clearance and a decrease in Hf volume of distribution was correlated with an increased binding of Hf to plasma lipoproteins in the post-prandial state compared with the fasted state. In addition, they demonstrated that the concentration that is inhibitory in 50% of test subjects (IC_{50}) of Hf within an in vitro culture of *Plasmodium falciparum* was significantly decreased when incubated in the presence of 10% post-prandial serum.[11] Taken together, these studies suggest that the effect of human dylipidemias (aberrant plasma lipoprotein and lipid concentrations) on the plasma distribution of Hf merit further investigation.

Most patients infected with malaria may exhibit disturbances in their lipid metabolism resulting in modified lipoprotein−lipid composition,[8] so we conducted studies to

* Corresponding author. Telephone: 604-822-4889. Fax: 604-822-3035. E-mail: Kwasan@unixg.ubc.ca.
† Division of Pharmaceutics and Biopharmaceutics.
‡ Victorian College of Pharmacy.

10.1021/js980353k CCC: $18.00
Published on Web 01/05/1999

determine whether the human plasma distribution of Hf was influenced by changes in lipoprotein concentration and composition. Our working hypothesis was that the association of Hf with different lipoprotein classes would be influenced by the relative abundance of these lipid−protein complexes and apolar lipid content. In addition, because Hf is lipophilic, we believed that lipid transfer protein I (LTP I), an endogenous glycoprotein responsible for the transfer of lipids between lipoproteins,[12] may influence Hf lipoprotein distribution in a similar manner as it regulates the transfer of AmpB[13] and CSA[14] between HDL and LDL.

Materials and Methods

Chemicals and Plasma—Halofantrine was provided by Smith-Kline Beecham Pharmaceuticals (King of Prussia, PA). Sodium bromide was purchased from Sigma Chemical Company (St. Louis, MO). Liquid chromatography grade acetonitrile and *tert*-butyl methyl ether (TBME) were obtained from Fisher Canada (Montreal, Quebec). Electrophoresis grade sodium dodecyl sulfate (SDS) was obtained from Eastman Kodak (Rochester, NY). Fasted human plasma samples from hypolipidemic, normolipidemic, and a hyperlipidemic subjects were obtained from the Vancouver Red Cross (Vancouver, British Columbia). Ten microliters of 0.4 M ethylenediaminetetraacetic acid, pH 7.1 (EDTA; Sigma Chemical Company) was added to 1.0 mL of whole blood. In this study, a hypolipidemic plasma sample was defined as having a total plasma cholesterol of <130 mg/dL and total plasma triglyceride of <100 mg/dL, a normolipidemic plasma sample was defined as having a total plasma cholesterol of 130−200 mg/dL and total plasma triglyceride of 100−200 mg/dL, and a hyperlipidemic plasma sample was defined as having a total plasma cholesterol of >350 mg/dL and total plasma triglyceride of >280 mg/dL.[1] For all Hf plasma distribution studies, Hf was dissolved in 100% methanol. The addition of methanol alone did not modify lipoprotein−lipid composition or plasma LTP I activity (data not shown).

Lipoprotein Separation—The plasma was separated into its HDL, LDL, triglyceride-rich lipoproteins (TRL), which consists of VLDL and chylomicrons, and lipoprotein deficient plasma (LPDP) fractions by ultracentrifugation.[15,16] Briefly, human plasma (3.0 mL) samples were placed in centrifuge tubes and their solvent densities were adjusted to 1.006 g/mL by sodium bromide. Following centrifugation (L8−80M; Beckman Canada) at 50 000 rpm for 18 h at 4 °C, the TRL-containing and TRL-deficient plasma fractions were recovered. The TRL-deficient plasma fraction was readjusted to a density of 1.063 g/mL and respun at 50 000 rpm for 18 h at 4 °C to separate the LDL-rich and TRL/LDL-deficient plasma fractions. This fraction was readjusted to a density of 1.21 g/mL and respun at 50 000 rpm for 18 h at 4 °C to separate the HDL-rich and lipoprotein-deficient plasma (LPDP) fractions.

Isolation and Purification of Lipid Transfer Protein (LTP I)—LTP I was purified from human lipoprotein-deficient plasma as has been previously described.[12] Briefly, citrated human plasma was made lipoprotein deficient by the dextran−$MnCl_2$ procedure of Burstein and co-workers.[17] LTP I was then partially purified by sequential chromatography on phenyl-Sepharose and carboxy methyl cellulose gel (CM-52, Whatman Inc., Chifton, NJ). Partially purified LTP I (1.05 mg protein/mL), enriched 800-fold relative to lipoprotein-deficient plasma, was stored at 4 °C in 0.01% disodium EDTA, pH 7.4. The CM-cellulose fraction of LTP I was used in all experiments.

Radiolabeling of Plasma Lipoproteins—Human LDL was labeled by the lipid dispersion technique as previously described.[12] Briefly, human plasma was incubated with a lipid dispersion containing egg phosphatidylcholine (PC), triglyceride (5 mol %), and [^{3}H]cholesteryl ester (CE) (12 mol %) at 37 °C for 20−24 h in the presence of LTP I and diethyl (*p*-nitrophenyl) phosphate. Then the LDL fractions were isolated from the total lipoprotein precipitate by centrifugation as previously described. LDL had a specific activity of 3.423×10^6 cpm/mL (1352 cpm/μg of total cholesterol).

Lipid Transfer Assays—To assess the LTP I activity within the different human plasma samples used in this study, the following protocol was used. Lipid (CE) transfer was performed within the lipoprotein-deficient plasma samples as has been previously described.[14,18] Typically, 10 μg (total cholesterol) of radiolabeled donor (^{3}H−CE LDL) and unlabeled acceptor (HDL) are incubated ± LTP I source (which are the different delipidated human plasma samples used in this study), pH 7.4, for 90 min at 37 °C. Lipid transfer between donor and acceptor lipoprotein is then quantitated by scintillation counting. The fraction of lipid and drug transferred (kt) was calculated as described by Pattnaik and Zilversmit:[19]

$$k_t = -\ln(1 - A_t/D_0) \quad (1)$$

where D_0 and A_t are the amounts of radioactivity in the donor at time 0 and in the acceptor at time t, respectively. The constant k is the fraction of label transferred per unit time (t). Acceptor radioactivity in the absence of LTP (usually < 2−3%) is subtracted before calculating k_t values. Calculations assume steady-state conditions, where all lipid transfer is an exchange process. To minimize calculation errors due to mass transfer, all values were determined from assays in which the extent of radiolabel transfer was small (≤15%).

Quantification of Halofantrine—Plasma lipoprotein and lipoprotein-deficient samples containing Hf (1-mL aliquot) were mixed with 2 mL of acetonitrile and 8 mL of TBME; the mixture was vortexed for 30 s after the addition of acetonitrile and TBME and centrifuged (2000x g for 2 min). The supernatant was transferred to another tube, dried under nitrogen at 30 °C, and reconstituted with 0.5 mL of acetonitrile. The reconstituted extractant was analyzed against an external standard calibration curve for Hf by a high-pressure liquid chromatography (HPLC) procedure developed by Humberstone and co-workers.[20] The internal standard used to account for variation between samples is 2,4-dichloro-6-trifluoromethyl-9-{1-(2-(dibutylamino)ethyl)}-phenanthrenemethanol.[20] The HPLC system consisted of a Beckman model 110A pump, a Shimadzu SIL-9A autoinjector, and a Shimadzu SPD-6A variable wavelength detector. The detector was set at a wavelength of 257 nm, with absorbance sensitivity of 0.05 absorbency units, full scale. Results were recorded on a Shimadzu C−R3A chromatopac integrator. For chromatographic separation, a ultrasphere ODS column (4.6 mm × 25 cm) packed with trimethylsilyl particles (particles of 5 μm in diameter) was used at ambient temperatures. The mobile phase consisted of 75:25 (v/v) acetonitrile:water with 0.2% (w/v) SDS and 0.2% (V/v) glacial acetic acid at a flow rate of 1.5 mL min^{-1}. This assay had a limit of quantitation for Hf of 39 ng/mL and external calibration curves in total plasma, lipoprotein, and lipoprotein-deficient fractions that were linear in a concentration range of 39−5000 ng/mL of Hf (r > 0.90), with an intraday coefficient of variation of 5−8%.

Determination of Plasma Lipoprotein Triglyceride, Cholesterol, and Protein Concentrations—Total plasma triglycerides (TG), cholesterol, and protein concentrations were determined by enzymatic assays purchased from Sigma Diagnostics (St. Louis Mo.) as previously described.[17] The external calibration curve for plasma and lipoprotein triglyceride was linear in a concentration range 10−300 mg/dL (r > 0.95), for cholesterol was linear in a concentration range 10−450 mg/dL (r > 0.96), and for protein was linear in a concentration range of 5−2000 mg/dL (r > 0.90). Free cholesterol was determined using an enzymatic assay purchased from Boehringer Mannheim and was linear in a concentration range 1−100 mg/dL (r > 0.90). Cholesteryl ester concentration was determined by calculating the difference between total and free cholesterol.

Halofantrine (Hf) Distribution Studies in Specific Human Plasma Samples of Varying Lipoprotein Concentration and Composition and LTP I Activity—To gain an understanding on how lipoprotein lipid and protein concentration and LTP I influences the plasma distribution of Hf, Hf (1000 ng/mL) was incubated in 3 mL of plasma samples (total amount of Hf in plasma was 3000 ng) from three different patients (hypo-, normo-, and hyperlipidemic) of varying total and lipoprotein cholesterol, triglyceride, and protein concentrations (Table 1) and composition (Table 2) for 60 min at 37 °C. A Hf concentration of 1000 ng/mL was chosen as a value broadly representative of serum concentrations expected in a clinical enviroment.[21] Following incubation, the plasma was cooled to 4 °C to prevent any drug redistribution (data not shown) and separated into its lipoprotein and lipoprotein-deficient fractions by density gradient ultracentrifugation, and each fraction was quantified for Hf by HPLC.[20] To ensure that the distribution of Hf found in each of these fractions was a result of its association with each lipoprotein or lipoprotein-deficient

Table 1—Fasted Total and Lipoprotein Plasma Cholesterol (Esterified + Unesterified), Triglyceride, and Protein Concentrations in Plasma Samples from Three Individual Patients[a]

patient profile	TRL, mg/dL	LDL, mg/dL	HDL, mg/dL	total, mg/dL
		cholesterol (esterified + unesterified)		
hypolipidemic	20.6 ± 2.6	70.8 ± 3.1	32.3 ± 1.7	123.7 ± 5.6
normolipidemic	43.9 ± 1.8*	108.2 ± 9.9*	44.7± 6.1*	196.9 ± 4.0*
hyperlipidemic	112.6 ± 9.4*	180.7 ± 16.1*	105.2 ± 13.9*	398.5 ± 18.1*
		triglyceride		
hypolipidemic	31.1± 2.1	22.7 ± 1.1	21.4 ± 3.4	75.1 ± 2.1
normolipidemic	92.1 ± 8.5*	45.3 ± 7.8*	33.0 ± 3.6*	170.4 ± 4.8*
hyperlipidemic	153.5 ± 16.9*	80.3 ± 11.3*	61.4 ± 6.6*	295.1 ± 18.6*
		protein		
hypolipidemic	7.4 ± 1.2	25.0 ± 2.3	132.4 ± 11.8	164.7 ± 11.8
normolipidemic	34.8 ± 2.8*	94.4 ± 2.8*	217.6 ± 9.0*	346.8 ± 10.2*
hyperlipidemic	77.9 ± 6.8*	156.3 ± 11.1*	936.9 ± 111*	1171 ± 115*

[a] Data are expressed as mean ± standard deviation ($n = 4$ replicates for hypolipidemic; $n = 6$ replicates for normolipidemic and hyperlipidemic). Abbreviations: TRL, triglyceride rich lipoproteins, which includes very low-density lipoproteins and chylomicrons; LDL, low-density lipoproteins; HDL, high-density lipoproteins. (*) $p < 0.05$ versus hypolipidemic patient profile.

Table 2—Lipoprotein Composition of Plasma from Hypolipidemic, Normolipidemic, and Hyperlipidemic Patients[a]

lipoprotein fraction	hypolipidemic	normolipidemic	hyperlipidemic
	triglyceride rich lipoproteins		
TC/TP (wt/wt)	2.8 ± 0.3	1.2 ± 0.1*	1.5 ± 0.2*
TG/TP (wt/wt)	4.3 ± 1.0	2.5 ± 0.1*	2.0 ± 0.3* **
TG/TC (wt/wt)	2.2 ± 0.4	2.9 ± 0.1*	1.4 ± 0.1* **
	low-density lipoproteins		
TC/TP (wt/wt)	2.9 ± 0.3	1.2 ± 0.1*	1.2 ± 0.1*
TG/TP (wt/wt)	0.9 ± 0.1	0.5 ± 0.1*	0.5 ± 0.1*
TG/TC (wt/wt)	0.30 ± 0.03	0.4 ± 0.1	0.44 ± 0.05*
	high-density lipoproteins		
TC/TP (wt/wt)	0.25 ± 0.02	0.13 ± 0.03*	0.12 ± 0.03*
TG/TP (wt/wt)	0.16 ± 0.01	0.11 ± 0.02*	0.07 ± 0.01* **
TG/TC (wt/wt)	0.66 ± 0.06	0.87 ± 0.17	0.59 ± 0.07**

[a] Data are expressed as mean ± standard deviation ($n = 4$ replicates for hypolipidemic and $n = 6$ replicates for normolipidemic and hyperlipidemic); (*) $p < 0.05$ versus hypolipidemic; (**) $p < 0.05$ versus normolipidemic; TC, total cholesterol (esterified + unesterified); TG, total triglycerides; TP, total protein; wt/wt, weight/weight; plasma type, hypolipidemic (total cholesterol <130 mg/dL and triglyceride < 100 mg/dL); normolipidemic (total cholesterol 130–200 mg/dL and triglyceride 100–200 mg/dL); hyperlipidemic (total cholesterol > 350 mg/dL and triglyceride > 280 mg/dL).

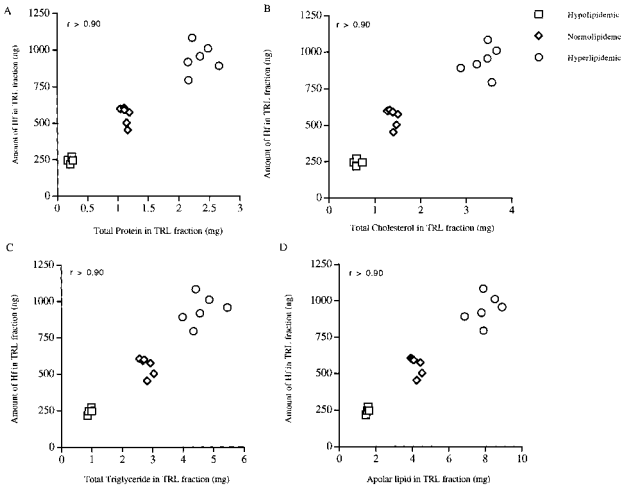

Figure 1—Distribution of Hf at 1000 ng/mL incubated for 60 min at 37 °C in hypolipidemic, normolipidemic, or hyperlipidemic plasma samples: (A) triglyceride-rich lipoprotein (TRL) protein; (B) TRL cholesterol, (C) TRL TG; and (D) TRL apolar lipid (cholesteryl ester and triglyceride) content versus the amount of Hf within the TRL fraction.

fraction and not a result of the density of the drug, the density profile of Hf reconstituted in 100% methanol and incubated in lipoprotein-deficient plasma was determined by ultracentrifugation. The majority of Hf (>85%) was found in the density range >1.21 g/mL (data not shown), suggesting that the Hf distribution within the ultracentrifuge tubes following incubation in human plasma is not a function of drug density.

In addition, to provide further evidence that LTP I may facilitate the movement of Hf between lipoprotein fractions, the lipoprotein distribution of Hf within normolipidemic human plasma (containing 1.0 μg protein/mL of LTP I), which has been supplemented with exogenous LTP I (0.67 μg protein/mL), was determined.

Data and Statistical Analysis—Correlation coefficients between the amount of Hf recovered within the TRL, HDL, and LDL plasma fractions and the amount of cholesterol, triglyceride, and protein within these fractions (Figures 1–3), proportion of apolar lipid within each lipoprotein fraction (Figure 4), and LTP I activity (Figure 5) were determined using Pearson's test. Differences in the human plasma distribution of Hf following incubation in human plasmas of varying lipid and protein concentrations were determined by a two-way analysis of variance (PCANOVA; Human Systems Dynamics). Critical differences were assessed by Neuman–Keuls posthoc tests. Differences were considered significant if p was <0.05. All data are expressed as mean ± standard deviation.

Results and Discussion

Total and Lipoprotein Lipid and Protein Levels in Plasma from Human Subjects—The differences in total and lipoprotein plasma cholesterol (esterified + unesterified), triglyceride, and protein concentrations and composition between hypolipidemic, normolipidemic, and hyperlipidemic human subjects chosen for this study are reported in Tables 1 and 2.

Distribution of Halofantrine (Hf) Following Incubation in Plasma from Human Subjects with Varying Lipid Concentrations—Table 3 reports the plasma distribution of Hf at 1000 ng/mL within plasma obtained from hypolipidemic, normolipidemic, and hyperlipidemic human subjects following incubation for 60 min at 37 °C. A significantly greater percentage of Hf was recovered within the TRL fraction following incubation in hyperlipidemic and normolipidemic patient plasma for 60 min at 37 °C than following incubation in hypolipidemic patient plasma. At the same time, a significantly lower percentage of Hf was recovered within the HDL fraction following incubation in hyperlipidemic and normolipidemic patient plasma samples than following the incubation in hypolipidemic patient plasma samples. In addition, a significantly higher percentage of Hf was recovered within the TRL fraction and significantly lower percentage of Hf was recovered in the HDL and LPDP fractions following incubation in hyperlipidemic compared with normolipidemic patient plasma samples.

Table 3—Distribution of Halofantrine Hydrochloride (Hf·HCl) at 1000 ng/mL within Fasted Plasma from Three Individual Patients Following Incubation for 60 min at 37 °C (following incubation plasma samples were assayed by high-pressure liquid chromatography for drug in each of the lipoprotein and lipoprotein-deficient plasma fractions)[a]

patient profile	TRL fraction, %[b]	LDL fraction, %	HDL fraction, %	LPDP fraction, %	percent recovery[c]	LTP I activity, %k_t
hypolipidemic ($n = 4$ replicates)	8.2 ± 0.7	17.5 ± 1.8	12.2 ± 3.3	59.1 ± 3.4	97.0 ± 2.6	2.2 ± 0.8
normolipidemic ($n = 6$ replicates)	18.5 ± 2.1*	15.6 ± 3.2	11.1 ± 1.9*	53.5 ± 5.2	98.7 ± 2.8	11.6 ± 0.6*
hyperlipidemic ($n = 6$ replicates)	31.4 ± 3.3* **	21.0 ± 4.4	4.9 ± 1.0* **	37.5 ± 4.8* **	94.6 ± 4.8	14.6 ± 2.5*

[a] Data are expressed as mean ± standard; (*) $p < 0.05$ vs hypolipidemic patients; (**) p, 0.05 versus normolipidemic patients. [b] Percent of initial Hf·HCL concentration. [b] Percent of initial drug incubated; LPDP, lipoprotein-deficient plasma; HDL, high-density lipoprotein; LDL, low-density lipoprotein; TRL, triglyceride-rich lipoproteins, which includes very-low-density lipoproteins and chylomirons; LTP I, lipid transfer protein I; k, fraction of labeled lipid transferred; t, time; plasma type, hypolipidemic (total cholesterol < 130 mg/dL and triglyceride < 100 mg/dL); normolipidemic (total cholesterol 130–200 mg/dL and triglyceride 100–200 mg/dL); hyperlipidemic (total cholesterol > 350 mg/dL and triglyceride > 280 mg/dL).

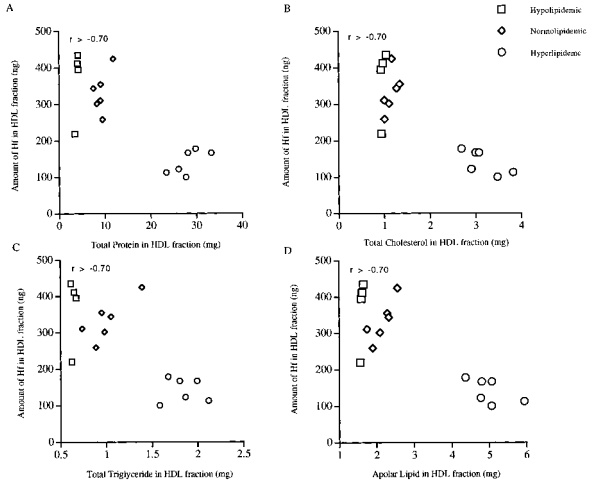

Figure 2—Distribution of Hf at 1000 ng/mL incubated for 60 min at 37 °C in hypolipidemic, normolipidemic, or hyperlipidemic plasma samples: (A) high-density lipoprotein (HDL) protein; (B) HDL cholesterol; (C) HDL TG; and (D) HDL apolar lipid (cholesteryl ester and triglyceride) content versus the amount of Hf within the HDL fraction.

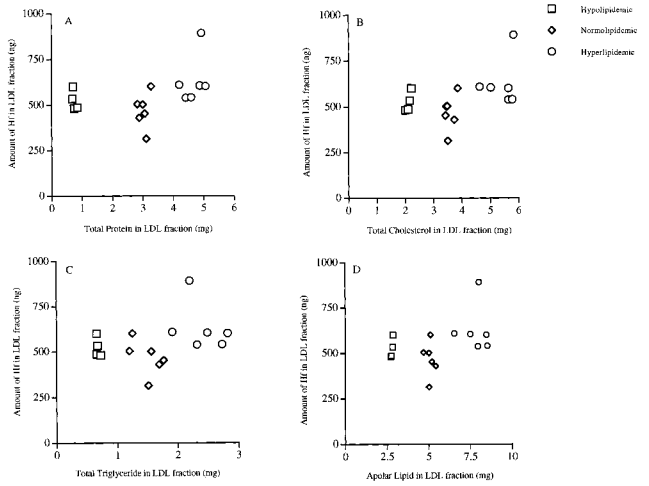

Figure 3—Distribution of Hf at 1000 ng/mL incubated for 60 min at 37 °C in hypolipidemic, normolipidemic, or hyperlipidemic plasma samples: (A) low-density lipoprotein (LDL) protein; (B) LDL cholesterol; (C) LDL TG; and (D) LDL apolar lipid (cholesteryl ester and triglyceride) content versus the amount of Hf within the LDL fraction.

When correlations between the amount of Hf recovered within the TRL, LDL, and HDL plasma fractions and the amount of cholesterol, triglyceride, and protein were calculated for all three patient plasma subgroups, the following relationships were observed. As TRL cholesterol, triglyceride, protein, and apolar lipid (cholesteryl esters and triglycerides) levels increased, the amount of Hf recovered in this fraction proportionally increased (Figure 1; $r > 0.70$). However, as HDL cholesterol, triglyceride, protein, and apolar lipid levels increased, the amount of Hf recovered in this fraction proportionally decreased (Figure 2; $r > 0.70$). Although no correlation between LDL lipid and protein levels and the amount of Hf recovered in this fraction was observed (Figure 3), a positive correlation between the proportion of apolar lipid and percentage of Hf recovered within each lipoprotein fraction was observed within all three plasma groups (Figure 4; $r > 0.70$).

We have further observed that although HDL cholesterol, triglyceride, and protein concentrations increased 3-fold, 3-fold, and 7-fold, respectively, from hypolipidemia through to hyperlipidemia (Table 1), the percent (Table 3)

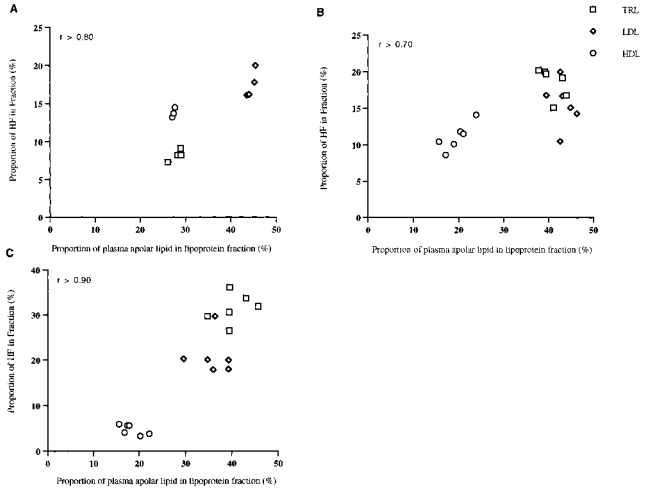

Figure 4—(A) Correlation between the percentage of Hf recovered in triglyceride-rich (TRL), low-density (LDL), and high-density lipoprotein (HDL) fractions in hypolipidemic human plasma and the proportional distribution of apolar lipids (cholesteryl esters and triglycerides) within the individual lipoprotein fractions. (B) Correlation between the percentage of Hf recovered in TRL, LDL, and HDL fractions in normolipidemic human plasma and the proportional distribution of apolar lipids (cholesteryl esters and triglycerides) within the individual lipoprotein fractions. (C) Correlation between the percentage of Hf recovered in TRL, LDL, and HDL fractions in hyperlipidemic human plasma and the proportional distribution of apolar lipids (cholesteryl esters and triglycerides) within the individual lipoprotein fractions.

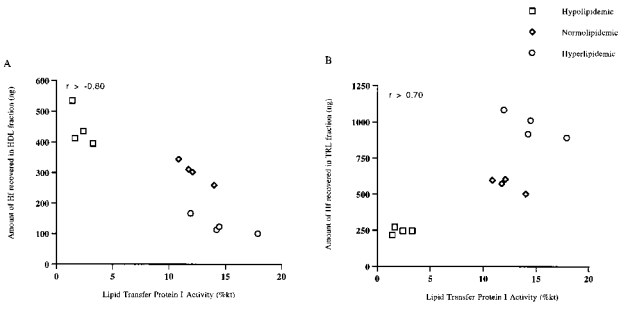

Figure 5—Lipid transfer protein I activity in hypolipidemic, normolipidemic, or hyperlipidemic plasma samples versus the amount of Hf within the (A) high-density lipoprotein (HDL) and (B) triglyceride-rich lipoprotein (TRL) fractions.

Table 4—Influence of LTP I on the Distribution of Halofantrine Hydrochloride (Hf·HCl) at 1000 ng/mL within Normolipidemic Human Plasma Following Incubation for 60 min at 37 °C (following incubation, plasma samples were assayed by high-pressure liquid chromatography for drug in each of the lipoprotein and lipoprotein-deficient plasma fractions)[a]

drug compound	TRL plasma fraction, %[b]	LDL plasma fraction, %	HDL plasma fraction, %	LPDP fraction, %	percent recovery
Hf·HCL	19.9 ± 2.7	20.8 ± 2.5	17.1 ± 1.1	42.1 ± 2.7	83.2 ± 4.2
Hf·HCL + LTP I	44.9 ± 2.7*	12.7 ± 2.0*	7.9 ± 1.2*	34.6 ± 1.9*	98.3 ± 8.9*

[a] Data are expressed as mean ± standard deviation ($n = 6$); (*) $p < 0.05$ vs Hf·HCl; 33 μL CM-LTP I (containing 0.67 μg of LTP I) added to 1 mL of plasma. [b] Percent of initial Hf·HCL concentration. [c] Percent of initial drug incubated; LPDP, lipoprotein-deficient plasma; HDL, high-density lipoprotein; LDL, low-density lipoprotein; TRL, triglyceride-rich lipoproteins, which includes very low-density lipoproteins and chylomicrons; LTP I, lipid transfer protein I; normolipidemic human plasma had a total cholesterol of 161 mg/dL and endogenous LTP I concentration of 1.05 μg protein/mL.

and amount (Figure 2) of Hf recovered within the HDL fraction significantly decreased. However, in these same plasmas, TRL cholesterol, triglyceride, and protein concentrations increased 5.5-fold, 5-fold, and 10-fold, respectively, from hypolipidemia through to hyperlipidemia (Table 1). This resulted in a significant and proportional increase in the percent (Table 3) and amount (Figure 1) of Hf recovered within the TRL fraction. These findings suggest that Hf lipoprotein distribution may be regulated by mass plasma lipoprotein triglyceride concentrations and the number of TRL particles present within plasma. Thus, Hf moved from one lipoprotein class to another and its movement could be influenced by different disease states, such as malaria, and adjunct therapies, such as Intralipid infusion,[3] where lipoprotein composition and plasma concentrations are altered. Furthermore, not only are triglyceride mass and particle number important factors in determining Hf lipoprotein distribution, but to which lipoprotein subfraction changes in composition ocurr may also be important in determining to which component the drug binds. It further appears that TRL may be more effective at binding Hf than either HDL or LDL as you increase lipoprotein lipid-load and particle number.

Influence of Lipid Transfer Protein I (LTP I) on the Plasma Distribution of Halofantrine (Hf)—The LTP I activity within the plasma of these patients were determined by measuring the transfer rate of [^{3}H]CE from LDL to HDL. As the total plasma and lipoprotein lipid concentrations increased from hypolipidemia through to hyerlipidemia, LTP I activity increased from 2.2 ± 0.8% k_t to 14.6 ± 2.5% k_t (Table 3). Furthermore, as LTP I-mediated transfer of CE increased, the amount of Hf recovered in the HDL fraction decreased (Figure 5A), whereas the amount of Hf recovered in the TRL fraction increased (Figure 5B). In addition, a significantly lower percentage of Hf was recovered in the LDL, HDL, and LPDP fractions and a significantly greater percentage of Hf was recovered in the TRL fraction compared with controls when fasted normolipidemic plasma containing 1 μg protein/mL of LTP I was supplemented with 0.67 μg protein/mL of exogenous LTP I (Table 4).

Taken together, these studies demonstrate that as LTP I activity increases, the proportion of Hf associated with the TRL fraction increases ($r > 0.70$) and the proportion of Hf associated with HDL decreases ($r > 0.80$). Because LTP I is the protein that catalyzes the transfer exchange of apolar lipids CE from CE-rich lipoproteins (HDL and LDL) for TG from TG-rich lipoproteins (i.e., VLDL and chylomicrons), our findings suggest that Hf plasma distribution may be related to its lipoprotein apolar lipid content. This suggestion is further supported by the observation within hypo- ($r > 0.80$), normo- ($r = 0.70$), and hyperlipidemic ($r > 0.90$) plasma samples that a proportionally greater percentage of Hf was recovered in those lipoprotein fractions that contained a larger proportion of apolar lipid (Figure 4). These findings are in agreement with our previous studies in pre- and postprandial plasma samples from beagles and humans,[9] where it was concluded that the mechanism of Hf association with plasma lipoprotein was primarily by way of solubilization in the apolar lipid core.

Summary

In conclusion we have determined that Hf associates with lipoproteins upon entrance into the plasma component of the bloodstream and that the distribution of Hf among lipoproteins is defined by the relative levels of individual lipoproteins and the proportion of apolar lipid content within each lipoprotein fraction, and is influenced by LTP I. Furthermore, the amount of Hf recovered in the TRL and HDL fractions correlates to lipoprotein lipid and protein mass and LTP−I activity. The alterations in plasma lipoprotein concentrations, including decreases in HDL-cholesterol and elevations in TRL-triglyceride concentrations,[8] often exhibited by patients with malaria, raises the possibility of altered efficacy and/or toxicity of drugs, such as Hf, which associate with lipoproteins. Recently, Humberstone et al.[11] demonstrated that the IC_{50} of Hf was significantly increased when incubated in the presence of 10% post-prandial serum (which contains elevated TRL triglyceride serum concentrations) compared with normolipidemic serum in a continuous in vitro culture of *Plasmodium falciparum*. In addition, there is an apparent linkage between excessively high plasma Hf concentrations and cardiac toxicity in patients with or without a preexisting cardiopathy.[22] As higher plasma concentrations of Hf are typically observed after post-prandial administration, distribution of Hf into post-prandial lipoproteins (particularly TRL) may contribute to the cardiac side effects of Hf observed in these patients. Future studies are warranted to investigate the pharmacological implications of the predominant association of Hf with TRL when total plasma TG concentrations are elevated.

References and Notes

1. Davis, R. A.; Vance, J. E. Structure, assembly and secretion of lipoproteins. In *Biochemistry of lipids, lipoproteins and membranes;* Vance, D. E.; Vance, J. E., Eds.; Elsevier: New York, 1996; pp 473−493.
2. Wasan, K. M.; Vadiei, K.; Lopez-Berestein, G.; Luke, D. R. Pharmacokinetics, tissue distribution, and toxicity of free and liposomal amphotericin B. *J. Infect. Dis.* **1990**, *161*, 562−566.
3. Wasan, K. M.; Grossie, Jr., V. B.; Lopez-Berestein, G. Concentrations in serum and tissue distribution of free and liposomal amphotericin B in rats on continuous Intralipid infusion. *Antimicrob. Agents Chemother.* **1994**, *38*, 2224−2226.
4. Le Maire, M.; Tillement, J. P. Role of lipoproteins and erythrocytes in the in vitro binding and distribution of cyclosporin A in the blood. *J. Pharm. Pharmacol.* **1982**, *34*, 715−718.
5. Wasan, K. M.; Morton, R. E. Differences in lipoprotein concentration and composition modify the plasma distribution of free and liposomal annamycin. *Pharm. Res.* **1996**, *13*, 462−468.

6. Wasan, K. M.; Perez-Soler, P. Distribution of free and liposomal annamycin within human plasma is regulated by plasma triglyceride concentrations but not by lipid transfer protein. *J. Pharm. Sci.* **1995**, *84*, 1094−1100.
7. Wasan, K. M.; Pritchard, P. H.; Ramaswamy, M.; Wong, W.; Donnachie, E. M.; Brunner, L. J. Differences in lipoprotein lipid concentration and composition modify the plasma distribution of cyclosporine. *Pharm. Res.* **1997**, *14*, 1613−1620.
8. Cenni, B.; Meyer, J.; Brandt, R.; Betschart, B. The antimalarial drug halofantrine is bound mainly to low and high-density lipoproteins in human serum. *Br. J. Clin. Pharmacol.* **1995**, *39*, 519−526.
9. McIntosh, M. P.; Porter, C. J. H.; Wasan, K. M.; Ramaswamy, M.; Charman. W. N. Differences in the lipoprotein binding profile of halofantrine in fed and fasted human or beagle plasma are dictated by the respective masses of core apolar lipoprotein lipid. *J. Pharm. Sci*., in press.
10. Humberstone, A. J.; Porter, C. J. H.; Edwards, G.; Charman, W. N. Distribution of halofantrine between plasma lipoprotein fractions after IV administration to pre- and postprandial beagle dogs. *Pharm. Res.* **1995**, *12*, S-356 (abstract).
11. Humberstone, A. J.; Porter, C. J. H.; Edwards, G.; Charman, W. N. Effect of altered serum lipid concentrations on the IC_{50} of halofantrine against *Plasmodium falciparum*. *J. Pharm. Sci.* **1998**, *87*, 256−258.
12. Morton, R. E.; Zilversmit, D. B. Purification and characterization of lipid transfer protein(s) from human lipoprotein-deficient plasma. *J. Lipid Res.* **1982**, *23*, 1058−1067.
13. Wasan, K. M.; Morton, R. E.; Rosenblum, M. G.; Lopez-Berestein, G. Decreased toxicity of liposomal amphotericin B due to association of amphotericin B with high-density lipoproteins: Role of lipid transfer protein. *J. Pharm. Sci.* **1994**, *83*, 1006−1010.
14. Wasan, K. M.; Ramaswamy, M.; Wong, W.; Pritchard, P. H. Lipid transfer protein I facilitated transfer of cyclosporine from low- to high-density lipoproteins is only partially dependent on its cholesteryl ester transfer activity. *J. Pharmacol. Exp. Ther.* **1998**, *284*, 509−605.
15. Havel, R. J.; Eder, H. A.; Bragdon, J. H. The distribution and chemical composition of ultracentrifugally separated lipoproteins in human serum. *J. Clin. Invest.* **1955**, *34*, 1345−1353.
16. Ramaswamy, M.; Zhang, X.; Burt, H. M.; Wasan, K. M. The human plasma distribution of free paclitaxel and paclitaxel associated with diblock copolymers. *J. Pharm. Sci.* **1997**, *86*, 460−464.
17. Burstein, M.; Scholnick, H. R.; Morfin, R. Rapid method for the isolation of lipoproteins from human serum by precipitation with polyanions. *J. Lipid Res.* **1970**, *11*, 583−595.
18. Wasan, K. M.; Ramaswamy, M.; Haley, J.; Dunn, B. P. Administration of long-term tamoxifen therapy modifies the plasma lipoprotein−lipid concentration and lipid transfer protein I activity in postmenopausal women with breast cancer. *J. Pharm. Sci.* **1997**, *86*, 876−879.
19. Pattnaik, N. M.; Zilversmit, D. B. Interaction of cholesteryl ester exchange protein with human plasma lipoproteins and phospholipid vesicles. *J. Biol. Chem*. **1979**, *254*, 2782−2786.
20. Humberstone, A. J.; Currie, G. J.; Porter, C. J. H.; Scanlon, M. J.; Charman, W. N. A simplified liquid chromatography assay for the quantitation of halofantrine and desbutylhalofantrine in plasma and identification of a degradation product of desbutylhalofantrine formed under alkaline conditions. *J. Pharm. Biomed. Anal.* **1995**, *13*, 265−272.
21. Karbwang, J.; Na Bangchang, K. Clinical pharmacokinetics of halofantrine. *Clin. Pharmacokinet.* **1994**, *27*, 104−119.
22. Monlun, E.; Le Metayer, P.; Szwandt, S.; Neau, D.; Longy Boursier, M.; Horton, J.; Le Bras, M. Cardiac complications of halofantrine: a prospective study of 20 patients. *Trans. Roy Soc. Trop. Med. Hyg.* **1995**, *89*, 430−433.

Acknowledgments

This work was supported in part by the University of British Columbia Development Fund and SmithKline Beecham Pharmaceuticals Inc. (UK). The authors thank Dr. John Horton for his interest and support of these studies and Dr. Andrew Humberstone for his initial discussions and feedback.

JS980353K

Process Control in a High Shear Mixer-Granulator Using Wet Mass Consistency: The Effect of Formulation Variables

ANNE FAURE,[†,‡] IAN M. GRIMSEY,[†] RAY C. ROWE,[†,§] PETER YORK,[*,†] AND MIKE J. CLIFF[§]

Contribution from *Drug Delivery Group, Postgraduate Studies in Pharmaceutical Technology, School of Pharmacy, University of Bradford, Bradford BD7 1DP, United Kingdom, and ZENECA Pharmaceuticals, Alderley Park, Macclesfield, Cheshire, United Kingdom.*

Received August 20, 1998. Accepted for publication November 9, 1998.

Abstract □ This work investigates the relationships between the wet mass consistency/viscosity of samples prepared in a mixer-granulator and physical properties of the dry granules produced from the wet mass; namely, size distribution, bulk density (Hausner ratio), friability, and flow avalanching behavior. The correlation between the consistency of the wet mass and the downstream dry granule properties confirms that consistency is the key parameter to control in wet granulation by mechanical agitation. Variations in the formulation affect the dimensionless power relationship of the mixer-granulator considered; that is, the equivalence between wet mass consistency and mixer net power consumption, which is actually the parameter used to monitor the wet granulation process. The same variations in formulation also affect the relationships between wet mass consistency and dry granule properties.

Introduction

Over recent years, a strategy based on the use of dimensionless numbers has been designed to allow a better control and scale-up of wet granulation processes in pharmaceutical mixer-granulators.[1−4] The granulation end point is classically detected by monitoring the power consumption of the mixer-granulator. In this new approach, a dimensionless power relationship is determined that summarizes the overall effect of various process parameters linked to the wet mass and to the mixer-granulator itself. Hence, knowing the wet mass characteristics wanted and the conditions in which the mixer is to be operated, the dimensionless power relationship is employed to give the corresponding target power consumption value that will signal the end point of the granulation.

However, several assumptions are made in this approach. In particular, the wet mass has to be considered as a continuous phase, which is described solely by the composition of its dry formulation, its wet bulk density, and viscosity. The viscosity of the wet mass is assessed using a mixer torque rheometer, an instrument that has been specifically developed to quantify the rheological consistency of the pharmaceutical wet masses.[4,5] It has been demonstrated that wet mass consistency was linearly proportional to wet mass viscosity,[5] while offering the advantage of being easier to measure. Intrinsically, it is also assumed in the methodology that if the wet mass quality can be reproduced, through the control of the wet mass consistency, then the quality of the dry granules produced downstream from the wet mass will also be controlled. This assumption presupposes that there exists a link between the wet mass consistency and the dry granule characteristics.

The objective of this work was to verify this assumption by proving the existence of a relationship between the wet mass consistency and several dry granule properties judged important with regards to tableting. The effect of formulation on the dimensionless power relationship of a given mixer-granulator will also be investigated.

Experimental Section

The wet mass samples were produced in a pharmaceutical, high-shear mixer-granulator (Aeromatic Fielder PMA 100 L, Eastleigh, Hampshire, UK) using five different hydrophilic formulations, coded as 'R', 'L', 'P', 'C', and 'D' and defined in Table 1. Lactose 450 mesh (DMV International, Veghel, The Netherlands), starch (National Starch and Chemical GmbH, Neustadt, Germany), pregelatinized starch (PGS, National Starch and Chemical GmbH, Neustadt, Germany), and dibasic calcium phosphate dihydrate (DCPD, Calipharm, UK) were generously supplied by Zeneca Pharmaceuticals. Lactose 200 mesh was a gift from DMV International, Veghel, The Netherlands. Poly(vinylpyrrolidone) (PVP K25) was supplied by BASF, Ludwigshafen, Germany.

Wet massing runs were carried out at different impeller speeds, whereas water was sprayed at a constant rate. The spray nozzle and the water flow rate were chosen to ensure a quick distribution of the water among the mix. Samples were withdrawn at regular intervals to give a range of increasing consistency values and were immediately analyzed for their bulk density and consistency.

The consistency was determined using a mixer torque rheometer (Caleva MTR, Sturminster-Newton, Dorset, UK) as previously described by Rowe and Parker,[4] run at a shaft speed of 50 rpm. A baseline was recorded for 20 s, then 35 g of wet sample was introduced and mixed for 30 s, and then data were recorded for 30 s. The wet mass consistency of the sample was calculated as the mean torque value recorded with the sample in the mixer less the mean torque value of the baseline recording. All reported values were the average of two determinations.

To obtain dry granules for further analysis, the wet mass samples were subsequently processed, by first passing through a 1000 μm screen, then tray-drying in an oven at 40 °C for 24 h, and finally screening once again through a 850 μm sieve. The undersized fractions were analyzed for size distribution (by sieve analysis); apparent bulk density (aerated and tapped to derive their Hausner ratio); flow (using an Aero-Flow, Amherst Process Instruments, Hadley, MA), based on an avalanching principle;[6] and friability index (using a modified test procedure in a Roche tablet friability test apparatus). The densities were determined in a tapping apparatus similar to that described in the European Pharmacopoeia (second edition, V.5.5.4.). The Aero-Flow measures the time intervals between avalanches generated within a granule sample placed in the slow rotating drum of the apparatus. The assay was made with the 1−600-μm fractions of the samples. The quantity used varied according to the density of the formulation, with 25 g for the lactose-based and 40 g for the DCPD-based formulations. Compilation of the frequency and irregularity of

* Corresponding author. Phone: (+44) 1274 384 738. Fax: (+44) 1274 384 769. E-mail: P.York@bradford.ac.uk.
† Drug Delivery Group.
§ ZENECA Pharmaceuticals.
‡ Present address: DMV International, Veghel, The Netherlands.

10.1021/js9803454 CCC: $18.00 Published on Web 01/05/1999

Table 1—Composition of the Different Powder Mixes Granulated[a]

formulation	lactose/DCPD	maize starch, %	PGS/PVP	composition
R	450 mesh 80%	18	PGS 2%	reference formulation
L	200 mesh 80%	18	PGS 2%	same source of lactose but different grade, with larger particles
P	450 mesh 80%	18	PVP 2%	same as reference formulation except binder (water soluble grade of PVP)
C	DCPD 80%	18	PGS 2%	filler replaced by an inorganic, water-insoluble but still hydrophilic filler
D	450 mesh DCPD 40% + 40% 450 mesh lactose	18	PGS 2%	intermediate composition between 'R' and 'C' formulations

[a] % indicated are on a weight basis.

these time intervals was then used to describe the flow behavior of the sample. In the friability test, 10 g of sample was used regardless of formulation, and the Roche tablet friabilator was run 5 min at 90 rpm with a sample and five small glass balls. The glass balls had a mean diameter of 16 mm and a density of 2.34 g/cm^3. They were preferred to lighter materials (plastic and wooden balls) to maximize the differences in results obtained from various granule samples. The friability index was taken as $100 - x$%, where x is the percentage of the original sample fraction 250–600 μm retained by a 250 μm sieve after testing. Similar methods are encountered in the literature with various drum speeds, sample sizes, and sieve fractions, and presence or absence of inert balls.[7–9] Mechanically stronger granules produce a lower friability index.

Results and Discussion

The dimensionless power relationship of the mixer-granulator gives the relationship between the power consumption of the mixer and the wet mass consistency. The following expression will be used:[2]

$$\log_{10} \mathrm{Np} = a + b^{*}\log_{10} (\Psi\mathrm{Re}^{*}\mathrm{Fr}^{*}\text{fill ratio}) \qquad (1)$$

where Np is the Power number

$$\mathrm{Np} = \frac{\Delta P}{\rho N^3 R^5} \qquad (2)$$

ΨRe is the pseudo Reynolds number

$$\Psi\mathrm{Re} = \frac{\rho N R^2}{\mu} \qquad (3)$$

Fr is the Froude number

$$\mathrm{Fr} = \frac{R N^2}{g} \qquad (4)$$

and fill ratio indicates the fraction of bowl working capacity occupied by the wet mass, and can be represented, for example, by[2]

$$\frac{\rho R_\mathrm{B}^3}{m} \qquad (5)$$

The dimensionless numbers 2 to 5 are defined with the following notations:

ΔP = the net power consumption of the mixer-granulator (W)

(total power consumption less power required to stir the dry mix)

m = the amount of wet mass (kg)

ρ = the wet mass bulk density (kg·m^{-3})

μ = the wet mass consistency (Nm)

N = the impeller rotational speed (s^{-1})

R = the impeller radius (m)

R_B = the bowl radius (m)

g = the gravitational constant (9.81 ms^{-2})

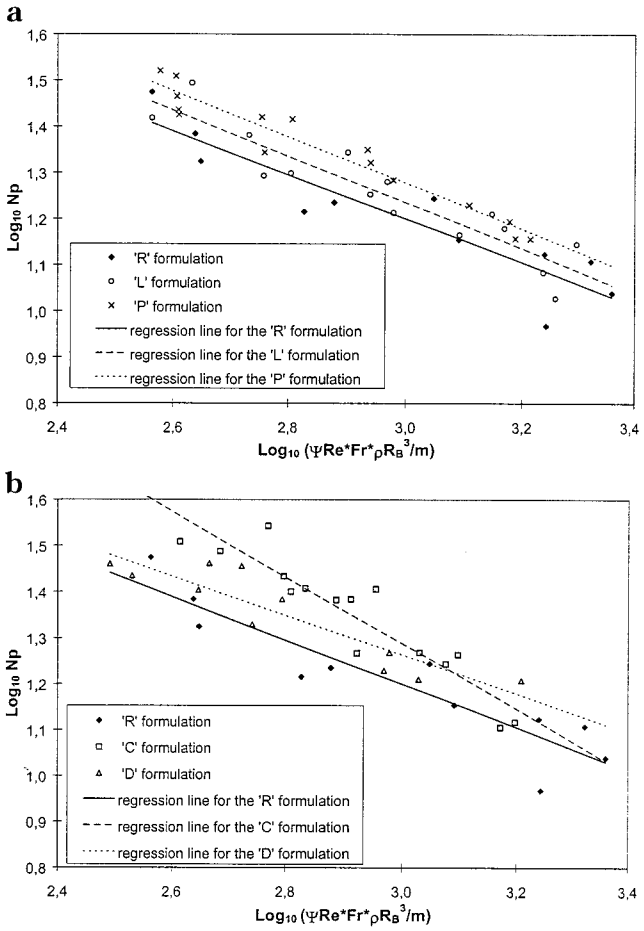

Figure 1—Scale-up relationships obtained for the five formulations tested in the Fielder PMA 100 L mixer-granulator.

Data from the experimental granulation runs were used to determine the dimensionless power relationship of the Fielder PMA 100 L mixer-granulator and to investigate the effect of formulation on this relationship. The results are graphically presented in Figures 1a and b. The statistical analysis on the regression lines was compiled using a statistical software package (SPSS 6 for Windows, SPSS UK Ltd, Chertsey, Surrey, UK) and the results are summarized in Table 2.

No statistical difference can be seen between the regression lines of the three lactose formulations. This result indicates that the dimensionless power relationship is little affected by the change of binder, from PGS to PVP, or by the change of filler particle size from lactose 450 mesh to lactose 200 mesh.

The slope and intercept of the regression line for the 'C' formulation, DCPD based, are distinct from these of the corresponding lactose 'R' formulation. Note, however, that as the confidence limits are determined at ± 1 standard deviation, the observations made are only at 68% confidence. At 95% confidence (i.e., $p = 0.05$), with the confi-

Table 2—Scale-up Regression Line Results[a]

formulation	a	σ_a	interval of confidence for a[b]	b	σ_b	interval of confidence for b	r^2[c]	n[d]
'R'	–0.473	0.067	[–0.540; –0.406]	2.620	0.202	[2.418; 2.822]	0.847	11
'L'	–0.500	0.057	[–0.557; –0.443]	2.734	0.170	[2.564; 2.904]	0.855	15
'P'	–0.499	0.037	[–0.536; –0.462]	2.775	0.105	[2.670; 2.880]	0.935	15
'C'	–0.717	0.079	[–0.796; –0.638]	3.439	0.230	[3.209; 3.669]	0.864	15
'D'	–0.426	0.064	[–0.490; –0.362]	2.542	0.178	[2.364; 2.720]	0.833	11

[a] $\text{Log}_{10}\text{Np} = a\ \log_{10}[\Psi\text{Re}\cdot\text{Fr}\cdot\rho R_B^3/m] + b$. [b] The confidence limits were calculated at ± one standard deviation (σ). [c] Regression coefficient. [d] Number of data points.

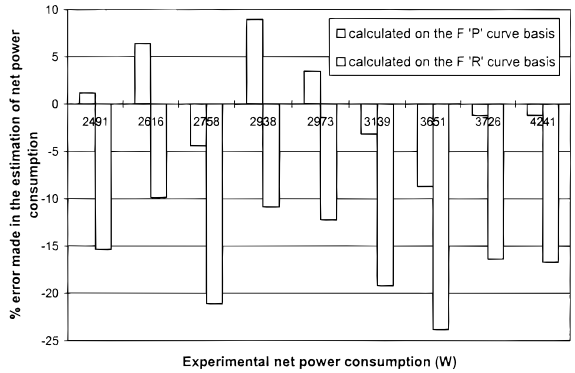

Figure 2—Percentage of error made on the net power consumptions of the 'P' formulation samples when the dimensionless power relationship of this formulation and of the 'R' formulation are used.

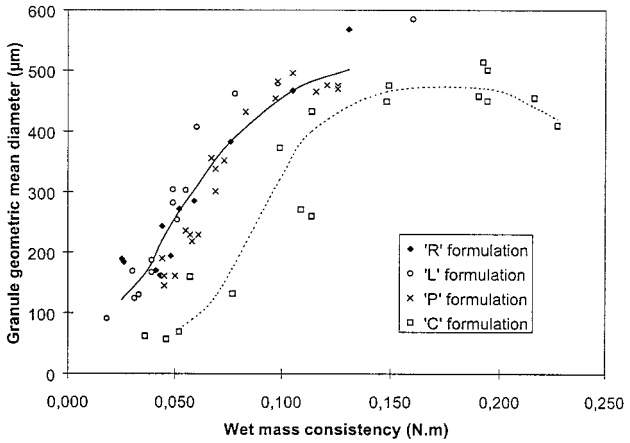

Figure 3—Relationship between the wet mass consistency and the dry granule geometric mean diameter by weight.

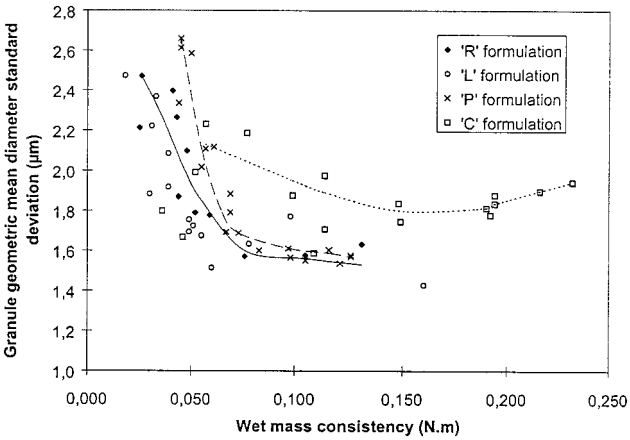

Figure 4—Relationship between the wet mass consistency and the dry granule size distribution standard deviation.

dence limits at ±1.96 standard deviation, the comparisons between slope and intercepts of the 'C' and 'R' regression lines are inconclusive.

When half the DCPD in the 'C' formulation is replaced by lactose 450 mesh ('D' formulation), the effect of this variation of filler on the slope and intercept of the regression line is again not significant. Interestingly the 'D' formulation does not behave intermediate to the 'C' and 'R' formulations but, on the contrary, would tend to present a curve similar to these of the lactose formulations.

To verify the quality of the model, or in other words the accuracy of the target net power consumption deduced from the dimensionless power relationship of the bowl, the case of the 'P' formulation was further studied. Figure 2 represents the percentage of error made in the estimation of ΔP with regards to the real value of ΔP measured experimentally, when the dimensionless power relationships specific to this formulation and the 'R' formulation are respectively used. Figure 2 shows that the dimensionless power relationship specific to the 'P' formulation permits a good prediction of the net power consumption, usually within 5% of error. On the other hand if the relationship established for the 'R' formulation is used, then the predicted power consumption value is systematically underestimated by around 10−20%. For scale-up purposes (i.e., when considering other geometrically similar bowls in the same series of mixer-granulators), it is therefore important to determine the dimensionless power relationship specific to the formulation considered to determine workable power consumption predictions.

In the remainder of this work, the dry granules obtained from the granulation runs on the different formulations were compared to study the link between the consistency of the mass prior to drying and the quality of the downstream granules, and to investigate once again the effect of varying the formulation.

Figures 3 to 6 illustrate the relationships found between the wet mass consistency and different dry granule properties; they are, geometric mean diameter by weight and its standard deviation, Hausner ratio, and friability index. With these tests no significant differences are seen between the three lactose formulations investigated, despite the change in binder composition (PVP or PGS) or in filler particle size (volume median diameter of lactose 450 and 200 mesh were respectively found to be 26 and 44 μm by laser diffraction, Malvern Instruments, Malvern, Worcestershire, UK). Only the granule size distribution of the 'P' formulation is slightly wider than that of the other two lactose formulations, at low levels of granulation (i.e., low wet mass consistency values).

The DCPD-based formulation, 'C', shows a distinct trend for granule size distribution and friability. Higher wet mass consistency values are required to obtain dry granules of a given size compared with the lactose formulation. The 'C' formulation is also more friable than its lactose counterparts, probably due to the absence of a 'secondary binder' effect. DCPD is indeed insoluble in water, the solvent used for granulation, whereas lactose is partially soluble and contributes therefore to the strength of the final dry bridges. The 'D' formulation, made up in equal parts of lactose 450 mesh and DCPD, was only analyzed for

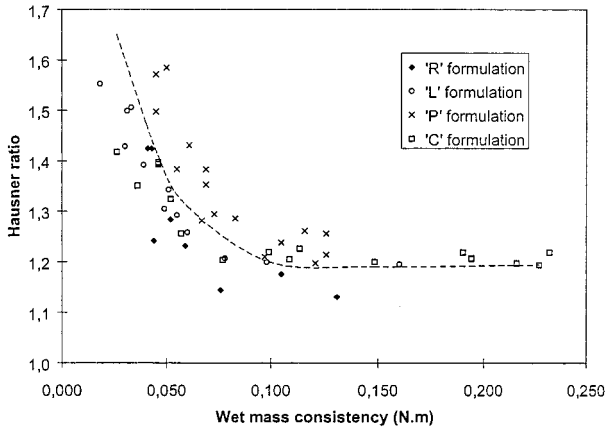

Figure 5—Relationship between the wet mass consistency and the dry granule Hausner ratio.

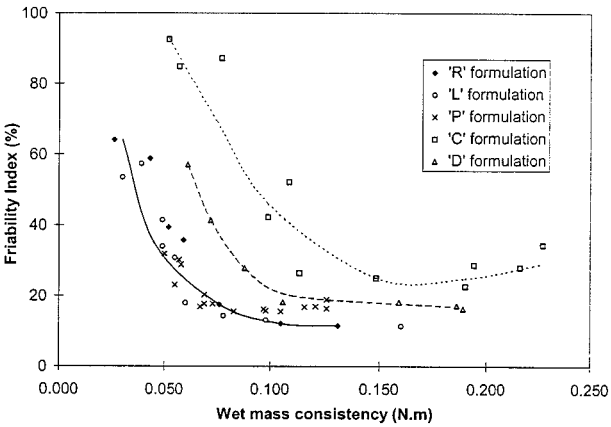

Figure 6—Relationship between wet mass consistency and the dry granule friability index.

friability. It behaved somewhat intermediate to the 'R' and 'C' formulations, except at high wet mass consistency values, where the level of moisture is such that the lactose contribution to the granule strength was almost comparable to a pure lactose formulation. The differences found between the lactose- and DCPD-based formulations are unlikely to be due to the variation in initial particle size (volume median diameter of 14 μm for DCPD), as there was already no difference in the wet mass consistency/dry granule properties relationships between the 'R' and 'L' formulations.

Overall, it is observed that the dry granule properties considered vary almost linearly with the consistency of the original wet mass, up to approximately 0.08 Nm for the lactose-based formulations, and 0.12 Nm for the 'C' formulation. Above these respective values, further addition of binder liquid (water) does not significantly affect the granule growth and densification (granule geometric mean diameter, standard deviation, and Hausner ratio all roughly level off). Additionally, the mechanical strength of the dry granules stops improving at exactly the same levels of wet mass consistency.

The flow avalanching behavior of the granules was analyzed using the Aero-Flow. As an example, the patterns obtained for different samples prepared from one granulation run with the 'P' formulation are shown in Figure 7a. These graphical representations are compiled by plotting the time between avalanches number n and $n+1$ ('time n+1') against the time between avalanches number $n-1$ and n ('time n'), for $1 < n < n_t - 1$, where n_t is the total number of avalanches recorded during the analysis. Such plots are characterized by their centroid, representing the

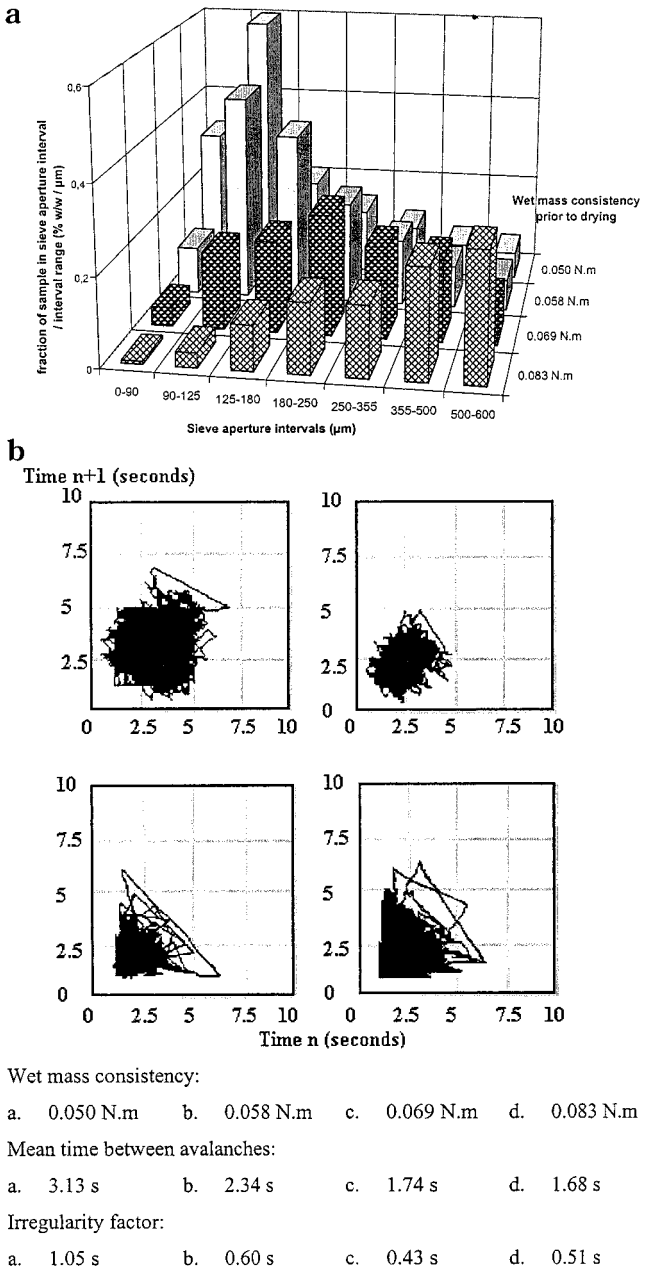

Wet mass consistency:

a. 0.050 N.m b. 0.058 N.m c. 0.069 N.m d. 0.083 N.m

Mean time between avalanches:

a. 3.13 s b. 2.34 s c. 1.74 s d. 1.68 s

Irregularity factor:

a. 1.05 s b. 0.60 s c. 0.43 s d. 0.51 s

Figure 7—Example of granule size distribution and corresponding flow patterns observed on four granule samples of increasing wet mass consistency (taken for the same granulation run at 180 rpm with the 'P' formulation).

mean time between avalanches, and the scatter around the centroid (irregularity factor). Free-flowing materials will give a dense pattern (small irregularity factor), close to the origin of the axes (frequent avalanches). The link between the granule size distribution of each of these samples and their flow avalanching behavior is shown in Figure 7b. Flow improves with increasingly bigger granule size, but as the fines almost disappear, the flow of the corresponding sample reverses back to less regular.

It is therefore concluded that a single parameter, the wet mass consistency, can be used to describe a wet mass and the dry granules that will ultimately be generated from it. In this case study of five formulations, it is clearly unnecessary to carry on wet massing beyond the 0.08 Nm consistency value for the lactose-based formulations or 0.12 Nm for the 'C' formulation, as further addition will only lengthen the drying process but not significantly modify the dry granule properties. Hence, the optimal dry granules

should be probed among the batches with consistencies in the 0.02−0.08 and 0.02−0.12 Nm ranges, respectively.

In conclusion, this work has shown that the wet mass consistency, as determined by mixer torque rheometry, is an essential parameter in the development of pharmaceutical wet granulation processes. It links the 'wet' and 'dry' stages of the operation, in terms of downstream production of dry granules of reproducible, optimized properties. This finding also reinforces the strategy of the scaleup methodology presented in the *Introduction* of this paper; that is, the transfer of a wet granulation process to a different manufacturing scale should require the reproduction of the same wet mass consistency and bulk density. In addition, this work suggests that some changes in the formulation can lead to the modification of the dimensionless power relationship. This suggestion was particularly evident when the filler was changed from a soluble to an insoluble hydrophilic material. Although for the limited range examined particle size and binder composition appeared not to be critical factors, in practice, the prediction of the target endpoint power consumption will only be reasonable if the dimensionless power relationship specific to the formulation studied is employed. The individual behavior of the materials is not able to be summed up to predict the wet massing behavior of a mixture of these materials, as demonstrated for the case of the 'D' formulation.

References and Notes

1. Cliff, M. J.; Parker, M. D. Scale-up in mixer-granulators. *Proceedings of the 12th Interphex Conference*; **1990**, *5*, 17−32.
2. Faure, A.; Grimsey, I. M.; York, P.; Rowe, R. C.; Cliff, M. J. A methodology for the optimization of wet granulation on a model planetary mixer. *Pharm. Technol. Dev.* **1998**, *3(3)*, 413−422.
3. Landin, M.; York, P.; Cliff, M. J.; Rowe, R. C.; Wigmore, A. J. Scale-up of a pharmaceutical granulation in fixed bowl mixer-granulators. *Int. J. Pharm.* **1996**, *133*, 127−131.
4. Rowe, R. C.; Parker, M. D. Mixer torque rheometry: an update. *Pharm. Technol. Eur.* **1994**, *6(3)*, 74−82.
5. Parker, M. D.; Rowe, R. C.; Upjohn, N. G. Mixer torque rheometry: a method for quantifying the consistency of wet granulations. *Pharm. Technol. Int.* **1990**, *2(8)*, 50−62.
6. Kaye, B. H.; Gratton-Liimatainen, J. Effect of flow agents in the rheology of a plastic powder. *Part. Syst. Charact.* **1995**, *12*, 194−197.
7. Reading, S. J.; Spring, M. S. The effect of binder film characteristics on granule and tablet properties. *J. Pharm. Pharmacol.* **1984**, *36*, 421−426.
8. Cutt, T.; Fell, J. T.; Rue, P. J.; Spring, M. S. Granulation and compaction of a model system. I. Granule properties. *Int. J. Pharm.* **1986**, *33*, 81−87.
9. Kokubo, H.; Sunada, H. Effect of process variables in the properties and binder distribution of granules prepared by a high-speed mixer. *Chem. Pharm. Bull.* **1996**, *45(6)*, 1069−1072.

Acknowledgments

Part of the experimental data presented in this paper have been the subject of a poster presentation at the Third World Congress on Particle Technology, Brighton, UK, 7−9 July 1998, and published in the proceedings of the conference.

JS9803454

Existence of a Mannitol Hydrate during Freeze-Drying and Practical Implications

LIAN YU,* NATHANIEL MILTON, EDWARD G. GROLEAU, DINESH S. MISHRA, AND RONALD E. VANSICKLE

Contribution from *Eli Lilly and Company, Lilly Research Laboratories, Indianapolis, Indiana 46285.*

Received August 7, 1998. Accepted for publication November 10, 1998.

Abstract □ We report thermal and crystallographic evidence for a previously unknown mannitol hydrate that is formed in the process of freeze-drying. The mannitol hydrate was produced by freeze-drying pure mannitol solutions (1–4% w/v) using the following cycle: (1) equilibration at –5 °C for 1 h; (2) freezing at –40 °C; (3) primary drying at –10 °C for 15 h; and (4) secondary drying at 10 °C for 2 h and then 25 °C for 5 h. This crystal form was also observed upon freeze-drying in the presence of sorbitol (1% w/v). The mannitol hydrate showed a distinct X-ray powder diffraction pattern, low melting point, and steplike desolvation behavior that is characteristic of crystalline hydrates. The mannitol hydrate was found to be metastable, converting to anhydrous polymorphs of mannitol upon heating and exposure to moisture. The amount of the mannitol hydrate varied significantly from vial to vial, even within the same batch. The formation of mannitol hydrate has several potential consequences: (1) reduced drying rate; (2) redistribution of the residual hydrate water during accelerated storage to the amorphous drug; and (3) vial-to-vial variation of the moisture level.

Introduction

The crystalline[1−11] and amorphous[12] forms of D-mannitol, a commonly used pharmaceutical excipient, have been extensively studied. The crystallization and polymorphic behaviors of mannitol have also been investigated in frozen aqueous solutions,[13−17] with an aim to understand and control the freeze-drying process. Unlike many excipients (e.g., sorbitol and disaccharides), mannitol has a strong tendency to crystallize from a frozen aqueous solution, both during cooling and reheating. The vial breakage phenomenon[13,14] is a striking illustration of this tendency. Mannitol has been observed to continue to crystallize after freeze-drying, especially as a result of heat and moisture,[18,19] which indicates that the freeze-drying process can produce a partially amorphous and partially crystalline material. The crystallization of mannitol during freeze-drying can lead to different anhydrous polymorphs (α, β, and δ) and their mixtures as a result of different formulation and processing conditions,[15] which leaves room for polymorphic transformations during storage. To the best of our knowledge, hydrated crystal forms of mannitol have not been reported.[20]

The formation of a crystalline hydrate by an excipient during freeze-drying may have several practical consequences. The difficulty of removing bound water from a crystal lattice can significantly limit the drying rate. Certain hydrates lose water without significantly altering the initial lattice structures ("isomorphic dehydration")[21] and lead to materials that are highly hygroscopic and undergo structural relaxation during storage. The residual water that is not removed by freeze-drying may be a potential threat to product stability if it is released during storage, especially under "accelerated" conditions.

We present here thermal and crystallographic evidence for a mannitol hydrate that is formed during freeze-drying and discuss the practical implications in terms of process design and product stability.

Experimental Section

Freeze-Drying—A laboratory freeze-drier (FTS Systems Inc.) was used. The following conditions produced the "mannitol hydrate" as characterized below: (1) equilibration at −5 °C for 1 h; (2) freezing at −40 °C; (3) primary drying at −10 °C for 15 h; and (4) secondary drying at 10 °C for 2 h and then 25 °C for 5 h. The cooling rate not controlled during freezing, and it took approximately 3 h to reach −40 °C. The chamber pressure was set to 100 μm of Hg throughout the drying process. Mannitol solutions were prepared at several concentrations (1, 2, and 4 w/v %) by dissolving mannitol (99+%, ACS reagent, Sigma; USP quality) in deionized water. The freeze-drying vials (tubing type manufactured by Wheaton) were 5 mL with 18.4 mm i.d. The fill volume was 2.0 mL/vial. The samples were stored at −20 °C before analysis.

XRD—A Siemens D5000 X-ray diffractometer was used, which was equipped with a Cu Kα source(λ = 1.54056 Å) operating at a tube load of 50 kV and 40 mA. The divergence slit size was 0.6 mm, the receiving slit 1 mm, and the detector slit 0.1 mm. Data were collected by a Kevex solid-state (SiLi) detector. The freeze-dried cake was broken, spread over the sample holder, and gently pressed before analysis. Each sample was scanned between 4 and 35° (2θ) with a step size of 0.03° and a maximum scan rate of 2 s/step.

DSC—Differential scanning calorimetry (DSC) was conducted in sealed Al pans at 10 °C/min using a Seiko DSC 210 under 50 mL/min nitrogen purge. Samples (5−10 mg) were either loosely packed into sample pans or first pressed into pellets using a stainless steel pellet-maker of local design. Sample preparation was carried out in a dry glovebag maintained at <5% RH.

TG/DTA—Simultaneous thermal gravimetric analysis (TGA) and differential temperature analysis (DTA) were conducted at 10 °C/min in open Al pans using a Seiko TG/DTA 220 under 150 mL/min nitrogen purge. Three to five milligrams were used for each analysis.

Results and Discussions

Figure 1 (curve 1) shows the XRD pattern of a freeze-dried mannitol sample from a 4% w/v solution. In addition to peaks that belong to the δ (major) and β (minor) polymorphs of mannitol,[22] additional peaks (marked by asterisks and listed in Table 1) were observed that could not be attributed to any known mannitol polymorphs. Heating this sample to 70 °C for 30 min eliminated the additional peaks (Figure 1, curve 2), with the remaining peaks attributable to the δ and β mannitol. These observations indicate the existence of a metastable crystal form of mannitol that was produced during freeze-drying and

* Corresponding author. Tel. (317) 276 1448. Fax (317) 277 5519. E-mail yu_lian@lilly.com.

10.1021/js980323h CCC: $18.00
Published on Web 12/19/1998

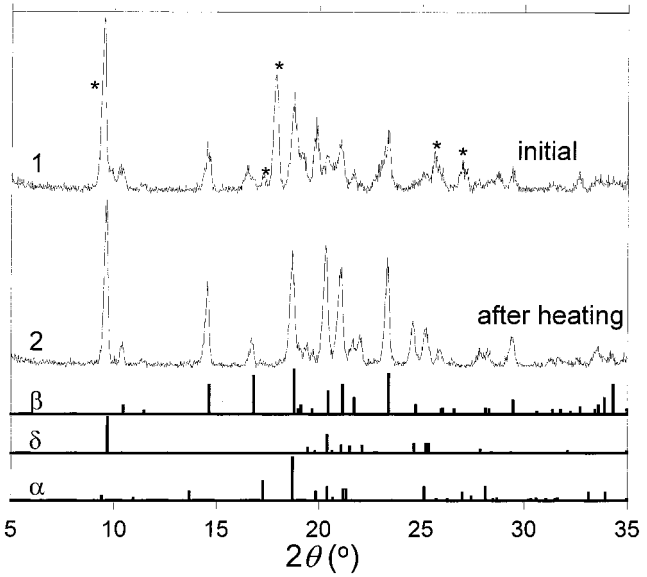

Figure 1—X-ray powder diffraction patterns of a freeze-dried mannitol sample (curve 1) and the same sample after heating at 70 °C for 30 min (curve 2). Curve 1 contains peaks that do not belong to any known mannitol polymorphs, whereas all peaks in curve 2 are attributable to the δ and β polymorphs of mannitol. The α-polymorph pattern is also shown for comparison.

Table 1—X-ray Powder Pattern for the Mannitol Hydrate

2θ, deg	9.6	16.5	17.9	25.7	27.0
I/I_0	0.8[a]	0.2	1[b]	0.3	0.2

[a] Overlapping the (020) reflection of δ-mannitol ($2\theta = 9.7°$). [b] Best i.d. peak.

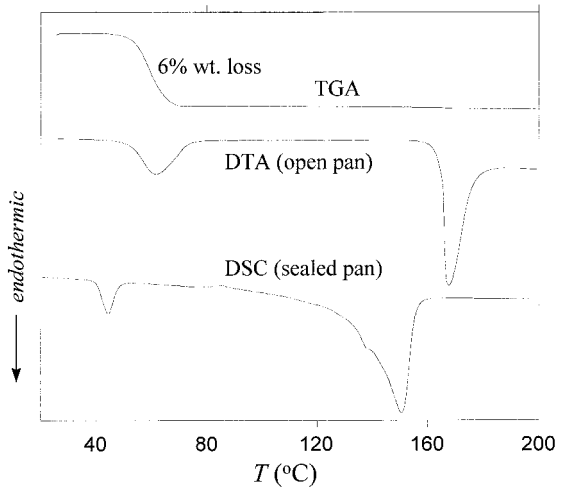

Figure 2—TGA (top), DTA (middle), and DSC (bottom) data of a freeze-dried mannitol sample. The TGA and DTA data were recorded simultaneously in an open sample pan, which show the melt/desolvation behavior of a crystalline hydrate. The DSC data was recorded in a hermetically sealed sample pan, which shows the homogeneous melting of the hydrate.

capable of converting to anhydrous mannitol polymorphs upon heating.

Figure 2 shows the thermal characteristics of the same sample described above. TGA (top curve) showed a steplike weight loss near 50 °C. The simultaneously conducted DTA (middle curve) showed a well-defined endotherm coinciding with the weight loss, which was followed by the melting of the anhydrous mannitol (mp 169 °C). DSC conducted in hermetically sealed pan (bottom curve) showed a sharp endotherm slightly below the desolvation onset.

The thermal data indicate that the crystal form transformation during heating (Figure 1) was accompanied by the loss of solvent (water). The steplike TGA loss and the well-defined DTA endotherm suggest the removal of structural water from a crystalline hydrate, rather than loosely bound ("free") water. This interpretation is supported by the sealed-pan DSC data. The use of sealed sample pans prevented the simultaneous evaporation of water during melting, making it possible to observe a sharp, homogeneous melting of the crystalline hydrate. The broad endothermic event following the sharp hydrate melting in the DSC trace can be attributed to the temperature-depressed melting of anhydrous mannitol crystals in the presence of water. We conclude therefore that a mannitol hydrate was formed in the process of freeze-drying and survived what appeared a "typical" drying cycle. This crystal form was metastable, converting to anhydrous polymorph(s) of mannitol upon heating.

Conditions of Formation—Using the same drying cycle, we have observed the mannitol hydrate under different formulation conditions: mannitol concentrations ranging from 1 to 4% w/v, with or without sorbitol (1% w/v), and in a drug formulation.[23] The same X-ray pattern assigned to the mannitol hydrate (Table 1) has also been observed by Cavatur and Suryanarayanan using in situ powder X-ray diffractometry.[24]

Anhydrous mannitol crystals are nonhygroscopic at room temperature, gaining less than 1% moisture at 90% RH.[25] This indicates that hydrate formation from anhydrous crystals is unlikely upon moisture exposure at the room temperature. The DSC data of Martini et al.[16] indicate that upon cooling a 10% w/v mannitol solution, ice forms (with substantial supercooling) before mannitol crystallizes. These observations, along with the previous failure to crystallize the mannitol hydrate at the room temperature or above,[20] suggest that the formation of the mannitol hydrate is likely a low-temperature phenomenon, relevant in particular to freeze-drying.

We have observed significant vial-to-vial variations in the amount and stability of the mannitol hydrate, even within the same batch. The relative intensity of the hydrate pattern ranged from comparable to that shown in curve 1 (Figure 1) to barely detectable or rapidly diminishing during measurement; the TGA losses ranged from 1 to 6%, and the onset of TGA loss ranged from 40 to 60 °C. The mannitol hydrate produced in certain vials could withstand mild heat (40 °C), humidity (60% RH) and compression (in DSC sample preparation), while in others it was easily destroyed, even by gentle compression. Although the drying cycle used in this study seemed a reasonable one, more aggressive secondary drying (same temperature but longer drying time) did eliminate traces of the mannitol hydrate and resulted in anhydrous mannitol crystals.

Several factors may contribute to the vial-to-vial variation in the amount and stability of the mannitol hydrate. First, the hydrate is formed in a low-temperature, concentrated solution, conditions that are not favorable for producing well-developed crystals in a reasonable processing time. Second, the ice crystallization temperature can vary as a result of the cooling rate[16] and thus the vial location in a drier. Other more subtle factors can also affect the onset of ice crystallization (e.g., defects on the vial surface). Such variability can influence the degree of freeze concentration and the ice structure and, in turn, the subsequent crystallization of mannitol. Finally, the hydrate formation is in competition with the crystallization of the anhydrous polymorphs (α, β, or δ), directly or through subsequent solid−solid conversion. Depending on the rate of anhydrous crystallization, the hydrate amount will vary. We suspect that these effects acting in concert contributed to the vial-to-vial variation and the previous failure to detect the mannitol hydrate.

Practical Implications—The formation of the mannitol hydrate during freeze-drying has several practical implications. First, the rate of water removal may be reduced due to strongly bound water that resides in the crystal lattice. In certain hydrates, such as the mannitol hydrate, the structural water cannot be fully removed without destroying the crystal lattice, a process that may require more aggressive or atypical drying conditions (e.g., longer drying time and higher temperature). Depending on the detailed mechanism of formation, it may be necessary, for example, to anneal the frozen solution to promote crystallization of the anhydrous form, thereby reducing or eliminating the mannitol hydrate.

Second, the residual hydrate water that is not fully removed by freeze-drying may pose a long-term threat to product stability, as the hydrate water can be released and redistributed, especially in "accelerated" storage, to the often amorphous drug and thus increases the potential for chemical and physical changes. Herman et al. have shown that methylprednisolone sodium succinate (MPSS) stored at accelerated conditions and formulated with mannitol is chemically less stable than materials formulated with lactose.[26] The difference in chemical stability was attributed to mannitol crystallization and the redistribution of water within the freeze-dried cake which promoted the hydrolysis of MPSS. Roos and Karel have shown that as amorphous lactose crystallizes and releases water, the glass transition temperature of the remaining amorphous material is depressed and the crystallization process accelerated.[27] It is conceivable, therefore, that the release of hydrate water during accelerated storage may also complicate the interpretation of stability data and cause a premature termination of an otherwise promising formulation.

Finally, our observations indicate that certain vial-to-vial variation in the water level may be associated with the formation of the mannitol hydrate.

Conclusions

We have reported thermal and crystallographic evidence for the formation of a previously unknown mannitol hydrate in the freeze-drying process. The mannitol hydrate can survive a "typical" drying cycle, but can be converted to anhydrous polymorph(s) of mannitol on gentle heating and more aggressive secondary drying. Potential consequences of the mannitol hydration formation include reduced drying rate, moisture release during accelerated storage, and vial-to-vial variation in the water level.

References and Notes

1. Marwick, T. C. An X-ray Study of Mannitol, Dulcitol and Mannose. *Nature* **1931**, *127*, 11−12.
2. McCrea, G. W. An X-ray Study of Mannitol. *Nature* **1931**, *127*, 162−163.
3. Rye, A.; Sorum, H. Crystalline Modifications of D-Mannitol. *Acta Chem. Scand.* **1952**, *6*, 1128−1129.
4. Berman, H. M.; Jeffrey, G. A.; Rosentein, R. D. The Crystal Structures of the α′ and β Forms of D-Mannitol. *Acta Crystallogr.* **1968**, *B24*, 442−449.
5. Kim, H. S.; Jeffrey, G. A.; Rosenstein, R. D. The Crystal Structure of the K Form of D-Mannitol. *Acta Crystallogr.* **1968**, *B24*, 1449−1455.
6. Walter-Levy, L. Sur les varietes crystallines du D-mannitol. *C. R. Acad. Sc. Paris* **1968**, *267*, 1779−1782.
7. Debord, B.; Lefebvre, C.; Guyot-Hermann, A. M.; Hubert, J.; Bouche, R.; Guyot, J. C. Study of Different Crystalline Forms of Mannitol: Comparative Behaviour under Compression. *Drug Dev. Ind. Pharm.* **1987**, *13*, 1533−1546.
8. Jones, F. T.; Lee, K. S. The Optical and Crystallographic Properties of Three Phases of Mannitol. *Microscope* **1970**, *18*, 279−285.
9. Grindley, T. B.; McKinnon, M. S.; Wasylishen, R. E. Towards Understanding ^{13}C-N.M.R. chemical shifts of Carbohydrates in the Solid State. The Spectra of D-Mannitol Polymorphs and of DL-Mannitol. *Carbohydr. Res.* **1990**, *197*, 41−52.
10. Pitkanen, I.; Perkkalainen, P.; Rautiainen, H. Thermoanalytical Studies of Phases of D-Mannitol. *Thermochim. Acta* **1993**, *214*, 157−162.
11. Burger, A.; Hetz, S.; Weissnicht, A. On the Polymorphism of Mannitol. *Eur. J. Pharm. Biopharm.* **1994**, *40(Suppl.)*, 21S.
12. Yu, L.; Mishra, D. S.; Rigsbee, D. R. Determination of the Glass Properties of D-Mannitol Using Sorbitol as an Impurity. *J. Pharm. Sci.* **1998**, *87*, 774−777.
13. Willaims, N. A.; Lee, Y.; Polli, G. P.; Jennings, T. A. The Effect of Cooling Rate on Solid-Phase Transitions and Associated Vial Breakage Occurring in Frozen Mannitol Solutions. *J. Parenteral Sci. Technol.* **1986**, *40*, 135−141
14. Williams, N. A.; Dean, T. Vial Breakage by Frozen Mannitol Solutions: Correlation with Thermal Characteristics and Effect of Stereoisomerism, Additives and Vial Configuration. *J. Parenteral Sci. Technol.* **1991**, *45*, 94−100.
15. Kim, A. I.; Akers, M. J.; Nail, S. L. The Physical State of Mannitol after Freeze-Drying: Effects of Mannitol Concentration, Freezing Rate, and a Noncrystallizing Cosolute. *J. Pharm. Sci.* **1998**, *87*, 931−935.
16. Martini, A.; Kume, S.; Crivellente, M.; Artico, R. Use of Subambient Differential Scanning Calorimetry to Monitor the Frozen-State Behavior of Blends of Excipients for Freeze-Drying. *PDA J. Pharm. Sci. Technol.* **1997**, *51*, 62−67.
17. Cavatur, R. K.; Suryanarayanan, R. Characterization of Frozen Aqueous Solutions by Low-Temperature X-ray Powder Diffractometry. *Pharm. Res.* **1998**, *15*, 194−199.
18. Kovalcik, T.; Guillory, J. K. The Stability of Cyclophosphamide in Lyophilized Cakes. Part I. Mannitol, Lactose, and Sodium Bicarbonate as Excipients. *J. Parenteral Sci. Technol.* **1988**, *42*, 29−39.
19. Isutsu, K.; Yoshioka, S.; Terao, T. Effect of Mannitol Crystallinity on the Stabilization of Enzymes during Freeze-Drying. *Chem. Pharm. Bull.* **1994**, *42*, 5−8.
20. Pitkanen et al. wrote in 1993, "We took efforts to crystallize hydrous forms, but did not succeed" (ref 10).
21. Stephenson, G. A.; Groleau, E. G.; Kleemann, R. L.; Xu, W.; Rigsbee, D. R. Formation of Isomorphic Desolvates: Creating a Molecular Vacuum. *J. Pharm. Sci.* **1998**, *87*, 536−542.
22. The Powder Diffraction File. International Centre for Diffraction Data, 12 Campus Blvd., Newtown Square, PA 19073-3273.
23. Yu, L.; Milton, N. Unpublished result.
24. Cavatur, R. K.; Suryanarayanan, R. Characterization of Phase Transitions During Freeze-Drying by in Situ Powder X-ray Powder Diffractometry, presentation abstract submitted to the AAPS Annual Meeting and Exposition, Nov 15−19, 1998, San Francisco, CA.
25. Wade, A.; Weller, P. J., Eds. *Handbook of Pharmaceutical Excipients*, 2nd ed.; American Pharmaceutical Association: Washington, D.C., 1994.
26. Herman, B. D.; Sinclair, B. D.; Milton, N.; Nail, S. L. The Effect of bulking Agent on the Solid-State Stability of Freeze-Dried Methylprednisolone Sodium Succinate. *Pharm. Res.* **1994**, *11*, 1467−1473.
27. Roos, Y.; Karel, M. Crystallization of Amorphous Lactose. *J. Food Sci.* **1992**, *57*, 775−777.

Acknowledgments

We thank Russell A. Miller for assistance in freeze-drying and Dr. Raj Suryanarayanan for helpful discussions.

JS980323H

Stability and Surface Activity of Lactate Dehydrogenase in Spray-Dried Trehalose

MICHAEL ADLER AND GEOFFREY LEE*

Contribution from *Department of Pharmaceutical Technology, Friedrich-Alexander-University, Erlangen, Germany.*

Received August 5, 1998. Accepted for publication November 25, 1998.

Abstract □ The stability of the model protein lactate dehydrogenase (LDH) during spray-drying and also on subsequent dry storage was examined. Trehalose was used as a carrier. The spray-drying temperatures T_{inlet} and T_{outlet} have a measurable effect on LDH inactivation. Low T_{inlet} produced the least process inactivation, but gave a high residual moisture content making the protein's storage stability poor. High T_{inlet} reduced residual moisture and improved storage stability, but at the cost of high process inactivation. As already found for other systems, addition of a surfactant (in this case polysorbate 80) could ameliorate process inactivation of LDH at T_{inlet} = 150 °C. Surfactant had, however, a deleterious effect on storage stability of LDH, the vital factor being the molar ratio of surfactant/protein in the dried product. By using electron spectroscopy it was shown that LDH has a 10 times higher surface concentration in the dried trehalose particles than expected for a homogeneous distribution. Surface tension measurements at the water/air interface proved that LDH is surface active, although the Gibbs equation appeared to be inapplicable. Calculations of spray-droplet formation time and drying time indicate than the extent of diffusion-driven LDH adsorption to the liquid/air interface is sufficient to account for the measured amount of LDH inactivation during spray-drying. The presence of 0.1% polysorbate 80 to the spray solution prevents LDH from appearing at the surface of the dried particles. As a negative control, the phosphatide Lipoid E 80 does not prevent the appearance of LDH in the surface according to electron spectroscopy and does not therefore prevent LDH inactivation during spray-drying at T_{inlet} = 150 °C.

Introduction

It is just 6 years since Broadhead et al.[1] concluded in their review article that the full potential of spray-drying of pharmaceutical proteins had yet to be exploited. Since then, a number of papers and patents have addressed the question of spray-drying to produce protein formulations suitable for pulmonary delivery. In most cases, spray-drying of an aqueous solution of the bulk protein led to substantial protein aggregation or inactivation.[2] The addition of stabilizing adjuvants as carriers, typically carbohydrates or amino acids, reduces the extent of protein inactivation during spray-drying. Sucrose (0.25 M), for example, reduced the formation of methemoglobin on spray-drying hemoglobin at an inlet air-temperature of 100 °C from 50% to <4%.[3] Trehalose, arginine, and sucrose completely ameliorated the activity loss of spray-dried β-galactosidase.[4] Both trehalose and sucrose have, however, been reported to be difficult to spray-dry, at least in the placebo state. The latter is extremely hygroscopic[5] whereas the former has been reported to form fused, sticky aggregates at an inlet air-temperature of 90 °C, unsuitable as a protein carrier.[6]

This paper presents part of our work investigating the relationship between process stability, storage stability, and surface activity of proteins in spray-dried powders. The question of process stability of proteins during spray-drying has already been addressed in the papers cited above. The problem of subsequent storage stability of the proteins has, however, received less attention. Broadhead et al.[4] reported that trehalose as a carrier produced the best storage stability of β-galactosidase at ambient temperatures. We wished to reconcile this report with the above-cited difficulty in producing dry spray-dried trehalose particles.[6] For pulmonary application, where the maximum powder-dose is severely limited,[7] the spray-drying of pure proteins appears attractive. Recombinant human growth hormone could, for example, be successfully spray-dried at an inlet air-temperature of 90 °C without a carrier, although only with addition of polysorbate 20 and/or $ZnCl_2$ to the spray solution.[8] The storage stability of such spray-dried proteins having no carrier has, however, yet to be addressed and will certainly be protein-specific. The use of a glass-forming carrier will surely be necessary for many proteins.

We selected lactate dehydrogenase (LDH) as a model protein. It is known to be sensitive to thermal treatment and has the distinct advantage that its enzyme *activity* can be measured directly and not just its degree of aggregation. To reconcile the conflicting reports in the literature regarding its suitability,[4,6] we used trehalose as a carrier. Its high glass transition temperature in the dried state renders trehalose an efficient stabilizer of proteins on storage,[9] even when containing relatively high residual moisture contents. We examined the influence of spray-drying temperatures on both the process and storage stability of LDH in spray-dried trehalose. The results are discussed in terms of the residual water contents and glass transition temperatures of the spray-dried powders. As has been already reported for other proteins,[8] surfactant could reduce loss of LDH activity occurring during the process of spray-drying. We show, however, that polysorbate 80 has an unexpectedly deleterious effect on storage stability of LDH. Surface tension measurements show that LDH is strongly surface-active. A particular feature of this work is the use of electron spectroscopy to assay the surface layer of the spray-dried LDH/trehalose particles. Using this method we find the first unequivocal evidence of protein exclusion from an interface on spray-drying with surfactant. The addition of lecithin did not induce protein exclusion from the interface and did not therefore prevent loss of LDH activity during spray-drying.

Materials and Methods

Materials—Porcine lactate dehydrogenase (LDH) of molecular weight approximately 144 kDa was obtained from Boehringer Mannheim (Mannheim, Germany). This suspension in 3 M $(NH_4)_2$-

* Address correspondence to: Prof Geoffrey Lee, Lehrstuhl für Pharmazeutische Technologie, Cauerstr. 4, 91058 Erlangen, Germany. Tel.: (49) 9131/85 295 52, Fax: (49) 9131/85 295 45, Email: lee@pharmtech.uni-erlangen.de.

10.1021/js980321x CCC: $18.00 Published on Web 01/14/1999

SO_4 was dialyzed immediately before use at 4 °C against 0.1 M phosphate buffer of pH 7 using a regenerated cellulose membrane (MW cutoff 12000−14000). The LDH activity of the dialysate was determined by the assay described later. Trehalose dihydrate was used as received from Sigma Chemicals (Munich, Germany). Polysorbate 80 of MW approximately 1300 and HLB value 15 was obtained from ICI (Sandhofen, Germany). Lipoid E 80 is an egg yolk lecithin obtained from Lipoid (Ludwigshafen, Germany) and was used without further refinement. Miglyol 812 came from Pharma Zentrale (Herdeke, Germany), and Span 85 from ICI. Water was double distilled from an all-glass apparatus.

Spray-Drying—Trehalose dihydrate was dissolved either in water or the diluted, dialyzed LDH solution in pH 7 phosphate buffer. Polysorbate 80 was added as appropriate. Fifty milliliters of the resulting trehalose or trehalose/LDH solution (with or without polysorbate 80) was spray-dried on a Büchi model 190 laboratory spray-dryer operated in the cocurrent mode. The liquid feed rate was 4 mL/min (0.24×10^{-3} m^3/h) through a pneumatic nozzle (0.7 mm diameter) driven at 6 bar air pressure. Cooling water was circulated through a jacket around the nozzle. The atomizing-air flow rate was 0.7 m^3/h, and the aspirator vacuum was 38 mbar. It was possible to control only the inlet air-temperature (T_{inlet}) on the machine we used; the outlet air-temperature (T_{outlet}) could only be measured. Spray-drying was performed under the following four sets of conditions: T_{inlet}/T_{outlet} = 90 °C/60 °C; T_{inlet}/T_{outlet} = 110 °C/70 °C; T_{inlet}/T_{outlet} = 130 °C/80 °C; T_{inlet}/T_{outlet} = 150 °C/95 °C. Unless otherwise stated, the spray solution contained 10% w/w total solids (trehalose + LDH + surfactant), giving a maximum theoretical yield of 5 g of powder per 50 mL of spray solution used in one experiment.

Characterization of Spray-Dried Powders—The residual moisture contents of the spray-dried powders were determined by Karl Fischer Titration (Schott Instruments). Powder samples (50−100 mg) were dissolved in water-free methanol/formamide (1:1) prior to titration. The thermal transitions of the powders were examined on a Polymer Laboratories differential scanning calorimeter. Samples (10 mg) were first sealed in Al pans and then repeatedly cooled and heated between −20 °C and 150 °C at 10 °C/min. Each sample's glass transition temperature, T_g, was determined from the midpoint of the endothermic shift on the DSC trace. Wide-angle X-ray diffraction was performed at 25 °C ± 1 °C on a Phillips Model TW 1730, with Cu Kα radiation of λ = 0.15418 nm at 40 kV/30 mA. The external morphology of the spray-dry powders was examined using scanning electron microscopy (SEM) on an Amray 1810 T microscope. The powders were gold sputtered on an Al sample holder.

Laser Diffractometry—The particle size distributions of the spray-dried powders were determined using a Coulter Model LS 130 Laser Diffractometer. Each dry powder sample was initially deaggregated by dispersion in a 1% w/w solution of Span 85 in Miglyol 812 using an ultrasonic bath for 4 min. This dispersion was placed in the small volume accessory of the diffractometer, and the laser light scattering intensity was evaluated by Fraunhofer analysis.[10]

Electron Spectroscopy for Chemical Analysis (ESCA)—This technique was used to quantify the surface coverage of the spray-dried powders with LDH. Using ESCA it is possible to identify quantitatively the elements present in the surface of dried particles.[11] Briefly, the powder sample is exposed to an X-ray beam, and electrons contained in the near-surface region of the solid (approximately 10 nm) that have a binding energy less than the photon energy will be ejected from the atom. The kinetic energy of the ejected electrons will be equal to the difference between photon energy and binding energy, allowing for an instrument response function. As the binding energy is characteristic of the atom from which it is ejected, the elements present in the specimen can be identified quantitatively.[12]

To determine the surface coverages of the spray-dried powders with LDH, we analyzed the surface atomic concentrations of the elements C, O, and N. We assume only that the ratio of elements found in a dried powder sample is a linear combination of the ratio of elements occurring in the pure components comprising the sample.[11] In this fashion the concentration of LDH in the outermost 10 nm-thick layer of the spray-dried powder can be calculated. A photoelectron spectrometer (Physical Electronics) was used with an Al Kα X-ray source. The pressure in the sample chamber was reduced to below 0.1 μbar bar. The detector (electron kinetic energy analyzer) was operated with a pass energy of 188 eV, and the ESCA spectra were determined using a step size of 1.0 eV. Each spray-dried powder sample was placed in the indentation of the machine's sample holder. The result of each ESCA analysis is expressed as a spectrum of counts/s at the detector versus binding energy in eV.

Table 1—Properties of Trehalose Powders Spray-Dried under Different Conditions of T_{inlet}/T_{outlet}[a,b]

T_{inlet} [°C]	T_{outlet} [°C]	yield [%]	water content [% w/w]	T_g [°C]
110	70	58	3.5	72
130	80	65	2.4	86
150	95	78	2.6	84

[a] Spray solution contained 10% w/w total solids. [b] Liquid feed rate was 4 mL/min, and atomizing air flow rate was 0.7 m^3/h.

Process and Storage Stability of LDH—The residual LDH activity in the trehalose powders was determined immediately after spray-drying and also after various storage times at 4 °C, 25 °C, 40 °C, and 60 °C in sealed glass vials over P_2O_5. The LDH activity assay was conducted as follows: 2.5 mL of phosphate buffer (0.1 M, pH 7), 0.1 mL of pyruvate (0.02 M), and 0.05 mL of NADH (11 mM) were first mixed in a quartz cuvette at 25 °C. LDH solution (0.05 mL) to be tested was then added with mixing. The extinction of the solution was measured at λ = 365 nm over 5 min using a Kontron Uvikon 810 UV−vis photometer with water bath for temperature control. The enzymatic activity [units/mL] could be calculated from the measured rate of change in extinction per min [$\Delta E/\Delta t$]. The residual LDH activities were expressed on a scale between 0 and 100% of the LDH activity of the spray solution determined immediately before spray-drying. Both trehalose and polysorbate strongly influenced the LDH assay and were accounted for by running appropriate blank references.

Surface Tension Measurements—The surface tension of LDH in water was measured at 25 °C ± 0.1 °C and at various concentrations using a thermostated Krüss K 10 Tensiometer equipped with a Wilhelmy plate. The surface tension was measured at various time points up to 60 min. The LDH concentrations were determined from UV-extinction of the solutions at λ = 280 nm by using $E^{0.1\%}_{280nm}$ 1.40 cm^{-1} mL mg^{-1}.[13]

Results and Discussion

Spray-Drying of Protein-Free Trehalose—The reported "sticky" nature of trehalose spray-dried at T_{inlet}/T_{outlet} = 90 °C/60 °C[6] could be overcome by the simple expedient of increasing T_{inlet} to improve product quality, as can be deduced from Broadhead's earlier work.[4] At T_{inlet}/T_{outlet} = 150 °C/95 °C a respectable yield (for the Büchi) of almost 80% is obtained, and the product has a residual moisture content of 2.6% with a T_g of > 80 °C (Table 1). Clearly, use of a low T_{inlet} = 90 °C[6] appears intuitively attractive to reduce possible protein inactivation by thermal stress during spray drying. The consequences of increasing T_{inlet} to 150 °C to obtain a drier product on LDH's process and storage stability will be seen presently. The advantage of using trehalose compared with other nonreducing sugars such as sucrose is also evident from Table 1. A residual moisture of 2.6% is still high compared with freeze-drying the same product, and this value would depress the T_g of sucrose down to approximately 40 °C.[9] By virtue of its high T_g in the dried state (T_g = 115 °C),[14] the relatively high residual moisture contents achievable with spray-drying still yield T_g's of >80 °C. This could be of advantage for the process stability of a protein and certainly will be propitious for its storage stability.[9]

Hancock and Zografi[15] showed that the plasticizing effect of water on various amorphous pharmaceutical solids could be accurately described by the simple Gordon−Taylor model of perfect volume-additivity and no interactions between water and the amorphous solid. Figure 1 shows the T_g's of the spray-dried trehalose powders plotted versus weight fraction residual moisture in the range 0 to ap-

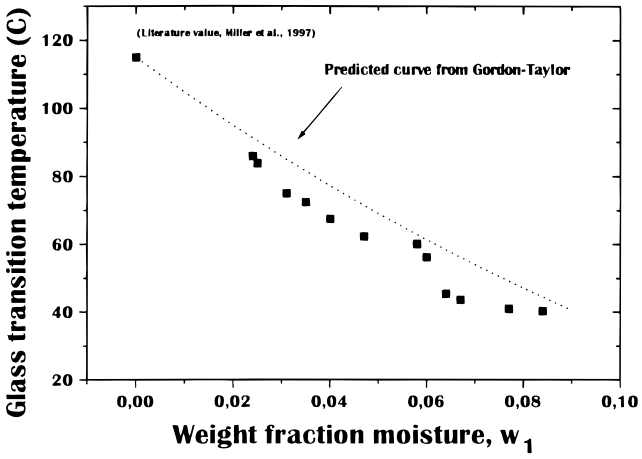

Figure 1—Variation in glass transition temperature (T_g) with weight fraction residual moisture content (w_1) of the spray-dried trehalose powders. Spray solutions contained 10% w/w total solids (trehalose dihydrate). Liquid feed rate was 4 mL/min, and atomizing air flow rate was 0.7 m^3/h. The solid squares are the individual results from the spray-dried powders. The dotted line is the curve calculated from the Gordon–Taylor equation for the water/trehalose system: $T_{g,mix} = (w_1T_g^1 + Kw_2T_g^2)/w_1 + Kw_2$, $K = (T_g^1\rho_1/T_g^2\rho_2)$. The following values were used: water $T_g^1 = 135$ K (–138 °C) $\rho_1 = 1.00 \times 10^3$ kg/m^3; trehalose $T_g^2 = 388$ K (115 °C) $\rho_1 = 1.47 \times 10^3$ kg/m^3; $K_{water/trehalose}$: = 0.237.

proximately 9% w/w water. These different residual water contents were obtained by varying T_{inlet}/T_{outlet} accordingly. The experimentally determined T_g's lie consistently below the curve predicted from the Gordon−Taylor equation (Figure 1). This deviation from ideality is, however, less than that observed for the sucrose−water system.[15] We expect the system trehalose−water to be very nonregular in terms of solution theory by virtue of hydrogen bonding. Bearing this in mind, the relatively small negative deviation from ideality in Figure 1 is surprising. As noted by Hancock and Zografi,[15] however, such nonideality obviously does not have a strong influence on the free volume of the water−glass mixtures.

The scanning electron micrograph (SEM) for trehalose spray-dried at T_{inlet}/T_{outlet} = 150 °C/95 °C (Figure 2a) shows almost perfectly spherical particles with smooth surfaces. This is the typical picture for other spray-dried sugars such as lactose and mannitol[6,7] that are not loaded with higher molecular weight ingredients such as proteins or polymers. No change in particle morphology could be observed with change in T_{inlet}/T_{outlet} in the range examined here. In a literature report, partly fused agglomerates were found with trehalose prepared at T_{inlet}/T_{outlet} = 90 °C/60 °C.[6] Although the product at T_{inlet}/T_{outlet} = 110 °C/70 °C showed no indication of particle fusion, any fused aggregates formed during the process were retained on the inner walls of the cyclone, accounting for the small yield of 58% at this T_{inlet}. Under all spray-drying conditions examined here the trehalose particles were fully amorphous, the wide-angle X-ray diffractograms showing the typical amorphous halo (Figure 2b). Although the particle size determined by laser diffraction was independent of T_{inlet}/T_{outlet}, decreasing the total solids concentration of the spray solution led to reduced particle size of the dried product (Figure 2c). Total solids (10% w/w) give, for example, an average particle diameter of 3.5 μm. If the fine particle dose of a powder is defined as that ≤6 μm,[7] it is approximately 72% with 10% w/w solids content. Such spray-dried powders are, therefore, attractive for pulmonary application, as noted before.[7] This would need to be confirmed, however, by measurements of the aerodynamic particle size using a suitable impactor. If the spray droplet size is independent of the total solids content of the spray solution in the range used

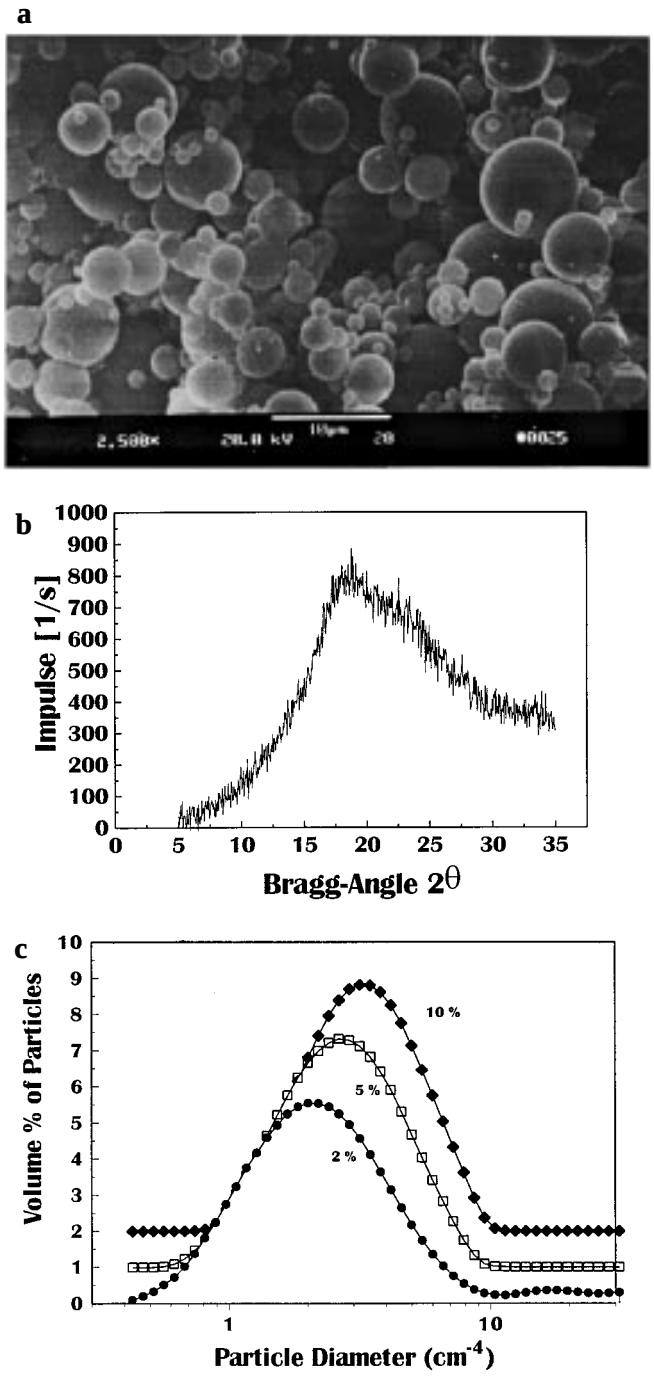

Figure 2—Spray-dried trehalose prepared at T_{inlet}/T_{outlet} = 150 °C/95 °C. (A) Scanning electron micrograph of magnification 2500×. (B) Wide-angle X-ray scattering diffractogram showing characteristic amorphous halo. (C) Influence of total solids content of spray solution on particle size distribution determined by laser diffraction. With decreasing total solid content from 10 through 5 to 2%, the size distribution is shifted to lower diameters.

here, then reducing the total solids content should produce smaller particles, as also observed in Figure 2c.

On dry storage (over P_2O_5) at room temperature, the residual moisture content of the spray-dried particles prepared at T_{inlet}/T_{outlet} = 150 °C/95 °C remained constant over at least 43 days (Table 2). Accordingly, T_g also remained unchanged. The powder remained fully amorphous (X-ray diffractogram not shown, but identical to Figure 2b), indicating that these spray-dried trehalose particles retain their glass properties on suitable dry storage. Uptake of moisture into spray-dried lactose particles[7] induced massive particle aggregation with subse-

Table 2—Properties of Spray-Dried Trehalose Powders on Dry Storage over P_2O_5[a]

storage time [days]	water content [% w/w]	T_g [°C]
0	2.6 ± 0.2	84
1	2.5 ± 0.1	83
8	2.5 ± 0.2	84
15	2.6 ± 0.1	84
43	2.4 ± 0.1	85

[a] Powder prepared at T_{inlet}/T_{outlet} = 150 °C/95 °C and as given in Table 1. n = 3.

quent major reduction in fine particle dose. When used as a protein carrier, it is vital, however, that adjuvents such as trehalose retain their amorphous glassy character on storage.

Spray-Drying of LDH in Trehalose—We distinguish between process stability and storage stability of the model protein LDH in the spray-dried trehalose. *Process stability* defines the extent of inactivation of LDH during spray-drying and can be quantified by measuring residual LDH activity in the powder immediately after spray-drying. Possible causes for protein unfolding and inactivation during spray-drying are shearing stress in the nozzle, thermal stress during droplet drying in the spray-drying tower, and adsorption at the greatly expanded liquid/air interface of the spray solution on atomization.[8] Recent work by Maa et al.[16] indicates that unfolding and aggregation of recombinant human growth hormone (rhGH) during spray-drying was induced primarily by adsorption at the liquid/air interface created during spraying; shearing and thermal stresses were considered to be of minor importance. Figure 3 shows the behavior of the spray-dried LDH/trehalose powders. A low dry-particle protein loading of 0.3% w/w LDH was purposefully chosen to maximize the possible stabilizing effects of the trehalose. Under the mild process conditions of T_{inlet}/T_{outlet} = 90 °C/60 °C (Figure 3a), a loss of approximately 11% LDH activity is caused by the spray-drying process. More vigorous process conditions increase this activity loss up to approximately 25% with T_{inlet}/T_{outlet} = 150 °C/95 °C (Figure 3b–d). It follows that thermal stress must play some part in LDH inactivation, since shearing stress and, presumably, liquid/air interfacial adsorption during the short time required for atomization will be independent of T_{inlet}/T_{outlet}. Only droplet drying time will decrease at higher T_{inlet}/T_{outlet}.[17] The spherical smooth particles of pure trehalose (cf. Figure 2a) are changed with the 0.3% dry-particle LDH loading to show a slightly dimpled appearance (Figure 4a). This is typical for the effects of a high molecular weight additive such as a polymer[18] or a protein.[6] Increasing the dry-particle loading to 5% LDH for T_{inlet}/T_{outlet} = 150 °C/95 °C reduces the percent inactivation of LDH during spray-drying from approximately 25% with 0.3% LDH to approximately 11% (Figure 5a). This represents, however, an increase in the absolute amounts of LDH inactivated from 0.075 mg LDH/mL of spray solution (with 0.3% LDH dry-particle loading) to 0.55 mg LDH/mL of spray solution (with 5% LDH dry-particle loading). Also, the SEM of 5% LDH dry-particle loading shows an extremely wrinkled appearance (Figure 4b). If the primary cause of this LDH inactivation during spray-drying is adsorption at the liquid/air interface of the nebulized spray solution, then the amount adsorbed evidently increases with greater LDH concentration in the spray solution, indicating a diffusion-controlled process.

Some light can be shed on the likelihood of adsorption-induced inactivation by comparing the rates of droplet formation, droplet drying, and LDH adsorption. As shown in the Appendix, the spray droplets formed under the conditions used in these experiments had an average diameter of 8.5 μm and an almost instantaneous formation time, t_f, at the tip of the pneumatic nozzle of 5×10^{-6} ms. The subsequent droplet drying process is slower and occurs in two periods:[19] a constant-rate period until solid phase

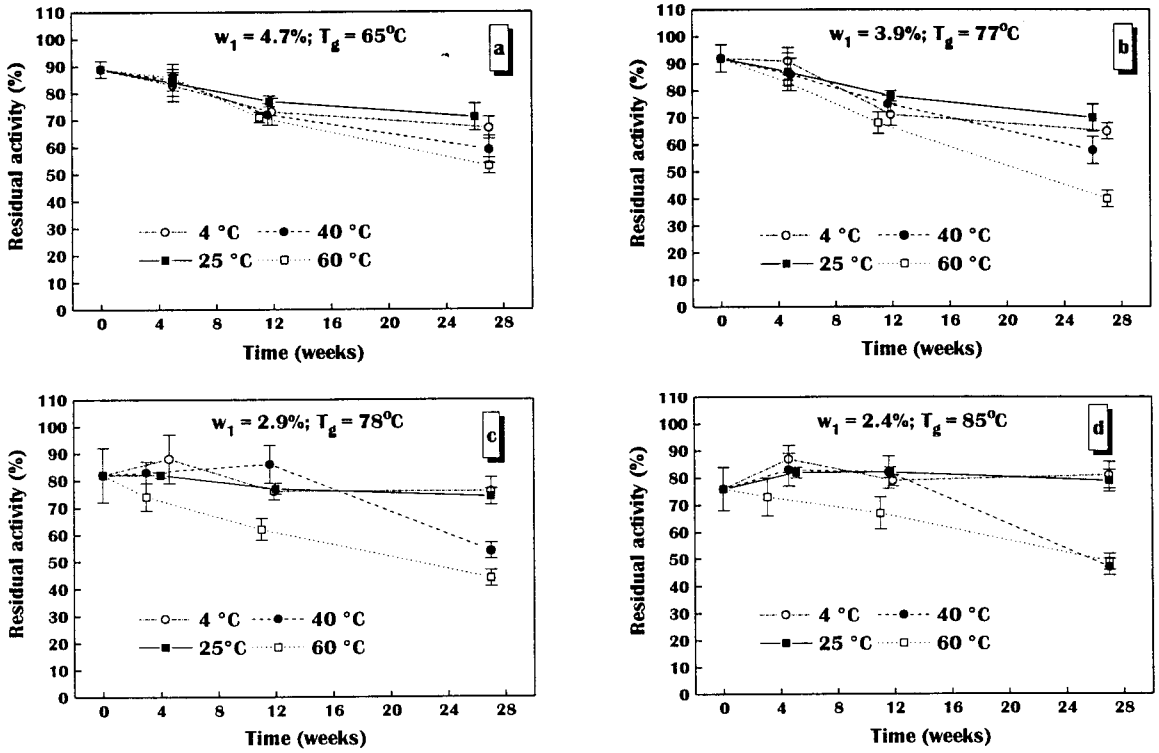

Figure 3—Effect of process temperatures (T_{inlet}/T_{outlet}) on process and storage stability of LDH in spray-dried trehalose powders. The trehalose was initially dry-particle loaded with 0.3% w/w LDH. The spray solution contained 10% total solids (trehalose dihydrate). Liquid feed rate was 4 mL/min, and the atomizing air flow rate was 0.7 m³/h. In each figure the corresponding values for residual water content (w_1) and glass transition temperature (T_g) are given. (A) T_{inlet}/T_{outlet} = 90 °C/60 °C; (B) T_{inlet}/T_{outlet} = 110 °C/70 °C; (C) T_{inlet}/T_{outlet} = 130 °C/80 °C; (D) T_{inlet}/T_{outlet} = 150 °C/95 °C.

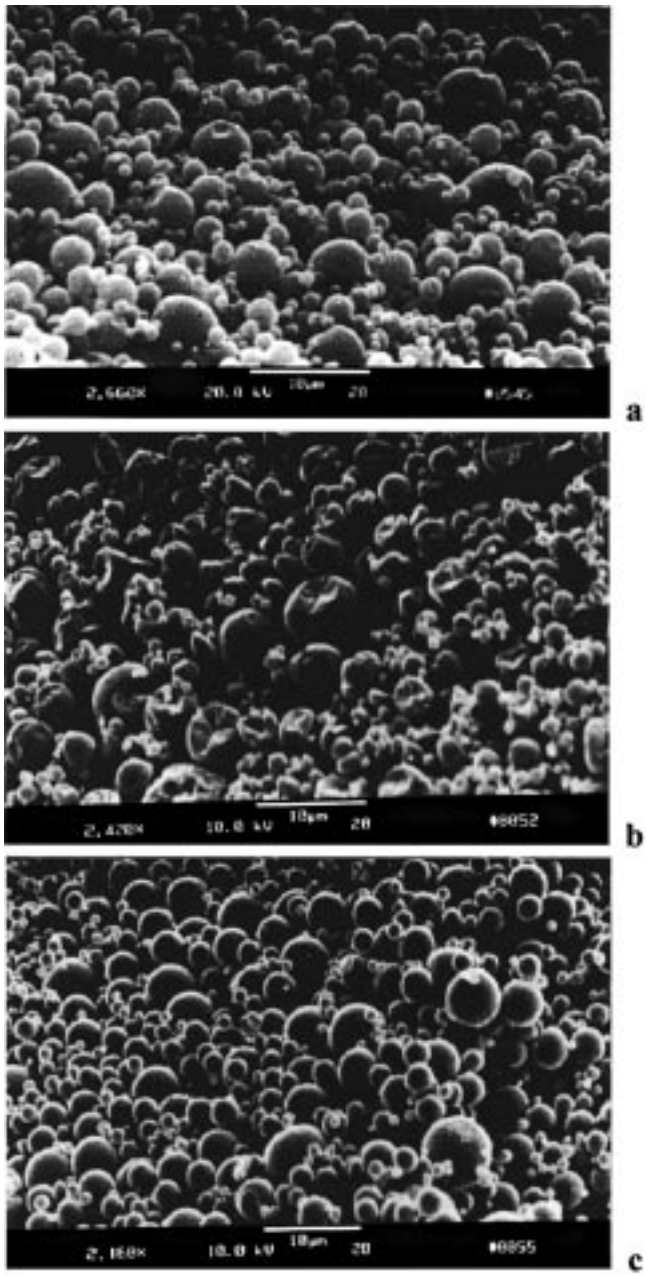

Figure 4—Scanning electron micrographs of trehalose powders spray-dried at T_{inlet}/T_{outlet} = 150 °C/95 °C. The spray solutions contained 10% w/w total solids. (A) Trehalose dry-loaded with 0.3% LDH. (B) Trehalose dry-loaded with 5% LDH. (C) Trehalose dry-loaded with 5% LDH; spray solution also contained 0.1% w/w polysorbate 80.

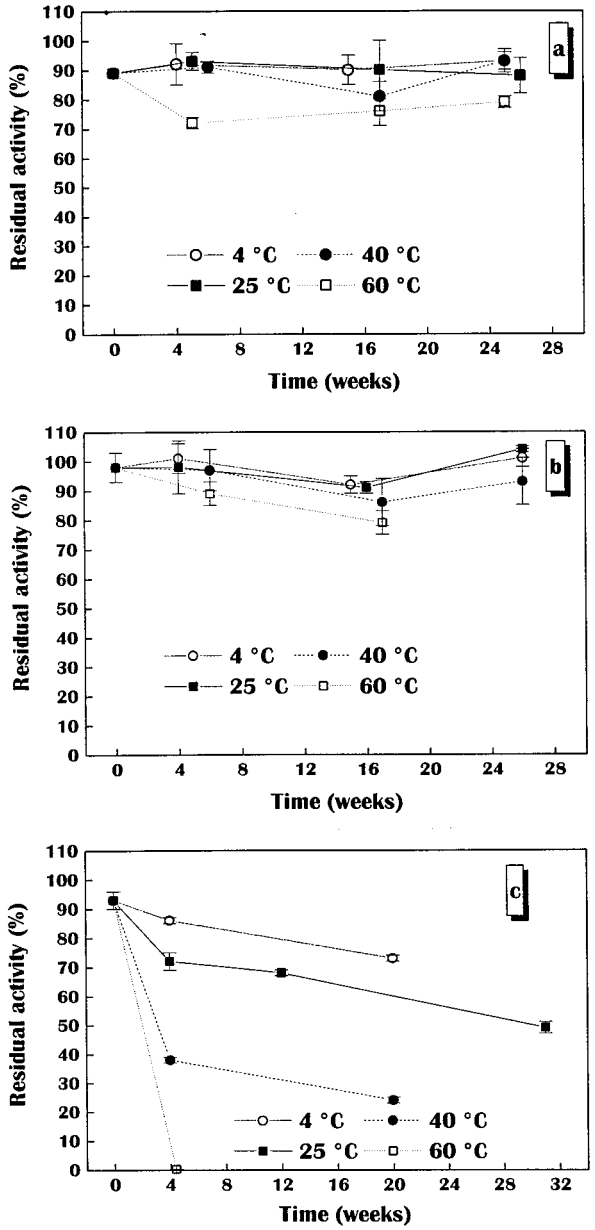

Figure 5—Process and storage stability of LDH in various spray-dried trehalose powders. The process temperatures were T_{inlet}/T_{outlet} = 150 °C/95 °C. The liquid feed rate was 4 mL/min, and the atomizing air flow rate was 0.7 m³/h. (A) 5% w/w dry-particle loading of LDH in trehalose, 10% total solids in spray solution, 0% polysorbate 80 (P 80); (B) 5% w/w dry-particle loading of LDH in trehalose, 10% total solids in spray solution, 0.1% w/w P 80 solution concentration = P 80/LDH molar ratio (27:1); (C) 0.3% w/w dry-particle loading of LDH in trehalose, 2% total solids in spray solution, 0.1% w/w P 80 solution concentration = molar ratio P 80/LDH (1890:1).

starts to form at the droplet surface, followed by a falling-rate period where particle diameter does not change further. As calculated in the Appendix, the droplet evaporation times for an 8.6 μm diameter water droplet containing 10% w/w dissolved solid in the constant-rate period, t_{cr}, and the falling-rate period, t_{fr}, are 0.4 and 1.1 ms, respectively (see Table 3). These process times can be used to calculate the amounts of LDH which could be adsorbed at the liquid/water interface [mg/m²] during droplet formation and drying. Figure 6a shows the air/water surface tension (γ) plot for LDH determined after 0.5 h and 1 h equilibration time. It is clear that this protein is surface active with a surface excess of Γ = 221 mg/m² calculated from the slope using the Gibbs equation. This value is 2 orders of magnitude larger than the saturated monolayer surface concentrations of β-casein (MW = 24000), lysozyme (MW = 14500), and bovine serum albumin (MW = 67000)

Table 3—Results of Calculated Times for Spray Droplet Formation, t_f, and Drying Times in Constant-Rate, t_{cr}, and Falling-Rate, t_{fr}, Periods (see Appendix for calculations)

time	calculated value, ms
t_f	5×10^{-6}
t_{cr}	0.41
t_{fr}	1.07

determined by a radio-tracer method.[20] Despite the higher molecular weight of LDH (144000 for the tetrameter), a Γ of 221 mg/m² is unreasonable. As previously found with human serum albumin, the Gibbs equation evidently cannot be applied to γ versus log C_B data for proteins in this concentration region.[21] It is more useful to examine

Table 4—Calculation of Diffusivity, D, and Surface Excess Concentration, Γ, for LDH in Water from Plot of Surface Pressure, $\Pi(t)$, versus $\sqrt{t}$ According to eq 1

LDH bulk concentration [mg/mL]	slope $d\Pi(t)/dt^{1/2}$ [N/m·s$^{1/2}$]	D [m^2/s]	Γ_f [mg/m^2]	Γ_{cr} [mg/m^2]	LDH adsorbed up to critical point [mg/mL solution]
0.43	1.2×10^{-4}	2.1×10^{-10}	5×10^{-4}	0.14	0.1

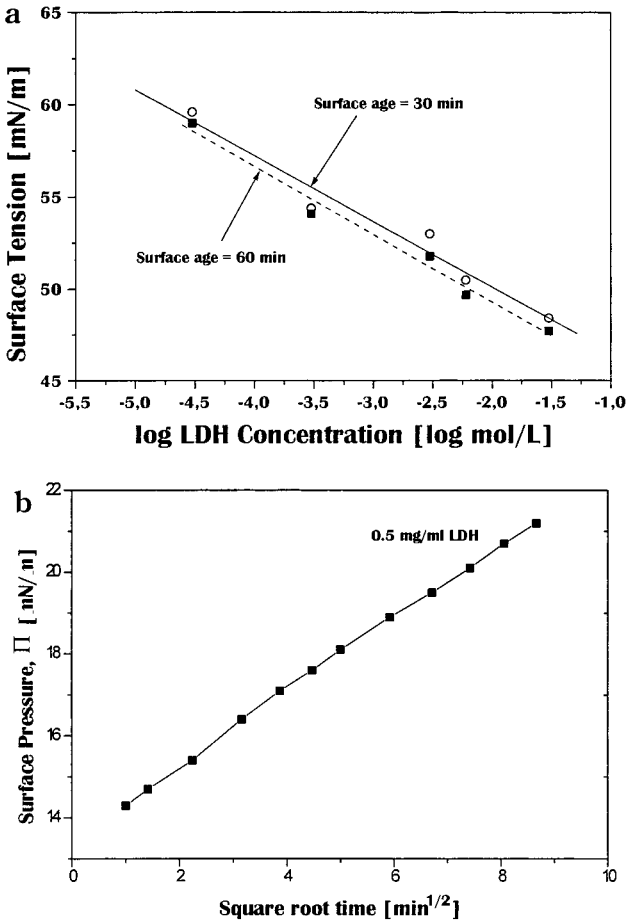

Figure 6—(A) Plot of surface tension versus log LDH concentration in water. From the Gibbs equation, $\Gamma = -[\, d\gamma/d \ln c] \times 1/RT$, the surface excess, Γ, is 221 mg/m^2. (B) Change in surface pressure (Π) with time for 0.43 mg/mL LDH (■) solution in water determined with Wilhelmy plate.

the time-dependence of γ. Adsorption of protein molecules at a liquid/air interface is diffusion-controlled up to approximately 10% surface saturation:[22]

$$\Pi(t) = \Gamma(t)RT = 2RTC_B\sqrt{\frac{Dt}{\pi}} \qquad \Gamma \le 0.1\Gamma_{sat} \quad (1)$$

where Π is the surface pressure ($= \gamma_{solvent} - \gamma_{solution}$), C_B is the protein's bulk concentration, and D is its diffusivity. Figure 6b shows a plot of Π versus $\sqrt{t}$ for an LDH solution in water of $C_B = 0.43$ mg/mL, this being approximately that LDH concentration in the spray solutions used to produce a dry-particle protein loading of 0.3%. The values for $\Pi(t)$ fit well to a straight line in accordance with eq 1 and yield calculated diffusivity of 2.7×10^{-10} m^2/s (see Table 4). This is in the same order of magnitude as found for β-casein and lysozyme.[22] If LDH can diffuse to the liquid/air interface only until the critical point is reached where solid forms at the droplet surface, the total time available for protein adsorption on spraying will be: $t_f + t_{cr}$ (see Table 3). The surface excess concentrations of LDH at the end of droplet formation, Γ_f, and at the critical point, Γ_{cr}, can now be calculated directly from eq 1 and are given in Table 4.

Table 5—Influence of T_g on % LDH-Inactivation Loss on Storage after 27 Weeks at 4 °C, 25 °C, 40 °C, and 60 °C[a]

storage temp [°C]	% LDH-inactivation loss at T_g [°C]: 65 °C	77 °C	78 °C	85 °C
4	25	29	7	0
25	20	24	10	0
40	37	37	34	38
60	40	57	46	36

[a] Values calculated from results in Figure 3.

The calculated total excess amount of LDH adsorbed at the liquid/air interface up to the critical point is clearly more than sufficient to account for the measured LDH-inactivation during spray-drying. With 0.3% LDH dry-particle loading, an LDH-inactivation of 0.075 mg LDH/mL spray solution was measured (Figure 3d), whereas 0.1 mg LDH/mL spray solution could be adsorbed at the spray droplet surface according to this calculation (Table 4). Thus approximately 75% of the theoretical amount of excess adsorbed LDH is therefore inactivated during spray-drying. The interfacial adsorption and inactivation of LDH during spray-drying thus appear feasible.

The *storage stability* of a protein in an amorphous solid will depend in a complex fashion on residual moisture content and T_g.[23] In an early study[3] it was found that those carriers which gave the best protein process stability also gave the best storage stability. The effect on T_{inlet}/T_{outlet} on the balance between process and storage stability has, however, not yet been clarified. Figure 3 shows that the influence of T_{inlet}/T_{outlet} on storage stability is the opposite of that seen with process stability. The high residual moisture content and low T_g of the dried product obtained with T_{inlet}/T_{outlet} = 90 °C/60 °C are associated with a continual decline in LDH activity at all four storage temperatures (Figure 3a). At 25 °C, for example, the LDH loses approximately 15% activity during 26 weeks of storage. Raising T_{inlet}/T_{outlet} reduces the residual moisture content, increases T_g, and improves the storage stability of the LDH, with no loss of LDH activity being seen after 26 weeks of storage at 25 °C for the product spray-dried at T_{inlet}/T_{outlet} = 150 °C/95 °C (Figure 3d). Degradation of proteins in amorphous solids is thought to follow fast kinetics (VTF or WLF) in the rubbery state and slow kinetics (Arrhenius) in the glassy state.[23] Only the samples stored at 4 °C and 25 °C show, however, a trend to less LDH-inactivation with increasing T_g of the carrier (Table 5). Those stored at 40 °C and 60 °C show no dependence of LDH-inactivation on the T_g. These inconsistencies underline the complexity of protein stability in a solid carrier. Protein degradation at storage temperatures below a formulation's T_g can, for example, depend on the presence of non-native protein structure in the dried state,[24] as has been demonstrated for freeze-dried LDH.[25] Also, the mechanism of protein degradation may be temperature dependent, making application of Arrhenius redundant. These aspects were not, however, considered further in this work.

Process and storage stability of LDH in the spray-dried powders are thus seen to be at odds. By decreasing T_{inlet}/T_{outlet} to improve the process stability of LDH, its storage stability (at least at 4 °C and 25 °C) is worsened. This is a result of either reduced T_g[23] or reduced degree of native

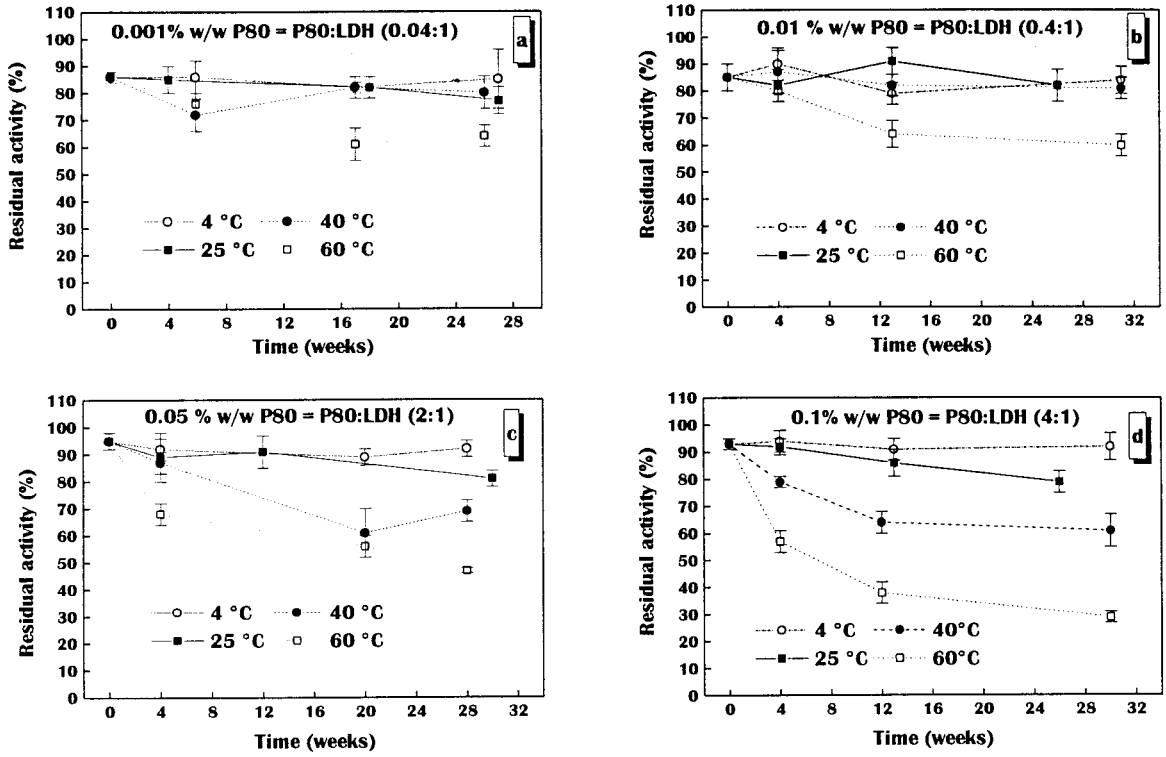

Figure 7—Influence of added Polysorbate 80 (P 80) concentration on process and storage stability of LDH in spray-dried trehalose powders. The trehalose was initially dry-particle loaded with 0.3% w/w LDH. The spray solution contained 10% total solids and was dried at T_{inlet}/T_{outlet} = 150 °C/95 °C. The liquid feed rate was 4 mL/min, and the atomizing air flow rate was 0.7 m³/h. (A) 0.001% w/w P 80 solution concentration = molar ratio P 80/LDH (4.4:1); (B) 0.01% w/w P 80 solution concentration = molar ratio P 80/LDH (44:1); (C) 0.05% w/w P 80 solution concentration = molar ratio P 80/LDH (222:1); (D) 0.1% w/w P 80 solution concentration = molar ratio P 80/LDH (444:1).

structure in the solid immediately after drying.[24] The physicochemical state of the spray-dried powders was stable at all four storage temperatures (over P_2O_5) examined here. There was no change in either residual moisture content (± 0.3% w/w), T_g (± 2 °C), or the X-ray diffractogram up to 27 weeks of storage (cf. Table 2). This was also the case for the powder whose T_g = 65 °C lies only marginally above the highest storage temperature of 60 °C. The incipient formation of a rubbery state without the additional uptake of moisture was evidently insufficient to promote crystallization of the trehalose after 27 weeks. Although not examined in this study, we expect storage under humid conditions to produce major changes in stability of both carrier[7] and protein.[26]

Influence of Polysorbate 80 on LDH Inactivation—It is known that nonionic surfactants can reduce aggregation of proteins during spray-drying at or above the critical micelle concentration of the surfactants in solution.[8,16] The addition of polysorbate 20 to spray solutions of rhGH reduced the total extent of rhGH aggregation during spray-drying at T_{inlet}/T_{outlet} = 90 °C/60 °C from approximately 45% to <18%.[8] Both of these values were reduced at higher protein concentrations in the spray solution. A similar effect is seen with polysorbate 80 on the process stability of LDH in the spray-dried trehalose powders (Figure 7). These results were all obtained for the powder spray-dried at T_{inlet}/T_{outlet} = 150 °C/95 °C. Recall that in the absence of polysorbate 80 some 25% loss in LDH activity occurred during spray-drying under these conditions (cf. Figure 3d). Again we must distinguish between *process stability* and *storage stability* of the LDH. Increasing polysorbate 80 solution-concentration in the spray solution progressively ameliorates the inactivation of LDH during the spray-drying process. At and above a polysorbate 80 solution-concentration of 0.05% w/w, the LDH inactivation has been reduced to approximately 5% during spray-drying (Figure 7c,d). The value of 0,05% w/w surfactant is the same critical surfactant concentration for protein stability found previously for polysorbate 20 and rhGH.[8] The current opinion is that the liquid–air interface of the spray-droplets is preferentially occupied by the surfactant rather than the protein,[8,16] reducing protein unfolding and aggregation during spray-drying. In accord with this idea, the addition of 0.1% polysorbate 80 to the spray solution (Figure 4c) changes the dimpled appearance of trehalose particles dry-loaded with 0.3% LDH (cf. Figure 4a) to the perfect sphericity and smoothness seen with pure trehalose (cf. Figure 2a). This can be explained by a reduction in surface tension of the spray droplets containing surfactant, which alters the balance of surface-to-viscous forces influencing droplet shape during drying.[18]

The effect of polysorbate 80 on the storage stability of LDH in the spray-dried trehalose is unexpected, although its presence in the concentrations examined here influenced neither residual moisture content nor T_g. Recall from Figure 3d that with a T_{inlet}/T_{outlet} = 150 °C/95 °C and a resulting T_g of 84 °C, LDH was storage stable at 4 °C and 25 °C up to 27 weeks. This behavior is retained with 0.001% polysorbate 80 in the spray solution (Figure 7a). Increasing polysorbate 80 solution concentration produces, however, a change in protein stability behavior. The good storage stability at 4 °C remains unaltered; at higher storage temperatures the presence of polysorbate 80 causes a reduction in stability. At polysorbate 80 solution concentrations ≥ 0.05%, we find a clear temperature-dependence of the LDH storage stability (Figure 7c,d). The higher concentrations of polysorbate 80 evidently promote inactivation of LDH within the trehalose glass on storage. The illuminating factor here is the molar ratio of polysorbate 80/LDH present in the dried particles. The low dry-particle LDH loading (0.3% w/w) of trehalose used for the data in Figure 4 makes this ratio large at the higher polysorbate

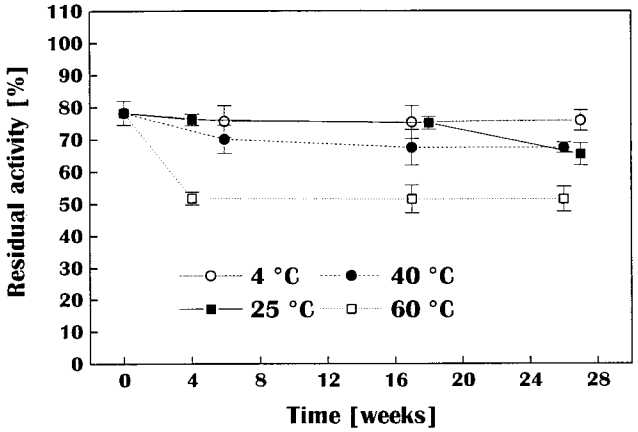

Figure 8—Influence of 0.01% w/w added Lipoid E 80 on process and storage stability of LDH in spray-dried trehalose powders. The trehalose was initially dry-loaded with 0.3% w/w LDH. The spray solution contained 10% total solids and was dried at T_{inlet}/T_{outlet} = 150 °C/95 °C.

80 concentrations. A high molar ratio of polysorbate 80/LDH of 444:1 exists, for example, in the dry product obtained with 0.1% polysorbate 80 in the spray solution, and LDH shows poor storage stability (Figure 7d). By increasing the dry-particle LDH loading to 5% (Figure 5b), 0.1% polysorbate 80 in the spray solution is now equivalent to a mole ratio of 27:1, and LDH is storage stable again. The opposite effect is achieved by reducing the total solids content of the spray solution to 2% with a dry-particle LDH loading of 0.3% and 0.1% polysorbate 80 in the spray solution. This yields the very high molar ratio of polysorbate 80/LDH of 1890:1 in the dry product, which causes extreme LDH instability on storage (Figure 5c). It is conceivable that this instability on storage is a result of peroxide contaminants known to be present in surfactants. These would be present in sufficient quantities to react with LDH in the solid trehalose particles. Care needs therefore to be exercised when adding surfactants to spray-drying solutions. The dependence on the molar ratio of surfactant/protein in the dried product means, however, that protein storage instability caused by the surfactant will not be noticeable with spray-dried pure proteins containing surfactant[8] where the surfactant/protein molar ratio will be smaller than here.

As a negative control we also examined the effect of egg lecithin added to the spray solution on LDH process and storage stability. Lipoid E 80 contains approximately 80% phosphatidylcholine and forms liposomes in water. We chose this material assuming that the single unilamellar vesicles formed would not be adsorbed at the liquid/air interface of the spray droplets and could not therefore stabilize LDH during spray-drying. Subsequent measurements showed, however, that Lipoid 80 reduced the γ of water to approximately 26 mN m^{-1} in the concentration range used in the spray solutions. We attribute this to interfacial adsorption of more water-soluble lyso-derivatives present within the Lipoid E 80. Figure 8 shows how the addition of ≥0.01% w/w solution concentration of Lipoid E 80 indeed fails to ameliorate the approximately 25% loss in LDH activity seen during spray-drying at T_{inlet}/T_{outlet} = 150 °C/95 °C (cf. Figure 3d without colloid). We conclude that the liposomes are not adsorbed at the liquid/air interface of the spray droplets sufficiently to prevent LDH being inactivated. The water-soluble lyso-derivatives evidently also do not stabilize LDH, although it is not clear why this is so. There is a reduction in storage stability of the dry product on addition of Lipoid E 80, but this negative effect (Figure 8) is less pronounced than with polysorbate 80 (cf. Figure 7b).

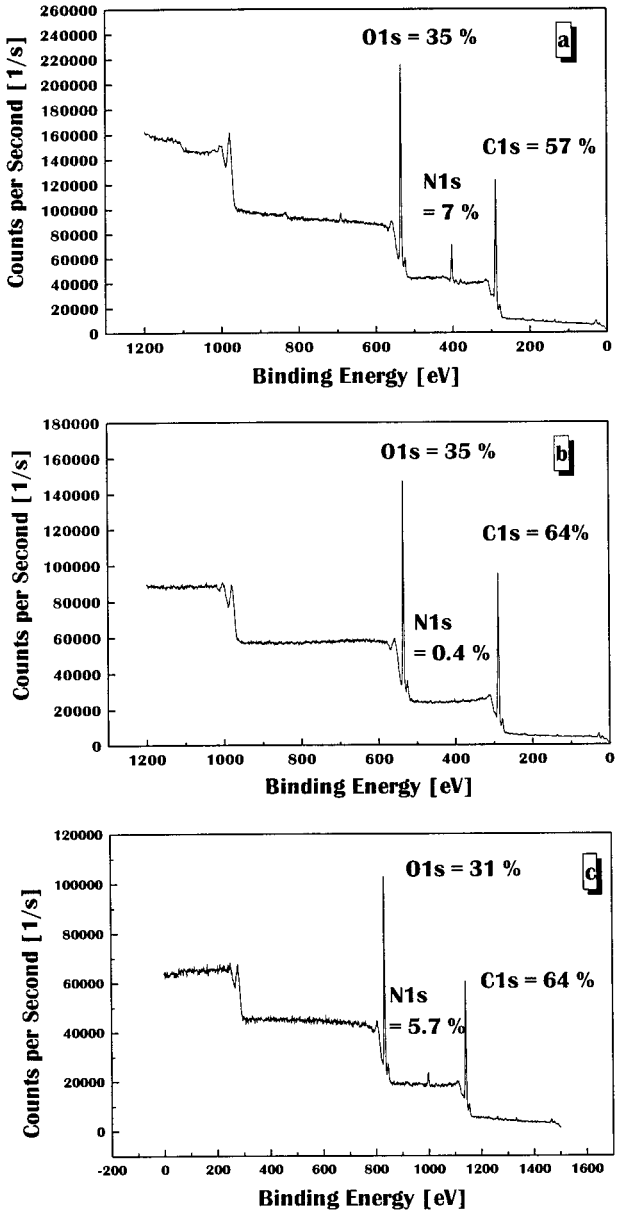

Figure 9—ESCA results for spray-dried trehalose powders dry-loaded with 5% w/w LDH. (A) 0% added polysorbate 80; (B) 0.1% added polysorbate 80 solution concentration; (C) 0.1% added Lipoid E 80 solution concentration.

ESCA Examination of LDH in Trehalose (5:95)—All ESCA measurements had to be carried out with 5% LDH dry-particle loading of the trehalose to ensure sufficient sensitivity to the elements being sought. Figure 9a shows the result for spray-dried LDH/trehalose (T_{inlet}/T_{outlet} = 150 °C/95 °C) in the absence of any added surfactant or colloid. The binding energy profile shows three elemental peaks that are of interest, viz. the 1 s electrons of O, N, and C. From the integrated peak heights the percentage surface-layer coverage of the dried product with each of these elements was calculated and is shown in the figure. The N peak is unequivocally indicative of the presence of LDH in the outer 10 nm of surface of the spray-dried particles. According to the ESCA result, 7 atomic weight % of this surface layer is composed of N (Figure 9a). LDH contains approximately 15 wt % N, although this could not be measured directly by ESCA, since pure solid LDH is not readily obtainable from the LDH-suspension used here. The spray-dried powder is loaded with 5 wt % LDH, so it follows that the surface-layer should contain approximately 0.75 wt % N, if the LDH were homogeneously distributed

throughout each uniformly solid particle. The result is, however, 10 times higher than this value and means that LDH is concentrated within the outer surface-layer of the spray-dried trehalose particles. This cannot be an artifact resulting from the formation of hollow particles, since this would not alter the concentration ratio of trehalose to LDH in the solid phase. The calculations presented above showed that there is sufficient time during droplet formation and drying to allow diffusion-mediated adsorption of LDH to the liquid/air interface. There seems no reason to believe that the rapidly *contracting* liquid/air interface during spray droplet drying up to the critical point would further alter the concentration of LDH at the resulting particle surface. As a result of this process we find the substantial inactivation of LDH during spray-drying seen in Figure 3.

The addition of 0.1% polysorbate 80 to the spray solution reduces the surface coverage with N to <0.4 atomic weight % (Figure 9b). The LDH present in the surface-layer of the spray-dried particles is thus greatly reduced in the presence of the surfactant. The N-coverage of 0.4% is indeed less than that value of 0.75% expected for a homogeneous distribution of LDH throughout a uniformly solid particle. It could also be a result of trace amounts of atmospheric N_2 adsorbed to the particle surface. The presence of surfactant at the liquid/air interface of the spray droplets thus hinders adsorption of LDH there. Owing to its much smaller molecular weight, the polysorbate 80 will diffuse faster to the liquid/air interface than does the LDH. Thus, in that range between 0% and 0.1% solution-concentration where polysorbate 80 progressively reduces LDH inactivation during spray-drying (cf. Figure 7), it also has to a great extent prevented the concentration of LDH in the surface-layer of the dried product. This result provides the first direct and quantitative evidence of the previously accepted stabilizing mechanism of the surfactant on proteins during spray-drying[8,16]

The ESCA result with Lipoid E 80 and LDH is also satisfactory. Recall that addition of Lipoid E 80 to the spray solution in the concentration ≥ 0.01% w/w did not influence inactivation of LDH during spray-drying (Figure 5b). The ESCA result in Figure 9c shows also no reduction in surface coverage of the spray-dried LDH/trehalose particles with N on the addition of 0.1% solution concentration of Lipoid E 80. Lipoid E 80 does not therefore prevent adsorption of LDH at the liquid/air interface of the spray solution and cannot therefore protect LDH against inactivation at T_{inlet}/T_{outlet} = 150 °C/95 °C. This is seen despite the aforementioned reduction in γ of the spray solution with Lipoid E 80. Neither liposomes nor surface-active impurities lead to LDH protection. Whatever the cause, the ESCA results for polysorbate 80 and Lipoid E 80 confirm that surfactants reduce the presence of proteins at the solid particle surface on spray-drying.

Conclusions

The main object of this work was to distinguish between process stability and storage stability of LDH in spray-dried trehalose. The influence of process conditions run contrary to one another: those process conditions that produce good process stability yield poor storage stability. The same behavior is found with addition of surfactant: this improves process stability but is deleterious to storage stability. A particular feature of this work was the use of ESCA to prove that polysorbate 80 prevents LDH appearing in the surface of the spray-dried particles. This could be correlated with a reduction in LDH inactivation during spray-drying. The negative result with Lipoid E 80 confirms this stabilizing mechanism. The relevant equations indicate that the concentrated presence of LDH in the surface of surfactant-free trehalose particles is a result of diffusion-driven adsorption of LDH at the liquid/air interface during spray droplet formation and drying.

Table 6—Comparison of Spraying Conditions and Resulting Spray Droplet Diameter

	from ref 6	in this work
liquid feed rate [m^3/h]	3×10^{-4}	2.4×10^{-4}
air flow rate [m^3/h]	0.9	0.7
air/liquid mass ratio[a]	3.61	3.35
spray droplet diameter [μm]	7.5 (measured)	8.6 (calcd)

[a] $= \dfrac{\text{air flow rate [m}^3\text{/h]} \times \text{air density (1.204)[kg/m}^3\text{]}}{\text{liquid feed rate [m}^3\text{/h]} \times \text{liquid density (1000 or 1407)[kg/m}^3\text{]}}$

Appendix

1. Calculation of Average Spray Droplet Volume—The relation between the diameter of a spray droplet, D_w, and the diameter of the resulting solid particle after drying, D_d, is given by:[27]

$$D_w = 2\left(\frac{\left(\frac{D_d}{2}\right)^3 \rho_2}{W_2}\right)^{1/3} \quad \text{(A1)}$$

where ρ_2 is the density of the solid and W_2 is the total solids' content of the spray solution. For the 10% w/w trehalose solution spray-dried at T_{inlet}/T_{outlet} = 150 °C/95 °C, D_d = 3.5 μm (from Figure 2c), and ρ_2 = 1470 kg/m^3 and W_2 = 100 kg/m^3. Equation A1 predicts a value of 8.6 μm for D_w, which agrees closely with measured values of droplet size at the same air/liquid mass ratio using laser diffraction (see Table 6).[6]

2. Calculation of Spray Droplet Formation Time—The formation time of a single spray droplet, t_f, at the tip of a pneumatic nozzle is given by:

$$t_f = \frac{\text{droplet volume [m}^3\text{]}}{\text{feed rate [m}^3\text{/h]}} \quad \text{(A2)}$$

For a droplet volume of $^4/_3\pi(4.3 \times 10^{-6})^3 = 3.33 \times 10^{-16}$ m^3 and a feed rate of 0.24×10^{-3} m^3/h, eq A2 gives a value for t_f of 5×10^{-6} ms, illustrating the almost instantaneous nature of droplet formation.

3. Calculation of Spray Droplet Drying Time—The drying of spray droplet containing dissolved trehalose in water can be divided into two phases. In the initial constant-rate period, the water concentration at the droplet surface and hence the rate of evaporation, dW/dt, are constant:[19]

$$\frac{dW}{dt}\Big|_{cr} = \frac{2\pi k_d D_{av} \Delta T}{\lambda} \quad \text{(A3)}$$

where ΔT is the log mean temperature difference:

$$\Delta T = \frac{(T_{inlet} - T_{wb}^{inlet})(T_{outlet} - T_{wb}^{outlet})}{\ln(T_{inlet} - T_{wb}^{inlet})/(T_{outlet} - T_{wb}^{outlet})} \quad \text{(A4)}$$

with T_{wb}^{inlet} being the wet-bulb temperature of the spray droplet surface and T_{wb}^{outlet} is the wet-bulb temperature of the dried particle surface. For the spray-dried trehalose, T_{inlet} = 150 °C, T_{wb}^{inlet} = 55 °C (from enthalpy/humidity chart), T_{outlet} = 95 °C, and T_{wb}^{outlet} = 55 °C, giving a value for ΔT of 64 °C. k_d is the thermal conductivity of the water vapor in the stagnant layer around the droplet = 0.567 kcal/m h °C at 64 °C. D_{av} is the average droplet/particle

diameter = 6.05 μm, and λ is the latent heat of vaporization of water = 540 kcal/kg. For these values, $dW/dt = 2.56 \times 10^{-6}$ kg/h according to eq A3. The total mass of water removed in the constant-rate period, ΔW_{cr}, is given by:

$$\Delta W_{cr} = \frac{4}{3}\pi(r_w^3 - r_d^3)\rho W_1 \quad \text{(A5)}$$

where r is droplet/particle radius, ρ is the density of the trehalose/water solution (1047 kg/m^3), and W_1 is the water content of the spray solution (0.9 kg/kg). Equation A5 gives for ΔW_{cr} a value of 2.93×10^{-13} kg. The drying time of the droplet in the constant-rate period, t_{cr}, is then given by:[19]

$$t_{cr} = \frac{\Delta W_{cr}}{dW/dt|_{cr}} = 0.41 \text{ ms} \quad \text{(A6)}$$

In the following falling-rate period, solid is present in the surface and the particle size is assumed not to change further. The rate of evaporation, $dW/dt|_{fr}$, decreases and is given by

$$\frac{\Delta W}{dt}|_{fr} = \frac{dW'}{dt} \times \text{wt of dry particle} \quad \text{(A7)}$$

where:

$$\frac{dW'}{dt} = \frac{12 k_d \Delta T}{\lambda D_c^2 \bar{\rho}_s} \quad \text{(A8)}$$

k_d is the thermal conductivity of the drying air around the particle = 0.0238 kcal/h m °C at approximately 64 °C. D_c is the critical particle diameter = D_d. $\bar{\rho}_s$ is the average particle density during the falling-rate period = 1374 kg/m^3. For these values eqs A7 and A8 give $dW/dt|_{fr} = 6.48 \times 10^{-8}$ kg/h. The mass of moisture removed in the falling-rate period, ΔW_{fr}, is given by the difference between moisture content at the critical point and the end moisture content:

$$\Delta W_{fr} = (2.00 \times 10^{14}) - (8.25 \times 10^{-16}) = 1.92 \times 10^{-14} \text{ kg} \quad \text{(A9)}$$

The drying time of the particle in the falling-rate period, t_{fr}, is then given by:

$$t_{fr} = \frac{\Delta W_{fr}}{dW/dt|_{fr}} = 1.07 \text{ ms} \quad \text{(A10)}$$

The results are summarized in Table 3. The extremely short drying times are a consequence of the small droplet size and high T_{inlet}. As a comparison, the drying time of a pure water droplet of the same diameter[17] yields:

$$t = \frac{\lambda \rho_1}{r k_d \Delta T} \int_0^{D_w} D\,dD = 0.5 \text{ ms} \quad \text{(A11)}$$

References and Notes

1. Broadhead, J.; Rouan, S.; Rhodes, C. The spray drying of pharmaceuticals. *Drug Devel. Ind. Pharm.* **1992**, *18*, 1169−1206.
2. Mumenthaler, M.; Hsu, C.; Pearlman, R. Feasibility study on spray-drying protein pharmaceuticals: recombinant human growth hormone and tissue-type plasminogen activator. *Pharm. Res.* **1994**, *11*, 12−20.
3. Labrude, P.; Rasolomanana, M.; Vigneron, C.; Thirion, C.; Chaillot, B. Protective effect of sucrose on spray drying of oxyhemoglobin. *J. Pharm. Sci.* **1989**, *78*, 223−229.
4. Broadhead, J.; Rouan, S.; Hau, I.; Rhodes, C. The effect of process and formulation variables on the properties of spray-dried β-galactosidase. *J. Pharm. Pharmacol.* **1994**, *46*, 458−467.
5. Woodruff, E.; Andersen, V. US Patent 3704169, 1972.
6. Maa, Y.; Costantino, H.; Nguyen, P.; Hsu, C. The effect of operating and formulation variables on the morphology of spray-dried protein particles. *Pharm. Devel. Technol.* **1997**, *2*, 213−223.
7. Broadhead, J.; Rouan, S.; Rhodes, C. The deposition of spray-dried β-galactosidase from dry powder inhaler devices. *Drug Devel. Ind. Pharm.* **1996**, *22*, 813−822.
8. Maa, Y.; Nguyen, P.; Hsu, S. Spray-drying of air−liquid interface sensitive recombinant human growth hormone. *J. Pharm. Sci.* **1998**, *87*, 152−159.
9. Franks, F.; Hatley, S. Material science and the production of shelf stable biologicals. *Biopharm.* **1994**, *4*, 38−55.
10. Schuhmann, R.; Müller R. Size analysis using diffraction with PIDS technique. *Pharm. Ind.* 1996
11. Fäldt, P.; Bergenstähl, B. The surface composition of spray-dried protein-lactose powders. *Colloids Surf.* **1994**, *90*, 183−190.
12. Fäldt, P.; Bergenstähl, B.; Carlsson, G. The surface coverage of fat on food powders analyzed by ESCA. *Food Structure* **1993**, *12*, 225−234.
13. Girg, R.; Rudolph, R.; Jaenicke, R. Analysis of lactate dehydrogenase. *FEBS Lett.* **1983**, *163*, 132−135.
14. Miller, D.; de Pablo, J.; Corti, H. Thermophysical properties of trehalose and its concentrated aqueous solutions. *Pharm. Res.* **1997**, *14*, 578−590.
15. Hancock B.; Zografi, G. The relationship between the glass transition temperature and the water content of amorphous pharmaceutical solids. *J. Pharm. Sci.* **1994**, *11*, 471−477.
16. Maa, Y.; Hsu, C., Protein denaturation by combined effect of shear and air−liquid interface. *Biotechnol. Bioeng.* **1997**, *54*, 503−512.
17. Masters, K. *Spray Drying Handbook*, 5th ed.; Langman Scientific & Technical: Harlow, UK, 1991; p 314, eq 8.8.
18. Alexander, K. Factors governing surface morphology in the spray-drying of foods. Unversity of California, Berkely, Ph.D. thesis, 1978.
19. Masters, K. *Spray Drying Handbook*, 5th ed.; Langman Scientific & Technical: Harlow, UK, 1991; pp 330−338, eq 8.44.
20. Graham, D., Pillips, M. Proteins at liquid interfaces. I: Kinetics of adsorption and surface denaturation. *J. Colloid Interface Sci.* **1979**, *70*, 403−414.
21. Chen, P.; Prokop, R.; Susnar, S.; Neumann, A. Interfacial tensions of protein solutions using axisymmetric drop shape analysis. In *Proteins at Liquid Interfaces*; Möbius, D., Miller, R., Eds.; Elsevier: New York, 1998; pp 303−340.
22. Magdassi, S.; Kamyshny, A. Surface Activity of Proteins. In *Surface activity and functional properties of proteins*; Magdassi, S., Ed.; Marcel Dekker: New York, 1995; pp 1−38.
23. Hancock, G.; Zografi, G. Characteristics and Significance of the amorphous state in pharmaceutical systems. *J. Pharm. Sci.* **1997**, *86*, 1−12.
24. Chang, B.; Beauvais, R.; Dong, A.; Carpenter, J. Physical factors affecting the storage stability of freeze-dried Interleukin-I Receptor Antagonist: Glass transition and protein conformation. *Arch. Biochem. Biophys.* **1996**, *331*, 249−258.
25. Carpenter, J.; Prestrelski, S.; Arakawa, T. Separation of freezing and drying induced denaturation of lyophilised proteins using stress-specific stabilization. *Arch. Biochem. Biophys.* **1993**, *303*, 456−464.
26. Maa, Y.; Nguyen, P.; Andya, J.; Dasovich, N.; Sweeney, T.; Shire, S.; Hsu, C. Effect of spray-drying and subsequent processing conditions on residual moisture content and physical/biochemical stability of protein inhalation powders. *Pharm. Res.* **1998**, *15*, 768−775.
27. Hickey, A.; Concessio, N.; Oort, M.; Platz, R.. Factors influencing the dispersion of dry powders as aerosols. *Pharm. Technol.* **1994**, August, 58−64.

Acknowledgments

We thank Michael Unger and Christian Bram from the Department of Materials Science for assistance with the ESCA measurements. Parts of this work were presented by M.A. at the Annual Meeting of the AAPS in Boston (1997) and the 2nd World Meeting on Pharmaceutics, Biopharmaceutics and Pharmaceutical Technology in Paris (1998). We thank one of the anonymous reviewers for some very helpful comments regarding protein adsorption kinetics (eq 1).

JS980321X

Inulin Hydrogels as Carriers for Colonic Drug Targeting. Rheological Characterization of the Hydrogel Formation and the Hydrogel Network

L. VERVOORT,[†] I. VINCKIER,[‡] P. MOLDENAERS,[‡] G. VAN DEN MOOTER,*[,†] P. AUGUSTIJNS,[†] AND R. KINGET[†]

Contribution from *Laboratorium voor Farmacotechnologie en Biofarmacie, K.U. Leuven, 3000 Leuven, Belgium, and Departement Chemische Ingenieurstechnieken, K.U. Leuven, 3001 Leuven, Belgium.*

Received July 10, 1998. Final revised manuscript received October 20, 1998.
Accepted for publication November 25, 1998.

Abstract □ Free radical polymerization converts aqueous solutions of methacrylated inulin into cross-linked hydrogels. The purpose of this work was to study the hydrogel formation and to characterize the fully cured hydrogels. The gelation process of aqueous solutions of methacrylated inulin was monitored as a function of time by means of linear oscillatory shear measurements, at a fixed frequency and amplitude. The fully cured inulin hydrogels were characterized by measurement of the frequency-dependency of the linear elastic modulus *G′*. The effects of the degree of substitution and feed concentration of methacrylated inulin on both the gelation kinetics and the rigidity of the obtained hydrogels were determined. The effect of the concentration of the initiators of the radical polymerization reaction has been studied as well. The weight fraction of polymer which was not incorporated in the hydrogel networks was determined using the anthrone reaction, and physical chain entanglements were determined by solution viscosity measurements. The gelation kinetics and the elastic modulus were proportional to the degree of substitution and feed concentration of methacrylated inulin. Increasing concentrations of radical-forming compounds also accelerated the hydrogel formation, but lowered the elastic modulus of the obtained hydrogels. The amount of polymer chains incorporated in the hydrogel network seemed to be especially influenced by the degree of substitution of the derivatized inulin, and for a feed concentration of 27% w/w of methacrylated inulin, entanglements have to be accounted for. The gelation kinetics and the elastic modulus of inulin hydrogels are not only affected by the degree of substitution and the feed concentration of methacrylated inulin, but also by the concentration of the initiators of the free radical polymerization reaction.

Introduction

Inulin hydrogels were developed as carriers for colonic drug targeting. Inulin is a storage polysaccharide found in many plants such as garlic, onion, artichoke, and chicory.[1] It consists of β 2−1 linked D-fructose molecules, and the majority of the fructose chains have a glucose unit at the reducing end. The β 2−1 glycosidic bond is not significantly hydrolyzed by the endogenous secretions of the human digestive tract,[2] but bacteria residing in the colon, and more specifically *Bifidobacteria*, are able to ferment inulin.[3−5] *Bifidobacteria* constitute up to 25% of the normal gut flora of man and animals.[6] Hence, inulin was selected as candidate polymer for the development of a colon-specific drug delivery systems.

* Author to whom correspondence should be addressed. Laboratorium voor Farmacotechnologie en Biofarmacie, Campus Gasthuisberg, O+N, Herestraat 49, B-3000 Leuven, Belgium. Tel.: 32-(0)16-34.58.30. Fax.: 32-(0)16-34.59.96. E-mail: guy.vandenmooter@med.kuleuven.ac.be.
[†] Laboratorium voor Farmacotechnologie en Biofarmacie.
[‡] Department Chemische Ingenieurstechnieken.

Inulin hydrogel formation has been previously described by Vervoort et al.[7] Vinyl groups were incorporated in the fructose chains by reaction of inulin with glycidyl methacrylate at room temperature using 4-(dimethylamino)-pyridine as catalyst. Transesterification occurred during the reaction of inulin with glycidyl methacrylate, since the obtained reaction product was characterized as methacrylated inulin (MA-IN) instead of glyceryl methacrylated inulin. This confirmed the findings which have been published previously by van Dijk-Wolthuis et al.[8] for the derivatization of dextran with glycidyl methacrylate. By varying the molar ratio of glycidyl methacrylate to inulin, the degree of substitution (DS), i.e., the amount of methacryloyl groups per 100 fructose units, of MA-IN could be tuned. Aqueous solutions of MA-IN were subsequently converted into cross-linked three-dimensional networks by free radical polymerization using ammonium persulfate (APS) and *N,N,N′,N′*-tetramethylethylenediamine (TMEDA) as radical generating compounds. Figure 1 gives a schematic representation of the derivatization reaction of inulin with glycidyl methacrylate and MA-IN hydrogel formation.

This work describes the rheological characterization of the synthesized inulin hydrogels as well as the hydrogel formation process. The influence of the degree of substitution and feed concentration of MA-IN, and the concentration of radical-generating compounds, were studied. The rheological data are correlated with previously obtained results with respect to the equilibrium-swelling degree of the inulin hydrogels and the in vitro enzymatic degradation of the devices.

Experimental Section

Materials—Chicory inulin (Raftiline HP; average degree of polymerization between 22 and 25) was kindly provided by Orafti (Tienen, Belgium), and was used for the synthesis of methacrylated inulin. APS was supplied by UCB (Leuven, Belgium) and TMEDA by Sigma (St. Louis, MO). Anthrone was obtained from ICN Biomedicals (Ohio) and D(−)-fructose from Merck (Darmstadt, Germany). For details about the materials used for the synthesis of MA-IN, reference is made to Vervoort et al.[7] For the rheological experiments, MA-IN solutions with feed concentration of 16%, 22%, and 27% w/w were prepared in 0.5 M phosphate buffer pH 6.5. MA-IN with three different degrees of substitution was used: DS = 4.4, 12.1, and 22.3.

Rheological Experiments—Dynamic oscillatory measurements were performed on a strain-controlled rheometer (Rheometrics Mechanical Spectrometer RMS705), equipped with a parallel plate geometry (diameter 25 mm). To avoid slippage of the sample, the plates were covered with sand-paper. The temperature was kept constant at 20 °C by a fluids bath. MA-IN solutions were prepared and immediately after adding the radical-generating compounds, the solutions were poured onto the lower plate (cup) of the rheometer, after which the upper plate was positioned at a gap of 1 mm. The free surface of the sample was

10.1021/js9802796 CCC: $18.00
Published on Web 01/13/1999

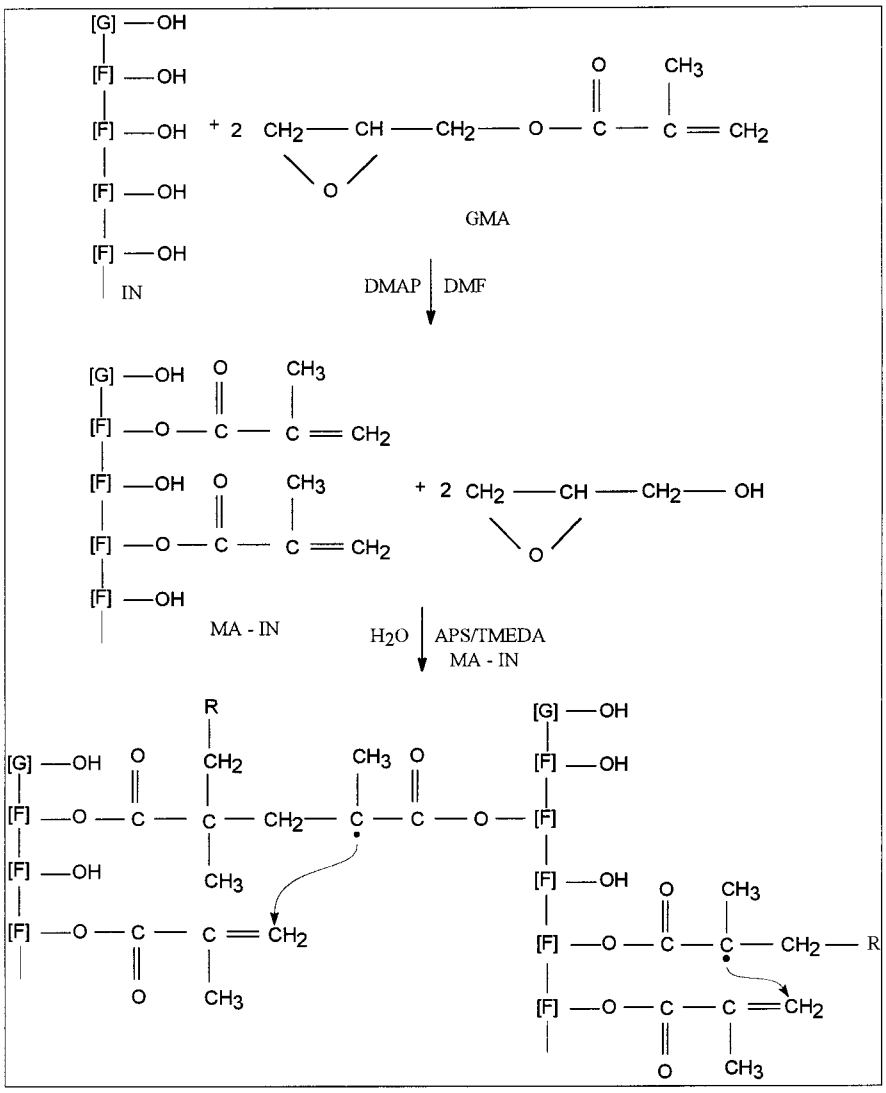

Figure 1—Schematic representation of the synthesis of MA-IN and the formation of inulin hydrogels. ([F]-OH = fructosyl unit; [G]-OH = glucosyl unit; IN = inulin; GMA = glycidyl methacrylate; DMAP = 4-(dimethylamino)pyridine; DMF = *N,N*-dimethylformamide; MA-IN = methacrylated inulin; APS = ammonium persulfate; TMEDA = *N,N,N′,N′*-tetramethylethylenediamine; R = initiator.)

covered with a mineral oil of low viscosity to prevent evaporation of the solvent during the experiment. The loading procedure took 160 s, after which the dynamic measurements started.

Small strain oscillations at a fixed frequency (4 rad/s) were applied to the samples to monitor the hydrogel formation. The strain was kept low enough to avoid interference with the formation of the MA-IN networks. After completion of the gelation process, a frequency sweep experiment was performed to characterize the fully cured MA-IN hydrogels. Before the latter experiment, the excess of gel at the rim of the geometry was removed to minimize errors due to edge effects. The dynamic behavior could be recorded over a frequency range from 0.01 to 10 rad/s. A linearity check was performed on every hydrogel to ensure that all measurements were probing the linear behavior of the hydrogels (results not shown).

Determination of Weight Fraction of Soluble Material (sol fraction)—The weight fraction of soluble material of a hydrogel (sol fraction) is defined as the amount of polymer chains, which are not incorporated in the hydrogel network and which can consequently be extracted and separated from the hydrogel.[9] To determine this sol fraction, MA-IN hydrogels of known dry weight were prepared and washed in demineralized water to extract the polymer chains, which are not attached to the hydrogel network. The sol fraction was calculated as the weight ratio of extracted material to initial material. The amount of extracted sugars was determined by means of the anthrone method,[10,11] and for the calculations, the degree of substitution of MA-IN used to prepare the respective hydrogels was taken into account.

The anthrone reagent was prepared by dissolving 50 mg of anthrone in a mixture of 28 mL of water and 72 mL of concentrated sulfuric acid. This freshly prepared reagent (2.5 mL) was mixed with 0.3 mL of collected samples of the hydrogel washing water containing the polymer chains, which were not incorporated in the hydrogel network. The samples were incubated for 10 min at 100 °C followed by cooling to room temperature. Finally, the absorbance of the samples was read spectrophotometrically with a HP 8452A spectrophotometer (Hewlett-Packard, Santa Clara, CA) at 625 nm. Since the same absorption is given by a sugar compound as if it was first hydrolyzed and then determined,[12] fructose solutions with concentrations ranging from 0.08 to 0.2 mg fructose/mL were used to construct a calibration line. Beside fructose, inulin also contains glucose units, but this does not compromise the anthrone method for sol fraction determination since equal amounts of glucose and fructose give identical absorption values.[12]

Determination of the Intrinsic Viscosity—To investigate whether chain entanglements, which can act as additional intermolecular cross-links, occur in the MA-IN solutions of different feed concentration, the intrinsic viscosity of MA-IN DS 12.1 was determined by solution viscosity measurements using an Ubbelohde suspended-level capillary viscometer (Schott Geräte, Hofheim, Germany). Efflux times of MA-IN solutions in 0.5 M phosphate buffer pH 6.5 were determined at 20 °C, and the respective reduced viscosities were calculated. The intrinsic viscosity was obtained by extrapolating the plot of the obtained values of reduced viscosity against the MA-IN concentration to infinite

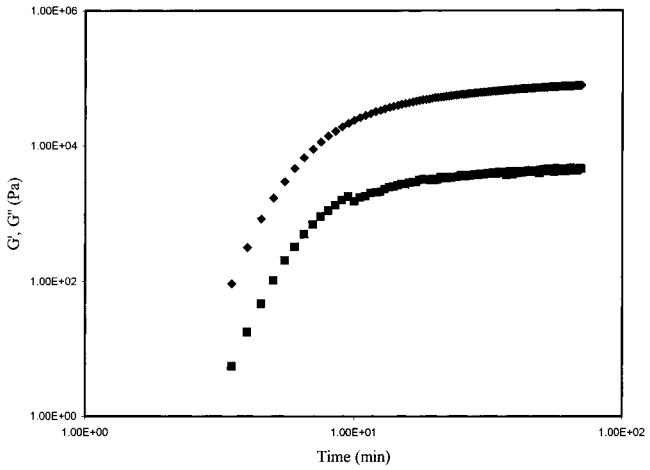

Figure 2—G' (◆) and G'' (■) as a function of polymerization time for hydrogel formation of a 27% w/w MA-IN DS 12.1 solution. (Concentration of APS = 17.5 μmol/mL buffer and TMEDA = 39.4 μmol/mL buffer.)

dilution according to the Huggins equation:

$$\eta_{red} = [\eta] + k[\eta]^2 c \quad (1)$$

with η_{red} the reduced viscosity, $[\eta]$ the intrinsic viscosity expressed in dL/g, k the Huggins constant, and c the concentration of the MA-IN solutions expressed in g/dL.

Results and Discussion

The addition of the radical-generating compounds APS and TMEDA to aqueous MA-IN solutions results in free radical polymerization. Dynamic rheological measurements at a fixed frequency and amplitude were performed during this process in order to follow the gradual formation of a three-dimensional network. The formation of intermolecular cross-links should show up in an increase of the elastic modulus G' as a function of time. G' is a measure of the energy stored and recovered per cycle of oscillatory deformation and represents the elastic behavior of the material.[13] Beside intermolecular cross-links, the radical polymerization reaction probably also introduces loops or intramolecular cross-links, loose ends or chains incorporated in the network by a single bond, unattached material or sol fraction, and physical chain entanglements in the network. These structures hardly contribute to an increase in G'.[14–16] The viscous modulus G'', on the other hand, is a measure of energy dissipation per cycle of sinusoidal deformation[13] and represents the viscous behavior of the system under investigation. The viscosity is known to be sensitive to the molecular weight of polymer chains. Figure 2 shows a plot of G' and G'' versus time, representing the gelation process of a 27% w/w MA-IN DS 12.1 solution. From the point on where the moduli have increased sufficiently to be measurable, G'' is an order of magnitude smaller than G'. This was the case for all hydrogel formulations tested. Since the fully cured hydrogels exhibited no or only a limited frequency dependence of G' (Figure 3), it can be assumed that a network has indeed been formed by the radical reaction. The profile of G' versus time (Figure 2) can thus be interpreted as the gradual formation of a hydrogel network from a MA-IN solution. The three stages commonly encountered in hydrogel formation can be distinguished from the evolution of G' in time: a pregelation period, in which no measurable increase in G' is seen, a gelation period showing a rapid increase in G', and a postgelation period in which G' hardly changes anymore and reaches a constant value. During the pregelation period free radicals are formed and reaction within and between chains starts. The incorporation of the MA-IN polymers in a three-dimensional network takes place during the gelation period while gelation is ending during the post-gelation period.

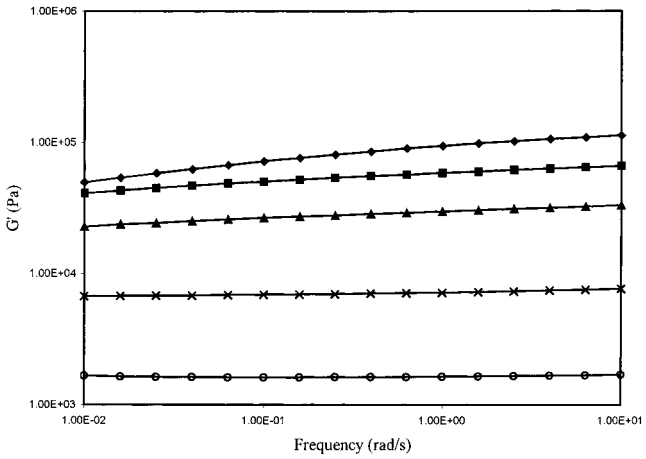

Figure 3—G' as a function of frequency for fully cured MA-IN hydrogels with different degree of substitution and feed concentration (○ = DS 4.4; 27%, × = DS 12.1; 16%, ▲ = DS 12.1; 22%, ■ = DS 12.1; 27%, ◆ = DS 22.3; 27%). (Concentration of APS = 17.5 μmol/mL buffer and TMEDA = 39.4 μmol/mL buffer.)

Table 1—Time (min, loading procedure included) To Reach 50% of G' end for Hydrogels of Different Composition ([APS] = 17.5 μmol/mL buffer, [TMEDA] = 39.4 μmol/mL buffer)

hydrogel composition		
DS	feed concn (% w/w)	time (min)
4.4	27	60.5
12.1	16	21.3
12.1	22	18.8
12.1	27	16.8
22.3	27	15.8

Table 2—Time (min, loading procedure included) To Reach 50% of G' end for Hydrogels Prepared from 16% w/w Solutions of MA-IN DS 12.1 as a Function of the Concentrations of APS and TMEDA (μmol/mL buffer)

[APS]	[TMEDA]	time (min)
17.5	39.4	21.3
17.5	78.7	13.1
17.5	157.4	4.6
70.1	39.4	3.8

To quantify a characteristic time for network formation, the time needed to reach 50% of the final value of G' (G' end) has been determined. Table 1 lists the results as a function of the degree of substitution and the feed concentration of MA-IN. It can be concluded that increasing the degree of substitution or the feed concentration accelerates the gelation process, implying that the radical cross-linking reaction is promoted by increasing concentrations of reactive vinyl groups. The characteristic time for network formation is also influenced by the concentration of the initiators of the polymerization reaction as is shown in Table 2. TMEDA is believed to exert a promoting effect on the vinyl polymerization initiated by persulfate attributed to an acceleration of the homolytic scission of the latter compound.[17,18] Increasing the concentration of the radical-generating compound APS, and thus introducing more free radicals in the reaction solution, also decreases the gelation time. To verify whether the accelerating effect of the

Table 3—Pregelation Period (min, loading procedure included) and Slope (Pa/min) of the Curves of G' versus Time ($0.1 < G'/G'$ end < 0.6), Indicative for the Gelation Period, for Hydrogels Prepared from 16% w/w Solutions of MA-IN DS 12.1 as a Function of Varying Concentrations of APS and TMEDA (μmol/mL buffer)

[APS]	[TMEDA]	pregelation period (min)	slope (Pa/min)
17.5	39.4	6.57	265.70
17.5	78.7	3.86	267.45
17.5	157.4	1.03	709.14
70.1	39.4	0.29	780.00

initiators was caused by shortening either the pregelation or the gelation period, both periods were separately defined, and the effect of the initiator concentration was studied. The pregelation period was defined as the time needed to reach 1% of G' end. The slope of the curves of G' versus time ($0.1 < G'/G'$ end <0.6) was considered as an indication of the rate of gelation. Table 3 illustrates that increasing initiator concentrations accelerate both stages of hydrogel formation: using high concentrations of APS and TMEDA, intermolecular cross-link formation is detectable almost immediately after mixing the two compounds with the MA-IN solutions, and the gelation process is characterized by a steep rise in G'.

From this kinetic study, it was concluded that the formation of MA-IN hydrogels can be performed within 2.5 h, because cross-linking of MA-IN chains will have ended in this period of time, at least for the range of degree of substitution and feed concentration studied.

If an ideal three-dimensional network is formed by the radical polymerization, the elastic modulus G' is independent of frequency. This frequency-independent elastic modulus is called the equilibrium elastic modulus G_e and is a measure of the structure that has been formed by the cross-linking reaction. Several theories, such as the affine theory, the phantom theory, the constrained junction model, or the Langley−Graessley model,[19−21] have been developed to relate the macroscopic elastic modulus of a polymeric network to its molecular structure. From these theories, it can generally be concluded that G_e is proportional to the number of moles of elastic chains, i.e., chains attached to the network with both ends, per volume unit of the network (ν) according to the following equation:

$$G_e \sim \nu RT \qquad (2)$$

with R the gas constant and T the absolute temperature.

Determination of G_e can thus give an idea about the concentration of elastic network strands and hence about the amount of intermolecular cross-links formed.

For the cross-linked materials under investigation, the frequency dependence of the elastic modulus is shown in Figure 3 over three decades in frequency. For hydrogels prepared from MA-IN with low degree of substitution (27% w/w solution with DS = 4.4) or low feed concentration (16% w/w solution with DS = 12.1), the values of G' appear to be almost independent of frequency. To a first approximation, these hydrogels can thus be considered as ideal networks, and the constant value of G' consequently represents the equilibrium elastic modulus G_e. However, the other hydrogels tested show a slight decrease of G' with decreasing frequency, indicating that relaxation (rearrangements) can still occur in the network. For these systems, G_e could not be determined. Nevertheless, it may be concluded that the amount of elastic chains per volume unit of the network increases with increasing degree of substitution and feed concentration, since both parameters definitely have an increasing effect on G'. These observations support the results of the equilibrium degree of swelling study and the in vitro enzymatic degradation study of the MA-IN hydrogels.[22,23] The decreased equilibrium swelling and the decreased enzymatic degradation of the hydrogels with increasing degree of substitution or feed concentration of MA-IN can be attributed to the increased intermolecular cross-linking density (higher G' values) of the networks, which increases the contractility of the hydrogels, resulting in a restriction of expansion upon swelling, and which reduces the permeability of the networks toward degrading enzymes.

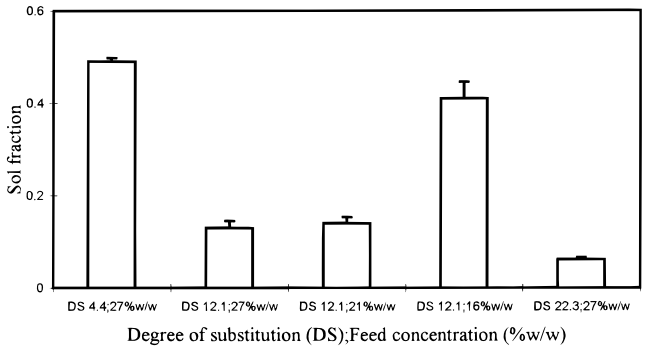

Figure 4—Weight fraction of soluble material (sol fraction) for MA-IN hydrogels with different compositions.

The observed frequency dependence of G' can possibly be attributed to imperfections in the structure of the network.[19] Loose ends, loops, and MA-IN chains which are not incorporated in the network, can relax, causing a decrease in G' at low frequencies.

It was first checked whether the presence of a sol fraction can explain the relaxation in G'. As gelation of the MA-IN solutions took place between the plates of the rheometer, the chains which are not incorporated in the hydrogel network, have not been removed. Figure 4 shows the sol fractions of MA-IN hydrogels of different feed composition. As expected, the sol fraction is reduced with an increasing amount of reactive groups per chain (DS): more chains will participate in the network when there are more groups present which can link them to the network. The effect of concentration on sol fraction can be understood from the promoting effect of dilution on intramolecular cross-linking, which does not incorporate chains in the network. The probability that bonds will be formed between different chains of the system is proportional to the probability that these chains lie in the same small volume-element[14] and therefore increases with concentration. Hence, the hydrogels prepared from a 16% w/w solution (MA-IN DS = 12.1) exhibited a higher sol fraction when compared with the more concentrated solutions (22 and 27% w/w). However, comparison of the data from Figure 3 and Figure 4 clearly indicates that the sol fraction data cannot explain the frequency dependence of G': the samples with the higher sol fraction do not correspond to the samples with the more pronounced frequency dependence of G'.

A second possible explanation for the observed decrease of G' is the relaxation of loose ends and loops. MA-IN solutions of high feed concentration form dense networks in a short period of time compared with more diluted solutions (Figure 3 and Table 1). As mentioned above, intermolecular cross-links are predominantly formed starting from a concentrated solution, whereas intramolecular cross-link formation is promoted by a diluted solution. Due to the higher extent of intermolecular cross-linking in case of a concentrated solution, the mobility of the polymer chains can be restricted to such an extent that full conversion of the vinyl groups can be impeded. Consequently, more loose ends may remain in the hydrogel network, and these are able to relax on the time scales

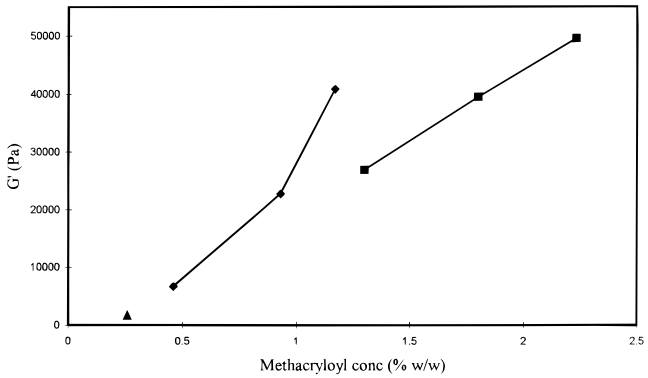

Figure 5—*G′* as a function of the real methacryloyl concentration in the hydrogel network prepared from MA-IN DS 4.4 (▲), DS 12.1 (◆), and DS 22.3 (■).

probed by the oscillatory experiments. In addition, when the feed concentration of MA-IN exceeds the critical concentration at which MA-IN chains start to overlap, physical chain entanglements are formed which promote intermolecular cross-linking even more. Moreover, the entanglements themselves can be considered as additional intermolecular cross-links, contributing to an increase in *G′* and additionally limiting chain mobility thereby restricting full conversion of the vinyl groups.

A rule of thumb for predicting when concentration effects will become important is when the coil overlap parameter $c[\eta]$, with c the concentration of the polymer solution (g/dL) and $[\eta]$ the intrinsic viscosity of the polymer (dL/g), is near unity.[24] Consequently, it can be postulated that:

$c[\eta] < 1$: the polymer coils are isolated one from another, and the solution can be considered as a particle solution;

$c[\eta] = 1$: the polymer coils begin to overlap;

$c[\eta] > 1$: the polymer coils form entanglements, and the solution can be considered as a network solution.

The intrinsic viscosity of MA-IN DS 12.1 is 0.038 dL/g as determined by solution viscosity measurements. This implies that for the highest feed concentration (density = 1.14 g/mL), entanglements have to be accounted for, which may increase the amount of loose ends.

Unfortunately, the degree of conversion of MA-IN during hydrogel formation could not be determined, neither by FT-IR nor by solid state ^{13}C NMR spectroscopy.[7] But van Dijk-Wolthuis et al.[18] described indeed a low final percentage conversion of the methacryloyl groups of methacrylated dextran upon free radical polymerization at a high initial concentration of methacrylated dextran compared with a low initial concentration.

With respect to the effect of degree of substitution on the observed frequency dependence of *G′*, the same remark can be made as for the effect of the feed concentration. Solutions of MA-IN with a high degree of substitution are converted rather fast in rigid networks (high value of *G′*), implying again that full conversion of the double bonds may be impeded and loose ends may remain. A high degree of substitution additionally promotes cyclization or the formation of loops,[25] which can also relax during the rheological experiments.

To investigate the relative amount of inter- to intramolecular cross-links, G_e, being a measure of the intermolecular cross-links, was plotted in Figure 5 as a function of the methacryloyl concentration, a measure of the amount of reactive sites. For the perfect networks, G_e was considered whereas for the imperfect networks *G′* at a frequency of 0.01 rad/s was taken. Since the sol fraction of the systems under investigation is not negligible (Figure 4), the real methacryloyl concentration in the network, i.e., the concentration corrected for the not incorporated polymer

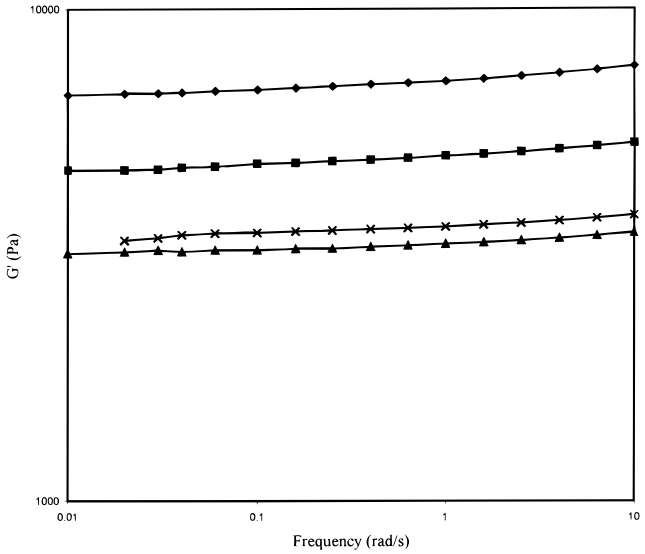

Figure 6—*G′* as a function of frequency for MA-IN hydrogels with DS 12.1 and feed concentration 16% w/w prepared with different concentrations of APS and TMEDA (μmol/mL buffer). ([APS]; [TMEDA] = 17.5; 39.4 (◆), 17.5; 78.7 (■), 17.5; 157.4 (▲), and 70.1; 39.4 (×).)

chains, has been considered. Determination of the sol fraction of hydrogels prepared from 16% and 22% w/w solutions of MA-IN DS 4.4 could not be performed, as these hydrogels were too weak to manipulate. Hence, only one value for DS 4.4 is depicted in Figure 5. Figure 5 clearly illustrates that increasing amounts of reactive vinyl groups in the polymerization reaction (increased feed concentration) results in the increased formation of intermolecular cross-links, confirming the conclusions from Figure 3. In addition, this figure suggests that for the same methacryloyl concentration, hydrogels prepared from MA-IN with a low degree of substitution exhibit higher values of *G′* than hydrogels from MA-IN with a higher degree of substitution. In other words, to form an equal amount of intermolecular cross-links, higher substituted MA-IN may need a higher amount of polymerizable groups, since reactive sites may be lost by intramolecular cross-linking or perhaps may not have reacted at all (lower degree of conversion). These observations agree with the remarks made in order to explain the frequency dependence of *G′*.

Finally, the effect of the concentration of the initiating species APS and TMEDA on the resulting structure of the hydrogel has been investigated. Figure 6 represents the dynamic behavior of fully cured networks prepared from 16% w/w solutions of MA-IN DS 12.1 with various initiator concentrations. Apparently, hydrogels prepared with higher initiator concentrations exhibit lower values of *G′*, at least for the range of concentrations studied. This can be explained by the fact that the higher concentrations of initiators result in the formation of an increased number of radicals in the initiation step of the radical polymerization reaction. Consequently, the number of active centers formed on the inulin chains is also increased, implying that less unreacted vinyl groups are left to cross-link the chains, which results in lower *G′* values.

Conclusions

Oscillatory shear measurements, performed on inulin solutions during the gelation process as well as on fully cured hydrogels, showed that the degree of substitution and feed concentration of MA-IN, and the concentration of the initiating species of the free radical polymerization reaction (APS and TMEDA), all affect the gelation process and the

rigidity of the obtained hydrogels. A higher degree of substitution or feed concentration cause an acceleration of the network formation. The resulting hydrogels are characterized by a higher mechanical strength (higher G' values), arising from the increased amount of intermolecular cross-links formed. Increasing concentrations of APS and TMEDA also shorten the process of hydrogel formation, but result in hydrogels with lower G' values.

References and Notes

1. Van Loo, J.; Coussement, P.; De Leenheer, L.; Hoebregs, H.; Smits, G. On the presence of inulin and oligofructose as natural ingredients in the western diet. *Crit. Rev. Food Sci. Nutr.* **1996**, *36*, 525−552.
2. Dysseler, P.; Hoffem, D. Inulin, an alternative dietary fiber. Properties and quantitative analysis. *Eur. J. Clin. Nutr.* **1995**, *49*, S145−S152.
3. Gibson, G. R.; Roberfroid, M. B. Dietary modulation of the human colonic microbiota: introducing the concept of prebiotics. *J. Nutr.* **1995**, *125*, 1401−1414.
4. Roberfroid, M. B. Dietary fiber, inulin, and oligofructose: a review comparing their physiological effects. *Crit. Rev. Food Sci. Nutr.* **1993**, *33*, 103−148.
5. Wang, X.; Gibson, G. R. Effects of the in vitro fermentation of oligofructose and inulin by bacteria growing in the human large intestine. *J. Appl. Bacteriol.* **1993**, *75*, 373−380.
6. McKellar, R. C.; Modler, H. W. Metabolism of fructooligosaccharides by *Bifidobacterium spp*. *Apl. Microbiol. Biotechnol.* **1989**, *31*, 537−541.
7. Vervoort, L.; Van den Mooter, G.; Augustijns, P.; Busson, R.; Toppet, S.; Kinget, R. Inulin hydrogels as carriers for colonic drug targeting. I. Synthesis and characterization of methacrylated inulin, and hydrogel formation. *Pharm. Res.* **1997**, *14*, 1730−1737.
8. van Dijk-Wolthuis, W. N. E.; Kettenes-van den Bosch, J. J.; van der Kerk-van Hoof, A.; Hennink, W. E. Reaction of dextran with glycidyl methacrylate: An unexpected transesterification. *Macromolecules* **1997**, *30*, 3411−3413.
9. Peppas, N. A.; Barr-Howell, B. D. Characterization of the cross-linked structure of hydrogels. In *Hydrogels in medicine and pharmacy*; Peppas, N. A., Ed.; CRC Press: Boca Raton, FL, 1986; Vol. I, pp 27−56.
10. White, R. P.; Samson, F. E.; Kan, L. Determination of inulin in plasma and urine by use of anthrone. *J. Lab. Clin. Med.* **1954**, *March*, 475−478.
11. Summerfield, A. L.; Hortin, G. L.; Smith, C. H.; Wilhite, T. R.; Landt, M. Automated enzymatic analysis of inulin. *Clin. Chem.* **1993**, *39*, 2333−2337.
12. Morris, D. L. Quantitative determination of carbohydrates with Dreywood's anthrone reagent. *Science* **1948**, *107*, 254−255.
13. Ferry, J. D. Illustrations of viscoelastic behavior of polymeric systems. In *Viscoelastic properties of polymers*; Ferry, J. D., Ed.; John Wiley & Sons: New York, 1961; pp 21−40.
14. James, H. M.; Guth, E. Theory of the increase in rigidity of rubbers during cure. *J. Chem. Phys.* **1947**, *15*, 669−683.
15. Langley, N. R. Elastically effective strand density in polymer networks. *Macromolecules* **1968**, *1*, 348−352.
16. Tonelli, A. E.; Helfand, E. Elastically ineffective cross-links in rubbers. *Macromolecules* **1974**, *7*, 59−63.
17. Feng, X. D.; Guo, X. Q.; Qiu, K. Y. Study of the initiation mechanism of the vinyl polymerization with the system persulphate/N,N,N′,N′-tetramethylethylenediamine. *Makromol. Chem.* **1988**, *189*, 77−83.
18. van Dijk-Wolthuis, W. N. E.; Franssen, O.; Talsma, H.; van Steenbergen, M. J.; Kettenes-van den Bosch, J. J.; Hennink, W. E. Synthesis, characterization, and polymerization of glycidyl methacrylate derivatized dextran. *Macromolecules* **1995**, *28*, 6317−6322.
19. Patel, S. K.; Malone, S.; Cohen, C.; Gillmor, J. R.; Colby, R. H. Elastic modulus and equilibrium swelling of poly(dimethylsiloxane) networks. *Macromolecules* **1992**, *25*, 5241−5251.
20. Gottlieb, M.; Macosko, C. W.; Benjamin, G. S.; Meyers, K. O.; Merrill, E. W. Equilibrium modulus of model poly(dimethylsiloxane) networks. *Macromolecules* **1981**, *14*, 1039−1046.
21. Gnanou, Y.; Hild, G.; Rempp, P. Molecular structure and elastic behavior of poly(ethyleneoxide) networks swollen to equilibrium. *Macromolecules* **1987**, *20*, 1662−1671.
22. Vervoort, L.; Van den Mooter, G.; Augustijns, P.; Kinget, R. Inulin hydrogels. I. Dynamic and equilibrium swelling properties. *Int. J. Pharm*., accepted for publication.
23. Vervoort, L.; Rombaut, P.; Van den Mooter, G.; Augustijns, P.; Kinget, R. Inulin hydrogels. II. In vitro degradation study. *Int. J. Pharm*., in press.
24. M. Tirrel. Rheology of polymeric liquids. In *Rheology. Principles, measurements and applications*; Macosko, C. W., Ed.; VCH Publishers: New York, 1994; pp 475−514.
25. De Smedt, S. C.; Lauwers, A.; Demeester, J.; Van Steenbergen, M. J.; Hennink, W. E.; Roefs, S. P. F. M. Characterization of the network structure of dextran glycidyl methacrylate hydrogels by studying the reological and swelling behavior. *Macromolecules* **1995**, *25*, 5082−5088.

Acknowledgments

The authors acknowledge Orafti (Tienen, Belgium) for the gift of Raftiline HP, Sigrid De Schouwer for her help in performing the rheological experiments, and Prof. W. E. Hennink for cooperation concerning initiation in the derivatization method of inulin.

JS9802796

Controlled Release of Human Immunoglobulin G. 1. Release Kinetics Studies

CHI-HWA WANG,*,† KAMALESH SENGOTHI,† AND TIMOTHY LEE‡

Contribution from *Department of Chemical Engineering and Department of Surgery, National University of Singapore, 10 Kent Ridge Crescent, Singapore - 119260.*

Received August 17, 1998. Accepted for publication November 3, 1998.

Abstract □ The release of human immunoglobulin G (IgG) using ethylene–vinyl acetate copolymer (EVAc) as a polymer carrier was studied by fabricating them into two commercially available dosage forms: slab and microsphere. A first-order flux decay model and two hierarchical models concerned with the mass transfer coefficient on the slab surface were used to describe the mechanism of release kinetics and the results compared. These models gave insight to some of the important physical parameters of drug release such as the diffusion coefficient, time constant of release, and initial flux. It was found that the release mechanism varies with time, and hence no single model can be used to predict the release profile for the entire period of study. A controlled release study by matrix coating was also done. The results obtained were utilized to examine the suitability of a particular dosage form (matrix geometry) of IgG for clinical applications. The release data compared with the standard methods of IgG therapy proves localized drug delivery to be a major boon for immunodeficient patients.

Introduction

The survival of the human race depends largely on the body's defense mechanism. Better known as humoral immune response, the production of antibodies in response to foreign bodies or "antigens" determines the state of health of any individual. Individuals falling short of this response are said to be immunodeficient and require immune therapy for treatment. This led to the development of γ-globulin therapy about three decades ago.[1] Immunoglobulin G (IgG), a very high molecular weight protein molecule, constitutes the major fraction of the γ-globulin repertoire, and its mean normal serum concentration is of the order 5.4−16.1 g/L. Replacement therapy using IgG is a common feature for patients suffering from hypogammaglobulinemia[2] and for those patients suffering from cancer, burns, and other disorders due to secondary IgG deficiencies. IgG has also been used in the development of efficient immunotherapeutic agents for the treatment of tumors, by the fusion of genetic engineering and hybridoma technology.[3] They function as carriers of drug molecules, which are directed toward a specific antigenic target site located in various parts of the human body.

Classical methods of IgG therapy are done either by intravenous injection or by intramuscular injection.[1] Intramuscular administration of IgG has been in vogue since the early 1950s. However limitations in this therapy, which include the painful method of injection, the persistence of discomfiture, the reduced elevation of serum IgG levels after injection etc. led to the usage of intravenous injection as an alternative in the 1980s. Although the method proved to be effective in certain areas such as an immediate rise in the serum IgG level after infusion, it had its own detrimental effects by introducing certain painful side effects. Further, the dose required for treatment and the frequency of therapy was substantially high, particularly if the treatment is for a tumor. IgG immunotherapy is employed in coordination with the radiation therapy and surgery for extreme cases of tumor. Inspite of these methodologies, the recurrence of malignancies at a site near the original location could not be prevented.[4] This can, however, be avoided if the tumor-bearing region is exposed to increasing doses of radiation and immunotherapy. However, both methodologies have their own defect. Excessive radiation might also affect the normal tissues, and a higher dose of drug might result in systemic toxicity.

A suitable alternative is the use of drug-incorporated polymer matrixes with controlled release applications, which has attracted considerable attention since its practicality was demonstrated.[5] The method is highly attractive due to its reduced dose handling and the drastic reduction in treatment frequency. Controlled delivery of antibody to the mucosal tissue of rats by topical application has been already studied by Kuo et al.[6] Cleek et al.[7] studied the release characteristics of γ-globulin molecules from biodegradable microspheres. Extensive efforts have been put into searching for a suitable polymer carrier and the variety of factors that affect the release kinetics of drug−polymer systems. A nonbiodegradable and hydrophobic polymer, EVAc (ethylene−vinyl acetate copolymer) has been chosen as a drug carrier in many drug−polymer systems because of its proven biocompatibility.[8,9]

In this report, we study the in vitro release kinetics of IgG by using two commercially available dosage forms: the slab and the microsphere. Due to the geometric difference, the release pattern obtained for the two cases will be different, thereby serving as dosage forms for patients with different dose specificities and natures of compliance. Since IgG is naturally present in humans along with other proteins, the in vitro analysis was carried out based on perfusion immunoassay using a high performance liquid chromatography (HPLC) system. We have chosen this method because of its ability to detect specific proteins in a relatively fast and highly automated fashion, as compared to the method of the enzyme-linked immunosorbent assay.[10] The results obtained from the release kinetics were then compared with the conventional methods of therapy and the features discussed.

Materials and Methods

Materials—EVAc polymer (40% vinyl acetate content) (Scientific Polymer Products, Inc. Ontario, NY), IgG crystals (Venoglobulin-I, 2.5 g vial with reconstitution kit, Alpha Therapeutic

* Corresponding author. Telephone: 65-8745079. Fax: 65-7791936. E-mail: chewch@nus.edu.sg.
† Department of Chemical Engineering.
‡ Department of Surgery.

10.1021/js9803407 CCC: $18.00
Published on Web 01/13/1999

Co., Los Angeles, CA), Protein A/G standard (PerSeptive Biosystems Inc., Framingham, MA).

Methods—*Fabrication of IgG-EVAc Systems*—To prevent the possible denaturation of IgG at high temperatures, which may occur during the classical methods of compression molding and injection molding, a solvent-casting method was chosen for fabrication of drug−polymer systems. The EVAc polymer, which is in the form of pellets, was cleaned as described by Langer et al.[8] It was then dissolved in methylene chloride in a mass ratio of 1:9. IgG crystals were sieved with Endecotts test sieve (250 μm) to obtain the desired size fraction. The amount of IgG powder corresponding to the required drug loading was then weighed out accurately (± 0.0001 g) and added to 10 mL of the resultant EVAc−methylene chloride solution. The drug−polymer suspension was then molded into two geometrical shapes, viz. microsphere and slab as reported in Sefton et al.[11] and Rhine et al.,[12] respectively. Briefly, the drug−polymer suspension was poured into a Petri dish (for slab fabrication) and precooled at −70 °C for 15 min. The dish containing the matrix was initially cooled at −70 °C for 10 min before transferring it to −20 °C. After 2 days, the matrix was kept under mild vacuum for an additional 2 days under room temperature. The resulting matrix was found to be a thin film ~1 mm in thickness. Square slabs with specific dimensions were cut off from the matrix. In the case of microsphere fabrication, the suspension was extruded using a disposable 3 mL syringe fitted with a 16 gauge (BioLaboratories, Singapore) needle into cold absolute ethanol (placed in a container of liquid nitrogen). After leaving for 24 h, the absolute ethanol solution was replaced in order to remove the methylene chloride by liquid−liquid extraction phenomena. The beads that were obtained were finally vacuum-dried for 4 h before using for release study. Microspheres were also prepared using the 19 gauge and 23 gauge sized needles.

Fabrication of Coated IgG−EVAc Matrixes—The slabs that were obtained as per the previous procedure were submerged in 10% EVAc solution for 2 min. Before dipping, one of the 1 × 0.1 cm^2 sides of each slab was covered with a carbon adhesive tape to make it coating free. The slabs were then taken out, and the tape was removed and dried at room temperature for 5 min. Finally, they were dried under mild vacuum at room temperature for 24 h. The same procedure was carried out for slabs coated in 20% and 30% EVAc solution.

In Vitro Release Kinetics Study—Each slice of slab was weighed and submerged in separate beakers containing 2 mL of 0.1 M phosphate buffer, pH 7.4, containing 0.1 M sodium phosphate and 0.15 M sodium chloride (prepared using the PBS pack obtained from Pierce, Rockford, IL) and 4 mg/L gentamicin sulfate (Sigma Diagnostics, St. Louis, MO) which acts as an antibiotic against microbes. A release study was carried out at 37 °C for 1 h. The slices were then removed by forceps, blotted dry by tissue, and then transferred to a fresh buffer solution. Phosphate buffers (2 mL) were analyzed by HPLC to determine the IgG concentration. The same procedure was repeated at specific time intervals. When the releasing was for more than 1 h, the slices were soaked in 10 mL of phosphate buffer to provide the "infinite sink" condition. Buffers (10 mL) were also used to determine the concentrations and to give a clear picture on the percentage of drug that had been released each day. For the case of microspheres, a 50 mg aliquot of microspheres was weighed accurately and subjected to the release study as mentioned above.

HPLC Analysis—The quantification of IgG release was done using the HPLC system (Perkin-Elmer Corporation, Norwalk, CT) and PA Immunodetection sensor cartridge (PerSeptive Biosystems Inc., Framingham, MA). The loading buffer (0.01 M phosphate buffer), pH 7.4, containing 0.12 M sodium chloride and 0.0027 M potassium chloride, was prepared from PBS packs obtained from Sigma Diagnostics while the elution buffer was prepared from 0.15 M sodium chloride, pH adjusted to 2.3 using 6 M HCl. The IgG sample with an injection volume of 50 μL was pumped through the sensor cartridge. The nontarget components of the assay gave the first peak of the chromatography. With the switch of loading buffer to the elution buffer, the IgG−Protein G complexes were dissociated, and IgG was eluted out of the cartridge, which gave the second peak of the chromatography. The sample peak area was obtained by subtracting the chromatogram of the blank from that of the sample. The mass of IgG released was then obtained on comparison with a calibration curve of the peak area plotted against the mass of IgG standard sample taken.

Data Analysis—The decay in the flux of IgG is approximated by a first-order process with a characteristic time constant τ, given by the relation

$$\frac{F}{F_0} = \exp\left(\frac{-t}{\tau}\right) \tag{1}$$

where F is the molar flux as a function of time and F_o is the initial flux. Further, two models of mass transfer were used to analyze the release mechanism of IgG from the polymer matrix. The first one (model I) assumes an infinitely high coefficient of matter transfer on the surface. Hence, making use of the classical Fickian equation for release from slab (thin film):

$$\frac{\partial C_i}{\partial \mathrm{t}} = D_i \frac{\partial^2 C_i}{\partial x^2} \tag{2}$$

where C_i is the IgG concentration in the EVAc matrix as a function of time and position, x is the position within the polymer matrix, and D_i is the diffusion coefficient for IgG transport within the EVAc matrix and assuming that (i) the IgG concentration is uniform throughout the matrix at time $t = 0$ i.e., $C_i = C_i^0$ at $t = 0$, for all x, and (ii) the surface concentration of IgG is maintained at a constant concentration at times $t > 0$, eq 2 can be solved for C_i[13] as a function of x and t. On integrating over the thickness of the film, the amount (mass) of IgG released Q_t from the slab at time t can be obtained. This can be further simplified to obtain the relation for Q_t at short and long times based on the value of Q_t/Q_T

$$\frac{Q_t}{Q_T} = \frac{4}{L}\left(\frac{D_i t}{\pi}\right)^{0.5} \quad \text{for} \quad Q_t/Q_T \le 0.5 \tag{3}$$

$$\frac{Q_T - Q_t}{Q_T} = \frac{8}{\pi^2}\exp\left(-\frac{\pi^2 D_i t}{L^2}\right) \quad \text{for} \quad Q_t/Q_T \ge 0.55 \tag{4}$$

where Q_T is the amount of IgG released at infinite time,[14] and L is the thickness of the slab. The diffusion coefficient D_i for IgG transport in the porous polymer matrix for short and long times were determined by comparing the experimental results to eqs 3 and 4, respectively.

The second model (model II) assumes a finite coefficient of matter transfer on the surface. Starting from eq 2 for a slab of thickness $2L$, the model similar to the previous one, assumes uniform initial concentration of IgG (C_i^0) for all x. The boundary condition representing the loss of IgG at the slab surface is given by eq 5,

$$t > 0 \quad -D_i\left|\frac{\partial C_i}{\partial x}\right| = h(C_s - C_e) \qquad x = \pm L \tag{5}$$

where h is the coefficient of matter (IgG) transfer, C_s is the concentration of IgG at the surface, and C_e is the concentration of IgG required to maintain equilibrium with the medium. Equation 2 can be solved for C_i[13] as a function of x and t making use of the given initial and boundary conditions. On integration over the slab thickness, a relation between the amount (mass) of IgG released Q_t from the slab at time t and the amount released after infinite time Q_T can be obtained.[15]

$$\frac{Q_T - Q_t}{Q_T} = \sum_{n=1}^{\infty} \frac{2N^2}{\beta_n^2(\beta_n^2 + N^2 + N)}\exp\left(-\frac{\beta_n^2 D_i t}{L^2}\right) \tag{6}$$

where N is the dimensionless number given by eq 7

$$N = \frac{Lh}{D_i} \tag{7}$$

and β_n is the positive root of eq 8

$$\beta \times \tan\beta = N \tag{8}$$

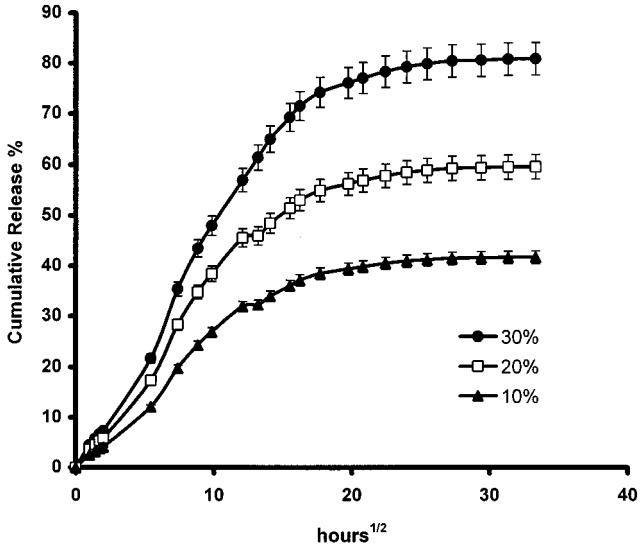

Figure 1—Fraction of IgG released for the 10, 20, and 30% loaded cases, respectively, for the slab geometry. Each point is an average of six data points. Standard error of the mean of release at each time point is 4%.

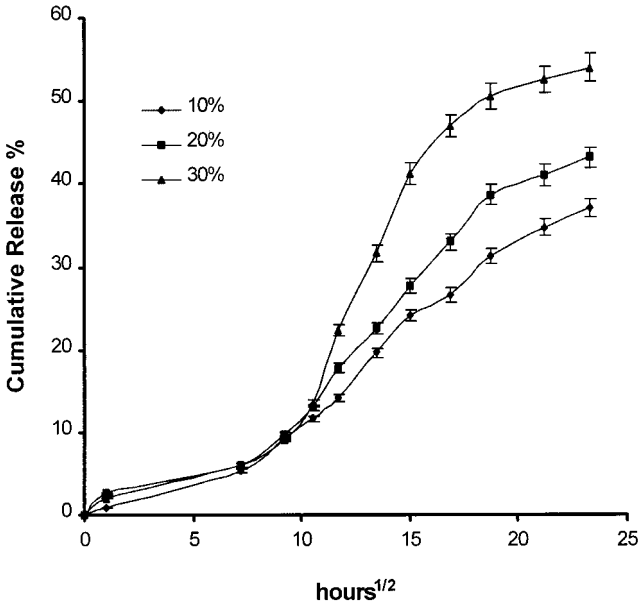

Figure 2—Fraction of IgG released for the 10, 20, and 30% loaded cases, respectively, for the microsphere geometry. Each point is an average of four data points. Standard error of the mean of release at each time point is 3–6%.

The transfer coefficient h and the diffusion coefficient D_i were then determined by fitting the experimental data to eq 6 coupled with eqs 7 and 8.

Results and Discussion

Release Studies—Preliminary studies carried out for different drug loading showed that drug release increased with increased drug loading for both geometries as shown in Figures 1 and 2, respectively. The initial steep slope for the slab geometry is mainly due to the release of drug molecules present on the exterior surface of the matrix that is followed by a stage in which the drug gradually diffuses through the polymer backbone to the exterior of the matrix and therefore a corresponding decrease in the release rate. The possibility of drug dissolution in the buffer followed by diffusion through the solvent-filled pores cannot be completely ignored. Further, since the solubility or the saturation concentration of IgG is less than the drug loading, dissolution in the solvent-filled pores plays a very important role in the initial period of release, whereas the latter period of release is predominated by the diffusion through the pores and channels formed in the matrix.[16]

The very high molecular weight of the IgG molecule restricts its release through the tortuous path within the matrix. Hence, in the presence of the available tortuous path formed by the preceding molecules, the later molecules find their way to the exterior much more easily, and therefore the release rate is gradually maintained but in a decreasing trend because of the increased distance for release. This feature continues until one of the following two limiting cases exist: (1) the path available for the drug to be released becomes more tortuous, and (2) decrease in the available drug content to utilize the existing release path. As a result, the curve tends to be asymptotic at very high time intervals. Thus, the drug release is explained by these two stages, which alternates between each other to give a sustained release. However, this can be avoided by altering the matrix geometry to compensate for the increasing distance for diffusion by increased drug concentration in order to achieve a zero-order release pattern.[17]

On observing the fraction of drug released for slabs from Figure 1, we find that the cumulative drug release rises in proportion with the square root of time for the first 15 days followed by a decline in the release percent. About 81% of the drug was observed to be released after 46 days for the 30% loaded case during which the 10 and 20% loaded cases released approximately 40 and 60% IgG, respectively. It is clearly noted that the drug release follows a square root of time kinetics in the initial period, which might vary for different drug loading and experimental conditions. Since then, the flux deteriorates, following an intermediate transitional order for the next fortnight finally tending toward zero after 45 days. In the case of microspheres, the drug release is initially in the lag period (Figure 2) after which the release gradually improves until an asymptotic behavior exists. The lag period might be due to the role of dissolution playing the rate-limiting step in the release kinetics. An important feature noted in the release profiles is the sigmoidal nature of the curve, and this nature increases for increasing drug loading. Furthermore, the release mechanism of a microsphere approximates that of a slab for smaller drug loading at all times and for higher drug loading at longer times (data not shown). Hence, the geometry of the drug−polymer matrix plays an essential role in deciding the type of release mechanism.

Henceforth, the discussion will be based on the 30% IgG loaded slab and microsphere matrixes (16 gauge size, unless mentioned otherwise) for more rigorous analysis on the release kinetics. In addition, this percentage loading exhibits some agreement with the required dosage levels of drug that has to be maintained in patients suffering from primary immunodeficiency disease.[18] An explanation of this statement is given later in this article.

The decrease in the molar flux of IgG calculated as moles of IgG released perpendicular to a square centimeter of surface area per second from the matrix was found to fit well to the exponential eq 1. F_o and τ were analyzed for slab matrixes with different dimensions (represented by the ratio of surface area to volume [S/V]), with the same thickness using eq 1. The initial flux and time constant for the different cases tabulated in Table 1 agree reasonably well with respect to each other. Further, the release profiles for the slabs with different S/V ratios shown in Figure 3 were in reasonable agreement with each other, thereby confirming the uniformity in drug distribution and the reproducibility of the release kinetics.[12] This is due to the release occurring primarily in the direction perpen-

Table 1—Initial Fluxes and Time Constants Calculated for Slabs of Different Dimensions

S/V (cm^{-1})	initial flux F_0 ($mol/cm^2 \cdot s$) $\times 10^{12}$	time constant (h)
22	1.244 ± 0.03	154.74 ± 1.56
24	1.318 ± 0.025	157.999 ± 2.10
30	1.334 ± 0.026	158.643 ± 1.89

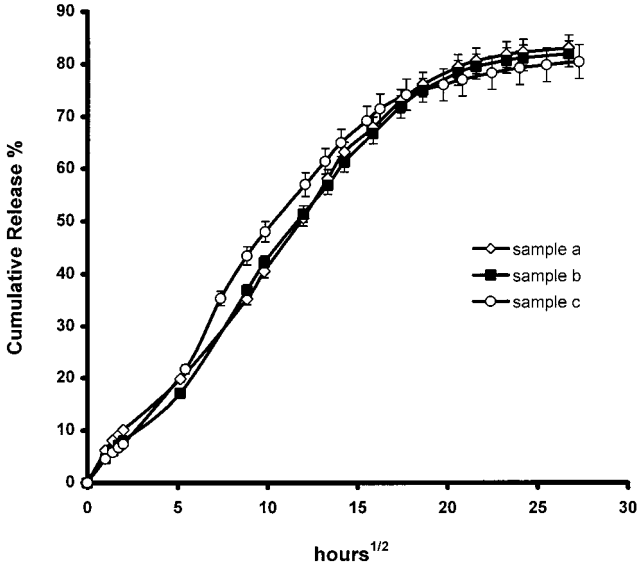

Figure 3—Cumulative percent of IgG release for different sized slab matrixes of 30% IgG loading. (Sample a: 30 cm^{-1}; sample b: 24 cm^{-1}; sample c: 22 cm^{-1}). Each point is an average of four data points, and the error of the mean of the release at each time point is less than 4%.

Table 2—Experimentally Determined Parameter Values for Short and Long Times of Release for the Case of a Slab Using Model One[a]

Q_t/Q_T	D_i (cm^2/s)	tortuosity
≤ 0.50	1.82×10^{-9}	341
≥ 0.55	1.89×10^{-9}	328

[a] $L = 0.1$ cm.

dicular to the thickness of the film. However, this cannot be true for cases in which the thickness is comparable to the other slab dimensions. For example, similar release studies carried out for different sized cubic samples (data not shown) showed variations in their kinetics.

Fitting of the experimental data to model I, i.e., eqs 3−4, show that the diffusion coefficient is almost a constant (see Table 2) with respect to time. The calculated D_i for IgG release through the EVAc backbone agrees reasonably well with the D_{eff} (0.9×10^{-9} cm^2/s) reported by Saltzman et al.[19] for IgG. The slight variation between the two values might be attributed to factors such as the difference in the percentage loading of IgG, the molecular weight of EVAc used, and the matrix geometry. The tortuosity value in the table was obtained on dividing the aqueous diffusion coefficient[20] of IgG (6.2×10^{-7} cm^2/s) by the experimentally determined diffusion coefficient.[21] Hence, it is noted that the path for drug diffusion in the polymer matrix becomes more complicated by an order of ~ 2 on comparison to unrestricted diffusion in free liquid. This seems to be quite practical on comparison with the tortuosity values obtained in similar experimental runs[22] for other biomolecules. The tortuosity value essentially takes into account all the properties of the polymer−drug and their interactions. In the case of model II, the experimental data was fitted to eq 6 by taking the diffusion coefficient developed in model I as an initial estimate, and refining the values of the

Table 3—Experimentally Determined Parameter Values for Model Two[a]

coefficient of matter transfer (h)	6.89×10^{-5} cm/s
diffusion coefficient (D_i)	2.06×10^{-9} cm^2/s
tortuosity	301

[a] $L = 0.05$ cm.

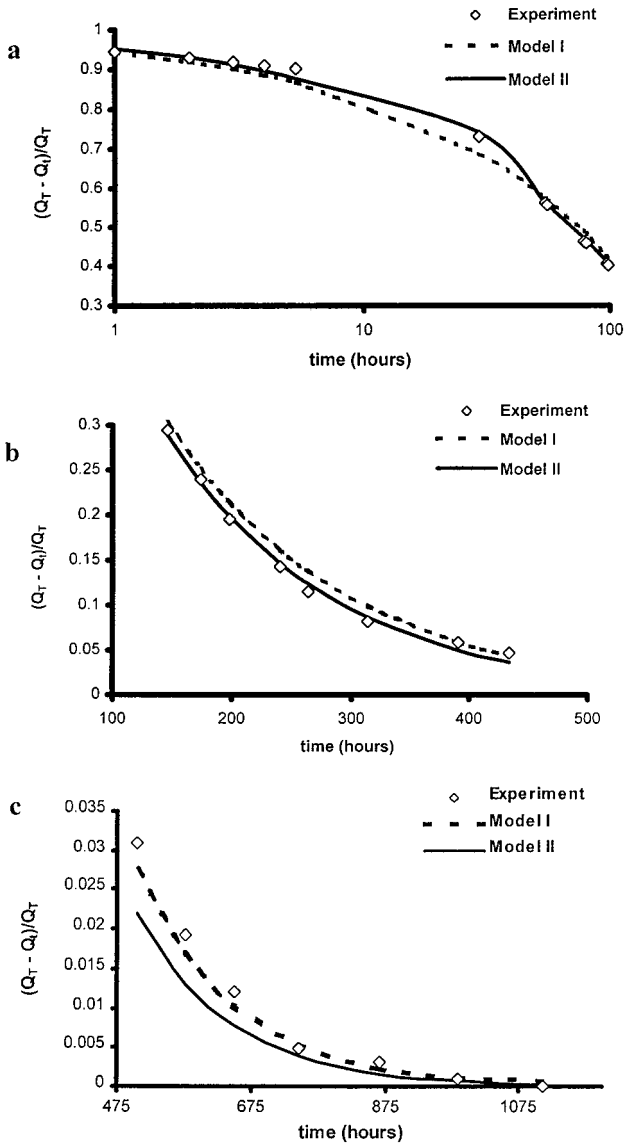

Figure 4—Fraction of IgG released from slab matrixes for (a) time less than 100 hours, (b) between 100 and 500 h, and (c) greater than 500 h.

dimensionless number N and its corresponding β_n by using a standard nonlinear optimization tool. The diffusion coefficient and the matter transfer coefficient that are finally obtained are shown in Table 3. The diffusion coefficient shows a slight deviation from that obtained for model I. Figure 4 gives the variation of the predicted model results from the experimental values. It is clearly seen from Figures 4a and 4b, that model II assuming finite coefficient of matter transfer on the surface is a better model on comparison to model I. Considering the fact that the experiment was conducted under stagnant conditions, the assumption that the rate of matter transfer to the surface by diffusion is equal to the rate at which it leaves the surface proves to be a more realistic model on comparison to model I which assumes all the matter brought to the surface to attain equilibrium with the medium concentration in an infinitesimally short time. Hence, model II approximates itself to model I when we assume an infinite

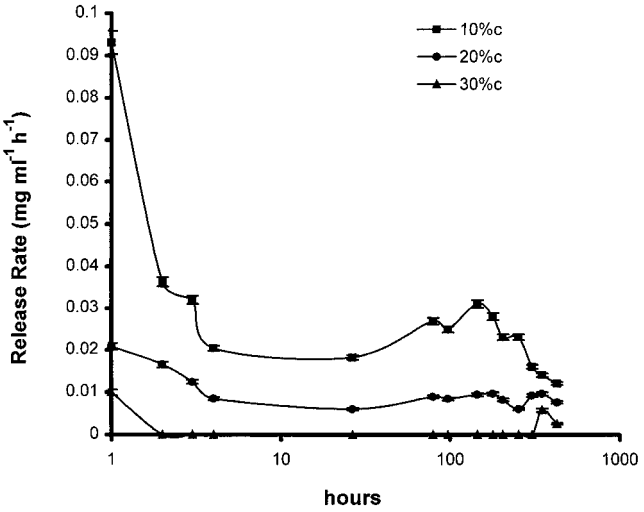

Figure 5—Release rate of IgG from EVAc-coated matrixes. 10, 20 and 30%c refers to 10, 20, and 30% EVAc coating, respectively. Each point is the mean of four data points, and the standard errors of the mean of release at each time point are within 4.5%.

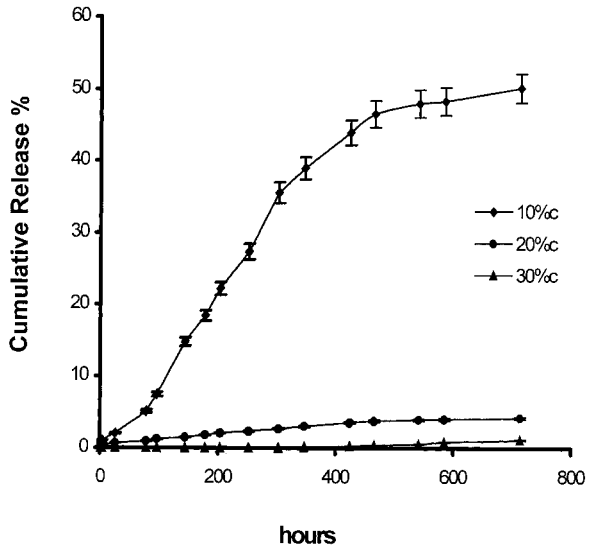

Figure 6—Cumulative percent release of IgG from 10, 20, and 30% coated matrixes. The symbolic representations and the standard errors are the same as those of Figure 5.

matter transfer coefficient ($h \rightarrow \infty$ and $N \rightarrow \infty$) on the surface. However, a slight deviation of the fitting of model II when compared to model I at higher time i.e., $t > 500$ h (Figure 4c) might be due to the experimental conditions involved and the limitations imposed by model II when the surface concentration C_s tends toward the equilibrium concentration C_e. This error observed is practically negligible, considering the fact that more than 76% of IgG has been released at that point of time (Figures 4a and 4b), and the rate of release is so low enough that the fraction of drug released is only 3% during the period greater than 400 h (Figure 4c).

Coating of matrixes (slab) in polymer solution significantly controlled the release rate as seen in Figure 5 which shows the release rate of IgG from matrixes coated in 10%, 20%, and 30% EVAc solution. The profile obtained is not as smooth as that got for uncoated matrixes. The sudden rise and fall in the release rate might be due to the EVAc coating, which, although initially impermeable to the IgG molecules, gradually forms a porous network due to the entry of the buffer solution, thereby bringing about the release of IgG molecules. Hence, a sudden rise in the release rate occurs, which then decreases because of the existence of one of the two limiting cases that have already been mentioned in this paper for uncoated matrixes. From Figure 6, we find that only about 50% and 4% of IgG has been released from the 10 and 20% coated matrixes after 700 h. In fact, the release of IgG from the 20% coated matrix is almost following a time-independent release profile, and this will continue until the coating gives way to porous networks for the IgG molecules to diffuse out. Coating of 30% EVAc polymer solution (or rather a paste because of its highly viscous nature) does not show any measurable release for the first 2 weeks after which the release gradually followed the 20% coating case.

From a clinical viewpoint, one of the primary objectives of sustained release is to maintain the required drug concentration at a reduced dosage level in patients. The usual dose of immunoglobulin for a primary immunodeficiency disease is 200 mg/kg of a patient's body weight[23] normally administered once per month by intravenous infusion (ivi). Although the minimum concentration of IgG necessary for protection has not yet been established, Pirofsky[18] has reported that an ivi of 150 mg/kg to a patient will result in the increase of serum IgG concentration to approximately 300 mg/dL which decays or is used up completely over a span of 28 days. Extrapolating from our experimental data, we find that a slab polymer drug matrix of dose 2.771 mg/kg (assuming an average patient weight as 50 kg) can give the same residual IgG concentration as the 150 mg/kg ivi case and can persist for a period more than one month before resulting in the decrease of concentration for a period of at least 2 months. This dose is found approximately 54 times less than the apparent ivi dose reported by Pirofsky.[18] Therefore a 3.704 mg/kg dose of the polymer–drug matrix can bring about the same effect as the conventional ivi of 200 mg/kg. Since it is a 30% loaded matrix, the total mass of the matrix administered to a 50 kg patient will be 617.5 mg. Hence, approximately six slabs of ~100 mg each will solve the process. Although the comparison above will be valid only if we get the exact relation between the in vitro and in vivo study, this work serves as a preliminary step in identifying the role played by controlled drug delivery to attenuate the problems faced by some of the conventional methods of drug treatment.

The methodology employed in the fabrication of microspheres is a nonaqueous encapsulation protocol in contrast to the commonly used double emulsion encapsulation technique.[24] The nonaqueous methodology is advantageous because it enhances the stability or the structural conformation of IgG, thereby protecting the native structure of the biomolecule as mentioned by Costantino et al.[25] The dehydrated proteins on suspension in organic solvents are conformationally rigid, and the chances of moisture induced aggregation are drastically reduced. Further, the question posed on the deteriorating activity of the protein under such conditions and the ways to overcome them have been discussed by Klibanov.[26] However, the study of IgG stability will be a very interesting topic for future investigations in this field.

All the release kinetics were studied under stagnant conditions (i.e. no shaking), since the implanted materials are localized in a rigid manner as in the case of a drug–polymer matrix being compactly placed and held inside the resection cavity of the pathological site.[27] Studies correlating the in vivo and in vitro release are few, and they greatly depend on the physiological environment in which the wafer has been placed, the presence of fluid remaining around the site, and the type of wafer involved. The initial flux F_o and the time constant of release τ are some of the few in vitro parameters that researchers use in their in

vivo model analysis.[28] The F_o and τ values in the case of slabs are given in Table 1. In the case of microspheres, the 30% loaded case had an initial flux value of 3.13×10^{-13} g·mol/cm^2·s and a time constant of 320.19 h with a deviation of less than 5%. The higher value of time constant and the lower value of F_o are due to the lag period experienced in the initial period of release. Hence, patients who cannot withstand high doses of IgG at the beginning can be recommended for the microsphere dosage form, and the slab dosage form can be recommended for the opposite case.

In general, the exact mechanism by which the IgG molecules are released through the EVAc into the buffer is based on a combination of different factors such as dissolution of the drug in the buffer, the relaxation rate of the polymer chains, the diffusion rate of the drug molecule through the polymer backbone, the experimental conditions involved, and last on the nature of the polymer, drug, and their interactions. This study serves as another step to elucidate the mechanism of release of macromolecules through an EVAc backbone and tries to identify the dosage form suitable for different type of patients.

Conclusions

The in vitro release kinetics of IgG−EVAc system fabricated by a solvent-casting method was studied for slab and microsphere geometry. Mass loading of IgG was found to affect the release rates significantly for both geometries. Release experiments conducted for the 30% loaded slab matrixes showed that the release rate followed a classical Fickian type of diffusion until 75% drug release (or for time $t < 15$ days) and gradually approaches the time-independent release for $t > 30$ days. Experiments conducted with matrixes of different surface areas showed a similar release pattern, and reproducible initial release flux and time constants were obtained. The one-dimensional pattern of drug release was the cause for reproducible results. Coating significantly controls the release rate of IgG from the matrix with the 20% EVAc-coated matrix providing a quasi-zero order drug release. Microsphere geometry gives a release pattern similar to the slab geometry, except for the initial lag time followed by Fickian type of diffusion. A model incorporating the finite matter coefficient of transfer on the surface seems to be more accurate than another model, which has an infinite matter transfer coefficient on the surface. The temporal variation of the diffusion coefficient was not significant. On correlating the experimental results with clinical data, it was worth noting that the polymeric implant dosage form can reduce the dose administration drastically compared with standard dosage forms.

References and Notes

1. Dwyer, J. M. Thirty years of supplying the missing link. *Am. J. Med*. **1984**, *76*, 46−52.
2. French, M. A. H. Serum immunoglobulins in disease diagnosis and management. In *Immunoglobulins in Health and Disease*; French, M. A. H., Ed.; MTP Press Ltd.: Lancaster, England, 1986; pp 123−142.
3. Jain, R. K. Physiological barriers to delivery of Monoclonal antibodies and other macromolecules in tumors. *Cancer Res. (Suppl)* **1990**, *50*, 814s−819s.
4. Hochberg, F. H.; Pruitt, A. Assumptions in the radiotherapy of gliobastoma. *Neurology* **1980**, *30*, 907−911.
5. Langer, R. S.; Folkman, J. Polymers for the sustained release of proteins and other macromolecules. *Nature* **1976**, *263*, 797−799.
6. Kuo, P. Y.; Sherwood, J. K.; Saltzman, W. M. Topical antibody delivery systems produce sustained levels in mucosal tissue and blood. *Nature Biotech*. **1998**, *16*, 163−167.
7. Cleek, R. L.; Ting, K. C.; Eskin, S. G.; Mikos, A. G. Microparticles of poly (DL-lactic-*co*-glycolic acid)/poly (ethylene glycol) blends for controlled drug delivery. *J. Controlled Release* **1997**, *48*, 259−268.
8. Langer, R. S.; Brem, H.; Tapper, D. Biocompatibility of polymeric delivery systems for macromolecules. *J. Biomed. Mater. Res.* **1981**, *15*, 267−277.
9. Yang, M. B.; Tarmargo, R. J.; Brem, H. Controlled delivery of 1,3-bis(2-chloroethyl)-1-nitrosourea from ethylene-vinyl acetate copolymer. *Cancer Res.* **1989**, *49*, 5103−5107.
10. Fulton, S. P.; Meys, M.; Varady, L.; Jansen, R.; Afeyan, N. B. Antibody quantitation in seconds using affinity perfusion chromatography. *BioTechniques* **1991**, *11*, 226−231.
11. Sefton, M. V.; Brown, L. R.; Langer, R. S. Ethylene vinyl acetate copolymer microspheres for controlled release of macromolecules. *J. Pharm. Sci.* **1984**, *73*, 1859−1861.
12. Rhine, W. D.; Hsieh, D. S. T.; Langer, R. S. Polymers for sustained macromolecular release: Procedures to fabricate reproducible delivery systems and control release kinetics. *J. Pharm. Sci.* **1980**, *69*, 265−269.
13. Crank, J. *The mathematics of diffusion*, 2nd ed.; Clarendon Press: Oxford, England, 1975.
14. Vergnaud, J. M. *Liquid transport processes in polymeric materials*; Prentice Hall, Inc.: New Jersey, 1991.
15. Vergnaud, J. M. *Controlled Drug Release of Oral Dosage Forms*; Ellis Horwood Ltd.: West Sussex, England, 1993.
16. Gurny, R.; Doelker, E.; Peppas, N. A. Modelling of sustained release of water-soluble drugs from porous, hydrophobic polymers. *Biomaterials* **1982**, *3*, 27−32.
17. Hsieh, D. S. T.; Rhine, W. D.; Langer, R. S. Zero-order controlled release polymer matrixes for micro- and macromolecules. *J. Pharm. Sci.* **1983**, *72*, 17−22.
18. Pirofsky, B. Intravenous Immunoglobulin therapy in hypogammaglobulinemia. *Am. J. Med.* **1984**, *76*, 53−60.
19. Saltzman, W. M.; Sheppard, N. F.; McHugh, M. A.; Dause, R. B.; Pratt, J. A.; Dodrill, A. M. Controlled antibody release from a matrix of poly (ethylene-*co*-vinyl acetate) fractionated with a supercritical fluid. *J. Appl. Polym. Sci.* **1993**, *48*, 1493−1500.
20. Radomsky, M. L.; Whaley, K. J.; Cone, R. A.; Saltzman, W. M. Macromolecules released from polymers: diffusion into unstirred fluids. *Biomaterials* **1990**, *11*, 619−624.
21. Saltzman, W. M.; Langer, R. S. Transport rates of proteins in porous materials with known microgeometry. *Biophys. J.* **1989**, *55*, 163−171.
22. Miller, E. S.; Peppas, N. A. Diffusional release of water-soluble bioactive agents from ethylene vinyl acetate copolymers. *Pharm. Res.* **1983**, *22*, 303−315.
23. Immune Globulin intravenous (human) Venoglobulin-I lyophilized: Product information. Alpha Therapeutic Corporation: Los Angeles, CA, 1995.
24. Cohen, S.; Yoshioka, T.; Lucarelli, M.; Hwang, L. H.; Langer, R. S. Controlled Delivery Systems for Proteins Based on Poly (Lactic/Glycolic Acid) Microspheres. *Pharm. Res.* **1991**, *8*, 713−720.
25. Costantino, H. R.; Griebenow, K.; Mishra, P.; Langer, R. S.; Klibanov, A. M. Fourier transform infrared spectroscopic investigation of protein stability in the lyophilized form. *Biochim. Biophys. Acta*. **1995**, *1253*, 69−74.
26. Klibanov, A. M. Why are enzymes less active in organic solvents than in water? *Trends Biotechnol.* **1997**, *15*, 97−101.
27. Guilford Pharmaceuticals, Gliadel WAFER, 1995.
28. Wang, C.-H.; Li, J. Three-Dimensional Simulation of IgG Delivery to Tumors. *Chem. Eng. Sci.* **1998**, *53*, 3579−3600.

Acknowledgments

This work has been supported by the National Medical Research Council, Singapore, under the grant number NMRC/0232/1997 (RP970658N). We also thank the Green Cross Corporation, Singapore, and Alpha Therapeutic Corporation, Los Angeles, CA, for providing the Venoglobulin-I sample. The technical support by Hsin Min Wong is also greatly appreciated.

JS9803407

Controlled Release of Human Immunoglobulin G. 2. Morphological Characterization

CHI-HWA WANG,*,† KAMALESH SENGOTHI,† HSIN MIN WONG,† AND TIMOTHY LEE‡

Contribution from *Department of Chemical Engineering and Department of Surgery, National University of Singapore, 10 Kent Ridge Crescent, Singapore - 119260.*

Received November 2, 1998. Accepted for publication November 3, 1998.

Abstract □ Human immunoglobulin G (IgG) serves as an important chemotherapeutic agent for a number of immunological ailments and as a carrier in the targeted delivery of other therapeutic agents. This paper deals with the characterization of IgG-dispersed monolithic matrixes of different geometries, prepared using a nonbiodegradable polymer carrier EVAc. The morphological changes associated with the matrix during drug release was studied using scanning electron microscopy, polarizing microscopy, atomic force microscopy, and X-ray photoelectron microscopy, and the results were compared. The study answered the burst effect problem significantly and illustrated the potential of these techniques in understanding the morphological structure of matrixes and mode of release kinetics.

Introduction

The topic of controlled drug release has received significant contributions from the scientific world ever since the work of Langer and Folkman in the mid-1970s.[1] A number of different types of polymers[2−6] have been used for the controlled release studies, and the mode of release varies with the polymer type. Although release kinetics studies and the fitting of experimental data to model equations would give us some understanding of the type of release mechanism involved, the results obtained can be ascertained by conducting matrix characterization studies for matrixes during different stages of drug release. Release kinetics of immunoglobulin G (IgG), from a nonbiodegradable EVAc polymer, have been discussed elsewhere.[7] It was noted that dissolution plays a significant role during the initial stages of release, while diffusion predominates in the later period. This variation in the release mechanism necessitated the use of combination of models to describe the release behavior. In this report, an extensive study has been made in the morphological characterization of these matrixes both in the qualitative and quantitative sense. A variety of techniques such as the scanning electron microscopy, atomic force microscopy, polarizing microscopy, and X-ray photoelectron microscopy were used for matrix characterization.

Scanning electron microscopy (SEM) still serves as a preliminary surface characterization technique for numerous drug delivery systems.[3,8−10] The technique is greatly appreciated when applied to biodegradable systems in which marked changes in matrix morphology occur with release. However, in the present study, nonbiodegradable EVAc matrixes of different geometries under varied stages of release were examined under SEM for both the surface and cross-section analysis.

Atomic force microscopy (AFM) is used to study the surface features of polymeric materials by visualizing their morphology, nanostructure, molecular order, and surface compositional mapping in heterogeneous samples with a resolution down to the atomic level.[11] The need to choose AFM for matrix characterization is because of its attractive feature of obtaining two- and three-dimensional topographical features of material surfaces at extremely high resolution in either vacuum, liquid, or ambient atmospheres. AFM is a mechano-optical instrument, which detects atomic-level forces ($\sim nN$) through optical measurements of movements of a very sensitive cantilever tipped with a hard, pyramid-shaped crystal that moves along surfaces. Typical working mode of AFM is the contact mode, where the AFM tip remains (more or less) in contact with the surface (some friction may be observed). Most AFMs have vertical resolution below 0.1 nm range, whereas lateral resolution is usually lower due to the sharp tip and the small loading force involved.

Polarizing microscopy (PM), when equipped with a hot stage, is a valuable tool for measuring phase transitions and crystallization kinetics. When the sample is placed between two crossed polarizing filters, different colors based on varying thickness, texture, stress level, and bond arrangement of polymer chains can be observed. The first polarizing filter polarizes or limits the vibration of light waves to one plane. When the polarized light passes through the polymer, its direction of polarization is altered depending on the thickness and texture of the polymer. The final direction of polarization determines whether light of a certain wavelength can pass through the second polarizing filter. The importance of this technique lies in the fact that it is able to qualitatively analyze the change in IgG concentration on the EVAc matrix surface.

X-ray photoelectron microscopy (XPS) is by far the most widely used surface spectroscopic instrument. When a surface is irradiated with soft X-ray photons, electrons from inner shells can be ejected with a definite binding energy. Therefore, XPS is capable of elemental analysis since no two atoms of the periodic table exhibit the same set of binding energies. Qualitative analysis of the elements can be easily performed by wide scans, in which all the available energy range is explored. Quantitative elemental analysis is performed by detail scans, where a small portion of the binding energy range is acquired with a higher spectral resolution than in the wide scans.

The characterization studies were performed for matrixes in different stages of drug release. The results obtained were then used to get a reasonable explanation for the type of release mechanism and the extent of drug distribution in the matrix.

Materials and Methods

IgG-EVAc systems of different geometries, viz. slabs, microspheres, and cubes, were fabricated as described in a previous

* Corresponding author. Telephone: 65-8745079. Fax: 65-7791936. E-mail: chewch@nus.edu.sg.
† Department of Chemical Engineering.
‡ Department of Surgery.

10.1021/js980443p CCC: $18.00
Published on Web 01/13/1999

Table 1—Mean Diameter of Microspheres of Different % IgG Loadings

microsphere type	mean diameter[a] (mm)	standard deviation
10% IgG loading	1.09	0.082
20% IgG loading	1.19	0.065
30% IgG loading	1.20	0.101

[a] Average of 20 beads.

paper.[7] Blank matrixes (without IgG) were also fabricated in a similar manner. The different matrixes were then subjected to release in 0.1 M phosphate buffer, pH 7.4, for a time span of 3 to 8 weeks. They were then removed by forceps, blotted dry by tissue, and subjected to characterization studies.

Scanning Electron Microscopy (SEM)—Samples of slab and microsphere were stuck on to metallic cylinders by making use of a double-sided carbon adhesive tape, which were then sputter-coated using an ion sputtering device (JFC-1100E, JEOL Co., Tokyo, Japan) and observed under SEM (JSM-T330A, JEOL Technics Co. Ltd., Tokyo, Japan).

Atomic Force Microscopy (AFM)—Samples of slab were cut into thin sections using a surgical blade (Hecos, Shanghai, China) and observed under AFM (Topometrix, TMX-2000, Topometrix Corp., Santa Clara, CA). Explorer AFM was used as the stage type and the image resolution was fixed at 200 × 200 pixels under forward scan direction and 0° rotation with system calibration. In addition, this instrument employs a "double cross" cantilever, which restricts the motion of the tip to the "Z" direction (normal to the sample surface). Scanning was done using an E449701 type scanner at the rate 200 μm/s, and the sample bias was fixed at 1 mV. Microspheres, because of their natural curvature, are difficult to be observed under AFM and hence are not shown.

Polarizing Microscopy (PM)—Samples of slab and microsphere were observed under PM-BX50 (Olympus, Japan). A 530 nm sensitive tint plate (U-TP530) was used as a test plate compensator, which resulted in a magenta background for the pictures taken. A hot stage (Cole-Parmer Digital Hot Plate, Model no. 8207C-2 Vernon Hills, IL) was used to increase the specimen temperature at selected rates, and the system was capable of taking a time series of photographs while holding the sample at a constant temperature. Visual observations of specimen transitions and the temperatures at which they occur may be recorded.

X-ray Photoelectron Spectroscopy (XPS)—Samples of slab were observed under XPS (VG ESCALAB MKII spectrometer) with Mg Kα (1253.6 eV, 120W) as X-ray source and neutral C1s (284.6 eV) as BEs reference to determine the elemental composition of the matrix. The take-off angle was set at 75°, and the chamber pressure was maintained at $\leq 1 \times 10^{-8}$ mbar. FWHM was kept constant for all the components. To investigate the distribution of IgG on the surface of IgG/EVAc system, a combined XPS method of wide scan with detail scan was employed. Elemental ratios of O/C and N/C were calculated by the method of detail scan. For the purpose of comparison with 30% IgG film sample, we also grinded it into fine powder using a mortar and pestle and then measured its XPS value.

Results and Discussion

(a) Particle Size Analysis—In the present study, the dependence of microsphere size on the needle size and the drug loading (which affects the viscosity and surface tension of the solution) was examined by maintaining a uniform extrusion rate (2−3 mL/min). The microsphere particle size was measured using the Nikon SMZ-1 microscope. The size distribution was compared for spheres with different drug loadings and for spheres with different diameters prepared using different sized needles. The results are tabulated in Tables 1 and 2. It is quite clear that the size increases as drug loading is increased and as needle size is increased. In spite of the size being in the range of 1000 μm, we can still consider these beads as microspheres since their size is within the range ca. 50 nm−2 mm.[12]

(b) SEM—Observations of the SEM pictures for slabs (Figure 1) show that the EVAc−IgG unreleased (Figure 1a)

Table 2—Mean Diameter of Microspheres Prepared Using Different Needle Sizes for the Blank (without IgG) and the 20% IgG-Loaded Cases

	mean diameter[a] (mm)		standard deviation	
needle size	blank	20% loading	blank	20% loading
16 gauge	0.99	1.19	0.071	0.065
19 gauge	0.88	0.95	0.097	0.062
23 gauge	0.68	0.81	0.096	0.049

[a] Average of 20 beads.

matrix surface was uniform without any clear demarcation of the IgG molecules in the matrix. The matrix surface, which can be described as an extended, highly loose globular, viscous, cloudy surface was found to be spread uniformly over and within the matrix (Figure 1b). This could not be seen in the blank sample of EVAc polymer (no drug case) matrix, which was made up of a clear continuous phase. Even the cross-section of the blank showed a clear phase distribution without the presence of any matrix deformities or pores. In the case of EVAc−IgG matrix subjected to release for 45 days (Figure 1c), the deformation of the continuous polymer phase can be clearly observed. The deformation might be due to the swelling of the dispersed IgG particles upon uptake of diffusant.[13] Further, cracks and channels, possibly due to the interconnection of the pores were also observed in the cross-section of Figure 1d. Figures 1e−h are the SEM pictures of 30% loaded cubic samples. Compared with the slab samples, the unreleased sample (Figure 1e) exhibits a similar continuous undeformed phase, whereas the cross-section (Figure 1f) reveals the presence of "pocket-filled IgG cluster" like structures. Surface (Figure 1g) and cross-section (Figure 1h) of the sample subjected to release for two months reveal deformities as expected. However, the cross-section reveals distinct pores rather than channels (seen in Figure 1d), which can be attributed to the difference in geometry between the two cases.

SEM pictures of microsphere are shown in Figure 2. The thready polymer entanglements are clearly visible in Figure 2a. Figure 2b shows a portion of the blank sample cut off. It was noticed that the cross-section of the blank exhibits a hollow region. This feature might be due to the evaporation of methylene chloride from the matrix during its fabrication. The 30% loaded sample in Figure 2c shows certain complications in the surface morphology. Again, the cross-section in Figure 2d of the loaded sample before release shows a hollow region. However, no pores are visible on the matrix surface. The sample subjected to release for three weeks in Figure 2e shows a little bit of swelling, and minute pores or channels can be noticed (possibly due to the relaxation of the polymer chains). Finally, Figure 2f, a cross-section of the loaded sample taken in the transverse direction, after three weeks of release, reveals pores along with the expected hollow region observed along the side. Hence, a common feature noted in all the three geometries is the increase of matrix porosity with prolonged exposure to the release medium. Since the polymer is hydrophobic and nonbiodegradable, the occurrence of such deformities such as pores and cracks can be attributed due to the drug−solvent interaction—dissolution of the drug in the solvent, swelling of the drug due to solvent uptake, and gradual diffusion through the solvent-filled pores and channels.

(c) AFM—AFM pictures of the slab samples are shown in Figure 3. Observation of the blank sample (Figure 3a) shows a smooth, flat surface. The numerous tiny spots, which appear on the figure, are not pores but are rather microscopic depressions on the surface due to the evaporation of the solvent. On observing the IgG-loaded sample

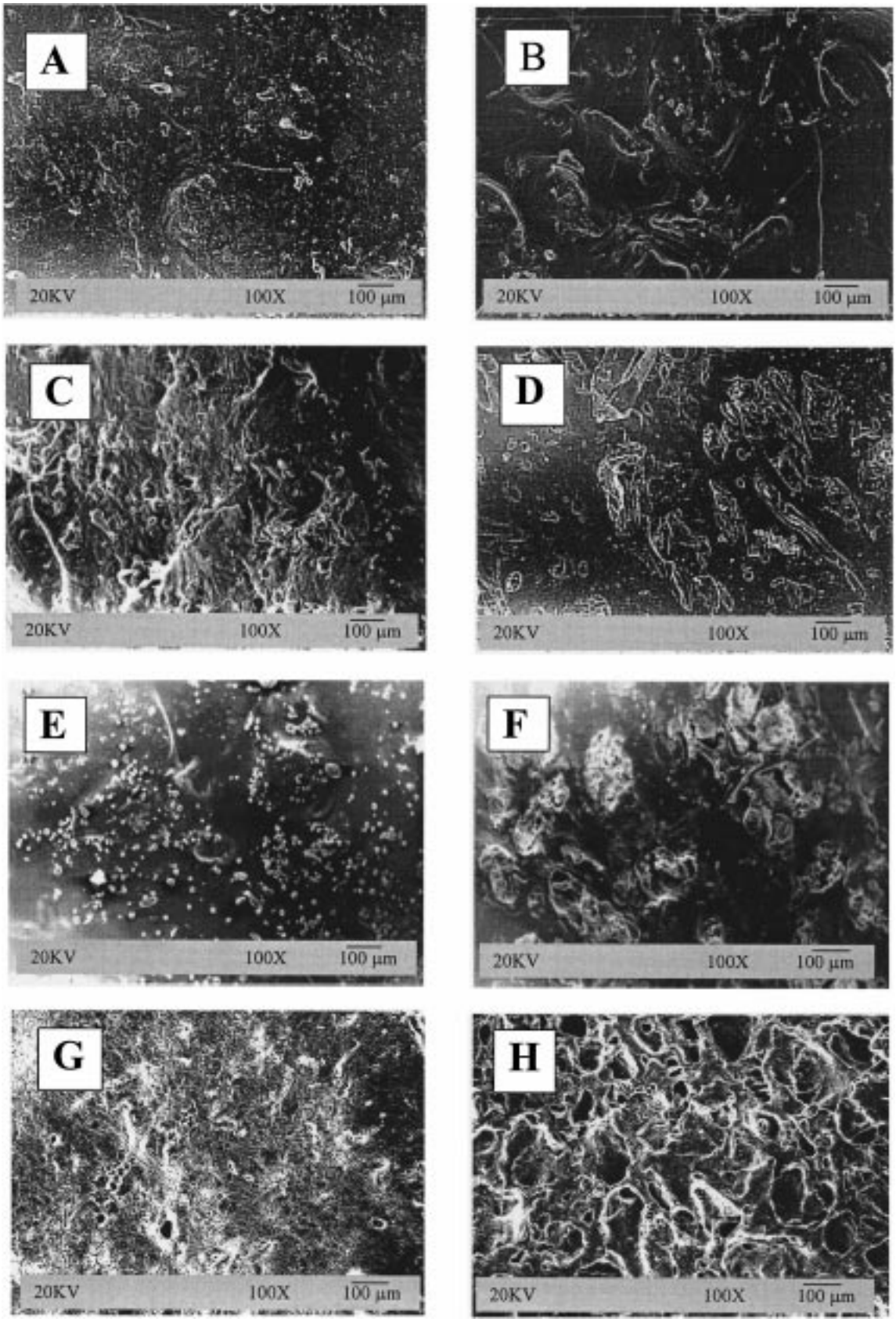

Figure 1—Scanning electron microscopy photographs of 30% IgG loading for (a) slab, before release, (b) slab cross-section, before release, (c) slab, after 45 days of release, (d) slab cross-section, after 45 days release, (e) cube, before release, (f) cube cross-section, before release, (g) cube, after 2 months of release, (h) cube cross-section, after 2 months of release. All pictures are of 200× magnification.

before release (Figure 3b), we find that the surface has a fluffy appearance with numerous bumps and undulations. The depressions seen on the blank sample have been completely filled up, and a homogeneous matrix surface could be observed. The dark spot appearing on the far corner of the figure is just an artifact created due to the

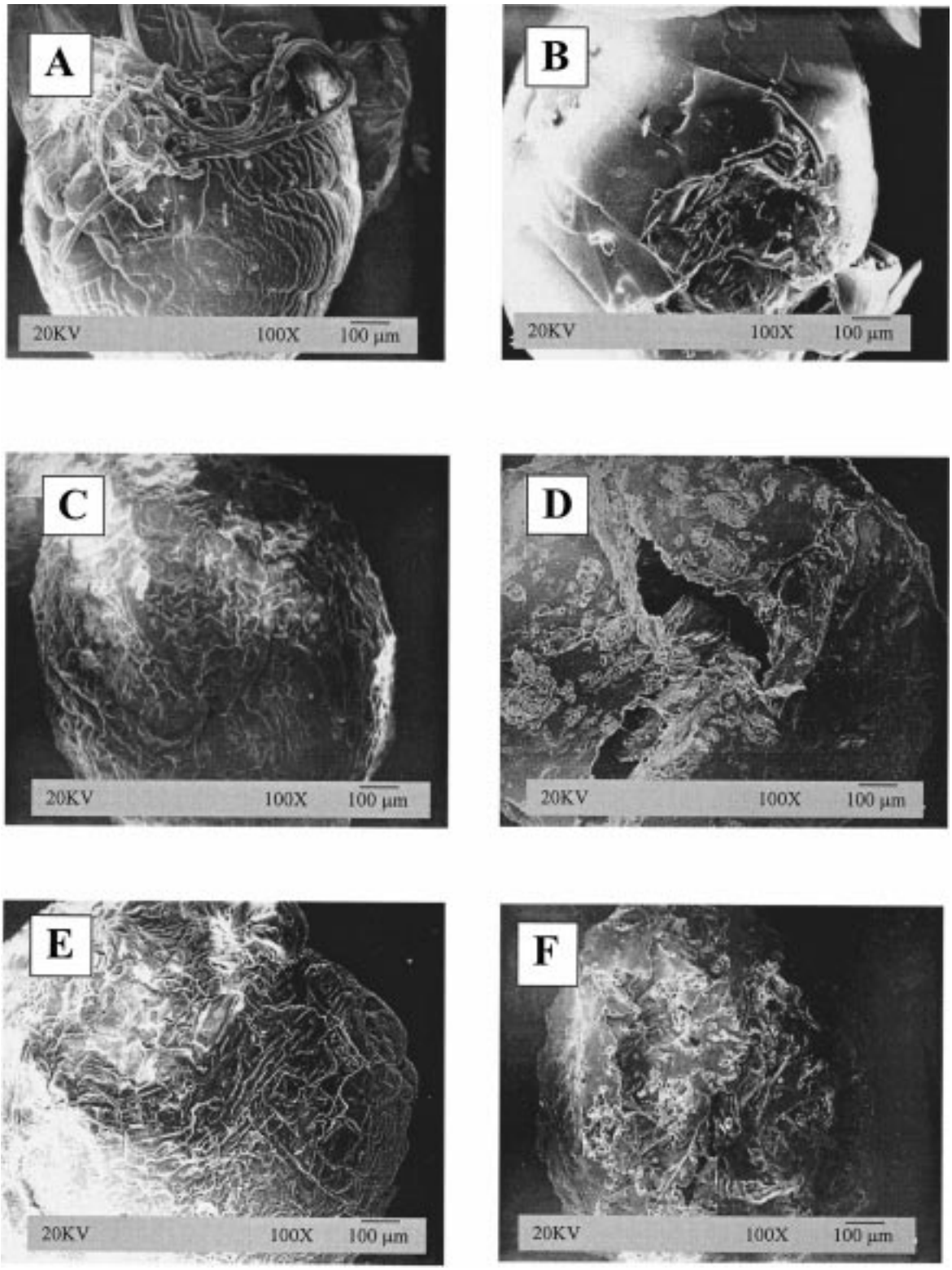

Figure 2—Scanning electron microscopy photographs of microspheres for (a) blank, (b) cross-section of blank, (c) 30% IgG loading, before release, (d) cross-section of 30% IgG loading, before release, (e) 30% IgG loading, after 3 weeks of release, (f) cross-section of 30% IgG loading, after 3 weeks release. All pictures are of 100× magnification.

sectioning of the sample for AFM studies. Figure 3c is an AFM picture of the sample subjected to release for 30 days. We can clearly see pores on the surface, with occasional strips of fluffy mass seen in the before release sample. AFM results confirm the nonbiodegradable nature of the EVAc polymer and backs the SEM results of drug dissolution into the buffer-filled pores followed by diffusion.

(d) PM—The PM pictures of the slab can be viewed in Figures 4a–c. The blank sample can be observed in Figure 4a. The sample placed between two crossed polarizing filters gives different shades of colors depending on the depths at which the light penetrates, and the colors are reflected based on the refractive index of the component. The complexity of the structure increases with the drug loading as shown in the 30% drug-loaded sample before release (Figure 4b). Numerous opaque dark spots could be

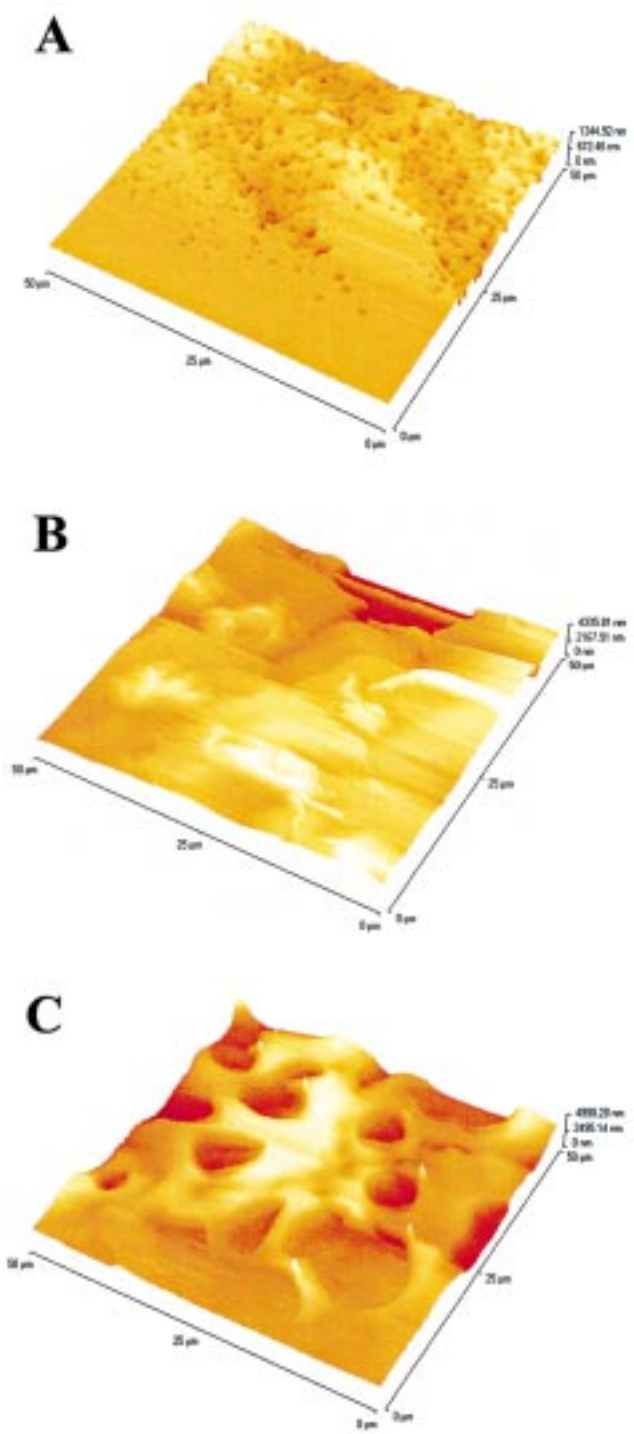

Figure 3—Atomic force microscopy pictures of slabs for (a) blank, (b) 30% IgG loading, before release, (c) 30% IgG loading, after 30 days release.

observed which are not present in the blank sample. The fact that these are IgG clusters cannot be completely ignored. This assumption is further strengthened by the reduction of such a structural feature in the sample subjected to release for 45 days, as shown in Figure 4c. A thorough analysis of the dark spots on Figure 4b was done by magnifying them and comparing with the PM pictures of raw IgG molecules and they did show similar structure (Figure 5). PM pictures of microspheres can be viewed in Figures 4d–f. The blank sample in Figure 4d shows some similarity with the SEM picture in Figure 2a with respect to the external morphology. In fact, higher magnification of Figure 4d reveals the presence of some polygonal structures on the matrix surface, which could also be observed in the SEM at higher magnifications. Similar to Figure 4b, dark spots can be observed in the 30% drug-loaded sample before release (Figure 4e) which are likely to be IgG molecules, but the decreased concentration of these spots when compared to the slab surface (Figure 4b) is attributed to the dosage form involved. The reduced black spot concentration on the microsphere surface also answers the decrease in burst effect observed for this geometry when compared to the case of slab geometry. The black spot concentration decreases with the release of IgG molecules, as shown in the sample subjected to release for 3 weeks (Figure 4f). However, this decrease is not as pronounced with respect to the relative decrease in concentration of black spots from Figure 4b to 4c. This is quite logical looking at the fact that only about 55% of IgG has been released after 3 weeks for a microsphere when compared to the 81% release observed for the slab after 46 days.[7]

(e) XPS—The wide scan and detail scan XPS pictures are shown in Figure 6. Theoretically, the photoelectron binding energy E_b is given by the following relation[14]

$$E_b = h\nu - E_k - \phi \qquad (1)$$

where $h\nu$ is the photon energy of the X-ray source (1253.6 eV in the present case), E_k is the kinetic energy of the photoelectron, and ϕ is the spectrometer work function (defined as the energy required to remove the uppermost electrons).

Examination of blank sample by wide scan XPS showed that the main elements of EVAc were C (carbon) and O (oxygen), without N (nitrogen), as seen in Figure 6a, while the wide scan XPS of pure IgG showed the presence of a N1s peak along with C1s and O1s peaks, thereby indicating the presence of nitrogen in pure IgG (Figure 6d). The peak of N1s is centered near 399.0 eV (Table 3), a value characteristic of the amino group from a protein. Hence, we may assume the concentration of nitrogen determined by the XPS method as an indirect measure of IgG concentration on the surface of the IgG–EVAc system. Interestingly, 30% IgG-loaded samples, exhibited a stronger N1s peak for its grinded version (Figure 6b) than its film version (Figure 6c). Further, detail scans of XPS revealed that the powdered sample had a higher N/C ratio than the film sample (Table 3). The reduced surface concentration of IgG in the film sample can be due to the relatively faster migration of EVAc to the surface compared to IgG during the evaporation of methylene chloride, which was ultimately reflected in the results due to the surface specific detection property of XPS. On the other hand, the sample obtained by grinding the film to a fine homogeneous blend of powder, exhibited an increased concentration of IgG on the surface, resulting in a stronger N1s peak in the wide scan XPS and a corresponding increase in the N/C ratio. Since XPS can be used to measure the elemental composition present on sample surfaces alone, we utilized this aspect to our advantage in trying to get an explanation for the "burst effect" or the increased release rate of drugs at the initial time period. Since most of the element nitrogen (N) is present in the IgG molecule (constituting about 85% wt in the Venoglobulin-I sample[15] used for the release study), an analysis of the N/C composition for the slab sample (top surface) and its grinded version (sample grinded to get a flat layer) will give the approximate IgG composition in the top surface of the slab and the overall IgG composition of the slab. The percentage of IgG present on the top surface calculated in this manner was found almost equal to the fraction of IgG released in the first hour (with an error less than 10%). Hence the burst effect might

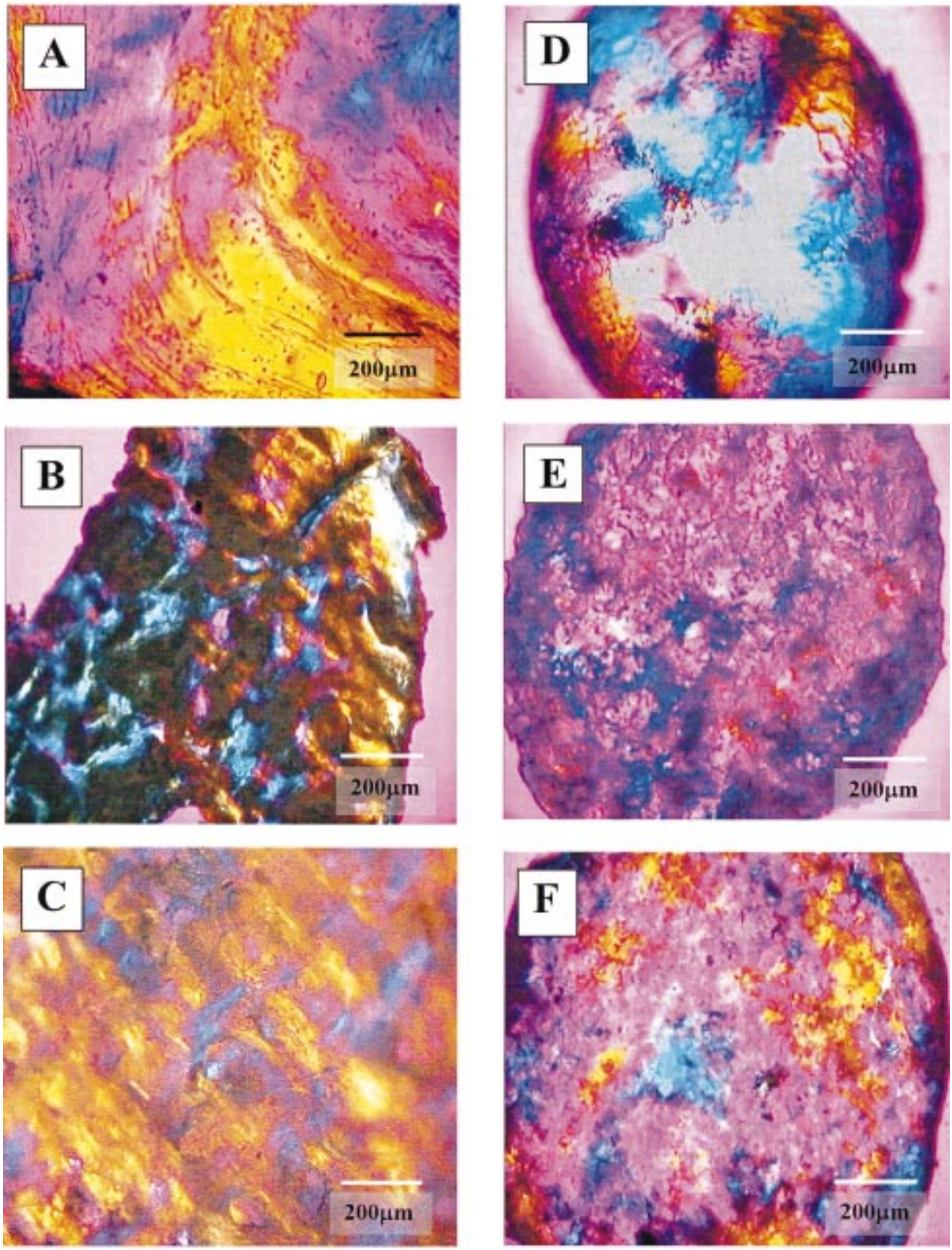

Figure 4—Polarizing microscopy pictures for (a) slab, blank, (b) slab, 30% IgG loading, before release, (c) slab, 30% IgG loading- after 45 days release, (d) microsphere, blank, (e) microsphere, 30% IgG loading, before release, (f) microsphere, 30% IgG loading, after 3 weeks of release.

be primarily due to the surface concentration of IgG molecules, and this can be avoided by the use of coated matrixes.

The utilization of microspheres of size range in the order of 800 to 1100 μm prevents phagocytosis by macrophages. Immunologically speaking, macrophages play an important

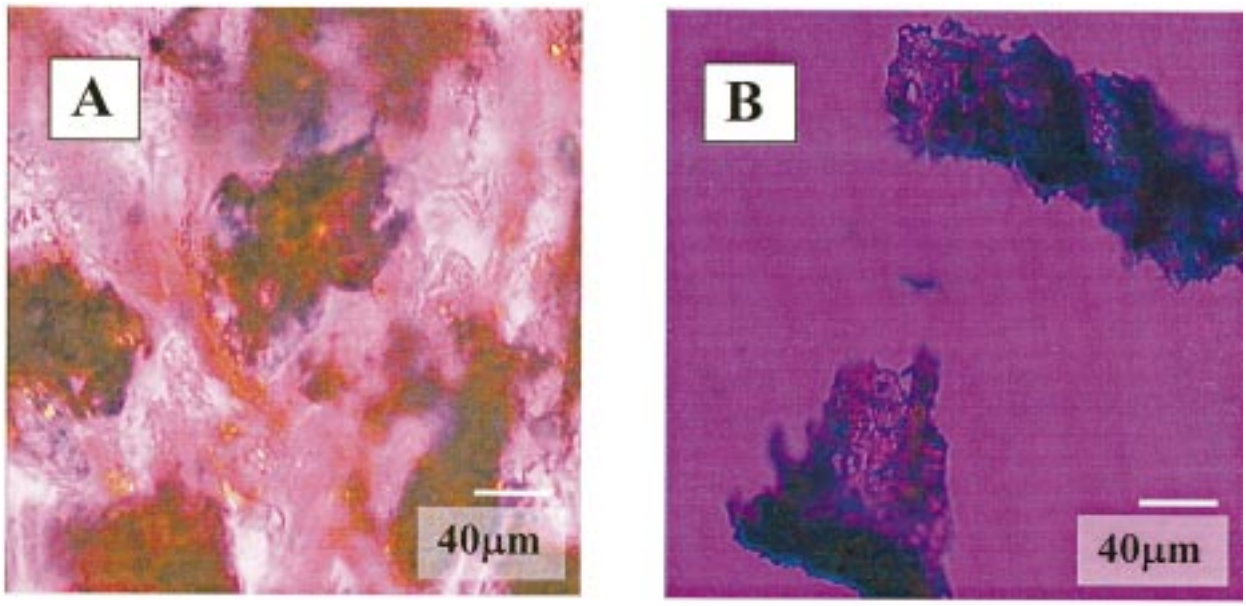

Figure 5—Polarizing microscopy pictures of (a) black spot on the matrix surface, (b) raw IgG clusters.

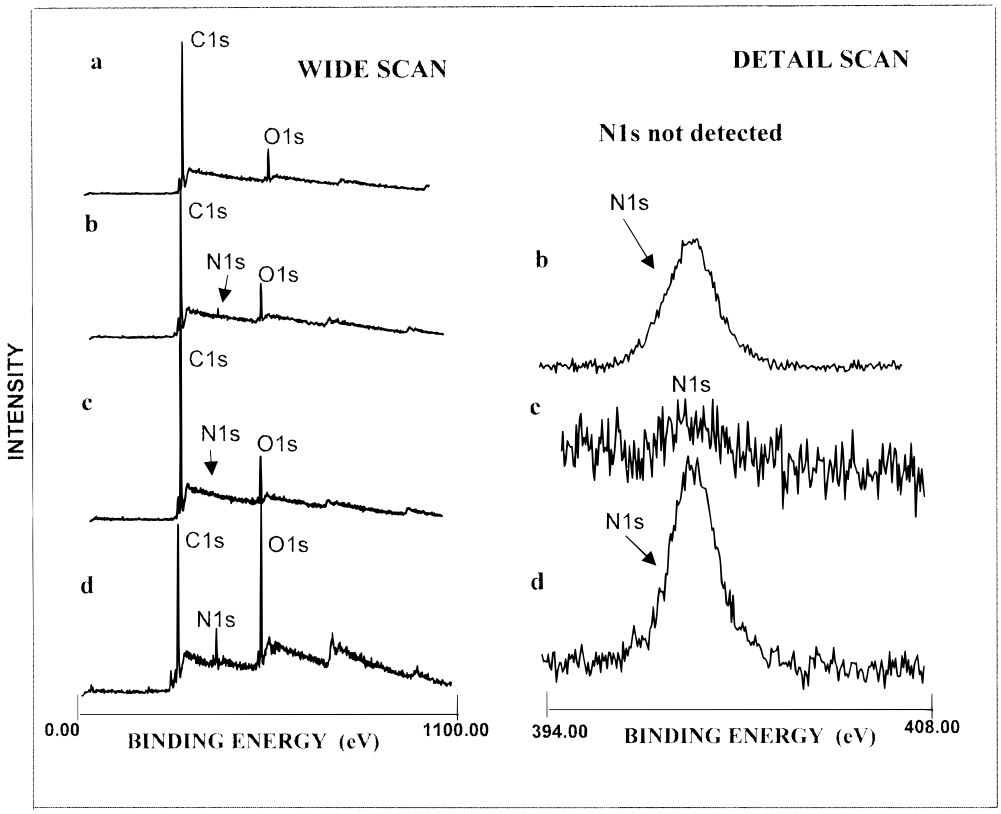

Figure 6—XPS spectrum for (a) blank, (b) 30% IgG loading, before release, powder, (c) 30% IgG loading, before release, film, (d) pure IgG.

Table 3—Detail Scan Data of XPS for Different Samples

sample	binding energy N1s (eV)	N/C	O/C
blank	–	–	0.1249
30% IgG-loaded film	399.10	0.0024	0.1323
30% IgG-loaded powder	399.52	0.0395	0.1799
IgG powder	400.00	0.1361	0.4328

role in the body's defense mechanism by engulfing or phagocytosing foreign bodies or antigenic particles and triggering the formation of antibodies to act against these antigens. Hence, microspheres of size range less than 800 μm have an increased probability of being engulfed by macrophages, which triggers the formation of anti-antibodies, thereby affecting the basic principle of treatment. This explains the role of microsphere size selection for therapeutic purposes.

Conclusions

Matrix characterization studies were performed using SEM, AFM, PM, and XPS. SEM and AFM studies gave a clear picture of the type of morphological changes encountered by the matrix in the release study. The results

indicate that the drug release mechanism is controlled by diffusion−dissolution irrespective of the matrix geometry. PM studies gave insight into the extent of IgG distribution in the polymer matrix while XPS results showed that the burst effect observed in the release studies during the initial period might be due to the surface concentration of IgG molecules. These characterization studies would therefore serve as supporting evidence to the in vitro release kinetics studies for IgG release through an EVAc backbone.

References and Notes

1. Langer, R. S.; Folkman, J. Polymers for the sustained release of proteins and other macromolecules. *Nature* **1976**, *263*, 797−799.
2. Miller, E. S.; Peppas, N. A. Diffusional release of water-soluble bioactive agents from ethylene vinyl acetate copolymers. *Pharm. Res.* **1983**, *22*, 303−315.
3. Cohen, S.; Yoshioka, T.; Lucarelli, M.; Hwang, L. H.; Langer, R. S. Controlled Delivery Systems for Proteins Based on Poly (Lactic/Glycolic Acid) Microspheres. *Pharm. Res.* **1991**, *8*, 713−720.
4. Kim, C. Compressed Donut-Shaped Tablets with Zero-Order Release Kinetics. *Pharm. Res.* **1995**, *12*, 1045−1048.
5. Wada, R.; Hyon, S.-H.; Ikada, Y. Kinetics of diffusion mediated drug release enhanced by matrix degradation. *J. Controlled Release* **1995**, *37*, 151−160.
6. Leong, K. W.; Brott, B. C.; Langer, R. S. Bioerodible polyanhydrides as drug carrier matrixes. I: Characterization, degradation and release characteristics. *J. Biomed. Mater. Res.* **1985**, *19*, 941−955.
7. Wang, C.-H.; Sengothi, K.; Lee, T. Controlled Release of Human Immunoglobulin-G. 1. Release Kinetics Study. *J. Pharm. Sci.* **1998**, *88*, 215−220.
8. Dang, W.; Daviau, T.; Brem, H. Morphological Characterization of Polyanhydride Biodegradable Implant Gliadel During in Vitro and in Vivo Erosion Using Scanning Electron Microscopy. *Pharm. Res.* **1996**, *13*, 683−691.
9. Chiba, M.; Hanes, J.; Langer, R. S. Controlled protein delivery from biodegradable tyrosine-containing poly (anhydride-*co*-imide) microspheres. *Biomaterials* **1997**, *18*, 893−901.
10. Iwata, M.; McGinity, J. W. Dissolution, Stability, and Morphological Properties of Conventional and Multiphase Poly (DL-Lactic-Co-Glycolic Acid) Microspheres Containing Water-Soluble Compounds. *Pharm. Res.* **1993**, *10*, 1219−1227.
11. Pizziconi, V. B.; Page, D. L.; Connolly, C. T.; Diamond, P. A. Scanning probe microscopy imaging and characterization of biological structures from biomolecules to living cells. In *Atomic force microscopy/Scanning tunneling microscopy*; Cohen, S. H., Bray, M. T., Lightbody, M. L., Eds.; Plenum Press: NewYork, 1994; pp 19−42.
12. Arshady, R. Microspheres for biomedical applications: preparation of reactive and labeled microsphere. *Biomaterials* **1993**, *14*, 5−15.
13. Hsu, T. T. P.; Langer, R. S. Polymers for the controlled release of macromolecules: Effect of molecular weight of ethylene vinyl acetate copolymer. *J. Biomed. Mater. Res.* **1985**, *19*, 445−460.
14. Burke, G. M.; Wurster, D. E.; Berg, M. J.; Veng-Pedersen, P.; Schottelius, D. D. Surface Characterization of Activated Charcoal by X-ray Photoelectron Spectroscopy (XPS): Correlation with Phenobarbital Adsorption data. *Pharm. Res.* **1992**, *9*, 126−130.
15. Immune Globulin intravenous (human) Venoglobulin-I lyophilized: Product information. Alpha Therapeutic Corporation: Los Angeles, CA, 1995.

Acknowledgments

This work has been supported by the National Medical Research Council, Singapore, under the grant number NMRC/0232/1997 (RP970658N). We also thank Professors Neal T.-S. Chung, Si-Shen Feng, and En-Tang Kang for their advice and help on the PM, AFM, and XPS measurements, respectively. The technical support by Dr.Gan Daoji is also greatly appreciated.

JS980443P

Prediction of Partition Coefficient Based on Atom-Type Electrotopological State Indices

JARMO J. HUUSKONEN,[†] ALESSANDRO E. P. VILLA,[‡] AND IGOR V. TETKO*[,‡,§]

Contribution from *Division of Pharmaceutical Chemistry, Department of Pharmacy, POB 56, FIN-00014 University of Helsinki, Finland, Laboratoire de Neuro-Heuristique, Institut de Physiologie, Université de Lausanne, Rue du Bugnon 7, Lausanne, CH-1005, Switzerland, and Biomedical Department, Institute of Bioorganic & Petroleum Chemistry, Murmanskaya 1, Kiev-660, 253660, Ukraine.*

Received June 29, 1998. Accepted for publication October 28, 1998.

Abstract □ The aim of this study was to determine the efficacy of atom-type electrotopological state indices for estimation of the octanol–water partition coefficient (log *P*) values in a set of 345 drug compounds or related complex chemical structures. Multilinear regression analysis and artificial neural networks were used to construct models based on molecular weights and atom-type electrotopological state indices. Both multilinear regression and artificial neural networks provide reliable log *P* estimations. For the same set of parameters, application of neural networks provided better prediction ability for training and test sets. The present study indicates that atom-type electrotopological state indices offer valuable parameters for fast evaluation of octanol–water partition coefficients that can be applied to screen large databases of chemical compounds, such as combinatorial libraries.

Introduction

The logarithm of the partition coefficient between octanol and water, log *P*, is extensively used to describe lipophilic or hydrophobic properties of chemical compounds. It has been shown that log *P* is a useful parameter to correlate transport properties of drug molecules, interactions between drugs and receptors, and changes in the structure of drugs with various biochemical or toxic effects of these compounds.[1] The measurement of log P throughout the synthesis of the compound and its subsequent experimental determination is time-consuming and expensive. Hence, there is a strong interest in the structure-based prediction of log P for rational development of new drugs before potential drug compounds have been synthesized.

Several approaches for computing log P on the basis of chemical structure have been proposed. Among others there are two essentially empirical methods for the estimation of log P: Rekker's *f* constant method and Leo and Hansch's fragment approach.[3] Both methods divide a compound into basic fragments and calculate its log P by the summation of the hydrophobic contributions of each fragment. However, the difficulties of these methods is how to fragment a molecule, especially large drug molecules, into basic fragments. New fragment methods (atomic fragments) were developed to overcome this problem.[4−6] These methods are conceptually simple and are able to give fast and accurate estimations for diverse organic compounds. However, correction factors are usually needed for complex structures to compensate for the interactions between functional groups.

Recently, Kier and Hall[7,8] introduced electrotopological state (E-state) indices for molecular structure description in which both electronic and topological characteristics are combined together. The E-state can be used in a group contribution manner and has been found to be useful in structure−property relationship studies. Using only these indices and neural network modeling, Hall and Story[9] were able to predict the boiling points and critical temperatures for a set of heterogeneous organic compounds.

In our recent studies we suggested methods for estimations of aqueous solubility, log S, of structurally related[10] and diverse sets[11] of drug compounds based on molecular topology and neural network modeling. The present study shows that the same indices can be successfully used to estimate log P coefficients, another important solubility property of drug compounds for drug design studies.

Experimental Section

Three hundred twenty-six drugs or related compounds from different structural classes were randomly selected from the Hansch−Leo compilation.[12] The partition coefficients of these compounds were represented as logarithm values, log P, and were in the range −2.11−5.9, corresponding to urea and thioridazine, respectively. This data set was divided into a training set of 300 compounds and a test set of 26 compounds (selected at random). An additional test set of 19 compounds[13] was included in the present study to compare our approach with currently available ones.

Structural parameters were calculated by Molconn-Z software (Hall Associated Consulting, Quincy, MA). Molecular weights and 32 atom-type E-state indices were calculated for each analyzed compound by SMILES line notation code. These 33 parameters were analyzed using multilinear regression (MLR) analysis and artificial neural networks (ANNs). MLR analysis was done with the SPSS package (v. 5.1, SPSS Inc., Chicago, IL) running on a Pentium PC. The ANNs employed in this study were fully connected feed-forward back-propagation networks with one hidden layer and bias neurons. ANN training was accomplished using the SuperSAB algorithm.[14] The logistic $f(x) = 1/(1+e^{-x})$ activation function was used both for hidden and output nodes. All calculated parameters and the set of parameters optimized by MLR were used for neural network training. The number of neurons in the hidden layer was optimized as indicated in the *Results* section. One single output node was used to code log P values.

The avoidance of overfitting/overtraining has been shown to be an important factor for improvement of generalization ability and correct selection of variables in neural networks studies.[14,15] The Early Stopping over an Ensemble technique was used in the current study to accomplish this problem. A detailed description of this approach can be found elsewhere.[14,15] In brief, each analyzed ensemble was composed of $M = 100$ networks. The values calculated for analyzed cases were averaged over all M neural networks, and their means were used for computing statistical

* Address to whom all correspondence should be addressed. FAX: ++41-21-692.5505. E-mail: itetko@eliot.unil.ch.
[†] Division of Pharmaceutical Chemistry.
[‡] Laboratoire de Neuro-Heuristique.
[§] Biomedical Department.

10.1021/js980266s CCC: $18.00
Published on Web 01/05/1999

coefficients with targets. We used a subdivision of the initial training set into two equal learning/validation subsets. The first set was used to train the neural network, whereas the second one was used to monitor the training process measured by root-mean-square error. An early stopping point determined as a best fit of a network to the validation set was used to stop the neural network learning. It was shown that a neural network trained up to an early stopping point provided better prediction ability than a network trained to the error minimum for the learning set.[10,14] Thus, statistical parameters calculated at the early stopping point were used. The training was terminated by limiting the network run to 10 000 epochs (total number of epochs) or after 2000 epochs (local number of epochs) following the last improvement of root-mean-square error at the early stopping point.

The computer code for the ANN was programmed in ANSI C++. The calculations were performed at HP Workstation Cluster at the Swiss Center for Scientific Computing.

The quality of the models was tested in two ways. An analysis of predictive ability was done in terms of both predictive q^2 and actual prediction. Predictive q^2 in leave-one-out cross-validation was defined as

$$q^2 = (\mathrm{SSY} - \mathrm{PRESS})/\mathrm{SSY} \quad (1)$$

Here, SSY is the sum of squares of the deviation between the observed log P values and their mean value and PRESS is the prediction error sum of squares obtained from leave-one-out (LOO) procedure. The standard deviation s_{LOO} was also considered. This coefficient was defined as

$$s_{LOO} = [\mathrm{PRESS}/n]^{1/2} \quad (2)$$

where n was the number of compounds in the model. In addition, the two test sets already described were used to estimate the actual prediction of the models using square of correlation coefficient r^2 and standard deviation s.

Results and Discussion

A total of 32 atom-type E-state indices (Table 1) and molecular weights were used as parameters for analysis by MLR and ANNs. Stepwise and backward methods were employed in the regression analysis and the following 19 parameters yielded a satisfactory statistical model:

$$\log P = 0.228\ (\pm 0.021)\ \mathrm{SsCH_3} + 0.294\ (\pm 0.072)\ \mathrm{SdCH_2} + 0.275\ (\pm 0.023)\ \mathrm{SssCH_2} + 0.171\ (\pm 0.011)\ \mathrm{SaaCH} + 0.221\ (\pm 0.053)\ \mathrm{SsssCH} - 0.190\ (\pm 0.063)\ \mathrm{SdssC} + 0.215\ (\pm 0.044)\ \mathrm{SaasC} + 0.246\ (\pm 0.047)\ \mathrm{SaaaC} - 0.093\ (\pm 0.016)\ \mathrm{SsNH_2} - 0.198\ (\pm 0.028)\ \mathrm{SssNH} - 0.051\ (\pm 0.013)\ \mathrm{SaaN} - 0.360\ (\pm 0.039)\ \mathrm{SsssN} + 0.013\ (\pm 0.004)\ \mathrm{SdO} - 0.035\ (\pm 0.013)\ \mathrm{SssO} + 0.071\ (\pm 0.006)\ \mathrm{SsF} + 0.264\ (\pm 0.068)\ \mathrm{SdS} + 0.199\ (\pm 0.098)\ \mathrm{SssS} + 0.444\ (\pm 0.185)\ \mathrm{SaaS} + 0.187\ (\pm 0.025)\ \mathrm{SsCl} - 0.468\ (\pm 0.124).$$

$$(n = 300,\ r^2 = 0.87,\ s = 0.68,\ F = 87.5,\ q^2 = 0.83,\ s_{LOO} = 0.71) \quad (3)$$

where n is the number of compounds used in the fit, F is the overall F-statistics for the addition of each successive term, and values in parentheses are the 95% confidence limit of each coefficient. The correlation analysis for parameters in eq 3 showed that all pairwise correlations were $R < 0.5$, indicating a low multicollinearity as well.

For neural network studies, a preliminary analysis using all available parameters was done to determine the optimal number of neurons in the hidden layer chosen in the set 2, 3, 5, 7, 10, 15, and 30. The performance of neural networks was evaluated by LOO statistical coefficients calculated at early stopping point for the training data set. We found that q^2 increased (i.e., $q^2 = 0.824 \pm 0.002$, 0.825 ± 0.002, 0.829 ± 0.003) when the number of neurons in the hidden layer was changed from 2 to 5. However, further increase in the number of hidden neurons from 7 to 30 did not influence the prediction ability of neural networks (i.e., $q^2 = 0.829 \pm 0.002$, 0.828 ± 0.003, 0.829 ± 0.002, 0.830 ± 0.003). Thus, we fixed the number of neurons in the hidden layer equal to 5.

Neural networks represents essentially nonlinear methods of data analysis. However, the use of ANNs for the same set of parameters provided a prediction ability similar to that of MLRs for compounds in the training set. In LOO cross-validation procedures, ANNs gave $q^2 = 0.84$ and $s_{LOO} = 0.69$ for the same set of parameters as in regression analysis, and $q^2 = 0.83$ and $s_{LOO} = 0.70$ for all calculated parameters. The prediction ability of the MLR model given by the PRESS statistics, $s_{LOO} = 0.71$, is only 0.03 log units

Table 1—The Atom-Type E-State Indices[a] Used in Multilinear Regression and Neural Network Models

			index value				
no.	symbol[b]	atom type[c]	min	max	training set	test set	MLR[d]
1	$SsCH_3$	—CH_3	0	12.9	158[e]	33	
2	$SdCH_2$	=CH_2	0	4.0	7	2	
3	$SssCH_2$	—CH_2—	–1.0	14.7	170	36	
4	StCH	≡CH	0	5.7	4	0	X
5	SdsCH	=CH—	0	6.0	60	5	X
6	SaaCH	..CH..	0	26.0	256	43	
7	SsssCH	—CH<	–4.7	3.1	107	18	
8	StC	≡C—	0	2.8	5	2	X
9	SdssC	>C=	–3.1	3.1	153	27	
10	SaasC	..C..	–3.8	6.8	225	42	
11	SaaaC	..C..	0	8.1	51	3	
12	SssssC	>C<	–6.8	0.5	70	11	X
13	$SsNH_2$	—NH_2	0	17.2	72	11	
14	SssNH	—NH—	0	8.1	100	22	
15	StN	≡N	0	10.2	2	2	X
16	SdsN	=N—	0	8.1	17	6	X
17	SaaN	..N..	0	19.8	77	7	
18	SsssN	>N—	0	7.6	95	24	
19	SddsN	—N≪	–0.7	0	6	0	X
20	SsOH	—OH	0	43.3	118	16	X
21	SdO	=O	0	47.6	167	26	
22	SssO	—O—	0	21.9	63	16	
23	SaaO	..O..	0	5.7	9	0	X
24	SsF	—F	0	39.9	26	3	
25	SsSH	—SH	0	4.1	3	0	X
26	SdS	=S	0	10.7	6	1	
27	SssS	—S—	0	3.7	24	8	
28	SaaS	..S..	0	1.7	7	0	
29	SdssS	=S<	–1.0	0	1	0	X
30	SddssS	>S≪	–8.9	0	29	3	X
31	SsCl	—Cl	0	12.2	23	9	
32	SsBr	—Br	0	3.4	1	0	X

[a] According to Hall and Kier.[8] [b] S states for the sum of the E-state values for a certain atom type or group; the sum for the hydroxyl groups is SsOH, for the ether or ester oxygen it is SssO, and for the keto oxygen it is SdO. [c] The formula of the atom type or group; the bond types between the heavy atoms are s = single (—), d = double (=), and a = aromatic (..). [d] The parameters that were eliminated in MLR regression are marked by X. [e] The number of compounds with the index.

Table 2—Comparison of the Predictive Ability of MLR and ANN Models

			training set		test set 1		test set 2	
model	params	#[a]	q^2	s_{LOO}	r^2	s	r^2	s
MLR	regressed	19	0.83	0.71	0.87	0.71	0.83	0.68
ANN1	regressed	19	0.84	0.69	0.90	0.62	0.84	0.62
ANN2	all	33	0.83	0.70	0.91 (0.93)[b]	0.60 (0.50)	0.87 (0.91)	0.57 (0.46)

[a] The number of input parameters in the model. [b] The results after excludance of loratidine and flufenamic acid are shown in the parentheses.

Table 3—Experimental and Estimated Log *P* Values for the Test Sets

A. test set 1

no.	compound	log P_{exp}	predicted	
			MLR	ANN2
1	acyclovir	–1.56	–1.70	–1.52
2	adrenalin	–1.37	0.10	–0.66
3	pyridoxine	–0.77	0.08	–0.59
4	isoniazid	–0.70	–0.14	–0.39
5	metaraminol	–0.27	0.46	–0.01
6	theophylline	–0.02	–0.22	–0.40
7	atenolol	0.16	1.13	0.83
8	sulpride	0.57	0.93	1.21
9	mescaline	0.78	1.25	1.18
10	primidone	0.91	0.97	0.82
11	carbutamide	1.01	0.85	0.76
12	ampicillin	1.35	0.91	1.12
13	clonidine	1.59	2.17	1.45
14	nalorphine	1.86	1.90	1.96
15	phenoxymethylpenicillin	2.09	1.40	1.67
16	hydrocortisoneacetate	2.19	2.01	2.05
17	lorazepam	2.39	3.81	3.28
18	dibenzepin	2.50	2.81	2.81
19	phenazine	2.84	2.71	2.38
20	ketoprofen	3.12	4.29	3.80
21	chlorpheniramine	3.38	4.61	4.19
22	disulfiram	3.88	4.06	3.18
23	fenethazine	4.20	2.84	3.39
24	methoxypromazine	4.90	4.15	4.26
25	trifluorperazine	5.03	4.95	4.57
26	loratidine	5.20	4.54	3.38

B. test set 2[a]

no.	compound	log P_{exp}	ANN2	XLOGP[b]	Moriguchi[b]	Rekker[b]	CLOGP[b]
1	chlorthiazide	–0.24	0.39	–0.58	–0.36	–0.68	–1.24
2	cimetidine	0.40	0.19	0.20	0.82	0.63	0.21
3	procainamide	0.88	1.32	1.27	1.72	1.11	1.11
4	trimethoprim	0.91	0.52	0.72	1.26	–0.07	0.66
5	chloramphenicol	1.14	1.29	1.46	1.23	0.32	0.69
6	phenobarbital	1.47	1.86	1.77	0.78	1.23	1.37
7	atropine	1.83	2.43	2.29	2.21	1.88	1.32
8	lidocaine	2.26	2.65	2.47	2.52	2.30	1.36
9	phenytoin	2.47	2.63	2.23	1.80	2.76	2.09
10	diltiazem	2.70	3.36	3.14	2.67	4.53	3.55
11	propranolol	2.98	3.22	2.98	2.53	3.46	2.75
12	diazepam	2.99	3.18	2.98	3.36	3.18	3.32
13	diphenhydramine	3.27	4.11	3.74	3.26	3.41	2.93
14	tetracaine	3.73	2.70	2.73	2.64	3.55	3.65
15	verapamil	3.79	4.33	5.29	3.23	6.15	3.53
16	haloperidol	4.30	4.41	4.35	4.01	3.57	3.52
17	imipramine	4.80	4.47	4.26	3.88	4.43	4.41
18	chlorpromazine	5.19	4.85	4.91	3.77	5.10	5.20
19	flufenamic acid	5.25	3.81	4.45	3.86	5.81	5.58

[a] This set was originally proposed by Moriguchi et al.[13] [b] The results calculated by XLOGP, CLOGP, and Moriguchi's and Rekker's methods are from ref 4.

higher than for the fitting model. Such a small increase indicates a robustness of the model.

The generalization ability of ANNs for the test sets was higher than that of MLR (Table 2). As in the case of the training set, the best predictions were calculated using all parameters. The results calculated using ANNs for the test set 2 ($n = 19$, $r^2 = 0.87$, $s = 0.57$) are comparable with those found using other known methods, such as CLOGP ($r^2 = 0.94$, $s = 0.44$), XLOGP ($r^2 = 0.89$, $s = 0.54$), and Moriguchi's method ($r^2 = 0.87$, $s = 0.63$), and are better than that of the Rekker's method ($r^2 = 0.84$, $s = 0.79$) (see Table 3).

The analysis of residuals showed that there were several compounds with a large calculation error in the training set. The compounds with a residual >1.4 log units, that is two times the standard deviation, are shown in Table 4. We found that two compounds in the analyzed test sets, loratidine (Test set 1) and flufenamic acid (Test set 2), were also characterized by high ANN prediction errors of 1.82 and 1.44 log units, respectively (Table 3). The elimination of these compounds from the test sets significantly improves prediction ability of ANNs (Table 2).

The low prediction ANN ability for loratidine and flufenamic acid and some other compounds from the training set can be explained by an analysis of the residuals. These two compounds have experimental log P values near to the largest value (5.90) in the training set. Let us note that for log P > 5.0, there were four compounds with large residual errors in the training set. However there were in total only seven compounds with such log P values in our training dataset. Thus, >50% of compounds with log P > 5.0 were poorly predicted. This result suggests that the

Table 4—Compounds with Large Prediction Errors in the Training Set

			MLR		ANN2	
no.	compound[a]	log P_{exp}	log P_{calc}	resid	log P_{calc}	resid
4	methotrexate	–1.85	–0.84	–1.01	0.09	–1.94
6	penicillamine[a]	–1.78	–0.07	–1.71	0.14	–1.93
10	riboflavine	–1.46	0.00	–1.46	–0.24	–1.22
11	α-methylnoradrenalin	–1.43	0.11	–1.54	–0.36	–1.07
15	thiourea	–1.08	0.51	–1.59	0.62	–1.70
22	phenformin	–0.83	0.45	–1.28	0.58	–1.41
56	cephalotin	0.00	1.60	–1.60	1.41	–1.41
64	ranitidine	0.27	1.16	–0.89	1.77	–1.50
102	triamteren	0.98	–0.66	1.64	–0.72	1.70
119	minoxidil	1.24	–0.39	1.63	–0.46	1.69
144	2,4-dihydroxybencoic acid	1.63	0.29	1.34	–0.39	2.01
150	timolol	1.83	0.36	1.47	–0.08	1.91
174	clobazam	2.12	3.32	–1.20	3.52	–1.40
183	ketamine	2.18	3.20	–1.02	3.64	–1.46
190	salicylic acid	2.26	0.81	1.45	0.54	1.72
207	thiophenol	2.52	1.43	1.09	0.64	1.88
222	LSD	2.95	1.46	1.49	1.42	1.52
228	papaverine	2.95	4.11	–1.16	1.61	1.45
251	piroxicamine	3.06	1.79	1.27	1.75	1.68
261	dextromoramide	3.61	4.68	–1.07	2.40	1.50
293	DES	5.07	3.65	1.42	3.02	2.04
294	mefenic acid	5.12	3.22	1.90	3.19	1.93
294	tolfenamic acid	5.17	3.56	1.61	3.64	1.53
300	thioridazine	5.90	4.97	0.93	4.50	1.40

[a] Compounds with absolute value of residuals >1.4 log units (two times the standard deviation of the prediction error) for MLR and ANNs are shown.

number of analyzed molecules with high log P values did not provide a representative training data set for correct application of the analyzed methods and the training set should be extended by including more compounds with high log P values.

The atom-type E-state indices are used in a manner similar to group additive schemes. Each atom in the molecular graph is presented by an E-state value that encodes the intrinsic electronic state of the atom perturbed by the electronic influence of all atoms in the molecule within the context of topological character of the molecule. Thus, the E-state for a given atom (or atom type) varies from molecule to molecule and depends on the detailed structure of the molecule. An analysis of residuals (Table 4) provided some hints of which structural features makes difficulties for the proposed method. There were four carboxylic acids (2,4-dihydroxybencoic acid, salicylic acid, mefenic acid, and tolfenamic acid) and hydroxyl-containing compounds (riboflavine, α-methylnoradrenalin, pyridoxamine, and DES), which all have a large calculation error. Also, both of the compounds with a large calculation error in the test sets contain a carbonyl group; that is, loratidine contains the ester carbonyl and flufenamic acid has a carboxylic acid group.

The reason for low prediction results for the compounds just mentioned can be explained by the fact that all E-state values calculated for hydroxyl groups are used to calculate only one parameter, SsOH, and no division for different types (i.e., alcohol, phenols, and carboxylic acids) is made. Likewise, the parameter SdO accounts for carbonyl oxygen, making no distinction between neighbor atom type (i.e., carboxylic acids, amides, ketones, and esters). The effects of the atom group could be considered similarly to the group contribution approach.[5,6,16] In this approach, contribution values are calculated separately for hydroxyl groups in aliphatic and aromatic compounds and for carbonyl oxygen-containing compounds, the division is made between carboxylic acids, esters, aldehydes, ketones, and amides. In both cases, the contribution values varied considerably, depending on the type of the atom group. Nearly all compounds with a large calculation error in our training set contain different types of hydroxyl and carbonyl compounds. Thus, it might be possible that the atom-type E-state index values for hydroxyl (SsOH) and carbonyl (SdO) groups are not enough to discriminate them according to their binding environment. We suggest that the usefulness of E-state formalism could be improved by taking into account the binding environment of an atom type, especially in the case of hydroxyl and carbonyl groups, like in Meylan's atom/fragment contribution method[5] and in Klopman's group contribution approach.[6,16]

The atom-type E-state indices are similar to some extent to the group contribution variables (e.g., numbers of $-CH_2-$ groups instead of $SssCH_2$). It is possible to assume that the same results would be calculated if these variables were used instead of the atom-type E-state indices. The numbers of atom-types computed using Molconn-Z software and the molecular weights were fitted as input parameters for MLR and ANNs. The best MLR model calculated using stepwise and backward methods contained the following 15 indices:

$$\log P = 0.163\ (\pm 0.072)\ ISsCH_3 + 0.164\ (\pm 0.038)\ ISssCH_2 + 0.128\ (\pm 0.037)\ ISaaCH + 0.260\ (\pm 0.062)\ ISaasC + 0.471\ (\pm 0.090)\ ISaaaC - 0.766\ (\pm 0.162)\ ISsNH_2 - 0.454\ (0.126)\ ISssNH - 0.522\ (\pm 0.264)\ ISdsN - 0.457\ (\pm 0.095)\ ISaaN - 0.465\ (\pm 0.119)\ ISsssN - 0.361\ (0.107)\ ISsOH - 0.516\ (0.122)\ ISssO + 0.254\ (\pm 0.111)\ ISsF - 0.472\ (\pm 0.231)\ SddssS + 0.0046\ (\pm 0.0012)\ MW + 0.145\ (\pm 0.234)$$

$$(n = 300,\ r^2 = 0.55,\ s = 1.18,\ F = 23.4,\ q^2 = 0.49,\ s_{LOO} = 1.23) \quad (4)$$

where I refers to the number of groups corresponding to the appropriate atom-type E-state index and MW is the molecular weight (Table 2). The prediction ability of this

equation was $r^2 = 0.59$, $s = 1.26$ and $r^2 = 0.13$, $s = 1.67$ for test sets 1 and 2, respectively. ANNs computed similar results; that is, $q^2 = 0.48$, $s_{LOO} = 1.24$ for the training set and $r^2 = 0.59$, $s = 1.29$ and $r^2 = 0.22$, $s = 1.74$ for test sets 1 and 2, respectively. Thus, both MLR and ANN methods provided significantly worse results if the group contribution variables were used instead of atom-type E-state indices. To understand these results, recall that the atom-type E-state indices account both for electronic and topological characteristics of the molecular structure. It is also important that the range of the atom-type E-state indices (Table 1) is considerably larger than that calculated by counts of the number of corresponding groups. This fact also significantly contributes to the performance and high prediction ability of models based on the atom-type E-state indices.

The most important advantage of the present approach is that only 32 parameters and no corrections factors were used for coding each molecule, whereas other methods require hundreds of parameters.[2−6,17] We are well aware of the shortcoming of the present model. Topological indices cannot account for three-dimensional and conformational effects, which may play a major role for solubility properties of chemical compounds, as recently suggested by Palm and co-workers.[18] However, topological indices are attractive because they can be easily and rapidly calculated from the structures of analyzed compounds. This feature makes it possible to obtain fast estimations of the solubility properties of compounds belonging to large databases, such as virtual combinatorial libraries. Probably, these indices can also be used to improve the prediction ability of other methods that are based on calculation of theoretical descriptors derived from the molecular structures of compounds.[19,20]

The prediction of partition coefficients using atom-type E-state indices is accurate and provides reliable log P estimations that are comparable to those obtained by other methods. An advantage of the proposed approach is that the atom-type E-state indices can be quickly and easily estimated directly from the chemical structure of analyzed compounds. Moreover, the number of parameters is small. Thus, the present approach introduces a fast method for estimation of log P of chemical compounds.

References and Notes

1. Hansch, C.; Leo, A. *Substituent Constants for Correlation Analysis in Chemistry and Biology*, Wiley: New York, 1979.
2. Rekker, R. E. *Hydrophobic Fragment Constant*, Elsevier: New York, 1977.
3. Leo, A.; Jow, P.; Silipo, C.; Hansch, C. Correlation of Hydrophobic Constant (log P) from π and ×a6 Constants. *J. Med. Chem.* **1975**, *18*, 865−868.
4. Wang, R.; Fu, Y.; Lai, L. A. New Atom-Additive Method for Calculating Partition Coefficients. *J. Chem. Inf. Comput. Sci.* **1997**, *37*, 615−621.
5. Meylan, W. M.; Howard, P. H. Atom/Fragment Contribution Method for Estimating Octanol−Water Partition Coefficients. *J. Pharm. Sci.* **1995**, *83*, 83−92.
6. Klopman, G.; Li, J.-Y.; Wang, S.; Dimayuga, M. Computer Automated log P Calculations Based on an Extended Group Contribution Approach. *J. Chem. Inf. Comput. Sci.* **1994**, *34*, 752−781.
7. Kier, L. B.; Hall, L. H. An Electrotopological-State Index for Atoms in Molecules. *Pharm. Res.* **1990**, *7*, 801−807.
8. Hall, L. H.; Kier, L. B. Electrotopological State Indices for Atom Types: A Novel Combination of Electronic, Topological and Valence State Information. *J. Chem. Inf. Comput. Sci.* **1995**, *35*, 1039−1045.
9. Hall, L. H.; Story, C. T. Boiling Point and Critical Temperature of a Heterogeneous Data Set: QSAR with Atom Type Electrotopological State Indices Using Artificial Neural Networks. *J. Chem. Inf. Comput. Sci.* **1996**, *36*, 1004−1014.
10. Huuskonen, J.; Salo, M.; Taskinen, J. Neural Network Modeling for Estimation of the Aqueous Solubility of Structurally Related Drugs. *J. Pharm. Sci.* **1997**, *86*, 450−454.
11. Huuskonen, J.; Salo, M.; Taskinen, J. Aqueous Solubility Prediction of Drugs Based on Molecular Topology and Neural Network Modeling. *J. Chem. Inf. Comput. Sci.* **1998**, *38*, 450−456.
12. Hansch, C.; Leo, A.; Hoekman, D. *Exploring QSAR: Hydrophobic, Electronic, and Steric Constants*, American Chemistry Society: Washington, 1995; Vol. 2.
13. Moriguchi, I.; Hirono, S.; Nakagome, I.; Hirano, H. Comparison of Reliability of log P Values for Drugs Calculated by Several Methods. *Chem. Pharm. Bull.* **1994**, *42*, *976−978*.
14. Tetko, I. V.; Livingstone, D. J.; Luik, A. I. Neural Network Studies. 1. Comparison of Overfitting and Overtraining. *J. Chem. Inf. Comput. Sci.* **1995**, *35*, 826−833.
15. Tetko, I. V.; Villa, A. E. P. Efficient Partition of Learning Data Sets for Neural Network Training. *Neural Networks* **1997**, *10***,** 1361−1374.
16. Klopman, G.; Wang. S.; Balthasar, D. M. Estimation of Aqueous Solubility of Organic Molecules by the Group Contribution Approach. Application to the Study of Biodegradiation. *J. Chem. Inf. Comput. Sci.* **1992,** *32*, 474−482.
17. Gombar, V. K.; Enslein, K. Assessment of N−Octanol/Water Partition Coefficient: When is the Assessment Reliable? *J. Chem. Inf. Comput. Sci.* **1996,** *36*, 1127−1134.
18. Palm, K.; Stenberg, P.; Luthman K.; Arthursson, P. Polar Molecular Surface Properties Predict the Intestinal Absorption of Drugs in Human. *Pharm. Res.* **1997**, *14*, 568−571.
19. Haeberlin, M.; Brinck, T. Prediction of Water-Octanol Partition Coefficients Using Theoretical Descriptors Derived from the Molecular Surface Area and the Electrostatic Potential. *J. Chem. Soc., Perkin Trans. 2* **1997**, 289−294.
20. Bodor, N.; Buchwald, P. Molecular Size Bazed Approach to Estimate Partition Properties for Organic Solutes. *J. Phys. Chem.* **1997**, *101*, 3404−3412.

Acknowledgments

This study was partially supported by the Technology Development Center in Finland (TEKES), INTAS-Ukraine grant 95-0060, and Swiss National Science Foundation grant FNRS 2150-045689.95. The authors thank the reviewers for their helpful remarks that improved the clarity and significance of our study.

JS980266S

Pharmacodynamic Analysis of the Electrocardiographic Interaction between Disopyramide and Erythromycin in Rats

ERIKA HANADA,[†] HISAKAZU OHTANI,[†] HAJIME KOTAKI,[‡] YASUFUMI SAWADA,[§] HITOSHI SATO,[†] AND TATSUJI IGA*[,†]

Contribution from *Department of Pharmacy, the University of Tokyo Hospital, Faculty of Medicine, the University of Tokyo, Hongo, Bunkyo-ku, Tokyo 113-8655, Japan, Department of Pharmacy, the Research Hospital, the Institute of Medical Science, the University of Tokyo, Shirokanedai, Minato-ku, Tokyo 108–8639, Japan, and Faculty of Pharmaceutical Sciences, Kyushu University, Maidashi, Higashi-ku, Fukuoka city, Fukuoka 812-0054, Japan.*

Received June 19, 1998. Final revised manuscript received October 27, 1998.
Accepted for publication November 4, 1998.

Abstract □ Disopyramide (DP) is known to induce QT prolongation and Torsades de Pointes (TdP) when administered concomitantly with erythromycin (EM). To define and evaluate quantitatively the arrhythmogenic risk of the concomitant administration of DP and EM, we investigated the influence of EM on the pharmacokinetics and pharmacodynamics of DP in rats. The time profiles of change in QT interval and plasma concentration of each drug were evaluated during and after constant intravenous infusion of DP (6.0 or 15.0 mg/kg/h), EM (4.0 or 8.0 mg/kg/h), and coadministration of DP and EM (DP 6.0 mg/kg/h plus EM 4.0 mg/kg/h). Each agent induced QT prolongation at plasma concentrations within the therapeutic range in humans. DP-induced QT prolongation was proportional to its plasma concentration. In the case of EM, the E_{max} model with an "effect compartment" could explain the relationship between plasma EM concentrations and changes in QT interval. Although coadministration of EM with DP gave enhanced QT prolongation compared to dosing with DP alone, EM did not affect the pharmacokinetics of DP. In conclusion, it was shown that a pharmacodynamic interaction contributes to the electrocardiographic adverse reaction (i.e., QT prolongation) induced by coadministration of DP and EM in rats.

Introduction

Disopyramide (DP), a class Ia antiarrhythmic agent, is used for tachyarrhythmia and prolongs action potential duration (APD) in cardiac myocytes. In recent years, it has been reported that concomitant administration of DP and erythromycin (EM), a macrolide antibiotic, induced Torsades de Pointes (TdP) associated with electrocardiographic QT prolongation.[1,2] In humans, DP is metabolized mainly by the liver into the major metabolite, mono-N-dealkylated disopyramide (MND).[3] Since EM, which is known to inhibit CYP3A4,[4] is reported to inhibit the metabolism of DP,[5] this oxdation enzyme is thought to be from the CYP 3A subfamily, paticularly CYP3A4. This inhibition may lead to elevated plasma DP concentration, and resultant toxicity such as QT prolongation. However, one case of TdP associated with QT prolongation resulting from the coadministration of DP and EM without an elevation of plasma DP concentration was also reported.[1] Therefore, the elevation of plasma DP concentration may not completly explain this adverse reaction. In fact, EM itself is known to induce QT prolongation or TdP.[6–8] Lin et al.[9] reported a case of TdP associated with QT prolongation induced by the concomitant use of quinidine and EM without an increase of plasma quinidine concentrations; they concluded that the adverse reaction caused by quinidine and EM coadministration might be based on their pharmacodynamic interaction. However, the significance of the pharmacodynamic interaction between DP and EM remains to be evaluated quantitatively.

Since EM is well-known as a metabolic inhibitor, the interaction between DP and EM might be initially considered based on metabolic inhibition. However, as far as a pharmacodynamic interaction is involved, monitoring of plasma DP concentrations only should underestimate the risk of adverse reactions. In this case, it is necessary to investigate this interaction not only from the pharmacokinetic aspect but also from the pharmacodynamic one. The aim of this study, therefore, was to define and evaluate quantitatively the risk of QT prolongation induced by DP and EM in an animal model, where rats were employed to estimate the ECG abnormality, including QT prolongation.[9]

Materials and Methods

1. Materials and Animals—DP was purchased from Wako Pure Chemical Industries (Osaka, Japan). MND and *p*-chlorodisopyramide were kindly provided from Russel Uclaf (Paris, France). Erythromycin base (EM) was obtained from Dai Nippon Pharmaceutical Co. (Osaka, Japan). Acetonitrile, methanol, and dichloromethane were of HPLC grade from Wako Pure Chemical Industries. Other reagents of analytical grade were also purchased from Wako Pure Chemical Industries. Male Sprague−Dawley rats weighing 250−350 g were purchased from Nippon Bio-Supp. Center (Tokyo, Japan) and used for the experiments.

2. Pharmacodynamic Studies—Drug solutions used for pharmacodynamic studies were prepared as follows: DP was solubilized by physiological salt solution (PSS; NaCl: 135 mM, $NaHCO_3$: 11.9 mM, KCl: 5.4 mM, $CaCl_2$: 1.8 mM, $MgCl_2$: 1.0 mM) with 1 mol equiv of H_3PO_4. EM was easily dissolved in PSS. For coadministration experiments, EM were dissolved in DP phosphate solution described above (nearly pH 7.0). EM was comfirmed to be stable in all the solutions for intravenous administration. Each solution was infused into the jugular vein of rats as below by means of a syringe pump (Model 975, Harvard Apparatus, MA) at an infusion rate of 1.05 mL/h.

Rats were anesthetized with a mixture of urethane and α-chlorarose (1.1 mg/kg and 27.5 mg/kg i.p., respectively). The precordial and limb hair were removed using a hair-removing cream (Hair Remover, Kanebo, Tokyo). The trachea, jugular vein, and carotid artery were cannulated with polyethylene tubing. After cannulation, the animals were restrained in a supine position on a heatpad, and the electrodes were noninvasively fastened. The body temperature was maintained at 37.5 ± 0.5 °C throughout the experiment.

After stabilization of the ECG and body temperature, PSS was infused into the jugular vein for 10 min. Subsequently, DP (6 or

* Coresponding author: Tel: 81-3-3815-5411 ext 5281.
[†] Department of Pharmacy, University of Tokyo.
[‡] Institute of Medical Science, University of Tokyo.
[§] Kyushu University.

10.1021/js980256r CCC: $18.00
Published on Web 12/30/1998

15 mg/kg/h), EM (4 or 8 mg/kg/h), and the mixture of these agents (DP 6 mg/kg/h + EM 8 mg/kg/h) or PSS only (for control) was infused for 90 min. ECG was recorded 10 min before the start of infusion (−10 min), and 0, 1−7, 10, 15, 20, 30, 45, 60, 75, 90−97, 100, 105, 110, 120, 135, 150, 165, and 180 min after the start of infusion. The ECG was examined by a procedure previously reported.[10] Briefly, signals from the bipolar lead II were amplified by means of an electric amplifier (AB-621G, Nihon-Koden, Tokyo), stored in a personal computer (PC-9801VX, NEC, Tokyo) via A/D converter (Analog-Pro Jr., Canopus Electric, Kobe) at a sampling rate of 500 Hz and analyzed with Wave Master II (Canopus Electric, Kobe). Signals from the pressure transducer joined to the cannula of carotid artery were amplified by means of a pressure amplifier (AP-621G, Nihon-Kohden, Tokyo) and recorded by a pen recorder (WI-681G, Nihon-Kohden, Tokyo). ECG parameters such as heart rate and QT interval were derived manually from the average wave shape of recordings for 10 s. Blood was collected after the last recording of ECG to verify that the plasma drug concentration was equivalent to that in pharmacokinetic studies.

3. Pharmacokinetic Studies—*Pharmacokinetics during and after infusion of DP or EM*—Pharmacokinetic studies were performed in animals different from those used in the pharmacodynamic experiments in order to avoid any influence of blood sampling on ECG. Each drug solution was infused in the same manner as the pharmacodynamic experiments. Blood samples were collected from the carotid artery at 2, 5, 15, 45, 90, 92, 95, 105, 135, and 180 min after the start of drug administration. Blood samples were centrifuged to obtain plasma at 1500*g* for 10 min and determined by a procedure described below.

Pharmacokinetics after Portal Vein Administration of DP—Rats were fasted overnight before the experiment. Polyethylene cannula were inserted and fixed into the pyloric vein, the femoral vein and artery under ether anesthesia. The body temperature was maintained at 37.5 ± 0.5 °C throughout the experiment. After recovery from anesthesia, physiological saline or 50 mg/kg of EM was injected into the femoral vein at 5 min before the administration of DP. Then, 20 mg/kg of DP was injected into the portal vein. Each drug solution was prepared as follows: EM was solubilized in phosphate buffer solution (pH 4.0) (0.04 M KH_2PO_4, 0.04 M H_3PO_4), and DP was easily dissolved in physiological saline.

Blood samples (150 μL) were collected at 1, 3, 5, 15, 30, 60, 120, and 180 min after the DP administration and immediately centrifuged at 1500*g* for 10 min. Urine samples were collected for the intervals of 0−3, 3−24, and 24−48 h after the drug administration. The plasma and urine samples were stored at −20 °C until assay.

4. Effects of EM on Plasma Free Fraction (f_p) of DP—The plasma free fraction of DP (f_p) was determined in the presence or absence of EM by an ultrafiltration method. Drug-free blood was collected through the portal vein, heparinized, and centrifuged (1500g, 10 min) to separate plasma. DP was dissolved in plasma to make the concentrations of 0.1, 3.0, 6.0, and 15.0 μg/mL. To examine the influence of EM on f_p of DP, EM was added to the plasma samples containing EM to give a final concentration of 63 μg/mL. After preincubation at 37 °C for 5 min, an aliquot (500 μL) of the sample was put into the reservoir of an ultrafiltration device (Centrifree, Amicon, MA). Thereafter, it was centrifuged at 1000*g* for 2 min at 37 °C to obtain ultrafiltrate. The volume of the ultrafiltrate was measured as less than 15% of the original sample (500 μL). The concentration of DP in each fraction was determined as described below. The f_p value was calculated by dividing the DP concentration in the ultrafiltrate by that in the retained sample.

5. Determination of DP, MND, and EM Concentration—DP and MND concentrations in plasma or urine were determined using an HPLC method reported previously by Mayer et al.[11] with a minor modification. Briefly, an aliquot (50 μL) of plasma or urine sample was pipetted into a 10-mL glass tube. After addition of 50 μL of the internal solution (0.6 μg/mL *p*-chlorodisopyramide solution in 0.01 M HCl) and 2 mL of dichloromethane, the mixture was made alkaline with 5 μL of 1 M NaOH and then shaken for 10 min by a mechanical shaker. After centrifugation (10 min, 1500*g*), the lower organic layer was transferred into a 10-mL glass tube and evaporated to dryness under a stream of dry nitrogen at ambient temperature. The dry residue was dissolved into 50 μL of mobile phase, and 20 μL was applied onto the HPLC system.

HPLC was performed with a UV detector (UV−vis DETECTOR SPD-10A, Shimazu, Kyoto, Japan) and a C_{18} reversed-phase column (Cosmosil-packed column 5-C_{18}, 150 mm × 4.6 mm i.d., particle size 5 μm, Nacalai Tesque, Kyoto, Japan). Assay was carried out at ambient temperature. The mobile phase consisted of aqueous solution (0.125 M HCl, 0.125 M sodium 1-octanesulfonate, 0.072 M triethylamine) and acetonitrile (70:30, v/v). The flow rate was 1.0 mL/min, and the detection wavelength was set at 263 nm. The lower limit of reliable detection of this method was 0.1 μg/mL for DP and 0.05 μg/mL for MND. The plasma EM concentrations were determined by an HPLC-ECD method described previously.[12]

6. Pharmacokinetic−Pharmacodynamic Analyses of QT prolongation—The effects of DP and EM on QT interval were analyzed from both pharmacokinetic and pharmacodynamic aspects. The QT interval was defined as the time from the start of the QRS complex to the end of the T wave, at which the amplitude of the T wave declined to 10% of its maximum. The effect of a drug at each time was expressed as the deviation from the value before the drug administration (ΔQT). Mean QT interval just before the start of drug administration was 61.6 ± 0.98 ms (n = 24). The PR interval was defined as the time from the start of the P wave to the apex of the R wave.

The time profiles of plasma DP concentration (C_p) were analyzed by a conventional two-compartment open with a first-order elimination model described previously.[13] Pharmacokinetic parameters were estimated by simultaneous fitting of the data at each infusion rate.

Then, the relationship between the plasma concentration of DP and the effect of DP on QT prolongation (E_{DP}) was analyzed, assuming a linear relation as follows:

$$E_{DP} = KC_p \quad (1)$$

where C_p is the plasma DP concentration and K is the slope.

The time profiles of plasma EM concentration were also analyzed by a conventional two-compartment model described previously.[13] Pharmacokinetic parameters of α, β, k_{10}, k_{21}, and V_1 were estimated by simultaneous computer-fitting of the data at each infusion rate.

For the pharmacokinetic−pharmacodynamic analysis of EM, the "effect compartment model"[14] was applied because a delay of QT prolongation was observed. The drug concentration (C_e) in the effect compartment is described by equations reported by Holford and Sheiner.[14]

Then the relationship between C_e and the effect of EM on QT prolongation (E_{EM}) was analyzed. The E_{max} model was employed to relate C_e to E_{EM} as follows:

$$E_{EM} = \frac{E_{max}C_e}{EC_{50} + C_e} \quad (2)$$

where E_{max} is the maximum effect, and EC_{50} represents the concentration which gives half-maximal effect.

For coadministration of EM and DP, we assumed that the effect of the coadministration on QT prolongation (E_{DP+EM}) was estimated from the additive model described below.

$$E_{DP+EM} = E_{DP} + E_{EM} \quad (3)$$

Results

ECG Effects and Pharmacokinetics of DP—Figure 1 represents the time profiles of the change in QT interval (ΔQT) and the plasma DP concentration during and after the constant intravenous infusion of DP. The QT interval was prolonged in response to the increase in plasma DP concentration without a lag-time. After the end of the infusion, the QT interval was shortened as the plasma DP concentration declined. DP induced a dose-dependent prolongation of QT interval within the dose range tested; changes in QT prolongation at 90 min after the start of the infusion were 17.50 ± 1.94 ms and 38.50 ± 5.00 ms at the dosing rates of 6 mg/kg/h and 15 mg/kg/h, respectively. In addition, DP induced a significant prolongation of PR

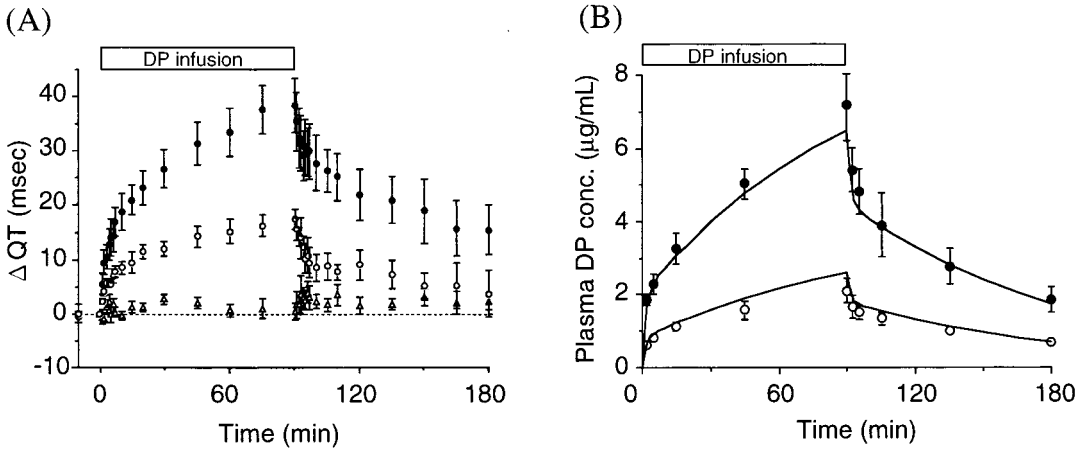

Figure 1—Time profiles of the change in QT interval (A) and the plasma concentration of DP (B) during and after i.v. infusion of DP. The solid lines in panel (B) are the fitting lines ●: DP 15 mg/kg/h, ○: DP 6 mg/kg/h, △: vehicle (mean ± SEM, $n = 3$–4).

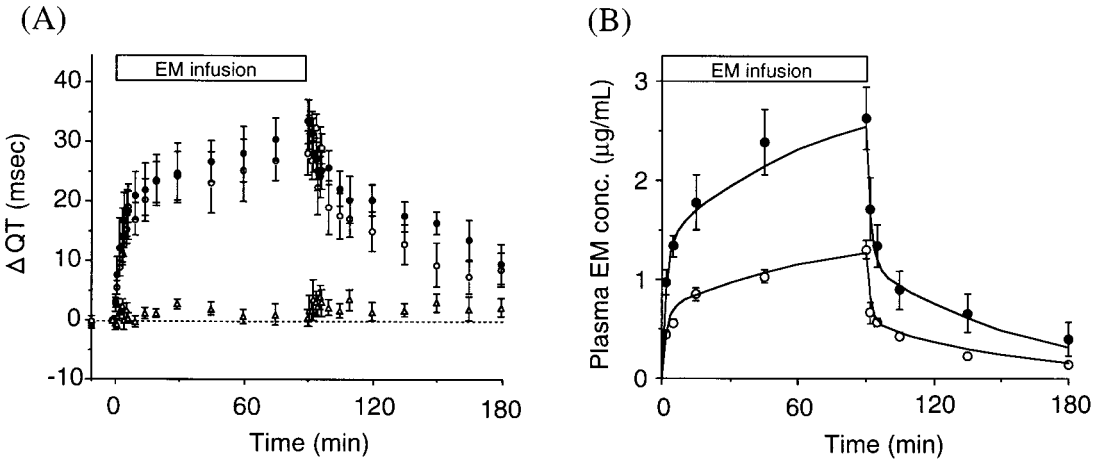

Figure 2—Time profiles of the change in QT interval (A) and the plasma concentration of EM (B) during and after i.v. infusion of EM. The solid lines in panel (B) are the fitting lines ●: EM 8 mg/kg/h, ○: EM 4 mg/kg/h, △: vehicle (mean ± SEM, $n = 3$–4).

interval and a slight prolongation of QRS interval (data not shown).

ECG Effects and Pharmacokinetics of EM—The time profiles of the change in QT interval (ΔQT) and the plasma EM concentration during and after the constant intravenous infusion of EM are shown in Figure 2. Although EM also evoked an obvious QT prolongation as observed in the case of DP, ceasing the infusion did not give an immediate shortening of the QT interval despite the prompt decrease in the plasma EM concentration. This observation indicates the presence of a delay in QT prolongation against plasma EM concentration. Within the EM concentration range under the present experimental conditions, saturation of the effect on QT interval was observed; changes in QT prolongation at 90 min after the start of the infusion were 28.20 ± 3.65 ms and 33.50 ± 3.75 ms at the dosing rates of 4 mg/kg/h and 8 mg/kg/h, respectively. Other ECG parameters, PR and QRS intervals, were not significantly altered (data not shown).

Pharmacokinetic–Pharmacodynamic Analyses of QT Prolongation—Figure 3 represents the relationship between plasma DP concentration and change in QT interval, and Figure 4 shows the relationship between EM concentration in plasma and change in QT interval. With regard to DP, as neither a delay nor saturation of QT prolongation was observed, the linear model (eq 1) was applied to the relationship between plasma DP concentration and E_{DP} (Figure 3). As judged from the anticlockwise hysteresis and saturation of the relationship in Figure 4, the E_{max} model with the effect compartment (eq 2) was

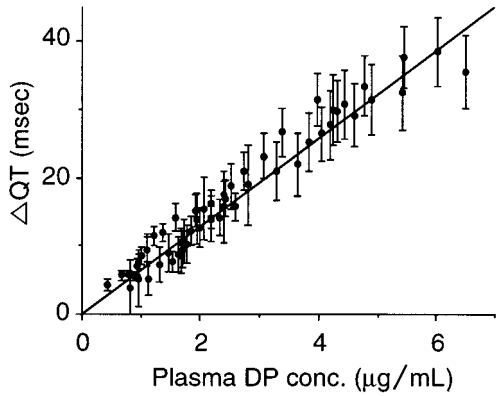

Figure 3—Relationship between the plasma concentration of DP and the change in QT interval. The solid line shows fitting curve calculated from eq 1 (mean ± SEM, $n = 4$).

successfully employed. The pharmacodynamic parameters for DP and EM are listed in Table 1.

Electrocardiographic Interaction on ECG Induced by DP and EM—Figure 5 represents the time profiles of the change in QT interval during and after the infusion of DP, EM, and their combination. The coadministration of DP and EM induced a larger QT prolongation than the administration of each drug alone. The simulation curves line calculated from eq 3 were in good agreement with the observed data. Although an electrocardiographic (ECG) interaction was seen between these drugs (right panel of

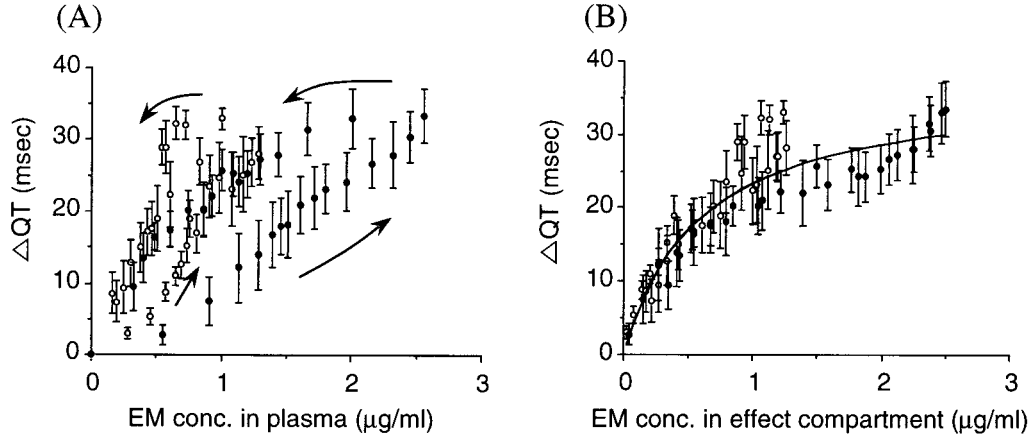

Figure 4—Relationship between the drug concentration of EM in plasma (A) or in effect compartment (B) and the change in QT interval. The solid line in panel (B) shows the fitting curve calculated from eq 2 (mean ± SEM, $n = 4$). ●: EM 8 mg/kg/h, ○: EM 4 mg/kg/h.

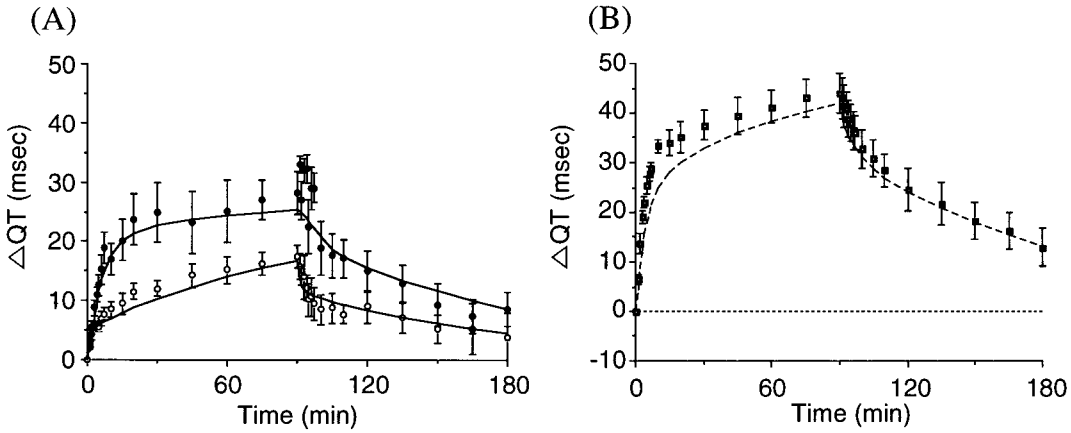

Figure 5—Changes in QT interval after the administration of DP or EM alone (A) and their concomitant administration (B). The solid lines in panel (A) are the fitting curves. The dotted line in panel (B) is the predicted curve calculated from eq 3 (mean ± SEM, $n = 4$). ●: DP 6 mg/kg/h, ○: EM 4 mg/kg/h, □: DP 6 mg/kg/h + EM 4 mg/kg/h.

Table 1—Pharmacodynamic Parameters for DP- or EM-Induced QT Prolongation (mean ± SD)

Parameter	DP	EM
K (ms·mL/μg)	6.45 ± 0.06	-
k_{e0} (min^{-1})	-	0.158 ± 0.023
E_{max} (ms)	-	37.10 ± 2.04
EC_{50} (mg/mL)	-	0.587 ± 0.091

Figure 5), EM did not affect the plasma concentration of DP and vice versa. This result led us to further investigate the pharmacokinetics of DP in the coadministration of EM.

Pharmacokinetic Interactions of DP and EM—Figure 6 represents the time profiles of plasma concentrations of DP and its metabolite, MND, after the portal vein administration of DP in the presence or absence of EM. The time profile of DP was described by a conventional two-compartment open model. Although the plasma concentration of MND reached maximum at 5 min after the administration of DP, the concentration of the metabolite was less than one tenth of that of the parent drug. After the administration of DP, 26.2 ± 2.1% of the dose was excreted as unchanged drug, while 4.1 ± 0.9% was excreted as MND in the urine within 24 h. Table 2 lists the pharmacokinetic parameters, which are in agreement with the published data.[15,16]

EM did not significantly change the pharmacokinetic parameters of DP, and both the plasma concentrations and the urinary excretion of the metabolite, MND, were not also significantly changed. Moreover, the plasma free fraction

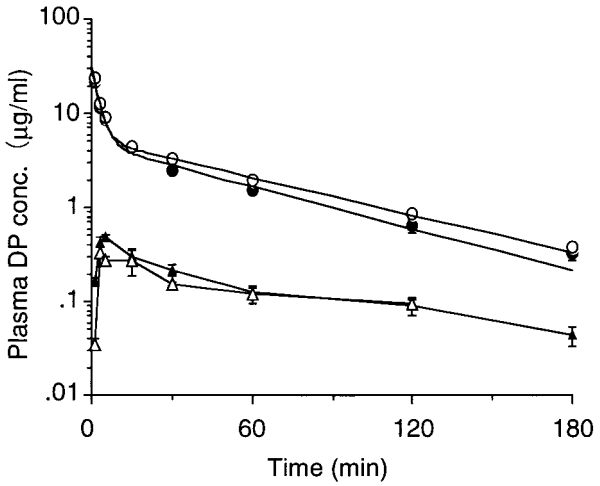

Figure 6—Time profiles of DP (circles) or MND (triangles) after portal vein administration of DP 20 mg/kg without (open symbols) or with (filled symbols) EM pretreatment (50 mg/kg i.v.) (mean ± SEM, $n = 4$). The solid lines of DP are the fitting curves calculated from two-exponential equation.

of DP (f_p), 0.800−0.875, was almost constant over the concentration range of 0.05−15.0 μg/mL and was not significantly changed in the presence of EM.

Discussion

In recent years, QT prolongation induced by noncardiovascular drugs has received much attention. Such drug-

Table 2—Pharmacokinetic Parameters of DP after Portal Vein Administration of DP (20 mg/kg) with or without EM Coadministration (50 mg/kg i.v.) to Rats

parameter	DP alone	DP + EM
V_{dss} (mL/kg)	2770 ± 100	2693 ± 155
AUC (μg/min/mL)	349 ± 28	413 ± 19
$t_{1/2}$ (β) (min)[a]	41.2 ± 3.3	45.5 ± 2.2
CL_{tot} (mL/min/kg)	57.9 ± 4.0	48.4 ± 2.31
CL_R (mL/min/kg)[b]	13.2 ± 1.7	12.2 ± 1.8

[a] $t_{1/2}$ (b): plasma eliminatiom half-life time for DP (mean ± SEM, $n = 5$). [b] CL_R: renal clearance of DP.

induced QT prolongation may be accentuated by coadministration of an antiarrhythmic agent, which itself prolongs QT interval. For instance, some cases have been reported that DP, coadministered with EM, caused TdP associated with QT prolongation,[1,2] a life-threatening adverse reaction. It is therefore important to investigate the interactions between antiarrhythmics and noncardiovascular agents which have the possibility of prolonging the QT interval.

Correction of QT Interval by Heart Rate—Since heart rate is known to affect the QT interval in humans, QTc, derived from "Bazett's formula", is widely applied in evaluation of QT prolongation. In this study, EM did not change the heart rate, whereas DP induced bradycardia, probably resulting from the blockade of sodium channels. However, Hayes et al. demonstrated that the QT interval is independent of heart rate in rats, in contrast to humans, rabbits, and guinea pigs.[17] In addition, it has been reported that the actual QT interval, without any correction for heart rate, may be preferable the QTc in heralding TdP.[18] Therefore, in this study, we employed the actual QT interval for evaluation of arrhythmogenic potency.

QT Prolongation Induced by DP or EM—In the present study, the administration of DP or EM alone induced a significant QT prolongation. DP is known to block sodium channels and potassium channels of cardiac myocytes and delay repolarization, which leads to prolongation of action potential duration (APD) and QT interval.[19] In our study in rats, DP induced QT prolongation within its therapeutic range (2.0−5.0 μg/mL). This range coincides with the concentrations where APD prolongation was reported on cardiac muscle of guinea pigs or rats by whole-cell voltage clamp technique.[20−23] Although MND, a major metabolite of DP, is documented to possess one-fourth the anticholinergic potency of DP,[24,25] it is virtually inactive in QT prolongation.[23,26] Therefore, MND was excluded from the further kinetic analysis.

EM is also known to inhibit potassium channels in ventricular myocytes.[27−29] This blockade may lead to delayed repolarization and prolongation of QT interval. However, the detailed mechanism has not been thoroughly elucidated.

An anticlockwise hysteresis was observed between plasma EM concentration and effect on QT prolongation, which indicates a delay of QT prolongation. The E_{max} model with "effect compartment" may adequately explain the relationship (Figure 3B). This hysteresis could be due to several factors, including delayed distribution of EM to the effect site, which is assumed to be potassium channels of ventricular myocytes. The binding site for EM in the potassium channel has not been identified yet. However, there is a possibility that the binding site is located in the intracellular or transmembrane domain of the channel and that it may take several minutes for the drug to reach the effect site, as speculated from the delay of QT prolongation. A possible explanation for this anticlockwise hysteresisis is the generation of an active metabolite of EM. While EM is reported to be active in QT prolongation, it is not reported whether the metabolite of EM is active or not. No major metabolites of EM were detected by ECD, so that we could not investigate metabolite pharmacokinetics. However, when we examined the time course of EM concentrations in the ventricle, it showed a delayed distribution of EM into the ventricle at the distribution rate similar with k_{eo} (data not shown).

In this study, EM induced a significant QT prolongation within the therapeutic range of plasma EM concentrations (0.5−3.0 μg/mL). Using the in vitro patch clamp technique, it has been reported that a higher concentration (up to 100 μM; 73.4 μg/mL) is necessary for EM to prolong the action potential duration (APD) or reduce potassium current (delayed rectifier potassium current).[27−29] Rubart et al.[27] discussed that the concentrations of EM required to induce early after-depolarizations (EADs) in vitro are higher than those in vivo. Antzelevitch et al.[29] demonstrated that APD prolongation was evoked at a relatively low concentration of EM (10 μM) in canine M cells, but the concentration was still above the therapeutic range. In the present study, even if the plasma protein binding of EM (16.9% for rats) was taken into consideration, the concentration which evoked QT prolongation in vivo was still lower than that reported in vitro,[27−29] indicating that the potency of EM for APD prolongation or potassium current blockade in ventricular myocytes in vitro may be weaker than that for QT prolongation in vivo. Further investigation is required to clarify the mechanism and sources of this discrepancy. A possible explanation is that the EM concentration near the potassium channels is different between in vivo and in vitro conditions, due to different cellular uptake and/or intracellular distribution under these conditions.

As no saturation was observed for DP-induced QT prolongation, the relationship between plasma DP concentration and change in QT interval was analyzed by a linear pharmacodynamic model (eq 1). Although we also employed the E_{max} model, the linear model showed a better goodness of fit than the E_{max} model. Doses of DP beyond the therapeutic range were not experimentally feasible due to adverse effects on rats. It is of interest that different pharmacodynamic models were applied to DP and EM: the linear model for DP and the E_{max} model for EM. Similar cases have been reported for other agents which induce QT prolongation, i.e., the relationship between drug concentration and change in QT interval was explained by the linear model for quinidine and an E_{max} model for terfenadine.[10] Whiting et al.[30] have also reported that the change in QT interval is linearly correlated with plasma DP concentration. Both DP and quinidine were reported to block several types of potassium channels on ventricular myocytes,[22,31] leading to a complex, stepwise inhibition, which may result in a linear relation between drug concentration and change in QT interval.

Pharmacodynamic Interaction between DP and EM—Enhanced QT prolongation was observed after coadministration of EM and DP compared to that after each administration of these drugs (Figure 5). However, the plasma concentrations of each agent were not changed by each other. This indicates that the interaction on ECG between these drugs can be attributed to their pharmacodynamic interaction, not a pharmacokinetic one, at least in the present experimental setting. Thus, a clinically important pharmacodynamic interaction between EM and DP can be observed without affecting pharmacokinetics.

The observed data after coadministration of EM and DP were simulated by simple addition of QT prolongations after separate EM and DP administrations. The simulated line is below the observed data during the administration. Then, at each point, we compared the ΔQT (ΔQT_{DP+EM}) in concomitant administration with the additional ΔQT (ΔQT_{DP}

$+ \Delta QT_{EM}$) using the Student *t*-test. As a result, significant differences were observed only at 4 and 5 min. Therefore, we cannot completely define this interaction as additive. However, we are not sure that the interaction between DP and EM is antagonistic. The clinical significance of the present study is that enhanced QT prolongation was shown in concomitant administration compared to individual administrations.

Effects of EM on Pharmacokinetics of DP—The pharmacokinetic parameters of DP obtained here were is close agreement with those noted in previous studies.[15,16] Since the total plasma clearance of DP was large and thought to be blood flow-limited, we evaluated the effects of EM on the pharmacokinetics of DP following portal vein administration of DP.

In the portal vein dosing of DP, EM pretreatment did not significantly change the pharmacokinetic parameters of DP (Table 2). In addition, no effect of EM on the plasma protein binding of DP was observed. In addition, the blood-to-plasma concentration ratio of DP (R_B) was also evaluated and it was not significantly changed by EM. While the plasma binding of DP is known to saturate within the therapeutic range in humans,[32] it was almost constant in rats under the current experimental range (0.05−15.0 μg/mL), suggesting interspecies difference in the plasma protein binding of DP, in accordance with a previous reports.[16]

Although it is expected that EM might cause the elevation of DP plasma concentrations in humans by metabolic inhibition, no pharmacokinetic interaction was seen in rats. The most likely explanation for these results may be interspecies differences in the metabolism of DP. In fact, the urinary excretion of MND, a major metabolite yielded by CYP3A, proved to be lower (up to 4% of the dose) in rats than in humans. It has also been reported[16,33] that in rats about 20% of the dose was excreted into urine as phenol and methoxyphenol metabolites, while these metabolites are not detected in humans. Therefore, the contribution of the metabolic pathway of DP, which EM could inhibit, to the total clearance may be lower in humans than in rats. The EM concentration in liver was enough compared to its inhibition constant (IC_{50} = 70 μg/mL) in vitro.[5] Another potential explanation for the lack of pharmacokinetic interaction between EM and DP is a setereoselective metabolism. DP is a racemic mixture of *R*(−) and *S*(+) enantiomers, and those clearances are reported to be different.[34] If EM inhibits one of the enantiomers, increase in AUC of DP as a racemic mixture may not reach significance. Echizen et al.[35] showed that the enantiomers share an enzyme in humans and mice, and that EM inhibited their metabolism equally in mice but not equally in human microsomes. However, no data are available for rats in vivo or in vitro. Since DP is used as a racemic mixture in clinical settings, the clinical significance of our study may not be diminished.

Other explanation is the administration route-dependency. EM was intravenously administered in this study. However, the repeated oral administration of EM might be required to induce the metabolic inhibition of CYP3A.[36] In addition, when orally administered, the intestinal metabolisms by CYP3A may be inhibited, which may lead to further increase in the DP concentrations if DP is metabolized by intestinal CYP3A.

Prediction of QT Prolongation in Humans—It has been reported[26,30,37−40] that DP prolongs the QT interval within the therapeutic range of plasma concentration (2.0−5.0 μg/mL) in humans. The findings obtained in the present study were consistent with the above reports. On the other hand, the plasma concentrations of EM have not been reported where QT prolongation or TdP occurred, possibly because of difficulty in the determination of EM concentration in plasma. Therefore, the quantitative relationship between concentration of EM and its effect on QT interval in clinical settings remains unknown. An EM-induced QT prolongation is reported[5] to occur not only after i.v. administration of a high dose (up to 1 g/body) in many cases, but also after oral administration of EM.[41] In the case of oral administration, plasma EM concentration is considered to be lower than in the case of i.v. injection, suggesting a possibility that EM may also induce QT prolongation within or near therapeutic plasma concentrations (0.5−3.0 μg/mL), which correlates well with the range examined in our present study. In addition, orally administered EM is also known to induce TdP associated with QT prolongation after concomitant treatment with quinidine.[9] Thus, our method presented here may be useful for predicting drug-induced QT prolongation in clinical settings, at least in a qualitative manner.

In conclusion, the present study suggests that pharmacodynamic interaction may increase the risk of QT prolongation after coadministration of DP and EM in humans. In concomitant treatment of DP and EM, therefore, it is our recommendation for patients' safety that ECG should be monitored periodically as necessary.

References and Notes

1. Ragosta, M.; Weihl, A. C.; Rosenfeld, L. E. Potentially fatal interaction between erythromycin and disopyramide. *Am. J. Med.* **1989**, *86*, 465−466.
2. Kawamoto, T.; Emoto, C.; Yoshino, T.; Maruyama, T.; Tamura, R.; Komuro, R.; Ishikawa, K. A case of torsade de pointes occurred by interaction between erythromycin and disopyramide. *Shinzou* **1993**, *25(6)*, 696−701.
3. Karim, A. The pharmacokinetics of norpace. *Angiology* **1975**, *26(S-1)*, 85−98
4. Periti, P.; Mazzei, T.; Mini, E.; Novelli, A. Pharmacokinetic drug interactions of macrolides. *Clin. Pharmacokinet.* **1992**, *23(2)*, 106−131.
5. Echizen, H.; Kawasaki, H.; Chiba, K.; Tani, M.; Ishizaki, T. A potent inhibitory effect of erythromycin and other macrolide antibiotics on the mono-N-dealkylation metabolism of disopyramide with human liver microsomes. *J. Pharmacol. Exp. Ther.* **1993**, *264(3)*, 1425−1431.
6. Brandriss, M. W.; Richardson, M. S.; Barold, S. S. Erythromycin-induced QT prolongation and polymorphic ventricular tachycardia (Torsades de Pointes): Case report and review. *Clin. Infect. Dis.* **1994**, *18*, 995−998.
7. Gitler, B.; Bergeer, L. S.; Buffa, S. D. Torsades de pointes induced by erythromycin. *Chest* **1994**, *105(2)*, 368−372.
8. Orban, Z.; MacDonald, L. L.; Peters, M. A.; Guslits, B. Erythromycin-induced cardiac toxicity. *Am. J. Cardiol.* **1995**, *75*, 859−861.
9. Lin, J. C.; Quasny, H. A. QT prolongation and development of torsades de pointes with the concomitant administration of oral erythromycin base and quinidine. *Pharmacotherapy* **1997**, *17(3)*, 626−630.
10. Ohtani, H.; Hanada, E.; Yamamoto, K.; Sawada, Y.; Iga, T. Pharmacokinetic-pharmacodynamic analysis of the electrocardiographic effects of terfenadine and quinidine in rats. *Biol. Pharm. Bull.* **1996**, *19(9)*, 1189−1196.
11. Mayer, F.; Kramer, B. K.; Res, K. M.; Kuhlkamp, V.; Liebich, H. M.; Risler, T.; Seipel, L. Simplified, rapid and inexpensive extraction procedure for a high-performance liquid chromatographic method for determination of disopyramide and its main metabolite mono-N-dealkylated disopyramide in serum. *J. Chromatogr.* **1991**, *572*, 339−345.
12. Hanada, E.; Ohtani, H.; Kotaki, H.; Sawada, Y.; Iga, T. Determination of erythromycin concentrations in rat plasma and liver by high-performance liquid chromatography with amperometric detection. *J. Chromatogr. B* **1997**, *692*, 478−482.
13. Wagner, J. G. *Fundamentals of Clinical Pharmacokinetics*; Intelligence Publication Ins.: Hamilton, Illinois, 1975; pp 90−102.
14. Holford. N. H. G.; Sheiner L. B. Undertanding the Dose−Effect Relationship; Clinical Application of Pharmacokinetic-Pharmacodynamic Models. *Clin. Pharmacokinet.* **1981**, *6*, 429−453.

15. Ito, T.; Takahashi, Y.; Tomidokoro, K.; Nishino, T.; Fukuzawa, Y.; Chiba, K.; Miyazaki, S.; Takada, M. The mechanism of the renal excretion of disopyramide in rats (I). *Yakugaku Zasshi* **1992**, *112(5*), 336−342.
16. Cook, C. S.; Karim, A.; Sollman, P. Stereoselectivity in the metabolism of disopyramide enantiomers in rat and dog. *Drug Metab. Dispos*. **1982**, *10(2)*, 116−121
17. Hayes, E.; Pugsley, M. K.; Penz, W. P.; Adaikan, G.; Walker, M. J. A. Relationship between QaT and RR intervals in rats, guinea pigs, rabbits, and primates. *J. Pharmacol. Toxicol. Med*. **1994**, *32(4)*, 201−207.
18. Keren, A.; Tzivoni, D.; Gavish, D.; Levi, J.; Gottlieb, S.; Benhorin, J.; Stern, S. Etiology, warning signs and therapy of torsade de pointes. A study of 10 patients. *Circulation* **1981**, *64*, 1167−1174.
19. Schanne, O. F.; Bkaily, G.; Dumais, B.; Boutin, L. Disopyramide phosphate effects on slow and depressed fast responses. *Can. J. Physiol. Pharmacol*. **1986**, *64*, 487−491.
20. Kus, T.; Sasyniuk, B. I. Electrophysiological actions of disopyramide phosphate on canine ventricular muscle and Purkinje fibers. *Circulation Res*. **1975**, *37*, 844−854.
21. Campbell, T. J. Kinetics of onset of rate-dependent effects of class I antiarrythmic drugs are important in determining their effects on refractoriness in guinea-pig ventricle, and provide a theoretical basis for their subclassification. *Cardiovasc. Res*. **1983**, *17*, 344−352.
22. Hiraoka, M.; Kuga, K.; Kawano, S.; Sunami, A.; Fan, Z. New observations on the mechanisms of antiarrythmic actions of disopyramide on cardiac membranes. *Am. J. Cardiol*. **1989**, *64*, 15J-19J.
23. Vanhoutte, F.; Vereecke, J.; Carmeliet, E.; Verbeke, N. Effects of the enantiomers of disopyramide and its major metabolite on the electrophysiological characteristics of the guinea-pig papillary muscle. *Naunyn-Schmiedeberg's Arch. Pharmacol*. **1991**, *344*, 662−673.
24. Grant, A. M.; Marshall, R. J.; Ankier, S. I. Some effects of disopyramide and its N-dealkylated metabolite on isolated nerve and cardiac muscle. *Eur. J. Pharmacol*. **1978**, *49*, 389−394.
25. Boucher, M.; Chassaing, C.; Herbet, A.; Duchene-Marullas, P. Interactions with the cardiac cholinergic system: Effects of disopyramide and its mono-N-dealkylated metabolite. *Life Sci*. **1992**, *50(20)*, PL161−166.
26. Bergfeldt, L.; Gustafsson, K. S.; Dahlqvist, R. Comparative class I electrophysiologic and anticholinergic effects of disopyramide and its main metabolite (mono-N-dealkylated disopyramide) in healthy humans. *Cardiovasc. Drug. Ther*. **1992**, *6*, 529−537.
27. Rubart, M.; Pressler, M. L.; Pride, H. P.; Zipes, D. P. Electrophysiological mechanisms in a canine model of erythromycin-associated long QT syndrome. *Circulation* **1993**, *88(4)*, 1832−44.
28. Daleau, P.; Lessard, E.; Groleau, M.-F.; Turgeon, J. Erythromycin blocks the rapid component of the delayed rectifier potassium current and lengthens repolarization of guinea pig ventricular myocytes. *Circulation* **1995**, *91(12)*, 3010−16.
29. Antzelevitch, C.; Sun, Z.-Q.; Zhang, Z.-Q.; Yan, G.-X. Cellular and ionic mechanisms underlying erythromycin-induced long QT intervals and torsade de pointes. *J. Am. Coll. Cardiol*. **1996**, *28(7)*, 1836−48.
30. Whiting, B.; Holford, N. H. G.; Sheiner, L. B. Quantitative analysis of the disopyramide concentration-effect relationship. *Br. J. Clin. Pharmacol*. **1980**, *9*, 67−75.
31. Coraboeuf, E.; Deroubaix, E.; Escande, D.; Coulombe, A. Comparative effects of three class I antiarryhythmic drugs on plateau and pacemaker currents of sheep cardiac Purkinje fibers. *Cardiovasc. Res*. **1988**, *22*, 375−384.
32. Lima, J. J.; Boudoulas, H.; Blanford, M. Concentration-dependence of disopyramide binding to plasma protein and its influence on kinetics and dynamics. *J. Pharmacol. Exp. Ther*. **1981**, *219(3)*, 741−747.
33. Karim, A.; Ranney, R. E.; Karaychy, S. Species differences in the biotransformation of a new antiarrhythmic agent: disopyramide phosphate. *J. Pharmacothuet. Sci*. **1972**, *61(6)*, 888−893.
34. Corre, P.; Gibassier, D.; Sado, P.; Verge, R. L. Human pharmacokinetics and metabolism of disopyramide enantiomers. *Eur. J. Drug Met., Pharmacokinet*. **1991**, *3*, 233−237.
35. Echizen, H.; Mochizuki, K.; Tani, M.; Ishizaki, T. Interspecies Differences in Enantioselective Mono-N-Dealkylation of Disopyramide by Human and Mouse Liver Microsomes. *J. Pharmacol. Exp. Ther*. **1993**, *268(3)*, 1518−1525.
36. Delaforge, M.; Jaouen, M.; Mansuy, D. The cytochrome P-450 metabolite complex derived from troleandomycin: properties in vitro and stability in vivo. *Chem. Biol. Interact*. **1984**, *15*, 371−376.
37. Piscitelli, D. A.; Fisher, J. H.; Schoen, M. D.; Hoon, T. J.; Bauman, J. L. Bioavailability of total and unbound disopyramide: implications for clinical use of the immediate and controlled-release dosage forms. *J. Clin. Pharmacol*. **1994**, *34*, 823−828.
38. Sadanaga, T.; Ogawa, S.; Okada, Y.; Tsutsumi, N.; Iwanaga, S.; Yoshikawa, T.; Akaishi, M.; Handa, A. Clinical evaluation of the use-dependent QRS prolongation and the reverse use-dependent QT prolongation of class I and class III antiarrythmis agents and their value in predicting efficacy. *Am. Heart J*. **1993**, *126(1)*, 114−121.
39. Longmore, J.; Berry, J. L.; Szabadi, E.; Bradshaw, C. M. A comparison of the anticholinergic effects of two formulations of disopyramide in healthy volunteers. *Eur. J. Clin. Pharmacol*. **1990**, *39*, 305−309.
40. Endresen, K.; Amlie, J. P.; Forfang, K. Effects of disopyramide on repolarization and intraventricular conduction in man. *Eur. J. Clin. Pharmacol*. **1988**, *35*, 467−474.
41. Freedman, R. A.; Anderson, K. P.; Green, L. S.; Mason, J. W. Effect of erythromycin on ventricular arrhythmias and ventricular repolarization in idiopathic long QT syndrome. *Am. J. Cardiol*. **1987**, *59*, 168−169.

JS980256R

Hydrogen Bonding. 47. Characterization of the Ethylene Glycol–Heptane Partition System: Hydrogen Bond Acidity and Basicity of Peptides

MICHAEL H. ABRAHAM,*,† FILOMENA MARTINS,‡ ROBERT C.MITCHELL,§ AND COLIN J.SALTER§

Contribution from *Department of Chemistry, University College London, 20 Gordon Street, London, WC1H OAJ, UK, Grupo de Estrutura e Reactividade Quimica, Department of Chemistry, University of Lisbon, Cc. Bento da Rocha Cabral 14, 1250 Lisboa, Portugal, and SB Pharmaceuticals, New Frontiers Science Park (North), Third Avenue, Harlow, Essex, CM19 5AW, UK.*

Received June 9, 1998. Accepted for publication October 19, 1998.

Abstract □ Twelve measured ethylene glycol–heptane partition coefficients, P_{eh}, have been combined with 20 measured literature values and 44 indirectly determined values to give a set of 76 values. Excluding one value for benzamide, the log P_{eh} values are correlated through our general solvation equation, log $P_{eh} = 0.336 - 0.075R_2 - 1.201\pi_2^H - 3.786\ \Sigma\alpha_2^H - 2.201\ \Sigma\beta_2^H + 2.085V_x$ with $r^2 = 0.966$, sd $= 0.28$, and $F = 386$. The solute descriptor R_2 is the excess molar refraction, π_2^H is the dipolarity/polarizability, $\Sigma\alpha_2^H$ and $\Sigma\beta_2^H$ are the overall hydrogen bond acidity and basicity, and V_x is the McGowan volume. The log P_{eh} equation has then been used to obtain descriptors for eleven peptides, all of which are end-protected. It is shown that for these end-protected peptides, hydrogen bond basicity makes a greater contribution to log P_{eh} than does hydrogen bond acidity.

Introduction

Karls et al.,[1] in 1991, showed that the hydrogen bond number of Stein[2] was useful in the correlation of absorption of a series of peptides in rats. The peptides, I−VII, are shown in Figure 1, and the hydrogen bond numbers, H#, are in Table 1. The latter are simply calculated from the total number of C=O and N−H groups, with NH_2 counted as two. Burton et al.[3] used the same seven peptides to study permeability across Caco-2 cell monolayers and showed graphically that there was a reasonable correlation between log k_{caco} and the Δlog P parameter of Seiler.[4] The latter is obtained from water−octanol and water−alkane partition coefficients through eq 1,

$$\Delta\log P = \log P_{oct} - \log P_{alk} \quad (1)$$

Burton et al.[3] did not explore the H# numbers, but investigated the use of a novel partitioning system, that of ethylene glycol−heptane:

$$P_{eh} = [\text{concn in heptane}]/[\text{concn in ethylene glycol}] \quad (2)$$

They showed that for the seven peptides there was a reasonable plot of log P_{eh} against Δlog P, and argued that since Δlog P could be taken as a measure of the hydrogen bond or desolvation potential of a solute, so could log P_{eh}. The various partition coefficients that were determined[3] for the seven peptides are given in Table 1; the alkane used was isooctane. In later work it was shown[5] that permeabilities of the seven peptides across an in vitro model of the blood−brain barrier (BBB) or from physiologic saline to rat brain could be correlated with H# or Δlog P or log P_{eh}. The hydrogen bonding capacity of the peptides was suggested to be the major factor governing both the in vitro and the perfusion in vivo permeabilities.

Table 1—Hydrogen Bond Numbers and Partition Coefficients for Peptides[a]

peptides	H#	log P_{oct}	log P_{iso}[b]	log P_{eh}
I	5	0.05	–4.92	–5.46 (–5.57)
II	7	1.19	–5.29	–6.52 (–6.28)
III	9	2.30	–5.02	–7.10 (–7.16)
IV	8	2.63	–4.20	–6.28
V	7	2.53	–3.10	–5.14
VI	6	2.92	–1.67	–4.20
VII	5	3.24	–0.69	–2.86
VIII	8			(–6.00)
IX	8			(–5.76)
X	7			(–4.35)
XI	5			(–3.44)

[a] log P values from ref 3; values in parentheses from ref 6. [b] P_{iso} refers to partition between water and isooctane.

To characterize the ethylene glycol−heptane partitioning system, Paterson et al.[6] measured log P_{eh} values for a set of 20 standard compounds, and correlated these values with the solvatochromic parameters of Kamlet et al..[7] The log P_{eh} values are in Table 2, nos. 1−20, and the correlation equation was:

$$\log P_{eh} = 0.30 - 1.53\pi^* - 4.41\alpha - 1.69\beta + 2.79V_I \quad (2)$$
$$n = 19,\ r^2 = 0.984,\ \text{sd} = 0.19,\ F = 223$$

In eq 2, π^* is the solute dipolarity/polarizability, α is the solute hydrogen bond acidity, β is the solute hydrogen bond basicity, and V_I is the solute intrinsic volume in (cm^3 mol^{-1})/100. Benzamide was left out of the correlation, hence n, the number of data points, is 19; the only other statistic given[6] was $r^2 = 0.980$, where r is the correlation coefficient. We have rerun the correlation and find $r^2 = 0.984$ (the value of 0.980 is the adjusted value), the standard deviation sd $= 0.19$ and the F-statistic $F = 223$, as shown above.

Paterson et al.[6] pointed out that eq 2 shows that the most important coefficient is the solute hydrogen bond acidity. However, this does not mean that the term in α always dominates; this will depend on the various parameter values for any given solute. Although the solvatochromic parameters of Kamlet et al.[7] are useful, there are difficulties in that parameters for many solutes have to be estimated, and that there is no protocol for the estimation of parameters for new structures such as peptides I−VII. In addition, although Paterson et al.[6] selected a reasonable set of compounds, the number is minimal for a four-

† University College London.
‡ University of Lisbon.
§ SB Pharmaceuticals.

10.1021/js980242l CCC: $18.00 Published on Web 12/10/1998

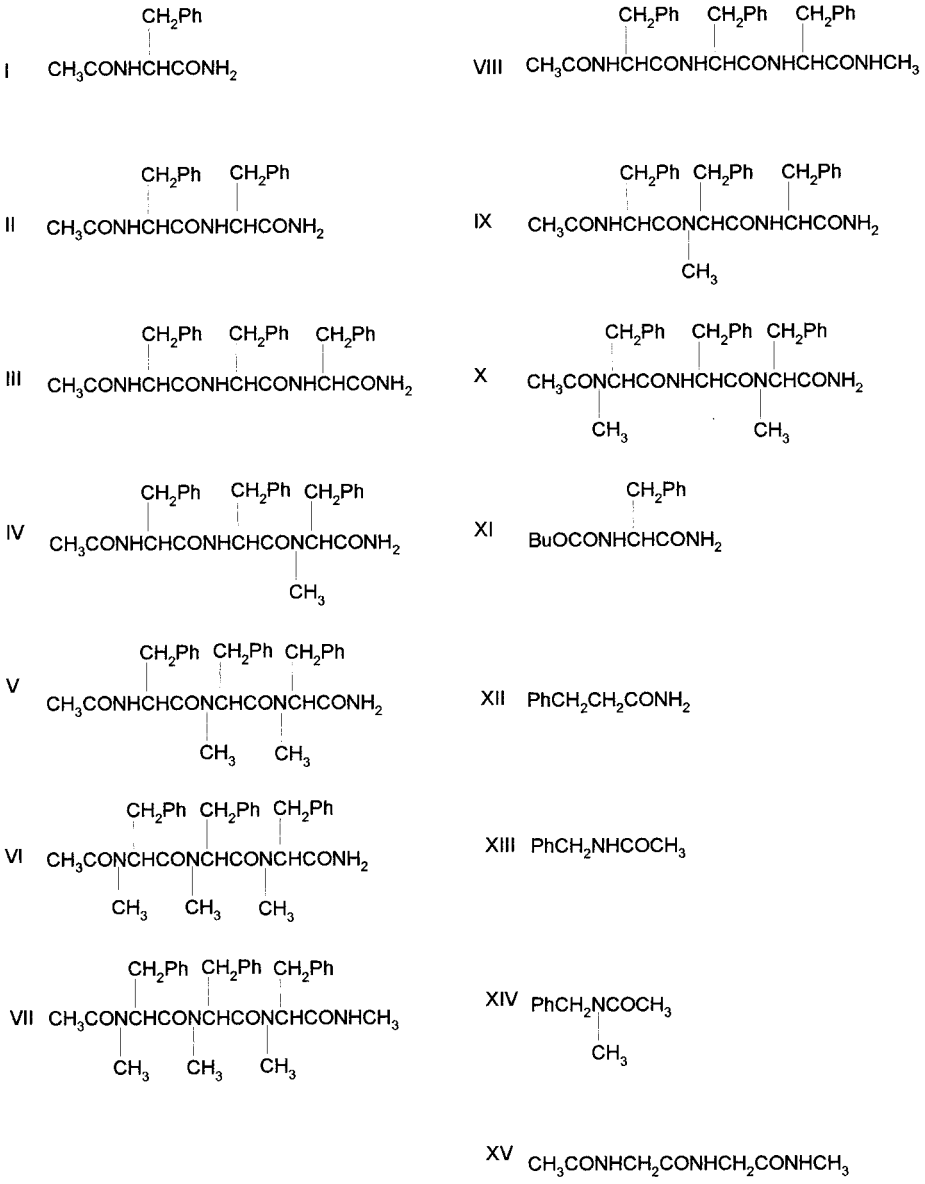

Figure 1—The structures of the peptides.

parameter equation, and the range of the various descriptors is not very large.

We therefore set out to expand the number and nature of the solutes, to characterize the ethylene glycol–heptane system through the solvation equation and the solvation parameters of Abraham,[8] and to compare coefficients in the correlation equation with those for many other partitioning systems that have been thus characterized.[9] Once this has been done, our aim is to determine solvation parameters for the peptides I–VII, and then to ascertain the factors that influence partitioning of peptides in the ethylene glycol–heptane system.

Experimental Section

Ethylene glycol was Fisons Analytical Reagent, and heptane was Fisher Scientific Analytical Reagent. Partition experiments were carried out with mutually saturated solvents. The various solutes were from Sigma or Aldrich, except for benzyl alcohol, zolantidine, and clonidine which were in-house specimens. Preliminary experiments showed that the maximum water content of the ethylene glycol was 0.11% by Karl Fischer titration, either with fresh solvent or after shaking the solvent in a separating funnel with a significant air space. Since the ethylene glycol did not appear to be particularly hydroscopic, no special precautions were taken to exclude water. A number of partition experiments were carried out on benzyl alcohol, with different combinations of sonication and tumbling. Results showed that 15 min sonication using a SEMAT ultrasonic bath followed by mixing for 1 h on a mechanical flask tumbler was sufficient to reach equilibrium.

Partition measurements were carried out by dissolving the solute in presaturated ethylene glycol. In the case of compounds obtained as salts (imipramine hydrochloride, mepyramine maleate, and clonidine hydrochloride) solid potassium hydroxide was first dissolved in the ethylene glycol at a concentration of 1.0 mg ml^{-1}. A known volume of the ethylene glycol solution was transferred to a Nalgene FEP bottle, and a known volume of preequilibrated heptane was added. The phases were mixed, as above, and allowed to separate, with centrifugation for 3 min at 3000 rpm, if necessary. The ethylene glycol solutions before and after partitioning were analyzed by UV spectrometry. In all case, determinations were carried out in duplicate, using different volume ratios of ethyene glygol:heptane. The volume ratios were chosen so that the initial and final absorbances were significantly different. In the case of pentachlorophenol and anthracene, solubility in ethylene glycol was very low. The compounds were therefore initially dissolved in heptane, and it was this phase that was analyzed before and after partitioning. Results are in Table 2 under compounds nos. 21–32.

Table 2—Solute Descriptors and Values of log P_{eh}

no.	solute	R_2	π_2^H	$\Sigma\alpha_2^H$	$\Sigma\beta_2^H$	V_x	log P_{eh}	no.	solute	R_2	π_2^H	$\Sigma\alpha_2^H$	$\Sigma\beta_2^H$	V_x	log P_{eh}
1	benzene	0.610	0.52	0.00	0.14	0.7164	0.475	39	carbon dioxide	0.000	0.28	0.05	0.10	0.2809	0.320
2	toluene	0.601	0.52	0.00	0.14	0.8573	0.994	40	methane	0.000	0.00	0.00	0.00	0.2495	1.080
3	bromobenzene	0.882	0.73	0.00	0.09	0.8914	0.970	41	ethane	0.000	0.00	0.00	0.00	0.3904	1.360
4	methyl phenyl ether	0.708	0.75	0.00	0.29	0.9160	0.673	42	propane	0.000	0.00	0.00	0.00	0.5313	1.270
5	benzaldehyde	0.820	1.00	0.00	0.39	0.8730	–0.131	43	butane	0.000	0.00	0.00	0.00	0.6722	1.750
6	acetophenone	0.818	1.01	0.00	0.48	1.0139	–0.051	44	2-methylpropane	0.000	0.00	0.00	0.00	0.6722	1.550
7	propyl phenyl ketone	0.797	0.95	0.00	0.51	1.2957	0.660	45	hexane	0.000	0.00	0.00	0.00	0.9540	2.370
8	butyl phenyl ketone	0.795	0.95	0.00	0.50	1.4366	0.950	46	heptane	0.000	0.00	0.00	0.00	1.0949	2.590
9	heptyl phenyl ketone	0.720	0.95	0.00	0.50	1.8593	1.720	47	octane	0.000	0.00	0.00	0.00	1.2358	2.820
10	benzonitrile	0.742	1.11	0.00	0.33	0.8711	–0.274	48	2,2,4-trimethylpentane	0.000	0.00	0.00	0.00	1.2358	2.580
11	benzamide	0.955	0.96	0.26	0.41	0.8162	–1.250	49	nonane	0.000	0.00	0.00	0.00	1.3767	2.990
12	nitrobenzene	0.871	1.11	0.00	0.28	0.8906	0.015	50	cyclohexane	0.305	0.10	0.00	0.00	0.8454	2.050
13	benzamide	0.990	1.50	0.49	0.67	0.9728	–3.690	51	methylcyclohexane	0.244	0.06	0.00	0.00	0.9863	2.310
14	acetanilide	0.870	1.40	0.50	0.67	1.1133	–2.740	52	ethylcyclohexane	0.263	0.10	0.00	0.00	1.1272	2.540
15	phenol	0.805	0.89	0.60	0.30	0.7751	–2.460	53	ethene	0.107	0.10	0.00	0.07	0.3474	0.890
16	4-ethylphenol	0.800	0.90	0.55	0.36	1.0569	–1.800	54	propene	0.103	0.08	0.00	0.07	0.4883	0.950
17	4-chlorophenol	0.915	1.08	0.67	0.20	0.8975	–2.750	55	2-methylbut-2-ene	0.159	0.08	0.00	0.07	0.7701	1.890
18	2-nitrophenol	1.015	1.05	0.05	0.37	0.9493	–0.258	56	hex-1-ene	0.078	0.08	0.00	0.07	0.9110	2.020
19	benzyl alcohol	0.803	0.87	0.39	0.56	0.9160	–1.780	57	hept-1-ene	0.092	0.08	0.00	0.07	1.0519	2.230
20	pyridine	0.631	0.84	0.00	0.52	0.6753	–1.070	58	oct-1-ene	0.094	0.08	0.00	0.07	1.1928	2.460
21	propanone	0.179	0.70	0.04	0.49	0.5470	–0.490	59	buta-1,3-diene	0.320	0.23	0.00	0.10	0.5862	0.970
22	butanone	0.166	0.70	0.00	0.51	0.6879	–0.050	60	2-methylbuta-1,3-diene	0.313	0.23	0.00	0.10	0.7271	1.540
23	anthracene	2.290	1.34	0.00	0.28	1.4544	0.960	61	cyclohexene	0.395	0.20	0.00	0.10	0.8024	1.800
24	hexafluorobenzene	0.088	0.66	0.00	0.00	0.8226	1.550	62	ethyne	0.190	0.25	0.21	0.15	0.3044	–0.110
25	3,5-dichlorophenol	1.020	1.00	0.91	0.00	1.0199	–2.070	63	1,4-dioxane	0.329	0.75	0.00	0.64	0.6810	–0.320
26	pentachlorophenol	1.220	0.87	0.96	0.01	1.3871	–0.920	64	butanone	0.166	0.70	0.00	0.51	0.6879	–0.120
27	antipyrine	1.320	1.50	0.00	1.48	1.5502	–2.280	65	ammonia	0.139	0.35	0.14	0.62	0.2084	–1.320
28	clonidine	1.847	1.83	0.35	1.08	1.5317	–1.800	66	trimethylamine	0.140	0.20	0.00	0.67	0.6311	–0.450
29	mepyramine	1.819	1.92	0.00	1.59	2.3870	0.000	67	nitromethane	0.313	0.95	0.06	0.31	0.4237	–1.170
30	imipramine	1.480	1.75	0.00	1.19	2.4020	0.910	68	ethanol	0.246	0.42	0.37	0.48	0.4491	–1.840
31	zolantidine	2.689	2.64	0.40	1.38	2.9946	–1.470	69	benzene	0.610	0.52	0.00	0.14	0.7164	0.910
32	deoxycorticosterone	1.740	3.50	0.14	1.31	2.6802	–1.520	70	toluene	0.601	0.52	0.00	0.14	0.8573	1.190
33	neon	0.000	0.00	0.00	0.00	0.0850	0.780	71	ethylbenzene	0.613	0.51	0.00	0.15	0.9982	1.400
34	argon	0.000	0.00	0.00	0.00	0.1900	1.030	72	*o*-xylene	0.663	0.56	0.00	0.16	0.9982	1.370
35	xenon	0.000	0.00	0.00	0.00	0.3290	1.120	73	*m*-xylene	0.623	0.52	0.00	0.16	0.9982	1.440
36	hydrogen	0.000	0.00	0.00	0.00	0.1086	0.810	74	*p*-xylene	0.613	0.52	0.00	0.16	0.9982	1.460
37	nitrogen	0.000	0.00	0.00	0.00	0.2222	1.160	75	propylbenzene	0.604	0.50	0.00	0.15	1.1391	1.660
38	nitrous oxide	0.068	0.35	0.00	0.10	0.2810	0.610	76	isopropylbenzene	0.602	0.49	0.00	0.16	1.1391	1.600

Results and Discussion

Characterization of the Ethylene Glycol–Heptane System—We use the solvation equation of Abraham,[8] as shown in eq 3:

$$\log SP = c + rR_2 + s\pi_2^H + a\Sigma\alpha_2^H + b\Sigma\beta_2^H + vV_x \quad (3)$$

The solute descriptor R_2 is excess molar refraction, π_2^H is the polarizability/dipolarity, $\Sigma\alpha_2^H$ and $\Sigma\beta_2^H$ are the overall or effective hydrogen bond acidity and basicity, and V_x is the characteristic volume of McGowan[10] in units of $(cm^3\ mol^{-1})/100$. As solutes we used the 20 compounds studied by Paterson et al.,[6] nos. 1–20 in Table 2, and we also measured log P_{eh} for another 12 compounds, nos. 21–32 in Table 2, by the standard shake-flask method, as described above. The 12 compounds were chosen specifically to increase the range of the descriptors; inclusion of the drugs nos. 28–32, and of deoxycortisone, very considerably extends the range. However, there is still room for improvement because over solutes nos. 1–32, the lowest value of π_2^H is 0.52 for benzene, and the lowest value of V_x is 0.5470 for propanone. Since the solubility of ethylene glycol in heptane is very small,[6] we felt that the partition coefficient between these equilibrated phases could be obtained through solubility of gases and vapors in the two pure solvents, eq 4:

$$\log P_{eh} = \log L_h - \log L_e \quad (4)$$

where log L_h and log L_e are the Ostwald solubility coefficients (or gas–liquid partition coefficients) in heptane[11–23] and ethylene glycol[13–16,22–29] at 298 K. Values of log P_{eh} could thus be obtained for 44 extra solutes (nos. 33–76 in Table 2) some with zero values of π_2^H, and with V_x as low as 0.0850 for neon; details are in Table 3. The range of descriptors over the total 72 solutes is now very large indeed; values are collected in Table 2. We note that three of the solutes in set 1–32 are duplicated in set 33–76 (benzene, toluene, and butanone) so that we have 76 data points for 73 solutes. Application of eq 3 to the 76 data points in Table 2 showed that again benzamide was a marked outlier. It is hard to believe that both the Kamlet and the Abraham set of descriptors for benzamide are wrong, and so it is possible that the log P_{eh} value is in error. We did not carry out a determination of log P_{eh} for benzamide ourselves, because the value quoted (–3.69) is lower than we can measure by our shake flask and UV analytical method. Omission of benzamide leads to the correlation eq 5; the sd values for the coefficients are also given.

$$\log P_{eh} = 0.336(0.067) - 0.075(0.134)R_2 - 1.201(0.140)\pi_2^H - 3.786(0.177)\Sigma\alpha_2^H - 2.201(0.163)\Sigma\beta_2^H + 2.085(0.097)V_x \quad (5)$$

$$n = 75,\ r^2 = 0.966,\ \text{sd} = 0.28,\ F = 386$$

Table 3—Indirect Calculation of log P_{eh}

no.	solute	log L_e[13–16,22–29]	log L_h[11–23]	log P_{eh}
33	neon	–0.45	–1.23	0.78
34	argon	–1.41	–0.38	1.03
35	xenon	–0.47	0.65	1.12
36	hydrogen	–1.75	–0.94	0.81
37	nitrogen	–1.81	–0.65	1.16
38	nitrous oxide	–0.13	0.48	0.61
39	carbon dioxide	–0.02	0.30	0.32
40	methane	–1.14	–0.06	1.08
41	ethane	–0.63	0.73	1.36
42	propane	0.03	1.30	1.27
43	butane	0.21	1.96	1.75
44	2-methylpropane	0.14	1.69	1.55
45	hexane	0.54	2.91	2.37
46	heptane	0.85	3.44	2.59
47	octane	1.13	3.95	2.82
48	2,2,4-trimethylpentane	0.77	1.81	2.58
49	nonane	1.43	1.56	2.99
50	cyclohexane	1.07	3.12	2.05
51	methylcyclohexane	1.20	3.51	2.31
52	ethylcyclohexane	1.52	4.06	2.54
53	ethene	–0.37	0.52	0.89
54	propene	0.33	1.28	0.95
55	2-methylbut-2-ene	0.56	2.45	1.89
56	hex-1-ene	0.79	2.81	2.02
57	hept-1-ene	1.07	3.30	2.23
58	oct-1-ene	1.33	3.79	2.46
59	buta-1,3-diene	0.99	1.96	0.97
60	2-methylbuta-1,3-diene	0.82	2.36	1.54
61	cyclohexene	1.39	3.19	1.80
62	ethyne	0.50	0.39	–0.11
63	1,4-dioxane	3.27	2.95	–0.32
64	butanone	2.64	2.52	–0.12
65	ammonia	2.25	0.93	–1.32
66	trimethylamine	2.24	1.79	–0.45
67	nitromethane	3.09	1.92	–1.17
68	ethanol	3.48	1.64	–1.84
69	benzene	2.02	2.93	0.91
70	toluene	2.28	3.47	1.19
71	ethylbenzene	2.49	3.89	1.40
72	*o*-xylene	2.67	4.04	1.37
73	*m*-xylene	2.51	3.95	1.44
74	*p*-xylene	2.49	3.95	1.46
75	propylbenzene	2.68	4.34	1.66
76	isopropylbenzene	2.59	4.19	1.60

The rR_2 term is statistically not significant and can be omitted to give:

$$\log P_{eh} = 0.343(0.066) - 1.247(0.112)\pi_2^H - 3.807(0.172)\Sigma\alpha_2^H - 2.194(0.162)\Sigma\beta_2^H + 2.065(0.089)V_x \quad (6)$$

$$n = 75,\ r^2 = 0.966,\ \text{sd} = 0.28,\ F = 488$$

These equations confirm the finding of Paterson et al.[6] that the *a*-coefficient is numerically the largest coefficient. However, as pointed out above, this does not necessarily mean that solute hydrogen bond acidity is the major factor that influences log P_{eh}. In any case, solute hydrogen bond acidity is not the only factor, as shown by the large *s*-, *b*-, and *v*-coefficients. Indeed, it is chemically unreasonable to suggest that solute hydrogen bond basicity, for example, will have little effect on log P_{eh}. The *b*-coefficient is related to the difference in solvent hydrogen bond acidity of ethylene glycol and heptane. Since ethylene glycol is a reasonably strong hydrogen bond acid, and heptane has no acidity, there must be a considerable difference in solvent hydrogen bond acidity, and this must give rise to a substantial *b*-coefficient in the solvation equation.

Table 4—Coefficients in Eq 3 for Various Systems

log SP	*c*	*r*	*s*	*a*	*b*	*v*
log P_{oct}	0.088	0.562	–1.054	0.034	–3.460	3.814
log P_{cyc}	0.127	0.816	–1.731	–3.778	–4.905	4.646
log P_{iso}	0.288	0.382	–1.668	–3.639	–5.000	4.561
log P_{eh}	0.336	–0.075	–1.201	–3.786	–2.201	2.085
-Δlog *P*	0.039	0.254	–0.677	–3.822	–1.445	0.832

Table 5—Values of R_2 and V_x, and Calculated Descriptors for Peptides I–VII from Three Simultaneous Equations

peptide	R_2	V_x	π_2^H	$\Sigma\alpha_2^H$	$\Sigma\beta_2^H$
I	1.453	1.6519	4.01	0.64	0.85
II	2.466	2.7979	5.18	0.73	1.60
III	3.479	3.9439	6.41	0.68	2.33
IV	3.441	4.0848	6.46	0.50	2.36
V	3.403	4.2257	6.91	0.12	2.40
VI	3.365	4.3666	7.68	–0.18	2.20
VII	3.302	4.5075	6.33	–0.30	2.66

We can compare the coefficients in eq 5 with those for a number of partitions,[9,30] as shown in Table 4. For convenience we give coefficients for $-\Delta\log P$. There is certainly a connection between the coefficients for log P_{eh} and $-\Delta\log P$, so it is not surprising that log P_{eh} and $-\Delta\log P$ are linearly related for a series of similar solutes, e.g., peptides I–VII, as shown by Burton et al.[3] However, there are considerable differences between the *b*- and *v*-coefficients in the two partition systems. Hence a relationship between log P_{eh} and $\Delta\log P$ for peptides I–VII may not be general, especially as these peptides have particularly large volumes and large basicities (as shown later).

Analysis of the Hydrogen Bonding Capacity of Peptides—To our knowledge, there are no published studies on quantitative determinations of either the hydrogen bond acidity or the hydrogen bond basicity of peptides. It is therefore of some interest to attempt to determine the solvation descriptors, including $\Sigma\alpha_2^H$ and $\Sigma\beta_2^H$, for peptides I–VII. Once the solvation descriptors are known, it is possible to determine quantitatively the factors that influence the distribution of the peptides.

For the peptides I–VII, both R_2 and V_x can be calculated from structure. The former is obtained by the summation of fragments of known R_2 value,[9] and the latter by McGowan's method of atomic fragments.[10] There remain three descriptors that have to be determined, π_2^H, $\Sigma\alpha_2^H$, and $\Sigma\beta_2^H$. Now if there are available for a given peptide log *P* values in three different partition systems for which the coefficients in eq 3 are known, all three descriptors can be calculated from a set of three simultaneous equations. In Table 1 are log *P* values for the peptides in three partition systems, and in Table 4 are the required coefficients. The calculated descriptors are in Table 5, together with the necessary R_2 and V_x values. There is no point in giving any calculated log *P* values, because the descriptors reproduce the three log *P* values exactly. The obtained descriptors can be compared with descriptors calculated by simple addition of fragment values. We take π_2^H, $\Sigma\alpha_2^H$, and $\Sigma\beta_2^H$ as follows: for a primary amide (1.30, 0.55, and 0.70), for a secondary amide (1.30, 0.40, and 0.70), and for the CH_2Ph group (0.51, 0.00, and 0.15). The calculated descriptors for the mono-, di-, and tripeptides I, II, and III are in Table 6. Values of π_2^H from the fragment addition and the simultaneous equations agree quite well, compare Tables 5 and 6, but $\Sigma\alpha_2^H$ and $\Sigma\beta_2^H$ from the simultaneous equations are much lower than those from fragment addition.

Table 6—Calculated Descriptors from Fragment Values

peptide	π_2^H	$\Sigma\alpha_2^H$	$\Sigma\beta_2^H$
I	3.11	0.95	1.95
II	4.92	1.35	2.82
III	6.73	1.75	3.69

Table 7–Revised Descriptors for Peptides I–VII

				calculated log P[a]		
peptide	π_2^H	$\Sigma\alpha_2^H$	$\Sigma\beta_2^H$	oct	iso	eh
I	3.90	0.65	0.89	0.04	–4.94	–5.43
II	5.20	0.67	1.63	1.05	–5.27	–6.38
III	6.60	0.64	2.27	2.30	–5.08	–7.05
IV	6.45	0.50	2.37	2.62	–4.20	–6.26
V	6.60	0.16	2.48	2.59	–3.13	–5.10
VI	6.50	0.00	2.50	3.13	–1.85	–4.12
VII	6.10	0.00	2.55	3.88	–0.82	–3.45

[a] Oct is water–octanol, iso is water–isooctane, eh is ethylene glycol–heptane.

This might be due to peptide conformations in which intramolecular hydrogen bonding takes place, or in which there is restricted access of solvent molecules to hydrogen bond sites. In either case, $\Sigma\alpha_2^H$ and $\Sigma\beta_2^H$ will be lower than expected.

Even taking these effects into account, some of the obtained descriptors by the simultaneous equation method are not very reasonable. The negative $\Sigma\alpha_2^H$ values for VI and VII have no physical meaning, and π_2^H for VI seems too large. There are a number of possible reasons. First, the determination of very negative log P values is difficult, and the observed log P values may have a larger error than usual. Second, there are numerous possible combinations of the three descriptors that will all give calculated log P values in reasonable accord with the observed values. Third, although we have considerably extended the range of descriptors by incorporation of compounds nos. 21−32 (Table 2), some of the peptides still lie outside this range. Hence small variations in the coefficients of the log P_{eh} equation could lead to large differences in calculated descriptors. We therefore take the descriptors in Table 5 as a first estimate only and then calculate a revised set that (i) will reproduce quite well the observed log P values, and (ii) will be chemically more reasonable. In particular we have assigned $\Sigma\alpha_2^H$ as zero for VI and VII, instead of the negative quantities in Table 5. From the fragment values in Table 6, the difference in π_2^H between I and II and between II and III would be around 1.80 units. However, we find that such an adjustment leads to poorer fits of calculated and experimental log P values, and as a compromise we take the difference as 1.5 units. Also, we expect π_2^H for the tripeptides III−VII to be nearly the same. The revised descriptors are in Table 7, together with the calculated log P values using the revised descriptors. Results are very good for peptides I−VI, with observed and calculated log P values being in good agreement, but for peptide VII, the agreement is not so good. The general trend of the descriptors for I−VII, Table 7, now seems more reasonable than those from the simultaneous equations, Table 5, especially regarding π_2^H and $\Sigma\beta_2^H$.

We can test whether the assigned descriptors for I−VII are compatible with those in Table 2 by incorporating the peptides into the log P_{eh} regression. The resulting equations are very close to eq 5 and eq 6. If only peptides I−VI are used, the regression equation coefficients are almost exactly the same as those in eq 5, or in eq 6:

Table 8—Calculated Descriptors for Peptides VIII–XIV

						calculated log P		
peptide	R_2	V_x	π_2^H	$\Sigma\alpha_2^H$	$\Sigma\beta_2^H$	oct	iso	eh
VIII	3.441	4.0848	6.55	0.41	2.35	2.58	–3.93	–6.00
IX	3.441	4.0848	6.40	0.40	2.34	2.77	–3.60	–5.76
X	3.403	4.2257	6.45	0.03	2.45	2.84	–2.26	–4.36
XI	1.263	2.1333	3.50	0.45	1.01	1.77	–2.02	–3.44
XII	1.060	1.2546	1.65	(0.40)	0.82	0.91	–1.89	–2.43
XIII	1.000	1.2546	1.54	(0.30)	0.83	0.95	–1.42	–1.94
XIV	0.960	1.3955	1.60	0.00	0.89	1.18	–0.10	–0.71

$$\log P_{eh} = 0.336(0.061) - 0.063(0.109)R_2 - 1.218(0.070)\pi_2^H - 3.788(0.157)\Sigma\alpha_2^H - 2.192(0.144)\Sigma\beta_2^H + 2.087(0.092)V_x \quad (7)$$

$$n = 81,\ r^2 = 0.986,\ \text{sd} = 0.27,\ F = 1043$$

$$\log P_{eh} = 0.339(0.061) - 1.231(0.066)\pi_2^H - 3.816(0.149)\Sigma\alpha_2^H - 2.206(0.141)\Sigma\beta_2^H + 2.063(0.082)V_x \quad (8)$$

$$n = 81,\ r^2 = 0.986,\ \text{sd} = 0.27,\ F = 1315$$

The range of descriptors in eq 7 and eq 8 is now so large that it is possible to estimate new values of log P_{eh} for a very large number of compounds; we suggest eq 7 or eq 8 rather than eq 5 or eq 6 be used for this purpose.

Paterson et al.[6] also gave values of log P_{eh} (Table 1) and log P_{oct} (the latter graphically) for peptides VIII−XI. We can use the same procedure as that used for peptides I−VII to assign descriptors. Thus for VIII, π_2^H is expected to be around 6.5−6.6 and $\Sigma\beta_2^H$ to be near to 2.4, by analogy with III, VI, and VII. For IX there is a direct analogy with IV ($\pi_2^H = 6.45$ and $\Sigma\beta_2^H = 2.37$), and for X there is an analogy with V ($\pi_2^H = 6.6$ and $\Sigma\beta_2^H = 2.48$). Our assigned descriptors are in Table 8, together with log P values calculated from the descriptors; there is quite good agreement with the expected values. For XI, it is more difficult to estimate descriptors, but by comparison of *N*-alkylamides and alkylcarbamates we expect that π_2^H for XI should be somewhat less than that for I ($\pi_2^H = 3.9$). If we take π_2^H as 3.5, then the descriptors shown in Table 8 for XI are obtained.

Conradi et al.[31] also investigated peptides XII−XIV in terms of hydrogen bond numbers, H#, but gave no partition coefficients. We can use our usual method of addition of fragments, together with known values of log P_{oct} for XII (0.91),[32,33] and XIII (0.95),[33] to estimate the descriptors shown in Table 8. There is not enough data to obtain reliable $\Sigma\alpha_2^H$ values for XII and XIII, and so the calculated values for log P_{iso} and log P_{eh} are provisional only.

Inspection of Table 7 reveals surprising trends especially with the descriptor $\Sigma\alpha_2^H$. For the mono-, di-, and tripeptides I, II, and III, π_2^H and $\Sigma\beta_2^H$ increase regularly with the number of amide groups, but $\Sigma\alpha_2^H$ remains constant even though the number of acidic (CO)N−H bonds is increased. This is not at all due to our assignment of descriptors, because the same trends are shown in Table 5. *N*-Methylation of III decreases the hydrogen bond acidity, as expected, but VI and VII would still be predicted to have some hydrogen bond acidity; yet from the results in Table 5 we have had to assign zero values of $\Sigma\alpha_2^H$. Our calculated descriptors for VIII−X show the same trend: $\Sigma\alpha_2^H$ decreases with increasing *N*-methylation, but the actual values are smaller than expected. Borchardt et al.[34,35] have shown how the secondary β-turn structure of peptides can influence their lipophilicity, as log P_{oct}, but

Table 9—An Analysis of the Factors That Influence Log P_{eh} for Peptides, Based on Eq 5

peptide	rR_2	$s\pi_2^H$	$a\Sigma\alpha_2^H$	$b\Sigma\beta_2^H$	vV_x	log P_{eh} calcd[a]	log P_{eh} obsd
I	–0.11	–4.68	–2.46	–1.96	3.44	–5.43	–5.46
III	–0.26	–7.93	–2.42	–5.00	8.22	–7.05	–7.10
VI	–0.26	–7.80	0.00	–5.50	9.10	–4.12	–4.20
XI	–0.07	–4.29	–1.66	–2.21	4.44	–3.45	–3.44

[a] With $c = 0.336$ in eq 5, and the descriptors in Table 7.

Table 10—Values of log *k* for Permeability of Peptides

peptide	log k_{mono}[a]	log k_{mono}[b]	log k_{mono}[c]	log k_{situ}[d]
I	–5.04	–5.05	–5.43	–5.74
II	–5.72	–5.65	–5.67	–6.77
III	–6.23	–6.71	–5.89	–7.06
IV	–5.47		–5.66	–6.68
V	–5.20		–5.51	–6.16
VI	–4.69		–5.12	–5.96
VII	–4.47		–4.89	–4.94
VIII	–6.10			
IX	–5.39			
X	–4.82			
XI	–4.05			
XII		–3.37		
XIII		–3.68		
XIV		–3.39		

[a] *k* cm/s for permeability across Caco-2 cell monolayers, ref 6. [b] *k* cm/s for permeability across Caco-2 cell monolayers, ref 14. [c] *k* cm/s for permeability across BBMEC monolayers, ref 5. [d] *k* cm/s for in situ rat perfusion from saline, ref 5.

the most direct evidence of the effect of structure on hydrogen-bonding potential is provided by Price et al.[36] These workers examined the peptide XV and calculated the electrostatic maxima and minima around the van der Waals surface, with the peptide in both an extended conformation and a helical conformation. In the extended conformation, only one substantial electrostatic maximum was found, and in the helical conformation only two maxima were found, yet the peptide possesses three acidic (CO)N−H bonds. The lack of maxima in the extended conformation was attributed to N−H bonds being parallel and coplanar with neighboring C═O groups, resulting in cancelation of potentials of opposite magnitude. In the helical conformation, the N−H in the terminal CONHMe group is in close proximity to the oxygen in the MeCONH group, again producing a cancelation of potentials.[36] Our findings can possibly be explained by similar effects that result in the loss of electrostatic maxima.

Interestingly, in the extended conformation of XV there are three substantial electrostatic minima, corresponding to the three C═O groups, and in the helical conformation there are two very large electrostatic minima corresponding to C═O(1)/C═O(2) and C═O(2)/C═O(3).[36] Hence cancellation of electrostatic potentials can result in almost complete loss of electrostatic maxima while still retaining substantial electrostatic minima. Our calculated descriptors seem to follow this trend; VI and VII have no hydrogen bond acidity, yet $\Sigma\beta_2^H$ gradually increases along the series III − VII, with increasing *N*-methylation.

Once descriptors for the peptides are available, it is possible to assess quantitatively the factors that influence values of log P_{eh} for peptides. In Table 9 is a term-by-term breakdown of eq 5 for a representative selection of peptides I−XIV. The most interesting finding is that solute hydrogen bond acidity is NOT the main factor that influences the value of log P_{eh}. Even for peptides I and III, with large values of $\Sigma\alpha_2^H$, the $a\Sigma\alpha_2^H$ term is numerically smaller than the dipolarity/polarizability and volume terms. And with the sole exception of peptide I, all the peptides I−XIV have a smaller $a\Sigma\alpha_2^H$ term than the hydrogen bond basicity term $b\Sigma\beta_2^H$. This illustrates that examination of coefficients is not enough to assess the contribution of the different terms in eq 5, or in eq 3, generally. Only a term-by-term analysis, such as that in Table 9, allows the contribution of each term to be found.

Paterson et al.[6] and Conradi et al.[31,37] determined permeability of Caco-2 cell monolayers for the fourteen peptides I−XIV, Table 10. For 10 of these peptides, there was a good correlation ($r^2 = 0.943$) of log k_{mono} against the hydrogen bond number H#.[34] We have repeated the correlation for all fourteen peptides and find $r^2 = 0.857$, still quite reasonable. However, such a correlation does not distinguish between effects of hydrogen bond acidity and hydrogen bond basicity. To establish these effects, a correlation equation and descriptors for the solutes concerned are required. Unfortunately, the number and variety of solutes is too small to yield a definitive correlation equation through the solvation equation, eq 3.

References and Notes

1. Karls, M. S.; Rush, B. D.; Wilkinson, K. F.; Vidmar, T. J.; Burton, P. S.; Ruwart, M. J. Desolvation Energy; a Major Determinant of Absorption but not Clearage of Peptides in Rats. *Pharm. Res.* **1991**, *8*, 1477−1481.
2. Stein, W. D. *The Movement of Molecules Across Cell Membranes*; Academic Press: New York, 1967; pp 65−91.
3. Burton, P. S.; Conradi, R. A.; Hilgers, A. R.; Ho, N. F. H.; Maggiora, L. L. The Relationship between Peptide Structure and Transport Across Epithelial Membranes. *J. Controlled Release* **1992**, *19*, 87−92.
4. Seiler, P. Interconversion of Lipophilicities from Hydrocarbon/water Systems into the Octanol/Water System. *Eur. J. Med. Chem.* **1974**, *9*, 473−479.
5. Chikale, E. G.; Ng, K.-Y.; Burton, P. S.; Borchardt, R. T. Hydrogen Bonding Potential as a Determinant of the in vitro and in situ Blood-brain Barrier Permeability of Peptides. *Pharm. Res.* **1994**, *11*, 412−419.
6. Paterson, D. A.; Conradi, R. A.; Hilgers, A. R.; Vidmar, T. J.; Burton, P. S. A Nonaqueous Partition System for Predicting the Oral Absorption Potential of Peptides. *Quant. Struct.-Act. Relat.* **1994**, *13*, 4−10.
7. Kamlet, M. J.; Doherty, R. M.; Abboud, J.-L. M.; Abraham, M. H.; Taft, R. W. Solubility − A New Look. *CHEMTECH* **1986**, 566−576.
8. Abraham, M. H. Scales of Solute Hydrogen-bonding: Their Construction and Application to Physicochemical and Biochemical Processes. *Chem. Soc. Rev.* **1993**, *22*, 73−83.
9. Abraham, M. H.; Chadha, H. S. *Lipophilicity in drug action and toxicology*; Pliska, V., Testa, B., van de Waterbeemd, H., Eds.; VCH: Weinheim, 1996; pp 311−337.
10. Abraham, M. H.; McGowan, J. C. The Use of Characteristic Volumes to Measure Cavity Terms in Reversed Phase Liquid Chromatography. *Chromatographia* **1987**, *664*, 243−246.
11. Clever, H. L.; Battino,; Saylor, J. H.; Gross, P. M. The Solubility of Helium, Neon, Argon and Krypton in some Hydrocarbon Solvents. *J. Phys. Chem.* **1957**, *61*, 1078−1082.
12. Brunner, E. Solubility of Hydrogen in 10 Organic Solvents at 298.15, 323.15 and 373.15 K. *J. Chem. Eng. Data* **1985**, *30*, 269−273.
13. Battino, R.; Rettich, T. R.; Tominaga, T. The Solubility of Nitrogen and Air in Liquids. *J. Phys. Chem. Ref. Data* **1984**, *13*, 563−600.
14. *Oxides of Nitrogen. Solubility Data series Vol. 8*; Young, C. L., Ed.; Pergamon Press: Oxford, 1981.
15. *Ammonia, Amines, Phosphines, Arsine, Stibine, Silane, Germane and Stannane in Organic Solvents. Solubility Data Series Vol. 21*; Young, C. L., Fogg, P. G. T., Eds.; Pergamon Press: Oxford, 1985.
16. Wilhelm, E.; Battino, R. Thermodynamic Functions of the Solubilities of Gases in Liquids at 25 °C. *Chem. Rev.* **1973**, *73*, 1−9.
17. Milanova, E; Cave, G. C. B. Limiting Activity Coefficients in Dilute Solutions of Nonelectrolytes. I. Determination for Polar-Nonpolar Binary Mixtures by a Novel Apparatus, and a Solubility Parameter Treatment of Results. *Can. J. Chem.* **1982**, *60*, 2697−2706.

18. Thomas, E. R.; Newman. B. A.; Long, T.C.; Wood, D.A.; Eckert, C.A. Limiting Activity Coefficients of Nonpolar and Polar Solutes in both Volatile and Nonvolatile Solvents by Gas Chromatography. *J. Chem. Eng. Data* **1982**, *27*, 399−405.
19. Rytting, J. H.; Huston, L. P.; Higuchi, T.. Thermodynamic Group Contributions for Hydroxyl, Amino and Methylene Groups. *J. Pharm. Sci.* **1978**, *67*, 615−618.
20. Jadot, R. Determination de Constants de Henry par Chromatographie. *J. Chim. Phys.* **1972,** 1036−1040.
21. Hayduk, W.; Minhas, B. S. Diffusivity and Solubility of 1,3-Butadiene in Heptane and Other Properties of Heptane-Styrene and Aqueous Potassium Laurate Solutions. *J. Chem. Eng. Data* **1987**, *32*, 285−290.
22. Bruckl, N.; Kim, J. I. Gibbs Free Energies of Solute Solvent Interactions for He, Ne, Ar, Kr, Xe, H_2, CH_4, SF_6, C_2H_4, CO_2, and C_2H_2 in Various Solvents: Comparison of Theoretical Prediction with Experiment. *Z. Phys. Chem. Neue Folge* **1981**, *126*, 133−150.
23. Park, J. H.; Hussam, A.; Couasnon, P.; Fritz, D.; Carr, P. W. Experimental Reexamination of Selected Partition Coefficients from Rohrschneider's Data Set. *Anal. Chem.*, **1987**, *59*, 1970−1976.
24. Fernandez-Prini, R.; Crovetto, R.; Gentili, N. Solubilities of Inert Gases in Ethylene Glycol. *J. Chem. Thermodyn.* **1987**, *19*, 1293−1298.
25. Brunner, E. Solubility of Hydrogen in Alcohols. *Ber. Bunsen-Ges. Phys. Chem.* **1979**, *83*, 715−721.
26. Hayduk, W.; Laudie, H. Solubilities of Gases in Water and Other Associated Solvents. *AIChE J.* **1973**, *19*, 1233−1238.
27. Vernier, P.; Raimbault, C.; Renon, H. Proprietes Thermodynamiques des Solutions Infiniment Diluees D′Hydrocarbures dans les Solvants Polaires. *J. Chim. Phys.* **1969**, *66*, 429−436.
28. Lenoir, J.-Y.; Renault, P.; Renon, H. Gas Chromatographic Determination of Henry's Constants of 12 Gases in 19 Solvents. *J. Chem. Eng. Data* **1971**, *16*, 340−342.
29. Arancibia, E. L.; Catoggio, J. A. Gas Chromatographic Study of Solution and Adsorption of Hydrocarbons on Glycols. *J. Chromatogr.* **1982**, *238*, 281−290.
30. Abraham, M. H.; Chadha, H. S.; Whiting, G. S.; Mitchell, R. C. Hydrogen Bonding. 32. An Analysis of Water-Octanol and Water-Alkane Partitioning and the Δlog *P* Parameter of Seiler. *J. Pharm. Sci.* **1994,** *83*, 1085−1100.
31. Conradi, R.A.; Hilgers, A.R.; Ho, N.F. H.; Burton, P.S.. The Influence of Peptide Structure on Transport Across Caco-2 Cells. *Pharm. Res.* **1991**, *8*, 1453−1460.
32. Leo, A. *The Medicinal Chemistry Project*; Pomona College: Claremont, CA 91711.
33. Sangster, J. A *Databank of Evaluated Octanol−Water Partition Coefficients*; Sangster Research Laboratories: Montreal, Quebec, Canada H3G 2A4, 1994.
34. Knipp, G. T.; Vander Velde, D. G.; Siahaan, T. J.; Borchardt, R. T. The Effect of β-Turn Structure on the Passive Diffusion of Peptides Across Caco-2 Cell Monolayers. *Pharm. Res.* **1997**, *14*, 1332−1340.
35. Sorensen, M.; Steenberg, B.; Knipp, G. T.; Wang, W.; Steffansen, B.; Frokjaer, S.; Borchardt, R.T. The Effect of β-Turn Structure on the Permeation of Peptides Across Monolayers of Bovine Brain Microvessel Endothelial cells. *Pharm. Res.* **1997**, *14*, 1341−1348.
36. Apaya, R. P.; Bondi, M.; Price, S. L. The Orientation of N−H···O═C and N−H···N Hydrogen Bonds in Biological Systems: How Good is a Point Charge as a Model for a Hydrogen Bonding Atom *J. Comput.-Aided Mol. Des.* **1997**, *11*, 479−490.
37. Conradi, R. A.; Hilgers, A. R.; Ho, N. F. H.; Burton, P. S. The Influence of Peptide Structure on Transport Across Caco-2 Cells. II. Peptide Bond Modification Which Results in Improved Permeability. *Pharm. Res.* **1992**, *9*, 435−439.

Acknowledgments

F. Martins thanks the North Atlantic Treaty Organization for a postdoctoral fellowship, the Department of Chemistry, University of Lisbon, for leave of absence, and Junta Nacional Investigaceo Cientisica Technologica for financial support under project PBIC/P/QUI/2199/95. We are grateful to Dr. Sarah L. Price for her helpful comments on electrostatic maxima and minima of peptides.

JS980242L

Application of Surface-Coated Liposomes for Oral Delivery of Peptide: Effects of Coating the Liposome's Surface on the GI Transit of Insulin

KAZUNORI IWANAGA,*,† SATOSHI ONO,† KOHJI NARIOKA,† MASAWO KAKEMI,† KAZUHIRO MORIMOTO,‡ SHINJI YAMASHITA,§ YUKIHIRO NAMBA,|| AND NAOTO OKU⊥

Contribution from *Department of Pharmaceutics, Osaka University of Pharmaceutical Sciences, 4-20-1 Nasahara, Takatsuki, Osaka 569-1094, Japan, Department of Pharmaceutics, Hokkaido College of Pharmacy, Hokkaido, Japan, Department of Pharmaceutics, Faculty of Pharmaceutical Sciences, Setsunan University, Osaka, Japan, Cosmetic Ingredients Laboratory, Lipid Division, Nippon Fine Chemical Co., Ltd, Tokyo, Japan, and Department of Radiobiochemistry, School of Pharmaceutical Sciences, University of Shizuoka, Shizuoka, Japan.*

Received June 2, 1998. Final revised manuscript received November 24, 1998.
Accepted for publication November 30, 1998.

Abstract □ We prepared two kinds of surface-coated liposomes and investigated their potencies as oral dosage forms for peptide drugs by focusing on their effects on the gastrointestinal (GI) transit of drugs. The surface of the liposomes was coated with poly(ethylene glycol) 2000 (PEG-Lip) or the sugar chain of mucin (Mucin-Lip). As a model peptide drug, insulin was encapsulated in these liposomes. Coating the surface with poly(ethylene glycol) was found to reduce the transit rate of liposomes in the small intestine after oral administration to rats in vivo. Mucin-Lip was retained in the stomach longer than PEG-Lip or uncoated liposomes. The effect of surface coating on the intestinal transit of liposomes was determined by means of in situ single pass perfusion in the rat small intestine. Statistical moment analysis was applied to the outflow pattern of both liposomes and encapsulated insulin. The mean transit time (MTT) and deviation of transit time (DTT) in the intestinal tract were calculated. The MTT of PEG-Lip was much longer than those of uncoated liposomes and Mucin-Lip and was significantly shortened after removal of the intestinal mucous layer. These results indicated that PEG-Lip interacts strongly with the intestinal mucous layer, leading to its slow transit in the intestine. In contrast, coating the liposome's surface with mucin did not affect either the MTT or DTT of liposomes in the intestine. This result is in accordance with the in vivo observation that Mucin-Lip was highly retained in the stomach, but not in any region of the small intestine in vivo. Both the MTT and DTT values of insulin encapsulated in PEG-Lip and Mucin-Lip were almost the same as those of liposomes themselves, suggesting that surface-coated liposomes retained insulin in the intestinal tract. However, MTT and DTT of insulin were significantly shorter than those of uncoated liposomes because these liposomes degraded and released significant amounts of insulin during single pass perfusion. The ability of surface-coated liposomes, especially of PEG-Lip, to interact with the mucus layer and slow the transit rate in the GI tract is considered desirable for oral delivery of peptide drugs. Modification of the liposomal surface with appropriate materials, therefore, should be an effective method by which to achieve the oral delivery of peptide drugs.

A number of peptide and protein drugs with high therapeutic potency have been developed. Most of these, however, can be administered only by injection due to their instability in the gastrointestinal (GI) tract and poor absorption. Recently, particulate systems such as liposomes, emulsions, and micro- or nanosized polymer particles have attracted a great deal of attention as possible oral dosage forms for such peptide drugs.[1−3] Among these particulate systems, liposomes possess the advantage that they are composed of physiological materials, e.g. phospholipids. Since Patel and Ryman reported the significant hypoglycemic effect of orally administered insulin encapsulated in liposomes,[4] many studies have been carried out to evaluate the potency of liposomes. However, the degradation of liposomes in the GI tract through the interaction with bile salts sometimes obscured the effects of liposomes on drug absorption. To circumvent this problem, we reported previously that liposomes coated with poly(ethylene glycol) 2000 (PEG-Lip) or the sugar chain of mucin (Mucin-Lip) became resistant to digestion by bile salts and were useful for oral delivery of peptide drugs. The oral administration of insulin encapsulated in PEG-Lip, in particular, showed a greatly enhanced and sustained hypoglycemic effect in rats in comparison to insulin encapsulated in normal liposomes.[5] It was revealed that the increased resistance of surface-coated liposomes against digestion by bile salts leads to the increased stability of insulin in the GI tract.

However, it is not possible to explain the enhanced and prolonged hypoglycemic effects of insulin only by the increase in stability because many other factors affect intestinal absorption of peptides. Kimura et al.[6] reported that the oral administration of insulin incorporated in poly(vinyl alcohol)-gel spheres significantly increased its bioavailability due to the decreased gastrointestinal transit rate of insulin. In this study, therefore, the effects of surface-coated liposomes on the oral absorption of peptide drugs were analyzed from the viewpoint of their effects on the gastrointestinal transit of drugs.

Experimental Section

Materials—Dipalmitoylphosphatidylcholine (DPPC), cholesterol (CHOL) and distearoylphosphatidylethanolamine−poly(ethylene glycol) 2000 (DSPE-PEG), were gifts from Nippon Fine Chemical Co., Ltd. (Tokyo, Japan). Bovine insulin (25.7 IU/mg) and stearylamine (SA) were purchased from Sigma Chemical Co. (St. Louis, MO). [^{14}C]DPPC (113.4 mCi/mmol) was obtained from New England Nuclear (Boston, MA). All other chemicals used were of analytical grade. Cetyl-mucin, one of the surface-coating materials, was synthesized as previously reported.[5] Briefly, mucin from pig stomach was trypsinized for 5 h at 37 °C, treated with proteinase K for another 40 h after adjusting to pH 8.0, and centrifuged and filtered to obtain the sugar portion of mucin. Further purification was carried out using Sepharose CL-2B column chromatography. The cetyl group was grafted to the sugar chain domain of mucin using cetyl bromide and triethylamine.

* Corresponding author. Tel, fax: +81-726-90-1049. e-mail: iwanaga@oysun01.oups.ac.jp.
† Osaka University of Pharmaceutical Sciences.
‡ Hokkaido College of Pharmacy.
§ Setsunan University.
|| Nippon Fine Chemical Co.
⊥ University of Shizuoka.

10.1021/js980235x CCC: $18.00
Published on Web 01/14/1999

Table 1—Lipid Composition of Liposomes Used in This Study[a]

	DPPC	Chol	SA	cetyl-mucin (mg/mL)	DSPE-PEG
(+)-Lip	10	10	1	–	–
mucin-Lip	10	10	1	1	–
PEG-Lip	10	10	–	–	1

[a] Each value was expressed as a molar ratio.

Preparation of Surface-Coated Liposomes—The sugar chain portion of mucin and poly(ethylene glycol) (PEG) were used as surface-coating materials. The compositions of liposomes are listed in Table 1. Liposomes were prepared according to the method of Bangham[7] with some modifications. Briefly, a mixture of DPPC, cholesterol, and surface-coating material (cetyl-mucin or DSPE-PEG) dissolved in chloroform was evaporated to dryness in a rotary evaporator. The lipid film was further dried in vacuo for 8 h to remove the solvent completely. Then the lipid film was hydrated with phosphate-buffered saline (PBS, pH 7.4) containing insulin. After three cycles of freeze−thawing, the liposomal suspension was diluted with PBS to adjust the lipid concentration. Just before the experiment, the liposomal suspension was centrifuged three times at 15000 rpm for 10 min to remove untrapped drugs. The entrapment efficiency of insulin in uncoated liposome, Mucin-Lip, and PEG-Lip was 31.4 ± 6.0%, 35.3 ± 5.9%, 37.7 ± 4.8%, respectively. The size distribution of liposomes was measured by electrophoretic light scattering photometer, ELS-800 (Otsuka Electronics Co. Ltd., Japan). The mean particle size of uncoated liposome, Mucin-Lip, and PEG-Lip was 348 ± 148 nm, 453 ± 165 nm, 479 ± 187 nm, respectively.

In Vivo Oral Administration Experiment—Male Wistar rats, weighing 250−300 g, were obtained from Japan SLC, Inc. (Shizuoka, Japan). Suspensions of liposomes in which the membranes were labeled with [^{14}C]DPPC were orally administered to rats (1 mL/rat). At predetermined time points, rats were anesthetized with sodium pentobarbital, and then the gastrointestinal tract was excised and divided into eight regions, i.e., stomach, duodenum, proximal jejunum, middle jejunum, distal jejunum, ileum, cecum, and colon. The contents of each region were washed with 10 mL of saline, and aliquots of each sample were placed in scintillation vials. Then, 10 mL of Clearsol (Nacalai Tesque, Kyoto, Japan) was added, and the radioactivity of each sample was measured using a liquid scintillation analyzer, LSA 1600 CA (Packard). The remaining amount of liposomes in each region was calculated and expressed as the mean % against the total recovery. The total recovery of radioactivity was more than 91% of the dose applied for each experiment.

In Situ Single Pass Perfusion Experiment—In situ local intestinal perfusion was carried out according to the method of Kakutani[8] with some modifications. The rats were fasted for 12 h and then anesthetized by intraperitoneal injection of sodium pentobarbital (40 mg/kg body weight). An abdominal incision was made, and both the duodenum and proximal jejunum (20 cm below the duodenum) were cannulated and ligated tightly. After preperfusion with PBS (pH7.4) for 10 min, 0.15 mL of test solutions including 1 mg/mL insulin, insulin in PBS (Solution; pH7.4), or liposomal suspensions were injected into the line of perfusion flow as a pulse using a three-position valve. The outflow perfusate was collected into preweighed tubes. In the early stages of the experiment, the samples were collected every 15 s, while at later stages sampling was performed every 30 s. After weighing each sample, the concentration of intact insulin was determined by HPLC. Bovine serum albumin labeled with Evans' blue (EB-BSA) was used as a nonabsorbable marker.[9] The recovery ratio of EB-BSA in outflow perfusate was more than 95% of the dose applied, and the coefficient of variability was 3.3%. When determining the transit of liposomes, diphenylhexatriene (DPH) was used as a liposomal membrane marker, and the concentration of DPH in the perfusate was measured spectrofluorometrically.

Determination of Insulin—Insulin was assayed by reverse phase HPLC on a LiChrospher 300 RP-8 column (250 × 4.0 mm, 10 μm). The HPLC consisted of a Shimadzu model LC-10As pump, SPD-6A UV spectrophotometric detector, and C-R6A integrator. The mobile phase was a mixture of 0.1% trifluoroacetic acid/acetonitrile = 60/40% (v/v) and was run at a flow rate of 1 mL/min. The UV detector was set at 210 nm.

Interaction between Liposomes and Intestinal Mucous Layer—To remove mucous fluid,[10] dithiothreitol solution (20 mM in PBS, pH 7.4) was injected into the perfused region of the rat jejunum. Thirty minutes after injection, dithiothreitol was washed out with PBS. Thereafter, in situ perfusion was carried out as described above. It was confirmed that 20 mM of dithiothreitol solution did not induce damage to the intestinal epithelial (data not shown).

Moment Analysis—Statistical moment analysis[8] was applied to the data obtained from the single pass perfusion experiment. The mean transit time (MTT) and the deviation of transit time (DTT) of insulin or liposomes were calculated from their outflow patterns. Briefly, the zero order moment (S_0) was calculated from the area under the time versus amount (% of dose) in the perfusate curve. Similarly, the first-order moment (S_1) and the second-order moment (S_2) were calculated from the area under the time versus time × amount curve and the time versus time × amount^2 curve, respectively. Then, MTT and DTT were calculated from the following equations.

$$\mathrm{MTT} = S_1/S_0$$

$$\mathrm{VTT} = (S_2/S_0) + (\mathrm{MRT})^2$$

$$\mathrm{DTT} = (\mathrm{VTT})^{1/2}$$

where VTT is variance of transit time. DTT, the square root of VTT, was used here, since VTT was too large.

Results

GI Transit of Liposomes in Vivo—Figure 1 shows the time course of remaining radioactivity (% of recovered) of [^{14}C]DPPC in each region of the GI tract after oral administration of liposomes to rats. Positively charged liposomes ((+)-Lip) were used as a control because among uncoated liposomes only (+)-Lip enhanced the absorption of insulin.[5] Although all kinds of liposomes examined reached the distal jejunum at 0.5 h postadministration, their transit patterns in the GI tract were markedly different. In the case of (+)-Lip, about 20% of liposomes were detected in the ileum at 1 h, and most were in the cecum at 2 h post-administration. On the other hand, Mucin-Lip was retained in the stomach for a longer time and then spread throughout the whole jejunum. When PEG-Lip was administered, about 30% remained in the distal jejunum even at 2 h post-administration, and 25% was still detected in the ileum at 3 h. The retention of PEG-Lip in both the distal-jejunum and ileum was remarkable compared to those in other regions.

Intestinal Transit of Insulin and Liposomes in Situ—The outflow pattern of insulin administered in liposomal form is shown in Figure 2. Both (+)-Lip and Mucin-Lip showed sharp peaks of insulin outflow, whereas a broad peak was observed after administration of PEG-Lip. In (+)-Lip and Mucin-Lip, insulin was detectable up to 250 and 495 s after administration, respectively. However insulin was continuously detected until the last sampling time point in PEG-Lip. Moment analysis was applied to these data to compare the differences in the intestinal transit patterns of insulin incorporated in the three kinds of liposomes. As summarized in Table 2, the recovery ratio of insulin was the highest in Mucin-Lip and the lowest in (+)-Lip. PEG-Lip showed 2-fold longer MTT than (+)-Lip or Mucin-Lip, reflecting the slow transit of insulin encapsulated in PEG-Lip. From the comparison of DTT, it was demonstrated that insulin encapsulated in PEG-Lip spread widely in the intestinal tract.

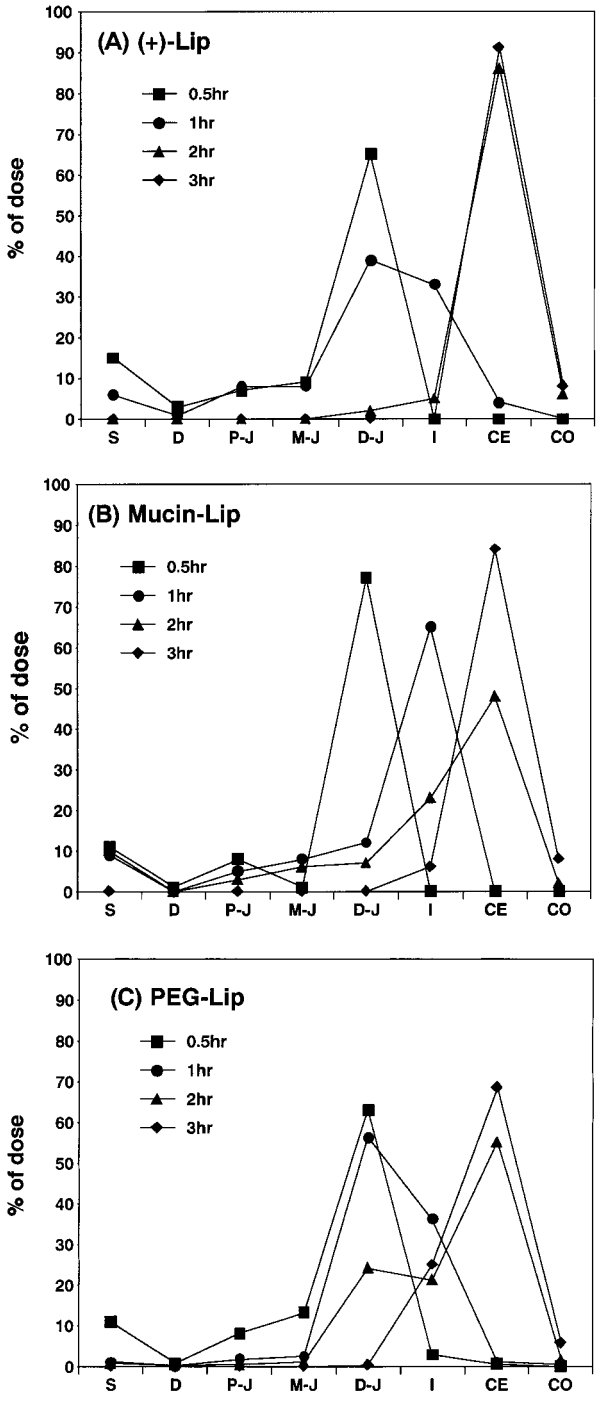

Figure 1—Time course of remaining radioactivity (% of recovered) of [^{14}C]-DPPC in the GI tract (A) (+)-Lip, (B) Mucin-Lip, (C) PEG-Lip. S, stomach; D, duodenum; P-J, proximal jejunum; M-J, middle jejunum; D-J, distal jejunum; I, ileum; CE, cecum; CO, colon. Data are expressed as means of 4–6 experiments.

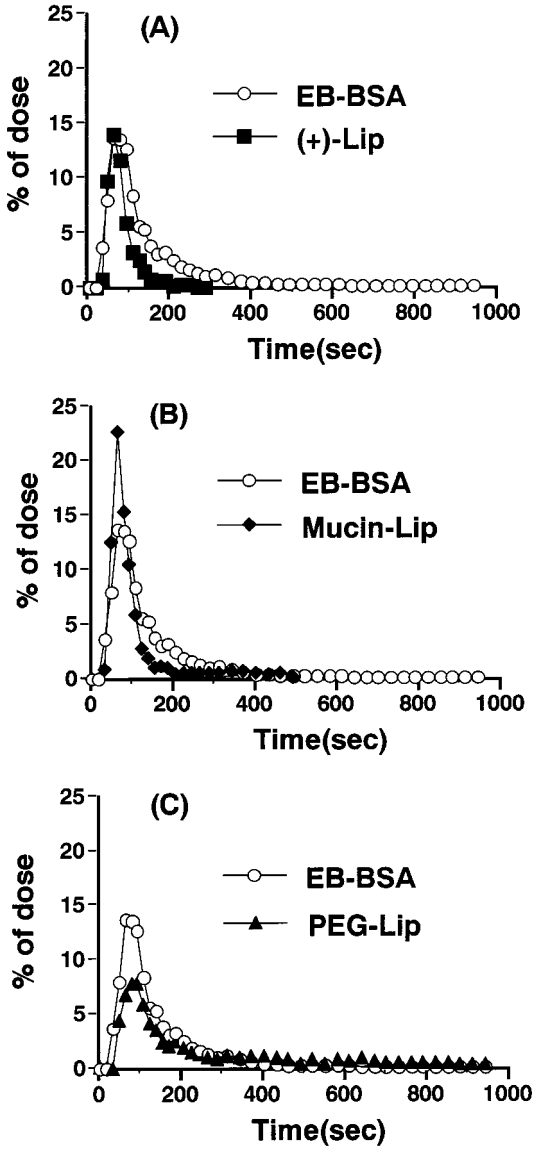

Figure 2—Typical outflow pattern of insulin obtained from in situ single pass perfusion experiment: (A) (+)-Lip, (B) Mucin-Lip, (C) PEG-Lip.

Table 2—Moment Parameters for Intestinal Transit of Insulin and Liposomes

		recovery[c] (%)	MTT[c] (s)	DTT[c] (s)
(+)-Lip	liposome	65.36 ± 4.56	111.96 ± 8.79	107.02 ± 13.41
	insulin	52.57 ± 4.67[b]	86.38 ± 2.63[b]	34.96 ± 1.32[b]
mucin-Lip	liposome	70.43 ± 5.07	99.22 ± 5.90	83.64 ± 17.42
	insulin	80.71 ± 5.29[a]	103.54 ± 12.52[a]	81.11 ± 14.02[a]
PEG-Lip	liposome	77.92 ± 2.93[a]	198.57 ± 22.16[a]	179.85 ± 22.54[a]
	insulin	64.54 ± 1.19[a,b]	201.58 ± 19.44[a]	165.48 ± 8.06[a]

[a] Significant at $p < 0.05$ vs (+)-Lip. [b] Significant at $p < 0.05$ between liposome and insulin. [c] Results were expressed as the mean ± SE of 5–8 experiments.

The intestinal transit of liposomes themselves was also investigated by labeling the liposomal membrane with diphenylhexatriene (DPH). Moment parameters for outflow patterns of liposomes are also listed in Table 2. After administration of Mucin-Lip and PEG-Lip, there were no significant differences in MTT or DTT between liposomes and insulin. In contrast, both MTT and DTT of liposomes were significantly longer than those of insulin in (+)-Lip. These results suggested that most of the insulin passed through the intestinal tract in liposomal form in the surface-coated liposomes, while in (+)-Lip significant amounts of insulin were released from liposomes in the intestinal loop.

Effect of Removal of the Mucous Layer on the Intestinal Transit of Liposomes—The effect of pretreatment of the intestine with dithiothreitol, which can remove the mucous layer from the epithelial surface, on the intestinal transit of surface-coated liposomes was investigated. As listed in Table 3, this pretreatment did not cause any significant changes in the recovery ratio of either type of liposomes. However, a marked decrease was observed

Table 3—Effects of Intestinal Mucous Layer on the Transit of Liposomes

		recovery[b] (%)	MTT[b] (s)	DTT[b] (s)
mucin-Lip	control	70.43 ± 5.07	99.22 ± 5.90	83.64 ± 17.42
	treated	61.20 ± 3.72	81.27 ± 3.97	97.41 ± 16.49
PEG-Lip	control	77.92 ± 2.93	198.57 ± 22.16	179.85 ± 22.54
	treated	76.25 ± 5.07	127.59 ± 18.70[a]	128.38 ± 15.28[a]

[a] Significant at $p < 0.05$ between control and treated. [b] Results were expressed as the mean ± SE of 5–8 experiments.

in MTT and DTT of PEG-Lip following pretreatment with dithiothreitol.

Discussion

We have reported that coating the surface of liposomes with poly(ethylene glycol) or the sugar chain of mucin increased the potency of liposomes as a tool for oral delivery of peptide drugs.[5] Insulin encapsulated in surface-coated liposomes showed enhanced and sustained hypoglycemic effects after oral administration. It was revealed that surface coating resulted in liposomes that resisted digestion by bile salts, leading to the stabilization and slow release of insulin in the GI tract. However, many factors other than drug stability affect the absorption profile of peptide drugs. Surface coating with these materials may also affect the intestinal transit of liposomes through interaction with the intestinal wall. Therefore, we investigated the behavior of surface coated liposomes in the GI tract in vivo and also in situ by focusing on the effect on liposomal transit.

When liposomes were orally administered to rats in vivo, uncoated liposomes, (+)-Lip, showed rapid transit to distal parts of the intestine, suggesting the weak interaction of liposomes themselves with the intestinal wall. Although surface coating reduced the transit rate of liposomes, PEG-Lip and Mucin-Lip showed different behavior in the GI tract (Figure 1). Mucin-Lip was retained in the stomach longer than other liposomes. As the surface of the stomach is completely covered with a mucin layer, this may be caused by the interaction between mucin on the surface of the stomach and that of the liposomes. In contrast, PEG-Lip was markedly retained in the lower region of the intestine rather than in the stomach, suggesting the higher affinity of poly(ethylene glycol) to the surface of the small intestine. These results indicated that the behavior of liposomes in the GI tract depends on the features of the surface-coating materials.

To elucidate this in further detail, we investigated the effect of coating the surface of liposomes on the intestinal transit by means of in situ perfusion experiments. The recovery ratio of insulin after administration of (+)-Lip was significantly lower than that after administration of surface-coated liposomes (Table 2). Furthermore, both the MTT and DTT of insulin encapsulated in (+)-Lip were different from those of the liposomes themselves. On the other hand, there were no significant differences in MTT or DTT between liposomes and insulin after administration of surface-coated liposomes. Therefore, it is obvious that (+)-Lip degraded and released insulin during transit through the intestinal tract, while surface-coated liposomes retained insulin in the intestine. These results are consistent with our observation that insulin encapsulated in surface-coated liposomes was much more stable than that in uncoated liposomes in the intestinal fluid in vitro.[5] Shegal and Rogers et al.[11] reported that coating the surface of liposomes with *O*-palmitoylpullulan was an effective way to avoid the interaction of the liposomal lipid membrane with bile salts. Also, Zeisig et al.[12] reported that the thickness of the fixed aqueous layer on the surface of liposomes was increased by coating the surface with poly(ethylene glycol). This fixed aqueous layer on PEG-Lip could protect the lipid membrane against digestion by bile salts. Since the surface of Mucin-Lip was covered with the long sugar chain, this also prevented the digestion of liposomes in the intestinal tract.

Neither the MTT nor DTT of Mucin-Lip were significantly different from those of (+)-Lip, indicating that surface coating with mucin did not affect the transit rate of liposomes in the small intestine. This result was supported by the observation that Mucin-Lip was highly retained in the stomach rather than in the intestine after oral administration in vivo.

In contrast, it is apparent from the much longer values of MTT and DTT that PEG-Lip strongly interacts with the intestinal wall. The viscosity and mucoadhesiveness of the liposomal formulation may be the most important factors affecting intestinal transit. Since coating the liposome's surface with poly(ethylene glycol) only slightly affected their viscosity (data not shown), it could be speculated that increased mucoadhesiveness decreased the intestinal transit rate and caused the wide spread distribution patterns of PEG-Lip observed in vivo. Hassan et al.[13] reported that the adhesive force of poly(ethylene glycol) to mucin is comparable to that of other neutral polymers. Also, Ascentiis et al.[14] reported that the mucoadhesiveness of methacrylate polymer microparticles was increased by the copolymerization of methacrylate with poly(ethylene glycol). The increased mucoadhesiveness of PEG-Lip was also confirmed by in situ perfusion experiments using rat intestine in which the mucous layer had been removed. Both the MTT and DTT of PEG-Lip were significantly shortened by removal of the intestinal mucous layer, whereas those of Mucin-Lip were changed only slightly (Table 3). This result clearly indicated that poly(ethylene glycol) interacts with intestinal wall through adhesion to the mucous layer. Rao et al. reported that the mucoadhesiveness of glass beads coated with hydrophilic polymers decreased following removal of the mucous layer.[15] Furthermore, since the amounts of mucous fluid in both the distal-jejunum and ileum are richer than those in other regions, the marked retention of PEG-Lip in these regions in vivo (Figure 1) may reflect its strong interaction with the mucous layer. Ilan et al.[16] reported that the intestinal absorption of desmopressin was enhanced by using mucoadhesive submicron emulsion. They speculated that coating the surface of the emulsion with Carbopol-940 caused a strong interaction between the emulsion and the mucous layer and increased the retention of the emulsion in the intestinal tract, resulting in the enhanced absorption of desmopressin. Lehr et al.[17] also reported that the intestinal absorption of 9-des-glycinamide, 8 arginine vasopressin (DGAVP) was enhanced by using mucoadhesive microspheres in the rat intestine in vitro. Thus, for oral delivery of peptide drugs, the slow transit of the formulation in the intestinal tract, such as PEG-Lip in this study, should be desirable.

In conclusion, Mucin-Lip adhered preferentially to the surface of the stomach. PEG-Lip moved along the GI tract slowly and spread widely in the small intestine because of the strong interaction with the intestinal mucous layer, leading to the enhanced and prolonged hypoglycemic effects of insulin. These findings clearly demonstrated that the surface coating of liposomes is a useful method for oral delivery of peptide drugs.

References and Notes

1. Fukunaga, M.; Miller, M.; Deftos, L. J. Liposome-entrapped calcitonin and parathytoid hormone are orally effective in rats. *Horm. Metab. Res.* **1991**, *23*, 166−167.
2. Rao, S.; Ritschel, W. A. Colonic drug delivery of small peptides. *S.T.P. Pharma. Sci.* **1995**, *5*, 19−29.
3. Damge, C.; Hillaire-Buys, D.; Puech, R.; Hoeltzel, A.; Michel, C.; Ribes, G. Effects of orally administered insulin nanocapsules in normal and diabetic dogs. *Diab. Nutr. Metab.* **1995**, *8*, 3−9.
4. Patel, H. M.; Ryman, B. E. Oral administration of insulin by encapsulation within liposomes. *FEBS Lett.* **1976**, *62*, 60−63.
5. Iwanaga, K.; Ono, S.; Narioka, K.; Morimoto, K.; Kakemi, M.; Yamashita, S.; Nango, M.; Oku, N. Oral delivery of insulin by using surface coating liposomes: Improvement of stability of insulin in GI tract. *Int. J. Pharm.* **1997**, *157*, 73−80.
6. Kimura, T.; Sato, K.; Sugimoto, K.; Tao, R.; Murakami, T.; Kurosaki, Y.; Nakayama, T. Oral administration of insulin as poly(vinyl alcohol)-gel spheres in diabetic rats. *Biol. Pharm. Bull.* **1996**, *19*, 897−900.
7. Bangham, A. D.; Standish, M. M.; Watkins, J. C. Diffusion of univalent ions across the lamellae of swollen phospholipids. *J. Mol. Biol.* **1965**, *13*, 238−252.
8. Kakutani, T.; Yamaoka, K.; Hashida, M.; Sezaki, H. A new method for assessment of drug disposition in muscle: application of statistical moment theory to local perfusion systems. *J. Pharmacokin. Biopharm.* **1985**, *13*, 609−631.
9. Freedman, F. B.; Johnson, J. A. Equilibrium and kinetic properties of the Evans blue-albumin system. *Am. J. Physiol.* **1969**, *216*, 675−681.
10. Tockman, M. S.; Qiao, Y.; Li, L.; Zhao, G.; Sharma, R.; Cavenaugh, L. L.; Erozan, Y. S. Safe separation of sputum cells from mucoid glycoprotein. *Acta Cytol.* **1995**, *39*, 1128−1136.
11. Shegal S.; Rogers, J. A. Polymer-coated liposomes: improved liposome stability and release of Cytosine arabinoside(Ara-C). *J. Microencapsulation* **1995**, *12*, 37−47.
12. Zeisig, R.; Shimada, K.; Hirota, S.; Arndt, D. Effect of sterical stabilization on macrophage uptake in vitro and on thickness of the fixed aqueous layer of liposomes made from alkylphosphocholines. *Biochim. Biophys. Acta* **1996**, *1285*, 237−245.
13. Hassen, E. E.; Gallo, J. M. A simple rheological method for the *in vitro* assessment of mucin-polymer bioadhesive bond strength. *Pharm. Res.* **1990**, *7*, 491−495.
14. Ascentiis, A. D.; Colombo, P.; Peppas, A. A. Screening of potentially muco-adhesive polymer microparticles in contact with rat intestinal mucosa. *Eur. J. Pharm. Biopharm.* **1995**, *41*, 229−234.
15. Rao, K. V. R.; Buri, P. A novel in situ method to test polymers and coated microparticles for bioadhesion. *Int. J. Pharm.* **1989**, *52*, 265−270.
16. Ilan, E.; Amselem, S.; Weisspapir, M.; Schwarz, J.; Yogev, A.; Zawoznik, E.; Friedman, D. Improved oral delivery of desmopressin via a novel vehicle: muco-adhesive submicron emulsion. *Pharm. Res.* **1996**, *13*, 491−495.
17. Lehr, C. M.; Bouwstra, J. A.; Kok, W.; De Boer, A. G.; Tukker, J. J.; Verhoef, J. C.; Breimer, D.; Junginger, H. E. Effects of the muco-adhesive polymer poly-carbophil on the intestinal absorption of a peptide drug in the rat. *J. Pharm. Pharmacol.* **1992**, *44*, 402−407.

Acknowledgments

We thank Dr. Nango (Nagoya Institute of Technology) for synthesis of Cetyl-mucin. We also thank Ms. K. Doi and Ms. N. Saito (University of Shizuoka) for their technical assistance.

JS980235X

Enhancement of Paracellular Drug Transport with Highly Quaternized *N*-Trimethyl Chitosan Chloride in Neutral Environments: In Vitro Evaluation in Intestinal Epithelial Cells (Caco-2)

AWIE F. KOTZÉ,*,†,‡ MAYA M. THANOU,‡ HENRIK L. LUEBEN,‡,§ A. G. DE BOER,¶ J. COOS VERHOEF,‡ AND HANS E. JUNGINGER‡

Contribution from *Department of Pharmaceutics, Potchefstroom University for Christian Higher Education, Potchefstroom, 2520, Republic of South Africa, Department of Pharmaceutical Technology, Leiden/Amsterdam Center for Drug Research, Leiden University, P.O. Box 9502, 2300 RA Leiden, The Netherlands, LTS Lohmann Therapie-Systeme GmbH, D-56605 Andernach, Germany, and Department of Pharmacology, Leiden/Amsterdam Center for Drug Research, Leiden University, P.O. Box 9503, 2300 RA Leiden, The Netherlands.*

Received June 1, 1998. Accepted for publication October 2, 1998.

Abstract □ Previous studies have established that a partially quaternized derivative of chitosan, *N*-trimethyl chitosan chloride (TMC), can be used as an absorption enhancer for large hydrophilic compounds across mucosal surfaces. This study evaluates and compares the effects of the degree of quaternization of TMC, in a neutral environment, on the permeability of intestinal epithelial cells in vitro, where normal chitosan salts are ineffective as absorption enhancers. The effects of TMC-H [61.2% quaternized, (0.05–1.5% w/v)], TMC-L [12.3% quaternized, (0.5–1.5% w/v)], and chitosan hydrochloride [0.5–1.5% w/v] on the transepithelial electrical resistance (TEER) and permeability, for the hydrophilic model compound [^{14}C]-mannitol, of intestinal epithelial Caco-2 cell monolayers, were investigated at pH values of 6.20 and 7.40. The viability of the monolayers was checked with the trypan blue exclusion technique. At a pH of 6.20, all the polymers caused a pronounced reduction (37–67% at 0.5% w/v concentrations) in the TEER of Caco-2 cells. On the contrary, at a pH of 7.40, only TMC-H was able to decrease the TEER values, even in a concentration as low as 0.05% w/v (35% reduction). Comparable results were obtained with the permeation of [^{14}C]mannitol. Large increases in the transport rate (18–23-fold at 0.5% w/v concentrations) were found at pH 6.20, whereas only TMC-H was able to increase the permeation of [^{14}C]mannitol at pH 7.40 (31–48-fold at 0.05–1.5% w/v concentrations of TMC-H). For all the polymers studied, no deleterious effects to the cells could be demonstrated with the trypan blue exclusion technique. It is concluded that highly quaternized TMC is a potent absorption enhancer and the potential use of this polymer, especially in neutral and basic environments where normal chitosan salts are not effective, is expected to be an important contribution to the development of effective delivery systems for hydrophilic compounds such as peptide drugs.

Introduction

The potential use of chitosan as an absorption enhancer across mucosal surfaces has been well documented in recent years. Chitosan salts such as chitosan glutamate and chitosan hydrochloride have been shown to increase the absorption of a number of hydrophilic compounds and peptide drugs both in vitro and in vivo.[1−7] Apart from its mucoadhesive properties,[8] chitosan acts mainly by opening the tight junctions between epithelial cells to allow for the paracellular transport of these large hydrophilic molecules. Such an action is believed to be due to an interaction of a positively charged amino group on the C-2 position of chitosan with negatively charged sites on the cell membranes, which results in a structural reorganization of the tight junction-associated proteins.[1,6]

Chitosan has an apparent pK_a value between 5.5 and 6.5, and a certain amount of acid is required to transform the glucosamine units into the positively charged, water-soluble form. At neutral and basic pH values, the chitosan molecules will lose their charge and therefore the potential use of this polymer, especially in more neutral and basic environments such as those found in the large intestine and colon, is limited. It has been shown recently that a partially quaternized (12%) derivative of chitosan, *N*-trimethyl chitosan chloride (TMC), was also able to significantly increase the transport of hydrophilic compounds, such as [^{14}C]mannitol (MW 182.2), fluorescein isothiocyanate-labeled dextran (MW 4400), and [^{14}C]poly(ethylene glycol) (MW 4000), and the peptide drugs buserelin (MW 1300), 9-desglycinamide, 8-L-arginine vasopressin (MW 1412), and insulin (MW 5778) in Caco-2 cell monolayers at acidic pH values (4.40−6.20).[9−11] It was suggested that TMC most likely has the same mechanism of action on the junctional complex as other chitosan salts.[10] The derivative TMC (12% quaternized) was not as effective as other chitosan salts, such as chitosan glutamate and chitosan hydrochloride. This lesser efficacy was explained by its charge density, which was determined by the degree of quaternization, and by a partial hiding of the positive charge on the amino group by the attached methyl groups.[10,11] However, the much higher aqueous solubility of TMC may compensate for its lesser efficacy. TMC has proved to be very soluble over a wide pH range (pH 1−9) up to 10% w/v concentrations, even at degrees of quaternization as low as 10%.[9−10]

Our hypothesis is that TMC with higher degrees of quaternization may be more effective as an absorption enhancer to increase the paracellular transport of hydrophilic compounds at neutral pH values. The aim of the present study was to synthesize TMC with different degrees of quaternization (low and high) and to evaluate and compare the effect of these polymers with the effect of chitosan hydrochloride on the permeability of intestinal

* Corresponding author. Telephone: 27 18 2992249. Fax.: 27 18 2992251. E-mail: FMSAFK@PUKNET.PUK.AC.ZA.
† Department of Pharmaceutics, Potchefstroom University for Christian Higher Education.
‡ Department of Pharmaceutical Technology, Leiden/Amsterdam Center for Drug Research.
§ LTS Lohmann Therapie-Systeme GmbH.
¶ Department of Pharmacology, Leiden/Amsterdam Center for Drug Research.

10.1021/js980233c CCC: $18.00 Published on Web 12/05/1998

epithelial cells in vitro for increased transport of a hydrophilic compound at slightly acidic and neutral pH values (6.20 and 7.40).

Experimental Section

Synthesis and Characterization of *N*-Trimethyl Chitosan Chloride (TMC)—Two batches of TMC, one with a low and one with a high degree of quaternization, were synthesized from sieved fractions (<500 μm) of chitosan (degree of acetylation ca. 25%; Pronova Biopolymer, Drammen, Norway) based on the method of Domard et al.[12] and Sieval et al.[13] Briefly, the experimental conditions are reductive methylation of chitosan with iodomethane in a strong basic environment at 60 °C. The batch with the lower degree of quaternization (TMC-L) was prepared in a single-step reaction of 60 min. To obtain TMC with the higher degree of quaternization (TMC-H), the basic reaction was repeated twice with the product obtained after the first step.[13] The counterion (I^-) was exchanged to Cl^- by dissolving the quaternized polymers in a aqueous solution of NaCl. The final products were obtained by precipitation and washing with ethanol. The polymers were characterized by nuclear magnetic resonance (NMR) spectroscopy, and the degree of quaternization of the respective polymers was calculated from ^{1}H NMR spectra (600 MHz) obtained with a Bruker DMX-600 spectrometer.[13]

Cell Cultures—Caco-2 cells (passages 88 and 93−94) were seeded on tissue-culture-treated polycarbonate filters (area 4.7 cm^2 and 0.33 cm^2) in Costar Transwell 6- and 24-well plates (Costar Europe Ltd., Badhoevedorp, The Netherlands) at a seeding density of 10^4 cells/cm^2. Dulbecco's Modified Eagle's Medium (DMEM, pH 7.40; Sigma, Bornem, Belgium), supplemented with 1% nonessential amino acids, 10% foetal bovine serum, benzylpenicillin G (160 U/mL), and streptomycin sulfate (100 μg/mL) (all obtained from Sigma), was used as culture medium. The medium was changed every second day. Cell cultures were kept at 37 °C in an atmosphere of 95% air and 5% CO_2. Filters were used for transepithelial electrical resistance measurements (24-well plates) and transport experiments (6-well plates), 21−23 days after seeding.[3,14,15]

Measurement of the Transepithelial Electrical Resistance (TEER)—The effect of TMC-H (0.05−1.5% w/v), TMC-L (0.5−1.5% w/v) and chitosan hydrochloride (0.5−1.5% w/v; SEACURE CL 210 from Pronova Biopolymer, Drammen, Norway) on the TEER of the Caco-2 cell monolayers was measured every 20 min with a Millicell ERS meter (Millipore Corp., Bedford, MA) connected to a pair of thin, side-by-side electrodes suitable for use in the small 24-well culture plates.[3,14,15] The effect of these polymers on the TEER was measured at both pH 6.20 and 7.40. The polymer solutions were prepared in serum-free DMEM, and the pH was adjusted to 6.20 with 0.1 M HCl or to 7.40 with 0.1 M NaOH. Because of the insolubility of chitosan hydrochloride at a pH of 7.40, the resulting polymer preparation was used as a dispersion of chitosan hydrochloride in DMEM. Two hours before the start of each experiment, the medium in the acceptor compartment was removed and replaced with DMEM buffered at pH 7.40 with 25 mM HEPES [*n*-(2-hydroxyethyl) piperazine-*N*-(2-ethanesulfonic acid; Sigma]. Measurements started 1 h prior to incubation on the apical side of the cells with the respective polymer solutions. After 2 h, the polymer solutions were carefully removed, and cells were washed three times with and replaced by serum-free DMEM (pH 6.20 or 7.40). The TEER was measured for an additional hour to study the reversibility of the effect of the polymer solutions. Control experiments were done under the same conditions without polymers. Average TEER values for untreated cell monolayers were in the range 200−300 Ω·cm^2 at both pH 6.20 and 7.40.[6] At the end of each experiment, the solutions in both the apical and basolateral sides of the cell compartments were checked for any changes in pH. Experiments were done in triplicate at 37 °C in an atmosphere of 95% air and 5% CO_2.

Permeability Studies with [^{14}C]Mannitol—[^{14}C]Mannitol (MW 182.2; specific radioactivity 57 mCi/mmol) was obtained from Amersham Life Science (Little Chalfort, UK). The transport of [^{14}C]mannitol across Caco-2 cell monolayers was studied as described previously.[3,9,10] The polymers were dissolved in serum-free DMEM containing the radioactive marker and the pH was adjusted to 6.20 with 0.1 M HCL or to 7.40 with 0.1 M NaOH. Chitosan hydrochloride was used as a dispersion in DMEM at pH 7.40. Solutions with TMC-H (0.05−1.5% w/v), TMC-L (0.5−1.5% w/v), and chitosan hydrochloride (0.5−1.5% w/v) were added on the apical side of the monolayers. The medium in the acceptor compartment was DMEM buffered at pH 7.40 with 40 mmol/L HEPES. Samples of 200 μL were taken every 20 min for 4 h from the basolateral side. Samples taken from the basolateral side were replaced with an equal volume of DMEM with HEPES. Control experiments were run in every experiment with solutions containing the radioactive markers without the dissolved polymers. At the end of each experiment the pH of the solutions from both the apical and basolateral sides were checked for any changes in pH. All experiments were done in triplicate in an atmosphere of 95% air and 5% CO_2 at 37 °C. The radioactivity applied to the cells was determined in 200-μL samples of the solutions tested and background radioactivity was determined in 200-μL samples of DMEM and HEPES without the radioactive marker. The radioactivity present in the samples was determined after adding 3 mL of scintillation cocktail (Ultima Gold) in a liquid scintillation counter (Tri −Carb 1500, Packard Instrument Company, Meridan, CT). Results were corrected for dilution and expressed as cumulative transport at time t.[3,9−11]

Viability of Caco-2 Cell Monolayers—Both the apical and basolateral sides of the cell monolayers were rinsed twice with 0.01 M phosphate-buffered saline (PBS, pH 7.40) after completion of all the TEER and transport experiments. The cell monolayers were incubated apically with a solution of 0.1% trypan blue (Sigma) in PBS.[3,9,10] The basolateral medium was PBS. After 30 min, the medium was removed from both sides of the cell monolayers and examined by light microscopy for exclusion of the marker. Cells excluding trypan blue were considered to be viable. Cells incubated for 5 min with 0.5% w/v sodium dodecyl sulfate in PBS and stained with trypan blue were used as a reference for uptake of the marker.

Data Analysis and Statistical Evaluation—From the permeation profiles of [^{14}C]mannitol, apparent permeability coefficients (P_{app}) were calculated according to the following equation:

$$P_{app} = dQ/dt/(A \cdot 60 \cdot C_0)$$

where P_{app} is the apparent permeability coefficient (cm s^{-1}), dQ/dt is the permeability rate (amount permeated per min), A is the diffusion area of the monolayer (cm^2), and C_0 is the initial concentration of the marker molecule. The regression coefficients (r^2) obtained from the curve fits were generally between 0.9 and 1.00. Transport enhancement ratios (R) were calculated from P_{app} values by:

$$R = P_{app}(\text{sample})/P_{app}(\text{control})$$

Statistical differences were determined using one-way analysis of variance (ANOVA) and Sheffe's F-test for multiple comparisons. Differences between groups were considered to be significant at $p < 0.05$.

Results

Synthesis and Characterization of TMC—The initial chitosan used to prepare TMC was only soluble in acidic solutions, but after quaternization it became highly soluble in water at every pH.[9,10,13] By repeating the reaction steps, polymers with different degrees of quaternization were obtained. The degree of quaternization was calculated from ^{1}H NMR spectra.[12,13] After an initial 60 min, a polymer (TMC-L) with a degree of quaternization of 12.3% was recovered. Longer reaction times (up to 6 h) do not yield polymers with higher degrees of quaternization.[9] Repeating the basic reaction twice, under the same conditions, with the polymer recovered after an initial 60 min, gave a highly quaternized product (TMC-H) with a degree of quaternization of 61.2%. At this degree of quaternization, the^{13}C and ^{1}H NMR spectra showed additionally some extent of methylation on the 3- and 6-hydroxyl groups of chitosan, but the polymer recovered was still perfectly soluble in water at pH values between 1 and 9.[13]

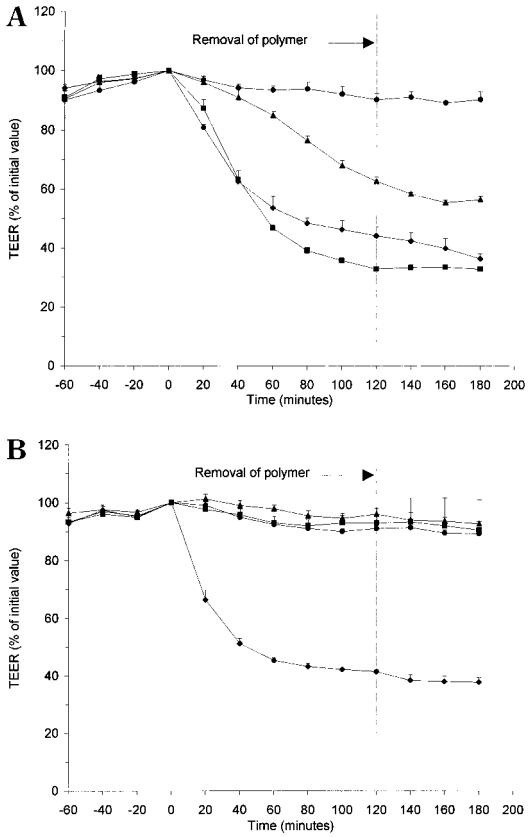

Figure 1—(A) The effects of 0.5% w/v concentrations of TMC-L, TMC-H, and chitosan hydrochloride on the TEER of Caco-2 cell monolayers at a pH of 6.20. (B) The effects of 0.5% w/v concentrations of TMC-L, TMC-H, and chitosan hydrochloride on the TEER of Caco-2 cell monolayers at a pH of 7.40. Each point represents the mean ± SD of three experiments. Key: (●) control; (▲) TMC-L; (◆) TMC-H; (■) chitosan hydrochloride; dotted line (- - -) represents start of reversibility experiment.

Effect on the TEER of Intestinal Epithelial Cells—The effects of 0.5% w/v concentrations of TMC-H, TMC-L, and chitosan hydrochloride on the TEER of the Caco-2 cell monolayers at pH 6.20 and 7.40 are shown in Figures 1A and 1B, respectively. At pH 6.20, incubation with these polymers resulted in a pronounced reduction in TEER values compared with the control group. After 2 h incubation, the reduction in TEER was in the following order: chitosan hydrochloride (67.1 ± 0.6%) > TMC-H (55.9 ± 3.1%) > TMC-L (37.3 ± 1.4%). Higher polymer concentrations (1.0 and 1.5% w/v) did not cause any further significant decreases in the TEER.

At pH 7.40, only TMC-H was able to decrease the TEER of the cell monolayers (Figure 1B). Neither TMC-L nor chitosan hydrochloride, even in concentrations of 1.5% w/v, was able to cause any significant decreases in TEER values compared with the control group. Incubation of the monolayers with TMC-H resulted in a pronounced decrease in the TEER of the cell monolayers. After 2 h incubation, the reduction in TEER was as followed: 43.1 ± 2.5% at 0.1% w/v TMC-H, 45.6 ± 3.7% at 0.25% w/v TMC-H, 58.6 ± 0.7% at 0.5% w/v TMC-H, 60.1 ± 3.1% at 1% w/v TMC-H, and 63.1 ± 2.1% at 1.5% w/v TMC-H. Even in a concentration as low as 0.05% w/v, TMC-H was able to reduce the TEER by 34.8 ± 4.1%.

Reversibility of the effect of 0.5% w/v concentrations of these polymers on TEER could not be demonstrated at any pH value (Figures 1A and 1B). Complete removal of the polymers, without damaging the cells, proved to be problematic due to the high viscosity and mucoadhesivity of the polymer solutions. Furthermore, the repeated washing of the cells and the short time allowed for recovery may also be reasons why significant reversibility of the effect could not be demonstrated. However, in concentrations <0.5% w/v of TMC-H, a clearer tendency to recover to initial values was observed. Staining with trypan blue after completion of all the TEER experiments did not result in any visible intracellular uptake of the marker, indicating that the cells were still viable after incubation with these polymers.

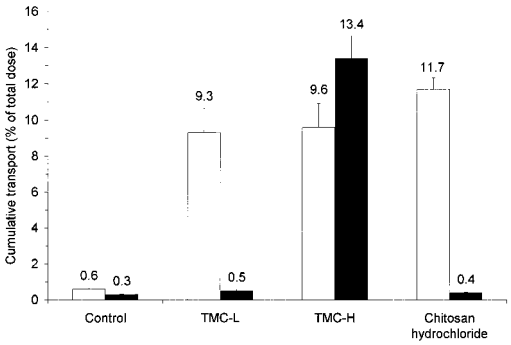

Figure 2—The effect of 0.5% w/v concentrations of TMC-L, TMC-H, and chitosan hydrochloride on the cumulative transport of [^{14}C]mannitol in Caco-2 cell monolayers at pH 6.20 (white bars) and pH 7.40 (black bars). Each point represents the mean ± SD of three experiments.

Effect on [^{14}C]Mannitol Transport—In Figure 2 the cumulative amounts of [^{14}C]mannitol transported after 4 h in the presence of the respective polymers (0.5% w/v) are given at both pH 6.20 and 7.40. From the permeation profiles of [^{14}C]mannitol at the different polymer concentrations and the two pH values, apparent permeability coefficients (P_{app}) values and transport enhancement ratios (R) were calculated (Table 1). Under the conditions described, only negligible amounts of [^{14}C]mannitol were transported in the control groups. At pH 6.20, all the polymers caused a marked accumulation of the marker molecule in the acceptor compartments. As evident from Figure 2, no major differences in the permeability of [^{14}C]-mannitol were found between TMC-L, TMC-H, and chitosan hydrochloride at 0.5% w/v concentrations. At this concentration, the permeability of [^{14}C]mannitol was increased 20-fold (TMC-H), 18-fold (TMC-L), and 23-fold (chitosan hydrochloride) compared with the control group (Table 1). Similar results were obtained at higher concentrations of TMC-L and TMC-H (1.0 and 1.5% w/v). With chitosan hydrochloride, a concentration-dependent increase in [^{14}C]mannitol transport was observed (14.6 ± 1.2% and 19.8 ± 3.8%, of the total dose applied, at 1.0 and 1.5% w/v concentrations, respectively). Apparently, chitosan hydrochloride is more effective than TMC-L and TMC-H at a pH of 6.20.

In agreement with the TEER results, only TMC-H was able to increase the transport of [^{14}C]mannitol at a pH of 7.40. The cumulative amounts of [^{14}C]mannitol transported at 0.05−1.5% w/v concentrations of TMC-H are depicted in Figure 3. These values represent a 31- to 48-fold increase in the permeation of [^{14}C]mannitol (Table 1). The efficiency of TMC-H at this pH value is evident from these results. Even in a concentration as low as 0.05% w/v, the permeability of [^{14}C]mannitol was increased 31-fold.

In all the permeation curves, both at pH 6.20 and 7.40, the transport of [^{14}C]mannitol from the donor to the acceptor compartment was relative steady, as evident from the slope of the individual concentration curves. This result indicates unhindered paracellular diffusion of this hydrophilic compound through opened tight junctions. No evidence of trypan blue inclusion into the intracellular spaces

Table 1—Effect of TMC-H, TMC-L, and Chitosan Hydrochloride on the Permeability of [^{14}C]Mannitol

		TMC-H		TMC-L		chitosan hydrochloride	
pH	polymer concentration (% w/v)	$P_{app} \times 10^{-7}$ (cm s^{-1})[a]	R	$P_{app} \times 10^{-7}$ (cm s^{-1})	R	$P_{app} \times 10^{-7}$ (cm s^{-1})	R
6.20	control	0.72 ± 0.09	1	0.72 ± 0.09	1	0.72 ± 0.09	1
	0.10	12.81 ± 2.56[b]	18	n.d.[c]		n.d.	
	0.25	13.32 ± 0.58[b]	19	n.d.		n.d.	
	0.50	14.28 ± 2.14[b]	20	13.15 ± 1.54[b]	18	16.38 ± 0.68[b,d]	23
	1.00	16.14 ± 0.72[b]	22	10.73 ± 1.87[b]	15	20.82 ± 1.07[b,d]	29
	1.50	14.44 ± 1.80[b]	20	11.32 ± 0.80[b]	16	31.03 ± 3.16[b,d]	43
7.40	control	0.47 ± 0.04	1	0.47 ± 0.04	1	0.47 ± 0.04	1
	0.05	14.69 ± 2.90[b]	31	n.d.		n.d.	
	0.10	14.06 ± 2.85[b]	30	n.d.		n.d.	
	0.25	15.10 ± 2.20[b]	32	n.d.		n.d.	
	0.50	20.14 ± 1.44[b]	43	0.63 ± 0.08	1	0.56 ± 0.09	1
	1.00	22.57 ± 1.89[b]	48	0.85 ± 0.08	2	0.51 ± 0.02	1
	1.50	15.13 ± 1.76[b]	32	1.07 ± 0.89	2	0.67 ± 0.04	1

[a] P_{app} = apparent permeability coeficient; each value represents the mean ± SD of 3 experiments. [b] Significantly different from control ($p < 0.05$). [c] n.d., Not determined. [d] Significantly different from all other treatmeants in group ($p < 0.05$).

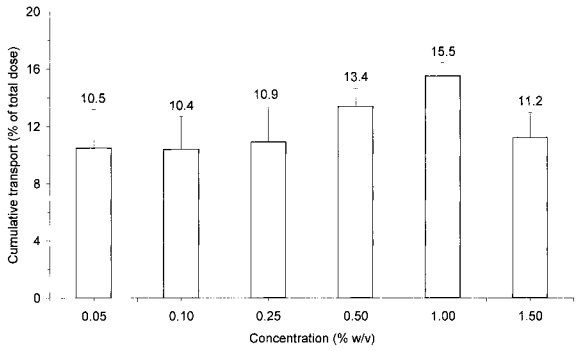

Figure 3—The effect of different concentrations of TMC-H on the cumulative transport of [^{14}C]mannitol in Caco-2 cell monolayers at a pH of 7.40. Each point represents the mean ± SD of three experiments.

of the cells was found when cells were stained with this dye after completion of all the transport studies.

Discussion

The results of this study show that both chitosan hydrochloride and TMC, with different degrees of quaternization, are potent absorption enhancers at a pH of 6.20. These polymers were able to decrease the TEER of the Caco-2 cell monolayers markedly. Measurement of TEER is believed to be a good indication of the tightness of the junctions between epithelial cells. The apparent difference in effect between chitosan hydrochloride and TMC could be explained in terms of their respective charge densities. The amino group on the C-2 position of TMC is a much larger unit, due to the attached methyl groups, compared with the amino group on the C-2 position of chitosan hydrochloride. With chitosan hydrochloride, about 10 wt % constitute the salt part and therefore the charge density is much higher as for TMC. Additionally, the attached methyl groups on TMC may partially shield the positive charge and steric effects may also influence the configuration of the TMC molecule where chitosan hydrochloride probably exists in a linear configuration at acidic pH values when the amino group is protonated. A clear comparison between these polymers is not possible because the equivalent amounts of free chitosan base could not be calculated, especially for TMC because NMR spectra showed that some amino groups are still dimethylated, depending on the degree of quaternization of the respective TMC sample.

In agreement with the reduction in TEER at a pH of 6.20, the permeation of the hydrophilic model compound [^{14}C]mannitol was also increased markedly, indicating enhanced paracellular transport. Because of their positive charge, cationic macromolecules such as chitosan and TMC can interact with the anionic components of the glycoproteins on the surface of epithelial cells. Cationic macromolecules can displace cations from electronegative sites on cell membranes, which require coordination with cations for dimensional stability.[16] It is also known that the interior of the tight junction channel are hydrated and contained fixed negative sites. Changes in the concentration of certain ions in the pore could result in alteration in tight junction resistance leading to opening of the pore with increased paracellular permeability.[17] It has been reported that chitosan is able to induce a redistribution in cytoskeletal F-action, thereby resulting in a structural reorganization of tight junction associated proteins such as ZO-1.[1,6] TMC probably acts in a similar way to open the tight junctions.[10]

At a pH of 7.40 only TMC-H was able to decrease the TEER of the cell monolayers. In agreement with this reduction in measured TEER, the permeation of [^{14}C]-mannitol was substantially increased even in concentrations as low as 0.05% w/v. Chitosan hydrochloride has an apparent pK_a value of 5.5−6.5 and, at a pH of 7.40, it probably exists in a more coiled configuration with no protonated amino groups that can interact with the cell surfaces or tight junctions. With TMC-L, the charged density has not reach the threshold concentration to induce interaction with the anionic components of the glycoproteins at the surface of the cells or with the fixed negative charges within the aqueous tight junctions. Additionally, the attached methyl groups may partially shield the positive charge from significant interaction with the cell membranes or tight junctions. TMC-H, on the other hand, has a much higher proportion of quaternary amino groups that seems to be sufficient to interact with anionic components on the cell membranes or the negative sites within the tight junctions.

Because of the high viscosity and mucoadhesive character of chitosan hydrochloride and TMC, it is unlikely that all the polymer solution could be removed without damaging the cells. Therefore, reversibility of the effect of these polymers on the TEER could not be established. Nevertheless, the absence of intracellular trypan blue staining, after prolonged incubation with these polymers, implies that the Caco-2 cells remained undamaged and functionally intact. This implication is in agreement with results obtained in a recent study where Caco-2 cell monolayers were tested with the propidium iodide nucleic stain for their viability after 4 h of incubation with TMC (40 and 60% quaternized) at different concentrations up to 1.0% w/v. In all cases, the monolayers were able to exlude propidium iodide.[18]

In summary, our study shows that the insolubility of chitosan and chitosan salts prevents these polymers from being effective as absorption enhancers at neutral pH values. It has been shown that TMC, already at very low degrees of quaternization, is superior in water solubility compared with chitosan and chitosan salts.[9,10] The degree of quaternization of TMC is demonstrated to play an important role in its ability to open the tight junctions of intestinal epithelial cells. Highly quaternized TMC proves to be a very potent absorption enhancer, especially at neutral pH values. The use of this chitosan derivative may be a valuable contribution to the development of selective and effective delivery systems for hydrophilic compounds such as peptide drugs, especially in neutral and basic environments where normal chitosan salts are ineffective.

References and Notes

1. Artursson, P.; Lindmark, T.; Davis, S. S.; Illum, L. Effect of chitosan on the permeability of monolayers of intestinal epithelial cells (Caco2). *Pharm. Res.* **1994**, *11*, 1358−1361.
2. Illum, L.; Farraj, N. F.; Davis, S. S. Chitosan as a novel nasal delivery system for peptide drugs. *Pharm. Res.* **1994**, *11*, 1186−1189.
3. Borchard, G.; Lueβen, H. L.; De Boer, A. G.; Verhoef, J. C.; Lehr, C- M.; Junginger, H. E. The potential of mucoadhesive polymers in enhancing intestinal peptide drug absorption. III. Effects of chitosan glutamate and carbomer on epithelial tight junctions in vitro. *J. Controlled Release* **1996**, *39*, 131−138.
4. Lueβen, H. L.; De Leeuw, B. J.; Langemeÿer, M. W. E.; De Boer, A. G.; Verhoef, J. C.; Junginger, H. E. Mucoadhesive polymers in peroral drug delivery. VI. Carbomer and chitosan improve the intestinal absorption of the peptide drug buserelin in vivo. *Pharm. Res.* **1996**, *13*, 1668−1672.
5. Schipper, N. G. M.; Vårum, K. M.; Artursson, P. Chitosans as absorption enhancers for poorly absorbable drugs. 1: Influence of molecular weight and degree of acetylation on drug transport across human intestinal epithelial (Caco-2) cells. *Pharm. Res.* **1996**, *13*, 1686−1692.
6. Schipper, N. G. M.; Olsson, S.; Hoogstraate, J. A.; De Boer, A. G.; Vårum, K. M.; Artursson, P. Chitosans as absorption enhancers for poorly absorbable drugs 2: Mechanism of absorption enhancement. *Pharm. Res.* **1997**, *14*, 923−929.
7. Lueβen, H. L.; Rental, C.-O.; Kotzé, A. F.; Lehr, C.-M.; De Boer, A. G.; Verhoef, J. C.; Junginger, H. E. Mucoadhesive polymers in peroral peptide drug delivery. IV. Polycarbophyl and chitosan are potent enhancers of peptide transport across intestinal mucosae *in vitro*. *J. Controlled Release* **1997**, *45*, 15−23.8.
8. Lehr, C.-M.; Bouwstra, J. A.; Schacht, E. H.; Junginger, H. E. In vitro evaluation of mucoadhesive properties of chitosan and some other natural polymers. *Int. J. Pharm.* **1992**, *78*, 43−48.
9. Kotzé, A. F.; Lueβen, H. L.; De Leeuw, B. J.; De Boer, A. G.; Verhoef, J. C.; Junginger, H. E. N-Trimethyl chitosan chloride as a potential absorption enhancer across mucosal surfaces: In vitro evaluation in intestinal epithelial cells (Caco-2). *Pharm. Res.* **1997**, *14*, 1197−1202.
10. Kotzé, A. F.; Lueβen, H. L.; De Leeuw, B. J.; De Boer, A. G.; Verhoef, J. C.; Junginger, H. E. Comparison of the effect of different chitosan salts and N-trimethyl chitosan chloride on the permeability of intestinal epithelial cells (Caco-2). *J. Controlled Release* **1998**, *51*, 35−46.
11. Kotzé, A. F.; De Leeuw, B. J.; Lueβen, H. L.; De Boer, A. G.; Verhoef, J. C.; Junginger, H. E. Chitosans for enhanced delivery of therapeutic peptides across intestinal epithelia: i*n vitro* evaluation in Caco-2 cell monolayers. *Int. J. Pharm.* **1997**, *159*, 243−253.
12. Domard, A.; Rinaudo, M.; Terrassin, C. New method for the quaternization of chitosan. *Int. J. Biol. Macromol.* **1986**, *8*, 105−107.
13. Sieval, A. B.; Thanou, M.; Kotzé, A. F.; Verhoef, J. C.; Brussee, J.; Junginger, H. E. Preparation and NMR-characterization of highly substituted N-trimethyl chitosan chloride. *Carbohydr. Polym.* **1998**, in press.
14. Noach, A. B. J.; Kurosaki, Y.; Blom-Roosemalen, M. C. M.; De Boer, A. G.; Breimer, D. D. Cell-polarity dependent effect of chelation on the paracellular permeabilty of confluent Caco-2 cell monolayers. *Int. J. Pharm.* **1993**, *90*, 229−237.
15. Hurni, M. A.; Noach, A. B. J.; Blom-Roosemalen, M. C. M.; De Boer, A. G.; Nagelkerke, J. F.; Breimer, D. D. Permeability enhancement in Caco-2 cell monolayers by sodium salicylate and sodium taurodihydrofusidate: Assessment of effect reversibility and imaging of transepithelial transport routes by confocal laser scanning microscopy. *J. Pharmacol. Exp. Ther.* **1993**, *267*, 942−950.
16. Siegel, S. M.; Daly, O. Regulation of betamycin efflux from beet root by poly-l-lysine, Ca-ion and other substances. *Plant Physiol.* **1966**, *41*, 1429−1434.
17. Madara, J. L. Intestinal absorptive cell tight junctions are linked to cytoskeleton. *Am. J. Physiol.* **1987**, *253*, C171−C175.
18. Thanou, M.; Kotzé, A. F.; Scharringhausen, T.; Lueβen, H. L.; De Boer, A. G.; Verhoef, J. C.; Junginger, H. E. Effect of degree of quaternization of N-trimethyl chitosan chloride for enhanced transport of hydrophilic compounds across intestinal Caco-2 cell monolayers. *J. Controlled Release (Special Issue)*, in press.

Acknowledgments

This study was supported in part by grants from The South African Druggist Group, the Foundation for Pharmaceutical Education of the Pharmaceutical Society of South Africa, and the State Scholarship Foundation of Greece. The authors thank John Beliën and Alex Sieval for their help in the synthesis of TMC.

JS980233C

The Versatility of Polysorbate 80 (Tween 80) as an Ionophore

CHARLES J. THOMAN*

Contribution from *Department of Chemistry and Biochemistry, University of the Science in Philadelphia,† 600 S. 43rd Street, Philadelphia, Pennsylvania 19104.*

Received May 21, 1998. Final revised manuscript received September 2, 1998.
Accepted for publication November 11, 1998.

Abstract □ A number of experiments were performed to illustrate the unusual versatility of Polysorbate 80 (Tween 80) as an ionophore. New ions shown to be transported by it from and to water layers through a model membrane (CH_2Cl_2) include H_3O^+, Li^+, Pb^{2+}, Co^{2+}, piperidinium ion, guanidinium ion, and Paraquat, while two complex ions resisted transport under the conditions used. "Reverse" transport of lipophilic guests (azobenzene, azulene, ferrocene) from and to organic solvents through water was also promoted by Tween 80, but C_{60} was not carried. Three water molecules were transported per molecule of KSCN by the Tween.

Introduction

Previous work has shown that Polysorbate 80 (**1**, Tween 80), a popular surfactant and solubilizing agent used in biochemical, chemical, and pharmacological research and in the food and cosmetic industries, is an effective ionophore,[1] can be used as a phase transfer catalyst,[2] and affects the serum concentrations of calcium ions of rats when included in their diets.[3] It also exhibits, as do poly(ethylene glycol) 1000 and 18-crown-6, an unusual inverse temperature effect on the rates of transport of potassium thiocyanate through a model membrane.[4]

The present work was undertaken to illustrate the versatility of Polysorbate 80 as an ionophore. It was already known that it is more stable in basic solutions than the tetraalkylammonium salts, and both cheaper and less toxic than the crown ethers.[1] We set out to expand the number and types of ions carried by it, to settle the question of how ions are carried ("naked" or hydrated), and to discover if the "reverse" transport of lipophilic guests through water could be achieved.

Too often, Polysorbate 80 has been used as a surfactant and solubilizing agent in living systems under the assumption that it was totally inert and had no further physiological activity or influence. To test this assumption, we hope to be able to answer the following questions. Is Polysorbate 80 able to transport, not only benign ions, but also potentially dangerous ones (e.g. heavy metal ions), across a membrane? Is it able to transport organic ions as well? Is it able to, not only solubilize into aqueous bodily compartments neutral organic entities, but also to facilitate their movements through membranes into other aqueous compartments, such as cells? How inert and innocuous is Polysorbate 80?

Experimental Section

Materials—Thiocyanate salts, azobenzene, azulene, ferrocene, Paraquat, Methyl Thymol Blue, and Carbon Soot were purchased from Aldrich and, except for the Soot, used without further purification. Polysorbate 80 was obtained from Fisher Chemical. Spectra were recorded on a Milton Roy Spectronic 301.

Transport Studies—The experimental setup has been described elsewhere.[1] A lower layer of 150 mL of approximately 0.8 mM **1** in CH_2Cl_2 in a 600 mL beaker supports an inner layer of 40 mL of 0.1 M aqueous metal or organic thiocyanate and an outer layer of 0.02 M $Fe(NO_3)_3$ in 0.20 M HNO_3, the latter two layers separated by a glass "cup". The rate of transport is monitored by measuring the increase in the absorbance at 480 nm of the red complex ion $Fe(SCN)^{2+}$ formed in the outer layer with time.

Two exceptions to the above procedure should be noted. Since $Pb(SCN)_2$ is only very slightly soluble in water, $Pb(NO_3)_2$ was used as the salt, and the outer layer changed to a 0.1 mM solution of methyl thymol blue in 0.05 mM succinic acid buffer (pH 5.8).[5]

In the case of the transport of hydronium ions, the inner layer consisted of various concentrations of aqueous HNO_3, and the outer layer of distilled water. Transport was monitored by measuring the pH of the outer layer.

Transport of Water Molecules—These experiments were conducted in a dry bag in an atmosphere of dry N_2. The inner layer consisted of 40 mL of 0.1 M aqueous KSCN and the outer layer of 25 mL of D_2O. At regular intervals, including at time zero, 2.0 mL samples of the outer layer were removed and placed in stoppered NMR tubes. At the end, the tubes were removed from the dry bag and the intensity of the absorption peak for H_2O at 4.65 ppm monitored a minimum of six times. Then, 1.5 mL of each sample was mixed in a UV cuvette with 1.5 mL of 0.02 M $Fe(NO_3)_3$ in 0.20 M HNO_3, and the absorption of the resultant solution followed at 480 nM.

The standard curve used to convert the UV absorptions to concentrations was that used previously.[1] A standard curve to ascertain the transport of H_2O into the D_2O of the outer layer was made by adding microliter samples of distilled, deionized H_2O to 2.0 mL samples of D_2O and measuring the intensity of the absorption in the NMR at 4.65 ppm; its $r = 0.9985$.

Blank experiments were run without KSCN in the inner layer but with Tween in the lower layer, and also without either present.

Transport of Paraquat—The colorless Paraquat can be monitored using the intensely colored radical cation which absorbs at 605 nm formed when it is oxidized by alkaline sodium dithionite.[6] A standard curve was prepared by measuring the absorption of a series of solutions made by adding 1.0 mL of aqueous Paraquat solutions to 1.0 mL of freshly prepared 0.5% sodium dithionite in 0.5 M ammonia buffer (pH 9); its coefficient of correlation was 0.9992. Timely 1.0 mL samples of the distilled water in the outer layer were taken during the experiment and, at the end, all added sequentially to 1.0 mL samples of a freshly prepared dithionite solution and the absorption read at 605 nm (dithionite solutions are unstable and must be prepared just before adding to the transported samples).

"Reverse" Transport of Lipophilic Guests—In these cases, the lower layer consisted of 150 mL of 0.643 mM aqueous Polysorbate 80; the inner layer of 40 mL of 0.100 M solute (azobenzene, azulene, or ferrocene) in the organic solvent (either hexane or isooctane); and the outer layer of 50 mL of the same pure solvent. Transport was monitored by measuring the absorption of the colored species themselves (azobenzene at 436 nm, azulene at 633 nm, and ferrocene at 442 nm) with time in the outer layer. Standard curves were constructed for each of the solutes: for azobenzene, $A = 0.00887 + 0.1834[AZB]$, $r = 0.9945$; for azulene, $A = -0.000963 + 0.3405[Azl]$, $r = 0.9981$; for ferrocene, $A = 0.0113 + 90.65[Fer]$, $r = 0.9928$.

* Corresponding author. (215)895-1158, fax (215)596-8543, e-mail c.thoman@usip.edu.
† Formerly Philadelphia College of Pharmacy and Science.

10.1021/js980216n CCC: $18.00
Published on Web 12/19/1998

Table 1—Fluxes of Ions via Polysorbate 80[a]

ion	n[b]	$10^8 \times$ flux (mol/s/m^2 ± SD
K^+	9	4.94 ± 0.65
Na^+	7	1.26 ± 0.23
NH_4^+	6	2.67 ± 0.31
Li^+	4	0.40 ± 0.05
H_3O^+[c]	4	0.83 ± 0.13
$(H_2N)_2C{=}NH_2^+$ (guanidinium)	3	5.44 ± 0.19
$C_5H_{10}NH^+$ (piperidinium)	5	14.11 ± 0.61
Ca^{2+}	6	0.72 ± 0.22
Co^{2+}	4	5.43 ± 0.12
Pb^{2+}[d]	3	1.81 ± 0.08
$Ni(NH_3)_6^{2+}$	3	0.00
$Cr(NH_3)_6^{3+}$	3	0.00
2 (Paraquat)[e]	3	0.0034 ± 0.0015

[a] Unless otherwise indicated, using 0.8 mM Tween in CH_2Cl_2 as the lower layer, 0.1 M thiocyanate salt as the inner layer, and 0.02 M $Fe(NO_3)_3$ in 0.20 M HNO_3 as the outer layer at 23 °C and 125 rpm. [b] Number of determinations. [c] Using 0.1 M HNO_3 as the inner layer and distilled, deionized water as the outer layer. [d] Using 0.10 M $Pb(NO_3)_2$ as the inner layer and 0.10 mM methyl thymol blue in 0.05 mM succinic acid buffer (pH 5.8) as the outer layer. [e] Using 0.0778 M Paraquat as the inner layer and distilled, deionized water as the outer layer.

A 0.006 M solution of buckminsterfullerene (C_{60}) in toluene was prepared according to the method of Scrivens et al.[7] and 40 mL of it used as the inner layer. Distilled water constituted the outer layer. A standard curve was constructed using the absorption of C_{60} at 598 nm.[8] Transport was monitored at the same wavelength.

Results and Discussion

Ion Transport—The number and type of ions shown to be transported by Polysorbate 80 was increased considerably. The original work[1] had studied four biochemically important ions (K^+, Na^+, NH_4^+, Ca^{2+}). In this work, smaller ions were used (Li^+, H_3O^+), as well as, for the first time, heavy metal ions (Co^{2+}, Pb^{2+}). Some larger organic ions (piperidinium ion, guanidinium ion) are transported, while several complex ions [hexamminecobalt(III)$^{2+}$ and hexamminenickel(II)$^{2+}$] are not. Methyl viologen, better known as Paraquat (**2**), a divalent cation in which the charges are separated, was also transported, but at a considerably lower rate (about 1/150) than any of the other ions. The fluxes of all these ions are summarized in Table 1.

The reluctance of the complex ions to be transported is probably due to the fact that the charges on the metals are so deeply buried within the six ammine groups that no interaction with the oxygen atoms of the Polysorbate 80 is possible, this despite the fact that the ammonium ion itself is easily transported. Chia et al.[9] reported a similar lack of transport of the hexamminecobalt(III)$^{2+}$ using the sodium salt of lasalocid as the ionophore; they did, however, effect transport if the receiving layer was spiked with ammonium ion (Lindoy et al.[10] also did this). The much lower rate of transport of the Paraquat may be related to the much greater size and weight that it represents; e.g. the length of the Paraquat molecule is about 10.2 Å compared to a length of only 4.9 Å for piperidinium ion. Apparently, the Tween can completely sequester the latter, but not the former. Also, it may be able to envelope only one of the positively charged nitrogen positions on the Paraquat molecule, leaving the other free to resist removal from the aqueous layer (the positive charges are about 7.1 Å apart).

Leaving Paraquat aside, the ions that are transported move at similar rates. An exception is the piperidinium ion, whose flux is three or more times greater than the other monopositive ions. The reason for this may be that this ion has a lipophilic end that can facilitate solution in the model membrane; even the guanidinium ion cannot do this, because the positive charge is distributed throughout the molecule by resonance. Still, this general similarity in fluxes is in contrast to the situation using cyclic ionophores such as the crown ethers, where the correspondence between the size of the cavity and the diameter of the ion is of such importance, so that ions that can fit comfortably within the cavity are transported much more easily than those that are too big or too small for a snug fit. Over a large range of sizes, the poly(ethylene oxide) arms of the Polysorbate 80 are able to envelope many dissimilar ions with similar effectiveness, making it inherently more versatile than the cyclic ionophores.

Table 2—Fluxes[a] of "Reverse" Transport via Polysorbate 80[b]

guest	concn, M	$10^8 \times$ flux (hexane)	$10^8 \times$ flux (isooctane)
azobenzene	0.0125	3.36 ± 0.72	
	0.025	3.69 ± 1.36	3.77 ± 0.41
	0.050	4.40 ± 1.36	4.45 ± 0.59
	0.075	5.35 ± 0.86	
	0.100	6.32 ± 1.18	6.53 ± 0.21
		(r = 0.9969)[c]	(r = 0.9955)[c]
azulene[d]	0.0125	0.90 ± 0.22	0.89 ± 0.09
	0.025	2.16 ± 0.46	2.06 ± 0.33
	0.050	4.33 ± 0.24	4.38 ± 0.60
	0.075	6.63 ± 0.51	6.70 ± 0.59
		(r = 0.9907)[c]	(r = 0.9973)[c]
ferrocene	0.038		1.53 ± 0.22
	0.077		2.68 ± 0.22
	0.107		3.44 ± 0.71
	0.128		4.03 ± 0.58
			(r = 0.9993)[c]
buckminsterfullerene (C_{60})	0.006	0.00 (toluene)	

[a] Mol/s/m^2 ± SD, with a minimum of three determinations at each concentration. [b] Using 150 mL of 0.8 mM aqueous Polysorbate 80 as the lower layer, 40 mL of the guest at the stated concentrations in the stated solvent as the inner layer, and 50 mL of the same pure solvent as the outer layer, at 23 °C and 150 rpm. [c] Coefficient of correlation of the plot of concentration versus flux. [d] Diederich and Dick[14] report a transport rate for azulene from 0.02 M azulene in hexane through a 0.5 mM cyclophane-type ionophore in water to hexane at 20–22 °C of 8.6×10^{-6} mol/L/h; they do not reduce this to a flux.

"Reverse" Transport of Lipophilic Guests—One of the major uses of Polysorbate 80 has been to solubilize in water compounds that are otherwise insoluble in it. This led us to believe that lipophilic guests, with very low solubilities, might be able to be transported by Polysorbate 80 from an initial organic layer through an aqueous layer and into a final organic layer. A few examples exist of such "reverse" transport involving specifically constructed hosts (e.g. calixarenes[11,12] and cyclophanes[13,14]) with limited versatility. We chose as our guests strongly colored organic molecules whose absorptions in the visible region could act as their own means of detection.

The results of these experiments are shown in Table 2. Three quite different types of substances (azobenzene, azulene, and ferrocene) were transported with fluxes comparable to those of the ions transported (cf. Table 1). Initially, hexane was used as the organic solvent, but its relatively high volatility led to problems (an adjustment of volume in the upper layers before each reading). These problems were solved by changing to the less volatile solvent isooctane.[15]

With regular ion transport, the flux is first order in the salt. We determined the orders of the transports of our three organic guests in the usual way (using the slope of the line obtained by plotting ln k versus ln c), with the following results: 0.3−0.4 order for azobenzene, 1.20−1.25 order for azulene, and 0.74 order for ferrocene. This indicates that the rate-determining step of the process, the

Table 3—Transport of Water with Ions through a Model Membrane

components	n^a	$10^8 \times$ flux^b for H_2O^c	$10^8 \times$ flux^b for KSCN^d
H_2O	4	16.18 ± 1.13	
H_2O + Tween	3	18.88 ± 0.68	
H_2O + Tween + KSCN	4	22.29 ± 2.48	1.11 ± 0.12

[a] Number of determinations. [b] Mol/s/m^2 ± SD. [c] Determined by integration of the NMR peak at 4.65 ppm in the D_2O outer layer. [d] Determined by the absorption of the $Fe(SCN)^{2+}$ complex at 480 nm.

formation of the complex at the initial organic solvent–water interface, is not simple, but complex, depending to some extent on the shape and the size of the guest. Further work is needed to explain these orders.

It is apparent that Polysorbate 80 is as adept at transporting hydrophobic molecules through an aqueous layer as it is in carrying ions through an organic layer. Such versatility is not possible with many artificial (e.g. crown ethers and analogues) or naturally occurring (e.g. valinomycin, monensin, etc.) ionophores, whose cyclic or pseudocyclic structures restrict them to one basic conformation featuring a hydrophilic cavity and a lipophilic exterior. In addition, as is the case with other "octopus" compounds,[12] the size of the guests carried by Polysorbate 80 is not limited by a cavity of a specific size. The relatively free poly(oxyethylene) arms of one or more molecules[11] can envelope and carry guests of widely varying dimensions.

These results should act as a caveat in the use of Polysorbate 80 in living systems. There is always the possibility that the movement of organic molecules that are small enough through membranes can be facilitated by the Tween, causing interference at best and risk at worst. One such example, involving a study of the effect of 11-hydroxy-Δ^9-tetrahydrocannabinol on the tachycardia of an excised rat heart, has already been documented.[16]

Are Tween Transported Ions Hydrated or Not—One of the reasons given for the increased rates of reaction produced by phase transfer catalysis (beyond the fact that the reacting species are in the same phase) is the fact that the ions transported to the organic phase are "naked", i.e., not hydrated, or at least are less hydrated, than they were in the aqueous phase. Polysorbate 80 has been used as a phase transfer catalyst,[2] and so an experiment was set up to ascertain whether and to what extent water was transported through an organic layer with the cations and their counterions.

The results are shown in Table 3. Two blanks were run. In the first case, no salt was present in the inner layer and no Polysorbate 80 in the lower layer. Despite this fact, water was transported under the usual conditions of the experiment with a significant flux (16.18×10^{-8} mol/s/m^2). The second blank involved no salt in the inner layer, but Polysorbate 80 in the lower layer; the flux of water rose to 18.88×10^{-8} mol/s/m^2, an increase of about 17%.

When KSCN was present in the inner layer and Polysorbate 80 in the lower layer, the flux of the salt was shown to be 1.11×10^{-8} mol/s/m^2 and that of the water 22.29×10^{-8} mol/s/m^2. Since the flux of the water without the presence of the salt was 18.88×10^{-8} mol/s/m^2, the KSCN would be responsible for a water flux of the difference, 3.41×10^{-8} mol/s/m^2. This means that, for each mole of KSCN transported, about three moles of water are transported [$(22.29 \pm 2.48 - 18.88 \pm 0.68) \div 1.11 \pm 0.12 = 3.07 \pm 1.32$]. It is not clear at present whether this water is transported by the cation, the counterion, or a combination of the two. In a similar case, Dang and Kollman[17] postulate on theoretical grounds that three water molecules adhere to the potassium ion in its complex with 18-crown-6. Still, it is clear that the ions in the organic layer, while not truly "naked", are nonetheless considerably unclothed compared to their situation in water.

References and Notes

1. Thoman, C. J. The Ionophoric Properties of Polysorbate 80 (Tween 80). *J. Pharm. Sci.* **1986**, *75*, 983.
2. Thoman, C. J.; Habeeb, T. D.; Huhn, M.; Korpusik, M.; Slish, D. F. The Use of Polysorbate 80 (Tween 80) as a Phase Transfer Catalyst. *J. Org. Chem.* **1989**, *54*, 4476.
3. Thoman, C. J.; Vermeulen, L. A.; Coffee, A. M.; DeSanto, R. J. Effect of Dietary Polysorbate 80 on the Serum Concentrations of Calcium and Magnesium in the Rat. *J. Agric. Food Chem.* **1993**, *41*, 714.
4. Thoman, C. J. The Effect of Temperature on the Transport Capabilities of Some Common Ionophores. *J. Am. Chem. Soc.* **1985**, *107*, 1437. This work has recently been confirmed: Borowitz, G. B. et al. Metal Cation Transport Studies Comparing Dibenzo-18-Crown-6 (DB18C6) with N,N,N′,N′-Tetrakis(*n*-propyl)-2,3-naphthalenedioxydiacetamide (Npr). *J. Inclusion Phenom. Mol. Recogit. Chem.* **1998**, *30*, 271.
5. Cheng, K. L., Ueno, K., Imamura, T., Eds. *CRC Handbook of Organic Analytical Reagents*; CRC Press: Boca Raton, FL, 1982; pp 231–238.
6. Perez-Ruiz, T.; Martinez-Lozano, C.; Tomas, V. Simultaneous Flow Injection Determination of Diquat and Paraquat in Foodstuffs, Natural Waters and Biological Fluids. *Intern. J. Environ. Anal. Chem.* **1991**, *44*, 243.
7. Scrivens, W. A.; Bedworth, P. V.; Tour, J. M. Purification of Gram Quantities of C_{60}. A New, Inexpensive and Facile Methodol. *J. Am. Chem. Soc.* **1992**, *114*, 7917.
8. Allemand, P.-M. et al. Two Different Fullerenes Have the Same Cyclic Voltametry. *J. Am. Chem. Soc.* **1991**, *113*, 1050.
9. Chia, P. S. K. et al. Supramolecular Transport of Metal Ammine and Amine Complexes by the Natural Ionophore Lasalocid A. The Selective Enantiomeric Transport of Chiral Metal Complexes. *J. Am. Chem. Soc.* **1991**, *113*, 2533.
10. Lindoy, L. F.; Walker, G. W.; Everett, G. W. Supramolecular Transport of Metal Complexes. Chiroselective Membrane Transport of Metal Amine Complexes by a Polyether Ionophore, Lasalocid A. *J. Am. Chem. Soc.* **1990**, *112*, 3659.
11. Shinkai, S. et al. Hexasulfonated Calix[6]arene Derivatives: A New Class of Catalysts, Surfactants and Host Molecules. *J. Am. Chem. Soc.* **1986**, *108*, 2409.
12. Alam, I.; Gutsche, C. D. Calixerenes. 24. Complexation by Water-soluble Calixarenes. *J. Org. Chem.* **1990**, *55*, 4487.
13. Diederich, F. Molecular Recognition in Aqueous Solution. *J. Chem. Educ.* **1990**, *67*, 813.
14. Diederich, F.; Dick, K. A New Water Soluble Cyclophane Type Host–Guest Complexation with Aromatic Guests in Aqueous Solution and Acceleration of the Transport of Arenes Through an Aqueous Phase. *J. Am. Chem. Soc.* **1984**, *106*, 8024
15. Rethwisch, D. G.; Subramanian, A.; Yi, G.; Dordick, J. S. Enzyme Facilitated Transport of Organic Acids Through Liquid Membranes. *J. Am. Chem. Soc.* **1990**, *112*, 1649.
16. B. Manno: private communication..
17. Dang, L. X.; Kollman, P. A. Free Energy of Association of the 18-Crown-6: K^+ Complex in Water: A Molecular Dynamics Simulation. *J. Am. Chem. Soc.* **1990**, *112*, 5716.

Acknowledgments

Thanks are due to Dr. Durai Sabapathi for statistical analyses, and to Mark A. Miller and Richard Freeman for preliminary work.

JS980216N

Powder Densification. 1. Particle–Particle Basis for Incorporation of Viscoelastic Material Properties

SUSAN K. LUM*,† AND WENDY C. DUNCAN-HEWITT†,‡

Contribution from *Faculty of Pharmacy, University of Toronto, 19 Russell Street, Toronto, Ontario, Canada M5S 2S2.*

Received January 9, 1998. Accepted for publication November 9, 1998.

Abstract □ The present investigation was undertaken to examine the basic unit of densification: the particle–particle indentation. The true interparticle contact area that is established during densification ultimately determines the quality of the tablet compact. By examining the interfacial contact between mutually indenting viscoelastic particles, the process of contact evolution may be represented in mathematical form through extension of the classical Hertzian elastic contact description to encompass material viscoelastic terms. In this way, the time-dependent response of materials to applied loads may be addressed explicitly. The effects of rates of applied loading and maximum load levels were also considered. This analysis was based on viscoelastic stress data collected using an instrumented Instron analyzer during the densification of PMMA/coMMA, a pharmaceutical polymeric coating material. A crossed cylinder matrix compaction geometry was used to simulate the geometry of two mutually indenting spherical particles. Numerical and graphical solutions delineating the relationship between contact area evolution and the prescribed loading force are presented. This particle–particle description of the contacting interface serves as a unit basis for describing the entire powder bed. The powder bed may ultimately be modeled as a collection of these particles in contact.

Introduction

Oral administration is the most common route of drug delivery for systemic circulation. The tablet is the leading oral form; it's simplicity, portability, and economic value enhances patient compliance. Tablets exist in diverse forms, ranging from conventional disintegrating forms to advanced modified-release systems, but all are formed through a common pathway, namely, through powder densification.

Powder densification consists of sequential and concurrent processes where particles are brought into intimate contact, interparticulate bonds are formed, and dimensional changes occur as a result of stress redistribution. Time-dependent phenomena inherent in these processes may govern the ultimate quality of the compact produced. Permanent densification occurs when stress exceeds the elastic strain limit of a given material. The extent of this nonrecoverable deformation depends on the time in which the applied stress exceeds this material yield stress. It is viscoelastic theory that serves to quantitate this time dependence and provide a description of the relationship between the strain rate of the material in a plastic state and the stress required to produce that strain rate.

The compaction of powders is a complex process. The rate at which compacts are formed determines the final tablet strength and viability.[1−4] With the advent of modern processes, the high speeds of compaction emphasize the time-dependent component of material behavior. This complexity is reflected in the large-scale manufacturing of tablets where problems of low tablet strength, capping and sensitivity to material batch variability exist and are translated into costly overruns. Resolution of these problems often involves multiple formulation adjustments based on empirical knowledge rather than the reasoned use of physical data; improving the theoretical understanding of the compaction process would enable a more rational approach to the formulation of tablets.[5]

It is conjectured that problems arise during tablet production as a consequence of viscoelasticity combined with poor interparticle bonding. The amount of elastic recovery of the particles depends on the release of elastic strain during decompression and tends to disrupt interparticle bonds. This stress relaxation is a function of the viscoelasticity of the material, which in turn is influenced by the speed of compression and decompression. At high compaction speeds, the internal stress after compaction is high and the propensity of the material for elastic recovery is considerably higher than at low compaction speeds.

Existing approaches to assess powder compaction have mainly tried to quantify compression in an empirical form. The equations proposed to empirically fit compaction data with parameters such as punch and die wall stresses and tablet porosity[6−9] offer little insight into the physical basis for particle interaction. Therefore, they remain descriptive rather than predictive of powder densification.

A predictive model of compaction must explicitly incorporate material viscoelastic terms into a working description of densification. Analytical models that describe densification from the deformation of particles serve to facilitate the selection of production process parameters such as pressure, temperature, and time. The present investigation was undertaken to examine the basic unit of densification: the particle−particle interaction. By defining the contact between mutually indenting viscoelastic particles, the compact may ultimately be modeled as a collection of these particles in contact and in this way address the time-dependent response of materials to applied loads.

Rationale

In random close packing of a powder bed, point contacts exist between adjacent particles. The density of the powder increases through processes that flatten these contacts between particles. The degree of interparticle bonding and bond strength, which which determines the ultimate quality of a tablet, is assumed to be largely governed by the magnitude of the true interparticle contact area created during densification. This process of contact evolution may be represented in mathematical form through amelioration of the classical Hertzian elastic contact description to encompass material viscoelastic terms. In this way, a

* Author to whom all correspondence should be sent. Telephone: (416) 978−2889. Fax: (416) 978-8511. E-mail: susan.lum@utoronto.ca.
† Faculty of Pharmacy.
‡ Consultant, Grian Facilitations, http://www.grian.com, 1929 Howard Drive, Amarillo, TX, 79106.

10.1021/js980010m CCC: $18.00
Published on Web 01/15/1999

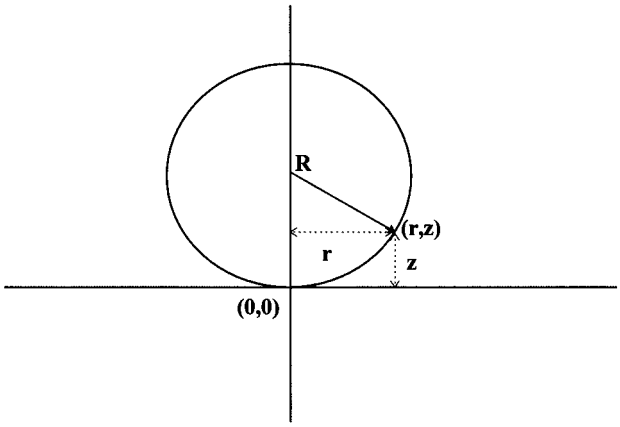

Figure 1—Schematic for the 2-D projection of a contact area. The equation of a translated circle with respect to the origin in the *x*–*y* Cartesian coordinate plane at a point designated (*r*,*z*) (where *R* is the radius of the circle) and where one assumes that $2R \gg z$ is $\therefore z \cong r^2/2R$. This is valid for cases where deformations are small.

quantitative measure of the contact deformation between mutually indenting viscoelastic particles may be defined.

Theoretical Section

The time-dependent stress and indentation behavior of the test matrixes were modeled in terms of a standard linear viscoelastic rheological form transposed into the classical elastic description of contact. Components of the theory underlying this contact deformation may be found interspersed in the literature for specific geometries.[10,11] The following derivation of the theory describing the contact between spherical particles of a viscoelastic material, as applied to these studies, is developed in detail for the integral understanding of the resultant model.

Boundary Conditions for the Deformation between Two Spherical Bodies in Contact—The geometry of the surface of undeformed spheres near the center of contact are smooth surfaces that can be described with sufficient accuracy, as shown in Figure 1, by

$$z_1 = \frac{r^2}{2R_1} \qquad z_2 = \frac{r^2}{2R_2} \tag{1}$$

and the mutual distance between points is

$$z_1 + z_2 = r^2\left(\frac{1}{2R_1} + \frac{1}{2R_2}\right) = \frac{r^2(R_1 + R_2)}{2R_1R_2} \tag{2}$$

If the spheres are compressed together by a normal force *P*, there will be a local deformation near the point of contact producing contact over a small surface with a circular boundary, hence, the surface of contact arises.

Let w_1 and w_2 be the deformations of the two spheres owing to the contact pressure, *a* the radius of the contact region, and α be the total distance of approach of the two spheres from the state of point contact. The deformed configuration is shown in Figure 2. The condition

$$w_1 + w_2 = \alpha - (z_1 + z_2) \tag{3}$$

is to be satisfied at each point in the contact region. By eq 2

$$w_1 + w_2 = \alpha - \left(\frac{r^2(R_1 + R_2)}{2R_1R_2}\right) \tag{4}$$

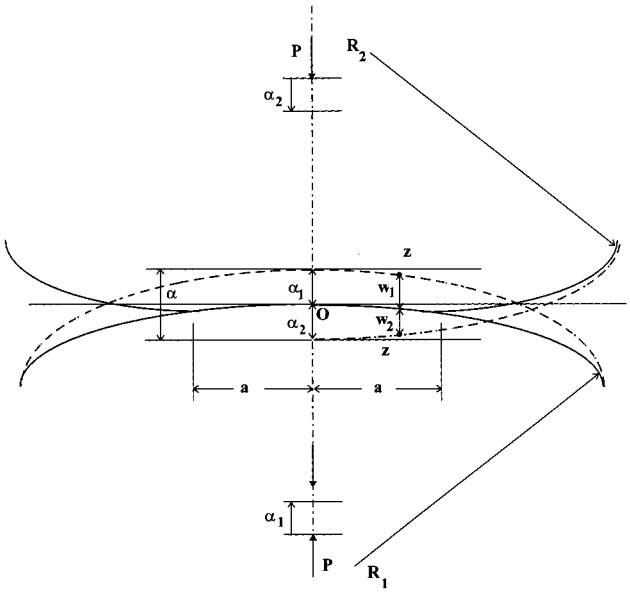

Figure 2—Schematic for the deformation between two spheres from the state of point contact. The deformed configuration is shown with dotted lines indicating the distance of approach of either sphere.

If points lie outside the contact area so that they do not touch it follows that

$$w_1 + w_2 > \alpha - \left(\frac{r^2(R_1 + R_2)}{2R_1R_2}\right) \tag{5}$$

from geometry alone.

Pressure between Two Spheres in Contact—The distribution of pressure transmitted between the two bodies at their surface of contact must be such that the resultant displacements normal to that surface satisfy eq 4 within the contact area and eq 5 outside it. Because the contact region is comparatively much smaller than the dimensions of the bodies ($r \ll R_1$ and R_2), the relation between the surface deflection of each body and the contact pressure can be represented approximately by the solution for surface deflection of a semi-infinite body with pressure distributed on part of its surface. The errors incurred by assuming that the spheres are half-spaces are smaller than those due to the assumption of infinitesimal strains.[12]

Let $a(t)$ be the radius of the contact region and $\alpha(t)$ the total distance of approach. For a given concentrated force acting on a boundary plane of a semi-infinite solid, the displacement is given by[11]

$$w_{z=0} = \frac{q(1 - v^2)}{\pi E r} \tag{6}$$

where *w* is the total displacement, *q* is the intensity of pressure between the bodies in contact, *v* is the Poisson's ratio, *E* is the elastic modulus, and *r* is the distance from the center.

In the case of an uniform load distributed over the area of a circle of radius *a*, if a point D is within the loaded area, the displacement produced is found by superposition. The load on the shaded element in Figure 3 which represents the surface of contact, is $qs\mathrm{d}\psi\mathrm{d}s$. The displacement in the direction of the load is then

$$\frac{(1 - v^2)q}{\pi E}\frac{s\mathrm{d}\psi\mathrm{d}s}{s} = \frac{(1 - v^2)q}{\pi E}\mathrm{d}\psi\mathrm{d}s \tag{7}$$

If there is no pressure between the bodies, we have contact

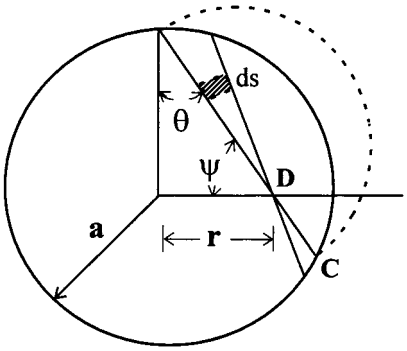

Figure 3—Sketch of a circular contact region of radius *a*. This is the surface of contact over which an uniform load has been distributed.

at one point O. Points D and C are on a meridian section of the spheres, on the plane tangent at O, at a very small distance r (r is small in comparison with R_1 and R_2) from the axis.

The total deflection of a point on the circular contact surface is then obtained by double integration

$$w = \frac{(1 - \upsilon^2)}{\pi E} q \int\int \mathrm{d}\psi \mathrm{d}s \tag{8}$$

because the length of the cord indicated by $bc = 2r = 2a \cos\theta$ and because $r = a \cos\theta = \sqrt{a^2 - r^2 \sin^2\psi}$ the area of the circle $= \pi r^2 = \pi(a^2 - r^2 \sin^2\psi)$ and ψ varies from 0 to $\pi/2$ (see *Appendix I*):

$$\therefore w = \frac{(1 - \upsilon^2)}{\pi E} q \pi \frac{\pi}{4}(2a^2 - r^2) \tag{9}$$

Expressions for the Displacement and Radius of the Contact Surface— Let $(1 - \upsilon^2)/\pi E = k_1 + k_2$ and assume a Hertzian pressure distribution wherein the scale[11] representing the pressure distribution is the constant q_0/a. Thus from eqs 4 and 9, for two same sized spheres in contact,

$$\therefore (k_1 + k_2)\frac{q_0}{a}\frac{\pi^2}{4}(2a^2 - r^2) = w = \alpha - \frac{r^2}{R} \tag{10}$$

Which is then solved by making a term-by-term equivalence between the left- and right-hand sides of this equation

$$\therefore \alpha = \frac{(k_1 + k_2)}{2} q_0 \pi^2 a \tag{11}$$

And because

$$\frac{1}{R} = \frac{(k_1 + k_2)}{4a} q_0 \pi^2 \tag{12}$$

$$\therefore a = \frac{(k_1 + k_2)}{4} q_0 \pi^2 R \tag{13}$$

By adopting the Hertzian pressure distribution assumption (see *Appendix II*),

$$q_0 = \frac{3P}{2\pi a^2} \tag{14}$$

which relates the maximum pressure, q_0, to the loading force, P. We thus find

$$a^3 = \frac{3}{8}\pi(k_1 + k_2)PR \tag{15}$$

by substituting eq 14 into eq 13.

Extension to the Viscoelastic Case—Solutions to the contact problem must accommodate mixed boundary conditions, assigned depending on whether the point in question lies inside or outside of the contacting region. Within the contacting area, the sum of the surface displacements of the two bodies must satisfy constraints to ensure perfect contact, whereas the surface traction must vanish outside of the contact area.

At first reckoning it may appear that Laplace transforms could be useful in addressing the viscoelastic or time-dependent contact case by removing the time variable in the governing equations and boundary conditions. Hence, the problem may be reduced to a corresponding elastic problem with the Laplace transform variable as a parameter. The desired viscoelastic solution would then be an inversion of the solution to the corresponding elastic case.

Viscoelastic contact regions, however, vary with time. Some points initially outside of the region of contact may fall later into the contacting region as the result of the growing indentation area. For these points, neither the traction nor the displacement may be prescribed completely throughout the development of the problem; the transform method may not be used directly to supply a solution to the problem.

Notwithstanding, it has been shown through inductive reasoning that the contact problem in elasticity may be generalized to include the contact of viscoelastic bodies with a restriction that the indentation must be monotonically increasing. Lee and Radok[13] treated a range of problems that fall outside the scope of the transform method by taking a family of solutions of the elastic problem with the parameter time, with the same boundary conditions as the viscoelastic problem, and replacing the elastic constants with the appropriate viscoelastic operators in the expression for stress components. The results comprise tractable mathematical equations for evaluating the stress components for the viscoelastic body.

In the elastic case of mutual indenting spheres, as shown in eqs 11–15, the normal contact pressure $p(r,t)$ of the assumed elastic half space is the relation[14,15]

$$p(r,t) \propto \frac{4}{\pi R}\frac{G}{1 - \upsilon}\sqrt{a^2(t) - r^2} \tag{16}$$

where G is the shear modulus, υ is the Poisson's ratio, and $a(t)$ is the contact area radius. Time appears only as a parameter prescribing the current radius of contact in this quasistatic approach. The elastic constants do not contain time explicitly and so when they are replaced by general linear operators, the solution at any time t depends solely on the instantaneous value of the boundary condition and not on the history of the process.

The viscoelastic counterpart of this Hertzian problem in elasticity as deduced from the elastic solution is then

$$P[p(r,t)] = \frac{4}{\pi R} Q[f(r,t)] \tag{17}$$

where $f(r,t) = \sqrt{a^2(t) - r^2}$, P, and Q are linear operators in the time variable.

The problem is now defined by a normal surface traction $p(r,t)$ and a zero shear traction and is amenable to analysis by the Laplace transform procedure. The transformed

surface pressure

$$\bar{p}(r,s) = \frac{4}{\pi R}\frac{\bar{Q}}{\bar{P}}\bar{f}(r,s) \tag{18}$$

is then related to $\bar{Q}$, $\bar{P}$, the transformed form of the operators. If integral operators are used, the convolution theorem then determines the transformed form.

This procedural manipulation of the operators is valid as long as the contact area does not decrease. In any physically reasonable contact problem of this type, to satisfy the restriction of the Hertz theory, the region of contact will be limited to a finite area. The transformed pressure given by eq 18 is thus nonzero only inside this maximum region of the contact. If the radius of contact increases to a maximum and then decreases to zero, then the normal deflection of the entire surface would reduce to zero, contradicting the reality of viscoelastic material behavior. Delayed elastic and viscous components of strain would be expected to leave a residual indentation after contact has ceased.

The reason for this paradoxical result is that if $a(t)$ passes through a maximum and decreases, then the corresponding $p(r,t)$ usually passes through zero and takes on negative or tensile values. When $a(t)$ then decreases, a residual tensile surface traction is left at the points formerly in the contact region, which violates the contact condition that outside the current region of contact the surface traction should be zero. This dilemma does not arise with nondecreasing $a(t)$ because the zero initial condition for all earlier times guarantee zero traction outside the region of contact.

What follows is a derivation of the formula for the extension of the contact problem to linear viscoelastic spheres. To reduce the complexity of the problem, a number of assumptions were adopted. It was assumed that both bodies in contact were isotropic, homogeneous, and linearly viscoelastic. The material properties were characterized by creep or relaxation functions. Moreover, the surfaces were considered smooth to neglect the effect of friction. Small strains were assumed, as evidenced in the preceding derivations where the area of contact is small in comparison with the dimensions of the contacting bodies. The indentation area should furthermore increase monotonically with time. And finally, shear and dynamic and intermolecular force effects were neglected.

Rheological Model for Viscoelastic Case—The behavior of viscoelastic materials under uniaxial loading may be represented by means of conceptual models composed of elastic and viscous elements. Such rheological forms are useful as analogues for stress and strain. The basic elements of springs and dashpots also assists in the conceptualization of the material behavior.

An ideal helicoidal spring element would be perfectly linear and massless, representing Hooke's Law:

$$\sigma(t) = E\epsilon(t) \tag{19}$$

where E is the modulus of elasticity with dimension (force/length^2). The spring has a creep function $H(t - \tau)/E$ and a relaxation function $EH(t - \tau)$. The dashpot as an ideal viscous element extends at a rate proportional to the force applied, according to Newton's Law:

$$\dot{\epsilon}(t) = \frac{\sigma(t)}{\eta} \tag{20}$$

where $\dot{\epsilon} = \partial\epsilon/\partial t$ is the rate of strain and η is the viscosity coefficient with dimension (force × time × length^{-2}).

Different combinations of springs and dashpots afford flexibility in portraying different responses. Whereas simple

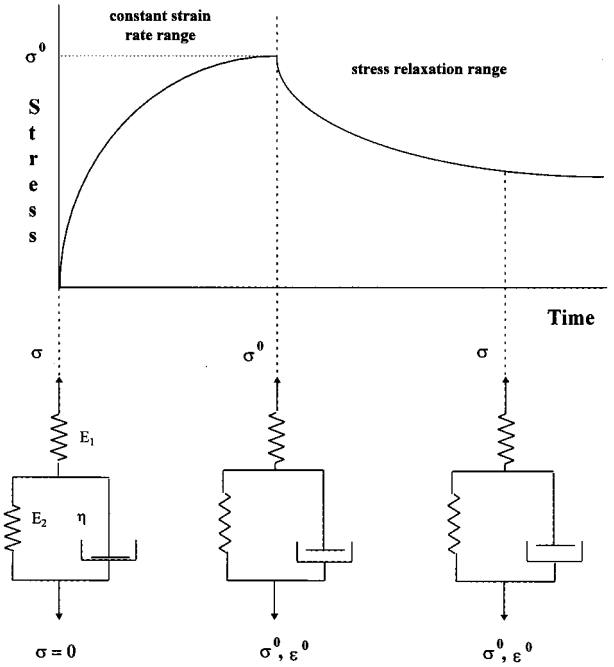

Figure 4—Illustration of the stress–time relation in association with a standard three-parameter rheological model.

models are inadequate representations of real viscoelastic behavior, a three-parameter, standard model consisting of two springs and a dashpot has successfully portrayed real material behavior.[17,18] A standard model was thus employed in the extension of the description of particle contact to the viscoelastic case.

In operational form, this standard model (Figure 4) appears as

$$E_1\eta\dot{\epsilon} + E_1E_2\epsilon = \sigma(E_1 + E_2) + \eta\dot{\sigma} \tag{21}$$

By integrating over a strain history $\epsilon(t)$

$$\therefore \sigma(t) = \epsilon(t)\frac{E_1E_2}{E_1 + E_2} + \frac{E_1^2}{E_1 + E_2}\int_0^t e^{-\frac{(t-\tau)(E_1+E_2)}{\eta}}\dot{\epsilon}(\tau)d\tau \tag{22}$$

Wherein the creep function is

$$\phi(t) = \frac{1}{E_1} + \frac{1}{E_2}(1 - e^{-\frac{tE_2}{\eta}}) \tag{23}$$

and the relaxation function is

$$\Psi(t) = E_1e^{-\frac{t(E_1+E_2)}{\eta}} + \frac{E_1E_2}{E_1 + E_2}(1 - e^{-\frac{t(E_1+E_2)}{\eta}}) \tag{24}$$

Linear Viscoelasticity—Many materials, notably polymers, exhibit time-dependent behavior in their relationships between stress and strain. The common features of a three-parameter or standard solid viscoelastic behavior includes an initial elastic response to an applied or eliminated stress, a delayed elastic response, and a permanent strain that is acquired through the action of creep.

Linear viscoelastic relationships are valid for small strains and assume the principle of superposition holds:[16] a stress history of

$$\sigma(\tau) = \sigma_1(\tau) + \sigma_2(\tau) \qquad \tau \ni (\tau_0,t) \tag{25}$$

corresponds to a strain history of

$$\epsilon(\tau) = \epsilon_1(\tau) + \epsilon_2(\tau) \quad (26)$$

Materials often exhibit linear behavior at low stresses and nonlinear viscoelastic behavior at high stresses.

The stress–strain relations for a linear viscoelastic material are commonly expressed as a relaxation function, $\Psi(t)$. This function, as already deduced from a standard spring-dashpot model, expresses the stress response to a step change in strain.

Viscoelastic Case Analysis—As the preceding contention shows, the interfacial description of two linearly viscoelastic spheres in normal contact may be described mathematically by replacing the elastic constant of the elastic solution by the integral operator from the viscoelastic stress–strain relations. For simplicity, the case of an isotropic, homogeneous, incompressible, and linearly viscoelastic material in the absence of shear is considered. These stipulations facilitate the analytical solution for the case of indentation of smooth viscoelastic spheres; the three-dimensional constitutive equations can be simplified to allow for the application of one pair of viscoelastic operators, p and q, as described by the stress–strain differential equation (see *Appendix III*):[19]

$$\left(\sum_0^m p_k \frac{\mathrm{d}^k}{\mathrm{d}t^k}\right)\sigma = \left(\sum_0^n q_k \frac{\mathrm{d}^k}{\mathrm{d}t^k}\right)\epsilon \quad (27)$$

The condition of very small strains permits the use of linear viscoelastic theory, although it is not a necessary restriction in the treatment detailed by Lee and Radok.[13] The elastic constants can be replaced by viscoelastic terms in the method of analysis for contact of smooth bodies of arbitrary linear viscoelastic materials, just as the Hertz solution applies for arbitrary smooth elastic bodies.[13] The form of the viscoelastic operator can be expressed in terms of the creep compliance or relaxation function found in eqs 23 or 24.

Thus, the contact between spherical particles may be described by substituting the viscoelastic operator ($\Psi(t)$, eq 24) for the elastic constants in the elastic solution found in eq 15. We then have

$$a^3(t) = \frac{3}{8}\pi R \int_0^t \left\{\frac{1}{E_1} + \frac{1}{E_2}\left(1 - \mathrm{e}^{-\frac{(t-t')E_2}{\eta}}\right)\right\}\frac{\mathrm{d}}{\mathrm{d}t'}P(t')\mathrm{d}t' \quad (28)$$

and

$$p(r,t) = \frac{\pi R}{4}\int_0^t \left\{E_1 \mathrm{e}^{-\frac{t-t'}{\tau}} + \frac{E_1E_2}{E_1+E_2}\left(1 - \mathrm{e}^{-\frac{t-t'}{\tau}}\right)\right\} \times \frac{\mathrm{d}}{\mathrm{d}t'}(a^2(t') - r^2)^{1/2}\,\mathrm{d}t' \quad (29)$$

where

$$\tau = \frac{\eta}{E_1 + E_2} \quad (30)$$

is a descriptor of viscoelastic material behavior. These equations, therefore, delineate then an explicit relation between contact area evolution and the applied contact force; a relation that will form the basis for the superposition of such contacts in summation over the entire powder bed.

Experimental Section

Instrumentation—An Instron 4206 stress–strain analyzer, housed in a climate-controlled room (T = 26 °C, RH = 45 ± 6%), was instrumentized through the addition of a 12-bit 10 mV unipolar A/D data acquisition board (PC-LPM-16, National Instruments, Austin, TX). With an op-amp added in line, the voltage signals from up to 8 channels exiting the control console were digitized for collection on a 486-DX clone. The commercial software provided with the board was modified to facilitate signal collection; the testing force was monitored at 250 points per second and averaged over 25 points to reduce spurious fluctuations associated with noise.

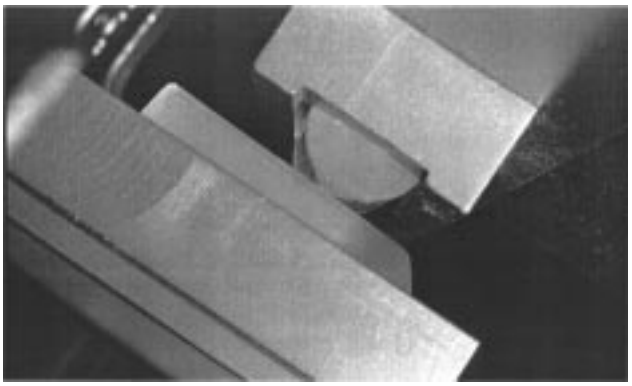

Figure 5—PMMA/coMAA cylinders displayed in crossed cylinder compaction geometry. Matrixes are mounted in stainless steel holders, which in turn are clamped to the platens within the Instron assembly.

Rods to be tested were oriented either axially or radially in stainless steel holders that were machined to fit the contour of the halved rods and that clamped directly onto the upper and lower base platens of the Instron. The test samples were held in compression and the forces experienced by the samples were measured as that transmitted by the load cell. The configuration is displayed in Figure 5.

The 5 kN, 150 kN reversible load cells, and the Instron itself were serviced and calibrated by the source company (Instron) prior to beginning experimental testing. Signal output to the board was calibrated to the force displayed on the console by verifying emitted voltages with a digital multimeter (Beckman 4.5 digit model 800). This calibration extended beyond the experimental applied forces associated with the displacement measurements and served to establish both the calibration factor and the linearity of response ($r^2 > 0.999$).

Materials—Inhibitor-free methyl methacrylate (MMA; Fischer, lot no. 911696) and methacrylic acid (MA; Aldrich, lot no. 07015EZ) were used as they were received. 2,2′-Azobisisobutyronitrile (AIBN; Analychem Corp. Ltd., Markham, Ontario, lot no. 413286) was recrystallized from isopropyl alcohol, and the HPLC grade tetrahydrofuran (THF) (Fischer, lot. no. 904140) was freshly distilled prior to use.

Specimen Synthesis—Ideal contact between two spheres is difficult to achieve experimentally, so the geometry was approximated by the contact of crossed cylinders at 90°. Poly(methyl methacrylate)/comethacrylic acid (PMMA/coMAA), an amorphous acrylic polymer similar to the commercial pharmaceutical Eudragit, was chosen as the model material for study. Although the flow and material properties of PMMA alone are well documented, the copolymer material is more commonly employed in pharmaceutical coating and encapsulation.

PMMA/coMAA cylinders were prepared by free radical bulk polymerization of a 1:1 mole ratio mixture of inhibitor-free MMA and inhibitor-free MAA using recrystallized AIBN as the initiator. The mixture was deaerated by repeated freeze thawing under an argon blanket, and the polymerization was carried out in sealed 13-mm diameter glass molds under Argon at 25°C for 4 weeks (Atmos environmental bag, Sigma Chemical Company, St. Louis, MO). During solidification, the molds were continuously agitated to minimize porosity from trapped gas bubbles (Psycrotherm Incubator shaker model R-27, ser. 8695; NewBrunswick Scientific Company Inc., New Brunswick, NJ). The resulting cylinders were purified by extracting any residual monomer, side products, or initiator by Soxhlet reflux (MeOH/water, 60/40 by volume). Rods were halved longitudinally, polished, and used together as the opposing upper and lower contact elements in compression (wire saw and diamond impregnated wire blades, 0.010" diameter, South Bay Technology, San Clements, CA; Crystal Bay crocus abrasive

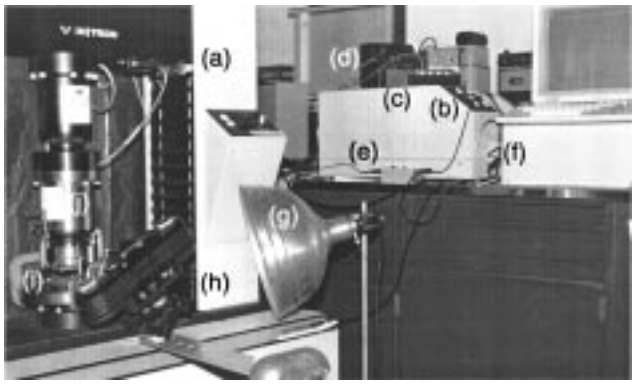

Figure 6—Instrumentation associated with compressional loading of polymer matrixes and concomitant photomicroscopy survey of contacting region: (a) Instron 4206; (b) Instron control console; (c) op-amp for signal transduction; (d) timing relay; (e) single switch or continuous relay; (f) 486DX for automated data acquisition and control, equipped with A/D board; (g) contrast illumination; (h) bulk loaded camera driven through electronic relay; (i) samples mounted within platens; and (j) reversible load cell.

cloth, 3M Canada Inc., London, Ontario, Canada). A nominal aspect ratio (length-to-diameter ratio) of at least 2:1 was chosen to avoid complications of edge effects or barreling during compression. Care was also taken that the material did not come into contact with water or any contaminant while the specimens were being prepared or during subsequent handling and testing; mainly by storage with desiccant under an argon blanket. The samples for this study were annealed at 170 °C for 2 h prior to deformation testing.

Polymer Characterization—Changes in material morphology and properties among sample matrixes were controlled by annealing and monitored by microhardness and acoustic testing as described elsewhere.[20] The mean diameters of five indentations per sample were used to calculate the Knoop hardness values and the corresponding elastic moduli, which averaged 11.3 ± 3.9 MPa and 5.67 ± 0.2 GPa, respectively, at 25 °C. The copolymer was further characterized by a variety of means as reported previously: [21] solid density measurements at various temperatures by stereopycnometer yielded $\rho = 1.20$ g/mL at 20 °C (SE = ±0.001 g/mL), differential scanning calorimetry scans showed a $T_g \sim 175$ °C and no evidence of crystallinity, copolymer composition was checked by Fourier transform infrared (FTIR) spectroscopy, and the viscosity average and weight average molecular weight were determined, respectively, by capillary viscometry and low angle laser light scattering, $M_w \sim 5 \times 10^5$.

Contact Deformation—Compaction between two cylinders was performed on the instrumentized Instron already described at four rates ranging from 1 to 10 mm/min and at four loads ranging from 3.0 to 4.5 kN. Stress relaxation was also monitored for 20 min after the peak load was achieved. At least three runs were performed at each load level and nominal strain rate. The contacting surface radius was determined concomitantly by optical means.

Growth of the contact area, produced by the forces applied to the mutually indenting rods, was measured photomicroscopically with an automated camera system equipped with a custom 10-mm microlens. The camera was mounted on a tripod parallel to the interface of the contacting matrixes, loaded with bulk film, and driven frame by frame by synchronized relay (Nikon F-250, Nippon Kogaku, Japan; TMAX 100 black and white film, Kodak, Canada; Nikon film winder cassette; Intervalomeer HN−I with single or continuous relay and motor driver, HN1 Anglophoto Ltd, Montreal). The timing of the relay and subsequent shutter interval was checked by stopwatch and matched to the timing of the force-data acquisition. High contrast photos were taken of the contact zone at 90° to the axis of compression at 1 s intervals, processed, magnified, and measured (Mitotuyo 500−133 vernier calipers). The instrumentation is depicted in Figure 6 for purposes of visualization. The data from these measurements were analyzed according to methods described next.

Data Analysis—*Force−Time Signal*—Below 0.6 kN on all preliminary and subsequent curves, a distortion was evident in the applied force that produced a replicate kink in the force−time plot across all applied loads and nominal strains. This artifact was attributable to the operational system of the Instron employed. Although hydraulically loaded systems provide an instantaneous force to the testing area, screw-loaded systems must overcome the give or stiffness of the machine before actual loading occurs. The screw-loaded Instron 4206 was employed because of its availability.

The force−time signals relayed to file were smoothed at <0.6 kN. The 0.6 kN value itself corresponds roughly to the 7.5% limit of sensitivity specification for the 5 kN reversible load cell employed for the majority of the experimental runs. Fortran subroutines were written to handle the data sets. The collected force signals were converted by the calibration already noted fitted to a power form by nonlinear regression following a Marquardt algorithm, and back extrapolated at 0.6 kN to the proper abscissa point to offset the time-lag associated with the screw loading.

In the nonlinear least-squares fitting, a chi squared merit function was defined and a best-fit parameter determined by its minimization. The iterative minimization proceeded from trial values input for the parameter following a Marquardt subroutine method (template[22]), which varies smoothly between the extremes of the inverse-Hessian method and the method of steepest descent. Several initial values were iterated through to safeguard against convergence onto a local rather than a global minimum. For each of the 4 × 4 matrix experiments repeated in triplicate, the best fit was assessed by minimization of the sum of squares, comparison of the multiple correlation coefficient, and examination of the residuals and the standard error associated with the estimate of the coefficient to the power form.

The resultant equations for the 4 × 4 design, of the form force $P(\text{time}) = \text{coefficient}*(\text{time-lag time})^{\text{power}}$ were amassed and assessed for correlations with the prescribed load levels and nominal strain rates. Multiple linear regression was applied in both forward and backward substitution forms for various combinations and permutations of the load level and crosshead rates. The best aggregate description was determined on the basis of assessment of the adjusted R, the standard error of the estimate, and the mean square residuals.

Radial Growth Data—The measured contact radii were normalized by the initial apparent contact radius that occurs as a result of the weight of the upper rod resting on the lower. Although the timing relay between photos was calibrated by stopwatch, minor variations accruing from the finite shutter speed time necessitated checking the timing intervals between radii measurements. This calculation was accomplished given the peak force time signal and the number of frames advanced. Accounting also for measurement magnification, and the lag-time associated with screw loading, the radii data provided normalized radius growth with time curves in triplicate for the 4 × 4 design (for various nominal strain rates and ultimate loading levels).

Calculation of Material Viscoelastic Parameters—Relaxation or creep compliance functions are traditionally measured by creep tests, in which constant strain rates or stresses are applied to achieve constant stresses or strain rates, respectively, at various elevated temperatures. These measurements require long loading times to reach steady state, which may change either the geometry of the specimen or the microstructure and hence the stress−strain relation. Changes such as these are especially important in porous powder materials which tend to densify during indentation creep testing.

Following the method of Hsueh,[23,24] the viscosity and the two elastic moduli of a three-parameter model constructed to represent a viscoelastic material were determined from the experimental stress−time curve generated from short-term loading at a constant strain rate ($\dot{\epsilon}_0$) followed by a period of stress relaxation. By decomposing the stress−time curve into the applied periods of strain, then for $\dot{\epsilon} = \dot{\epsilon}_0$,

$$\sigma(t) = \left(\frac{E_1}{E_1 + E_2}\right)^2 \eta\epsilon_0[1 - \exp^{-\frac{(E_1 + E_2)}{\eta}t}] + \frac{E_1E_2}{E_1 + E_2}\dot{\epsilon}_0 t \qquad (31)$$

During the stress relaxation phase, $\dot{\epsilon} = 0$ and

$$\sigma(t) = \sigma_\infty + (\sigma_f - \sigma_\infty) \exp^{-(t - t_i)\frac{(E_1 + E_2)}{\eta}} \qquad (32)$$

where

$$\sigma_\infty = \frac{E_1 E_2}{E_1 + E_2}\dot{\epsilon}_0 t_f$$

$$\therefore \sigma(t) = A[1 - \exp^{-\frac{t}{\tau}}] + \sigma_\infty \frac{t}{t_f} \quad (33)$$

for $t > t_f$, where $\tau = \eta/(E_1 + E_2)$, and $A = (E_1/E_1 + E_2)^2 \eta \dot{\epsilon}_0$.

Examination of the stress–time curve provides estimates for t_f, the time at which stress relaxation begins, σ_∞, the limiting stress, and, by plotting ln $(\sigma - \sigma_\infty)$ vs $(t - t_f)$, an estimate for τ. The subsequent application of nonlinear (Marquardt) regression to the stress data, following the form of eq 33, yields a value for A. Simple algebraic manipulation of A, τ, and σ_∞ therefore returns:[24]

$$E_1 = \frac{1}{\tau \dot{\epsilon}_0}\left(A + \frac{\sigma_\infty \tau}{t_f}\right) \quad (34)$$

$$E_2 = \frac{\sigma_\infty}{\dot{\epsilon}_0 t_f}\left(1 + \frac{\sigma_\infty \tau}{A t_f}\right) \quad (35)$$

and

$$\eta = \frac{1}{\epsilon_0}\left(A + \frac{2\sigma_\infty \tau}{t_f} + \frac{\sigma_\infty^2 \tau^2}{A t_f^2}\right) \quad (36)$$

as estimates for substitution into the equational definition (eq 24) for the relaxation function.

Solution of Viscoelastic Case Equations—The premise of this study was to mathematically describe the link between applied load and the evolution of particle–particle contact area between spherical bodies during densification. In this way, the material response may be incorporated in the mathematical description. The experimental data described in the preceding sections measured specific contact area growth resulting from specified applied loads, which then serve as input boundaries for the mathematical relation described in the set of eqs 27–30.

Decomposition of the stress–time curves into applied periods of strain allowed for the estimation of the variables comprising the relaxation modulus operator ($\Psi(t)$, eq 24). The radius of the contacting area (eq 28) was then to be solved for a prescribed loading force–time with substitution of this viscoelastic operator $\Psi(t)$. Application of integration by parts (see *Appendix IV*) provided a simplified form of the equation

$$a^3(t) = \frac{3}{8}\pi R\left\{\frac{P(t)}{E_1} - \left(\frac{1}{E_1} + \frac{1}{E_2} - \frac{1}{E_2}e^{-\frac{tE_2}{\eta}}\right)P_0\right\} + \int_0^t \frac{P(t')}{\eta} e^{-\frac{(t-t')E_2}{\eta}} dt' \quad (37)$$

which was then processed using the numerical quadrature algorithm of a commercial high-performance numeric computation and visualization software program (MATLAB, The MathWorks, Inc., Natrick, MA). The initial processing was performed with a Fortran numerical quadrature subroutine,[22] which was cumbersome compared with the speed with which the commercial form using a recursive adaptive Newton-Cotes 8 panel rule was able to ameliorate the calculations.

A best-fit polynomial form for the contact area–time description was then returned as input into the equation form describing the pressure distribution within the sphere. Equations 29–30 were likewise simplified to

$$p(r,t) = \frac{8}{\pi R}\left\{(a^2(t) - r^2)^{1/2}E_1 - (a_0^2 - r^2)^{1/2}\frac{(E_1^2 e^{-\frac{t}{\tau}} + E_1 E_2)}{E_1 + E_2} - \int_0^t (a^2(t') - r^2)^{1/2} \cdot \frac{E_1^2}{(E_1 + E_2)\tau} e^{-\frac{(t-t')}{\tau}} dt'\right\} \quad (38)$$

where $\tau = \eta/(E_1 + E_2)$, and processed in MATLAB.

Results and Discussion

The primary motivation for studying the particle level contact was the need to ascertain a time-dependent material function for subsequent modeling analysis. With the focus of this study centered on the interaction zone between two particles under mutual deformation, the loading force under which our experimental matrixes were subjected and the resultant experimental area growths were monitored. The applied loading force curves are depicted in Figures 7 and 8 inclusive. Each displayed curve represents the average of several large experimental datasets; the experimental standard deviation for selected points along a curve are shown in Figure 9 for clarity. In accordance with the geometry of the load application, the applied force experienced within the contact zone matches that which was applied externally through the Instron apparatus. The effect of the applied nominal strain rates is clearly shown in the force versus time series of Figure 7. As expected, the time to achieve a defined maximum load was inversely proportional to the crosshead speed, and, within experimental error, the ratio of such times mirrored the ratios of the respective strains (1:2:5:10) applied.

Force–time curves were replotted in Figure 8 for each nominally applied strain rate. Within experimental error, then, the maximum load level itself may be inferred as a function of the time under which the cylinders are compressed and hence not wholly independent of the applied rate of strain. The fitted coefficients for the power form of the force–time curves are summarized in Table 1. From multiple regression analyses, the prescribed loading force–time, $P(t)$, rate dependence may be embodied in the equational form

$$P(t) = (2.859 \times 10^{-2}\dot{\epsilon} + 3.233 \times 10^{-3}\dot{\epsilon}^2)(t - \text{lagtime})^{1.1} \quad (39)$$

where $\dot{\epsilon}$ is the applied strain rate. The value $R^2_{adj} = 98.34$, SE = 0.0424, mean absolute error equals 0.0246, and the mean square residual is 1.802×10^{-3}.

Radial contact growth curves derived from triplicate runs are displayed with error bars representing the replicate variability in Figures 10a–d inclusive. The effect of the applied nominal strain rates is clearly revealed in the sequence of plots where the strain rate differs in achieving a standard maximum load. This rate dependence is analogous to that which was manifest in the force–time series; that is, the time required to attain a specified dilation was inversely proportional to the applied crosshead speed and, within experimental error, the ratio of these times were roughly 1:2:5:10.

By replotting the radial growth curves in Figures 11a–d for each nominally applied strain rate, the effect of the maximum load level achieved is evidently once again a function of the time spent under compression. Each curve series held at a constant strain rate resembles a collinear plot within experimental error. The errors associated with higher strain rates are larger in relation to the points shown at lower strains because there is a finite time required to measure, process, and handle the photographs capturing the changing radial area.

The experimental radial growth data curves were subjected to simple regression fitting (minimization of least squares), and the coefficients of the normalized radial growth, $a(t)$, fitted to the square root of time are tabulated in Table 2.

The solution of the constitutive differential equation describing the behavior during a stress relaxation experiment to yield the relaxation function parameters is not an easy task. For simple models comprised of one to three

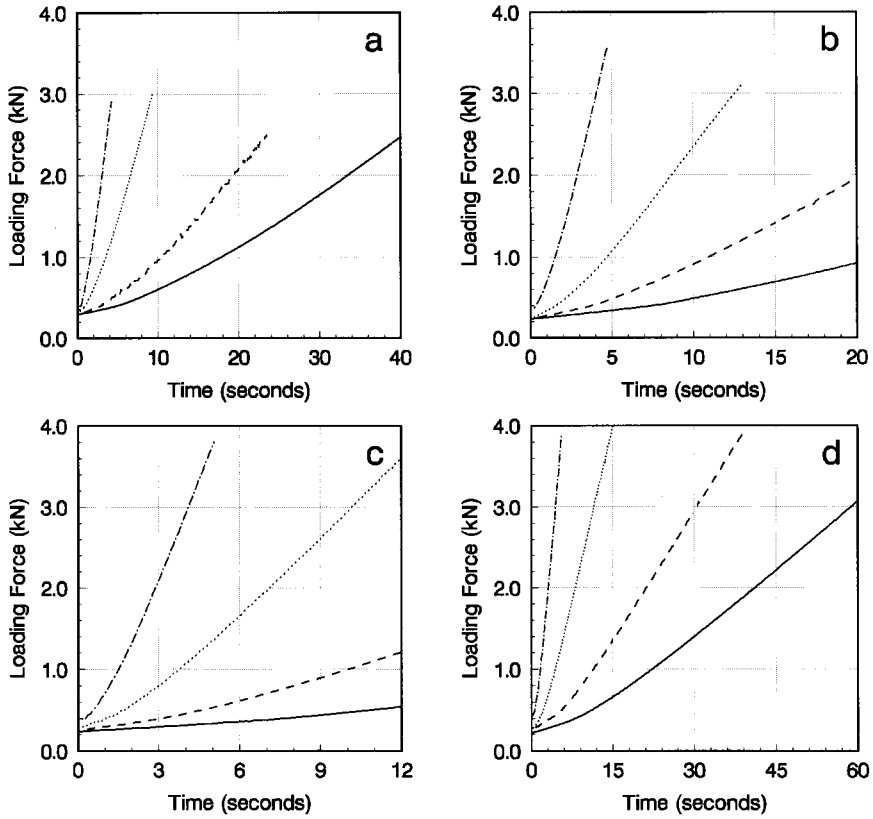

Figure 7—Applied load–time curves for various strain rates imposed on the mutually indenting matrixes: to a maximum load level of (a) 3.0 kN; (b) 3.5 kN; (c) 4.0 kN; and (d) 4.5 kN. Key: (—) 1 mm/min; (– – –) 2 mm/min; (•••) 5 mm/min; (- - -) 10 mm/min.

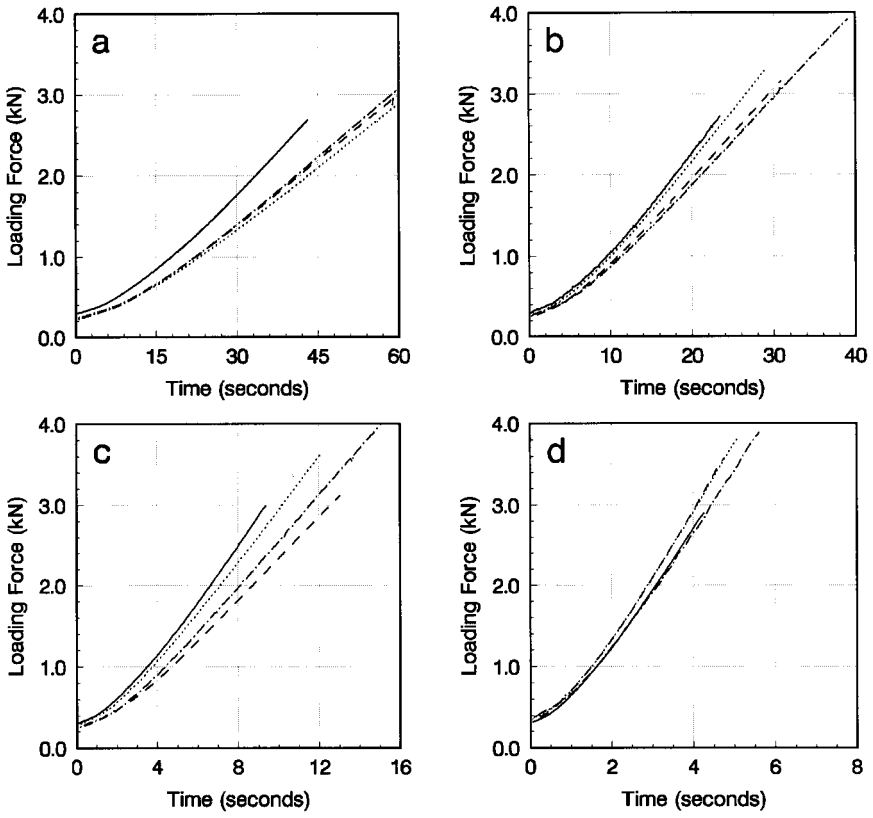

Figure 8—Applied load–time curves at specified strain rates and various loading levels for the cylinders in crossed compaction: loading at (a) 1 mm/min; (b) 2 mm/min; (c) 5 mm/min; and (d) 10 mm/min. Key: (—) 3.0 kN; (– – –) 3.5 kN; (•••) 4.0 kN; (- - -) 4.5 kN.

elements, the relaxation function may be formulated using hybrid parameters, which also allows a valid conversion to the creep compliance at the same point and at the same time.[25] In more complex models, the relaxation force equalizes differently in time and direction using parts of the springs, dashpots, and Kelvin elements differentially

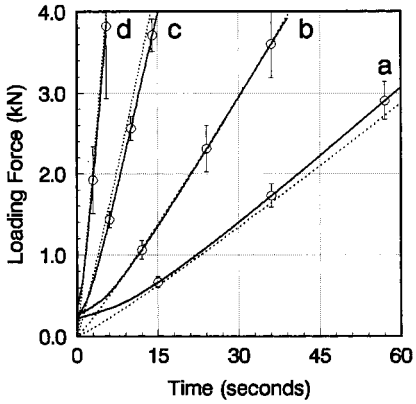

Figure 9—Loading force–time plots of the results obtained from use of the applied strain rates (a) 1 mm/min, (b) 2 mm/min, (c) 5 mm/min, and (d) 10 mm/min, to a maximum of 4.5 kN. Displayed in dotted form are the resultant curves predicted for the prescribed loading at these various strain rates. Selected experimental datapoints depicting the standard deviations between triplicate runs are highlighted.

Table 1—Force–Time Loading Phase of PMMA/CoMAA Matrices[a]

strain rate (mm/min)	maximum load (kN)	average coefficient of fit ($\times 10^{-2}$)	average lag time (s)
1	3.0	4.239 ± 0.57	34.17 ± 3.22
1	3.5	3.431 ± 0.14	19.74 ± 0.10
1	4.0	3.288 ± 0.62	21.12 ± 0.76
1	4.5	3.370 ± 0.35	19.49 ± 1.38
2	3.0	8.382 ± 0.81	13.72 ± 5.16
2	3.5	7.250 ± 0.77	11.00 ± 0.47
2	4.0	8.047 ± 1.71	13.28 ± 4.43
2	4.5	6.966 ± 1.02	9.990 ± 1.35
5	3.0	25.28 ± 0.58	7.040 ± 0.19
5	3.5	18.49 ± 3.37	4.300 ± 0.47
5	4.0	23.36 ± 2.97	4.000 ± 0.34
5	4.5	20.13 ± 1.44	4.460 ± 1.17
10	3.0	58.69 ± 4.32	3.410 ± 0.21
10	3.5	62.33 ± 2.23	2.820 ± 0.93
10	4.0	59.68 ± 4.72	2.330 ± 1.17
10	4.5	58.20 ± 15.95	2.520 ± 1.01

[a] $P(t)$ = coefficient*(t – lag time)$^{1.1}$. Average fitted coefficients reported are calculated from triplicate runs in each case. Standard deviations reported reflect the matrix-matrix variability.

until a forceless condition arises. Consequently, in the time-dependent domain, no simple relation between the creep compliance and the relaxation function may be found.[25]

Extraction of the relaxation function parameters, based on a standard three-element model from compaction load-time experiments, was preferred over the use of traditional measured creep tests over long times and elevated temperatures. As previously inferred, such tests would necessitate recasting specimen geometry or induce unwonted alterations in the material microstructure. A method used in material science to evaluate the viscosity and the two elastic modules of a three-parameter model during a combined experiment consisting of deformation with a constant strain rate followed by stress relaxation was adopted as a suitable means of evaluation of the PMMA/coMAA $\Psi(t)$ parameters. The crossed cylinder compactions performed consisted of the prerequisite deformation, load-time monitoring under a set crosshead speed, and relaxation monitoring under constant strain. The assumption of the equivalence of a constant crosshead speed with a constant nominal strain rate is a best first approximation. This method is consistent with an engineering definition of strain[26] ($\epsilon = \Delta l/l_0$, where Δl is the change in distance, l is the postfacto length, and l_0 is the original specimen length) rather than that of true strain [$\epsilon_t = \int dl/l_0 = \ln(l/l_0)$].

Table 2—Normalized Radial Growth with Time during Loading Phase of PMMA/CoMAA Matrices[a]

strain rate (mm/min)	maximum load (kN)	intercept of fit ($\times 10^{-2}$)	coefficient of fit ($\times 10^{-1}$)
1	3.0	–0.198 ± 2.0	1.201 ± 0.04
1	3.5	–8.500 ± 3.0	1.349 ± 0.05
1	4.0	–2.723 ± 1.5	1.256 ± 0.02
1	4.5	–14.47 ± 2.2	1.416 ± 0.03
2	3.0	–8.836 ± 3.9	1.845 ± 0.11
2	3.5	–11.54 ± 2.8	1.884 ± 0.07
2	4.0	–16.50 ± 3.6	1.955 ± 0.09
2	4.5	–11.55 ± 2.6	1.862 ± 0.05
5	3.0	–18.68 ± 7.2	3.679 ± 0.29
5	3.5	–6.614 ± 2.0	3.163 ± 0.09
5	4.0	–18.06 ± 3.1	3.528 ± 0.13
5	4.5	–5.969 ± 4.4	3.255 ± 0.16
10	3.0	–2.216 ± 7.0	5.171 ± 0.33
10	3.5	–4.783 ± 5.4	6.477 ± 0.25
10	4.0	–3.845 *	5.682 *
10	4.5	–2.135 *	5.312 *

[a] $a(t)$ = intercept + coefficient × $\sqrt{t}$. Average fitted coefficients reported are calculated from triplicate runs in each case. Standard errors reported reflect the matrix–matrix variability.

Others[25] have used solely numerical means for decomposing tabletting load–time curves. In both convolution and deconvolution processes of estimating viscoelastic model parameters, the numerical stability of the regression methods are problematic. The limited accuracy of the numerical transactions and the uncertainty of the initial condition estimates necessitates validation with well-defined, known theoretical material data. This necessity is especially true in the case of powder-type consolidation because volume reduction itself augments viscoelastic features.[25]

Figure 12 serves to illustrate the use of the decomposition method for the determination of the three-parameter viscoelastic terms for one specific case. The procedure is visually elucidated in terms of the decomposition of the stress relaxation curve into components in the development and provides an example of the nonlinear regression analysis used to determine the estimates in the summation process.

The derived parameters required for the relaxation modulus calculation are then summarized in Tables 3 and 4 per the method already described. These parameters serve as input variables in merely defining the viscoelastic operator over a limited time frame and by no means can be used to define $\Psi(t)$ over the time spectrum in its entirety.

Evaluation of the relaxation modulus (eq 24) with the parameters derived in Table 4 is shown in Figure 13. In physical terms, the relaxation modulus represents the time-dependent analogue of the equilibrium shear modulus, which in itself is a ratio of a stress to a corresponding strain measured in an experiment with a specific time pattern. The shape and magnitude of the log–log plots are consistent with that expected for an un-cross-linked polymer network of high molecular weight:[18] at short times, $\Psi(t)$ approaches a limiting value that represents the rigidity of the chain in the absence of backbone rearrangements, and at long times, $\Psi(t)$ falls rapidly for the un-cross-linked networks and eventually vanishes. A mechanical model analogue would translate this behavior as the relaxation of all the springs in an array. Alternatively, in molecular terms, this configuration corresponds to the resumption of random average configurations by the macromolecular coils that have been divested from the constraints originally imposed on them. The external dimensions of the sample in question may remain deformed at long times during this

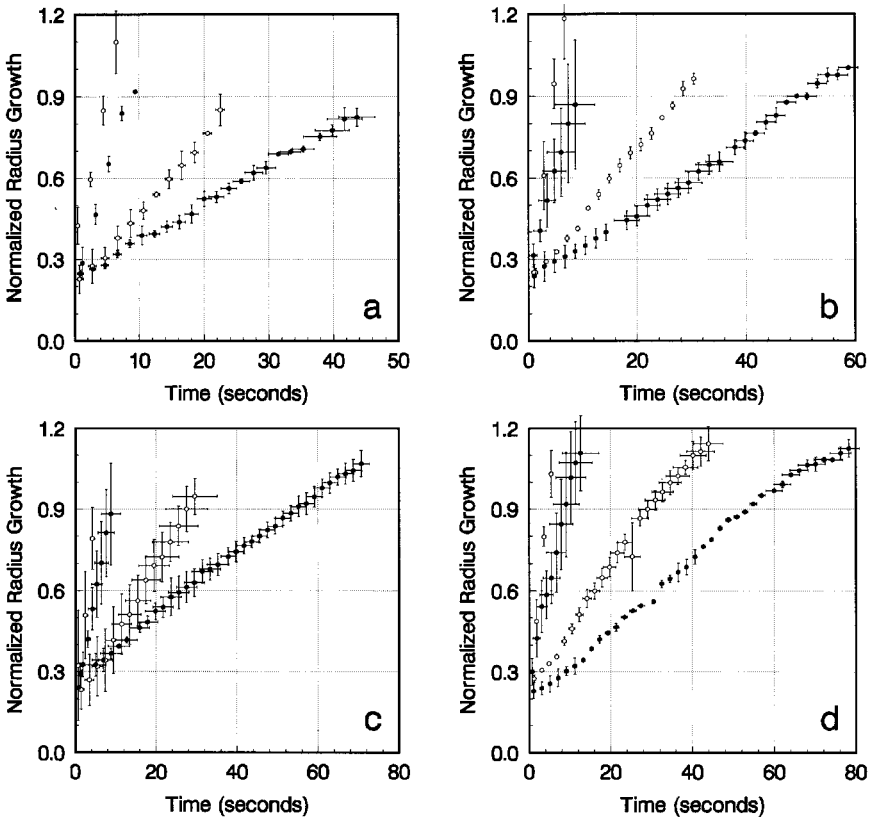

Figure 10—Averaged radial contact growth-time series for various strain rates measured concomitantly: to a maximum load level of (a) 3.0 kN; (b) 3.5 kN; (c) 4.0 kN; and (d) 4.5 kN.

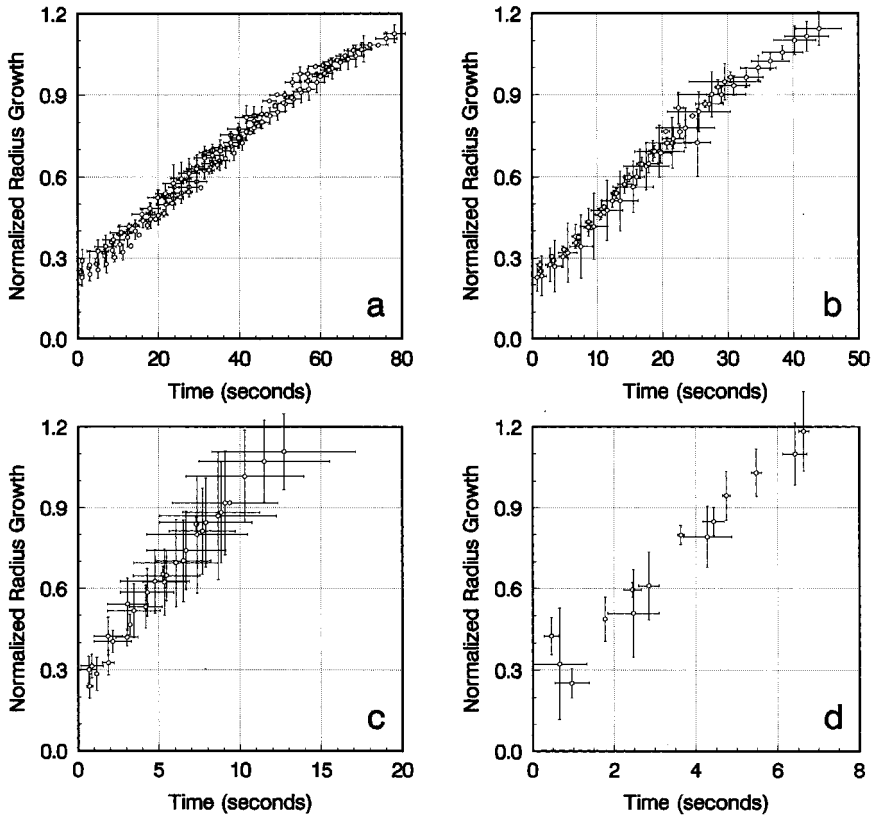

Figure 11—Radial contact growth–time series for the cylinders in crossed compaction at specified strain rates: loading at (a) 1 mm/min; (b) 2 mm/min; (c) 5 mm/min; and (d) 10 mm/min.

resumption of molecular motion; the residual deformation is the result of the flow contribution to what is essentially a creep experiment.

The magnitude of the compressionally derived modulus depicted in Figure 13 is lower than that reported for PMMA[14] achieved by tension experimentation. This dif-

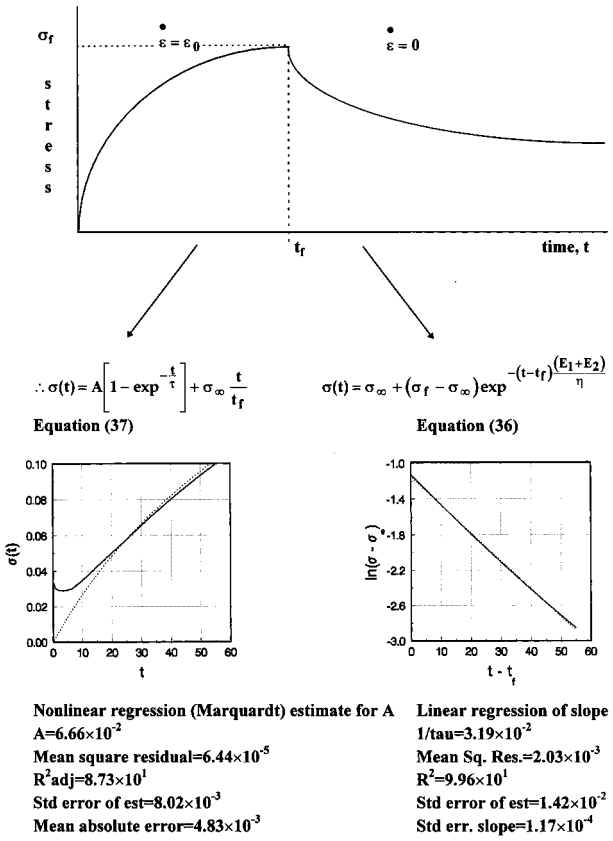

Figure 12—Schematic of the decomposition of the stress–time curve for the case of a load level of 3.0 kN achieved through loading at 1 mm/min. Evaluation of the viscosity and modulus components of a three-parameter model follows that described by Hsueh.[23]

ference is not unexpected, because of the experimental configurational differences and the differences between the two experimental time patterns. At intermediate times depicted in each curve of the figure, the stress shown gradually falls as the distortion of the chain backbones compensates through Brownian motion; segments would adjust first with respect to other closely neighboring segments and then with respect to those farther removed. The modulus falls off sharply thereafter in the region time scale of the terminal zone.

The time dependent operator $\Psi(t)$ displays the effects of the applied strain rates 1, 2, 5, and 10 mm/min shown through the superposition of curves a−d. The trend is in accord with the anticipated rate effect, that is, the inflection time marking the terminal zone is abbreviated with higher strain rates, while the inflection times are elongated with lower strains.

The parameters tabulated in Table 4 served as input for the calculation of the relaxational modulus and thereby the predicted radial contact growth for a prescribed load−time application. Numerical quadrature of the transformed eq 37 predicts a resultant contact growth that has been superimposed on the experimental dataset in Figure 14. The predicted curves are further tabulated using simple least squares regression in Table 5. Although the predicted curve lies within the range of experimental error, deviation from the measured growth may be due to error in the steps taken for the approximation of the specific relaxational modulus form. Indeed, assessing the fit of the predicted curves to this experimental set would not be a valid means of evaluating the utility of the model form as a predictive tool. An independent particle densification series based on stepped load, which was not itself used in the evaluation of the stress relaxation curves from which the relaxation operator was interpolated, would be required; such an assessment will form the basis for subsequent study.

In assessing the viscoelastic operator parameters derived in Table 4, it is clear that the value of the arbitrary maximum load level at which replicate runs were held is a complex function of the time under which loading occurs in a fashion similar to that deduced for load−time and radial growth−time curves. The nominal strain rate under which the matrixes were subjected serves as a better independent measure of the time-dependent behavior of each of the modulus parameters that comprise the $\Psi(t)$ operator. Multiple regression analysis of these tabulated parameters offers a best fit for E_1, E_2, and η when stratifying for specific load levels achieved. For the 4.5 kN levels, as an example,

$$E_1 = 1.70 \times 10^{-3} + 1.60 \times 10^{-3}\dot{\epsilon} - 4.47 \times 10^{-4}\dot{\epsilon}^2 + 3.62 \times 10^{-4}\dot{\epsilon}^3 - 5.58 \times 10^{-7}\dot{\epsilon}^4$$

$$E_2 = 5.21 \times 10^{-4} + 4.28 \times 10^{-5}\dot{\epsilon} - 5.69 \times 10^{-5}\dot{\epsilon}^2 + 6.96 \times 10^{-6}\dot{\epsilon}^3 - 1.15 \times 10^{-7}\dot{\epsilon}^4$$

$$\eta = 5.30 \times 10^{-1} - 1.71 \times 10^{-1}\dot{\epsilon} + 3.67 \times 10^{-2}\dot{\epsilon}^2 - 2.91 \times 10^{-3}\dot{\epsilon}^3 + 4.47 \times 10^{-5}\dot{\epsilon}^4$$

represents a parametrization set that may be used for interpolative prediction within the experimental boundaries delineated in the origin of the dataset. The values of E_1, E_2, and η represent theoretical estimates of the stiffness and flowability of the viscoelastic material. Together, these values form a mathematical construct of the viscoelastic behavior of the material that allows for prediction of the material behavior under different testing conditions. In a viscoelastic body, all of the stresses, strains, and displacements occurring are time dependent, whereas in an elastic solid under constant load, these parameters are independent of time. The values of these spring moduli and dashpot viscosity may provide an estimate of elastic parameters that represent the limiting case of a viscoelastic material. This theory is elucidated in *Appendix V*. Obviously, caution must be exercised in attempting to extrapolate beyond the strain rates prescribed because the size of the dataset lends insufficient power to that function.

The pressure distribution within the two mutually indenting viscoelastic three-parameter model spheres was also found by substituting the relaxation modulus function solved from eq 24 and $a(t)$ as derived from eq 37 into eq 38 and performing the integrations. The computations were carried out for each of the cases indicated in Table 4; the results are plotted in Figures 15a and b for the case of 4.5 kN at both 1 and 10 mm/min loading. These simplified sketches display a two-dimensional projection of the matrix solution which forms a three-dimensional contour (radius, time) in the Cartesian plane. From this schematic, one may infer that immediately following load application, there is an instantaneous elastic response from which the initial contact radius arises. This contact size then grows with time as discussed in preceding sections. It is apparent that the pressure distribution is similar to the Hertz elastic form given by

$$p = p_0\left(1 - \left(\frac{r}{a}\right)^2\right)^{-1/2} \qquad (40)$$

in which the maximum pressure is in the center of the contact area. As time progresses during loading, the balance of relaxation, contact, and load growth favors an

Table 3—Calculation of Material Viscoelastic Parameters Per Method of Hsueh[23]

4 × 4 matrix element code	peak time t_f (s)	relaxation stress σ_∞ (MPa) ($\times 10^{-2}$)	tau^{-1} ($\times 10^{-2}$)	coefficient A ($\times 10^{-2}$)	E_1 ($\times 10^{-3}$)	E_2 ($\times 10^{-3}$)	η ($\times 10^{-1}$)
11a	54.87	4.670	3.186 (0.01)	6.664 (0.80)	2.974	1.192	1.308
11b	46.00	6.716	5.794 (0.02)	4.567 (0.84)	4.107	2.265	1.100
11c	43.01	7.448	7.769 (0.06)	3.998 (0.82)	4.838	2.697	0.970
12a	64.31	2.359	1.443 (0.01)	20.03 (0.97)	3.258	0.413	2.544
12b	68.09	2.683	1.545 (0.01)	17.46 (0.91)	3.092	0.452	2.293
13a	70.16	3.684	0.909 (0.002)	32.61 (1.37)	3.489	0.618	4.519
13b	105.67	2.967	1.054 (0.002)	28.96 (1.18)	3.332	0.307	3.453
13c	75.9	2.707	0.639 (0.001)	24.00 (1.34)	1.890	0.440	3.656
14a	91.44	3.291	0.804 (0.001)	27.62 (1.16)	2.580	0.418	3.731
14c	77.63	3.981	0.928 (0.001)	29.13 (1.30)	3.215	0.610	4.124
21a	25.66	8.042	11.46 (0.09)	5.224 (0.85)	4.560	2.388	0.606
21b	23.37	4.512	3.359 (0.01)	17.57 (1.10)	3.916	1.281	1.547
21c	27.61	5.568	7.219 (0.04)	7.890 (1.00)	3.856	1.365	0.723
22b	37.49	2.959	1.517 (0.006)	46.99 (1.36)	3.959	0.438	2.899
22c	34.35	2.335	1.200 (0.005)	43.81 (1.33)	2.969	0.384	2.793
22d	30.76	3.289	1.416 (0.004)	40.12 (1.33)	3.376	0.635	2.832
23a	34.74	2.614	1.293 (0.003)	38.14 (1.11)	2.842	0.434	2.534
23c	28.79	11.09	14.70 (0.20)	5.407 (0.86)	5.901	2.861	0.596
23d	45.95	1.502	0.827 (0.001)	44.68 (1.03)	2.012	0.178	2.646
24a	45.69	3.541	1.344 (0.004)	44.26 (1.47)	3.362	0.438	2.827
24b	50.92	2.161	0.843 (0.001)	58.80 (1.72)	2.690	0.230	3.465
24c	38.91	4.266	1.566 (0.002)	46.24 (1.73)	4.168	0.631	3.065
31a	9.54	5.072	18.23 (0.12)	6.809 (0.93)	3.545	1.519	0.278
31b	9.27	3.664	11.39 (0.09)	11.40 (1.00)	3.387	1.031	0.388
31c	9.27	2.247	5.632 (0.02)	22.37 (1.10)	3.005	0.578	0.636
32a	18.12	0.685	1.211 (0.002)	79.53 (1.79)	2.003	0.079	1.718
32b	13.62	0.740	1.058 (0.002)	135.3 (1.87)	2.971	0.113	2.915
32c	12.95	1.029	1.425 (0.003)	109.1 (1.85)	3.269	0.167	2.410
33a	11.92	1.102	1.660 (0.004)	90.27 (1.62)	3.182	0.196	2.035
33b	15.19	0.308	0.639 (0.002)	165.1 (1.52)	2.152	0.041	3.430
33c	12.89	1.358	2.294 (0.006)	59.04 (1.61)	2.920	0.227	1.372
34a	16.54	0.975	1.111 (0.002)	123.8 (2.03)	2.869	0.123	2.694
34b	18.82	0.788	1.021 (0.002)	113.8 (1.97)	2.408	0.087	2.443
34c	16.25	0.946	1.205 (0.002)	117.2 (2.14)	2.939	0.121	2.540
41b	4.69	2.982	13.26 (0.08)	19.96 (0.97)	3.282	0.788	0.307
41c	4.18	1.809	7.021 (0.03)	45.45 (1.11)	3.624	0.491	0.586
42a	4.75	5.175	25.50 (0.25)	10.98 (0.87)	3.888	1.514	0.212
42c	4.63	2.411	8.886 (0.03)	31.88 (1.04)	3.354	0.616	0.447
42d	4.85	2.428	12.03 (0.06)	25.19 (1.00)	3.532	0.583	0.342
43a	5.12	5.662	24.86 (0.25)	11.24 (0.92)	3.901	1.543	0.219
43c	5.69	2.797	12.78 (0.08)	25.36 (1.00)	3.733	0.566	0.336
43d	5.71	5.986	38.39 (0.33)	7.463 (0.78)	3.914	1.432	0.139
44a	8.91	2.309	7.612 (0.03)	23.30 (1.10)	2.033	0.297	0.306
44b	5.61	8.089	40.28 (0.31)	8.776 (1.14)	4.976	2.030	0.174
44c	5.51	3.954	14.84 (0.14)	23.12 (1.29)	4.148	0.868	0.338

Table 4—Calculation of Material Viscoelastic Parameters[a]

strain rate (mm/min)	maximum load (kN)	average E_1 ($\times 10^{-3}$)	average E_2 ($\times 10^{-3}$)	average η ($\times 10^{-1}$)
1	3.0	3.973 ± 0.94	2.052 ± 0.78	1.126 ± 0.17
1	3.5	3.175 ± 0.12	0.433 ± 0.03	2.418 ± 0.18
1	4.0	2.904 ± 0.88	0.455 ± 0.16	3.873 ± 0.57
1	4.5	2.897 ± 0.45	0.514 ± 0.14	3.927 ± 0.28
2	3.0	4.111 ± 0.39	1.678 ± 0.62	0.959 ± 0.51
2	3.5	3.435 ± 0.50	0.486 ± 0.13	2.841 ± 0.05
2	4.0	3.585 ± 2.05	1.158 ± 1.48	1.925 ± 1.15
2	4.5	3.407 ± 0.74	0.433 ± 0.20	3.119 ± 0.32
5	3.0	3.312 ± 0.28	1.043 ± 0.47	0.434 ± 0.18
5	3.5	2.748 ± 0.66	0.119 ± 0.04	2.348 ± 0.60
5	4.0	2.751 ± 0.54	0.155 ± 0.10	2.279 ± 1.05
5	4.5	2.739 ± 0.29	0.110 ± 0.02	2.559 ± 0.13
10	3.0	3.453 ± 0.24	0.640 ± 0.21	0.446 ± 0.20
10	3.5	3.591 ± 0.27	0.905 ± 0.53	0.333 ± 0.12
10	4.0	3.849 ± 0.10	1.180 ± 0.54	0.232 ± 0.10
10	4.5	3.719 ± 1.52	1.065 ± 0.88	0.273 ± 0.09

[a] Average fitted coefficients reported are calculated from triplicate runs in each case. Standard deviations reported reflect the matrix–matrix variability.

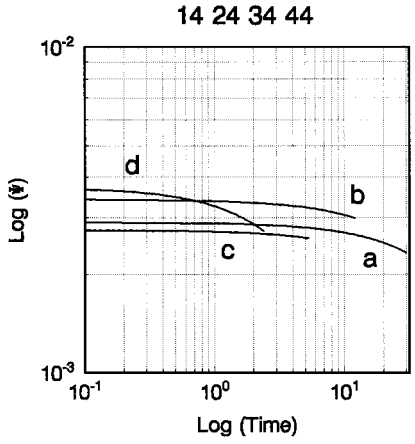

Figure 13—log–log plot of the relaxational modulus–time curves calculated for compaction at the rates of loading at (a) 1 mm/min, (b) 2 mm/min, (c) 5 mm/min, and (d) at 10 mm/min, to a maximum load of 4.5 kN.

expanding pressure distribution. Variation in the loading rate results in a marginally greater magnitude of pressure distributed in a similar fashion. The time-dependent effect, therefore, would appear to consist of the growth in the contact from its initial to its final size; the stresses at any instant in the process being distributed according to elastic theory.

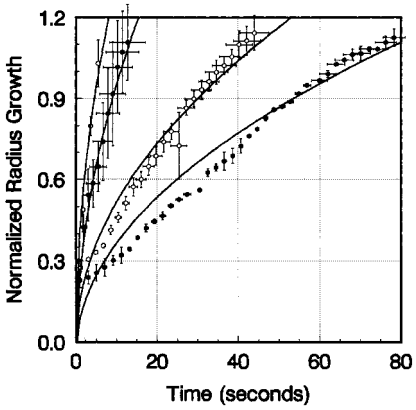

Figure 14—Predicted radial growth curves for various strain rates imposed on the compact to a loading level of 4.5 kN: loading at (a) 1 mm/min, (b) 2 mm/min, (c) 5 mm/min, and (d) 10 mm/min.

Table 5—Predicted Normalized Radial Growth with Time During Loading Phase of PMMA/coMAA Matrices[a]

strain rate (mm/min)	intercept of fit ($\times 10^{-2}$)	coefficient of fit ($\times 10^{-2}$)
1	–4.005 (0.25)	12.846 (0.06)
2	–0.741 (0.10)	16.577 (0.04)
5	–7.281 (0.30)	32.381 (0.17)
10	–0.941 (0.18)	42.564 (0.15)

[a] Average fitted coefficients and standard errors reported are calculated for a maximum loading level of 4.5 kN.

Conclusions

The present investigation was undertaken to examine the basic unit of densification: the particle–particle interaction. Emphasis was placed on the contact interface between two spheres under compression as interparticulate bonding inherently occurs whenever an area of true contact is established between two solids; the interfacial energy is always less than the surface energy of the two surfaces which form the interface. The degree of cohesion within a tablet was assumed to be largely governed by the magnitude of this true interparticle contact area created during densification.

The interfacial description of two linearly viscoelastic spheres in normal contact was described mathematically by replacing the elastic constant of the elastic solution by the integral operator from the viscoelastic stress–strain relations. An explicit relation was delineated between contact area evolution and the applied or prescribed contact force in a 4 × 4 matrix of varying strain and load level. The analysis of the extended Hertzian solution with experimentally determined input parameters yielded two-dimensional surface plots which map the evolution of these variables of local contact force, area growth, and pressure functions with time and applied strain rate at specified maximum loads. Within the context of the experimental time frame, these relations form the basis for the superposition of such contacts in summation over the entire powder bed.

By defining the contact between mutually indenting viscoelastic particles, the compact may ultimately be modeled as a collection of these particles in contact and in this way address the time-dependent response of materials to applied loads. This summation to describe a tabletting powder is the subject of the second paper in this series.

Acknowledgments

This work was abstracted in part from a dissertation submitted by S.L. to the Graduate School, University of Toronto, in partial fulfillment of the Doctor of Philosophy degree. The authors thank and acknowledge the financial assistance of MRC in the form of a grant (to W.D.H.) and a studentship (to S.L.) in supporting this study.

Appendix I

As the length of the cord $bc = 2r = 2a \cos\theta$, $r = a \cos\theta$ since $a \sin\theta = r \sin\psi$

$$a^2 \sin^2\theta = r^2 \sin^2\psi$$

$$a^2(1 - \cos^2\theta) = r^2 \sin^2\psi$$

$$a^2 - a^2 \cos^2\theta = r^2 \sin^2\psi$$

$$a^2 \cos^2\theta = a^2 - r^2 \sin^2\psi$$

$$\therefore a \cos\theta = \sqrt{a^2 - r^2 \sin^2\psi}$$

$$\therefore \text{area of circle} = \pi r^2 = \pi(a^2 - r^2 \sin^2\psi)$$

$$\therefore w = \frac{(1 - \upsilon^2)}{\pi E} q\pi \int_0^{\pi/2} (a^2 - r^2 \sin^2\psi)\mathrm{d}\psi$$

Appendix II

Pressure Applied to a Circular Region—When axisymmetrical pressure distributions of the form

$$q = q_0\left(1 - \frac{r^2}{a^2}\right)^n$$

are applied to a circular region of radius a, the displacements at surface points and the stresses at internal points due to this pressure distribution may be found in closed form.

In the particular case where $n = 1/2$, the pressure distribution is referred to as the "Hertz pressure" given by Hertz theory. This pressure is exerted between two frictionless purely elastic solids of revolution in contact.

As the total loading or compressive force, P, relates to this pressure, q, via

$$P = \int_0^a q(r) 2\pi r \mathrm{d}r$$

then

$$p = \frac{2\pi q_0}{a} \int_0^a (a^2 - r^2)^{1/2} r \mathrm{d}r$$

let $u = a^2 - r^2$, $\mathrm{d}u = -2r\mathrm{d}r$, $r\mathrm{d}r = -1/2\ \mathrm{d}u$, and $a^2 = u + r^2$

$$\therefore P = \frac{2\pi q_0}{a} \int_0^1 u^{\frac{1}{2}}\left(-\frac{1}{2}\right)\mathrm{d}u = \left[-\frac{2\pi q_0}{3a} u^{\frac{3}{2}}\right]_0^a = \left[-\frac{2\pi q_0}{3a}(a^2 - r^2)^{\frac{3}{2}}\right]_0^a = \frac{2}{3}\pi q_0 a^2$$

$$\therefore \text{force} \propto \text{maximum pressure}$$

$$\therefore q_0 = \frac{3P}{2\pi a^2}$$

Appendix III

Derivation of Simplified Three-Dimensional Form for Viscoelastic Constitutive Description[19]—When a problem has more than one stress component, then a generalization of the viscoelastic law to the three-dimensional form may be needed. If a viscoelastic material is

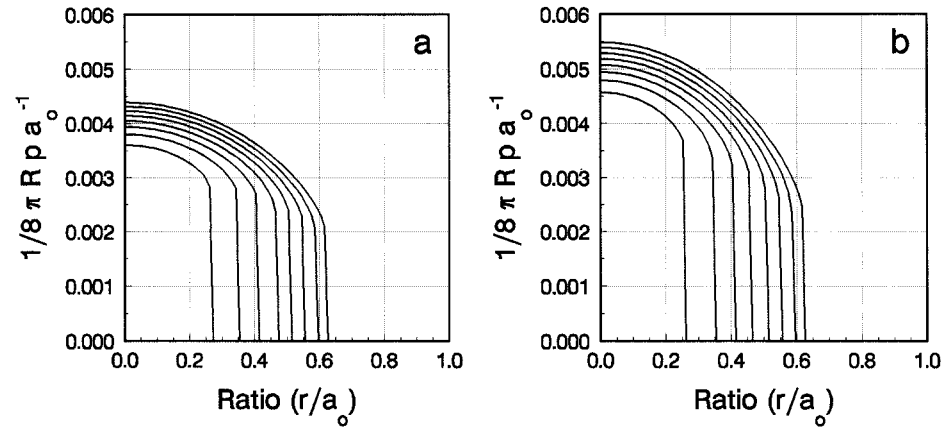

Figure 15—Solution of the pressure equations predicts a stress distribution similar to the elastic form. (a) two-dimensional surface contour plot of the pressure distribution for loading at 1 mm/min to the 4.5 kN level; and (b) loading at 10 mm/min to the 4.5 kN level.

isotropic, a hydrostatic stress must produce a dilatation and no distortion. The stress and strain are related by the differential equation

$$\sigma + p_1\dot{\sigma} + p_2\ddot{\sigma} + \ldots = q_0\epsilon + q_1\dot{\epsilon} + \ldots \qquad \text{(III.1)}$$

$$\left(\sum_0^m p_k \frac{\mathrm{d}^k}{\mathrm{d}t^k}\right)\sigma = \left(\sum_0^n q_k \frac{\mathrm{d}^k}{\mathrm{d}t^k}\right)\epsilon \qquad \text{(III.2)}$$

or, shorter, by

$$P''\sigma = Q''\epsilon \qquad \text{(III.3)}$$

On the other hand, if shear is present, then the shear strain coupled with isotropy of the material requires that

$$\left(\sum_0^{m'} p'_k \frac{\mathrm{d}^k}{\mathrm{d}t^k}\right)\hat{\sigma} = \left(\sum_0^{n'} q'k \frac{\mathrm{d}^k}{\mathrm{d}t^k}\right)\hat{\epsilon} \qquad \text{(III.4)}$$

or

$$P'\hat{\sigma} = Q'\hat{\epsilon} \qquad \text{(III.5)}$$

where $\hat{\sigma}$ and $\hat{\epsilon}$ correspond to the components of the stress and strain deviators.

The operator pairs P'', Q'', and P' and Q', which describe the viscoelastic material, are entirely independent of each other. To each pair, the relation stated in eq 23 or 24 is applicable for a standard three element model.[19] These operator pairs for different rheological models are also summarized in Flugge (Table 1.2; pp 22−23)[19] and in Muller (pp 108, 110, 112, 119, 121).[25]

In uniaxial tension, there is only one stress, σ_x; and strain has three components, the axial strain ϵ_x and the lateral contractions $\epsilon_y = \epsilon_z$. As the operators are assumed linear and time invariant, the commutative properties yields

$$(P''Q' + 2Q''P')\sigma_x = 3Q''Q'\epsilon_x \qquad \text{(III.6)}$$

$$(\mathrm{P}''\mathrm{Q}' - Q''P')\sigma_x = 3Q''Q'\epsilon_y \qquad \text{(III.7)}$$

for applied uniaxial stress. By analogy,

$$(Q''P' + 2P''Q')\epsilon_x = 3P''P'\sigma_x \qquad \text{(III.8)}$$

$$(Q''\mathrm{P}' - P''Q')\epsilon_x = 3P''P'\sigma_y \qquad \text{(III.9)}$$

follows for applied uniaxial strain (in stress relaxation experiments).

Equations III.6−III.9 serve as the viscoelastic equivalent of a complete statement of Hooke's law for uniaxial tension. Interpretation requires special choices for the operators.

As stated by Flugge (p 167),[19] although the shear deformation may be rather large, the change of volume measured by E is always very limited. It seems therefore, reasonable to neglect the latter completely and to assume $E = 0$. This corresponds to $P'' = 0$ and $Q'' = 1$. The constitutive equations for uniaxial stress in tension are then

$$2P'\sigma_x = 3Q'\epsilon_x \text{ and } -P'\sigma_x = 3Q'\epsilon_y \qquad \text{(III.10)}$$

and for applied uniaxial strain,

$$2Q'\epsilon_x = 3P'\sigma_x \text{ and } -Q'\epsilon_x = 3P'\sigma_y \qquad \text{(III.11)}$$

Appendix IV

$$a^3(t) = \frac{3}{8}\pi R\int_0^t\left\{\frac{1}{E_1} + \frac{1}{E_2}(1 - \mathrm{e}^{-\frac{(t-t')E_2}{\eta}})\right\}\frac{\mathrm{d}}{\mathrm{d}t'}P(t')\mathrm{d}t' \qquad (28)$$

integration by parts $uv - \int v\mathrm{d}u$: let

$$u = \frac{1}{E_1} + \frac{1}{E_2} - \frac{1}{E_2}\mathrm{e}^{-\frac{(t-t')E_2}{\eta}} \quad \therefore \mathrm{d}u = -\frac{1}{E_2}\cdot\frac{E_2}{\eta}e^{-\frac{(t-t')E_2}{\eta}}\mathrm{d}t'$$

$$\mathrm{d}v = \frac{\mathrm{d}}{\mathrm{d}t'}P(t')\mathrm{d}t' \quad \mathrm{v} = P(t')$$

$$\therefore a^3(t) = \frac{3}{8}\pi R\left[\left(\frac{1}{E_1} + \frac{1}{E_2} - \frac{1}{E_2}\,\mathrm{e}^{-\frac{(t-t')E_2}{\eta}}\right)(P(t'))\right]_0^t - \int\frac{P(t')}{-\eta}\mathrm{e}^{-\frac{(t-t')E_2}{\eta}}\mathrm{d}t'$$

$$\therefore a^3(t) = \frac{3}{8}\pi R\left\{\frac{P(t)}{E_1} - \left(\frac{1}{E_2} + \frac{1}{E_2} - \frac{1}{E_2}\mathrm{e}^{-\frac{tE_2}{\eta}}\right)P_0\right\} + \int_0^t\frac{P(t')}{\eta}\mathrm{e}^{-\frac{(t-t')E_2}{\eta}}\mathrm{d}t'$$

calculate $a(t)$ per given $P(t)$.

Similarly,

$$p(r,t) = \frac{4}{\pi R}\int_0^t\left\{E_1\mathrm{e}^{-\frac{t-t'}{\tau}} + \frac{E_1E_2}{E_1+E_2}(1 - \mathrm{e}^{-\frac{t-t'}{\tau}})\right\}\times \frac{\mathrm{d}}{\mathrm{d}t'}(a^2(t') - r^2)^{1/2}\,\mathrm{d}t'$$

where

$$\tau = \frac{\eta}{E_1 + E_2} \tag{30}$$

let

$$u = \frac{1}{E_1 + E_2} \cdot E_1^2 e^{-\frac{(t - t')}{\tau}} + \frac{E_1 E_2}{E_1 + E_2}$$

$$\therefore \mathrm{d}u = \frac{E_1^2}{(E_1 + E_2)\tau} \mathrm{e}^{-\frac{(t - t')}{\tau}} \mathrm{d}t'$$

and

$$\mathrm{d}v = \frac{\mathrm{d}}{\mathrm{d}t'}(a^2(t') - r^2)^{1/2} \mathrm{d}t' \quad \therefore v = (a^2(t') - r^2)^{1/2}$$

$$p(r,t) = \frac{8}{\pi R}\left\{(a^2(t) - r^2)^{1/2} E_1 - (a_0^2 - r^2)^{1/2} \frac{(E_1^2 e^{-\frac{t}{\tau}} + E_1 E_2)}{E_1 + E_2} - \right.$$

$$\left. \int_0^t (a^2(t') - r^2)^{1/2} \frac{E_1^2}{(E_1 + E_2)\tau} \mathrm{e}^{-\frac{(t - t')}{\tau}} \mathrm{d}t' \right\}$$

Appendix V

Derivation of Elastic Parameters as a Limiting Case[19]—In a viscoelastic body, all of the stresses, strains, and displacements occurring under load are time dependent. The elastic solid is then a limiting case of a viscoelastic material. The moduli of the springs of the rheological model do not correspond simply to Young's modulus because time, temperature, and stress dependence are overt considerations. If, for example, one considers a material tested in tension, the plot of the compliance would show that the ratio $\epsilon_x/-\epsilon_y$ varies with time. This time dependence indicates that the concept of Poisson ratios etc. are not very meaningful for a viscoelastic material.[19]

The linear elastic law (Hooke's law) in the form (III.1; see *Appendix III*) would render the four operators as multiplicative constants and the formulation of the stress deviation as[19]

$$\sigma_x = \frac{E}{(1 + \nu)(1 - 2\nu)}[(1 - \nu)\epsilon_x + \nu(\epsilon_y + \epsilon_z)] \tag{V.1}$$

The differential operators P and Q can be replaced by polynomials $\rho(s)$ and $\vartheta(s)$ in considering an elastic body, hence,[19]

$$\rho''(s)\bar{\sigma} = \vartheta''(s)\bar{\epsilon} \tag{V.2}$$

$$\rho'(s)\bar{\sigma} = \vartheta'(s)\bar{\epsilon} \tag{V.3}$$

where $\bar{\sigma}$ and $\bar{\epsilon}$ are the Laplace transforms of the time-dependent stresses and strains. These algebraic relations define the limits of their elastic counterparts if[19]

$$3K \rightarrow \frac{\vartheta''(s)}{\rho''(s)} \quad 2G \rightarrow \frac{\vartheta'(s)}{\rho'(s)} \tag{V.4}$$

$$E \rightarrow \frac{3\vartheta'\vartheta''}{2\rho'\vartheta'' + \vartheta'\rho''} \quad \nu \rightarrow \frac{\rho'\vartheta'' - \vartheta'\rho''}{2\rho'\vartheta'' + \vartheta'\rho''} \tag{V.5}$$

For a standard (three-parameter material), a reduced or effective modulus $E_R(t, \tau)$ offers estimates of an instantaneous $E_R(\tau_0,\tau_0)$ and an asymptotic modulus $E_R(\infty,\tau)$:[17]

$$E(\tau_0,\tau_0) = \frac{1}{E_1} \quad E(\infty,\tau_0) = \frac{E_1 E_2}{E_1 + E_2} \tag{V.6}$$

List of Symbols

$\dot{\epsilon}_0$	constant strain rate
$\dot{\epsilon}$	rate of strain
τ	interval within domain t, also designated $\eta/(E_1 + E_2)$
υ	Poisson's ratio
σ_∞	limiting stress during stress relaxation
$\Phi(t)$	creep function
$\epsilon(t)$	strain which varies with time
$\sigma(t)$	stress which varies with time
$\Psi(t)$	the relaxation modulus function, a viscoelastic operator
α, α_1, α_2	total distance of approach of two spheres, of each sphere designated 1 and 2
σ_f	stress at time corresponding to beginning of stress relaxation (strain rate = 0)
Δl	change in distance
ϵ_t	true strain
A	coefficient = $(E_1/E_1 + E_2)^2\eta\dot{\epsilon}_0$
a, $a(t)$	particle contact radius (radius of circular contact region) varying with time
E	elastic modulus
E_1, E_2, η	elastic moduli of the springs and viscosity coefficient of the dashpot of a standard rheological model
K, G	bulk, and shear modulus
$k_1 + k_2$	elastic constant term = $(1 - \upsilon^2)/\pi E$ upon substitution
l	length
l_0	original specimen length
$P(t)$	applied compressive force acting normal to the surface
p, $p(r,t)$	normal contact pressure which varies with contact radius and time
q, q_0	concentrated pressure, maximum pressure
r	distance from sphere center, x coordinate of point (r,z) of indenting sphere, $r \ll R$
R, R_1, R_2	radius of curvature, of the indenting spheres designated 1 and 2, respectively
t'	dummy time variable within interval t
t_f	time at which stress relaxation begins, total strain is held constant
w_1, w_2	deformation of sphere 1 and 2 owing to contact pressure
x, y, z	Cartesian coordinates
z_1, z_2	Cartesian coordinate projection of deforming surface points, designated 1 and 2

References and Notes

1. Hoag, S. W.; Rippie, E. G. Thermodynamic analysis of energy dissipation by pharmaceutical tablets during stress unloading. *J. Pharm. Sci.* **1994**, *83*, 903−908.

2. Paronen, P.; Ilkka, J. Porosity-pressure functions. In *Pharmaceutical powder compaction technology, Drugs and the pharmaceutical sciences series, 71*, Alderborn, G.; Nystrom, C., Eds.; Marcel Dekker: Inc.: New York, 1996; p 69.
3. Rippie, E. G.; Danielson, D. W. Viscoelastic stress/strain behavior of pharmaceutical tablets: analysis during unloading and postcompression periods. *J. Pharm. Sci.* **1981**, *70*, 476−481.
4. York, P. J. A consideration of experimental variables in the analysis of powder compaction behavior. *Pharm. Pharmacol.* **1979**, *31*, 244−246.
5. Duncan-Hewitt, W. C.; Papadimitriopoulos, E. Deformation kinetics of KBr crystals predict tablet stress relaxation. *J. Pharm. Sci.* **1994**, *83*, 91−95.
6. Celik, M.; Okutgen, E.; A feasibility study for the development of a prospective compaction functionality test and the establishment of a compaction data bank, *Drug Dev. Ind. Pharm.* **1993**, *19 (17&18)*, 2309−2334.
7. Pinto, J. F.; Podczeck, F; Newton, J. M.; Investigations of tablets prepared from pellets produced by extrusion and spheronisation. II. Modeling the properties of the tablets produced using regression analysis. *Int. J. Pharm.* **1997**, *152*, 7−16.
8. Rue, P. J.; Rees, J. E. Limitations of the Heckel relation for predicting powder compaction mechanisms. *J. Pharm. Pharmacol.* **1978**, *30*, 642−643.
9. Toure, P.; Puisieux, F.; Duchene, D.; Carstensen, J. T. Energy terms in tablet compression cycles. *Powder Technol.* **1980**, *26*, 213−216.
10. Johnson, K. L. *Contact mechanics*; Cambridge University: New York; 1985; p 542.
11. Timoshenko, S.; Goodier, J. N. *Theory of Elasticity*, third ed.; McGraw-Hill: New York; 1970; pp 409−420.
12. Gladwell,G. M. L. *Contact Problems in the Classical Theory of Elasticity*; Sijthoff and Noordhoff: Alphen aan den Rijn; 1980; p 95.
13. Lee, E. H.; Radok, J. R. M. The contact problem for viscoelastic bodies. *J. Appl. Mech.* **1960**, 438−444.
14. Lee, E. H.; Rogers, T. G. Solution of viscoelastic stress analysis problems using measured creep or relaxation functions. *J. Appl. Mech.* **1963**, 127−133.
15. Lee, E. H. Stress analyis in viscoelastic bodies. *Quart. Appl. Math.* **1955**, *13*, 183−190.
16. Radok, J. R. M. Viscoelastic stress analysis. *Quart. Appl. Math.* **1957**, *15*, 198−202.
17. Creus, G. J. Viscoelasticity- -Basic theory and applications to concrete structures. In *Lecture notes in engineering, 16*; Brebbia, C. A.; Orszag, S. A., Eds.; Springer-Verlag: New York, 1985; pp 18−42.
18. Ferry, J. D. *Viscoelastic Properties of Polymers*, second ed.; John Wiley & Sons: New York, 1970.
19. Flugge, W. *Viscoelasticity*, second ed., Springer-Verlag: New York, 1975; pp 22−23, 165−167.
20. Lum, S. K.; Duncan-Hewitt, W. C. A comparison of elastic moduli derived from theory, microindentation and ultrasonic testing. *Pharm. Res.* **1996**, *13*, 1739−1745.
21. Lum, S. K.; Duncan-Hewitt, W. C. Deformation kinetics analysis of polymeric matrixes. *Pharm. Res.* **1996**, *13*, 692−700.
22. Vetterling, W. T.;Teukolsky, S. A.;Press, W. H.;Flannery, B. P. *Numerical Recipes Example Book (Fortran)*, second ed.; Cambridge University: New York, 1992; p 245.
23. Hsueh, C.-H. Mathematical model of viscosity measurements for viscoelastic solids. *J. Am. Ceram. Soc.* **1986**, *69*, C48−C49.
24. Berg, G.; Grau, P. Estimating the viscosity of viscoelastic solids based on a three-parameter model. *J. Am. Ceram. Soc.* **1989**, *72*, 2187−2188.
25. Muller, F. Viscoelastic models. In *Pharmaceutical Powder Compaction Technology, Drugs and the pharmaceutical sciences series, 71*; Alderborn, G.; Nystrom, C., Eds.; Marcel Dekker: New York, 1996; pp 108−130.
26. Askeland, D. R. *The Science and Engineering of Materials*, PWS−Kent Publishing: Boston, 1984; pp 122, 128.

JS980010M

Dose-Dependent Plasma Clearance of MK-826, a Carbapenem Antibiotic, Arising from Concentration-Dependent Plasma Protein Binding in Rats and Monkeys

BRADLEY K. WONG,* PATRICK J. BRUHIN, AND JIUNN H. LIN

Contribution from *Drug Metabolism, WP75-100, Merck Research Laboratories, West Point, Pennsylvania 19486.*

Received May 29, 1998. Final revised manuscript received September 22, 1998.
Accepted for publication October 2, 1998.

Abstract □ After intravenous administration of MK-826, a new carbapenem antibiotic, the compound exhibited nonlinear pharmacokinetics in rats and monkeys. In both species, time-averaged plasma clearance (based on total concentrations) increased about 5-fold over the 10- to 180-mg/kg dose range. MK-826 was extensively plasma protein bound in rat and monkey plasma, and the extent of binding was concentration dependent at plasma concentrations achieved after administration of these doses. Rosenthal analysis of the plasma protein binding indicated that there were two classes of binding sites. The binding capacity of the primary site was comparable to the plasma albumin concentration, which suggested that this primary site consisted of a single site on albumin. The extent of binding of MK-826 to rat albumin was similar to that in whole plasma. Clearance values based on unbound concentrations appeared independent of dose from 10 to 180 mg/kg, which is consistent with saturation of protein binding as the primary cause of the nonlinear pharmacokinetic behavior.

Introduction

MK-826 is a carbapenem antibiotic intended for the parenteral treatment of bacterial infections (see Figure 1).[1] Preliminary studies indicate that MK-826 is bound extensively to plasma proteins. Saturable plasma protein binding can lead to nonlinear pharmacokinetic behavior.[2,3] In the present studies, dose-dependent clearance of MK-826 was observed following intravenous (iv) administration to rats and monkeys. This clearance was explained by concentration-dependent protein binding to two different classes of plasma binding sites that probably reside on albumin.

Experimental Section

Synthesis—MK-826 (formula weight of monosodium salt, 497.4) was synthesized at Merck Research Laboratories (Rahway, NJ).

Animal Studies—Male Sprague–Dawley rats weighing 0.240 to 0.280 kg were purchased from Taconic Farms (Germantown, NY) and housed under standard conditions with free access to food and water. On the day prior to drug administration, a silicone rubber/polyethylene cannula was implanted in a jugular vein while the rats were under pentobarbital [40 mg/kg, intraperitoneally (ip)] anesthesia.[4]

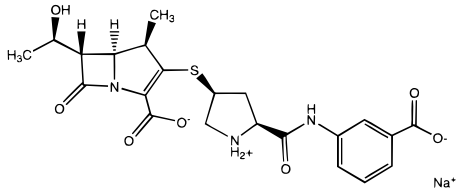

Figure 1—Chemical structure of MK-826.

Intravenous doses of MK-826 (monosodium salt dissolved in saline) of 10, 30, 60, and 180 mg/kg were administered by bolus injection into the jugular vein cannula to four rats per dose level. Male rhesus monkeys weighing 4.2 to 6 kg (Charles River, Key Lois, FL, $n = 4$) received the same dose levels as in the rat study, iv via a cephalic or saphenous vein. The rat study was of noncrossover design, but the monkeys received the MK-826 doses in a crossover fashion at least 1 week apart. Blood samples were drawn from rats before and 1, 3, 5, 15, and 30 min, and 1, 2, 3, and 4 h after the iv administration of MK-826. In the monkey studies, blood samples were obtained predose and at 5 and 30 min, and 1, 2, 4, 6, 12, 16, and 24 h post dose. Heparin was added to the blood samples to prevent clotting, and the resultant plasma was immediately frozen on dry ice. When stored at −70 °C, the compound was stable in plasma for at least 44 days; all assays were completed within that time.

Protein Binding—Protein binding of MK-826 was measured in triplicate in rat and monkey plasma by ultrafiltration over the 10- to 2000-μg/mL concentration range as previously described.[5] This range includes the concentrations observed in vivo; after the administration of the a 180-mg/kg dose to rats and monkeys, the concentration in plasma at the initial sampling time was about 1000 μg/mL. Briefly, stock solutions of MK-826 in water were added to freshly drawn plasma (pH 7.4) at 1% of total volume. After incubation at 37 °C for 10 min, aliquots of plasma were transferred to ultrafiltration devices (30 000 molecular weight cutoff; Centrifree, Amicon, Danvers, MA) and centrifuged at 1500 x g for 15 min. The binding of MK-826 to albumin was assessed similarly using solutions of rat (fraction V, fatty acid free) and rhesus (fraction V, not fatty acid free, Sigma) albumin (40 mg/mL). Concentrations of MK-826 in plasma and ultrafiltrate were determined by a liquid chromatographic method. A preliminary study showed that nonspecific binding of MK-826 to the ultrafiltration device was minor (<4%).

The binding capacity and association constants were estimated by fitting the protein binding data to the following equation that describes two classes of sites:

$$\frac{B}{U} = \frac{n_1P_1 \times K_1}{1 + K_1 \times U} + \frac{n_2P_2 \times K_2}{1 + K_2 \times U} \quad (1)$$

where B and U are the concentration of bound and unbound MK-826; n_1P_1 and n_2P_2 are the binding capacities or concentrations of

* Corresponding author. Telephone: 215-652-5644. Fax: 215-993-3533. E-mail: bradley_wong@merck.com.

10.1021/js980232k CCC: $18.00
Published on Web 12/11/1998

Table 1—Pharmacokinetic Parameters of MK-826 Based on Total Plasma Concentrations[a]

	rat			monkey		
dose, mg/kg	dose-normalized AUC, (μg x min/mL)/(mg/kg)	*CL*, mL/min/kg	terminal $t_{1/2}$, min	dose-normalized AUC, (μg x min/mL)/(mg/kg)	*CL*, mL/min/kg	terminal $t_{1/2}$, min
10	$203 \pm 50^{a,b,c}$	$5.17 \pm 1.30^{a,b,c}$	25 ± 9	$3458 \pm 696^{a,b,c}$	$0.299 \pm 0.061^{a,b,c}$	301 ± 24
30	$107 \pm 10^{c,d}$	$9.34 \pm 0.83^{c,d}$	34 ± 10	$1475 \pm 302^{b,e}$	$0.700 \pm 0.142^{b,e}$	290 ± 25
60	$97.1 \pm 11.8^{b,c}$	$10.4 \pm 1.3^{b,e}$	35 ± 5	$1276 \pm 181^{c,f}$	$0.795 \pm 0.102^{c,f}$	314 ± 38
180	$38.1 \pm 9.5^{a,d,e}$	$27.5 \pm 6.9^{a,d,e}$	48 ± 9	$594 \pm 53^{a,e,f}$	$1.70 \pm 0.15^{a,e,f}$	282 ± 13

[a] Shown as the mean (SD) of $n = 4$ per group. Dose-normalized AUC, *CL*, and terminal $t_{1/2}$ were evaluated by one-way ANOVA and Tukey's multiple comparison test. Values bearing the same superscript were judged to be different at $p < 0.05$. Abbreviations: AUC, area under the concentration–time curve from time 0 to infinity; *CL*, time-averaged plasma clearance. Values for half-lives are harmonic mean. Standard deviation was calculated using the jackknife method.[10]

the first and second classes of binding sites, respectively; and K_1 and K_2 are the association constants for the first and second classes of binding, respectively.[6] This analysis assumes that the classes of binding sites are mutually independent. The nonlinear regression analysis was performed with the RS/1 computer program (version 4.2, BBN Software) using a weighting factor of $1/y^2$.

Pharmacokinetic Analysis—Because of blood sample volume constraints, unbound concentrations were calculated from total concentrations in plasma (measured in vivo after administration of MK-826) using the binding capacities and association constants for the binding of MK-826 to plasma proteins. The relationship between bound and unbound concentrations for two classes of binding sites is described by

$$B = \frac{n_1P_1 \times K_1 \times U}{1 + K_1 \times U} + \frac{n_2P_2 \times K_2 \times U}{1 + K_2 \times U} \quad (2)$$

Substitution for bound concentration (Bound = Total − Unbound) permits calculation of unbound concentrations from total concentrations. In this study, $K_2 \times U \ll 1$, so eq 2 reduces to

$$(n_2P_2 \times K_2 \times K_1 + K_1) \times U^2 + (n_1P_1 \times K_1 + n_2P_2 \times K_2 - T \times K_1 + 1) \times U - T = 0 \quad (3)$$

which is a quadratic equation with one positive solution for unbound concentration. This equation for calculating the unbound concentrations for a drug that has two classes of binding sites is similar to that reported previously for a drug with single binding site.[2]

The terminal $t_{1/2}$ of MK-826 was determined by linear regression of the log-linear portion of the plasma concentration—time profile. Clearance (*CL*), based on either total or unbound plasma concentrations, was calculated as

$$CL = \text{Dose/AUC} \quad (4)$$

where AUC is the area under the curve from time zero to infinity. Clearance based on total concentration was shown to be dose-dependent, so these are time-averaged values. The standard method of calculating the volume of distribution at steady state (Vd_{ss}) based on total drug concentrations is invalid when nonlinear protein binding exists because it overestimates the steady-state distribution volume of total drug.[7,8] However, a corrected distribution volume $\overline{Vd^{t}_{ss}}$ may be calculated that theoretically better reflects the distribution volume of total drug at steady state:[8]

$$\overline{Vd^{t}_{ss}} = \overline{f_p} \times \overline{Vd^{n}_{ss}} \quad (5)$$

where $\overline{f_p}$ corresponds to the area-weighted average fraction unbound in the plasma[7] and $\overline{Vd^{u}_{ss}}$ is the steady-state distribution volume for unbound drug calculated by the standard method from the unbound concentrations.[7,8]

Liquid Chromatographic Method for MK-826—Plasma concentrations of MK-826 were measured by a direct-injection, column-switching method with UV absorption detection at 298 nm. Briefly, two columns connected by a switching valve provided automated sample cleanup and analysis; the columns were a Phenomenex (Torrance, CA) C18 Maxil-10 extraction column (50 × 4.6 mm) and a Whatman (Clifton, NJ) C18 Partisphere analytical column (125 × 4.6 mm). Plasma, buffered by the addition of one volume of 1 M 2-[*N*-morpholino]ethanesulfonate (pH 6.5) buffer, was injected directly onto the extraction column. Endogenous interfering components were diverted to waste for 5 min, and then from 5 to 10 min the mobile phase was switched to transfer MK-826 from the extraction column to the analytical column. Mobile phase for the extraction column consisted of 0.025 M sodium phosphate (pH 6.5) buffer at a flow rate of 2 mL/min. The analytical mobile phase consisted of the preceding buffer and acetonitrile (95/5, v/v) at a flow rate of 2 mL/min. Under these conditions, the retention time of MK-826 was 12 min. Replicate analysis of calibration standards and spiked quality control samples ($n = 5$ per concentration) indicated that the method provided >90% accuracy and variability of <10% over the 0.1- to 100-μg/mL concentration range.

Statistical Analysis—One-way analysis of variance (ANOVA) was used to assess the effect of dose on pharmacokinetic parameters. A log transformation of data was made when unequal variances across dose levels were detected. Differences between dose levels were evaluated using the Tukey multiple comparison test.[9]

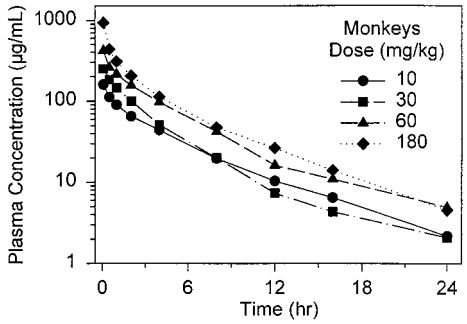

Figure 2—Mean plasma concentrations of MK-826 in rhesus monkeys after iv administration of 10 to 180 mg/kg.

Table 2—Binding Capacities and Association Constants for the Protein Binding of MK-826 in Rat and Monkey Plasma[a]

animal	n_1P_1, M	K_1, M^{-1}	n_2P_2, M	K_2, M^{-1}
rat	2.89×10^{-4}	9.07×10^{4}	8.50×10^{-3}	2.17×10^{2}
monkey	6.52×10^{-4}	11.5×10^{4}	1.36×10^{-3}	1.37×10^{2}

[a] Symbols: n_1P_1 and n_2P_2 are the binding capacities or concentrations of the first and second class of binding sites, respectively; K_1 and K_2 are the association constants for the primary and secondary classes of binding sites, respectively.

Results and Discussion

Following the iv administration of MK-826 to rats, plasma concentrations increased less than dose-proportionally, as shown by the dose-normalized AUC that decreased with dose (Table 1). Over this 18-fold range of doses, the dose-normalized AUC decreased by 5- to 6-fold. This decrease was due to a 5-fold increase in the time-averaged plasma clearance. A similar dose-dependent trend was observed in monkeys. Because for drugs with a low extraction ratio the plasma clearance is proportional to the

Table 3—Pharmacokinetic Parameters of MK-826 Based on Unbound Concentrations in Rats and Monkeys[a]

	rat			monkey		
dose, mg/kg	dose-normalized unbound AUC, (μg x min/mL)/(mg/kg)	*CL*, mL/min/kg	terminal $t_{1/2}$, min	dose-normalized unbound AUC (μg x min/mL)/(mg/kg)	*CL*, mL/min/kg	terminal $t_{1/2}$, min
10	9.60 ± 2.38	110 ± 30	28 ± 9	55.6 ± 12.2	18.7 ± 4.3[a]	295 ± 21
30	7.44 ± 0.69	136 ± 12	31 ± 5	30.6 ± 7.0	33.9 ± 7.2[a]	270 ± 18
60	8.50 ± 0.85	119 ± 14	33 ± 4	40.5 ± 9.3	25.6 ± 5.1	282 ± 5
180	6.70 ± 1.92	159 ± 46	39 ± 4	42.2 ± 5.8	24.0 ± 2.9	267 ± 13

[a] Abbreviations and superscripts are as given in footnote to Table 1.

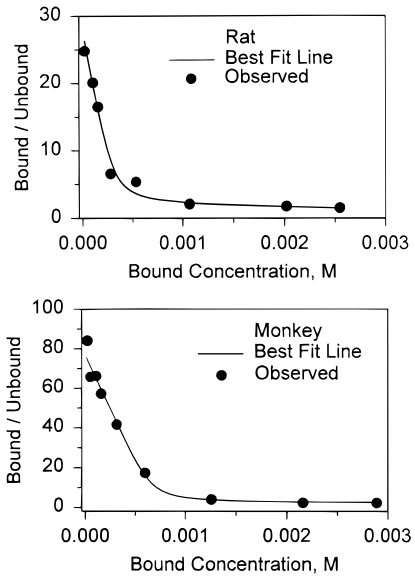

Figure 3—Rosenthal analysis of the protein binding of MK-826 in rat and monkey plasma.

unbound fraction in plasma, the concentration dependence of plasma protein binding was examined as a potential mechanism for the nonlinear clearance.

MK-826 was bound extensively to rat and monkey plasma proteins and the extent of protein binding was concentration dependent. In rat plasma, the unbound fraction was ca. 4% and remained constant up to 75 μg/mL; however, the unbound fraction increased to 40% at 2000 μg/mL. In monkey plasma, the unbound fraction in the linear range was 1.5% and then increased to 32% at 2000 μg/mL. The nonlinear binding range extended to concentrations achieved in the dose proportionality study (Figure 2). Rosenthal plots of the bound/unbound concentration ratio versus bound concentration were biphasic, consistent with two different classes of binding sites (Figure 3). When the data were fit to the equation describing two classes of binding sites, there was good agreement between the theoretical and observed values (the residual errors were ≤11% and there was no systematic deviation between the observed and calculated values). The binding capacities of the primary binding sites (n_1P_1) in rat and monkey plasma were 289 and 652 μM, respectively (Table 2), values which are comparable to physiological albumin concentrations.[11] Binding capacity is the product of the number of binding sites per protein molecule times the protein concentration, so this similarity implied that the higher affinity binding was to a single site on albumin. The binding of MK-826 (25 μg/mL) to rat albumin was assessed directly and found to be extensive (2.0 ± 0.1% unbound fraction, $n = 3$). Binding of MK-826 to monkey albumin also was extensive, however, the unbound fraction was higher than the free fraction in plasma (18 ± 0.5% versus 1.5 ± 0.2%). The reason for this result is unknown but could be due to the presence of endogenous competitive displacers, such as fatty acids, that form during the isolation of albumin.

Pharmacokinetic parameters based on unbound concentrations would be independent of dose if saturation of plasma protein binding was the primary cause of the dose-dependent plasma clearance. Determination of the association constants and binding capacities for the plasma protein binding permitted the calculation of unbound pharmacokinetic parameters from total plasma concentrations. In rats, dose-normalized AUC and clearance based on calculated unbound concentrations in plasma appeared independent of dose, confirming that the concentration-dependent plasma protein binding was the primary cause of the nonlinear plasma clearance (Table 3). The unbound clearance in rats was very high (110−159 mL/min/kg) and exceeded hepatic blood flow. However, preliminary studies in rats indicate that dehydropeptidase-I, an enzyme that is present in highest concentration in rodent lungs and kidneys, is important to the clearance of MK-826 in this species (data not shown). Kinetic analysis of unbound concentrations showed similar results in monkeys over the dose range examined, although the unbound clearance at 30 mg/kg appeared slightly higher than in the other dose groups. During the initial period after administration of MK-826 (30 min in mice and 4 h in monkeys after 180 mg/kg), the unbound fraction in the nonlinear dose range was increased because the concentrations achieved saturated the primary albumin binding site. Clearance based on total concentrations increased because of the higher unbound fraction available for elimination.

Despite the dose-dependent plasma clearance, terminal half-life was dose independent because this parameter reflected decline during a period when concentrations were within the linear protein binding range. The calculated steady-state distribution volume (Vd_{ss}^{t}), corrected for the nonlinear protein binding, was relatively unchanged with dose (ranges of means across the dose levels were 145−151 and 84−122 mL/kg in rats monkeys, respectively). This result suggested that despite the saturation of plasma protein binding, the net shift of MK-826 out of the plasma into the tissues was minor.

In summary, the dose-dependent increases in plasma clearance of MK-826 in rats and monkeys were shown to be the result of concentration-dependent plasma protein binding. Initial clinical studies suggest that after high doses of MK-826, the AUC in plasma also increases less than dose proportionally.[12]

References and Notes

1. Pelak, B. A.; Gerckens, L. S.; Scott, P. M.; Gill, C.; Pacholok, C.; Lynch, L.; Dorso, K.; Kohler, J.; Shungu, D.; Kropp, H. Antibacterial profile of L-749, 345 (ZD-4433), a new potent 1-beta-methyl carbapenem. *Abstr. 36th Intersci. Conf. Antimicrob. Agents and Chemother.* **1996**, 120.
2. Stoeckel, K.; McNamara, P. J.; Brandt, R.; Plozza-Nottebrock, H.; Ziegler, W. H. Effects of concentration-dependent plasma

protein binding on ceftriaxone kinetics. *Clin. Pharmacol. Ther.* **1981**, *29*, 650−657.
3. Lin, J. H.; Hooke, K. F.; Yeh, K. C.; Duggan, D. E. Dose-dependent pharmacokinetics of diflunisal in rats. Dual effects of protein binding and metabolism. *J. Pharmacol. Exp. Ther.* **1985**, *235*, 402−406.
4. Weeks, J. R.; Davis, J. D. Chronic intravenous cannulas for rats. *J. Appl. Physiol.* **1964**, *10*, 540−542.
5. Judd, R.; Pesce, A. J. Free drug concentrations are constant in serial fractions of plasma ultrafiltrate. *Clin. Chem.* **1982**, *28*, 1726−1727.
6. Rosenthal, H. E. A graphic method for the determination and presentation of binding parameters in a complex system. *Anal. Biochem.* **1967**, *20*, 525−532.
7. McNamara, P. J.; Gibaldi, M.; Stoeckel, K. Volume of distribution terms for a drug (ceftriaxone) exhibiting concentration-dependent protein binding. I. Theoretical considerations. *Eur. J. Clin. Pharmacol.* **1983**, *25*, 399−405.
8. McNamara, P. J.; Gibaldi, M.; Stoeckel, K. Volume of distribution terms for a drug (ceftriaxone) exhibiting concentration-dependent protein binding II. Physiological significance. *Eur. J. Clin. Pharmacol.* **1983**, *25*, 407−412.
9. Zar, J. H. Biostatistical Analysis, 2nd ed.; Prentice-Hall: Englewood Cliffs, NJ 1984.
10. Lam, F. C.; Hung, C. T.; Perrier, D. G. Estimation of variance for harmonic mean half-lives. *J. Pharm. Sci.* **1985**, *74*, 229−231.
11. *Handbook of Laboratory Animal Science*, Vol. II, Melby, E. C., Jr.; Altman, N. H., Eds.; CRC: Cleveland, OH, 1974; pp 365−405.
12. Majumdar, A.; Birk, K.; Blum, R. A.; Cairns, A. M.; Conroy, J.; Mendel, C. M.; Musson, D.; Rogers, J. D. Pharmacokinetics of L-749, 345, a carbapenem antibiotic, in healthy male and female volunteers. *Abstr. 36th Intersci. Conf. Antimicrob. Agents and Chemother.* **1996**, 122.

Acknowledgments

The authors thank Ms. Janice Brunner and Mr. Sam White for assistance with the monkey studies.

JS980232K

A publication of the **American Pharmaceutical Association** and the **American Chemical Society**

JOURNAL OF
Pharmaceutical Sciences

March 1999
Volume 88, Number 3

RESEARCH ARTICLES

Effects of Additives on the Stability of *Humicola lanuginosa* Lipase during Freeze-Drying and Storage in the Dried Solid

LOTTE KREILGAARD,[†§] SVEN FROKJAER,[†] JAMES M. FLINK,[‖] THEODORE W. RANDOLPH,[⊥] AND JOHN F. CARPENTER*

Contribution from *Department of Pharmaceutical Sciences, School of Pharmacy, University of Colorado Health Sciences Center, Denver, Colorado 80262, and Department of Pharmaceutics, The Royal Danish School of Pharmacy, Copenhagen, Denmark.*

Received October 5, 1998. Accepted for publication December 2, 1998.

Abstract □ The effects of various classes of additives on the stability of a protein with a relatively hydrophobic surface, *Humicola lanuginosa* lipase (HLL), during lyophilization and storage in the dried solid, were investigated. Prior to lyophilization, it was found that 1 M trehalose or 1% (wt/vol) Tween 20 caused the protein to precipitate. Infrared spectroscopy indicated that trehalose "salted-out" native HLL, whereas Tween 20 induced non-native aggregates. Optimal recovery of native protein in the initial dried solid was obtained in the presence of additives which formed an amorphous phase and which had the capacity to hydrogen bond to the dried protein (e.g., trehalose and sucrose). Additives which crystallized during lyophilization (e.g., mannitol) or which remained amorphous, but were unable to hydrogen bond to the dried protein (e.g., dextran), afforded less stabilization relative to that seen in the absence of additives. Optimal storage stability in the dried solid required that both protein unfolding during lyophilization was minimized and that the formulation was stored at a temperature below its T_g value. Crystallization of sucrose during storage greatly reduced the storage stability of HLL. This was attributed to the increased moisture content and the reduced T_g value in the remaining amorphous phase containing the protein. Sucrose crystallization and the resulting damage to the protein were inhibited by decreasing the mass ratio of sucrose:protein.

Introduction

Mechanisms that are proposed to account for stabilization of proteins acutely during lyophilization and long-term during storage in the dried solid are based mainly upon studies using globular proteins with a typical hydrophilic surface. It has been found that, in addition to formation of an amorphous phase in the dried solid, the ability of the additive to hydrogen bond to the dried protein and thus act as a water substitute also is required for optimal protection of a protein during the lyophilization process.[1] Furthermore, it has been found that long-term storage stability depends on two factors: (1) formation of a an amorphous phase containing protein and additive and maintenance of the formulation glass transition temperature (T_g) above the storage temperature, and (2) preservation of native, aqueous protein secondary structure during lyophilization.[2−4]

To determine if the same mechanisms may account for stabilization of a soluble, globular protein which has a much more hydrophobic surface than proteins typically studied, the current study investigates the effects of additives with selected properties on the acute and long-term stability of lyophilized *Humicola lanuginosa* lipase (HLL). HLL is a well-characterized protein[5,6] that has a predominantly hydrophobic surface exposed to the solvent, as determined by hydrophobicity plots.[7] HLL is used as an

* To whom correspondence should be addressed. Phone: (303) 315 6075. Fax: (303) 315 6281. E-mail address: John.Carpenter@UCHSC.edu. Department of Pharmaceutics, School of Pharmacy, Box C238, University of Colorado Health Sciences Center, 4200 E. 9th Ave., Denver, CO 80262.

[†] Department of Pharmaceutics, The Royal Danish School of Pharmacy, Copenhagen, Denmark.

[§] Current address: Department of Analytical Chemistry and Formulation, Immunex Corporation, Seattle, WA 98101.

[‖] Pharmaceutical Development − Technology, Biopharmaceuticals Division, Novo Nordisk A/S, 2820 Gentofte, Denmark.

[⊥] Department of Chemical Engineering, University of Colorado, Boulder, CO 80309, USA.

10.1021/js980399d CCC: $18.00
Published on Web 01/15/1999

enzymatic detergent additive[8] and has shown potential as a therapeutic protein for exocrine pancreatic insufficiencies.[9] The additives tested were mannitol, dextran, trehalose, and sucrose.

Sugars are often used to stabilize proteins during lyophilization and during subsequent storage in the dried solid. However, similar to other reports,[10−12] we have recently observed that crystallization of a sugar from the amorphous state during storage can drastically reduce protein storage stability.[2] Crystallization of amorphous sugars is usually only observed on a reasonable time scale of weeks to months during storage at temperatures close to or above the formulation T_g value.[13] Crystallization can be due to increased moisture contents (e.g., because of moisture transfer from the vial stopper to the dried formulation)[14,15] or simply due to prolonged storage.[16] Recently, it has been shown that proteins, at an adequately high protein:sugar mass ratio, are able to prevent crystallization of either sucrose[17] or trehalose[18] from the dried solid. However, since the T_g value of sucrose is much lower than that of trehalose at similar moisture contents,[19,20] it is expected that sucrose may crystallize at lower temperatures than trehalose. Thus, another objective of the current study is to determine the effects of varying protein: sugar mass ratios on the capacity of HLL to inhibit crystallization of sucrose or trehalose during storage.

In addition to issues involving sugar crystallization, it is generally of interest to investigate the relative stabilizing effects of sucrose or trehalose on the acute and long-term stability of proteins. This topic has been the subject of many publications.[12,19−21] Trehalose has been shown to provide improved storage stability at high storage temperatures to proteins[2,22] and to liposomes[20] compared to that provided by sucrose. However, no study to date has addressed the relative effectiveness of the disaccharides as stabilizers for a protein with a relatively hydrophobic surface, such as HLL.

Materials and Methods

Materials—Recombinant *Humicola lanuginosa* lipase (HLL), expressed in *Aspergillus oryzae*,[5] was a kind gift from Novo Nordisk A/S (Bagsværd, Denmark). The protein was obtained as a lyophilized, additive-free powder containing >95% HLL (by activity assay). Potassium phosphate, mannitol, dextran (*Leuconostoc mesenteroides*, Strain no. B-512, Average MW 162 kDa) and poly(oxyethylene) sorbitan monolaurate (Tween 20) were obtained from Sigma Chemical Co. (St. Louis, MO). Sucrose and trehalose were purchased from Pfanstiehl Laboratories (Waukegan, IL). All other chemicals and reagents were obtained from Sigma Chemical Co. (St. Louis, MO), except as indicated below.

Formulation Preparation—HLL was dissolved in 10 mM potassium phosphate buffer (pH 10, at 23 °C) at 4 mg/mL ($E_{280\ nm}$ (1%) = 14.68)[6] and mixed in a 1:1 (vol:vol) ratio with the respective additive solutions (prepared at twice the desired concentration using phosphate buffer) to obtain a final HLL concentration of 2 mg/mL and the final desired additive concentration. Formulations were subsequently aliquotted (1.0 mL) into 5 mL lyophilization vials (21 mm ID) (West Company, Lionsville, PA).

Lyophilization—The protein formulations were lyophilized in a FTS Durastop μP microprocessor controlled freeze-drier (Stoneridge, NY) as previously described.[2] After drying was complete, the vials were capped under vacuum using butyl stoppers from the West Company (formulation no. 4416) (Lionsville, PA). None of the formulations showed any evidence of cake collapse following lyophilization.

Storage Studies—Following lyophilization, vials were incubated at 40 or 60 °C and analyzed following 0, 14 days, 1 and 3 months. Control formulations were stored at −80 °C and analyzed following 3 months. Following storage, formulations were rehydrated to 1 mg/mL HLL with deionized, distilled water and filtered to remove insoluble aggregates, and the filtrate was analyzed as described below. Triplicate vials from each formulation were assayed at each time point. No differences were seen between formulations assayed at $t = 0$ and the control formulations stored at −80 °C (results not shown).

Analytical Methods—*Size exclusion high performance liquid chromatography (HPLC-SEC)* was performed by using a Dionex HPLC (Sunnyvale, CA) equipped with a GP40 gradient pump and an AD20 detector, using a detection wavelength of 215 nm. The amount of native, monomeric protein molecules and non-native soluble aggregates were quantitated using a Zorbax G250 column (MACMOD Analytical Inc., Chadds Ford, PA) eluted with 1 M sodium phosphate in phosphate-buffered saline solution (120 mM sodium chloride, 2.7 mM potassium chloride, 10 mM monobasic potassium phosphate; pH 7.4, at 23 °C) at a flow rate of 1.0 mL/min. Between 1 and 20 μg of protein were injected onto the column. The masses of native, monomeric HLL and soluble aggregates were calculated based on peak areas eluting at 11.2 min and between 9.1 and 11.0 min, respectively. Results were expressed as percentage of the native, monomeric protein mass present in solution prior to freeze-drying.

The amount of the protein-forming insoluble aggregates was calculated and reported as previously described.[2] To test whether protein could also be lost from solution due to adsorption to the vial or stopper during lyophilization and rehydration, the total protein content was estimated by a Bradford assay using bicinchoninic acid (BCA) (Pierce, Rockford, IL) as a reagent. For all preparations, 100% of the protein was recovered in the rehydrated formulations (data not shown), indicating that minimal protein was lost due to adsorption to surfaces.

HLL Activity Assay—HLL activity was assessed by the ability of the protein to hydrolyze tributyrin according to a slightly modified method originally described by Holmquist et al.[5,6] The amount of sodium hydroxide (Merck, Damstadt, Germany) required to neutralize hydrolyzed tributyrin (Merck, Damstadt, Germany) was monitored as a function of time employing a pH-stat titrator. The substrate solution (pH 7, at 30 °C) containing tributyrin (0.159 M) and gum arabic (0.094%, wt/vol) in water was emulsified using a blender for 20 s and subsequently stirred using a magnetic stir plate for 20−30 min. The HLL formulations were dissolved in 0.01 M glycine (Merck, Damstadt, Germany) (pH 10.6, at 23 °C) to yield a final concentration of approximately 1 mg/mL. The reaction was started by the addition of HLL solution to a stirred, thermostated (30 °C) substrate solution. The pH was maintained automatically with sodium hydroxide (0.05−0.1 M) using a Titralab 90 (Radiometer, Copenhagen, Denmark) equipped with an ABU900 autoburet (Radiometer, Copenhagen, Denmark) connected to a Titration Manager TIM900 (Radiometer, Copenhagen, Denmark). The amount of base required to maintain pH at 7.0 during 5 min of titration was recorded and used to calculate the hydrolytic activity of a given HLL formulation. Results are reported as mean values (± standard deviation) of three vials assayed in duplicate.

The enzymatic activity of HLL in solution prior to lyophilization was not determined. However, acute recovery of enzymatic activity in the lyophilized and rehydrated formulations averaged 97% ± 5% compared to a standard solution of freshly prepared HLL (1 mg/mL), and this value was therefore used as initial recovery of enzymatic activity at $t = 0$.

Karl Fisher Moisture Analysis—The relative amount of moisture was determined by preparing samples in a dry nitrogen purged glovebox and assaying for water content using a Mettler DL37 KF coulometer (Hightstown, NJ) as previously described,[2] except that slightly larger aliquots (2−5 mL) of a 1:1 (vol:vol) methanol: formamide mixture were used to dissolve the dried formulations compared to that previously used (1 mL aliquots).

X-ray Diffraction—X-ray powder diffraction was recorded with a Guinier powder diffraction camera, XDC-700 (Incentive Research & Development AB), using Cr $K\alpha_1$ (l = 2.290 Å) radiation. Small amounts of dried solid (5−10 mg) was placed in a sample disk, and the sample was subjected to radiation for approximately 30−45 min. The film was developed, and crystallization was detected as distinct band patterns characteristic for the crystallized material (sucrose).

Sodium dodecyl lauryl sulfate polyacrylamide gel electrophoresis (SDS−PAGE), using nonreduced and reduced samples, was performed as previously described.[2] The gels showed a faint band corresponding to the molecular weight of a dimer in all stored and rehydrated formulations which had more than 20% soluble aggregates, as determined by size-exclusion chromatography (data

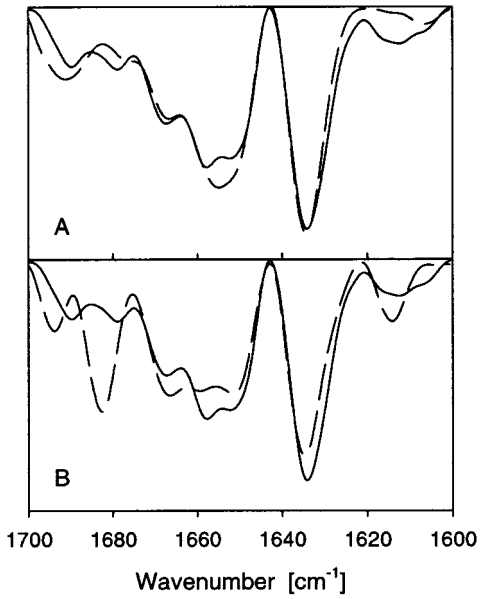

Figure 1—Area-normalized, second derivative infrared amide I spectra of native, aqueous HLL in buffer alone (10 mM phosphate buffer, pH 10, at 23 °C) (—) and of HLL precipitate (---) induced by 1 M trehalose (A) or 1% (wt/vol) Tween 20 (B).

not shown). The band was present in both nonreduced and reduced samples assayed by SDS−PAGE, indicating that the covalently bonded dimer is formed by mechanisms other than disulfide scrambling. No bands corresponding to low molecular weight fragmentation products were observed (not shown).

Infrared (IR) Spectroscopy—Infrared spectra of liquid and dried HLL formulations were recorded at 23 °C using a Nicolet Magna 550 infrared spectrometer (Madison, WI) as previously described.[2] Spectra were processed according to previously established criteria.[23]

Differential scanning calorimetric (DSC) analysis was also conducted as previously described[2] using a Perkin-Elmer DSC-7 (Norwalk, CT). Briefly, samples were heated at 10 °C/min to a final temperature of 180 °C. Selected samples were then cooled and reheated to 50−100 °C above the glass transition temperature to ensure reversibility of the glass transition. The degree of crystallinity of PEG or mannitol was calculated by dividing the enthalpy per gram of PEG or mannitol in an experimental formulation by the value obtained for the respective reference material and multiplying the result by 100.[2] Reference materials were taken from the supplier's bottle (Sigma Chemical Co., St. Louis, MO).

Results and Discussion

Effect of Additives on Secondary Structure in Solution—To determine if the presence of an additive induced secondary structural changes in HLL prior to lyophilization, protein infrared spectra in the conformationally sensitive amide I region were compared. The second derivative spectrum for the protein prepared in buffer alone is shown in Figure 1. The component bands can be assigned as follows:[24] bands at 1631, 1635, and 1689 cm^{-1} are due to β-sheet, the band at 1649 cm^{-1} is due to random elements, the band at 1657 cm^{-1} is due to α-helix, and the bands at 1668 and 1679 cm^{-1} are often assigned to turn structures. The spectra for the protein prepared in the presence of 1 M sucrose, 0.5 M mannitol, or 5% (wt/vol) dextran were essentially identical to that for the protein in buffer alone (data not shown). Thus, these additives do not alter the secondary structure of the protein in solution.

However, unexpectedly, in the presence of 1 M trehalose or 1% (wt/vol) Tween 20, the protein formed a white precipitate. Such behavior has not been reported previously in several studies of more typical globular proteins with relatively hydrophilic surfaces and may thus be attributed to the surface hydrophobicity of HLL. To gain insight into the process causing precipitation, we used infrared spectroscopy to study the protein secondary structure. The spectrum for the precipitate formed in 1 M trehalose was very similar to that for native, soluble protein, indicating that precipitation did not alter protein secondary structure (Figure 1A). Diluting the solution with buffer caused the precipitate to dissolve completely (data not shown). Thus, it appears that trehalose can "salt-out" HLL. Reversible precipitation and retention of native protein secondary structure in precipitates have previously been noted for interferon-γ salted-out with PEG,[25] and for lactate dehydrogenase, chymotrypsinogen, bovine serum albumin, and insulin salted-out with poloxamer.[26]

Salting-out of proteins by additives can be explained by the Timasheff preferential exclusion mechanism. The salting-out agents are preferentially excluded from the protein surface, which increases protein chemical potential and reduces solubility.[27] Interestingly, HLL remained soluble in 1 M sucrose but was salted-out with 1 M trehalose. Sucrose and trehalose have both been shown to be preferentially excluded to a similar degree from the surface of ribonuclease A, a protein with a more typical predominantly hydrophilic surface.[27,28]

The preferential interactions of sugars with a protein with a more hydrophobic surface such as HLL have not been studied. However, trehalose has been found to interact less favorably with poly(ethylene glycol) (PEG) than does sucrose.[29] PEG attains a more hydrophobic surface at higher temperatures due to conformational alterations.[30] Izutsu and colleagues found that trehalose depressed the cloud point of PEG (i.e., the temperature above which PEG separates as a precipitate from an aqueous solution) to a greater degree than sucrose. The lower solubility of PEG in the presence of trehalose is thought to be due to a greater repulsion between PEG and trehalose than between PEG and sucrose.[29] In turn, this difference has been attributed to differences between sucrose and trehalose stereochemistry.[30,31] That of trehalose fosters a larger volume of hydration and thus a more favorable interaction with water and a less favorable interaction with apolar molecules. Therefore, trehalose is expected to interact less favorably with hydrophobic molecules such as PEG or HLL than does sucrose.

Contrary to the trehalose-induced precipitate, the precipitate induced by Tween 20 did not dissolve upon dilution in buffer (data not shown), and the infrared spectrum of the protein precipitate was substantially altered compared to that of native HLL (Figure 1B). The presence of large infrared bands at 1614 and 1696 cm^{-1} are due to an intermolecular β-sheet,[32,33] suggesting that the precipitated protein was composed of non-native aggregates. Aggregation via the formation of non-native β-sheet structure is commonly seen for proteins under denaturing conditions such as high temperature, extremes in pH, or the presence of chaotrophs such as urea, guanidine hydrochloride, or thiocyanate.[32,33] Thus, in contrast to the "salting-out" noted in the presence of trehalose, Tween 20 alters the native conformation to a sufficient degree that the non-native molecules form intermolecular contacts and precipitate. Interaction of HLL with the Tween 20 micelle−water interface and/or direct binding of Tween 20 to the protein's surface may be responsible for perturbation of the native protein structure. For proteins with a more typical hydrophilic surface such as Factor XIII[2] and subtilisin,[34] Tween 20 does not alter the native structure of the protein.

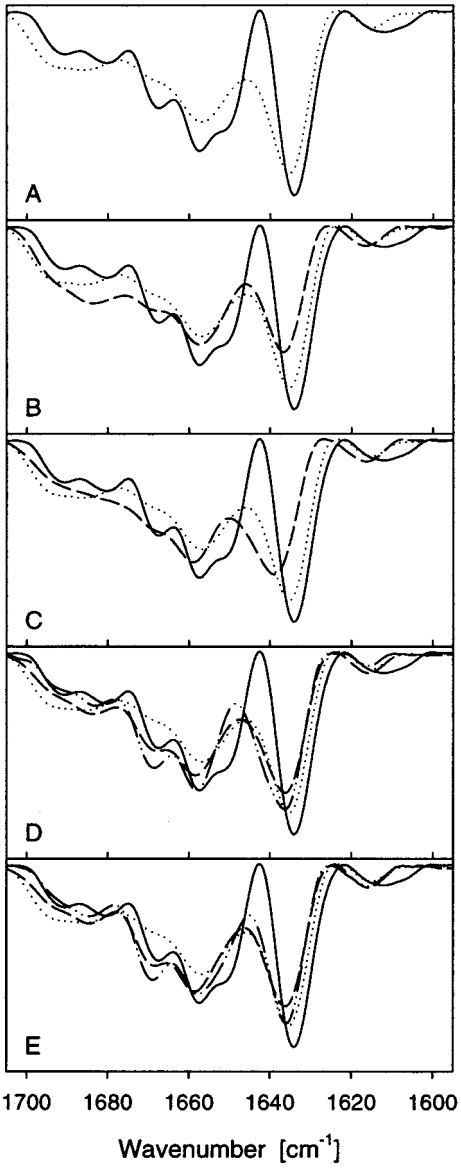

Figure 2—Area-normalized second derivative infrared amide I spectra of HLL in the native, aqueous state (—) and when lyophilized in the absence of additives (•••), or in the presence of additives (---): No additives (A), 300 mM mannitol (B), 5% (wt/vol) dextran (C), 50 mM (---) or 300 mM (–••–) trehalose (D), or 50 mM (---) or 300 mM (–••–) sucrose (E).

Thus, it appears that the effects of additives on the structure and solubility of the hydrophobic protein HLL in aqueous solution are quite different from those noted with more typical soluble, globular proteins that have a more hydrophilic surface exposed to the solvent. The next question we addressed is whether different behaviors also are manifested during the lyophilization process.

Acute Stability during Freeze-Drying and Rehydration—To assess initially the effects of freeze-drying, HLL was lyophilized in the absence of additives. Figure 2A shows that the infrared spectrum of the dried protein was substantially altered relative to that of the native, aqueous protein. In general, the components bands in the amide I region for the spectrum of the dried protein appeared broader and had decreased resolution. This is typical of many lyophilized proteins.[2,35] In addition, there was a decrease in absorbance of the bands at 1635, 1649, 1657, and 1668 cm^{-1} which was compensated for by an increase in absorbance at 1645 cm^{-1} and in the region from 1684 to 1694 cm^{-1} (Figure 2A). Together, these changes indicated that HLL was unfolded in the dried solid. Upon rehydration, however, 100% native, monomeric protein was recovered (Table 1). Thus, it appeared that refolding of HLL was favored over aggregation during rehydration.[35]

Table 1—Lyophilized Formulation Characteristics

formulation	% native monomer[a]	glassy[b]	T_g,[b] °C	% moisture[a]
no additives	100 ± 0.5	yes	nd[c]	<0.5
300 mM mannitol	93 ± 1.8	no	na[d]	1.3 ± 0.5
5% (wt/vol) dextran	96 ± 1.8	yes	nd[c]	0.6 ± 0.3
50 mM trehalose	98 ± 1.6	yes	95	0.9 ± 0.7
300 mM trehalose	95 ± 1.2	yes	100	0.5 ± 0.1
50 mM sucrose	102 ± 1.2	yes	70	1.0 ± 0.5
300 mM sucrose	99 ± 0.3	yes	70	1.2 ± 0.6

[a] Values are reported as mean of three vials from each formulation (±standard deviation). Native, monomer recovery was determined by size exclusion chromatography. Moisture content was determined by Karl Fisher titration and reported as % (g H_2O/100 g dried solid). [b] Determined by differential scanning calorimetry (see Methods). [c] nd = no glass transition detectable. Previous literature[42,43] indicates that the T_g may be above the highest storage temperature (60 °C). [d] na = not applicable, mainly crystalline material.

To determine if the water replacement mechanism shown to account for protection of more hydrophilic proteins during lyophilization[2–4] also accounts for protection of more hydrophobic proteins, HLL was lyophilized in the presence of representative additives, which previously have been shown to (1) remain amorphous and hydrogen bond to the dried protein (trehalose or sucrose),[1] (2) fail to protect due to crystallization (mannitol),[10] or (3) remain amorphous, but fail to protect the protein because steric hindrance eliminates effective hydrogen bonding to the dried protein (dextran).[36]

The second derivative amide I infrared spectra for the protein dried with 300 mM mannitol or 5% (wt/vol) dextran were more perturbed than that for HLL lyophilized without additives (Figure 2B,C). There was a further decrease in absorbance at 1635 cm^{-1} and greater band broadening. In addition, the recovery of native, monomeric protein was slightly less with mannitol than that noted for the protein lyophilized without additives (Table 1). Dextran had little effect on the recovery of native, monomeric protein (Table 1).

Differential scanning calorimetric analysis (see Methods) documented that 85% of the mannitol mass was crystallized in the dried solid (not shown). Apparently the remaining 15% of mannitol, corresponding to a 4:1 mass ratio of mannitol:HLL, did not afford protection to the protein during lyophilization. This is consistent with results observed for more hydrophilic proteins.[2,10]

In contrast, differential scanning calorimetry showed that dextran was completely amorphous in the dried solid containing HLL (data not shown). The failure of amorphous dextran to inhibit protein unfolding may be due to steric hindrance making it unable to hydrogen bond with the dried protein. In addition, potential separation of dextran and protein into separate dextran-rich and protein-rich amorphous phases[37] could have caused greater damage to the protein during lyophilization.

Finally, the effects of sucrose and trehalose were tested. Both disaccharides formed amorphous phases (Table 1) during lyophilization and are known to have the ability to hydrogen bond to the protein during dehydration.[1,35] Infrared spectra of HLL lyophilized in the presence of either concentration (50 or 300 mM) of trehalose (Figure 2D) or sucrose (Figure 2E) were more nativelike than those of HLL lyophilized without additives (Figure 2A). The bands near 1648, 1657, and 1668 cm^{-1} were better resolved, and the absorbance in the region from 1684 to 1694 cm^{-1}

was reduced to a level more closely resembling that seen in the spectrum of the native, aqueous protein (Figure 2D,E). The spectrum of HLL lyophilized with sucrose (Figure 2E) had slightly less broadening of the 1635 cm^{-1} band compared to that seen in the spectrum of HLL lyophilized with trehalose (Figure 2D), suggesting that structural preservation by sucrose was somewhat better than that by trehalose. Thus, despite the less favorable interaction between HLL and trehalose than between HLL and sucrose in aqueous solution, similar levels of structural protection are noted during freezing-drying and rehydration. Also, slightly better band resolution was achieved in spectra of HLL lyophilized in the presence of 300 mM disaccharide compared to formulations prepared in 50 mM disaccharide (Figure 2D,E). Preliminary studies showed band resolution in the spectra of the dried protein increased when HLL was lyophilized with increasing disaccharide concentrations ranging from 10 to 300 mM (unpublished results). Finally, more than 95% of native, monomeric protein was recovered after rehydration of HLL formulations lyophilized with either disaccharide (Table 1). Taken together, these results indicate that sucrose and trehalose are far superior to mannitol and dextran at inhibiting lyophilization-induced unfolding of HLL.

Long-Term Storage Stability—It has been proposed that storage stability of a protein in the dried solid only depends on using an amorphous additive and on maintaining the formulation at a temperature below its T_g value.[38] However, in the only three published studies (with interleukin-1 receptor antagonist, Factor XIII, and interleukin-2), in which both protein structure and glass transition temperature of the dried solid have been determined,[2–4] it was found that long-term stability of a protein in the dried solid depended both on minimizing protein unfolding during the lyophilization process as well as on storage at a temperature below the formulation T_g value. If the only requirement for storage stability of HLL is that formulations must be stored in the amorphous solid at temperatures below the T_g value,[38] then formulations containing either dextran, trehalose, or sucrose should show optimal stability (Table 1). If, in addition, preservation of native structure in the dried solid is also important,[2–4] then only trehalose and sucrose should provide optimal stability (Figure 2).

However, storage stability of a dried protein may also be compromised if the sugar additive crystallizes during storage.[11,12] Sugar crystallization usually occurs at temperatures close to or above the formulation T_g value and can be minimized by increasing the mass ratio of protein to sugar.[17,18] Since the initial T_g values of the trehalose containing HLL formulations were 25–30 °C higher than those of the sucrose-containing formulations (Table 1), it would be expected that during storage at 40 and 60 °C, HLL formulations containing sucrose (especially at the higher initial sucrose concentration) would be more prone to sugar crystallization than those containing trehalose.

HLL was stored without additives to assess the storage stability of the protein alone. The additive-free formulation had a residual moisture level of less than 0.5% (g H_2O/g dried solid) (Table 1). Similar to what has been observed for other proteins,[2,17] a glass transition for the HLL formulation was not discernible by differential scanning calorimetric analysis (data not shown). The glass transition temperature of dried HLL was probably well above either storage temperature, since dried protein T_g values have been estimated to be between 100 and 200 °C.[39] Thus, if storage in the amorphous solid at temperatures below the T_g value was the only important factor accounting for long-term storage stability of the hydrophobic protein, it would be expected that HLL without additives would exhibit good storage stability.

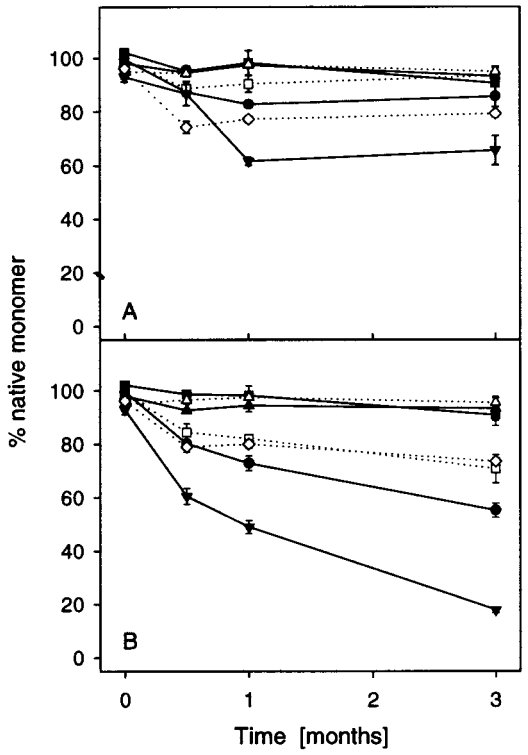

Figure 3—Recovery of native, monomeric HLL as a function of time as determined by size exclusion chromatography. The recovery was determined as the percentage of native, monomeric protein relative to that present in solution prior to lyophilization. Formulations were stored at 40 °C (A) or 60 °C (B) in the absence of additives (solid circle) or in the presence 300 mM mannitol (solid triangle, down), 5% (wt/vol) dextran (open diamond), 50 mM trehalose (solid triangle, up), 300 mM trehalose, (open triangle, up), 50 mM sucrose (solid square), or 300 mM sucrose (open square). Each data point represents the mean of 3 vials ± standard deviation.

Following rehydration of the formulation, which had been stored for 14 days at either 40 and 60 °C, loss of native, monomeric HLL (Figure 3) was seen. This was mainly due to formation of insoluble aggregates in the formulation stored at 40 °C (Figure 5A) and formation of approximately equal amounts of soluble and insoluble aggregates at 60 °C (Figures 4B, 5B). Larger effects were noted in the formulation stored at 60 °C than at 40 °C (Figures 3–6). There was a much larger loss of hydrolytic activity (Figure 6) compared to loss of native, monomeric protein (Figure 3) after 3 months storage. This suggested that chemical degradation in addition to physical degradation (aggregation) was taking place. Chemical degradation such as deamidation and oxidation has previously been observed in lyophilized protein formulations during storage of the dried solid.[40] Taken together, these results document that storage of HLL at temperatures below the T_g value was not sufficient to ensure optimal storage stability, similar to that noted for several other more hydrophilic proteins.[2,3,40,41]

To determine if the damage assessed after storage and rehydration was accompanied by structural alterations in the dried solid, infrared spectra of the dried formulations stored at either temperature were recorded. Figure 7A shows that the structural alterations initially induced during the lyophilization process were augmented after storage for 3 months at either 40 or 60 °C. Absorbances of the bands at 1635 and 1657 cm^{-1} were further decreased, and this was compensated for by a further increase in absorption in the 1684 to 1694 cm^{-1} region. The modest increase in absorbances at 1694 cm^{-1} might be due to an

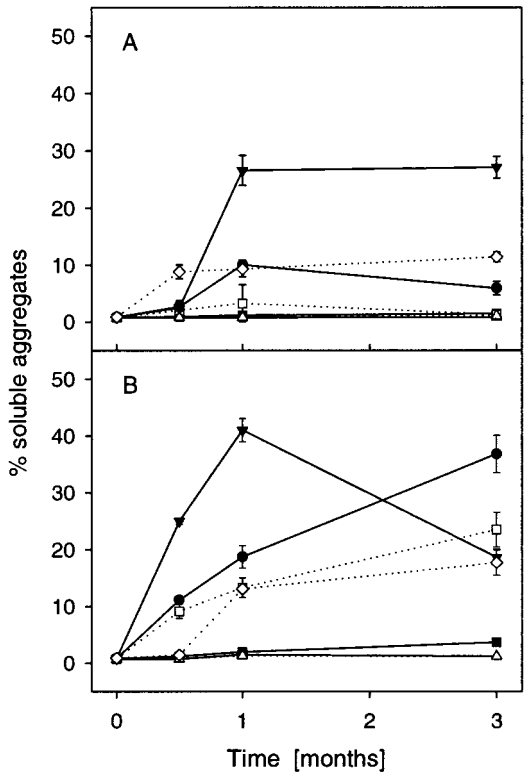

Figure 4—Formation of soluble aggregates as a function of time as determined by size exclusion chromatography. The amount of soluble aggregates formed was determined as the amount of soluble aggregates present in the stored and rehydrated formulations relative to the initial amount of native, monomeric protein present in solution prior to lyophilization. Formulations were stored at 40 °C (A) or 60 °C (B) in the absence of additives (solid circle) or in the presence 300 mM mannitol (solid triangle, down), 5% (wt/vol) dextran (open diamond), 50 mM trehalose (solid triangle, up), 300 mM trehalose, (open triangle, up), 50 mM sucrose (solid square), or 300 mM sucrose (open square). Each data point represents the mean of 3 vials ± standard deviation.

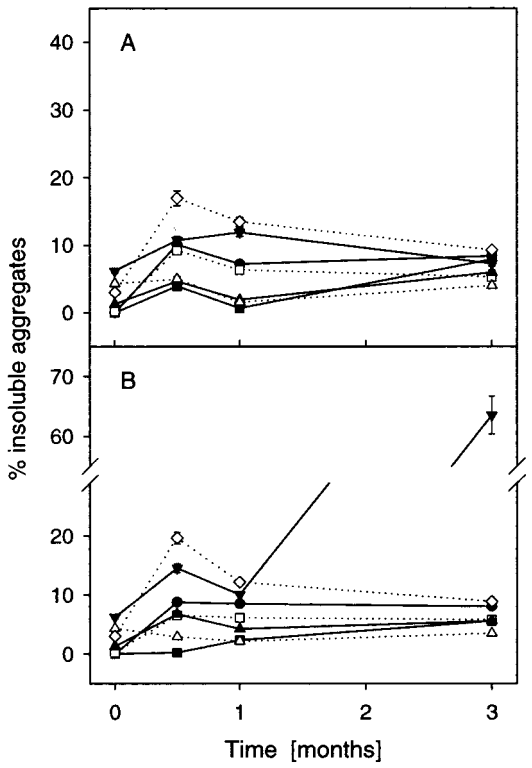

Figure 5—Formation of insoluble aggregates as a function of time. The amount of insoluble aggregates present in the stored and rehydrated formulations was calculated as the difference between the initial mass of native, monomeric protein present in solution prior to lyophilization minus the mass of recovered soluble protein (native, monomeric protein and soluble aggregates). Formulations were stored at 40 °C (A) or 60 °C (B) in the absence of additives (solid circle) or in the presence 300 mM mannitol (solid triangle, down), 5% (wt/vol) dextran (open diamond), 50 mM trehalose (solid triangle, up), 300 mM trehalose, (open triangle, up), 50 mM sucrose (solid square), or 300 mM sucrose (open square). Each data point represents the mean of three vials ± standard deviation.

intermolecular β-sheet, reflective of the formation of protein aggregates in a small fraction of the dried protein molecules.[32,33,35] However, the much greater formation of soluble aggregates noted after rehydration of the formulation stored at 60 °C compared to that measured for the formulation stored at 40 °C (Figure 4) was not reflected in the infrared spectra of the dried protein, which were very similar. Thus, it appears that aggregation during rehydration was more pronounced for the formulation stored at 60 °C.

Compared to the formulation prepared without additive, the formulation prepared with 300 mM mannitol had a greater loss of native, monomeric protein (Figure 3) and of hydrolytic activity (Figure 6) and increased formation of both soluble and insoluble aggregates during storage at either 40 or 60 °C. The one exception was the formulation stored at 60 °C which showed a decrease in the amount of soluble aggregates (Figure 4B) between 1 and 3 months storage concomitant with a large increase in the amount of insoluble aggregates (Figure 5B). Similar to that seen in the absence of additives, there was a larger decrease in recovery of hydrolytic activity (Figure 6) than that of native, monomeric protein (Figure 3), indicating that chemical degradation, in addition to physical degradation, was taking place.

Interestingly, secondary structural changes were not observed following storage for 3 months at either temperature (Figure 7B). It may have been that the amorphous mannitol in the formulation provided spatial separation between the protein molecules, thus preventing protein structural changes, resolvable by infrared spectroscopy, in the dried solid. The extensive aggregation noted after rehydration, however, indicated that mannitol was not able to inhibit aggregation during rehydration.

The poor storage stability of HLL lyophilized in the presence of mannitol is consistent with previous studies, which have shown that additives, which crystallized during lyophilization, afforded poor storage stability to several proteins.[2,10–12] The cause of the increased degradation of HLL in the mannitol formulation compared to that in the formulation without additives was not clear. There was not any increase in mannitol crystallinity during storage, based on analysis of the formulation with differential scanning calorimetry (data not shown). However, even though a glass transition was not apparent in the thermograms of the mannitol formulations, it may be that the T_g value of the amorphous solid of this formulation was lower than that for the formulation prepared without additives, resulting in reduced storage stability of the mannitol formulation.

To assess the effect of forming an amorphous solid with a T_g value above the storage temperature, HLL was stored in the presence of 5% (wt/vol) dextran. The amorphous solid formed in the presence of dextran had a moisture content of 0.6% (Table 1). No glass transition was detected by differential scanning calorimetric analysis (data not shown). Dextrans are known to form amorphous solids with T_g values increasing with the molecular weight of the dextran.[42] Since dextran with an average molecular weight of 40 kDa and a moisture content of 4% has previously been shown to exhibit a glass transition at temperatures corresponding to 90−100 °C,[43] it is assumed that the T_g value

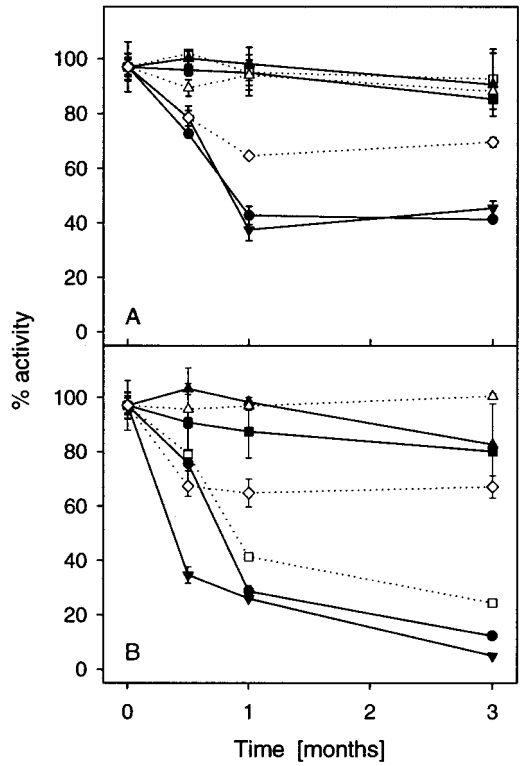

Figure 6—Recovery of hydrolytic activity as a function of time as determined by the activity assay. The recovery of hydrolytic activity was determined as the hydrolytic activity of the stored and rehydrated formulations relative to the initial hydrolytic activity of a given formulation prior to lyophilization. Formulations were stored at 40 °C (A) or 60 °C (B) in the absence of additives (solid circle) or in the presence 300 mM mannitol (solid triangle, down), 5% (wt/vol) dextran (open diamond), 50 mM trehalose (solid triangle, up), 300 mM trehalose, (open triangle, up), 50 mM sucrose (solid square), or 300 mM sucrose (open square). Each data point represents the mean of 3 vials ± standard deviation.

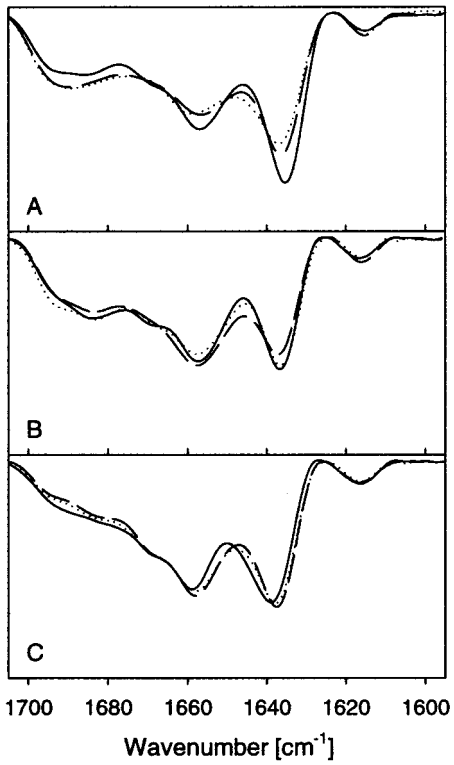

Figure 7—Effect of 3 months storage at 40 °C (•••) or 60 °C (---) on the area-normalized, second derivative amide I infrared spectra of lyophilized HLL. Changes were compared to those induced during lyophilization (—). Formulations were lyophilized and stored in the absence of additives (A), or in the presence of 300 mM mannitol (B), or 5% (wt/vol) dextran (C).

of the current dextran formulation (average molecular weight of dextran = 162 kDa) was well above either storage temperature used in the current study.

Dextran did not substantially improve recovery of native, monomeric protein (Figure 3) nor decrease the formation of aggregates (Figures 4, 5) following rehydration of the formulation stored at 40 °C compared to that observed for the formulation without additives. However, a slight improvement in recovery of hydrolytic activity (Figure 6) was observed in the dextran-containing formulation stored at 40 °C. In addition, dextran slightly improved storage stability of the formulation stored at 60 °C compared to that observed in the formulation without additives (Figures 3–6). At both storage temperatures, loss of hydrolytic activity (Figure 6) following storage and rehydration was not much larger than the loss of native, monomeric protein (Figure 3), suggesting that dextran may stabilize against putative chemical degradation to a greater degree than that seen in the absence of additives.

Figure 7C shows that potential secondary structural changes arising during storage in the dried solid were not detectable with infrared spectroscopy. This is consistent with the results observed for Factor XIII[2] and interleukin-2.[4] Dextran may inhibit structural transitions in the dried solid because it forms an amorphous phase with a high T_g value, which restricts alterations in protein conformation, and also because amorphous dextran is able to spatially separate protein molecules in the dried solid.[38]

The partially improved stability of HLL in the presence of dextran is attributed to storage in an amorphous solid at temperatures substantially below the T_g value of the dextran formulation, suggesting that the same criterion, which is necessary for storage stability of hydrophilic proteins, also is important for hydrophobic proteins. However, also similar to that observed for hydrophilic proteins,[2] this mechanism alone did not appear to be sufficient for optimal storage stability of HLL.

Both concentrations of trehalose (50 mM or 300 mM) formed an amorphous cake with a low moisture content and a T_g value substantially greater than either storage temperature (Table 1), and afforded optimal stability following 3 months storage at either temperature (Figures 3–6). Minor structural alterations were induced during storage in the dried solid in the presence of either concentration of trehalose (Figure 8A,B). These alterations, however, were not reflected in the recovery of either native, monomeric (Figure 3) nor hydrolytically active molecules (Figure 6) in the stored and rehydrated formulations. This may have been because trehalose afforded an environment conducive to refolding upon rehydration.[4]

The increased storage stability relative to that noted with dextran is attributed to the greater retention of native protein structure during the initial lyophilization process (Figure 2). Thus, as has been documented for more hydrophilic proteins, for the relatively hydrophobic HLL, storage at a temperature below the T_g value of the amorphous phase as well as preservation of native structure during lyophilization are critical for storage stability.

Sucrose at either concentration (50 mM or 300 mM) formed an amorphous solid with an initial T_g value above the highest storage temperature (Table 1). In addition, sucrose was able to minimize lyophilization-induced structural alterations (Figure 2E). Figures 3–6 show that the formulation containing 50 mM sucrose stored at either temperature and also the formulation containing 300 mM sucrose stored at 40 °C were as effective at stabilizing HLL

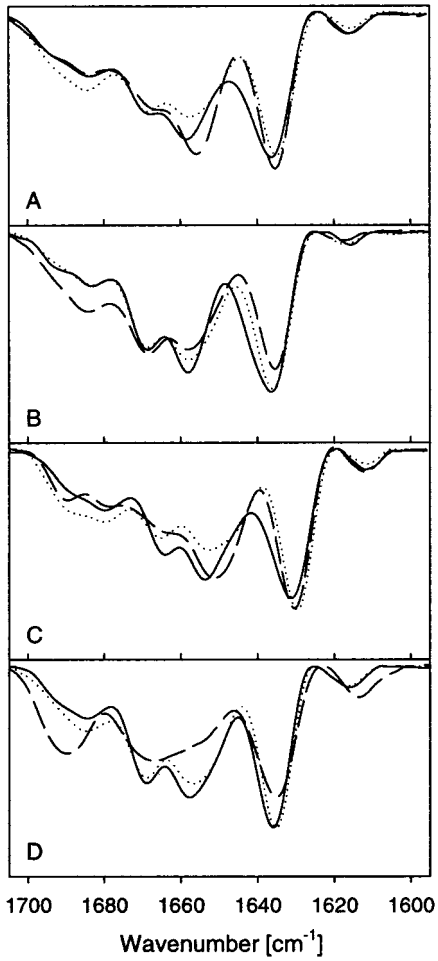

Figure 8—Effect of 3 months storage at 40 °C (•••) or 60 °C (---) on the area-normalized, second derivative amide I infrared spectra of lyophilized HLL. Changes were compared to those induced during lyophilization (—). Formulations were lyophilized and stored in the presence of 50 mM trehalose (A), 300 mM trehalose (B), 50 mM sucrose(C), or 300 mM sucrose (D).

as either concentration of trehalose. However, at 60 °C, 300 mM sucrose afforded minimal stability.

Relatively small secondary structural changes were seen in the formulation containing 50 mM sucrose following storage at either temperature and in the formulation containing 300 mM sucrose stored at 40 °C (Figure 8C,D). However, the infrared spectrum of the protein stored with 300 mM sucrose at 60 °C showed substantial alterations (Figure 8D). Decreases in absorbances at 1635 and 1657 cm^{-1} were indicative of loss of native structure. In addition, increased absorbances at 1614 and 1695 cm^{-1} were due to intermolecular β-sheet formation, which suggested that aggregation was occurring in the dried solid during storage.[35] These changes were consistent with the large amount of aggregates formed upon rehydration.

Thus, at the higher storage temperature (60 °C) sucrose was able to stabilize HLL at high protein:sucrose ratio corresponding to 12% protein [g protein/g (protein+sucrose)] but not at low protein: sucrose ratio (2% protein). Differential scanning calorimetric analysis showed similar initial T_g values for the sucrose containing HLL formulations (Table 1), independent of initial protein:sucrose ratio. Similarly, Sarciaux and Hageman[17] also found that somatotropin (rbSt) did not affect the T_g value of an rbSt formulation containing sucrose at protein weight fractions below 30% (g protein/ g dried formulation). However, they did notice that increasing the concentration of rbSt at lower protein weight fractions (4−10% protein) resulted in an

Table 2—Moisture Content and Glass Transition Temperatures following 3 Months Storage

formulation	% moisture[a] (40 °C)	% moisture[a] (60 °C)	T_g,[b] (40 °C)	T_g,[b] (60 °C)
no additives	13.2 ± 0.8	11.3 ± 2.0		
300 mM mannitol	1.7 ± 0.4	1.4 ± 0.2		
5% (wt/vol) dextran	4.9 ± 0.3	6.5 ± 0.8		
50 mM trehalose	7.1 ± 0.8	4.7 ± 0.5	81	85
300 mM trehalose	2.6 ± 0.2	3.3 ± 0.4	79	87
50 mM sucrose	5.1 ± 1.3	5.9 ± 0.9	46	50
300 mM sucrose	3.1 ± 0.5	1.1 ± 0.2	52	nd[c]

[a] Moisture content of formulations stored at either 40 or 60 °C were determined by Karl Fisher titration (% [g H_2O/100 g dried solid]) and are reported as mean of three vials from each formulation (±standard deviation). [b] Glass transition temperatures (T_g) of formulations stored at either 40 or 60 °C were determined by differential scanning calorimetry (see Methods) and are reported as an average temperature of two vials from each formulation. [c] nd = no glass transition detectable.

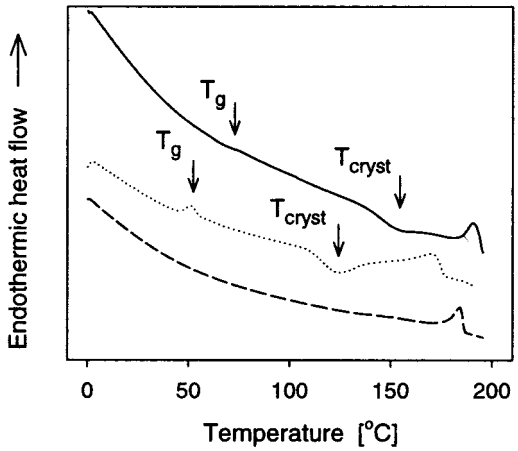

Figure 9—Differential scanning calorimetric thermograms of HLL formulations lyophilized with 300 mM sucrose: Immediately after lyophilization (—), or after 3 months storage at 40 °C (•••) or 60 °C (---). Formulations containing amorphous sucrose prior to thermal scans (top and middle thermograms) exhibited a second-order transition corresponding to a glass transition (T_g) and an exothermic peak (T_{cryst}) corresponding to sucrose crystallization during heating in the calorimeter. The formulation containing crystalline sucrose prior to thermal scanning did not exhibit either of these thermal events (lower thermogram). The endothermic peak at the glass transition of the formulation stored at 40 °C (•••) is due to enthalpic relaxation.

increase in the crystallization temperature of sucrose. Thus, for the current study, although no measurable effect were resolved based on the initial T_g values (Table 1), the differences in storage stability of the two sucrose formulations may be due to inhibition of sucrose crystallization in the formulation containing the greatest weight fraction of HLL.

Crystallization of a sugar commonly requires storage at or above the formulation T_g value.[13] Although the initial T_g values of the dried disaccharide formulations were all above the highest storage temperature (Table 1), during storage the formulations showed an increase in moisture content and a concomitant decrease in the T_g values (Table 2), presumably due to moisture transfer from the stopper.[44]

Differential scanning calorimetric analysis indicated that the decrease in T_g values for both of the trehalose formulations and for the formulation containing low concentrations of sucrose was not accompanied by crystallization of sugar (not shown). In contrast, after 3 months of storage at 60 °C, the 300 mM sucrose formulation did not show a glass transition nor was a crystallization exotherm observed in the thermogram (Figure 9). For comparison, these features were clearly apparent in thermograms for the corresponding formulation immediately after lyophilization or after

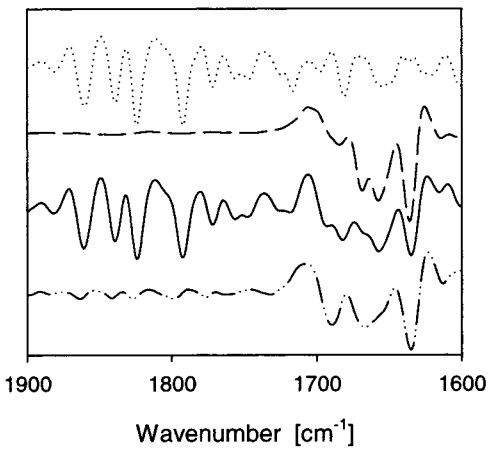

Figure 10—Area-normalized second derivative infrared spectra (1900 cm^{-1} to 1600 cm^{-1}) of crystalline sucrose obtained from the supplier's bottle (•••) and of HLL, lyophilized in the presence of 300 mM sucrose, immediately after lyophilization (---), and after 3 months storage at 60 °C (—). Subtraction of the crystalline sucrose spectrum from the spectrum of HLL lyophilized with 300 mM sucrose, stored at 60 °C for 3 months, resulted in a nearly flat baseline from 1900 cm^{-1} – 1700 cm^{-1} (–••–), ensuring that absorbance in the amide I region (1700 cm^{-1} – 1600 cm^{-1}) was due only to protein.

storage at 40 °C (Figure 9). Thus, for the 300 mM sucrose formulation, the amorphous saccharide had crystallized during storage at 60 °C. This conclusion was confirmed with X-ray powder diffraction, which showed that sucrose crystallization was initiated in the formulation containing 300 mM sucrose following 1 month storage at 60 °C and increased further after 3 months of storage (data not shown). There was not any crystalline sucrose detectable by X-ray powder diffraction in the 300 mM sucrose formulation immediately after lyophilization. And there was no indication of crystalline sucrose in the formulation containing 50 mM sucrose, even after 3 months of storage at 60 °C (data not shown).

Further evidence for sucrose crystallization was obtained by infrared spectroscopy. We have previously shown that sucrose crystallization can be detected by analyzing the second derivative IR spectra in the 1900−1700 cm^{-1} region.[2] Figure 10 shows the second derivative IR spectra of crystalline sucrose obtained from the supplier's bottle and of noncrystalline and crystalline sucrose containing HLL formulations. Both the spectrum of pure crystalline sucrose and that of the HLL formulation containing crystalline sucrose (300 mM sucrose formulation stored for 3 months at 60 °C) had strongly absorbing bands at 1860, 1839, 1824, and 1792 cm^{-1}. In contrast to this, spectra of HLL containing only amorphous sucrose (e.g., immediately after lyophilization) showed a straight baseline in the 1900−1700 cm^{-1} region (Figure 10). Since crystalline sucrose also absorbed slightly in the amide I region (1700−1600 cm^{-1}), it was necessary to subtract the spectrum of crystalline sucrose from that of the HLL formulation containing crystalline sucrose. The subtraction result showed a relatively flat baseline between 1900 and 1700 cm^{-1}, indicating that absorption of the resultant spectrum in the amide I region was due to protein only (Figure 10).

The increased damage to HLL associated with crystallization of sucrose most likely is due to the fact that crystalline sucrose is anhydrous.[45] Thus, as sucrose crystallizes the relative mass of water remaining in the amorphous phase will increase. As a result, the T_g value of the remaining amorphous material will decrease, resulting in compromised protein stability. Similar results were noted with formulations of Factor XIII in which sucrose crystallized.[2]

Finally, the formulation containing 50 mM sucrose stored at 60 °C for 3 months had a final T_g value below the storage temperature (Table 2), yet no sucrose crystallization was observed. This may have been due to several factors. First, when stored at a temperature near the T_g value, the formulation may collapse, but not crystallize.[42] Second, as explained above, increased weight fractions of protein in a dried solid may increase the crystallization temperature without affecting the T_g value.[17,18] Thus, it may have been that the crystallization temperature of sucrose in the current HLL formulation remained above the highest storage temperature (60 °C).

Conclusion

The precipitation of HLL—by salting-out action of trehalose and denaturing action of Tween—documents that the effect of excipients on this relatively hydrophobic protein are much different than those seen with proteins with more typical predominantly hydrophilic surfaces. Despite this difference, the same mechanisms accounting for both acute and long-term storage stability of hydrophilic proteins also accounted for stability of HLL. First, optimal acute stability during lyophilization of HLL required the formation of an amorphous phase containing protein and additive. In addition, the additive should possess the ability to hydrogen bond and thus act as a water substitute during dehydration. However, since the protein favored refolding over aggregation upon rehydration, damage to HLL during lyophilization was best resolved in the dried solid by infrared spectroscopy. Next, formation of an amorphous phase with a T_g value above storage temperature and preservation of native structure during lyophilization were both necessary criteria for storage stability. However, as was seen for hydrophilic proteins,[10−12] crystallization of an amorphous saccharide during storage resulted in poor storage stability. Crystallization of sucrose could be prevented by increasing the protein:sucrose mass ratio, which presumably resulted in an increase in the crystallization temperature. Finally, the superior stabilization afforded by trehalose compared to that afforded by sucrose was attributed to the higher T_g value of the trehalose-containing formulation.

References and Notes

1. Carpenter, J. F.; Crowe, J. H. An infrared spectroscopic study of the interactions of carbohydrates with dried proteins. *Biochemistry* **1989**, *28*, 3916−3922.
2. Kreilgaard, L.; Frokjaer, S.; Flink, J. M.; Randolph, T. W.; Carpenter, J. F. Effect of additives on the storage stability of recombinant human factor XIII during freeze-drying and storage in the dried solid. *Arch. Biochem. Biophys.* **1998**, *360*, 121−134.
3. Chang, B. S.; Beauvais, R. M.; Dong, A.; Carpenter, J. F. Physical factors affecting the storage stability of freeze-dried interleukin-1 receptor antagonist: glass transition and protein conformation. *Arch. Biochem. Biophys.* **1996**, *331*, 249−258.
4. Prestrelski, S. J.; Pikal, K. A.; Arakawa, T. Optimization of lyophilization conditions for recombinant human interleukin-2 by dried-state conformational analysis using Fourier-transform infrared spectroscopy. *Pharm. Res.* **1995**, *12*, 1250−1259.
5. Boel, E.; Huge-Jensen, I. B. Recombinant Humicola lipase and process for the production of recombinant humicola lipases. European Patent Office Publication No: 0 305 216.
6. Holmquist, M.; Martinelle, M.; Clausen, I. G.; Patkar, S.; Svendsen, A.; Hult, K. Trp89 in the lid of *Humicola lanuginosa* lipase is important for efficient hydrolysis of tributyrin. *Lipids* **1994**, *29*, 599−603.
7. Naver, H.; Løvborg, U. The importance of noncharged amino acids in antibody binding to *Humicola lanuginosa* lipase. *Scand. J. Immunol.* **1995**, *41*, 443−448.

8. Huge-Jensen, I. B.; Gormsen, E. Enzymatic detergent additive. European Patent Office Publication No: 0 285 068.
9. Huge-Jensen, B. Recombinantly produced lipases for therapeutical treatment. Patent Cooperation Treaty, International Publication No: WO 91/18623.
10. Izutsu, K.; Yoshioka, S.; Terao, T. Effect of mannitol crystallinity on the stabilization of enzymes during freeze-drying. *Chem. Pharm. Bull. (Tokyo)* **1994**, *42*, 5−8.
11. Izutsu, K.; Yoshioka, S.; Kojima, S. Physical stability and protein stability of freeze-dried cakes during storage at elevated temperatures. *Pharm. Res.* **1994**, *11*, 995−999.
12. Cardona, S.; Schebor, C.; Buera, M. P.; Karel, M.; Chirife, J. Thermal stability of invertase in reduced-moisture amorphous matrixes in relation to glassy state and trehalose crystallization. *J. Food Sci.* **1997**, *61*, 105−112.
13. Roos, Y.; Karel, M. Plasticizing effects on water on thermal behavior and crystallization of amorphous food models. *J. Food Sci.* **1991**, *56*, 38−43.
14. Makower, B.; Dye, W. B. Equilibrium moisture content and crystallization of amorphous sucrose and glucose. *J. Agric. Food Chem.* **1956**, *4*, 72−77.
15. Hancock, B. C.; Zografi, G. The relationship between the glass transition temperature and the water content of amorphous pharmaceutical solids. *Pharm. Res.* **1994**, *11*, 471−477.
16. To, E. C.; Flink, J. M. "Collapse", a structural transition in freeze-dried carbohydrates. I. Evaluation of analytical methods. *J. Food Technol.* **1978**, *13*, 551−565.
17. Sarciaux, J. M.; Hageman, M. J. Effects of bovine somatotropin (rbSt) concentration at different moisture levels on the physical stability of sucrose in freeze-dried rbSt/sucrose mixtures. *J. Pharm. Sci.* **1997**, *86*, 365−371.
18. French, D. L.; McAuley, A. J.; Chang, B.; Niven, R. W. Moisture-induced state changes in spray-dried trehalose/protein formulations. *Pharm. Res.* **1995**, *12*, S-83.
19. Green, J. L.; Angell, C. A. Phase relations and vitrification in saccharide-water solutions and the trehalose anomaly. *J. Phys. Chem.* **1989**, *93*, 2880−2882.
20. Crowe, L. M.; Reid, D. S.; Crowe, J. H. Is trehalose special for preserving dry biomaterials? *Biophys. J.* **1996**, *71*, 2087−2093.
21. Miller, D. P.; de Pablo, J. J.; Corti, H. Thermophysical properties of trehalose and its concentrated aqueous solutions. *Pharm. Res.* **1997**, *14*, 578−590.
22. Duddu, S. P.; Dal Monte, P. R. Effect of glass transition temperature on the stability of lyophilized formulations containing a chimeric therapeutic monoclonal antibody. *Pharm. Res.* **1997**, *14*, 591−595.
23. Dong, A.; Huang, P.; Caughey, W. S. Protein secondary structures in water from second-derivative amide I infrared spectra. *Biochemistry* **1990**, *29*, 3303−3308.
24. Dong, A.; Caughey, W. S. Infrared methods for study of hemoglobin reactions and structures. *Methods Enzymol.* **1994**, *232*, 139−175.
25. Kendrick, B. S.; Cleland, J. L.; Lam, X.; Nguyen, T.; Randolph, T. W.; Manning, M. C.; Carpenter, J. F. Aggregation of recombinant human interferon gamma: kinetics and structural transitions. *J. Pharm. Sci.* **1998**, *87*, 1069−1076.
26. Stratton, L. P.; Dong, A.; Manning, M. C.; Carpenter, J. F. Drug delivery matrix containing native protein precipitates suspended in a poloxamer gel. *J. Pharm. Sci.* **1997**, *86*, 1006−1010.
27. Lee, J. C.; Timasheff, S. N. The stabilization of proteins by sucrose. *J. Biol. Chem.* **1981**, *256*, 7193−7201.
28. Xie, G.; Timasheff, S. N. The thermodynamic mechanism of protein stabilization by trehalose. *Biophys. Chem.* **1997**, *64*, 25−43.
29. Izutsu, K.; Yoshioka, S.; Kojima, S.; Randolph, T. W.; Carpenter, J. F. Effects of sugars and polymers on crystallization of poly(ethylene glycol) in frozen solutions: phase separation between incompatible polymers. *Pharm. Res.* **1996**, *13*, 1393−1400.
30. Sjöberg, Å.; Karlström, G.; Tjerneld, F. Effects on the cloud point of aqueous poly(ethylene glycol) solutions upon addition of low molecular weight saccharides. *Macromolecules* **1989**, *22*, 4512−4516.
31. Galema, S. A.; Høiland, H. Stereochemical aspects of hydration of carbohydrates in aqueous solutions. 3. Density and ultrasound measurements. *J. Phys. Chem.* **1991**, *95*, 5321−5326.
32. Dong, A.; Kendrick, B. S.; Kreilgard, L.; Matsuura, J.; Manning, M. C.; Carpenter, J. F. Spectroscopic study of secondary structure and thermal denaturation of recombinant human factor XIII in aqueous solution. *Arch. Biochem. Biophys.* **1997**, *347*, 213−220.
33. Allison, S. D.; Dong, A.; Carpenter, J. F. Counteracting effects of thiocyanate and sucrose on chymotrypsinogen secondary structure and aggregation during freezing, drying, and rehydration. *Biophys. J.* **1996**, *71*, 2022−2032.
34. Kendrick, B. S.; Meyer, J. D.; Matsuura, J. E.; Carpenter, J. F.; Manning, M. C. Hydrophobic ion-pairing as a method for enhancing structure and activity of lyophilized subtilisin BNP′ suspended in isooctane. *Arch. Biochem. Biophys.* **1997**, *347*, 113−118.
35. Prestrelski, S. J.; Tedeschi, N.; Arakawa, T.; Carpenter, J. F. Dehydration-induced conformational transitions in proteins and their inhibition by stabilizers. *Biophys. J.* **1993**, *65*, 661−671.
36. Allison, S. D.; Randolph, T. W.; Chang, B. S.; Carpenter, J. F. Unpublished results.
37. Randolph, T. W. Phase separation of excipients during lyophilization: Effects on protein stability. *J. Pharm. Sci.* **1997**, *86*, 1198−1203.
38. Franks, F.; Hatley, R. H. M.; Mathias, S. F. Materials science and the production of shelf-stable biologicals. *BioPharm* **1991**, *4*, 38−55.
39. Angell, C. A. Formation of glasses from liquids and biopolymers. *Science* **1995**, *267*, 1924−1939.
40. Pikal, M. J.; Dellerman, K. M.; Roy, M. L.; Riggin, R. M. The effects of formulation variables on the stability of freeze-dried human growth hormone. *Pharm. Res.* **1991**, *8*, 427−436.
41. Tanaka, T.; Takeda, R.; Miyajama, R. Cryoprotective effect of saccharides on denaturation of catalase during freeze-drying. *Chem. Pharm. Bull.* **1991**, *39*, 1091−1094.
42. To, E. C.; Flink, J. M. "Collapse", a structural transition in freeze-dried carbohydrates: II. Effect of solute composition. *J. Food. Technol.* **1978**, *13*, 567−581.
43. te Booy, M. P.; de Ruiter, R. A.; de Meere, A. L. Evaluation of the physical stability of freeze-dried sucrose-containing formulations by differential scanning calorimetry. *Pharm. Res.* **1992**, *9*, 109−114.
44. Pikal, M. J.; Shah, S. Moisture transfer from stopper to product and resulting stability implications. *Dev. Biol. Stand.* **1992**, *74*, 165−177.
45. Flink, J. M. Structure and structure transitions in dried carbohydrate materials. In *Physical Properties of Foods*; Peleg, M., Bagley, E. B., Eds.; AVI Publishing Co.: Westport, CT, 1983; pp 473−521.

Acknowledgments

We gratefully acknowledge the gift of HLL from Novo Nordisk A/S. In addition, we thank Mette Bergø from The Royal Danish School of Pharmacy, for performing the HLL activity assays. The research was supported by grants from H. C. Ørsted's Travel Grant, The Danish Pharmacy Association's Foundation, Pharmacist Julius Wael's and cand. pharm. Helga Wael's Foundation, and NSF (BES 9505301).

JS980399D

Nucleation and Crystallization Kinetics of Hydrated Amorphous Lactose above the Glass Transition Temperature

ERIC A. SCHMITT,* DEVALINA LAW, AND GEOFF G. Z. ZHANG

Contribution from *Pharmaceutical Products Division, Abbott Laboratories, Abbott Park, Illinois 60064.*

Received September 25, 1998. Final revised manuscript received December 8, 1998.
Accepted for publication December 15, 1998.

Abstract □ The crystallization kinetics of amorphous lactose in the presence and absence of seed crystals were investigated at 57.5% relative humidity. Isothermal crystallization studies were conducted gravimetrically in an automated vacuum moisture balance at several temperatures between 18 and 32 °C. The crystallization rate constants were then determined from Johnson–Mehl–Avrami (JMA) treatment and isothermal activation energies were obtained from Arrhenius plots. Based on microscopic observations, a reaction order of 3 was used for JMA analysis. The nonisothermal activation energies were determined by differential scanning calorimetry using Kissinger's analysis. Isothermal activation energies for amorphous lactose with and without seed crystals were 89.5 (±5.6) kJ/mol and 186.5 (±17.6) kJ/mol, respectively. Nonisothermal activation energies with and without seed crystals were 71 (±7.5) kJ/mol and 80.9 (±8.9) kJ/mol, respectively. The similarity of the isothermal and nonisothermal activation energies for the sample with seeds suggested that crystallization was occurring by growth from a fixed number of preexisting nuclei. Markedly different isothermal and nonisothermal activation energies in the absence of seeds suggested a site-saturated nucleation mechanism, and therefore allowed calculation of an activation energy for nucleation of 317 kJ/mol.

Introduction

Increases in the dissolution rate and bioavailability of poorly soluble drugs can often be achieved by using metastable amorphous preparations.[1−4] Nevertheless, the use of amorphous oral dosage forms, such as solid dispersions, has seen very limited commercial application. One reason for this limited use is undoubtedly the physical instability of such formulations. Since the amorphous state is thermodynamically unstable compared to the crystalline state, there is a tendency for conversion to the crystalline form. When the conversion occurs during manufacturing or normal storage, product failure can result from the reduced dissolution rate of the crystalline form. If the advantages of metastable amorphous drugs in solid oral dosage forms are to be fully utilized, it is vital to understand the crystallization process, develop methods to stabilize the amorphous phase, and evaluate potential crystallization inhibitors in a timely manner.

The crystallization of amorphous materials can also be detrimental to parenteral products. For example, in protein lyophilization, disaccharides have been shown to stabilize the tertiary structure during the removal of water.[5] One requirement for this stabilizing effect is that the disaccharide form an amorphous phase with the dried protein. It follows that crystallization of the amorphous disaccharide would result in increased protein denaturization. Thus, understanding the transition from amorphous to crystalline states and the stabilization of amorphous phases is also important for parenteral product development.

Spray-dried lactose is widely used in solid dosage forms, and it is probably the most commonly used metastable amorphous material in the pharmaceutical industry. The crystallization of amorphous lactose, particularly during tableting operations[6] and storage of micronized powders,[7] has been reported as an industrial problem. Recent reports in the pharmaceutical literature have discussed amorphous lactose crystallization; however, these studies have not addressed the kinetics.[8−10] This may be a result of the complicating issue of mutarotation between the α- and β-forms of lactose and the ensuing crystal form issues.

Sucrose, another disaccharide, is much less complicated and fairly well studied. Over the years, the crystallization of amorphous sucrose alone and with additives has been studied by various isothermal and nonisothermal techniques including X-ray diffraction,[11] gravimetry,[12−14] and differential scanning calorimetry.[11,15] It is somewhat surprising that other than the statistical approach taken by Van Scoik and Carstensen,[13] crystallization rate constants, and the separation of kinetic parameters for nucleation and growth, are not readily obtained from the literature. Johnson−Mehl−Avrami theory has been used for the determination of crystallization rate constants of materials in frozen solution[16] and for the crystallization of amorphous lactose[17] and amorphous indomethacin;[18] however, none of these studies focused on the separation of nucleation and growth processes.

Determination of the kinetic parameters associated with crystallization of amorphous lactose with and without seed crystals is the focus of the current investigation. The use of isothermal and nonisothermal techniques, combined with microscopic observations, allowed elucidation of the nucleation mechanisms and calculation of activation energies associated with nucleation and growth. The methods and results reported here for lactose form the foundation for later studies on potential crystallization inhibitors.

Theoretical Section

Johnson−Mehl−Avami (JMA) theory describes many solid-state reactions that occur through a process of nucleation and growth such as crystallization.[19−23] For isotropic growth in m dimensions, the general form of the JMA equation is:

$$\alpha(t) = 1 - \exp[-\int_0^t g[\int_\tau^t Y(\Theta)\mathrm{d}\Theta]^m I(\tau)\mathrm{d}\tau] \qquad (1)$$

where α is the fraction crystallized, $Y(\Theta)$ represents the growth rate for all m dimensions of growth, g is a geometric

* To whom correspondence should be addressed: Eric A. Schmitt, Abbott Laboratories, D-4P3, Blg. AP9, 100 Abbott Park Rd., Abbott Park, IL 60064-6122, TEL: (847) 938-4835, FAX: (847) 938-4434, e-mail: eric.schmitt@abbott.com.

10.1021/js980387s CCC: $18.00
Published on Web 02/05/1999

Table 1—Summary of the Meanings of Isothermal and Nonisothermal Apparent Activation Energies from Woldt[26] [a]

nucleation mechanism	reaction order (n)	isothermal apparent E_a	nonisothermal apparent E_a
continuous	$m+1$	$(E_a^N + mE_a^G)/(m+1)$	$(E_a^N + mE_a^G)/(m+1)$
fixed number	m	E_a^G	E_a^G
site saturated	m	$(E_a^N + mE_a^G)/m$	E_a^G

[a] The superscripts N and G refer to nucleation and one-dimensional growth, respectively.

constant, and $I(\tau)$ is the nucleation rate. Equation 1 can be reduced to the following simplified form:[24−26]

$$\alpha = 1 - e^{-(k(t - t_o))^n} \quad (2)$$

where, k is the crystallization rate constant (time^{-1}), t is time, t_o is the induction time, and n is the reaction order which depends on the nucleation mechanism and the number of dimensions in which growth is occurring. After assigning the appropriate order, the linearized form of eq 2

$$[-\ln(1 - \alpha)]^{1/n} = k(t - t_o) \quad (3)$$

can be used for determining isothermal induction times and rate constants.

If nucleation and growth rates are functions of temperature only (i.e. not position or time dependent), then three general mechanisms of nucleation can be considered: continuous (which reduces to constant rate under isothermal conditions), fixed number of nuclei, and site-saturated nucleation.[26] Continuous nucleation means that nuclei continue to form and grow throughout the transformation. Fixed number nucleation occurs when growth proceeds from a fixed number of preexisting nucleation sites. The number of nuclei is independent of the experimental conditions. The term site-saturated nucleation is a hybrid of the previous two cases. In this situation all nuclei are present at the beginning of the isothermal process, and additional nuclei do not form during the transformation, but the absolute number of nuclei depend on the temperature. One example of this would be if the rate of growth was much greater than the rate of nucleation.

Starting with eq 1 and assuming only Arrhenius dependence of growth and nucleation rates, Woldt derived the meanings of activation energies determined from isothermal and nonisothermal experiments.[26] After corrections for the differences in the units of k between Woldt's representation and eq 3, the meanings of reaction orders and apparent activation energies determined isothermally and nonisothermally can be summarized as shown in Table 1. Thus, if growth occurs in the same number of dimensions, the apparent E_a obtained isothermally and nonisothermally should be identical under fixed number and continuous nucleation. A more interesting situation arises if nucleation occurs through a site-saturated mechanism. In this case different apparent activation energies will be obtained under isothermal and nonisothermal conditions, and the underlying activation energies for nucleation and growth, E_a^N and E_a^G, can be determined. Therefore, the combination of isothermal and nonisothermal methods of determining activation energies for crystallization can, in theory, provide insight into the underlying mechanism of crystallization.

Experimental Section

Materials—Anhydrous lactose was purchased from Quest International (Norwich, NY). Lactose monohydrate was purchased from Van Waters and Rogers (Bedford Park, IL).

Crystallization Conditions—The International Conference on Harmonization (ICH) has recommended 60 ± 5%RH as a humidity condition for long-term stability testing of pharmaceutical products.[27] Since 57.5% RH is easily achieved at 25 °C using saturated aqueous solutions of NaBr, this was the humidity condition chosen for crystallization studies. Preliminary studies showed that amorphous lactose absorbed ca. 14% water at 57.5% RH, resulting in a glass transition temperature (T_g) for the hydrated material of ca. 5 °C. For comparison, the T_g of dry amorphous lactose is ca. 114 °C. Since all crystallization experiments were conducted at least 13 °C above the T_g, the assumption of Arrhenius dependence of nucleation and growth rates employed in Woldt's analysis should be valid.

Preparation and Characterization of Amorphous Lactose—All amorphous samples were prepared by spray-drying (Buchi mini spray dryer, model B-191) freshly prepared aqueous solutions of anhydrous lactose (10% w/v). The inlet air temperature was set to 150 °C and the other parameters were adjusted to give an outlet air temperature of ca. 80 °C. Spray drying was started exactly 4 min after addition of water to the lactose powder and lasted for 12.5 min. The amorphous nature of the product was assessed by X-ray powder diffraction (XRPD) and differential scanning calorimetry (DSC). The amorphous product was then observed by polarized light microscopy (PLM) at a magnification of 332× to check for the presence of seed crystals. One batch of amorphous lactose showed no evidence of crystals by any of the techniques. A second batch appeared amorphous by XRPD and DSC, but small crystallites could be observed by PLM indicating that nucleation occurred during processing stage. Therefore, two batches of amorphous lactose were studied: one which had previously nucleated designated as "with seeds" and one which did not show evidence of nucleation designated as "without seeds".

Polarimetry—The proportion of α and β diastereomers in the raw material, spray-dried product, and recrystallized amorphous material was estimated by polarimetry (Jasco DIP-370 digital polarimeter). Briefly, a standard curve was constructed from the literature values for specific rotation of pure α and β forms.[28] Solutions (1% w/v) were prepared and optical rotation measurements made as a function of time. The specific rotation values were plotted versus time and the y-intercept, which gave the specific rotation at $t = 0$, was used in the standard curve to estimate the α/β content of the solid materials.

Differential Scanning Calorimetry—The DSC experiments employed a Mettler DSC 30 (Mettler-Toledo Inc., Highstown, NJ) or a TA Instruments model 2920 DSC (TA Instruments, Inc. New Castle, DE). Both instruments used aluminum sample pans and were purged with dry nitrogen at 50 mL/min. The DSC cell constants were calibrated with indium and temperature calibrations were performed using indium (single point) or indium, lead and zinc (three point). For nonisothermal crystallization studies, amorphous lactose samples (ca. 2−3 mg) were weighed into sample pans and stored over a saturated aqueous solution of NaBr. After exactly 2 h, the pans were hermetically sealed and immediately scanned in the DSC. The nonisothermal E_a was determined by Kissinger analysis[29,30] at scanning rates of 7.5, 10, 15, 20, and 25 °C/min.

A comparison of the crystallization products from isothermal and nonisothermal crystallization was also performed by DSC. Crystals obtained from isothermal crystallization were scanned from 25 to 300 °C at rates between 7.5 and 25 °C/min using DSC pans with a pinhole. The pinhole was used so that any water could be removed in a reproducible manner and not interfere with the melting transitions. The nonisothermal crystallizations were conducted at rates of 7.5−25 °C/min in hermetically sealed pans as used in Kissinger analysis. However, immediately after the crystallization exotherm a pinhole was placed in the pan and the scan continued to observe the dehydration and melting behavior of the product. The composition of the crystallization products obtained during Kissinger analysis and gravimetric analysis were then compared by using the magnitudes of the α-monohydrate dehydration peak at ca. 145 °C and the α-anhydrous melting peak at ca. 215 °C.

Gravimetry—Crystallization kinetics were determined gravimetrically at 57.5% RH using a vacuum moisture balance (VTI Corporation, Hialeah, FL). The balance was calibrated prior to each run, and the accuracy of the relative humidity was periodically checked by measuring the water uptake of PVP K-90 at 80% RH. Samples weighing approximately 15 mg were used for all but

Table 2—Results of Solution Polarimetry Studies Used to Estimate α/β Composition of Solid Materials

sample	specific rotation[a] (deg/g/dm)	calcd % α
lactose, monohydrate	89	99
starting material	46	20
spray dried	48	24
recrystallized @ 57.5%RH	51	29

[a] Specific rotation values are calculated on an anhydrous lactose basis.

one experiment with seeds at 29 °C which used a 6 mg sample to check for possible sample size effects. All samples were dried under vacuum at 50 °C until a constant weight was maintained. After the instrument reached the desired experimental temperature, the humidity was rapidly increased to 57.5% and maintained at that level for the duration of the experiment. Sample weight was monitored as a function of time, and the weight loss associated with crystallization was used for the determination of crystallization kinetics. The first step in data reduction was transforming the raw data into fraction crystallized (α) versus corrected time as follows:

$$\alpha = \left(\frac{\mathrm{Wt}_{\max} - \mathrm{Wt}_t}{\mathrm{Wt}_{\max} - \mathrm{Wt}_{\mathrm{final}}}\right), \quad t_{\mathrm{corrected}} = t - t_{\mathrm{drying}} \qquad (4)$$

The α and $t_{\mathrm{corrected}}$ values in the region between $\alpha = 0.15$ and $\alpha = 0.85$ were then fit using eq 3. Crystallization rate constants determined between 18 and 32 °C were used to calculate the apparent activation energies of samples with and without seed crystals.

Microscopy Studies—The crystallization process was observed with a polarized light microscope fitted with a video camera, VCR, and video printer. Constant humidity chambers were constructed using a standard microscope slide, a cover slip, and an O-ring as follows: A greased O-ring was placed on a slide and a small drop of a saturated salt solution placed inside the O-ring. A thin layer of amorphous lactose was pressed on the inside surface of the cover slip, which was then placed on top of the O-ring forming a closed constant humidity chamber suitable for microscopic analysis. The crystallization at room temperature and 57.5% RH was then recorded on the VCR at magnifications of 166× and 332×.

Results and Discussion

Polarimetry—The extrapolated specific rotation values and calculated α/β compositions of various types of lactose are given in Table 2. An increase in α content of 4% is observed on going from crystalline anhydrous lactose to the spray-dried amorphous product. Crystallization of the amorphous material at 57.5% RH results in another 5% increase in α content. Errors in the determination of α content primarily result from different moisture contents of the samples which, based on prior experience, we estimate to be on the order of ca. 2%. The equilibrium distribution of α and β anomers in aqueous lactose solutions has been reported as 37.3% α and 62.7% β at 20 °C.[28] The data in Table 2 suggest that exposure of lactose samples to liquid water or 57.5% RH results in a drift toward the equilibrium composition. However, the increase in α content during isothermal crystallization is small and therefore its impact on the kinetic parameters is considered to be insignificant.

Microscopy—The crystallization of amorphous lactose was observed using polarized light microscopy. For the sample without seeds, visible crystallites formed after a short induction time. Subsequent crystal growth occurred from these "nuclei" with no new "nuclei" appearing in the amorphous regions. Similar observations were made in the presence of seed crystals. Since new crystals should constantly form during the growth phase with continuous nucleation, these findings served to rule out the possibility

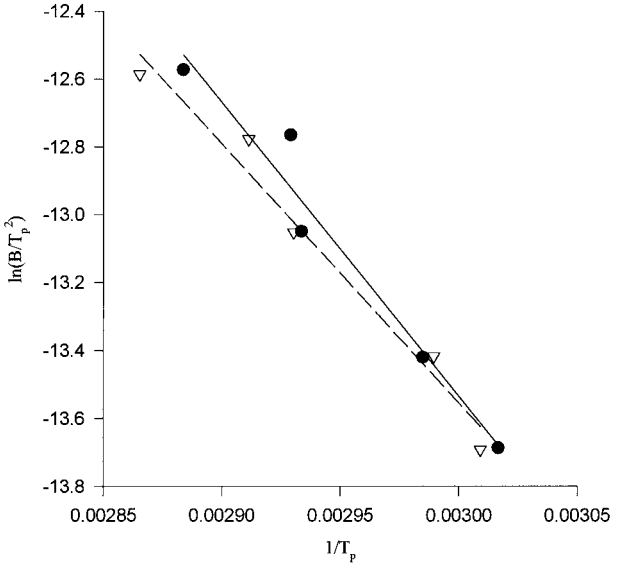

Figure 1—Kissinger plot of the nonisothermal crystallization of amorphous lactose equilibrated at 57.5% RH. Circles, solid line = without seeds; triangles, dashed line = with seeds.

of this mechanism. Table 1 shows that for both fixed number and site-saturated nucleation mechanisms the reaction order is equal to the dimensions of growth. We assume three-dimensional crystal growth and therefore use an order (n) of 3 for fitting gravimetric data to eq 3. Combining this information with the analysis described in the theoretical section should allow elucidation of the nucleation mechanisms in the presence and absence of seed crystals.

Differential Scanning Calorimetry—In Kissinger's analysis, E_a is determined by measuring peak crystallization temperature (T_p) at several heating rates (β), in K/s. The slope of a plot of $\ln(\beta/T_p^2)$ versus $1/T_p$ is $-E_a/R$. Figure 1 shows representative Kissinger plots for lactose at 57.5% RH. Each point in Figure 1 represents a single DSC experiment. The nonisothermal activation energies were 71 (±7.5) and 81 (±8.9) for samples with and without seed crystals, respectively. The reported values represent the averages of three or four Kissinger plots, and the uncertainties are the standard deviations.

As discussed in the theoretical section, the actual meaning of this activation energy may be elucidated by comparing the isothermal and nonisothermal determinations. However, it is possible that effects such as changes in the relative humidity inside the DSC pan during heating could affect the process. Therefore, before a comparison can be made we must have some assurance that the same process is occurring under isothermal and nonisothermal conditions. To support this requirement, DSC thermograms of isothermally recrystallized amorphous lactose and nonisothermally recrystallized amorphous lactose are shown in Figure 2. Both recrystallized lactose samples show an endotherm at ca. 145 °C which is indicative of the dehydration of α-lactose monohydrate. Integration of these endotherms gives values of 55.4 and 58.7 J/g for the isothermal and nonisothermal crystallization products, respectively. A comparison of the previous dehydration endotherms to that obtained for pure α-lactose monohydrate under identical experimental conditions indicates that approximately 33−35% of the sample crystallized as α-lactose monohydrate under both isothermal and nonisothermal conditions.[31] This is in excellent agreement with the proportion of α-lactose in the crystallized product as estimated by polarimetry (29%). The small endotherm at ca. 215 °C represents melting of the α-anhydrous crystal and is

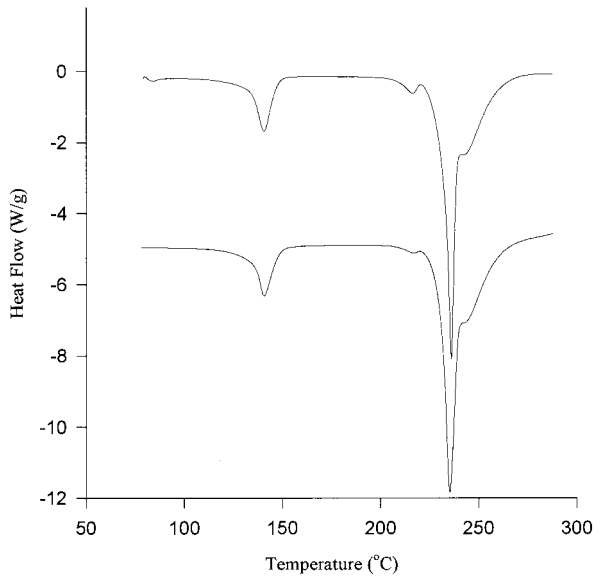

Figure 2—DSC thermograms of amorphous lactose crystallized at 57.5% RH under isothermal and nonisothermal conditions.

slightly larger in the nonisothermal crystallization products. Using a method similar to that described for estimating the amount of α-lactose monohydrate it is estimated that less than 2% α-anhydrous is formed isothermally and that slightly more, but less than 5%, is formed nonisothermally. The DSC-estimated composition of the crystallization products did not depend on the presence of seeds or the heating rate used during nonisothermal crystallization. Given that the difference in crystal composition between isothermal and nonisothermal crystallizations is only on the order of a few percent a significant affect on the activation energy determinations is not expected.

Gravimetry—Isothermal crystallization processes can be followed by techniques including X-ray powder diffraction, isothermal calorimetry, and gravimetry. The large difference in hygroscopicity between the amorphous and crystalline lactose at 57.5% RH made gravimetry an acceptable technique for this study. Other methods such as isothermal calorimetry or X-ray powder diffraction may be better suited for more hydrophobic drug molecules where the difference in hygroscopicity between amorphous and crystalline states is negligible. A representative plot of the raw moisture balance output obtained at 25 °C is shown in Figure 3a. The raw data transformed into fraction crystallized as a function of time shown in Figure 3b give the typical sigmoidal curve expected for reactions occurring through nucleation and growth. Figure 3c shows the experimental data and fit of eq 3 with $n = 3$ in the region $0.15 < \alpha < 0.85$.

One important assumption when determining crystallization kinetics from gravimetric data is that the weight loss is crystallization rate limited, and not limited by evaporation. This assumption was tested by comparing crystallization rate constants at 25 °C and 52.5, 57.5, and 62.5% RH. Since evaporation will occur at a slower rate at higher RH, the observed crystallization rate constants should decrease with increasing RH if weight loss is evaporation limited. Table 3 shows that the rate constants increased markedly with RH as is expected for crystallization rate limited weight loss. The similarity of rate constants obtained for two different sample sizes (Figure 4, 29 °C with seeds) also supports crystallization limited weight loss and suggests sample size has minimal effects on the observed rate constants.

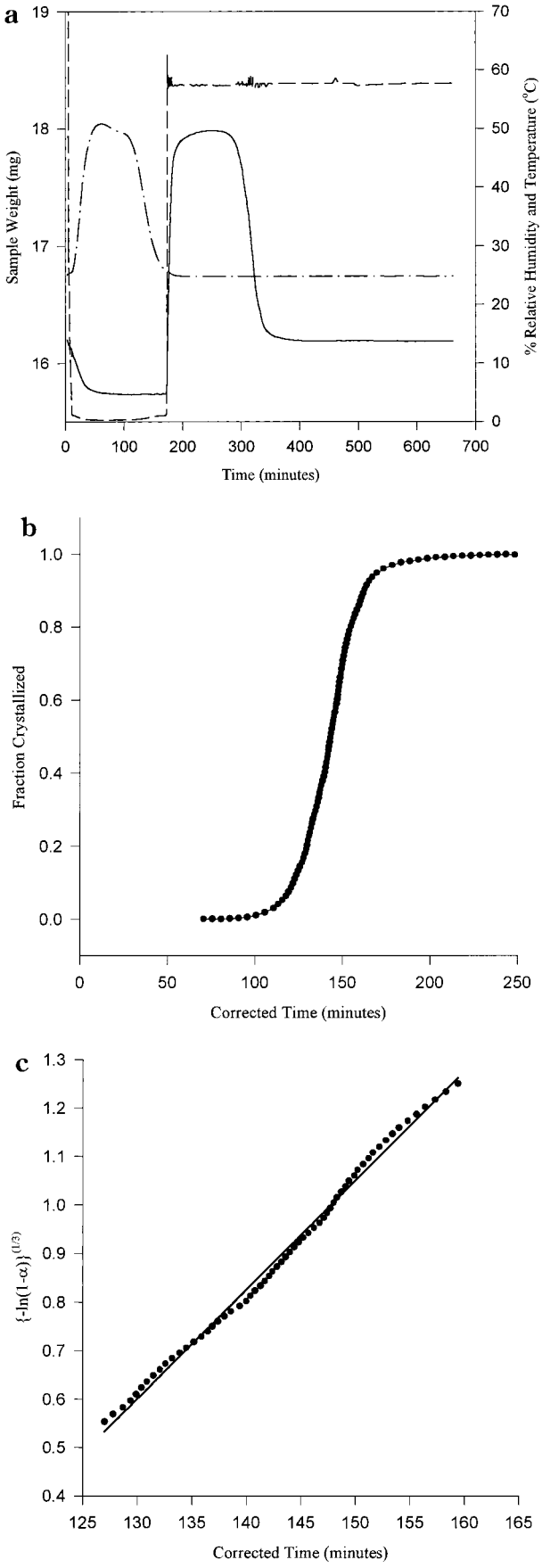

Figure 3—(a) Plot of typical gravimetric data showing sample temperature (dash–dot), sample weight (solid), and percent relative humidity (dashed) as a function of time. (b) Plot of transformed raw data. (c) JMA plot of transformed gravimetric data.

Table 3—Crystallization Rate Constants Determined at 25 °C as a Function of Relative Humidity

% relative humidity	k (min^{-1})
52.5	0.0056
57.5	0.0155, 0.0224
62.5	0.0466

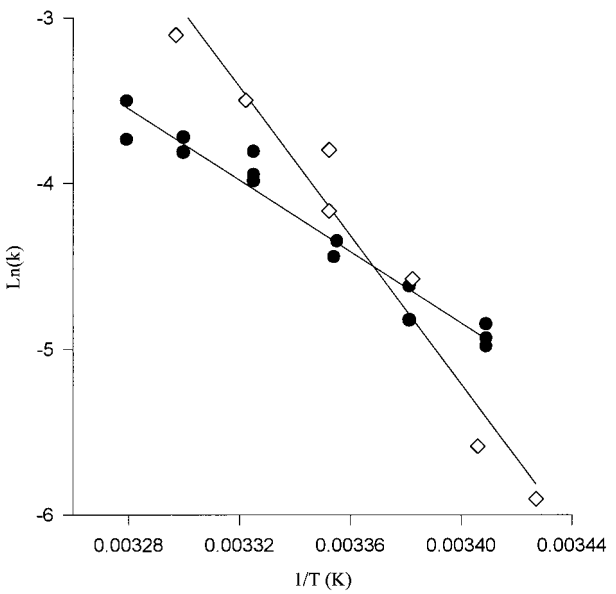

Figure 4—Arrhenius plots of JMA rate constants determined gravimetrically at 57.5% relative humidity. Solid circles = with seeds; open squared = without seeds. The solid lines show the least squares linear fit.

Arrhenius plots of the crystallization rate constants (Figure 4) gave isothermal activation energies with and without seeds of 89.5 (±5.6) and 187 (±17.6) kJ/mol, respectively. The uncertainties represent one estimated standard error obtained from regression analysis.

Comparison of Isothermal and Nonisothermal Activation Energies—Table 4 shows that amorphous lactose containing seed crystals gives essentially the same activation energies by isothermal and nonisothermal techniques. Remembering that continuous nucleation has been ruled out by microscopy, reference to Table 1 reveals that equivalent isothermal and nonisothermal activation energies are expected for growth from a fixed number of preexisting nuclei. Under the fixed number nucleation mechanism, the activation energy determined isothermally or nonisothermally is that for growth. In the absence of seed crystals there is a marked difference between activation energies obtained from isothermal and nonisothermal experiments (Table 4). As shown in Table 1 this result supports a site-saturated nucleation mechanism. Both fixed number and site-saturated nucleation mechanisms should give an activation energy for growth under nonisothermal conditions, and the results obtained with and without seeds (71 ± 7.5 and 81 ± 8.9, respectively) support this assertion.

The process of crystal growth can be separated into bulk diffusion and surface integration steps.[32] It has been shown experimentally that for sucrose crystallization from solution, the activation energies for diffusion are on the order of 25−33 kJ/mol while activation energies for surface incorporation are 67−84 kJ/mol.[33] The activation energies for lactose crystal growth determined here compare very favorably with the range cited for surface incorporation. This comparison suggests that under the conditions studied the crystal growth rate of lactose is limited by surface incorporation rather than diffusion.

Table 4—Comparison of Isothermal and Nonisothermal Activation Energies Determined in the Presence and Absence of Seed Crystals

sample	isothermal E_a (kJ/mol)	nonisothermal E_a (kJ/mol)
seeds present	89.5 ± 5.6	71 ± 7.5
seeds absent	187 ± 18	81 ± 8.9

With site-saturated nucleation and three-dimensional growth, the E_a values obtained isothermally and nonisothermally are given by $(E_a^N + 3E_a^G)/3$ and E_a^G, respectively. Using the experimentally determined apparent E_a values for samples without seeds we can calculate the activation energy for nucleation as $E_a^N = 317$ kJ/mol. The relative value of this activation energy compared to that obtained for growth seems intuitively correct; however, no literature values are available for a direct comparison of the magnitude. By separating the activation energies for nucleation and growth it may be possible to ascertain how various excipients affect nucleation and growth processes during crystallization. This knowledge could allow directed inhibition of nucleation, growth, or both during product development.

Another method for determining an apparent E_a^N involves using the reciprocal of the induction time in an Arrhenius plot.[34] When the induction time data calculated from the intercept and slope of the JMA plots were analyzed in this manner, apparent activation energies of 112 (±15) and 104 (±7.5) kJ/mol were obtained. The fact that equivalent activation energies were obtained with and without seeds seriously calls into question the use of this apparent activation energy for evaluating nucleation. These results may suggest that activation energies determined from induction times may be related to the slow growth of initial nuclei, so-called germ nuclei, into growth nuclei rather than the actual nucleation step as recently discussed by Jacobs.[35]

Conclusions

Under the crystallization conditions used in this report, amorphous lactose appears to give a mixed product consisting of ca. 30% α-monhydrate, 70% β-anhydrous, and possibly a small amount of α-anhydrous crystal forms. Growth rates appear to be limited by surface incorporation rather than diffusion, and in the absence of seed crystals nucleation appears to occur though a site-saturated mechanism. Gravimetry was shown to be useful method for determining crystallization rate constants and induction times of lactose. The combination of isothermal and nonisothermal activation energies allowed investigation of both crystal growth and nucleation mechanisms and led to the separation of activation energies for nucleation and growth. Finally, the relationship between induction-time-based activation energies and nucleation has been questioned. Additional studies employing additives are needed to determine if the separation of activation energies for nucleation and growth allows a more mechanistic understanding of the role of additives in stabilizing or destabilizing amorphous phases.

References and Notes

1. Mullins, J. D.; Mack, T. J. Some Pharmaceutical Properties of Novobiocin. *J. Am. Pharm. Assoc.* **1960**, *49*, 245−248.
2. Shefter, E.; Higuchi, T. Dissolution Behavior of Crystalline Solvated and Nonsolvated Forms of Some Pharmaceuticals. *J. Pharm. Sci.* **1963**, *52*, 781−791.
3. Fukuoka, E.; Makita, M.; Yamamura, S. Some Physicochemical Properties of Glassy Indomethacin. *Chem. Pharm. Bull.* **1986**, *34*, 4314−4321.

4. Fukuoka, E., Makita, M.; Yamamura, S. Glassy State of Pharmaceuticals. II. Bioinequivalence of Glassy and Crystalline Indomethacin. *Chem. Pharm. Bull.* **1987**, *35*, 2943−2948.
5. Carpenter, J. F.; Pikal, M. J.; Chang, B. S.; Randolph, T. W. Rational design of stable lyophilized protein formulations: some practical advice. *Pharm. Res.* **1997**, *14*, 969−975.
6. Huettenrauch, R. Molecular Pharmaceutics as the Basis of Modern Formulation. *Acta Pharm. Technol.* **1978**, Suppl. 6, 55−127.
7. Bystrom K.; Briggner, L.-E., Microcalorimetry − A Novel Technique for Characterization of Powders. In *Respiratory Drug Delivery IV*; Byron, P. R., Dalby, R. N., Farr, S. J., Eds.; Virginia Commonwealth University: Richmond, VA, 1994; pp 297−302.
8. Buckton, G.; Darcy, P. The influence of additives on the recrystallisation of amorphous spray dried lactose. *Int. J. Pharm.* **1995**, *121*, 81−87.
9. Darcy, P.; Buckton, G. The influence of heating/drying on the crystallisation of amorphous lactose after structural collapse. *Int. J. Pharm.* **1997**, *158*, 157−164.
10. Stubberud, L.; Forbes, R. T. The use of gravimetry for the study of the effect of additives on the moisture-induced recrystallisation of amorphous lactose. *Int. J. Pharm.* **1998**, *163*, 145−156.
11. Palmer, K. J.; Dye, W. B.; Black, D. X-ray diffractometer and microscopic investigation of amorphous Sucrose. *J. Agric. Food Chem.* **1956**, *4*, 77−81.
12. Makower, B.; Dye, W. B. Equilibrium moisture content and crystallization of amorphous sucrose and glucose. *J. Agric. Food Chem.* **1956**, 4, 72−77.
13. Van Scoik, K.; Carstensen, J. T. Amorphous-to-crystalline transformation of sucrose. *Pharm. Res.* **1990**, *7*, 1278−1281.
14. Saleki-Gerhardt, A.; Zografi, G. Nonisothermal and isothermal crystallization of sucrose from the amorphous state. *Pharm. Res.* **1994**, *11*, 1166−1173.
15. Shamblin, S. L.; Huang, E. Y.; Zografi, G. The effects of co-lyophilized polymeric additives on the glass transition temperature and crystallization of amorphous sucrose. *J. Therm. Anal.* **1996**, *47*, 1567−1579.
16. Gatlin, L. A. Kinetics of phase transitions in a frozen solution. *Dev. Biol. Stand.* **1991**, *74*, 93−104.
17. Jouppila, K.; Kansikas, J.; Roos, Y. H. Glass transition, water plasticization, and lactose crystallization in skim milk powder. *J. Dairy Sci.* **1997**, *80*, 3152−3160.
18. Andronis, V.; Yoshioka, M.; Zografi, G. Effects of Sorbed Water on the Crystallization of Indomethacin from the Amorphous State. *J. Pharm. Sci.* **1997**, 86, 346−351.
19. de Bruijn, T. J. W.; de Jong, W. A.; van den Berg, P. J. Kinetic Parameters in in Avrami−Erofeev Type Reactions from Isothermal and Non-Isothermal Experiments *Themochim. Acta.* **1981**, *45*, 315−325.
20. Johnson, W. A. and Mehl, R. F. Reaction Kinetics in Processes of Nucleation and Growth. *Trans. Am. Inst. Min. Eng.* **1939**, *135*, 416−442.
21. Avrami, M. Kinetics of phase change. I. General theory. *J. Chem. Phys.* **1939**, *7*, 1103−1112.
22. Avrami, M. Kinetics of phase change. II. Tranformation-time relations for random distribution of nuclei. *J. Chem. Phys.* **1940**, *8*, 212−224.
23. Avrami, M. Granulation, phase change, and microstructure. Kinetics of phase change. III. *J. Chem. Phys.* **1941**, *9*, 177−184.
24. Maffezzoli, A.; Kenny, J. M.; Torre, L. On the physical dimensions of the Avrami constant. *Thermochim. Acta* **1995**, *269/270*, 185−190.
25. Two different forms of the JMA equation are found in the literature, eq 3 and $-\ln(1-\alpha) = k^*(t-t_o)^n$. Maffezzoli et al.[23] have advocated using the form given in eq 3 so that rate constants will have consistent units of time^{-1}. Care should be taken when comparing kinetic parameters in the literature to ensure the same forms of the JMA equation are being used. The results are different but can be converted using $k^{*1/n} = k$ and $E^*_a/n = E_a$. The physical meaning of the two constants is that k^* is an overall value for all dimensions and k is for one dimension.[18]
26. Wolt, E. The Relationship Between Isothermal and Nonisothermal Description of Johnson−Mehl−Avrami−Kolmogorov Kinetics. *J. Phys. Chem. Solids* **1992**, *53*, 521−527.
27. Stability testing of new drug substances and products. In *Proceedings of the Third International Conference on Harmonization*; D'arcy, P. F., Harron, D. W. G., Eds.; Greystone Books Ltd.: Antrim, N. Ireland. 1996; Appendix 3.
28. Morrissey, P. A. Lactose: Chemical and Physicochemical Properties. In *Developments in Dairy Chemistry-3: Lactose and Minor Constituents*; Elsevier Applied Science Publishers: New York, 1985; pp 1−34.
29. Kissinger, H. E. Variation of peak temperature with heating rate in differential thermal analysis. *J. Res. Nat. Bur. Stand.* **1956**, *57*, 217−221.
30. Kissinger, H. E. Reaction Kinetics in Differential Thermal Analysis. *Anal. Chem.* **1957**, *29*, 1702−1706.
31. Khankari, R. K.; Law, D.; Grant, D. J. W. Determination of water content in pharmaceutical hydrates by differential scanning calorimetry. *Int. J. Pharm.* **1992**, *82*, 117−127.
32. Mullin, J. W. *Crystallization*; Butterworth Heinemann: Oxford, 1992.
33. Hartel, R. W. Solid−Liquid Equilibrium: Crystallization in Foods. In *Physical Chemistry of Foods*; Marcel Dekker: New York, 1992; pp 47−81.
34. Van Scoik, K. G.; Carstensen, J. T. Nucleation phenomena in amorphous sucrose systems. *Int. J. Pharm.* **1990**, *58*, 185−196.
35. Jacobs, P. W. M. Formation and Growth of Nuclei and the Growth of Interfaces in the Chemical Decomposition of Solids: New Insights. *J. Phys. Chem. B* **1997**, *101*, 10086−10093.

Acknowledgments

The authors thank Drs. Luk Li and Michael Chang of Abbott Laboratories Hospital Products Division for use of the spray dryer and Prof. David J. W. Grant for helpful comments and discussions.

JS980387S

Polymorph Determination for the GP IIb/IIIa Antagonist, Roxifiban, Using a Combination of Electron Diffraction and Synchrotron X-ray Powder Diffraction Techniques

Z. G. Li,*,† R. L. Harlow,† C. M. Foris,† H. Li,‡ P. Ma,‡ R. D. Vickery,§ M. B. Maurin,§ and B. H. Toby||

Contribution from *Central Research & Development, Science & Engineering Laboratory, Experimental Station, DuPont Company, Wilmington, Delaware 19880-0228, Chemical Process R&D, DuPont Pharmaceuticals Company, Deepwater, New Jersey 08023-0999, Pharmacy R&D, DuPont Pharmaceuticals Company, P.O.Box 80400, Wilmington, Delaware 19880-0400, and Center for Neutron Research E151/235, National Institute of Standards & Technology, Gaithersburg, Maryland 20899..*

Received August 12, 1998. Accepted for publication December 4, 1998.

Abstract □ Unit cell parameters of two polymorphs of roxifiban have been determined by a combination of transmission electron microscopy (TEM) single-crystal and synchrotron X-ray powder diffraction techniques. While it was difficult to differentiate the two forms by their standard X-ray diffraction patterns, the high-resolution synchrotron patterns clearly showed striking differences. Unit cells for the two forms required the use of cell parameters derived from TEM diffraction patterns. The two unit cells are, not surprisingly, very similar except for a doubling of one of the axes for form II. The combined use of TEM and synchrotron patterns appears to be a good general approach for characterizing complex (low-symmetry, large unit cell) polymorphs.

Introduction

The term polymorph refers to substances that have the same chemical formula but different crystal structures. Polymorphism has played an important role in drug development, production, and litigation. Synthesized and crystallized under different conditions, polymorphs may have different physical and chemical properties as well as bioavailabilities. Steroids, sulfonamides, and barbiturates are some well-known examples[1] of compounds that have two or more polymorphs. Recently, the polymorphic behavior of Abbott-79175 was detailed.[2] The conventional techniques used to identify polymorphs are X-ray diffraction, optical microscopy, DSC, IR, and solid-state NMR. However, these techniques sometimes fail to differentiate definitively between two structurally similar polymorphs, so more advanced techniques are required. The advanced techniques were applied to roxifiban:

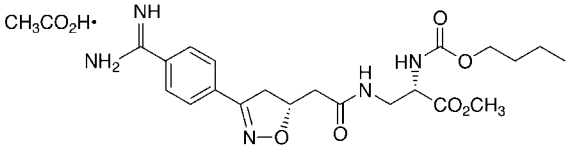

The GP IIb/IIIa receptor antagonist, roxifiban, is a very promising cardiovascular drug discovered recently at DuPont Pharmaceuticals.[3,4] Extensive human clinical trials are presently in progress. It was suspected at one point that different crystalline phases, labeled form I and form II, were being obtained when the synthesis/crystallization conditions were varied. Bulk and tapped densities, for example, were found to vary from 0.23 and 0.37 g/mL for form I to 0.07 and 0.19 g/mL for form II, respectively. These differences were of some concern given the low drug load in the solid dosage form.

Conventional X-ray single-crystal diffraction and polarized microscopy, two traditional methods employed to characterize the physical forms of drug compounds in development, were of no value in distinguishing between the two forms because of the relatively small crystallite sizes of the materials. Even powder diffraction patterns of forms I and II of roxifiban showed few differences when collected on a commercial diffractometer; although there is some intensity variation among peaks in general, there were only 1−2 additional peaks that were truly unique to form II. These differences in the two patterns could easily be explained away either as an effect of preferred orientation (since the crystals have a needle habit) or by the presence of impurity phases.

Unit cell parameters and atomic coordinates of crystalline polymorphs can routinely be determined by single-crystal X-ray diffraction techniques if suitably large crystals are available. However, many organic compounds tend to grow needle and platelike crystals that never achieve a large enough volume for single-crystal studies. Such was the case with forms I and II of roxifiban: diffraction patterns from a few small "single-looking" crystallites produced just enough spots to clearly show that these crystals were generally twinned or agglomerated. Because the single-crystal technique was not available in this case, both TEM and synchrotron powder diffraction techniques were employed in the hope of at least determining the unit cells for the two forms. If all of the peaks in the individual powder patterns of forms I and II can be accounted for by appropriate indexing of the peaks based on their unit cell parameters, then one can assume with high probability (a) that the two forms do indeed exist and, therefore, can be distinguished and (b) that the peaks are not from contaminant phases.

While it is possible to obtain unit cell information from powder X-ray diffraction data by "trial-and-error" techniques either manually or through the use of automated indexing software, chances for successful determination are less likely if the unit cell has low symmetry and a large volume. Unit cells are easily determined by single-crystal techniques because the diffraction spots are spread out in a three-dimensional pattern. Because the powder spectrum is a projection of these spots into a one-dimensional set of peaks, wrong unit cells are often determined when low-resolution commercial powder patterns are used as input.

* Corresponding author. Phone: 302-695-3323; Fax: 302-695-1351; e-mail: zhigang.li@usa.dupont.com.
† Central Research & Development, DuPont Co.
‡ Chemical Process R&D, DuPont Pharmaceuticals Co.
§ Pharmacy R&D, DuPont Pharmaceuticals Co.
|| NIST.

10.1021/js9803306 CCC: $18.00
Published on Web 01/26/1999

High-resolution powder diffractometers at synchrotron sources produce patterns that are more easily indexed, but complicated patterns of the type produced by many organic crystals are still difficult to analyze. In electron diffraction, two-dimensional patterns can be obtained from crystals which are very small (submicron or less in size). This is a big advantage in determining some of the unit cell parameters, but generally it is difficult (crystals are generally plates or needles) to obtain all three of the necessary projections to determine all the parameters. Another disadvantage is that organic materials are usually beam sensitive and, for this reason, electron diffraction has not been extensively used on pharmaceuticals. Recently, however, the development of very sensitive CCD detectors has allowed electron diffraction patterns of beam-sensitive materials to be recorded in a few seconds using very low electron currents. In this report, we describe the utility of our newly developed "hybrid" characterization technique[5,6] to pharmaceuticals, coupling the analysis of the synchrotron powder data with information obtained from TEM diffraction patterns to characterize the unit cell parameters of the two forms of roxifiban.

Experimental Section

High-resolution, X-ray powder diffraction patterns for various samples of roxifiban were obtained at the Advanced Photon Source, a DOE User Facility located at Argonne National Laboratory, Chicago, IL. The samples were initially mounted in capillaries although flat-plate samples were later used to obtain patterns with increased Bragg intensities. Patterns were collected on a Huber diffractometer at beamline DND-5BMB. A Si(111) double-crystal monochromator, a Si(111) analyzer, and slits on the order of 1 × 8 mm were used in conjunction with a scintillation counter to achieve the highest possible resolution and signal/noise ratio. Peaks in the patterns were deconvolved using GPLSFT, and indexing was attempted using the program TREOR. GSAS was used to test possible unit cells.

A JEM-2000EX (at 200 kV accelerated voltage) microscope, equipped with a Gatan 1024 × 1024 CCD camera, was used to characterize these materials. The samples were directly deposited on conventional TEM grids. The TEM technique has the primary advantage of being able to examine individual crystallites, and thus it can circumvent the problems of contaminant phases. This technique can exploit the special geometric shapes of these crystallites, many of which have plate and fiberlike habits. In particular, unit cell information perpendicular to the plate direction can be obtained: a typical diffraction pattern might contain the *h*0*l* zone, for example, from which the *a**, *c**, and β* parameters can be obtained.

While these two techniques were individually valuable for partial definitions of the unit cell, neither give data from which the complete unit cell could readily be determined. The determination of roxifiban polymorphs required a combination of transmission electron microscopy (TEM) and synchrotron X-ray diffraction capabilities.

Results

Electron Microscopy (EM)—Figure 1 shows scanning electron microscopy images comparing the morphologies of forms I and II. Both forms I and II contain very small crystals which prevent the use of conventional single crystal X-ray techniques. It is clear that the crystals of form II are more fiberlike. Figure 2 is a low magnification TEM view of form I and II crystals, confirming the SEM results. Figure 3 shows a higher magnification image of a single Form II crystal and its diffraction pattern. TEM results indicate that *d*(100), *d*(001), and β* of both forms I and II are, respectively, around 5.0 Å, 9.2 Å, and 81°.

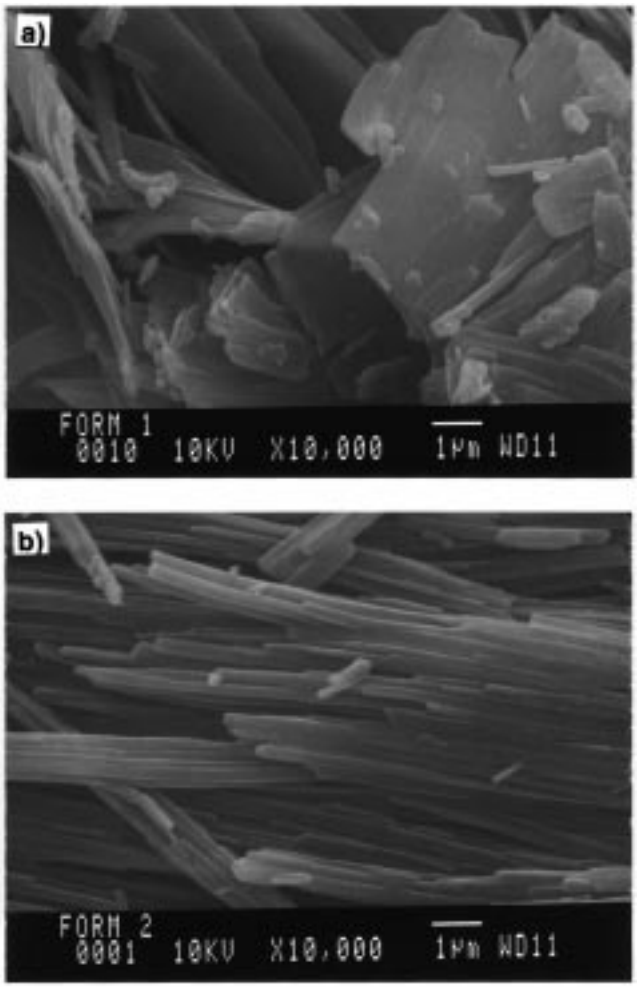

Figure 1—Scanning electron microscopy images of forms I and II. The crystals of form II are seen to be much more fiberlike.

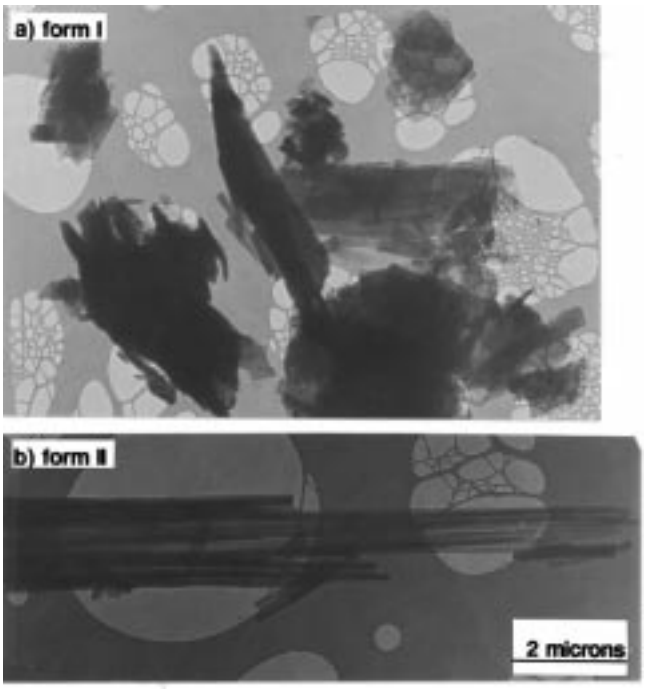

Figure 2—Low magnification TEM images of (a) form I and (b) form II crystals.

Synchrotron X-ray Powder Diffraction (S-XRPD)—*Transmission Mode*—It was revealed that the S-XRPD

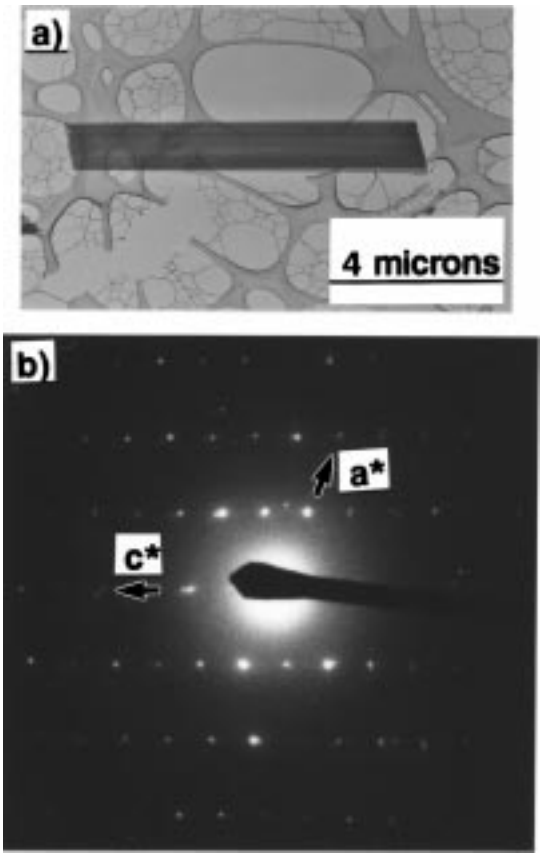

Figure 3—(a) TEM image and (b) diffraction pattern of a single form II crystal.

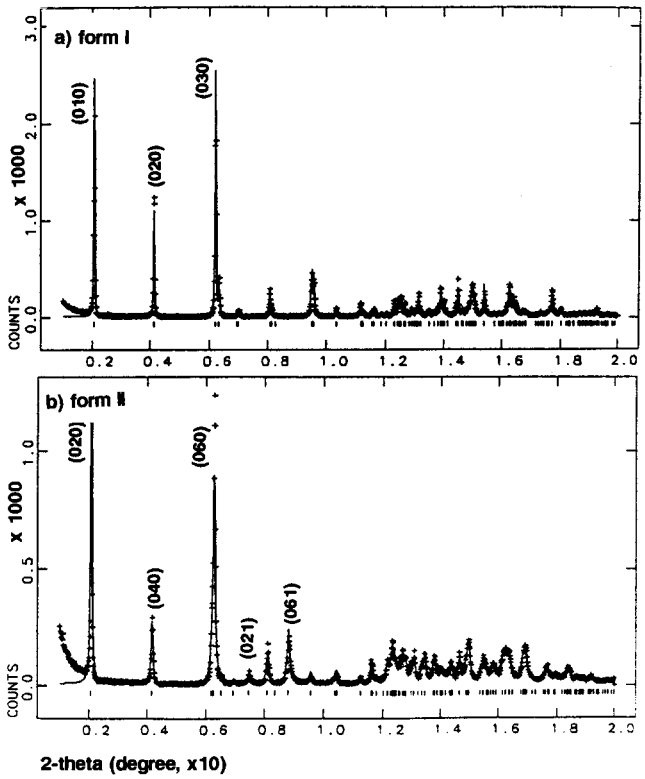

Figure 4—Synchrotron X-ray diffraction patterns (wavelength of 1.00006 Å) of (a) form I and (b) form II. In both cases, the "+" marks represent the observed data points; the solid line is the result of a LeBail fit using the unit cell parameters. The "tick" marks are the locations of the expected reflections. The two extra peaks in the low-angle region of the form II pattern which clearly differentiate it from the pattern of form I are labeled as the (021) and (061) reflections. It can clearly be seen that the match of the derived unit cells and the experimental data points is excellent.

diffraction pattern of form I and form II run with a 1.5 mm capillary were indeed different with two extra diffraction peaks in the lower angle range. Since the large capillary samples should be relatively free of preferred orientation, it was assumed at this point that the major differences in the patterns were a clear indication that the extra peaks in form II were not simply due to preferred orientation effects.

Reflection Mode—Because the intensities of the diffraction lines using the capillary mode were relatively weak, we recollected the patterns in reflection mode using large and deep flat-plate sample holders on samples that were carefully ground. Figure 4 shows the resulting S-XRPD patterns for forms I and II and points out the two extra peaks in the low-angle region of form II which (vide infra) distinguish it from form I. Although we had expected serious problems from preferred orientation effects, the relative intensities of the peaks in the reflection mode were, in fact, very similar to those measured in the capillary mode (without grinding the samples, the relative intensities in reflection mode were very different and strong, preferred orientation effects were very obvious).

Unit Cell of Form I—An attempt was made to determine the unit cell of form I since the peaks were reasonably sharp and the phase appeared pure. TEM work had suggested that the cell was probably of low symmetry, either monoclinic or triclinic, with two of the three cell axes in the neighborhood of 5.0 and 9.2 Å with an interaxial angle of 81°. Synchrotron patterns had shown that the third axis was very long, ca. 27−28 Å. Given the number of atoms in the molecule, one can estimate that the volume per molecule is in the vicinity of 648 Å^3 which would be compatible with two molecules per cell. Indexing was attempted first in the triclinic study giving several hits with one in particular that had dimensions of 6 × 9 × 28 Å. Placing the trial cell into the program RMANDEX showed a nearly perfect fit to all of the peaks. The cell parameters were then refined with CELLREF, and ultimately these numbers were used in a LeBail fit routine in GSAS. Figure 4a shows the quality of the fit for the full pattern. The refined triclinic ($Z = 2$, with space group P1 because the compound is stereochemically pure) unit cell parameters are given below:

	a	*b*	*c*	α	*β*	*γ*	*V*
value:	5.0235	28.075	9.2954	98.533	98.498	92.244	1279.7
σ:	0.0005	0.002	0.0009	0.006	0.009	0.008	0.2

Unit Cell of Form II—Several lines in the low-angle regions of the pattern are unique to the form II pattern, and if their origin could be established, then it might be possible to determine its unit cell. The form II pattern was displayed in RMANDEX[7] using the same unit cell established for form I as a starting point because TEM results indicated that a^*, c^*, and β^* values of forms I and II were very similar. It became immediately clear that the unique peaks in the pattern could not be indexed unless one of the cell edges was doubled. Doubling the volume requires that four molecules must reside in the cell, and, in that case, the cell would likely be monoclinic with space group $P2_1$. The long axis, ca. 28 Å, was the obvious choice for *b* (the unique axis of the monoclinic cell) because the TEM diffraction pattern suggested that 5−9 Å projection still had the 81° angle. Fixing the α and *γ* angles to 90° and adjusting the *a* and *c* axes as well as the *β* angle soon gave a cell which could account for the unique lines in the form II pattern. This cell was then refined using the LeBail fit

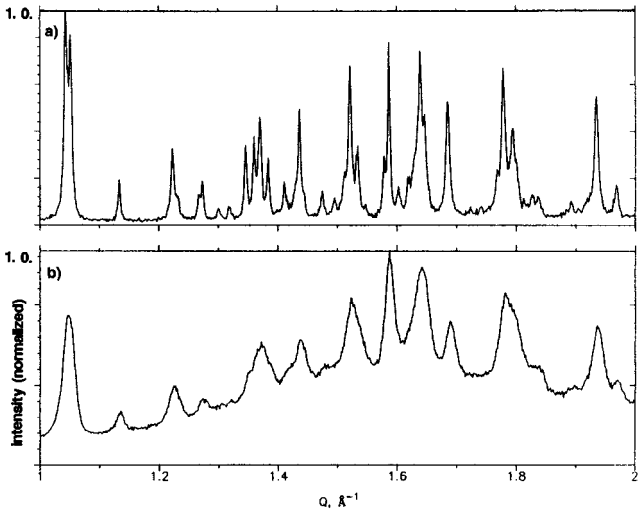

Figure 5—A partial comparison of a (a) synchrotron pattern of form II collected using a wavelength of 1.00006 Å with a (b) conventional X-ray diffraction pattern using Cu Kα radiation in a region where there are many overlapping peaks. The patterns are plotted as a function of $Q = 2\pi/d = 4\pi \sin \theta/\lambda$ to removal the effects of using different wavelengths.

routine in GSAS. The fit is shown in Figure 4b. The final monoclinic unit cell is:

	a	*b*	*c*	*β*	*V*
value:	4.992	54.77	9.372	99.15	2529.9
σ:	0.002	0.02	0.003	0.04	1.5

Conclusions

Conventionally, there are two ways to differentiate polymorphs: single-crystal or powder X-ray diffraction. The former requires fairly large crystals which, in many cases, are very difficult to obtain; the latter is often ambiguous if only visual comparisons of the patterns are made. Successful indexing of a powder pattern, however, strongly suggests that a pattern represents a single, pure phase and can be used as strong evidence for the existence of individual polymorph. We have used a combination of electron and X-ray diffraction techniques to differentiate the polymorphs of roxifiban by demonstrating that they have different, but closely related, unit cell parameters. To our knowledge, this represents the first time this combination of techniques has been used to differentiate two polymorphs of a pharmaceutical drug substance.

The success of this study was critically dependent on the use of a synchrotron diffraction pattern to obtain reliable indexing and accurate lattice parameters. Figure 5 compares the diffraction patterns of form II using (a) S-XRPD and (b) commercial X-ray diffractometer (C-XRD). The much higher resolution of the S-XRPD pattern is clear: the separation of the nearly overlapped peaks was critical to the indexing and to the refinement of the unit cell parameters of the two polymorphs.

Given that the patterns match so closely in the low-angle region, it is not surprising that the unit cell parameters of forms I and II are quite similar. The two extra peaks found in the low-angle region of form II are a consequence of the fact that the *b*-axis, and hence the unit cell volume, is approximately double that of form I. A schematic representation of the two unit cells is shown in Figure 6. It is reasonable to suggest that the long axis of the molecules must be aligned with the *b* axis in both cases. In fact, given that the form I cell is triclinic with space group *P*1 (and hence the origin of the cell is arbitrary), it might be possible to determine its structure by placing a pair of "optimized"

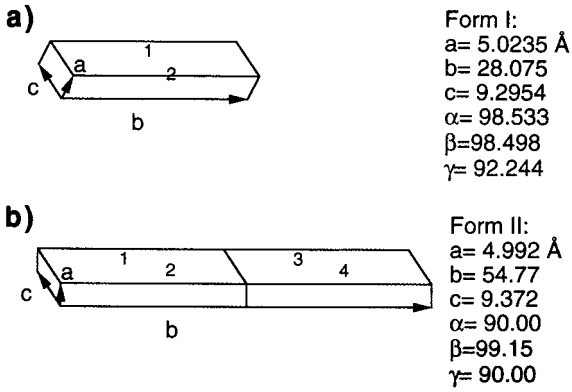

Figure 6—Schematic representation of unit cells of (a) form I with two molecules per cell and (b) form II with four molecules per cell. The molecules presumably align themselves approximately parallel with the very long *b*-axes.

molecules of roxifiban in the unit cell and adjusting their orientations. The task would be complicated by the number of flexible torsion angles in the molecule and by the fact that it is actually a salt, but it may be possible.

Because most crystallites which fail to grow to sizes that would make them amenable to routine single-crystal diffraction techniques have either platelike or needlelike habits, this combined use of TEM and synchrotron powder diffraction techniques should be applicable to similar structural problems in the pharmaceutical industry. Although access to synchrotron powder diffraction beamlines is presently somewhat limited, the use of synchrotron data for the differentiation of these two polymorphs was absolutely critical to the success of this study. In the future, access to such beamlines will be more readily available as more synchrotrons come on line and as better detector systems for powder diffraction are developed.[8]

References and Notes

1. Byrn, S. R. *The Solid State Chemistry of Drugs*; Academy Press: New York, 1982.
2. Li, R.; Mayer, P. T.; Trivedi, J. S.; Fort, J. J. Polymorphism and Crystallization Behavior of Abbott-79175, a Second-Generation 5-Lipoxygenase Inhibitor. *J. Pharm. Sci.* **1996**, *85*, 773−780.
3. Chu, C. B.; Wityak, J.; Sielecki, T. M.; Pinto, D. J.; Batt, D. G.; Cain, G. A.; Sworin, M.; Rockwell, A. L.; Roderick, J. J.; Wang, S. W.; Orwat, M. J.; Frietze, W. E.; Bostrom, L. L.; Liu, J.; Higley, C. A.; Rankin, F. W.; Tobin, A. E.; Emmett, G.; Lalka, G. K.; Sze, J. Y.; Di Meo, S. V.; Mousa, S. A.; Thoolen, M. J.; Racanelli, A. L.; Hausner, E. A.; Reilly, T. M.; DeGrado, W. F.; Wexler, R. R.; Olson, R. E. Discovery of an Orally Active Series of Isoxazoline Glycoprotein IIb/IIIa Antagonists. *J. Med. Chem.* **1997**, *40*, 2064−2084.
4. Zhang, L.; Chung, J. C.; Costello, T. D.; Valvis, I.; Ma, P.; Kauffman, S.; Ward, R. The Enantiospecific Synthesis of an Isoxazoline. A RGD Mimic Platelet GPIIb/IIIa Antagonist. *J. Org. Chem.* **1997**, *63*, 2466−2470.
5. Li, Z. G.; Harlow, R. L.; Gardner, K. H.; Liang, L.; Dorset, D. L.; Zou, J. M. Plate- and Needlelike Crystal Structure Determination by Combining Electron and Synchrotron Diffraction. In *Proceedings in Microscopy and Microanalysis 1995*; Bailey, G. W., Ellisman, M. H., Henniger, R. A., Zaluzec, N. J., Eds.; Jones and Begell Publishing: New York, 1995; pp 152−153.
6. Li, Z. G.; Harlow, R. L.; Herron, N.; Horowitz, H. S.; McCarron, E. M. Unit Cell Information for δ- and γ-$VOPO_4$. *J. Catal.* **1997**, *171*, 506−508.
7. Program to visually display a measured powder diffraction pattern and to overlay it with the calculated positions of peaks derived from the unit cell dimensions. As the cell dimensions are altered, the calculated positions are adjusted in real time. Further information can be obtained from one of the authors (B.H.T.).
8. Harlow, R. L. Synchrotron Usage by Industry. In *Industrial Powder Diffraction*; Chung, F. H., Smith, D. K., Eds.; Marcel Dekker: New York, submitted.

Acknowledgments

We would like to thank K. Gardner, K. Lehman, A. McGhie, W. Marshall, J. Freida, J. Longacre, and W. Stewart for their collaboration and/or technical assistance. Portions of this work were performed at the DuPont-Northwestern-Dow Collaborative Access Team (DND-CAT) Synchrotron Research Center located at Sector 5 of the Advanced Photon Source. DND-CAT is supported by the E.I. DuPont de Nemours & Co., The Dow Chemical Company, the U.S. National Science Foundation through Grant DMR-9304725, and the State of Illinois through the Department of Commerce and the Board of Higher Education Grant IBHE HECA NWU 96. Use of the Advanced Photon Source was supported by the U.S. Department of Energy, Basic Energy Sciences, Office of Energy Research under Contract No. W-31-102-Eng-38.

JS9803306

Pharmacokinetic Analysis of 6-Monoamino-β-cyclodextrin after Intravenous or Oral Administration to Rats Using a Specific Enzyme Immunoassay

CHRISTOPHE CRÉMINON,*† FLORENCE DJEDAÏNI-PILARD,‡ RAYMOND VIENET,† CHRISTOPHE PÉAN,‡ JEAN-MARC GROGNET,† JACQUES GRASSI,† BRUNO PERLY,‡ AND PHILIPPE PRADELLES†

Contribution from *CEA, DRM, Service de Pharmacologie et d'Immunologie, CEA-Saclay F-91191 Gif s/Yvette, France, and CEA, DRECAM, Service de Chimie Moléculaire, CEA-Saclay F-91191 Gif s/Yvette, France.*

Received July 23, 1998. Final revised manuscript received November 9, 1998.
Accepted for publication December 1, 1998.

Abstract □ We have developed a highly sensitive enzyme immunoassay for 6-monoamino-β-CD (mono(6-amino-6-deoxy)cyclomaltoheptaose) and its parent compound (β-CD) with a detection limit in the 100 pg/mL range. The polyclonal antibodies obtained are highly specific for the β-cyclodextrin core and do not recognize other cyclic cyclodextrins (i.e., α- and γ-CD) or linear analogues. This enzyme immunoassay can be used to quantify 6-monoamino-β-CD in rat urine and plasma. Using this immunoassay, we have evaluated the main pharmacokinetic parameters of 6-monoamino-β-CD after iv administration to the rat of a 25 mg/kg dose. Since this method is strictly specific to the native β-CD form, we have demonstrated that the molecule rapidly disappeared from plasma but is probably distributed in the tissues. The urinary route appears as the predominant way of elimination since almost all the administered drug is recovered in urine. Finally, analysis of the same molecule after oral administration to the rat (25 mg/kg) demonstrates low plasma levels and that about 1% of the administered dose is excreted in urine. These experiments demonstrate the high stability of the β-CD core irrespective of the method of administration. This immunological method could provide relevant information on the fate of β-CD and some derivatives for drug delivery using different modes of administration (oral, parenteral, transmucosal, or dermal).

Introduction

Cyclo-malto-oligosaccharides (cyclodextrins or CDs) are natural molecules with the unique feature of trapping small organic compounds in their hydrophobic cavity. Such inclusion complexes induce modifications of the physical properties of the "guest" molecules, particularly in terms of their solubility and stability.[1] Pharmaceutical applications of cyclodextrins and derivatives are aimed at increasing the bioavailability and reducing the side-effects of drugs.[2] CDs can overcome formulation problems encountered with some drugs using classical pharmaceutical excipients, which explains the increasing number of CD-based formulations appearing on the market. Some CD derivatives may prove useful in delivery of hydrophilic compounds such as peptides[3] or oligonucleotides.[4,5]

However, the use of CD molecules as drug carriers or stabilizers requires safety evaluation. Investigation of the biological fate of CDs as well as toxicological issues must be considered before approval of these new excipients by regulatory agencies. Nephrotoxicity of α- and β-CD[6] as well as the hemolytic character of β-CD[7] severely hamper their potential use in pharmaceutical applications, at least for parenteral administration. However, the availability of different substituted analogues with better safety profiles (as recently reviewed[8]) broadens the range of administration. We recently described the decreased hemolytic properties of 6-monoamino-β-CD compared with the parent compound.[9] Using a competitive enzyme immunoassay which is both sensitive and specific for the cyclic structure of 6-monoamino-β-CD, we have investigated the fate of this compound after iv and oral administration to the rat (both at a single 25 mg/kg dose). After parenteral administration, the main pharmacokinetic parameters of 6-monoamino-β-CD were determined and indicated little metabolism and major elimination by the urinary route. It was shown that in the rat, after oral intake, a small but not inconsiderable proportion of 6-monoamino-β-CD is detected in plasma and eliminated in urine.

The data presented support the potential use of 6-monoamino-β-CD and demonstrate the efficiency of immunological methods in specifically monitoring such compounds for safety evaluation.

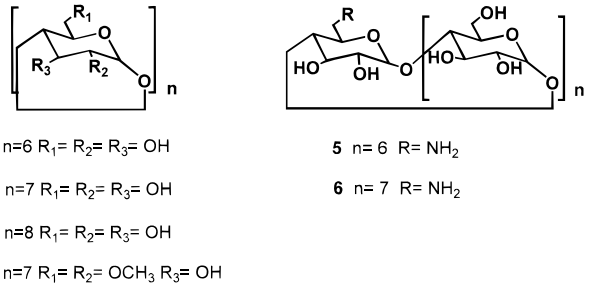

1 n=6 R_1= R_2= R_3= OH
2 n=7 R_1= R_2= R_3= OH
3 n=8 R_1= R_2= R_3= OH
4 n=7 R_1= R_2= OCH_3 R_3= OH
5 n= 6 R= NH_2
6 n= 7 R= NH_2

Scheme 1—Structure of the Linear and Cyclic Maltooligosaccharides Used in the Present Study: **1**, α-CD; **2**, β-CD; **3**, γ-CD; **4**, (2,6)-Dimethyl-β-CD; **5**, 6-Monoamino-β-CD; **6**, 6-Monoamino-γ-CD

Materials and Methods

Reagents and Buffer—Unless otherwise stated, all reagents were of analytical grade, from Sigma (St Louis, MO). The linear and cyclic oligosaccharides used are presented in Scheme 1. β-CD and α-, γ-CD were gifts from Roquette Frères (Lestrem, France) and Wacker (Germany), respectively. 6-Monoamino-β-CD[10] was prepared from 6-*O*-*p*-tolylsulfonyl cyclomaltoheptaose[11] according to a modified procedure.[12,13] 6-Monoamino-γ-CD was obtained in

* Corresponding author. Phone: 33-1-69081314; Fax: 33-1-69085907: E-mail: Creminon@dsvidf.cea.fr.
† Service de Pharmacologie et d'Immunologie.
‡ Service de Chimie Moléculaire.

10.1021/js9802998 CCC: $18.00
Published on Web 02/11/1999

three steps from the parent CD as described elsewhere.[14] Maltoheptaose was obtained from Fluka AG (Basel, Switzerland). Heptakis-(2,6-di-*O*-methyl)cyclomaltoheptaose was obtained from Janssen (Beerse, Belgium) and was recrystallized five times in MeOH to over 99% purity. The chemical and optical purity of the different compounds was checked by ^{1}H NMR, mass spectroscopy, and chemical analysis.

Acetylcholinesterase (AChE, EC 3.1.1.7) from the electric organs of the electric eel *Electrophorus electricus* was purified by affinity chromatography[15] and used in its G4 form for 6-monoamino-β-CD labeling. AChE activity was measured using the colorimetric method of Ellman et al.[16]

All reagents used for immunoassays were diluted in the following buffer (EIA buffer): 0.1 M potassium phosphate buffer pH 7.4 containing 0.9% NaCl, 1 mM EDTA, 0.1% bovine serum albumin (BSA), and 0.01% sodium azide. The washing buffer was a 10 mM phosphate buffer containing 0.05% Tween 20.

Apparatus—Solid-phase EIA was performed in 96-well microtiter plates (Immunoplate Maxisorb with certificate, Nunc, Denmark) using automatic Titertek microtitration equipment (washer, dispenser and reader) from Labsystems (Helsinki, Finland).

Antiserum Production—For the production of antibodies, 6-monoamino-β-CD was covalently linked to bovine serum albumin (BSA) by means of glutaraldehyde as previously described.[17]

Preparation of the Enzymatic Tracer—6-Monoamino-β-CD was covalently coupled to AChE using the heterobifunctional reagent *N*-succinimidyl-4-(*N*-maleimidomethyl)-cyclohexane-1-carboxylate (SMCC) as previously described.[17] This method involved the reaction of thiol groups previously introduced into 6-monoamino-β-CD (by reaction of its primary amino group with *N*-succinimidyl-*S*-acetylthioacetate (SATA) in alkaline medium) with maleimido groups incorporated into the enzyme.

Competitive EIA Procedure—Competitive EIA was performed as described elsewhere for various molecules.[18−20] Microtiter plates were coated with mouse monoclonal anti-rabbit IgG antibodies in order to ensure separation of bound and free moieties of the enzymatic tracer during the immunological reaction. Before use, the plates were washed with 0.01 M phosphate buffer (pH 7.4) containing 0.05% Tween 20. The total volume of the immunological reaction was 150 μL, each component (enzymatic tracer, diluted rabbit polyclonal antisera, and cyclodextrin standard) being added in a 50 μL volume. 6-Monoamino-β-CD-AChE enzyme conjugate was used at a concentration of 2 Ellman units/mL (for Ellman unit definition, see ref 19). The working dilution for the rabbit antiserum was determined by performing serial dilution experiments.

After 18-h incubation at 4 °C, the plates were washed and the enzyme activity of the bound immunological complex was revealed by addition of 200 μL of enzymatic substrate and chromogen (Ellman's reagent[16]) to each well. After 1 h of gentle shaking in the dark at room temperature, the absorbance at 414 nm in each well was measured automatically. Results are given in terms of $B/B_0 \times 100$ as a function of the dose (logarithmic scale), B and B_0 representing the bound enzyme activity in the presence or absence of competitor, respectively. A linear log−logit transformation was used to fit the standard curve.[21] The sensitivity of the assay was characterized by the dose of 6-monoamino-β-CD inducing a 50% lowering of the binding observed in the absence of competitor (B/B_0 50%). Nonspecific binding represented less than 0.1% of the total enzyme activity. Finally, the minimum detectable concentration (MDC) was taken as the concentration of competitor inducing a significant decrease (three standard deviations in B_0). All determinations were made in duplicate and quadruplicate for B_0.

To characterize the specificity of the antibodies, standard curves were plotted using various derivatives of malto-oligosaccharides. The results are expressed in terms of percentage cross-reactivity (CR) [(dose of 6-monoamino-β-CD B/B_0 50%/dose of analogue B/B_0 50%) × 100].

For rat plasma samples, a methanol precipitation procedure was performed before the assay. Four volumes of cold methanol were added to the sample before centrifugation (2500 rpm, 10 min). The pellet was discarded and the supernatant dried under vacuum using a SpeedVac apparatus (Savant, Farmingdale, NY) before reconstitution with EIA buffer. Standard curves were plotted by spiking control plasma samples with known amounts of 6-monoamino-β-CD and demonstrated more than 95% recovery of the molecule in the supernatant.

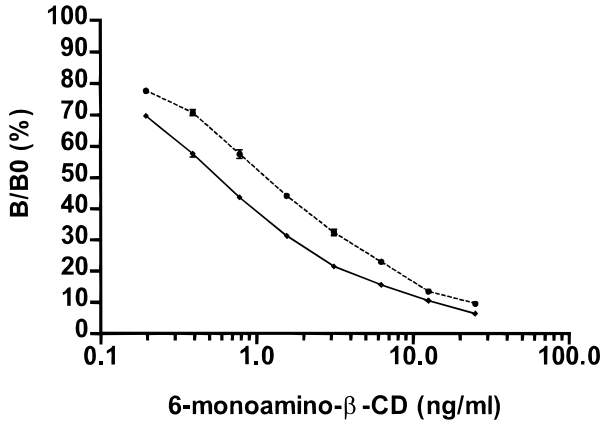

Figure 1—Standard curve for 6-amino-β-cyclodextrin enzyme immunoassay performed in rat urine (full line) and EIA buffer after methanol extraction of rat plasma (dotted line).

Animal Experiments—Experiments were performed on 10-week-old (325 ± 60 g) male Sprague−Dawley rats (Iffa Credo, Les Oncins, France) which throughout the study had free access to water and to a commercial feed (DO4, UAR, Villemoisson, France). The rats were acclimatized for 4 days in individual metabolic cages before experiments. Rats were anaesthetized (one-third O_2, two-thirds NO_2, and 4% fluothane) and catheters were placed in the right femoral artery and vein, passed up into the abdominal vessels, and their free extremity exteriorized at the back of the neck. One day after surgery, a single intravenous dose of 6-monoamino-β-CD (25 mg/kg) in saline solution (47.4 mg/mL) was injected into four rats via the venous catheter. Oral administration of 6-monoamino-β-CD (25 mg/kg) in saline solution (50.1 mg/mL) was performed on four other rats using a 1 mL tuberculin syringe and a 16 gauge gavage needle.

Blood (200 μL) was sampled at various times (0, 5, 10, 15, 20, 30 min, 1 h, 2 h, 4, 8, and 24 h) at the arterial catheter. The blood was centrifuged, and the resulting plasma kept frozen at −20 °C until assay. The pellets containing red blood cells were reinjected after dilution (1/2) with saline dilution through the venous catheter. During the experiment, the rats were housed individually in glass metabolic cages which allowed separate collection of urine and feces. Urine was collected at 4, 8, and 24 h.

Pharmacokinetic Evaluation—A specific computer program (Siphar from SIMED, Créteil, France), designed for nonlinear regression of pharmacokinetic data, was used to fit plasma concentrations. Pharmacokinetic parameters were evaluated using a noncompartmental approach as previously described.[22] The area under the plasma concentration curve (AUC) was determined using the trapezoidal lin-log rule and extrapolated to infinity. The apparent elimination rate constant (k_e) was determined by the decay of the plasma concentration at the four last values (between 30 min and 4 h). Clearance was calculated from the dose divided by the AUC. The apparent volume of distribution was determined using the relation Cl/k_e. Quantities eliminated in urine (Q_e) were evaluated over 0−24 h. Urinary clearance was calculated on the basis of $Cl_u = Q_e/AUC$. Values are expressed as mean ± SD.

Results

Sensitivity and Specificity of the Assay—Using the 6-amino-β-CD-AChE tracer, we optimized the antiserum dilution for the assay. A typical routine standard curve for this assay in EIA buffer using antiserum (no. L1076SAB) at 1/50000 initial dilution is presented in Figure 1. The sensitivity at B/B_0 50% is about 550 pg/mL (25.4 fmol/well) with a minimum detectable concentration close to 110 pg/mL (4.8 fmol/well). The specificity of this assay was demonstrated by testing against different compounds. Parent cyclodextrin (β-CD) gave a full response (90% of cross-reactivity), whereas neither substituted β-CD (i.e. heptakis(2,6-di-*O*-methyl)-β-CD) nor other native or modified CD (i.e. α-CD, γ-CD, and 6-monoamino-γ-CD) displayed any significant cross-reactivity (<0.1%). Linear maltoheptaose was not recognized at all by the antibodies.

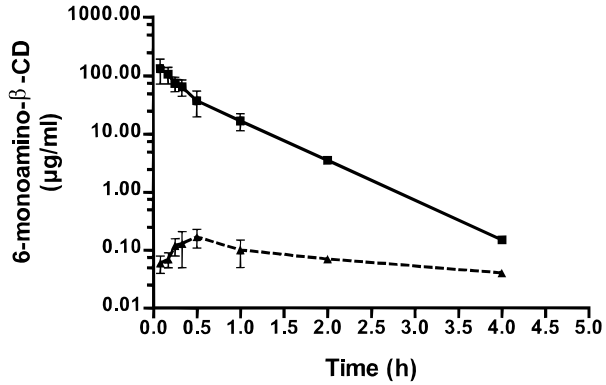

Figure 2—Analysis of plasma levels using specific immunoassay after administration of 6-monoamino-β-cyclodextrin (25 mg/kg) to rats by iv (full line) or oral intake (dotted line). Each value represents the mean ± SD of four rats.

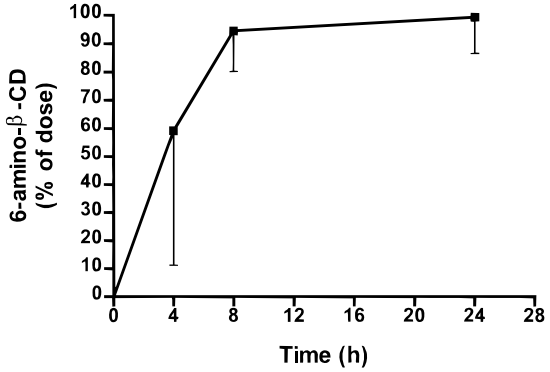

Figure 3—Cumulative urinary excretion of 6-monoamino-β-cyclodextrin after iv administration (25 mg/kg) to rats. Each value represents the mean ± SD of four rats.

All these experiments demonstrated the strict specificity of this assay for the cyclic core of β-CD. Recognition of the molecule by the antibodies seems to involve the secondary hydroxyl rim since the 2,6-di-methyl-β-CD derivative was not detected.

Before performing the pharmacokinetic experiments, we tested the analytical characteristics of the immunomethod in different biological fluids. Rat urine and plasma samples were spiked with known concentrations of 6-monoamino-β-CD. While the assay works properly for urine samples, we observed a lack of reproducibility for undiluted plasma samples. We thus applied a methanol precipitation protocol (see Methods), which provided good reproducibility with only a small change in sensitivity (Figure 1; minimum detectable concentration close to 180 pg/mL). Under these conditions, the precision of the assay is very satisfactory since the coefficients of variation (%) were 8.7, 5.6, and 9.6 within assays and 9.1, 6.1, and 9.8 between assays, for 10, 2, 0.3 ng/mL of 6-amino-β-CD, respectively.

Pharmacokinetic Measurements for 6-Monoamino-β-CD after iv Administration—After a single injection at 25 mg/kg, 6-monoamino-β-CD was detected for up to 4 h in plasma. The 8 and 24 h plasma samples presented no detectable immunoreactivity (except for a single rat for which we measured values of 60 ± 20 ng/mL and 50 ± 30 ng/mL of 6-monoamino-β-CD in the 8 and 24 h samples, respectively). In urine, meaningful concentrations were observed, remaining higher than 20 μg/mL in the 8−24 h collection period. The mean plasma concentration curve and cumulative urinary excretion of iv administered 6-monoamino-β-CD are presented in Figures 2 and 3, respectively. The main pharmacokinetic parameters are listed in Table 1. 6-Monoamino-β-CD disappears rapidly from plasma, as demonstrated by a short half-life (21 min) and MRT (28 min). The apparent volume of distribution (V_d) corresponds to 20% of the total body weight and is close to the plasma and the interstitial volume. This indicates that 6-monoamino-β-CD probably penetrates into tissues to some extent. Most if not all administered compound is eliminated in urine (100% at 24 h) with an apparent urinary clearance close to the systemic clearance. This clearance value is close to the renal glomerular filtration rate.[23]

Table 1—Main Pharmacokinetic Parameters[a] of 6-Monoamino-β-CD after Intravenous Administration (25 mg/kg) to Rats

parameters		rat 1	rat 2	rat 3	rat 4	mean ± SD
$T_{1/2}$	min	20	24	20	19	21 ± 2
MRT	min	28	34	19	29	28 ± 5
Cl_s	mL·min^{-1}·kg^{-1}	5.3	6.3	5.4	10.5	6.9 ± 2.1
AUC (0–inf)	μg·mL^{-1}·h	83.9	72.2	80.8	40.4	69.3 ± 17.2
V_d	mL·kg^{-1}	149	220	153	287	202 ± 56
Q_{el} (0–24 h)	% dose	85	103	95	115	100 ± 11
Cl_u (0–24 h)	mL·min^{-1}·kg^{-1}	4.5	6.4	5.1	12.2	7.1 ± 3.1

[a] Abbreviations: $T_{1/2}$, half-life; MRT, mean residence time; Cl_s, systemic clearance; AUC (0–inf), area under the curve from 0 to infinity; V_d, apparent volume of distribution; Q_{el} (0–24 h), eliminated quantity during 24 h; Cl_u (0–24 h) urinary clearance.

Table 2—Main Pharmacokinetic Parameters[a] of 6-Monoamino-β-CD after Oral Administration (25 mg/kg) to Rats

parameters		rat A	rat B	rat C	rat D	mean ± SD
C_{max}	μg·mL^{-1}	0.15	0.14	0.25	0.13	0.17 ± 0.06
T_{max}	min	30	30	30	30	30
AUC (0–inf)	μg·mL^{-1}·h	0.15	0.25	0.58	0.40	0.35 ± 0.19
Q_{el} (0–24 h)	% dose	0.76	0.68	1.80	0.12	0.84 ± 0.70

[a] Abbreviations: C_{max}, maximal concentration; T_{max}, time of maximal concentration; AUC (0–inf), area under the curve from 0 to infinity; Q_{el} (0–24 h), eliminated quantity during 24 h.

Oral Administration of 6-Monoamino-β-CD—We detected 6-monoamino-β-CD in plasma and urine of all the rats who had received a single oral 25 mg/kg dose. The plasma kinetics measurements are presented in Figure 2 (dotted line), and the main pharmacokinetic parameters are listed in Table 2. The plasma concentration exhibited a maximal value of 170 ± 60 ng/mL at 30 min after administration. 6-Monoamino-β-CD data were presented over the 4 h after oral intake, since it was undetectable in the 8 and 24 h samples. Cumulative urinary elimination of 6-monoamino-β-CD represented 0.84 ± 0.7% of the initial dose. 6-Monoamino-β-CD could still be assayed in the 8−24 h urine (concentration and amount ranging from 0.16 to 11.53 μg/mL and from 1.5 to 71.8 μg, respectively). The bioavailability of 6-monoamino-β-CD was 0.5% and 0.89% as calculated from AUC(0−inf) and Qel (0−24 h), respectively.

Discussion

We have determined the main pharmacokinetic parameters of a β-CD derivative, 6-monoamino-β-CD, which was shown to be less hemolytic than the parent compound, after iv administration at a single 25 mg/kg dose. These results were obtained using a sensitive and specific enzyme immunoassay. Due to the high specificity of this method toward the intact β-CD core, we have demonstrated that little metabolism of this compound occurs. Indeed, 6-monoamino-β-CD is rapidly eliminated from the systemic circulation and is almost totally eliminated via the urinary route, rather like the parent compound.[24] However, in contrast with previous observations for β-CD,[24] 6-monoamino-β-CD has an apparent volume of distribution of 202 mL/

kg, pointing to a probable extravascular distribution, in select tissues or storage pools. The urinary clearance is close to the systemic clearance and appeared close to the glomerular filtration rate.

Using the same immunoanalytical method, we also analyzed the fate of 6-monoamino-β-CD in the rat after oral intake (25 mg/kg). We demonstrated the presence of detectable amounts of the intact molecule in plasma, with a maximal concentration observed 30 min after administration. The molecule is then eliminated via the urinary route. Although 6-monoamino-β-CD was detected in both plasma and urine of the 4 treated rats, large variations were observed; the extent of gastrointestinal absorption of this molecule depends on the individual animal. The cumulative amount of intact CD excreted represents 0.84 $\pm$ 0.7% of the dose. These observations are in agreement with previous reports on orally administered β-CD[25,26] using either radiolabeled compound or a sensitive HPLC technique.[27] Thus, chemical modification does not seem to induce major changes in the pharmacokinetic behavior of the molecule compared with the parent compound. Finally, we have calculated a low oral bioavailability for this molecule, indicating only minimal absorption.

To our knowledge, this is the first full description of the pharmacokinetic analysis of this β-cyclodextrin derivative after iv and oral administration to the rat. A specific analytical method such as the presently described enzyme immunoassay may yield valuable information on the fate of cyclodextrin(s) used for pharmaceutical applications, irrespective of the mode of administration (parenteral and oral for the present study but dermal or transmucosal applications can also be investigated). Moreover, we have observed that this assay retains its analytical characteristics when applied to human urine and plasma samples (data not shown). We are currently developing similar specific immunoassays for methyl derivatives of β-CD, i.e., heptakis-(2, 6-di-*O*-methyl)cyclomaltoheptaose (DIMEB) and heptakis-(2,3,6-tri-*O*-methyl)cyclomaltoheptaose (TRIMEB) which may provide further important data for pharmaceutical applications.

References and Notes

1. Loftsson, T.; Brewster, M. Pharmaceutical applications. 1. Drug solubilization and stabilization. *J. Pharm. Sci.* **1996**, *85*, 1017−1025.
2. Stella, V.; Rajewski, R. Cyclodextrins: their future in drug formulation and delivery. *Pharm. Res.* **1997**, *14*, 556−567.
3. Schipper, N.; Verhoef, J.; De Lannoy, L.; Romeijn, S.; Brakkee, J.; Wiegant, V.; Gispen, W.; Merkus F. Nasal administration of an ACTH(4−9) peptide analogue with dimethyl-beta-cyclodextrin as an absorption enhancer: pharmacokinetics and dynamics. *Br. J. Pharmacol.* **1993**, *110*, 1335−1340.
4. Zhao, Q.; Temsamani, J.; Agrawal, S. Use of cyclodextrin and its derivatives as carrier for oligonucleotide delivery. *Antisense Res. Rev.* **1995**, *5*, 185−192.
5. Zhao, Q.; Temsamani, J.; Iadarola, P.; Agrawal, S. Modulation of oligonucleotide-induced immune stimulation by cyclodextrin analogues. *Biochem. Pharmacol.* **1996**, *52*, 1537−1544.
6. Frank, D.; Gray, J.; Weaver, R. Cyclodextrin nephrosis in the rat. *Am. J. Pathol.* **1976**, *83*, 367−382.
7. Shiotani, K.; Uehata, K.; Irie, T.; Uekama, K.; Thompson, D.; Stella, V. Differential effects of sulfate and sulfobutyl ether of beta-cyclodextrin on erythrocyte membranes in vitro. *Pharm. Res.* **1995**, *12*, 78−84.
8. Irie, T.; Uekama, K. Pharmaceutical applications of cyclodextrins. III. Toxicological issues and safety evaluation. *J. Pharm. Sci.* **1997**, *86*, 147−162.
9. Bost, M.; Lainé, V.; Pilard, P.; Gadelle, A.; Defaye, J.; Perly, B. The hemolytic properties of chemically modified cyclodextrins. *J. Inclus. Phenom. Mol. Recogn.* **1997**, *29*, 57−63.
10. Petter, R.; Salek, J.; Sikorski, C.; Kumaravel, G.; Lin, F. Cooperative binding by aggregated mono-6-(alkylamino)-β-cyclodextrins. *J. Am. Chem. Soc.* **1990**, *112*, 3860−3868.
11. Takahashi, K.; Hattori, K.; Toda, F. Monotosylated α and β-cyclodextrins prepared in an alkaline aqueous solution. *Tetrahedron Lett.* **1984**, *25*, 3331−3334.
12. Djedaïni-Pilard, F.; Desalos, J.; Perly, B. Synthesis of a new molecular carrier: N(Leu-enkephalin)yl-6-amido-6-deoxycyclomaltoheptaose. *Tetrahedron Lett.* **1993a**, *34*, 2457−2460.
13. Djedaïni-Pilard, F.; Perly, B. Utilisation de cyclodextrines aminées pour la solubilisation aqueuse de composés hydrophobes, en particulier de molécules pharmaceutiquement actives. French Patent 93-15472, 1993b.
14. Djedaïni-Pilard, F.; Azaroual-Bellanger, N.; Gosnat, M.; Vernet, D.; Perly, B. Potential formation of intramolecular inclusion complexes in peptido-cyclodextrins as evidenced by NMR spectroscopy. *J. Chem. Soc., Perkin Trans. 2* **1995**, 723−730.
15. Massoulié, J.; Bon, S. Affinity chromatography of acetylcholinesterase: the importance of hydrophobic interactions. *Eur. J. biochem.* **1976**, *68*, 531−539.
16. Ellman, G.; Courtney, K.; Andres, V.; Featherstone, R. A new and rapid colorimetric determination of acetylcholine esterase activity. *Biochem. Pharmacol.* **1961**, *7*, 88−95.
17. Créminon, C.; Pilard, F.; Grassi, J.; Perly, B.; Pradelles, P. A sensitive and specific enzyme immunoassay for cyclomaltoheptaose and some derivatives. *Carbohydr. Res.* **1994**, *258*, 179−186.
18. McLaughlin, L.; Wei, Y.; Stockman, P.; Leahy, K.; Needleman, P.; Grassi, J.; Pradelles, P. Development, validation and application of an enzyme immunoassay (EIA) of atriopeptin. *Biochem. Biophys. Res. Commun.* **1987**, *144*, 469−476.
19. Pradelles, P.; Grassi, J.; Chabardes, D.; Guiso, N. Enzyme immunoassays of adenosine cyclic 3′,5′-monophosphate and guanosine cyclic 3′,5′-monophosphate using acetylcholinesterase. *Anal. Chem.* **1989**, *61*, 447−453.
20. Grassi, J.; Frobert, Y.; Pradelles, P.; Chercuitte, D.; Gruaz, D.; Dayer, J.-M.; Pradelles, P. Production of monoclonal antibodies against interleukin-1α and -1β; Development of two enzyme immunoassays (EIA) using acetylcholinesterase and their application to biological media. *J. Immunol. Methods* **1989**, *123*, 193−210.
21. Rodnard, D.; Lewald, J. Computer analysis of radioligand assay and radioimmunoassay data. *Acta Endocrinol.* **1970**, *64*, 79−103.
22. Gibaldi, M.; Perrier, D. In *Pharmacokinetics in drugs and the pharmaceutical sciences*; Marcel Dekker: New York, 1982; pp 15−48.
23. Bivin, W.; Crawford, M.; Brewer, N. In *The laboratory rat: biology and diseases*; Barker, H., Lindsey, J., Weisbroth, S., Eds; Academic Press: New York, 1979; Vol. 1, pp 90−95.
24. Frijlink, H.; Visser, J.; Hefting, N.; Oosting, R.; Meijer, D.; Lerk, C. The pharmacokinetics of beta-cyclodextrin and hydroxypropyl-beta-cyclodextrin in rat. *Pharm. Res.* **1990**, *7*, 1248−1252.
25. Gerloczi, A.; Fonagy, A.; Keresztes, P.; Perlaky, L.; Szejtli, J. Absorption, distribution, excretion and metabolism of orally administered 14C-beta-cyclodextrin in rat. *Arzneim. Forsch.* **1985**, *35*, 1042−1047.
26. Kubota, Y., Fukuda, M.; Muroguchi, M.; Koizumi, K. Absorption, distribution and excretion of beta-cyclodextrin and glucosyl-beta-cyclodextrin in rats. *Biol. Pharm. Bull.* **1996**, *19*, 1068−1072.
27. Kubota, Y., Fukuda, M.; Ohtsuji, K.; Koizumi, K. Microanalysis of beta-cyclodextrin and glucosyl-beta-cyclodextrin in human plasma by high-performance liquid chromatography with pulsed amperometric detection. *Anal. Biochem.* **1992**, *201*, 99−102.

Acknowledgments

The expert technical assistance of M.-C. Nevers, C. Pavard, and M. Plaisance throughout this work was particularly appreciated.

JS9802998

Multivariate Quantitative Structure–Pharmacokinetic Relationships (QSPKR) Analysis of Adenosine A_1 Receptor Agonists in Rat

PIETER H. VAN DER GRAAF,[†] JONAS NILSSON,[‡,§] ERNO A. VAN SCHAICK,[†,$] AND MEINDERT DANHOF*[,†]

Contribution from *Division of Pharmacology, Leiden/Amsterdam Center for Drug Research, P.O. Box 9503, 2300RA Leiden, The Netherlands, and Department of Medicinal Chemistry, University Centre for Pharmacy, Antonius Deusinglaan 1, 9713 AV Groningen, The Netherlands.*

Received July 21, 1998. Final revised manuscript received October 21, 1998.
Accepted for publication October 26, 1998.

Abstract □ The aim of this study was to investigate the feasibility of a quantitative structure–pharmacokinetic relationships (QSPKR) method based on contemporary three-dimensional (3D) molecular characterization and multivariate statistical analysis. For this purpose, the programs SYBYL/CoMFA, GRID, and Pallas, in combination with the multivariate statistical technique principal component analysis were employed to generate a total of 16 descriptor variables for a series of 12 structurally related adenosine A_1 receptor agonists. Subsequently, the multivariate regression method, partial least squares, was used to predict clearance (CL), volume of distribution (Vd_{SS}) and protein binding (fraction unbound, f_U). The QSPKR models obtained could account for most of the variation in *CL*, Vd_{SS}, and f_U ($R^2 = 0.82$, 0.61 and 0.78, respectively). Cross-validation confirmed the predictive ability of the models ($Q^2 = 0.59$, 0.41 and 0.62 for *CL*, Vd_{SS}, and f_U, respectively). In conclusion, we have developed a multivariate 3D QSPKR model that could adequately predict overall pharmacokinetic behavior of adenosine A_1 receptor agonists in rat. This methodology can also be used for other classes of compounds and may facilitate the further integration of QSPKR in drug discovery and preclinical development.

Introduction

Since the pioneering work of Hansch and co-workers,[1] quantitative structure−activity relationships (QSAR) analysis has become a widely used tool in the design of modern drugs. In recent years, sophisticated alternatives for traditional "Hansch-type" QSAR methods have been developed, in particular in the area of three-dimensional (3D) molecular characterization and multivariate data analysis.[2−4] In contrast to these developments in the QSAR field, the vast majority of quantitative structure−pharmacokinetic relationships (QSPKR[5]) studies have only focused on univariate correlations of individual pharmacokinetic parameters with lipophilicity and ionization, and it has been well established that log *P* and pK_A are important determinants of drug absorption, distribution, protein binding and elimination (for example[3,6−10]). A major drawback of such QSPKR models is that they provide no insight into the influence of other physicochemical properties and therefore their conceptual and predictive value is rather limited. However, despite these limitations, only a few attempts have been made to develop more comprehensive multivariate QSPKR models that predict pharmacokinetics on the basis of various molecular physiocochemical descriptors.[11,12] Furthermore, most QSPKR studies have primarily focused on the prediction of single parameters instead of multivariate modeling of overall pharmacokinetic behavior.[6] Therefore, in the present study we have started to explore the possibilities of generating QSPKR models based on contemporary QSAR methods of 3D molecular characterization and multivariate statistical analysis. The 3D molecular descriptor methods, SYBYL/CoMFA[13] and GRID,[14] in combination with the multivariate statistical techniques, principal component analysis (PCA) and partial least squares (PLS[15,16]), were used to build models for simultaneous prediction of the primary pharmacokinetic parameters, clearance (*CL*), volume of distribution at steady-state (Vd_{SS}), and protein binding (fraction unbound, f_U) for a series of structurally related adenosine A_1 receptor agonists in rat. The pharmacokinetic data were obtained during the course of a program focused on the design of partial agonists for the adenosine A_1 receptor[17,18] as reported previously.[19−23]

Materials and Methods

Chemicals—All compounds used in this study are analogues of the endogenous purine nucleoside, adenosine (Figure 1). Compound **1** is the reference adenosine A_1 receptor agonist, N^6-cyclopentyladenosine (CPA[19]). Compounds **2**−**4** and **5**−**9** are deoxyribose[20] and 8-alkylamino-substitued CPA analogues,[22] respectively. In addition to the CPA analogues, another widely used adenosine A_1 receptor agonist, R−N^6-phenylisopropyladenosine (R−PIA,[21] **10**) was included as well as the novel compounds **11** and **12** as hydrophilic and lipophilic non-CPA analogues, respectively.[23]

Pharmacokinetic Experiments—Details of the pharmacokinetic experiments have been published previously.[19−23] Briefly, 2 days before experimentation, the right femoral artery and the right jugular vein of male Wistar rat (200−250 g) were cannulated for the collection of blood samples and administration of drugs, respectively. Conscious, freely moving rats received an intravenous infusion of vehicle (20% DMSO/water) or compound over 15 min. Serial arterial blood samples were taken over a period of at least 100 min, hemolyzed immediately, and stored at −35 °C until HPLC analysis of blood concentrations.

Compartmental analysis of blood concentration−time profiles was performed by fitting the data to a biexponential equation from which systemic clearance (*CL*) and volume of distribution at steady state (Vd_{SS}) were calculated.[19] The fraction unbound drug in blood (f_U) was determined using standard ultrafiltration methods. The pharmacokinetic parameters for all 12 compounds included in the study are summarized in Table 1.

Molecular Modeling—The 3D structures of the compounds were provided by Dr A. P. IJzerman (Division of Medicinal Chemistry, Leiden/Amsterdam Center for Drug Research), based on the adenosine A_1 receptor model published before.[24]

Generation of Molecular Descriptors—In both the SYBYL/CoMFA[13] (Molecular Modeling Software 6.3, Tripos Inc., St. Louis,

* Corresponding author. Telephone: ++-31-71-5276211. Fax: ++-31-71-5276292. E-mail: m.danhof@lacdr.leidenuniv.nl.
[†] Division of Pharmacology.
[‡] Department of Medicinal Chemistry.
[§] Current affiliation: Pharmacia & Upjohn, Department of Structural Chemistry, Uppsala, Sweden.
[$] Current affiliation: Janssen Research Foundation, Department of Clinical Pharmacokinetics, Beerse, Belgium.

10.1021/js980294a CCC: $18.00
Published on Web 01/12/1999

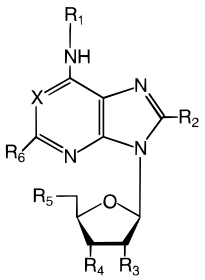

	R_1	R_2	R_3	R_4	R_5	R_6	X
1	cyclopentyl	H	OH	OH	OH	H	N
2			H				
3				H			
4					H		
5		NH-CH_3					
6		NH-CH_2CH_3					
7		NH-$(CH_2)_2CH_3$					
8		NH-$(CH_2)_3CH_3$					
9		NH-cyclopentyl					
10	phenylisopropyl						
11	(p-sulfophenyl)						
12						Cl	C

Figure 1—Chemical structure of the adenosine A_1 receptor agonists. For the sake of clarity, only the modifications compared with the reference compound **1** (CPA) are indicated.

Table 1—Pharmacokinetic Parameters for the Adenosine A_1 Receptor Agonists[a]

compound[a]	CL (mL/min/kg)[b]	Vd_{SS} (mL/kg)[c]	f_U (%)[d]
1	76	320	72
2	33	1050	63
3	58	660	68
4	55	740	61
5	65	1000	24
6	81	860	16
7	92	1000	23
8	72	1190	15
9	62	1130	11
10	24	940	41
11	5.6	365	67
12	62	1155	17

[a] Compound numbers correspond to the chemical strucutres shown in Figure 1. [b] Clearance. [c] Volume of distribution at steady state. [d] Fraction unbound.

MO) and GRID[14] (Molecular Discovery Ltd., University of Oxford, U.K.) programs, a grid large enough to enclose all the aligned ligands is utilized. In each grid point, interactions between a probe atom and the target molecules are calculated. SYBYL/CoMFA and GRID use different force fields and different types of probe atoms, and the interactions are calculated differently. Interactions accounted for in the GRID force field are steric, electrostatic and hydrogen bonding interactions represented by the Lennard−Jones energy (E_{ste}), the Coulombic energy (E_{ele}) and a hydrogen bonding (E_{hb}) term, respectively. In contrast to SYBYL/CoMFA, where the interaction energies (i.e., E_{ste} and E_{ele}) are considered separately, the sum of all the different interaction energies is calculated in each grid point with GRID. An attractive interaction between the probe atom and the ligand produces a negative field (E_{tot}), whereas a repulsive interaction is positive

$$E_{tot} = E_{ele} + E_{ste} + E_{hb} \quad (1)$$

Different probes reflect different types of interactions and may selectively be included to mimic specific interactions between the ligand and the target protein,[14,25,26] and often more than one probe is necessary for a complete description of the interactions involved in the ligand−protein interaction.

The second type of descriptors considered were molecular surface volumes, such as, POP1, POT0, and POM1 (see Table 2), corresponding to the volumes (Å^3) of the electrostatic potential surfaces at the charge levels plus one, zero, and minus one, respectively (SYBYL 6.1, Molecular Modeling Software 6.3, Tripos Inc., St. Louis, MO).

The third type of descriptors were the electronic descriptors [heat of formation (HEFO), electronic energy (ELEN), dipole moment (DIPO), filled levels (FILE), and ionization potentials (IOPO)], obtained from Mopac 6.0 (SYBYL 6.1) AM1 single point calculations[27] with the keywords SCF1, MULLIK, AM1 and T = 3600 activated (Table 2). Four steric descriptors were included in the present investigation, namely the core−core repulsion (COCO), molecular weight (MW) and the areas and the volumes enclosed by the Connolly surfaces, COAR and COVO, respectively. The Connolly surface area (solvent accessible area) is defined as the area a theoretical water molecule (1.4 Å in diameter) produces when it moves over the van der Waals surface of a ligand.

Finally, the log *P* descriptor (the logarithm of the partition coefficient, *P*, between 1-octanol and water) was estimated with the Prolog *P* module (CDR database) of the Pallas program (version 1.2, CompuDrug Chemistry Ltd., Budapest, Hungary), which utilizes a modification of the method presented by Rekker and De Kort,[28] where the contributions of the hydrophobic molecular fragment constants are added. It is well-known that different methods of calculation may yield different theoretical estimates of log *P*. Therefore, we also calculated log *P* with the ATOMIC5 database of the Pallas program, which is based on a modification of the work of Ghose and Crippen.[29] Although the estimates varied slightly between the two methods, the correlation was high (r = 0.88) and the slope and intercept of the best-line fit were not significantly different from unity and zero, respectively. Hence, for the sake of simplicity only estimates based on the CDR database were used in the present analysis, and the log *P* parameter should be interpreted as such. In other cases, however, it might be advantageous to include several log *P* estimates calculated by different methods in the model.

Principal Component Analysis (PCA)—Principal component analysis (PCA) was used in the first stage of the study to replace the original molecular descriptors generated in the GRID program by so-called "3D principal properties" (3DPPs, see *Results*) and to summarize in a graphical manner the information contained in the dataset. Details of PCA can be found in numerous references.[15,16] Briefly, let **X** be a matrix with *m* rows and *n* columns, representing a dataset of *m* compounds with *n* descriptor variables ($\mathbf{X} = [\mathbf{x_1}, \mathbf{x_2}, ..., \mathbf{x_n}]$). In PCA, the original *n* descriptors in **X** are replaced by a limited number (*a*) of new variables, called principal components (PCs), which are linear combinations of the columns in **X**. Algebraically, PCA decomposes **X** in *a* PCs as follows

$$\mathbf{X} = \mathbf{t_1}\,\mathbf{p_1}^T + \mathbf{t_2}\,\mathbf{p_2}^T + ... + \mathbf{t_a}\,\mathbf{p_a}^T + \mathbf{E} \quad (2)$$

where the $\mathbf{t_i}$ and $\mathbf{p_i}$ vectors are known as the principal components scores and variable loadings, respectively, and **E** is the residual matrix not described by the model. Each consecutive PC is calculated orthogonal to all previous PCs and accounts for a decreasing percentage of the variation in **X**. The purpose of PCA is to describe the complete dataset with less PCs than original descriptors without significant loss of information. Plots of scores and loadings obtained from the first few PCs can then be made to reveal the relationships between objects (compounds) and variables (descriptors), respectively.

Partial Least Squares (PLS) Regression—Partial least squares (PLS) is a relatively new multivariate statistical method that has become the most widely used regression tool in the area of QSAR.[16] PLS is a generalization of ordinary multiple linear regression (MLR) and can be seen as a least-squares regression extension of PCA. Like MLR, PLS aims to provide a statistical model that describes biological properties (**y**) in terms of the descriptor variables in matrix **X**. In contrast to MLR, PLS can deal with high correlations between the descriptor variables in **X** (collinearity) and with the situation where the number of descriptors exceeds the number of compounds ($n > m$), which is often the case in QSAR/QSPKR). A detailed description of the PLS algorithm can be found in the review by Geladi and Kowalski.[15]

For the interpretation of the model, it is particularly useful that PLS models can be expressed in terms of regression coefficients ($\mathbf{b_{PLS}}$):

Table 2—Physicochemical Descriptors[b] Used for the QSPKR Analysis of the Adenosine A_1 Receptor Agonists[a]

compound	1 3DPP1	2 3DPP2	3 3DPP3	4 POP1	5 POT0	6 POM1	7 HEFO	8 ELEN	9 DIPO	10 FILE	11 IOPO	12 COAR	13 COVO	14 MW	15 COCO	16 log *P*
1	109.0	–40.2	14.9	1120	12 116	18 426	–27.3	–32 308	4.21	65	8.63	322.4	322.2	335.4	27 785	0.12
2	105.1	–30.2	8.5	1094	13 202	18 272	10.2	–29 569	3.36	62	8.66	317.1	313.2	319.4	25 367	0.64
3	100.9	–38.1	16.8	1232	9 511	17 683	12.4	–29 811	5.13	62	8.56	316.0	313.4	319.4	25 609	0.64
4	96.2	–33.8	5.6	1108	11 548	17 689	15.5	–29 995	3.48	62	8.65	313.9	312.0	319.4	25 793	1.22
5	–117.1	5.4	–5.1	1461	10 162	17 713	148.3	–38 336	6.96	71	7.64	334.1	337.4	364.4	33 444	0.92
6	–130.9	4.0	–5.4	1512	11 248	18 820	142.9	–40 810	7.12	74	7.63	348.2	357.0	378.4	35 763	1.44
7	–154.7	–5.5	5.6	1545	11 366	18 828	140.8	–43 295	7.08	77	7.62	363.0	374.7	392.5	38 092	1.96
8	–156.4	–3.4	–1.0	1583	12 177	19 393	185.0	–46 016	7.03	80	7.62	374.1	389.1	406.5	40 659	2.48
9	–158.2	–1.7	–1.7	1619	12 210	19 412	160.0	–48 099	7.00	82	7.62	379.5	398.9	418.5	42 613	2.63
10	93.7	131.7	63.8	1335	14 004	19 957	25.5	–38 180	4.17	74	8.63	374.2	376.0	385.4	33 119	1.11
11	112.1	51.9	–116.7	1374	12 110	18 324	–99.3	–40 984	8.70	77	8.85	364.2	361.9	423.4	35 234	–2.23
12	100.3	–40.1	14.7	1178	11 994	18 766	–41.0	–34 615	3.71	78	8.59	340.6	342.2	368.8	29 798	1.67

[a] Compound numbers refer to the chemical structures shown in Figure 1. [b] Abbreviations: 3DPP, three-dimensional principal property; COAR, area enclosed by Connolly surface; COCO, core–core repulsion; COVO, volume enclosed by Connolly surface; DIPO, dipole moment; ELEN, electronic energy; FILE, filled levels; HEFO, heat of formation; IOPO, ionization potential; log *P*, logarithm of partition coefficient; MW, molecular weight; POM1, volume of electrostatic potential surface at charge level minus one; POP1 volume of electrostatic potential surface at charge level plus one; and POT0, volume of electrostatic potential surface at charge level zero.

$$\mathbf{y} = \mathbf{X}\mathbf{b}_{\mathbf{PLS}} + \mathbf{F} \tag{3}$$

where **F** is the residual matrix. As in the case of MLR, the regression coefficients can be used to determine the influence of each variable in **X** in the model.[30]

A crucial step in the development of PLS models is the determination of the number of significant components.[4,15] Although it is possible to calculate as many PLS components as the number of descriptors in the **X** matrix, the use of too many components will result in a model that fits the data well but has poor predictability. Cross-validation has become the method of choice to determine the optimal number of components in PLS[25,26,30] and was also used in the present study. Briefly, with cross-validation, a PLS model is developed with a group of compounds omitted from the dataset. Subsequently, the model is used to predict the dependent variable (y_{pred}) for the omitted compounds and the differences between actual (y_{obs}) and predicted values are calculated. This procedure is repeated several times until all compounds have been omitted once. The predictive ability of the model can then be quantified with the Q^2 statistic:[25,26,30]

$$Q^2 = 1 - \sum (y_{ipred} - y_{iobs})^2 / \sum (y_{iobs} - y_{mean})^2 \tag{4}$$

The optimum number of PLS components is given by the number of components that maximizes Q^2. A model with good predictive capability will have a Q^2 close to unity, whereas a negative value for Q^2 indicates that the model does not predict better than random. Formally, real predictability can only be validated with an external test set, which is not included in the calibration process of the model. However, even in QSAR studies in which it is usually easier to test a large number of compounds than in pharmacokinetic experiments, it is common to test predictability by cross-validation because the dataset is often too small to be split into a training and test set. A compromise between an external test set and leave-one-out cross-validation as used in the present study is leave-more-out cross-validation where multiple compounds are left out simultaneously several times, like in bootstrapping. However, this method still requires rather large datasets and we therefore decided to use the leave-one-out method; that is, compounds were omitted one by one.

The Q^2 value can be compared with the R^2 statistic which indicates the fraction of the variation accounted for by the model:[25,26,30]

$$R^2 = 1 - \sum (y_{icalc} - y_{iobs})^2 / \sum (y_{iobs} - y_{mean})^2 \tag{5}$$

The R^2 values range between zero (meaningless model) and unity (perfect correlation). The value of R^2 increases with the number of components included in the model, and the PLS regression model converges toward the MLR solution when the number of components is identical to the number of variables in the **X** matrix. In that case, the fraction explained variance is maximal but the model is usually overfitted, that is, the predictability is poor (low Q^2). On the other hand, an underfitted model with too few PLS components does not account for sufficient variation (low R^2). Eriksson and Johansson[30] have suggested that a difference between R^2 and Q^2 values of >0.3 is indicative of an inappropriate model.

The outcomes of PCA and PLS are dependent on the scaling of the variables. In the present study we always employed the autoscaling procedure, that is, all variables were scaled to unit variance and centered around the mean.[15]

All PLS and PCA calculations were performed with the PLS_Toolbox version 1.5.2 (Eigenvector Research, Inc., Manson WA) using the MATLAB software package version 4.2c.1 (The MathWorks Inc., Natick MA).

Computer Hardware—The generation of the 3D molecular descriptors was carried out on a R4600 Indy Silicon Graphics workstation. All other calculations were done on standard Pentium personal computers.

Results

Generation and PCA of Molecular Descriptors—The grid created in GRID enclosed all the aligned ligands with 4 Å with a resolution of 1 Å in all directions and consisted of 9025 points. For each of the 12 compounds, interactions with three probes (CA2+, C3, and OH2) were calculated at each grid point, thus yielding three grids with 9025 data points for each compound (i.e., a total of 27 075 data points per compound). Prior to the multivariate analysis, the grids were unfolded to row vectors, which were subsequently combined to form a 12 × 27 075 matrix. A PCA was performed on this matrix to reduce this large set of data into a smaller number of new, orthogonal (uncorrelated) variables. The first three PCs explained 91% of the total variance in the data, indicating that the original 27 075 GRID variables could be replaced by the score vectors associated with these PCs without significant loss of information. These scores vectors can be regarded as "principal properties" (PP) of the compounds and, because they were derived from a 3D structure analysis, will be referred to as "3DPPs". The 3DPPs for the first, second, and third PC (3DPP1, 3DPP2, and 3DPP3, respectively) are given in Table 2 together with the other descriptors, which were obtained as described in the *Methods* section.

Subsequently, a PCA was performed on the combined data of Table 2 to obtain insight into the relationships between descriptors and compounds. One-, two-, and three-component models described 60, 79, and 94% of the total variance, respectively. The plot of the scores of the compounds for the first two PCs reveals three clusters: the first one with the reference ligand CPA (**1**), the deoxyribose

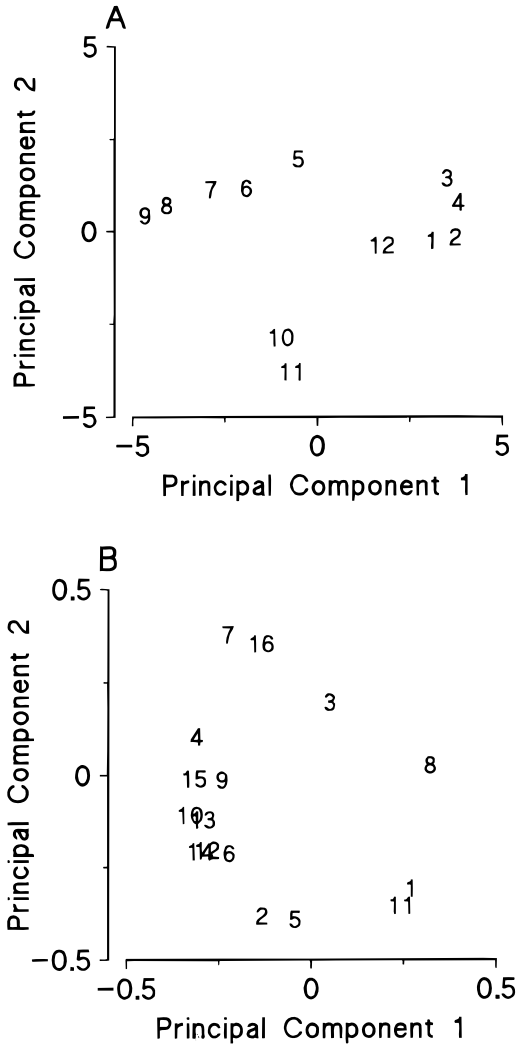

Figure 2—Graphical representation of the first two principal components, which explained 79% of the total variance of the data given in Table 2. (A) Plot of the scores of the 12 adenosine A_1 receptor agonists. Numbers correspond to the compounds shown in Figure 1. (B) Plot of the loadings of the 16 molecular descriptors. Numbers correspond to the descriptor variables in Table 2.

analogues **2**, **3**, and **4**, and the lipophilic non-CPA analogue **12**; a second cluster with the 8-alkylamino-substitued CPA analogues **5**, **6**, **7**, **8**, and **9**; and a third cluster with R−PIA (**10**) and the hydrophilic non-CPA analogue **11** (Figure 2A). From the loading plot for the first two PCs, one clear cluster can be recognized that contains the steric descriptors 12 (COAR), 13 (COVO), 14 (MW), and 15 (COCO), the electronic descriptors 9 (DIPO) and 10 (FILE), and the molecular surface volumes 4 (POP1) and 6 (POM1, Figure 2B). The clustering of the remaining descriptors is less clear. It is of interest to note, however, that 3DPP1 and 3DPP2 seem to be closely associated with IOPO and POT0, respectively (Figure 2B).

Correlation between Pharmacokinetic Parameters and Molecular Descriptors—Correlation coefficients were calculated between the pharmacokinetic parameters and each of the molecular descriptors using the MATLAB program. All three pharmacokinetic parameters were significantly correlated ($P < 0.05$) with HEFO ($r = 0.63$, 0.63, and −0.75 for *CL*, Vd_{SS}, and f_U, respectively) and log *P* ($r = 0.66$, 0.80 and −0.74 for *CL*, Vd_{SS} and f_U, respectively). In the case of Vd_{SS}, no other significant correlations were found, whereas *CL* displayed additional significant correlations with 3DPP1 ($r = -0.62$) and IOPO ($r = -0.68$), and f_U had significant correlations with 3DPP1 ($r = 0.81$), IOPO ($r = 0.81$), POP1 ($r = -0.75$), ELEN ($r = 0.73$), FILE ($r = -0.68$), COAR ($r = -0.61$), COVO ($r = -0.69$), MW ($r = -0.59$), and COCO ($r = -0.74$).

Table 3—Summary of the Results of the Prediction of *CL*, Vd_{SS}, and f_U of the Adenosine A_1 Receptor Agonists (Table 1) using PLS

pharmacokinetic parameter	no. of components[a]	Q^2	R^2
CL	4	0.59	0.82
Vd_{SS}	2	0.41	0.61
f_U	2	0.62	0.78

[a] Number of PLS components were determined using leave-one-out cross-validation (see *Methods* for details).

PLS Regression—PLS regression models to predict *CL*, Vd_{SS}, and f_U were built using the 16 descriptor variables listed in Table 2. The results of the analysis are summarized in Table 3 and plots of the observed versus predicted values are shown in Figure 3. With the exception of Vd_{SS} for **1** and f_U for **12**, most of the variation in the pharmacokinetic parameters could be accounted for by the PLS models (R^2 values 0.6−0.8). Furthermore, the moderate differences between R^2 and Q^2 (∼0.2 for each model) found using cross-validation indicate adequate model predictability and number of PLS components (Table 3). The relationship between R^2 and Q^2 with increasing number of PLS components is exemplified for *CL* in Figure 4.

Figure 5 shows the weighted PLS regression coefficients, which provide insight into the contribution of each descriptor to the modeling of the pharmacokinetic parameters. For example, 3DPP2 (descriptor 2) has a high impact on *CL* but is relatively unimportant in the models for Vd_{SS} and f_U. On the other hand, lipophilicity has considerable, but opposite, influence on both Vd_{SS} and f_U; that is, the log *P* regression coefficient is positive for the former and negative for the latter.

Discussion

To date, QSPKR studies have mainly focused on the relationship between pharmacokinetic properties and single, conventional physiocochemical parameters. To our knowledge, this study is the first example of the application of the molecular descriptor techniques, SYBYL/CoMFA and GRID, in combination with multivariate analysis methods, PCA and PLS, for the prediction of pharmacokinetic properties. Our multivariate approach has several advantages compared with the conventional methodologies employed in previously published QSPKR studies. First, the use of a whole series of advanced molecular descriptors instead of a single "classical" physicochemical property may yield more comprehensive 3D QSPKR models that can provide better insight into the relationship between chemical structure and pharmacokinetic behavior and a better and more robust prediction. Second, our approach can be used to predict multiple parameters and thus overall pharmacokinetic profile. Third, this approach could allow for integrated QSPKR−QSAR analysis and thus for simultaneous optimization of pharmacodynamic and pharmacokinetic properties at a very early stage of drug discovery. This integration could become a feasible strategy in the light of the emerging in vivo high-throughput screening technologies[31−33] that could provide considerable savings of laboratory animals, time, and money.

In the current study, QSPKR models were obtained for the prediction of three main pharmacokinetic parameters (*CL*, Vd_{SS}, and f_U) of a series of 12 adenosine A_1 receptor agonists. It should be noted that the present study was primarily focused on the development of methodology and

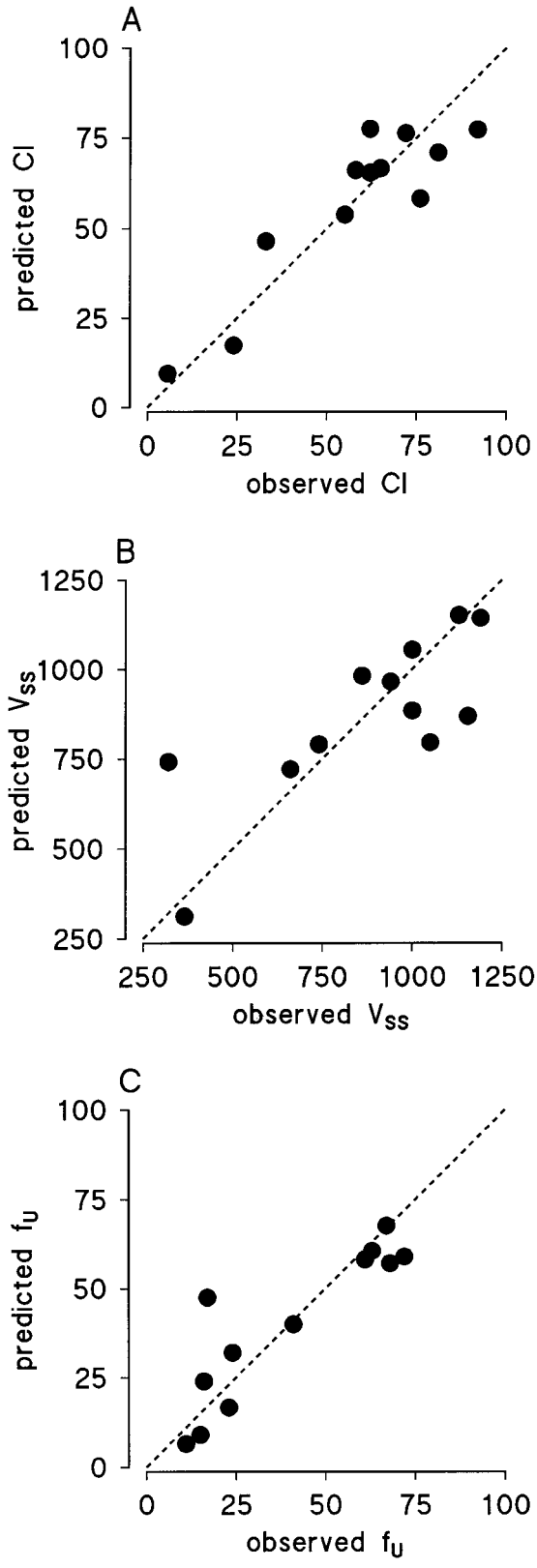

Figure 3—Relationship between observed and predicted (A) *CL*, (B) Vd_{SS}, and (C) f_U using the PLS models summarized in Table 3. The dashed lines represent lines of identity.

the number of compounds used for the modeling was limited. However, despite the relatively small dataset, the predictive ability of the QSPKR model as judged by leave-one-out cross validation was fair (i.e., difference between R^2 and Q^2 was ~0.2 in each case). The between-ligand variation in the pharmacokinetic parameters was accounted for in an adequate manner by the models in most cases (Figure 3). The exceptions were the predictions of Vd_{SS} for CPA (**1**, predicted 742 mL/kg, observed 320 mL/kg) and f_U for **12** (predicted 47%, observed 17%). At present we have no explanation for these outliers, but in the case of CPA, the overestimation of Vd_{SS} may at least in part be due to variability in the experimental estimate because we have recently[23] obtained a >30% higher value (421 mL/kg). Furthermore, the use of the standard PLS algorithm implies the assumption of a linear relationship between molecular descriptors and pharmacokinetic parameters. If this assumption would not be valid, nonlinear variations of PLS might provide better predictions. However, the nonlinear algorithms with polynomial, spline, or neural-network inner relations as implemented in the MATLAB PLS_Toolbox have not yet been widely applied and require further validation.

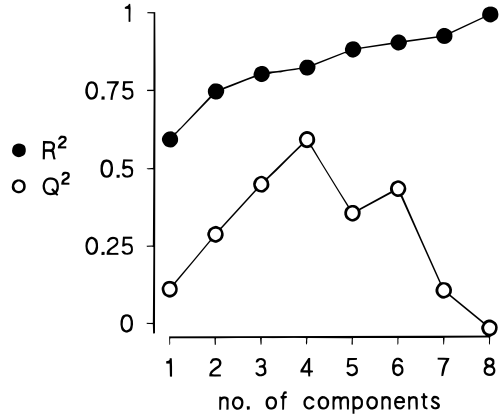

Figure 4—Effect of increasing the number of PLS components in the model for *CL* on the values of R^2 and Q^2. In this case, the optimum number of components was found to be 4 (Table 3).

The GRID program was used to generate 3D molecular descriptors in this study. Because GRID generates datasets with a very large number (27 075 in the present study) of highly correlated variables, it is desirable to employ some form of data pretreatment to reduce the number of datapoints in the descriptor matrix. Because it was found that three principal components could describe >90% of the total variance in the GRID matrix, we decided to replace the original variables with these principal components (3DPPs). An advantage of the use of principal properties, particularly when the number of compounds is relatively small, is that it is much more efficient in reducing the number of variables than other data pretreatment methods generally used in conjunction with GRID, such as D-optimal variable preselection.[25,26] Furthermore, being principal components, the 3DPPs display no collinearity. Another advantage is that the 3DPPs can be related to other molecular descriptors, which allows for a physicochemical interpretation of the GRID analysis. In the present study, it was found that the first and second 3DPP were closely associated with IOPO and POT0, respectively (Figure 2B). To our knowledge, this is the first example where such a relationship between GRID and physicochemical properties is shown.

A qualitative interpretation of the QSPKR models can be made on the basis of the PLS weighted regression coefficients (Figure 5). High values of 3DPP2 and the related descriptor POT0, and to a lesser degree 3DPP1 and the related descriptor IOPO, are associated with low *CL*. In contrast, high values of 3DPP3 and POM1 result in an increase of *CL*. The influences on *CL* of the remaining molecular properties, including log *P* (as calculated), appear to be less important (Figure 5A).

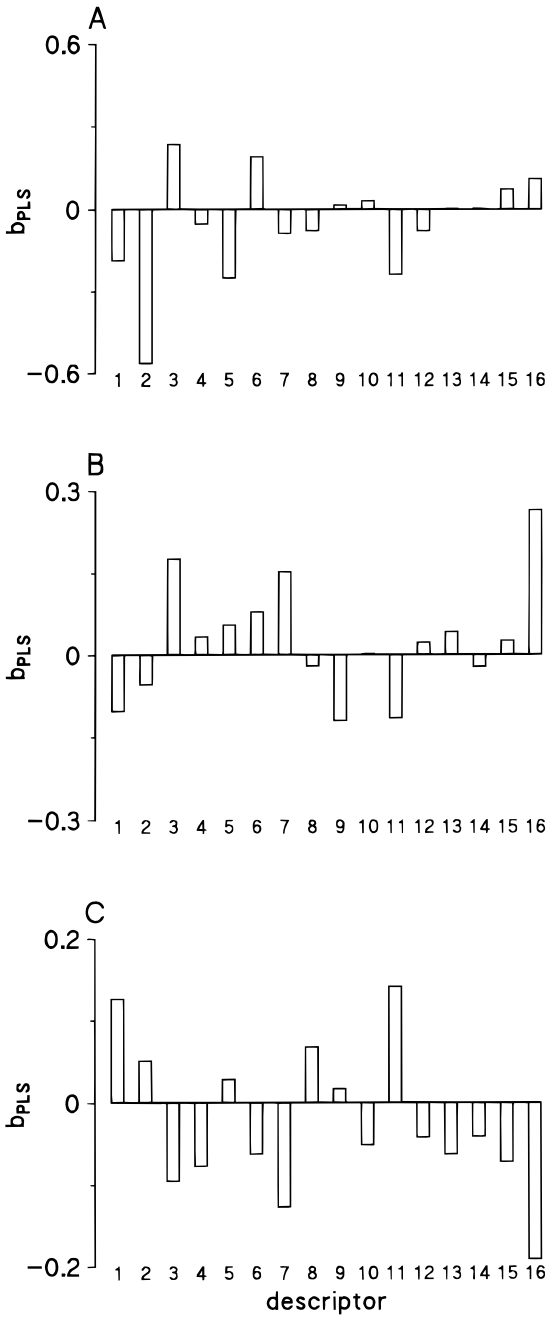

Figure 5—Weighted PLS regression coefficients (b_{PLS}) for (A) *CL*, (B) Vd_{SS}, and (C) f_U. Numbers correspond to the descriptor variables in Table 2.

In the case of Vd_{SS}, the high value of the regression coefficient for log *P* is consistent with many previously published reports that high lipophilicity is associated with large Vd_{SS}.[7] However, from Figure 5B it can be seen that 3DPP3 and HEFO are also important factors that are positively correlated with Vd_{SS}, whereas increased values of 3DPP1, IOPO, and DIPO will reduce Vd_{SS}.

Figure 5C shows that many factors contribute to the model for f_U, which would be expected on the basis of the high number of significant correlations found previously (see *Results*). The most influential factors are log *P* and to a lesser degree HEFO, which are negatively correlated, and the two related descriptors 3DPP1 and IOPO, which are positively correlated with f_U. This result confirms the conclusion made by others that lipophilicity is a key determinant of protein binding but that other physicochemical features, in particular electronic properties, also play an important role.[7]

To date, MLR has been used successfully as a regression technique in many QSPKR studies. The main disadvantage of MLR compared with PLS is that it performs very poorly in the case of collinearities among descriptor variables and that it can only be applied when the number of compounds exceeds the number of descriptors by at least a factor 3−5.[15,30] Therefore, PLS has replaced MLR as method of choice in modern QSAR studies and it may be expected that this will also happen in the area of QSPKR when the methods presented in this paper are developed further and applied to large datasets with even more molecular descriptors (for example original GRID points) and pharmacokinetic properties. The main appeal of MLR is that it may yield models that are apparently easy to interpret. When a dependent variable is strongly correlated with one of the independent variables, it should, in general, be possible to generate a simple MLR model based on the influential descriptor and one or two additional orthogonal variables that explain a fraction of the variation similar to that explained by PLS. For example, on the basis of the strong influence of log *P* on Vd_{SS} and f_U, one can calculate the simple MLR relationships $Vd_{SS} = 236.2 + 181.6 \log P + 1.2$ MW and $f_U = 92.4 - 15.4 \log P - 6.4$ DIPO which yield R^2 values (0.67 and 0.77, respectively) that are as good as the ones obtained with PLS (Table 3). However, the molecular diversity of the ligands in this study was limited, and it may be expected that the chances of finding such simple relationships will decrease with increasing complexity of the dataset. Furthermore, multivariate QSPKR modeling should aim to predict overall pharmacokinetic behavior, whereas MLR on the basis of a few descriptors may only provide an adequate alternative for PLS for some of the parameters of interest. In the present case, for example, the best MLR model for *CL* on the basis of log *P* and one other descriptor ($CL = 156.5 + 12.9 \log P - 0.01$ POT0) predicted poorly compared to PLS ($R^2 = 0.65$ and 0.82, respectively).

Herman and Veng-Pedersen[11] have suggested that QSPKR models need not be limited to congeneric series but can be used to predict distribution kinetics of a wide variety of drugs. However, in our view, QSPKR and QSAR models should generally be regarded as having "local validity" only, that is, their utility is restricted to series of chemically related ligands with similar biological properties. Hence, we believe that QSPKR modeling may be particularly useful to analyze pharmacokinetic databases of structural analogues obtained in the early stages of drug development programs. Obviously, the aim is always to develop a model that predicts the pharmacokinetic parameters of the whole set of compounds as well as possible. However, the limitations of a QSPKR model may be just as valuable and the outliers that are poorly predicted may provide new insight into the mechanisms underlying the pharmacokinetic processes. For this purpose, however, a more physiological approach than the one used in the present study should be adopted in which the dependent variables represent intrinsic pharmacokinetic properties of individual organ systems rather than overall pharmacokinetic behavior.[10,34]

In conclusion, in the present paper we have described a QSPKR method based on 3D molecular characterization and multivariate statistical analysis. By using this method, we obtained a model that could adequately predict overall pharmacokinetic behavior of 12 adenosine A_1 receptor ligands in rat. Notwithstanding the fact that analysis of a larger dataset would be required to draw any general conclusion about the pharmacokinetic behavior of adenosine analogues, these first results obtained with a relatively small number of ligands warrant further validation and application of multivariate 3D QSPKR on larger datasets of other classes of compounds. In combination with emerg-

ing methods for high-throughput in vivo pharmacokinetic screening of mixtures of structurally related compounds[31−33] and with novel approaches in physiologically based pharmacokinetic modeling,[10,34] multivariate 3D QSPKR may become a useful tool in drug discovery and preclinical development.

References and Notes

1. Hansch, C.; Fujita, T. rho-sigma-pi Analysis. A method for the correlation of biological activity and chemical structure. *J. Am. Chem. Soc.* **1964**, *86*, 1616−1626.
2. van de Waterbeemd, H. *Chemometric Methods in Molecular Design*, VCH: Weinheim, 1995.
3. Kubinyi, H. The quantitative analysis of structure−activity relationships. In *Burger's Medicinal Chemistry and Drug Discovery*; Wolff, M. E., Ed.; John Wiley & Sons: New York, 1995; pp 497−571.
4. Kubinyi, H. QSAR and 3D QSAR in drug design. Part 2: Applications and problems. *Drug Discovery Today* **1997**, *2*, 538−546.
5. Others have used the abbreviation "QSPR" for this purpose, but to avoid confusion, we propose to reserve this term for "quantitative structure−property relationships".[2]
6. Toon, S.; Rowland, M. Strucure-pharmacokinetic relationships among the barbiturates in the rat. *J. Pharmacol. Exp. Ther.* **1983**, *225*, 752−763.
7. Mayer, J. M.; van de Waterbeemd, H. Development of quantitative structure-pharmacokinetic relationships. *Environ. Health Perspect.* **1985**, *61*, 295−306.
8. Yamada, Y.; Ito, K.; Nakamura, K.; Sawada, Y.; Iga., T. Prediction of therapeutic doses of beta-adrenergic receptor blocking agents based on quantitative structure-pharmacokinetic/pharmacodynamic relationship. *Biol. Pharm. Bull.* **1993**, *16*, 1251−1259.
9. Gobburu, J. V. S.; Shelver, W. H. Quantitative structure-pharmacokinetic relationships (QSPR) of beta blockers derived using neural networks. *J. Pharm. Sci.* **1995**, *84*, 862−865.
10. Blackey, G. E.; Nestorov, I. A.; Arundel, P. A.; Aarons, L. J.; Rowland, M. Quantitative structure-pharmacokinetics relationships: I. Development of a whole-body physiologically based model to characterize changes in pharmacokinetics across a homologous series of barbiturates in the rat. *J. Pharmacokinet. Biopharm.* **1997**, *25*, 277−312.
11. Herman, R. A.; Veng-Pedersen, P. Quantitative structure-pharmacokinetic relationships for systemic drug distribution kinetics not confined to a congeneric series. *J. Pharm. Sci.* **1994**, *83*, 423−428.
12. Cupid, B. C.; Beddell, C. R.; Lindon, J. C.; Wilson, L. D.; Nicholson, J. K. Quantitative structure-metabolism relationships for substituted benzoic acids in the rabbit: prediction of urinary excretion of glycine and glucuronide conjugates. *Xenobiotica* **1996**, *26*, 157−176.
13. Cramer III, R. D.; Patterson, D. E.; Bunce, J. D. Comparative molecular field analyses (COMFA). 1. Effects of shape on binding of steroids to carrier proteins. *J. Am. Chem. Soc.* **1988**, *110*, 5959−5967.
14. Goodford, P. Multivariate characterization of molecules for QSAR analysis. *J. Chemom.* **1996**, *10*, 107−117.
15. Geladi, P.; Kowalski, B. R. Partial least squares: a tutorial. *Anal. Chem. Acta* **1985**, *185*, 1−17.
16. Cecchetti, V.; Filipponi, E.; Fravolini, A.; Tabarrini, O.; Bonelli, D.; Clementi, M.; Cruciani, G.; Clementi, S. Chemometric methodologies in a quantitative structure−activity relationship study: the antibacterial activity of 6-aminoquinolones. *J. Med. Chem.* **1997**, *40*, 1698−1706.
17. IJzerman, A. P.; van der Wenden, E. M.; Roelen, H. C. P. F.; Mathôt, R. A. A.; Von Frijtag Drabbe Künzel, J. K. Partial agonists for adenosine receptors. In *Perspectives in Receptor Research*; Giardinà, D.; Piergentili, A.; Pigini M., Eds.; Elsevier Science B. V.: Amsterdam, 1996; pp 181−192.
18. Van der Graaf, P. H.; Van Schaick, E. A.; Mathôt, R. A. A.; IJzerman, A. P.; Danhof, M. Mechanism-based pharmacokinetic-pharmacodynamic modeling of the effects of N^6-cyclopentyladenosine analogues on heart rate in rat: estimation of in vivo operational affinity and efficacy at adenosine A_1 receptors. *J. Pharmacol. Exp. Ther.* **1997**, *283*, 809−816.
19. Mathôt, R. A. A.; van Schaick, E. A.; Langemeijer, M. W. E.; Soudijn, W.; IJzerman, A. P.; Danhof, M. Pharmacokinetic-pharmacodynamic relationship of the cardiovascular effects of adenosine A_1 receptor agonist N^6-cyclopentyladenosine in the rat. *J. Pharmacol. Exp. Ther.* **1994**, *268*, 616−624.
20. Mathôt, R. A. A.; van der Wenden, E. M.; Soudijn, W.; IJzerman, A. P.; Danhof, M. Deoxyribose analogues of N^6-cyclopentyladenosine (CPA): partial agonists at the adenosine A_1 receptor in vivo. *Br. J. Pharmacol.* **1995**, *116*, 1957−1964.
21. Mathôt, R. A. A.; van den Aarsen, B. C.; Soudijn, W.; Breimer, D. D.; IJzerman, A. P.; Danhof, M. Pharmacokinetic-pharmacodynamic modelling of the cardiovascular effects of R- and S−N^6-phenylisopropyladenosine (PIA) in conscious normotensive rats. *J. Pharmacol. Exp. Ther.* **1995**, *273*, 405−414.
22. van Schaick, E. A.; Mathôt, R. A. A.; Gubbens-Stibbe, J. M.; Langemeijer, M. W. E.; Roelen, H. C. P. F.; IJzerman, A. P.; Danhof, M. 8-Alkylamino substituted analogues of N^6-cyclopentyladenosine (CPA) are partial agonists for the cardiovascular adenosine A_1 receptors in vivo. *J. Pharmacol. Exp. Ther.* **1997**, *283*, 800−809.
23. van Schaick, E. A.; Kulkarni, C.; Von Frijtag Drabbe Künzel, J. K.; Mathôt, R. A. A.; Cristalli, G.; IJzerman, A. P.; Danhof, M. Time course of action of three adenosine A_1 receptor agonists with differing lipophilicity in rats: comparison of pharmacokinetic, hemodynamic and EEG effects. *Naunyn-Schmiedeberg's Arch. Pharmacol.* **1997**, *356*, 827−837.
24. IJzerman, A. P.; Van Galen, P. J. M.; Jacobson, K. A. Molecular modeling of adenosine receptors. I. The ligand binding site on the A_1 receptor. *Drug Design Discov.* **1992**, *9*, 49−67.
25. Nilsson, J.; Wikström, H.; Smilde, A.; Glase, S.; Pugsley, T.; Cruciani, G.; Pastor, M.; Clementi S. GRID/GOLPE 3D quantitative structure−activity relationship study on a set of benzamides and naphthamides, with affinity for the dopamine D_3 receptor subtype. *J. Med. Chem.* **1997**, *40*, 833−840.
26. Nilsson, J.; Homan, E. J.; Smilde, A. K.; Grol, C. J.; Wikström, H. A multiway 3D QSAR analysis of a series of (S)-N-[(1-ethyl-2-pyrrolidinyl)methyl]-6-methoxybenzamides. *J. Computer-Aided Mol. Design* **1998**, *12*, 81−93.
27. Dewar, M. J. S.; Zoebisch, E. G.; Healy, E. F.; Stewart, J. J. P. A new general purpose quantum mechanical molecular model. *J. Am. Chem. Soc.* **1985**, *107*, 3902−3909.
28. Rekker, R. F.; De Kort, H. M. The hydrophobic fragmental constant: an extension to a 1000 data point set. *Eur. J. Med. Chem.* **1979**, *6*, 479−488.
29. Ghose A. K.; Crippen G. M. Atomic physicochemical parameters for three-dimensional structure-directed quantitative structure−activity relationships. I. Partition coefficients as a measure of hydrophobicity. *J. Comput. Chem.* **1986**, *7*, 565−577.
30. Eriksson, L.; Johansson, E. Multivariate design and modeling in QSAR. *Chemom. Intell. Lab. Syst.* **1996**, *34*, 1−19.
31. Berman, J.; Halm, K.; Adkison, K.; Shaffer, J. Simultaneous pharmacokinetic screening of a mixture of compounds in the dog using API LC/MS/MS analysis for increased throughput. *J. Med. Chem.* **1997**, *40*, 827−829.
32. Olah, T. V.; McLoughlin, D. A.; Gilbert J. D. The simultaneous determination of mixtures of drug candidates by liquid chromatography atmospheric pressure chemical ionization mass spectrometry as an in vivo drug screening procedure. *Rapid Commun. Mass Spectrom.* **1997**, *11*, 17−23.
33. Korfmacher, W. A.; Cox, K. A.; Bryant, M. S.; Veals, J.; Ng, K.; Watkins, R.; Lin, C.-C. HPLC-API/MS/MS: a powerful tool for integrating drug metabolism into the drug discovery process. *Drug Discovery Today* **1997**, *2*, 532−537.
34. Nestorov, I. A.; Aarons, L. J.; Rowland, M. Physiologically based pharmacokinetic modeling of a homologous series of barbiturates in the rat: a sensitivity analysis. *J. Pharmacokinet. Biopharm.* **1997**, *25*, 413−448.

JS980294A

Use of "N-in-One" Dosing to Create an in Vivo Pharmacokinetics Database for Use in Developing Structure–Pharmacokinetic Relationships

JOEL E. SHAFFER,*,† KIMBERLY K. ADKISON,‡ KATHY HALM,‡,|| KEVIN HEDEEN,‡ AND JUDD BERMAN§

Contribution from *Departments of Receptor Biochemistry, Research Bioanalysis & Drug Metabolism, and Medicinal Chemistry, Glaxo Wellcome Inc., 5 Moore Drive, Research Triangle Park, North Carolina 27709.*

Received July 20, 1998. Final revised manuscript received November 30, 1998.
Accepted for publication December 1, 1998.

Abstract □ The purpose of this work was (1) to determine if useful in vivo pharmacokinetic data could be obtained after simultaneous administration of 5–22 compounds of a chemically congeneric series to dogs and (2) to determine if structure–pharmacokinetic relationships could be derived from such studies. Mixtures of structurally related α-1 antagonist compounds (**5**–**22**) were administered intravenously to conscious dogs. Blood samples were taken over the next 24 h and analyzed by LC/MS to determine plasma levels and pharmacokinetics of each compound. The pharmacokinetics of 17 of these compounds were also determined after individual administration. Results obtained in the N-in-One format for 17 compounds correlated well with results obtained when these same compounds were administered individually. The N-in-One method is a useful method for obtaining pharmacokinetic data on 5–20 molecules in a single animal at one time. The increased throughput in obtaining important pharmacokinetic information should enhance the drug discovery process. In addition, it was possible to determine the extent to which various chemical substitutions did or did not affect pharmacokinetic parameters.

Introduction

Success in drug discovery increasingly relies on the ability to rapidly identify quality molecules that possess the desired attributes of bioavailability, chemical tractability, selectivity, and potency. Combinatorial chemistry and high throughput biochemical screening techniques should have a major impact on the process of generating and identifying potent and selective compounds in drug discovery.[1] The identification of compounds that possess the desired pharmacokinetic (oral bioavailability, clearance, volume of distribution, and half-life) and pharmacodynamic profile has become a time-consuming process in drug discovery programs. While in vivo studies are expensive to conduct, they are also extremely informative. Thus, substantial enhancements in the capacity to characterize molecules in vivo could help relieve a bottleneck in the current drug discovery process.

Increased throughput in in vivo pharmacokinetic screening has recently been reported by (a) dosing mixtures of compounds to a single animal and (b) by pooling samples from singularly administered compounds prior to analysis.[2–8] Both methods capitalize on tandem liquid chromatography/mass spectrometry (LC/MS) as a sensitive and specific method for analysis. We have referred to the former method as N-in-One dosing, where N is the number of compounds coadministered. The N-in-One approach provides an opportunity to study the pharmacokinetics of several compounds under identical conditions while minimizing sample processing time, analysis time, and the number of animals required. Initial reports have shown the method applicable to (a) a wide range of structural classes of compounds, (b) iv and oral dosing, (c) compounds that are renally and/or metabolically eliminated, and (d) a wide variety of species including mice, rats, dogs, and monkeys.

This contribution expands on a previous report of increased capacity of in vivo pharmacokinetic evaluations.[2] This paper reports results of N-in-One studies of 5−22 α-1a antagonist compounds that provided sufficiently good estimates of pharmacokinetic such that compound progression decisions could be made. In addition, structure-pharmacokinetics relationships were developed to help define molecular changes that do and that do not alter pharmacokinetics.

Methods

Compounds—All compounds were synthesized at Glaxo Wellcome and gave satisfactory analysis by TLC, ^{1}H NMR, mass spectrometry, and elemental analysis.[11]

Pharmacokinetic Study—*N-in-One Dosing*—Male mongrel dogs (weight range 15−20 kg) were fasted overnight and fitted with two temporary cephalic vein cannulae on the day of study. Each dog received 5−22 compounds per dose session. Dose solutions involving mixtures of five or less compounds were prepared by dissolving compounds in 50 mM sodium acetate buffer (pH 4.5). Dose solutions with more than five compounds were prepared by dissolving compounds in 100 mM sodium acetate buffer containing 30% propylene glycol and 1% Tween 80 at a concentration of 0.3 mg each compound/mL. The dose solution was infused over 5 min into the right cephalic vein cannula. Each compound was given at a dose level of 0.25 mg/kg body weight (5-in-One) or 0.3 mg/kg body weight (>5-in-One). Blood samples (4 mL) were obtained from the left cephalic vein cannula in heparinized syringes at 0 (predose), 5, 15, 30, 45 min, 1, 1.5, 2, 4, 6, 8, and 24 h after the infusion began. The plasma was separated from the red blood cells by centrifugation and frozen until APCI LC/MS/MS or APCI LC/MS analysis.

Individual Dosing—Male mongrel dogs (weight range 15−21 kg) were fasted overnight and then fitted with two temporary cephalic vein cannulae on the day of study. Each compound was dissolved in 50 mM sodium acetate buffer (pH 4.5) at a concentration of 1.0 mg/mL and administered at a dose of 1 mg(base)/kg body weight via a 5 min intravenous infusion into the right cephalic vein. Blood was sampled, and plasma was obtained and stored as described above until analysis by HPLC with fluorescence detection. Each compound was studied in one dog, except for compounds **19** and **59** which were studied in four and two dogs, respectively. This

* Corresponding author. Phone 919-483-3059, Fax 919-483-6465, e.mail Joel_Shaffer@Glaxowellcome.com.
† Receptor Biochemistry.
‡ Research Bioanalysis & Drug Metabolism.
§ Medicinal Chemistry.
|| Current address: ThermoQuest Finnigan, 355 River Oaks Parkway, San Jose, CA 95134.

10.1021/js980292q CCC: $18.00
Published on Web 02/04/1999

Table 1—Pharmacokinetics of Compound 19 in Individual and N-in-One Studies[a]

	n	half-life (min)	clearance (mL/min/kg)	volume of distribution (mL/kg)
individual studies	4	248 ± 37	0.8 ± 0.3	202 ± 101
N-in-One studies	9	326 ± 96	0.9 ± 0.3	272 ± 99

[a] Data are mean ± standard deviation for the number of observation shown. $p > 0.05$ using Student's *t*-test.

research complied with national legislation and with company policy on the Care and Use of Animals.

Sample Analysis—*N-in-One Dosing*—Calibration standards were prepared at each calibration level for each compound by spiking blank dog plasma over the range of 1 to 2300 ng/mL. Aliquots of the standards and samples (200 μL) were precipitated with 400 μL of acetonitrile that contained an internal standard (compound **18** or **9**) at a concentration of 400 ng/mL. After vortexing and centrifugation, the resulting supernatant was transferred to a clean tube and evaporated to dryness under nitrogen at 35 °C.

The analysis was performed on a Finnigan TSQ-700 mass spectrometer with Atmospheric Pressure Chemical Ionization (APCI). The residues were reconstituted in mobile phase (200 μL), centrifuged, and injected onto either a 3 μm, 50 × 4.6 mm (5-in-One study) or a 5 μm, 250 × 4.6 BDS Hypersil C18 column (>5-in-One studies). The mobile phase consisted of 5 mM ammonium acetate (pH 4.0) and acetonitrile at a flow rate of 1 mL/min. The percentage of acetonitrile was adjusted in each study to retain the mixture from the column void volume and elute all compounds within a k' range of about 1−10. The first 2 min of the HPLC effluent were diverted to waste to minimize contamination of the APCI source. Detection was by selected reaction monitoring (SRM) in positive ion mode for the 5-in-One study. A more generic approach using MS rather than MS/MS was used for quantitation of larger mixtures by scanning in selected ion monitoring mode (SIM). A longer column was necessary for mixtures >5 compounds to increase selectivity and afford more specificity because SIM was used. The run time per sample was 6 min for the 5-in-One study and a maximum of (approximately) 30 min for the other N-in-One studies.

Individual Dosing—Plasma calibration standards were constructed from 5 to 200 ng/mL for each compound. Aliquots of standards and samples (50−100 μL) were precipitated with two volumes of acetonitrile (no internal standard) and prepared as described above. Samples above 200 ng/mL were diluted prior to protein precipitation. The plasma extracts were reconstituted in mobile phase (100 mL) and injected onto a Keystone BDS Hypersil C18 (150 × 3 mm, 3 μm) HPLC column at a temperature of 30 °C. The compounds were eluted with a 25 mM ammonium acetate buffer (pH = 4.5) and acetonitrile mobile phase at a flow rate of 0.5 mL/min. The compounds were detected using a fluorescence detector. The mobile phase composition and wavelength settings were varied to optimize conditions for each compound.

Pharmacokinetic and Statistical Analysis—The clearance (CL), steady-state volume of distribution (V_{ss}), and elimination phase half-life ($t_{1/2}$) of each compound were derived from the respective plasma concentration versus time curve using noncompartmental methods. Statistical comparisons between groups were done by an unpaired *t* test. Results in Tables 2−6 reflect pharmacokinetic data from 1 to 4 dogs in individual or N-in-One format.

Results

Comparison of Pharmacokinetics after Individual and N-in-One Dosing—Table 1 compares the pharmacokinetic parameters of compound **19** when dosed individually to those obtained when coadministered with 4−21 other compounds. There was no statistical difference for any parameter between the two methods. Figure 1 shows the linear regression analyses for the plasma elimination half-life, clearance and steady-state volume of distribution of 17 compounds when measured by both individual and N-in-One methods. There was good agreement in the pharmacokinetic parameters, particularly clearance, obtained from N-in-One dosing and individual dosing.

Table 2—Pharmacokinetic Data for Compounds 1–15[a]

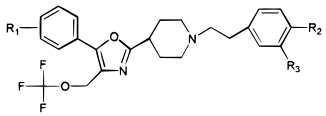

Cmpd	R1	R2	R3	CL (mL/min/kg)	t1/2 (min)	Vss (mL/kg)
1	4H	OMe	H	14	59	785
2	4H	OMe	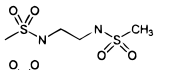	2.0	144	151
3	4H	OMe	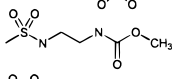	9.1	144	647
4	4H	Ome	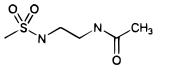	10	156	600
5	4H	Ome	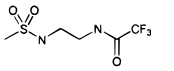	26	72	2035
6	4H	Ome	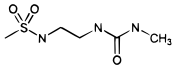	6.8	72	210
7	4H	OMe		11	120	1102
8	4H	OMe	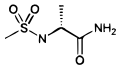	11	114	930
9	4H	OMe	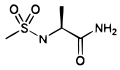	22	107	1241
10	4H	OMe	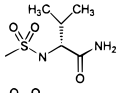	28 ± 8	123 ±47	4133 ±2514
11	4H	OMe	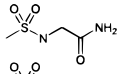	18	135	3175
12	4F	OMe	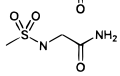	11	432	4778
13	4H	OMe	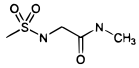	22	144	3450
14	4H	OMe	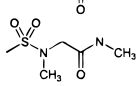	25 ±4	101 ±34	3004 ±651
15	4F	OMe	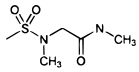	12	204	2907

[a] Data are present as the mean ± the standard deviation. Compound 19 data is mean of $n = 4$ individual dogs, compounds 26, 27, 31, 33, 48, and 59 are $n = 3$ observations from either individual dogs or from an N-in-One study; the remaining means are $n = 2$ (if standard deviation is shown) otherwise $n = 1$.

Pharmacokinetic data from all studies (individual and N-in-One dosed) are compiled in Tables 2−6. Mean data are presented in cases where the compound was dosed in more than one dog or was studied by both N-in-One and individual dosing. The range of pharmacokinetic values obtained from this chemical series was fairly large. For example, CL ranged from 0.3 to 44 mL/min/kg (146-fold); $t_{1/2}$ ranged from 45 to 1072 min (24-fold); and V_{ss} ranged from 41 to 14178 mL/kg (346−fold). The extent of protein binding was determined for 21 molecules. These were highly protein bound molecules which ranged from 92−99.94% bound (133-fold variation in unbound fraction).

Effect of Chemical Modifications on Pharmacokinetic Properties—*Effect of 4-F on Left-Hand Phenyl Ring*—There are several examples of pairs of molecules (**11, 12; 14, 15; 18, 19; 30, 31; 35, 36; 55, 56; 19, 21**) where the

Table 3—Pharmacokinetic Data from Compounds 16–29[a]

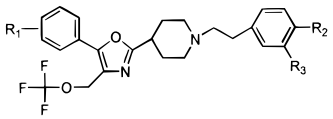

Cmpd	R1	R2	R3	CL (mL/min/kg)	t1/2 (min)	Vss (mL/kg)
16	4F	OMe	H	7.9	318	2677
17	4F	OMe	F	6.7	324	2233
18	4H	OMe		4.5 ±0.7	85 ±1	523 ±199
19	4F	OMe		0.8 ±0.3	248 ±37	202 ±101
20	3F	OMe		5.0	90	523
21	4Cl	OMe		0.9 ±0.3	336 ±64	417 ±218
22	3F,4Me	OMe		5.4	67	626
23	2F,3F	OMe		2.6	45	242
24	2F,5F	OMe		5.3 ±0.9	109 ±68	616 ±21
25	2F,4F	OMe	H	8.9 ±3.7	130 ±23	1595 ±812
26	3F,4F	OMe		2.0 ±0.8	333 ±118	643 ±374
27	2F,4F	OMe		1.0 ±0.7	287 ±86	334 ±110
28	2F,3F,4F	Ome		0.6 ±0.4	429 ±182	240 ±182
29	2F,4F,5F	OMe		2.3	138	372

[a] See footnote of Table 2.

Table 4—Pharmacokinetic Data from Compounds 30–39[a]

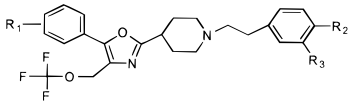

Cmpd	R1	R2	R3	CL (mL/min/kg)	t1/2 (min)	Vss (mL/Kg)
30	4H	OEt		2.8 ±0.9	129 ±72	375 ±82
31	4F	OEt		0.8 ±0.5	264 ±86	186 ±35
32	2F,4F	OEt		1.1 ±0.8	176 ±57	172 ±95
33	4F	OEt	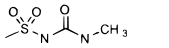	0.3 ±.2	286 ±103	2017 ±3314
34	4F	OEt		11	144	1950
35	4H	OEt	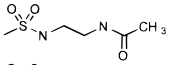	16	126	1992
36	4F	OEt	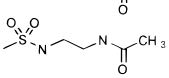	5.5	126	675
37	4F	OEt	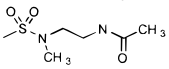	14	66	1539
38	4F	OEt	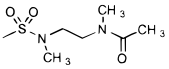	18	54	1806
39	4F	OEt	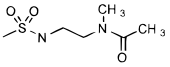	9	71	516

[a] See footnote of Table 2.

only structural difference was the presence or absence of a F-substitution in the 4-position of the phenyl ring at the 5-position of the oxazole ring. In each case, the effect of the 4-F substitution was to reduce CL, although the magnitude varied from a 36% decrease (**55, 56**) to greater than 5-fold decrease (**18, 19**). CL was reduced in all cases despite the fact that CL of the non-F molecules varied from 2.8 to 44 mL/min/kg. Similar effects on CL were obtained when a chlorine was placed in the 4-position. The CL of **21,** the 4-chloro compound, was similar to **19**, the 4-F analogue (0.9 vs 0.8). In contrast, a 4-methyl substitution did not reduce clearance. The CL of compound **22** increased with 4-methyl substitution compared to its di-F analogue (**26**) (2.0 vs 5.4 mL/min/kg). The position of the halogen appeared to be important in determining the CL of the compound. The presence of F in the 3-position (**20**) did not decrease CL as much as a 4-position F- or Cl-substitution. The CL for **19** was 6 times less than its 3-F homologue (**20**). The importance of 4-position halogenation in lowering CL was also evident in a series of compounds with multiple halogenations on the left-hand side phenyl. The CL of the 2,4-F compound (**27**) was one-half that of the 2,3-F (**23**) and one-quarter that of the 2,5-F compound (**24**). Compounds **19**−**21**, **23**−**24**, and **26**−**29** contain one or more halogen substitutions on the left-hand phenyl ring (either F or Cl) with R_2 = methoxy and R_3 = SO_2NH_2. Of these nine compounds, three compounds (**20**, **23**, and **24)** have H in the 4-position with 0−3 fluorines in other positions on the ring. The remaining six compounds are all 4-halogen compounds. The CL values for **20, 23**, and **24** are 5.0, 2.5, and 5.3 mL/min/kg, respectively, whereas the CL of the other six compounds are lower, ranging from 0.7 to 2.3 mL/min/kg. On the basis of metabolites identified from bile samples of dogs dosed with compound **11**, it is likely that the halogen-substitution on the 4-position blocked a common hydroxylation pathway of metabolism on the left-hand side phenyl ring resulting in a decrease in metabolic clearance.

The effect on V_{ss} of F-substitution on the left-hand phenyl varied. V_{ss} decreased in five pairs of examples of 4-position halogenation from 16 to 66%; however, V_{ss} increased 50% for **12** compared to **11**. The net effect of 4-F substitution on $t_{1/2}$ was mixed depending on the magnitude of change in CL and volume. For example, compounds **11** and **19** experienced a 200% increase in their $t_{1/2}$ whereas **36** and **56** saw essentially no change. 4-Chloro or 4-methyl substitution did not change V_{ss}. No trends were observed in the modest changes in V_{ss} for multiply halogenated compounds. Changes in $t_{1/2}$ thus followed from the changes in CL for these compounds.

*Effect of F-Substitution on Right-Hand Phenyl Ring (**16, 17**; **40, 41**; **41, 42**)*—The placement of F on the right-hand phenyl ring at R_2 or R_3 led to changes in pharmacokinetic parameters that were inconsistent with what was observed with left-hand phenyl ring substitution. Comparisons of **16, 17** as well as **40, 41** and **41, 42** show that putting F in both the R_3 (meta) position with R_2 = methoxy (**16, 17**) or

Table 5—Pharmacokinetic Data from Compounds 40–54[a]

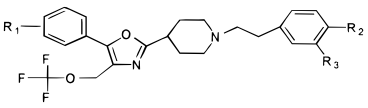

Cmpd	R1	R2	R3	CL (mL/min/kg)	t1/2 (min)	Vss (mL/kg)
40	4F	H	H	4.1	720	2743
41	4F	F	H	7.4	107	884
42	4F	F	F	3.3	89	246
43	4F	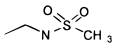	H	6.2 ±1.7	653 ±112	5101 ±757
44	4F	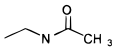	H	5.7	486	3350
45	4F		H	17	78	2419
46	4F		H	6.4	846	6192
47	4F		H	34 ±1	324 ±51	14178 ±6375
48	4F	NH_2	H	6.3 ±1.5	1072 ±502	8052 ±1493
49	4F	NMe	H	6.6	894	5584
50	4F		H	24	66	1725
51	4F	NO_2	H	10	126	838
52	4F	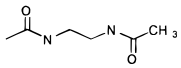	H	18	240	5298
53	4F	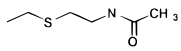	H	11	78	828
54	4F	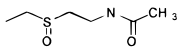	H	14 ±10	211 ±7	3632 ±2819

[a] See footnote of Table 2.

Table 6—Pharmacokinetic Data from Compounds 55–66[a]

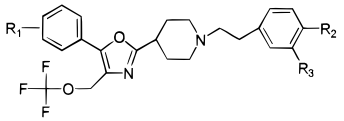

Cmpd	R1	R2	R3	CL (mL/min/kg)	t1/2 (min)	Vss (mL/kg)
55	H		H	44	108	4967
56	4F		H	28	114	3655
57	4F		H	33	126	5085
58	4F		H	8.4	252	2102
59	4F	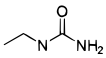	H	2.5 ±1.4	982 ±110	3128 ±1376
60	4F	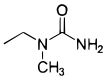	H	5.9	468	2795
61	4F	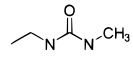	H	26 ±0	95 ±10	3375 ±1053
62	4F	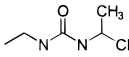	H	6.1	270	1808
63	4F	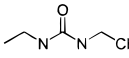	H	12	282	3024
64	4F	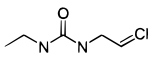	H	19 ±3	244 ±122	4173 ±330
65	4F		H	9.3	648	7754
66	4F	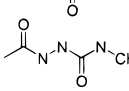	H	8.0 ±0.6	570 ±187	4308 ±1852

[a] See footnote of Table 2.

at R_3 with R_2 = H (**40, 41**) had either no effect on or increased CL (CL = 7.9 vs 6.7 mL/min/kg; 4.1 vs 7.4 mL/min/kg, respectively). However, putting F in both the R_3- and R_2-position (**41, 42**) reduced CL by 55% (7.4 vs 3.3 mL/min/kg). The addition of F to R_2 (**40, 41**) or addition of F to both R_2 and R_3 (**40**, **42**) decreased V_{ss}. A modest decrease in V_{ss} was also observed when F was substituted at R_3 in the R_2 = methoxy series (**16**, **17**).

*Effect of Adding SO_2NH_2 to R_3 or R_2 (**1, 18; 25, 27; 19, 47**).* Placing a sulfonamide in the R_3 position decreased CL from 14 to 4.5 mL/min/kg (comparing **1** and **18**, respectively). The V_{ss} also decreased (51%), and $t_{1/2}$ was increased from 59 to 85 min. When this same chemical modification was made to **25**, a larger decrease in CL was observed (from 8.9 to 1.0 mL/min/kg for compounds **25** and **27**, respectively). V_{ss} also decreased from 1595 to 344 mL/kg and there was little effect on $t_{1/2}$. In sharp contrast, when the sulfonamide was placed at the R2 position (**47**) CL increased from 0.8 to 34 mL/min/kg, a 42-fold increase compared to **19**. V_{ss} was also dramatically increased from 202 (**19**) to 14178 mL/kg (**47**), a 70-fold increase. However, the dramatic alterations in CL and V_{ss} led to a relatively modest 31% decrease in $t_{1/2}$ from 248 to 324 min.

Effect of Substituted SO_2NH_2 in R_3-position—Substitution on the sulfonamide in the R_3-position when R_2 = methoxy (**2**−**11**, **13**, **14**, **18**) resulted in higher CL values for all compounds compared to the unsubstituted **18** with the exception of **2** which had a CL about one-half that of **18**. The V_{ss} also tended to be higher for substituted compounds (523 mL/kg for **18** and ranging from 600 to 3464 mL/kg for all others) except for compounds **2** and **6** which had lower V_{ss} values of 151 and 210 mL/kg, respectively. Similar effects (increased CL and V_{ss}) were observed with substituted sulfonamides in the 4-F series (**12, 15** compared to **19**) when R_2 = methoxy. For example, compound **15** had a larger CL (12 mL/min/kg) and a larger V_{ss} (2407 mL/kg) than its unsubstituted counterpart **19** (0.8 mL/min/kg, 202 mL/kg). Similarly, substitution on the sulfonamide in the R_2-position in the R_3 = ethoxy series **(30, 35; 31, 35, 36**−**39)** usually led to increases in CL (0.8−2 mL/min/kg compared to 5.5−18 mL/min/kg) and an increase in V_{ss} (1992 compared 375 mL/kg; or 516−1806 compared to 186 mL/kg). The notable exception in this case was **33,** an *N*-methyl sulfonylurea, which had the lowest CL (0.3 mL/min/kg) of not only all of the substituted sulfonamides, but also of all the 66 compounds presented in this paper, and a very low V_{ss} of 123 mL/kg. Protein binding was determined on five of the compounds in this N-substituted sulfonamide series and free fraction was greater for all the substituted molecules compared to that of the unsubstituted analogue. This may partly explain the larger volumes and the higher clearances. The higher clearances may also arise from increased metabolism (N-dealkylation) of the sulfonamide substitution, a metabolic pathway that was

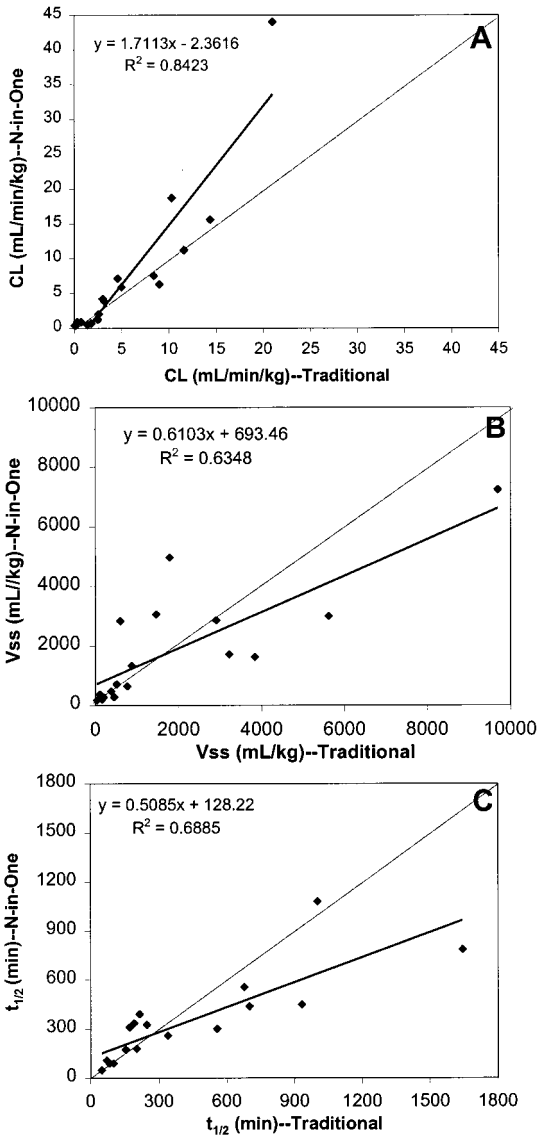

Figure 1—Linear regression (bold line) of CL, V_{ss}, and $t_{1/2}$ data for 17 compounds by both individual and N-in-One methods.

observed in in vitro dog microsomal metabolism studies of several compounds including compound **11**. Finally, one pair of enantiomers was synthesized by substituting *R*- or *S*-alanine on the R_3 sulfonamide. One enantiomer (**8**) had 50% lower CL compared to its opposite enantiomer (**9**). V_{ss} was 27% lower and $t_{1/2}$ was little changed (114 vs 107 min for **8** vs **9**, respectively).

Effect of Chemical Modifications to R3-Sulfonamide Substitutions—Methylation of the sulfonamide nitrogen (**37**) or the acetamide nitrogen (**39**) or both (**38**) increased the CL of the compound compared to that of **36**. When both nitrogens were methylated (**39**), CL was increased more than that of a single methylation (18 vs 9.0 or 14 mL/min/kg). V_{ss} was also increased when the sulfonamide nitrogen is methylated (**37** or **38**), but not when the acetamide alone was methylated (**39**). The net effect on $t_{1/2}$ was a consistent decrease of about 50% comparing **36** to **37**–**39**.

When the amide nitrogen was methylated (**13**), CL was not changed much (22%) compared to the unmethylated compound (**11**). When both the amide and sulfonamide nitrogens were methylated (**14**), the CL was still similar to when one nitrogen was methylated (**11**). However, comparing the 4-F compounds **12** and **15,** CL was unaffected when both nitrogens were methylated (11 to 12 mL/min/kg). No consistent changes were noted in V_{ss}, and no major differences in $t_{1/2}$ were observed in these series. Finally**,** replacement of a methyl group with a trifluromethyl group on the R_3 sulfonamide (**4, 5**) resulted in a 160% increase in CL, 239% increase in V_{ss}, and a 50% reduction in $t_{1/2}$.

*Comparison of Ethoxy- vs Methoxy-Substitution at R_2 (**4, 35; 18, 30; 19, 31; 25, 32**)*—No consistent change in pharmacokinetic properties was observed when the size of the alkyl group on R_2 was increased from methyl to ethyl. The notable structural difference between these compounds is that **30**–**32** are unsubstituted sulfonamides, whereas **35** has a ethylene acetamide moiety on its sulfonamide nitrogen. The direction and magnitude of change in pharmacokinetic parameters may be related to the size of the R_3 substituent. For the pair of substituted sulfonamides (**4**, **35**) the CL increased by 60% and the V_{ss} increased by 232% when the methoxy was changed to ethoxy. For the unsubstituted sulfonamides **(18, 30; 19, 31)**, the CL and V_{ss} decreased or were unchanged. The net effect of these changes on $t_{1/2}$ was minimal, except in the case of **30**.

Effect of Adding an N-Methyl Group to R_2 Amide[56–58]—In this example of *N*-methylation, addition of a methyl group to the amide of **56** to generate **57** had little effect on CL, V_{ss}, or on $t_{1/2}$. In contrast to the earlier two examples of methylation at the R_3-substituent, adding a second methyl group (**58**) dramatically reduced the CL from 33 mL/min/kg (**57**) to 8.4 mL/min/kg (about 4-fold). V_{ss} also drops by more than 50% (from 5085 mL/kg to 2102 mL/kg) which attenuates the increase in $t_{1/2}$ to 138% (from 126 to 252 min).

Effect of Adding an N-Methyl Group to Right-Hand Aniline: Comparing NH_2 to NO_2—When the aniline nitrogen was methylated (**49**), CL was not greatly altered compared to **48** (6.3 to 6.6 mL/min/kg). V_{ss} and $t_{1/2}$ were unaffected as well. Adding a second methyl group (**50**) caused CL to increase by almost 4-fold (from 6.3 to 24 mL/min/kg) with a further decrease in V_{ss} (from 8052 to 1725 mL/kg) and a decrease in $t_{1/2}$ by 94% to only 66 min. Oxidation of the amine to a nitro group (**51**) also increased CL by 59% and decreased V_{ss} by 90% compared to **48** and hence also resulted in a large decrease in $t_{1/2}$ of 84%.

*Effect of Alkyl Substitution on the Terminal Nitrogen of the Phenylmethyleneurea on R_2 (**59**–**64**)*—Single methylation of the proximal nitrogen resulted in an increase in CL of 136% (**59** compared to **60**), a modest decrease in V_{ss}, and a large decrease in $t_{1/2}$ of 52% (from 982 to 468 min). When the terminal nitrogen was methylated, the effect on CL was even greater going from 2.5 to 26 mL/min/kg (**59** compared to **61**), and there was little effect on V_{ss} (from 3128 to 3375 mL/kg). The net effect on $t_{1/2}$ was a dramatic reduction from 982 to 95 min (**59**, **61**). When larger alkyl groups were added to the terminal nitrogen of **59**, the effect was still a net increase in CL and decrease in $t_{1/2}$, but the magnitude of the changes were not as great compared to the effect of adding a single methyl group.

*Comparing Methylene Acetamide to Methylene Sulfonamide or Acetal at R_2 (**40**, **43**–**45**)*—Placing an acetal group at R_2 (**45**) increased CL from 4.1 to 17 mL/min/kg relative to no substitution (**40**). V_{ss} was not greatly affected (2743 vs 2419 mL/kg) and $t_{1/2}$ was, therefore, greatly reduced (78 vs 720 min). Extending the acetal to a methylene acetamide (**44**) resulted in a lower CL value of 5.7 mL/min/kg and a higher V_{ss} value of 3350 mL/kg leading to an intermediate $t_{1/2}$ of 486 min. When the methylene acetamide was replaced with a bulkier methylene sulfonamide (**43**), CL (6.2 mL/min/kg) remained essentially the same as **44** and V_{ss} increased still further to 5101 mL/kg. The $t_{1/2}$ is 653

min, which is the longest $t_{1/2}$ of this group of compounds, yet still less than the unsubstituted compound (**40**).

Effect of Other R_2 Substitutions—Comparing the pharmacokinetics of the sulfonamide to the sulfone in the R_2-position, the sulfonamide (**47**) had a 5-fold higher CL and 2-fold higher V_{ss} than the methyl sulfone (**46**). The $t_{1/2}$ was lowered by a factor of 1.6-fold, comparing **47** to **46**. Oxidation of the thioether (**53**) to its sulfoxide (**54**) resulted in a slight increase in CL (from 11 to 14 mL/min/kg) whereas V_{ss} quadrupled, going form 828 to 3632 mL/kg. The effect on $t_{1/2}$ was a 171% increase going from 78 to 211 min. Extension of the urea in the R_2-position (**65**) with a methylene group (**59**) led to a >3-fold increase in CL (2.5 to 9.3 mL/min/kg) and a 37% increase in V_{ss}. The $t_{1/2}$ was decreased by 42%.

Discussion

The original goal of this effort was to determine if N-in-One studies could be used to rapidly determine pharmacokinetic consequences of changes in chemical structure within a congeneric chemical series. In essence, that goal was achieved. This conclusion is supported by the linear regression analysis on the pharmacokinetic parameters for 17 compounds studied by the individual method of one compound in one dog or in various N-in-One studies. It is also supported by the work with **19** which was examined in all nine N-in-One studies and in four separate single drug studies (Table 1).

A second feature of this work was to permit the development of structure−pharmacokinetic relationships with the 66 compounds tested using this method. Of the 66 compounds, 22 were examined in at least two dogs as mixtures or individually. The general robustness of the data afforded the opportunity to make hypotheses about structure−pharmacokinetic relationships that would suggest further study or the resynthesis of compounds to investigate the hypothesis. There are some caveats and limitations to using this method. It is not clear if it applies uniquely to this set of compounds or if the method applies to all compound mixtures. More studies by us and others will be needed to answer this question. A number of limitations have been previously cited[2] and those apply here as well.

In the research program from which these compounds were derived, the desired criteria for the three PK variables were: CL < 5 mL/min/kg, $t_{1/2}$ > 240 min and V_{ss} < 1000 mL/kg. At the other extreme, compounds having either CL > 15 mL/min/kg, $t_{1/2}$ < 120 min, or V_{ss} > 3000 mL/kg were judged unacceptable. Of the 66 compounds studied, there were only five molecules which met all three pharmacokinetic criteria (four in the R_2 = methoxy series, and one in the R_2 = ethoxy series). On the other hand, only two compounds had unacceptable values for all three parameters and these were in the series where R_2 = H. This led to the conclusion that continued modification of compounds with R_2 = methoxy or ethoxy would lead to compounds with the best pharmacokinetic profile. In addition, halogen substitution at the 4-position of the left-hand-side phenyl and removal of substitutions on the R_3-sulfonamide consistently resulted in compounds with lower CL. However, the latter did not appreciably increase the half-life of the compound, since removal of the sulfonamide substitution also consistently led to compounds with reduced volumes of distribution. Compound **33** appears to be unique in pharmacokinetic terms since most N-substituted sulfonamides (**2**−**15; 35**−**39**) had CL values between 2 and 34 mL/min/kg, yet for **33** the CL was 0.3 mL/min/kg, the lowest value obtained for all of the molecules examined. Compound **33** was studied in three dogs with consistent results and therefore raises the question as to why this methylsulfonylurea had such a low (and desirable) CL.

Another example with unexpected results is compound **46** and **47**, which differ only in one being a methyl sulfone, whereas **47** is a sulfonamide in that position. Despite this similarity, there is a 5-fold difference in CL. The explanation for this difference is not clear. Neither the clogP values (3.4 and 3.2, respectively), nor different electron-withdrawing effects (σ values of 0.68 vs 0.62 via Hammett equation) seem likely explanations. One possibility is that glucuronidation may be an additional elimination pathway for the sulfonamide thus contributing the higher clearance. This example highlights the value in doing the N-in-One approach to generate data that can lead in directions that would not have been anticipated from first principles.

Both in vitro drug metabolism and cell permeation studies and in vivo pharmacokinetic experimentation will be needed in order to more fully expand our current understanding of the various factors governing pharmacokinetics.[9,10] It is envisioned that the enhanced capacity to generate qualitative and quantitative pharmacokinetics and drug metabolism data will provide information that will enable the iterative generation and refinement of predictive rules regarding the many factors that govern pharmacokinetics.

References and Notes

1. Ecker, D. J.; Crooke, S. T. Combinatorial drug discovery: which methods will produce the greatest value? *Bio/Technology* **1995**, *3*, 351−60.
2. Berman, J.; Halm, K.; Adkison, K.; Shaffer, J. Simultaneous Pharmacokinetic Screening of a Mixture of Compounds in the Dog Using APCI/LC/MS/MS Analysis for Increased Throughput. *J. Med. Chem.* **1997**, *40*, 827−829.
3. Olah, T. V.; MCLoughlin, D. A.; Gilbert, J. D. The simultaneous determination of mixtures of drug candidates by liquid chromatography atmospheric pressure chemical ionization mass spectrometry as an in vivo drug screening procedure. *Rapid Commun. Mass Spectrom.* **1997**, *11*, 17−23.
4. Allen, M. C.; Shah, T. S.; Day, W. W. Rapid determination of oral pharmacokinetics and plasma free fraction using cocktail approaches: Methods and application. *Pharm. Res.* **1998**, *15*, 93−97.
5. Toon, S.; Rowland, M. Structure-Pharmacokinetic Relationships Among the Barbiturates in the Rat. *J. Pharmacol. Exp. Ther.* **1983**, *225*, 752−763.
6. Henschel, L.; Hoffmann, A. Assessment of Biotransformation Capacity After Oral Administration of Various Model Substances as a Cocktail. *Z. Gastroenterol.* **1991**, *29*, 645−649.
7. Jenner, P. J.; Ellard, G. A.; Gruer, P. J. K.; Aber, V. R. A comparison of the blood levels and urinary excretion of ethionamide and prothionamide in man. *J. Antimicrob. Chemother.* **1984**, *13*, 267−277.
8. Jenner, P. J.; Smith, S. E. Plasma levels of ethionamide and prothionamide in a volunteer following intravenous and oral dosages. *Lepr. Rev.* **1987**, *58*, 31−37.
9. Guttendorf, R. J. The Emerging Role of A.D.M.E. in Optimizing Drug Discovery and Design. http://www.awod.com/netsci/Science/Special/feature06.html, Feb 1996.
10. Rodrigues, A. D. Preclinical Drug Metabolism in the Age of High-Throughput Screening: An Industrial Perspective. *Pharm. Res.* **1997**, *14*, 1504−1510.
11. Andrews, R. C., Brown, P. J., Cadilla, R., Drewry, D. H., Luzzio, M. J., Marron, B. E. and Nobel, S. A. Preparation and formulation of piperdinyloxazoles as α/c adrenergic receptor antagonists. PCT Int. Appl. WO 9616049, 81 pp, CODEN: P1XXD2.

Acknowledgments

We acknowledge the many scientists who contributed to this work. The chemists who made the compounds: David Drewry, Rudolfo Cadilla, Deanna Garrison, Michael Foley, Yolanda Gray-Nunez, Patrick Maloney, Brian Marron, David Deaton, Steven Frye, Debra Lake, Michael Evans, Michael Luzzio, Terry Smalley and Robert Noe. The in vitro metabolism scientists: Archie Sinhababu and Deanna Garrison. The bioanalytical scientists: Caroline Stafford, Michelle Brosnan, and Bob St. Claire. The in vivo scientists: Bajin Han, Don Anderson, and Jim Liacos. The formulation scientists: Tony Tong and Mike Jozwiakowski. Those who gave their advice and suggestions: Arthur Moseley, Frank Lee, Steve Unger, Mike McNulty, and Dhiren Thakker.

JS980292Q

Development of HPLC Conditions for Valid Determination of Hydrolysis Products of Cisplatin

MAHMOUD EL-KHATEEB,[†] TREVOR G. APPLETON,*[,†] BRUCE G. CHARLES,[‡] AND LAWRENCE R. GAHAN[†]

Contribution from *Department of Chemistry and School of Pharmacy, The University of Queensland, Brisbane, Queensland 4072, Australia.*

Received July 15, 1998. Final revised manuscript received November 3, 1998.
Accepted for publication December 15, 1998.

Abstract □ In water, the antineoplastic drug cisplatin, *cis*-[$PtCl_2(NH_3)_2$] (**1**) hydrolyses slowly to the aqua complexes *cis*-[$Pt(NH_3)_2Cl(H_2O)]^+$ (**2**) and, to a small extent, *cis*-[$Pt(NH_3)_2(H_2O)_2]^{2+}$ (**3**), which are thought to play an important role in the metabolism of cisplatin. HPLC is a useful technique for monitoring **2** and **3**, but only if the components of the mobile phase used in the reverse phase HPLC technique are unreactive toward these aqua complexes under the conditions of the experiment. ^{15}N Nuclear magnetic resonance (NMR) with samples highly enriched (>98%) in ^{15}N has been used to check the reactivity of **2** and **3** toward substances commonly used as components of the mobile phase. The results reported herein indicate that acetonitrile, often used as an organic modifier, reacts readily with **2** and **3**. Methanol, also commonly employed, is much less reactive. Carboxylic acids RCO_2H (R = CH_3, H, CF_3), which are frequently used to adjust pH of the mobile phase, also react readily with **2** and **3**. Trifluoromethanesulfonic acid ("triflic acid"), CF_3SO_3H, is unreactive. Neither hexanesulfonic acid nor sodium dodecyl sulfate (SDS), used as "ion-pairing agents", reacts significantly with **2** or **3** under the experimental conditions, but SDS gives better peak separation. Commercial SDS must, however, be purified from chloride contamination. From our studies, optimal conditions for HPLC separation of **1**, **2**, and **3**, with a C_{18} stationary phase at 37 °C, require an aqueous mobile phase with 3% v/v methanol, 0.05 mM SDS, and pH 2.5 (adjusted with triflic acid). This technique was then used to measure levels of **1**, **2**, and **3** in ultrafiltered serum after incubation for various times with cisplatin at 37 °C.

Introduction

Cisplatin (*cis*-diamminedichloroplatinum(II), *cis*-[$PtCl_2(NH_3)_2$] (**1**)) is a widely used antineoplastic drug which is effective against a number of tumors, although its beneficial effects are balanced by significant toxicities.[1] There have been a number of studies of the pharmacokinetics of intact cisplatin,[2,3] but very little is yet known about the pharmacokinetic disposition of the metabolites and hydrolysis products of cisplatin.

The solution chemistry of cisplatin and its analogues has now been extensively explored. The hydrolysis reactions of cisplatin, for example, have been well-studied[4−9] and are summarized in Scheme 1. In an aqueous solution of cisplatin (**1**) with pH < 5, one of the bound chloride ions dissociates, to give *cis*-[$Pt(NH_3)_2Cl(H_2O)]^+$ (**2**), until an equilibrium is set up between **1**, **2**, and the liberated chloride ion. A second chloride ion may dissociate, to give *cis*-[$Pt(NH_3)_2(H_2O)_2]^{2+}$ (**3**), but little of this complex will form unless chloride ion is removed from the solution (e.g., with silver ion).[7] The coordinated water molecules in **2** and **3** may be deprotonated to give hydroxo complexes *cis*-[$Pt(NH_3)_2Cl(OH)$] (**4**), *cis*-[$Pt(NH_3)_2(OH)(H_2O)]^+$ (**5**), and *cis*-[$Pt(NH_3)_2(OH)_2$] (**6**). The acid dissociation constants of **2** and **3** are such that, under physiological conditions, the hydrolysis products will be predominately, but not totally, in the forms **4** and **5**,[6,9,10] with equilibria lying more toward the hydrolysis products than in acid solution. The solution chemistry near pH 7 can be further complicated by the tendency to form hydroxo-bridged oligomers, [{$Pt(NH_3)_2(\mu\text{-}OH)\}_n]^{n+}$ (n = 2,3)[4,5,11−13] and [{$Pt(NH_3)_2\}_2(\mu\text{-}Cl)(\mu\text{-}OH)]^{2+}$.[6] Such species are unlikely to form from mononuclear compounds in solutions with pH < 5, or at the low concentrations of platinum compounds used in vivo, but if present in the initial formulation of platinum compounds dinuclear compounds may persist in both these situations.[5]

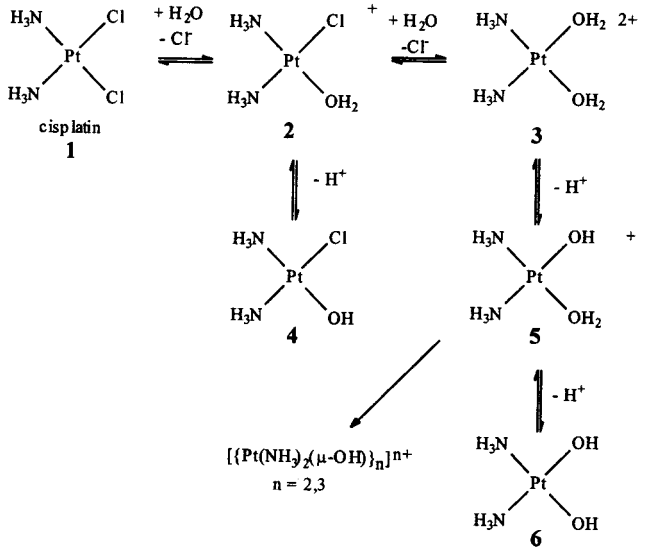

Scheme 1

The rate constants for these hydrolysis reactions, in both acidic and alkaline solutions, have been measured by Miller and House.[7−9] The reactions are relatively slow, with many hours required after cisplatin is dissolved before equilibrium is established. There will also be little change in the composition of a solution during the time required for a HPLC run or for a ^{15}N NMR spectrum to be obtained (up to 20 min).

The reactions which cisplatin undergoes in vivo may be divided into three main classes:

(1) Simple hydrolysis reactions of the type shown in Scheme 1.

(2) Reactions involving coordination of small molecules (and ions) to platinum. The species involved may be inorganic, such as phosphate, or small organic molecules such as amino acids or peptides.

[†] Department of Chemistry.
[‡] School of Pharmacy.

10.1021/js980287m CCC: $18.00 Published on Web 02/11/1999

(3) Binding of platinum to macromolecules, such as DNA (believed to be primarily responsible for the antitumor activity of platinum drugs).[14−16]

Rather different techniques are required to study the products of these three types of reactions. HPLC techniques are well-suited for study of both small molecule adducts and hydrolysis products. Because of the fundamental role played by hydrolysis in much of the reaction chemistry of cisplatin, and because of the challenge presented by the high reactivity of platinum aqua complexes, we considered it desirable to develop techniques to reliably detect the hydrolysis products in vitro and in vivo. This is the subject of this paper, with later contributions focusing on small molecule adducts.

A number of papers have described reversed-phase HPLC conditions for detecting and monitoring cisplatin hydrolysis products.[17−19] Necessary components of the HPLC system are the stationary phase, the mobile phase, and the detection system. From this previous work, it is clear that a stationary phase consisting of silica particles bonded to C_8 or C_{18} hydrocarbon is suitable. Convenient UV detection is adequate for development of HPLC techniques and checking retention times for model compounds. The use of anionic hydrophobic ion-pairing reagents in the mobile phase, such as sodium dodecyl sulfate (SDS) or hexanesulfonate,[17,19] is clearly effective in giving good peak separation for cationic species. However, the mobile phases used by these workers have been chosen without sufficient regard for the high reactivity of the cisplatin hydrolysis products, so that they contain components that are capable of reacting with platinum aqua complexes. For example, Andersson et al.[18] used a mobile phase containing phosphate buffer, although phosphate is known to react readily with platinum aqua complexes.[5,20,21] De Waal et al.[22] and, more recently, Heudi et al.[23] showed that on-column reactions occur between phosphate and cisplatin hydrolysis products. Wenclawiak and Wollman[24] used micellar electrokinetic capillary chromatography to separate cisplatin from other platinum antitumor drugs (carboplatin and lobaplatin) as well as cisplatin hydrolysis products, using SDS and phosphate−borate or phosphate buffers. Shearan et al.[25] also used phosphate buffers in the separation of cisplatin and hydrolysis products on alumina. It is very likely that some of the peaks observed in each of these studies were actually due to platinum phosphate complexes. Daley-Yates and McBrien[17] used acetonitrile as an organic modifier in their mobile phase, yet acetonitrile is known to interact with platinum aqua complexes, with the well-known "platinum amide blues" forming as the ultimate products under some circumstances.[26] Zhao et al.[19] used mobile phases containing carboxylic acids (trifluoroacetic, formic) although acetate is known to react readily with platinum aqua complexes,[5] which raises the possibility that carboxylato complexes were formed while solutions were passed down the column, in the experiments reported by Zhao et al.[19] Heudi et al.,[23] however, obtained no evidence for reaction of formic acid with cisplatin hydrolysis products in their experiments.

The ambiguities in interpretation of results arising from the possibility of reactions between platinum aqua complexes and the mobile phase may be responsible for some literature conclusions which are surprising in the light of evidence from other sources. For example, Zhao et al.[19] concluded that *cis*-$[Pt(NH_3)_2(H_2O)_2]^{2+}$ (**3**) was present in significant proportions with *cis*-$[PtCl_2(NH_3)_2]$ (**1**) and *cis*-$[Pt(NH_3)_2Cl(H_2O)]^+$ (**2**) when **1** was allowed to stand in acidic aqueous solution. This does not agree with the result of Miller and House,[7] that only small quantities of **3** are present with **1** and **2** under these conditions. Andersson et al.[18] reported that clearance time of **2** (in equilibrium with *cis*-$[Pt(NH_3)_2Cl(OH)]$ (**4**)) in vivo is greater than that of intact cisplatin (**1**), even though the aqua complex **2** would be expected to be more reactive toward potential ligands than **1**. Daley-Yates and McBrien[17] concluded that the concentration of the diaqua complex **3** increased markedly in plasma (despite the rich ligand environment) and suggested that the hydrolysis reaction was catalyzed in plasma! The possibility of accidental equality of retention times of different species was not considered.

In the present work, potential components of the mobile phase were carefully checked for reactivity with **2** and **3**, both by monitoring HPLC traces and by obtaining ^{15}N nuclear magnetic resonance (NMR) spectra of solutions containing the platinum ammine complexes highly enriched in ^{15}N (>98% ^{15}N, nuclear spin quantum number I = $^1/_2$). ^1H-decoupled ^{15}N NMR lines are characteristically very sharp, and the ^{15}N chemical shift, δ_N, is very sensitive to the ligands bound to platinum, especially the ligand trans to the ammine group.[27] Conditions were then determined which optimized the separation of HPLC peaks from **1**, **2**, and **3** with the use of a mobile phase containing only substances which are unreactive toward these complexes under the conditions used. These conditions were then used to monitor concentrations of *cis*-$[Pt(NH_3)_2Cl(H_2O)]^+$ (**2**) in solutions of ultrafiltered plasma incubated with cisplatin (**1**) at 37 °C.

Experimental Section

Platinum Ammine Complexes—Literature methods[4,5] were used for the preparation of *cis*-$[PtCl_2(NH_3)_2]$ (**1**), *cis*-$[Pt(NH_3)_2(ONO_2)_2]$, with both normal isotopic composition and with high enrichment (>98%) in ^{15}N, with $(^{15}NH_4)_2SO_4$ used as the source of labeled ammonia. As previously described,[4,5] warming *cis*-$[Pt(NH_3)_2(ONO_2)_2]$ with water gives a solution of *cis*-$[Pt(NH_3)_2(H_2O)_2](NO_3)_2$, with a trace only of *cis*-$[Pt(NH_3)_2(ONO_2)(H_2O)](NO_3)$ present in dilute solution.[5] To avoid the presence of traces of unreacted silver ion, preparations of *cis*-$[Pt(NH_3)_2(ONO_2)_2]$ were usually carried out with a slight deficiency of silver nitrate, so that a small quantity of *cis*-$[Pt(NH_3)_2Cl(H_2O)]^+$ (**2**) was also present in these solutions. As noted in Results below, samples of *cis*-$[Pt(NH_3)_2(ONO_2)_2]$ for HPLC use must be freshly prepared (within 24 h) to avoid the appearance of additional HPLC peaks. A solution containing >90% *cis*-$[Pt(^{15}NH_3)_2Cl(H_2O)]^+$ (**2**), with *cis*-$[PtCl_2(^{15}NH_3)_2]$ (**1**) as an impurity, was prepared by a refinement of the procedure previously described.[6] *cis*-$[Pt(^{15}NH_3)_2(ONO_2)_2]$ (30 mg, 85.0 μmol) was dissolved in 2 mL of distilled water. Solid sodium chloride (6.0 mg, 102.5 μmol) was dissolved in 10 mL of distilled water. The sodium chloride solution was added very slowly to the stirred solution of *cis*-$[Pt(^{15}NH_3)_2(H_2O)_2](NO_3)_2$ (dropwise, over 2.5 h). The solution was then filtered, and the composition of the solution was checked by ^{15}N NMR. The total platinum concentration of this solution was 7.08 mM. The composition of this solution (far from equilibrium) did not change significantly on standing at 25 °C for 4 h, but after longer times the concentration of **2** decreased as concentrations of **1** and **2** increased. Cooling the solution hastened the loss of **2** through this chloride ion redistribution.

Other Materials—HPLC-grade methanol and acetonitrile (EM Science), trifluoromethanesulfonic acid ("triflic acid")(Aldrich, 98%, appropriately diluted), trifluoroacetic acid (Merck, >98%), formic acid (Ajax), acetic acid (Ajax), and sodium hexanesulfonate (Sigma, 98%) were used without further purification. Sodium dodecyl sulfate (SDS) from different suppliers (e.g., ICN) contained sufficient chloride to affect the HPLC results (notified on labels as 0.01%), and so a chloride-free solution was prepared as follows. Solid SDS (5 g) was dissolved in 20 mL of deionized water, and 17 mg of silver trifluoromethanesulfonate ($Ag(CF_3SO_3)$) was added to precipitate choride as silver chloride. The solution was filtered and then passed down a column of cation-exchange resin (Amberlite IR120) in the H^+ form. The eluted solution was diluted to 1 L with deionized water to give a chloride-free solution with SDS concentration 17.35 mM. It was stored in a refrigerator at 5 °C and diluted as required for use in HPLC. Since semimicro

combination electrodes used for pH determination leaked significant quantities of chloride ion into solutions in which they were immersed, the adjustment of pH to 2.5 was carried out with the aid of narrow-range indicator strips (Merck Acilit) with the colors on the strip calibrated against solutions whose pH was measured with the use of a glass electrode.

HPLC Instrumentation—The HPLC system consisted of a pump (Waters model 510), an automatic injector (Waters model 712 WISP), a Waters stainless steel analytical column (3.9 mm i.d. × 300 mm), packed with Bondapak C18, 10 μm particle size, a variable-wavelength detector (Waters model 484), and a chart recorder (Omniscribe, Houston Instruments). The column was maintained at 37 °C.

HPLC Experiments—In a typical experiment, 0.8−1.0 mg of the platinum complex was dissolved in 4 mL of the mobile phase, and 100 μL of the solution was injected onto the column. Flow rate was 0.5 mL min^{-1} and column temperature 37 °C. The wavelength for the detector was set at 305 nm. At this wavelength, the platinum complexes absorb strongly, but many organic molecules in plasma absorb weakly. To determine the relationship between the integrated area of the HPLC peak and concentration for the platinum compounds, solutions were prepared over a range of concentrations, and a 100 μL aliquot was injected onto the column. Elution was with the mobile phase described above, with SDS concentration 0.5 mM. For **2** and **3**, the solutions were prepared by diluting stock solutions respectively of **2** (prepared as described above) and of *cis*-$[Pt(NH_3)_2(H_2O)_2](NO_3)_2$ (prepared by dissolving a weighed quantity of solid *cis*-$[Pt(NH_3)_2(ONO_2)_2]$). For cisplatin (**1**), each solution was prepared by dissolving a weighed quantity of *cis*-$[PtCl_2(NH_3)_2]$ in a measured volume of water. To minimize hydrolysis, an aliquot was injected onto the column immediately after the solid dissolved.

NMR Experiments—^{1}H-Decoupled 20.2-MHz ^{15}N NMR spectra were obtained with a Bruker ACF-200 spectrometer, equipped with a 5-mm QUAD (^{1}H, ^{13}C, ^{19}F, ^{15}N) probe, with conditions as previously described, including use of the DEPT pulse sequence to enhance signal sensitivity.[28] Spectra are referenced relative to a 5 M solution of $(^{15}NH_4)_2SO_4$ in 1 M sulfuric acid, in a coaxial capillary. Shifts to lower nuclear shielding (higher frequency) are positive. In a typical experiment using *cis*-$[Pt(^{15}NH_3)_2(ONO_2)_2]$ as the starting material, 40 mg of the compound was dissolved in 1 mL of warm water, followed by addition of the mobile phase component.

Incubation of Cisplatin with Ultrafiltered Serum—A sample of human plasma was ultrafiltered from substances with molecular weight >10000 in a Millipore ultrafree MC centrifuge at 6000 G for 30 min. The plasma was incubated at 37 °C with cisplatin at a concentration of 0.2 mg/mL. After the appropriate time, 100 μL of the solution was injected onto the HPLC column. For comparison, samples of plasma without added cisplatin were incubated under identical conditions.

Results

^{15}N NMR Spectra of 2 and 3 in Aqueous Trifluoromethanesulfonic Acid Solution—It is desirable that HPLC separations on platinum(II) aqua complexes be carried out in acid solution. The pK_a values for water bound to platinum(II) in such complexes lie between 5 and 8,[6] so that, at pH-values greater than 5, the protonation state of the complex may be uncertain unless conditions are precisely controlled. Furthermore, hydroxo-bridged oligomers may form, causing undesirable complications.[4−6,11−13] The effectiveness of the anionic hydrophobic ion-pairing agent used in the HPLC mobile phase would also be expected to be optimal when the coordinated aqua ligands are fully protonated, giving maximum positive charge to the complexes. To adjust the pH to a suitable value (e.g., 2.5) it is desirable that an acid be used whose anion is known to be incapable of binding to platinum(II) in aqueous solution. We have previously shown[5] that perchlorate ion does not react with platinum(II) aqua complexes. Although the likelihood of forming potentially explosive compounds from the aqueous solutions studied is remote, as a matter of principle, we prefer to use alternatives if available. Thus,

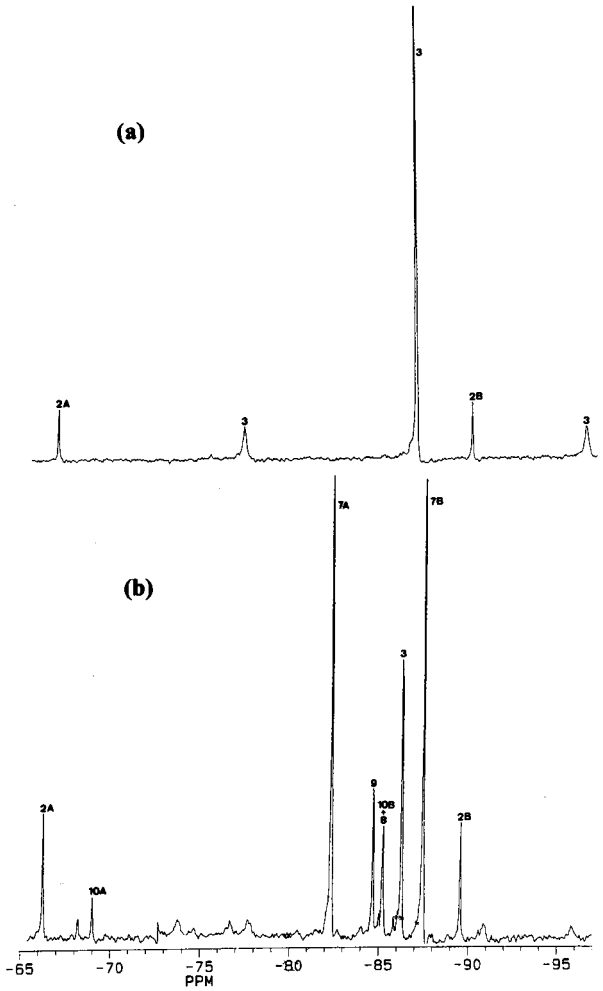

Figure 1—^{1}H-Decoupled 20.2-MHz ^{15}N NMR spectra of solutions obtained by dissolving *cis*-$[Pt(^{15}NH_3)_2(ONO_2)_2]$ in 1 M aqueous solutions of (a) triflic acid, (b) acetic acid. Labels correspond to those in the schemes.

a 1 M solution of triflic acid was used to dissolve a sample of *cis*-$[Pt(^{15}NH_3)_2(-ONO_2)_2]$ containing a small proportion of *cis*-$[Pt(^{15}NH_3)_2Cl(-ONO_2)]$. The ^{15}N NMR spectrum of the resultant solution (Figure 1a) was readily interpreted as showing a singlet from *cis*-$[Pt(^{15}NH_3)_2(H_2O)_2]^{2+}$ (**3**) at −86.8 ppm with "satellite peaks" from coupling with ^{195}Pt (I = $^1/_2$, 34% abundance) ($J(^{195}Pt-^{15}N)$ 385 Hz). The satellite peaks were somewhat broadened through chemical shift anisotropy-induced relaxation of the ^{195}Pt nucleus.[29] These ^{15}N NMR parameters are close to those previously reported for **3**,[4,5] with the usual small dependence on "medium effects" (different counterions etc.). Weaker ^{15}N NMR peaks of equal intensity at −66.9 (labeled **2a** in Figure 1a) and −90.0 ppm (labeled **2b** in Figure 1a) were readily assigned to ^{15}N nuclei trans to chloride and to water in *cis*-$[Pt(^{15}NH_3)_2Cl(H_2O)]^+$ (**2**).[4,6,27] Even when the concentration of triflic acid was greatly increased, no peaks were observed that could be assigned to species containing coordinated triflate.

^{15}N NMR Spectra 2 and 3 in Aqueous Carboxylic Acid Solutions—Previously, it was shown[5] that *cis*-$[Pt(NH_3)_2(H_2O)_2](NO_3)_2$ reacts readily with acetate ion, forming predominantly *cis*-$[Pt(NH_3)_2(-OC(O)CH_3)(H_2O)]^+$ (**7**, R = CH_3), and *cis*-$[Pt(NH_3)_2(-OC(O)CH_3)_2]$ (**8**, R = CH_3) in solution, with $[\{Pt(NH_3)_2\}_2(\mu\text{-}OH)(\mu\text{-}O_2CCH_3)](NO_3)_2$ crystallizing from solution.[30] To determine whether carboxylate complexes are formed when free carboxylic acids are added to solutions of **3** and **2**, ^{15}N NMR spectra were obtained of solutions in 1 M aqueous solutions of RCO_2H (R = CH_3,

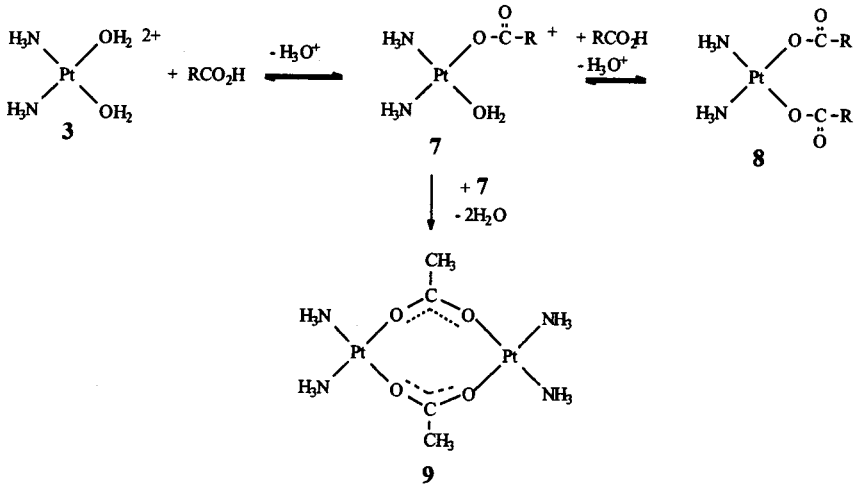

Scheme 2

H, CF_3). The spectrum of the solution containing acetic acid is shown in Figure 1b. In light of results obtained on related systems,[5] the major features of this spectrum may be explained in terms of the reactions shown in Scheme 2. The strongest peaks in the spectrum are assigned to ^{15}N trans to acetate (labeled **7A**, −82.1 ppm) and water (labeled **7B**, −87.2 ppm) in **7**. The peak at −85.0 may be assigned to **8**. The nearby peak at −84.5 ppm has not been reported previously. Since both of the ^{15}N nuclei appear to be equivalent, and in view of the propensity of acetate to form a bridge between platinum(II) atoms,[30] this peak has been assigned to the dinuclear complex $[\{Pt(^{15}NH_3)_2(\mu\text{-}O_2CCH_3)\}_2]^{2+}$ (**9**). The presence of a small proportion of *cis*-$[Pt(^{15}NH_3)_2Cl(H_2O)]^+$ (**2**) in the solution also allowed the simultaneous monitoring of the reaction of acetate with this species. It is clear from the spectrum that **2** reacted less overall with acetate than **3**, but the peak labeled **10A** (−68.8 ppm) could be assigned to ^{15}N trans to chloride in *cis*-$[Pt(^{15}NH_3)_2Cl(O_2CCH_3)]$ (**10**, R = CH_3) (Scheme 3). In additional experiments using higher proportions of **2** in the initial solution, the peak from ^{15}N trans to acetate in this complex was clearly observed at −84.7 ppm. In the spectrum shown in Figure 1b this peak (**10B**) is partially obscured by the peak from **8**. The spectrum also contained a small peak at −68.2 ppm from *cis*-$[PtCl_2(^{15}NH_3)_2]$ (**1**).

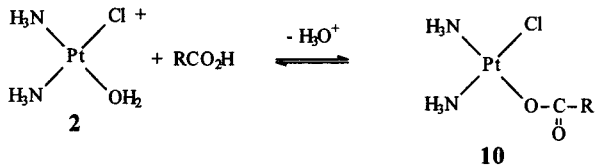

Scheme 3

The ^{15}N NMR spectra of analogous solutions with formic (R = H) and trifluoroacetic (R = CF_3) acids showed peaks analogous to those from the acetate complexes (R = H: **7**, −82.5, −88.3 ppm; **8**, −84.3 ppm. R = CF_3: **7**, −83.7, −87.5 ppm; **8**, −85.0 ppm). Although relative intensities indicated that there was less reaction with **2** and **3** than for acetate, the reaction was still significant.

^{15}N NMR Spectra of Solutions of 3 and 2 with Hydrophobic Ion-Pairing Agents—The agents which are in common use are sodium dodecyl sulfate, $Na^+(^-O_3SO(CH_2)_{11}CH_3)$, (SDS), and hexanesulfonic acid, $HO_3S(CH_2)_5CH_3$. Commercially available SDS usually contains traces of chloride (two brands tried each were labeled as containing up to 0.01% w/w chloride). Both HPLC experiments and NMR spectra showed that sufficient chloride was present to convert a significant amount of *cis*-$[Pt(NH_3)_2(H_2O)_2]^{2+}$ (**3**) into chloro complexes **2** and **1**. It was therefore necessary to remove chloride from the SDS solution before it could be used with the aqua complexes (see Experimental Section). Addition of excess chloride-free SDS to solutions containing *cis*-$[Pt(^{15}NH_3)_2(H_2O)_2]^{2+}$ (**3**) and *cis*-$[Pt(^{15}NH_3)_2Cl(H_2O)]^+$ (**2**) at pH 2.5 (adjusted with triflic acid) caused no additional peaks to appear from species containing coordinated SDS. Commercially available hexanesulfonic acid did not contain detectable chloride. With excess hexanesulfonic acid added to a solution of *cis*-$[Pt(^{15}NH_3)_2(H_2O)_2]^{2+}$ (**3**), a very small additional ^{15}N NMR peak appeared at −85.5 ppm which was probably from ammine trans to hexanesulfonate in a complex *cis*-$[Pt(^{15}NH_3)_2(-O_3S(CH_2)_5CH_3)(H_2O)]^+$ (the peak from ammine trans to water was probably obscured by the large peak from **3**). The extent of reaction was too small to affect significantly the HPLC experiments.

^{15}N NMR Spectra of Solutions of 3 and 2 with Aqueous Acetonitrile—Addition of even a small quantity of acetonitrile to an aqueous solution of *cis*-$[Pt(^{15}NH_3)_2(H_2O)_2]^{2+}$ (**3**) caused complete conversion to *cis*-$[Pt(^{15}NH_3)_2(NCCH_3)_2]^{2+}$ (^{15}N NMR singlet with satellites, δ_N −70.3 ppm, $J(^{195}Pt-^{15}N)$ 351 Hz). The monochloro complex **2** was similarly converted completely to *cis*-$[Pt(^{15}NH_3)_2Cl(NCCH_3)]^+$ (^{15}N trans to Cl^- −66.9 ppm, trans to acetonitrile −69.9 ppm). Although polynuclear paramagnetic "amide blues" form with more concentrated solutions of diammineplatinum(II) with aqueous acetonitrile,[24] these ^{15}N NMR spectra did not change over several days, probably because the solutions were too dilute for significant amide bridging to occur. Clearly, any acetonitrile used as an organic modifier would be expected to react completely with platinum(II) aqua complexes in HPLC experiments.

^{15}N NMR Spectra of Solutions of 3 and 2 with Aqueous Alcohols—The ^{15}N NMR spectrum of a solution of *cis*-$[Pt(^{15}NH_3)_2(H_2O)_2](NO_3)_2$ in a 2:1 (v/v) mixture of methanol and water showed an intense singlet with satellites from *cis*-$[Pt(^{15}NH_3)_2(H_2O)_2]^{2+}$ (**3**) at −87.0 ppm. A peak at −86.5 ppm assignable to ammine trans to nitrate in *cis*-$[Pt(^{15}NH_3)_2(-ONO_2)(H_2O)]^+$ was stronger than in a pure water solution,[5] but remained weak (from peak heights, the concentration of the nitrato complex was 7.5% of that of **3**; the peak from ammine trans to water in the nitrato complex would be expected to be obscured by that from **3**). Two small peaks with equal intensities, at −84.6 and −88.0, could be assigned to the complex with coordinated methanol, *cis*-$[Pt(^{15}NH_3)_2(CH_3OH)(H_2O)]^{2+}$. From peak heights, the concentration of the methanol complex was

Table 1—Variation of Retention Times for Cisplatin (1), *cis*-$[Pt(NH_3)_2Cl(H_2O)]^+$ (2), and *cis*-$[Pt(NH_3)_2(H_2O)_2]^{2+}$ (3) with Ion-Pairing Agent[a]

ion-pairing agent	concn (mM)	retention times (min)		
		1	2	3
SDS	0.05	6.2	12.0	5.2
SDS	0.50	6.4	18.0	4.4
hexanesulfonic acid	0.05	6.0	6.0	5.4
hexanesulfonic acid	0.50	8.1	7.2	6.2

[a] pH adjusted to 2.5 with triflic acid, 3% (V/V) methanol, column temperature 37 °C, flow rate 0.5 mL/min, detection wavelength 305 nm.

13% of that of **3** under these conditions. This ratio of methanol to water was very much greater than that used in our HPLC experiments. With methanol concentration of 5% v/v, the peaks from the methanol and nitrato complexes were of negligible intensity (<1% of the intensity of peaks from **3**). No peaks from methanol coordination were observed from a solution of *cis*-$[Pt(^{15}NH_3)_2Cl(H_2O)]^+$ (**2**) in 2:1 methanol/water.

In 2-propanol/water mixtures no peaks were observed from alcohol coordination, although there was again a small increase in the intensity of the peak from ammine trans to nitrate in the nitrato complex.

Separation of 1, 2, and 3 by Reversed-Phase HPLC—Solutions containing ^{15}N-labeled cisplatin, *cis*-$[PtCl_2(^{15}NH_3)_2]$ (**1**), *cis*-$[Pt(^{15}NH_3)_2Cl(H_2O)](NO_3)$ (**2**) (>90%), *cis*-$[Pt(^{15}NH_3)_2(H_2O)_2](NO_3)_2$ (**3**), and solutions containing mixtures of these complexes, were checked by ^{15}N NMR spectra, so that their compositions were known, and then injected onto the HPLC column. The mobile phase used in each case contained 3% (v/v) methanol, and the pH of the solution was adjusted to 2.5 with triflic acid. The ion-pairing agent used was either SDS (purified from chloride) or hexanesulfonic acid, at various concentrations. When the starting materials used were freshly prepared, the HPLC trace obtained in each case gave the number of peaks corresponding to the number of species present in solution, as revealed by the ^{15}N NMR spectra. Table 1 shows retention times for **1**, **2**, and **3** under some of the conditions used. Figure 2a is a chromatogram obtained for a solution containing all of the species, **1**, **2**, and **3**, with 0.5 mM SDS, and Figure 2b a chromatogram obtained for another solution, with 0.05 mM SDS. Figure 2c shows the chromatogram of a mixture of **1**, **2**, and **3** with 0.5 mM hexanesulfonate, and Figure 2d with 0.05 mM hexanesulfonate.

As expected, the retention time for the neutral compound cisplatin (**1**) was almost independent of the identity and concentration of the ion-pairing agent. With SDS as the ion-pairing agent, the retention time for **2** (which carries a single positive charge) was much longer than for **1** and also increased dramatically as the concentration of SDS was increased. The peak from **2** was always significantly broader than that from **1**. The retention time for **2** corresponding to a particular SDS concentration was reproducible if the column was thoroughly washed with mobile phase and then allowed to equilibrate for several hours between injections. With more rapid throughput of samples, there was some variation in the retention time for **2** (up to 2 min). With SDS as the "ion-pairing agent", **2** therefore effectively became a nonpolar species. By contrast, the retention time for **2** was relatively short when hexanesulfonate, with its shorter aliphatic chain, was used as the "ion-pairing agent". The retention time for **3** was short with both SDS and hexanesulfonate as the "ion-pairing agent", so that **3**, dipositively charged, remained a relatively polar species. The separation between peaks from

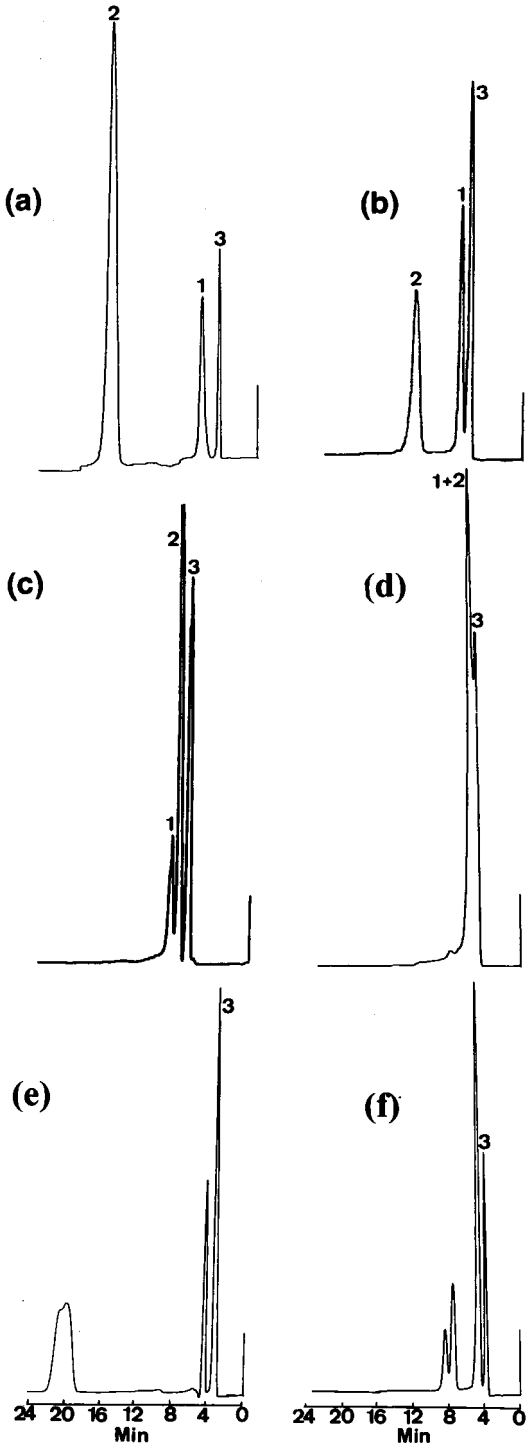

Figure 2—Chromatograms from aqueous solutions containing *cis*-$[PtCl_2(NH_3)_2]$ (**1**), *cis*-$[Pt(NH_3)_2Cl(H_2O)]^+$ (**2**), and *cis*-$[Pt(NH_3)_2(H_2O)_2]^{2+}$ (**3**) (total Pt concentration 0.5 mM), with mobile phase containing 3% (v/v) methanol, pH adjusted to 2.5 with the acid indicated, flow rate 0.5 mL/min (a) triflic acid, 0.5 mM SDS; (b) triflic acid, 0.05 mM SDS; (c) triflic acid, 0.5 mM hexanesulfonate; (d) triflic acid, 0.05 mM hexanesulfonate; (e) acetic acid, 0.5 mM SDS; (f) acetic acid, 0.05 mM SDS

1 and **3**, although always small, was always resolved (baseline resolution in Figure 2a). When chromatograms were obtained from solutions of *cis*-$[Pt(NH_3)_2(H_2O)_2](NO_3)_2$ made up using freshly prepared *cis*-$[Pt(NH_3)_2(ONO_2)_2]$, a single peak from **3** was observed when either ion-pairing agent was used. However, when a sample of *cis*-$[Pt(NH_3)_2(ONO_2)_2]$ was used which had been allowed to stand for 24 h or more, even when refrigerated and protected from light, chromatograms obtained using SDS showed a number of

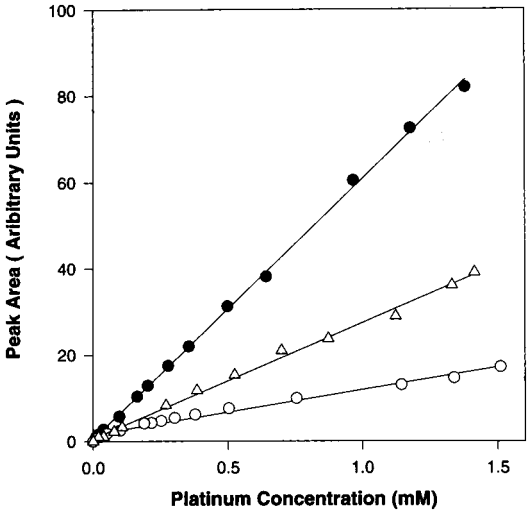

Figure 3—Relationship between integrated peak area and concentration of platinum complex in injected solution, under conditions described in text. In each case the line of best fit is drawn. (●) cisplatin (**1**); (○) *cis*-$[Pt(NH_3)_2(H_2O)_2]^{2+}$, (**3**); (△) *cis*-$[Pt(NH_3)_2Cl(H_2O)]^+$ (**2**).

broad peaks at very long retention times (>20 min). When hexanesulfonic acid was used, the same solutions showed a single, sharper peak, with longer retention time than peaks from **1**, **2**, or **3**. When ^{15}N-labeled sample was used, the ^{15}N NMR spectra of these solutions showed only the peaks from **3**. It is likely that reactions on the surface of solid *cis*-$[Pt(NH_3)_2(ONO_2)_2]$ formed traces of intensely absorbing oligomeric paramagnetic complexes which were responsible for these HPLC peaks. Since this problem could be avoided by the use of freshly prepared material, it was not further investigated. No such HPLC peaks were observed from solutions prepared from fresh *cis*-$[Pt(NH_3)_2(ONO_2)_2]$ which were then allowed to stand for long periods.

Figure 2e shows a chromatogram obtained from a solution initially containing **1**, **2**, and **3**, with the mobile phase containing 0.5 mM SDS and 3% (v/v) methanol, with the pH adjusted to 2.5 with acetic acid rather than triflic acid. For Figure 2f, the SDS concentration was 0.05 mM. Compared with the chromatograms obtained with triflic acid, there is an additional peak. Three of the observed peaks undoubtedly corresponded to **1**, **2**, and **3**, with the additional peak most likely representing a carboxylate complex formed on the column during elution. No attempt was made to assign these peaks to individual species, as, after these results, mobile phases containing carboxylic acids were simply avoided.

Quantitative Determination of 1, 2, and 3 by HPLC—HPLC traces were obtained for solutions which contained known concentrations of **1**, and the integrated area of the HPLC peak from **1** was measured under the standard conditions outlined above (mobile phase containing 3% methanol, 0.5 mM SDS, pH adjusted to 2.5 with triflic acid, column temperature 37 °C, detection wavelength 305 nm). A linear relationship was obtained between peak area and concentration (Figure 3). Similar relationships were obtained for **2** and **3** (Figure 3). The different line slopes are, of course, a result of the differing molar absorptivity coefficients of the three complexes at 305 nm. Such linear plots would not be expected if there were any covalent bonding interaction between the platinum aqua complexes and the stationary phase.

HPLC Detection of *cis*-$[Pt(NH_3)_2Cl(H_2O)]^+$ (2) from Ultrafiltered Plasma Incubated with Cisplatin—Samples were periodically removed from a solution of ultrafiltered human plasma incubated at 37 °C with cisplatin (**1**) and analyzed by HPLC using mobile phases

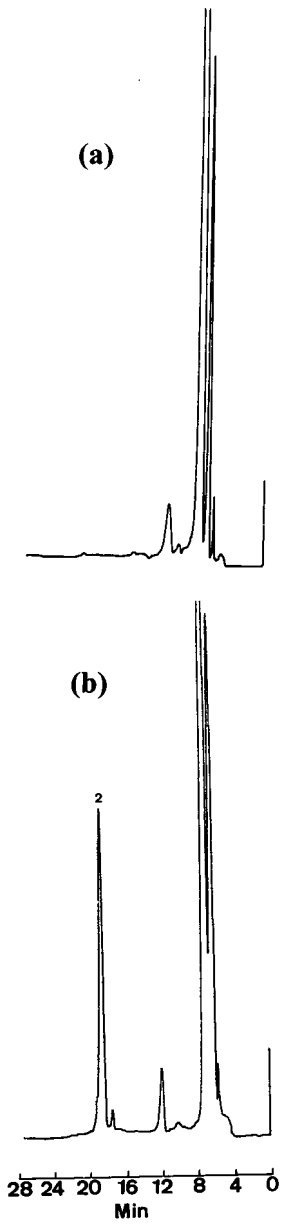

Figure 4—Chromatograms from ultrafiltered human plasma (100 μL injection, mobile phase 3% (v/v) methanol, pH adjusted to 2.5 with triflic acid, 0.05 mM SDS, detector wavelength 305 nm): (a) plasma allowed to stand 24 h at 37 °C; (b) plasma incubated with cisplatin (**1**) (0.2 mg/mL) for 24 h. The peak labeled "**2**" corresponds to *cis*-$[Pt(NH_3)_2Cl(H_2O)]^+$.

as described above (3% (v/v) methanol, pH adjusted to 2.5 with triflic acid) with SDS concentrations of 0.05 or 0.5 mM. Figure 4b shows a chromatogram (obtained with SDS concentration 0.05 mM), from ultrafiltered plasma incubated with cisplatin (**1**) at 37 °C for 24 h, while Figure 4a shows the chromatogram from a sample of plasma allowed to stand at 37 °C for the same time. At the detector wavelength, 305 nm, platinum complexes absorb strongly, but many organic molecules present in plasma have weak absorption. The chromatograms showed the growth, and then decline over several days, of a peak (labeled "**2**" in Figure 4b) with a retention time corresponding to that of *cis*-$[Pt(NH_3)_2Cl(H_2O)]^+$ (**2**). From Figure 4a, it is evident that platinum-free plasma did not give any significant peaks near this retention time, under the same conditions. The assignment of the peak to **2** was confirmed from the chromatogram obtained for the same solution with SDS concentration 0.5 mM, as a peak was now observed at retention time 34.4 min which corresponded to **2** under

these conditions (see Table 1). "Spiking" the plasma with a solution of **2** also caused a large increase in the intensity of the peak. It was, therefore, relatively easy to detect and monitor this species by HPLC analysis of the ultrafiltered plasma. Again, it should be mentioned that at the pH of the plasma, **2** would be largely deprotonated to *cis*-[Pt-$(NH_3)_2Cl(OH)]$ (**4**).

Although there were a number of intense peaks at short retention times from the plasma, there were no peaks in any of the chromatograms at a retention time corresponding to *cis*-$[Pt(NH_3)_2(H_2O)_2]^{2+}$ (**3**). This species and its partially deprotonated form *cis*-$[Pt(NH_3)_2(OH)(H_2O)]^+$ (**5**) are, therefore, not present in detectable concentrations in ultrafiltered plasma incubated with cisplatin.

Discussion

Many previous attempts to detect and monitor cisplatin hydrolysis products and metabolites by HPLC have been marred by a lack of appreciation of the reaction chemistry of these compounds. In the Introduction of this paper, reference has been made to a number of studies in which components were used in mobile phases which react readily with the platinum aqua complexes. There has seldom been unequivocal assignment of HPLC peaks to particular compounds. Checks for accidental superposition of peaks from different compounds have seldom been applied. If results are to be interpreted unambiguously we propose that the following conditions must be applied scrupulously:

(1) The use of any substance in a mobile phase which may react with one of the analytes under the analysis condition should be avoided. This includes the need to check for interfering impurities (such as the chloride present in commercially available SDS or which may leak from electrodes used to measure pH).

(2) Assignment of HPLC peaks to particular compounds should be based on check runs using solutions of known composition. For platinum(II) ammine complexes, ^{15}N NMR spectroscopy provides an excellent means for analysis of such solutions. If sufficient sample is obtainable from HPLC elution, analysis of this purified sample may be an acceptable alternative.

(3) There should be routine checks for accidental equivalence of retention times for different compounds. This may be done by HPLC analysis of the solution with two different mobile phases, which are known to give different retention times for the compound(s) of interest. This also provides confirmation of the assignment of a peak to a particular compound.

Our results have shown that it is possible to analyze for *cis*-$[Pt(NH_3)_2Cl(H_2O)]^+$ (**2**) and *cis*-$[Pt(NH_3)_2(H_2O)_2]^{2+}$ (**3**) (and their deprotonated forms) in aqueous solution and in ultrafiltered plasma while meeting these necessary conditions. The purpose of the experiments on ultrafiltered plasma described here was to show that HPLC peaks corresponding to **2** can be detected in ultrafiltered plasma. The cisplatin concentration used (0.2 mg/mL) was therefore relatively high—higher than would be present when cisplatin is administered as a drug. We are currently carrying out analyses in vitro and in vivo in which the platinum concentration is much lower.

References and Notes

1. *Platinum and Other Metal Coordination Compounds in Cancer Chemotherapy 2*, Pinedo, H. M.; Schornagel, J. H., Eds.; Plenum: New York, 1996.
2. Gormley, P. E.; Bull, J. M.; LeRoy, A. F.; Cysyk, R. L. Kinetics of *cis*-Dichlorodiammineplatinum. *Clin. Pharmacol. Ther.* **1979**, *25*, 351−357.
3. Erlichman, C.; Soldin, S. J.; Thiessen, J. J. Disposition of Total and Free Cisplatin on Two Consecutive Treatment Cycles in Patients with Ovarian Cancer. *Cancer Chemother. Pharmacol*, **1987**, *19*, 75.
4. Boreham, C. J.; Broomhead, J. A.; Fairlie, D. P. A ^{195}Pt and ^{15}N NMR Study of the Anticancer Drug, *cis*-Diamminedichloroplatinum(II), and its Hydrolysis and Oligomerization Products. *Aust. J. Chem.* **1981**, *34*, 659−664.
5. Appleton, T. G.; Berry, R. D.; Davis, C. A.; Hall, J. R.; Kimlin, H. A. Reactions of Platinum(II) Aqua Complexes. 1. Multinuclear (^{195}Pt, ^{15}N, and ^{31}P) NMR Study of Reactions between the *cis*-Diamminediaquaplatinum(II) Cation and the Oxygen-Donor Ligands Hydroxide, Perchlorate, Nitrate, Sulfate, Phosphate, and Acetate. *Inorg. Chem.* **1984**, *23*, 3514−3521.
6. Appleton, T. G.; Hall, J. R.; Ralph, S. F.; Thompson, C. S. M. NMR Study of Acid−Base Equilibria and Other Reactions of Ammineplatinum Complexes with Aqua and Hydroxo Ligands. *Inorg. Chem.* **1989**, *28*, 1989−1993.
7. Miller, S. E.; House, D. A. The Hydrolysis Products of *cis*-Diamminedichloroplatinum(II). 1. The Kinetics of Formation and Anation of the *cis*-Diammine(aqua)chloroplatinum(II) Cation in Acidic Aqueous Solution. *Inorg. Chim. Acta* **1989**, *161*, 131−137.
8. Miller, S. E.; House, D. A. The Hydrolysis Products of *cis*-Dichlorodiammineplatinum(II). 2. The Kinetics of Formation and Anation of the *cis*-Diamminedi(aqua)platinum(II) Cation. *Inorg. Chim. Acta* **1989**, *166*, 189−197.
9. Miller, S. E.; House, D. A. The Hydrolysis Products of *cis*-Dichlorodiammineplatinum(II). 3. Hydrolysis Kinetics at Physiological pH. *Inorg. Chim. Acta* **1990**, *173*, 53−60.
10. Berners-Price, S. J.; Frenkiel, T. A.; Frey, U.; Ranford, J. D.; Sadler, P. J. Hydrolysis Products of Cisplatin: pK_a Determinations via [^1H, ^{15}N] NMR Spectroscopy. *J. Chem. Soc., Chem. Commun.* **1992**, 789−791.
11. Faggiani, R.; Lippert, B.; Lock, C. J. L.; Rosenberg, B. Hydroxo-Bridged Platinum(II) Complexes. 1. Di-μ-hydroxo-bis[diammineplatinum(II)] Nitrate, $[(NH_3)_2Pt(OH)_2Pt(NH_3)_2](NO_3)_2$. Crystalline Structure and Vibrational Spectra. *J. Am. Chem. Soc.* **1977**, *99*, 777−781.
12. Lippert, B.; Lock, C. J. L.; Rosenberg, B.; Zvagulis, M.. Hydroxo-Bridged Platinum(II) Complexes. 4. Crystal Structure and Vibrational Spectra of Di-μ-hydroxo-bis[diammineplatinum(II)] Carbonate Dihydrate, $[(NH_3)_2Pt(OH)_2Pt(NH_3)_2](CO_3)0{\cdot}2H_2O$. *Inorg. Chem.* **1978**, *17*, 2971−2975.
13. Faggiani, R.; Lippert, B.; Lock, C. J. L.; Rosenberg, B. Hydroxo-Bridged Platinum(II) Complexes. 2. Crystallographic Characterization and Vibrational Spectra of *cyclo*-Tri-μ-hydroxo-tris[*cis*-diammineplatinum(II)] Nitrate. *Inorg. Chem.* **1977**, *16*, 1192−1196.
14. Lippert, B. Platinum Nucleobase Chemistry. *Prog. Inorg. Chem.* **1989**, *37*, 1−97.
15. Bancroft, D. P.; Lepre, C. A.; Lippard, S. J. ^{195}Pt NMR Kinetic and Mechanistic Studies of *cis*- and *trans*-Diamminedichloroplatinum(II) Binding to DNA. *J. Am. Chem. Soc.* **1990**, *112*, 6860−6871.
16. Sundquist, W. I.; Lippard, S. J. The Coordination Chemistry of Platinum Anticancer Drugs and Related Compounds with DNA. *Coord. Chem. Rev.* **1990**, *100*, 293−322.
17. Daley-Yates, P. T.; McBrien, D. C. H. Cisplatin Metabolites in Plasma, A Study of Their Pharmacokinetics and Importance in the Nephrotoxic and Antitumour Activity of Cisplatin. *Biochem. Pharmacol.* **1984**, *33*, 3063−3067.
18. Andersson, A.; Fagerberg, J.; Lewensohn, R.; Ehrsson, H. Pharmacokinetics of Cisplatin and Its Monohydrated Complex in Humans. *J. Pharm. Sci.* **1996**, *85*, 824−827.
19. Zhao, Z.; Tepperman, K.; Dorsey, J. G.; Elder, R. C. Determination of Cisplatin and Some Possible Metabolites by Ion-Pairing Chromatography with Inductively Coupled Plasma Mass Spectrometric Detection. *J. Chromatog. Biomed. Applic.* **1993**, *615*, 83−89.
20. Wood, F. E.; Hunt, C. T.; Balch, A. L. ^{195}Pt and ^{31}P Nuclear Magnetic Resonance Studies of the Binding of the *cis*-Pt-$(NH_3)_2^{2+}$ Moiety to Phosphate in Aqueous Solution. *Inorg. Chim. Acta* **1982**, *67*, L19−L20.
21. Appleton, T. G.; Berry, R. D.; Hall, J. R. 'Platinum Phosphate Blues'. A Comparison with 'Amide Blues'. *Inorg. Chim. Acta* **1982**, *64*, L229-L233.
22. DeWaal, W. A. J.; Maessen, F. J. M. J.; Kraak, J. C. Analysis of Platinum Species Originating from *cis*-Diamminedichloroplatinum(II) (Cisplatin) in Human and Rat Plasma by High-Performance Liquid Chromatography with On-Line Inductively Coupled Plasma Atomic Emission Spectrometric Detection. *J. Chromatogr.* **1987**, *407*, 253.

23. Heudi, O.; Caillieux, A.; Allain, P. Interactions Between Cisplatin Derivatives and Mobile Phase During Chromatographic Separation. *Chromatographia* **1997**, *44*, 19−24.
24. Wenclawiak, B. W.; Wollmann, M. Separation of Platinum-(II) Anti-tumour Drugs by Micellar Electrokinetic Capillary Chromatography. *J. Chromatogr. A* **1996**, *724*, 317−326.
25. Shearan, P.; Alvarez, J. M. F.; Zayed, N.; Smyth, M. R. High Performance Liquid Chromatography Separation of Cisplatin and Its Hydrolysis Products on Alumina and Application to Studies of their Interaction with Cysteine. *Biomed. Chromatogr.* **1990**, *4*, 78−82.
26. Gillard, R. D.; Wilkinson, G. Platinum Blue and Related Complexes. *J. Chem. Soc.* **1964**, 2835−2837.
27. Appleton, T. G.; Hall, J. R.; Ralph, S. F. ^{15}N and ^{195}Pt NMR Spectra of Platinum Ammine Complexes: Trans- and Cis-Influence Series Based on ^{195}Pt-^{15}N Coupling Constants and ^{15}N Chemical Shifts. *Inorg. Chem.* **1985**, *24*, 4685−4693.
28. Appleton, T. G.; Bailey, A. J.; Bedgood, D. R.; Hall, J. R. Amino Acid Complexes of Palladium(II). 1. NMR Study of the Reactions of the Diaqua(ethylenediamine)palladium(II) Cation with Ammonia, Betaine, and the Amino Acids $^{+}NH_3(CH_2)nCO_{2-}$ ($n = 1 - 3$). *Inorg. Chem.* **1994**, *33*, 217−226.
29. Lallemand, J.-Y.; Soulie, J.; Chottard, J.-C. Implication of ^{195}Pt Chemical Shift Anisotrophy Relaxation in NMR Studies of the Platinum Complexes. *J. Chem. Soc., Chem. Commun.* **1980**, 436−438.
30. Appleton, T. J.; Mathieson, M.; Byriel, K. A.; Kennard, C. H. L. Crystal Structure of (μ-acetato-O,O′)(μ-hydroxo)bis-(diammine)platinum(II) nitrate. *Z. Kristallogr.* **1998**, *213*, 247−248.

Acknowledgments

We thank Ms. Lynette Lambert for some assistance with NMR spectroscopy.

JS980287M

Interaction between Surface Active Drug (FK906:Rennin Inhibitor) and Cyclodextrins in Aqueous Solution

SATOSHI KITAMURA,* TOMOKO FUJIMURA, AND SHIGETAKA KOHDA

Contribution from *Analytical Research Laboratories, Fujisawa Pharmaceutical Co., Ltd. 1–6, Kashima 2-chome, Yodogawa-ku, Osaka 532-8514, Japan.*

Received July 9, 1998. Accepted for publication November 24, 1998.

Abstract □ The aggregation behavior of FK906, which is a peptide like hypertensive agent, in aqueous solution was studied by static light scattering, ^{1}H-nuclear magnetic resonance (NMR), and surface tension. These experiments showed a clear critical micelle concentration (cmc) at around 6.3×10^{-3} to 1.3×10^{-2} M of FK906 aqueous solution. The result of ^{1}H NMR experiments revealed that FK906 aggregates primarily by hydrophobic interactions involving the benzyl moiety. The Debye plots from light-scattering studies showed that the apparent molecular weight of aggregated FK906 molecule is 1670 which corresponds to 2–3 molecules of FK906. The effect of α- and β-cyclodextrins on the surface tension of FK906 aqueous solution was investigated. It appeared that the addition of α-cyclodextrin showed very small shift of cmc, but that of β-cyclodextrin shifted the cmc to much higher concentration. The investigation on the surface tension of FK906 aqueous solution in the presence of β-cyclodextrin indicated that FK906 forms a 1:1 complex with β-cyclodextrin. On the basis of these experiments, it appears that β-cyclodextrin has an ability to change the surface active property of FK906 in its aqueous solution. Therefore, it is expected that the addition of β-cyclodextrin to FK906 aqueous solution may prevent the adsorption onto container walls and/or reduce the local irritancy.

Introduction

Pharmaceuticals with both hydrophilic and hydrophobic groups show a surface active property. Surface active pharmaceuticals usually show critical micelle concentration (cmc) above that at which they tend to aggregate to form micelles in their aqueous solutions. This aggregation behavior of pharmaceuticals sometimes causes a completely different activity below and above the cmc, because the drug molecules exist as monomer below cmc and form aggregates above cmc. For example, the anesthetic potency as a function of drug in solution shows a decrease in activity at the cmc.[1] Furthermore, these surface active drugs sometimes present problems in pharmaceutical formulation. Typical examples are the adsorption of surface active drugs on to container walls, which may result in a loss of free drug at low concentration,[2] and erythrocytes from hemolysis.[3]

To overcome these pharmaceutical problems, many additives have been studied to change the molecular interaction of surface active drugs in their aqueous solutions. Methyl *p*-hydroxybenzoate is one of the example which has been regarded as an effective additive to prevent the gel formation caused by stacking self-association of doxorubicin at the aromatic rings and to shorten the dissolution time of its freeze-dried product.[4] Cyclodextrins also have been regarded as beneficial additives in the pharmaceutical area because they have an ability to protect erythrocytes from hemolysis and shape changes induced with surface active drugs.[5,6] Furthermore, some hydrophilic cyclodextrins, including maltosyl-β-cyclodextrin, inhibit the adsorption of bovine insulin to containers and its aggregation by interacting with hydrophobic regions of the peptide.[7]

Recently, the number of new drug candidates which have peptide-like structure has been increasing due to their specific biological activities. However, they have a risk of the above-mentioned problems in aqueous solution because they have hydrophilic as well as hydrophobic moieties in their structures.[8] Therefore, whether newly developed drugs are surface active or not is particularly significant in early stage since the concept of the preformulation should be established by taking into account the correlation between biological activities and physicochemical properties for these compounds.

In this report, FK906 ($C_{40}H_{63}N_7O_7$·HCl; mw: 790.44), which is a peptide-like synthetic rennin inhibitor, was used as a model compound since FK906 has polar and nonpolar groups, and its aqueous solution foams readily upon agitation. Thus, the aqueous solution properties of FK906 as a surface active drug were investigated by surface tension measurement, a light scattering study, and chemical shift observations in NMR spectra of samples in aqueous solution. The interaction between FK906 and cyclodextrins was also investigated to know whether cyclodextrins have an ability to change the surface active property of FK906.

Experimental Section

1. Materials—FK906 ($C_{40}H_{63}N_7O_7$·HCl; mw: 790.44), (2*S*,3*S*)-cyclohexyl-3-hydroxy-6-methyl-2-[Na-methyl-[(*S*)-2-[*N*-methyl-N-[2-(*N*-methyl-*N*-morpholinocarbonylamino)ethyl]-3-phenylpropinoil]-L-histidyl]aminoheptane hydrochloride, was synthesized at Fujisawa Pharmaceutical Co., Ltd. and used without further purification. The purity determined by area % with HPLC was 99.1%. All other reagents used were reagent grade.

2. Measurement of Static Light Scattering—Static light scattering of FK906 aqueous solution was measured at 25 °C using a light-scattering spectrophotometer (model DSL-7000, Otsuka Electronics Co., Osaka) equipped with an argon laser (488 nm). FK906 solution filtered through a membrane filter (pore size 0.2 μm) was used for static light scattering at a scattering angle of 45−135°. The refractive index increment of FK906 was measured at 25 °C using a differential refractometer (model DRM-1021, Otsuka Elecrtrocics Co., Osaka) at 633 nm. Solutions of FK906 ranging in concentration from 4 μg/mL to 80 mg/mL were prepared for static light-scattering measurement.

3. Measurements of ^{1}H-Nuclear Magnetic Resonance Spectra—^{1}H NMR spectra were measured at 25 °C on a 200 MHz nuclear magnetic resonance spectrometer (model AC 200P, Bruker) in deuterium oxide (D_2O) over a concentration range from 1 mg/mL to 50 mg/mL.

4. Measurement of Surface Tension—The surface tension was measured based on the Wilhelmy plate method with an automatic surface tensiometer (model CBVP-Z, Kyowa Seimitsu, Tokyo). The platinum plate was heated by an oxidizing flame before use. For the calculation of the surface tension of aqueous solution, the value of 72.0 mN/m was used as the surface tension

* To whom correspondence should be addressed.

10.1021/js980278d CCC: $18.00 Published on Web 01/30/1999

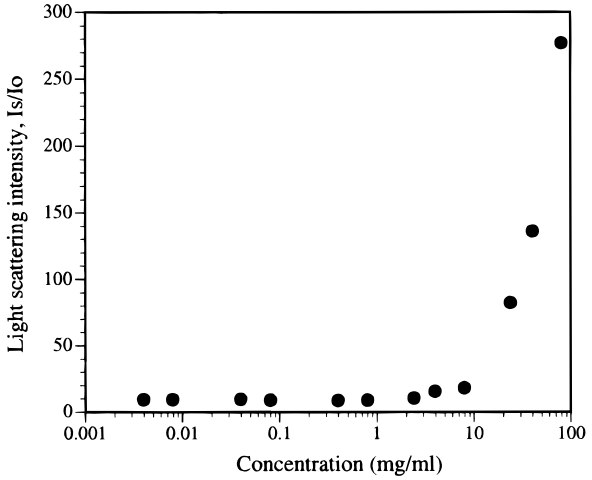

Figure 1—Effects of FK906 concentration on light-scattering intensity.

of pure water at 25 °C. The surface tension data for FK906 aqueous solution ranging from 1 μg/mL to 25 mg/mL were plotted against the logarithm of the concentration as the abscissa, and the intersection of the descending line and another one close to the horizontal was taken as the cmc. The effect of α- and β-cyclodextrins on the surface tension data for FK906 aqueous solution was also investigated according to the above-mentioned conditions.

Results and Discussion

1. Light Scattering Studies on Micelle Formation—Figure 1 shows the effects of FK906 concentration on light-scattering intensity at an angle of 90°. A rapid rise in the curve at around 10 mg/mL (1.3×10^{-2} M) is evidence of the aggregate formation of FK906 molecule.

This light-scattering method has another advantage of being able to obtain the molecular weight of a self-associated drug substance. Debye plots which are obtained from the light-scattering experiments were used to evaluate the apparent molecular weight of aggregated FK906. In this calculation, the following equations were used.

$$R\vartheta = A(n^2 I / {n_b}^2 I_0) \quad (1)$$

Where $R\vartheta$ is the Rayleigh ratio, A is the calibration constant of the apparatus, n and n_b are the refractive indices of water and toluene used for calibration, and I and I_0 are the intensities of scattered and introduced laser light, respectively. The apparent molecular weight of FK906 aggregates, mw, was determined according to eq 2:[9]

$$K(C - C_0)/(R\vartheta - R_0) - 2A_2(C - C_0) = 1/\mathrm{mw} \times P(\vartheta) \quad (2)$$

Where K is the optical constant, R_0 is the Rayleigh ratio at critical micelle concentration, C_0 is the second virial coefficient, and $P(\vartheta)$ can be assumed to be 1 when the particle size is small enough.

The apparent molecular weight of aggregated FK906 molecules obtained from Debye plots was 1670 which corresponds to 2 or 3 molecules of FK906. Although the aggregation number of FK906 molecules was much smaller than that of a reported drug substance such as a leukotriene D_4 receptor antagonist which aggregates more than 16000 molecules,[10] similar results to those from FK906 have been reported for some antibiotics[11] and nicotinamide.[12]

2. ^{1}H-Nuclear Magnetic Resonance Study—Figure 2 shows the ^{1}H NMR spectrum of FK906 in D_2O. Signal assignments of main moieties are also shown in Figure 2.

To evaluate the effect of aggregation on chemical shifts of the proton signals, the protons of benzyl, imidazoil, and

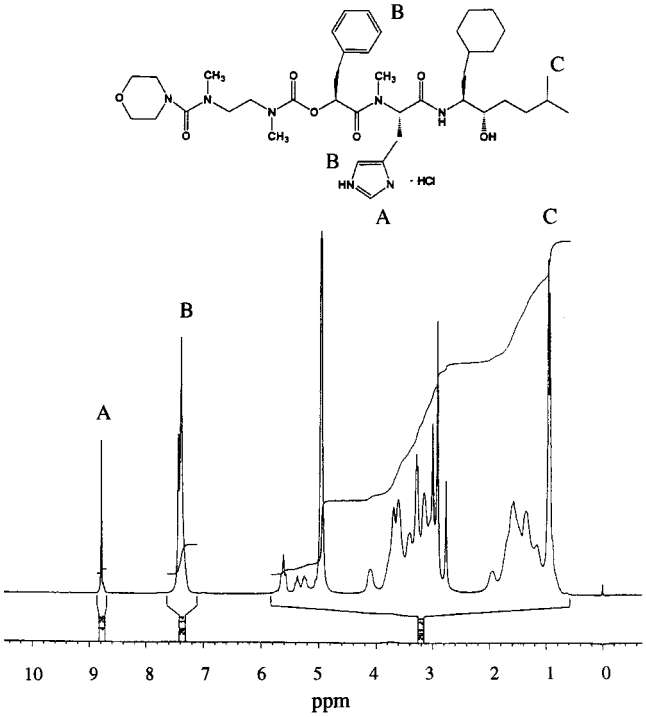

Figure 2—^{1}H NMR spectrum of FK906.

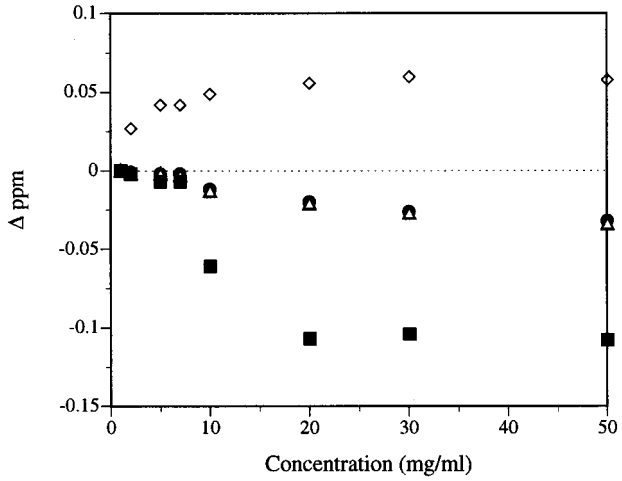

Figure 3—Concentration dependence of proton chemical shifts of FK906 in D_2O. ●, 0.76 ppm; △, 0.79 ppm; ■, 7.33 ppm; ◇, 8.52 ppm.

methyl groups were selected, since they are considered to have an important role to form micelle.[13,14] The concentration dependence of chemical shifts of above-mentioned protons are shown in Figure 3.

It appeared that by increasing the concentration of FK906 in solution, large upfield shifts were found for aromatic ring protons as compared with other protons. Furthermore, NMR studies also proved the existence of cmc for FK906 aqueous solutions, since plots of proton chemical shifts in Figure 3 showed a marked break at 10 mg/mL FK906 aqueous solution. From these chemical shifts of protons, the cmc value seems to be about 1.3×10^{-2} M. These results suggest that FK906 aggregates primarily by hydrophobic interaction involving the benzyl moiety.

3. Surface Tension Studies—Figure 4 shows the relation between the surface tension and the concentration of the aqueous FK906 solution.

The curve shows a general decline in surface tension with increase in drug concentration. The value of cmc was estimated as the point of intersection of the extension of

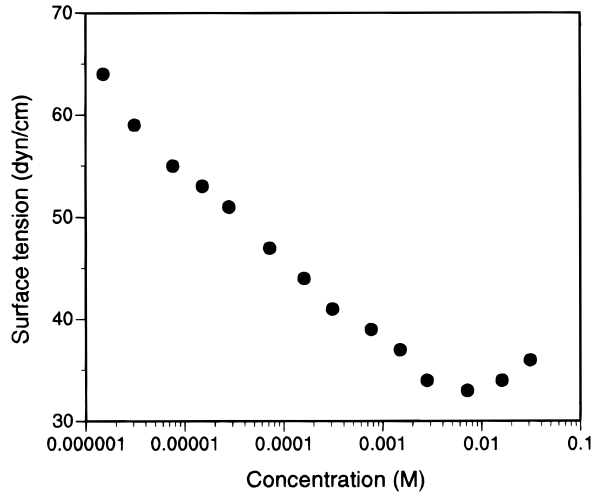

Figure 4—Effects of FK906 concentration on surface tension.

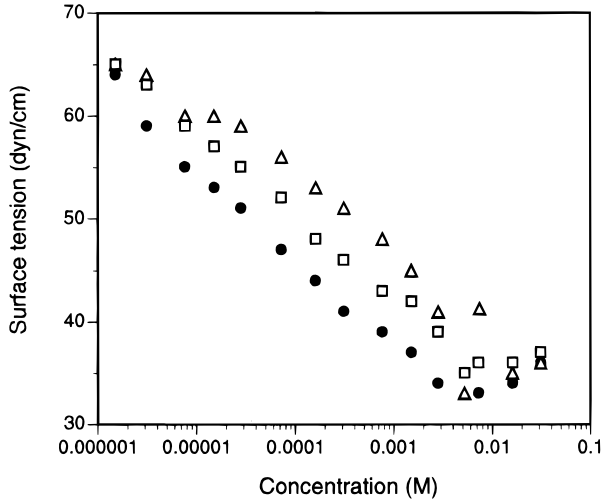

Figure 5—Dependence of FK906 concentration on the surface tension in the presence of cyclodextrins. ●, CyDs (0 M); △, β-Cy (5.0×10^{-3} M); □, α-CyD (6.7×10^{-3} M).

the gentle curve and the horizontal line. The cmc of FK906 in water was about 5 mg/mL (6.3×10^{-3} M) by the surface tension measurement.

These static light-scattering, NMR, and surface tension measurements apparently indicated that FK906 is a typical surface active product, and these experiments showed similar cmc values for FK906 in aqueous solution.

4. Effects of Cyclodextrins on Self-Association Behavior—It was expected that the surface tension measurement would indicate the formation of an inclusion complex of FK906 with cyclodextrins, because Funasaki et al.[15] reported that the binding constants of cyclodextrin–surfactant complexes were evaluated by surface tension data. Thus, surface tension measurements were used to evaluate the effects of α- and β-cyclodextrins on the surface tension property for FK906 aqueous solutions. Figure 5 shows the dependence of surface tension on the FK906 concentration in the presence of α- and β-cyclodextrins.

From Figure 5, some shifts of the surface tension curve can be seen when β-cyclodextrin was added to FK906 aqueous solution. Therefore, it was proved that β-cyclodextrin has an interaction with FK906 molecule. On the contrary, α-cyclodextrin showed only small shifts of surface tension curve, which indicated that the cavity size of α-cyclodextrin is too small to form a inclusion complex with FK906.

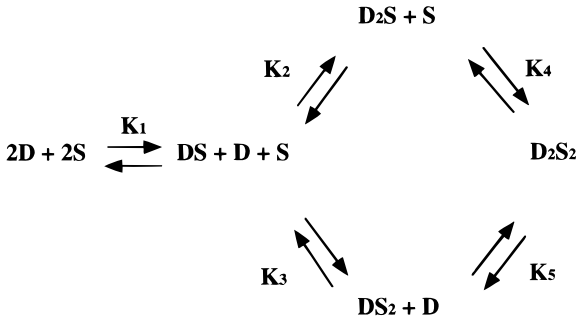

Figure 6—Scheme for the formation of the inclusion complex.

The following scheme (Figure 6) with regard to the complex formation between FK906 and β-cyclodextrin was introduced from a paper describing the complex formation between cyclodextrin and surfactants.[15]

In this scheme, β-cyclodextrin and FK906 were designated as D and S, respectively, and K_1 through K_5 represent the stability constants.

The each stability constant presented in Figure 6 is defined as follows:

$$K_1 = [DS]/[D][S] \quad (3)$$

$$K_2 = [D_2S]/[DS][D] \quad (4)$$

$$K_3 = [DS_2]/[DS][S] \quad (5)$$

$$K_4 = [D_2S_2]/[D_2S][S] \quad (6)$$

$$K_5 = [D_2S_2]/[DS_2][D] \quad (7)$$

where [D] represents the concentration of β-cyclodextrin and [S] is the concentration of FK906. In the case of FK906–β-cyclodextrin complex, a 2:2 complex of FK906 and β-cyclodextrin was assumed to be excluded because the binding constants of K_4 and K_5 reported for surfactant–cyclodextrin complex were almost zero. Thus, the total concentrations of β-cyclodextrin, C_D, and FK906, C_S, in the testing solution are expressed as follows:

$$C_D = [D] + [DS] + 2[D_2S] + [DS_2] = [D] + K_1[D][S] + 2K_1K_2[D]^2[S] + K_1K_3[D][S]^2 \quad (8)$$

$$C_S = [S] + [DS] + 2[D_2S] + [DS_2] = [S] + K_1[D][S] + 2K_1K_2[D]^2[S] + K_1K_3[D][S]^2 \quad (9)$$

By using the above equations, the next four cases are represented as follows:

Case 1: only DS is present.

$$\{C_D[S] - (C_S - [S])[S]\}K_1 = C_S - [S] \quad (10)$$

Case 2: DS and D_2S are present.

$$\{1 + 4K_1K_2C_D[S] - K_1^2[S]^2 - (1 - K_1[S])^2 + 8K_1K_2C_D[S]^{1/2}\}/8K_1K_2[S] + [S] - C_S = 0 \quad (11)$$

Case 3: DS and D_2S are present.

$$K_1K_3[S]^3 - K_1[1 + K_3(2C_D - C_S)][S]^2 + [1 + K_1(C_D - C_S)][S] - C_S = 0 \quad (12)$$

Case 4: DS, D_2S, and DS_2 are present.

$$\{1 + 4K_1K_2C_D[S] - K_1(K_1 + 2K_3)[S]^2 - 4K_1^2K_3^2[S]^4 - 3K_1^2K_3^2[S]^4 - (1 - K_1[S] - 3K_1K_3[S]^2) - [(1 + K_1[S] + K_1K_3[S]^2)^2 + 8K_1K_2C_D[S]^{1/2}\}/8K_1K_2[S] + [S] - C_S = 0 \quad (13)$$

Since the addition of β-cyclodextrin to the FK906 aqueous solution does not decrease the surface tension of water, the inclusion complexes can be expected to show less surface action than free FK906. Therefore, it can be assumed that the surface tension depends on only the concentration of free FK906 [S] even in the solution including β-cyclodextrin. As there is a good linearity between the surface tension and the concentration of FK906 below the cmc (see Figure 4), the concentration of free FK906 [S] is obtained from the surface tension of the sample solution.

From Figure 4, the concentration dependence of the surface tension for FK906 solution is written as the following equation.

$$\sigma = -3.77 \ln[S] + 11.5 \quad (14)$$

In this equation, σ represents the surface tension.

As the total concentration of β-cyclodextrin (C_D), the total concentration of FK906 (C_S), and the concentration of free FK906 [S] are known values, the best fit value for each stability constant was estimated from Akaike information criterion (AIC).[15]

The estimation of binding constants was carried out by minimizing the AIC value which is expressed in the following equation.

$$AIC = n \times \ln(ss) + 2r \quad (15)$$

$$ss = \sum_{i=1}^{n} (\sigma_{i,obsd} - \sigma_{i,calcd})^2 \quad (16)$$

In this equation, n, ss, and r represent that the number of data, sum of squares, and the number of constants, respectively. The minimum value of AIC obtained from this equation was selected and tabulated in Table 1.

It appeared that type 3 is the best of them in the case of β-cyclodextrin. However, this is an unrealistic model, since the value of K_3 is negative. Thus, it is concluded that FK906 forms a 1:1 inclusion complex with β-cyclodextrin, since type 1 is the second fit model among these models (K_1 = 2000). Spectroscopic (circular dichrorism spectra) analysis was performed to confirm the formation of inclusion complex of FK906 with β-cyclodextrin. As a result, the obtained spectra strongly supported the complex formation of FK906 with β-cyclodextrin. However, it was difficult to determine the exact molar ratio of FK906/β-cyclodextrin complex, since there were some deviations in the magnitude of circular dichrorism spectra. On the contrary, it is expected that surface tension method gives us rather detailed information to discuss the model of complex formation, since quantitative treatment for cyclodextrin−FK906 interactions including 1:1, 1:2, 2:1, and 2:2 complexes was taken into account.[15]

Conclusion

It was confirmed that FK906 shows aggregation behavior in aqueous solution. Three different experiments, ^{1}H NMR spectrometry, light scattering, and surface tension, showed almost the same cmc at 6.3×10^{-3} to 1.3×10^{-2} M. It appeared that the addition of β-cyclodextrin strongly affected the surface tension of FK906 aqueous solution. Furthermore, the surface tension measurement suggested that the aggregation of FK906 was prevented by the formation of an inclusion complex with β-cyclodextrin.

Therefore, it is expected that the addition of β-cyclodextrin to FK906 aqueous solution may solve the pharmaceutical problems such as toxicity which comes from the surface active property of FK906.

Table 1. Best Fit Value of Binding Constants for FK906 and β-Cyclodextrin

complexes	K_1	K_2	K_3	ss	A
(1) DS	2000	–	–	0.284	–11.8
(2) DS, D_2S	1000	0.11	–	1.26	606
(3) DS, DS_2	2500	–	–85	0.0119	–44.8
(4) DS, D_2S, DS_2	1700	0.11	24	0.425	–3.4

References and Notes

1. Florence, A. T. Surface chemical and micellar properties of drugs in solution. *Adv. Colloid Interface Sci.* **1968**, *2*, 115−149.
2. Song, D.; Hsu, L.-F.; Au, J. L.-S. Binding of taxol to plastic and glass containers and protein under in vitro conditions. *J. Pharm. Sci.* **1996**, *85*, 29−31.
3. Miller, T. L.; Buhler, D. R. Effect of hexachlorophene on monovalent cation transport in human erythrocytes, A mechanism for hexachlorophene-induced hemolysis. *Biochim. Biophys Acta* **1974**, *352*, 86−96.
4. Hayakawa, E.; Furuya, K.; Uno, H.; Kuroda, T.; Moriyama, M.; Kondo, A. Visible absorption and proton nuclear magnetic resonance studies on the self-association of doxorubicin in aqueous solution. *Chem. Pharm. Bull.* **1991**, *39*, 1009−1012.
5. Uekama, K.; Irie, T.; Sunada, M.; Otagiri, M.; Tsubaki, K. Protective effects of cyclodextrins on drug-induced hemolysis in vitro. *J. Pharm. Dyn.* **1981**, *4*, 142−144.
6. Irie, T.; Sunada, M.; Otagiri, M.; Uekama, K. Protective mechanism of β-cyclodextrin for the hemolysis induced with phenothiazine neuroleptics in vitro. *J. Pharm. Dyn.* **1983**, *6*, 408−414.
7. Tokihiro, K.; Irie, T.; Uekama, K. Varying effects of cyclodextrin derivatives on aggregation and thermal behavior of insulin in aqueous solution. *Chem. Pharm. Bull.* **1997**, *45*, 525−531.
8. Tsai, T.; Mehta, R. C.; DeLuca, P. P. Adsorption of peptides to poly(D,L-lactide-*co*-glycolide): 1. Effect of physical factors on the adsorption. *Int. J. Pharm.* **1996**, *127*, 31−42.
9. Fukahori, M.; Takatsuji, Y.; Yamakita, T.; Takahashi, H.; Sato, H.; Yotsuyanagi, T. Aggregate formation of p-hydroxybenzoic acid esters in aqueous solution. *Chem. Pharm. Bull.* **1996**, *44*, 245−248.
10. Thibert, R.; Mach, H.; Clas, S.-D.; Meisner, D. R.; Vadas, E. B. Characterization of the self-association properties of a leukotriene D_4 receptor antagonist, MK-0476. *Int. J. Pharm.* **1996**, *134*, 59−70.
11. Attwood, D.; Agarwal, S. P. Light scattering studies on micelle formation by some penicillins in aqueous solution. *J. Pharm. Pharmcol.* **1984**, *36*, 563−564.
12. Coffman, R. E.; Kildsig, D. O. Self-association of nicotinamide in aqueous solution: Light-scattering and vapor pressure osmometry studies. *J. Pharm. Sci.* **1996**, *85*, 848−853.
13. Florence, A. T.; Parfitt, R. T. Nuclear magnetic resonance studies on micelle formation by promethazine hydrochloride. *J. Pharm. Pharmacol.* **1970**, *22*, 121S−125S.
14. Thakkar, A. L.; Wilham, W. L. Self-association of benzylpenicillin in aqueous solution: ^{1}H Nuclear magnetic resonance study. *Chem. Commun.* **1971**, 320−322.
15. Funasaki, N.; Yodo, H.; Hada, S.; Neya, S. Stoichiometries and equilibrium constants of cyclodextrin−surfactant complexations. *Bull. Chem. Soc. Jpn.* **1992**, *65*, 1323−1330.

JS980278D

A Novel Protein Cross-Linking Reaction in Stressed Neutral Protamine Hagedorn Formulations of Insulin

RONALD C. BEAVIS,* MICHAEL D. KNEIRMAN, DAVID SHARKNAS, MARK A. HEADY, BRUCE H. FRANK, AND MICHAEL R. DEFELIPPIS

Contribution from *Lilly Research Laboratories, Eli Lilly and Company, Lilly Corporate Center, DC 3811, Indianapolis, Indiana 46285.*

Received June 22, 1998. Final revised manuscript received December 8, 1998.
Accepted for publication December 9, 1998.

Abstract □ The covalent insulin–protamine product molecules formed by heat stress in Neutral Protamine Hagedorn formulations of insulin and the insulin analogue [Lys^{B28},Pro^{B29}] were examined by mass spectrometry. The results demonstrated that the covalent cross-link between insulin and protamine was not caused by linkage through the protamine N-terminal amino group, as had been previously thought. Our results indicate that the linkage was formed between the side chain of a protamine arginine and a histidine in the insulin B chain, resulting in a net mass change of –5 Da, compared to the sum of the protamine and insulin molecular masses. A mechanism for this new type of covalent cross-linking reaction is proposed.

Introduction

The Neutral Protamine Hagedorn (NPH) formulation of insulin is the oldest and most successful example of a sustained release protein pharmaceutical product.[1] NPH[2] consists of insulin cocrystallized with a defined amount of the very basic protein protamine. The resulting microcrystalline suspension is administered to a patient parenterally. The crystals dissolve very slowly in the subcutaneous depot site, resulting in a protracted release of free insulin. The pharmacological properties of NPH have been thoroughly studied.[3]

The long history of the NPH formulation has led to careful examination of the products that form during long-term storage of this pharmaceutical preparation. Brange and co-workers[4−6] have examined these products in detail and determined that they fall into two general classes: modification of side chain moieties of insulin, and polymerization reactions that form both covalently cross-linked insulin dimers (CID) and covalently cross-linked insulin−protamine products (CIPP). The nature of the polymerization reactions that cause the insulin dimer products could not be directly determined by these studies. Brange et al.[4−6] speculate that the polymers were produced by the attack of an N-terminal amino group on a side chain amide group, resulting in the loss of ammonia and the formation of an isopeptide bond. This cross-linking reaction was referred to as either aminolysis or transamidation. It was further speculated that any of the six amide-containing residues of insulin could participate in these reactions leading to the observed chromatographic multiplicity of insulin dimer peaks. Formation of insulin−protamine polymer products was assumed to proceed by the same mechanism, i.e., transamidation between the N-terminus of protamine and any of the amide groups in insulin. The protamine used in pharmaceutical preparations of NPH does not have any amide moeities,[7] so there can be no reactions of this type between protamine and the N-termini of mature insulin.

Anderson and co-workers[8−10] have suggested a different reaction mechanism for the formation of covalent insulin dimers. Their mechanism requires the formation of a succinyl anhydride by the loss of ammonia from the C-terminal asparagine residue on the A-chain of insulin. Succinyl anhydride can then react with water to form $desamido_{A21}$-insulin. Alternatively, succinyl anhydride can react with a free amino group on the N-terminus of insulin's A or B chain to form a covalently linked dimer. This reaction can result in either a peptide or isopeptide bond linking the two chains together. Their work does not directly consider the formation of insulin−protamine products; however, it would be reasonable to assume that a highly reactive succinyl anhydride should cause a similar transacylation reaction with the free N-terminus of protamine.

Conventional reversed-phase HPLC methods result in many CID peaks and a rather ambiguous set of CIPP peaks. A size exclusion method has been recently developed to separate insulin from any covalent cross-linked products, in a solution formed by dissolving NPH insulin crystals in an acidic solution.[11] This method results in three resolved peaks: (1) monomeric insulin; (2) containing all CID species; and (3) containing all CIPP species. In this work, we have used this method to purify relatively large amounts of CIPP. The isolated material was characterized using a combination of mass spectrometry and standard protein chemistry techniques. Our results show that the CIPP peak consists of a mixture of many different insulin−protamine covalent dimers. We show that CIPP dimers are not linked by either a peptide or isopeptide bond. Instead, we propose that a condensation reaction occurs, involving any arginine group in protamine and the histidine groups on the B chain at position B5 or B10. This proposed reaction results in the loss of 5 Da, compared to the sum of the starting materials.

Experimental Section

Chemicals—NPH and NPL[12−14] (a similar preparation to NPH that uses the [Lys^{B28},Pro^{B29}] analogue of insulin) suspensions were obtained in house from Eli Lilly and Company (Indianapolis, IN) supplies. Chum salmon (*Oncorhynchus keta*) protamine was also obtained in house from Eli Lilly and Company (Indianapolis, IN). All chromatographic solvents were HPLC grade, except the water, which was obtained from a Milli-Q Plus water purification system (Millipore, Bedford, MA). Burdick & Jackson (Muskegon, MI) high purity grade water and acetonitrile were used for mass spectrometric sample preparation. The trifluoroacetic acid used was Sequanal grade (Pierce, Rockford, IL). *trans*-α-cyano-4-hydroxycinnamic acid[15] (Acros, Pittsburgh, PA) was dissolved as an ammonium salt, recrystallized with dilute hydrochloric acid and repeatedly washed with water prior to use as a MALDI matrix. Porcine trypsin was obtained from Promega (Madison, WI), and

10.1021/js9802603 CCC: $18.00
Published on Web 01/20/1999

endo-Glu-C was obtained from Sigma (St. Louis, MO). Ammonium bicarbonate (Fisher Scientific, Pittsburgh, PA) and dithiothreitol (Aldrich Chemical Co., Milwaukee, WI) were used in digesting the CIPP fractions.

Sample Preparation and Storage—One vial of NPH suspension contains the following ingredients: biosynthetic human insulin (3.5 mg/mL); protamine free base (0.27 mg/mL); dibasic sodium phosphate (3.78 mg/mL); glycerol (16 mg/mL); phenol (0.65 mg/mL); *m*-cresol (1.60 mg/mL); zinc oxide (to yield 0.025 mg/mL Zn^{2+}); water for injection. One vial of NPL suspension contains the following ingredients: biosynthetic [Lys^{B28},Pro^{B29}] human insulin analogue (3.5 mg/mL); protamine free base (0.30 mg/mL); dibasic sodium phosphate (3.78 mg/mL); glycerol (16 mg/mL); phenol (0.72 mg/mL); *m*-cresol (1.76 mg/mL); zinc oxide (as needed to yield 0.025/ml mg Zn^{2+}); water for injection.

CID and CIPP molecular species were generated in these vials of suspended crystals by heat stressing the sealed containers in normal atmospheric air for 3−6 months at 30−37 °C. These conditions normally promote mild oxidation of the tested protein, such as the formation of methionine sulfoxide, if methionine residues are present in the sequence.

Size Exclusion Chromatography—The method used has been previously described.[11] The chromatography system was composed of an AS-100T autosampler (BIO-RAD, Mountain View, CA), a Protein-Pak 125, 10 μm, 7.8 × 300 mm size exclusion column, a ConstaMetric 3500 pump (LDC Analytical, Riviera Beach, FL), and a variable wavelength UV detector (Applied Biosystems, Foster City, CA). The mobile phase was 65:20:15 5.74 mM l-arginine:acetonitrile:glacial acetic acid (v/v/v). The volume flow rate was 0.5 mL/min, the injection volume was 100 μL, and the column temperature was room ambient. The total run time for the method was approximately 40 min, and all peaks were collected manually. To improve CIPP recovery from dried fractions, the arginine was left out of the mobile phase for some sample collections. The absence of arginine from the mobile phase did not affect the method's ability to resolve the CIPP or CID peaks from monomeric insulin.

Enzymatic Digestion—Purified CIPP fractions were digested with trypsin by first vacuum evaporating 10 μL of a fraction in a 0.5 mL polypropylene Eppendorf tube, using a SpeedVac drying apparatus (Savant Instruments, Holbrook, NY), with no heating applied during drying. The resulting deposit was dissolved in 20 μL of 50 mM ammonium bicarbonate (pH = 8.0), and 1 μL of 0.1 g/L trypsin was added. The tube was incubated for 1 h at 37 °C. If the sample was to be reduced, sufficient dithiothreitol was added to bring its concentration to 10 mM and incubated for 20 min at 20 °C. For endo-Glu-C digestion, the same procedure was followed, except that 1 μL of 0.1 g/L endo-Glu-C was substituted for trypsin. All other relevant factors remained the same. Pharmaceutical grade biosynthetic human insulin was used as the control in all of the studies mentioned in this paper, with parallel digestions and analyses performed. The results of these controls were not included explicitly in the Results section, because they did not demonstrate any unexpected results.

Mass Spectrometry—ESI mass spectrometry was performed using an API-III triple quadrupole (PE-Sciex, Foster City, CA) equipped with a nanospray ion source. Data analysis of the ESI spectra was performed using *BioMultiView* (PE-Sciex, Foster City, CA), version 1.2. The MS/MS experiment described in the Results section was performed with *m*/*z* steps of 0.24 and 0.14 on the first and third quadrupoles, respectively. The collision gas used was argon.

MALDI mass spectrometry was performed using a Voyager linear time-of-flight mass spectrometer (PerSeptive Biosystems, Framingham, MA). The matrix material used was *trans*-α-cyano-4-hydroxycinnamic acid. Typical sample preparation[16] consisted of first preparing a stock solution of the matrix material—a saturated solution of the matrix in 2:1:0.001 water:acetonitrile: trifluroacetic acid (v/v/v), prepared at room temperature. This solution was mixed with the sample at a ratio of 10 parts matrix solution to 1 part sample solution (v/v), and a 1 μL aliquot of the mixture was dried on the sample stage of the mass spectrometer. Data analysis of the MALDI spectra was performed using *m*/*z* (ProteoMetrics, New York, NY), version 8.6. Molecular mass calculations were performed using *PAWS* (ProteoMetrics, New York, NY), version 8.3. All masses shown as labels in figures or in tables below are the true molecular mass for the peptide, calculated from the experimental *m*/*z* value by the following formula: $m = z \times (m/z - 1.0079)$. All peptide masses calculated correspond to the isotopically averaged, chemical mass of the peptide.

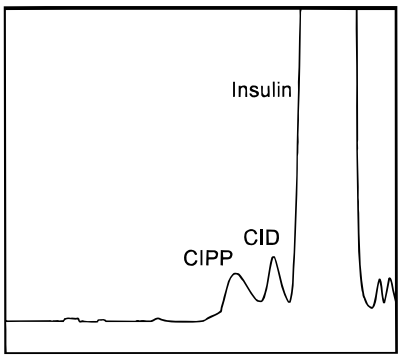

Figure 1—A typical size exclusion chromatogram of stressed NPH insulin, using the method described in the text. Free protamine was not recorded in this chromatogram because at the detector wavelength used (276 nm), protamine is transparent.

Table 1—The Molecular Masses of Chum Salmon Protamine

protamine variant	measured mass[a] (Da)	calculated mass[b] (Da)
1	4237	4236
2	4320	4319
3	4250	4250
4	4064	4064
5	4163	–
6	4418	–

[a] The measured masses were obtained by MALDI. [b] The calculated masses were obtained using the sequences and numbering system found in Hoffman,[7] except variants 5 and 6, which are reported here for the first time.

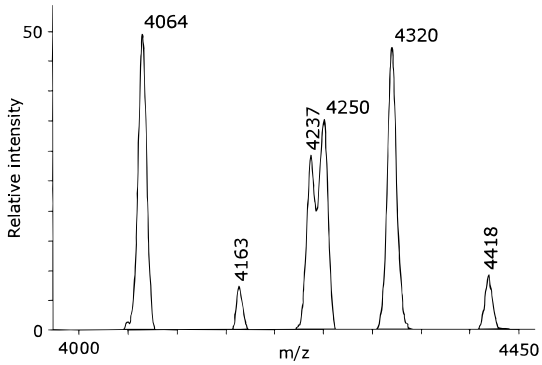

Figure 2—MALDI spectrum of protamine. See Table 1 for a comparison with known protamine sequences. The mass accuracy for the labeled peaks was ±1 Da.

Results

Figure 1 is a representative size exclusion chromatogram, demonstrating the resolution of the CID and CIPP species from insulin. Protamine, which is also present in the preparation, elutes just to the left of the CIPP peak. The detector wavelength used (276 nm) was chosen so that protamine itself is transparent, making the interpretation of the intensity of the CIPP peak unambiguous: the only absorption is the consequence of the presence of insulin[17] attached to one or more protamine molecules.

Even though protamine has considerable microheterogeneity[7] (see Table 1 and Figure 2), the size exclusion method produces only one peak corresponding to a dimer of itself with insulin. The presence of a single peak suggests that this product is the result of the addition of only one protamine molecule per insulin molecule. The mass spec-

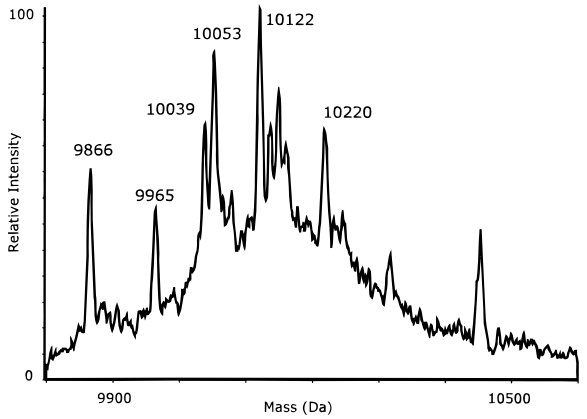

Figure 3—ESI spectrum of intact CIPP molecules. This spectrum was reconstructed from the multiply charged ion intensity pattern. The mass accuracy for the labeled peaks was ±1 Da.

Table 2—A Comparison of the Mass of the CIPP Dimer Observed by Electrospray Mass Spectrometry and the Molecular Mass Calculated by Simply Adding the Mass of Insulin to the Mass of a Protamine Variant (see Table 1)

observed dimer mass (Da)	assigned variant	protamine + insulin (Da)	Δ (Da)
10039	1	10044	–5
10122	2	10127	–5
10053	3	10058	–5
9866	4	9871	–5
9965	5	9971	–6
10220	6	10226	–6

trum in Figure 2 shows that the protamine used for the current study corresponded to known protamine sequences, although two new sequence variants (5 and 6) were discovered.

The reconstructed mass spectrum of the complete mixture of species found in the CIPP peak (see Figure 1) is shown in Figure 3. There are clearly many molecular species present in this mixture. Comparing the intensity distribution and molecular mass differences found in Figure 2 with those found in Figure 3, it was straightforward to assign which variant gave rise to a particular signal. For example, the lowest mass peak in Figure 3 (9866) is 99 Da lighter than the next peak (9965). This result corresponds to the same mass difference observed between the first two peaks in Figure 2. Table 2 shows the results of this correlation analysis. The first column is the observed mass of the CIPP species, column 2 is the assigned protamine variant, column 3 is the result of simply adding the mass of the protamine variant and insulin (5807.6 Da), and column 4 is the difference, $\Delta =$ (column 1) − (column 3). Examination of column 4 shows that the average mass loss in forming a CIPP dimer is ≈5 Da, regardless of which protamine variant is present in the CIPP dimer.

The spectrum shown in Figure 3 is the best electrospray spectrum obtained from CIPP material, but it still represents a very low intensity signal, relative to the baseline noise. MALDI produced much higher relative signal intensities for all CIPP samples, and it was the method of choice for analyzing these materials. In this case, however, the mass accuracy of the electrospray spectrum was sufficiently superior to the MALDI spectrum that it was used for the calculation shown in Table 2. The ionic species represented in Table 2 were those that were observed unambiguously in both the MALDI and electrospray spectra.

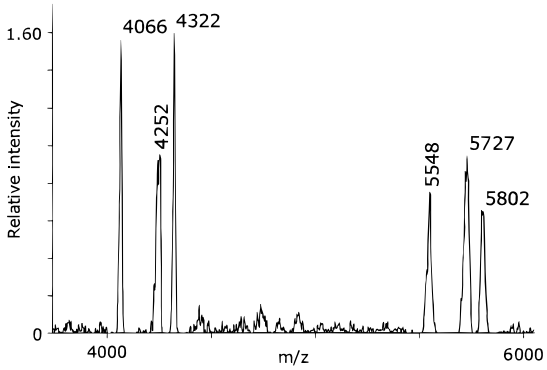

Figure 4—MALDI spectrum of CIPP, after treatment with endo-Glu-C and reduction with DTT. The mass accuracy for the labeled peaks was ±2 Da.

It is worth noting that even the purest CIPP fractions contained a significant amount of free protamine. The CIPP peak shown in Figure 1 elutes in the tail of the free protamine peak, which does not appear in the chromatographic trace because of the long wavelength chosen for the UV detector. All of the sample examined contained at least 30% free protamine, as estimated by MALDI-MS. Free protamine does not produce a useful signal in ESI-MS, so it could not be estimated by this method.

The nature of the cross-linking reaction was further investigated by performing a series of specific cleavages on the CIPP molecules and analyzing the results by mass spectrometry. The first of these cleavage reactions was to treat CIPP with the disulfide bond reducing reagent dithiothreitol and then cleave the resulting insulin A and B chains with the enzyme endo-Glu-C. This enzyme cleaves rapidly at the carboxy side of the peptide bond of glutamic acid residues, and more slowly at aspartic acid residues. Protamine does not contain any acidic residues, so it remains intact. The results of this cleavage are shown in Figure 4. The peaks in the mass range 4000−4400 Da correspond to unmodified protamine. The peaks in the mass range 5500−5900 Da correspond to protamine attached to the proteolytic fragment of insulin B chain, B[1−13]. These peaks also have $\Delta \approx -5$ Da. This result localizes the site of protamine attachment to somewhere in the first thirteen residues of the insulin B chain. Disulfide bond reduction was used to simplify the interpretation of the resulting molecular masses: the conditions used for this digestion reaction can promote disulfide shuffling.

One reasonable hypothesis regarding the attachment of protamine to insulin would be that the N-terminal amino group of protamine is involved in the cross-linking reaction. This hypothesis was tested by adding trypsin to the CIPP fraction, with the intention of cleaving all of the R−X (X ≠ P) bonds in protamine. The known protamine sequences[7] predicted that complete cleavage of all trypsin susceptible bonds would result in the dipeptide "PR" remaining attached to the insulin B chain. Dithiothreitol was added to the mixture after trypsin digestion to confirm that the modification was on the B chain.

Figure 5 shows the results of trypsin digestion followed by disulfide bond reduction. The signal $m/z = 2488$ and 3430 correspond to unmodified insulin B[1−22] and B[1−30], respectively. Table 3 assigns the signals for $m/z > 3430$ to possible tryptic fragments of the protamine sequences, along with the Δ value for each one of these assignments. Protamine produces many partially digested tryptic fragments with the same amino acid composition: the multiplicity per protamine molecule of possible fragments is given in the 4th column of Table 3, averaged over the known protamine sequences. The pattern of masses in the range $m/z = 2488-3327$ correspond to the same sequence

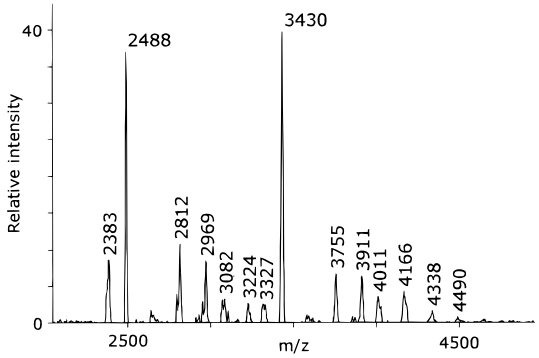

Figure 5—A portion of the MALDI mass spectrum of CIPP, following trypsin digestion and reduction with DTT. The mass accuracy for the labeled peaks was ±1 Da.

Table 3—Assignment of Tryptic Fragments of Protamine That Are Covalently Cross-Linked to the Human Insulin B Chain

measured mass (Da)	B chain + sequence	Δ (Da)	multiplicity[a]
3755	RR	–5	14
3911	RRR	–5	11
4011	PRRR	–5	2
4166	PRRRR; *or* RPRASR	–5	2
		–5	2
4338	RRRRGGR	–5	4

[a] Multiplicity indicates the number of different ways that a tryptic fragment with the same amino acid composition can be generated from the sequence of protamine.

and Δ assignments as in Table 3, except they are cross-linked to the tryptic fragment of insulin, B[1−22]. The signal at $m/z = 2383$ is the A chain of insulin.

The same types of experiments were performed using NPL formulations of the biosynthetic [Lys^{B28},Pro^{B29}] human insulin analogue. Identical results were obtained with the NPL formulation (data not shown).

Using the hypothetical reaction deduced in the section below, an MS/MS experiment was performed on CIPP material that had been subjected to a trypsin digestion, followed by a disulfide bond reduction and an endo-Glu-C digestion. The quadruply charged ion that would correspond to the B[1−13] cross-linked to the dipeptide RR less 5 Da ($m/z = 453.1$) was selected and MS/MS sequencing performed on that ion. The MS/MS data showed that the RR peptide was attached in the interval B[4−5]: the ion signals excluded all but these two residues as possible attachment sites. The interpretation of the signals from this MS/MS experiment was made possible by the deductions made below, rather than aiding in the formulation of these deductions, and therefore the data was not included in this study.

Discussion

The general strategy of using mass spectrometry on mixtures of peptides produced by enzymatic and chemical digests has been used to generate the main results in this study. The heterogeneity of the analytes and their physical properties make this approach the most viable method of gaining an understanding of the chemistry involved. Protamine and the protamine-insulin cross-linked species are very heterogeneous: there are at least 6 distinct protamine sequences and as many as 23 possible side chains that may participate in the proposed cross-linking reaction described below. Therefore, there are approximately 140 distinct molecular species that are being generically referred to as "CIPP". The samples that were analyzed in the course of this research were near the limits of detection for the mass spectrometric methods used, so any additional peak dilution caused by separating the individual components would compromise the quality of the data obtained from those peak fractions. Protamine-containing molecules do not separate well using reversed-phase separations because of the high solubility of protamine. Amino acid analysis was not useful for generating either positive or negative results because of the heterogeneity of the samples, their low concentrations, and the unusually high relative abundance of arginine in protamine-containing molecules, which leads to dynamic range problems in conventional amino acid analysis equipment.

Our results show that covalent CIPP species are present in stressed NPH insulin preparations and that they are very heterogeneous. The grossest level of heterogeneity results from the different sequences of protamine present in the initial preparation. The attachment site of protamine molecules to insulin is in the B chain of insulin. The results of endo-Glu-C digestion show that the protamine is linked to a residue somewhere within the first 13 amino acid residues of the insulin B chain. Tryptic digestion shows that the linkage can be made between B[1−13] and any arginine residue in protamine.

The value $\Delta = -5$ Da rules out the dimer formation reactions discussed by other authors[4−6,8−10] (see the Introduction). Transamidation reactions[4−6] result in the value $\Delta = -17$ Da. Succinyl anhydride-mediated reactions[8−10] result in $\Delta = -18$ Da. Cross-linking reactions resulting from the presence of low concentrations of aldehydes[4] would result in $\Delta \geq +12$ Da ($\Delta = +12$ is for the smallest aldehyde, formaldehyde). Protamine does not contain any cysteine residues, so disulfide cross-linking cannot occur.

The tryptic fragment assignments made in Table 3 rule out any dimer formation reaction involving the N-terminal amino group of protamine. If a free amino group was required to form the cross-link, then all of the sequences should begin with the N-terminal proline of the protamine sequence,[18] i.e., sequences beginning with the residues "PR ...". The observed sequences do not conform to this pattern. Instead they could come from any part of the protamine molecules, with fragments characteristic of both the N- and C-terminal region. Therefore, the protamine's N-terminal amino group cannot be involved in the dimer formation mechanism.

The fact that cross-linking to a single arginine residue is not observed (there is no signal at m/z = B chain + "R" − 5 Da) suggests that the cross-linking reaction involves the side chain of arginine in some way. The size of Δ suggests that the reaction involves the loss of 5 hydrogen atoms. This reaction would therefore not belong to the general class of condensation reactions typically found in protein chemistry. This different mechanism is probably brought about by the fact that this reaction is not a low temperature, solution phase reaction. Instead, this reaction occurs at elevated temperatures in the solid phase, i.e., within protamine-insulin crystals.

Inspection of the amino acid residues in the insulin B chain peptide B[1−13] can rule out a number of the residues for reaction with protamine. The sequence[16] is as follows:

FVNQHLCGSHLVE....

The side chains of phenylalanine, valine, leucine, and glycine residues are chemically inert under the conditions used to form CIPP. Therefore, the side chains of B1, B2, B6, B8, B11, and B12 do not participate in the reaction. The specificity of endo-Glu-C for cleaving at the carboxy side of glutamic acid residues implies that if B13 was modified there would be no cleavage at that site. The cleavage does occur; therefore B13 is not modified and does

not participate in the cross-linking reaction. Reactions known to occur with serine, asparagine, and glutamine residues all involve condensation reactions of their side chain amide groups, resulting in the loss of ammonia or water ($\Delta = -17$ or -18 Da). The results shown in Tables 2 and 3 rule out this type of reaction. Therefore residues B3, B4, and B9 do not participate in the formation of the CIPP observed in this study.

This simple process of elimination leaves the histidine residues, B5 and B10, and the cystine residue, B7-A7, as candidates to form of a cross-link with $\Delta = -5$ between a protamine guanidino group and insulin's B chain in a neutral pH, mildly oxidizing environment. There are no reactions that the authors are aware of (or can imagine) between an arginine guanidino group and a cystine residue that would result in this type of cross-linking under these conditions. Any reaction involving the oxidation of the sulfur atoms leading to a reactive product, such as cystine *S*-dioxide,[19] would result in $\Delta > 0$. A β-elimination reaction[20] involving that cystine could leave a reactive dehydroalanine at B7, but any reaction of that dehydroalanine with a guanidino group would result in $\Delta \leq -32$. These considerations eliminate the cystine residue and point to the involvement of at least one of the histidine residues.

Any dimer-forming reaction that occurs in the solid-state would be either assisted or inhibited by the geometry of insulin and protamine molecules in the NPH crystals. X-ray crystallographic examination of NPH crystals[21] shows that protamine does not occupy a single, well-oriented site in these crystals, due to its repetitive and heterogeneous structure. Electron density maps of these crystals show a region of protamine density at the interface between monomer 1 and the symmetry equivalent of monomer 3. It was suggested that the interactions between insulin and protamine molecules occurred via the guanidino groups of protamine's arginine residues and carboxylic acid containing residues in the insulin molecule. Contrary to this supposition, the actual structure shows that the most stable portions of the protamine electron density occur near the two histidine residues in the B chain, B5 and B10. The histidine residue B10 was also found to be responsible for the coordination of the zinc atoms in the assembled insulin hexamers.

Hydrogen bonding interactions between arginine and histidine side chains probably produce the localization observed in the X-ray crystal structure. Both histidine and arginine contain hydrogen bond donor and acceptor nitrogen atoms, because both contain singly bonded and doubly bonded nitrogens separated by one carbon atom. Therefore, there is the potential of forming two hydrogen bonds between these residues, which would lead to a significant stabilization of conformers that would allow the formation of these bonds in NPH crystals.

The most likely cross-linking reaction involves the imidazole group of histidine and the guanidino group of arginine, based on the combination of the known geometric association of insulin histidine and protamine arginine residues and the process of eliminating all of the other residues in the B[1−13] peptide. The mass lost during the reaction strongly suggests that two bonds are formed: a loss of four hydrogens leads to $\Delta = -4$, which is very close to the measured experimental value. However, the mechanism for this type of bond formation could not be probed directly in this system. Subsequently, the location of the cross-linking bridge was confirmed by LC/MS/MS (see Results) to be within the region B[4−5], supporting this hypothesis.

A number of reactions were considered for forming this cross-link, given the experimental constraints. Reactions involving the formation of a bridged tetrazine ring, and a

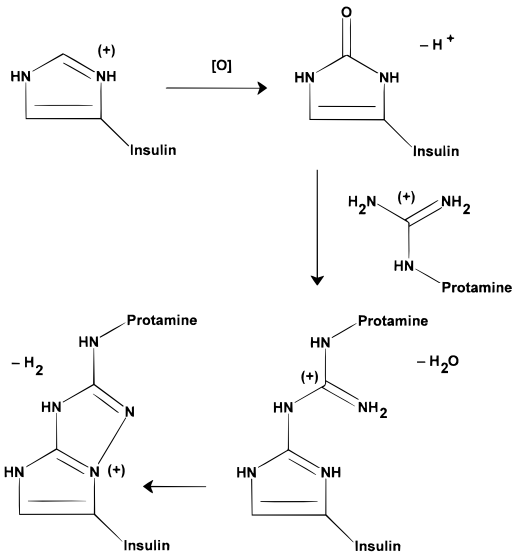

Figure 6—The proposed mechanism for the formation of the protamine-insulin cross-link, via an oxidation–reduction to form an imidazo[2,3-*b*]-1,2,4-triazolinium fused ring.[28]

number of other possible bridged rings were rejected because they would all result in violations of Bredt's rule.[22] One reasonable pathway to the formation of an appropriate cross-link is to postulate an initial oxidation of the histidine imidazole, as shown in Figure 6. This reaction, which forms imidazolone, is known to occur in histidine-containing peptides under oxidizing conditions.[23−25] This reaction has also been identified as a necessary step in the cross-linking of crystallins under oxidizing conditions.[26] The resulting imidazolone ring can be modified in several different ways, resulting in 2(3*H*)-, 2(5*H*)-, or 4(5*H*)-imidazolone.[27] Each of these exists as several tautomers,[26] by shifting a hydrogen to or from the keto group to form the tautomeric alcohol. The following discussion will center on the 2-imidazolone form because it has been observed in peptides.[23−25] Once the imidazolone derivative has been formed by oxidation, it is susceptible to a nucleophilic attack by one of the nitrogens in a protamine arginine side chain guanidino group. The final step in this tentative cross-linking mechanism is a further oxidation, as shown at the bottom of Figure 6.

This final step is necessary to explain the observed $\Delta = -5$ Da. The net result of the proposed reaction is the addition of oxygen (+16 Da), the loss of water (−18 Da), and the loss of H_2 (−2 Da), giving an overall $\Delta = -4$ Da. However, because the final product is positively charged, the additional proton that is normally assumed when making molecular mass calculations from experimentally determined *m/z* values is not necessary, resulting in the apparent loss of an additional proton, i.e., $\Delta = -5$ Da.

Conclusions

Whatever the exact mechanism, the results given in this paper clearly demonstrate that in the NPH formulation of insulin, the CIPP species formed are caused by a novel cross-linking reaction that occurs most rapidly under heat-stressed, mildly oxidizing conditions. Our observations do not agree with previous propositions as to the mechanism of CIPP formation, and they rule out most common condensation reactions that are known to occur between amino acid side chains. The site of the cross-linkage is proposed to be between any arginine side chain in protamine and the B[1−13] residues of insulin. We propose the reaction pathway indicated by Figure 6 as being consistent

with the experimental evidence. This mechanism may be the cause of dimer formation in other proteins, when they are stressed under similar conditions. Further work is ongoing to test this hypothesis.

References and Notes

1. Hagedorn, H. C.; Jensen, B. N.; Karup, N. B.; Wodstrup, I. Protamine Insulinate. *J. Am. Med. Assoc.* **1936**, *106*, 177−180.
2. The following abbreviations are used: NPH, neutral protamine Hagedorn; NPL, neutral protein LisPro; CID, covalent insulin dimer; CIPP, covalent insulin−protamine product; MALDI, matrix-assisted laser desorption/ionization; ESI, electrospray ionization; HPLC, high performance liquid chromatography. All molecular masses are reported in Daltons (Da). Mass-to-charge ratios (*m*/*z*) are dimensionless.
3. Felig, P. Landmark perspective: Protamine insulin. Hagedorn's pioneering contribution to drug delivery in the management of diabetes. *J. Am. Med. Assoc.* **1984**, *251*, 393−396.
4. Brange, J.; Havelund, S.; Hougaard, P. Chemical Stability of Insulin. 2. Formation of Higher Molecular Weight Transformation Products During Storage of Pharmaceutical Preparations. *Pharma. Res.* **1992**, *9*, 727−734.
5. Brange, J. Chemical stability of insulin. 4. Mechanisms and kinetics of chemical transformation in pharmaceutical formulation. *Acta Pharm. Nord.* **1992**, *4*, 209−222.
6. Brange, J.; Hallund, O.; Sørensen, E. Chemical stability of insulin. 5. Isolation, characterization and identification of insulin transformation products. *Acta Pharm. Nord.* **1992**, *4*, 223−232.
7. Hoffman, J. A.; Chance, R. E.; Johnson, M. G. Purification and Analysis of the Major Components of Chum Salmon Protamine Contained in Insulin Formulations Using High Performance Liquid Chromatography. *Protein Expression Purif.* **1990**, *1*, 127−133.
8. Darrington, R. T.; Anderson, B. D. Evidence for a Common Intermediate in Insulin Deamidation and Covalent Dimer Formation: Effects of pH and Analine Trapping in Dilute Acidic Solutions. *J. Pharm. Sci.* **1995**, *84*, 275−282.
9. Darrington, R. T.; Anderson, B. D. Effects of Insulin Concentration and Self-Association on the Partitioning of Its A-21 Cyclic Anhydride Intermediate to Desamido Insulin and Covalent Dimer. *Pharm. Res.* **1995**, *12*, 1077−1084.
10. Strickley, R. B.; Anderson, B. D. Solid-State Stability of Human Insulin II. Effect of Water on Reactive Intermediate Partitioning in Lyophiles from pH 2−5 Solutions: Stabilization against Covalent Dimer Formation. *J. Pharm. Sci.* **1997**, *86*, 645−653.
11. "Insulin Preparations, Injectable." PA/PH/Exp. 6I/T (96) 4, ANP. Test: Impurities with Molecular masses Greater Than That of Insulin. *Pharmeuropa* **1996**, *8(3)*.
12. DiMarchi, R. D.; Mayer, J. D.; Fan, L.; Brems, D. N.; Frank, B. H.; Green, L. K.; Hoffman, J. A.; Howey, D. C.; Long, H. B.; Shaw, W. N.; Shields, J. E.; Slieker, L. E.; Su, K. S. E.; Sundel, K. L.; Chance, R. E. Synthesis of a fast-acting insulin based on structural homology with insulin-like growth factor I. In *Peptides: Chemistry and Biology*; Smith, J. A., Rivier, J. E., Eds.; ESCOM: Leiden, 1992; pp 26−28.
13. Long, H. B.; Baker, J. C.; Belagaje, R. M.; DiMarchi, R. D.; Frank, B. H.; Green, L. K.; Hoffman, J. A.; Muth, W. L.; Pekar, A. H.; Reams, S. G.; Show, W. N.; Shields, J. E.; Slieker, L. J.; Su, K. S. E.; Sundel, K. L.; Chance, R. E. A−C−B human proinsulin: a novel insulin agonist and intermediate in the synthesis of human insulin. In *Peptides: Chemistry and Biology*; Smith, J. A.; Rivier, J. E., Eds.; ESCOM: Leiden, 1992; pp 88−90.
14. DeFelippis, M. R.; Bakaysa, D. L.; Bell, M. A.; Heady, Li, S.; Youngman, K. M.; Radziuk, J.; Frank, B. J. Preparation and Characterization of a Cocrystalline Suspension of [Lys^{B28},-Pro^{B29}]-Human Insulin Analogue. *J. Pharm. Sci.* **1998**, *87*, 170−176.
15. Beavis, R. C.; Chaudhary T.; Chait, B. T. α-Cyano-4-hydroxycinnamic acid as a matrix for matrix-assisted laser desorption mass spectrometry**.** *Org. Mass Spectrom.* **1992**, *27*, 156.
16. Beavis, R. C.; Chait, B. T. Matrix-assisted laser desorption ionization mass-spectrometry of proteins**.** *Methods in Enzymology*; Karger, B. L.; Hancock, W. S., Eds.; 1996; Vol. 270A, pp 519−551.
17. Sures, I.; Goeddel, D. V.; Gray, A.; Ullrich, A. Nucleotide sequence of human preproinsulin complementary DNA**.** *Science* **1980**, *208*, 57−59.
18. All 14 of the *Oncorhynchus sp.* protamine sequences currently available in GenBank (http://www.ncbi.nlm.nih.gov/Web/Genbank/index.html) begin with the sequence "PR...".
19. *The Merck Index*, 11th ed.; Budavari, S., Ed.; Merck & Co.: Rahway, NJ, **1989**; p 437.
20. Kosen, P. A. Disulfide bonds in proteins. In *Stability of Protein Pharmaceuticals, Part A, Chemical and Physical Pathways of Protein Degradation: Pharmaceutical Biotechnology;* Ahern, T. J., Manning, M. C., Eds.; Plenum Publishing: New York, 1992; Vol. 2, pp 31−67.
21. Balschmidt, P.; Benned Hansen, F.; Dodson, E. J.; Dodson, G. G.; Korber, F. Structure of Porcine Insulin Cocrystallized with Clupeine Z. *Acta Crystallogr.* **1991**, *B47*, 975−986.
22. Wiseman, J. R.; Pletcher, W. A. Bredt's rule. III. Synthesis and chemistry of bicyclo[3.3.1]non-1-ene**.** *J. Am. Chem. Soc.* **1970**, *92*, 956−962.
23. Uchida, K.; Kawakishi, S. Selective oxidation of imidazole ring in histidine residues by the ascorbic acid-copper ion system. *Jpn. Biochem. Biophys. Res. Commun.* **1986**, *138*, 659−65.
24. Lewisch, S. A.; Levine, R. L. Determination of 2-oxohistidine by amino acid analysis. *Anal. Biochem.* **1995**, *231*, 440−446.
25. Uchida, K.; Kawakishi, S. 2-Oxohistidine as a novel biological marker for oxidatively modified proteins. *FEBS Lett.* **1993**, *332*, 208−210.
26. Guptasarma, P.; Balasubramanian, D.;Matsugo, S.; Saito, I. Hydroxyl radical mediated damage to proteins, with special reference to the crystallins. *Biochemistry* **1992**, *31*, 4296−4303.
27. Hofman, K. *Imidazole and Its Derivatives: Part I*; Interscience Publishers: New York, 1953; pp 60−63.
28. Preston, P. N. *Condensed Imidazoles: 5−5 Ring Systems*; Interscience Publishers: New York, 1986; pp 330−345.

Acknowledgments

The authors are indebted to Al Pekar for his preparation of one of the samples used in this paper and to Christine O'Keefe for Edman sequencing work. They also thank Drs. Steve Baertschi, John Towns, and Ralph Riggin for their critical reviews and discussion of this manuscript.

JS9802603

Characterization of Racemic Species of Chiral Drugs Using Thermal Analysis, Thermodynamic Calculation, and Structural Studies

Z. JANE LI,[†,‡] MARK T. ZELL,[§] ERIC J. MUNSON,[§] AND DAVID J. W. GRANT*[,†]

Contribution from *Department of Pharmaceutics, College of Pharmacy, University of Minnesota, Weaver-Densford Hall, 308 Harvard Street SE, Minneapolis, Minnesota 55455-0343, and the Department of Chemistry, University of Minnesota, Smith Hall, Minneapolis, Minnesota 55455.*

Received May 12, 1998. Final revised manuscript received October 12, 1998.
Accepted for publication December 7, 1998.

Abstract □ The identification of the racemic species, as a racemic compound, a racemic conglomerate, or a racemic solid solution (pseudoracemate), is crucial for rationalizing the potential for resolution of racemates by crystallization. The melting points and enthalpies of fusion of a number of chiral drugs and their salts were measured by differential scanning calorimetry. Based on a thermodynamic cycle involving the solid and liquid phases of the enantiomers and racemic species, the enthalpy, entropy and Gibbs free energy of the racemic species were derived from the thermal data. The Gibbs free energy of formation, $\Delta G^{\circ}_{T_f}$, is always negative for a racemic compound, if it can exist, and the contribution from the entropy of mixing in the liquid state to the free energy of formation is the driving force for the process. For a racemic conglomerate, the entropy of mixing in the liquid state is close to the ideal value of R ln 2 (1.38 cal·mol^{-1}·K^{-1}). Pseudoracemates behave differently from the other two types of racemic species. When the melting points of the racemic species is about 30 K below that of the homochiral species, $\Delta G^{\circ}_{T_f}$ is approximately zero, indicating that the racemic compound and racemic conglomerate possess similar relative stabilities. The powder X-ray diffraction patterns and ^{13}C solid-state nuclear magnetic resonance spectra are valuable for revealing structural differences between a racemic compound and a racemic conglomerate. Thermodynamic prediction, thermal analysis, and structural study are in excellent agreement for identifying the nature of the racemic species.

Introduction

Chiral drugs comprise more than one-half of drugs approved worldwide.[1,2] In recent years, enantioselective production of chiral drugs has continued to grow at a rapid pace. Although catalytic asymmetric syntheses and biocatalytic resolutions have advanced steadily, resolution of racemates by crystallization (enantioselective crystallization) remains an important and the most economic process for the industrial-scale production and purification of single enantiomers.

A racemic species (also termed a racemate) can exist as a racemic compound, a racemic conglomerate, or a pseudoracemate (racemic solid solution), through different arrangements of equal numbers of moles of the opposite enantiomers in the crystalline state.[3] Characterization of the racemic species is a prerequisite for the design of industrial-scale resolution processes. Depending on the nature of the racemic species, different resolution techniques may be employed for the separation of the opposite enantiomers. Formation of a racemic conglomerate, consisting of homochiral crystals (same chirality),[4] facilitates resolution by crystallization. The outcome of a crystallization process, homochiral or heterochiral (differing chiralities), is governed by the nature of the solid−liquid-phase equilibrium that occurs in mixtures of enantiomers.[5] The formation of these different types of crystals is a result of difference in the structure and energetics between the homochiral and heterochiral crystals, which is the origin of chiral discrimination in the solid state.[6] For this reason, understanding the thermodynamic basis of the stereoselective interactions in these systems is essential for predicting and optimizing the course of resolution.

Construction of the binary phase diagram from simple measurements of the melting temperatures of the racemic species and of the corresponding enantiomers has traditionally been used for identifying the nature of the racemic species, usually a racemic compound (Figure 1a or 1b), or a racemic conglomerate (Figure 1c), or rarely a pseudoracemate (Figure 1d).[7,8] However, examination of melting temperatures alone may not be adequate in some cases, in particular when the racemic species exists either as a metastable racemic compound or as a metastable racemic conglomerate as in Figure 1c. The definitive identification of the structural differences between a racemic compound and the enantiomers usually comes from powder X-ray diffraction patterns, or from spectroscopic techniques, such as infrared and solid-state nuclear magnetic resonance (SSNMR) spectroscopy.

Questions arise as to the thermodynamic basis for the formation of different racemic species and as to the ability of the thermodynamic properties of chiral systems to serve as a reliable tool for the identification of racemic species. In view of the significant differences in the melting behavior of these racemic species (Figure 1), their thermodynamic properties must differ. These differences may be used to characterize the racemic species and may furthermore reveal the driving force for the formation of a racemic compound versus that of a racemic conglomerate or a pseudoracemate.

Although some studies on a number of chiral organic compounds have been carried out,[3,5] no investigation of this type has been reported for chiral pharmaceuticals. Therefore, the specific aims of this work are (1) to characterize various racemic species of chiral drugs using thermodynamic properties derived from calorimetric measurements, (2) to explore the thermodynamic factors determining the formation of homochiral and racemic crystals, (3) to identify the solid racemic phase by powder X-ray diffraction and by SSNMR, and to correlate the structural differences with the calculated thermodynamic quantities.

* Corresponding author. Tel (612) 624-3956. Fax (612) 625-0609. E-mail: grant001@maroon.tc.umn.edu.
† Department of Pharmaceutics.
‡ Present address: Process R & D, Pfizer Central Research, Groton, CT 06340.
§ Department of Chemistry.

10.1021/js980205u CCC: $18.00 Published on Web 02/09/1999

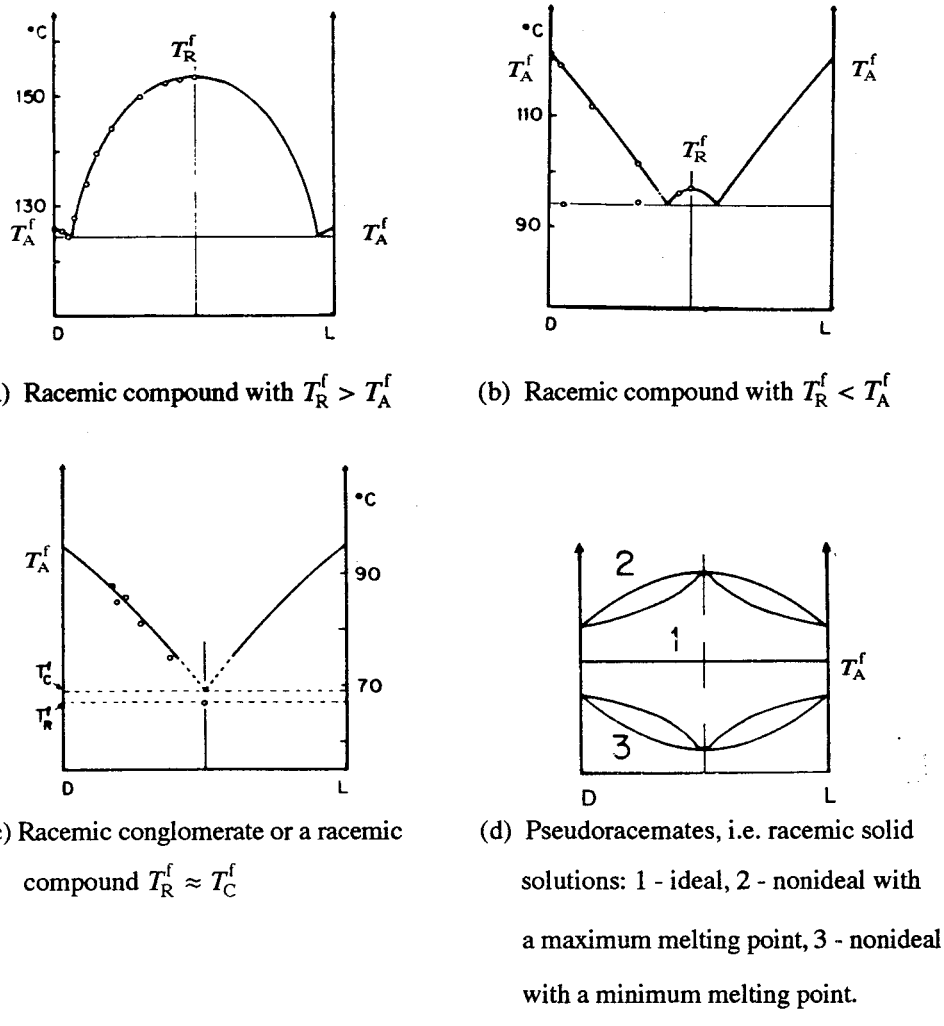

Figure 1—Typical phase diagrams of various racemic species[3] (reprinted with the permission of the copyright owner, Krieger Publishing Co.)

Twenty five chiral compounds of pharmaceutical interest were selected (see Table 1). Several compounds, specifically ephedrine and its derivatives and their salts, were prepared in this work, while others were collected from previously reported thermal analytical data of chiral drugs. These chiral compounds have various molecular structures and therapeutic applications, including several β-adrenergic antagonists, mucoregulating agents, and diagnostic agents. The overall goal of this work is to reveal unique thermodynamic properties of chiral solids of pharmaceutical interest.

Thermodynamics of Racemic Species—*Various Racemic Species.* Figure 1 shows three types of racemic species, sometimes termed racemates. However, because the term racemate has also been applied to racemic compounds only, use of the word racemate is avoided in this paper. A racemic conglomerate is an equimolar physical mixture of the individual homochiral crystals of the two opposite enantiomers. A racemic compound consists of crystals in which the two enantiomeric molecules of opposite chirality are paired up in the unit cell of the crystal lattice. A pseudoracemate consists of the two enantiomeric molecules of opposite chirality arranged more or less randomly in the same crystal lattice. All these three types are collectively termed racemic species in this work.

These structural differences in the solid state give rise to a difference in the energetics of the solid, which can be described by various thermodynamic properties that are either experimentally determined or derived quantities. To calculate the differences in the thermodynamic quantities between a racemic compound and its corresponding racemic conglomerate, Jacques et al.[3] developed a thermodynamic approach, using thermodynamic cycles. In the present work, the thermodynamic cycles of Jacques et al.[3] are modified and applied to the 25 racemic species studied. The thermodynamic cycle involving the two enantiomers, D and L, and their corresponding racemic species, R, is shown in Figure 2 for the enthalpy changes and in Figure 3 for the corresponding entropy changes.

Racemic Conglomerate—In a racemic conglomerate, if the enantiomers are perfectly immisible in the solid state, $\Delta H_s^m = 0$. Because of the structural similarity of the enantiomeric molecules, their liquid mixture is close to ideal, so that $\Delta H_l^m \approx 0$. The entropy of mixing of the enantiomers in the liquid state can be derived as described by Jacques et al.[3] and may be stated as follows:

$$\Delta S_l^m = \frac{\Delta H_R^f}{T_R^f} - \frac{\Delta H_A^f}{T_A^f} - \frac{\Delta H_R^f - \Delta H_A^f}{T_R^f - T_A^f} \ln\frac{T_R^f}{T_A^f} \qquad (1)$$

Equation 1 allows us to calculate the entropy of mixing of the liquid enantiomers from the enthalpies of fusion and

Table 1—List of the Chiral Compounds Used in This Study

compound[a]	acronym[a]	source[b]	thermal data	ref
(–)-norephedrine	(–)-NE	Sigma	this work	
(±)-norephedrine	(±)-NE	this work	this work	
(–)-norephedrine·HCl	(–)-NE·Cl	Sigma	this work	
(±)-norephedrine·HCl	(±)-NE·Cl	Sigma	this work	
(+)-norephedrine·HS	(+)-NE·S	this work	this work	
(±)-norephedrine·HS	(±)-NE·S	this work	this work	
(+)-pseudoephedrine	(+)-PE	Sigma	this work	
(±)-pseudoephedrine	(±)-PE	this work	this work	
(+)-pseudoephedrine·HCl	(+)-PE·Cl	Sigma	this work	
(±)-pseudoephedrine·HCl	(±)-PE·Cl	Sigma	this work	
(+)-pseudoephedrine·HS	(+)-PE·S		this work	10
(±)-pseudoephedrine·HS	(±)-PE·S		this work	10
(–)-ephedrine	(–)-E	Sigma	this work	
(±)-ephedrine	(±)-E	Sigma	this work	
(–)-ephedrine·HCl	(–)-E·Cl	Sigma	this work	
(±)-ephedrine·HCl	(±)-E·Cl	Sigma	this work	
(–)-ephedrine·napsylate	(–)-E·NS	this work	this work	11
(±)-ephedrine·napsylate	(±)-E·NS	this work	this work	11
(–)-methylephedrine	(–)-ME	Sigma	this work	
(±)-methylephedrine	(±)-ME	this work	this work	
(–)-ibuprofen	(–)-IB	Ethyl	this work	
(±)-ibuprofen	(±)-IB	Ethyl	this work	
(–)-mandelic acid	(–)-MA	Sigma	this work	
(±)-mandelic acid	(±)-MA	Sigma	this work	
(–)-propranolol·HCl	(–)-PN·Cl	Sigma	this work	
(±)-propranolol·HCl	(±)-PN·Cl	Sigma	this work	
(–)-propranolol	(–)-PN		this work	12
(±)-propranolol	(±)-PN		this work	12
(+)-atenolol	(+)-AN	Aldrich	this work	
(±)-atenolol	(±)-AN	Sigma	this work	
(+)-alprenolol	(+)-APN			12
(±)-alprenolol	(±)-APN			12
(–)-*trans*-sobrerol	(–)-t-SB			13
(±)-*trans*-sobrerol	(±)-t-SB			13
(–)-*cis*-sobrerol	(–)-c-SB			13
(±)-*cis*-sobrerol	(±)-c-SB			13
(–)-bevantolol	(–)-BT			8
(±)-bevantolol	(±)-BT			8
(–)-bevantolol·HCl	(–)-BT·Cl			8
(±)-bevantolol·HCl	(±)-BT·Cl			8
(–)-pindolol	(–)-PD			8
(±)-pindolol	(±)-PD			8
(–)-iopanoic acid	(–)-IA			14
(±)-iopanoic acid	(±)-IA			14
(–)-dropropizine	(–)-DPP			15
(±)-dropropizine	(±)-DPP			15
(–)-sulpiride	(–)-SP			16
(±)-sulpiride	(±)-SP			16
(–)-dexrazoxane	(–)-DZ			17
(±)-dexrazoxane	(±)-DZ			17
(–)-4-hydroxy-2-pyrrolidone	(–)-HPL			18
(±)-4-hydroxy-2-pyrrolidone	(±)-HPL			18

[a] Cl and S represent the chloride and salicylate anions, respectively. [b] Sigma Chemical Co. (St. Louis, MO); Ethyl Corporation (Baton Rouge, LA); Aldrich Chemical Co. (Milwaukee, WI).

melting points, as measured by differential scanning calorimetry (DSC). If the enantiomeric molecules are randomly mixed in the liquid state, the entropy of mixing is ideal and its value is given by:

$$\Delta S_l^{\mathrm{m}} = R \ln 2 = 1.38 \text{ cal·mol}^{-1}\text{·K}^{-1} \qquad (2)$$

For a number of racemic conglomerates, the average entropy of mixing of the enantiomers in the liquid state was found to be 1.33 ± 0.14 cal·mol^{-1}·K^{-1}, indicating that mixing of the enantiomers is nearly ideal in the liquid state.[3] The small deviation from the ideal value may be attributed to the possibility that the corresponding enthalpy of mixing, ΔH_l^{m}, may not be exactly zero.

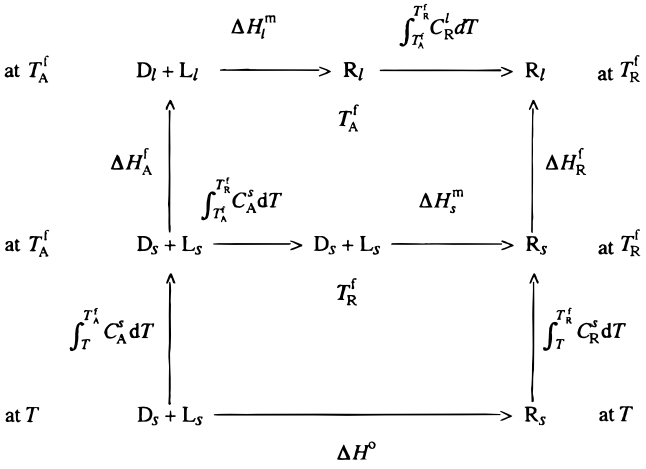

Figure 2—The enthalpy changes during various stages of a thermodynamic cycle involving the enantiomers, D and L, and the racemic species, R, where ΔH^{f}, C^{l}, C^{s} and T^{f} represent the enthalpy of fusion, heat capacity of the liquid and solid, and melting temperature, respectively. The subscript A denotes the enantiomer and R the racemic species; and the subscripts *l* and *s* denote the liquid and solid state, respectively. ΔH^{m} and ΔH° represent the enthalpy of mixing and the enthalpy of formation, respectively.

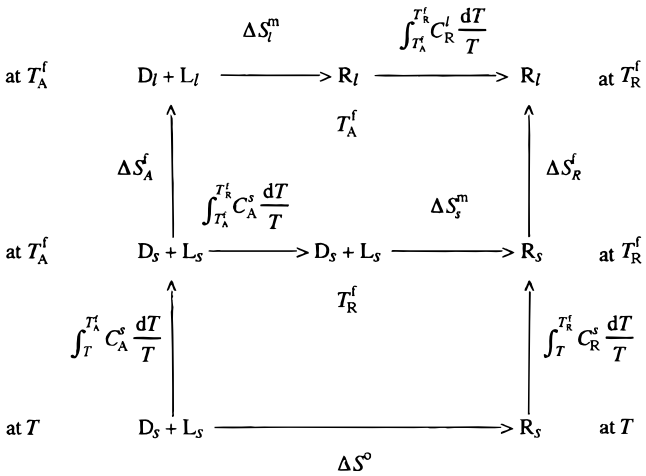

Figure 3—The entropy changes during various stages of a thermodynamic cycle involving the enantiomers, D and L, and the racemic species, R, where ΔS^{f}, C^{l}, C^{s}, and T^{f} represent the entropy of fusion, heat capacity of the liquid and solid, and melting temperature, respectively. The subscript A denotes the enantiomer and R the racemic species; the subscript *l* and *s* denote the liquid and solid state, respectively. ΔS^{m} and ΔS° represent the entropy of mixing and the entropy of formation, respectively.

Racemic Compound—The stability of a racemic compound can be defined by the Gibbs free energy change, $\Delta G°$, of solid-state transformation, corresponding to the "reaction" between the crystals of the two enantiomers, D and L, in the racemic conglomerate to yield crystals of the racemic compound, R:

$$\mathrm{D_s} + \mathrm{L_s} \rightarrow \mathrm{R_s}$$

where the left-hand side refers to the racemic conglomerate, which consists of an equimolar mixture of crystals of D and L, and the subscript, s, refers to the solid, i.e., the crystalline state. For a stable racemic compound, *this free energy change must be negative*. For this purpose, $\Delta G°$ is the Gibbs free energy of formation of the racemic compound from the two opposite enantiomers. $\Delta G°$ may be also expressed as a function of the corresponding enthalpy of formation, $\Delta H°$, and entropy of formation, $\Delta S°$:

$$\Delta G° = \Delta H° - T\Delta S° \qquad (3)$$

The thermodynamic quantities in eq 3 are not directly measurable, but can be determined from calorimetry data using eqs 4a−7b, as discussed below.

Assuming that the above "reaction" occurs at the melting point of that species (racemic species or enantiomer) which has the lower melting point, eqs 4a−7b may be derived to calculate the thermodynamic properties for the formation of a racemic compound. The enthalpies of fusion, ΔH^f, and the melting temperature, T^f, of both the racemic compound, R, and its enantiomer, A (in subscript), are determined experimentally. As shown in Figure 1a and 1b, the two situations, $T^f_A < T^f_R$ and $T^f_A > T^f_R$, are presented separately.

Enthalpy of formation:

$$\Delta H^\circ_{T^f_A} = \Delta H^f_A - \Delta H^f_R + (C^l - C^s_R)(T^f_R - T^f_A), \quad \text{when } T^f_A < T^f_R \quad (4a)$$

$$\Delta H^\circ_{T^f_R} = \Delta H^f_A - \Delta H^f_R + (C^l - C^s_A)(T^f_R - T^f_A), \quad \text{when } T^f_A > T^f_R \quad (4b)$$

Entropy of formation

$$\Delta S^\circ_{T^f_A} = \Delta S^f_A - \Delta S^f_R + R \ln 2 + (C^l - C^s_R)\ln \frac{T^f_R}{T^f_A}, \quad \text{when } T^f_A < T^f_R \quad (5a)$$

$$\Delta S^\circ_{T^f_R} = \Delta S^f_A - \Delta S^f_R + R \ln 2 + (C^l - C^s_A)\ln \frac{T^f_R}{T^f_A}, \quad \text{when } T^f_A > T^f_R \quad (5b)$$

Substituting the enthalpy of formation and the entropy of formation into eq 3 affords the free energy of formation, $\Delta G°$. The contribution from the terms containing the heat capacities in eqs 4 and 5 is always small and is effectively negligible.[3] Taking the difference in the melting points, $\Delta T = T^f_R - T^f_A$, and neglecting the small difference in the heat capacities, the free energy of formation is given by:

$$\Delta G^\circ_{T^f_A} \cong -\Delta S^f_R \Delta T - T^f_A R \ln 2, \text{ when } T^f_A < T^f_R, \text{ i.e., } \Delta T > 0 \quad (6a)$$

$$\Delta G^\circ_{T^f_R} \cong -\Delta S^f_A \Delta T - T^f_R R \ln 2, \text{ when } T^f_A > T^f_R, \text{ i.e., } \Delta T < 0 \quad (6b)$$

When, as in Figure 1a, the racemic compound melts at a higher temperature than its enantiomers, represented by eq 6a, $\Delta G° < 0$, suggesting that the formation of the racemic compound is always thermodynamically favorable in this situation. Figure 1b and eq 6b, however, present a more complicated situation. When $\Delta T < 0$, eq 6b is applicable and the first term on the right becomes positive. As ΔT becomes increasingly negative, $\Delta G°$ becomes less negative, eventually approaching zero (as ΔT approaches −30 K, to be considered later following eqs 7a and 7b). When $\Delta G°$ is zero or positive, there is no driving force for the formation of a racemic compound, and the racemic species remain as a racemic conglomerate as shown in Figure 1c. In other words, no "reaction" occurs between the enantiomers, when the racemic species is a racemic conglomerate.

Equations 4a−6b are valid only at the melting temperature of the enantiomers (or of the racemic species). In the pharmaceutical sciences, however, we are more interested in the thermodynamic values, especially $\Delta G°$, below the melting temperatures, e.g., at 25 °C or 37 °C. Extrapolation of the thermodynamic quantities from the melting temperature to another temperature, T, requires knowledge of the heat capacity terms. Accordingly, $\Delta G°$ at any temperature T, ΔG°_T, can be derived from the thermodynamic cycles in Figures 2 and 3:

$$\Delta G^\circ_T = \Delta G^\circ_{T^f_A} + \Delta\Delta S(T^f_A - T) + (C^l - C^s_R)\left[T^f_R - T^f_A - T \ln \frac{T^f_R}{T^f_A}\right] + (C^s_A - C^s_R)\left[T^f_A - T - T \ln \frac{T^f_A}{T}\right]$$

where

$$\Delta\Delta S = \Delta S^f_A - \Delta S^f_R + R \ln 2, \text{ when } T^f_A < T^f_R \quad (7a)$$

$$\Delta G^\circ_T = \Delta G^\circ_{T^f_R} + \Delta\Delta S(T^f_R - T) + (C^l - C^s_A)\left[T^f_R - T^f_A - T \ln \frac{T^f_R}{T^f_A}\right] + (C^s_A - C^s_R)\left[T^f_R - T - T \ln \frac{T^f_R}{T}\right]$$

where

$$\Delta\Delta S = \Delta S^f_A - \Delta S^f_R + R \ln 2, \text{ when } T^f_A > T^f_R \quad (7b)$$

The magnitude of the last three terms is relatively small. In the case of eq 7a, ΔG°_T is likely to remain negative over a wide temperature range below the melting point. However, when the free energy of formation at T^f_R in eq 7b has a small negative value close to zero (see examples in Tables 3), the sign of ΔG°_T may become positive depending on the sign of the sum, i.e., the relative magnitudes, of the last three terms. This possibility, arising from eq 7b, provides a thermodynamic basis for the melting point phase diagrams, shown in Figure 1c, and for the solubility diagrams of chiral systems that display a transformation from a racemic compound to a racemic conglomerate at certain temperatures.[3,9]

Materials and Methods

Materials—The names, acronyms, and sources of the chiral compounds used in this study are listed in Table 1. Some of these compounds were prepared by the methods described in the next paragraph. Others were purchased from chemical suppliers, with reported purity exceeding 99%, and were used as received.

Crystallization—(+)-Norephedrinium salicylate, (+)-NE·S, was obtained by dissolving equimolar quantities of (+)-norephedrine and salicylic acid in anhydrous ether followed by complete drying to yield a solid mass. The purity of (+)-NE·S was verified by a single sharp exotherm in the DSC curve and also by a single thermal event in the derivative of heat flow versus temperature. (+)-Pseudoephedrinium salicylate, (+)-PE·S, was prepared by crystallization.[10,11]

The racemic species of NE, E, PE, NE·S, PE·S, and ME, listed in Table 1, were prepared by dissolving equimolar quantities of the two enantiomers in methanol or ethanol and allowing the solvent to evaporate completely at room temperature (22.5 °C).

Differential Scanning Calorimetry (DSC)—Measurement of melting point and enthalpy of fusion of the crystalline chiral compounds was performed using a Du Pont 910 differential scanning calorimeter equipped with a data station (Thermal

Table 2—Physical Properties of Homochiral and Racemic Species

no.[a]	code name[a]	T^f(R)[b] (°C)	T^f(A)[b] (°C)	ΔT^f (°C)	ΔH^f(R)[b] (kcal/mol)	ΔH^f(A)[b] (kcal/mol)	$\Delta\Delta H^f$ (kcal/mol)	$\Delta\Delta S^{fc}$ (cal/mol·K)
1	NE	101.1	51.2	49.8	6.241	3.792	2.449	4.99
2	NE·Cl	195.9	172.8	23.1	6.924	4.839	2.085	3.91
3	NE·S	117.3	101.4	15.9	7.120	5.559	1.561	3.39
4	PE	117.9	119.2	–1.3	8.149	7.636	0.513	1.38
5	PE·Cl	166.0	182.9	–16.9	6.738	6.680	0.058	0.70
6	PE·S	108.2	131.2	–23.0	7.769	8.752	–0.983	–1.27
7	E	77.5	39.7	37.8	6.953	4.141	2.812	6.59
8	E·Cl	190.8	219.1	–28.3	8.348	7.577	0.771	2.60
9	E·NS	170.4	170.6	–0.2	9.203	7.878	1.325	3.00
10	ME	62.8	88.01	–25.2	6.358	7.304	–0.946	–1.30
11	IB	77.7	54.0	23.7	6.142	4.278	1.864	4.43
12	MA	120.6	131.5	–10.9	6.398	6.147	0.251	1.06
13	PN·Cl	163.4	194.6	–31.2	9.322	8.605	0.717	2.96
14	PN	92.3	71.5	20.8	10.385	8.665	1.720	3.28
15	AN	150.2	147.2	–3.0	8.523	8.789	–0.266	–0.48
16	APN	58.0	25.3	32.7	8.512	5.684	2.828	6.66
17	t-SB	131.7	150.4	–18.7	8.22	8.29	–0.07	0.73
18	c-SB	105.7	109.7	–4.0	6.18	5.54	0.64	1.84
19	BT	87.4	75.1	12.3	10.97	10.33	0.64	0.76
20	BT·Cl	134.5	154.8	–20.3	9.68	11.03	–1.35	–2.03
21	PD	169.7	92.5	77.2	13.84	6.14	7.70	14.46
22	IA	153.8	165.6	–11.8	6.62	6.21	0.41	1.35
23	SP	177.8	186.3	–8.5	11.03	10.04	0.98	2.59
24	DZ	234.2	194.4	39.8	10.75	9.04	1.71	1.85
25	HPL	121.6	156.6	–35.0	6.39	6.81	–0.42	0.34

[a] Numbers are given to identify the entries; code names are the acronyms explained in Table 1. [b] R and A denote the racemic species and its enantiomers, respectively. For entries 1–10, thermal analysis was carried out in this work, the standard deviation being less than 2.5%. [c] Entropy of fusion was obtained as $\Delta H^f/T^f$ of the corresponding homochiral or racemic species, but only the differences, $\Delta\Delta S^f$, are given.

Analyst 2000, TA instruments, New Castle, DE). The temperature axis and the cell constant were calibrated with indium (~3 mg, 99.99%, peak maximum at 156.6 °C and heat of fusion 28.4 J/g). Samples of 3.5 ± 0.5 mg in crimped aluminum pans were heated at a rate of 10 °C/min, and the peak melting temperature was recorded. All samples were measured in triplicate, and the standard deviations were less than ± 2.5%. Any small variations in the enthalpy of fusion as a result of differences in crystallinity of the homochiral and racemic species were expected to be negligible. The errors in determining the enthalpy of fusion when followed by possible decomposition were practically canceled out in the calculations, because small deviations in the baseline after melting occurred in the melt state for both the pure enantiomers and the racemic species.

Powder X-ray Diffraction (PXD) Pattern—Experimental PXD patterns of the compounds, both racemic and homochiral crystals, were determined at room temperature using a powder diffractometer (Model D-500, Siemens, Germany) with Cu Kα radiation at 30 mA, 45 kV. The sample was packed into an aluminum holder and scanned with the diffraction angle 2θ increasing from 2 to 30°, with a step size of 0.02°/min and counting time of 1 s per step.

^{13}C Solid-State Nuclear Magnetic Resonance (SSNMR) Spectroscopy—^{13}C SSNMR spectra were acquired at 75.743 MHz using a Chemagnetics CMX-300 spectrometer (Fort Collins, CO) and a Chemagnetics Pencil probe equipped with a 7.5 mm magic-angle spinning system using zirconia rotors. All spectra were acquired with cross polarization, magic-angle spinning, and high power ^{1}H decoupling. Spinning speeds were typically 5–6 kHz. Between 1024 and 2048 transients were acquired with a repetition delay of 3 s, contact time of 5 ms, and pulse width of 4 ms. No apodization was applied to the free induction decay prior to the Fourier transform.

Results and Discussion

Thermal Properties and Thermodynamic Calculations—To compare the thermodynamic properties of the enantiomers and their racemic species, the melting temperatures and enthalpy of fusion of the 25 chiral compounds are compiled in Table 2. The difference in melting temperature, ΔT^f, enthalpy of fusion, $\Delta\Delta H^f$, and entropy of fusion, $\Delta\Delta S^f$, of the two species are also given in Table 2 and are illustrated in Figure 4. Entry numbers, instead of compound names, are used for unbiased analysis and

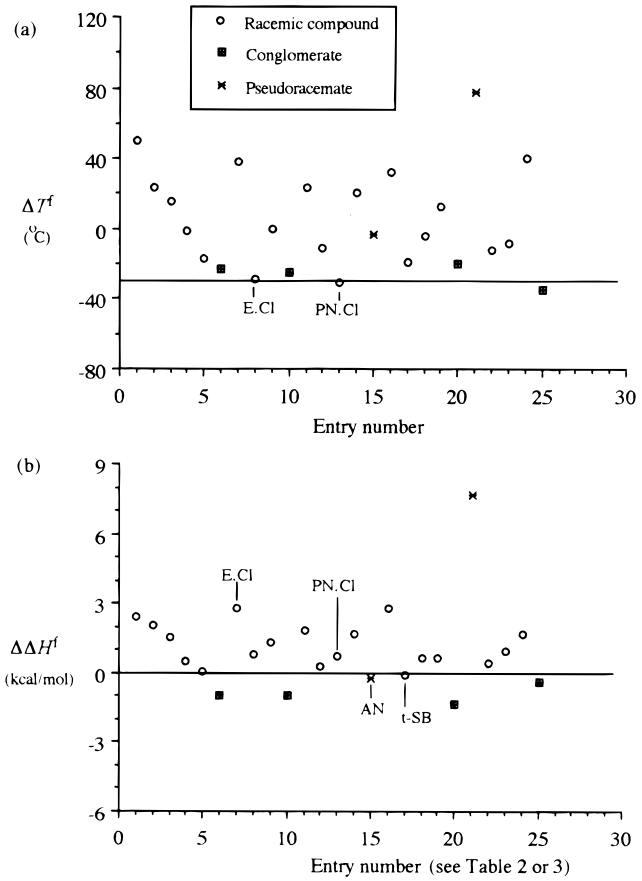

Figure 4—Differences between homochiral and racemic species in (a) the melting points, ΔT^f, and (b) the enthalpies of fusion, $\Delta\Delta H^f$.

Table 3—Comparison of the Experimental Thermal Properties and the Calculated Thermodynamic Properties of Racemic Species

		thermal properties			thermodynamic properties			
no.[a]	code name[a]	ΔT^f (°C)	$\Delta\Delta H^f$ (kcal/mol)	$\Delta\Delta S^f$ (cal/mol·K)	$\Delta H^{\circ b}$ (kcal/mol)	$\Delta S^{\circ b}$ (cal/mol·K)	$\Delta G^{\circ c}$ (kcal/mol)	ΔS^{md} (cal/mol·K)
1	NE	49.8	2.449	4.99	–1.453	–3.61	–1.278	–2.039
2	NE·Cl	23.1	2.085	3.91	–1.623	–2.53	–0.955	–0.648
3	NE·S	15.9	1.561	3.39	–1.244	–2.02	–0.805	–0.688
4	PE	–1.3	0.513	1.38	–0.539	0.00	–0.513	0.067
5	PE·Cl	–16.9	0.058	0.70	–0.396	0.68	–0.357	0.566
6	PE·S	–23.0	–0.983	–1.27	0.523	2.65	***–0.027***	***1.231***
7	E	37.8	2.812	6.59	–2.057	–5.22	–1.180	–1.895
8	E·Cl	–28.3	0.771	2.60	–1.336	–1.22	–0.204	0.986
9	E·NS	–0.2	1.325	3.00	–1.329	–1.62	–0.607	0.008
10	ME	–25.2	–0.946	–1.30	0.442	2.68	***0.048***	***1.418***
11	IB	23.7	1.864	4.43	–1.390	–3.05	–0.865	–1.074
12	MA	–10.9	0.251	1.06	–0.469	0.32	–0.376	0.429
13	PN·Cl	–31.2	0.717	2.96	–1.341	–1.58	***–0.027***	***1.370***
14	PN	20.8	1.720	3.28	–1.304	–1.90	–1.066	–1.572
15	AN	–3.0	–0.266	–0.48	0.206	1.86	–0.516	0.146
16	APN	32.7	2.828	6.66	–2.174	–5.28	–1.252	–2.337
17	t-SB	–18.7	–0.07	0.73	–0.304	0.65	–0.191	0.900
18	c-SB	–4.0	0.64	1.84	–0.720	–0.46	–0.464	0.161
19	BT	12.3	0.64	0.76	–0.394	0.61	–0.854	–1.044
20	BT·Cl	–20.3	–1.35	–2.03	0.944	3.41	***–0.038***	***1.205***
21	PD	77.2	7.70	14.46	–6.156	–13.08	–2.917	–4.653
22	IA	–11.8	0.41	1.35	–0.646	0.030	–0.421	0.404
23	SP	–8.5	0.98	2.59	–1.152	–1.21	–0.435	0.432
24	DZ	39.8	1.71	1.85	–0.913	–0.47	–1.487	–1.657
25	HPL	–35.0	–0.42	0.34	–0.281	1.03	***0.011***	***1.361***

[a] Numbers are given to identify the entries; code names are the acronyms explained in Table 1. [b] Enthalpy and entropy of formation were calculated according to eqs 4 and 5, respectively. [c] ΔG° was calculated by eq 6; those values that are approximately zero are shown in bold italics. [d] Entropy of mixing in the liquid state was calculated by eq 1, those values that are close to the ideal value are shown in bold italics.

convenience. The errors in the values of ΔH^f and T^f from literature references in Table 1 are less than 5%, if reported.

If ΔT^f approaches −30 K, the racemic species is likely to be a racemic conglomerate, such as PE·S, ME, BT·Cl and HPL, identified as the filled squares in Figure 4a. This generalization is not conclusive for (±)-PN·Cl and (±)-E·Cl, which are racemic compounds. The nature of these racemic species was determined by a comparison of the experimental PXD pattern with the PXD pattern calculated from the crystal structures, as derived from single-crystal X-ray analysis.[19a] Positive values of $\Delta\Delta H^f$, i.e., $\Delta H^f_R > \Delta H^f_A$, are found for all the racemic compounds, including (±)-PN·Cl and (±)-E·Cl, reflecting their preferential formation (Figure 4b). The racemic compound of t-SB is an exception to this trend; the very small negative value of $\Delta\Delta H^f$ (−0.07 kcal·mol^{-1}) may lie within experimental error.[13] For those racemic species that are identified as racemic conglomerates, e.g. PE·S, ME, BT·Cl, and HPL, their $\Delta\Delta H^f$ values are negative.

Two chiral compounds in this study do not belong to the above series. Pindolol, (PD entry 21) forms a pseudoracemate with a maximum melting point (Figure 1d(2)), and shows exceptionally large values of ΔT^f = 77.2 K and of $\Delta\Delta H^f$ = 7.7 kcal·mol^{-1}.[8] Atenolol (AN entry 15), whose racemic species was not identified, has a negative value of $\Delta\Delta H^f$, similar to those of racemic conglomerates, but has a small value of $-\Delta T^f$ (3.0 K), too small for a stable racemic conglomerate.[12] The formation of a pseudoracemate is suggested for (±)-AN.

Large differences in the melting points (ΔT^f approaching −30 K) between the homochiral and racemic species have been observed for all the racemic conglomerates examined and for a few of the racemic compounds. Therefore, the melting point phase diagram is not an adequate single criterion for identifying the nature of the racemic species. A positive value of $\Delta\Delta H^f$ may be a more reliable indicator of the formation of a racemic compound, which evidently is the enthalpically favorable species. This finding is consistent with the conclusion from lattice energy calculations that the racemic compound has a greater stabilization energy than the individual enantiomers.[19a,b]

Thermodynamic Properties of Racemic Species—The thermodynamic quantities for the formation of the racemic compound and the entropy of mixing of the enantiomers in the liquid state for racemic conglomerates were derived from the equations shown previously. Assuming that the nature of the racemic species is unknown, the thermodynamic calculations were carried out for all 25 chiral compounds in Table 3 to reveal any trends in the calculated values for different racemic species.

Table 3 presents the calculated thermodynamic values, ΔH°, ΔS°, ΔG°, and ΔS^m_l. The ΔH° and ΔS° values were calculated using eqs 4 and 5 assuming an average heat capacity difference of 20 cal·mol^{-1}·K^{-1} for ($C^l - C^s$) in each case.[20] The ΔG° values were obtained using eq 6, in which the heat capacity terms are neglected because they practically cancel in the free energy of formation as explained in the preceding section. The entropy of mixing in the liquid state, ΔS^m_l, was calculated by eq 1.

Comparison of the data in Table 3 reveals that ΔG° and ΔS^m_l show interesting trends between different racemic species, but the trends in the enthalpy of formation and the entropy of formation between racemic species are difficult to interpret.

Free Energy Formation, ΔG°—The calculated ΔG° values are shown in Figure 5. The free energy of formation for racemic compounds, ΔG°, is negative for 23 of the 25 entries, because, as expected, the majority of the racemic species are racemic compounds. However, not every negative ΔG° indicates a racemic compound.

In Figure 5, the five ΔG° values within the range of −0.05 to 0.05 kcal·mol^{-1} correspond to the four compounds (entries 6, 11, 20,[21] 25 in Table 3) which are identified as racemic conglomerates; the fifth is the racemic compound

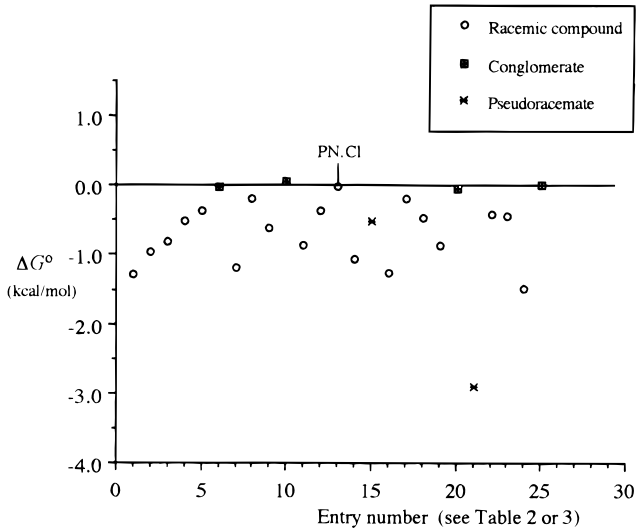

Figure 5—The free energy of formation, $\Delta G°$, of the racemic compound.

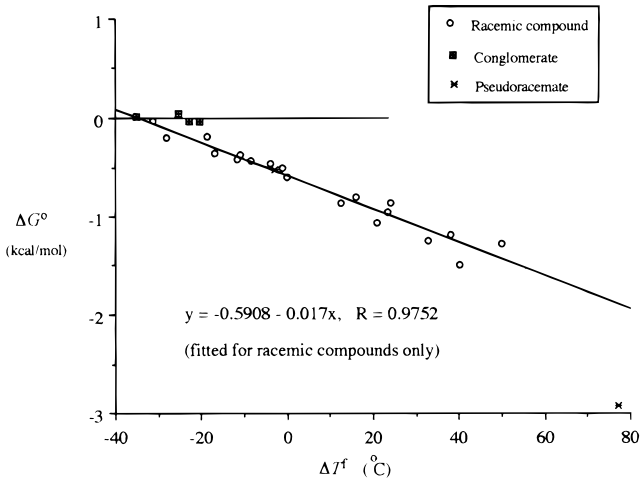

Figure 6—A plot of free energy of formation of racemic compounds, $\Delta G°$, as a function of the difference in melting temperatures, ΔT^f.

of PN·Cl (entry 13 in Table 3). Although PN·Cl forms a racemic compound, its thermodynamic properties are similar to those of racemic conglomerates. The fact that its $\Delta G°$ value is close to zero (-0.027 kcal·mol^{-1}) indicates lack of driving force for the formation of the racemic compound, (±)-PN·Cl. Such a small value may be within experimental error. In such a case, it is proposed that the formation of the racemic compound may be reversed under controlled conditions. Thus, to achieve resolution of this type of racemate by crystallization, the kinetic factors may be very important to offset the possible formation of the racemic compound.

Combining eqs 6a and 6b, a general expression for $\Delta G°$ as a function of the difference in melting points, ΔT^f, can be derived:

$$\Delta G°_{T^f} = -\Delta S^f \Delta T^f - T^f R \ln 2, \text{ where } \Delta T = T^f_R - T^f_A \quad (8)$$

ΔS^f and T^f are the mean entropy of fusion and the mean melting temperature, respectively, of the racemic compounds in the series studied. Figure 6 demonstrates a significant linear correlation for the 19 racemic compounds used in this study. In Figure 6, the negative free energy of formation (reflecting the stability) of a racemic compound is proportional to the difference in the melting temperatures between the racemic compound and its enantiomers.

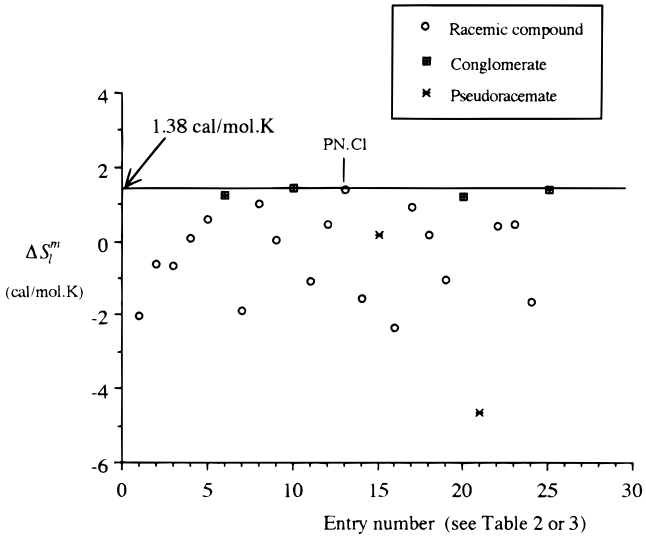

Figure 7—The entropy of mixing in the liquid state, ΔS^m_l.

This apparent linearity was observed previously for a number of organic racemic compounds.[3,5,22] According to eq 8, the slope of the regression line can be identified as the mean entropy of fusion, $\langle \Delta S^f \rangle = 17.04$ cal·mol^{-1}·K^{-1}. Similarly, the intercept represents the contribution of the ideal entropy of mixing, $\Delta S^m_l = 1.38$ cal·mol^{-1}·K^{-1}, at the average melting temperature of $\langle T^f \rangle = 427$ K (154 °C).

In eq 8, as ΔT^f approaches -30 K, the $\Delta G°$ values become close to zero. The entropy of mixing term, the second term on the right, is always negative and contributes to stabilize the racemic compound over its enantiomers. When the pure enantiomer and the racemic compound have the same melting temperature, $\Delta T^f = 0$, the racemic compound is stabilized by a $\Delta G°$ value of -0.59 kcal·mol^{-1}. This result suggests that the entropy of ideal mixing in the liquid state is the driving force for the formation of racemic compounds.

The calculated $\Delta G°$ values for all the racemic conglomerates (PE·S, ME, BT·Cl, and HPL) are approximately zero, which may serve as an indicator for identifying racemic conglomerates. However, the $\Delta G°$ value may be close to zero for racemic compounds, such as (±)-PN·Cl. To identify the nature of the racemic species which show $\Delta T^f \sim -30$ K, further characterization by X-ray diffraction and/or spectroscopic methods is necessary.

Entropy of Mixing in the Liquid State, ΔS^m_l—Values of the entropy of mixing in the liquid state, calculated by eq 1 are given in Table 3 and are shown in Figure 7. The average value of ΔS^m_l for the racemic conglomerates (PE·S, ME, BT·Cl, and HPL) is 1.30 ± 0.10 cal·mol^{-1}·K^{-1}, close to the ideal entropy of mixing of liquid enantiomers ($R \ln 2 = 1.38$ cal·mol^{-1}·K^{-1}). The small deviations of the entropy of mixing of the liquid enantiomers from the ideal value for racemic conglomerates may be related to deviation of these systems from the assumption that the corresponding enthalpy of mixing has the ideal value of zero. For racemic species which are not racemic conglomerates, with the exception of (±)-PN·Cl, their ΔS^m_l values (<1.0 cal·mol^{-1}·K^{-1}) deviate significantly from, and are smaller than, the ideal value. In other words, the assumptions made for racemic conglomerates are invalid for racemic compounds.

Pseudoracemates, i.e., Racemic Solid Solutions—A single, macroscopically homogeneous, crystalline phase may occasionally be formed by mixtures of the two enantiomers in any proportion, i.e., a racemic solid solution, termed a pseudoracemate. This miscibility in the solid state may be demonstrated by the melting point phase diagrams

shown in Figure 1d. Three types of solid solution are observed: (1) ideal, (2) nonideal with a maximum melting, and (3) nonideal with a minimum melting temperature. The few available crystallographic data show that the lattice parameters of a solid solution are very similar to that of the enantiomers, though not identical. In addition, each type of solid solution may be related to a given structural type, namely disordered for type 1, short range ordered for type 3, and nonstatistical inverse symmetry for type 2.[3]

The melting point phase diagram with no eutectic melting shows that the chiral compound pindolol, PD (entry 21 in Tables 2 and 3), forms a type 2 solid solution.[8] The calculated thermodynamic quantities of this pseudoracemate have unusually large negative values in comparison with the other compounds in this study. These unusual values are indicative of the unique properties of the racemic species. In the structure of this type of solid solution, one enantiomer can substitute for the other at one site only, forming a real (nonstatistical) inverse symmetry element.[3] The structure of this pseudoracemate may be similar to that of the racemic compound. The maximum difference in melting temperature of the pseudoracemate of PD, $\Delta T^f = 77.2$ K in Table 1, suggests more favorable interactions between the paired enantiomers in the racemic solid than in the single enantiomers.

The racemic species of atenolol, AN (entry 15 in Tables 2 and 3), was found to be a quasi-ideal solid solution ($\Delta T^f = -3$ K, not zero). Its negative $\Delta\Delta H^f$ (-0.266 kcal·mol^{-1}) seems to follow the trend of racemic conglomerates, but ΔT^f is small and $\Delta G°$ is negative, suggesting a nonconglomerate phase. The DSC trace of mixtures containing unequal amounts of the two enantiomers of AN showed no eutectic melting, which supports the predication from thermodynamic calculations that the racemic species of AN is a racemic solid solution. Unlike PD, AN with small ΔT^f corresponds to a quasi-ideal solid solution of type 1. The structure of a type 1 solid solution is almost identical to that of the pure enantiomer with the two enantiomers randomly occupying the lattice sites. Such a structural feature implies negligible differences in the intermolecular interactions between molecules with the same or opposite handedness in the solid state, i.e., lack of chiral recognition in the solid state.

Characterization of Racemic Species by Powder X-ray Diffractometry and ^{13}C Solid-State Nuclear Magnetic Resonance Spectroscopy—Powder X-ray diffractometry (PXD) and ^{13}C solid-state nuclear magnetic resonance (SSNMR) spectroscopy are two complementary techniques for the structural characterization of powder samples.[23,24] PXD patterns reveal differences of long range order in the packing of the crystal lattice. SSNMR spectra, on the other hand, can probe the short range order of the molecular environments in the solid and can effectively differentiate dynamic or static disorders.[25] The information from ^{13}C chemical shifts can be particularly useful for identifying conformational changes and structural differences, especially when they are difficult to recognize from the PXD patterns.

A number of racemic species in this study were investigated using both PXD patterns and ^{13}C SSNMR spectra. The PXD patterns of the enantiomers and of their racemic species for all the available compounds were first determined and compared. The two opposite enantiomers have identical PXD patterns because their crystal structures are identical, apart from their handedness which confers mirror symmetry. On the other hand, a racemic compound has a PXD pattern different from that of the two enantiomers. A close match of the 2θ values of the peaks in the PXD patterns of the enantiomers and of their racemic species indicates the same crystal structure, suggesting that the racemic species is a racemic conglomerate. Differences in in relative intensity of the PXD patterns may arise from differences in crystallinity and/or preferred orientation. A pseudoracemate displays a PXD pattern closely resembling that of the enantiomers but with some peak broadening. In this work, the findings from the PXD patterns were further confirmed by the ^{13}C SSNMR spectra.

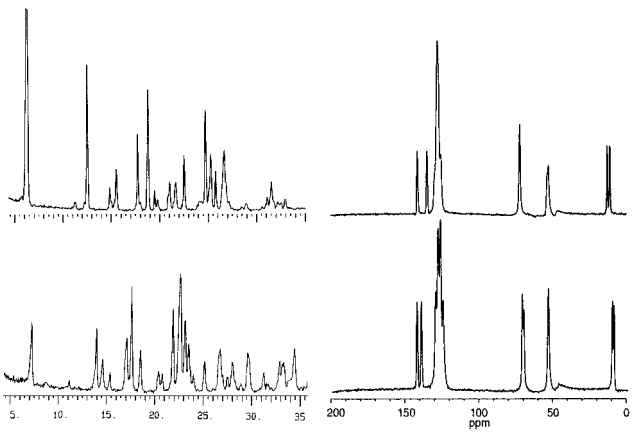

Figure 8—Powder X-ray diffraction patterns (left) and ^{13}C solid-state nuclear magnetic resonance spectra (right) of the racemic compound (upper traces) and of the (–)-enantiomer (lower traces) of norephedrine hydrochloride (NE·Cl).

The PXD patterns and SSNMR spectra of the enantiomers and of their racemic species, for the three possible racemic species: racemic compound, racemic conglomerate, and pseudoracemate, are illustrated in Figures 8, 9, and 10, respectively.

Figure 8 refers to a racemic compound, norephedrine hydrochloride, (±)-NE·Cl (entry 2 in Tables 2 and 3). The PXD pattern of the enantiomer is significantly different from that of the racemic compound. Likewise, the ^{13}C chemical shifts for the enantiomer and the racemic compound are markedly different. For both the homochiral and racemic crystals, the asymmetric unit contains two molecules with different conformations[19a] which are crystallographically nonequivalent.[26] Each carbon in the molecule should theoretically have two chemical shifts, one for each conformation. However, the chemical shifts for two conformations may or may not differ substantially to give distinct peaks. In this case the two peaks are distinguishable for both the aliphatic carbons and the substituted aromatic carbons.

An example of a racemic conglomerate, methylephedrine (ME entry 10), is given in Figure 9. Most of the peak positions in the PXD patterns show a good match between (−)-ME and (±)-ME. Difference in peak intensity may be ascribed to preferred orientation of the thin plates (−)-ME. The ^{13}C chemical shifts in the SSNMR spectra of the homochiral and racemic species agree well, except for the two *N*-methyl carbons. Crystallographically, the two *N*-methyl carbons are nonequivalent in the unit cell, so two peaks are expected. The two *N*-methyl carbons of the racemic species show two peaks. In (−)-ME, the two *N*-methyl carbon signals coalesce into one broad peak. The relatively broad peaks of the *N*-methyl carbons indicate mobility of the methyl groups. In conjunction with X-ray data, NMR results suggest that (±)-ME is a racemic conglomerate, although the nature of the small difference for the *N*-methyl carbons is unclear.

The PXD pattern of atenolol (AN entry 15) in Figure 10 also demonstrates no substantial differences between the enantiomers and the racemic species; only minor differ-

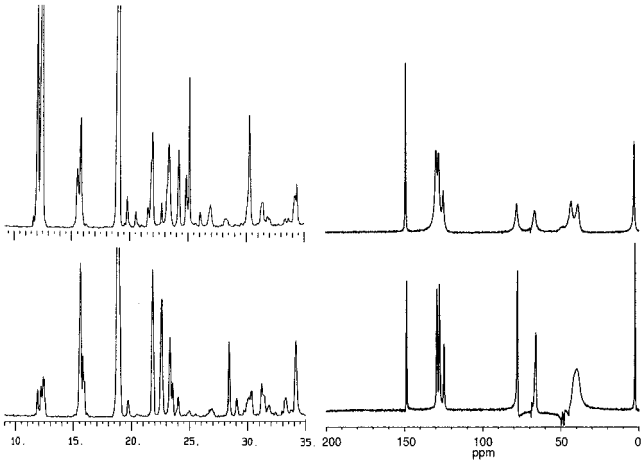

Figure 9—Powder X-ray diffraction patterns (left) and ^{13}C solid-state nuclear magnetic resonance spectra (right) of the racemic conglomerate (upper traces) and of the (–)-enantiomer (lower traces) of methylephedrine (ME).

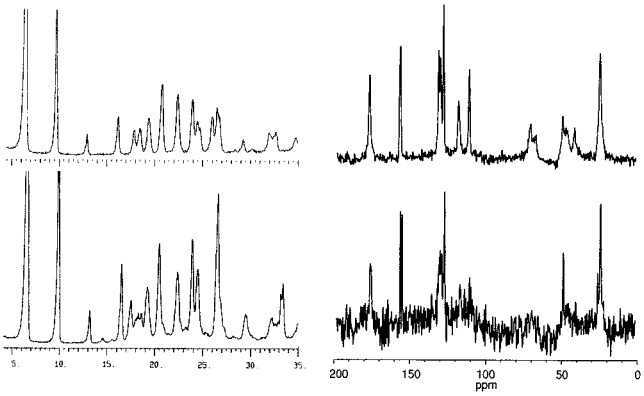

Figure 10—Powder X-ray diffraction patterns (left) and ^{13}C solid-state nuclear magnetic resonance spectra (right) of the pseudoracemate (upper traces) and of the (–)-enantiomer (lower traces) of atenolol (AN).

ences are noted at 17.5° and 33.3° 2θ. Most of the ^{13}C chemical shifts of the enantiomer and racemic species match well, but a few peaks in (−)-AN are difficult to detect above the noise in the spectrum. The reasonably good agreement between the two PXD patterns and between the two SSNMR spectra for racemic and enantiomeric AN suggests that these two forms have very similar crystal structures. The minor differences observed are attributed to decreased crystallinity of the single enantiomer, (−)-AN. Moreover, both the DSC analyses and the thermodynamic calculations indicate that the racemic species of AN is a pseudoracemate, confirming the deduction made above.

In summary, the structural identification of the chiral compounds studied has, in all cases, confirmed the nature of the racemic species suggested by the thermodynamic calculations. However, for differentiation between a racemic conglomerate and a pseudoracemate, PXD and SSNMR may not be adequate. Identification of the pseudoracemate is then shown by the absence of eutectic melting in DSC.

Phase Diagrams and Thermodynamic Aspects—Among the 25 chiral pharmaceutical compounds included in this study as a subset of chiral compounds, 19 racemic species are racemic compounds, corresponding to a 76% frequency. The lower frequency of racemic compounds among these 25 chiral drugs, as compared with 90% among chiral organic compounds in general, is partly explained by the sample collection, of which seven are salts. Nevertheless, this lower frequency of racemic compounds may reflect their occurrence among chiral pharmaceuticals because many drugs are formulated as salt forms.

Several compilations of racemic and enantiomeric pairs of organic chiral compounds have been published.[3,5,22,27] In many respects, the results of the thermodynamic calculations in this study with 25 chiral pharmaceutical compounds are in general agreement with those reported previously for a much larger set of other organic compounds.[3]

The free energy calculations show that the entropy of mixing is the driving force for the formation of racemic compounds. This interpretation can be given from a different point of view in terms of phase separation. Considering crystallization of a racemic conglomerate from a racemic liquid, separation of the two enantiomers as homochiral crystals is not entropically favorable. In some cases, this entropic cost for the phase separation may be merely compensated by the slightly lower enthalpy of the pure crystalline enantiomer as compared with the racemic compound, resulting in an approximately zero value of $\Delta G°$, indicating approximately equal stability of the racemic compound and racemic conglomerate. Hence, crystallization of conglomerates is unlikely to be thermodynamically favored in most cases, but may be controlled by the kinetics of the solid−liquid interface as well as by nucleation and crystal growth.

Emphasis has been placed on those systems whose racemic species are ambiguous in nature, particularly racemic conglomerates or racemic compounds for which $\Delta T^f \approx -30$ K. The reason for this emphasis is that this type of system is particularly important in the resolution of racemates by crystallization. In theory, such systems exist as a thermodynamic equilibrium between the racemic conglomerate and the racemic compound. It may be possible to vary the temperature and kinetic factors to steer the crystallization in the desired direction, so as to facilitate the separation of enantiomers by crystallization. For example, the small difference in the stability of the racemic compound and enantiomeric crystals in the racemic conglomerate may give rise to a significant difference in their solubilities at certain temperatures, which may be utilized for preferential crystallization.[3,9]

It is known that conversion of a free acid or base into a salt increases the likelihood of a racemic conglomerate.[3] In the present study, all the hydrochloride salts in Table 2 show substantially smaller values of ΔT^f values than their free bases or acids. The thermodynamic calculations show that the negative free energy change, $\Delta G°$, approaches zero as $T_R^f - T_A^f$ approaches −30 K. This result provides the thermodynamic basis for the greater frequency of racemic conglomerates among the salts than among the free acids or bases, corresponding to a significant reduction of the difference in melting point between the racemic and homochiral species.

The use of salts to facilitate the resolution of racemates has been attempted.[9] Conglomerates, resolvable by preferential crystallization, were sought by Coquerel and coworkers[28] among various salts of fenfluramine, whose *R* enantiomer is an anorectic agent, and among norfenfluramine, its precursor. Numerous salts of these bases with achiral acids were tested, and several were found to form conglomerates, resolvable by preferential crystallization. Another proposed method for increasing the occurrence of racemic conglomerates is the use of a pressure-induced transition of a racemic compound to a conglomerate.[5] Both methods rely on a significant reduction of the difference in melting point between the racemic compound and its enantiomers. Therefore, a rational procedure for the resolution of racemates by crystallization requires, first, the conversion of the chiral drug into a suitable salt with $T_R^f - T_A^f$ approaching −30 K, and second, a search for the optimal crystallization conditions to facilitate separation

of the two enantiomers by thermodynamic and kinetic factors, such as solubility differences at various temperatures or nucleation, which may be probed by seeding with homochiral crystals.

Conclusions

The free energy of formation of a racemic compound from its pure enantiomers is always negative, indicating that the racemic compound, if it exists, is the thermodynamically favored racemic species. For a racemic conglomerate the entropy of mixing of the two enantiomers in the liquid state is close to the ideal value of R ln 2 (1.38 cal·mol^{-1}·K^{-1}). In comparison to racemic compounds and racemic conglomerates, unusual thermodynamic behavior was observed for racemic solid solutions. Furthermore, thermodynamic calculations reveal that the contribution of the nonideal entropy of mixing to the free energy of formation is the driving force for the formation of racemic compounds. The results show that the combination of thermal analysis with thermodynamic calculations provides a powerful tool to identify the three racemic species: racemic compound, racemic conglomerate, and racemic solid solution. A dynamic equilibrium exists between the racemic compound and the racemic conglomerate when the difference in the melting points between the racemic and homochiral species, ΔT^{f}, approaches −30 K and ΔG°_{Tf} becomes approximately zero. Structural studies using powder X-ray diffraction patterns and solid-state NMR are valuable for distinguishing between a racemic compound and either a racemic conglomerate or a pseudoracemate. Thermal analysis can be used to differentiate between a pseudoracemate and the other two types of racemic species. A preliminary report of this work has been presented as a poster at the 1996 Annual Meeting of the American Association of Pharmaceutical Scientists.[29]

References and Notes

1. Millership, J. S.; Fitzpatrick, A. Commonly used chiral drugs: a survey. *Chirality* **1993**, *5*, 573−576.
2. Stinson, S. C.; Chiral drugs. *Chem. Eng. News* **1995**, *October 9*, 44−47. Chiral drugs. *Chem. Eng. News* **1997**, *October 20*, 38−70.
3. Jacques, J.; Collet, A.; Wilen, S. H. *Enantiomers, Racemates and Resolutions*; John Wiley and Sons: New York, 1981 (reprint edition 1991, reissued with corrections, Krieger Publishing Co.: Malabar, FL, 1994).
4. A homochiral crystal is composed of a single enantiomer, whereas a heterochiral crystal contains both opposite enantiomers in the crystal lattice. A racemic conglomerate is an equimolar physical mixture of homochiral crystals of both enantiomers, while a racemic compound and a pseudoracemate are heterochiral crystals. In a racemic compound, the two opposite enantiomers are paired up in the unit cell of the crystal lattice, whereas in a pseudoracemate the opposite enantiomers are arranged more or less randomly as a solid solution.
5. Collet, A.; Ziminski, L.; Garcia, C.; Vigné-Maeder, F. Chiral discrimination in crystalline enantiomer systems: Facts, interpretations, and speculations. In *NATO ASI series − Supramolecular Stereochemistry*; Siegel, J. S., Ed.; Kluwer Academic: The Netherlands, 1995; pp 91−110.
6. Li, Z. J.; Grant, D. J. W. Relationship between crystal properties and physicochemical properties of chiral drugs. *J. Pharm. Sci.* **1997**, *86*, 1073−1078.
7. Prankerd, R. J.; Elsabee, M. Thermal analysis of chiral drug mixtures: The DSC behavior of mixtures of ephedrine·HCl and pseudoephedrine·HCL enantiomers. *Thermochim. Acta* **1995**, *248*, 147−160.
8. Neau, S. H.; Shinwari, M. K.; Hellmuth, E. W. Melting point phase diagrams of free base and hydrochloride salts of bevantolol, pindolol and propranolol. *Int. J. Pharm.* **1993**, *99*, 303−310.
9. Eliel, E. L.; Wilen, S. H.; Mander, L. N. *Stereochemistry of Organic Compounds*; John Wiley and Sons: New York, 1994.
10. Duddu, S. P.; Fung, F. K.-Y.; Grant, D. J. W. Effects of crystallization in the presence of the opposite enantiomer on the crystal properties of (*SS*)-(+)-pseudoephedrinium salicylate. *Int. J. Pharm.* **1996**, *127*, 53−63.
11. Li, Z. J.; Grant, D. J. W. Effects of excess enantiomers on the crystal properties of a racemic compound: ephedrinium 2-naphthalenesulfonate. *Int. J. Pharm.* **1996**, *137*, 21−31.
12. Touitou, E.; Chow, D. D.; Lawter, J. R. Chiral β-blockers for transdermal delivery. *Int. J. Pharm.* **1994**, *104*, 19−28.
13. Bettinetti, G.; Giordano, F.; Fronza, G.; Italia, A.; Pellegata, R.; Villa, M.; Ventura, P. Sobrerol enantiomers and racemates: solid-state spectroscopy, thermal behavior and phase diagrams. *J. Pharm. Sci.* **1990**, *79*, 470−475.
14. Pitre, D.; De Amici, M.; Colombo, M.; Gallo, G. G.; Nebuloni, M. Further characterization of the solid forms of iopanoic acid and its enantiomers. *Arch. Pharm.* **1992**, *32*, 385−388.
15. Pitre, D.; Stradi, R. Racemic modification of (*R,S*)-3-(4-phenyl-1-piperazinyl)-1,2-propandiol and melting point diagram. *Arch. Pharm.* **1990**, *323*, 23−25.
16. Pitre, D.; Valoti, E. Physical properties of sulpiride and its (*S*)-enantiomer. *Arch. Pharm.* **1987**, *320*, 859−861.
17. Vigevani, A.; Zampieri, M.; Pellizzato, R. Thermal behavior and binary phase diagram of (*S*)-(+)-4,4′-(1-methyl-1,2-ethandiol)-bis-(2,6-piperazinedione) (dex-razoxane), a cardioprotective agent, and its (*R*)-(−)-enantiomer. *J. Pharm. Biomed. Anal.* **1992**, *10*, 31−36.
18. Di Silvestro, G.; Palmisano, G.; Pellegata, R. Phase diagram of (*R*)- and (*S*)-hydroxy-2-pyrrolidone mixtures: A new case of a conglomerate forming system. *J. Pharm. Sci.* **1993**, *82*, 758−760.
19. (a) Li, Z. J. *Implications of Chirality in the Physicochemical Properties and Crystallization of Chiral Drugs*, Ph.D. Thesis, University of Minnesota, 1997. (b) Li, Z. J.; Grant, D. J. W. A molecular modeling study of chiral drug crystals: structural analysis and lattice energy calculations. *Pharm. Res.* **1996**, *13 Suppl.*, S-340, PDD-7430.
20. Comparative heat capacities between the solid and liquid states of enantiomers and racemic species have rarely been determined. From the few available data, the average value of $C^{l} - C^{s}_{AorR}$ approximately 20 cal·mol^{-1}·K^{-1} (see ref 3).
21. Entry 20 is BT·Cl, which was identified as a racemic conglomerate from the melting point phase diagram,[8] but no structural analysis was given. Because the material is not commercially available, further testing could not be performed.
22. Brock, C. P.; Schweizer, W. B.; Dunitz, J. D. On the validity of Wallach's rule: On the density and stability of racemic crystals compared with their chiral counterparts. *J. Am. Chem. Soc.* **1991**, *113*, 9811−9820.
23. Bugay, D. E. Solid-state nuclear magnetic resonance spectroscopy: theory and pharmaceutical applications. *Pharm. Res.* **1993**, *10*, 317−327.
24. Byrn, S. R. *Solid-State Chemistry of Drugs*; Academic Press: New York, 1982.
25. Etter, M. C.; Hoye, R. C.; Vojta, G. A. Solid-state NMR and X-ray crystallography: complementary tools for structure determination. *Cryst. Rev.* **1988**, *1*, 281−338.
26. Maciel, G. E.; Jagannathan, N. R.; Frye, J. S. Solid-state NMR: opportunities and challenges. In *NMR and X-ray Crystallography: Interfaces and Challenges*; Etter, M. C., Ed.; *Trans. Am. Crystallogr. Assoc.* **1988**, *24*, 1−23.
27. Mason, S. F. *Molecular Optical Activity and Chiral Discriminations*; Cambridge University Press: Cambridge, UK, 1982; p 171.
28. Coquerel, G.; Perez, G.; Hartman, P. Croissance d'un énantiomère en milieu quasi-racémique: cas du dichloroacétate de norfenfluramine. *J. Cryst. Growth* **1988**, *88*, 511−521.
29. Li, Z. J.; Grant, D. J. W. Thermal analysis as a method for characterizing racemic species. *Pharm. Res.* **1996**, *13 Suppl.*, S-340, PDD-7429.

Acknowledgments

The authors thank Professor Ferdinando Giordano for reading the draft manuscript and for providing useful suggestions, and the Pharmaceutical Research and Manufacturers of America Foundation for an Advanced Predoctoral Fellowship for Z. J. Li.

JS980205U

CHO/hPEPT1 Cells Overexpressing the Human Peptide Transporter (hPEPT1) as an Alternative in Vitro Model for Peptidomimetic Drugs

HYO-KYUNG HAN,[†] JULIE K. RHIE,[†,‡] DOO-MAN OH,[†] GO SAITO,[†] CHENG-PANG HSU,[†] BARBRA H. STEWART,[§] AND GORDON L. AMIDON*,[†]

Contribution from *College of Pharmacy, The University of Michigan, Ann Arbor, Michigan 48109-1065, and Pharmacokinetics and Drug Metabolism Department, Parke-Davis Pharmaceutical Research, Division of Warner-Lambert Company, Ann Arbor, Michigan 48105.*

Received March 19, 1998. Final revised manuscript received December 8, 1998.
Accepted for publication December 9, 1998.

Abstract □ The present study characterized Chinese hamster ovary cells overexpressing a human intestinal peptide transporter, CHO/hPEPT1 cells, as an in vitro model for peptidomimetic drugs. The kinetic parameters of Gly-Sar uptake were determined in three different cell culture systems such as untransfected CHO cells (CHO–K1), transfected CHO cells (CHO/hPEPT1) and Caco-2 cells. V_{max} in CHO/hPEPT1 cells was approximately 3-fold higher than those in Caco-2 cells and CHO–K1 cells, while K_m values were similar in all cases. The uptake of β-lactam antibiotics in CHO/hPEPT1 cells was three to twelve fold higher than that in CHO–K1 cells, indicating that CHO/hPEPT1 cells significantly enhanced the peptide transport activity. However, amino acid drugs also exhibited high cellular uptake in both CHO–K1 and CHO/hPEPT1 cells due to the high background level of amino acid transporters. Thus, cellular uptake study in CHO/hPEPT1 cells is not sensitive enough to distinguish the peptidyl drugs from amino acid drugs. The potential of CHO/hPEPT1 cells as an in vitro model for peptidomimetic drugs was also examined through the inhibition study on Gly-Sar uptake. Peptidomimetic drugs such as β-lactam antibiotics and enalapril significantly inhibited Gly-Sar uptake whereas the nonpeptidyl compounds, L-dopa and α-methyldopa, did not compete with Gly-Sar for cellular uptake within the therapeutic concentrations. In conclusion, the present study demonstrates the further characterization of CHO/hPEPT1 cells as an uptake model as well as inhibition study and suggests their utility as an alternative in vitro model for drug candidates targeting the hPEPT1 transporter.

Introduction

Since peptide transporters are potential targets for improving oral drug absorption through chemical modification due to the broad substrate specificity,[1,2] an efficient screening tool is necessary for rapid evaluation of peptidyl drug candidates arising from rational drug design.

The advantages of in vitro cell cultures over conventional techniques have been summarized by Audus et al.,[3] which include (a) rapid evaluation of the permeability and metabolism of a drug, (b) the opportunity to characterize the molecular mechanism(s) of drug absorption /or drug metabolism, (c) rapid evaluation of strategies for enhancing drug absorption and minimizing drug metabolism, (d) the opportunity to use human cells, rather than animal tissues, and (e) the opportunity to minimize time-consuming, expensive, and sometimes controversial animal studies. Therefore, mammalian cell cultures are increasingly attractive to pharmaceutical scientists as a suitable in vitro model for drug transport and metabolism studies.

Caco-2 cells are well-characterized[4] and currently the most widely used in vitro cell culture system for intestinal drug transport studies. However, this cell line exhibits various transport systems other than peptide transporters,[5,6] and it may be difficult to distinguish the responsible transport system for the test compound. In addition, the expression level of peptide transporters in Caco-2 cells is low, variable, and rather insufficient for the screening of peptidyl drug candidates.[7] The advances in the cloning of peptide transporters and recombinant DNA technology have recently triggered several attempts to develop a cell culture model having enhanced peptide transport activity.[8−14] For instance, a human intestinal peptide transporter, hPEPT1, has been functionally expressed in HeLa cells[13] and also stably transfected into the CHO cells.[14] These overexpression systems provide the analytical advantage in verifying possible drug candidates with transport activity mediated via hPEPT1 transporter. Since the stable transfected cell line, CHO/hPEPT1 has been characterized only through inhibition studies using some peptidyl compounds,[14] further characterization is necessary for its wide application as a screening tool of peptidomimetic drugs.

In the present study, the functional expression level of hPEPT1 transporter in CHO/hPEPT1 cells was evaluated by the kinetic study of Gly-Sar uptake and compared with those in untransfected CHO cells (CHO−K1) and Caco-2 cells. The potential of CHO/hPEPT1 cells as a screening tool was examined through the uptake and the inhibition studies using both peptidyl and nonpeptidyl compounds as substrates of the hPEPT1 transporter.

Experimental Section

Materials—Glycyl-[^{3}H]-sarcosine (specific radioactivity, 400 mCi/mmol) was purchased from Moravek Biochemicals Inc. (Brea, CA). Cephalexin, cephradine, cefaclor, ampicillin, enalapril, glycylsarcosine, L-dopa, and α-methyldopa were purchased from Sigma Chemical Co. (St. Louis, MO). All tissue culture reagents were obtained from Gibco (Grand Island, NY). Other chemicals were either analytical or HPLC grade.

Cell Cultures—CHO/hPEPT1 cells were cultured in F-12 nutrition mixture (HAM) containing 10% fetal bovine serum (FBS), penicillin (100 U/ml)/streptomycin (100 mg/mL), and 200 mg/mL G418. CHO−K1 cells were cultured in the same media without G418. Caco-2 cells were routinely maintained in Dulbecco's modified Eagle's medium (DMEM) containing 10% FBS, 1% nonessential amino acids, 1 mM sodium pyruvate, 1% L-glutamine, and penicillin (100 U/ml)/streptomycin (100 mg/mL). All cells were

* To whom correspondence should be addressed. E-mail: glamidon@umich.edu, Phone: 734-764-2440, Fax: 734-763-6423.
† University of Michigan.
‡ Present address: NIH−NIGMS/FDA-CBER-DCGT, Bethesda, Maryland 20892.
§ Parke-Davis Pharmaceutical Research.

10.1021/js980132e CCC: $18.00 Published on Web 01/23/1999

maintained in an atmosphere of 5% CO_2 and 90% relative humidity at 37 °C.

Kinetic Study of Gly-Sar Uptake in the Different Cell Culture Systems—CHO/hPEPT1 cells were seeded in 12-well culture plates at a density of 10^5 cells/cm^2. At 2 days postseeding, the cells were washed twice with pH 6.0 uptake buffer containing 1 mM $CaCl_2$, 1 mM $MgCl_2$, 150 mM NaCl, 3 mM KCl, 1 mM NaH_2PO_4, 5 mM D-glucose, and 5 mM MES. Gly-Sar solution was prepared at seven different concentrations (0.01 mM to 50 mM, 0.4 μCi/mL). Each drug solution was added to each well and incubated at 25 °C. At each time point, cells were washed with ice-cold pH 6.0 uptake buffer three times to stop the cellular uptake. One milliliter of 1.5% ice-cold Triton X solution was added to each well and incubated for 30 min at 25 °C. Cells were harvested and transferred into vials containing 4 mL of the scintillation cocktail. Samples were analyzed by a scintillation counter, and the protein amount of each sample was measured by the method of Lowry et al.[15] Kinetic parameters of Gly-Sar uptake were also determined in CHO−K1 cells and Caco-2 cells following the same protocol as was performed in CHO/hPEPT1 cells.

Uptake Study in Both Untransfected and Transfected CHO Cells. Cells were seeded in six-well culture plates (9.6 cm^2, growth area) at a density of 10^5 cells/cm^2. At 2 days postseeding, the medium was removed and cells were washed twice with pH 6.0 uptake buffer. Independent studies were performed for each drug solution at 1 mg/mL made in pH 6.0 uptake buffer. At each time point (10, 20, 30, 45, 60, 90 min), drug solution was removed and cells were washed three times with ice-cold pH 6.0 uptake buffer. One milliliter of Milli-Q water was added to each well and incubated for 30 min at 25 °C. Cells were harvested and sonicated for 1−2 min. $ZnSO_4$ solution (8%, 200 mL) was added to the cell lysate, vortexed rigorously, and centrifuged for 5 min at 3000 rpm. After filtration of the supernatant through a membrane filter (0.45 mm), samples were analyzed by HPLC. The protein amount of each sample was determined by the method of Lowry et al.[15]

Inhibition of Gly-Sar Uptake in CHO/hPEPT1 Cells. Cells were seeded in 12-well culture plates at a density of 10^5 cells/cm^2. At 2 days postseeding, the cells were washed twice with pH 6.0 uptake buffer. Each inhibitor solution (0.01 mM to 50 mM) containing ^{3}H-Gly-Sar (20 mM, 0.4 μCi/ml) was added to each well and incubated for 30 min at 25 °C. After removing the drug solution, the cells were washed with ice-cold pH 6.0 uptake buffer three times to stop the cellular uptake. One milliliter of 1.5% ice-cold Triton X solution was added to each well and incubated for 30 min at 25 °C. Cells were harvested and transferred into vials containing 4 mL of scintillation cocktail. Samples were analyzed by a scintillation counter (Beckman instruments Inc., Model LS-9000), and the protein amount of each sample was measured by the method of Lowry et al.[15]

HPLC Assay—The instrument consists of a pump (Waters, Model 510, Milford, MA) and automatic sampler (Model 712 WISP, Waters) and an UV detector (Waters, 990 Photodiode Array Detector, Milford, MA). Data acquisition and integration was carried out using the Millennium software. All compounds were separated on a reversed phase C-18 column (Beckman Ultrasphere, 5 μm, 4.6 × 250 mm) under the conditions published by Walter et al.[16]

Data Analysis—*Estimate of IC_{50}*—In this study, IC_{50} is defined as the drug concentration to show the 50% inhibition of Gly-Sar uptake. As described by De Lean et al.,[17] it was determined from nonlinear regression of dose−response curve by the Sigma Plot program (Jandel Scientific, San Rafael, CA) using the equation $f = (a - d)/(1 + (x/c)^b) + d$, where a and d represent the maximum and minimum uptake, respectively, x is the inhibitor concentration, and b is the slope factor.

Determination of K_m and V_{max}—K_m and V_{max} for the uptake of each drug was determined by the nonlinear regression of $V = V_{max} \cdot C/(K_m + C) + K_dC$, where K_dC represents a diffusional uptake rate.

Statistical differences between two means were evaluated using a *t*-test assuming unequal variance.

Results and Discussion

Uptake Kinetics of Gly-Sar in the Different Cell Culture Systems—Due to the broad substrate specificity of the peptide transporter, a wide range of structurally unrelated molecules have exhibited significant binding affinity and are transported by the peptide transporter.[18−21] Therefore, chemical modification targeting a peptide transporter to improve oral drug absorption is increasingly attractive to the pharmaceutical scientists. Thus, an efficient and rapid screening tool is needed to support the drug discovery process targeting the peptide transporters. The present study quatitatively evaluated the enhancement of peptide transport activity in CHO/hPEPT1 cells through the kinetic study of Gly-Sar uptake. Kinetic parameters of Gly-Sar uptake were determined in CHO/hPEPT1 cells and compared with those in untransfected CHO cells and Caco-2 cells which is the most prevalent in vitro cell culture system for intestinal drug absorption (Figure 1). As summarized in Table 1. K_m values for Gly-Sar uptake are similar in all three systems, which are comparable to those in other literatures.[11,22] V_{max}/K_m was 380 for CHO/hPEPT1 cells, which is 2-fold higher than that for CHO−K1 cells and four times higher than that for Caco-2 cells. Compared with K_d that indicates the contribution of passive diffusion, V_{max}/K_m was approximately 210-fold, 24-fold, and 17-fold higher in CHO/hPEPT1 cells, CHO−K1 cells and Caco-2 cells, respectively, indicating that Gly-Sar uptake was predominantly carrier-mediated. Furthermore, as shown in Eadie−Hofstee plot (Figure 2), the cellular uptake of Gly-Sar appeared to be mediated by a single transporter, even though there are more than one peptide transporters in CHO/hPEPT1 cells (i.e., hPEPT1 and endogenous peptide transporter) and Caco-2 cells (i.e., PEPT1 and HPT1). This is probably due to the wide overlap of the substrate specificity among peptide transporters and consequently similar affinity of Gly-Sar to each peptide transporter. Taken all together, the Gly-Sar kinetic study indicated that CHO/hPEPT1 cells significantly enhanced the capacity of the peptide transport system while retaining the substrate specificity and that this system may be useful as an in vitro model for the rapid screening of peptidyl drugs.

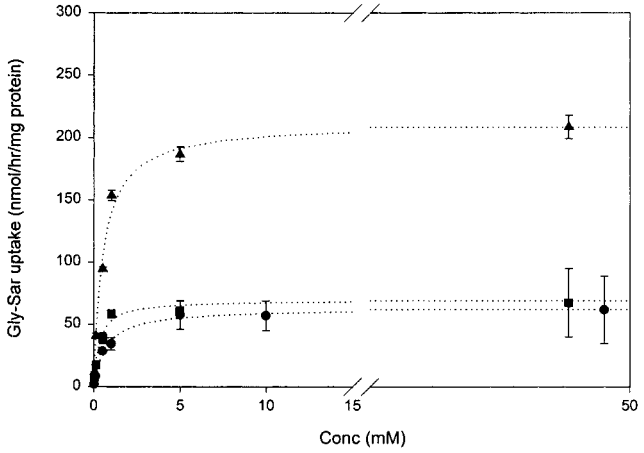

Figure 1—Kinetic study of Gly-Sar uptake in the different cell culture systems ($n = 3$, mean ± SE). (▲) CHO/hPEPT1 cells; (■) CHO–K1 cells; (●) Caco-2 cells.

Table 1—Kinetic Parameters of Gly-Sar Uptake in Three Different Cell Lines ($n = 3$, mean ± SE)

	CHO/hPEPT1	CHO–K1	Caco-2
K_m (mM)	0.5 ± 0.1	0.3 ± 0.1	0.7 ± 0.1
V_{max} (nmol/h/mg protein)	211.2 ± 16.4	69.5 ± 6.4	62.5 ± 2.9
K_d (nmol/h/mg protein/mM)	1.8 ± 0.4	7.7 ± 0.2	5.5 ± 0.1

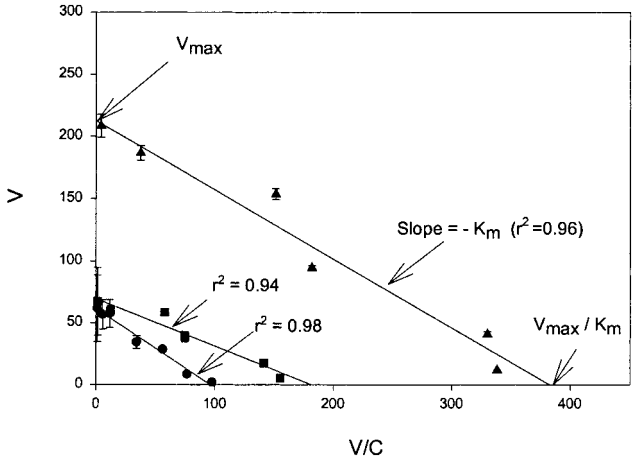

Figure 2—The Eadie-Hofstee plot of Gly-Sar uptake in the different cell culture systems ($n = 3$, mean ± SE). *V* and *C* represent the uptake rate (nmol/h/mg protein) and Gly-Sar concentration (mM), respectively. (▲) CHO/hPEPT1 cells; (■) CHO–K1 cells; (●) Caco-2 cells.

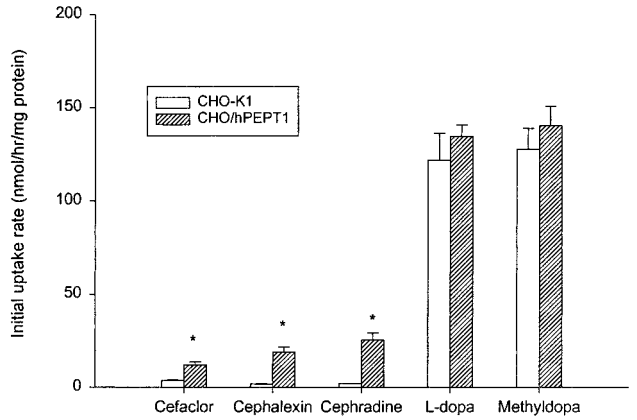

Figure 3—Cellular uptake of peptidyl and nonpeptidyl drugs in CHO/hPEPT1 cells (hatched bars) and in CHO–K1 cells (open bars) ($n = 3$, mean ± SE). (*) indicates $p < 0.01$.

Uptake Studies in Both Transfected and Untransfected CHO Cells—The validity of CHO/hPEPT1 cells as an uptake model was examined using nonpeptidyl drugs as well as peptidyl compounds. Cellular uptake of β-lactam antibiotics was evaluated in CHO/hPEPT1 cells and compared with that in CHO−K1 cells. Initial uptake rate of each drug was determined from the linearity of time versus uptake curve. Estimated uptake ratio between CHO/hPEPT1 cells and CHO−K1 cells (uptake $rate_{CHO/hPEPT1}$/uptake $rate_{CHO-K1}$) was 3.3 for cefaclor, 10.3 for cephalexin, and 12.1 for cephradine (Figure 3). The cellular uptake of β-lactam antibiotics was significantly ($p < 0.01$) increased in CHO/hPEPT1 cells compared with that in CHO−K1 cells. These results demonstrated that CHO/hPEPT1 cells greatly enhanced peptide transport activity via the transfection of hPEPT1 gene.

The cellular uptake of L-dopa and α-methyldopa which are known to be substrates of amino acid transporters[23,24] was also evaluated in both CHO/hPEPT1 cells and CHO−K1 cells. As shown in Figure 3, amino acid analogues, L-dopa and α-methyldopa, showed significant cellular uptake in both CHO−K1 cells and CHO/hPEPT1 cells which were even higher than β-lactam antibiotics. These results implicated that CHO/hPEPT1 cells expressed a high background level of the amino acid transport system which is inherited from the native CHO cells. This explanation is also supported by other report that CHO cells exhibited some amino acid transport systems such as system A, ASC, and L.[25] For clarification, the expression level of amino acid transporters in CHO/hPEPT1 cells should be further evaluated by using antibodies specific for these transporters. Collectively, due to the high expression of amino acid transporters, uptake study alone in CHO/hPEPT1 cells is insufficient for screening peptidomimetic drug candidates.

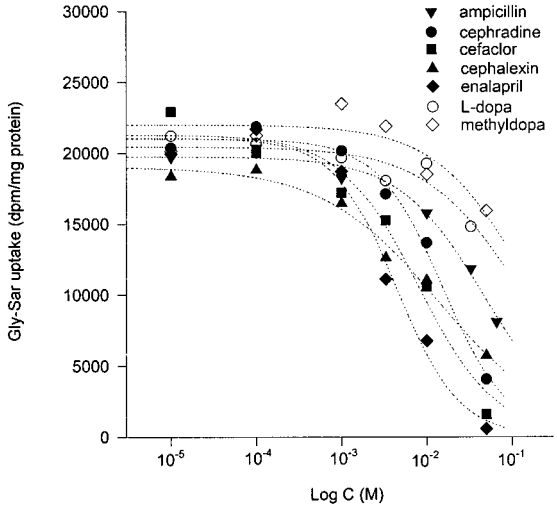

Figure 4—Inhibition of Gly-Sar uptake in CHO/hPEPT1 cells (mean ± SE): two independent studies were done for each inhibitor and every independent study had $n = 3$. Log *C* represents the inhibitor concentration.

Table 2—Inhibition Effect of Peptidomimetic Drugs on Gly-Sar Uptake in CHO/hPEPT1 Cells

	IC_{50} (mM)[a]
Gly-Sar	0.7 ± 0.1
enalapril	4.5 ± 0.7
cefaclor	8.2 ± 1.8
cephalexin	13.7 ± 3.0
cephradine	15.3 ± 2.4
ampicillin	47.4 ± 6.0
L-dopa	141.2 ± 40.4
methyldopa	151.6 ± 21.4

[a] IC_{50} was determined from two independent studies, and each study has $n = 3$, mean ± SE.

Inhibition of Gly-Sar Uptake in CHO/hPEPT1 Cells—The potential of CHO/hPEPT1 cells as a rapid screening tool for peptidyl drug candidates was further examined through inhibition studies using peptidomimetic drugs (e.g., β-lactam antibiotics, enalapril) as well as nonpeptidyl drugs such as L-dopa and α-methyldopa (Figure 4). IC_{50} was determined as the drug concentration to demonstrate 50% inhibition of Gly-Sar uptake and summarized in Table 2. While L-dopa and α-methyldopa did not inhibit Gly-Sar uptake within the therapeutic concentrations, β-lactam antibiotics and enalapril exhibited significant inhibition of Gly-Sar uptake (low IC_{50}), implying that Gly-Sar and the peptidyl derivatives share the same peptide transport system for cellular uptake. Lower IC_{50} indicates higher binding affinity to the peptide transporter, and thus enhancement of peptide transporter-mediated absorption is expected from lower IC_{50} values. Carrier-mediated permeability values (P_C*) of β-lactam antibiotics and enalapril from our previous studies[26–28] were compared with inhibition effects on the peptide transporter (Figure 5). As shown in Figure 5, IC_{50} values of peptidomimetic drugs were reciprocally correlated to the intestinal permeability in rats ($r^2 = 0.91$, $p < 0.05$). These results suggest that inhibition studies on Gly-Sar uptake in CHO/hPEPT1 cells may rapidly elucidate the ability of a drug to interact with the hPEPT1 transporter.

Generally speaking, inhibition studies are not always a good predictor for the actual cellular uptake of drug candidates, since binding to a transporter does not neces-

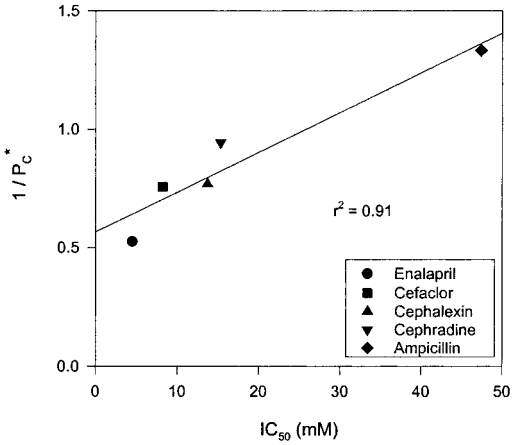

Figure 5—Correlation between IC_{50} in CHO/hPEPT1 cells and the intestinal permeability in rats: P_c * represents the dimensionless carrier-mediated permeability in rats. Permeability data were selected from refs 25–27.

sarily guarantee drug transport into cells. However, false positives may do little harm in the discovery of drug candidates for oral administration, since they can be excluded by further evaluation. Therefore, competitive inhibition studies in CHO/hPEPT1 cells as well as Caco-2 cells could be used for the initial screening of promising candidates from the various drug derivatives, and then more rigorous studies are necessary for further screening of drug candidates.

In conclusion, our present study can be summarized as follows. First, CHO/hPEPT1 cells significantly enhanced peptide transport activity via overexpression of hPEPT1 gene. Second, due to the high background level of amino acid transporters, the cellular uptake study alone in CHO/hPEPT1 cells is insufficient for the screening of peptidyl drugs. Third, inhibition study in CHO/hPEPT1 cells can be served as an alternative in vitro model to support the drug discovery process targeting the peptide transporter.

References and Notes

1. Walter, E.; Kissel, T.; Amidon, G. L. The intestinal peptide carrier: A potential transport system for small peptide derived drugs. *Adv. Drug Del. Rev.* **1996**, *20*, 33−58.
2. Bai, J. P. F.; Stewart, B. H.; Amidon, G. L. Gastrointestinal Transport of Peptide and Protein Drugs and Prodrugs, *Handbk. Exp. Pharmacol.* **1994**, *110*, 189−206.
3. Audus, K. L.; Bartel, R. L.; Hidalgo, I. J.; Borchardt, R. T. The use of cultured epithelial and endothelial cells for drug transport and metabolism studies. *Pharm. Res.* **1990**, *7*, 435−449.
4. Hidalgo, I. J.; Raub, T. J.; Borchardt, R. T. Characterization of the Human Colon Carcinoma Cell Line(Caco-2) as a Model System for Intestinal Epithelial Permeability. *Gastroenterology* **1989**, *96*, 736−749.
5. Tamai, I.; Takanaga, H.; Maeda, H.; Sai, Y.; Ogihara, T.; Higashida, H.; Tsuji, A. Participation of a proton-cotransporter, MCT1, in the intestinal transport of monocarboxylic acids. *Biochem. Biophys. Res. Commun.* **1995**, *214*, 482−489.
6. Mesonero, J.; Matosin, M.; Cambier, D.; Rodriguez-Yoldi, M. J.; Brot-Laroche, E.; Sugar-dependent expression of the fructose transporter GLUT5 in Caco-2 cells. *Biochem. J.* **1995**, *312*, 757−762.
7. Chong, S.; Dando, S. A.; Soucek, K. M.; Morrison, R. A. In vitro permeability through Caco-2 cells is not quantitatively predictive of in vivo absorption for peptide-like drugs absorbed via the dipeptide transporter system. *Pharm. Res.* **1996**, *13*, 120−123.
8. Fei, Y. J.; Kanai, Y.; Nussberger, S.; Ganapathy, V.; Leibach, F. H.; Romero, M. F.; Singh, S. K.; Boron, W. F.; Hediger, M. A. Expression cloning of a mammalian protein-coupled oligopeptide transporter. *Nature* **1994**, *386*, 563−566.
9. Liu, W.; Ramamoorthy, S.; Fei, Y. J.; Ganapathy, N. E.; Hediger, M. A.; Ganapathy, V.; Leibach, F. H. Molecular cloning of PEPT2, a new member of the H^+/peptide cotransporter family from human kidney. *Biochim. Biophys. Acta.* **1995**, *1235*, 461−466.
10. Dantzig, A. H.; Hoskins, J.; Tabas, L. B.; Bright, S.; Shepard, R. L.; Jenkins, I. L.; Duckworth, D. C.; Sportsman, J. R.; Mackensen, D.; Rosteck P. R., Jr.; Skatrud, P. L. Association of intestinal peptide transport with a protein related to the cadherin superfamily, *Science* **1994**, *264*, 430−433.
11. Liang, R.; Fei, Y. J.; Prasad, P. D.; Ramamoorthy, S.; Han H.; Yang-Feng, T. L.; Hediger, M. A.; Ganapathy, V.; Leibach, F. H. Human intestinal H^+/peptide cotransporter: cloning, functional expression and chromosomal localization *J. Biol. Chem.* **1995**, *270*, 6456−6463.
12. Terada, T.; Saito, H.; Mukai, M.; Inui, K. Characterization of stably transfected kidney epithelial cell line expressing rat H+/Peptide cotransporter PEPT1: localizaion of PEPT1 and transport of beta-lactam antibiotics. *J. Pharmacol. Exp. Ther.* **1997**, *281*, 1415−1421.
13. Ganapathy, M. E.; Brandsch, M.; Prasad, P. D.; Ganapathy, V.; Leibach, F. H. Differential recognition of β-lactam antibiotics by intestinal and renal peptide transporters, PEPT 1 and PEPT 2. *J. Biol. Chem.* **1995**, *270*, 25672−25677.
14. Covitz, K. Y., Amidon, G. L. Sadee, W. Human dipeptide transporter, hPEPT1, stably transfected into chinese hamster ovary cells., *Pharm. Res.* **1996**, *13*, 1631−1634.
15. Lowry, O. H.; Rosebrough, N. J.; Farr, A. L.; Randall, R. J. Protein measurement with the Folin phenol reagent. *J. Biol. Chem.* **1951**, *193*, 265−275.
16. Walter, E.; Janich, S.; Roessler, B. J.; Hilfinger, J. M.; Amidon, G. L.; HT29-MTX/Caco-2 cocultures as an in vitro model for the intestinal epithelium: in vitro-in vivo correlation with permeability data from rats and humans. *J. Pharm. Sci.* **1996**, *85*, 1070−1076.
17. De Lean, A.; Munson, P. J.; Rodbard, D. Simultaneous analysis of families of sigmoidgand assay and physiological dose−response curves. *Am. J. Physiol.* **1978**, *235*, E97−102.
18. Kramer, W.; Girbig, F.; Gutjaha, U.; Kleemann, H.-W.; Leipe, I.; Urbach, H.; Wagner, A. Interaction of renin inhibitors with the intestinal uptake system for oligopeptides and beta-lactam antibiotics. *Biochim. Biophys. Acta* **1990**, *1027*, 25−30.
19. Hu, M.; Subramanian, P.; Mosberg, H. I.; Amidon, G. L. Use of the peptide carrier system to improve the intestinal absorption of L-α-methyldopa: carrier kinetics, intestinal permeabilities, and in vitro hydrolysis of dipeptidyl derivatives of L-α-methyldopa. *Pharm. Res.* **1989**, *6*, 66−70.
20. Dantzig, A. H.; Bergin, L. Uptake of the cephalosporin, cephalexin, by a dipeptide transport carrier in the human intestinal cell line, Caco-2. *Biochim. Biophays. Acta*, **1990**, *1027*, 211−217.
21. Han, H−k.; de Vrueh, R. L. A.; Rhie, J. K.; Covitz, K.-M. Y.; Smith, P. L.; Lee, C.-P.; Oh, D.-M.; Sadée, W.; Amidon, G. L. 5′-Amino Acid Esters of Antiviral Nucleosides, Acyclovir and AZT, Are Absorbed by the Intestinal PEPT1 Peptide Transporter. *Pharm. Res.* **1998**, *15*(8), in press.
22. Mackenzie, B.; Loo, D. D. F.; Fei, Y.-J.; Liu, W.; Ganapathy, V.; Leibach, F. H.; Wright, E. M. Mechanisms of the human intestinal H^+-coupled oligopeptide transporter hPEPT1. *J. Biol. Chem.* **1996**, *271*, 5430−5437.
23. Stenbaek, O., Myhre, E., Rugstad, H. E., Arnold, E.; Hansen, T. Pharmaco-kinetics of methyldopa in healthy man. *Eur. J. Clin. Pharmacol.* **1977**, *12*, 117−123.
24. Shindo, H.; Komai, T.; Kawai, K. Studies on the metabolism of D- and L-isomers of 3,4-dihydroxyphenylalanine (DOPA). V. Mechanism of intestinal absorption of D- and L-DOPA-^{14}C in rats. *Chem. Pharm. Bull. (Tokyo)* **1973**, *21*, 2031−2038.
25. Shotwell, M. A.; Jayme, D. W.; Kilberg, M. S.; Oxender, D. L. Neutral amino acid transport systems in Chinese hamster ovary cells. *J. Biol. Chem.* **1981**, *256*, 5422−5427.
26. Friedman, D. I.; Amidon, G. L. Passive and carrier-mediated intestinal absorption components of two angiotensin converting enzyme (ACE) inhibitor prodrugs in rats: enalapril and fosinopril. *Pharm. Res.* **1989**, *6*, 1043−1047.
27. Sinko, P. J.; Amidon, G. L. Characterization of the oral absorption of β-lactam antibiotics. I. Cephalosporins: Determination of intrinsic membrane absorption parameters in the rat intestine in situ. *Pharm. Res.* **1988**, *5*, 645−650.
28. Oh, D.-M.; Sinko, P. J.; and Amidon, G. L., Characterization of the oral absorption of several aminopenicillins: Determination of intrinsic membrane absorption parameters in the rat intestine in situ. *Int. J. Pharm.* **1992**, *85*, 181−187.

Acknowledgments

We appreciate Dr. W. Sadée and Dr. K. M. Covitz (University of California, San Francisco) for providing the CHO-K1 and CHO/hPEPT1 cells. This work was supported by NIH/NIGM grant No. GM 37188 and a grant from Parke-Davis Pharmaceutical Research.

JS980132E

Activity–Stability Considerations of Trypsinogen during Spray Drying: Effects of Sucrose

STELIOS T. TZANNIS*,† AND STEVEN J. PRESTRELSKI‡

Contribution from *Biopharmaceutical R&D, ALZA Corporation, 950 Page Mill Road, Palo Alto, California 94303.*

Received January 9, 1998. Accepted for publication November 25, 1998.

Abstract □ The preparation and processing of protein pharmaceuticals into powders may impose significant stresses that could perturb and ultimately denature them. In many cases their stabilization through added excipients is necessary to yield native and active proteins. In this study, the effect of spray drying on the structure and activity of a model protein (trypsinogen) was investigated. In the absence of excipients, spray drying resulted in small losses of its enzymatic activity. Protein conformational rearrangements in the solid state (observed via FTIR) and irreversible aggregation (upon reconstitution) constituted the major degradation pathways. The irreversible unfolding in the solid state was also confirmed by solution calorimetric studies that indicated a decreased thermal stability of the spray-dried protein after reconstitution. The presence of sucrose, a thermal and dehydration stress stabilizer, induced a concentration-dependent protective effect. Protein protection was afforded even at low carbohydrate concentrations, while at specific mass ratios (sucrose-to-protein = 1:1) complete activity preservation was achieved. However, at the high end of sucrose concentrations, a small destabilization was evident, indicating that excluded volume effects may be undesirable during preparation of protein microparticles via spray drying. The profile of both the protein conformational changes and thermal stability in the solid state closely followed that of the incurred activity losses, indicating that protein stabilization during dehydration is crucial during processing of these polypeptides.

Introduction

The increased needs for accurate, on-site, and controlled delivery of therapeutic peptides and proteins have led to novel strategies for their release.[1,2] However, their application and successful commercial development may require the formulation of these labile pharmaceutics into alternative forms to improve their bioavalability as well as to achieve stability levels beyond the conventional shelf life requirements. One such approach is their preparation into solid microparticle forms. In the particular case of pulmonary delivery via dry powder inhalers, this requirement becomes even more important since the efficient deposition to the lung, and therefore the therapeutic benefit, requires particles in the range of 1 to 3 μm.[3–5] Further, to minimize physical and chemical degradation reactions and maintain the finished product's physical properties during long-term storage, the protein powders must be produced and maintained at low moisture contents.[6–9]

Several methods have been employed for microparticle production including spray drying,[10,11] spray freeze-drying,[12] ball or jet milling of lyophilized powders, precipitation in supercritical antisolvents,[13] and coprecipitation with water-soluble starch.[14] Of these, spray drying appears to be one of the most promising because of its capacity to produce particles with appropriate characteristics, narrow particle size distribution, process simplicity, and energy efficiency. Moreover, previous efforts have demonstrated the feasibility of its use for processing of pharmaceutical proteins.[11] In contrast to lyophilization, which utilizes freezing and sublimation processes to produce a cake during an energy-intensive and time-consuming process, spray drying is a fast and cost-effective dehydration process. During this operation, heat from a preheated gas stream is used to evaporate microdispersed droplets produced by atomization of a continuous liquid feed.

Among the main drawbacks in the production of protein solid state formulations are the severe stresses that may be imposed during processing. Previous studies have indicated that lyophilization, although it exerts significantly smaller thermal effects than spray drying, can have a significant impact on the structure and stability of several proteins.[15–17] Due to their nature, the processes involved in spray drying impose several stresses that can potentially destabilize labile biological molecules such as proteins. During atomization, proteins are exposed to high pressure and to potentially harmful air–liquid interfaces; both such stresses are known to compromise protein structural integrity[11,18] and decrease their enzymatic or biological activity.[18–20] Previous studies have suggested that heating and subsequent dehydration during the drying step constitute the major degradative stresses.[10] In particular, the outlet temperature during spray drying has been correlated with activity losses of heat-sensitive materials.[10,21,22] Although sucrose would be expected to aggravate interfacial denaturation during atomization via an increase of the solution surface tension,[23,24] it is known to exert an effective baroprotective effect.[25] Finally, well documented is the ability of disaccharides to preserve protein structure and activity in the solution state via their excluded volume effects,[24–26] as well as during thermal and dehydration stresses.[15,16,19,28]

In this effort, the effect of spray drying on the stability of a model protein, trypsinogen, and the impact of a common thermal and dehydration stress stabilizer, sucrose, were investigated. Through a variety of biophysical, chromatographic, and thermal methods of analysis, the degradation pathways of the protein in the presence and absence of sucrose during processing were investigated. Further, through examination of the conformation of spray-dried trypsinogen and its stability both in the solid state and after complete rehydration, we attempted to discern activity–stability relationships for the protein in the sucrose-containing microparticles. The results of the present study are expected to have further implications in production and stabilization of spray-dried pharmaceutical proteins.

* Author to whom all correspondence should be addressed.
† Inhale Therapeutic Systems, 150 Industrial Road, San Carlos, CA 94070. Tel: (650) 631 3276; Fax: (650) 631 3276; email: stelios.tzannis@inhale.com.
‡ Powderject Technologies, Inc., 6511 Dumbarton Circle, Fremont, CA 94555.

10.1021/js980011e CCC: $18.00
Published on Web 02/06/1999

Experimental Section

Chemicals—Trypsinogen (1× crystallized, dialyzed against 1 mM HCl and lyophilized; lot no. 38E273N), trypsin (2× crystallized, dialyzed against 1 mM HCl, and lyophilized; lot no. M5K669) and lysozyme (2× crystallized, dialyzed, and lyophilized) were purchased from Worthington Biochemical Corporation (Freehold, NJ). Myoglobin, ovalbumin (crystallized and lyophilized), and bovine serum albumin (Cohn fraction V, 96% purity) and ultrapure sucrose (>99.5% purity via HPLC, lot no. 35H03582) were purchased from Sigma Chemical Co. (St. Louis, MO). All proteins were used without further purification. Potassium phosphate, calcium chloride, and sodium chloride salts were purchased from J. T. Baker (Phillipsburg, NJ). FTIR grade potassium bromide was purchased from Aldrich Chemicals (St. Louis, MO).

Experimental Design—Protein solutions were spray-dried at different protein-to-sucrose mass ratios in order to examine and compare the processing effect on protein stability as well as to determine the optimum range of sucrose concentrations within which the maximum stabilizing effects are exerted. The carbohydrate-to-protein weight ratios examined in this study were no sucrose, 0.25:1, 0.5:1, 1:1, 2:1, 4:1 and 8:1, which correspond to sucrose concentrations of 0, 0.015, 0.029, 0.058, 0.117, 0.234, and 0.47 M, respectively. All the results in this study are reported in terms of sucrose-to-protein mass ratios.

Spray Drying—Trypsinogen particles were prepared by spray drying in a Yamato mini spray dryer model ADL-31 (Yamato Scientific, Orangeburg, NY). The proteinaceous solutions (at different sucrose mass ratios) were prepared at constant protein concentration of 2% w/v in 1 mM HCl. The pH of all prepared solutions ranged from 3.05 to 3.15; this low pH is necessary to minimize autolysis of the enzyme.[29] Before operation, they were filtered through 0.2-μm nylon filters to remove contaminants or aggregates formed during the solution preparation. The solutions were continuously fed to the spray dryer at an approximate flow rate of 3 mL/min and were dried at an inlet temperature of 120 °C; outlet temperatures ranged from 85 to 90 °C. Both the drying and atomization processes utilized room air with relative humidities (RH) that during the experiments ranged between 35% and 55%. Powders were collected in a collection vessel through a cyclone trap and were then aliquoted in lyophilization vials into a drybox (Ray Products, Inc., El Monte, CA); the latter was operated under constant nitrogen purge, providing an atmosphere of 1% to 10% RH. The vials were then capped, sealed, and stored at −20 °C until further analysis.

Particle Size Analysis—The particle size of the spray-dried trypsinogen−sucrose powders prepared for this study was determined with a Horiba LA-900 (Irvine, CA) laser light size analyzer. Small amounts of powders were dispersed in an excess of poly(ethylene glycol) 400 by overnight stirring. The suspension concentration was adjusted to attain optimal obscuration. The samples were then analyzed in a static mode; measurements were repeated in triplicates over a 20-min period, to ensure that no dissolution or powder agglomeration occurred. The size distribution was expressed in terms of volume median diameter, particle size range, and span. The latter represents a measure of the width of the volume distribution relative to the median diameter and was defined as [D(v, 90)-D(v, 10)]/D(v, 50), where D(v, 90), D(v, 50), and D(v, 10) are the equivalent volume diameters at 90, 50, and 10% cumulative volume, respectively.

Moisture Analysis—The moisture content of the spray-dried trypsinogen powders was analyzed via Karl Fisher titration; assays were performed on an Aquatest 10 Karl Fisher Coulorimetric Titrator (Seradyn, Indianapolis, IN), that was calibrated with anhydrous methanol. The moisture content of the protein microparticles was monitored in triplicate using a methanol-extraction protocol. One milliliter of anhydrous methanol was added in 2-mL lyophilization vials containing known amounts (approximately 10 to 50 mg) of powder. The vials were then subjected to brief sonication and mild shaking, to facilitate the moisture extraction process. For the moisture determinations, 200 to 500 μL of the samples were injected in the Karl Fischer coulorimeter. The moisture content was calculated after subtraction of the background moisture of methanol, and results were expressed on a percent total weight basis.

Protein Concentration Determination—Protein concentration in solution was determined by UV/vis spectroscopy; spectra were recorded on a Beckman model DU 640 (Beckman Instruments Inc., Fullerton, CA) spectrophotometer equipped with an automatic six-cell holder, set up with the appropriate transport mechanism. The cells were thermostated via a constant temperature Neslab circulator, model RTE-111M (Neslab Instruments Inc., Newington, NH). Spectra were recorded at 25 °C between 240 and 400 nm at 50-second intervals with a scan speed of 240 nm/min using 1-cm path length quartz cuvettes. Protein concentrations were determined using the absorbance at 280 nm of the light scattering-corrected spectra and an extinction coefficient of 1.54 mL mg^{-1} cm^{-1};[30] light scattering corrections were performed using a built-in function.

Enzymatic Activity Assay—The proteolytic activity of trypsinogen was determined via an appropriate modification of an established assay.[31,32] Briefly, trypsinogen activity was analyzed by first activation to trypsin by addition of the equivalent of 20 μg of trypsin to a 1 mL solution of 0.5 mg/mL trypsinogen in 10 mM Tris-HCl, 20 mM $CaCl_2$ with 100 mM KCl, pH 8.0. Activation was allowed to reach a maximum by incubating for 4 h at room temperature. The activation process was then stopped by addition of 10 μL of 1 N HCl. The activity determination reaction was initiated by adding 33 μL of an appropriate dilution of the activated trypsinogen to 967 μL of *p*-toluenesulfonyl-L-arginine methyl ester (TAME) (Worthington Biochemical Corp., Freehold, NJ). Enzymatic activity rates were followed by the rate of absorbance increase at 247 nm for 5 min at 25 °C. All activity assays were performed in triplicate, and the reported results were corrected for the intrinsic trypsin activity in the reaction mixture.

Aggregation Status—The presence and amount of soluble (covalent and noncovalent aggregates) in the spray-dried trypsinogen powders were determined via size exclusion HPLC analysis as follows: the stationary phase was a 300 Å, 30 cm × 7.8 mm Progel-TSK Supelco column (molecular weight range 10−120 kDa). The mobile phase consisted of a 10 mM phosphate buffer at pH 7.4 prepared in deionized water; the flow rate was set at 0.5 mL/min. Typically, 10 μL of the spray-dried protein samples reconstituted at approximately 5 mg/mL in 1 mM HCl were loaded onto the column and were eluted with the mobile phase at a flow rate of 0.5 mL/min. Experiments were performed on a Waters (Bedford, MA) system equipped with a 626 model pump and a 996 photodiode array detector. Prior to determination, the samples were loaded to a 717 Plus autosampler (Waters, Bedford, MA), which was thermostated at 4 °C; the column was maintained at room temperature. Trypsin, lysozyme, myoglobin, bSA, and ovalbumin were used as internal standards for molecular weight determination. The relative amount of monomeric trypsinogen was determined by comparison of the percent peak area to that of a standard solution of the protein.

In an effort to examine the presence of insoluble aggregates, 0.5 mL of the reconstituted solutions was centrifuged at 12000 rpm for 20 min in an Eppendorf centrifuge model 5415C (Brinkmann Instruments, Westbury, NY). The supernatant (400 μL) was carefully removed and filtered through 0.2 μm nylon filters; the filtrate was then diluted in 1 mM HCl, and its concentration was determined via UV−vis spectroscopy. The amount of insoluble (covalent and noncovalent) trypsinogen aggregates was determined via mass balance from the protein concentration before and after the centrifugation and filtration steps. All determinations were performed in triplicate.

Protein Secondary Structure—The secondary structure of the spray-dried trypsinogen powders was determined via Fourier transform infrared (FTIR) spectroscopy. FTIR spectra were recorded on a Nicolet Magna 550 spectrophotometer (Madison, WI) equipped with a DTGS detector. The spectrometer and the sample compartment were continuously purged, at a constant rate of 50 ft^3/min, with air that was dried via a Balston air-dryer (Whatman, Pleasanton, CA). Double-sided interferograms (1024) were collected in the 4000−900 cm^{-1} range at 4 cm^{-1} resolution, coadded, apodized with a Happ−Genzel function, and Fourier transformed.

Solution state FTIR spectra were recorded at room temperature in the transmission mode using CaF_2 windows with a 6 μm Mylar spacer (Graseby Specac, Smyrna, GA). The spectral solvent contributions in the solution state were removed by subtraction of a solvent spectrum, which was recorded under identical conditions; spectral subtractions were performed with the OMNIC software (Nicolet, Madison, WI) Version 2.0. The subtractions were performed in order to remove the combination water band at 2150 cm^{-1}. The resulting spectra, as well as the calculated second derivative spectra, were smoothed with a nine-point Savitzky-

Table 1—Particle Size and Size Distribution of Spray-Dried Trypsinogen-Sucrose Powders[a]

sucrose:trypsinogen mass ratio	median diameter[b] (μM)	size range (μM)	span[c]
no sucrose	5.0 ± 2.2	1.1–17.4	1.04 ± 0.02
0.25:1	5.2 ± 2.3	1.3–17.4	1.14 ± 0.03
0.5:1	5.6 ± 2.3	1.5–19.9	1.05 ± 0.03
1:1	5.7 ± 2.8	1.5–26.1	1.06 ± 0.01
2:1	6.4 ± 1.8	1.5–17.3	0.91 ± 0.05
4:1	6.0 ± 1.9	1.5–39.2	1.36 ± 0.04

[a] Values represent averages and standard deviations of triplicate measurements. [b] Volumetric median diameter (D(v, 50)). [c] Span = [D(v, 90) − D(v, 10)]/D(v, 50), where D(v, 90), D(v, 50), and D(v, 10) are the equivalent volume diameters at 90, 50, and 10% cumulative volume, respectively.

Golay convolution window. FTIR spectra of trypsinogen powders were collected in the transmission mode using KBr pellets via a computer-controlled automatic sample wheel (Spectra Tech Inc., Shelton, CT). Both the original absorbance spectra and their second derivatives were smoothed via a nine-point Savitzky-Golay window. The spectral second derivatives in the amide I region (1600−1700 cm^{-1}) were used for the calculation of correlation coefficients (r^2 values).[16] These coefficients provide an estimate of the deviation of the structure of the examined sample from the native state by comparison of the second derivatives of the examined sample with that of the native protein in solution.

Solution State Protein Stability—The thermal stability of the trypsinogen−sucrose solution formulations before and after spray drying followed by reconstitution at 20 mg/mL in 1 mM HCl was examined by differential scanning calorimetry. Approximately 750 μL of protein solutions were loaded on preweighed stainless steel pans, were hermetically sealed, and were loaded on the sample compartment of a model 4207 Calorimetry Sciences DSC (Provo, UT). For each measurement a blank cell was loaded with 750 μL of 1 mM HCl solution at the appropriate sucrose concentration. The samples, after a 30-min equilibration step at 10 °C, were heated to 90 °C at a rate of 60 °C/hr and were subsequently cooled at the same rate down to 10 °C.

The midpoint of temperature denaturation ($T_{unfolding}$) was determined at the peak maximum, while the enthalpies of the transitions ($\Delta H^0_{unfolding}$ and $\Delta H^0_{folding}$ for the unfolding and refolding reaction, respectively) were determined by integration of the heat capacity curves after subtraction of a polynomial baseline drawn between 30 and 75 °C.

Powder Thermal Stability—The thermal stability of trypsinogen in the spray-dried formulations was determined by the endotherm ($T_{melting}$) obtained by solid state differential scanning calorimetry (DSC). The endothermic thermal transitions were assigned to protein denaturation, as per previous literature studies.[33−35] For the data analysis, we also assumed complete miscibility of protein and sucrose in the solid state formulations, as demonstrated in previous studies of lyophilized sucrose-protein mixtures.[36] The experiments were performed on a Pyris 1 Perkin-Elmer DSC (Norwalk, CT) equipped with an intracooler; the instrument was calibrated with indium before sample analysis. Approximately 10−20 mg of the samples was loaded under ambient conditions in sealed aluminum pans. After a short preequilibration at 10 °C, the samples were heated to 200 °C at a heating rate of 5 °C/min. All measurements were performed in triplicate.

Results

Particle Size Analysis—The size distribution analysis of the spray-dried trypsinogen−sucrose particles is given in Table 1. The results indicate that spray drying of trypsinogen produces a homogeneous monomodal distribution of protein particles of an approximate diameter of 5 μm and a narrow size distribution (1.1−17.4 μm). The addition of sucrose appears to have a rather minor effect on the particle dimensions. At the highest sucrose mass ratio examined (total solids loading of 180 mg/mL), the median particle diameter reached 6.6 ± 1.9 μm. The small deviations of the particle size with the addition of sucrose would be expected since the primary determinant of the final particle size is the atomization process, indicating the suitability of this process for microparticle production.

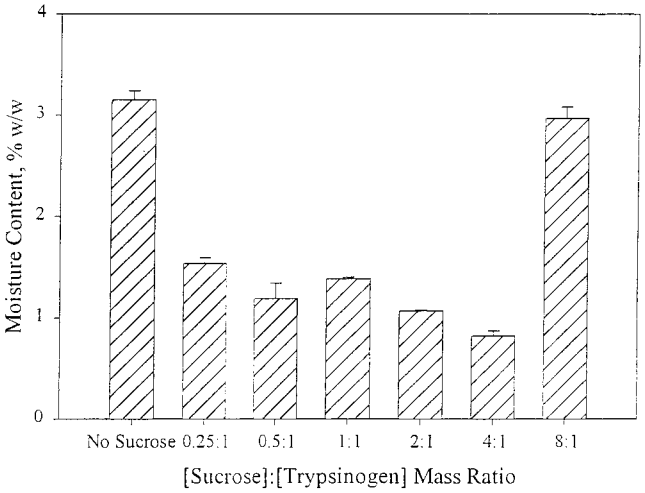

Figure 1—The effect of sucrose on the moisture contents of the spray-dried trypsinogen formulations. Error bars represent (±) one standard deviation of triplicate determinations.

Moisture Content—The moisture content of the spray-dried trypsinogen powders as a function of the protein-to-sucrose mass ratio is shown in Figure 1. The results suggest that even in the absence of secondary drying processes, such as oven drying (which has been employed as a complimentary process following an incomplete drying operation[37]), spray drying can provide powders of low moisture contents.

The final moisture content achieved when trypsinogen was spray-dried in the absence of excipients is 3.1 ± 0.1% w/w (or 3.2 ± 0.2% w/w on a dry protein basis). This amount is even lower than the calculated equivalent water monolayer value of 5.4%; these calculations assume the attachment of one water molecule per charged amino acid.[38] However, this approximation assumes that all charged amino acids are accessible to water vapor. Moreover, spray drying is a flash process, and therefore the obtained moisture contents do not reflect an equilibrium value.

Gradual addition of sucrose progressively decreases the attained moisture content. This is surprising, as one would expect that the presence of a hygroscopic substance like sucrose would increase the amount of residual sorbed moisture. This decrease indicates a possible specific hydrogen bonding interaction between the two substances. At the highest end of sucrose concentrations examined (mass ratio of 8:1), however, the final moisture content increased to 2.9 ± 0.1% w/w; the increased relative humidity during collection and aliquoting may have contributed to this increase.

Activity Profile—The effect of spray drying on the activity profile of trypsinogen at different sucrose mass ratios is shown in Figure 2. When processed in the absence of excipients, trypsinogen loses part of its enzymatic activity, as compared to the unprocessed material (85.1 ± 3.3%). However, the addition of sucrose to the spray-dried solution appears to exert a concentration-dependent stabilizing effect.

Even small amounts of sucrose, sucrose-to-protein mass ratio of 0.25:1, appear to partially stabilize the protein, which recovers part of its initial activity. Increasing concentrations of the carbohydrate further protect trypsinogen in a concentration-dependent fashion. At equal mass ratios of protein and sucrose, the complete restoration of the initial enzymatic activity (99.9 ± 1.5%) was achieved,

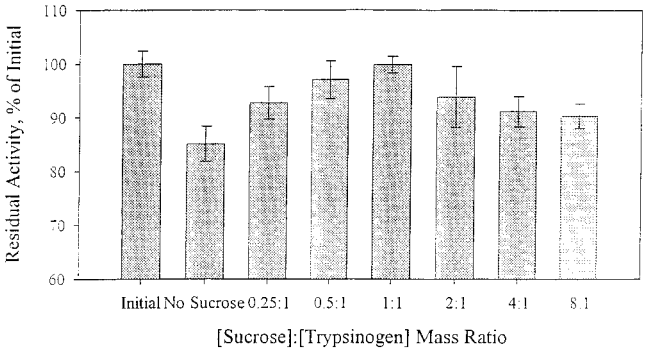

Figure 2—The effect of sucrose on the residual activity of trypsinogen after spray drying. Error bars represent (±) one standard deviation of triplicate determinations.

indicating the complete stabilization of the protein. However, at higher sucrose mass ratios, a small destabilization of trypsinogen is evident. The destabilizing effect is intensified with increasing sucrose concentrations, since the recovered activity of trypsinogen in the spray-dried formulations decreases with increasing sucrose mass ratio. At the high end of the examined carbohydrate concentrations (sucrose-to-protein mass ratios of 4:1 and 8:1), the activity losses approach those observed in the absence of the carbohydrate (91.13 ± 2.82% and 90.33 ± 2.3% of initial, respectively), implying the vast elimination of the protective action of sucrose.

The presence of sucrose in the assay reaction mixture does not have any effect by itself on the determined enzymatic activity of trypsinogen (data not shown). Thus, the observed activity profiles of the spray-dried protein powders truly represent the effects of sucrose on the protein stability during processing rather than an effect of the carbohydrate on the enzymatic activity assay.

Aggregation Profile—The size exclusion chromatography results indicate the presence of high and low molecular weight trypsinogen products in the starting material after reconstitution at pH 3.0; only 89.3 ± 0.3% of the commercial preparation is monomeric trypsinogen. Part of the protein forms an aggregate; the main species appearing to be a dimer (9.6 ± 0.5%). Smaller fragments (approximate molecular weights of 8−12 kDa) account for the remainder of the material. The amount of monomeric and aggregated trypsinogen after reconstitution of the spray-dried powders, relative to the starting material, is shown in Figures 3a,b, respectively. When trypsinogen is spray-dried in the absence of sucrose, it fails to completely recover its initial monomeric state upon reconstitution, as indicated by the decrease of the relative peak area corresponding to the native protein. This loss represents an 8.4 ± 0.3% reduction in the relative amount of the monomeric protein as compared with the unprocessed material; this decline is fully accounted for by an increase of the relative concentration of the dimer (+8.3 ± 0.5%) after spray drying.

Addition of sucrose decreases the extent of aggregation in a concentration-dependent manner. Even small amounts of sucrose partially inhibit dimerization. Increasing concentrations of the carbohydrate progressively diminish the dimer content, up to a sucrose-to-protein mass ratio of 1:1, at which almost complete stabilization of the native protein is achieved. The monomeric state is fully retained at all higher sucrose concentrations examined (up to the highest examined mass ratio of 8:1).

In contrast, formation of insoluble aggregates does not appear to be an operative degradation pathway, as indicated by the small amounts of these species, as shown in Figure 3b. Although some insoluble aggregates were detected when trypsinogen was spray-dried without sucrose and at a sucrose-to-protein mass ratio of 8:1 (1.3 ± 2.0% and 1.64 ± 2.6%, respectively, relative to the unprocessed material) these values are well within the errors of the HPLC analysis method. To further identify the nature of aggregates, we performed SDS−PAGE electrophoresis under both native and reduced conditions. The results (not shown) indicated the absence of covalent disulfide bonds in the high molecular weight species, supporting the formation of hydrophobic aggregates.

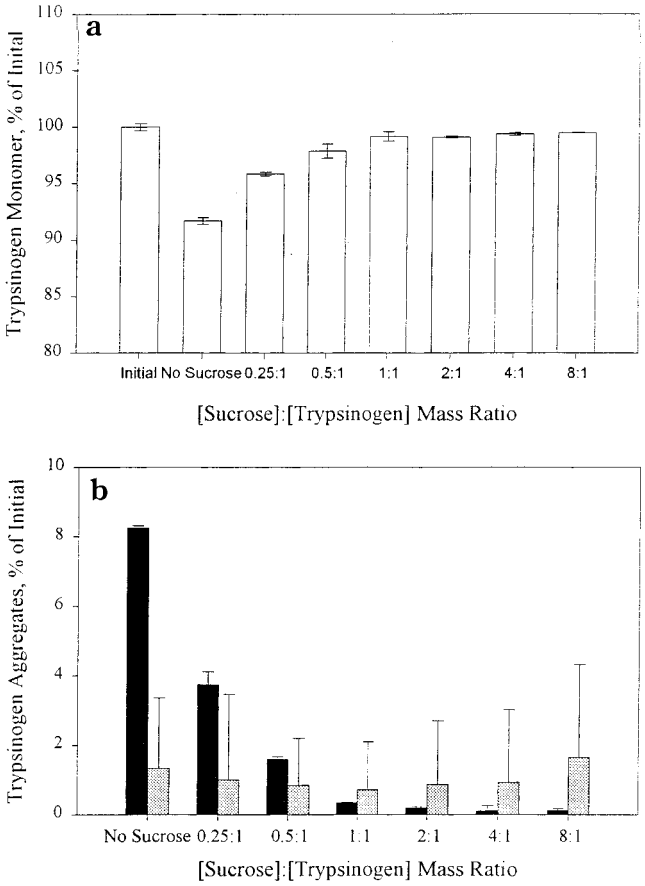

Figure 3—Aggregation status of trypsinogen following spray drying at different sucrose mass ratios and subsequent reconstitution at 5 mg/mL in 1 mM HCl: (a) Relative amount of monomer; (b) Relative amounts of dimer (black bars) and insoluble aggregates (grey bars). Error bars represent (±) one standard deviation based on triplicate determinations.

Solid State Secondary Structure—The second derivative spectra of the amide I band of trypsinogen in the spray-dried powders are displayed in Figure 4, and the calculated correlation coefficients are given in Table 2. The second derivative of the amide I band of native trypsinogen denotes the presence of a major β-sheet band centered at 1636 cm^{-1}, and other components at 1664 and 1685 cm^{-1} signifying primarily β-turn structures. When trypsinogen is spray-dried in the absence of sucrose, it undergoes a significant departure from its native solution structure. As indicated in Figure 4, the second derivative of the amide I band has lost its sharp features as the separation between the bands has diminished. Moreover, the major bands appearing in the native spectrum have all been shifted: the characteristic β-sheet band is shifted approximately 7 cm^{-1} to 1642 cm^{-1}, indicating a rearrangement of the native β-sheet structures of the protein molecule. A similar shift, but of smaller magnitude (+5 cm^{-1}), is evident for the high frequency β-turn band, which is now located at 1689 cm^{-1}. This overall departure from the native state is depicted in the low value of the computed correlation coefficient (0.54 ± 0.05).

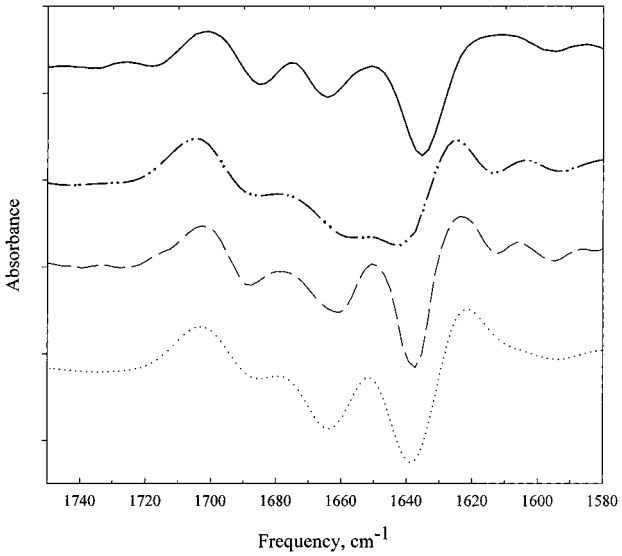

Figure 4—Amide I second derivatives of native trypsinogen in solution (solid line), and in the solid state after spray drying: in the absence of sucrose (– • • –), and with sucrose at 1:1 (– –) and 8:1 (• • • •) mass ratios.

Table 2—Correlation Coefficient Analysis of the Second Derivative Spectra of Spray-Dried Trypsinogen-Sucrose Powders

sucrose:trypsinogen mass ratio	correlation coefficient[a]
no sucrose	0.54 ± 0.05
0.25:1	0.74 ± 0.04
0.5:1	0.88 ± 0.01
1:1	0.93 ± 0.01
2:1	0.87 ± 0.06
4:1	0.78 ± 0.06

[a] Values represent averages and standard deviations of triplicate measurements.

Upon addition of sucrose in the spray-dried trypsinogen formulation (carbohydrate-to-protein mass ratios of 0.25:1−1:1), there is significant recovery of native structural features, as indicated by the increased values of the correlation coefficient. The most remarkable effect is the restoration of the sharpness of the spectral features in the amide I region. Further, the band shifts observed in the absence of sucrose are now, at least partially, reversed. As such, the major β-sheet band has shifted by +3−5 cm^{-1} to 1638 cm^{-1}, closer to its initial position in solution. Likewise, the composite band is centered at 1662 (+2 cm^{-1}) and the high frequency β-turn band at 1688 (+2 cm^{-1}). The observed band shifts occur rather abruptly upon sucrose addition, though a minor improvement appears with increasing sucrose concentration. The profile of the observed spectral restoration of the native structural features is further depicted in the profile of the correlation coefficients (0.8−0.93).

However, upon addition of larger amounts of sucrose in the protein formulation, a small destabilization of the native structure is evident, as indicated by the decreased values of correlation. This observation is in agreement with the determined residual activity results. Moreover, as indicated in Figure 5, the profile of the observed structural alterations of the spray-dried powders follows closely that of the enzymatic activity retention with titrating amounts of sucrose ($r^2 = 0.84$). This correlation provides corroborative evidence that the protein structural deformation in the solid state may be at least partially responsible for the incurred activity losses. Further, it provides indirect evidence that some of the protein molecules may not be

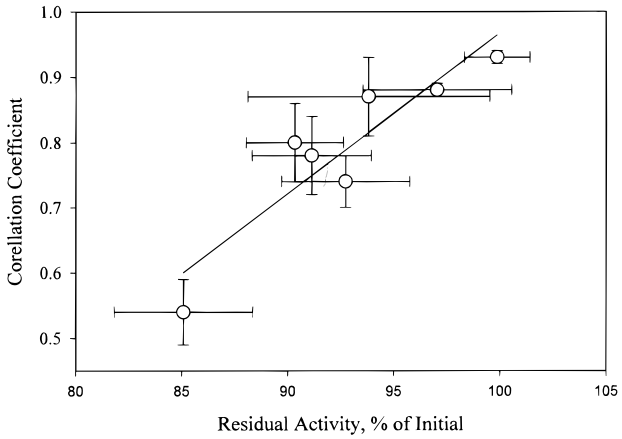

Figure 5—Correlation between the FTIR correlation coefficients and the residual trypsinogen activity after spray drying ($r^2 = 0.84$). Error bars represent (±) one standard deviation based on triplicate determinations.

Table 3—Solid State Thermal Stability of the Spray-Dried Trypsinogen-Sucrose Powders

sucrose:trypsinogen mass ratio	T_{onset}[a] (°C)	$T_{melting}$[a] (°C)	$\Delta H_{melting}$[a] (J/gr)
no sucrose	122.5 ± 3.4	143.5 ± 3.4	54.4 ± 12.5
0.25:1	139.7 ± 2.5	165.7 ± 2.1	92.6 ± 8.9
0.5:1	159.5 ± 1.7	173.7 ± 2.3	139.9 ± 11.5
1:1	182.7 ± 2.5	190.6 ± 3.3	174.8 ± 14.2
2:1	172.1 ± 2.1	180.6 ± 1.1	214.9 ± 16.6
4:1	138.7 ± 4.1	158.6 ± 5.3	214.5 ± 15.3

[a] Values represent averages and standard deviations of triplicate measurements.

able to refold to their native, fully active state upon reconstitution.

Solid State Thermal Stability—The denaturation temperature ($T_{melting}$) of trypsinogen in the spray-dried powders is given as a function of the sucrose mass ratios in Table 3. The results indicate that spray drying induces a significant destabilizing effect on trypsinogen, as indicated by the decrease in the denaturation temperature, which reaches 143.5 ± 3.4 °C in the absence of sucrose. However, in agreement with the activity assays and size exclusion results, the addition of sucrose exerts a concentration-dependent stabilizing effect. When small amounts of sucrose were added to the trypsinogen solution before processing, they induced a structural stabilization of the protein in the solid state, as indicated by the continuous increase of its denaturation temperature. The maximum stabilization occurs, in agreement with the enzymatic activity determinations, at a sucrose-to-protein mass ratio of 1:1, as indicated by the highest denaturation temperature of 190.6 ± 3.3 °C.

However, further addition of sucrose decreases $T_{melting}$, indicating a reduction in the thermal stability of trypsinogen in the spray-dried powders (denaturation temperatures of 158.6 ± 5.3 °C and 161.6 ± 3.3 °C at sucrose-to-protein mass ratios of 4:1 and 8:1 respectively). The overall profile of the thermal stability of the protein in the solid state closely resembles that observed for the activity of the reconstituted protein, indicating again that the mechanism of the incurred enzymatic activity losses proceeds via reduction of the protein stability in the solid state. As indicated in the linear regression shown in Figure 6, there appears to be a good correlation between these two phenomena, as indicated by the high value of the obtained correlation coefficient ($r^2 = 0.88$). In agreement with the similar correlation of the FTIR results, this observation provides additional evidence for the involvement of solid-

Table 4—Effect of Sucrose on the Thermal Stability of Trypsinogen in Solution, before and after Spray Drying and Reconstitution in 1 mM HCl

sucrose:trypsinogen mass ratio	before spray drying			after spray drying		
	$T_{unfolding}$,[a] (°C)	$\Delta H_{unfolding}$a (kcal/mol)	$(\Delta H_{fold}/\Delta H_{unfold})^a$ (×100, %)	$\Delta H_{unfolding}$a (kcal/mol)	$\Delta H_{unfolding}$a (kcal/mol)	$(\Delta H_{fold}/\Delta H_{unfold})^a$ (×100, %)
no sucrose	61.8 ± 0.3	87.2 ± 5.4	86.9 ± 7.5	59.3 ± 0.3	75.4 ± 3.3	52.8 ± 3.9
0.25:1	61.5 ± 0.2	79.4 ± 4.7	78.7 ± 6.5	60.4 ± 0.5	80.3 ± 3.3	63.3 ± 6.1
0.5:1	61.9 ± 0.1	83.3 ± 0.7	78.8 ± 3.8	60.4 ± 0.18	3.9 ± 5.3	63.0 ± 5.7
1:1	62.0 ± 0.2	81.3 ± 2.1	72.0 ± 5.1	61.1 ± 0.3	83.1 ± 9.3	73.5 ± 12.0
2:1	62.3 ± 0.1	82.7 ± 3.3	82.9 ± 11.9	59.7 ± 0.3	77.9 ± 3.4	78.6 ± 1.1
4:1	62.9 ± 0.2	82.4 ± 1.6	75.7 ± 3.0	58.2 ± 0.2	79.0 ± 3.8	75.1 ± 3.8

[a] Values represent averages and standard deviations of triplicate measurements.

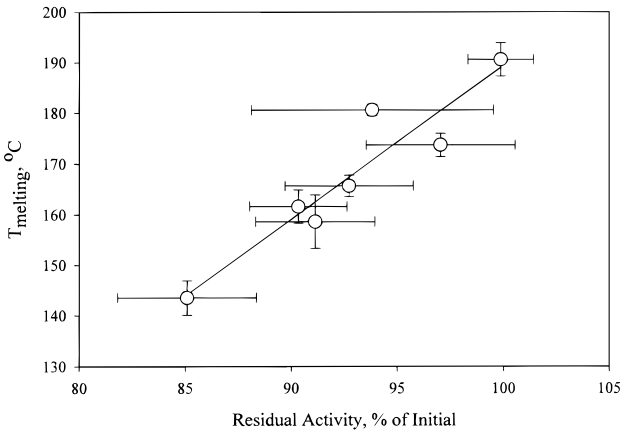

Figure 6—Correlation between the thermal denaturation temperature of trypsinogen in the solid state ($T_{melting}$) and the residual trypsinogen activity after spray drying ($r^2 = 0.88$). Error bars represent (±) one standard deviation based on triplicate determinations.

state destabilization in the mechanism of the induced activity losses of trypsinogen.

Solution Thermal Stability—The above observations prompted the further examination of the possibility of the involvement of irreversible (upon reconstitution) protein denaturation in the activity losses. We examined this hypothesis by determining the solution state thermal stability of trypsinogen at different sucrose mass ratios before spray drying and after reconstitution of the spray-dried powders. The results, which are shown in Figures 7a,b and given in Table 4, indicate the multiple effects of sucrose on the thermal stability of the protein before and after processing and reconstitution.

In the solution state, the midpoint of the thermal unfolding of trypsinogen occurs at 61.8 ± 0.3 °C. Unfolding of this protein appears to be a two-state transition as indicated by the similitude of the experimental enthalpy of the transition and that calculated by the van't Hoff equation: indeed, a second derivative of the thermogram (data not shown) indicates the presence of a single transition. Further, the transition appears to be highly reversible, as indicated by the large value of the ratio of the enthalpies of the unfolding and folding transitions ($\Delta H_{unfold}/\Delta H_{fold}$ = 86.9 ± 7.5%). Addition of small amounts of sucrose (up to a mass ratio of 1:1) does not appear to have a significant impact on the thermal stability of the protein, as indicated by the rather small deviations of both the temperature and enthalpy of unfolding. However, higher concentrations of sucrose appear to exert a protein-stabilizing effect. The magnitude of this phenomenon is largest at the highest sucrose mass ratio (8:1), as indicated by the 2.6 ± 0.1 °C elevation of $T_{unfolding}$.

The thermal stability of trypsinogen when spray-dried without sucrose and reconstituted at the initial conditions was compromised, as indicated by the decreased $T_{unfolding}$ (59.3 ± 0.3 °C). Although the enthalpy of unfolding does not change significantly, spray drying appears to exert a significant effect on the reversibility of the transition: only 52.8 ± 3.9% of the unfolded protein can reversibly refold after thermal treatment. This indicates that a significant proportion of the protein molecules was significantly perturbed from the native state during spray drying. When small amounts of sucrose (mass ratios of 4:1−1:1) were incorporated in the spray-dried formulation however, the reduction of the thermal stability of the protein molecules was alleviated, as indicated by the smaller decrease of trypsinogen's $T_{unfolding}$. The minimal destabilization appears to occur at a sucrose-to-protein mass ratio of 1:1, in agreement with the previous observations with the residual activity and solid state thermal stability analyses. However, higher sucrose concentrations fail to stabilize the protein, as indicated by the decreased values of the unfolding temperatures. Again, minimal stability is observed at the highest sucrose mass ratio, as indicated by the reduction of $T_{unfolding}$ by 5.8 ± 1.6 °C and $\Delta H_{unfolding}$ by 12.9 ± 5.4 kcal/mol relative to the native protein. The destabilization becomes even more profound when we compare it with the $T_{unfolding}$ of the same formulation prior to spray drying.

Discussion

The preparation of solid state protein formulations frequently results in their destabilization due to the stresses imposed on them during processing.[15,16] Trypsinogen appears to follow this trend when processed for microparticle production via spray drying. Protein aggregation, a frequently encountered pathway of protein destabilization during solid-state processing,[39,40] upon reconstitution can account only in part (55.8 ± 2.7%) for the observed activity losses. Another destabilization pathway must be responsible for the unaccounted inactivation. The loss of the native protein structure, as observed by the FTIR correlation analysis, during processing along with the observation of decreased stability of the reconstituted protein offers a potential elucidation of the unaccounted activity losses: it is possible that some of the spray-dried protein has departed from its native state and fails to recover its structural integrity, conformational stability, and enzymatic activity upon reconstitution. This argument is further supported by the decrease of the enthalpy of unfolding of trypsinogen after spray drying: from 87.2 ± 5.4 before to 75.4 ± 3.3 kcal/mol after processing. This represents a 13.6 ± 5.4% decrease of $\Delta H_{unfolding}$, which is, within experimental error, close to the extent of the observed activity losses (14.9 ± 3.2%). Therefore, the amount of native protein available to unfold has decreased by 13.6% after spray drying; part of this reduction must be due to the aggregated protein (8.4 ± 0.3%), while the rest can be assigned to irreversibly unfolded protein (5.5 ± 2.1%). The reason for the irreversibility is rather unclear;

it is possible that a chemical degradation reaction of a folding-crucial residue during spray drying may have impaired the correct folding of the protein upon reconstitution. Alternatively, the protein may have reached a partially unfolded state representing a local energetic minimum along its folding pathway, which cannot be overcome after reconstitution.

The addition of sucrose appears to exert a concentration-dependent stabilization effect. At low to moderate sugar-to-protein mass ratios (up to 1:1), sucrose stabilizes the protein. The stabilization appears to occur through impediment of the aggregation pathway, as indicated by the sucrose concentration-dependent decrease of the aggregated molecules, along with a stabilization of the native structure of the protein, as shown by the increased values of the FTIR correlation coefficients during processing. The stabilizing action of disaccharides has been well documented in studies of protein lyophilization.[15,16,28] In addition, sucrose and trehalose have been shown to efficiently protect hemoglobin (from oxidation via protection of its native structure)[19] and β-galactosidase during spray drying.[20]

The solution calorimetry studies of the commercial protein preparation indicated that at high concentrations, sucrose stabilizes the native state of trypsinogen. This finding is in agreement with previous studies that reported a rise of the thermal transition temperature of α-chymotrypsin, chymotrypsinogen, and ribonuclease-A upon addition of sucrose.[27] Moreover, there appears to be a linear dependence of the transition temperature on the concentration of added sucrose ($r^2 = 0.98$); a similar correlation was also suggested by Lee and Timasheff[27] on the three above-mentioned proteins. Again in agreement with these studies, the observed stabilizing effect of sucrose does not appear to be enthalpic in nature, as indicated by the little variation of the $\Delta H_{\text{unfolding}}$. The same authors[27] concluded that the stabilizing effect of sucrose arises from an increase in the apparent activation energy for the thermal perturbation of the proteins, which in turn reflects changes in the physicochemical properties of the system and in particular of the solvent structure. This is a manifestation of the excluded volume effects exerted by sucrose, which, as a natural consequence of the Le Chatelier principle, become evident at these concentrations of the carbohydrate.

However, at this concentration regime (above 2:1, or 0.117 M), the protective action of sucrose appears to have somewhat dissipated, as there is a substantial reduction of the activity of trypsinogen in the spray-dried formulations. The activity losses cannot be assigned to protein aggregation, since the protein remains essentially monomeric; this provides corroborative evidence that protein dilution in the solid matrix by the addition of sucrose molecules is the aggregation-stabilizing mechanism. Nor is a gross conformational change evident in the FTIR spectra, but rather a small departure from the native state, as indicated by the decreased values of the determined correlation coefficients. Yet, the stability of the protein in the spray-dried formulations has been considerably compromised as indicated by the decreased values of T_{melting}, shown by solid-state DSC. Upon reconstitution of these formulations, the protein fails to recover its conformational integrity, as indicated by the decreased $T_{\text{unfolding}}$ and enthalpies of unfolding. Although the activity losses in this sucrose formulation regime are smaller than those incurred in the absence of sucrose, the $T_{\text{unfolding}}$ results indicate a larger destabilization of the protein when high amounts of sucrose are incorporated in the formulation. Further, the decrease of $\Delta H_{\text{unfolding}}$ after processing provides an additional indication of the extent of the departure of the protein from its native state: at a sucrose-to-protein mass

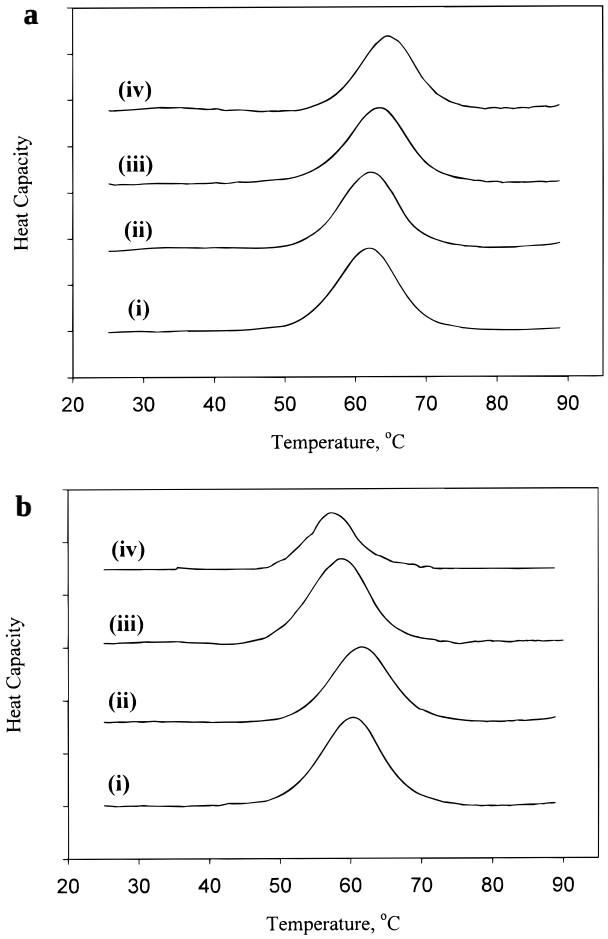

Figure 7—DSC thermograms of trypsinogen–sucrose formulations before (a) and after (b) spray drying: (i) in the absence of sucrose, and at [sucrose]:[trypsinogen] mass ratios of (ii) 1:1, (iii) 4:1 and 8:1.

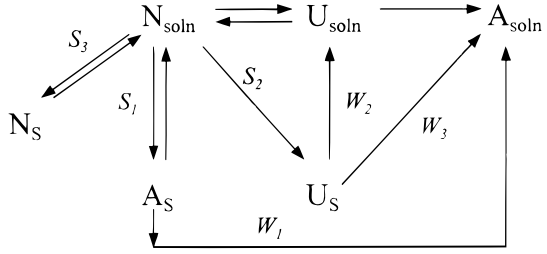

Figure 8—Proposed protein degradation mechanism during spray drying. Subscripts S and soln denote the native (N), unfolded (U), and aggregated (A) protein molecules in the solid and solution states, respectively.

ratio of 8:1 the enthalpy of unfolding has decreased from 86.2 ± 7.3 to 75.7 ± 0.5 kcal/mol, indicating an approximate decrease of 12.2% of the unfolding enthalpy. This value is again in good agreement with the incurred activity losses, indicating that irreversible structural destabilization of trypsinogen in the solid state is the degradation pathway at this end of sucrose concentrations.

Our observations seem to support the destabilization mechanism illustrated in Figure 8. Spray drying of a native protein (N_{soln}) may result in partial protein aggregation (state A_S) and unfolding (state U_S) in the solid state, via pathways S_1 and S_2, respectively. These states are supported by the intermolecular β-sheet band observed in the FTIR spectra and by the departure from the native state into a state of reduced conformational stability (observed by solid-state DSC and FTIR) data, respectively. Alternatively, some protein molecules may still retain their native state in the solid, as illustrated via pathway S_3 (state N_S).

After rehydration, some of the intermolecular contacts persist, leading to formation of soluble, hydrophobic aggregates (state A_{soln}) via pathway W_1. Moreover, some of the unfolded molecules in the solid state fail to adopt their native structure and stability and remain partially unfolded in solution (state U_{soln}) via pathway W_2. Alternatively, some unfolded molecules may participate in self-association reactions via pathway W_3. Finally, molecules that retained their native conformation and structural integrity are able to return in their native solution state (N_{soln}). Addition of sucrose appears to stabilize the protein by blocking both pathways S_1 and S_2, as indicated by both decreased aggregation, nativelike conformationally stable structures in the solid state. However, high concentrations of sucrose, while still effective in impeding aggregation, fail to efficiently stabilize the protein structure in the solid state, rendering pathway S_2 operative.

A consideration of the nature of the destabilizing stresses is particularly interesting. Protein denaturation at the air−liquid interface has been previously considered as the potential degradation pathway of human growth hormone (hGH) during spray drying.[11] Since it is well established that sucrose increases the surface tension of water,[23,24,27] one would expect that its presence would lead to preferentially increased interfacial interactions and consequent destabilization. Yet, the observed stabilizing action of sucrose contradicts this hypothesis, thereby discounting the presence of interfacial inactivation phenomena. Neither heat appears to be the destabilizing stress. If thermal stresses were responsible for the observed destabilization, then, based on the solution DSC results, it would be expected that addition of sucrose at 1:1 mass ratio would not significantly impact the stability of trypsinogen during processing. However, this is contrast with our observations, which indicated complete stabilization of the protein during spray drying at this mass ratio of sucrose, thereby ruling out the involvement of thermal stresses on trypsinogen destabilization. Finally, pressure-induced denaturation during atomization does not appear to be an operative destabilization pathway, since the addition of high concentrations of sucrose, a well-known baroprotectant,[25] would be expected to provide adequate stabilization, which is inconsistent with our observations. The elimination of these potential stresses provides corroborative evidence that dehydration is the major stress responsible for the observed structural destabilization of trypsinogen during spray drying. These observations are in agreement with studies of protein lyophilization, which indicated that the dehydration was the major stress responsible for protein denaturation.[16,41]

Protein destabilization in the solid state in the presence of large amounts of protectants has been previously observed during lyophilization of β-galactosidase with mannitol.[39] The observed activity losses were assigned to excipient crystallization in the solid state. It was thought that the decreased stabilizing effect of crystallized protectants was due to the preferential replacement of the protein−excipient with excipient−excipient interactions. Moreover, this process frequently results in increased water content of the protein-rich phase arising from its exclusion from the excipient crystals, eventuating increased protein molecular mobility and therefore a higher propensity for degradation and inactivation.

The results further indicate that spray drying of trypsinogen under conditions where excluded volume effects dominate results in compromised protein stability and resultant reduction of its enzymatic activity. If crystallization or phase separation were responsible for the protein destabilization, as was previously observed with lyophilized β-galactosidase,[39] these must arise from the exclusion of sucrose from the protein surface. As a result of this phenomenon, the sucrose molecules preferentially interact with themselves (presumably via hydrogen bonding) rather than with the protein surface, leading to the formation of separate phases: a protein-rich and a sucrose-rich phase. Indeed, exclusion is a form of phase separation at the molecular level; this separation precedes the processing step. Despite the high surface area produced during atomization, the solution distribution of each excipient in the droplets should not be expected to alter dramatically, and the microphase separation should remain. This implies that during the spray drying process, the sucrose molecules are not available to hydrogen bond efficiently with the protein, since they remain in their carbohydrate-rich regions, resulting in insufficient protection of the protein. We therefore hypothesize that it is the solution separation that is responsible for the departure from the native state and the decreased stability patterns in the solid state. This hypothesis suggests that when the dispersed droplets are dried, a similar molecular-level separation must exist in each dried particle. These observations indicate that, at high sucrose concentrations, excluded volume effects are destabilizing during protein processing in microparticles via spray drying. These are phenomena that warrant further exploration.

References and Notes

1. Langer, R. S. New Methods of Drug Delivery. *Science* **1990**, *249*, 1527−1533.
2. Robinson, J. R. Controlled Drug Delivery. Past, Present and Future, In *Controlled Drug Delivery. Challenges and Stretegies*; Park, K., Ed.; American Chemical Society: Washington, D. C., 1997; pp 1−6.
3. Gupta, P.; Hickey, A. J. Contemporary Approaches in Aerosolized Drug Delivery to the Lung. *J. Controlled Release* **1991**, *17*, 129−148.
4. Patton, J. S.; Platz, R. M. Pulmonary Delivery of Peptides and Proteins for Systemic Action. *Adv. Drug Deliv. Rev.* **1992**, *8*, 179−196.
5. Adjei, A.; Garren, J. Pulmonary Delivery of Peptide Drugs: Effects of Particle Size on Bioavailability of Leuprolide Acetate in Healthy Human Male Volunteers. *Pharm. Res.* **1990**, *7*, 565−569.
6. Hageman, M. J. Water Sorption and Solid-State Stability of Proteins, In *Stability of Protein Pharmaceuticals. Part A: Chemical and Physical Pathways of Protein Degradation*; Ahern, T. J., Manning, M. C., Eds.; Plenum Press: New York, 1992; pp 273−309.
7. Strickley, R. G., Anderson, B. D. Solid-State Stability of Human Insulin II. Effect of Water on Reactive Intermediate Partitioning in Lyophiles from pH 2−5 Solutions: Stabilization Against Covalent Dimer Formation. *J. Pharm. Sci.* **1997**, *86*, 645−653.
8. Liu, W. R., Langer, R., Klibanov, A. M. Moisture-Induced Aggregation of Lyophilized Proteins in the Solid State. *Biotechnol. Bioeng.* **1991**, *37*, 177−184.
9. Hageman, M. J. The Role of Moisture in Protein Stability. *Drug Dev. Ind. Pharm.* **1988**, *14*, 2047−2070.
10. Broadhead, J.; Edmond-Rouan, S. K.; Rhodes, C. T. The Spray Drying of Pharmaceuticals. *Drug Dev. Ind. Pharm.* **1996**, *22*, 813−822.
11. Mumenthaler, M.; Hsu, C. C.; Pearlman, R. Feasibility Study on Spray-Drying Protein Pharmaceuticals: Recombinant Human Growth Hormone and Tissue Plasminogen Activator. *Pharm. Res.* **1994**, *11*, 12−20.
12. Mumenthaler, M.; Leuenberger, H. Atmospheric Spray-Freeze-Drying: A Suitable Alternative in Freeze-Drying Technology. *Int. J. Pharm.* **1991**, *72*, 97−110.
13. Winters, M. A.; Knutson, B. L.; Debenedetti, P. G.; Sparks, G.; Przybycien, T. M.; Stevenson, C. L.; Prestrelski, S. J. Precipitation of Proteins in Supercritical Carbon Dioxide. *J. Pharm. Sci.* **1996**, *85*, 586−594.
14. Randen, N.; Nilson, J.; Edman, P. Copecipitation of Enzymes with Water-Soluble Starch − An Alternative to Freeze-Drying. *J. Pharm. Pharmacol.* **1988**, *40*, 763−766.
15. Prestrelski, S. J.; Arakawa, T.; Carpenter, J. F. Structure of Proteins in Lyophilized Formulations Using Fourier Transform Infrared Spectroscopy. In *Formulation and Delivery of Proteins and Peptides*, Cleland, J. L., Langer, R., Eds;

American Chemical Society Symposium Series 567: 1994; pp 148−169.
16. Prestrelski, S. J.; Tedeschi, N.; Arakawa, T.; Carpenter, J. F. Dehydration-Induced Conformational Transitions in Proteins and Their Inhibition by Stabilizers. *Biophys. J*. **1993**, *65*, 661−671.
17. Griebenow, K.; Klibanov, A. M. Lyophilization-Induced Reversible Changes in the Secondary Structure of Proteins. *Proc. Natl. Acad. Sci. U.S.A.* **1995**, *92*, 10969−10976.
18. Tzannis, S. T.; Hrushesky, W. J. M.; Wood, P. A.; Przybycien, T. M. Irreversible Inactivation of Interleukin-2 in a Pump-Based Delivery Environment. *Proc. Natl. Acad. Sci. U.S.A.* **1996**, *93*, 5460−5465.
19. Labrude, P.; Rasolomanana, M.; Vigneron, C.; Thirion, C.; Chaillot, B. Protective Effect of Sucrose on Spray Drying of Oxyhemoglobin. *J. Pharm. Sci*. **1989**, *78*, 223−229.
20. Broadhead, J.; Edmond Rouan, S. K.; Hau, I, Rhodes, C. T. The effect of Process and Formulation Variables on the Properties of Spray-Dried β-Galactosidase. *J. Pharm. Pharmacol*. **1994**, *46*, 458−467.
21. Daemen, A. L. H.; van der Stege, H. J. The Destruction of Enzymes and Bacteria During The Spray Drying of Milk and Whey. 2. The Effect of The Drying Conditions. *Neth. Milk Dairy J*. **1982**, *36*, 211−229.
22. Wijhuizen, A. E.; Kerkhof, P. J. A. M.; Bruin, S. Theoretical Study of the Inactivation of Phosphatase During Spray Drying of Skim Milk. *Chem. Eng. Sci*. **1979**, *34*, 651−660.
23. Lin, T. Y., Timasheff, S. N. On the Role of Surface Tension in the Stabilization of Globular Proteins. *Protein Science* **1996**, 5, 372−381.
24. Kita, Y.; Arakawa, T.; Lin, T.-Y.; Timasheff, S. N. Contribution of the Surface Free Energy Perturbation to Protein−Solvent Interactions. *Biochemistry*, **1994**, *33*, 15178−15189.
25. Dumay, E. M.; Kalichevsky, M. T.; Cheftel, J. C. High-Pressure Unfolding and Aggregation of β-Lactoglobulin and the Baroprotective Effects of Sucrose. *J. Agric. Food Chem*. **1994**, *42*, 1861−1868.
26. Arakawa, T.; Timasheff, S. N. Stabilization of Protein Structure by Sugars. *Biochemistry* **1982**, *21*, 6536−6544.
27. Lee, J. C.; Timasheff, S. N. The Stabilization of Proteins by Sucrose. *J. Biol. Chem*. **1981**, *256*, 7193−7201.
28. Carpenter, J. F.; Crowe, J. H. An Infrared Spectroscopic Study of the Interactions of Carbohydrates with Dried Proteins. *Biochemistry* **1989**, *28*, 3916−3922.
29. Prestrelski, S. J., Byler, D. M., Liebman, M. N. Comparison of Various Molecular Forms of Bovine Trypsin: Correlation of Infrared Spectra with X-ray Crystal Structures. *Biochemistry* **1991**, *30*, 133−143.
30. Worthington Biochemical Corporation, Worthington Enzyme Manual: Enzymes and Related Biochemicals. Worthington, V., Ed.; New Jersey, 1993; pp 374−375.
31. Hummel, B. C. W. A Modified Spectrophotometric Determination of Chymotrypsin, Trypsin, and Thrombin. *Can. J. Biochem. Physiol*. **1959**, *37*, 1393−1397.
32. Worthington Biochemical Corporation, **1996**−**97** Catalog, p 183.
33. Bell, L. N., Hageman, M. J., Muraoka, L. M. Thermally Induced Denaturation of Lyophilized Bovine Somatotropin and Lysozyme as Impacted by Moisture and Excipients. *J. Pharm. Sci*. **1995**, *84*, 707−712.
34. Fujita, Y., Noda, Y. The Effect of Hydration on the Thermal Stability of Ovalbumin as Measured by Means of Differential Scanning Calorimetry. *Bull. Chem. Soc. Jpn*. **1981**, *54*, 3233−3234.
35. Rüegg, M., Moor, U., Lukesch, A., Blanc, B., Hydration and Thermal Denaturation of β-Lactoglobulin. A Calorimetric Study, *Biochim. Biophys. Acta* **1975**, *400*, 334−342.
36. Sarciaux, J.-M. E., Hageman, M. J. Effects of Bovine Somatotropin (rbST) Concentration at Different Moisture Levels on the Physical Stability of Sucrose in Freeze-Dried rbST/Sucrose Mixtures. *J. Pharm. Sci*. **1997**, *86*, 365−371.
37. Maa, Y.-F., Nguyen, P.-A., Andya, J., Dasovich, N., Sweeney, T. D., Shire, S. J., Hsu, C. C. Effects of Spray Drying and Subsequent Processing Conditions on Residual Moisture Content and Physical/Biochemical Stability of Protein Inhalation Powders, *Pharm. Res*. **1998**, *15*, 768−775.
38. Leeder, J. D.; Watt, J. C. The Stoichiometry of Water Sorption by Proteins. *J. Coll., & Interface Sci*. **1974**, *48*, 339−344.
39. Izutsu, K.; Yoshioka, S.; Terao, T. Decreased Protein-Stabilizing Effects of Cryoprotectants Due to Crystallization. *Pharm. Res*. **1993**, *10*, 1232−1237.
40. Costantino, H. R.; Langer, R.; Klibanov, A. M. Solid-Phase Aggregation of Proteins Under Pharmaceutically Relevant Conditions. *J. Pharm. Sci*. **1994**, *83*, 1662−1669.
41. Carpenter, J. F.; Prestrelski, S. J.; Arakawa, T. Separation of Freezing- and Drying-Induced Denaturation of Lyophilized Proteins Using Stress-Specific Stabilization. I. Enzyme Activity and Calorimetric Studies. *Arch. Biochem. Biophys*. **1993**, *303*, 456−464.

Acknowledgments

The authors thank Drs. Bill Van Osdol and Joan Huey-Dow (ALZA Corporation) for their valuable assistance in solution calorimetry and particle size analyses, respectively, and Perkin-Elmer for the support in the solid state DSC measurements and analysis.

JS980011E

Moisture Effects on Protein–Excipient Interactions in Spray-Dried Powders. Nature of Destabilizing Effects of Sucrose

STELIOS T. TZANNIS*,† AND STEVEN J. PRESTRELSKI‡

Contribution from *Biopharmaceutical Research & Development, ALZA Corporation, 950 Page Mill Road, Palo Alto, California 94303.*

Received January 9, 1998. Accepted for publication November 23, 1998.

Abstract □ The preparation of stable solid protein formulations presents significant challenges. Ultimately, the interactions between incorporated excipients and the pharmaceutical protein determine the formulation stability. In this study, moisture was utilized to probe the interactions between a model protein, trypsinogen, and sucrose in the solid state, following spray drying. Through investigation of the physical properties of the spray-dried formulations, we attempted to elucidate the mechanisms underlying the previously observed[1,2] stabilizing and destabilizing effects of the carbohydrate during spray drying. Both dynamic and equilibrium moisture uptake studies indicated the presence of an optimal protein–sugar hydrogen bonding network. At low sucrose contents, a preferential protein–sucrose hydrogen bonding interaction was dominant, resulting in protein stabilization. However, at high carbohydrate concentrations, preferential sugar–sugar interactions prevailed, resulting in a phase separation within the formulation matrix. The preferential incorporation of the sucrose molecules in a sugar-rich phase reduced the actual amount of the carbohydrate available to interact with the protein and thereby decreased the number of effective protein–sucrose contacts. As a consequence, the protein could not be effectively protected during spray drying. We hypothesize that the observed phase separation at this sucrose concentration regime originates from its exclusion from the protein in solution before spray drying, further accompanied by preferential clustering of the sucrose molecules.

Introduction

The development of solid state dosage forms of biopharmaceutical molecules presents considerable challenges since the processing environments impose severe stresses that may destabilize and ultimately denature these labile biomolecules. Previous studies have indicated that lyophilization can extensively perturb the structure and diminish the activity and physical stability of several proteins.[3−5] Similarly, spray drying and precipitation in supercritical antisolvents, methods frequently used for production of protein microparticles, have been shown to disrupt the native structure and compromise the enzymatic activity of various proteins.[1,2,6−10] Indeed, the processes involved in spray drying impose stresses that can potentially have detrimental effects on protein stability: pressure effects and exposure to air−liquid interfaces during atomization, as well as heat and dehydration stresses during the drying process, have all shown capacity to denature proteins.[1,3−5,11]

In many cases, formulation excipients are required to preserve the protein native structure and stability in the solid state and to ensure physical stability during either long-term storage or delivery. Research efforts over the past decade have indicated that carbohydrates, and in particular disaccharides, can provide significant protection during lyophilization by preserving the native protein structure during the dehydration process.[3,4,12] Similarly, sucrose and trehalose have shown efficacy in stabilizing several proteins, such as trypsinogen, lysozyme, and soybean trypsin inhibitor (STI) during spray drying.[1,2,13,14] The stabilization was shown to occur via preservation of the native protein structure in the solid state along with impediment of protein aggregation on reconstitution.[1,2] Although the formation of a glassy matrix has been proposed as a stabilization mechanism, the "water replacement" theory is the only one that accounts for specific interactions between the proteins and carbohydrates in a mechanistic fashion. In terms of the latter, disaccharide-induced protein stabilization during drying is thought to occur via hydrogen bonding between sugar and protein molecules, thereby satisfying the hydrogen bonding requirements of the protein during the dehydration step.[3,4,12,15,16]

However, our previous studies[1,2,13,14] have shown that at high concentrations of both disaccharides, the stabilizing effects were partially dissipated: at increasing sucrose-to-protein mass ratios the activity losses approached those observed in the absence of the excipient. Similar activity profiles were observed for STI and trypsinogen when spray-dried in excess of trehalose.[13,14] The incurred losses could not be accounted by aggregation or major conformational perturbations, leading to the hypothesis of process-mediated, irreversible enzyme destabilization.[1]

In effort to account for the destabilizing carbohydrate effects, moisture was used to probe the interactions between trypsinogen and sucrose in the solid state following spray drying. The utilization of moisture as a probe is of particular interest since water is a key determinant of both the solid matrix integrity and the excipient−protein interactions. Dynamic and equilibrium moisture sorption analyses were used to characterize the nature and strength of trypsinogen−sucrose interactions, while physicochemical and thermal methods of analysis were used to probe the state of sucrose in the solid state. The phenomenon of the reduced stabilization of trypsinogen during spray drying at high sucrose concentrations was also examined. The results presented in this study are expected to improve the understanding of protein−excipient interactions in the solid state and to aid the design of stable spray-dried protein formulations, with implications for other solid-state processing methodologies.

Experimental Section

Chemicals—Trypsinogen (1× crystallized, dialyzed against 1 mM HCl and lyophilized; Lot no. 38E273N) was purchased from Worthington Biochemical Corporation (Freehold, NJ). Ultrapure

* Author to whom all correspondence should be addressed.
† Inhale Therapeutic Systems, 150 Industrial Road, San Carlos, CA 94070. Tel: (650) 631 3276; Fax: (650) 631 3276; email: stelios.tzannis@inhale.com.
‡ Powderject Technologies, Inc., 6511 Dumbarton Circle, Fremont, CA 94555.

10.1021/js9800127 CCC: $18.00
Published on Web 02/04/1999

sucrose (>99.5% purity via HPLC, Lot no. 35H03582) was purchased from Sigma Chemical Company (St. Louis, MO). Lithium chloride, potassium carbonate, potassium phosphate, calcium chloride, and sodium chloride salts were purchased from J. T. Baker (Phillipsburg, NJ). Barium chloride and ammonium chloride were purchased from Mallinckrodt (St. Louis, MO).

Experimental Design—Protein powders were prepared by spray drying formulations at different sucrose-to-protein mass ratios: no sucrose, 0.25:1, 0.5:1, 1:1, 2:1, 4:1, 8:1, and no protein, which correspond to sucrose concentrations of 0, 0.015, 0.029, 0.058, 0.234, 0.47, and 0.53 M, respectively. In all cases, the protein concentration was held constant at 20 mg/mL. All results in this study are reported in terms of sucrose-to-protein mass ratios.

Spray Drying—Trypsinogen particles were prepared by spray drying in a Yamato minispray dryer model ADL-31 (Yamato Scientific, Orangeburg, NY). The proteinaceous solutions were prepared in 1 mM HCl, achieving a pH around 3.1 for all formulations in order to minimize the autolysis of the enzyme.[1,17] The solutions were continuously fed to the spray dryer at an approximate flow rate of 3−5 mL/min and were dried at an inlet temperature of 120 °C; outlet temperatures ranged from 85 to 90 °C. Powders were aliquoted in lyophilization vials in a drybox (Terra Universal, Anaheim, CA) at <1% relative humidity (% RH).

Particle Size Analysis—The particle size of the spray-dried powders was determined with a Malvern Mastersizer S (Southborough, NH) laser-light scattering analyzer. Small amounts of powders were dispersed in an excess of octanol; the suspension concentration was properly adjusted to attain optimal obscuration. The samples were then analyzed in a static mode; measurements were repeated in triplicate over a 20-min period, to ensure that no dissolution or powder agglomeration occurred. The size distribution was expressed in terms of volume median diameter, particle size range, and span.

Moisture Analysis—The moisture content of the spray-dried powders was analyzed via Karl Fisher titration; assays were performed on an Aquatest 10 Karl Fisher Coulorimetric Titrator (Seradyn, Indianapolis, IN), calibrated with anhydrous methanol. The moisture content of the protein microparticles was monitored in triplicate using a methanol extraction protocol.

Moisture Sorption Isotherms—Dynamic moisture sorption isotherms were determined by gravimetric measurement of water uptake using an Integrated Microbalance System, model MB-300G (VTI Corporation, Hialeah, FL), equipped with a digital Cahn ultra-microbalance model 13200-1 (Cahn Instruments, Madison, WI). The microbalance was calibrated with poly(vinylpyrollidone) (PVP) standard. The temperature of the sample chamber throughout the experiment was maintained at 37 °C by circulating water from a constant temperature Neslab circulator, model RTE-100 (Neslab Instruments Inc., Newington, NH) in a water jacket built around the sample compartment. Five to ten milligrams of sample was loaded onto the microbalance, carefully minimizing the sample exposure to ambient conditions. The powder was first subjected to a drying cycle, in which the residual water was removed by vacuum, until equilibrium was attained; the equilibrium criteria were set to reflect sample weight fluctuations of less than 5 μg (representing <1% of the loaded sample) within 5 min. Following drying, the samples were exposed to incremental changes in relative humidity from 0 → 95 → 0% RH at 5% RH intervals. The %RH level was automatically incremented only after complete sample equilibration at each RH level, as dictated by the set equilibrium conditions of less than 3 μg weight change every 10 min with a maximum equilibration time of 400 min. All sorption profiles were determined in triplicate.

The monolayer amount of sorbed water molecules was calculated by a fit of the adsorption data between 0 and 30% RH to the two-state Brunauer−Emmet−Teller (BET) equation[18]

$$W = \frac{W_m C_B (P/P_o)}{1 - (P/P_o)[1 - (P/P_o) + C_B(P/P_o)]} \quad (1)$$

where W is the weight of water adsorbed per unit weight of dry solid at a relative pressure of P/P_o, P and P_o are the vapor pressure and saturation vapor pressure of water, respectively, at the experimental temperature, W_m is the monolayer capacity of the adsorbent, and C_B is a constant related to the heat of adsorption. The latter provides an indication of the affinity of water molecules for the solid sample[19,20] and is given by:[18,21]

$$C_B = k \exp\frac{H_1 - H_L}{RT} \quad (2)$$

where H_1 is the heat of adsorption of the first vapor molecule adsorbed to a substrate site, H_L is the heat of condensation of bulk adsorbate, R is the universal gas constant, T is the absolute temperature, and k is a constant, usually assumed to be close to unity.[21] The approximate water sorption-based sample surface area was calculated from the BET monolayer value assuming 12.5 Å^2 for the cross-sectional area of each water molecule.[19]

BET Surface Area Measurements—The measurements were carried out on a Gemini 2360 surface area analyzer (Micromeritics Instrument Corporation, Norcross, GA) based on the multi-point BET gas adsorption method. For each measurement 0.4−1.5 g of spray-dried powders were loaded onto the sample holder. The surface area was determined using nitrogen as the adsorbate at five different relative pressures (P/P_o range of 0.1−0.3). Prior to the measurements, the samples were degassed under high vacuum at room temperature for at least 24 h, until no further gas or vapor evolved, as judged by the stabilization of the instrument readings.

Equilibrium Sorption Experiments—The spray-dried samples were stored for 10 days at room temperature in sealed desiccators equilibrated with the appropriate saturated salt solutions. The humidity was maintained at 12, 43, 75, and 84% RH with saturated aqueous solutions of LiCl, K_2CO_2, NH_4Cl, and $BaCl_2$, respectively. The physical state of the powders was characterized by X-ray diffraction and thermal analysis.

Powder Thermal Stability—The thermal stability of the spray-dried formulations was determined by the glass transition (T_g) and crystallization exotherms (T_{cryst}) obtained by solid state DSC. The experiments were performed on a TA Instruments (New Castle, DE), Model 2920 DSC, which was calibrated with indium prior to sample analysis. Approximately 10−50 mg of the samples were loaded under environmentally controlled conditions in 50-μL hermetically sealed aluminum pans. After a short preequilibration step at −20 °C, the samples were heated to 200 °C. In effort to deconvolute relaxation events during the glass transition, the samples were analyzed by modulated DSC (MDSC) at a heating rate of 5 °C/min with a modulation frequency of ±2 °C every 60 s. The glass transition temperatures were extracted in triplicate using the transition midpoints.

X-ray Diffraction Experiments—X-ray diffractograms (Coors Ceramics Analytical Laboratory, Golden, CO) were collected using a Scintag Pad X θ-θ diffractometer under the following conditions: copper tube operated at 45 kV, 40 mA; goniometer radius 250 mm; beam divergence slits of 6 and 1 mm and scatter and receiving slits of 0.5 and 0.3 mm; germanium solid state detector bias 1000 V; the PHA was set to accept only K-α radiation. The samples were loaded on a zero-background quartz plate mounted on a special sample holder. Diffractograms were collected between 3° and 90° 2θ at a scan speed of 2.0° 2θ per minute and a chopper increment of 0.03° 2θ. The temperature at the time of the experiments was approximately 23−25 °C. The percent crystallinity of the samples was calculated by numerical integration of the sample and amorphous X-ray diffraction data over the 5−80° range. After background subtraction, utilizing a cubic spline fit, the integrated peak areas were determined using a Lorentzian profile fitting routine, and % crystallinity was assessed by calculating the relative percentage of crystalline peak areas to the total area under the diffractograms.[22]

Results

Particle Size Analysis—The size distribution analysis of the spray-dried particles is given in Table 1. In agreement with our previous observations,[1,14] spray drying of the trypsinogen−sucrose formulations produced a homogeneous monomodal distribution of an approximate diameter of 3−5 μm and a narrow range (0.8−20 μm). The addition of sucrose had a rather minor effect on the particle average diameter: a small increase of the particle size was observed with increasing amounts of added sucrose, however, within the error of the measurements.

Moisture Content—The moisture content of the spray-dried trypsinogen powders as a function of the protein-to-

Table 1—Particle Size and Size Distribution of Spray-Dried Trypsinogen–Sucrose Powders[a]

sucrose:trypsinogen mass ratio	median diameter[b] (μm)	span[c]	$(SSA)_{estimated}$[d] (m^2/g)
no sucrose	3.1 ± 2.2	1.03 ± 0.02	2.3 ± 0.6
0.25:1	3.2 ± 1.3	1.04 ± 0.02	2.1 ± 0.5
0.5:1	3.6 ± 2.3	1.15 ± 0.03	1.5 ± 0.4
1:1	3.7 ± 2.8	1.26 ± 0.03	1.4 ± 0.4
2:1	4.6 ± 1.8	1.11 ± 0.01	0.7 ± 0.2
4:1	4.9 ± 0.9	1.26 ± 0.02	0.6 ± 0.2
8:1	5.2 ± 1.9	1.16 ± 0.03	0.5 ± 0.1

[a] Values represent averages and standard deviations of triplicate measurements. [b] Volumetric median diameter (D(v, 50)). [c] Span = [D(v, 90) − D(v, 10)]/D(v, 50), where D(v, 90), D(v, 50), and D(v, 10) are the equivalent volume diameters at 90, 50, and 10% cumulative volume, respectively. [d] Nominal specific particle surface area estimated based on the particle size distribution.

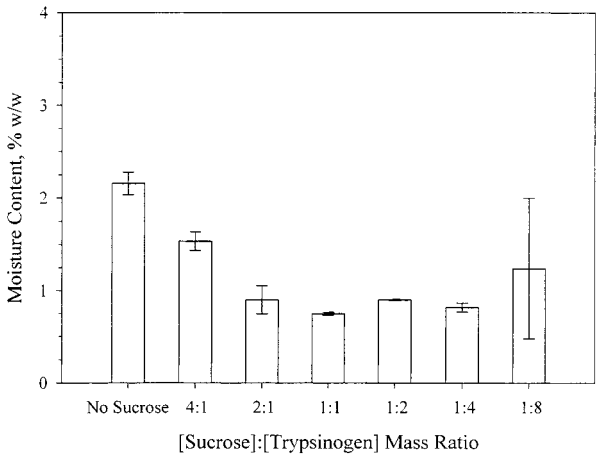

Figure 1—The effect of sucrose on the moisture contents of the spray-dried trypsinogen formulations. Error bars represent (±) one standard deviation of triplicate determinations.

sucrose mass ratio is shown in Figure 1. In agreement with our previous studies,[1,14] spray drying yielded powders of very low residual moisture. The moisture content achieved when trypsinogen was spray-dried in the absence of sucrose was 2.2 ± 0.1% w/w. This is lower than the calculated water monolayer value of 5.4% w/w, which assumes the attachment of one water molecule per charged amino acid, as suggested by Leeder et al.[23]

The addition of sucrose, up to a sucrose-to-protein mass ratio of 1:1, progressively decreased the attained moisture content; thereafter, it remained constant up to the highest sucrose concentration examined. The observed reduction in the final moisture content indicates that the dehydration process is more efficient in the presence of sucrose. This could indicate an increase of the effective heat transfer coefficient as a consequence of the increased surface tension of the droplets, caused by the addition of sucrose. Alternatively, it may reflect facilitation of the removal of water, thereby providing an indirect indication of specific hydrogen bonding interactions between the spray-dried components.

Particle Surface Area Analysis—The nitrogen adsorption analysis results are given in Table 2. The surface area of pure protein particles was 14.5 ± 0.02 m^2/g, which is larger than what would be expected for perfectly spherical particles of this volumetric size distribution (given in Table 1). Since nitrogen sorption is a purely surface phenomenon, this suggests that the particle surface is not perfectly smooth or alternatively the presence of blowholes and cracks. Upon addition of sucrose the surface area decreased: at a sucrose mass ratio of 1:1, it became half of that in the absence of the carbohydrate, while at the highest sugar mass ratio examined, the mean particle surface area decreased 4-fold. A similar trend was observed for the estimated values of W_m, which decreased with increasing sucrose content, thereby providing further evidence of a decrease in the available surface sites for nitrogen adsorption. Scanning electron microscopy (SEM) analysis (data not shown) confirmed that this was due to the increased smoothness of the sucrose-containing particles compared to the wrinkled surface of those in the absence of the carbohydrate; no cracks or blowholes were observed. In contrast, the affinity of the adsorbate for the particle surface did not appear to change with the addition of sucrose, as suggested by the relatively invariable values of the constant C^N_B, indicative of similar heats of nitrogen adsorption to the particle surface.

Dynamic Moisture Sorption Isotherms—The moisture adsorption/desorption isotherms are shown in Figures 2a–f and the BET analysis results are given in Table 2. Spray-dried trypsinogen in the absence of sucrose exhibited a sigmoidal-Type II adsorption isotherm (Figure 2a), which is characteristic of amorphous protein and protein–sugar systems.[24–31] The estimated monolayer of 5.3 ± 0.6 g/100 g solid is in excellent agreement with that calculated by assuming strong adsorption sites on the protein surface (5.4 g/100 g solid). This suggests that at the monolayer, approximately 67 ± 5 water molecules are bound per trypsinogen molecule. The adsorption curve also indicates that the amount of moisture sorbed in the multilayer region (>20–25% w/w) is much larger than what would be expected from the particle surface area. This is also implied by the calculated water sorption-based specific surface area, which is much larger than that determined by the nitrogen adsorption experiments. These observations provide corroborative evidence that moisture actually penetrates into the amorphous solid in contrast to the purely surface-limited adsorptive phenomenon.[20,30] Absorption phenomena have been previously described for lyophilized lysozyme, recombinant bovine somatotropin (rbST), ovalbumin, β-lactoglobulin, and microcrystalline cellulose.[24,30,32,33] The moisture sorption profile of trypsinogen also revealed the presence of hysteresis $[W^{desorption} - W^{adsorption}]_{RH}$ between the sorption and desorption isotherms, which is generally thought to be a consequence of water absorption. The hysteresis loop appeared at 80% RH and closed at 0% RH, indicating the complete reversibility of water sorption, under the experimental conditions.

On addition of low-to-moderate concentrations of sucrose (carbohydrate-to-protein mass ratios of 2:1 and 1:1), the sorption curves retained their Type II profile, as shown in Figures 2b and 2c, respectively. However, the amount of moisture sorbed at low vapor pressures appeared to decrease with increasing sucrose content, and it reached a minimum at a mass ratio of 1:1. This was also reflected in the values of W_m, which decreased to 4.8 ± 0.1, 4.6 ± 0.1, and 4.4 ± 0.1 g H_2O/100 g solid at sucrose-to-protein mass ratios of 0.25:1, 0.5:1, and 1:1, respectively, indicating a reduction of the number of sorbed water molecules per unit weight of the solid at monolayer conditions. The same trend was observed for the water sorption-based particle surface areas, which, however, remained higher than the actual surface areas, indicating that absorption is still the main mode of water interaction with the solid. The gradual addition of sucrose appears to also progressively reduce the magnitude of the hysteresis loop: the loop areas decreased from 135 ± 4.4 units in the absence of sucrose, to 103.2 ± 9.9 and 93.2 ± 3.3 units for sucrose-to-protein mass ratios of 0.25:1 and 0.5:1, respectively. The hysteresis loop disappeared at a mass ratio of 1:1 (area of 1.2 ± 1.1 units).

In contrast, at high sucrose contents (mass ratios > 1:1),

Table 2—Gas and Moisture Sorption BET Analysis of Spray-Dried Trypsinogen–Sucrose Formulations

sucrose:trypsinogen mass ratio	gas sorption analysis			moisture sorption analysis			
	surface area,[a] (m^2/g)	W_m[a] (gr/100 g solid)	C^N_B[a]	app. surface area,[b] (m^2/g)	W_m[b] (gr/100 g solid)	C^W_B[b]	ΔW_m[e]
no sucrose	14.5 ± 0.02	3.3 ± 0.01	32.1 ± 0.01	224.3 ± 18.6	5.3 ± 0.5	12.4 ± 0.9	0
0.25:1	–	–	–	202.3 ± 11.8	4.8 ± 0.1	6.2 ± 0.5	0.5 ± 0.1
0.5:1	9.3 ± 0.01	2.1 ± 0.01	29.4 ± 0.01	199.9 ± 7.4	4.6 ± 0.1	4.7 ± 0.2	0.7 ± 0.1
1:1	7.6 ± 0.01	1.7 ± 0.01	29.3 ± 0.01	185.4 ± 13.4[c]	4.4 ± 0.1[c]	5.6 ± 0.5[c]	0.9 ± 0.1
2:1	6.5 ± 0.01	1.5 ± 0.01	27.6 ± 0.01[4]	196.9 ± 2.8	4.7 ± 0.1	6.2 ± 0.7	0.6 ± 0.1
4:1	5.5 ± 0.01	1.3 ± 0.01	28.1 ± 0.01	228.5 ± 20.1[d]	5.1 ± 0.6[d]	4.4 ± 0.6[d]	0.2 ± 1.1
8:1	3.6 ± 0.01	0.8 ± 0.01	29.9 ± 0.01	244.5 ± 80.8[d]	5.4 ± 0.4[d]	3.5 ± 0.5[d]	–0.1 ± 0.4

[a] Standard errors represent standard deviations from the fit of the five-point gas sorption curve. [b] Values represent averages and standard deviations of triplicate measurements ($n = 3$) except [c]$n = 2$, and [d]$n = 5$. [e] $\Delta W_m = W_m^{protein} - W_m^{protein/sucrose}$.

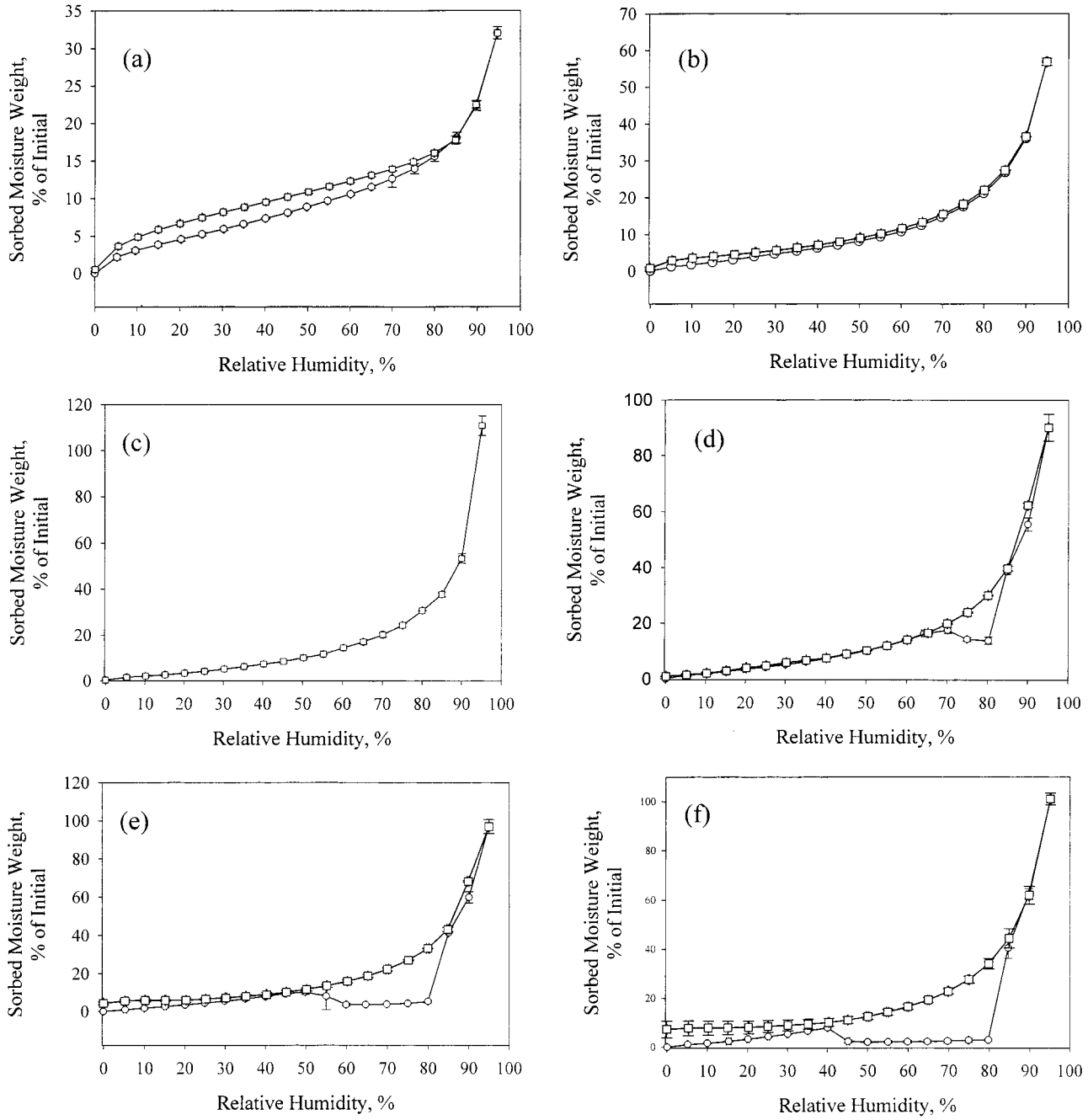

Figure 2—Dynamic moisture absorption (○) and desorption (□) isotherms of spray-dried trypsinogen-sucrose formulations (a) in the absence of sucrose, and sucrose-to-protein mass ratios of (b) 0.25:1, (c) 1:1, (d) 2:1, (e) 4:1, and (f) 8:1. Error bars represent (±) one standard deviation of triplicate determinations.

the amount of sorbed moisture at low vapor pressures increased with increasing sucrose concentration. This was also reflected in the increasing values of the water-based BET surface areas as well as the estimated equivalent monolayer values. The latter gradually increased from 4.4 ± 0.1 g/100 g solid at a mass ratio of 1:1, to 4.7 ± 0.1, 5.1

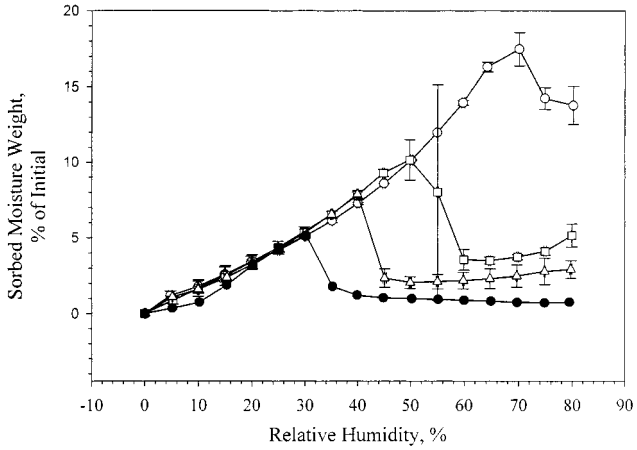

Figure 3—Comparison of the sucrose crystallization phenomenon for the spray-dried formulations at sucrose-to-trypsinogen mass ratios of (a) 2:1, (b) 4:1, (c) 8:1, and (d) in the absence of protein. Error bars represent (±) one standard deviation based on triplicate determinations.

± 0.6 and 5.4 ± 0.4 g/100 g solid at mass ratios of 2:1, 4:1, and 8:1, respectively. Therefore, at this sucrose concentration regime, the available water sorption sites progressively increased with increasing sucrose content. At the highest sucrose-to-protein mass ratio, W_m reached the value determined for the spray-dried pure protein, potentially implying that all the initial sorption sites in the mass of the solid have been reinstated. This is further demonstrated by the decreasing value of the constant C^W_B, which indicates a decline of the heat of water sorption, and thereby decreased affinity of water for the particles, with increasing sucrose concentrations.

One of the most significant features of the sorption isotherms at this sucrose concentration regime is the discontinuity appearing at high vapor pressures. For the 2:1 formulation, the discontinuity occurred at approximately 75% RH. This break is thought to be due to the release of water following the phase transition of sucrose from the amorphous glass to its crystalline state.[24,31,34–36] The formed crystals persisted up to 80% RH; upon further increase of the vapor pressure, the powder resumed its sorptive behavior, as large amounts of water were absorbed: this is indicative of the dissolution of the sucrose crystals and the formation of a saturated solution.[31,35,36] On reversal of the sorption driving force, this formulation exhibited a desorption pathway that followed closely the absorption curve. With the exception of the absence of the discontinuity in the desorption curve, no hysteresis phenomena were observed, and therefore sorption of moisture was fully reversible, as also indicated by the return to the initial conditions.

Crystallization was also observed at all higher sucrose concentrations (Figures 2e,f). However, it occurred at lower critical RH: 55 and 45% for the spray-dried samples at sucrose-to-protein ratios of 4:1 and 8:1, respectively. The crystallization process began at moisture contents of 10.2 ± 1.4 and 7.9 ± 0.3% w/w and completed at 80% RH at 5.1 ± 0.76 and 2.9 ± 0.6% w/w for the 4:1 and 8:1 formulations, respectively. In agreement with the observations with the 2:1 formulation, the sucrose crystals dissolved and the powders resumed their sorptive behavior at 85% RH. However, the desorption isotherms of these samples did not follow the absorption portions, while the loops did not close upon return to the initial conditions, potentially indicating irreversible changes in the state of the powder during the sorption process. In comparison, in the adsorption isotherm of spray-dried pure sucrose (Figure 3) the crystallization discontinuity occurred at approximately 30–35% RH. The crystallization process began at a moisture content of 5.4 ± 0.6% and completed at 0.8 ± 0.3% w/w. This result is very similar to that observed in previous studies of sucrose crystallization by Saleki–Gerhardt et al.,[34] which indicated crystallization of sucrose at approximately 32% RH (equilibrium water content of 6% w/w) at 25 °C, which is within experimental error from our observations.

Table 3—Glass Transitions of the Spray-Dried Sucrose–Trypsinogen Powders before and after Exposure to Controlled Relative Humidity Levels[c]

sucrose:trypsinogen mass ratio	glass transition (T_g)[a]		
	no. exposure	12%	43%
0.25:1	80.4 ± 1.3	44.2 ± 0.8	ND[b]
1:1	75.1 ± 1.9	44.6 ± 0.5	ND[b]
2:1	71.3 ± 1.9	39.2 ± 1.6	5.6 ± 2.7
4:1	69.5 ± 2.7	39.9 ± 2.9	3.1 ± 1.1
8:1	67.4 ± 2.6	42.3 ± 3.4	ND[b]

[a] No glass transitions were detected for the samples exposed to 75 and 84% RH. [b] No glass transitions were detected.

The results, as illustrated in Figure 3, indicate that increased sucrose concentration in the spray-dried mixtures facilitates its moisture-induced crystallization. From a different perspective, the addition of protein inhibits the carbohydrate state transition, as indicated by the decreasing critical crystallization RH with increasing protein concentration in the solid matrix. Similar results have been reported for binary mixtures of sucrose with other proteins, such as recombinant consensus interferon (rConIFN) and recombinant human granulocyte colony stimulating factor (rhG-CSF),[37] rbST,[38] and several polymers, such as starch and celluloses.[39] However, in the case of the rbST–sucrose system, the exact value of the critical %RH of sucrose crystallization at different protein contents was generally higher than that observed in our studies; the different experimental temperatures as well as the differences of the initial states of the spray-dried and lyophilized powders may account for the observed differences.

X-ray Diffraction Analysis—The diffractograms of all spray-dried formulations (results not shown) were characterized by two broad humps and the absence of any sharp peaks over the entire 2θ range, which are indicative of their amorphous nature, confirming the water sorption findings. Even at the highest sucrose-to-protein mass ratio of 8:1, the carbohydrate retained its amorphous character, as would be expected from the nature of the process and the very low moisture contents attained. These results are in agreement with previous studies that indicated the amorphous character of spray-dried rConIFN and rhG-CSF formulations even when they were prepared at high concentrations of trehalose (90% w/w).[37]

Powder Thermal Analysis—The glass transitions of the spray-dried sucrose–trypsinogen formulations, as obtained by DSC thermal analysis, are given in Table 3. The glass transition of the spray-dried pure trypsinogen could not be determined. This is a common problem with protein glasses in the absence of excipients,[37,38] which presumably arises from their large internal heterogeneity and results in an extremely broad distribution of their relaxation times.[40] However, the determination of T_g was possible for the sucrose-containing formulations. In all thermograms, only a single glass transition was observed, implying the complete miscibility of the protein and sucrose in the amorphous matrixes or, alternatively, that a second phase, if present, exists in small amounts that cannot be detected by DSC. Increasing sucrose concentrations gradually decreased the glass transition from 80.4 ± 1.3 °C at a mass ratio of 2:1 to 68.4 ± 3.2 °C for the 8:1 formulation. This observation provides further evidence of the miscibility of

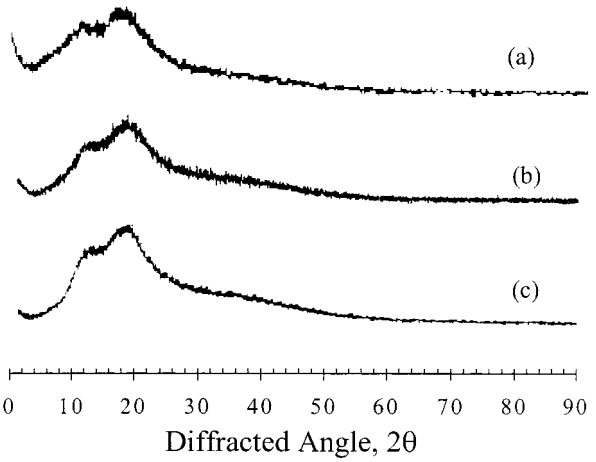

Figure 4—X-ray diffractograms of spray-dried trypsinogen formulations before exposure to elevated moisture: (a) in the absence of sucrose and at sucrose-to-protein mass ratios of (b) 0.5:1, (c) 1:1, (d) 2:1, (e) 4:1, and (f) 8:1.

the two formulation components in the solid matrix.[38] In contrast with the other spray-dried powders, the formulation at a sucrose-to-protein mass ratio of 8:1 exhibited a stress relaxation endotherm, indicating increased molecular mobility of its components.[34]

The formulations at high sucrose concentrations further exhibited an exothermic transition, which is characteristic of sucrose recrystallization. The exact temperature and magnitude of the transition, however, varied with the formulation: 173.9 °C, 160.4 °C, and 142.9 °C for the formulations at sucrose-to-protein mass ratios of 2:1, 4:1, and 8:1, respectively. These results are in agreement with previous studies,[38] and further confirm the hypothesis of protein-induced inhibition of sucrose crystallization, as observed in the dynamic moisture sorption experiments.

Equilibrium Water Sorption Studies—These studies were performed to confirm the dynamic sorption isotherms, which do not represent true equilibrium events; the "non-equilibrium" attributes arise from the limitations of user-defined equilibrium criteria of the "dynamic sorption" experiments prevent the system from reaching true equilibrium. The diffractograms of the moisture-exposed samples are shown in Figures 5–7, and the sample crystallinity analysis is given in Table 4. The X-ray diffraction analysis of the moisture-exposed samples confirmed the dynamic sorption experiments, indicating the appropriateness of this technique. When the spray-dried particles were exposed to 12% RH, the formulations retained their amorphous character; the diffractograms illustrated in Figure 4 are characterized by two broad humps and the absence of any sharp features. This is expected from the dynamic moisture sorption studies, which indicated the absence of any state changes in all formulations at this %RH level. Further, these results are in agreement with moisture sorption studies of protein–disaccharide systems, which demonstrated the absence of state transitions (for both sucrose and trehalose) upon exposure to low relative humidities.[37,38] However, the absorbed water plasticized the solid matrixes, as indicated by the decreased glass transitions given in Table 3. For all examined powders, T_g was reduced to almost half of its original value, while all formulations exhibited a relaxation endotherm during the glass transition.

As indicated in Figure 5, even after exposure to 43% RH most spray-dried powders (sucrose-to-protein mass ratios of 1:1, 2:1, and 4:1) remained amorphous, again in good agreement with the dynamic moisture sorption studies. In contrast, the diffractogram of the highest sucrose-containing powder (8:1) exhibited crystalline patterns dominated

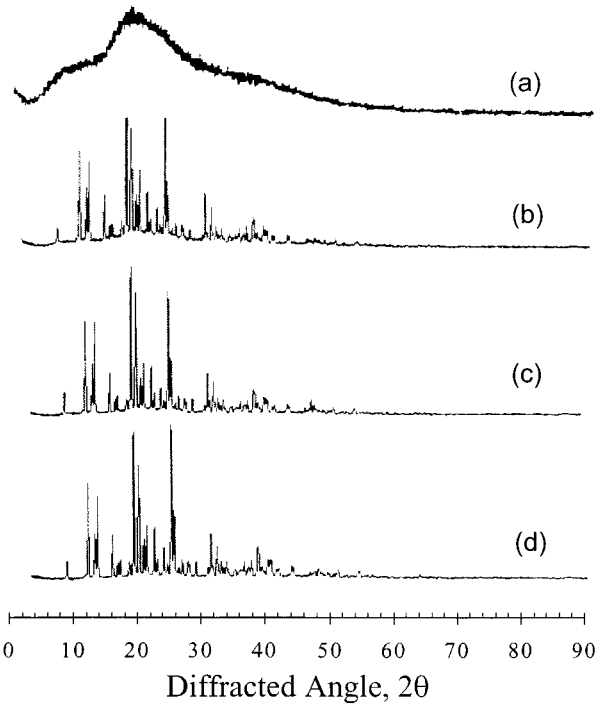

Figure 5—X-ray diffractograms of spray-dried trypsinogen formulations after equilibrium exposure to 12% RH for 10 days. Formulations are at sucrose-to-protein mass ratios of (a) 2:1, (b) 4:1, and (c) 8:1.

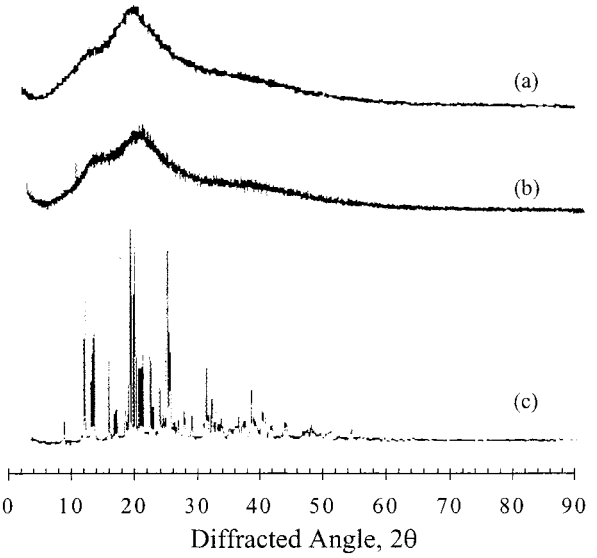

Figure 6—X-ray diffractograms of spray-dried trypsinogen formulations after equilibrium exposure to 43% RH for 10 days. Formulations illustrated are at sucrose-to-protein mass ratios of (a) 2:1, (b) 4:1, and (c) 8:1.

by sharp peaks located at 11.6°, 12.8°, 18.8°, and 24.7°, which are indicative of sucrose crystals.[39] The incurred phase transformation was expected, since the dynamic sorption results indicated the occurrence of a crystallization event at 40–45% RH. Sample crystallinity was determined at 76% w/w solid, indicating that under these conditions, most of the sucrose in the formulation has crystallized. As illustrated in Table 3, the formulation T_gs further decreased, as would be expected by the increased amounts of sorbed water.

Even after exposure to 75% RH, no state transition became apparent for the 1:1 formulation (Figure 6a), indicating that when the protein concentration in the solid matrix exceeds this mass ratio, the crystallization of sucrose can be completely inhibited. These findings are in

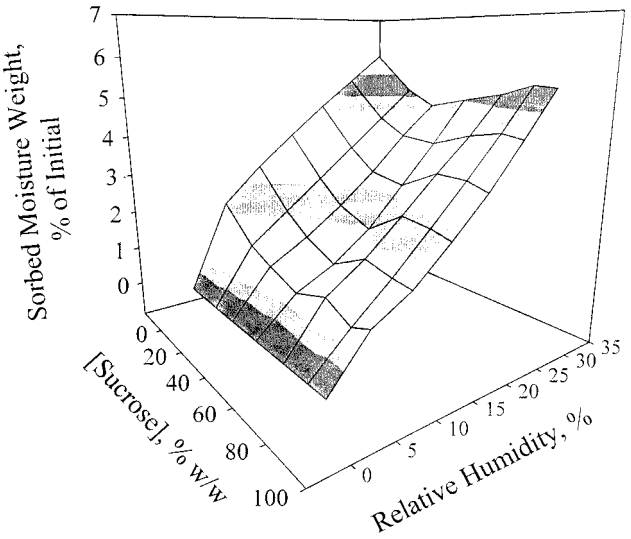

Figure 7—X-ray diffractograms of spray-dried trypsinogen formulations after equilibrium exposure to 74% RH for 10 days. Formulations illustrated are at sucrose-to-protein mass ratios of (a) 1:1, (b) 2:1, (c) 4:1, and (d) 8:1.

Table 4—Crystallinity of Spray-Dried Trypsinogen–Sucrose Formulations before and after Exposure to Controlled Relative Humidity Environments[a]

sucrose:trypsinogen mass ratio	no exposure	% crystallinity			
		12%	43%	75%	84%
1:1	0[a]	ND[b]	ND[b]	0[a]	0[a]
2:1	0[a]	0[a]	0[a]	51	0[a]
4:1	0[a]	0[a]	0[a]	71	44
8:1	0[a]	0[a]	76	85	71

[a] No crystalline peaks were detected. Samples are characterized as 100% amorphous. [b] Sample crystallinity was not determined.

agreement with literature studies which concluded that sucrose crystallization is entirely inhibited when the protein concentration in the spray-dried rConIFN and rhG-SCF formulations exceeded 50%.[37] In contrast, the sucrose in the 2:1 and 4:1 formulations underwent crystallization upon exposure to 75% RH, as indicated by the diffraction patterns shown in Figures 6b-c. These were identical to those observed for the 8:1 formulation at 43% RH. Again, these results conform well with those obtained from the dynamic sorption studies, which showed sucrose crystallization phenomena at 55 and 75% RH, respectively. However, the extent of crystallization varied, as indicated by the quantitative crystallinity estimates of 51%, 67%, and 82% for the 2:1, 4:1, and 8:1 formulations, respectively. These findings suggest that the amount of crystallizable sucrose increases with increasing concentration of the excipient in the solid matrix. No glass transitions were detected for the formulations exposed to 75% RH. This is probably due to the crystallization of most of the sucrose in the formulations, which renders the amount of the remaining amorphous material insufficient for detection of its T_g via DSC.

Finally, upon exposure of the formulations to 84% RH, the crystallinity patterns were partially disrupted, as indicated by the decreased intensity of the diffractogram peaks. As a consequence, the determined crystallinity percentages dropped to 44% and 71% for the 4:1 and 8:1 formulations, respectively, while the crystalline patterns completely disappeared for the 2:1 sample. These findings are in good agreement with the previous studies which demonstrated decreased crystallinity levels of sucrose on exposure to 84% RH, due to the crystal dissolution and the formation of saturated solutions at this vapor pressure.[39]

Discussion

It is well documented that pharmaceutical solids tend to adsorb significant amounts of water over a wide range of relative humidities. The presence of water can accelerate degradation phenomena in the solid state, such as deamidation, oxidation, disulfide cross-linking, and Maillard reactions.[41] In particular for proteins, water can affect a complex matrix of protein motions, ranging from oscillatory and rotational movement of individual amino acid groups, to segmental motions and internal fluctuations that increase their dynamic mobility and thereby decrease their conformational stability.[41,42] Moreover, the sorbed water may have a tremendous impact on both the physical properties of the processed material. In terms of the latter, water sorption plasticizes the solid matrix, reduces its T_g,[43] and may induce excipient crystallization and alter its morphology, physicochemical properties, and physical characteristics,[44] phenomena that can all deteriorate product stability or even diminish proper delivery.

In agreement with previous studies,[37,45] the X-ray diffraction results suggest that spray drying of trypsinogen, even in the presence of increasing amounts of sucrose, results in the formation of amorphous microparticles. In this state, proteins are devoid of long-range intermolecular interactions or orientation, although they maintain their specific short-range interactions.[41] Upon exposure to different relative humidity levels, the protein-based powders take up large amounts of water, illustrative of their amorphous nature. Water sorption confers increased mobility, which may be regarded as an increase in the dynamic fluctuations of the protein, as demonstrated for trypsin, a protein that has a significant degree of homology with trypsinogen.[46]

Similarly with amorphous polymers, water sorption in all spray-dried trypsinogen−sucrose formulations occurs via penetration into the disordered solid and is not limited to surface adsorption.[41] This was demonstrated by the large excess of moisture taken up by the solid at high vapor pressures and the lack of dependence of the water uptake on the specific surface area of the samples.[43] The absorption process is further elucidated by comparison of the surface areas obtained from the nitrogen adsorption studies with those calculated from fits of the BET equation to the moisture sorption isotherms; although the former are highly dependent on particle size and physical state of the solid, the latter are unaffected by these properties. The very large H_2O/N_2 surface area ratios obtained for all spray-dried formulations are consistent with the water penetration hypothesis.

This explanation is also consistent with the sorption hysteresis, observed for formulations at the low sucrose concentration regime. Hysteresis has been described for many amorphous systems.[27] Although it was first suggested to originate from capillary condensation, it was later thought to be caused by chemisorption in rigid materials, and by water−polymer interactions in nonrigid solids (such as proteins).[27] Specifically for proteins, hysteresis phenomena have also been attributed to conformational rearrangements that involve a structural relaxation or even a phase change, which can be facilitated by increasing free volume and mobility of the protein during sorption.[44,47] It has been previously hypothesized that it provides an indication of the existence of the protein in a kinetically metastable, dynamically constrained state, which arises from the macroscopic swelling due to the penetration of water in the solid matrix.[25,41,44,47] The extent of the hysteresis loop in our experiments, decreased with increasing sucrose concentration, indicating the decreased plasticization of the amorphous solid by water. Alternatively, the protein con-

formational changes should be less dramatic in the presence of sucrose; this is confirmed by our previous studies, which indicated that trypsinogen gradually maintains a more nativelike conformation in the presence of increasing amounts of sucrose.[1] Finally, since hysteresis is related to the glass transition of the solid at the specified RH,[44] it is possible that its decreased magnitude may also relate to variations of $\Delta T = T - T_g(\mathrm{RH})$ during the sorption process for the different trypsinogen−sucrose formulations. The disappearance of the hysteresis loop at a sucrose-to-protein mass ratio of 1:1, formulation at which the protein fully recovers its native structure and activity,[1] further underscores the utility of this parameter in correlating solid behavior with protein conformation and structural dynamics.

The hygroscopic nature of both trypsinogen and sucrose would forecast a cumulative water sorption capacity of their physical mixtures. However, comparison of the actual amounts of sorbed water at low (<35%) relative humidities indicated a concentration-dependent effect of sucrose. At low mass ratios of the disaccharide, the sorptive capacity of the powders actually decreased, in good agreement with literature studies.[26,48] This observation indicates that addition of sucrose contributes to the blockage of potential sorption sites in the binary solid matrix, providing evidence of specific hydrogen bonding interactions between the two components. This analysis further supports the expressed "water replacement" hypothesis.[3,4,12] The interaction is also confirmed by the decreased heat of sorption with increasing sucrose concentration. Moreover, the facility of the replacement of protein−sucrose interactions by water, as represented by the amount of sorbed water at low vapor pressures (<35%) can provide an estimate of the extent (and perhaps the strength) of their interactions. The latter is illustrated in the three-dimensional mesh plot of Figure 7 as a function of the sucrose concentration and vapor pressure. It becomes apparent that the extent of interaction increases with increasing sucrose concentration and becomes maximal at equal mass ratios; thereafter in decreases, as the sorptive capacity of the formulation increases, potentially implying the preferential replacement of the stabilizing protein−sugar contacts.

The existence of specific protein−sucrose interactions was further confirmed by examination of the estimated BET monolayer of water. The importance of this parameter stems from its correlation with the onset of internal protein flexibility.[49,50] Moreover, the water content at the monolayer has been directly linked to the free energy changes induced by water sorption and its concomitant changes in the protein structure,[43] while it can provide information on the relative affinity of the water for the substrate. The decreased value of W_m, upon sucrose addition, confirmed the specific protein−sucrose hydrogen bonding interactions. Similar to our previous observations, W_m became minimal at a sucrose-to-protein mass ratio of 1:1, while it increases at higher sucrose contents, reaching its value for the pure protein at the highest sucrose content.

This explanation is in agreement with our enzymatic activity results,[1] which indicated the sucrose-induced stabilization of trypsinogen up to a mass ratio of 1:1, with subsequent reduction of its protective effects at excess concentrations of the carbohydrate. Moreover, the profile of monolayer values closely follows that of the activity losses of the protein during spray drying, potentially indicating that sucrose−protein interactions in the solid matrix are responsible for both stabilizing and destabilizing effects of the disaccharide. Assuming that the relative values of W_m are proportional to the number of component−water interactions, a relative estimate of the sucrose-occupied sites on the protein surface could be obtained by

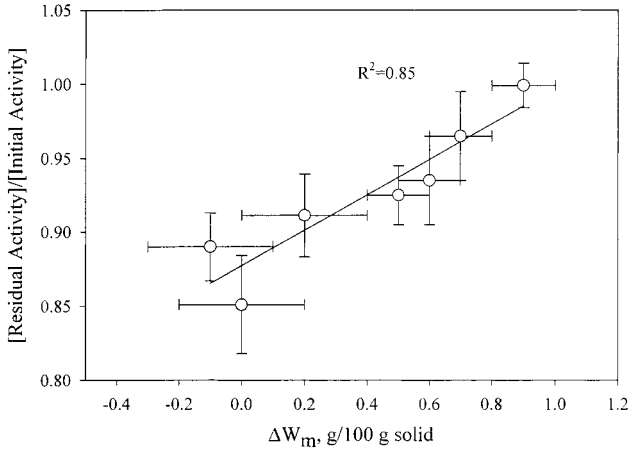

Figure 8—3-D mesh plot of the effect of sucrose and %RH of exposure on the moisture uptake by the spray-dried trypsinogen–sucrose powders.

subtracting the number of water-accessible hydrogen bonding sites of the protein/sucrose mixture ($W_m^{\text{protein/sucrose}}$) from the total number of water-accessible hydrogen bonding sites on the protein in the absence of sucrose (W_m^{protein}), $\Delta W_m = W_m^{\text{protein}} - W_m^{\text{protein/sucrose}}$. From the values of ΔW_m, which are given in Table 2, it follows that at conditions of excess sucrose, the hydrogen bonds between the two components actually decrease and finally reach depletion. This interpretation would support the finding of reduced stability of trypsinogen at the high sugar concentration regime.[1] Indeed, as illustrated in Figure 8, a good correlation ($R^2 = 0.85$) exists between ΔW_m and the residual activity of trypsinogen after spray drying, confirming this hypothesis and implying the replacement of the stabilizing protein−sugar interactions.

Sucrose Crystallization and Inhibition Phenomena—Our moisture sorption experiments indicated that pure, amorphous sucrose can undergo an amorphous-to-crystalline state change at a moisture level of 5.8% w/w. Sucrose crystallization was initiated presumably by sorption of sufficient moisture that reduced its T_g below the operating temperature of 37 °C; in the spray-dried particles crystallization is thought to start at the particle surface and rapidly propagate in the interior.[51] The crystals persisted until approximately 85% RH, which is close to the saturation water activity ($a_w = 0.86$) of sucrose.[27] It is interesting to consider the structure of sucrose in the crystals. In sufficiently diluted solutions, all eight available hydroxyl groups of sucrose form bonds with water molecules.[52−54] However, in concentrated solutions, the high flexibility of the bond joining the two glucose and fructose units promotes the formation of two intramolecular and several intermolecular hydrogen bonds.[53] At this concentration regime, aggregation phenomena occur between sucrose molecules, which now exist in clusters, and under the appropriate conditions will create the stable three-dimensional nucleus.

Although crystallization events were absent at sucrose-to-protein mass ratios lower than 1:1, they became apparent at higher mass ratios of the disaccharide, after exposure to intermediate or high relative humidities. The critical RH of crystallization of these formulations were higher than that observed for the pure compound, denoting the inhibitive role of the protein: increasing concentrations of the protein more effectively inhibit the state transition of the disaccharide, as also indicated by the increasing T_{cryst} with increasing trypsinogen content. From a different perspective, and as illustrated in Figure 3, increasing sucrose concentrations facilitate crystallization, approaching that of the pure compound. Despite the small differences in the

actual critical RH levels, similar results on the inhibitive role of protein in the growth of sucrose crystals were previously described for the rbST−sucrose lyophilized system.[38] It is well documented that impurities decrease the overall growth rate of crystals and change their morphology, as they can block the crystal faces, or even modify the solution characteristics and affect the supersaturation level of sucrose.[52,53] The inhibition of sucrose crystal growth in the presence of high amounts of trypsinogen could reflect the absence of nuclei or even their poisoning by the protein. At low relative protein concentrations, there is less protein available for growth inhibition, while the capacity of the protein phase to compete for water sorption is reduced. In this case, and when adequate water is sorbed to increase the mobility of the sucrose molecules, nuclei can form and grow in the absence of inhibiting interactions. Once nucleation takes place, crystallization occurs rapidly.[55]

For crystallization to proceed, the presence of significant sucrose−sucrose contacts in the solid matrix is imperative. It is therefore conceivable that these are responsible for replacing the stabilizing protein−sugar interactions and could account for the altered interactions of the solid with water. We further assessed the validity of this hypothesis to investigated the nature of this phenomenon.

Phase Separation Phenomena and Origin Hypothesis—Quantitative estimates of the maximum amount of crystallizable sucrose in the formulations can be obtained by the X-ray estimates at conditions of maximal crystal content, 75% RH. Even under these conditions, the X-ray-estimated fractions of crystalline material (within the 5−10% error of the method) cannot fully account for the total amount of sucrose in the formulations, indicating the simultaneous presence of amorphous sugar. Since sucrose crystallization would be inhibited by the presence of protein, it can be assumed that the crystallizable sugar matrix is devoid of protein. This provides evidence for the separation of the dried solid into two distinct phases: a protein-rich and a sugar-rich phase. In the former, amorphous phase, sucrose molecules are in contact with protein, which inhibits their crystallization. In contrast, the second, crystallizable phase, is devoid of protein, so when the system acquires sufficient mobility upon moisture sorption, crystallization is induced. This implies that in the spray-dried material, the phase-separated, crystallizable sucrose does not contribute to the stabilization of the protein, due to its exclusion from it. Assuming that the determined crystallinity fractions provide, within error, a representation of the mass fraction of the crystallized sucrose, we could then obtain via a mass balance an estimate of the actual amounts of amorphous sucrose in the formulations; the analysis is illustrated in Table 5. Using this approach, the amount of protein-interacting, amorphous sucrose was calculated at 15.7, 13.0, and 6.9% w/w for formulations 2:1, 4:1, and 8:1. The analysis indicates that as the mass fraction of sucrose in the formulation increases, there is less available carbohydrate to interact with the protein. The actual amounts of active, protein-interacting sucrose are smaller than expected, based on the formulated mass ratios, as indicated in Table 5. In fact, the effective mass ratios are below the maximally stabilizing mass ratio of 1:1, indicating the inadequate protection of the protein, in agreement with the decreased stability of trypsinogen at these sucrose mass ratios.[1] Moreover, despite the small variability of the observed effects, the phenomenon of partial dissipation of the protective effects of disaccharides has been observed with other proteins,[13,14] indicating a global phenomenon rather than an isolated, protein-specific event.

The onset of the phase separation and crystallization phenomena, with respect to the sucrose content, in the solid formulations coincides with that of the excluded volume effects of the sugar in the solutions before spray drying.[1] Excluded volume phenomena arise from the preferential separation of the carbohydrate from the protein surface; they represent by default phase-separation events at the molecular level. We hypothesize that this distribution of phase-separated formulation components in solution before spray drying is not significantly disturbed during the atomization step, resulting in the formation of protein-rich and sugar-rich phases in the formed particles. The low moisture contents achieved during spray drying prohibited sucrose crystallization in the formulations; however, when the viscosity of the solid matrix decreased upon water sorption, crystal formation was promoted. Further, as discussed above, the protein-excluded sucrose molecules in the solution phase may exist as aggregates, promoting nuclei formation. The presence of aggregate clusters is favored at high concentrations of the disaccharide, as reflected in the reduced hydration number of sucrose: it decreases from 10 to 12 (mol of water/mol of sugar) at sucrose concentrations < 2% w/w, to 5 (mol of water/mol of sugar) at concentrations between 10 and 50% w/w.[54] While the formulated solutions at low sucrose concentrations (mass ratios < 1:1) reside in the former, those prepared at high sucrose concentrations (mass ratios > 1:1) lie in the latter regime, indicating the possible presence of phase-separated, aggregated sucrose in the pre-spray drying solutions.

The proposed mechanisms are in agreement with previous studies on the destabilization of β-galactosidase during lyophilization in the presence of an excess amount of mannitol and inositol;[56,57] however, our results indicate that it is not crystallization per se, but the preceding phase separation event that is responsible for the destabilizing phenomena. It is important to note, however, that the initial protein concentration during spray drying may play an important role, as it may dramatically influence both the starting solution equilibria and the interactions with the excipient in the solid state. More work is required in this direction to understand the concentration dependence of the protein−excipient interactions in the solid state.

Our results suggest that utilization of high concentrations of excipients during preparation of solid state protein formulations may not always be desirable, as even ordinarily stabilizing excipients (such as the commonly utilized disaccharides) may not guarantee the expected stabilization. This becomes particularly important when excipients

Table 5—Nominal and Effective Sucrose Concentrations in the Spray-Dried Trypsinogen–Sucrose Powders

[sucrose: TGN]$_{nominal}$ mass ratio	sucrose[a] (% mass$_{total}$)	free sucrose[b] (% mass$_{total}$)	bound sucrose[c] (% mass$_{total}$)	[sucrose: TGN]$_{effective}$[d] mass ratio
no sucrose	0	0	0	no sucrose
0.25:1	20.0	0	20.0	0.25:1
0.5:1	33.3	0	33.3	0.5:1
1:1	50.0	0	50.0	1:1
2:1	66.7	51.0	15.7	0.47:1
4:1	80.0	71.0	9.0	0.45:1
8:1	88.9	85.0	3.9	0.35:1

[a] Nominal sucrose concentration (% w/w) on a percent total solids basis ($f^{sucrose}_{set}$). [b] Crystallizable sucrose, percent total solids basis. The value represents X-ray diffraction percent crystallinity estimates, under the assumption that sucrose is the only crystallizable formulation component ($f^{sucrose}_{free} = f^{XRD}_{crystalline}$). [c] Noncrystallizable sucrose, percent total solids basis. The value is extracted from a mass balance from the crystallizable sucrose X-ray diffraction estimates ($f^{sucrose}_{bound} = (f^{sucrose}_{set} - f^{sucrose}_{free})$. [d] The "effective" sucrose-to-protein mass ratio is calculated from the mass ratio of noncrystallizable (protein-bound) sucrose to total protein ($f^{sucrose}_{bound}/f^{protein}_{total}$).

that exert excluded volume effects are utilized. Formulation components that exhibit increased capacity for exclusion from the protein surface will have a high tendency to phase separate and will preferentially interact with themselves rather than the protein. Moreover, they may undergo undesirable phase transformations that may decrease product stability. This becomes of particular significance during the administration of pharmaceutical products with sustained release delivery systems, such as polymeric injectable depots or implantable micropumps, because of the exposure of the formulation to increased water levels at the physiologic temperature of 37 °C.

References and Notes

1. Tzannis, S. T.; Prestrelski, S. J. Activity-Stability Considerations of Trypsinogen during Spray Drying: Effects of Sucrose, *J. Pharm. Sci*. **1999**, *88*, 351−359.
2. Tzannis, S. T. Stabilization of Proteins during Spray Drying, Protein Stability Conference, Breckenridge, CO, July 16−18, 1998.
3. Prestrelski, S. J.; Arakawa, T.; Carpenter, J. F. Structure of Proteins in Lyophilized Formulations Using Fourier Transform Infrared Spectroscopy. In *Formulation and Delivery of Proteins and Peptides*, Cleland, J. L., Langer, R., Eds.; ACS Symposium Series 567; American Chemical Society: Washington, DC, 1994; pp 148−169.
4. Prestrelski, S. J.; Tedeschi, N.; Arakawa, T.; Carpenter, J. F. Dehydration-Induced Conformational Transitions in Proteins and Their Inhibition by Stabilizers. *Biophys. J*. **1993**, *65*, 661−671.
5. Griebenow, K.; Klibanov, A. M. Lyophilization-induced Reversible Conformational Changes in the Secondary Structure of Proteins. *Proc. Natl. Acad. Sci. U.S.A*. **1995**, *92*, 10969−10976.
6. Winters, M. A.; Knutson, B. L.; Debenedetti, P. G.; Sparks, G.; Przybycien, T. M.; Stevenson, C. L.; Prestrelski, S. J. Precipitation of Proteins in Supercritical Carbon Dioxide. *J. Pharm. Sci*. **1996**, *85*, 586−594.
7. Mumenthaler, M.; Hsu, C. C.; Pearlman, R. Feasibility Study on Spray-Drying of Protein Pharmaceuticals: Recombinant Human Growth Hormone and Tissue-Type Plasminogen Activator. *Pharm. Res*. **1994**, *11*, 12−20.
8. Labrude, P.; Rasolomanana, M.; Vigneron, C.; Thirion, C.; Chaillot, B. Protective Effect of Sucrose on Spray Drying of Oxyhemoglobin. *J. Pharm. Sci*. **1989**, *78*, 223−229.
9. Broadhead, J.; Edmond Rouan, S. K.; Hau, I, Rhodes, C. T. The Effect of Process and Formulation Variables on the Properties of Spray-Dried β-Galactosidase. *J. Pharm. Pharmacol*. **1994**, *46*, 458−467.
10. Broadhead, J.; Edmond-Rouan, S. K.; Rhodes, C. T. The Spray Drying of Pharmaceuticals. *Drug Dev. Ind. Pharm*. **1996**, *22*, 813−822.
11. Tzannis, S. T.; Hrushesky, W. J. M.; Wood, P. A.; Przybycien, T. M. Irreversible Inactivation of Interleukin-2 in a Pump-Based Delivery Environment. *Proc. Natl Acad. Sci. U.S.A*. **1996**, *91*, 5460−5465.
12. Carpenter, J. F.; Prestrelski, S. J.; Anchordoquy, T. J.; Arakawa, T. Interactions of Stabilizers with Proteins During Freezing and Drying. In*Formulation and Delivery of Proteins and Peptides*. Cleland, J. L., Langer, R., Eds.; ACS Symposium Series 567; American Chemical Society: Washington, DC, 1994; pp 134−147.
13. Tzannis, S. T.; Meyer, J. D.; Prestrelski, S. J. Secondary Structure Considerations during Protein Spray Drying. 213th ACS National Meeting, San Francisco, CA, April 13−17, 1997; American Chemical Society: Washington, DC, 1997.
14. Tzannis, S. T. Spray Drying of Protein Pharmaceuticals: Powder Characteristics and Stability Considerations. Presented at Conference of Formulations and Drug Delivery II, La Jolla, CA, October 5−8, 1997.
15. Carpenter, J. F.; Crowe, J. H. An Infrared Spectroscopic Investigation of the Interactions of Carbohydrates with Dried Proteins. *Biochemistry* **1989**, *28*, 3916−3922.
16. Carpenter, J. F.; Prestrelski, S. J.; Arakawa, T. Separation of Freezing- and Drying-Induced Denaturation of Lyophilized Proteins Using Stress-Specific stabilization. I. Enzyme Activity and Calorimetric Studies. *Arch. Biochem. Biophys*. **1993**, *303*, 456−464.
17. Prestrelski, S. J., Byler, D. M., Liebman, M. N. Comparison of Various Molecular Forms of Bovine Trypsin: Correlation of Infrared Spectra with X-ray Crystal Structures. *Biochemistry* **1991**, *30*, 133−143.
18. Brunauer, S.; Emmett, P. A.; Teller, E. Adsorption of Gases in Multimolecular Layers. *J. Am. Chem. Soc*. **1938**, *60*, 309−319.
19. Teng, C. D.; Zarrintan, M. H.; Groves, M. J. Water Vapor Adsorption and Desorption Isotherms of Biologically Active Proteins. *Pharm. Res*. **1991,** *8*, 191−195.
20. Zografi, G. States of Water Associated with Solids. *Drug Dev Ind. Pharm*. **1988**, *14*, 1905−1926.
21. Kontny, M. J.; Zografi, G. Sorption of Water by Solids. In *Physical Characterization of Pharmaceutical Solids*; Brittain, H. G., Ed.; Marcel Dekker Inc.: New York, 1995; pp 387−418.
22. Andres, M. C.; Bugay, D. E.; McKenzie, A. T.; Remick, D. M.; Stahly, G. P.; Thomas, A. S. Quantitative X-ray Powder Diffraction Analysis: A Comparison of Data Analysis Techniques. *PharmSci* **1998**, *1*, S-23.
23. Leeder, J. D.; Watt, J. C. The Stoichiometry of Water Sorption by Proteins. *J. Colloid Interface Sci*. **1974**, *48*, 339−344.
24. Hageman, M. J. The Role of Moisture In Protein Stability. *Drug Dev. Ind. Pharm*. **1988**, *14*, 2047−2070.
25. Bizot, H.; Buleon, A.; Mouhous-Riou, N.; Multon, J. L. Some Factors Concerning Water Vapour Sorption Hysteresis on Potato Starch. In *Properties of Water in Foods*; Simatos, P., Multon, J. L., Eds.; NATO-AST Series E: Applied Sciences, No. 90, Martinus Nijhoff Publishers: Dordrecht, The Netherlands, 1985; pp 83−93.
26. Chinachoti, P.; Steinberg, M. P. Interaction of Sucrose with Gelatin, Egg Albumin and Gluten in Freeze-Dried Mixtures as Shown by Water Sorption. *J. Food Sci*. **1988**, *53*, 932−934.
27. Chinachoti, P.; Steinberg, M. P. Moisture Hysteresis is due to Amorphous Sugar. *J. Food Sci*. **1986**, *51*, 453−455.
28. Chinachoti, P.; Schmidt, S. J. Solute-Polymer−Water Interactions and their Manifestations. In *Water Relationships in Foods: Advances in the 1980s and Trends for the 1990s*; Levine, H., Slade, L., Eds.; Plenum Press: New York, 1991; pp 561−583.
29. Kuntz, I. D.; Kauzmann, W. Hydration of Proteins and Polypeptides. *Adv. Prot. Chem*. **1974**, *28*, 239−345.
30. Hageman, M. J.; Possert, P. L.; Bauer, J. M. Prediction and Characterization of Water Sorption Isotherm for Bovine Somatotropin. *J. Agric. Food Chem*. **1992**, *40*, 342−347.
31. Saltmarch, M.; Lanuza, T. P. Influence of Relative Humidity on the Physicochemical State of Lactose in Spray-Dried Sweet Whey Powders. *J. Food Sci*. **1980**, *45*, 1231−1236.
32. Benson, S. W.; Ellis, D. A.; Zwansig, R. W. Surface Areas of Proteins. III. Adsorption of Water. *J. Am. Chem. Soc*. **1950**, *72*, 2102−2105.
33. Nakai, Y.; Fukuoka, E.; Kakajima, S.; Hasegawa, J. Crystallinity and Physical Characterization of Microcrystalline Cellulose. *Chem. Pharm. Bull*. **1977**, *25*, 96−101.
34. Saleki-Gerhardt, A.; Zografi, G. Non-Isothermal and Isothermal Crystallization of Sucrose from the Amorphous State. *Pharm. Res*. **1994**, *11*, 1166−1173.
35. Makower, B.; Dye, W. B. Equilibrium Moisture Content and Crystallization of Amorphous Sucrose and Glucose. *Agric. Food Chem*. **1956**, *4*, 72−77.
36. Warburton, S.; Pixton, S. W. The Moisture Relations of Spray Dried Skimmed Milk. *J. Stored Prod. Res*. **1978**, *14*, 143−158.
37. French, D. L.; McAuley, A. J.; Chang, B.; Niven, R. W. Moisture Induced State Changes in Spray-Dried Trehalose/Protein Formulations. *Pharm. Res*. **1995**, *12*, S83.
38. Sarciaux, J.-M. E.; Hageman, M. J. Effects of Bovine Somatotropin (rbST) Concentration at Different Moisture Levels on the Physical Stability of Sucrose in Freeze-Dried rbST/Sucrose Mixtures. *J. Pharm. Sci*. **1997**, *86*, 365−371.
39. Chinachoti, P.; Steinberg, M. P. Crystallinity of Sucrose by X-ray Diffraction as Influenced by Absorption versus Desorption, Waxy Maize Starch Content and Water Activity. *J. Food Sci*. **1986**, *51*, 456−459.
40. Green, J. L.; Fan, J.; Angell, C. A. The Protein-Glass Analogy: Some Insights from Homopeptide Comparisons. *Biophys. Chem*. **1994**, *98*, 13780−13790.
41. Hageman, M. J. Water Sorption and Solid-State Stability of Proteins. In *Stability of Protein Pharmaceuticals. Part A: Chemical and Physical Pathways of Protein Degradation*. Ahern, T. J., Manning, M. C., Eds.; Plenum Press: New York, 1992; pp 273−309.
42. Bone, S. Dielectric Studies of Native, Unfolded and Intermediate Forms of β-lactamase. *Phys. Med. Biol*. **1994**, *39*, 1801−1809.
43. Zografi, G.; Hancock, B. Water-Solid Interactions in Pharmaceutical Systems. In *Proceedings of 53rd International Congress of Pharmaceutical Sciences*; Tokyo, Japan, Elsevier: New York, 1994.

44. Levine, H.; Slade, L. Water as a Plasticizer: Physicochemical Aspects of Low Moisture Polymeric Systems. In *Water Science Reviews*; Franks, F., Ed.; Cambridge University Press: Cambridge, UK, 1987; Volume 3, pp 79−185.
45. White, G. W.; Cakebread, S. H. The Glassy State In Certain Sugar-Containing Foods. *J. Food. Technol.* **1966**, *1*, 73.
46. Parak, F. Correlations of Protein Dynamics with Water Mobility: Mössbauer Spectroscopy and Microwave Absorption Methods. *Methods Enzymol.* **1986**, *127*, 196−206.
47. Morozov, V. N.; Morozova, T. Y.; Kachalova, G. S.; Myachin, E. T. Interpretation Of Water Desorption Isotherms Of Lysozyme. *Int. J. Biol. Macromol.* **1988**, *10*, 329−336.
48. Costantino, H. R.; Curley, J. G.; Wu, S.; Hsu, C. C. Water Sorption Behavior of Lyophilized Protein−Sugar Systems and Implications for Solid-State Interactions. *Int. J. Pharm.* **1998**, *166*, 211−221.
49. Poole, P. L.; Finey, J. L. Sequential Hydration of Dry Proteins: A Direct Difference IR Investigation of Sequence Homologues Lysozyme and α-Lactalbumin. *Biopolymers* **1984**, *23*, 1647−1666.
50. Rupley, J. A.; Gratton, E.; Careri, G. Water and Globular Proteins. *Trends Biochem. Sci.* **1983**, *8*, 18−22.
51. Palmer, K. J.; De, W. B.; Black, D. X-ray Diffractometer and Microscopic Investigation of Crystallization of Amorphous Sucrose. *Agric. Food Chem.* **1956**, *4*, 77−81.
52. Vaccari, G.; Mantovani, G. Sucrose Crystallization, In *Sucrose: Properties and Applications*; Mathlouthi, M., Reiser-Cedus, P., Eds.; Chapman & Hall: New York, 1995; pp 33−74.
53. Mathlouthi, M. Amorphous Sugar. In *Sucrose: Properties and Applications*; Mathlouthi, M., Reiser-Cedus, P., Eds.; Chapman & Hall: New York, 1995; pp 75−100.
54. Flink, J. M. Structure and Structure Transitions in Dried Carbohydrate Materials. In *Physical Properties of Foods*; Peleg, M., Bagley, E. B., Eds.; AVI Publishing Co.: New York, 1984; pp 473−521.
55. Van Scoik, K. G.; Carstensen, J. T. Nucleation Phenomena in Amorphous Sucrose Systems. *Int. J. Pharm.* **1990**, *58*, 185−196.
56. Izutsu, K.; Yoshioka, S.; Terao, T. Decreased Protein Stabilizing Effects of Cryoprotectants due to Crystallization. *Pharm. Res.* **1993**, *10*, 1233−1238.
57. Izutsu, K.; Yoshioka, S.; Kojima, S. Physical Stability and Protein Stability of Freeze-Dried Cakes during Storage at Elevated Temperatures. *Pharm. Res.* **1994**, *11*, 995−999.

Acknowledgments

The authors thank Wei Zhang, Joan Huey-Dow, and Tom Piercy (ALZA Corporation) for their assistance in the modulated DSC and surface area measurements.

JS9800127

A Method for Quantifying Differential Expansion within Hydrating Hydrophilic Matrixes by Tracking Embedded Fluorescent Microspheres

JEREMY ADLER,† ARVIND JAYAN, AND COLIN D. MELIA*

Contribution from *School of Pharmaceutical Sciences, University of Nottingham, Nottingham NG7 2RD, UK.*

Received September 25, 1997. Final revised manuscript received October 20, 1998.
Accepted for publication December 7, 1998.

Abstract □ A method is described for quantifying the pattern of deformation within a matrix and is demonstrated by analyzing the expansion of polymer hydrophilic matrix tablets. The fundamental features of the method are the incorporation of nondiffusing markers into the matrix and the subsequent tracking of these markers during deformation. Since the markers are too large to diffuse, their individual movement reflects the translocation of the surrounding matrix, and the separation between pairs of markers reveals any perturbation in the intervening area. By tracking many markers, the pattern of deformation within a matrix can be ascertained. The method was demonstrated on hydrating hydrophilic matrix tablets, using fluorescent microspheres as nondiffusing markers which were observed with a confocal laser scanning microscope. Analysis of the tracks showed a wave of expansion moving from the exterior toward the core, with the greatest and earliest expansion found in the outer regions. The results also showed that even as deeper layers started to expand the outer layers continued to swell.

Introduction

Many materials undergo alterations in size during their production or use and while it is relatively easy to measure gross dimensional changes[1,2] it is much harder to establish the pattern of internal deformation. Deformation can vary from the isotropic expansion of an evenly heated metal bar to the contraction of drying gels or the hydration of hydrophilic matrix (HM) tablets, both of which are anisotropic, despite the homogeneity of the original material. The experimental difficulty lies in following and quantifying differential deformation, for which there appear to be no established methods.

Hydrophilic matrix tablets are used as controlled release formulations.[3] Their performance depends on the rapid formation of a coherent gel layer around the tablet on hydration. An intact gel layer restricts the further ingress of water and controls drug release by acting as a diffusional barrier and by limiting erosion. The gel layer is inhomogeneous,[4] varying between a water rich exterior and an initially dry core.[4] The common USP dissolution methods used to assess the performance of HM tablets measure only rates of drug release. However, the underlying processes are dynamic and complex, involving interactions between water, polymer, the drug, and ions, all in an expanding and eroding matrix. Similarly, in the food industry, syneresis of gels is estimated by reweighing[5] or from volume changes. These measures adequately describe overall performance but do not expose the underlying processes.

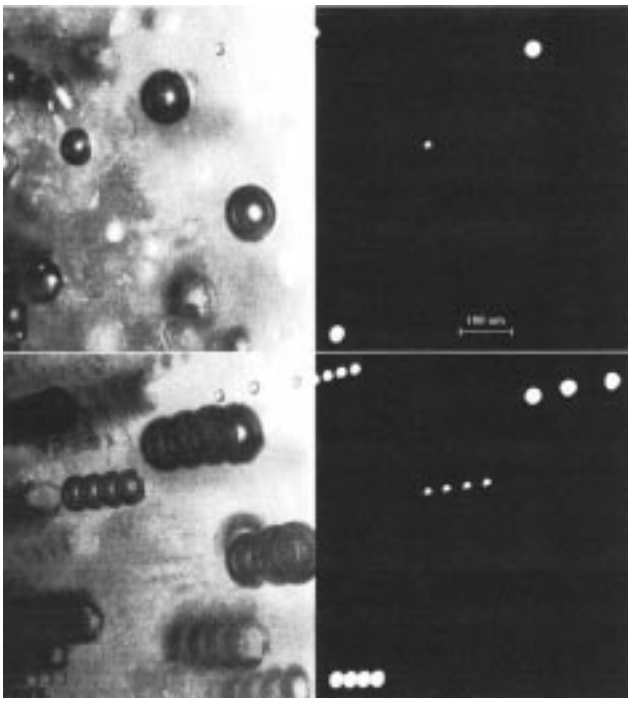

Figure 1—The left panels show (transmitted light image) air bubbles and microspheres, and the right panels (fluorescence image) microspheres only, in the gel layer of an HPMC tablet. The lower panels show a superimposed sequence of four images, showing movement. The bottom left image (transmitted light) is a minimum projection, and the bottom right (fluorescence) a maximum projection. Two sizes of fluorescent microspheres are apparent diameters of 2 μm and 22 μm.

In studying the performance of gel or tablet matrixes, the real goal is to expose the underlying mechanisms and advance from using experiments to observe the performance of specific formulations, to the experimental validation of predictive mathematical models. To confirm and validate such models, experimental methods are required that generate data which fully describes their properties and behavior. With this in mind we have been developing techniques to examine the internal performance of matrixes.[6−8]

We have reported on the presence of air bubbles[9] in HM tablet gel layers and have subsequently observed that these bubbles move as the gel layer continues to expand (Figure 1). Similarly undissolved particulates within a gel are also translocated (Figure 2). In this paper we consider how this observable movement can be used to map the internal performance of matrixes, and we describe a novel method in which nondiffusing markers are embedded within a tablet matrix and tracked during hydration. These tracks are then used to establish where and when expansion occurs. A fundamental assumption is that the influence of Brownian motion on our markers is minimal and that any

* Corresponding author. Telephone +44 (0)115−9515032. Facsimile +44 (0)115−9515102. Email colin.melia@nottingham.ac.uk.
† Current address, RHM Technology Ltd, Lincoln Rd, High Wycombe, HP12 3QR, UK.

10.1021/js970376j CCC: $18.00 Published on Web 01/23/1999

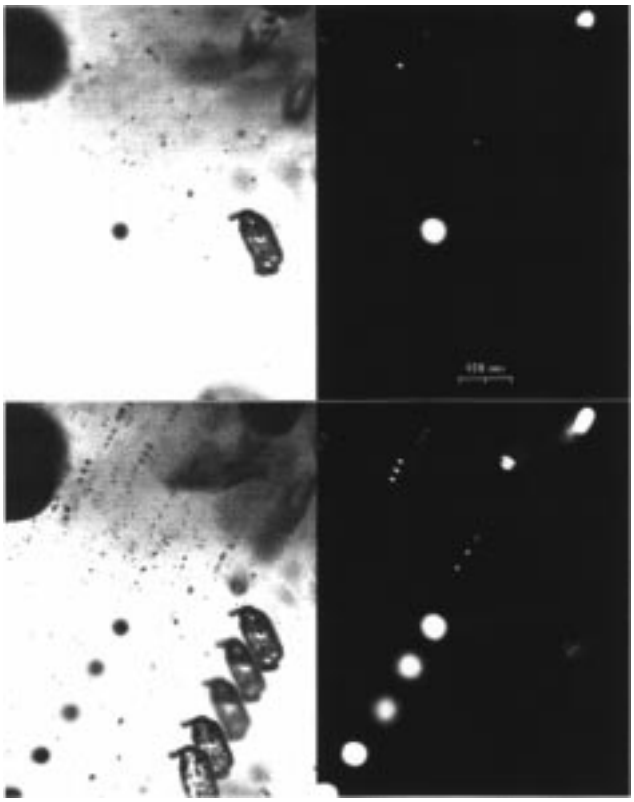

Figure 2—Left panels (transmitted light) show particulates and microspheres, and the right panels (fluorescence image) microspheres in the gel layer of a HPMC tablet. The lower two panels show a superimposed sequence of five images: the bottom left image is a minimum projection, and the bottom right image is a maximum projection. Two sizes of fluorescent microspheres are apparent, diameters of 22 μm and 2 μm.

movement of the markers therefore mirrors movement of the surrounding matrix.

Tracking the positions of individual embedded markers shows the changing location of these points within the matrix. However, their movement is not necessarily a consequence of a localized deformation: when a train moves, all the carriages also move but without any local or even overall deformation. Similarly a difference in velocity between markers does not necessarily reveal different degrees of local expansion: stretching a rubber band, with one fixed end, produces the greatest extension at the free end while the fixed end remains almost stationery, but the local expansion is nonetheless uniform. However, local expansion can be measured from the changing distance between a pair of markers, because their relative separation reflects any perturbation in the intervening zone, and it therefore becomes possible to move from measuring the translocation of markers to the measurement of localized deformation.

In summary, this study examines the use of nondiffusing markers to follow localized deformation within hydrating hydrophilic matrix tablets.

Experimental Section

Materials—Five millimeter diameter flat-faced circular tablets were prepared by direct compression of 40−63 μm sieve fractions of hydroxypropylmethylcellulose (HPMC) (Methocel K4M, Dow Europe, Germany) or xanthan gum (Satiaxane CX90, Sanofi Biopolymers France) containing 0.125% w/w latex microspheres, 2 μm and 22 μm average diameter, labeled with Nile red (Polymer Labs Ltd, UK). The microspheres, supplied in 10% w/v suspension in water, were dried by evaporation and then mixed with the dry polymer by trituration prior to tableting. Tablets were manufactured at a compression force of 1.2−1.5 kN using a Manesty F3 single-punch tablet press (Manesty machines, Speke, UK). Additional HPMC tablets were prepared containing different quantities of microspheres (0, 0.025, 0.05, 0.1, and 0.2% w/w).

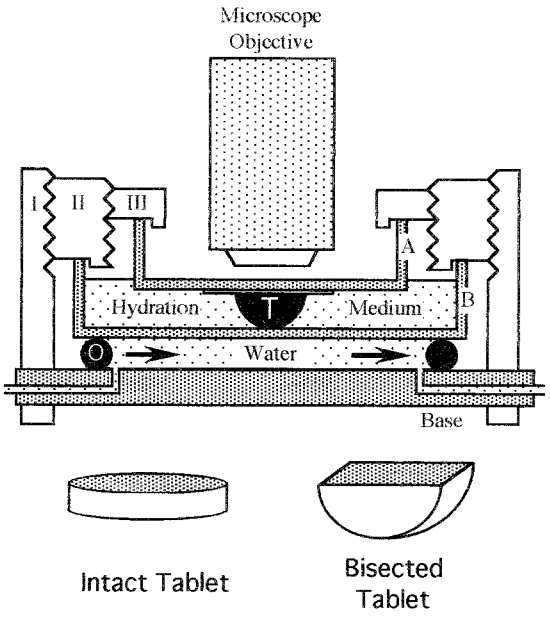

Figure 3—Tablet hydration cell: A bisected tablet (t) is shown placed between two Petri dishes (A and B) and held in place by three concentric brass rings (I, II, III). There is a silicon rubber membrane between Petri dish A and the tablet surface. The lower chamber, formed by compression of an O ring between the base and Petri dish B, can be perfused to maintain a constant temperature. Intact or bisected tablets were mounted in the cell, with a flat surface presented to the microscope objective.

Tablet Hydration Cell—Consisted of three interlocking brass rings (I, II, and III), two Petri dishes, and a transparent Perspex (poly(methyl methacrylate) base (Figure 3). Rotation of the upper two rings fixed a tablet between the two Petri dishes, enabling the observation of the upper surface of the tablet during hydration. The hydration medium was added to the chamber formed between the two Petri dishes. To prevent the hydration medium penetrating between the upper Petri dish (diameter 35 mm) and the upper surface of the tablet, a 200 μm transparent silicon rubber membrane was inserted between the tablet and the underside of the upper Petri dish. Temperature control was achieved by (i) preheating the hydration medium and (ii) circulating water through a bottom chamber formed by the compression of a silicon rubber O ring between the lower Petri dish and the Perspex base.

Tablets were hydrated at 37 °C in degassed distilled water. Two different orientations (Figure 3, bottom) of the tablets were used: (i) intact tablets face down for examination of radial expansion and (ii) bisected tablets with their exposed surface facing upward for both radial and axial expansion.

Confocal Laser Scanning Microscopy (CLSM)—Sequential images (768 × 512 pixels with 8-bit intensity) were generated using a MRC600 confocal microscope (Bio-Rad, Hemel Hempstead, UK) based on a Nikon Labophot upright microscope using the YHS filter with excitation at 565 nm and a ×1 microscope objective. Images were taken with the microscope focused 100 μm below the silicone/tablet interface.

The method relies on following individual microspheres through a series of images, but small movements in the *z* axis can take a microsphere outside the plane of focus, making tracking difficult. This problem was ameliorated by generating each image from a maximum projection of four almost synchronous images taken at increasing (20 μm step) depths. In a projection, homologous pixels from each image are compared and either the most intense (a maximum projection) or the least intense (a minimum projection) retained in the final image.

The confocal microscope was also used to generate transmitted light images which showed the initial edge of the dry tablet and the outer limit of the gel layer after hydration. These images were obtained using a light collector beneath the hydration cell. Changes in the extent of the gel layer were used to compare water uptake

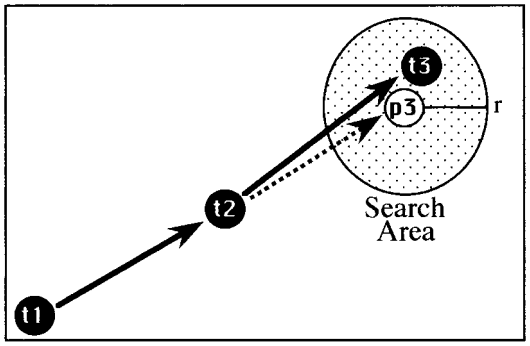

Figure 4—The tracking method: the two previous positions (t1 and t2) are used to predict the next location (p3), which is used as the center of a search area (radius r) for the actual subsequent location (t3).

in the series of tablets containing different fractions of microspheres.

Image Processing—In the CLSM images, the fluorescent microspheres appeared as areas of high intensity against a dark background, with each microsphere covering several pixels. Ideally each microsphere should be tracked from its center to the next center; however, it is possible that the brightest single pixel may not occur at the center. To ensure that the tracking was from center to center, a local averaging of the image preceded each search. For a bright object of a similar size to the distance used by the local area average, the brightest pixel is forced to center. The fluorescence image of the microsphere typically covered about 20 pixels and an equally weighted local average over a 5×5 pixel block was used. The centers were located to the nearest pixel.

Tracking Microspheres—Software was developed around a Semper 6.4 (Synoptics, Cambridge, UK) kernel operating on a Sprynt 40 processing board (Synoptics, Cambridge, UK). The objective was to determine the *x,y* coordinates of identified particles throughout a sequence of images. Figure 4 shows how the location of a microsphere in two preceding images (t1 and t2) was used to predict the next location (p3), and this predicted location then became the center for a local search (radius *r*) for the particle, producing the actual location (t3). Once the location of the microsphere had been established in several images, the predicted location was then based on the preceding three images, which proved to be more accurate. The initial location of each particle (t1) was input using a mouse from a prehydration image, and the second location (t2) was also input manually from either the first post-hydration image or from a maximum projection image, which sometimes made it easier to establish the direction of a track. After the first two locations had been established, the subsequent tracking was undertaken by the software alone. The search radius around the predicted location was either 8 pixels or half the length of the predicted movement, whichever was the greater. This choice of search radius depended upon the density of microspheres and was a compromise between checking a small enough area to exclude a second microsphere, and using a sufficiently large area to accommodate substantial changes in velocity.

Provision was made in the tracking software for automatically discontinuing the search for microspheres that exceeded the limits of the image (once part of the search area fell outside the image) and also for the rejection of manifestly incorrect tracks. These can occur when a second more intense microsphere appears in the search area and the search algorithm then latches onto an incorrect path.

Analysis—After tracking was completed, the initial location and subsequent path taken by each microsphere was stored as a sequential list of *x,y* coordinates from which the speed of each microsphere was obtained. However, our primary interest lies in determining where and when the matrix deforms. As discussed previously, the movement per se of a single microsphere does not reveal the local rate of expansion in the matrix, but this can be determined from the relative position of a pair of microspheres. However, when considering the radial expansion of flat-faced cylindrical tablets, which are radially symmetrical, the distance of each microsphere from the center of the tablet can replace the *x,y* coordinates. This then permits the grouping of microspheres into bands of similar radii. Within each band the radius of each microsphere was expressed as a ratio to its original radius, and the mean ratio multiplied by the nominal radius of the band then produced the average radius. The changes in the average radius of each band and difference in radii between adjacent bands were used to measure overall expansion and local expansion. The coordinates of the tablet center were derived from the curvature of the tablet edge. When bisected tablets were observed, the movements of individual microspheres were separated into radial and axial vectors.

Results

The images obtained showed that it was practical to incorporate and detect fluorescent microspheres in HM tablets. The compression used during tableting did not seem to fracture or fragment the microspheres, and their distribution appeared to be random. Sequential CLSM images of hydrating HM tablets showed that individual microspheres could be followed for long periods.

In Figures 1 and 2 individual fluorescent microspheres and their movement are apparent. The individual microspheres, polymer particles, and air bubbles appeared to move linearly and in concert. The speed (the distance between successive occurrences) of microspheres within a few hundred micrometers of each other differs, which we attribute to different rates of local expansion of the matrix. In the lower panels of Figure 2 a blurring of the polymer particle and the large microsphere is apparent, and in the maximum projected image (bottom, left) there are five occurrences of the large microsphere but only three occurrences of the smaller microspheres. We attributed these variations to small movements in the *z* axis that took smaller objects outside the focal plane and defocused the larger objects. Problems associated with small movements in the *z* axis were minimized by using only the larger 22 μm microspheres in subsequent experiments and by using a maximum projection of four images taken at different depths.

Figure 5 (upper) shows that individual microspheres can be clearly seen in a dry tablet. The maximum projections (Figure 5 center and Figure 9 upper) contain the combined sequence of images and revealed linear tracks, apparently radiating away from the center of the tablet. The tracks of individual microspheres, shown in the maximum projected images in Figures 5, 8, and 9 are either linear or gently curving and are in the direction of expansion. Their linearity shows that Brownian motion had minimal influence. The overall pattern of movement and the continuing proximity of microspheres to the edge of the gel layer indicate that the microspheres were carried along with the hydrating polymer.

Individual microspheres, shown by their paths in the maximum projected images in Figures 5, 8, and 9, cover markedly different distances depending on their initial position in the tablet. The actual distance covered is the path length minus the diameter of the microsphere, but this is an overall measure taken over the full duration of the experiment; a more detailed assessment requires tracking individual microspheres through the whole sequence of images.

The tracking software proved able to follow a substantial number of microspheres. However, some microspheres moved outside the plane of focus of the confocal images and were lost; others were not apparent in the first image and only appeared in subsequent images, either by moving into the plane of focus or becoming visible as a transparent gel layer replaced the relatively opaque dry polymer. The greatest problems occurred with microspheres on the edge of the tablet, which move very rapidly in the initial 2 min after hydration making them difficult to track, and with

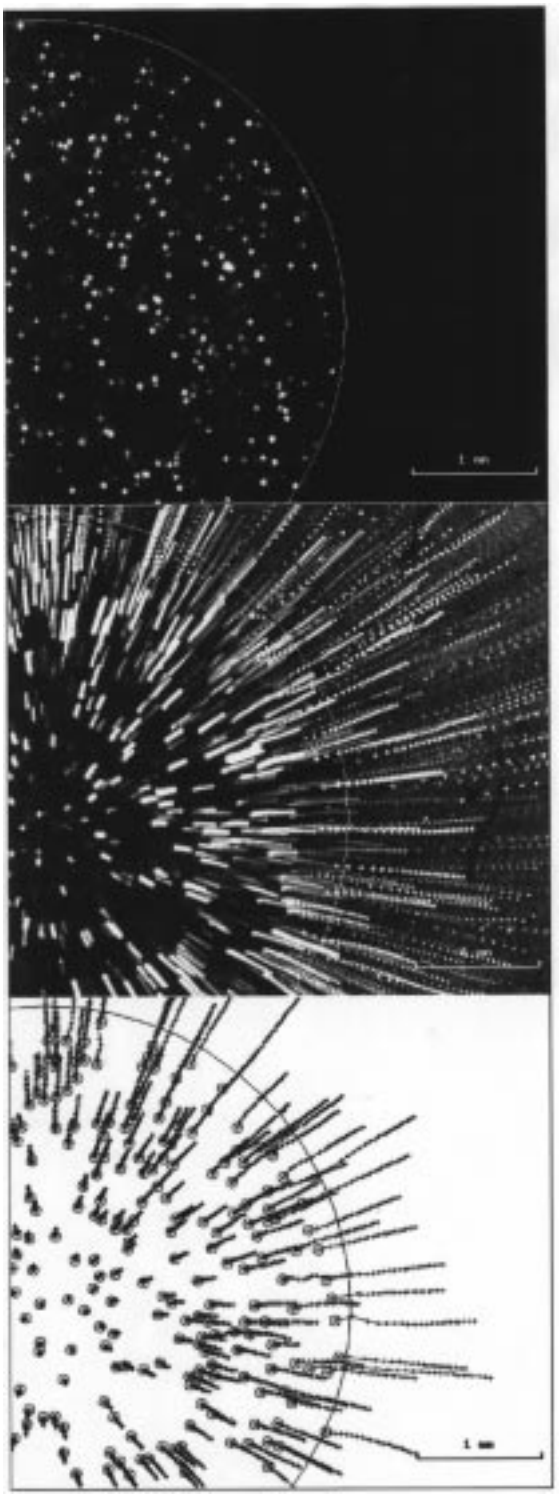

Figure 5—Radial expansion of a xanthan tablet. Upper panel: a confocal microscope image showing fluorescent microspheres within a dry tablet. Center panel: a maximum projected image showing the paths taken by microspheres during the 40 min following hydration. Lower panel: the mapped tracks of identified microspheres starting from their original locations. The original edge of the tablet is superimposed on each image.

pairs of microspheres that were too close to be easily separated. The complete tracks of 211 microspheres that were followed from the first image appear in Figure 5 lower panel.

It is apparent that the movement of individual microspheres depends on their proximity to the initial edge of the tablet and declines further into the tablet. This is made clear in Figure 6 when the individual movements are

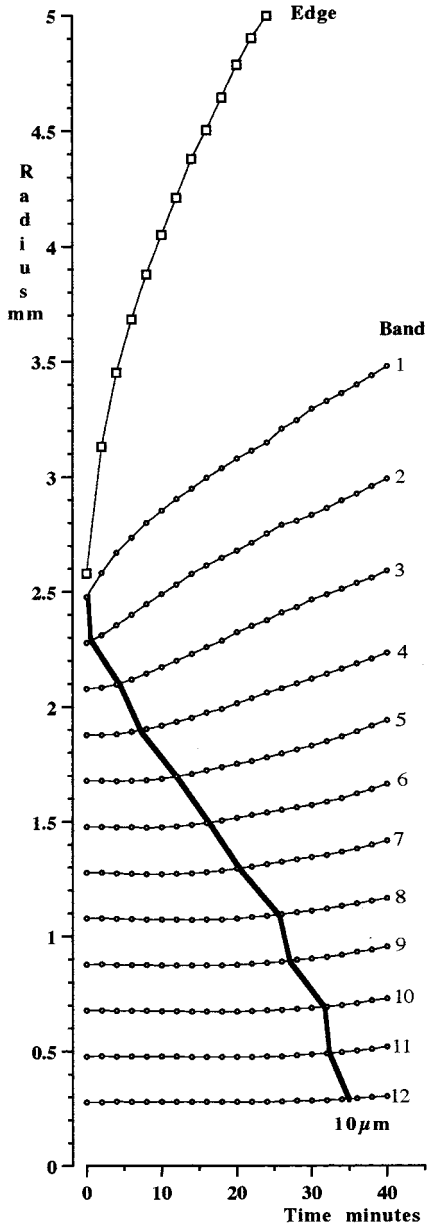

Figure 6—The expansion within a xanthan tablet undergoing hydration, shown as the growth of a series of 200 μm concentric bands radiating from the tablet center. Band 1 is the outermost and band 12 the innermost. $y = 0$ mm is the tablet center. The movement of the outermost edge of the tablet is also shown. The thick line links the time points when each band first moved by 10 μm.

pooled by assigning microspheres into a series of 200 μm wide bands at increasing distance from the tablet edge. The outer bands move earlier and faster, but even the deepest bands finally undergo some movement. An estimate of when each band began to move was obtained by marking the time when a 10 μm displacement first occurred. This reveals the ingress of a wave of expansion which reached the innermost band after 36 min. This was a surprising finding since the gelatinous layer formed around the tablet only extends over the first few bands.

The outer edge of the gel, shown in Figure 6, appears to expand much more dramatically than the microspheres in the outermost 200 μm band. This is a consequence of underestimating the expansion of the outer band due to difficulties in tracking microspheres that originate close to the tablet edge. The rapid expansion made following these microspheres difficult.

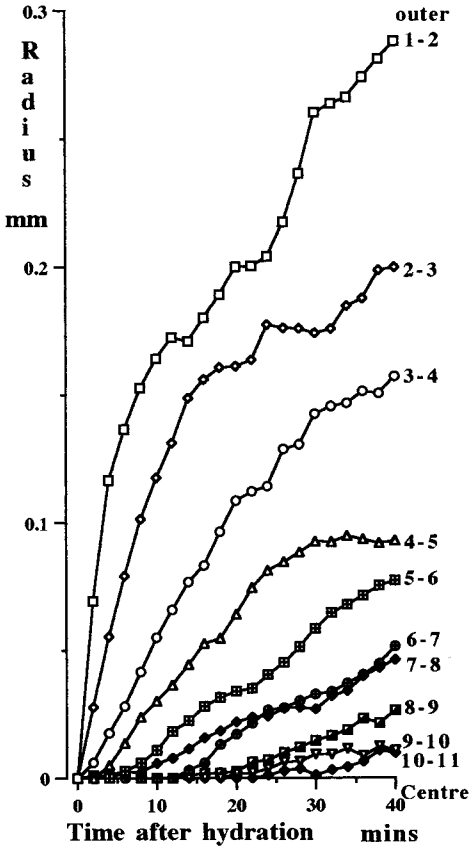

Figure 7—The differential expansion between adjacent concentric bands in a hydrating xanthan tablet, determined by subtracting the movement of the adjacent inner band. Each band is 200 μm thick and band 1-2 is the outermost.

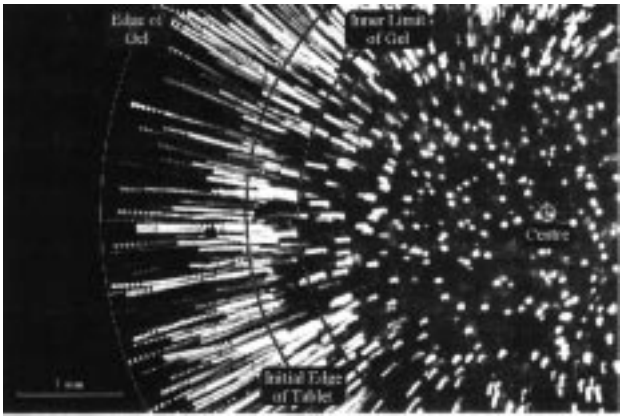

Figure 8—Tracks made by fluorescent microspheres in a xanthan tablet hydrating in 0.05 M NaCl over 80 min. The image is a maximum projection. Also marked is the initial location of the tablet edge and the final limits, inner and outer, of the gel layer.

The progressively increasing radius of each band could correspond to expansion within the band, to displacement following the expansion of deeper areas of the matrix, or to a combination of both mechanisms. In Figure 7 the analysis is extended by subtracting the radius of the adjacent inner band from each band, leaving the endogenous expansion. This shows that expansion progressively decreases deeper within the tablet and that the outer band is still expanding at the end of the experiment.

To determine the relative penetration of the gel layer into a tablet and the depths at which the movement of microspheres occurred, the gel layer of a hydrated tablet was gently removed with a small spatula and the size of the residual core measured. The core of the tablet was hard and appeared dry. In Figure 8 the initial tablet edge and the limits of the gel layer are superimposed on the tracks of the embedded microspheres. The extended tracks of microspheres beyond the inner limit of the gel layer shows that expansion had occurred deep in the core of the tablet though had not yet reached the center.

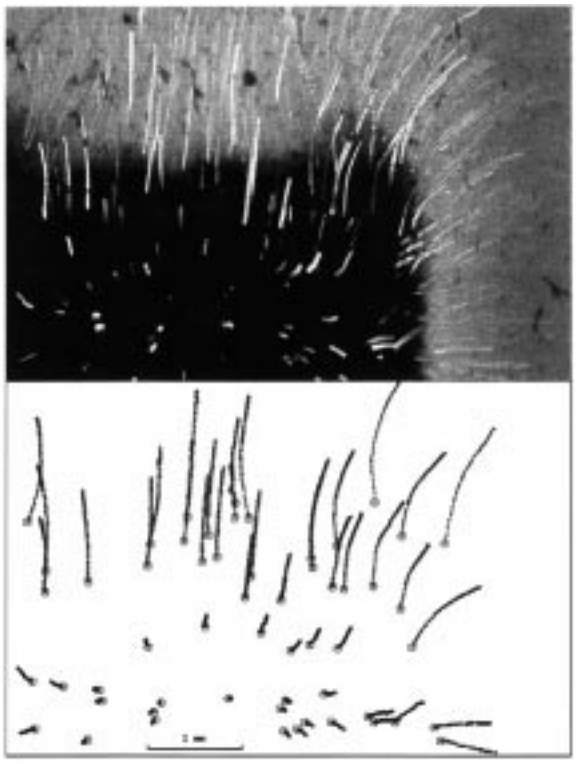

Figure 9—The expansion of a bisected hydroxypropylmethylcellulose tablet after hydration. Upper panel: a maximum projected image showing the paths followed by microspheres following hydration. The inclusion of the fluorophore Congo red in the hydration medium makes the gel layer apparent. Lower panel: the mapped tracks of identified microspheres, starting from their original locations. Axial movements are in the vertical plane and radial movements in the horizontal plane.

When a bisected hydroxypropylmethylcellulose (HPMC) tablet was examined (Figure 9), the pattern of microsphere movements was more complex, with some microspheres taking curved paths, rather than the linear trajectories seen with intact tablets. Curved tracks predominated at the corners of the tablet, reflecting the interplay between axial and radial expansion. More unexpected were the tracks of some microspheres that originated slightly away from the corners and, while predominantly moving axially, had an initial inward radial component that was later replaced by an outward component. We suspect that this pattern may be due to an inward pressure exerted by the more rapidly expanding corners of the tablet that cause a slight short-lived radial compression. The larger surface area at the corners increases their exposure to water and accordingly leads to a greater rate of expansion, which produces a dumbbell shape.[10]

Examination of tablets containing different amounts of microspheres (0−2.0% w/w) showed no discernible difference in their rates of expansion when recorded at 4 min intervals and followed over 60 min, with each performed in duplicate.

Discussion

We have demonstrated that it is possible to closely follow events within a hydrating tablet and to follow its expansion in the *x* and *y* axes but not concurrently in the *z* axis.

The hydration cell, by preventing direct access by water to the upper face of the tablet, effectively makes observation of only this face serve to cover a range of depths from the outer limit of gel layer to the center of the tablet. Prevention of direct hydration of the upper face is critical because (i) the formation of an overlying gel layer would quickly exceed the imaging depth of even a confocal microscope, (ii) the opacity of the unhydrated polymer would prevent imaging below the unhydrated surface, and (iii) the accurate measurement of depth[11] is especially difficult through layers of progressively changing refractive index. The prevention of direct hydration was achieved with a silicon rubber membrane between the upper surface of the tablet and the upper Petri dish and is further enhanced once a gel layer has formed around the edge of a tablet, which seals any residual gaps and prevents water flowing across the upper surface. By imaging 100 μm below the silicon rubber/tablet interface, we probably avoid any interference between the polymer and the membrane. However, an interaction can only be precluded either by imaging at much greater depths, which is unfortunately impractical, or by comparison of the experimental observations with similar observations from an unrelated technique, which is currently unavailable.

The use of intact tablets measures radial expansion while bisected tablets permit the measurement of both radial and axial expansion. Intact tablets, when confined in our hydration cell, model a tablet of infinite axial thickness in which only radial expansion can occur. The curved and faster trajectories seen with microspheres at the corners of bisected tablets is probably due to their exposure to external water from two surfaces and generates the dumbbell shape commonly observed with flat-faced circular tablets. The bisected tablet is a better model of in vivo hydration since it shows both axial and radial expansion; however, the analysis of the tracks is much more difficult, and this approach requires the physical cutting of tablets, which may alter their performance.

Our measurements of expansion were made in unstirred water, unlike the standard USP procedures for measuring drug release which place tablets in a rotating cage or a medium stirred by a paddle. Our experiment was therefore a simplification of a tablet undergoing drug release since erosion of the tablet was greatly reduced; however, it does demonstrate that complex measurements are possible within these tablets. The hydration cell could be modified to permit both agitation of the hydrating medium and also to allow fluid sampling to determine drug release rates, thereby providing a more complete picture of in vitro release.

A major assumption underlying the use of markers is that they remain trapped within the matrix and do not move independently. The linearity of their tracks, in contrast to the random walks seen with Brownian motion, confirms our expectation, based on their mass and the viscosity of the gel that diffusion does not contribute significantly to their movement. Also we found no evidence that the initial inrush of water carried microspheres deeper into the matrix. An additional assumption was that the presence of the microspheres does not alter the performance of the matrix; the small fraction of the matrix occupied by the chemically inert microspheres makes this assumption plausible, and experiments showed that the expansion of tablets was unaffected by the presence microspheres.

Early experiments tested silver granules, observed by reflection, as nondiffusing markers, but their lower intensity and irregular shape made tracking difficult and they proved less satisfactory than fluorescent microspheres. Undissolved particles of polymer and air bubbles could potentiallly be used as markers, but air bubbles are only found in hydrated regions of the gel layer and are unevenly distributed, while the irregular shape of undissolved polymer particles makes precise tracking difficult. Both air bubbles and polymer particles can only be observed with transmitted light which would preclude observation in the poorly hydrated tablet core which is opaque.

The tracking software combined with CLSM imaging was able to follow individual microspheres. Similar tracking of particulates has been employed to measure the motion of individual particles on cell surfaces,[12] sperm motility,[13] and rates of mucocillary clearance.[14] The use of a predictive tracking strategy is only appropriate because the random walks seen with simple diffusion are not seen. Our analysis requires that each microsphere is tracked from its initial location, prior to hydration, over the whole image sequence. This proved difficult for microspheres originating close to the tablet edge, because the dramatic initial swelling makes finding the subsequent location very difficult. Increasing the frequency of images over the first few minutes reduces this problem, though the changing time intervals need to be incorporated into the predictive part of tracking strategy.

To summarize the pattern of expansion, the tracks of individual microspheres were grouped into bands of similar depth and the normalized movements of each microsphere were combined to obtain the changing radius of each band (Figure 6). This treats each band as homogeneous, which is reasonable given the radial symmetry of the expansion and the relatively macroscopic level of investigation. Within each band microspheres appeared to be randomly distributed and each band contained many microspheres; however, it should be noted that the shrinking area covered by bands closer to the center of the tablet progressively reduces the number of associated microspheres and therefore the accuracy of the measurements. This could be ameliorated by calculating the location of each microsphere to subpixel accuracy.[15] In the outermost band the assumption of homogeneity of deformation is combined with the difficulty of tracking the outermost microspheres and produces an underestimate of the expansion. While this is lessened by the ability to follow the outer gel edge, it could be reduced by using thinner bands and by using more frequent imaging in the initial period after hydration.

Overall we are able to quantify deformation throughout a HM tablet and confirm that expansion reaches deep into the tablet, well in advance of the limits of gel layer. Expansion of the core, especially in HPMC matrix tablets has been reported previously,[16] but this is the first direct observation made of the internal dynamics of the process. The underlying mechanism is unclear, but we suspect either the effect of water vapor moving ahead of the gel front or that the gelation of the exterior reduces the mechanical integrity of the tablet, releasing stresses stored during compression. Prolonged exposure to water vapor alone has been reported to cause axial expansion of HM tablets[1] albeit over a longer time scale.

It is also apparent that the outer layers of the these tablets expanded dramatically and still continued to expand as deeper layers began to hydrate. In tablets made from HPMC we have observed how rapid water uptake of the constituent polymer particles then retards the total water uptake by the whole tablet,[17] but the time scale for this process may differ between polymers. In addition, we would anticipate finding, and being able to experimentally differentiate between, hydrated matrixes with similar gel layer thicknesses, but which have resulted from different patterns of internal expansion. This could result in different polymer distribution within the gel layer and altered controlled release properties.

Our method has similarities to studies of HM tablets with magnetic resonance imaging that were used to follow gross changes in the size of the gel layer[18] and map water mobility[19] but cannot establish the local expansion within the gel or dry core. At present, MRI imaging also has poorer temporal and spatial resolution than CLSM.

There is considerable scope for extending the use of embedded microspheres. We have used them to measure syneresis in gels,[20] and the technique would be suitable for examining dehydration shrinkage. The method could also be used to examine selected areas at much higher magnifications, to isolate localized inhomogeneities that undoubtedly exist. The development of techniques for imaging deep within matrixes would make it feasible to measure deformations in three dimensions.

Through measuring internal events within HM tablets we believe it will become possible to elucidate the complex events that underlie their performance. Although the suggestion that "I have yet to see any problem, however complicated, which when looked at in the right way, did not become still more complicated"[21] might be considered to apply, we submit that the dynamics of drug release from HM tablets are inherently complex and require models of similar complexity founded on similarly detailed experimental observations.

References and Notes

1. Mitchell, K.; Ford, J. L.; Armstrong, D. J.; Elliott, P. N. C.; Hogan J. E; Rostron, C. The influence of drugs on the properties of of gels and swelling characteristics of matrixes containing methylcellulose or hydroxypropyl methycellulose. *Int. J. Pharm.* **1993**, 165−173.
2. Colombo, P.; Catellani, PL.; Peppas, N. A.; Maggi,. L.; Conte, U. Swelling characteristics of hydrophilic matrixes for controlled release new dimensionless number to describe the swelling and release behavior *Int. J. Pharm.* **1992**, 88, 99−109.
3. Melia, C. D. Hydrophilic Matrix Sustained Release Systems based on Polysaccharide Carriers. *Crit. Rev. Ther. Drug Carrier Syst.* **1991**, *8*(4), 395−421.
4. Melia, C. D.; Hodsdon, A. C.; Davies, M. C.; Mitchell, J. R. Polymer concentration profiles across the surface gel layer of xanthan, alginate and HPMC matrix systems. *Proc. Int. Symp. Cont. Relat. Bioact. Mater.* **1994**, *21*, 724−725.
5. Nakayama T., Kawasaki M., Niea E., Hamada I. Compression creep behaviour and syneresis water of agar-agar and actomysin gels. *J. Food Sci.* **1978**, *43*(5), 1430−1432.
6. Cutts, L. S.; Hibberd, S.; Adler, J.; Davies, M. C.; Melia, C. D. Characterising drug release processes within controlled release dosage forms using the confocal laser scanning microscope. *J. Controlled Release* **1996**, *42*, 115−124.
7. Cutts, L. S.; Roberts, P. A.; Adler, J.; Davies, M. C.; Melia, C. D. Measurement of diffusion coefficients using the confocal laser scanning microscope. *J. Microsc.* **1995**, *180*, 131−139.
8. Adler, J.; Rajabi-Siahboomi A. R.; Davies, M. C.; Melia, C. D. Differential expansion of the core within hydrating HPMC hydrophilic matrix tablets. *J. Pharm. Pharmacol.* **1993**, *45*, 1150.
9. Melia, C. D.; Rajabi-Siahboomi, A. R.; Hodsdon, A. C.; Adler, J.; Mitchell, J. R. Structure and behaviour in hydrophilic matrix sustained release dosage forms: 1. Origin and mechanism of formation of gas bubbles in the hydrated surface layer. *Int. J. Pharm.* **1993**, *100*, 263−269.
10. Bowtell, R. W.; Sharp, J. C.; Mansfield, P.; Rajabi-Siahboomi, A. R.; Melia, C. D. NMR Microscopy of hydrating hydrophilic matrix pharmaceutical tablets. *J. Magn. Reson. Imag.* **1994**, *12*, 36−364.
11. Carlsson, K. Factors influencing imaging quality in confocal microscopy. *J. Microsc.* **1991**, *163*, 167−178.
12. Gelles, J.; Schnapp, B. J.; Sheetz, M. P. Tracking kinesin-driven movements with nanometre-scale precision. *Nature* **1988**, *331*, 450−453.
13. Holt, W. V.; Moore, H. D. M.; Hillier, S. G. Computer-assisted measurement of sperm swimming speed in human semen: correlation of results with in vitro fertilization assays. *Fertil. Steril.* **1985**, *44*, 112−119.
14. Aspden, T. J.; Adler, J.; Davis, S. S.; Skaugrud, O.; Illum, L. Chitosan as a nasal delivery system − evaluation of the effect of chitosan on mucociliary clearance rate in the frog palate model. *Int. J. Pharm.* **1995**, *122*, 69−78.
15. Jobbagy, A.; Furnee. E. H. Marker centre estimation algorithms in CCD camera based motion analysis. *Med. Biol. Eng. Comp.* **1994**, *32*, 85−91.
16. Rajabi-Siahboomi, A. R.; Bowtell, R. W.; Mansfield, P.; Henderson, A.; Davies, M. C.; Melia, C. D. Structure and behaviour in hydrophilic matrix sustained release dosage forms: 2. NMR-imaging studies of the dimensional changes in the gel layer and core of HPMC matrixes undergoing hydration. *J. Controlled Release* **1994**, *31*, 121−128.
17. Rajabi-Siahboomi, A. R.; Nokhodchi, A. *Proceedings of the 4th United Kingdom Association of Pharmaceutical Scientists (UKAPS) Conference*; UKAPS: Cardiff, 1995; p 45.
18. Rajabi-Siahboomi, A. R.; Adler, J.; Davies, M. C.; Melia, C. D. Particle swelling and the mechanism of failure of HPMC matrixes. *Proceedings of the 3rd United Kingdom Association of Pharmaceutical Scientists (UKAPS) Conference*; UKAPS: Cardiff, 1994; p 21.
19. Rajabi-Siahboomi, A. R.; Bowtell, R. W.; Mansfield, P.; Davies, M. C.; Melia, C. D. Structure and behaviour in hydrophilic matrix sustained release dosage forms: 4. Studies of self-diffusion water mobility and diffusion coefficients in the gel layer of HPMC tablets using NMR imaging. *Pharm. Res.* **1996**, *13*, 376−380.
20. Cutts, L. S.; Adler, J.; Mitchell, J. R.; Hill, S.; Davies, M. C.; Melia, C. D. Time dependent changes in drug transport within the gel layer of hydrophilic matrix tablets. *Proceedings of the 4th United Kingdom Association of Pharmaceutical Scientists (UKAPS)*; UKAPS: London, 1995; p 44.
21. Anderson, P. In *A Dictionary of Scientific Quotations*; Mackay, A. L., Ed.; Adam Hilger: New York, 1991; p 3.

Acknowledgments

This work was funded by Hydra, a MAFF/DTI Link scheme.

JS970376J

Differences in the Lipoprotein Binding Profile of Halofantrine in Fed and Fasted Human or Beagle Plasma Are Dictated by the Respective Masses of Core Apolar Lipoprotein Lipid

MICHELLE P. MCINTOSH,[†] CHRISTOPHER J. H. PORTER,[†] KISHOR M. WASAN,[‡] MANISHA RAMASWAMY,[‡] AND WILLIAM N. CHARMAN*,[†]

Contribution from *Department of Pharmaceutics, Victorian College of Pharmacy, Monash University (Parkville Campus), 381 Royal Parade, Parkville, Victoria 3052, Australia, and Division of Pharmaceutics and Biopharmaceutics, Faculty of Pharmaceutical Sciences, The University of British Columbia, Vancouver, British Columbia V6T 1Z3, Canada.*

Received April 3, 1998. Final revised manuscript received November 16, 1998.
Accepted for publication November 20, 1998.

Abstract □ Halofantrine hydrochloride (Hf) is an orally active, highly lipophilic antimalarial indicated for the treatment of multi-drug resistant *Plasmodium falciparum.* In this study, we have examined the binding profile of Hf to the various classes of human and beagle plasma lipoproteins as such interactions have been implicated in a post-prandial plasma lipoprotein-induced decrease in the total clearance and volume of distribution of Hf. The distribution of Hf within plasma was dominated by interaction with the various classes of plasma lipoproteins, and the characteristics and extent of binding were markedly different between species and between pre- and post-prandial plasma. In an attempt to understand the basis for the differential binding of Hf to the various lipoprotein fractions, the relationship between the proportion of Hf associated with each lipoprotein fraction (as a function of the respective mass of protein, triglyceride, cholesterol, and phospholipid) was investigated. The data indicated that the distribution of Hf between plasma lipoproteins was highly correlated with the apolar lipid load of individual plasma lipoprotein fractions suggesting that the mechanism of association was primarily via solubilization in the lipoprotein apolar lipid core. These data suggest that acute changes in plasma lipoprotein profiles, such as encountered post-prandially or in disease states such as malaria, will likely have an impact on the plasma lipoprotein binding of Hf.

Introduction

Halofantrine hydrochloride (Hf) is an orally administered, highly lipophilic phenanthrenemethanol antimalarial indicated for the treatment of acute infections caused by multi-drug resistant *Plasmodium falciparum* and *Plasmodium vivax*.[1] Absorption of Hf after fasted oral administration is poor and highly variable, although the extent of absorption is markedly enhanced when administered post-prandially.[2,3] The primary biopharmaceutical consequence of post-prandial Hf administration is improved solubilization within the bile salt rich post-prandial intestinal environment leading to enhanced absorption.[2] An interesting secondary consequence of post-prandial administration is an apparent plasma lipoprotein-induced decrease in the clearance and volume of distribution of Hf.[4]

The distribution of Hf within beagle plasma is dominated by interaction with plasma lipoproteins, with the characteristics and extent of the binding reflecting the relative pre- and post-prandial lipoprotein profiles.[4,5] In beagles, a significant temporal relationship was noted between the association of Hf with lipoproteins and the post-prandial reduction in total clearance (15%) and volume of distribution (21%).[4] This effect was most likely mediated via a reduction in the free fraction of Hf in plasma which occurred secondarily to increased binding to plasma lipoproteins.[4]

The profile of plasma lipoproteins varies widely between and within individuals as a function of age, gender, co-administered drugs, diet, and disease states including alcoholism, diabetes, and acute malaria,[6,7] thereby raising the possible specter of altered therapeutic profiles of highly lipoprotein-bound drugs (such as Hf) under these circumstances.[8] For example, it was recently demonstrated that the IC_{50} of Hf determined in continuous in vitro culture of *P. falciparum* was significantly increased when incubated in the presence of 10% post-prandial serum.[9] From a drug targeting standpoint, as high-density lipoproteins (HDL) are a major phospholipid source which can support the intra-erythrocytic stage of parasite reproduction,[10] the possibility of HDL-associated uptake of Hf into infected erythrocytes has been suggested.[11] From a toxicological standpoint, there appears to be a linkage between excessively high plasma Hf concentrations and cardiac side effects (typically observed as a lengthening of the QTc interval) in patients with a preexisting cardiopathy.[12] As excessively high plasma concentrations of Hf are typically observed after post-prandial administration, elucidation of the distribution of Hf between post-prandial lipoproteins may contribute to a better understanding of the possible factors contributing to the changed QTc profiles.

In this study, we have extended our previous preliminary examination[5] of the in vivo lipoprotein binding of Hf in beagle plasma to pre- and post-prandial human plasma. In an attempt to understand the basis for the differential binding of Hf across lipoprotein fractions, the relationship between the proportion of Hf associated with each lipoprotein fraction (as a function of the respective mass of protein, triglyceride, cholesterol and phospholipid) was investigated between species in pre- and post-prandial states.

Materials and Methods

Chemicals—Halofantrine hydrochloride and Hf base were obtained from SmithKline Beecham Pharmaceuticals (Brentford, Middlesex, U.K.). Acetonitrile (Mallinckrodt, Paris, KY) and *tert*-butyl methyl ether (Fluka, Buchs, Switzerland) were HPLC grade, and sodium dodecyl sulfate (SDS, Eastman Kodak, Rochester, NY) was electrophoresis grade. All other chemicals were at least AR grade, and water was obtained from a Milli-Q (Millipore, Bedford, MA) water purification system.

* To whom correspondence should be addressed. Phone: +61 3 9903 9519. Fax: +61 3 9903 960. E-mail: bill.charman@vcp.monash.edu.au.
[†] Monash University.
[‡] The University of British Columbia.

10.1021/js980152g CCC: $18.00
Published on Web 01/23/1999

Plasma Incubation Studies—Blank plasma was taken from healthy male beagle dogs after either an overnight fast or 4 h after ingestion of 400 g of standard canned dog food (average composition: 2.5% fat, 7.5% protein) supplemented with 50 mL of soybean oil (a representative long-chain triglyceride). Human plasma was obtained from a healthy male volunteer after either an overnight fast or 4 h after ingestion of a lipid rich meal (fat content greater than 50 g: MacDonalds Big Mac and french fries). Blood samples were collected into sterile tubes, anti-coagulated with 1.5 mg mL^{-1} Na_2EDTA, and centrifuged at 2000 rpm for 15 min, and the plasma stored at 4−8 °C. For incubation studies, fresh blank plasma (used within 3 h of collection) was prewarmed to 37 °C and spiked with drug dissolved in ethanol (10 μL of ethanol per mL of plasma) to provide a final drug concentration of 1000 ng mL^{-1} (Hf base equivalents). The addition of up to 50 μL of ethanol per mL of plasma does not have a discernible affect on plasma lipoprotein concentrations or their respective composition or integrity.[13] The spiked plasma samples were incubated at 37 °C for 60 min in a temperature-controlled water bath, and the samples were gently swirled manually at 5 min intervals. At the conclusion of the incubation period, samples were placed in an ice bath for at least 5 min prior to immediate density gradient ultracentrifugation.

The Hf distribution profiles from the in vitro spiking studies were compared with the distribution profile of Hf in a plasma sample taken from a fasted male beagle (3 yr, 18 kg) 30 min after intravenous administration of a 2 mg kg^{-1} dose of Hf base prepared in Intralipid.[14]

Lipoprotein Separation—After incubation of plasma with Hf, 1 mL plasma samples were fractionated by single spin density gradient ultracentrifugation as previously described.[5,15] Briefly, stock buffer for density gradient solutions contained 0.1% NaN_3, 0.2% Na_2EDTA, and 1.2% Tris base dissolved in distilled water adjusted to pH 7.4, which was stored at room temperature after filtration. Density gradient solutions were prepared by adding appropriate quantities of KBr to a plasma background solution, and the solution densities were confirmed using refractometry. The density gradient was formed in a 4 mL centrifuge tube (Seton Scientific, Sunnyvale, CA), and the samples were centrifuged at 15 °C for 19 h at 58 000 rpm (Sorvall OTD65B Ultracentrifuge, Newtown, CT) using a SW 60 rotor (Beckman, CA). Plasma samples were separated into the following fractions: triglyceride rich lipoproteins (TRL, which includes VLDL and chylomicrons), low-density lipoproteins (LDL), high-density lipoproteins (HDL), and lipoprotein deficient plasma (LPDP). In a minor modification to our previous technique,[4,5] the majority of TRL was first recovered from the top of the centrifuge tube by needle aspiration of 2 × 200 μL aliquots. This modification improved the separation of post-prandial TRL and minimized potential contamination of the more dense fractions with TRL. The LDL, HDL, and the LPDP fractions were then obtained using a fraction collection system (Beckman, CA) where a high-density solution (Fluorinert, Sigma Chemicals, St Louis, MO) was pumped into the bottom of each centrifuge tube at 24 mL h^{-1}, the eluent was collected from the top of the tube and passed through a UV detector set at 280 nm (to identify peak elution via monitoring of lipoprotein-associated protein), prior to the automated collection of 18 × 200 μL aliquots.

Each aliquot was analyzed for total protein (TP), total cholesterol (CH), free cholesterol (FC), triglyceride (TG), and phospholipid (PL) using commercial enzymatic colorimetric kits (Bohringer Mannheim, Germany) running on a Cobas BIO clinical analyzer (Roche, Basle, Switzerland). The analyzer was externally calibrated for each run and quality control samples were run on a weekly basis. In aliquots from beagle plasma, the amount of cholesteryl ester (CE) was calculated as the difference between the measured CH and FC values, whereas in aliquots from human plasma the mass of CE was calculated as a fixed percentage of the measured TC value for each individual lipoprotein fraction.[16]

The individual cholesterol and triglyceride concentration profiles in each aliquot were used to define the respective TRL, LDL, HDL, and LPDP fractions. Typically, the two aspirated aliquots were combined with the initial two aliquots obtained using the fraction recovery system (i.e., aliquots 3 and 4) and designated as the TRL fraction, aliquots 5−11 were combined for the LDL fraction, aliquots 12−17 were combined for the HDL fraction, and aliquots 18−20 were combined for the LPDP fraction.

Analysis of Hf in Lipoprotein Fractions—The concentration of Hf in plasma and individual lipoprotein fractions was determined using a validated assay.[17] Due to the logistical difficulty in obtaining sufficient quantities of blank lipoproteins to routinely prepare standard curves for each individual lipoprotein fraction, spiked blank plasma was used to prepare standard curves on a daily basis. The validity of this approach was confirmed by the similarity in the ratio of the peak area/concentration values (<5%) from standard curves prepared using either plasma or specifically isolated lipoprotein.

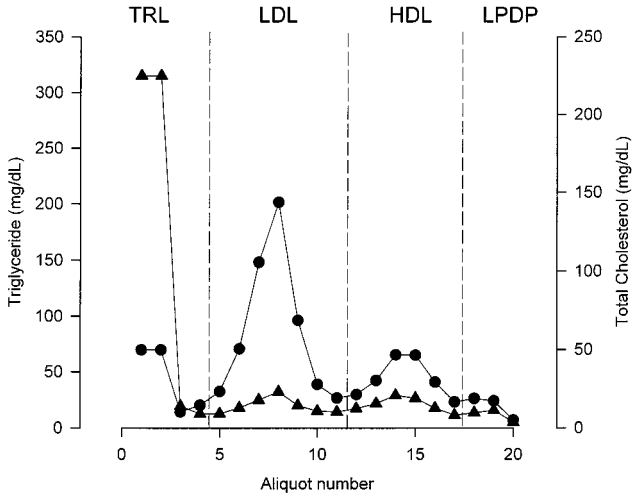

Figure 1—Representative profile of total cholesterol (●) and triglyceride (▲) concentrations as a function of fractionation aliquot obtained after density gradient ultracentrifugation of 1 mL of post-prandial human plasma. Aliquots 1–4 were combined for the TRL fraction, aliquots 5–11 for the LDL fraction, aliquots 12–17 for the HDL fraction, and aliquots 18–20 were designated as the LPDP fraction.

Compositional Analysis of LP Fractions—To explore the basis for the distribution of Hf between lipoprotein fractions, the compositional profile of individual lipoprotein fractions based on measured PL, CH, FC, CE, TG, and TP values were assessed in the following manner. The mass of apolar lipid, which effectively constitutes the hydrophobic core of lipoproteins, was calculated for each respective fraction as the sum of the CE and TG content. The volume of the hydrophobic core was calculated assuming individual lipoprotein particles to be spherical, with each lipoprotein fraction having a similar gross structure including a 20.5 Å thick surface monolayer as previously described.[18] The following average values[16] for the density (ρ) and average radius (r) of human lipoproteins were used to calculate the volume of the hydrophobic core and the surface area of individual human lipoprotein fractions: VLDL, r = 275 Å, ρ = 989 mg mL^{-1}; LDL, r = 100 Å, ρ = 1042 mg mL^{-1}; HDL, r = 37.7 Å, ρ = 1136.5 mg mL^{-1}. The volume and surface area values of lipoprotein fractions from beagle plasma could not be estimated as published density and radius data were not available.

Results

The lipoprotein fraction isolation procedure employed in the current study was modified to better separate the increased quantities of TRL present in post-prandial plasma compared with our previous technique designed for pre-prandial plasma.[4,5] Figure 1 depicts a typical separation profile of post-prandial human plasma when monitored using the TG and TC concentrations present in individual fractionation aliquots. Importantly, there was distinct separation of TG associated with the sequential TRL and LDL fractions indicating an excellent separation profile.

The distribution of Hf between lipoprotein fractions obtained after in vitro spiking of pre-prandial beagle plasma with an ethanolic Hf·HCl solution, or from a blood sample taken from a pre-prandial beagle after intravenous administration of Hf base (sample taken at 30 min post-dosing as this afforded a plasma Hf concentration of approximately 1000 ng mL^{-1}), are presented in Table 1.

Table 1—Percentage Distribution of Hf between Plasma Lipoprotein Fractions[a] (Mean ± SD, $n = 3$) Obtained after in Vitro Incubation of Fasted Beagle Plasma with Hf·HCl Dissolved in Ethanol (10 μL/mL Plasma) and from an in Vivo Plasma Sample Taken from a Fasted Beagle 30 min after Intravenous Administration of 2 mg kg^{-1} Hf Base

treatment	TRL	LDL	HDL	LPDP	recovery (%)[b]
in vitro incubation of fasted plasma with Hf·HCl	3.3 ± 0.9	10.1 ± 0.8	51.2 ± 4.4	35.4 ± 2.7	93.8 ± 3.7
in vivo plasma sample after IV administration of Hf base	3.2 ± 0.5	8.9 ± 0.4	52.3 ± 1.2	35.2 ± 1.4	101.3 ± 1.4

[a] TRL, triglyceride rich lipoproteins which include VLDL and chylomicrons; LDL, low-density lipoproteins; HDL, high-density lipoproteins; LPDP, lipoprotein deficient plasma. [b] Recovery is defined as the % mass of drug recovered after plasma fractionation divided by the mass of drug present in the original sample (as either the in vitro spike or the plasma Hf concentration in the in vivo sample).

Table 2—Percentage Distribution of Halofantrine (Hf) between Plasma Lipoprotein Fractions[a] (Mean ± SD, $n = 3$) Obtained after in Vitro Incubation of 1000 ng mL^{-1} Hf·HCl with Plasma Obtained from Pre- and Post-prandial Human Subjects, and Pre- and Post-prandial Beagles

lipoprotein fraction	percentage distribution of Hf			
	in human plasma		in beagle plasma	
	pre-prandial	post-prandial	pre-prandial	post-prandial
TRL	17.3 ± 1.2	39.7 ± 1.2[b]	3.3 ± 0.9	26.6 ± 2.0[b]
LDL	31.5 ± 0.2	18.6 ± 1.0[b]	10.1 ± 0.8	7.5 ± 1.1[b]
HDL	6.1 ± 0.6	6.5 ± 2.4	51.2 ± 4.4	37.5 ± 0.9[b]
total LP binding	54.8 ± 0.9	64.8 ± 3.2[b]	64.6 ± 2.7	71.5 ± 1.4[b]
LPDP	45.2 ± 0.9	35.2 ± 3.2[b]	35.4 ± 2.7	28.5 ± 1.4[b]
% recovery[c]	99.1 ± 4.4	109.1 ± 1.6	93.8 ± 3.7	90.2 ± 4.0

[a] TRL, triglyceride rich lipoproteins which include VLDL and chylomicrons; LDL, low-density lipoproteins; HDL, high-density lipoproteins; LPDP, lipoprotein deficient plasma. [b] Significantly different to the corresponding pre-prandial value ($p < 0.05$). [c] Recovery is defined as the % mass of drug recovered after plasma fractionation divided by the mass of drug present in the original sample.

Greater than 90% of Hf present in either plasma sample was accounted for in the TRL, LDL, HDL, and LPDP fractions. The utility of the in vitro spiking procedure was confirmed by the similar distribution profiles of Hf between the various lipoprotein fractions isolated from either the in vitro or in vivo samples.

Table 2 describes the lipoprotein distribution of Hf in spiked pre- and post-prandial human and beagle plasma when incubated with Hf using the validated in vitro procedure. The distribution of Hf in beagle and human plasma was dominated by significant binding to lipoproteins as 54.8% of Hf was lipoprotein bound in fasted human plasma, and 64.6% was lipoprotein bound in fasted beagle plasma. Additionally, there were increases in the extent of Hf binding by lipoproteins in pre-prandial compared with the post-prandial state (an 18.2% increase in human plasma, and a 10.7% increase in beagle plasma).

Although the extent of lipoprotein binding of Hf was similar between man and dog, analysis of the distribution of Hf between individual lipoprotein fractions indicated substantial species differences. For example, a much larger proportion of the plasma concentration of Hf was carried in TRL and LDL fractions in human plasma compared with beagle plasma, whereas the proportion of Hf carried in HDL was 6−8-fold higher in beagle plasma compared with human plasma (Table 2).

Assessment of the distribution of Hf between pre- and post-prandial lipoprotein classes demonstrated increased amounts of drug associated with the lipid rich TRL fraction of post-prandial plasma with an average 2-fold increase observed in human plasma, and a 8-fold increase in beagle plasma. In contrast, there were decreases in the proportion of Hf associated with post-prandial LDL and LPDP fractions in human and beagle plasma, and HDL in beagle plasma. The proportion of Hf in human HDL was low (6%) and apparently unchanged in pre- and post-prandial human, whereas a much larger proportion of Hf was associated with HDL in pre-prandial beagle plasma (51%) which decreased in the post-prandial state.

The mass of TG, CH, FC, CE, PL, and TP determined in each lipoprotein fraction isolated from the Hf spiked pre- and post-prandial human and beagle plasma are presented in Table 3, with the values for human lipoproteins being similar to literature reports.[19] Data are also presented describing the individual quantities of apolar lipid (i.e. TG + CE) and total lipid (TC + TG + PL) present in the various isolated lipoprotein fractions.

Discussion

In a preliminary communication, we demonstrated that Hf was highly associated with lipoproteins in beagle plasma, and that the characteristics of association were altered when the concentration profile of plasma lipids increased post-prandially.[5] The primary change was an increased proportion of Hf associated with TRL in post-prandial plasma, and from a pharmacokinetic standpoint, this was accompanied by a reduction in drug clearance and volume of distribution which most likely arose through reduction in the plasma free fraction of drug.[4] In this study, we have examined the association of Hf with human plasma lipoproteins (as a possible indicator of similar effects in humans) and explored correlations between the association of Hf with lipoproteins and the mass of protein, triglyceride (TG), cholesterol (CH), and phospholipid (PL) within specific lipoprotein classes as a possible predictor of the basis for the interaction.

It was only possible to study the association of Hf with human plasma lipoproteins in an in vitro setting as an acceptable intravenous formulation for human administration was not available,[20] and potential toxicity concerns precluded post-prandial oral administration to healthy volunteers.[12] Consequently, it was necessary to demonstrate the equivalence of a plasma spiking methodology which afforded a Hf lipoprotein binding profile representative of the in vivo situation.

Employing beagles as a test species, the data in Table 1 indicates that the binding profile of Hf across lipoprotein fractions in plasma sampled after intravenous drug administration was essentially identical to that obtained after fractionation of plasma spiked with Hf, thereby indicating the equivalence of the spiking methodology. Similar in vivo and in vitro lipoprotein distribution profiles have been reported for cyclosporin when small volumes of ethanol were used as the plasma spiking solvent.[21]

Application of this spiking methodology to pre- and post-prandial human plasma, and subsequent fractionation of plasma into TRL, LDL, HDL, and LPDP subgroups, indicated that Hf was also significantly bound to pre- and post-prandial human plasma lipoproteins although the distribution profile was markedly different to that observed in beagles (Table 2). Broadly, the proportion of Hf associated with the TRL and LDL fractions was higher in humans compared with beagles, whereas the proportion of Hf associated with HDL was much higher in beagles. These findings reflect the broad species differences in lipoprotein profiles (Table 3) where a larger proportion of human plasma lipid is carried by TRL and LDL fractions,

Table 3—Quantities of Plasma Lipids and Protein from Isolated Lipoprotein Fractions (Mean ± SD, $n = 3$) in Pre- and Post-prandial Human and Beagle Plasma (Lipoprotein Fractions Are the Same as Those Used To Determine the Distribution of Hf Described in Table 2)

	human plasma		beagle plasma	
lipoprotein composition (mg mL^{-1})	pre-prandial	post-prandial	pre-prandial	post-prandial
TRL fraction				
total cholesterol	0.20 ± 0.01	0.27 ± 0.02[a]	0.05 ± 0.00	0.07 ± 0.00[a]
cholesterol ester	0.13 ± 0.01	0.17 ± 0.01[a]	0.05 ± 0.00	<0.05
free cholesterol	0.07 ± 0.00	0.09 ± 0.01[a]	<0.05	0.11 ± 0.00[a]
triglyceride	0.38 ± 0.05	1.38 ± 0.05[a]	0.12 ± 0.00	0.87 ± 0.02[a]
phospholipid	0.11 ± 0.07	0.20 ± 0.07	0.04 ± 0.00	0.14 ± 0.00[a]
protein	<0.15	<0.15	<0.15	<0.15
apolar lipid (TG + CE)	0.51 ± 0.06	1.55 ± 0.06[a]	0.17 ± 0.00	0.84 ± 0.01[a]
total lipid (TC + TG + PL)	0.68 ± 0.12	1.86 ±0.14[a]	0.21 ± 0.00	1.09 ± 0.02[a]
apolar lipid/total plasma lipid (%)	15.43 ± 1.64	36.38 ± 1.44[a]	3.28 ± 0.04	13.10 ± 0.19[a]
apolar lipid/plasma apolar lipid (%)	25.33 ± 1.41	52.05 ± 2.53[a]	10.70 ± 0.40	35.50 ± 1.71[a]
LDL fraction				
total cholesterol	0.89 ± 0.06	0.86 ± 0.02	0.24 ± 0.00	0.23 ± 0.00
cholesterol ester	0.72 ± 0.05	0.69 ± 0.02	0.18 ± 0.00	0.19 ± 0.00
free cholesterol	0.17 ± 0.01	0.17 ± 0.00	0.05 ± 0.00	0.05 ± 0.00
triglyceride	0.29 ± 0.00	0.24 ± 0.03	0.14 ± 0.01	0.17 ± 0.01
phospholipid	0.41 ± 0.17	0.30 ± 0.07	0.25 ± 0.01	0.26 ± 0.02
protein	0.20 ± 0.20	0.20 ± 0.00	<0.15	<0.15
apolar lipid (TG + CE)	1.01 ± 0.05	0.93 ± 0.05	0.32 ± 0.01	0.35 ± 0.01
total lipid (TC + TG + PL)	1.59 ± 0.21	1.40 ± 0.08	0.63 ± 0.01	0.66 ± 0.03
apolar lipid/total plasma lipid (%)	30.72 ± 2.93	21.84 ± 1.94	6.09 ± 0.22	5.53 ± 0.13
apolar lipid/plasma apolar lipid (%)	50.41 ± 1.12	31.18 ± 1.12[a]	19.90 ± 0.29	15.00 ± 0.84[a]
HDL fraction				
total cholesterol	0.40 ± 0.03	0.37 ± 0.02	1.41 ± 0.06	1.32 ± 0.03
cholesterol ester	0.32 ± 0.02	0.30 ± 0.02	1.09 ± 0.06	1.00 ± 0.02
free cholesterol	0.08 ± 0.00	0.07 ± 0.00	0.31 ± 0.00	0.33 ± 0.01
triglyceride	0.16 ± 0.01	0.21 ± 0.04	0.04 ± 0.00	0.17 ± 0.13
phospholipid	0.47 ± 0.12	0.46 ± 0.11	3.03 ± 0.07	3.16 ± 0.05
protein	2.20 ± 0.92	2.07 ± 0.81	3.43 ± 0.08	3.21 ± 0.05
apolar lipid (TG + CE)	0.48 ± 0.03	0.50 ± 0.05	1.13 ± 0.07	1.17 ± 0.10
total lipid (TC + TG + PL)	1.03 ± 0.14	1.03 ± 0.10	4.47 ± 0.05	4.66 ± 0.05
apolar lipid/total plasma lipid (%)	14.78 ± 1.33	11.77 ± 1.61	21.20 ± 1.20	18.30 ± 1.61
apolar lipid/plasma apolar lipid (%)	24.26 ± 0.29	16.78 ± 1.42[a]	69.40 ± 0.65	49.50 ± 2.54[a]
whole plasma				
total lipid (TC + TG + PL)	3.30 ± 0.46	4.28 ± 0.28	5.31 ± 0.07	6.40 ± 0.02[a]
total apolar lipid (TG + CE)	2.00 ± 0.14	2.99 ± 0.07[a]	1.63 ± 0.08	2.36 ± 0.09[a]

[a] Significantly different to the corresponding pre-prandial value ($p < 0.05$).

whereas HDL are the major lipid carrier in dogs. The post-prandial state induced significant changes in the distribution of Hf between plasma lipoprotein fractions, with increased proportions of Hf in the TRL fractions in both human and beagle plasma at the expense of a species-dependent decrease in the proportion of Hf in LDL and HDL fractions (Table 2). Unfortunately, toxicity concerns and related ethical issues precluded our assessment of the post-prandial pharmacokinetics of Hf in human volunteers. However, as the in vitro studies identified increased post-prandial lipoprotein binding of Hf in human plasma, this suggests the possibility of a potential decrease in clearance and volume of distribution (as observed in the beagle studies).[4]

Historically, methods used to quantify drug–lipoprotein interactions have been modifications of classical protein binding experiments. Typically, individual association constants (K) and the number of binding sites (n) associated with drug–lipoprotein binding are generated from study of the interaction between a drug substrate and isolated fractions using Scatchard-type analyses. Subsequently, an indication of the overall lipoprotein binding profile is obtained from the product of the affinity constant, the apparent number of binding sites and the estimated concentration of each lipoprotein class in plasma.[22] The lipoprotein binding profile of drugs such as anthracycline,[23] ticlopidine and PCR2362,[24] nicardipine,[25] propranolol,[22] and etretinate and acitretin[26] have been assessed in this manner. In contrast to the majority of drug–plasma protein interactions, the nature of the lipoprotein association profiles for these compounds is nonsaturable, which only allows for calculation of the overall binding capacity from the product of the association constant and the number of binding sites. In each of the above examples, the order of the lipoprotein binding capacity (expressed per mole of lipoprotein) was VLDL > LDL > HDL, and the binding was seemingly related to the size and/or overall lipid content of the lipoprotein subclasses. In each case, it was suggested that the nonsaturable nature of the binding, and the apparent correlation of the binding capacity with the size and/or lipid content of the lipoproteins indicated that the binding interaction was solubilization-based rather than a specific binding phenomenon.

To investigate solubilization as the basis for the interaction of Hf with the various lipoprotein fractions, correlations were investigated between the amount of Hf present in individual fractions and the corresponding mass of total protein, phospholipid, triglyceride, and apolar lipid in human and beagle plasma lipoproteins (Figures 2 and 3, respectively). In beagle and human plasma, the Hf distribution profile was poorly correlated with individual lipoprotein surface constituents (protein and phospholipid), reasonably correlated with TG profiles in human compared with beagle lipoproteins, and better correlated with the mass of the apolar lipid core (TG + CE) in both human and beagle lipoprotein fractions.

As representative dimensions were available for the various lipoprotein fractions in human plasma,[16] this

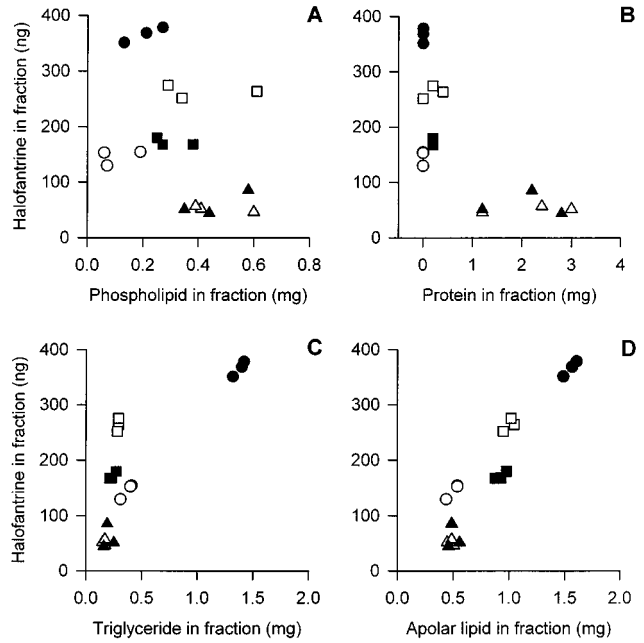

Figure 2—Correlation between the mass of Hf present in pre-prandial (open symbols) and post-prandial (closed symbols) HUMAN plasma lipoprotein fractions and the mass of specific lipoprotein components present in the individual TRL (●); LDL (■), and HDL (▲) fractions. (A) Correlation with the mass of phospholipid per fraction ($r^2 = 0.14$). (B) Correlation with the mass of protein per fraction ($r^2 = 0.50$). (C) Correlation with the mass of triglyceride per fraction ($r^2 = 0.66$). (D) Correlation with the mass of apolar lipid per fraction ($r^2 = 0.88$).

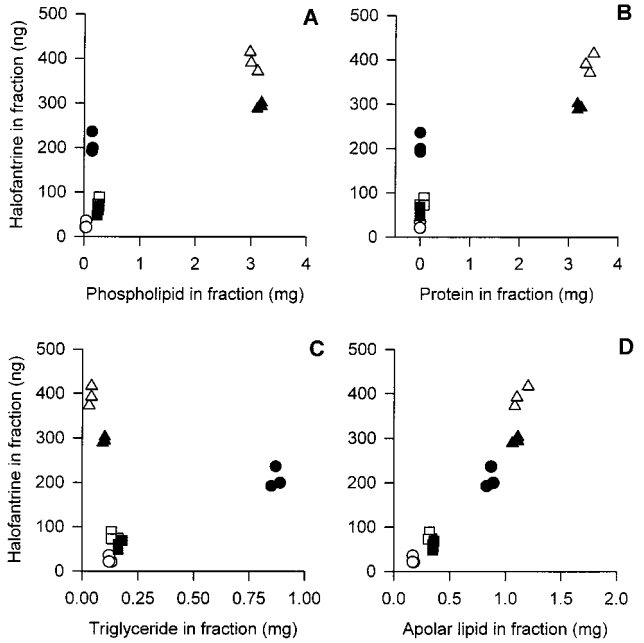

Figure 3—Correlation between the mass of Hf present in pre-prandial (open symbols) and post-prandial (closed symbols) BEAGLE plasma lipoprotein fractions and the mass of specific lipoprotein components present in the individual TRL (●); LDL (■) and HDL (▲) fractions. (A) Correlation with the mass of phospholipid per fraction ($r^2 = 0.79$). (B) Correlation with the mass of protein per fraction ($r^2 = 0.81$). (C) Correlation with the mass of triglyceride per fraction ($r^2 = 0.01$). (D) Correlation with the mass of apolar lipid per fraction ($r^2 = 0.93$).

enabled estimation of the surface area and hydrophobic core volume parameters for each lipoprotein fraction in human plasma. Figure 4 presents the relationship between the mass of Hf present in each fraction and these calculated parameters. There was a poor correlation with the respective surface area of individual fractions, but an improved correlation with the calculated volume of the hydrophobic core of the lipoprotein fractions.

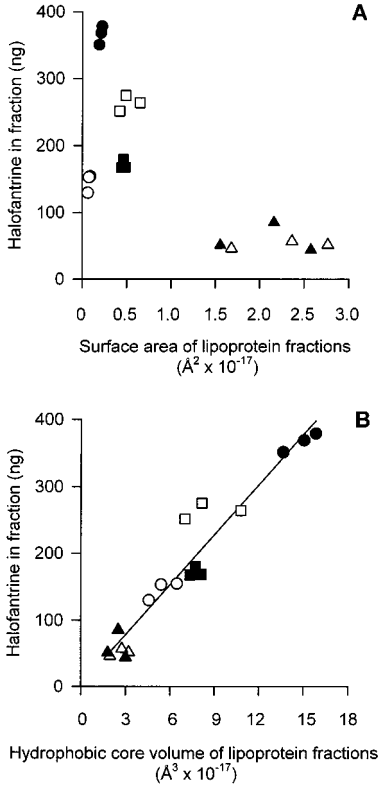

Figure 4—Correlation between the mass of Hf present in individual pre-prandial (open symbols) and post-prandial (closed symbols) HUMAN lipoprotein fractions (TRL (●), LDL (■), HDL (▲)) and the calculated surface area of the individual lipoprotein fractions ((A) $r^2 = 0.52$) and the calculated volume of the hydrophobic core of the individual lipoprotein fractions ((B) $r^2 = 0.93$).

The positive correlation between the mass of Hf in each lipoprotein fraction and the mass of apolar lipid as depicted in Figures 2 and 3, and the calculated volume of the hydrophobic core presented in Figure 4, was consistent with solubilization of Hf in the apolar lipid core and inconsistent with a specific interaction with surface groups or apolipoproteins. Furthermore, the correlation parameters were similar for all lipoprotein groups in human and beagle plasma (Figures 2 and 3), indicating that the binding/solubilization of Hf was independent of the lipoprotein fraction, relative lipid load, and species. These data indicated that the quantity of Hf solubilized per mg of lipoprotein apolar lipid was effectively constant regardless of the overall lipoprotein composition. On first inspection, these data were surprising as significant compositional differences exist between TRL, LDL, and HDL and across species. However, although the percentage composition of lipoproteins varies with the changing particle sizes (e.g. smaller lipoproteins such as HDL have proportionally more surface material such as PL and protein), the nature of the hydrophobic apolar core lipids is largely invariant such that their capacity to solubilize Hf was proportional to the respective mass of apolar lipid.

These data suggest that the trend governing the association of Hf with lipoprotein fractions was the quantity of apolar lipid in each of the respective fractions. Although the decreased proportion of Hf present in post-prandial LDL compared with pre-prandial LDL (despite the mass of LDL apolar lipid remaining relatively constant) (Tables 2 and 3) appears to contradict this scenario (Table 2), the actual driving force behind the lipoprotein distribution of Hf was the *proportional* distribution of lipids across the

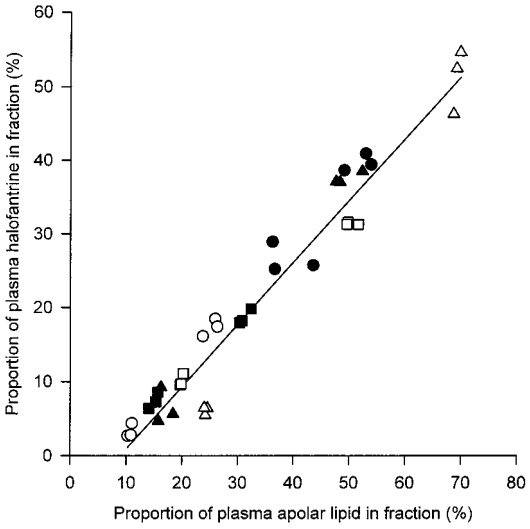

Figure 5—Combined correlation between the proportion of Hf distributed between lipoprotein fractions (TRL (●), LDL (■), HDL (▲)) in human and beagle plasma and the proportional distribution of apolar lipid (TG + CE) within the individual lipoprotein fractions from pre-prandial (open symbols) and post-prandial plasma (closed symbols). The correlation coefficient was 0.95.

lipoprotein fractions and not their absolute masses. Therefore, although the mass of apolar lipid in LDL was similar between pre- and post-prandial states, the proportion of apolar plasma lipid carried by LDL decreased due to the increased quantity of apolar lipid present in the TRL fraction. From consideration of the proportional distribution of apolar lipid, Figure 5 presents the combined correlation between the proportion of Hf between lipoprotein fractions from pre- and post-prandial beagle and human plasma and the proportional distribution of apolar lipid across the individual fractions. The significant correlation between these parameters across species, lipoprotein fractions, and pre- and post-prandial states supports the contention that the apolar lipid content of the individual lipoprotein fractions is the basis for the lipoprotein distribution of Hf.

For drugs with significant lipoprotein binding, the overall binding profile can be estimated from the product of the binding capacity per mole (nK) and the concentration of each individual lipoprotein fraction in plasma. Therefore, as the relative concentrations of plasma lipoprotein fractions are VLDL ($\approx$0.1 μM) < LDL ($\approx$1 μM) < HDL ($\approx$11 μM),[23,24,26] the distribution profile of lipophilic drugs often reflects the relative lipoprotein concentrations such that a larger proportion of the drug is carried by HDL or LDL as observed for ticlopidine,[24] nicardipine,[25] diclofenac,[27] and propranolol.[22] Employing this approach, Cenni and co-workers[28] recently determined the in vitro binding constants (nK) of Hf to human serum constituents (LDL and HDL, human serum albumin α_1-acid glycoprotein) and predicted that a significant proportion of Hf in plasma would be associated with lipoproteins. On the basis of the calculated binding constants, Cenni and co-workers predicted that approximately 67% of Hf in serum would be associated with LDL, about 25% with HDL and that the unbound fraction of Hf in blood would be as low as 0.4%. The marked differences between the data reported in this study and the predicted Hf distributions described by Cenni and co-workers[28] are likely to be (at least in part) a result of an erroneous assumption of minimal Hf binding to TRL. This assumption was based on results of preliminary gel filtration chromatography studies for Hf binding to serum constituents where the recovery of Hf was only 40%. Therefore, the low recovery of Hf from the preliminary gel filtration studies may have clouded the accuracy of the binding profile such that significant binding of Hf with constituents such as TRL was not observed. We believe that the direct method of estimating the plasma lipoprotein binding profile of Hf in plasma employed in the current study yields a more accurate estimate of the overall lipoprotein binding and plasma distribution of Hf.

In summary, the results from this study extends to human plasma the previously identified changes in the post-prandial distribution of Hf in beagle plasma, and raises the possibility of a decrease in Hf clearance and volume of distribution in post-prandial compared with pre-prandial human subjects. The data from this study indicate that the distribution of Hf among plasma lipoproteins was highly correlated with the apolar lipid load of individual plasma lipoprotein fractions thereby suggesting that the mechanism of Hf association with plasma lipoprotein was primarily via solubilization in the apolar lipid core. Furthermore, these findings suggest that acute changes in plasma lipoprotein distributions, such as encountered post-prandially or in disease states such as malaria, may markedly affect the plasma lipoprotein binding of Hf (and other highly lipophilic drugs).

References and Notes

1. Horton, J.; Parr, S. N.; Bokor, L. C. Clinical experience with halofantrine in the treatment of malaria. *Drugs Exp. Clin. Res.* **1990**, *16*, 497−503.
2. Humberstone, A. J.; Porter, C. J. H.; Charman, W. N. A physicochemical basis for the effect of food on the absolute oral bioavailability of halofantrine. *J. Pharm. Sci.* **1996**, *85*, 525−529.
3. Milton, K. A.; Edwards, G.; Ward, S. A.; Orme, M. L.; Breckenridge, A. M. Pharmacokinetics of halofantrine in man: effects of food and dose size. *Br. J. Clin. Pharmacol.* **1989**, *28*, 71−77.
4. Humberstone, A. J.; Porter, C. J. H.; Edwards, G. A.; Charman, W. N. Association of halofantrine with post-prandially derived plasma lipoproteins decreases its clearance relative to administration in the fasted state. *J. Pharm. Sci.* **1998**, *87*, 936−942.
5. Humberstone, A. J.; Porter, C. J. H.; Edwards, G.; Charman, W. N. Distribution of halofantrine between plasma lipoprotein fractions after IV administration to pre- and post-prandial beagle dogs. *Pharm. Res.* **1995**, *12*, S-356 (abstract).
6. Schaefer, E. J.; Levy, R. I. Pathogenesis and management of lipoprotein disorders. *N. Engl. J. Med.* **1985**, *312*, 1300−1310.
7. Mohanty, S.; Mishra, S. K.; Das, B. S.; Satpathy, S. K.; Mohanty, D.; Patnaik, J. K.; Bose, T. K. Altered plasma lipid pattern in *falciparum* malaria. *Ann. Trop. Med. Parasitol.* **1992**, *86*, 601−606.
8. Wasan, K. M.; Cassidy, S. M. Role of plasma lipoproteins in modifying the biological activity of hydrophobic drugs. *J. Pharm. Sci.* **1998**, *87*, 411−424.
9. Humberstone, A. J.; Cowman, A. F.; Horton, J.; Charman, W. N. Effect of altered serum lipid concentrations on the IC_{50} of halofantrine against *Plasmodium falciparum*. *J. Pharm. Sci.* **1998**, *87*, 256−258.
10. Grellier, P.; Rigomier, D.; Clavey, V.; Fruchart, J. C.; Schrevel, J. Lipid traffic between high-density lipoproteins and *Plasmodium falciparum*-infected red blood cells. *J. Cell Biol.* **1991**, *112*, 267−277.
11. Cenni, B. *Plasmodium falciparum*: Characteristics of halofantrine accumulation in vitro in parasitised red blood cells. Ph.D. Thesis, Swiss Tropical Institute, Basle, Switzerland, 1994,
12. Monlun, E.; Le Metayer, P.; Szwandt, S.; Neau, D.; Longy Boursier, M.; Horton, J.; Le Bras, M. Cardiac complications of halofantrine: a prospective study of 20 patients. *Trans. R. Soc. Trop. Med. Hyg.* **1995**, *89*, 430−433.
13. Ramaswamy, M.; Zhang, X.; Burt, H. M.; Wasan, K. M. Human plasma distribution of free paclitaxel and paclitaxel associated with diblock copolymers. *J. Pharm. Sci.* **1997**, *86*, 460−464.
14. Porter, C. J. H.; Charman, S. A.; Charman, W. N. Lymphatic transport of halofantrine in the triple cannulated anaesthetised rat model: effect of lipid vehicle dispersion. *J. Pharm. Sci.* **1996**, *85*, 351−356.

15. Redgraves, T. G.; Roberts, D. C. K.; West, C. E. Separation of plasma lipoproteins by density-gradient ultracentrifugation. *Anal. Biochem.* **1975**, *65*, 42−49.
16. Florence, A. T.; Halbert, G. W. Lipoproteins and microemulsions as carriers of therapeutic and chemical agents. In *Lipoproteins as carriers of pharmacological agents*; Shaw. J. M., Ed.; Marcel Dekker Inc.: New York, 1991; pp 141−174.
17. Humberstone, A. J.; Currie, G. J.; Porter, C. J. H.; Scanlon, M. J.; Charman, W. N. A simplified liquid chromatography assay for the quantitation of halofantrine and desbutylhalofantrine in plasma and identification of a degradation product of desbutylhalofantrine formed under alkaline conditions. *J. Pharm. Biomed. Anal.* **1995**, *13*, 265−272.
18. Shen, B. W.; Scanu, A. M.; Kezdy, F. J. Structure of human serum lipoproteins inferred from compositional analysis. *Proc. Natl. Acad. Sci. U.S.A.* **1977**, *74*, 837−841.
19. Meydani, M.; Cohn, J. S.; Macauley, J. B.; McNamara, J. R.; Blumberg, J. B.; Schaefer, E. J. Postprandial changes in the plasma concentration of α- and γ-tocopherol in human subjects fed a fat-rich meal supplemented with fat-soluble vitamins. *J. Nutr.* **1989**, *119*, 1252−1258.
20. Krishna, S.; ter Kuile, F. O.; Supanaranond, W.; Pukrittayakamee, S.; Teja-Isavadharm, P.; Kyle, D. E.; White, N. J. Pharmacokinetics, efficacy and toxicity of parenteral halofantrine in uncomplicated malaria. *Br. J. Clin. Pharmac.* **1993**, *36*, 585−591.
21. Sgoutas, D.; MacMahon, W.; Love, A.; Jerkunica, I. Interaction of cyclosporin A with human lipoproteins. *J. Pharm. Pharmacol.* **1986**, *38*, 583−588.
22. Glasson, S.; Zini, R.; D'Athis, P.; Tillement, J. P.; Boissier, J. R. The distribution of bound propranolol between the different human serum proteins. *Mol. Pharmacol.* **1980**, *17*, 187−191.
23. Chassany, O.; Urien, S.; Claudepierre, P.; Bastian, G.; Tillement, J. P. Binding of anthracycline derivatives to human serum lipoproteins. *Anticancer Res.* **1994**, *14*, 2353−2355.
24. Glasson, S.; Zini, R.; Tillement, J. P. Multiple human serum binding of two thienpyridinic derivatives, ticlopidine and PCR 2362, and their distribution between HSA, α-acid glycoprotein and lipoproteins. *Biochem. Pharmacol.* **1982**, *31*, 831−835.
25. Urien, S.; Albengres, E.; Comte, A.; Kiechel, J. R.; Tillement, J. P. Plasma protein binding and erythrocyte partitioning of nicardipine in vitro. *J. Cardiovasc. Pharmacol.* **1985**, *7*, 891−898.
26. Urien, S.; Claudepierre, P.; Meyer, J.; Brandt, R.; Tillement, J. P. Comparative binding of etretinate and acitretin to plasma proteins and erythrocytes. *Biochem. Pharmacol.* **1992**, *44*, 1891−1893.
27. Chamouard, J. M.; Barre, J.; Urien, S.; Houin, G.; Tillement, J. P. Diclofenac binding to albumin and lipoproteins in human serum. *Biochem. Pharmacol.* **1985**, *34*, 1695−1700.
28. Cenni, B.; Meyer, J.; Brandt, R.; Betschart, B. The antimalarial drug halofantrine is bound mainly to low- and high-density lipoproteins in human serum. *Br. J. Clin. Pharmacol.* **1995**, *39*, 519−526.

Acknowledgments

This work was supported, in part, by SmithKline Beecham Pharmaceuticals (U.K.). The authors thank Dr. John Horton for his interest and support of these studies, Dr. Andrew Humberstone for initial discussions, and M.P.M. gratefully acknowledges scholarship support provided by an Australian Postgraduate Award.

JS980152G

A publication of the American Pharmaceutical Association and the American Chemical Society

JOURNAL OF Pharmaceutical Sciences

April 1999
Volume 88, Number 4

Characterization of Tolbutamide Polymorphs (Burger's Forms II and IV) and Polymorphic Transition Behavior

KENYA KIMURA, FUMITOSHI HIRAYAMA, AND KANETO UEKAMA*

Contribution from *The Faculty of Pharmaceutical Sciences, Kumamoto University, 5-1 Oe-honmachi, Kumamoto 862-0973, Japan.*

Received September 17, 1998. Accepted for publication January 20, 1999.

Abstract □ Burger's two polymorphs of tolbutamide (TB), an oral hypoglycemic agent, were obtained by spray-drying the drug dissolved in a mixed solvent of ethanol/dichloromethane (Form IV) and allowing Form IV to stand at constant temperatures and humidities (Form II). These polymorphs were characterized by various physical methods [e.g., powder X-ray diffractometry, differential scanning calorimetry, infrared spectrometry, and solid-state carbon-13 nuclear magnetic resonance (^{13}C NMR) spectroscopy] and compared with two other TB polymorphs Forms I and III. The ^{13}C NMR spectra showed that the chemical shift and the peak shape of resonance associated with the toluene and *n*-butyl moieties of TB were different for each of the four polymorphs, whereas the carbonyl carbon was unchanged, indicating different conformations and molecular motions of the toluene and *n*-butyl moieties in the solid states. Form IV converted itself to Form II within 3 h when it was stored at 45 °C and 75% relative humidity (RH) and, in turn, Form II transformed to Form I at higher temperatures. The conversion of Form IV to Form II proceeded according to a zero-order equation (Polany–Winger equation), and that of Form II to Form I according to a first-order equation. The increase in RH accelerated the polymorphic transition of Form IV. Both the apparent dissolution rate and the solubility of Form IV were nearly identical with those of Form II, because the former changed to the latter during the dissolution, but their dissolution rates and solubility were higher than those of Forms I and III. These dissolution characteristics of TB polymorphs were reflected in the oral absorption behavior in dogs; that is, the bioavailability increased in the order Form I < Form III < Form II ≈ Form IV.

Introduction

Pharmaceutical solids can exist in different crystal forms, such as crystalline, amorphous, or glass, and also in solvated or hydrated states.[1−3] Because of the difference in molecular packing, polymorphic forms of solid drugs influence their dissolution rate, solubility, stability, bioavailability, pharmaceutical manufacturing, etc.[4−6] Therefore, some of the most important components of pharmaceutical solid formulation are the detection of as many polymorphs as possible, as well as their characterizations and selection of the desired ones. Tolbutamide [1-butyl-3-{4-methylphenylsulfonyl)urea, TB] is an oral hypoglycemic agent used clinically in the treatment of insulin-dependent diabetic patients.[7] Early studies have suggested that TB has several polymorphs in the solid states.[8−17] For example, Simmons et al.[8] reported the presence of two polymorphs, whereas Burger et al.[9] and Traue et al.[14] suggested the existence of four polymorphs. The Simmons's Forms A and B are identical with the Burger's Form I and III, respectively, and have been well characterized. However, Burger's Forms II and IV have been not fully characterized; for example, the diffraction pattern of the Georgarakis's Form II is different from that of the Al-Saieq's Form II but resembles that of Form IV.[11,15] In this study, two polymorphs (Forms II and IV) of TB were prepared and characterized by various physical methods [e.g., powder X-ray diffractometry (PXRD), differential scanning calorimetry (DSC), infrared (IR) spectrometry, and solid-state carbon-13 nuclear magnetic resonance (^{13}C NMR) spectroscopy] and compared with the TB polymorphs Forms I and III reported by Simmons et al.[8] Furthermore, the polymorphic transition behavior of Form IV was investigated. Because TB is a poorly water-soluble drug with several different polymorphs, its tablets are obligated to pass the dissolution test in Japanese Pharmacopoeia.[18] The dissolution and in vivo absorption behavior of Form IV in dogs were compared with those of Forms I, II, and III.

* To whom correspondence should be addressed. Telephone and fax: (+81-96)-371-4160. E-mail: uekama@gpo.kumamoto-u.ac.jp.

10.1021/js980376z CCC: $18.00
Published on Web 03/11/1999

Experimental Section

Materials—TB (purity > 99%) and chlorpropamide were donated by Nippon Hoechst-Marion-Roussel Ltd. (Tokyo, Japan) and Ono Pharmaceutical Company (Osaka, Japan), respectively. Other chemicals and solvents were of analytical reagent grade, and deionized double-distilled water was used throughout the study.

Apparatus—The PXRD patterns were measured with a Rigaku Rint-2500 diffractometer (Tokyo, Japan) under the following conditions: Ni-filtered Cu−Kα radiation (1.542 Å), a voltage of 40 kV, a current of 40 mA, a divergent slit of 1.74 mm (1°), a scattering slit of 0.94 mm (1°), a receiving slit of 0.15 mm, and a goniometer angular increment of 1°/min. The theoretical diffraction profiles on the basis of single-crystal X-ray analysis data were drawn using the teXsan crystallographic software package of Molecular Structure Corporation[19] on a Silicone Graphics IRIS Indigo work station (U.S.A.). The DSC analyses were carried out using a Perkin-Elmer DSC-7 thermal analyzer (Norwalk, CT) with a data analysis system (DEC station 325C computer, U.S.A.), operated with sample weights of 5 mg and a scanning rate of 10 °C/min. The heat fusion was calibrated with indium (purity, 99.999%; melting point, 156.4 °C; ΔH 28.47 mJ/mg; heating rate, 10 °C/min). Fourier transform infrared (FT-IR) spectra were recorded using a JEOL JIR-6500 FT-IR spectrometer (Tokyo, Japan) on samples prepared with KBr. The solid-state ^{13}C NMR spectra were taken on a JEOL JNM EX-270 spectrometer with a cross polarization/magic angle spinning (CP/MAS) accessory (Tokyo, Japan). The operating conditions were 270 MHz (^1H) and 25 °C. The CP radio frequency field strength was about 56 kHz, the contact time was 5 ms and the MAS rate was 6 kHz. The ^{13}C NMR chemical shifts were measured with respect to the resonance of tetramethylbenzene (17.3 ppm downfield from the resonance of tetramethylsilane). The chemical shift of TB was assigned according to the report of Ueda et al.[20] Crystal appearance was observed with a scanning electron microscope (SEM) instrument (Hitachi-Akashi S-501, Tokyo, Japan), after crystals were mounted onto an SEM sample stub with double-sided sticky tape and coated with gold by a direct current sputter technique.

Preparation of TB Polymorphs—Form I of TB was prepared according to the method of Simmons;[8] that is, TB (5 g) was dissolved in benzene (10 mL) at 70 °C, and then hexane (5 mL) was slowly added. The resulting solution was allowed to stand at room temperature. Form III was prepared by dissolving TB (5 g) in ethanol (10 mL) at 60 °C, slowly adding warm water, and allowing the resulting solution to stand at room temperature.[8] Form II was prepared by storing Form IV at 60 °C, 75% RH for 10 min. Form IV was prepared by the spray-drying method; that is, TB was dissolved in the mixed solvent ethanol/dichloromethane (1.2:1 v/v, 150 mL) and subjected to spray-drying, using a Pulvis GA32 Yamato spray-drier (Tokyo, Japan) under the following conditions: an air flow rate of 0.4 m^3/min, an air pressure of 1.0 kgf/cm^3, and inlet and outlet temperatures of 85 and 55 °C, respectively.

Aging Studies—The test powder (about 300 mg, <100 mesh) was placed in glass containers in desiccators at constant humidity (saturated solutions of potassium acetate, sodium bromide dihydrate, and sodium chloride at 22%, 50% and 75% RH, respectively), and then stored in incubators at constant temperatures (35−70 °C).[21,22] The phase change of TB crystals was monitored by PXRD.

Dissolution Studies—The dissolution rate of TB polymorphs was measured according to the dispersed amount method.[23] A fixed amount (100 mg, <100 mesh) of TB polymorphs was put into 25 mL of Japanese Pharmacopoeia XIII (JP XIII) second fluid (pH 6.8) and stirred at 91 rpm at 37 °C. At appropriate intervals, an aliquot (1.0 mL) was withdrawn with a cotton plugged pipet and analyzed for TB spectrophotometrically at 230 nm. To monitor the polymorphic change of TB during the dissolution, DSC curves were made of the powder suspended in the medium after drying under reduced pressure for 1 day.

Absorption Studies—The absorption studies were carried out using male beagle dogs (9−11 kg) that were fasted for 24 h before drug administration. The sample (equivalent to 100 mg/body) was wrapped in a wafer and administered orally with water (50 mL), using a catheter. Blood samples (1 mL) were withdrawn from the cephalic vein with a heparinized injection syringe and centrifuged at 1100 × g for 10 min. The plasma (0.2 mL) was added to the solution containing an internal standard, chlorpropamide (1.0 mg/mL, 0.5 mL), and extracted with ethyl ether (4.0 mL). The organic phase (3.0 mL) was evaporated, the residue was dissolved in acetonitrile (0.1 mL), and TB was determined by high-performance liquid chromatography (HPLC) with an Hitachi L-600 pump and a 635A UV detector (Tokyo, Japan), a Yamamura YMC AQ-312 ODS column (5 μm, 6 × 150 mm, Kyoto, Japan), a mobile phase of acetonitrile/0.05 M NaH_2PO_4 solution (45:55 v/v), a flow rate of 1.6 mL/min, and detection at 230 nm.

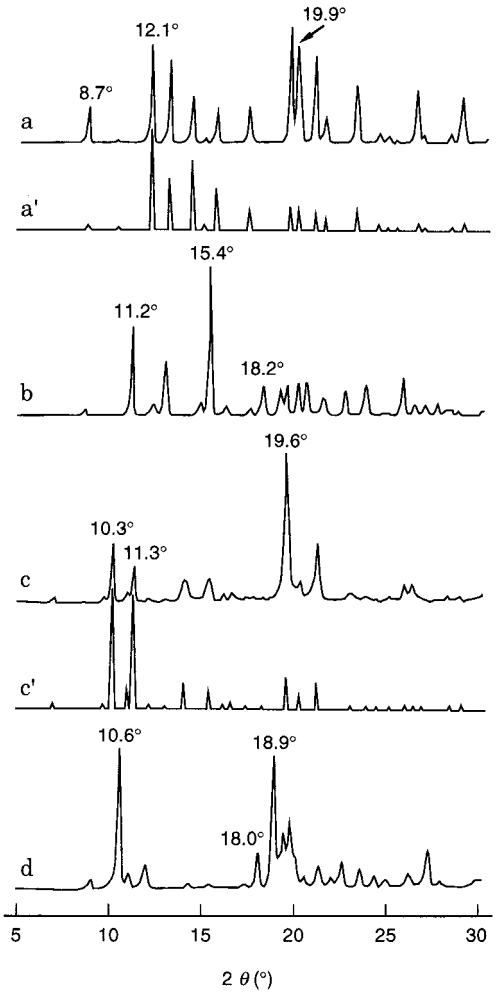

Figure 1—PXRD patterns of TB polymorphs: (a) Form I; (a′) theoretical profile of Form I; (b) Form III; (c) Form II; (c′) theoretical profile of Form II; (d) Form IV.

Results and Discussion

Characterization of TB Polymorphs—Figure 1 shows PXRD patterns of the TB solids (Forms I, II, III, and IV). Form IV was prepared by spray-drying TB using the mixed solvent ethanol/dichloromethane (1.2:1 v/v) and Form II was prepared by storing Form IV at 60 °C, 75% RH (see *Experimental Section*). Form I of TB gave diffraction peaks at 8.7, 12.1, and 19.9°, and this pattern coincided in diffraction angle and with the computer-simulated pattern drawn on the basis of single-crystal data of Form I reported by Donaldson et al.[24] The difference in diffraction intensity at 2θ = about 20° may be ascribed to the difference in crystal habit of the two samples. Rowe and Anderson reported that Form III is less soluble than Form I in water at 37 °C; thus, Form III is a stable form at room temperature, although the difference in free energy of the two forms is small.[25] Form III gave diffraction peaks at 11.2, 15.4, and 18.2° and Form II at 10.3, 11.3 and 19.6°. The diffraction pattern of Form II was identical in diffraction angle to the computer-simulated pattern drawn on the

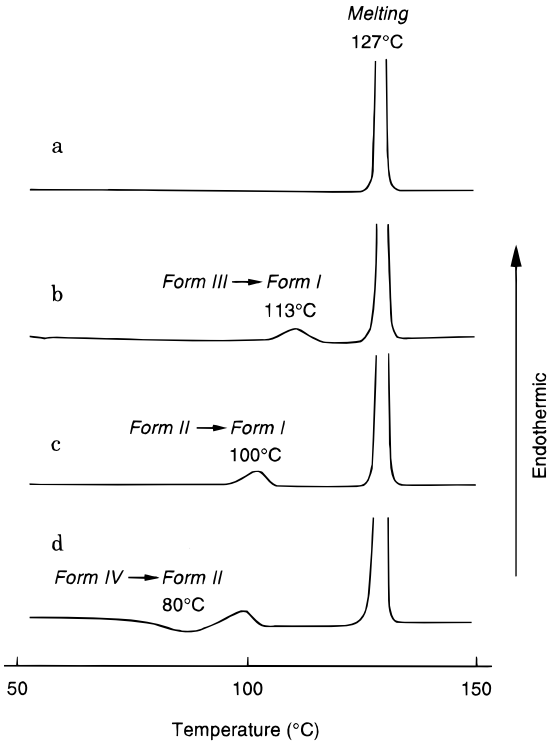

Figure 2—DSC thermograms of TB polymorphs: (a) Form I; (b) Form III; (c) Form II; (d) Form IV.

basis of single-crystal data of Form II, which was analyzed in our laboratory and will be reported elsewhere.[26] The difference in diffraction intensity may be also ascribed to the difference in crystal habit of the two samples. On the other hand, the spray-dried TB gave two strong diffraction peaks at 10.6 and 18.9° and a small peak at 18.0°, which were clearly different from those of Forms I, II, and III, although its diffraction pattern resembled that of Form II. These results suggest that the spray-dried TB is one of polymorphs of TB and its internal structure may resemble that of Form II. These polymorphs of TB, Forms II and IV, were further characterized by other physical methods.

Figure 2 shows DSC curves of Forms I, II, III, and IV. Form I showed an endothermic peak at 127 °C due to melting. Form III gave two peaks at 113 and 127 °C. The latter peak is due to the melting of Form I and the former peak is due to the melting of Form III followed by the crystallization of Form I, because the PXRD pattern of Form III heated to about 110 °C coincided with that of Form I. Form II showed a similar polymorphic transition behavior; that is, the melting of Form II and crystallization of Form I at 100 °C and the melting of Form I at 127 °C. On the other hand, Form IV showed an exothermic peak at 80 °C, followed by endothermic peaks at 100 and 127 °C. The PXRD pattern of Form IV heated to 80 °C was identical to that of Form II, indicating that the 80 °C peak is due to the transition of Form IV to Form II, the 100 °C peak is due to the melting of Form II and crystallization of Form I, and the 127 °C peak is due to the melting of Form I. The conversion of Form IV to Form II was apparently accompanied by no liquification, whereas that of Form II to Form I is a crystallization from the liquified Form II. The enthalpy changes (ΔH) for the conversion of Form IV to Form II and the melting of Form I were 1.2 and 27.2 kJ/mol, respectively. The apparent ΔH values for the conversion of Forms III and II to Form I were 1.9 and 1.5 kJ/mol, respectively, although they contain the combined ΔH changes of fusion and crystallization processes.

Figure 3 shows SEM pictures of the four TB polymorphs.

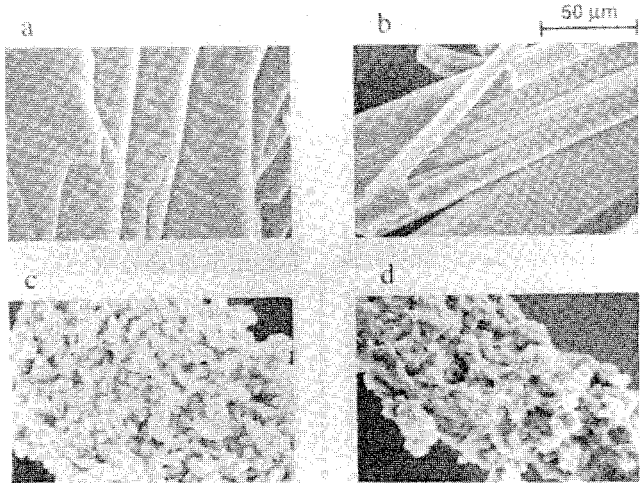

Figure 3—Scanning electron micrographs of TB polymorphs: (a) Form I; (b) Form III; (c) Form II; (d) Form IV.

Form I is in the form of plate crystals with a microscopically layered sheet structure and Form III consists of needlelike crystals, with both forms having smooth surfaces. Form II, an aggregate, consists of small solid particles, whereas Form IV has a rodlike structure, with many pores and clusters of small particles on the surface, and its appearance resembles that of Form II.

The solid-state ^{13}C NMR spectroscopic studies were employed to gain insight into the internal structure of TB polymorphs. Figure 4 shows ^{13}C NMR spectra of Forms I, II, III, and IV measured in a CP/MAS mode. The chemical shifts are listed in Table 1. These ^{13}C NMR signals were assigned according to the spectrum of TB in solution.[20] In Form I, the butyl and methyl carbons gave sharp peaks, suggesting a definite conformation[24] as described later, whereas the benzene carbons gave rather broad peaks with a shoulder, suggesting that each *ortho*- and *meta*-carbon is magnetically unequivalent and the broadening of the C2 carbon may arise from a magnetic fluctuation due to a rotation of the methyl group. Form III gave chemical shifts similar to those of Form I, although the signals of the *ortho*-(C4 and C6) and *meta*-(C3 and C7) carbons became sharp whereas those of the C10−C12 carbons split. These results suggest that the conformation of TB in Form III is very similar to that in Form I, but with different motional freedom as reflected by the observed NMR peak splitting. On the other hand, the chemical shifts of the butyl moiety in Forms II and IV were significantly different from those in Forms I and III, although the benzene ring had similar chemical shifts; that is, C10 carbon: 31.8 ppm (Form I), 30.9 and 31.9 ppm (Form III), 35.2 and 33.4 ppm (Form II), and 33.8 ppm (Form IV); C12 carbon: 13.6 ppm (Form I), 12.7 and 12.0 ppm (Form III), 15.8 and 13.7 ppm (Form II), and 16.1 ppm (Form IV). Our results on the single-crystal analysis of Form II[26] and the reported result of Form I[24] indicate that the butyl moiety of TB is in a trans conformation in Form II crystals (C9−C10−C11−C12 dihedral angle = 178.6°) but it is in a gauche conformation in Form I crystals (the dihedral angle = 101.3°). Therefore, the shift difference of the butyl moiety can be ascribed to this conformational alteration. The chemical shifts of TB in Form IV were very similar to those in Form II, although the signals of the *ortho*- and *meta*-carbons became sharp. These results indicate that the conformation of TB in Form IV is almost the same as that of Form II, but the environment around the benzene ring may differ; that is, there may be some vacant space that allows the ring to rotate due to the looser packing of crystals in Form IV. The FT-IR spectroscopic studies supported this conclusion; that

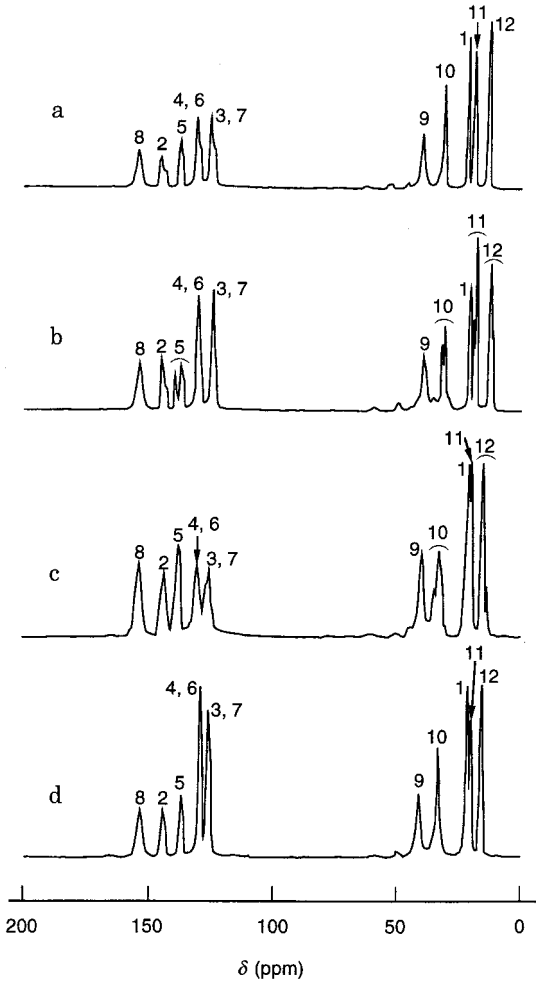

Figure 4—^{13}C CP/MAS NMR spectra of TB polymorphs at 25 °C (see Table 1 for the carbon numbering of TB): (a) Form I; (b) Form III; (c) Form II; (d) Form IV.

Table 1—^{13}C NMR Chemical Shifts (ppm)[a] of TB Polymorphs at 25 °C

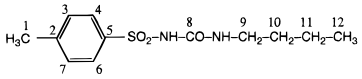

carbon	solution in 2 N NaOD	solid state Form I	Form III	Form II	Form IV
1	21.6	21.8	20.9	21.7	22.1
2	144.9	145.8	145.1	144.2	144.8
3, 7	127.0	126.2	125.0	126.2	127.2
4, 6	130.1	131.8	131.0	130.9	130.4
5	136.7	138.1	139.8, 137.4	138.6	137.5
8	151.3	155.0	154.1	154.3	154.0
9	40.2	40.1	39.2	40.2	41.5
10	31.6	31.8	31.9, 30.9	35.2, 33.4	33.8
11	19.9	19.4	19.5, 18.6	20.6	20.7
12	13.7	13.6	12.7, 12.0	15.8, 13.7	16.1

[a] Downfield from the resonance of tetramethylsilane.

is IR absorption bands of the functional groups involving in the intermolecular hydrogen bonding of TB molecules, such as the imino (NH, 3328 cm^{-1}), carbonyl (CO, 1703 and 1660 cm^{-1}), and sulfonyl (SO_2, 1336 and 1159 cm^{-1}) groups, showed insignificant differences in the wavelength between the four TB polymorphs, suggesting the similar hydrogen bonding network.[24,26] On the other hand, the spectral shapes of the stretching absorption band of alkyl portion around 2950−3000 cm^{-1} and the aromatic CH stretching

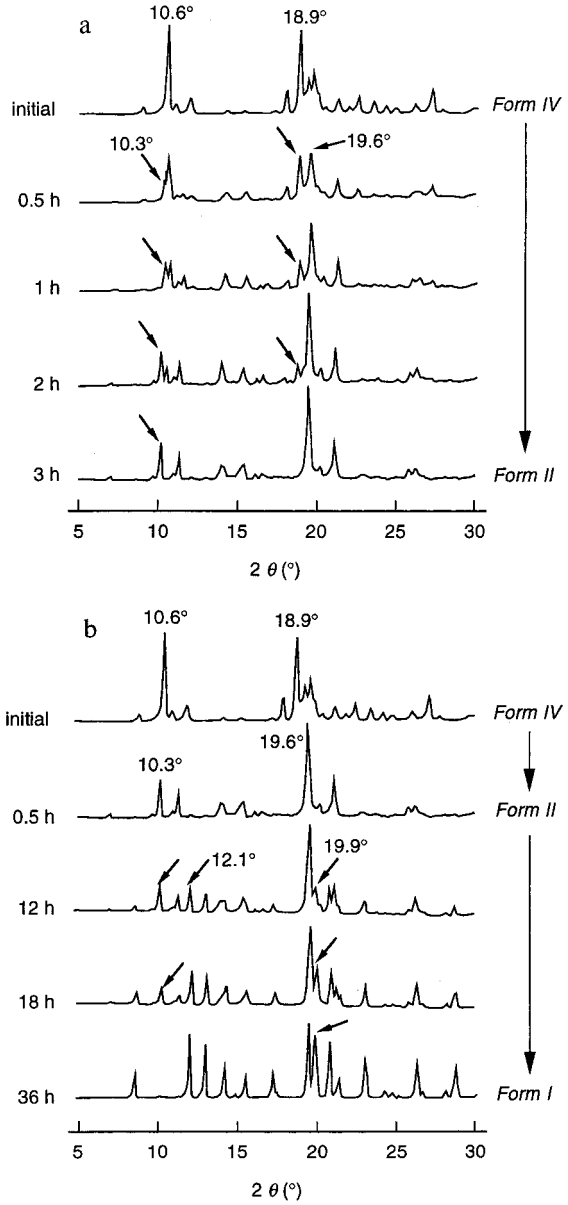

Figure 5—Changes of PXRD pattern of Form IV during storage at (a) 45 °C and 75% RH and (b) 60 °C and 75% RH.

band around 800−850 cm^{-1} were different between the four polymorphs. As judged by the peak intensities of 816 and 843 cm^{-1}, our Forms I, II, III, and IV are identical with Burger's Forms I, II, III, and IV, although it is difficult to completely identify the latter because no diffraction data are given in his paper.[9] However, it is apparent from the diffraction data, that Al-Saieq's[11] Form IV corresponds to our Form II and Georgarakis's[15] Form II corresponds to our Form IV.

Transition Behavior of Form IV—The isothermal transition behavior of Form IV was investigated because it may be easily converted to Form II, which has a similar crystal structure. Figure 5 shows changes in the PXRD pattern of Form IV during storage at 45 and 60 °C at 75% RH. During the storage at 45 °C (Figure 5a), the diffraction peaks characteristic of Form IV at 2θ = 10.6° and 18.9° decreased, whereas those of Form II at 10.3° and 19.6° increased. The longer storage at the higher temperature (Figure 5b) gave diffraction peaks characteristic of Form I at 12.1° and 19.9°, indicating the transition of Form IV to Form I via Form II. Figure 6 shows the time courses for the conversion of Form IV to Forms II and I on storage at

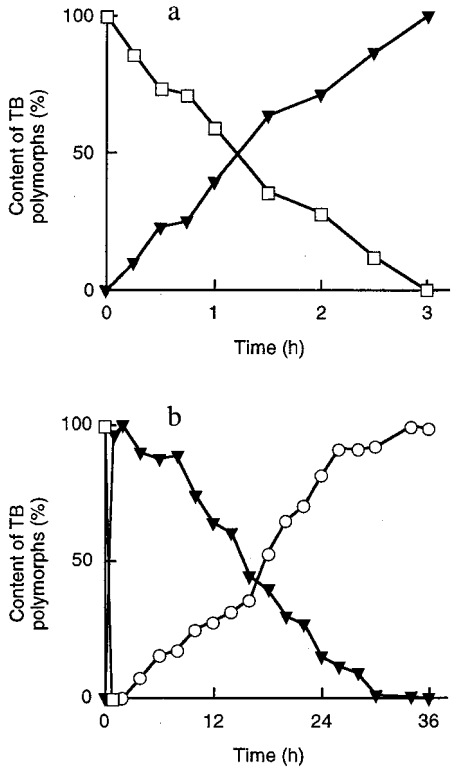

Figure 6—Time courses for conversion of Form IV to Form II and Form I during storage at (a) 45 °C and 75% RH and (b) 60 °C and 75% RH. Key: (○) Form I; (▼) Form II; (□) Form IV.

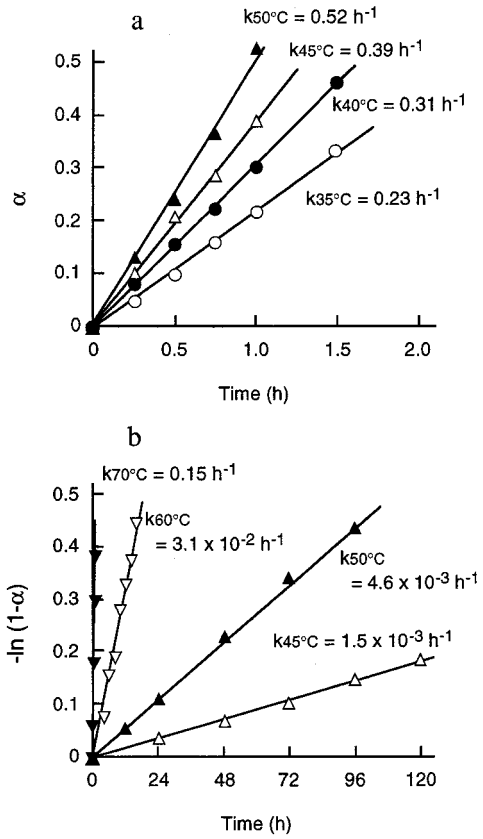

Figure 7—Plots of α and [–ln(1 – α)] for transitions of (a) Form IV to Form II and (b) Form II to Form I at 75% RH. Key: (○) 35 °C; (●) 40 °C; (△) 45 °C; (▲) 50 °C; (▽) 60 °C; (▼) 70 °C.

the conditions just stated. The contents of each polymorph were determined from the following diffraction intensity ($2\theta = 19.9°$ for Form I, 10.3° for Form II, and 18.9° for Form IV). Form IV was converted completely to Form II in 3 h with storage at 45 °C, 75% RH, whereas at 60 °C, Form IV rapidly changed to Form II within 30 min and Form II slowly changed to Form I in 30 h. These polymorphic transition−time profiles were analyzed according to the Hancock and Sharp equation (eq 1):[27]

$$\ln [-\ln(1 - \alpha)] = m \ln t + \ln B \qquad (1)$$

where m is the intrinsic value for various theoretical equations of solid-state decomposition, α is the fraction of the total sample converted to the other polymorph, based on the X-ray relative intensities, t is the storage time, and B is a constant. The plot of $\ln[-\ln(1 - \alpha)]$ versus $\ln t$ using the data of $\alpha = 0.1-0.5$ gave straight lines of $m = 1.23 \pm 0.06$ (mean ± SE, $n = 4$, correlation coefficient (r) = 0.998) for the conversion of Form IV to Form II at 45 °C and 75% RH, and $m = 0.99 \pm 0.04$ ($n = 4$, $r = 0.997$) for that of Form II to Form I at 60 °C and 75% RH. The m value of 1.23 indicates that the Form IV-to-II transition proceeds according to a zero-order mechanism (a criterion for zero-order transition: $m = 1.24$)[27] and its rate obeys the equation of $\alpha = kt$. On the other hand, the m value of 0.99 indicates that a random nucleation on each particle is a rate-determining step for the Form II-to-Form I transition (a criterion for this conversion is $m = 1.0$)[27] and its rate obeys the equation of $-\ln(1 - \alpha) = kt$. Therefore, the polymorphic transition rates of Form IV to Form II and Form II to Form I were analyzed, respectively according to the aforementioned equations, and the results at various temperatures are shown in Figure 7. The plots of α or $-\ln(1 - \alpha)$ versus t were confirmed to be linear, and the transition rate constants (k, see Figure 7) were obtained from the slopes. The Arrhenius plots of these rate constants gave straight lines ($r = 0.999$), from which the activation energies of 44 and 166 kJ/mol were obtained for the transitions of Form IV to II and Form II to I, respectively. These results indicate that the energy barrier of the transition of Form IV to Form II is very low, because the internal structure of Form IV, including the conformation of TB, is similar to that of Form II, whereas that of Form II to Form I is rather high because the crystal system and the conformation of TB are different between Form II (monoclinic, $P2_1/n$, $a = 11.815$ Å, $b = 9.069$ Å, $c = 13.981$ Å, $\beta = 104.50°$)[26] and Form I (orthorhombic, $Pna2_1$, $a = 20.223$ Å, $b = 7.831$ Å, $c = 9.090$ Å)[24] crystals. The transition behavior of Form IV at different humidity conditions (22, 50, and 75% RH) and 50 and 60 °C was investigated, and the rate constants were obtained from the linear plots of α and $-\ln(1 - \alpha)$ versus t for the Form IV-to-Form II transition and the Form II-to-Form I transition, respectively, as follows: $k = 0.16$, 0.52, and 1.01 h^{-1} for the Form IV-to-Form II transition at 50 °C, and $k = 0.0030$, 0.012, and 0.031 h^{-1} for the Form II-to-Form I transition at 60 °C. The transition rate increased as the humidity increased, presumably because TB dissolves in adsorbed water on the crystal surface, which may consequently promote the nucleation and growth of crystals.

Dissolution and Absorption Behavior of Polymorphs—Figure 8 shows dissolution profiles of TB polymorphs in the JP XIII second fluid (pH 6.8), measured by the dispersed amount method at 37 °C. The dissolution rate of Form III was slightly faster than that of Form I, whereas those of Forms IV and II were significantly faster than that of Form I. The dissolution rate of Form IV was almost the same as that of Form II. The Form IV powder in the dissolution medium was taken out, dried, and subjected to DSC measurements to gain insight into phase changes of Form IV during the dissolution. As is apparent from the change in DSC curves in Figure 9, Form IV transformed

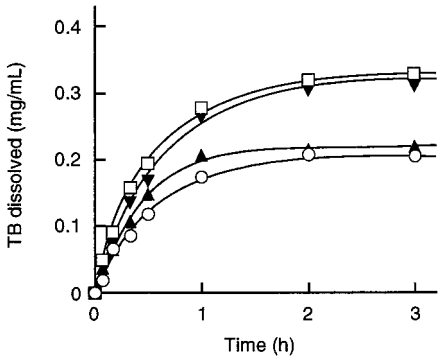

Figure 8—Dissolution profiles of TB polymorphs (equivalent to 100 mg TB) in JP XIII second fluid at 37 °C, measured by the dispersed amount method at 91 rpm. Key: (○) Form I; (▲) Form III; (▼) Form II; (□) Form IV. Each point represents the mean of 3 experiments.

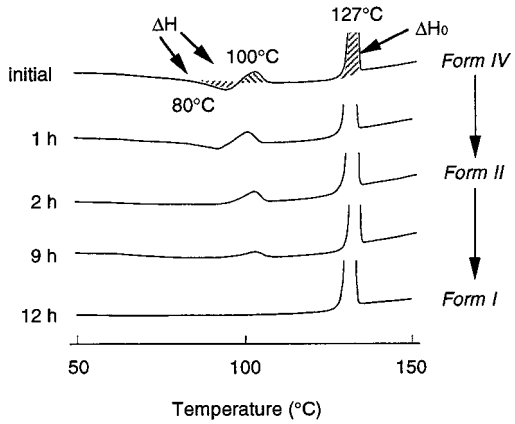

Figure 9—DSC thermograms of Form IV during dissolution in JP XIII second fluid at 37 °C, measured by the dispersed amount method at 91 rpm.

into Form I via Form II during the dissolution. The apparent first-order transition rate constants of Form IV to Form II and Form II to Form I under the dissolution test condition (dispersed amount method, JP XIII second fluid, powder size < 100 mesh, 37 °C, 91 rpm) were determined by plotting the data of $\ln(\Delta H/\Delta H_0)$ versus time, where ΔH_0 is the enthalpy change for fusion of total Form I at 127 °C. The enthalpy changes (ΔH) of the exothemic peak at about 80 °C during 0−2 h were used for calculation of the rate constant of the Form IV-to-Form II transition, and those of the adjacent endothermic peak (about 100 °C) after 2 h were used for the rate constant calculation of the Form II-to-Form I transition. The first-order plot of both transitions gave a straight line ($r = 0.998$), from which the rate constants of 0.45 and 0.087 h^{-1} for the transitions of Form IV to Form II and Form II to Form I, respectively, were obtained. Therefore, the insignificant difference in the dissolution rate between Forms IV and II can be attributed to the phase change of Form IV to Form II within about 2 h under experimental conditions. Figure 10 shows the plasma TB level−time profiles after oral administration of TB polymorphs in dogs. Their bioavailability parameters are summarized in Table 2. The oral bioavailability of TB increased in the order Form I ≪ Form III < Form II ≈ Form IV, and that of Forms IV and II was >2-fold higher than that of Form I, reflecting the in vitro dissolution behavior of the polymorphs.

Conclusion

In this study, we fully characterized polymorphs of TB (Burger's Forms I, II, III, and IV) by various physical methods such as XRPD, solid-state ^{13}C NMR, FT-IR, and thermal analysis. The results indicate that Form IV has an internal structure and conformation that resemble closely those of Form II. Because of this similarity, Form IV was easily converted to Form II under both isothermal and nonisothermal conditions. The dissolution rate of Form IV was almost identical to that of Form II because of the conversion to Form II during the dissolution. This dissolution property of Form IV was clearly reflected in the oral bioavailability of TB in dogs. The present systematic characterization of TB polymorphs will be useful for identification of solid TB and gives a rational basis for the design of solid TB formulations.

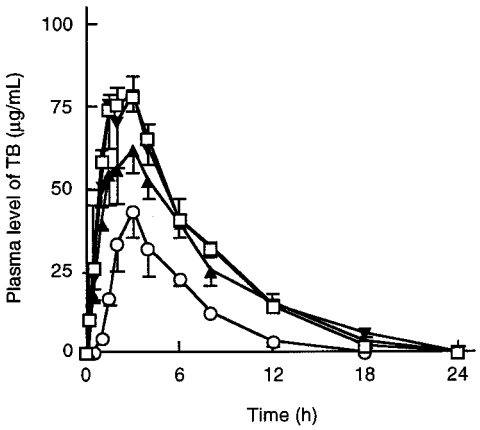

Figure 10—Plasma levels of TB after oral administration of TB polymorphs (equivalent to 100 mg/body TB) in dogs. Key: (○) Form I; (▲) Form III; (▼) Form II; (□) Form IV.

Table 2—Bioavailability Parameters of TB after Oral Administration of TB Polymorphs (Equivalent to 100 mg/body TB) in Dogs[a]

Form	t_{max} (h)[b]	C_{max} (μg/mL)[c]	AUC (h·μg/mL)[d]	MRT (h)[e]	F (%)[f]
I	3.0 ± 0.0	43.6 ± 7.1	226.1 ± 34.6	5.1 ± 0.1	19.2 ± 3.6
III	2.7 ± 0.3	62.1 ± 6.1	489.0 ± 64.7**	6.1 ± 0.3**	41.6 ± 6.7**
II	2.2 ± 0.4	84.8 ± 9.3*	590.0 ± 74.7**	6.0 ± 0.3**	50.2 ± 7.8**
IV	2.7 ± 0.3	80.5 ± 2.8**	576.0 ± 33.6*	5.5 ± 0.2	49.0 ± 3.5**

[a] Each value represents the mean ± SE of 3 dogs; significant difference from Form I is noted as follows: (*) $p < 0.05$; (**) $p < 0.01$. [b] The time required to reach the maximum plasma level. [c] The maximum plasma level. [d] The area under the plasma level versus time curve up to 24 h post-administration. [e] The mean residence time in plasma. [f] The extent of bioavailability compared with the AUC value of intravenously administered TB.

Supporting Information Available— Four figures of TB polymorphs (FT-IR spectra and conversion plots). This material is available free of charge via the Internet at http://pubs.acs.org.

References and Notes

1. Haleblian, J.; McCrone, W. Pharmaceutical applications of polymorphism. *J. Pharm. Sci.* **1969**, *58*, 911−929.
2. Brittain, H. G.; Bogdanowich, S. J.; Bugay, D. E.; Vincentis, J. D.; Lewen, G.; Newman, A. W. Physical characterization of pharmaceutical solid. *Pharm. Res.* **1991**, *8*, 963−973.
3. Borka, L. Review on crystal polymorphism of substances in the european pharmacopoeia. *Pharm. Acta Helv.* **1991**, *66*, 16−22.
4. Shibata, M.; Kokubo, H.; Morimoto, K.; Morisaka, K.; Ishida, T.; Inoue, M. X-ray structural studies and physicochemical properties of cimetidine polymorphism. *J. Pharm. Sci.* **1983**, *72*, 1436−1442.
5. Matsuda, Y.; Kawaguchi, S.; Kobayashi, H.; Nishijo, J. Physicochemical characterization of spray-dried phenylbutazone polymorphs. *J. Pharm. Sci.* **1984**, *73*, 173−179.
6. Hirayama, F.; Usami, M.; Kimura, K.; Uekama, K. Crystallization and polymorphic transition behavior of chloramphenicol palmitate in 2-hydroxypropyl-β-cyclodextrin matrix. *Eur. J. Pharm. Sci.* **1997**, *5*, 23−30.

7. Thomas, R. C.; Ikeda, G. J. The metabolic fate of tolbutamide in man and in the rat. *J. Med. Chem.* **1966**, *9*, 507−510.
8. Simmons, D. L.; Ranz, R. J.; Gyanchandani, N. D.; Picotte, P. Polymorphism in pharmaceuticals II (tolbutamide). *Can. J. Pharm. Sci.* **1972**, *7*, 121−123.
9. Burger, A. Zur polymorphie oraler antidiabetika. *Sci. Pharm.* **1975**, *43*, 161−168.
10. Burger, A.; Ramberger, R. On the polymorphism of pharmaceuticals and other molecular crystals. II. Applicability of thermodynamic rules. *Mikrochim. Acta* **1979**, 273−316.
11. Al-Saieq, S. S.; Riley, G. S. Polymorphism in sulphonylurea hypoglycaemic agents: I. Tolbutamide. *Pharm. Acta Helv.* **1981**, *56*, 125−129.
12. Leary, J. R.; Ross, S. D.; Thomas, M. J. K. On characterization of the polymorphs of tolbutamide. *Pharm. Weekblad. Sci. Ed.* **1981**, *3*, 62−66.
13. Umeda, T.; Ohnishi, N.; Yokoyama, T.; Kuroda, T.; Kita, Y.; Kuroda, K.; Tatsumi, E.; Matsuda, Y. A kinetic study on the isothermal transition of polymorphic forms of tolbutamide and mefenamic acid in the solid state at high temperatures. *Chem. Pharm. Bull.* **1985**, *33*, 2073−2078.
14. Traue, J.; Kala, H.; Köhler, M.; Wenzel, U.; Wiegeleben, A.; Förster, B.; Pollandt, P.; Pintye-Hódi, K.; Szabó-Révész, P.; Selmeczi, B. Untersuchungen zur polymorphie von arzneistoffen in pulvern und tabletten. *Pharmazie* **1987**, *42*, 240−241.
15. Georgarakis, M. Untersuchungen zur polymorphie von tolbutamid. *Pharmazie* **1989**, *44*, 209−210.
16. Olives, A. I.; Martin, M. A.; del Castillo, B.; Barba, C. Influence of the presence of trace amounts of metals on the polymorphism of tolbutamide. *Int. J. Pharm.* **1996**, *14*, 1069−1076.
17. Stephenson, G. A.; Pfeiffer, R. R.; Byrn, S. R. Solid-state investigation of the tautomerism of acetohexamide. *Int. J. Pharm.* **1997**, *146*, 93−99.
18. *The Japanese Pharmacopeia XIII*; Japanese Pharmacopeial Conversion, Inc.: Tokyo, 1996; pp 116−121.
19. *teXsan: Single-Crystal Structure Analysis Package*, Vesion 1.6 (1993), Molecular Structure Corporation: The Woodlands, TX.
20. Ueda, H.; Nagai, T. Solid-state nuclear magnetic resonance spectroscopy and Raman spectroscopy of inclusion compound of tolbutamide with β-cyclodextrin. *Chem. Pharm. Bull.* **1981**, *28*, 1415−1421.
21. Carr, D. S.; Hariss, B. L. Solutions for maintaining constant relative humidity. *Ind. Eng. Chem.* **1949**, *41*, 2014−2015.
22. Nyqvist, H. Saturated salt solutions for maintaining specified relative humidities. *Int. J. Pharm. Technol. Prod. Mfr.* **1983**, *4*, 47−48.
23. Nogami, H.; Nagai, T.; Yotsuyanagi, Y. Dissolution phenomena of organic medicinals involving simultaneous phase changes. *Chem. Pharm. Bull.* **1969**, *17*, 499−509.
24. Donaldson, J. D.; Leary, J. R.; Ross, S. D.; Thomas, M. J. K. The structure of the orthorhombic form of tolbutamide (1-*n*-butyl-3-*p*-toluenesulphonylurea). *Acta Crystallogr.* **1981**, *B27*, 2245−2248.
25. Rowe, E. L.; Anderson, B. D. Thermodynamic studies of tolbutamide polymorphs. *J. Pharm. Sci.* **1984**, *73*, 1673−1675.
26. Kimura, K.; Hirayama, F.; Arima, H.; Uekama, K. in preparation.
27. Hancock, J. D.; Sharp, J. H. Method of comparing solid-state kinetic data and its application to the decomposition of kaolinite, brucite, and $BaCO_3$. *J. Am. Ceram. Soc.* **1972**, *55*, 74−77.

JS980376Z

Transport of the δ-Opioid Receptor Agonist [D-Penicillamine^{2,5}] Enkephalin Across the Blood–Brain Barrier Involves Transcytosis[1]

RICHARD D. EGLETON AND THOMAS P. DAVIS*

Contribution from *Department of Pharmacology, The University of Arizona, College of Medicine, LSN 533, 1501 N. Campbell Avenue, Tucson, Arizona 85724.*

Received October 14, 1998. Accepted for publication January 6, 1999.

Abstract □ The delta opioid receptor antagonist [D-penicillamine^{2,5}]-enkephalin (DPDPE) is an enzymatically stable peptide analogue of Met-enkephalin. DPDPE uses a saturable transport mechanism to cross the blood-brain barrier (BBB), though the exact mechanism is not fully understood. The aim of the present study was to identify the mechanism by which DPDPE enters the brain. The effect of phenylarsine oxide (PAO), an endocytosis inhibitor, on the transport of [^{3}H]DPDPE was investigated using both in vitro and in situ transport studies. Two in vitro models of the BBB utilizing primary bovine brain microvascular endothelial cells (BBMEC) were studied. [^{3}H]DPDPE permeability across monolayers of BBMEC grown on polycarbonate filters was studied. PAO significantly reduced the permeability of [^{3}H]-DPDPE across the monolayer. PAO also reduced the uptake of [^{3}H]-DPDPE into BBMEC cells, without affecting binding to the cells. The in situ perfusion model of the BBB was also studied, PAO reduced DPDPE uptake by the brain in a dose-dependent manner. These studies indicate that DPDPE enters the brain via an energy-dependent transcytotic mechanism.

Introduction

The blood-brain barrier (BBB), consisting of the cerebral capillary endothelial cells, restricts the entry of solutes into the brain. There are, however, a number of transport mechanisms that peptide drugs can utilize to enter the brain.[2] For example biphalin ([Tyr-D-Ala-Gly-Phe]$_2$), an enkephalin analogue, uses the large neutral amino acid transporter to enter the brain.[3] The cyclic somatostatin analogue, CTAP (D-Phe-Cys-Tyr-D-Trp-Arg-Thr-Pen-Thr) enters the brain via a diffusional mechanism.[4]

[D-Penicillamine^{2,5}] enkephalin (DPDPE, Tyr-D-Pen-Gly-Phe-D-Pen) is a δ-opioid receptor agonist that is conformationally constrained by a disulfide bridge between the two D-Pen moieties.[5] Conformationally constraining the peptide results in a higher enzymatic stability in both brain and serum[6,7] compared with the endogenous enkephalins.[8] In the bovine brain microvascular endothelial cell (BBMEC) model of the BBB, DPDPE had a higher permeability than most other opioid peptides studied.[9]

In situ perfusion studies have shown that DPDPE accumulates in the brain significantly better than the BBB-impermeable marker sucrose.[10] This accumulation is partially saturable.[10] The saturable component follows Michaelis–Menten kinetics with a maximum velocity (V_{max}) of 51.1 ± 13.2 pmol·min^{-1}·g^{-1}, and a Michaelis–Menten constant (K_m) of 45.6 ± 27.6 μM, and the nonsaturable component has a K_d of 0.6 ± 0.3 μL·min^{-1}·g^{-1}.[11] Further studies show that DPDPE does not use a number of previously reported peptide transporters, including the enkephalin transporter and the insulin transporter.[11] DPDPE uptake is also not dependent on any δ-opioid receptor-mediated mechanism.[11] Recent studies have shown an important role for endocytosis in the transport of peptides and proteins across the BBB,[12] and phenylarsine oxide (PAO) has been shown to inhibit saturable endocytotic mechanisms.[13] In this study, we investigated the role of endocytosis in the transport of DPDPE in BBMEC monolayers and into the rat brain.

Experimental Procedures

In Vitro BBMEC Permeability Studies. BBMEC cells were isolated from the cerebral cortex gray matter as previously described.[14,15] Isolated BBMECs, suspended in culture media, were seeded onto 25-mm polycarbonate membrane filters (Costar Nucleopore 10 μm; Costar Corp., Cambridge, MA) that had previously been coated with rat-tail collagen and human fibronectin. After the cells had grown to confluence (10–12 days), the BBMEC monolayers were used for transendothelial transport studies of [^{3}H]DPDPE in the presence and absence of PAO. The PAO was administered to both chambers commencing at the preincubation period.

Polycarbonate filters with confluent BBMEC monolayers were placed in side-by-side diffusion chambers (Crown Glass Company, Somerville, NJ) kept at 37 °C. Both sides of the diffusion cell chamber contained phosphate buffered saline (PBS) (122 mM NaCl, 3 mM KCl, 25 mM Na_2PO_4, 1.3 mM K_2HPO_4, 1.4 mM $CaCl_2$, 1.2 mM $MgSO_4$, 10 mM glucose, 10 mM HEPES pH 7.4) that was continuously stirred. At 15, 30, 60, 90, and 120 min, after the addition of 1 mL of [^{3}H]DPDPE (0.33 μCi·mL^{-1}) to the donor chamber, 200 μL samples were removed from the receiver chamber. An equal volume of fresh PBS was added to the sampled chamber to maintain a constant volume during sampling. Four milliliters of Budget Solve Scintillation Cocktail (RPI, Mount Prospect, IL) was added to each sample, and the samples were counted for radioactivity using a Beckman Beta counter model LS 5000 TD (Fullerton, CA).

The effect of phenylarsine oxide on the basal permeability of the BBMEC membranes was studied using [^{14}C]sucrose. [^{14}C]-Sucrose has a very low permeability across BBMEC-coated membranes and is used to access basal permeability.

In Vitro BBMEC Uptake Studies. BBMEC cells were grown to confluence on 24 well plates (Falcon, Becton Dickinson, Lincoln Park, NJ) precoated with rat tail collagen and human fibronectin. Growth media was removed, and the cells were preincubated with assay buffer (122 mM NaCl, 3 mM KCl, 25 mM Na_2PO_4, 1.3 mM K_2HPO_4, 1.4 mM $CaCl_2$, 1.2 mM $MgSO_4$, 10 mM glucose, 10 mM HEPES pH 7.4). After 20 min, 0.33 μCi of [^{3}H]DPDPE was added to each well. The cells were then incubated for 5–30 min at 37 °C on a shaker table. After the set time, the radioactive buffer was removed and the cells were washed three times with ice cold assay buffer and then incubated for 4 min with an acid buffer (0.2 M acetic acid in 0.2 M NaCl[16]). The acid wash was performed to strip any of the DPDPE from the external surface of the cell. Therefore, any radioactivity that remains with the cell has been taken into the cell itself. After 4 min, the acid wash was removed and the cells were incubated with a 1% Triton-X-100 for 30 min. Samples (100 μL) from both the acid wash and the Triton-X-100 wash were prepared for radioactive sampling by adding 4 mL of Budget Solve

* Corresponding author. Telephone: (520)-626-7643. Fax: (520)-626-4053. E-mail: davistp@u.arizona.edu.

10.1021/js980410+ CCC: $18.00
Published on Web 03/02/1999

Scintillation Cocktail to each sample, and the samples were counted for radioactivity using a Beckman Beta counter model LS 5000 TD (Fullerton, CA). The remaining samples were assayed for protein using a Pierce BCA-protein kit.

The effect of PAO on [^{3}H]DPDPE uptake was studied at the 20-min time point. PAO (10−200 μM) was added to the cells during the preincubation and throughout the experimental time course. The experiment was repeated as already described.

In Situ Rat Brain Perfusion. The following experimental protocol was approved by the Institutional Animal Care and Use Committee at the University of Arizona. Adult Sprague−Dawley rats (weighing 250−350 g) were anesthetized with 1 mL·kg^{-1} of a cocktail of acepromazine (0.6 mg·mL^{-1}), ketamine (3.1 mg·mL^{-1}), and xylasine (78.3 mg·mL^{-1}), and then heparinized (10 000 U·Kg^{-1}). The neck vessels were exposed, and the right common carotid artery was cannulated with fine silicon tubing connected to a perfusion system. The perfusion fluid was a modified Krebs-Henseleit Ringers[17] [117.0 mM NaCl, 4.7 mM KCl, 0.8 mM $MgSO_4 \cdot 3H_2O$, 24.8 mM $NaHCO_3$, 1.2 mM KH_2PO_4, 2.5 mM $CaCl_2 \cdot 6H_2O$, 10 mM D-glucose, 39% dextran (MW 70 000), and 1% bovine serum albumin] that had been aerated with 5% CO_2, 95% O_2 and warmed to 37 °C. The right jugular vein was sectioned at the start of the perfusion. Once the correct perfusion pressure of 90.8 ± 5.3 mmHg and perfusion flow rate of 3.1 mL·min^{-1} were obtained, the contralateral carotid artery was cannulated and perfused in the same manner. The [^{3}H]DPDPE or [^{14}C]sucrose, along with various concentrations of PAO (10−200 μM), 100 μM DPDPE, or 100 μM DPDPE + 100 μM PAO, was then infused via a slow-drive syringe pump (model 22, Harvard Apparatus, South Natick, MA) into the inflowing mammalian Ringers solution. After 20 min, the perfusion was terminated and the animals were sacrificed by decapitation. The brain was removed, choroid plexi were excised, and brain samples taken and weighed. Perfusion fluid samples were taken from the carotid cannulae immediately at the termination of the perfusion.

Brain tissue samples and 100 μL of perfusion fluid were prepared for liquid scintillation counting by 12 h of solubilization in 1 mL of tissue solubilizer (TS-2; Research Products, Mount Pleasant, IL). After solubilization, 100 μL of 30% acetic acid was added to each sample to eliminate chemiluminescence, followed by 4 mL of Budget Solve Scintillation Cocktail (Research Products). The samples were counted for radioactivity (model LS 5000 TD counter; Beckman Instruments, Fullerton, CA).

Materials. *Radiolabeled Substances.* [^{3}H] Tyr^1 DPDPE (42 Ci·mmol^{-1}) was obtained from Chiron Mimotopes Peptide Systems (San Diego, CA), under the direction of the National Institute on Drug Abuse. [^{14}C]Sucrose (672 mCi·mmol^{-1}) was purchased from NEN Research Products (Boston, MA).

Nonradiolabeled Substances. DPDPE was provided by Chiron Mimotopes Peptide Systems under the direction of the National Institute on Drug Abuse. PAO was purchased from Sigma (St. Louis, MO). All other chemicals were supplied by Sigma (St. Louis, MO) unless otherwise stated.

Expression of Results. *In Vitro BBMEC Permeability.* The flux of peptide was determined by the linear regression of picomoles of DPDPE appearing in the receiver chamber versus time in minutes. The apparent permeability constant (*PC*) was then calculated as

$$PC = \text{flux}/(AC_{DO}) \quad (1)$$

where flux is the gradient of the linear regression, *A* is the surface area of the membrane (0.636 cm^2), and C_{DO} is the initial concentration in the donor chamber.

In Vitro BBMEC Uptake. The flux of peptide into the cells was determined by the linear regression of picomoles of DPDPE per milligram of protein associated with the cells versus time in minutes. The cell-associated radioactivity was composed of two components, the acid-sensitive (representing [^{3}H]DPDPE bound to the cell surface) and the acid-insensitive uptake (representing the radioactivity within the cell).

In Situ Perfusion. The amount of radioactivity in the whole brain was expressed as the percentage ratio of the tissue concentration (C_{Tissue}, in dpm/g) to the concentration in the perfusion fluid (C_{Perf}, in dpm/mL).

$$R_{Tissue}\,(\%) = C_{Tissue}/C_{Perf} \times 100$$

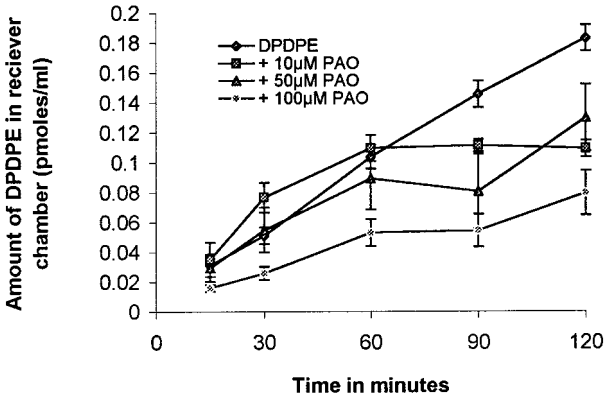

Figure 1—The permeability of [^{3}H]DPDPE across BBMEC monolayers. Each point represents the mean and SEM of 12 individual BBMEC confluent monolayers on filters. Concentrations of phenylarsine oxide (PAO) from 10 to 100 μM led to significant inhibition of [^{3}H]DPDPE permeability across the monolayers.

Table 1—Permeability Coefficient (*PC*) Values Calculated for [^{3}H]DPDPE in the Presence of 10–100 μM PAO[a]

PAO, μM	$PC \times 10^{-4}$ cm·min^{-1} (± SEM)	level of significance
0	9.31 (0.62)	—
10	3.73 (1.86)	$p < 0.05$
50	4.97 (1.24)	$p < 0.05$
100	3.54 (0.62)	$p < 0.01$

[a] *PC* values calculated from Figure 1 were compared using ANOVA and Newman–Keuls analysis; there was no significant difference between the concentrations of PAO used.

Unidirectional rate constants, K_{in} (μL·min^{-1}g^{-1}) were determined by single time point analysis as described previously,[18] where *T* is the time in minutes

$$K_{in} = C_{Tissue}\,(T)/C_{perf}T$$

The blood−brain unidirectional transfer constants determined in this manner were corrected for vascular space by subtracting the [^{14}C]sucrose R_{Brain} from the [^{3}H]DPDPE R_{Brain} values.

Statistical Analysis. For all experiments, the data were presented as the mean and SEM All concentration effects of PAO on the [^{3}H]DPDPE transport were compared by ANOVA, followed by Newman−Keuls using the Pharmacological Calculation System (PCS) statistical analysis program.[19] Linear regressions were carried out using the PCS statistical analysis program, and compared by the method of Bailey.[20]

Results

In Vitro BBMEC Permeability of [^{3}H]DPDPE. The effect of PAO on the basal permeability of BBMEC monolayers to [^{14}C]sucrose was studied. There was no effect on sucrose permeability across the membranes with 10, 50, or 100 μM PAO (data not shown). The permeability of [^{3}H]-DPDPE across BBMEC monolayers grown on collagen/fibronectin-coated polycarbonate filters and the effect of 10, 50, and 100 μM PAO were studied. Figure 1 shows the permeability of [^{3}H]DPDPE with time. The *PC* values calculated from Figure 1 (Table 1) show that all concentrations of PAO led to a significant decrease in the rate of [^{3}H]DPDPE permeability across the membrane. The amount of DPDPE in the receiver chamber was significantly lower at all time points in the presence of 100 μM PAO ($p < 0.01$ at all time points). Also, the values at 100 μM PAO were significantly lower than the values for 10 μM PAO for all but the 120-min time point ($p < 0.05$ for 10 and 90 min, $p < 0.01$ for 30 and 60 min). The 50 μM concentration of PAO significantly reduced DPDPE permeability at all time points studied ($p < 0.05$ at 15 and 60 min, $p < 0.01$ at 30,

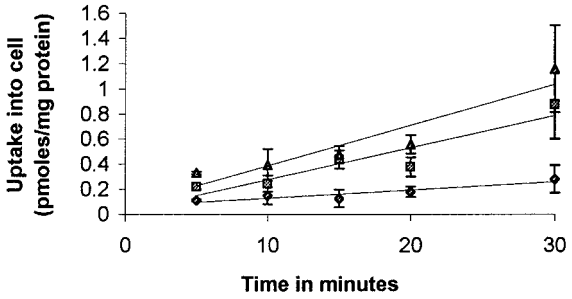

Figure 2—The time-dependent uptake of [^{3}H]DPDPE into BBMEC monolayer cells. Each point represents the mean and SEM of eight wells. Triangles represent the total amount of DPDPE associated with the cells, and diamonds represent the acid-sensitive and squares represent the acid-insensitive fractions of the binding.

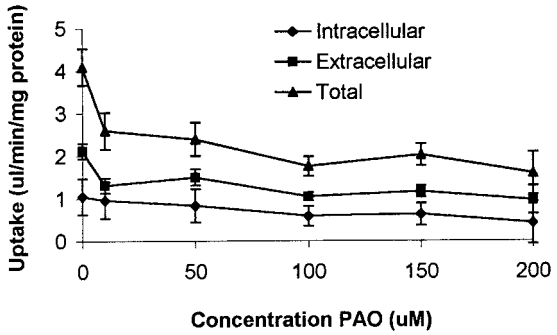

Figure 3—The effects of PAO (10–200 μM) on the total cell association of DPDPEs and acid-sensitive/acid-insensitive fractions at the 20-min time point. Each point represents the mean and SEM of eight wells.

60, and 90 min) and was significantly different from 10 μM PAO at the 30- and 60-min time points ($p < 0.01$ and $p < 0.05$, respectively). A solution 10 μM PAO reduced DPDPE permeability at the 90- and 120-min time point ($p < 0.05$ and $p < 0.01$, respectively).

In Vitro BBMEC Uptake of [^{3}H]DPDPE. In the in vitro BBMEC model of the BBB, [^{3}H]DPDPE uptake is linear with time with an uptake rate of 32.3 ± 0.7 fmol·min^{-1}·mg^{-1} protein (Figure 2). The total uptake could be split into two components, the binding of [^{3}H]DPDPE to the external membrane (acid sensitive), with a rate of 6.5 ± 0.15 fmol·min^{-1} ·mg^{-1} protein; and the internalized fraction (acid insensitive), with a rate of 25.6 ± 0.59 fmol·min^{-1}·mg^{-1} protein. The uptake of [^{3}H]DPDPE was significantly decreased at all concentrations of PAO (Figure 3). The acid-sensitive fraction showed no significant difference in [^{3}H]DPDPE binding to the cell except at the 200-μM PAO concentration ($p < 0.05$), whereas the acid-insensitive uptake fraction was significantly reduced.

In Situ Perfusion. The effects of phenylarsine oxide concentrations ranging from 10 to 200 μM on the basal permeability of the BBB to [^{14}C]sucrose were studied. PAO had no significant effect on the basal permeability of the BBB (Figure 4) at the concentrations used. All subsequent in situ figures have had the sucrose space subtracted.

The transport of [^{3}H]DPDPE across the BBB was studied during in situ brain perfusion with various (10−200 μM) concentrations of PAO. Addition of PAO decreased the uptake of [^{3}H]DPDPE into the rat brain in a dose-dependent manner (Figure 5, Table 2). The [^{3}H]DPDPE uptake was decreased by 27% ($p < 0.05$) at 10 μM, 43% ($p < 0.01$) at 50 μM, 73% ($p < 0.01$) at 100 μM, 80% ($p < 0.01$) at 150 μM, and 49% ($p < 0.01$) at 200 μM PAO. The effects at both 100 and 150 μM were significantly different from those at 10 μM ($p < 0.05$ for both).

Addition of 100 μM nonradioactive DPDPE led to a significant inhibition of [^{3}H]DPDPE uptake ($p < 0.01$)

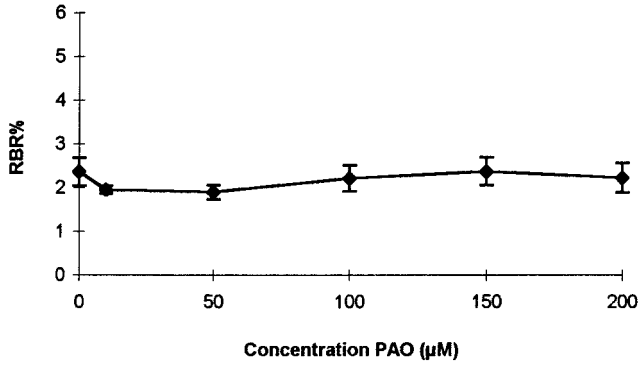

Figure 4—The effects of DPDPE and PAO on the permeability of the rat BBB to [^{14}C]sucrose. Each bar represents the mean and SEM of 4–6 animals. Concentrations of 100 μM DPDPE and 100 μM PAO had no significant effect on the permeability of the BBB to sucrose.

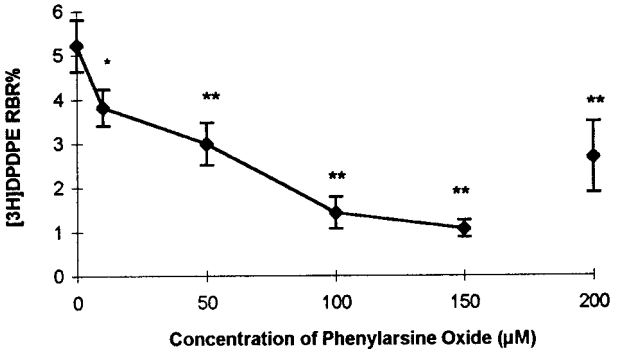

Figure 5—Dose-dependent inhibition of [^{3}H]DPDPE in situ uptake by rat brains of 10–200 μM PAO. Each point represents the mean and SEM of 4–6 animals. Statistical significance is indicated by (*) $p < 0.05$ and (**) $p < 0.01$ (using ANOVA followed by Newman–Keuls ad hoc test with the sucrose space subtracted).

Table 2—Unidirectional Transfer Constants (K_{in}) for [^{3}H]DPDPE in the Presence of Various Concentrations of PAO[a]

PAO, μM	K_{in} (μL·min^{-1}·g^{-1}) ± SEM	percent change (p value)
0	2.61 ± 0.29	—
10	1.91 ± 0.21	27% ($p < 0.05$)
50	1.49 ± 0.27	43% ($p < 0.01$)
100	0.71 ± 0.17	73% ($p < 0.01$)[b]
150	0.53 ± 0.10	80% ($p < 0.01$)[b]
200	1.30 ± 0.39	51% ($p < 0.05$)

[a] The unidirectional transport constants (K_{in}) for [^{3}H]DPDPE calculated from Figure 5 and the percent decrease in the constants with 10–200 μM PAO. Concentrations of PAO from 50 to 200 μM led to significant decreases in the K_{in} values (K_{in} values compared by ANOVA, followed by Newman–Keuls test). [b] This value is also significantly different from 10 μM PAO data at $p < 0.05$.

(Figure 6). Co-administration of both PAO and cold DPDPE led to no additive inhibition of [^{3}H]DPDPE uptake.

Discussion

In this study, we investigated the role of a saturable endocytotic mechanism in the transport of DPDPE (a cyclized opioid peptide) into the brain, using a three-model BBB paradigm. It is assumed with each of the three models that the receiver chamber, cells, or brain are acting as a sink (i.e., that the transport of DPDPE will be in one direction only). We also assume that the transport will be linear. The concentration of peptide that we used in this study is 7.6 pM. This concentration is considerably lower than the half-saturation constant of the peptide transporter, which is 45.5 μM.[11] Thus, the concentration we use

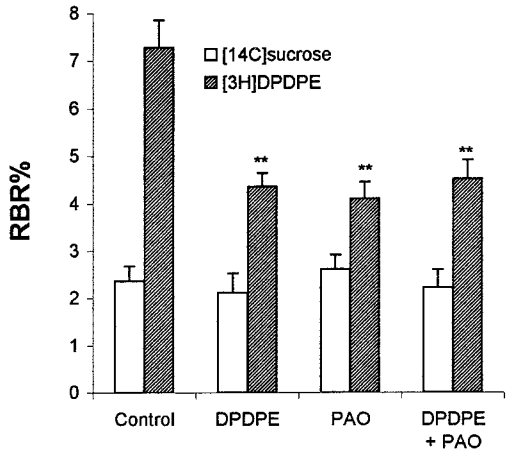

Figure 6—The effects of a combination of 100 μM PAO and 100 μM DPDPE on the uptake of [^{3}H]DPDPE by rat brain. Each bar represents the mean and SEM of 4–6 animals. Addition of PAO, DPDPE, and the combination to the perfusate led to a significant decrease in [^{3}H]DPDPE uptake. There was no significant difference between the three treatment groups.

is 10^{-6} lower than the concentration required to saturate the transport. This concentration is thus reasonable and we assume that the sink conditions will occur, if the amount of peptide in the donor solution remains higher than the amount of peptide in the receiver chamber. In this study, only a small percentage of the peptide actually crosses into the receiver chamber, cell, or brain. If the concentration of peptide used in a study is lower than the K_m value, it is likely that the process will remain linear.

The trivalent monosubstituted organoarsenic compound, PAO has been shown to inhibit endocytosis via clathrin coated pits[21] and has been used to study receptor-mediated endocytosis at concentrations of 0.1 to 100 μM.[16] The major toxic effect of PAO is the inhibition of cellular pyruvate dehydrogenase, which results in a decrease in ATP production via the citric acid cycle.[22] Viability of MDCK cells in the presence of PAO was maintained in the presence of 5 mM glucose.[22] In all of our models, of the BBB the concentration of glucose was 10 mM. Most of the other toxic effects of PAO are generally seen at longer time points than those used in this study and can be related to its long-term inhibition of endocytosis.

The first model of the BBB that was investigated in the present study was the in vitro permeability of [^{3}H]DPDPE across BBMEC monolayers. In general, this model of the BBB is used to study the transport of nonradioactive peptides across the BBB, and the typical concentrations used (i.e., 500 μM) will result in the predominant mode of transport being diffusion. In this report, we used [^{3}H]-DPDPE with a specific activity of 42 Ci·mM^{-1}, and 0.33 μCi was added to each of the donor chambers (i.e., approximately 7.6 pM compared with 500 μM of peptide added in cold experiments). This low pmolar concentration of [^{3}H]DPDPE is similar to that used in the in situ model and thus makes comparison easier. If we assume a cerebrovascular surface area of 100 cm^2·g^{-1},[23] the permeability surface area constant (*PC*) for the in situ [^{3}H]DPDPE is 1.46 ± 0.31 cm·min^{-1} $\times$ 10^{-5} compared with a cold 500 μM in vitro value of 49.24 ± 2.78 cm·min^{-1} $\times$ 10^{-4}.[9] This result is a 337-fold difference. In contrast, when the in vitro study is carried out with [^{3}H]DPDPE, the *PC* value is 9.31 ± 0.62 cm·min^{-1} $\times$ 10^{-4}, which is a 64-fold difference. From the previous in situ studies[10,11] it is known that the K_m for DPDPE is 45.6 ± 27.6 μM. Therefore, in the control DPDPE permeability studies, any transport system expressed by the cells would be thoroughly saturated at the 500 μM concentration. However, in the present study, the [^{3}H]-DPDPE is at a concentration of 7.6 pM, which would not saturate the transporters. Therefore, it is likely that a larger proportion of the permeability across the membranes is due to a transport mechanism other than diffusion. Previous studies have used this model to study the transport of insulin[24] and angiotensin II.[13] These peptides are biologically important and use receptor-mediated transcytosis to enter the brain. Furthermore, both of these previous studies used concentrations of PAO similar to those used in this study, and neither group reported any adverse affects of PAO on the membranes or cells studied. In the present study, PAO lead to a significant decrease in the permeability of DPDPE across BBMEC monolayers (Figure 1). The basal permeability of the monolayers to [^{14}C]sucrose was not effected by PAO (data not shown), indicating that the monolayer was not adversely affected by the PAO. In previous studies, it has been shown that the presence of high glucose will protect cell viability against PAO,[22] and 10 mM glucose was used in these experiments. The higher concentration of PAO (100 μM) led to an inhibition at all time points of DPDPE permeability. There was a dose-dependent effect on the inhibition between the 10 and 100 μM concentrations. The 10 μM concentration significantly inhibited the permeability of [^{3}H]DPDPE only at 90 and 120 min. The [^{3}H]DPDPE (7.6 pM) permeability in the presence of 100 μM PAO was significantly different from the 10 μM PAO concentration at all time points except the 120-min time point.

The uptake of [^{3}H]DPDPE into confluent monolayers of BBMEC cells was also studied. The uptake of DPDPE by the cells was linear with time (Figure 2). To assess the actual uptake into the cell, an acid wash was carried out. The peptide that was acid sensitive represented the amount of peptide bound to the outer membrane of the cells. The acid-sensitive fraction remained fairly consistent throughout the time-course of the uptake, with no significant difference in binding to the cells at any time point. PAO has been shown to cross-link vicinal sulfydryl groups to form stable ring structures, thus inhibiting the internalization of receptors.[25] However, it is also possible that PAO could be preventing DPDPE from binding to sites on the membrane responsible for its uptake. PAO (10−200 μM) significantly reduced the uptake of [^{3}H]DPDPE (Figure 3), without affecting the acid-sensitive portion (except at 200 μM). Thus it is evident that PAO was preventing internalization rather than cell surface binding of the DPDPE. Similar results have been seen with other peptides, such as angiotensin II in rat myometrial cells[26] and BBMEC.[13]

For both of the in vitro models of the BBB, the cells were grown without co-culture with astrocytes or astrocyte-conditioned media. A number of groups have reported improved BBB characteristics due to addition of either astrocytes or media from astrocytes.[27,28] However, in studies carried out in this laboratory, we have found no significant change in either trans-endothelial resistance or sucrose crossing of monolayers due to either astrocyte-conditioned media or co-culture.[29] In fact, our sucrose space and trans-endothelial resistance measurements indicate that we have a tighter in vitro BBB than those reported by other groups who use co-culture.[27,28]

The in situ perfusion model used in this study has been previously utilized to study the transport of a number of peptide neuropharmaceuticals across the BBB.[3,4,10,30] The basal permeability of the BBB has been extensively studied using inert nontransported substances such as sucrose. In this study, the sucrose space was measured to assess the effect of PAO on the basal permeability of the BBB. The values measured ranged from 0.12 ± 0.002 to 0.13 ± 0.002 μL·min^{-1}·g^{-1} for basal and PAO-treated rats, respectively. These values are well within the range of normal sucrose spaces reported previously in the literature.[31,17,10] It is thus

Table 3—Comparison of *PC* Values from Literature and Those Calculated from This Study for DPDPE

model of BBB	*PC*, cm·min^{-1}	reference
BBMEC permeability with 500 μM DPDPE	49.24×10^{-4}	Weber et al., 1993
BBMEC permeability with [^{3}H]DPDPE	9.31×10^{-4}	present study
in situ with [^{3}H]DPDPE	1.46×10^{-5}	Williams et al., 1996
	2.61×10^{-5}	present study
uptake studies with [^{3}H]DPDPE	9.56×10^{-5}	present study

clear that, within the experimental parameters studied, PAO has no significant effect on the basal permeability of the BBB for a 20-min exposure. Furthermore, 100 μM DPDPE did not significantly affect the vascular space under the current experimental conditions. The uptake of DPDPE was inhibited in a dose-dependent manner by 10−150 μM PAO (Figure 5.). The inhibition caused by 100 μM PAO was not significantly different from that caused by 100 μM DPDPE, and no additive effect was observed on co-administration (Figure 6). At the 200 μM concentration of PAO, there was a slight yet not statistically significant rise in the uptake of DPDPE into rat brains. This rise was obviously not due to an increased basal permeability of the BBB because at the same concentration there was no increase in the sucrose space of the brain. Furthermore, a similar effect was not seen in the cellular uptake model.

PAO has been shown to have similar effects on the uptake/transport of DPDPE in two in vitro and one in situ model of BBB transport. It is generally difficult to compare in vivo and in vitro studies of the BBB. However, in this study, all the chemicals used were similar and the isotope was from the same batch and equivalent concentrations of isotope were used in each experiment. To make comparison of the three models easier, the flux and K_{in} values were converted to a *PC* value that was already described for the in situ experiments. The *PC* values for the uptake were calculated on the assumption that the mean protein value was 59.6 μg of protein per well (based on 162 individual wells) and the surface area of the wells is fixed at 2 cm^2. The *PC* values from this study and others (Table 3.) show that the BBMEC uptake studies have *PC* values 3.6 times higher than the in situ studies.

PAO has been used at concentrations ranging from 1 to 100 μM in a number previous studies and has resulted in variable levels of inhibition on receptor-mediated endocytosis. For example, Bradley et al.[32] showed that the receptor-mediated endocytosis of low-density lipoprotein by human umbilical vein endothelial cells was reduced 66% by 1 μM PAO. Wiley et al.[16] used a range of PAO concentrations (10^{-4}−10^{-7} M) to inhibit receptor-mediated endocytosis of EGF by human fibroblast cells, finding that there was almost total inhibition at 10 μM. In contrast, angiotensin II receptor-mediated transcytosis across endothelial cells was significantly decreased by 25 μM PAO, though it required 100 μM PAO to significantly reduce uptake into the cell.[13] These differences in the required concentrations of PAO to cause an effect may be linked to the differences in the endocytotic rate constants for each receptor studied and to the number of receptors expressed in a given system. For example, EGF receptors have endocytotic rate constants ranging from 0.03 to 0.3 min^{-1}, depending on cell type.[33] Also, receptor distribution and density varies from cell type to cell type, for example, the transferrin receptor is constitently expressed at a high density on the BBB endothelial cells and relatively low in other capillary beds.[34] The fact that we were unable to totally inhibit the permeability across BBMEC cells on filters is not surprising. The *PC* value takes into account the diffusion across the membranes between cells (by calculating the *PC* value from linear regression), however, it does not divide the transport into saturable and nonsaturable mechanisms. The evidence that we present in this study is that the saturable component of DPDPE transport is inhibited by PAO, thus implicating clathrin-dependent receptor-mediated endocytosis. It has been shown that DPDPE also uses a nonsaturable diffusional mechanism to cross the BBB.[11] This mechanism would not be affected by PAO and thus should not be inhibited. Therefore, we would be more surprised if we totally inhibited all DPDPE transport.

Together with data from previous studies, we can now state that DPDPE crosses the BBB in part via an endocytotic (transport) mechanism. PAO has been shown to inhibit some fluid phase endocytosis[25] at higher concentrations. Although this form of endocytosis may explain some of the DPDPE transport, it would not explain the saturable component of the transport. Furthermore, if the PAO were indeed inhibiting the nonsaturable component of the transport, it would be reasonable to assume that addition of a high concentration of DPDPE to the in situ media would lead to an additive inhibition. This assumption is evidently not the case (Figure 6), and the likely saturable mechanism is endocytosis. The two saturable forms of endocytosis are adsorptive endocytosis and receptor-mediated endocytosis. In an earlier study, the competitive adsorptive endocytosis inhibitor poly-L-lysine failed to reduce DPDPE uptake into rat brain,[11] suggesting that DPDPE does not bind to the anion-rich sites in the cell membrane and thus does not use classical adsorptive endocytosis. DPDPE has been shown to have a K_m in the micromolar range,[11] which is indicative of a carrier-mediated rather than receptor-mediated process.[35] This result would indicate that the mechanism of DPDPE uptake is unlikely to be via a normal receptor-mediated endocytotic effect. However, DPDPE transport could be explained by DPDPE binding specifically to a protein/receptor in an area that has a high basal endocytotic rate (for example, clathrin-coated pits) and entering the cell via receptor turnover rather than stimulating its own endocytosis. PAO has previously been shown to reduce the basal endocytotic rate in 3T3 cells[25] and could inhibit DPDPE uptake in this manner. Furthermore, insulin, which binds to its receptor (in clathrin-coated pits) and is internalized, leads to an increase in the basal endocytotic rate and also increases DPDPE uptake.[11]

In conclusion, the present study demonstrates that DPDPE enters the brain via an endocytotic mechanism that is saturable and can be inhibited in a dose-dependent fashion by PAO. The understanding of the transport of DPDPE is important for several reasons. First, a number of opioid peptides based on the structure of DPDPE are currently being developed and studied for analgesia therapy. Second, the disulfide bridge between two D-amino acids has become a common strategy for stabilizing the peptide backbone of peptide pharmaceuticals. By studying the transport of DPDPE, we will be able to determine whether cyclization via disulfide bridges results in a common transport mechanism for peptide drugs.

References and Notes

1. This work was supported by NIDA grants no. DA-06284 and RO1-DA-11271.
2. Egleton, R. D.; Davis, T. P. Bioavailability and transport of peptides and peptide drugs into the brain. *Peptides* **1997**, *18*, 1431−1439.
3. Abbruscato, T. J.; Thomas, S. A.; Hruby, V. J.; Davis, T. P. Brain and spinal cord distribution of biphalin: Correlation

with opioid receptor density and mechanism of CNS entry. *J. Neurochem.* **1997**, *69*, 1236−1245.
4. Abbruscato, T. J.; Thomas, S. A.; Hruby, V. J.; Davis, T. P. Blood-brain barrier permeability and bioavailability of a highly potent and μ-selective opioid receptor antagonist, CTAP: Comparison with morphine. *J. Pharm. Exp. Ther.* **1997**, *280*, 402−409.
5. Mosberg, H. I.; Hurst, R.; Hruby, V. J., Gee, K.; Yamamura, H. I.; Galligan, J. J.; Burks, T. F. Bis-penicillamine enkephalins possess highly improved specificity toward delta opioid receptors. *Proc. Natl. Acad. Sci., U.S.A.* **1983**, *80*, 5871−5874.
6. Weber, S. J.; Greene, D. L.; Sharma, S. D.; Yamamura, H. I.; Kramer, T. H.; Burks, T. F.; Hruby, V. J.; Hersh, L. B.; Davis, T. P. Distribution and analgesia of [3H][D-Pen2, D-Pen5] enkephalin and two halogenated analogues after intravenous administration. *J. Pharm. Exp. Ther.* **1991**, *259*, 1109−1117.
7. Weber, S. J.; Greene, D. L.; Hruby, V. J.; Yamamura, H. I.; Porreca, F.; Davis, T. P. Whole body and brain distribution of [3H]cyclic[D-Pen2, D-Pen5] enkephalin after inraperitoneal, intravenous, oral and subcutaneous administration. *J. Pharm. Exp. Ther.* **1992**, *263*, 1308−1316.
8. Dupont, A.; Cusan, L.; Garon, M.; Alvarado-Urbina, G.; Labrie, F. Extremely rapid degradation of [3H] methionine-enkephalin by various rat tissues in vivo and in vitro. *Life Sci.* **1977**, *21*, 907−914.
9. Weber, S. J.; Abbruscato, T. J.; Brownson, E. A.; Lipkowski, A. W.; Polt, P.; Misicka, A.; Haaseth, R. C.; Bartosz, H.; Hruby, V. J.; Davis, T. P. Assessment of an in vitro blood-brain barrier model using several [Met5]enkephalin opioid analogues. *J. Pharm. Exp. Ther.* **1993**, *266*, 1649−1655.
10. Williams, S. A.; Abbruscato, T. J.; Hruby, V. J.; Davis, T. P. Permeability of a δ-opioid receptor selective enkephalin [D-penicillamine2,5]enkephalin, across the blood-brain and blood-cerebrospinal fluid barriers. *J. Neurochem.* **1996**, *66*, 1289−1299.
11. Thomas, S. A.; Abbruscato, T. J.; Hruby, V. J.; Davis, T. P. The entry of [D-penicillamine2,5]enkephalin into the central nervous system: saturation kinetics and specificity. *J. Pharm. Exp. Ther.* **1997**, *280*, 1235−1240.
12. Tamai, I.; Sai, Y.; Kobayashi, H.; Kamata, M.; Wakamiya, T.; Tsuji, A. Structure-internalization relationship for adsorptive-mediated endocytosis of basic peptides at the blood-brain barrier. *J. Pharmacol. Exp. Ther.* **1997**, *280*, 410−415.
13. Rose, J. M.; Audus, K. L. Receptor-mediated angiotensin II transcytosis by brain microvessel endothelial cells. *Peptides* **1998**, *19*, 1023−1030.
14. Audus, K. L.; Borchardt, R. T. Characterization of an in vitro blood-brain barrier model system for studying drug transport and metabolism. *Pharm. Res.* **1986**, *3*, 81−87.
15. Audus, K. L.; Borchardt R. T. Bovine brain microvessel endothelial cell monolayers as a model system for the blood-brain barrier. *Ann. N. Y. Acad. Sci.* **1987**, *507*, 9−18.
16. Wiley: H. S.; Cunningham, D. D. A cellular parameter for quantitating receptor mediated endocytosis. *J. Biol. Chem.* **1982**, *257*, 4222−4229.
17. Preston, J. E.; Al-Sarraf, H.; Segal, M. B. Permeability of the developing blood-brain barrier to 14C-mannitol using the rat in situ brain perfusion technique. *Dev. Brain Res.* **1995**, *87*, 69−76.
18. Zlokovic, B. V.; Begley, D. J.; Djuricic, B. M.; Mitrovic, D. M. Measurement of solute transport across the blood-brain barrier in the perfused guinea-pig brain: Method and application to *N*-methylaminoisobutyric acid. *J. Neurochem.* **1986**, *46*, 1444−1451.
19. Tallarida, R. J.; Murray, B. M. *Analysis of Variance. Manual of Pharmacologic Calculations with Computer Programs*, 2nd ed.; Springer-Verlag: New York, 1987; pp 110−124.
20. Bailey, N. T. J. *Regression Analysis. Statistical Methods in Biology*; English University Press: London, 1959; pp 91−99.
21. Roosterman, D.; Roth, A.; Kreienkamp, H. J.; Richter, D.; Meyerhof, W. Distinct agonist-mediated endocytosis of cloned rat somatostatin receptor expresssed in insulinoma cells. *J. Neuroendocrinol.* **1997**, *9*, 741−751.
22. Liebl, B.; Muckter, H.; Doklea, E.; Reichl, F. X.; Fichtl, B.; Forth, W. Influence of glucose on the toxicity of oxophenylarsine in MDCK cells. *Arch. Toxicol.* **1995**, *69*, 421−424.
23. Pardridge, W. M.; Triguero, D.; Yang, J. P. A. Comparisons of in vitro and in vivo models of transcytosis through the blood-brain barrier. *J. Pharm. Exp. Ther.* **1990**, *253*, 884−891.
24. Miller, D. W.; Keller, B. T.; Borchardt, R. T. Identification and distribution of insulin receptors on cultured bovine brain microvessel endothelial cells: Possible function in insulin processing in the blood-brain barrier. *J. Cell Physiol.* **1994**, *161*, 333−341.
25. Frost, S. C.; Lane, M. D.; Gibbs, E. M. Effect of phenylarsine oxide on fluid phase endocytosis: Further evidence for activation of the glucose transporter. *J. Cell. Physiol.* **1989**, *141*, 464−474.
26. Lazari, M. F.; Porto, C. S.; Freymuller, E.; Abreu, L. C.; Picarelli, Z. P. Receptor-mediated endocytosis of angiotensin II in rat myometrial cells. *Biochem. Pharmacol.* **1997**, *54*, 399−408.
27. Dehouck, M. P.; Jolliet-Riant, P.; Bree, F.; Fruchart, J. C.; Cecchelli, R.; Tillement, J. P. Drug transfer across the blood-brain barrier: Correlation between in vitro and in vivo models. *J. Neurochem.* **1992**, *58*, 1790−1797.
28. Raub, T. J.; Kneutzel, S. I.; Sawada, G. A. Barrier tightening by a factor released from astroglioma cells. *Exp. Cell. Res.* **1992**, *199*, 330−340.
29. Abbruscato, T. J.; Davis, T. P. Combination of hypoxia/aglycemia compromises blood-brain barrier integrity. *J. Pharm. Exp. Ther.*, in press.
30. Egleton, R. D.; Abbruscato, T. J.; Thomas, S. A.; Davis, T. P. Transport of opioid peptides into the central nervous system. *J. Pharm. Sci.* **1998**, *87*, 1433−1439.
31. Zlokovic, B. V.; Banks, W. A.; Kadi, H. E.; Erchegyi, J.; Mackic, J. B.; McComb, J. G.; Kastin, A. J. Transport, uptake and metabolism of blood-bourne vasopressin by the blood-brain barrier. *Brain Res.* **1992**, *590*, 213−218.
32. Bradley, J. R.; Johnson, D. R.; Pober, J. S. Four different classes of inhibitors of receptor mediated endocytosis decrease tumour necrosis factor-induced gene expression in human endothelial cells. *J. Immunol.* **1993**, *150*, 5544−5555.
33. Koenig, J. A.; Edwardson, J. M. Endocytosis and recycling of G protein-coupled receptors. *Trends Pharmacol. Sci.* **1997**, *18*, 276−287.
34. Jefferies, W. A.; Brandon, M. R.; Hunt, S. V.; Williams, A. F.; Gatter, K. C.; Mason, D. Y. Transferrin receptor on the endothelium of brain capillaries. *Nature* **1984**, *312*, 162−163.
35. Zlokovic, B. V.; Hyman, S.; McComb, J. G.; Lipovac, M. N.; Tang, G.; Davson, H. Kinetics of arginine-vasopressin uptake at the blood-brain barrier. *Biochim. Biophys. Acta* **1990**, *1025*, 191−198.

JS980410+

Validation of a Biophysical Drug Absorption Model by the PATQSAR System†

MARIVAL BERMEJO, VIRGINIA MERINO, TERESA M. GARRIGUES, JOSÉ M. PLA DELFINA, ANTONIO MULET,‡ PATRICK VIZET,§,|| GERARD TROUILLER,§ AND CHRISTIANE MERCIER*,||

Contribution from *Department of Pharmaceutics, Faculty of Pharmacy, University of Valencia, Spain.*

Received September 15, 1998. Final revised manuscript received December 30, 1998.
Accepted for publication January 8, 1999.

Abstract □ Absorption rate constants (in situ rat gut technique) and in vitro antibacterial activities of twenty fluoroquinolones have been evaluated. A biophysical model that relates the absorption of the compounds with their lipophilicity was fitted. The model considers the absorption process from the intestinal lumen as the sum of two resistances in series: aqueous diffusional barrier and lipoidal membrane. Even if partitioning into the membrane and membrane diffusion are both enhanced for lipophilic compounds, the absorption rate constant is limited by the aqueous diffusion. To estimate the influence of structural modifications on each property and to establish the role of lipophilicity in controlling in situ absorption and in vitro antibacterial activity, the PATQSAR search system is used to construct structure–property relationships. The structural models, which explain 99% of the total variance of each physicochemical property and 96% of each in vitro biological activity, provide an explicit and precise interpretation of lipophilicity, absorption, and antimicrobial activity. The results confirm the important role of lipophilicity in controlling absorption, as pointed out by the biophysical model for the piperazinyl series, and suggest the introduction of electronic factors in order to extend the model to heterologues. They also justify the mechanism by which quinolones are assumed to induce antibacterial activity.

Introduction

Absorption−lipophilicity correlations can help to explain absorption mechanisms by passive diffusion. The Plá-Delfina and Moreno absorption model[1] considers that in the small intestine diffusion can occur by two parallel paths: the aqueous pores and the lipoidal membrane. The actual absorption rate represents the sum of the rate constants governing the penetration into the lipoidal membrane and across the aqueous pores. When the molecular weight of the compounds is above approximately 250 Da, diffusion by the aqueous pathway becomes impossible, and the absorption is reduced to membrane penetration. In this case, the Higuchi-Ho equation[2] is able to describe in more detail the two steps involved in absorption. This equation considers that there are two resistances in series associated with the stagnant aqueous layer and the lipoidal barrier. In the present study, a lipophilicity−absorption relationship for homologous series of compounds is established by means of a previously published[3] modification of the Higuchi-Ho equation, to check its utility and predictive potentialities.

In the field of computer-aided design, we have developed an interactive graphic system, PATQSAR (Population Analysis by Topology-based QSAR), based on the topological DARC/PELCO methodology,[4−6] for predicting physicochemical or biological properties of molecules, starting from their characteristic structural elements and the appropriate experimental data. With a view to validating the absorption−lipophilicity correlation established with the compartmental model and to gaining insight into the mechanism by which fluoroquinolones induce antimicrobial activity, we use our general QSAR search procedure to construct structure−absorption, structure−lipophilicity, and structure−activity correlations.

Materials and Methods

Test Compounds—Sixteen 6-fluoro-7-piperazinyl quinolones derived from norfloxacin and ciprofloxacin by progressive alkylation of *N′*-piperazinyl,[7] as well as four additional compounds, one homologue and three related heterologues, were provided by Cenavisa S. A. Laboratories (I+D Department, Reus, Spain).[8]

Each compound was identified by its infrared spectrum. Purity was checked by ion-pair reversed phase HPLC and shown to be above 99.9% in all cases. The names, structures, and molecular weights of the compounds are given in Table 1. The piperazinyl quinolones exhibited a pK_{a1} between 5.5 and 6.5, and a pK_{a2} between 7.5 and 8.5, and at the working pH (7.00) they were in their zwitterionic form. The heterologues have only one pK_a value between 6.0 and 7.0.

Absorption Studies—*Biological Technique*—The in situ rat gut technique, adapted as previously described,[9,10] was performed using the whole small intestine of male Wistar rats weighing 210−295 g (six animals per compound). To prevent enterohepatic recycling, the bile duct was cannulated before the perfusion. An isotonic saline solution was prepared and buffered to pH 7.00 by addition of 10% (v/v) of 0.066 M Sörensen phosphate solution. This concentration prevents the disturbing effects of phosphates on the intestinal membrane[11] while maintaining the ionization of the substances. Test solutions were prepared immediately before use by dissolving a fixed amount of each compound in the vehicle solution (w/v), depending on its solubility. The concentrations, shown in Table 1, are low enough to avoid precipitation in the lumen during the absorption tests. After dissolving the xenobiotic, the pH of the solution was checked and readjusted when necessary. The perfusate was sampled into silanized glass tubes at fixed times after 5 min, at intervals of 5 min. All samples were analyzed immediately.

Water Reabsorption Studies—The volume of the perfused solutions at the end of the experiments was significantly reduced (up to 20%), and a correction became necessary in order to calculate the absorption rate constants accurately. If this process is not considered, the disappearance from the gut is underestimated and the absorption rate constant is incorrectly calculated. Water reabsorption is an apparent zeroth-order process.[10,12] A method based on direct measurement of the remaining volume of the test solution was employed.[7] The volume V_0 at the beginning of the experiment for each compound was determined on groups of three animals, while the volume V_t at each time t was measured on every animal used. The corrected concentration C_t, which represents the concentration in the gut that would exist in the absence of the water reabsorption process, was deduced from the concentration C_e analyzed in the sample at the same time t, by the following equation:

* Corresponding author: Christiane Mercier, ITODYS, 1 rue Guy de la Brosse, 75005 Paris, France. Phone: 33-1-44276803. Fax: 33-1-44276814. E-mail: mercier@itodys.jussieu.fr.

† The results were presented in part at the Fourth International Conference on Drug Absorption, June 13−15, 1997, Edinburgh, UK.

‡ Department of Food Technology, Polytechnic University of Valencia, Spain.

§ Centre d'Etudes du Bouchet, France.

|| ITODYS, Université Paris VII, France.

10.1021/js980370+ CCC: $18.00
Published on Web 03/05/1999

Table 1—Names, Structures, Molecular Weights and Perfusion Concentrations of Substituted 6-Fluoroquinolones

Additional 6-fluoroquinolones

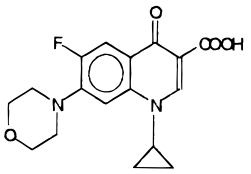

NV 8804, 1-cyclopropyl-6-fluoro-1,4-dihydro-7-(4-morpholinyl)-4-oxo-3-quinoline carboxylic acid
Perfusion concentration 50μg/mL MW=330

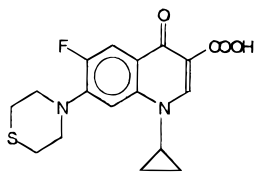

NV 8919, 1-cyclopropyl-6-fluoro-1,4-dihydro-7-(4-thiomorpholinyl)-4-oxo-3-quinoline carboxylic acid
Perfusion concentration 11μg/mL MW=349

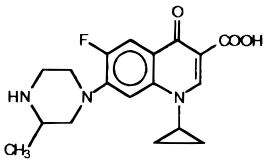

CNV 97100, 1-cyclopropyl-6-fluoro-1,4-dihydro-7-(3-methyl-1-piperazinyl)-4-oxo-3-quinoline carboxylic acid
Perfusion concentration 100μg/mL MW= 345

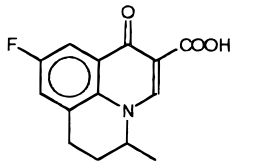

Flumequine, 9-fluoro-6,7-dihydro-5-methyl-1-oxo-1H,5H-pyrido[3,2,1-ij] quinoline-2-carboxylic acid
Perfusion concentration 100μg/mL MW= 261

6-fluoro-7-piperazinylquinolones

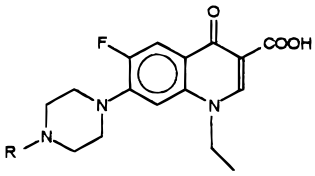

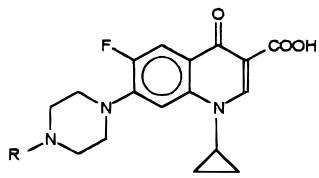

R		MW	Perfusion concentration (μg/mL)	R		MW	Perfusion concentration (μg/mL)
H-	Norfloxacin, 1-ethyl-1,4-dihydro-4-oxo-6-fluoro-7-(N-piperazinyl)-3-quinoline carboxylic acid	319	100	H-	Ciprofloxacin, 1-cyclopropyl-1,4-dihydro-4-oxo-6-fluoro-7-(N-piperazinyl)-3-quinoline carboxylic acid	331	100
CH_3-	N'-methylnorfloxacin	333	100	CH_3-	N'-methylciprofloxacin	345	100
CH_3-CH_2-	N'-ethylnorfloxacin	347	100	CH_3-CH_2-	N'-ethylciprofloxacin	359	100
CH_3-$(CH_2)_2$-	N'-propylnorfloxacin	361	100	CH_3-$(CH_2)_2$-	N'-propylciprofloxacin	373	100
CH_3-$(CH_2)_3$-	N'-butylnorfloxacin	375	100	CH_3-$(CH_2)_3$-	N'-butylciprofloxacin	387	80
CH_3-$(CH_2)_4$-	N'-pentylnorfloxacin	389	50	CH_3-$(CH_2)_4$-	N'-pentylciprofloxacin	401	50
CH_3-$(CH_2)_5$-	N'-hexylnorfloxacin	403	25	CH_3-$(CH_2)_5$-	N'-hexylciprofloxacin	415	40
CH_3-$(CH_2)_6$-	N'-heptylnorfloxacin	417	6	CH_3-$(CH_2)_6$-	N'-heptylciprofloxacin	429	6

$$C_t = C_e \frac{V_t}{V_0} \qquad \text{(eq 1)}$$

Absorption Rate Constants—The absorption rate constants k_a were determined by nonlinear regression analysis of the corrected concentrations C_t versus time, using Sigma Plot 2.0 (Jandel Scientific), as it had been previously established that the process follows first-order kinetics. To prevent adsorption on the intestinal mucosa and residual sample dilution effects,[10,13] only the calculated values after 5 min, listed in Table 2, were used for regression, as it was found that after that time adsorption equilibrium was generally reached.

Lipophilicity Indexes—*Partition Coefficients*—Bulk phase partition coefficients, *P*, between *n*-octanol (Merck analytical grade) and of 0.066 M Sörensen phosphate buffer, pH 7.00, were determined for each compound of the series. Six values per compound were used to establish the average value to be used in the correlations. These values are reported in previous papers.[3,14]

Number of Methylene Groups—This was used as a lipophilicity index free of the influence of solvent interactions. Provided that a perfect homologous series is studied, it has been demonstrated to be equivalent to other indexes such as partition coefficients, *P*,[1,15] or capacity factors, *K*.

Analysis of the Samples—An original HPLC procedure was used to quantify the solute concentration in both biological and partition samples. The analysis was carried out on a Novapak C18 column (3.9 × 150 mm), using as mobile phase a mixture of methanol and 15 mM phosphate buffer, adjusted to pH 2.4 with orthophosphoric acid. The percentage of each component of the mobile phase was selected for each compound of the series in order to obtain the best chromatographic resolution. The equipment consisted of a Series III Hewlett-Packard quaternary pump, a Rheodyne injector, a 1046 Hewlett-Packard fluorescence detector, and a 3395 Hewlett-Packard integrator. Quantification was done by fluorometry, with excitation and emission wavelengths of 338 and 425 nm, respectively. This technique offers a high degree of selectivity and specificity. The procedure was validated for inter- and intraday runs before use. Accuracy was estimated from the percentage error associated with measuring 5 to 8 standards, analyzed at least three times. Accuracy was demonstrated to be

Table 2—Observed and Calculated Partition Coefficients, Absorption Rate Constants, and in Vitro Antibacterial Activities

compound	log *P*			k_a (h^{-1})	log k_a		log 1/MIC *E. coli*		log 1/MIC *Staph.*	
	P	obsd	calcd eq 3		obsd	calcd eq 4	obsd	calcd eq 5	obsd	calcd eq 6
norfloxacin	0.03[b]	–1.55 (0.03)[b]	–1.60	0.42[b]	–0.38 (0.07)[b]	–0.32	1.00[b]	1.03	0.30	0.33
N′-methylnorfloxacin	1.88[b]	0.27 (0.01)[b]	0.22	1.92[b]	0.28 (0.04)[b]	0.32	1.00[b]	1.03	0.30	0.33
N′-ethylnorfloxacin	2.36[b]	0.37 (0.01)[b]	0.48	2.75[b]	0.44 (0.03)[b]	0.46	0.70[b]	0.75	0.30	0.33
N′-propylnorfloxacin	11.28[b]	1.05 (0.01)[b]	1.01	4.07[b]	0.61 (0.04)[b]	0.60	0.40[b]	0.47	0.00	0.05
N′-butylnorfloxacin	30.34[b]	1.48 (0.02)[b]	1.54	5.59[b]	0.75 (0.02)[b]	0.74	0.40[b]	0.20	–0.30	–0.23
N′-pentylnorfloxacin	127.67[b]	2.11 (0.02)[b]	2.08	5.69[b]	0.76 (0.04)[b]	0.74	0.40[b]	0.20	–0.30	–0.51
N′-hexylnorfloxacin	515.95[b]	2.71 (0.01)[b]	2.61	5.98[b]	0.78 (0.05)[b]	0.74	–0.20[b]	–0.08	–0.60	–0.80
N′-heptylnorfloxacin	1664.69[c]	3.22 (0.02)[b]	3.14	6.00[b]	0.78 (0.04)[b]	0.74	–0.51[b]	–0.35	–1.20	–1.07
ciprofloxacin	0.08[c]	–1.12 (0.02)[c]	–1.07	0.63	–0.20 (0.06)	–0.26	1.60	1.58	0.60	0.61
N′-methylciprofloxacin	1.42[c]	0.15 (0.06)[c]	0.22	2.55	0.41 (0.04)	0.38	1.60	1.58	0.60	0.61
N′-ethylciprofloxacin	3.38[c]	0.53 (0.01)[c]	0.48	3.52	0.55 (0.03)	0.52	1.30	1.30	0.60	0.61
N′-propylciprofloxacin	11.86[c]	1.07 (0.01)[c]	1.01	4.79	0.68 (0.05)	0.66	1.00	1.03	0.30	0.33
N′-butylciprofloxacin	35.30[c]	1.55 (0.04)[c]	1.54	5.69	0.76 (0.03)	0.80	0.70	0.75	0.30	0.05
N′-pentylciprofloxacin	116.04[c]	2.06 (0.01)[c]	2.07	6.04	0.78 (0.02)	0.80	0.70	0.75	–0.30	–0.23
N′-hexylciprofloxacin	361.71[c]	2.56 (0.02)[c]	2.61	6.03	0.78 (0.04)	0.80	0.40	0.47	–0.60	–0.51
N′-heptylciprofloxacin	1043.96[c]	3.02 (0.04)[c]	3.14	6.08	0.78 (0.04)	0.80	0.40	0.20	–0.90	–0.80
CNV8919	54.71	1.74 (0.02)	1.76	7.52	0.88 (0.03)	0.87				
flumequine	9.38	0.97 (0.02)	0.96	6.87	0.84 (0.04)	0.82				
CNV97100	0.09	–1.07 (0.06)	–1.07	1.24	0.09 (0.07)	0.09				
CNV8804	9.37	0.97 (0.01)	0.96	7.10	0.85 (0.06)	0.87				
mean SD[a]		(0.02)			(0.04)					

[a] SD: standard deviation. [b] Data from ref 3. [c] Data from ref 14.

better than 15%, regardless of the analyte concentration. Precision was calculated as the coefficient of variation of five determinations over the same standards, and it was shown to be better than 5%. Linearity was established over the range of concentrations present in the samples for every compound (correlation coefficients always over 0.999).

In Vitro Antibacterial Activity—The lowest concentration of the drug that inhibited the growth of 90% of the strains on agar was taken as the minimum inhibitory concentration, MIC_{90}. It was determined on 100 strains of *Escherichia coli*, using the agar plate dilution method. The procedure was validated by means of the following typified strains: *Pseudomonas aeruginosa* ATCC 27853, *E. coli* ATCC 25922, *Streptococcus faecalis* ATCC 29212, and *Staphilococcus aureus* ATCC 29213. The assay was carried out following the specifications of the National Committee for Clinical Laboratory Standards.[16] Mueller-Hinton agar plates were prepared with known concentrations of the quinolone tested, covering a suitable range. The bacterial suspension was then inoculated into the plates with a Steers replicator. The plates were cultured at 37 °C for 20 h and evaluated immediately thereafter.

Fitting of Models to the Data—To test the pertinence of the absorption rate constants for establishing correlations, their values were compared with each of those by means of ANOVA after the homogeneity of the variance had been tested using the Cochran test.

Absorption−Lipophilicity Relationship—A biophysical compartmental model, which considers the total resistance to passive absorption as the sum of two resistances in series, was fitted. As previously pointed out,[3] the partial resistances correspond to the aqueous resistance, produced by the stagnant aqueous layer and to the lipoidal resistance due to the membrane. The original equation[2,3,17] was adapted assuming that the permeability in the aqueous layer depends inversely on the square root of the molecular weight and that the permeability in the membrane lipoidal phase is related to lipophilicity. The equation can be written as follows:

$$k_a = \frac{CP^d}{1 + E\sqrt{M}P^d} \qquad \text{(eq 2)}$$

where *C*, *d*, and *E* are fitting parameters. Curve fitting was carried out only for perfectly homologous compounds. All fitting operations were run on a computer using the PCNONLIN 4.0 program. For more complicated fitting models, PCNONLIN was used instead of Sigma Plot because it is a more powerful software which uses several algorithms to optimize the objective function, provides more statistical information about the parameters obtained, and gives the standard deviation of the predicted values. To appreciate the goodness of fit, the correlation coefficients between the experimental and model-predicted k_a values were calculated. Precision in the estimation of the parameters, and the standard deviation, *s*, were also used as criteria for evaluating the results.

Structural Models—Four correlations were run on the compounds and the available data for each property. The experimental population consisted of 20 compounds for the absorption rate and partition coefficients, and 16 for in vitro antibacterial activity. The models were established by using PATQSAR,[18] a system for QSAR search based on the DARC/PELCO topological procedure.[4−6]

Data are encoded directly by an interactive procedure. The compounds are represented as ordered chromatic graphs. Their superposition generates the population trace, which contains all the elements required for constructing the initial structural variable automatically. Compounds are described by a vector of discrete structural variables, which have values of 0 or 1 depending on their absence from or presence in the molecule, respectively.

These primary variables can be further combined into more complex ones:

Interaction variables designate the simultaneous existence of two or more basic structural elements, each of which can exist without the other; they are written as $V_1{*}V_2$;

Exclusion variables designate the existence of a basic element in the absence of another one, which can exist simultaneously; they are represented as $V_1{*}\overline{V_2}$;

Equivalence variables make elements, which belong to homogeneous series and have closely similar effects on the property, equivalent; they are written as $V_1 = V_2$.

Optimal correlations were sought on the basis of the criterion of experimental precision (± 0.04 for log k_a and ± 0.02 for log *P*). For each model an exploratory correlation was run on the available data with all the topochromatic "sites" as parameters, i.e., atoms and bonds different from the common structure or "focus". Deviations from additivity were taken into account by introducing interaction sites. Regularities, which allow certain structural effects to be generalized, were detected by introducing equivalence sites. At each step the new SAR is set up by multiple linear regression analysis. A stepwise module is available to detect the most significant parameters.

Results and Discussion

Lipophilicity Indexes—The *n*-octanol/water partition coefficients listed in Table 2 undoubtedly constitute the most classic index. To study the effect of alkylation on lipophilicity, the relationships between log *P* and the number of methyl groups of homologous compounds were established for each series. Statistical comparison (*t* test) of their slopes demonstrated that they are the same. Therefore, the overall correlation is shown in Figure 1. In such a correlation the intercept should represent the log *P* value of the parent compounds of the series (i.e. norfloxacin and ciprofloxacin), but it does not. This can be interpreted as the result of specific interactions between these elements and the solvent, promoted by the absence of the methyl substituent. This effect has been reported for many parent

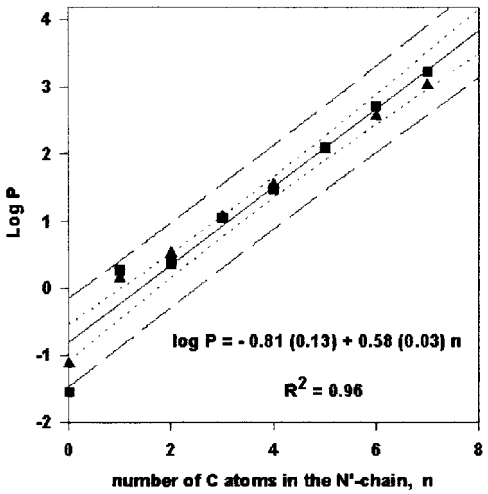

Figure 1—Relationship between partition coefficient and number of methylene groups for *N′*-alkylnorfloxacin (■) and *N′*-alkylciprofloxacin (▲). The dotted and dashed lines represent the 95% confidence (•••) and prediction (- - -) intervals, respectively.

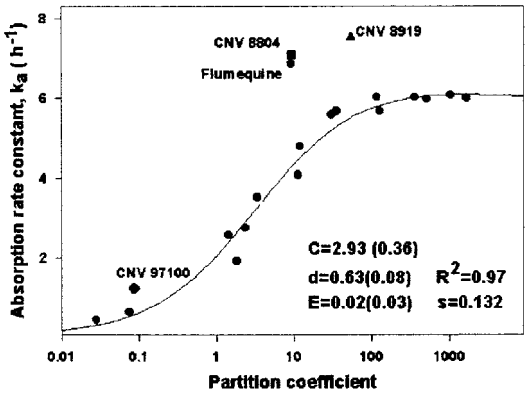

Figure 2—Relationship between absorption and partition coefficient for perfectly homologous compounds. The line represents the best fit of eq 2: $k_a = (2.60P^{0.72})/(1 + 0.02M^{1/2}P^{0.72})$. The points associated with the heterologues are superimposed: CNV 8804 (■); CNV 8919 (▲); flumequine (●).

compounds of very different homologous series. The methyl derivatives, on the contrary, show higher lipophilicity indexes than predicted. This effect, known as the "first element effect", can easily be explained if we consider the fact that the methyl group has a larger volume than the hydrogen of the parent ring. Therefore, the substituent significantly reduces the water to *n*-octanol transfer energy. Obviously, this substituent produces greater changes than subsequent alkylation. Finally, the slope of the correlation, which represents $\Delta\pi$ for the series, is in good agreement with Hansch's predictions.

Absorption–Lipophilicity Correlation—Applying the biophysical model to the 17 6-fluoro-7-piperazinylquinolones leads to a very significant absorption–lipophilicity correlation ($R^2 = 0.97$) represented in Figure 2 where the fitting parameters are listed along with the statistical data. As can be seen, the absorption rate constant increases with lipophilicity up to a certain value because of the limiting effect of water diffusion through the stagnant layer. Therefore, there is a practical limit to the lipophilicity that improves the intestinal absorption rate. The k_a and P values of the three heterologous compounds have also been plotted in Figure 2. Their absorption rate constants are higher than those predicted by the correlation from their lipophilicity index. This could be due to the electronic changes that the new substituents introduce into the molecule, which probably modify their interactions with the absorptive membrane. Nevertheless, the optimal values for lipophilicity that could be predicted reproduce the value obtained by the correlation for homologous compounds.

Structural Models—*Lipophilicity–Structure Model*—The results are displayed on the population trace diagram in Table 3. The relationship can be written:

$$\log P = 0.96(\pm 0.04) - 2.56(\pm 0.05)\ \text{N}\bigcirc\text{N} + 0.81(\pm 0.03)\ \text{S}\bigcirc\text{N}$$

$$+1.82(\pm 0.05)C_1 + 0.27(\pm 0.01)C_2 + 0.54(\pm 0.02)\sum_{i=3}^{7} C_i + 0.54(\pm 0.02)\ \text{CH}_2\!\curvearrowright\! {}^{*}\overline{C_1}$$

$R^2 = 0.99$ F = 2556 s = 0.07 df = 16 n = 20 (eq. 3)

where:

ΣC_i groups the chain-lengthening atoms; $\text{CH}_2\!\curvearrowright\! {}^{*}\overline{C_1}$ represents the methylene bridge in the absence of chain-lengthening on the piperazinyl ring: the contribution of the methylene bridge is zero when C_1 is present.

The structural elements, whose contributions are 0.27, 0.54, and 0.81, are grouped in an equivalence variable where they are weighted as indicated below:

$$C_2 = 1,\ C_3 = C_4 = C_5 = C_6 = C_7 = \text{CH}_2\!\curvearrowright\! {}^{*}\overline{C_1} = 2,\quad \text{S}\bigcirc\text{N} = 3$$

Contributions of the different heterocycles take into account the absence of the flumequine moiety represented by the dotted line in Table 3.

The lipophilicity, as expected, is markedly reduced by introducing a piperazinyl ring at position 7. Replacing the N′ nitrogen of this ring by a different heteroatom, oxygen or sulfur, produces a more lipophilic molecule. The lipophilicity is decreased by a higher electron-donating effect of the substituent which enhances its solvation by water. It is greatly increased upon methylation of the *N′*-piperazinyl nitrogen (+1.82) and regularly enhanced by lengthening or branching of the *N*-alkyl chains (+0.54) except in the β positions with respect to the N′ nitrogen. The contribution of the first methyl to total lipophilicity is about three times that of the chain-lengthening atoms. This can be explained by the fact that secondary amines have a higher polarity and affinity for the aqueous phase and interact with it more easily. Replacing the hydrogen by a donor substituent, such as the methyl group, reduces the transfer energy from water into *n*-octanol.[19] The small contribution of the β chain-lengthening atom (0.27) compensates the first element effect. Replacing the *N*-ethyl by a *N*-cyclopropyl in position 1 increases lipophilicity by the same 0.54 value but has no effect in the presence of a N′-chain. The influence of the methylene bridge is quantified by the interaction–exclusion variable. Surprisingly, introducing a methyl group on the piperazinyl ring at the β position with respect to the N′ nitrogen has no effect.

Absorption–Structure Model. The relationship presented in Table 4 can be expressed as:

$$\log k_a = 0.82(\pm 0.02) - 1.13(\pm 0.03)\ \text{N}\bigcirc\text{N} + 0.06(\pm 0.02)\ \text{CH}_2\!\curvearrowright$$

$$+0.35(\pm 0.04)\ C_0 + 0.64(\pm 0.03)\ C_1 + 0.14(\pm 0.01)\sum_{i=2}^{4} C_i$$

$R^2 = 0.99$ F = 387 s = 0.04 df = 14 n = 20 (eq. 4)

In this case the interaction variable is not necessary because the membrane behaves as a less discriminative partitioning system than *n*-octanol/water.

The 7-piperazinyl group reduces both lipophilicity and absorption, as this implies an increase in polarity.[19] Again, replacing the nitrogen of the piperazinyl ring by a different heteroatom, oxygen or sulfur, enhances both lipophilicity

Table 3—Structure–Lipophilicity Model

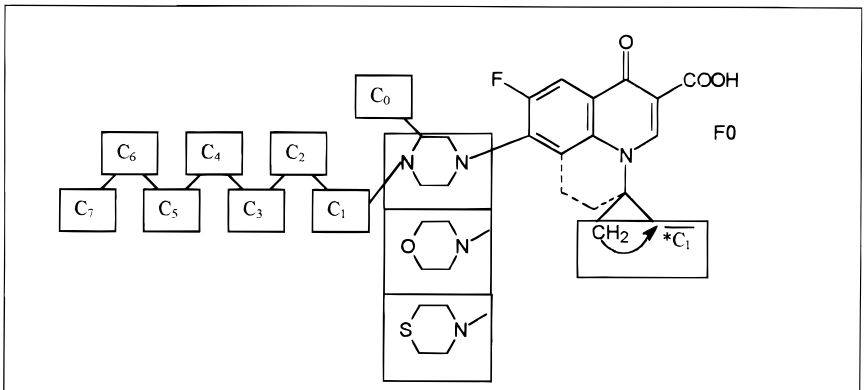

Structural elements	Lipophilicity contributions	Structural elements	Lipophilicity contributions
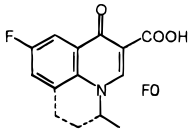	0.96 (± 0.04)	C_0	0.00
		C_1	1.81 (± 0.05)
		C_2	0.27 (± 0.01)
		C_3	0.54 (± 0.02)
	2.56[a] (± 0.05)	C_4	0.54 (± 0.02)
	0.00[a]	C_5	0.54 (± 0.02)
	0.81[a] (± 0.03)	C_6	0.54 (± 0.02)
	0.54[b] (± 0.02)	C_7	0.54 (± 0.02)

[a] Contributions of the heterocyclic rings take into account the absence of the flumequine moiety represented by the dashed line. [b] Contribution of the methylene bridge is zero when C_1 is present.

and absorption. However, the relative contributions are not the same. Starting from flumequine whose lipophilicity is a little higher than absorption, introducing the 7-piperazinyl group decreases lipophilicity (−2.56) much more than absorption (−1.13) while introducing a morpholinyl or a thiopiperidyl group either has no effect on both properties or increases lipophilicity (+0.81) markedly and does not influence absorption. Introducing a methylene bridge into the *N*-ethyl side chain strengthens this effect, leading to heterologues having a higher lipophilicity than absorption, in contrast to the first terms of the piperazinyl series. This could explain why they were found as outliers in the biophysical model. It suggests that absorption is an increasing function of lipophilicity which must be modulated by electronic factors.

In the piperazinylquinolones, each chain-lengthening atom that increases lipophilicity produces an increase in absorption up to four carbons. The relative contributions are also reproduced: the first methyl group produces a bigger increase than any other, as previously seen for log *P*, and further elongation produces a uniform absorption increase. However, in this case the scheme changes, the three last chain-lengthening atoms have no effect on absorption and can be ignored. This fact can be understood if we consider the biophysical model. As stated by Higuchi-Ho, adjacent to the intestinal membrane there is an aqueous diffusion barrier, whose thickness creates an aqueous resistance to solute diffusion which has to be overcome before partitioning into the membrane. This step represents the absorption rate-limiting process. Even if partitioning into the membrane and membrane diffusion are enhanced for lipophilic compounds, the absorption rate has a practical limit fixed by the aqueous diffusion,[3] as is clear from the zero contribution of the three last chain-lengthening elements.

Additionally, introducing a 3′-methyl group or a 1-cyclopropyl has a slightly different effect on absorption and lipophilicity: 3′-methyl, which has no influence on lipophilicity, increases absorption weakly; 1-cyclopropyl, which has no influence on absorption, increases lipophilicity but only for the first term.

Structure–Antibacterial Activity Models—The results are displayed on the population trace diagrams in Tables 5 and 6. The equations can be written:

$$\log(1/MIC)_{E.Coli} = 1.03\,(\pm 0.03) - 0.28\,(\pm 0.01)\sum_{\substack{i=2\\ i\neq 6}}^{7} C_i + 0.56\,(\pm 0.02)\ \ CH_2$$

$$R^2 = 0.96 \quad F = 371 \quad s = 0.11 \quad df = 14 \quad n = 16 \qquad \text{(eq.5)}$$

The two structural elements are grouped in an equivalence variable, where they are weighted as indicated:

$$C_2 = C_3 = C_4 = C_5 = C_7 = -1, \quad CH_2 = 2.$$

$$\log(1/MIC)_{Staph.} = 0.33\,(\pm 0.04) - 0.28\,(\pm 0.02)\sum_{i=3}^{7} C_i + 0.28\,(\pm 0.02)\ \ CH_2$$

$$R^2 = 0.96 \quad F = 323 \quad s = 0.12 \quad df = 14 \quad n = 16 \qquad \text{(eq. 6)}$$

In this case, the two structural elements grouped in the equivalence variable are weighted:

Table 4—Structure–Absorption Model

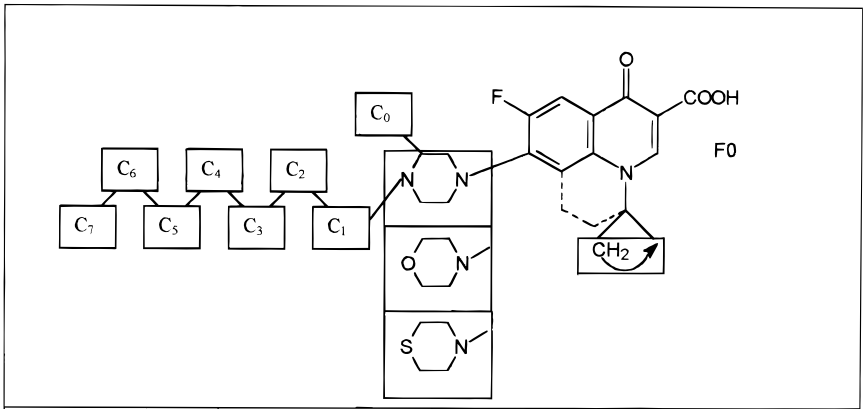

Structural elements	Absorption contributions	Structural elements	Absorption contributions
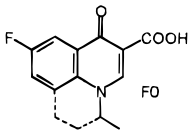	0.82 (± 0.02)	C_0	0.35 (± 0.05)
		C_1	0.64 (± 0.03)
		C_2	0.14 (± 0.01)
		C_3	0.14 (± 0.01)
	- 1.13[a] (± 0.05)	C_4	0.14 (± 0.01)
	0.00[a]	C_5	0.00
	0.00[a]	C_6	0.00
	0.06 (±0.02)	C_7	0.00

[a] Contributions of the heterocyclic rings take into account the absence of the flumequine moiety represented by the dashed line.

Table 5—Structure–Antibacterial Activity Model for *Escherichia coli*

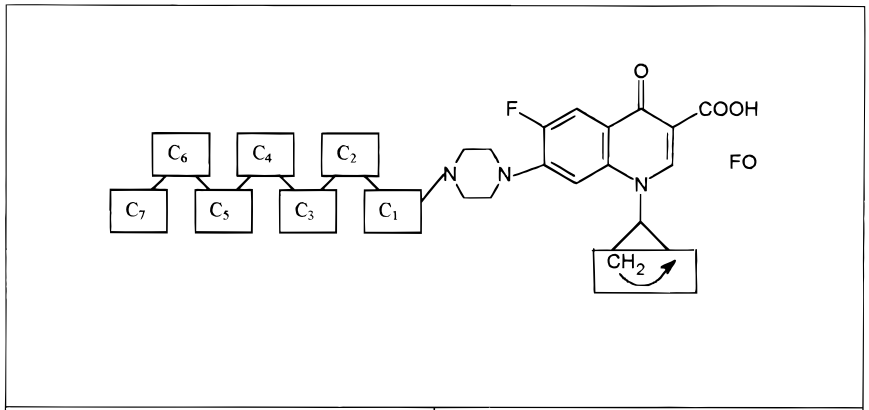

FO		1.03 (± 0.03)	
C_1	0.00	C_5	- 0.28 (± 0.01)
C_2	- 0.28 (± 0.01)	C_6	0.00
C_3	- 0.28 (± 0.01)	C_7	- 0.28 (± 0.01)
C_4	- 0.28 (± 0.01)		0.56 (± 0.02)

$$C_3 = C_4 = C_5 = C_6 = C_7 = -1, \quad \text{CH}_2 = 1$$

As can be observed, only replacing the ethyl by a cyclopropyl substituent enhances the antimicrobial activity. This effect has been reported previously.[19,20] Nevertheless, in these studies the step concerned in the mechanism, either the cellular penetration or an interaction between

Table 6—Structure–Antibacterial Activity Model for *Staphilococcus aureus*

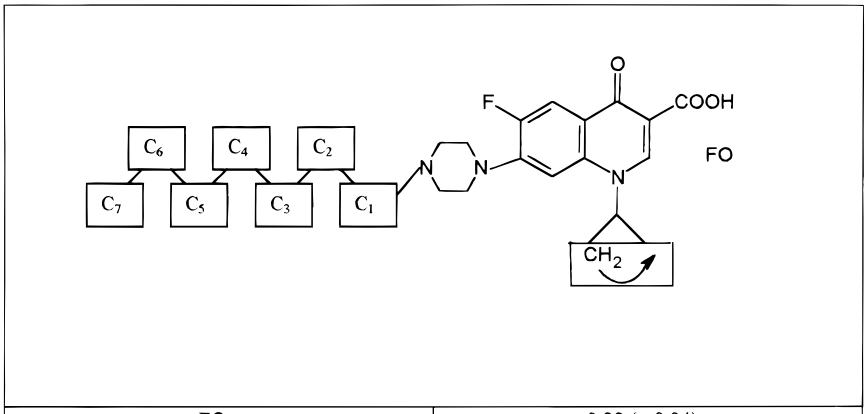

FO		0.33 (± 0.04)	
C_1	0.00	C_5	- 0.28 (± 0.02)
C_2	0.00	C_6	- 0.28 (± 0.02)
C_3	- 0.28 (± 0.02)	C_7	- 0.28 (± 0.02)
C_4	- 0.28 (± 0.02)	CH_2	0.28 (± 0.02)

the cyclopropyl group and the DNA or bacterial girase binding site, was not clarified. On the other hand, it can be noted that the activity on both strains is decreased by lengthening the *N*′-alkyl chain. According to the structure–lipophilicity model, these structural effects are not related to cellular penetration, as the methylene bridge has no influence on lipophilicity, and chain-lengthening increases it. Thus, antibacterial activity is enhanced by a *N*-cyclopropyl which could help to bind the molecule to the DNA or to the bacterial girase. It is decreased by steric hindrance of the *N*′-alkyl chain which could hinder access of the molecule to the enzyme or its intercalation in the DNA.

Conclusion

Two strategies are used to identify the properties which influence in situ absorption. In the first, the influence is assessed quantitatively by searching for correlations between absorption and lipophilicity. Within the series of closely related piperazinyl fluoroquinolones, lipophilicity appears as a strong determinant factor, and the results validate our previous biophysical model. Although the three heterologues are found as outliers, the biophysical model is still able to predict the lowest value of lipophilicity for a maximum absorption. In the second strategy, we construct structural models by using the PATQSAR approach and deduce the influence, starting from a simultaneous analysis of absorption and lipophilicity. The results confirm that absorption is increased by higher lipophilicity up to a limit due to N′-chain lengthening which could hinder membrane penetration by steric hindrance. Moreover, they suggest that electronic factors could be introduced into the biophysical model in order to reflect the marginal behavior of the heterologues.

The PATQSAR approach confirms some of the hypotheses of the biophysical absorption model and suggests its extension, thus demonstrating that they are complementary. Moreover, its use to identify the properties which influence antibacterial activity suggests the role of steric factors. This system is therefore a powerful tool for interpreting physicochemical and biological data and for optimizing certain processes, such as in situ absorption and antibacterial activity.

References and Notes

1. Plá-Delfina, J. M.; Moreno, J. Intestinal absorption-partition relationship: a tentative functional nonlinear model. *J. Pharmacokin. Biopharm*. **1981**, *9*, 191–215.
2. Suzuki, A.; Higuchi, W. I.; Ho, N. F. H. Theoretical model studies of drug absorption and transport in the gastrointestinal tract. II. *J. Pharm. Sci.* **1970**, *59*, 644–651.
3. Merino, V.; Freixas, J.; Bermejo, MV.; Garrigues, T. M.; Moreno, J.; Plá Delfina, J. M. Biophysical models as an approach to study passive absorption in drug development: 6-fluoroquinolones. *J. Pharm. Sci.* **1995**, *84*, 777–782.
4. Sobel, Y.; Vizet, P.; Chemob, S.; Barbieux, F.; Mercier, C. Enhancing the flexibility and adaptability of the DARC structural representation for computer-aided Drug Design. *SAR and QSAR in Environ. Res.* **1998**, *9*, 83–109.
5. Mercier, C.; Sobel, Y.; and Dubois, J. E. DARC/PELCO method: a topological tool for QSAR search and its reliable predictive capability. In *Chemical Graph Theory;* Bonchev, D., Rouvray, D. H., Eds.; Gordon and Breach: Philadelphia, 1992, pp 199–257.
6. Mercier, C.; Fabart, V.; Sobel, Y.; Dubois, J. E. Modeling alcohol metabolism with the DARC/CALPHI system. *J. Med. Chem*. **1991**, *34*, 934–942.
7. Koga, H. Structure–activity relationships of antibacterial 6,7- and 7,8-disubstituted 1-alkyl-1,4-dihydro-4-oxoquinoline-3-carboxylic acids. *J. Med. Chem*. **1980**, *23*, 1358–1363.
8. Cenavisa, S. A. Spanish Patent 8,901,480, 1989.
9. Doluisio, J. T.; Billups, N. F.; Dittert, L. W.; Sugita, E. T.; Swintosky, J. V. Drug absorption. I. An in situ rat gut technique yielding realistic absorption rates. *J. Pharm. Sci.* **1969**, *58*, 1196–1199.
10. Martín-Villodre, A.; Plá-Delfina, J. M.; Moreno, J.; Pérez-Buendía, M. D.; Miralles-Mir, J.; Collado, E. F.; Sánchez-Moyano, E.; Del Pozo, A. Studies on the reliability of a bihyperbolic functional absorption model. I. Ring substituted anilines. *J. Pharmacokin. Biopharm*. **1986**, *14*, 615–633.
11. Morishita, T.; Yamazaki, M.; Yata, N.; Kamada, A. Studies on absorption of drugs. Physicochemical factors affecting the absorption of sulfonamides from the rat small intestine. *Chem. Pharm. Bull.* **1973**, *21*, 2309–2322.

12. Gabus-Sannié, C.; Buri, P. Étude comparative des méthodes de determination du volume d′eau absorbé lors de la perfusion de l′intestin grêle du rat. *S. T. P. Pharma* **1987**, *3*, 856−860.
13. Doluisio, J. T.; Crouthamel, W. G.; Tan, G. H.; Swintosky, J. V.; Dittert, L. W. Drug absorption. III. Effect of membrane storage on the kinetics of drug absorption. *J. Pharm. Sci.* **1970**, *59*, 72−76.
14. Merino, V.; Martín-Algarra, R.; Rocher, A.; Garrigues, T. M.; Freixas, J.; Polache, A. Effects of ethanol on intestinal absorption of drugs I. In situ studies with ciprofloxacin analogues in normal and chronic alcohol fed rats. *Alcohol Clin. Exp. Res.* **1997**, *41*, 1996−2000.
15. Plá-Delfina, J. M.; Pérez Buendía, J. M.; Casabó, V. G.; Peris Ribera, J. E.; Martín Villodre, A. Absorption-partition relationships for true homologous series of compounds as a possible approach to study mechanism of surfactants in absorption. I. Aromatic amines in rat colon. *Int. J. Pharm.* **1987**, *37*, 49−64.
16. NCCLS Document M 100-S, Vol. 6, No. 21. National Committee for Clinical Laboratory Standards (NCCLS): Villanova, Philadelphia, 1986.
17. Ho, N. F. H.; Park, J. Y.; Morozowich, W.; Higuchi, W. I. Physical model approach to the design of drugs with improved intestinal absorption. In *Design of Biopharmaceutical Properties through Prodrugs and Analogues*; American Pharmaceutical Association: Washington, D.C., 1977; pp 136−227.
18. Vizet, P. PATQSAR, version 2.55, **1997**.
19. Takacs-Novak, K.; Jozan, M.; Hermecz, I.; Szasz, G. Lipophilicity of antibacterial fluoroquinolones. *Int. J. Pharm.* **1992**, *79*, 89−96.
20. Bryskier, A.; Chantot, J. F. Classification and structure−activity relationships of fluoroquinolones. *Drugs* **1995**, *49*, 16−28.
21. Wolfson, J. S.; Hoopert, D. Pharmacokinetics of quinolones: newer aspects of antimicrobial agents. *Chemotherapy* **1985**, *28*, 581−586.

Acknowledgments

The present work is a part of a research project carried out with a grant from CICYT (SAF96-1710) from the Education and Science Ministry (Spain) and from the Defense Ministry (France). The authors are indebted to the Education, Culture and Science Department of Valencian Generalitat for a grant (Marival Bermejo). The authors are also indebted to Mr. J. Freixas of Cenavisa for supplying the compounds studied and some of the MIC data.

JS980370+

Colloidal and Thermal Characteristics of Concentrated Dispersions of Polymethacrylate-Based Latices for Aqueous Enteric Coating

MATTIAS PAULSSON[†] AND SATISH K. SINGH[*,‡,§]

Contribution from *Department of Pharmacy, Division of Pharmaceutics, Uppsala University, Uppsala Biomedical Centre, Box 580, S-751 23 Uppsala, Sweden, and Department of Pharmaceutical Technology, Pharmacia & Upjohn AB, S-751 82 Uppsala, Sweden.*

Received August 31, 1998. Accepted for publication December 10, 1998.

Abstract □ We have used rheological and thermal methods to study the colloidal characteristics of a widely used technical latex. The dispersions of poly(methacrylic acid–ethyl acrylate) (Eudragit L100-55) were found to be stabilized by a combination of electrostatic and steric mechanisms termed as electrosteric stabilization. The electrosteric stabilization is considered to arise in part from dissolved polymer chains with charged carboxylic groups extending out into the continuous phase. The presence of dissolved polymer chains in the dispersion implies that coalescence and interpenetration will be facilitated during film formation, enabling a smooth continuous film to be formed. The extent of the stabilization layer and an effective hard-sphere volume was estimated to discuss the steady shear and viscoelastic properties in this context. The glass transition temperature (T_g) of the particles making up the dispersion has also been determined as a function of sorbed moisture and modeled by the Gordon–Taylor equation modified for specific interaction between water, surfactant, and polymer. This parameter at high moisture content can be used as a first approximation to the minimum film-forming temperature (MFT). Change in T_g (and thus MFT) with moisture content implies that the coating process must be controlled so as to produce a rate of drying slow enough to allow coalescence to occur.

Introduction

The release of drug from a solid dosage form is often tailored by applying a polymeric coating. Water-based rate-controlling polymer films are generally made by spraying an aqueous polymeric dispersion (latex) onto the dosage form (tablet or multiparticulates) and then evaporating the water, a process not unlike film formation from water-borne paints. Commonly used aqueous coating polymers within the pharmaceutical industry are cellulose derivatives and acrylic polymers. These latices are characterized by low viscosity, even at relatively high solid content.[1]

The mechanism of film formation from aqueous latex dispersions has been discussed for almost half a century. The evolution of the theories of film formation can be followed through a number of interesting papers.[2−5] Rheology,[4,6] scanning electron microscopy,[4,6] and lately atomic force microscopy[4,7] are primary techniques that have been employed for studying dispersions and film formation. Latex dispersions are subject to a range of shear rates during the coating process ranging from 10^5 s^{-1} during atomization to 10^{-2} s^{-1} during leveling. The process of deformation and coalescence is a function of polymer viscoelasticity.[2] In this work, we have applied rheology to study a commercial latex dispersion based on a methacrylic acid−ethyl acrylate (MAEA) copolymer and relate its characteristics to the first stages of film formation in pharmaceutical processing.

Film formation from polymer dispersions is correlated to the glass transition temperature (T_g) of the polymer and the temperature of operation in relation to the minimum film-forming temperature (MFT) of the latex.[8] The MFT is the minimum temperature above which a continuous and clear film is formed during drying.[2,8] While film formation does not imply that interdiffusion of polymer chains between adjacent particles must occur,[7,9] coalescence and interpenetration would be required for the formation of a strong film.[5] This flexibility is influenced by additives (plasticizers) as well as water (moisture) content of the polymer and can be detected as a reduction in both the T_g and the MFT. While both these parameters are apparently similar, T_g is a fundamental property of the material while MFT is an ill-defined parameter[10] reflecting latex morphology[11] and even particle size in some cases[2]. T_g can, however, be used as a first approximation for the MFT. (Data from Heuts et al.[8] gives the ratio of MFT to T_g as ranging between 0.8 and 1.1 for single stage acrylic dispersions, while data from Hoy[12] gives a ratio of 0.95). The T_g (and MFT) of the sprayed latex will change with moisture content, and a poor film will be formed if the MFT rises above operating temperature due to too rapid a drying. We have therefore determined the moisture adsorption isotherm for the dry commercial latex dispersion and measured the T_g of as a function of moisture content.

Materials and Methods

A spray-dried aqueous dispersion of methacrylic acid−ethyl acrylate (MAEA) copolymer (MW 250 000) with the commercial name Eudragit L100-55 was used (Röhm GmbH, Darmstadt, Germany). The as-received Eudragit L100-55 also contains 0.7% sodium lauryl sulfate (SLS) and 2.3% Polysorbate 80 based on solid substance, added to function as emulsifiers.

Dispersions were made by adding NaOH to the latex particle agglomerates in water and dispersing in accordance with Lehmann.[1] The dispersion is stable when 3−6% of the carboxylic groups of the copolymer are ionized; at greater than 20% ionization, the polymer particles would dissolve.[1] A suitable ratio of alkali and polymer was found to be 90 g of polymer/g of NaOH. This ratio was determined by measuring the viscosity and stability of the dispersions with constant polymer content but varying alkali concentration. Low pH gave an unstable dispersion while high pH's resulted in a rapid increase in viscosity due to dissolution of polymer. Dispersions were considered to be stable if no sedimentation could be detected in 24 h by visual inspection. The pH of the dispersions ranged between 5.1 and 5.3 (see Table 1). By keeping the NaOH−MAEA ratio constant, stable dispersions over a wide

* Corresponding author.
† Uppsala University.
‡ Pharmacia & Upjohn AB.
§ Present address: Pharmacia & Upjohn, Inc. 7207-259-277, 7000 Portage Rd., Kalamazoo, MI 49001-0199. Fax: +1-616-833-6743. E-mail: satish.singh@am.pnu.com.

10.1021/js9803555 CCC: $18.00
Published on Web 03/13/1999

Table 1—Estimation of the Effective Hydrodynamic Volume Fraction. The Increase of Effective Particle Radius (Δ) is Obtained from a Krieger–Dougherty Data Fit ($n = 3$)

ϕ	ϕ_{eff}	η_r	Δ (nm)	pH
0.255 ± 0.0003	0.456618	54.4	21.43325	5.27 ± 0.05
0.292 ± 0.004	0.493944	124	19.15116	5.20 ± 0.02
0.335 ± 0.005	0.492656	120	13.71898	5.13 ± 0.06
0.353 ± 0.002	0.571702	3810	17.43521	5.19 ± 0.06
0.355 ± 0.01	0.592429	60800	18.61404	5.13 ± 0.06
0.364 ± 0.02	0.599142	533000	18.07085	5.14 ± 0.07
0.392 ± 0.008	0.60186	3140000	15.36387	5.09 ± 0.05

range of solids content could be made. A suggested procedure for preparation of the dispersion requires a ratio of 71 g of polymer/g of NaOH along with 10% triethyl citrate at a final pH of ~5.[1] The ready-to-use commercial 30% dispersion Eudragit L30 D from Röhm has a pH of 2.5. At this pH, however, a 30% dispersion of the spray dried L100-55 is not stable and sediments immediately.

True polymer concentration of the latices was determined by "Loss on drying", method d (383 K, 3 h), in accordance with Ph. Eur. 1979. Taking into account the mass of compounds that did not evaporate and knowing the density of Eudragit L100-55, 1.18 g/cm^3 (data from manufacturer), the volume fraction of polymer, ϕ, was calculated.

The ζ potential of the particles was measured using a Malvern Zetasizer 4 (Malvern Instruments Ltd, Malvern, UK). Measurements were performed 24 h after preparation, on three samples from each dispersion. The latex dispersions were diluted 160-fold in an acetate buffer with similar pH and ionic strength (~10^{-2} M) prior to measurement due to their high turbidity. The used ionic strength is an estimate, since the exact degree of ionization of the carboxylic groups on the polymer is unknown.

Steady-state rheological measurements were carried out using a Bohlin VOR Rheometer (Bohlin Reologi, Lund, Sweden), a controlled strain instrument, with a double gap measuring system (DG 24/27) for dispersions of low viscosity or a concentric cylinder (C25) for dispersions of intermediate viscosity. A controlled stress instrument (Stresstech Rheometer, Reologica Instruments, Lund, Sweden) with a concentric cylinder (CC15) measuring system was used for all the dynamic viscoelastic measurements. The frequency range of 0.0001-90 Hz with a constant stress of 0.5 Pa was used. This stress is such that resulting deformation lies within the linear viscoelastic region of all dispersions measured. All measurements were performed at 298 K. Unwanted drying out and film formation at the surface of the sample were prevented by covering the measuring cups with a vapor trap. The intrinsic viscosity was determined using an Ostwald capillary viscometer at 298 K.

The glass transition temperature of the spray-dried Eudragit L100-55 was determined using modulated temperature differential scanning calorimetry (MTDSC) on a Seiko DSC220C instrument upgraded with a SSC5300 analysis system. Other operational conditions are described by Singh et al.;[13] the instrument operational parameters used were a heating rate of 3 K/min, an amplitude of 1 K, and a frequency of 0.02 Hz. The T_g of the MAEA copolymer in question here could not be detected using a conventional DSC.

To examine the effect of moisture on the glass transition temperature, samples were stored for 3−4 weeks in desiccators with constant humidity atmosphere at room temperature. The constant relative humidity atmospheres, in the range 31−95% RH, were created using saturated salt solutions.[14] Dried polymer samples were weighed (5−10 mg) into aluminum DSC pans and placed in these desiccators for equilibration. Prior to measurement, the pans were quickly sealed with crimping covers.

The water content of the MAEA powder equilibrated at the specified relative humidity was measured by Karl Fischer (coulometry) analysis (Metrohm 737 KF Coulometer, Metrohm AG, Herisau, Switzerland).

The glass transition temperature (at various moisture contents) can also be determined by an isothermal dynamic vapor sorption (DVS) method.[15] The sample is loaded onto a quartz pan of a microbalance located in a controlled gas flow environment, where the relative humidities (0−95%) can be accurately specified while the weight gain is continuously registered (DVS-1, Surface Measurement Systems, Marlow, UK). DVS was performed on the MAEA sample at one temperature (313 K) only to confirm the results of the MTDSC measurements.

Results and Discussion

The surface charge of particles in dispersions has a strong influence on both the stability and the flow behavior of the dispersion. Since the MAEA particles carry carboxylic groups, the particles will be negatively charged at the pH of the experiments (Table 1). This is confirmed by measuring the ζ potential of the particles. At $\phi = 0.25$ the ζ potential was -42 ± 1.9 mV, and at $\phi = 0.34$ the value was -43 ± 1 mV. There was a small tendency of the ζ potential to increase with increasing the polymer content. This was, however, within the uncertainty of the method. All the dispersions were therefore considered to have the same ζ potential. The ζ potential of the ready-to-use Eudragit L30D was -14 ± 3 mV in a dilution buffer of pH 2.5 and ionic strength 10^{-2} M.

In addition to the charges on the particles and the probable presence of dissolved polymer chains, the dried latex contains surface active substances that could in principle contribute to the steric stabilization of the dispersion.[16,17] Some simple experiments were performed in order to gain some insight into the interparticle repulsion/stabilization mechanism. Addition of small amounts of salt (e.g. KCl) instantaneously affected the stability causing the dispersion to flocculate irreversibly. The same effect was seen when the pH was lowered slightly. This is a typical feature of electrostatically stabilized dispersions. The freeze−thaw stability of the dispersion was good, however, which usually indicates steric stabilization.[18] Thus, a combination of electrostatic and steric stabilization is indicated for the dispersion.

From the above experiments it is also clear that the dispersion tested here cannot be described as hard spheres. The data also does not fit Einstein's law for hard spheres since the measured intrinsic viscosity, [η], is 4.7, compared to the expected hard-sphere intrinsic viscosity of 2.5. [For comparison, Raynaud et al.[19] report an intrinsic viscosity of 3.65 for a sterically stabilized dispersion of particle diameter 250 nm, while Krieger and Dougherty[20] report 3.44 for a dispersion with rigid uncharged particles with a diameter of 110 nm]. It is apparent that the effective hydrodynamic radius of the particles is increased by the adsorbed surfactants, dissolved polymer chains, and/or electroviscous effects from surface charges, forming a stabilization layer. An estimate of the effective hydrodynamic radius can be made using the expression

$$[\eta] = 2.5\left[\frac{a_H}{a}\right]^3 \quad (1)$$

where a is the core or true radius of the particles while a_H is the effective hydrodynamic radius. The (number) average particle radius of the dispersions, containing 10−40 wt % polymer is 100 nm although the particle size distribution is fairly broad ranging from 60 to 200 nm[1]. The thickness of the stabilization layer calculated from eq 1 is 23 nm.

Steady-State Shear Flow Behavior—The steady-state shear viscosity of various volume fractions of Eudragit L100-55 latex dispersions as a function of applied shear rate is plotted in Figure 1. The dispersion with lowest ϕ's showed Newtonian behavior. All dispersions above a volume fraction of $\phi = 0.4$ showed a more or less pronounced shear thinning behavior. The extent of shear thinning increased with increasing volume fraction. At very low shear rates a plateau is evident, which is an approximation of the zero shear viscosity. The experimental

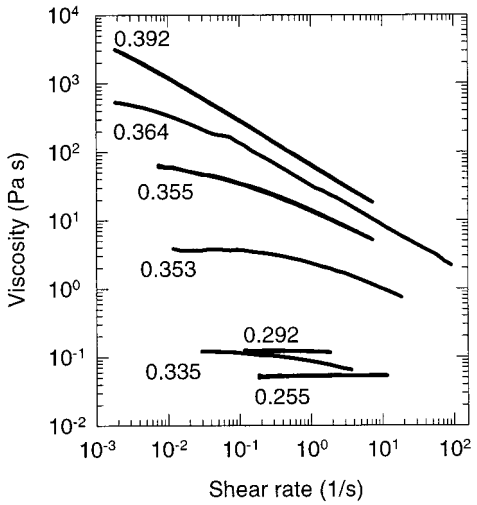

Figure 1—Steady-state shear flow curves of MAEA dispersions as a function of applied shear for increasing polymer volume fractions, ϕ ($n = 3$; see Table 1 for standard deviations). Data from controlled strain instrument.

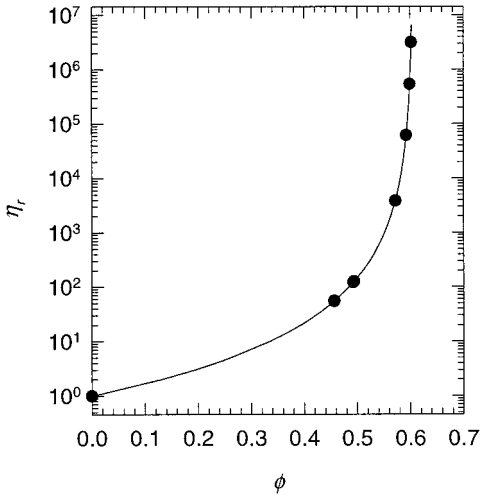

Figure 2—The low shear relative viscosity as a function of effective volume fraction for MAEA dispersions (●) fitted to the Krieger–Dougherty model, eq 3, with $[\eta] = 4.7$ and $\phi_{eff,m} = 0.605$. Data from controlled strain instrument.

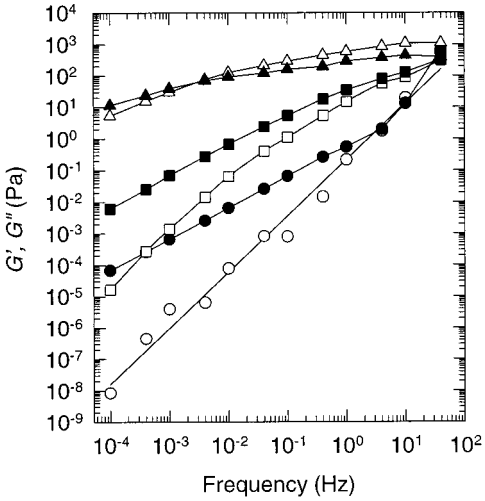

Figure 3—The storage (open symbols) and loss (closed symbols) moduli of $\phi = 0.33$ (○, ●), $\phi = 0.35$ (□, ■), and $\phi = 0.39$ (△, ▲) dispersions. Data from the controlled stress instrument.

set up could not detect the low-shear plateau for the dispersion with the highest solid content.

On the basis of previously discussed electrostatic and steric stabilization mechanism, an effective volume fraction, ϕ_{eff}, can be defined[6] such that

$$\phi_{eff} = \phi\left(1 + \frac{\Delta}{a}\right)^3 \quad (2)$$

where a is the particle radius (= 100 nm) and Δ is the increase of the effective particle radius due to contributions from the stabilization mechanisms (Debye length and/or adsorbed layer). With the above correction, the dispersion can be modeled as a hard-sphere system. The semiempirical Krieger−Dougherty equation[20] can then be used to correlate the relative viscosity, η_r, at low shear (approximation of the zero-shear viscosity from Figure 1) to the effective volume fraction

$$\eta_r = \left(1 - \frac{\phi_{eff}}{\phi_{eff,m}}\right)^{-[\eta]\phi_{eff,m}} \quad (3)$$

$[\eta]$ is the intrinsic viscosity and $\phi_{eff,m}$ is the maximum packing fraction. The value of $[\eta]$ from capillary viscometry = 4.7. The value used for $\phi_{eff,m} = 0.605$, corresponding to a hexagonally packed sphere structure (loose packing, coordination number 8). [The dispersion has a honeycomb-like structure in the last stages before the water layer disappears and the particles begin to deform and possibly coalesce.[21] Roulstone et al. propose a close-packed hexagonal structure for this stage with a maximum packing fraction of 0.74;[22] however, their conclusion is based on cast films where the particles have a longer time to achieve such a structure. Heterodispersity can also lower the packing efficiency[10]]. The value of Δ used to fit the experimental data points in Figure 2 to eq 3 are tabulated in Table 1, in accordance with Prestidge and Tadros.[23] At the low volume fractions, the effective thickness of the stabilization layer, Δ, is estimated to be 21 nm. The thickness of this stabilization layer decreases gradually with increasing volume fraction (Table 1). This is not surprising since the layer is compressed with increasing volume fractions as the particles approach each other closely. This compression causes the dispersion to display an increasingly elastic behavior as discussed below.

Viscoelastic Behavior—The viscoelastic response of the MAEA dispersion, in terms of the storage (G') and loss (G'') moduli, is shown in Figure 3 for three volume fractions. For $\phi = 0.33$ ($\phi_{eff} = 0.49$) which corresponds to a less-than-close packing fraction, G'' is considerably larger than G' at low frequencies. When the frequency is increased, the difference between the moduli decreases and at a critical value called the crossover frequency ~1 Hz, they are equal.

Increase in G' with frequency is a function of the relaxation time scale, τ_r, of the suspension in relation to the experimental time scale. At low frequencies, the experimental time of the order of $\tau \approx 1/\omega$ is longer than the relaxation time allowing the perturbed structure to relax during oscillation. The applied energy is thus dissipated, resulting in a large loss modulus or viscous behavior. With increasing frequency, τ becomes of the order of τ_r, resulting in a combined viscous and elastic response. Further increases in frequency will thus result in a predominantly elastic response i.e.,

$$G^* \approx G' = G_\infty$$

implying that the viscoelastic properties do not change at higher frequencies.[24]

With increasing volume fraction the average distance between the particles decreases causing increasing overlap of the stabilization layers surrounding the particles and

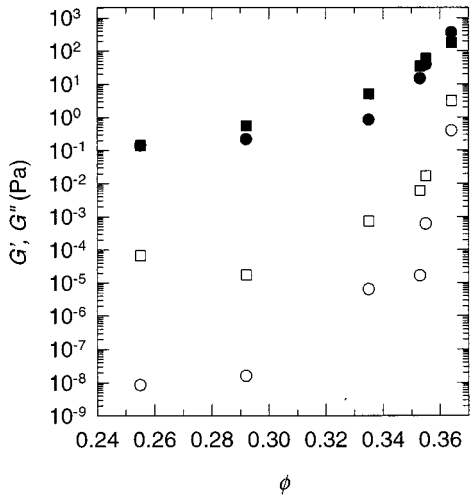

Figure 4—The storage (○, ●) and loss (□, ■) moduli at 10^{-4} Hz (open symbols) and 1 Hz (closed symbols) as a function of increasing volume fraction. Data from the controlled stress instrument.

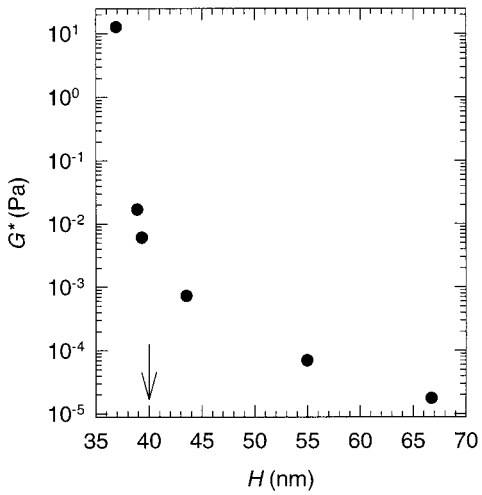

Figure 5—Complex modulus (at 10^{-4} Hz) as a function of the mean interparticle spacing from eq 5. The arrow shows the estimated point where the particles start overlapping. Data from the controlled stress instrument.

therefore increasing the elasticity (G'). This is apparent in Figure 3 for $\phi = 0.39$ ($\phi_{eff} = 0.60$). G' and G'' of this dispersion is almost frequency independent. A much lower crossover frequency is obtained, ≈0.002 Hz, since the dispersion is unable to scatter the applied energy due to its high solid content and begins to show elastic behavior at low levels of perturbation.

At low volume fractions ($\phi = 0.33$) the dispersion follows the Maxwell model, implying that one relaxation process dominates the dynamic properties of the latex in solution. The implication is that transient structures (stabilization layer) existing in the system at these concentrations are similar. [The slope of $G'(\omega)$ in Figure 3 is 1.8, and the slope of $G''(\omega)$ is 1.1, compared to 2 and 1, respectively, as required by the model]. The dispersions with higher volume fractions, however, do not fit the Maxwell model: for $\phi = 0.39$ ($\phi_{eff} = 0.60$), the slope for $G'(\omega)$ is 0.4 and for $G''(\omega)$ is 0.27 in Figure 3. This is not surprising since stabilization layer overlap and the resulting interactions introduce a new type of "cross-link" in the dispersion.

The variation of G' and G'' with volume fraction at two different frequencies of oscillation are shown in Figure 4, where an increase in solid content increases G'' and particularly G'. The phase angle shift is almost 90° for the lowest volume fractions but increases to approximately 45°, at $\phi = 0.36$ ($\phi_{eff} = 0.60$). Results from both frequencies confirm that the close-packing volume fraction for the present system occurs at $\phi_{eff} = 0.60$, above which the system behaves as a gel.[23]

The reciprocal crossover frequency (in rad/s) can be used to approximate the relaxation time, assuming that the material follows the Maxwell model of viscoelastic fluids. The relaxation time increases with the volume fraction and typical values of the relaxation time are 0.1 s for the low ($\phi_{eff} = 0.49$) concentration increasing to ~75 s for the high solid dispersions ($\phi_{eff} = 0.60$). To put these in perspective, characteristic process times for spraying are of the order of 10-5 s, while that for leveling of an applied film is 100 s. These times thus agree well with the characteristic relaxation times of the dispersions at the relevant concentrations. To further relate the viscoelastic properties to the deformation and possible coalescence processes, we resort to the modified viscoelastic model[9] for film formation by Eckersley and Rudin.[2] According to this model, film formation requires

$$G'(t) \leq \frac{34\sigma}{a} \tag{4}$$

where σ is the surface tension of water in the capillaries between particles, while $G'(t)$ is the time-dependent elastic shear modulus of the polymer. Using $\sigma = 30$ mN/m and 200 nm as the largest particle size in the dispersion gives a critical upper limit for elastic modulus of 5.1×10^6 Pa. Figure 4 shows that this criteria is satisfied by the present dispersion.

The mean interparticle spacing in a dispersion, H, is a measure of the closeness of approach of these particles and can be expressed as

$$H = 2a\left[\left(\frac{\phi_{eff,m}}{\phi_{eff}}\right)\right] \tag{5}$$

In Figure 5, we have plotted the complex modulus G^* (at 1 Hz) against H calculated from eq 5 using values of ϕ from Table 1 and $\phi_m = 0.605$ as indicated above. It is clearly apparent that as the interparticle spacing falls below 40 nm, G^* increases markedly due to the stabilization layers beginning to overlap. An estimate of the thickness of this layer is therefore = $^1/_2H$, i.e., approximately 20 nm. This value compares well to the Δ-value in Table 1 for the low volume fractions, as well as the estimate from intrinsic viscosity using eq 1.

The Debye double layer thickness, $1/\kappa$, in the present system (water at 298 K)

$$\kappa = 3.288\sqrt{I} \quad (\text{in nm}^{-1}) \tag{6}$$

gives a fairly thin double layer of the order of 3 nm, due to the ionic strength estimated as 10^{-2} M. The large value of κ_a (≈ 30) suggests that primary electroviscous effects would be small. Secondary electroviscous effects, while not significant at low volume fractions, may, however, play a role in increasing the viscosity at the high volume fractions considered here. In the literature, such effects have been attributed to the formation of (temporary) doublets of like-charged particles which allow energy to be dissipated when rotating in or when destroyed by shear.[25] Examining the possible steric contributions to the stabilization layer suggests that the surfactants added to the latex particles (Polysorbate 80 and SLS) cannot extend out 20 nm from the surface of the particles. This and the fairly high ζ potential imply that alternative explanations are needed to rationalize the extent of the stabilization layer (which is in agreement when calculated from the various methods). This layer must arise due to dissolved latex polymer chains

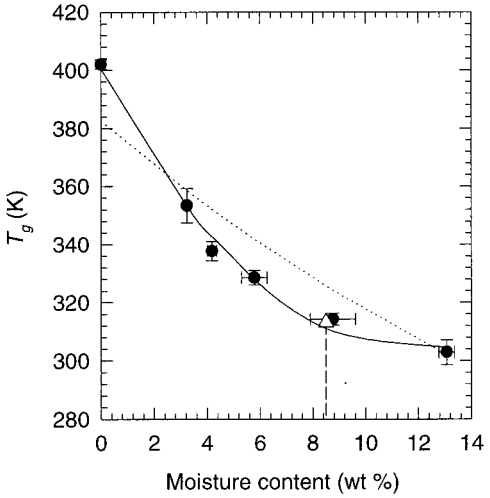

Figure 6—Influence of moisture content on T_g for spray-dried MAEA dispersion from MTDSC (●). The dotted line is calculated from eq 7 while the continuous line is a data fit using eq 9. Standard deviations are shown for both T_g and the moisture content. Results of T_g determination by DVS (Δ) at 40 °C (313 K) is marked with a line.

Table 2—Moisture Sorption Isotherm at 25 °C, and the Glass Transition Temperature (T_g) of Eudragit L 100-55 (Methacrylic Acid–Ethyl Acrylate Copolymer) ($n = 3$)

rel humidity (%)	equilibrium moisture content by KF (wt %)	equilibrium moisture content by DVS (wt %)	T_g by MTDSC (K)
0	0	0	402 ± 1.6
31	3.24 ± 0.05	3.68	353 ± 5.8
42	4.19 ± 0.17	4.70	338 ± 3.3
58	5.78 ± 0.48	6.70	329 ± 2.5
90	8.76 ± 0.86	10.9	314 ± 2.0
95	13.1 ± 0.29	13.8	303 ± 4.2

which allow the charged carboxyl groups to extend further out from the surface. The alkyl chain of anionic SLS can also adsorb to the surface of the latex as well as bind to the dissolved chains extending the charged headgroup into the surrounding phase, effectively increasing the (negative) surface charge. The picture we have of the latex is thus one with a charged "hairy" surface, electrosterically stabilized.[26] The presence of the adsorbed neutral surfactant (as well as dissolved polymer) can influence the adsorption characteristics of the ions in the diffuse layer as well as shifting the shear plane away from the surface. Contribution to the latter effect due to Polysorbate 80 will not be very strong since the amount added is small, allowing the adsorbed layer to be approximated as free draining; any contribution due to dissolved latex polymer is, however, difficult to estimate. Change in the ion distribution in the diffuse layer can be caused by excluded volume effect leading to an extension of the double layer and thereby an increase in the surface potential of the particle.[25]

Moisture Sorption and Thermal Analysis—MAEA is an amorphous polymer and takes up water in a humid environment. The moisture sorption isotherm at 298 K is tabulated in Table 2 and shows good agreement between the two (KF and DVS) techniques. The particles absorb up to 13% moisture when exposed to high relative humidity. The data seems to follow a typical Type II isotherm for multilayer physical adsorption on nonporous solids.

The corresponding T_g of the MAEA particles (measured by MTDSC) equilibrated at a range of relative humidities is also shown in Table 2 and plotted in Figure 6. The glass transition temperature of the particles is substantially lowered after exposure to moisture, as is to be expected. Lehmann[1] reports the MFT of redispersed MAEA latex is 291 K, the MFT of the ready-to-use Eudragit L30D dispersion is 300 K, and the T_g of the dry polymer is 380 K. We find that the T_g (at high moisture content; Figure 6) is a good first approximation of the MFT. The data also suggests that since the T_g (and thus MFT) rises rapidly with decreasing water content, the process of film formation should be complete before the sprayed material is dried to such an extent that the MFT rises above operating temperature. A balance is therefore required between spray rate, temperature, and drying air flow. It also implies that the MFT of (and T_g for hydrophilic) latex systems must be related to the moisture content, and determined by the humidity of the drying air in which it is measured.

The data from the Dynamic Vapor Sorption measurement performed at 313 K agrees well with the MTDSC data as shown in Figure 6. A glass transition event at this temperature is detected when the moisture content of the polymer is approximately 9%. However, no such event is observed when the experiment is performed at 298 K. The plasticizing effect of sorbed moisture is not sufficient to lower the T_g to 298 K.

Monotonic variations of the T_g with composition in mixtures/blends are often modeled by the modified Gordon−Taylor equation which is based on free volume effects under the assumption that there are no specific interactions between the components. For a three-component mixture, this can be written as

$$T_{gmix} = \frac{w_1 T_{g1} + K_{12} w_2 T_{g2} + K_{13} w_3 T_{g3}}{w_1 + K_{12} w_2 + K_{13} w_3} \quad (7)$$

where w_1, w_2, and w_3 are the weight fractions of the three components, and T_{g1}, T_{g2}, and T_{g3} are the corresponding pure component glass transition temperatures. Constants K_{12} and K_{13} are ratios of free volumes of components and can be estimated from

$$K_{ij} = \frac{\rho_i T_{gi}}{\rho_j T_{gj}} \quad (8)$$

where ρ_i represents density of component i.

We expect that the MAEA copolymer has specific interactions with water including deprotonation of the carboxylic groups. Similarly, hydrophobic portions of Polysorbate 80 will have an increased affinity for the latex surface. To account for these interactions, quadratic and third-power interaction terms are added to eq 7, giving

$$T_{gmix} = \frac{w_1 T_{g1} + K_{12} w_2 T_{g2} + K_{13} w_3 T_{g3}}{w_1 + K_{12} w_2 + K_{13} w_3} + Q_{12} w_1 w_2 + Q_{13} w_1 w_3 + Q_{123} w_1 w_2 w_3 \quad (9)$$

where Q_{12}, Q_{13}, and Q_{123} are empirical interaction parameters reflecting the strength and type of interactions.[27,28] We denote MAEA, water and Polysorbate 80 as components 1, 2, 3 with T_{g1}, T_{g2}, and T_{g3} as the glass transitions temperatures of pure MAEA, water (= 135 K),[29] and Polysorbate 80 (= 207 K), respectively. The T_g of Polysorbate 80 was measured in this work, but the same could not be done for pure MAEA since the MAEA available was preblended with surfactants. While an extensive dialysis procedure could in principle remove all added surfactant, we chose to estimate this parameter (T_{g1}) from the data at 0% RH. We have neglected any plasticizing effect of SLS because of the small amount added. Using a two-component version of eq 7 on T_g data at 0% RH gives T_{g1} = 412 K. (Specific gravity of Polysorbate 80 = 1.08 and of MAEA = 1.18). Utilizing this parameter in eq 7 to calculate the T_{gmix}

of the blend at various moisture contents gives a theoretical glass transition that does not agree with the experimental data (Figure 6). However, using eq 9 with Q_{12} and Q_{123} as curve-fitting parameters allows the data to be modeled well as shown in Figure 6. (It was found that the parameter Q_{13} could be dropped without any effect on the goodness of fit). The value obtained for parameter Q_{12} is positive while that for Q_{123} is negative. While Kwei et al. have presented arguments based on intermolecular force parameters to explain the negative values of such parameters,[30] we will simply ascribe these to be empirical parameters that enable the data to be modeled and underline the importance of specific interaction terms in our system.

Conclusions

In the first part of this study, we have used the techniques and methods of colloid science and applied them to a technical latex, widely used in the pharmaceutical industry. The dispersions are found to be electrostatically and sterically stabilized. The stabilization is considered to arise in part from dissolved polymer chains with charged groups that extend out into the bulk continuous phase. The extent of the stabilization layer was estimated to be around 20 nm, giving an effective hard-sphere volume that can be used to relate the steady shear and viscoelastic properties to the film formation phenomena. The presence of dissolved polymer chains in the dispersion implies that coalescence and interpenetration will be facilitated during film formation.

The results generated here provide a baseline to evaluate the effect of normal coating additives such as plasticizers, colorants, flavorants, buffering agents etc., on dispersion stability and film-forming ability. While such studies increase our understanding of the systems in question, they also point to the complexity and limitations in the strict application of techniques and models based on ideal and simplified systems. Technical dispersions present a challenge because of their heterodispersity and the combination of mechanisms involved.

The glass transition temperature of the particles making up the dispersion has then been determined as a function of sorbed moisture and modeled by the Gordon−Taylor equation modified for specific interaction between water, surfactant, and polymer. Our data and that in the literature suggests that the high-moisture content T_g can be used as a first approximation for the MFT. Change in T_g (and thus MFT) with moisture content implies that the process must be controlled so as to produce a rate of drying slow enough to allow coalescence to occur. A curing stage is generally added to assist in the coalescence and interpenetration of the sprayed polymer chains. Knowledge of the moisture sorption and T_g data can be used to determine the conditions of this stage especially for heat labile substances.

References and Notes

1. Lehmann, K. Chemistry and application properties of polymethacrylate coating systems. In *Aqueous Polymeric Coatings for Pharmaceutical Dosage Forms*, 2nd ed.; McGinity, J. W., Ed.; Marcel Dekker: New York, 1997; pp 101−176.
2. Eckersley, S. T.; Rudin, A. Mechanism of Film Formation from Polymer Latexes. *J. Coat. Technol.* **1990**, *62*, 89−100.
3. Lin, F.; Meier, D. J. A study of latex film formation by atomic force microscopy. 1. A comparison of wet and dry conditions. *Langmuir* **1995**, *11*, 2726−2733.
4. Lin, F.; Meier, D. J. A study of latex film formation by atomic force microscopy. 2. Film formation vs rheological properties: Theory and experiment. *Langmuir* **1996**, *12*, 2774−2780.
5. Dobler, F.; Hall, Y. Mechanism of latex film formation. *Trends Polym. Sci.* **1996**, *5*, 145−151.
6. Tadros, T. F. Use of viscoelastic measurements in studying interactions in concentrated dispersions. *Langmuir* **1990**, *6*, 28−35.
7. Wang, Y.; Juhué, D.; Winnik, M. A.; Leung, O. M.; Goh, M. C. Atomic force microscopy study of latex film formation. *Langmuir* **1992**, *8*, 760−762.
8. Heuts, M. P. J.; le Fêbre, R. A.; van Hilst, J. L. M.; Overbeek, G. C. Influence of morphology on film formation of acrylic dispersions. *Film formation in waterborne coatings*; Provder, T., Ed.; ACS Symposium Series, 648, American Chemical Society: Washington, DC, 1996; pp 271−285.
9. Brown, G. L. Formation of films from polymer dispersions. *J. Polym. Sci.* **1956**, *22*, 423−434.
10. Keddie, J. L.; Meredith, P.; Jones, R. A. L.; Donald, A. M. Kinetics of film formation in acrylic latices studied with multiple-angle-of-incidence ellipsometry and environmental SEM. *Macromolecules* **1995**, *28*, 2673−2682.
11. Lippold, B. C.; Lippold, B. H.; Sutter, B. K.; Gunder, W. Properties of aqueous, plasticizer-containing ethyl cellulose dispersions and prepared films in respect to the production of oral extended release formulations. *Drug Dev. Ind. Pharm.* **1990**, *16*, 1725−1747.
12. Hoy, K. L. Estimating the effectiveness of latex coalescing aids. *J. Paint. Technol.* **1973**, *45*, 51−56.
13. Singh, S. K.; Jalali, A. F.; Aldén, M. Modulated temperature differential scanning calorimetry for examination of tristearin polymorphism. I. Effect of operational parameters. *J. Am. Oil Chem. Soc.*, in press.
14. Nyqvist, H. Saturated salt solutions for maintaining specified relative humidities. *Int. J. Pharm. Technol. Prod. Manuf.* **1983**, *4*, 47−48.
15. Buckton, G.; Darcy, P. Water mobility in amorphous lactose below and close to the glass transition temperature. *Int. J. Pharm.* **1996**, *136*, 141−146.
16. Florence, A. T.; Rogers, J. A. Emulsion stabilization by nonionic surfactants: experiment and theory. *J. Pharm. Pharmacol.* **1971**, *23*, 153−169.
17. Zapata, M. I.; Feldkamp, J. R..; White, J. L.; Hem, S. L. Use of the tension cell to monitor particle interactions in suspensions. *Drug Dev. Ind. Pharm.* **1989**, *15*, 1933−1941.
18. Zapata, M. I.; Feldkamp, J. R..; Peck, G. E.; White, J. L.; Hem, S. L. Mechanism of freeze−thaw instability of aluminum hydroxycarbonate and magnesium hydroxide gels. *J. Pharm. Sci.* **1984**, *73*, 3−8.
19. Raynaud, L.; Ernst, B.; Vergé, C.; Mewis, J. Rheology of aqueous latices with adsorbed stabilizer layers. *J. Colloid Interface Sci.* **1996**, *181*, 11−19.
20. Krieger, I. M.; Dougherty, T. J. A mechanism for nonnewtonian flow in suspensions of rigid spheres. *Trans. Soc. Rheol.* **1959**, *3*, 137−152.
21. Barnes, H. A.; Hutton, J. F.; Walters, K. Rheology of suspensions. In *An Introduction to Rheology;* Elsevier B. V.: Amsterdam, 1989; pp 115−139.
22. Roulstone, B. J.; Wilkinson, M. C.; Hearn, J.; Wilson, A. J. Studies on polymer latex films: I. A study of latex film morphology. *Polym. Int.* **1991**, *24*, 87−94.
23. Prestidge, C.; Tadros, T. F. Viscoelastic properties of aqueous concentrated polystyrene latex dispersions containing grafted poly(ethylene oxide) chains. *J. Colloid Interface Sci.* **1988**, *2*, 660−665.
24. Bergström, L. Rheology of concentrated suspensions. In *Surface and Colloid Chemistry in Advanced Ceramics Processing;* Pugh, R. J., Bergström, L., Eds.; Marcel Dekker Inc.: New York, 1994; pp 193−244.
25. Hunter, R. J. Charge and potential distribution at interfaces. In *Zeta Potential in Colloid Science, Principles and Applications*; Academic Press: London, 1981; Ch. 2, 5, 8.
26. Peula, J. M.; Santos, R.; Forcada, J.; Hidalgo-Alvarez, R.; de Las Nieves, F. J. Study on the colloidal stability mechanisms of acetal-functionalized latexes. *Langmuir* **1998**, *14*, 6377−6384.
27. Kwei, T. K. The effect of hydrogen bonding on the glass transition temperatures of polymer mixtures. *J. Polym. Sci., Polym. Lett. Ed.* **1984**, *22*, 307−313.
28. Hancock, B. C.; Zografi, G. The relationship between the glass transition temperature and the water content of amorphous pharmaceutical solids. *Pharm. Res.* **1994**, *11*, 471−477.
29. Sugisaki, M.; Suga, H.; Seki, S. Calorimetric study of the glassy state. 4. Heat capacities of glassy water and cubic ice. *Bull. Chem. Soc. Jpn.* **1968**, *41*, 2591−2599.
30. Kwei, T. K.; Pearce, E. M.; Pennacchia, J. R.; Charton, M. Correlation between the glass transition temperatures of polymer mixtures and intermolecular force parameters. *Macromolecules* **1987**, *20*, 1174−1176.

JS9803555

In Vitro Investigation of Ionic Polysaccharide Microspheres for Simultaneous Delivery of Chemosensitizer and Antineoplastic Agent to Multidrug-Resistant Cells†

ZHI LIU, XIAO YU WU,* AND REINA BENDAYAN

Contribution from *Faculty of Pharmacy, 19 Russell Street, University of Toronto, Toronto, Ontario, Canada M5S 2S2.*

Received August 14, 1998. Final revised manuscript received December 9, 1998.
Accepted for publication January 8, 1999.

Abstract □ Insufficient intratumoral concentration of therapeutic agents and multidrug resistance are major factors responsible for failure of treatment of solid tumors. Simultaneous delivery of chemosensitizing and antineoplastic agents by microspheres could lead to enhanced chemotherapy of multidrug-resistant (MDR) tumors. Ionic polysaccharide microspheres derived from dextran were used to load chemosensitizers (e.g., verapamil) and anticancer drugs such as vinblastine. High drug loading was achieved for both a single agent and dual agents. The equilibrium drug loading was dependent on the ratio of the microspheres (MS) to the drug, as well as the relative affinity of the agents to the MS in the case of dual agents. The drug release from drug–MS involved hydration and swelling of the MS in addition to ion exchange. The effectiveness of MS-delivered chemosensitizers in the reversal of drug resistance was evaluated by measuring the uptake of [^{3}H]vinblastine by MDR cells (CH^{R}C5). The concomitant delivery of verapamil with vinblastine by the MS led to a 6–7-fold increase in the uptake of vinblastine, a level similar to the uptake obtained with free drug solutions. The results suggest that the antineoplastic and chemosensitizing agents were released effectively from the MS and the bioactivity of the chemosensitizer was preserved during the process.

Introduction

The efficacy of cancer chemotherapy may be limited by the drug toxicity, drug concentration achievable in the tumor, and the development of multidrug resistance (MDR). The maximum systemic drug concentration is set by the drug toxicity to the normal tissues (e.g., leukopenia of vinblastine, and cardiotoxicity and immunosuppressive activity of doxorubicin). In addition, it is difficult to obtain an effective therapeutic drug level in solid tumors because of higher intratumoral pressure and poor blood supply.[1] Therefore, targeted drug delivery has been extensively investigated to increase the drug exposure of the tumor relative to that of normal tissues. Of all the targeting approaches, the most direct one is the intratumoral or intra-arterial injection of drug solutions to the tumor site.[2−4] This technique, however, is often associated with significant systemic exposure due to rapid egress of the drug from the tumor mass. To maintain the intratumoral drug concentration and reduce the systemic exposure, slow-release formulations, especially in the form of microspheres (MS), have been utilized in the place of free drug solutions.[5−14]

To date, slow-release MS have been tested in regional cancer chemotherapy in over a thousand patients worldwide[6−9] as a potential, effective treatment of solid tumors in the liver, kidney, breast, lung, head, and neck. Pharmacokinetic and pharmacodynamic studies in animals and humans have shown enhanced drug exposure of tumors and diminished systemic toxicity as compared with organ perfusion with free drug solutions.[2−14] Moreover, there is little indication of increased local toxicity in most studies.[5,7,8] Despite these positive results, a considerable percentage of chemotherapy failure is still observed in animal tumor models and in clinical trials, which may be partly attributed to MDR to chemotherapy.[8,15−19]

It has been demonstrated that chronic exposure of cancer cells to sublethal concentrations of chemotherapeutic agents can lead to the outgrowth of the MDR phenotype.[15−19] MDR, characterized by diminished cellular drug accumulation, usually derives from an increased rate of drug efflux by specific membrane proteins [e.g., P-glycoprotein (P-gp)[16−19]]. Integration of MDR-reversing agents, such as verapamil and cyclosporins, in conventional chemotherapy has been used for treatment of MDR tumors.[18−22] However, there has been limited success in clinical trials, especially in the treatment of solid tumors, which is believed to be a consequence of insufficient drug concentration in the tumors.[23,24] We hypothesized that simultaneously delivery of both chemosensitizing and antineoplastic agents to the tumor sites by MS could increase local drug concentration and thus enhance the therapeutic efficacy while reducing the systemic side effects.

Among the numerous methods for incorporating drugs into MS, loading of ionic drugs into ion-exchange MS is of particular interest because of their high drug-loading capacity and ease of the loading process.[25−28] Furthermore, biocompatible and biodegradable materials, such as polysaccharides and albumin, can be used to prepare the MS.[5,25,29] The biodegradable MS drug carriers are more suitable for in vivo application than nonbiodegradable polystyrene MS, although the latter have also led to positive therapeutic results.[26−28]

Our group has initiated the development of microspherical delivery systems for enhanced therapy of MDR tumors via regional, simultaneous delivery of chemosensitizing and antineoplastic agents.[30,31] The purpose of this work was to undertake in vitro characterization and evaluation of MS for simultaneous delivery of the dual agents to MDR cells. Ionic polysaccharide MS derived from cross-linked dextran were chosen as the drug carriers because of their biocompatibility and biodegradability.[29,32−34] More importantly, the original material, dextran, has been applied in vivo as a blood expander for years. Although the cross-linked dextran MS have not been approved officially, they have been used clinically in cancer therapy[32,33] and wound treatment[34] without observed adverse effects. To achieve a sustained release of the therapeutic agents and retention of the MS in the tumor or the arteries leading to the tumor

* Corresponding author. Telephone: (416)978-5272. Fax: (416)978-8511. E-mail: xywu@phm.utoronto.ca.

† Part of the results was presented at the AAPS Annual Meeting (Boston, MA, 1997).

10.1021/js9803353 CCC: $18.00
Published on Web 03/16/1999

while maintaining the ease of injection, MS with diameters ranging from 40 to 125 μm were selected. As our previous work suggested,[35,36] the therapeutic agents may interfere with each other or redistribute among the MS after having been released into a confined compartment in the tumor, thus altering their bioavailability. To elucidate the possible mutual effect of the dual agents on the release kinetics, the competitive loading and release of the dual agents were investigated. Moreover, because of the concern about loss of biological activity of the agents during the process of loading and release, in vitro efficacy of the agents in the reversal of MDR was evaluated using an MDR model cell line with high expression of P-gp.

Experimental Section

Characterization of the Microspheres. The morphology of the MS before and after drug loading was examined by microscopy. The diameters of the MS with or without a loaded drug were measured by a Wild M420 stereomicroscope equipped with a Wild MMS 235 digital optical accessory and an automated camera.[35] The swelling kinetics and swelling ratio were determined based on the diameter change measured by microscopy.

Drug Loading into the Microspheres. Cross-linked dextran MS containing sulfonic groups (Sephadex SP C-25, Pharmacia) were washed several times with deionized water prior to use. Vinblastine sulfate and verapamil hydrochloride (Sigma Chemical Company) were used in this study because the former is a P-gp substrate and broadly used anticancer drug and the latter is a well-known effective chemosensitizer for P-gp-mediated MDR. In a typical loading process, 0.05 g of the dry, ionic MS were added to 10 mL of 0.5% verapamil aqueous solution. After incubation at room temperature for predetermined time intervals, the MS were separated by centrifugation, and the drug concentration in the supernatant was analyzed by ultraviolet−visible (UV−VIS) spectrophotometry (Hewlett-Packard 8452A) at wavelengths of 270 nm for vinblastine and 278 nm for verapamil. When the drug absorption reached equilibrium (after ~30 h), the MS were harvested by centrifugation and washed extensively with deionized water. The amount of drug loaded was calculated from the difference between the initial drug concentration and the final one after incubation with the ion-exchange MS. Unbound drug in the washout was also determined by spectrophotometry for the calibration of the drug loading. The MS were then lyophilized. In the case of loading of dual agents (i.e., vinblastine and verapamil), the same procedures were applied except that the drug assay was carried out by high performance liquid chromatography (HPLC; see next section).

Analysis of Drug Mixture by HPLC. Because of the interference of UV absorbance of the two drugs, for the studies of competitive drug loading and dual-agent release, the concentration of vinblastine and verapamil in the solution was analyzed using a Waters HPLC system including a spectrophotometer (Model 481), an HPLC pump (Waters 501), and a System Interface Module. The mobile phase consisted of phosphate buffer (ionic strength, 0.1 M; pH 7.0), tetrahydrofuran, and methanol, with a volume ratio 0.43:0.41:0.16. Vinblastine and verapamil were separated in a reverse-phase column (Norva-pak C-18, Waters) by the mobile phase at a flow rate of 0.6 mL/min. The drug concentration in the solution was determined based on the standard curves by a UV detector at a wavelength of 270 nm.

In Vitro Drug Release. Release rate of vinblastine and verapamil from single-agent-loaded and dual-agent-loaded MS was determined at 37 °C with the addition of 1.4 mg of dry MS in 10 mL of pH 7.4 phosphate buffer with ionic strength of 0.05 M. At predetermined time intervals, the suspension was centrifuged and the supernatant was analyzed by spectrophotometry or by HPLC. The release kinetics of both agents from dual-agent-loaded MS was also studied at 37 °C in an Earle's Balanced Salt Solution (EBSS), a pH 7.4 buffer solution commonly used in studies of drug uptake by cultured cells. The solution consists of $CaCl_2$ (1.8 mM), KCl (5.3 mM), $MgS0_4$ (0.8 mM), NaCl (138 mM), Na_2HP0_4 (1.0 mM), D-glucose (5.5 mM), *N*-hydroxyethylpiperazine-*N*′-2-ethanesulfonic acid (HEPES; 20 mM), and Trizma base to bring the pH to 7.4. In this case, the concentration of the individual drugs in the dual-agent solution was monitored by spectrophotometry (for verapamil) and liquid scintillation counting (for [^{3}H]vinblastine).

Tissue Cell Culture and Drug Accumulation Studies. Parent (AUXB1) and MDR (CH^RC5) Chinese hamster ovary (CHO) cells were initially grown in Dr. V. Ling's laboratory.[37,38] The resistant cell line, CH^RC5, is chosen because it expresses high levels of P-gp and has been shown to be resistant to a variety of structurally unrelated drugs, such as vinblastine and doxorubicin. The cells were grown in plastic culture flasks containing alpha minimal essential medium (α-MEM), 10% fetal bovine serum, and 0.5% penicillin-streptomycin at 37 °C, under an atmosphere of 95% air and 5% CO_2. Subculture of the cells was undertaken by trypsinization with 0.05% trypsin-EDTA when a confluent monolayer was formed.

Drug accumulation tests were carried out using monolayer cells grown on 24-well plates.[39] Initially, the accumulation of vinblastine over time by the parent and resistant cells was determined in the absence (control) or presence of chemosensitizers. Cyclosporin A (20 μM, a gift from Sandoz Canada) and verapamil hydrochloride (50 μM) were used as the chemosensitizers to verify the MDR characteristic of the resistant cells. Drug uptake was initiated in the presence or absence of a chemosensitizer by the addition of 0.5 mL of an EBSS containing 21 nM [^{3}H]vinblastine sulfate (11.7 Ci/mmol, Moravek Biochemicals) with 1/3 ^{3}H-labeled and 2/3 cold drug. At various time intervals (e.g., 0.5, 1, and 2 h), drug accumulation by the monolayer cells was stopped by aspirating the medium and washing the cells twice with an excess of ice-cold 0.16 N NaCl. The cells were then lysed with 1 mL of 1 N NaOH for 30 min and then transferred to scintillation vials containing 0.5 mL of 2 N HCl. Radioactivity was measured by a standard liquid scintillation technique using a Beckman Scintillation Counter and the standard Beckman scintillation fluid cocktail "Ready Safe". The protein concentration of the cells was determined by a colorimetric method using bovine serum albumin as a standard.[40]

The effect of blank MS and MS-immobilized agent(s) on the cellular uptake of vinblastine was determined using the same method as already described. Typically, in the place of a free drug solution, 0.5 mL of EBSS containing 0.2 wt % MS were introduced to the monolayer cells followed by the addition of 0.5 mL EBSS containing 21 nM vinblastine. After the medium was aspirated, the MS were removed by washing with an excess of ice-cold 0.16 N NaCl.

Cell Viability Tests. Cell viability in the presence of blank MS was tested by the standard trypan blue method. This procedure monitors the integrity of the plasma membrane. An aliquot (100 μL) of CH^RC5 cells incubated with the blank MS at various times was rapidly added to an equal volume of 0.8% trypan blue solution in isotonic saline and examined by optical microscopy. The percentage of nonviable cells was evaluated from the percentage of cells taking up the stain.

Statistical Analysis. For the drug uptake studies, each experiment was performed using at least two different sets of cultured cells. Within each experiment, the experimental data points were determined in quadruplicate. The results are expressed as means ± SD from data obtained from at least two separate experiments. Two-way analysis of variance (ANOVA) was applied to compare the results from different experiments. A value of $p < 0.05$ is considered statistically significant.

Results and Discussion

Characterization of the Microspheres. *Morphology of the Microspheres.* Figure 1 shows the microscopic photographs of the unloaded (Figure 1a) and verapamil (VER)-loaded (Figure 1b) dry MS with the same magnification. As illustrated, the process of drug loading did not rupture the MS. Instead, the surface of the MS became smoother and the size of the MS became larger, indicating an increase in the volume of the MS due to the drug loading.

Swelling of the MS in Various Media. Equilibrium swelling and swelling rate are two important parameters associated with the release mechanism and kinetics of a solute from hydrogels. The MS used in this study are essentially polyelectrolyte hydrogels. Therefore, their swelling in various media, such as deionized water, 0.05 M pH

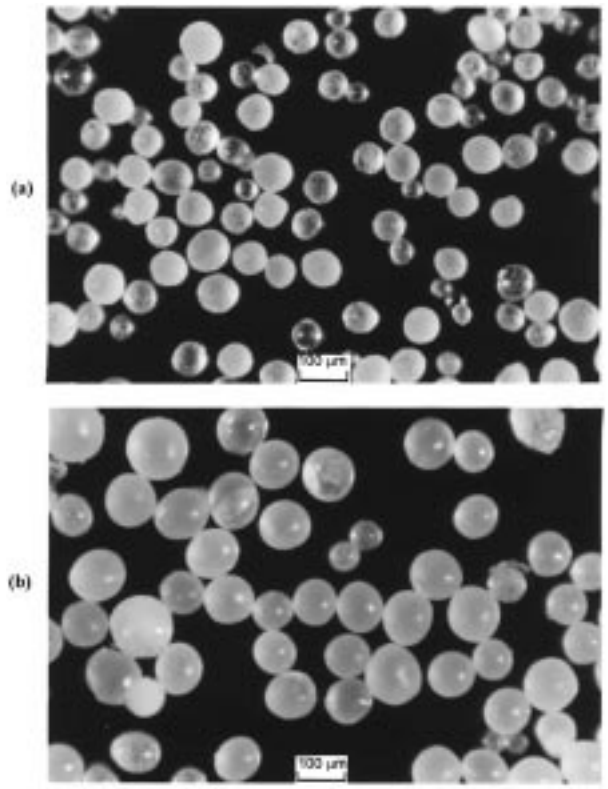

Figure 1—Microscopic photographs of (a) unloaded and (b) verapamil-loaded MS in dry state.

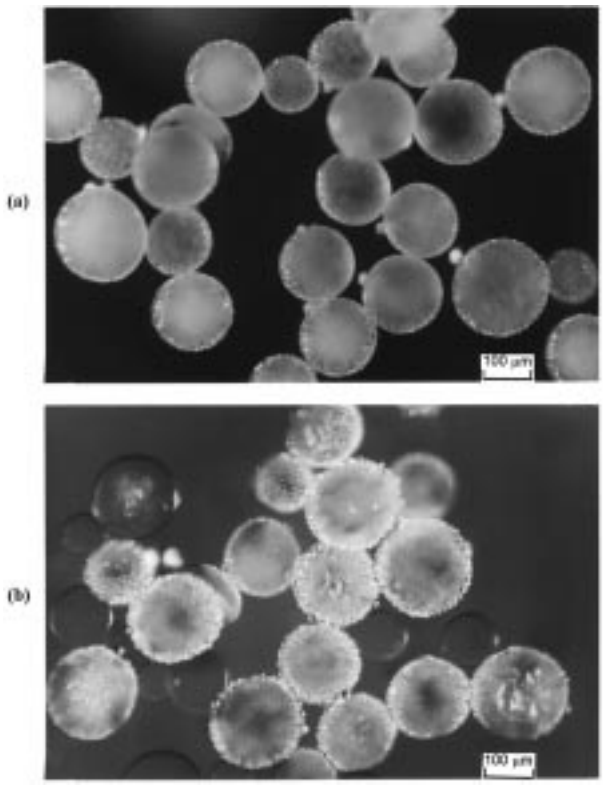

Figure 2—Microscopic photographs of verapamil-loaded MS in 0.05 M pH 7.4 buffer solution at room temperature for (a) 5 min and (b) 20 min.

7.4 phosphate buffer (Fisher Scientific), and 0.9% NaCl, was investigated microscopically. The MS without loaded drug swelled instantaneously like "pop corns" in all three media. Their swelling ratio, H, defined as the volume of the MS at the swollen state divided by the volume at the dry state, was 12−13. In contrast, the drug-loaded MS exhibited slower swelling and a much smaller swelling ratio, especially in deionized water. The VER-loaded MS reached the equilibrium swelling ($H \approx 3$) in deionized water in about 30 min, with a clear swelling or solvent penetration front, like the observation with hydrophobic gels.[41] In the isotonic saline and the buffer solution, the maximal size ($H \approx 6$) was observed within 3−10 min, followed by a size reduction. The peak size may be an indication of an initial swelling-dominated stage and thereafter solute depletion, which is typical in hydrophobic hydrogel loaded with high drug content.[42] The diminished swelling ratio and rate for drug-loaded MS suggest an increased hydrophobicity of the MS due to the bound drug molecules (i.e., VER) that are more hydrophobic than Na^+ present in the unloaded MS. In pH 7.4 buffer solution, the swelling or penetration front disappeared, probably as a result of quick ion exchange of the drug with the counterions (i.e., K^+ or Na^+), which converts the hydrophobic drug−MS complex into hydrophilic MS.

Microscopic photographs of the VER-loaded MS in the buffer solution for 5 and 20 min are shown in Figures 2a and 2b, respectively. It was observed that oily droplets accumulated on the surface of the MS at a later time. The droplets disappeared as more buffer solution was added and more vigorous shaking was applied. This result may be ascribed to small volume of the solution and insufficient mixing during the examination of microscopy. It implies that the rate of removal of the released drug from the MS surface is lower than the drug release from the MS, resulting in the drug accumulation on the surface. This accumulation may be the case in the body cavities, such as a solid tumor, where circulation of the body fluid is poor.[35,36]

Interestingly, the oily droplets were absent when 0.9% NaCl was used as a releasing medium. Moreover, the boundary of undissolved drug that was observed in the pH 7.4 buffer solution disappeared in the saline. These results agree with the observations of the dependence of the drug moving front on the drug solubility,[41] suggesting that the solubility of verapamil salts may vary with its salt form. In a NaCl solution, the released verapamil salt is in a chloride form, whereas in the phosphate buffer, it is in a phosphate form. The latter may exhibit lower solubility than the former. Based on this observation, it may be concluded that in the present system, ion exchange is a major mechanism of the drug release from the MS, but drug solubility and drug diffusion away from the surface of the MS into the bulk fluid may play important roles in the release kinetics.

Determinants of Drug Loading. To obtain optimal drug loading, several factors influencing the amount of drug bound to the MS were investigated, including incubation time, ratio of MS to drug (M/D), drug affinity to the MS, and initial drug concentration.

Effect of Incubation Time. Curve A in Figure 3 depicts the fraction of remaining verapamil in the solution as a function of time for the MS incubated in a 0.025-mg/mL verapamil solution. A rapid decrease in the remaining drug is seen in the initial 10 h, followed by a slower change in the subsequent 10 h. A plateau in the curve after 20 h indicates an equilibrium state. A similar trend was also observed for vinblastine. Therefore, incubation was carried out for 30 h for all the drug loading to ensure completion of the process. The fraction of the drug loaded into the MS, as shown by curve B in Figure 3, follows typical first-order sorption kinetics, suggesting that the drug loading is essentially a diffusion-controlled process like drug release.[43]

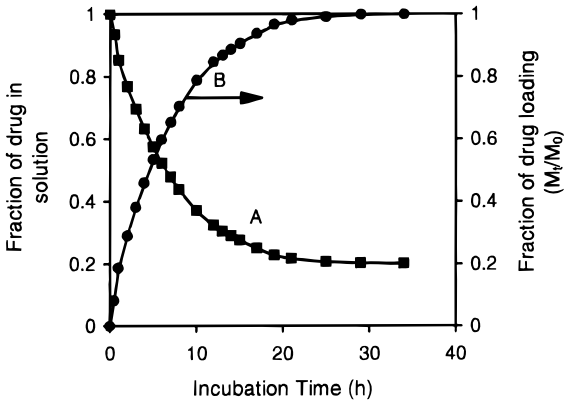

Figure 3—Dynamics of verapamil absorption into the MS through ion exchange. The initial concentration of verapamil is 0.025 mg/mL; curve A, Fraction of drug remains in the solution; curve B, fraction of drug loaded into the MS calculated using the amount of drug loaded at time *t* divided by the equilibrium amount of drug loaded. Experiments in Figures 3–6 were performed as described in the Experimental Section (SD < 10%).

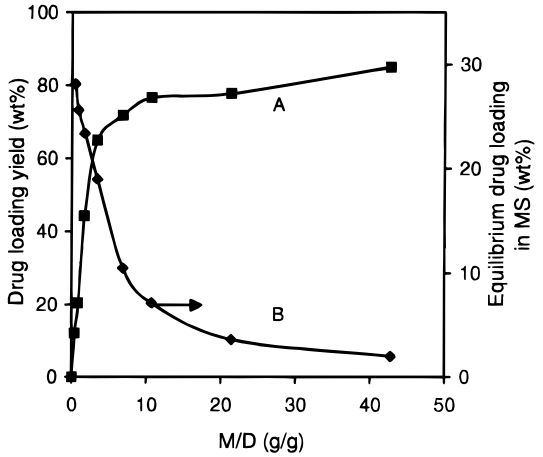

Figure 4—Effect of the MS/drug ratio (M/D) on the equilibrium level of verapamil loaded and the yield of the loading. The initial verapamil concentration is 0.05 mg/mL.

Although swelling of the dry MS is observed, the swelling in an aqueous medium is very quick compared with the drug absorption, as discussed previously.

Effect of Ratio of Microspheres to Drug. The amount of MS relative to drug is an important factor influencing the equilibrium drug content and the yield of drug loading. However, there has been little work in this area, though various conditions have been used by different researchers.[25−28] Using verapamil as a model drug, the effect of the M/D ratio was investigated. The yield of drug loading and the equilibrium level of verapamil loaded are plotted against the M/D ratio in Figure 4. As the M/D ratio increases, the yield of drug loading increases while the equilibrium level of drug loaded decreases (Curve A). This result indicates that to raise the equilibrium drug content in the MS, one has to sacrifice the loading efficiency. Therefore, a compromise approach is to control the M/D ratio between 1 and 3 and thus the drug content can reach ~30% and the yield of drug loading is in the range 40−60%.

Effect of Drug Concentration. The effect of drug concentration on the equilibrium drug content was investigated for initial verapamil concentrations ranging from 10 to 85 mg/mL at an M/D ratio of 1. In this wide range of verapamil concentrations, the equilibrium loading is only slightly reduced from 24 to 22%. This observation is not abnormal. At a fixed M/D ratio, the amount of drug bound to MS is determined by the competition between the drug and the counterions (e.g., Na^+). Addition of water to the mixture causes an equal dilution of both cations, but the equilibrium constant remains unchanged. Consequently, the amount of drug bound to the MS undergoes little change.

Relative Affinity of Vinblastine and Verapamil. The relative affinity of vinblastine (VIN) and verapamil (VER) was determined by the sorption method. The competitive sorption of VIN and VER was carried out using known amounts of MS (e.g., M/D ratio = 1.5) in the solution of dual agents with various VIN/VER ratios. The separation and assay of the dual agents were performed with HPLC. The dual agents were effectively separated with a retention time of 5.95 min for VIN and 6.82 min for VER.

When the MS are added to a solution containing a cationic drug, the drug competes with Na^+ to bind to the MS as illustrated by the following formula

$$\mathrm{Re{-}SO_3^-\ Na^+ + DRUG^+ \rightleftharpoons Re{-}SO_3^-\ DRUG^+ + Na^+}$$

The equilibrium of ion exchange determines the maximum of the drug loaded into the MS, which can be correlated with selective coefficients that are expressed by the following equations[44]

$$K_{VIN} = \frac{[VIN]_m[Na]_s}{[VIN]_s[Na]_m} \quad (1)$$

$$K_{VER} = \frac{[VER]_m[Na]_s}{[VER]_s[Na]_m} \quad (2)$$

where K_{VIN} and K_{VER} are the selectivity coefficients for the drug and the competing ions, Na^+; and the subscripts m and s denote the concentration in the microspheres and in the solution, respectively. In the process of absorption of dual agents, the Na^+ concentration in the solution and the MS should be the same in eqs 1 and 2. Therefore, the relative selectivity coefficient of VIN and VER, K_R, can then be obtained from eq 3

$$K_R = \frac{K_{VIN}}{K_{VER}} = \frac{[VIN]_m/[VER]_m}{[VIN]_s/[VER]_s} \quad (3)$$

By plotting the [VIN]/[VER] ratio in the MS against that in the solution at the equilibrium as illustrated by Figure 5, the value of K_R was estimated from the slope of the straight line to be 1.25. The K_R value greater than unity reflects slightly higher affinity of VIN to the MS than that of VER.

Kinetics of Drug Release. Figure 6a shows the release profiles of verapamil and vinblastine from single-agent-loaded MS in 0.05 M pH 7.4 buffer at 37 °C. It appears that verapamil is released completely within 2 h and vinblastine by 3 h. Similarly, Figure 6b illustrates a higher release rate of verapamil than vinblastine from the dual-agent-loaded MS. In EBBS, the same trend was also observed. The lower release rate of vinblastine may be a reflection of its higher affinity to the MS in addition to its larger molecular size. When the MS loaded with the drugs without drying were added to the release medium, the release rate was increased significantly. This result suggests that hydration of the MS or the polymer relaxation may play some role in the kinetics of drug release. Microscopic studies revealed a short period time of swelling of the MS, as discussed previously. The completion of the swelling was within 10 min which was relatively short compared with other hydrogel beads[41,42] because of their much smaller diameter and higher hydrophilicity. Never-

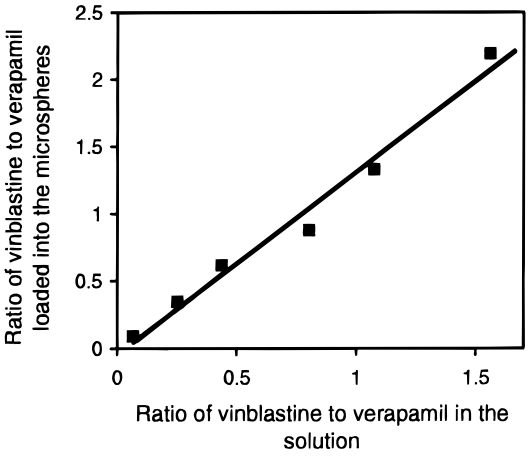

Figure 5—A plot of [VIN]/[VER] ratio in the MS against that in the solution at the equilibrium (M/D = 1.5, the total drug loading is ~20 wt %). The relative selective coefficient of vinblastine is evaluated from the slope of the straight line (K_R = 1.25).

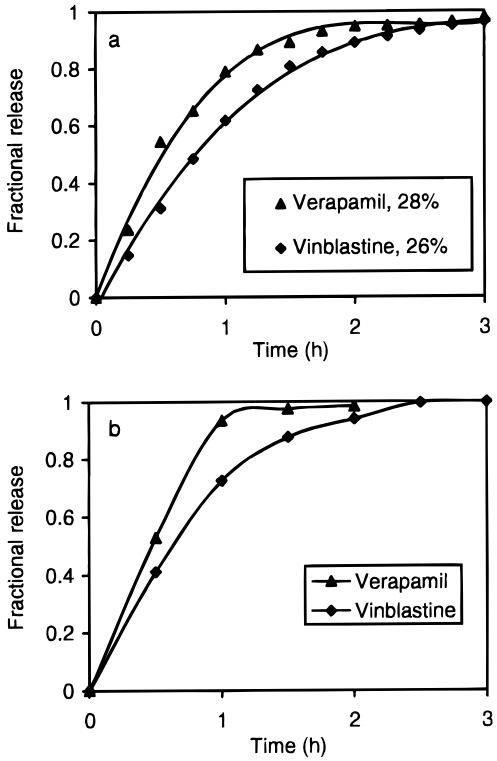

Figure 6—Fractional release of vinblastine and verapamil in 0.05 M pH 7.4 buffer at 37 °C as a function of time from (a) single-agent-loaded MS (drug loading for verapamil is 28 wt % and for vinblastine is 26 wt %); and (b) dual-agent-loaded MS (the total drug loading is ~20 wt %).

theless, this time span is about 10% of the total release time of the drug (i.e., VER). Therefore, the hydration of the MS is not negligible in the present system.

In Vitro Evaluation of the MS Delivery System. *Drug Resistance of CH^{R}C5 Monolayer Cells.* The effectiveness of CH^{R}C5 monolayer cells as a MDR cell model was investigated by measuring drug uptake by the cells in the absence (control) and presence of a chemosensitizer, either verapamil (50 μM) or cyclosporin A (20 μM). Figure 7a shows that in the presence of verapamil or cyclosporin A, the cellular uptake of vinblastine by CH^{R}C5 cells significantly ($p < 0.01$) increases 7 and 9 times, respectively. In contrast, only up to 3-fold ($p < 0.01$) increase in drug uptake by nonresistant cells, AUXB1, is observed in the

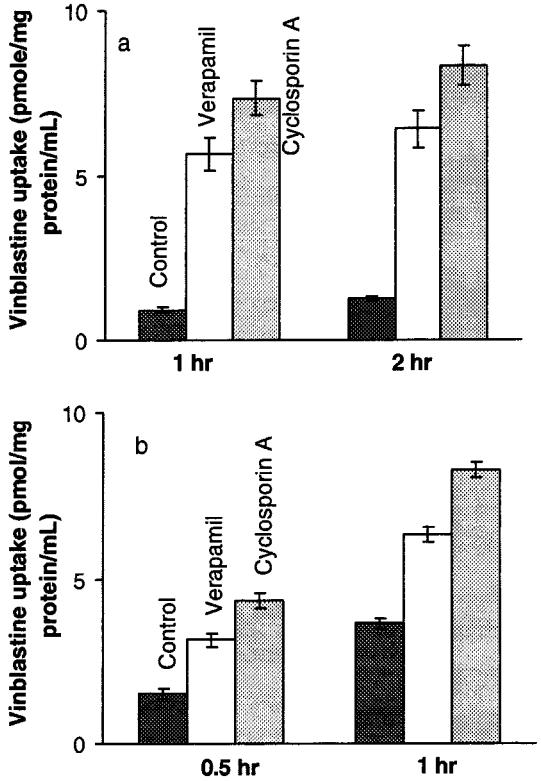

Figure 7—Vinblastine uptake by (a) MDR (CH^{R}C5) monolayer cells and (b) parent cells (AuxB1) after incubation for 1 h and 2 h. The bars represent control (i.e., without a chemosensitizer), with addition of verapamil (50 μM), and with addition of cyclosporin A (20 μM). The concentration of vinblastine used in the uptake is 21 nM with 1/3 radiolabeled and 2/3 cold drug. Results are expressed as mean ± SD from at least two different experiments. A statistically significant difference between the control and the uptake in the presence of chemosensitizers was found ($p < 0.01$) for Figure 7a and 7b.

presence of chemosensitizers (Figure 7b). These results confirm that CH^{R}C5 cell line grown as a monolayer is an effective model for the in vitro evaluation of chemosensitization.

Effect of Blank Microspheres on Cell Viability and Cellular Drug Uptake. Cell viability in the presence of blank MS was comparable to the control (data not shown), suggesting that the blank MS did not cause cell toxicity. As shown in Figure 8a, in the presence of the blank MS and absence of chemosensitizers, the cellular drug uptake (bar 2) does not statistically differ from the control (bar 1; $p > 0.05$). In the presence of chemosensitizers (bar 3: 50 μM verapamil, and bar 4: 20 μM cyclosporin A), the blank MS do not have any significant effect on the drug uptake as evidenced by the equivalent efficacy of MDR reversal in the absence (Figure 7a, bars 2 & 3) and presence of the MS (Figure 8a, bars 3 & 4). As presented in Section 2, the relative equilibrium loading of vinblastine to verapamil is 1.25; that is, the amount of vinblastine loaded in the MS can reach 1.25 times of that of verapamil if both are of the same concentration in the solution. However, the concentration of vinblastine used in the uptake studies is 21 nM, which is about or less than the one-thousandth of the concentration of the chemosensitizers (20 and 50 μM). Therefore, the competitive binding of vinblastine with verapamil to the MS is expected to be negligible.

Effectiveness of the Chemosensitizer Delivered by the Microspheres. Two different approaches of delivering chemosensitizers and anticancer drugs to MDR cells were evaluated: (1) verapamil-loaded MS plus free vinblastine (bar 2 in Figure 8b), and (2) vinblastine- and-verapamil-

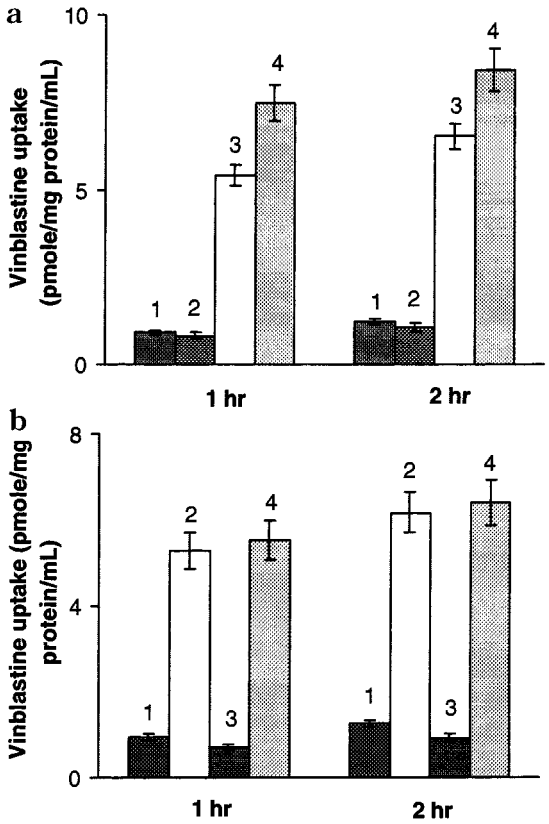

Figure 8—(a) Effect of blank MS on vinblastine uptake by MDR (CH^RC5) monolayer cells at 1 and 2 h. The bars represent (1) control; (2) blank MS; (3) free verapamil plus the blank MS; and (4) free cyclosporin A plus the blank MS. The concentration of vinblastine used is the same as in Figure 7. Results are expressed as mean ± SD from at least two different experiments. A statistically significant difference between the control and the uptake in the presence of chemosensitizers/blank MS was found for bar 3 and bar 4 ($p < 0.01$). (b) Effect of different microspherical formulations on vinblastine uptake by MDR (CH^RC5) monolayer cells. The bars represent (1) control; (2) verapamil-loaded MS plus free vinblastine (21 nM); (3) vinblastine-loaded MS; and (4) vinblastine- and-verapamil-loaded MS. Results are expressed as mean ± SD from at least two different experiments. A statistically significant difference between the control and the uptake in the presence of chemosensitizer-loaded MS was found for bar 2 and bar 4 ($p < 0.01$).

loaded MS (bar 4 in Figure 8b). For comparison, a control (bar 1) and vinblastine-loaded MS (bar 3) are also presented in the figure. In the absence of verapamil, the drug uptake in the presence of vinblastine-loaded MS (bar 3) is almost the same ($p > 0.05$) as the control. In contrast, the verapamil-loaded MS (Figure 8b, bar 2) exhibit a comparable efficacy in the reversal of MDR as free verapamil (Figure 7a, bar 2), suggesting that the bioactivity of the chemosensitizer has been preserved. Moreover, the MS loaded with both verapamil and vinblastine display a significant ($p < 0.01$) enhancement of drug uptake up to 7-fold, a level achieved with free drug solutions.

The diameter of the MS ranges from 40 to 125 μm in dry form (even larger in wet form), much bigger than the size of CHO cells, so it is unlikely that the increase in drug uptake is due to the phagocytosis of the particles by the cells. On the other hand, the blank MS have no effect on drug uptake. Therefore, the enhancement of the drug uptake is likely a reflection of the effect of the chemosensitizer released from the MS. These results demonstrate that the bioactivity of the MS-loaded verapamil in reversing MDR remains unchanged in both formulations of single-agent and dual-agent loading. The results also suggest that both antineoplastic and chemosensitizing agents are released from the MS effectively.

Conclusion

The ionic polysaccharide MS possess a fairly good loading capacity for ionic chemosensitizer and anticancer drug. The loading of a single agent or dual agents could readily reach 28 wt %. The amount of drug loaded was influenced by the M/D ratio and drug affinity to the MS. Release rate of the loaded drugs was likely controlled by ion exchange; that is, the counterions diffuse in and the ionic drugs diffuse out of the MS. However, hydration of the MS, solubility of the drug, as well as the rate of drug leaving the surface of the MS each might play an important role in release kinetics. The delivery system appeared effective at releasing both antineoplastic and chemosensitizing agents in vitro. More importantly, similar enhancement of anticancer drug uptake was achieved with the MS-delivered chemosensitizer as that with the free drug, suggesting that the biological activity of the chemosensitizer was preserved. To further evaluate the therapeutic efficacy of the new formulation, in vivo investigation is presently being undertaken using an animal tumor model.

References and Notes

1. Jain, R. K. Barriers to drug delivery in solid tumors. *Sci. Am.* **1994**, *July*, 58−65.
2. Andrews, P. M.; Johnson, J. L., Jr. Regional chemotherapy in an experimental model of Wilms' tumor in rats. *Cancer Chemother. Pharmacol.* **1989**, *23*, 31−34.
3. Bast, R. C.; Segerling, M.; Ohanian, S. H.; Greens, S. L.; Zbar, B., Rapp, H. J.; Borsos, T. Regression of established tumors and induction of tumor immunity by intratumor chemotherapy. *JNCI* **1976**, *56*, 829−834.
4. McLaughlin, C. A.; Cantrell, J. L.; Ribi, E.; Goldberg, E. P. Intratumor chemotherapy with Mytomycin and components from Myobacterium in regression of line 10 tumor in Guinea pigs. *Cancer Res.* **1978**, *38*, 1311−1317.
5. Chen, Y.; Burton, M. A.; Gray, B. N. Pharmaceutical and Methodological Aspects of Microparticles. In *Microspheres and Regional Cancer Therapy*; Willmot, N., Daly, J. M., Eds.; CRC Press: Boca Raton, FL, 1994; pp 1−29.
6. Kato, T. Foreword. In *Microspheres and Regional Cancer Therapy*, Willmot, N., Daly, J. M., Eds.; CRC Press: Boca Raton, FL, 1994.
7. Deurloo, M. J. M.; Bohlken, S.; Kop, W.; Lerk, C. F.; Hennink, W.; Bartelink, H.; Begg, A. C. Intratumoral administration of Cisplatin in slow-release device: I. Tumor response and toxicity. *Cancer Chemother. Pharmacol.* **1990**, *27*, 135−140.
8. Anderson, J. H.; McArdle, C. S.; Cooke, T. G.; Microparticulate carriers as a therapeutic option in regional cancer therapy: Clinical consideration, In *Microspheres and Regional Cancer Therapy*. Willmot, N., Daly, J. M., Eds.; CRC Press: Boca Raton, FL, 1994; pp 57−70.
9. Kato, T.; Sato, K.; Sasaki, R.; Kakinuma, H.; Moriyama, M. Targeted cancer chemotherapy with arterial microcapsule chemoembolization: Review of 1013 patients. *Cancer Chemother. Pharmacol.* **1996**, *37*, 289−296.
10. Murata, T.; Akagi, K.; Imamura, M.; Nasu, R.; Kimura, H.; Nagata, K.; Tanaka, Y. Studies on hyperthermia combined with arterial therapeutic blockade for treatment of tumors: (Part III) Effectiveness of hyperthermia combined with arterial chemoembolization using degradable starch microspheres on advanced liver cancer. *Oncol Rep.* **1998**, *5*, 709−12.
11. Sugiyama, T.; Kumagai, S.; Nishida, T.; Ushijima, K.; Matsuo, T.; Yakushiji, M.; Hyon, S. H.; Ikada, Y. Experimental and clinical evaluation of cisplatin-containing MS as intraperitoneal chemotherapy for ovarian cancer. *Anticancer Res.* **1998**, *18*, 2837−42.
12. Hagiwara, A.; Sakakura, C.; Shirasu, M.; Yamasaki, J.; Togawa, T.; Takahashi, T.; Muranishi, S.; Hyon, S.; Ikada, Y. Therapeutic effects of 5-fluorouracil microspheres on peritoneal carcinomatosis induced by Colon 26 or B-16 melanoma in mice. *Anticancer Drugs* **1998**, *9*, 287−289.
13. Tokuda, K.; Natsugoe, S.; Shimada, M.; Kumanohoso, T.; Baba, M.; Takao, S.; Nakamura, K.; Yamada, K.; Yoshizawa, H.; Hatate, Y.; Aikou, T. Design and testing of a new cisplatin form using a base material by combining poly-D, L-lactic acid and poly(ethylene glycol) acid against peritoneal metastasis. *Int. J. Cancer* **1998**, *76*, 709−712.

14. Ciftci, K.; Hincal, A. A.; Kas, H. S.; Ercan, T. M.; Sungur, A.; Guven, O.; Ruacan, S. Solid tumor chemotherapy and in vivo distribution of fluorouracil following administration in poly(L-lactic acid) microspheres. *Pharm. Dev. Technol.* **1997**, *2*, 151−160.
15. Pastan, I.; Gottesman, M. Multiple-drug resistance in human cancer. *N. Engl. J. Med.* **1987**, *316*, 1388−1393.
16. Kessel, D. *Resistance to antineoplastic drugs*; CRC Press: Boca Raton, FL, 1989.
17. Cole, S. P. C.; Bhardwaj, G.; Gerlach, J. H.; Mackie, J. E.; Grant, C. E.; Almquist, K. C.; Stewart, A. J.; Kurtz, E. U.; Duncan, A. M. V.; Deeley, R. G. Overexpression of a transporter gene in a multidrug-resistant human cancer cell line. *Science* **1992**, *258*, 1650−1654.
18. Georges, E.; Sharom, F. J.; Ling, V. Multidrug resistance and chemosensitization: Therapeutic implications for cancer therapy. In *Advances in Pharmacology*, V21; Academic Press: New York, 1990.
19. Fan, D.; Beltran, P. J.; O′Brian, C. A. Reversal of Multidrug Resistance. In *Reversal of Multidrug Resistance*; Kellen, J. A., Ed.; CRC Press: Boca Raton, FL, 1994.
20. Slater, L. M.; Murray, S. L.; Wetzel, M. W.; Wisdom, R. M.; DuVall, E. M. Verapamil restoration of daunorubicin responsiveness in daunorubicin-resistant Ehrlich ascites carcinoma. *J. Clin. Invest.* **1982**, *70*, 1131−1134.
21. Ozols, R. F.; Cunnion, R. E.; Klecker, R. W., Jr.; Hamilton, T. C.; Ostchega, Y.; Parrillo, J. E.; Young, R. C. Verapamil and adriamycin in the treatment of drug-resistant ovarian cancer. *J. Clin. Oncol.* **1987**, *5*, 641−647.
22. Bartlett, N. L.; Lum, B. L.; Fisher, G. A.; Brophy, N. A.; Ehsan, M. N.; Halsey, J.; Sikic, B. I. Phase I trial of doxorubicin with cyclosporine as a modulator of multidrug resistance. *J. Clin. Oncol.* **1994**, *12*, 835−842.
23. Murren, J. R.; Hait, W. N. Why have not we cured multidrug resistant tumors? *Oncol. Res.* **1992**, *4*, 1−6.
24. Raderer, M.; Scheithauer, W. Clinical trials of agents that reverse multidrug resistance. *Cancer* **1993**, *72*, 3553−3563.
25. Goldberg, E. P.; Iwata, H.; Longo, W. Hydrophilic albumin and dextran ion-exchange MS for localized chemotherapy. In *Microspheres and Drug Therapy, Pharmaceutical, Immunological and Medical Aspects*; Davis, S. S.; Illum, L.; McVie, J. G.; Tomlinson, E., Eds.; Elsevier Science: New York, 1984; pp 309−325.
26. Chen, Y.; Burton, M. A.; Codde, J. P.; Napoli, S.; Martins, I. J.; Gray, B. N. Evaluation of ion-exchange microspheres as carrier for the anticancer drug doxorubicin: In *vitro* studies. *J. Pharm. Pharmacol.* **1992**, *44*, 211−215.
27. Codde, J. P.; Burton, M. A.; Kelleher, D. K.; Archer, S. G.; Gray, B. Reduced toxicity of adriamycin by incorporation into ion exchange microspheres: A therapeutic study using a rat liver tumour model. *Anticancer Res.* **1990**, *10*, 1715−1718.
28. Codde, J. P.; Lumsden, A. J.; Napoli, S.; Burton, M. A.; Gray, B. N. A comparative study of the anticancer efficacy of doxorubicin carrying MS and liposomes using a rat liver tumour model. *Anticancer Res.h* **1993**, *13*, 539−543, and *14-(11)*, S-281.
29. Kamath, K. R.; Park, K. Biodegradable hydrogels in drug delivery. *Adv. Drug Deliv. Rev.* **1993**, *11*, 59−84.
30. Wu, X. Y.; Liu, Z.; Bendayan, R. Development of a particulate delivery system with surface-immobilized chemosensitizer. *Pharm. Res.* **1996**, *13*(*9*), S-303.
31. Liu, Z.; Wu, X. Y.; Bendayan, R. Enhanced drug uptake by multidrug resistant cells via simultaneous delivery of chemosensitizer and therapeutic agent. *Pharm. Res.* **1997**, *14(11)*, S-281.
32. Wang, J.; Li, L. S.; Feng, Y. L.; Yao, H. M.; Wang X. H. Permanent hepatic artery embolization with dextran MS in 131 patients with unresectable hepatocellular carcinoma. *Chin. Med. J.* **1993**, *106*, 441−445.
33. Dion, J. E.; Rankin, R. N.; Vinuela, F.; Fox, A. J.; Wallace, A. C.; Mervart, M. Dextran microsphere embolization: experimental and clinical experience with radiologic-pathologic correlation. Work in progress. *Radiology* **1986**, *160*, 717−721.
34. Chakravarthy, D.; Rodway, N.; Schmidt, S.; Smith, D.; Evancho, M.; Sims, R. Evaluation of three new hydrocolloid dressings: Retention of dressing integrity and biodegradability of absorbent components attenuate inflammation. *J. Biomed. Mater. Res.* **1994**, *28*, 1165−1173.
35. Wu, X. Y.; Eshun, G.; Zhou, Y. Effect of interparticulate interaction on kinetics of drug release in microsphere ensembles. *J. Pharm. Sci.* **1998**, *87*, 586−593.
36. Wu, X. Y.; Zhou, Y.; Eshun, G. Effects of drug accumulation and particulate separation on drug release kinetics. *Proceed. Intern. Symp. Control. Relat. Bioact. Mater.* **1998**, *25*, 449−450.
37. Ling, V.; Thompson, L. H. Reduced permeability in CHO cells as a mechanism of resistance to colchicine. *J. Cell. Physiol.* **1974**, *83*(*1*), 103−116.
38. Carlsen, S. A.; Till, J. E.; Ling, V. Modulation of membrane drug permeability in Chinese hamster ovary cells. *Biochim. Biophys. Acta* **1976**, *455*(*3*), 900−912.
39. Bendayan, R.; Lo, B.; Silverman, M. Characterization of cimetidine tranport in LLCPK_1 cells. *J. Am. Soc. Nephrol.* **1994**, *5*(*1*), 75−84.
40. Bradford, M. M. A rapid and sensitive method for quantitation of microgram quantities of protein utilizing the principle of protein dye binding. *Anal. Biochem.* **1976**, *15*, *2*, 248−254.
41. Lee, P. I. Diffusion-controlled matrix systems. In *Treatise on Controlled Drug Delivery*; Kydonieus, A., Ed., Marcel Dekker: New York, 1992.
42. Kim, C.-J.; Lee, P. I. Effect of loading on swelling-controlled drug release from hydrophobic polyelectrolyte gel beads. *Pharm. Res.* **1992**, *9*, 1268−1274.
43. Schacht, E.; Goethals, E.; Gyselinck, P.; Thienpont, D. Polymer drug combinations. VI. Sustained release of levamisole from ion-exchange resins. *J. Pharmacie Belgique* **1982**, *37*(*3*), 183−188.
44. Borodkin, S. Ion Exchange Resin Delivery System. In *Polymers for Controlled Drug Delivery*; Tarcha, P. J., Ed.; CRC Press: Boca Raton, FL, 1991; pp 215−230.

Acknowledgments

The authors sincerely thank the following individuals and organizations: Dr. V. Ling, Dr. S. Ito, and Dr. J. Ballinger for kindly providing the cell lines; Sandoz Canada for generously donating cyclosporin A; the Faculty of Pharmacy and the Connaught Fund at the University of Toronto for financial support to X.Y.W.; and the University of Toronto for providing an Open Scholarship to Z.L.

JS9803353

Pore Induction in Human Epidermal Membrane during Low to Moderate Voltage Iontophoresis: A Study Using AC Iontophoresis

S. KEVIN LI,* ABDEL-HALIM GHANEM, KENDALL D. PECK, AND WILLIAM I. HIGUCHI

Contribution from *Department of Pharmaceutics and Pharmaceutical Chemistry, University of Utah, Salt Lake City, Utah 84112.*

Received August 13, 1998. Accepted for publication December 18, 1998.

Abstract □ The present study aimed to investigate new pore induction as a flux-enhancing mechanism in human epidermal membrane (HEM) with low to moderate voltage electric fields. The extent of pore induction and the effective pore sizes of these induced pores were to be assessed using a low frequency (12.5 Hz) low to moderate voltage (2.0 to 4.0 V) square-wave alternating current (ac) "passive" permeation method (ac iontophoresis). This ac approach was to allow for inducing and sustaining a state of pore induction in HEM while permitting no significant transport enhancement via electroosmosis; thus, transport enhancement entirely due to new pore induction (enhanced passive permeation) was to be assessed without any contributions from electroosmosis. Good proportionality between the increase in HEM permeability and its electrical conductance was found with the "passive" transport data obtained during square-wave ac iontophoresis using urea as the model permeant. Typically, at 3.0 to 4.0 V, HEM conductance increases (and permeability increases) ranged from around 3- to 30-fold. These results appear to be the first *direct* evidence that new pore induction in HEM is a significant flux enhancing mechanism under moderate voltage conditions. The extents of pore induction in HEM under low frequency moderate voltage (2.0 to 3.0 V) ac, pulsed direct current (dc), and continuous dc were also compared. The extents of pore induction from square-wave ac and pulsed dc were generally of the same order of magnitude but somewhat less than that observed during continuous dc iontophoresis at the same applied voltage and duration, suggesting less extent of pore induction with reversing polarity or when a brief delay is provided between pulses to allow for membrane depolarization. The average effective pore sizes calculated for the induced pores from the experimental data with urea and mannitol as probe permeants and the hindered transport theory were 12 ± 2 Å, which are of the same order of magnitude as those of preexisting pores determined from conventional passive diffusion experiments.

Introduction

Previous studies have provided insights regarding iontophoretic transdermal transport mechanisms of ionic and polar compounds with human epidermal membrane (HEM). It has been shown that the alteration of HEM barrier properties during low to moderate voltage iontophoresis is consistent with the induction of new pores (or new pathways) with the observed increase in HEM electrical conductance correlating with the increase in HEM permeability.[1] The occurrence of pore induction during low to moderate voltage iontophoresis was hypothesized in even earlier studies,[2−5] but other explanations for the decrease in electrical resistance and the increase in permeability during iontophoresis could not be justifiably excluded.[5−9] Also, some recent reports have continued to take the view that significant new pore induction in HEM can occur only at high voltages and that (at conventional voltages employed in iontophoresis) "iontophoresis primarily involves electrically driven transport through *fixed* pathways across the stratum corneum".[10−12]

In a recent study with HEM, the size of the pores induced during low to moderate voltage iontophoresis was estimated with neutral permeants in electroosmosis experiments.[13] However, because electroosmosis depends on the sign and magnitude of the pore surface charge density, pore size estimation based on these data are considered to be compromised by possible variable pore surface charge density in HEM.

As will be shown, square-wave ac iontophoresis can be used as a tool in characterizing the barrier properties of human skin during iontophoresis and pore induction. A method based on ac iontophoresis may be employed to study the state of pore induction in the absence of flux enhancement from electroosmosis and from electrophoresis. Particularly, the characteristics of the pores induced in HEM during iontophoresis (pulsed dc, square-wave ac, and/or continuous dc) may be investigated with this ac iontophoresis strategy regardless of possible pore surface charge distributions because transport enhancement due to pore induction can be isolated from the additional enhancement due to electroosmosis and electrophoresis.

The present study aimed to investigate pore induction as a flux-enhancing mechanism during low to moderate applied voltage iontophoresis with HEM. An ac "passive" permeation method (i.e., square-wave ac iontophoresis) was to be developed and used to quantify the extent of pore induction and the effective size of the pores induced. The effects of square-wave ac and pulsed dc on the barrier properties of HEM were also to be compared with continuous dc iontophoresis.

Experimental Section

Materials—Radiolabeled [^{14}C]urea and [^{3}H]mannitol were purchased from New England Nuclear (Boston, MA) and American Radiolabeled Chemicals (St. Louis, MO). Human epidermal membrane (HEM) was supplied by TheraTech Inc. (Salt Lake City, UT). HEM was prepared by heat separation[14] with human skin (from the back, abdomen, or thigh) obtained from Ohio Valley Tissue and Skin Bank (Cincinnati, OH) and was frozen immediately for later used. Millipore GVWP filters (0.22 μm pore diameter) were purchased from Millipore Corporation (Bedford, MA). Phosphate-buffered saline (PBS) at 0.1 M ionic strength and pH 7.4 containing 0.02% sodium azide was prepared by reagent grade chemicals and distilled deionized water.

General Experimental Setup—Iontophoresis studies were carried out in a side-by-side two-chamber diffusion cell (diffusional surface area of around 0.8 cm^2 and chamber volume of 2 or 4 mL) using a four-electrode potentiostat system (JAS Instrumental Systems, Inc., Salt Lake City, UT) as described previously[15] and a waveform programmer (JJ 1276, JAS Instrument Systems, Inc., Belmont, NC) at 37 °C. The counter electrodes were Ag−AgCl. Unless otherwise specified, dc iontophoresis was conducted with

* To whom correspondence should be addressed. E-mail address: kevin.li@m.cc.utah.edu.

10.1021/js980331y CCC: $18.00 Published on Web 02/20/1999

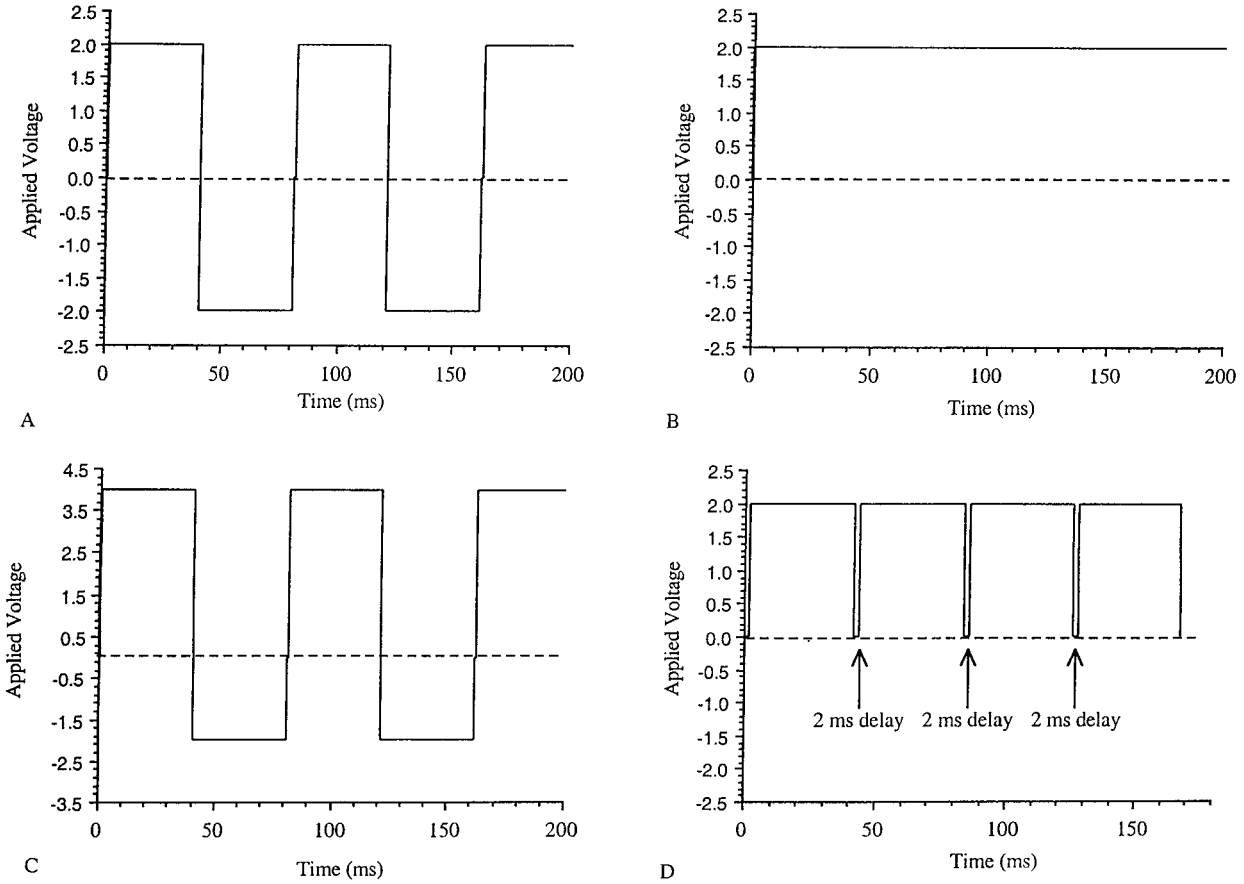

Figure 1—Representative waveform diagrams. (A) 2.0 V 12.5 Hz square-wave ac iontophoresis, (B) 2.0 V continuous dc iontophoresis, (C) superposition of a 1.0 V dc and 12.5 Hz 3.0 V square-wave ac iontophoresis, (D) 2.0 V pulsed dc iontophoresis with 2 ms delay.

the anode in the donor chamber and cathode in the receiver chamber. The electrical conductance of the membrane was monitored by an oscilloscope (Model 2211, Tektronix Inc., Beaverton, OR). Initial electrical conductance was determined by applying a 100 mV potential drop across the membrane. In each transport experiment, the receiver and donor chambers were filled with PBS and PBS premixed with tracer levels of radiolabeled permeants. An appropriate amount of receiver solution sample (1 mL sample for the 2 mL diffusion cells and 1 or 2 mL for the 4 mL diffusion cells) was withdrawn at predetermined time intervals and replaced with fresh PBS, and a 10 μL donor sample was also withdrawn at the same time. These samples were mixed with 10 mL of scintillation cocktail (Ultima Gold, Packard, Meriden, CT) and assayed in a liquid scintillation counter. The apparent permeability coefficients (P) in each experiment were calculated by:

$$P = \frac{1}{C_D A}\frac{dQ}{dt} \quad (1)$$

where A is the membrane surface area, t is time, Q is the amount of permeant transported into the receiver chamber, and C_D is the concentration of permeant in the donor chamber. The pH of the solutions in the donor and receiver chambers was checked after each iontophoresis run.

Nuclepore Membrane Studies—Nuclepore membranes (polycarbonate membrane, 7.5 nm pore radius, 0.001 porosity) were used (the control) to examine the "passive" permeation technique (i.e., square-wave ac iontophoresis) before applying the method to HEM. An assembly of 50 Nuclepore membranes (Nuclepore Corp., Pleasanton, CA) was mounted between the two side-by-side diffusion half-cells. These studies were divided into two stages with mannitol as the permeant. Stage I was passive permeation. In stage II, one of the following protocols was carried out: square-wave ac iontophoresis (amplitude of 1.0 or 2.0 V and frequency ranging from 1.25 to 50 Hz), continuous 0.5 V dc iontophoresis, or a protocol of superposition of 12.5 Hz 2.0 V ac and 0.5 V continuous dc iontophoresis. The duration of the ac transport experiments was around 3 to 5 h. Representative waveforms are shown in Figure 1. Radiolabeled [^{3}H]mannitol was the model permeant in the experiments.

HEM Electrical Resistance Studies—Prior to carrying out the HEM permeant transport studies, a set of experiments were conducted to assess the extent of pore induction in HEM under the low frequency (12.5 Hz) ac voltage regimens and to compare the results to continuous dc and pulsed dc regimens. See General Experimental Setup. HEM supported with a Millipore filter[16] was mounted between the two half-cells of the diffusion cell. HEM was allowed to equilibrate in PBS at 37 °C for 12 to 40 h until its conductance became essentially constant with time before the experiments. The purpose of incubating HEM in PBS was to establish a steady baseline (an essentially constant HEM conductance with time, determined with 100 mV) for comparison studies; changes in HEM electrical conductance are generally observed in the first 10 h (sometimes up to 20 h) of the incubation even though HEM conductance usually does not change by more than a factor of 2 (usually decreases and sometimes increases) during this period. It has been shown that after this equilibration phase, the barrier properties of HEM can remain stable for up to 5–7 days.[16] After this equilibration phase, the following protocol of consecutive runs with a given HEM was employed: 2.0 V 12.5 Hz square-wave ac (which is alternating 40 ms pulses) for 10 s; 2.0 V 40 ms square-wave dc pulses with 1, 2, or 3 ms delay between pulses for 10 s; continuous 2.0 V dc for 10 s; then returning back to 2.0 V 12.5 Hz ac for 10 s. Other similar protocols were also employed with the first and last runs always the same to ensure reversibility/reproducibility in a given set of consecutive runs with a single HEM. Similar experiments were carried out with 3.0 V instead of 2.0 V. HEM electrical resistance was monitored by measuring the current[17] with the oscilloscope throughout the sequence of runs.

HEM Transport Studies—For the iontophoresis/transport studies with HEM, the same experimental setup was used (as above). The receiver and donor chambers were filled with PBS and PBS premixed with trace amounts of the radiolabeled [^{3}H]mannitol

and/or [^{14}C]urea. Mannitol and urea were chosen as the model permeants in the present study because they have well-characterized diffusion properties and are polar nonelectrolytes that essentially transport across the stratum corneum via the pore pathways.[14,18] The apparent permeability coefficients for HEM were calculated with eq 1. The present HEM investigation was divided into three levels of analyses (studies A, B, and C). In study A, the effective radii of the pores induced during square-wave ac iontophoresis were deduced and compared with those of the preexisting pores. In study B, a 1 min 4.0 V prepulse was provided before the square-wave ac run to better match the extent of pore induction to that with continuous dc iontophoresis because the extent of pore induction under continuous dc iontophoresis was generally found to be somewhat higher than that under the same voltage ac iontophoresis (see HEM Electrical Resistance Studies in the Results section and Pulsed and Continuous Iontophoresis in the Discussion section). The objective of study C was to examine whether the pores induced under square-wave ac iontophoresis are similar to those induced under continuous dc iontophoresis.

As part of study A, some preliminary experiments were performed with urea as the only probe permeant. These experiments with urea alone were aimed to establish a HEM permeability vs resistance correlation for square-wave ac iontophoresis. The main experiments in study A were done using urea and mannitol as dual permeants to permit estimating the effective radii of the induced pores. Study A involved three stages. Stage I was a passive permeation run. Stage II was 2.0 V 12.5 Hz square-wave ac and 3.0 V 12.5 Hz square-wave ac iontophoresis when urea was involved alone and when urea and mannitol were the dual permeants, respectively. The duration of stage II ranged from 2 to 5 h depending on the electrical resistance of HEM (around 2 h for the lower resistance and around 5 h for the higher resistance HEM samples). Stage III was a passive permeation run carried out again after the iontophoresis run when the electrical resistance of HEM became constant with time.

Study B also involved three stages. Stage I was passive transport run. Stage II was 4.0 V dc iontophoresis for 1 min (prepulse) followed by a square-wave ac iontophoresis run (3.0 or 4.0 V at 12.5 Hz) for a duration ranging from 1.5 to 6 h. Again, stage III was a passive permeation experiment after iontophoresis when the electrical resistance of HEM became constant with time.

Study C involved five stages. Stage I was a passive permeation run. Stage II was continuous dc iontophoresis (2.0 or 3.0 V; duration of around 0.5 to 1.5 h). Immediately after the continuous dc iontophoresis, stage III was square-wave ac iontophoresis (3.0 or 4.0 V at 12.5 Hz; around 2 to 6 h) following a 4.0 V dc 1 min prepulse. In stage IV, square-wave ac iontophoresis (3.0 or 4.0 V at 12.5 Hz) was superimposed over 1.0 V continuous dc for a duration ranging from around 1.5 to 3 h. The various waveforms used in stages II, III, and IV are illustrated in Figure 1. Stage V was a passive permeation run after the electrical resistance of HEM became constant with time.

Theory and Effective Pore Radius Calculation—Methods of estimating the effective pore radii for the pore pathway in HEM have been described previously for passive permeation[18] and iontophoresis[13] using the hindered transport theory. Briefly, the steady-state iontophoretic flux ($J_{\Delta\psi}$) for a nonionic permeant through HEM can be described by a convective transport model derived from the modified Nernst–Planck theory:[13]

$$J_{\Delta\psi} = \frac{C_D \epsilon W v}{1 - \exp[-Wv(\Delta x)/(HD)]} \quad (2)$$

where ϵ is the combined porosity and tortuosity factor for the membrane, v is the average velocity of the convective solvent flow, H and W are the hindered transport factors for passive diffusion and for transport due to the convective solvent flow induced by electroosmosis, Δx is the effective membrane thickness, C_D has been previously defined in eq 1, and D is the permeant diffusion coefficient taken from the literature.[18] Assuming a single pore size (radius, R_p) and a cylindrical pore geometry in the membrane, the hindrance factor for Brownian diffusion (H) and the hindrance factor for pressure-induced parabolic convective solvent flow (W) can be expressed by:[19]

$$H(\lambda) = (1 - \lambda)^2(1 - 2.104\lambda + 2.09\lambda^3 - 0.948\lambda^5) \quad (3)$$

$$W(\lambda) = (1 - \lambda)^2(2 - (1 - \lambda)^2)\left(1 - \frac{2}{3}\lambda^2 - 0.163\lambda^3\right) \quad (4)$$

when the ratio of solute radius to pore radius (r/R_p) is small (i.e. $\lambda = r/R_p < 0.4$). The hydration radii (Stokes–Einstein radii, r) of the permeants can be obtained from the literature.[18]

At the convection limit (convective flow transport ≫ passive diffusion), eq 2 reduces to:

$$J_{\Delta\psi} = \epsilon W v C_D \quad (5)$$

In the case of passive diffusion, the appropriate relation is:

$$J_{\text{passive}} = \frac{DC_D\epsilon H}{\Delta x} \quad (6)$$

Fluxes for nonionic permeants with square-wave ac iontophoresis in the present study are expected to be well approximated by eq 6, because the electroosmosis contribution to the flux is expected to be negligible at the ac frequencies used (see Nuclepore Membrane Studies in the Results section and the last paragraph in HEM Transport Studies in the Discussion section). In this situation, the effective pore radii for HEM can be estimated from the ratio of urea and mannitol fluxes with eq 6 as in the passive diffusion experiments:

$$\frac{J_m}{J_u} = \frac{H_m}{H_u}\frac{D_m}{D_u} \quad (7)$$

where the subscripts m and u represent the probe permeants mannitol and urea, respectively. The limitations of eqs 5–7 and the uncertainties of estimating the effective pore radii have been previously discussed.[13,18]

The electrical resistance of HEM (R) in PBS is expected to be proportional to its thickness and inversely proportional to its effective porosity:

$$R \propto \frac{\Delta x}{\epsilon H} \quad (8)$$

From eqs 6 and 8 and taking logarithms,

$$\log P = -\log R + c \quad (9)$$

where c is a constant. Equation 9 shows that the electrical resistance of HEM can be expressed as a function of its permeability for the conducting ions. A plot of the logarithm of the permeant permeability coefficient of a membrane vs the logarithm of membrane electrical resistance yielding a slope of − 1.0 would therefore suggest similar transport pathways for the permeant and the conducting ions across the membrane under the specified experimental conditions.

Results

Nuclepore Membrane Studies—The studies with Nuclepore membrane (Figure 2) served to validate the instrumentation (i.e., the four electrode potentiostat system and the waveform programmer) and provided a baseline for the transport studies with HEM. The resistance of an assembly of 50 Nuclepore membranes was found to be essentially the same over the range of applied voltage conditions and the frequency range in the present study (data not shown). The plateau value of the current observed on the oscilloscope display after a brief (within 1 ms) transient period was used to calculate the electrical resistance (the resistance portion of a parallel capacitance and resistance model circuit[20]). Results for mannitol transport with square-wave ac iontophoresis (ranging from 1.25 to 50 Hz), continuous dc iontophoresis (0.5 V), and square-wave ac (2.0 V at 12.5 Hz) superimposed with continuous dc iontophoresis (0.5 V) are summarized in Figure 2. As can be seen, the mannitol

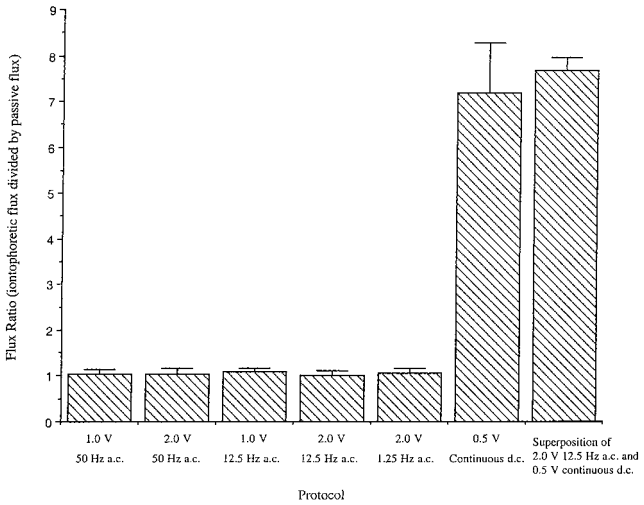

Figure 2—Mannitol flux ratios (iontophoretic flux divided by passive flux) during square-wave ac iontophoresis, continuous dc iontophoresis, and superposition of 12.5 Hz square-wave ac and continuous dc iontophoresis for an assembly of 50 Nuclepore membranes are plotted against the respective experimental protocols. Each bar represents the mean and standard deviation of $n \geq 3$.

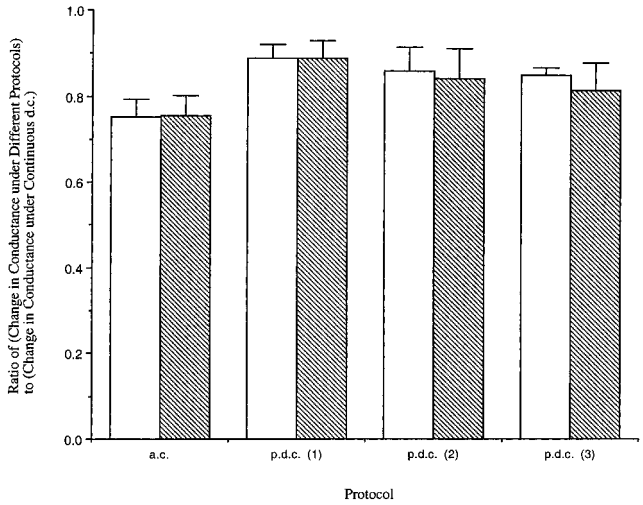

Figure 3—Effects of square-wave ac and pulsed dc iontophoresis on the barrier properties of HEM relative to those of continuous dc at 2.0 V (open bar) and 3.0 V (striped bar). The changes in HEM conductance under different protocols divided by the changes in conductance during continuous dc iontophoresis (for individual HEM samples) were plotted against different protocols. Changes in conductance were determined by conductance (i.e., $1/R$ ($1/k\Omega$)) at 10 s into the iontophoresis run minus the conductance before the iontophoresis run. Abbreviations: ac, 12.5 Hz square-wave ac iontophoresis; pdc, 40 ms square-wave pulsed dc iontophoresis with a brief delay (numbers, ms, in brackets) between each pulse. Each data bar represents the mean ± 95% confidence interval ($n \geq 3$).

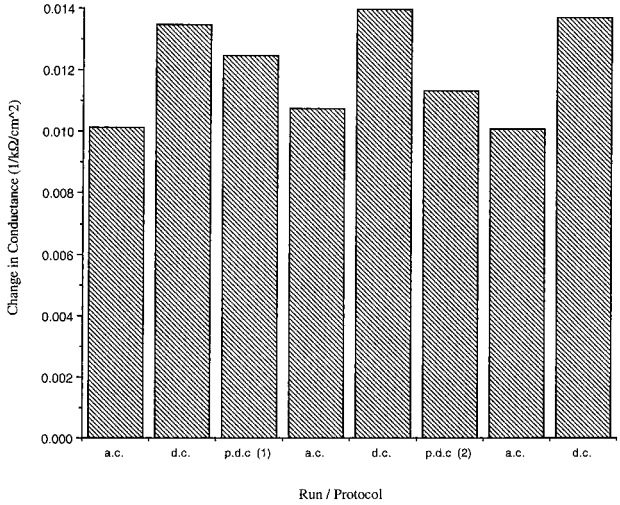

Figure 4—Representative data from a 2.0 V HEM resistance study with a single HEM. The initial electrical resistance of this HEM sample was 71 kΩ cm^2. The HEM electrical resistance just before an iontophoresis run (original or after recovery from the preceding run) was 72 ± 3 kΩ cm^2 (mean ± SD, ranging from 68 to 75 kΩ cm^2). The changes in HEM electrical conductance (changes in $1/R$ from before to the end of the iontophoresis run) are plotted against the different iontophoresis protocols from left to right in the order in which they were carried out. Abbreviations: ac, 12.5 Hz square-wave ac iontophoresis; dc, continuous dc iontophoresis; pdc, 40 ms square-wave pulsed dc iontophoresis with a brief delay (numbers, ms, in brackets) between each pulse.

fluxes with square-wave ac iontophoresis at the voltage conditions in the present study and at frequency ranging from 1.25 to 50 Hz were essentially the same as the fluxes in passive diffusion, in good agreement with predictions based on eq 6 as discussed earlier. This demonstrates that, at sufficiently high frequencies (≥1.25 Hz in the case of the present Nuclepore membrane) under the applied voltage conditions and duration studied, ac iontophoresis does not enhance the transport of permeants across membranes. The results in Figure 2 represent the concept underpinning the HEM studies in the next section.

The flux enhancement with 0.5 V continuous dc superimposed with square-wave ac (2.0 V at 12.5 Hz) was essentially the same as that with 0.5 V continuous dc iontophoresis. The fluxes with 0.5 V continuous dc iontophoresis were more than 7 times higher than those with square-wave ac iontophoresis and passive diffusion; the enhancement factor determined in the present 0.5 V continuous dc iontophoresis experiments is consistent with previous results.[21]

HEM Electrical Resistance Studies—Figure 3 summarizes the results of the experiments designed to compare the extent of pore induction in HEM during 12.5 Hz ac and pulsed dc iontophoresis with continuous dc iontophoresis. A total of 19 HEM samples were involved in this study, with each sample taken successively through several 10 s runs as described in the Experimental section. Figure 4 shows representative results of consecutive experimental runs with a HEM sample. As can be seen in Figure 3, the increases in the electrical conductance with 12.5 Hz ac and with pulsed dc were generally less than (Student's *t*-test of 95% confidence level), but of the same order of magnitude of that observed with continuous dc at the same applied voltages (2.0 or 3.0 V). In general, the increase in the electrical conductance with 12.5 Hz ac was around 75% of that with continuous dc. In these experiments, as the delay time between pulses was increased, the pore induction approached that found with 12.5 Hz ac.

HEM Transport Studies—Typical examples of transport enhancement results of studies A and C are presented in Figures 5 and 6, respectively. Figure 5 gives data of urea flux and electrical conductance for stage II of study A, where 3.0 V 12.5 Hz square-wave ac was applied for approximately 250 min. As can be seen here, both the electrical resistance and the corresponding flux generally attained near plateau values within 1 h, the plateaus representing around an 8-fold increase in conductance relative to the initial value. Results similar to those in study A were observed in study B. In the example presented in Figure 6 (an example of study C), stage II was 2.0 V dc iontophoresis for around 50 min; stage III was 4.0 V dc for 1 min followed by 3.0 V square-wave ac iontophoresis for 2 h; stage IV was superposition of 1.0 V dc over 3.0 V 12.5 Hz ac iontophoresis. It is seen in this example that there was significant pore induction during stage II but little or no further change in the state of pore induction during stages III and IV. Also can be noted in

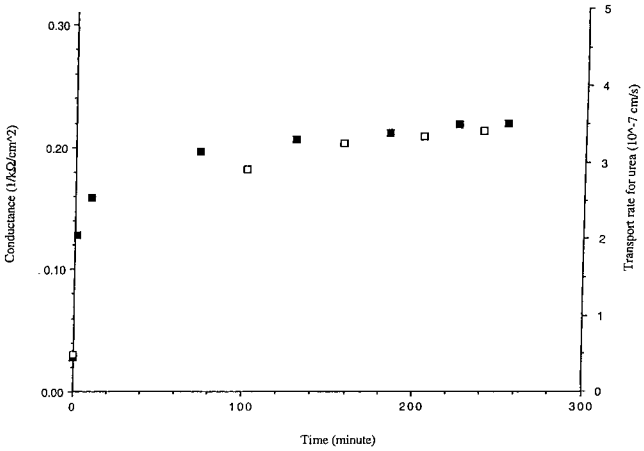

Figure 5—Representative HEM conductivity data ((kΩ cm^2)$^{-1}$), closed symbols, and HEM transport data for urea, open symbols, in study A (stage II: 3.0 V 12.5 Hz square-wave ac iontophoresis). Data are from skin sample 9.

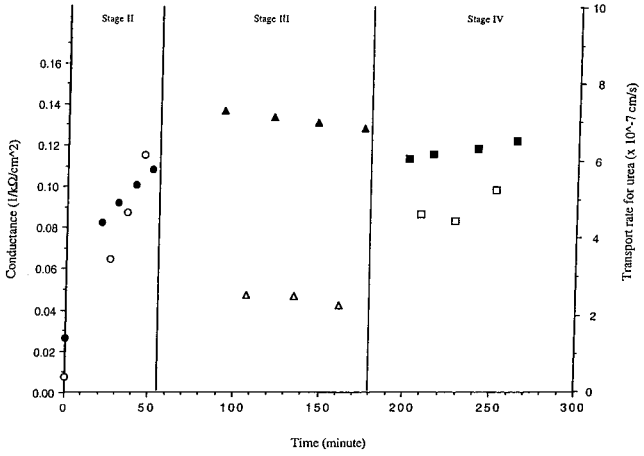

Figure 6—Representative HEM conductivity data ((kΩ cm^2)$^{-1}$), closed symbols, and HEM transport data for urea, open symbols, in study C (stage II: 2.0 V dc iontophoresis; stage III: 4.0 V 1 min followed by around 2 h 3.0 V square-wave ac iontophoresis; stage IV: superposition of 1.0 V dc and 3.0 V 12.5 Hz square-wave ac iontophoresis). Symbols: stage II, circles; stage III, triangles; stage IV, squares. Data are from skin sample 17.

Figure 6 are the relatively constant electrical resistance values and the corresponding fluxes in stages III and IV. In stage II, a lag between the increase in transport rate and the increase in conductance can be seen; this lag was noted in four of the six HEM samples of study C.

Table 1 shows the HEM electrical resistance decreases and HEM permeability increases that occurred with the modest applied 12.5 Hz square-wave ac voltages (stage II of studies A and B and stage III of study C). HEM electrical resistance and HEM permeability generally did not change by more than 25% during the conventional passive diffusion runs (stage I of studies A, B, and C). During square-wave ac iontophoresis of 2.0 to 4.0 V (stage II of studies A and B and stage III of study C), both the HEM permeability and the HEM conductance increased by up to around 30-fold relative to conventional passive diffusion runs (stage I of studies A, B, and C). Figure 7 is a plot of the Table 1 data, and it clearly reveals the relationship between the increase in HEM urea permeability and the increase in HEM electrical conductance during square-wave ac iontophoresis.

The effective pore radii estimated using the urea and mannitol flux data and the hindered transport theory in studies A and B are summarized in Table 2, and those for study C are in Table 3. The effective pore radii for HEM deduced in the passive transport experiments are consis-

Table 1—HEM Electrical Resistance (*R*) and Urea Permeability Coefficient (*P*) during 12.5 Hz Square-Wave ac Iontophoresis (stage II of studies A and B, stage III of study C) and during Passive Permeation Runs (stage I of studies A, B, and C) in Studies A, B, and C

skin sample	study	*R*, stage I (kΩ cm^2)	*P*, stage I $\times 10^8$ (cm/s)	*R*, during ac iontophoresis (kΩ cm^2)[a]	*R* ratio (*R*, stage I: *R*, during iontophoresis)	*P* ratio (*P*, during ac iontophoresis: *P*, stage I)
1	A	43	3.4	14	3.2	3.1
2	A	15	12	5.8	2.5	2.5
3	A	53	3.6	20	2.7	2.4
4	A	128	0.73	26	5	6
5	A	200	0.62	19	13	12
6	A	14	10.3	3.3	4.3	4.3
7	A	66	2.1	4.0	16	17
8	A	31	4.8	3.7	8	9
9	A	38	4.8	4.6	8	7
10	B	23	4.9	6.7	3.5	4.4
11	B	15	10.2	2.3	7	6
12	B	22	8.5	5.3	3.6	3.1
13	B	23	6.4	5.4	4.2	4.4
14	B	21	8.5	2.8	7	6
15	B	24	5.7	0.9	28	29
16	C	59	2.4	7.8	8	9
17	C	39	4.0	7.6	5	6
18	C	22	7.7	3.5	6	6
19	C	26	7.4	0.9	28	27
20	C	30	5.1	4.7	7	9
21	C	81	1.8	3.6	24	25

[a] Data taken from near the plateau region after the initial decrease (see Figures 5 and 6).

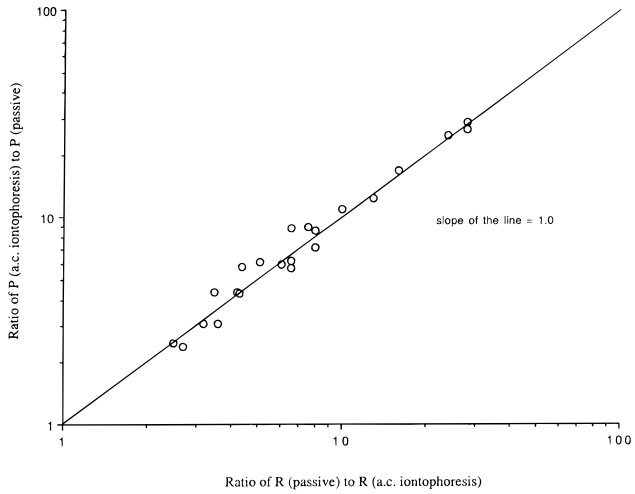

Figure 7—A correlation between the increase in HEM permeability for urea and the increase in HEM conductance in studies A, B, and C. The ratios of passive permeability to permeability during the 12.5 Hz square-wave ac iontophoresis ("passive" permeation) are plotted against the ratios of electrical conductance in passive diffusion study to the conductance in the square-wave ac iontophoresis study.

tent with those determined previously by Peck et al.[18] In Tables 2 and 3, the effective pore radii deduced for the induced pores under the electric field are seen to be of the same order of magnitude as those of the preexisting pores involved in passive diffusion. Results obtained in study B in which the extent of pore induction was expected to be increased by a 1 min dc prepulse before the square-wave ac transport run are similar to those from study A. Also seen in Table 3 are the generally somewhat smaller effective pore sizes calculated from the electroosmotic transport data obtained with continuous dc iontophoresis (stage II of study C; mean ± SD = 8.5 ± 1.4 Å, $n = 6$) when compared to those of the preexisting pores deduced from passive transport runs (stage I of studies A, B, and C; mean

Table 2—Effective Pore Radii Determined for the 12.5 Hz Square-Wave AC Iontophoresis (stage II) and Passive Permeation (stages I and III) Runs in Studies A and B

skin sample	study	protocol[a]	effective pore radius (Å)[b]		
		stage II	stage I	stage II	stage III
6	A	3 V ac	13	10	15
7	A	3 V ac	23	8.5	18
8	A	3 V ac	13	9	11
9	A	3 V ac	15	11	12
10	B	4 V dc 1 min then 3 V ac	19	9.5	12
11	B	4 V dc 1 min then 3 V ac	24	13	17
12	B	4 V dc 1 min then 3 V ac	13	13	13
13	B	4 V dc 1 min then 4 V ac	12	10	11
14	B	4 V dc 1 min then 4 V ac	13	12	13
15	B	4 V dc 1 min then 4 V ac	18	9	12.5

[a] Stages I and III were passive diffusion experiments. [b] Equation 3 was used.

$\pm$ SD $= 14 \pm 4$ Å, $n = 16$) and those deduced from the square-wave ac iontophoresis runs (stage II of studies A and B, stage III of study C; mean $\pm$ SD $= 12 \pm 2$ Å, $n = 16$). The effective radii of the pores induced by an ac electric field during square-wave ac iontophoresis (stage II of studies A and B and stage III of study C) seem to be smaller, but only marginally, than those of the preexisting pores determined in the passive diffusion runs (stage I of studies A, B, and C). The results (mean $\pm$ SD $= 8 \pm 1$ Å, $n = 6$) from stage IV of study C involving the superposition of square-wave ac (3.0 or 4.0 V) for pore induction with 1 V continuous dc as the driving force for transport (i.e., electroosmosis) were essentially the same as those from continuous dc iontophoresis alone (stage II of study C). No significant differences were observed between the effective pore radii obtained in the passive permeation runs before (stage I of studies A to C; mean $\pm$ SD $= 14 \pm 4$ Å, $n = 16$) and after the application of the electric fields (stage III of studies A and B and stage V of study C; mean $\pm$ SD $= 13 \pm 2$ Å, $n = 16$). It should be noted that the effective pore radii deduced with continuous dc iontophoresis (stage II of study C) are consistent with the results obtained in a previous study.[13] Finally, the recovery of HEM barrier properties after the application of the electric field in the ac protocol was observed to be generally faster and more complete than those after continuous dc iontophoresis (see Table 4).

Discussion

HEM Transport Studies—The effective pore sizes of HEM have important implications on the delivery of large molecules (such as oligonucleotides and polypeptides), and this has been discussed previously.[13,18] Recent findings in the effective pore sizes during low to moderate voltage iontophoresis with continuous dc electroosmotic transport may be complicated by possible variable pore surface charge density in HEM.[13] Because HEM transport enhancement with ac iontophoresis in the present experiments is basically due to the induction of new pores and not due to electroosmosis (see *Nuclepore Membrane Studies* in the *Results* section and the last paragraph in this section), possible pore charge density distributions in HEM would not affect the deduced effective pore radii with the ac protocol. Also, the same equation (eq 3) has been used in the pore radii determination with the ac iontophoresis data as in the case of the passive transport data; hence, any uncertainties arising from the use of eq 3 would likely be essentially the same for the passive and the ac situations, especially when the pore sizes are essentially the same. Thus, it is rather safe to conclude that the effective pore sizes of the pores induced in the ac experiments are close to those deduced for the preexisting pores. The situation is more complicated when the effective pore sizes deduced from the electroosmotic transport data obtained during continuous dc iontophoresis (stage II of study C) are compared to either those deduced from ac iontophoresis (stage II of studies A and B and stage III of study C) or those deduced from passive diffusion (stage I of studies A, B, and C). The smaller effective pore sizes deduced from the electroosmosis data presented in Table 3 (stages II and IV of study C) are likely the result of one or both of two possible explanations: (a) because of the directionality of the convective solvent flow during HEM electroosmosis, clearly negatively charged pores must dominate. However, there can exist a distribution of negative, positive, and neutral pores,[22] and, conceivably, negatively charged induced pores may possess smaller effective pore sizes than the neutral and/or positively charged pores; (b) the alternative explanation is that eq 4 likely has different limitations (than eq 3) in the calculation of effective pore sizes. These limitations in the region of $\lambda \geq 0.4$ have not been well investigated from the experimental standpoint[19] and raise the question of the magnitude of the actual uncertainty in the effective pore sizes presented in Tables 3 and 4 where λ values range from around 0.1 to 0.6. Only further independent studies on the quantitative applicability of eqs 3 and 4 can provide a more quantitative assessment of this issue. In the meantime, eqs 3 and 4 may be employed as a first approximation in the range of $\lambda \geq 0.4$. It is of interest to note that calculations carried out based on a mathematically more rigorous approximation of the centerline theory for $0 \leq \lambda \leq 1.0$[19] show differences of only 10 to 20% from those of eqs 3 and 4 at $\lambda \approx 0.6$.

It is noteworthy that the pore size estimates from stage II of study C are essentially the same as those from stage IV. This together with the resistance data (initial, stage II, stage III, and stage IV in Tables 1 and 3) suggest that pores induced by dc alone (stage II of study C) have characteristics similar to those induced by 12.5 Hz ac (stage IV of study C, where the 3.0 or 4.0 V ac component prevails over the 1.0 V dc component with regard to pore induction).

The correlation in Figure 7 is consistent with the results obtained in a previous study[1] and demonstrates the appropriateness of using the changes in HEM electrical resistance to represent the increase in accessible porosity/tortuosity during iontophoresis. The results in Figure 7 accordingly provide the first direct quantitative evidence of pore induction under the modest voltage conditions. Also, because the average effective pore sizes of the transport pathways during ac iontophoresis and the effective sizes of the preexisting pores are essentially the same (Tables 3 and 4), the increase in HEM permeability and the corresponding increase in HEM conductance (up to around a 30-fold increase) shown in Table 1 and Figure 7 under the ac conditions can best be interpreted as electric field induction of new pores in HEM rather than the enlargement of the preexisting pores.

Another important result of the present study is revealed in Figure 8. Here, the permeability coefficient (P) for the 12.5 Hz ac iontophoresis runs (square symbols) are plotted against electrical resistance (R) together with the corresponding conventional passive permeation data obtained before (circle symbols) and after (triangle symbols) ac iontophoresis. What is significant is that the passive permeation data fall upon the same line (slope $= -1.0$). This, together with the results in Figure 7, is further support that HEM transport enhancement under the present ac conditions is entirely due to enhanced "passive" permeation resulting from pore induction with negligible contribution from electroosmosis. The slope of -1.0 is what

Table 3—HEM Electrical Resistance (*R*) and Effective Pore Radii Determined for DC Iontophoresis (stage II), 12.5 Hz Square-Wave AC Iontophoresis (stage III), Superposition of 12.5 Hz Square-Wave AC and DC Iontophoresis (stage IV), and Passive Permeation (stages I and V) Runs in Study C

skin sample	protocol[a]			effective pore radius (Å)					*R* (kΩ cm²)[d]		
	stage II	stage III	stage IV	stage I[b]	stage II[c]	stage III[b]	stage IV[c]	stage V[b]	stage II	stage III	stage IV
16	2 V dc	4 V dc 1 min, then 3 V ac	superposition of 3 V ac with 1 V dc	10	8	12	7	12	10	7.8	8.2
17	2 V dc	4 V dc 1 min, then 3 V ac	superposition of 3 V ac with 1 V dc	11	9	13	8	14	9.6	7.6	8.3
18	2 V dc	4 V dc 1 min, then 3 V ac	superposition of 3 V ac with 1 V dc	12	10	13	8.5	15	4.1	3.5	4.7
19	3 V dc	4 V dc 1 min, then 4 V ac	superposition of 4 V ac with 1 V dc	13	7	11.5	7	11	1.0	0.9	0.71
20	3 V dc	4 V dc 1 min, then 4 V ac	superposition of 4 V ac with 1 V dc	11	10	18	9	15	6.7	4.7	6.0
21	3 V dc	4 V dc 1 min, then 4 V ac	superposition of 4 V ac with 1 V dc	10	7	11	7	9	5.0	3.6	3.2

[a] Stages I and V were passive diffusion experiments. [b] Equation 3 was used. [c] Equation 4 was used. [d] Average resistance values.

Table 4—Comparison of the Effects of Square-Wave AC and Continuous DC Iontophoresis upon the Barrier Properties of HEM in Iontophoresis Transport Studies

12.5 Hz square-wave ac protocol[a]				continuous dc[b]			
initial resistance of HEM sample (kΩ cm²)	voltage	drop in resistance[c]	recovery[d]	initial resistance of HEM sample (kΩ cm²)	voltage	drop in resistance[c]	recovery[d]
43	2 V	69	93	16	2 V	89	70
15	2 V	60	69	27	2 V	98	31
53	2 V	63	79	18	2 V	73	78
23	4 V/3 V[e]	71	92	73	2 V	92	53
15	4 V/3 V[e]	85	70	57	4 V/2 V[e]	98	40
				18	4 V/2 V[e]	95	38
24	4 V/4 V[e]	96	61	123	4 V/2 V[e]	98	12
23	4 V/4 V[e]	76	81				

[a] Duration of iontophoresis was around 2–5 h. [b] Data obtained from Li et al.;[13] duration of iontophoresis was 50 min. [c] As percent of initial electrical resistance (data from the close to plateau region after the initial decrease). [d] As percent of initial electrical resistance after the iontophoresis run when resistance became constant with time (after more than 10 h). [e] First value is the dc voltage of the 1 min prepulse and the second value is the ac voltage (in 12.5 Hz ac iontophoresis) in the present study or dc voltage (in continuous dc iontophoresis) from a previous study.[13]

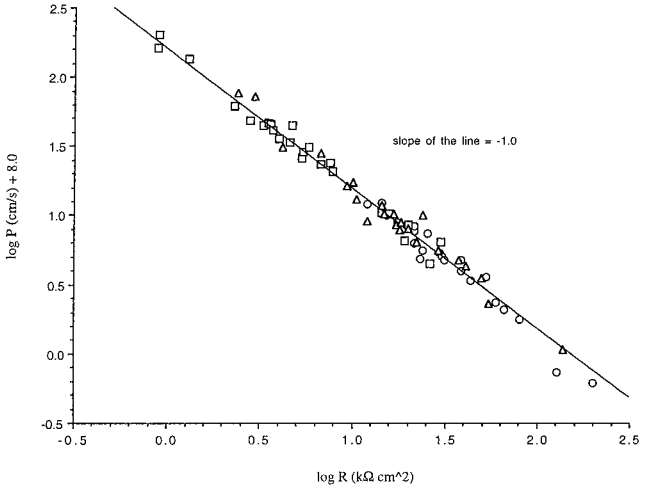

Figure 8—A correlation between HEM electrical resistance and its permeability for urea in studies A, B, and C. Symbols: passive permeation before iontophoresis, circles; 12.5 Hz square-wave ac iontophoresis ("passive" permeation), squares; passive permeation after iontophoresis, triangles.

would be expected when the transport pathways for the conducting ions in PBS during iontophoresis correlate with both the preexisting and the induced pathways for urea passive transport in HEM (see eq 9 and ref 13). The results in Figure 8 are evidence that the electrical current increases that take place during moderate voltage low-frequency ac iontophoresis is the direct result of pore induction in the stratum corneum and not due to some other transient electrical effects[5–8] such as a complex potential-dependent energy barrier for transport at the membrane–solution interface or effects arising from time dependent membrane polarization, the latter being likely important only for much shorter time frames (e.g., in the order of a millisecond[7]) than that of the present situation. These findings support the pore induction hypothesis made in previous studies with applied voltages ≥ 1 V.[1–5]

Electroporation of HEM at Low to Moderate Voltages (2 to 4 V), Yes or No—Although the issue of the sites of pore induction in human skin at low to moderate voltages is beyond the scope of the present investigation, possible mechanisms and skin morphology proposed in the literature[1,4,23–24] for the increase in skin electrical conductance observed in the present study may be discussed. Previously, Inada et al.[1] hypothesized that the increase in HEM electrical conductance at 1 to 4 V is similar to the reversible electrical breakdown found with lipid bilayer membranes and that pore formation may occur transepidermally or via the cells lining the appendageal ducts. For transepidermal electrical breakdown, the electric field across HEM under an applied potential of 2 V for an average of 15 to 20 corneocyte layers in the stratum corneum was estimated to be in the order of 40 kV/cm when the voltage drop was assumed to be concentrated across the intercellular lipid bilayers rather than the conductive corneocytes. Thinner portions of the stratum corneum may experience a higher field strength and thus may disproportionally contribute to electroporation. This calculated electric field strength (40 kV/cm) is in the order of the magnitude of, but probably at the lower end of the range of, field strengths needed to induce electrical breakdown of lipid bilayer membranes, estimated to be around 50 to 200 kV/cm based on a bilayer thickness of around 10 nm and a "threshold voltage" of around 50 to 200 mV over periods of seconds[25,26] to minutes.[27] The "threshold" voltage used in the above estimation for membrane electroporation is strongly dependent on the duration of the applied electric field and the particular type of the membrane. The view of reversible breakdown of the epithelial cell bilayers lining the appendages was offered earlier by Kasting and Bow-

man[5] as a possible explanation for the time-dependent, nonlinear, current−voltage relationship observed in their skin electrical resistance study. The number of bilayers involved in this case is much smaller than that of full thickness stratum corneum, and accordingly the electric field strengths attainable in the bilayers lining the appendages could be much greater and much more than sufficient to induce electroporation. Chizmadzhev et al.[23] has come to a similar conclusion in a recent quantitative examination of this problem. Under applied potentials of a few volts, Chizmadzhev et al. state that the "time-dependent, nonlinear current−voltage characteristics of the skin can be attributed to electroporation" associated with the epithelial cells lining skin appendages. Their analysis "confirms skin electroporation at low voltages", which is in agreement with the views of Kasting and Bowman[5,6] and Inada et al.[1] The results in Figures 7 and 8 of the present study clearly support electroporation at these low to moderate voltage conditions.

Pulsed and Continuous Iontophoresis—Although pulsed dc iontophoresis transport experiments were not conducted in the present investigation, the results of the present HEM electrical resistance study impact upon the understanding of pulsed dc iontophoresis, and some discussion here is instructive. Pulsed dc iontophoresis has been an aspect of interest in transdermal iontophoresis partly because of the possible advantage of less skin irritation than that with continuous dc iontophoresis[28,29] and the belief by some researchers that it may provide greater transport enhancement than conventional continuous dc iontophoresis via mechanisms that are unique in pulsed iontophoresis.[30] Some previous studies have reported that higher or equal fluxes are observed under continuous dc iontophoresis relative to pulsed dc iontophoresis,[7,29,31−32] but other studies have suggested higher transport rates or greater pharmacological effects under pulsed dc iontophoresis.[33,34] These differing results demonstrate the need for more systematic mechanistic studies to compare the effects of pulsed dc and continuous dc upon the barrier properties of skin.

Results from the present electrical resistance study can provide a better understanding of the mechanism(s) of pore induction in human skin during pulsed and/or continuous dc iontophoretic enhanced transdermal delivery. A particular advantage of the protocols used in the present study has been that of minimizing the influence of skin-to-skin variabilities. By utilizing the same HEM sample for successive experiments, the influence of the variabilities has been reduced and more meaningful results were obtainable. The merit of this approach is illustrated by the relatively small data scatter in Figure 3 (contrast this with the large variations seen in Table 4 for the effects of pulsed dc and continuous dc on the barrier properties of HEM).

Because HEM conductance was shown to be directly proportional to the "passive" permeability of HEM (Figures 7 and 8), the electrical conductance results presented in Figure 3 suggest that continuous dc iontophoresis generally induces a greater extent of pore induction than those observed during pulsed dc and ac iontophoresis at the same level of applied voltage (2.0 to 3.0 V) and duration. The present electrical conductance data are consistent with the study by Yamamoto and Yamamoto.[35] The generally larger extent of pore induction in HEM observed during continuous dc iontophoresis than in pulsed and ac iontophoresis under the applied voltage conditions in the present study is believed to be at least in part due to the depolarization/recovery of the membrane allowed between each ac square-wave pulse and is consistent with the hypothesis of pore induction at the bilayer level in HEM. The dc square-wave pulsed iontophoresis (with a 1, 2, or 3 ms delay between each pulse) induced a lesser extent of pore induction than those by continuous dc (Figure 3) and approached those by 12.5 Hz square-wave ac; this also supports the hypothesis that depolarization between the pulses (ac or dc) allows for depolarization/recovery of the membrane during iontophoresis, and hence, lessen the extent of pore induction. This depolarization/recovery between pulses may also lead to the observed faster (data not shown) and more complete (Table 4) recovery of HEM barrier properties after ac and pulsed dc iontophoresis than those after continuous dc iontophoresis. It should be noted that the results presented in Figure 3 are for the particular case of consecutive 10 s runs, and the differences between continuous dc and pulsed dc are rather modest. For longer duration and at higher applied voltages, there may be greater differences between continuous dc and pulsed dc and/or ac. More work is needed in this area.

References and Notes

1. Inada, H.; Ghanem, A.-H.; Higuchi, W. I. Studies on the effects of applied voltage and duration on human epidermal membrane alteration/recovery and the resultant effects upon iontophoresis. *Pharm. Res.* **1994**, *11*, 687−697.
2. Sims, S. M.; Higuchi, W. I.; Srinivasan, V. Skin alteration and convective solvent flow effects during iontophoresis: I. neutral solute transport across human skin. *Int. J. Pharm.* **1991**, *69*, 109−121.
3. Sims, S. M.; Higuchi, W. I.; Srinivasan, V. Skin alteration and convective solvent flow effects during iontophoresis: II. monovalent anion and cation transport across human skin. *Pharm. Res.* **1992**, *9*, 1402−1409.
4. Keister, J. C.; Kasting, G. B. A kinetic model for ion transport across skin. *J. Membr Sci.* **1992**, *71*, 257−271.
5. Kasting, G. B.; Bowman, L. A. Electrical analysis of fresh, excised human skin: a comparison with frozen skin. *Pharm. Res.* **1990**, *7*, 1141−1146.
6. Kasting, G. B.; Bowman, L. A. DC electrical properties of frozen, excised human skin. *Pharm. Res.* **1990**, *7*, 134−143.
7. Bagniefski, T.; Burnette, R. R. A comparison of pulsed and continuous current iontophoresis. *J. Controlled Release* **1990**, *11*, 113−122.
8. Dinh, S. M.; Lao, C. W.; Berner, B. Upper and lower limits of human skin electrical resistance in iontophoresis. *AIChE J.* **1993**, *39*, 2011−2018.
9. Prausnitz, M. R. The effects of electric current applied to skin: a review for transdermal drug delivery. *Adv. Drug Deliv. Rev.* **1996**, *18*, 395−425.
10. Jadoul, A.; Preat, V. Electrically enhanced transdermal delivery of domperidone. *Int. J. Pharm.* **1997**, *154*, 229−234.
11. Pliquett, U.; Langer, R.; Weaver, J. C. Changes in passive electrical properties of human stratum corneum due to electroporation. *Biochim. Biophys. Acta* **1995**, *1239*, 111−121.
12. Vanbever, R.; Boulenge, E. L.; Preat, V. Transdermal delivery of fentanyl by electroporation I. Influence of electrical factors. *Pharm. Res.* **1996**, *13*, 559−565.
13. Li, S. K.; Peck, K. D.; Ghanem, A.-H.; Higuchi, W. I. Characterization of the transport pathways induced during low to moderate voltage iontophoresis in human epidermal membrane. *J. Pharm. Sci.* **1998**, *87*, 40−48.
14. Peck, K. D.; Ghanem, A.-H.; Higuchi, W. I. The effect of temperature upon the permeation of polar and ionic solutes through human epidermal membrane. *J. Pharm Sci.* **1995**, *84*, 975−982.
15. Srinivasan, V.; Higuchi, W. I.; Su, M.-H. Baseline studies with the four-electrode system: the effect of skin permeability increase and water transport on the flux of a model uncharged solute during iontophoresis. *J. Controlled Release* **1989**, *10*, 157−165.
16. Peck, K. D.; Ghanem, A.-H.; Higuchi, W. I.; Srinivasan, V. *Int. J. Pharm*. Improved stability of the human epidermal membrane during successive permeability experiments. **1993**, *98*, 141−147.
17. Tregear, R. T. *Physical Functions of Skin*. Academic Press: New York, 1966; pp 53−57.
18. Peck, K. D.; Ghanem, A.-H.; Higuchi, W. I. Hindered diffusion of polar molecules through and effective pore radii estimates of intact and ethanol treated human epidermal membrane. *Pharm. Res.* **1994**, *11*, 1306−1314.
19. Deen, W. M. Hindered transport of large molecules in liquid-filled pores. *AlChE. J.* **1987**, *33*, 1409−1425.

20. Sandifer, J. R. *Ion-Transfer Kinetics: Principles and Applications*, VCH: New York, 1995; Ch. 4.
21. Peck, K. D.; Srinivasan, V.; Li, S. K.; Higuchi, W. I.; Ghanem, A.-H. A quantitative description of the effect of molecular size upon electroosmotic flux enhancement during iontophoresis for a synthetic membrane and human epidermal membrane. *J. Pharm. Sci.* **1996**, *85*, 781−788.
22. Pikal, M. J. *Pharm. Res.* Transport mechanisms in iontophoresis. I. A theoretical model for the effect of electroosmotic flow on flux enhancement in transdermal iontophoresis. **1990**, *7*, 118−126.
23. Chizmadzhev, Y. A.; Indenbom, A. V.; Kuzmin, P. I.; Galichenko, S. V.; Weaver, J. C.; Potts, R. O. Electrical properties of skin at moderate voltages: contribution of appendageal macropores. *Biophys. J.* **1998**, *74*, 843−856.
24. Chizmadzhev, Y. A.; Zarnitsin, V. G.; Weaver, J. C.; Potts, R. O. Mechanism of electroinduced ionic species through a multilamellar lipid system. *Biophys. J.* **1995**, *68*, 749−765.
25. Chang, D. C.; Chassy, B. M.; Saunders: J. A.; Sowers, A. E. *Guide to Electroporation and Electrofusion*; Academic Press: New York, 1992.
26. Neumann, E.; Sowers, A. E.; Jordan, C. A. *Electroporation and Electrofusion in Cell Biology*; Plenum Press: New York, 1989.
27. Donlon, J. A.; Rothstein, A. The cation permeability of erythrocytes in low ionic strength media of various tonicities. *J. Membr. Biol.* **1969**, *1*, 37−52.
28. Okabe, K.; Yamaguchi, H.; Kawai, Y. New iontophoretic transdermal administration of the beta-blocker metoprolol. *J. Controlled Release* **1986**, *4*, 79−85.
29. Hirvonen, J.; Hueker, F.; Guy, R. H. Current profile regulates iontophoretic delivery of amino acids across the skin. *J. Controlled Release* **1995**, *37*, 239−249.
30. Pikal, M. J.; Shah, S. Study of the mechanisms of flux enhancement through hairless mouse skin by pulsed dc iontophoresis. *Pharm. Res.* **1991**, *8*, 365−369.
31. Numajiri, S.; Sakurai, H.; Sugibayashi, K.; Morimoto, Y.; Omiya, H.; Takenaka, H.; Akiyama, N. Comparison of depolarizing and direct current systems on iontophoretic enhancement of transport of sodium benzoate through human and hairless rat skin. *J. Pharm. Pharm.* **1993**, *45*, 610−613.
32. Preat, V.; Thysman, S. Transdermal iontophoretic delivery of sufentanil. *Int. J. Pharm.* **1993**, *96*, 189−196.
33. Knoblauch, P.; Moll, F. In vitro pulsatile and continuous transdermal delivery of buserelin by iontophoresis. *J. Controlled Release* **1993**, *26*, 203−212.
34. Liu, J. C.; Sun, Y.; Siddiqui, O.; Chien, Y. W.; Shi, W.-M.; Li, J. Blood glucose control in diabetic rats by transdermal iontophoresis delivery of insulin. *Int. J. Pharm.* **1988**, *44*, 197−204.
35. Yamamoto, T.; Yamamoto, Y. Nonlinear electrical properties of skin in the low-frequency range. *Med. Biol. Eng. Comput.* **1981**, *19*, 302−310.

Acknowledgments

This research is supported by NIH Grant GM 43181 and an Advanced Predoctoral Fellowship in Pharmaceutics awarded to S. Kevin Li from the Pharmaceutical Research and Manufacturers of America Foundation. The authors thank Professor Paul C. Fife for helpful discussion and TheraTech, Inc. for supplying the human epidermal membrane.

JS980331Y

Chemical Stability of an Ester Prodrug of a Glycoprotein IIb/IIIa Receptor Antagonist in Solid Dosage Forms

SHERIF I. FARAG BADAWY,* REED C. WILLIAMS, AND DONNA L. GILBERT

Contribution from *Pharmaceutical R&D, DuPont Pharmaceuticals Company, Experimental Station, P.O. Box 80400, Wilmington, Delaware 19880-0400.*

Received August 12, 1998. Accepted for publication January 21, 1999.

Abstract □ DMP 754 is an ester prodrug of a glycoprotein IIb/IIIa receptor antagonist that undergoes ester and amidine hydrolysis in the presence of excipients. A means for the stabilization of DMP 754 was needed for the formulation of a stable drug product. Incorporation of a pH modifier in the formulation was used to control the microenvironment pH to coincide with that of maximum stability for DMP 754. Stability of tablets and capsules manufactured by (a) trituration process, (b) dry granulation process, and (c) wet granulation process was evaluated in HDPE bottles. Formulations manufactured by the dry and wet granulation processes contained disodium citrate as the pH modifier. Although aqueous wet granulation of a hydrolyzable drug is usually avoided, tablets and capsules manufactured by wet granulation were more stable in this case than those manufactured by the dry granulation process. This was attributed to the more uniform distribution of the pH modifier. Although the compression process resulted in enhanced degradation of the binary blend of DMP 754 and anhydrous lactose, tablets manufactured by the wet granulation process were more stable than capsules manufactured by the same process. Decreasing excipient-to-drug ratio enhanced the stability of tablets manufactured by the wet granulation process.

Introduction

DMP 754, the acetate salt of (*R*)-methyl 3-[[[3-[4-(aminoiminomethyl)phenyl]-4,5-dihydro-5-isoxazolyl]acetyl]amino]-*N*-(butoxycarbonyl)-L-alanine, is an ester prodrug of platelet IIb/IIIa glycoprotein receptor antagonist.[1,2] DMP 754 drug substance is crystalline and was found to exhibit good stability in the solid state. DMP 754 degradation in the solid state was significantly enhanced in the presence of different excipients, and the rate of degradation was proportional to the excipient:drug ratio. Among all the fillers tested, anhydrous lactose showed the lowest rate of DMP 754 degradation. However, DMP 754 showed significant degradation in the presence of anhydrous lactose at high excipient-to-drug ratios. A means for the stabilization of DMP 754 in solid dosage forms was needed since it is a potent drug that is present at low concentration in the drug product. The two main degradation products isolated in the solid state (Figure 1) were the ester hydrolysis product (XV459) and the amidine hydrolysis product (SJ459). Enhanced hydrolysis of DMP 754 in the presence of lactose was attributed, at least partly, to lactose catalysis, since lactose was shown to provide concentration-dependent catalysis of ester and amidine degradation in solution.[3] While catalysis of esters by sugars and polyhydric alcohols in aqueous solutions was reported,[4] this effect was not previously shown for the amidine group.

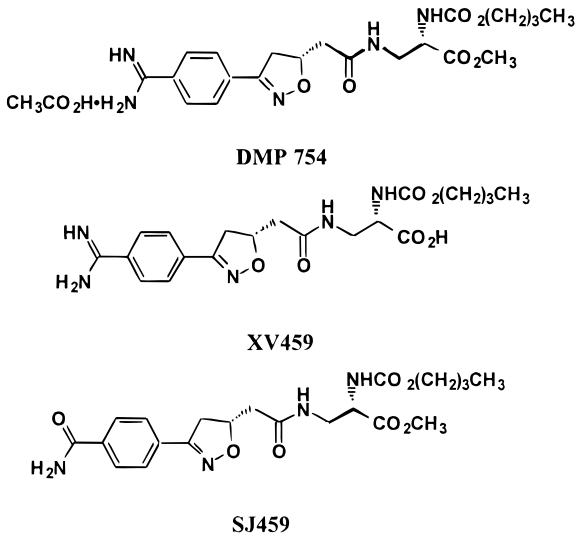

Figure 1—Structure of DMP 754 and degradation products, XV459 and SJ459.

Hydrolysis rate of DMP 754 in the presence of lactose was found to be dependent on the microenvironment pH. The hydrolysis rates of the ester and amidine groups of DMP 754 in lactose blends were altered by incorporation of acidic components in the blend. The use of pH modifiers to decrease the degradation rate in the solid state was previously reported.[5,6] However, the rationale for the choice of particular pH modifier was generally lacking. The effect of an acid on the microenvironment pH of DMP 754 was predicted by the saturated solution pH of the acid.[3] The ester group attained maximum stability with acids having saturated solution pH of approximately 4. On the other hand, the amidine group showed increased stability with the more acidic modifiers having saturated solution pH values as low as 0.4. Hydrolysis rate of amidines was reported to decrease as the acidity of the reaction medium increased.[7] Disodium citrate (saturated solution pH of 4.6) was the only acid tested that improved the stability of both groups. Stability of DMP 754 in the solid state can, therefore, be improved by the use of an appropriate acid that adjusts the microenvironmental pH to approximately 4.

The purpose of this study was to develop a stable oral solid dosage form for DMP 754. The formulation and manufacturing process were selected to maximize DMP 754 stability. Disodium citrate was included in the formulation as a pH modifying agent, in an attempt to control the microenvironment pH to that of maximum stability for DMP 754 as mentioned earlier. The effect of the manufacturing process on DMP 754 stability was also evaluated. Although aqueous wet granulation is usually avoided for a hydrolyzable drug,[8] both dry and wet processes were evaluated for the manufacture of DMP 754 drug product. Method of incorporation of a pH modifier can affect the

* Corresponding author. Phone: 302-695-9116. Fax: 302-695-7592. E-mail: sherif.i.badawy@dupontpharma.com.

10.1021/js9803297 CCC: $18.00
Published on Web 03/02/1999

Table 1. Summary of DMP 754 Formulations

ingredients	concentration (% w/w)						
	physical blends		dry granulation	wet granulation			
DMP 754	0.33	0.33	0.33	0.33	0.8	1.7	0.33
disodium citrate	0	2.5	2.5	2.5	2.5	2.5	0
povidone	0	0	0	2.0	2.0	2.0	2.0
lactic acid	0	0	0	0	0	0	0.0083
magnesium stearate	0	0	1.0	1.0	1.0	1.0	1.0
anhydrous lactose	99.67	97.17	96.17	94.17	93.7	92.8	96.66
tablet or capsule strength (mg)	0.1	0.1	0.2	0.2	0.5	1.0	0.1
weight of tablet or capsule content (mg)	30	30	60	60	60	60	30

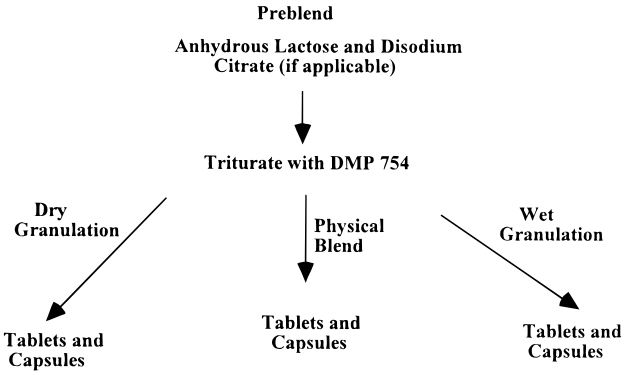

Figure 2—Summary of the manufacturing processes for DMP 754.

stability of the drug product.[6] Initially, the effect of compression and encapsulation on DMP 754 stability was examined for binary blends with anhydrous lactose. The effect of processing on the stability of drug product containing disodium citrate was then evaluated. Thus, stability of DMP 754 tablets and capsules containing disodium citrate and manufactured by a dry granulation (slugging) process or a wet granulation process was assessed.

Materials and Methods

Materials—DMP 754 was obtained from the Chemical Processing Research and Development Department of DuPont Pharmaceuticals Company and used as received. Mean particle size of DMP 754 was 11.5 μm. Anhydrous lactose, NF (Quest International Inc., Norwich, NY), was used as the filler. Disodium citrate sesquihydrate was supplied by Aldrich Chemical Co. (Milwaukee, WI). Other excipients used were magnesium stearate, NF (Mallinckrodt, St. Louis, MO), and povidone, USP (ISP, Wayne, NJ). HPLC grade trifluoroacetic acid (TFA) and glacial acetic acid were obtained from J. T. Baker, Phillipsburgh, NJ. HPLC grade acetonitrile (ACN) was obtained from EM Science (Gibbstown, NJ).

Equipment—Turbula T2C mixer (Willy A. Bachofen AG, Basel, Switzerland); Carver press (Fred S. Carver Inc., Menomonee Falls, WI); V-blender (Patterson-Kelley, East Stroudsburg, PA); Stokes single station press (Pennwalt Corporation, Warminster, PA); Key KG-5 high shear granulator (Key International, Englishtown, NJ); Zanasi AZ5 capsule filling machine (IMA, Fairfield, CT).

Methods—Table 1 summarizes the different DMP 754 formulations. Figure 2 shows a summary of the different manufacturing processes. Strength (or concentration) of DMP 754 in the various formulations represents that of the free base. Potency of DMP 754 was corrected for the assay value of the free base in the drug substance (use as value).

1. Preparation of Blends—A blend containing DMP 754 (0.33% w/w), disodium citrate (2.5% w/w), and anhydrous lactose (97.17% w/w), was prepared by a trituration process. DMP 754 was triturated with anhydrous lactose/disodium citrate preblend in a mortar and pestle using a geometric dilution technique. Another blend of DMP 754 (0.33% w/w) and anhydrous lactose (99.67% w/w) without disodium citrate was also prepared by a similar trituration process.

2. Preparation of Capsules and Tablets from the Binary Blend with Anhydrous Lactose—A binary blend of DMP 754 and anhydrous lactose, prepared by the above-mentioned method, was hand-filled into size 1 hard gelatin capsules (Capsugel, Greenwood, SC). Tablets were also manufactured by direct compression of the binary blend (no magnesium stearate) using the Carver press.

3. Preparation of Capsules and Tablets by the Dry Granulation Process—Capsules and tablets, 0.2 mg strength, containing 2.5% disodium citrate were prepared by a dry granulation process. Disodium citrate, DMP 754, and anhydrous lactose were blended with three-fourths the quantity of magnesium stearate using a V-blender with I-bar. The discharged blend from the V-blender was compressed into tablets (slugs) with a target weight of 200 mg on a Stokes single station press. The slugs were hand-screened through a 25-mesh screen and blended with the remaining amount of magnesium stearate in the V-blender. The resulting granulation was filled into size 3 hard gelatin capsules on the Zanasi capsule filling machine, or compressed into tablets on the Stokes single station press.

4. Preparation of Capsules and Tablets by the Wet Granulation Process—A formulation containing 2.5% disodium citrate was also manufactured by a wet granulation process. DMP 754 was blended with anhydrous lactose in the bowl of the high shear granulator. The blend was then granulated with an aqueous solution containing disodium citrate and povidone (pH of granulating solution was adjusted to 4 with 1 N hydrochloric acid). The wet granulation was screened through 8-mesh screen and dried in a vacuum oven at 40 °C to a moisture NMT 1.0% (determined by loss on drying at 105 °C). The dried granulation was screened through a 25-mesh screen and blended with magnesium stearate in a V-blender. The granulation was filled into hard gelatin capsules, or compressed into tablets similar to the dry granulation formulation. Various tablet strengths (0.2, 0.5, and 1.0 mg) were manufactured by the wet granulation process. Tablet weight was kept constant and the different strengths were obtained by changing the excipient-to-drug ratio.

In addition, DMP 754 tablets were manufactured by the above wet granulation process without disodium citrate. The formulation contained 0.0083% lactic acid added to the granulating solution. The pH of granulating solution was adjusted to 4 with 0.1 N sodium hydroxide. The formulation was similar to that mentioned above for the 0.2 mg tablets except for the substitution of lactic acid for disodium citrate.

5. Stability of Blends, Tablets and Capsules—Blends, tablets, and capsules were packaged into 40-cc high density polyethylene (HDPE) bottles capped with child-resistant caps. A 180 mg amount of the blend was accurately weighed into a bottle without desiccant, and the bottle was capped, torqued, and induction sealed. Capsules and tablets were packaged into the HDPE bottle in counts of ten or six, respectively, with or without desiccant (0.6 g silica gel). The packaged HDPE bottles were stored in stability chambers at 30 °C/60% RH and/or 40 °C/75% RH. The bottles were pulled at different time intervals, and the contents were analyzed for DMP 754 and degradation products by the HPLC method described below.

6. Analytical Method—An HPLC system equipped with automatic sampler, heated column compartment, gradient elution pump, and variable wavelength UV detector set at 280 nm (Model 1050/Hewlett Packard) was used for analysis of the blend, capsule, and tablet samples. The reverse phase HPLC assay method utilized a Waters Symmetry C-18 column (15 × 0.4 cm, 5 μm packing) with a mobile phase of 18:82 ACN/0.05% TFA in water

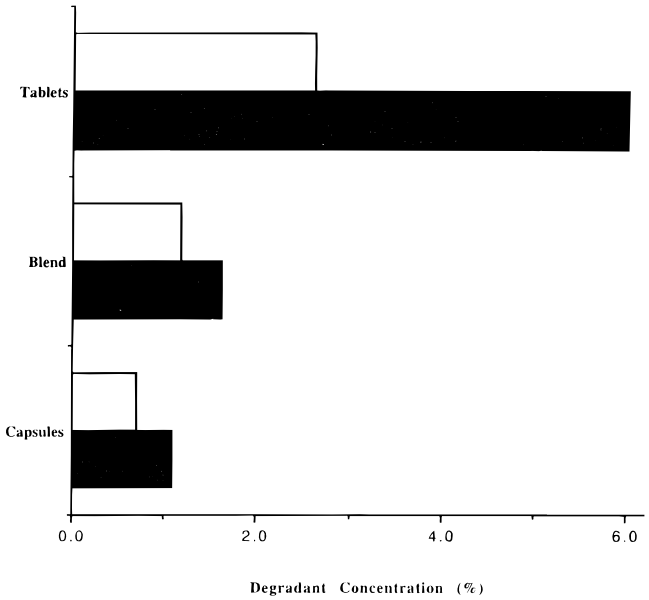

Figure 3—Percent degradation products of DMP 754 in binary blends (without magnesium stearate) after four weeks at 40 °C/75% RH. SJ459, (□); XV459, (■).

delivered at a flow rate of 1.5 mL/min and column temperature of 35 °C. The degradation products method also used a Waters Symmetry C-18 column with gradient elution of the mobile phase from 10:90 to 60:40 ACN/0.05% TFA in water over 30 min at a flow rate of 1.5 mL/min and a column temperature of 35 °C.

The blend samples were prepared by adding 30 mL of 14:86 ACN/0.05% glacial acetic acid in water to the HDPE bottles containing the blends and shaking for 30 min. The solution was then filtered as needed through 0.45 μm syringeless filter (Whatman, Clifton, NJ). In the case of tablets and capsules, 10 dosage units were dissolved in 14:86 ACN/0.05% glacial acetic acid in water, and the solution was filtered through the 0.45 μm syringeless filter. An external standard method was used for the assay and degradation products analysis.

The HPLC method was validated for linearity, accuracy, precision, limit of quantitation, and specificity. Studies with spiked placebo samples showed recoveries of 99.5% with method repeatability of 0.6% RSD. Specificity was determined by stressing samples with heat and light and by chromatographing known impurities; no peaks were found to coelute with the known degradants. Studies with degraded samples showed mass balance of drug substance and degradation products. Methods were linear over the range of study, and limit of quantitation of degradants was measured to be 4 ng/mL which was equivalent to 0.02% of drug substance in blends. Samples showed no degradation in the extraction solvent for up to 4 days.

7. X-ray Microanalysis—Citrate distribution in the tablets manufactured by the dry and wet granulation processes was evaluated by determining the sodium distribution on the tablet surface using X-ray analysis in the electron microscope. Citrate exists as sodium salt in the formulation, and therefore sodium distribution is expected to reflect the extent of citrate distribution in the sample. Intact tablet samples were mounted on aluminum stubs, carbon-coated, and examined using a Cameca electron microprobe fitted with a Wavelegth Dispersive Spectrometry (WDS) detector.

8. Moisture Uptake Studies—Moisture uptake by the granulation was determined at 25 °C using VTI MB 300G Integrated Microbalance System (VTI Corporation) from 40% RH to 90% RH with desorption to 10% RH. All transitions were in incremental steps of 10% RH.

Results and Discussion

1. Stability of DMP 754 Binary Blends with Anhydrous Lactose—Encapsulation and compression affected the stability of DMP 754 in the binary blend with anhydrous lactose. The encapsulation of the lactose/DMP 754 blend into hard gelatin capsules decreased drug degradation. The stabilizing effect of encapsulation was comparable for the ester and the amidine groups. The encapsulation of the blend reduces the surface area of the blend exposed to the environment and can decrease the rate of penetration of water vapor into the powder bed. The capsule shell can also act as a barrier that water vapor has to penetrate before it reaches the blend. This is particularly true if the gelatin shell is more hygroscopic than the blend and can consequently act as a "desiccant". Thus, encapsulation can prolong the time that it takes the moisture content of powder bed to equilibrate with water vapor pressure at 75% RH, which may be the reason for the improved stability of blends encapsulated into hard gelatin shells. To the contrary, tableting of the DMP 754/lactose blend enhanced drug degradation (Figure 3). Tableting increases the number of contact points between lactose and DMP 754. This would possibly enhance lactose catalysis and also increase the rate of moisture transfer between lactose and the drug, thus resulting in an increased rate of drug degradation in the tablets as compared to the blends. Despite the low concentration of moisture associated with anhydrous lactose (approximately 0.5% at 75% RH), this moisture corresponds to high water:drug molar ratio due to the small amount of DMP 754 in the blend and the low

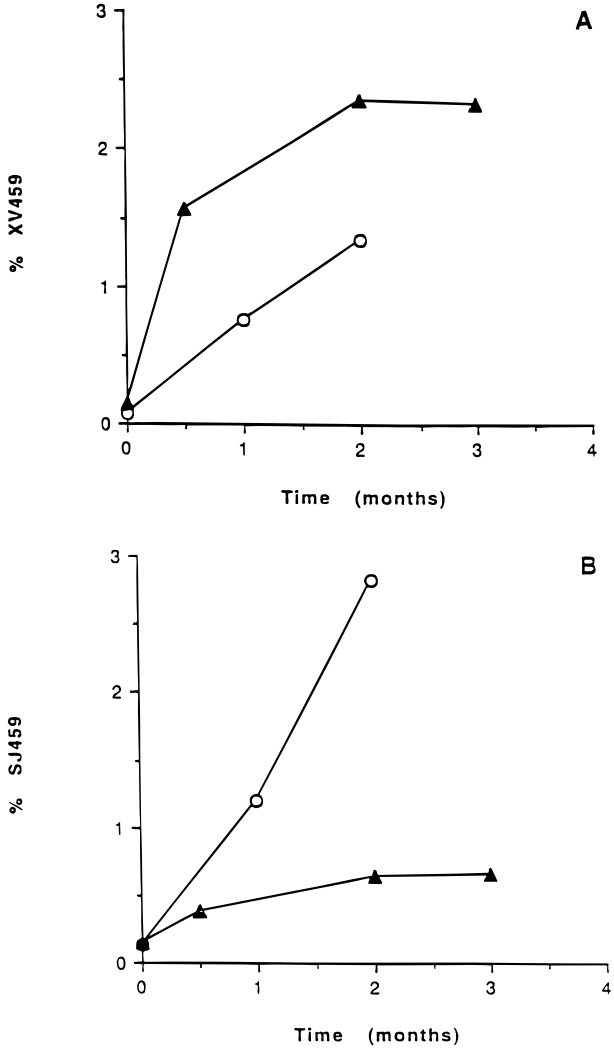

Figure 4—Percent degradation products of DMP 754: (a) XV459 and (b) SJ459 in blend with 2.5% disodium citrate, (○); and capsules with 2.5% disodium citrate manufactured by the dry granulation process, (▲); packaged in HDPE bottles without desiccant and stored at 40 °C/75% RH.

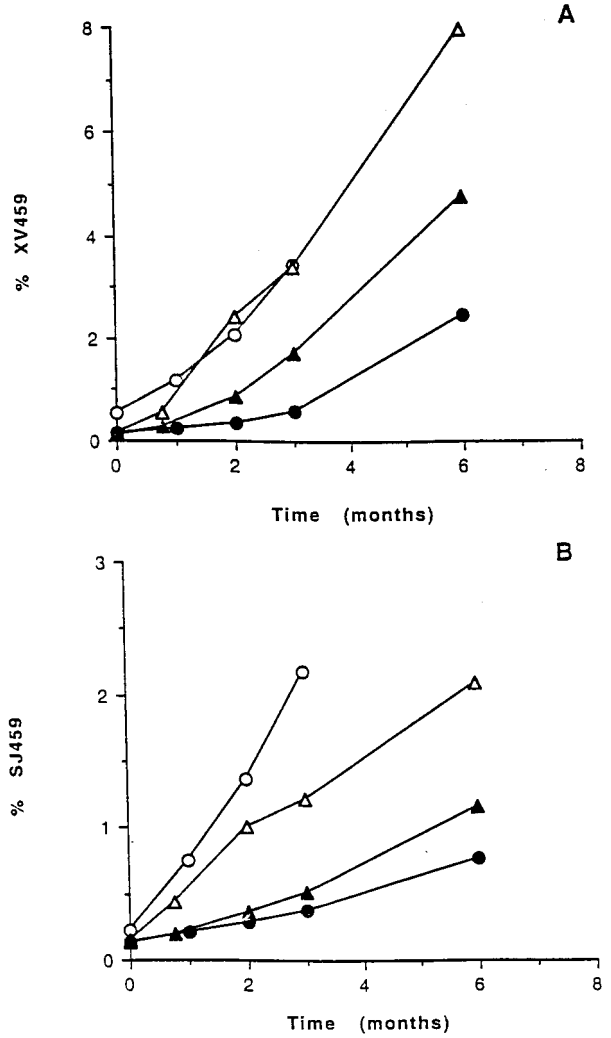

Figure 5—Percent degradation products of DMP 754: (a) XV459 and (b) SJ459 in capsules and tablets packaged in HDPE bottles with desiccant and stored at 40 °C/75% RH. Capsules manufactured by wet granulation process, (▲); capsules manufactured by dry granulation process, (△); tablets manufactured by wet granulation process, (●); tablets manufactured by dry granulation process, (○).

molecular weight of water. The destabilizing effect of tableting appeared to be more pronounced for ester hydrolysis than amidine hydrolysis. Thus, processing influences the stability of DMP 754.

2. Stability of DMP 754 Drug Product Manufactured by Dry Granulation Process—Capsules containing disodium citrate manufactured by dry granulation showed enhanced ester hydrolysis compared to the corresponding blend with disodium citrate in the same packaging configuration at 40 °C/75% RH. On the other hand, the dry granulation process resulted in diminished amidine hydrolysis compared to the blend (Figure 4). The dry granulation process for capsules involves the destabilizing effect of slugging (compression) and the stabilizing effect of encapsulation as mentioned above. On the basis of results from the binary blends, capsules manufactured by the dry granulation process would be expected to have higher ester and amidine degradation rates since the destabilizing effect of tableting was shown to be more pronounced than the stabilizing effect of encapsulation for both groups. The same effect of the dry granulation process on stability was also observed for a similar formulation without disodium citrate. Thus, the effect of the dry granulation process on amidine hydrolysis was not predicted by the blend studies. It is possible that this discrepancy may be due to magnesium stearate, which is not present in the binary blend. Magnesium stearate is known to have the ability to coat individual particles in a pharmaceutical formulation.[9] This can act as a barrier that protects DMP 754 from lactose catalysis, which is an important factor in the solid-state hydrolysis of the amidine group.[3]

Tablets manufactured by the dry granulation process showed comparable ester stability to the corresponding capsule formulation manufactured by the same process in the same packaging configuration at 40 °C/75% RH. However, the amidine group appeared to be even less stable in the tablet formulation (Figure 5).

3. Stability of DMP 754 Drug Product Manufactured by the Wet Granulation Process—DMP 754 capsules, 0.2 mg, manufactured by wet granulation process were more stable when stored at 40 °C/75% RH compared to capsules manufactured by the dry granulation process in the same packaging configuration (Figure 5). A similar trend was also observed at 30 °C/60% RH. The rates of

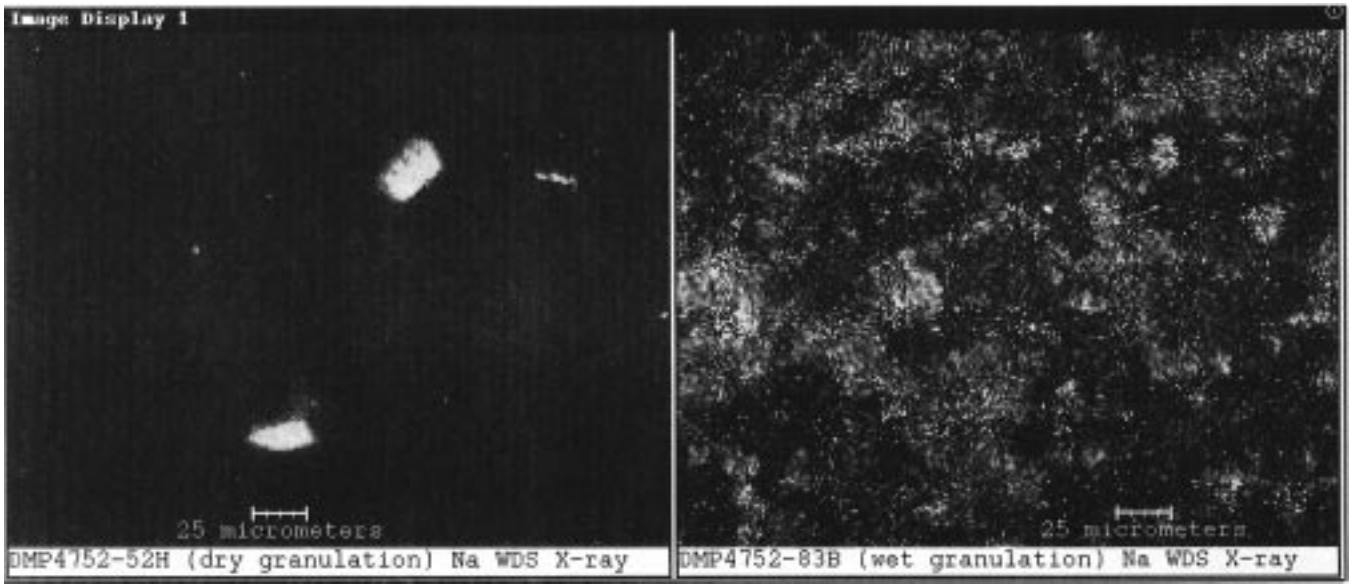

Figure 6—Distribution of sodium in DMP 754 tablets manufactured by dry granulation (left) and wet granulation (right). The intensity of the white areas is proportional to sodium concentration.

Table 2. Degradation of DMP 754 in Tablets and Capsules after 3 Months at 40 °C/75% RH

	disodium citrate concentration (%)	strength (mg)	moisture content (%)[a]	degradation product	
				XV459	SJ459
capsules/dry granulation	2.5	0.2	0.7	3.41	1.22
tablets/dry granulation	2.5	0.2	0.7	3.44	2.18
capsules/wet granulation	2.5	0.2	2.5	1.72	0.51
tablets/wet granulation	2.5	0.2	1.5	0.59	0.37
tablets/wet granulation	2.5	0.5	1.2	0.46	0.32
tablets/wet granulation	2.5	1.0	1.4	0.28	0.25
tablets/wet granulation	0[b]	0.1	1.5[c]	1.36[c]	2.00[c]

[a] Moisture of tablet or capsule content determined by Karl Fischer assay after 3 months at 40 °C/75% RH. [b] Contains 0.0083% lactic acid. [c] Two months timepoint.

degradation of the ester and amidine groups were lower for the wet granulation capsules than for the dry granulation capsules. The higher stability of capsules manufactured by wet granulation may be explained by the more uniform distribution of the citrate in this formulation. Adding the citrate to the granulating solution leads to intimate contact of this acidic component with the drug and other formulation components, resulting in a better control of the microenvironment pH. The granulating solution wets the particles, and when the water evaporates, the citrate is in close contact with the formulation constituents. Sodium distribution was found to be more diffuse in the wet granulation sample compared to localized distribution in the dry granulation sample, thus suggesting a more uniform distribution of the citrate in the former formulation (Figure 6).

Moisture content of capsules manufactured by the wet granulation process was higher than those manufactured by the dry granulation process. Capsule moisture content at time zero, determined by a Karl-Fisher titration, was found to be 0.6% and 2.0% for the dry and wet formulations, respectively. The moisture content of capsules manufactured by wet granulation was also higher than those manufactured by dry granulation after 3 months of storage at 40 °C/75% RH (Table 2). The higher moisture content of the wet granulation formulation is attributed to two reasons. First, partial conversion to lactose monohydrate during the wet granulation process was observed by X-ray diffraction of the granulation manufactured by the wet process. Second, the formulation manufactured by the wet granulation process was found to be more hygroscopic than the dry granulation formulation as determined by moisture sorption−desorption isotherms for the two formulations. Percent weight gain of the granulation upon the increase of relative humidity from 40% to 90% was 1.7% and 6.5% for the dry and wet formulations, respectively. Although the increased hygroscopicity of a formulation is generally expected to increase the degradation rate of a moisture sensitive drug, the effective microenvironment pH control in the case of the wet granulation formulation was a key factor for the stability of this formulation. The microenvironment pH control in the case of the wet granulation formulation was probably able to compensate for the increased hygroscopicity, resulting in a more stable dosage form than the less hygroscopic dry granulation formulation, which lacked effective pH control.

DMP 754 tablets, 0.2 mg, compressed from the granulation manufactured by the wet process were more stable than the capsules filled with the same granulation at 40 °C/75% RH (Figure 5). DMP 754 degradation was more pronounced at 40 °C/75% RH than at 30 °C/60% RH. At both conditions, ester and amidine hydrolysis rates were lower in the tablet dosage form. The higher degradation rate in the case of capsules may be due to the moisture associated with capsule shell. Due to the hygroscopic nature of the formulation manufactured by wet granulation, moisture may be transferred from the capsule shell to the granulation, which is in direct contact with the gelatin shell. Capsules manufactured by wet granulation showed higher moisture content than tablets (Table 2). In the case of the wet granulation formulation, compression did not demonstrate the destabilizing effect observed for the dry blends. Increasing the number of contact points in the case of granulation manufactured by the wet process did not result in enhanced degradation, probably due to the control of microenvironment pH. Stability of tablets manufactured by the wet granulation process increased with the decrease of the excipient-to-drug ratio. Thus, the

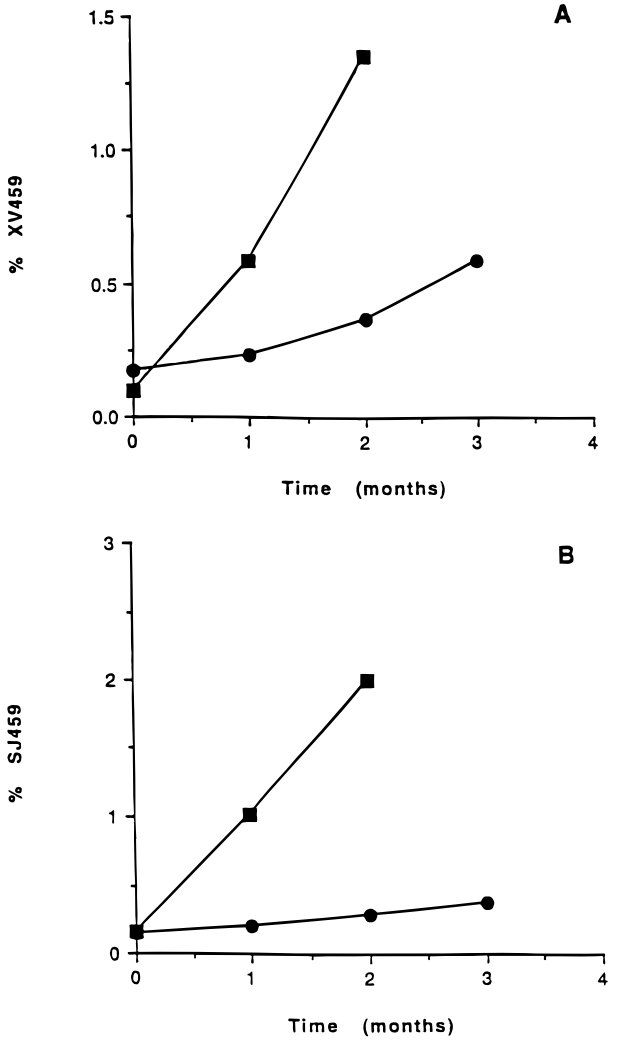

Figure 7—Percent degradation products of DMP 754: (a) XV459 and (b) SJ459 in tablets manufactured by the wet granulation process. Tablets are packaged in HDPE bottles with desiccant and stored at 40 °C/75% RH. Tablets containing 2.5% disodium citrate, (●); tablets without disodium citrate, (■).

1.0 mg tablet showed the least degradation among the three strengths followed by the 0.5 mg tablet, while the 0.2 mg tablet demonstrated the highest rate of degradation (Table 2).

The stabilizing effect of disodium citrate was further demonstrated by the instability of tablets without disodium citrate. Although this formulation was manufactured using a granulating solution buffered to pH 4 with lactate, these tablets showed a higher degradation rate than for the tablets with disodium citrate (Figure 7). The very low concentration of lactate (0.0083% of the total weight of the formulation) was probably insufficient to control the microenvironment pH in the tablets. This was shown by measuring the pH of a slurry prepared by mixing 0.5 g of the granulation with 0.5 g of water. The pH values of the slurries prepared from the granulations with disodium citrate and lactate were found to be 4.4 and 7.7, respectively.

Conclusions

A stable solid dosage form containing a pH modifying agent was developed for DMP 754. The choice of the manufacturing process was critical to the stability of the drug product. The stability of DMP 754 in the dosage form was maximized by the inclusion of the pH modifying agent and the selection of the appropriate manufacturing process. Method of incorporation of an acidic ingredient affects its ability to control the microenvironment pH of a hydrolyzable drug such as DMP 754 and, hence, the stability of the drug product. Depending on the nature of the moisture-sensitive drug and the formulation, the dry granulation process may not be the process of choice. The wet granulation process can yield a more stable drug product for a hydrolyzable drug if the formulation contains a pH modifying agent that controls the pH of the microenvironment. Excipient-to-drug ratio can also be modified in order to maximize drug product stability.

References and Notes

1. Mousa, S. A.; Bozarth, J.; Forsythe, M.; Xue, C. B.; Wityak, J.; Olson, R.; Thoolen M. J.; Reilly, T. M. Discovery of a Novel Non Peptide Antiplatelet GPIIb/IIIa Receptor Antagonist, DMP 754: Receptor Binding Afffinity and Specificity. *Circulation* **1996**, *94(8)*, I-513.
2. Racanelli, A. L.; Kapil, R. P.; Mousa, S. A.; Reilly T. M.; Thoolen, M. J. Oral Antiplatelet Effects of DMP 754 in Dogs and Nonhuman Primates. *Circulation* **1996**, *94(8)*, I-98.
3. Badawy, S. I. F.; Williams, R. C.; Gilbert, D. L. Effect of Different Acids on Solid State Stability of an Ester Prodrug of a Glycoprotein IIb/IIIa Receptor Antagonist. Accepted for publication in *Pharm. Dev. Technol.*, in press.
4. Kallion, R. B.; Stella, V. J. The Nucleophilicity of Dextrose, Sucrose, Sorbitol and Mannitol with *p*-Nitrophenyl Esters in Aqueous Solution. *Int. J. Pharm*. **1990**, *66*, 149−155.
5. Brandl, M.; Magill, A.; Rudraraju, V.; Gordon, M. S. Approaches for Improving the Stability of Ketorolac in Powder Blends. *J. Pharm. Sci*. **1995**, *84(10)*, 1151−1153.
6. Gu, L.; Strickley, R. G.; Chi L. H.; Chowhan, Z. T. Drug-Excipient Incompatibility Studies of the Dipeptide Angiotensin-Converting Enzyme Inhibitor, Moexipril Hydrochloride: Dry Powder vs Wet Granulation. *Pharm. Res*. **1990,** *7(4)*, 379−383.
7. De Wolfe, R. H. Kinetics and Mechanisms of Reactions of Amidines. In *The Chemistry of Amidines and Imidates*; Patai, S., Ed.; John Wiley & Sons Ltd.: New York, 1975; p 354.
8. Carstensen, J. T. *Drug Stability: Principles and Practice*; Marcel Dekker Inc.: New York, 1990; p 165.
9. Peck, G. E.; Baley, G. J.; McCurdy, V. E. Tablet Formulation and Design. In *Pharmaceutical Dosage Forms: Tablets*; Liberman, H. A., Lachman, L., Schwartz, J. B., Eds.; Marcel Dekker Inc.: New York, 1989; Vol. 1, p 111.

Acknowledgments

The authors are thankful to Janet F. Edwards and Kathleen L. Reilly for their assistance in the HPLC analysis and to James L. Long and Anthony J. Gawronski for their help with the manufacturing process. The authors also thank C. Michel for performing the X-ray microanalysis and R. Vickery for his help with the moisture uptake studies.

JS9803297

Dissolution Specifications Based on Release Rates

ZEEV ELKOSHI*

Contribution from *Teva Pharmaceutical Industries Ltd., P.O. Box 353, Kfar-Sava 44102, Israel.*

Received August 6, 1998. Accepted for publication January 4, 1999.

Abstract □ A procedure based on release rates is proposed for the establishment of dissolution specifications that ensure the bioequivalence of a test and a reference product. This procedure, which confines C_{max} (the maximum concentration of the drug in vivo) and AUC_∞ (the area under the time–concentration curve, extrapolated to infinity) values within any desired range (relative to a reference product), can be used as an alternative to the methods presented in the FDA guidance[1] or the USP.[2] The method is appropriate for zero-order or first-order release products with linear Level A in vitro/in vivo correlations (IVIVC). Based on the result that the relative difference in C_{max} must always be smaller than the relative difference in the absorption rate constants (for any test and reference products of a given drug), the "minimum range" specifications are set. These specifications, which are identical for both zero-order and first-order release products, are of general validity. They depend only on the relative extents of release, but are otherwise drug or formulation independent. For certain extended release products demonstrating a constant release rate that is unaffected by dissolution conditions (thus allowing the assumption of Level A IVIVC), the "minimum range" dissolution limits are applicable even when in vivo data is not available. If the reference product in vivo data is available, wider limits (which are product specific) may be set. If the drug disposition is monoexponential, the specifications generated are the widest possible. They are termed the "ideal" specifications. In the case of a multiexponential disposition, the limits set by the procedure will (generally) not be the widest possible. Although the method is based on one-compartment models, it is essentially model independent in the sense that microscopic modeling is redundant for its application.

Introduction

In the presence of in vitro/in vivo correlations (IVIVC), dissolution specifications are important as a means of controlling drug bioavailability and thus can be used as a substitute for human bioequivalence studies. A recently published FDA guidance deals with the application of IVIVC for the setting of dissolution specifications for extended release (ER) products.[1] This guidance includes a section concerning specifications based on the release rate of the product. The section, however, is very brief and refers only to products presenting a zero-order release rate. No method for the establishment of the specifications is included.

The present work proposes a procedure for the determination of rate specifications that ensures the bioequivalence of a tested product and a reference product. This procedure presents an alternative approach to the methods proposed by the USP[2] and FDA guidance.[1] The procedure assumes zero- or first-order release rates and linear Level A IVIVC. Generally, IVIVC are established with in vivo data. Under certain conditions, however, when the rate and extent of release of an ER product are unaffected by dissolution conditions (such as, pH, stirring rate, etc.), linear Level A IVIVC are anticipated (assuming that drug release is the rate-limiting step in the process of in vivo drug absorption).[3] In these cases the procedure is applicable, even in the absence of in vivo data. If the reference product in vivo data are available, the dissolution specifications can be widened.

Although this method is based on monoexponential disposition models, it is also applicable when a multiexponential disposition is involved. The method is essentially model independent in the sense that microscopic modeling is not needed.

The bioequivalence metrics required today by most regulatory agencies are AUC_∞ (the area under the time−concentration curve, extrapolated to infinity) and C_{max} (the maximum concentration of drug in vivo). The specifications produced by the proposed procedure may bound both metrics of a tested product, within any desired range, relative to a reference product, thus ensuring their bioequivalence. In this text, a range of ±20% for both metrics is used.

Setting Dissolution Specifications

Dissolution limits are used as a batch-to-batch quality control means. If in vitro dissolution data are related to in vivo data, these in vitro limits can then be used to control the bioavailability of a tested product, relative to that of a reference product (with a known bioavailability). In this way, the bioequivalence of the two products can be guaranteed in vitro.

Bioavailability and bioequivalence are usually assessed in terms of the C_{max} and AUC_∞ metrics. Most regulatory agencies consider two drugs as bioequivalent when they differ by no more than ±20% with respect to each of these metrics. Hence, dissolution limits that control a ±20% difference between the test metrics and the reference metrics will ensure the bioequivalence of the products. Under these circumstances, quality control is meaningful in terms of the in vivo performance of the drug. Dissolution limits that are set in this way may also be used for a selection of a generic substitute or for the approval of manufacturing changes (drug formulation, drug substance, manufacturing site, etc.).

Dissolution limits that are too wide may allow the approval of batches that are bioinequivalent to a reference product. Limits that are too tight, on the other hand, may lead to the rejection of a large number of production batches. It is desired, therefore, to use the widest possible dissolution specifications that are also consistent with the allowed differences between the test and reference metrics of bioequivalence.

Two sets of dissolution specifications are presented: the "minimum range" and the "ideal" specifications. These two sets are first investigated under the constraint of equal extents of release (between the test and reference products).

* Author to whom all correspondence should be addressed. Telephone: 972-9-7648260. Fax: 972-9-7648636. E-mail address: zeev-e@teva.co.il.

10.1021/js980322p CCC: $18.00
Published on Web 03/13/1999

Then, dissolution specifications for test and reference drugs with different extents of release are considered.

It is assumed throughout this text that linear level A IVIVC are present.

The "Minimum Range" Specifications—The "minimum range" specifications are the widest (relative) dissolution limits that are common to all reference products with IVIVC. Being common to all reference products, the "minimum range" limits must be tighter than the widest feasible dissolution limits for any individual product. Hence, the origin of the name.

It is useful to introduce, at this point, two dimensionless variables, x and y.

For a one-compartment model with zero-order absorption (Appendix A):

$$x = k_{el}D/k_o = k_{el}T \quad (1)$$

where D is the dose absorbed, k_o is the zero-order absorption rate constant, k_{el} is a first-order elimination constant, and T is the duration of the absorption process. Then

$$C_{max} = \frac{D}{Vx}(1 - e^{-x}) \quad (2)$$

where V is the compartment volume.

For a one-compartment model with a first-order absorption (Appendix B):

$$y = k_{el}/k_a \quad (3)$$

where k_a is a first-order absorption constant. Then, by eq B6:

$$C_{max} = \frac{D}{V}y^{y/(1-y)} \quad (4)$$

It is proved in Appendixes A and B that the sensitivity of C_{max} to changes in the rate constant value grows as x or y increase. This result was previously noticed numerically, for the first-order case.[5] The sensitivity reaches a maximum value as $\{x \text{ or } y\} \rightarrow \infty$, where a change in k_o or k_a leads to a change in C_{max} of exactly the same relative value. This, in turn, leads to the conclusion that the in vivo limits $\{\Delta k_o/k_{o(r)} \text{ or } \Delta k_a/k_{a(r)}\} = \pm 0.2$ ensure the condition $|\Delta C_{max}|/C_{max(r)} < 0.2$, where Δ is the test to reference difference and the subscript "r" stands for a reference product. This conclusion is based on the assumption that the test and the reference products are absorbed to the same extent.

If linear level A IVIVC are present, the in vivo absorption rate constants must be linearly related to the in vitro dissolution rate constants. Similarly the (in vivo) extent of absorption must be linearly related to the in vitro extent of release. Therefore, the in vitro condition:

$$-0.2 < \frac{\Delta k_{do}}{k_{do(r)}} \text{ or } \frac{\Delta k_{da}}{k_{da(r)}} < +0.2 \quad (5)$$

where k_{do} or k_{da} are the zero- or first-order dissolution rate constants, respectively, will generally confine the C_{max} value of the test product within ±20% of the reference product value. As before, the Δ sign stands for the test-to-reference difference.

Equation 5 presents the "minimum range" rate specifications when the test and reference products are released to the same extent. The "minimum range" specifications are of general validity because they are not product specific. They are valid even when the drug disposition is multiexponential, as demonstrated in Appendixes C and D. The "minimum range" specifications may be applied for any drug product with established IVIVC. They are particularly useful for certain ER products, where drug release is slow enough and well controlled (see the Discussion). With these products, IVIVC are *expected*. Hence, in these particular cases (and in these cases only), the "minimum range" specifications may be used even when in vivo data are not available.

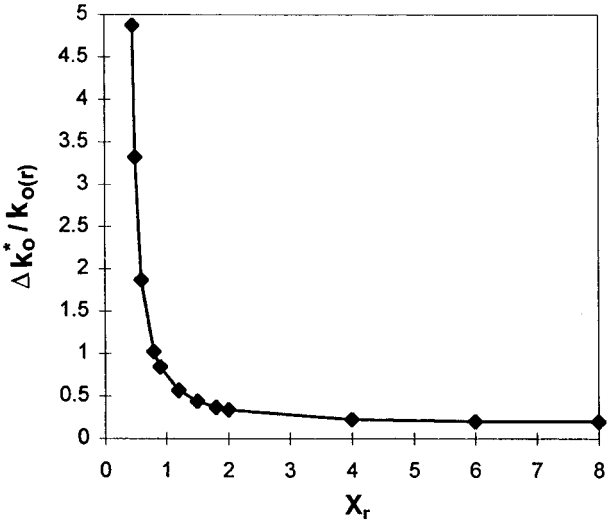

Figure 1—The relative difference in the (zero-order) absorption rate constant values correlating to a standard +20% difference in the C_{max} values, as a function of x_r. The line presents $\Delta k_o^*/k_{o(r)}$ values estimated by the use of eq A11. In the presence of linear IVIVC, the same line defines the upper limit of the "ideal" specifications.

The "Ideal" Specifications—The "ideal" specifications are the widest possible specific dissolution limits that ensure the bioequivalence of any test drug relative to a specific reference product. Similar to the "minimum range" specifications, the "ideal" specification may be applied for any drug product with established IVIVC. However, the "ideal" specifications are dependent on x_r or y_r, which renders the "ideal" specifications product specific.

The widest specific limits of the in vivo absorption rate constants are set in Appendix A (eqs A11 and A12) and Appendix B (eqs B14 and B15) by a test-fitting procedure, assuming one-compartment models with zero- or first-order absorption, respectively. The test and reference products are assumed to be absorbed to the same extent. If linear level A IVIVC are present, the in vivo absorption rate constant (k_o or k_a) is linearly related to the in vitro dissolution rate constant (k_{do} or k_{da}). Similarly, the extent of in vivo absorption is linearly related to the extent of in vitro release.

Hence, when absorption is *zero-order*, the "ideal" dissolution limits are as follows:

Upper limit ($\Delta C_{max}/C_{max(r)} = +0.2$):

$$\Delta k_{do}^*/k_{do(r)} = 0.0018722x_r^{-9.097} + 0.52492x_r^{-2.003} + 0.2 \quad (6)$$

Lower limit ($\Delta C_{max}/C_{max(r)} = -0.2$):

$$\Delta k_{do}^*/k_{do(r)} = -0.35753e^{-4.4507x_r} - 0.44063e^{-1.0255x_r} - 0.2 \quad (7)$$

These limits are presented by the lines in Figures 1 and 2.

When absorption is *first-order*, the "ideal" dissolution limits are as follows:

Upper limit ($\Delta C_{max}/C_{max} = +0.2$):

$$\Delta k_{da}^*/k_{da(r)} = 0.277y_r^{-0.767} + 0.0271y_r^{-3.005} + 0.2 \quad (8)$$

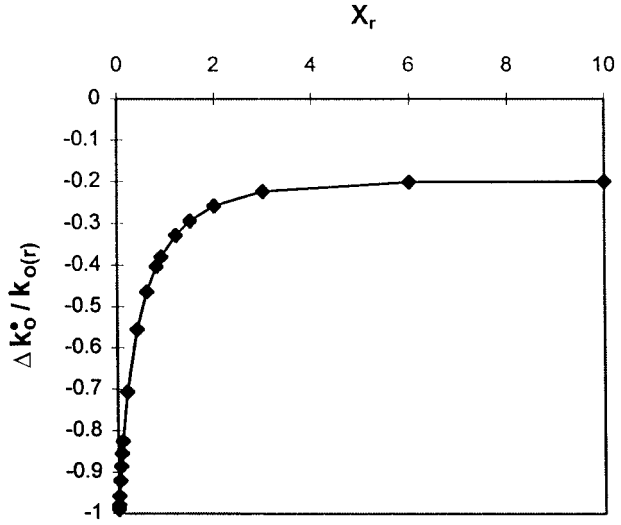

Figure 2—The relative difference in the (zero-order) absorption rate constant values correlating to a standard –20% difference in the C_{max} values, as a function of x_r. The line presents $\Delta k_0^*/k_{0(r)}$ values estimated by the use of eq A12. In the presence of linear IVIVC, the same line defines the lower limit of the "ideal" specifications.

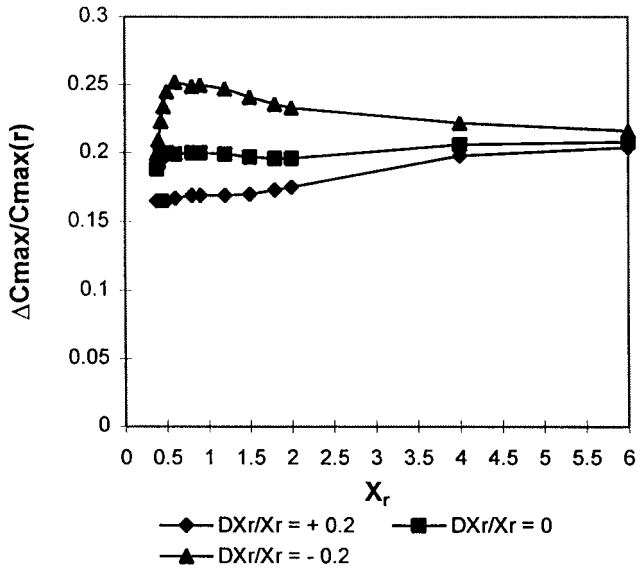

Figure 3—$\Delta C_{max}/C_{max(r)}$ values generated for the zero-order case by using $\Delta k_0^*/k_{0(r)}$ values (defined by eq. A11) in eqs. A5 and A6. The effects of +20% or –20% errors in the estimation of x_r ($Dx_r/x_r = +0.2$ or $Dx_r/x_r = -0.2$) are also included.

Lower limit ($\Delta C_{max}/C_{max(r)} = -0.2$):

$$\Delta k_{da}^{\bullet}/k_{da(r)} = -0.299e^{-26.4y_r} - 0.348e^{-3.128y_r} - 0.146e^{-0.165y_r} - 0.2 \quad (9)$$

These limits are presented by the lines in Figures 3 and 4. Again, Δ is the test-to-reference difference. The (*) and (•) superscripts are reminders that +20% and −20% differences in C_{max}, respectively, are involved.

The use of eqs 6−9 ensures a difference of exactly +20% or −20% between the C_{max} values of the test and reference products. Thus, the range of the rate specifications is the widest possible for each reference product, which renders the "ideal" specifications product specific.

Equations 6 and 8 diverge for $x_r < 0.38$ and $y_r < 0.07$ respectively, indicating that an increase of >20% in C_{max} is *impossible* for x or y values low enough to satisfy these conditions. This leads to the conclusion that a rate-related

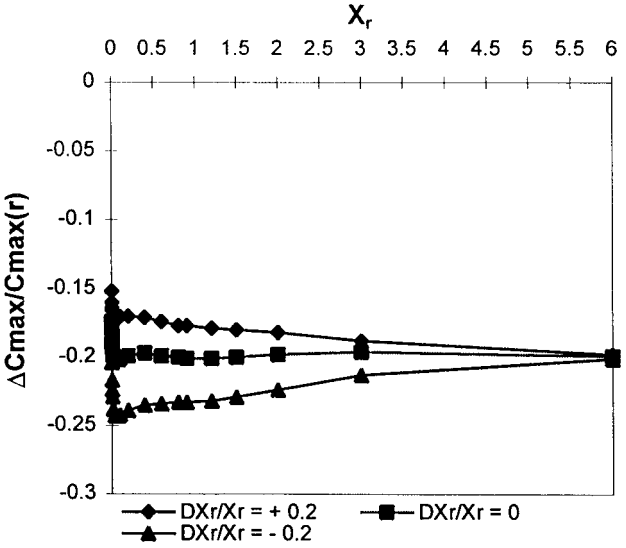

Figure 4—$\Delta C_{max}/C_{max(r)}$ values generated for the zero-order case by using $\Delta k_0^*/k_{0(r)}$ values (defined by eq A12) in eqs. A5 and A6. The effects of +20% or –20% errors in the estimation of x_r ($Dx_r/x_r = +0.2$ or $Dx_r/x_r = -0.2$) are also included.

dose-dumping is impossible when $x < 0.38$ in the zero-order case, or $y < 0.07$ in the first-order case (see Appendixes A and B).

Like the "minimum range" specifications, the "ideal" specifications are particularly useful for ER products with a well-controlled drug release. In these cases, the "ideal" limits may be applied when the reference product in vivo data are the only in vivo data available (see the Discussion).

Equations 6−9 are useful, even when the disposition of the drug is multiexponential. In this case (as described in Appendixes C and D), k_e in x_r or y_r should be replaced by α_1, the largest macroscopic disposition rate constant. The specifications defined this way are, in general, tighter than the "ideal" specifications (which are not feasible when disposition is multiexponential) and wider than the "minimum range" specifications.

Dissolution Specifications when Products are Absorbed to a Different Extent. It has been postulated so far that both the test and the reference products are released (and hence absorbed) to the same extent. The equations used for the dissolution specifications may be generalized to include the effect of a difference in the extent of release (Appendix E). The "minimum range" specifications in this case are

$$\left.\begin{aligned} -0.2 < \frac{\Delta A}{A_r} < 0.2 \\ -0.2 - \frac{\Delta A}{A_r} < \frac{\Delta k_{do}}{k_{do(r)}} \text{ or } \frac{\Delta k_{da}}{k_{da(r)}} < 0.2 - \frac{\Delta A}{A_r} \end{aligned}\right\} \quad (10)$$

where A is the extent of in vitro release and Δ is the test-to-reference difference.

The "ideal" specifications are generalized by the use of eqs E6 and E7. One of the following two equations should be solved (numerically) to estimate Q, depending on whether the absorption is zero- or first-order:

When absorption is zero-order

$$\frac{1 - e^{-Qx_r}}{Q(1 - e^{-x_r})} - 1 + \frac{\Delta A}{A_r} = \pm 0.2 \quad (11)$$

When absorption is first-order

$$\frac{Qy_r^{Qy_r/(1-Qy_r)}}{y_r^{y_r/(1-y_r)}} - 1 + \frac{\Delta A}{A_r} = \pm 0.2 \qquad (12)$$

where the (+) sign is related to the upper dissolution limit and the (−) sign to the lower dissolution limit.

The "ideal" dissolution limits are then defined by

$$\{\Delta k_{do}/k_{do(r)} \text{ or } \Delta k_{da}/k_{da(r)}\} = 1/Q - 1 \qquad (13)$$

If multiexponential disposition is involved, k_{el} in x_r or y_r (eq 11 or 12) should be replaced by α_1, the largest macroscopic disposition rate constant. In that case, as before, the generated limits are, in general, tighter than the "ideal" limits (which are not feasible, when disposition is multiexponential) and wider than the "minimum range" limits.

Discussion

The conclusion that a 20% change in the value of the in vivo rate constant cannot lead to more than a 20% change in the value of C_{max} is a fundamental result of this work. In the presence of linear IVIVC, this result enables the setting of in vitro "minimum range" dissolution limits that are unspecific to the product and hence are of a general validity. If in vivo data related to the reference product are available, x_r or y_r can be estimated, and the dissolution limits may be widened (by the use of eqs 6−9). The dissolution limits in this case are product specific. The generated limits widen as the x_r or y_r values decrease.

The determination of the in vitro/in vivo correlation coefficients is not required for any of the proposed sets of specifications but in vivo data are generally needed to verify IVIVC. However, when IVIVC are *expected*, the "minimum range" specifications may be set even in the absence of in vivo data. Similarly, when IVIVC are expected, the "ideal" specifications may be set even when only the reference product in vivo data are available. IVIVC are highly probable when the drug release is sufficiently slow and well controlled (i.e., when it is unaffected by dissolution conditions such as pH, stirring rate, ionic strength, surfactant concentration, etc.) Roxatidine controlled/modified-release capsules[3] and the nifedipine push−pull osmotic pump[6,7] are examples. Thus, the proposed specifications, which are valid for any drug product with established IVIVC, are particularly useful when IVIVC are expected. This is not true for methods of setting release specifications based on convolution/deconvolution or modeling techniques where the particular in vitro/in vivo correlation coefficients are required.

It should be emphasized that the availability of in vivo data is always desired, even when linear IVIVC are expected. If in vivo data are available, the validity of the linear IVIVC assumption may be assessed. In addition, wider dissolution limits can be set because x_r or y_r may be evaluated.

Once linear IVIVC have been established (or assumed), dissolution limits are easily set. The "minimum range" limits may always be set with the help of a simple desk calculator. This simplicity is true also with the "ideal" limits when both the test and the reference products are released to the same extent. However, a best-fit procedure is needed to set the "ideal" specifications when the products are released to a different extent.

An interesting and practical result of this work is the observation that for $x < 0.38$ in the zero-order case, or $y < 0.07$ in the first-order case, a rate-dependent dose-dumping (an increase of >20% in C_{max}) is impossible (Appendixes A and B). In other words, formulations with $x < 0.38$ or $y < 0.07$ are dose-dumping proof.

The methods just described do not deal with any microscopic rate constants. The only values derived from the in vivo data are the largest disposition rate constant and either the first-order absorption rate constant or the duration of the zero-order "infusion". All of these are macroscopic constants that do not require any microscopic modeling. In this respect, the procedure is model independent.

For products with a first-order release, it is extremely important to correctly identify the absorption exponential term. A wrong identification (in a "flip-flop" situation) may lead to an underestimation of $y_1(=\alpha_1/k_a)$. The generated dissolution limits, in this case, will allow deviations of the C_{max} value from the ±20% range.

Only when IVIVC prevail can dissolution data be used as a surrogate for the in vivo performance of the drug. From practical experience, the majority of dissolution profiles can be closely approximated by zero- or first-order rates of release. To demonstrate linear Level A IVIVC, the patterns of in vitro release and in vivo absorption profiles must be similar, which means that mainly zero- or first-order in vivo absorption profiles can linearly be correlated with the in vitro data. The more complex absorption curves originating due to the changing physiological environment along the gastrointestinal tract, (usually) cannot be linearly correlated with the (simple) in vitro release curves. Hence, a procedure for the establishment of dissolution specifications, that deals with zero-or first-order release rates (like the one proposed in this work) covers most cases with linear Level A IVIVC.

References and Notes

1. Guidance for Industry, *Extended Release Oral Dosage Forms: Development, Evaluation, and Application of In Vitro/In Vivo Correlations*. CDER, Food and Drug Administration, USA, 1997.
2. *The United States Pharmacopeia (USP 23)*; United States Pharmacopeial Convention: Rockville, MD, 1995; p 1929.
3. Frick, A.; Möller, H.; Wirbitzki, E. Biopharmaceutical characterization of oral controlled/modified-release drug products. In vitro/in vivo correlation of roxatidine. *Eur. J. Pharm. Biopharm*. **1998**, *46*, 313−319.
4. Gibaldi M.; Perrier. D. *Pharmacokinetics*, 2nd ed.; Marcel Dekker: New York and Basel, 1982.
5. Rostami-Hodjegan, A.; Jackson, P. R.; Tucker, G. T. Sensitivity of indirect metrics for assessing "rate" in bioequivalence studies-moving the "goalposts" or changing the "game". *J. Pharm. Sci.* **1994**, *83*, 1554−1556.
6. Grundy, J. S.; Foster, R. T. The nifedipine gastrointestinal therapeutic system (GITS): Evaluation of pharmaceutical, pharmacokinetic and pharmacological properties. *Clin. Pharmacokinet*. **1994**, *30(1)*, 28−51.
7. Swanson, R. D., Barclay, B. L., Wong, P. S., Theeuwes, F. Nifedipine gastrointestinal therapeutic system. *Am. J. Med.* **1987**, *83 (Suppl. 6B)*, 3−9.

Acknowledgments

The author is indebted to Dr. Daniel Teitel for editing the manuscript. The assistance of Mrs. Lea Avivi, Mrs. Sarie Nir, and Mr. Michael Cogan is gratefully acknowledged.

Appendix A: One-Compartment Model with Zero-Order Absorption

Consider a one-compartment open model with a zero-order absorption. Define the dimensionless variable x

$$x = k_{el}\, T \qquad (A1)$$

where T is the duration of the absorption process (the

"infusion" time) and k_{el} is a first-order elimination constant. Then

$$C_{max} = \frac{D}{Vx}(1 - e^{-x}) \quad \text{(A2)}$$

where D is the dose absorbed and V is the compartment volume.[4]

The following question is addressed: How is a (macroscopic) difference between the (zero-order) absorption rate constants of two products related to the difference in their C_{max} values? Equation A1 may be rewritten as

$$x = \frac{k_{el}\, D}{k_o} \quad \text{(A3)}$$

where k_o is the zero-order absorption rate constant. Consider test and reference products with equal D, V, and k_{el} values.

The absorption rate constant of the test product, $k_{o(t)}$, has a different value from that of the reference product, $k_{o(r)}$.

Define

$$Q = \frac{x_t}{x_r} = \frac{k_{o(r)}}{k_{o(t)}} \quad \text{(A4)}$$

Then

$$\frac{\Delta k_o}{k_{o(r)}} = \frac{k_{o(t)} - k_{o(r)}}{k_{o(r)}} = \frac{1}{Q} - 1 \quad \text{(A5)}$$

By eqs A2 and A4

$$\frac{\Delta C_{max}}{C_{max(r)}} = \frac{C_{max(t)} - C_{max(r)}}{C_{max(r)}} = \frac{1 - e^{-Qx_r}}{Q(1 - e^{-x_r})} - 1 \quad \text{(A6)}$$

At the limit, as $x_r \to \infty$

$$\lim_{x_r \to \infty} \frac{\Delta C_{max}}{C_{max(r)}} = \frac{1}{Q} - 1 = \frac{\Delta k_o}{k_{o(r)}} \quad \text{(A7)}$$

Hence, as $x_r \to \infty$, the relative difference in C_{max} is equal to the relative difference in k_o.

Derive x with respect to k_o

$$\frac{dx}{dk_o} = -\frac{k_{el} D}{k_o^{\,2}} = -\frac{x}{k_o} \quad \text{(A8)}$$

The infinitesimal relative difference in C_{max} is defined by

$$\frac{dC_{max}}{C_{max}} = \frac{C'_{max}}{C_{max}} dx = -\frac{C'_{max}\, x}{C_{max}} \frac{dk_o}{k_o} = \left[\frac{1 - e^{-x}(x+1)}{1 - e^{-x}}\right] \frac{dk_o}{k_o} \quad \text{(A9)}$$

where eq A8 was used, and C'_{max} is the derivative of C_{max} with respect to x.

Define

$$F(x) = \frac{1 - e^{-x}(x+1)}{1 - e^{-x}} \quad \text{(A10)}$$

It may be proven (Appendix F) that $F(x)$ is a positive and monotone increasing function of x for $x > 0$.

As $x \to \infty$, $F(x)$ assumes its maximal value and therefore, for a constant value of dC_{max}/C_{max}, dk_o/k_o is minimal (by its absolute value) at that limit.

It is demonstrated in Appendix G that the macroscopic quantity $|\Delta k_o|/k_{o(r)}$ corresponding to a constant value of $|\Delta C_{max(r)}|/C_{max}$, assumes a minimum value as $x_r \to \infty$.

This value, which is equal (by eq A7) to $|\Delta C_{max}|/C_{max(r)}$ is a lower boundary to $|\Delta k_o|/k_{o(r)}$ (at any x_r) that corresponds to a constant relative difference between the C_{max} values. In other words, a relative difference of $\pm q$ in k_o corresponds to a relative difference in C_{max}, which is less than q by its absolute value. When $x_r \to \infty$, this relative difference in C_{max} approaches q (by its absolute value).

Hence, the in vivo limits $\Delta k_o/k_{o(r)} = \pm 0.2$ ensure the condition: $|\Delta C_{max}|/C_{max(r)} < 0.2$. These limits will be termed the "minimum range" limits. The "minimum range" limits are the widest (relative) rate constant limits common to all reference products. Being common to all reference products, the "minimum range" limits must be tighter than the widest feasible rate constant limits for any individual product. Hence the origin of the name.

Using eqs A5 and A6 it is possible to estimate (numerically) the value of $\Delta k_o/k_{o(r)}$ correlating to a certain relative difference in $C_{max,}$ as a function of x_r. Figure 1 depicts the best fitted $\Delta k_o/k_{o(r)}$ values related to $\Delta C_{max}/C_{max(r)}$ value of $+0.2$. An asterisk was added as a reminder that a standard $+20\%$ difference in C_{max} is involved.

For $x_r < 0.38$, $\Delta k_o^*/k_{o(r)}$ values diverge. This result means that an infinite relative increase in the $k_{o(r)}$ value is needed when $x_r < 0.38$ to observe a $+20\%$ change in C_{max}. Therefore, dose-dumping (due to a difference in the drug release rate) is not expected when $x_r < 0.38$. This is a consequence of the fact that for $x_r < 0.38$, C_{max} is closer to its maximal value (at $x \sim 0$) by $<20\%$.

The data presented in Figure 1 fit the equation

$$\Delta k_o^*/k_{o(r)} = 0.0018722 x_r^{-9.097} + 0.52492 x_r^{-2.003} + 0.2 \quad \text{(A11)}$$

The $\Delta k_o^*/k_{o(r)}$ values estimated with eq A11 are presented by the line in Figure 1. The accuracy of eq A11 was tested by using $\Delta k_o^*/k_{o(r)}$ values estimated by eq A11 in eqs A5 and A6 to evaluate $\Delta C_{max}/C_{max(r)}$. With 20 x_r values in the range $\{0.38 < x_r < 100\}$ the relative difference in C_{max} was close to 0.2 (ranging from 0.189 to 0.209), as presented in Figure 3. Figure 2 depicts the best fitted $\Delta k_o/k_{o(r)}$ values related to a $\Delta C_{max}/C_{max(r)}$ value of -0.2. The $(\bullet)$ superscript is a reminder that a standard -20% difference in C_{max} is involved. The data presented in Figure 2 fit the equation

$$\Delta k_o^\bullet/k_{o(r)} = -0.35753 e^{-4.4507 x_r} - 0.44063 e^{-1.0255 x_r} - 0.2 \quad \text{(A12)}$$

The fit is presented by the line in Figure 2. The accuracy of eq A12 was examined by using the values generated by this equation in eqs A5 and A6 to evaluate $\Delta C_{max}/C_{max(r)}$. The relative difference between the C_{max} values was close to -0.2 [from (-0.190) to (-0.202)] for 20 x_r values in the range $\{0.008 < x_r < 100\}$, as presented in Figure 4.

Equations A11 and A12 define the relative differences in the absorption rate constant values that are consistent with exactly $+20\%$ or -20% difference between the C_{max} values. Therefore, these equations constitute *the widest* possible absorption rate constant limits that ensure the bioequivalence of test and reference products. Hence, they will be termed the zero-order absorption "ideal" limits. The "ideal" limits are specific to each reference product.

An error in the estimation of $\Delta k_o^*/k_{o(r)}$ or $\Delta k_o^\bullet/k_{o(r)}$ by eqs A11 or A12 may result from a misevaluation of x_r. This misevaluation will lead to $\Delta C_{max}/C_{max(r)}$ values different from the expected values of $\sim +0.2$ or ~ -0.2, respectively. Figure 3 includes the effects of $+20\%$ or -20% errors in the estimation of x_r on the value of $\Delta C_{max}/C_{max(r)}$, when its

expected value is $\sim +0.2$ (i.e. when eq. A11 is used for an estimation of $\Delta k_o^*/k_{o(r)}$). In a similar way, Figure 4 includes the effect of +20% or −20% errors in the estimation of x_r on the value of $\Delta C_{max}/C_{max(r)}$ when its expected value is ~ -0.2 (i.e., when eq A12 is used for an estimation of $\Delta k_o^\bullet/k_{o(r)}$). An overestimation of x_r will lead to $|\Delta C_{max}|/C_{max(r)} < 0.2$. In this case, the $\Delta k_o^*/k_{o(r)}$ and $\Delta k_o^\bullet/k_{o(r)}$ values estimated with eqs A11 and A12 will lead to $\Delta C_{max}/C_{max(r)}$ values within the assumed boundary. However, when x_r is underestimated, $|\Delta C_{max}|/C_{max(r)} > 0.2$. The effect of an error in the estimation of x_r is especially pronounced for low values of x_r. Therefore, when the precise value of x_r is uncertain, it is good practice to use its highest estimated value to evaluate $\Delta k_o^*/k_{o(r)}$ or $\Delta k_o^\bullet/k_{o(r)}$. The resultant $\Delta C_{max}/C_{max(r)}$ value will then probably be confined within the ± 0.2 limits.

If the x_r value is unknown, using the "minimum range" rate limits: $\Delta k_o/k_{o(r)} = \pm 0.2$ will ensure the condition: $|\Delta C_{max}|/C_{max} < 0.2$.

Generally, it is desired to set the widest limits (on a variable) that are consistent with a certain constraint. The "ideal" limits are always wider than the "minimum range" limits. On the other hand, the "ideal" limits may be used only when the reference in vivo rate constants are known.

Appendix B: One-Compartment Model with First-Order Absorption

Consider a one-compartment open model with first-order absorption. The parameter C_{max} is given by[4]

$$C_{max} = \frac{k_a D}{V(k_a - k_{el})}(e^{-k_{el}t_{max}} - e^{-k_a t_{max}}) \qquad (B1)$$

where k_a is a first-order absorption constant. The parameter t_{max} is given by

$$t_{max} = \frac{1}{k_a - k_{el}}\ln[k_a/k_{el}] \qquad (B2)$$

Define the dimensionless variable y

$$y = k_{el}/k_a \qquad (B3)$$

Then, by eq B2,

$$e^{-k_{el}t_{max}} = y^{y/(1-y)} \qquad (B4)$$

$$e^{-k_a t_{max}} = y^{1/(1-y)} \qquad (B5)$$

Using eqs B4 and B5 in eq B1 produces

$$C_{max} = \frac{D}{V} y^{y/(1-y)} \qquad (B6)$$

It is of interest to investigate the effect of a (macroscopic) difference between the (first-order) absorption rate constants of two products on their relative C_{max} values. Consider test and reference products with equal D, V, and k_{el} values. The first-order rate constant of the test product, $k_{a(t)}$ has a different value from that of the reference product, $k_{a(r)}$.

Define

$$Q = \frac{y_t}{y_r} = \frac{k_{a(r)}}{k_{a(t)}} \qquad (B7)$$

Then

$$\frac{\Delta k_a}{k_{a(r)}} = \frac{k_{a(t)} - k_{a(r)}}{k_{a(r)}} = \frac{1}{Q} - 1 \qquad (B8)$$

Equation B8 is identical to eq A5 except that here first-order constants are involved. By the use of eq B6,

$$\frac{\Delta C_{max}}{C_{max(r)}} = \frac{C_{max(t)} - C_{max(r)}}{C_{max(r)}} = \frac{y_t^{y_t/(1-y_t)} - y_r^{y_r/(1-y_r)}}{y_r^{y_r/(1-y_r)}} = \frac{(Qy_r)^{Qy_r/(1-Qy_r)} - y_r^{y_r/(1-y_r)}}{y_r^{y_r/(1-y_r)}} = \frac{(Qy_r)^{Qy_r/(1-Qy_r)}}{y_r^{y_r/(1-y_r)}} - 1 \qquad (B9)$$

At the limit as $y_r \to \infty$,

$$\lim_{y_r \to \infty} \frac{\Delta C_{max}}{C_{max(r)}} = \frac{1}{Q} - 1 = \frac{\Delta k_a}{k_{a(r)}} \qquad (B10)$$

Equation B10 is identical to eq A7. By eq B10, as $y_r \to \infty$, the relative difference in C_{max} is equal to the relative difference in k_a.

Derive y with respect to k_a

$$\frac{dy}{dk_a} = -\frac{k_{el}}{k_a^2} = -\frac{y}{k_a} \qquad (B11)$$

The infinitesimal relative difference in C_{max} is defined by

$$\frac{dC_{max}}{C_{max}} = \frac{C'_{max}}{C_{max}}\,dy = -\frac{C'_{max}}{C_{max}}\,y\,\frac{dk_a}{k_a} = \left[\frac{(y - 1 - \ln y)y}{(1-y)^2}\right]\frac{dk_a}{k_a} \qquad (B12)$$

where eq B11 was used and C'_{max} is the derivative of C_{max} with respect to y (derivation of eq B6).

Define

$$G(y) = \frac{(y - 1 - \ln y)y}{(1-y)^2} \qquad (B13)$$

It may be proven (see Appendix H) that $G(y)$ is a positive and monotone increasing function of y, for $y > 0$ ($y \neq 1$). Therefore, as $y \to \infty$, $G(y)$ assumes a maximal value. Hence, by eq B12, for a constant value of dC_{max}/C_{max}, dk_a/k_a is minimal (by its absolute value) as $y \to \infty$, exactly as in the zero-order model when $x \to \infty$.

By replacing x with y and k_o with k_a in Appendix G, it is demonstrated that the macroscopic quantity $|\Delta k_a|/k_{a(r)}$, corresponding to a constant value of $|\Delta C_{max}|/C_{max(r)}$ assumes a minimum value as $y_r \to \infty$, just as in the zero-order model when $x_r \to \infty$. This value, which is equal (by eq B10) to $|\Delta C_{max}|/C_{max(r)}$, is a lower boundary of the absolute value of $|\Delta k_a|/k_{a(r)}$ (at any y_r) that corresponds to a constant relative difference in C_{max}. In other words, a relative difference of $\pm q$ in k_a corresponds to a relative difference in C_{max} that is less than q by its absolute value. When $y_r \to \infty$, this relative change in C_{max} approaches q (by its absolute value). Hence the in vivo "minimum range" limits $\Delta k_a/k_{a(r)} = \pm 0.2$, ensure the condition $\Delta C_{max}/C_{max(r)} < 0.2$, just as in the zero-order case.

Using eqs B8 and B9, it is possible to estimate (numerically) the value of $\Delta k_a/k_{a(r)}$ corresponding to a certain relative difference in C_{max} as a function of y_r. Figure 5 depicts the best fitted $\Delta k_a/k_{a(r)}$ values related to a $\Delta C_{max}/C_{max(r)}$ value of ± 0.2. Like before, the asterisk stands for a standard +20% difference in C_{max}. For $y_r < 0.07$, the $\Delta k_a/k_{a(r)}$ values diverge, indicating that under this condition, a

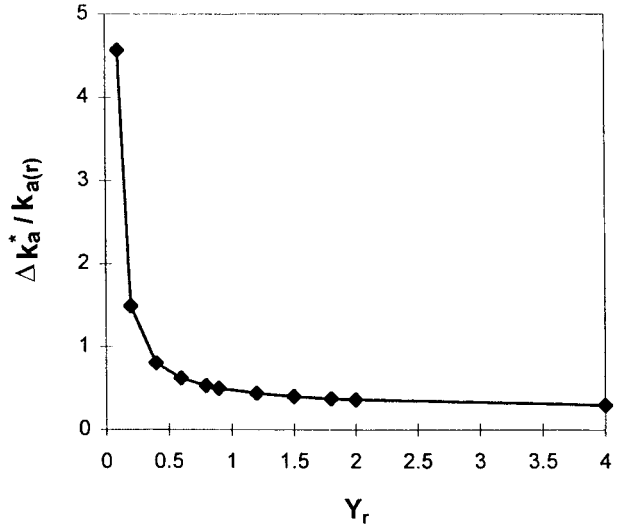

Figure 5—The relative difference in the (first-order) absorption rate constant values correlating to a standard +20% difference in the C_{max} values, as a function of y_r. The line presents $\Delta k_a^*/k_{a(r)}$ values estimated by the use of eq B14. In the presence of linear IVIVC, the same line defines the upper limit of the "ideal" specifications.

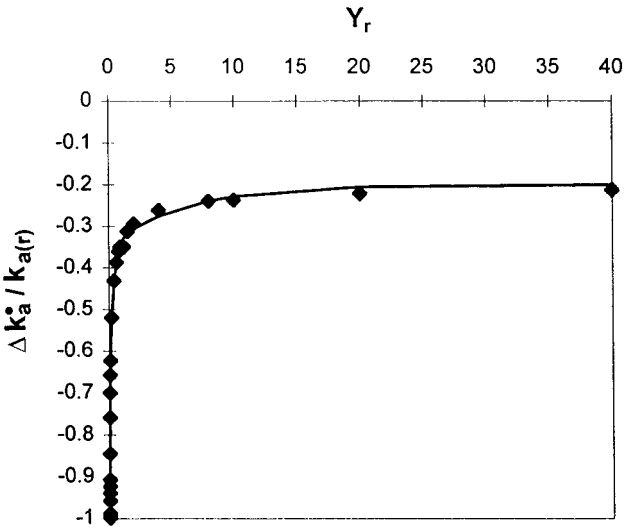

Figure 6—The relative difference in the (first-order) absorption rate constant values correlating to a standard –20% difference in the C_{max} values, as a function of y_r. The line presents $\Delta k_a^\bullet/k_{a(r)}$ values estimated by the use of eq B15. In the presence of linear IVIVC, the same line defines the lower limit of the "ideal" specifications.

+20% difference in C_{max} (a dose-dumping due to a difference in the release rates) is impossible. This is a consequence of the fact that, for $y_r < 0.07$, C_{max} is closer to its maximal value (at $y \sim 0$) by <20%.

The data presented in Figure 5 fit the equation

$$\Delta k_a^*/k_{a(r)} = 0.277 y_r^{-0.767} + 0.0271 y_r^{-3.005} + 0.2 \qquad \text{(B14)}$$

The $\Delta k_a^*/k_{a(r)}$ values estimated with eq B14 are presented by the line in Figure 5. The accuracy of eq B14 was tested by using the estimated $\Delta k_a^*/k_{a(r)}$ values in eqs B8 and B9 to evaluate $\Delta C_{max}/C_{max(r)}$. Twenty y_r values in the range $\{0.07 < y_r < 100\}$ were examined. The relative difference in C_{max} was close to 0.2 (from 0.184 to 0.201), as presented in Figure 7.

Figure 6 depicts the best fitted $\Delta k_a/k_{a(r)}$ value related to a $\Delta C_{max}/C_{max(r)}$ value of −0.2. The (•) superscript, as in the zero-order model, stands for a standard −20% difference

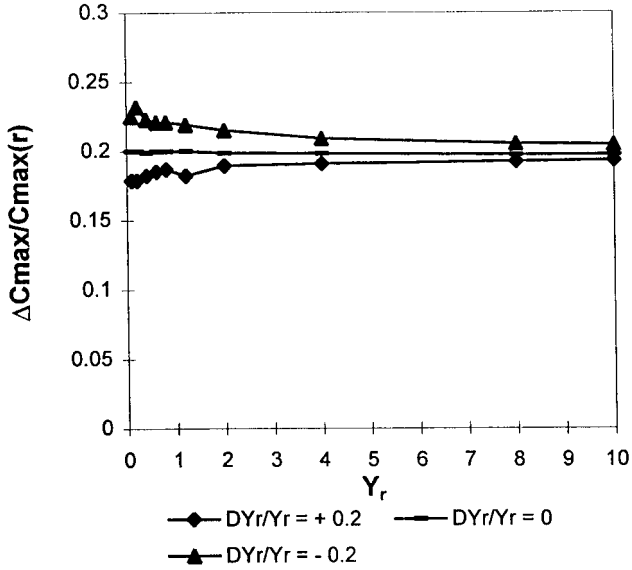

Figure 7—$\Delta C_{max}/C_{max(r)}$ values generated for the first-order case by using $\Delta k_a^*/k_{a(r)}$ values (defined by eq B14) in eqs. B8 and B9. The effects of +20% or −20% errors in the estimation of y_r ($Dy_r/y_r = +0.2$ or $Dy_r/y_r = -0.2$) are also included.

in C_{max}. The data presented in Figure 6 fit the equation

$$\Delta k_a^\bullet/k_{a(r)} = -0.299\, e^{-26.4 y_r} - 0.348\, e^{-3.128 y_r} - 0.146\, e^{-0.165 y_r} - 0.2 \qquad \text{(B15)}$$

The fit is presented by the line in Figure 6. The accuracy of eq B15 was examined, like before, by using the values generated by this equation in eqs B8 and B9 to evaluate $\Delta C_{max}/C_{max(r)}$. With 20 y_r values examined in the range $\{0.004 < y_r < 100\}$, the $\Delta C_{max}/C_{max(r)}$ values were between −0.186 and −0.212, as presented in Figure 8.

Like eqs A11 and A12, eqs B14 and B15 define the relative differences in the absorption rate constant values, consistent with exactly +20% or −20% differences between the C_{max} values. Therefore, these equations provide *the widest* possible rate constant limits that ensure the bioequivalence of the test and reference products. They will be termed the first-order absorption "ideal" limits. These limits are specific to each reference product.

An error in the estimation of $\Delta k_a^*/k_{a(r)}$ or $\Delta k_a^\bullet/k_{a(r)}$ by eqs B14 or B15 may result from a misevaluation of y_r. This misevaluation will lead to $\Delta C_{max}/C_{max(r)}$ values different from the expected values of $\sim +0.2$ or ~ -0.2, respectively. Figure 7 presents the effects of +20% or −20% errors in the estimation of y_r on the value of $\Delta C_{max}/C_{max(r)}$, when its expected (standard) value is $\sim +0.2$ (i.e., when eq B14 is used for the estimation of $\Delta k_a^*/k_{a(r)}$). In a similar way, Figure 8 presents the effect of +20% or −20% errors in y_r on the value of $\Delta C_{max}/C_{max(r)}$ when its expected (standard) value is ~ -0.2 (i.e., when eq B15 is used for an estimation of $\Delta k_a^\bullet/k_{a(r)}$). As in the zero-order case, an overestimation of y_r will lead to $\Delta C_{max}/C_{max(r)}$ values within the boundaries assumed. However, when y_r is underestimated, $\Delta C_{max}/C_{max(r)} > 0.2$. As before, the effect of an error in y_r is especially pronounced for low y_r values.

When the precise value of y_r is uncertain, it is a good practice to use its highest estimated value in eqs B14 and B15. If the y_r value is unknown, the "minimum range" limits $\Delta k_a/k_{a(r)} = \pm 0.2$ should be used. The "ideal" limits are always wider. They are, however, feasible only when the reference in vivo data are available.

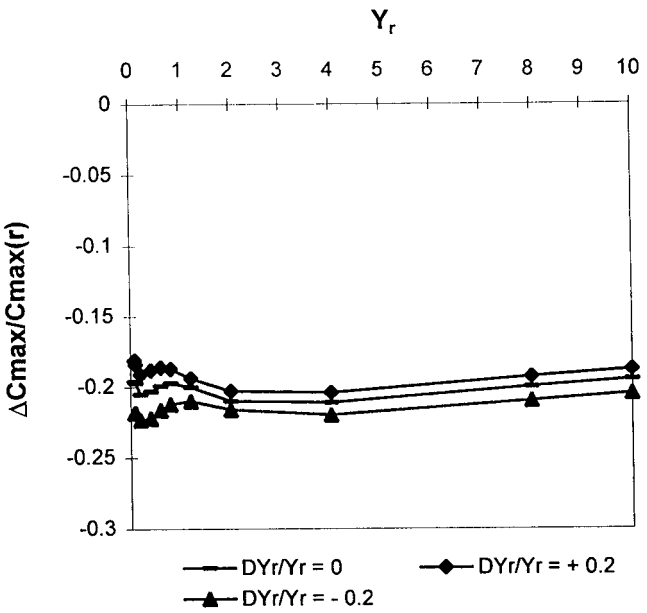

Figure 8—$\Delta C_{max}/C_{max(r)}$ values generated for the first-order case by using $\Delta k_a^{\bullet}/k_{a(r)}$ values (defined by eq. B15) in eqs B8 and B9. The effects of +20% or –20% errors in the estimation of y_r ($Dy_r/y_r = +0.2$ or $Dy_r/y_r = -0.2$) are also included.

Appendix C: Multicompartment Model with Zero-Order Absorption

When the disposition phase of a drug with a zero-order absorption is appropriately described by n exponential terms, with n first-order rate constants: $\alpha_1 > \alpha_2 > \ldots > \alpha_n$, the dependence of C_{max} on the zero-order rate constant is specific to the kinetic model involved. Consider an n-compartment model with a zero-order absorption and m (microscopic) first-order disposition rate constants k_j (j = 1, ... m). When elimination occurs from the central compartment, the concentration in this compartment (while absorption is continuing) is given by[4]

$$C(t) = \frac{D/T}{V_c}\sum_{l=1}^{n}\frac{(1-e^{-\alpha_l t})\prod_{i=2}^{n}(E_i-\alpha_l)e^{-\alpha_l t}}{-\alpha_l\prod_{\substack{i=1\\ i\neq l}}^{n}(\alpha_i-\alpha_l)} \qquad (C1)$$

where V_c is the volume of the central compartment and E_i is the sum of the exit rate constants from the i^{th} compartment. The parameter α_l can be expressed in terms of the k_j values (it is not dependent on other physical constants). Because α_l has the same dimensions as k_j (time^{-1}), α_l is a homogeneous function of the first degree with respect to the k_j values. That is, α_l (k_1, ..., k_m) satisfies the identity

$$\alpha_l(qk_1,....qk_m) = q\alpha_l(k_1,....k_m) \qquad (C2)$$

where q is any number.

Equations C1 and C2 imply

$$C(D/V_cT,k_1,....,k_m,t) = C(qD/V_cT,qk_1,...,qk_m,t/q) \qquad (C3)$$

When $t = T$, we have

$$C_{max} = C(D/V_cT,k_1,...k_m,T) = C(qD/V_cT,qk_1,...,qk_m,T/q) \qquad (C4)$$

Using $q = T$ in eq (C4) provides

$$C_{max} = C(D/V_c, k_1T,,...k_mT) \qquad (C5)$$

Therefore, C_{max} is dependent on the m dimensionless variables: k_1T, ... k_mT and on D/V_c. The same conclusion may be reached when the elimination is not from the central compartment or when the concentration involved is that of a peripheral compartment.

The one-compartment model discussed in Appendix A is a special case with $m = 1$ and $k_1 = k_{el}$. As demonstrated

$$C_{max}\text{ (one compartment)} = C(D/V_c, x) \qquad (C6)$$

where $x = k_{el}\ T$.

If a one-compartment model is used (as an approximation) to describe the kinetics of a drug with n exponential disposition terms, the best-fitted disposition rate constant must be smaller than α_1 (and larger than α_n).

Define

$$x_1 = \frac{\alpha_1 D}{k_o}(=\alpha_1 T) \qquad (C7)$$

If $x_{1(r)}$ is used instead of x_r in eq A6, it is reasonable to believe that

$$\frac{|\Delta C_{max}|}{C_{max(r)}} < \frac{1-e^{-Qx_{1(r)}}}{Q(1-e^{x_{1(r)}})} - 1 \qquad (C8)$$

because the $x_{1(r)}$ is an upper boundary of x_r. For the same reason, using $x_{1(r)}$ values as defined by eq C7 in eqs A11 or A12 will generate $|\Delta C_{max}|/C_{max(r)} < 0.2$.

Four different compartment models (with a zero-order absorption) were used to assess this assumption: a classical two-compartment model, a classical three-compartment model, a two-compartment model with a central absorption and a peripheral elimination, and a three-compartment model with a central absorption and a peripheral elimination. Values between 0 and 1 were randomly assigned to the disposition rate constants of each model. For this purpose, a computerized random number generator was used. Ten sets of disposition rate constants were thus produced for each model. For the two-compartment models, the values of the three microscopic disposition rate constants were assigned in this same way. For the three-compartment models, the values of the three macroscopic rate constants and of two of the microscopic rate constants were similarly assigned.

Five absorption rate constant values were defined such that

$$x_{1(r)} = 0.1,\ 0.5,\ 1.5,\ 5,\ 30 \qquad (C9)$$

where eq C7 was used to define $x_{1(r)}$. In this way, a total of 50 different sets of constants were generated for each model.

Equations A11 and A12 with $x_{1(r)}$ substituted for x_r, were utilized to produce $k^*_{o(t)}$ (the upper boundary of $k_{o(t)}$) or $k^{\bullet}_{o(t)}$ (the lower boundary of $k_{o(t)}$). These values were introduced into the model to estimate $C_{max(t)}$.

In each of the four models examined, the inequality

$$|\Delta C_{max}|/C_{max(r)} < 20\% \qquad (C10)$$

was verified for all 50 data sets. The values for $|\Delta C_{max}|/C_{max(r)}$ were in the range of ~ 1% to 19%. Hence, eqs A11 and A12 (the zero-order "ideal" limits) may be used to assess the absorption rate limits for products with a zero-order absorption and a multiexponential disposition.

The relative rate limits defined by eqs A11 and A12 are wider than ±20% for any finite value of $x_{r(1)}$. Because eq C10 holds when the limits are wider than 20%, it will certainly hold when the relative rate is limited to ±20% (in each of the four models used, for each of the sets of data examined). Thus, the validity of the "minimum range" rate limits is verified for products with a zero-order absorption and a multiexponential disposition.

Appendix D: Multicompartment Model with First-Order Absorption

For the case of multiexponential disposition, consider an *n*-compartment model with a first-order absorption (k_a) and m(microscopic) first-order disposition rate constants k_j ($j = 1,...m$). When the elimination occurs from the central compartment, the concentration in the central compartment is given by[4]

$$C = \frac{k_a D}{V_c} \frac{\prod_{i=2}^{n}(E_i - k_a)}{\prod_{i=1}^{n}(\alpha_i - k_a)} e^{-k_a t} + \frac{k_a D}{V_c} \sum_{l=1}^{n} \frac{\prod_{i=2}^{n}(E_i - \alpha_l)}{(k_a - \alpha_l)\prod_{\substack{i=1 \\ i \neq l}}^{n}(\alpha_i - \alpha_l)} e^{-\alpha_l t} \quad \text{(D1)}$$

where α_l is a first-order macroscopic disposition constant, V_c is the volume of the central compartment, and E_i is the sum of the exit rate constants from the i^{th} compartment.

By eqs C2 and D1, the following identity is satisfied

$$C(D/V_c, k_a, k_1,...,k_m, t) = C(D/V_c, qk_a, qk_1,...,qk_m, t/q) \quad \text{(D2)}$$

where q can be any number.

Therefore, under the transformations

$$k_a \rightarrow qk_a$$

$$k_1 \rightarrow qk_1$$

$$\vdots$$

$$k_m \rightarrow qk_m$$

The value of the untransformed function (at any time point t) is equal to the value of the transformed function (at time point t/q). In particular, the maximum value of the untransformed function (at t_{max}) is equal to the maximum value of the transformed function (at t_{max}/q). Hence

$$C(D/V_c, k_a, k_1,...k_m, t_{max}) = C(D/V_c, qk_a, qk_1,...qk_m, \hat{t}_{max}) \quad \text{(D3)}$$

where $\hat{t}_{max}$ is the time correlating to maximum value of the transformed function.

Therefore, C_{max} is a function of the following variable

$$C_{max} = C(D/V_c, qk_a, qk_1,...,qk_m) \quad \text{(D4)}$$

However, its value is independent of the value of q. The parameter t_{max} is not included among the variables in eq D4 because C_{max} is defined at $t = t_{max}$ (C_{max} is not a function of t_{max}).

Using $q = 1/k_a$ in eq D4 provides

$$C_{max} = C(D/V_c, k_1/k_a,...,k_m/k_a) \quad \text{(D5)}$$

C_{max} is therefore dependent on the m dimensionless variables ($k_1/k_a,...k_m/k_a$) and on D/V_c. The same conclusion may be reached when the elimination is not limited to the central compartment, or when the concentration involved is that of a peripheral compartment.

In the one-compartment case

$$C_{max} = C(D/V_c, k_1/k_a) \quad \text{(D6)}$$

This is demonstrated by eq B6 (with $k_1 = k_{el}$).

Define

$$y_1 = \frac{\alpha_1}{k_a} \quad \text{(D7)}$$

where α_1 is the largest first-order (macroscopic) disposition rate constant. If $y_{1(r)}$ is used instead of y_r in eq B9, it is reasonable to believe that

$$\frac{|\Delta C_{max}|}{C_{max}} < \frac{Qy_{1(r)}^{Qy_{1(r)}/(1-Qy_{1(r)})}}{y_{1(r)}^{y_{1(r)}/(1-y_{1(r)})}} - 1 \quad \text{(D8)}$$

because y_1 is an upper boundary of y. For the same reason, using $y_{1(r)}$ values as defined by eq D7 in eqs B14 or B15 will generate $|\Delta C_{max}|/C_{max} < 0.2$.

For assessing this assumption, the four compartment models used in Appendix C, were utilized with a first-order absorption. The procedure of assigning values to the disposition rate constants was identical to that previously used. The five absorption rate constant values were defined such that

$$y_{1(r)} = 0.1,\ 0.5,\ 1.5,\ 5,\ 30 \quad \text{(D9)}$$

where eq D7 was used to define $y_{1(r)}$. Equations B14 and B15 with $y_{1(r)}$ substituted for y_r were used to produce $k^*_{a(t)}$ (the upper boundary of $k_{a(t)}$) or $\Delta k^{\bullet}_{a(t)}$ (the lower boundary of $k_{a(t)}$). These values were introduced into the model to estimate $C_{max(t)}$.

As in the zero-order models, with each of the four models examined, the inequality

$$|\Delta C_{max}|/C_{max} < 20\% \quad \text{(D10)}$$

was verified for all 50 data sets. Hence, eqs B14 and B15 (the first-order "ideal" limits) may be used to evaluate the absorption rate limit for products with a first-order absorption and a multiexponential disposition.

The relative rate limits defined by eqs B14 and B15 are wider than ±20% for any finite value of $y_{1(r)}$. Hence, it is clear that limiting the relative rate to ±20% will also lead to eq D10 in each of the four models used and for each of the data sets examined. Thus, the "minimum range" limits are applicable for products with a first-order absorption and a multiexponential disposition.

Appendix E: The Effect of a Difference in the Extent of Absorption

It has been postulated, so far, that both test and reference products are absorbed to the same extent. Suppose that each product is absorbed to a different extent.

By the zero-order or the first-order models (mono- or multiexponential disposition), C_{max} may be presented as

$$C_{max} = D \cdot E(z) \tag{E1}$$

where D is the dose absorbed and z stands for either x or y, depending on the model used. The function E depends on the particular model.

Therefore

$$dC_{max} = \frac{\partial C_{max}}{\partial D} dD + \frac{\partial C_{max}}{\partial z} dz \tag{E2}$$

Using eq E1 in eq E2, we get

$$\frac{dC_{max}}{C_{max}} = \frac{dD}{D} + \left[\frac{dC_{max}}{C_{max}}\right]_D \tag{E3}$$

By eq E3, the total relative difference in C_{max} is the sum of the relative difference in D and the "partial" relative difference in C_{max} (when D = constant).

Hence, when the test and reference products are absorbed to a different extent, eq A6 for the zero-order case is generalized as

$$\frac{\Delta C_{max}}{C_{max(r)}} = \frac{1 - e^{-Qx_r}}{Q(1 - e^{-x_r})} - 1 + \frac{\Delta D}{D_r} \tag{E4}$$

Similarly, eq B9 for the first-order case is replaced by

$$\frac{\Delta C_{max}}{C_{max(r)}} = \frac{(Qy_r)^{Qy_r/(1-Qy_r)}}{y_r^{y_r/(1-y_r)}} - 1 + \frac{\Delta D}{D_r} \tag{E5}$$

For the zero-order model, at the limit as $x_r \to \infty$

$$\lim_{x_r \to \infty} \frac{\Delta C_{max}}{C_{max(r)}} = \frac{1}{Q} + 1 + \frac{\Delta D}{D_r} = \frac{\Delta k_o}{k_{o(r)}} + \frac{\Delta D}{D_r} \tag{E6}$$

Similarly, for the first-order model when $y_r \to \infty$

$$\lim_{y_r \to \infty} \frac{\Delta C_{max}}{C_{max(r)}} = \frac{1}{Q} + 1 + \frac{\Delta D}{D_r} = \frac{\Delta k_a}{k_{a(r)}} + \frac{\Delta D}{D_r} \tag{E7}$$

Equations E6 and E7 are generalizations of eqs A7 and B10, respectively.

Appendix F: The Function *F(x)*

By eq A10

$$F(x) = \frac{1 - e^{-x}(x + 1)}{1 - e^{-x}}$$

Define

$$f(x) = 1 - e^{-x}(x + 1) \tag{F1}$$

Then

$$f'(x) = xe^{-x} > 0 \text{ for } x > 0 \tag{F2}$$

By eq F1

$$f(0) = 0 \tag{F3}$$

Hence, eq F2 implies

$$f(x) > 0 \text{ for } x > 0 \tag{F4}$$

It is also true that

$$1 - e^{-x} > 0 \quad \text{when} \quad x > 0 \tag{F5}$$

Therefore

$$F(x) = \frac{f(x)}{1 - e^{-x}} > 0 \quad \text{when} \quad x > 0 \tag{F6}$$

Derive $F(x)$ with respect to x

$$F'(x) = \frac{e^{-x}(e^{-x} + x - 1)}{(1 - e^{-x})^2} \tag{F7}$$

Define

$$p(x) = e^{-x} + x - 1 \tag{F8}$$

Then

$$p'(x) = 1 - e^{-x} > 0 \quad \text{when} \quad x > 0 \tag{F9}$$

By eq F8, $p(0) = 0$. Therefore eq F9 implies

$$p(x) > 0 \quad \text{when} \quad x > 0 \tag{F10}$$

It is also true that

$$\frac{e^{-x}}{(1 - e^{-x})^2} > 0 \quad \text{for any } x \tag{F11}$$

Therefore

$$F'(x) = \frac{e^{-x}p(x)}{(1 - e^{-x})^2} > 0 \quad \text{when} \quad x > 0$$

Hence $F(x)$ is a positive monotone increasing function of x for $x > 0$.

Appendix G: The Asymptotic Behavior of $\Delta k_o/k_{o(r)}$

$$\int_r^t \frac{dC_{max}}{C_{max}} = \ln \frac{C_{max(t)}}{C_{max(r)}} = \ln\left(\frac{\Delta C_{max}}{C_{max(r)}} + 1\right) \tag{G1}$$

A constant value of the integral on the left-hand side of eq G1 corresponds to a constant value of $\Delta C_{max}/C_{max(r)}$.

It was proven that the infinitesimal quantity dk_o/k_o, corresponding to a constant infinitesimal relative difference in C_{max} (dC_{max}/C_{max}), is minimal (by its absolute value) as $x \to \infty$. Therefore, the integrated form $\int_r^t dk_o/k_o$ corresponding to a constant value of $\int_r^t dC_{max}/C_{max}$ must also assume a minimum value as $x_r \to \infty$.

Because

$$\int_r^t \frac{dk_o}{k_o} = \ln \frac{k_{o(t)}}{k_{o(r)}} \tag{G2}$$

$|\ln(k_{o(t)}/k_{o(r)})|$, corresponding to a constant value of $\Delta C_{max}/C_{max(r)}$, has a minimum value as $x_r \to \infty$.

When $k_{o(t)}/k_{o(r)} > 1$, both $k_{o(t)}/k_{o(r)}$ and $|k_{o(t)}/k_{o(r)} - 1|$ attain a minimum value as $x_r \to \infty$. When $k_{o(t)}/k_{o(r)} < 1$, $k_{o(t)}/k_{o(r)}$ is maximal as $x_r \to \infty$, whereas $|k_{o(t)}/k_{o(r)} - 1|$ is minimal at this limit.

Hence $|k_{o(t)}/k_{o(r)} - 1|$ $(=|\Delta k_o|/k_{o(r)})$ corresponding to a constant value of $|\Delta C_{max}|/C_{max(r)}$, is minimal as $x_r \rightarrow \infty$.

Appendix H: The Function *G(y)*

By eq B13

$$G(y) = \frac{(y - 1 - \ln y)y}{(1 - y)^2}$$

Define

$$g(y) = y - 1 - \ln y \tag{H1}$$

Then

$$g'(y) = \frac{y - 1}{y} \tag{H2}$$

By eq H2

$$g'(y) > 0 \quad \text{for} \quad y > 1 \tag{H3}$$

$$g'(y) < 0 \quad \text{for} \quad 0 < y < 1 \tag{H4}$$

By eq H1 $g(y = 1) = 0$; hence, eq H3 implies

$$g(y) > 0 \quad \text{for} \quad y > 1 \tag{H5}$$

For the same reason, eq H4 implies

$$g(y) > 0 \quad \text{for} \quad 0 < y < 1 \tag{H6}$$

Therefore

$$G(y) = \frac{g(y)}{(1 - y)^2} y > 0 \quad \text{for} \quad y > 0 \tag{H7}$$

Derive $G(y)$ with respect to y

$$G'(y) = \frac{(y - 1 - \ln y)(1 + y) - (1 - y)^2}{(1 - y)^3} \tag{H8}$$

Define

$$h(y) = (y - 1 - \ln y)(1 + y) - (1 - y)^2 \tag{H9}$$

Then

$$h'(y) = 1 - \ln y - y^{-1} \tag{H10}$$

Suppose $h'(y) = 0$, then by eq H10

$$\ln y = \frac{y - 1}{y} \tag{H11}$$

Equation H11 is satisfied when $y = 1$. Therefore, $y = 1$ is a solution for $h'(y) = 0$. We shall prove that $y = 1$ is the only solution for $h'(y) = 0$ $(0 < y < \infty)$:

When $y > 0$, both $\ln y$ and $(y - 1)/y$ are monotone increasing functions of y, as demonstrated by eqs H12 and H13

$$[\ln y]' = \frac{1}{y} \tag{H12}$$

$$\left[\frac{y - 1}{y}\right]' = \frac{1}{y^2} \tag{H13}$$

By eqs H12 and H13

$$[\ln y]' > \left[\frac{y - 1}{y}\right] \quad \text{for} \quad y > 1 \tag{H14}$$

$$[\ln y]' < \left[\frac{y - 1}{y}\right] \quad \text{for} \quad 0 < y < 1 \tag{H15}$$

Therefore, for $y > 1$, $\ln y$ increases (with y) faster than $(y - 1)/y$, and the functions do not cross each other. For $0 < y < 1$, $\ln y$ decreases (when y decreases) slower than $(y - 1)/y$ and again, both functions do not cross. Therefore, $y = 1$ is the only solution for $h'(y) = 0$ $(0 < y < \infty)$.

A second differentiation of $h(y)$ with respect to y, provides

$$h''(y) = \frac{1}{y} + \frac{1}{y^2} \tag{H16}$$

At $y = 1$

$$h''(y = 1) = 0 \tag{H17}$$

Therefore $y = 1$ is an inflection point of $h(y)$. Because $y = 1$ is the only point where eq H11 holds, $h(y)$ is monotone for $0 < y < \infty$. By substituting any positive value $(\neq 1)$ for y in eq H10, it is found that

$$h'(y) < 0 \tag{H18}$$

Therefore, $h(y)$ is a monotone decreasing function of y for $0 < y < \infty$.

By eq H9

$$h(y = 1) = 0 \tag{H19}$$

Hence

$$h(y < 1) > 0 \tag{H20}$$

$$h(y > 1) < 0 \tag{H21}$$

Therefore

$$G'(y) = \frac{h(y)}{(1 - y)^3} > 0 \quad \text{for} \quad 0 < y < \infty \ (y \neq 1)$$

It may be concluded that $G(y)$ is a positive and monotone increasing function of y for $0 < y < \infty$ $(y \neq 1)$ and it is undefined at $y = 1$.

JS980322P

Uptake and Excretion of Sodium Taurocholate by the Isolated Perfused Neonatal Sheep Liver

PAUL J. GOW,[†] SAARD TREEPONGKARUNA,[‡] MICHAEL S. CHING,[*,†] HANY GHABRIAL,[†] ARTHUR SHULKES,[‡] RICHARD A. SMALLWOOD,[†] CHUN J. JIN,[†] AND DENIS J. MORGAN[§]

Contribution from *Departments of Medicine and Surgery, Austin and Repatriation Medical Centre, West Heidelberg, 3081, Victoria, Australia, and Victorian College of Pharmacy, Monash University, Parkville, 3052, Victoria, Australia.*

Received August 3, 1998. Final revised manuscript received December 8, 1998.
Accepted for publication December 10, 1998.

Abstract □ We present a model for perfusion of the isolated perfused neonatal sheep liver which allows examination of drug disposition by the intact organ. We studied the disposition of sodium taurocholate (TC) in seven neonatal lambs (ages 2–11 days) and compared the results with earlier data from the perfused fetal sheep liver (Ring, J. A. et al. *Biochem. Pharmacol*. **1994**, *48*, 667–674). Measurements of perfusion pressure, oxygen consumption, lactate:pyruvate ratio, bile flow, and liver histology indicated that the preparation was both viable and stable over a 2 h period. [^{14}C]-labeled TC was added to the reservoir by constant infusion (30 μmol/h) and the ductus venosus shunt quantitated by injection of [^{153}Gd]-labeled microspheres. Shunt-corrected hepatic extraction ratio of TC was 0.56 ± 0.14 (fetal 0.23 ± 0.16, $p < 0.005$) and clearance of TC was 0.92 ± 0.35 mL/min/g liver (fetal 0.44 ± 0.23 mL/min/g, $p < 0.01$). We conclude that the isolated perfused neonatal sheep liver is a useful experimental model which will facilitate the study of the developmental physiology and pharmacology of the liver. There is considerable maturation of the biliary excretion of TC between the late fetal and early neonatal periods in the lamb.

Introduction

Sodium taurocholate (TC) is a principal bile salt in many mammalian species, including humans.[1] In the adult, TC undergoes an efficient enterohepatic circulation from bile to small intestine, active reabsorption from the terminal ileum, and then hepatic uptake and re-excretion into bile. TC is highly cleared from portal plasma by the liver cell and concentratively excreted into bile.[2] In contrast to many highly cleared drugs, TC is taken up by the liver by an active or facilitated transport process[3] and is then actively secreted into bile.[2]

Several studies have examined TC transport in the developing liver, both in late fetal and neonatal life.[4−7] In general they have shown, in several species, that hepatic transport processes of TC appear to be immature in the fetus and neonate. The same can also be said of many drug metabolic processes.[8,9] One of the difficulties encountered in studying fetal hepatic function in vivo is the inability to obtain samples consistently from, for example, hepatic outflow vessels or the bile duct. This leads to difficulties in defining fetal hepatic clearance and differentiating this from placental transfer and subsequent clearance by maternal organs. To overcome these problems we have recently developed the in-situ isolated, perfused fetal sheep liver model.[4] This has allowed detailed study of TC transport and the metabolism of a number of drugs by the fetal liver near term.[10,11]

The present study details the development of an analogous model in the neonatal sheep. This allows direct comparison of a variety of hepatic functions at various times before and after birth, a period of dramatic physiological change. We present here the findings on neonatal TC transport and compare them with our earlier data from late fetal life.

Experimental Section

Materials and Reagents—[^{14}C]TC (99% pure by TLC, 1.7 GBq/mmol) and [^{153}Gd] microspheres (37-185 MBq/g) were purchased from NEN (Boston, MA). D-Glucose and unlabeled TC (sodium salt) were obtained from Sigma Chemical Co. (St. Louis, MO), and bovine serum albumin (fraction V) from the Commonwealth Serum Laboratories (Melbourne, Victoria, Australia). Hartman's solution and sodium heparin were purchased from David Bull laboratories (Melbourne, Victoria, Australia).

Animals and Surgical Procedure—The experiments were approved by the Austin and Repatriation Medical Centre (ARMC) Animal Welfare Ethics Committee. Experiments were conducted in seven neonatal sheep between 2 and 11 days of age (2, 2, 3, 6, 8, 10, and 11 days). Pregnant ewes were supplied by a contracted local farmer and delivered to the animal house at least 2 weeks before the scheduled parturition date. All lambs were born by natural delivery at the ARMC and fed naturally by their mothers.

Anaesthesia was induced with intravenous sodium thiopental, a tracheostomy performed, and the lamb intubated and ventilated. Anaesthesia was maintained with halothane. A midline abdominal incision was performed and the remnant of the umbilical vein ligated. The portal vein, hepatic artery, bile duct, and superior mesenteric vein were located, and the gall bladder was isolated by ligating the cystic duct. The bile duct was cannulated (internal diameter (i.d.) 1.0 mm, external diameter (o.d.) 1.5 mm) and left to drain externally into a collection tube. Loose ties were applied around the portal vein, hepatic artery, and superior mesenteric vein. The inferior vena cava above the renal veins was located and a loose tie applied. A midline thoracotomy was performed to expose the suprahepatic inferior vena cava, and a loose tie was applied. A silastic inflow cannula (o.d. 6 mm, i.d. 4.5 mm, with an in-line small preliver bubble trap) primed with Hartman's solution at 37 °C, containing sodium heparin (5 units/mL), was then prepared for portal vein cannulation.

The superior mesenteric vein was ligated distally and cannulated with the inflow cannula via a proximal incision. The cannula was passed down the superior mesenteric vein to the portal vein, visually confirmed to be in the correct position and then secured. The supra-hepatic inferior vena cava was cannulated (o.d. 8 mm, i.d. 6 mm) and left to drain externally. The loose ties around the hepatic artery and inferior vena cava above the renal veins were secured, isolating the liver, which was flushed with heparinized Hartman's solution until it had uniformly blanched. Perfusion was commenced by connecting the primed perfusion circuit to the

* Corresponding author. Telephone: 61 3 9496 2252, Fax: 61 3 9497 4554, e-mail: ching@austin.unimelb.edu.au.
[†] Department of Medicine, Austin and Repatriation Medical Centre.
[‡] Department of Surgery, Austin and Repatriation Medical Centre.
[§] Monash University.

10.1021/js9803151 CCC: $18.00
Published on Web 03/04/1999

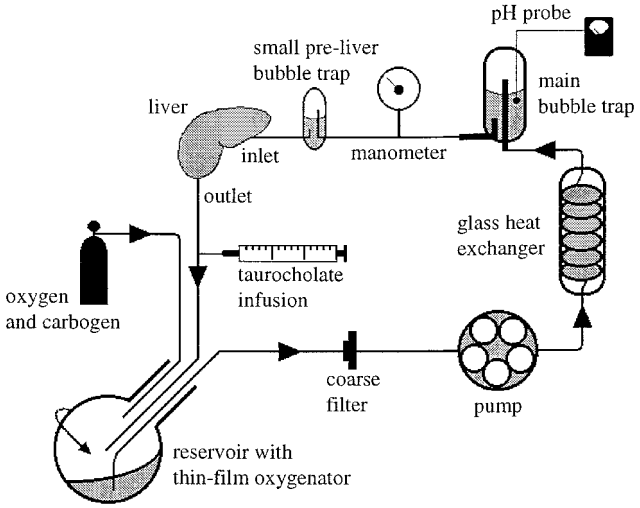

Figure 1—Diagram of the isolated neonatal liver perfusion circuit.

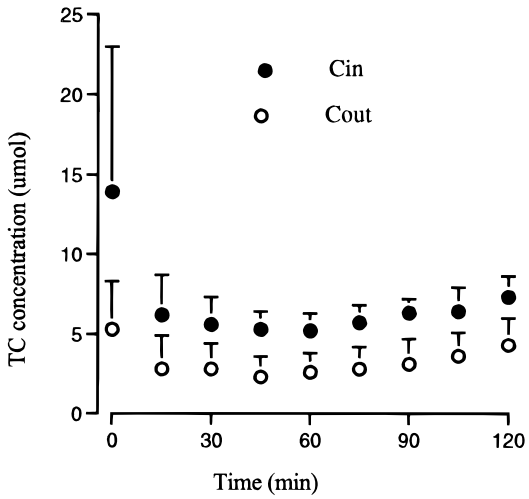

Figure 2—Mean concentration (and standard deviation) of TC in inflow and outflow cannulae.

silastic inflow cannula, and the distal end of the outflow catheter was connected to the reservoir to complete the recirculating system. The liver was perfused in situ and covered with saline-soaked gauze. The lamb was sacrificed by an overdose of sodium thiopental injected into the left ventricle.

Perfusion Circuit—The perfusate volume was 1000 mL and comprised Krebs-Henseleit buffer pH 7.4, bovine serum albumin 1% w/v, D-glucose 0.1% w/v, washed human red blood cells 20% v/v, and Hepes 5 mM. The perfusion circuit (Figure 1) was based on our perfused fetal liver preparation.[4] Modifications were made as follows to improve and simplify the method of perfusate oxygenation and perfusate sampling. The reservoir was a 3 L spherical glass flask with a ground glass neck. To this was connected a hollow glass stalk 30 cm long (i.d. 25.4 mm, o.d. 31.75 mm) with a ground glass connector to the reservoir. The reservoir with stalk was mounted at a 60° angle using a Corning model 349/2 rotary evaporator apparatus which constantly rotated at 40 rpm to mix the perfusate and form a thin perfusate film on the inside of the reservoir for oxygenation. Entering the stalk were three stiff, nonrotating Teflon tubes; one tube was immersed into the perfusate as the liver portal supply, another tube as the venous return from the liver, and the third tube positioned so as to constantly oxygenate the reservoir air space.

A peristaltic pump (Masterflex No. 7521-25 Cole-Palmer Instrument Co., Chicago, IL) provided a flow rate of approximately 200 mL/min, and flow was accurately quantitated at the conclusion of each experiment. The perfusate was kept at a temperature of 37 °C by recirculating water through a glass heat exchanger from a 15 L water bath. Perfusate pH was maintained at 7.40 by mixing humidified carbogen (95% oxygen, 5% carbon dioxide) in addition to the delivered oxygen via a T-piece, as required. TC was delivered into the reservoir at 30 μmol/h (4 mL/h of 7.5 mM TC solution) by a syringe pump (Sage Instruments No. 355, Cambridge, MA).

Viability and Stability—An initial equilibration time of 15 min was followed by a perfusion time of 120 min. The perfusion pressure of the liver was determined by subtracting the circuit pressure obtained before connection of the circuit to the liver from the pressure reading with the liver in place. Oxygen delivery and consumption were calculated using an AVL 995 blood gas analyzer (AVL Medical Instruments, Switzerland) every 30 min by sampling perfusate inflow to and outflow from the liver. At the conclusion of each experiment, samples of the left and right lobes of the liver were taken and fixed in 10% formalin solution for later histological examination. The perfusate lactate:pyruvate ratio was measured spectrophotometrically in samples collected at 0, 30, 60, 90 and 120 min using a commercially available kit (kit nos. 826-A and 726, Sigma Chemical Co, St Louis, MO).

Experimental Design—After the initial 15 min equilibration, a bolus loading dose of 30 μmol (4 mL of 7.5 mM solution, specific activity 111Bq/mmol) [^{14}C]TC was injected into the reservoir, followed by a constant infusion of 30 μmol/h of [^{14}C]TC (4 mL/h of 7.5 mM solution) for 120 min. Samples (5 mL) from the inflow and outflow cannulae were then taken every 15 min for the duration of the experiment. Reservoir volume was maintained by replacing sampled perfusate with an equal volume of blank perfusate. All bile was collected via the common bile duct cannula into preweighed tubes in 30 min aliquots. Volume of bile was calculated by weight, assuming a specific gravity of 1.0 g/mL. Perfusate (whole blood perfusate including red blood cells) and bile radioactivity was determined by liquid scintillation counting on a Packard 1900CA liquid scintillation analyzer as described previously.[12]

Hepatic Distribution of Perfusate Flow—Latex microspheres 15 μm in diameter labeled with [^{153}Gd] were used to determine the ductus venosus flow shunting through the liver, the proportion of flow to left and right lobes, and the evenness of liver perfusion as previously described.[13] Briefly, 200 μL [^{153}Gd] of the microsphere preparation (approximately 2 million microspheres) were injected into the inflow cannula, and the outflow perfusate was collected in 10 s aliquots for 60 s, by which time all microspheres not distributed to the liver had eluted. The liver was then removed from the carcass and divided into left and right lobes (via Cantlie's line, a line joining the middle of the gallbladder fossa to the left of the inferior vena cava posteriorly), and the lobes were individually weighed. The lobes were then divided further into 2−4 g sections which were subjected to γ counting using a Packard Cobra 5005C γ counter at an energy window of 85−115 keV. The proportion of perfusate shunted through the ductus venosus was taken as the ratio of total counts in outflow perfusate to the sum of total counts in outflow perfusate and liver tissue.

Calculations and Statistics—The hepatic extraction ratio (E) at steady state (using the 60−90 min interval, Figure 2) was calculated as:

$$E = C_{in} - C_{out}/C_{in}$$

where C_{in} is TC concentration in the inflow cannula, and C_{out} is TC concentration in the outflow cannula from the liver. Where a ductus venosus shunt was present, a corrected hepatic extraction ratio (E^*) was calculated to take into account the fraction of perfusate shunting through the ductus venosus:

$$E^* = E/(1 - S)$$

where S is the fraction of the perfusate shunted, calculated from the portal injection of microspheres. Total clearance of TC from perfusate (CL) was calculated as:

$$CL = EQ$$

where Q is perfusate flow rate. Biliary clearance of TC at steady state (using the 60−90 min interval, CL_{bile}) was calculated as:

$$CL_{bile} = v/C_{ss}$$

where v is the mean excretion rate of TC into bile at steady state,

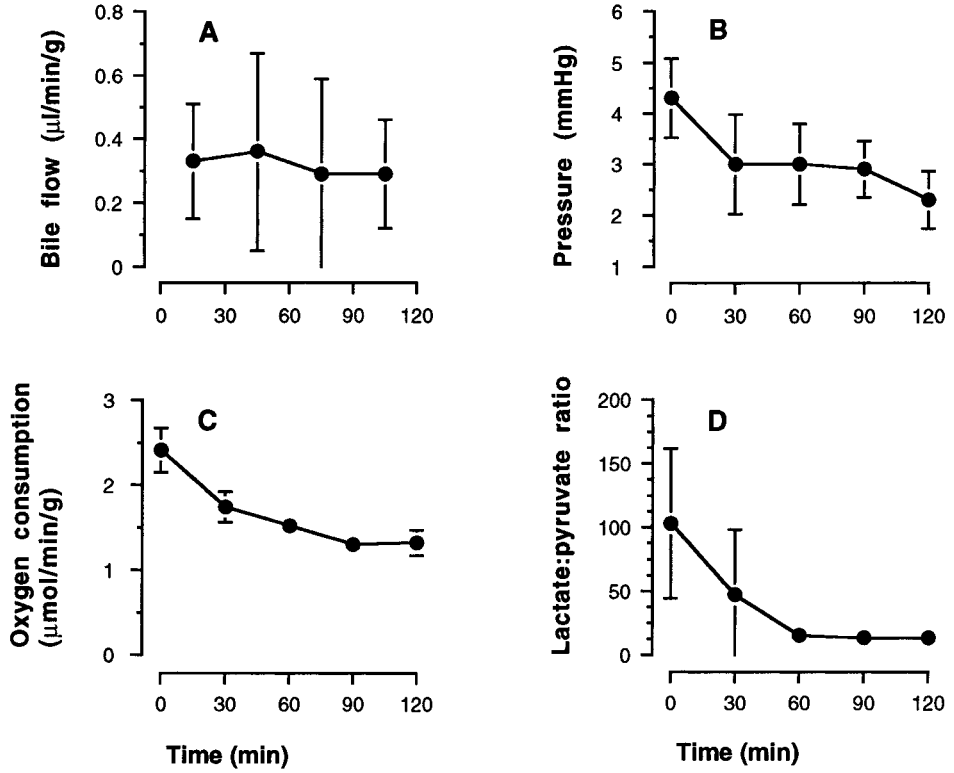

Figure 3—Physiological parameters (mean and standard deviation) versus time: (A) bile flow, (B) perfusion pressure, (C) oxygen consumption, (D) perfusate lactate:pyruvate ratio.

Table 1—Distribution of Perfusate Flow in Neonatal Liver

		liver weight (g)			perfusate flow (mL/g/min)	
neonatalage (days)	shunt (%)	left lobe	right lobe	total	left lobe	right lobe
2	15.2	45.8	52.8	96.6	1.67	2.96
2	18.2	41.3	52.2	91.5	1.83	2.92
3	1.6	72.8	90.3	163.1	1.17	1.37
6	1.4	73.8	62.9	136.7	1.31	1.53
8	2.0	41.3	50.2	91.5	1.83	2.92
10	0	71.2	67.1	138.4	0.84	2.21
11	3.0	56.3	52.6	108.9	1.58	2.72
Mean ± SD	5.9 ± 7.5	62.6 ± 14.7	66.4 ± 17.7	129.0 ± 30.8	1.39 ± 0.33	2.11 ± 0.79

and C_{ss} is the mean steady-state perfusate concentration in the inflow cannula.

Data are expressed as mean ± standard deviation. Correlations between variables were examined by linear regression analysis, and differences between groups of data were examined by unpaired *t*-test. A p value less than 0.05 was considered statistically significant.

Results

Liver Viability and Stability—Liver appearance was satisfactory in that the liver remained a uniform red color throughout the perfusion and there were no areas of hepatic capsular distension or exudation. Light microscopy of liver tissue showed no evidence of hypoxic damage or sinusoidal congestion. The whole liver was shown to have been grossly perfused by the presence of microspheres in all liver samples. Bile flow throughout the experiment was stable at 0.32 ± 0.24 µL/min/g of liver (as shown by linear regression) (Figure 3 A). Mean perfusion pressure was 3 mmHg and did not change significantly (as shown by linear regression) throughout the experimental period (Figure 3B). Overall mean oxygen consumption was 1.67 ± 0.44 µmol/min/g, falling from an initial rate of 2.41 ± 0.68 µmol/min/g liver to be stable over the latter 90 min of the perfusion at a rate of 1.48 ± 0.40 µmol/min/g liver (Figure 3C). The lactate:pyruvate ratio did not rise during the experiment, indicating that hepatic oxygenation did not deteriorate (Figure 3D).

Hepatic Distribution of Perfusate Flow—Ductus venosus flow as a proportion of total perfusate flow is shown in Table 1. The two neonates aged 2 days had ductus venosus shunts of 15.2 and 18.2%, and the five older lambs had shunts of less than 3% of perfusate flow (Table 1). Perfusate flow was 39.5 ± 8.5% to the left lobe of the liver and 60.5 ± 8.5% to the right lobe. The right lobe received a somewhat greater flow per gram of tissue (2.11 ± 0.79 mL/g/min) than the left lobe (1.39 ± 0.33 mL/g/min, $p < 0.05$).

Taurocholate Elimination—Mean C_{in} and C_{out} concentrations are depicted in Figure 2. Data for steady-state calculations were taken from the time period 60–90 min. Mean steady-state hepatic extraction of TC, calculated after taking into account shunted perfusate flow, was 0.56 ± 0.14; TC was concentratively secreted into bile (bile:plasma concentration ratio up to 5000). The total clearance of TC at steady state was 0.92 ± 0.35 mL/min/g liver (Table 2),

Table 2—Kinetics of Taurocholate Elimination

neonatal age (Days)	TC extraction	shunt-corrected TC extraction	bile/perfusate TC ratio	total TC clearance (mL/min/g)	biliary clearance of TC (mL/min/g)
2	0.43	0.51	785	1.01	0.65
2	0.46	0.56	1787	1.12	0.80
3	0.44	0.45	5241	0.56	0.60
6	0.32	0.33	2308	0.45	0.34
8	0.70	0.71	5828	0.85	0.53
10	0.61	0.61	3906	0.92	0.55
11	0.71	0.73	5529	1.51	1.49
Mean ± SD	0.52 ± 0.15	0.56 ± 0.14	3626 ± 2014	0.92 ± 0.35	0.71 ± 0.37

which was significantly higher than biliary clearance of TC (0.71 ± 0.37 mL/min/g liver, $p < 0.05$, Table 2). There was no significant correlation between hepatic extraction ratio, total clearance or biliary clearance of TC, and neonatal age over the age range studied.

Discussion

The isolated perfused liver (IPL) has proved a valuable experimental model in enhancing our understanding of the pharmacology and physiology of the liver.[14] Studies with this model complement those using isolated organelles or hepatocytes, and studies in whole animals. The IPL preserves the structural and functional integrity of the liver, while eliminating the confounding elements of metabolism and elimination by other organs.[14] Moreover, it allows ready access to hepatic inflow and outflow vessels and to the biliary tree.

The IPL model which we recently established to examine hepatic function in the fetal sheep[4] has proved particularly valuable in facilitating access to fetal hepatic blood vessels and bile ducts and in eliminating placental transport and maternal metabolism as confounding factors. The development of the neonatal IPL model described in the present study represents a modification of the approach used to establish the fetal model. The neonatal IPL is equally robust and stable over a 2 h experimental period, and the two preparations allow direct comparison of fetal and neonatal hepatic function.

The neonatal IPL has a stable bile flow comparable to other perfused liver models,[4,15] and maintains a low perfusion pressure,[16] a low lactate:pyruvate ratio, and a steady oxygen consumption after an early fall from a high initial level (Figure 3). The high initial reading was probably occasioned by increased tissue oxygen extraction consequent upon a transient acidosis after flushing the system with Hartman's solution. The absence of any later increase in lactate:pyruvate ratio, and normal histology, indicate that there has been no significant tissue hypoxia.[17] Moreover the mean level of oxygen consumption was significantly greater than that in the fetus (1.67 ± 0.44 versus 0.86 ± 0.07 μmol/min/g liver $p < 0.005$)[4] and approximates that previously reported in the neonatal and adult sheep liver in vivo.[18]

In the early neonatal period there was still appreciable shunting of blood through the ductus venosus (Table 1), although the degree of shunting was considerably less than in the near-term fetus (35 ± 18%[4]). By 6 days the ductus venosus had all but closed. This accords with previous observations in the sheep in vivo.[16,19] Nonetheless, it will be important in using this neonatal model, as in the fetal IPL, to measure and correct for the degree of ductus venosus shunting.

It is of interest that, on a weight basis, the right lobe of the liver appeared to be more generously perfused than the left (Table 1) whereas in the fetus, perfusion rates are similar.[4] This may reflect increasing resistance to flow in the portal sinus, and one consequence may be the disproportionate growth of the right lobe that is seen in the neonatal period.[16]

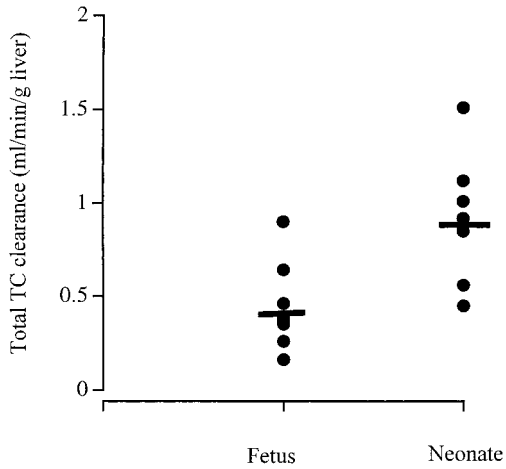

Figure 4—Total clearance of TC in neonatal liver (this study) and fetal liver (data from: Ring, J. A. et al. *Biochem. Pharmacol*. **1994**, *48*, 667–674).

In the adult human and rat, TC extraction approaches unity,[20,21] but no data are available in the adult sheep. In late fetal life, the hepatic extraction ratio (E^*) of 0.23 ± 0.16[4] indicates that at this stage of the liver's development TC is a low clearance compound. Within days of birth, TC extraction ratio had risen 2-fold to 0.56 ± 0.14 ($p < 0.005$), which represents an intermediate level of clearance. This increase in hepatic extraction ratio around the time of birth was accompanied by an increase in mean total TC clearance from 0.44 to 0.92 mL/min/g liver ($p < 0.01$, Figure 4). These results indicate a substantial change in the efficiency of hepatic TC transport, although there is further development in TC uptake and biliary excretion before the functions are fully mature.[21]

Values for total TC clearance were significantly greater than biliary clearance of TC in this study. The likely explanation is that although TC levels had reached steady state in perfusate (Figure 4), transport of TC into bile may not have reached steady state.

We conclude that the sheep neonatal IPL is a useful experimental model which will facilitate the study of the developmental physiology and pharmacology of the liver. Our study shows that there is considerable maturation of the biliary excretion of TC between the late fetal and early neonatal period in the lamb.

References and Notes

1. Haslewood, G. A. D. Distribution of bile salts in the animal Kingdom. In *The Biological importance of Bile Salts*. Neuberger A., Tatum E. L., Eds.; North-Holland publishing Co.: Amsterdam, 1978; pp 77–118.

2. Reichen J. Physiology of bile formation and of the motility of the biliary tree. In*Oxford Textbook of Hepatology*. McIntyre N., Benhamou J. P., Bircher J., Rizzetto M., Rodes J., Eds., Oxford university press: Oxford, 1991; 87−94.
3. Inoue, M.; Kinne, R.; Tran, T.; Arias, I. M. Taurocholate transport by the rat liver sinusoidal membrane vesicles: evidence of sodium co-transport. *Hepatology*. **1982**, 2, 572−579.
4. Ring, J. A.; Ghabrial, H.; Ching, M. S.; Potocnik, S.; Shulkes, A.; Smallwood, R. A.; Morgan, D. J. Hepatic uptake and excretion of [^{14}C] sodium taurocholate by the isolated perfused fetal sheep liver. *Biochem. Pharmacol*. **1994**, 48, 667−674.
5. Jackson, B. T.; Smallwood, R. A.; Piasecki, G. J.; Rauschecker, F. J.; Lester, R. Fetal bile salt metabolism I. The metabolism of sodium cholate-^{14}C in the fetal dog. *J. Clin. Invest*. **1971**, 50, 1286−1287.
6. Smallwood, R. A.; Brown, A. G.; Piasecki, G. J.; Jackson, B. T.; Lester, R. Fetal bile salt metabolism II. Hepatic excretion of endogenous bile salt and of a taurocholate load.*J. Clin. Invest*. **1972**, 51, 1388−1397.
7. Suchy, F. J.; Bucuvalas, J. C.; Goodrich, A. L.; Moyer, M. S.; Blitzer, B. L. Taurocholate transport and Na^+- K^+ ATPase activity in fetal and neonatal rat liver plasma membrane vesicles. *Am. J. Physiol*. **1986**, 251, G665−673.
8. Wang, L. H.; Rudolph, A. M.; Benet, L. Z. Comparative study of Acetaminophen disposition in sheep at three developmental stages: the fetal, neonatal and adult periods. *Dev. Pharmacol. Ther*. **1990**, 14, 161−179.
9. Wang, L. H.; Zakin, D.; Rudolph, A. M.; Benet, L. Z Developmental alterations in hepatic UDP− Glucuronsyltransferase. *Biochem. Pharmacol*. **1986**, 35, 3065−3070.
10. Ring, J. A.; Ghabrial, H.; Ching, M. S.; Shulkes, A.; Smallwood, R. A.; Morgan, D. J. Fetal hepatic propranolol metabolism. Studies in the isolated perfused fetal sheep liver. *Drug Metab. Dispos*. **1995**, 23, 190−196.
11. Ring, J. A.; Ghabrial, H.; Ching, M. S.; Shulkes, A.; Smallwood, R. A.; Morgan, D. J. Conjugation of para-nitrophenol by isolated perfused fetal sheep liver. *Drug Metab. Dispos*. **1996**, 24, 1378−1384.
12. Ching, M. S.; Morgan, D. J.; Smallwood, R. A. Models of hepatic elimination: implications from studies of the simultaneous elimination of taurocholate and diazepam by isolated rat liver under varying conditions of binding. *J. Pharmacol. Exp. Ther*. **1989**, 250, 1048−1054.
13. Heymann, M. A.; Payne, B. D.; Hoffman, J. I.; Rudolph, A. M. Blood flow measurements with radionuclide-labeled particles. *Prog. Cardiovasc. Dis*. **1977**, 20, 55−79.
14. Gores, G. J.; Kost, L. J.; LaRusso, N. F. The isolated perfused rat liver: conceptual and practical consideration. *Hepatology*. **1986**, 6, 511−517.
15. Linzell, J. L.; Setcheil, B. P.; Lindsay, D. B. The isolated perfused liver of the sheep: an assessment of its metabolic, synthetic and excretory functions. *Q. J. Exp. Physiol. Cogn. Med. Sci*. **1971**, 56, 53−71.
16. Botti, J. J.; Edelstone, D. I.; Caritis, S. N.; Mueller-Heubach, E. Portal vein blood flow distribution to liver and ductus venosus in newborn lambs. *Am. J. Obstet. Gynecol*. **1982**, 144, 303−308.
17. Jones, D. B.; Mihaly, G. W.; Smallwood, R. A.; Webster, L. K.; Morgan, D. J.; Madsen, N. P. Differential effects of hypoxia on the disposition of propranolol and sodium taurocholate by the isolated perfused rat liver.*Hepatology*. **1984**, 4, 461−466.
18. Apatu, R. S. K.; Barnes, R. J. Blood flow to and measurement of glucose and lactate by the liver in vivo in fetal, newborn and adult sheep. *J. Physiol*. **1991**, 436, 341−347.
19. Zink, J.; Van Pettern, G. R. Time course of closure of the ductus venosus in the newborn lamb. *Pediatr. Res*. **1980**, 14, 1−3.
20. Klaassen, C. D.; Watkins, J. B. Mechanisms of bile formation, hepatic uptake and biliary excretion. *Pharmacol. Rev*. **1984**, 36, 1−67.
21. Smallwood, R. H.; Morgan, D. J.; Mihaly, G. W.; Jones, D. B.; Smallwood, R. A. Effects of plasma protein binding on elimination of taurocholate by isolated perfused rat liver: comparison of venous equilibrium, undistributed and distributed sinusoidal, and dispersion models. *J. Pharmacokinet. Biopharm*. **1988**, 16, 377−397.

Acknowledgments

This study was supported in part by grants from the N.H.& M.R.C. (Australia) and the Clive and Vera Ramaciotti Foundations. P.J.G is funded by a N.H.&M.R.C. (Australia) Medical Postgraduate Research Scholarship and A.S. is a N.H.& M.R.C. (Australia) Principal Research Fellow.

JS9803151

Comparison of the Biodistribution in Mice of ^{111}Indium Oxine Encapsulated into Poly(lactic-*co*-glycolic)-D,L-85/15 and Poly(epsilon Caprolactone) Nanocapsules

L. MARCHAL-HEUSSLER,[†] P. THOUVENOT,[‡] M. HOFFMAN,[§] AND P. MAINCENT*[,§]

Contribution from *Novartis Pharma, Pharmaceutical Development, Basel, Switzerland, Centre Hospitalo-Universitaire, Service de Médecine Nucléaire, Nancy, France, and Faculté de Pharmacie, Laboratoire de Pharmacie Galénique, 5, rue Albert Lebrun, B. P. 403, 54000 Nancy, France.*

Received July 28, 1998. Final revised manuscript received December 7, 1998.
Accepted for publication December 10, 1998.

Abstract □ Poly(lactic-*co*-glycolic)-D,L-85/15 (PLAGA) nanocapsules and poly(epsilon caprolactone) (PCL) nanocapsules were labeled with a relatively long half-life compound that is usually used in humans; that is, ^{111}In-labelled oxine (^{111}In oxine). This labeling technique led to a high ^{111}In oxine entrapment efficiency and good stability during dialysis against phosphate buffer and phosphate buffered albumin solution. Because of these characteristics, the nanocapsules biodistribution was followed up after intravenous administration for up to 96 h by determining the gamma activity in the tissues after sampling. The administration of the PCL-encapsulated ^{111}In oxine led to a decrease in the blood radioactivity and an increase in the liver radioactivity compared with the solution. This effect was even more pronounced with the PLAGA nanocapsules. Finally, the activity level in other tissues, such as the kidneys, the lungs, and the spleen, appeared to be rather low and only slightly affected by the encapsulation into one or the other polymer.

Introduction

Most research in the field of drug targeting is being carried out with either liposomes or polymeric micro- or nanoparticles. However, it has been demonstrated that submicron vesicular structures, the so-called nanocapsules, are of great interest for the delivery of lipophilic drug substances. The ability of nanocapsules to improve the biopharmaceutical properties of lipophilic drug substances has been studied using different routes of administration; namely, the intravenous (iv), oral, and ophthalmic routes.[1,2] Follow-up studies with nanocapsules made of different polymers after iv administration are useful to characterize the influence of physicochemical parameters on the ability of the carriers to escape the mononuclear phagocyte system (MPS). Nevertheless, the biodistribution of poly(lactic-*co*-glycolic)-D,L-85/15 (PLAGA) and poly(epsilon caprolactone) (PCL) nanocapsules in mice after iv administration has still not been described.

Biodistribution studies of colloidal carriers are usually performed with either liposomal lipids, polymers, or encapsulated drug labeled with beta emitters[3] or carbon-14.[4,5] For example, the biodistribution of radiolabeled cyclosporine incorporated into poly(isobutyl cyanoacrylate) nanocapsules has been described.[6] However, mainly because of safety reasons, preliminary phases of clinical trials can hardly be performed with such labeled dosage forms.

Therefore, colloidal carriers incorporating gamma emitters have been prepared and injected in humans by different routes of administration, such as the iv or the pulmonary route. Although most of these colloids are found in the MPS after iv administration,[7−9] the potential of gamma scintigraphy study techniques has been outlined by Rolland et al.[8] and by Gahnem et al. in humans[9] using poly(cyanoacrylate) nanoparticles labeled with Indium-111 and technetium-99m, as well as by Thanoo et al.[10] using ^{111}In oxine-labeled microspheres. In these studies, the particle distribution in the body was followed as a function of time.

Nevertheless, the labeling technique appears to be critical. Indeed, binding efficiency and radioactive half-life have a great impact onto the feasibility of the experiments, whereas stability of the labeling greatly influences the reliability of the data. For example, the binding efficiency of technetium-99m or iodide-125 to cyanoacrylates nanoparticles or to cellulose derivative microparticles, respectively, is poor; moreover, the technetium-99m gamma emitter has a relatively short half-life (6 h), which implies the use of highly radioactive preparations for a distribution follow-up of ≈12 h. Finally, noncovalent gamma emitter−carrier binding is susceptible to desorption due to dilution or particle degradation, especially in a blood protein environnement. Poly(butylcyanoacrylate) nanoparticles have been successfully labeled with ^{111}In by an adsorption process by Kreuter et al.,[11] but the stability of the binding has not been demonstrated. Discrimination between particles and the released free emitter biodistribution then appears to be difficult.

The objectives of the present work were to directly label polymeric nanocapsules with a relatively long half-life compound usually used in humans i.e., ^{111}In oxine (half-life, 2.8 days). Additionally, the labeling was to be done by an easy, fast, and reproducible method and the binding was to be stable in a blood environment. The potential of the labeling technique to follow up the distribution of the nanocapsules in the body after iv administration was evaluated in mice. Finally, the biodistribution of two different types of nanocapsules (PLAGA and PCL) were compared.

Experimental Section

Chemicals—Copolymer of lactic and glycolic acid (PLAGA MW 40 000) was kindly furnished by Medisorb (Cincinnati, OH). Polyepsilon caprolactone (MW 60 000) was purchased from Aldrich Chemical (Saint Quentin Fallavier, France), olive oil and ^{111}In

* Corresponding author. Telephone: 33-3-83-17-88-48. Fax: 33-3-83-17-88-79. E-mail: maincent@pharma.u-nancy.fr.
[†] Novartis Pharma.
[‡] Centre Hospitalo-Universitaire.
[§] Faculté de Pharmacie.

10.1021/js980307k CCC: $18.00
Published on Web 03/12/1999

Table 1—Mean Diameter, Zeta Potential, and ^{111}In Oxine Encapsulation Ratio of PLAGA and PCL Nanocapsules

nanocapsules	mean diameter ± standard deviation, nm	zeta potential ± standard deviation, mV	^{111}In oxine encapsulation ratio, %
PLAGA	340 ± 12	–25 ± 1.1	94
PCL	454 ± 8	–29 ± 1.1	95

oxine (^{111}In oxine, 1 mCi/mL) were purchased from Cooper (Melun, France) and Oris Industrie (Saclay, France), respectively. Pluronic F68 was a gift from BASF (Paris, France). All reagents were analytical grade and used as received.

Preparation of Labeled Nanocapsules—the commercial indium oxine is an aqueous solution containing <0.1 μg of radioactive indium atoms complexed by 50 mg of hydroxy-8-quinoleine (i.e., oxine). According to the first step of the preparation process, the lipophilic marker was partioned upon shaking for 20 min between the aqueous radioactive phase (0.25 mL) and olive oil (0.7 mL). Up to 80% of the radioactive compound transferred into the olive oil. After separation by centrifugation, 0.5 mL of olive oil was used for further processing.

PLAGA and PCL nanocapsules were prepared according to the method of Fessi et al.[12] Briefly, 0.125 g of polymer was dissolved in 20 mL of acetone. After dissolution of the polymer, the radioactive oily phase was mixed with the acetonic phase. This radioactive organic solution was mixed with 50 mL of an aqueous solution containing 0.25 g of Pluronic F68 as a stabilizer. Acetone was evaporated under reduced pressure, and the final volume of the suspension was adjusted to 15 mL. The final polymer concentration in the suspension was 0.83% (w/v).

Indium Oxine Incorporation Ratio—Gel permeation chromatography was performed to assess the incorporation ratio of the radioactive compound in the nanocapsules. Briefly, an aliquot (0.1 mL) of the suspension was passed through a Sephadex G75 column (3 × 16 cm). The suspension was eluted with a 0.9% NaCl solution at a rate of 1 mL/min. Samples were collected at the bottom of the column, and the radioactive content of each sample was counted with a gamma counter. An aliquot of 0.1 mL of pure indium oxine solution was also eluted at the same conditions and served as a reference. The activity of each sample was expressed as a percentage of the total activity of the suspension counted before the sample was passed through the column.

Characterization of the Nanocapsules—The particle diameter was determined by photon correlation spectroscopy (Malvern 4600, Malvern, France) and the zeta-potential by LASER doppler velocimetry (Zetamaster, Malvern, France). All suspensions were diluted with a 10^{-6} M NaCl, pH 6.5 aqueous solution to maintain a constant ionic strength and an adequate concentration of particles.

Biodistribution Studies of the Indium Oxine Formulations—Studies were carried out in Swiss male mice weighing ≈20 g. A 0.1 mL volume of ^{111}In-labelled nanocapsules was injected by iv bolus into the tail vein. After various time intervals up to 96 h after administration, five mice per time point were sacrified by cervical fracture. The blood, liver, spleen, lungs, and kidneys were removed, washed with 0.9% NaCl solution, and accurately weighed. A group of five mice also received a 0.1 mL bolus dose of ^{111}In oxine aqueous solution by the same administration route. Along with standards prepared from the injected materials, the total radioactivity in the blood and the organs was measured on an auto-gamma well counter (Beckman Gamma 4000, Munich, Germany). The raw radioactive data were corrected for the half-life of the marker and presented as the percentage of the administered dose per gram of tissue. Statistical analysis was performed using the ANOVA test (Fischer, $p < 0.05$). The ^{111}In oxine half-life in the blood was calculated with a noncompartmental model.

Results and Discussion

Preparation and Labeling of the Nanocapsules—as shown in Table 1, the preparation method led to the production of PLAGA and PCL nanocapsules of 340 ± 12 and 454 ± 8 nm, respectively, as well as a high gamma emitter encapsulation efficiency. Both PLAGA and PCL nanocapsules gel permeation elution profiles show that >90% of the total ^{111}In oxine radioactivity was associated with the combined fractions of nanocapsules. Thus, the manufacturing process of labeled nanocapsules appears to be fairly independent of the polymer used. Although the gamma emitter is water soluble at this low concentration, most of it did not diffuse from the oil into the acetone/water phase during the manufacturing process, nor during the elution of the nanocapsules from the gel permeation column. The release of ^{111}In oxine upon high dilution in aqueous medium is fairly low. These results are not in favor of a diffusion process driven by Fick's Law but rather by the partition effect. The partitioning effect has also been considered as one of the driving force of the release process of drugs from the oily core of nanocapsules into outer phases, such as blood or intestinal fluids.[13] Moreover, it has been proposed that the intraocular penetration of drugs encapsulated in PCL nanocapsules after topical application is partly related to the partition of the drug between the oily inner phase of the capsules and the lipophilic corneal epithelium.[2]

The in vitro stability of the labeling of PCL nanocapsules in an albumin or buffer environment was investigated, earlier in our laboratory[14] and was shown to be high. The release kinetics of ^{111}In oxine from PCL nanocapsules during dialysis against albumin aqueous solution or phosphate buffer were compared with the free ^{111}In oxine solution, and the results showed that ^{111}In oxine diffuses very slowly out of the capsules into the albumin solution or the buffered outer phase. After 4 h, <5% of the aqueous (i.e., nonencapsulated) solution of the gamma emitter is still present into the dialysis bag compared with 100% of the encapsulated gamma emitter. This labeling technique, therefore, leads to high ^{111}In oxine entrapment efficiency and good stability against dilution and partitionning. The method is easy, fast, and reproducible. Because of these characteristics, the nanocapsules biodistribution can be followed-up after iv administration either by gamma scintigraphy imaging or by determining the gamma activity in the tissues after sampling. Moreover, the study can be performed for up to 96 h because of the relative long half-life of indium oxine. Finally, the gamma dose used under these conditions is relatively safe because the same low dose is used for diagnosis purposes in humans.

Biodistribution of Indium Oxine after Intravenous Administration—Depending on the drug dosage form (solution or nanocapsules), the distribution of the ^{111}In oxine appears to be very different. A comparison of the radioactivity detected in the blood and the other tissues at the earlier sampling time shows that most of the ^{111}In oxine solution was distributed into the blood and the liver (Figures 1 and 2). However, the administration of the PCL-encapsulated ^{111}In oxine led to a decrease in the blood activity and an increase in the liver activity compared with the solution (Figures 1 and 2). This effect was even more pronounced after administration of the PLAGA nanocapsules. In that latter case, 60−70% of the administered dose reached the liver. The activity level in other tissues, such as kidneys, lungs, and spleen, appeared to be unaffected by the encapsulation into one or the other polymer (Tables 2, 3, 4). These results are in good agreement with results obtained with ^{14}C-labeled colloidal carriers. Indeed, it was previously shown that a high proportion of the nanoparticles were quickly taken up by the liver after iv administration.[1,7−10,15] The plasma half-life of such carriers usually ranges from 1 to 10 min,[15] but could be extended up to >10 h if nanoparticles are precoated with Pluronic F108.[16]

In addition, it appears that the ^{111}In oxine radioactivity kinetics in the blood as well as in the liver are, quite similarly, independent of the dosage form. Indeed, the blood

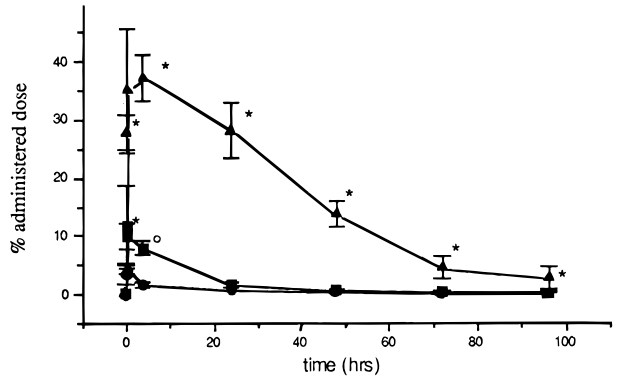

Figure 1—Chronological blood ^{111}In oxine activity after iv administration of the ^{111}In oxine solution, the PLAGA nanocapsules, and the PCL nanocapsules. Key: (●) PLAGA nanocapsules, (■) PCL nanocapsules, (▲) ^{111}In oxine solution; (*) = statistically different at 95% compared with PLAGA and PCL nanocapsules; (○) statistically different at 95% compared with PLAGA nanocapsules (one-factor ANOVA *F* test).

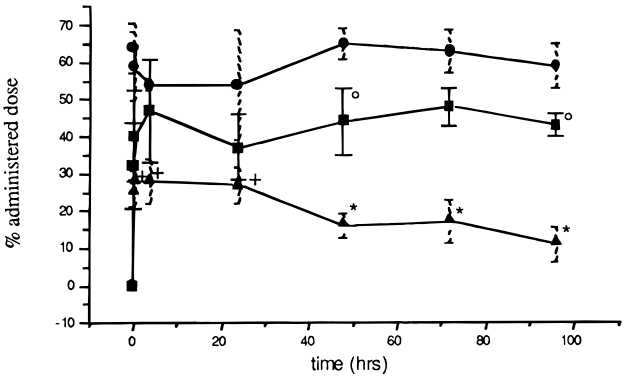

Figure 2—Chronological liver ^{111}In oxine radioactivity after iv administration of the ^{111}In oxine solution, the PLAGA nanocapsules, and the PCL nanocapsules. Key: (●) PLAGA labeled nanocapsules; (■) PCL nanocapsules; (▲) ^{111}In oxine solution; (*) statistically different at 95% compared with PLAGA and PCL nanocapsules; (○) statistically different at 95% compared with PLAGA ; (+) statistically different at 95% compared with PCL nanocapsules (one-factor ANOVA *F* test).

Table 2—Mean Percentages of ^{111}In Oxine Administered Dose in Lungs As a Function of Time after Administration[a]

	lungs		
time (h)	solution (SD)	PCL (SD)	PLAGA (SD)
0.00	0	0	0
0.25	7 (1.1)	18.5 (9.2)	6 (2.6)
0.50	5.4 (1.4)	7.5 (6.8)	4.8 (1.4)
4.00	4.7 (2.0)	4.8 (1.7)	4.0 (1.3)
24.00	5.1 (1.7)	2.9 (0.8)	1.5 (1.1)
48.00	2.9 (0.6)	1.1 (0.6)	1.6 (0.2)
72.00	1.2 (0.7)	0.9 (0.2)	1 (0.6)
96.00	0.8 (0.4)	0.8 (0.3)	1 (0.5)

[a] $n = 5$, values have been corrected according to the half-life of ^{111}In.

radioactivity after administration of the solution, the PCL nanocapsules, and the PLAGA nanocapsules followed a monoexponential decline with a half-lives of 23, 25, and 28 h, respectively. In the kidneys, the marker radioactivity declined slowly after administration of either the solution or the encapsulated forms. It has been previously demonstrated that after iv administration of an indium oxine solution, the indium oxine is quickly bound to the plasma transferin. After adsorption, the marker is taken up by the liver cells through the transferin receptor, and a progressive elimination of the marker from the blood occurs. Indeed, the elimination of the marker from the blood is driven by the availability of free transferin receptors. The

Table 3—Mean Percentages of ^{111}In Oxine Administered Dose in Spleen As a Function of Time after Administration[a]

	spleen		
time (h)	solution (SD)	PCL (SD)	PLAGA (SD)
0.00	0	0	0
0.25	8 (2.3)	1.6 (1.4)	2.8 (0.2)
0.50	7.9 (3.6)	1.4 (0.6)	2.7 (0.6)
4.00	13.3 (2.9)	1.8 (0.2)	2.9 (0.5)
24.00	4.8 (2.2)	1.7 (0.4)	3.4 (0.8)
48.00	2.5 (0.7)	2.3 (0.4)	3.6 (0.9)
72.00	9.4 (5.5)	2.2 (0.2)	3.6 (0.9)
96.00	7.2 (6.6)	2.0 (0.9)	3.3 (0.4)

[a] $n = 5$; values have been corrected according to the half-life of ^{111}In.

Table 4—Mean Percentages of ^{111}In Oxine Administered Dose in Kidneys As A Function of Time after Administration[a]

	kidneys		
time (h)	solution (SD)	PCL (SD)	PLAGA (SD)
0.00	0	0	0
0.25	11.2 (3.9)	5.5 (2.9)	4.1 (0.9)
0.50	8.1 (1.0)	7.9 (5.3)	3.5 (1.7)
4.00	10.4 (2.7)	8.8 (4.6)	2.8 (1.0)
24.00	11.2 (3.5)	7.5 (1.1)	3.3 (0.7)
48.00	7.5 (2.2)	5.1 (0.6)	2.4 (0.5)
72.00	4.8 (1.1)	5.5 (0.2)	2.0 (0.5)
96.00	4.0 (0.7)	4.5 (1.3)	2.0 (0.5)

[a] $n = 5$, values have been corrected according to the half-life of ^{111}In.

marker is continuously internalized and released into the liver cells where the complex is disrupted and the hydrophilic indium molecule is eliminated. However, the biodistribution process of encapsulated indium oxine appears to be very different. It seems that it mainly proceeds through a rapid liver uptake. The uptake of nanocapsules by the liver is nonspecific, mediated by the opsonization of the particles after contact with the plasma proteins, and leads to a higher uptake of the marker compared to the solution. After internalization of the nanocapsules, the indium oxine is released and reduced to its hydrophilic form. This form is then eliminated, as demonstrated by the activity in the kidneys.

Although a high proportion of both PLAGA and PCL nanocapsules were quickly taken up by the liver after iv administration, the biodistribution profiles of the two carriers were different. These differences are apparent in the blood and the liver distribution, whereas the distribution of the carriers in the other tissues does not seem to depend on the polymer used. Both the proportion of the carrier that was detected in the tissues as well as the elimination rate of the carrier from the tissues have to be considered. Indeed, until 20 h after administration of the nanocapsules, a higher gamma activity was detected in the blood after administration of PCL nanocapsules compared with PLAGA nanocapsules. However, the gamma emittor encapsulated either in PLAGA or in PCL nanocapsules was eliminated at a similar rate from the blood (25 and 28 h, respectively). In the liver, we found a higher proportion of ^{111}In oxine after administration of PLAGA nanocapsules than after administration of PCL nanocapsules but, again, both were eliminated at a slow and similar rate. Previously, it was demonstrated that particle size, zeta potential, and surface hydrophilicity greatly influence the kinetics of the elimination of particles from the blood.[4,5,13,15–18] Because following internalization into the liver the release rate from the two types of nanocapsules are similar, one can assume that the longer residence time of PCL nanocapsules in blood compared with that of the PLAGA nanocapsules

results from the lower liver uptake mediated by the adsorption of opsonins onto the carriers. Budhi et al.[5] have shown that larger polystyrene particles were eliminated from the blood faster than smaller ones. In our study, the size as well as the zeta potential of the two types of nanocapsules are similar. In addition, both polymers are considered to be hydrophobic. However, the glass transition temperature of the PCL is far lower that of the PLAGA (−53 and +42 °C, respectively). The PCL nanocapsules surface is therefore less rigid than the PLAGA nanocapsules surface at temperatures <42 °C (e.g., 37 °C, body temperature). Both types of nanocapsules have been prepared in the presence of Pluronic F68 as stabilizer, but the interaction of the stabilizer with the polymer during the formation of the polymeric wall could be influenced by the physical state of the polymer. The rubbery state of PCL at room temperature (≈20 °C, manufacturing temperature) could facilitate the anchor of the stabilizer into the polymeric wall. As already demonstrated,[19−21] the presence of block copolymers, such as Pluronic F68, promotes a decrease in the interaction with liver-specific opsonins, which in turn leads to a slower blood clearance and a lower liver uptake. Because the uptake of the two types of nanocapsules is similar in the spleen, it seems that the difference in the interaction with spleen-specific opsonins is less pronounced. The preferential adsorption of liver- and spleen-specific opsonins onto polymeric colloidal carriers has nevertheless not been demonstrated. Polymers with a glass transition temperature lower than the manufacturing temperature and/or 37 °C, like PCL, appear therefore to be a potential interesting polymer in the development of colloidal carriers. Because of its rubbery state at 37 °C, this polymer could be an alternative to PLAGA. In particular, higher plasma drug level could be achieved for a prolonged period of time after administration of PCL colloidal carriers prepared only with hydrophilic surfactant. This procedure could be an alternative to stealth PLAGA colloidal carriers, at least for the first 24 h, during which the hydrophilic part is covalently bound onto the polymer.

References and Notes

1. Fawaz, F.; Bonini, F.; Guyot, M.; Lagueny, A. M.; Fessi, H.; Devissaguet. J. P. Influence of poly(DL-lactide) nanocapsules on the biliary clearance and enterohepatic circulation of indomethacin in the rabbit. *Pharm. Res.* **1993**, *10*, 750−756.
2. Marchal-Heussler, L.; Sirbat, D.; Hoffman, M.; Maincent, P. Poly(epsilon-caprolactone) nanocapsules in carteolol ophthalmic delivery. *Pharm. Res.* **1993**, *10*, 386−390.
3. Kiwada, H. Plasma factors affecting disposition of liposomes. *Adv. Drug. Del. Rev.* **1997**, *24*, 193−199.
4. Bazile, D.; Prudíhomme, C.; Bassoullet, M. T.; Marlard, M.; Spenlehauer, G.; Veillard, M. Stealth MePEG-PLA nanoparticles avoid uptake by mononuclear phagocytes system. *J. Pharm. Sci.* **1995**, *84*, 493−498.
5. Simon, B. H.; Ando, H. Y.; Gupta, P. K. Circulation time and body distribution of C14-labeled amino-modified polystyrene nanoparticles in mice. *J. Pharm. Sci.* **1995**, *84*, 1249−1253.
6. Bonduelle, S.; Pimienta, C.; Benoit, J. P.; Lenaerts, V. Body distribution in mice of intravenously injected radiolabeled cyclosporin associated with polyisohexylcyanoacrylate nanocapsules or nanospheres. *Eur. J. Pharm. Biopharm.* **1995**, *41*, 27−30.
7. Scherphof, G. L. Modulation of pharmacokinetic behavior of liposomes. *Adv. Drug. Del. Rev.* **1997**, *24*, 179−191.
8. Rolland, A.; Collet, B.; Le Verge, R.; Toujas, L. Blood clearance and organ distribution of intravenously administered polymethacrylic nanoparticles in mice. *J. Pharm. Sci.* **1989**, *78*, 481−484.
9. Gahnem, G. E.; Joubran, C.; Arnould, R.; Lejeune, F.; Fruhling, J. Labeled polycyanoacrylate nanoparticles for human in vivo use. *Appl. Radiat. Isot.* **1993**, *44*, 1219−1224.
10. Thanoo B. C.; Doll W. J.; Metha R. C.; Digenis, G. A.; Deluca, P. P. Biodegradable indium-111 labeled microspheres for in vivo evaluation of distribution and elimination. *Pharm. Res.* **1995**, *12*, 2060−2064.
11. Kreuter, J.; Wilson, C. G.; Fry, J. R.; Paterson, P.; Ratcliffe, J. H. Toxicity and association of polycyanoacrylate nanoparticles with hepatocytes. *J. Microencapsul.* **1984**, *1*, 253−257.
12. Fessi, H.; Puisieux, F.; Devissaguet, J. P.; Ammoury, N.; Benita, S. Nanocapsule formation by interfacial polymer deposition following solvent displacement. *Int. J. Pharm.* **1989**, *55*, R1−R4.
13. Ammoury, N.; Fessi, H.; Devissaguet, J. P.; Dubrasquet, M.; Benita, S. Jejunal absorption, pharmacological activity and pharmacokinetic evaluation of indomethacin-loaded poly(d,l-lactide) and poly(isobutyl-cyanoacrylate) nanocapsules in rats. *Pharm. Res.* **1991**, *8*, 101−105.
14. Kedzierewicz, F.; Thouvenot, P.; Monot, I.; Hoffman, M.; Maincent, P. Influence of different physicochemical conditions on the release of indium oxine from nanocapsules. *J. Biomed. Mater. Res.* **1998**, *39*, 588−593.
15. Lescure, F.; Seguin, C.; Breton, P.; Bourrinet, P.; Roy, D.; Couvreur, P. Preparation and characterization of novel poly-(methylidene malonate 2.1.2.)-made nanoparticles. *Pharm. Res.* **1994**, *11*, 1270−1277.
16. Tan, J. S.; Butterfield, D. E.; Voycheck, C. L.; Caldwell, K. D.; Li, J. T. Surface modification of nanoparticles by PEO/PPO block copolymers to minimize interactions with blood components and prolong blood circulation in rats. *Biomaterials* **1993**, *14*, 823−833.
17. Sahli, H.; Japon-Bretandière, J.; Fischer, A. M.; Sternberg, C.; Spenlehauer, G.; Verrechia, T.; Labarre, D. Interactions of poly(lactic acid) and poly(lactic acid-*co*-ethylene oxide) nanoparticles with the plasma factors of coagulation system. *Biomaterials* **1997**, *18*, 281−288.
18. Borchard, G.; Kreuter, J. The role of serum complement on the organ distribution of intravenously administered poly-(methyl methacrylate) nanoparticles: effect of precoating with plasma and with serum complement. *Pharm. Res.* **1996**, *13*, 1055−1058.
19. Blunk, T.; Hochstrasser, D. F.; Sanchez, J. C.; Muller, B. W.; Muller, R. H. Colloidal carriers for intravenous drug targeting: plasma protein adsorption patterns on surface-modified latex particles evaluated by two-dimensional polyacrylamide gel electrophoresis. *Electrophoresis* **1993**, *14*, 1382−1387.
20. Stolnik, S.; Dunn, S. E.; Garnett, M. C.; Davies, M. C.; Coombes, A. G. A.; Taylor, D. C.; Irwing, M. P.; Purkiss, S. C.; Tadros, T. F.; Davis, S. S.; Illum, L. Surface modification of poly(lactide-*co*-glycolide) nanospheres by biodegradable poly(lactide)-poly(ethylene glycol) copolymers. *Pharm. Res.* **1994**, *11*, 1800−1808.
21. Alyantdin, R. N.; Petrov, V. E.; Langer, K.; Berthold, A.; Kharbevich, D. A.; Kreuter, J. Delivery of loperamide across the blood-brain barrier with polysorbate 80-coated polybutylcyanoacrylate nanoparticles. *Pharm. Res.* **1997**, *14*, 325−328.

Acknowledgments

The authors thank Mrs. D. Corvi for helpful technical assistance and APRAB for financial support.

JS980307K

Effect of Surface Charge on the Stability of Oil/Water Emulsions during Steam Sterilization

GAYSORN CHANSIRI,[†] ROBERT T. LYONS,[‡] MAHESH V. PATEL,[§] AND STANLEY L. HEM*

Contribution from *the Department of Industrial and Physical Pharmacy, Purdue University, West Lafayette, Indiana 47906.*

Received July 20, 1998. Final revised manuscript received November 18, 1998.
Accepted for publication February 1, 1999.

Abstract □ Intravenous lipid emulsions are used for total parenteral nutrition and as carriers for lipophilic drugs. Exposure to the high temperature (121 °C) required for steam sterilization may cause coalescence and an increase in droplet size. The purpose of this study was to investigate whether an increase in the electrostatic repulsive force between oil droplets produced by formulation modification improves the thermal stability of lipid emulsions during autoclaving. The addition of a small amount, 0.66 or 1.32 mmol/kg (mm), of purified anionic phospholipid fractions (phosphatidic acid, phosphatidylglycerol, or phosphatidylinositol) to the standard formula increased the ζ potential from its normal value of –11 mV to –39 mV. Emulsions with the larger negative ζ potential did not exhibit any change in oil droplet size or distribution during steam sterilization at 121 °C for 15 min. The autoclaved emulsions having the larger negative ζ potential did not exhibit any evidence of coalescence when samples were stored for 1 month at 4 °C, room temperature, or 40 °C. Reduction of the negative surface charge of the oil droplets by the addition of stearylamine confirmed that the surface charge was an important factor, as emulsions having a reduced negative surface charge separated into two phases during autoclaving.

Introduction

Lipid emulsions have a long history of safe use as a source of intravenous nutrition. They have been used more recently for the intravenous administration of lipid-soluble drugs. Intravenous lipid emulsions must be sterile. The preferred sterilization process is steam sterilization. Exposure to the high temperature, 121 °C, required for steam sterilization may cause an increase in the mean droplet size.[1] The droplet size is important for the safe use of intravenous lipid emulsions, as the smallest capillaries have a diameter of 5 μm.[2−5] The desirable size range of oil droplets administered intravenously is approximately 0.4 to 1 μm,[2−5] which is approximately the same size as naturally occurring chylomicron in the blood.

Intravenous lipid emulsions are stabilized by a combination of forces such as electrostatic, hydration, and steric repulsive forces. Egg phospholipid, the emulsifier in most intravenous lipid emulsions, is a mixture of nonionic and anionic phospholipids. The anionic components have apparent pK_a values between 3 and 4[6] and contribute an electrostatic repulsive force within the pH range of intravenous lipid emulsions, i.e., pH 8.0−9.0. It has been proposed that phospholipids form a liquid crystal interfacial film structure at the oil−water interface by adsorption of water.[7] The phospholipid molecule can attach to itself up to 39 water molecules, resulting in a great increase in molecular volume.

The hydration and steric repulsive forces, which depend on adsorption, are inversely related to temperature. Thus, these stabilizing forces are less effective during exposure to 121 °C during steam sterilization. On the other hand, the electrostatic repulsive force is inversely related to the dielectric constant of the medium.[8] In the case of lipid emulsions, the medium is water and its dielectric constant decreases as temperature increases. Therefore, the electrostatic repulsive force is larger at elevated temperatures than at room temperature.

The electrostatic repulsive force has been increased in phospholipid-stabilized o/w emulsions by the addition of oleic acid, phosphatidylserine, phosphatidylglycerol, or phosphatidic acid.[9−13] Most of the studies focused on reducing the rate of coalescence when the lipid emulsion was mixed with electrolytes in an admixture for total parenteral nutrition. In general, the stability of emulsions to the addition of electrolytes was directly related to the magnitude of the negative surface charge. Yamaguchi et al.[13] reported that when the ζ potential of a lipid emulsion was increased from −8 to −18 mV by the addition of 17.5 mM oleic acid, the emulsion exhibited no change in mean particle size after autoclaving at 121 ° C for 20 min. The mean particle size of the control emulsion (without the added oleic acid) increased from 0.20 to 0.32 μm during autoclaving. No information was presented regarding the particle size distribution. Thus, although the mean droplet size (as measured by photon correlation spectroscopy) did not change during autoclaving, coalescence may have occurred. A second technique capable of monitoring droplets larger than 1 μm, such as single-particle optical sensing, was needed to determine if coalescence occurred during autoclaving.

This study was undertaken to determine if the formulation of o/w emulsions can be modified by the addition of purified anionic phospholipid fractions to increase the naturally occurring negative surface charge and if emulsions having a larger negative surface charge will undergo less coalescence during steam sterilization.

Experimental Section

Miglyol 812 is a neutral oil composed of caprylic and capric triglyceride (Huls, Hillside, NJ). Olive oil was obtained from ICN Biomedical, Aurora, OH. Egg phospholipid was a gift of Pharmacia & Upjohn, Clayton, NC. Phosphatidic acid, phosphatidylcholine, phosphatidylglycerol, and phosphatidylinositol were obtained from Avanti Polar Lipid, Alabaster, AL. Stearylamine was obtained from Sigma Chemical Co., St. Louis, MO.

* Corresponding author. Tel: 765-494-1451. Fax: 765-494-6545. E-mail: jglass@pharmacy.purdue.edu.
[†] Faculty of Pharmacy, Silpakorn University, Nakornpathom, Thailand.
[‡] Pharmacia & Upjohn, Inc., Clayton, NC 27520.
[§] Lipocine, Inc., Salt Lake City, UT 84103.

10.1021/js980293i CCC: $18.00
Published on Web 03/02/1999

Table 1—Effect of Autoclaving on the Properties of the Standard Emulsion

	before autoclaving	after autoclaving
acid value, mg KOH/g emulsion	0.247 ± 0.003	0.348 ± 0.009
pH	8.0 ± 0.0	7.2 ± 0.0
ζ potential, mV	−10.5 ± 2.4	−23.6 ± 0.8
Mean diameter, μm	0.28 ± 0.01	0.40 ± 0.00
Volume of oil present as droplets larger than 1 μm, % v/v	0.060 ± 0.005	0.473 ± 0.046

The following formula was the standard emulsion used in this study: Miglyol 812 10 g olive oil 10.0 g; butylated hydroxytoluene 0.2 g; egg phospholipid 1.2 g; glycerol 2.4 g; doubly distilled water, qs 100.0 g.

The emulsion was produced by preparing the aqueous phase by dispersing the egg phospholipid in a solution of glycerol and water using a constant speed stirrer at 1500 rpm. Nitrogen was bubbled into the glycerol and water solution for 15 min before the egg phospholipid was added. The oil phase was prepared by combining Miglyol 812 and olive oil and bubbling nitrogen into the solution for 15 min. Butylated hydroxytoluene was dissolved in the oil phase. A primary emulsion was prepared by mixing the oil and aqueous phases for 10 min using a high speed mixer with a propeller blade (Multimix 4642, Braun). The primary emulsion was passed through a microfluidizer (Model 110 Y, Microfluidics Corp., Newton, MA) five times at 20000 psi. The cooling coil and interaction chamber were packed with ice. The final pH of the emulsion was adjusted to 8.0 by the addition of 0.5 to 1.0 mL of 0.1 N NaOH per 300 g of emulsion.

The temperature of emulsions produced by the microfluidizer has been reported to increase by 5 °C for each pass when no cooling is used.[14,15] The use of ice on the cooling coil and interaction chamber in this study controlled the temperature of the discharged emulsion in the range of 16 to 22 °C.

The emulsion was packaged in 10 mL vials (Type 1 glass) and sealed with a pulp and plastic screw cap. The emulsion was purged with nitrogen before sealing. Samples of the emulsion in the 10 mL vials were autoclaved for 15 min at 121 °C, 15 psi.

The pH of the emulsion and the results of all of the other tests were reported as the mean of four measurements from two sample vials. The acid value was determined by a standard procedure and is expressed as the milligrams of potassium hydroxide required to neutralize the free acids in 1 g of emulsion.[16] The mean droplet diameter was determined by dynamic light scattering (Nicomp 370, Particle Sizing Systems, Santa Barbara, CA) and was based upon volume weighting. The emulsion was diluted 1:100 immediately before measurement with doubly distilled water that had been passed through a 0.22 μm membrane filter. This dilution procedure was selected after a preliminary experiment indicated that the mean droplet diameter remained the same when measured immediately after dilution or 10, 15, or 30 min after dilution. The percentage of oil present as droplets larger than 1 μm was determined using a single-particle optical sensing system (Accusizer 770, Particle Sizing Systems, Santa Barbara, CA). The emulsion was diluted immediately before measurement with doubly distilled water that had been passed through a 0.22 μm membrane filter. The dilution ratio was adjusted to obtain a droplet count between 3000 and 8000 droplets/mL. The ζ potential was determined by Doppler electrophoretic light scattering analysis (DELSA 440, Coulter, Hialeh, FL). The emulsion was diluted with 0.01 M HEPES buffer at pH 7.5 (Fisher, Fairlawn, NJ) which contained 5 mM NaCl.

Results and Discussion

The effect of autoclaving at 121 °C for 15 min on the properties of the standard emulsion is presented in Table 1. The acid value increased following autoclaving, indicating the formation of free fatty acids. It is likely that the elevated temperature accelerated the hydrolysis of the oil phase and the egg phospholipid used as the emulsifier. The rate of hydrolysis of phospholipids has been found to follow the Arrhenius equation in the temperature range of 5 to 90 °C.[17] The fatty acids formed by the hydrolysis of egg phospholipid are probably also responsible for the decrease in pH observed after autoclaving. The ζ potential became more negative following autoclaving. This may be the result of the increased fatty acid concentration and/or the redistribution of the egg phospholipid from the aqueous phase where it is present as liposomes to the interface during autoclaving.[18]

Table 2—Effect of Adding Egg Phospholipid Fractions (0.66 or 1.32 mm) on the ζ Potential

egg phospholipid fraction added	ζ potential ± SD, mV	
	0.66 mm	1.32 mm
none	−10.5 ± 2.4	−10.5 ± 2.4
phosphatidylcholine	−12.2 ± 3.4	
phosphatidic acid	−35.1 ± 1.7	−38.4 ± 1.4
phosphatidylglycerol	−39.4 ± 1.2	−40.0 ± 1.8
phosphatidylinositol	−32.7 ± 0.3	−37.3 ± 0.4

Autoclaving caused an increase in the mean droplet size from 0.28 to 0.40 μm. It is likely that coalescence occurred during exposure to 121 °C which resulted in an increased mean droplet size. Further evidence that coalescence occurred is the increase in the percentage of oil present as droplets larger than 1 μm. This parameter is more critical for safety than the mean droplet size, as the smallest capillary has a diameter of 5 μm.[2–5] Some oil droplets which formed during autoclaving became large enough to rise to the surface of the emulsion and were seen without magnification as oil droplets on the surface.

Egg phospholipid is a mixture of many components.[19] The major components are phosphatidylcholine (PC) and phosphatidylethanolamine which exhibit no net charge at physiological pH. The minor components, which comprise 2−5% of the total lipid, are phosphatidylserine, phosphatidic acid (PA), phosphatidylglycerol (PG), phosphatidylinositol (PI), sphingomyelin, cholesterol, and lysophosphatidylcholine. Phosphatidylserine, PA, PG, and PI are negatively charged at pH 7.0. Along with free fatty acids, these anionic fractions are probably responsible for the negative ζ potential of the standard emulsion (Table 1).

The effect of increased negative ζ potential on the physical stability of the standard emulsion during autoclaving was tested by adding approximately 0.05% w/w (0.66 millimolal (mm)) of purified egg phospholipid fractions which are anionic (PA, PG, or PI). The nonionic fraction, PC, was included at the same concentration as a control. As seen in Table 2, the addition of 0.66 mm of the anionic fractions caused the ζ potential to increase from −11 mV to approximately −39 mV. The nonionic egg phospholipid fraction, PC, did not cause a statistically significant change in the ζ potential. The formula modification did not affect the production of the emulsion as the mean droplet diameter of the emulsions containing an additional 0.66 mm of nonionic or anionic egg phospholipid fractions was the same as the standard formulation (Figure 1).

The effect of increased electrostatic repulsive force was seen when the emulsions containing 0.66 mm egg phospholipid fractions were autoclaved. The mean droplet size of the emulsions having a larger negative ζ potential (PA, PG, PI) were unchanged during autoclaving (Figure 1). In contrast, the mean droplet size increased during autoclaving in the standard emulsion and the emulsion containing additional nonionic fraction, PC. The change in mean droplet diameter during autoclaving for the standard emulsion and the emulsion containing additional PC was statistically significant at *p*-values of 0.001 and 0.003, respectively.

Table 3—Effect of Adding 0.66 mm Egg Phospholipid Fractions on the Free Fatty Acid Content, pH, and ζ Potential Following Autoclaving at 121 °C for 15 min

egg phospholipid fraction added	acid value, mg KOH/g emulsion		pH[a]		ζ potential mV	
	before autoclaving	after autoclaving	before autoclaving	after autoclaving	before autoclaving	after autoclaving
none	0.247 ± 0.003	0.348 ± 0.009	8.0	7.2	–10.5 ± 2.4	–23.6 ± 0.8
phosphatidylcholine	0.236 ± 0.002	0.359 ± 0.005	8.0	7.2	–12.2 ± 3.4	–22.4 ± 0.5
phosphatidic acid	0.275 ± 0.003	0.319 ± 0.004	8.0	7.4	–35.1 ± 1.7	–37.7 ± 1.5
phosphatidylglycerol	0.270 ± 0.004	0.303 ± 0.002	8.0	7.3	–39.4 ± 1.2	–40.3 ± 0.8
phosphatidylinositol	0.269 ± 0.007	0.303 ± 0.005	8.0	7.1	–32.7 ± 0.3	–35.2 ± 3.0

[a] The standard deviation was ± 0.0.

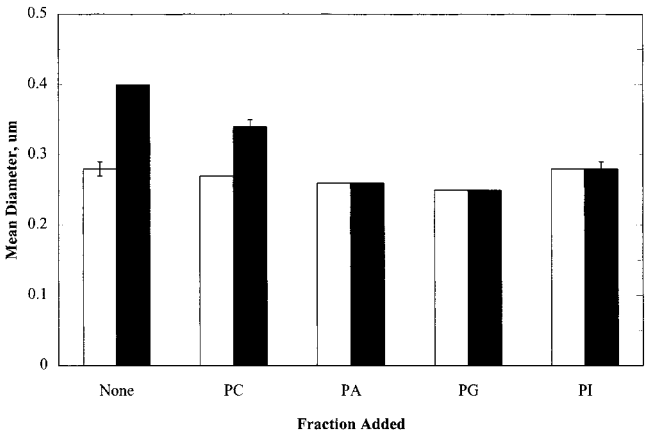

Figure 1—Effect of adding 0.66 mm egg phospholipid fractions on the mean droplet size following autoclaving at 121 °C for 15 min. The standard deviation is indicated on each bar when its value was greater than 0.00. Key: open bar, before autoclaving; hatched bar, after autoclaving; PC, phosphatidylcholine; PA, phosphatidic acid; PG, phosphatidylglycerol; PI, phosphatidylinositol.

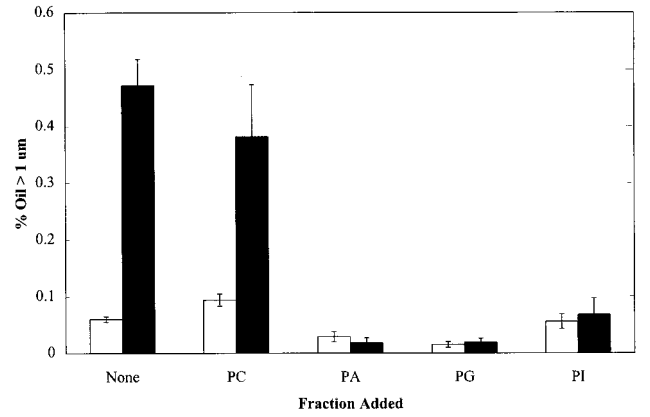

Figure 2—Effect of adding 0.66 mm egg phospholipid fractions on the percentage of oil present as droplets larger than 1 μm following autoclaving at 121 °C for 15 min. The standard deviation is indicated on each bar. Key: open bar, before autoclaving; hatched bar, after autoclaving; PC, phosphatidylcholine; PA, phosphatidic acid; PG, phosphatidylglycerol; PI, phosphatidylinositol.

The enhanced physical stability of the emulsions having an increased negative ζ potential was also seen when the percentage of oil present as droplets larger than 1 μm was determined (Figure 2). The three emulsions containing 0.66 mm anionic egg phospholipid fractions and having an increased negative ζ potential exhibited no change in the percentage of oil present as droplets larger than 1 μm as a result of autoclaving. This behavior is in sharp contrast to the standard formulation and the formulation containing an additional 0.66 mm PC. The percentage of oil present as droplets larger than 1 μm in these emulsions increased from less than 0.1 to 0.4 during autoclaving. Oil droplets were also visible on the surface of the standard emulsion and the emulsion containing additional PC. The three emulsions having a larger negative ζ potential did not have any visible oil droplets on the surface after autoclaving. Thus, the hypothesis that additional electrostatic repulsive force would inhibit coalescence during autoclaving was supported.

Table 4—Mean Droplet Size[a] of Autoclaved Emulsions Containing 0.66 mm Egg Phospholipid Fractions during Storage at 4 °C, Room Temperature (rt), and 40 °C

egg phospholipid fraction added	mean diameter, μm			
	initial	1 mo, 4 °C	1 mo, RT	1 mo, 40 °C
none	0.40	0.41	0.40	0.41
phosphatidylcholine	0.34	0.33	0.33	0.34
phosphatidic acid	0.26	0.26	0.26	0.26
phosphatidylglycerol	0.25	0.25	0.25	0.25
phosphatidylinositol	0.28	0.28	0.28	0.28

[a] All standard deviations were ± 0.01 or less.

Exposure to the elevated temperature of autoclaving caused hydrolysis of the egg phospholipid in the standard emulsion which was seen as an increase in the acid value, a decrease in the pH, and an increase in the negative ζ potential (Table 1). These parameters changed in a similar way during autoclaving of the emulsions containing additional egg phospholipid fractions (Table 3).

The effect of a higher concentration of added anionic egg phospholipid fractions was studied by repeating the experiments using 1.32 mm (approximately 0.10%) egg phospholipid fractions. The ζ potentials of the emulsions containing 1.32 mm PA, PG, and PI (Table 2) were −38.4, −40.0, and −37.3 mV, respectively. These values are only slightly increased in comparison to the values obtained when half that amount was added (Table 2). The mean droplet size of emulsions containing 1.32 mm PA, PG, or PI did not change during autoclaving. The percentage of oil present as droplets greater than 1 μm also did not change in these emulsions during autoclaving. Thus, increasing the concentration of added anionic egg phospholipid fractions above 0.66 mm (approximately 0.05%) did not significantly increase the surface charge or improve the physical or chemical stability of the emulsion to autoclaving.

The autoclaved standard emulsion and emulsions containing an additional 0.66 mm egg phospholipid fractions were stored at 4 °C, room temperature, and 40 °C for 1 month. As seen in Table 4, the mean droplet size of all of the emulsions was stable at all three temperatures. Likewise, the percentage of oil present as droplets larger than 1 μm did not significantly change during the storage period (Table 5). Thus, the addition of small amounts of anionic egg phospholipid fractions to reduce the rate of coalescence during autoclaving did not adversely affect the rate of coalescence during storage.

The preceding experiments demonstrate that the thermal stability of o/w emulsions can be improved by increasing the electrostatic repulsive forces between oil droplets.

Table 5—Percentage of Oil Present as Droplets Larger than 1 μm in Autoclaved Emulsions Containing 0.66 mm Egg Phospholipid Fractions During Storage at 4 °C, Room Temperature (rt), and 40 °C

egg phospholipid fraction added	% oil present as droplets larger than 1 μm, % v/v ± SD			
	initial	1 mo, 4 °C	1 mo, rt	1 mo, 40 °C
none	0.473 ± 0.046	0.452 ± 0.037	0.235 ± 0.028	0.352 ± 0.027
phosphatidylcholine	0.382 ± 0.092	0.452 ± 0.067	0.395 ± 0.073	0.399 ± 0.062
phosphatidic acid	0.018 ± 0.009	0.015 ± 0.002	0.025 ± 0.002	0.009 ± 0.002
phosphatidylglycerol	0.019 ± 0.007	0.016 ± 0.009	0.010 ± 0.003	0.010 ± 0.001
phosphatidylinositol	0.068 ± 0.029	0.022 ± 0.002	0.032 ± 0.008	0.019 ± 0.001

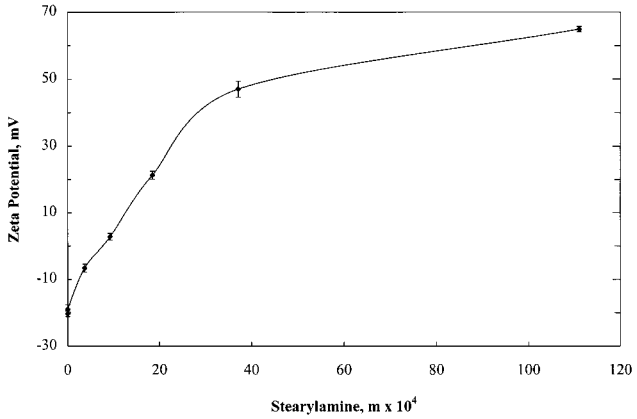

Figure 3—ζ potential of emulsions containing various concentrations of stearylamine. The standard deviation is indicated for every emulsion.

Table 6—Effect of Autoclaving at 121 °C for 15 min on the Mean Droplet Size of Emulsions Containing Stearylamine

experiment	concentration of stearylamine, mm	mean droplet diameter ± SD, mm	
		before autoclaving	after autoclaving
1	0	0.27 ± 0.01	0.37 ± 0.00
1	0.371	0.75 ± 0.02	cracked[a]
1	0.925	0.62 ± 0.00	cracked[a]
1	1.85	0.40 ± 0.01	cracked[a]
2	0	0.27 ± 0.00	0.42 ± 0.01
2	3.71	0.29 ± 0.00	0.28 ± 0.00
2	11.1	0.28 ± 0.00	0.27 ± 0.00

[a] The emulsion had separated into two phases.

To verify that the surface charge plays an important role in the stability of o/w emulsions, emulsions were prepared which had reduced negative ζ potentials as well as positive ζ potentials. The ζ potential of the standard emulsion containing 1.2% egg phospholipid was modified by incorporating concentrations of stearylamine ranging from 0.371 to 11.1 mm. The emulsions were prepared and autoclaved as two experiments. The first experiment consisted of the standard emulsion and emulsions containing 0.371, 0.925, and 1.85 mm stearylamine. The second experiment consisted of the standard emulsion and emulsions containing 3.71 and 11.1 mm stearylamine.

The ζ potential of the standard emulsion in the first experiment was −20.3 ± 0.8 mV and −19.0 ± 1.4 mV in the second experiment (Figure 3). Addition of 0.371 mm (approximately 0.01%) stearylamine reduced the negative ζ potential to −6.6 mV. This result indicates that the interface contains both anionic egg phospholipid fractions and stearylamine. The mean droplet diameter of this emulsion (Table 6) prior to autoclaving was larger (0.75 μm) than the standard emulsion. The mean droplet diameter prior to autoclaving was also larger than the standard emulsion when 0.925 and 1.85 mm stearylamine was included in the formulation. However, emulsions containing 3.71 or 11.1 mm of stearylamine exhibited initial mean droplet diameters which were virtually identical to the standard emulsion. This behavior suggests that coalescence occurred prior to autoclaving in the emulsions containing 0.371, 0.925, and 1.85 mm stearylamine.

Table 7—Effect of Autoclaving at 121 °C for 15 min on the Percent of Oil Present as Droplets Larger than 1 μm in Emulsions Containing Stearylamine

experiment	concentration of stearylamine, mm	% oil present as droplets larger than 1 mm ± SD	
		before autoclaving	after autoclaving
1	0	0.005 ± 0.000	0.115 ± 0.077
1	0.371	0.257 ± 0.119	cracked[a]
1	0.925	0.237 ± 0.079	cracked[a]
1	1.85	0.201 ± 0.030	cracked[a]
2	0	0.051 ± 0.008	0.486 ± 0.067
2	3.71	0.099 ± 0.024	0.103 ± 0.038
2	11.1	0.019 ± 0.001	0.029 ± 0.10

[a] The emulsion had separated into two phases.

The standard emulsions without added stearylamine (Table 6) exhibited the same increase in mean droplet size during autoclaving as was reported in Table 1. The emulsion with a reduced negative ζ potential (0.371 mm stearylamine) coalesced to such a degree during autoclaving that it completely separated into two phases. The surface charge of the emulsions became positive (+2.8 mV) when the concentration of stearylamine was 0.925 mm or higher (Figure 3). The ζ potential was +64.9 mV at the highest stearylamine concentration (11.1 mm). Only the two emulsions having the highest positive ζ potentials failed to exhibit an increase in mean droplet size during autoclaving (Table 6). These two emulsions were also the only ones which did not exhibit an increase in the percent oil present as droplets larger than 1 μm (Table 7). Although there was no significant change following autoclaving in the mean droplet size or percentage of oil present as droplets greater than 1 μm in the emulsions containing 3.71 or 11.1 mm stearylamine, examination of the surface of the emulsions after autoclaving revealed that the emulsion containing 11.1 mm stearylamine was more stable. No oil droplets were observed on the surface of the emulsion containing 11.1 mm stearylamine after autoclaving. In contrast, oil droplets were visible on the surface of the emulsion containing 3.71 mm stearylamine after autoclaving.

The thermal instability of the emulsions containing 0.371 or 0.925 mm stearylamine may be attributed to the small surface charge, −6.6 or + 2.8 mV, respectively. The electrostatic repulsive forces present in these emulsions may be insufficient to prevent coalescence during autoclaving. The emulsion containing 1.85 mm stearylamine had a ζ potential of +21.3 mV. The absolute value of the ζ potential was similar to the standard emulsions (−20.3 and −19.0 mV). Since the standard emulsion never separated into two phases during autoclaving (Tables 1 and 6), it was

surprising that the emulsion containing 1.85 mm stearylamine cracked during autoclaving. Previous experiments showed that autoclaving the standard emulsion caused the formation of free fatty acids and increased the negative ζ potential (Table 1). Thus, it is likely that the positive ζ potential of the emulsion containing 1.85 mm stearylamine became less positive during autoclaving. It is believed that the reduced positive ζ potential did not provide enough electrostatic repulsive force to prevent coalescence. Unfortunately, the ζ potential of this emulsion after autoclaving could not be measured because the emulsion separated into two phases during autoclaving.

The emulsions containing 3.71 and 11.1 mm stearylamine did not separate during autoclaving. Measurement of the ζ potential after autoclaving yielded reduced positive ζ potentials of $+7.5 \pm 0.9$ and $+31.5 \pm 1.5$ mV, respectively. The formation of free fatty acids may explain why the emulsion containing 11.1 mm stearylamine exhibited better thermal stability than the emulsion containing 3.71 mm stearylamine. The ζ potential of the emulsion containing 11.1 mm stearylamine was always greater than +31.5 mV during autoclaving while the ζ potential of the emulsion containing 3.71 mm stearylamine decreased to a minimum ζ potential of +7.5 mV during autoclaving.

Conclusions

This study demonstrates the important role of the electrostatic repulsive force in the thermal stability of o/w emulsions. We have shown that positively charged egg phospholipid emulsions are not desirable, as the positive ζ potential is neutralized during autoclaving. In commerce, o/w emulsions stabilized by egg phospholipid are autoclaved at an alkaline pH (pH 8−9) in order to maintain an adequate negative ζ potential for thermal stability.

Formulation modification by the addition of small amounts of anionic phospholipid fractions is a convenient means of increasing the ζ potential. This approach may be an attractive alternative to alterations of the autoclaving process when coalescence occurs during steam sterilization. The results of this study may also be relevant to observed batch-to-batch differences in the stability of egg phospholipid to autoclaving. As a natural product, the composition of egg phospholipid may vary in terms of nonionic and anionic components. All other factors being equal, one lot of egg phospholipid having a larger fraction of anionic components may produce a more stable emulsion at elevated temperatures than another lot having a smaller fraction.

The mechanical properties of the interfacial film may also be an important factor in the thermal stability of o/w emulsions. This factor will be investigated in a subsequent study.

References and Notes

1. Chaturvedi, P. R.; Patel, N. M.; Lodhi, S. A. Effect of Terminal Heat Sterilization on the Stability of Phospholipid-Stabilized Submicron Emulsions. *Acta Pharm. Nord.* **1992**, *4*, 51−55.
2. Hansrani, P. K.; Davis, S. S.; Groves, M. J. Preparation and Properties of Sterile Intravenous Emulsions. *J. Parenter. Sci. Technol.* **1983**, *37*, 145−150.
3. Collins-Gold, L. C.; Lyons, R. T.; Bartholow, L. C. Parenteral Emulsions for Drug Delivery. *Adv. Drug Delivery Rev.* **1990**, *5*, 189−208.
4. Mehta, R. C.; Head, L. F.; Hazrati, A. M.; Parr, M.; Rapp, R. P.; DeLuca, P. P. Fat Emulsion Particle-Size Distribution in Total Nutrient Admixtures. *Am. J. Hosp. Pharm.* **1992**, *49*, 2749−2755.
5. Chanana, G. D.; Sheth, B. B. Particle Size Reduction of Emulsions by Formulation Design I: Effect of Polyhydroxy Alcohols. *J. Parenter. Sci. Technol.* **1993**, *47*, 130−134.
6. Arias, C.; Rueda, C. Comparative Study of Lipid Systems from Various Sources by Rotational Viscometry and Potentiometry. *Drug Dev. Ind. Pharm.* **1992**, *18*, 1773−1786.
7. Shchipunov, Y. A.; Kolpakov, A. F. Unusual Processes of Phospholipid Dispersion Formation by the Action of an External Electric Field. *Colloids Surfaces* **1993**, *76*, 15−22.
8. Everett, D. H. *Basic Principles of Colloid Science*; Royal Society of Chemistry: London, 1988; pp 16−53.
9. Washington, C.; Chawla, A.; Christy, N.; Davis, S. S. The Electrokinetic Properties of Phospholipid-Stabilized Fat Emulsions. *Int. J. Pharm.* **1989**, *54*, 191−197.
10. Rubino, J. T. The Influence of Charged Lipids on the Flocculation and Coalescence of Oil-in-Water Emulsions. I: Kinetic Assessment of Emulsion Stability. *J. Parenter. Sci. Technol.* **1990**, *44*, 210−215.
11. Rubino, J. T. The Influence of Charged Lipids on the Flocculation and Coalescence of Oil-in-Water Emulsions. II: Electrophoretic Properties and Monolayer Film Studies. *J. Parenter. Sci. Technol.* **1990**, *44*, 247−252.
12. Muchtar, S.; Levy, M. Y.; Sarig, S.; Benita, S. Stability Assessment of a Fat Emulsion Prepared with an Original Mixture of Purified Phospholipids. *STP Pharma. Sci.* **1991**, *1*, 130−136.
13. Yamaguchi, T.; Nishizaki, K.; Itai, S.; Hayashi, H.; Ohshima, H. Physicochemical Characterization of Parenteral Lipid Emulsion: Influence of Cosurfactants on Flocculation and Coalescence. *Pharm. Res.* **1995**, *12*, 1273−1278.
14. Washington, C. New Technology for Emulsion Production. *Manuf. Chem.* **1988**, *59*, 49−55.
15. Washington, C.; Davis, S. S. The Production of Parenteral Feeding Emulsions by Microfluidizer. *Int. J. Pharm.* **1988**, *44*, 169−176.
16. *United States Pharmacopoeia*, 23rd ed.; United States Pharmacopoeial Convention: Rockville, MD, 1995; p 1738.
17. Herman, C. J.; Groves, M. J. Hydrolysis Kinetics of Phospholipids in Thermally Stressed Intravenous Lipid Emulsion Formulations. *J. Pharm. Pharmacol.* **1992**, *44*, 539−542.
18. Groves, M. J.; Herman, C. J. The Redistribution of Bulk Aqueous Phase Phospholipids During Thermal Stressing of Phospholipid-Stabilized Emulsions. *J. Pharm. Pharmacol.* **1992**, *45*, 592−596.
19. Lehninger, A. L.; Nelson, D. L.; Cox, M. M. *Principles of Biochemistry*, 2nd ed.; Worth: New York, 1993; pp 241−248.

Acknowledgments

This study was supported by the government of Thailand and the NSF Industry/University Cooperative Research Center in Pharmaceutical Processing.

JS980293I

Cocaine and Alcohol Interactions in the Rat: Effect on Cocaine Pharmacokinetics and Pharmacodynamics

WEI-JIAN PAN[†,‡] AND MOHSEN A. HEDAYA*[,†]

Contribution from *Pharmacology/Toxicology Graduate Program, Department of Pharmaceutical Sciences, College of Pharmacy, Washington State University, Pullman, Washington 99164-6510.*

Received July 13, 1998. Final revised manuscript received October 22, 1998.
Accepted for publication January 20, 1999.

Abstract □ The effect of alcohol coadministration on cocaine pharmacokinetics and pharmacodynamics was investigated in awake, freely moving rats. Cocaine plasma and brain extracellular fluid (ECF) concentration–time profiles were characterized after intraperitoneal (ip) administration of 30 mg/kg cocaine to rats that were pretreated with either normal saline or alcohol at 5 g/kg in a balanced crossover experimental design. The neurochemical response to cocaine administration, measured as the change in dopamine concentration in the nucleus accumbens (N ACC) and the change in the mean arterial blood pressure were monitored simultaneously. Intragastric alcohol administration significantly increased cocaine systemic bioavailability after ip administration from 0.550 ± 0.044 to 0.754 ± 0.071. Also, the absorption rate constant increased from 0.199 ± 0.045 to 0.276 ± 0.059 min^{-1} due to alcohol coadministration; however, this increase was not significant. Alcohol inhibition of cocaine metabolism caused an increase in cocaine elimination half-life from 26.3 ± 3.6 to 40.0 ± 8.1 min. Also, cocaine tissue distribution was enhanced by alcohol, resulting in a significant increase in cocaine volume of distribution. Analysis of the brain cocaine concentration–neurochemical effect relationship by the sigmoid-E_{max} pharmacodynamic model showed that E_{max} increased from 850 ± 200 to 1550 ± 640% of baseline due to alcohol coadministration, whereas EC_{50} decreased from 3400 ± 580 to 2000 ± 650 ng/mL, indicating higher cocaine potency in the presence of alcohol. The estimates of the indirect inhibitory pharmacodynamic model used to examine the plasma cocaine concentration–change in blood pressure relationship were not significantly different after the two treatments. These results indicate that alcohol significantly alters cocaine absorption, distribution, and elimination, resulting in higher and prolonged cocaine plasma concentration. Alcohol coadministration also potentiates the neurochemical response to cocaine administration.

Introduction

The pharmacological activities of cocaine include central nervous system (CNS), cardiovascular, and local anesthetic effects.[1] Cocaine inhibits catecholamine reuptake in the brain, leading to higher catecholamine concentration and producing cocaine stimulant effects.[2] Cocaine can also inhibit peripheral catecholamine reuptake leading to higher peripheral catecholamine concentrations that are primarily responsible for cocaine sympathomimetic effects.[3] It is also believed that cocaine may produce its sympathomimetic effect by a central mechanism.[4] The local anesthetic effect of cocaine results from blocking the sodium channel in sensory neurons, a mechanism that can affect the cardiac action potential leading to slower heart rate and slower cardiac conduction at high cocaine concentrations.[5] The sympathomimetic and the local anesthetic effects of cocaine can lead to opposite effects on the cardiovascular functions, which is responsible for the large variability in the cardiovascular effects of cocaine.[6,7]

Concurrent cocaine and alcohol use is one of the most frequently abused drug combinations.[8] The popularity of this drug combination arises primarily from the fact that abusers of this drug combination experience more intense and longer lasting euphoric effects, while the unpleasant disphoria experienced with cessation of cocaine use is reduced.[9] However, concurrent cocaine and alcohol abuse is associated with serious medical problems. This drug combination was identified as the most frequent substance abuse pattern found among individuals presented to emergency rooms with substance abuse-related problems (Drug Abuse Warning Network, 1991). Also, epidemiological studies of cocaine fatalities have indicated that combined cocaine and alcohol abuse results in 18-fold increase in the risk of sudden death compared with cocaine abuse alone.[10] Although the observed effects of this drug combination may result from the pharmacological effects of cocaine in addition to those of alcohol, several investigations have shown that alcohol can significantly alter the pharmacokinetics of cocaine.[11−14]

Alcohol coadministration with cocaine in experimental animals and humans has been shown to inhibit the metabolism of cocaine,[15,16] increase the plasma and brain cocaine concentrations,[14] and lead to the formation of the pharmacologically active metabolite cocaethylene.[11−14] In controlled human studies, concurrent cocaine and alcohol administration have been shown to increase the plasma cocaine concentrations in addition to the formation of cocaethylene.[17,18] Cocaine area under the plasma concentration−time curve (AUC_p) and the maximum cocaine plasma concentration ($C_{p\ max}$) after administration of alcohol and cocaine were significantly higher than those after administration of cocaine only.[11−13,17] Because good correlation between the pharmacokinetics and pharmacological effects of cocaine has been reported,[19−21] alteration in cocaine pharmacokinetics has been implicated, at least in part, for the increased incidence of cocaine-related toxicities after combined abuse of cocaine and alcohol.

The primary objective of this study was to investigate the effect of alcohol coadministration on the pharmacokinetics and the pharmacological effects of cocaine in the rat. This objective was achieved by comparing cocaine absorption, distribution, and elimination when administered alone and in combination with alcohol. Both the neurochemical response measured as the change in dopamine concentration in the nucleus accumbens (N ACC) and the change in mean arterial blood pressure after the two treatments were

* Corresponding author. Phone: (509)-335-5622. Fax: (509)-335-0162. E-mail: hedaya@mail.wsu.edu. Current address (effective May 15, 1999): College of Pharmacy, Tanta University, Tanta, Egypt.
† Pharmacology/Toxicology Graduate Program.
‡ Current address: Clinical Pharmacokinetics and Toxicokinetics, Abbott Laboratories, Abbott Park, Illinois 60064-6104.

10.1021/js980282p CCC: $18.00 Published on Web 03/12/1999

monitored simultaneously. This is the first investigation that examined the effect of alcohol coadministration on cocaine pharmacokinetics and pharmacological activities simultaneously in the same group of experimental animals.

Materials and Methods

Chemicals and Reagents—Cocaine hydrochloride, bupivacaine, 1-heptanesulfonic acid, and sodium fluoride were purchased from Sigma Chemical (St. Louis, MO). Acetonitrile and chloroform were supplied by Burdick and Jackson Laboratory (Muskegon, MI). The dehydrated-200 proof ethyl alcohol (USP) was purchased from McCormick Distilling (Weston, MO). Methanol, citric acid, EDTA, monobasic sodium phosphate, sodium hydroxide, and monobasic ammonium phosphate were obtained from J. T. Baker (Phillipsburg, NJ). All solvents were of high-performance liquid chromatographic (HPLC) grade, and all chemicals were of analytical reagent (AR) grade.

Animal Care and Preparation. Male Wistar rats (250−350 g, Simonsen Laboratories, Gilroy, CA) were maintained on a 12 h light/dark cycle and were given Purina chow pellets and water ad libitum for at least 7 days before use in the experiments. All operating procedures on animals were in accordance with the Guide for the Care and Use of Laboratory Animals (National Institutes of Health Publication No. 85-23, revised 1985) and were approved by the institutional animal care and use committee. The details of the animal preparation procedures were described previously.[22] Briefly, for the cocaine ip experiment, rats were prepared under aseptic condition while fully anesthetized by implanting a microdialysis cranial probe, cannulating the femoral arteries, and inserting abdominal and gastric catheters. For the cocaine iv experiment, all the procedures were similar except that the abdominal catheter was not implanted and only one femoral artery and one femoral vein were cannulated.

Cocaine and Alcohol Administration—A stock solution of cocaine (10 mg/mL) in normal saline was used for cocaine administration. For the ip cocaine experiment, the administered dose was 30 mg/kg, and for the iv cocaine experiment, the dose was 6.8 mg/kg. These doses were chosen because they are well below the cocaine dose that is lethal in 50% of the tested rats (LD_{50} 17 mg/kg for iv, and 75 mg/kg for ip, Material Safety Data Sheet, University of Washington, Seattle, 1995). Also, these doses should achieve measurable plasma and brain concentrations of cocaine and its metabolites over the period of the experiment. The alcohol dose (5 g/kg) was chosen to achieve an alcohol plasma concentration in the range of concentrations observed in humans after moderate drinking based on the reported alcohol pharmacokinetic parameters in rats.[23] Cocaine was administered ip via the abdominal catheter and iv via the femoral vein cannula, whereas alcohol was administered through the gastric catheter. This animal model allows cocaine and alcohol administration and collection of samples without the need to hold the rat, thereby avoiding the effect of animal handling on the monitored pharmacodynamic parameters.

Cocaine Pharmacokinetic and Pharmacodynamic Studies—*Cocaine ip Treatment*—Eight male Wistar rats were randomly chosen and were prepared following the surgical procedures just outlined. After the recovery period, each rat was treated with cocaine+normal saline and cocaine+alcohol in a balanced crossover experimental design with 48-h washout period between treatments. Four of the rats received cocaine+normal saline first followed by cocaine+alcohol after the washout period and the other four received cocaine+alcohol then cocaine+normal saline. In all the experiments, rats were pretreated with normal saline or alcohol 20 min before cocaine administration.

On the day of the experiment, one of the femoral artery cannulae was connected to a pressure transducer linked to a portable physiological monitor (Model VSM1, Physio-control, Redmond, WA) for monitoring the mean arterial blood pressure. Meanwhile, the effluent of the microdialysis probe (1 μL/min) was collected every 20 min into an HPLC autosampler vial spiked with 20 μL of dopamine mobile phase, and 5 μL was injected immediately into an HPLC with electrochemical detection (HPLC−EC) for dopamine analysis. This procedure was repeated until a stable basal dopamine concentration was detected (<10% difference in dopamine concentration in three consecutive collections). Once a stable dopamine baseline was achieved, the rat received either 10 g/kg of normal saline or 5 g/kg of alcohol (50% v/v in normal saline) through the gastric catheter. Twenty minutes later, 30 mg/kg of cocaine was administered ip through the abdominal catheter. This lag time was necessary to allow alcohol absorption into the systemic circulation before cocaine administration.[23] After cocaine administration, 10 blood samples, each of 0.2 mL, were collected through the femoral artery cannula at 2, 5, 10, 15, 30, 60, 90, 120, 180, and 240 min into vacutainers pretreated with heparin and sodium fluoride to avoid cocaine hydrolysis by the plasma esterases. Plasma samples were obtained by centrifugation and were stored at −20 °C until analysis for cocaine and its metabolites by HPLC with ultraviolet detection (HPLC−UV). The effluent of the microdialysis probe was continuously collected every 20 min throughout the experiment in HPLC autosampler vials containing 20 μL of the mobile phase for dopamine analysis (pH 4). This mobile phase was added to increase the stability of dopamine, cocaine, and cocaine metabolites in the collected samples. After mixing the vial content, 5 μL was injected immediately into the HPLC-EC system for dopamine analysis, and the remainder was analyzed for cocaine and its metabolites by HPLC−UV. The concentrations of cocaine and cocaine metabolites in the brain ECF were determined from the microdialysis probe effluent concentrations after correcting for the probe recovery, which was determined from an in vitro experiment.[24] The mean arterial blood pressure was continuously monitored during the entire experiment.

After the two treatments just described, four of these eight rats received a third treatment that consisted of alcohol (5 g/kg, 50% v/v in normal saline) through the gastric catheter. The purpose of this alcohol treatment was to determine the range of alcohol plasma concentrations achieved after alcohol administration during the pharmacokinetic experiment. Serial blood samples were obtained after alcohol administrations, and the plasma samples, each of 100 μL, were analyzed immediately for their alcohol content utilizing the Abbott ADx Analyzer (Abbott Diagnostic, Chicago, IL) as described previously.[13]

Cocaine iv Treatment. This experiment was performed to estimate the absolute bioavailability of cocaine after ip cocaine administration with and without alcohol pretreatment. Also, the results of this experiment were used to validate the pharmacokinetic model used in the analysis of the effect of alcohol pretreatment on cocaine pharmacokinetics. In this experiment, 12 male Wistar rats were randomly chosen and were prepared as already outlined.[22] After the recovery period, each rat received cocaine+normal saline and cocaine+alcohol in a balanced crossover design with a 48-h washout period between treatments. The rats received either normal saline (10 g/kg) or alcohol (5 g/kg, 50% v/v in normal saline) through the gastric catheter followed 20 min later by iv cocaine (6.8 mg/kg) via the femoral vein cannula. After cocaine administration, 10 blood samples, each of 0.2 mL, were collected through the femoral artery cannula at 2, 5, 10, 15, 30, 60, 90, 120, 180, and 240 min into vacutainers pretreated with heparin and sodium fluoride. Plasma samples were obtained by centrifugation and were stored at −20 °C until analysis for cocaine and its metabolites by HPLC−UV. The effluent of the microdialysis probe was continuously collected every 20 min and was analyzed for cocaine and its metabolites by HPLC−UV immediately after each collection.

Analytical Methods—*Cocaine and its Metabolites*—Plasma and microdialysis probe effluent were analyzed for cocaine and its metabolites by the method developed in our laboratory.[25] This is an isocratic HPLC method that involves extraction of cocaine and its metabolites from plasma samples with chloroform and utilizes bupivacaine as an internal standard. This method is sensitive enough to quantitate cocaine and its metabolites in concentrations as low as 25 ng/mL in 100-μL plasma samples, with a coefficient of variation of <10%. The brain ECF concentrations of cocaine and its metabolites were determined by the same method, except that the probe effluent was injected directly into the HPLC−UV system without any pretreatment.

Dopamine—The effluent of the microdialysis probe was injected directly into an HPLC system equipped with an electrochemical detector for dopamine analysis (Coulochem detector Model 5100A, guard cell Model 5020, and analytical cell Model 5014A, ESA, Bedford, MA). The mobile phase consisted of 0.1 M citrate, 0.075 M monobasic sodium phosphate, 36 mg/L of EDTA, 303 mg/L of 1-heptanesulfonic acid, and 5.5% methanol (v/v). The pH of the

mobile phase was adjusted to pH 4 with sodium hydroxide pellets. On the coulochem detector, the potential for the guard cell was set at −0.20 V, whereas those for detectors 1 and 2 were set at +0.30 and −0.15 V, respectively. Quantitation of dopamine was achieved on a Supelcosil LC-18-DB column (250 × 2.1 mm i.d., 5 μm), and the flow rate was 0.3 mL/min. The signal from detector 2 was analyzed with an electronic integrator (Hewlett-Packard, Model 3390, Palo Alto, CA). Because the change in dopamine ECF concentration after cocaine administration was expressed as percentage of baseline, dopamine probe recovery, which was necessary to calculate the actual concentration of dopamine in the brain ECF, was not determined.

Pharmacokinetic Analysis—A two-compartment pharmacokinetic model with elimination from the central compartment was used to analyze the effect of alcohol on cocaine absorption, distribution, and elimination after ip administration. This model assumes that cocaine absorption, distribution, and elimination follow first-order kinetics, and that the brain is part of the peripheral tissue compartment. The following equations were used to describe cocaine concentrations in the central (eqs 1 and 2) and the peripheral (eqs 3 and 4) compartments after a single ip (eqs 1 and 3) and iv administration (eqs 2 and 4):[26]

$$C_p = \frac{FD_{ip}k_a}{V_c}\left[\frac{(k_{21}-k_a)}{(\alpha-k_a)(\beta-k_a)}e^{-k_a t} + \frac{(k_{21}-\alpha)}{(k_a-\alpha)(\beta-\alpha)}e^{-\alpha t} + \frac{(k_{21}-\beta)}{(k_a-\beta)(\alpha-\beta)}e^{-\beta t}\right] \quad (1)$$

$$C_p = \frac{D_{iv}}{V_c(\alpha-\beta)}[(\alpha-k_{21})e^{-\alpha t} + (k_{21}-\beta)e^{-\beta t}] \quad (2)$$

$$C_b = \frac{FD_{ip}k_a k_{21}}{V_t}\left[\frac{e^{-k_a t}}{(\alpha-k_a)(\beta-k_a)} + \frac{e^{-\alpha t}}{(k_a-\alpha)(\beta-\alpha)} + \frac{e^{-\beta t}}{(k_a-\beta)(\alpha-\beta)}\right] \quad (3)$$

$$C_b = \frac{D_{iv}k_{12}}{V_t(\beta-\alpha)}(e^{-\alpha t} - e^{-\beta t}) \quad (4)$$

where D_{ip} and D_{iv} are cocaine doses for ip and iv administrations, F is cocaine bioavailability after ip administration, C_p and C_b are cocaine concentrations in the central (plasma) and tissue (brain ECF) compartments, respectively, V_c and V_t are volumes of distribution of the central and tissue compartments, k_a is cocaine first-order absorption rate constant after ip administration, k_{12} is the first-order transfer rate constant from the central to the tissue compartment, k_{21} is the first-order transfer rate constant from the tissue to the central compartment, k_{10} is the first-order elimination rate constant from the central compartment, and α and β are the hybrid first-order rate constants for the distribution and elimination processes, respectively.[26,27]

Plasma and brain ECF cocaine concentrations for each rat after ip cocaine with or without alcohol coadministration were fitted simultaneously to the two integrated equations that describe the plasma and brain ECF concentration−time profiles (eq 1 and 3). The pharmacokinetic model parameters were estimated by nonlinear regression analysis utilizing PCNONLIN (Version 4.0, SCI Software, Lexington, KY). Other pharmacokinetic parameters such as the total body clearance (*TBC*), the volumes of distribution at steady state and during the elimination phase (V_{dss} and $V_{d\beta}$), and the areas under cocaine plasma (AUC_p) and brain ECF (AUC_b) concentration−time curves were calculated from the estimated parameters.[27] The systemic bioavailability of cocaine after ip administration with and without alcohol pretreatment was calculated by comparing the corresponding AUC_p after iv and ip cocaine administrations.

Pharmacodynamic Analysis—*Neurochemical Response*—The sigmoid-E_{max} pharmacodynamic model was used to describe the relationship between the brain ECF cocaine concentration and the percent change in the brain ECF dopamine concentration.[22] The mathematical expression that describes the concentration−effect relationship for the sigmoid-E_{max} model is the following:

$$E = E_0 + \frac{E_{max}C_b^n}{EC_{50}^n + C_b^n} \quad (5)$$

where E is the effect measured as the percent change in dopamine basal concentration, E_0 is the baseline effect measured as the basal dopamine concentration, E_{max} is the maximum effect measured as the maximum change in dopamine concentration, EC_{50} is the brain ECF cocaine concentration when the observed effect is 50% of E_{max}, C_b is the brain ECF cocaine concentration, and n is the sigmoidicity factor. The pharmacodynamic model parameters were estimated by fitting the percent change in dopamine level and the cocaine concentration in the brain ECF at different time points to eq 5. The basal dopamine concentration was kept constant (100%) during the analysis. Nonlinear regression analysis was performed utilizing PCNONLIN.

Mean Arterial Blood Pressure Response—The relationship between the plasma cocaine concentration and the change in mean arterial blood pressure after ip cocaine administration followed counterclockwise hysteresis loop. The mean arterial blood pressure did not return to its baseline value at the end of the 4-h experiment.[21,22] This result indicates that under the condition of our investigation, there was no direct relationship between cocaine plasma concentration and the change in mean arterial blood pressure. Therefore, the indirect pharmacodynamic response model was utilized to characterize this relationship.[28,29] We chose the model that can describe indirect drug response resulting from inhibition of a mediator because cocaine effect on blood pressure results primarily from inhibition of catecholamine reuptake at the peripheral nerve endings leading to higher peripheral catecholamine concentration, which is responsible for the vasopressor effect of cocaine. The mathematical expression that describes the model for the change in the pharmacological response and the drug concentration is:

$$\frac{dR}{dt} = k_{in} - k_{out}\left(1 - \frac{I_{max}C_p^n}{IC_{50}^n + C_p^n}\right)R \quad (6)$$

where R is the observed response (percent change in mean arterial blood pressure), k_{in} is the apparent zero-order rate constant for response production, k_{out} is the first-order rate constant for response dissipation, I_{max} is the maximum inhibition of the factor that produces the effect, IC_{50} is the plasma cocaine concentration that leads to 50% inhibition of the factor that produces the effect, C_p is the plasma cocaine concentration at the time of the observed response, and n is the sigmoidicity factor.[28,29] The maximum response that will be achieved when D_{ip} is very large or IC_{50} approaches zero is the following:

$$R_{max} = \frac{R_0}{1 - I_{max}} \quad (7)$$

where R_{max} is the maximum response and R_0 is the basal response (100%).

The indirect pharmacodynamic model parameters were estimated by fitting the percent change in mean arterial blood pressure and the plasma cocaine concentration at different time points to eq 6. Nonlinear regression analysis was performed utilizing PCNONLIN.

Statistical Analysis—The pharmacokinetic and pharmacodynamic parameters obtained after cocaine+normal saline and cocaine+alcohol treatments were analyzed using the Statistical Analysis System (SAS Institute Inc., Cary, NC). The balanced crossover design of our investigation is equivalent to the two-way factorial experiment (2 × 2) with repeated measures on the cocaine treatment factor. The plasma and brain ECF cocaine concentration−time profiles, the percent change in dopamine brain ECF concentration−time profiles, and the percent change in mean arterial blood pressure−time profiles after the two treatments were analyzed with two-way analysis of variance with repeated measures on both factors using SAS. Treatments (cocaine+normal saline or cocaine+alcohol) and time were considered as the between subject-variability. Multiple comparison with Bonferroni correction was conducted to examine the difference between

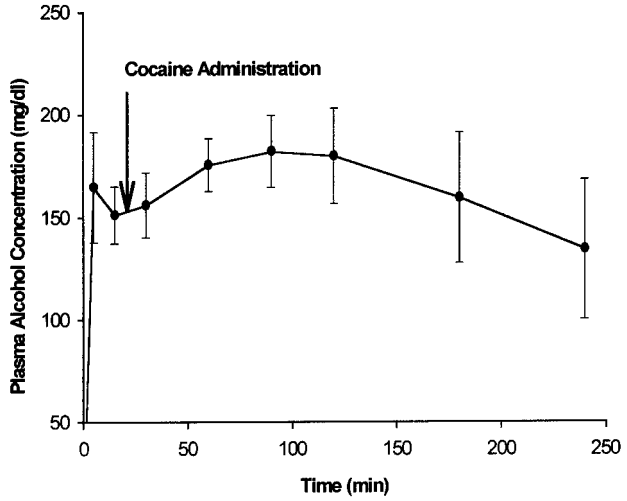

Figure 1—Plasma alcohol concentration–time profile after 5 g/kg of alcohol po ($n = 4$, data are presented as mean ± SE).

treatments at each time point. Differences of $P < 0.05$ were considered significant.

Results

Alcohol was rapidly absorbed after intragastric administration and its plasma concentration declined very slowly because alcohol elimination has been shown to follow zero-order kinetics in rodents.[13] The average plasma alcohol concentrations in the four rats that received 5 g/kg of alcohol intragastrically ranged from 140 to 180 mg/dL (0.14−0.18%) during the 4-h sampling period (Figure 1). This range of alcohol concentrations is similar to that observed in humans after moderate alcohol drinking.

The plasma concentration−time profile of cocaine after a single iv administration declined biexponentially with an average elimination half-life of 28.6 ± 3.5 min. After ip administration, cocaine was absorbed rapidly from the abdominal cavity, reaching the maximum plasma concentration within 10−15 min, and then the concentration declined, with an average elimination half-life of 26.3 ± 3.6 min. Meanwhile, the brain ECF cocaine concentration increased rapidly, reaching its maximum value within 10−20 min after iv administration and within 20−40 min after ip administration, and then declined parallel to the concentration in plasma (Figures 2A and 2B). Cocaethylene was detected in plasma and brain ECF only when cocaine was given with alcohol. Although other cocaine metabolites, including benzoylecgonine and norcocaine, were measured in both plasma and brain ECF in this study, the effect of alcohol on cocaine metabolic profile will be discussed in detail in a separate publication.

Pharmacokinetic studies that involved administered cocaine doses similar to those used in our investigation have shown that cocaine follows linear pharmacokinetics, which validates the first assumption of our proposed model.[13,14,30] The assumption that the brain is part of the peripheral compartment was validated by comparing the estimates for the pharmacokinetic parameters obtained from fitting the plasma concentrations to eq 2 with those obtained from fitting the plasma and brain concentrations simultaneously to eqs 2 and 4. Agreement between the estimated parameters using the two fitting procedures should indicate that the brain is indeed part of the peripheral compartment. The plasma and brain ECF concentrations obtained after iv cocaine administration were used in this validation. The average estimates for k_{12}, k_{21}, k_{10}, and V_c in 12 rats obtained from fitting eq 2 only

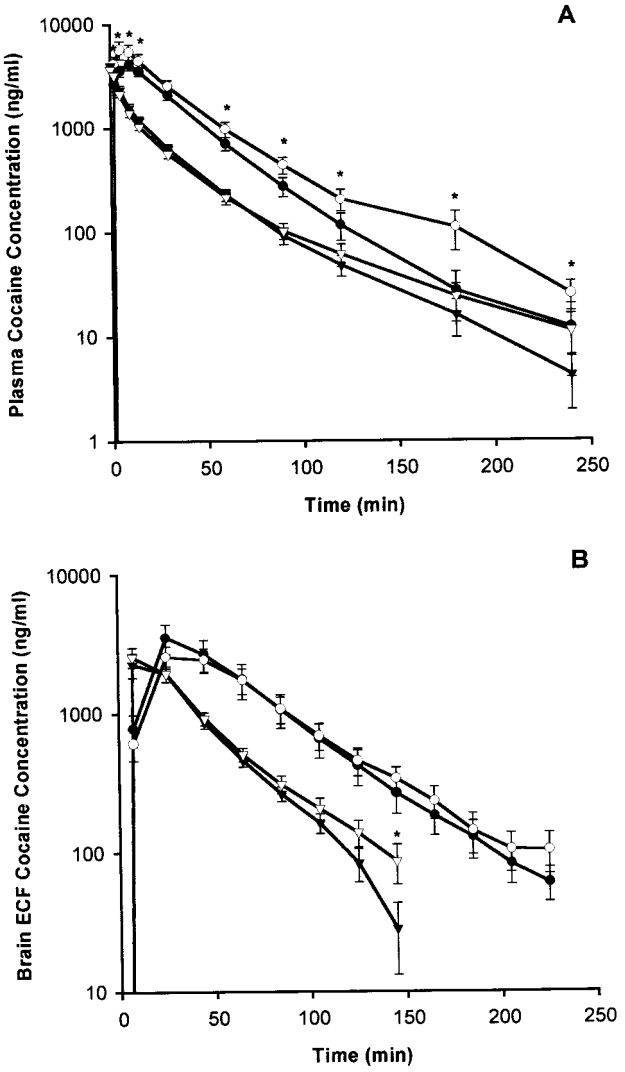

Figure 2—Plasma concentration–time profile of cocaine in plasma (A) and brain (B) after administration of 6.8 mg/kg cocaine iv (▼), 6.8 mg/kg of cocaine iv plus 5 g/kg alcohol po (▽), 30 mg/kg of cocaine ip (●), and 30 mg/kg of cocaine ip plus 5 g/kg alcohol po (○). Each point represents the mean ± SE from 12 rats (iv) and 8 rats (ip). Key: (*) significantly different from the cocaine+ normal saline treatment ($p < 0.05$).

were 0.094 min^{-1}, 0.097 min^{-1}, 0.075 min^{-1}, and 1.63 L/kg, respectively. The average estimates for k_{12}, k_{21}, k_{10}, and V_c in the same 12 rats obtained from fitting eq 2 and 4 simultaneously were 0.082 min^{-1}, 0.093 min^{-1}, 0.073 min^{-1}, and 1.76 L/kg, respectively. Statistical analysis showed that the estimated pharmacokinetic parameters from the two fitting procedures were not different. However, the precision of the parameter estimates was better when the plasma and brain concentrations were used simultaneously. These findings indicate that the brain is a representative part of the peripheral compartment in the proposed pharmacokinetic model and that fitting the plasma and brain data simultaneously improves the precision of the parameter estimation. The fact that the brain is part of the peripheral compartment in the pharmacokinetic model indicates that cocaine distribution to the brain is not instantaneous. As a result, the proposed pharmacokinetic model should adequately describe cocaine absorption, distribution, and elimination after ip administration. A representative example of the simultaneous fitting of the measured plasma and brain ECF cocaine concentrations after ip cocaine administration to eqs 1 and 3 is shown in Figure 3.

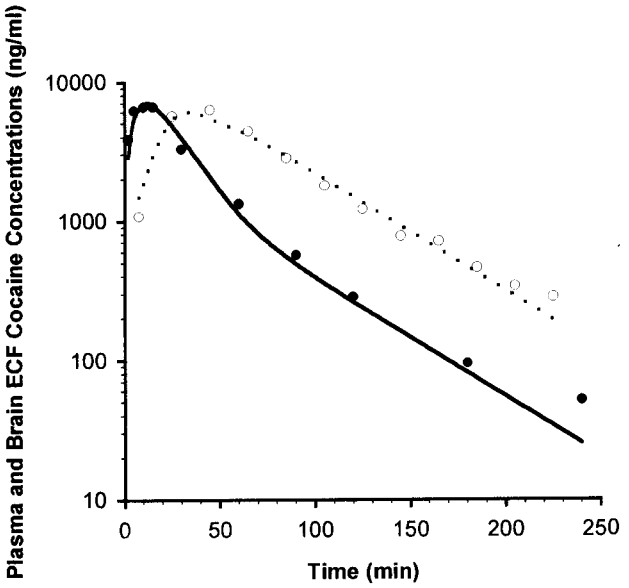

Figure 3—A representative example of the simultaneous fitting of the observed plasma (●) and brain ECF (○) cocaine concentration–time profiles after administration of 30 mg/kg of cocaine ip. The symbols represent the actual experimental data and the line represent the model-fitted curve.

Table 1—Pharmacokinetic Parameters for Cocaine after ip Administration in Wistar Rats (Mean ± SE, $n = 8$)

pharmacokinetic parameter	cocaine treatment: cocaine (ip)[a] + normal saline (po)	cocaine treatment: cocaine (ip)[a] + alcohol (po)
AUC_p (μg-min/mL)	154 ± 12	219 ± 34[c]
AUC_b (μg-min/mL)	224 ± 70	205 ± 47
AUC_b/AUC_p	1.35 ± 0.28	0.98 ± 0.17[c]
TBC (mL/min/kg)	203 ± 16[b]	158 ± 21[b]
t_{max} (min)	10.63 ± 0.63	7.50 ± 0.97[c]
$C_{p\,max}$ (ng/mL)	4100 ± 460	5900 ± 1060[c]
F	0.550 ± 0.044	0.754 ± 0.071[c]
k_a (min^{-1})	0.199 ± 0.045	0.276 ± 0.059
$\alpha_{t1/2}$ (min)	10.9 ± 2.1	10.2 ± 1.7
$\beta_{t1/2}$ (min)	26.3 ± 3.6	40.0 ± 8.1[c]
k_{12} (min^{-1})	0.021 ± 0.014	0.042 ± 0.023
k_{21} (min^{-1})	0.043 ± 0.006	0.036 ± 0.007
k_{10} (min^{-1})	0.056 ± 0.007	0.055 ± 0.011
V_c (L/kg)	2.12 ± 0.25	2.41 ± 0.37
V_{dss} (L/kg)	2.82 ± 0.37	4.11 ± 0.66[c]
$V_{d\beta}$ (L/kg)	4.07 ± 0.56	5.90 ± 0.91[c]
V_t (L/kg)	2.04 ± 0.48	3.50 ± 0.97[c]

[a] Cocaine dose, 30 mg/kg, ip; alcohol dose, 5 g/kg, po. [b] Presented as *TBC/F*. [c] Significantly different from the cocaine+normal saline treatment ($P < 0.05$).

The proposed pharmacokinetic model was used to examine the effect of alcohol coadministration on cocaine pharmacokinetics by comparing the pharmacokinetic parameters estimated after cocaine+normal saline and cocaine+alcohol. The estimated cocaine pharmacokinetic parameters after ip administration with and without alcohol pretreatment are summarized in Table 1. Alcohol pretreatment significantly affected the extent of cocaine absorption after ip cocaine administration. The absolute bioavailability of cocaine significantly increased from 0.550 ± 0.044 after cocaine+normal saline to 0.754 ± 0.071 after cocaine+alcohol. Although cocaine absorption rate, measured as the first-order absorption rate constant, was not significantly faster after alcohol pretreatment, the time to achieve the maximum plasma cocaine concentration was significantly shorter than that after administration of cocaine+normal saline. This result is an indication of a faster rate of cocaine absorption after alcohol pretreatment.

Table 2—Pharmacodynamic Parameters of Cocaine in Wistar Rats (Mean ± SE, $n = 8$)

pharmacodynamic parameter	cocaine treatment: cocaine (ip)[a] + normal saline (po)	cocaine treatment: cocaine (ip)[a] + alcohol (po)
A. neurochemical		
E_{max} (% of baseline)	850 ± 200	1550 ± 640
EC_{50} (ng/mL)	3400 ± 580	2000 ± 650[b]
n	1.23 ± 0.17	2.31 ± 0.29[b]
B. Cardiovascular		
k_{in} (% of baseline/min)	23.8 ± 5.1	36.0 ± 13.0
k_{out} (min^{-1})	0.218 ± 0.047	0.31 ± 0.11
I_{max}	0.304 ± 0.033	0.307 ± 0.035
IC_{50} (ng/mL)	6700 ± 2100	5600 ± 710
R_{max} (% of baseline)	146 ± 6.9	148 ± 8.9
n	3.0 ± 1.5	3.6 ± 1.9

[a] Cocaine dose, 30 mg/kg; alcohol dose, 5 g/kg. [b] Significantly different from the cocaine+normal saline treatment group ($p < 0.05$).

Alcohol pretreatment also resulted in a significant prolongation of cocaine elimination half-life from 26.3 ± 3.6 min after cocaine+normal saline to 40.0 ± 8.1 min after cocaine+alcohol treatment. Similarly, the estimated cocaine elimination half-life after iv administration significantly increased from 28.6 ± 3.5 min after cocaine+normal saline to 37.3 ± 4.7 min after cocaine+alcohol. The estimated apparent *TBC* of cocaine decreased from 203 ± 16 mL/min/kg after cocaine+normal saline to 158 ± 21 mL/min/kg after cocaine+alcohol; however, this difference was not significant. Another interesting finding of this study is that the brain-to-plasma distribution ratio, measured as the ratio of the cocaine AUC in the brain ECF to the cocaine AUC in plasma, decreased significantly from 1.35 ± 0.28 after cocaine+normal saline to 0.98 ± 0.17 after cocaine+alcohol. Also, alcohol pretreatment resulted in a significant increase in the volume of distribution of cocaine.

After cocaine administration, the brain ECF dopamine concentration increased and reached its maximum value within 20−40 min, then it gradually declined to its baseline value at the end of the 4-h experiment period. Dopamine concentration−time profile followed closely the cocaine concentration−time profile in the N ACC. Alcohol coadministration with cocaine caused significantly higher dopamine concentrations in the N ACC, and the rate of decline of dopamine concentration to its baseline level was slower compared with that after cocaine+normal saline (Figure 4A). The relationship between the brain ECF cocaine concentration and the percent change in dopamine concentration was described using the sigmoid-E_{max} pharmacodynamic model. A representative example of the sigmoid-E_{max} model-fitted curve is shown in Figure 4B. The average estimate for E_{max} increased by ≈80% when alcohol was administered with cocaine, however, this difference was not statistically significant. Also, after cocaine+alcohol, the estimated EC_{50} was significantly smaller and the sigmoidicity factor *n* was significantly larger than those after cocaine+normal saline. A summary of the pharmacodynamic parameters is shown in Table 2.

The mean arterial blood pressure increased rapidly after cocaine administration and then declined slowly and did not return to its baseline value at the end of the 4-h experiment (Figure 5A). Because alcohol alone caused, on average, a 5−10% decrease in blood pressure, we partitioned this effect from the combined effect of cocaine+alcohol when these drugs were administered together (Figure 5A). The corrected percent change in mean arterial blood pressure−time profile was used for pharmacodynamic

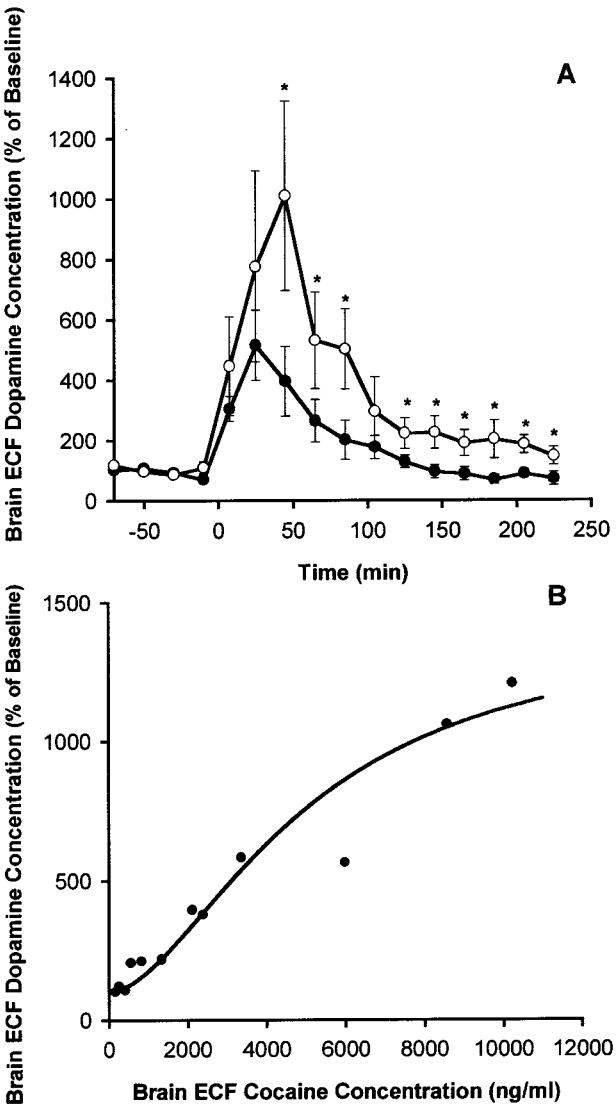

Figure 4—(A) Brain ECF dopamine concentration–time profiles after administration of 30 mg/kg of cocaine ip (●) and 30 mg/kg of cocaine ip plus 5 g/kg of alcohol po (○). Each point represents the mean ± SE from 8 rats. (B) A representative example of the relationship between the percent change in brain dopamine concentration and cocaine brain ECF concentration after ip administration of 30 mg/kg cocaine to the rat. The symbols represent the observed values and the line represents the sigmoid-E_{max} model-fitted curve. Key: (*) significantly different from the cocaine+normal saline treatment ($p < 0.05$).

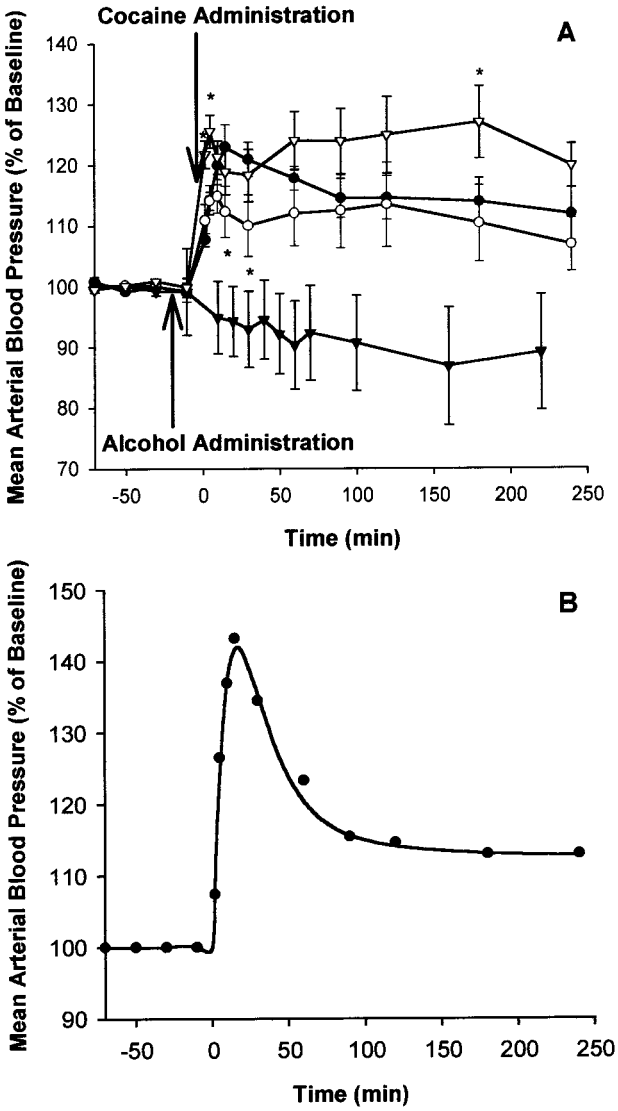

Figure 5—(A) Percent change in mean arterial blood pressure after administration of 30 mg/kg of cocaine ip (●), 30 mg/kg of cocaine ip plus 5 g/kg of alcohol po (○), and 5 g/kg of alcohol po (▼). The mean arterial blood pressure–time profile with cocaine and alcohol coadministration after partitioning the effect of alcohol is also presented (▽). Each point represents the mean ± SE from 8 rats (only 4 rats for alcohol po). (B) A representative example of the percent change in mean arterial blood pressure–time profile after ip administration of 30 mg/kg cocaine to the rat. The solid circles (●) represent the observed values and the line represents the indirect inhibitory pharmacodynamic response model-fitted curve. Key: (*) significantly different from the cocaine+normal saline treatment ($p < 0.05$).

modeling. A representative example of the observed values and the indirect inhibitory pharmacodynamic response model-fitted curve is shown in Figure 5B. Table 2 shows that the estimated parameters for the proposed pharmacodynamic model were not different after cocaine+normal saline and cocaine+alcohol.

Discussion

The pharmacokinetic model used to describe cocaine disposition in our investigation is a two-compartment model with first-order absorption, distribution, and elimination. The proposed two-compartment pharmacokinetic model used in our investigation was adequate in describing cocaine pharmacokinetics as indicated by the good agreement between the experimental data points and the model predicted curves. Examination of the cocaine plasma concentration−time profile and the brain ECF concentration−time profile showed the existence of a short delay in the appearance of cocaine in the brain. This delay represents the distribution of cocaine to the brain, which has been shown to be part of the peripheral compartment in the proposed model. The experimental design in the current investigation involved serial sampling of both plasma and brain ECF that represent the central and the peripheral compartments, respectively. This design allowed characterization of the absorption, distribution, and elimination of cocaine after ip administration, and examination of the effect of alcohol pretreatment on these processes.

Cocaine undergoes significant presystemic elimination, which is the main cause of its incomplete bioavailability after ip administration. Alcohol coadministration significantly increased the systemic bioavailability of cocaine due to the inhibition of cocaine presystemic metabolism. This conclusion is indicated because the maximum concentration of benzoylecgonine, one of the major cocaine metabolites, was lower after cocaine+alcohol administration in the

current study (data not shown) and in pervious investigations.[13,17] Similar inhibition of the presystemic metabolism by alcohol has been reported for drugs that undergo significant first-pass effect.[31,32] This increase in cocaine bioavailability was reflected by the significant increase in its *AUC* and $C_{p\ max}$ after cocaine+alcohol compared with those values after cocaine+normal saline. Although the increase in cocaine first-order absorption rate constant was not significant after cocaine+alcohol, the time to achieve maximum cocaine plasma concentration was significantly shorter. This result indicates that alcohol may enhance the rate of cocaine absorption, which is consistent with what we have reported previously.[13]

Alcohol coadministration significantly increased the volume of distribution of cocaine. The results of our investigation showed that V_c did not change due alcohol administration with cocaine, however both V_{dss} and $V_{d\beta}$ increased significantly. Cocaine has been shown to bind primarily to albumin and alpha-1-acid glycoprotein in serum.[33] Also, cocaine is extensively distributed to tissues such as kidney, brain, liver, heart, and placenta.[34] The significant increase in cocaine volume of distribution due to alcohol coadministration is caused by increased cocaine tissue distribution, which may have resulted from altering the binding of cocaine in plasma and tissues.[35] These results are not contradictory to the decreased brain-to-plasma *AUC* ratio when cocaine was administered with alcohol. Because the microdialysis technique used for the determination of cocaine brain ECF concentration measures only the free (unbound) cocaine concentration in the brain ECF. This free concentration is dependent on the total cocaine concentration and the cocaine bound fraction in the brain, which may be altered due to alcohol coadministration. We have previously reported that alcohol coadministration with cocaine increased the brain ECF concentration of cocaine.[14] However, alcohol was administered by a constant-rate iv infusion in that study, and the plasma alcohol concentration achieved at the end of the 4-h experiment period was on average 365 mg/dL. This result may suggest that more severe alcohol intoxication can lead to higher brain and plasma cocaine concentrations that may augment cocaine pharmacological effects and toxicity.

Alcohol coadministration has been shown to inhibit cocaine metabolism in vivo and in mouse and human liver preparations in vitro.[15−17] The decrease in *TBC* due to alcohol coadministration in our investigation was barely insignificant. However, cocaine elimination half-life was significantly prolonged due to alcohol coadministration. The increase in cocaine volume of distribution in addition to the insignificant reduction of the cocaine TBC contributed to the significantly prolonged cocaine half-life. These findings suggest that the enhanced cocaine systemic bioavailability and the prolonged cocaine elimination half-life are the major factors responsible for the significantly higher and prolonged cocaine plasma concentrations after cocaine+alcohol.

It has been reported previously that drug abusers often experience more intense and longer lasting euphoric effect after simultaneous use of cocaine and alcohol.[9] Controlled human studies have shown that, compared with either cocaine or alcohol administration alone, the combination of cocaine and alcohol seemed to produce more marked subjective effects especially in the feelings related to well-being.[17,18] Results from the current investigation also showed that the increase in dopamine concentration in the N ACC after cocaine+alcohol was significantly higher and its rate of decline to the baseline was slower than that after cocaine+normal saline. Several factors may contribute to the higher dopamine concentration in the N ACC. Cocaethylene, a pharmacologically active metabolite formed only when both cocaine and alcohol are administered, has been shown to possess cocaine-like effects and can increase dopamine concentration after administration in experimental animals.[34−38] Another contributing factor may be related to alcohol administration because alcohol has been shown to increase dopamine brain concentrations after acute or chronic administrations in experimental animals.[39] It is also possible that the increased tissue distribution of cocaine due to alcohol pretreatment may result in higher (bound + free) brain tissue concentration of cocaine, which can lead to higher dopamine concentrations.

The relationship between cocaine brain ECF concentration and the change in N ACC dopamine level can be described by the sigmoid-E_{max} pharmacodynamic model.[22] Our pharmacodynamic analysis showed that the estimated E_{max} was higher after cocaine+alcohol compared with after cocaine+normal saline, however, this difference was not significant. On the other hand, EC_{50} was significantly lower after cocaine+alcohol compared with after cocaine+normal saline. This result means that the same brain ECF cocaine concentration will produce higher neurochemical response after coadministration of alcohol, which is consistent with the more intense and longer lasting euphoric effects experienced by subjects after combined abuse of cocaine and alcohol.[9] This higher response may be caused by the pharmacologically active metabolite cocaethylene, which is formed only when cocaine is administered with alcohol. The contribution of cocaine metabolites to the observed pharmacological activities after administration of cocaine and alcohol will be discussed in detail in a separate publication. Other possibilities for the enhanced neurochemical responses when cocaine is administered with alcohol may include the effect of alcohol and the increased cocaine brain tissue distribution as was discussed previously.

The cardiovascular activities of cocaine are mainly due to its sympathomimetic effects. These include an increase in blood pressure, QRS duration, and heart rate.[1] However, at higher cocaine concentrations, the sodium channel blocking effect of cocaine can slow the cardiac conduction and result in slower heart rate.[5] In this study, the immediate increase in mean arterial blood pressure achieved after cocaine administration is mainly due to the sympathomimetic vasopressor effect of cocaine. Alcohol coadministration did not have any significant effect on the change in the mean arterial blood pressure after cocaine administration. Studies conducted in humans also showed that the change in arterial systolic and diastolic blood pressures after administration of cocaine and alcohol was similar to that of cocaine only.[17] The lack of difference in the vasopressor response after the two treatments despite the higher cocaine plasma concentrations after cocaine+alcohol may be attributed to the effect of alcohol on the cardiovascular system. Alcohol caused an average 5−10% reduction in the mean arterial blood pressure in the rats that received alcohol only. This reduction means that the change in the mean arterial blood pressure in response to cocaine administration was larger after cocaine+alcohol (if the effect of alcohol is partitioned) compared with that after cocaine+normal saline. The higher and the prolonged cocaine plasma concentration in addition to the formation of cocaethylene after cocaine+alcohol treatment may be responsible for the higher response to cocaine after cocaine+alcohol.

Several previous studies reported that the relationship between plasma cocaine concentration and the change in the mean arterial blood pressure showed a counterclockwise hysteresis.[21,22,40] This hysteresis indicates that there is no direct relationship between cocaine plasma concentration and the change in the mean arterial blood pressure.

When direct concentration−effect relationship does not exist, indirect pharmacodynamic response models,[28,29] or the use of an effect compartment may be useful in the pharmacodynamic analysis.[41] The indirect pharmacodynamic response model used to describe the relationship between cocaine plasma concentration and the change in blood pressure adequately characterized this relationship. This adequacy is evident from the agreement between the observed results and the model-fitted curve. Table 2 shows that the maximum inhibitory effect of cocaine on neurotransmitter reuptake was increased by 2.30% when alcohol was administered with cocaine. Also, alcohol coadministration increases the potency of cocaine as reflected by the 20% reduction in IC_{50}. This difference in the blood pressure response to cocaine after the two treatments may have clinical and biological significance despite the fact that the difference is statistically insignificant.[6] This difference may also explain the increased incidence of cardiovascular toxicity after abusing this drug combination.

The cocaine dose used in the ip administration experiment (30 mg/kg) is in the range of doses used frequently in the pharmacological investigations of cocaine. The plasma cocaine concentrations achieved after administration of this dose was higher than the plasma cocaine concentration observed in human studies. However, this dose was well tolerated by the rats and there was no visible evidence of acute adverse effects. The choice of this dose was necessary to precisely determine the pharmacokinetic behavior of cocaine in plasma and brain ECF and to characterize the cocaine concentration−pharmacological effects relationship over a wide range of cocaine concentrations. It will be important to determine if the outcome of the interactions between cocaine and alcohol is dependent on the dose of cocaine and/or alcohol.

In conclusion, alcohol coadministration increases the rate and extent of cocaine absorption after ip administration and increases the tissue distribution of cocaine as manifested by the increase in cocaine volume of distribution. Meanwhile, cocaine elimination is inhibited resulting in longer cocaine half-life. The combined effect of these pharmacokinetic changes produces higher and prolonged cocaine plasma concentrations. The pharmacologically active metabolite cocaethylene is detected in both plasma and brain ECF only when cocaine and alcohol are administered together. Alcohol coadministration also augments the pharmacological activities of cocaine, especially its CNS effects. Because of the existence of good relationships between cocaine brain and plasma concentrations and the neurochemical and cardiovascular responses to cocaine administration, the changes in cocaine pharmacokinetics are, at least partially, responsible for the changes in cocaine effects after administration of this drug combination.

References and Notes

1. Johanson, C. E.; Fischman, M. W. The Pharmacology of Cocaine Related to Its Abuse. *Pharmacol. Rev.* **1989**, *41*, 3−52.
2. Ritz, M. C.; Lamb, R. J.; Goldberg, S. R.; Kuhar M. J. Cocaine Receptors on Dopamine Transporters Are Related to Self-administration of Cocaine. *Science* **1987**, *237*, 1219−1223.
3. Jain, R. K.; Jain, M. K.; Bachenheimer, L. C.; Visner, M. S.; Hamosh, P.; Tracy, C. M.; Gillis R. A. Factors Determining Whether Cocaine Will Potentiate The Cardiac Effects of Neurally Released Norepinephrine. *J. Pharmacol. Exp. Ther.* **1990**, *252*, 147−153.
4. Kiritsy-Roy, J. A.; Halter, J. B.; Gordon, S. M.; Smith, M. J.; Terry, L. C. Role of The Central Nervous System in Hemodynamic and Sympathoadrenal Responses to Cocaine in Rats. *J. Pharmacol. Exp. Ther.* **1990**, *255*, 154−160.
5. Beckman, K. J.; Parker, R. B.; Hariman, R. J.; Gallastegui, J. L.; Javaid, J. I.; Bauman, J. L. Hemodynamic and Electrophysiological Actions of Cocaine: Effects of Sodium Bicarbonate as an Antidote in Dogs. *Circulation* **1991**, *83*, 1799−1807.
6. Foltin, R. W.; Fischman, M. W.; Levin, F. R. Cardiovascular Effects of Cocaine in Humans: Laboratory Studies. *Drug Alcohol Depend.* **1995**, *37*, 193−210.
7. Schindler, C. W.; Tella, S. R.; Erzouki, H. K.; Goldberg, S. R. Pharmacological Mechanisms in Cocaine's Cardiovascular Effects. *Drug Alcohol Depend.* **1995**, *37*, 183−191.
8. Grant, B. F.; Harford, T. C. Concurrent and Simultaneous Use of Alcohol with Sedatives and with Tranquilizers: Results of A National Survey. *J. Subst. Abuse* **1990**, *2*, 1−14.
9. Hearn, W. L.; Flynn, D. D.; Hime, G. W.; Rose, S.; Cofino, J. C.; Mantero-Atienza, E.; Wetli C. V.; Mash, D. C. Cocaethylene: A Unique Cocaine Metabolite Displays High Affinity for The Dopamine Transporter. *J. Neurochem.* **1991**, *56*, 698−701.
10. Rose, S.; Hearn, W. L.; Hime, G. W.; Wetli, C. V.; Ruttenber, A. J.; Mash, D. C. Cocaine and Cocaethylene Concentrations in Human Post Mortem Cerebral Cortex. *Neurosci. Abstr.* **1990**, *16*, 6−14.
11. Perez-Reyes, M.; Jeffcoat, A. R. Ethanol/Cocaine Interaction: Cocaine and Cocaethylene Plasma Concentrations and Their Relationship to Subjective and Cardiovascular Effects. *Life Sci.* **1992**, *51*, 553−563.
12. McCance-Katz, E. F.; Price, L. H.; McDougle, C. J.; Kosten, T. R.; Black, J. E.; Jatlow, P. I. Concurrent Cocaine-Ethanol Ingestion in Humans: Pharmacology, Physiology, Behavior, and The Role of Cocaethylene. *Psychopharmacology* **1993**, *111*, 39−46.
13. Hedaya, M. A.; Pan, W. J. Cocaine and Alcohol Interactions in Naive and Alcohol-Pretreated Rats. *Drug Metab. Dispos.* **1996**, *24*, 807−812.
14. Hedaya, M. A.; Pan, W. J. Effect of Alcohol Coadministration on Cocaine Plasma and Brain Concentrations in the Rat. *Drug Metab. Dispos.* **1997**, *25*, 647−650.
15. Dean, R. A.; Harper, E. T.; Dumaual, N.; Stoeckel, D. A.; Bosron, W. F. Effects of Ethanol on Cocaine Metabolism: Formation of Cocaethylene and Norcocaethylene. *Toxicol. Appl. Pharmacol.* **1992**, *117*, 1−8.
16. Roberts, S. M.; Harbison, R. D.; James, R. C. Inhibition by Ethanol of the Metabolism of Cocaine to Benzoylecgonine and Ecgonine Methyl Ester in Mouse and Human Liver. *Drug Metab. Dispos.* **1993**, *21*, 537−541.
17. Farre, M.; Torre, R.; Llorente, M.; Lamas, X.; Ugena, B.; Segura, J.; Cami, J. Alcohol and Cocaine Interactions in Humans. *J. Pharmacol. Exp. Ther.* **1993**, *266*, 1364−1373.
18. Farre, M.; Torre, R.; Gonzalez, M. L.; Teran, M. T.; Roset P. N.; Menoyo, E.; Cami, J. Cocaine and Alcohol Interactions in Humans: Neuroendocrine Effects and Cocaethylene Metabolism. *J. Pharmacol. Exp. Ther.* **1997**, *283*, 164−176.
19. Hurd, Y. L.; Kehr, J.; Ungerstedt, U. In Vivo Microdialysis as a Technique to Monitor Drug Transport: Correlation of Extracellular Cocaine Levels and Dopamine Overflow in the Rat Brain. *J. Neurochem.* **1988**, *51*, 1314−1316.
20. Nicolaysen, L. C.; Pan, H. T.; Justice Jr., J. B. Extracellular Cocaine and Dopamine Concentrations Are Linearly Related in Rat Striatum. *Brain Res.* **1988**, *456*, 317−323.
21. Hedaya, M. A.; Pan, W. J. Cocaine Pharmacokinetics/Pharmacodynamics in Awake Freely Moving Rats. *Pharm. Res.* **1997**, *14*, 1099−1102.
22. Pan, W. J.; Hedaya, M. A. An Animal Model for Simultaneous Pharmacokinetic/Pharmacodynamic Investigations: Application to Cocaine. *J. Pharmacol. Toxicol. Meth.* **1998**, *39*, 1−8.
23. Lim, R. T., Jr.; Gentry, R. T.; Ito, D.; Yokoyama, H.; Baraona, E.; Lieber, C. S. First-Pass Metabolism of Ethanol is Predominantly Gastric. *Alcohol Clin. Exp. Res.* **1993**, *17*, 1337−1344.
24. Menacherry, S.; Hubert, W.; Justice, J. B., Jr.; In Vivo Calibration of Microdialysis Probes for Exogenous Compounds. *Anal. Chem.* **1992**, *64*, 577−583.
25. Pan, W. J.; Hedaya, M. A. Sensitive and Specific High-Performance Liquid Chromatographic Assay with Ultraviolet Detection for the Determination of Cocaine and Its Metabolites in Rat Plasma. *J. Chromatogr. B Biomed. Sci. Appl.* **1997**, *703*, 129−138.
26. Welling, P. G. *Pharmacokinetics: Processes, Mathematics, and Applications*, 2nd ed.; American Chemical Society: Washington, D. C., 1997; pp 271−296.
27. Gibaldi, M.; Perrier, D. *Pharmacokinetics*, 2nd ed.; Marcel Dekker: New York, 1982; pp 45−111.
28. Sharma, A.; Jusko, W. J. Characterization of Four Basic Models of Indirect Pharmacodynamic Responses. *J. Pharmacokinet. Biopharm.* **1996**, 24, 611−635.
29. Krzyzanski, W.; Jusko, W. J. Mathematical Formalism for the Properties of Four Basic Models of Indirect Pharmacodynamic Responses. *J. Pharmacokinet. Biopharm.* **1997**, *25*, 107−123.

30. Pan, H. T.; Menacherry, S.; Justice, J. B., Jr. Differences in the Pharmacokinetics of Cocaine in Naive and Cocaine-Experienced Rats. *J. Neurochem.* **1991**, *56*, 1299−1306.
31. Dorian, P.; Sellers, E. M.; Reed, K. L.; Warsh, J. J.; Hamilton, C.; Kaplan, H. L.; Fan, T. Amitriptyline and Ethanol: Pharmacokinetic and Pharmacodynamic Interaction. *Eur. J. Clin. Pharmacol.* **1983**, *25*, 325−331.
32. Girre, C.; Hirschhorn, M.; Bertaux, L.; Palombo, S.; Dellatolas, F.; Ngo, R.; Moreno, M.; Fournier, P. E. Enhancement of Propoxyphene Bioavailability by Ethanol: Relation to Psychomotor and Cognitive Function in Healthy Volunteers. *Eur. J. Clin. Pharmacol.* **1991**, *41*, 147−152.
33. Bailey, D. N. Cocaine and Cocaethylene Binding in Human Serum. *Am. J. Clin. Pathol.* **1995**, *104*, 180−186.
34. Bailey, D. N. Cocaine and Cocaethylene Binding to Human Tissues: A Preliminary Study. *Ther. Drug Monit.* **1996**, *18*, 280−283.
35. Sands, B. F.; Knapp, C. M.; Ciraulo, D. A. Interaction of Alcohol with Therapeutic Drugs and Drugs of Abuse. In *The Pharmacology of Alcohol Abuse*; Kranzler, H. R., Ed.; Springer-Verlag: Berlin, 1995; pp 475−512.
36. Jatlow, P.; Elsworth, J. D.; Bradberry, C. W.; Winger, G.; Taylor J. R.; Russell, R.; Roth, R. H. Cocaethylene: A Neuropharmacologically Active Metabolite Associated with Concurrent Cocaine-Ethanol Ingestion. *Life Sci.* **1991**, *48*, 1787−1794.
37. Katz, J. L.; Terry, P.; Witkin, J. M. Comparative Behavioral Pharmacology and Toxicology of Cocaine and Its Ethanol-Derived Metabolite, Cocaine Ethyl-Ester (Cocaethylene). *Life Sci.* **1992**, *50*, 1351−1361.
38. Woodward, J. J.; Mansbach, R.; Carroll, F. I.; Balster, R. L. Cocaethylene Inhibits Dopamine Uptake and Produces Cocaine-Like Actions in Drug Discrimination Studies. *Eur. J. Pharmacol.* **1991**, *197*, 235−236.
39. Pecins-Thompson, M.; Peris, J. Behavioral and Neurochemical Changes Caused by Repeated Ethanol and Cocaine Administration. *Psychopharmacology* **1993**, *110*, 443−450.
40. Evans, S. M.; Cone, E. J.; Henningfield, J. E. Arterial and Venous Cocaine Plasma Concentrations in Humans: Relationship to Route of Administration, Cardiovascular Effects and Subjective Effects. *J. Pharmacol. Exp. Ther.* **1996**, *279*, 1345−1356.
41. Sheiner, L. B.; Stanski, D. R.; Vozeh, S.; Miller, R. D.; Ham, J. Simultaneous Modeling of Pharmacokinetics and Pharmacodynamics: Application to d-Tubocurarine. *Clin. Pharmacol. Ther.* **1979**, *25*, 358−371.

Acknowledgments

This work was supported by a grant from the National Institute of Neurological Disorder and Stroke (NS/OD36399-01).

JS980282P

Cocaine and Alcohol Interactions in the Rat: Contribution of Cocaine Metabolites to the Pharmacological Effects

WEI-JIAN PAN[†,‡] AND MOHSEN A. HEDAYA*[,†]

Contribution from *Pharmacology/Toxicology Graduate Program, Department of Pharmaceutical Sciences, College of Pharmacy, Washington State University, Pullman, Washington 99164-6510.*

Received July 13, 1998. Final revised manuscript received October 22, 1998.
Accepted for publication January 20, 1999.

Abstract □ The pharmacokinetics and pharmacodynamics of cocaine and its three metabolites, benzoylecgonine, norcocaine, and cocaethylene, were investigated in awake, freely moving rats. This work was performed to examine the effect of alcohol coadministration on the metabolic profile of cocaine and to determine the contribution of cocaine metabolites to the pharmacological responses observed after cocaine administration. The plasma and brain extracellular fluid concentration–time profiles were characterized after intravenous (iv) administration of cocaine and the three metabolites in a crossover experimental design. The neurochemical response, measured as the change in dopamine concentration in the nucleus accumbens, and the cardiovascular responses, measured as the change in the mean arterial blood pressure, heart rate, and QRS interval, were monitored simultaneously. Cocaethylene had the highest brain-to-plasma distribution ratio, followed by cocaine, norcocaine, and benzoylecgonine. The estimated total body clearances for cocaine, benzoylecgonine, norcocaine, and cocaethylene were 140 ± 19, 14.7 ± 1.2, 130 ± 19, and 111 ± 16 mL/min/kg, respectively. Alcohol coadministration increased the formation of norcocaine, decreased the formation of benzoylecgonine, and resulted in the formation of the pharmacologically active metabolite cocaethylene. When cocaine was administered with alcohol, 12.9 ± 3.1% to 15.3 ± 2.9% of the cocaine dose was converted to cocaethylene. Benzoylecgonine did not have any central nervous system or cardiovascular activities after iv administration. Compared with cocaine, norcocaine and cocaethylene had more potent and prolonged effects on the neurochemical, heart rate, and QRS interval responses, and were equipotent in increasing the mean arterial blood pressure. These results indicate that changes in the cocaine metabolic profile and the formation of the pharmacologically active metabolite cocaethylene are, at least partially, responsible for the more intense and longer lasting effects reported after using this drug in combination with alcohol.

Introduction

Cocaine metabolism involves both hydrolysis and oxidation pathways. Benzoylecgonine is formed by spontaneous hydrolysis or as a result of enzymatic hydrolysis by serum and liver microsomal carboxylesterases.[1,2] When both cocaine and alcohol are present, the same enzymes are responsible for the formation of cocaethylene via ethyl transesterification.[2] Ecgonine methyl ester is formed via hydrolysis of the cocaine phenyl ester group by serum and liver cholinesterases.[1,2] Formation of norcocaine is catalyzed by either cytochrome P-450 enzymes or flavin adenine dinucleotide (FAD)-containing monooxygenases.[3−5] Further oxidative metabolism of norcocaine by cytochrome P-450 enzymes yields reactive metabolites that are implicated in the norcocaine-mediated hepatotoxicity of cocaine.[5]

Cocaine is a short-term sympathomimetic psychostimulant that produces marked physiological and behavioral effects in both humans and experimental animals. The pharmacological consequences of cocaine consumption include central nervous system (CNS) stimulant effects manifested by euphoria, increase in locomotor activity, and stereotypy.[6] The cardiovascular activities of cocaine are mainly due to its sympathomimetic effects, which include an increase in blood pressure, QRS duration, and heart rate. However, at higher cocaine concentrations, the sodium channel blocking effect of cocaine can slow the cardiac conduction and result in slower heart rate. The mechanism of the effects of cocaine is believed to be the binding of cocaine to the neurotransmitter reuptake sites, leading to accumulation of the neurotransmitters in the synaptic cleft.[7] The locomotor activity and the reinforcement effects of cocaine are believed to be mediated by the increased brain extracellular (ECF) dopamine concentrations.[8] The major toxicities of cocaine abuse include addiction, cardiac arrhythmia, myocardial ischemia, myocarditis, aortic dissection, cerebral vasoconstriction, seizure, and trauma that leads to death.[9] The proposed mechanism for the cardiac arrhythmia and conduction disturbances associated with cocaine overdose is the blockage of cardiac sodium channels by cocaine.[10,11]

The two major metabolites of cocaine, benzoylecgonine and ecgonine methyl ester, do not have any cocaine-like stimulant activity when administered to experimental animals. However continuous intravenous (iv) infusion of benzoylecgonine and ecgonine methyl ester in doses of 0.45 and 1.5 mg/kg/min, respectively, for 30 min to anesthetized rats have been shown to significantly increase the blood pressure without affecting either the heart rate or the QRS duration.[11] Norcocaine can cause a CNS stimulant effect in rats after intracerebroventricular administration and has higher affinity for inactivated cardiac sodium channels than cocaine in guinea pig cardiac myocytes.[10,12] Norcocaine is also hepatotoxic in both animals and humans.[5,13] Cocaethylene is a CNS stimulant and has cardiovascular effects comparable to those of cocaine in rats and rabbits.[11,14]

Alcohol coadministration with cocaine has been shown to alter the metabolic profile of cocaine, leading to the formation of cocaethylene and increasing the fraction of cocaine dose converted to norcocaine.[15] The changes in cocaine pharmacokinetics and metabolic profile has been implicated in the more intense and longer-lasting cocaine pharmacological effects observed after abusing this drug combination.[16] The primary objective of this study was to investigate the pharmacokinetics and pharmacodynamics of cocaine and its three metabolites, benzoylecgonine,

* Corresponding author. Phone: (509)-335-5622. Fax: (509)-335-0162. E-mail: hedaya@mail.wsu.edu. Current address (effective May 15, 1999): College of Pharmacy, Tanta University, Tanta, Egypt.
† Pharmacology/Toxicology Graduate Program.
‡ Current address: Clinical Pharmacokinetics and Toxicokinetics, Abbott Laboratories, Abbott Park, Illinois 60064-6104.

10.1021/js980283h CCC: $18.00
Published on Web 03/12/1999

norcocaine, and cocaethylene, in the rat. This work was important to determine the effect of alcohol coadministration on the metabolic profile of cocaine and to evaluate the contribution of cocaine metabolites to the pharmacological effects of cocaine. In this study, the pharmacokinetics of cocaine and its metabolites were characterized after iv administration of the four compounds to the rat in a crossover experimental design. Meanwhile, the neurochemical response, measured as the change in dopamine concentration in the nucleus accumbens (N ACC), and the cardiovascular responses, measured as changes in mean arterial blood pressure, heart rate, and QRS interval, were monitored simultaneously after each drug administration. This is the first study that examined the pharmacokinetics and pharmacodynamics of cocaine metabolites and compared the effect of cocaine and its metabolites on the pharmacological activities in the same group of experimental animals.

Materials and Methods

Chemicals and Reagents—Benzoylecgonine, norcocaine hydrochloride, and cocaethylene hydrochloride were obtained from Research Biochemicals International (Natick, MA). Cocaine hydrochloride was purchased from Sigma Chemical (St. Louis, MO).

Animal Care and Preparation—Male Wistar rats (250−350 g, Simonsen Laboratories, Gilroy, CA) were used in this investigation. All animal preparation procedures were in accordance with the *Guide for the Care and Use of Laboratory Animals* (National Institutes of Health Publication No. 85-23, revised 1985) and were approved by the institutional animal care and use committee at Washington State University. The details of the animal preparation procedures were described previously.[17,18]

Administration of Cocaine and its Metabolites—Stock solutions of cocaine (10 mg/mL), benzoylecgonine (5 mg/mL), norcocaine (1.5 mg/mL), and cocaethylene (3 mg/mL) in normal saline were prepared and used for the experiment. Drugs were administered iv through the femoral vein cannula at doses of 0.02 mmol/kg (for cocaine) and 0.01 mmol/kg (for benzoylecgonine, norcocaine, and cocaethylene) in a crossover experimental design. The cocaine dose was chosen because it is well below the dose of cocaine that is lethal in 50% of the tested rats (LD_{50}) after iv administration (0.05 mmol/kg, Material Safety Data Sheet, University of Washington, Seattle, 1995). The dose of 0.01 mmol/kg for benzoylecgonine, norcocaine, and cocaethylene was chosen based on the preliminary studies conducted in our laboratory to determine the tolerable doses of these metabolites in the rat. The doses of cocaine and its metabolites used in this experiment should achieve measurable plasma and brain concentrations of these compounds for at least 2 h after drug administration.

Pharmacokinetic and Pharmacodynamic Studies—Nine male Wistar rats were randomly chosen and were prepared following the surgical procedures described previously.[17,18] After the recovery period, the rats were treated with cocaine, benzoylecgonine, norcocaine, and cocaethylene in a crossover experimental design, with a 24-h washout period between treatments.

On the day of the experiment, one of the femoral artery cannulae was connected to a pressure transducer linked to a blood pressure analyzer (Digi-Med model 190, Micro-Med, Louisville, KY) for monitoring the mean arterial blood pressure and heart rate. The three exposed tips of the insulated wires of the 3-electrode EKG cable were connected to the sinus rhythm analyzer (Digi-Med model 200, Micro-Med, Louisville, KY) in Lead-II setting for monitoring the cardiac electrical activity. The signals from the two analyzers were collected, updated, and averaged every 1 min by a system integrator (Digi-Med model 200, Micro-Med, Louisville, KY) and were stored in a computer for subsequent analysis. Meanwhile, the brain microdialysis effluent was collected every 20 min (at 1 μL/min) in HPLC autosampler vials containing 20 μL of dopamine mobile phase. After mixing the vial content, 5 μL was injected immediately into an HPLC equipped with an electrochemical (EC) detector for dopamine analysis. This procedure was repeated until a stable basal dopamine concentration was detected (<10% difference in dopamine concentration in three consecutive samples). Once a stable dopamine baseline was achieved, the rat received iv cocaine (or one of the three metabolites) through the femoral vein cannula. After drug administration, 10 blood samples each of 0.2 mL were collected through the femoral artery cannula at 2, 5, 10, 15, 30, 60, 90, 120, 180, and 240 min in heparin- and sodium fluoride-pretreated vacutainers to avoid cocaine and cocaethylene hydrolysis by plasma carboxylesterases. Plasma samples were obtained by centrifugation and were stored at −20 °C until analysis for cocaine and its metabolites by HPLC with ultraviolet (UV) detection. The effluent of the microdialysis probe was continuously collected every 20 min throughout the experiment in HPLC autosampler vials containing 20 μL of dopamine mobile phase (pH 4). This procedure was to maintain dopamine, cocaine, and its metabolites under acidic condition so as to reduce their spontaneous oxidation and hydrolysis. After mixing the vial content, 5 μL was injected immediately into the HPLC−EC system for dopamine analysis, and the remainder was analyzed for cocaine and its metabolites by HPLC−UV. The mean arterial blood pressure, the heart rate, and the QRS interval were continuously monitored during the entire experiment. Nine rats received all three metabolites in a crossover experimental design, whereas only six of these rats received cocaine in addition to the three metabolites.

The pharmacokinetic parameters for each of the cocaine metabolites estimated in the current study were utilized to investigate the effect of alcohol on cocaine metabolic profile. This was achieved by estimating the fraction of the cocaine dose converted to each of the metabolites when cocaine was administered alone and in combination with alcohol. The results obtained from a previous pharmacokinetic experiment, which involved iv and intraperitoneal (ip) cocaine administrations, were used in this analysis.[18] The pharmacological effects observed after the administration of benzoylecgonine, norcocaine, and cocaethylene were used to determine the contribution of these metabolites to the overall cocaine pharmacological effects when cocaine was administered alone and in combination with alcohol.

Analytical Methods—*Cocaine and Its Metabolites*—Plasma and microdialysis probe effluents were analyzed for cocaine and its metabolites by the method developed in our laboratory.[19] This method is sensitive enough to quantitate cocaine and its metabolites in concentrations as low as 0.075 nmol/mL in 100-μL plasma samples, with coefficient of variation of <10%. The brain ECF concentrations of cocaine and its metabolites were determined by the same method, except that the probe effluent was injected directly into the HPLC−UV system without any pretreatment. The actual concentrations of cocaine and its metabolites in the brain ECF were determined from the probe effluent concentration after correcting for the probe recovery, which was determined from an in vitro calibration experiment.

Dopamine—The microdialysis probe effluent was injected directly into an HPLC system equipped with an EC detector for dopamine analysis immediately after collection. The details of the analytical procedures used for dopamine determination in the microdialysis probe effluent were described previously.[18]

Pharmacokinetic Analysis—A two-compartment pharmacokinetic model with elimination from the central compartment was used to analyze the distribution and elimination of cocaine and its metabolites after iv administration.[18] This model assumes that the distribution and elimination of these compounds follow first-order kinetics, and that the brain is part of the peripheral tissue compartment. The plasma and brain ECF drug concentrations for each rat after administrations of each compound were fitted simultaneously to the equations that describe the plasma and brain ECF concentration−time profiles.[18] The pharmacokinetic model parameters were estimated by nonlinear regression analysis utilizing PCNONLIN (Version 4.0, SCI Software, Lexington, KY). Other pharmacokinetic parameters such as the total body clearance (TBC), the volumes of distribution at steady state and during the elimination phase (Vd_{ss} and Vd_{β}), and the area under the drug plasma (AUC_p) and brain ECF (AUC_b) concentration−time curves were calculated from the estimated parameters.[20]

The fraction of the cocaine iv dose converted to each metabolite (f_m) was calculated using eq 1:[21]

$$f_m = \frac{AUC_{\text{iv cocaine}}(m)TBC(m)}{D_{iv}} \quad (1)$$

where $AUC_{\text{iv cocaine}}(m)$ is the area under the plasma metabolite

concentration−time curve after iv administration of cocaine, D_{iv}, is cocaine dose, and TBC(m) is the total body clearance of the metabolite after iv administration of cocaine, which is assumed to be equal to the estimated metabolite TBC after administration of the preformed metabolite. For ip cocaine administration, the fraction of the cocaine dose converted to the metabolite (f_m) was also calculated using eq 1 after substituting $AUC_{iv\ cocaine}(m)$ and D_{iv} by $AUC_{ip\ cocaine}(m)$ and D_{ip}.

Pharmacodynamic Analysis—*Neurochemical Response*—The linear pharmacodynamic model was used to describe the relationship between the brain ECF drug concentration and the change in the brain ECF dopamine concentration. The mathematical expression that describes the concentration−effect relationship for the model is the following:

$$E = E_o + \text{slope}\ C_b \tag{2}$$

where E is the effect measured as the percent change in dopamine concentration, E_0 is the baseline effect measured as the basal dopamine concentration, Slope is the percent increase in the measured dopamine concentration caused by every unit increase in the brain ECF drug concentration (C_b). In this model, the slope is a measure of the potency of the drug. The pharmacodynamic model parameters were estimated by fitting the percent change in dopamine level and the drug concentration in the brain ECF at different time points to eq 2. The basal dopamine concentration was kept constant (100%) during the linear regression analysis.

Cardiovascular Responses—The relationship between the plasma drug concentration and the change in the mean arterial blood pressure, heart rate, and QRS interval after iv administration of the four compounds was characterized by the mechanism-based pharmacodynamic response model as described previously.[22,23] The mathematical expression that describes the model for the change in the pharmacological response and the drug concentration is the following:

$$\frac{dR}{dt} = k_{in} - k_{out}\left(1 - \frac{I_{max}C_p^{\,n}}{IC_{50}^{\,n} + C_p^{\,n}}\right)R \tag{3}$$

where R is the observed response (for example the percent change in mean arterial blood pressure), k_{in} is the apparent zero-order rate constant for response production, k_{out} is the first-order rate constant for response dissipation, I_{max} is the maximum inhibition of the factor that produces the effect, IC_{50} is the plasma drug concentration that leads to 50% inhibition of the factor that produces the effect, C_p is the plasma drug concentration at the time of the observed response, and n is the sigmoidicity factor. At very high drug concentration or at the maximum inhibition, the maximum response can be estimated as follows[22,23]

$$R_{max} = \frac{R_0}{1 - I_{max}} \tag{4}$$

where R_{max} is the maximum response and R_0 is the basal response (100%).

The pharmacodynamic model parameters were estimated by fitting the percent change in each of the monitored cardiovascular functions and the plasma concentrations of cocaine and its metabolites at different time points to eq 3. Nonlinear regression analysis was performed utilizing PCNONLIN.

Statistical Analysis—Cocaine and its metabolites were administered to the rats in a crossover experimental design. The estimated pharmacodynamic parameters for the neurochemical and the cardiovascular effects of each compound were compared by the paired t test. Also, the effect of alcohol coadministration with cocaine on the pharmacokinetic parameters of each metabolite were compared by the paired t test. Differences of $p < 0.05$ were considered significant.

Results

The plasma and the brain concentration−time profiles of cocaine, benzoylecgonine, norcocaine, and cocaethylene after a single iv bolus administration are illustrated in Figure 1. For these four compounds, the plasma concentration declined biexponentially and the brain ECF concentration increased rapidly and then declined parallel to the concentration in plasma during the elimination phase. The distribution half-lives of cocaine and its metabolites were not significantly different from each other and they ranged from 4.48 ± 0.51 to 6.4 ± 1.1 min. On the other hand, benzoylecgonine had the longest elimination half-life, followed by norcocaine, cocaethylene, and cocaine. Benzoylecgonine had the smallest TBC, followed by cocaethylene, norcocaine, and then cocaine. The brain-to-plasma distribution ratio, measured as AUC_b/AUC_p, was the highest for cocaethylene, followed by cocaine, norcocaine, and benzoylecgonine. A summary of the model-estimated pharmacokinetic parameters of cocaine, benzoylecgonine, norcocaine, and cocaethylene is listed in Table 1.

After iv administration of cocaine, norcocaine, and cocaethylene, the brain ECF dopamine concentration increased and reached its maximum value within 20−40 min, then it gradually declined to its baseline value after 2 h when the brain ECF drug concentration approached zero. The dopamine concentration−time profile followed the drug concentration−time profile in the N ACC. Benzoylecgonine, however, did not cause any significant change in N ACC dopamine concentration (Figure 2A). The relationship between the brain ECF drug concentration and the percent change in dopamine concentration was determined with the linear pharmacodynamic model. Representative examples of the linear model-fitted lines in one rat after iv administration of cocaine, norcocaine, and cocaethylene are shown in Figure 2B. Norcocaine and cocaethylene were more potent than cocaine with respect to the neurochemical effect, and the average model-estimated slopes for these two compounds were 3.7 and 2.5 times larger than that of cocaine (Table 2).

The mean arterial blood pressure increased rapidly after cocaine administration and then declined slowly and did not return to its baseline value when plasma drug concentration approached zero (Figure 3A). The effect of cocaine on the mean arterial blood pressure was higher than that of norcocaine and cocaethylene, however, this difference was due to the higher cocaine dose. The pharmacodynamic analysis showed that there was no difference in the estimated IC_{50} and R_{max} for the effect of cocaine, norcocaine, and cocaethylene on the mean arterial blood pressure, which indicates that there is no differences in the potency and the maximum intrinsic activity of these three compounds (Table 2). Norcocaine and cocaethylene caused larger reductions in heart rate even though their doses were 50% lower than that of cocaine (Figure 3B). The higher potency of these two cocaine metabolites was reflected in their significantly lower IC_{50} compared with that of cocaine (Table 2). For the QRS response, norcocaine and cocaethylene were more potent than cocaine, as indicated by their lower IC_{50} (Table 2). Benzoylecgonine did not have any significant effect on the mean arterial blood pressure, heart rate, or QRS interval (Figures 3A−C). Representative examples of the observed cardiovascular response values and the indirect pharmacodynamic response model-fitted curves for one rat after administration of cocaine and its metabolites in a crossover experimental design are shown in Figures 4A−C. All estimated parameters of cocaine and its metabolites for the pharmacodynamic model are summarized in Table 2.

In one of our previous cocaine pharmacokinetic studies, we administered cocaine iv and ip to rats with and without alcohol.[18] The plasma and brain ECF concentration−time profiles of cocaine and its metabolites after ip cocaine with and without the coadministration of alcohol are shown in Figure 5. After ip cocaine alone, both benzoylecgonine and norcocaine were detected in the plasma and the brain (Figures 5A & B). In the presence of alcohol, the pharma-

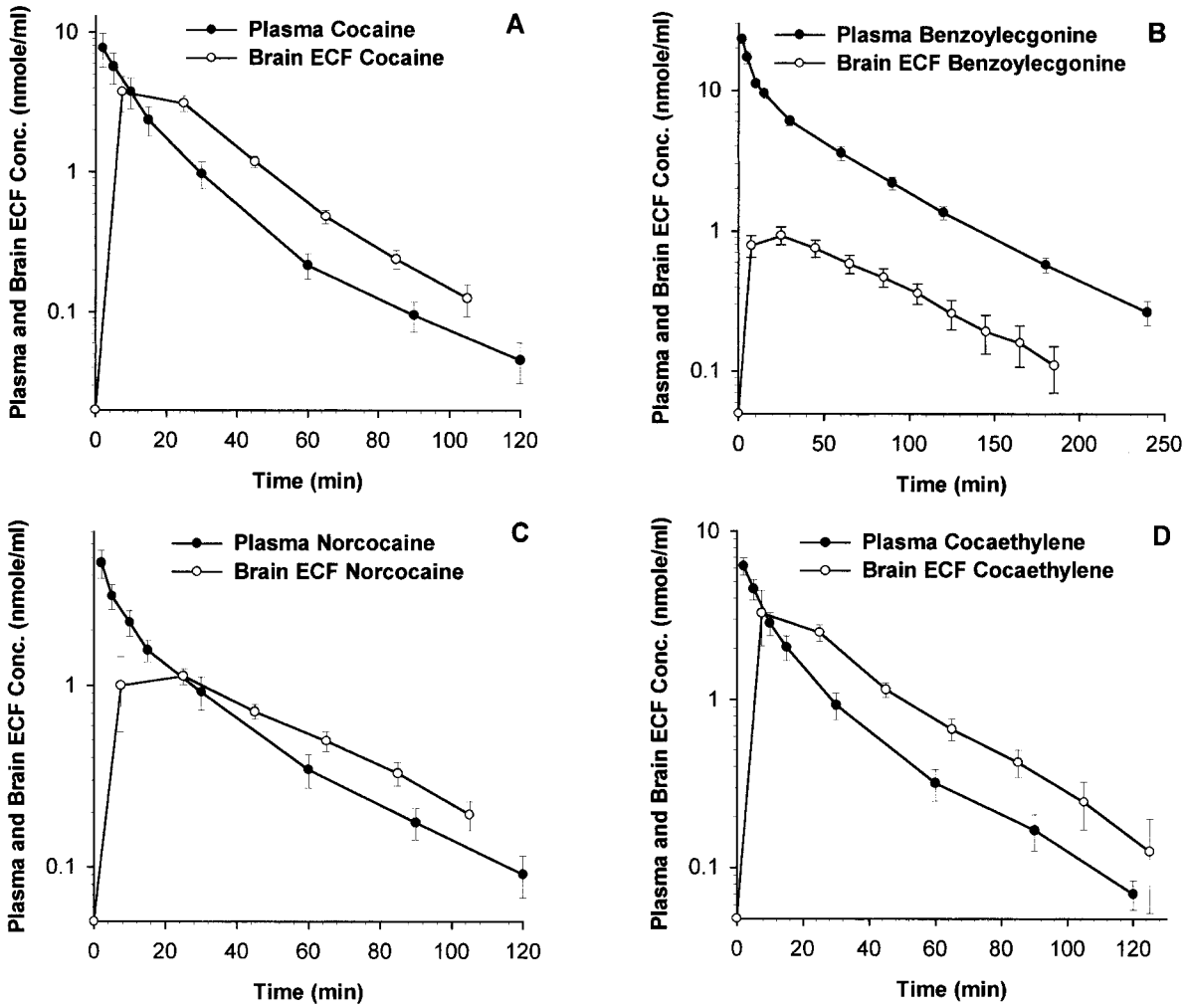

Figure 1—Plasma (●) and brain ECF (○) concentration–time profiles of cocaine and its metabolites after administration of 0.02 mmol/kg cocaine iv (A), 0.01 mmol/kg benzoylecgonine iv (B), 0.01 mmol/kg norcocaine iv (C), and 0.01 mmol/kg cocaethylene iv (D) to the rat. (Data presented as mean ± SE; $n = 6$ for cocaine and $n = 9$ for the metabolites.)

Table 1—Pharmacokinetic Parameters of Cocaine, Benzoylecgonine, Norcocaine, and Cocaethylene after iv Administration of 0.02 mmol/kg of cocaine and 0.01 mmol/kg of Each of the Cocaine Metabolites to the Rat[a]

	administered compound			
pharmacokinetic parameter	cocaine	benzoylecgonine	norcocaine	cocaethylene
AUC_p (nmol·min/mL)	157 ± 19	720 ± 55	93 ± 15	108 ± 16
AUC_b (nmol·min/mL)	170 ± 23	94 ± 13	78.5 ± 9.6	149 ± 26
AUC_b/AUC_p	1.18 ± 0.26	0.147 ± 0.032	0.97 ± 0.14	1.44 ± 0.17
TBC (mL/min/kg)	140 ± 19	14.7 ± 1.2	130 ± 19	111 ± 16
$\alpha_{t1/2}$ (min)	6.2 ± 1.3	4.48 ± 0.51	6.4 ± 1.1	5.35 ± 0.97
$\beta_{t1/2}$ (min)	15.8 ± 1.5	46.7 ± 2.9	38.3 ± 5.1	25.0 ± 3.1
k_{12} (min^{-1})	0.025 ± 0.014	0.081 ± 0.013	0.072 ± 0.033	0.097 ± 0.052
k_{21} (min^{-1})	0.085 ± 0.018	0.070 ± 0.010	0.087 ± 0.047	0.093 ± 0.033
k_{10} (min^{-1})	0.076 ± 0.007	0.041 ± 0.002	0.059 ± 0.004	0.080 ± 0.006
V_c (L/kg)	1.96 ± 0.34	0.364 ± 0.033	2.22 ± 0.30	1.43 ± 0.20
Vd_{ss} (L/kg)	2.48 ± 0.60	0.808 ± 0.065	4.06 ± 0.52	2.34 ± 0.31
Vd_β (L/kg)	3.28 ± 0.64	1.00 ± 0.12	6.54 ± 0.84	4.14 ± 0.88

[a] Values are presented as mean ± SE; $n = 6$ for cocaine; $n = 9$ for metabolites.

cologically active metabolite cocaethylene was formed and it was detected in both plasma and the brain (Figures 5C & D). The effect of alcohol coadministration on the metabolic profile of cocaine was determined utilizing the pharmacokinetic parameters of cocaine metabolites determined in the current study, and the results are summarized in Table 3.

Compared with iv cocaine alone, alcohol coadministration caused significant inhibition of cocaine metabolism to benzoylecgonine. This effect is shown in the significant reduction in benzoylecgonine AUC_p and $C_{p\ max}$. Also, the fraction of the administered cocaine dose converted to benzoylecgonine was significantly reduced from 0.432 ± 0.047 to 0.237 ± 0.038, and the formation clearance of this cocaine metabolite was decreased from 47.2 ± 4.0 to 27.2 ± 4.0 mL/min/kg. Alcohol coadministration also led to a slight increase in the formation of norcocaine, and cocaethylene was formed only when alcohol was administered

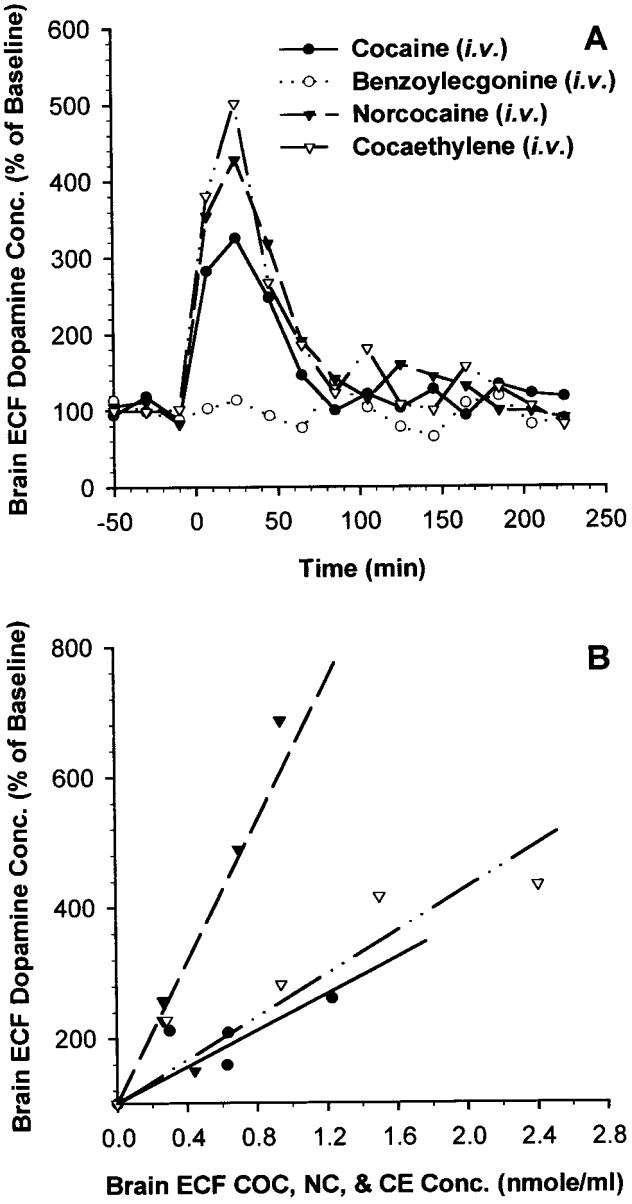

Figure 2—(A) The brain ECF dopamine concentration–time profiles after administration of 0.02 mmol/kg cocaine iv (●), 0.01 mmol/kg benzoylecgonine iv (○), 0.01 mmol/kg norcocaine iv (▼), and 0.01 mmol/kg cocaethylene iv (▽) to the rat. Each point represents the mean from six rats. (B) Representative examples of the relationship between the percent change in the brain ECF dopamine concentrations and cocaine (●), norcocaine (▼), and cocaethylene (▽) brain ECF concentrations after iv administration of these compounds in one rat in a crossover experimental design. The symbols represent the observed values and the lines represent the linear model-fitted curves.

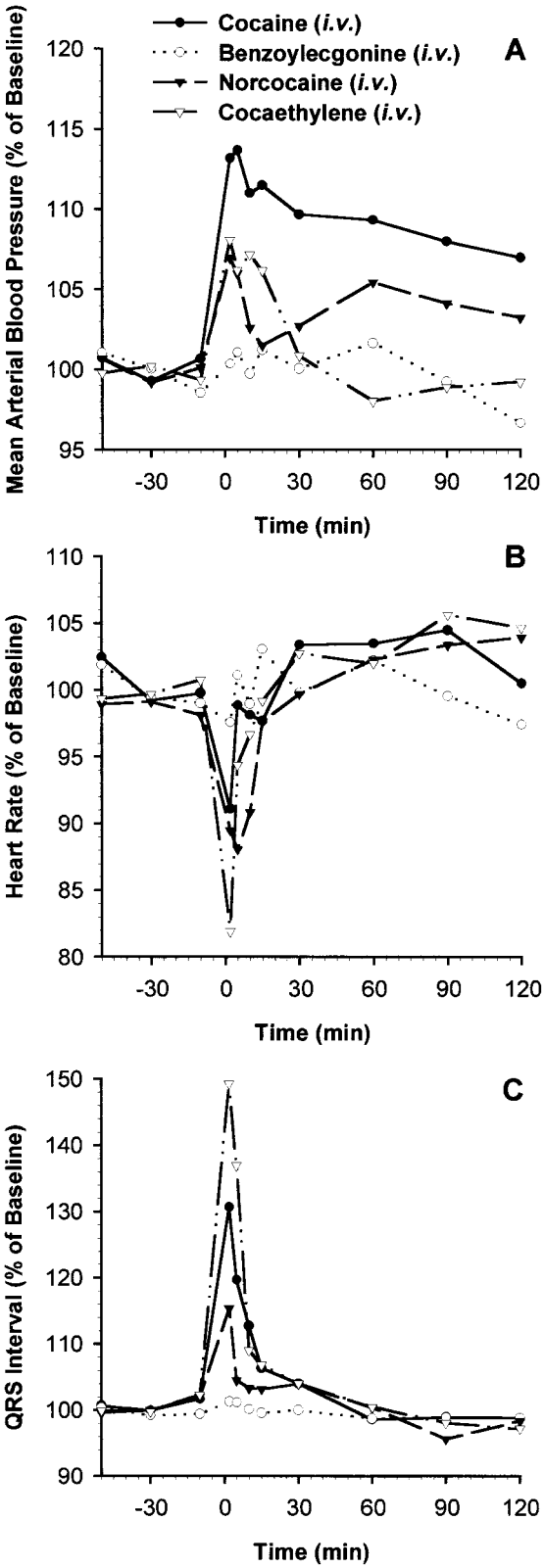

Figure 3—Percent change in the mean arterial blood pressure (A), heart rate (B), and QRS interval (C) after administration of 0.02 mmol/kg cocaine iv (●), 0.01 mmol/kg benzoylecgonine iv (○), 0.01 mmol/kg norcocaine iv (▼), and 0.01 mmol/kg cocaethylene iv (▽) to the rat. Each point represents the mean from six rats.

with cocaine. The fraction of cocaine iv dose converted to cocaethylene was 0.129 ± 0.031. When cocaine was given ip, alcohol coadministration caused significant reduction in benzoylecgonine $C_{p\ max}$. However, no changes were found in the fraction of the cocaine dose converted to benzoylecgonine. There was about a 40% increase in the formation of norcocaine, and 15.3 ± 2.9% of the cocaine dose was metabolized to cocaethylene.

Discussion

In the present study, we investigated the pharmacokinetics and pharmacodynamics of cocaine and its three metabolites simultaneously after iv bolus administration of these compounds to awake, freely moving rats. Our results showed that the highly hydrophilic cocaine metabolite benzoylecgonine had the highest AUC_p, whereas its AUC_b was the lowest. The brain-to-plasma distribution ratio of benzoylecgonine was the lowest among the four

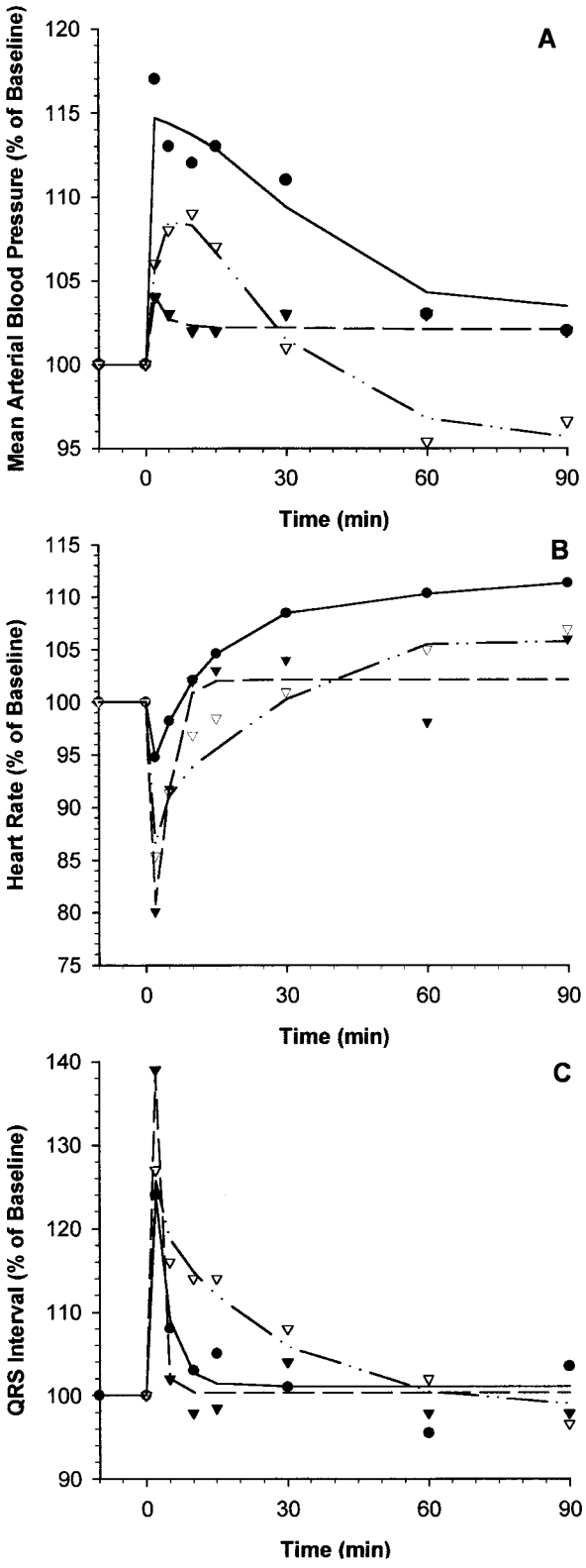

Figure 4—Representative examples of the percent change in the time profiles of the mean arterial blood pressure (A), heart rate (B), and QRS interval (C) after administration of 0.02 mmol/kg cocaine iv (●), 0.01 mmol/kg norcocaine iv (▼), and 0.01 mmol/kg cocaethylene iv (▽) to one rat in a crossover experimental design. The symbols represent the observed values and the lines represent the pharmacodynamic model-fitted curves.

compounds under investigation. Benzoylecgonine iv administration did not have any effect on dopamine levels in the N ACC or on the monitored cardiovascular functions. The absence of the CNS effect after an iv bolus dose of

Table 2—Pharmacodynamic Parameters after iv Administration of Cocaine (0.02 mmol/kg) and Its Metabolites (0.01 mmol/kg) to the Rat (Mean ± SE)

pharmacodynamic parameter	compound		
	cocaine	norcocaine	cocaethylene
	A. neurochemical		
Slope (%/nmol/mL)	85 ± 18	314 ± 97[b]	211 ± 73
	B. cardiovascular		
	mean blood pressure		
k_{out} (min^{-1})	1.38 ± 0.86	1.95 ± 0.93	1.72 ± 0.80
I_{max}	0.277 ± 0.087	0.231 ± 0.051	0.239 ± 0.094
IC_{50} (nmol/mL)	8.4 ± 3.1	7.2 ± 3.4	4.7 ± 2.4
R_{max} (% of baseline)	152 ± 22	133 ± 8.6	146 ± 24
	heart rate		
k_{out} (min^{-1})	3.02 ± 0.77	1.92 ± 0.75	3.44 ± 0.36
I_{max}[a]	0.359 ± 0.072	0.273 ± 0.075	0.45 ± 0.11[c]
IC_{50} (nmol/mL)	12.5 ± 4.7	1.83 ± 0.47[b]	6.6 ± 1.4[c]
R_{max} (% of baseline)[a]	165 ± 16	147 ± 18	248 ± 69[c]
	QRS interval		
k_{out} (min^{-1})	5.31 ± 0.45	0.94 ± 0.20[b]	2.91 ± 0.98[c]
I_{max}	0.63 ± 0.18	0.26 ± 0.14	0.47 ± 0.13
IC_{50} (nmol/mL)	14.4 ± 5.0	3.4 ± 1.5	5.8 ± 1.7
R_{max} (% of baseline)	490 ± 260	149 ± 35	227 ± 74

[a] Presented as absolute values. [b] Significantly different from the cocaine treatment ($p < 0.05$, paired t test). [c] Significantly different from the norcocaine treatment ($p < 0.05$, paired t test).

benzoylecgonine may be explained by the low brain distribution of this hydrophilic metabolite because intracerebroventricular administration of benzoylecgonine has been shown to produce stimulant effect in awake Sprague-Dawley rats.[12] A previous investigation has shown that benzoylecgonine can increase the blood pressure after iv infusion of 0.45 mg/kg/min for 30 min to anesthetized rats; however, the dose of benzoylecgonine used in that investigation was much higher than the dose used in our experiment.[11]

Cocaethylene has the highest brain-to-plasma distribution ratio, followed by cocaine, norcocaine, and then benzoylecgonine, which is the same rank order of the lipophilicity of these four compounds. This result indicates that the brain distribution of these compounds is probably via passive diffusion across the blood–brain barrier. Norcocaine and cocaethylene administration resulted in higher dopamine concentration in the N ACC compared with after cocaine administration. The brain ECF concentration–neurochemical effect relationships for cocaine, norcocaine, and cocaethylene after iv administration were best described by the linear pharmacodynamic model, even though we used the sigmoid-E_{max} pharmacodynamic model to describe the brain ECF concentration–neurochemical effect relationship after ip cocaine administration.[17] The reason for this discrepancy is that the iv dose used in the current investigation was much lower than the ip dose that resulted in lower brain ECF concentration of cocaine and its metabolites. It was not possible to characterize the sigmoid-E_{max} relationship because all the observed brain ECF concentrations were in the lower linear portion of this relationship. The linear pharmacodynamic model showed that norcocaine and cocaethylene were more potent than cocaine in dopamine reuptake inhibition. This result was consistent with the higher dopamine concentrations observed after norcocaine and cocaethylene administration despite the fact that cocaine dose was twice that of norcocaine and cocaethylene. This finding indicates that after cocaine administration with alcohol, despite the lower concentrations of norcocaine and cocaethylene, these metabolites may be significantly contributing to the observed neurochemical response to cocaine administration due to

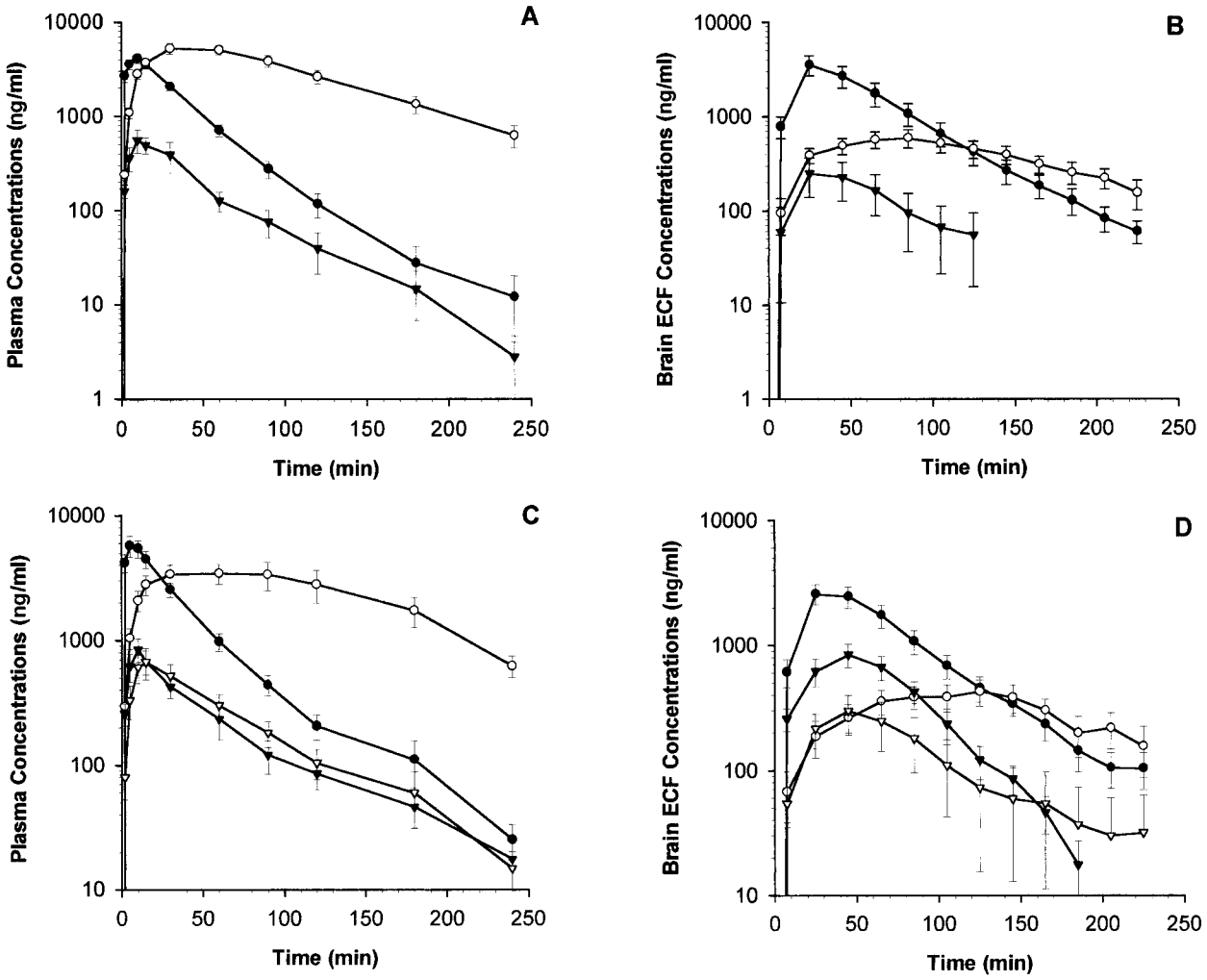

Figure 5—Plasma (A, C) and the brain (B, D) ECF concentration–time profiles of cocaine (●), benzoylecgonine (○), norcocaine (▼), and cocaethylene (▽) after administration of 0.088 mmol/kg cocaine ip (A, B) and 0.088 mmol/kg cocaine ip plus 5 g/kg alcohol po (C, D) to the rat in a balanced crossover experimental design. (Data presented as mean ± SE, $n = 8$.)

Table 3—Cocaine Metabolite Pharmacokinetics after Cocaine iv and ip Administrations Alone or In Combination with Alcohol (Mean ± SE)

pharmacokinetic parameter	cocaine (iv) + NS (po)[a]	cocaine (iv) + alcohol (po)[a]	cocaine (ip) + NS (po)[b]	cocaine (ip) + alcohol (po)[b]
		cocaine		
AUC_p (nmol·min/mL)	187 ± 17	174 ± 114	453 ± 35	644 ± 100[c]
$C_{p\,max}$ (nmol/mL)	10.9 ± 1.1	11.0 ± 0.7	12.1 ± 1.4	17.4 ± 3.1[c]
TBC (mL/min/kg)	118 ± 12	125 ± 12	112 ± 4	106 ± 5
		benzoylecgonine		
AUC_p (nmol·min/mL)	587 ± 64	420 ± 130[c]	2000 ± 210	2020 ± 430
$C_{p\,max}$ (nmol/mL)	4.33 ± 0.50	1.59 ± 0.27[c]	15.0 ± 1.8	10.8 ± 2.3[c]
f_m	0.432 ± 0.047	0.237 ± 0.038[c]	0.326 ± 0.036	0.336 ± 0.071
f_m TBC (mL/min/kg)	47.2 ± 4.0	27.2 ± 4.0[c]	34.9 ± 3.8	33.3 ± 4.3
		norcocaine		
AUC_p (nmol·min/mL)	2.3 ± 1.2	3.0 ± 1.1	79 ± 19	110 ± 23
$C_{p\,max}$ (nmol/mL)	0.155 ± 0.029	0.198 ± 0.044	1.64 ± 0.43	2.41 ± 0.51[c]
f_m	0.015 ± 0.008	0.017 ± 0.007	0.116 ± 0.028	0.162 ± 0.033
f_m *TBC* (mL/min/kg)	1.46 ± 0.74	2.01 ± 0.86	12.4 ± 3.0	16.3 ± 2.7
		cocaethylene		
AUC_p (nmol·min/mL)		23.2 ± 5.6		122 ± 23
$C_{p\,max}$ (nmol/mL)		0.259 ± 0.043		1.78 ± 0.48
f_m		0.129 ± 0.031		0.153 ± 0.029
f_m TBC (mL/min/kg)		16.2 ± 4.4		15.3 ± 1.9

[a] Balanced crossover experiment, $n = 12$; cocaine dose, 0.02 mmol/kg; alcohol dose, 5 g/kg. [b] Balanced crossover experiment, $n = 8$; cocaine dose, 0.088 mmol/kg; alcohol dose, 5 g/kg. [c] Significantly different from cocaine + normal saline ($p < 0.05$, paired t test).

their higher potency. Also, factors that can alter the formation of these two metabolites, such as genetic polymorphism and drug-drug interactions, may change the overall neurochemical response to cocaine administration.

Analysis of the cardiovascular effects observed after administration of cocaine and its metabolites showed that cocaine, norcocaine, and cocaethylene have similar potency and maximum intrinsic activity on the mean arterial blood pressure. Both norcocaine and cocaethylene were more potent than cocaine in reducing the heart rate and prolonging the QRS interval. This result is consistent with the previous experimental results obtained in vitro using cardiac myocytes.[10,24] Meanwhile, k_{out} was the smallest for norcocaine, so that the dissipation of the heart rate response was the slowest when rats were treated with norcocaine. Norcocaine and cocaethylene also had smaller k_{out} values compared with cocaine, which means slower dissipation of the QRS response after administration of these two compounds. These pharmacodynamic results were consistent with the pharmacokinetic findings because norcocaine and cocaethylene have longer elimination half-lives and lower TBCs when compared with cocaine. The pharmacodynamic model-predicted higher potency of cocaethylene and norcocaine with respect to their effect on heart rate is consistent with the higher responses observed after administration of these two metabolites. These findings indicate that norcocaine and cocaethylene should be contributing to the cardiovascular responses to cocaine administration because of their higher potency.

The fraction of the cocaine iv dose converted to benzoylecgonine was reduced by >50% when iv cocaine was administered with alcohol. However, the formation of benzoylecgonine was not reduced after ip administration of cocaine with alcohol. The difference in the fraction of the iv and the ip doses of cocaine metabolized to benzoylecgonine (0.43 for iv versus 0.33 for ip) indicates that less benzoylecgonine is formed during the presystemic metabolism of cocaine compared with the systemic metabolism of cocaine. Coadministration of alcohol results in increased cocaine bioavailability after ip administration, which will lead to the formation of more benzoylecgonine and may mask the effect of alcohol coadministration on benzoylecgonine formation. This result may explain the small difference in the fraction of cocaine dose metabolized to benzoylecgonine after cocaine ip alone and after cocaine ip and alcohol.

Norcocaine formation after ip cocaine administration was ≈8 times more than that after iv cocaine administration. This difference may be caused by more norcocaine formation during the presystemic metabolism when cocaine was given ip. The reason for this result is that the formation of norcocaine is catalyzed by either cytochrome P-450 enzymes (CYP2B and CYP3A subfamilies) or FAD-containing monooxygenase.[3] These enzymes, especially the CYP3A subfamily, have different expressions and activities in the gut and liver isoforms.[25] Norcocaine formation increased by 10 and 40% due to alcohol coadministration with iv and ip cocaine administration, respectively. Our pharmacodynamic analysis showed that norcocaine is more potent than cocaine in its neurochemical, heart rate, and QRS interval effects. Norcocaine AUC in plasma was ≈1−2% as large as cocaine AUC after iv cocaine administration and was ≈17% as large as cocaine AUC after ip cocaine administration. Because of the higher potency of norcocaine this metabolite significantly contributes to the observed neurochamical and cardiovascular effects after ip cocaine administration because 11−16% of cocaine dose is converted to norcocaine. However, after iv cocaine administration, which is the route of administration relevent to human cocaine abuse, the contribution of norcocaine to the neurochamical and cardiovascular effects may not be significant because only 1−2% of the administered iv cocaine dose is converted to norcocaine.

The hepatotoxicity of norcocaine is believed to be the result of its further oxidative metabolism by CYP2Bs, either through redox cycling between *N*-hydroxynorcocaine and norcocaine nitroxide or the production of an unidentified reactive metabolite.[5,26] The hepatic toxicity of norcocaine may be synergized by alcohol because both of these drugs act on the central lobular area of the liver.[27] In addition to potentiation of cocaine-induced hepatocellular toxicity through CYP2E1-dependent oxidative stress, alcohol could also enhance cocaine bioactivation through induction of other P-450 enzymes, such as the CYP2B and 3A subfamilies.[26,28] In our investigation, the increase in norcocaine formation due to a single dose of alcohol was ≈10% after iv cocaine administration and 40% after ip cocaine administration. This difference may indicate that the increase in cocaine hepatotoxicity when given in combination with alcohol is not exclusively dependent on the increased norcocaine formation especially after iv cocaine administration.

Approximately 13 to 15% of the cocaine doses were converted to cocaethylene when cocaine was administered iv or ip in combination with alcohol. Presystemic and systemic metabolism led to similar fractional conversion of cocaine to cocaethylene. Our pharmacodynamic analysis showed that cocaethylene is ≈2−3 times more potent than cocaine in its neurochemical, heart rate, and QRS interval effects. The pharmacokinetic analysis showed that cocaethylene AUC in plasma and brain were ≈15−20% as large as those of cocaine after administration of cocaine and alcohol. Because of its higher potency, cocaethylene should be significantly contributing to the pharmacological effects observed in response to combined cocaine and alcohol administration even if cocaethylene concentration in brain and plasma is much lower than that of cocaine.

In conclusion, benzoylecgonine does not possess any significant CNS or cardiovascular activities after iv administration with the dose used in our investigation. Norcocaine and cocaethylene are more potent than cocaine with respect to their neurochemical, heart rate, and QRS interval effects. However, cocaine, norcocaine, and cocaethylene are equipotent with respect to their effect on the mean arterial blood pressure. Alcohol coadministration causes the formation of the pharmacologically active metabolite cocaethylene, reduces the formation of the inactive metabolite benzoylecgonine, and increases the formation of norcocaine. Because of its higher potency, cocaethylene should have significant contribution to the observed pharmacological effects after administration of cocaine and alcohol. Also, modification of the cocaine metabolic profile, such as that due to drug−drug interactions, can lead to significant modification of the observed cocaine pharmacological effects. Because our investigation has been performed in rodents and differences in cocaine pharmacokinetics and pharmacodynamics in different species have been reported, the clinical significance of these finding warrants further investigation.

References and Notes

1. Stewart, D. J.; Inaba, T.; Lucassen, M.; Kalow, W. Cocaine Metabolism: Cocaine and Norcocaine Hydrolysis by Liver and Serum Esterases. *Clin. Pharmacol. Ther.* **1979**, *25*, 464−468.
2. Dean, R. A.; Christian, C. D.; Sample, R. H.; Bosron, W. F. Human Liver Cocaine Esterases: Ethanol-Mediated Formation of Ethylcocaine. *FASEB J.* **1991**, *5*, 2735−2739.
3. Kloss, M. W.; Rosen, G. M.; Rauckman, E. J. N-Demethylation of Cocaine to Norcocaine. Evidence for Participation by Cytochrome P-450 and FAD-Containing Monooxygenase. *Mol. Pharmacol.* **1983**, *23*, 482−485.
4. Roberts, S. M.; Harbison, R. D.; James, R. C. Human Microsomal N-oxidative Metabolism of Cocaine. *Drug Metab. Dispos.* **1991**, *19*, 1046−1051.

5. Poet, T. S.; McQueen, C. A.; Halpert, J. R. Participation of Cytochromes P4502B and P4503A in Cocaine Toxicity in Rat Hepatocytes. *Drug Metab. Dispos.* **1996**, *24*, 74−80.
6. Johanson, C. E.; Fischman, M. W. The Pharmacology of Cocaine Related to Its Abuse. *Pharmacol. Rev.* **1989**, *41*, 3−52.
7. Ritz, M. C.; Lamb, R. J.; Goldberg, S. R.; Kuhar, M. J. Cocaine Receptors on Dopamine Transporters Are Related to Self-administration of Cocaine. *Science* **1987**, *237*, 1219−1223.
8. Roberts, D. C.; Koob, G. F.; Klonoff, P.; Fibiger, H. C. Extinction and Recovery of Cocaine Self-Administration Following 6-Hydroxydopamine Lesions of the Nucleus Accumbens. *Pharmacol. Biochem. Behav.* **1980**, *12*, 781−787.
9. Marzuk, P. M.; Tardiff, K.; Leon, A. C.; Hirsch, C. S.; Stajic, M.; Portera, L.; Hartwell, N.; Iqbal, M. I. Fatal Injuries after Cocaine Use as a Leading Cause of Death Among Young Adults in New York City. *N. Engl. J. Med.* **1995**, *332*, 1753−1757.
10. Crumb, W. J., Jr.; Clarkson, C. W. Characterization of the Sodium Channel Blocking Properties of the Major Metabolites of Cocaine in Single Cardiac Myocytes. *J. Pharmacol. Exp. Ther.* **1992**, *261*, 910−917.
11. Erzouki, H. K.; Baum, I.; Goldberg, S. R.; Schindler, C. W. Comparison of the Effects of Cocaine and Its Metabolites on Cardiovascular Function in Anesthetized Rats. *J. Cardiovasc. Pharmacol.* **1993**, *22*, 557−563.
12. Schuelke, G. S.; Konkol, R. J.; Terry, L. C.; Madden, J. A. Effect of Cocaine Metabolites on Behavior: Possible Neuroendocrine Mechanisms. *Brain Res. Bull.* **1996**, *39*, 43−48.
13. Shuster, L.; Garhart, C. A.; Powers, J.; Grunfeld, Y.; Kanel, G. Hepatotoxicity of Cocaine. *NIDA Res. Monogr.* **1988**, *88*, 250−275.
14. Jatlow, P.; Elsworth, J. D.; Bradberry, C. W.; Winger, G.; Taylor, J. R.; Russell, R.; Roth, R. H. Cocaethylene: A Neuropharmacologically Active Metabolite Associated with Concurrent Cocaine-Ethanol Ingestion. *Life Sci.* **1991**, *48*, 1787−1794.
15. Farre, M.; Torre, R.; Llorente, M.; Lamas, X.; Ugena, B.; Segura, J.; Cami, J. Alcohol and Cocaine Interactions in Humans. *J. Pharmacol. Exp. Ther.* **1993**, *266*, 1364−1373.
16. Hearn, W. L.; Flynn, D. D.; Hime, G. W.; Rose, S.; Cofino, J. C.; Mantero-Atienza, E.; Wetli, C. V.; Mash, D. C. Cocaethylene: A Unique Cocaine Metabolite Displays High Affinity for the Dopamine Transporter. *J. Neurochem.* **1991**, *56*, 698−701.
17. Pan, W. J.; Hedaya, M. A. An Animal Model for Simultaneous Pharmacokinetic/Pharmacodynamic Investigations: Application to Cocaine. *J. Pharmacol. Toxicol. Meth.* **1998**, *39*, 1−8.
18. Pan, W. J.; Hedaya, M. A. Cocaine and Alcohol Interactions in the Rat: Effect on Cocaine Pharmacokinetics and Pharmacodynamics. *J. Pharm. Sci.* **1999**, *88*, 459−467.
19. Pan, W. J.; Hedaya, M. A. Sensitive and Specific High-Performance Liquid Chromatographic Assay with Ultraviolet Detection for the Determination of Cocaine and Its Metabolites in Rat Plasma. *J. Chromatogr. B Biomed. Sci. Appl.* **1997**, *703*, 129−138.
20. Gibaldi, M.; Perrier, D. *Pharmacokinetics*, 2nd ed.; Marcel Dekker: New York, 1982, pp 45−111.
21. Houston, J. B. Drug Metabolite Kinetics. *Pharmacol. Ther.* **1982**, *15*, 521−552.
22. Sharma, A.; Jusko, W. J. Characterization of Four Basic Models of Indirect Pharmacodynamic Responses. *J. Pharmacokinet. Biopharm.* **1996**, *24*, 611−635.
23. Krzyzanski, W.; Jusko, W. J. Mathematical Formalism for the Properties of Four Basic Models of Indirect Pharmacodynamic Responses. *J. Pharmacokinet. Biopharm.* **1997**, *25*, 107−123.
24. Xu, Y. Q.; Crumb, W. J. Jr.; Clarkson, C. W. Cocaethylene, A Metabolite of Cocaine and Ethanol, Is a Potent Blocker of Cardiac Sodium Channels. *J. Pharmacol. Exp. Ther.* **1994**, *271*, 319−325.
25. Parkinson, A. Biotransformation of Xenobiotics, in *Casarett & Doull's Toxicology: The Basic Science of Poisons*, 5th ed.; Klaassen, C. D., Ed.; McGraw-Hill: New York, 1996; pp 113−186.
26. Boelsterli, U. A.; Göldlin, C. Biomechanisms of Cocaine-Induced Hepatocyte Injury Mediated by the Formation of Reactive Metabolites. *Arch. Toxicol.* **1991**, *65*, 351−360.
27. Smith, A. C.; Freeman, R. W.; Harbison, R. D. Ethanol Enhancement of Cocaine-Induced Hepatotoxicity. *Biochem. Pharmacol.* **1981**, *30*, 453−458.
28. Boelsterli, U. A.; Lanzotti, A.; Göldlin, C.; Oertle, M. Identification of Cytochrome P-450IIB1 as A Cocaine-Bioactivating Isoform in Rat Hepatic Microsomes and in Cultured Rat Hepatocytes. *Drug Metab. Dispos.* **1992**, *20*, 96−101.

Acknowledgments

This work was supported by a grant from the National Institute of Neurological Disorder and Stroke (NS/OD36399-01).

JS980283H

Influence of Calcium Ions on the Structure and Stability of Recombinant Human Deoxyribonuclease I in the Aqueous and Lyophilized States

BEI CHEN,[†] HENRY R. COSTANTINO,[‡] JUN LIU,[†] CHUNG C. HSU,[†] AND STEVEN J. SHIRE*,[†]

Contribution from *Pharmaceutical Research and Development, Genentech, Inc., 1 DNA Way, South San Francisco, California 94080.*

Received July 7, 1998. Accepted for publication January 13, 1999.

Abstract □ The effect of calcium ions on the structure and stability of recombinant human DNase I (rhDNase) in the aqueous and solid (lyophilized) states was investigated. Fourier transform infrared (FTIR) spectroscopy was used to examine the overall secondary structure, while chemical stability was monitored in terms of deamidation and soluble aggregate formation at 40 °C. The exogenous calcium was removed by EGTA. This process can remove all but approximately one calcium ion per protein molecule. Analysis of the FTIR spectra in the amide III region in either the aqueous or lyophilized state demonstrated that removal of exogenous Ca^{2+} by EGTA-treatment had little effect on the secondary structure (and lyophilization-induced rearrangement thereof). For the aqueous solution, circular dichroism was used as an independent technique and confirmed that there was no large overall change in the secondary or tertiary structure upon the removal of calcium. The primary degradation route for the aqueous protein was deamidation. For the EGTA-treated protein, there was also severe covalent aggregation, e.g., formation of intermolecular disulfides facilitated by the cleavage of Cys173-Cys209. The aggregates exhibited a markedly different secondary structure compared to the native protein. For instance, the β-sheet band observed at ca. 1620 cm^{-1} wavenumber in the amide I second derivative spectra was increased. Enzymatic activity was completely lost upon aggregation, consistent with the cleavage of the aforementioned native disulfide. For the protein lyophilized in the presence of Ca^{2+}, there was no increase in deamidated species during solid-state storage; however, some aggregation was observed. For the lyophilized EGTA-treated protein, aggregation was even more pronounced, and there was some loss in enzymatic activity upon reconstitution. Thus, the removal of calcium ions by EGTA-treatment decreased the stability of rhDNase in both the aqueous and solid states even though no large overall calcium-induced structural changes could be observed by the techniques used in this study.

Introduction

It has been established that divalent metal cations, particularly Ca^{2+}, play an important role in the structure and function of deoxyribonuclease I (DNase).[1] For the bovine-derived molecule (bDNase), it was shown that the removal of Ca^{2+} from aqueous solution induced changes in the secondary structure, as evidenced in the far-UV circular dichroism spectrum, although no change was seen by sedimentation velocity analysis.[2] In addition, the presence of Ca^{2+} has been shown to increase bDNase's resistance to proteolysis (e.g., by trypsin),[2,3] play a role in refolding the reduced protein,[4] and impart stability toward pH-induced structural alterations.[5] The biological activity of bDNase is lost upon the removal of calcium ions.[1,6] According to Price,[7] bDNase has two strongly binding Ca^{2+} sites and several weakly binding ones. Similar results have demonstrated the importance of Ca^{2+} for the structure and function of the homologous recombinant human form of DNase (rhDNase).[8]

Suck and co-workers[9−11] have examined the structure of bDNase by X-ray crystallography. The protein has a mixed α/β composition, with a hydrophobic core of two, six-stranded β-pleated sheets flanked by α-helices and extensive loop regions. The electron density map also revealed two Ca^{2+} bound to the native protein, one located in a flexible loop formed by residues Gly100 to Gly105, and another in the loop formed by residues Asp201 to Cys209. Both sites are located in proximity to cystine bridges, one between Cys101 and Cys104 and the other between Cys173 and Cys209. The latter disulfide bridge, which is essential for enzymatic activity, is protected against reduction in the presence of Ca^{2+}.[4] It was hypothesized that the stabilizing effects of Ca^{2+} were due to configurational restraints imposed by binding of the cation in the flexible loop regions.[9,10] The putative catalytic Ca^{2+} binding site is located in the proximity of residues Glu78 and His134 at the active center.[11] The X-ray crystal structure of rhDNase has also been determined and is very similar to the bovine form.[8,12]

In the present investigation, we have focused on the effect of removal of exogenous Ca^{2+} on rhDNase structure and biochemical stability, in particular, aggregation and deamidation. The protein was studied both in aqueous solution and the freeze-dried form. The latter is often considered as a common dosage for biopharmaceuticals since many deleterious processes are retarded upon the removal of water (and thus shelf life can be extended).[13] The data reveal that the influence of Ca^{2+} on the rhDNase molecule observed for the aqueous solution also persists following lyophilization and storage in the solid state.

Materials and Methods

Materials—rhDNase (a glycosylated protein with MW ~ 32.7 kDa) was produced at Genentech, Inc. (South San Francisco). Deamidation is the major route of degradation of the protein in aqueous solution. The degradation happens during the manufacturing process, resulting in the starting material with ~60% deamidation. All other chemicals were of reagent grade and purchased from commercial suppliers.

Protein Lyophilization—rhDNase was provided in an aqueous solution consisting of ~18 mg/mL protein, 150 mM NaCl, and 1 mM $CaCl_2$ at pH ~ 6.5 ± 0.5. To remove calcium ions, this solution was exhaustively dialyzed against 1 mM EGTA (pH ~ 6.5 ± 0.5) at 5 °C. It should be noted that it is difficult to completely remove bound Ca^{2+}, and even after exhaustive dialysis against the chelating agent, there is approximately one calcium ion bound per rhDNase molecule.[8] Samples were filtered (0.22 μm, Millipore-

* To whom correspondence should be addressed.
[†] Genentech, Inc.
[‡] Current address: Alkermes, Inc., 64 Sidney Street, Cambridge, MA 02139.

10.1021/js980273g CCC: $18.00
Published on Web 03/12/1999

GV) and filled (2 mL) in 3-cc glass vials. The lyophilization cycle consisted of freezing for 4 h at −55 °C, followed by drying at a chamber pressure of 50 μm Hg and a shelf temperature which was ramped at a rate of 10 °C/h to a maximum of 25 °C and held for 50 h. A Leybold (Germany) model GT20 freeze-dryer was used. The moisture content of lyophilized samples was 6 ± 3%. There was no observed moisture transfer from the stoppers during storage (7 ± 2% after incubation for 24 months at 15 °C).

Determination of rhDNase Aggregation—Size exclusion chromatography (SEC) was used to monitor protein monomer, fragments, and soluble aggregates. A Hewlett-Packard 1090L system was used with a silica-based TSK Gel2000SWxl column (Tosohaas, Japan). Sample loadings were approximately 50 μg, and the flow rate for the mobile phase (phosphate-buffered saline; 5 mM sodium phosphate, pH 7.3, and 150 mM NaCl) was 0.5 mL/min. Molecular weight standards (BioRad) consisting of thyroglobulin (670 kDa), γ-globulin (158 kDa), ovalbumin (44 kDa), myoglobulin (17 kDa), and cyanocobalamin (1.35 kDa) were used to calibrate the column. Silver-stained SDS−PAGE, under both reducing and nonreducing conditions, was employed to further examine protein fragments, monomer, and aggregates.

Determination of rhDNase Deamidation—The extent of deamidation of rhDNase was measured using tentacle ion-exchange chromatography.[14] Samples (~50 μg) were loaded on a LiChrosphere column (EM Separations) equilibrated with 1 mM $CaCl_2$, 0.1% acetate buffer, pH 4.7, and eluted with a linear gradient of 0−50% of 1 M sodium chloride in the same buffer. The flow rate was 0.8 mL/min.

Enzymatic Activity Assay—Measurement of rhDNase enzymatic activity was accomplished via a colorimetric method (using DNA complexed with methyl green as a substrate).[15] The activity of experimental samples was determined (in triplicate) relative to a rhDNase standard. Data are expressed as % specific activity, i.e., concentration of rhDNase determined by activity assay divided by that based on UV absorption of the sample.

Circular Dichroism (CD)—CD spectra were measured and analyzed as described previously.[8] All spectra were taken at a concentration of ~0.6 mg/mL rhDNase at room temperature using an Aviv 60DS spectropolarimeter. A 1-cm cylindrical cell was used for CD measurement above 250 nm with a 5-s averaging time for each data point taken at 0.5 nm interval and bandwidth of 0.2 nm. A 0.01-cm cell was used for CD measurement below 250 nm with a 5-s averaging time for each data point taken at 0.5 nm interval and bandwidth of 1.5 nm. Ellipticity values were converted to mean residue weight ellipticity using a mean weight of 112.8 for the protein.

Fourier transform Infrared (FTIR) Spectroscopy and Estimation of Secondary Structure—FTIR spectra were measured using an ATI-Mattson Galaxy 5022 IR spectrophotometer as described previously.[16] A total of 256 scans at 4 cm^{-1} resolution using Happ-Ganzel apodization were averaged to obtain each spectrum. Aqueous samples were measured using a 15-μm spacer between CaF_2 windows in a liquid cell (Spectra-Tech). The spectrum of pure water was subtracted out using Nicolet OMNIC 3.1 software in order to obtain the pure aqueous protein spectrum. Lyophilized samples were measured as KBr pellets (~1 mg of protein per 200 mg of KBr, pressure into a pellet at 5 kpsi compaction pressure); these conditions were shown not to induce any artifactual alterations in rhDNase secondary structure.[16] Spectra were analyzed by second derivatization (with smoothing equivalent to an approximate 10 cm^{-1} span) to determine the number of spectral bands and their approximate locations (OMNIC 3.1 software). Using this information as a starting point, the original spectra in the amide III region (1320−1220 cm^{-1}) were Gaussian curve-fitted using GRAMS/32 software (Galactic Industries), following the strategy detailed by Griebenow and Klibanov.[17] The secondary structure contents were calculated from the areas of the individual assigned bands and their fraction of the total area in the amide III region.[16,17] Data are presented as the average and deviation of at least three determinations. Secondary structure was also assessed and confirmed by qualitative examination of the second derivative amide I spectra (1700−1620 cm^{-1}).[18]

Results and Discussion

Effect of Ca^{2+} on Secondary Structure of rhDNase by Fourier transform Infrared (FTIR) Spectroscopy—

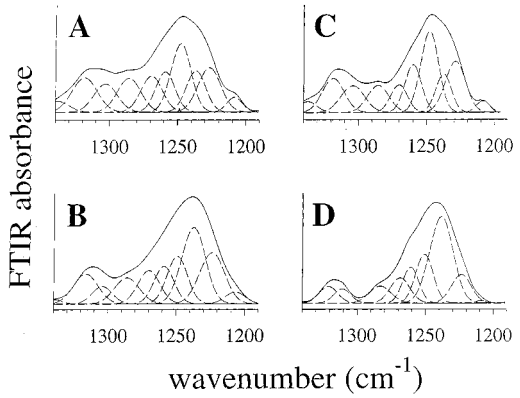

Figure 1—IR spectra for rhDNase I in the amide III region and their Gaussian curve-fitting: (A) in aqueous solution (EGTA-treated, no incubation); (B) in the lyophilized powder (EGTA-treated, no incubation); (C) deamidated form (aqueous protein incubated in 1 mM $CaCl_2$ for 120 days at 40 °C); (D) aggregated form (aqueous EGTA-treated protein incubated in the absence of exogenous calcium ions for 120 days at 40 °C). The solid and dotted curves represent the superimposed original spectra and curve-fit, and the dashed curves are individual Gaussian bands.

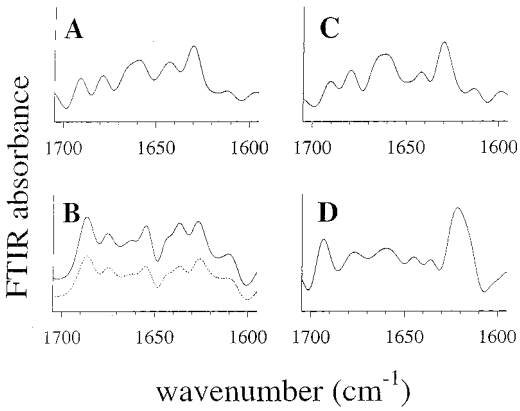

Figure 2—Inverted second derivative of the amide I IR spectra of rhDNase I: (A) in aqueous solution (EGTA-treated, no incubation); (B) lyophilized untreated power (solid line), and lyophilized EGTA-treated power (dotted line) (no incubation for either sample); (C) deamidated form (aqueous protein incubated in 1 mM $CaCl_2$ for 120 days at 40 °C); (D) aggregated form (aqueous EGTA-treated protein incubated in the absence of exogenous calcium ions for 120 days at 40 °C).

Recently, we examined the structure of rhDNase employing Fourier transform infrared (FTIR) spectroscopy, which allows for estimation of protein secondary structure in both aqueous and solid states.[16] It was seen that there was a dehydration-induced structural change, specifically a loss in α-helix and increase in β-sheet structures. Such alterations may be a common occurrence for proteins upon the removal of water.[17,18] In the present investigation, we have further extended FTIR spectroscopy to examine the effect of removing exogenous calcium ions on the protein structure in aqueous solution and also upon drying.

The FTIR spectrum, in the conformationally sensitive amide III region,[17] was measured for rhDNase in aqueous solution following EGTA-treatment to remove exogenous calcium ions (Figure 1A). The spectrum appears very similar to the protein in aqueous solution containing calcium ions, as presented earlier.[16] The amide I second derivative spectrum (Figure 2A) shows similar numbers of peaks and peak positions, but slightly different peak intensities, as for the spectrum for rhDNase with calcium reported previously.[16] To quantitate the structure in terms of the overall secondary structure, Gaussian curve-fitting of the original amide III spectra was employed.[17] A summary of the data is presented in Table 1 and shows that

Table 1—FTIR Analyses of Various rhDNase I Samples[a]

sample	secondary structure (%)		
	α-helix	β-sheet	other[b]
aqueous solution, with Ca^{2+}[c,d]	21 ± 2	23 ± 3	56 ± 6
aqueous solution, EGTA-treated	20 ± 2	26 ± 2	54 ± 3
lyophilized, with Ca^{2+}[d]	13 ± 2	41 ± 3	46 ± 2
lyophilized, EGTA-treated	14 ± 2	45 ± 3	41 ± 3
deamidated form[e]	21 ± 1	25 ± 2	54 ± 2
aggregated form[f]	10 ± 1	44 ± 4	46 ± 3

[a] The secondary structure of rhDNase was calculated by Gaussian curve-fitting the original amide III spectra. [b] Other secondary structure includes random coil and turns, and extended chains. [c] The aqueous solution contained 1 mM calcium chloride. [d] Data from ref 16. [e] Aqueous protein incubated in 1 mM $CaCl_2$ for 120 days at 40 °C. [f] Aqueous EGTA-treated protein incubated in the absence of exogenous calcium ions for 120 days at 40 °C.

removal of exogenous calcium had little effect on the overall secondary structure. The mixed α/β secondary structure estimated from the amide III FTIR spectra is in agreement with that predicted from consideration of the X-ray crystal structure of native rhDNase,[8,12] which is similar to bDNase.[9–11] As an independent method, we also employed circular dichroism (CD) to examine the structure of rhDNase in aqueous solution (data not shown). The secondary structure of rhDNase in the presence and absence of calcium as revealed by the far-UV CD were the same. Furthermore, the near-UV CD indicated that there was no change in the tertiary structure for the protein in the presence and absence of calcium ions. Therefore, data from two independent techniques, FTIR spectroscopy and CD, indicate that the removal of calcium does not affect the solution structure of rhDNase.

It is intriguing that a previous study on bDNase concluded that there was some change in the protein conformation upon addition of calcium based on circular dichroism (CD) data.[2] It was found that the addition of calcium (10^{-4} to 10^{-2} M) to bDNase resulted in an intensification of the CD bands with major peaks centered at 275 and 284 nm. It was also found that as the pH was decreased (from pH 8 to pH 3), the change in the CD spectrum (change in ellipticity at 215 nm) induced by 10^{-3} M $CaCl_2$ was eliminated. It was hypothesized that the affinity of bDNase for binding calcium was greatly decreased due to protonation of the amino acid side chains involved in binding calcium.[2] The explanation for the difference in the effect of calcium observed for rhDNase herein compared to the earlier bDNase study is uncertain. The two protein forms have a high structural homology, including the ability to bind calcium ions.[1,8–12] In our current study, we started with rhDNase in the presence of 1 mM $CaCl_2$. Even after exhaustive dialysis in the presence of the chelating agent EGTA, there is still approximately one calcium ion bound per rhDNase molecule.[8] In the bDNase study, no information was provided regarding the calcium level of the starting material. It is possible that the binding of calcium is less strong for bDNase, leading toward a more complete removal. A direct comparison of rhDNase and bDNase starting from the same, known level of calcium on the protein is necessary to shed light on this issue.

Chan et al.[20] have studied the thermal denaturation of rhDNase as a function of calcium ion concentration by solution differential scanning calorimetry (DSC). It was found that there was a significant increase in T_m and H_m (putative "melting" temperature and enthalpy corresponding to an endothermic event associated with protein denaturation) as the exogenous calcium ion concentration was increased. Furthermore, this event was associated with unfolding and irreversible aggregation of rhDNase. It was hypothesized that the effect was due to stabilization of rhDNase structure in its native state and protection of disulfides near calcium binding sites (which may be involved in aggregation via intermolecular disulfide formation). The latter effect has been well-established for bDNase and is also likely to play a role in the thermal denaturation of rhDNase. The former effect, if true, may be minor since there was quantitatively a similar percentage of ordered secondary structures found for the protein in the presence of calcium and following EGTA-treatment. It should be noted that such solution DSC studies, while valuable in obtaining information regarding denaturation at elevated temperatures, cannot necessarily be used as an indication of stability in aqueous solution at lower temperatures, or upon freeze-drying. The binding of calcium may stabilize rhDNase via mediation of the free energy of denaturation. For the classic, native-to-denatured state transition, the native state would be favored (lowered free energy) if it binds calcium more strongly than the denatured state. This view is consistent with an increase in T_m, without calcium-induced changes in protein conformation at lower (e.g., ambient) temperatures.

Next, we examined the secondary structure of solid (lyophilized) rhDNase. The amide III spectra (Figure 1B depicts data for the protein that was EGTA-treated prior to freeze-drying) clearly indicate that some structural perturbations occurred upon drying. These alterations were quantified by curve-fitting of the original spectra, as summarized in Table 1. It can be seen that there was a significant decrease in α-helical structures and increase in β-sheets for the EGTA-treated protein. To further confirm this change, we also examined the second-derivative amide I spectra for the aqueous (Figure 2A) and lyophilized (dashed line in Figure 2B) EGTA-treated protein. These data also reveal alterations upon lyophilization, in particular, augmentation of the band centered at approximately 1691 cm^{-1}, which likely indicates increased β-sheets in the solid state as a result of increased protein−protein interactions.[18] The nature and extent of the drying-induced structural alterations for the lyophilized EGTA-treated protein were similar to that for rhDNase freeze-dried from aqueous solution containing 1 mM calcium chloride (Figure 2).[16]

Therefore, although calcium ions increase rhDNase structural stability with respect to thermal unfolding, there was little effect on the stability toward dehydration-induced structural perturbation. This result is similar to that presented in a previous investigation of the enzyme lysozyme.[21] In that study, the protein lyophilized from a series of pHs from 1.9 to 5.1, corresponding to a wide range in T_m values from 45 °C to 75 °C (determined by solution DSC), exhibited very similar structural rearrangements upon lyophilization (estimated from FTIR spectra in the amide III region).[21]

Effect of Ca^{2+} on Protein Stability in the Aqueous and Lyophilized States—As described by Shire,[8] the dominant degradation pathway for rhDNase in current liquid formulation is deamidation of Asn74. The pseudo-first-order rate constants are not affected by the starting levels of deamidation of the protein (data not shown). Furthermore, deamidation, which results in partial loss of the enzymatic activity, does not significantly alter the protein's structure, as evidenced in the far- and near-UV CD.[8]

Figure 3A depicts data for the deamidation of rhDNase in aqueous solution at the accelerated stability condition of 40 °C. This condition is well below the T_m for rhDNase, even in the absence of calcium ions.[20] As expected, based on previous data,[8] the molecule readily deamidated. The starting material was already largely deamidated (about 60%), and complete deamidation was observed after 120

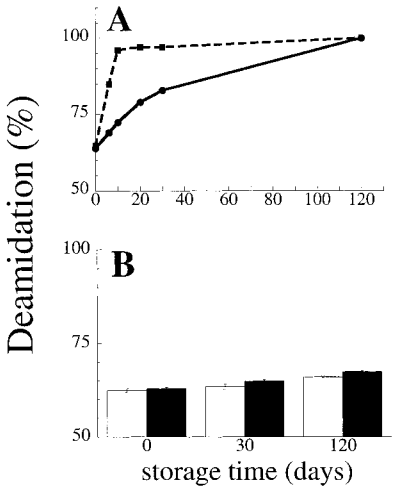

Figure 3—Deamidation of rhDNase at 40 °C: (A) in aqueous solution: solid line depicts data for untreated protein in the presence of 1 mM $CaCl_2$ and dashed line represents EGTA-treated protein in the absence of exogenous calcium ions (note that all error bars are too small to be seen); and (B) in the lyophilized untreated powder (open symbols) and lyophilized EGTA-treated powder (filled symbols).

days at 40 °C for the protein in the presence of 1 mM $CaCl_2$ (dashed line in Figure 3A). For this latter sample, which was fully deamidated (and did not exhibit any significant aggregate formation as discussed below), we measured the amide III FTIR spectra (Figure 1C) and estimated the secondary structure (Table 1), in addition to qualitative inspection of the amide I second derivative spectra (Figure 2C). Despite the conversion of asparagine to isoaspartate (i.e., the placement of an extra methylene group in the peptide backbone), there was no difference in the secondary structure, consistent with previous data obtained by CD.[8]

Deamidation was then monitored for the EGTA-treated protein which was incubated in aqueous solution without calcium ions (solid line in Figure 3A). In the absence of calcium, the degradation occurred even more rapidly compared to the protein in the presence of calcium ions. There was nearly complete deamidation seen after only a 10-day incubation at 40 °C. This result is different from that observed previously under a milder condition.[8] In that investigation, rhDNase was treated with EDTA to remove calcium and reformulated in isotonic 10 mM phosphate buffer. Deamidation of rhDNase under this condition did not increase significantly compared to untreated samples over ~0.5 year stored at 25 °C.[8]

We also examined the protein by size-exclusion chromatography (SEC), which was useful in detecting soluble aggregate formation. For the protein in the aqueous solution of 1 mM $CaCl_2$, there was virtually no aggregation observed by SEC, even after 120 days at 40 °C (filled symbols in Figure 4A). However, for the case of the protein in aqueous solution in the absence of calcium, there was rapid deterioration, with nearly complete aggregation following only 30 days of incubation (open symbols in Figure 4A).

Therefore, the data show that the removal of calcium ions results in increased rates of both deamidation and soluble aggregate formation in aqueous solution. These findings are consistent with results of bDNase, demonstrating that the removal of calcium was associated with increased rates of proteolysis (e.g., by trypsin),[2,3] susceptibility toward pH-induced structural alterations,[5] and reduction of the Cys173-Cys209 disulfide.[4] The latter may play a role in covalent aggregation via intermolecular disulfide formation. Majority of aggregates as observed by SDS−PAGE were dissociable in the presence of free thiol

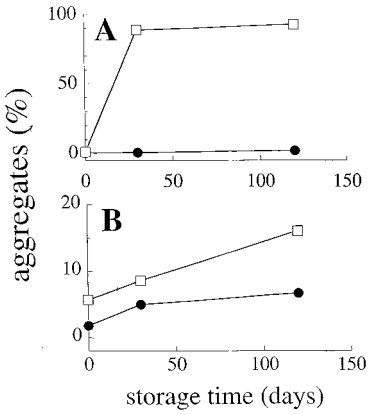

Figure 4—Aggregation of rhDNase at 40 °C: (A) in aqueous solution; (B) in the lyophilized powder. Filled symbols depict data for untreated protein in the presence of 1 mM $CaCl_2$, and open symbols represent EGTA-treated protein in the absence of exogenous calcium ions (note that all error bars are too small to be seen).

Table 2—Enzymatic Activities of Various rhDNase I Samples[a]

sample	enzymatic activity after incubation at 40 °C for[b] 0 days	30 days	120 days
aqueous solution, with Ca^{2+}[c]	100 ± 12	67 ± 5	58 ± 2
aqueous solution, EGTA-treated	90 ± 9	<9	<6
lyophilized, with Ca^{2+}	100 ± 13	89 ± 4	89 ± 2
lyophilized, EGTA-treated	92 ± 6	75 ± 6	53 ± 5

[a] Enzymatic activity was determined by the methyl green assay. [b] Data are expressed as % specific activity, or the amount of protein determined by the activity assay divided by that based on UV absorption of the sample. [c] The aqueous solution contained 1 mM calcium chloride.

agent (data not shown). Therefore, these aggregates were linked by disulfides.

Since reduction of the Cys173-Cys209 disulfide is known to affect the enzymatic activity, we used the methyl green assay[15] to probe the integrity of the active site of the molecule. For the protein in aqueous solution containing 1 mM calcium chloride, there was a substantial drop in activity, up to about 40% loss after 120 days at 40 °C (Table 2), even though there was no significant aggregation observed (Figure 4A). In this case, the drop in activity is a result of increased deamidation (Figure 3A), which is known to result in decreased activity.[8]

If the disulfide bridge Cys173-Cys209 had been cleaved for aqueous rhDNase in the absence of calcium ions, then it follows that the enzymatic activity would be lost, based on observations for the bovine-derived protein.[4] Thus, we measured the enzymatic activity of the EGTA-treated protein in aqueous solution without calcium ions. As predicted, there was over 90% loss of enzymatic activity after only 30 days of incubation (Table 2), concomitant with the aggregation of the molecule (Figure 4A). These data, along with the confirmation of the presence of disulfides in the rhDNase aggregates, strongly support the view that removal of calcium from binding sites near native disulfides made these areas more susceptible to cleavage and ultimately intermolecular bond formation. The increased susceptibility toward deamidation in the absence of calcium may be linked to increased configurational freedom as a result of the disulfide cleavage and/or exchange.

It was interesting to also examine the secondary structure of the rhDNase aggregates (generated by incubation of EGTA-treated protein for 120 days in aqueous solution). To this end, we measured the amide III FTIR spectra for the rhDNase aggregates (Figure 1D) which showed sig-

nificant perturbation compared to the protein prior to incubation, particularly an increase in the β-sheet band centered at approximately 1238 cm^{-1} (Figure 1D). Estimation of the secondary structure (Table 2) confirmed that there was an increase in the overall β-sheet content in the aggregates. Protein aggregates tend to have increased β-sheet contents, largely intermolecular in nature.[18] This was also confirmed in the amide I second derivative spectra (Figure 2D) which exhibited a band at $\sim$1620 cm^{-1}. It has been reported that this band indicates the presence of intermolecular aggregates, and has been correlated with protein aggregation.[18]

Having established the influence of calcium ions on the solution structure/stability of rhDNase, we then next examined the lyophilized form of the protein. Generally, proteins exhibit superior stability in the dehydrated state due to several factors, such as the increase in molecular rigidity upon dehydration, which should retard deleterious reactions.[22,23] The level of deamidation (Figure 3B) shows that there was no significant increase in the extent of deamidation, regardless of the absence of calcium. This result may stem from the fact that deamidation is a hydrolytic process, i.e., requires water;[24] it is logical then, that removal of water would coincide with reduction of deamidation.

Figure 4B depicts the formation of aggregates for rhDNase in the solid state. It can be seen that for the protein lyophilized from the aqueous solution containing Ca^{2+}, there was slight aggregation ($\sim$7% after 120 days at 40 °C). Note that under this condition in aqueous solution, there was essentially no aggregation observed. Therefore, from the standpoint of intermolecular processes, i.e., aggregation, the protein exhibited inferior stability in the solid compared to the aqueous state; the reverse was true for the intramolecular process of deamidation. This finding is consistent with the view that the proximity of protein molecules in the dried state facilitates intermolecular pathways over intramolecular ones.[25]

For the EGTA-treated protein, the extent of solid-state aggregation was more substantial (Figure 4B), although not as severe as observed for the aqueous solution (Figure 4A). Thus, in this case (EGTA-treated), superior stability was observed for the lyophilized protein. As expected, there was also significant loss in rhDNase enzymatic activity for the EGTA-treated protein (Table 2), whereas there was little change for the protein lyophilized from 1 mM $CaCl_2$. From the data it is clear that the activity loss does not directly correspond to the loss of monomer, suggesting that some monomers have become inactivated (e.g., cleavage of Cys173-Cys209). As was the case for the protein aggregates in aqueous solution, the aggregates generated in the solid-state had over 50% disulfide-bonded character, as revealed by reducing and nonreducing SDS−PAGE.

The data clearly demonstrate that the removal of calcium destabilizes rhDNase in the solid state. This result is intriguing considering the conjecture that protein biochemical stability is linked to the glass transition temperature (T_g) of the formulation.[24] Although it is difficult to measure the T_g for pure proteins,[26] it is expected that the T_g for rhDNase is much higher than that of calcium. Therefore, removal of calcium should raise the T_g, yet the data show that rhDNase stability was decreased. The other component present in our system, namely water, also has a very low T_g and is known to destabilize proteins.[22,23] Another possibility to explain the effect of calcium is that its removal results in increase in residual moisture level and/or increase in moisture over storage (e.g., moisture transfer from the lyophilization stopper). To check this, we measured the moisture levels of lyophilized rhDNase in the presence and absence of calcium after a storage period of 24 months at 15 °C. We found there was no significant difference in moisture levels between the samples in the presence and absence of calcium. In addition, the average moisture level ($n = 10$) was found the same as previous data,[16] suggesting that no moisture transferred from the stopper over time. These data strongly suggest that for the case of rhDNase the stabilizing influence of calcium is due to some specific effect (e.g., binding) rather than mediated by influence on the T_g of the system.

In addition to the formulation, the reconstitution medium may also affect protein stability. For instance, Zhang et al.[27] have studied the effect of additives in the reconstitution medium on aggregation and activity of lyophilized recombinant interleukin-2 and ribonuclease A. It was found that additives such as 0.05% sodium polyphosphate or 0.5% sulfated β-cyclodextrin increased recovery of activity of RNase (from 62% to 97% and 77%, respectively) after storage of the lyophilized proteins for three weeks at 45 °C. In the current investigation, we tested whether the addition of calcium in the reconstitution medium (but not the dried formulation) could influence rhDNase stability. EGTA-treated samples were stored for 2 years at 40 °C and then reconstituted in the absence and presence of calcium (1 mM $CaCl_2$). The data revealed the same activity loss, 60 $\pm$ 2% vs 55 $\pm$ 5%, and increase in aggregates, 17 $\pm$ 1% vs 15 $\pm$ 2% for the protein reconstituted in the absence and presence of calcium, respectively. This excludes the possibility that rhDNase is stabilized solely by calcium binding during the reconstitution step.

Both EGTA-treated and nontreated rhDNase exhibited similar alterations in their structure upon lyophilization as determined by FTIR spectroscopy, yet the two had different stability. This suggests that the predominant mechanism of solid-state instability, aggregation, did not depend on the overall secondary structure. If similar mechanisms hold for the aqueous and solid states, then it is likely that the local structure near a labile site, for instance, Cys173-Cys209, is influenced by calcium ions (such an effect is not detectable by examination of overall secondary structure by FTIR spectroscopy).

In summary, this investigation reports the effect of calcium ions on the structure and stability of rhDNase in the aqueous and solid (lyophilized) states. The data reveal that the removal of calcium ions by EGTA-treatment had little effect on the secondary structure (and lyophilization-induced rearrangement thereof) as determined by FTIR spectroscopy. The CD spectra also confirmed that the removal of calcium did not alter the secondary or tertiary structure for the aqueous protein. The primary degradation route for the aqueous protein at 40 °C was deamidation. There was also rapid aggregation observed for the aqueous EGTA-treated protein, presumably via a mechanism not related to the overall structure, but rather a labile site, e.g., reduction of Cys173-Cys209. For the protein lyophilized in the presence of calcium, there was some aggregation observed at 40 °C; thus the solid-state stability was actually worse than that in aqueous solution. For the EGTA-treated protein lyophilized in the absence of calcium, solid-state aggregation was much more pronounced compared to protein in the presence of calcium. Thus, the removal of calcium ions by EGTA-treatment has a similar effect on the structure and stability of rhDNase in both the aqueous and solid states.

References and Notes

1. Moore, S. Pancreatic DNase. In *The Enzymes Vol. XIV*; Academic Press: San Diego, CA, 1981; pp 281−295.
2. Poulos, T. L.; Price, P. A. Some effects of calcium ions on the structure of bovine pancreatic deoxyribonuclease A. *J. Biol. Chem.* **1972**, *247*, 2900−2904.

3. Price, P. A.; Liu, T.-Y.; Stein, W. H.; Moore, S. Properties of chromatographically purified bovine pancreatic deoxyribonuclease. *J. Biol. Chem*. **1969**, *244*, 917−923.
4. Price, P. A.; Stein, W. H.; Moore, S. Effect of divalent cations on the reduction and re-formation of the disulfide bonds of deoxyribonuclease. *J. Biol. Chem*. **1969**, *244*, 929−932.
5. Lizarraga, B.; Sanchez-Romero, D.; Gil, A.; Melgar, E. The role of Ca^{2+} on pH-induced hydrodynamic changes of bovine pancreatic deoxyribonuclease A. *J. Biol. Chem*. **1978**, *253*, 3191−3195.
6. Price, P. A. The essential role of Ca^{2+} in the activity of bovine pancreatic deoxyribonuclease. *J. Biol. Chem*. **1975**, *250*, 1981−1986.
7. Price, P. A. Characterization of Ca^{2+} and Mg^{2+} binding to bovine pancreatic deoxyribonuclease A. *J. Biol. Chem*. **1972**, *247*, 2895−2899.
8. Shire, S. J. Stability characterization and formulation development of recombinant human deoxyribonuclease I [Pulmozyme®, (Dornase alpha)]. In *Formulation, Characterization and Stability of Protein Drugs*; Pearlman, R., Wang, Y. J., Eds.; Plenum Press: New York, 1996; pp 393−426.
9. Suck, D.; Oefner, C.; Kabsch, W. Three-dimensional structure of bovine pancreatic DNase I at 2.5 Å resolution. *EMBO J*. **1984**, *3*, 2423−2430.
10. Oefner, C.; Suck, D. Crystallographic refinement and structure of DNase I at 2 Å resolution. *J. Mol. Biol*. **1986**, *192*, 605−632.
11. Suck, D.; Oefner, C. Structure of DNase I at 2.0 Å resolutions suggests a mechanism for binding to and cutting DNA. *Nature* **1986**, *321*, 620−625.
12. Wolf, E.; Frenz, J.; Suck, D. Structure of human pancreatic DNase at 1.8 Å resolution. *Protein Sci*. **1995**, *4*, 115.
13. Nail, S. J. Formulation of Proteins and Peptides. In *Controlled Drug Delivery. Challenges and Strategies*; Park, K., Ed.; American Chemical Society: Washington, D. C., 1997; pp 185−203.
14. Cacia, J.; Quan, C. P.; Vassar, M.; Sliwkowski, M. B.; Frenz, J. Protein sorting by high-performance liquid chromatography. I. Biomimetic interaction chromatography of recombinant human deoxyribonuclease I on polyionic stationary phases. *J. Chromatogr*. **1993**, *634*, 229−239.
15. Sinicropi, D.; Baker, D. L.; Prine, W. S.; Shiffer, K.; Shak, S. Colorimetric determination of DNase I activity with a DNA-methyl green substrate. *Anal. Biochem*. **1994**, *222*, 351−358.
16. Costantino, H. R.; Chen, B.; Liu, J.; Hsu, C. C.; Shire, S. J. Fourier transform infrared (FTIR) spectroscopic investigation of the secondary structure of recombinant human DNase I in the aqueous and dried states. *Pharm. Pharmacol. Commun*. **1998**, *4*, 391−395.
17. Griebenow, K.; Klibanov, A. M. Lyophilization-induced changes in the secondary structure of proteins. *Proc. Natl. Acad. Sci U.S.A*. **1995**, *92*, 10969−10976.
18. Dong, A.; Prestrelski, S. J.; Allison, S. D.; Carpenter, J. F. Infrared spectroscopic studies of lyophilization and temperature-induced protein aggregation. *J. Pharm. Sci*. **1995**, *84*, 415−424.
19. Bloemendal, M.; Johnson, W. C. Structural information on proteins from circular dichroism spectroscopy: Possibilities and limitations. In *Physical Methods to Characterize Pharmaceutical Proteins*; Herron, J. N., Crommelin, D. J. A., Eds.; Plenum Press: New York, 1995; pp 65−93.
20. Chan, H.-K.; Au−Yeung, K.-L.; Gonda, I. Effects of additives on heat denaturation of rhDNase in solution. *Pharm. Res*. **1996**, *13*, 756−761.
21. Costantino, H. R.; Griebenow, K.; Mishra, P.; Klibanov, A. M. Fourier transform infrared (FTIR) spectroscopic investigation of protein stability in the lyophilized form. *Biochim. Biophys. Acta* **1995**, *1253*, 69−74.
22. Hageman, M. J. Water sorption and solid-state stability of proteins. In *Stability of Protein Pharmaceuticals. Part A. Chemical and Physical Pathways of Protein Degradation*; Ahern, T. J., Manning, M. C., Eds.; Plenum Press: New York, 1992; pp 273−309.
23. Costantino, H. R.; Langer, R.; Klibanov, A. M. Solid-phase aggregation of proteins under pharmaceutically relevant conditions. *J. Pharm. Sci*. **1994**, *83*, 1662−1669.
24. Cleland J. L.; Powell, M. F.; Shire, S. J. The development of stable protein formulations. A close look at protein aggregation, deamidation, and oxidation. *Crit. Rev. Ther. Drug Carrier Syst*. **1993**, *10*, 307−377.
25. Hageman, M. J.; Bauer, J. M.; Possert, P. L.; Darrington, R. T. Preformulation studies oriented towards sustained delivery of recombinant somatotropins. *J. Agric. Food Chem*. **1992**, *40*, 348−355.
26. Bell, L. N.; Hageman, M. J.; Muraoka, L. M. Thermally induced denaturation of lyophilized bovine somatrotropin and lysozyme as impacted by moisture and excipients. *J. Pharm. Sci*. **1995**, *84*, 707−712.
27. Zhang, M. Z.; Pikal, K.; Nguyen, T.; Arakawa, T.; Prestrelski, S. J. The effect of the reconstitution medium on aggregation of lyophilized recombinant interleukin-2 and ribonuclease A. *Pharm. Res*. **1996**, *13*, 643−646.

Acknowledgments

The authors thank Sylvia Wu for assistance in lyophilization, Dee Ann Henderson for technical support, Dennis Brooks for helping with moisture content determination, Tom Bewley and Tom Patapoff for critical reading and valuable suggestion about modification of the manuscript, and Tue Nguyen for project support.

JS980273G

Atmospheric Oxidation of Poly(oxyethylene) Alcohols. Identification of Ethoxylated Formates as Oxidation Products and Study of Their Contact Allergenic Activity

MARGARETA BERGH,* LI PING SHAO, KERSTIN MAGNUSSON, ELISABETH GÄFVERT, J. LARS G. NILSSON, AND ANN-THERESE KARLBERG

Contribution from *Department of Occupational Medicine, Dermatology, National Institute for Working Life, Solna, Sweden.*

Received May 18, 1998. Final revised manuscript received November 19, 1998.
Accepted for publication December 15, 1998.

Abstract □ Ethoxylated alcohols are widely used as surfactants. In the present study we have continued our investigations on the degradation with time upon air exposure of the ethoxylated alcohols at normal storage and handling. As a result, a new group of ethoxylated formates with the general formula $C_{12}H_{25}(OCH_2CH_2)_nOCHO$ ($n = 0–4$) was identified in $C_{12}H_{25}(OCH_2CH_2)_5OH$ stored and handled at room temperature. To facilitate the identification work, reference compounds were synthesized. The formates showed no allergenic activity in the sensitization studies performed. In previous investigations on the same ethoxylated alcohol, we have identified formaldehyde and ethoxylated aldehydes among the oxidation products formed. Formaldehyde is a common contact allergen, and the ethoxylated aldehydes were shown to have a sensitizing capacity of the same magnitude as formaldehyde. The instability of the ethoxylated alcohols and formation of oxidation products may give an allergenic contribution to hand eczema caused by work with water and surfactants. To investigate the clinical significance in man an appropriate diagnostic patch testing in exposed humans is required.

Introduction

The ethoxylated surfactants have wide applications and are used in, for example, household cleaners, laundry products, pharmaceuticals, and industrial and institutional cleaners. In 1993 the total consumption of ethoxylated alcohols was estimated to about 313000 tons in Western Europe.[1] The number of oxyethylene groups in nonionic ethoxylated surfactants determines application behavior, e.g. detergency, emulsification, and wetting, at a given temperature in all formulation work.

In recent studies[2−4] we have shown that oxidation products were rapidly formed from ethoxylated nonionic surfactants during storage and handling at room temperature in daylight and also during storage in dark. We detected peroxides,[2,4] formaldehyde,[2,4] and a series of ethoxylated aldehydes[3] among the oxidation products in our studies on Tween 80 (sorbitan monooleate)[2] and ethoxylated fatty alcohols.[3,4] The ethoxylated surfactants have so far been considered to be stable products at normal storage and handling.[5] The products are usually stored at room temperature, since they become semisolid at lower temperatures. However, ethoxylated surfactants are polyethers and as such susceptible to oxidation at air exposure. This autoxidation is theoretically discussed in the surfactant literature.[6] The proposed mechanism for autoxidation is a free radical mechanism initiated by minor amounts of free radicals present or catalyzed by metal salts, e.g. copper sulfate.[6] Peroxides and hydroperoxides are the primary oxidation products followed by formation of carbonyl compounds as secondary oxidation products.[7]

The prevalence of contact allergy in the general population in Europe is about 10%. Of those sensitized, about 2−4% have ongoing allergic contact dermatitis, which is the consequence of exposure to environmental chemicals.[8] About 90% of occupational contact dermatitis is located on the hands, and half of all work-related hand eczemas are caused by work with surfactants and water.[9] Most diagnoses of contact dermatitis from wet work are considered to be irritant dermatitis.[10] The diagnosis of allergy is difficult to exclude from irritancy in cases of chronic dermatitis. Surfactants are irritants, partially due to their ability to solubilize lipid membranes, since they possess both lipophilic and hydrophilic regions in their structures.[10] In our recent studies we found that the oxidation products identified after air exposure of ethoxylated surfactants had allergenic properties. Formaldehyde is a well-known contact allergen, and the ethoxylated aldehydes (Figure 1) were shown to be contact allergens in experimental sensitization studies.[3] In the literature some cases are reported of allergic contact dermatitis due to ethoxylated nonionic surfactants and emulsifiers.[11,12] Formaldehyde is described to be a significant allergen in women with hand eczema caused by occupational and domestic exposure.[13] Thus, allergenic oxidation products in ethoxylated surfactants may cause hand eczema or aggravate an ongoing irritant dermatitis in wet work.

In our previous studies on the identification of oxidation products formed from ethoxylated alcohols we have for the first time shown the formation of ethoxylated aldehydes with allergenic properties.[3] In the present study we have further investigated the autoxidation of the pure ethoxylated dodecyl alcohol, $C_{12}H_{25}(OCH_2CH_2)_5OH$ (below referred to as $C_{12}E_5$) by gas chromatography (GC) analysis during one year. We have identified a new group of oxidation products formed, the ethoxylated formates, and studied their allergenic activity.

Experimental Section

Chemicals—Tetraethylene glycol (99%) was obtained from Aldrich (Steinheim, Germany). Triethylene glycol (99%), formic acid (98−100%), 1-dodecanol (98%), 1-bromododecane, *p*-toluenesulfonic acid (99%), and dimethyl sulfoxide (DMSO) were obtained from Kebo Lab AB (Stockholm, Sweden). Sodium hydride (60% dispersion in mineral oil, toluene-soluble bags) was obtained from Acros Chimica N.V. (Geel, Belgium). Triethylene glycol mono *n*-dodecyl ether $C_{12}H_{25}(OCH_2CH_2)_3OH$ (CAS Reg. no. 3055-94-5) (referred to as $C_{12}E_3$) and pentaethylene glycol mono *n*-dodecyl

* Corresponding author. Phone: + 46 8 730 9919. Fax: + 46 8 730 9892. e-mail: mbergh@niwl.se.

10.1021/js980210y CCC: $18.00
Published on Web 02/17/1999

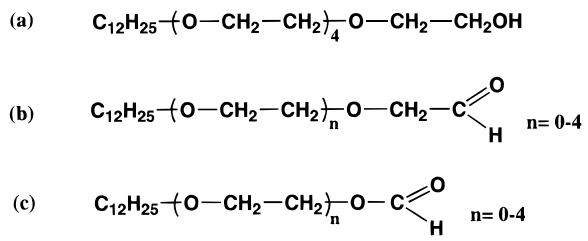

Figure 1—(a) Ethoxylated alcohol (pentaethylene glycol mono *n*-dodecyl ether) $C_{12}E_5$. (b) The earlier identified ethoxylated aldehydes in air exposed $C_{12}E_5$. (c) In the present study the identification and sensitizing capacity of the ethoxylated formates are presented.

ether $C_{12}H_{25}(OCH_2CH_2)_5OH$ (CAS Reg. no. 3055-95-6) (referred to as $C_{12}E_5$) were purchased from Nikko Chemicals CO., Ltd. (Tokyo, Japan). The purity was stated to be 98% by the producer, which was confirmed with GC analysis. The other ethoxylated alcohols were synthesized as described below. Standard chemicals were of p.a. quality.

Instrumentation and Mode of Analysis—FT-IR spectra were recorded with a Perkin-Elmer 16 PC FT-IR instrument using a sealed liquid cell with KBr windows. NMR spectroscopy was performed on a JEOL EX 270 instrument in $CDCl_3$ using tetramethylsilane as internal standard. GC analyses were carried out on a Hewlett-Packard HP 5890 gas chromatograph with a flame ionization detector (FID). The gas chromatograph was equipped with a fused silica capillary column (25 m × 0.22 mm i.d) coated with 0.2 μm CP-sil 8 CB (Chrompack, Middelburg, The Netherlands). Nitrogen was used as carrier gas at a linear gas velocity of 22 cm/s. An ELDS laboratory data system from Chromatography Data System Inc. (Svartsjö, Sweden) was used for registration and processing of the detector signal.

Mass spectrometric (MS) analyses were performed on a Finnigan Incos 50 quadrapole instrument equipped with a Varian 3400 gas chromatograph with an on-column injector. The MS analyses were carried out in electron impact (EI) and positive ion chemical ionization (PCI) modes. Introduction of the sample into the ion source was made via GC using on-column technique. The gas chromatograph was equipped with a fused silica capillary column (25 m × 0.25 mm i.d.) coated with 0.2 μm CP-sil 8 CB (Chrompack, Middelburg, The Netherlands), and helium was used as carrier gas. The temperature programming of the gas chromatograph oven was as follows: 35 °C for 1.0 min followed by a temperature increase of 10 °C/min up to 295 °C. The GC-MS transferline was held at 310 °C. The ion source was held at a temperature of 150 °C and the electron energy was 70 eV in the EI mode. In PCI mode the ion source was held at 80 °C, the electron energy was 110 eV, and the ion source pressure was about 1 Torr. At chemical ionization, methane of >99.995% purity was used as reagent gas, and the instrument was tuned by optimizing the reactant ions (CH_5^+, $C_2H_5^+$, and $C_3H_5^+$) to an approximate ratio of 5:4:1. The MS scan range in all analyses was *m*/*z* 50−600, and the scan cycle time was 0.6 s.

Synthesis—*Preparation of Dodecylethoxylated Alcohols **1**−**3***—Sodium hydride (0.80 g, 5.5 mmol) was stirred in DMSO (dry, 8 mL) at room temperature for 30 min. The appropriate glycol $H(OCH_2CH_2)_nOH$ (n = 1, 2, or 4) (77 mmol) was added slowly, and the mixture was stirred at room temperature under nitrogen for 2 h. 1-Bromododecane (5.0 g, 20 mmol) was added dropwise, and the mixture was heated at 90 °C overnight under nitrogen. The reaction mixture was dissolved in ethyl acetate and washed with water. The organic phase was dried over $MgSO_4$ and evaporated. The crude product was chromatographed on a silica gel column eluted with an increasing content of ethyl acetate 4−6% in hexane, followed by 20% methanol in ethyl acetate. The products **1**−**3** were obtained as clear oils in 57−66% yield and identified with FT-IR, NMR, and MS.

$C_{12}H_{25}OCH_2CH_2OH$ (1). Yield: 66%. FT-IR (neat): 3370 (O−H), 2850 and 2950 cm^{-1} (C−H). ^{1}H NMR ($CDCl_3$): δ 3.72 (tr, 2H, CH_2O), 3.53 (tr, 2H, CH_2O), 3.42 (tr, 2H, $CH_2CH_2CH_2O$), 2.11 (s, 1H, O**H**), 1.58 (m, 2H, $CH_2CH_2CH_2O$), 1.26 (m, 18H, (CH_2)$_9$) 0.85 (tr, 3H, CH_3). ^{13}C NMR ($CDCl_3$): δ 71.68, 71.43 ((CH_2O)$_2$), 61.85 (*C*H_2OH), 31.90 ($CH_3CH_2CH_2$), 29.63 (5 C:s), 29.47, 29.33 ((CH_2)$_7$), 26.09 (*C*H_2CH_2O), 22.66 (CH_3CH_2), 14.05 (*C*H_3). GC-MS-PCI *m*/*z* (% rel inten): 231 [M + 1]$^+$ (17), 230 M$^+$ (2), 229 [M − 1]$^+$ (17), 169 [$C_{12}H_{25}$]$^+$ (16), 63 [$HOCH_2CH_2OH_2$]$^+$ (100).

$C_{12}H_{25}(OCH_2CH_2)_2OH$ (2). Yield: 59%. FT-IR (neat): 3467 (O−H), 2850 and 2950 cm^{-1} (C−H). ^{1}H NMR ($CDCl_3$): δ 3.78−3.65 (m, 8H, (CH_2O)$_4$), 3.47 (tr, 2H, $CH_2CH_2CH_2O$), 2.85 (s, 1H, O**H**), 1.58 (m, 2H, $CH_2CH_2CH_2O$), 1.24 (m, 18H, (CH_2)$_9$), 0.87 (tr, 3H, CH_3). ^{13}C NMR ($CDCl_3$): δ 72.49, 71.56, 70.40, 70.08 (*C*H_2O)$_4$, 61.73 (*C*H_2OH), 31.86 ($CH_3CH_2CH_2$), 29.58 (2 C:s), 29.58 (3 C:s), 29.42, 29.29 ((*C*H_2)$_7$), 25.99 ($CH_2CH_2CH_2O$), 22.62 (CH_3CH_2), 14.05 (*C*H_3). GC-MS-PCI *m*/*z* (% rel inten): 275 [M + 1]$^+$ (53), 274 M$^+$ (3), 273 [M − 1]$^+$ (19), 166 [$C_{12}H_{22}$]$^+$ (23), 107 [$HO(CH_2CH_2O)_2H_2$]$^+$ (100).

$C_{12}H_{25}(OCH_2CH_2)_4OH$ (3). Yield: 57%. FT-IR (neat): 3374 (O−H), 2847 and 2948 cm^{-1} (C−H). ^{1}H NMR ($CDCl_3$): δ 3.63−3.56 (m, 16H, (CH_2O)$_8$), 3.40 (tr, 2H, $CH_2CH_2CH_2O$), 2.74 (s, 1H, O**H**) 1.55 (m, 2H, $CH_2CH_2CH_2O$), 1.22 (m, 18H, (CH_2)$_9$), 0.80 (tr, 3H, CH_3). ^{13}C NMR ($CDCl_3$): δ 72.46, 71.45, 70.51, 70.48, 70.48, 70.46, 70.24, 69.93 (*C*H_2O)$_8$, 61.57 (*C*H_2OH), 31.59 ($CH_3CH_2CH_2$), 29.30 (5C:s), 29.15, 29.01 (*C*H_2)$_7$, 25.73 ($CH_2CH_2CH_2O$), 22.30 (CH_3CH_2), 13.69 (*C*H_3). GC-MS-PCI *m*/*z* (% rel inten): 363 [M + 1]$^+$ (100), 362 M$^+$ (9), 361 [M − 1]$^+$ (61), 195 [$HO(CH_2CH_2O)_3$-$CH_2CH_2OH_2$]$^+$ (54), 177 [$(CH_2CH_2O)_4H$]$^+$ (12), 166 [$C_{12}H_{22}$]$^+$ (8), 133 [$(CH_2CH_2O)_3H$]$^+$ (16), 89 [$(CH_2CH_2O)_2H$]$^+$ (17), 45 [CH_2CH_2-OH]$^+$ (28).

*Preparation of Ethoxylated Formates **4**−**8***—Samples of the appropriate alcohol **1**−**3** and $C_{12}E_3$(4 mmol) were heated at 85 °C in formic acid (10 mL) with *p*-toluenesulfonic acid as catalyst for 4 h.[14−16] The reaction mixture was neutralized with a saturated (10 M) sodium hydroxide solution and washed with water, dried over $MgSO_4$, and concentrated in a vacuum. The crude product was chromatographed on a silica gel column eluted with an increasing content of ethyl acetate 30−70% in dichloromethane to give the pure ethoxylated formates **4**−**8** as clear oils in 80−100% yield. Identification was performed with FT-IR, NMR, and MS.

$C_{12}H_{25}OCHO$ (4). Yield 100%. FT-IR (neat): 2924 and 2854 (C−H aliphatic), 1732 (C=O), 1180 cm^{-1} (C−O). ^{1}H NMR ($CDCl_3$): δ 8.03 (s, 1H, OC*H*O), 4.14 (tr, 2H, CH_2OCHO), 1.63 (m, 2H, CH_2CH$_2$O), 1.29 (m, 18H, (CH_2)$_9$), 0.85 (tr, 3H, CH_3). ^{13}C NMR ($CDCl_3$): δ 161.35 (O*C*HO), 64.26 (*C*H_2O), 32.04 ($CH_2CH_2CH_3$), 29.67 (5C:s), 29.47 29.31 ((*C*H_2)$_7$), 25.93 (*C*H_2CH_2O), 22.80 (*C*H_2-CH_3), 14.24 (*C*H_3). GC-MS-PCI *m*/*z* (% rel inten): 215 [M + 1]$^+$ (2.62), 213 [M − 1]$^+$ (5.25), 169 [$C_{12}H_{25}$]$^+$ (69.2).

$C_{12}H_{25}OCH_2CH_2OCHO$ (5). Yield 95%. FT-IR (neat): 2924 and 2852 (C−H), 1732 (C=O), 1180 cm^{-1} (C−O). ^{1}H NMR ($CDCl_3$): δ 8.10 (s, 1H, OC*H*O), 4.31 (tr, 2H, CH_2OCHO), 3.67 (tr, 2H, CH_2O), 3.47 (tr, 2H, CH_2CH_2O), 1.58 (m, 2H, CH_2CH$_2$O), 1.26 (m, 18H, (CH_2)9), 0.87 (tr, 3H, CH_3). ^{13}C NMR ($CDCl_3$): δ 161.01 (O*C*HO), 71.55, 68.21, 63.13 (*C*H_2O)$_3$, 31.90 ($CH_2CH_2CH_3$), 29.58 (5C:s), 29.43, 29.32 ((CH_3)$_7$), 26.02 (*C*H_2CH_2O), 22.68 (CH_2CH_3), 14.24 (*C*H_3). GC-MS-PCI *m*/*z* (% rel inten): 259 [M + 1]$^+$ (30.5), 258 M$^+$ (0.39), 257 [M − 1]$^+$ (1.77), 169 [$C_{12}H_{25}$]$^+$ (6.32), 73 [CH_2CH_2-OCHOH]$^+$ (100).

$C_{12}H_{25}(OCH_2CH_2)_2OCHO$ (6). Yield 92%. FT-IR (neat): 2900 and 2850 (C−H), 1732 (C=O), 1180 cm^{-1} (C−O). ^{1}H NMR ($CDCl_3$): δ 8.09 (s, 1H, OC*H*O), 4.33 (tr, 2H, CH_2OCHO), 3.75−3.60 (m, 6H, (CH_2O)$_3$), 3.52 (tr, 2H, CH$_2$CH_2O), 1.57 (m, 2H, CH_2CH$_2$O), 1.25 (m, 18H, (CH_2)$_9$), 0.87 (tr, 3H, CH_3). ^{13}C NMR ($CDCl_3$): δ 161.07 (O*C*HO), 71.73, 70.80, 70.15, 68.98, 63.18 (*C*H_2O)$_5$, 32.04 ($CH_2CH_2CH_3$), 29.74 (5C:s), 29.59, 29.47 (*C*H_2)$_7$, 26.20 (*C*H_2CH_2O), 22.80 (CH_2CH_3), 14.24 (*C*H_3). GC-MS-PCI *m*/*z* (% rel inten): 303 [M + 1]$^+$ (38.0), 302 M$^+$ (8.45), 301 [M − 1]$^+$ (17.6), 275 [M + 1 − 28]$^+$ (5.63), 166 [$C_{12}H_{22}$]$^+$ (19.7), 135 [$H_2(OCH_2CH_2)_2OCHO$]$^+$ (71), 73 [$H_2OCH_2CH_2OCHO$]$^+$ (95.8).

$C_{12}H_{25}(OCH_2CH_2)_3OCHO$ 7. Yield 90%. FT-IR (neat): 2945 and 2835 (C−H), 1724 (C=O), 1180 cm^{-1} (C−O). ^{1}H NMR ($CDCl_3$): δ 8.09 (s, 1H, OC*H*O), 4.32 (tr, 2H, OCH_2OCHO), 3.75−3.56 (m, 10H, (CH_2O)$_5$), 3.44 (tr, 2H, CH$_2$CH_2O), 1.55 (m, 2H, CH_2CH$_2$O), 1.25 (m, 18H, (CH_2)$_9$), 0.88 (tr, 3H, CH$_3$). ^{13}C NMR ($CDCl_3$): δ 160.93 (O*C*HO), 71.51, 70.66, 70.62, 70.55, 70.01, 68.82, 63.00 (*C*H_2O)$_7$, 31.88 ($CH_2CH_2CH_3$), 29.58 (5C:s), 29.45, 29.31 ((CH$_2$)$_7$), 26.06 (*C*H_2CH_2O), 22.64 (*C*H_2CH_3), 14.09 (*C*H_3). GC-MS-PCI *m*/*z* (% rel inten): 347 [M + 1]$^+$ (29.2), 346 M$^+$ (2.89), 345 [M − 1]$^+$ (13.6), 317 [M + 1 − 28]$^+$ (4.82), 179 [$(CH_2CH_2O)_3H$]$^+$ (49.5), 166 [$C_{12}H_{22}$]$^+$ (21.91), 73 [CH_2CH_2OCHO]$^+$ (100).

$C_{12}H_{25}(OCH_2CH_2)_4OCHO$ (8). Yield 80% FT-IR (neat): 2942 and 2845 (C−H), 1732 (C=O), 1178 cm^{-1} (C−O). ^{1}H NMR ($CDCl_3$): δ 8.10 (s, 1H, OC*H*O), 4.33 (tr, 2H, CH_2OCHO), 3.76−3.60 (m, 14 H, (CH_2O)$_7$), 3.45 (tr, 2H, CH$_2$CH_2O), 1.58 (m, 2H, CH_2CH$_2$O), 1.26

(m, 18H, $(CH_2)_9$), 0.89 (tr, 3H, CH_3). ^{13}C NMR ($CDCl_3$): δ 160.94 (OCHO), 71.52, 70.58 (5C, s), 70.10, 68.81, 63.00 $(CH_2O)_9$, 31.88 ($CH_2CH_2CH_3$), 29.55 (5C:s), 29.45, 29.31 $(CH_2)_7$, 26.04 (CH_2CH_2O), 22.64 (CH_2CH_3), 14.07 (CH_3). GC-MS-PCI *m/z* (% rel inten): 391 $[M + 1]^+$ (8.12), 390 M^+ (1.63), 389 $[M - 1]^+$ (11.8), 363 $[M + 1 - 28]^+$ (90.2), 223 $[H(OCH_2CH_2)_4OCHO]^+$ (36.3), 166 $[C_{12}H_{22}]^+$ (24.0), 133 $[(CH_2CH_2O)_2H]^+$ (17.8), 73 $[CH_2CH_2OCHO]^+$ (100).

Storage and Handling of Ethoxylated Alcohols—Two samples of undiluted $C_{12}E_5$ (98%) were used in the experiment. Sample 1 (5 g) was stored in a closed 10 mL vessel in darkness at room temperature (20−22 °C) for 12 months. Sample 2 (5 g) was stirred gently in an open 10 mL Erlenmeyer flask in daylight at room temperature (20−22 °C) for 1 h, 4 times a day, during 12 months, mimicking what we considered normal handling in laboratories and industries. The top of the flask was covered with aluminum foil to prevent contamination and to diminish the evaporation.

Detection of Oxidation Products in Ethoxylated Alcohols—Samples 1 and 2 were analyzed with GC-MS analysis using the synthesized references.

Samples 1 and 2 were also analyzed with GC every fourth week after start of the exposure. The content of the ethoxylated formates in samples 1 and 2 was quantified using the synthesized reference compounds. Aliquots of 2 × 10 mg were taken out from each sample. Two sample preparations (1.0 mg/mL) from each sample were prepared and dissolved in dichloromethane, methyl stearate was added as internal standard, and a duplicate analysis on each sample was performed. On-column injections (1 μL) were made at an injector temperature of 35 °C. The column oven was kept at 35 °C for 2 min whereafter the temperature of the column was raised with a rate of 10 °C/min to 210 °C. The column temperature was then raised with a rate of 5 °C/min to a final value of 240 °C which was kept for 10 min.

Studies on the Sensitizing Capacity of 5—The sensitization experiment was performed using female Dunkin-Hartley guinea pigs (weight 250−300 g) from AB Sahlins Försöksdjursfarm, Malmö, Sweden. The animals were kept on a standard diet from Beekey, North Humberside, England, and water *ad libitum*. The animals were randomly assigned to one exposed, group 1 ($n = 15$), and one control group, group 2 ($n = 15$).

The sensitization study was performed according to the Cumulative Contact Enhancement Test (CCET) method[17] in a modified form with closed epidermal challenge testing.[18,19] At induction the animals received an occlusive epidermal application on the shaved upper back on days 0, 2, 7, and 9. About 200 mg of the test material was applied on pieces of filter paper (4 × 2 cm) at each of the four inductions. The FCA injections at the third induction were omitted according to our earlier experience of sensitization studies on surfactants.[3] Challenge testing was performed on day 21 on the shaved left flank using Finn Chambers (aluminum chambers, 8 mm i.d from Epitest, Helsinki, Finland) with approximately 15 mg of the test material applied in each chamber.

The exposed group was induced with **5** 10% w/w (2.6×10^{-4} mol/g) in water, while the animals in the control group received water alone. Both groups were challenged with 10, 5, and 1% w/w (2.6×10^{-4}, 1.3×10^{-4}, and 2.6×10^{-5} mol/g) of **5** in water, with $C_{12}E_5$ 5% (1.3×10^{-4} mol/g) in water, and $C_{12}E_4OCH_2CHO$ 1% w/w (2.5×10^{-5} mol/g) in water (Table 1). Water was applied as a vehicle control. The chambers were removed after 24 h, and the reactions were assessed at 48, 72, and 96 h after start of the exposure. The minimum criterion for a positive reaction was a confluent erythema.

The experiment was performed with the equimolar concentrations for induction and challenge as used in the experiments with the ethoxylated aldehyde, $C_{12}H_{25}(OCH_2CH_2)_4OCH_2CHO$.[3] The challenge concentrations of **5** were in pretests shown to be nonirritating in three untreated guinea pigs. Patch testing with concentrations 20−1% of **5** in water gave no skin reactions after 48 and 72 h. The experiment was approved by the local ethics committee.

Statistical Analyses—The result from the animal experiment was analyzed with Fisher's exact test. The number of reactions to each applied test substance in the exposed animals was compared with the number of reactions in the control group. A p value <0.05 was statistically significant.

Table 1—Sensitizing Potential of Compound 5 and Cross-Reactivity Studies with $C_{12}E_5$ and an Ethoxylated Aldehyde in Guinea Pigs Using the Modified CCET Method without Adjuvant

	no. of animals with positive reaction after exposure[a]					
	5 (% w/w in water)			C12E5[b]	aldehyde[c]	
guinea pigs	10	5	1	5	1	water
	Group 1[d]					
exposed ($n = 15$)						
48 h	0	0	0	1[a]	1	0
72 h	0	0	0	2	2	0
96 h	0	0	0	1	1	0
	Group 2					
controls ($n = 15$)						
48 h	0	0	0	0	1	1
72 h	0	1	0	1	1	1
96 h	0	0	0	1	0	1

[a] The figures are the number of animals with confluent erythema 48, 72, and 96 h after application of the test material. [b] Ethoxylated alcohol, $C_{12}E_5$, 5% (w/w in water). [c] Ethoxylated aldehyde with four ethylenoxide groups, $C_{12}H_{25}(OCH_2CH_2)_4OCH_2OCHO$, 1% (w/w in water). [d] Induction: 10% (w/w in water) of **5** in water.

Results

Spectral Characteristics—In FT-IR the specific hydroxyl resonance of the synthesized alcohols **1**−**3** was observed at 3370−3467 cm^{-1}. The FT-IR spectra of the synthesized ethoxylated formates **4**−**8** had a specific carbonyl resonance at 1724−1732 cm^{-1} and the C−O resonance at 1180 cm^{-1} from the ester group.[15] The NMR signals were compared with literature data for poly(oxyethylene) alcohols[20,21] and formates[16] and accorded with structures **1**−**3** and **4**−**8**. MS analyses in the GC-EI mode yielded no molecular ions of the ethoxylated alcohols and formates. Aliphatic ethers normally exhibit weak molecular ion peaks.[22] In the GC-MS-PCI analyses of the synthesized alcohol ethoxylates, **1**−**3**, the molecular ion M^+ and $[M + 1]^+$ and $[M - 1]^+$ ions were observed. Cleavage of the ethoxylated chain led to fragments of the general formula $[(CH_2CH_2O)_nH]^+$. These data, together with the FT-IR and NMR data are consistent with the structures **1**−**3**. In the GC-MS-PCI analyses of the synthesized formates **4**−**8** the molecular ion M^+ and $[M + 1]^+$ and $[M - 1]^+$ ions were observed together with specific fragments with the general formula $[(CH_2CH_2O)_nH]^+$ and $[CH_2CH_2O)_nOCHO]^+$. The $[M - 1]^+$ ion fragment corresponded to α-cleavage. No adducts with methane, $[(M + C_2H_5)^+]$ and $[(M + C_3H_5)^+]$ were seen. These data, together with the FT-IR and NMR data are consistent with the structures **4**−**8**, $C_{12}H_{25}(OCH_2CH_2)_n$-OCHO, $n = 1-4$.

Detection of Oxidation Products in Ethoxylated Alcohols—The ethoxylated formates, $C_{12}H_{25}(OCH_2CH_2)_n$-OCHO, $n = 1-4$, were all detected in samples 1 and 2 of $C_{12}E_5$ with GC-MS-PCI analyses using **4**−**8** as reference compounds. The alcohols, $C_{12}H_{25}(OCH_2CH_2)_nOH$ ($n = 1-4$), were identified in samples 1 and 2 of $C_{12}E_5$ with GC-MS-PCI analyses using $C_{12}E_3$ and the synthesized alcohols **1**−**3** as reference compounds.

The amount of the identified formates increased continuously with time. The formates seem to be rapidly formed since they were detected in small amounts in the GC analysis already in a newly opened bottle of the pure ethoxylated alcohol. The limits of detection for the substances **1**−**5** in the GC-analysis were estimated to be in the range 0.001−0.05 ng/μL using a signal-to-noise ratio 3:1 (S/N = 3). The total content of formates in $C_{12}E_5$ was 3.3% in the sample stored in a closed vessel in darkness (sample 1) and 4.0% in the sample handled in daylight (sample 2) after 12 months. The content of the individual

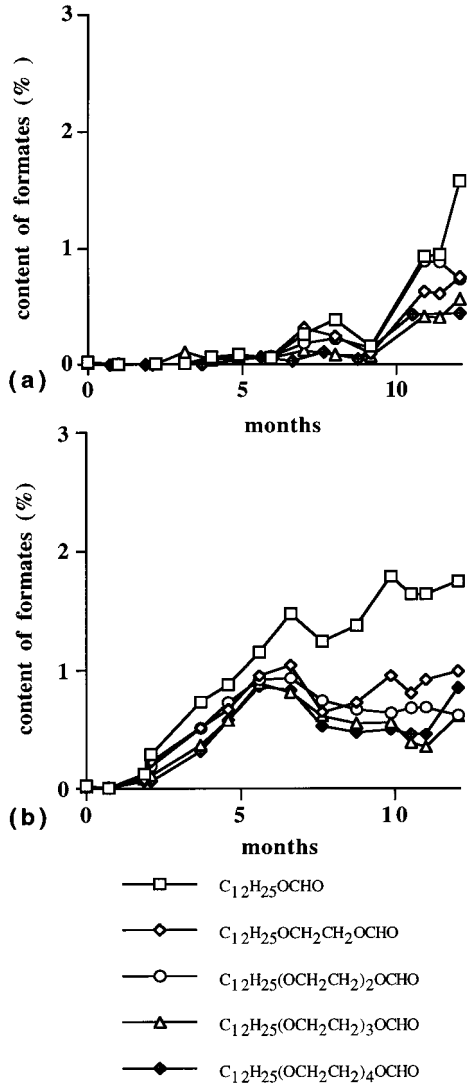

Figure 2—The content (%) of the individual ethoxylated formates **4**–**8** at different time points in $C_{12}E_5$: (a) sample 1 stored in a closed vessel in darkness at room temperature; (b) sample 2 stored and handled in daylight at room temperature.

formates in samples 1 and 2 is shown in Figure 2. Formate **4**, $C_{12}H_{25}OCHO$, was formed in the highest concentration. All calculations were performed relative to the internal standard. The coefficient of variation (CV) was below 10% at repeated measurements ($n = 10$). Duplicate analyses were performed of each sample. Approximately 5% of the total sample volume (5 g) was used for analysis, which was not regarded to contribute to the degradation. Figure 3 shows the GC separation of oxidation products in sample 2 air exposed for 12 months. The oxidation products that we have identified are assigned in the chromatogram with retention times corresponding to homologue retention characteristics accordning to boiling point.

Sensitizing Capacity of 5—No sensitizing response was observed to **5** in the animal experiment (Table 1). No cross-reactivity was observed to the corresponding alcohol, $C_{12}E_5$, or to the ethoxylated aldehyde, $C_{12}H_{25}(OCH_2CH_2)_4OCH_2CHO$. Some irritation was seen when the animals were tested with the alcohol and the aldehyde.

Discussion

Air exposure during storage and handling of the pure ethoxylated alcohol $C_{12}E_5$ at room temperature results in

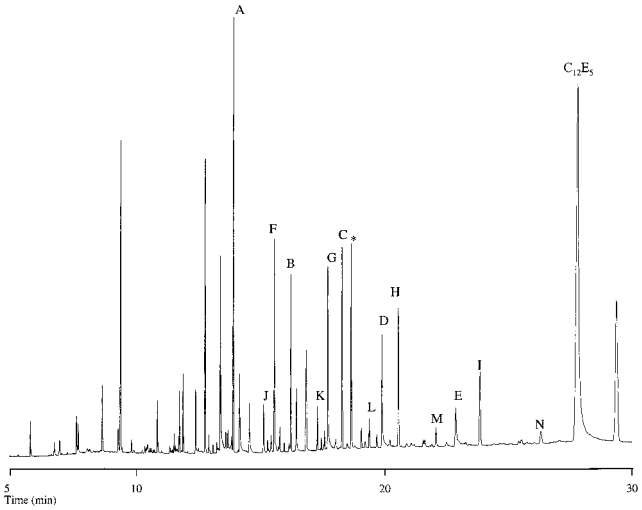

Figure 3—GC chromatogram showing the separation of different degradation products formed at air exposure of $C_{12}E_5$. The peak from the original ethoxylated alcohol is assigned $C_{12}E_5$, peaks A–E are the homologue series of ethoxylated formates, $C_{12}H_{25}(OCH_2CH_2)_nOCHO$ $n = 0$–4, eluting in the order of boiling point; peaks F–I are the homologue series of ethoxylated alcohols, $C_{12}H_{25}(OCH_2CH_2)_nOH$ $n = 1$–4, eluting in the order of boiling point; peaks J–N are the homologue series of ethoxylated aldehydes, $C_{12}H_{25}(OCH_2CH_2)_nOCH_2CHO$ ($n = 0$–4), eluting in the order of boiling point. The peak assigned * is the internal standard, methyl stearate, with a retention time of 18.63 min.

a number of degradation products as illustrated by the gas chromatogram in Figure 3. Among the oxidation products identified, some have significant allergenic properties. So far, nonionic ethoxylated surfactants have been regarded as stable products and are normally stored at room temperature, since they become semisolid at lower temperatures.[5] The practical consequence will be that a product containing ethoxylated alcohols can have quite a different chemical composition after storage and handling compared to the original product. In addition to an increase of their harmful effects on skin[3] with time, there might also be a change in their surface active properties.[25] To avoid significant decomposition, the pure ethoxylated alcohols must be stored in the refrigerator (8 °C), which was demonstrated in a previous study.[4]

To the best of our knowledge, ethoxylated formates are described here for the first time. The formates, $C_{12}H_{25}(OCH_2CH_2)_nOCHO$, $n = 0-4$, were identified and their structures elucidated in the oxidation mixture of $C_{12}E_5$. Prior to the identification work, the dodecyl poly(oxyethylene) formates that theoretically might be formed were synthesized and used as reference compounds in the analyses. The major formate, $C_{12}H_{25}OCHO$ (**4**), is apparently formed due to cleavage between the poly(oxyethylene) groups and the alkyl chain. The ethoxylated aldehydes earlier identified[3] are formed by cleavage of the poly(oxyethylene) chain resulting in loss of oxyethylene units and also by oxidation of the terminal hydroxyl group yielding the dominant ethoxylated aldehyde, $C_{12}H_{25}(OCH_2CH_2)_4OCH_2CHO$. This indicates that the autoxidation proceeds with parallel and different mechanisms.

The amount of ethoxylated formates increased with time of air exposure as determined with GC analysis. Different compounds are predominant in the degradation mixture depending on the time of air exposure. In our previous studies[2–4] the formation of peroxides, formaldehyde and ethoxylated aldehydes was shown. The amount of peroxides was determined with the unspecific iodometric titration method[23] whereas the aldehydes were quantified using GC- and LC methods. Peroxides were initially formed followed by formation of formaldehyde and the ethoxylated alde-

hydes as secondary oxidation products. There was a decrease in the content of peroxides after a certain time during the oxidation process, while the content of aldehydes steadily increased.[2−4] The ethoxylated alcohols, $C_{12}H_{25}(OCH_2CH_2)_nOH$, ($n = 1-4$) that we identified in the oxidation mixture with GC-MS may be formed by decomposition of the corresponding peroxides or hydroperoxides, since alkyl hydroperoxides are reported to decompose to alcohols at temperatures above 90 °C.[24] The boiling point of $C_{12}E_5$ is in the range of 202−216 °C. Therefore, the commonly used GC technique involves injection via a split/splitless injector at a temperature of 280 °C. Despite the use of on-column injection technique in this study to avoid degradation of thermally unstable compounds at injection, the hydroperoxides were not detected with GC-MS. The hydroperoxides could have decomposed in the column when the column temperature increased during the analysis. To identify ethoxylated hydroperoxides alternative methods have to be employed.

In the predictive sensitization studies, Freund's complete adjuvant (FCA) is often used. FCA consists of Arlacel (mannide mono-oleate), a sorbitan emulsifier to promote a stable water-in-oil emulsion, and dried heat-killed *Mycobacterium tuberculosis* organisms to enhance the nonspecific immune response and raise the sensitivity of the method.[26] However, also an increased irritability of the skin may be seen. Determination of the sensitizing potential of chemicals, such as surfactants, with irritating properties is difficult. The challenge testing should be performed with the chemical in nonirritating concentrations which might then be too low to detect an allergenic effect. In our investigation of the sensitizing capacity of the ethoxylated aldehydes[3] two parallel CCET protocols were used, one with intradermal FCA injections and one without. No increased allergenic activity was observed when FCA was administered, but an increased irritation was initially seen in the FCA-treated controls compared to the non-FCA-treated. A dose−response relationship was seen in both experiments. Thus, in our subsequent experiments with ethoxylated alcohols[4] and formates no FCA treatment was performed. In these experiments the compounds showed no significant allergenic activity (Table 1). Some irritation was seen showing the difficulties when testing with irritants. However, irritation in some of the control animals can also be observed in sensitization studies of other substances.[17]

Since alcohols and esters are rare sensitizers, the absence of a sensitizing capacity for the ethoxylated formate was not surprising.[27] To cause sensitization, a compound (hapten) has to penetrate the skin and react with macromolecules in the skin to form a complete antigen that is recognized as foreign. Molecules which can function as haptens in allergic contact dermatitis are either electrophilic or have structures that can easily form radicals.[27] Such molecules are able to react with the nucleophilic skin proteins forming stable covalent bonds. In our studies, three ethoxylated compounds have so far been tested for their contact allergenic properties, i.e., $C_{12}E_5$,[4] $C_{12}H_{25}(OCH_2CH_2)_4OCH_2CHO$[3] and $C_{12}H_{25}(OCH_2CH_2)_4OCHO$. The alcohol has no electrophilic properties, and contact allergenic activity could not be observed.[4] The formate has a very low reactivity as electrophile, whereas the aldehyde is an apparent electrophilic group. In our tests, only the aldehyde[3] showed contact allergenic activity which is in accordance with its electrophilic properties.

In a sample of $C_{12}E_5$ stored at room temperature only 70% of the original product remained after 6 months. Similar analysis after 12 months storage was not performed. The results in this study together with earlier investigations of the autoxidation of $C_{12}E_5$ show that the content of the identified oxidation products constitutes less than 10% of the total content in the product after 6 months. This indicates that a major part of the oxidation and degradation products from $C_{12}E_5$ still remains to be identified in the complex oxidation mixture. Our data indicates that the composition of ethoxylated alcohols may change rather rapidly upon storage. It has not been a topic of this study to investigate this in detail, but our data support that a stability study is requested.

It is important to further investigate the skin effects of the widely used ethoxylated surfactants, since a majority of the cases of occupational dermatits is caused by work with water and surfactants. Various types of ethoxylated surfactants are also used as emulsifiers in creams and lotions used on the skin. The clinical significance to man will require an appropriate diagnostic patch testing in exposed humans. The sensitizing capacity of other oxidation/degradation products will be studied and also the influence of oxidation on the skin-irritating properties.

References and Notes

1. Modler, F.; Willhalm, R.; Yoshida, Y. Surfactants, household detergents and their raw material. In *CEH (Chemical Economics Handbook)*; Stanford Research Institute: Palo Alto, CA, 1994; pp 583.8001A−583.0003J.
2. Bergh, M.; Magnusson, M.; Nilsson, J. L. G.; Karlberg, A.-T. Contact allergenic activity of Tween 80 before and after air exposure. *Contact Dermatitis* **1997**, *37*, 9−18.
3. Bergh, M.; Shao, L. P.; Gäfvert, E.; Nilsson, J. L. G.; Karlberg, A.−T. Contact allergens from surfactants. Atmospheric oxidation of polyoxyethylene alcohols, formation of ethoxylated aldehydes and their allergenic activity. *J. Pharm. Sci.* **1998**, *87*, 276−282.
4. Bergh, M.; Magnussson, K.; Nilsson J. L. G.; Karlberg, A.-T. Formation of formaldehyde and peroxides by air oxidation of high purity polyoxyethylene surfactants. *Contact Dermatitis* **1998**, *39*, 14−20.
5. Evetts, S.; Kovalski, C.; Levin, M.; Stafford, M. High-temperature stability of alcohol ethoxylates. *JOACS* **1995**, *72*, 811−816.
6. Donbrow, M. Stability of the polyoxyethylene chain. In *Surfactant Science Series volume 23, Nonionic surfactants: Physical chemistry*; Schick, M. J., Ed.; Marcel Dekker, Inc.: New York, 1987; pp 1011−1067.
7. Decker, C.; Manchal, J. Polyoxyéthylène: produits d'oxidation et schéma cinétique. *Makromol. Chem.* **1973**, *66*, 155−178.
8. Hypersensitivity induced by chemicals: Report on a WHO consultation. In *Allergic hypersensitivities induced by chemicals: recommendations for prevention*. Vos, J. G., Younes, M., Smith, E., Eds.; CRC Press: Boca Raton, FL, 1996; pp 3−18.
9. Rycroft, R. J. G. Occupational contact dermatitis. In *Textbook of Contact Dermatitis*, 2nd ed.; Rycroft, R. J. G., Menné, T., Frosch, P. J., Eds.; Springer-Verlag: Berlin, 1995; pp 343−357.
10. Effendy, I.; Maibach, H. I. Surfactants and experimental irritant contact dermatitis. *Contact Dermatitis* **1995**, *33*, 217−225.
11. Dooms-Goossens, A.; Blockeel, I. Allergic contact dermatitis and photoallergic contact dermatitis due to soaps and detergents. *Clin. Dermatol.* **1996**, *14*, 67−76.
12. Pasche-Koo, F.; Piletta, P.-A.; Hunziker, N.; Hauser, C. High sensitization rate to emulsifiers in patients with chronic leg ulcers. *Contact Dermatitis* **1994**, *31*, 226−228.
13. Cronin; E. Formaldehyde is a significant allergen in women with hand eczema. *Contact Dermatitis* **1991**, *25*, 276−282.
14. Dymicky, M. A general method for the preparation of formates. *Org. Prep. Proc. Int.* **1982**, *14*, 177−181.
15. Martinez, J.; Laur, J. Active esters of formic acid as useful formylating agents: Improvements in the synthesis of formyl-amino acid esters, N-α-Formyl-Met-Leu-Phe-OH, and Formyl-Met- Lys-Pro-Arg, a phagocytosis stimulating peptide. *Synthesis* **1982**, *11*, 979−981.
16. Bhart, I.; William, R.; Gelbaum L. T. Methanol-formic acid esterification equilibrium in sulfuric acid solution: Influence of Sodium Salts. *Ind. Eng. Chem. Res.* **1993**, *32*, 981−985.
17. Tsuchyia, S.; Kondo, M.; Okamoto, K.; Takase, Y. The cumulative contact enhancement test. In *Contact Allergy Test in Guinea Pigs*; Andersen, K. E., Maibach, H. I., Eds.; Karger: Basel, **1985**; pp 208−219.

18. Boman, A.; Karlberg A−T.; Wahlberg, J. E. Experiences with Freund's complete adjuvant test (FCAT) when screening for contact allergens in colophony. *Contact Dermatitis* **1988**, *18*, 25−29.
19. Karlberg, A.-T.; Gäfvert, E.; Hagelthorn, G.; Nilsson, J. L. G. Maleopimaric acid − a potent sensitizer in modified rosin. *Contact Dermatitis* **1990**, *22*, 193−201.
20. Ribeiro, A. A.; Dennis, E. A. Motion in nonionic micelles and mixed micelles with phospholipids- C-13 spin−lattice relaxation study on p- tert-octylphenylpolyoxyethylene ethers. *J. Phys. Chem*. **1976**, *80*, 1746−1753.
21. Ribeiro, A. A.; Dennis, E. A. A carbon −13 and proton nuclear magnetic resonance study on the structure and mobility of nonionic alkyl polyoxyethylene ether micelles. *J. Phys. Chem*. **1977**, *81*, 957−963.
22. McLafferty, F. W.; Turecek, F. Detailed mechanisms of ion fragmentation. *Interpretation of mass spectra*; University Science Books: Mill Valley: CA, 1993; pp 261−264.
23. *European Pharmacopoeia III*; Council of Europe: 67075 Strasbourg Cedex, ISBN 9287129916; p 2.5.5.
24. Foglia, A.; Sibert, L. S.; Vail, P. D. Gas−liquid and high-performance liguid chromatographic analysis of aliphatic hydroperoxides and dialkyl hydroperoxides. *J. Chromatogr*. **1993**, *637*, 157−165.
25. Blute, I.; Svensson, M.; Holmberg, K.; Bergh, M.; Karlberg, A.-T. Solution behavior of a surfactant aldehyde − the oxidation product of an alcohol ethoxylate. *Colloids Surf., A*, in press.
26. Herbert, W. J. Handbook of Experimental Immunology. In *Application of Immunological Methods*; Weir, D. M., Ed.; Blackwell Scientific Publications: Cambridge, MA, 1979; Vol. 3, pp A 3.1−A 3.12.
27. Roberts, D. W.; Lepoittevin, J.-P. Hapten-protein interactions. In *Allergic contact dermatitis. The molecular basis*; Lepoittevin, J.-P., Basketter, D. A., Goossens, A., Karlberg A−T., Eds.; Springer-Verlag: Berlin, 1998; pp 81−111.

Acknowledgments

We would like to thank Gunnel Hagelthorn for her skillful assistance with the animal testing. Financial support from the Swedish Council for Work Life Research is gratefully acknowledged.

JS980210Y

A publication of the American Pharmaceutical Association and the American Chemical Society

JOURNAL OF Pharmaceutical Sciences

May 1999
Volume 88, Number 5

MINIREVIEW

Solid-State Chemical Stability of Proteins and Peptides

M. C. LAI† AND E. M. TOPP*

Contribution from *Department of Pharmaceutical Chemistry, The University of Kansas, 2095 Constant Ave., Lawrence, Kansas 66047.*

Received September 16, 1998. Final revised manuscript received March 5, 1999.
Accepted for publication March 11, 1999.

Abstract ☐ Peptide and protein drugs are often formulated in the solid-state to provide stabilization during storage. However, reactions can occur in the solid-state, leading to degradation and inactivation of these agents. This review summarizes the major chemical reactions affecting proteins and peptides in the solid-state: deamidation, peptide bond cleavage, oxidation, the Maillard reaction, β-elimination, and dimerization/aggregation. Physical and chemical factors influencing these reactions are also discussed. These include temperature, moisture content, excipients, and the physical state of the formulation (amorphous vs crystalline). The review is intended to serve as an aid for those involved in formulation, and to stimulate further research on the determinants of peptide and protein reactivity in the solid-state.

Introduction

In the last two decades, proteins and peptides have become an important class of potent therapeutic drugs. However, their susceptibility to chemical degradation in solution presents a challenge in the development of stable protein pharmaceuticals.[1] As a result, many polypeptide drugs are formulated as lyophilized or freeze-dried products to prolong their shelf life.[2−4] While a "dry" formulation is generally more stable than the corresponding aqueous formulation, chemical degradation reactions can still occur.[2−4] In some cases, protein stability in the solid state is less than or comparable to that in solution.[5,6]

Factors that may impact the chemical stability of proteins and peptides in the solid-state include residual moisture and the excipient(s) used in a formulation. Excipients, such as polymers, are often included in protein and peptide formulations to protect the drug from degradation during processing and/or storage or to act as a matrix for controlled release. This review presents an overview of the chemical degradation reactions common to proteins and peptides in the solid state, and of our current knowledge regarding the effects of formulation and storage factors on peptide and protein stability in these systems.

The degradation pathways of proteins in the solid state can be classified into two types: chemical and physical. Chemical instability involves covalent modification of a protein or amino acid residue to produce a new molecule via bond cleavage, bond formation, rearrangement, or substitution. These chemical processes include such reactions as deamidation at asparagine (Asn) and glutamine (Glu) residues,[7] oxidation of sulfur atoms at cysteine (Cys) and methionine (Met) residues, disulfide exchange at Cys, and hydrolysis of aspartate (Asp) and glutamate (Glu) residues.[8] Physical instability refers to changes in the three-dimensional conformational integrity of the protein and does not necessarily involve covalent modification. These physical processes include denaturation, aggregation, precipitation, and adsorption to surfaces.[1] Chemical instabilities, such as deamidation and disulfide bond cleavage, may lead to physical instabilities, and vice versa. The physical instabilities of proteins will not be discussed in detail here, since the focus is chemical instability. The reader may refer to a recent article on the physical instability of proteins for further discussion.[9] Instead, this review will discuss reactions and factors that contribute to the chemical instability of proteins and peptides in the solid-state.

The different types of chemical reactions that contribute

* To whom correspondence should be addressed. Phone: (785) 864-3644. Fax: (785) 864-5736. e-mail: topp@ ukans.edu.
† Current address: Bristol Myers Squibb, New Brunswick, NJ.

10.1021/js980374e CCC: $18.00
Published on Web 04/14/1999

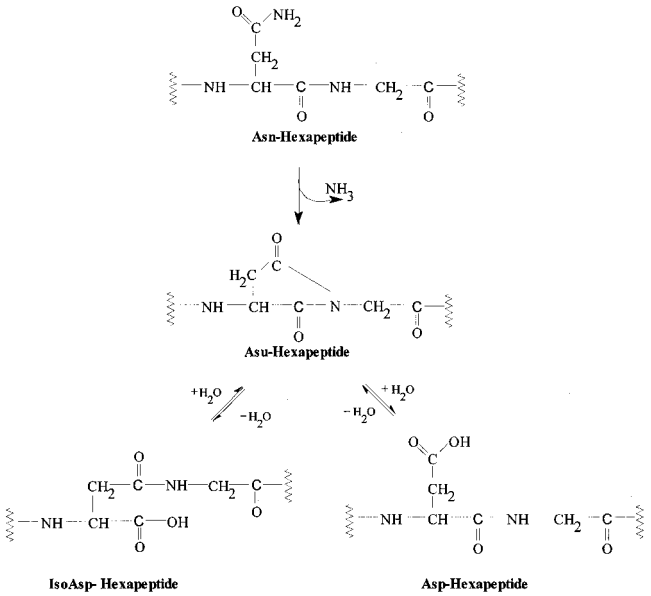

Scheme 1—Deamidation.

to protein and peptide instability in the solid-state are first presented. These include deamidation, peptide bond cleavage, oxidation, the Maillard reaction, β-elimination, and covalent dimerization or aggregation. In the next section, formulation factors that affect chemical stability, such as temperature, moisture, and excipients, are discussed. The review concludes with a summary and a discussion of the implications for future research.

Solid-State Reactions of Peptides and Proteins

Deamidation—Chemical instability in the solid state due to deamidation has been observed for human growth hormone (hGH),[4,10] recombinant human interleukin-1 receptor antagonist,[11] recombinant bovine somatotropin (growth hormone),[12] and insulin.[13,14] While there have been numerous mechanistic studies of protein and peptide deamidation in solution,[7,15–19] few such studies have been reported for deamidation in the solid state. Two studies which provide a mechanistic perspective on deamidation in solids are summarized below.

The stability and mechanism of degradation of the Asn-hexapeptide (Val-Tyr-Pro-Asn-Gly-Ala) were studied in solid formulations lyophilized from acidic solutions ranging from pH 3–5. The main degradation pathway for Asn-hexapeptide in the pH 3 formulation is deamidation via hydrolysis of the Asn side chain to produce the Asp-hexapeptide, which is further hydrolyzed at the Asp-Gly amide bond to generate a small quantity of tetrapeptide (Scheme 1).[18] As the pH of the solution prior to lyophilization increases from 3 to 5, intramolecular attack of the carbonyl center of the Asn side chain by the amide nitrogen of the succeeding amino acid to form a cyclic imide intermediate becomes more prominent, as evidenced by an increase in the cyclic imide in the product distribution (Scheme 1).[18] In solution at pH 5, the cyclic imide is hydrolyzed to form the isoAsp-hexapeptide, which is the dominant degradation product;[15] however, the isoAsp-hexapeptide was not observed in the solid state.[18] The absence of the isoAsp-hexapeptide in the product distribution may be due to the low level of water available for hydrolysis in the solid state. The mechanism of deamidation for the Asn-hexapeptide in the solid state was found to be similar to that in solution.[18] In an extension of this work, we have recently investigated the deamidation of this peptide in solid poly(vinyl alcohol) and poly(vinyl pyrrolidone) matrixes.[20–22] As in the lyophilized peptide, the mechanism of deamidation appears to be similar to that in solution, but the kinetics and product distribution are altered, particularly in matrices of low water content.

Human insulin has also been observed to undergo deamidation in the solid-state via a mechanism similar to that in solution.[13] In insulin formulations lyophilized from acidic solutions (pH 3–5), the rate-determining first step involves intramolecular nucleophilic attack of the C-terminal Asn_{A21} carboxylic acid onto the side-chain amide carbonyl to release ammonium and to form a reactive cyclic anhydride intermediate, which can further react with various nucleophiles.[13] The cyclic anhydride intermediate may react with water to form [desamido$_{A21}$] insulin,[13] and may also react with another molecule of insulin to form covalent dimers.[13] While the cyclic imide intermediates formed during Asn-hexapeptide deamidation in the solid state were observed to accumulate,[23] the cyclic anhydride intermediate formed during insulin deamidation did not.[13] Strickley and Anderson were able to verify that insulin deamidation proceeds via formation of a cyclic anhydride by using aniline trapping of the intermediate.[13] Consistent with these findings, Pikal and Rigsbee observed that the deamidation of human insulin occurs predominantly at Asn_{A21}, except at high relative humidity when deamidation at Asn_{B3} is more prevalent.[14]

Similar to the degradation of the Asn-hexapeptide discussed previously, the solid-state degradation of a model Asp-hexapeptide (Val-Tyr-Pro-Asp-Gly-Ala) is dependent on the pH of the bulk solution prior to lyophilization. This value is often referred to as the "pH" of the solid, since the true hydrogen ion activity is difficult to measure and pH is technically undefined in the solid-state. Under acidic conditions ("pH" 3.5 and 5.0), the Asp-hexapeptide mainly decomposes to produce a cyclic imide intermediate via base-catalyzed intramolecular cyclization.[23] Hydrolysis of the Asp-Gly amide bond also occurs but to a lesser extent. Under neutral and basic conditions ("pH" 6.5 and 8.0), the Asp-hexapeptide degrades exclusively via intramolecular cyclization to produce the Asu-hexapeptide, which is further hydrolyzed to form the isoAsp-hexapeptide.[23] At "pH" 8, the isoAsp-hexapeptide is the dominant degradation product,[23] similar to that observed in solution.[24]

Peptide Bond Cleavage—A second common degradation pathway for peptides and proteins involves cleavage of the peptide bond. Representative pathways of peptide bond cleavage are shown in Scheme 2. Lyophilized human relaxin formulated with glucose can undergo hydrolytic cleavage of the C-terminal serine (Ser) residue on the B-chain (Trp_{28}-Ser_{29}-COOH) upon storage at 40 °C.[25] This observation was supported by a reduction in molecular mass corresponding to the loss of Ser from fragment T5-T9 of relaxin, as verified by liquid chromatography/mass spectroscopy (LC/MS) and tryptic digest.[25] Li et al. proposed that this cleavage involved an initial reaction of the Ser hydroxyl group with glucose followed by subsequent hydrolysis of the Trp-Ser bond via a cyclic intermediate.[25]

In the solid state, the major degradation pathway of aspartame (α-aspartylphenylalanine methyl ester, APM) is intermolecular cyclization to form exclusively diketopiperazine (DKP) with the elimination of methanol.[26] In solution, the degradation of aspartame at neutral and basic pH also occurs mainly via cyclization to form diketopiperazine (DKP) or hydrolysis at the ester linkage to form α-aspartylphenylalanine (AP) and methanol.[27] Since water was absent in the aspartame solid-state study, no hydrolysis products were observed.[26]

The instability of the undecapeptide substance P (SP) in the solid state also proceeds through diketopiperzine

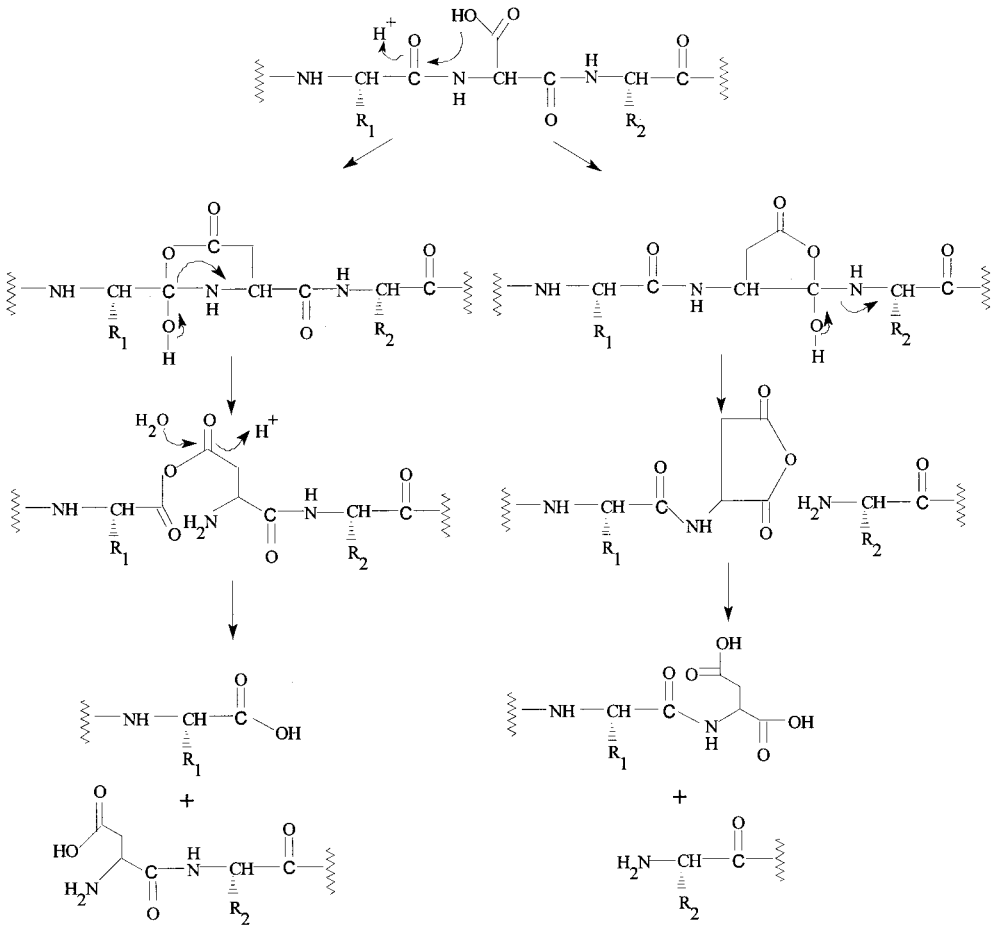

Scheme 2—Proteolysis.

formation. The main pathway of decomposition consists of the sequential release of N-terminal dipeptides via their diketopiperazines, cyclo(Arg-Pro) and cyclo(Lys-Pro).[28] Under the conditions studied, the release of N-terminal dipeptides dominates over other possible routes of spontaneous modification, such as oxidation and deamidation.[28]

Oxidation—The side chains of His, Met, Cys, Trp, and Tyr residues in proteins are potential sites for oxidation (Scheme 3).[1] A major chemical decomposition pathway for human growth hormone (hGH) in the solid state is methionine oxidation at Met_{14} to form the sulfoxide.[10] Even with minimal oxygen (~0.05%) in the vial headspace, decomposition via oxidation is comparable to or greater than that due to the alternative reaction of deamidation.[4] Storage of lyophilized hGH in an oxygen atmosphere results in greater decomposition than storage in a nitrogen atmosphere.[29] As in solution, atmospheric oxygen can easily oxidize Met residues in the solid state, leading to chemical instability and loss of biological activity.

Human insulin-like growth factor I (hIGF-I), lyophilized from phosphate buffer, also undergoes oxidation at its Met residue.[30] There were no significant differences in reaction rates (second-order kinetics) between solution and solid states.[30] However, Met oxidation in the solid-state constitutes a greater fraction of the total protein modification than in solution.[30] Both oxygen content and light exposure affect the oxidation rate.[30] Exposure to light increases the oxidation rate by a factor of 30.[30] This increase in oxidation rate with exposure to light and oxygen suggests that photooxidation and molecular oxygen may be involved in the generation of radicals. However, no further experiments were conducted to determine the nature of the radicals involved or the mechanism of Met oxidation in the solid state.

The oxidative deamidation of a cyclic hexapeptide, acetylcysteine-asparagine-(5,5-dimethyl-4-thiazolidinecarbonyl)-(4-(aminomethyl)phenylalanine)-glycine-aspartic acid-cysteine cyclic disulfide, in a lyophilized mannitol formulation does not appear to depend on molecular oxygen as a reactive species.[31] The oxidation reaction occurs at the aminomethyl phenylalanine moiety to form a benzaldehyde derivative.[31] This oxidative degradant is not detected in the neat solid drug stored under atmospheric oxygen, suggesting that oxygen is not involved in the reaction.[31] Instead, the decomposition of the heptapeptide may be due to a reaction with reducing sugar impurities in the mannitol excipient.[31] The proposed mechanism involves (1) formation of a Schiff base from the peptide primary amine reacting with the carbonyl of the aldehydic group on the reducing sugar, (2) tautomerization to a more stable configuration, conjugated with the phenyl group, and (3) hydrolytic cleavage of the new Schiff base to generate the observed aldehyde derivative.[31] The first part of this proposed reaction, the formation of the Schiff base, proceeds via a mechanism similar to the Maillard reaction, discussed below.

Maillard Reaction—The food industry has studied extensively the nonenzymatic browning of food due to the Maillard reaction, which results from reducing sugars reacting with either amino or free amine groups in proteins, leading to changes in both the chemical and physiological properties of the proteins (Scheme 4).[32] The first phase of the Maillard reaction involves a condensation reaction between the carbonyl of a reducing sugar and an amino group to form an N-substituted glycosylamine, which then converts to a Schiff base and a molecule of water.[33] Subsequent cyclization and isomerization (Amadori rearrangement) result in derivatives which cause discoloration

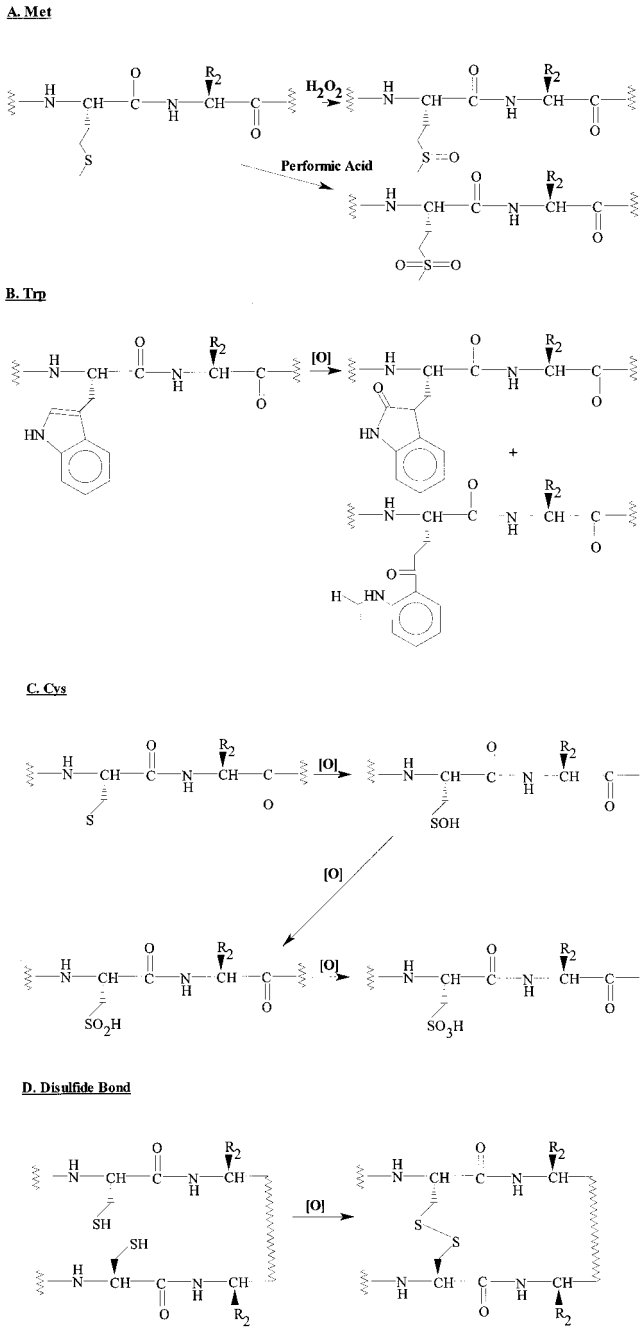

Scheme 3—Oxidation.

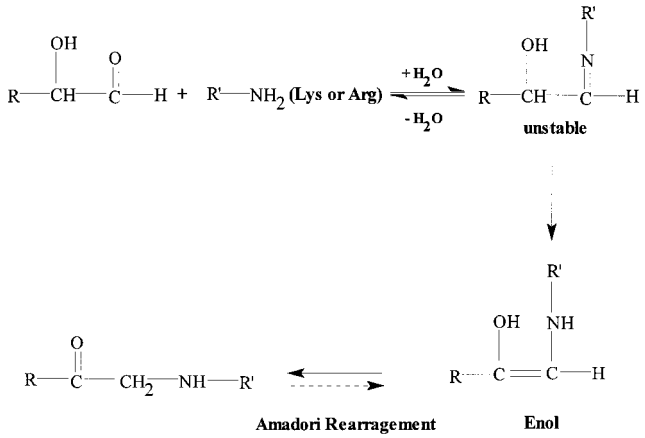

Scheme 4—Maillard Reaction.

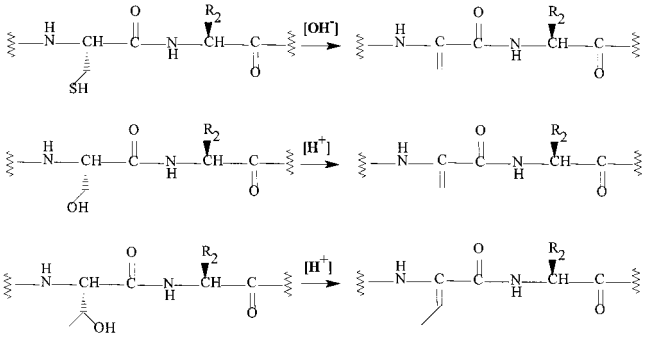

Scheme 5—β Elimination.

(nonenzymatic browning) of the formulation.[33] This type of covalent modification is a problem in the solid state because the initial aminocarbonyl condensation reaction to form the Schiff base is accelerated in the low moisture range.[25,34]

Lyophilized human relaxin (Rlx) formulated with glucose was observed to degrade via the Maillard reaction to form adducts with glucose.[25] The resulting adducts were shown by liquid chromatography/mass spectroscopy (LC/MS) to contain up to four glucose molecules covalently attached to Rlx.[25] With tryptic digestion, the individual reaction sites on Rlx were identified as including Lys_{A9}, Lys_{B9}, and Arg_{B17}.[25] The fourth reaction site was hypothesized to be either Lys_{A17} or Arg_{B13} on the T2-T7 fragment, which showed a broadened peak on the tryptic map, but positive identification was not possible using mass spectroscopy.[25]

A review of the food literature prior to 1966 by Goldblith and Tannenbaum revealed that lysine loss in foods is primarily due to the Maillard reaction.[35] Lysine is usually lost more rapidly than the other amino acids because of its free ϵ-amino group, which will react easily with the carbonyl of reducing sugars.[33] However, other residues, such as arginine, asparagine, and glutamine, have been observed to react with reducing sugars also.[25,34]

***β*-Elimination**—Lyophilized bovine insulin has been observed to degrade rapidly with increased water content to produce both covalent and noncovalent aggregates after incubation at 50 °C at various relative humidities.[36] Costantino et al. hypothesized that the reducible covalent interactions were due to thiol-catalyzed disulfide exchange.[36] They speculated that these free thiol groups resulted from the β-elimination of intact disulfide bonds in insulin.[36] The proposed mechanism for β-elimination involves hydroxide ion catalyzed cleavage of a carbon–sulfur bond (cysteine) (Scheme 5A), resulting in two new residues, dehydroalanine and thiocysteine.[36] Dehydroalanine can then react with lysine to form a lysinoalanine cross-link, while thiocysteine can undergo further decomposition to form thiol-containing products, such as hydrosulfide ions (free thiols).[36] A 5-fold increase in the level of free thiols was measured in lyophilized insulin after incubation at 50 °C and 96% relative humidity.[36] The free thiols formed during solid state aggregation were predominantly low molecular weight (<3000 Da), perhaps hydrosulfide ions.[36]

Covalent Dimerization and Aggregation—Dimerization and aggregation differ from the other types of degradation reactions discussed in this review in that they are not the result of a single chemical change. In fact, many different types of chemical or physical changes can induce the formation of dimers or aggregates. A brief description of chemically induced dimerization and aggregation is included here because of its importance in the pharmaceutical industry, and because much of the published literature on protein stability uses aggregate formation as

a key stability indicator. Dimerization or aggregation via covalent cross-linkage can be categorized into two types: reducible (via disulfide exchange) and nonreducible.

Reducible Dimerization and Aggregation—Lyophilized bovine serum albumin, ovalbumin, glucose oxidase, and β-lactoglobulin were observed to form covalent intermolecular disulfide linkages via a thiol−disulfide interchange reaction (Scheme 3D).[37,38] Liu et al. postulated that the intermolecular thiol−disulfide interchange results from the ionized thiol on one albumin molecule attacking the disulfide linkage of another albumin molecule:

$$P_1{-}S^- + P_2{-}S{-}S{-}P_2 \rightarrow P_1{-}S{-}S{-}P_2 + P_2{-}S^-$$

where P1 and P2 are the first and second protein molecules.[37] Thiolate ions rather than thiols are the reactive species in this reaction, since a decrease in the initial solution pH resulted in a slower aggregation rate while an increase in pH led to a more rapid reaction.[37] Free thiols are both necessary and sufficient for the moisture-induced aggregation to occur, since S-alkylated BSA (no free sulfhydryl groups) does not undergo aggregation.[37]

Moisture-induced aggregation of bovine insulin occurred via both noncovalent and covalent interactions. The covalent interactions were reportedly due to intermolecular disulfide bonds as evidenced by the dissolution of 21% of the aggregates upon treatment with a reducing agent, 10 mM dithioerythritol, and 1 mM EDTA to prevent its autoxidation.[36] Costantino et al. postulated that β-elimination produced free thiols which can subsequently catalyze the reshuffling of intact protein disulfides and lead to intermolecular disulfide cross-linkage.[36]

Chemical instability in the solid state can also occur after proteins first experience physical instability, such as denaturation or unfolding. Lyophilized recombinant human keratinocyte growth factor (rhKGF) is prone to aggregation at elevated temperatures.[39] Its aggregation pathway is proposed to proceed initially with unfolding of the protein, leading to formation of large soluble aggregates, which can form disulfide bonds.[39] Finally, these precipitates are converted to scrambled disulfides and/or nondisulfide cross-linked oligomers. Recombinant human albumin (rHA) also undergoes intermolecular thiol−disulfide interchange.[40] The unfolding or loss of tertiary structure in lyophilized rHA is suspected to have initiated the covalent thiol−disulfide exchange.[40] The covalent aggregation of ovalbumin, glucose oxidase, and β-lactoglobulin have also been linked to initial protein physical instability, such as protein unfolding.[37]

Nonreducible Dimerization and Aggregation—Lyophilized human insulin can undergo covalent dimerization at the Asn_{A21} site to form [Asp_{A21}-Phe_{B1}] and [Asp_{A21}-Gly_{A1}] insulin dimers.[13] This dimerization occurs after deamidation of the C-terminal Asn_{A21} forms a reactive cyclic anhydride intermediate that further reacts with the free N-terminal amine of another insulin molecule to yield dimers.[13] Lyophilized tumor necrosis factor (TNF) is also susceptible to the formation of cross-linked aggregates consisting of dimers, trimers, and higher oligomers, which were nonreducible when treated with β-mercaptoethanol.[41]

Another protein that forms nonreducible dimers in the solid state is recombinant bovine somatotropin (rbSt). When lyophilized rbSt was stored at 30 °C and 96% RH, the rate of loss of monomeric rbSt was greater than or equal to the rate of loss in solution.[12] Covalent dimers accounted for 80−90% of the total degradation products observed, with the remaining 20−10% attributed to deamidation/cleavage. The fractional amount of nonreducible dimers was only 23−26% in solution.[12] Most of the covalent dimers were not reducible with β-mercaptoethanol, indicating that the covalent bonds were not disulfide bonds.[12] Hageman et al. hypothesized that such covalent interaction could be due to the condensation of a lysine ϵ-amine and a carbonyl side chain of either Asp or Glu.[12]

A similar mechanism was proposed for the degradation of lyophilized ribonuclease A due to the formation of soluble and insoluble aggregates during storage at 45 °C. These aggregates were not dissociable using an anionic detergent (sodium dodecyl sulfate) and a reducing agent (2-mercaptoethanol), indicating that the aggregates were covalently attached but not through disulfide bonds.[42] Originally, protein oxidation was believed to be the cause of the aggregation since exposure to oxygen and light increased the solid-state aggregation rate of ribonuclease A.[43] Upon further investigation, Townsend et al. postulated that these covalent linkages did not result from an oxidation reaction but from the lysine residues reacting with asparagine or glutamine in a manner similar to the mechanism proposed by Hageman et al. for rbSt.[44] The loss of free lysine residues in the insoluble aggregates, as determined by amino acid analysis, is consistent with this mechanism.[44]

A loss of lysine and histidine residues also was observed by Schwendeman et al. in studies of the moisture-induced aggregation of tetanus and diphtheria toxoids.[45] In this case, however, aggregation was thought to be caused by formaldehyde-induced cross-linking of the proteins, since the aggregates were not soluble under either reducing (10 mM dithiothreitol, 1 mM EDTA) or denaturing (6 M urea) conditions, and since the toxoids had been treated with formaldehyde ("formalinized") during production.[45] The authors proposed a mechanism for the formation of stable intermolecular cross-links in this system and established methods for stabilizing the toxoid formulation against this reaction. Effective stabilization methods included succinylation, treatment with sodium borohydride, and addition of sorbitol.[45]

Factors Influencing Protein and Peptide Chemical Instability in Solids

The importance of temperature, moisture, and formulation excipients in determining the solid-state stability of small molecule drugs has been widely reported and accepted.[45−47] However, the effects of these factors on the solid state chemical stability of proteins and peptides are not as widely reported or understood. In addition to these factors, there is a growing literature that suggests that the hydrogen ion activity in the solid-state may have a significant influence on peptide and protein stability, paralleling the influence of pH in the solution state. The physical state of the solid (e.g., glassy vs rubbery) also has been shown to affect protein reactivity in the solid state. This section reviews published reports of the effects of these factors on peptide and protein stability in the solid state: temperature, moisture, excipients, hydrogen ion activity, and the physical state of the solid.

Temperature—The exposure of solid protein and peptide formulations to elevated temperatures generally decreases chemical stability by accelerating almost all chemical degradation reactions. For example, the deamidation of the Asn-hexapeptide increases with increasing temperature in the solid-state, with the formation of the cyclic imide intermediate becoming more favored over the direct hydrolysis of the Asn side chain.[18] In general, the increase in degradation rates with temperature did not follow an Arrhenius relationship within the temperature range studied (40−70 °C).[18] This suggests that acceleration of chemical reaction kinetics due to temperature is not solely responsible for the rate increase.

High-temperature inactivation of proteins often results from the destruction of disulfide bonds in cystine via β-elimination.[1] Consistent with this, the aggregation of insulin, in which β-elimination is the first step, was observed to increase with increasing temperature.[36] Increases in temperature have been observed to increase the rate of covalent cross-linking in the solid state for rbSt,[12] bovine insulin,[36] and tumor necrosis factor.[41] Most degradation reactions, such as deamidation,[18] peptide bond cleavage,[23,26] the Maillard reaction,[33] and oxidation[49] are accelerated by increasing temperature.

The increases in chemical instability with temperature may be due to increased mobility in the system or lowering of the activation barrier for reaction. In particular, significant changes in mobility may occur when the temperature range of interest includes the glass transition temperature (T_g) of an amorphous solid. In this case, changes in temperature affect not only the intrinsic reactivity of the degrading species, as observed in the solution state, but also the medium in which the reaction occurs. The relationship between the glass transition temperature (T_g) and reactivity is discussed below, under "Physical State of the Solid".

Moisture—Residual moisture is often thought to be responsible for protein and peptide chemical instability in the solid-state. In general, lyophilized protein formulations are more stable at lower water contents.[2] For example, the rate of degradation of the Asp-hexapeptide increases as the formulation vial moisture content increases.[23] Likewise, the deamidation of the Asn-hexapeptide increases as water content increases from 0.5% to 2%.[18] However, further increases in water content of up 3% do not significantly affect the rate of degradation.[18]

A similar effect of water on the deamidation of insulin was observed. The rate of degradation of lyophilized human insulin increases steeply with water content at low levels of hydration, approaching apparent plateaus at water contents greater than 20%.[13] The rate constants in the plateau region are comparable to those in solution.[13] The rate of rbSt loss due to deamidation and dimerization also increased with increased water content.[12] Increasing the relative humidity from 75% to 96% doubled the rate of rbSt loss.[12] However, the fractional amount of nonreducible dimers formed remained constant at around 80% and was independent of water content over the range studied.[12]

The covalent aggregation of bovine serum albumin (BSA) in the solid state greatly depends on water content.[38] Freeze-dried BSA was more prone to aggregation in the moistened solid state than in solution and exhibited a maximum at a very low moisture level.[38] The aggregation of BSA in solution increased with increasing ratio of water to protein.[38] Jordan et al. proposed that the increase in aggregation rate is related to the increase in water mobility with increasing ratios of water to protein.[38] Lyophilized recombinant human interleukin-1 receptor antagonist (rhIL-1ra) formulated with 2% glycine, 1% glycerol, and 10 mM citrate buffer at pH 6.5 exhibited maximum relative instability at a moisture content of around 0.8% (w/w) and the least stability at water contents less than 0.5% or around 3.2% (w/w).[11] A similar bell-shaped relationship between covalent aggregation and water content has been observed for ovalbumin, glucose oxidase, and β-lactoglobulin.[37]

A few other types of chemical instabilities appear to exhibit this bell-shaped relationship between degradation kinetics and moisture content. A bell-shaped dependence on moisture content also was observed for the aggregation of rHA via thiol-disulfide exchange, with maximum aggregation corresponding to 47 g water/100 g dry protein (96% RH).[40] The Maillard reactions usually have maximum rates in the low-moisture range.[34] Insulin,[50] casein,[51] and blood plasma proteins[52] in "dry" systems containing glucose show a maximum in the range of 40−80% RH (10−20% water content).[2]

This bell-shaped relationship between water content and reaction rate is often attributed to the effect of water on molecular mobility and reactant concentration. At low moisture levels, the Maillard reaction is less rapid because the diffusion and mobility of reactants are restricted.[2,34,52] As water content increases, molecular mobility increases, leading to enhanced reactant mobility which should facilitate the reaction.[37] At higher water contents, the reaction rates decrease due to dilution of the reactants by water.[37,53] Liu et al. observed that the addition of various types of polymers (carboxymethyl-cellulose, dextran, poly(ethylene glycol)) as diluents also appeared to hinder the aggregation of BSA.[37]

While residual water can often increase chemical degradation rates, under some conditions it can suppress a chemical reaction. Pikal et al. observed that the oxidation of a lyophilized hGH formulation was affected by increases in headspace oxygen at low moisture levels but not at higher moisture contents.[29] This may be due to water's possible antioxidant properties. Water may be either an antioxidant or an oxidant depending on the system.[32] Generally, oxidation in foods reaches a maximum at low water content and decreases as water content increases.[2]

In addition to having an effect on solid-state degradation rates, water may also affect the reaction pathways. For example, the formation of the cyclic imide intermediate during deamidation of the Asn-hexapeptide at pH 5 was favored over direct hydrolysis as water content increased.[18] The low moisture environment of the solid-state can generate product distributions which differ from those of the solution state.[18] The main product in the degradation of the Asp-hexapeptide in solids lyophilized from pH 3.5 and 5 solutions is the cyclic imide hexapeptide.[23] In contrast, the dominant degradation product in solution at pH 3.5 is the tetrapeptide and at pH 5.0 is the isoAsp-hexapeptide.[24] Thus, the reduced moisture in the lyophilized solids appears to suppress the hydrolysis of the Asu-hexapeptide intermediate to form the isoAsp-hexapeptide and that of the Asp-Gly peptide bond to form the tetrapeptide.

We have observed similar shifts in the product distribution in our recent studies of Asn-hexapeptide deamidation in poly(vinyl pyrrolidone) and poly(vinyl alcohol) matrices.[21] In addition, the order of the reaction with respect to water content differs in these two polymers: it is first-order in poly(vinyl pyrrolidone), but second order in poly(vinyl alcohol).[21] Since it is unlikely that the molecular deamidation mechanism differs significantly in the two systems, the results suggest that the role of water extends beyond that of reactant and may involve plasticization of the polymer matrices.

So, while the importance of water in chemical reactions is well recognized, the exact relationship between solid-state chemical instability and water content is often difficult to delineate and is dependent on the type of degradation reaction(s). This difficulty in determining the mechanism by which water affects the chemical stability of proteins and peptides in the solid state is in part due to the various roles water can play in promoting chemical reactivity. Water can act as (1) a reactant, (2) a medium or solvent, and (3) a plasticizer to increase molecular mobility.[2,47,54] Discriminating among these possible effects is difficult, particularly since more than one effect may be important in a given system.

Excipients—Proteins are often formulated with excipients, such as sugars and polymers, to protect them during

Table 1—Types of Polyalcohols Used as Pharmaceutical Excipients

polyhydric alcohols	nonreducing sugars	reducing sugars
mannitol	dextran	fructose
sorbitol	sucrose	glucose (dextrose)
	trehalose	lactose
		maltodextrin
		maltose

freeze-drying and storage. Polymeric "excipients" may also be used to form a matrix for controlled release. The types of excipients used and their effects on the chemical stability of proteins and peptides are varied. For example, a wide range of excipients, such as heparin, sulfated polysaccharides, anionic polymers, and citrate, decreased the rate of covalent aggregation in recombinant human keratinocyte growth factor (rhKGF) at elevated temperatures.[39] On the other hand, while EDTA inhibited disulfide formation in aggregates, it was not as effective in stabilizing rhKGF.[39] In this section, three categories of excipients will be discussed since they comprise the majority used in solid formulations: polyalcohols, polymers, and buffer salts.

Polyalcohols—Sugars and polyols are the most commonly used excipients in lyophilized protein and peptide formulations.[55] Table 1 lists the different types of polyalcohols used as pharmaceutical excipients. These sugars and polyols are often added to lyophilized formulations to protect and stabilize the proteins against decomposition during processing and storage. TNF formulated with dextran, sucrose, trehalose, or 2-hydroxypropyl-β-cyclodextrin, which are amorphous, formed fewer nonreducible dimers than TNF formulated without an excipient.[41] The covalent dimerization of human insulin was markedly decreased by incorporation into a glassy matrix of trehalose.[56] The stability of lyophilized recombinant human interleukin-1 receptor antagonist (rhIL-1ra) was greatly improved by increasing the concentration of sucrose in the formulation.[11] Sucrose stabilized rhIL-1ra against chemical degradation better than trehalose.[11] Examination of a series of polyalcohols in this system showed the following order of decreasing ability to stabilize the protein: sucrose > trehalose > sorbitol > no excipient > maltose.[11] In a recent study of Asp-Pro bond cleavage in Physalaemin and Hamburger peptides, stabilization was provided by glassy polyols in the order: sucrose > Ficoll (low mw) > Byco A, Ficoll (high mw) > dextran.[57] The authors attributed the stabilizing ability of the polyols to the density of the matrix, with greater packing density leading to improved stability.

Some of these excipients, such as maltose in the rhIL-1ra example above, may have a destabilizing effect. For example, the oxidative deamidation of a cyclic heptapeptide was observed in formulations containing mannitol, but not in solution or in the neat solid (no excipient).[31] The extent of oxidative degradation increases with increasing mannitol content after 12 weeks of storage at 40 and 60 °C.[31] These researchers postulated that the cyclic heptapeptide was reacting with a reducing sugar impurity in the mannitol.[31] Thus, the lower stability of the rHIL-1ra maltose formulation may have been due to the rhIL-1ra reacting with maltose, a reducing sugar.

Reducing sugars are known to react with proteins and peptides via the Maillard reaction (formation of Schiff base) as well as other side reactions.[2,25,55] Rapid covalent modification of lyophilized human relaxin was observed in the presence of glucose.[25] The glucose appeared to have reacted with lysine and arginine residues via the Maillard reaction to form covalent adducts.[25] A significant amount of serine cleavage from the C-terminal of the B-chain of relaxin was also identified.[25] A high glucose content may be necessary for cleavage to occur, since the hydrolytic cleavage of relaxin stored in concentrated glucose solutions occurred to a lesser extent than in the solid state.[25] In contrast, formulating relaxin with nonreducing sugars such as mannitol and trehalose produced stable, lyophilized formulations.[25]

In addition to oxidation and deamidation products, human growth hormone formulated with lactose produced an additional product not observed in either the freshly freeze-dried lactose formulation or in any of the other formulations studied. The researchers postulated that the product was due to an adduct of lactose and hGH, either the glycosylamine or the corresponding Schiff base.[4] As stated above, the use of reducing sugars in lyophilized formulations is problematic due to their propensity to react with proteins via the Maillard reaction, especially at lysine and arginine residues.

Polymers—Polymeric excipients may influence the reactivity of peptides and proteins through direct chemical interactions or by altering the physical state (e.g., glassy vs rubbery) of the system. This section addresses chemical interactions between polymeric excipients and incorporated proteins. The effects of polymers on the physical state of the matrix are discussed below.

Many of the published studies on the chemical effects of polymers on peptides and proteins involve the lactide/glycolide copolymers. These polymers are of particular interest because they are biocompatible and biodegradable and are therefore used commonly in implantable devices.

The stability of atriopeptin III (APIII) encapsulated in poly(D,L-lactide-*co*-glycolide) (PLG) microspheres was studied and compared to that of APIII alone at 40 °C.[58] When microspheres were shaken in neutral buffer solution, APIII was completely degraded in 5 days. In neutral buffer alone, APIII degraded with a half-life of 8.7 days.[58] After 8 days at 95% relative humidity, 20% of APIII in the microspheres had degraded.[58] Concentrated APIII showed no degradation after 2 weeks, and dilute APIII in water showed no loss after one month.[58] Different degradation peaks were observed for APIII in microspheres and APIII alone.[58] It was concluded that PLG catalyzes the degradation of APIII, and the mechanism of this degradation appears to be different from that seen for APIII alone in buffer.[58] This suggests that the polymer environment has a significant effect on the chemical stability of this protein.

Park and co-workers also found this to be the case for the stability of carbonic anhydrase and bovine serum albumin during release from a polymer matrix immersed in buffered medium at 37 °C.[59] Carbonic anhydrase encapsulated in poly(D,L-lactic acid-*co*-glycolic acid) (PLGA) microspheres was released in an inactive form.[59] Severe hydrolysis of unreleased and released proteins was observed.[59] It was postulated that the hydrolysis was due to an acidified medium created by the degradation of the PLGA microspheres.[59] The degradation of the PLGA microspheres occurs via random chain scission of an ester linkage in the polymer backbone, which produces water soluble oligomers with carboxylic acid end groups that affect medium pH.[59] As the microspheres degraded, the pH of the medium decreased from 7 to 3 over 40 days.[59] Park et al. also suggest that the protonated carboxylic acid end group of the lactic and glycolic acid fragments may react with the carbonyl group of the amide linkage in the proteins, leading to cleavage of the peptide backbone.[59] So, in addition to having an environmental effect, polymers may also have a direct catalytic effect on the chemical stability of proteins in solids.

In contrast to these reports of a detrimental effect of lactide-glycolide polymers on protein stability, there have been several reports of successful protein formulation in

these polymers.[60−62] Cleland et al. describe the stability of recombinant human growth hormone (rhGH) during release from PLGA microspheres into isotonic buffer.[60] Rates of oxidation, diketopiperazine formulation, and deamidation in the microspheres were comparable to those in solution controls, and rates of aggregation were only slightly greater than in solution.[60] The authors infer that the pH within the microspheres is comparable to that in the surrounding buffer, and that rapid buffer equilibration may prevent a pH decrease in this system.[60] In related studies, rhGH was stabilized in a PLGA microsphere formulation by the formation of an insoluble complex with zinc.[61] In vitro studies showed that microsphere encapsulation did not alter rhGH activity in this system, and in vivo studies in rats and monkeys showed sustained delivery of rhGH for up to one month.[61] The discrepancies in protein stability in PLGA systems suggest that factors other than the polymer choice will influence drug stability. These may include the properties of the protein drug itself, other formulation variables, and the interaction of the formulation with the release matrix (e.g., buffer, tissue).

Limited information is available on the chemical effects of other polymeric excipients on peptide and protein stability. Recent studies in our laboratories suggest that the Asn-hexapeptide forms a reversible complex with poly(vinyl pyrrolidone) when stored in matrixes of this polymer at elevated temperature and low matrix moisture content.[63] Formation of the complex results in a reduction in Asn-hexapeptide degradation to the cyclic imide, but release of the Asn-hexapeptide from the complex requires more than 1 week in dialysis studies at neutral pH.[63] The chemical nature of this complex is under investigation. Protein binding to dextrans in lyophilized proteins has also been suspected.[64] After exposure to aqueous media for more than 2 weeks, recombinant bovine somatotropin (rbSt) and zinc insulin were released intact and active from microspheres composed of sucrose and poly[1,3-bis(*p*-carboxyhydroxy)-hexane anhydride], which is a very hydrophobic polymer.[65] Ron et al. postulated that the hydrophobic polymer prevented the entry of water into the microspheres[65] and thus protected rbSt from moisture induced decomposition, such as covalent dimerization and deamidation.[12]

Buffer Salts—Buffer salts are often included in solid formulations of peptides and proteins in an attempt to control the hydrogen ion activity, or the protonation state of the functional groups on the protein. In solution, buffer salts may have a catalytic effect on many protein degradation reactions, apart from their effect on pH. In this section, we review the limited evidence for specific chemical effects of buffers in the solid state. The effects of solid-state hydrogen ion activity on reactivity are discussed in the next section.

There is some evidence that phosphate buffers have a catalytic effect on protein degradation. In a study on lyophilized RNase, Townsend and DeLuca prepared lyophilized formulations from solutions containing varying concentrations of sodium phosphate buffer.[66] While a buffer-free formulation showed a 10% loss in activity over 120 days of storage at 45 °C, a formulation lyophilized from a 0.2 M buffer solution showed a nearly 40% loss in activity during the same period.[66] Similarly, Pikal et al. showed an effect of sodium phosphate buffer concentration on the chemical degradation and aggregation of lyophilized human growth hormone.[4] Mechanisms suggested for this effect include the catalysis of oxidation reactions by heavy metal contaminants in the buffer salts,[66] and the preferential crystallization of phosphate buffer components during freeze-drying, leading to pH shifts.[4] It should be noted that sodium phosphate buffers are thought to be particularly prone to preferential crystallization, and often are avoided in lyophilized protein formulations for this reason.[67] Acetate buffers are also avoided in lyophilized formulations, since volatilization of acetate species during freeze-drying may alter the buffer composition in the solid.

Buffer species themselves may be chemically unstable in solid formulations, producing degradation products that interact with peptides and proteins. Recent studies in our laboratories examined the deamidation of the Asn-hexapeptide in lyophilized matrixes containing PVP and Tris buffer.[68] We observed the formation of a new peak in HPLC chromatograms, which mass spectral analysis showed to be a formaldehyde adduct of the tyrosine residue on the aspartate or isoaspartate deamidation product. The presence of formaldehyde was shown to be associated with the inclusion of Tris buffer in the formulation, since no formaldehyde was detected when Tris was omitted or replaced with other buffers.[68] We hypothesize that degradation of Tris [tris(hydroxymethyl)aminomethane] occurs on storage of this formulation, liberating formaldehyde, which then reacts with the tyrosine residue on the peptide.[68]

Hydrogen Ion Activity—In the solution state, pH is used as a simple indicator of hydrogen ion activity. While pH is not defined in the solid state, there is a strong correlation between the chemical stability of proteins and peptides in the solid state and the pH of the solution prior to lyophilization. This value is often termed the "apparent pH" of the solid and is often given the abbreviated designation, "pH", with the quotation marks signifying that the value is apparent.

The deamidation rate of the Asn-hexapeptide increases as the solution pH prior to freeze-drying increases from 5 to 8.[18] The "pH" of the Asn-hexapeptide formulation solution also appears to dictate the extent to which the peptide stability depends on other variables, such as moisture level and temperature.[18] The deamidation of lyophilized human insulin is also quite sensitive to "pH".[13,14] Increases in the oxidation of hGH,[4,29] the β-elimination of cysteine in bovine insulin,[36] and the formation of nonreducible dimers of tumor necrosis factor[41] in the solid state all increase with formulation "pH". Interestingly, while no dimers were observed at "pH" 4, the biological activity of TNF at "pH" 4 was significantly lower than at higher "pH's".[41]

The increase in the rate of covalent dimerization of rbSt with increasing "pH" is attributed to the deprotonation of the lysine residues, which are more nucleophilic when deprotonated. Interestingly, the fractional amount of nonreducible dimers formed during rbSt degradation remained constant at around 80%, independent of "pH" over the range studied (pH 5−10).[2,69] Lyophilized recombinant human interleukin-1 receptor antagonist (rhIL-1ra) formulations containing citrate were less likely to form noncovalent aggregates than those with phosphate.[11] The researchers postulated that the destabilizing effect of phosphate buffer may be due to the selective crystallization of the dibasic salt, which would expose the protein to a low "pH".[11]

To avoid drastic pH shifts, the weight ratio of buffer to other solutes should remain low.[3] The addition of ionic agents such as NaCl should also be kept at a minimum or avoided. While NaCl does not affect "pH", the chemical stability of hGH in freeze-dried formulations was decreased by the presence of NaCl.[4] The researchers attributed the destabilizing effect of NaCl on hGH to a specific ion effect, due primarily to the chloride ion.[4] The effect of NaCl on hGH may also be due to a salt effect on "pK_a".

The Physical State of the Solid—The state of a pharmaceutical solid depends on the temperature, composition (drug and excipient), moisture, and on the time allotted to the experiment. While the effects of tempera-

ture, moisture, and formulation composition on chemical instability were presented independently above, their influences on the solid-state chemical stability of proteins and peptides are often synergistic. These variables combined determine the physical bulk state of solid protein and peptide formulations. The bulk state of a formulation (crystalline versus amorphous) has been linked to various cases of protein and peptide chemical instability in the solid-state.[4,13,18]

Crystalline—Crystalline solids possess long range molecular order with the molecules structured in fixed geometric units. In contrast, amorphous solids have irregular packing and lack long range order. For small molecule drugs in the solid-state, the crystalline drug is generally less prone to chemical decomposition than the amorphous form.[14,70] However, the crystalline state may not be more stable for protein and peptide formulations. Oliyai et al. found that the Asp-hexapeptide was more stable in a lactose matrix (amorphous) than in mannitol (crystalline).[23] Interestingly, the lactose formulation had a greater affinity for water (a higher water content) than the mannitol formulation, yet the peptide was significantly more stable in the lactose matrix than in mannitol.[23] Excipients that were more hygroscopic were generally better at stabilizing rHA against aggregation, suggesting that the stabilization arises primarily from interactions between the excipient and water rather than between the excipient and the protein.[40]

The stability of crystalline and amorphous insulin (neat solid) was also investigated at various water contents. For crystalline insulin, deamidation at the Asn_{A21} site increases rapidly with increases in water content.[14] In contrast, the deamidation of amorphous insulin was nearly independent of moisture content (up to 15%).[14] Crystalline human insulin was less stable than amorphous insulin, independent of the water content over the range studied.[14]

Solid formulations which are at least partially amorphous appear to best protect proteins and peptides against chemical instability.[4] Lyophilized human growth hormone (hGH) formulated in a partially amorphous excipient system (glycine:mannitol) was less susceptible to chemical degradation and aggregation than hGH formulated in either totally amorphous (dextran) or crystalline (mannitol) systems.[4] So, while a partially amorphous system is necessary to stabilize hGH, an amorphous system is not a sufficient condition for stability.[4] Pikal et al. postulated that a partially amorphous system allows molecular interaction with the protein and/or acts as "sink" for residual water.[4]

While residual moisture generally leads to chemical instability, the relative stability of proteins and peptides in solid formulations cannot be judged solely on the basis of the amount of water present, as seen in the above cases. The nature of the excipient, such as its crystallinity and affinity for water, appears to be important as well.

Amorphous—Depending on temperature, structure, and composition, amorphous solids such as polymers exhibit widely different physical and mechanical properties.[71] At low temperature and moisture, amorphous solids are brittle, hard, and highly viscous, and are said to be in the "glassy" state. In the glassy state, molecular motion is largely restricted to vibrations and short-range rotational motion.[71] As the temperature and/or moisture content increases, the solids undergo a transition from a glassy state to the so-called "rubbery" state, which is characterized by decreased viscosity and increased elasticity. The glass transition temperature (T_g) is defined as the temperature at which the solid softens because of the onset of long-range coordinated molecular motion.[71] The T_g varies greatly among different amorphous pharmaceutical solids and is dictated by such factors as composition and moisture content, since water may act as a plasticizer to increase bulk mobility and decrease T_g.

Researchers have speculated that chemical reactions which involve molecular mobility, such as bimolecular reactions, are unlikely to occur in the glassy state due to the limited mobility.[72] As the solid system becomes more rubbery ($T > T_g$) and mobility increases, the reaction rates would then greatly increase.[72] Lyophilized rhIL-1ra formulations with T_g's ranging from 20 to 56 °C were stored for several weeks at temperatures above and below their T_g's.[73] The decomposition of rhIL-1ra, both via deamidation and aggregation, was greatly accelerated at temperatures above T_g (rubbery state).[73] However, the rate of degradation also increased in some formulations whose T_g's were above the storage temperature (glassy state).[73]

Other instances of protein and peptide degradation in the glassy state have been documented. The aggregation of hGH has been found to occur in formulations stored at temperatures well below their glass transition temperature.[4] The dimerization and deamidation of insulin have been observed in the glassy state;[13] however, the actual formulation T_g was not measured in this study. Recently, the fission of the Asp-Pro bond in Physalaemin and Hamburger peptides has been detected in water soluble glasses (e.g., dextrose, Ficoll, sucrose) below their T_g.[57] Thus, while proteins and peptides are generally more stable in the glassy state, chemical degradation reactions can still occur. Although mobility is limited in the glassy state, glassy pharmaceutical solids may experience significant molecular mobility at temperatures up to 50 °C below their glass transition temperature.[74] Furthermore, significant rotational and translational mobility was shown to exist for water in solid poly(vinyl pyrrolidone), even at very low water contents (glassy state).[75]

The increase in reactivity with water content is often attributed to water's ability to plasticize or increase the molecular mobility of the bulk structure and thus the reactants. The decomposition of a freeze-dried monoclonal antibody–vinca conjugate has been correlated with formulation T_g.[76] However, since water activity and content were not kept constant, other factors which may contribute to this instability cannot be ruled out. In contrast, the degradation of aspartame in the solid-state correlates better with water activity and content than with T_g.[77] In recent studies of Asn-hexapeptide deamidation in poly(vinyl pyrrolidone) matrices, we have attempted to discriminate between water's effects on T_g (i.e., as a plasticizer) and its solvent effects by adding glycerol to the matrix as a secondary plasticizer.[22] This enabled us to generate systems with constant T_g and varying water activity, or with constant water activity and varying T_g. Interestingly, the deamidation rate showed a single log-linear correlation with T_g for matrices in the rubbery state, while in the glassy state this correlation resulted in multiple parallel lines with intercepts dependent on matrix water activity.[22] These results suggest that for this system, water acts primarily as a plasticizer in the rubbery state, but acts both as a plasticizer and a solvent or reaction medium in the glassy state. Taken together, these conflicting reports on water's role as a plasticizer demonstrate the complexity of these systems and the attendant difficulty in gaining a mechanistic understanding of the chemical reactivity of incorporated proteins and peptides.

Summary and Commentary

The results discussed above highlight the difficulty in determining the mechanisms of protein chemical instability in the solid-state. Protein decomposition in the solid state

can occur through multiple degradation pathways, involving both physical and chemical instabilities, as observed for rbSt and insulin. Since chemical instability can also lead to physical instability and vice versa, it can be difficult to determine the mechanism of chemical degradation in proteins. Furthermore, non-peptide/protein components of these solid-state formulations may have multiple effects. Residual moisture and polymeric excipients, for example, may influence matrix mobility (T_g), may participate directly or indirectly in degradation reactions, and may influence the "pH" or other properties of the reaction medium. Multiple effects caused by a single additive make mechanistic definition difficult.

Consideration of the available literature in this area suggests several avenues for additional research. Most notably, it is clear that the determinants of protein and peptide reactivity in the solid-state have not been fully characterized. While pH, temperature, and buffer composition are known to be critical in solution, different or additional factors may be important in the solid-state. These may include mobility in the matrix, hydrogen ion activity, and protein secondary and tertiary structure. Additional research relating to each of these factors is warranted.

For example, while mobility in a solid polymer matrix is often characterized using the glass transition temperature (T_g), this measurement describes the mobility of the matrix as a whole and not its specific components. Ultimately, the degradation of peptides and proteins in these systems is more likely to depend on the mobility of the drug molecules themselves or of specific amino acid residues within them, rather than on the "bulk" mobility described by T_g, particularly when the drug loading is low. Recent research has begun to address this question,[78,79] but continued effort will be required to establish a measure of solid-state mobility that is predictive of reactivity. In addition, mobility is likely to be more important for bimolecular reactions involving large molecules (e.g., protein aggregation) than for unimolecular reactions (e.g., succinimide formation) or bimolecular reactions involving relatively small, mobile reactants (e.g., oxidation). An understanding of the factors that produce a "mobility-limited reaction" in the solid state would aid in formulation, since stabilization strategies that reduce mobility (e.g., inclusion of glass-forming excipients) are most likely to be effective for these reactions. Reaction mechanism and reactant molecular weight are likely to be among these factors.

Hydrogen ion activity (i.e., pH) is important in the solution state degradation of many peptides and proteins, but its role in the solid-state remains unclear. At present, there is no convenient measure of hydrogen ion activity in these solid systems, so examination of its effects has relied on correlation with "effective" pH. These studies have suggested that the "pH" dependency in the solid state parallels its solution state counterpart. However, it is reasonable to expect that a reaction that is pH-driven in solution may be controlled by other factors, such as mobility, in a glassy solid. Examination of the dependence of solid-state "pH" rate profiles on other matrix properties would be useful, as would the development of methods to measure hydrogen ion activity in solid formulations.

Finally, the effects of protein secondary and tertiary structure on reactivity and reaction mechanism should be examined. In solution, secondary structure has been shown to affect deamidation rate,[80] and protein aggregation in the solid state has been attributed to adsorption-induced unfolding.[62] In addition, a recent study has demonstrated the utility of infrared spectroscopy to determine protein secondary structure in PLGA matrixes.[81] However, there is a lack of information on the effects of protein structure on chemical reactivity in solids. Such information is important not only for chemical routes of protein degradation, but also because physical modes of degradation, such as aggregation, are often associated with chemical changes. Information on the interaction of protein structural domains with matrix properties (such as mobility and water content) to produce degradation would help to identify labile residues in solid protein formulations a priori. Stabilization strategies could then be directed in a rational way toward the modification of protein structure and/or formulation variables.

References and Notes

1. Manning, M. C.; Patel, K.; Borchardt, R. T. Stability of protein pharmaceuticals. *Pharm. Res.* **1989**, *6*, 903−918.
2. Hageman, M. J. Water sorption and solid-state stability of proteins. In *Stability of Protein Pharmaceuticals, Part A: Chemical and Physical Pathways of Protein Degradation*; Ahern, T. J., Manning, M. C., Eds.; Plenum Press: New York, 1992; pp 273−309.
3. Carpenter, J. F.; Pikal, M. J.; Chang, B. S.; Randolph, T. W. Rational design of stable lyophilized protein formulations: Some practical advice. *Pharm. Res.* **1997**, *14*, 969−975.
4. Pikal, M. J.; Dellerman, K. M.; Roy, M. L.; Riggin, R. M. The effects of formulation variables on the stability of freeze-dried human growth hormone. *Pharm. Res.* **1991**, *8*, 427−436.
5. Pearlman, R.; Nguyen, T. J. Pharmaceutics of protein drugs. *Pharm. Pharmacol.* **1992**, *44*, 178−185.
6. Strickley, R. G.; Visor, G. C.; Lin, L.; Gu, L. Unexpected pH effect on the stability of moexipril lyophilized powder. *Pharm. Res.* **1989**, *6*, 971−975.
7. Bhatt, N.; Patel, K.; Borchardt, R. T. Chemical pathways of peptide degradation. I. Deamidation of adrenocorticotropic hormone. *Pharm. Res.* **1990**, *7*, 593−598.
8. Creighton, T. E. *Proteins: Structures and Molecular Properties*, 2nd ed.; W. H. Freeman and Company: New York, 1993; pp 464−469.
9. Costantino, H. R.; Langer, R.; Klibanov, A. M. Solid-phase aggregation of proteins under pharmaceutically relevant conditions. *J. Pharm. Sci.* **1994**, *83*, 1662−1669.
10. Becker, G. W.; Tackitt, P. M.; Bromer, W. W.; Lefeber, D. S.; Riggin, R. M. Isolation and characterization of a sulfoxide and a desamido derivative of biosynthetic human growth hormone, *Biotechnol. Appl. Biochem.* **1988**, *10*, 326−337.
11. Chang, B. S.; Reeder, G.; Carpenter, J. F. Development of a stable freeze-dried formulation of recombinant human interleukin-1 receptor agonist. *Pharm. Res.* **1996**, *13*, 243−249.
12. Hageman, M. J.; Bauer, J. M.; Possert, P. L.; Darrington, R. T. Preformulation studies oriented toward sustained delivery of recombinant somatotropins. *J. Argicul. Food Chem.* **1992**, *40*, 348−355.
13. Strickley, R. G.; Anderson, B. D. Solid-state stability of human insulin. I. Mechanism and the effect of water on the kinetics of degradation in lyophiles from pH 2−5 solutions. *Pharm. Res.* **1996**, *13*, 1142−1153.
14. Pikal, M. J.; Rigsbee, D. R. The stability of insulin in crystalline and amorphous solids: observation of greater stability for the amorphous form. *Pharm. Res.* **1997**, *14*, 1379−1387.
15. Patel, K.; Borchardt, R. T. Chemical pathways of peptide degradation. II. Kinetics of deamidation of an asparaginyl residue in a model hexapeptide. *Pharm. Res.* **1990**, *7*, 703−711.
16. Geiger, T.; Clarke, S. Deamidation, isomerization and racemization at asparaginyl and aspartyl residues in peptides. *J. Biol. Chem.* **1987**, *262*, 785−794.
17. Patel, K.; Borchardt, R. T. Chemical pathways of peptide degradation. III. Effect of primary sequence on the pathways of deamidation of asparaginyl residues in hexapeptides. *Pharm. Res.* **1990**, *7*, 787−793.
18. Oliyai, C.; Patel, J.; Carr, L.; Borchardt, R. T. Solid-state stability of lyophilized formulations of an asparaginyl residue in a model hexapeptide. *J. Parenteral Sci. Technol.* **1994**, *48*, 67−173.
19. Heckman, C.; DeMond, W.; Dixit, T.; Mauch, S.; Nuechterlein, M.; Stepaneko, A.; Williams, J. D.; Ye, M. Isolation and identification of peptide degradation products of heat stressed pramlintide injection drug product. *Pharm. Res.* **1998**, *15*, 650−659.
20. Lai, M. C.; Schowen, R. L.; Borchardt, R. T.; Topp, E. M. Chemical stability of peptides in polymers. I. Deamidation

of a model hexapeptide in poly(vinyl alcohol) hydrogels and xerogels. *J. Peptide Res.* **1999**, submitted.
21. Lai, M. C.; Hageman, M. J.; Schowen, R. L.; Borchardt, R. T.; Laird, B. B.; Topp, E. M. Chemical Stability of Peptides in Polymers. 2. Discriminating between Solvent and Plasticizing Effects of Water on Peptide Deamidation in Poly(vinyl pyrrolidone). *J. Pharm. Sci.* **1998**, submitted.
22. Lai, M. C.; Hageman, M. J.; Schowen, R. L.; Borchardt, R. T.; Topp, E. M. Chemical Stability of Peptides in Polymers. 1. Effect of Water on Peptide Deamidation in Poly(vinyl alcohol) and Poly(vinyl pyrrolidone) Matrixes. *J. Pharm. Sci.* **1998**, submitted.
23. Oliyai, C.; Patel, J. P.; Carr, L.; Borchardt, R. T. Chemical pathways of peptide degradation. VII. Solid-state chemical instability of an aspartyl residue in a model hexapeptide. *Pharm. Res.* **1994**, *11*, 901−908.
24. Oliyai, C.; Borchardt, R. T. Chemical pathways of peptide degradation. IV. Pathways, kinetics, and mechanism of degradation of an aspartyl residue in a model hexapeptide. *Pharm. Res.* **1993**, *10*, 95−102.
25. Li, S.; Patapoff, T. W.; Overcashier, D.; Hsu, C.; Nguyen, T. H.; Borchardt, R. T. Effects of Reducing Sugars on the Chemical Stability of Human Relaxin in the Lyophilized State. *J. Pharm. Sci.* **1996**, *85*, 873−877.
26. Leung, S. S.; Grant, D. J. W. Solid-State Stability Studies of Model Dipeptides: Aspartame and Aspartylphenylalanine. *J. Pharm. Sci.* **1997**, *86*, 64−71.
27. Bell, L. N.; Labuza, T. P. Aspartame degradation as a function of "water activity". In *Water Relationships in Foods: Advances in the 1980s and Trends for the 1990s*; Levine, H., Slade, L., Eds.; *Advances in Experimental Medicine and Biology*; Plenum: New York, 1991; Vol. 302, pp 337−350.
28. Kertscher, U.; Bienert, M.; Krause, E.; Sepetov, N.F.; Mehlis, B. Spontaneous chemical degradation of Substance P in the solid phase and in solution. *Int. J. Pept. Protein Res.* **1993**, *41*, 207−211.
29. Pikal, M. J.; Dellerman, K.; Roy, M. L. Formulation and stability of freeze-dried proteins: Effects of moisture and oxygen on the stability of freeze-dried formulations of human growth hormone. *Dev. Biol. Stand.* **1991**, *74*, 21−38.
30. Fransson, J.; Florin-Robertsson, E.; Axelsson, K.; Nyhlen, C. Oxidation of human insulin-like growth factor I in formulation studies: Kinetics of methionine oxidation in aqueous solution and in solid state. *Pharm. Res.* **1996**, *13*, 1252−1257.
31. Dubost, D. C.; Kaufman, M. J.; Zimmerman, J. A.; Bogusky, M. J.; Coddington, A. B.; Pitzenberger, S. M. Characterization of a solid-state reaction product from a lyophilized formulation of a cyclic heptapeptide. A novel example of an excipient-induced oxidation. *Pharm. Res.* **1996**, *13*, 1811−1814.
32. Hageman, M. J. The role of moisture in protein stability. *Drug Dev. Ind. Pharm.* **1988**, *14*, 2047−2070.
33. Labuza, T. P.; Saltmarch, M. The nonenzymatic browning reaction as affected by water in foods. In *Water Activity: Influences on Food Quality*; Rockland, L. B., Stewart, G. F., Eds; Academic Press: New York, 1981; pp 605−650.
34. Eichner, K.; Ciner-Doruk, M. Formation and decomposition of browning intermediates and visible sugar-amine browning reactions. In *Water Activity: Influences on Food Quality*; Rockland, L. B., Stewart, G. F., Eds; Academic Press: New York, 1981; pp 567−603.
35. Goldblith, S. A.; Tannenbaum, S. R. The nutritional aspects of the freeze-drying of foods. In *Procedings of the 7th International Congress on Nutrition* Pergamon Press: Oxford, 1966; Vol. 4, pp 432−445.
36. Costantino, H. R.; Langer, R.; Klibanov, A. M. Moisture-induced aggregation of lyophilized insulin. *Pharm. Res.* **1994**, *11*, 21−29.
37. Liu, W. R.; Langer, R.; Klibanov, A. M. Moisture-induced aggregation of lyophilized proteins in the solid state. *Biotechnol. Bioeng.* **1991**, *37*, 177−184.
38. Jordan, G. M.; Yoshioka, S.; Terao, T. The aggregation of bovine serum albumin in solution and in the solid state. *J. Pharm. Pharmacol.* **1994**, *46*, 182−185.
39. Chen, B. L.; Arakawa, T.; Morris, C. F.; Kenney, W. C.; Wells, C. M.; Pitt, C. G. Aggregation pathway of recombinant human keratinocyte growth factor and its stabilization. *Pharm. Res.* **1994**, *11*, 1581−1587.
40. Costantino, H. R.; Langer, R.; Klibanov, A. M. Aggregation of a lyophilized pharmaceutical protein, recombinant human albumin: Effect of moisture and stabilization by excipients. *Biotechnology* **1995**, *13*, 493−496.
41. Hora, M. S.; Rana, R. K.; Smith, F. W. Lyophilized formulations of recombinant tumor necrosis factor. *Pharm. Res.* **1992**, *9*, 33−36.
42. Townsend, M. W.; DeLuca, P. P. Use of lyoprotectants in the freeze-drying of a model protein, ribonuclease A. *J. Parent. Sci. Technol.* **1988**, *42*, 190−199.
43. Townsend, M. W.; Byron, P. R.; DeLuca, P. P. Effects of formulation additives on the degradation of freeze-dried ribonuclease A. *Pharm. Res.* **1990**, *7*, 1086−1091.
44. Townsend, M. W.; DeLuca, P. P. Nature of aggregates formed during storage of freeze-dried ribonuclease A. *J. Pharm. Sci.* **1991**, *80*, 63−66.
45. Schwendeman, S. P.; Costantino, H. R.; Gupta, R. K.; Siber, G. R.; Klibanov, A. M.; Langer, R. Stabilization of tetanus and diptheria toxoids against moisture-induced aggregation. *Proc. Natl. Acad. Sci. U.S.A.* **1995**, *92*, 11234−11238.
46. Connors, K. A.; Amidon, G. L.; Stella, V. J. *Chemical Stability of Pharmaceuticals*, 2nd ed.; John Wiley & Sons: New York, 1986; pp 115−134.
47. Ahlneck, C.; Zografi, G. The molecular basis of moisture effects on the physical and chemical stability of drugs in the solid state. *Int. J. Pharm.* **1990**, *62*, 87−95.
48. Carstensen, J. T. Effect of moisture on the stability of solid dosage forms. *Drug. Dev. Ind. Pharm.* **1988**, *14*, 1927−1969.
49. Karel, M.; Yong, S. Autoxidation-initiated reactions in foods. In *Water Activity: Influences on Food Quality*; Rockland, L. B., Stewart, G. F., Eds.; Academic Press: New York, 1981; pp 511−530.
50. Lea, C. H.; Hannan, R. S. Studies of the reaction between proteins and reducing sugars in the "dry" state. *Biochim. Biophys. Acta* **1949**, *3*, 313−325.
51. Lea, C. H.; Hannan, R. S.; Greaves, R. I. N. The reaction between proteins and reducing sugars in the "dry" state: Dried human blood plasma. *Biochim. Biophys. Acta* **1950**, *4*, 626−629.
52. Schwartz, H. M.; Lea, C. H. The reaction between proteins and reducing sugars in the "dry" state: Relative reactivity of the alpha- and epsilon-amino groups of insulin, *Biochem. J.* **1952**, *50*, 713−716.
53. Duckworth, R. B.; Allison, J. Y.; Clapperton, H. A. A. The aqueous environment for chemical change in intermediate moisture food. In *Intermediate Moisture Foods*; Davies, R., Birch, G. G., Parker, K. J., Eds.; Elsevier Applied: London, 1975; pp 89−99.
54. Shalaev, E. Y.; Zografi, G. How Does Residual Water Affect the Solid-State Degradation of Drugs in the Amorphous State? *J. Pharm. Sci.* **1996**, *85*, 1137−1141.
55. Wang, Y. J.; Hanson, M.A Parenteral formulations of proteins and peptides: Stability and stabilizers. *J. Parenter. Sci. Technol.* **1988**, *10*, 3−26.
56. Strickley, R. G.; Anderson, B. D. Solid-State Stability of Human Insulin. 2. Effect of Water on Reactive Intermediate Partitioning in Lyophiles from pH 2−5 Solutions: Stabilization against Covalent Dimer Formation. *J. Pharm. Sci.* **1997**, *86*, 645−653.
57. Streefland, L.; Auffret, A. D.; Franks, F. Bond cleavage reactions in solid aqueous carbohydrate solutions. *Pharm. Res.* **1998**, *15*, 843−849.
58. Johnson, R. E.; Lanaski, L. A.; Gupta, V.; Griffin, M.J.; Needham, T. E.; Zia, H. Stability of atriopeptin III in poly-(D,L-lactide-*co*-glycolide) microspheres. *J. Controlled Release* **1991**, *17*, 61−68.
59. Park, T. G.; Lu, W.; Crotts, G. Importance of in vitro experimental conditions on protein release kinetics, stability and polymer degradation. *J. Controlled Release* **1995**, *33*, 211−222.
60. Cleland, J. L.; Mac, A.; Boyd, B.; Yang, J.; Duenas, E. T.; Yueng, D.; Brooks, D.; Hsu, C.; Chu, H.; Mukku, V.; Jones, A. J. S. The stability of recombinant human growth hormone in poly(lactic-*co*-glycolic acid) (PLGA) microspheres. *Pharm. Res.* **1997**, *14*, 420−425.
61. Johnson, O. L.; Jaworowicz, W.; Cleland, J. L.; Bailey, L.; Charnis, M.; Duenas, E.; Wu, C.; Shepard, D.; Magil, S.; Last, T.; Jones, A. J. S.; Putney, S. D. The stabilization and encapsulation of human growth hormone into biodegradable microspheres. *Pharm. Res.* **1997**, *14*, 730−735.
62. Putney, S. D.; Burke, P. A. Improving protein therapeutics with sustained-release formulations. *Nature Biotechnol.* **1998**, *16*, 153−157.
63. Berglund, P. The effect of temperature on peptide deamidation in polymer matrixes. Master's Thesis, Danish Royal School of Pharmacy, Copenhagen, 1998.
64. Yoshioka, S.; Aso, Y.; Kojima, S. Dependence of the molecular mobility and protein stability of freeze-dried gamma-globulin formulations on the molecular weight of dextran. *Pharm. Res.* **1997**, *14*, 736−741.
65. Ron, E.; Turek, T.; Mathiowitiz, E.; Chasin, M.; Hageman, M.; Langer, R. Controlled release of polypeptides from polyanhydrides. *Proc. Natl. Acad. Sci. U.S.A.* **1993**, *90*, 4176−4180.

66. Townsend, M. W.; DeLuca, P. P. Stability of ribonuclease A in solution and the freeze-dried state. *J. Pharm. Sci.* **1990**, *79*, 1083−1086.
67. Pikal, M. J. Excipients for lyophile formulations. 1998 Walter F. Enz Lecture, presented at The University of Kansas, Department of Pharmaceutical Chemistry, July 30, 1998.
68. Song, Y.; Borchardt, R. T.; Schowen, R. L.; Topp, E. M. Effect of pH on peptide deamidation in polymeric matrixes, presented at the American Association of Pharmaceutical Scientists Midwest Regional Meeting, Chicago, IL, May 17, 1999.
69. Davio, S. R.; Hageman, M. J. Characterization and formulation considerations for recombinantly derived bovine somatotropin. In *Stability and Characterization of Protein and Peptide Drugs: Case Histories*; Wang, Y. J., Pearlman, R., Eds.; Plenum Press: New York, 1993; pp 59−89.
70. Carstensen, J. T.; Morris, T. Chemical stability of indomethacin in the solid amorphous and molten states, *J. Pharm. Sci.* **1993**, 82, 657−659.
71. Sperling, L. H. *Introduction to Physical Polymer Science*; John Wiley & Sons: New York, 1986.
72. Levine, H.; Slade, L. The glassy state phenomenon in food molecules. In *The Glassy State in Foods*; Blanshard, J. M. V., Lillford, P. J., Eds.; Nottingham Press: Nottingham, 1993; pp 35−101.
73. Chang, B. S.; Beauvais, R. M.; Dong, A.; Carpenter, J. F. Physical factors affecting the storage stability of freeze-dried interleukin-1 receptor antagonist: Glass transition and protein conformation. *Arch. Biochim. Biophys.* **1996**, *331*, 249−258.
74. Hancock, B. C.; Zografi, G. Molecular mobility of amorphous pharmaceutical solids below their glass transition. *Pharm. Res.* **1995**, *12*, 799−806.
75. Oksanen, C. A.; Zografi, G. Molecular mobility in mixtures of absorbed water and solid poly(vinyl pyrrolidone). *Pharm. Res.* **1993**, *10*, 791−799.
76. Roy, M. L.; Pikal, M. J.; Rickard, E. C.; Maloney, A. M. The effects of formulation and moisture on the stability of a freeze-dried monoclonal antibody-vinca conjugate: A test of the WLF glass transition theory. *Dev. Biol. Standard.* **1992**, *74*, 323−340.
77. Bell, L. N.; Hageman, M. J. Differentiating between the effects of water activity and glass transition dependent mobility on a solid-state chemical reaction: Aspartame degradation. *J. Agric. Food Chem.* **1994**, *42*, 2398−2401.
78. Yoshioka, S.; Aso, Y.; Kojima, S. The effect of excipients on the molecular mobility of lyophilized formulations, as measured by glass transition temperature and NMR relaxation-based critical mobility temperature. *Pharm. Res.* **1999**, *16*, 135−140.
79. Yoshioka, S.; Aso, Y.; Nakai, Y.; Kojima, S. Effect of High Molecular Mobility of Poly(vinyl alcohol) on Protein Stability of Lyophilized γ-Globulin Formulations. *J. Pharm. Sci.* **1998**, *87*, 147−151.
80. Xie, M.; Schowen, R. L. Secondary Structure and Protein Deamidation. *J. Pharm. Sci.* **1999**, *88*, 8−13.
81. Yang, T. H.; Dong, A.; Meyer, J.; Johnson, O. L.; Cleland, J. L., Carpenter, J. F. Use of Infrared Spectroscopy to Assess Secondary Structure of Human Growth Hormone within Biodegradable Microspheres. *J. Pharm. Sci.* **1999**, *88*, 161−165.

Acknowledgments

The authors express their appreciation to Rong Li of the University of Kansas, Department of Pharmaceutical Chemistry, for preparing the reaction schemes. Financial support for our work in this area has been provided by a Takeru Higuchi predoctoral fellowship to M.C.L., by an NIGMS Biotechnology Training grant, by Pharmacia & Upjohn, Inc., and by NIH grant GM-54195.

JS980374E

Freeze-Drying above Room Temperature

MARC S. TESCONI, KIARESH SEPASSI, AND SAMUEL H. YALKOWSKY*

Contribution from *Department of Pharmaceutical Science, College of Pharmacy, University of Arizona, Tucson, Arizona 85721.*

Received December 10, 1998. Accepted for publication February 22, 1999.

Abstract □ This study investigates the use of solid, organic compounds to lyophilize drugs without conventional freeze-drying equipment. The aim of the investigation is to find a pharmaceutically acceptable solvent or solvent combination that is appropriate for freeze-drying on the basis of its ability to (1) solubilize hydrophobic drugs, (2) provide a stable environment for water-sensitive compounds, (3) be rapidly and completely removed from the product under vacuum, and (4) produce cakes that are readily reconstituted. A eutectic formed from 1,1,1-trichloro-2-methyl-2-propanol (chlorobutanol) hemihydrate and dimethyl sulfone ($DMSO_2$) is determined to be a suitable medium.

Introduction

The formulation of certain parenteral drugs as reconstitutable freeze-dried products offers the advantages of improved stability, dissolution rate, dosing accuracy, and sterility. However, freeze-drying is generally restricted to drugs that are water soluble and/or stable to hydrolysis for at least the time required for freezing. Compounds that hydrolyze rapidly are poor candidates because the amount of drug that remains in the dried product is likely to depend on the time required to freeze the sample. Hydrophobic nonelectrolytes are poor candidates because they require either large volumes of water or significant amounts of cosolvent to yield the desired quantity of drug in a reasonably sized container. Although cosolvents usually improve both stability and solubility, they can cause incomplete freezing and a drying stage that involves the simultaneous sublimation of ice and evaporation of liquid residue.[1] The resultant dried product is often very dense and difficult to reconstitute. Furthermore, since a surface skin is often produced when an incompletely frozen medium evaporates, drying times can be extended beyond the point of practicality.

It is also important to consider that if sublimation temperatures are significantly lower than normal to keep the medium frozen, then the condensing temperature required to recover the solvents may be lower than the −55 °C minimum of the lyophilizer.

The current study investigates the feasibility of using organic solvents that are solids at room temperature to lyophilize hydrophobic and water-sensitive compounds without conventional freeze-drying equipment. The aim of this investigation is to find a solvent or solvent combination that is suitable for freeze-drying on the basis of its ability to (1) solubilize hydrophobic drugs, (2) provide a stable environment for water-sensitive compounds, (3) be rapidly and completely removed from the product under vacuum, and (4) produce cakes that are easily reconstituted using pharmaceutically acceptable cosolvents.

* To whom correspondence should be addressed. Tel: (520) 626-1289. Fax: (520) 626-4063. E-mail: yalkowsky@pharmacy.arizona.edu.

Materials

Solvents were selected from the *Handbook of Pharmaceutical Excipients*[2] and *The Merck Index*[3] on the basis of their having low toxicity, melting points between 35 and 120 °C, and relatively low molecular weights. The compounds chosen for the study are listed in Table 1.

All compounds were >98% pure and were used as received from their respective suppliers except for anhydrous chlorobutanol, which was prepared by dehydration of a chlorobutanol hemihydrate melt.

Approach

The individual solvents in Table 1 were experimentally determined to be either too high melting to ensure solute stability or too nonpolar to solubilize semipolar compounds. Solvent combinations that formed eutectics were sought for their intermediate polarities and lower melting temperatures. The selection of a eutectic medium for freeze-drying involved seven steps: (1) screening solvent combinations for eutectic formation; (2) determination of the eutectic compositions; (3) measurement of sublimation rates; (4) assessment of solubilizing ability; (5) selection of an optimal medium; (6) freeze-drying sample compounds; and (7) analysis of freeze-dried products. Each of these steps is described below.

Experimental and Results

1. Eutectic Formation—The solvents in Table 1 were combined in a 1:1 mole ratio in quantities sufficient to yield approximately 2 g of material. The mixtures were melted, and those systems that exhibited solvent miscibility and stability were allowed to cool at room temperature for 2 h. These were refrigerated for 24 h at 4 °C to ensure complete solidification and then brought to room temperature. Samples that appeared "wet" were deleted from the study. Core samples of approximately 5 mg were taken from the remaining solids and analyzed with a DuPont Instruments model 910 differential scanning calorimeter using closed sample pans and a heating rate of 10 °C/min. Solvent combinations that exhibited a single, well-defined eutectic melt between 35 and 75 °C were considered further.

2. Eutectic Composition—The eutectic compositions were estimated using the van't Hoff equation

10.1021/js980478p CCC: $18.00
Published on Web 04/14/1999

Table 1—Compounds Used in This Study

compds used as solvents	T_m (°C)	compds used as solvents	T_m (°C)
coumarin	69	chlorobutanol (hemihydrate)	78
imidazole	90	chlorobutanol (anhydrous)[a]	97
2-amino-4-picolene	100	vanillin	82
2-aminopyridine	58	ethyl vanillin	77
salicylamide	140	ethyl paraben	116
tiglic acid	64	2-furoic acid	133
2-amino-5-nitrothiazole	187	other compounds	
menthol	35	anthracene	219
dimethyl sulfone	109	caffeine	238
camphene	51	fluasterone	175
thymol	52	progesterone	130
urea	133	coronene	438
salicylic acid	158	phenytoin	297
camphor	180	1,1-dicyano-3-nitrobenzyl-1-propene	161

[a] Prepared by dehydration of chlorobutanol hemihydrate.

$$\ln X_A = \frac{\Delta_{fus}H_A}{R}\left(\frac{1}{T_m} - \frac{1}{T_{eut}}\right) \quad (1)$$

with the molar heat of fusion, $\Delta_{fus}H_A$, determined by differential scanning calorimetry (DSC). In eq 1, X_A represents the mole fraction of component A, T_m is the melting point of pure component A, and T_{eut} is the eutectic melting temperature. Once the calculated mole fractions were determined (with $X_B = 1 - X_A$), solvent ratios slightly above and below the estimated value were prepared and a closer approximation of the eutectic composition was made experimentally using DSC. The eutectic composition was obtained as the mole ratio that produced a single melting endotherm. Hot stage microscopy was used to confirm the DSC results.

3. Sublimation Rates—Samples of the eutectics weighing ~50 mg were sublimed at 10 °C below their eutectic melting points at ~0.3 mmHg pressure. Evaporation rates were measured using a DuPont Instruments model 951 thermogravimetric analyzer. Two evaporation rates were observed in most cases. The greater first rate is due to the sublimation of both solvents. The second rate is due to the sublimation of the less volatile component after the more volatile solvent has been removed. The results for the most readily sublimed solvent combinations are given in Table 2.

4. Solubilizing Ability—To test the ability of the binary systems to solubilize both semipolar and nonpolar compounds, 20 mg of anthracene, caffeine, coronene, phenytoin, progesterone, and urea were added separately to 1 mL volumes of the eutectic melts at temperatures within 5 °C above their respective melting temperatures. All of the solvent systems were able to solubilize this quantity of the solutes. Solubility parameters were also calculated for the eutectic melts using the method of Adjel et al.[4] for combined solvent systems with group contribution values of cohesive energy density and molar volume from Fedors.[5] The solubility parameters shown in Table 3 are in the range of most drugs, which suggests that the melts are good solvents for drugs.

5. Premier Eutectic for Freeze-Drying—The chlorobutanol hemihydrate–dimethyl sulfone ($DMSO_2$) eutectic was found to be the most suitable media for freeze-drying on the basis of nontoxicity, solubilizing ability, and rate of solvent removal. As shown in Table 2, the eutectic is formed at a mole ratio of 60% chlorobutanol hemihydrate and 40% dimethyl sulfone, and it has a melting temperature of 50 °C. Figure 1 shows a phase diagram constructed from DSC analysis of several solvent ratios.

6. Freeze-Drying—The five compounds shown in Figure 2, progesterone, coronene, Fluasterone, phenytoin, and 1,1-dicyano-3-nitrobenzyl-1-propene, were lyophilized from the chlorobutanol hemihydrate–$DMSO_2$ eutectic. Samples were prepared in 10 mL freeze-drying vials with orifices of ~2 cm^2 by dissolving 30 mg of solute in 5 g of the eutectic melt at 60 °C. These were allowed to solidify for 2 h at 25 °C. The samples were then placed in a large Erlenmeyer flask that was connected to a vacuum pump. The base of the flask was submerged in a water bath that was heated by a hot plate. The solvents were sublimed at approximately 0.3 mmHg pressure using two drying stages:

stage 1: 40 °C, 6.5 h (−450 mg/cm^2-h: primarily chlorobutanol hemihydrate)

stage 2: 60 °C, 6.5 h (−150 mg/cm^2-h: $DMSO_2$)

The stage times were roughly equal in this study because both the mass and evaporation rate ratios are 3:1. However, the evaporation rate ratio is likely to vary with the temperatures and pressures used.

7. Freeze-Dried Product Analysis—*Residual Solvent*—Thermogravimetric (TG) analysis was used to measure the amount of residual solvent remaining in the cakes. Samples of ~10 mg were placed under vacuum and heated at a rate of 10 °C/min. The TG scans of the cakes and the solvents are shown in Figure 3. The analysis indicates that the cakes contain less than 1% residual solvent. The profiles for pure chlorobutanol–hemihydrate (-×-) and pure $DMSO_2$ (-+-) in Figure 3 indicate the temperatures at which weight loss due to residual solvent would be expected.

Solute Stability—The investigational compound 1,1-dicyano-3-nitrobenzyl-1-propene has a half-life in water of approximately 20 min, which precludes its freeze-drying by conventional methods. High-performance liquid chromatography was used to analyze the product immediately following lyophilization from the eutectic and after 15 months of storage at room temperature. Assays were performed using a Beckman System Gold HPLC with a Pinnacle ODS amine column (5 μm, 250 mm × 4.6 mm i.d., Restek, Bellefonte, PA) and a mobile phase consisting of 500 parts water, 500 parts acetonitrile, and 3 parts acetic acid at a pH of 3.45. A Beckman model 110A pump was used to maintain a flow rate of 1.0 mL/min. Ultraviolet detection was made using a Kratos Analytical Spectroflow model 757 detector at a wavelength of 300 nm. Quantification of drug in the effluent was made using a Hewlett-Packard model 3394 integrator. The relative retention times of 1,1-dicyano-3-nitrobenzyl-1-propene and its major degradation product are 3.4 and 2.8 min, respectively. No

Table 2—Compositions, Melting Temperatures, and Relative Evaporation Rates (at 10 °C below the Melting Temperatures) of the Eutectics

	solvents			sublimation rate[a] × 10^{-3}	
mol % A	A	B	T_{eut}	A +B	B
75	coumarin	salicylamide	58	0.6	0.0
65	2-amino-4-picolene	salicylamide	73	3.2	0.1
50	imidazole	coumarin	56	0.8	0.5
80	2-aminopyridine	salicylamide	46	1.3	0.0
24	2-amino-4-picolene	2-aminopyridine	44	1.3	1.3
60	chlorobutanol (hemihydrate)	dimethyl sulfone	50	7.9	0.8

[a] Expressed as a fraction of the estimated sublimation rate of ice at –10 °C and 0.3 mmHg (~10 mg/mm^2 min).

Table 3—Solubility Parameters for the Most Promising Solvent Combinations

solvents		solubility parameter of the eutectic melt
A	B	
coumarin	salicylamide	13.5
2-amino-4-picolene	salicylamide	11.8
imidazole	coumarin	12.5
2-aminopyridine	salicylamide	12.1
2-amino-4-picolene	2-aminopyridine	11.1
chlorobutanol (hemihydrate)	dimethyl sulfone	10.0

degradation was detected in the freeze-dried cake immediately after lyophilization or after 15 months of storage at room temperature.

Cake Structure and Particle Size—Figure 4a,b contains photomicrographs of the freeze-dried cakes of phenytoin and coronene, respectively, that were taken using a SPOT camera and a Leica DMLP polarizing microscope. The fiberlike structures in the phenytoin cake are loose aggregates of crystals that are approximately 1−2 μm long. The coronene cake is composed of bundles of roughly 5−10 crystals. The coronene crystals are the largest in the test set, having an average length of approximately 50 μm. The cakes of the other three compounds are similar in overall appearance and contain particles that range from 5 to 15 μm.

Reconstitution—The phenytoin cake was reconstituted using Millipore water adjusted to pH 12. Dissolution was complete with a single shake of the vial. With the exception of coronene, the other compounds were reconstituted using ethanolic solutions in which they were soluble. The progesterone cake was reconstituted using 8 mL of a 60% ethanol, 10% dimethylacetamide, and 30% water solution. The 1,1-dicyano-3-nitrobenzyl-1-propene and Fluasterone cakes were reconstituted using 8 mL of a nonaqueous 50% ethanol and 50% poly(ethylene glycol) 400 solution due to their low water solubilities, which are on the order of 1 μg/mL. For hydrophobic drugs such as these, the composition of the vehicles that are used for reconstitution, whether aqueous solutions or cosolvent concentrates, will depend on the solubilities of the drugs.

In all of the above cases, dissolution of the cakes was complete with 1−2 s of shaking. Note that coronene, which is not a therapeutic agent, was not soluble in pharmaceutical cosolvents.

Discussion

Solid organic solvents were successfully used to lyophilize hydrophobic and water-sensitive compounds. Because the solvents used for the freeze-drying medium were solids at room temperature, the process could be conducted without refrigeration and without conventional freeze-drying equipment. This also facilitated solvent collection, which was accomplished without using a cooled condenser.

A eutectic comprised of two solvents was used in order to achieve good solubilization of drugs in a medium with a moderate melting temperature. The latter property is required because drugs must be dissolved in a medium above its melting temperature and drug stability is compromised if that temperature is high. Since a eutectic is composed of two pure solid phases, these solvents are removed relatively independently of one another according to their vapor pressures. Consequently, two drying stages were used: one at 40 °C to remove (primarily) the more volatile chlorobutanol−hemihydrate and one at 60 °C to remove the $DMSO_2$. Note that these stages do not cor-

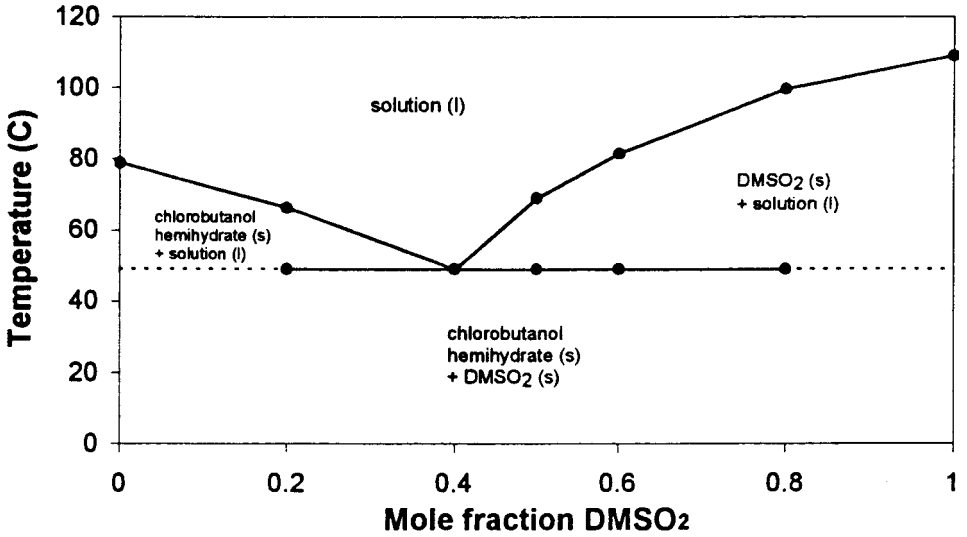

Figure 1—Chlorobutanol hemihydrate–$DMSO_2$ phase diagram.

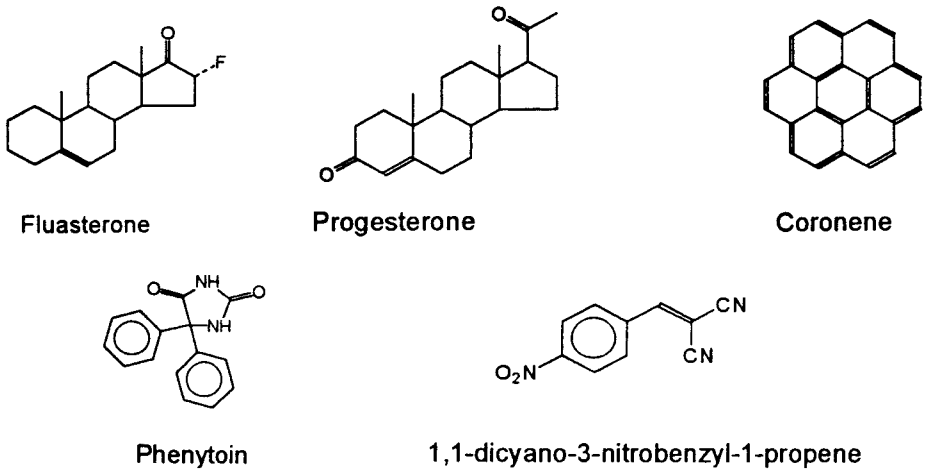

Figure 2—Compounds that were freeze-dried from the chlorobutanol hemihydrate–$DMSO_2$ eutectic.

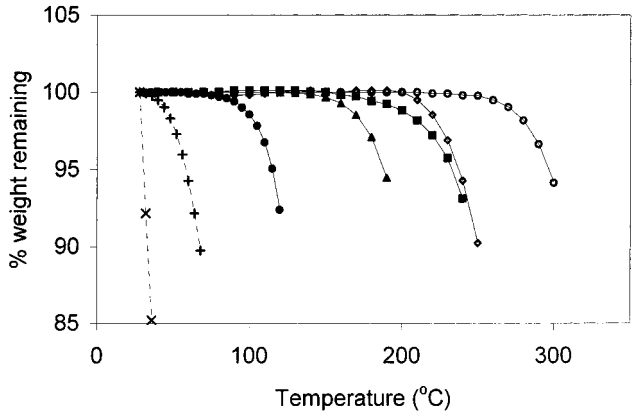

Figure 3—TG analysis of the pure solvents and the freeze-dried cakes: (×) chlorobutanol; (+) $DMSO_2$; (●) 1,1-dicyano-3-nitrobenzyl-1-propene; (▲) Fluasterone; (■) phenytoin; (◇) progesterone; (○) coronene.

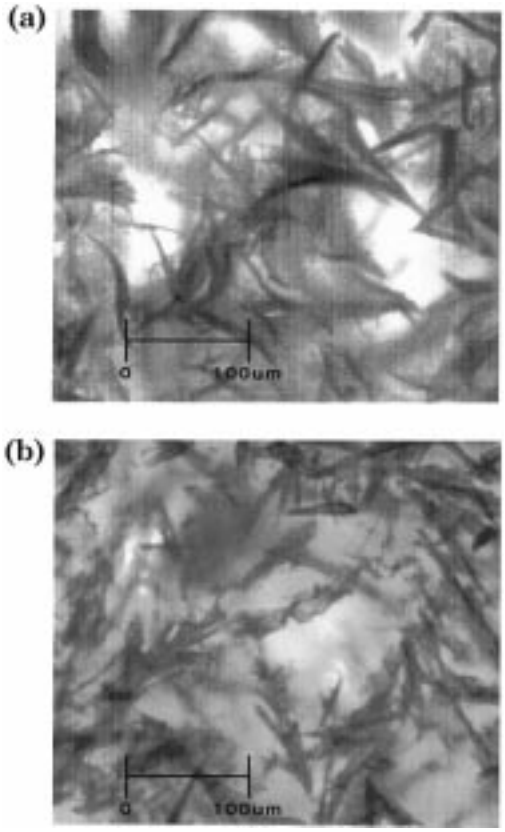

Figure 4—(a) Phenytoin cake. (b) Coronene cake.

respond to the drying stages used for ice in which the first removes frozen water and the second removes bound water.

Thermogravimetric analysis showed that the freeze-dried products did not contain significant amounts of residual solvent. This indicates that the 60 °C used to sublime the bulk $DMSO_2$ was sufficient to remove bound solvent. However, 60 °C is a relatively high temperature compared to what is normally used in freeze-drying, and care must be taken to avoid drug loss. It may be necessary to use lower temperatures and longer drying times when freeze-drying volatile compounds.

One of the major concerns in this study was that the structure of the eutectic should not be significantly altered by the presence of solute. The eutectic contains ~3.6% water that is believed to exist primarily in the form of chlorobutanol−hemihydrate crystals. If a dissolved drug caused the anhydrous form of chlorobutanol to crystallize on cooling, it could lead to incomplete freezing or variable solvent sublimation rates. Analysis of a eutectic containing 5% phenytoin indicated that the eutectic structure is largely unaffected by the presence of this solute. Figure 5a,b shows the DSC traces of the eutectic and the eutectic with 5% phenytoin, respectively. The similarity of the DSC traces suggests that the eutectic microstructures are the same.

The likeness of the photomicrographs of the eutectic and the eutectic with 5% phenytoin in Figure 6a,b, respectively, provides additional evidence for a stable eutectic structure. Hot-stage microscopy indicated that the apparent coarseness in the eutectic with phenytoin is due to presence of drug crystals in the solid. After fusion of the solvents at 50 °C, small, needlelike phenytoin crystals remain in the melt. These dissolved by 70 °C on heating the melt at a rate of 10 °C/min.

Evidence that a hydrated form of chlorobutanol exists in the eutectic is provided by the different thermal properties of the solid formed from the anhydrous chlorobutanol−$DMSO_2$ mixture at a 60:40 mole ratio. DSC and hot-stage microscopic analysis of the anhydrous chlorobutanol−$DMSO_2$ solid indicate a fusion event at 35 °C that is not exhibited by the solid formed from the hemihydrate. However, when 3.6% water is added to the anhydrous melt, the solid that is produced on cooling exhibits the same thermal properties as the solid prepared from the hemihydrate, i.e., a melting point of 50 °C without a 35 °C transition. Physically, the anhydrous solid is much softer than the hydrous form. The former also appears translucent, whereas the hydrous form (the eutectic) is a white

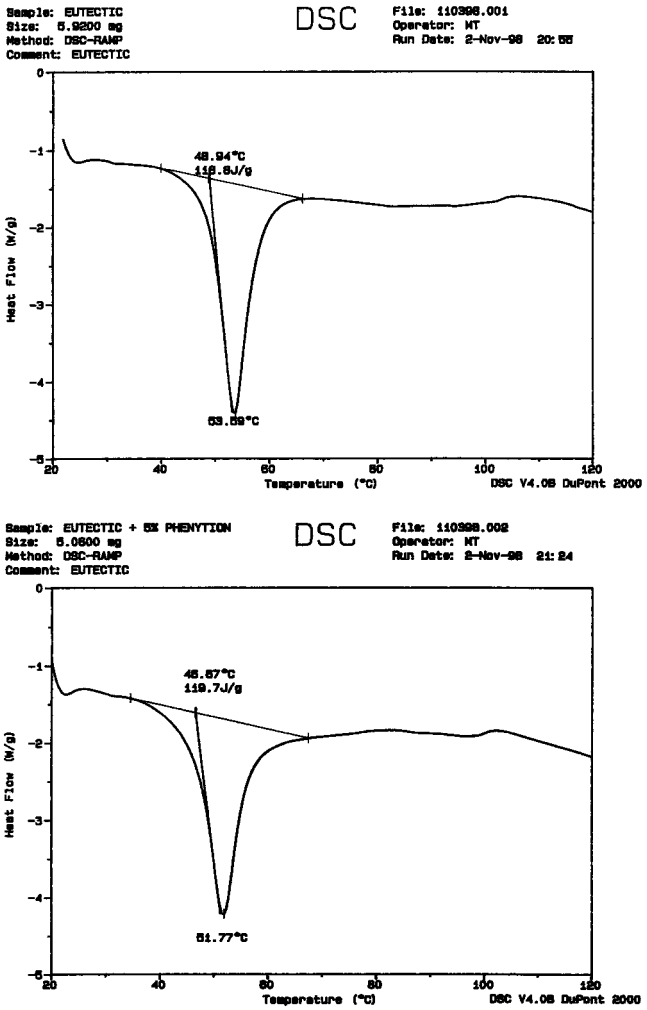

Figure 5—(a) DSC scan of the eutectic. (b) DSC scan of the eutectic + 5% phenytoin.

solid. Both properties may be due to the anhydrous form being incompletely frozen at room temperature. The physical properties of the hydrous eutectic also return with the addition of water to the anhydrous melt.

Thermogravimetric analysis indicated that the cakes produced in this study contained less than 1% residual solvent. Although human toxicity data are scarce, the available data suggest that trace amounts of the solvents which may remain in the freeze-dried products are well below harmful levels. Borody[6] found that plasma concentrations of chlorobutanol as high as 100 μg/mL produced sluggishness and slowed speech, but did not produce liver disease or abnormal electrolyte levels. Others have reported adverse reactions to high doses such as cardiovascular effects following the intravenous administration of heparin preserved with chlorobutanol, neurological effects following the administration of large doses of morphine with the preservative, and hypersensitivity reactions.[2] However, chlorobutanol is currently used in the U.S. as a parenteral preservative in concentrations of up to 0.5% in injectable (e.g., methadone, epinephrine, oxytocin, thiamine), opthalmic (e.g., pilocarpine, epinephrine, phospholine iodide), otic (e.g., Cresylate, Cerumenex), and cosmetic products. It is also the active ingredient in a nonprescription sleep aid (Seducaps: chlorobutanol 150 mg, salicylamide 300 mg) that is available in several countries outside of the United States.[2,7] The lethal dose of chlorobutanol is estimated to be 500 mg/kg[2].

Dimethyl sulfone is an oxidation product of dimethyl sulfoxide (DMSO) and is its major metabolite in all species

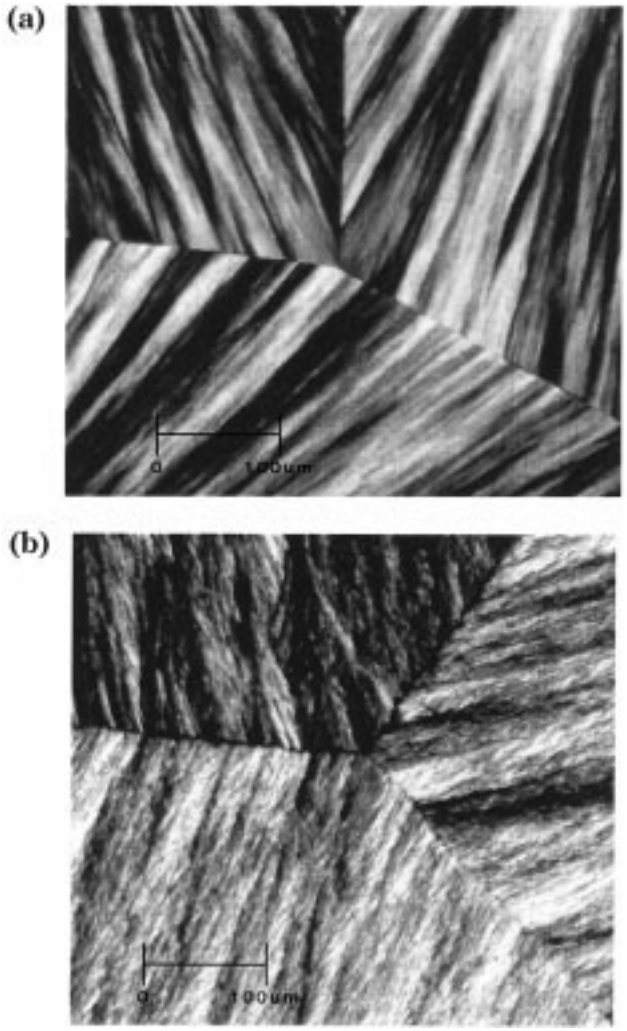

Figure 6—(a) Eutectic viewed with polarized light after crystallization between a glass slide and coverslip. (b) Eutectic with 5% phenytoin.

studied.[8] $DMSO_2$ was first identified as a natural constituent of biological systems in 1934 when Pfiffner and Vars isolated it from beef adrenals.[9] It was later isolated from beef blood and milk, and it has been indicated that human intake from these sources may be as high as a few milligrams daily.[8] The latter figure is consistent with Williams et al.'s finding of 4−11 mg of $DMSO_2$ in 24-h samples of human urine[10] and a reported circulating blood concentration of 0.2−0.5 ppm in the adult male.[11]

$DMSO_2$ has recently been tested for efficacy in the treatment of interstitial cystitis[11] without findings of any adverse effects. Bertken[8] also reported that a man who ingested approximately 4 g of $DMSO_2$ daily for 3 months suffered no ill effects. The only (related) report of toxicity that was found in the literature, other than the detrimental effects of $DMSO_2$ on nematode gamete production,[12] implicated dimethyl sulfate ($DMSO_4$) in a 1994 death.[13] However, as indicated by the authors of that paper, there is no established precedent for the direct conversion of $DMSO_2$ to $DMSO_4$.

Conclusion

The chlorobutanol hemihydrate−dimethyl sulfone ($DMSO_2$) eutectic was determined to be a suitable medium for lyophilizing drugs that are poorly water soluble and/or highly water sensitive. The eutectic is formed at a 60:40 mole ratio (75:25 weight ratio) and has a melting point of

50 °C. Lyophilization can be accomplished without refrigeration, and thus, without conventional freeze-drying equipment, because the melting point is above room temperature. The solvents are rapidly and thoroughly removed under vacuum with moderate heating. Two drying stages were used in the current study, both at a pressure of 0.3 mmHg. The first stage was at 40 °C to primarily remove the chlorobutanol hemihydrate, and the second was at 60 °C to remove the bulk of the $DMSO_2$. Each drying stage required approximately 6.5 h using standard 10 mL freeze-drying vials and solvent volumes of ~5 mL. The cakes produced from the eutectic contain <1% residual solvent and are rapidly reconstituted. Trace amounts of residual solvent are below harmful levels.

References and Notes

1. Seager, H.; Taskis, C. B.; Syrop, M.; Lee, T. J. Structure of Products Prepared by Freeze-Drying Solutions Containing Organic Solvent. *J. Parenter. Sci. Technol.* **1985**, *39*, 161−181.
2. *The Handbook of Pharmaceutical Excipients*; Wade, A., Weller, P. J., Eds.; The Pharmaceutical Press: London, 1994.
3. *The Merck Index*, 12th ed.; Budavari, S., Ed.; Merck Research Laboratories: Whitehouse Station, NJ, 1996.
4. Adjei, A.; Newburger, J.; Martin, A. Extended Hildebrand Approach: Solubility of Caffeine in Dioxane−Water Mixtures. *J. Pharm. Sci.* **1980**, *69*, 659−661.
5. Fedors, R. F. A Method for Estimating Both the Solubility Parameters and Molar Volumes of Liquids. *Polym. Eng. Sci.* **1974**, *14*, 147−154.
6. Borody, T.; Chinwah, P. M.; Graham, G. G.; Wade, D. N.; Williams, K. N. Chlorobutanol Toxicity and Dependence. *Med. J. Australia.* **1979**, *7*, 288.
7. Nordt, S. P. Chlorobutanol Toxicity. *Ann. Pharmacother.* **1996**, *30*, 1179−1180.
8. Bertken, R. "Crystalline DMSO": $DMSO_2$. Arthritis Rheum. **1983**, *26*, 693−4.
9. Pfiffner, J. J.; Vars, H. M. Extraction Studies on Adrenal Cortical Hormone; Disrtibution Studies. *J. Biol. Chem.* **1934**, *106*, 645.
10. Williams, K. I. H.; Burstein, S. H.; Layne, D. S. Dimethyl Sulfone: Isolation forom Human Urine. *Arch. Biochem. Biophys.* **1966**, *113*, 251−252.
11. Childs, S. J. Dimethyl Sulfone ($DMSO_2$) in the Treatment of Interstitial Cystitis. *Urol. Clin. North Am.* **1994**, *21*, 85−88.
12. Goldstein, P.; Magnano, l.; Rojo, J. Effects of Dimethyl Sulfone ($DMSO_2$) on Early Gametogenesis in *Caenorhabditis Elegans*: Ultrastructural Aberrations and Loss of Synaptonemal Complexes from Pachytene Nuclei. *Reprod. Toxicol.* **1992**, *6*, 149−159.
13. Grant, P. M.; Haas, J. S.; Whipple, R. E.; Andrensen, B. D. A Possible Chemical Explanation for the Events Associated with the Death of Gloria Ramirez at Riverside General Hospital. *Forensic Sci. Int.* **1997**, *87*, 219−237.

JS980478P

Solubilization of Ionized and Un-ionized Flavopiridol by Ethanol and Polysorbate 20

PING LI,[†] S. ESMAIL TABIBI,[‡] AND SAMUEL H. YALKOWSKY*,[†]

Contribution from *Department of Pharmaceutical Sciences, College of Pharmacy, University of Arizona, Tucson, Arizona 85721, and Pharmaceutical Resources Branch, National Cancer Institute, NIH, Bethesda, Maryland 20892.*

Received November 6, 1998. Accepted for publication February 8, 1999.

Abstract □ Because the ionized species is more polar than its un-ionized counterpart, it is often assumed that the ionized species of the drug does not make a meaningful contribution to solubilization by either cosolvents or surfactants. This report extends previous studies on solubilization of the ionic species by a combination of pH control and complexation to pH control and micellization and to pH control and cosolvency. The total aqueous solubility is expressed as the addition of the concentration of all contributing species: free un-ionized drug [D_u], free ionized drug [D_i], un-ionized drug micelle [D_uM], and ionized drug micelle [D_iM] for surfactant, and free un-ionized drug [D^c_u] and free ionized drug [D^c_i] for cosolvent. The equations indicate that under certain conditions the ionized species can be more important in determining the drug total solubility than the un-ionized species. Flavopiridol, a weak base, is used to test these newly generated equations. As expected, the micellar partition coefficient and solubilization power for ionized flavopiridol are both less than those of the un-ionized species. However, at acidic pH, the solubilities of the ionized drug in surfactant micelles [D_iM] and in cosolvent–water [D^c_i] are both much greater than that of the un-ionized drug. This difference is because the solubilization of the ionized drug is proportional to its aqueous solubility, and its solubility [D_i] can be as much as 24-fold greater than that of the free un-ionized species [D_u].

Introduction

The control of pH with either a cosolvent, a surfactant, or a complexant is often used to improve the aqueous solubility of drugs.[1] It is commonly believed that the un-ionized species makes the major contribution to the improvement of the total aqueous drug solubility.[2] In a recent study we found that a change of pH favoring ionization of the drug significantly increased not only the solubility of the drug in water but also the amount of the drug solubilized by the complexant.[3] In fact, the ionized species were shown to be solubilized to a greater extent than the un-ionized species.[3−6]

In this report, we extend our studies on the role of the ionized species in improving aqueous solubility to pH control combined with either cosolvency or micellization. The newly developed equations are verified using flavopiridol [5,7-dihydroxy-8-(4-*N*-methyl-2-hydroxy-pyridyl)-6′-choloroflavone hydrochloride], a derivative of rohitukine that has been developed for the treatment of breast cancer, as a model drug. The drug is weakly basic with an apparent pK_a of 5.68 and a low intrinsic solubility of 0.025 mg/mL for its zwitterionic form.[7]

* To whom correspondence should be addressed.
[†] Department of Pharmaceutical Sciences.
[‡] Pharmaceutical Resources Branch.

Background

Solubilization by Surfactant—A surfactant or surface-active agent has two distinct regions: one polar and one nonpolar. When it is added to aqueous media, the surfactant molecules orient themselves to form micellar aggregates, provided their concentration exceeds the critical micellar concentration (cmc).[1] Because the interiors of these micelles are much less polar than water, they can more effectively dissolve the nonpolar drug molecules. As a result, the apparent aqueous solubility is increased.

For a given surfactant solution there is an equilibrium among four species: un-ionized drug [D_u], ionized drug [D_i], un-ionized drug in the micelle [D_uM], and ionized drug in the micelle [D_iM]. The total concentration of the drug [D^{tot}] is

$$[D^{tot}] = [D_u] + [D_i] + [D_uM] + [D_iM] \quad (1)$$

For a basic drug, the concentrations of the ionized drug and the un-ionized drug are related by the Henderson−Hasselbalch equation

$$[D_i] = [D_u]10^{(pK_a - pH)} \quad (2)$$

The value of [D_uM] is related to the micellar partition coefficient for the un-ionized species κ_u and the micellar concentration [C_m] by[1]

$$[D_uM] = \kappa_u[D_u][C_m] \quad (3)$$

Note that [C_m] is equal to the total surfactant concentration when the cmc is small enough to be ignored. Similarly, the value of [D_iM] is related to the micellar partition coefficient for the ionized species κ_i by

$$[D_iM] = \kappa_i[D_i][C_m] \quad (4)$$

Therefore eq 1 can be expanded to

$$[D^{tot}] = [D_u] + [D_u]10^{(pK_a - pH)} + \kappa_u[D_u][C_m] + \kappa_i[D_u]10^{(pK_a - pH)}[C_m] \quad (5)$$

Equation 5 indicates that the total drug aqueous solubility is a function of [D_u], pK_a, κ_u, κ_i, [C_m], and solution pH. The ionized species will be solubilized to a greater extent than the un-ionized species (i.e., [D_iM] > [D_uM]) if $\kappa_i[D_i] > \kappa_u[D_u]$. This condition will be met if $\kappa_i 10^{(pK_a - pH)} > \kappa_u$ (i.e., if pK_a − pH > log κ_u − log κ_i). This equation is similar to a previously developed equation that describes solubilization by pH control and complexation.[3]

Solubilization by Cosolvent—Unlike surfactants, cosolvents form homogeneous solutions with water. These solutions act as new solvents that have polarities between

10.1021/js980433o CCC: $18.00 Published on Web 04/02/1999

that of water and the pure cosolvents. In any cosolvent–water mixture, the concentrations of the un-ionized species $[D^c_u]$ and the ionized species $[D^c_i]$ are in equilibrium as described by eq 2. The total solubility in the mixed solvent $[D^{tot}]$ is

$$[D^{tot}] = [D^c_u] + [D^c_i] \quad (6)$$

The value of $[D^c_u]$ is related to the volume fraction of cosolvent f in the mixture and the solubilizing power for the un-ionized drug σ_u by[1,2]

$$[D^c_u] = [D_u]10^{\sigma_u f} \quad (7)$$

Similarly, the value of $[D^c_i]$ is related to the solubilizing power for the ionized drug σ_i by

$$[D^c_i] = [D_i]10^{\sigma_i f} \quad (8)$$

Equation 8 can be expressed as

$$[D^c_i] = [D_u]10^{(pK_a - pH)}10^{\sigma_i f} \quad (9)$$

Substituting eqs 7 and 9 into eq 6 gives

$$[D^{tot}] = [D_u]10^{\sigma_u f} + [D_u]10^{(pK_a - pH)}10^{\sigma_i f} \quad (10)$$

The total drug solubility in a mixed solvent can therefore be described in terms of $[D_u]$, σ_u, σ_i, pK_a, f, and solution pH. In general, the solubilizing power of the cosolvent for the ionized species (σ_i) is smaller than that of the un-ionized species (σ_u). As a result, the un-ionized species is often assumed to be primarily responsible for the improvement of the total drug solubility. However, eq 10 indicates that the solubilization of the ionized species can be more important than that of the un-ionized species in determining the total drug solubility. In fact, the concentration of the ionized species will exceed that of the un-ionized species if the difference between the pK_a of the drug and the solution pH is greater than the difference between the solubilization powers of the cosolvent for the un-ionized species and that of the cosolvent for the ionized species (i.e., $pK_a - pH > \sigma_u - \sigma_i$).

In this report, the effect of the ionized species on the total drug solubility by either micellization or cosolvency (as predicted by eqs 5 and 10, respectively) is confirmed using a weakly basic drug, flavopiridol.

Materials and Methods

Materials—Flavopiridol was provided by the National Cancer Institute and used as received. All other chemicals were reagent grade and purchased from Sigma (St. Louis, MO) or Aldrich (St. Louis, MO) and used without further purification. Citrate-phosphate buffers were prepared according to Scientific Tables.[8] Samples for the solubilization studies were prepared in a series of either polysorbate 20 or ethanol solutions at concentrations of 0, 1.25, 2.5, 5, 10, and 20% in citrate-phosphate buffers at pH 4.3, 5.0, and 8.4.

Methods—*Solubility Determination*—An excess amount of flavopiridol was added to vials containing 0.5 mL of an aqueous solution of either polysorbate 20 or ethanol. The sample vials were then rotated at 20 rpm using an end-over-end mechanical rotator (Glas-Col Laboratory Rotator, Terre Haute, IN) at 25 °C for 6 days. Samples with drug crystals present were considered to have reached their equilibrium solubility and were removed from the rotator. The samples were filtered through a 0.45-μm filter and the pH at equilibrium was measured before performing the HPLC analysis.

HPLC Analysis—The HPLC assay used an EPS C18 column (100 cm × 4.6 mm, Alltech, Deerfield, IL) with a mobile phase composed of acetonitrile and 50 mM phosphate buffer at pH 3.0 (ratio, 35:65). The flow rate was controlled at 1 mL/min (125 Solvent Module, Beckman), and the effluent was detected at 263 nm (168 detector, Beckman). All experimental data are the average of duplicate values, with a relative standard deviation of <3%.

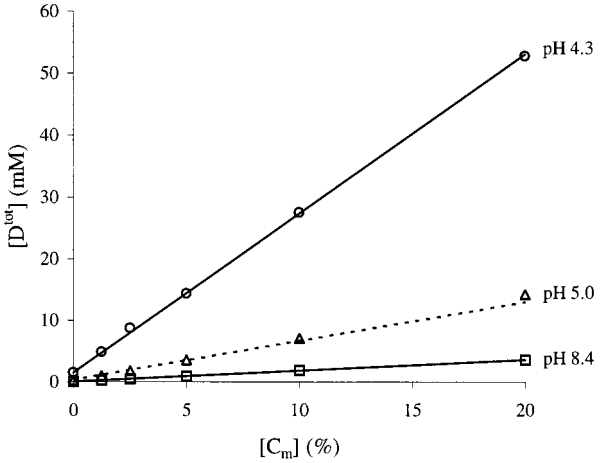

Figure 1—Experimentally determined total aqueous flavopiridol solubilities $[D^{tot}]$ (symbols) in polysorbate 20 solutions $[C_m]$ at different pHs.

Table 1—Results Determined with Equations 2, 3, and 4

pH	total $[D^{tot}]$	free un-ionized $[D_u]$	micelled un-ionized $[D_uM]$	free ionized $[D_i]$	micelled ionized $[D_iM]$
8.4	1.85	0.06	1.79	0.00	0.00
5.0	6.92	0.06	1.79	0.29	4.78
4.3	27.3	0.06	1.79	1.44	24.0

Results and Discussions

Solubilization by Surfactant—In Figure 1, the experimental total aqueous solubility is plotted against the concentration of polysorbate 20 at pH 4.3 (open circles) and pH 8.4 (open squares). Although linearity between the drug aqueous solubility and the surfactant concentration is observed at both pHs, the solubilization slopes are quite different. The solubilization slope at pH 4.3 is ≈15-fold higher than the slope at pH 8.4.

These solubilization slopes can be used to calculate polysorbate 20 micellar partition coefficients for un-ionized and ionized flavopiridol via eq 5. The calculated values are $\kappa_u = 333.3\ M^{-1}$ and $\kappa_i = 185.4\ M^{-1}$, respectively. The lower micellar partition coefficient for the ionized drug is obviously due to its greater affinity for water.

With $[D_u]$, pK_a, κ_u, and κ_i, we can calculate $[D_i]$, $[D_uM]$, and $[D_iM]$ at any given combination of surfactant concentration and solution pH by using eqs 2, 3, and 4, respectively. Table 1 lists these values and the experimental total drug solubility for a 10% surfactant concentration at pH 8.4, 5.0, and 4.3. The highest total drug solubility is achieved at pH 4.3 where most of the drug is ionized. At this pH $[D_i]$ accounts for 5% of total solubility and $[D_iM]$ accounts for ≈88%. The high concentration of the $[D_iM]$ is primarily responsible for the higher total solubility in the acidic solution than in the neutral solution. Note that $[D_uM]$ remains constant at all pH conditions because it is only determined by $[D_u]$ and κ_u, both of which are pH independent.

Solubilization by Cosolvent—Figure 2a shows the experimental aqueous solubility of flavopiridol versus the concentration of ethanol at pH 4.3 (open circles) and pH 8.4 (open squares). Unlike the linear surfactant solubilization curves, the drug solubility increases exponentially

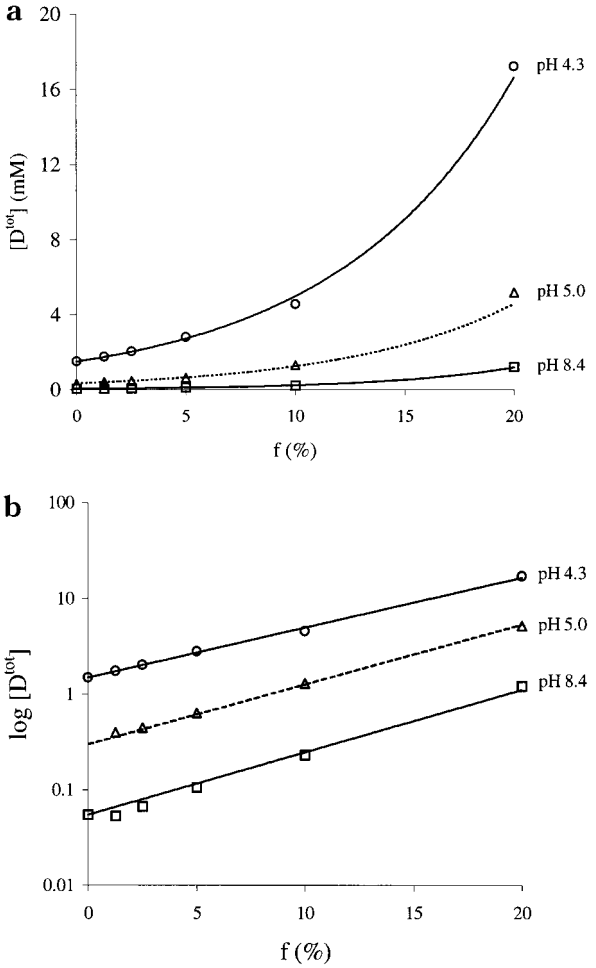

Figure 2—(a) Experimentally determined total aqueous flavopiridol solubilities [D^{tot}] (symbols) in ethanol solutions [*f*] at different pHs. (b) Schematic plot of the semilogarithmical total aqueous solubility of flavopiridol log[D^{tot}] against ethanol volume fraction *f*.

Table 2—Results Determined with Equations 7 and 9

pH	total [D^{tot}]	un-ionized [D^c_u]	ionized [D^c_i]
8.4	0.25	0.25	0.00
5.0	1.19	0.25	0.94
4.2	4.98	0.25	4.73

as the cosolvent concentration increases. Again, the solubilization curves are different at different solution pHs. The drug solubilities in both water and 10% ethanol solution at pH 4.3 are ≈20-fold greater than that at pH 8.4.

Figure 2a can be re-plotted semilogarithmically, as is seen in Figure 2b, where nearly parallel linear relationships between log[D^{tot}] and cosolvent volume fraction are evident at both pHs. This linearity persists up to 20% cosolvent. The slopes at pH 4.3 and 8.4 show that σ_u and σ_i are quite similar, with values of 0.06 and 0.05% $^{-1}$, respectively.

Table 2 lists the experimental total drug solubility [D^{tot}] in 10% cosolvent and the values of [D^c_u] and [D^c_i] calculated with eqs 7 and 9. As in surfactant solubilization, the total drug solubility in cosolvent is much higher at pH 4.3 than that at pH 8.4. Although the solubility of flavopiridol increases by nearly the same factor at both pH values, the amount of drug solubilized is much greater at the lower pH. This difference occurs because the concentration of ionized drug [D^c_i] far exceeds the concentration of the un-ionized drug [D^c_u] in the solution at pH 4.3. It is also noted that the value of [D^c_u] is pH independent.

Validation of Equations—The solubilities (dotted lines), calculated with eq 5 for polysorbate 20 solution and with eq 10 for ethanol solution, are compared with the experimental solubility data (open triangles) at pH 5.0 in Figures 1 and 2, respectively. The strong agreement between the predicted and the observed solubility data supports the validity of both eq 5 and eq 10.

Conclusion

A pH change that favors the ionization of the drug not only increases the solubility of the ionized species in water, but also increases the solubility of the ionized species in both micelles and cosolvent. This result is independent of the values of the micellar partition coefficient and the solubilization power. Furthermore, the solubilities of the ionized species in the micelles and cosolvent can exceed those of the un-ionized species.

For micellization:

$$[D_iM] > [D_uM], \text{ if } (pK_a - pH) > (\log \kappa_u - \log \kappa_i)$$

For cosolvency:

$$[D^c_i] > [D^c_u], \text{ if } (pK_a - pH) > (\sigma_u - \sigma_i)$$

Note that these relationships are similar to the following relationship, which was previously derived for complexation

$$[D_iL] > [D_uL], \text{ if } (pK_a - pH) > (\log K_u - \log K_i)$$

where K_u and K_i are complexation constants for the un-ionized and ionized solutes, respectively, and [D_uL] and [D_iL] are the concentrations of the corresponding complexes.

References and Notes

1. Martin, A. *Physical Pharmacy*, 4th ed.; Lea & Febiger: Philadelphia, PA, 1993; pp 234−236, 259−260.
2. Alvarez-Nunez, F. A.; Yalkowsky, S. H. Solubilization of Diazepam. *PDA J. Pharm. Sci. Technol.* **1998**, *52*, 33−36.
3. Li, P.; Tabibi, S. E.; Yalkowsky, S. H. Combined effect of complexation and pH on solubilization. *J. Pharm. Sci.* **1998**, *87*, 1535−1537.
4. Johnson, M. D.; Hoesterey, B. L.; Anderson, B. D. Solubilization of a tripeptide HIV protease inhibitor using a combination of ionization and complexation with chemically modified cyclodextrins. *J. Pharm. Sci.* **1994**, *83*, 1142−1146.
5. Tinwalla, A. Y.; Hoesterey, B. L.; Xiang, T. X.; Lim. K.; Anderson, B. D. Solubilization of thiazolobenzimidazole using a combination of pH adjustment and complexation with 2-hydroxypropyl-β-cyclodextrin. *Pharm. Res.* **1993**, *10*, 1136−1143.
6. Okimoto, K.; Rajewski, R. A.; Uekama, K.; Jona, J. A.; Stella, V. J. The interaction of charged and uncharged drugs with neutral (HP-βCD) and anionically charged (SBE7-β-CD) β-cyclodextrins. *Pharm. Res.* **1996**, *13*, 256−264.
7. Dannenfelser, R. M.; Surakitbanharn, Y.; Tabibi, S. E.; Yalkowsky, S. H. Parenteral formulation of flavopiridol (NSC-649890). *PDA J. Pharm. Sci. Technol.* **1995**, *50*, 356−359.
8. Diem, K.; Lentner, C. *Scientific Tables*, 7th ed.; Geigy Pharmaceuticals: Ardsley, NY, 1974; pp 280−282.

Acknowledgments

This work was performed under contract no. N01-CM-27757 from the National Cancer Institute.

JS980433O

A Novel Microbial Infection-Responsive Drug Release System

MASAO TANIHARA,*,† YOSHIHISA SUZUKI,‡ YOSHIHIKO NISHIMURA,‡ KYOKO SUZUKI,‡ YOSHIMI KAKIMARU,§ AND YOSHIHARU FUKUNISHI||

Contribution from *Graduate School of Materials Science, Nara Institute of Science and Technology, 8916-5 Takayama, Ikoma, Nara 630-0101, Department of Plastic and Reconstructive Surgery, Faculty of Medicine, Kyoto University, Kyoto 606-8507, Medical R&D, Kuraray Company, Ltd., Okayama 710-8622, and R&D Department, Kuraray Chemical Company, Ltd., Okayama 705-0025, Japan.*

Received October 23, 1998. Accepted for publication February 3, 1999.

Abstract □ The aim of this study was to construct a novel drug delivery system suitable for controlled release of antibiotics. There is a need for devices that release antibiotics only during microbial infection, because prophylactic or prolonged use of antibiotics leads to serious problems, such as renal and liver toxicity and the emergence of drug-resistant bacteria (e.g., meticillin-resistant *Staphylococcus aureus*). We found previously that *Staphylococcus aureus*-infected wound fluid showed high thrombin-like activity; therefore, in this study we designed an antibiotic release system triggered by thrombin activity. We synthesized an insoluble polymer–drug conjugate in which gentamicin was bound to poly(vinyl alcohol) hydrogel through a newly developed thrombin-sensitive peptide linker. The conjugate released gentamicin when it was incubated with *Staphylococcus aureus*-infected wound fluid, with thrombin and leucine aminopeptidase, or with human plasma and Ca^{2+}, whereas no biologically active gentamicin was released when the conjugate was incubated with noninfected wound fluid, with leucine aminopeptidase alone, with thrombin alone, or with plasma. Furthermore, the conjugate reduced the bacterial number in an animal model of *Staphylococcus aureus* infection. These results demonstrated that the conjugate has sufficient specificity and excellent potential as a stimulus-responsive, controlled drug release system.

Introduction

Improper usage of antibiotics is very serious because of the appearance of renal and liver toxicity and the emergence of drug-resistant bacteria (e.g., meticillin-resistant *Staphylococcus aureus*).[1−4] In the ideal case, the proper amount of antibiotics is used at the site and during the period of the infection. For this purpose, many kinds of drug delivery systems have been investigated, including several antibiotic-impregnated polymer systems;[5−11] however, these systems are not appropriate for controlled release of antibiotics. Therefore, a system that detects the occurrence of bacterial infection and releases the proper amount of antibiotics relative to the degree of infection is needed. In this study, we constructed a system in which antibiotics are bound to an insoluble polymer matrix through a linker that acts as an infection sensor.

First, we investigated biological signals, such as enzyme activities, which appeared in infected wound fluid and found a remarkable increase of thrombin-like activity in *Staphylococcus aureus* (SA)-infected wounds.[12] This enzyme activity was thought to be mainly attributed to staphylocoagulase produced by SA, which forms an enzymatically active complex with prothrombin named staphylothrombin.[13] Second, we developed a novel peptide linker, Gly-(D)-Phe-Pro-Arg-Gly-Phe-Pro-Ala-Gly-Gly, which could connect insoluble polymer matrix and drug, and was specifically cleaved by thrombin.[14] The ideal insoluble polymer matrix should be biocompatible, noninflammative, and nontoxic, and should have good mechanical properties. A new hydrogel made of a poly(vinyl alcohol) derivative was synthesized in this study. Introduction of carboxyl groups to partially saponified polyvinyl pivalate gave a transparent, soft, and high-water-content hydrogel that is cross-linked by hydrophobic bonds between tertiary butyl groups in pivalate.[15]

Our preliminary study revealed that gentamicin was selectively released from the device when it was incubated with infected wound fluid and that the device showed bacteriocidal effect in vitro.[12] In this report, we describe the synthesis of the device combining these components to attain a suitable polymer−drug conjugate system, and the specificity of drug release properties in vitro and bacteriocidal effect in vivo. The results showed that the device is sufficiently potent and specific for treating SA-infected wounds.

Methods

Materials—Gentamicin sulfate, thrombin (human plasma, EC 3.4.21.5), and leucine aminopeptidase (cytosol, Type V: Porcine kidney, EC 3.4.11.1) were purchased from Sigma Chemical Company, St. Louis, MO. Fluorogenic peptide substrates, WSCD (1-ethyl-3-(3-dimethyl-aminopropyl)-carbodiimide hydrochloride), and HOSu (*N*-hydroxysuccinimide) were from Peptide Institute Inc., Minoh, Osaka, Japan. Other reagents were from Wako Pure Chemicals, Doshomachi, Osaka, Japan. Peptide linker (Gly-(D)-Phe-Pro-Arg-Gly-Phe-Pro-Ala-Gly-Gly) was synthesized by Peptide Institute Inc.; purity: 95.0%, as determined by reversed-phase HPLC [column: YMC PACK ODS-A (4.6 mm i. d. × 150 mm) + (4.0 mm i. d. × 10 mm); eluent: 10− 60% acetonitrile gradient (25 min) in 0.1% trifluoroacetic acid−water, flow rate: 1 mL/min, detection: 220 nm OD). Amino acids analyzed (calcd): Arg 1.00 (1), Pro 1.99 (2), Gly 4.01 (4), Ala 1.01 (1), Phe 1.99 (2). Mass analysis: 962.8 $[M + H]^+$ (calcd for $[M + H]$: 962.5).

Synthesis of PVA−Linker−Gentamicin (Scheme 1)—*Polyvinyl Pivalate* (***1***)—Freshly distilled vinyl pivalate (200 g, 1.56 mol) was dissolved in 70 g of methanol in a reaction vessel, and purged with nitrogen gas with stirring. The mixture was heated to 60 °C, and 2, 2′-azobis(isobutylonitrile) (0.04 g, 0.24 mmol) in 5 g of methanol was added to start the polymerization. When the polymerization ratio reached 40%, about 5 h after starting of the polymerization, the reaction mixture was cooled to 20 °C. Several volumes of *tert*-butyl alcohol were added to the reaction mixture, and residual vinyl pivalate was distilled off under reduced pressure. Then several volumes of tetrahydrofuran were added and *tert*-butyl alcohol was distilled off under reduced pressure. Finally the solution of polyvinyl vivalate in tetrahydrofuran (concentration: 45.7 wt %) was obtained. Yield: 78 g (39%).

* Corresponding author. Telephone: +81-743-72-6120. Fax: +81-743-72-6129. E-mail: mtanihar@ms.aist-nara.ac.jp.
† Graduate School of Materials Science.
‡ Department of Plastic and Reconstructive Surgery.
§ Medical R&D.
|| R&D Department.

10.1021/js980418j CCC: $18.00
Published on Web 04/02/1999

*Partially Saponified Poly(vinyl alcohol) (**2**)*—Fifty grams of the solution of polyvinyl vivalate in tetrahydrofuran was heated to 60 °C with stirring in a reaction vessel equipped with a reflux condenser. The vessel was purged with nitrogen gas, and 20 g of a 25% solution of KOH was added. After the reaction mixture was kept at 60 °C for 6 h, it was neutralized by adding 5.5 g of acetic acid and 5.5 g of methanol. The solidified product, partially saponified poly(vinyl alcohol), was washed with methanol using a Soxhlet extractor and dried under reduced pressure. Yield: 10.7 g (46.8%), P = 1650, determined by [η] of the polyvinyl acetate at 30 °C, which was acetylated after full saponification of the partially saponified poly(vinyl alcohol), according to the following equation:

$$P = \{[\eta] \times (1000/7.94)\}^{(1/0.62)} \quad (1)$$

The saponified ratio was 0.811, determined from 500 MHz ^{1}H NMR (d_6-dimethyl sulfoxide): δ (ppm) 1.11 (s, 9H, $C(CH_3)_3$, integration: 89 au), 1.4−1.77 (complex, 2H, CH_2, integration: 106 au).

*Carboxylated Poly(vinyl alcohol) Hydrogel (PVA−COOH) (**3**)*—Ten grams of partially saponified poly(vinyl alcohol) was dissolved in 300 g of dimethyl sulfoxide at 70 °C, followed by the addition of succinic anhydride (1.64 g, 16.4 mmol) and pyridine (0.64 g, 8.1 mmol). After the reaction mixture was kept at 70 °C for 4 h, it was cast in a glass tray, followed by hydration in a humidified chamber. After 1 or 2 days of incubation in a humidified chamber, a sheet of transparent hydrogel (PVA−COOH) was obtained. This hydrogel was thoroughly washed with water to remove the residual reagents. The water content of the hydrogel was 91 wt % and the carboxyl group content was 12 μmol/g-hydrogel (= 1.3×10^{-4} mol/g-dry weight).

*Poly(vinyl alcohol) Hydrogel−Peptide Linker Conjugate (PVA−Linker) (**4**)*—PVA−COOH (10 g, 0.12 mmol carboxyl group) was washed several times with dimethylformamide, and to the resultant dimethylformamide-swollen gel, HOSu (46 mg, 0.4 mmol) and WSCD (81 mg, 0.42 mmol) in 10 mL of dimethylformamide were added, followed by shaking overnight. The gel was washed several times each with dimethylformamide and water, followed by the addition of the peptide linker, Gly-(D)-Phe-Pro-Arg-Gly-Phe-Pro-Ala-Gly-Gly (116 mg, 0.12 mmol), in 10 mL of 20 mM phosphate buffer (pH 7.0). After shaking the reaction mixture overnight, the resultant PVA−linker was washed several times with phosphate buffered saline (PBS, 10 mM phosphate, 150 mM NaCl, pH 7.4) and Gly-HCl buffer (0.1 M, pH 2.5), and then washed several times with 20 mM phosphate buffer (pH 7.0). The yield of this coupling reaction was ~80%, as determined by HPLC analysis of the residual peptide linker in the reaction mixture.

*Poly(vinyl alcohol) Hydrogel−Peptide Linker−Gentamicin Conjugate (PVA−Linker−Gentamicin) (**5**)*—PVA−linker (10 g) was immersed in 10 mL of 20 mM phosphate buffer (pH 7.0), and gentamicin (1.28 g, 1.68 mmol) and WSCD (46 mg, 0.24 mmol) were added, followed by overnight shaking. The resultant product, PVA−linker−gentamicin, was thoroughly washed with phosphate buffered saline (PBS) and water until the concentration of total organic carbon of the supernatant decreased below 10 ppm.

Bacterial Culture—*Staphylococcus aureus* (FDA209P, Institute of Fermentation Osaka, Osaka, Japan) was used. This strain was stored in trypticase soy broth with glycerol (20%) at −70 °C. Before the experiments, the strain was grown in Brain-Heart Infusion (BHI) broth overnight at 37 °C on a rotary shaker. The concentration of cells was measured by turbidity at 600 nm, and adjusted to the desired concentration by diluting with PBS.

SA-Infected Wounds—Male Wistar rats weighing 150 to 200 g were acclimatized to laboratory conditions for 7 days prior to use. The animals were fed a standard commercial rat chow ad libitum and housed individually in facilities that complied with the requirements of the Kyoto University Animal Experiment Committee, with controlled temperature (22−23 °C) and light (12 h light/12 h darkness). Each rat was anesthetized with an intraperitoneal injection of sodium pentobarbital (65 mg/kg). The dorsal paravertebral fur was then removed with electric clippers and a depilatory agent. The skin was cleansed with an iodophor solution followed by a 70% alcohol rinse. Air was sucked into a syringe through a sterile cotton filter, and 10 mL of air was injected into the loose subcutaneous tissue between the shoulders of the rat. One day after creation of the air pouch, 3 g of PVA−linker−gentamicin (n = 8) or PVA−COOH (n = 8) was inserted into the pouch with 5 mL of a suspension of 10^5 SA per milliliter in PBS. After 4 h, the bacterial number in the fluid from each pouch was estimated by limiting dilution methods using BHI agar plates.

Sampling of wound fluids was done by almost the same method just described except for the following points. One day after creation of the air pouch, animals were randomly assigned to the infected wound group or the noninfected wound group, and 10 mg of Montmorillonite clay soil fraction, a well-known infection-potentiating factor,[16] was inserted into each air pouch instead of PVA−COOH or PVA−linker−gentamicin as already described. Five days after creation of the infected air pouch, the animals were anesthetized as already described, and the wounds were opened. The pus was removed and the inner surface of the pouch was gently wiped with wet gauze to expose the fresh wound bed. Freeze-dried agarose sponges were inserted into the pouch to absorb the wound fluid, and the incision was closed. After 20 min, the pouch was reopened. The wound fluid contained in the agarose sponges was weighed and the amount of fluid obtained from the pouch during 20 min was calculated. The fluid contained in the agarose sponges was stored at −150 °C until assay. Simultaneously, the wound tissues were removed, weighed, and used to count the bacterial number by limiting dilution methods using BHI agar plates. Then, all the animals were sacrificed with an overdose of pentobarbital.

Assay for Enzymatic Activity of Infected Wound Fluid and Plasma—The wound fluid contained in the agarose sponges was extracted by addition of 9 volumes of PBS and filtered by centrifugation. Plasma was also diluted by addition of 9 volumes of PBS with or without 10 mM Ca^{2+}. Thrombin-like activity and aminopeptidase activity were measured using the fluorogenic peptide substrates (0.2 mM) Boc-Val-Pro-Arg-MCA[17,18] (MCA = 4-methylcoumaryl-7-amide) and Ala-MCA,[19] respectively. Enzymatic activity was calculated from the fraction of each substrate hydrolyzed after incubation for 30 min at 25 °C.

Assay of Gentamicin Release—The wound fluid in the agarose sponges was extracted by addition of two volumes of PBS and filtered by centrifugation. After incubation of 0.05 g of PVA−linker−gentamicin with 250 μL of the wound fluid, Ca^{2+}-supplemented plasma, plasma, or enzyme solution for 24 h at 37 °C, the supernatant was used to measure the concentration of gentamicin by the following two methods.

Width of Zone of Inhibition of SA Growth on BHI Agar Plates—Seventy-five microliters of the supernatant was adsorbed onto a paper disk, the disk was placed on a BHI agar plate inoculated with SA, and the plate was incubated overnight at 37 °C. The concentration of gentamicin was calculated from the width of the zone of inhibition around the disk compared with the widths of zones around standard gentamicin solutions with concentrations from 0 to 30 μg/mL of solution.

2. Fluorescence Polarization Immunoassay (FPIA)—A fully automatic FPIA apparatus (TDX analyzer, DAINABOT, Tokyo, Japan) and the corresponding reagents kit for gentamicin were used.

Statistical Analysis—All statistical evaluations were performed by unpaired t test and analysis of variance (ANOVA). All values were expressed as mean ± standard deviation.

Results

Enzymatic Activity in SA-Infected Wound Fluid—We found significantly elevated thrombin-like activity in SA-infected wound fluid compared with the level in noninfected wound fluid (Table 1). On the other hand, SA-infected wound fluid did not differ from noninfected wound fluid in aminopeptidase activity. Therefore, the thrombin-like activity in wound fluid seemed to be a specific signal of SA-infection. The amount of wound fluid also increased significantly in SA-infected wounds compared with noninfected wounds. The elevated thrombin-like activity in SA-infected wound fluid may be attributable to both α-thrombin and staphylothrombin.[12] Furthermore, high levels of aminopeptidase activity existed in both noninfected and SA-infected wound fluid.

Table 1—Enzymatic Activities and Weight of Exudate From Infected Wounds[a]

variable	digested substrate (nmol/30 min) non-infected ($n = 16$)	SA-infected ($n = 12$)
thrombin-like activity	0.376 ± 0.104	0.518 ± 0.084**
alanine amino peptidase activity	0.938 ± 0.372	1.402 ± 0.206*
amount of exudate (g/wound)	0.190 ± 0.051	0.449 ± 0.116***
bacterial number (CFU/mL)	0	5900***

[a] Key to statistical significance: (*) $p > 0.05$, not significant compared with non-infected control; (**) $p < 0.01$, significant compared with non-infected control; (***) $p < 0.001$, significant compared with non-infected control.

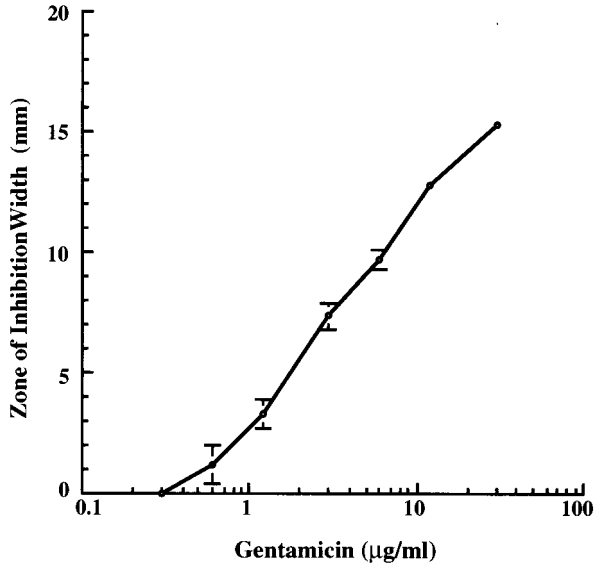

Figure 1—A representative standard curve showing the relationship between the width of the zone of inhibition and concentration of gentamicin. Each value represents mean ± SD of two or three experiments.

Gentamicin Release from PVA–Linker–Gentamicin—one representative standard curve showing the relationship between the width of the zone of inhibition and gentamicin concentration is shown in Figure 1. Because such curves showed a linear relation in the concentration range from 1 to 30 μg/mL, the concentration of released gentamicin was calculated from the width of the zone of inhibition using the standard curve obtained in each experiment.

As shown in Scheme 2, at least two enzyme activities were needed for gentamicin release from PVA–linker–gentamicin. That is, the Arg–Gly bond in the peptide linker was cleaved, and the resultant Gly-Phe-Pro-Ala-Gly-Gly gentamicin was released and digested by aminopeptidase to produce free gentamicin. Figure 2 shows the dose dependence of gentamicin release on thrombin concentration in the presence of leucine aminopeptidase (LAP). Almost no gentamicin was released without thrombin, as measured by both the zone of inhibition and FPIA methods. The amount of gentamicin released increased with increasing thrombin concentration, and seemed to reach a maximum at a thrombin concentration of 2 U/mL. At concentrations of thrombin >4 U/mL, gentamicin release measured by zone of inhibition decreased. LAP may be deactivated by excess thrombin.

The effects of LAP on gentamicin release in the presence of thrombin at 8 U/mL are shown in Figure 3. Gentamicin release was nearly undetectable in the absence of LAP when measured by the zone of inhibition method; however, a considerable amount of gentamicin released was detected by FPIA. This discrepancy seemed to arise from the difference of the specificity of the two methods. Because Gly-Phe-Pro-Ala-Gly-Gly-gentamicin is not biologically active, it was not detected by the zone inhibition method. In contrast, the anti-gentamicin antibody used in FPIA could bind with Gly-Phe-Pro-Ala-Gly-Gly-gentamicin; therefore, it was detected as gentamicin by FPIA.

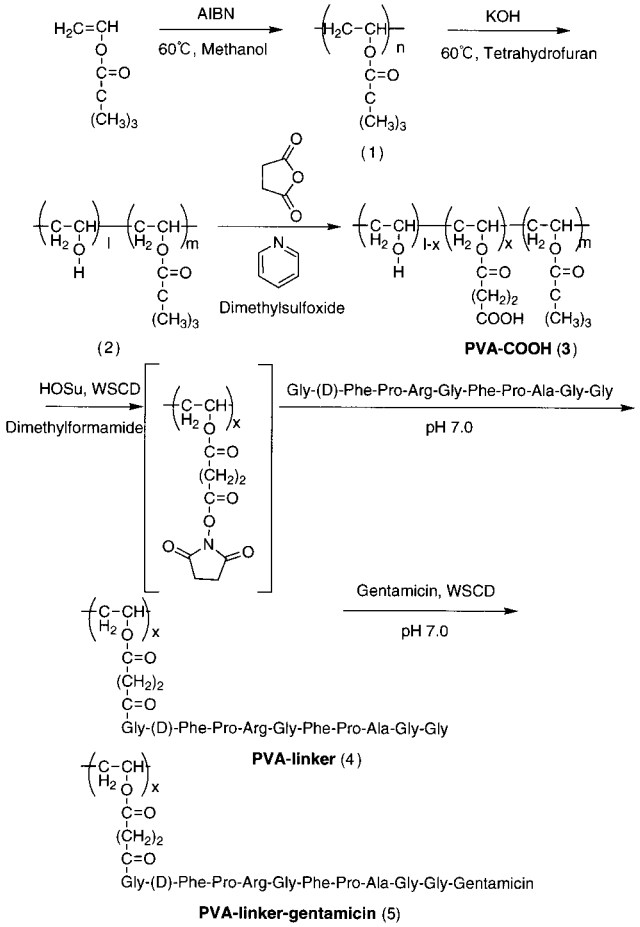

Scheme 1—Synthesis of PVA-linker-gentamicin.

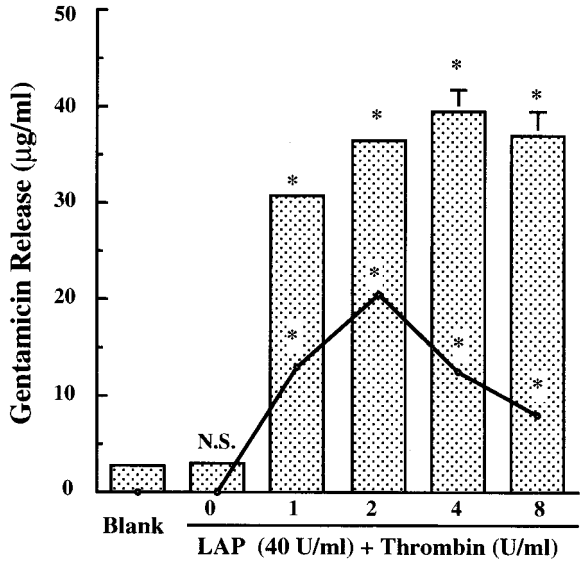

Figure 2—Dose dependence of gentamicin release on thrombin concentration in the presence of LAP: FPIA (bar); zone of inhibition (–○–). Each value represents mean ± SD of triplicate experiments. The data marked with * are significantly high values compared with blank ($p < 0.001$), calculated by ANOVA. N. S. denotes no significant difference compared with blank ($p > 0.05$), calculated by ANOVA.

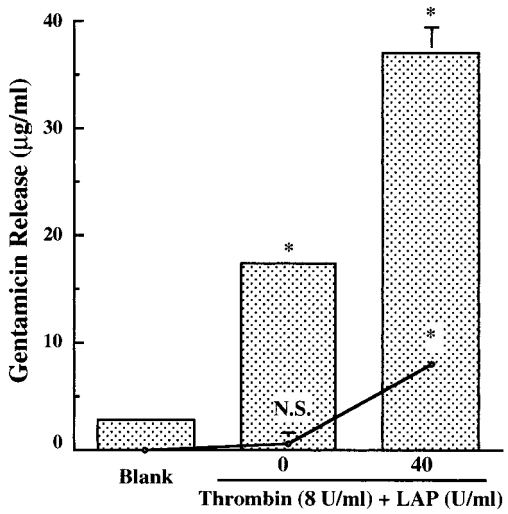

Figure 3—Effects of LAP on gentamicin release in the presence of thrombin: FPIA (bar); zone of inhibition (–○–). Each value represents mean ± SD of triplicate experiments. The data marked with * are significantly high values compared with blank ($p < 0.001$), calculated by ANOVA. N. S. denotes no significant difference compared with blank ($p > 0.05$) calculated by ANOVA.

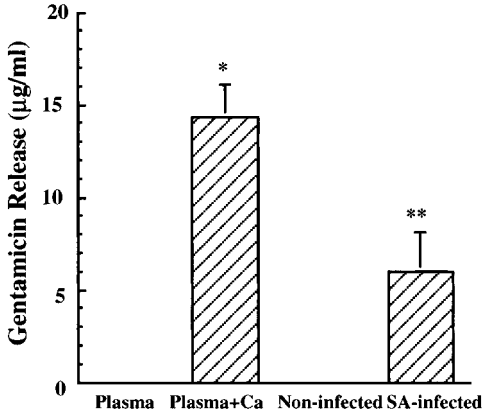

Figure 4—Gentamicin release detected by the zone of inhibition assay when PVA–linker–gentamicin was incubated with Ca^{2+}-supplemented human plasma ($n = 3$) or plasma alone ($n = 3$) in glass tubes, and SA-infected ($n = 13$) or noninfected wound fluid ($n = 3$). Key: (*) plasma + Ca shows a significantly higher value than plasma ($p < 0.001$), by the unpaired t test. (**) SA-infected wound fluid shows a significantly higher value than noninfected wound fluid ($p < 0.001$), calculated by the unpaired t test.

Figure 4 shows the release of biologically active gentamicin when PVA−linker−gentamicin was incubated with Ca^{2+}-supplemented human plasma and plasma alone in glass tubes. Because Ca^{2+} addition to human plasma in glass tubes causes thrombin activation, biologically active gentamicin was released. In plasma alone there was no thrombin activity; therefore, gentamicin release was not detected. Figure 4 also shows that PVA−linker−gentamicin could release biologically active gentamicin when it was incubated with SA-infected wound fluid, however, it could not release a detectable amount of gentamicin when incubated with noninfected wound fluid.

In Vivo Bacteriocidal Effect—The logarithm of the bacterial number (1.96 ± 0.79 CFU/mL, $n = 8$, $p < 0.001$) in an animal model of SA-infection in rats in which PVA−linker−gentamicin was applied was significantly lower than that in rats in which PVA−COOH was applied (5.74 ± 0.29 CFU/mL, $n = 8$) or that in rats in which no treatment was administered (3.76 ± 0.37 CFU/mL, $n = 9$). This result showed that PVA−linker−gentamicin was effective in vivo.

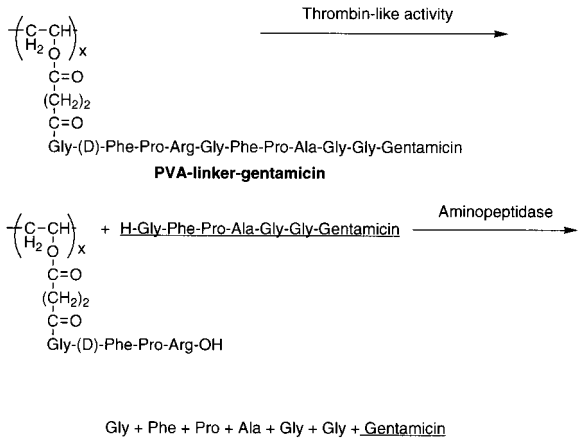

Scheme 2—Gentamicin release from PVA-linker-gentamicin by enzymes.

Discussion

LAP is a typical aminopeptidase present in human serum at a concentration of 8−12 mU/mL.[20] It is thought that LAP is also contained at about the same concentration in wound fluid. Actually, aminopeptidase activity was present in wound fluid and its activity was not changed by SA infection. Therefore, Gly-Phe-Pro-Ala-Gly-Gly-gentamicin produced from PVA−linker−gentamicin by the thrombin-like activity in SA-infected wound fluid was rapidly digested by aminopeptidase, and biologically active free gentamicin was generated. It was also shown that active gentamicin was released from PVA−linker−gentamicin in Ca^{2+}-supplemented human plasma; however, no active gentamicin was released by incubation in human plasma alone (Figure 4). When PVA−linker−gentamicin was incubated with only PBS, human plasma, or LAP, gentamicin release was not detected by either the zone of inhibition or FPIA methods (Figures 2 and 4). These results clearly show that significant contaminations of free gentamicin and peptide linker−gentamicin were not present in the PVA−linker−gentamicin.

Because the amount of released gentamicin was dependent on the thrombin concentration (Figure 2) and thrombin-like activity increases with SA-infection,[12] PVA−linker−gentamicin was expected to release an amount of active gentamicin proportional to the degree of SA-infection. In fact, PVA−linker−gentamicin did release biologically active gentamicin in SA-infected wound fluid (Figure 4), and showed a bacteriocidal effect in the animal model of SA infection. A considerable amount of thrombin-like activity was detected in noninfected wound fluid (Table 1); however, no gentamicin release was detected (Figure 4). This result might be because of failure to reach the threshold of the concentration of thrombin-like activity that could digest the macromolecular substrate, PVA−linker−gentamicin, and/or the threshold of gentamicin concentration that could be detected by the zone of inhibition assay (Figure 1).

The zone of inhibition method depends on the biological activity of intact gentamicin. In contrast, the FPIA method uses antibody that binds immunologically active gentamicin and therefore detects molecules that retain the required antigenic properties of gentamicin, such as, peptide-attached gentamicin, amino acid-attached gentamicin, and damaged gentamicin, as well as intact gentamicin. This point is very important in the study of drug delivery systems because there is a considerable chance that released drug may be damaged by the modification. In our synthesis of PVA−linker−gentamicin, shown in Scheme 1, the possibility of damaging the drug is minimized. According to the reaction shown in Scheme 2, PVA−linker−gentamicin can release intact gentamicin (Figures 2−4) in

the presence of thrombin and LAP. These results demonstrated that PVA−linker−gentamicin is an ideal system for the controlled release of this antimicrobial drug.

Systemic and local administration of antibiotics for wound infection is well established. The efficacy of antibiotics, however, depends on factors such as the pharmacokinetics, the timing of infusion, tissue concentrations, and the antibacterial spectrum of the drug. Because systemic administration of antibiotics is associated with certain drawbacks, such as systemic toxicity and poor penetration into severely infected or necrotic tissues, many physicians favor the use of local antibiotics and other topical measures. Controlled local delivery of antibiotics has been shown to reduce the number of microorganisms with minimal side effects compared with systemic administration. Thus, we have developed a new local, controlled-release system of an antibiotic stimulated by bacterial infection. PVA−linker−gentamicin showed specific release of gentamicin in SA-infected wound fluid and caused a significant reduction in SA number in vivo. These results show that this system allows gentamicin to be released at specific times and locations, namely, when and where SA infection occurs. Because PVA−COOH is a potential occlusive dressing material, it is expected that PVA−linker−gentamicin would inhibit bacteria from colonizing the dressing surface when applied to wounds infected with SA. In addition, if proteinases specific to each bacterium could be used for the triggering signal, different spectra of antibiotics could be released from the same material, depending on the strain of bacterium. That is, for bacterium X, use of bacterium-specific proteinase Y and proteinase Y-sensitive linker Z, would result in release of bacterium X-specific antibiotic. Furthermore, it may also be possible to make tumor-specific devices by utilizing peptide linkers sensitive to tumor-producing enzymes, such as some collagenases.[21,22]

References and Notes

1. Gold, H. S.; Moellering, R. C., Jr. Antimicrobial-drug resistance. *N. Engl. J. Med.* **1996**, *335*, 1445−1453.
2. Goldfarb, J. New antimicrobial agents. *Pediatr. Clin. North. Am.* **1995**, *42*, 717−735.
3. Acar, J. F. Problems and changing patterns of resistance with gram-negative bacteria. *Rev. Infect. Dis.* **1985**, *7*, 545−551.
4. Hayward, C. M.; Griffin, G. E. Antibiotic resistance: the current position and the molecular mechanism involved. *Br. J. Hosp. Med.* **1994**, *52*, 473−478.
5. Langer, R. New methods of drug delivery. *Science* **1990**, *249*, 1527−1533.
6. Gerhart, T. N.; Roux, R. D.; Hanff, P. A.; Horowitz, G. L.; Renshaw, W. C.; Hayes, W. C. Antibiotic-loaded biodegradable bone cement for prophylaxis and treatment of experimental osteomyelitis in rats. *J. Orthop. Res.* **1993**, *11*, 250−255.
7. Gref, R.; Minamitake, Y.; Peracchia, M. T.; Trubetskoy, V.; Torchilin, V.; Langer, R. Biodegradable long-circulating polymeric nanospheres. *Science* **1994**, *263*, 1600−1603.
8. Price, J. S.; Tencer, A. F.; Arm, D. M.; Bohach. G. A. Controlled release of antibiotics from coated orthopedic implants. *J. Biomed. Mater. Res.* **1996**, *30*, 281−286.
9. Gombotz, W. R.; Pettit, D. K. Biodegradable polymers for protein and peptide drug delivery. *Bioconjug. Chem.* **1995**, *6*, 332−351.
10. Johnson, O. L.; Cleland, J. L.; Lee, H. J.; Charnis, M.; Duenas, E.; Jaworowicz, W.; Shepard, D.; Shahzamani, A.; Jones, A. J. S.; Putney, S. D. A month-long effect from a single injection of microencapsulated human growth hormone. *Nature Med.* **1996**, *2*, 795−799.
11. Putnam, D. A.; Shiah, J. G.; Kopecek, J. Intracellulary biorecognizable derivatives of 5-fluorouracil. Implications for site-specific delivery in the human condition. *Biochem. Pharmacol.* **1996**, *52*, 957−962.
12. Suzuki, Y.; Tanihara, M.; Nishimura, Y.; Suzuki, K.; Kakimaru, Y.; Shimuzu, Y. A novel wound dressing with an antibiotic delivery system stimulated by microbial infection. *ASAIO J.* **1997**, *43*, M854−M857.
13. Kawabata, S.; Iwanaga, S. Structure and function of staphylothrombin. *Semin. Thromb. Hemost.* **1994**, *20*, 345−350.
14. Tanihara, M.; Suzuki, Y.; Nishimura, Y.; Suzuki, K.; Kakimaru, Y. Thrombin-sensitive peptide linkers for biological signal-responsive drug release systems. *Peptides* **1998**, *19*, 421−425.
15. Tanihara, M.; Fukunishi, Y.; Kinoshita, H. Wound dressing. U.S. Patent **1997**, 5679371.
16. Rodeheaver, G.; Pettry, D. P.; Turnbull, V.; Edgerton, M. T.; Edlich, R. F. Identification of the wound infection-potentiating factors in soil. *Am. J. Surg.* **1974**, *128*, 8−14.
17. Morita, T.; Kato, H.; Iwanaga, S.; Takada, K.; Kimura, T. New fluorogenic substrates for alpha-thrombin, factor Xa, kallikreins, and urokinase. *J. Biochem.* (*Tokyo*) **1977**, *82*, 1495−1498.
18. Kawabata, S.; Miura, T.; Morita, T.; Kato, H.; Fujikawa, K.; Iwanaga, S.; Takada, K.; Kimura, T.; Sakakibara, S. Highly sensitive peptide-4-methylcoumaryl-7-amide substrates for blood-clotting proteases and trypsin. *Eur. J. Biochem.* **1988**, *172*, 17−25.
19. Mantle, D.; Hardy, M. F.; Lauffart, B.; McDermott, J. R.; Smith, A. I.; Pennington, R. J. Purification and characterization of the major aminopeptidase from human skeletal muscle. *Biochem. J.* **1983**, *211*, 567−573.
20. Matsushima, M.; Takahashi, T.; Ichinose, M.; Miku, K.; Kurokawa, K.; Takahashi, K. Structural and immunological evidence for the identity of prolyl aminopeptidase with leucyl aminopeptidase. *Biochem. Biophys. Res. Commun.* **1991**, *178*, 1459−1464.
21. Ben'itez-Bribiesca, L.; Mar'tinez, G.; Ru'iz, M. T.; Gut'ierrez-Delgado, F.; Utrera, D. Proteinase activity in invasive cancer of the breast. Correlation with tumor progression. *Arch. Med. Res.* **1995**, *26*, S163−168.
22. Tamakoshi, K.; Kikkawa, F.; Nawa, A.; Ishikawa, H.; Mizuno, K.; Tamakoshi, A.; Yamagata, S.; Suganuma, N.; Tomoda, Y. Characterization of extracellular matrix-degrading proteinase and its inhibitor in gynecologic cancer tissues with clinically different metastatic form. *Cancer* **1995**, *76*, 2565−2571.

Acknowledgments

This work was supported by a grant for Scientific Research from the Ministry of Education of Japan, and a grant for "Research for the Future" Program (JSPSRFTF 96I00204) from the Japan Society for the Promotion of Science.

JS980418J

Correlation of Aqueous and Lipid Solubilities with Flux for Prodrugs of 5-Fluorouracil, Theophylline, and 6-Mercaptopurine: A Potts–Guy Approach

WILLIAM J. ROBERTS AND KENNETH B. SLOAN*

Contribution from *Department of Medicinal Chemistry, P.O. Box 100485, University of Florida, Gainesville, Florida 32610.*

Received October 23, 1998. Final revised manuscript received February 22, 1999.
Accepted for publication March 1, 1999.

Abstract □ The Potts and Guy equation that has been used to predict permeability coefficients for molecules being delivered from aqueous vehicles has been transformed to accommodate lipid vehicles that are less polar than skin, and polar vehicles that are less polar than water. Solubilities in pH 4.0 aqueous buffer (S_{AQ}), solubilities in isopropyl myristate (S_{IPM}), and molecular weights (MW) of prodrugs of 5-fluorouracil (5-FU), theophylline (Th), and 6-mercaptopurine (6-MP) have been regressed against their fluxes from suspensions in IPM (J_M). Seven series ($n = 39$) of alkylcarbonyloxymethyl (ACOM), alkyloxycarbonyl (AOC), alkylcarbonyl (AC), and alkylaminocarbonyl (AAC) prodrugs were used to determine the best fit to the transformed Potts and Guy equation (eq 6): $\log J_M = x + y \log S_{IPM} + (1 - y)\log S_{AQ} - z$ MW. The estimated values for x, y, and z were –0.193, +0.525, and +0.00364, respectively, with $r^2 = 0.945$ for $n = 39$. Inclusion of a miscellaneous series comprised of the parent drugs and a branched alkyl chain prodrug gave an equally good fit only if 6-MP was excluded from the analysis. The best performer (largest J_M) in each series was usually correctly identified. The values for x, y, and z were consistent with values obtained by Potts and Guy, but the inclusion of the $(1 - y)\log S_{AQ}$ term in eq 6 and the value for y, shows that water solubility is almost as important as lipid solubility in predicting flux. There were no significant changes in predicted $\log J_M$ or x_i for each series if their $\log J_M$ or x_i were calculated using y and z coefficients obtained for solutions to eq 6 from which the data for the series had been excluded. This suggests that the data from all the series is homogeneous. Data from Kasting, Smith, and Cooper for S_{IPM}, S_{PG}, and MW of unrelated molecules were regressed against their fluxes from propylene glycol (PG) using eq 7: $\log J_M = x + y \log S_{IPM} + (1 - y) \log S_{PG} - z$ MW. The estimated values for x, y, and z were –1.673, +0.599, and +0.00595, respectively, with $r^2 = 0.852$ for $n = 28$. These values for x, y, and z are also consistent with those previously reported by Potts and Guy, and, together with the results for fluxes from IPM, show the general utility of the transformed Potts and Guy equation in predicting flux from vehicles other than water and in showing the importance of solubility in a polar solvent as well as a nonpolar solvent in predicting flux.

Introduction

It has become obvious that the water as well as the lipid solubility of a permeant plays an important role in determining the rate of diffusion through biological membranes. Nowhere is this fact more obvious than in the results from diffusion cell experiments where prodrugs designed to enhance topical delivery—or flux—of a parent drug have been evaluated.[1] Examples where different types of promoieties have been used with one parent drug,[2–5] or where one type of promoiety has been used with a number of different parent drugs,[5–8] show that, for an homologous series of more lipid soluble prodrugs, the more water soluble member or members of the series are the more efficient at delivering the parent drug topically. Although the greatest accumulation of data supporting this axiom exists for prodrugs of heterocycles such as a fluorouracil (5-FU),[2–5] theophylline (Th),[8] 6-mercaptopurine (6-MP),[6,7] and arabinofuranosyladenine,[9,10] ample supporting data can also be found from experiments using prodrugs of lipophilic drugs such as levonorgestrel[11] and indomethacin.[12] In one comparison of variables affecting flux, the axiom holds regardless of the polarity of the vehicle used to deliver the prodrug,[6,7] while in another comparison, the axiom holds regardless of the type of skin that is used in the experiments—mouse[2–8] or human skin.[11]

It would be useful to develop a model that could predict the effect of changes in water and lipid solubilities of prodrugs on the topical delivery of their parent drugs. A large portion of the published data on the delivery of parent drugs by prodrugs has been obtained using suspensions of the prodrugs in isopropyl myristate (IPM) as the donor phase where the IPM and aqueous (AQ) solubilities of the prodrugs were variables and flux was measured.[1] On the other hand, many models that have been developed to predict flux actually use measurements of permeability coefficients of drugs obtained using concentrations of drugs in vehicles (usually water) significantly less than saturation as the donor phase, and where the partition coefficient and size of the drug were the variables.[13] In this paper we transform a model that had been developed previously for predicting permeability coefficients of drugs into a model where the aqueous as well as lipid solubilities of prodrugs are variables for predicting the flux of their parent drugs and vehicles other than water can be accommodated.

Development of the Model

Most models used to predict flux or solubility normalized flux—permeability coefficient (P)—have focused on the effects of lipid solubility [either directly as S_{LIPID} or in the form of partition coefficient ($K_{LIPID:AQ}$)] and size [as it affects diffusivity] on flux. Typical of these treatments is eq 1 derived by Kasting, Smith, and Cooper from data developed in their laboratories and published in 1987[14] where J_M is the maximum flux obtained by applying saturated propylene glycol solutions of permeants to the membrane (human skin), S_{MEM} is the solubility of the permeant in the membrane, $D°$ is the diffusivity in the membrane of a

$$\log J_M = \log(D°/L) + \log S_{MEM} - (\beta/2.303)V \quad (1)$$

* To whom correspondence should be addressed. Tel 352-846-1957, fax 352-392-9455, e-mail: sloan@cop.health.ufl.edu.

10.1021/js980419b CCC: $18.00 Published on Web 04/06/1999

hypothetical molecule having zero molecular volume, h (we will use L) is the diffusion path length, V is the van der Waals volume, and β is a constant that is characteristic of the skin.

Since it is very difficult to measure the solubility of the permeant in the membrane, the authors[14] examined several S_{LIPID} substitutes for S_{MEM} and suggested that S_{OCT} (measured solubility in octanol) gave a better correlation with J_M than S_{IPM} (measured solubility in isopropyl myristate) or S_i (calculated ideal solubility). The assumption was that some sort of lipid solubility alone was sufficient to characterize solubility of permeants in and their flux through the membrane. The other assumption was that J_M was independent of the vehicle because saturated solutions were used as donor phases where the thermodynamic activities of the permeants were the same. This assumed there was no effect of the vehicle on the barrier properties of the skin. Analysis of their unique data set of 36 compounds fitted to eq 1 gave $r^2 = 0.74$ for the correlation of J_M with the model. This data set was unique because propylene glycol, not water, was used as the vehicle or donor phase. Substitution of molecular weight for the molecular volume gave a similar fit.

Subsequently, several groups developed models that were based on permeability coefficients obtained from data from combinations of series from different laboratories[15–17] where water was used as the vehicle. One model frequently referenced is that represented by eq 2 developed by Potts and Guy and published in 1992.[13] In eq 2 K_P (we will use P) is permeability coefficient, $K_{OCT:AQ}$ is the partition coefficient between octanol and water, MW is the molecular weight, $\beta°$ is a constant similar to β in eq 1 but which

$$\log P = \log(D°/L) + f \log K_{OCT:AQ} - \beta° MW \qquad (2)$$

includes a conversion factor for the substitution of MW for molecular volume, and f accounts for the difference between K_m (partitioning between membrane and vehicle) and $K_{OCT:AQ}$ (partitioning between octanol and water): i.e., $K_m = (K_{OCT:AQ})^f$. From the data sets analyzed using eq 2, the values for $D°/L$ and $\beta°$ that were obtained were consistent with physical properties of the skin, and $r^2 = 0.83$ was obtained for the correlation of P with this model for $n = 42$. A somewhat poorer correlation ($r^2 = 0.67$) was obtained using the larger data set ($n = 93$) of Flynn.[18]

Although no positive dependence of log P on S_{AQ} was discussed, an inverse dependence derives from the definition of $K_{OCT:AQ} = C_{OCT}/C_{AQ}$ (where C_{OCT} and C_{AQ} are the equilibrium concentrations of the permeant in octanol and water, respectively), if it is assumed that $K_{OCT:AQ}$ for the permeant is approximately equal to its solubility ratio ($SR_{OCT:AQ}$) in the same solvents (S_{OCT}/S_{AQ}). On the other hand, Potts and Guy[13] discuss that one interpretation of skin transport for molecules of very high lipophilicites (low S_{AQ}) is that the rate-determining step becomes the slow transfer from the lipophilic stratum corneum to the aqueous, viable epidermis and upper dermis, i.e., low water solubility can become rate-determining. Significant conclusions from this analysis were that the limiting barrier, the stratum corneum, could be adequately characterized as a lipid-like barrier alone, and that an aqueous-polar (pore) pathway across the barrier was not necessary to explain the flux of the more water soluble members of the data set.

Improvements in eq 2 have been obtained by a number of groups[19–22] by defining permeant partitioning between membrane/water or organic phase/water from a transfer free energy model where R_2 is molar refractivity, MV is the molar volume, π is the dipolarity/polarizability, and H_d and H_a are the hydrogen bond donor and hydrogen bond acceptor activity, respectively, of the solute. Substitution of eq 3 for $K_{OCT:AQ}$ in eq 2 gives log P values that are independent of the organic phase/water partition coefficients and dependent on the physicochemical properties of the permeant alone. For a monofunctional group subset of their previous data set, Potts and Guy in 1995[20] showed that R_2 and π could be omitted from the analysis giving eq 4 to predict log P with $r^2 = 0.94$. Negative values were

$$\log K_{ORG} = a_1 MV + a_2 \pi + a_3 H_d = a_4 H_a + a_5 R_2 \qquad (3)$$

$$P = (a_1 - \beta)MV + a_3 H_d + a_4 H_a + \log(D°/L) \qquad (4)$$

found for a_3 and a_4 suggesting, for permeants delivered from water, that hydrogen bond donating or accepting abilities exhibited by the permeant were inversely related to stratum corneum (SC) permeation. Hence, water solubility was also inversely related to SC permeation.

Equation 4 or similar models give the best correlation with experimental results but do not offer a mechanism for incorporating water solubility (S_{AQ}) directly as a variable. Similarly, although all of the data in the Kasting, Smith, and Cooper permeation set[14] were from experiments where J_M values were measured, eq 1 does not have S_{AQ} as a variable. On the other hand, eq 2 offers the opportunity to substitute other K values for K_m besides $K_{OCT:AQ}$ and to include the effect of vehicle on flux in the model. Since[23]

$$K_{MEM:IPM} = K_{MEM:AQ}/K_{IPM:AQ}$$

and[24]

$$K_{MEM:AQ} = (K_{IPM:AQ})^f$$

then

$$K_{MEM:IPM} = (K_{IPM:AQ})^f/K_{IPM:AQ} \qquad (5)$$

Substitution of eq 5 into eq 2 for $K_{OCT:AQ}$ gives

$$\log P = \log(D°/L) + f \log S_{IPM} - f \log S_{AQ} - \log S_{IPM} + \log S_{AQ} - \beta° MW$$

or

$$\log P = \log(D°/L) + f \log S_{IPM} - \log S_{IPM} + (1 - f)\log S_{AQ} - \beta° MW$$

Addition of log S_{IPM} to both sides gives

$$\log J = \log(D°/L) + f \log S_{IPM} + (1 - f)\log S_{AQ} - \beta° MW$$

Substitution of x for log $D°/L$, y for f, z for $\beta°$, and assuming that saturated IPM donor phases are used in the diffusion experiments gives

$$\log J_M = x + y \log S_{IPM} + (1 - y) \log S_{AQ} - z\ MW \qquad (6)$$

which is the transformation of the Potts and Guy model, given in eq 2, that will be used in this analysis.

To fit the Kasting, Smith, and Cooper[14] data to the same type of equation, two different substitutions were made. Instead of using the identity $K_{MEM:AQ} = (K_{IPM:AQ})^y$ where IPM has been substituted for MEM, the identity $K_{MEM:AQ} = (K_{IPM:PG})^y$ has been used where PG has been substituted for AQ, and IPM has been substituted for MEM. Then, instead of adding log S_{IPM} to both sides of eq 2, log S_{PG} has been added to both sides of eq 2 to give eq 7 using the same

substitutions as in eq 6. $(K_{OCT:PG})^y$ can also be substituted for $(K_{IPM:PG})^y$ to give a similar equation.

$$\log J_M = x + y \log S_{IPM} + (1 - y) \log S_{PG} - z\,MW \qquad (7)$$

Experimental Section

The methods used to determine the values for flux (J_M), solubilities (S_{IPM}, S_{AQ}), and partition coefficients between IPM and water ($K_{IPM:AQ}$) are described in the original papers for each series of prodrugs: 1-alkylcarbonyloxymethyl-5-FU (ACOM-5-FU),[5] 1-alkyloxycarbonyl-5-FU (AOC-5-FU),[3] 1-alkylcarbonyl-5-FU (AC-5-FU),[4] 1-alkylaminocarbonyl-5-FU (AAC-5-FU),[2] 7-alkylcarbonyloxymethyltheophylline (ACOM-Th),[8] 6-alkylcarbonyloxymethyl-6-MP (6ACOM-6-MP),[7] and 6,9-bis(alkylcarbonyloxymethyl)-6-MP (6,9ACOM-6-MP).[6] In each series only straight chain homologues were completely characterized and evaluated except for the ACOM-5-FU series where one branched chain homologue was characterized and evaluated: 1-pivaloyloxymethyl-5-FU (pivACOM-5-FU). Solubilities (S_{IPM}, S_{AQ}) and partition coefficients ($K_{IPM:AQ}$) are listed in Table 1. S_{AQ} values were calculated from $S_{IPM}/K_{IPM:AQ}$ values where available. Where $K_{IPM:AQ}$ values were not available, directly measured S_{AQ} values were used. In one case where the reported $K_{IPM:AQ}$ value for one member of a series, octylaminocarbonyl-5-FU, was inconsistent with other literature values and did not fit the trend in the remaining data for that series; the literature value,[25] which did fit the trend, was used as well as the corresponding calculated S_{AQ}. The J_M values listed in Table 1 were obtained using female hairless mice (SKH-hr-1) obtained from Temple University Skin and Cancer Hospital or from Charles River. The mice were sacrificed by cervical dislocation. Their skins were removed by blunt dissection and then placed epidermal side up in Franz type diffusion cells thermostated to 32 °C in contact with pH 7.1 phosphate buffer receptor phase. The buffer contained 0.11% formaldehyde as a preservative to prevent microbial growth and maintain the integrity of the skins during the course of the experiment.[8] The surface area of the diffusion cells was 4.9 cm^2, and the receptor phase volume was 20 mL. After contact with the receptor phase for 48 h to condition the skins, aliquots of a suspension of the prodrug in IPM (usually 0.5 mL) were applied to the epidermal side of three skins ($n = 3$) for 48 h. The receptor phases were continuously stirred during the entire experiment and were changed every 3 h during the time when steady-state fluxes were measured which was usually from 19 to 33 h. Variation in flux values was less than 30% except from the 6ACOM-6-MP series where the variation was less than 50%.

The solubilities, partition coefficients, and flux values for the parent drugs (5-FU,[2] Th,[8] 6-MP[6]) and the one branched alkyl chain prodrug (pivACOM-5-FU)[5] are also listed in Table 1 as a separate, miscellaneous series.

The multiple linear regression model depicted in eq 6 was fit to various combinations of the sets of data in Table 1 using the SPSS 7.5 statistical software package.

The J_M values in $\mu g\ cm^{-2}\ h^{-1}$ from Kasting, Smith, and Cooper[14] were converted to $\mu mol\ cm^{-2}\ h^{-1}$ values and the S_{IPM} and S_{PG} (solubilities in propylene glycol) values were converted to millimolar values before converting them to their respective log values and analyzing them using eq 7. The multiple linear regression model depicted in eq 7 was fit to the Kasting, Smith, and Cooper data using the SPSS 7.5 statistical software package. The data for salt forms of amines and for benzyl alcohol were omitted from the analysis to give $n = 28$ instead of $n = 36$.

Results

The log J_M, MW, log S_{IPM}, and log S_{AQ} data for the 39 straight chain alkyl prodrugs from Table 1 comprising seven series of prodrugs ($n = 39$ set) were fit to eq 6 using the SPSS nonlinear function. The parameter estimates for the $n = 39$ set (solution 1) were $x = -0.193$ (± 0.199), $y = +0.525$ (± 0.029), and $z = +0.00364$ (± 0.00084) with $r^2 = 0.945$ (Table 2). Using these estimated values for x, y, and z from solution 1, predicted log J_M values were calculated and are listed in Table 3. The average error or residual for predicting log J_M (experimental log J_M − predicted log J_M = Δ log J_M, data not shown) was 0.126 log units for all log J_M values. The average Δ log J_M value for each series is listed in boldface in the predicted log J_M column in Table 3 and quantitates the variation in Δ log J_M among members of each series and among the different series. The largest Δ log J_M values for members within a series were obtained for the longer alkyl chain members of the ACOM-, AOC-, AC-, and AAC-5-FU series. The largest average error in predicting log J_M values for a series was obtained for the AAC-5-FU series while the smallest was for the 6,9ACOM-6-MP series. The best performing member in each series (highest value for log J_M) was correctly identified in each series except for the 6ACOM-6-MP series, but in that series

Table 1—Molecular Weight (MW), Log Solubilities in Isopropyl Myristate (S_{IPM}), Log Solubilities in pH 4.0 Buffer (S_{AQ}), Log Partition Coefficients between IPM and pH 4.0 Buffer ($K_{IPM:AQ}$), and Log Maximum Flux Values from IPM Donor Phases (J_M)

compounds[a]	MW	log S_{IPM}[b,c]	log S_{AQ}[b,d]	log $K_{IPM:AQ}$	log J_M[e]
ACOM-5-FU					
C_1	202	0.517	2.26	–1.74	0.46
C_2	216	0.993	2.22	–1.23	0.58
C_3	230	1.158	1.63	–0.47	0.41
C_4	244	1.170	1.10	0.08	0.11
C_5	258	1.167	0.35	0.82	–0.25
C_7	286	1.000	–0.77	1.77	–0.92
C_9	314	0.631	–2.51[c]	3.14[f]	–1.82
AOC-5-FU					
C_1	188	0.328	2.05	–1.72	0.42
C_2	202	1.117	2.24	–1.12	0.77
C_3	216	1.182	1.63	–0.45	0.36
C_4	230	1.529	1.37	0.16	0.35
C_6	258	2.186	0.70	1.48	0.19
C_8	286	1.561	–0.89	2.46	–0.53
AC-5-FU					
C_1	172	1.344	2.08	–0.73	0.97
C_2	186	1.561	1.68	–0.12	0.63
C_3	200	1.241	0.81	0.43	0.11
C_4	214	1.593	0.54	1.05	0.00
C_5	228	2.052	0.47	1.58	0.04
C_7	256	2.044	–0.84	2.88	–0.22
AAC-5-FU					
C_1	187	–0.524	0.57	–1.09	–0.68
C_2	201	0.446	0.89	–0.44	–0.22
C_3	215	1.093	0.95	0.14	–0.13
C_4	229	1.391	0.71	0.68	–0.29
C_8	285	1.670	–1.52[g]	3.19[f]	–1.22
ACOM-Th					
C_1	252	0.439	1.29	–0.85	–0.24
C_2	266	0.467	0.67	–0.20	–0.51
C_3	280	1.405	1.02	0.38	0.03
C_4	294	1.643	0.72	0.93	–0.23
C_5	308	1.891	0.44	1.45	–0.33
6ACOM-6-MP					
C_1	224	0.022	0.86[c]	–0.83[f]	–0.69
C_2	238	0.362	0.61[c]	–0.25[f]	–0.67
C_3	252	0.517	0.31[c]	0.21[f]	–0.58
C_4	266	0.624	–0.10[c]	0.73[f]	–0.66
C_5	280	0.566	–0.63[c]	1.19[f]	–1.26
C_7	308	0.618	–1.61[c]	2.23[f]	–1.88
6,9ACOM-6-MP					
C_1	296	0.722	0.46[c]	0.26[f]	–0.64
C_2	324	1.527	0.22[c]	1.30[f]	–0.63
C_3	352	1.959	–0.71[c]	2.67[f]	–0.85
C_4	380	2.241	–1.33[c]	3.57[f]	–0.99
miscellaneous					
5-FU	130	–1.308	1.93[c]	–3.24[f]	–0.62
pivACOM-5-FU	244	0.891	0.90	–0.01	–0.52
Th	180	–0.469	1.66[c]	–2.13[f]	–0.32
6-MP	152	–1.650	0.05[c]	–1.71[f]	–2.42

[a] C_1, C_2, etc., indicate the number of carbons in the alkyl chain. [b] Units of mM. [c] Measured directly. [d] Calculated from $S_{AQ} = S_{IPM}K_{IPM:AQ}$. [e] Units of $\mu mol\ cm^{-2}\ h^{-1}$. [f] Calculated from $K_{IPM:AQ} = S_{IPM}/S_{AQ}$. [g] From reference 25.

Table 2—*x*, *y*, *z*, and Associated r^2 Values for Solutions to Equation 6 and to Equation 7

solution: database	*n*	*x* (± SD)	*y* (± SD)	*z* (± SD)	r^2
1: all n-alkyl prodrugs	39	–0.193 (0.199)	0.525 (0.029)	+0.00364 (0.00084)	0.945
2: $n = 39$ + miscellaneous	43	–0.401 (0.243)	0.530 (0.035)	+0.00293 (0.00103)	0.924
3: $n = 43$ – (6-MP)	42	–0.211 (0.203)	0.534 (0.029)	+0.00364 (0.00086)	0.937
4: $n = 39$ – (ACOM-5-FU)	32	–0.211 (0.193)	0.508 (0.031)	+0.00362 (0.00082)	0.942
5: $n = 39$ – (AOC-5-FU)	33	–0.210 (0.203)	0.523 (0.030)	+0.00359 (0.00084)	0.944
6: $n = 39$ – (AC-5-FU)	33	–0.100 (0.285)	0.532 (0.038)	+0.00400 (0.00116)	0.943
7: $n = 39$ – (AAC-5-FU)	34	–0.081 (0.201)	0.548 (0.029)	+0.00409 (0.00083)	0.955
8: $n = 39$ – (ACOM-Th)	34	–0.260 (0.222)	0.521 (0.033)	+0.00333 (0.00095)	0.950
9: $n = 39$ – (6ACOM-6-MP)	33	–0.198 (0.206)	0.525 (0.030)	+0.00361 (0.00087)	0.933
10: $n = 39$ – (6,9ACOM-6-MP)	35	–0.287 (0.253)	0.518 (0.032)	+0.00322 (0.00108)	0.943
11: all *n*-alkyl prodrugs, $z = +0.00610$	39	0.388 (0.031)	0.590 (0.020)	+0.00610 fixed	0.931
12: $n = 39$ – (AC-5-FU and AAC-5-FU)	28	0.427 (0.325)	0.605 (0.042)	+0.00607 (0.00130)	0.961
13: Kasting et al.	28	–1.673 (0.363)	0.599 (0.126)	+0.00595 (0.00124)	0.852
14: Kasting et al.	28	–1.969 (0.395)	0.849 (0.250)	+0.00673 (0.00146)	0.807

the top four performers were not statistically different from each other.[7] Solution 1 identified the C_2 member of the 6ACOM-6-MP series as the best performer while the C_3 member was actually the best performer experimentally. Using the estimated values for *y* and *z* from solution 1, the values of x_i for the members of each series that were required to give the experimental log J_M values were calculated and are given in Table 3. The average x_i for all members of all series was −0.193 with a standard deviation of ±0.155 log units. The average x_i value and SD for each series of prodrugs are also given in Table 3 and quantitate variations in x_i among the members of each series and among the different series. The largest SD of x_i was seen in the AAC-5-FU series, followed by that in the AOC- and AC-5-FU series. Figure 1 shows a plot of experimental log J_M values versus predicted log J_M values (eq 6) using all 39 prodrugs (solution 1).

Predicted log J_M values and calculated x_i values for the parent drugs and pivACOM-5-FU (miscellaneous series) were determined using the solution 1 fit to eq 6 as above for the $n = 39$ set. Those predicted log J_M and calculated x_i values are given in Table 3. The Δ log J_M value for 6-MP was over twice as large as the next largest Δ log J_M value and almost six times larger than the average for all Δ log J_M values: average Δ log $J_M = 0.146$ log units for all log J_M values, $n = 43$. Similarly, the calculated x_i value for 6-MP was twice as large as any other calculated x_i value. Figure 1 also shows the fit of the members of the miscellaneous series to the solution 1 fit to eq 6. When the log J_M, MW, log S_{IPM}, and log S_{AQ} data for the miscellaneous series were added to the $n = 39$ set to give an $n = 43$ set (solution 2, Table 2) and eq 6 was fit to that data, the correlation coefficient decreased to $r^2 = 0.924$ from $r^2 = 0.945$, and the estimated values for *x*, *y*, and *z* changed to −0.401, +0.530, and +0.00293, respectively. If the data for 6-MP was removed from the set (solution 3, Table 2) the values for *x* and *z* returned to approximately their solution 1 values, and the value for *y* stayed reasonably constant.

Equation 6 was then fit to the log J_M, MW, log S_{IPM}, and log S_{AQ} data for the seven series of straight chain alkyl prodrugs using the SPSS nonlinear function, but using only six of the series in each fitting. This systematically excluded a different series each time to give a total of seven sets of parameter estimates for eq 6 (solutions 4−10). This was done to correct for overly optimistic measures of fit which result from using the same data to both calibrate the model (estimate its parameters) and assess the error of prediction. The estimates for *x*, *y*, *z*, and associated r^2 values for these seven sets are given in Table 2. Using these estimated values for *x*, *y*, and *z* for solutions 4−10, predicted log J_M values were calculated for each member of the series that had been excluded from determining that solution to eq 6. Those predicted log J_M values for solutions 4−10 are given in Table 3. The average error for predicting log J_M (Δ log J_M, data not shown) was 0.132 log units for all log J_M values, $n = 39$. The average Δ log J_M value for each series is listed in boldface in the predicted log J_M column in Table 3. The largest average error in predicting log J_M values for the series excluded from obtaining the solution to eq 6 was for the AAC-5-FU series. Using the estimated values for *y* and *z* for each of the seven solutions to eq 6 generated by excluding the data from one series of prodrugs, values for x_i which were required to give the experimental log J_M values were calculated for each member of the series that had been excluded. These calculated x_i values for solutions 4−10 are given in Table 3. The average x_i for all members of all series was −0.193 with a standard deviation of ±0.173 which was essentially identical with the average x_i value and standard deviation from solution 1. The results in Table 2 show that the estimated *x*, *y*, and *z* values from solution 7 (exclusion of the AAC-5-FU series) exhibited the largest differences from the estimated *x*, *y*, and *z* values from solution 1. The estimated value for *z* from solutions 4−10 are all quite close to the estimated values of *z* from solution 1 and to several of those reported by Potts and Guy[13] for fits to data from combinations of series from different laboratories (+0.0042 ± 0.0001, $n = 19$; +0.0050 ± 0.0003, $n = 42$; +0.0061 ± 0.0006, $n = 93$).

Using the Potts and Guy value that is most frequently quoted for *z* of +0.0061, a solution to eq 6 was obtained using the $n = 39$ set: solution 11 Table 2, $x = +0.388$, $y = +0.590$. Using the estimated values for *x* and *y* from solution 11 and *z* fixed at 0.0061, predicted log J_M values were calculated and are listed in Table 3. The average error for predicting log J_M (Δ log J_M, data not shown) was 0.141 log units for all log J_M values, $n = 39$. The average Δ log J_M value for each series is listed in boldface in the predicted log J_M column in Table 3. The predicted log J_M values for the miscellaneous series were also calculated using the coefficients from solution 11. Figure 2 shows the fit of the $n = 39$ prodrug set and the members of the miscellaneous series to a plot of experimental log J_M versus predicted log J_M based on solution 11. Using the estimated value for *y* and the fixed value for *z*, values for x_i which were required to give the experimental log J_M values were calculated for all the members of all the series. Those x_i values are given in Table 3. The average x_i for all members of all series was +0.413 with a standard deviation of ±0.187 log units. Excluding the data for the AC- and AAC-5-FU series, the solution 12 fit to eq 6 gave estimated values for *x*, *y*, and *z* (no longer fixed) which are given in Table 2.

Equation 7 was fit to the log J_M, MW, log S_{IPM}, and log S_{PG} data for the 28 molecules comprising the Kasting, Smith, and Cooper[14] data set (with the amine salts and

Table 3—Predicted log J_M and Calculated x_i Values for Calculated Solutions to Equation 6

	pred[a] log J_M	calcd[b] x_i	pred[a] log J_M	calcd[b] x_i	pred[a] log J_M	calcd[b] x_i
ACOM-5-FU	sol 1[c]		sol 4[c]		sol 11[c]	
C_1	0.41	–0.15	0.43	–0.18	0.38	0.46
C_2	0.60	–0.21	0.60	–0.23	0.57	0.40
C_3	0.35	–0.13	0.35	–0.15	0.33	0.46
C_4	0.05	–0.13	0.04	–0.14	0.04	0.46
C_5	–0.36	–0.09	–0.38	–0.08	–0.36	0.49
C_7	–1.08	–0.04	–1.12	–0.02	–1.08	0.55
C_9	–2.20	0.19	–2.26	–0.24	–2.19	0.75
average	**0.12**[d]	–0.08	**0.14**[d]	–0.08	**0.13**[d]	0.51
SD		0.13		0.16		0.12
AOC-5-FU	sol 1[c]		sol 5[c]		so1 1[c]	
C_1	0.26	–0.04	0.26	–0.04	0.27	0.53
C_2	0.72	–0.14	0.72	–0.14	0.73	0.43
C_3	0.41	–0.24	0.41	–0.24	0.43	0.32
C_4	0.42	–0.27	0.42	–0.27	0.45	0.29
C_6	0.35	–0.35	0.34	–0.35	0.39	0.19
C_8	–0.84	0.11	–0.85	0.11	–0.80	0.66
average	**0.13**[d]	–0. 16	**0.13**[d]	–0.16	**0.14**[d]	0.40
SD		0.17		0.17		0.17
AC-5-FU	sol 1[c]		sol 6[c]		sol 11[c]	
C_1	0.87	–0.10	0.90	–0.03	0.98	0.37
C_2	0.75	–0.31	0.77	–0.24	0.86	0.16
C_3	0.11	–0.19	0.14	–0.12	0.23	0.27
C_4	0.12	–0.31	0.14	–0.24	0.24	0.14
C_5	0.28	–0.43	0.30	–0.36	0.40	0.03
C_7	–0.45	0.04	–0.43	0.11	–0.31	0.48
average	**0.14**[d]	–0.22	**0.14**[d]	–0.14	**0.18**[d]	0.24
SD		0.17		0.17		0.16
AAC-5-FU	sol 1[c]		sol 7[c]		sol 11[c]	
C_1	–0.88	0.00	–0.88	0.11	–0.83	0.54
C_2	–0.27	–0.15	–0.26	–0.05	–0.21	0.38
C_3	0.05	–0.37	0.07	–0.28	0.11	0.15
C_4	0.04	–0.52	0.06	–0.43	0.10	0.00
C_8	–1.08	–0.34	–1.02	–0.28	–0.99	0.16
average	**0.18**[d]	–0.27	**0.20**[d]	–0.19	**0.20**[d]	0.24
SD		0.20		0.21		0.21
ACOM-Th	sol 1[c]		sol 8[c]		sol 11[c]	
C_1	–0.27	–0.16	–0.25	–0.24	–0.36	0.51
C_2	–0.60	–0.10	–0.59	–0.18	–0.69	0.57
C_3	0.01	–0.18	0.03	–0.26	–0.07	0.49
C_4	–0.06	–0.36	–0.04	–0.45	–0.14	0.30
C_5	–0.11	–0.41	–0.09	–0.50	–0.19	0.25
average	**0.11**[d]	–0.24	**0.10**[d]	–0.33	**0.13**[d]	0.42
SD		0.13		0.14		0.14
6ACOM-6-MP	sol 1[c]		sol 9[c]		so1 1[c]	
C_1	–0.59	–0.30	–0.59	–0.31	–0.61	0.30
C_2	–0.58	–0.28	–0.58	–0.29	–0.60	0.32
C_3	–0.70	–0.08	–0.69	–0.09	–0.72	0.53
C_4	–0.88	0.03	–0.88	0.03	–0.91	0.64
C_5	–1.21	–0.25	–1.21	–0.25	–1.24	0.37
C_7	–1.73	–0.34	–1.73	–0.35	–1.77	0.27
average	**0.12**[d]	–0.20	**0.12**[d]	0.21	**0.11**[d]	0.41
SD		0.15		0.15		0.15
6,9ACOM-6-MP	sol 1[c]		sol 10[c]		sol 11[c]	
C_1	–0.67	–0.16	–0.65	–0.29	–0.81	0.55
C_2	–0.47	–0.36	–0.44	–0.48	–0.60	0.36
C_3	–0.78	–0.26	–0.75	–0.39	–0.90	0.43
C_4	–1.03	–0.15	–0.99	–0.29	–1.16	0.55
average	**0.08**[d]	–0.23	**0.08**[d]	–0.36	**0.11**[d]	0.47
SD		0.10		0.10		0.10
miscellaneous	sol 1[c]				sol 11[c]	
5-FU	–0.44	–0.38			–0.39	0.15
pivACOM-5-FU	–0.19	–0.53			–0.21	0.07
Th	–0.30	–0.21			–0.31	0.37
6-MP	–1.59	–1.01			–1.50	–0.52

[a] Units of μmol cm^{-2} h^{-1}. [b] Units of cm h^{-1}. [c] Solutions from Table 2. [d] Average $\triangle$ log J_M for series.

benzyl alcohol data deleted) using the SPSS nonlinear function. The solution 13 for the fit to eq 7 gave $x = -1.673 \pm 0.363$, $y = +0.599 \pm 0.236$, $z = +0.00595 \pm 0.00124$, and $r^2 = 0.852$. If log S_{OCT} was substituted for log S_{IPM}, solution 14 was obtained which gave a poorer fit ($r^2 = 0.807$), although z stayed relatively constant. Figure 3 shows the fit of the $n = 28$ data set from Kasting, Smith, and Cooper[14] to eq 7 solution 13.

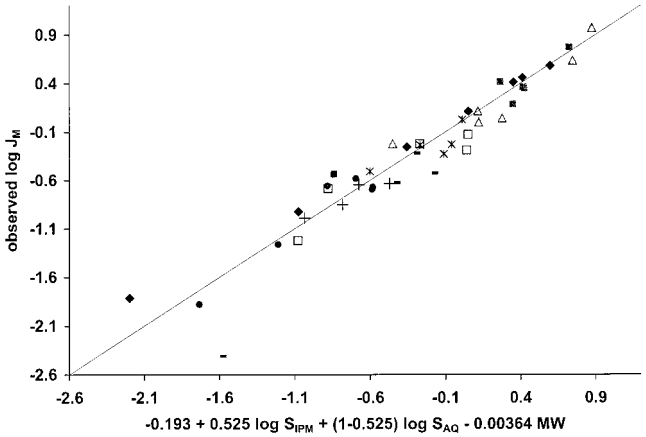

Figure 1—Fit of 39 prodrugs and the miscellaneous series to solution 1: ACOM-5-FU (◆), AOC-5-FU (■), AC-5-FU (△). AAC-5-FU (□), ACOM-Th (∗), 6ACOM-6-MP (●), 6,9ACOM-5-FU (+), miscellaneous (–).

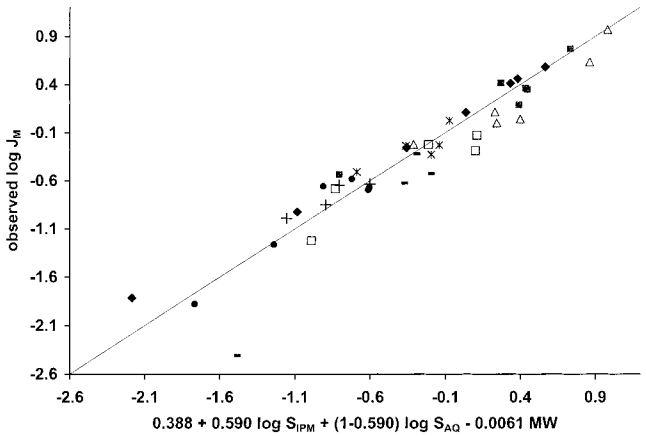

Figure 2—Fit of 39 prodrugs and the miscellaneous series to solution 11: ACOM-5-FU (◆), AOC-5-FU (■), AC-5-FU (Δ). AAC-5-FU (□), ACOM-Th (∗), 6ACOM-6-MP (●), 6,9ACOM-5-FU (+), MISCELLANEOUS (–).

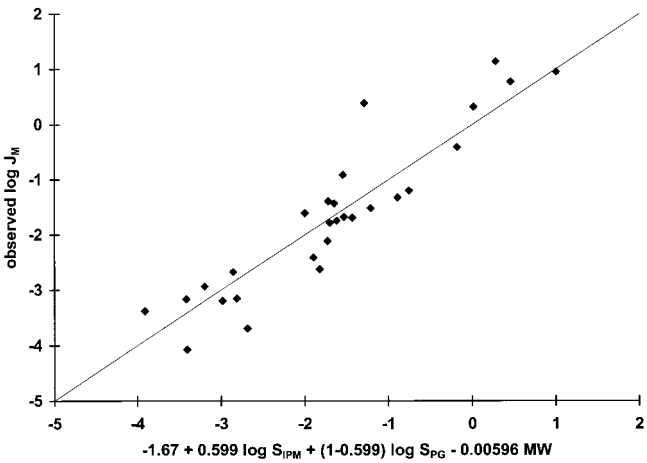

Figure 3—Prediction of log J_M from Kasting, Smith, and Cooper data, solution 13.

Discussion

Transformation of the Potts and Guy model[13] was done not only to include S_{AQ} as a variable in predicting flux but

also to accommodate donor phases other than water in the model. One of the key features of the Potts and Guy model is the substitution of $(K_{OCT:AQ})^f$ for K_m where K_m is the partition coefficient between the biological membrane, skin, and water. A more specific representation of K_m would be $K_{MEM:AQ} = (K_{LIPID:AQ})^f$ where water (AQ) is defined as the polar phase, and lipids, which can be different from octanol, are defined as appropriate nonpolar phase substitutes for skin (MEM). However, since $K_m D°/L$ is equal to the permeability coefficient (P), in the Potts and Guy model the polar phase is also the donor phase in the diffusion cell experiments which measure flux. This presents a significant limitation to the extension of the Potts and Guy model to predict P (or J) where the donor phase is a lipid or a polar phase other than water. The key substitution cannot be made if the donor phase is also a lipid such as isopropyl myristate (IPM) or even octanol. Taking the example where IPM is used as the donor phase, K_m is the partition coefficient between skin and IPM and a lipid/aqueous partition coefficient cannot be substituted for K_m.

There are three important features of the transformation of the Potts and Guy model into the model represented by eq 6. The first feature is the use of the identity of $K_{MEM:IPM}$ with $K_{MEM:AQ}/K_{IPM:AQ}$ which had previously been established by Surber et al.[23] Use of this identity allows substitution of the experimental partition coefficient, $K_{MEM:IPM}$, by the partition coefficient used by Potts and Guy in developing their model, $K_{MEM:AQ}$, and by a partition coefficient, $K_{IPM:AQ}$, containing two variables available from the published data on the prodrugs: S_{AQ} and S_{IPM}. This assumes that the solubility ratio, $SR_{IPM:AQ} = S_{IPM}/S_{AQ}$, can be substituted for partition coefficient, K. The second feature is the use of the identity of $K_{MEM:AQ}$ with $(K_{LIPID:AQ})^f$ where the membrane phase cannot only be replaced by another lipid phase such as octanol, which is similar in polarity, but also by lipids such as ether,[17] or in this case IPM, which are much less polar than skin or octanol. In this case $K_{MEM:AQ} = (K_{IPM:AQ})^f$. The coefficient f is used to account for the difference between the partitioning domain presented by IPM and that presented by the permeation limiting barrier in the skin: the stratum corneum. The third feature is the use of saturated solutions of the permeants in the donor phases. This allows all of the prodrugs to be evaluated at the same thermodynamic activity.

The estimated values for x, y, and z obtained for solution 1 to eq 6 using data from the seven series of straight chain alkyl prodrugs are consistent with the values obtained by Potts and Guy.[13] The value for y is 0.525 ± 0.029 which is consistent with the f value of 0.48 ± 0.05 obtained by Potts and Guy when they performed multiple linear regression of log P (K_P) values upon log $K_{ETHER:AQ}$ and MW from the data of Ackerman et al.[17] A y value of 1.0 would indicate that IPM is a good substitute for the partitioning domain of the stratum corneum (SC) lipids. On the other hand, the y values when IPM or ether is used are significantly less than 1.0, which suggests that they are both much less polar than the partitioning domain of the SC and in fact are less polar than octanol for which y (f) values of from 0.82 to 0.70 were obtained.[13] This order of polarity follows from the solubility parameters of ether, IPM, skin, and octanol: 7.4,[26] 8.5,[26] 10.0,[27] and 10.3[26] $(cal/cm^3)^{1/2}$, respectively. Since ether and IPM exhibit similar solubility parameter values, one would expect them to behave similarly and to be significantly less polar than octanol or skin.

Cohen and co-workers[27] have estimated a macroscopic value of $\delta = 9.7-10.0$ $(cal/cm^3)^{1/2}$ for the solubility parameter of porcine skin. However, the fact that the y value for octanol as the SC substitute is less than 1.0 suggests that the SC is more polar than $\delta = 9.7-10.0$ $(cal/cm^3)^{1/2}$ and may be as large as 12 $(cal/cm^3)^{1/2}$.

The value for z of $+0.00364 \pm 0.00084$ is also consistent with the $\beta°$ value of $+0.0019 \pm 0.0008$ obtained by Potts and Guy[13] in their analysis of the Ackerman et al. data,[17] where mouse skin was used as the diffusion cell membrane and $K_{ETHER:AQ}$ was used instead of $K_{OCT:AQ}$. It is also consistent with the $\beta°$ value of $+0.0050 \pm 0.0003$ obtained by Potts and Guy for the $n = 42$ combined data from Schuplein and Blank[15] and Roberts et al.[16] Although the value for z most often quoted from the paper of Potts and Guy is the value of $+0.0061 \pm 0.0006$ obtained using the data collected by Flynn,[18] it was obtained from a regression analysis that only yielded an $r^2 = 0.67$.

Although the estimated values for y and z from the prodrug data set are consistent with those previously obtained by Potts and Guy data from combinations of series from different laboratories, the value for x obtained here is different from that obtained by Potts and Guy by a factor of approximately 10^6. This difference can be attributed to differences in the way the flux data was obtained and the units used to present the data. The prodrug J_M data has been presented in units of μmol cm^{-2} h^{-1} instead of units of μmol cm^{-2} s^{-1}. This introduces a factor of 3.6×10^3. In addition, since x defines D, any experimental difference that affects D will result in differences in x. The prodrug J_M data were obtained using hairless mouse skin instead of using human skin. Hairless mouse skin may be as much as 10 times more permeable than human skin,[28] using experimental conditions similar to the ones used to collect the prodrug flux data. Finally, isopropyl myristate (IPM) was used as the vehicle (donor phase) in the diffusion cell experiments used to obtain the prodrug J_M values. IPM has been shown[29−31] to irreversibly change hairless mouse skin so that it is 50 to 100 times more permeable than it would be if there were no interactions between the skin and vehicle. Taking all three factors into account gives an x value of the same order of magnitude as that obtained by Potts and Guy. Considering all the differences in the experimental details between the way the data in the two data sets were obtained, this is a good agreement.

A plot of experimental log J_M values versus predicted log J_M values from solution 1 for the prodrug series is shown in Figure 1. The largest differences between experimental and calculated values for log J_M (Δ log J_M) were found for the C_9 member of the ACOM-5-FU, the C_8 member of AOC-5-FU, and the C_4 member of AAC-5-FU series: Δ log $J_M = 0.31$ to 0.38 log units. Inclusion of the fit of the data from the miscellaneous series to solution 1 in Figure 1 shows that 6-MP is an obvious outlier (Δ log $J_M = 0.83$) to solution 1 and that pivACOM-5-FU (Δ log $J_M = 0.33$) is only predicted as well as the worst predicted members of the straight chain alkyl series. When the data from the miscellaneous series was included in the data used to determine a solution (solution 2, Table 2) to eq 6 the fit was worse ($r^2 = 0.924$) and x and z changed substantially from their solution 1 values. Exclusion of the data for 6-MP from the solution to eq 6 gave estimated values for x, y, and z (solution 3, Table 2) which were consistent with those from solution 1. Thus, there is no reason to exclude parent drugs (except for 6-MP) or branched alkyl chain prodrugs from analysis of the data for the straight alkyl chain prodrugs using eq 6.

To determine if any of the data from individual series were inconsistent with the remaining data set, solutions 4−10 to eq 6 were obtained in which each series was individually excluded from the entire data set one series at a time. Using solutions 4−10 from Table 2, predicted log J_M and x_i values were calculated for the excluded series and compared with the predicted log J_M and x_i values calculated from solution 1 for the excluded series (Table 3). There was no substantial change in the differences

between the experimental log J_M and predicted log J_M values calculated from solution 1 and predicted log J_M calculated from solutions 4−10. Also there were no significant differences between the average x_i values calculated for each of the individual series using solution 1 compared to the average x_i values calculated using solutions 4−10. Thus, the data from each of the series is consistent with the remaining series.

When the Potts and Guy value for z was used to obtain a solution (solution 11, Table 2) for the $n = 39$ data set fit to eq 6, there were significant changes in the average x_i value for all the series and the AC- and AAC-5-FU series together gave average x_i values that were significantly different ($p < 0.01$) from the average of all the other series (Table 3). If the data from AC- and AAC-5-FU series were excluded from the $n = 39$ data set and a solution (solution 12, Table 2) was obtained for the fit of that $n = 28$ data set to eq 6, the estimated values for x, y, and z were consistent with those from solution 11. The value for z remained the same even though it was not fixed in solution 12 and was free to optimize. Solution 12 gave the best fit to the data ($r^2 = 0.961$) but at the expense of excluding the AC- and AAC-5-FU data and possibly biasing estimation of x, y, and z to give values that are not representative of all the prodrugs. Thus, the best solution to eq 6 for all the data is solution 1 or 3.

To determine if the data from diffusion cell experiments where donor phases other than IPM and membranes other than hairless mouse skin were used could be analyzed by a transformation of the Potts and Guy model, eq 7 was fit to the data from Kasting, Smith, and Cooper to give solution 13 in Table 2. The value for z obtained (+0.00595) is consistent with the previous values obtained when water or IPM were the donor phases. Thus, the dependency (z) of diffusivity on molecular weight (size) of the solute is not changed by properties of the vehicle or the membrane used. The value for y obtained by substitution of $(K_{IPM:PG})^y$ for $K_{MEM:AQ}$ is consistent with the value of y obtained when $(K_{IPM:AQ})^y$ was substituted for $K_{MEM:AQ}$. Thus PG does not behave significantly differently from AQ as a donor phase. Finally, the value for x estimated from the Kasting, Smith, and Cooper data is about 2 orders of magnitude more negative than that from the IPM data. Since human skin was used in the Kasting, Smith, and Cooper diffusion cell experiments and PG, which does not irreversibly change the skin, was used as the donor phase, there could be as much as 3 orders of magnitude difference between the IPM and PG data. Thus, the x value from solution 13, where PG was the donor phase, is also consistent with those where IPM or AQ were the donor phases.

It is probable that some error is introduced into the model as a result of hydrolysis of the prodrugs to parent drug during their diffusion through the skin. Partial hydrolysis would tend to give increased values of experimental total flux compared to predicted values of flux because two species (parent drug and intact prodrug) would be diffusing independently. In this analysis no attempt was made to account for hydrolysis since rates for the hydrolyses of the prodrugs in skin homogenates were not available. However, neglect of hydrolysis has resulted in a good fit and a simple equation with good predictive value.

The results presented here show for the first time that S_{AQ} is an important variable to incorporate into a model that is to be used to predict the topical delivery of drugs and prodrugs. In addition, the importance of S_{AQ} in determining the best correlation between permeation of 5-FU and its prodrugs in Caco-2 cells and various physicochemical parameters has also recently been identified.[32] Thus, S_{AQ} is an important physicochemical parameter for predicting flux not only through skin but also membrane models for intestinal absorption.

Conclusion

Transformation of the Potts and Guy equation gives an eq 6 that can accommodate vehicles as donor phases that are less polar than skin and that can predict maximum flux values from aqueous and lipid solubilities (instead of partition coefficients) and molecular weights. The values for the coefficients estimated by fitting eq 6 to the values of fluxes from IPM through hairless mouse skin, solubilities in IPM and AQ and molecular weights from the prodrug literature were consistent with the values previously reported by Potts and Guy. In addition, the value for the coefficient defining the contribution of IPM and AQ solubilities to predictions of flux showed that water solubility was almost as important as IPM or lipid solubility. The Potts and Guy equation was also transformed into eq 7 to accommodate a vehicle that was more polar than skin but not as polar as water and a membrane other than hairless mouse skin, i.e., human skin. The values for the coefficients estimated by fitting eq 7 to the values of fluxes from PG through human skin, solubilities in IPM and PG and molecular weights from the data set of Kasting, Smith, and Cooper were also consistent with the values previously reported by Potts and Guy. These results support the conclusion that the coefficients have physical meaning in the diffusion process and that equations of the type developed by Potts and Guy have general utility in predicting flux when suitably transformed.

References and Notes

1. Sloan, K. B. Functional group considerations in the development of prodrug approaches to solving topical delivery problems. In *Prodrugs: Topical and Ocular Drug Delivery*; Sloan, K. B., Ed.; Marcel Dekker: New York, 1992; pp 17−116.
2. Sloan, K. B.; Getz, J. J.; Beall, H. D.; Prankerd, R. J. Transdermal of 5-fluorouracil (5-FU) by 1-alkylaminocarbonyl-5-FU prodrugs through hairless mouse skin: physicochemical characterization of prodrugs and correlations with transdermal delivery. *Int. J. Pharm.* **1993**, *93*, 27−36.
3. Beall, H. D.; Prankerd, R. J.; Sloan, K. B. Transdermal delivery of 5-fluorouracil (5-FU) through hairless mouse skin by 1-alkyloxycarbonyl-5-FU prodrugs: physicochemical characterization of prodrugs and correlations with transdermal delivery. *Int. J. Pharm.* **1994**, *111*, 223−233.
4. Beall, H. D.; Sloan, K. B. Transdermal delivery of 5-fluorouracil (5-FU) by 1-alkylcarbonyl-5-FU prodrugs. *Int. J. Pharm.* **1996**, *129*, 203−210.
5. Taylor, H. E.; Sloan, K. B. 1-Alkylcarbonyloxymethyl Prodrugs of 5-Fluorouracil (5-FU): Synthesis, Physicochemical Properties and Topical Delivery of 5-FU. *J. Pharm. Sci.* **1998**, *87*, 15−20.
6. Waranis, R. P.; Sloan, K. B. The effect of vehicle and prodrug properties and their interactions on the delivery of 6-mercaptopurine through skin: bisacyloxymethyl-6-mercaptopurine prodrugs. *J. Pharm. Sci.* **1987**, *76*, 587−595.
7. Waranis, R. P.; Sloan, K. B. Effects of vehicles and prodrug properties and their interactions on the delivery of 6-mercaptopurine through skin: S^6-acyloxymethyl-6-mercaptopurine prodrugs. *J. Pharm. Sci.* **1988**, *77*, 210−215.
8. Kerr, D. P.; Roberts, W. J.; Tebbett, I. R.; Sloan, K. B. 7-Alkylcarbonyloxymethyl prodrugs of theophylline: topical delivery of theophylline. *Int. J. Pharm.* **1998**, *167*, 37−48.
9. Baker, D. C.; Kumar, S. D.; Waites, W. J.; Arnett, G.; Shannon, W. M.; Higuchi, W. I.; Lambert, W. J. Synthesis and Evaluation of a Series of 2′-*O*-Acyl Derivatives of 9-β-D-Arabinofuranosyladenine as Antiherpes Agents. *J. Med. Chem.* **1984**, *27*, 270−274.
10. Shannon, W. M.; Arnett, G.; Baker, D. C.; Kumar, S. D.; Higuchi, W. I. Evaluation of prodrugs of 9-β-D-arabinofuranosyladenine for therapeutic efficacy in the topical treatment of genital herpesvirus infections in guinea pigs. *Antimicrob. Agents Chemother.* **1983**, *24*, 706−712.

11. Friend, D.; Catz, P.; Heller, T.; Reid, J., Baker, R. Transdermal delivery of levonorgestrel II: effect of prodrug structure on skin permeability in vitro. *J. Controlled Release* **1988**, *7*, 251−261.
12. Bonina, F. R.; Montenegro, L.; DeCapraris, P.; Bousquet, E.; Tirendi, S. 1-Alkylazacycloalkane-2-one esters as prodrugs of indomethacin for improved delivery through human skin. *Int. J. Pharm*. **1991**, *77*, 21−29.
13. Potts, R. O.; Guy, R. H. Predicting skin permeability. *Pharm. Res.* **1992**, *9*, 663−669.
14. Kasting, G. B.; Smith, R. L.; Cooper, E. R. Effect of lipid solubility and molecular size on percutaneous absorption. In *Skin Pharmokinetics*; Shroot, B., Schaefer, H., Eds.; Karger: Basel, 1987; pp 138−153.
15. Scheuplein, R. J.; Blank, I. H. Molecular structure and diffusional processes across intact skin. Report to the U. S. Army Chemical R and D Laboratories: Edgewood Arsenal, MD, 1967.
16. Roberts, M. S.; Anderson, R. A.; Swarbrick, J. Permeability of human epidermis to phenolic compounds. *J. Pharm. Pharmacol.* **1977**, *29*, 677−683.
17. Ackerman, C.; Flynn, G. L.; Smith, W. M. Ether-water partitioning and permeability through hairless mouse skin in vitro. II. Hydrocortisone 21-*n*-alkyl esters, alkanols and hydrophilic compounds. *Int. J. Pharm*. **1987**, *36*, 67−71.
18. Flynn, G. L. Physicochemical determinants of skin absorption. In *Principles of Route-to-Route Extrapolation for Risk Assessment*; Gerrity, T. R., Henry, C. J., Eds; Elsevier: New York, 1990; pp 93−127.
19. Abraham, M. H.; Chadha, H. S.; Mitchell, R. C. The factors that influence skin penetration of solutes. *J. Pharm. Pharmacol*. **1995**, *47*, 8−16.
20. Potts, R. O.; Guy, R. H. A predictive algorithm for skin permeability: the effect of molecular size and hydrogen bond activity. *Pharm. Res.* **1995**, *12*, 1628−1633.
21. Roberts, M. S.; Pugh, W. J.; Hadgraft, J.; Watkinson, A. C. Epidermal permeability-penetrant structure relationships: 1. An analysis of methods of predicting penetration of monofunctional solutes from aqueous solutions. *Int. J. Pharm*. **1995**, *126*, 219−233.
22. Pugh, W. J.; Roberts, M. S.; Hadgraft, J. Epidermal permeability-penetrant structure relationship: 3. The effect of hydrogen bonding interactions and molecular size on diffusion across the stratum corneum. *Int. J. Pharm*. **1996**, *138*, 149−165.
23. Surber, C.; Wilhelm, K. P.; Hori, M.; Maibach, H. I.; Guy, R. H. Optimization of topical therapy: partitioning of drugs into stratum corneum. *Pharm. Res.* **1990**, *7*, 1320−1324.
24. Diamond, J. M.; Katz, Y. Interpretation of nonelectrolyte partition coefficients between dimyristoyl lecithin and water. *J. Membr. Biol*. **1974**, *17*, 127−154.
25. Sasaki, H.; Takahashi, T.; Mori, Y.; Nakamura, J.; Shibasaki, J. Transdermal delivery of 5-fluorouracil and its alkylcarbamoyl derivatives. *Int. J. Pharm*. **1990**, *60*, 1−9.
26. Barton, A. F. M. Solubility Parameters. *Chem. Rev.* **1975**, *75*, 731−753.
27. Leron, Z.; Cohen, S. Percutaneous absorption of alkanoic acids II. Application of regular solution theory. *J. Pharm. Sci*. **1984**, *73*, 538−542.
28. Sherertz, E. F.; Sloan, K. B.; McTiernan, R. G. Transdermal delivery of 5-fluorouracil through skin of hairless mice and humans in vitro: a comparison of the effect of formulation and a prodrug. *Arch. Dermatol. Res.* **1990**, *282*, 463−468.
29. Sloan, K. B.; Koch, S. A. M.; Siver, K. G.; Flowers, R. P. Use of solubility parameters of drug and vehicle to predict flux through skin. *J. Invest. Dermatol*. **1986**, *87*, 244−252.
30. Sherertz, E. F.; Sloan, K. B.; McTiernan, R. G. Use of theoretical partition coefficients determined from solubility parameters to predict permeability coefficients for 5-fluorouracil. *J. Invest. Dermatol*. **1987**, *89*, 147−151.
31. Waranis, R. P.; Siver, K. G.; Sloan, K. B. The solubility parameter of vehicles as a predictor of relative vehicle effects on the diffusion of 6-mercaptopurine. *Int. J. Pharm*. **1987**, *36*, 211−222.
32. Buur, A.; Trier, L.; Magnusson, C.; Artursson, P. Permeability of 5-fluorouracil and prodrugs in Caco-2 cell monolayers. *Int. J. Pharm*. **1996**, *129*, 223−231.

Acknowledgments

These studies were supported by NIH grant R15 CA67230. Dr. Jane Pendergast of the University of Florida was consulted on the statistical analyses.

JS980419B

Sites of Elimination and Pharmacokinetics of Recombinant [^{131}I]Lepirudin in Baboons

S. M. MEIRING,*,† M. G. LÖTTER,‡ P. N. BADENHORST,† E. BUCHA,§ G. NOWAK,§ AND H. F. KOTZÉ†

Contribution from *Department of Haematology and Cell Biology, University of the Orange Free State, P.O. Box 339 (G2), Bloemfontein, Republic of South Africa, Department of Medical Physics, University of the Orange Free State, Bloemfontein, Republic of South Africa, and Max-Planck Gessellschaft, Pharmacological Haemostaseology, Friedich Schiller University, Jena, Germany.*

Received October 12, 1998. Final revised manuscript received January 28, 1999.
Accepted for publication February 4, 1999.

Abstract □ Lepirudin has a short half-life, and only 50–60% of the intravenously administered dose is excreted by the kidneys. The fate of the remainder is unknown. We designed a study to determine the fate of this lepirudin. In each of six baboons, [^{131}I]lepirudin was given intravenously as a bolus or infused over 30 min, 24 h apart. The in vivo redistribution of [^{131}I]lepirudin was determined and quantified by scintillation camera imaging. In all studies, the half-life of [^{131}I]lepirudin, as determined from the disappearance of radioactivity, was 21 ± 3 min. The half-life determined from the disappearance of lepirudin, measured by the Ecarin Clotting Time (ECT) method, was similar at 23 ± 8 min. Results obtained with the labeled lepirudin are therefore comparable with those obtained using the plasma concentration of lepirudin. When lepirudin was administered as a bolus, the half-life was 18 ± 4 min, and lepirudin was cleared from the plasma at a rate of 42 ± 12 mL/min and by the kidneys at 23 ± 2 mL/min. Following infusion over 30 min, the half-life and total and renal clearances were not significantly different. In both studies, between 50 and 60% of the administered lepirudin was excreted by the kidney. Studies on sacrificed baboons showed that appreciable amounts of lepirudin were present in the bile, indicating the liver as a contributor to the elimination of lepirudin.

Introduction

Hirudin is regarded as the most potent direct inhibitor of thrombin and its recombinant form, lepirudin ([leu^1, Thr^2]-63-disulfatohirudin), has the same physiochemical characteristics and biochemical properties as the native protein.[1,2] Lepirudin is a 65 amino acid polypeptide (7 kDa) produced by transfected yeast cells.[1] The interaction between hirudin and thrombin results in the formation of a stable, noncovalent stoichiometric 1:1 complex that inhibits all functions of thrombin.[1,2] Apart from its inhibition of coagulation, it also inhibits platelet-dependent arterial-type thrombosis when given in high enough dosages.[3−5] Although the pharmacokinetics of lepirudin is well-known, there are still some unresolved issues. It is generally accepted that lepirudin is mainly excreted in an unchanged form by the kidneys.[1,6] However, approximately 40 to 50% of injected protein cannot be accounted for in the urine. The sites of metabolism and/or uptake of this lepirudin are unknown. We designed this study to investigate the metabolism and fate of lepirudin in baboons.

* Corresponding author. Telephone: 0027-51-4053039. Fax: 0027-51-4441036. E-mail: GNHMSMM@MED.UOVS.AC.ZA.
† Department of Haematology.
‡ Department of Medical Physics.
§ Max-Planck Gessellschaft.

Subjects and Methods

Experimental Animals—Eight male baboons (Papio ursinus) supporting permanent femoral arteriovenous shunts (A-V shunts) of silicone rubber tubing[7,8] were used. The animals were sedated with intramuscular ketamine hydrochloride (10 mg/kg body mass, Centaur Laboratories, South Africa) to enable handling. Anesthesia was maintained with subsequent administrations when necessary. One hundred milliliters of saline were given intravenously (iv) to each baboon 30 min before the start of a study to ensure that they were normovolaemic.

Experimental Protocol—Six baboons received [^{131}I]lepirudin as an iv bolus of 0.3 mg/kg as well as an infusion at a rate of 0.01 mg/kg/min for 30 min on separate days. The treatment requirements were such that an equal number of baboons received the bolus or infusion on each day. The lepirudin (HBW 023, Hoechst AG, Frankfurt and Behringwerke AG, Marburg, Germany) was labeled with 131-iodine (^{131}I; Radiochemical Centre, Amersham, UK) using the IODO-GEN method.[9] Labeling efficiency was 98 ± 1%. It is important to note that only labeled lepirudin was infused and that we determined the plasma concentration of the labeled lepirudin (see later). Therefore, when reference is made to lepirudin, it refers to the results obtained from the plasma concentration as determined using the ECT method.[10] Similarly, reference to labeled lepirudin refers to results obtained from radioactive count rates of [^{131}I]lepirudin.

Scintillation Camera Imaging—Imaging of the in vivo distribution of labeled lepirudin was done with a Large Field of View Scintillation Camera fitted with a high-energy collimator. Image analysis was done with an A^3-MDS data processing system that was interfaced with the camera. Imaging was done in two phases; they are, a dynamic image acquisition phase and a static acquisition phase.

Dynamic Image Acquisition—The baboons were positioned in front of the detector of the camera so as to include the kidneys, bladder, liver, and spleen in the field of view. Dynamic image acquisition, consisting of 3-min images (64 × 64 word mode) for 120 min (infusion study) and 90 min (bolus study), started simultaneously with the infusion of [^{131}I]lepirudin. For analysis, a region of interest was selected for the kidneys, the bladder, the spleen, and the liver, and the radioactivity in each region was expressed as a percentage of injected [^{131}I]labeled lepirudin, which was estimated by the geometrical mean method of quantification (see Static Image Acquisition). The radioactive count rates of the left and right kidneys were summed to obtain total kidney radioactivity.

Static Image Acquisition and Quantification of In Vivo Distribution of [^{131}I]Lepirudin—After the dynamic image acquisition, static anterior and posterior images of 3 min (64 × 64 word mode) were acquired of the head, thorax and abdomen, and legs. A background image was also acquired to correct whole body and region of interest (organ) radioactivity for background radioactivity. Before treatment on the second day, anterior and posterior images of the thorax and abdomen were acquired to determine and correct for residual ^{131}I radioactivity as a result of infusion of [^{131}I]lepirudin on the previous day.

To obtain anterior and posterior whole body radioactivity, the radioactivity in the head, thorax and abdomen, and legs was

10.1021/js980407q CCC: $18.00
Published on Web 04/15/1999

corrected for background radioactivity and/or residual radioactivity and summed. Regions of interest for the kidneys, bladder, spleen, and liver were selected to determine organ radioactivity. On the first day of the experiment, these radioactivities were corrected for background radioactivity. On the second day, organ radioactivity was corrected for background radioactivity and residual radioactivity, measured before the infusion of [^{131}I]lepirudin. The in vivo organ distribution of [^{131}I]lepirudin was quantified by the geometric mean method.[11]

Blood Collection and Analysis—Blood, 4.5 mL in 0.5 mL of a 3.2% sodiumcitrate solution, was collected before a study was started and then every 15 min thereafter. The radioactivity in 1 mL of plasma was determined in a gamma counter. Plasma levels of lepirudin were determined by the ECT method, which was specifically developed to measure hirudin levels in plasma and body fluids.[10] The activated partial thromboplastin time (aPTT) was measured with a fibrinometer (Clotex II, Hyland Division, Travenol Laboratories, Costa Mesa, CA), and reagents were supplied by the same company. The aPTT was measured to give an indication of the level of anticoagulation achieved and to show that the labeled lepirudin was functional.

To determine if the labeling procedure affected the function of [^{131}I]lepirudin, unlabeled and labeled lepirudin were added to plasma obtained from 4 baboons. Plasma concentrations were 2.5 and 5.0 μg/mL of lepirudin. In addition, a 50/50 mixture of labeled and unlabeled protein was also used. The aPTT was determined on all samples.

Urine Collection and Analysis—Urine was collected into a urine-collecting bag with a Teflon-coated latex Foley catheter (GRS Medicals, Kelvin, SA) for up to 24 h and analyzed for lepirudin by the ECT method.[10] The total amount of lepirudin was calculated from the total urine volume and the concentration in urine.

Urine was also analyzed by sodium dodecylsulfate polyacrylamide gel electrophoresis (SDS-PAGE). Samples analyzed were [^{131}I]lepirudin, urine without [^{131}I]lepirudin (native urine), [^{131}I]-lepirudin added to native urine, and urine collected from the treated baboons. The results strongly suggest that [^{131}I]lepirudin was excreted in an unchanged form. The results are not given.

Calculations—*Plasma Half-Lives of Lepirudin and [^{131}I]-Lepirudin*—The elimination half-lives of lepirudin and [^{131}I]-lepirudin were calculated by adjusting a one-phase exponential function to the appropriate phases of the log−linear plasma concentration−time and radioactive count rate−time profiles by the method of least-squares analysis. The value k, in the function $C_{max} \times e^{-kt}$, was thus found, where C_{max} is the maximum lepirudin concentration or maximum radioactive count rate in plasma. The half-lives were calculated as $t_{1/2} = 0.693/k$.

Total Clearance of Lepirudin and [^{131}I]Lepirudin—For the constant *infusion*, total clearance (CL_{total}) was calculated by dividing the rate of infusion (mg/min or radioactive count rate/min) by the maximum concentration of lepirudin or radioactive count rate in the plasma. To estimate the maximum plasma concentration or plasma radioactive count rate, an exponential association function was fitted to the data points obtained during the infusion period and extrapolated to maximum (i.e., an estimate of steady-state levels).[12]

For the *bolus* injection, CL_{total} was calculated by dividing the total dose, or the total counts injected, by the area under the curve ($AUC_{0-\infty}$) of the plasma lepirudin concentration (μg/mL)−time or plasma radioactivity (radioactive count rate/ml)−time profiles. The area under the plasma concentration−time and plasma radioactive counts rate−time curves up to 90 min (AUC_{0-90}) were calculated using the trapezoid rule. The curves were extrapolated to ∞ using the formula $AUC_{0-\infty} = AUC_{0-90} + C_p^*/k_e$, where C_p^* is the plasma lepirudin concentration or plasma radioactive count rate at the last sampling time (90 min). The terminal rate constant (k_e) was determined from the slope of the terminal portion of the log-linear C_p versus time curve.

Renal Clearance of [^{131}I]Lepirudin—For the constant *infusion*, renal clearance (CL_{renal}) was calculated by dividing the rate of appearance of [^{131}I]lepirudin in the bladder (radioactive count rate/min) by the maximum counts in the plasma. The latter was estimated by fitting an exponential association function to the available radioactive count rate/mL−time profiles and extrapolated to estimate the maximum value where a steady state was reached.

For the *bolus* injection, CL_{renal} was calculated by dividing the maximum radioactive count rate in the bladder by $AUC_{0-\infty}$ of the plasma radioactivity (radioactive count rate/mL)−time profiles.

Extravascular Clearance—The plasma clearance of lepirudin by the extravascular compartment was estimated by calculating the difference between the total clearance and the renal clearance.

Determination of Sites of Lepirudin Accumulation in Sacrificed Baboons—Two baboons were used. The one baboon was sacrificed after 30 min of infusion of [^{131}I]lepirudin. The other one received no lepirudin and was sacrificed to obtain organs and body fluids that served as controls for immunohistochemistry and lepirudin determinations, respectively. The baboons were deeply anesthetized. The test baboon was exsanguinated through the arterial side of the A-V shunt. About 2 L of saline at 37 °C were simultaneously infused under pressure (140 mmHg) into the venous side of the shunt to replace the blood that was lost.

Ex Vivo Quantification of the Distribution of [^{131}I]Lepirudin—The liver, spleen, kidneys, and bladder of the sacrificed baboons were immediately excised by careful dissection. Residual radioactivity in the body and that present in the liver, spleen, kidneys, and bladder were determined by scintillation camera imaging.[11] Images of 3 min (64 × 64 word mode) were acquired. Organ radioactivity was then expressed as a percentage of total body radioactivity, obtained by summation of residual and organ radioactivities.

Organ Biopsies—Biopsies of the kidneys (cortex and medulla), spleen, and liver were collected to establish the location of the lepirudin by using immunohistochemistry techniques. A primary antibody, rabbit anti-hirudin antibody (diluted 1:100 in PBS; Celsus Laboratories, Cincinnati, OH) was added to thin processed sections of the tissues and incubated for 60 min. A secondary goat anti-rabbit antibody (Signet kit, Johnson & Johnson, Johannesburg, Republic of South Africa) was added to bind to the primary antibody and a third antibody complex, a peroxidase−antiperoxidase immune complex, was used as the marker complex. These antibody complexes become visible when the tissues are exposed to the substrate diaminobenzidine. By adding hydrogen peroxide to the diaminobenzidine solution, a brown precipitate forms where lepirudin is present. Light microscopy was used to interpret the stains. Lightmicrographs of all tissues were enlarged 200 times and examined for the presence of lepirudin in cells.

Biopsies of the kidneys, liver, and spleen were also homogenized in saline and centrifuged at 8000 g for 24 h. The ECT method[10] was used to test for the presence of lepirudin in the supernatant of the homogenates.

Collection and Analysis of Duodenal and Gastric Juices and Bile—Duodenal and gastric juices and bile were collected from the sacrificed baboons to test for the presence of lepirudin by the ECT method.[10]

Statistics—Statistical comparison was done using Student's t test for paired data. Values of $p < 0.05$ were considered significant. The results are expressed as mean ± 1 standard deviation (SD).

Results

Changes in aPTT and Pharmacokinetics of Lepirudin—In the in vitro studies, concentrations of 2.5 and 5.0 μg/mL lepirudin lengthened the aPTT to 87 ± 4 and 174 ± 5 s. [^{131}I]Lepirudin, at the same concentrations, lengthened the aPTT to 92 ± 4 and 180 ± 6 s. When labeled and unlabeled lepirudin were mixed, the aPTT lengthened to 90 ± 3 and 178 ± 4 s. The difference in measurements was not significant. The labeling process therefore does not affect the function of lepirudin.

The in vivo changes in aPTT are summarized in Table 1. The labeled hirudin was biologically active because it caused a 2−3-fold lengthening in the aPTT. When lepirudin infusion was stopped and following the bolus injection, the aPTT rapidly shortened to reach near pre-infusion values after 90 min.

The changes in circulating lepirudin and labeled lepirudin are summarized in Figure 1. Following infusion or the bolus injection, the plasma levels of lepirudin and [^{131}I]-lepirudin decreased rapidly. In all studies, the plasma half-life of lepirudin was 24 ± 9 min. When calculated from the

Table 1—Changes in APTT[a]

time (min)	infusion	bolus
–30	40 ± 4	–
–10	–	–
0	131± 20	42 ± 6
30	79 ± 10	98 ± 16
60	64 ± 9	74 ± 13
90	56 ± 8	64 ± 12

[a] Results are given in seconds and are expressed as mean ± 1 SD.

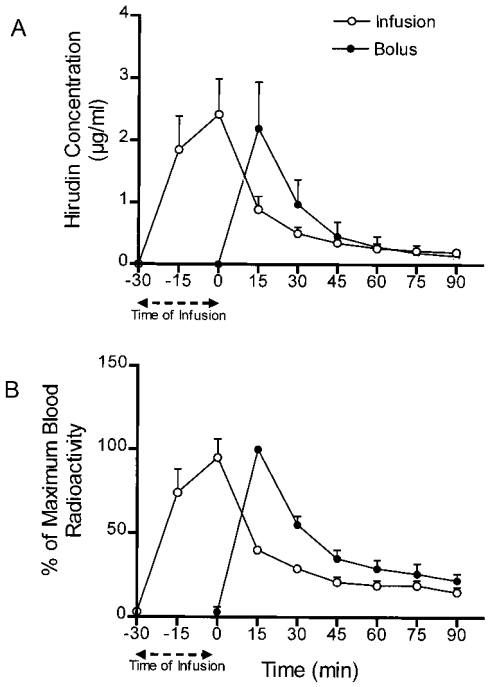

Figure 1—Dynamic changes of (A) plasma lepirudin and (B) [^{131}I]lepirudin following infusion (open circles) or bolus administration (black circles). Values are given as a mean ± 1 SD.

Table 2—Total, Renal, and Extravascular Clearance of Lepirudin and [^{131}I]Lepirudin

route	clearance	r-Lepirudin	[^{131}I]Lepirudin
infusion	total	49 ± 16	52 ± 10
	renal	–	32 ± 10
	extravascular	–	20 ± 8
bolus	total	42 ± 12	45 ± 12
	renal	–	23 ± 2[b]
	extravascular	–	22 ± 12

[a] Values are given in mL/min and are expressed as mean ± 1 SD. [b] $p < 0.05$, infusion versus bolus (Student's *t* test for paired data).

disappearance of radioactivity from the blood, it was 21 ± 6 min. The difference was not statistically significant ($p > 0.05$). After infusion of [^{131}I]lepirudin was stopped, lepirudin was eliminated from the plasma with a half-life of 23 ± 8 min ([^{131}I]lepirudin = 21 ± 3 min). When the same amount of [^{131}I]lepirudin was given as a bolus, the half-life was 18 ± 4 min ([^{131}I]lepirudin = 19 ± 8 min). The mean difference in the half-lives between infused and bolus injected lepirudin was 5 ± 10 min. The 95% confidence interval of between −5 and 16 min indicates that the difference was not statistically significant.

Total, renal, and extravascular clearance of lepirudin is summarized in Table 2. Total clearance was ≈45 mL/min, whether it was calculated from the data obtained from the concentration of lepirudin or from labeled lepirudin. Between 51 and 61% of this lepirudin was cleared by the kidneys.

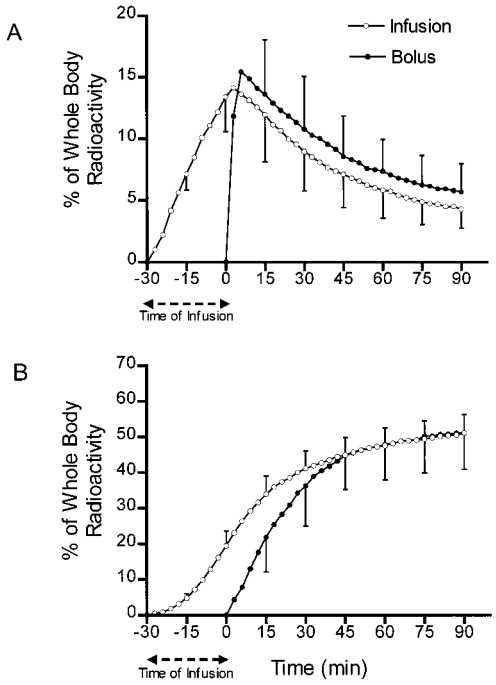

Figure 2—Dynamic changes of [^{131}I]lepirudin in the (A) kidneys and (B) bladder following infusion (open circles) and bolus administration (black circles). The radioactivity is expressed as a mean percentage ± 1 SD of whole body radioactivity at the end of each study.

Table 3—Organ Distribution of [^{131}I]Lepirudin at the End of Treatment

organ	infusion	bolus
kidneys	4.3 ± 1.5	5.7 ± 2.3
bladder	51.2 ± 5.2	51.2 ± 10.3
liver	1.7 ± 0.8	1.8 ± 0.9
spleen	3.6 ± 2.4	3.0 ± 2.7

[a] Percent of whole body radioactivity at the end of each study. Values are given as mean ± 1 SD.

Table 4—ECT of Bile and Duodenal and Gastric Juices, and of the Supernatant of Homogenized Kidney, Liver, and Spleen Tissue[a]

sample	ECT, s
bile	229
gastric juice	49
duodenal juice	39
kidney	77
liver	44
spleen	49

[a] Control values for the ECT method are between 38 and 40 s.

In Vivo Distribution of [^{131}I]Lepirudin—The changes in radioactivity in the kidneys and bladder are summarized in Figure 2, and the in vivo organ distribution at the end of the study in Table 3. Only ≈5% of total injected [^{131}I]-lepirudin was quantified in the liver and the spleen. The results obtained in the sacrificed baboon, 0.1% of the injected radioactivity in the spleen and 1.5% in the liver, also showed that the liver and spleen contained little [^{131}I]-lepirudin. Between 50 and 60% of the injected labeled lepirudin could be accounted for in the bladder. At the end of infusion or shortly after the bolus was injected, the kidneys contained ≈15% of the injected radioactivity (Figure 2A).

The presence of lepirudin in the bile and gastric and duodenal juices of the sacrificed baboon was measured by the ECT method, and the results are shown in Table 4. Of these, only the bile contained appreciable amounts as indicated by the markedly longer than normal ECT results.

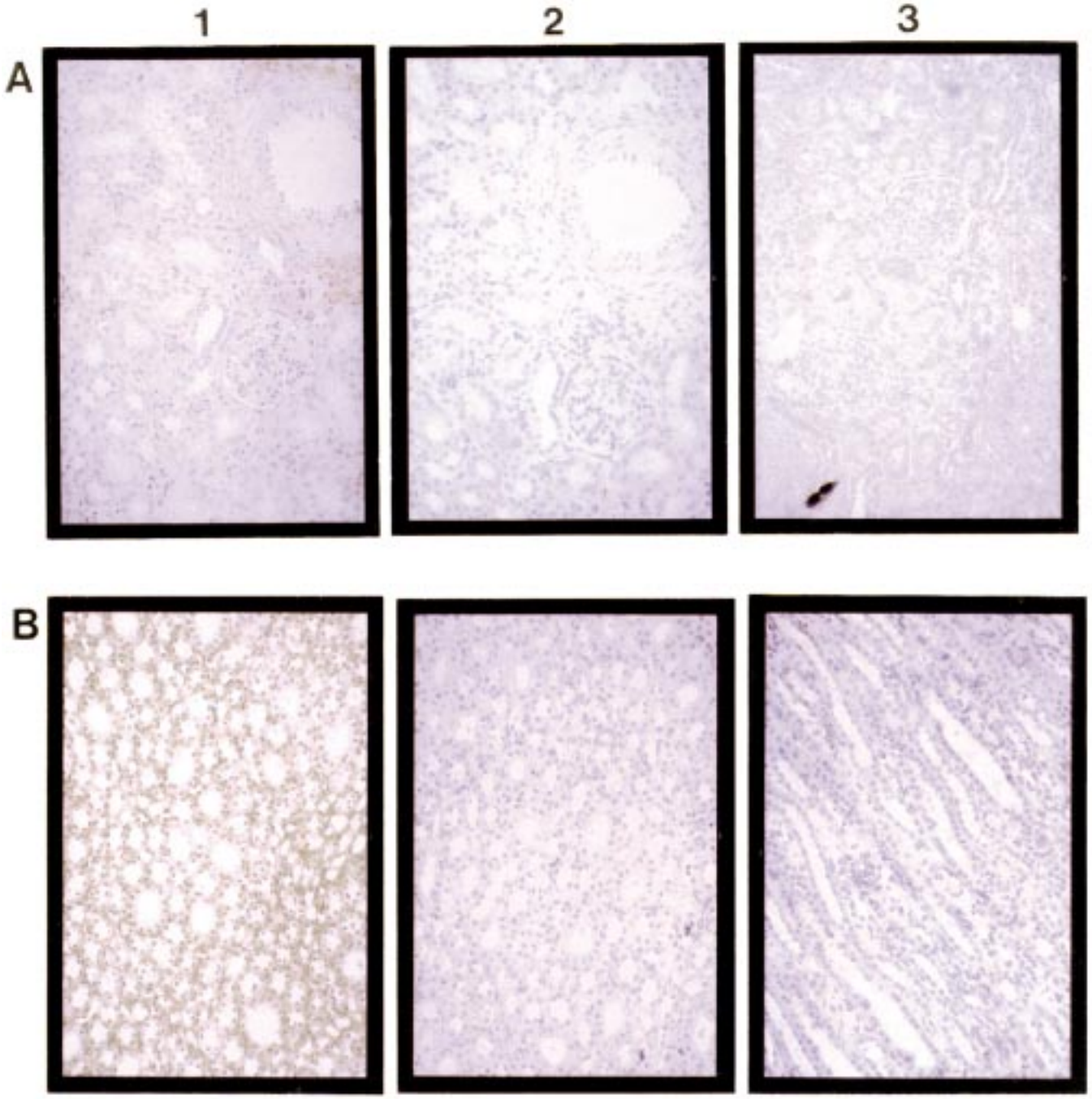

Figure 3—Light micrographs (enlarged 200X) of the (A) renal cortex and (B) medulla. A1 and B1 are from baboons that received lepirudin. A2 and B2 are negative controls where no anti-hirudin antibody was used. A3 and B3 show the renal cortex and medulla of the control baboon that did not receive lepirudin but was treated with anti-hirudin antibody.

The amount of lepirudin excreted by the kidneys was calculated from the total urine volume and the concentration of r-hirudin in urine. In two cases (1 × bolus study and 1 × infusion study), very little urine could be collected. The results are nevertheless given. After infusion of labeled lepirudin, 2.2 ± 1.9 mg of lepirudin was excreted, after the bolus 2.2 ± 1.5 mg was excreted. This amount was ≈54% of the total dose of lepirudin given.

Immunohistochemisty—The results are presented in Figures 3 and 4. The kidney, liver, and spleen of the baboon that was not treated with lepirudin stained negative when the tissues were incubated with the anti-hirudin antibody (Figure 3, A3 and B3, and Figure 4, A3 and B3). This result indicates that these tissues did not contain proteins that interact with the antibody. Kidney, spleen, and liver tissue from baboons treated with lepirudin also stained negative when the tissues were not incubated with the antibody (Figure 3, A2 and B2, and Figure 4, A2 and B2), indicating that the positive staining obtained in the test samples was not a result of the staining procedure.

In the renal cortex, the cytoplasm of the epithelial cells of the convoluted tubules, the cytoplasm of the endothelial cells of the blood vessels, and the connective tissue stained for lepirudin. The glomeruli stained negative (Figure 3, A1). The renal medulla stained intensely. It is likely that lepirudin was present in the epithelium of the thick and thin segments of the loop of Henly and the collecting tubes. The cytoplasm of the endothelial cells of the vas recta and the connective tissues between the cells stained strongly (Figure 3, B1).

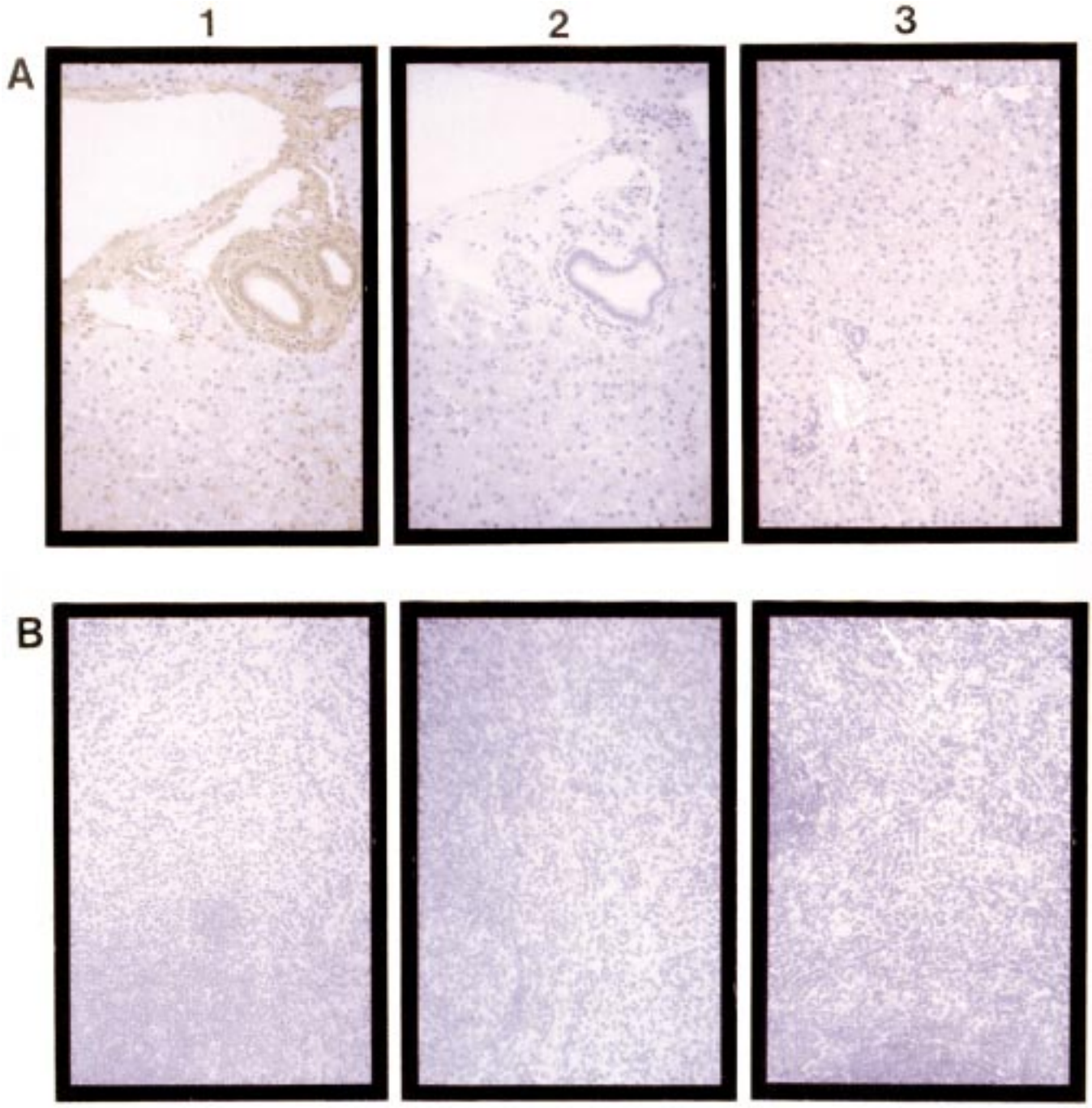

Figure 4—Light micrographs (enlarged 200X) of the (A) liver and (B) spleen. A1 and B1 are from baboons that received lepirudin. A2 and B2 are negative controls where no anti-hirudin antibody was used. A3 and B3 show the liver and spleen of the control baboon that did not receive lepirudin but was treated with anti-hirudin antibody.

The spleen did not stain for lepirudin (Figure 4, A1). On the other hand, staining of liver is ambiguous (Figure 4, B1). The cytoplasm of the hepatocytes did not stain strongly, but the cytoplasm of the endothelial cells of the hepatic artery and portal vein and that of the epithelial cells of the bile duct stained strongly.

Discussion

In a study of this nature, where the pharmacokinetics and mechanism of clearance of a compound labeled with a radioisotope is studied, it is vital that the labeled compound reacts in the same way as the native compound. There are several lines of evidence to show that the behavior of lepirudin, when labeled with ^{131}I, was not markedly affected by the labeling procedure. First, treatment with the labeled lepirudin lengthened the aPTT 3−4-fold (Table 1). In addition, when unlabeled and labeled hirudin, either alone or as a 50/50 mixture, were added to plasma in vitro, the lengthening in aPTT was equivalent. This result indicated that the labeled lepirudin was functional. Second, when the half-life was measured from the radioactive count rate in blood, it was 21 ± 6 min, which was not significantly different from that estimated for lepirudin (24 ± 9 min). These estimates were also not significantly different from that obtained in another study.[5] Third, after 90 min of treatment with labeled lepirudin, no accumulation of ^{131}I was imaged in the thyroid or spleen, both of which rapidly

remove free iodine in plasma.[13] It is therefore reasonable to conclude that labeling of lepirudin with ^{131}I did not adversely affect the function and plasma clearance of lepirudin and that the ^{131}I remained bound to the lepirudin. The results obtained with the labeled lepirudin can therefore be compared with those of lepirudin, and conclusions relating to the pharmacokinetics of lepirudin can be made from the results obtained with labeled lepirudin.

It is evident that lepirudin was mainly excreted by the kidneys (Figures 2A and B). Between 50 and 60% of the injected lepirudin was detected in the bladder 90 min after it was injected (Table 3), which agrees with results obtained in humans and rhesus monkeys.[6,14,15] Because the clearance of lepirudin approximates that of creatinine in humans, it was proposed that excretion be by glomerular filtration.[14,15] We used immunohistochemical techniques in an attempt to verify this proposal (Figure 3). The results were rather confusing and do not confirm glomerular filtration. Glomeruli in the renal cortex did not stain for lepirudin. Tissue surrounding the glomerulus and the blood vessel did stain. Even more surprising was the fact that the tubuli in the medulla, and especially the epithelial cells lining the tubules, stained intensely, which suggests tubular reabsorption and secretion. A well-planned study to investigate glomerular filtration and possible tubular reabsorption and secretion is called for. Such a study will provide definitive answers about the mechanisms by which the kidneys excrete lepirudin.

It is generally accepted that the fraction of lepirudin that is not excreted by the kidneys is distributed in the extravascular compartment.[14] The in vitro results in this study however showed that the liver plays a part in the catabolism of lepirudin and that lepirudin was excreted in the bile. Although we could not quantify appreciable quantities of [^{131}I]labeled lepirudin in the liver (Table 3), immunohistochemical studies showed that lepirudin was present in the hepatocytes and the tissues surrounding the blood vessels and bile ducts. The finding that lepirudin was present in the bile means that it has to be excreted into the digestive system. We explain the absence of lepirudin in the duodenal juices (Table 4) and the finding that lepirudin was not present in the feces of normal humans 24 h after it was administered[15] by digestion and absorption of lepirudin by the enzymes present in the duodenum. It is reasonable to assume that the 40% of administered lepirudin that was not excreted by the kidneys, could be excreted by the liver into the bile. However, a well-planned study is needed to quantify the contribution of the liver to the clearance of lepirudin from plasma. It is further evident that the spleen plays no part in the catabolism of lepirudin (Table 3, Figure 4).

The plasma elimination half-life of lepirudin was 18 ± 4 min when it was injected as a bolus. When the same quantity was infused over 30 min, the estimated half-life was not significantly different (23 ± 8 min). This result is similar to the estimated half-life that we determined in baboons where different dosages of lepirudin were infused over 30 min.[5] The half-lives estimated in the baboons are shorter than the 55−70 min measured in humans, rhesus monkeys, rats, rabbits, and dogs.[6,15−17] We have no easy explanation for this discrepancy.

The total clearance of lepirudin from plasma was ≈45 mL/min, whether the same amount was infused or given as a bolus. Similar results were obtained when clearance was calculated from the radioactive radioactive count rates (Table 2). This value is not very different from that determined in rhesus monkeys,[18] but differs greatly from the results reported for humans, rats, rabbits, and dogs.[6,15] Labeled lepirudin, infused over 30 min, was cleared by the kidneys at a significantly higher rate than that administered as a bolus (Table 2). However, when renal clearance was expressed as a percentage of plasma clearance, 62 ± 16% of infused lepirudin was cleared by the kidneys. The corresponding value for bolus administrated lepirudin, 55 ± 15%, was not significantly different ($p > 0.05$, Student's *t* test for paired data). Thus, although the rate of clearance was different, the relative contribution of the kidneys to plasma clearance was the same. It is important to note that in rhesus monkeys that received a bolus of lepirudin, renal clearance also contributed ≈50% to plasma clearance.[18] These results are similar to those obtained in this study. The method of administration of the labeled lepirudin did not affect the extravascular clearance (Table 2).

In summary, whether 0.3 mg/kg of labeled lepirudin was infused over 30 min or given as a bolus, it did not influence its plasma half-life and clearance. This result suggests that the study was performed with plasma concentrations below the maximum threshold levels of excretion of lepirudin by the kidneys. The mode of administration did not affect the clearance of lepirudin from plasma, nor that by the kidneys or the extravascular compartment. The kidneys were the main sites of excretion of lepirudin, where between 50 and 60% was excreted, probably by tubular secretion. It has been speculated that the remainder may be catabolized by the kidneys and that the methods used to determine lepirudin are unable to recognize the degradation products.[6,14,18,19] The quantification of the percentage labeled lepirudin found in the bladder argues against renal catabolisation. If the labeled lepirudin was catabolized, much more than 50 to 60% of administered labeled lepirudin would have been detected in the bladder at the end of the study. In addition, SDS-PAGE suggested excretion in an unchanged form. A surprising finding was that the bile contained appreciable amounts of lepirudin.

References and Notes

1. Adkins, J. C.; Wilde, M. I. Lepirudin: A review of its potential place in the management of thrombotic disorders. *Biodrugs* **1998**, *10*, 227−255.
2. Harvey, R. P.; Degryse, E.; Stefani, L.; Schamber, F.; Cazenave, J. P.; Courtney, M.; Tolsthev, P.; Lecocq, J. P. Cloning and expression of c DNA coding for the anticoagulant hirudin from the blood sucking leech, *Hirudo medicinalis*. *Proc. Natl. Acad. Sci. U.S.A.* **1986**, *83*, 1084−1088.
3. Kelly, A. B.; Marzec, U. M.; Krupski, W.; Bass, A.; Cadroy, Y.; Hanson, S. R.; Harker, L. A. Hirudin interruption of heparin-resistant arterial thrombus formation in baboons. *Blood* **1991**, *77*, 1006−1012.
4. Kotzé, H. F.; Lamprecht, S.; Badenhorst, P. N. A 4-h infusion of recombinant hirudin results in long-term inhibition of arterial-type thrombosis in baboons. *Blood* **1995**, *85*, 3158−3163.
5. Kotzé, H. F.; Lamprecht, S.; Van Wyk, V.; Roodt, J. P.; Badenhorst, P. N. Differences in platelet-dependent thrombosis and thrombin production does not affect the pharmacokinetics of r-hirudin (HBW 023) in baboons. *Thromb. Haemost.* **1995**, *73*, 1308 (abstract).
6. Nowak, G. Pharmacokinetics of hirudin. *Semin. Thromb. Hemost.* **1991**, *17*, 145−149.
7. Harker, L. A.; Hanson, S. R. Experimental arterial thromboembolism in baboons: Mechanism, quantification, and pharmacologic prevention. *J. Clin. Invest.* **1979**, *64*, 559−569.
8. Hanson, S. R.; Kotzé, H. F.; Savage, B.; Harker, L. A. Platelet interactions with Dacron vascular grafts. *Arteriosclerosis* **1985**, *5*, 595−603.
9. Salacinski, P. R. P.; Mclean, C.; Sykes, J. E. C.; Clement-Jones, V. V.; Lowry, P. J. Iodination of proteins, glycoproteins and peptides using a solid-phase oxidising agent, 1,3,4,5-tetrachloro-3α, 6α-diphenyl glycoluril (IODO-GEN). *Anal. Biochem* **1981**, *117*, 136−146.

10. Nowak, G.; Bucha, E. Quantitative determination of hirudin in blood and body fluids. *Semin. Thromb. Hemost.* **1996**, *22*, 197−202.
11. Kotzé, H. F.; Lötter, M. G.; Badenhorst, P. N.; Heyns, A. du P. Kinetics of ^{111}In-platelets in the baboons. II. In vivo distribution and sites of sequestration. *Thromb. Haemost.* **1985**, *53*, 408−410.
12. Lyer, L.; Koza, M.; Iqbal, O.; Calabria, R.; Fareed, J. Studies on the pharmacokinetics and pharmacodynamics of recombinant hirudin (rHV-Lys47) after intravenous and subcutaneous administration in dogs. *Thromb. Res.* **1993**, *69*, 259−269.
13. Saha, G. B. Uses of radiochemicals in nuclear medicine. In *Fundamentals of Nuclear Pharmacy*; Saha, G. B., Ed.; Springer-Verlag: New York, 1992; pp 227−241.
14. Markwardt, F.; Nowak, G.; Stürzebecher, J.; Griessbach, U.; Walsmann, P.; Vogel, G. Parmacokinetics and anticoagulant effect of hirudin in man. *Thromb. Haemost.* **1984**, *52*, 160−163.
15. Meyer, B. H.; Luus, H. G.; Müller, F. O.; Badenhorst, P. N.; Röthig, H.−J. The pharmacology of recombinant hirudin, a new anticoagulant. *S. Afr. Med. J.* **1990**, *78*, 268−270.
16. Markwardt, F.; Fink, G.; Kaiser, B.; Klöking, H, P.; Nowak, G.; Richter, M.; Stürzebecher, J. Pharmacological survey of recombinant hirudin. *Pharmazie* **1988**, *43*, 202−207.
17. Nowak, G.; Markwardt, F.; Fink, E. Pharmacokinetic studies with recombinant hirudin in dogs. *Folia Haematol.* **1988**, *115*, 70−74.
18. Grötsch, H.; Hropot, M.; Berscheid, G.; Crause, P.; Malerczyk, G.; Apidopoulos, G.; Haun, G.; Husak, B. Pharmacokinetic investigations of the α-human thrombin-hirudin complex in rhesus monkeys. *Thromb. Res.* **1992**, *66*, 271−275.
19. Grötsch, H.; Hropot, M. Degradation of rDNA hirudin and α-human thrombin-lepirudin complex in liver and kidney homogenates from rat. *Thromb. Res.* **1991**, *64*, 763−767.

JS980407Q

Influence of the Treatment Protocol upon the in Vivo Efficacy of Cidofovir (HPMPC) and of Acyclovir (ACV) Formulations in Topical Treatment of Cutaneous HSV-1 Infection in Hairless Mice

MOHSEN I. AFOUNA, SAMIR C. MEHTA,[†] ABDEL-HALIM GHANEM, WILLIAM I. HIGUCHI,* EARL R. KERN,[‡] ERIK DECLERCQ,[§] AND HAMED H. EL-SHATTAWY[||]

Contribution from *Department of Pharmaceutics and Pharmaceutical Chemistry, University of Utah, 30 So. 2000 E, Salt Lake City, Utah 84112; GlaxoWellcome Inc., 5 Moore Dr., Research Triangle Park, North Carolina 27709; The Department of Pediatrics, University of Alabama at Birmingham, Birmingham, Alabama 35294; Rega Institute for Medical Research, Katholieke Universiteit Leuven, B-3000 Leuven, Belgium; and the Department of Pharmaceutics, Al-Azhar University, Nasr City, Cairo, Egypt.*

Received October 12, 1998. Final revised manuscript received February 9, 1999. Accepted for publication February 22, 1999.

Abstract □ In recent studies we found that the topical effectiveness of acyclovir (ACV) formulations was a single-valued function of *C**—the target site free drug concentration. The topical efficacy was the same when the therapy was initiated 0, 1, or 2 days after intracutaneous herpes simplex virus type-1 (HSV-1) inoculation in hairless mice. The purpose of the present study was to examine the hypothesis that the topical effectiveness of cidofovir (HPMPC) would not be a single valued function of *C** and that it would be dependent upon when the therapy was initiated relative to the time of viral infection. Formulations of HPMPC and ACV in 95% DMSO as a vehicle were used. Hairless mice intracutaneously infected with HSV-1 were used, and 20 μL of the test formulation was topically applied twice a day. In protocol A, the treatment was continued until the fourth day after virus inoculation, whereas in protocol B the treatment was terminated on the day of virus inoculation. Treatment was initiated on various days ranging from day −6 to day 4, and the lesions were scored on day 5. Treatment of ACV according to protocol A proved efficacious whether started as early as 6 days before virus inoculation or later, whereas the efficacy of ACV was annihilated if applied following protocol B. For HPMPC, on the other hand, the in vivo efficacies were found to be strongly dependent on how early the therapy was initiated, and significant efficacy was observed even when the treatment was terminated on the day of virus inoculation. This difference was attributed to the virus-independent intracellular phosphorylation of HPMPC and slow clearance of its metabolites from the cell. It was also noted that, similar to ACV, for HPMPC the topical efficacy is likely to be a function of *C** for a fixed protocol. However, unlike for ACV, for HPMPC the efficacy was not a single-valued function of *C**.

Introduction

In a previous study,[1] we found that the topical effectiveness of acyclovir (ACV) formulations was essentially the same when the therapy was initiated 0, 1, or 2 days after intracutaneous herpes simplex virus type-1 (HSV-1) inoculation in hairless mice. Also, a good relationship was found between the free drug concentration at the skin target site (*C**) calculated from in vitro flux data and the in vivo antiviral efficacy for a variety of ACV formulations (i.e., topical efficacy was found to be a single-valued function of *C**).[2] We have hypothesized that this relatively straightforward behavior exhibited by ACV is the consequence of the relatively rapid local pharmacokinetics that ACV may exhibit at the cellular level. A long-term objective of this research has been to investigate the *C** concept using other anti-herpes model drugs that are similar to, as well as different from, ACV. A recent report assessed the relationship of *C** with the in vivo efficacy of (*E*)-5-(2-bromovinyl)-2-deoxyuridine (BVDU), an antiherpetic drug with a mechanism of action similar to that of ACV.[3] Cidofovir ((*S*)-1-(3-hydroxy-2-phosphonylmethoxypropyl)-cytosine or HPMPC) represents a new class of broad-spectrum antiviral agents that are active against a broad range of herpes viruses and exhibit rather slow cellular kinetics; particularly noteworthy is that the active metabolites are retained intracellularly for a very long time.[4] The purpose of the present study was to examine the hypothesis that because of the slow cellular pharmacokinetics, the topical effectiveness of HPMPC formulations would be strongly dependent upon when therapy is initiated relative to the time of virus infection and that, accordingly, the final outcome may not be a single-valued function of *C**.

Materials and Methods

Animals—Female hairless mice strain SKH/HR1 (Charles River, Bloomington, MA), 6−8 weeks old with average body weight of 22−27 g, were used throughout this study.

Virus—Samples from the same batch of herpes simplex virus type-1, strain E-377, with a final titer of 4×10^7 PFU/mL, were used for inoculation. They were stored at −70 °C in aliquots until used. The preparation and assay methods of the virus have been previously reported.[5]

Drug Formulations—HPMPC was generously provided by Gilead Sciences, Inc. (Foster City, CA). ACV was obtained from Thera Tech, Inc. (Salt Lake City, UT). DMSO was purchased from Baker Chemical Company (Phillipsburg, NJ). The formulations were made with 0.5 and 1% HPMPC and 0.1% ACV in 95% DMSO as a vehicle and 1% hydroxypropyl cellulose (Klucel, Hercules, Wilmington, DE) was added as a thickening agent.

In Vitro Flux Measurement and *C Predictions**—For the in vitro determination of HPMPC and ACV fluxes and *C** predictions, a combined in vivo−in vitro experimental procedure reported earlier[1,6] was adopted and performed in triplicate for each formulation. Briefly, a finite dose of 20 μL of the test formulation was applied over a rectangular skin area of 2 cm^2 on the animal

* To whom correspondence should be addressed.
[†] GlaxoWellcome Inc.
[‡] University of Alabama.
[§] Rega Institute for Medical Research.
[||] Al-Azhar University.

10.1021/js980406y CCC: $18.00 *Published on Web 04/14/1999*

Table 1—Treatment Protocols Followed for the in Vivo Efficacy Experiments. X Indicates Two Applications on that Day

	protocol A							protocol B			
	–6A	–4A	–3A	–2A	–1A	0A	1A	–6B	–4B	–2B	0B
day –6	X							X			
day –5	X							X			
day –4	X	X						X	X		
day –3	X	X	X					X	X		
day –2	X	X	X	X				X	X	X	
day –1	X	X	X	X	X			X	X	X	
day 0 (virus inoculation)	X	X	X	X	X	X					
day 1	X	X	X	X	X	X	X				
day 2	X	X	X	X	X	X	X				
day 3	X	X	X	X	X	X	X				
day 4	X	X	X	X	X	X	X				
day 5	scoring	scoring	scoring	scoring	scoring	scoring	scoring	scoring	scoring	scoring	scoring

dressed in a Velcro jacket twice a day for 2 days. The in vivo pretreatment was followed by the in vitro flux experiment in which the pretreated skin was excised from the animal and mounted on a Franz diffusion cell. Flux measurements were carried out as reported earlier[1] after applying a 10 μL/cm^2 dose of the test formulation. ACV and HPMPC concentrations were analyzed using the previously reported reversed phase HPLC methods.[2,7]

The cumulative amount of the test drug transported into the receiver chamber was plotted as a function of time, and the instantaneous flux J was estimated from the slope of the line connecting the two consecutive points. The instantaneous C^* estimates were then calculated using the following equation.

$$C^* = J/P_D \quad (1)$$

where J is the skin flux and P_D is the in vivo dermis permeability coefficient of the drug. The details of the derivation of this equation have been reported in our previous study.[8] A P_D value of 1.4×10^{-3} cm/s was obtained for ACV. Since the molecular size of HPMPC is sufficiently close (for the present purpose) to that of ACV, it was deemed reasonable to use the in vivo P_D value of ACV for HPMPC as a good approximation.

In Vivo Antiviral Efficacy Studies—The in vivo antiviral efficacy was evaluated using a group of 8–10 hairless mice per experiment, and an average of two to six experiments were performed for each drug formulation. In each experiment a group of animals treated with a placebo formulation similar to the test formulation without the drug was always included as a negative control. For the purpose of these experiments, the animals were dressed in a Velcro jacket. The details of dressing the animals in the Velcro jacket and of virus inoculation have been described earlier.[2] Two general treatment protocols were followed. For both protocols, 20 μL of the test formulation was topically applied twice a day. In protocol A, the treatment was continued until the fourth day after virus inoculation, whereas in protocol B the treatment was terminated on the day of virus inoculation. The day of virus inoculation was always considered as day 0. Treatment was initiated on various days ranging from day −6 to day 4, as outlined in Table 1. The lesions were scored on day 5 as previously described,[9] and the antiviral efficacies were calculated using the following equations:[1]

$$\text{topical efficacy (\%)} = \frac{N_{St} + N_J + N_{NR}}{N_{Th} + N_{St} + N_J + N_{NR}} \times 100 \quad (2)$$

$$\text{systemic efficacy (\%)} = \frac{N_{NR}}{N_{Th} + N_{St} + N_J + N_{NR} + N_M} \times 100 \quad (3)$$

where N_{Th}, N_{St}, N_J, N_{NR}, and N_M are the number of animals corresponding to each of the five lesion categories and represent the cases where the lesion passes through (Th), stops (St) at the edge of, jumps (J) over, does not reach (NR), or misses (M) the treatment area, respectively.

During the treatment protocol coded −6A, the dosing was performed over 11 days, and hence the animal was dressed with the Velcro jacket for that period of time. This raised the question of the possible effect of stress (induced due to prolonged dressing in Velcro jackets) on the efficacy results. To assess this, an experiment was performed in which the animals were dressed in Velcro jackets on day −6 and the treatment with 0.5% HPMPC was initiated on day 1. The results of this experiment were compared with the results obtained with protocol coded 1A (where the dressing in the jacket and the treatment were both initiated on day 1). The results of these two experiments were comparable indicating that prolonged dressing in the Velcro jacket did not compromise the efficacy results (data not shown). The same conclusion was drawn from separate experiments with 0.1% ACV formulation.

Table 2—Mean C^* Estimates ($n = 3$) for 0.5% and 1% HPMPC and 0.1% ACV Formulations

formulation	C^* (μg/mL)	SD
0.5% HPMPC	1.2	0.14
1% HPMPC	2.13	0.38
0.1% ACV	0.12	0.02

Results

Table 2 shows the mean C^* estimates obtained from the combined in vivo–in vitro experiments for the three topical formulations. For HPMPC, an increase in the applied concentration resulted in an increase in the predicted C^* levels. The saturation solubility of HPMPC in DMSO was >10%, and hence an increase in the applied concentration resulted in essentially a proportional increase in the flux, which in turn resulted in proportionally higher C^* levels. These results are consistent with those previously observed with other anti-herpes agents such as ACV and BVDU.[2,3]

Figure 1 shows the results (mean ± SD) of our preliminary experiments with 1% HPMPC in 95% DMSO as vehicle. For this formulation, when the therapy was initiated 1 day after virus inoculation (and continued for 4 days, protocol 1A), around 45% topical efficacy and 0% systemic efficacy was observed. However, when the treatment was initiated sooner, high efficacies were obtained, rising to ~100% topical efficacy and ~45% systemic efficacy when the treatment was started 2 days before virus inoculation (and continued for 4 days after virus inoculation, protocol coded −2A).

To further extend these findings, we investigated the effect of starting the treatment even sooner (up to 6 days before virus inoculation). Also, a lower HPMPC level (of 0.5%) was employed to provide a greater dosage range, and therefore greater differentiation in the effects. Figure 2A presents the results of these experiments. As can be seen here, in general the earlier the treatment was initiated, the higher were the topical and systemic efficacies with both reaching a maximum of 100% with protocol coded −6A (treatment initiated 6 days prior to virus inoculation).

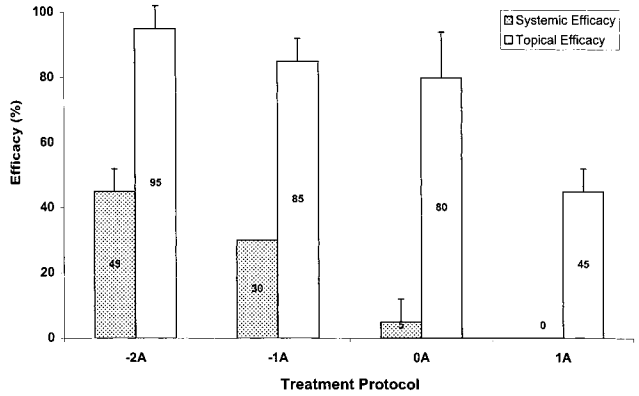

Figure 1—The topical and systemic efficacy of 1% HPMPC in 95% DMSO as a function of the treatment protocol ($n = 3$).

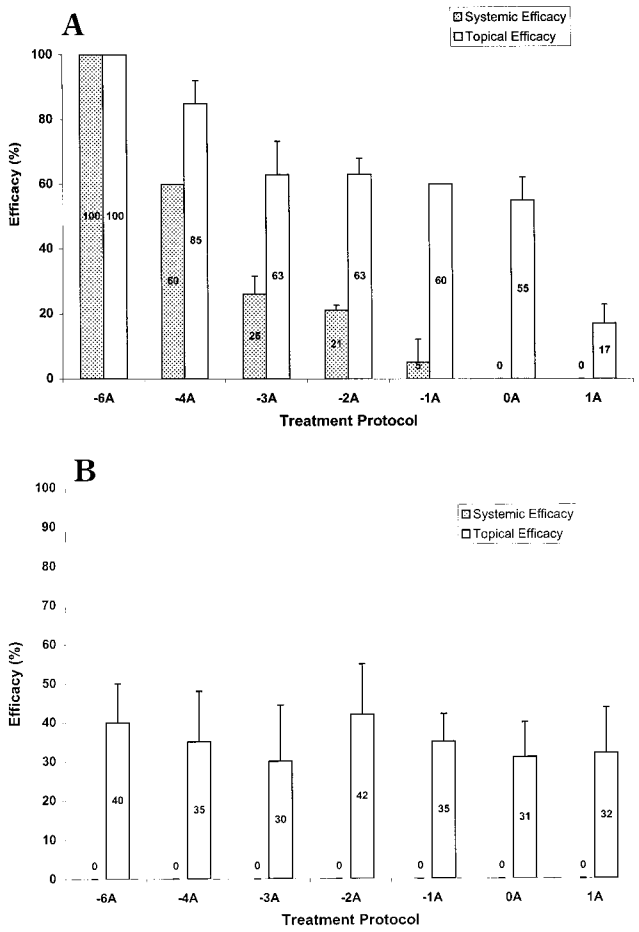

Figure 2—The topical and systemic efficacy of (A) 0.5% HPMPC and (B) 0.1% ACV in 95% DMSO as a function of the treatment protocol ($n = 3$–6).

A remarkable contrast is seen when the HPMPC results are compared to the ACV results. Figure 2B presents the results of similar experiments with 0.1% ACV. The figure clearly shows that treatment with ACV beginning as early as 6 days before virus inoculation (protocol coded −6A) had no effect on the outcomes when compared to the standard experiment of beginning the treatment 1 day after virus inoculation (protocol coded 1A). Clearly, the strong time dependency seen with HPMPC is absent with ACV.

In another series of experiments, the antiviral efficacies of 0.5% HPMPC and 0.1% ACV were tested as per protocol B (Figures 3A and 3B, respectively). In these experiments, the treatment was stopped on the day of virus inoculation. There was consequently no application of the drug formulation during the period of virus replication. Once again, there was a sharp difference in the outcomes with ACV and HPMPC. For ACV, terminating the treatment on the day of virus inoculation essentially rendered the treatment completely ineffective (Figure 3B), indicating that the application of ACV was required during the time of virus replication. However, for HPMPC, this was not the case. Topical efficacies ranging from 25 to 60% were found when the treatment was initiated 2−6 days prior to virus inoculation and stopped on the day of virus inoculation (Figure 3A). HPMPC applied prior to the infection acted prophylactically and continued to act against viral replication even though no HPMPC was applied during the time when the infection was progressing. The efficacy seen in this case seemed to be related to the duration of the exposure prior to the treatment, a longer duration of exposure with a given HPMPC formulation resulting in higher efficacy. For example, the topical efficacy obtained with 2 days (−2B) and 6 days (−6B) of exposure were 25 and 61%, respectively.

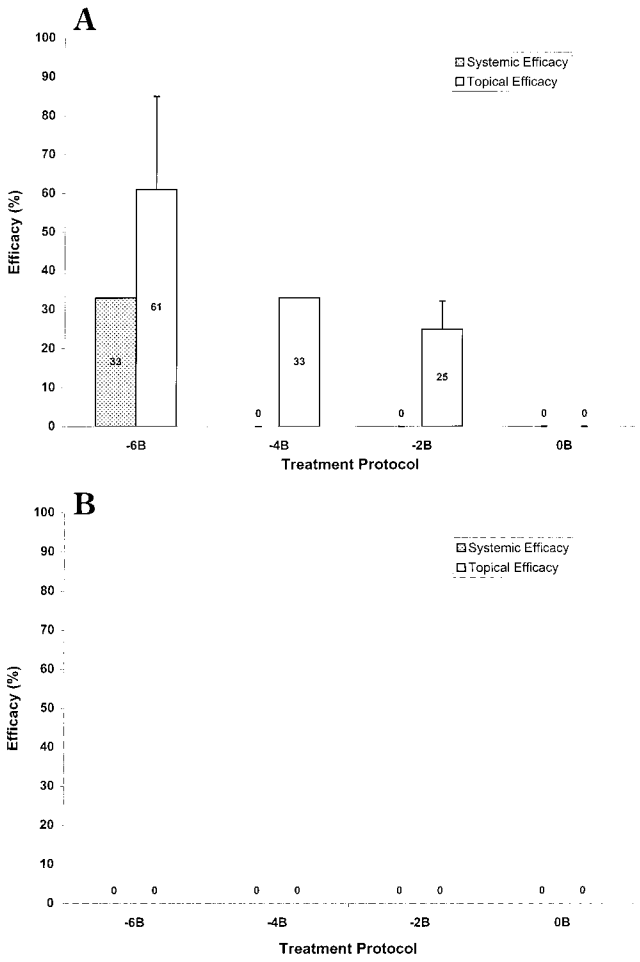

Figure 3—The topical and systemic efficacy of (A) 0.5% HPMPC and (B) 0.1% ACV in 95% DMSO as a function of the treatment protocol ($n = 2$).

Discussion

For ACV as the anti-herpes agent, starting treatment early did not alter its efficacy against cutaneous HSV-1 infections. These results extend the earlier work of Lee et al.,[1] who, employing controlled delivery transdermal systems, found that topical efficacy was independent of whether ACV treatment was started on day 0, 1, or 2 after

virus inoculation. The present data show that initiating treatment with ACV several days prior to virus inoculation essentially has the same effect as initiating treatment 1 day after virus inoculation. These results are consistent with our earlier findings[2] that topical efficacy of ACV formulations is a single valued function of *C** and can be explained by the relatively rapid pharmacokinetics of ACV at the cellular level.

Cell culture studies have shown that ACV is converted to its mono-, di-, and triphosphorylated forms (ACVp, ACVpp, and ACVppp, respectively) in cells infected with HSV-1.[10] The initial phosphorylation of ACV to ACVp is catalyzed by the HSV-1-induced thymidine kinase. Subsequent phosphorylation to ACVpp and ACVppp is carried out by cellular enzymes. In the uninfected cells, phosphorylation of ACV occurs to a very limited degree. The end product of phosphorylation, ACVppp, is a selective inhibitor of viral DNA polymerase and is the active metabolite responsible for efficacy.

The intracellular concentration of the active metabolite (species) can be regarded as a function of (a) *C** (extracellular drug concentration), (b) the rate of cellular uptake of the drug, (c) the rate of conversion of the drug to the active species, and (d) the rate of elimination of the active species. When the treatment with ACV is started prior to virus inoculation, step c is very slow. The uninfected cells lack the virally induced thymidine kinase which is responsible for conversion of ACV to ACVp (a required precursor for the active species). The rate of formation of ACVppp in the uninfected cells is approximately several orders of magnitude smaller than that in the infected cells.[11] On the other hand, step d, the rate of elimination of active species, is fairly rapid for ACV. In cell culture studies, the levels of ACVppp declined rapidly after the removal of the drug from the medium. The initial half-life of the triphosphate was 1.2 h in the absence of ACV in the medium with the levels reaching a plateau after 6 h.[11] The combined effect of the above would mean that the intracellular levels of the active species of ACV are negligible until the infection sets in. This can explain the results obtained with protocol B, where no protective effect was seen when ACV was applied as pretreatment only. With protocol A there was no additional effect afforded by ACV pretreatment. It should also be noted that in the infected cells, steps b−d are relatively rapid for ACV, and a steady state is reached quickly. Due to this rapid uptake and elimination, the intracellular level of the active ACV species and its efficacy seems to be a single-valued function of *C**, the extracellular drug concentration.

HPMPC is somewhat different from ACV in its mechanism of action. HPMPC is a nucleoside phosphonate (thus a nucleotide) analogue, in a way similar to ACVp. In cells, HPMPC is phosphorylated by host enzymes to its mono- and diphosphates (HPMPCp and HPMPCpp, respectively). HPMPCpp (similar to ACVppp) is a selective inhibitor of viral DNA polymerase and is the active species responsible for efficacy.[12] The HPMPCp−choline adduct is another intracellular moiety identified in cell culture studies. A significant difference from ACV is that the phosphorylation is carried out by the host cell enzymes and is therefore not dependent on virus infection. It has been shown that following treatment with a fixed extracellular HPMPC concentration, levels of HPMPCp, HPMPCpp, and HPMPCp−choline adduct in the cells infected with HSV-1 are the same as those in the uninfected cells.[12] This allows the opportunity for building up metabolites prior to virus infection and priming the cells to resist viral replication. It would also explain, at least in part, the results of Figure 3A where pretreatment with HPMPC acted prophylactically to resist a subsequent virus infection.

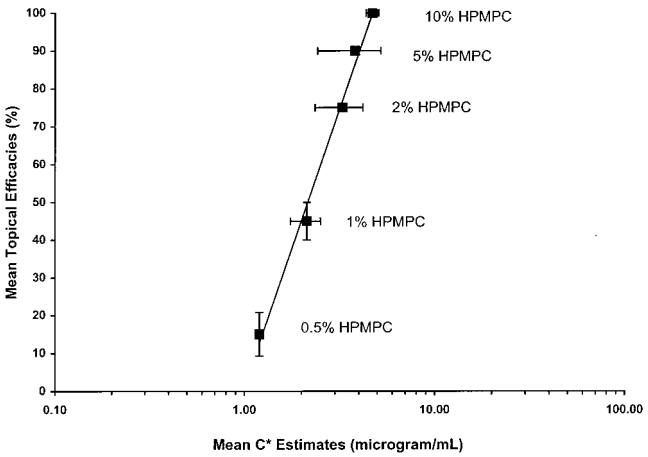

Figure 4—The topical efficacy of HPMPC as a function of *C**. The mean *C** estimates for different concentrations of HPMPC were obtained from combined in vivo–in vitro experiments ($n = 3$). The in vivo efficacies were obtained using protocol coded 1A ($n = 1$–6) (see text for details).

Another difference between ACV and HPMPC is their rate of cellular uptake and rate of conversion to the active metabolites. In cell culture studies (for ACV), the intracellular levels of ACVppp reach a maximum after 8 h of exposure of the cells to ACV.[11] For HPMPC, the intracellular levels of HPMPCpp continued to rise for 24 h after the cells were exposed to HPMPC.[13,14] More notable is the fact that the clearance of the metabolites of HPMPC from the cells is extremely slow. Various studies reported the intracellular half-life of HPMPCpp to be in the order of 17−24 h.[12−14] The long intracellular half-life of HPMPCpp after the extracellular drug is removed would be expected to lead to persistence of antiviral activity. The intracellular half-life of HPMPCp−choline adduct was reported to be >48 h. The long intracellular half-life of this adduct may produce an intracellular reservoir of drug from which the active metabolite is slowly released. This may contribute to the long duration of antiviral action of HPMPC. These facts further explain the protective effects seen with HPMPC pretreatment in Figure 3A. Also, because of the slow build-up of the metabolites and their slow elimination, it is expected that longer duration of exposure would result in higher levels of the active species and a correspondingly higher efficacy. This pattern is clearly seen in Figures 2A and 3A.

It must be noted that as for ACV, the intracellular concentration of active species of HPMPC, and in turn its in vivo efficacy, is also a function of its extracellular concentration or *C**. It was reported in cell culture studies that the HPMPCpp concentration inside the cell increased in response to increased extracellular HPMPC concentrations, and it was speculated that the antiviral efficacy should show dose responsiveness.[12] Results obtained for the treatment of HSV-1 infection with HPMPC in a murine model support this theory.[15] In a separate series of experiments we observed that for a fixed protocol coded 1A, increasing the dose of HPMPC from 0.5% to 10% resulted in an increase in the *C** values from 1.2 μg/mL to 4.7 μg/mL, which in turn resulted in an increase in topical efficacy from 17% to 100% (Figure 4). These results are very similar to those obtained with ACV.[2] However, for HPMPC, although efficacy is a function of *C**, it is not a single-valued function of *C**. Apart from *C**, the rate of its cellular uptake, rate of conversion to its active metabolites, and rate of elimination of active metabolites all have an effect on the efficacy. In conclusion, for ACV, because of the rela-

tively rapid pharmacokinetics, the intracellular level of the active metabolites as well as the in vivo efficacy may be time-independent and a single-valued function of the *C**. In contrast, for HPMPC, the in vivo efficacy is strongly time dependent and is not a single-valued function of *C** because of slow cellular kinetics of the drug and its active metabolites.

References and Notes

1. Lee, P. H.; Su, M. H.; Kern, E. R.; Higuchi, W. I. Novel animal model for evaluating topical efficacy of antiviral agents: Flux versus efficacy correlations in the acyclovir treatment of cutaneous herpes simplex virus type-1 (HSV-1) infection in hairless mice. *Pharm. Res.* **1992**, *9*, 979−989.
2. Mehta, S. C.; Afouna, M. I.; Ghanem, A-H.; Higuchi, W. I.; Kern, E. R. Relationship of skin target site free drug concentration (C*) to the in vivo efficacy: An extensive evaluation of the preditive value of the C* concept using Acyclovir as a model drug. *J. Pharm. Sci.* **1997**, *86*, 797−801.
3. Afouna, M. I.; Mehta, S. C.; Ghanem, A-H.; Higuchi, W. I.; Kern, E. R., DeClercq, E.; El-Shattawy, H. Assessment of correlation between skin target site free drug concentration and the in vivo topical antiviral efficacy in hairless mice for (*E*)-5-(2-bromovinyl)-2′-deoxyuridine and Acyclovir formulations. *J. Pharm. Sci.* **1998**, *87*, 917−921.
4. Hitchcock, M. J. M. Cidofovir, a new agent with potent anti-herpesvirus activity. *Antiviral Chem. Chemother.* **1996**, *7*, 115−127.
5. Kern, E. R.; Overall, J. C.; Glasgow, L. A. Herpesvirus hominis infection in newborn mice. I. An experimental model and therapy with iododeoxyuridine. *J. Infect. Dis.* **1973**, *128*, 290−299.
6. Patel, P. J.; Ghanem, A−H.; Higuchi, W. I.; Srinivasan, V.; Kern, E. R. Correlation of in vivo topical efficacies with in vitro predictions using acyclovir formulations in the treatment of cutaneous HSV-1 infections in hairless mice: An evaluation of the predictive value of C* concept. *Antiviral Res.* **1996**, *29*, 279−286.
7. Cundy, K. C.; Petty, B. G.; Flaherty, J.; Fisher, P. E.; Polis, M. A.; Wachsman, M.; Lietman, P. S.; Lalezari, J. P.; Hitchcock, J. M.; Jaffe, H. S. Clinical pharmacokinetics of cidofovir in human immunodeficiency virus-infected patients. *Antiviral Chem. Chemother.* **1995**, *39*, 1247−1252.
8. Imanidis, G.; Song, W. Q.; Lee, P. H.; Suh, M. H.; Kern, E. R.; Higuchi, W. I. Estimation of skin target site acyclovir concentrations following controlled (trans)dermal drug delivery in topical and systemic treatment of cutaneous HSV-1 infections in hairless mice. *Pharm. Res.* **1994**, *11*, 1035−1041.
9. Gonsho, A.; Imanidis, G.; Vogt, P.; Kern, E. R.; Tsuge, H.; Su, M. H.; Choi, S. H.; Higuchi, W. I. Controlled (trans)-dermal delivery of an antiviral agent (acyclovir). I: An in vivo animal model for efficacy evaluation in cutaneous HSV-1 infections. *Int. J. Pharm.* **1990**, *65*, 183−194.
10. Fyfe, J. A.; Keller, P. M.; Furman, P. A.; Miller, R. L.; Elion, G. B. Thymidine kinase from herpes simplex virus phosphorylates in the new antiviral compound, 9-(2-hydroxyethoxymethyl)guanine. *J. Biol. Chem.* **1978**, *253*, 8721−8727.
11. Furman, P. A.; De Miranda, P.; St. Clair, M. H.; Elion, G. B. Metabolism of acyclovir in virus-infected and uninfected cells. *Antimicrob. Agents Chemother.*, **1981**, *20*, 518−524.
12. Ho, H.-T.; Woods, K. L.; Bronson, J. J.; De Boeck, H.; Martin, J. C.; Hitchcock, M. J. M. Intacellular metabolism of the antiherpes agent (S)-1-(3-hydroxy-2-phosphonylmethoxypropyl)cytosine. *Mol. Pharmacol.* **1992**, *41*, 197−202.
13. Cihlar, T.; Vortuba, I.; Horska, K.; Liboska, R.; Rosenberg, I.; Holy, A. Metabolism of (S)-1-(3-hydroxy-2-phosphonylmethoxypropyl)cytosine (HPMPC) in human embryonic lung cells. *Coll. Czech. Chem. Commun.* **1992**, *41*, 661−671.
14. Aduma, P.; Connelly, M. C.; Srinivas, R. V.; Fridland, A. Metabolic diversity and antiviral activities of acyclic nucleoside phosphonates. *Mol. Pharmacol.* **1995**, *47*, 816−822.
15. DeClercq, E.; Holy, A. Efficacy of (S)-1-(3-hydroxy-2-phosphonylmethoxypropyl)cytosine in various models of herpes simplex virus infection in mice. *Antimicrob. Agents Chemother.* **1991**, *35*, 701−706.

Acknowledgments

This study was supported by a grant-in-aid from Thera Tech, Inc., and by NIH Grant A1 20161. The authors thank Gilead Sciences, Inc., for kindly supplying the HPMPC.

JS980406Y

Spectrophotometric Determination of Acidity Constants of 4-Dedimethylamino Sancycline (Col-3), A New Antitumor Drug

SIRIRAT PINSUWAN,[†] FERNANDO A. ALVAREZ-NÚÑEZ,[‡] S. ESMAIL TABIBI,[§] AND S. H. YALKOWSKY*,[‡]

Contribution from *Department of Pharmaceutical Technology, Prince of Songkla University, Songkhla, Thailand, 90112, Department of Pharmaceutical Sciences, College of Pharmacy, University of Arizona, Tucson, Arizona 85721, and National Cancer Institute, National Institutes of Health, Pharmaceutical Resources Branch, Bethesda, Maryland 20892-7446.*

Received October 2, 1998. Final revised manuscript received February 10, 1999.
Accepted for publication February 16, 1999.

Abstract □ A spectrophotometric technique was used to determine the acidity constants of 4-dedimethylamino sancycline (Col-3), a new antitumor drug. The apparent pK_a values of Col-3 in 0.5% methanol aqueous media at approximately 25 °C with a constant ionic strength of 0.2 were calculated manually and graphically to be 5.64 ± 0.17 (pK_{a1}) and 8.35 ± 0.07 (pK_{a2}). In addtion, the computer program SQUAD was used to confirm Col-3 pK_a values. The pK_a values obtained by SQUAD were pK_{a1} 5.63 ± 0.14 and pK_{a2} 8.39 ± 0.04. These results are in agreement with the tetracycline-like structure of Col-3.

1. Introduction

4-Dedimethylamino sancycline (Col-3) is a new synthetic derivative obtained by chemical synthesis from sancycline methiodide. Col-3 exhibits in vitro and in vivo activity as an inhibitor of matrix metalloproteinases, tumor invasion, and metastasis of a variety of tumor types. Due to its oral biovailability, Col-3 has been formulated for oral administration by the National Cancer Institute (NCI).

Col-3 can be classified as the simplest tetracycline. Structurally, it differs from tetracycline by the absence of the 4-dimethylamino, 6-hydroxyl, and 6-methyl groups. The chemical structures of Col-3, sancycline, and tetracycline are presented in Figure 1.

Due to the absence of the 4-dimethylamino group, Col-3 cannot exist as a zwitterion and, therefore, differs from the tetracyclines in its acid−base properties. The main goal of this study is to determine the macroscopic acid dissociation constants of Col-3. Spectrophotometry was chosen for the determination of pK_a values of Col-3 because it is too insoluble ($S_w \approx 0.01$ mg/mL) for potentiometry, and also the ionized and neutral forms of this compound absorb differently in the UV/vis regions of the spectrum.

2. Materials and Methods

2.1. Materials—Col-3 was used as received from the National Cancer Institute (Bethesda, MD). Methanol was Burdick & Jackson (Muskegon, MI) HPLC grade. Phosphoric acid, monosodium phosphate, disodium phosphate, and sodium chloride were purchased from Sigma Chemical Co. (St. Louis, MO) and used without further purification.

2.2. Instrumentation—pH measurements were performed using a Corning pH meter (model no. 140) equipped with a combination glass electrode filled with potassium chloride gel. A Beckman DU-640 UV spectrophotometer was used for Spectral scan and fixed wavelength measurements.

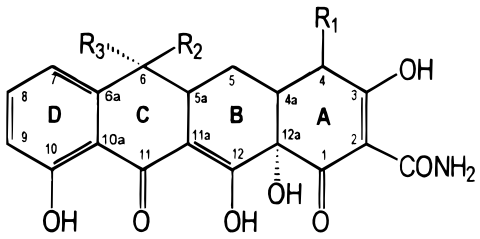

	R_1	R_2	R_3
Tetracycline	$N(CH_3)_2$	OH	CH_3
Sancycline	$N(CH_3)_2$	H	H
Col-3	H	H	H

Figure 1—Chemical structure of Col-3, sancycline, and tetracycline.

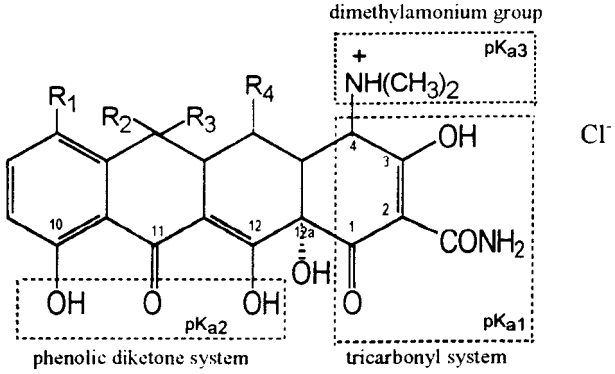

Figure 2—Structural groupings in the tetracyclines.

2.3. Methods—Aliquots of stock solution of Col-3 in methanol were added to buffers ranging from pH 2 to 11. All buffers were prepared with 0.05 M phosphate buffer and adjusted to an ionic strength of 0.2 with sodium chloride. Buffer solutions were spiked with 20 μL of the stock solution to produce 5.0 μg/mL (1.3×10^{-5} M) solutions with a final methanol concentration of 0.5%. The absorbance vs wavelength profiles of the resulting solutions were immediately obtained. All determinations were performed in duplicate at room temperature (approximately 25 °C).

3. Results and Discussion

It has been determined that the tetracycline antibiotics contain three ionizable groups[1−3] as shown in Figure 2. The first dissociation constant is due to the tricarbonyl system consisting of C1, C2, and C3 and their substitutes, the

* To whom correspondence should be addressed.
[†] Prince of Songkla University.
[‡] University of Arizona.
[§] National Cancer Institute.

10.1021/js980398l CCC: $18.00 Published on Web 04/02/1999

Table 1—The pK_a Values of the Tetracyclines in Aqueous Solution at 25 °C

	R_1	R_2	R_3	R_4	pK_{a1}	pK_{a2}	pK_{a3}
tetracycline	H	CH_3	OH	H	3.3	7.7	9.5
chlortetracycline	Cl	CH_3	OH	H	3.3	7.4	9.3
demeclocycline	Cl	H	OH	H	3.3	7.2	9.3
oxytracycline	H	CH_3	OH	OH	3.3	7.3	9.1
doxacycline	H	H	CH_3	OH	3.4	7.7	9.7
minocycline	$N(CH_3)_2$	H	H	H	2.8	7.8	9.3

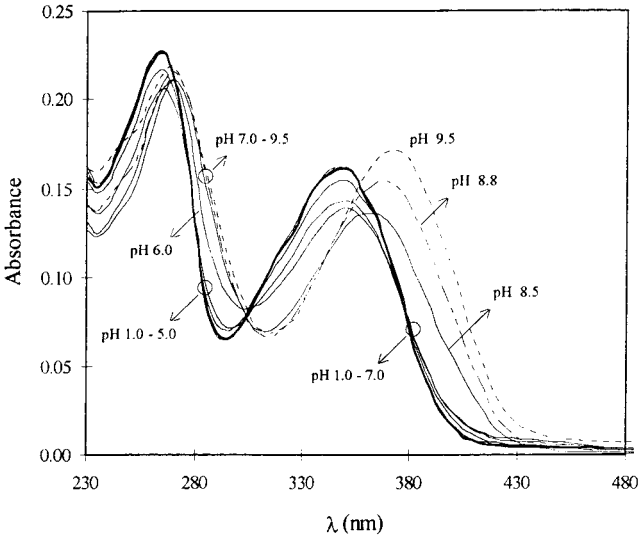

Figure 3—Absorbance vs wavelength profiles of Col-3 at different pH values.

second due to the phenolic diketone system consisting of C10, C11, C12 and their substitutes, and the third relates to the dimethylammonium functional group at C4.[2,3] The approximate pK_a values for each of these groups in some tetracycline derivatives are shown in Table 1.[1,3]

Col-3 has the first two of the acidic groupings of the tetracyclines. However, due to the absence of the dimethyammonium functional group at C4, Col-3 does not possess the third pK_a. The two pK_a values suggest that this drug can exist depending on the pH species as either the un-ionized, a monovalent anion, or a divalent anion. The UV/vis absorption spectra of Col-3 in aqueous solutions at various pH values are plotted in Figure 3.

As with most of the tetracyclines, an absorption band at about 260 nm is due to the β-tricarbonyl system, while a visible band at about 360 nm is produced by the phenolic diketone moiety.[4–7] Both anionic sites are stabilized by resonance, and they are separated from each other by carbon 12a. This sp^3 hybrid atom isolates the two light-absorbing regions and makes it possible to determine their pK_a values independently by spectrophotometry.

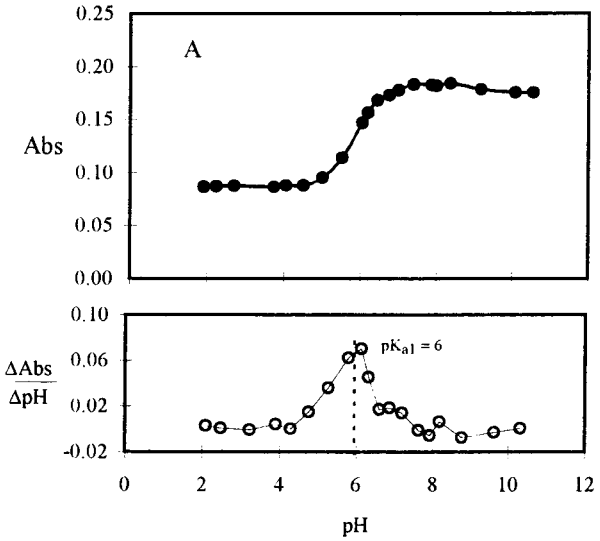

Figure 4—pH–absorbance profile of Col-3 at 286 nm (A) and the first derivative of absorbance respective to pH (B).

In this investigation, absorptions between 275 and 300 nm of the first band and between 370 and 390 nm of the second band were chosen as the analytical wavelengths for determining the first and the second pK_a values, respectively. These two wavelength intervals were chosen due to their maximum absorbance changes with pH.

The absorbance–pH curve of Col-3 at 286 nm is shown in Figure 4. The profile shows that the absorbance of the drug increases in the pH range of 4.0 to 7.0 and is constant below pH 4 and above pH 7.0. At this wavelength, the absorbance of the ionized species is higher than that of the un-ionized species, while the mono- and divalent species cannot be differentiated. The first pK_a of Col-3 was calculated at 275–300 nm using:

$$pK_a = pH + \log \frac{A_i - A}{A - A_u} \quad (1)$$

where A_i and A_u are the absorbance of the ionized and the un-ionized species, respectively. The results are shown in Table 2. The calculated pK_{a1} (5.64) is approximately equal to the pK_a determined using the derivative graph shown in Figure 4B.

Similarly, the second pK_a was calculated using the absorbance changes at 370–390 nm over the pH range of 7.39 to 8.37. At these wavelengths, the absorbance of divalent species is higher than that of the monovalent species, while the un-ionized and monovalent species cannot be differentiated. Thus, eq 1 can be used to calculate the second pK_a. The results are shown in Table 2. Both methods eq 1 and derivative graph were used to determine

Table 2—Spectroscophotometric Determined pK_a Values of Col-3 at Several Wavelengths and pH Values

	pK_{a1} at λ										pK_{a2} at λ								
pH	275	280	281	282	284	286	288	290	295	300	370	374	376	378	380	382	384	386	390
5.53	5.84	5.75	5.75	5.76	5.73	5.74	5.72	5.71	5.74	5.77									
6.06	5.69	5.74	5.73	5.71	5.71	5.72	5.73	5.74	5.73	5.76									
6.20	5.63	5.69	5.66	5.71	5.68	5.69	5.71	5.70	5.68	5.60									
6.45	6.04	6.00	5.93	5.98	5.94	5.94	5.93	5.92	5.98	6.06									
6.75	5.12	5.54	5.48	5.51	5.53	5.60	5.60	5.60	5.39	4.90									
7.39											8.26	8.24	8.23	8.23	8.23	8.23	8.24	8.24	8.24
7.86											8.35	8.35	8.35	8.35	8.35	8.35	8.35	8.36	8.36
8.00											8.42	8.41	8.41	8.41	8.42	8.42	8.42	8.42	8.42
8.37											8.39	8.39	8.40	8.39	8.40	8.39	8.39	8.39	8.39
	average pK_{a1} = 5.64 ± 0.17										average pK_{a2} = 8.35 ± 0.07								

the second pK_a as previously. The calculated value of 8.35 is again in good agreement with the value determined from the derivative graph.

From the results, the spectroscopically determined pK_a values of Col-3 are 5.64 (pK_{a1}) and 8.35 (pK_{a2}). Notice that its second pK_a value which corresponds to the loss of a proton from the phenolic diketone moiety is closed to those of the tetracyclines (∼7.8). However, the first pK_a value, which is due to the loss of a proton from the tricarbonyl methane system, is shown to be over two pH units higher than that those of the tetracyclines (∼3.3). This difference is due to the absence of the electron-withdrawing dimethylammonium group at the C-4. A similar increase of the pK_a value of this system due to the absence of the dimethylammonium group is found in desdedimethylaminotetracycline, which has a pK_a value of 5.94. In addition to the above methods, the computer program SQUAD (Stability QUotients from Absorbance Data) was used to confirm Col-3 pK_a values.[8] SQUAD calculates overall stability constant values such as pK_a values by means of a nonlinear least-squares approach. The data fed to SQUAD are absorption spectra, Col-3 total concentration, and a chemical model to describe the system (i.e., $H_2A \rightarrow HA^- + H^+ \rightarrow A^{2-} + 2H^+$). The p$K_a$ values obtained by SQUAD were pK_{a1} 5.63 ± 0.14 and pK_{a2} 8.39 ± 0.04. Note that the manually calculated (Table 2) and computer caluculated (SQUAD) pK_a values are in good agreement.

4. Conclusions

The macroscopic acid dissociation constants of Col-3 were determined by means of a spectrophotometric technique. The apparent pK_a values of Col-3 in 0.5% methanol aqueous media at approximately 25 °C with a constant ionic strength of 0.2 were calculated manually and graphically to be 5.64 ± 0.17 (pK_{a1}) and 8.35 ± 0.07 (pK_{a2}). The SQUAD calculated vales were pK_{a1} 5.63 ± 0.14 and pK_{a2} 8.39 ± 0.04. These results are in agreement with the tetracycline-like structure of Col-3.

References and Notes

1. Martin, A. R. Antibiotics In *Wilson and Gisvold's Textbook of Organic Medicinal and Pharmaceutical Chemistry*, 9th ed.; Delgado, J. N., Remers, W. A., Eds.; J. B. Lippincott Company: Philadelphia, 1991; pp 282−292.
2. Rigler, N. E.; Bag, S. P.; Leyden, E.; Sudmeier, J. L.; Reilley, C. N. Determination of Protonation Scheme of Tetracycline Using Nuclear Magnetic Resonance *Anal. Chem.* **1965**, *37*, 872−875.
3. Stephens, C. R.; Murai, K.; Brunings, K. J.; Woodward, R. B. Acidity Constants of the Tetracycline Antibiotics *J. Am. Chem. Soc.* **1956**, *78*, 4155−4158.
4. Ali, S. L. Tetracycline Hydrochloride *Anal. Profile Drug Subst.* **1984**, *13*, 597−652.
5. McCormick, J. R. D.; Fox, S. M.; Smith, L. L.; Bitler, B. A.; Reichenthal, J.; Origoni, V. E.; Muller, W. H.; Wimterbottom, R.; Doerschuk, A. P. Studies of the Reversible Epimerization Occurring in the Tetracycline Family: The Preparation, Properties, and Proof of Structure of Some 4-Epi-tetracyclines *J. Am. Chem. Soc.* **1957**, *79*, 2849−2858.
6. Regna, P. P.; Solomons, I. A.; Murai, K.; Timreck, E.; Bruning K. J.; Lazier, W. A. The Isolation and General Properties of Terramycin and Tetramycin Salts *J. Am. Chem. Soc.* **1951**, *73*, 4212−4215.
7. Sterphens, C. R.; Conover, L. H.; Pasternack, R.; Hochstein, F. A.; Moreland, W. T.; Regna, P. P.; Pilgrim, F. J.; Brunings, K. J.; Woodward, R. B. The Structure of Aureomycin *J. Am. Chem. Soc.* **1954**, *76*, 3568−3575.
8. Legget, D. J.; McBryde, W. A. E. General Computer Program for the Computation of Stability Constants from Absorbance Data. *Anal. Chem.* **1975**, *47*, 1065−1070.

Acknowledgments

This work was performed in part under NCI contract no. CM-77109. We thank the CONACYT and the UNAM of México. Also, the work of Dr. Alberto Rojas-Hernández and Ms. Mi Jin Kim is appreciated.

JS980398L

Analysis Program Based on Finite Element Method, MULTI(FEM), for Evaluation of Dose-Dependent Local Disposition of Drug in Liver

KAZUYA FUKUMURA, KIYOSHI YAMAOKA,* MITSUO HIGASHIMORI, AND TERUMICHI NAKAGAWA

Contribution from *Graduate School of Pharmaceutical Science, Kyoto University, Sakyo-ku, Kyoto 606-8501, Japan.*

Received September 17, 1998. Final revised manuscript received January 27, 1999.
Accepted for publication February 22, 1999.

Abstract □ A curve-fitting program based on the Finite Element Method, MULTI(FEM), was developed to model nonlinear local disposition of a drug in the liver under non-steady-state conditions. The program was written in FORTRAN on an IBM-compatible personal computer. The validity of MULTI(FEM) was confirmed by analyzing the outflow kinetics of oxacillin (a model drug) following a pulse input to isolated, perfused rat livers, according to both linear and nonlinear dispersion models. Four dose levels (300, 1000, 3000, and 5000 μg) of oxacillin were administered to observe the dose-dependency in the hepatic local disposition. First, the individual outflow time-profiles at the same dose were averaged, and the average time-profile was analyzed by MULTI(FEM) based on linear dispersion models to yield a single curve fit. The fitted parameters at each dose level were compared with parameters estimated using MULTI(FILT), a program based on fast inverse Laplace transform, to analyze linear pharmacokinetics. The estimated parameters by MULTI(FEM) were in good agreement with those by MULTI(FILT). The apparent elimination rate constant (k_e) decreased with an increase in dose, whereas other parameters showed no discernible dependency on an increase of dose. Second, the average outflow time-profiles at the four dose levels were simultaneously analyzed by MULTI(FEM) based on dispersion models featuring Michaelis–Menten elimination. The outflow time-profiles of oxacillin were well approximated by a two-compartment dispersion model with central Michaelis–Menten elimination. The maximum elimination rate constant (V_{max}) and the Michaelis constant (K_m) were estimated to be 1520 μg/mL/min and 41.3 μg/mL, respectively. Thus, the capability of MULTI(FEM) was demonstrated in evaluating capacity-limited local disposition in the liver.

Introduction

The liver is an essential organ for the metabolism and elimination of drugs. After oral administration, a drug absorbed into the portal system may be eliminated to a large extent during its first pass through the liver. Thus, the liver shields the body from the excess inflow of xenobiotics into the systemic circulation. However, hepatic clearance can exhibit capacity-limited kinetics. Therefore, when the portal drug concentration is extremely high and/or metabolic function is compromised by a hepatic malfunction or drug−drug interaction, a greater fraction of the absorbed dose escapes into the systemic circulation, bypassing first-pass hepatic elimination. Thus, the evaluation of capacity-limited (nonlinear) disposition in the liver is crucial for understanding the influence of dose and absorption kinetics on drugs which undergo significant first-pass metabolism.

In situ liver perfusion experiments following infusion or bolus injection have often been used to assess hepatic local disposition of drugs in vivo. The time-profile of drug outflow from the liver following a pulse input is more informative of intrahepatic disposition than data obtained at steady state. The well-stirred and parallel-tube models offer straightforward analysis of steady-state kinetic data from perfusion experiments.[1−6] In contrast, the dispersion model[5−11] and the distribution model[5,6,12−15] have been developed to explain the outflow time-profile following a pulse input. The dispersion model equations with flexible initial and boundary conditions can explain a variety of outflow drug kinetics at non-steady-state.[7,9] A local disposition model that features several linear dispersion processes has been proposed to analyze the distribution of a drug in the perfused rat hindlimb.[16] However, the dispersion model equations, which are second-order partial differential equations, are difficult to solve analytically. Linear mass-balance rate equations can readily be solved by the Laplace transform. MULTI(FILT)[9−11,18] is one well-recognized computer program for curve-fitting that is based on the transformed equations. However, no analysis program is available to quantitatively evaluate dose-dependent, non-steady-state, local disposition kinetics which are expressed by nonlinear partial differential equations.

Thus, the purpose of the present investigation is to develop a new curve-fitting program, MULTI(FEM), based on the Finite Element Method which has been used in structural[19,20] and hydrodynamic analyses.[21−23] MULTI(FEM) enables the use of local disposition models described by nonlinear partial differential equations with dispersion terms. To confirm the validity of MULTI(FEM), a rat liver perfusion experiment was performed at several dose levels of oxacillin to represent a typical local disposition system of a drug. First, linear dispersion models were adopted in the fitting of data at each dose level, and the estimated parameters were compared with those by MULTI(FILT). Second, outflow time-profiles at the different doses (300, 1000, 3000, and 5000 μg), which were confirmed to exhibit dose-dependent (nonlinear) kinetics, were simultaneously analyzed by MULTI(FEM) based on dispersion models with Michaelis−Menten elimination.[24]

Theory

Five dispersion models (two linear and three nonlinear) were considered. The linear dispersion models involve one-compartment model and two-compartment models with either central and peripheral elimination. However, it is known that the linear two-compartment models, unlike nonlinear models, are not kinetically distinct, because the parameters in the two-compartment model with central elimination are convertible (mapable) to those with peripheral elimination.[9] Thus, the only central elimination process is adopted in our analysis of the linear two-compartment dispersion model. In contrast, the nonlinear two-compartment model with central elimination is kineti-

* Corresponding author. Tel: +81-(0)75−753−4531. Fax: +81-(0)-75-753-4578. E-mail: yamaoka@pharm.kyoto-u.ac.jp.

10.1021/js9803757 CCC: $18.00
Published on Web 04/02/1999

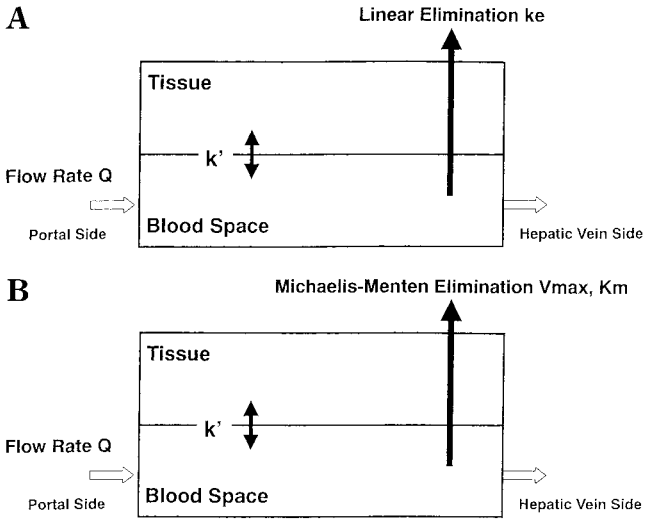

Figure 1—One-compartment dispersion model with linear elimination (A) and nonlinear elimination (B).

cally distinguishable from that with peripheral elimination. Therefore, the one-compartment model with Michaelis–Menten elimination and two-compartment models with central and peripheral Michaelis–Menten elimination were considered as the nonlinear dispersion models.

One-Compartment Dispersion Model—In the one-compartment dispersion model, complete mixing between perfusate and hepatic tissues is assumed as shown in Figure 1A. The equation of this model with linear elimination is described by

$$(1 + k')\frac{\partial C(t,v)}{\partial t} = D_c\frac{\partial^2 C(t,v)}{\partial v^2} - Q\frac{\partial C(t,v)}{\partial v} - k_e C(t,v) \quad (1)$$

where C(t,v) is the perfusate concentration in the liver, Q is the perfusate flow rate, k' is the partition ratio which is the measure of extent of drug partition into the hepatic tissue, D_c is the corrected dispersion coefficient, v is the volume axis, and k_e is the first-order elimination rate constant.

For a pulse input, eq 1 can be solved by Laplace transform under the initial and boundary conditions given by eq 2. The image equation is given by eq 3.[9]

$$C(0,v) = 0, \quad C(t,0) = \frac{M}{Q}\delta(t) \quad \text{and} \quad C(t,\infty) = 0 \quad (2)$$

$$\tilde{C}(s) = \frac{M}{Q}\exp\left[\left\{\frac{Q}{2D_c} - \sqrt{\left(\frac{Q}{2D_c}\right)^2 + \frac{k_e + (1 + k')s}{D_c}}\right\}V_B\right] \quad (3)$$

where V_B is the blood volume which was assumed to be 15.5% of liver weight.[25,26]

If the drug is eliminated according to Michaelis–Menten equation as shown in Figure 1B, the one-compartment dispersion model is described by

$$(1 + k')\frac{\partial C(t,v)}{\partial t} = Dc\frac{\partial^2 C(t,v)}{\partial v^2} - Q\frac{\partial C(t,v)}{\partial v} - \frac{V_{max}}{K_m + C(t,v)}C(t,v) \quad (4)$$

where V_{max} is the maximal elimination rate, and K_m is the Michaelis constant. It is noted here that V_{max} and K_m are the lumped parameters which reflect the transfer of a drug from the sinusoid to the tissue space, the uptake into hepatocytes by active transport, and the enzymatic activity in hepatocytes.

Two-Compartment Dispersion Model—A two-compartment dispersion model with linear elimination from central compartment, as shown in Figure 2A, is described by eq 5. The equilibrium distribution phase, which is kinetically included in the central compartment of the liver, was predicted in the previous paper using BOF-4272, a drug for treatment of hyperuricemia.[26]

$$\begin{cases} \dfrac{\partial C_1(t,v)}{\partial t} = Dc\dfrac{\partial^2 C_1(t,v)}{\partial v^2} - Q\dfrac{\partial C_1(t,v)}{\partial v} - \\ \qquad k_{12}C_1(t,v) + \epsilon k_{21}C_2(t,v) - keC_1(t,v) \\ \dfrac{\partial C_2(t,v)}{\partial t} = \dfrac{1}{\epsilon}k_{12}C_1(t,v) - k_{21}C_2(t,v) \end{cases} \quad (5)$$

where C_1(t,v) and C_2(t,v) are the concentrations in the central and peripheral compartments, respectively, k_{12} and k_{21} are the forward and backward transfer rate constants between central and peripheral compartments, ϵ is the volume ratio of peripheral compartment to central compartment, and k_e is the first-order elimination rate constant. Under the initial and boundary conditions given by eq 6 for a pulse input of drug, the image equation for the central compartment is described by eq 7.[9]

$$C_1(0,v) = 0, \quad C_2(0,v) = 0, \quad C_1(t,0) = \frac{M}{Q}\delta(t), \quad C_1(t,\infty) = 0 \quad \text{and} \quad C_2(t,0) = 0 \quad (6)$$

$$\tilde{C}(s) = \frac{M}{Q}\exp\left[\left\{\frac{Q}{2Dc} - \sqrt{\left(\frac{Q}{2Dc}\right)^2 + \frac{1}{Dc}\left(s + k_{12} + k_e - \frac{k_{12}k_{21}}{s + k_{21}}\right)}\right\}V_B\right] \quad (7)$$

where V_B is the volume of central compartment. It is noted that the volume ratio ϵ disappears in eq 7.

A two-compartment dispersion model with central Michaelis–Menten elimination (Figure 2B) is described by eq 8.

$$\begin{cases} \dfrac{\partial C_1(t,v)}{\partial t} = Dc\dfrac{\partial^2 C_1(t,v)}{\partial v^2} - Q\dfrac{\partial C_1(t,v)}{\partial v} - \\ \qquad k_{12}C_1(t,v) + \epsilon k_{21}C_2(t,v) - \dfrac{V_{max}}{K_m + C_1(t,v)}C_1(t,v) \\ \dfrac{\partial C_2(t,v)}{\partial t} = \dfrac{1}{\epsilon}k_{12}C_1(t,v) - k_{21}C_2(t,v) \end{cases} \quad (8)$$

A two-compartment dispersion model with peripheral Michaelis–Menten elimination (Figure 2C) is described by eq 9.

$$\begin{cases} \dfrac{\partial C_1(t,v)}{\partial t} = Dc\dfrac{\partial^2 C_1(t,v)}{\partial v^2} - Q\dfrac{\partial C_1(t,v)}{\partial v} - \\ \qquad k_{12}C_1(t,v) + \epsilon k_{21}C_2(t,v) \\ \dfrac{\partial C_2(t,v)}{\partial t} = \dfrac{1}{\epsilon}k_{12}C_1(t,v) - k_{21}C_2(t,v) - \\ \qquad \dfrac{V_{max}C(t,v)}{K_m + C_2(t,v)} \end{cases} \quad (9)$$

Although eqs 4, 8, and 9 are not solvable by Laplace transform, a numerical solution can be achieved with MULTI(FEM).

Danckwerts's condition[27] given by eq 10 is adopted as the boundary condition in MULTI(FEM), because it is easily programmed in MULTI(FEM).

$$Dc\left(\frac{\partial C(t,v)}{\delta v}\right)_{v=0} = QC(t,0) \quad \text{and} \quad Dc\left(\frac{\partial c(t,v)}{\partial v}\right)_{v=V_B} = 0 \tag{10}$$

Numerical Procedure

MULTI(FEM) written in Microsoft FORTRAN (ver. 3.2) was newly developed on a IBM-compatible personal computer (PentiumII, 266 MHz and 96 MB). Equations 3 and 7, which are given as Laplace-transformed equations, were numerically solved by fast inverse Laplace transform (FILT).[9−11] Equations 1 and 5, which are given as linear partial differential equations, were numerically solved by MULTI(FEM). The outflow time-profiles following the same dose of oxacillin (300, 1000, 3000, or 5000 μg) were averaged, and the average time-profile at each dose was fitted by MULTI(FILT) and MULTI(FEM) based on the linear dispersion model. Equations 4, 8, and 9, which are given as nonlinear partial differential equations, were fitted by MULTI(FEM) simultaneously to all four average time-profiles at the different doses.

Ten sets of outflow time courses at the four dose levels were generated by adding 10% random normal errors to theoretical curves calculated from parameter values estimated by MULTI(FEM). The generated time courses were fitted by MULTI(FEM), and the estimated parameters were compared with the original parameters to verify the stability of MULTI(FEM).

Materials and Methods

Chemicals—Oxacillin was purchased from Sigma Chemical Co. (St. Louis, MO). Sodium pentobarbital solution (NEMBUTAL forcanimal injection, Abbott Laboratories, Chicago, IL) was used to anesthetize the rats. All other reagents used for preparing the perfusate and HPLC mobile phase were of guaranteed reagents grade or HPLC grade.

Animals—Male Wistar rats weighing 200−240 g were purchased from Shimizu Experimental Materials Co. (Kyoto, Japan). All rats were maintained on standard rat chow, and water was allowed ad libitum before the experiments.

Single-Pass Perfusion Experiment Using Rat Liver—Isolated rat livers were prepared and perfused according to the Mortimore method[28] using Krebs-Ringer bicarbonate buffer (pH 7.4) containing 10 mM glucose and saturated with 95% O_2−5% CO_2. The bile duct was cannulated with a polyethylene tube (PE10). The perfusate was maintained at 37 °C and delivered by a roller pump (RP-NP2, Furue Science Co., Ltd., Tokyo, Japan) through a polyethylene cannula (1.67 mm o.d.) placed in the portal vein. The perfusate flow rate was 14.6−15.6 mL/min, and the recoveries of perfusate were greater than 99%. The bile flow rate was measured to monitor the viability of the liver. The liver perfusion data were rejected when the bile flow rate was less than 4 μL/min. At 20 min after the operation, a 250 μL volume of oxacillin in saline solution (1.2 mg/mL, $n = 3$; 4.0 mg/mL, $n = 3$; 12.0 mg/mL, $n = 2$; 20 mg/mL, $n = 3$) was injected into the liver using a six-way valve injector. The outflow sample was collected at intervals of 1 s. After the perfusate collection, the validity of the perfusion experiment was confirmed by uniform coloration and decoloration of the liver after injection of Evans Blue. The lag time was calculated from the total void volume (half volume of the injector tube plus full volume of the catheter) divided by the perfusate flow rate, and was subtracted from sampling times. The liver weights were 8.66−12.0 g.

Analytical Procedure—The perfusate sample (0.2 mL) was diluted up to 10-fold with blank perfusate, when oxacillin concentration was too high. Acetonitrile (0.3 mL) was added to the sample (0.2 mL) to precipitate proteins, and an aliquot of the supernatant (15 μL) obtained by centrifugation at 2000 rpm was injected into HPLC. An HPLC system (LC-10A series, Shimadzu Company, Kyoto, Japan) was equipped with the Chemcosorb 5-ODS−H reversed-phase column (5 μm, 150 × 4.6 mm i.d., Chemco Scientific Company, Ltd., Osaka, Japan). The HPLC conditions described by Yano et al.[9] were modified as follows. The mobile phase consisted of a 1:1 (v/v) mixture of 100 mM sodium acetate buffer (pH5.2)/methanol. Mobile phase flow rate, detection wavelength, and column temperature were 1.0 mL/min, 220 nm, and 40 °C, respectively. The peak area was recorded on Chromatopack C-R6A (Shimadzu Company). A linear calibration plot was made over the oxacillin concentration range of 1.0−300 μg/mL, according to the method of the variance-stabilizing transformation.[29] Accuracy and precision were within 10% at all concentrations.

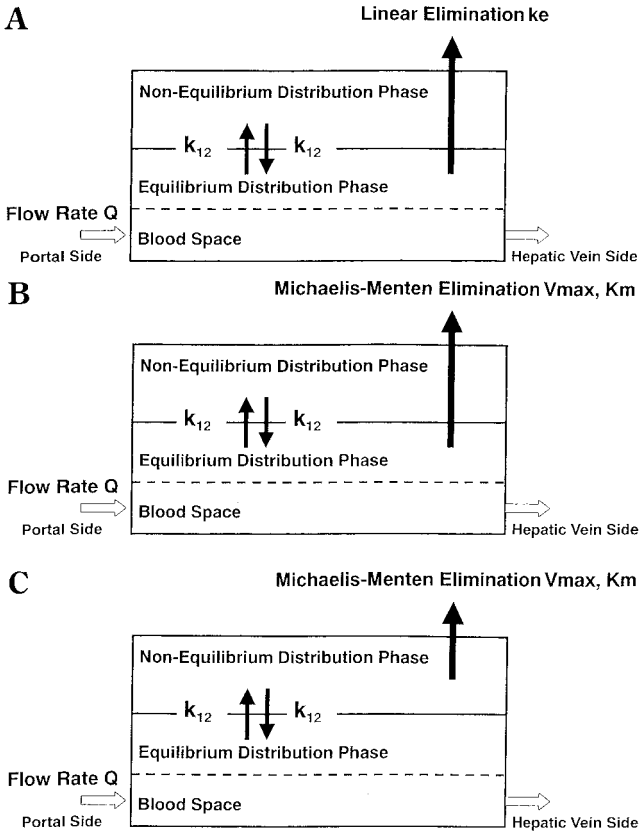

Figure 2—Two-compartment dispersion model with linear elimination (A), with central Michaelis–Menten elimination (B), and with peripheral Michaelis–Menten elimination (C).

Results and Discussion

Figure 3 presents the average outflow time-profiles and the predicted time courses by MULTI(FILT) and MULTI(FEM) based on a two-compartment dispersion model with linear elimination. Table 1 shows the parameter estimates. The curve fittings based on the one-compartment dispersion model gave much larger Akaike's Information Criterion (AIC)[30] values than those based on the two-compartment model and were deemed unacceptable. The predicted time courses by MULTI(FILT) and MULTI(FEM) agreed well with the experimental data points. The pharmacokinetic parameters by MULTI(FEM) coincided well with those by MULTI(FILT), which demonstrates the validity of MULTI(FEM). It is noted in Table 1 that k_e increases with a decrease in dose from 5000 to 300 μg, whereas other parameters show no systematic change with dose. Thus, this suggested that the average outflow time-profiles at the four dose levels would be better described by a dispersion model with capacity-limited elimination.

Figure 4 shows the outflow time profiles of oxacillin and the curves predicted by MULTI(FEM) fit to the two-

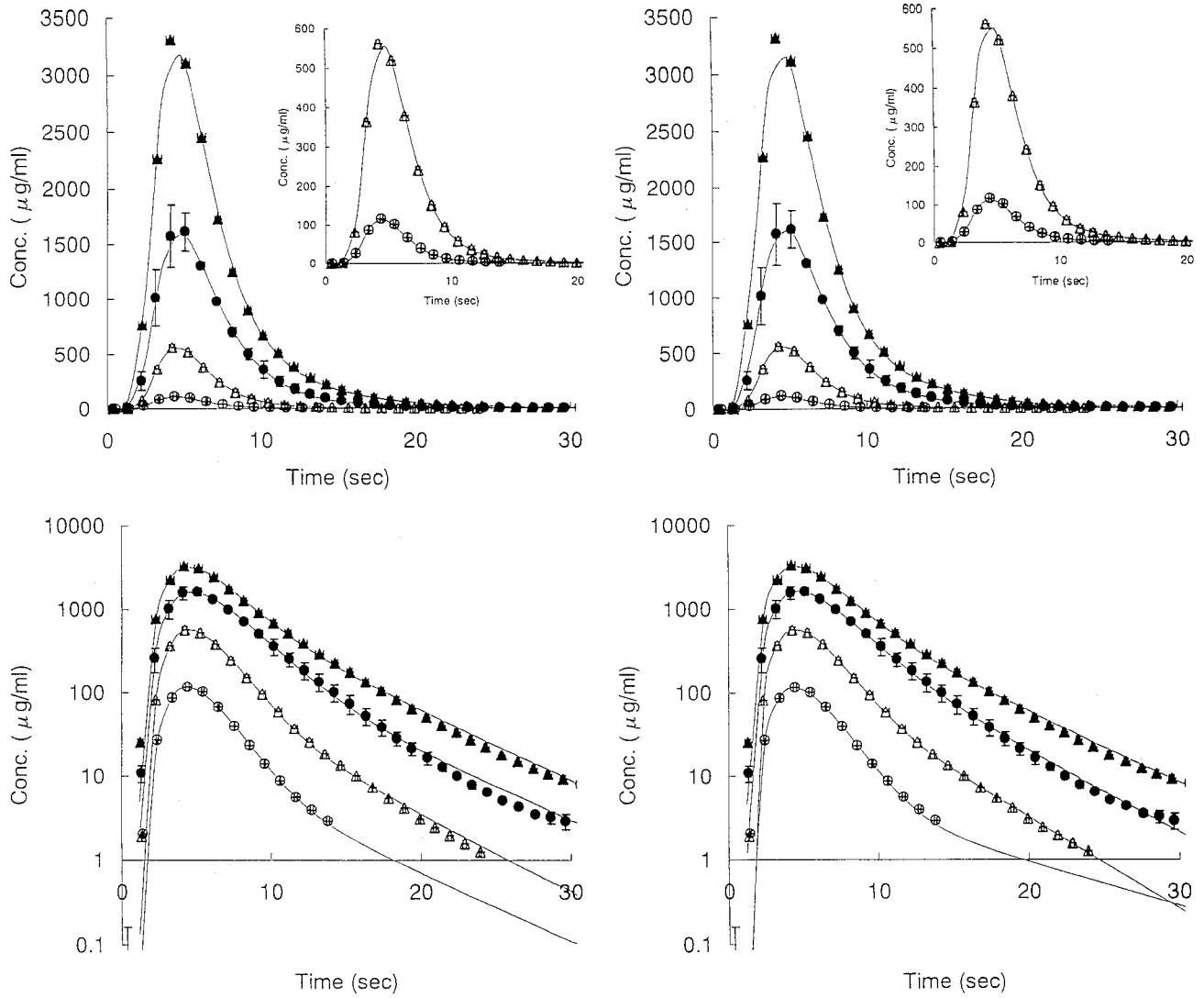

Figure 3—Outflow time-profiles averaged at 300 μg (○, $n = 3$), 1000 μg (△, $n = 3$), 3000 μg (●, $n = 2$) and 5000 μg (▲, $n = 3$) doses of oxacillin and theoretical curves predicted by MULTI(FILT) (left) and MULTI(FEM) (right). The time-profiles are given by means and standard deviations in two-compartment dispersion model with linear elimination. The bottom figures and the inserts at the top show the semilogarithmic and the expanded plots, respectively.

Table 1—Kinetics Parameters of Oxacillin Calculated Using MULTI(FILT) and MULTI(FEM) in Two-Compartment Dispersion Model with Linear Elimination

	dose (μg)			
	5000	3000	1000	300
	MULTI(FILT)			
D_c (mL^2/min)	1.93	2.37	1.63	1.71
V_B (ml)	1.46	1.63	1.49	1.51
k_{12} (min^{-1})	2.19	0.929	1.19	1.02
k_{21} (min^{-1})	13.4	11.7	13.8	11.7
k' (= k_{12}/k_{21})	0.163	0.0796	0.0856	0.0871
k_e (min^{-1})	1.01	2.52	4.14	8.80
	MULTI(FEM)			
D_c (mL^2/min)	2.10	2.40	1.68	1.95
V_B (mL)	1.45	1.58	1.47	1.53
k_{12} (min^{-1})	2.31	1.53	1.54	0.881
k_{21} (min^{-1})	13.9	15.2	16.4	7.44
k' (= k_{12}/k_{21})	0.167	0.101	0.0942	0.118
k_e (min^{-1})	1.05	2.58	4.24	8.65

compartment dispersion models with Michaelis–Menten elimination from the central compartment and from the peripheral compartment. The local disposition parameters estimated from curve-fittings are shown in Table 2. Because AIC assumed a smaller value for the central elimination model (AIC = 854) than for the peripheral elimination model (AIC = 996), the two-compartment dispersion model with central capacity-limited elimination was considered to better represent the outflow time-profiles of oxacillin. The maximum elimination rate constant (V_{max}) and the Michaelis constant (K_m) were estimated to be 1520 μg/mL/min and 41.3 μg/mL, respectively. Since the AIC based on the nonlinear one-compartment model was much larger than those based on two-compartment models, the results were not presented. To verify the stability of MULTI(FEM) fits, 10 sets of outflow time courses at four dose levels were generated by adding 10% random normal errors to theoretical curves calculated using mean parameter estimates from the earlier data fitting. The generated time courses were fitted by MULTI(FEM). The parameter values from the fit of noise-added data (D_c: 2.20 ± 0.18 mL^2/min, V_B: 1.50 ± 0.02 mL, k_{12}: 3.45 ± 0.21min^{-1}, k_{21}: 10.8 ± 0.49min^{-1}, k′: 0.319 ± 0.026, V_{max}: 1520 ± 120 μg/mL/min and K_m: 41.5 ± 6.8 μg/mL) were in good agreement with the original parameter estimates (D_c: 2.14 mL^2/min, V_B: 1.49 mL, k_{12}: 3.45 min^{-1}, k_{21}: 10.7 min^{-1}, k': 0.322, V_{max}: 1520 μg/mL/min and K_m: 41.3 μg/mL), respectively.

In conclusion, dose-dependency kinetics in local organ disposition kinetics at steady state[2,3] has been well-

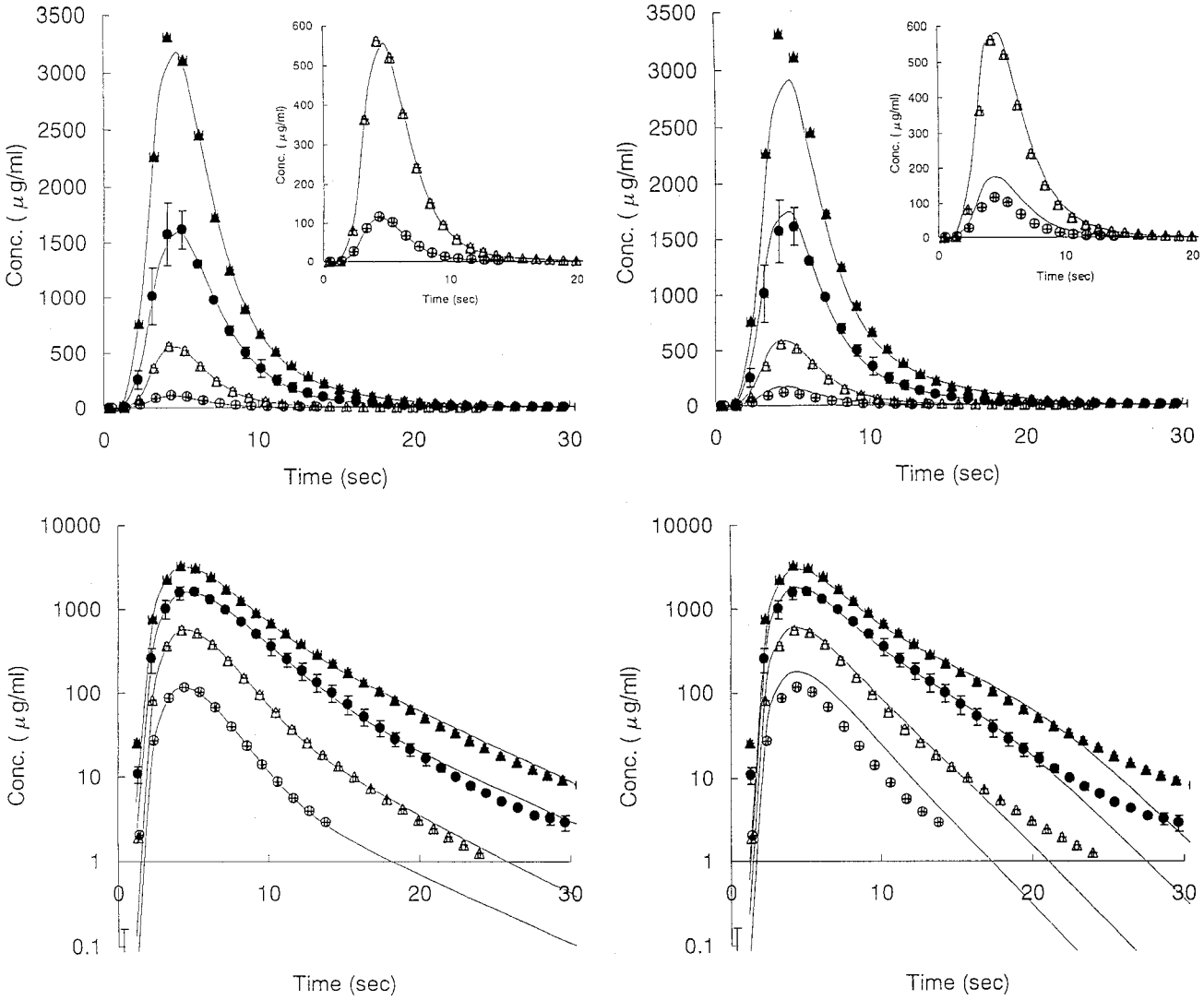

Figure 4—Outflow time-profiles of oxacillin (300 μg (○, $n = 3$), 1000 μg (○, $n = 3$), 3000 μg (●, $n = 2$), 5000 μg (▲, $n = 3$)) and theoretical curves predicted by MULTI(FEM) based on two-compartment dispersion models with Michaelis–Menten elimination from central compartment (left) and from peripheral compartment (right). The time-profiles are given by means and standard deviations. The bottom figures and the inserts at the top show the semilogarithmic and the expanded plots, respectively.

Table 2—Kinetics Parameters of Oxacillin Calculated Using MULTI(FEM) in Two-Compartment Dispersion Model with Central and Peripheral Michaelis–Menten Elimination

	central	peripheral
D_c (mL^2/min)	2.14	1.84
V_B (mL)	1.49	1.45
k_{12} (min^{-1})	3.45	4.93
k_{21} (min^{-1})	10.7	7.45
k' (= k_{12}/k_{21})	0.322	0.662
V_{max} (μg/mL/min)	1520	4250
K_m (μg/mL)	41.3	200
AIC	854	996

characterized, but investigations of the disposition under transient or non-steady-state conditions have been scarce. MULTI(FEM) enables the evaluation of dose-dependent drug clearance kinetics in the hepatic perfusion system following a pulse input, i.e., to allow detailed description of intrahepatic Michaelis−Menten disposition kinetics in the liver. The present analysis further showed that the central and peripheral elimination models can be distinguished based on perfusate outflow data under the nonlinear condition. With the availability of MULTI(FEM), the dispersion model may be applicable to analyzing the dose-dependency in other perfused organ experiments, such as those with intestine and kidney.

References and Notes

1. Wilkinson, G. R.; Shand, D. G. A Physiological Approach to Hepatic Drug Clearance. *Clin. Pharmacol. Ther.* **1975**, *18*, 377−390.
2. Ishida, R.; Suzuki, K.; Masubuchi, Y.; Narimatsu, S.; Fujita, S.; Suzuki, T. Enzymatic Basis for the Non-Linearity of Hepatic Elimination of Propranolol in the Isolated Perfused Rat Liver. *Biochem. Pharmacol.* **1992** *44*, 2281−2288.
3. Kukan, M.; Woolf, T. F.; Meluš, M.; Bezek, Š. Characterization of Nonlinear Elimination of the Xanthine-Related Drug Ethimizol in 3-Methylcholanthrene-Induced Rat Liver by the "Parallel-Tube" Model. *Drug Metab. Dispos.* **1993**, *21*, 547−550.
4. Pang, K. S.; Rowland, M. Hepatic Clearance of Drugs. II. Experimental Evidence for Acceptance of the "Well-Stirred" Model over the "Parallel Tube" Model Using Lidocaine in the Perfused Rat Liver in Situ Preparation. *J. Pharmacokin. Biopharm.* **1977**, *5*, 655−680.
5. Roberts, M. S.; Donaldson, J. D.; Rowland, M. Model of Hepatic Elimination: Comparison of Stochastic Models to Describe Residence Time Distributions and to Predict the Influence of Drug Distribution, Enzyme Heterogeneity, and

Systemic Recycling on Hepatic Elimination. *J. Pharmacokin. Biopharm.* **1988**, *17*, 41−83.
6. Saville, B. A.; Gray, M. R.; Tam, Y. K. Models of Hepatic Drug Elimination. *Drug Metab. Reviews* **1992**, *24*, 49−88.
7. Roberts, M. S.; Rowland, M. Hepatic Elimination−Dispersion Model. *J. Pharm. Sci.* **1985**, *74*, 585−587.
8. Roberts, M. S.; Rowland, M. A Dispersion Model of Hepatic Elimination: 1. Formulation of the Model and Bolus Considerations. *J. Pharmacokin. Biopharm.* **1986**, *14*, 227−260.
9. Yano, Y.; Yamaoka, K.; Aoyama, Y.; Tanaka, H. Two-Compartment Dispersion Model for Analysis of Organ Perfusion System of Drugs by Fast Inverse Laplace Transform (FILT). *J. Pharmacokin. Biopharm.* **1989** *17*, 179−202.
10. Yano, Y.; Yamaoka, K.; Minamide, T.; Nakagawa, T.; Tanaka, H. Evaluation of Protein Binding Effect on Local Disposition of Oxacillin in Rat Liver by a Two-Compartment Dispersion Model. *J. Pharm. Pharmacol.* **1990** *42*, 632−636.
11. Yano, Y.; Yamaoka, K.; Yasui H.; Nakagawa, T. Effect of Perfusion Rate on the Local Disposition of Cefixime in Liver Perfusion System Based on Two-Compartment Dispersion Model. *Drug Metab. Dispos.* **1991**, *19*, 1022−1027.
12. Goresky, C. A.; Bach, G. G.; Nadeau, B. E. On the Uptake of Materials by the Intact Liver. *J. Clin. Invest.* **1973**, *52*, 991−1009.
13. Tsao, S. C.; Sugiyama, Y.; Sawada, Y.; Nagase, S.; Iga, T.; Hanano, M. Effect of Albumin on Hepatic Uptake of Warfarin in Normal and Analbuminemic Mutant Rats: Analysis by Multiple Indicator Dilution Method. *J. Pharmacokin. Biopharm.* **1986**, *14*, 51−64.
14. Miyauchi, S.; Sugiyama, Y.; Sawada, Y.; Morita, K.; Iga, T.; Hanano, M. Kinetics of Hepatic Transport of 4-Methylumbelliferone in Rats. Analysis by Multiple Indicator Dilution Method. *J. Pharmacokin. Biopharm.* **1987**, *15*, 25−38.
15. Tsao, S. C.; Sugiyama, Y.; Sawada, Y.; Iga, T.; Hanano, M. Kinetic Analysis of Albumin-Mediated Uptake of Warfarin by Perfused Rat Liver. *J. Pharmacokin. Biopharm.* **1988**, *16*, 165−181.
16. Oliver, R. E.; Heatherring, A. C.; Janes, A. F.; Rowland, M. A Physiologically Based Pharmacokinetic Model Incorporating Dispersion Principles to Describe Solute Distribution in the Perfused Rat Hindlimb Preparation. *J. Pharmacol. Biopharm.* **1997**, *25*, 389−412.
17. Sato, H.; Sugiyama, Y.; Sawada, Y.; Iga, T.; Sakamoto, S.; Fuwa, T.; Hanano, M. Dynamic Determination of Kinetic Parameters for the Interaction between Polypeptide Hormones and Cell-Surface Receptors in the Perfusate Rat Liver by the Multiple-Indicator Dilution Method. *Proc. Natl. Acad. Sci. U.S.A.* **1988**, *85*, 8355−8359.
18. Yano, Y.; Yamaoka, K.; Tanaka, H. A Nonlinear Least Squares Program, MULTI(FILT), Based on Fast Inverse Laplace Transform for Microcomputers. *Chem. Pharm. Bull.* **1989**, *37*, 1035−1038.
19. Turner, M. J.; Clough, R. W.; Martin, H. C.; Topp, L. J. Stiffness and Deflection Analysis of Complex Structures. *J. Aeronaut. Sci.* **1956**, *23*, 805−823.
20. McMeeking, R. M.; Rice, J. R. Finite Element Formulations for Problems of Large Elastic-Plastic Deformation. *Int. J. Solids Struct.* **1975**, *11*, 601−616.
21. Hughes, T. J. R.; Liu, W. K.; Brooks, A. Finite Element Analysis of Incompressible Viscous Flows by the Penalty Function Formulation. *J. Comput. Phys.* **1979**, *30*, 1−60.
22. Gresho, P. M.; Chan, S. T.; Lee, R. T.; Upson, C. D. A Modified Finite Element Method for Solving the Time-Dependent, Incompressible Navier−Stokes Equations. Part 1: Theory and Part 2: Applications. *Int. J. Numer. Methods Fluids* **1984**, *4*, 557−598, 619−640.
23. Baker A. J.; Pepper D. W. *Finite Elements 123*; McGraw-Hill: New York, 1991.
24. Michaelis, L.; Menten, M. L. Die Kinetik der Invertinwirkung. *Biochem. Z.* **1913**, *49*, 333−369.
25. Blouin, A.; Bolender, R. P.; Welbel, E. R. Distribution of Organelles and Membranes between Hepatocytes and Nonhepatocytes in The Rat Liver Parenchyma. A Stereological Study. *J. Cell Biol.* **1977**, *72*, 441−455.
26. Nishimura, M.; Yamaoka, K.; Naito, S.; Nakagawa, T. Effect of Temperature in Perfusate on Local Hepatic Disposition of BOF-4272, a New Xanthine Oxidase Inhibitor. *Biol. Pharm. Bull.* **1996**, *19*, 1197−1202.
27. Danckwerts, P. V. Continuous Flow Systems Distribution and Residence Time. *Chem. Eng. Sci.* **1953**, *2*, 1−13.
28. Mortimore, G. E.; Tietze, F.; Stetten, D., Jr. Metabolism of Insulin-I^{131} Studies in Isolated, Perfused Rat Liver and Hindlimb Preparations. *Diabetes* **1959**, *8*, 307−314.
29. McLean, A. M.; Ruggirello, D. A.; Banfield, C.; Gonzalez, M. A.; Bialer, M. Application of a Variance-Stabilizing Transformation Approach to Linear Regression of Calibration Lines. *J. Pharm. Sci.* **1990**, *79*, 1005−1008.
30. Yamaoka, K.; Nakagawa, T.; Uno, T. Application of Akaike's Information Criterion (AIC) in the Evaluation of Linear Pharmacokinetic Equations. *J. Pharmacokin. Biopharm.* **1978**, *6*, 165−175.

JS9803757

Synthesis, Stereoselective Enzymatic Hydrolysis, and Skin Permeation of Diastereomeric Propranolol Ester Prodrugs

CHANDRASEKHAR UDATA, GIRIDHAR TIRUCHERAI, AND ASHIM K. MITRA*

Contribution from *Division of Pharmaceutical Sciences, School of Pharmacy, University of Missouri, Kansas City, Missouri 64110-2499.*

Received August 31, 1998. Final revised manuscript received February 9, 1999.
Accepted for publication February 12, 1999.

Abstract □ Four diastereomeric propranolol ester prodrugs (1*S*2*S*, 1*S*2*R*, 1*R*2*S*, 1*R*2*R*) were synthesized by treating pure *R*- and *S*-propranolol hydrochloride with pure enantiomers *R*- and *S*-phenylbutyryl chloride. A HPLC technique using α-1 acid glycoprotein (chiral AGP) column was developed to study the racemization of propranolol enantiomers during synthesis and hydrolysis studies. A reversed phase HPLC method was also developed to simultaneously analyze propranolol and the ester prodrug. Hydrolysis of these esters was studied in different rat tissue homogenates, i.e., liver, intestine, plasma, skin, brain, and pure plasma cholinesterases, i.e., butyryl cholinesterase (EC 3.1.1.8) and acetyl cholinesterase (EC 3.1.1.7). In vitro percutaneous permeation studies across full thickness shaved rat skin were performed using standard side-by-side diffusion cells at 37 °C. The disappearance of the diastereomeric ester prodrugs in rat tissue homogenates followed apparent first-order kinetics and was stereoselective. The ratio of brain to plasma hydrolytic rate constants are 27.8, 5.58, 6.07, and 2.97 for 1*S*2*S*, 1*R*2*R*, 1*R*2*S*, and 1*S*2*R* esters, respectively. Hydrolysis of all four diastereomeric ester prodrugs was faster by acetyl cholinesterase than butyryl cholinesterase and is stereoselective. The permeability coefficients [$K_p \times 10^3$ (cm h^{-1})] are 1.40 ± 0.30, 1.41 ± 0.27, 42.20 ± 1.24, 29.26 ± 3.41, 16.27 ± 3.12, 12.99 ± 2.84 for (*R*)-propranolol, (*S*)-propranolol, 1*S*2*S*, 1*R*2*S*, 1*S*2*R*, and 1*R*2*R* ester prodrugs, respectively. The results indicate that the 1*R*2*S* diastereomeric ester prodrug of propranolol shows greatest stability in liver and intestinal tissues while it exhibits fairly rapid conversion in plasma. The results also suggest the configuration on the second chiral carbon atom to be the determinant in the rate of hydrolysis of all the diastereomeric prodrugs in all biological media examined. The K_p of all four prodrugs markedly increased compared to that of the parent drug, with 1*S*2*S* showing a 30-fold increase in skin permeability, the highest among all four prodrugs.

Introduction

Propranolol (PL), an adrenergic β-blocker, is a widely accepted and clinically effective cardiovascular agent, indicated in the treatment of angina pectoris, hypertension, and cardiac arrhythmia. Very low and variable bioavailability of the drug follows oral administration, which may be attributed to extensive stereoselective hepatic first-pass metabolism.[1−4] Alternative noninvasive administration modes including rectal,[5] transdermal,[6] and nasal[7,8] routes have been explored to improve the systemic bioavailability of propranolol. These routes can allow the drug to reach the systemic circulation, bypassing the liver and escaping first-pass metabolism. Since one of the major metabolites is the *O*-glucuronide of PL,[9] O-acylation of PL may be a potentially useful way to reduce presystemic metabolism, as has already been demonstrated.[10,11]

The transdermal route of administration also allows systemic drug absorption bypassing hepatic first-pass effects, thus achieving higher bioavailability of the drug.[6,12] However, relative impermeability of lipoidal stratum corneum, the outermost keratinized layer of skin, offers considerable resistance to the permeation of PL through the skin. The prodrug approach represents an alternative and promising method of enhancing the skin permeability of drugs by increasing their lipophilicity. Permeability characteristics of individual enantiomers of chiral species in comparison to their racemates have been studied in some detail recently. Wearly et al.[13] reported that the maximum flux of a new antifungal compound from a saturated solution, through human cadaver skin, was 1 order of magnitude lower for the racemic compound than that of either of its enantiomers. Roy et al.[14] compared the permeability of pure enantiomers of keterolac acid, a potent analgesic, through human cadaver skin, and showed that there was no significant difference in the intrinsic permeability coefficients of the racemic compound and the enantiomers. Touitou et al.[15] proposed the Melting Temperature Membrane Transport concept, which showed the simple dependence of permeation flux ratio on the melting behavior of chiral compounds.

Propranolol has two optical isomers, dextro-PL ((*R*)-PL) and levo-PL ((*S*)-PL). The drug shows stereoselective activity, i.e., the S-isomer is 100 times more potent than the R-isomer as a β blocker.[16] A number of studies have demonstrated stereoselective disposition of the drug in various species including man[17] and dog.[18] In addition, Stoschitzky et al.,[19] reported that half the dose of optically pure (*S*)-propranolol generates an equally effective β-adrenergic receptor agonist activity relative to the racemic mixture and that (*R*)-PL inhibits thyroid hormone activity.

Esterases are ubiquitous in nature and have broad substrate specificity. Stereoselective hydrolysis of ester prodrugs including PL prodrugs is largely dependent on the type of species and the tissue of origin.[20−25] Variability in the esterase content may have a significant effect on the rate of regeneration, tissue uptake, and disposition of the prodrug. Thus, consideration of stereoselectivity during prodrug design is very important. The chirality of a compound is critical to receptor-binding interactions: therefore, differences in biological activity are common. Chirality can also effect the way in which molecules fit together in a crystal structure. Diastereomers may differ in crystal structure and may cause differences in melting point and thereby differences in solubilities.[13] Therefore, diastereomeric prodrugs having at least two chiral centers may

* Address for correspondence: Ashim K. Mitra, Professor and Chair, Division of Pharmaceutical Sciences, University of Missouri—Kansas City, 5005 Rockhill Rd., Kansas City, MO 64110. Phone: 816-235-1615. Fax: 816-235-5190. E-mail: amitra@cctr.umkc.edu.

10.1021/js980358h CCC: $18.00
Published on Web 03/31/1999

significantly alter the permeation of the enantiomeric parent drug.

This research article describes the influence of a chiral promoiety on the stereoselective hydrolysis and permeation of *R* and *S* propranolol prodrugs. Specifically the stereoselective hydrolysis and skin permeation of four diastereomeric PL ester prodrugs have been studied. 2-Phenylbutyryl chloride was chosen as a model chiral promoiety for the syntheses of four diastereomeric ester prodrugs of PL, as it offers both chirality and the aromatic group, which would aid in increasing the lipophilicity considerably.

Materials and Methods

Materials—The pure (*R*)- and (*S*)-propranolol hydrochloride, (*R*)- and (*S*)-2-phenylbutyric acids and pure esterases, acetyl cholinesterase (EC 3.1.1.7) and butyryl cholinesterases (EC 3.1.1.8), were obtained from Sigma Chemical Co. (St. Louis, MO). All other reagents were of analytical grade and used as received (Fisher Scientific).

Animals—Male Sprague Dawley rats (250−275 g) were obtained from Harlan Sprague Dawley, Indianapolis, IN. Animals were fasted overnight prior to conducting any experiment. Water was allowed ad libitum.

Synthesis of Acid Chloride—The acid chloride was synthesized by slightly modifying a previously published report.[26] Briefly, pure (*R*) or (*S*)-2-phenylbutyric acid (200 mg) was mixed with thionyl chloride (0.24 mL) (freshly redistilled) at 0 °C and then kept at 70 °C for 30 min. Dry benzene was added, and the mixture was evaporated to dryness. Another portion of dry benzene was then added, and the mixture was reevaporated to remove the last traces of thionyl chloride. The residue was dissolved in 2.4 mL of dry benzene and stored in the refrigerator in a glass-stoppered flask. The new acid chloride bands in the IR spectra appeared at about 1810 cm^{-1} with the concomitant disappearance of hydroxyl bands. The purity of the acid chloride was determined by TLC, HPLC, and ^1H NMR. No significant ($p > 0.05$) difference in the optical activity between the acid {$[\alpha]^{20}_D = -94/+93.8$ ($c = 0.9$, $C_6H_5CH_3$)} and acid chloride {$([\alpha]^{20}_D = -94.8/+94$ ($c = 0.9$, C_6H_5-CH_3)} was noticed for a particular enantiomer.

Synthesis of Propranolol Diastereomeric Ester Prodrugs—The synthetic method is a slight modification of the methods described previously.[27,28] Pure (*R*)- and (*S*)-propranolol HCl (100 mg, 0.34 mmol) was dissolved in chloroform and heated under reflux conditions for 5 h with pure (*S*)- or (*R*)-2-phenylbutyryl chloride (1.36 mmol). Excess acid chloride was removed under high vacuum, and the residue was repeatedly treated with toluene and evaporated to dryness to ensure removal of any remaining acid chloride. The diastereomeric esters were obtained as an oily residue. The ν_{max} at 1810 cm^{-1} in the IR spectrum due to acid chloride disappeared over 3 h and a strong ν_{max} at 1740 cm^{-1} due to O-acylation appeared. The structural identity and purity of the diastereomeric esters were confirmed by IR, ^1H NMR, mass spectrometry, TLC, and HPLC.

Solubility Determination—A normal equilibrium solubility determination was undertaken in 0.01 M acetate buffer (pH 4.0, 25 °C). To 1 mL of buffer, 2−3 mg of hydrochloride salts of ester prodrug or 300 mg of propranolol HCl was added. The samples were sonicated for 60 min at room temperature and subsequently shaken mechanically in a temperature-controlled water-bath at 25 °C for 16 h. The solution was then filtered through a 0.2 mm filter (Millipore) and, after dilution, the solubility of each diastereomer was determined by reversed phase HPLC. The solubility of each diastereomer was also determined in DMSO/acetate buffer mixture used in the skin permeation study according to the procedure outlined above.

Measurement of Partition Coefficient—Partition coefficients of propranolol and the prodrugs were determined in 1-octanol/pH 4.0 phosphate buffer ($\mu = 0.155$) since the prodrugs are most stable at pH 4.0. Aqueous buffer solution and 1-octanol were mutually presaturated at 25 °C before use. Propranolol or the prodrug concentration in pH 4.0 buffer was measured by a reversed phase HPLC method before and after shaking with equal volume of 1-octanol for 1 h. The partition coefficients were determined as the ratios between the concentrations measured in 1-octanol and pH 4.0 phosphate buffer.

Preparation of Liver and Intestinal Homogenates—Rats were sacrificed by decapitation and the upper two-thirds of the small intestine and liver were removed rapidly, washed with ice-cold 0.15 M KCl, blotted to dryness, and weighed. The intestine was cut into approximately 5 cm long sections, and the subsequent tissue manipulations were conducted at 4 °C. Fat and omentum from the small intestine were removed, and the lumen was washed with saline. The mucosal layer was collected by scraping with a glass slide. The mucosal cells and the liver were homogenized in five volumes of 1.15% KCl with a tissue homogenizer (Biospec) and then centrifuged at 10000*g* for 20 min at 4 °C. To adjust the protein content (2 mg/mL in liver sample and 1.5 mg/mL in intestine sample), the supernatant fraction was diluted with 1.15% KCl solution. Blood was collected in heparinized tubes, and plasma was separated by centrifugation (10000*g*) for 15 min at 4 °C. The protein content in the tissue homogenates was estimated by the method of Lowry et al.[29]

Preparation of Rat Brain Homogenate—Animals (male rats, Sprague−Dawley) were sacrificed by decapitation, and brains were removed and homogenized in ice-cold 1.15% KCl (w/v) solution [brain tissue/solution, 1:4] with a homogenizer (Tissue Tearor, Biospec). The homogenate was centrifuged at 9000*g* for 20 min. The supernatant fraction containing soluble and microsomal esterases was stored in aliquots at −80 °C until further use. Protein contents were determined by the method of Lowry et al. with bovine serum albumin as the standard.

Preparation of Skin Homogenate Fractions—All operations were carried out at 0−4 °C. After sacrificing the animal by decapitation, cutaneous strips were removed from the back and the abdomen. Fat and the surrounding muscular tissues as well as capillaries adhering to the dermis were removed. The skin was minced and mixed with 10 volumes of cold Tris-HCl buffer (pH 7.4) containing 0.15 M KCl and homogenized for 10 min. The whole homogenate was filtered with a funnel through buffer-soaked cotton and centrifuged at 10 000*g* for 20 min at 0−4 °C to remove mitochondria and nuclei. The postmitochondrial fraction was centrifuged at 100 000*g* for 1 h with a Beckman TL 100 ultracentrifuge, and the cytosolic supernatant was separated. The microsomes obtained from the pellet were resuspended in 5 mL of Tris buffer. Washed microsomes were isolated by recentrifugation at 100 000*g* for 1 h.

Hydrolysis Studies—*In Buffer*—Stock solution of diastereomeric ester prodrugs (0.05 M) was prepared in dimethyl sulfoxide. An aliquot (20 μL) was added to 10 mL of preincubated (37 °C) buffer solution (pH 7.4, $\mu = 0.155$) in a shaker water bath to initiate the hydrolysis reaction. At appropriate time intervals, samples (100 μL) were withdrawn and directly analyzed by HPLC.

In Plasma—Five microliters of stock solution of each diastereomeric prodrug was added to 2.5 mL of fresh plasma preincubated at 37 °C for 5 min to initiate the reaction. At appropriate time intervals 20 μL samples were withdrawn and immediately added to 100 μL of acetonitrile kept in an ice−water bath to precipitate the plasma proteins. The mixture was vortexed and centrifuged at 10 000*g* for 10 min at 4 °C. The supernatant was separated and stored at 4 °C until analysis by HPLC.

In Liver, Intestinal, and Brain Homogenates—Stock solutions of the liver, mucosal cells, and brain homogenate preparations were diluted to approximately 1 mg/mL protein content with ice-cold phosphate buffer (pH 7.4; $\mu = 0.155$). The rest of the procedure was similar to that described for hydrolysis in plasma.

In Skin Preparations—Protein concentrations of the cytosol and microsomal fractions were adjusted to 2 mg/mL with ice-cold pH 7.4 phosphate buffer ($\mu = 0.155$). The rest of the procedure was similar to that described for hydrolysis in plasma.

In Pure Esterase—Pure cholinesterases, i.e., buytyryl and acetyl, were diluted with phosphate buffer (100 mM, pH 7.4) to a suitable protein concentration (1 mg/mL) and were used to study the hydrolysis kinetics of diastereomeric propranolol esters. The rest of the procedure is similar to that described above.

Chromatography—A Beckman 100 A liquid chromatographic system equipped with a fluorescence spectrophotometer (Schoeffel FS 970) was used at excitation (λ_{ex}) and emission (λ_{em}) wavelengths of 290 and 340 nm, respectively. Propranolol and diastereomeric ester prodrug concentrations were determined with a C_{18} Novapak column (150 mm × 3.9 mm i.d., 5 mm, Waters). A chiral AGP column (100 mm × 4 mm, 5 mm, Alltech) was used to separate enantiomers of propranolol. The eluent systems were composed of acetonitrile: 2% v/v acetic acid (70:30), pH 4.0 adjusted with

ammonia (C_{18} column), and 20 mM ammonium acetate buffer (pH 4.1)/acetonitrile (98:2) (AGP column). A constant flow rate of 1.5 mL/min (C_{18} column), and 1.0 mL/min (AGP column) was maintained. The chromatographic separations were carried out at ambient temperature. Samples of 20 μL were injected onto the chromatograph. The retention times were 11.5, 13, 14.5, and 17 min for 1*S*2*R*, 1*S*2*S*, 1*R*2*R*, and 1*R*2*S*, respectively.

In Vitro Permeation Study—In vitro percutaneous permeation study was performed with a side-by-side diffusion cell apparatus. The rats were sacrificed by decapitation, and the hair of the abdominal region was removed immediately using an animal clipper (Oster A2) and a razor. A rectangular section of dorsal skin was excised from the animal with surgical scissors. Adhering fat and visceral debris were removed from the undersurface with tweezers. The excised skin was immediately mounted between the half-cells, with the dermis side in contact with the receptor fluid (0.01 M acetate buffer, pH 4). The area of skin available for diffusion was 0.636 cm^2. The prodrugs (7.5 mg) 1*S*2*S*, 1*S*2*R*, and 1*R*2*R* were solubilized in 7% v/v DMSO, and the volume was subsequently adjusted to 3 mL with 0.01 M pH 4 acetate buffer and added to the donor half-cell. The 1*R*2*S* prodrug (7.5 mg) was solubilized in 20% DMSO since this prodrug was the least soluble one. The saturation solubility of the prodrugs, determined in the buffer−DMSO system, was used for calculating the permeability. The solubility of the prodrugs in these systems ranged from 1 mM (1*R*2*S*) to 1.6 mM (1*S*2*S*). Enantiomer transport of propranolol hydrochloride from actate buffer (pH 4.0) was studied using 230 mM donor concentration. The half-cells were maintained at 37 °C connected to a circulating water bath (Isotemp, 1016P, Fischer Scientific). A 200 μL sample was withdrawn periodically for 24 h and replaced with equal volume of buffer. The fractions were stored at 4 °C until analyzed by HPLC for regenerated propranolol and the intact prodrugs. Cumulative amount of propranolol and the prodrugs transported (sum of intact prodrug and regenerated propranolol) was plotted against time, and the flux was obtained from the apparent steady-state linear portion of the graph.

The permeability coefficients of propranolol and its prodrugs were calculated[30] by

$$K_p = J_s/C_s$$

where K_p is the permeability coefficient, J_s is the steady-state flux, and C_s is the saturation solubility of the prodrugs in the buffer−DMSO system or PL in acetate buffer.

Statistical Analysis—Results of hydrolysis and permeation experiments were expressed as the mean ± SD. The student's *t* test was applied, where necessary, to evaluate significance of difference.

Results and Discussion

A major problem associated with the preparation of *O*-acetyl derivatives of propranolol and similar O,N-bifunctional compounds is the competing *N*-acetyl reactions. Indeed, the previously reported hemisuccinate derivative of propranolol has been shown to have the N- rather than the *O*-acetyl structure.[31] Irwin and Belaid[28] showed that O-acetylation is possible only by allowing the reaction of propranolol hydrochloride to take place with an appreciable, i.e., 4−5-fold, excess of the acid chloride without a catalyst. Under either synthetic or hydrolysis reaction conditions racemization at any one/two of the chiral centers of the prodrug can occur. It has been reported that, oxazepam undergoes racemization in aqueous medium.[32] The factors and the implications of racemization of enantiomers were discussed in detail elsewhere.[33] Such possible racemization was checked by reversed phase HPLC. Racemization of propranolol after prodrug hydrolysis is also possible, and this was also cross-checked under chiral column HPLC conditions. Interestingly, neither O to N transfer nor racemization were observed during synthesis or hydrolysis of the prodrugs.

Physicochemical Properties—Physicochemical parameters, such as aqueous solubility, have been shown to influence membrane flux, therapeutic activity, and pharmacokinetic profiles of medicinal agents. Therefore the physicochemical properties of propranolol and the prodrugs are important, especially in determining loading and release properties from a transdermal therapeutic device. The ester derivatives of propranolol used in this study undergo chemical hydrolysis, particularly under alkaline conditions as described later. Therefore the compounds are relatively unstable for normal equilibrium aqueous solubility determination around neutral pH range. To overcome this problem, the solubility of the prodrugs was determined at pH 4 (acetate buffer; $\mu = 0.155$) in which the prodrugs are found to be most stable. Analysis by HPLC showed insignificant degradation (<0.05%) of the esters during the solubility determination. The physicochemical properties such as solubility and partition coefficients (PC) of the four diastereomeric prodrugs are shown in Table 1. Diastereomers by definition exhibit different physicochemical properties. However, as shown in Table 1, only 1*R*2*S* showed significantly ($p < 0.05$) different aqueous solubility compared to the other diastereomers. The aqueous solubilities of the PL diastereomeric esters decreased and the partition coefficients increased compared to those of PL. Lipophilicity is very important for transdermal permeation because the stratum corneum, the major barrier to drug permeation, is lipid in nature and generally favors the permeation of lipophilic drugs. It has also been reported recently that an effective dermal prodrug should possess not only high lipophilicity but also adequate aqueous solubility.[34]

Table 1—Solubility and Partition Coefficients (PC) of Propranolol and Its Diastereomeric Ester Prodrugs

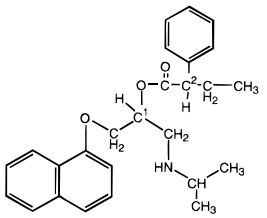

compound	solubility,[a] mg/mL	PC[b]
propranolol HCl	116.521[38]	2.50
1*S*2*S*	0.303 ± 0.031	11.85
1*R*2*R*	0.231 ± 0.005	17.90
1*S*2*R*	0.301 ± 0.021	11.00
1*R*2*S*	0.040 ± 0.006 *	20.70

[a] Determined in pH 4.0 acetate buffer at 25 °C. [b] Done in octanol–pH 4.0 phosphate buffer ($\mu = 0.155$) at 25 °C; *$p < 0.05$ compared to the other prodrugs.

Hydrolysis in Buffer and Tissue Preparations—Hydrolysis of all four diastereomeric prodrugs was investigated in aqueous solution at 37 °C over a wide pH range. At constant pH and temperature, the disappearance of the prodrugs displayed apparent first-order kinetics for several half-lives (data not shown). The prodrugs were completely hydrolyzed to propranolol in buffer (pH 1.2−8.0) although the propranolol prodrugs can undergo both hydrolysis and intramolecular aminolysis in alkaline solution.[35] The hydrolysis rate of prodrug increased with increasing pH. The shape of the pH−rate profile indicated proton- and hydroxyl-catalyzed degradation of the protonated prodrug together with a hydroxyl-catalyzed degradation of the unprotonated form. The V-shaped pH−rate profile (slope close to unity [0.78]) (Figure 1) indicated that water-catalyzed spontaneous degradation does not significantly contribute to the overall reaction. The maximum stability of the prodrugs was observed at around pH 4.0. No significant ($p > 0.05$) differences were observed among the hydrolytic rate constants of four diastereomeric PL ester

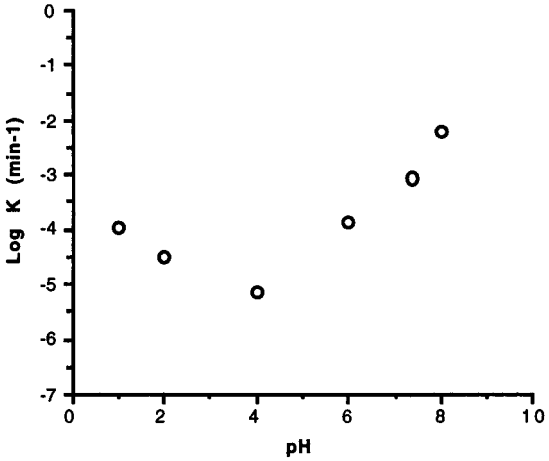

Figure 1—Typical pH–rate profile for the hydrolysis of diastereomeric ester prodrug (1*S*2*S*) in aqueous solution at 37 °C.

prodrugs in the phosphate buffer solution at a given pH, suggesting that H^+, OH^-, or spontaneous hydrolytic rate constants for an ester may not depend on the stereochemistry of the attached R group. The features of chemical kinetics are in agreement with those findings earlier reported for other propranolol esters.[20,35]

The first-order degradation of the diastereomeric ester prodrugs in plasma and liver homogenates is shown in Figure 2, and apparent first-order rate constants were determined from the slopes of the linear plots. Absence of any detectable peaks other than the propranolol and prodrug indicated the possibility of ester hydrolysis without rearrangement. Similar findings have been reported for other propranolol esters in rabbit serum.[36] The rate constants for the hydrolysis of four diastereomeric PL ester prodrugs with various tissue preparations are summarized in Table 2. Hydrolysis was accelerated by the addition of plasma or tissue homogenate, and stereoselectivity was observed. The order of hydrolytic rate constant of diastereomeric esters was found to be (1*S*2*S* < 1*R*2*S* < 1*R*2*R* < 1*S*2*R*) in plasma, and brain tissue homogenates. However, the order was changed in liver homogenates (1*R*2*S* < 1*S*2*S* < 1*S*2*R* < 1*R*2*R*) and intestinal homogenate (1*S*2*S* < 1*R*2*S* < 1*R*2*R* < 1*S*2*R*). The data clearly suggests that the configuration on the second chiral carbon atom (see prodrug structure in Table 1) to be the determinant in the rate of hydrolysis of all the diastereomeric prodrugs in all biological media examined (slowest 1X2S and fastest 1Y2R). The rate of hydrolysis of each diastereomer shows tissue dependency, with highest rate constants observed in intestinal homogenate and the lowest being in the plasma.

As judged from the rate constants shown in Table 2, the diastereomeric PL esters may be hydrolyzed mainly by esterases in the intestine and liver. These esterases consist of several isozymes, and esterase activity differs among various tissues. It was reported that oxazepam succinate was stereoselectively hydrolyzed and the selectivity differed between brain and liver.[37] This study clearly demonstrates that hydrolysis of diastereomeric PL prodrugs by plasma, liver, and intestine is stereoselective.

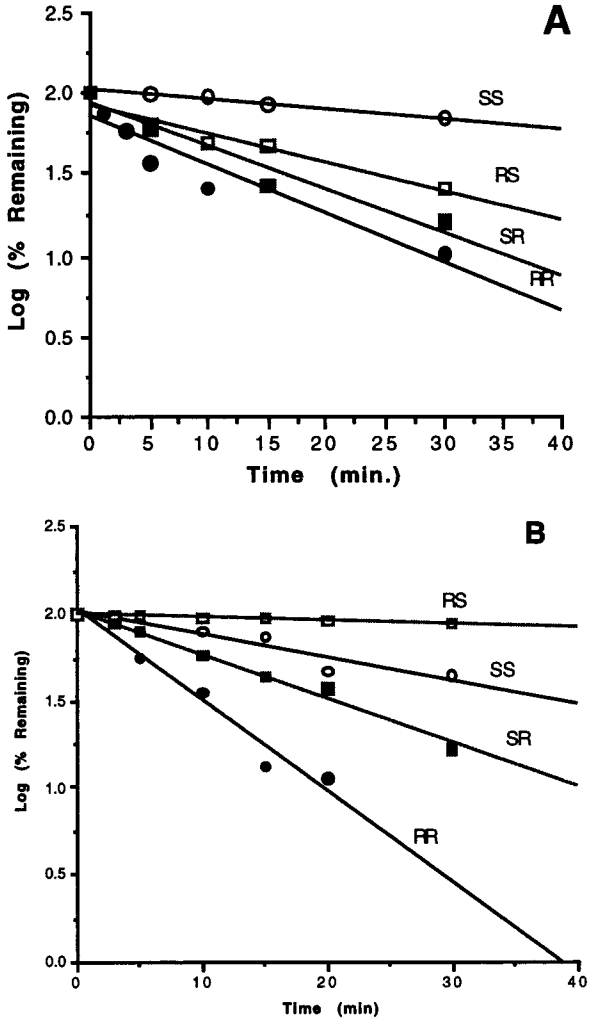

Figure 2—First-order plots for hydrolysis of diastereomeric propranolol ester prodrugs in plasma (A) and liver (B) homogenates.

In an attempt to characterize these differences, hydrolysis of these prodrugs was carried out with pure plasma esterases such as acetyl cholinesterase (EC 3.1.17) and butyryl cholinesterase (EC 3.1.1.8). The hydrolytic rate constants by these esterases were expressed in min^{-1} mg^{-1} and are tabulated in Table 2. It was found that the hydrolysis of all four diastereomeric ester prodrugs was faster by acetyl cholinesterase than by butyryl cholinesterase and was stereoselective.

The hydrolysis of these four diastereomeric ester prodrugs has also been studied in rat brain tissue homogenate, and results are shown in Table 2. Though there is no significant difference in the hydrolytic rate constants among the four diastereomeric ester prodrugs in the rat brain tissue homogenate, the plasma rate constants suggest significantly higher stability of the all diastereomers. In fact, when these rate constants were compared with those obtained in plasma, 1*S*2*S* prodrug was found to be 27 times

Table 2—Stereoselective Hydrolysis Rate Constants of Diastereomeric Ester Prodrugs of Propranolol in Different Rat Tissue Homogenates at 37 °C

	rate constants[a] ($\times 10^4$, min^{-1} mg^{-1} protein)							
prodrug	plasma	liver	intestine	brain	cytosol[c]	microsomes[c]	EC 3.1.1.7[b]	EC 3.1.1.8[b]
1*S*2*S*	1.89 ± 0.03	30.12 ± 0.18	83.64 ± 0.16	52.59 ± 0.99	0.003 ± 0.000	0.189 ± 0.020	1.32 ± 0.02	50.31 ± 1.21
1*R*2*R*	10.79 ± 0.13	129.10 ± 1.62	236.9 ± 3.27	60.29 ± 1.54	0.042 ± 0.005	0.090 ± 0.008	0.72 ± 0.01	32.43 ± 0.78
1*R*2*S*	9.12 ± 0.20	4.59 ± 0.09	84.18 ± 3.44	55.39 ± 0.01	0.015 ± 0.001	0.860 ± 0.008	0.15 ± 0.01	33.02± 0.66
1*S*2*R*	24.52 ± 0.37	97.72 ± 2.25	334.5 ± 5.64	73.01 ± 1.44	0.020 ± 0.002	0.183 ± 0.016	0.11 ± 0.01	41.18 ± 0.92

[a] Each value is the mean ± SD (n = 3). [b] Expressed as min^{-1} $units^{-1}$. [c] Skin.

Table 3—Calculated Flux (J_s) and Permeability (K_p) Values for Propranolol and the Prodrugs

compound	solubility in donor phase (μg/mL)[d]	J_s (μg cm^{-2} h^{-1})	$K_p \times 10^3$ (cm h^{-1})
(*R*)-propranolol	–	94.48 ± 11.09	1.40 ± 0.30
(*S*)-propranolol	–	95.61 ± 14.08	1.41 ± 0.27
1*S*2*S*	702 ± 48	29.63 ± 0.26	42.20 ± 1.24[b,c]
1*R*2*S*	450 ± 27	13.17 ± 0.16	29.26 ± 3.41[b,c]
1*S*2*R*	650 ± 39	10.58 ± 0.34	16.27 ± 3.12[b]
1*R*2*R*	628 ± 40	8.16 ± 1.24	12.99 ± 2.84[b]

[a] Each value is the mean ± SD ($n = 3$). [b] $p < 0.05$ compared to propranolol. [c] $p < 0.05$ compared to the other prodrugs. [d] Determined as described in Materials and Methods.

more stable in plasma (rate constant $0.189 \pm 0.03 \times 10^{-3}$ min^{-1} mg^{-1}), compared to the brain tissue (rate constant $5.259 \pm 0.99 \times 10^{-3}$ min^{-1} mg^{-1}), making it a likely prodrug candidate if brain targeting is needed for this drug.

Percutaneous Permeation—Topically applied drugs may be subject to considerable metabolic conversion. Simultaneous metabolism may affect the overall transport and disposition of the active species. It is possible to synthesize prodrugs, which permeate the skin more rapidly than the parent molecule, but are metabolized to the active form at the site of action. Simultaneous transport and metabolism after topical application of a drug is of interest to rationalize and develop a topical dosage form. Studies with propranolol have been conducted in the past using hairless mouse skin on the premise that there is no stereoselective penetration of propranolol.[38] In this study, shaved skin of male Sprague Dawley rats has been used. No stereoselective permeation of propranolol was observed. This is consistent with the findings of Heard et al., where no stereoselective permeation of propranolol through human skin was reported.[39]

All the diastereomeric ester prodrugs were hydrolyzed simultaneously during permeation and permeated as both intact prodrug and PL. To make the comparison simple only the total permeated amount (sum of intact prodrug and converted PL) of each diastereomeric prodrug was considered. The permeation parameters are shown in Table 3. The highest flux of the prodrugs was obtained with the 1*S*2*S* diastereomeric prodrug. The target rate of delivery (R_o) for propranolol and the prodrugs was calculated from reported values of the pharmacokinetic parameters for propranolol,[40] namely, clearance (Cl) and desired therapeutic steady-state concentration (C_{ss}) by:

$$R_o = C_{ss}\mathrm{Cl}$$

The clearance of (*S*)-propranolol is 16 mL min^{-1} kg^{-1}, and the required steady-state concentration for control of resistant ventricular arryhthmias is 1 μg mL^{-1}. Using these values, the target delivery rate for (*S*)-propranolol and its prodrugs is 0.672 mg h^{-1} and for (*R*)-propranolol and its prodrugs 67.2 mg h^{-1} for a 70 kg individual. This difference in delivery rate arises because the *S* isomer of propranolol is 100 times more potent than the *R* isomer. On the basis of this and the comparatively lower flux values obtained with the other prodrugs, the 1*S*2*S* prodrug is by far the best candidate for transdermal delivery. Taking into consideration the size of a patch for delivery, a patch size of 22.68 cm^2 is required for the 1*S*2*S* prodrug, and a size of 7.07 cm^2 is required for (*S*)-propranolol. Delivery of (*R*)-propranolol and its prodrugs is, however, problematic because of the relatively higher target for delivery and constraints in patch size.

From the in vitro diffusion studies, it appears that there is a 3- to 12-fold higher flux value associated with propranolol than with the prodrugs. However, it should be noted that the donor concentration of the 1*S*2*S* prodrug in the diffusion studies was approximately 1.6 mM and that of propranolol was 230 mM. The permeability coefficient (K_p) is independent of donor concentration and serves as an important parameter in comparing permeation potential. The K_p value was higher for all prodrugs compared to that of propranolol. From the flux and K_p values, it can be concluded that the 1*S*2*S* prodrug is promising in that it allows greater permeation with a lower concentration of the drug. This is preferable, since chances of skin irritation may be minimized.[38]

Hydrolysis of prodrugs in the cytosol and microsomal fraction of the skin were conducted to determine the location of the esterases. Stereoselective hydrolysis was observed in both fractions. The hydrolytic rate constants of the four diastereomeric ester PL prodrugs are summarized in Table 2. The prodrugs were hydrolyzed to a lesser extent in the cytosol as compared to microsomes. An interesting observation was that the prodrugs made with (*S*)-2-phenylbutyryl chloride were hydrolyzed to a lesser

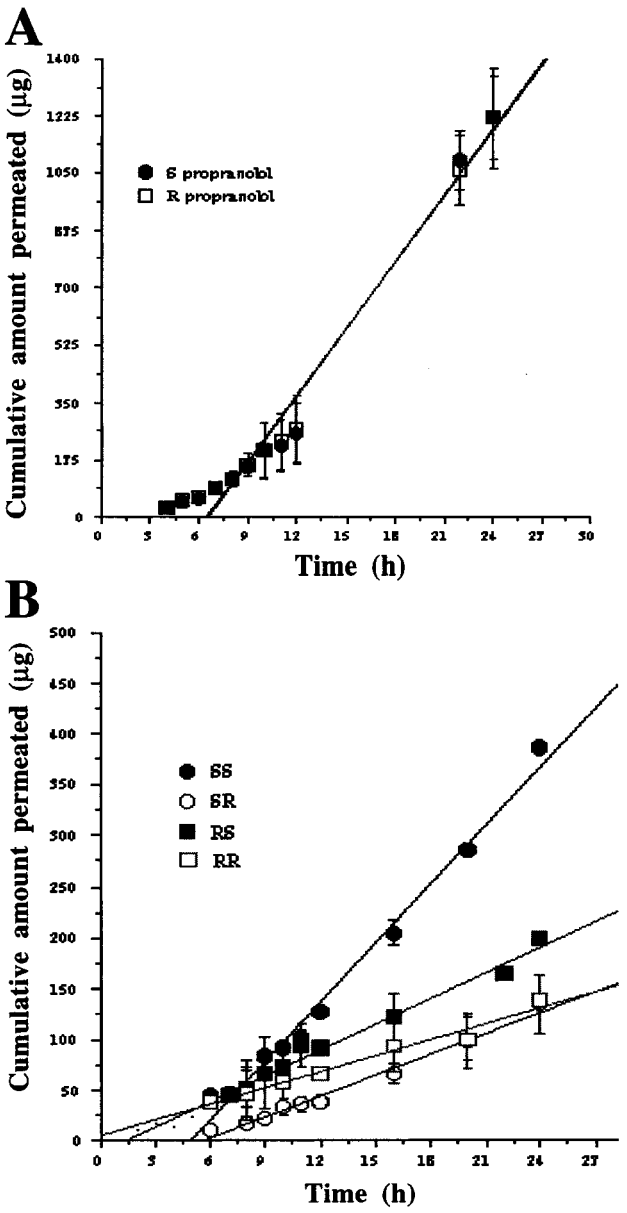

Figure 3—Penetration of propranolol enantiomers (A) and diastereomeric prodrugs (intact prodrug and transported propranolol) (B) across full thickness rat skin at 37 °C.

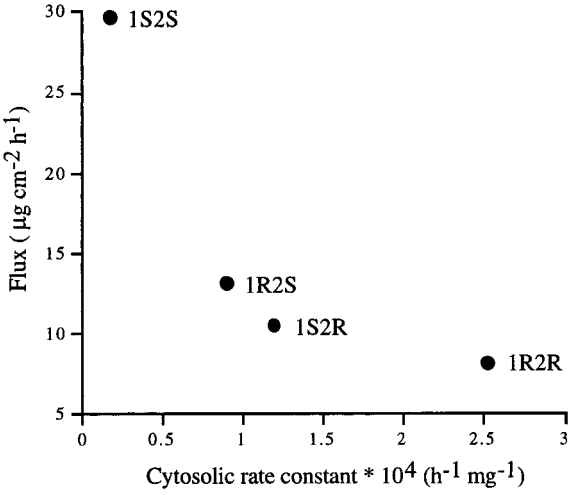

Figure 4—Plot showing inverse relationship between flux and skin cytosolic rate constants.

extent in the cytosol than those made with (*R*)-2-phenylbutyryl chloride. This assumes significance in light of the fact that the *S* isomer of propranolol is 100 times more potent than the *R* isomer. These prodrugs being more efficient at avoiding metabolism further help in improving the skin permeation of propranolol.

In Figure 3, the cumulative amount of propranolol and the diastereomeric ester prodrugs (sum of intact prodrug and regenerated propranolol) transported through the full thickness rat skin was plotted against time. It appears that all four drugs impart increase in lipophilicity as compared to parent PL as indicated by their PC data. The hydrolysis data in conjunction with the flux data clearly suggests that the prodrug, which has optimum stratum corneum partitioning and exhibits the most resistance to enzymatic hydrolysis, is able to cause the highest permeation. As shown (Figure 4), the transdermal fluxes may be inversely related to their skin cytosolic enzymatic rate constants. Therefore, a design of prodrugs should not only involve optimization of physicochemical parameters, i.e., lipophilicity and aqueous solubility, but must also include optimum evaluation of biochemical stability by membranes containing degradative enzymes.

References and Notes

1. Paterson, J. W.; Connolly, M. E.; Dollery, C. T.; Hayes A.; Cooper R. G. The Pharmacodynamics and metabolism of propranolol in man. *Pharmacol. Clin.* **1970**, *2*, 127−133.
2. Shand, D. G.; Rangno, R. E. The disposition of propranolol I. Elimination during oral absorption in man. *Pharmacology* **1972**, *7*, 159−168.
3. Silber, B.; Holford, N. H. G.; Riegelman, S. Stereoselective disposition and glucuronidation of propranolol in humans. *J. Pharm. Sci.* **1982**, *71*, 699−704.
4. Walle, T.; Walle, U. K.; Wilson, M. J.; Fagan, T. C.; Gaffney, T. E. Stereoselective ring oxidation of propranolol in man. *Br. J. Clin. Pharmacol.* **1984**, *18*, 741−747.
5. Iwamoto, K.; Watanabe, J. Avoidance of first-pass metabolism of propranolol after rectal administration as a function of the absorption site. *Pharm. Res.* **1985**, *1*, 53−54.
6. Ogiso, T.; Shintani, M. Mechanism for the enhancement effect of fatty acids on the percutaneous adsorption of propranolol. *J. Pharm. Sci.* **1990**, *79*, 1065−1071.
7. Hussain, A.; Foster, T.; Hirai, S.; Kashihara, T.; Botenhrst, R.; Jones, M. Nasal absorption of propranolol in humans. *J. Pharm. Sci.* **1980**, *69*, 1240.
8. Vyas, S. P.; Bhatnagar, S.; Gogoi, P J.; Jain, N. K. Preparation and characterization of HSA-propranolol microspheres for nasal administration. *Int. J. Pharm.* **1991**, *69*, 5−12.
9. Ehrsson, H. Identification of diastereomeric propranolol-O-glucuronides by gas chromatography−mass spectrometry. *J. Pharm. Pharmacol.* **1975**, *27*, 971−973.
10. Garceau, Y.; Davis, I.; Hasegawa, J. Plasma propranolol levels in beagle dogs after administration of propranolol hemisuccinate ester. *J. Pharm. Sci.* **1978**, *67*, 1360−1363.
11. Anderson, B. D.; Chu, W. W.; Galinsky, R. E. Reduction of first-pass metabolism of propranolol after oral administration of ester prodrugs. *Int. J. Pharm.* **1988**, *43*, 261−265.
12. Chien, Y. W. In *Peptide and protein drug delivery*; Lee, V. H. L., Ed.; Marcel Dekker: New York, 1990; pp 667−690.
13. Wearly, L.; Antonacci, B.; Cacciapuoti, A.; Assenza, S.; Chaudry, I.; Eckhart, C.; Levine, N.; Loebenberg, D.; Norris, C.; Parmegiani, R.; Sequeira, J.; Yarosh-Tomaine, T. Relationship among physicochemical properties, skin permeability, and topical activity of the racemic compound and pure enantiomers of a new antifungal. *Pharm. Res.* **1993**, *10*, 136−140.
14. Roy, S. D.; Chatterjee, D. J.; Manoukian, E.; Divor, A. Permeability of pure enantiomers of ketorolac through human cadaver skin. *J. Pharm. Sci.* **1995**, *84*, 987−990.
15. Touitou, E.; Chow, D. D.; Lawter, J. R. Chiral β-blockers for transdermal delivery. *Int. J. Pharm.* **1994**, *104*, 19−28.
16. Barret, A. M.; Cullum, V. A. The biological properties of the optical isomers of propranolol and their effects on cardiac arrhythmia. *Br. J. Pharm.* **1968**, *34*, 43−45.
17. Von Bahr, C.; Hermansson, J.; Tawara, K. Plasma levels of (+) and (−)-propranolol and 4-hydroxypropranolol after administration of (±)-propranolol in man. *Br. J. Clin. Pharmacol.* **1982**, *14*, 79−82.
18. Walle T.; Walle, U. K. Stereoselective oral bioavailability of (±) propranolol in the dog. A GC-MS study using a stable isotope technique. *Res. Commun. Chem. Pathol. Pharmacol.* **1979**, *23*, 453−464.
19. Stoschitzky, K.; Lindner, W.; Egginger, G.; Brunner, F.; Obermayer-Pietsch, B.; Passath, A.; Klein, W. Racemic (R, S)-propranolol versus half-dosed optically pure (S)-propranolol in humans at steady state: Hemodynamic effects, plasma concentrations, and influence on thyroid hormone levels. *Clin. Pharmacol. Ther.* **1992**, *51*, 445−453.
20. Takahashi, K.; Haginaka, J.; Tamagawa, S.; Yasuda, H.; Katagi, T.; Mizuno, N. Stereoselective hydrolysis of O-acetyl propranolol as prodrug in human serum. *J. Pharm. Pharmacol.* **1992**, *42*, 356−357.
21. Takahashi, K.; Tamagawa, S.; Haginaka, J.; Yasuda, H.; Katagi, T.; Mizuno, N. Stereoselective hydrolysis of O-acetyl propranolol as prodrug in rat tissue homogenates. *J. Pharm. Sci.* **1992**, *81*, 226−227.
22. Kamal, A.; Rao, A. B.; Rao, M. V. Stereoselective metabolism of 3-isopropyl-5-(1-naphthoxymethyl) oxazolidine, a prodrug of propranolol. *J. Biochem. Pharmacol.* **1991**, *41*, 1393−1395.
23. Maksay, G.; Tegey, Z.; Otvos, L. Stereospecificity of esterases hydrolyzing oxazepam acetate. *J. Pharm. Sci.* **1978**, *67*, 1208−1210.
24. Liu, K.; Guengerich, F. P.; Yang, S. K. Enantioselective hydrolysis of lorazepam 3-acetate by esterases in human and rat liver microsomes and rat brain S9 fraction. *Drug Metab. Dispos.* **1991**, *19*, 609−613.
25. Mosher, G. L.; McBee, J.; Shaw, D. B. Esterase activity toward the diastereomers of cofuroxine axetil in the rat and dog. *Pharm. Res.* **1992**, *5*, 687−689.
26. Hammarstrom, S.; Hamberg, M. Steric analysis of 3-,4,3- and 2-hydroxy acids and various alkanols by gas−liquid chromatography. *Anal. Biochem.* **1973**, *52*, 169−179.
27. Crowther, A. F.; Smith, L. H. Beta-Adrenergic blocking agents. II. Propranolol and related 3-amino-1-naphthoxy-2-propanols. *J. Med. Chem.* **1968**, *11*, 1009−1013.
28. Irwin, W. J.; Belaid, K. A. Drug delivery by ion-exchange. Part I: ester prodrugs of propranolol. *Drug Dev. Ind. Pharm.* **1987**, *13*, 2017−2031.
29. Lowry, O. H.; Rosebrough, N. J.; Farr A. L.; Randall, R. J. Protein measurement with the folin phenol reagent. *J. Biol. Chem.* **1951**, *193*, 265−275.
30. Komatsu, H.; Suzuki, M. Percutaneous absorption of butylparaben through guinea pig skin in vitro. *J. Pharm. Sci.* **1979**, *68*, 596−598.
31. Nelson, W. L.; Walker, R. B. The structure of propranolol hemisuccinate. *Res. Commun. Chem. Path. Pharmacol.* **1978**, *22*, 435.
32. Yang, S. K.; Lu, X. Racemization kinetics of enantiomeric oxazepams and stereoselective hydrolysis of enantiomeric oxazepam 3-acetates in rat liver microsomes and brain homogenates. *J. Pharm. Sci.* **1989**, *78*, 789−795.
33. Reista, M.; Testa B.; Carrupt, P. A.; Jung, M.; Schurig, V. Racemization, enantiomerization, diastereomerization, and epimerization: Their meaning and pharmacological significance. *Chirality* **1995**, *7*, 396−400.
34. Waranis, R. P.; Sloan, K. B. Effects of vehicle and prodrug properties and their interactions on the delivery of 6-mercaptopurine through skin: Bisacyloxymethyl-6-mercaptopurine prodrugs. *J. Pharm Sci.* **1987**, *76*, 587−595.

35. Buur, A.; Bundgaard, H.; Lee, V. H. L. Prodrugs of propranolol: hydrolysis and intramolecular aminolysis of various propranolol esters and an oxazolidin-2-one derivative. *Int. J. Pharm.* **1988**, *42*, 51−60.
36. Irwin W. J.; Belaid, K. A. Drug-delivery by ion-exchange. Hydrolysis and rearrangement of ester pro-drugs of propranolol. *Int. J. Pharm.* **1988**, *46*, 57−67.
37. Salmona, M.; Saronis, C.; Bianchi, R.; Marcucci, F.; Mussini, E. In vitro hydrolysis of oxepam succinate half-ester by a stereospecific soluble esterase from different animal species. *J. Pharm. Sci.* **1974**, *63*, 222−225.
38. Ahmed, S.; Imai, T.; Otagiri, M. Stereoselective hydrolysis and penetration of propranolol prodrugs: In vitro evaluation using hairless mouse skin. *J. Pharm. Sci.* **1995**, *84*, 877−883.
39. Heard, C. M.; Watkinson, A. C.; Brian, K. R.; Hadgraft, J. *Int. J. Pharm.* **1993**, *90*, R5−R8.
40. Colangelo, P. M.; Blouin, R. A.; Steinmetz, J. E.; McNamara, P. J.; DeMaria A. N.; Wedlund, P. J. Age and propranolol stereoselective disposition in humans. *Clin. Pharmacol. Ther.* **1992**, *51*, 489−494.

Acknowledgments

This work was supported by a grant from Hoechst Marion Roussel, Kansas City, MO.

JS980358H

Development and Validation of a Method for the Analysis of a Pharmaceutical Preparation by Near-Infrared Diffuse Reflectance Spectroscopy

MARCELO BLANCO,* JORDI COELLO, ALBA EUSTAQUIO, HORTENSIA ITURRIAGA, AND SANTIAGO MASPOCH

Contribution from *Departamento de Química, Unidad de Química Analítica, Universidad Autónoma de Barcelona, E-08193 Bellaterra, Barcelona, Spain*

Received August 17, 1998. Final revised manuscript received January 21, 1999.
Accepted for publication January 25, 1999.

Abstract ☐ A near-infrared (NIR) spectroscopic method based on the use of a fiber optical probe for the analysis of a commercially available pharmaceutical preparation is proposed. The analyte is identified by comparison with a second-derivative spectral library, using the correlation coefficient as the discriminating parameter. Once a sample has been positively identified, the active principle is quantified with partial least-squares (PLS) calibration. The proposed method was validated for use as a control method; to this end, the selectivity of the identification process, and the repeatability, intermediate precision, accuracy, linearity, and robustness of the active principle quantitation, were assessed.

Introduction

"Quality" is gaining crucial significance in many fields, where it is becoming a necessity rather than a secondary goal as in former times. Achieving and ensuring quality entails strict control of raw materials, production processes (via the analysis of intermediate products), and end-products. Controlling every single step and product involved in a manufacturing process entails performing a large number of analyses. Conventional analytical methodologies involve pretreating the sample, which accounts for most of the time expended in the analysis, produces most of the errors arising during the control process, and uses substantial amounts of reagents and solvents. This has promoted the development of expeditious, reliable alternative methodologies, enabling thorough control of a production process via the simultaneous determination of several parameters.

Near-infrared (NIR) spectroscopy is gaining wide acceptance in the pharmaceutical industry as both the expeditiousness with which information can be obtained and the fact that the NIR signal depends on the chemical composition and physical properties of the sample make this technique widely applicable.[1,2] The most important physical properties that affect the spectra of pharmaceutical samples are the particle size and granulation, bringing about modifications on the spectrum like shifts or drifts of the baseline.

One of its most appealing applications of NIR is the use of a fiber optical probe coupled to the spectrophotometer to make measurements with no sample preparation, thereby avoiding the need for reagents and solvents. Although the most common use of fiber optical probes in routine analyses is the identification of raw materials,[3] its potential for quantitative analyses has also been demonstrated.[4−6]

As regards qualitative applications, NIR spectroscopy has solved various problems such as preliminary investigations in the analysis of mixtures or discrimination among similar products;[7] more widespread, however, is the identification of pure chemicals by reference to an existing spectral library.[3,4,8] In this work, we used the correlation coefficient as the discriminating parameter to identify the spectrum for the unknown sample with one in the library.

As far as quantitative analysis is concerned, NIR spectroscopy allows the determination of active principles and/or excipients in various pharmaceutical preparations by use of different multivariate calibration techniques[9] (e.g. multiple linear regression, principal component regression) of which partial least-squares (PLS) regression, used in this work, is the most widely employed choice. In quantitative analysis the modification on the spectra due to the physical properties are minimized by applying spectral pretreatments (derivatives, SNV, MSC, etc.) and/or including variability in the calibration to model it; using these procedures it is expected that the physical characteristics of the sample do not affect on the prediction capability of the model.

One more advantage of the use of NIR is the possibility to identify and quantify a sample using the same experimental data. Mathematically both methods are independent; spectral pretreatment used in each method is optimized to get the best results. For the quantification method we optimized the spectral mode to get the best prediction capability, but for the identification procedure we used the second derivative because it is the usual method that the commercial softwares includes. After defining the spectral mode needed in each method (identification or quantitative) in routine analysis, the software automatically transforms the absorbance spectral data of the recorded spectrum to the proper spectral mode previously defined for each method.

Once a new analytical protocol has been developed, it must be validated if it is to be accepted for use in routine analyses; in this way, the method is guaranteed to perform in such a way as to provide quality results every time.

There are several reported guidelines for the practical validation of analytical methods.[10,11] Official ones such as those issued by the United States Pharmacopeia (USP),[12] the International Conference on Harmonization (ICH),[13] or the Food and Drug Administration (FDA)[14] provide a framework for the validation process. As a rule, methods for regulatory submission must include studies on specificity, linearity, accuracy, precision, range, quantitation limit, and robustness.

* Corresponding author. Tel.: 34 93 581 13 67; fax: 34 93 581 24 77, e-mail: iqan8@blues.uab.es.

10.1021/js980338f CCC: $18.00
Published on Web 03/11/1999

The ICH has lately made strong harmonization efforts aimed at validating methods for the control of formulations and substances. However, chemists continue to be faced with the problem that every existing regulation of this type is concerned with the validation of chromatographic methods. The lack of officially endorsed methodologies where sample treatment differs markedly from that of a chromatographic procedure makes validation a process for which no preset rules exist.

The objective of this work is the development and validation of a NIR quantitative method. To carry out this objective, two requirements are necessary. First, the validation regulation demands a guarantee of the sample identity before quantifying the sample. Second, once a method is established, conventional tests are adapted to the specific NIR needs in order to demonstrate their suitability.

Experimental Section

Samples—A pharmaceutical preparation (CBIC) commercially available in granular form contains ferrous lactate dihydrate (770 mg/g as anhydrous ferrous lactate) as active principle, and sodium croscarmellose (50 mg/g) and talc (20 mg/g) as excipients. Samples of the pure components and of the pharmaceutical preparation from different production batches were supplied by Laboratorios Menarini S.A.

Apparatus and Software—The spectra were recorded on a NIRSystems 5000 near-infrared spectrophotometer equipped with a reflectance detector and an AP6645 ANO3P fiber optical probe. The instrument was governed by the software package NSAS v. 3.30, from Perstorp Analytical, NIRSystems, which includes modules for acquisition and treatment of NIR spectra. It also includes IQ,[2] a program for developing the routine qualitative and quantitative analyses.

A Turbula Type T2C shaker mixer from WAB (Basel, Switzerland) was used to homogenize laboratory-made solid samples.

Calibration was performed by using the commercially available multivariate calibration software package Unscrambler v. 5.03, from Camo AS (Trondheim, Norway), which enables principal component analysis (PCA) and partial least-squares regression (PLS) and has additional capabilities for variable selection and outlier detection. The NIR spectra processed by this program were previously exported in JCAMP format from the spectrophotometer.

Sample Preparation—Two types of samples (laboratory and production) were used. Laboratory samples were prepared by weighing variable amounts of the active pure principle and adding different amounts of sodium croscarmellose and talc until the appropiate ferrous lactate concentration was obtained; the active principle content varied evenly over a concentration range about ±15% of the nominal value (viz. 650−850 mg/g). Each sample was shaken about 1 h and then a NIR spectrum was recorded; the shaking process was repeated again for 10 min and then a second NIR spectrum was recorded. When two consecutively recorded spectra were identical, the sample was considered homogeneous; otherwise, the shaking process was repeated.

The production samples were granulated samples obtained from different production batches, and their NIR spectra were recorded without any treatment.

Recording of NIR Spectra—The spectrum for each sample was recorded over the wavelength range 1100−2500 nm by inserting the fiber optical probe into the containers where the samples were received, so preparation of the sample for the analysis it was not necessary.

All samples were recorded in triplicate; after each single measurement the powder was stirred with the aid of a spatula to record different parts of the sample. The average of the three spectra for each sample was used for analysis.

Figure 1 shows the NIR spectrum for each individual component of the pharmaceutical preparation, together with that for a production sample.

Reference Method—The active principle in the pharmaceutical was determined by measuring the ferrous ion in ferrous lactate by redox titration[15] with Ce^{4+} ion. An amount of ca. 0.2 g of sample was supplied with 100 mL of 1:50 H_2SO_4:H_2O, 0.5 g of $NaHCO_3$, and 1−2 drops of ferroin (indicator) and titrated with a previously standardized 0.1 M Ce^{4+} solution.[16] The active principle content in each sample was obtained as the average of three determinations by the reference volumetric method.

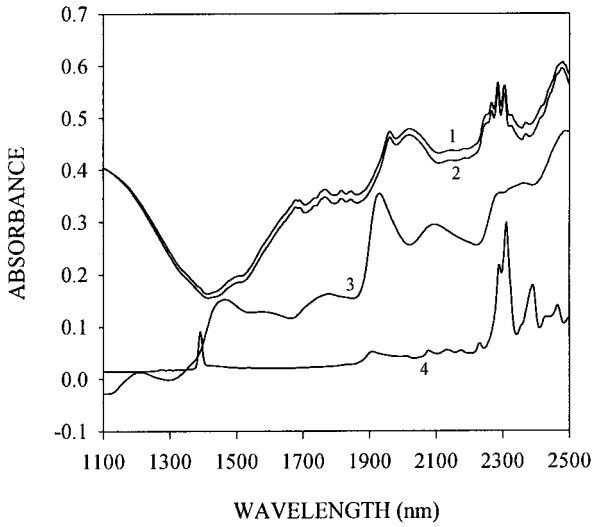

Figure 1—NIR spectra for a production sample and the pure components of the pharmaceutical. (1) Production sample. (2) Ferrous lactate dihydrate. (3) Sodium croscarmellose. (4) Talc.

The ferrous lactate content in the laboratory samples was calculated from weights of the pure components used to prepare them.

Data Processing—*Identification*—Samples were identified by comparison of their spectra with standard spectra in a reference library. To this end, a library containing spectra for the pharmaceutical preparation, the active principle, and the excipients was compiled; for each product, a set of sample spectra that met the specifications and represented all the variability in the manufacturing process were available. The library was constructed from second-derivative spectra in order to facilitate discrimination among different products and decrease spectral variability due to scattering.

Similarity between products was expressed through the correlation coefficient or match index, ρ_{jk}, given by

$$\rho_{jk} = \frac{\sum_{i=1}^{p}(x_{ij} - \bar{x}_j)(x_{ik} - \bar{x}_k)}{\sqrt{\sum_{i=1}^{p}(x_{ij} - \bar{x}_j)^2}\sqrt{\sum_{i=1}^{p}(x_{ik} - \bar{x}_k)^2}}$$

where the subscripts k and j denote the sample and product reference spectra, respectively, acquired at p wavelengths, x_{ik} and x_{ij} are measured values of the sample and the product reference at wavelength i, and $\bar{x}_j$ is the value of the average spectrum j over all p wavelengths.

The match index ranges between −1 and +1. A value of +1 indicates perfect similarity between the unknown product and a product in the library. However, random noise associated to measurements may preclude obtainment of this value, so an identification threshold must usually be established.

Quantitative Analysis—All models tested were based on the PLS algorithm[17] and constructed by cross-validation, using as many segments as samples in the calibration set. All were constructed for the spectral range 1100−2200 nm and thus avoided the upper zone of the spectrum and hence the high background noise associated with the use of a fiber optical probe. The number of significant PLS components was taken to be the minimum number for which the prediction error sum of squares (PRESS) was not significantly different from the lowest PRESS value.[18]

The quality of the results was assessed in terms of the relative standard error of prediction,[19]

$$\mathrm{RSEP}(\%) = \sqrt{\frac{\sum_{i=1}^{n}(C_{\mathrm{LAB}_i} - C_{\mathrm{NIR}_i})^2}{\sum_{i=1}^{n} C_{\mathrm{LAB}_i}^2}}$$

where C_{LAB_i} is the reference concentration and C_{NIR_i} the PLS calculated concentration.

Results and Discussion

The proposed analytical procedure uses a single spectral measurement for the simultaneous qualitative (identification) and quantitative analysis of a commercially available pharmaceutical preparation.

Unknown samples are identified by comparing their spectra with the average spectrum for each product in a library. If the sample is positively identified, then its active principle content is automatically quantified by reference to a previous PLS calibration.

After the proposed method was developed, it was validated for use as a routine control method.

Identification—A library consisting of 45 spectra for four different products, viz. the pharmaceutical preparation (five different CBIC production batches) and its three pure components (ferrous lactate dihydrate, sodium croscarmellose, and talc) was compiled. The spectra in the library were all recorded over the 1134−2200 nm range and converted into their second derivatives to lessen the effects of scattering. The library thus obtained exhibited no internal conflicts and correctly identified every spectrum used for self-validation.

All production samples studied (calibration and prediction sets) exhibited correlation coefficients between 0.95 and 1. An unknown sample was assumed to be positively identified if its correlation coefficient exceeded the established threshold (0.95). If any sample surpassed such a threshold for more than one product in the library, it was positively matched to that with the highest coefficient.

Quantitative Analysis—Available samples were split into a calibration set and a prediction set. The calibration set consisted of laboratory samples and samples from different batches of the pharmaceutical preparation (see Table 1). The laboratory samples used for calibration spanned the whole concentration range of interest in a uniform manner; these samples are powdered, and do not have the same physical properties that the real samples (granulation) have, so production samples were included in the calibration set in order to introduce the variability of the manufacturing process. Generally, a calibration set composed of only laboratory samples causes high prediction errors in production samples; in this case, using a calibration set composed of laboratory samples alone (12 samples) the prediction of production samples always gave underestimated results (except one) and a RSEP = 3.8%, an error that we considered too high.

To improve the prediction, we introduced production samples in the calibration set.[6,20] The Principal Component Analysis (PCA) was used to select the production samples to include to the calibration set. A PCA of second derivative spectra was calculated using the eight production samples available when the calibration was constructed; as can be seen from Figure 2, the samples selected were those exhibiting the greatest variability in a plot of the first component against the second, which, together, accounted for 89% of the variance. After this selection, the calibration set was composed of 17 samples, 12 of which were laboratory-made and 5 from production batches; the prediction set was composed of 19 samples, 9 laboratory-made samples, and 10 production batches.

Absorbance, first-derivative, and second-derivative PLS

Table 1—Determination of Ferrous Lactate by Use of the Proposed NIR Spectroscopic Method and Reference Method

sample	reference method (mg/g)	NIR method (mg/g)
	Calibration Set	
1	671	668
3	685	688
5	701	697
7	720	720
9	739	745
11	758	759
13	777	780
15	795	805
17	816	813
19	831	832
20	841	839
21	850	846
K-4M	791	784
K-11	778	780
K-16	771	765
K-18	771	770
K-19	754	757
		RSEP(C) = 0.6%
	Prediction Set	
2	677	673
4	694	694
6	710	712
8	730	729
10	747	747
12	766	769
14	786	784
16	805	813
18	813	816
K-9M	750	759
K-11M	770	765
K-12	777	765
K-14	765	763
K-17	761	763
K-20	765	760
K-21	756	760
K-22	763	754
K-23	761	758
K-24	771	759
		RSEP(P) = 0.8%

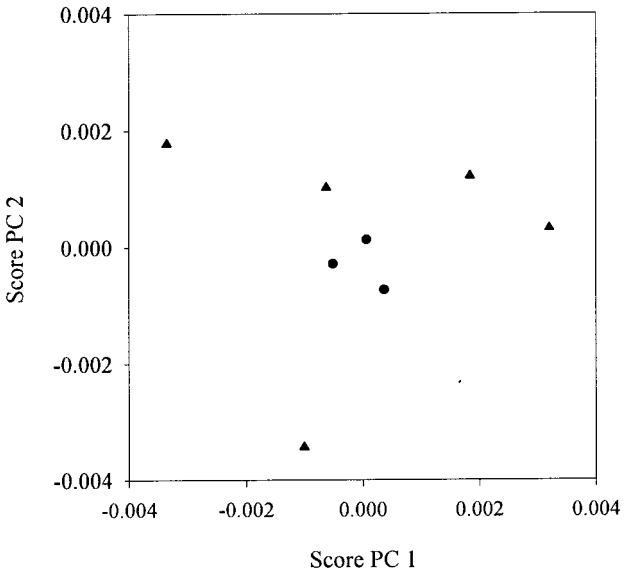

Figure 2—Scores plot for the first and second principal component of the production samples. (▲) Calibration samples. (●) Prediction samples.

Table 2—Relative Standard Error of Prediction (%) for the Calibration and Prediction Sets [RSEP(C) and RSEP(P), respectively]

	PLS-components	RSEP(C)	RSEP(P)
absorbance	5	1.2	2.9
derivative 1	4	0.6	0.8
derivative 2	5	0.5	0.9

Table 3—Correlation Coefficient Found in the Identification of Unknown Samples Using the Spectral Library

	samples analyzed			
products included in the library	CBIC	ferrous lactate dihyd	croscarmellose sodium	talc
CBIC	0.984	0.989	0.056	0.056
ferrous lactate dihyd	0.974	0.997	–0.056	0.000
croscarmellose sodium	0.054	–0.060	0.999	–0.017
talc	0.049	–0.002	–0.012	0.997

models were tested. Table 2 shows the relative standard error of prediction (RSEP) for the different quantitative models studied. As can be seen, the best results were provided by derivative models, with no significant differences between first- and second-derivative ones. A quantitation model based on first-derivative spectra was chosen as optimal, as it was more simple; it used one fewer PLS component and gave slightly lower errors than the rest. As can be seen from the results (Table 1), this calibration model allows the accurate prediction of real-world samples with no adverse effect on the quantitation of laboratory samples.

The specification limit for acceptance of the active principle content in the pharmaceutical was ±5% of the nominal value, which is clearly larger than the prediction errors obtained with the optimum calibration procedure for the production samples; in fact, none of the samples assayed provided a relative error in excess of 1.5%. Therefore, the proposed calibration procedure is precise enough for use as a control methodology.

Validation of the Procedure—There is no universally accepted procedure for validating a quantitative method by NIR spectroscopy. In this work, we adapted the ICH general guidelines[13] to the purpose. The specific aspects of the NIR method that differ most markedly from the usual regulatory analysis are the use of a multivariate calibration method and the need for no sample pretreatment, i.e. sample spectra are directly recorded.

The factors considered in validating the proposed method included selectivity in the identification step, and repeatability, intermediate precision, accuracy, linearity, and robustness in the quantitation step. The concentration range spanned by the calibration is another parameter usually examined for validation; however, the use of PLS regression to determine the active principle entails the a priori selection of the concentration range of interest. During the validation process, solid evidence was obtained that the resulting quantitation errors were acceptable throughout the concentration range studied.

Identification—*Sensitivity*—The proposed method is able to positively identify the pharmaceutical and distinguish it from its pure components.

The identification selectivity of the proposed method was assessed by comparing the results of the NIR analysis of CBIC samples with those for the active principle and excipients in the pharmaceutical. Table 3 shows the correlations for a production sample and samples of the pure components with the different products included in the spectral library. As can be seen, the production sample was identified as CBIC (the material for which the highest correlation coefficient, in excess of 0.95, was obtained).

Table 4—Correlation Coefficients for Different Production Batches Relative to Products in the CBIC Library and Ferrous Lactate Dihydrate

sample	CBIC	lactate ferrous dihydrate
K-17	0.959	0.955
K-12	0.984	0.983
K-14	0.977	0.973
K-11M	0.973	0.967
K-20	0.967	0.964
K-21	0.960	0.954
K-22	0.959	0.955
K-24	0.980	0.977
K-9M	0.983	0.972
K-23	0.985	0.982

Table 5—Study of Repeatability. NIR Results of 12 Analyses of the Same Production Batch

measurement	ferrous lactate (mg/g)
1	773
2	775
3	773
4	771
5	772
6	777
7	774
8	778
9	773
10	777
11	776
12	775
	mean: 774
	CV: 0.3%

Table 6—Study of Intermediate Precision. NIR Results Obtained by Two Different Analysts on Three Different Days

sample		day 1	day 2	day 3	
1	operator 1	760	751	760	
	operator 2	748	757	761	$CV_{global} = 0.7\%$
2	operator 1	754	751	758	
	operator 2	749	763	755	$CV_{global} = 0.7\%$

The closeness of the correlation coefficients between CBIC and ferrous lactate dihydrate reveals that the two products are very similar. To avoid conflicting identifications, Table 4 shows the correlation coefficients with CBIC and ferrous lactate dihydrate of the different production batches not used in compiling the library. No spurious identifications were made provided the established criterion was adhered to by virtue of the small spectral differences introduced by the presence of excipients in the pharmaceutical.

Quantitative Analysis—*Repeatability*—The repeatability of the proposed method was evaluated by performing 12 determinations of a production batch. Table 5 shows the results obtained from measurements made by the same operator on the same day. The active principle contents obtained in the 12 determinations exhibited a coefficient of variation CV = 0.3%, which is well below the usual accepted limits (<1%).

Intermediate Precision—The intermediate precision was assessed on two different production samples by evaluating two variable parameters in the routine control of the preparation, namely, day and operator. Table 6 shows the quantitative results obtained from measurements made by

Table 7—Study of Accuracy. NIR and Reference Results, Together with Relative Errors (%)

sample	NIR method (mg/g)	reference method (mg/g)	relative error (%)
K-9M	750	759	–1.2
K-11M	770	765	0.6
K-12	777	765	1.5
K-14	765	763	0.3
K-17	761	763	–0.3
K-20	765	760	0.6
K-21	756	760	–0.5
K-22	763	754	1.1
K-23	761	758	0.3
K-24	771	759	1.5

two different analysts on three different days. As can be seen, the coefficient of variation for the two samples studied was slightly higher than that obtained in the repeatability study as a result of new sources of variation being introduced in the analyses; in any case, the CV values were within accepted limits for this type of test (<2%).

The variability between days and that between operators were evaluated jointly by two-way analysis of variance (ANOVA), which revealed that neither source produced any systematic errors.

Accuracy—Because the results could be affected by physical properties of the samples, the accuracy of the proposed procedure was only evaluated in production batches. For this purpose, the NIR results were compared with those provided by a well-characterized (reference) method.

A paired *t* test[21] was used to check whether the mean value and that held as true (viz. the average value provided by the volumetric method) were significantly different. From the results for 10 samples (Table 7), a t_{exp} value of 1.41 was obtained (the t_{tab} value for $P = 0.05$ and 9 degrees of freedom is 2.26). Because $t_{exp} < t_{tab}$, the results provided by NIR spectroscopy and the reference method are not significantly different.

Linearity—Linearity is usually estimated by evaluating the goodness of the variation of the analytical signal as a function of the analyte concentration.[10] With multivariate calibration (e.g. PLS regression), however, an alternative test suited to the methodology in question must be used. To determine the linearity of the proposed method, the NIR and reference results were compared via the following equation:

$$\text{NIR value} = a + b \times \text{reference value}$$

The samples used to check for linearity should span the whole concentration range studied, which is known to be the case with production samples only. To include samples of variable concentration with physical features as close as possible to those of the production samples, under- and overdosed samples were prepared in the laboratory. Such samples were obtained by adding variable amounts of the active principle or excipients, respectively, to samples from different production batches and homogenizing them in the shaker mixer before their NIR spectra were recorded. Their active principle contents were determined by using the reference procedure.

Table 8 shows the results for the 16 samples studied (5 of which were production samples and 11 samples used to assess linearity). As can be seen, the results provided by both techniques were quite consistent throughout the concentration range studied. A plot of NIR concentration against reference concentration was linear, with a slope of 1.03 ± 0.06, an intercept of -20 ± 51, and a correlation coefficient $r = 0.994$. The curve has an origin and a slope

Table 8—Study of Linearity. NIR and Reference Results, Together with Relative Errors (%)

sample	reference method (mg/g)	NIR method (mg/g)	relative error (%)
1	669	674	0.7
2	681	675	–0.9
3	721	726	0.7
4	737	732	–0.7
5	740	746	0.8
6	742	750	1.0
7	756	760	0.5
8[a]	761	758	–0.3
9[a]	761	763	0.3
10[a]	765	763	–0.3
11[a]	770	767	–0.4
12[a]	770	765	–0.6
13	794	799	0.7
14	804	818	1.7
15	832	835	0.4
16	837	841	0.4

[a] Production samples.

not significantly different from zero and one, respectivity, so the proposed method is subject to no systematic or matrix errors in relation to the reference method over the concentration range studied.[22]

Finally, a paired *t* test between the values provided by the two methods[21] was carried out in order to check whether the NIR method provided accurate results throughout the calibration range. The t_{exp} value thus obtained for the samples of Table 8 was 1.45 (t_{tab} for $P = 0.05$ and 15 degrees of freedom is 2.13); since $t_{exp} < t_{tab}$, the average results provided by the two methods are not significantly different.

Robustness—The proposed NIR method involves no sample pretreatment, so the only experimental variables potentially affecting the results are those inherent in the spectrophotometer, which are set before any spectra are recorded.

The proposed analytical method can be validated by comparing its results with those of a reference method over a period of time. The production samples analyzed in the accuracy study were manufactured over a 4-month period. Also, after the proposed method was accepted as a valid control method, an overall 10 production batches have been analyzed over a period of 8 months. The results exhibit more than acceptable accuracy (the average error relative to the theoretical value is 1.3%) and coefficients of variation (1.5%). The method is thus quite robust.

Conclusions

A near-infrared spectroscopic method for a commercially available pharmaceutical preparation that affords direct analyses of untreated samples in the solid phase was developed. The analytical process involves the identification of the unknown sample and the quantitation of the active principle in the pharmaceutical. Identification relies on the correlation coefficient; the method allows the positive identification of the pharmaceutical and discriminates it from its pure components, and also even from the active principle, which is the major component. After the sample is identified, PLS regression allows the quantitation of the active principle with a prediction error well below the accepted limit for the pharmaceutical.

The method was validated by determining its selectivity, precision, linearity, and robustness. The results demonstrate that the proposed NIR spectroscopic method for the identification and determination of ferrous lactate in the pharmaceutical preparation CBIC is a valid alternative to

existing methods for this purpose and that it allows the successful analytical control of its production process.

References and Notes

1. Corti, P.; Dreassi, E.; Lonardi, S. Near Infrared Reflectance Analysis: Features and Applications in Pharmaceutical and Biomedical Analysis. *Il farmaco* **1993**, *48* (1), 3−20.
2. Blanco, M.; Coello, J.; Iturriaga, H.; Maspoch, S.; de la Pezuela, C. Near-infrared spectroscopy in the pharmaceutical industry. *Analyst* **1998**, *123*, 135R−150R.
3. Khan, P. R.; Jee, R. D.; Watt, R. A.; Moffat, A. C. The identification of Active Drugs in Tablets using Near Infrared Spectroscopy. *J. Pharm. Sci.* **1997**, *3*, 447−453.
4. Blanco, M.; Coello, J.; Iturriaga, H.; Maspoch, S.; de la Pezuela, C.; Russo, E. Control Analysis of a Pharmaceutical Preparation by Near-infrared Reflectance Spectroscopy. A Comparative Study of a Spinning Module and Fibre Optic Probe. *Anal. Chim. Acta* **1994**, *298*, 183−191.
5. Blanco, M.; Coello, J.; Iturriaga, H.; Maspoch, S.; de la Pezuela, C. Strategies for Constructing the Calibration Set in the Determination of Active Principles in Pharmaceuticals by Near Infrared Diffuse Reflectance Spectrometry. *Analyst* **1997**, *112*, 761−765.
6. Blanco, M.; Coello, J.; Iturriaga, H.; Maspoch, S.; de la Pezuela, C. Quantitation of the Active Compound and Major Excipients in a Pharmaceutical Formulation by Near Infrared Diffuse Reflectance Spectroscopy with Fibre Optical Probe. *Anal. Chim. Acta* **1996**, *333*, 147−156.
7. Wu, W.; Walczak, B.; Massart, D. L.; Prebble, K. A.; Last, I. R. Spectral Transformation and Wavelength Selection in Near-infrared Spectra Classification. *Anal. Chim. Acta* **1995**, *315*, 243−255.
8. Shah, N. K.; Gemperline, P. J. Combination of the Mahalanobis Distance and Residual Variance Pattern Recognition Techniques for Classification of Near-infrared Reflectance Spectra. Anal. Chem. **1990**, *62*, 465−470.
9. Martens, H.; Naes, T. *Multivariate Calibration*; Wiley: New York, 1991.
10. Green, J. M. A Practical Guide to Analytical Method Validation. *Anal. Chem. News Features* **1996**, *68*, 305A−309A.
11. Huber, L. Validation of Analytical Methods: Review and Strategy. *LC-GC Int.* **1998**, *11* (2), 96−105.
12. *U. S. Pharmacopeia 23*; United States Pharmacopeial Convention, Inc., 1994; pp 1982−1984.
13. Harmonised Tripartite Guideline: Validation of Analytical Procedures Methodology, International Conference on Harmonisation (ICH), The European Agency for the Evaluation of Medicinal Products, London, 1996.
14. *Reviewer Guidance, Validation of Chromatographic Methods*; Center of Drug Evaluation and Research, Food and Drug Administration: Washington, D.C., 1994.
15. Vogel, A. I. *A text-book of quantitative inorganic analysis including elementary instrumental analysis*; Longman group limited: London, 1961; p 322.
16. Koltoff, I. M.; Sandell, E. B.; Meehan, E. J.; Bruckenstein, S. *Quantitative Chemical analysis*; The Macmillan Company: London, 1969; p 838.
17. Geladi, P.; Kowalski, B. Partial Least-squares Regression: a Tutorial. *Anal. Chim. Acta* **1986**, *185*, 1−17.
18. Haaland, D. M.; Thomas, E. V. Partial Least-squares Methods for Spectral Analyses. Relation to other Quantitative Calibration Methods and the Extraction of Qualitative Information. *Anal. Chem.* **1988**, *60*, 1193−1202.
19. Otto, M.; Wegscheider, W. Spectrophotometric Multicomponent Analysis Applied to Trace Metal Determinations. *Anal. Chem.* **1985**, *57*, 63−69.
20. Riley, M. R.; Arnold M. A.; Murhammer D. W. Matrix-Enhanced Calibration Procedure for Multivariate Calibration Models with Near-Infrared Spectra. *Appl. Spectrosc.* **1998**, *52* (10), 1339−1347.
21. Miller, J. C.; Miller J. N. *Statistics for analytical chemistry*; Chalmers R. A., Masson M., Eds., Ellis Horwood Series in Analytical Chemistry: Chichester, 1984; p 56.
22. Miller, J. C.; Miller J. N. *Statistics for analytical chemistry*, Chalmers R. A., Masson M., Eds., Ellis Horwood Series in Analytical Chemistry: Chichester, 1984; p 102.

Acknowledgments

The authors are grateful to Spain's DGICyT (Project PB 96-1180) and to the Direcció General de Recerca de la Generalitat de Catalunya (1995 SGR-50) for funding this work. A. Eustaquio acknowledges additional financial support in the form of an FPI grant from the Ministerio de Educación y Ciencia. Laboratorios Menarini S.A. are also gratefully acknowledged for kindly supplying the pharmaceutical samples studied, as are our students I. Valverde and A. Villar for their cooperation in the laboratory experiments.

JS980338F

An Alternative Method for the Estimation of the Terminal Slope When a Few Data Points Are Available

ARISTIDES DOKOUMETZIDIS,[†] ATHANASSIOS ILIADIS,[‡] AND PANOS MACHERAS*,[§]

Contribution from *Department of Physics, University of Athens, Athens, Greece, Department of Pharmacokinetics, University of Mediterranee, Marseilles, France, and Department of Pharmacy, University of Athens, Panepistimiopolis, 15771 Athens, Greece.*

Received August 3, 1998. Final revised manuscript received November 24, 1998.
Accepted for publication January 19, 1999.

Abstract □ Phase plane plots are graphical expressions for differential equations ploting the state derivative d*c*/d*t* versus the state *c*. Using these plots, we developed a novel method for the estimation of the terminal slope from time–concentration data. The values of the derivatives used for the construction of the phase plane plots were calculated by two different methods of numerical differentiation. The first method (D1) is based on the classical calculation of slope of the line connecting two successive data points. The alternative method (D2) relies on an initial second-order polynomial interpolation utilizing three successive data points followed by the calculation of the derivative at each one of the concentration values. A forced-through-zero linear regression of the phase plane plot data is used to derive an estimate for the slope. For comparative purposes, the standard approach based on the semilogarithmic plot was also applied. For a hypothetical drug absorbed by first-order process into a one-compartment model, simulated time–concentration data disturbed by a Gaussian zero mean random error with various coefficients of variation were generated. Various sampling schedules, with two, three, four, or five data points, were utilized for the estimation of the terminal slope. Performances of the proposed methods on simulated data were expressed by means of root-mean-squared error, bias, and standard deviation. In all cases, D2 was superior to D1. The D2 method outperforms the standard method in that it furnishes estimates closer to the real values in all cases when two data points and in most cases when three data points were used. All methods behave similarly when four or five data points were used.

Introduction

The estimation of the terminal slope in time (*t*)–concentration (*c*) data can play an important role in pharmacokinetic, bioavailability, and bioequivalence studies. Routinely, this estimation is accomplished on the semilogarithmic plot of *c* vs *t*, where the slope is determined by the best line fitting the data. In some cases, two or three data points have been used to derive an estimate for the terminal slope.[1–6] Although the use of two data points to estimate terminal slope by log-linear regression is not statistically or theoretically justified, the method can be quite satisfactory when limited experimental error is encountered. However, a poor estimate may be obtained when the experimental error is high because measurements in the proximity of the least quantifiable concentration have been carried out and/or sampling has not been continued for a long enough time to ensure that absorption or disposition processes do not disturb the elimination process.

In the present study, a novel method is proposed for the estimation of the terminal slope. The method relies on the phase plane plot, which has been used for the analysis of various kinetic phenomena.[7–10] Moreover, phase plane plots of dye-dilution curves have been used to determine the cardiac output.[11] Also, this method was utilized recently for the discernment of absorption kinetics.[12]

Theoretical Section

In our previous study,[12] it was proven that for drugs obeying one-compartment model disposition and irrespective of the absorption kinetics, the slope of the terminal segment of the phase plane plot (d*c*/d*t* vs *c*) corresponds to the elimination rate constant. Similarly, when the computation was applied to a two-compartment model, this slope was equal to the smaller hybrid rate constant.[12] This observation applies to drugs following multiexponential disposition; for example

$$c(t) = \sum_{i=1}^{z} A_i e^{-\lambda_i t} \tag{1}$$

where A_i are fictitious constants in concentration units and λ_i ($i = 1, ..., z$) are hybrid rate constants ($\lambda_1 > \lambda_2 > ... > \lambda_z$). As time goes toward infinity, all but the terminal exponential term in eq 1 vanish and the latter is reduced to

$$c(t) = A_z e^{-\lambda_z t} \tag{2}$$

Taking the derivative of eq 2, we have

$$\frac{dc(t)}{dt} = -\lambda_z A_z e^{-\lambda_z t} = -\lambda_z c(t) \tag{3}$$

where λ_z is the terminal slope, which plays an important role in kinetic data analysis for determining the terminal half-life.

The last equation indicates that the negative slope of the last segment of the phase plane curve (d*c*/d*t* vs *c*) corresponds to the terminal slope. Obviously, the final state of the system ($t \rightarrow \infty$), when all the drug has been eliminated, corresponds to $c = 0$ and $dc/dt = 0$ [i.e., the last point of the phase plane is always the point (0,0)]. These observations encouraged us to examine the potential of estimating the terminal slope using the terminal limb of the phase plane curve and taking into consideration the last point (0,0), which is exact (Figure 1).

Methods

To illustrate feasibility of the proposed method and to evaluate its performances with respect to other computational approaches, a simulation study was undertaken. To this end, the one-

* To whom correspondence should be addressed. Phone: +30-1-7274675-8. Fax: +30-1-7244191. E-mail: macheras@pharm.uoa.gr.
[†] Department of Physics.
[‡] Department of Pharmacokinetics.
[§] Department of Pharmacy.

10.1021/js980317l CCC: $18.00 Published on Web 04/03/1999

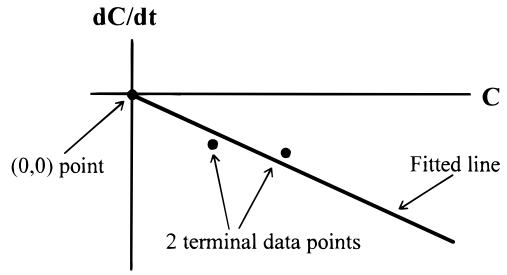

Figure 1—Schematic representation of the estimation of the terminal slope using the phase plane plot. In this example, two data points are used; the regression line is forced through (0,0), which is not an actual data point but a theoretical asymptotic limit for infinite time. The slope of the line is equal to $-k_e$.

compartment model was used associated with first-order absorption process. At time t, concentrations $c(t)$ are given by the following equation:

$$c(t) = \frac{fD}{V} \cdot \frac{k_a}{k_a - k_e} \cdot (e^{-k_e t} - e^{-k_a t}) \quad (4)$$

For normalization, the coefficient $[f \cdot D/V]$ is set to unity. The parameters k_a and k_e are absorption and elimination rate constants, respectively. Equation 4 was used to simulate concentrations in the following 5-factor controlled experimental protocol.

1. Model Parameters—One k_e value was set to reflect a 7 h half-life. Two k_a values set to reflect 1.7 and 4.6 h half-lives. Thus, the elimination rate constant was set to $k_e = 0.1\ h^{-1}$ while low and high $[k_a/k_e]$ ratios, equal to 1.5 and 4, respectively, were used.

2. Sampling Schedules—Short and long sampling schedules were examined [{6, 8, 12, 16, 20, 24} and {16, 20, 24, 28, 32, 36} h]; that is, the sampling lasts for 3.4 and 5.1 half-lives, respectively.

3. Measurement Error—Using eq 4, concentrations were computed at the sampling times and then they were corrupted by a Gaussian random zero mean measurement error. The error was variable with 5 levels of coefficient of variation (CV) at 10, 20, 30, 40, and 50%.

4. Computational Methods—The phase plane plots were constructed using two alternative methods of numerical differentiation. The first method (D1) is based on the classical calculation of slope of the line connecting two successive data points. This slope corresponds to the derivative for the mid-time point of the two data points considered. The alternative method (D2) is based initially on a second-order polynomial interpolation utilizing three successive data points. Further, the derivative is calculated at each one of the three time points considered. The method D2 as well as its application to the present study are described in the Appendix. Finally, a forced-through-zero linear regression analysis utilizing two, three, four, or five (dc/dt, c) data points is performed. In other words, a line of the form $y = ax$ is used for the fitting; the slope of this line provides an estimate for $-\lambda_z$ or for $-k_e$ for the model considered in this study. For comparative purposes, the data were also analyzed by the standard method (S) using linear regression on the semilogarithmic plot.

5. Data Analysis—Separate analyses were carried out utilizing either the last two, three, four, or five data points for both sampling schedules examined.

For each combination of the first two controlled factors (model parameters and sampling schedule) and at each one of the 5 levels of CV, 1000 measurements errors were randomly obtained and used to disturb the error-free simulated concentrations. Because of the high range of CV used, simulated data leading to positive slopes were excluded from the calculations for all methods studied. However, additional simulations were carried out to ensure a total of 1000 runs with negative slopes in all cases examined.

Simulations were done with Mathematica. The results of this simulation study were evaluated statistically. The root-mean-square error (RMSE), which provides the spread of the measures around the theoretical value ($0.1\ h^{-1}$) of the terminal slope, was calculated. Further, RMSE was split into its two components, namely, (i) the standard deviation (std), which evaluates the spread of the measures around their average value, and (ii) the bias, which provides the difference of the average of the measures from the theoretical value.

Results

For various combinations of the controlled factors utilizing either two or three data points (Figure 2) shows the results for RMSE, std, and bias. All results were derived only from data with negative slopes. The number of simulations leading to data with positive slopes increased as the level of the % CV increased for all combinations of the rest-controlled factors. Overall, the range of the percentages of data with positive slopes was 0−1.4, 0−15.2, 1−32.1, 5.6−42.8, and 18.5−57.0% for 10, 20, 30, 40, and 50% CV, respectively.

When two data points were utilized and irrespective of the CV levels, D2 yielded the lower RMSE and std values; in contrast, S yielded the higher RMSE and std values (Figure 2). In general, the higher the CV levels, the lower the performances of the methods in terms of RMSE and std. As far as the bias is concerned, D2 is the less dependent method on the CV levels.

When three data points were utilized, the performances of the methods were less dependent on the CV level (Figure 2). Moreover, in both sampling schedules, D2 method performs slightly better.

When four or five data points were utilized, the performances (not shown) of the methods were again less dependent on the CV level. All methods exhibit similar performance in terms of RMSE, std, and bias for all scenarios examined.

Discussion

The D1 and D2 methods based on the phase plane plot were developed for the estimation of the terminal slope. These methods were evaluated statistically and compared with the standard approach (S).

Two important arguments in support of the proposed D1 and D2 methods can be pointed out. First, the evaluation of the terminal slope in both methods relies on the slope of the "real terminal" segment of the phase plane curve irrespective of the sampling design applied. Second, the slope of this segment is drastically influenced by the theoretical (0,0) datum point; that is, the forced-through-zero linear regression (Figure 1).

When two data points were used, the proposed methods (D1 and especially D2) perform better than the S approach for all combinations of controlled factors examined. In particular, the D2 method had remarkably smaller RMSE, std, and bias than the D1 and S methods. The superiority of the D1 and D2 methods with respect to the S approach should be attributed to the considerable contribution of the exact datum point (0,0) in determining the slope of the regression line in the phase plane plot. In fact, the regression line (i) passes through this errorless datum point and (ii) satisfies the least squares condition for the other two (dc/dt, c) data points. These observations should be considered in conjunction with the low std and the negligible bias of the D2 method when applied to the long sampling interval conditions. Hence, the best performance of the D2 method is noted when two data points near the end of the sampling schedule are used. The poorer characteristics of the D1 method in comparison with the D2 method are most likely associated with the refined methodology used for the calculation of the derivatives in the D2 method. In addition, the D2 method utilizes the same number, whereas the D1 method utilizes one less of the data points (dc/dt, c) than the available (c, t) data points.

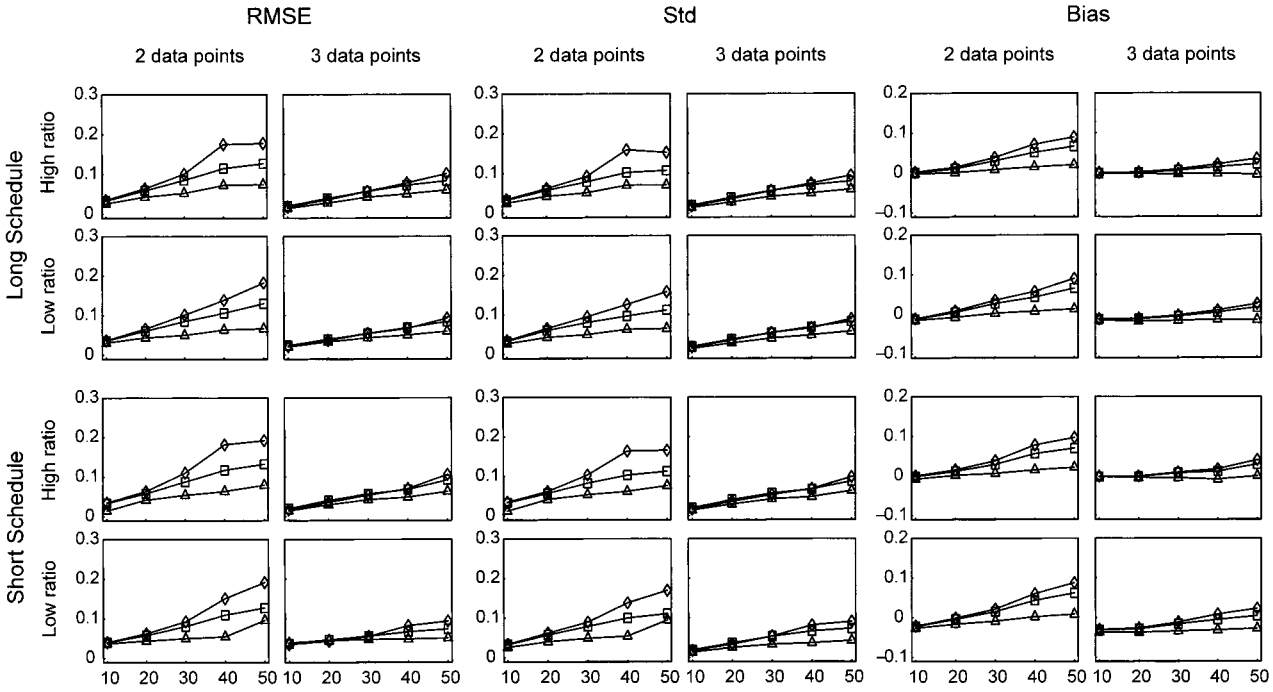

Figure 2—For all combinations of the controlled factors and for the three methods S, D1, and D2, utilizing either two or three data points, the RMSE, the std, and the bias are shown as a function of CV of measurement errors. Key: (◇) method S; (□) method D1; (△) method D2.

The D2 method draws power from the computational method that adds another data point at 0,0. Clearly, this power is more dramatic with few data points.

When three data points were used, the D2 method is marginally superior to the others for both sampling schedules. Methods D1 and S exhibit higher dependence on the CV levels for all parameters studied (Figure 2). This higher dependence is so despite the diminished contribution of the errorless datum point (0,0), which is now one out of four data points in determining the slope. However, for the worst scenario (short schedule-low ratio of rate constants), the D2 method underestimates the true value of k_e (Figure 2).

We recently used the phase plane approach jointly with the D1 method in investigating the absorption kinetics.[12] The results of the present study comparing the D1 and D2 methods in estimating the terminal slope allow someone to infer that the analytical power of the phase plane approach in investigating the absorption kinetics will be improved if the D2 method is used in place of the D1 method. Indeed, we carried out a number of simulations (results not shown), and the D2 method was superior.

For the sake of completion, one should add that the forced-through-zero classical linear regression analysis applied to the phase plane plot data does not take into account the error associated with the *x*-variable (*c* in abscissa). Special procedures are used in the literature in those situations where both variables are subject to error.[13,14] To this end, we applied the D2 method to our simulated data utilizing the geometric mean functional relationship (GMFR)[14] approach to linear regression for fitting. For the same sets of data, the GMFR approach did not provide better estimates for k_e when compared with the estimates derived from the classical linear regression. It seems likely that the error associated with the *y*-variable (d*c*/d*t* in ordinate) is considerably higher than the corresponding for *x*-variable (concentration *c*) and, therefore, the GMFR approach does not offer any advantage over the classical regression for the proper analysis of data.

Conclusions

The phase plane methods D1 and D2 perform better than the semilogarithmic approach for all scenarios examined when two or three data points are used for the estimation of the terminal slope. When four or five data points are available, all methods, D1, D2, and S, behave similarly.

The D2 method described here appears to be a robust approach to provide a reliable estimate for the terminal slope when two or three data points are available. Although essentially new, the D2 method can be handled computationally by simple calculations of the derivative at the various time points using interpolation techniques, such as spline functions, Lagrange polynomials, etc.[15] It should be emphasized that the technique of Lagrange polynomials used here provides a unique polynomial for a given (*c*,*t*) data set and, therefore, the method developed is not user dependent.

Appendix

The D2 method relies on the general problem of finding the Lagrange interpolating polynomial,[15] which is equal to the function describing the time course of drug in the body at a certain number of specified time points; that is, the experimental data points (c_j, t_j). We use three successive data points ($j = 1, 2, 3$) and derive the unique quadratic polynomial $c = pt^2 + qt + h$, which passes through these points.

The polynomial coefficients *p*, *q*, and *h* can be calculated by solving the following system:

$$\left.\begin{aligned} pt_1^2 + qt_1 + h &= c_1 \\ pt_2^2 + qt_2 + h &= c_2 \\ pt_3^2 + qt_3 + h &= c_3 \end{aligned}\right\} \qquad \text{(A1)}$$

Furthermore, the derivative dc_j/dt at any of these three points c_j is given by

$$\frac{dc_j}{dt} = 2pt_j + q \qquad j = 1, 2, 3 \tag{A2}$$

Solving the system A1 and replacing in A2 we obtain the following required derivatives:

$$\frac{dc_j}{dt} = c_1\left[\frac{2t_j - t_2 - t_3}{(t_1 - t_2)(t_1 - t_3)}\right] + c_2\left[\frac{2t_j - t_1 - t_3}{(t_2 - t_1)(t_2 - t_3)}\right] + c_3\left[\frac{2t_j - t_1 - t_2}{(t_3 - t_1)(t_3 - t_2)}\right] \tag{A3}$$

for every middle point of the data set $j = 2$. For the first and the last data points of the set that are not surrounded by other points, j is taken to be 1 and 3, respectively.

It is well-known that the derivative is more accurately calculated at the middle point.[15] In the present study, we took advantage of this fact and calculated all the derivatives of the data points used for the estimation of k_e by applying $j = 2$ in eq A3; for example, for the sampling schedule {6, 8, 12, 16, 20, 24} h, the derivatives at 8, 12, 16, and 20 h were calculated from the triplets (6, 8, 12), (8, 12, 16), (12, 16, 20), and (16, 20, 24) h, respectively. Unavoidably, the derivatives at the final points were calculated with eq A3 using $j = 3$ [e.g., for the sampling schedule just mentioned, the derivative at 24 h was calculated from the triplet (16, 20, 24) h].

References and Notes

1. Hamaguchi, T.; Shinkuna, D.; Yamanaka, Y.; Mitsuno, N. Bioavailability of mefenamic acid: influence of food and water intake. *J. Pharm. Sci.* **1986**, *75*, 891−893.
2. Sanders, S. N.; Michaelis, K.; Maurette, J. M.; Jaeger, H. Relative bioavailability of two spray formulations of nitroglycerin. *J. Pharm. Sci.* **1986**, *75*, 244−246.
3. Macheras, P.; Reppas, C. Studies on drug-milk freeze-dried formulations I: Bioavailability of sulfamethizole and dicumarol formulations. *J. Pharm. Sci.* **1986**, *75*, 692−696.
4. Midha, K. K.; Chakraborty, R.; Schwede, E. M.; Hawes, G.; McKay, J. W.; Hubbard, J. K.; Cooper, M.; Moore, M. Comparative bioavailability of two tablet formulations of phluphenazine dihydrochloride in drug-free psychiatric patients. *J. Pharm. Sci.* **1990,** *79*, 3−8.
5. Cefali, E. A.; Baufieled, C. R.; Gonzalez, M. A.; Wagner, J. G. In vivo determination of zero-order absorption from a transdermal glycerol trinitrate system. *Eur. J. Pharm. Biopharm*. **1993**, *39*, 140−143.
6. Liu, X.; Brouwer, K. L. R.; Pollack, G. M. A modified residual method to estimate the zero-order absorption rate constant in a one-compartment model. *Bioph. Drug Dispos*. **1997**, *18*, 93−101.
7. Tchernichovski, O.; Golani, I. A phase plane representation of rat exploratory behavior. *J. Neurosci. Meth*. **1995**, *62*, 21−27.
8. Cooke, J. D.; Brown, S. H. Phase plane tracking: a new method for shaping movements. *Brain Res. Bull.* **1986**, *16*, 435−437.
9. Karagueuzian, H. S.; Khan, S. S.; Denton, T. A.; Gotoh, M.; Mandel, W. J.; Diamond, G. A. Phase plane plot of electrograms as a marker of ventricular electrical instability during acute ischemia: initial experimental results and potential clinical applications. *Pacing Clin. Electrophysiol*. **1992**, *15*, 2188−2193.
10. Fonseca-Costa, A.; Magrassi, P.; Zin, W. A.; Romeo, L. J. M., Jr. Detection and quantification of small right-to-left shunts by the phase-plane method. *Am. J. Physiol*. **1984**, *247*, H517−H522.
11. Fonseca-Costa, A.; Zin, W. A. Cardiac output and mean transit time using the phase plane of dye-dilution curves. *Am. J. Physiol*. **1979**, *236*, H798−H801.
12. Dokoumetzidis, A.; Macheras, P. Investigation of absorption kinetics by the phase plane method *Pharm. Res.* **1998**, *14*, 1262−1269.
13. Seber, S. A. F.; Wild, C. J. Errors-in-variables models. In *Nonlinear Regression*; Wiley: New York, 1989; Ch.10.
14. Valsami, G.; Macheras, P. The geometric mean functional relationship approach to linear regression in pharmaceutical studies: application to the estimation of binding parameters. *Pharm. Sci.* **1995**, *1*, 551−554.
15. Burden, R. L.; Faires, J. D. *Numerical Analysis*; PWS Publishing: Boston, 1993; p 159.

Acknowledgments

Supported in part by the General Secretariat for Research and Development (PENED Grant 70/3/2824).

JS980317L

Synthesis, Stability, and Pharmacological Evaluation of Nipecotic Acid Prodrugs

FRANCESCO PAOLO BONINA,*,† LOREDANA ARENARE,‡ FRANCESCO PALAGIANO,‡ ANTONELLA SAIJA,§ FELICE NAVA,|| DOMENICO TROMBETTA,§ AND PAOLO DE CAPRARIIS‡

Contribution from *Dipartimento di Scienze Farmaceutiche, Facoltà di Farmacia, Università di Catania, Catania, Italy, Dipartimento di Chimica Farmaceutica e Tossicologica, Facoltà di Farmacia, Università di Napoli Federico II, Napoli, Italy, and Dipartimento Farmaco-Biologico, Facoltà di Farmacia, and Istituto di Farmacologia, Facoltà di Medicina e Chirurgia, Università di Messina, Messina, Italy.*

Received July 27, 1998. Final revised manuscript received January 20, 1999.
Accepted for publication January 22, 1999.

Abstract □ Nipecotic acid (**1**), one of the most potent in vitro inhibitors of neuronal and glial γ-amino butyric acid (GABA) uptake, is inactive as an anticonvulsant when administered systemically. To obtain in vivo active prodrugs of (**1**), we synthesized four new nipecotic acid esters (**3**–**6**), which were obtained by chemical conjugation with glucose, galactose, and tyrosine. These compounds were assayed to evaluate their in vitro chemical and enzymatic hydrolysis. In addition, their anticonvulsant activity was evaluated in vivo in Diluted Brown Agouti (DBA)/2 mice, an excellent animal model for the study of new anticonvulsant drugs. Esters (**3**–**6**) appeared stable, at various temperatures, in a pH 7.4 buffered solution and showed susceptibility to undergoing in vitro enzymatic hydrolysis. Intraperitoneally injected nipecotic acid (**1**) and esters (**3**–**5**) did not protect mice against audiogenic seizures; conversely, nipecotic tyrosine ester (**6**) showed a significant dose-dependent anticonvulsant activity. The in vivo protective activity of the ester (**6**) and the inefficiency of nipecotic acid (**1**) in the same experimental conditions suggest that this ester prodrug could be actively transported intact across the blood–brain barrier, beyond which it could be hydrolyzed.

Introduction

Several potentially central nervous system (CNS)-active drugs have relatively unfavorable physicochemical characteristics that hinder their transport into the brain. In fact, the brain microvessel endothelium provides a barrier to the passive transport of hydrophilic drugs into the brain. Several strategies have been developed to overcome this problem.[1−3] The prodrug approach represents a very promising method to enhance drug delivery to the brain. In fact, prodrugs are normally inactive and must generate active drug at their target by enzymatically or chemically mediated cleavage of their promoiety. The development of CNS-active prodrugs has been generally aimed at obtaining an improvement in the lipophilic character of the drug by transiently masking ionized group(s) of the parent drug. However, the preferential delivery of drugs or their derivatives to brain may be improved by using endogenous facilitated transport systems present at the blood−brain interface. Thus, chemical conjugation of potentially CNS-active drugs with an amino acidic or glycoside moiety actively transported across the blood−brain barrier (BBB) represents a plausible means of improving their brain delivery by providing suitable substrates for active membrane transport. In particular, conjugation with tyrosine or glucose has recently been shown to be a successful means of selective drug delivery; for example, phosphonoformate-L-tyrosine conjugate is actively transported,[4] by means of active amino acid carriers, through monolayers of porcine brain microvessel endothelial cells, and a glycosyl phosphotriester prodrug of 3′-azido-3′-deoxythymidine (AZT) shows good delivery to the CNS.[5] Similarly, conjugating glucose or galactose to poorly absorbable drugs can improve their intestinal absorption by means of glucose transport carriers in the small intestine;[6−8] for example, tocopherol conjugation to a monocarboxylate or glycoside moiety has appeared to provide suitable substrates for active erythrocyte membrane transport.[9]

Nipecotic acid (**1**) is one of the most potent in vitro inhibitors of neuronal and glial γ-aminobutyric acid (GABA) uptake.[10] Disorders such as Parkinson's disease, Huntington's chorea, and epilepsy may result from abnormalities in the GABA system and, thus, enhancement of the activity of GABA may be a useful treatment for these disorders. Unfortunately, nipecotic acid is a highly polar compound that does not easily penetrate the BBB, and is therefore inactive as an anticonvulsant when administered systemically.[11,12]

Successful prodrugs of nipecotic acid should be readily transported into the CNS and hydrolyzed there to the parent drug. Several esters of nipecotic acid (e.g., alkyl-, substituted phenyl-, and triaryl-nipecotic esters) have been synthesized with the goal to increase drug lipophilicity and have been reported to have varying degrees of anticonvulsant activity and to inhibit in vitro GABA uptake after conversion to the parent drug.[13−15]

The purpose of our research was to synthesize new nipecotic acid esters (**3**−**6**) obtained by chemical conjugation with essential nutrients, such as glucose, galactose, or tyrosine, that are actively transported across the BBB. These compounds were assayed to evaluate their in vitro chemical stability and enzymatic hydrolysis. In addition, their anticonvulsant activity was evaluated in vivo in Diluted Brown Agouti (DBA)/2 mice, an excellent animal model for the study of certain kinds of epilepsy and for testing new anticonvulsant drugs.[16,17]

Methods and Materials

Materials—Nipecotic acid was obtained from Sigma Chemical Company, Boc-L-tyrosine was purchased from Fluka Chemical Company. All other reagent chemicals were from Aldrich Chemical Company.

* Author to whom correspondence should be addressed at Dipartimento di Scienze Farmaceutiche, Viale A. Doria 6, 95125 Catania, Italy. Phone/Fax: 0039-095-222258. E-mail: boninaf@mbox.unict.it.
† Dipartimento di Scienze Farmaceutiche.
‡ Dipartimento di Chimica Farmaceutica e Tossicologica.
§ ipartimento Farmaco-Biologico.
|| Istituto di Farmacologia.

10.1021/js980302n CCC: $18.00
Published on Web 03/19/1999

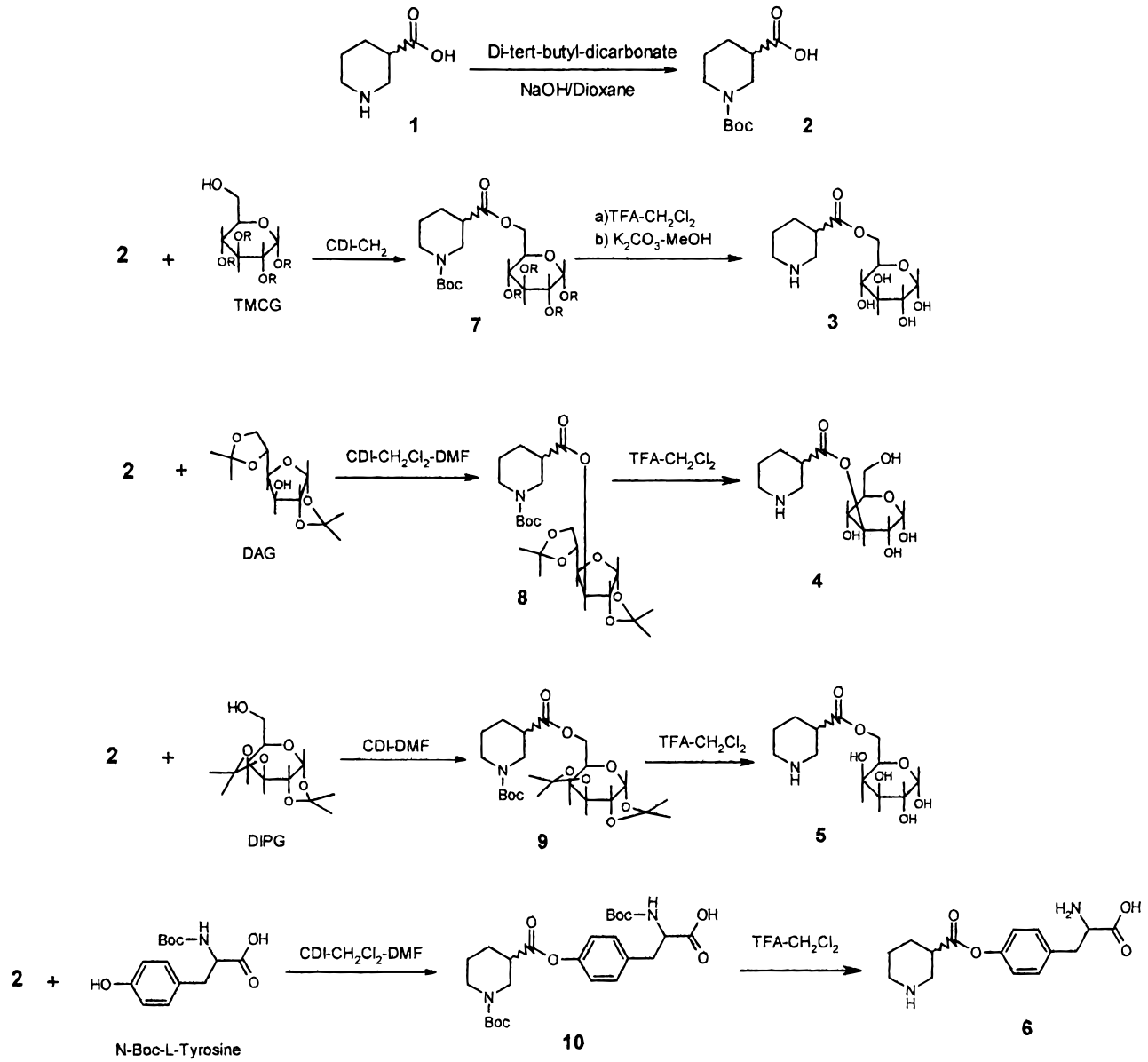

Scheme 1—Synthesis of nipecotic acid eters (**3**–**6**): synthetic routes and chemical structures of the obtained compounds (abbreviations: TMCG, 1,2,3,4-tetramethylcarbonate-D-glucose; DAG, diacetone-D-glucose; DIPG, 1,2,3,4-diisopropylidene-D-galactose).

Liquid Chromatographic (LC) grade acetonitrile and water, used in high-performance liquid chromatography (HPLC), were obtained from Merck and Carlo Erba, respectively.

Apparatus—Melting points were taken on Buchi 510 capillary melting point apparatus and are uncorrected.

The ^{1}H NMR and ^{13}C spectra were recorded on a Bruker WM 250 and on a Bruker AMX 500, respectively, using $CDCl_3$ as solvent. Chemical shifts are reported in ppm (δ) relative to tetramethylsilane as internal standard for ^{1}H NMR and in ppm relative to the solvent for ^{13}C NMR. Elemental analyses were performed on a Carlo Erba model 1108 elemental analyzer.

The flash chromatography was performed on Merck silica gel (0.040−0.063 mm) column. The HPLC apparatus consisted of a Varian 5000 system (Varian, Walnut Creek, CA) equipped with a 20-μL loop and an HP 1046A fluorescence detector (Hewlett-Packard, D-76337 Waldbrom, Germany). Integration of the chromatographic peaks was achieved with a 4290 integrator (Varian).

General Synthetic Method—All esters (**3**−**6**) were prepared as outlined in Scheme 1.

Initially we started from *N*-Boc nipecotic acid (**2**) obtained by treatment of (**1**) with di-*tert*-butyl-dicarbonate. Esterification of (**2**), in the presence of 1,1[1]-carbonyldiimidazole (CDI), with 1,2,3,4-*O*-tetramethyl carbonate-D-glucose (TMCG), diacetone-D-glucose (DAG), 1,2:3,4-di-*O*-isopropylidene-D-galactopyranose (DIPG), or *N*-Boc-L-tyrosine, afforded the corresponding esters (**7**−**10**). These esters, submitted to deprotection, allowed us to obtain compounds **3**−**6**.

N-Boc-Nipecotic Acid (2)—Nipecotic acid (**1**; 1 g, 7.75 mmol) was dissolved in dioxane (10.7 mL) and NaOH solution (1 N, 9.6 mL, 9.6 mmol). The resulting solution was stirred for 5 h, with the addition of the di-*tert*-butyl-dicarbonate (1.9 g, 10.0 mmol). The solvent was evaporated, and the resulting aqueous mixture was layered with ethyl acetate (EtOAc; 15 mL). Then, 1 N HCl solution was added with vigorous stirring until the pH of the aqueous phase was 2. The layers were separated, and the aqueous layer was extracted with EtOAc (3 × 10 mL). The EtOAc phases were combined, washed with brine (6 mL), dried over Na_2SO_4, filtered, and concentrated to give 1.42 g of (**2**) as a white solid (80% yield).

^{1}H NMR ($CDCl_3$): δ 4.1 + 3.85 (m, 2H, 2-H), 3.05 + 2.85 (m, 2H, 6-H), 2.50 (m, 1H, 3-H), 2.05 + 1.72 (m, 2H, 4-H), 1.70 + 1.46 (m, 2H, 5-H), 1.45 (m, 9H, -Boc).

N-Boc-Nipecotic Acid (1′,2′,3′,4′−O-Tetramethyl carbonate)-D-glucopyranos-6′-yl Ester (7)—To a stirred solution of *N*-Boc nipecotic acid (**2**; 1 g, 4.36 mmol) in CH_2Cl_2-dimethyl formamide (DMF) (9:1, 30 mL) was added CDI (706 mg, 4.36 mmol), and the mixture was stirred for 1 h at room temperature (RT). A solution of 1,2,3,4-tetramethyl carbonate-D-glucose (TMCG; 2.17 g, 5.26 mmol) in CH_2Cl_2/DMF (1:5, 30 mL) was added in a dropwise manner and

stirred for 24 h at RT. Most of the DMF was removed in vacuo, and the reaction mixture was taken up in EtOAc (30 mL), washed with water (20 mL) and brine (20 mL), and dried. Solvent was removed in vacuo and the crude was purified by flash chromatography eluting with hexane/EtOAc (6:4) to provide 1.90 g of (**7**) as a pale yellow oil (69.5% yield).

^{1}H NMR ($CDCl_3$): δ 6.00 (m, 1H, 1^1-H), 5.40 (m, 1H, 3^1-H), 4.92 (m, 1H, 2^1-H), 4.60 (m, 2H, 6^1-H), 4.15 (m, 2H, 4^1-H and 5^1-H), 4.05 + 3.85 (m, 2H, 2-H); 3.65 + 2.75 (m, 2H, 6-H), 3.55 (m, 12H, methyl carbonate groups), 2.55 (m, 1H, 3-H), 2.15 + 1.80 (m, 2H, 4-H), 1.45 + 1.35 (m, 2H, 5-H), 1.20(m, 9H, Boc).

Nipecotic Acid D*-glucos-6′-yl Ester* (**3**)—To a solution of **7** (1.90 g, 3.04 mmol) in CH_2Cl_2 (5 mL), 5 mL of trifluoroacetic acid (TFA) was added, and the mixture was stirred at RT for 2 h. Evaporation of the solvent gave a residue that was poured into a saturated solution of $NaHCO_3$ (20 mL) and extracted with $CHCl_3$ (3 × 15 mL). The organic layers were dried over Na_2SO_4 and concentrated in vacuo. This material (1.5 g) was taken directly into the next reaction without further purification. To a solution of crude (1.5 g) in MeOH (10 mL) was added K_2CO_3 (100 mg), and the mixture was stirred at RT for 12 h. Evaporation of the solvent gave a residue that was taken up in water and neutralized with 6 N aqueous HCl, diluted with more water, and washed with $CHCl_3$.The aqueous layers were concentrated in vacuo, and the residue was submitted to cation-exchange chromatography, eluting with 10% pyridine in water to give 610 mg of (**3**) (69% yield) as a pale yellow solid (mp 145−146 °C).

^{1}H NMR (D_2O): δ 4.65 (m, 1H, 1^1-H), 4.60 (m, 1H, 3^1-H), 3.70 (m, 1H, 2^1-H), 3.50 (m, 3H, 6^1-H and 5^1-C), 3.15 (m, 3H, 3^1-C and 2-H), 2.95 + 2.75 (m, 2H, 6H), 2.45 (m, 1H, 3-H), 1.90 + 1.65 (m, 2H, 4-H), + 1.55 (m, 2H, 5-H).

^{13}C NMR (D_2O + MeOD): δ 172 (−COOR), 96.84 (C-1^1), 76.86−76.66 (C-3^1), 75.71 (C-2^1), 75.31−75.08 (C-5^1), 70.56 (C-4^1), 63.57−63.33 (C-6^1), 48.78 (C-2), 45.02−44.91 (C-6), 39.57 (C-3), 26.63 (C-5), 21.98 (C-4).

*N-Boc Nipecotic Acid Diacetone-*α*-*D*-glucofuranos-3′-yl Ester* (***8***)—To a stirred solution of *N*-Boc-nipecotic acid (**2**; 1 g, 4.36 mmol) in CH_2Cl_2/DMF (9:1, 30 mL) was added CDI (706.97 mg, 4.36 mmol), and the mixture was stirred for 1 h at RT. A solution of DAG (1.36 g, 5.23 mmol) in CH_2Cl_2/DMF (9:1, 30 mL) was added in a dropwise manner and stirred for 24 h at RT. Most of the DMF was removed in vacuo, and the reaction mixture was taken up in EtOAc (30 mL), washed with water (20 mL) and brine (20 mL), and dried. Solvent was removed in vacuo, and the crude was purified by flash chromatography, eluting with hexane/Et_2O (8:2) to provide 1.34 g of **8** as a white oil (65% yield).

^{1}H NMR ($CDCl_3$): δ 5.85 (m, 1H, 1^1-H), 5.25 (m, 1H, 3^1-H), 4.41 (m, 1H, 2^1-H), 4.15 (m, 3H, 6^1-H and 5^1-H), 4.05 (m, 1H, 4^1-H), 3.95 (m, 2H, 2-H), 2.85 + 2.72 (m, 2H, 6-H), 2.48 (m, 1H, 3-H), 2.00 + 1.70 (m, 2H, 4-H), 1.70 + 1.55 (m, 2H, 5-H), 1.40 (m, 21H, -Boc and ketals).

Nipecotic Acid D*-Glucos-3′-yl Ester* (***4***)—To a solution of (**8**; 1.34 g, 2.84 mmol) in CH_2Cl_2 (5 mL) was added TFA (5 mL), and the mixture was stirred at RT for 12 h. Evaporation of the solvent gave a residue that was taken up in water (20 mL) and neutralized with 10% aqueous NH_4OH, diluted with more water, and washed with $CHCl_3$ (3 × 15 mL). The aqueous layers were concentrated in vacuo, and the residue was submitted to cation-exchange chromatography, eluting with 10% pyridine in water to give 690 mg of **4** (84% yield) as a pale yellow solid (mp 135−136 °C).

^{1}H NMR (D_2O): δ (m, 1H, 1^1-H), 4.41 (m, 1H, 3^1-H), 3.65 (m, 1H, 2^1-H), 3.50 (m, 2H, 6^1-H), 3.21 (m, 1H, 5^1-H), 3.15 (m, 2H, 4^1-H), 3.15 + 3.03 (m, 2H, 2-H), 2.90 + 2.81 (m, 2H, 6-H), 2.42 (m, 1H, 3-H); 1.81 + 1.67 (m, 2H, 4-H), 1.51 (m, 2H, 5-H).

^{13}C NMR (D_2O + MeOD): δ 180.03 (−COOR), 97.17−93.30 (C-1^1), 77.96 (C-3^1), 77.06 (C-2^1), 75.44 (C-5^1), 70.85 (C-4^1), 61.87 (C-6^1), 48.53 (C-2), 46.78 (C-6), 39.44 (C-3), 26.60 (C-5), 22.01 (C-4).

*N-Boc-Nipecotic Acid (1′,2′:3′,4′-diisopropylidene)-*α*-*D*-galactopyranos-6′-yl Ester* (***9***)—To a stirred solution of *N*-Boc-nipecotic acid (**2**; 1 g, 4.36 mmol) in CH_2Cl_2/DMF (9:1, 30 mL) was added CDI (706 mg, 4.36 mmol), and the mixture was stirred for 1 h at RT. A solution of DIPG (1.36 g, 5.23 mmol) in CH_2Cl_2/DMF (1:5, 30 mL) was added in a dropwise manner and stirred for 24 h at RT. Most of the DMF was removed in vacuo, and the reaction mixture was taken up in EtOAc (30 mL), washed with water (20 mL) and brine (20 mL), and dried. Solvent was removed in vacuo, and the crude was purified by flash chromatography eluting with hexane/Et_2O (8:2) to provide 1.75 g of **9** (85% yield) as a white oil.

^{1}H NMR ($CDCl_3$): δ 5.50 (m, 1H, 1^1-H), 4.60 (m, 1H, 3^1-H), 4.32 (m, 1H, 2^1-H), 4.20 (m, 3H, 6^1-H and 5^1-H), 4.00 (m, 1H, 4^1-H), 2.95 (m, 2H, 2-H), 2.75 (m, 1H, 3-H), 2.75 + 2.50 (m, 2H, 6-H), 2.05 + 1.70 (m, 2H, 4-H), 1.55 + 1.40 (m, 2H, 5-H), 1.40 (m, 21H, Boc and ketals).

Nipecotic Acid D*-Galactos-6′-yl Ester* (***5***)—To a solution of **9** (1.75 g, 3.71 mmol) in CH_2Cl_2 (5 mL), TFA (5 mL) was added, and the mixture was stirred at RT for 2 h. Evaporation of the solvent gave a residue that was taken up in water (20 mL), neutralized with 10% aqueous NH_4OH, diluted with more water, and washed with $CHCl_3$ (3 × 15 mL). The aqueous layers were concentrated in vacuo, and the crude was submitted to cation-exchange chromatography, eluting with 10% pyridine in water to give 915 mg of **5** (84% yield) as pale yellow solid (mp 138−139 °C).

^{1}H NMR (D_2O): δ 4.95 (m, 1H, 1^1-H), 4.28 (m, 1H, 3^1-H), 3.60 (m, 1H, 2^1-H), 3.42 (m, 2H, 6^1-H), 3.35 (m, 1H, 5^1-H), 3.25 (m, 1H, 4^1-H), 3.10 + 2.95 (m, 2H, 2-H), 2.80 (m, 2H, 6-H), 2.33 (m, 1H, 3-H), 1.75 + 1.65 (m, 2H, 4-H), 1.45 (m, 2H, 5-H).

^{13}C NMR (D_2O + MeOD): δ 179.41 (−COOR), 96.72 (C-1^1), 75.15 (C-3^1), 72.04 (C-2^1), 70.40 (C-5^1), 68.82 (C-4^1), 60.97 (C-6^1), 46.01 (C-2), 43.99 (C-6), 40.76 (C-3), 25.73 (C-4), 21.01 (C-5).

*N-Boc-Nipecotic Acid N-Boc-*L*-Tyrosyl Ester* (***10***)—CDI (0.71 g, 4.37 mmol) was added to a solution of **2** (1 g, 4.37 mmol) in CH_2Cl_2/DMF (3:1, 50 mL), and the resulting mixture was stirred at RT. After disappearance of the starting materials (determined by thin-layer chromatography), *N*-Boc-L-tyrosine (1.11 g, 4.15 mmol) in CH_2Cl_2/DMF (3:1, 150 mL) was added in a dropwise manner to the mixture over 120 min, and stirring was then continued for 12 h. After evaporation of the solvent, the residue was taken up in EtOAc (60 mL) and washed with water (2 × 30 mL). The organic layer was dried on Na_2SO_4 and evaporated to give a residue (3 g) that was submitted to flash chromatography, eluting with $CHCl_3$/MeOH/AcOH (95:4.5:0.5) to afford the title compound (**10**) as a pale yellow oil (1.5 g, 71%).

^{1}H NMR ($CDCl_3$): δ 6.85 (d, 2H J = 7 Hz, 2^1-H and 6^1-H), 6.64 (d, 2H J = 7 Hz, 3^1-H and 5^1-H), 4.91 (br, 1H, −NH−Boc), 4.45 (m, 1H, 8^1-H), 4.15 + 3.80 (m, 2H, 2-H), 2.85 (m, 2H, 7^1-H), 2.84 + 2.75 (m, 2H, 6-H), 2.40 (m, 1H, 3-H), 2.00 + 1.43 (m, 2H, 4-H), 1.40 (m, 20H, 5-H and -Boc).

Nipecotic Acid L*-Tyrosyl Ester* (***6***)—To a solution of **10** (1.75 g, 3.71 mmol) in CH_2Cl_2 (5 mL), TFA (5 mL) was added, and the mixture was stirred at RT for 2 h. Evaporation of the solvent gave a residue that was taken up in water (20 mL), neutralized with 10% aqueous NH_4OH, diluted with more water, and washed with $CHCl_3$ (3 × 15 mL). The aqueous layers were concentrated in vacuo, and the crude was submitted to cation-exchange chromatography, eluting with 10% pyridine in water to give 760 mg of **6** (73% yield) as a white solid (mp 134−135 °C).

^{1}H NMR (DMSO): δ 7.30 (d, 2H J = 7 Hz, 2^1-H and 6^1-H), 7.20 (d, 2H J = 7 Hz, 3^1-H and 5^1-H), 4.00 (m, 1H, 7^1-H), 3.50 + 3.30 (m, 2H, 2-H), 3.19 (m, 2H, 6^1-H), 3.05 (m, 2H, 6-H), 2.95 + 1.82 (m, 2H, 4-H), 1.82 + 1.70 (m, 2H, 5-H).

^{13}C (DMSO): δ 173.50 (−COOH); 172.84 (−COO−), 156.35 (C-4^1), 134.64 (C-1^1), 131.75−131.63 (C-2^1 and C-6^1), 116.79 (C-3^1 and C-5^1), 55.87 (C-7^1), 44.96 (C-2), 44.84 (C-6), 39.20 (C-3), 36.31−36.06 (C-6^1), 25.52 (C-5), 21.73 (C-4).

Chemical Stability—Nipecotic ester solutions were prepared by dissolving an aliquot of **3**−**6** in pH 7.4 phosphate buffer to give a final concentration of ≈10^{-5} M. The solution was maintained at 37 °C, and aliquots were withdrawn every 2 h for the initial 12 h of incubation and successively every 12 h for 7 days. The disappearance of the nipecotic esters was followed by HPLC analysis using the method reported later. Pseudo-first-order rate constants for chemical hydrolysis were determined from slopes of linear plots obtained by reporting the logarithm of residual nipecotic ester against time. All experiments were carried out in triplicate.

Enzymatic Stability—Enzymatic hydrolysis of nipecotic esters (**3**−**6**) was determined using the procedure described in the literature.[18] Porcine liver esterase (obtained from Sigma) was diluted 10 times with phosphate buffer and used to hydrolyze nipecotic esters. Nipecotic ester solutions were prepared by dissolving an aliquot of **3**−**6** in phosphate buffer to give a final concentration of ≈10^{-5} M. The solution was maintained at 37 °C, and 325 μL of porcine esterase were added to achieve a concentration of 1.3 U/mL. Aliquots of 300 μL were withdrawn every hour for 16 h and combined with 600 μL of 0.01 N HCl in methanol. After centrifugation at 5000 × *g* for 5 min, an aliquot of supernatant was derivatized by the method reported later and

then monitored by HPLC. Pseudo-first-order rate constants for enzymatic hydrolysis were determined from the slopes of linear plots obtained by reporting the logarithm of residual nipecotic ester against time. All experiments were carried out in triplicate.

Analytical Procedures—For dansyl derivatization of nipecotic acid (**1**) and of **3**−**5**, 100 μL of sample or of stock standard solutions (prepared in pH 7.4 phosphate buffer) were combined with 9 μL of dansyl chloride (1.5 mg/mL in acetonitrile) and 100 μL of 80 mM Li_2CO_3, pH 9.5. The mixture was kept at room temperature for 2 h in darkness. The reaction was stopped by adding 10 μL of 2% methylamine hydrochloride solution. For derivatization of nipecotic tyrosine ester (**6**), 125 μL of sample or of stock standard solutions (prepared in pH 7.4 phosphate buffer) were combined with 55 μL of fluorescamine (2 mg/mL in acetone) and 125 μL of 120 mM phosphate buffer, pH 8.0; then, the mixture was mixed by vortex for a few minutes. An aliquot of derivatized drug solutions (20 μL) was analyzed by the chromatographic method described next.

HPLC analysis was performed with an ODS Hypersil column (particle size, 5 μm; 125 × 4 mm i.d.; Hewlett-Packard, D-76337 Waldbrom, Germany). The mobile phase consisted of sodium acetate buffer (100 mM)/acetonitrile (75:25). The flow rate was set at 1.0 mL/min. Each sample was filtered prior to injection with a Millex HV13 filter (Waters-Millipore Corporation, Milford, MA), and an aliquot (20 μL) was injected into the HPLC apparatus. Dansyl derivatives of nipecotic acid (**1**) and **3**−**5** were monitored at 330 nm (excitation wavelength) and 510 nm (emission wavelength), and the fluorescamine derivative of the nipecotic tyrosine ester (**6**) was monitored at 260 nm (excitation wavelength) and 470 nm (emission wavelength). The retention times of dansyl derivatives of **1** and **3**−**5** were 6.29, 6.7, 6.9, and 7.37 min, respectively. The retention time of the fluorescamine derivative of ester **6** was 4.65 min. The limit of sensitivity was <2 μM for detection of dansyl derivatives of **1** and **3**−**5** and <3 μM for detection of the fluorescamine derivative of the ester **6**.

Anticonvulsivant Activity—DBA/2 mice, purchased from Charles River (Calco, Como, Italy), were used to evaluate the anticonvulsant activity of **1** and **3**−**6**. The DBA strain of the house mouse, *Mus musculus*, inbred since 1909, has been known since 1947 to be susceptible to sound-induced seizures. Nearly 100% of the males and females of the DBA/2 strain undergo an age-dependent, often fatal, sequence of convulsions (a wild running phase, followed by clonic convulsions and tonic extensions, ending in respiratory arrest or full recovery) when initially exposed to a loud mixed-frequency sound (12−16 kHz; 90−120 dB) such as a door bell. The age of maximum susceptibility of the DBA/2 strain to the sound-induced seizures has been reported as 20−39 days, 21−28 days, or 16−26 days. Other strains of audiogenic mice often require acoustic priming in the neonatal period to attain a similar degree of seizure susceptibility.[19]

In our study, male DBA/2 mice (10 for each experimental group), 21−28 days old, were exposed to auditory stimulation (109 dB for 60 s or until tonic extension occurred), 30 min following injection of the drugs tested **1** and **3**−**6** or of a same volume of their vehicle. Compounds **1** and **3**−**5** were dissolved in isotonic phosphate buffer, pH 7.4; **6** was dissolved in 20% EtOH/H_2O (v/v). The injection volume (both for drug solutions and the vehicle alone) was 0.1 mL/10 g body weight.

The intensity of seizure response (SR) was assessed on the following scale: 0 = no response, 1 = wild running, 2 = clonus, 3 = tonus, and 4 = respiratory arrest. The maximum response was recorded for each animal. Rectal temperature was recorded immediately prior to auditory testing using an Elektrolaboratoriet thermometer type T.E.3. Behavioral changes (spontaneous activity, explorative behavior, tremor, spontaneous convulsions) were observed during the period between drug administration and auditory testing.

Statistical comparisons between controls and drug-treated groups were carried out with Fisher's exact probability test (incidence of seizure phases) and the Mann−Whitney U test. The percentage of incidence of each seizure phase was calculated for the different doses of the drugs administered. Fifty percent efficient doses (ED_{50}s) with 95% confidence limits (95% CL) of the nipecotic tyrosine ester (**6**) were estimated, concerning tonus and clonus phases, by the method of Litchfield and Wilcoxon.

Table 1—Chemical and Enzymatic Stability of Esters 3–6

drug	$t_{1/2}$ (h)[a]	
	pH 7.4 buffer	esterase (1.3 U/mL)
3	150.00	8.30
4	169.42	10.70
5	197.48	14.0
6	27.37	2.5

[a] $t_{1/2}$ was calculated from the equation: $t_{1/2} = (\ln 0.5)/K^1$, where K^1 is the pseudo-first-order rate constant.

Results and Discussion

Data concerning chemical and enzymatic stability of ester prodrugs **3**−**6** are reported in Table 1. Figure 1 and Figure 2 show the times courses of disappearance of nipecotic esters (**3**−**6**) in pH 7.4 buffer solution and in the presence of porcine esterase. When we evaluated their chemical stability, the compounds appeared stable in a pH 7.4 buffered solution; however, prodrugs **3**−**5** disappeared more slowly than the ester **6**.

To confirm that the tested prodrugs can be enzymatically hydrolyzed, we evaluated their stability in the presence of porcine esterase. The findings indicate that each of the four esters **3**−**6** is capable of being cleaved in vitro by esterase.

Half-life times concerning enzymatic stability were notably lower than those obtained in buffer solution. Moreover, we found a good correlation between chemical and enzymatic decomposition rates of the prodrugs examined.

Table 2 shows the results obtained in in vivo experiments with a genetically seizure-prone strain (DBA/2) of mice. DBA/2 mice are a useful model to test compounds acting on the GABAergic system;[20] furthermore, this model avoids the problem of possible effects of tested substances on the absorption or metabolism of the convulsant compound that arises with drug-induced seizures.[21,22] According to data reported by other authors, we confirmed that nipecotic acid (**1**; 0.75 mmol/kg), given systemically 30 min before sound exposure, possesses no anticonvulsant effect.[11,12] Also, **3**−**5**, intraperitoneally injected in the same experimental schedule at dose levels up to 0.75 mmol/kg, did not protect mice against all phases of audiogenic seizures. Conversely, when the ester prodrug **6** was administered systemically, a significant dose-dependent anticonvulsant activity was observed. In fact, a marked reduction in the incidence of each phase (wild running, clonus, tonus, respiratory arrest) of audiogenic seizures was evident at the dose levels studied (0.125, 0.17, 0.21, 0.25, 0.5, and 0.75 mmol/kg). Furthermore, no behavior alteration or change in rectal temperature in comparison with control animals were recorded after administration of **3**−**6** (data not shown).

The in vivo protective activity of systemically administered nipecotic tyrosine ester **6** against audiogenic seizures and the inefficiency of nipecotic acid (**1**) under the same experimental conditions suggest that this ester prodrug is transported intact across the BBB, beyond which it could be hydrolyzed. Tyrosine enters the brain through the large neutral amino acid transporter system. This system, present in the brain microvessel endothelial cells, has been extensively characterized and is of particular interest in the transport of amino acid drugs into the brain.[23,24] Moreover, Walker and co-workers[4] have recently demonstrated that a phosphonoformate−L-tyrosine conjugate possesses a high affinity for large amino acid transporters in monolayers of porcine brain microvessel endothelial cells and so might be a substrate for facilitated transport at the BBB. As to our findings, one tempting hypothesis is that the tyrosine moiety acts as a vector, which should allow

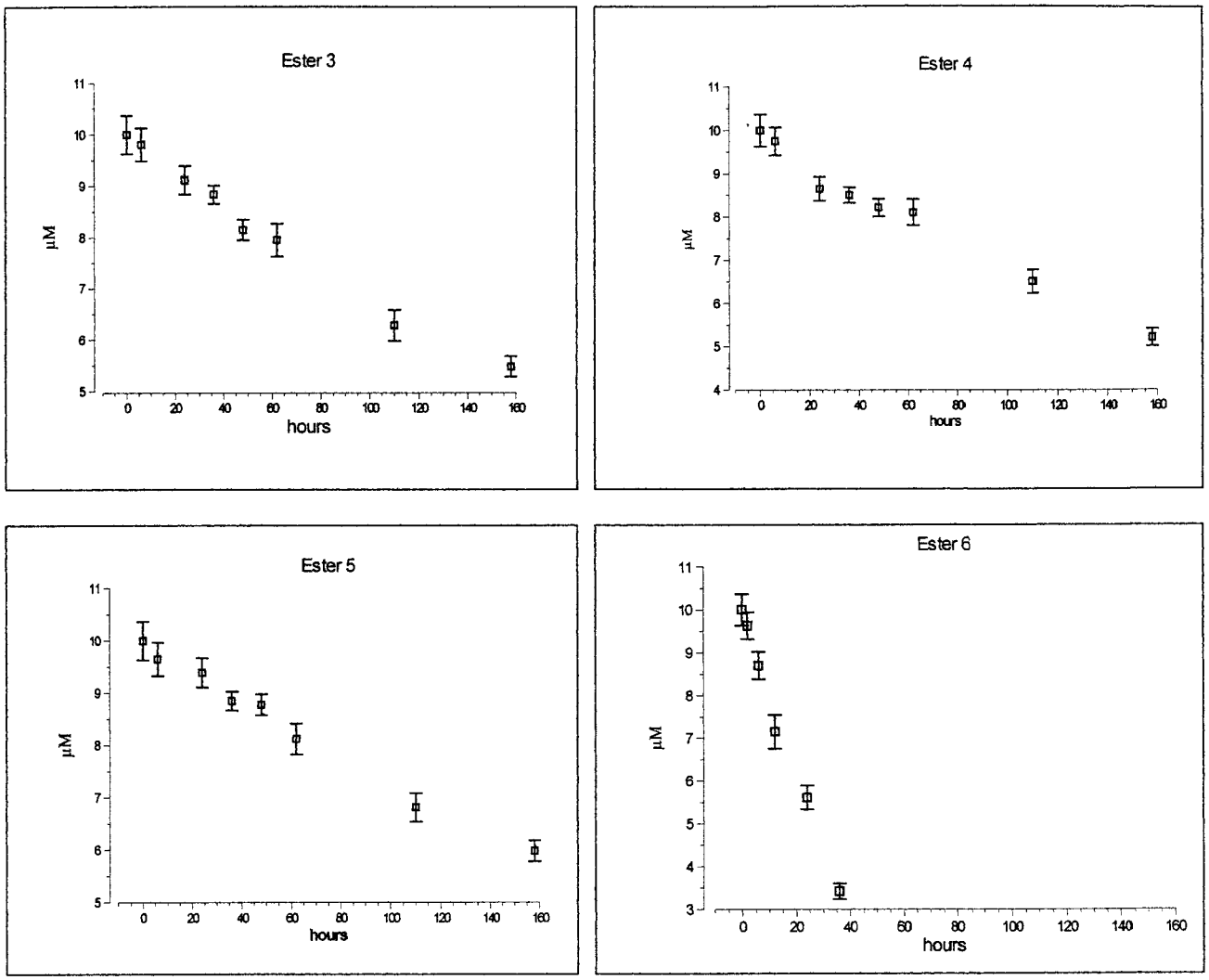

Figure 1—Time courses of disappearance of nipecotic esters (**3**–**6**) in pH 7.4 buffer solution obtained by plotting time (h) versus drug concentration (μM). Each point represents the mean ± SD of three experiments.

the transport of the nipecotic tyrosine ester (**6**) across the BBB; as the drug appears to achieve pharmacologically active concentrations in the brain, it could be supposed to be endowed with a high affinity for the amino acid carriers. Unfortunately, the almost absolute insolubility of nipecotic tyrosine ester (**6**) in water made it impossible to calculate its water/oil partition coefficient. Of course, further studies are needed to clarify if the ability of **6** to cross the BBB is dependent also on its lipophilicity. For example, Stark et al.[25] have demonstrated that des-tyrosine1-D-phenylalanine3-beta-casomorphin is able to cross the BBB by paracellular transport without using a carrier system. One could to point out that the nipecotic tyrosine ester (**6**) seems more potent than other lipophilic nipecotic acid esters, such as (+)ethyl nipecotate[12] or pivaloyloxymethyl ester;[11] however, its ED_{50}s calculated for tonus (ED_{50}, 0.130 mmol/kg; 95% CL, 0.115−0.146 mmol/kg) and clonus (ED_{50}, 0.173 mmol/kg, 95% CL, 0.162−0.186 mmol/kg) are very higher than those of tiagabine (a GABA uptake inhibitor, structurally related to nipecotic acid), as measured in the same experimental models[26] (tonus: ED_{50}, 1 μmol/kg; clonus: ED_{50}, 5 μmol/kg).

Furthermore, the present findings do not allow us to establish exactly whether the observed anticonvulsant activity of **6** could be due to nipecotic acid derived from its enzymatic hydrolysis or, partially at least, to the intact compound. However, several papers have provided information that the anticonvulsant effect and GABA uptake inhibition, induced by various esters of nipecotic acid, are mostly due to free nipecotic acid generated after hydrolysis in the brain.[27,28]

Similar results have also been reported for esters of isoguvacine, a GABA uptake inhibitor, structurally related to nipecotic acid.[29] Finally we can exclude that the observed anticonvulsant effect of **6** is due to the free promoiety (tyrosine) generated in the brain; in fact, tyrosine, systemically injected under the same experimental conditions at a dose level of 0.75 mmol/kg, elicited no protective effect against audiogenic seizures (data not shown).

Concerning prodrugs **3**−**5**, several possible explanations can be offered for their lack of anticonvulsant activity. First, β−D-glucose and galactose enter the brain through the transporter GLUT-1.[30] A high transporter affinity is required, so that a drug may be efficiently transported by the carrier across the BBB. Prodrugs **3**−**5** might have insufficient affinity for this carrier to achieve significant brain uptake and/or their transport through the BBB might be limited by competition with the endogenous substrate. In addition, the hydrophilic character of esters **3**−**5** would preclude their passive transport through the BBB.

Second, carbohydrate receptor-mediated targeting of drugs has been proposed as a potential method for site-specific delivery of drugs to cells possessing carbohydrate receptors on their surface. Several types of galactosylated drugs are reported to be interesting candidates for successful delivery to liver cells.[31] So, nipecotic derivatives

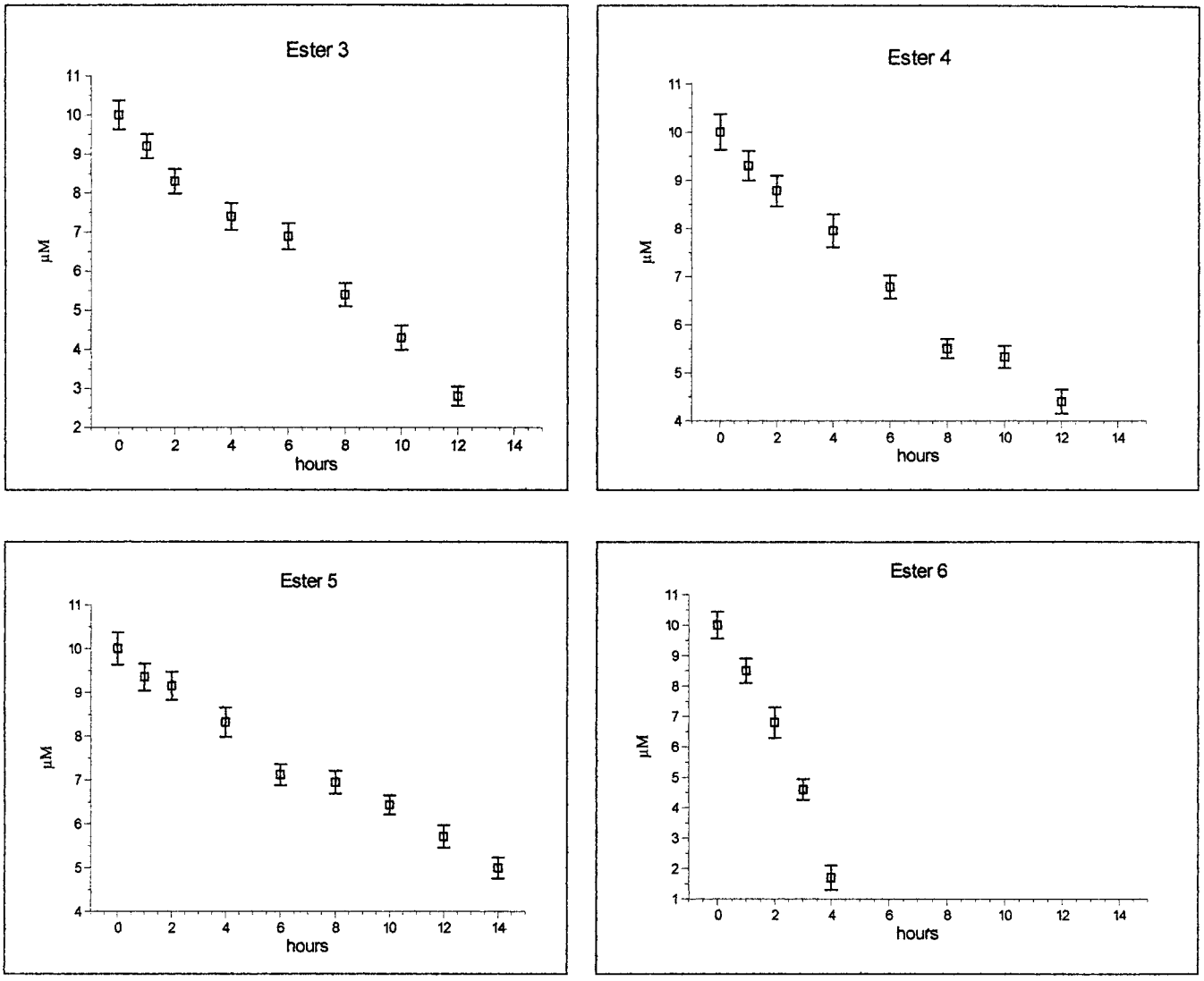

Figure 2—Time courses of disappearance of nipecotic esters (**3**–**6**) in the presence of porcine esterase obtained by plotting time (h) versus drug concentration (μM). Each point represents the mean ± SD of three experiments.

Table 2—Effects of Intraperitoneal Injection of 1, 3, 4, 5, and 6 on Audiogenic Seizures in DBA/2 Mice[a]

drug	dose, mmol/kg	% response					
		W.R.[b]	clonus	tonus	R.A.[b]	SR[b]	*n*[b]
controls A[c]	vehicle (0)	100	100	80	60	3.40	10
1	0.750	100	100	88.8	55.5	3.44	9
3	0.750	100	100	88.8	55.5	3.44	9
4	0.750	100	100	88.8	55.5	3.44	9
5	0.750	100	100	88.8	55.5	3.44	9
controls B[d]	vehicle (0)	100	100	87.5	50	3.37	8
6	0.125	75	75	50	25	2.25	8
6	0.170	60	50	40	10	1.6[e]	10
6	0.210	40	40	30	0	1.1[e]	10
6	0.250	20	20[d]	20[d]	0[d]	0.60[e]	10
6	0.500	20[d]	10[d]	0[d]	0[d]	0.30[e]	10
6	0.750	20[d]	20[d]	0[d]	0[d]	0.40[e]	10

[a] The incidence of each seizure phase is expressed as the percentage of mice in each group displaying that phase. [b] W.R. = wild running; R.A. = respiratory arrest; SR = seizure response expressed as arithmetic mean of the maximum individual response in each group; *n* = number of mice. [c] Mice given buffer, pH 7.4, 10 mL/kg, ip. [d] Mice given 20% EtOH/H_2O solution, 10 mL/kg, ip. [e] $p < 0.05$ from controls B, as assessed by Fisher's exact probability test. [f] $p < 0.05$ from controls B, as assessed by Mann–Whitney U test.

3−**5**, obtained by the conjugation with glucose and galactose, could be rapidly taken up and degraded by the liver after systemic injection. Therefore, these derivatives are hindered in the achievement of pharmacologically active concentrations in the brain.

Finally, a correlation between in vitro rates of enzymatic hydrolysis and its pharmacologic activity is generally expected for CNS-active prodrugs.[29] In fact, the rate of hydrolysis in plasma would have to be sufficiently slow to allow the prodrug to gain access to the brain, but not so slow as to remain inactive within the brain. Compounds **3**−**5** appeared much more resistant to enzyme-catalyzed hydrolysis ($t_{1/2}$ = 8.30, 10.70, and 14.0 h, respectively, for **3**, **4**, and **5**) than the prodrug **6** ($t_{1/2}$ = 2.5 h), but unlike **6** do not give protection against audiogenic seizures 30 min after administration. Moreover, no anticonvulsant effect was observed when audiogenic seizures were induced 1, 2, or 3 h after injection of **3**−**5** (data not shown). Further investigations would clarify if a significant pharmacological effect may be detectable at longer times after administration of the very slowly hydrolyzed esters **3**−**5**.

In conclusion, the present findings indicate that nipecotic tyrosine ester **6** is an excellent prodrug for potential application in the treatment of epilepsy and of other disorders resulting from abnormalities in the GABA system. Further studies are in progress to investigate the bioavailability of this compound and to clarify its mechanism of action.

References and Notes

1. Greig, N. H. Drug entry into the brain and its pharmacological manipulation. In: *Physiology and Pharmacology of the Blood-Brain Barrier*. Bradbury, M. W. B., Ed.; Springer-Verlag: New York, 1992; pp 487−524.
2. Robinson, P. J.; Rapoport, S. I. Transport of drugs. In: *Physiology and Pharmacology of the Blood-Brain Barrier*. Bradbury, M. W. B., Ed.; Springer-Verlag: New York, 1992; pp 279−300.
3. Greenwood, J. Experimental manipulation of the blood-brain and blood-retinal barriers. In: *Physiology and Pharmacology of the Blood-Brain Barrier*. Bradbury, M. W. B., Ed.; Springer-Verlag: New York, 1992; pp 459−486.
4. Walker, I.; Nicholls, D.; Irwin, W. J.; Freeman, S. Drug delivery via active transport at the blood-brain barrier: affinity of a prodrug of phosphonoformate for the large amino acid transporter. *Int. J. Pharm*. **1994**, *104*, 157−167.
5. Namane, A.; Gouyette, C.; Fillion, M.; Fillion, G.; Huynh-Dinh, T. Improved brain delivery of AZT using a glycosyl phosphotriester prodrug, *J. Med. Chem*. **1992**, *35*, 3039−3044.
6. Mizuma, T.; Ohta, K.; Hayashi, M.; Awazu, S. Intestinal active absorption of sugar-conjugated compounds by glucose transport system: implication of improvement of poorly adsorbable drugs, *Biochem. Pharmacol*. **1992**, *43*, 2037−2039.
7. Mizuma, T.; Ohta, K.; Hayashi, M.; Awazu, S. Comparative study of active absorption by the intestine and disposition of anomers of sugar-conjugated compounds. *Biochem. Pharmacol*. **1993**, *45*, 1520−1523.
8. Mizuma, T.; Ohta, K.; Awazu, S. The beta-anomeric and glucose preferences of glucose transport carrier for intestinal active absorption of monosaccharide conjugates. *Biochim. Biophys. Acta* **1994**, *1200*, 117−122.
9. Bonina, F. P.; Lanza, M.; Montenegro, L.; Salerno, L.; Smeriglio, P.; Trombetta, D.; Saija, A. Transport of alpha-tocopherol and its derivatives through erytrocyte membranes. *Pharm. Res*. **1996**, *13*, 1342−1346.
10. Krogsgaard-Larsen, P.; Johnston, G. A. R. Inhibition of GABA uptake in rat brain slices by nipecotic acid, various isoxazoles and related compounds. *J. Neurochem*. **1975**, *25*, 797−802.
11. Meldrum, B. S.; Croucher, M. J.; Krogsgaard-Larsen, P. GABA-uptake inhibitors as anticonvulsant agents. In: *Problems in GABA Research*; Okada, Y.; Roberts, E., Eds.; Exerpta Medica: Amsterdam, 1982; pp 182−191.
12. Horton, R. W.; Collins, J. F.; Anlezark, G. M.; Meldrum, B. S. Convulsant and anticonvulsant actions in DBA/2 mice of compounds blocking the reuptake of GABA. *Eur. J. Pharmacol*. **1979**, *59*, 75−83.
13. Hinko, C. N.; Seibert, K.; Crider, A. M. Anticonvulsant activity of the nipecotic acid ester, (±)-*m*-nitrophenyl-3-piperidinecarboxylate, *Neuropharmacology* **1984**, *23*, 1009−1014.
14. Hinko, C. N.; Crider, A. M.; Wood, J. D. A comparison of prodrug esters of nipecotic acid. *Neuropharmacology* **1988**, *27(5)*, 475−483.
15. Dhar, T. G.; Borden, L. A.; Tyagarajan, S.; Smith, K. E.; Branchek, T. A.; Weinshank, R. L.; Gluchowski, C. Design, synthesis and evaluation of substituted triaryl nipecptic acid derivatives as GABA uptake inhibitors: identification of a ligand with moderate affinity and selectivity for the cloned human Gaba transporter GAT.3. *J. Med. Chem*. **1994**, *37-(15)*, 2334−2342.
16. Chapman, A. G.; Croucher, M. J.; Meldrum, B. S. Evaluation of anticonvulsant drugs in DBA/2 mice with sound-induced seizures. *Arzneim.−Forsch./Drug Res*. **1984**, *34*, 1261−1264.
17. Seyfried, T. N.; Glaser, G. H. A review of mouse mutants as genetic models of epilepsy. *Epilepsia* **1985**, *26*, 143−150.
18. Bonina, F. P.; Montenegro, L.; Guerrera, F. Naproxen 1-alkylazacicloalkan-2-one esters as dermal prodrugs: in vitro evaluation. *Int. J. Pharm*. **1993**, *100*, 99−105.
19. Fischer, R. S. Animal models of the epilepsies. *Brain Res. Rev*. **1989**, *14*, 245−278.
20. Horton, R. W.; Prestwich, S. A.; Meldrum, B. S. Gamma-aminobutyric acid and benzodiazepine binding sites in audiogenic seizure-susceptible mice. *J. Neurochem*. **1982**, *39*, 864−870.
21. De Sarro, G. B.; Chimirri, A.; De Sarro, A.; Gitto, R.; Grasso, S.; Giusti, P.; Chapman. A. G. GYKI 52466 and related 2,3-benzodiazepines as anticonvulsant agents in DBA/2 mice. *Eur. J. Pharmacol*. **1995**, *294*, 411−422.
22. Suzdak, P. D.; Jansen, J. A. A review of the preclinical pharmacology of tiagabine: a potent and selective anticonvulsant GABA uptake inhibitor. *Epilepsia* **1995**, *36*, 612−626.
23. Smith, Q. R.; Momma, S.; Aoyagi, M.; Rapoport, S. I. Kinetics of neutral amino acid transport across the blood-brain barrier. *J. Neurochem*. **1987**, *49*, 1651−1658.
24. Reichel, A.; Begley, D. C.; Ermisch, A. Arginine vasopressin reduces the blood-brain transfer of L-tyrosine and L-valine: further evidence of the effect of the peptide on the L-system transporter at the blood-brain barrier. *Brain Res*. **1996**, *713*, 232−239.
25. Stark, H.; Van Bree, J. B.; de Boer, A. G.; Jaehde, U.; Breimer, D. D. In vitro penetration of des-tyrosine 1-D-phenylalanina-3-beta-casomorphin across the blood-brain barrier. *Peptides* **1992**, *13*, P47−51.
26. Dalby, N. O.; Nielsen, E. B. Comparison of the preclinical anticonvulsant profiles of tiagabine, lamotrigine, gabapentin and vigabatrin. *Epilepsy Res*. **1997**, *28*, 63−72.
27. Crider, A. M.; Tita, T. T.; Wood, J. D.; Hinko, C. N. Esters of nipecotic and isonipecotic acids as potential anticonvulsants. *J. Pharm. Sci*. **1982**, *71*, 1214−1219.
28. Nassereddine-Sebaei, M.; Crider, A. M.; Carrol, R. T.; Hinko, C. N. Determination of *m*-nitrophenol and nipecotic acid in mouse tissues by high-performance liquid chromatography after administration of the anticonvulsivant *m*-nitrophenyl-3-piperidinecarboxylate hydro-chloride. *J. Pharm. Sci*. **1993**, *82*, 39−43.
29. Falch, E.; Krogsgaard-Larsen, P. Esters of isoguvacine as potential prodrugs. *J. Med. Chem*. **1981**, *24*, 285−289.
30. Fuglsang, A.; Lomholt, M.; Gjedde, A. Blood-brain transfer of glucose and glucose analogues in newborn rats. *J. Neurochem*. **1986**, *46*, 1417−1428.
31. Takakura, Y.; Hashida, M. Macromolecular carrier systems for targeted drug delivery: pharmacokinetics considerations on biodistribution. *Pharm. Res*. **1996**, *13*, 820−831.

Acknowledgments

This paper was partially supported by the Italian M.U.R.S.T. (40%).

JS980302N

Simultaneous Investigation of Indinavir Nonlinear Pharmacokinetics and Bioavailability in Healthy Volunteers Using Stable Isotope Labeling Technique: Study Design and Model-Independent Data Analysis

KUANG C. YEH,*,† JULIE A. STONE,† ALEXANDRA D. CARIDES,‡ PAUL ROLAN,|| ERIC WOOLF,† AND WILLIAM D. JU§

Contribution from *Departments of Drug Metabolism and Biostatistics, Merck Research Laboratories, West Point, Pennsylvania 19486, Department of Clinical Pharmacology, Merck Research Laboratories, Rahway, New Jersey 07065, and Medeval Limited, University of Manchester, Lloyd Street North, Manchester, M15 6SH, England.*

Received June 6, 1998. Final revised manuscript received December 17, 1998.
Accepted for publication February 25, 1999.

Abstract □ Indinavir follows nonlinear pharmacokinetics upon oral administration at clinical doses. A study employing the stable isotope administration technique in a three-treatment design was conducted to identify the source of the nonlinearity and to determine the dose-dependency of systemic bioavailability. In treatment A, 400 mg of unlabeled indinavir (D_0) was coadministered orally with 16 mg of a hexadeutero analogue of indinavir (D_6) intravenously. In treatment B, 800 mg of D_0 po was coadministered with 16 mg of D_6 intravenously. In treatment C, 16 mg of iv D_6 was infused concurrently with 16 mg iv of D_0. Plasma concentrations of D_0 and D_6 were determined by an LC/MS/MS assay method. Concentrations of indinavir in plasma increased greater than dose-proportionally over the 400- to 800-mg dose range. No meaningful kinetic isotope effects were found in treatment C. Plasma concentrations of D_6 were dependent on the coadministered D_0-indinavir dose and were lowest in treatment C, higher in treatment A, and highest in treatment B. The bioavailability of indinavir was high (60–65%) and comparable between the 400- and 800-mg doses. There was a significant contribution of nonlinear kinetics in the systemic circulation to the observed disproportional increase in plasma concentrations following oral dosing. The high bioavailability at clinically relevant doses suggests a high degree of saturation of first-pass metabolism. These results further demonstrate that the concomitant administration technique in combination with the LC/MS/MS method can provide a realistic and reliable means of elucidating important pharmacokinetic properties of drug candidates during product development.

Introduction

Characterization of biopharmaceutical and pharmacokinetic attributes of a drug candidate is an integral part of the drug product development. When properly studied and evaluated, such information provides the scientific basis for the optimal definition of dosage regimens. Among the many important properties are the pharmacokinetics of drug absorption and disposition and their dependence on dose or concentration. Procedures for bioavailability assessment differ, depending on whether linear kinetics prevail in the therapeutically relevant concentration range.

For a drug exhibiting linear pharmacokinetics, as demonstrated by proportional increases in plasma concentration with dose, plasma clearance can be assumed to be independent of the concentration. Clinical studies for determination of the systemic bioavailability are often conducted in a crossover fashion. The bioavailability of the oral treatment relative to the reference intravenous treatment is estimated by comparing the dose-normalized areas under the drug concentration curve (AUC). The crossover study design eliminates the intersubject variation and results in improved reliability of the estimates.

For a drug with nonlinear disposition kinetics, its clearance is concentration-dependent, and the above-cited crossover bioavailability study design may not be valid.[1−4] Under special circumstances, concomitant administration of the intravenous reference dose and the oral dose may provide a viable approach of obtaining reliable bioavailability estimates.[1−3,5] In this approach, the reference treatment is distinguished from the oral treatment by the use of a tracer dose of the isotopically labeled drug.[2,4,6] With recent advances in the LC/MS/MS assay detector technology,[7,8] simultaneous tracking and quantitation of both the unlabeled and labeled analytes can be reliably achieved.[9,10] Due to its potential of high specificity and sensitivity, the technique is most useful when the labeled dose, given intravenously, is small in mass relative to that of the unlabeled dose given orally. With the concurrent dosing study design, the intrasubject variation is eliminated. Further, stable isotope-labeled analogues may be repetitively administered in clinical studies. The concurrent dosing design may also provide a means of identifying the source(s) of pharmacokinetic nonlinearity.

Indinavir, a potent HIV protease inhibitor, exhibited greater than dose-proportional increases in plasma concentrations following oral administration in clinical studies.[11,12] Possible causes of the observed nonlinearity include the dose-dependent absorption or first-pass metabolism, nonlinear systemic disposition, or both. Based on the LC/MS/MS assay technology, a clinical study was conducted to examine the source(s) of the nonlinearity and to compensate for the observed nonlinearity and thereby enabling estimates of the systemic bioavailability in the therapeutic dose range. The purpose of this communication is to present the design and findings of the study.

Materials and Methods

Equation 1 forms the basis of computing the bioavailability (F) of a given dose (D) based on the observed drug concentration ($C(t)$):

* Corresponding author: Phone: (215) 652-6117. Fax: (215) 993-3533. E-mail: kuang_yeh@merck.com.
† Department of Drug Metabolism, Merck Research Laboratories.
‡ Department of Biostatistics, Merck Research Laboratories.
§ Department of Clinical Pharmacology, Merck Research Laboratories.
|| Medeval Limited.

10.1021/js9802392 CCC: $18.00
Published on Web 03/31/1999

$$F_{po} = \frac{F_{iv} D_{iv} \int_0^\infty CL_{po}(t) C_{po}(t) dt}{D_{po} \int_0^\infty CL_{iv}(t) C_{iv}(t) dt} \quad (1)$$

where CL(t) is the clearance at time t, and subscripts iv and po denote the mode of administration. In general, the time profile of CL(t) is concentration-dependent and is unknown in a system where the disposition kinetics are nonlinear. The integrated quantities in eq 1 represent the respective amount of the drug which has been eliminated from the systemic circulation following the administration of test and reference treatments. In the present case, F_{iv} is assumed to be unity.

Upon simultaneous administration of a tracer intravenous dose and an oral dose, the systemically available drug from both doses is subject to the same time-course of clearance, CL(t):

$$F_{po} = \frac{D_{iv}}{D_{po}} \frac{\int_0^\infty CL(t) C_{po}(t) dt}{\int_0^\infty CL(t) C_{iv}(t) dt} \quad (2)$$

Under the situation where $C_{iv}(t)$ is an exact multiple of $C_{po}(t)$ at all times, the ratio of the two would remain constant:

$$z = \frac{C_{iv}(t)}{C_{po}(t)} \quad (3)$$

Substituting eq 3 into eq 2:

$$F_{po} = \frac{D_{iv}}{D_{po}} \frac{\int_0^\infty CL(t) C_{iv}(t) dt}{z \int_0^\infty CL(t) C_{iv}(t) dt} = \frac{D_{iv}}{z D_{po}} \quad (4)$$

Expressions similar to eqs 2 and 3 in bioavailability assessment under concurrent administration conditions have been discussed and reported previously.[5] In actual practice, due to differences in the absorption rate and infusion rate, eq 3 is virtually impossible to achieve since the ratio of the two concentrations will invariably fluctuate with time. As an approximation, an apparent z_{app} is defined as follows:

$$z_{app} = \frac{\int_0^\infty C_{iv}(t) dt}{\int_0^\infty C_{po}(t) dt} = \frac{AUC_{iv}}{AUC_{po}} \quad (5)$$

By analogy to eq 4, the bioavailability is estimated by the following:

$$F_{po} \cong \frac{D_{iv}}{z_{app} D_{po}} \quad (6)$$

In a nonlinear disposition system, the bioavailability computed with eq 6 would not be exact but would be an approximation. The degree of the imperfection would depend on the degree to which the concentration ratios, shown in eq 3, fluctuated with time. The magnitude of fluctuations in such a system might be minimized, but not eliminated, with properly designed clinical studies. To reduce the errors, other study designs, such as delaying the iv bolus or varying the infusion period to various fractions of plasma peak time (T_{max}), have been discussed previously.[5]

With the present approach, the estimation of bioavailability is based on the comparison of dose-normalized AUCs, and specific assumptions regarding the underlying mechanism(s) of the nonlinearity are not required. This represents a model-independent approach, with its computational procedures being identical to that of the conventional AUC method. It is worth noting that in a linear pharmacokinetic system, the accuracy of bioavailability estimation is independent of the fluctuations shown in eq 3.

Study Subjects and Dosing Regimens—The study was conducted as an open-label, three-period, single-dose study with 12 healthy subjects (6 males and 6 females, age range: 21 to 31 years; mean age, 25.3 years; weight range: 53 to 92 kg; mean weight, 70.9 kg). The protocol was approved by the Medeval Independent Ethics Committee, and informed consent was obtained from all subjects. The study subjects received doses of the unlabeled indinavir (D_0) as well as indinavir which was labeled with six deuterium atoms on the pyridomethyl side chain (D_6). The three treatments were as follows:

Treatment A: 400 mg D_0 orally as one 400-mg dry-filled capsule (DFC) plus 16-mg D_6 dose intravenously as an infusion.

Treatment B: 800 mg D_0 orally as two 400-mg DFC's plus 16-mg D_6 dose intravenously as an infusion.

Treatment C: Simultaneous intravenous infusion of 16 mg D_0 and 16 mg D_6 over 30 min.

Subjects fasted from midnight before drug administration and remained fasted until 2 h after the dosing. In treatments A and B, each oral D_0-indinavir dose was administered at 0 h with 240 mL water, and each intravenous D_6 dose was administered as a 30-min infusion, starting at 15 min and ending at 45 min following the ingestion of the oral dose. The infusion regimen was designed to minimize the fluctuations in the ratio between the expected plasma concentrations of D_0 and D_6 over time. Previous clinical studies[11–13] indicated an average T_{max} of 0.8 h and often with a lag time <0.25 h in absorption following oral administration.

Treatment C was designed to examine (a) the disposition kinetics of indinavir at concentrations significantly lower than that generally achieved following oral dosing; and (b) the possible in vivo enzymatic isotope effect on the metabolism (and therefore the systemic disposition) of indinavir. Depyridomethylation is known to be one of the CYP3A-mediated oxidative biotransformations of indinavir in humans.[14,15]

Treatments A and B were administered according to a randomized two-period crossover design. Treatment C was administered in the third period. All iv solutions contained 0.05 mg/mL of D_6-indinavir. In treatment C, the iv solution also contained 0.05 mg/mL of D_0-indinavir. All indinavir doses were expressed as the milligram equivalent of anhydrous free base of unlabeled drug.

Plasma samples for assay of indinavir were obtained in treatments A and B at 0 (predosing), 20, 25, 35 and 45 min, and at 1, 1.5, 2, 4, 6, 8, 10, 12, 16, and 24 h following oral dosing; and in treatment C at 0, 5, 10, 20, 30, and 45 min, and at 1, 1.5, 2, 4, 6, 8, 10, 12, 16, and 24 h postdosing. All samples were stored at −20 °C until assayed.

Analytical Method—Concentrations of D_0-indinavir and D_6-indinavir in plasma were quantified by an LC/MS/MS method.[16] Briefly, the analytes and internal standard were isolated from plasma via liquid−liquid extraction with methyl *tert*-butyl ether. Multiple reaction monitoring of the parent → product ion combinations of m/z 614 → 465, 620 → 471, and 654 → 505 were used to quantify D_0-indinavir, D_6-indinavir, and internal standard, respectively, in the resulting extracts. The method was validated over the concentration range of 1 to 200 ng/mL for each analyte, using 1-mL aliquots of plasma. Precision of the assay, as measured by the coefficient of variation, ranged from 0.9 to 4.3% and 0.9 to 6.2% for D_0-indinavir and D_6-indinavir, respectively. Indinavir concentrations were converted to a molar basis using molecular weights of 613.81 for D_0-indinavir and 619.81 for D_6-indinavir. The limit of quantification was 1.63 and 1.61 nM for D_0 and D_6, respectively.

Pharmacokinetic Analysis—Peak plasma concentration (C_{max}) and the time to peak plasma concentration (T_{max}) following oral administration were obtained by inspection. All AUC values were computed up to the last sampling time point at 24 h without extrapolation, and were obtained by the modified trapezoidal method using stable piecewise cubic polynomials.[17] For the intravenously administered plasma concentration data, AUC values were obtained as the sum of AUC up to the end of infusion and the AUC after the end of infusion. Plasma concentrations below the limit of quantification were treated as zero in all calculations. Apparent plasma clearance was computed as the quotient of D_6-dose/D_6-AUC.

To further investigate the effect of the fluctuations in concentration ratio on the bioavailability estimates, a second analysis of the data with a modeling approach was taken. The model composed of three compartments with saturable elimination from the central compartment and saturable distribution in one of the peripheral compartments. Nonlinear regression analysis was employed to obtain the best-fit model parameters. The bioavailabilities of the oral doses were estimated using a mass balance approach. The computational procedures and the results based on this analysis have been reported.[18]

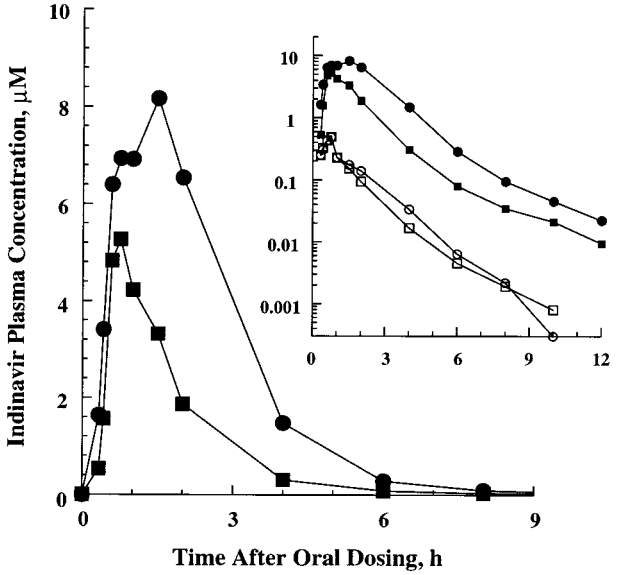

Figure 1—Mean plasma concentration profiles of D_0-indinavir following oral administration of D_0-indinavir in treatments A and B. Comparisons with the corresponding mean profiles of D_6-indinavir following intravenous administration of D_6-indinavir are shown in the inset. Key: ■ = 400 mg of D_0-indinavir po in treatment A; ● = 800 mg of D_0-indinavir po in treatment B; □ = 16 mg of D_6-indinavir iv in treatment A; ○ = 16 mg D_6-indinavir iv in treatment B.

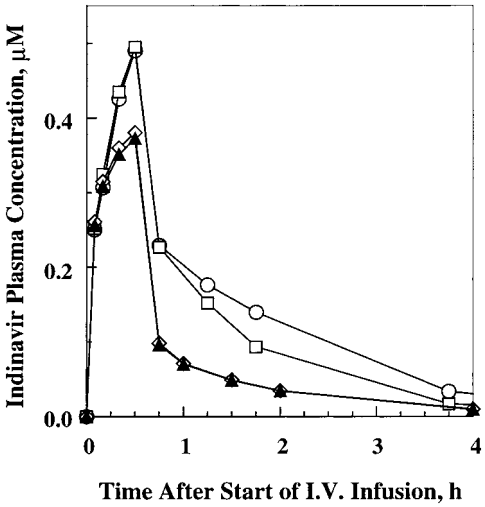

Figure 2—Comparisons of plasma concentration profiles of the intravenously administered indinavir from all three treatments. Key: □ = D_6 with 400 mg of oral indinavir in treatment A; ○ = D_6 with 800 mg of oral indinavir in treatment B; ◇ = D_6 in treatment C; ▲ = D_0 in treatment C.

Statistical Analysis—Statistical analysis was performed on the natural log-transformed individual bioavailability estimates based on dose-normalized D_6-AUC and D_0-AUC values. An ANOVA model for a two-period crossover design was used to test for the period effect. The systemic bioavailability for each treatment was estimated by the geometric mean (GM) ratio of the individual bioavailability estimates for that treatment. Ninety percent confidence intervals (CI) for the bioavailability estimates for each treatment were calculated on the log scale, and the limits were then exponentiated to yield the 90% CI for the GM ratio. To evaluate the kinetic isotope effect in treatment C, paired *t*-tests were performed to compare the AUC and the concentration at 30 min ($C_{30\ min}$) for D_0 and D_6. Dose-normalized geometric mean ratios and the corresponding 90% CI were similarly obtained.

Results

Concentration Profiles—Mean plasma concentration profiles of indinavir following the administration of oral and intravenous doses are shown in Figures 1 and 2. Summary values of the pharmacokinetic parameters are presented in Table 1.

The orally administered indinavir data in the present study were generally consistent with those observed previously following oral administration,[11,12] with the exception of a trend of a slightly prolonged T_{max} following the 800-mg dose in treatment B relative to that of the 400-mg dose in treatment A. As expected, there was a disproportionate increase in plasma concentrations; an increase of 2-fold in the dose from 400 to 800 mg resulted in a 2.67-fold increase in AUC. However, as a result of the delayed T_{max} following the 800-mg dose, C_{max} did not increase disproportionally as is generally seen over a wider dose range.[11] Plasma concentrations of D_0-indinavir and D_6-indinavir in treatment C were virtually superimposed. Differences between the D_6-AUC and D_0-AUC, although statistically significant, were small, suggesting the absence of meaningful kinetic isotope effect.

Plasma concentrations of the intravenously administered D_6-indinavir varied considerably with treatment and were dependent on the magnitude of the coadministered D_0-indinavir concentrations. The D_6-AUC values were highest when coadministered with the 800-mg oral dose in treatment B, lower with the 400-mg oral dose in treatment A, and lowest with the 16-mg D_0-indinavir iv dose in treatment C. Plasma concentrations at the end of the 30-min infusion also demonstrated a similar trend. Additionally, in the presence of coadministered D_0-indinavir in the two oral treatments, plasma concentrations of D_6-indinavir declined more slowly after the termination of infusion and near the plasma T_{max} for D_0-indinavir. Adjusted for the increase in D_6-AUC from treatment A to treatment B (ratio = 1.22), the net increase in D_0-AUC was reduced to 2.19-fold. These observations are consistent with nonlinearity in the systemic disposition kinetics contributing significantly to the disproportionate increase in D_0-indinavir concentrations over the 400- and 800-mg dose range.

Plasma Clearance—It was reported previously[11] that following oral administration, the indinavir terminal plasma concentration did not reach the log-linear phase until concentrations had declined to below ~0.1 to 0.5 μM. In the present study, the range of the total concentrations in treatment C (sum of D_0- and D_6-indinavir) did not completely fall within this range. However, concentrations generally did not exceed 0.8 μM and the computed apparent plasma clearance (1.29 L/min) was approaching the hepatic blood flow of 1.45 L/min. The decreased plasma clearances in treatments A and B reflected the increased D_6-AUC values in the presence of high concentrations of D_0-indinavir in these treatments and were consistent with the concentration-dependency of clearance in a nonlinear disposition system.

Bioavailability—The systemic bioavailability of indinavir appeared to be high, averaging 0.60 following the 400-mg dose, and 0.65 following the 800-mg dose. The corresponding values based on the modeling approach were 0.64 for both doses.[18] The dose-dependence of bioavailability values over this dose range was not statistically significant.

Discussion

This study was motivated by the desire to understand the underlying source(s) of the observed nonlinear pharmacokinetics in previous clinical studies and to examine the systemic bioavailability of indinavir. Recognizing the potential of bioavailability overestimation based on conventional crossover study design in a nonlinear system,[19] the concurrent administration technique was adapted for the present study. In addition, treatment C was incorpo-

Table 1—Geometric Mean of Pharmacokinetic Parameter Values and the Corresponding Ratios (90% CI) of Intravenously and Orally Administered Indinavir

analyte	pharmacokinetic measures	treatment A[e]	treatment B[f]	treatment C[g]
D_0 (po)	AUC_{0-24h}, μM·h	7.41	19.78	–
	AUC ratio[a]	–	2.67 (2.10, 3.40)	–
	C_{max}, μM	5.89	10.55	–
	C_{max} ratio[a]	–	1.79 (1.23, 2.53)	–
	T_{max}, h[b]	0.87 ± 0.40	1.20 ± 0.53	–
	T_{max} difference[a]	–	0.33 (0.0, 0.65)	–
	bioavailability	0.60 (0.54, 0.66)	0.65 (0.58, 0.72)	–
	bioavailability ratio[a]	–	1.09 (0.92, 1.29)	–
D_6 (iv)	apparent CL, L/min	0.85 (0.74, 0.98)	0.70 (0.62, 0.79)	1.29 (1.20, 1.38)
	AUC_{0-24h}, μM·h	0.510	0.620	0.337
	AUC ratio[c]	1.50 (1.32, 1.69)	1.83 (1.60, 2.09)	1.016 (1.010, 1.021)[d]
	AUC ratio[a]	–	1.22 (1.07, 1.39)	–
	C_{30min}, μM	0.472	0.478	0.377
	C_{30min} ratio[a]	–	1.01 (0.88, 1.17)	–
	C_{30min} ratio[c]	1.25 (1.04, 1.51)	1.27 (1.10, 1.46)	1.023 (1.016, 1.031)[d]

[a] Relative to treatment A. [b] Arithmetic mean ± SD. [c] Relative to the intravenous D_6 dose in treatment C. [d] Relative to the intravenous D_0 dose in treatment C. [e] Treatment A: 400 mg of D_0 orally plus 16 mg of D_6 intravenously. [f] Treatment B: 800 mg of D_0 orally plus 16 mg of D_6 intravenously. [g] Treatment C: Simultaneous 16 mg of D_0 and 16 mg of D_6 intravenously.

rated to serve as a reference for identifying the source of nonlinearity.

While there are a number of factors that could result in the nonlinear disposition kinetics, plasma protein binding did not appear to be a contributing factor in the present case. Binding of indinavir to plasma protein is not extensive (39% unbound) and is not dependent on concentration up to 80 μM, which is significantly higher than the C_{max} of 10.6 μM achieved following the 800-mg dose. Other potential causes include saturable elimination and tissue binding. A more detailed study on the mechanism(s) of the systemic nonlinearity can be found elsewhere (Stone et al., unpublished results).

Increasing the mass as a result of isotope labeling generally increases the bond stability in the drug molecule.[20,21] In the present case, the deuterium isotope was chosen to be incorporated on the pyridomethyl moiety of the indinavir because of its relative ease of chemical syntheses. Since the bond cleavage leading to depyridomethylation is one of the metabolic pathways for indinavir,[15] the possibility that the metabolic rate and therefore the overall disposition kinetics of indinavir might be perturbed could not be ruled out. The most desirable deuterated analogue of indinavir would have contained the labeling placed at the metabolically stable site of the molecule. However, such an ideal analogue of indinavir was not available at the time of the study. Any significant difference in the disposition kinetics of indinavir between the two analogues of the drug would have made the D_6 a poor surrogate for D_0 in data analysis.

Prior to initiation of the present human study, the potential for the isotope effect was examined. In vitro studies with D_6 using rat liver and human microsome preparations indicated modest decreases (~23%) in the formation of the dealkylated product.[13] Intravenous administration of a 1:1 mixture containing the D_0 and D_6 in rats at a total dose of 10 mg/kg indicated no discernible difference in plasma concentration profiles.[13] In vitro metabolism studies indicated depyridomethylation was only one of the multiple CYP3A4-mediated pathways in the oxidative metabolism of indinavir in humans.[15] These experiments suggested that the potential kinetic isotope effects in human would be negligible, which was confirmed by the data from treatment C of the present study.

The mass of the intravenous D_6-indinavir dose administered in treatments A and B was considerably lower than that of the D_0 oral doses. The D_0-AUC data observed in the present study did not appear inconsistent with the historical data,[11] suggesting the D_6 dose did not have significant effect on the absorption or disposition processes of the D_0 oral doses.

The first-pass metabolism of indinavir has been characterized to be mediated by the CYP3A isoform of the cytochrome P450 enzyme system, primarily in the liver but also to some extent in the intestine.[22,23] This same isozyme is also known to be involved in the metabolism of other protease inhibitors ritonavir, saquinavir, and nelfinavir. It has been recently reported[24] that protease inhibitors as a class are also substrates for p-glycoprotein (Pgp) which functions as a transmembrane efflux pump.[25–27] Thus, in addition to the first-pass metabolism, the apical expression of Pgp in the epithelial cells of the GI tract and on the bile canalicular surface of hepatocytes would function as biological barriers and further limit the absorption for this class of drugs. The high bioavailability results of the present study would suggest a reduced impact of the Pgp-mediated transporter system at clinically relevant doses of indinavir.[28,29]

The use of a constant-rate infusion rather than a bolus intravenous administration in the study was designed to reduce the magnitude of fluctuations in the D_6/D_0 concentration ratios and to improve the reliability of bioavailability estimates.[5] Ideally, the infusion rates may be controlled to match closely the rate of drug delivery to the systemic circulation. In actual practice, the superposition can only be approximated since the drug input after an oral dose is not known a priori. Figure 3 shows the (D_6/D_0) plasma concentration ratios following the two oral treatments. These data indicated relatively constant ratios after about 1.5 h post oral dosing. However, substantial fluctuations were noted during the earlier time points. Prior to the start of the infusion at 15 min, D_0-concentrations were unmatched with ratios effectively zero for a brief period. The ratios then increased rapidly and reached the maximum within 5 min once the D_6 infusion was initiated. It should be noted that a perfect alignment of T_{max} with the end of infusion would only reduce, but not eliminate, the fluctuations, due to the differences in the input rate between the two administration modes. The magnitude of errors associated with such imperfection has been reviewed using model simulations.[5]

Cross comparisons of the bioavailability estimates based on the present method and those based on the modeling approach[18] are presented in Figure 4. Although the two computational procedures differed from each other, the results were numerically comparable, confirming the im-

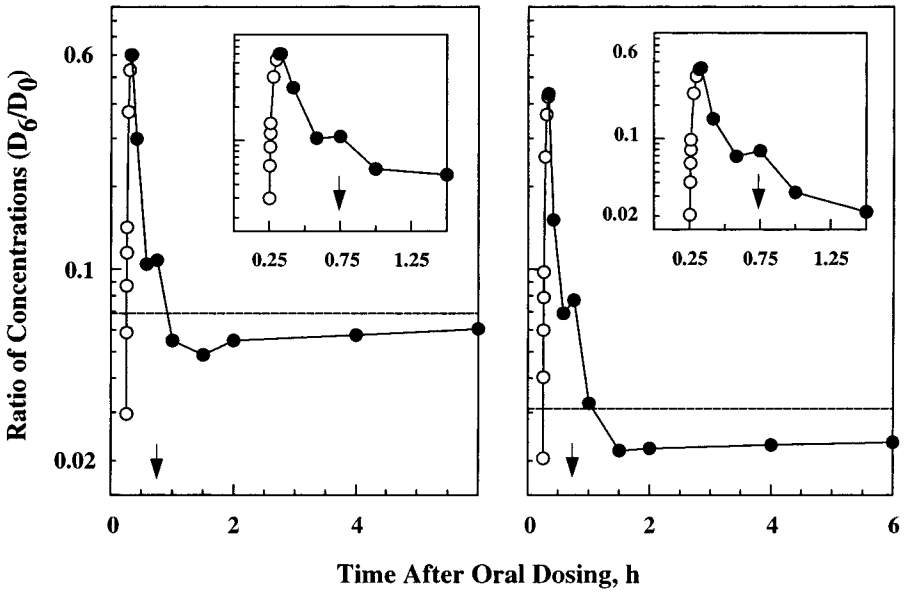

Figure 3—Ratios of plasma concentrations (D_6-indinavir/D_0-indinavir) following the administration of 16 mg of D_6-indinavir iv with 400 mg of D_0-indinavir po in treatment A (left panel) or with 800 mg of D_0-indinavir po in treatment B (right panel). Solid circles represent median ratios and open circles represent medians of simulated ratios during the first 5 min immediately after the initiation of the iv infusion. Simulated ratios were obtained using interpolated concentration values between 0 and 5 min for the po and iv curves, which were obtained by the piecewise cubic polynomial functions.[17] The arrows indicate the end of infusion at 0.75 h. The horizontal lines represent the apparent Z_{app} based on eq 5. The expanded initial ratios are shown in the insets.

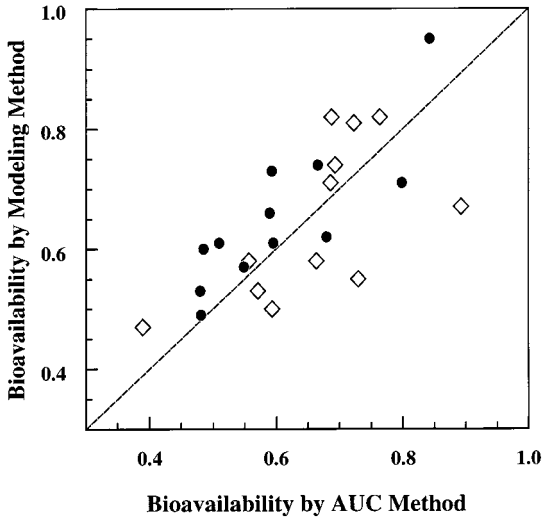

Figure 4—Comparison of the bioavailability estimates based on the present model-independent AUC method and that based on the kinetic modeling method.[18] The diagonal line represents the projected perfect agreement between the two estimation methods. Key: ● = 400-mg dose; ◇ = 800-mg dose.

portance of the delayed iv infusion regimen used in this study in reducing the imperfection of fluctuations in the (D_6/D_0) plasma concentration ratios. Lengthening the infusion period with a reduced input rate would likely have reduced the fluctuations at early time points (Figure 3) and improve the concordance between the two estimates for those data sets with greatly delayed T_{max}, although it also would have adversely affected the bioavailability estimates from the data sets with shorter T_{max}. On the other hand, errors in bioavailability estimates based on the modeling method would most likely arise from model miss-specification and thus would be model-dependent but would be less likely to be correlated with the D_0 T_{max}.

While the ratio of indinavir concentrations in blood to that in plasma was not available for humans, preclinical studies indicated the ratio to be approximately equal to unity for monkeys.[22] Thus, the plasma clearance and the blood clearance for indinavir could be assumed to be comparable for humans. It has been reported that the urinary excretion of intact indinavir constituted 5−12% of the dose over the 200−1000 mg dose range, indicating a significant contribution of hepatic metabolism to the overall elimination of the drug.[11,15] At low indinavir plasma concentrations, the extremely high clearance (1.29 L/min) relative to the hepatic blood flow of ∼1.45 L/min in man would suggest that at low doses, indinavir could be classified as a high hepatic extraction drug with low systemic bioavailability following oral administration,[30] and that dose-dependence of bioavailability would contribute significantly to the observed pharmacokinetic nonlinearity. In addition, the first-pass metabolism would gradually become more saturated with increasing doses, and as the doses approached the clinical range, the bioavailability would be high and would be only marginally dose-dependent.

In summary, the present study indicates that indinavir bioavailability was high (60−65%) and comparable over the 400−800 mg dose range and that there was a significant contribution of the nonlinearity in the systemic disposition to the observed nonlinear pharmacokinetics following oral administration. These results demonstrate that the concurrent administration approach can be used to identify the source(s) of pharmacokinetic nonlinearity and obtain bioavailability estimates in a nonlinear pharmacokinetic system. Characterizing important pharmacokinetic attributes of drug candidates during product development based on such an approach has become increasingly feasible as a result of recent advances in LC/MS/MS instrumentation.[31] The application of the model-independent method described in the present study requires that there is no kinetic isotope effect. The computed bioavailability is not exact and its reliability depends on the closeness of similarity between the plasma concentration profile following the test dose and that following the labeled tracer dose. However, the elaboration needed in the design and execution of such studies is compensated for by the simplicity in data analysis. With the conventional crossover study design, bioavailability in a nonlinear disposition system could only at best be estimated with a modeling

approach.[32] Additionally, due to the concentration-dependence in clearance, systemic bioavailability could be potentially overestimated unless the concentration ranges achieved in the intravenous treatment were sufficiently high and comparable to that achieved in the test treatment. For drugs with low aqueous solubility, it may not be feasible, if not impossible, to achieve the required plasma concentrations with clinically acceptable preparations.

References and Notes

1. Tozer, T. N.; Rubin, G. M. Saturable kinetics and bioavailability determination. In *Pharmacokinetics*; Welling, P. G., Tse, F. L. S., Eds.; Marcel Dekker: New York, 1988; pp 473−513.
2. Kasuya, Y.; Mamada, K.; Baba, S.; Matsukura, M. Stable isotope methodology for the bioavailability study of phenytoin during multiple-dosing regimens. *J. Pharm. Sci.* **1985**, *74*, 503−507.
3. Rubin, G. M.; Tozer, T. N. Theoretical considerations in the calculation of bioavailability of drugs exhibiting Michaelis−Menten elimination kinetics. *J. Pharmacok. Biopharm.* **1984**, *12*, 437−450.
4. Haskins, N. J.; Waddell, K. A.; Ford, G. C.; Spalton, P. N.; Walls, C. M.; Forrest, T. J.; Palmer, R. F. The absorption of disopyramide in animal determined using a stable isotope co-administration technique. *Biomed. Mass Spectrom.* **1980**, *7*, 80−83.
5. Rubin, G. M.; Waschek, J. A.; Pond, S. M.; Effeney, D. J.; Tozer, T. N. Concurrent intravenous administration of a labeled tracer to determine the oral bioavailability of a drug exhibiting Mechaelis-Menten metabolism. *J. Pharmacok. Biopharm.* **1987**, *6*, 615−631.
6. Brown, T. R. Stable isotopes in pharmacology studies: present and future. *J. Clin. Pharmacol.* **1986**, *26*, 485−489.
7. Covey, T. R.; Lee, E. D.; Henion, J. D. High-speed liquid chromatography/tandem mass spectrometry for the determination of drugs in biological samples. *Anal.Chem.* **1986**, *58*, 2453−2460.
8. McLoughlin, D. A.; Olah, T. V.; Ellis, J. D.; Gilbert, J. D.; Halpin, R. A. Quantitation of the $5HT_{1D}$ agonists MK-462 and Sumatriptan in plasma by liquid chromatography-atmospheric pressure chemical ionization mass spectrometry. *J Chromatogr. A* **1996**, *726*, 115−124.
9. Avery, M. J.; Mitchell, D. Y.; Falkner, F. C.; Fouda, H. G. Simultaneous determination of tenidap and its stable isotope analogue in serum by HPLC/atmospheric pressure chemical ionization tandem mass spectrometry. *Biol. Mass Spectrom.* **1992**, *21*, 353−357.
10. Barrish, A.; Olah, T. V.; Gatto, G. J.; Michel, K. B.; Dobrinska, M. R.; Gilbert, J. D. The use of stable isotope labeling and liquid chromatography/tandem mass spectrometry techniques to study the pharmacokinetics and bioavailability of the antimigraine drug, MK-0462 (rizatriptan) in dogs. *Rapid Commun. Mass Spectrom.* **1996**, *10*, 1033−1037.
11. Yeh, K. C.; Deutsch, P. J.; Haddix, H.; Hesney, H.; Hoagland, V.; Ju, W. D.; Justice, S. J.; Osborne, B.; Sterrett, A. T.; Stone, J. A.; Woolf, E.; Waldman, S. Single dose pharmacokinetics of indinavir and the effect of food. *Antimicrob. Agents Chemother.* **1998**, *42*, 332−338.
12. Bjornsson, T.; Chiou, R.; Deutsch, P.; Haddix, H.; Hoagland, V.; Justice, S.; Nessly, M.; Pomerantz, R.; Saag, M.; Squires, K.; Teppler, H.; Waldman, S.; Woolf, E, Yeh, K. C. Pharmacokinetics of indinavir. *Pharm. Res.* **1996**, *13* (*Suppl*), S485.
13. Merck Research Laboratories. Data on file, MRL. Unpublished results.
14. Chiba, M.; Hensleigh, M.; Nishime, J. A.; Balani, K. S.; Lin, J. H. Role of CYP3A4 in human metabolism of MK-639, a potent HIV protease inhibitor. *Drug Metab. Dispos.* **1996**, *24*, 307−314.
15. Balani, S. K.; Woolf, E. J.; Sturgill, M.; Deutsch, P. J.; Yeh, K. C.; Lin, J. H. Disposition of indinavir, a potent HIV-1 protease inhibitor, after oral dose in humans. *Drug Metab. Dispos.* **1996**, *24*, 1389−1394.
16. Woolf, E. J.; Matuszewski, B. K. Simultaneous Determination of Unlabeled and Deuterium-Labeled Indinavir in Human Plasma by HPLC with Tandem Mass Spectrometric Detection. *J. Pharm. Sci.* **1997**, *86*, 193−198.
17. Yeh, K. C.; Small, R. Pharmacokinetic evaluation of stable piecewise cubic polynomials as numerical integration functions. *J. Pharmacok. Biopharm.* **1989**, *17*, 721−740.
18. Stone, J. A.; Yeh, K. C.; Winchell, G. A. Development of a nonlinear compartmental model of indinavir pharmacokinetics. *Pharm. Res.* **1997**, *14* (*Suppl*), S-505.
19. Kempf, D. J.; Marsh, K. C.; Denissen, J. F.; McDonald, E.; Vasavanonda, S.; Flentge, C. A.; Green, B. E.; Fino, L.; Park, C. H.; Kong, X. P.; Wideberg, N. E.; Saldivar, A.; Ruiz, L.; Kati, W. M.; Sham, H. L.; Robins, T.; Stewart, K. D.; Hsu, A.; Plattner, J. J.; Leonard, J. M.; Norbeck, D. W. ABT-538 is a potent inhibitor of human immunodeficiency virus protease and has high oral bioavailability in human. *Proc. Natl. Acad. Sci.* **1995**, *92*, 2484−2488.
20. Brown, T. R.; van Langenhove, A.; Costello, C. E.; Biemann, K.; Greenblatt, D. J. Kinetic equivalence of stable-isotope-labeled and unlabeled phenytoin. *J. Clin. Pharmacol.* **1981**, *29*, 511−515.
21. Lu, A. Y. H.; Harada, N.; Miwa, G. T. Rate-limiting steps in cytochrome P450-catalyzed reactions: studies on isotope effects in the O-de-ethylation of 7-ethoxycoumarin. *Xenobiotica* **1984**, *14*, 19−26.
22. Lin, J. H.; Chiba, M.; Balani, S. K.; Chen, I.-W.; Kwei, G. Y−S.; Vastag, K. J.; Nishime, J. A. Species differences in the pharmacokinetics and metabolism of indinavir, a potent human immunodeficiency virus protease inhibitor. *Drug Metab. Dispos.* **1996**, *24*, 1111−1120.
23. Chiba, M.; Hensleigh, M.; Lin, J. H. Hepatic and intestinal metabolism of indinavir, an HIV protease inhibitor, in rats and human microsomes. *Biochem. Pharmacol.* **1997**, *53*, 1187−1195.
24. Kim, R. B.; Fromm, M. F.; Wandel, C.; Leake, B.; Wood, A. J. J.; Roden, D. M.; Wilkinson, G. R. The drug transporter p-glycoprotein limits oral absorption and brain entry of HIV-1 protease inhibitors. *J. Clin. Invest.* **1998**, *101*, 289−294.
25. Gottesman, M. M.; Pastan, I. Biochemistry of multidrug resistance mediated by the multidrug transporter. *Annu. Rev. Biochem.* **1993**, *62*, 385−427.
26. Watkins, P. B. The barrier function of CYP3A4 and p-glycoprotein in the small bowel. *Adv. Drug Delivery Rev.* **1997**, *27*, 161−170.
27. Wacher, V. J.; Wu, C.-Y.; Benet, L. Z. Overlapping substrate specificities and tissue distribution of cytochrome P450 3A and p-glycoprotein: implications for drug delivery and activity in cancer therapy. *Mol. Carcinogen.* **1995**, *13*, 129−134.
28. Hunter, J.; Hirst, B. H.; Simmons, N. L. Drug absorption limited by p-glycoprotein-mediated secretory drug transport in human intestinal epithelial Caco-2 cell layers. *Pharm. Res.* **1993**, *10*, 743−749.
29. Fricker, G.; Drewe, J.; Huwyler, J.; Gutman, H.; Beglinger, C. Relevance of p-glycoprotein for the enteral absorption of cyclosporin A: in vitro − in vivo correlation. *Br. J. Pharmacol.* **1996**, *118*, 1841−1847.
30. Rowland, M.; Tozer, T. N. *Clinical Pharmacokinetics Concepts and Applications*; Lea & Febiger: Baltimore, 1995.
31. Brewer, E.; Henion, J. Atmospheric Pressure Ionization LC/MS/MS Techniques for Drug Disposition Studies. *J. Pharm Sci.* **1998**, *87*, 395−402.
32. Cheng, H.; Schwartz, J. I.; Lin, C.; Amin, R. D.; Seibold, J. R.; Lasseter, K. C.; Ebel, D. L.; Tocco, D. J.; Rogers, J. D. The bioavailability and nonlinear pharmacokinetics of MK-679 in humans. *Biopharm. Drug Dispos.* **1994**, *15*, 409−418.

Acknowledgments

The authors are grateful to Drs. E. G. Mellilo and A. N. Jones for providing the deuterium-labeled indinavir, to Drs. S. N. Behrens and C. Anderson for providing the iv preparations and the corresponding preclinical safety and tolerability study, to Ms. D. Kaspareck, Ms. V. Hoagland, and Ms. D. S. Wyss for facilitating the clinical study, to Drs. W. F. Bayne, P. Deutsch, M. Dobrinska, K. C. Kwan, M. Rowland, and G. A. Winchell for helpful discussions during the conduct of the study, and to Dr. B. K. Matuszewski and Ms. I. Fu for assistance in providing the assay data.

JS9802392

Encapsulation and Release of Rhodium(II) Citrate and Its Association Complex with Hydroxypropyl-β-cyclodextrin from Biodegradable Polymer Microspheres

RUBEN DARIO SINISTERRA,[†,‡,§] VENKATRAM PRASAD SHASTRI,[*,†,§] RENATO NAJJAR,[||] AND ROBERT LANGER[*,†]

Contribution from *Chemical Engineering Department, Massachusetts Institute of Technology, 45 Carleton Street, Bldg. E25, Rm. 342, Cambridge, Massachusetts 02139, and Instituto de Química, Universidade de São Paulo, São Paulo Brazil.*

Received November 4, 1998. Final revised manuscript received February 5, 1999.
Accepted for publication February 8, 1999.

Abstract □ Rhodium(II) carboxylates and their derivatives constitute a promising class of second-generation transition metal compounds with anticancer properties. While most transition metal anticancer compounds chelate DNA and cause extensive chromosomal damage, rhodium(II) carboxylates act on the enzyme DNA polymerase α and hence cause minimal chromosomal damage. Rhodium(II) citrate, a recent member of the rhodium(II) carboxylate family is highly promising as an antitumor agent. However, due to its high water solubility, a high systemic dose is necessary to achieve efficacy. In this paper, we have explored the complexation of rhodium(II) citrate with hydroxypropyl-β-cyclodextrin as a means to improve encapsulation and release kinetics from poly(*dl*-lactic-co-glycolic) acid (PLGA) and poly(anhydride) microspheres. We observed that complexation of rhodium(II) citrate with hydroxypropyl-β-cyclodextrin significantly increased both the encapsulation efficiency and duration of release in both polymer systems.

Introduction

A class of promising second-generation transition metal anti-cancer compounds are the rhodium(II) [Rh(II)] carboxylates.[1−4] Most anti-cancer drugs induce chromosomal damage in treated cells (e.g., cisplatin), resulting in the formation of chromosomal lesions.[5] In contrast, rhodium(II) butyrate only slightly increases the incidence of chromatid gaps and breaks.[3] It is believed that its mode of inhibition of DNA synthesis is via the inhibition of enzyme(s) essential for DNA synthesis, such as DNA polymerase α, rather than DNA chelation. In general, inhibition of DNA synthesis by R-substituted Rh(II) carboxylates derivatives in vitro increases with increasing side chain lipophilicity in the order: Rh(II) methoxyacetate < acetate < propionate < butyrate.[2,5] However, the simple extension of the carboxylate chain (R group) is not effective in increasing the therapeutic effects of the drug. Thus it appears that for Rh(II) compounds to be efficacious, they have to exhibit some degree of water solubility.[6] However, Rh(II) butyrate and analogues are very toxic; Rh(II) carboxylates irreversibly inhibit enzymes that possess sulfydryl groups.[4] Recently, a new class of Rh(II) carboxylates [i.e., Rh(II) citrates] have been synthesized and shown to be promising compounds for chemotherapy.[7−9] However, due to the high water solubility of Rh(II) citrate, high systemic doses of the drug would be required to achieve efficacious concentrations in tumor sites. Therefore, it is useful to develop controlled release systems wherein the Rh(II)-complex is shielded from the extracellular milieu to minimize local toxicity and prolong drug action.

To address this problem we have examined the host: guest complexation approach using cyclodextrins to alter solubility and improve the encapsulation and release from polymer microspheres.

Experimental Section

Materials—Rhodium(II) citrate was prepared as described elsewhere.[7] Hydroxypropyl-β-cyclodextrin (HPBCD) was generously donated by Cerestar Company to VPS and had a degree of substitution of hydroxypropyl groups between 5 and 7. Poly(vinyl alcohol) (PVA) was purchased form Aldrich (MW, 70 000; 90% hydrolyzed) and used as received. The poly((*dl*)lactic-*co*-glycolic)-acid (PLGA; RG503, MW, 30 000) was purchased from Boehringer Ingelheim (Indianpolis, IN) and poly(1,3-bis(*p*-carboxyphenoxy)-propane-*co*-sebacic acid) (CPP:SA, 20:80; (MW, 70 000) was prepared as described elsewhere.[10] All other chemical were purchased from Aldrich Chemical and used as received.

Methods—*Preparation of the Association Compound between Rhodium(II) Citrate and HPBCD*—The association compound was prepared by mixing 292 mg of HPBCD and 200 mg of Rh(II) citrate in 20 mL of distilled water and stirring overnight. The resulting solution was then frozen in liquid N_2 and lyophilized into a free flowing powder.

Characterization of Rh(II) Citrate−HPBCD Association Complex—the formation of the association complex of Rh(II) citrate with HPBCD was studied by infrared (IR) spectroscopy and thermogravimetric (TG) analyses. The IR spectra were obtained on a Nicolet Magna IR-550 FTIR equipped with a liquid nitrogen cooled helium−neon laser. All samples were pressed as KBr pellets. The TG and differential thermogravimetric (DTG) curves were obtained on 5−10 mg of sample under dynamic nitrogen atmosphere using a Perkin-Elmer Series 7 thermogravimetric analyzer interfaced to a PC. The curves were analyzed using Perkin-Elmer TGA software.

Preparation of the Microspheres—Polymer microspheres were prepared by a solvent evaporation technique.[11] In brief, 200 mg of the polymer (PLGA or CPP:SA) was dissolved in 1 mL of

* Corresponding author. E-mail: prasha@mit.edu and rlanger@mit.edu.
† Chemical Engineering Department.
‡ Equally contributing authors.
§ Sabbatical Researcher from Chemistry Department of Federal University of Minas Gerais, Brazil, 31270-901. E-mail ruben@apolo.qui.ufmg.br, CAPES-Brazil.
|| Institute de Química.

10.1021/js9804314 CCC: $18.00
Published on Web 04/02/1999

methylene chloride. To this, 50 mg of the Rh(II) citrate or the association compound (corresponds to ≃20 mg of Rh(II) citrate) dissolved in 200 mL of water was added, and the solution was sonicated using a Vibra Cell ultrasonicator (Sonics and Materials, Danbury, CT, six pulses, 50% duty cycle, output 3) to prepare the first w/o microemulsion. The microemulsion was then dispersed in 100 mL of a 1% PVA solution with an homogenizer (Silverson L4R, Nottingham, England, 3/4 in. homogenization tip) at 5200 rpm for 1 min to stabilize the second emulsion (w/o/w). The PVA solution containing polymer microspheres was then stirred for 1.5 h to facilitate evaporation of methylene chloride (solvent) and induce hardening of the polymer microspheres. The microspheres were isolated by centrifugation at 1500 rpm for 5 min, subsequently washed three times with water to remove surface-adsorbed PVA, and finally resuspended in 2 mL of water and freeze-dried to a free powder. The size distribution of the microspheres was determined with a Coulter Counter multisizer.

Rhodium(II) Citrate Release Studies—the release studies were carried out on 10 mg of microspheres in 1.5 mL Eppendorf tubes containing 1 mL of phosphate buffer release medium (pH 7.4) at 37 °C. To ensure thorough mixing, the tubes were placed on a Labline orbital shaker. Sink conditions were maintained by periodically replacing the release medium with fresh release buffer throughout the duration of the study.

Quantification of Rhodium—The Rh(II) citrate released was quantified by visible spectroscopy (Beckman DU-6) and inductively coupled plasma mass spectrometry (ICP-MS). The visible absorbance was measured at 591 nm in 1X PBS using a quartz sample cell (1 cm path length). The calibration curve was established using known concentrations of Rh(II) citrate in 1X PBS. The loading in microspheres was determined by solvent extraction. In brief, 5.0 mg of microspheres (in triplicate) was first placed in 1 mL of methylene chloride to dissolve the polymer phase and then extracted with 1 mL of 1X PBS. The Rh(II) citrate, which was extracted in the aqueous phase, was quantified as described above.

Results and Discussion

Characterization of the Association Compound between the Rhodium (II) Citrate and HBCD—The formation of the association compound between Rh(II) citrate and HPBCD was verified by IR, TG, and DTG. The IR spectra of the association compound showed two important characteristics consistent with the formation of an associative complex between the Rh(II) citrate and HPBCD: (a) displacement of the IR band associated with the stretching the −OH bond to 3400 cm^{-1} in comparison with free HPBCD (3440 cm^{-1}) and (b) narrowing of this band due to the breakdown of hydrogen bonding in the CD cavity upon the release of the resident water molecules.[12,13]

The TG and DTG curves of Rh(II) citrate, HPBCD, and the association compound between Rh(II) citrate and HPBCD are shown in Figures 1a and 1b, respectively. The TG and DTG curves of Rh(II) citrate revealed an onset of mass loss beginning at 25 °C. However, significant changes in mass presumably due to the decomposition of the metal complex, occurred at 220 and 350 °C. In contrast, the TG and DTG curves of the Rh(II) citrate−HPBCD association compound showed only one thermal transition at higher temperature, around 310 °C, which was accompanied by an 80% mass loss. Thus, it appears that the thermal stability of Rh(II) citrate is improved significantly upon association with HPBCD. The increased thermal stability could have significant benefits when using high-temperature polymer processing techniques, such as compression or injection molding to manufacture polymer delivery devices.

Release of Rh(II) Citrate and its Association Complex with HPBCD from PLGA and CPP:SA Microspheres—The size distributions of PLGA and CPP:SA microspheres containing Rh(II) citrate and its association complex with HPBCD are shown in Table 1. An interesting observation was the significant enhancement of Rh(II) citrate encapsulation efficiency upon complexation with HPBCD. The encapsulation efficiency of the free Rh(II) citrate in PLGA microspheres was 30%, whereas that of the HPBCD complex system was 83%. Similarly, the encapsulation efficiencies of free Rh(II) citrate and Rh(II) citrate−HPBCD association complex in CPP:SA were 22 and 79%, respectively. This increase in loading efficiency upon complexation with HPBCD can be explained on the basis of the following observations.

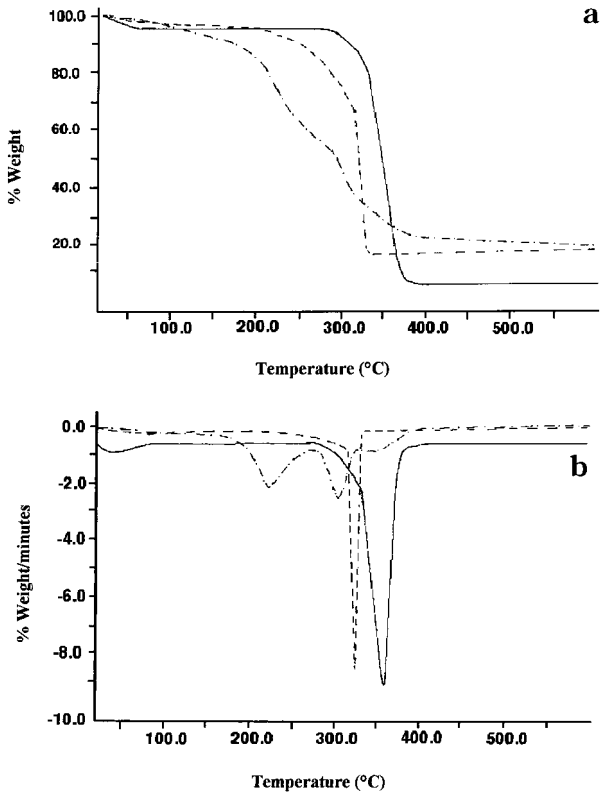

Figure 1—(a) TG curves of HPBCD (–), Rh(II) citrate (–•–•), and association complex between Rh(II) citrate and HPBCD (- - -). (b) DTG curves of HPBCD (–), Rh(II) citrate (–•–•), and association complex between Rh(II) citrate and HPBCD (- - -).

Table 1—Size Distribution and Percent Loading of PLGA and CPPSA Microspheres Containing Rh(II) Citrate and Rh(II) Citrate–HPBCD Association Complex

compound	polymer	size, μm	loading of Rh(II) citrate, %
Rh(II) citrate	PLGA	10.0	30.0
Rh(II) citrate	CPP:SA	20.5	22.4
Rh(II) citrate–HPBCD	PLGA	15.4	83.4
Rh(II) citrate-HPBCD	CPP:SA	25.0	79.2

The enhanced solubility of alkyl-substituted β-CD in comparison with the unsubstituted β-CD has been attributed to several factors, including breakdown of hydrogen bonding between CD molecules, changes in ring conformation, and lowering of the lattice free energy due to its enhanced interaction with surrounding water molecules.[14,15] However, the introduction of alkyl groups such as hydroxypropyl, can also increase the lipophilicity of substituted β-CDs in comparison with the unsubstituted β-CD. One possible mechanism could involve the delocalization of the hydrophobic core in the alkyl substituted β-CD toward the primary 6-CH_2OH hydroxy face.[16] Thus, it is plausible that the complexation of Rh(II) citrate with HPBCD can alter the partition coefficient of the Rh(II)

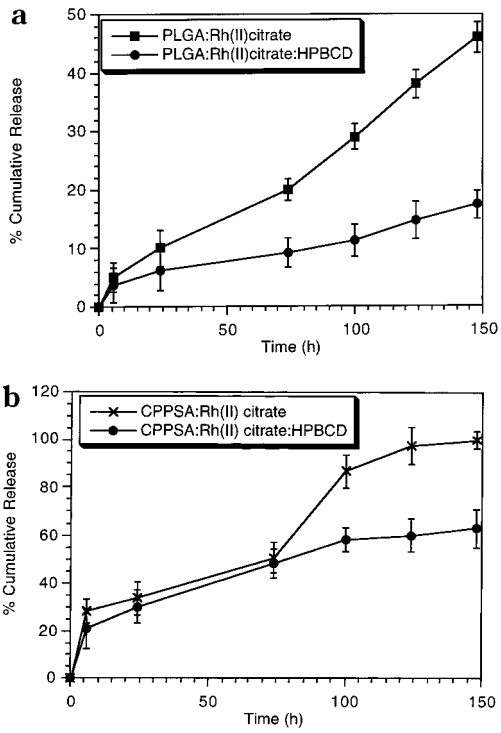

Figure 2—(a) Release of Rh(II) citrate and Rh(II) citrate–HPBCD from PLGA microspheres. (b) Release profiles of Rh(II) citrate and Rh(II) citrate–PBCD association complex from CPP:SA (20:80) microspheres. The error bars are represented as the standard deviation from the mean.

citrate molecule so as to bias its distribution in the hydrophobic polymer phase during microsphere preparation

The release profiles of Rh(II) citrate and its association complex with HPBCD from PLGA microspheres are shown in Figure 2a. The 'burst effect' (8 h) was almost identical in both the cases although the loading was nearly three times higher in the case of the Rh(II) citrate−HPBCD association complex. Beyond 24 h, near zero-order release kinetics was observed, with 45% of the encapsulated Rh-(II) citrate released at 148 h in comparison with 18% of the HPBCD complexed molecule. Thus, it appears that one can prolong the duration of release of small molecules from polymer microspheres by association with CDs.

Release profiles of Rh(II) citrate and Rh(II) citrate−HPBCD association complex from CPP:SA (20:80) microspheres are shown in Figure 2b. As in the PLGA system, the 'burst effect' was almost identical in both the cases, although the loading of the Rh(II) citrate−HPBCD association complex in the microspheres was nearly four times higher. As observed in the PLGA system, the association of Rh(II) citrate with HPBCD prolonged the duration of release from the CPP:SA microspheres as well. Whereas 100% of the encapsulated Rh(II) citrate was released at the end of 148 h, only 60% of HPBCD complexed molecule was released during the same period.

Finally, in this study we observed that although the size of the PLGA and CPP:SA microspheres containing Rh(II) citrate−HPBCD was larger (20.5 and 25.0 μm, respectively) when compared with microspheres containing uncomplexed Rh(II) citrate (10.0 and 15.4 μm, respectively), the cumulative release was lower in the former system. If one were to assume that the surface roughness of all the microspheres were similar, the lower cumulative release from the PLGA and CPP:SA microspheres containing the complexed Rh-(II) citrate is surprising, considering the fact that the surface area of these microspheres would be larger in comparison with the microspheres containing uncomplexed Rh(II) citrate. This result could be due to the decrease in the solubility of the Rh(II) citrate upon complexation with HPBCD, as discussed earlier.

References and Notes

1. Hughes, R. G.; Bear, J. L.; Kimball, A. P. Synergistic Effect of Rhodium(II) Acetate and Arabinosylcytosine on L_{210}. *Proc. Am. Assoc. Cancer Res.* **1972**, *13*, 120.
2. Erck, A.; Rainen, L.; Whileyman, J.; Chang, I. M.; Kimball, A. P.; Bear, J. L. Studies of Rhodium(II) Carboxylates as Potential Antitumor Agents. *Proc. Soc. Exp. Biol. Med.* **1974**, *145*, 1278.
3. Rao, P. N.; Smith, M. L.; Pathak, S.; Howard, R. A.; Bear, J. L. Rhodium(II) Butyrate: A Potential Anticancer Drug with Cell Cycle Type Phase-Specific Effects in HeLa Cell. *J. Nat. Cancer Inst.* **1980**, *64*, 905.
4. Bear, J. L.; Howard, R. A.; Dennis, A. M. Interactions of Rhodium(II) Carboxylates with Molecules of Biologic Importance. *Curr. Chemother.* **1974**, 1321.
5. Zwelling, L. A.; Andersen, I.; Kohn, K. W. DNA-Protein and DNA Interstrand Cross-Linking by Cis- and Trans-Platinum-(II) Diamminedichloride in L_{210} Mouse Leukemia Cell and Relation to Cytotoxicity. *Cancer Res.* **1979**, *39*, 365.
6. Howard, R. A.; Sherwood, E.; Erck, A.; Kimball, A. P.; Bear, J. L. Hydrophobicity of Several Rhodium(II) Carboxylates Correlated with Their Biologic Activity. *J. Med. Chem.* **1977**, *20*, 943.
7. Najjar, R.; Santos, F. S.; Seidel, W. Synthesis and Characterization of the Rhodium(II) Citrate Complex. *Anais da Acad. Brasileira de Ciencias* **1987**, *59*, 13.
8. Zyngier, S.; Kimura, E.; Najjar, R. Antitumor Effects of Rhodium(II) Citrate in Mice Bearing Ehrlich Tumors. *Brazilian J. Med. Biol. Res.* **1989**, *22*, 397.
9. Sinisterra, R. D.; Riebscheid, E. M.; Zyngier, S.; Maria, D. A.; Mistrone, R. J.; Couto, L. G.; Najjar, R. Antitumor Effects of Rhodium(II) Complexes on Mice Bearing Ehrlich Tumors. *Brazilian J. Med. Biol. Res.* **1994**, *27*, 91.
10. Domb, A. J.; Langer, R. Polyanhydrides I. Preparation of High Molecular Weight Polyanhydrides. *J. Polym. Sci.: Part A: Polym. Chem.* **1987**, *25*, 3373.
11. O'Donell, P. B.; McGinity, J. W. Preparation of Microspheres by Solvent Evaporation Technique. *Adv. Drug Del. Rev.* **1997**, *28*, 25.
12. (a) Szejtli, J. Utilization of cyclodextrins in industrial products and processes. *J. Mater. Chem.* **1997**, *7*(4) 575. (b) Szejtli, J. Chemistry, Physical and Biological Properties of Cyclodextrins. In *Comprehensive Supramolecular Chemistry*; Lehn, J. M., Atwood, J. L., Davies, J. E. D., Macnicol, D. D., Vogtle, F., Eds.; Pergamon: Oxford, 1996; Vol 9, Chapter 2, p 5.
13. Saenger, W. In *Inclusion Compounds*, Atwood, J. L., Davies, J. E. D., Macnicol, D. D., Eds.; Academic Press: London, 1984.
14. Uekuma, K.; Irie, T. Pharmaceutical Use of Cyclodextrins in Various Drug Formulations. In *Comprehensive Supramolecular Chemistry*; Lehn, J. M., Atwood, J. L., Davies, J. E. D., Macnicol, D. D., Vogtle, F., Eds.; Pergamon: Oxford, 1996; Vol 9, Chapter 15, p 451.
15. Tsuneji, N.; Haruhisa, U. Aspects of Drug Formulation with Cyclodextrins. In *Comprehensive Supramolecular Chemistry*; Lehn, J. M., Atwood, J. L., Davies, J. E. D., Macnicol, D. D., Vogtle, F., Eds.; Pergamon: Oxford, 1996; Vol 9, Chapter 14, p 441.
16. Lichtenthaller, F. W.; Immel, S. Lipophilicity Patterns of Cyclodextrins and nonglucose Cyclooligosaccharides. *Proc. Eight Int. Symp. Cyclodextrins* **1996**, 3.

Acknowledgments

The authors acknowledge the Ministry of Education of the Brazilian Government (CAPES) for partial support through a sabbatical Fellowship to RDS and the National Institutes of Health (GM 26698−18).

JS9804314

A publication of the American Pharmaceutical Association and the American Chemical Society

JOURNAL OF Pharmaceutical Sciences

June 1999
Volume 88, Number 6

RESEARCH ARTICLES

Disposition of Radioactivity after Injection of Liver-Targeted Proteins Labeled with ^{111}In or ^{125}I. Effect of Labeling on Distribution and Excretion of Radioactivity in Rats

FRANTISEK STAUD, MAKIYA NISHIKAWA, KENSUKE MORIMOTO, YOSHINOBU TAKAKURA, AND MITSURU HASHIDA*

Contribution from *Department of Drug Delivery Research, Graduate School of Pharmaceutical Sciences, Kyoto University, Sakyo-ku 606-8501, Kyoto, Japan.*

Received November 16, 1998. Accepted for publication March 26, 1999.

Abstract □ The effect of radiolabeling liver-specific proteins on the in vivo disposition of radioactivity was investigated. The suitability of ^{111}In and ^{125}I as radiolabels for protein disposition studies in vivo was examined. Galactosylated and cationized bovine serum albumin were labeled with either ^{125}I by the chloramine-T method or ^{111}In, using 1-(4-isothiocyanatobenzyl)ethylenediaminetetraacetic acid (SCN-BZ-EDTA) or diethylenetriaminepentaacetic acid (DTPA) as bifunctional chelating agents (BCAs) and administered intravenously to rats. ^{125}I radioactivity disappeared rapidly from the liver with subsequent excretion in the urine and bile, mainly in the TCA soluble fraction. ^{111}In-associated radioactivity, on the other hand, remained in the hepatic tissue in considerably higher amounts during the experiment and was excreted in the bile and urine to a lower extent when compared with ^{125}I. When the effect of BCA on excretion of ^{111}In radioactivity was compared, no significant differences were observed in the urinary clearances. However, biliary excretion was significantly higher for ^{111}In-SCN-BZ-EDTA-bound radioactivity. In conclusion, when compared with ^{125}I, ^{111}In labeling seems to more accurately characterize the in vivo distribution of liver-targeted proteins after their iv administration in rats and allows a more accurate pharmacokinetic evaluation to be performed.

Introduction

Since biologically active proteins are receiving much attention as potential therapeutic agents, there has been a need to modify their structure in order to overcome difficulties associated with their clinical application. Consequently, it is necessary to quantitatively describe the disposition of these proteins in the body using pharmacokinetic evaluation. Labeling a protein in question with a radionuclide is the easiest way to trace it in the organism, and a variety of methods have been employed to label proteins with a radionuclide. Among these, radioiodine isotopes are the most widely used protein radiolabels for imaging studies.[1] Proteins may be easily labeled with radioisotopes of iodine by several methods; however, certain limitations to the use of radioiodine for imaging applications have become apparent, especially their poor target retention of radioactivity.[2,4]

Several alternative methods of radiolabeling proteins and peptides have been examined to overcome these difficulties and to increase and retain enough radioactivity at target sites for a sufficient period of time. After introduction of bifunctional chelating agents (BCAs), ^{111}In has become a convenient radiometal which has been used by many investigators.[4] This radionuclide is commonly attached to a protein via ethylenediaminetetraacetic acid (EDTA) or, alternatively, via diethylenetriaminepentaacetic acid (DTPA). In addition, several other modifications of these BCAs have been investigated to improve labeling efficiency and in vivo stability.[5−8]

When internalized by cells, these proteins undergo intracellular catabolism with subsequent formation of radiolabeled metabolites. In particular, after endocytotic internalization, the ligand is delivered to the endosome and then to the lysosome. In the lysosomal compartment, most

* Corresponding author. Tel: +81-75-753-4525. Fax: +81-75-753-4575. E-mail: hashidam@pharm.kyoto-u.ac.jp.

10.1021/js9804415 CCC: $18.00
Published on Web 05/06/1999

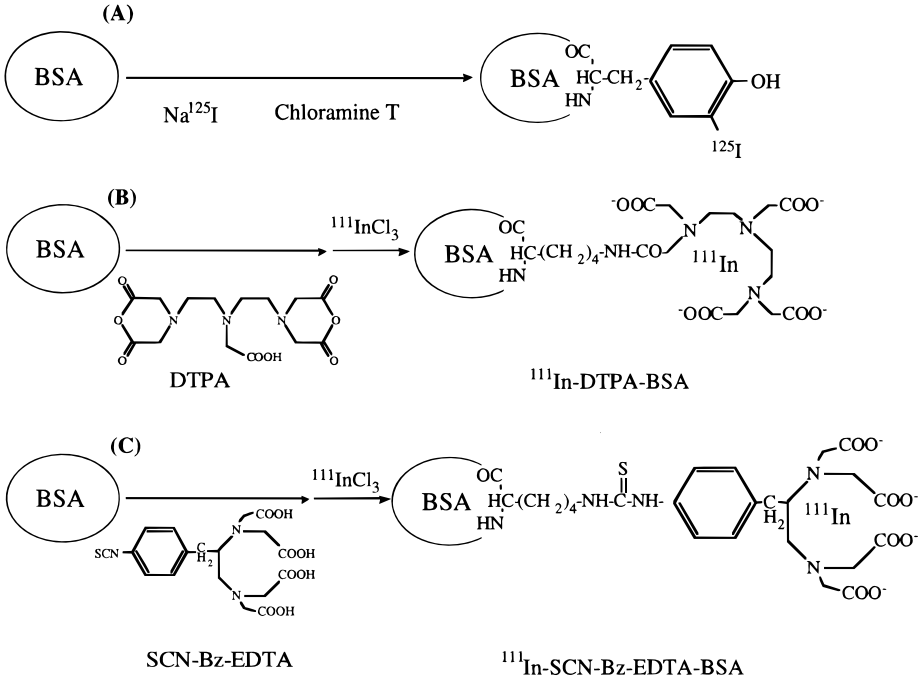

Figure 1—Chemical structures of BSA derivatives radiolabeled with (A) ^{125}I, (B) ^{111}In-DTPA, or (C) ^{111}In-SCN-BZ-EDTA.

of the ligand is degraded by proteases and glycosidases.[9] Obviously, further disposition of radioactivity within the body will be determined by the nature of the radiolabeled degradation product(s) formed, mainly by their physicochemical characteristics such as lipophilicity and molecular weight and/or by their possible affinity for a carrier-mediated transport system. This problem becomes especially marked in cases where proteins are intended to be preferentially taken up by liver cells. In the case of radioiodine-labeled proteins, the final radioactive metabolite is mono- or diiodotyrosine[10] which seems to escape from the liver at a very fast rate with consequent interference with the pharmacokinetic analysis.

The aim of the present study was to investigate and quantitatively compare the difference between ^{125}I and ^{111}In radiolabeling of liver-specific proteins in terms of the whole body disposition of radioactivity. Galactosylated bovine serum albumin (Gal-BSA) and cationized BSA (Cat-BSA) were employed as carrier proteins for hepatic cells. Both have been reported to be taken up preferentially by hepatic parenchymal cells, although the mechanism and rate by which they enter cells differ. Hepatic uptake of Gal-BSA occurs via asialoglycoprotein receptors, whereas Cat-BSA enters hepatocytes by adsorptive endocytosis based on universal electrostatic interaction with the cell surface (for review see refs 11 and 12). In the present study, ^{111}In was attached to the proteins using 1-(4-isothiocyanatobenzyl) EDTA (SCN-BZ-EDTA) or DTPA as chelating agents as described by Meares et al.[13] and Hnatowich et al.,[14] respectively. Radioiodination of both proteins by ^{125}I was achieved by the chloramine-T method.[15] Radiolabeled compounds were administered to rats as a bolus intravenous injection. The radioactivity in the plasma, bile, urine, and several organs was measured, and its movement within the body was described using clearance concepts.

Materials and Methods

Chemicals—BSA (fraction V) was purchased from Sigma Chemicals (St Louis, MO). SCN-BZ-EDTA and DTPA anhydride were obtained from Dojindo Laboratory (Kumamoto, Japan). ^{111}Indium chloride ([^{111}In]$InCl_3$) was supplied from Nihon Medi-Physics Co. (Takarazuka, Japan). Chloramine T was supplied by Nacalai Tesque (Kyoto, Japan). Sodium (^{125}I) iodide ([^{125}I]NaI) was purchased from DuPont/NEN Co. (Boston, MA). All other chemicals were obtained commercially as reagent-grade products.

Synthesis of BSA Derivatives—The method of Lee et al.[16] was used to introduce galactose residues into BSA. Briefly, cyanomethyl 2,3,4,6-tetra-*O*-acetyl-1-thio-D-galactopyranoside was treated with 0.01 M sodium methoxide at room temperature for 24 h, and the syrup of 2-imino-2-methoxyethyl 1-thio-D-galactopyranoside was obtained after evaporation of the solvent. This resultant syrup was quantitatively added to BSA (100 mg) in 10 mL of 50 mM borate buffer (pH 9.0). After 24 h at room temperature, the reaction mixture was concentrated by ultrafiltration and applied to a Sephadex G-25 column equilibrated with 0.1 M acetate buffer (pH 6.0) to remove the unreacted compound. The number of sugars incorporated into the albumin was determined by the phenol/sulfuric acid method calibrated with galactose.[17]

Cat-BSA was synthesized by covalent coupling of hexamethylendiamine to BSA according to the method reported by Pardridge et al.[18] In brief, 5 mL of 10% BSA in distilled water was slowly added to 30 mL of 2 M hexamethylendiamine at pH 6.5. 1-ethyl-(3-dimethylaminopropyl)carboimide hydrochloride (0.5 g) was added to the solution after 30 and 60 min, and the solution was kept at a pH of 6.5 by addition of 1 M HCl. The solution was stirred overnight and then dialyzed thoroughly against distilled water. The protein was purified by chromatofocusing using Polybuffer exchanger 94 resin and Polybuffer 96 elution buffer (Pharmacia, Uppsala, Sweden). The major protein peak eluted in the void volume and was collected and concentrated by ultrafiltration. The cationic nature of Cat-BSA was confirmed by its absorption on a CM-Sephadex C-50 anion exchanger.

^{125}I Labeling—A modified chloramine-T method[15] was used to label both proteins with ^{125}I. Twenty μL 0.4 M phosphate buffer (pH 7.5) and 20 μL 10-fold diluted [^{125}I]NaI were added to 20 μL the sample solution (1 mg/mL) and vortexed. Two times 20 μL chloramine-T diluted in ice-cold distilled water (3.8 mM) was added and vortexed for 30 s. Finally, 50 μL of sodium metabisulfite solution (2.5 mM) was added and vortexed for 30 s. The solution was applied to a PD-10 column (Pharmacia, Uppsala, Sweden) and eluted with phosphate buffer (0.25 M, pH 7.5) containing 0.2% BSA. The eluent was collected into plastic tubes and the radioactivity counted using a survey meter. Appropriate fractions were taken and stored at −80 °C until use. The specific activity of the obtained sample was 74 MBq/mg protein.

^{111}In Labeling of BSA Derivatives—^{111}In labeling of BSA derivatives was performed using DTPA and SCN-BZ-EDTA as the

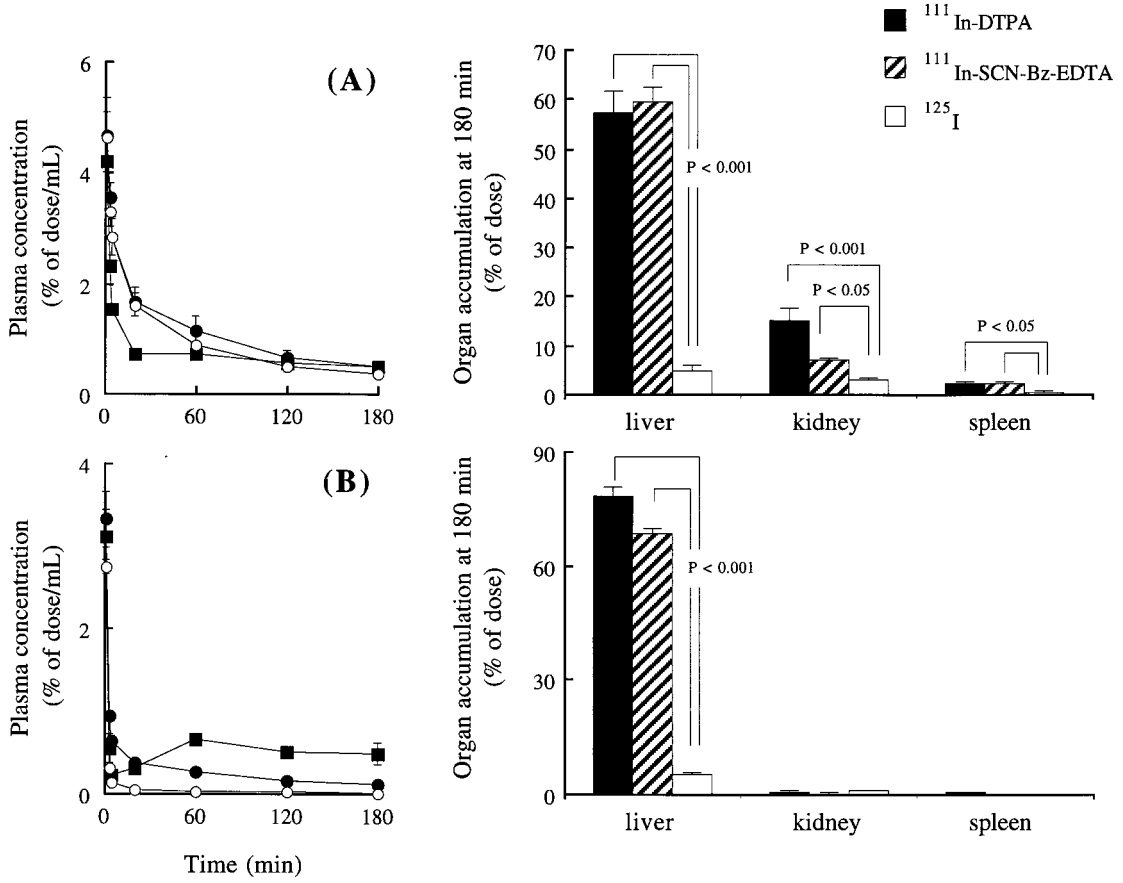

Figure 2—In vivo disposition of radioactivity after iv administration of Cat-BSA (A) and Gal-BSA (B) labeled with ^{111}In-DTPA (●), ^{111}In-SCN-BZ-EDTA (○), or ^{125}I (■). Data are expressed as mean ± SD of at least three experiments. Statistical significance was based on Student *t*-test.

bifunctional chelating agents by the method of Hnatowich et al.[14] and Meares et al.,[13] respectively.

Attachment of DTPA: Gal-BSA or Cat-BSA (2 mg) was dissolved in 1 mL of 4-(2-hydroxyethyl)-1-piperazineethane sulfonic acid buffer (0.1 M, pH 7.0), and a 2-fold molar excess of DTPA anhydride in 10 μL of dimethyl sulfoxide was added. After stirring 30 min at room temperature, the mixture was purified by gel-filtration chromatography using a Sephadex G-25 column (1 × 40 cm) and eluted with acetate buffer (0.1 M, pH 6.0) to separate the unreacted DTPA. Fractions containing DTPA−BSA were selected using spectrophotometry and concentrated by ultrafiltration.

Attachment of SCN-BZ-EDTA: Gal-BSA or Cat-BSA (5 mg) was dissolved in 1 mL of borate-buffered saline (50 mM, pH 8.5) and an equimolar amount of SCN-BZ-EDTA in 10 μL of dimethylformamide was added. After 24 h at 37 °C, the mixture was purified by gel-filtration chromatography using a Sephadex G-25 column (1 × 40 cm) and eluted with acetate buffer (0.1 M, pH 3.0) to separate the unreacted SCN-BZ-EDTA. The fractions containing SCN-BZ-EDTA-BSA were treated as described above.

Thirty microliters of $^{111}InCl_3$ solution was added to 30 μL of sodium acetate buffer (1 M, pH 6.0) and 60 μL of either the DTPA- (or SCN-BZ-EDTA)−BSA derivative was added to the mixture. After 30 min at room temperature (45 min at 37 °C, in the case of SCN-BZ-EDTA−BSA), the mixture was purified by gel filtration chromatography using a PD-10 column (Pharmacia, Uppsala, Sweden) and eluted with acetate buffer (0.1 M, pH 6.0). The appropriate fractions were selected based on their radioactivity and concentrated by ultrafiltration. The specific activity of the obtained samples was 37 MBq/mg protein.

In Vivo Animal Experiments—Prior to administration, trace amounts of radiolabeled proteins were diluted with saline, and the protein concentration was adjusted to 0.1 mg/mL by adding nonlabeled protein. Male Wistar rats (200 g) maintained on a standard rat food and water diet were anaesthetized by intraperitoneal administration of pentobarbital sodium at a dose of 50 mg/kg. Their urinary bladder and bile duct were cannulated using polyethylene and polyvinyl tubing to collect bile and urine samples, respectively. Then, 200 μL investigated protein was injected into the femoral vein at a dose of 0.1 mg/kg. Samples of blood, urine, and bile were collected throughout the 180 min of the experimental period. At the end of the experiment, each animal was killed by bleeding and the liver, kidney, and spleen were excised. Blood samples were centrifuged at 2000*g* for 2 min, and 100 μL of plasma was collected for analysis. The ^{111}In and ^{125}I radioactivity in the samples was measured in a well, NaI scintillation counter (ARC-500, Aloka, Tokyo, Japan).

Table 1—Physicochemical Properties of BSA and Its Derivatives Used in This Study

	molecular weight[a]	number of NH_2 groups[b]	number of galactose[c]	pI[d]
BSA	67000	60.0	–	4.2–4.8
Cat-BSA	70000	69.3	–	>9.0
Gal-BSA	69000	8.6	42	4.8–4.9

[a] Determined by size-exclusion chromatography (LC-6A, Shimadzu, Japan) using a Shim-pack Diol-300 column. [b] Determined by the TNBS method. [c] Determined by the phenol–sulfuric acid method. [d] Determined by chromatofocusing.

Organ Distribution of ^{125}I-Labeled BSA Derivatives—Male Wistar rats similar to these defined above were given 0.1 mg/kg ^{125}I-Cat-BSA or ^{125}I-Gal-BSA. Animals were sacrificed at 5, 20, or 60 min by bleeding, the liver, kidney, spleen, and thyroid were excised, and the radioactivity was measured as described above. Data from the interval of 180 min were adopted from the experiments described in the In Vivo Animal Experiments section.

Assessment of Degradation Products of ^{125}I-Labeled Proteins in Plasma, Bile, and Urine—To investigate the degradation products of ^{125}I-labeled proteins, the samples of plasma, bile, and urine were weighed, and an equivalent volume of 45% trichloracetic acid (TCA) was added. Samples were vortexed and centrifuged at 1500*g* for 10 min. Supernatant (100 μL) was separated into different tubes, and the radioactivity of the TCA-precipitable (protein) and TCA-soluble (degradation product) fractions was measured separately as described above.

Table 2—Apparent Volumes of Distribution, Distribution Half-Lives, AUCs, and Clearances of Cat-BSA and Gal-BSA Based on Radioactivity Concentrations/Amounts in Body Compartments[a,b]

compound	method of labeling	V_d (mL)	$t_{1/2}$ of distribution phase (min)	AUC (% of dose·min·mL^{-1})	CL_{total} (mL·h^{-1})	CL_{liver} (mL·h^{-1})	CL_{kidney} (mL·h^{-1})	CL_{spleen} (mL·h^{-1})	$CL_{thyroid}$ (mL·h^{-1})
Cat-BSA	^{111}In-DTPA	17.3	2.89*	244***,†	24.6***	17.8***	4.73††	0.71	—
	^{111}In-SCN-BZ-EDTA	17.7	2.87*	194***	31.0***	21.7***	2.51**	0.77	—
	^{125}I	16.1	1.76	42.5	141	7.07	4.42	0.83	1.55
Gal-BSA	^{111}In-DTPA	10.5	0. 831	12.3	487	382***	3.41**,††	—	—
	^{111}In-SCN-BZ-EDTA	10.9	0.613	15.0	401	324***	0.98***	—	—
	^{125}I	12.2	0.790	14.7	407	31.6	5.62	—	11.2

[a] Results of ^{125}I are based on the TCA-precipitable fractions of radioactivity in the plasma. [b] Statistical significance was based on Student *t*-test. * Compared with ^{125}I, † compared with ^{111}In-SCN-BZ-EDTA, *(†) $p < 0.05$, **(††) $p < 0.01$, *** $p < 0.001$.

Data Analysis—In this study, the radioactivity of particular samples and organs was employed to express the apparent organ uptake clearance of investigated proteins. The radioactivity of all samples and that of plasma was normalized to the % dose or % dose/mL, respectively. Plasma concentrations ($C_p(t)$) were analyzed by mono- or biexponential functions using the nonlinear least-squares program MULTI.[19] The one- or two-compartment model was chosen according to Akaike Information Criterion.

Total body clearance of radioactivity (CL_{total}) was calculated by:

$$CL_{total} = \frac{D}{AUC} \quad (1)$$

where D is the dose of radioactivity administered, and AUC is the area under the plasma concentration−time curve extrapolated to infinity.

Assuming zero or negligible leakage of radioactivity from organs, the apparent organ uptake clearance (CL_{organ}) may be expressed as:

$$CL_{organ} = \frac{X_{t_i}}{AUC_{t_0-t_i}} \quad (2)$$

where X_{t_i} is the amount of radioactivity in the organ of interest at the end of experiment and $AUC_{t_0-t_i}$ is the area under the curve over the time interval t_0 = administration of the compound and t_i = end of the experiment.[20] In studies with ^{125}I-labeled proteins, AUC of TCA-precipitable radioactivity was employed to estimate tissue uptake clearances.

Results

Characteristics of BSA Derivatives—Chemical structures of the radiolabeled proteins are depicted in Figure 1. Some physicochemical characteristics of BSA, Gal-BSA, and Cat-BSA are given in Table 1. The amount of galactose residues attached to BSA was estimated to be 42:1 (mol/mol). The BSA derivatives had nearly the same molecular weights as the original BSA as judged by gel-filtration chromatography. The isoelectric point of Cat-BSA indicated a highly positive charge caused by introduction of hexamethylenediamine into the BSA molecule.

Plasma Profile of ^{111}In and ^{125}I Radioactivity—The time-courses of the radioactivity in plasma and organ accumulation of radioactivity after injection of ^{111}In-DTPA, ^{111}In-SCN-BZ-EDTA, and ^{125}I-labeled compounds into rats are shown in Figure 2. Fast disappearance of radioactivity from the circulation was observed in all experiments and may be accounted for by the avid hepatic uptake of investigated proteins. In the case of Gal-BSA, the initial phase of plasma concentration did not seem to be influenced by the labeling method. However, in the later phase, ^{125}I radioactivity started to increase reaching a peak at 0.75% dose/mL at 60 min followed by a gradual decrease. In the case of Cat-BSA, on the other hand, the distribution patterns varied significantly depending on the labeling methods (see Table 2). Similarly, the latter phase of ^{125}I radioactivity in the plasma was influenced by the reappearance of a ^{125}I-metabolite in the circulation. This, however, did not result in the appearance of a peak. Kidney and spleen showed generally low radioactivity in the Cat-BSA studies and only negligible amounts were found in these organs in the Gal-BSA studies, 3 h after injection.

Biliary and Urinary Excretion of ^{111}In and ^{125}I Radioactivity—Statistically different features of urinary excretion of radioactivity were observed as far as the three methods of labeling are concerned (Figure 3). In the case of ^{111}In labeling, the total radioactivity excreted in the urine within the 180 min of the experimental period was less than 1% of the administered dose, regardless of the BCA used for labeling and regardless of the BSA derivative. On the other hand, the cumulative amount of ^{125}I radioactivity in the urine was 7.8% and 2.9% of the administered dose for Cat-BSA and Gal-BSA, respectively.

The biliary excretion of radioactivity after administration of radiolabeled Cat-BSA was highest for ^{125}I (2.2% of the administered dose) followed by ^{111}In-SCN-BZ-EDTA (1.1% of the dose) and ^{111}In-DTPA (0.3% of the dose). In the case of Gal-BSA, similarly, the radioactivity excretion of ^{111}In-DTPA-labeled compound was the lowest of all, representing 1.7% of the injected dose. There was no statistically significant difference in the biliary excretion of radioactivity of ^{111}In-SCN-BZ-EDTA and ^{125}I-labeled Gal-BSA (3.8% and 3.5% of the administered amount, respectively).

When the biliary excretion rate (BER) of radioactivity was investigated, differences in the rate of appearance of radioactivity in the bile were observed relating to the three methods of labeling (Figure 4). In particular, ^{125}I-bound radioactivity showed a rapid fall in BER after reaching a peak at 25 min. On the contrary, the rate of biliary excretion of ^{111}In-SCN-BZ-EDTA radioactivity, after reaching a maximum, was found to remain constant (Cat-BSA) or only fall gradually (Gal-BSA). The BER value of ^{111}In-DTPA radioactivity (BER_{DTPA}) during the last hour of the experimental period (calculated as the mean of the last three values) was significantly ($p < 0.001$) lower than that of ^{111}In-SCN-BZ-EDTA. The ratio BER_{DTPA}/BER_{EDTA} was 0.20 in the case of Cat-BSA and nearly identical for Gal-BSA (0.19).

Radioactivity Disposition of ^{125}I-Labeled BSA Derivatives and Their Metabolite(s)—The separation of TCA-precipitable ^{125}I radioactivity is shown in Figure 5. It can be seen that the increase in plasma radioactivity after injection of ^{125}I-Gal-BSA was exclusively caused by the appearance of a low molecular weight product in the circulation. Both the urinary and biliary excretion of ^{125}I radioactivity after the administration of ^{125}I-labeled Cat-BSA and Gal-BSA may also be accounted for by the excretion of a degradation product rather than the intact protein. In the urine, no TCA-precipitable radioactivity was detected.

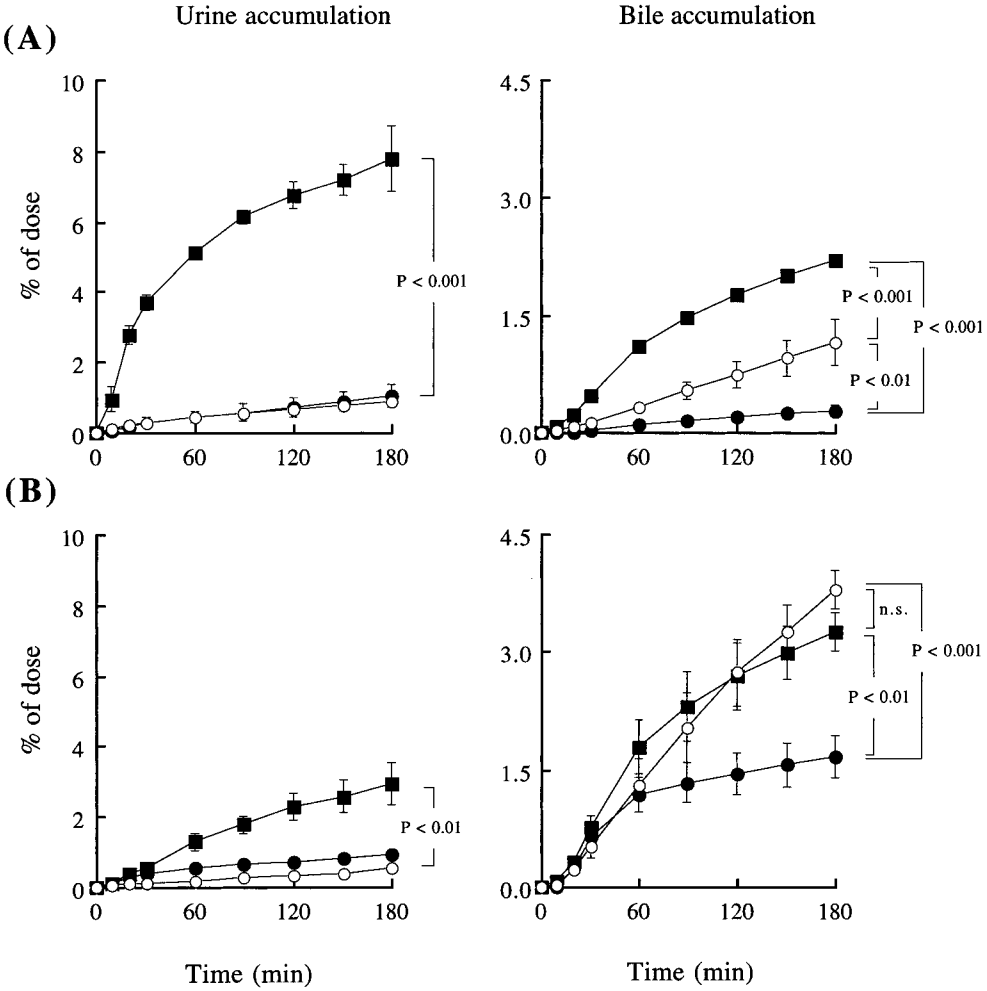

Figure 3—Time-courses of accumulation of radioactivity in the urine and bile after iv administration of Cat-BSA (A) and Gal-BSA (B) labeled with ^{111}In-DTPA (●), ^{111}In-SCN-BZ-EDTA (○), or ^{125}I (■). Data are expressed as mean ± SD of at least three experiments. Statistical significance was based on Student *t*-test; n.s. = statistically nonsignificant.

Apparent Organ Uptake Clearance after Intravenous Administration of BSA Derivatives Labeled with ^{111}In-DTPA, ^{111}In-SCN-BZ-EDTA, and ^{125}I—The apparent volumes of distribution, areas under the radioactivity concentration curve (AUC) and apparent organ uptake clearance of radiolabeled proteins after administration of the investigated compounds in rats are given in Table 2. The AUC of total radioactivity after administration of Cat-BSA was not significantly affected by the method of radiolabeling. However, in the case of Gal-BSA, a rapid release of ^{125}I-metabolite occurred (Figure 2), which resulted in significantly ($p < 0.001$) increased AUC of total radioactivity. When recalculated to infinity, the AUC of ^{125}I radioactivity was about 25 times larger than that of ^{111}In-labeled protein.

The apparent organ uptake clearance of ^{111}In-labeled compounds (regardless of the BCA employed) was consistent with the well-known mechanism of their hepatic uptake. Therefore, the CL_{liver} of ^{111}In-labeled Gal-BSA was very high, approaching the value of liver plasma flow (390 mL/h[21]) ^{111}In−Cat-BSA, on the other hand, was taken up by the liver at a significantly lower rate ($p < 0.001$), with CL_{liver} reaching only about 6% that of Gal-BSA. When ^{125}I was employed as a radiolabel, the apparent hepatic uptake clearance was statistically lower ($p < 0.001$) for both substances, representing approximately 35% of ^{111}In-labeled Cat-BSA. In the case of Gal-BSA, this difference was still more pronounced; the apparent hepatic uptake clearance of ^{125}I-labeled Gal-BSA was less than 10% that of ^{111}In-labeled Gal-BSA.

Statistically lower uptake and/or retention of ^{125}I radioactivity, when compared with ^{111}In, was also observed in the kidney. Uptake of radioactivity by the spleen was observed only for cationized proteins (2−3% of the administered dose), and only a negligible amount of radioactivity was detected in the spleen for the galactosylated proteins.

Time-Course of Organ Distribution of ^{125}I-Labeled BSA Derivatives—The time-courses of ^{125}I radioactivity distribution in the liver, kidney, spleen, and thyroid at 5, 20, 60, and 180 min after injection of ^{125}I−Cat-BSA and ^{125}I-Gal-BSA are shown in Figure 6. In both cases the radioactivity recovered in the liver, kidney, and spleen decreased with time. The most marked fall was seen in the liver during the first 60 min after injection. On the other hand, the thyroid showed an increasing tendency to accumulate ^{125}I radioactivity.

Schematic depiction of radioactivity disposition after administration of radiolabeled proteins in rats is shown in Figure 7.

Discussion

In the previous studies[6,22,23] it was pointed out that the radiolabeled metabolites of liver-specific proteins are the most important determinants of radioactivity elimination

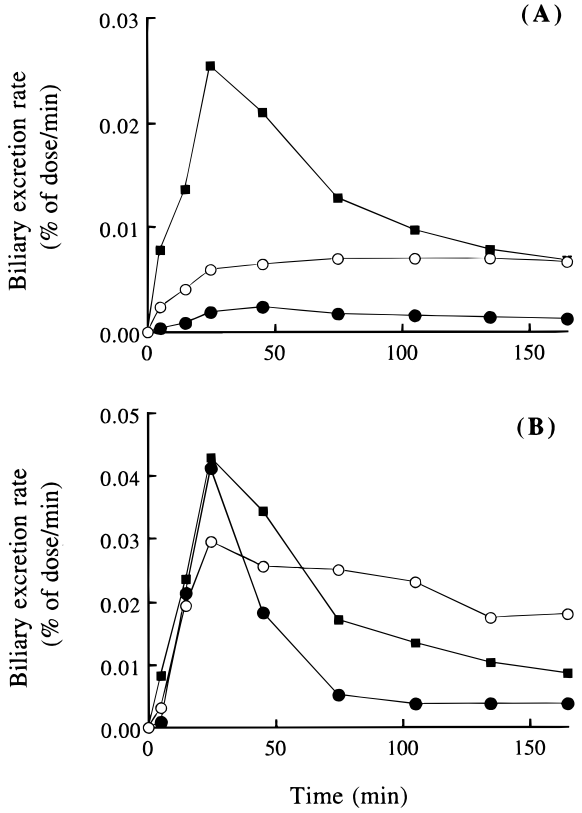

Figure 4—Biliary excretion rate of radioactivity after intravenous administration of radiolabeled Cat-BSA (A) and Gal-BSA (B) in rats. (●) ^{111}In-DTPA; (○) ^{111}In-SCN-BZ-EDTA; (■) ^{125}I. Data represent mean of three rats.

from the target site. Therefore, the choice of an appropriate radionuclide for protein labeling may be the critical step in studies where the body distribution of proteins is investigated and the interpretation of the obtained results is based on radioactivity measurements in various body compartments.

In the present study, we employed two radionuclides, ^{111}In and ^{125}I, to investigate the effect of the radioisotope on the whole body disposition of radioactivity. ^{125}I was attached to the tyrosine residues of proteins using the chloramine T method, and ^{111}In was incorporated into the protein using DTPA or SCN-BZ-EDTA as bifunctional chelating agents. Using these methods, two derivatives of BSA were radiolabeled, and the distribution and excretion of radioactivity was investigated. Gal-BSA and Cat-BSA were chosen as marker compounds because they are known to be taken up by the liver cells via receptor-mediated endocytosis and adsorptive endocytosis, respectively. Previously, we reported the different pharmacokinetics of liver uptake of these two derivatives in rat liver perfusion experiments.[24] Gal-BSA was found to enter the hepatocytes in a dose-dependent (nonlinear) manner with a very fast internalization rate. On the other hand, Cat-BSA was taken up by the liver cells more slowly (internalization constant was about 15% that of Gal-BSA) with a high capacity and was linear over a wide range of inflow concentrations.[24] Consistent results were also obtained in the present study. Both proteins were taken up by the liver in accordance with the type of chemical modification. The CL_{liver} of ^{111}In-labeled Gal-BSA was close to the hepatic plasma flow rate (390 mL/h[21]) and seemed to be limited by this value. On the other hand, the apparent CL_{liver} of ^{111}In-labeled Cat-BSA was significantly lower, representing about 5% that of Gal-BSA.

The fast disappearance of radioactivity from the plasma after intravenous administration of both compounds was caused preferentially by the hepatic uptake of the modified BSAs. In the case of Gal-BSA, there were no significant differences in the distribution phases among the labeling methods. Therefore, it seems plausible that the appearance of the protein in the liver was not influenced by the type of labeling. In the case of Cat-BSA, however, differences between ^{111}In and ^{125}I-labeled proteins were observed. In particular, the distribution half-lives of Cat-BSA labeled with ^{111}In were longer than that of ^{125}I−Cat-BSA (Table 2). We assume that this discrepancy was caused by the anionic character of the chelating agents introduced into the protein molecule. Consequently, the reduced positive charge of the complex resulted in a lower affinity of the protein for adsorptive endocytosis by hepatocytes. This assumption is further supported by the fact that when a 10-fold molar excess of SCN-BZ-EDTA was attached to Cat-BSA, the results obtained from in vivo experiments indicated markedly prolonged retention of radioactivity in the plasma ($t_{1/2\alpha}$ = 13.9 min) with a significantly reduced hepatic uptake clearance (CL_{liver} = 4.74 mL/h) (data not shown).

Significant differences were observed in the extent to which the radiolabel remained in the hepatic tissue. Three hours after drug administration, only a small portion of ^{125}I associated radioactivity was present in the liver (about 5% of the administered dose) when compared with ^{111}In (56−78% dose). Additional distribution experiments with iodine-labeled proteins have revealed a rapid disappearance of ^{125}I radioactivity from the liver within 1 h after drug administration (Figure 6). Then, when the apparent hepatic uptake clearances were calculated, iodinated proteins showed a CL_{liver} that represented only a small fraction of that of ^{111}In-labeled compounds. Therefore, it is evident that the hepatic uptake clearance of these two proteins cannot be simply estimated using ^{125}I radioactivity counts, ignoring the formation of radiolabeled metabolite(s) and radioactivity escaping from the liver. On the other hand, results obtained with ^{111}In-labeled proteins seem to adequately characterize the hepatic uptake of both Gal-BSA and Cat-BSA.

The reason iodine radioactivity escapes from the hepatic tissue much faster than indium radioactivity may be explained in terms of the metabolites that are produced within the hepatic cells. After internalization by the hepatocytes, the proteins are delivered to lysosomes where they undergo proteolytic cleavage and give raise to their metabolic products.[9] In the case of proteins labeled with iodine via tyrosine residues, the metabolites are likely to be mono- and/or diiodinated tyrosine.[10] Either the physicochemical properties or the possible affinity for a transporter system that may be present in the hepatocytes, as speculated by Gore et al.[25] and Duncan and Welch,[22] or a combination of both, enable these metabolites to leave the hepatocytes very easily. In addition, the metabolite may be converted to iodine by cytoplasmic deiodinase[26] and both radiolabeled monoiodtyrosine and iodine were found in blood in studies with ^{125}I-labeled asialofetuin.[27]

In the case of indium-labeled compounds with SCN-BZ-EDTA and DTPA as chelators, ^{111}In-SCN-BZ-EDTA-lysine and ^{111}In-DTPA-lysine were identified as the final metabolic products respectively.[28,23] Slow release of ^{111}In-DTPA-amino acid-associated radioactivity from the liver has previously been reported by Duncan and Welch[22] who pointed out that the compound, to leave the lysosomal compartment, had either to cross the lipid bilayer by simple diffusion or to use a transporter for amino acids. However, simple diffusion is greatly complicated by the ionic character of the chelate and the attached amino acid at intralysosomal pH (about 5.0); carrier-mediated amino acid transport is present for lysine, but the transfer is hindered

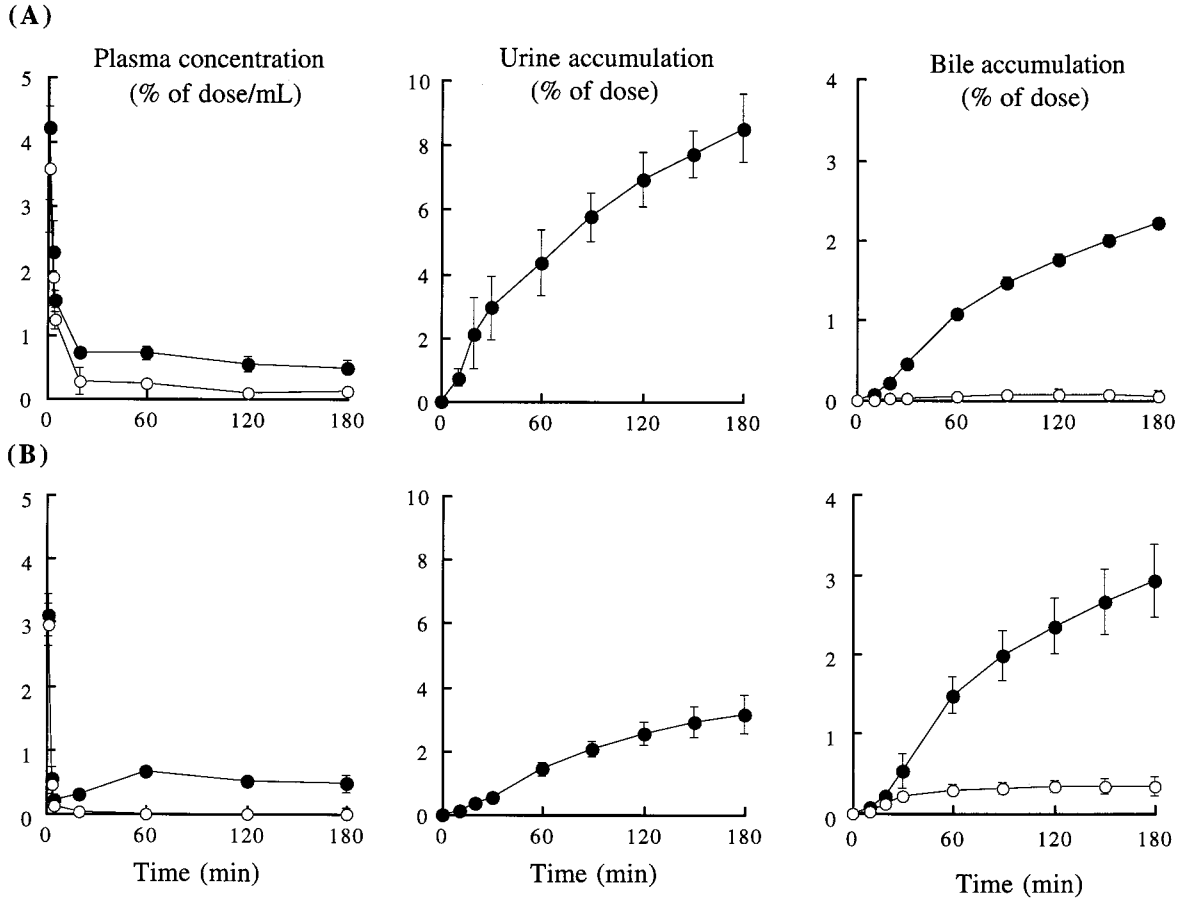

Figure 5—Body disposition of ^{125}I radioactivity; TCA-precipitable (○) and total radioactivity (●) of ^{125}I-labeled Cat-BSA (A) and ^{125}I-labeled Gal-BSA (B). In the urine, no TCA-precipitable radioactivity was detected. Data are expressed as mean ± SD of at least three experiments.

by derivatization of the ϵ-amine. Therefore, the possibility for ^{111}In-DTPA-amino acid to leave lysosomes/hepatocytes is rather limited.

In our study, the different mode and rate of hepatic uptake of both proteins resulted in a different disposition of ^{125}I-associated radioactivity. The internalization and degradation of Gal-BSA take place at a very fast rate. Consequent proteolytic degradation resulted in a rapid escape of radioactivity from the liver (Figure 6) and in the appearance of TCA-soluble ^{125}I radioactivity in the plasma and bile (Figure 5). As a result, the AUC of ^{125}I radioactivity in the plasma was 25 times larger than that of ^{111}In associated radioactivity. A similar course of iodine radioactivity has also been reported in rabbits after administration of ^{131}I-asialoorosomucoid.[29] However, the internalization of Cat-BSA and its delivery to the lysosomal compartment occur at a much slower rate when compared with Gal-BSA,[24] and the production of ^{125}I-metabolite(s) is supposed to be delayed. Therefore, it is unlikely that the fall in the liver radioactivity within 60 min of ^{125}I-Cat-BSA injection and the appearance of TCA-soluble radioactivity in the plasma and urine occurred only due to the formation of a metabolite in the lysosomes. We suppose that it might be caused by an enzymatic degradation (deiodination) of the protein in the plasma, or even when attached to the liver surface, with consequent glomerular filtration of ^{125}I or ^{125}I-radiolabeled metabolite. An attempt to distinguish between the ^{125}I radioactivity associated with protein and that of its degradation product has confirmed that the radioactivity in the urine was accounted for by a metabolite rather than an intact protein (Figure 5). However, the precise structure of the metabolite(s) has not been determined, and therefore we cannot speculate on the exact origin and pathways of the metabolite(s). Nevertheless, when compared with ^{111}In-labeled compounds, ^{125}I labeling resulted in a significantly higher accumulation of radioactivity in the urine in studies with both proteins. In addition, bifunctional chelating agents employed for attaching ^{111}In to protein molecules did not appear to affect the urinary excretion of ^{111}In radioactivity to a great extent.

When the biliary excretion rate was investigated (Figure 4), in the case of Gal-BSA, the curves of BER during the first 25 min followed nearly identical courses. As more than 90% of ^{125}I radioactivity in the bile was TCA-precipitable within 20 min of injection, we assume that during this period the protein avoided the lysosomal compartment and the radioactivity was excreted into the bile in protein-bound form, by means of transcytosis. In a different set of experiments, the gel separation of protein and metabolite-bound radioactivity in the bile in studies with ^{111}In-DTPA labeled Gal-BSA was performed. Similarly, it was found that 80−95% of radioactivity released into the bile was in protein-bound form within ca. 60 min after administration (unpublished results). After this interval, degradation of the protein in the lysosomal compartment occurred and the radiolabeled metabolites were leaving the hepatocytes at different rates in the following order: ^{125}I > ^{111}In-SCN-BZ-EDTA > ^{111}In-DTPA. This escape was in a good agreement with the theory of Duncan and Welch[22] described above. Similar patterns were also observed in the case of Cat-BSA. Interestingly, it was found that the ratio of BERs between ^{111}In-DTPA and ^{111}In-SCN-BZ-EDTA-associated radioactivity was nearly identical for both protein derivatives. Consequently, the cumulative amount of radioactivity in the bile during the 180 min experimental period has shown that, among the three methods of labeling

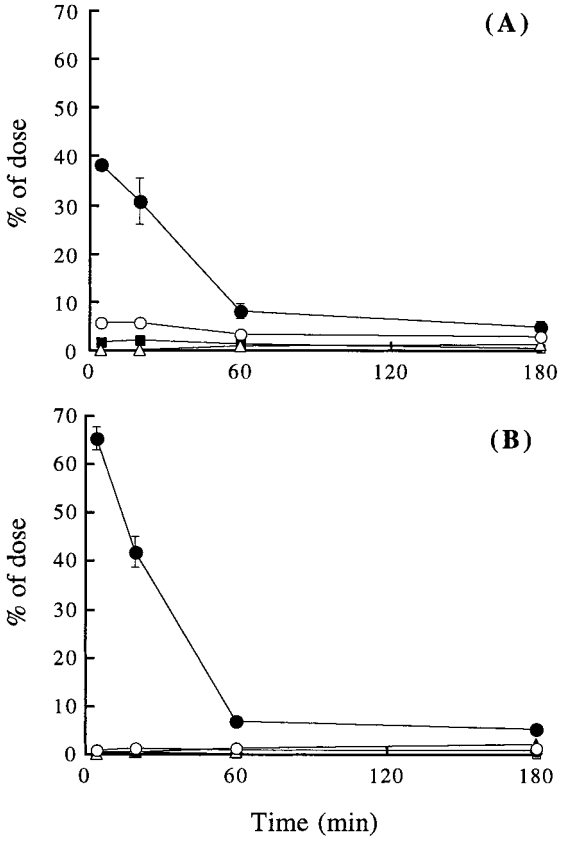

Figure 6—Time-courses of ^{125}I radioactivity distribution in rats after intravenous administration of ^{125}I-labeled Cat-BSA (A) and ^{125}I-labeled Gal-BSA (B). (●) liver, (○) kidney, (■) spleen, (△) thyroid. Data are expressed as mean ± SD of two experiments.

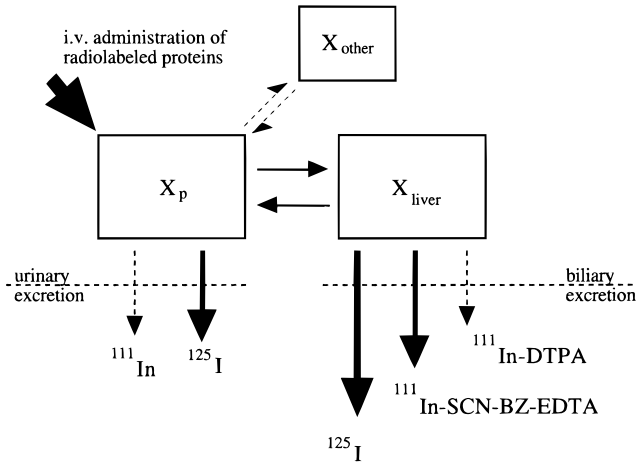

Figure 7—Schematic depiction of radioactivity disposition after intravenous administration of radiolabeled liver-specific protein in rat. X_p = radioactivity in the plasma; X_{liver} = radioactivity in the liver; X_{other} = radioactivity in other tissue.

employed, ^{111}In-DTPA-associated radioactivity appeared in the bile in the lowest amount, regardless of the protein derivative. ^{111}In-SCN-BZ-EDTA radioactivity was excreted into the bile in a higher amount than that of ^{111}In-DTPA. This is consistent with the previous results of Arano et al.[30] who reported faster biliary elimination of ^{111}In-SCN-BZ-EDTA-lysine in comparison with ^{111}In-DTPA-lysine. Also, a similar set of experiments performed in mice revealed comparable behavior of these radiolabels. However, the difference between ^{111}In-DTPA and ^{111}In-SCN-BZ-EDTA radioactivity was much more pronounced.[31] The faster elimination of ^{111}In-SCN-BZ-EDTA-labeled metabolite might also be explained in terms of the physicochemical properties of the radiometabolites. However, the detailed mechanism of the disappearance of these compounds from the liver cells remains to be elucidated.

For a more accurate estimation of the CL_{liver} of ^{125}I-labeled proteins, the more sophisticated approach of a pharmacokinetic analysis has been adopted in our previous study in mice.[31] TCA-precipitable fraction was employed for data analysis and the time-courses of radioactivity in the plasma and liver were simultaneously fitted to exponential equations to calculate the CL_{liver}. However, even this approach, requiring much more experimental data, did not produce satisfactory results due to the pattern of liver accumulation.

In conclusion, this study has confirmed a significant influence of the radioisotope employed in the labeling of the liver-specific proteins on the fate of the radioactivity in the body. ^{125}I radioactivity rapidly escaped from the target tissue and was excreted into bile and urine, thus interfering with the pharmacokinetic analysis to a great extent. Therefore, ^{125}I labeling was found inappropriate for distribution studies of Gal-BSA and Cat-BSA in rats. On the other hand, the results obtained with ^{111}In were consistent with the well-known behavior of these proteins in the organism and allowed pharmacokinetic analysis to be performed without correction for radiolabeled metabolites. In particular, because of the restricted release of ^{111}In-DTPA-labeled metabolite from the liver, among the three methods of radiolabeling investigated, ^{111}In radiolabeling using DTPA as a bifunctional chelating agent was found to be the most suitable for in vivo disposition studies of liver-specific proteins.

References and Notes

1. Fritzberg, A. R.; Beaumier, P. L. Targeted proteins for diagnostic imaging: Does chemistry make a difference? *J. Nucl. Med.* **1992**, *33*, 394−397.
2. Scheinberg, D. A.; Strand, M. Leucemic cell targeting and therapy by monoclonal antibody in a mouse model system. *Cancer Res.* **1982**, *42*, 44−49.
3. Fritzberg, A. R.; Berninger, R. W.; Hadley, S. W.; Wester, D. W. Approaches to radiolabeling of antibodies for diagnosis and therapy of cancer. *Pharm. Res.* **1988**, *5*, 325−334.
4. Hnatowich, D.; Layne, W. W.; Childs, R. L.; Lanteigne, D.; Davis, M. A.; Griffin, T. W.; Doherty, P. W. Radioactive labeling of antibody: a simple and efficient method. *Science* **1983**, *220*, 613−615.
5. Cole, W. C.; DeNardo, S. J.; Meares, C. F.; McCall, M. J.; DeNardo, G. L.; Epstein, A. L.; O'Brien, H. A.; Moi, M. K. Comparative serum stability of radiochelates for antibody radiopharmaceuticals. *J. Nucl. Med.* **1987**, *28*, 83−90.
6. Arano, Y.; Mukai, T.; Akizawa, H.; Uezono, T.; Motonari, H.; Wakisaka, K.; Wakisaka, K.; Kairiyama, C.; Yokoyama, A. Radiolabeled metabolites of proteins play a critical role in radioactivity elimination from the liver. *Nucl. Med. Biol.* **1995**, *22*, 555−564.
7. Arano, Y.; Uezono, T.; Akizawa, H.; Ono, M.; Wakisaka, K.; Nakayama, M.; Sakahara, H.; Konishi, J.; Yokoyama, A. Reassessment of diethylentriaminpentaacetic acid (DTPA) as a chelating agent for indium-111 labeling of polypeptides using a newly synthesized monoreactive DTPA derivative. *J. Med. Chem.* **1996**, *39*, 3451−3460.
8. Brandt, K. D.; Johnson, D. K. Structure−function relationships in indium-111 radioimmunoconjugates. *Bioconjugate Chem.* **1992**, *3*, 118−125.
9. Bridges, K.; Harford, J.; Ashwell, G.; Klausner, R. D. Fate of receptor and ligand during endocytosis of asialoglycoproteins by isolated hepatocytes. *Proc. Natl. Acad. Sci. U.S.A.* **1982**, *79*, 350−354.
10. Geissler, F.; Anderson, S. K.; Venkatesan, P.; Press: O. Intracellular catabolism of radiolabeled anti-mu antibodies by malignant B-cells. *Cancer Res.* **1992**, *52*, 2907−2915.
11. Hashida, M.; Nishikawa, M.; Takakura, Y. Hepatic targeting of drugs and protein by chemical modification. *J. Controlled Release* **1995**, *36*, 99−107.

12. Takakura, Y.; Mahato, R. I.; Nishikawa, M.; Hashida, M. Control of pharmacokinetic profiles of drug-macromolecule conjugates. *Adv. Drug. Delivery Rev.* **1996**, *19*, 377−399.
13. Meares, C. F.; McCall, M. J.; Reardan, D. T.; Goodwin, D. A.; Diamanti, C. I.; McTigue, M. Conjugation of antibodies with bifunctional chelating agents: isothiocyanate and bromoacetamide reagents, methods of analysis, and subsequent addition of metal ions. *Anal. Biochem.* **1984**, *142*, 68−78.
14. Hnatowich, D.; Layne, W. W.; Childs, R. L. The preparation and labeling of DTPA-coupled albumin. *Int. J. Appl. Radiat. Isot.* **1982**, *12*, 327−332.
15. Hunter, W. M.; Greenwood, F. C. Preparation of iodine-131 labeled human growth hormone of high specific activity. *Nature* **1962**, *194*, 495−496.
16. Lee, Y. C.; Stowell, C. P.; Krantz, M. J. 2-imino-2-methoxyethyl 1-thioglycoside: New reagents for attaching sugars to proteins. *Biochemistry* **1976**, *15*, 3956−3963.
17. Gray, G. R. The direct coupling of oligosacharides to proteins and derivatized gels. *Arch. Biochem. Biophys.* **1974**, *163*, 426−428.
18. Pardridge, W. M.; Kumagai, A. K.; Eisenberg, J. B. Chimeric peptides as a vehicle for peptide pharmacokinetical delivery through the blood-brain barrier. *Biochem. Biophys. Res. Commun.* **1987**, *146*, 307−313.
19. Yamaoka, K.; Tanigawara, Y.; Tanaka, H.; Uno, Y. A pharmacokinetic analysis program (MULTI) for microcomputer. *J. Pharmacobio-Dyn.* **1981**, *4*, 879−885.
20. Nishikawa, M.; Takakura, Y.; Hashida, M. Pharmacokinetic evaluation of polymeric carriers. *Adv. Drug Del. Rev.* **1996**, *21*, 135−155.
21. Bischoff, K. B.; Dedrick, R. L.; Zaharko, D. S.; Longstreth, J. A. Methotrexate pharmacokinetics. *J. Pharm. Sci.* **1971**, *60*, 1128−1133.
22. Duncan, J. R.; Welch, M. J. Intracellular metabolism of indium-111-DTPA-labeled receptor targeted proteins. *J. Nucl. Med.* **1993**, *34*, 1728−1738.
23. Franano, N. F.; Edwards, W. B.; Welch, M. J.; Duncan, J. R. Metabolism of receptor targeted ^{111}In-DTPA-glycoproteins: Identification of ^{111}In-DTPA-ϵ-lysine as the primary metabolic and excretory product. *Nucl. Med. Biol.* **1994**, *21*, 1023−1034.
24. Nishida, K.; Takino, T.; Eguchi, Y.; Yamashita, F.; Hashida, M.; Sezaki, H. Pharmacokinetic analysis of uptake process of lactosaminated albumin in rat liver constant infusion experiments. *Int. J. Pharm.* **1992**, *80*, 101−108.
25. Gore, S.; Morris, A. I.; Gilmore, I. T.; Maltby, P. J.; Thornback, J. R.; Billington, D. Differences in the intracellular processing of the radiolabel following the uptake of iodine-125- and technetium-99m-neogalactosylalbumin by the isolated perfused rat liver. *J. Nucl. Med.* **1991**, *32*, 506−512.
26. Koehrle, J.; Auf'mkolk, M.; Rokos, H.; Hesch, R. D.; Cody, V. Rat liver iodothyronine monodeiodinase. Evaluation of the iodothyronine ligand-binding site. *J. Biol. Chem.* **1986**, *26*, 11613−11622.
27. LaBadie, J. H.; Chapman, K. P.; Aronson, N. N. Jr. Glycoprotein catabolism in rat liver. Lysosomal digestion of iodinated asialo-fetuin. *Biochem. J.* **1975**, *152*, 271−279.
28. Arano, Y.; Mukai, T.; Uezono, T.; Wakisaka, K.; Motonari, H.; Akizawa, H.; Taoka, Y.; Yokoyama, A. A biological method to evaluate bifunctional chelating agents to label antibodies with metallic radionuclides. *J. Nucl. Med.* **1994**, *35*, 890−898.
29. Galli, G.; Maini, C. L.; Orlando, P.; Deleide, G.; Valle, G. A radiopharmaceutical for the study of the liver: ^{99m}Tc-DTPA-asialoorosomucoid. *J. Nucl. Med. Allied Sci.* **1988**, *32*, 110−116.
30. Arano, Y.; Mukai, T.; Uezono, T.; Motonari, H.; Wakisaka, K.; Yokoyama, A. Biological comparison of DTPA and SCN-benzyl-EDTA as chelating agents for indium labeling of antibodies. *J. Labeled. Compd. Radiopharm.* **1994**, *35*, 381−383.
31. Nishikawa, M.; Staud, F.; Takemura, S.; Takakura, Y.; Hashida, M. Pharmacokinetic Evaluation of Biodistribution Data Obtained with Radiolabeled Proteins in Mice. *Biol. Pharm. Bull.* **1999**, *22*, 214−218.

JS9804415

Oleate Salt Formation and Mesomorphic Behavior in the Propranolol/Oleic Acid Binary System

KIERAN J. CROWLEY,[†] ROBERT T. FORBES,*[†] PETER YORK,[†] HÅKAN NYQVIST,[‡] AND OLA CAMBER[‡]

Contribution from *Drug Delivery Group, Postgraduate Studies in Pharmaceutical Technology, The School of Pharmacy, University of Bradford, Bradford, BD7 1DP, U.K., and Analytical and Pharmaceutical R&D, Astra Arcus, Södertälje, S-151 85, Sweden.*

Received December 28, 1998. Accepted for publication February 23, 1999.

Abstract □ Thermal analysis of propranolol/oleic acid mixtures prepared by solvent evaporation enabled construction of the binary system phase diagram. This allowed both physical and chemical interactions to be identified, including complex formation at the equimolar composition. An incongruent melting complex with a characteristic reaction point was identified in excess oleic acid compositions, a common property of fatty acid/fatty acid salt binary systems. The equimolar complex was confirmed to be propranolol oleate using infrared spectroscopy. Wide-angle X-ray powder diffractometry demonstrated that propranolol oleate possessed long-range positional order (~25 Å *d* spacing) accompanied by a degree of disorder over shorter *d* spacings. Such a pattern suggested mesophase formation, explaining the unctuous nature of propranolol oleate at room temperature. Accurate measurement of the long-range *d* spacing was achieved using small-angle X-ray scattering, permitting differentiation of the three different phases identified (phase I: 25.4 Å, phase II: 24.6 Å, phase III: 25.4–25.5 Å). The implications of drug fatty acid salt formation and also mesomorphism in pharmaceutical systems are discussed.

Introduction

The numerous gastrointestinal physiological effects of lipids can be utilized to manipulate drug oral bioavailability. Examples include extension of the gastrointestinal transit time, modified drug absorption, and stimulation of lymphatic drug transport.[1] Owing to the regional nature of these effects, drug and lipid must be released in a localized and controlled manner. During the initial development stages of such an oral drug delivery system, one must establish the physicochemical properties of drug, lipid, and the drug/lipid combination so that an appropriate system is chosen.

Oleic acid is a long chain fatty acid of considerable interest in oral drug delivery, as it has been shown to participate in all of the aforementioned physiological effects.[2−4] An example of oral bioavailability enhancement following coadministration of oleic acid has been reported for the β-adrenoceptor blocking drug, propranolol.[5] Administration of a propranolol/oleic acid binary mixture with a propranolol/oleic acid/polymer sustained release ternary mixture led to 3-fold bioavailability enhancement in humans. Propranolol human oral bioavailability is approximately 30% due to extensive first pass metabolism.[6] In light of this, the effect of oleic acid is particularly significant because a postabsorption event appeared to be responsible. Stimulation of propranolol lymphatic transport was considered but a cannulated lymphatic animal model failed to identify sufficient lymphatic drug transport that could impact on drug first pass metabolism.[7] We have undertaken a physicochemical investigation of the propranolol/oleic acid binary system to identify alternative mechanisms of improved bioavailability caused by oleic acid coadministration.

Little is known about the solid-state physical and chemical properties of drug/fatty acid binary systems. The linear structure and polar properties of lipid molecules predispose them to mesophase formation.[8] The term mesophase defines all levels of molecular order that are intermediate of the fully ordered crystalline state and the liquid or amorphous state. Subcategories are present within this broad definition, an example of which is provided by high purity oleic acid. At −6 °C the fully ordered crystalline phase (γ) converts to a conformationally disordered crystalline mesophase (α), followed by melting to a neat phase at 13 °C.[9] The α-phase of oleic acid contains long range positional order in three-dimensions, but orientational disorder of the fatty acid chains is present within the lattice. Structures with a lower degree of positional order, in only one or two-dimensions, are classed as liquid crystalline.[10]

The aim of this study was to investigate the phase behavior of the propranolol/oleic acid binary system using thermal analysis, infrared spectroscopy, and X-ray crystallography. Construction of the binary system phase diagram allowed physical and chemical interactions to be identified. The analytical and pharmaceutical implications of complex formation and mesomorphism in the propranolol/oleic acid system are discussed.

Materials and Methods

Materials—Propranolol base was prepared by addition of excess sodium hydroxide to an aqueous solution of propranolol HCl (Sigma, Poole, U.K.), followed by extraction into chloroform and solvent evaporation. Thermal analysis of six batches found the propranolol base extrapolated onset of melting temperature (91.6 ± 0.6 °C) and melting enthalpy (148.4 ± 1.8 J/g) to be in good agreement with literature values (92.9 °C, 146.4 J/g).[11] Thermogravimetric analysis demonstrated 0.6% w/w (± 0.1, n=3) weight loss during heating at 10 °C/min from 25 to 150 °C, and water content was found to be less than 0.1% w/w (n = 3) using Karl Fischer titration. Binary mixtures of propranolol base and high purity oleic acid (>99%, Sigma, Poole, U.K.) ranging from 5 to 95% P (% P: molar percentage of propranolol base) were prepared by evaporation from chloroform under 900 mbar vacuum at 25 °C for 24 h to yield approximately 1 g product. Drug and fatty acid chemical structures are shown in Figure 1.

Methods—*Thermal Analysis*—Differential scanning calorimetry (DSC) was carried out using the Perkin-Elmer DSC-7 (Beaconsfield, U.K.). Binary mixtures were accurately weighed in the range 5−7 mg into stainless steel pans, hermetically sealed, and then

* To whom correspondence should be addressed. Tel 44-1274-384653. Fax 44-1274-234769. E-mail r.t.forbes@bradford.ac.uk.
[†] University of Bradford.
[‡] Astra Arcus.

10.1021/js9804967 CCC: $18.00
Published on Web 04/24/1999

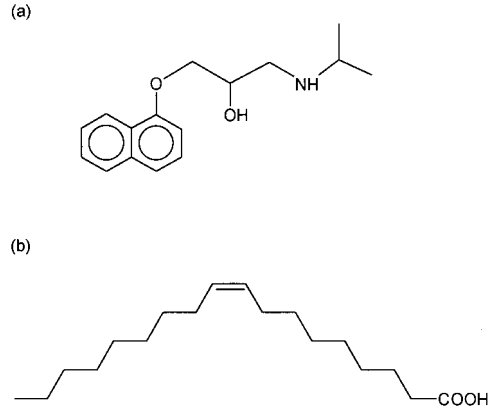

Figure 1—Chemical structures of (a) propranolol, (b) oleic acid.

stored at −17 to −15 °C for 18 h prior to analysis. Particle size control was not possible because many compositions were semisolid or liquid at room temperature. Cooled sample pans were rapidly transferred to the precooled DSC head and analyzed using varying heating rates from −30 to 110 °C. Temperature and enthalpy calibration was carried out using standard indium and zinc, with TAS-7 software for data analysis. All thermal event temperature values were the extrapolated onset temperature with the exception of the liquidus temperature calculation. This temperature represents the liquidus line of the phase diagram, the point above which a system is liquid. Peak melting temperature is therefore a more appropriate measure of the often broad liquidus endotherm and is used in this study.[12] DSC analyses were complemented with hot stage microscopy (HSM, Stanton Redcroft, London, U.K.) to confirm the nature of phase changes taking place.

Fourier Transform Infrared (FT-IR) Spectroscopy—FT-IR spectroscopy was carried out using a 6020 Galaxy spectrometer (Mattson, Newport Pagnell, U.K.) converting 250 scans over 4000 to 400 cm^{-1} at 4 cm^{-1} resolution to conventional frequency domain spectra. An attenuated total reflectance crystal (ATR crystal, Graseby-Specac, Orpington, U.K.) was used to allow analysis of solid, semisolid, and liquid samples. Samples were spread directly onto the crystal surface from chloroform solution and then analyzed at room temperature following solvent evaporation.

X-ray Crystallography—Wide-angle crystallographic data was obtained using a Siemens D5000 X-ray powder diffractometer (XRPD, Karlsruhe, Germany) with a Cu Kα radiation source at generator settings of 40 kV and 30 mA. XRPD diffractograms were obtained at 22 °C over 1−30° 2θ (2θ, the angle between incident and reflected X-rays) using a step size of 0.01° 2θ and a count time of 1 s. Small-angle X-ray scattering (SAXS) was also completed using the Kratky Compact Camera (M. Braun Graz Optical Systems, Graz, Austria). Samples approximately 1 mm thick were mounted in a transmission sample holder between mica windows and cooled below −15 °C for 18 h. The sample stage was cooled to 4 °C with an Anton Paar Peltier temperature control device before sample transfer to stage. The camera tube was evacuated to 0.1 mbar and data collected for 10 min, using Cu Kα radiation generated by the Philips 1830/40 generator at 40−45 kV and 35−40 mA. Measurements were made following 10 min isothermal holds to ensure sample temperature equilibration. Temperature control was accurate to ± 1 °C in the range 0 to 70 °C, with *d* spacings calibrated at 37 °C to 0.1 Å with tristearin.

Results

Thermal Analysis—Precooled propranolol/oleic acid binary mixtures prepared by solvent evaporation were analyzed using DSC. Representative DSC scans are shown in Figures 2a (excess propranolol) and Figure 3a (excess oleic acid). These data were used to construct the binary phase diagram, also presented in two parts (Figures 2b and 3b).

Binary mixtures containing excess propranolol were analyzed at 10 °C/min (Figure 2a). A new thermal event at 51 °C was present in all compositions increasing in

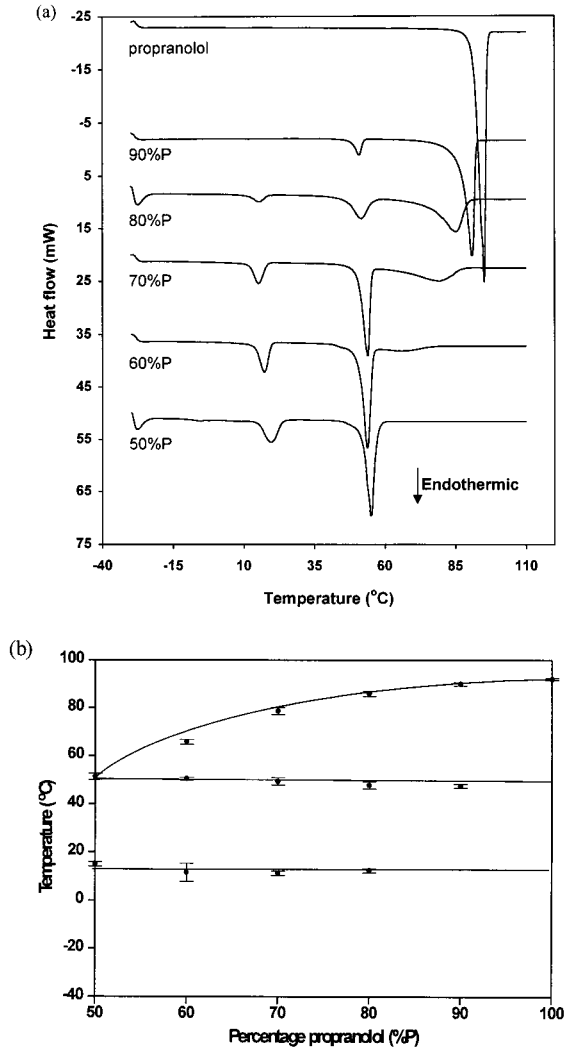

Figure 2—(a) DSC heating scans performed at 10 °C/min of propranolol/oleic acid binary mixtures containing excess propranolol (propranolol, 90% P, 80% P, 70% P, 60% P, 50% P). Compositions quoted as molar percentage % P. (b) Corresponding phase diagram. Three replicate DSC scans were used to obtain each phase transition temperature, the average of which is plotted with the standard deviation shown by an error bar.

magnitude as propranolol content decreased. The enthalpy of melting of excess propranolol decreased until absence at 50% P. The decreasing melting temperature of propranolol and also endotherm broadening suggested that solid propranolol was melting in a liquid phase. An initial melt at 51 °C followed by slow melting of excess propranolol was confirmed using HSM. Therefore, 51 °C corresponded to the solidus line of the phase diagram (the temperature below which the system was solid) and completion of excess propranolol melting represented the liquidus line. The 51 °C thermal event reached maximum enthalpy at 50% P, suggesting formation of an equimolar complex. The abbreviation POA is now used for this complex. The phase diagram indicated that propranolol had negligible solubility in molten POA immediately above the melting temperature of POA. Such a system is described as monotectic.[12] An endotherm at 13 °C also reached maximum enthalpy at POA, suggesting that POA underwent a phase change prior to melting at 51 °C. However, no macroscopic change could be observed when heating precooled POA using HSM.

Multiple thermal events in the second portion of the propranolol/oleic acid system were poorly resolved at 10 °C/min heating rate. Analysis at 2 °C/min provided improved thermal data presented in Figure 3a. The lower

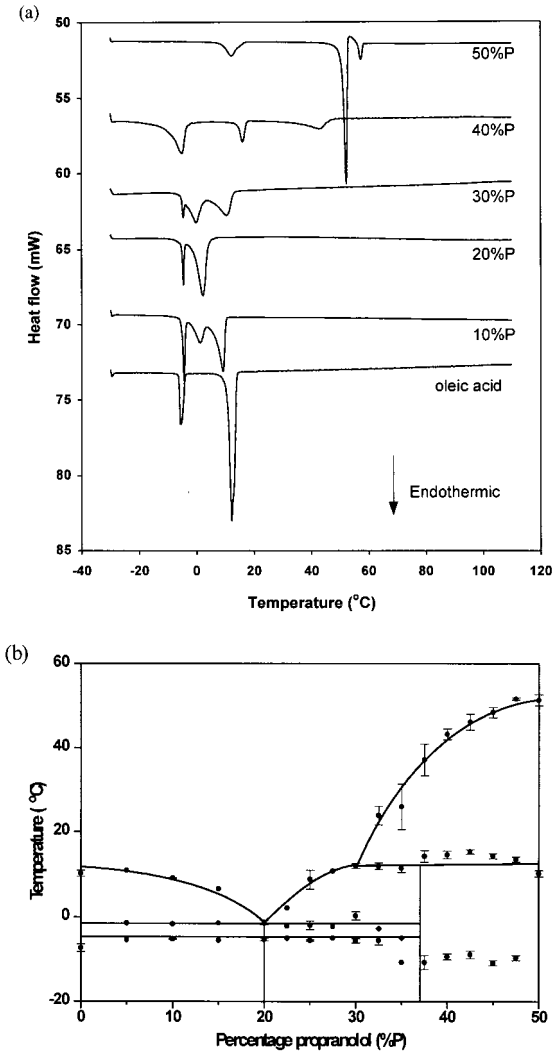

Figure 3—(a) DSC heating scans performed at 2 °C/min of propranolol/oleic acid binary mixtures containing excess oleic acid (50% P, 40% P, 30% P, 20% P, 10% P, oleic acid). Compositions quoted as molar percentage % P. (b) Corresponding phase diagram. For some compositions, three replicate DSC scans were used to obtain each phase transition temperature, the average of which is plotted with the standard deviation shown by an error bar.

heating rate produced a double endotherm at the POA melting event which is investigated in a following section. Eutectic system formation in excess oleic acid compositions was demonstrated by a depression in the liquidus line to a minimum of −1 °C, accompanied by eutectic melting at −1 °C in all 5−30% P compositions. The eutectic melt enthalpy was greatest at 20% P, the eutectic composition. The presence of the $\gamma-\alpha$ oleic acid phase transition at −6 °C in 5−30% P compositions confirmed eutectic system formation because an eutectic is a two-phase system in the solid state. This explains why the $\gamma-\alpha$ transition was present in compositions when the α-oleic acid melting endotherm was absent.

The absence of the eutectic melt in mixtures 35−47.5% P, plus the discontinuity in the liquidus arm of the phase diagram at approximately 30% P, indicated formation of a second complex. The complex did not undergo congruent melting (where both solid and liquid phase have the same chemical composition). When a complex is stable as a solid but is not stable as a liquid phase of the same composition, the process is described as an incongruent melt.[13] Such a melting process yields both a liquid and solid phase. This was apparent in the phase diagram (Figure 3b), and confirmation was obtained from the DSC curve for the

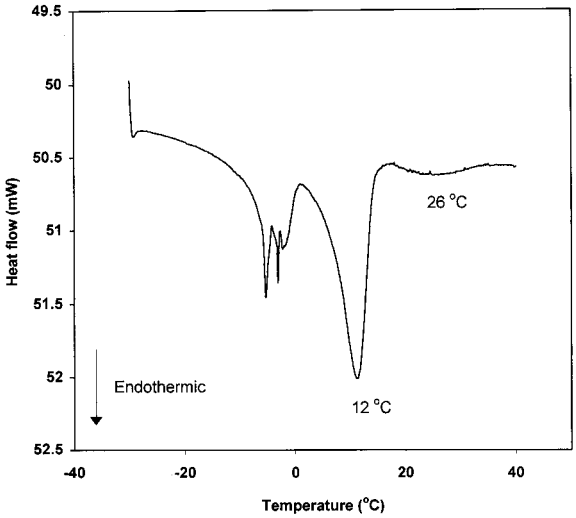

Figure 4—DSC heating scan performed at 2 °C/min of the 32.5% P binary mixture.

32.5% P composition shown in Figure 4. A complicated endothermic process between −6 and 0 °C indicated the presence of the eutectic melt and oleic acid polymorphism. According to the simple eutectic phase diagram,[12] an eutectic melt is followed by a single liquidus endotherm that represents the melt of the excess component. However, a second low enthalpy melting endotherm (peak temperature, 26 °C) could also be identified following the "liquidus" endotherm (peak temperature, 12 °C). The endotherm at 26 °C must be a product of the excess component melting event, confirming incongruent melting. The incongruent melting process of this complex, abbreviated as P/OA*, was as follows:

$$\text{P/OA* (s)} \rightarrow \text{POA (s)} + \text{oleic acid} \qquad (1)$$

The composition of the incongruent melting complex was approximately 35−37.5% P, as indicated on the phase diagram. The break in the liquidus curve at approximately 30% P, 12 °C, represented a reaction point and not the complex composition. Incongruent melting could not be identified using HSM because formation of a solid product during a melt cannot be distinguished from the final stages of a broad congruent melt. It was not possible to characterize the thermal event at approximately −10 °C due to inadequate low temperature equilibration. Incongruent melting processes are commonly identified in fatty acid/fatty acid salt systems, suggesting that the equimolar complex POA was propranolol oleate.[14]

Fourier Transform Infrared (FT-IR) Spectroscopy—The physical properties of propranolol/oleic acid binary mixtures varied widely with composition as indicated on the phase diagram, and so an ATR crystal was used for spectroscopic investigation at room temperature. Spectra obtained for propranolol, oleic acid, and POA are displayed in Figure 5. The high-intensity absorption band at 1710 cm^{-1} of oleic acid was due to asymmetric stretch of the C=O group present in the stabilized fatty acid dimer. O−H out of plane bending of the carboxyl dimer was also identified by an absorption peak at 910 cm^{-1}. Both peaks were absent in POA. The propranolol absorption band at 3270 cm^{-1} due to N−H stretch of the free base was also absent in POA. A new absorption band was present in POA at 1552 cm^{-1}. This suggested formation of a stabilized carboxylate anion (corresponding to asymmetric stretch of COO^-) as seen in propranolol laurate[15] and sodium oleate spectra.[16] FT-IR confirmed that the equimolar complex POA was propranolol oleate.

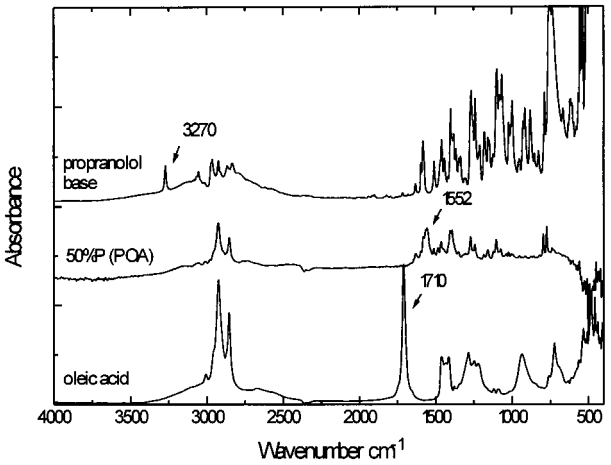

Figure 5—ATR FT-IR spectra of propranolol, 50% P (POA), and oleic acid at room temperature. The absence of secondary amine and carbonyl stretch bands at 3270 and 1710 cm^{-1}, respectively, and the presence of a new band at 1552 cm^{-1} (carboxylate anion) indicated salt formation.

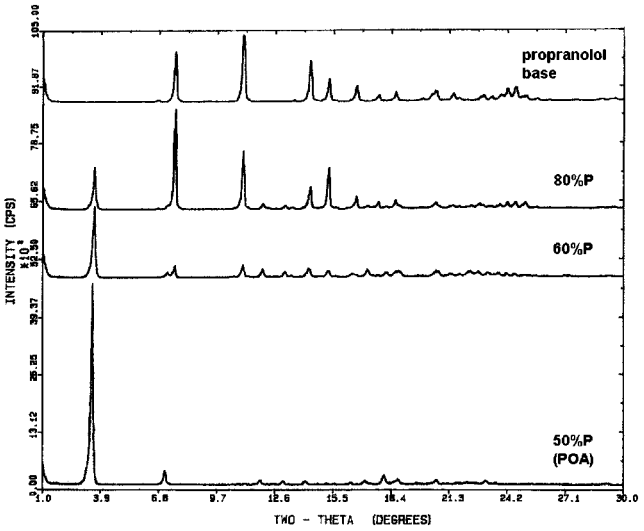

Figure 6—Wide-angle X-ray powder diffractometry (XRPD) patterns of propranolol, and binary mixtures 80% P, 60% P, and 50% P (POA) obtained over 1–30 °2θ at 22 °C.

Wide-Angle X-ray Powder Diffraction (XRPD)—POA existed as an unctuous waxlike solid at room temperature with pronounced birefringence when viewed under crossed polarized light, suggesting mesomorphism. Many phase changes in excess oleic acid compositions took place beneath 22 °C and could not be measured. XRPD diffractograms of 50, 60, 80% P and propranolol base were measured at 22 °C (Figure 6). As the quantity of excess propranolol decreased, the intensity of propranolol reflections reduced until absence at the equimolar composition. Increasing POA content was marked by a high-intensity reflection at 3.7° 2θ. The presence of both propranolol base and POA reflections at intermediate compositions indicated immiscibility of the two components in the solid state. This confirmed a two-phase monotectic system, as shown on the phase diagram (Figure 2b). The absence of high-intensity reflections in the 10−30° 2θ region of the POA spectrum indicated that this composition did not possess a rigid three-dimensional molecular lattice. Conversely, the absence of a broad "amorphous halo" in this region ruled out extensive molecular disorder. The high-intensity reflection at low angle demonstrated long-range positional order, approximate *d* spacing 24 Å. New reflections of much reduced intensity were present at 7.3 and 11.0° 2θ, corresponding to *d* spacings of 12.1 and 8.1 Å. These appeared to be higher order reflections originating from the ~24 Å repeat unit. The relationship between the primary reflection (~24 Å when $n = 1$) and higher order reflections (when $n = 2, 3, 4$, etc., from Bragg's Law $n\lambda = 2d \sin \theta$) can be used to identify mesophase structure. The ~24:12.1:8.1 Å ($1:^1/_2:^1/_3$) ratio of different order reflections for POA indicated a layered structure, such as lamellar or smectic.[17]

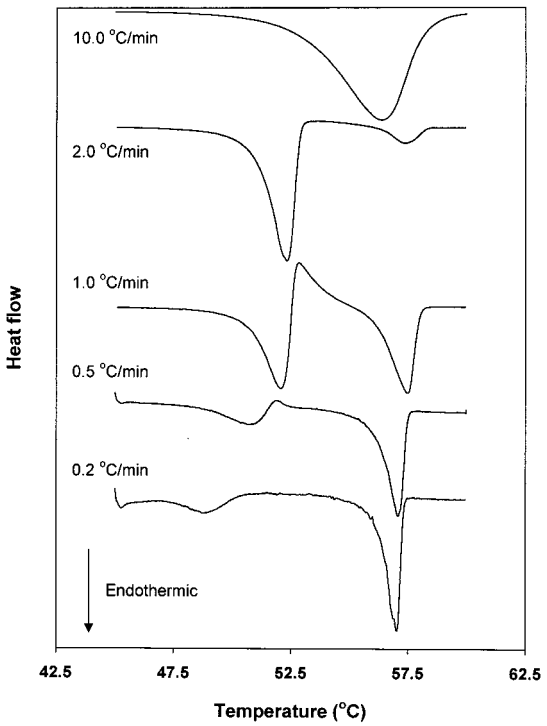

Figure 7—DSC heating scans of 50% P (POA) using variable heating rates (0.2, 0.5, 1.0, 2.0, and 10.0 °C/min). Reduced heating rate reduces the magnitude of thermal events so the heat flow scale is averaged to facilitate data interpretation.

Variable DSC Heating Rate Effect on POA Melting—Thermal analysis of precooled POA demonstrated an endothermic transition at 13 °C. The low-temperature POA solid phase was termed form I, and the phase present above 13 °C form II. A double endotherm at the POA form II melting temperature was observed when a DSC heating rate of 2 °C/min was used (Figure 3a). Further heating rate reduction led to identification of a third POA solid phase (III) that resolidified following form II melting (Figure 7). As heating rate was reduced, the magnitude of the higher temperature endotherm increased, because greater time was available for form III resolidification in a narrow temperature range. An isothermal period proceeding form II melting resulted in complete resolidification of form III. This permitted accurate measurement of melting temperature and enthalpy for this form in the absence of concurrent exothermic processes. At the lowest heating rate of 0.2 °C/min, the endothermic signal for form II melting was virtually absent due to simultaneous resolidification within the sample pan. HSM measurements were used to confirm simultaneous thermal events.

Small-Angle X-ray Scattering (SAXS)—In the absence of unique "fingerprint" XRPD patterns for POA forms I, II, and III, comprehensive thermal analysis provided the optimum tool for oleate salt mesophase characterization. Subtle changes in long-range positional order are commonplace during lipid phase changes (e.g., $\gamma-\alpha$ oleic acid phase transition).[18] SAXS analysis of POA I showed two signals corresponding to 25.4 and 12.7 Å (Figure 8a). The absence of high-intensity reflections at larger *d* spacings

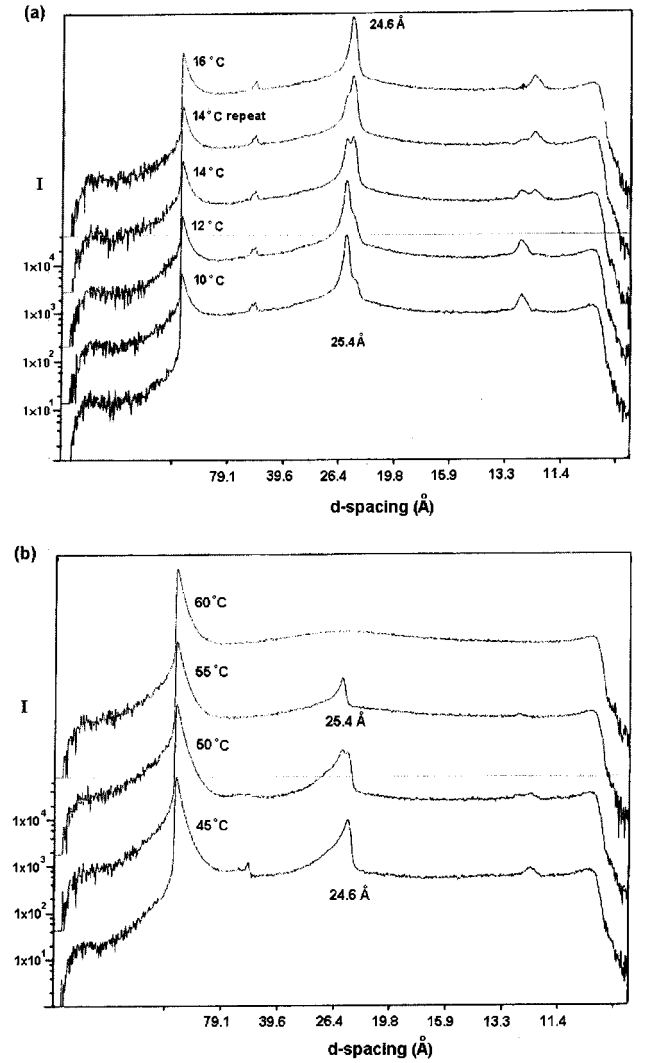

Figure 8—(a) Small-angle X-ray scattering (SAXS) patterns of precooled 50% P (POA) heated from 10 to 16 °C at 2 °C increments. (b) 50% P (POA) heated from 45 to 60 °C at 5 °C increments. For both plots, data collection time was 10 min with a 10 min interval between measurements to allow temperature equilibration.

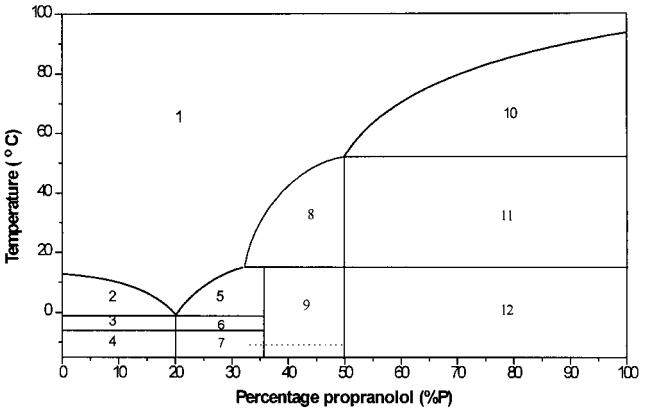

Figure 9—Propranolol/oleic acid binary system phase diagram. (**1**) miscible liquid phase, (**2**) α-oleic acid (s) and liquid, (**3**) α-oleic acid (s) and eutectic (s), (**4**) γ-oleic acid (s) and eutectic (s), (**5**) incongruent melting complex P/OA* (s) and liquid, (**6**) P/OA* (s) and eutectic containing α-oleic acid (s), (**7**) P/OA* (s) and eutectic containing γ-oleic acid (s), (**8**) equimolar complex POA II (s) and liquid, (**9**) P/OA* (s) and POA I (s), (**10**) propranolol (s) and liquid, (**11**) propranolol (s) and POA II (s), (**12**) propranolol (s) and POA I (s).

confirmed that the 25.4 and 12.7 Å signals represented the primary and secondary reflections. A decrease in the long-range repeating unit took place on I−II conversion, as indicated by a fall in reflections to 24.5 and 12.3 Å. A small but significant structural change was also identified following gradual heating through POA II melting point to enable form III resolidification (Figure 8b). The repeating unit in POA III was found to be 25.4/25.5 Å. Thermal and crystallographic properties of POA forms I, II, and III are summarized in Table 1.

Table 1—Summary of Propranolol Oleate Forms I, II, and III DSC (heating rate, 10 °C/min) and SAXS Data

form	temperature of melting/transition, °C (sd, $n = 6$))	enthalpy of transition, °C (sd, $n = 6$)	long-range *d* spacing, Å ($n = 3$)
I	13.1 (1.3)	23.9 (1.4)	25.4, 25.4, 25.4
II	51.4 (1.3)	77.3 (1.7)	24.6, 24.6, 24.6
III	55.7 (0.2)	58.7 (1.0)	25.5, 25.4, 25.5

Discussion

The propranolol/oleic acid binary phase diagram contained important information concerning physical interactions such as monotectic and eutectic systems and also chemical interactions (complex formation). The presence of an incongruent melting complex and reaction point is commonly reported in fatty acid/fatty acid salt binary mixtures.[14] In such systems "acid soap" complexes commonly form that undergo peritectic transformation at the reaction point. The peritectic transformation also marked by a reaction point, but the stable low-temperature solid phase is a solid solution.[19] The transformation temperature often corresponds to a thermotropic polymorphic change of the fatty acid salt, as was seen in the oleic acid/propranolol oleate (POA) portion of the phase diagram (Figure 3b). Solid solution formation was not identified in this system. However, the presence of multiple thermal events at many compositions obstructed accurate measurement of transition enthalpies which are required for such calculations, and so solid solution formation cannot be ruled out. The presence of incongruent melting in phase equilibria is significant because it leads to extremely slow equilibration on cooling. Such behavior is of great importance in the fields of ceramics and metallurgy, but is rarely reported in the pharmaceutical sciences with the following exceptions.[20−22] Incongruent melting complex formation in the propranolol/oleic acid system was thought to have contributed to the slow equilibration of binary mixtures in this region.

Incongruent melting can only be identified by interpretation of the phase diagram. DSC or HSM analysis of a single composition would consist of the incongruent melt followed by solid product melting, which would be interpreted as a two-phase solid sample undergoing separate melting processes. This melt is a single-step process, and so further decrease in heating rate will not alter the relative enthalpies of incongruent melt to solid product melt. However, the effect of heating rate was evident during DSC analysis of two simultaneous thermal events. A change in heating rate altered the relative magnitude of two simultaneous processes, causing marked changes in the DSC total heat flow signal (Figure 7). The latter example demonstrated the importance of complementing DSC data with HSM analysis under similar conditions.

It is emphasized that the phase diagram presented does not represent the equilibrium phase diagram for this system. In addition to the fact that phase behavior beneath −10 °C was not investigated, the impact of POA III formation was omitted. POA II was the most stable form

at room temperature, as shown by DSC analysis of 50−90% P compositions following 6 and 12 months. Therefore, the phase diagram presented was of practical relevance. XRPD indicated that POA II exhibited mesomorphic properties as seen by the presence of long range order accompanied by considerable molecular disorder over shorter distances. The fact that this phase underwent a high enthalpy melt, and that resolidification took place post-melting, strongly suggested that POA II was a conformationally disordered crystalline phase. Liquid crystalline transitions are generally of a lower enthalpy than the initial breakdown of three-dimensional order (crystalline phase) and do not revert to higher ordered structures on temperature increase.[10] XRPD data for POA III showed the absence of high intensity reflections at wide-angle, and so this phase was also classified as a conformationally disordered mesophase. XRPD data was not obtained for POA I so description of this phase is not possible. Nevertheless, SAXS enabled accurate measurement of the long-range repeating unit of all POA solid phases I, II, and III, for which small but significant differences were found.

Oral bioavailability improvement was reported following propranolol laurate administration,[23] and propranolol stearate modified drug entry into the systemic circulation following nasal administration.[24] Thus, the formation of propranolol oleate salt in the propranolol/oleic acid system is likely to have biopharmaceutical implications. In particular, oleate salt formation within the dosage form or in the gastrointestinal tract may have contributed to the increased bioavailability of a propranolol/oleic acid/polymer oral dosage form reported by Barnwell et al.[5] The encouraging effects of propranolol and fatty acid coadministration mean that such drug/lipid systems warrant further investigation, but their complicated phase behavior must be fully understood to enable optimal formulation.

Conclusion

The propranolol/oleic acid binary system phase diagram was constructed using thermal analysis, and equimolar complex and incongruent melting complex formation was demonstrated. The equimolar complex, POA, was identified as propranolol oleate using FT-IR. At room temperature, POA possessed substantial long range positional order accompanied by disorder over shorter *d* spacings as shown by XRPD. This phase (POA II) was classified as a conformationally disordered crystalline phase. SAXS allowed accurate measurement of the long-range repeating unit, leading to the identification of subtle structural changes following POA I, II, and III conversions. Formation of an oleate salt provides an interesting approach for oleic acid inclusion in solid oral dosage forms, but the propensity for complicated phase behavior must be considered. Characterization of the propranolol/oleic acid binary system has demonstrated that a thorough understanding of drug/lipid interactions is vital when formulating such materials.

References and Notes

1. Charman, W. N.; Porter, C. J. H.; Mithani, S.; Dressman, J. B. Physicochemical and physiological mechanisms for the effects of food on drug absorption. *J. Pharm. Sci.* **1997**, *86*, 269−281.
2. Brown, N. J.; Read, N. W.; Richardson, A.; Rumsey, R. D. E.; Bogentoft, C. Characteristics of lipid substances activating the ileal brake in the rat. *Gut* **1990**, *31*, 1126−1129.
3. Muranishi, S. Modification of intestinal absorption of drugs by lipoidal adjuvants. *Pharm. Res.* **1985**, *2*, 108−118.
4. Charman, W. N.; Stella, V. J. Transport of lipophilic molecules by the intestinal lymphatic system. *Adv. Drug Del. Rev.* **1991**, *7*, 1−14.
5. Barnwell, S. G.; Burns, S. J.; Higginbottom, S.; Whelan, I.; Corness, D.; Hay, G.; Rosenberg, E.; Attwood, D. Demonstration of the importance of biphasic oleic acid delivery for enhancing the bioavailability of propranolol in healthy volunteers. *Int. J. Pharm.* **1996**, *128*, 145−154.
6. Riddell, J. G.; Harron, D. W. G.; Shanks, R. G. Clinical pharmacokinetics of β-adrenoceptor antagonists. *Clin. Pharmacokin.* **1987**, *12*, 305−320.
7. White, D. G.; Story, M. J.; Barnwell, S. G. An experimental animal model for studying the effects of a novel lymphatic drug delivery system for propranolol. *Int. J. Pharm.* **1991**, *69*, 169−174.
8. Small, D. M., Ed. *Handbook of Lipid Reseach 4. The Physical Chemistry of Lipids*; Plenum Press: New York, 1988.
9. Kobayashi, M.; Kaneko, F.; Sato, K.; Suzuki, M. Vibrational spectroscopic study on polymorphism and order−disorder phase transition in oleic acid. *J. Phys. Chem.* **1986**, *90*, 6371−6378.
10. Leadbetter, A. J. Structural classification of liquid crystals. In *Thermotropic Liquid Crystals*; Gray, G. W., Ed.; J. Wiley and Sons: U.K., 1987; pp 1−27.
11. Neau, S. H.; Shinwari, M. K.; Hellmuth, E. W. Melting point phase diagrams of free base and hydrochloride salts of bevantolol, pindolol and propranolol. *Int. J. Pharm.* **1993**, *99*, 303−310.
12. Ford, J. L.; Timmins, P. *Pharmaceutical Thermal Analysis: Techniques and Applications*; Ellis Horwood: Chichester, U.K., 1989.
13. Atkins, P. W., Ed. *Physical Chemistry*, 6th ed.; Oxford University Press: U.K., 1998.
14. Cheda, J. A. R.; Ortega, F.; Sanchez-Arenas, A.; Cosio, A.; Fernandez-Garcia, M.; Fernandez-Martin, F.; Roux, M. V.; Turrion, C. Binary phase diagrams of lead(II) *n*-alkanoates and *n*-alkanoic acids. *Pure Appl. Chem.* **1992**, *64*, 65−71.
15. Ogiso, T.; Shintani, M. Mechanism for the enhancement effect of fatty acids on the percutaneous absorption of propranolol. *J. Pharm. Sci.* **1990**, *79*, 1065−1071.
16. Crowley, K. J. Unpublished results.
17. Harwood, J. L.; Padley, F. B. X-ray diffraction. In *The Lipid Handbook*, 2nd ed.; Gunstone, F. D., Harwood, J. L., Padley, F. B., Eds.; Chapman and Hall: London, 1994; pp 538−539.
18. Suzuki, M.; Ogaki, T. Crystallization and transformation mechanisms of α-, β-, and γ-polymorphs of ultrapure oleic acid. *J. Am. Oil Chem. Soc.* **1985**, *62*, 1600−1604.
19. McKie, D.; McKie, C. *Crystalline solids*; Nelson: Walton-on-Thames, U.K., 1980; pp 506−557.
20. El-Banna, H. M.; El-Gholmy, Z. A.; Hammouda, Y. Phase diagram and dissolution rate studies on hydrochlorothiazide-urea solid dispersions. *Pharm. Acta Helv.* **1980**, *55*, 244−248.
21. Grant, D. J. W.; Jacobson, H.; Fairbrother, J. E.; Patel, C. G. Phases in the paracetamol-phenazone system. *Int. J. Pharm.* **1980**, *5*, 109−116.
22. Winfield, A. J.; Al Saidan, S. M. H. Compound formation in phenobarbitone-urea systems. *Int. J. Pharm.* **1981**, *8*, 211−216.
23. Aungst, B. J.; Hussain, M. A. Sustained propranolol delivery and increased oral bioavailability in dogs given a propranolol laurate salt. *Pharm. Res.* **1992**, *9*, 1507−1509.
24. Hussain, A.; Hirai, S.; Bawarshi, R. Nasal absorption of propranolol from different dosage forms by rats and dogs. *J. Pharm. Sci.* **1980**, *69*, 1411−1413.

Acknowledgments

The support of the Analytical and Pharmaceutical Department at Astra Arcus AB, Sweden, is gratefully acknowledged for provision of a graduate research studentship for K.J.C., and for access to small-angle X-ray equipment.

JS9804967

Physicochemical Characterization and Preliminary in Vivo Efficacy of Bioadhesive, Semisolid Formulations Containing Flurbiprofen for the Treatment of Gingivitis

DAVID S. JONES,*,† CHRISTOPHER R. IRWIN,‡ A. DAVID WOOLFSON,† JASMINA DJOKIC,† AND VICKY ADAMS‡

Contribution from *The Pharmaceutical Sciences Group, School of Pharmacy, and Division of Restorative Dentistry (Periodontics), The Queen's University of Belfast, Medical Biology Centre, 97, Lisburn Road, Belfast BT9 7BL, Northern Ireland, United Kingdom.*

Received July 29, 1998. Final revised manuscript received November 30, 1998.
Accepted for publication February 1, 1999.

Abstract □ In this study, the physicochemical properties and preliminary in vivo clinical performance of formulations containing hydroxyethylcellulose (HEC; 3, 5, 10% w/w), poly(vinylpyrrolidone) (PVP; 3, 5% w/w), polycarbophil (PC; 1, 3, 5% w/w), and flurbiprofen (5% w/w) were examined. Flurbiprofen release into PBS pH 7.4 was performed at 37 °C. The mechanical properties (hardness, compressibility, adhesiveness, initial stress) and syringeability of formulations were determined using a texture analyzer in texture profile analysis (TPA) and compression modes, respectively. In general, the time required for release of 10 and 30% of the original mass of flurbiprofen ($t_{10\%}$, $t_{30\%}$) increased as the concentration of each polymeric component increased. However, in the presence of either 5 or 10% HEC and 5% PC, increased PVP concentration decreased both $t_{10\%}$, $t_{30\%}$ due to excessive swelling (and disintegration) of these formulations. Increased concentrations of HEC, PVP, and PC significantly increased formulation hardness, compressibility, work of syringe expression, and initial stress due to the effects of these polymers on formulation viscoelasticity. Similarly, increased concentrations of PC (primarily), HEC, and PVP increased formulation adhesiveness due to the known bioadhesive properties of these polymers. Clinical efficacies of formulations containing 3% HEC, 3% PVP, 3% PC, and either 0% (control) or 5% (test) flurbiprofen, selected to offer optimal drug release and mechanical properties, were evaluated and clinically compared in an experimental gingivitis model. The test (flurbiprofen-containing) formulation significantly reduced gingival inflammation, as evaluated using the gingival index, and the gingival crevicular fluid volume, whereas, these clinical parameters were generally increased in volunteers who had received the control formulation. There were no observed differences in the plaque indices of the two subject groups, confirming that the observed differences in gingival inflammation could not be accredited to differences in plaque accummulation. This study has shown both the applicability of the in vitro methods used, particularly TPA, for the rational selection of formulations for clinical evaluation and, additionally, the clinical benefits of the topical application of a bioadhesive semisolid flurbiprofen-containing formulation for the treatment of experimental gingivitis.

Introduction

Periodontal diseases are a group of inflammatory conditions affecting the supportive structures of the teeth, the gingiva, periodontal ligament, and alveolar bone. Inflammation of the gingiva is referred to as gingivitis whereas extension of inflammation into deeper tissues is termed periodontitis.[1] The inflammation is in response to plaque bacteria residing on both the tooth surface and beneath the gingiva in periodontal pockets. Treatment of the disease, aimed at arresting the progression of the destructive process and preventing recurrence, is mainly through the mechanical cleaning of the tooth surface. However, as specific bacteria are thought to play a major role in the disease process, antimicrobial agents have also been used as adjuncts to treatment, particularly in early-onset and refractory cases.[2−4] The potential side-effects of administering systemic antibiotics, and the inability of antiseptic mouthwashes to penetrate the periodontal pocket, have fueled interest in the sustained delivery of such agents within the pocket. The attributes of, and indeed problems associated with, such drug delivery systems have been described by several authors.[5−7] One particular problem common to many drug delivery systems designed for use in the oral cavity is poor retention at the site of application.[1,8] This problem may be resolved by the incorporation of bioadhesive polymers, i.e., polymers that exhibit characteristic adhesive interactions with biological membranes, within the drug delivery system.[8,9] In so doing, several authors have reported improved retention and, hence, clinical performance of topical formulations designed for the oral cavity.[10,11]

New insights into the mechanisms underlying periodontal disease have placed greater emphasis on the role of the host response, rather than bacterial aetiology, as the primary determinant of disease progression. Inflammatory mediators, including the arachadonic acid derivative prostaglandin E_2 (PGE_2), have been associated with the condition. Levels of PGE_2 in the periodontal tissues, which are significantly increased at diseased sites, are reduced following successful treatment and may be used as predictors of further tissue destruction.[12,13] As a result of these findings, a number of studies have investigated the potential use of nonsteroidal antiinflammatory drugs (NSAIDs) as an adjunct to mechanical cleaning in the treatment of periodontal diseases. Results from both animal[14,15] and human[16−19] studies have shown the clinical benefit of flurbiprofen in the treatment of periodontal diseases. Given the potential problems associated with systemic NSAID usage, topical application of these agents may be of clinical value in the treatment of periodontal disease.

Therefore, this study describes the physicochemical properties, i.e., drug release and mechanical properties, of candidate flurbiprofen-containing, controlled-release bioadhesive semisolids, important determinants of clinical performance. In addition, a preliminary in vivo evaluation of a formulation exhibiting optimal physiochemical proper-

* Corresponding author. Tel ++44 1232 245133 ext. 2011, fax ++44 1232 247794, e-mail d.jones@qub.ac.uk.
† School of Pharmacy.
‡ Division of Restorative Dentistry.

10.1021/js9803095 CCC: $18.00
Published on Web 04/13/1999

ties for the treatment of gingivitis, one of the periodontal diseases, is described.

Experimental Section

Materials—Flurbiprofen was a gift from Boots plc., Nottingham, England. Hydroxyethylcellulose (Natrosol HHX 250-Pharm), poly(vinylpyrrolidone) (Kollidon K90), and polycarbophil (Noveon AA-1) were donated by Aqualon LTD (Warrington, England), BASF (Ludwigshafen, Germany), and B. F. Goodrich Company, Cleveland, OH, respectively. All other chemicals were purchased from BDH Laboratory Supplies, Poole, England and were AnalaR, or equivalent, quality.

Methods—*Preparation of Flurbiprofen-Containing Formulations*—Initially, hydroxyethylcellulose (HEC; 3, 5, 10%w/w) was dissolved with stirring in the required amount of phosphate-buffered saline (PBS; pH 6.8, 0.03 M) using a mechanical stirrer. Poly(vinylpyrrolidone) (PVP; 3, 5% w/w), polycarbophil (1, 3, 5% w/w) and, finally, flurbiprofen (5.0% w/w, particle size <63 μm) were mixed thoroughly into this gel to form pharmaceutical semisolids. All formulations were stored in amber ointment jars at 4 °C until required.

In Vitro Release of Flurbiprofen—The release of flurbiprofen from the bioadhesive formulations into PBS (pH 7.2) at 37 °C was determined in triplicate using a Caleva 7ST dissolution apparatus with paddle stirrers (100 rev min^{-1}), as previously reported.[7,20] Formulations were retained within three-sided plastic molds and anchored to the bottom of the dissolution vessels, thus ensuring that drug release occurred principally from the top of the molds. Samples of the dissolution fluid were removed at predetermined intervals and their absorbances determined using ultraviolet spectroscopy at 290 nm. Flurbiprofen release was determined using a calibration curve, which was linear over the concentration range 1.0−100.0 μg mL^{-1} ($r > 0.99$, with zero intercept). The presence of formulation excipients was observed not to interfere with the analysis.

Drug release data generated from dissolution experiments were fitted to the general release equation (eq 1) using logarithmic transformations and least squares regression analysis, as previously described.[20−22]

$$\frac{M_t}{M_\infty} = kt^n \quad (1)$$

where M_t/M_∞ = the proportion of flurbiprofen released at time t, k = a constant incorporating structural and geometrical characteristics of the delivery system, and n = the release exponent, a measure of the primary mechanism of drug release.

Characterization of Bioadhesive, Flurbiprofen-Containing Semisolids Using Texture Profile Analysis—The method employed to characterize the mechanical properties of each formulation was texture profile analysis.[7,9,20] In brief, formulations were packed into identical 60 mL ointment jars to a fixed height, avoiding the introduction of air into the samples, and texture profile analysis performed using a Stable Micro Systems TA-XT2 texture analyzer (Haslemere, Surrey, UK). The analysis involved the double compression of the analytical probe (10 mm diameter) into each sample. The depth and rate of each compression were 15 mm and 2.0 mm s^{-1}, respectively, and a 15 s delay period between the end of the first and beginning of the second compression was allowed. All analyses were performed on four replicate samples. From the resultant force−time plot, several mechanical parameters may be determined, including[8] (1) product hardness (force required to attain a given deformation); (2) product adhesiveness (the work required to overcome the attractive forces between the surface of the sample and the surface of the probe with which the sample comes into contact) and compressibility (the force per unit time required to deform the product during the first compression of the probe); (3) product compressibility (the work required to deform the product during the first compression cycle of the probe); (4) initial stress (the resistance to probe compression over a defined time period, i.e., from 0.5 to 1.5 s of the initial compression.

Determination of the Work Required to Expel the Bioadhesive, Semisolid Formulations from a Syringe—The method employed to determine the work required to expel the formulations from a syringe (syringeability) has previously been reported by us.[7,20] Each formulation was packed into plastic syringes (of identical dimensions) to a preselected height (3 cm). The formulation was then expressed from the syringe using the Stable Micro Systems Texture Analyzer in compression mode and the work done determined by measuring the area under the resultant force−distance plot. Increased area under the force−distance plot is indicative of decreased ease of syringeability. All measurements were performed, at least, in quadruplicate.

Clinical Evaluation of Bioadhesive Semisolid Formulations in Experimental Gingivitis—The effects of two formulations containing 3% w/w HEC, 3% w/w PVP, 3% w/w PC and either 5% or 0% w/w (control) flurbiprofen on gingival inflammation were determined using an experimental gingivitis model, as described by Heasman et al.[17] Ethical approval for the study was obtained from the Faculty of Medicine Ethics Committee, The Queen's University of Belfast. Exclusion criteria for the study included use of, or allergy to, nonsteroidal, antiinflammatory drugs, recent antibiotic therapy, use of the contraceptive pill, pregnancy, gastric upset, smoking, inadequately attached gingiva, and crowding of the lower anterior teeth. Ten subjects were recruited, of whom nine successfully completed the study. Each subject was examined and, where required, dental prophylaxis was performed to ensure health of the gingival tissues. Each subject was provided with an individual bite guard designed to cover their lower six anterior teeth and associated attached gingiva. Subjects were instructed on normal toothbrushing techniques and asked to brush their teeth twice daily. Bite guards were worn during toothbrushing to allow plaque accumulation in the lower anterior region. During the third week of the study, subjects were given the test formulations and asked to apply 0.5 mL evenly over the attached gingiva around the lower six anterior teeth following toothbrushing at night for seven consecutive nights. Subjects continued to wear the bite guard during toothbrushing. Five subjects received the flurbiprofen-containing formulation, whereas the remainder received the control formulation, i.e., devoid of flurbiprofen. Both clinician and subject were unaware as to which formulation was administered. Clinical assessments were performed at weekly intervals over a three-week period. Plaque deposits were assessed at four surfaces (mesial, distal, labial, lingual) of each lower lateral incisor using the plaque index.[23] The level of inflammation in the gingival tissues was scored at the labial surfaces of the four lower incisor teeth using the gingival index (GI) on a ordinal scale of 0 to 3, as described by Loe and Silness.[24] The degree of inflammation was then recorded as the mean GI score for these four sites. Gingival crevicular fluid (GCF) was collected from the distal surfaces of the lower lateral incisors. Briefly, the area was isolated with cotton wool rolls and dried with a continuous air stream, and the GCF was collected onto a Periopaper strip inserted into the gingival sulcus for 30 s. The volume of GCF collected was determined using a Periotron 6000 (Louisville, KY).

Statistical Analysis of Results—The effects of HEC (3, 5, and 10% w/w), PVP (3 and 5% w/w), and PC (1 and 5% w/w) on the times required for the release of defined percentages (i.e., 10 and 30%) of the original mass of flurbiprofen from each formulation, formulation hardness, adhesiveness, compressibility, initial stress, and syringeability were evaluated statistically using a three-way Analysis of Variance (ANOVA, $p < 0.05$ denoting significance). In a subsequent analysis, the effects of increasing concentrations of PC from 1 to 3 to 5% w/w and HEC from 3 to 5 to 10% w/w on the release and mechanical properties of formulations containing 3% PVP were statistically evaluated using a two-way ANOVA.[8] Post-hoc statistical analyses of the means of individual groups were performed using Fischer's LSD test. In clinical studies, both the gingival indices, plaque indices, and gingival crevicular fluid of the two patient groups following the initial two-week study period, and the effects of flurbiprofen treatments and control treatments on gingival inflammation, gingival crevicular fluid volume, and plaque indices, were statistically compared and evaluated using a Mann−Whitney U-test. Finally, the differences in gingival inflammation, gingival crevicular fluid volume, and plaque indices of the patients over week two to three of the study period were statistically assessed using a Wilcoxon signed rank test. In all analyses, $p < 0.05$ denoted significance.

Results

Application of the generalized release equation to the flurbiprofen release data allowed calculation of the release

Table 1—Effects of Hydroxyethylcellulose (HEC), Poly(vinylpyrrolidone) (PVP), and Polycarbophil (PC) on the Time Required for the Release of Flurbprofen (10 and 30% of original drug loading) from Bioadhesive, Semisolid Formulations

concn of PC (% w/w)	concn of PVP (% w/w)	concn of HEC (% w/w)	time (h) required for release of flurbiprofen (mean ± sd)	
			10%	30%
1	3	3	1.27 ± 0.05	3.19 ± 0.12
1	3	5	3.26 ± 0.11	13.51 ± 0.81
1	3	10	4.90 ± 0.21	24.57 ± 1.99
1	5	3	1.72 ± 0.09	4.73 ± 0.19
1	5	5	5.52 ± 0.25	17.10 ± 1.11
1	5	10	10.00 ± 0.56	32.33 ± 1.92
3	3	3	2.17 ± 0.17	8.73 ± 0.56
3	3	5	7.08 ± 0.61	21.21 ± 3.32
3	3	10	17.11 ± 0.99	40.96 ± 2.27
5	3	3	3.30 ± 0.22	10.99 ± 1.01
5	3	5	14.27 ± 0.91	40.45 ± 1.69
5	3	10	28.41 ± 3.01	101.11 ± 7.22
5	5	3	5.54 ± 0.21	16.52 ± 1.11
5	5	5	6.17 ± 0.51	20.17 ± 1.24
5	5	10	16.53 ± 1.34	40.51 ± 2.51

exponent (n) which, for the formulations under investigation, ranged from 0.6 to 1.0. Therefore, in light of the disparity of release rates exhibited by these formulations, statistical analyses were performed on the times required for the release of 10 and 30% ($t_{10\%}$, $t_{30\%}$, Table 1) of the original loading of flurbiprofen from each formulation, as previously reported by us.[20] A wide range of values of $t_{10\%}$ and $t_{30\%}$ were exhibited by the formulations under examination. Maximum $t_{10\%}$ and $t_{30\%}$ values were observed in the formulation containing 10% HEC, 3% PVP, and 5% PC and were 28.41 ± 3.01 and 101.11 ± 2.22 h, respectively. Conversely, minimum $t_{10\%}$ and $t_{30\%}$ values were 1.27 ± 0.05 and 3.19 ± 0.12 h, respectively, and were associated with semisolids containing 3% HEC, 3% PVP, and 1% PC. Increasing the concentration of either HEC (from 3 to 5 and from 5 to 10% w/w) or alternatively PC (from 1 to 3 and from 5 to 10% w/w) significantly increased both $t_{10\%}$ and $t_{30\%}$. Conversely, the effect of PVP on the release of flurbiprofen from the semisolid formulations under examination was dependent on the concentrations of both HEC and PC. Thus, in formulations containing either 3, 5, or 10% HEC and 1, 3, or 5% PC, increasing the concentration of PVP from 3 to 5% w/w significantly increased $t_{10\%}$, $t_{30\%}$. Conversely, increasing the concentration of PVP in the formulations containing 5 or 10% HEC and 5% PC significantly reduced $t_{10\%}$, $t_{30\%}$. These disparate effects accounted for the observed interactions in the statistical analysis of the effects of polymeric components on these release parameters.

The effects of HEC, PVP, and PC on the mechanical (textural) properties and syringeability of the formulations under examination are presented in Tables 2 and 3, respectively. Increasing concentrations of each polymeric component (HEC, PVP, and PC) significantly increased each parameter investigated. Hence, the minimum values of hardness, adhesiveness, compressibility, initial stress, and work of syringeability were exhibited by the formulation containing 3% HEC, 3% PVP, and 1% PC and were 0.52 ± 0.02 N, 2.24 ± 0.14 N mm, 2.36 ± 0.16 N mm, 0.50 ± 0.06 × 10^6 dynes cm^{-2}, and 19.58 ± 0.46 N mm, respectively. Conversely, maximum values of hardness, adhesiveness, compressibility, initial stress, and work of syringeability were 9.12 ± 0.20 N, 13.02 ± 0.48 N mm, 49.82 ± 1.12, 10.01 ± 0.61 dynes cm^{-2}, and 113.78 ± 2.82 N mm, respectively, observed in the formulation containing the highest concentration of each polymer investigated, namely 10% HEC, 5% PVP and PC 5%. Interestingly, statistical interactions were observed in the Analysis of Variance concerning the effects of these polymeric components on each mechanical parameter. In these, the effects of PVP and PC on the mechanical properties of semisolids containing 10% HEC were significantly (and disproportionately) greater than those containing either 3 or 5% HEC.

Following the initial two week period, the gingival indices of the two patient groups were 0.75 ± 0.44 and 0.81 ± 0.54. This difference in the two patient groups was insignificant. The comparative effects of seven daily (nightly) applications of two formulations, each containing 3% HEC, 3% PVP, 3% PC and either 0 or 5% flurbiprofen on the level of inflammation, as determined using the gingival index, are presented in Figure 1. As determined by the gingival index, the level of gingival inflammation increased in two of the four volunteers treated with the control formulation, but reduced in four out of five subjects treated with the test formulation containing flurbiprofen. Mean gingival crevicular fluid levels were also reduced in four out of five subjects treated with the flurbiprofen-containing formulation, but also in three out of four control subjects (Table 4). However, the mean gingival crevicular fluid volume of subjects treated with flurbiprofen-treated formulations was significantly lower when compared to that of subjects in the control group. Finally, the plaque indices did not significantly change between week two and three of the study period in either patient group (Table 4). No patients reported any side-effects following application of either formulation.

Discussion

The formulations examined in this study exhibited wide ranges of both drug release and mechanical properties that were dependent on the concentrations of each polymeric component present. In light of the relative structural complexity of these systems, it is appropriate to discuss the observed physicochemical properties in relation to the physical state of each polymeric component. In all formulations, HEC (3, 5, 10% w/w) was initially dissolved to form a primary gel into which PVP was added until the saturation solubility of this component in the primary gel was exceeded. Further additions of PVP resulted in the emergence of a two-phase semisolid system in which this polymer was present both in solution and as a suspended solid within the HEC gel. Hence, in gels containing 3% HEC, PVP (3 and 5%) was soluble, whereas in gels containing 5% and 10% HEC, PVP existed both in solution and suspension, the ratio of the mass of dissolved to suspended PVP decreasing as the concentration of HEC was increased. Following its addition, as a direct consequence of its cross-linked structure, PC did not dissolve in the formulation but exhibited swelling, the extent of which was dependent on the amount of available water present in the formulations. Thus, as the concentrations of HEC (primarily) and PVP increased, the degree of swelling of PC decreased. The range of physicochemical properties exhibited by the formulations under examination may be due to the states of PVP and PC within the primary HEC gel. Similarly, in a previous publication, the states of these polymeric components, namely dissolved/dispersed (in the cases of HEC and PVP) or swollen/unswollen (PC) were reported to directly influence the viscoelastic properties of related formulations containing chlorhexidine designed for the treatment of localized infection.[25] Thus, the effects of each polymeric component on both the release of flurbiprofen and the mechanical properties of each formulation will be considered in light of the state of each polymeric component in these formulations.

Table 2—The Effects of Concentration of Hydroxyethylcellulose (HEC), Poly(vinylpyrrolidone) (PVP), and Polycarbophil (PC) on the Hardness, Adhesiveness, Compressibility, and Initial Stress of Formulations Containing Flurbiprofen (5% w/w), As Determined Using Texture Profile Analysis

concn of PC (% w/w)	concn of PVP (% w/w)	concn of HEC (% w/w)	hardness (N)	adhesiveness (N mm)	compressibility (N mm)	initial stress (dyn $cm^{-2} \times 10^6$)
1	3	3	0.52 ± 0.02	2.24 ± 0.14	2.36 ± 0.16	0.50 ± 0.06
1	3	5	1.18 ± 0.02	5.56 ± 0.08	5.74 ± 0.08	1.58 ± 0.12
1	3	10	6.00 ± 0.18	7.86 ± 0.28	14.74 ± 1.42	4.69 ± 0.46
1	5	3	0.64 ± 0.02	3.06 ± 0.20	2.96 ± 0.04	0.76 ± 0.06
1	5	5	1.38 ± 0.06	7.10 ± 0.38	8.82 ± 0.18	2.00 ± 0.03
1	5	10	6.62 ± 0.14	12.04 ± 0.76	29.94 ± 1.42	5.75 ± 0.12
3	3	3	0.91 ± 0.04	3.14 ± 0.21	4.00 ± 0.23	0.81 ± 0.02
3	3	5	1.89 ± 1.11	6.91 ± 0.42	7.23 ± 0.54	1.88 ± 0.11
3	3	10	7.14 ± 0.32	8.84 ± 1.04	17.84 ± 1.01	5.99 ± 0.33
5	3	3	1.40 ± 0.12	4.84 ± 0.30	6.70 ± 0.56	1.48 ± 0.10
5	3	5	2.71 ± 0.06	8.86 ± 0.28	22.54 ± 0.86	2.69 ± 0.31
5	3	10	8.88 ± 0.26	10.84 ± 1.04	42.98 ± 1.18	7.32 ± 0.50
5	5	3	1.64 ± 0.06	5.78 ± 0.22	7.90 ± 0.10	1.72 ± 0.05
5	5	5	3.41 ± 0.04	8.26 ± 0.62	16.84 ± 0.24	3.10 ± 0.30
5	5	10	9.12 ± 0.20	13.02 ± 0.48	49.82 ± 1.12	10.01 ± 0.61

Table 3—The Effects of Hydroxyethylcellulose (HEC), Poly(vinylpyrrolidone) (PVP), and Polycarbophil (PC) on the Syringeability[a] of Bioadhesive, Semisolid Formulations Containing Flurbiprofen

mean ± sd work (N mm) required to syringe formulations containing				
PC (% w/w)	PVP (% w/w)	HEC 3% w/w	HEC 5% w/w	HEC 10% w/w
1	3	58.74 ± 3.46	123.61 ± 10.22	241.47 ± 14.70
1	5	74.14 ± 4.01	151.05 ± 3.57	279.49 ± 10.24
3	3	79.99 ± 3.54	168.11 ± 7.11	298.31 ± 12.12
5	3	139.47 ± 14.16	191.40 ± 8.19	341.34 ± 8.46
5	5	163.91 ± 9.06	221.41 ± 9.27	379.00 ± 3.99

[a] Measured as the work required to express a defined amount of the formulation from a syringe of specified dimensions, as described in Materials and Methods.

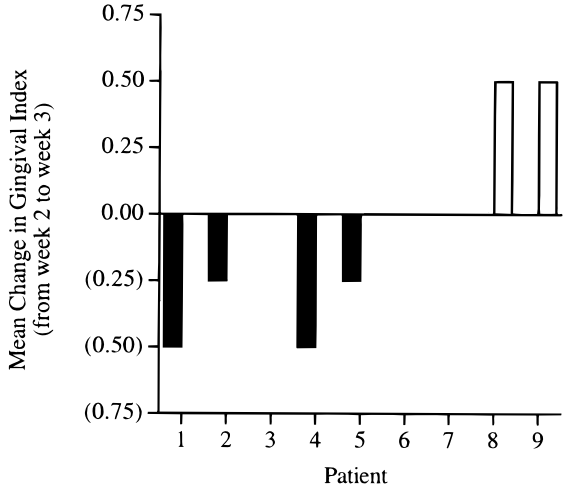

Figure 1—The effect of topical application of a test formulation (containing 5% w/w flurbiprofen, 3% w/w hydroxyethylcellulose, 3% w/w poly(vinylpyrrolidone), and 3% w/w polycarbophil) or a control formulation (containing 3% w/w hydroxyethylcellulose, 3% w/w poly(vinylpyrrolidone), and 3% w/w polycarbophil) for one week on the level of gingival inflammation (as evaluated using the gingival index) in clinical subjects. Subjects 1–5 received the test formulation whereas subjects 6–9 received the control formulation.

Increasing the concentration of HEC in aqueous gel systems has previously been reported to increase both gel elasticity (storage modulus) and, additionally, viscosity due to increased polymeric chain entanglement.[25,26] One consequence of these rheological alterations was observed in the effects of HEC on the release of flurbiprofen, in which the rate of drug diffusion through the polymer matrix and, hence, drug release was reduced. Similarly, in formulations containing 3% HEC (in which PVP was dissolved), increasing the concentration of PVP from 3 to 5% decreased flurbiprofen release due to the greater entanglement of dissolved polymeric chains. In general, the reduced release of flurbiprofen observed following increased formulation concentrations of PVP, in which this polymer was present in both the solid and solution phases in the primary HEC gel, may be due to the effects of both the increasing semisolid nature, and, hence, increased elasticity of these formulations.[25,26] A further retarding effect of PVP on drug release may be due to swelling following contact with dissolution fluid. These two mechanisms serve to enhance the elastic structure of the formulations, thereby decreasing the rate of drug diffusion through the semisolid matrix. Similarly, incorporation of PC into these formulations decreased flurbiprofen release, observations that may also be explained by the state of this polymer in each formulation. The extent of swelling of PC in the formulations under investigation was greatest in those formulations containing 3% HEC, 3% PVP, and 1% PC, as, first, the amount of free water, i.e., water not associated with the other polymeric components, was greatest in this system, and, second, the ratio of mass of free water to mass of PC was largest, thus allowing a greater percentage swelling of this polymer.

Table 4—The Effects of Application of Either a Control (devoid of flurbiprofen) or Test Formulation on the Gingival Crevicular Fluid Volume and Plaque Index of Subjects

		gingival crevicular fluid volume (periotron units)[c]		plaque index[c]	
treatment	patient number	prestudy (2 weeks)[d]	poststudy (3 weeks)[e]	prestudy (2 weeks)[d]	poststudy (3 weeks)[e]
flurbiprofen[a]	1	32.5	8.5	1.2	1.2
flurbiprofen[a]	2	12.5	4.5	1.0	0.6
flurbiprofen[a]	3	7.5	1.0	0.5	0.6
flurbiprofen[a]	4	14.0	12.0	0.8	0.8
flurbiprofen[a]	5	21.0	16.5	0.5	0.5
control[b]	6	38.0	16.0	1	1.1
control[b]	7	19.0	6.5	1	0.8
control[b]	8	14.5	35.0	0.5	0.5
control[b]	9	12.0	11.0	0.9	0.7

[a] Formulation contained 5% w/w flurbiprofen, 3% w/w hydroxyethylcellulose, 3% w/w poly(vinylpyrrolidone), and 3% w/w polycarbophil. [b] Formulation contained 3% w/w hydroxyethylcellulose, 3% w/w poly(vinylpyrrolidone), and 3% w/w polycarbophil. [c] All values are means. The coefficient of variation in all cases <6%. [d] Gingival crevicular fluid volume and plaque index at the end of the second week of the study. [e] Gingival crevicular fluid volume and plaque index at the end of the third week of the study.

In the swollen state, PC imparts both greater elasticity to the formulation, due to entanglement of the chains of poly(acrylic acid) with those of HEC and PVP, and also greater viscosity.[25] Thus, flurbiprofen release was further retarded. As the concentrations of HEC and PVP were increased in the formulations, the mass of free water available for swelling of PC decreased, and hence the percentage of unswollen PC particles increased. In this scenario, the greatest mass of unswollen particles of PC occurred in formulations containing 10% HEC, 5% PVP, and 5% PC. Following immersion in dissolution fluid, the unswollen particles of PC imbibed fluid and commenced swelling, the extent of which was dependent on the initial percentage of unswollen PC. This swelling process established the presence of a swelling front that opposed further ingress of dissolution fluid and hence retarded drug dissolution and diffusion. The presence of PC as dispersed, unswollen particles had a significantly greater retarding effect on drug release than when primarily present as swollen or partly swollen particles due to the influence of this extensive swelling front. In certain formulations, namely those in which the mass of unneutralized PC was greatest (i.e., HEC 5 or 10%, PVP 5%, PC 5%), the extent of swelling resulted in extension of the formulation beyond the retaining molds, leading to disintegration of the formulation. In this fashion, the surface area for drug dissolution and diffusion was significantly increased, and, as a result, the release of flurbiprofen from these formulations was greater than their counterparts containing 3% PVP. The role of formulation swelling on flurbiprofen release accounted for the statistical interactions between HEC and PC and between PVP and PC, as the concentration of HEC (primarily) and PVP directly influenced the state of PC in, and hence swelling of, the formulations. Therefore, as the mass of suspended solids within the formulations increased, there was a significant (and statistically unpredicted) effect on the release of flurbiprofen.

It is accepted that the mechanical properties of topical formulations will directly influence their clinical performance. Therefore, in the design of such systems, it is important to fully characterize these properties. Recently, we have successfully reported the use of texture profile analysis (TPA) for the mechanical characterization of a range of topical formulations, e.g., semisolids,[7,8] gels,[26] and creams,[27] and, consequently, this technique was employed for the characterization of the formulations examined in this study. In particular, TPA provides information for several relevant rheological parameters, including formulation hardness and compressibility, properties that may be related to both mouth feel and ease of removal of the formulation from the container and also ease of application of the formulation onto the proposed substrate,[8,26] initial stress, a measure of the stress required to initiate flow, and adhesiveness, a property that is related to bioadhesion.[8] Thus, both the versatility of sample consistencies that may be analyzed by TPA and the type of information provided by this technique have established its use in the development of topical formulations. In this current study, TPA has been successfully employed to characterize the range of flurbiprofen-containing formulations. Furthermore, the syringeabilities of formulations have been measured using a Texture Analyzer, as, in many cases, it is appropriate to apply formulations to remote supragingival sites/periodontal pockets using syringe systems. Once more, the wide ranges of hardness, compressibility, adhesiveness, initial stress, and work of syringeability exhibited by these formulations may be attributed to the state of the polymeric components.

Formulation hardness, compressibility, initial stress, and work of syringing are parameters that measure the resistance of the product to probe compression, and, indeed, their relationships with product viscosity have been reported previously.[8,29,30] Hence, the effects of HEC, PVP, and PC on these parameters may be directly related to their effects on product viscosity and, indeed, elasticity. Consequently, increasing the amount of dissolved HEC and PVP increased these mechanical properties due to increased elasticity and viscosity of the formulations,[25,26] resulting from the increasing entanglement of the polymeric chains. Increasing the mass of solid particles in the formulation, however, offers greater semisolid properties to the formulations and, hence, greater resistance to probe compression. Interestingly, statistical interactions were observed between HEC and PVP and between HEC and PC with respect to hardness, compressibility and work of syringeability that may again be explained by the state of each polymeric component in the formulations. In these interactions, the effects of PC and PVP on these parameters were significantly (and unexpectedly) greater in the presence of 10% HEC than either 3 and indeed 5% HEC. Thus, as the concentration of HEC increases, the mass of suspended PVP and unswollen PC increase, and thus the formulations adopted greater semisolid nature due to the increasing content of suspended solids. At lower concentrations of HEC, the effects of PVP and PC on formulation hardness, compressibility, and work to syringe may be attributed, in part, to the entanglement of the dissolved chains of HEC with PVP and also the swollen chains of PC. As the mass of solid particles increases, the relative contribution of chain entanglement to these mechanical properties decreases due to the overwhelming effects of the increasing mass of dispersed polymeric solid materials. The observed imbalance of the contribution of polymeric chain entanglement and suspended solid particles accounted for the statistical interactions.

In textural analysis, adhesiveness refers to the work required to overcome the attractive bonds between the sample and probe and is determined from the area under the force−distance curve in the tension section of the plot. However, at this point it is useful to record that the removal of the probe from the sample may involve the destruction of cohesive bonds within the sample in addition to the cleavage of bonds between the sample and probe. Interestingly, a correlation has been reported between the mucoadhesive properties of formulations and their adhesiveness,[8,26] and, consequently, quantification of adhesiveness provides a useful, rapid method by which the mucoadhesive properties of related formulations may be reliably ranked. In this current study, increasing concentrations of HEC, PVP, and PC significantly increased formulation adhesiveness. As these polymers have been described as bioadhesive,[9] these observations may be due to both their ability to form adhesive bonds (in a concentration-dependent fashion) with the probe in TPA, and to increase viscosity (tack) of the formulations, a property that has been reported to influence the adhesiveness of certain formulations.[8]

It is important to consider specifically the role of PC in the adhesiveness of the formulations under examination. PC possesses the ability to strongly interact with biological substrates, the degree of interaction being dependent on the number of unneutralized carboxylic acid groups on the poly(acrylic acid) chains.[8,9] In this study, and indeed in related earlier publications,[8,31] the contribution of unneutralized carboxylic acid groups to adhesiveness in TPA was confirmed. Hence, in formulations containing 3% HEC, 3% PVP, and 1% PC, the extent of neutralization, and hence swelling of PC, was greatest, and this formulation exhibited lowest adhesiveness. Conversely, in formulations where the amount of water available to neutralize PC is lowest, i.e.,

10% HEC, 5% PVP, and 5% PC, the mass of unneutralized (and hence unswollen) particles of PC was greatest, and hence adhesiveness is maximal. Given the correlation with mucoadhesion, this formulation would be expected to possess the greatest mucoadhesive properties of all formulations studied.[26] The statistical interactions observed between HEC and PC, PVP and HEC, and PVP and PC reflect once more the effects of the state of each polymeric component on formulation adhesiveness. Thus, the presence of solid polymeric particles may be associated with dramatic increases in adhesiveness due both to the effects on formulation viscosity (and hence tack) and additionally to the effects on the mass of free water present and, hence, the mass of unneutralized carboxylic acid groups in PC.

The ideal formulation for clinical examination for the treatment of periodontal diseases should possess a number of desirable attributes, including adequate prolonged and controlled release of therapeutic agent, ease of removal from the container, and ease of application to, and good retention at, the desired site. In addition, it should be comfortable to the patient during the residence period of the formulation. The various in vitro methods employed in this study have allowed quantification of all of these attributes. Hence, in vitro release methods defined the nature of the release of flurbiprofen from all formulations. The TPA parameters of hardness/compressibility and adhesiveness described the ease of removal from the container/ease of application to the desired site and product retention, respectively. Finally, acceptability of the product by the patient during the period of residence in the oral cavity may be conveniently described by hardness measurements in TPA, as previously reported,[28,31] whereas the syringeability of the formulations to, e.g., subgingival or remote supragingival regions, was conveniently described using a modified compression test.

Ideally, candidate formulations for clinical examination should exhibit low hardness, initial stress, compressibility, work of syringeability, yet high adhesiveness. However, as may be observed in Tables 2 and 3, increased formulation adhesiveness (and hence increased retention at the site of application) may be achieved by increasing the concentration of PC (primarily), HEC, and PVP. However, such increases also resulted in increased formulation hardness, compressibility, and work of syringing, undesirable formulation attributes. Therefore, in terms of mechanical properties, a compromise must be attained between formulation adhesiveness and formulation hardness, compressibility, and syringeability. Examples of formulations that exhibited acceptable mechanical properties included HEC 3%/PVP 3 or 5%/PC 1, 3 or 5% and HEC 5%/PVP 3%, PC 1 or 3%. Furthermore, in light of the proposed daily (nightly) administration of the formulation and based on information from related clinical studies,[14,17] the formulations containing 3% HEC, 3% PVP, and either 3 or 5% PC exhibited the required release properties, namely $t_{30\%}$ values of 8.73 $\pm$ 0.56 and 10.99 $\pm$ 1.01 h, respectively. Therefore, following consideration of both the mechanical and release properties, the formulation selected for clinical examination contained 3% HEC, 3% PVP, 3% PC, and 5% flurbiprofen. Initial clinical assessment of this formulation, using an experimental gingivitis model, indicated significantly beneficial effects in the treatment of gingivitis, as denoted by the improvement in the gingival index and the gingival crevicular fluid volume. Of further interest were the insiginificant differences in the plaque indices of the two patient groups during weeks 2 to 3 of this study period. Therefore, changes in gingival crevicular fluid volume could not be explained by differences in plaque accumulation. It is known that levels of the cyclooxygenase metabolites of arachadonic acid, PGE_2 and TxB_2, both of which are potent vasodilators, are elevated during the onset of gingival inflammation.[17] The clinical effects of flurbiprofen, an inhibitor of the cyclooxygenase pathway, observed in this study may thus be attributed to prolonged reduced levels of both mediators in the gingival tissue. Quantification of these levels is the subject of current clinical investigations.

In conclusion, a series of formulations containing HEC, PVP, PC, and flurbiprofen has been designed and characterized in vitro in terms of both flurbiprofen release and mechanical properties. The use of texture profile analysis to characterize the mechanical properties has been shown to be particularly useful as the mechanical parameters defined by this technique (e.g., hardness, compressibility, syringeability, adhesiveness) have direct relevance to both the potential clinical and sensory performance of these formulations.[8] A candidate formulation was chosen for clinical evaluation containing 3% HEC, 3% PVP, 3% PC, and 5% flurbiprofen that offered optimal flurbiprofen release over the proposed daily application of the product and, additionally, offered a compromise between formulation adhesiveness (and hence persistence at the site of application) and hardness (comfort during the period of application), and compressibility/syringeability (ease of removal from the container and ease of spreading/application to the inflamed site).

The comparative clinical efficacies of this chosen flurbiprofen-containing formulation and an otherwise identical placebo formulation (devoid of flurbiprofen) were evaluated in an experimental gingivitis model in nine volunteers, in which gingival inflammation was measured using the gingival index. Following seven nightly applications, volunteers who had received the flurbiprofen-containing formulation exhibited decreased gingival inflammation and gingival crevicular fluid volume, whereas those who had received the control formulation displayed increased gingival inflammation and gingival crevicular fluid volume. This preliminary clinical study has therefore shown the clinical improvements associated with the use of topical bioadhesive, flurbiprofen-containing semisolid formulations. The clinical efficacy of this formulation, including quantification of the concentrations of inflammatory mediators, is currently ongoing in multicentered clinical evaluations.

References and Notes

1. Addy, M. Local delivery of antimicrobial agents to the oral cavity. *Adv. Drug Deliv. Rev.* **1994**, *13*, 123−134.
2. Joyston-Bechal, S. Féderation Dentaire Internationale Technical Report No. 26. Topical and systemic antimicrobial agents in the treatment of chronic gingivitis and periodontitis. *Int. Dental J.* **1987**, *37*, 52−62.
3. Lindhe, J.; Haffajee, A. J.; Sokransky, S. S. Progression of periodontal disease in adult subjects in the absence of periodontal therapy. *J. Clin. Periodontol.* **1993**, *10*, 433−443.
4. Listgarten, M. A. Nature of periodontal diseases: pathogenic mechanisms. *J. Clin. Periodontol.* **1986**, *13*, 418−425.
5. Medlicott, N. J.; Rathbone, M. J.; Tucker, I. G.; Holborow, D. W. Delivery systems for the administration of drugs to the periodontal pocket. *Adv. Drug Deliv. Rev.* **1994**, *13*, 181−203.
6. Fiorellini, J. P.; Paquette, D. M. D. The potential role of controlled-release delivery systems for chemotherapeutic agents in periodontitis. *Periodontol. Restor. Dent.* **1992**, 63−79.
7. Jones, D. S.; Woolfson, A. D.; Djokic, J.; Coulter, W. A. Development and physical characterisation of bioadhesive semisolid, polymeric systems containing tetracycline for the treatment of periodontal diseases. *Pharm. Res.* **1996**, *13*, 1734−1738.
8. Jones, D. S.; Woolfson, A. D.; Brown, A. F. Textural analysis and flow rheometry of bioadhesive, antimicrobial oral gels. *Pharm. Res.* **1997**, *14* (4), 450−457.

9. Gandhi, R. B.; Robinson, J. A. Oral cavity as a site fo bioadhesive drug delivery. *Adv. Drug Deliv. Rev.* **1994**, *13*, 43−74.
10. Collins, A. E.; Deasy, P. B. Bioadhesive lozenge for the improved delivery of cetylpyridinium chloride. *J. Pharm. Sci.* **1990**, *79*, 116−119.
11. Mahdi, A. B.; Coulter, W. A.; Woolfson, A. D.; Lamey, P. J. Efficacy of bioadhesive patches in the treatment of recurrent apthous stomatitis. *Journal of Oral Pathology & Medicine* **1996**, *25* (8), 416−419.
12. Offenbacher, S.; Odle, B. M.; Van Dyke, T. E. Assay of cyclooxygenase products in crevicular fluid in periodontal health and disease. *J. Periodont. Res.* **1986**, *21*, 101−112.
13. Offenbacher, S.; Odle, B. M.; Braswell, L. D.; Johnson, H. G.; Hall, C. M.; McClure, H.; Orkin, J. L.; Strobert, E. A.; Green, M. D. Changes in cyclooxygenase metabolites in experimental periodontitis in macaca-mulatta. *J. Periodont. Res.* **1989**, *24*, 63−74.
14. Williams, R. C.; Offenbacher, S.; Jeffcoat, M. K.; Howell, T. H.; Johnson, H. G.; Hall, C. M.; Wechter, W. J.; Goldhaber, P. Indomethacin or flurbiprofen treatment of periodontitis in beagles − effects of crevicular arachadonic acid metabolites compared with effect on alveolar bone loss. *J. Periodont. Res.* **1988**, *23*, 134−138.
15. Williams, R. C.; Jeffcoat, M. K.; Howell, T. H.; Reddy, M. S.; Johnson, H. G.; Hall, C. M.; Goldhaber, P. Ibuprofen − an inhibitor of alveolar bone resorption in beagles. *J. Periodont. Res.* **1988**, *23*, 166−169.
16. Jeffcoat, M. K.; Williams, R. C.; Reddy, M. S.; English, R.; Goldhaber, P. Flurbiprofen treatment of human periodontitis − effect on alveolar bone height and metabolism. *J. Periodontol. Res.* **1988**, *23* (6), 381−385.
17. Heasman, P. A.; Collins, J. G.; Offenbacher, S. Changes in crevicular fluid levels of interleukin 1β, leucotriene B_4, prostagalndin E_2, thromboxane E_2, and tumour necrosis factor α in experimental gingivitis in man. *J. Periodont. Res.* **1993**, *28*, 241−247.
18. Heasman, P. A.; Benn, D. K.; Kelly, P. J.; Seymour, R. A.; Aitken, D. The use of topical flurbiprofen as an adjunct to nonsurgical management of periodontal disease. *J. Clin. Periodontol.* **1993**, *20*, 457−464.
19. Heasman, P. A.; Offenbacher, S.; Collins, J. G.; Edwards, G.; Seymour, R. A. Flurbiprofen in the prevention and treatment of experimental gingivitis. *J. Clin. Periodontol.* **1993**, *20*, 732−738.
20. Jones, D. S.; Woolfson, A. D.; Brown, A. F.; O'Neill, M. J. Mucoadhesive, syringeable drug delivery systems for controlled application of metronidazole to the periodontal pocket: In vitro release kinetics, syringeability, mechanical and mucoadhesive properties. *J. Contolled Release* **1997**, *49*, 71−79.
21. Gurny, R.; Doelker, E.; Peppas, N. A. Modelling of sustained release of water-soluble drugs from porous, hydrophobic polymers. *Biomaterials* **1982**, *3*, 27−32.
22. Medlicott, N. J.; Tucker, I. G.; Rathbone, M. J.; Holborow, D.; Jones, D. S. Chlorhexidine release from Poly(ϵ-caprolactone) films prepared by solvent evaporation. *Int. J. Pharm.* **1996**, *143* (1), 25−35.
23. Loe, H.; Silness, P. Periodontal disease in pregnancy (1). Prevealence and severity. *Acta Odont. Scand.* **1963**, *21*, 533−551.
24. Silness, J.; Loe, H. Periodontal disease in pregnancy (2). Correlation between oral hygiene and periodontal condition. *Acta Odont. Scand.* **1964**, *22*, 112−135.
25. Jones, D. S.; Woolfson, A. D.; Brown, A. F. Viscoelastic properties of bioadhesive, chlorhexidine-containing semisolids for topical application to the oropharynx. *Pharm. Res.* **1998**, *15* (7), 1131−1136.
26. Jones, D. S.; Woolfson, A. D.; Brown, A. F. Textural, viscoelastic and mucoadhesive properties of pharmaceutical gels composed of cellulose polymers. *Int. J. Pharm.* **1997**, *151*, 223−233.
27. Brown, A. F.; Jones, D. S.; Woolfson, A. D. The effects of emulsifier and drug (chlorhexidine) concentrations on the mechanical and viscoelastic properties of creams. *J. Pharm. Pharmacol.* **1997**, *49* (S4), 127.
28. Schwartz, N. O. Adaptation of the sensory textile profile method to skin care products. *J. Text. Studies* **1975**, *42*, 33−42.
29. Ferrari, F.; Bertoni, M.; Caramella, C.; La Manna, A. Description and validation of an apparatus for gel strength measurements. *Int. J. Pharm.* **1994**, *109*, 115−124.
30. Lucero, M. J.; Vigo, J.; Leon, M. J. The influence of antioxidants on the spreadability of α-tocopherol gels. *Drug Deliv. Ind. Pharm.* **1994**, *20*, 2315−2322.
31. Jones, D. S.; Woolfson, A. D.; Djokic, J. Texture profile analysis of bioadhesive polymeric semisolids: mechanical characterisation and investigation of interactions between formulation components. *J. Appl. Polym. Sci.* **1996**, *61* (12), 2229−2234.

JS9803095

Experimental and Theoretical Analysis of the Interaction of (±)-*cis*-Ketoconazole with β-Cyclodextrin in the Presence of (+)-L-Tartaric Acid

ENRICO REDENTI,*,† PAOLO VENTURA,† GIOVANNI FRONZA,‡ ANTONIO SELVA,‡ SILVIA RIVARA,§ PIER VINCENZO PLAZZI,§ AND MARCO MOR§

Contribution from *Chemical and Biopharmaceutical Department, Chiesi Farmaceutici S.p.A., Via Palermo, 26/A, I-43100 Parma, Italy, Centro di Studio del CNR sulle Sostanze Organiche Naturali, Dipartimento di Chimica, Politecnico di Milano, Via Mancinelli 7, I-20131 Milano, Italy, and Dipartimento Farmaceutico, Università degli Studi di Parma, Viale delle Scienze, I-43100 Parma, Italy.*

Received December 7, 1998. Accepted for publication March 17, 1999.

Abstract □ ^{1}H NMR spectroscopy was used for determining the optical purity of *cis*-ketoconazole enantiomers obtained by fractional crystallization. The chiral analysis was carried out using β-cyclodextrin in the presence of (+)-L-tartaric acid. The mechanism of the chiral discrimination process, the stability of the complexes formed, and their structure in aqueous solution were also investigated by ^{1}H and ^{13}C chemical shift analysis, two-dimensional NOE experiments, relaxation time measurements, and mass spectrometry experiments. Theoretical models of the three-component interaction were built up on the basis of the available NMR data, by performing a conformational analysis on the relevant fragments on ketoconazole and docking studies on the components of the complex. The model derived from a folded conformation of ketoconazole turned out to be fully consistent with the molecular assembly found in aqueous solution, as inferred from NOE experiments. An explanation of the different association constants for the complexes of the two enantiomers is also provided on the basis of the interaction energies.

Introduction

Ketoconazole, 1-acetyl-4-[4-[[2-(2,4−dichlorophenyl)-2-(1*H*-imidazol-1-yl-methyl)-1,3-dioxolan-4-yl]methoxy]phenyl]piperazine, is a potent, orally active broad-spectrum antifungal agent[1,2] which is marketed as a racemic mixture of the *cis*-(2*S*,4*R*) and -(2*R*,4*S*) enantiomers.

The (−)-stereoisomer is (2*S*,4*R*).[3] Both the enantiomers of ketoconazole (KC) were stereoselectively prepared,[3,4] as it has been claimed that the optically pure compounds are more effective than the racemic one for treating local and systemic fungal infections in humans.[5] One of the current active research areas in host−guest or supramolecular chemistry is chiral recognition by cyclodextrins (CDs). Both naturally occurring (α, β, and γ) and derivatized CDs are indeed extensively used in chromatography (bonded to the stationary phase or in the eluate) for the separation of enantiomers[6] and as chiral shift reagents for NMR determination of enantiomeric composition.[7,8] In this paper we report a ^{1}H NMR method for determining the optical purity of the ketoconazole enantiomers obtained by fractional crystallization. Chiral analysis was carried out using β-cyclodextrin (βCD) in the presence of (+)-L-tartaric acid (hereafter TA), as it has been found that simultaneous inclusion and salt formation yield complexes freely soluble in water. For instance, KC solubility is enhanced by several orders of magnitude, while that of βCD increases by more than 10 times.[9−13] The stability of the complexes formed and their structure in aqueous solution were investigated by NMR spectroscopy and ionspray tandem mass spectrometry.[14] In addition, a model of the KC:TA:βCD complex was built up by computational techniques, on the basis of the available NMR data, with the aim of elucidating the chiral discrimination process. Among the different conformations of KC, only those in accordance with intramolecular NOE cross-peaks were selected and submitted to docking studies. The intermolecular distances were measured and related to the intensities of NOE cross-peaks, allowing the selection of a unique interaction pattern. The energies of interaction between the components were calculated for the proposed complexes of both the enantiomers of KC.

Materials and Methods

(±)-*cis*-Ketoconazole was a kind gift from RGR Co. (Milan, Italy).

Samples of (+)-(2*R*,4*S*) (ee ≈ 98%) and (−)-(2*S*,4*R*)-ketoconazole ee ≈ 98%) were obtained from the racemate by fractional crystallization of the diastereomeric salts with (−)- and (+)-10-camphorsulfonic acid, respectively. The corresponding equimolar tartrate salts were prepared by freeze-drying their aqueous solutions. β-cyclodextrin (water content ≈ 10%) and D_2O (99.8%) were purchased from Roquette Co. (Lestrem, France) and from Merck Co. (Milan, Italy), respectively. All other reagents were of analytical grade. Solutions of 10 mM drug concentration and guest-to-host ratio at 1:1.5 were used unless otherwise specified.

NMR spectra were acquired on ACF 200 and ARX 400 spectrometers (Bruker, Karlsruhe, Germany). Chemical shifts were referred to external TSP (sodium, 3-(trimethylsilyl)propionate) at 0 ppm (accurate to ± 0.001 ppm). The phase-sensitive ROESY (Rotating-frame Overhauser Effect SpectroscopY) experiments were performed using a 3.5 kHz spin-lock field and a mixing time of 350 ms. T_1 relaxation time measurements were made using the inversion recovery method. Fifteen different τ delays varying from 0.05 to 10 s between 180° and 90° pulses were used. A regression procedure was used to fit the relaxation data to the exponential equation $M = \mathrm{Mo}(1 - 2e^{-\tau/t})$.

For the determination of the association constants k of the two enantiomers, the concentration of *rac*-ketoconazole tartrate was kept at 1 mM while that of βCD varied between 5 and 20 mM. The change in the chemical shift of the H20 proton, which splits upon βCD addition, was monitored during the titration. The data were evaluated according to the Foster−Fyfe[15] modification of the Benesi−Hildebrand equation:[16]

$$\Delta\delta_{obs}([B]_t)^{-1} = k(\Delta\delta_c - \Delta\delta_{obs})$$

* Corresponding author. Tel: ++39 0521 279662. Fax: ++39 0521 774468.
† Chiesi Farmaceutical S.p.A.
‡ Centro di Studio del CNR sulle Sostanze Organiche Naturali.
§ Università degli Studi di Parma.

10.1021/js980468o CCC: $18.00 Published on Web 04/24/1999

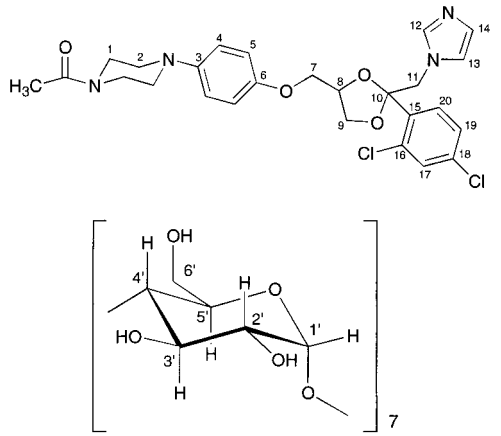

Figure 1—Hydrogen-labeling scheme for KC and βCD.

where $[B]_t$ is the total concentration of host, $\Delta\delta_{obs}$ is the difference between the chemical shift observed and the chemical shift of the free guest for a given proton, and $\Delta\delta c$ is the chemical shift difference (for a given proton) between the free guest and the pure complex.

The statistical analysis was performed by using SAS program version 3.1 (SAS Institute Inc., Cary, NC).

The mass spectra were acquired on a benchtop API 300 triple quadrupole mass spectrometer (Perkin-Elmer, Norwalk, CT), equipped with a standard API−Ionspray ionization source. Tandem MS experiments were carried out operating with a collision energy (E_{lab}) of 30 eV, using nitrogen as collision gas at a pressure of 8 mTorr. The 1:1:1 (+)-KC:TA:βCD and (−)-KC:TA:βCD samples were dissolved in 50/50 (v/v) water/acetonitrile and diluted to a concentration of 1000 ppm. The tandem MS analysis was repeated six times for each sample.

Molecular modeling studies were performed with the Sybyl 6.3 Software (Tripos Inc., 1699 South Hanley Rd., St. Louis, MO, 63144), running on a Silicon Graphics R4400 (200 MHz 64 Mb RAM) Indigo2 workstation. Three-dimensional models of (+)-TA and *cis*-KC were built and energy-minimized using the standard Tripos force field, with the Powell minimization method[17] and a convergence gradient of 0.05 kcal/mol·Å. The minimum-energy geometry of *cis*-(2*R*,4*S*)-KC was in good agreement with the crystal structure reported in Cambridge Structural Database (CSD) (ref code: KCONAZ),[18] with the exception of the torsion angle between the benzene and the piperazine rings; in fact, they lie on the same plane in the crystal structure and are perpendicular in the minimum-energy conformation obtained with Tripos force field. βCD structure was taken from CSD (ref code: BCDEXD10),[19] deleting the cocrystallized water molecules, and its geometry was kept fixed. Charges were calculated using the Gasteiger−Hückel method, giving an initial formal charge of +1 to the N^3 atom of the imidazole ring of KC and of −0.5 to the two O atoms of one of the carboxylic groups of TA, to simulate the same conditions of ionization as supplied in NMR studies (pH = 3.5); the dielectric function was dependent on 1/*r*.

A systematic conformational analysis on KC, with rotation of bonds C10−C11, C8−C7, C7−O with steps of 120°, and of O−C6 (Figure 1) with two steps of 90° (that is, with C7−O coplanar and perpendicular to the phenoxy ring), was performed in order to generate the possible KC conformations and was followed by energy minimization (with electrostatic term ignored). The orientations of the imidazole and the dichlorophenyl rings were not changed, nor were all possible conformations of the dioxolane and acetylpiperazine rings created (see Results and Discussion for a comment). Only those conformations having H−H distances lower than 3.5 Å for couples of protons giving high-intensity NOE cross-peaks were selected for subsequent docking studies.

Docking was performed with the DOCK routine of Sybyl, in a region of space including the three components of the complex, with a 0.5 Å grid resolution. Docking between KC (considered as the ligand in the docking routine) and βCD (considered as the site) was based on steric interaction energy only; the electrostatic contribution was considered for the subsequent docking of TA (ligand) onto the KC:βCD complex (site); during the docking procedure, the geometry of the site was kept fixed. Inter- and intramolecular distances were measured after energy minimization of the whole complex, with fixed geometry of the βCD ring (considered as an aggregate in Sybyl); for equivalent hydrogens, the minimum distance was chosen. βCD was eventually rotated around the axis connecting C15 and C18 of KC with steps of 30°, and the 12 resulting models were energy-minimized as reported.

MOLCAD[20] was used for the representation of the lipophilicity potential at the solvent accessible surface of KC and βCD.

Results and Discussion

NMR Studies—The formula of ketoconazole in Figure 1 shows the numbering system employed, which is different from the IUPAC notation. The spectral features of its tartrate salt in the absence and in the presence of βCD in 1.5 molar ratio are given in Table 1 and Table 2. An excess of the host was used in order to improve the separation between the pair of signals of the two enantiomers of the drug.

The difference between the enantiomers in the bound state and the free state ($\Delta\delta$) and the difference between the two bound states ($|\Delta\Delta\delta|$) are given in frequency units (Hz) rather than ppm, as, in this way, small changes can be better appreciated. In the ^{1}H NMR spectrum of (±)-*cis*-ketoconazole tartrate, on addition of βCD, two sets of resonances are observed for most of the protons or groups of equivalent protons, indicating that inclusion complex formation with βCD induces nonequivalence in the proton nuclei of the two enantiomers of the drug. As far as βCD is concerned, the ^{1}H resonances of the inner protons H3′ and H5′ show the diagnostic upfield shift due to the inclusion of the aromatic ring of the guest in the cavity.[21] Among the aromatic resonances, the largest shifts in δ were observed for the protons belonging to the imidazolium moiety, which also show splitting upon inclusion. The protons belonging to the dichlorophenyl moiety, which is the part of the molecule involved in the inclusion complex formation (vide ultra), experience smaller downfield shifts[22] and only the proton H20 shows splitting of the signal as well ($|\Delta\Delta\delta| = 8.8$ Hz). The upfield shift of the alkyl- and H4 aromatic protons may be due to conformational changes produced by the inclusion. Similar changes in the ^{13}C NMR spectra were also observed. Doubling of some of the aromatic resonances was observed, while only the C9 and C7 aliphatic carbons split. Analysis of the complexation-induced ^{13}C chemical shift changes allows some preliminary considerations on the geometry. According to Inoue,[23] the inclusion of the guest molecule into the CD cavity causes upfield shifts of the signals of the included carbons and downfield displacements of the signals of the carbons externally close to the rims of the truncated cone of CD. The changes observed for the carbons of the dichlorophenyl moiety may suggest that the insertion occurs from the wider rim of the cavity in such a way as to leave the carbons C15 and C18 exposed to the aqueous medium. The downfield shift of the carbon C16 is probably a consequence of the steric interaction[24] between the chlorine atom and the closely spaced hydrogens.

The coupling constants of the single enantiomers of KC were measured to check whether conformational changes were induced upon complexation. Since all values show no difference (Table 1) between the enantiomers, it seems to be the different orientation inside the cavity and/or outer-sphere interaction (intermolecular hydrogen bonds), rather than a different conformation of the enantiomers upon inclusion, that makes chiral discrimination possible. The more evident changes in differential chemical shifts for the signals of the imidazolium moiety in comparison to the signals of the dichlorophenyl moiety directly involved in the inclusion complex formation may indicate that the

Table 1—Tabulation of Coupling Constants (J) and ^{1}H Chemical Shifts (δ), for Free *rac*-Ketoconazole Tartrate and Its Multicomponent Complexes

assignment	J (Hz)	δ (±)-KC:TA	δ (+)-KC:TA:βCD	δ (–)-KC:TA:βCD	$\Delta\delta$ (Hz) (–)	$\Delta\delta$ (Hz) (+)	$\lvert\Delta\Delta\delta\rvert$
CH_3CO		2.186	2.154		–14.4		–
H2 (t)	$^3J = 4.8$	3.254	3.176	3.160	–37.6	–31.2	6.4
H2′ (t)	$^3J = 5.2$	3.314	3.225	3.213	–40.4	–35.6	4.8
H9 (dd)	$^2J = 10.8$ $^3J = 6.3$	3.549	hidden by CD signals				
H1 (t)[a]	$^3J = 7.0$	3.802	hidden by CD signals				
H1′ (t)[a]	$^3J = 6.8$	3.811	hidden by CD signals				
H7 (dd)[b]	$^2J = 8.8$ $^3J = 5.2$	3.859	3.948[c]	3.962[c]	41.2	35.6	5.6
H7′ (dd)[b]	$^2J = 8.8$ $^3J = 7.3$	3.966	4.009	3.933	–13.2	17.2	30.4
H9′ (dd)	$^2J = 10.8$ $^3J = 2.8$	4.064	4.100	4.065	0.4	14.4	14.0
H8 (m)		4.494	4.421	4.489	–2.0	–29.2	27.2
C*H*OH (s)		4.519	4.50		–7.6		–
H11	$^2J = 14.8$	4.913	4.931	4.958	18.0	7.2	11.8
H11′	$^2J = 14.8$	4.817	4.827	4.801	–6.4	4.0	10.4
H5 (d)	$J = 9.1$	6.973	6.940	6.934	–15.6	–13.2	2.4
H4 (d)	$J = 9.1$	7.241	7.121		–48.0		–
H14 (t)	$J = 1.6$	7.289	7.364	7.334	18.0	30.0	12.0
H19 (dd)	$J = 8.5$ $J = 2.1$	7.444	7.517	7.517	29.2		–
H13 (t)	$J = 1.6$	7.482	7.622	7.606	49.6	56.0	6.4
H17 (d)	$J = 2.1$	7.654	7.666		4.8		–
H20 (d)	$J = 8.5$	7.712	7.784	7.805	37.2	28.8	8.4
H12 (t)	$J = 1.6$	8.747	8.884	8.868	48.4	54.8	6.4

[a,b] Assignments may be interchanged. [c] ABX system

Table 2—Tabulation of ^{13}C Chemical Shifts (δ)

assignment	δ (±)-KC:TA	δ (+)-KC:TA:βCD	δ (–)-KC:TA:βCD	$\Delta\delta$ (+)	$\Delta\delta$ (–)	$\lvert\Delta\Delta\delta\rvert$
CH_3CO	22.711	22.652		–3.0		–
C1′	42.807	43.580		38.9		–
C1	47.396	48.253		43.1		–
C2	54.697	53.758		–47.3		–
C2′	55.030	54.710		–16.1		–
C11	55.220	54.828		–19.7		–
C9	68.371	68.455	68.800	4.2	21.6	17.4
C7	70.797	70.489	70.310	–15.5	–24.5	9.0
CHOH	75.031	75.233		10.2		–
C8	77.171	77.599		21.5		–
C10	109.609	109.395		–10.8		–
C5	118.527	118.551	118.504	1.2	–1.2	2.4
C13	121.238	121.310		3.6		–
C4	123.473	122.282		–59.9		–
C14	126.375	126.696		16.2		–
C19	130.013	129.491		–26.3		–
C20	132.487	132.285	132.178	–10.2	–15.5	5.3
C17	133.676	133.224		–22.7		–
C15	134.841	135.424	135.543	29.3	35.3	6.0
C16	135.102	135.876		39.0		–
C18	138.456	138.718	138.742	13.2	14.4	1.2
C12	138.622	139.027	139.075	20.4	22.8	2.4
C3	142.380	145.698	145.793	167.0	171.8	4.8
C6	158.456	156.875	156.792	–79.6	–83.7	4.1
CH_3CO	175.055	174.426		–31.7		–
COOH	178.242	178.659		21.0		–

strength of the "outer-sphere" interactions between the nitrogen atoms and the secondary hydroxyl groups probably plays the main role in the chiral discrimination process. For most of the signals, both the shielding and deshielding are more pronounced for the (–)-KC:TA:βCD complex than for the (+)-KC:TA:βCD complex, suggesting a stronger intermolecular interaction for the former enantiomer.

The H14 signal has the greatest potential for optical purity determination. It occurs as a pair of well-resolved narrow triplets (J = 1.6 Hz) of 12 Hz separation at 400 MHz, allowing the most accurate integration of each signal. Larger splitting in substrate resonance can be observed (e.g., H8 gives rise to a pair of well-resolved multiplet – $|\Delta\Delta\delta|$ = 27 Hz), but no attempts were made to determine the optical purity from these changes. By monitoring the H14 signal at 400 MHz, the resolved (–)-enantiomer turned out to contain about 2% of isomeric impurity (see Figure 2). The results we obtained would suggest that 1% optical purity measurements could be attainable by this method.

To further explore differences in these weakly bound diastereomeric complexes, T_1 measurements were made on free (±)-*cis*-ketoconazole tartrate and its βCD complex. The results are presented in Table 3. Only the protons for which it was possible to determine the T_1 values with sufficient accuracy (no overlapping with other signals) are reported. In general, the T_1 values for KC protons reduce in the presence of βCD in accordance with the fact that the correlation time of the guest increases upon complex formation. In particular, a dramatic reduction was observed for proton H17, which relaxes very slowly as it lacks nearby protons. Among the resonances which split, T_1 reduces more for protons H14 and H13 of the (–)-enantiomer; this difference in reduction may once again be attributed to a tighter binding of this enantiomer.

In the case of proton H20, both (–)- and (+)-form display equal reduction in T_1, confirming that the orientation of the dichlorophenyl ring inside the cavity is probably very similar for the two enantiomers. T_1 of the tartrate protons also reduces dramatically, suggesting that the counterion is strictly involved in the molecular assembly. Since complexes stability is important in determining chiral discrimination, a correlation was sought with the findings reported above, i.e., larger differences in shift and in T_1 reduction for the (–)-enantiomer. The two enantiomers of (±)-ketoconazole form 1:1 inclusion complexes as they possess only one binding site, i.e., the dichlorophenyl ring. The consistency of the stoichiometric model with the solubility diagram has also been reported in the litera-

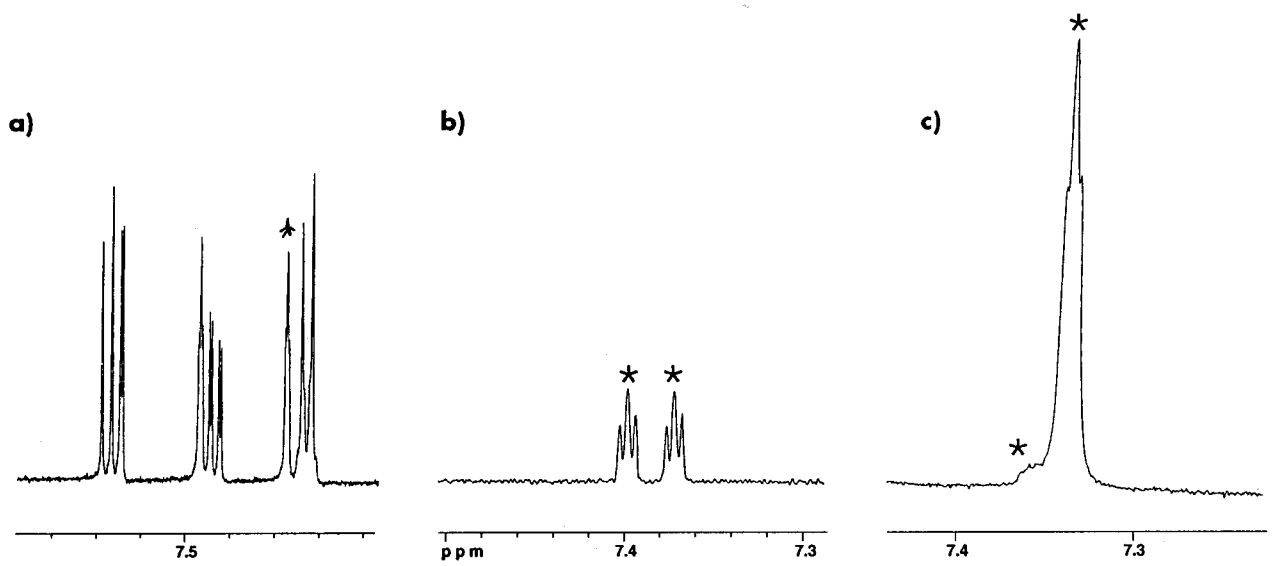

Figure 2—400 MHz H14 signal (*) of (a) (±)-KC:TA 1:1; (b) (±)-KC:TA:βCD 1:1:1.5; (c) (–)-KC:TA:βCD (ee = 98%).

Table 3—Tabulation of T_1 Values (s) for Some ^{1}H Resonances

assign-ment	T_1 (±)-KC:TA	T_1 (+)-KC:TA:βCD	T_1 (–)-KC:TA:βCD	ΔT_1 (+)	ΔT_1 (–)	$\lvert\Delta\Delta T_1\rvert$
H12	2.20	0.89	0.87	–1.31	–1.33	0.02
H20	1.18	0.30	0.30	–0.88		–
H17	10.76	0.60		–10.16		–
H13	1.78	0.83	0.61	–0.95	–1.17	0.22
H19	1.90	0.48		–1.42		–
H14	2.55	1.38	1.31	–1.17	–1.24	0.07
H4	0.70	0.37		–0.33		–
H5	0.77	0.46		–0.31		–
CH (tartrate)	5.70	1.83		–3.87		–
H2	0.46	0.23		–0.23		–
CH_3CO	0.95	0.64		–0.31		–

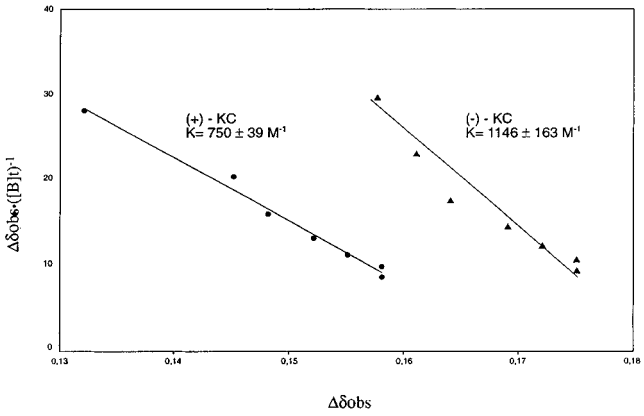

Figure 3—Change in the chemical shift of the H20 proton: (●) (+)-KC; (▲) (–)-KC.

ture.[12] Therefore, the association constants for the two complexes were evaluated by using the Foster–Fyfe equation (see Materials and Methods). The k at 25 °C, obtained from the slope of the straight lines, resulted as being 750 ± 100 M^{-1} for the (+)-enantiomer and 1146 ± 419 M^{-1} for the (–)-enantiomer (Figure 3). The test for heterogeneity of the slopes was positive, indicating that the difference in the complexes stability is statistically significant.

Finally, the stereochemistry of the two complexes was investigated by means of two-dimensional rotating frame NOE (ROESY) spectroscopy. An expansion of the spectrum of the complex of the (–)-enantiomer is reported in Figure 4. Both the enantiomers gave the same NOE pattern. A set of cross-peaks is observed between the inner protons H3′ and H5′ of βCD and the protons H17, H19, and H20, indicating that the inclusion occurs by accommodation of the dichlorophenyl ring. In addition, significant dipolar contacts are observed between H12, H13 (imidazolium), H4, and H5 (phenolic ring) with the H3′ proton of βCD, suggesting that the inclusion must occur from the wider-diameter side of the truncated cone of βCD. The H4 and H5 protons probably interact with H2′ of βCD as well, reflecting the major mobility of the phenolic ring around the "mouth" of the host. Anyway, an unambiguous interpretation is not possible as the signals H2′ and H5′ of βCD and H9 of KC are overlapped (vide ultra).

Mass Studies—Since some authors have recently drawn attention to the use of mass spectrometry for studying chiral selectivity in the inclusion complex formation,[25,26] the relative strength of the interaction binding of the two enantiomers was investigated by ionspray tandem mass spectrometry (ISMS/MS) experiments.[27] The positive ISMS spectra of the samples (Figure 5) exhibit the protonated 1:1:1 KC:TA:βCD (m/z 1815.5), which, upon collision, dissociate, yielding protonated KC:βCD complex (m/z 1665.6) and protonated KC (m/z 531.2). The ratio between the ion current of the two product ions is significantly higher for the (–)-enantiomer, suggesting that it forms a more stable inclusion complex than the other one in the gaseous phase. These findings are in agreement with the data obtained in aqueous solution (vide supra).

Molecular Modeling Calculations—Molecular modeling proved to be an excellent tool for the study of drug–cyclodextrin interaction.[28] The three components of the title complex, namely βCD, KC, and TA, can assume, in aqueous solution, a number of interconverting conformations and can perform different mutual interactions. For βCD alone, for example, the round-shaped conformation is not a minimum energy one, but can be regarded as the result of a time average in the ns-scale.[29] Given the high number of possible βCD conformations and the absence of a correction for the anomeric effect[29] in the Tripos force field here employed, the internal energy for the βCD molecule was not minimized, and its geometry was kept fixed in one of the crystal conformations reported in CSD.[19]

Although KC is a rather flexible compound, the complexation with βCD should select some of the allowed conformations which, in turn, could be identified by the analysis of the intramolecular NOEs (see Figure 4). Pos-

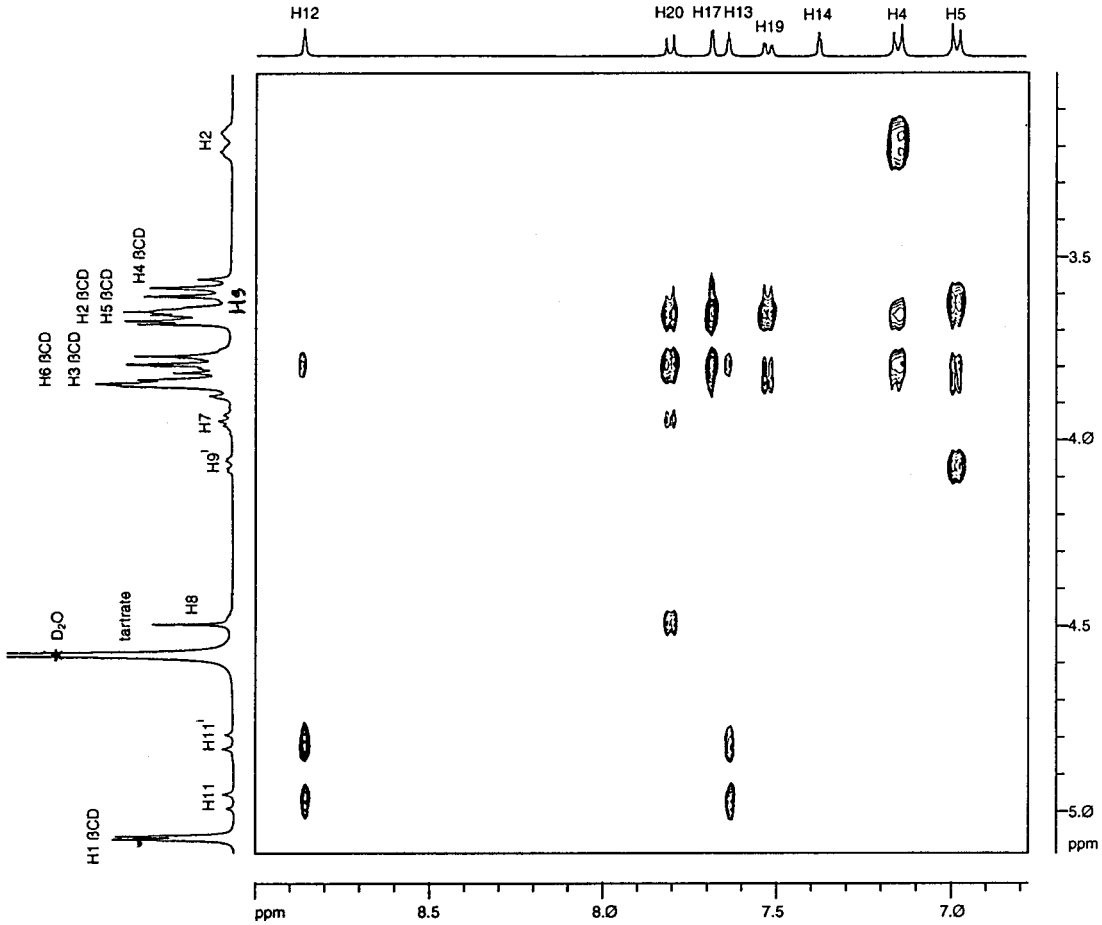

Figure 4—400 MHz ROESY spectrum of (–)-KC:TA:βCD 1:1:1.5.

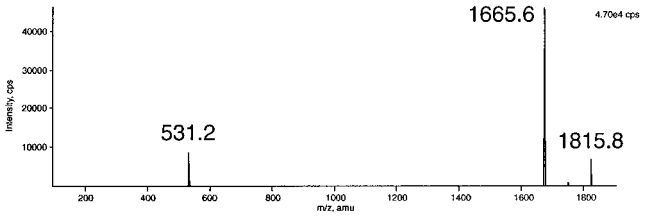

Figure 5—IS MS/MS spectrum of (–)-KC:TA:βCD 1:1:1.

sible conformations were thus chosen on the basis of the cross-peaks between the signals H20−H8, H20−H7, and H5−H9′ (the NMR signal marked as H9′ was assigned to the proton trans to H8). An intramolecular cross-peak between H9 (the dioxolane hydrogen opposite to the side chain) and H5 is also recognizable although it is partly overlapped with the intermolecular cross-peak between H5 and H2′ and/or H5′ of βCD; therefore, the relevant averaged distance was included in the conformation selection criteria. The minimum-energy conformations of KC were generated by rotation of the bonds, causing a variation in the mutual disposition of the fragments showing NOE interactions with βCD, i.e., the dichlorophenyl, the imidazole, and the side-chain phenyl rings. Some preliminary considerations allowed a reduction in the number of conformations to be generated. The dichlorophenyl ring has two possible orientations, with the plane of the ring perpendicular to the C10−C11 bond; the presence of a cross-peak between H20−H8 and H20−H7, but not between H20−H9′, prompted us to consider only the rotamers having H20 pointing toward H8. The imidazole ring is quite free to rotate around C11−N; we kept it in one of the possible orientations because its rotation caused slight variations

Table 4—Torsion Angles (deg) and Intramolecular Distances (Å) for the Conformers of (+)-KC Consistent with NOE Intramolecular Cross-peaks. For the (–)-enantiomer the Intramolecular Distances are the Same, and the Torsion Angles Are Opposite

	1	2	3	4	5	6
			Torsion Angles			
C15C10C11N	60.2	–56.1	178.5	60.7	–55.7	179.3
C9C8C7O	78.7	79.2	78.7	59.2	58.6	57.3
C8C7OC6	–60.4	–60.9	–61.6	56	56	55.2
C7OC6C5	104	103.6	103.7	–110.4	–110.6	–113.5
			Intramolecular Distances			
H20–H8	2.88	2.73	2.77	2.87	2.73	2.75
H20–H7[a]	4.18	4.10	4.13	4.25	4.17	4.20
H5–H9′[b]	3.21	3.23	3.24	2.95	2.88	2.83
H5–H9	3.01	3.01	3.00	2.65	2.68	2.77

[a] Measured from the H7 closer to H20. [b] H9′ is trans to H8.

in the spatial arrangement of the complex, compared to the uncertainty of the model. This means that each generated rotamer is representative of a family of conformations attainable from imidazole rotation. The same applies to the acetylpiperazine moiety, which gave no recognizable NOE interaction with βCD, and whose conformations were not explored. Rotation of the other four single bonds (see Materials and Methods) gave a set of 54 conformations, which were energy-minimized before the calculation of H5−H9 and H5−H9′ distances. Only six conformers, described in Table 4, had these two distances lower than 3.5 Å, and were submitted to docking studies.

While the intramolecular distances between hydrogen atoms of the isolated KC molecule are the same for the corresponding conformers of the two enantiomers (with

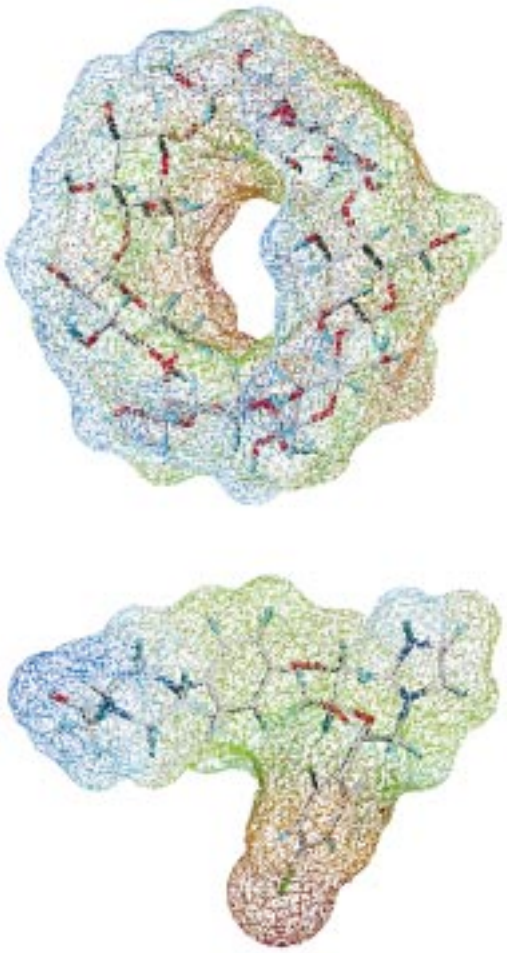

Figure 6—Lipophilicity potential contour maps of βCD, in the crystal structure conformation, and KC in conformation **3** (Table 4), colored according to a lipophilicity scale, ranging from blue (hydrophilic) to brown (lipophilic). Atom color codes – white: carbon; red: oxygen; blue: nitrogen; cyan: hydrogen; green: chlorine.

opposite torsional angles), the complexation with the chiral βCD molecule leads to different interactions for the (+)- and (−)-KC. The docking procedure described as follows was therefore performed on both the KC enantiomers. The analysis of NMR data, in particular NOEs, gives evidence that complexation occurs by involving the dichlorophenyl ring, which is inserted in the βCD cavity from the wider rim (vide supra). This is also supported by the lipophilicity potential of the host and guest molecules at their solvent accessible surface, which is maximum in correspondence to the dichlorophenyl ring and βCD cavity (Figure 6).

Only three (**1**, **2**, and **3**) of the six selected conformations of KC could be docked into the βCD, as the spatial disposition of the side chain, having the phenoxy ring stacked beneath the dichlorophenyl one, prevented the arrangement of βCD around the dichlorophenyl moiety for the other three conformations. The chosen conformations differed from each other only by the imidazolylmethyl group orientation around C10−C11 (Table 4). As a first step, KC was docked into the βCD cavity on the basis of the van der Waals contribution of intermolecular interactions; monoanionic tartrate was then docked onto the KC:βCD complex with the charged carboxylate group involved in a saline bond with the protonated imidazolium ring, and with the uncharged carboxylic group, in gauche conformation, pointing toward the βCD secondary hydroxyl groups, as suggested by the dramatic relaxation time variation of tartrate C−H signal. The multicomponent complexes thus obtained were energy minimized, always keeping the geometry of βCD fixed as it was in the crystal structure.

Table 5—Intra- and Intermolecular Distances (Å) for the Proposed Complexes of the Two Enantiomers of *cis*-KC with βCD and TA, Represented in Figure 7, and Mean Values for the 12 Models Obtained after Rotation of the βCD around the Dichlorophenyl Ring, with Steps of 30°

	(+)-KC:TA:βCD		(–)-KC:TA:βCD	
	starting geometry	mean (range)	starting geometry	mean (range)
Intramolecular Distances				
H20–H8	2.86	2.88 (2.47–3.15)	2.38	2.66 (2.38–3.20)
H20–H7	4.20	4.26 (3.99–4.52)	4.10	4.19 (3.95–4.59)
H5–H9′	3.32	3.24 (2.89–3.42)	3.09	3.18 (2.99–3.42)
H5–H9	2.79	3.07 (2.74–3.62)	3.30	3.27 (2.75–4.28)
Intermolecular Distances				
H20–H3′βCD	2.39	2.48 (2.26–2.85)	2.22	2.46 (2.22–3.10)
H20–H5′βCD	3.04	3.22 (2.78–4.16)	3.07	3.36 (2.73–4.82)
H19–H3′βCD	3.47	3.55 (2.49–4.32)	3.73	3.29 (2.25–4.07)
H19–H5′βCD	2.50	2.52 (2.34–2.86)	2.70	2.52 (2.37–2.73)
H17–H3′βCD	2.41	2.51 (2.38–2.84)	2.34	2.54 (2.31–3.10)
H17–H5′βCD	2.64	2.50 (2.35–2.74)	2.64	2.70 (2.35–3.44)
H12/H13–H3′βCD[a]	3.81	3.81 (3.03–4.45)	3.74	4.01 (3.32–5.72)
H4–H3′βCD	2.94	3.24 (2.51–4.47)	2.65	3.31 (2.63–4.83)
H4–H2–H5′βCD[b]	4.32[c]	4.67 (4.23–5.07)	4.90[d]	4.91 (4.12–5.45)
H5–H3′βCD	2.63	2.86 (2.42–3.92)	2.44	2.95 (2.37–4.40)
H5–H2′/H5′βCD[b]	4.81[d]	4.66 (4.22–5.41)	4.27[c]	4.74 (4.27–6.75)

[a] The lower distance between H12–H3βCD and H13–H3βCD is reported, since the imidazole ring was not rotated (see Results and Discussion). [b] The H2′βCD and H5′βCD ^{1}H NMR signals were overlapped, and a unique assignment of NOE cross-peaks was impossible; the lower distances are reported. [c] With H2′βCD. [d] With H5′βCD.

Intermolecular distances were calculated in order to select those complexes which were consistent with the NOE cross-peaks observed. The cross-peaks were thus grouped on the basis of their intensity, each group corresponding to a different distance range: H17−H3′βCD and H17−H5′βCD were considered strong (protons closer than 2.5 Å) intensity peaks; H20−H3′βCD, H20−H5′βCD, H19−H5′βCD were considered medium (closer than 3.5 Å) intensity peaks; H19−H3′βCD, H4−H3′βCD, H4−H2′/H5′βCD, H5−H3′βCD, H12−H3′βCD, H13−H3′βCD were considered weak (closer than 5 Å) intensity peaks.[30] The intensity of H5−H2′/H5′βCD cross-peak cannot be assigned unambiguously, being overlapped with the H5−H9 intramolecular peak; therefore, distances lower than 5 Å were considered acceptable (vide supra).

Analysis of the intermolecular distances gave similar results for the two KC enantiomers, allowing the selection of a multicomponent complex, corresponding to KC conformer **3** in Table 4, which was in full agreement with NOE data; the intra- and intermolecular distances of the best multicomponent complex are reported in Table 5. The most significant difference between this complex and the other two, built up from conformer **1** and **2** of KC, concerns H20−H5′βCD distance: for the (−)-enantiomer this was 3.1 Å in the complex of conformer **3**, and 4.4 and 4.6 Å in the other two, while for the (+)-enantiomer it was 3.0, 4.4, and 5.7 Å respectively. These differences reflect the lower degree of inclusion of the dichlorophenyl ring into the βCD cavity in the two discarded models; in fact, the inclusion is partially forbidden by the position of the imidazole ring which "bumps" against the rim of βCD.

The βCD structure used for the docking studies is not symmetrical; to better explore the possible mutual orientations of the components of the complex, βCD was rotated, with 12 steps of 30° around the dichlorophenyl ring, keeping the ketoconazole tartrate fixed. Analysis of the intermolecular distances, after energy minimization, showed

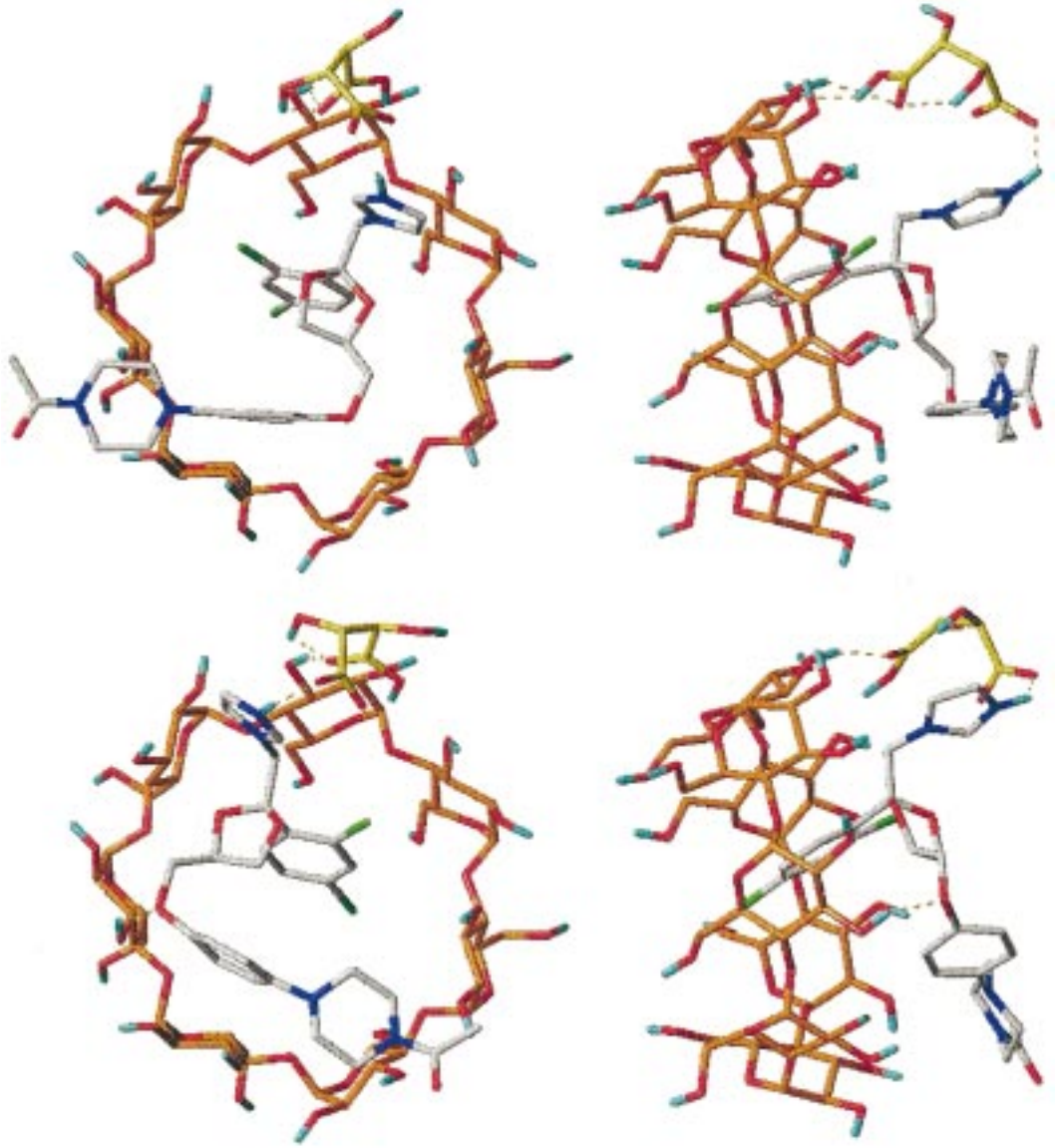

Figure 7—Representation of the multicomponent complex models for (+)- and (–)-KC (top and bottom, respectively) from the wider rim of βCD (left) and rotated by 90° on the *Y* axis (right); only polar hydrogens are displayed. Hydrogen bonds are indicated by dashed lines. Atom color codes – white: KC carbon; orange: βCD carbon; yellow: TA carbon; red: oxygen; blue: nitrogen; cyan: hydrogen; green: chlorine.

minor differences in some interatomic distances, compared to the starting geometry, but the mean values were still in agreement with the NOE cross-peak intensities, as reported in Table 5.

It has been stated that one of the major driving forces of drug−βCD complexation is a hydrophobic interaction between the guest molecule and the internal cavity of βCD.[31] Furthermore, the net entropy contribution was negligible in some cases,[28] but this fact could be attributed to the sum of entropy-favorable hydrophobic interaction and entropy loss due to conformational restriction. Under the hypothesis of similar entropy contribution for the two KC enantiomers, the interaction energy between the components, which is a rough estimate of the enthalpy contribution, can be regarded as an indication of different expected association constants. The interaction energy was therefore calculated for the multicomponent complexes of both the enantiomers of the selected KC conformation, to assess whether the higher association constant of the (−)-(2*S*,4*R*)-KC could be explained on the basis of tighter interactions. The energy values for the starting geometry of each complex, and the mean values calculated from the 12 models obtained after βCD rotation, are reported in

Table 6—Interaction Energies (kcal/mol) between the Components of the Proposed Multicomponent Complexes for the Two Enantiomers of *cis*-KC. Energy Contributes for the Starting Geometry and Mean Values Obtained Rotating the βCD around the Dichlorophenyl Ring with Steps of 30° Are Reported

	(+)-KC:TA:βCD		(–)-KC:TA:βCD	
contribute[a]	starting geometry	mean ± SEM	starting geometry	mean ± SEM
El. KC:βCD	–2.19	–3.20 ± 0.42	–4.43	–3.48 ± 0.20
El. TA:βCD	–1.90	–1.29 ± 0.62	–3.74	–1.51 ± 0.55
El. KC:TA	–42.68	–41.76 ± 0.48	–42.10	–41.19 ± 0.42
St. KC:βCD	–20.80	–22.90 ± 0.72	–25.17	–23.30 ± 0.78
St. TA:βCD	–1.70	–2.13 ± 0.18	–2.15	–2.25 ± 0.13
St. KC:TA	0.79	0.33 ± 0.38	0.13	–0.15 ± 0.13
total	–68.48	–70.94 ± 1.17	–77.46	–71.89 ± 1.59

[a] El. = electrostatic energy; St. = steric energy.

Table 6. Comparison between the two enantiomers in terms of interaction energies can only be considered on a qualitative basis, being related only to the complementarity of the van der Waals surfaces (steric) and to the attractive and repulsive interactions between the assigned partial charges

(electrostatic). While significant differences in the interaction energies were observed for the starting geometry of the two complexes, they were much less pronounced, considering the mean values calculated for the 12 rotated models. However, the complex of the (−)-enantiomer was still characterized by a higher mean total interaction energy, although the small difference was comparable to the SEM of the data. This difference of about 1 kcal/mol, consistent with the small difference of association constant, was mainly due to the steric interaction between βCD and KC, but also to the electrostatic interaction of βCD with KC and TA, while the total (steric and electrostatic) interaction energy between KC and TA was approximately constant.

The starting geometry of the complexes formed by the two KC enantiomers are represented in Figure 7. As can be observed, besides the insertion of the dichlorophenyl ring into the internal βCD cavity, two additional interaction points are represented by the tartrate, bridging KC and βCD, and by the phenoxy fragment, located near the wider rim of βCD. Therefore, enantioselectivity results from the inclusion of an aromatic ring into the βCD cavity, the strong electrostatic interaction between the imidazolium tartrate moiety and βCD hydroxyl groups, and the accessory interaction of the phenoxy fragment with the wider rim of βCD, in agreement with the rule suggested by Armstrong.[31]

The real situation should be represented by an ensemble of different interconverting relative dispositions of the components of the complex; however, the reported model can be considered highly representative, as βCD seems to select some of the possible conformations of KC, as indicated by the H5−H9 and H5−H9′ intramolecular NOE cross-peaks. The different states of the complex include (i) the unexplored conformations of KC; in particular, those resulting from the rotation of the imidazole ring around C11−N bond could be related to enantioselectivity, as suggested by the different relaxation time variations of the imidazole protons for the two KC enantiomers; (ii) different orientations of the tartrate molecule with similar energy content, corresponding to each imidazole rotation; this multiplicity makes the arrangement of the imidazolium tartrate bridging region less defined, and, as a consequence, we considered H12 and H13 as equivalent in the calculation of the intermolecular distances; (iii) different possible relative orientations of KC and βCD, which we partially explored by rotation of the βCD; inclusion of other fragments into the βCD cavity could also occur at high CD concentrations, but the calculated lipophilicity profiles and the NMR data indicate that complex formation preferably occurs by inclusion of the dichlorophenyl moiety.

The Tripos force field put the piperazine ring of KC perpendicular to the benzene ring, while in the crystal structure they lie roughly on the same plane. Moreover, 24 different compounds containing a piperazinylphenyl substructure reported in CSD have the two rings almost in the same plane. The coplanar disposition of the two rings in our multicomponent complex could also be suggested by the presence of the very intensive H4−H2 NOE cross-peak; in fact, the distance between the two hydrogens is significantly lower in the coplanar disposition than in the perpendicular one. While our studies were conducted with the geometry resulting from energy minimization by the force field, repeated runs performed imposing the crystal geometry to the non-H atoms of the piperazinylphenyl fragment gave similar results in terms of intermolecular distances and chiral recognition.

Conclusions

An interaction model for both enantiomers of *cis*-KC with βCD in the presence of (+)-L-tartaric acid was built on the basis of preliminary ^{1}H NMR and ^{13}C NMR data. The measured intra- and intermolecular distances are in qualitative agreement with 2D NOE cross-peak intensities. This model, which probably represents the predominant solution structure, indicates that the inclusion of the dichlorophenyl moiety into the βCD cavity occurs from its wider-diameter side. Tartaric acid is strictly involved in the recognition process by establishing electrostatic interaction with the imidazolium ring and hydrogen bonds with 2- and/or 3-hydroxyl groups of βCD. A third interaction site is represented by the phenoxy fragment, involved in van der Waals and electrostatic interaction with the wider rim of βCD, with the possibility of hydrogen bond formation. These sites allow the definition of a chiral interaction; in fact, the association constants for the two KC enantiomers are slightly different, the (−)-one giving rise to the stronger interaction, in agreement with the calculated interaction energies for our models. The results are also consistent with patterns of chiral interactions proposed in the literature,[31,32] where the interactions with the 2- and 3- hydroxyl groups at the wider rim of CD appear to be the key element for the chiral recognition process.

References and Notes

1. Heeres, J.; Backx, L. J. J.; Mostmans, J. H.; Van Cutsem, J. Antimycotic Imidazoles. 4. Synthesis and Antifungal Activity of Ketoconazole, a New Potent Orally Active Broad Spectrum Antifungal Agent. *J. Med. Chem.* **1979**, *22*, 1003−1005.
2. Heel, R. C.; Brogden, R. N.; Carmine, A.; Morley, P. A.; Speight, T. M.; Avery, G. S. Ketoconazole: a Review of its Therapeutic Efficacy in Superficial and Systemic Fungal Infections. *Drugs* **1982**, *23*, 1−36.
3. Rotsein, D. M.; Ketesz, D. J.; Walker, K.; Swinney, D. C. Stereoisomers of Ketoconazole: Preparation and Biological Activity. *J. Med. Chem.* **1992**, *35*, 2818−2825.
4. Camps, P.; Farres, X.; Garcia, M. L.; Ginesta, J.; Pascual, J.; Mauleon, D.; Carganico, G. Stereoselective Syntheses of Both Enantiomers of Ketoconazole from (R)- and (S)-Epichlorohydrin. *Tetrahedron: Asymmetry* **1995**, *6*, 1283−1294.
5. Gray, N. M. WO 94 14447-A1, 1994.
6. König, W. A.; Gehrcke, B.; Hochmuth, D. H.; Mlynek, C.; Hopf, H. Resolution of Chiral [2.2]Paracyclophanes by Enantioselective Gas Chromatography. *Tetrahedron: Asymmetry* **1994**, *5*, 347−350.
7. Greatbanks, D.; Pickford, R. P. Cyclodextrins as Chiral Complexing Agents in Water, and their Application to Optical Purity. *Magn. Reson. Chem.* **1987**, *25*, 208−215.
8. Casy, A. F.; Mercer, A. D. Application of Cyclodextrins to Chiral Analysis by ^{1}H NMR Spectroscopy. *Magn. Reson. Chem.* **1988**, *26*, 765−774
9. Selva, A.; Redenti, E.; Pasini, M.; Ventura, P.; Casetta, B. A study of the salts with organic hydroxyacids of the Terfenadine β-Cyclodextrin inclusion complex in solution by Ionspray mass spectrometry. *J. Mass Spectrom.* **1995**, *30*, 219−220.
10. Vikmon, M.; Szemán, J.; Szejtli, J.; Pasini, M.; Redenti, E.; Ventura, P. In *Proceedings of the 7th International Cyclodextrins Symposium;* Osa, T., Ed.; Komiyama: Tokyo, 1994; pp 480−483.
11. Loftsson, T.; Brewster, M. Pharmaceutical Applications of Cyclodextrins. 1. Drug Solubilisation and Stabilization. *J. Pharm. Sci.* **1996**, *85*, 1017−1025.
12. Esclusa-Diaz, M. T.; Gayo-Otero, M.; Perez-Marcos, M. B.; Vila-Lato, J. L.; Torres-Labandeira, J. J. Preparation and Evaluation of Ketoconazole-β-cyclodextrin Multicomponent Complexes. *Int. J. Pharm.* **1996**, *142*, 183−187.
13. Gerloczy, A.; Szeman, J.; Csabai, K.; Kolbe, I.; Jicsinzky, L.; Acerbi, D.; Ventura, P.; Redenti, E.; Szejtli, J. Pharmacokinetic Study of Orally Administered Ketoconazole and its Multicomponent Complex on Rabbits of Normal and Low Gastric Acidity. In *Proceedings of the Eighth International Symposium on Cyclodextrins*; Szejtli, J., Szente, L., Eds.;

Kluwer Academic Publishers: Dordrecht, 1996; pp 515−518.
14. Part of the work was presented at the 9th International Symposium on Cyclodextrins, Santiago de Compostela, Spain, May 31−June 3, 1998.
15. Foster, R.; Fyfe, C. A. Interaction of Electron Acceptors with Bases. Part 15.-Determination of Association Constants of Organic Charge-Transfer Complexes by N. M. R. Spectroscopy. *Trans Faraday Soc.* **1965**, *61*, 1926−1631.
16. Benesi, B. H.; Hildebrand, J. H. A Spectrophotometric Investigation of the Interaction of Iodine with Aromatic Hydrocarbons. *J. Am. Chem. Soc.* **1949**, *71*, 2703−2707.
17. Powell, M. J. D. Restart Procedures for the Conjugate Gradient Method. *Mathematical Programming* **1977**, *12*, 241−254.
18. Peters, O. M.; Blaton, N. M.; De Ranter, C. J. *cis*-1-Acetyl-4-(4-{[2-(2,4-dichlorophenyl)-2-(1H-1-imidazolylmethyl)-1,3-dioxolan-4-yl]methoxy}phenyl)piperazine: Ketoconazole. A Crystal Structure with Disorder. *Acta Crystallogr., Sect. B* **1979**, *35*, 2461−2464.
19. Lindner, K.; Saenger, W. Topography of Cyclodextrin Complexes. Part XVII. Crystal and Molecular Structure of Cycloheptaamylose Dodecahydrate. *Carbohydr. Res.* **1982**, *99*, 103−115.
20. Heiden, W.; Goetze, T.; Brickmann, J. Fast Generation of Molecular Surfaces from 3D Data Fields with an Enhanced "Marching Cube" Algorithm. *J. Comput. Chem.* **1993**, *14*, 246−250.
21. Demarco, P. V.,; Thakkar, A. R. Cyclohepta-amylose Inclusion Complexes. A Proton Magnetic Resonance Study. *J. Chem. Soc., Chem. Commun.* **1970**, 2−4.
22. Djedaini, F.; Lin, S.; Perly, B.; Wouessidjewe, D. High-field Nuclear Magnetic Resonance Techniques for the Investigation of a β-Cyclodextrin: Indomethacin Inclusion Complex. *J. Pharm. Sci.* **1990**, *79*, 643−646.
23. Inoue, Y., NMR Studies of the Structure and Properties of Cyclodextrins and their Inclusion Complexes. *Ann. Rep. NMR Spectrosc.* **1993**, *27*, 59−101.
24. Breitmaier, E.; Voelter, W. *Carbon-13 NMR Spectroscopy;* VCH Publishers: New York, 1989; p 115 and p 259.
25. Haskins, N. J.; Saunders: M. R.; Camilleri, P. The Complexation and Chiral Selectivity of 2-Hydroxypropyl-β-cyclodextrin with Guest Molecules as Studied by Electrospray Mass Spectrometry. *Rapid. Comm. Mass Spectrom.* **1994**, *8*, 423−426.
26. Pocsfalvi, G.; Liptak, M.; Huszthy, P.; Bradshaw, J. S.; Izatt, R. M.; Vekey, K. Characterization of Chiral Host−guest Complexation in Fast Atom Bombardment Mass Spectrometry. *Anal. Chem.* **1996**, *68*, 792−795.
27. Selva, A.; Redenti, E.; Ventura, P.; Zanol, M.; Casetta, B. A Study of β-Cyclodextrin/Ketoconazole/tartaric acid Multicomponent Noncovalent Association by Positive and Negative Ionspray Mass Spectrometry. *J. Mass Spectrom.* **1998**, *33*, 729−734.
28. Lipkowitz, K, B. Applications of Computational Chemistry to the Study of Cyclodextrins. *Chem. Rev.* **1998**, *98*, 1829−1873 and references cited therein.
29. Lipkowitz, K. B. Symmetry Breaking in Cyclodextrins: a Molecular Mechanics Investigation. *J. Org. Chem.* **1991**, *56*, 6357−6367.
30. Neuhaus, D.; Williamson, M. *The Nuclear Overhauser Effect in Structural and Conformational Analysis*; VCH Publishers: New York, 1989.
31. Armstrong, D. W.; Ward, T. J.; Armstrong, R. D.; Beesley, T. E. Separation of Drug Stereoisomers by the Formation of β-Cyclodextrin Inclusion Complexes. *Science* **1986**, *232*, 1132−1135.
32. Lipkowitz, K. B.; Raghothama, S.; Yang J. Enantioselective Binding of Tryptophane by α-Cyclodextrin. *J. Am. Chem. Soc.* **1992**, *114*, 1554−1562.

Acknowledgments

The authors are grateful to Gabriele Amari and Giuseppe Pispisa (Chiesi Farmaceutici) for their experimental support. Financial support from the Italian MURST (40% and 60%) is gratefully acknowledged.

JS980468O

Novel Sorbitan Monostearate Organogels

SUDAXSHINA MURDAN, GREGORY GREGORIADIS, AND ALEXANDER T. FLORENCE*

Contribution from *Centre for Drug Delivery Research, School of Pharmacy, University of London, 29–39 Brunswick Square, London, WC1N 1AX, UK.*

Received August 17, 1998. Final revised manuscript received December 16, 1998.
Accepted for publication March 2, 1999.

Abstract □ Sorbitan monostearate, a hydrophobic nonionic surfactant, gels a number of organic solvents such as hexadecane, isopropyl myristate, and a range of vegetable oils. Gelation is achieved by dissolving/dispersing the organogelator in hot solvent to produce an organic solution/dispersion, which, on cooling sets to the gel state. Cooling the solution/dispersion causes a decrease in the solvent–gelator affinities, such that at the gelation temperature, the surfactant molecules self-assemble into toroidal inverse vesicles. Further cooling results in the conversion of the toroids into rod-shaped tubules. Once formed, the tubules associate with others, and a three-dimensional network is formed which immobilizes the solvent. An organogel is thus formed. Sorbitan monostearate gels are opaque, thermoreversible semisolids, and they are stable at room temperature for weeks. The gels are affected by the presence of additives such as the hydrophilic surfactant, polysorbate 20, which improves gel stability and alters the gel microstructure from a network of individual tubules to star-shaped "clusters" of tubules in the liquid continuous phase. Another solid monoester in the sorbitan ester family, sorbitan monopalmitate, also gels organic solvents to give opaque, thermoreversible semisolids. Like sorbitan monostearate gels, the microstructure of the palmitate gels comprise an interconnected network of rodlike tubules. Unlike the stearate gels, however, the addition of small amounts of a polysorbate monoester causes a large increase in tubular length instead of the "clustering effect" seen in stearate gels. The sorbitan stearate and palmitate organogels may have potential applications as delivery vehicles for drugs and antigens.

Introduction

Gels are an intermediate state of matter, containing both solid and liquid components. The solid component comprises a three-dimensional network of interconnected molecules or aggregates which immobilizes the liquid continuous phase. Hydrogels have an aqueous continuous phase, and organogels have an organic solvent as the liquid continuous medium. Gels may also be classified based on the nature of the bonds involved in the three-dimensional solid network—chemical gels arise when strong covalent bonds hold the network together, and physical gels when hydrogen bonds and electrostatic and van der Waals interactions maintain the gel network.[1]

Interest in the physical organogel field has increased, with the discovery and synthesis of a number of substances able to gel organic solvents. Examples of such organogelators) include 12-*d*-hydroxyoctadecanoic acid (12-HOA),[2] D-homosteroidal nitroxide (SNO),[3] calixarenes,[4] 1,3:2,4-di-*O*-benzylidene-D-sorbitol (D-DBS),[5] ALS compounds (an Aromatic moiety attached by a Linker segment to a Steroidal group),[6] lecithin,[7] bis(2-ethylhexyl) sodium sulfosuccinate (AOT),[8] gelatin,[9] 2,3-bis-*n*-decyloxyanthracene (DDOA),[10] and some azobenzene cholesterol derivatives.[11] These organogels exhibit interesting properties such as acute temperature/moisture sensitivities,[12,8] the ability to solubilize guest molecules[12] and to act as templates[13] and nonaqueous media for synthesis,[14–19] uses for purification and separation purposes,[20] as transdermal delivery vehicles,[21] and as carriers for liquid crystals.[22] Some of these potential applications are discussed in a review by Hinze et al.[12]

We have previously reported the gelation of certain organic solvents, e.g. *n*-alkanes, cyclohexane, vegetable oils, isopropyl myristate by the nonionic surfactant, sorbitan monostearate (Span 60).[23–25] Gelation is achieved by dissolving/dispersing the gelator in the solvent at 60 °C and then cooling the resulting solution/suspension, which conseqently gels as thermoreversible organic systems that are opaque and semisolid with a smooth, silky "feel". Microscopical examination reveals a network of tubular aggregates in the liquid disperse phase. Since these aggregates were large enough to be visualized by a light microscope, we followed their formation and the establishment of a gel network as a hot suspension was cooled to the gel state, using hot-stage light microscopy. X-ray diffraction measurements have provided further information on the microstructure of the gels, and we report here the possible arrangement of the gelator molecules in the gel network. Other members of the sorbitan ester family were also studied as were the effects of additives with the aim of finding the structural features responsible for gelation.

Materials and Methods

Sorbitan monostearate was purchased from Sigma (UK) and used as received. Like most sorbitan esters, sorbitan monostearate is a mixture of sorbitan esters, with the stearate and palmitate esters predominating. Other sorbitan esters (sorbitan monolaurate, sorbitan monopalmitate, sorbitan monooleate, and sorbitan tristearate) were also purchased from Sigma (UK). Like sorbitan monostearate, these sorbitan esters are mixtures, their fatty acid compositions being as follows: sorbitan monolaurate, lauric acid ~50%, and the balance primarily myristic, palmitic, and linolenic acids; sorbitan monopalmitate, palmitic acid ~90%, and the balance primarily stearic acid; sorbitan monooleate, oleic acid ~75%, and the balance primarily linoleic, linolenic, and palmitic acids; sorbitan tristearate, stearic acid ~50%, and the balance palmitic acid. The polysorbates (polysorbates 20, 40, 60, 65, 80, and 85) were purchased from Fluka (UK). The organic solvents were all of analytical grade. Hexadecane, *cis*-decalin, *trans*-decalin, isopropyl myristate, ethyl oleate, ethyl formate, squalene, and the vegetable oils (cottonseed oil, soybean oil, sesame oil, corn oil, and olive oil) were bought from Fluka (UK); hexane and cyclohexane were purchased from Rathburn (UK); octane, isooctane, decane, dodecane, tetradecane, and octadecane were obtained from Sigma (UK); benzene and toluene were from BDH (UK). All the reagents were used as received, except for hexadecane, isopropyl myristate, and the vegetable oils, which were dried in a vacuum oven

* Corresponding author. Tel: 0171 753 5819. Fax: 0171 837 5092. E-mail: a.t.florence@ulsop.ac.uk.

10.1021/js980342r CCC: $18.00
Published on Web 04/21/1999

(Gallenkamp, UK) at room-temperature overnight to ensure the absence of any moisture which might affect gelation.

Gel Preparation—Sorbitan monostearate (10% w/v) was dispersed/dissolved in the organic solvent at 60 °C. The resulting dispersion/solution was then allowed to cool by standing at room temperature. An opaque, semisolid gel was obtained. To obtain gels containing polysorbate additives, sorbitan monostearate (10% w/v) and the polysorbate (2% w/v) were weighed into a vial, and the organic solvent was added. The mixture was heated in a water-bath at 60 °C and then allowed to cool and set to a gel at room temperature.

Light Microscopy—A light microscope (Nikon Microphot-FXA, Japan) was used, with attached camera (Nikon FX-35DX, Japan) or a high-speed camera (Microscope Service & Sales, UK) and a hot-stage (Linkam TC93, UK). A video recorder was also used to record the events in selected experiments.

Differential Scanning Calorimetry (DSC)—A Perkin-Elmer DSC7 (UK) differential scanning calorimeter was used to determine gelation temperatures. Samples were weighed into aluminum pans using a Perkin-Elmer AD-4 autobalance and the pans then sealed nonhermetically. The samples were heated at a rate of 10 °C/min from 20 °C to 70 °C. The melting point was taken as the temperature corresponding to the melting endotherm. The equipment was calibrated using indium, and low temperatures were maintained using liquid nitrogen.

X-ray Diffraction Studies—X-ray data on the gel sample was collected on a Siemens D500 diffractometer (in the Department of Crystallography, Birkbeck College) equipped with a copper tube and a quartz primary-beam monochromator giving a wavelength (λ) = 1.54056 Å. The X-ray tube was run at 45 kV and 30 mA. The sample was mounted in a flat-plate specimen holder and flattened with a glass microscope slide. The sample was spun about an axis normal to its flat-plate surface. Diffraction patterns were measured using a scintillation detector. The data were obtained for the 2θ range 1−35° in steps of 0.05° at 10 s per point.

Results and Discussion

Sorbitan Monostearate Gels—Sorbitan monostearate is a small (MW = 431), monoalkyl, lipophilic (HLB 4.7), nonionic surfactant (Scheme 1). A waxy solid with a grainy texture, it disperses in hexadecane (at 10% w/v) on heating at 60 °C to give a slightly turbid suspension. On cooling, the latter suspension sets to an opaque, white, semisolid gel with a smooth texture. Cooling the suspension results in reduced affinities between the solvent and the surfactant, and this appears to cause surfactant self-assembly into aggregates. The aggregates join with one another to form a three-dimensional network which captures the solvent. The latter is thus immobilized and a gel is formed, as the bulk viscosity is increased by the network.

Solvents Gelled by Sorbitan Monostearate—The solvent has a prime role in gel formation. It must provide the correct solubility/insolubility balance toward the gelator so that the latter is dissolved or dispersed at high temperatures and is sufficiently insoluble when the organic solution/suspension is cooled such that the gelator molecules self-assemble into aggregates or otherwise associate. We tested a number of solvents by incubating the gelator (10% w/v) in the solvent at 60 °C for 0.5 h and then cooling by standing at room temperature. Sorbitan monostearate gels alkanes (C > 5), e.g., hexane, cyclohexane, octane, decane, *cis*- and *trans*-decalins, dodecane, tetradecane, hexadecane, octadecane, the alkene squalene, vegetable oils, e.g., corn oil, sesame seed oil, olive oil, cottonseed oil, and the long-chain synthetic esters, isopropyl myristate, ethyl oleate, and ethyl myristate.

The ungellable solvents include the more polar alkanols, ethanol, 2-propanol, and butanol, and chloroform and dichloromethane, which dissolve sorbitan monostearate (10% w/v) on heating, but which allow the sorbitan ester to precipitate on cooling. Benzene and toluene proved to be too good solvents in which the surfactants do not gel.

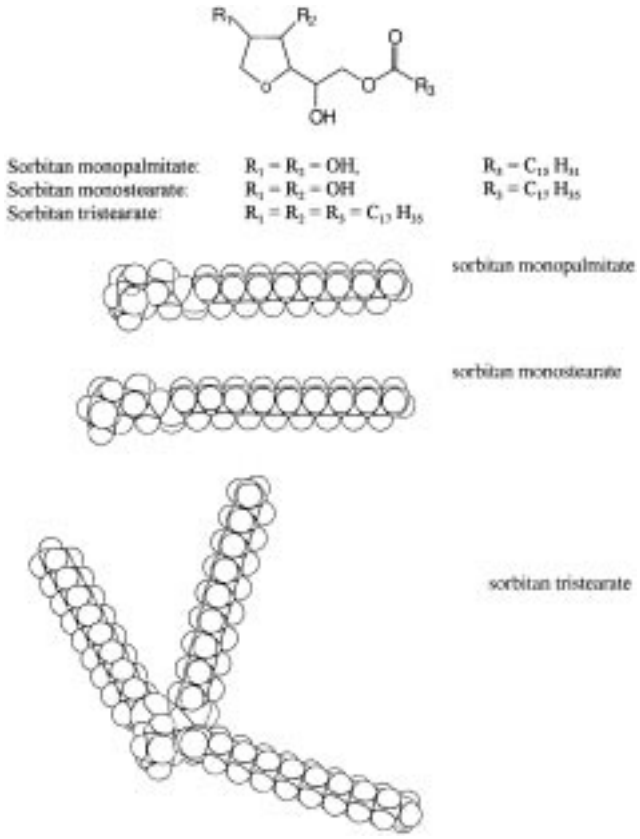

Scheme 1—Structures and Space-Filling Models of Some Sorbitan Ester Surfactants

Gelation Temperature—The gelation temperature of a hexadecane gel containing 10% w/v sorbitan monostearate was found to be 41−44 °C by differential scanning calorimetry. This relatively broad gelation temperature range is typical of physical organogels, involving the rupture of the junctions between aggregates and dissolution of the surfactant aggregates as the temperature rises, causing a corresponding increase in the surfactant solubility in the solvent. The melting point of the solid sorbitan monostearate is 51 °C. A melting point of the neat gelator higher than that of the gel seems to be a universal property of organogels. The organogel is thermoreversible, i.e., it melts on heating to the sol phase which can once again be gelled upon cooling. Heating and cooling cycles can be repeated a number of times without any appreciable change in gel properties.

Gelling Concentration—Sorbitan monostearate gels hexadecane at concentrations as low as 1% w/v (0.02 M). At this concentration, 170 solvent molecules are immobilized by each surfactant molecule. At lower concentrations, e.g., 0.2% w/v, a white fibrous gel mass is formed within the hexadecane solvent. The fibrous mass within the solvent becomes denser with increasing surfactant concentration until all the hexadecane is gelled. An increase in surfactant concentration was expected to cause a gradual increase in the viscosity of the bulk sample due to an isotropic dispersion of the increasing number of aggregates in the solvent until gelation occurred at the critical gelling concentration. It seems however, that aggregate−aggregate interactions are stronger than solvent−aggregate affinities, resulting in a preferential ordered flocculation of aggregates to form a three-dimensional network within the solvent. The surfactant network, anisotropically dispersed in the solvent, is then able to gel only that part of the solvent, and a fibrous gel mesh is observed within the

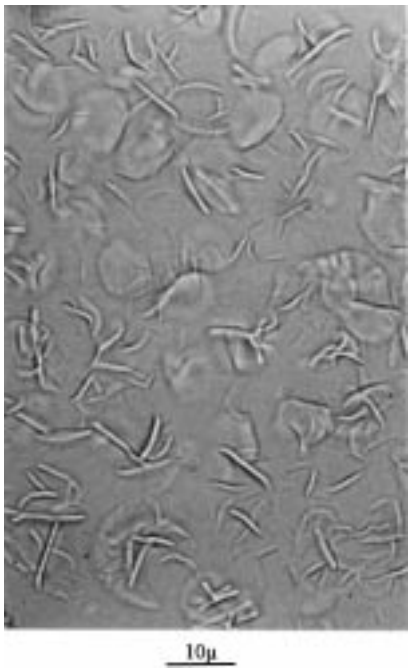

Figure 1—Organogel microstructure: tubular aggregates formed by the self-assembly of sorbitan monostearate molecules in hexadecane solvent.

excess solvent. The excess solvent is defined here as the fluid not gelled by the surfactant network.

This partial gelation within the excess solvent was most strikingly apparent in hexadecane. Other solvents such as isopropyl myristate, decane, corn oil, and squalene showed the anticipated isotropic dispersion of surfactant aggregates and a gradual increase in viscosity with increasing surfactant concentration until all the solvent was gelled. This difference in the gelation phenomenon with insufficient amounts of gelator, reflects the importance of the solvent, which influences the attractive forces between the gelator aggregate structures. In hexadecane, aggregate–aggregate interactions are maximized so that the aggregates join to form a meshwork which immobilizes part of the solvent. In other solvents, e.g., isopropyl myristate, the aggregate–aggregate interactions required for entanglement and formation of a three-dimensional network seem to be less favored, probably because of stronger solvent–aggregate attractions. The latter promote an isotropic dispersion of gelator aggregates in the solvent and consequently a progressive increase in the sample viscosity is observed upon increasing the sorbitan monostearate concentration until the critical gelling concentration is reached.

Gel Microstructure—Light microscopy of the organogels has revealed the surfactant aggregates to be rodlike tubules (Figure 1). The aggregates associate with others through contact points and a three-dimensional network is established which immobilizes the solvent. Figure 2 shows examples of gel networks in different solvents. The three-dimensional network acts as the gel skeleton. The importance of the contact points between tubules is seen when small amounts of ethanol are added to a gel sample. The contact points are disrupted with a consequent loss of the gel state even though tubules are still present.

Events Occurring at Gelation—In an attempt to understand the formation of tubular aggregates, the gelation process was followed microscopically as a hot suspension of sorbitan monostearate in isopropyl myristate was slowly cooled using a hot-stage. As the suspension cools and the solvent–surfactant affinities decrease, doughnut shaped, membrane-bound, inverse toroidal vesicular structures are seen to form as the sorbitan monostearate surfactant

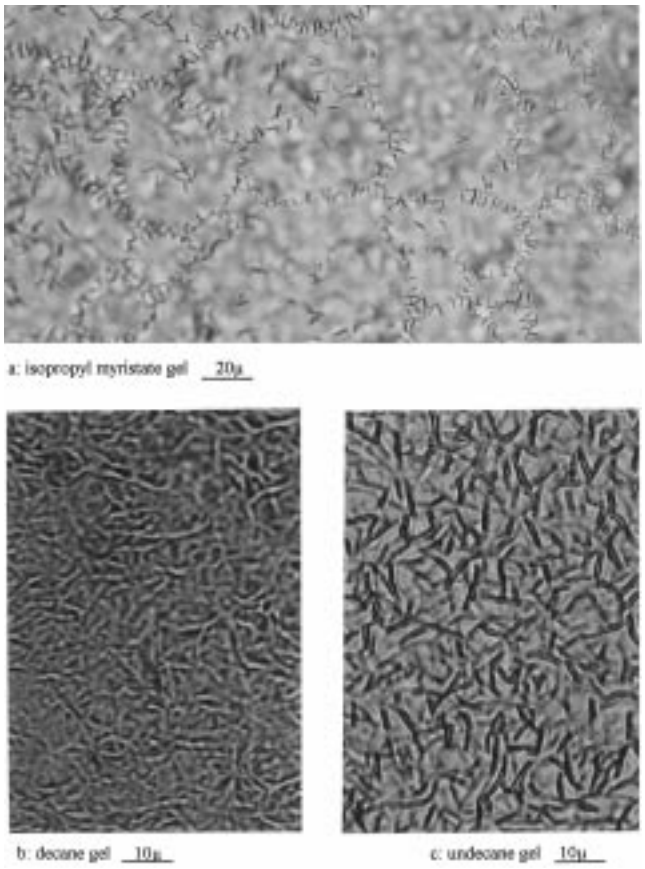

Figure 2—Examples of gel networks in different solvents.

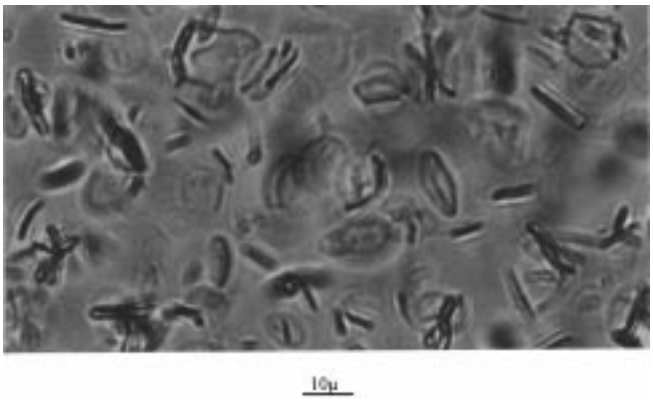

Figure 3—A photomicrograph of an isopropyl myristate formulation at the transition temperature between sol and gel phases. A number of toroidal vesicular structures can be seen.

molecules self-assemble. These toroidal vesicles (Figure 3) are in constant motion about their axis. Using a high-speed camera, one of the toroidal vesicles was photographed in quick succession as it rotated about its axis (Figure 4), and the toroidal rather than spherical shape of the vesicle was confirmed.

The toroids are short-lived structures, existing only at the gelation temperature (44–41 °C). Further cooling results in their conversion into tubules. The mechanism of such a change is not understood at present. The toroid might contract into a more tubular shape or it might split into one or more cylindrical segments, giving rise to the tubules seen in Figure 1. The latter structures are believed to be tubular and not toroidal vesicles lying perpendicular to the plane of the micrograph as the probability that all the toroidal vesicles would lie at such an angle is rather small.

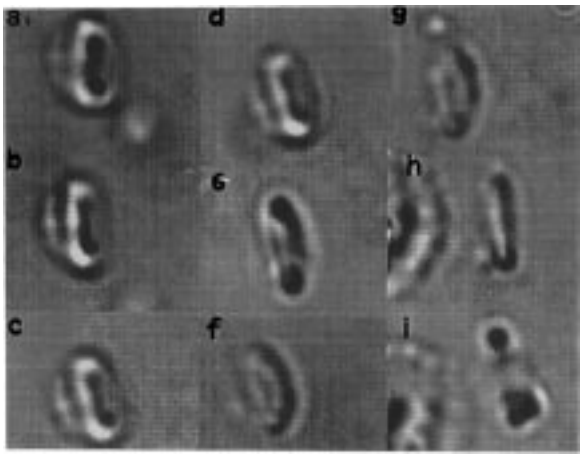

Figure 4—One of the inverse toroidal vesicular structures seen in Figure 3 was photographed in rapid succession as it rotated about its axis.

Formation of the surfactant aggregates is followed by random association between the aggregates and the establishment of junction points. The sequential pictures in Figure 5 obtained from a video recording of gelation demonstrates the migration of one aggregate to join another. From the sequential stills, the aggregate–aggregate interaction seems to be an active process, probably due to relatively strong forces of attraction between the surfactant assemblies and an overall negative energy change. Extensive joining of individual tubules finally creates a three-dimensional network which acts as the skeleton, "holds" the solvent, and forms the gel. Such flocculation of the surfactant aggregates and the obvious attractive forces among them (most clearly seen in Figures 2a and 5) suggest the existence of long-range forces of attraction in the system and provides another example of how large structures "seem to recognize each other's presence at rather great distances" as suggested by Adamson.[26] Further work is required to be done to more fully understand the energetics of gel formation.

Ultrastructure of Tubules and the Possible Molecular Organization of Surfactant Molecules—The toroids most probably consist of bilayers of surfactant molecules, in a fashion similar to other well-known vesicles—liposomes and niosomes. The difference lies in their toroidal shape and the inverted nature of the bilayers. Preferential self-assembly of surfactant molecules into toroidal vesicles may be due to the reduced membrane curvature required in toroids. Figure 6 shows a diagrammatic representation of such a toroidal vesicle consisting of surfactant bilayers. Assuming this surfactant organization is retained upon gelation, the tubules present in the gel would also consist of concentric sheets of bilayers (Figure 6). A bilayer organization of surfactant molecules in the tubules is suggested by X-ray diffraction measurements on a sorbitan monostearate/hexadecane gel, which show peaks corresponding to distances 5.9 and 0.4 nm. These distances relate to the bilayer thickness and the distance between two adjacent surfactant tails, respectively, as shown in Figure 6. These values agree with the corresponding to theoretical calculated distances (using Quanta and CHARMm software), which are 5.91 and 0.46 nm, respectively, assuming close packing of the surfactant molecules in the bilayers. Such an arrangement of the amphiphiles ensures the solvophobic headgroups are shielded from the organic solvent.

Gel Stability—The two markers of gel stability normally used are gelation temperature and gel lifetime. Gelation temperature usually increases with gelator concentration and is dependent on the solvent. The gel lifetime is the

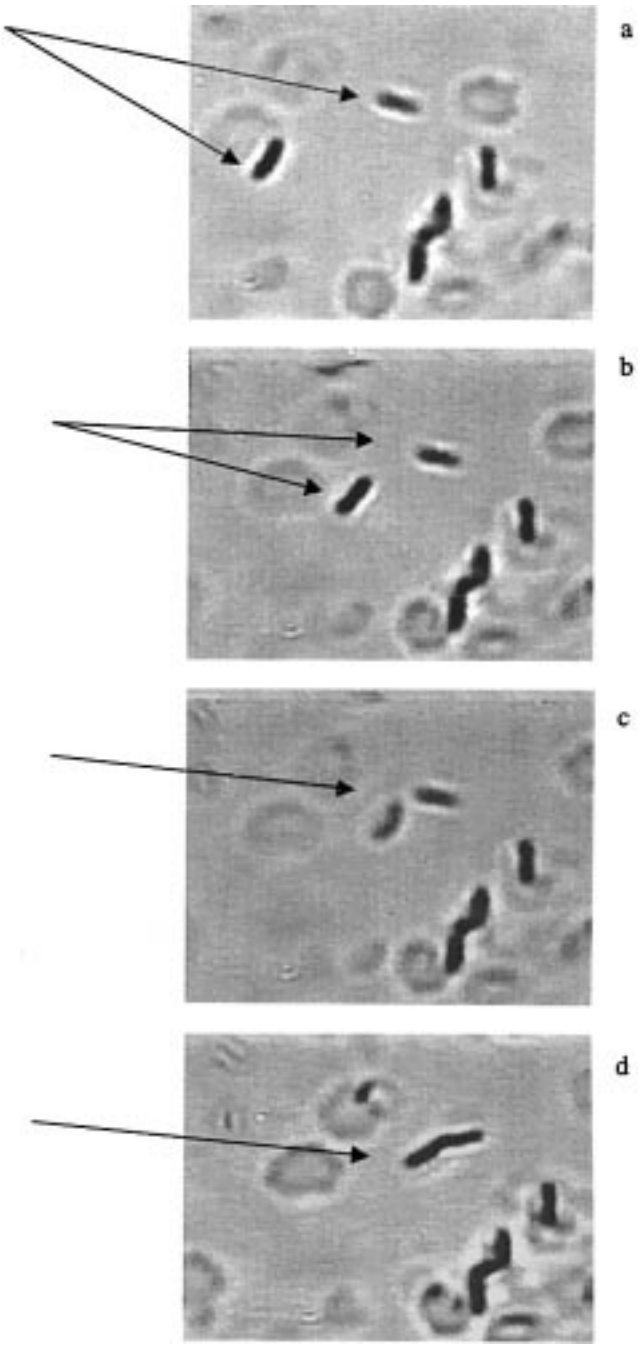

Figure 5—Sequential micrographs (a–d) show the migration of one surfactant aggregate to join another in the formation of the three-dimensional network.

length of time a gel remains intact when stored in sealed vessels at room temperature, without syneresis (the separation of the solid and liquid components). Like gelation temperature, the gel lifetime depends on gelator concentration and the solvent. A hexadecane gel containing 10% w/v sorbitan monostearate remains intact for a few weeks before syneresis occurs. Hexadecane gels also have a longer lifetime compared to isopropyl myristate and vegetable oil gels.

Gel stability was found to be drastically altered when small amounts of a second nonionic surfactant, polysorbate 20, was included in the formulation.

The Influence of Polysorbate Additives on Sorbitan Monostearate Gels—Small amounts of polysorbate 20 (Tween 20), a hydrophilic nonionic surfactant (HLB 16.7), was included in a sorbitan monostearate/hexadecane organogel when the latter was used as the continuous

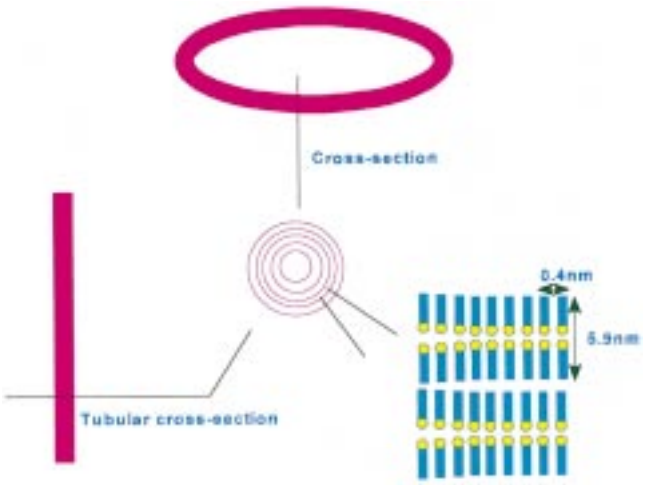

Figure 6—Diagrammatic representations of a surfactant tubule, its precursor, an inverse toroidal vesicle and the aggregates' cross-section. A segment of the cross-section has been magnified to show the suggested surfactant organization, i.e., inverse bilayers.

external oil phase in the formation of multiple emulsions.[24] It was anticipated that the addition of the hydrophilic polysorbate 20 would stabilize the emulsion due to the formation of mixed surfactant films at the w/o interface. This was indeed realized. Addition of polysorbate 20 also had interesting effects on the gel lifetime and stability.

Polysorbate 20 seems to enhance the solubility of sorbitan monostearate in hexadecane, such that a sorbitan monostearate/polysorbate 20/hexadecane system is a clear, transparent solution at 60 °C (compared to a slightly turbid suspension in the absence of polysorbate 20). The enhanced solubility is probably mediated via the formation of mixed inverse micelles of the two surfactants in the hexadecane solvent at high temperatures.

The transparent mixed surfactant solution cools to a semisolid, opaque gel which is similar in appearance to the gel without polysorbate 20. The gel lifetime and stability is, however, drastically improved. Hexadecane gels spiked with polysorbate 20 were found to be stable for months (compared to weeks in the absence of polysorbate 20) at room temperature without syneresis. Penetrometer studies also showed a slight increase in gel consistency upon the addition of polysorbate 20 (unpublished results). Such an enhanced gel stability seems to be a direct result of the enhanced solubility in the system described above. Inclusion of polysorbate 20 in hexadecane gel moves the solubility toward the optimum level required for stable gel formation.

This solubility-enhancing effect of polysorbate 20, is, however, not universal: solubility was enhanced in some solvents, but it was reduced in others. An enhanced solubility is always followed by improvement in gel lifetime and stability. Polysorbate 20 reduces the solubility of sorbitan monostearate in the shorter chain alkanes (C < 14) with consequent deterioration of the gels, as evidenced by syneresis. Polysorbate 20 has no effect in tetradecane. The solubility of sorbitan monostearate is increased in longer chain hydrocarbons, e.g., hexadecane, octadecane, and squalene, with a consequent enhancement of the gel formed. The long chain esters, ethyl oleate, isopropyl myristate, and ethyl myristate, and the vegetable oils also show an enhancement of the gel upon the addition of polysorbate 20. Table 1 recapitulates these findings. The key feature seems to be the size of the solvent molecule: a relatively large size or a long hydrocarbon chain seems to be required for polysorbate 20 to exert a beneficial effect on solubility and gelation. It is unclear at present why this should be so.

Table 1—The Effects of Polysorbate 20 on the Solubility of Sorbitan Monostearate in Hot Solvents (60 °C) and on the Resulting Gels

solvent	effects of polysorbate 20 on the solubility of sorbitan monostearate	effect of polysorbate 20 on gel lifetime and stability: enhancement (↑) or deterioration (↓)
hexane	↓	↓
cyclohexane	↓	↓
octane	↓	↓
isooctane	↓	↓
cis-decalin	↓	↓
trans-decalin	↓	↓
decane	↓	↓
dodecane	↓	↓
tetradecane	no effect	no effect
hexadecane	↑	↑
octadecane	↑	↑
squalene	↑	↑
ethyl oleate	no effect	↑
isopropyl myristate	no effect	↑
ethyl myristate	no effect	↑
cottonseed oil	no effect	↑
soybean oil	no effect	↑
sesame oil	no effect	↑
corn oil	no effect	↑
olive oil	no effect	↑

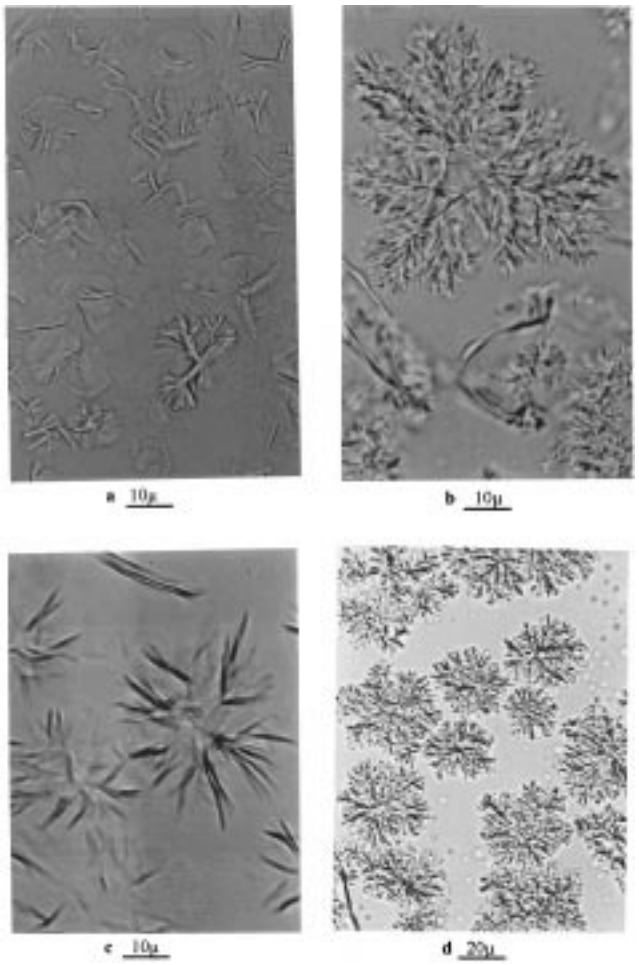

Figure 7—Microstructures of sorbitan monostearate gels: (a) absence of polysorbate surfactant, (b) + polysorbate 20, (c) + polysorbate 60, and (d) + polysorbate 80.

Gel microstructure is affected by the inclusion of polysorbate 20. Gels spiked with the hydrophilic surfactant comprise star-shaped "clusters" of surfactant tubules in the

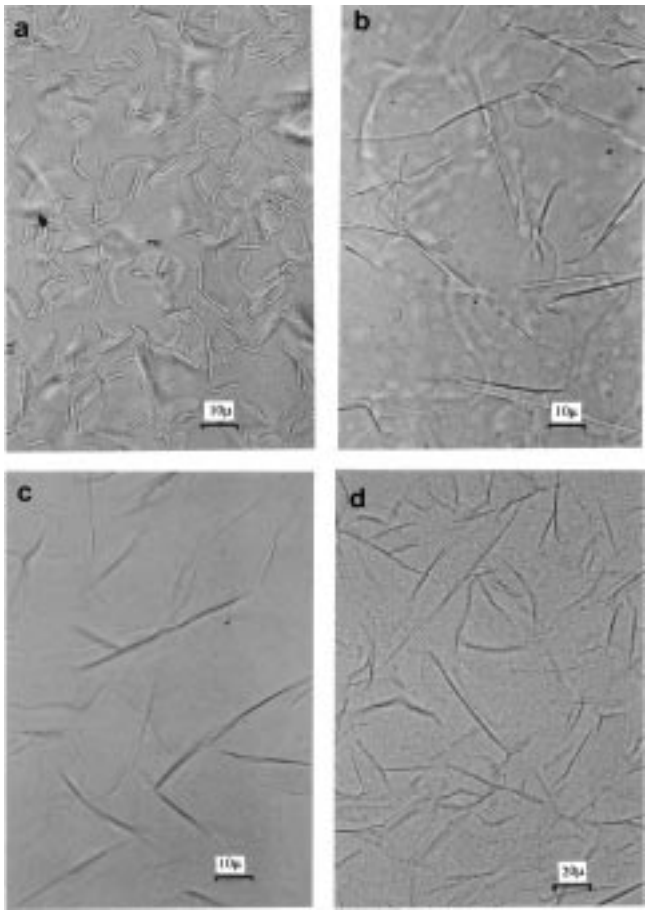

Figure 8—Microstructures of sorbitan monopalmitate gels: (a) absence of polysorbate surfactant, (b) + polysorbate 20, (c) + polysorbate 60, and (d) + polysorbate 80.

organic medium (Figure 7). On cooling a hot solution, these "clusters" were found to grow as an entity, rather like the opening of a clenched fist. The polysorbate 20 molecules are thought to become incorporated into the inverted surfactant bilayers and thus into the tubular aggregates.

The other polysorbates tested, polysorbate 40, 60, and 80 showed similar effects to polysorbate 20 in hexadecane gels. The solubility of sorbitan monostearate in hexadecane was enhanced, presumably due to the formation of mixed inverse micelles and the resulting more stable gels resulted from star-shaped clusters of surfactant tubules (Figure 7). The triesters, polysorbates 65 and 85, do not affect the solubility of sorbitan monostearate in hexadecane. It is possible that their large size and shape do not allow mixed micelle formation, and thus the solubility of the gelator is not enhanced.

The Gelling Abilities of Other Sorbitan Esters—To determine the key properties of sorbitan monostearate as an organogelator, other members of the sorbitan ester family which are in the solid state at room temperature, namely, sorbitan monopalmitate (Span 40) and sorbitan tristearate (Span 65), were investigated for any gelling ability. Sorbitan monopalmitate was found to gel hexadecane. The thermoreversible gel obtained is similar in appearance to sorbitan monostearate gel described, i.e., it is opaque, semisolid, with a smooth silky "feel" and the microstructure comprises rodlike tubular aggregates (Figure 8a). When gelation was followed using hot-stage microscopy, the surfactant tubules were found to be formed from toroidal vesicular precursors as described above for sorbitan monostearate.

Sorbitan tristearate does not gel hexadecane, but crystallizes out on cooling the hexadecane. The conical shape of the triester (Scheme 1) is not conducive to the formation of bilayers and thus tubule formation. Reports on vesicle formation by sorbitan tristearate in aqueous media could not be found in the literature. On the other hand, the cylindrical shape (Scheme 1) of the sorbitan monoesters (monostearate and monopalmitate) seems to allow molecular packing in bilayers such that the surfactant molecules can assemble into tubular aggregates responsible for gelation.

Sorbitan monopalmitate gels are less stable than the stearate gels at 10% w/v gelator concentration. Gelation temperature is lower, and syneresis occurs at a faster rate. As in the case of monostearate gels, the addition of polysorbate monoesters (polysorbates 20, 40, 60, and 80) increases the solubility of sorbitan monopalmitate in hexadecane, presumably via the formation of mixed inverse micelles, with consequent enhanced gel stability. The effects on the microstructures of the palmitate gels were, however, very different: the tubular length was drastically increased when the gels were spiked with polysorbates (Figure 8). These long tubules were formed from large toroidal vesicular precursors generated at the gelation temperature. Why the polysorbates have such widely different effects on the two sorbitan esters which only differ in their hydrocarbon chains by a C_2H_4 group remains to be solved.

References and Notes

1. Hermans, P. H. Reversible Systems. In *Colloid Science*; Kruyt, H. R., Ed.; Elsevier: Amsterdam, 1969; Vol II, pp 483−651.
2. Terech, P. 12-d-hydroxyoctadecanoic acid organogels − a small angle neutron scattering study. *J. Phys. II* **1992**, *2*, 2181−2195.
3. Terech, P. Structure of nonionic rodlike surfactant aggregates in apolar solvents − study of the influence of the nature of the solvent in steroid hydrocarbon organogels. *J. Phys.* **1989**, *50*, 1967−1982.
4. Aoki, M.; Nakashima, K.; Kawabata, H.; Tsutsui, S.; Shinkai, S. Molecular design and characterisations of new calixarene-based gelators of organic fluids. *J. Chem. Soc., Perkin Trans. 2* **1993**, 347−354.
5. Yamasaki, S.; Tsutsumi, H. The dependence of the polarity of solvents on 1,3/2,4-di-o-benzylidene-d-sorbitol gel. *Bull. Chem. Soc. Jpn*. **1995**, *68*, 123−127.
6. Lin, Y.; Kachar, B.; Weiss, R. G. Novel family of gelators of organic fluids and the structure of their gels. *J. Am. Chem. Soc.* **1989**, *111*, 5542−5551.
7. Scartazzini, R.; Luisi, P. L. Organogels from lecithins. *J. Phys. Chem*. **1988**, *92*, 829−833.
8. Xu, X. D.; Ayyagari, M.; Tata, M.; John, V. T.; McPherson, G. L. Formation of novel organogels by the addition of phenols to AOT micelles in isooctane. *J. Phys. Chem*. **1993**, *97*, 11350−11353.
9. Haering, G.; Luisi, P. L. Hydrocarbon gels from water-in-oil microemulsions. *J. Phys. Chem*. **1986**, *90*, 5892−5895.
10. Terech, P.; Bouas-Laurent, H.; Desvergne, J. P. Small molecular luminescent gelling agent 2,3-bis-*n*-decyloxyanthracene: rheological and structural study. *J. Colloid Interface Sci.* **1995**, *174*, 258−263.
11. Murata, K.; Aoki, M.; Suzuki, T.; Harada, T.; Kawabata, H.; Komori, T.; Ohseto, F.; Ueda, K.; Shinkai, S. Thermal and light control of the sol−gel phase transition in cholesterol-based organic gels. Novel helical aggregation modes as detected by circular dichroism and electron microscopic observation. *J. Am. Chem. Soc*. **1994**, *116*, 6664−6676.
12. Hinze, W. L.; Uemasu, I.; Dai, F.; Braun, J. M. Analytical and related applications of organogels. *Curr. Opin. Colloid Interface Sci.* **1996**, *1*, 502−513.
13. Petit, C.; Pileni, M. P. Synthesis of cadmium sulfide in situ in reverse micelles and in hydrocarbon gels. *J. Phys. Chem*. **1988**, *92*, 2282−2286.
14. Backlund, S.; Eriksson, F.; Hedstrom, G.; Laine, A.; Rantala, M. Lipase-catalyzed enantioselective esterifications using different microemulsion-based gels. *Colloid Polym. Sci*. **1996**, *274*, 540−547.

15. De Jesus, P. C.; Rezende, M. C.; Nascimento, M. G. Enzymatic resolution of alcohols via lipases immobilised in microemulsion-based gels. *Tetrahedron: Asymmetry* **1995**, *6*, 63−66.
16. Jenta, T. R. J.; Batts, G.; Rees, G. D.; Robinson, B. H. Biocatalysis using gelatin microemulsion-based organogels containing immobilized chromobacterium viscosum lipase. *Biotechnol. Bioeng.* **1997**, *53*, 121−131.
17. Nascimento, M. G.; Rezende, M. C.; Vecchia, R. D.; de Jesus, P. C.; Aguiar, L. M. Enzyme-catalysed esterifications in microemulsion-based organo gels. *Tetrahedron Lett.* **1992**, *33*, 5891−5894.
18. Scartazzini, R.; Luisi, P. L. Reactivity of lipase in an optically transparent lecithin-gel matrix. *Biocatalysis* **1990**, *3*, 377−380.
19. Stamatis, H.; Xenakis, A.; Provelegiou, M.; Kolisis, F. N. Esterification reactions catalyzed by lipases in microemulsions -the role of enzyme localization in relation to its selectivity. *Biotech. Bioeng.* **1993**, *42*, 103−110.
20. Crecchio, C.; Ruggiero, P.; Pizzigallo, M. D. R. Polyphenoloxidases immobilised in organic gels: properties and applications in the detoxification of aromatic compounds. *Biotechnol. Bioeng.* **1995**, *48*, 585−591.
21. Willimann, H.; Walde, P.; Luisi, P. L.; Gazzaniga, A.; Stroppolo, F. Lecithin organogel as matrix for transdermal transport of drugs. *J. Pharm. Sci.* **1992**, *81*, 871−874.
22. Seeboth, A.; Wustneck, R.; Kragel, J. Gel dispersed liquid-crystals. *Colloid Polym. Sci.* **1994**, *272*, 1151−1156.
23. Yoshioka, T.; Florence, A. T. Vesicle (niosome)-in-water-in-oil (v/w/o) emulsions: an in vitro study. *Int. J Pharm.* **1994**, *108*, 117−123.
24. Murdan, S.; Gregoriadis, G.; Florence, A. T. Nonionic surfactant based organogels incorporating niosomes. *STP Pharma Sci.* **1996**, 44−48.
25. Murdan, S. Nonionic surfactant based organogels: properties and potential as immunoadjuvants, 1998, Ph.D. Thesis, School of Pharmacy, University of London.
26. Adamson, A. W. The gentle force of entropy. *Science* **1998**, *280*, 655−657.

Acknowledgments

The authors thank Colin James and David McCarthy for assistance and Jeremy Cockcroft, Department of Crystallography, Birkbeck College, for carrying out the X-ray diffraction measurements.

JS980342R

Water-in-Sorbitan Monostearate Organogels (Water-in-Oil Gels)

SUDAXSHINA MURDAN,[†] BENEDICTE VAN DEN BERGH,[‡] GREGORY GREGORIADIS,[†] AND ALEXANDER T. FLORENCE*,[†]

Contribution from *Centre for Drug Delivery Research, School of Pharmacy, University of London, 29-39 Brunswick Square, London, WC1N 1AX, United Kingdom, and Leiden Amsterdam Centre for Drug Research, Gorlaeus Laboratories, Leiden University, Einsteinweg 55, P.O. Box 9502 2300RA, Leiden, The Netherlands.*

Received August 17, 1998. Final revised manuscript received December 16, 1998.
Accepted for publication March 2, 1999.

Abstract □ Novel multicomponent organogels containing an aqueous phase are described, and some properties which influence their potential as delivery devices for hydrophilic drugs and vaccines are discussed. The gel is produced by preparing a hot water-in-oil (w/o) emulsion using sorbitan monostearate, a nonionic surfactant which is also the organogelator, as the principal emulsifying agent. On cooling at room temperature, the w/o emulsion sets to an opaque, semisolid, thermoreversible organic gel. Cooling the emulsion results in a reduced solubility of the sorbitan monostearate in the oil, with a corresponding decrease in solvent–surfactant affinities, causing surfactant self-assembly into aggregates. The microstructure of the w/o gel is seen by light microscopy to consist of a network of tubules and fibrils (containing the aqueous phase) dispersed in the organic medium. X-ray diffraction and freeze-fracture studies suggest that the tubular aggregates in the w/o gel are made up of surfactant molecules arranged in inverted bilayers and that the aqueous phase is accommodated within these inverted bilayers, bound by the polar headgroups of the surfactant molecules. The presence of water in the tubular skeleton of the organic gels results in the establishment of percolating electroconductive aqueous channels in the organogel. Increasing the water content of a w/o gel causes the surfactant tubules to swell with a corresponding increase in conductivity until the tubules are saturated. Further increase in the water content results in the excess water accumulating in droplets within the organic medium and a decrease in conductivity as the gel integrity is compromised. The w/o gels (containing a model antigen, radiolabeled bovine serum albumin, in the aqueous phase) have demonstrated depot properties after intramuscular administration to mice, entrapped antigen being released over a period of days.

Introduction

Interest in organic gels has increased, and a number of applications of these nonaqueous systems are being investigated.[1] Examples include transdermal drug delivery devices,[2] biosynthetic media,[3−8] moisture sensors,[9,10] synthetic templates,[11] purification and separation media,[12] and carriers for liquid crystals.[13] We previously reported the gelation of organic solvents by the nonionic surfactant, sorbitan monostearate.[14] These are opaque, thermoreversible semisolids whose microstructures consist of interconnected tubular aggregates, which, as suggested by freeze-fracture and X-ray diffraction measurements, are assemblies of the gelator molecules arranged in bilayers.[15]

The nonionic surfactant-based organogels, comprising pharmaceutically acceptable excipients (sorbitan monostearate, polysorbate 20, and a biodegradable oil, e.g., isopropyl myristate) may have potential as delivery devices for hydrophobic and hydrophilic drugs and vaccines. The hydrophobic active entity can be dissolved or dispersed in the sol phase at high temperatures before gel formation on cooling. This ensures a homogeneous distribution of the active ingredient in the organogel. A hydrophilic substance (dissolved in an aqueous medium) may also be incorporated in the organogel, by adding the aqueous phase to the organic solution at high temperatures (60 °C). A water-in-oil (w/o) emulsion is thus produced, where discrete aqueous droplets, bounded by surfactant films, are dispersed in the continuous external oil phase. On cooling, the w/o emulsion is converted to the gel state i.e., a w/o organogel is produced. We have previously reported the preparation of organogels where the aqueous phase was a niosome suspension, such that a vesicle-in-water-in-oil (v/w/o) gel is produced.[14,16] An active agent such as dissolved or suspended drug or antigen can thus be delivered in vivo within a nonaqueous medium. The latter may present a barrier to the diffusion of the active after in vivo administration, and it was speculated that a w/o gel may act as an intramuscular/subcutaneous depot for hydrophilic drugs and vaccines. In turn, the addition of the aqueous phase alters the organic gel. In this paper we report on the effects of the addition of an aqueous phase on sorbitan monostearate organogels. The gelation mechanism, the location of the aqueous phase in the w/o gel, and the maximum amount of aqueous phase which can be incorporated in the gel are explored. The in vivo release rate of a model hydrophilic antigen from a w/o gel was investigated, and an aqueous solution and a w/o emulsion (liquid state) were used as controls.

Materials and Methods

Sorbitan monostearate, 5,6-dicarboxyfluorescein, and bovine serum albumin (BSA) were purchased from Sigma (UK) while polysorbate 20, hexadecane (analytical grade), and isopropyl myristate (analytical grade) were from Fluka (UK). ^{125}I used to radiolabel BSA was from Amersham Pharmacia Biotech (UK). All were used as received, except for hexadecane and isopropyl myristate which were dried at room temperature overnight in a vacuum oven (Gallenkemp, UK) to ensure the absence of moisture which might affect gelation. Ultrahigh quality (double distilled) water was used throughout. In-bred male Balb/c mice (weighing approximately 20 g) were from Bantin & Kingman, Hull, UK.

Organogel Preparation—Sorbitan monostearate (10% w/v) and polysorbate 20 (2% w/v) were weighed into a vial, and the organic solvent (hexadecane or isopropyl myristate) was added. The mixture was heated to 60 °C in a water-bath and a transparent organic solution was produced. After the latter sol was cooled at room temperature, an opaque, thermoreversible semisolid gel was obtained.

Preparation of w/o Gel—The aqueous phase (water/5,6-dicarboxyfluorescein solution/radiolabeled bovine serum albumin solution) was added dropwise to the oil phase (the gel prepared

* Corresponding author. Tel: 0171 753 5819. Fax: 0171 837 5092. E-mail: a.t.florence@ulsop.ac.uk.
[†] University of London.
[‡] Leiden University.

10.1021/js980343j CCC: $18.00 Published on Web 04/21/1999

above) while vortexing, both phases being at 60 °C. A w/o emulsion was obtained. On cooling at room temperature, the w/o emulsion gelled to an opaque, thermoreversible semisolid.

Preparation of w/o Emulsion—The aqueous phase (radiolabeled bovine serum albumin solution) was added dropwise to the oil phase (10% w/v sorbitan monooleate + 2% w/v polysorbate 20 in isopropyl myristate) while vortexing, both phases being at 60 °C. A water-in-oil (w/o) emulsion was obtained.

Light Microscopy—A light microscope (Nikon Microphot-FXA, Japan) with an attached camera (Nikon, FX-35DX, Japan) and a hot-stage (Linkam TC 93, UK) was used to analyze the gel microstructures.

X-ray Diffraction Studies—X-ray data on hexadecane organogels were collected on a Siemens D500 diffractometer (in the Department of Crystallography, Birkbeck College) equipped with a copper tube and a quartz primary-beam monochromator giving a wavelength $\lambda = 1.54056$ Å. The X-ray tube was run at 45 kV and 30 mA. Samples were mounted in a flat-plate specimen holder and flattened with a glass microscope slide. The sample was spun about an axis normal to its flat-plate surface, and diffraction patterns were measured using a scintillation detector. The data were obtained for the 2θ range 1−35° in steps of 0.05° at 10 s per point. A w/o gel containing 48 μL water per milliliter of gel was studied to investigate the effect of the added water on the surfactant organization in the tubular aggregates, and an anhydrous gel was used as control.

Freeze Fracture Investigations—The gel (containing 167 mL water/mL of hexadecane organogel) was sandwiched between copper plates and then quickly frozen using liquid propane (−180 °C). The frozen samples were loaded in a holder under liquid nitrogen, transferred to a Balzers BAF 400, and fractured at −150 °C. The frozen planes were replicated with platinum (2 nm) at an angle of 45° and with carbon (20 nm) from an angle of 90°. The replicas were then cleaned with distilled water, mounted on copper grids, dried, and examined using a transmission electron microscope.

Conductivity Measurements—A Wayne−Kerr conductivity bridge was used to measure the conductance of hexadecane gel samples containing increasing amounts of water. Two carbon electrodes (diameter 5 mm, 5 cm apart) were used while a constant voltage from a DC source was applied. Five conductance readings were taken for each gel sample, and the mean was calculated.

Intramuscular Administration—The presence of a depot property was investigated by measuring the amount of a model radiolabeled antigen, bovine serum albumin (BSA), which remains at the site after intramuscular injection. A biodegradable oil (isopropyl myristate) was used as the organic solvent in the w/o gel. An aqueous radiolabeled BSA solution and a w/o emulsion were used as controls. At time $t = 0$, each group of mice (15 mice/group) was injected intramuscularly with 50 μL of a formulation (each mouse received the same amount of radiolabeled BSA, around 108 Bq). Three mice from each group were killed at different times, t, postinjection, the injected leg was amputated, and the radioactivity in the leg was measured using a mini-γ counter. The count obtained was expressed as a percentage of the initial total radioactivity at time $t = 0$.

The injection technique was very important to ensure reproducibility, especially for the w/o gel; the latter was taken up into a glass syringe when hot and thus in the liquid state. The sol phase was then allowed to cool and set to the gel state (observed visually) before intramuscular administration. Both w/o gel and w/o emulsions were administered using glass syringes; plastic syringes were avoided as their rubber plunger tips absorb the oily vehicle and swell such that the force needed to expel and thus administer syringe contents would be dramatically increased, and the formulation would be altered through loss of oil.

Results and Discussion

Water-in-Oil Gel Formation—A w/o gel is prepared by first forming the w/o emulsion (the sol phase) at high temperatures: the aqueous phase at 60 °C is added dropwise to the oil phase (oil solution of the nonionic surfactants, sorbitan monostearate, and polysorbate 20), while vortexing. A w/o emulsion is produced, where the aqueous droplets, bound by surfactant interfacial films, are dispersed in the continuous external oil phase (Figure 1a). The hydrophilic nonionic surfactant, polysorbate 20, was included in the organosol prior to emulsion preparation, as it increases the gel lifetime[15] and enhances emulsion stability by forming mixed surfactant films with the sorbitan monostearate molecules at the w/o interface. On cooling, the w/o emulsion gels to an opaque, thermoreversible semisolid. Cooling results in a decrease in the solubility of the sorbitan monostearate gelator in the oil and consequently lowered solvent−gelator affinities. As a result, the surfactant molecules self-assemble into tubular aggregates (Figure 1b) which join and interact with one another. Junction points are established (Figure 1b), and a three-dimensional network is formed which immobilizes the oil phase. The fluorescent aggregates in Figure 1b indicate that the aqueous phase (in this case, fluorescent, 5,6-dicarboxyfluorescein solution), previously bound by the surfactant interfacial layer at 60 °C, is incorporated into the surfactant tubules upon gel formation. The w/o gel is physically stable for months at room temperature.

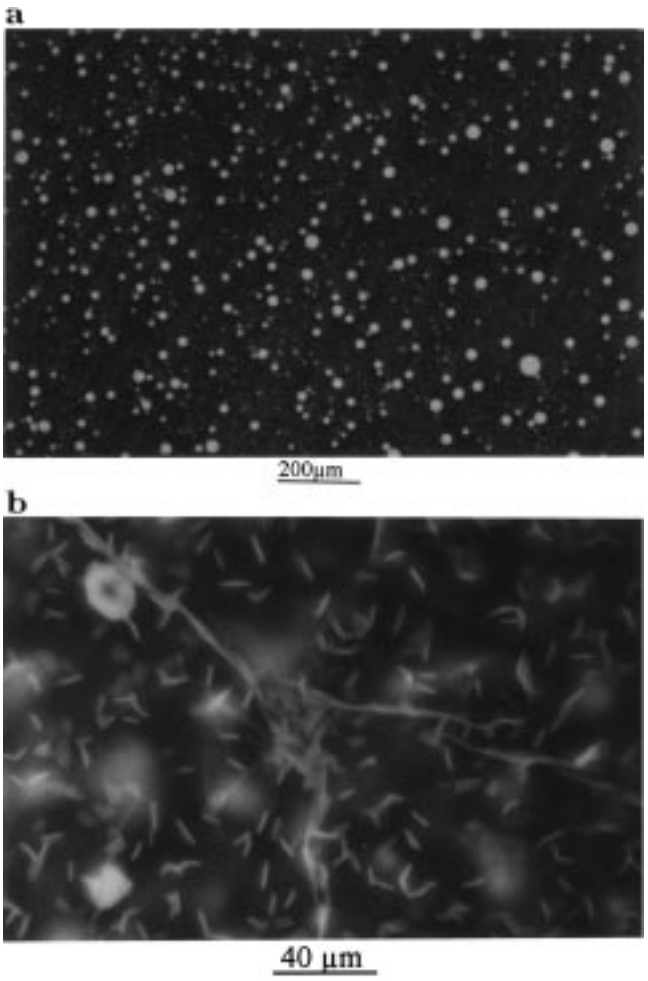

Figure 1—(a) The microstructure of a w/o emulsion at 60 °C: aqueous droplets (fluorescent CF solution) dispersed in the continuous oil phase. (b) The microstructure of a w/o gel at 25 °C: tubules and fibrils incorporating the aqueous fluorescent CF solution in the organic medium. Junction nodes are responsible for the integrity of the gel skeleton.

The w/o gel is thermoreversible: on heating it melts to a liquid w/o emulsion, as an increase in temperature causes a corresponding increase in the gelator solubility in the oil phase and the tubular aggregates disassemble. The w/o emulsion can, in turn, be cooled to the gel state. The gelation temperature (T_g) at which the w/o gel melted to the emulsion was found to be 41−44 °C by hot-stage microscopy.

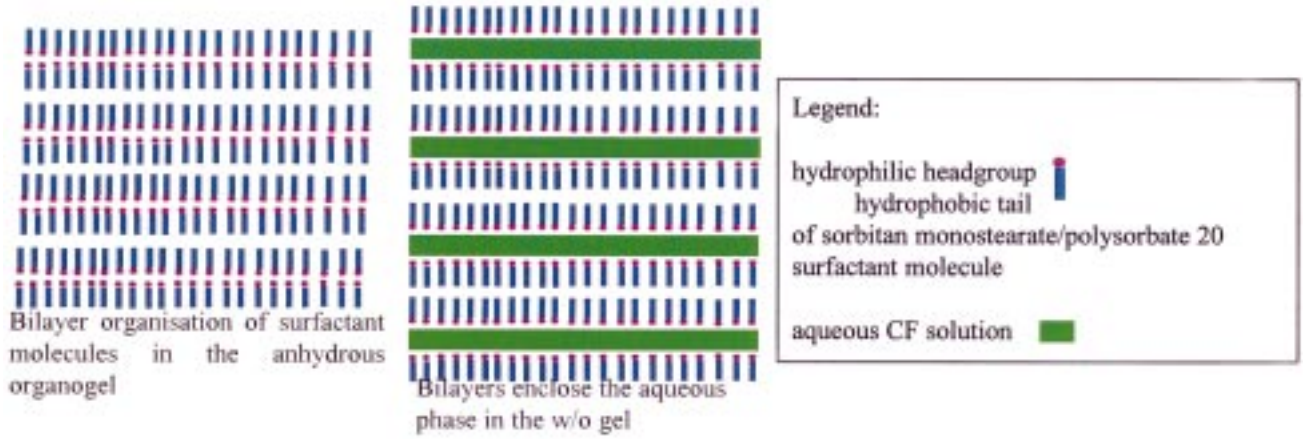

Figure 2—Schematic diagram shows the suggested location of aqueous phase within bilayers, bound by surfactant headgroups. The structures here are highly idealized.

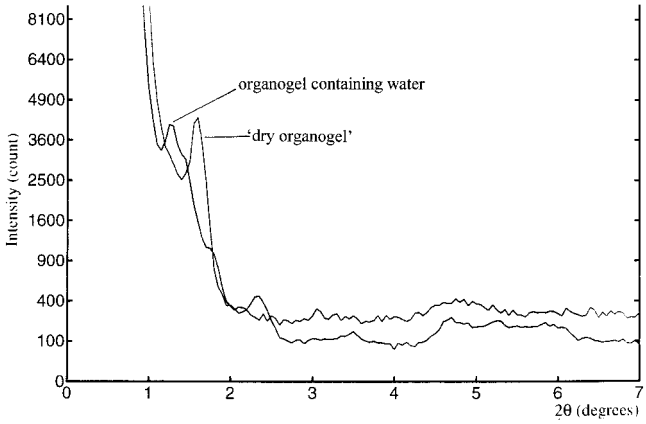

Figure 3—X-ray diffraction measurements show an increase in bilayer width upon the incorporation of an aqueous phase in the organic gel ($\downarrow \theta \equiv \uparrow$ distance).

Location of the Aqueous Phase within Surfactant Tubules—The tubular aggregates in sorbitan monostearate organogels are thought to be composed of surfactant molecules arranged in multiple inverted-bilayers (Figure 2). Such an arrangement was suggested by freeze-fracture investigations which revealed the presence of bilayers, and X-ray diffraction measurements which showed peaks at 5.9 and 0.4 nm. These values (relating to the bilayer width and the distance between two adjacent surfactant molecules, respectively) were found to correlate with the theoretical calculated values, 5.91 and 0.46 nm, obtained using the software QUANTA & CHARm (unpublished results).

Figure 1b shows the aqueous phase to be located within the tubular surfactant aggregates in the w/o organogel. The aqueous phase is most likely accommodated within the surfactant bilayers as schematically shown in Figure 2. The water molecules will also hydrogen bond with the surfactant headgroups, which may further stabilize the w/o gel. The water-in-bilayer hypothesis is supported by X-ray diffraction measurements which show an increased bilayer width, from 5.9 to 6.9 nm when water is incorporated in the gel (Figure 3). Freeze fracture microscopy also shows that the bilayered nature of the organogel is retained in the w/o gel (Figure 4).

Water in Tubules: Effect on Gel Microstructure and Electrical Conductivity—Water-in-oil gels containing increasing amounts of aqueous phase were prepared and examined using light microscopy to determine first the effect on gel microstructure and second, the maximum

Figure 4—Freeze-fracture micrograph shows a bilayered arrangement in a w/o gel sample.

amount of aqueous phase that can be incorporated in sorbitan monostearate/hexadecane organogels. Upon the addition of increasing amounts of water, the star-shaped clusters of surfactant tubules (Figure 5a) break up gradually, initially coexisting with individual tubules until all the clusters break and individual tubules and fibrils are seen in the medium. Further addition of water results in swollen tubules as their bilayers enclose increasing volumes of water (Figure 5b). Swelling of tubules is, however, a limited process as the bilayers can only enclose a certain amount of water while retaining their integrity. Excess water added after the saturation point has been reached, accumulates in droplets, bound by surfactant films (Figure 5, parts c and d). Addition of excessive amounts of water finally results in gel breakdown as aggregate integrity is lost, the surfactant molecules being in interfacial films

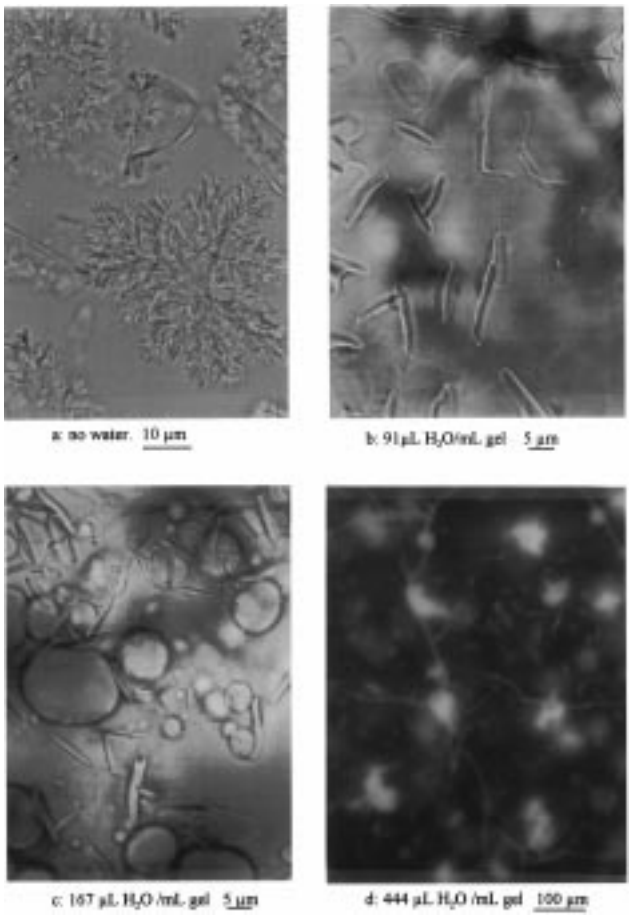

Figure 5—The changing microstructure of the w/o gel containing increasing amounts of water.

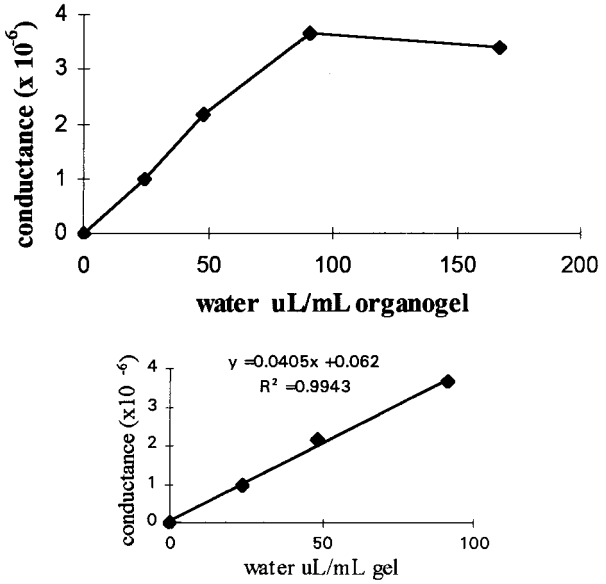

Figure 6—The electrical conductivity (1/Ω) of w/o gels containing increasing amounts of water (μL/mL organogel).

around the water droplets and in monomeric or spherical micellar form in the bulk oil.

The changing microstructures of the w/o gels is reflected in the electrical conductivity changes (Figure 6). The presence of water in the interconnected surfactant tubules results in the establishment of electroconductive aqueous channels in the organic gel. Electrical conductivity increases linearly with increasing amounts of water until a

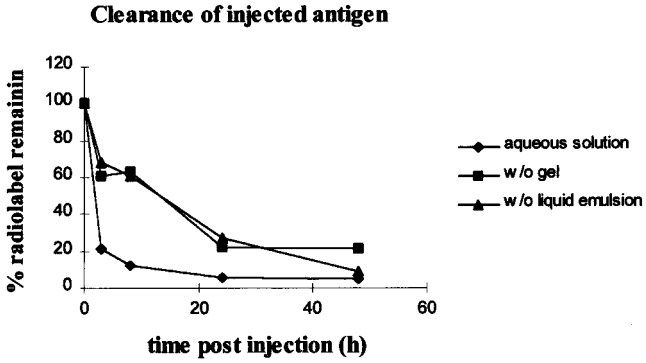

Figure 7—The clearance rates of radiolabeled model antigen after intramuscular administration in a w/o gel and controls, a w/o emulsion, and an aqueous solution.

peak is reached after which the conductivity decreases. The peak lies between 91 and 167 μL of water/mL of organogel and corresponds to the saturation level of water in surfactant bilayers in the tubules. This tallies with the light micrographs in Figure 5 which also indicate a saturation point between 91 and 167 μL water/mL of organogel. After the saturation point is reached, the distorted water droplets containing the excess aqueous phase cause a deterioration of the gel structure and integrity. This interferes with the electrical conductivity of the gel and the latter decreases, as part of the surfactant molecules are involved in interfacial films around the water droplets and fewer surfactant tubules providing aqueous channels are available for electrical conduction.

The Water-in-Oil Gel: A Delivery System for Drugs and Vaccines? The water-in-oil gel is a formulation in which hydrophilic drugs and vaccines may be administered in vivo, in an organic vehicle. Such incorporation may confer certain advantages to the active entity, e.g., the organic gel may present barriers to diffusion, such that after administration, the active entity, incorporated within the surfactant bilayers in the organogel is slowly released from the w/o gel, and a depot effect may be achieved.

To determine any depot effect after intramuscular injection, we measured the clearance rate of a model antigen (bovine serum albumin) administered in a w/o gel to mice. Figure 7 shows the clearance rates (defined as the rate at which injected antigen disappears from the site of injection) of BSA from a w/o gel and from the controls, aqueous solution, and w/o emulsion. After injection of the aqueous BSA solution, almost all the BSA is cleared within 8 h. On the other hand, the w/o emulsion and the w/o gel release the antigen slowly over a period of days. The clearance rate of antigen from the w/o emulsion is similar to that from the w/o gel except at 48 h postinjection, where the w/o gel is superior as a depot. After 48 h, 20% of the injected antigen is still present at the injection site. Gelling of the oil phase, though apparently not important in the initial stages of antigen clearance, seems to confer some advantage in increasing the duration of the antigen at the injection site.

After injection, the organic gel probably remains at the site of injection and assumes, like oils, a pea-shaped depot,[17] unlike aqueous formulations which spread along the muscle fibers. The local interstitial fluid then penetrates into the gel mass via the interconnected tubular network. This invasion of the interstitial fluid into the gel mass slowly breaks down the gel into smaller fragments. At the same time, emulsification occurs at the gel surface between the oil and the interstitial fluid and oil droplets bud off from the gel. The model hydrophilic solute is thus released as the gel slowly breaks into smaller fragments and erodes. This suggested release mechanism is based on

in vitro investigations where an aqueous solution was made to contact with a gel mass. This gel disintegration after administration explains why the depot effect achieved by the organogel is more transient than anticipated. A short depot effect may, however, be sufficient for certain applications, e.g., as immunoadjuvants, where a short depot action is thought to be effective in enhancing the immune response to antigens.[18]

Conclusions

We have reported the gelation of water-in-oil emulsions when a gelator, sorbitan monostearate, is used as the emulsifying agent. The w/o gels are thermoreversible semisolids whose microstructure consists of interconnected tubular aggregates within which the aqueous phase is trapped. The latter aqueous phase is believed to be entrapped within the inverted surfactant bilayers, bound by polar headgroups in the tubules. The presence of water in the surfactant tubules allows electrical conduction through the gel, conductivity being proportional to the aqueous content in the gel. The w/o gels enable the delivery of hydrophilic active entities within an organic medium, and we have demonstrated an in vivo depot over several days, but their longevity is compromised by the access of water to the system by percolation.

References and Notes

1. Hinze, W. L.; Uemasu, I.; Dai, F.; Braun, J. M. Analytical and related applications of organogels. *Curr. Opin. Colloid Interface Sci*. **1996**, *1*, 502−513.
2. Willimann, H.; Walde, P.; Luisi, P. L.; Gazzaniga, A.; Stroppolo, F. Lecithin organogel as matrix for transdermal transport of drugs. *J. Pharm. Sci.* **1992**, *81*, 871−874.
3. Scartazzini, R.; Luisi, P. L. Reactivity of lipase in an optically transparent lecithin-gel matrix. *Biocatalysis* **1990,** *3*, 377−380.
4. Nascimento, M. G.; Rezende, M. C.; Vecchia, R. D.; de Jesus, P. C.; Aguiar, L. M. Enzyme-catalysed esterifications in microemulsion-based organo gels. *Tetrahedron Lett.* **1992**, *33*, 5891−5894.
5. Stamatis, H.; Xenakis, A.; Provelegiou, M.; Kolisis, F N. Esterification reactions catalyzed by lipases in microemulsions -the role of enzyme localization in relation to its selectivity. *Biotech. Bioeng.* **1993**, *42*, 103−110.
6. Rees, G. D.; Jenta, T. R. J.; Nascimento, M. G.; Catauro, M.; Robinson, B. H.; Stephenson, G. R.; Olphert, R. D. G. Use of water-in-oil microemulsions and gelatin-containing microemulsion-based gels for lipase-catalysed ester synthesis in organic solvents. *Indian J. Chem.* **1993**, *32B*, 30−34.
7. De Jesus, P. C.; Rezende, M. C.; Nascimento, M. G. Enzymatic resolution of alcohols via lipases immobilised in microemulsion-based gels. *Tetrahedron Asymmetry* **1995**, *6*, 63−66.
8. Jenta, T. R. J.; Batts, G.; Rees, G. D.; Robinson, B. H. Biocatalysis using gelatin microemulsion-based organogels containing immobilized chromobacterium viscosum lipase. *Biotechnol. Bioeng.* **1997**, *53*, 121−131.
9. Xu, X. D.; Ayyagari, M.; Tata, M.; John, V. T.; McPherson, G. L. Formation of novel organogels by the addition of phenols to AOT micelles in isooctane. *J. Phys. Chem.* **1993**, *97*, 11350−11353.
10. Tata, M.; John, V. T.; Waguespack, Y. Y.; McPherson, G. L. Intercalation in novel organogels with a stacked phenol microstructure. *J. Am. Chem. Soc.* **1994**, *116*, 9464−9470.
11. Petit, C.; Pileni, M. P. Synthesis of cadmium sulfide in situ in reverse micelles and in hydrocarbon gels. *J. Phys. Chem.* **1988**, *92*, 2282−2286.
12. Crecchio, C.; Ruggiero, P.; Pizzigallo, M. D. R. Polyphenoloxidases immobilised in organic gels: properties and applications in the detoxification of aromatic compounds. *Biotechnol. Bioeng.* **1995**, *48*, 585−591.
13. Seeboth, A.; Wustneck, R.; Kragel, J. Gel dispersed liquid-crystals. *Colloid Polym. Sci.* **1994**, *272*, 1151−1156.
14. Murdan, S.; Gregoriadis, G.; Florence, A. T. Nonionic surfactant based organogels incorporating niosomes. *STP Pharma. Sci.* **1996**, *6*, (1), 44−48.
15. Murdan, S. Nonionic surfactant based organogels: their structures and potential as vaccine adjuvants. Ph.D. Thesis, 1998, School of Pharmacy, University of London.
16. Yoshioka, T.; Florence, A. T. Vesicle (niosome)-in-water-in-oil (v/w/o) emulsions: an in vitro study. *Int. J Pharm.* **1994**, *108*, 117−123.
17. Shaffer, L. W. The fate of intragluteal injections. *Arch. Dermatol. Syphilol.* **1929**, *19*, 347−364.
18. Freund, J. The mode of action of immunologic adjuvants. *Adv. Tuberc. Res.* **1956**, *7*, 130−148.

Acknowledgments

The authors thank David McCarthy and Colin James for assistance, and Jeremy Cockcroft, Department of Crystallography, Birkbeck College, for carrying out the X-ray diffraction measurements.

JS980343J

In Vitro Models of the Blood–Brain Barrier to Polar Permeants: Comparison of Transmonolayer Flux Measurements and Cell Uptake Kinetics Using Cultured Cerebral Capillary Endothelial Cells

MARK D. JOHNSON AND BRADLEY D. ANDERSON*

Contribution from *Department of Pharmaceutics and Pharmaceutical Chemistry, University of Utah, Salt Lake City, Utah 84112.*

Received July 31, 1998. Final revised manuscript received December 31, 1998.
Accepted for publication March 25, 1999.

Abstract □ Given that the cerebral microvasculature within the brain constitutes the rate-limiting barrier to drug entry, primary cultures of cerebral capillary endothelial cells would appear to offer a potentially useful model system for predicting drug delivery to the central nervous system. In the present study, the predictive capabilities of two potential models of the in vivo blood–brain barrier (BBB) to the passive diffusion of polar permeants were assessed. A comparison of the logarithms of the in vitro transmonolayer permeability coefficients ($P_{monolayer}$) for several polar permeants varying in lipophilicity (from this study and literature data) with the well-established relationship between the logarithms of the in vivo BBB permeability coefficients (log P_{BBB}) and permeant lipophilicity as measured by the logarithm of the octanol/water partition coefficient (log $PC_{octanol/water}$) demonstrated that in vitro permeation across these monolayers is largely insensitive to polar permeant lipophilicity as a result of the predominance of the paracellular component in the transmonolayer flux. Conversely, kinetic studies of uptake of the same compounds into monolayers yielded transfer rate constants (k_p) reflecting membrane permeability coefficients ranging over several orders of magnitude, similar to the variation in permeant lipophilicity. Furthermore, a linear relationship could be demonstrated between the logarithms of k_p and in vivo BBB log P (slope $= 1.42 \pm 0.35$; $r = 0.92$). In conclusion, this preliminary investigation suggests that monitoring the kinetics of cell uptake into cerebral capillary endothelial cell monolayers may be superior to transmonolayer flux measurements for predicting the passive diffusion of polar permeants across the BBB in vivo.

Introduction

An in vitro model of the blood−brain barrier (BBB) that could mimic its in vivo barrier properties and thus allow one to predict the outcome of in vivo experiments would be extremely useful. Assuming the rate-limiting barrier to drug uptake to be the cerebral microvasculature, primary cultures of cerebral capillary endothelial cells offer a potentially useful model system for predicting drug delivery to the CNS.[1,2] Indeed, recent studies have led several investigators to conclude that primary cultures of cerebrovascular endothelial cells exhibit a barrier function that correlates with BBB function in vivo.[3−5] In vivo, the BBB permeability depends on permeant lipophilicity in a manner consistent with predominantly transcellular diffusion even for permeants as polar as sucrose, which has a log octanol/water partition coefficient (log $PC_{octanol/water}$) of approximately −4.[6] The present study confirms, however, that transmonolayer permeabilities across primary cultures of BBB endothelial cells, a popular in vitro model of the BBB, fail to display the expected dependence on permeant lipophilicity for polar permeants having log $PC_{octanol/water} \leq 0$. This paper therefore explores the utility of monolayer uptake kinetics as an alternative to transmonolayer flux measurements in an attempt to identify a more reliable model of the BBB for predicting permeability coefficients of polar permeants.

Materials and Methods

Reagents—[1-^{3}H]Sucrose (20 Ci/mmol) was obtained from NEN Research Products, DuPont, Wilmington, DE. [^{14}C(U)]Sucrose (600 mCi/mmol) and [^{14}C]urea (59 mCi/mmol) were obtained from Moravek Biochemicals, Brea, CA. [1-^{3}H]Mannitol (15 Ci/mmol), [2-^{3}H]glycerol (30 Ci/mmol), and [1-^{14}C]acetamide (55 mCi/mmol) were obtained from American Radiolabeled Chemicals Inc., St. Louis, MO. All radiolabeled compounds were purchased >98% pure and were used without further purification. 3′-Azido-3′-deoxythymidine (zidovudine, 98% purity) was obtained from Aldrich Chemical Co., Milwaukee, WI. All other reagents were of analytical grade. Culture media consisted of minimum essential media (MEM)/F-12 Ham's nutrient mixture 1:1 (HyClone Laboratories, Logan, Utah) supplemented with 10 mM HEPES/13 mM sodium bicarbonate (pH 7.4), 100 μg/mL penicillin G (Sigma Chemical Co., St. Louis, MO), 100 μg/mL streptomycin (Sigma), 100 μg/mL heparin (170 units/mg), and 10% plasma-derived horse serum (HyClone Laboratories).

Isolation and Culture of Cerebrovascular Endothelial Cells—Capillary segments were isolated from bovine cerebral gray matter (Dale T. Smith & Sons Meat Packing Company, Draper, UT) by a two-step enzymatic dispersion treatment followed by centrifugation over preestablished 50% Percoll density gradients as described previously.[1] Sequential filtering of the preparation through 500 μm and 95 μm nylon mesh filters yielded a relatively purified and homogeneous capillary suspension containing 5−20 individual endothelial cells per cluster. The isolated microvessels were cultured immediately or stored at −70 °C in culture medium to which had been added DMSO (10% v/v). Microvessels were seeded onto various surfaces at approximately 50 000 cells/cm^2 and cultured at 37 °C under 95% humidity and 5% CO_2/95% air. Culture media were changed every other day.

Transmonolayer Flux Measurements—Microvessels were seeded onto fibronectin-coated Biocoat (Becton Dickinson) cell culture inserts (fibrillar collagen matrix, 10.5 mm diameter, $A =$ 0.9 cm^2, 1.0 μm pore size, 1.6×10^6 pores/cm^2) and cultured as described above. Confluent monolayers were obtained within 9−10 days as determined visually via an inverted microscope. To provide clearance for a magnetic stir bar between the bottom of the plate well (six-well companion plate) and the microporous membrane of the insert, a 2 mm thick shim (60.0 mm diameter) was placed around the top of the well. Culture media (9.6 mL) was placed in the plate well (receiver chamber), and 0.9 mL was added to the insert (donor chamber) to maintain hydrodynamic stability. The system was allowed to equilibrate for 15 min at 37 °C in an air incubator with continuous magnetic stirring. To initiate an experiment, the media in the insert was replaced with an equivalent volume of media containing [^{3}H]- or [^{14}C]-labeled and/or nonra-

* To whom correspondence should be addressed. Tel: (801) 581-4688. FAX: (801) 585-3614. E-mail: banderson@deans.pharm.utah.edu.

10.1021/js9803149 CCC: $18.00
Published on Web 04/30/1999

diolabeled solute(s). At selected time points, samples (100 μL) were removed from the receiver chamber and immediately replaced with an equal volume of media. After the experiment, the donor concentration was analyzed to verify its constancy (i.e., >97% of initial concentration) throughout the experiment.

In some cases, transmonolayer flux measurements were also conducted using a vertical diffusion chamber system (Corning Costar Corp., Cambridge, MA) and Snapwell inserts (Corning Costar Corp.). Brain microvessels were seeded onto the cell culture inserts, which were thinly coated with rat tail collagen (type I) cross-linked with ammonia fumes[2] and cultured as described above. The two-piece cell culture devices consisted of 12 mm diameter, 0.4 μm polycarbonate (10^8 pores/cm^2) or polyester (10^6 pores/cm^2) microporous membranes assembled in detachable rings. Confluent monolayers were typically obtained in 12−14 days, at which point the Snapwell insert ring was removed from the upper assembly and placed between the two halves of the diffusion chamber, thus minimizing cell monolayer disruption. Equal volumes (5 mL) of transendothelial assay buffer (122 mM NaCl, 25 mM $NaHCO_3$, 10 mM D-glucose, 3 mM KCl, 1.2 mM $MgSO_4$, 0.4 mM $NaHPO_4$, 1.4 mM $CaCl_2$, and 10 mM HEPES adjusted to pH 7.4 with NaOH)[1] were placed in both the donor (side facing the monolayer) and receiver sides. The chamber temperatures were maintained at 37 °C with a water-heated metal block. Both chambers were mixed using a 5% CO_2/95% O_2 airlift. After 15 min of equilibration, the donor chamber was spiked with 0.5 mL buffer containing [^{3}H]- or [^{14}C]-labeled and/or nonradiolabeled solute(s). An equal volume of assay buffer was simultaneously added to the receiver chamber. Aliquots (100 μL) of the receiver solution were removed at various times along with equal volumes from the donor solution to maintain constant hydrostatic pressure.

Apparent permeability−area products ($P_{app}A$) were obtained from the slopes of linear plots of permeant flux into the receiver compartment versus time, $\Delta M_R/\Delta t$, where ΔM_R ($= \Delta C_R V_R$) is the change in permeant mass over a given time interval,Δt, using the following relation:

$$P_{app}A = (\Delta M_R/\Delta t)/(C_D - C_R) \cong (\Delta C_R V_R/\Delta t)/C_D \qquad (1)$$

where C_R was the concentration in the receiver and C_D was the donor concentration. Constant donor concentrations and sink conditions, respectively, were maintained (i.e., $C_D - C_R \approx C_D$) by ensuring that less than 10% mass transfer occurred over the time of the assay and by using large buffer volumes (V_R) in the receiver chamber.

Monolayer permeability−area products, $P_{monolayer}A$, were determined from the following relationship:

$$1/P_{app}A = 1/P_{monolayer}A + 1/P_{insert}A \qquad (2)$$

where permeability−area values for the collagen-coated insert ($P_{insert}A$) were measured independently. Monolayer permeability coefficients, $P_{monolayer}$, were then obtained by dividing $P_{monolayer}A$ by the surface area of the insert (i.e., $A = 0.9$ cm^2, Biocoat system; $A = 1.13$ cm^2, Snapwell system). $P_{monolayer}$ includes contributions from both paracellular and transcellular flux of solute across the cell monolayer (i.e., $P_{monolayer} = P_{paracellular} + P_{transcellular}$).

Monolayer Uptake Experiments—Rat tail collagen (type I) was attached to tissue culture dishes (35 × 10 mm^2) with a cross-linking reagent, 1-cyclohexyl-3-(2-morpholinoethyl)carbodiimide-metho-*p*-toluenesulfonate (Aldrich) to provide a uniform and durable surface for cell attachment and growth that would withstand multiple media changes and the wash procedure.[7] Brain microvessels were seeded onto the treated dishes, and confluent monolayers were obtained 8−10 days after initial plating. Uptake was initiated by the addition of fresh culture media containing [^{3}H]- and/or [^{14}C]-labeled or nonradiolabeled compounds (sucrose, mannitol, urea, and zidovudine at donor concentrations of 1×10^{-6}, 2.1×10^{-7}, 5.1×10^{-5}, and 5.4×10^{-3} M, respectively). At selected times, uptake was terminated by the rapid (~1 s) removal of uptake solution using a pipettor followed by a series of washes (50 mL per wash) with ice-cold Dulbecco's phosphate-buffered saline solution (pH 7.4). Dishes were immersed repeatedly (4 times) in wash solution and gently agitated (5 s per wash). (Validation experiments using urea and zidovudine detected no change in cellular content after the first wash.) Cells were solubilized with 1 N NaOH (15 min at room temperature) and neutralized with an equivalent volume of 1 N HCl, and aliquots were analyzed for both permeant and protein content.

The mmoles solute per mg protein ($M(t)$) in each monolayer versus time (one monolayer per time point) were recorded. $M(t)$ includes potential contributions from both intracellular ($M_{monolayer}(t)$) and any residual extracellular or surface bound permeant (M_i) remaining after the washing procedure. Assuming that intracellular uptake is due to simple passive diffusion, the mass of permeant in the monolayer can be described by the following equation:

$$M(t) = M_{monolayer}(t) + M_i = C_D V_{monolayer}(1 - e^{-k_p t}) + M_i \qquad (3)$$

where the monolayer volume per mg protein is $V_{monolayer}$, k_p is the apparent first-order rate constant governing cell uptake ($k_p = P_{membrane}A_{monolayer}/V_{monolayer}$), and C_D is the donor concentration of permeant. Experimental uptake versus time profiles were fit by nonlinear least-squares regression analysis to obtain estimates of $V_{monolayer}$, k_p, and M_i.

Values of k_p for metabolizable compounds (i.e., glycerol and acetamide) were obtained from initial rates of cell uptake at glycerol donor concentrations of 2.9×10^{-7} and 1.0×10^{-3} M and acetamide donor concentrations of 0.9×10^{-6} to 1.6×10^{-5} M. Intracellular concentrations of permeant ($C_{monolayer}(t)$) were calculated by dividing the intracellular mass (mmole/mg protein) by $V_{monolayer}$ (7.2 μL/mg protein, determined above from the nonmetabolized permeants). Plots of concentration vs time for these permeants were fit to eq 4 by linear least-squares regression

$$C_{monolayer}(t) = k_p C_D t + C_i \qquad (4)$$

analysis to obtain the first-order rate constants for simple passive diffusion, k_p. Values of k_p for urea were also determined by this method over a concentration range of nearly 4 orders of magnitude (2×10^{-5} to 0.1 M) to compare the two kinetic methods and to examine the concentration dependence of the cellular uptake of urea.

Analytical Methods—Samples containing [^{3}H]- and/or [^{14}C]-radionuclides were diluted with liquid scintillation cocktail (Opti-Fluor) and analyzed with a Beckman LS 1801 scintillation counter. Samples containing zidovudine were quantified with a modular reversed-phase HPLC system (Supelcosil LC-18-S analytical column) with UV detection at 254 nm. The mobile phase consisted of 15% acetonitrile in phosphate buffer (pH = 7.4, $I = 0.02$). Protein content for each monolayer was determined by the Lowry method.[8]

Statistical and Regression Analyses—Statistical significance was determined using either a one-tailed or two-tailed Student's *t* test for unpaired data. Values were determined to be significantly different when $P \leq 0.05$. Nonlinear least-squares regression analysis was performed using a computer and commercially available software (SCIENTIST, MicroMath, Salt Lake City, UT).

Results And Discussion

Isolation and Culture of Cerebrovascular Endothelial Cells—The isolation and culture of cerebral microvascular endothelial cells have led to the development of in vitro models designed to rapidly and conveniently examine various aspects of BBB function.[2,9−11] Primary cultures of these cells retain many characteristics of their cerebral counterparts, including specific BBB and endothelial "markers", the absence of fenestrae, few micropinocytotic vesicles, an abundance of mitochondria, and well-developed junctional complexes.[1,2,12−14]

Bovine cerebral microvessels were isolated and characterized as described previously.[15] When seeded onto collagen-coated microporous surfaces, these cells showed excellent attachment and growth, with confluent monolayers forming within 8−10 days. Monolayers completely covered the insert, including along the edges, when examined microscopically and exhibited the characteristic spindle-shaped morphology described in the literature.[1,13] Furthermore, the permeability coefficients of polar permeants

Table 1—Physicochemical Properties and Permeability Coefficients (mean ± SD) for the Transmonolayer Flux of Various Polar Solutes

permeant	MW	$PC_{octanol/water}$	P_{app} (cm/min × 10^3)	P_{insert} (cm/min × 10^3)	$P_{monolayer}$ (cm/min × 10^3)	av log $P_{monolayer}$
sucrose	342	2.1×10^{-4} [a]	1.70 ± 0.46[e]	2.29 ± 0.05[e]	6.6	–2.56
			1.37 ± 0.24[f]	3.10[f,h]	2.4	
			1.09[g,h]	5.98[g,h]	1.3	
mannitol	182	3.4×10^{-3} [b]	1.50 ± 0.27[e]	3.03 ± 0.46[e]	3.0	–2.52
glycerol	92	1.1×10^{-2} [c]	3.59 ± 0.97[e]	5.01 ± 0.18[e]	13	–1.9
urea	60	2.6×10^{-2} [c]	3.47 ± 0.51[f]	6.03[f]	8.2	–2.25
			2.83[g,h]	10.56[g,h]	3.9	
acetamide	59	8.9×10^{-2} [c]	3.31 ± 0.31[e]	4.82 ± 0.59[e]	11	–1.96
zidovudine	267	1.1[d]	2.90 ± 0.20[e]	3.84 ± 0.26[e]	12	–2.02
			3.92[g,h]	8.14[g,h]	7.6	

[a] Ref 32. [b] Ref 33. [c] Ref 34. [d] Ref 35. [e] Biocoat system ($n = 3$ or 4 for P_{app}, except for zidovudine where $n = 2$; $n = 2$ for all P_{insert} values). [f] Vertical diffusion chamber system (Snapwell, polyester membrane); $n = 3$ unless otherwise specified. [g] Vertical diffusion chamber system (Snapwell, polycarbonate membrane). [h] Single determinations.

frequently used as paracellular markers (e.g., sucrose and mannitol) were comparable to those reported in the literature.[1,16,17]

To establish that the in vitro culture system is a useful model system for predicting in vivo BBB permeability coefficients for passively diffusing polar permeants, it is essential that the in vitro model exhibit comparable barrier properties and similar selectivity to permeant structure (e.g., lipophilicity) as that observed in vivo. As demonstrated below, monolayers of cultured endothelial cells are too leaky and therefore provide neither the barrier properties nor the selectivity to polar permeant structure found in vivo.

Transmonolayer Flux Measurements—To evaluate the reliability of transmonolayer flux measurements for predicting in vivo brain uptake rates of passively diffusing polar permeants, several model permeants, listed in Table 1, were selected for transmonolayer experiments. The compounds chosen had molecular weights <400 daltons and varied in lipophilicity as measured by $PC_{octanol/water}$ by nearly 4 orders-of-magnitude. With the exception of zidovudine, the permeants employed, namely, sucrose, mannitol, glycerol, urea, and acetamide, have been used in numerous cerebrovascular permeability studies in vivo or in situ in which their transfer across the BBB was shown to occur via simple passive diffusion.[18,19] Zidovudine has also been shown to cross monolayers of bovine capillary endothelial cells primarily via passive diffusion,[20] although there is substantial evidence that its in vivo brain efflux is at least partially carrier-mediated.[20–23] Zidovudine's stability in endothelial cell homogenate made it a useful model permeant for this study, and its inclusion extended the range of lipophilicity explored, as measured by $PC_{octanol/water}$, to 4 orders-of-magnitude (~10^{-4} to 1).

Plots of % of permeant in the receiver compartment ($100 \cdot C_R/C_D$) versus time for two representative permeants, mannitol and acetamide, in control (collagen-coated insert only) and transmonolayer flux experiments are shown in Figure 1. In all experiments, sink conditions were maintained, and consequently, linear profiles were observed, as demonstrated in Figure 1. As shown in Figure 1, fluxes across inserts containing monolayers were significantly ($P \leq 0.05$) smaller than those across inserts without monolayers, indicating the presence of additional barrier function due to the monolayers. Least-squares regression analyses of the permeability data were performed to obtain permeability coefficients for the inserts (P_{insert}) and for the monolayer/insert combinations (P_{app}), as displayed in Table 1. Transmonolayer permeability coefficients ($P_{monolayer}$), also shown in Table 1, were then obtained using eq 2 and the surface area of the insert.

log $P_{monolayer}$ values generated in Table 1 are plotted in Figure 2 versus log $PC_{octanol/water}$ for each of the six permeants. The dashed line in Figure 2 represents the in vivo relationship between the logarithm of the BBB permeability coefficient and log $PC_{octanol/water}$ according to eq 5,

$$\log P_{BBB} = -2.14 + \log PC_{octanol/water} \qquad (5)$$

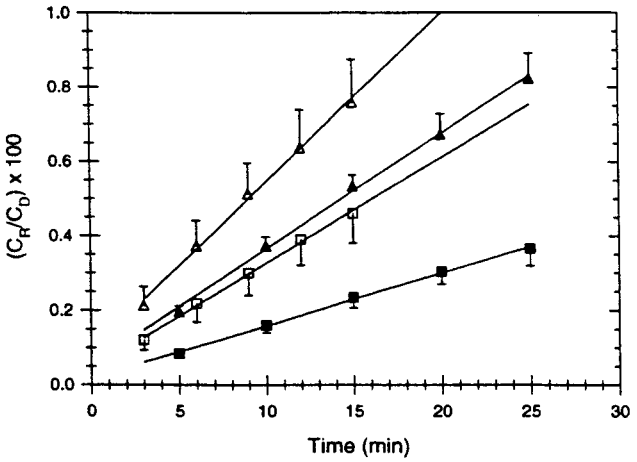

Figure 1—Representative transmonolayer flux ($100 \cdot C_R/C_D$) profiles of mannitol (squares) and acetamide (triangles) across cell culture inserts with (filled symbols) and without (open symbols) confluent monolayers attached. Each time point represents the mean ± SD of 2 or 3 individual experiments. The two solutes were present as a mixture. Donor concentrations of mannitol and acetamide were 8.9×10^{-8} and 3.1×10^{-5} M, respectively.

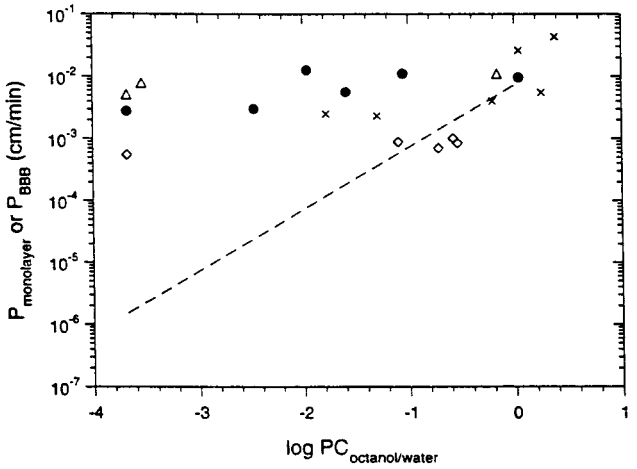

Figure 2—Semilogarithmic plots of $P_{monolayer}$ versus log $PC_{octanol/water}$ for polar permeants having log PC values less than one. Results are from several laboratories, including this one (●); van Bree et al. (x);[3] Pardridge et al. (△);[4] and Glynn and Yazdanian (◇).[24] The dashed line is adapted from the literature regression line for BBB permeability–area product in vivo from Fenstermacher.[6]

which was adapted from the regression line for the logarithm of BBB permeability−area product versus log $PC_{octanol/water}D_m$ published by Fenstermacher[6] by assuming a BBB surface area of 240 cm^2/g of brain tissue and a permeant diffusion coefficient (D_m) of 1×10^{-5} cm^2/s. The literature regression line was based on in vivo BBB permeability data for a variety of permeants, including some from this study. It applies to approximately the same lipophilicity range as that covered in Table 1. As is evident in eq 5 and from the dashed line in Figure 2, the passive permeability of similarly sized polar permeants across the BBB in vivo appears to depend approximately linearly on $PC_{octanol/water}$ (i.e., the slope of log P_{BBB} versus log $PC_{octanol/water}$ is ~1). This is the primary evidence for the conclusion by Fenstermacher[6] that passage across the BBB is transcellular, even for solutes as polar as sucrose. In stark contrast, the log $P_{monolayer}$ values exhibit virtually no dependence on log $PC_{octanol/water}$ within the range of lipophilicities explored, suggesting that the transmonolayer transfer of these solutes is mainly via a paracellular route (i.e., through leaks in the monolayer).

Because the extent of tight junction formation may vary with isolation technique, culturing conditions, etc., the results from several studies of the transmonolayer passage of low molecular weight permeants (log $PC_{octanol/water} < 1$) are also displayed in Figure 2, including data published by van Bree et al.,[3] Glynn and Yazdanian,[24] and Pardridge et al.[4] These data similarly show virtually no dependence of transmonolayer permeability on permeant lipophilicity for compounds having a log $PC_{octanol/water} < 1$. Again, paracellular diffusion appears to predominate in these experiments.

Several investigators have observed that the barrier properties of endothelial cell monolayer cultures can be better maintained by coculturing with astrocytes[25−27] or with a combination of astrocyte-conditioned media and treatment with agents that elevate cyclic AMP.[28] Raub, for example, was able to demonstrate that noncontact coculture of postconfluent bovine brain cerebral capillary endothelial cell monolayers with rat C_6 glioma cells reduced $P_{monolayer}$ for sucrose from 1.47×10^{-3} cm/min in primary cultures to 7.7×10^{-4} cm/min. An additional decrease to 1.5×10^{-4} cm/min was acheived with adenylate cyclase activators.[27] Dehouck et al. reported a sucrose permeability coefficient of 6.3×10^{-4} cm/min for monolayers in coculture.[25,29] These investigations indicate that some progress is evident in terms of improving barrier integrity by coculturing, but a comparison of these sucrose values with those shown in Figure 2 indicates that they are still orders-of-magnitude above the in vivo regression line.

Monolayer Uptake Experiments—Rate constants for permeant uptake into capillary endothelial cell monolayers (k_p), which reflect the product of the membrane permeability coefficient, P_m, and monolayer surface-area-to-volume ratio (i.e., $k_p = P_m A_{monolayer}/V_{monolayer}$), were determined by measuring the accumulation of permeant in confluent monolayers after normalizing for the protein content in each monolayer.

Displayed in Figure 3 are plots of % uptake ($100 \cdot M(t)/M_{monolayer}(\infty)$) versus time for the nonmetabolizable permeants sucrose, mannitol, urea, and zidovudine, along with the fitted curves obtained using eq 3. Independent estimates of monolayer volume, normalized to protein content, were obtained from each permeant as listed in Table 2. These estimates were not significantly different from each other as judged by their 95% confidence intervals and were therefore combined to give an average value of 7.2 ± 1.1 (SEM) μL/mg protein, which, given an average protein content of 0.17 ± 0.01 (SEM) mg protein per monolayer corresponds to an intracellular volume in the monolayer of ~1.2 μL.

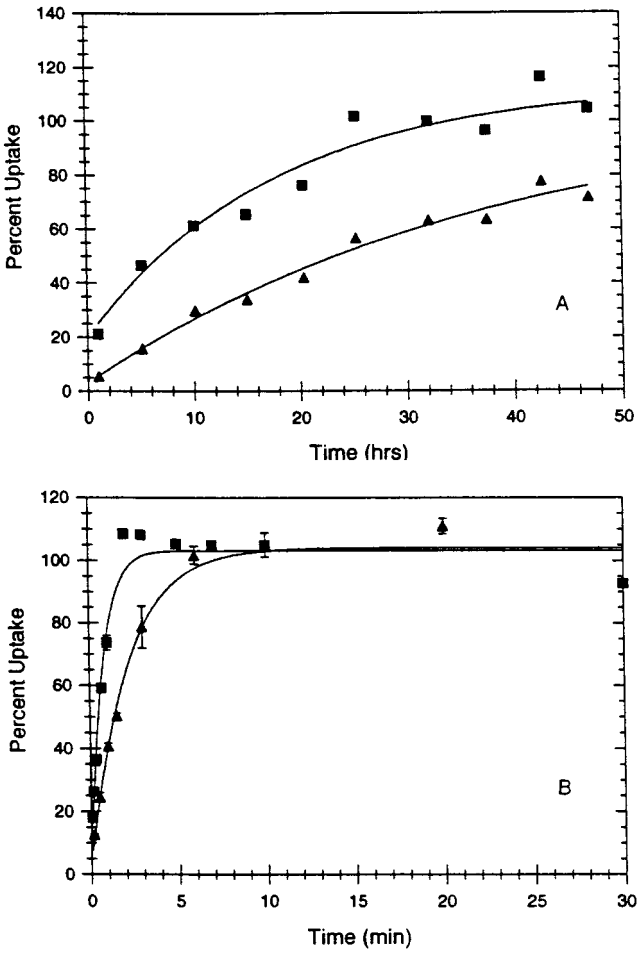

Figure 3—Percent uptake versus time profiles for (a) sucrose (▲) and mannitol (■) and (b) zidovudine (■) and urea (▲) into brain capillary endothelial cell monolayers. Each point represents an individual monolayer incubated at 37 °C for a given period of time in the presence of 1 mL of culture media containing 1.0×10^{-6} M sucrose, 2.1×10^{-7} M mannitol, 5.4×10^{-3} M zidovudine or 5.0×10^{-5} M urea, washed, and lysed for analysis. Values for urea (mean ± SD) represent duplicate measurements at each time point.

Table 2—Parameters Obtained from Monolayer Uptake Experiments for Various Polar Permeants

permeant	$V_{monolayer}$[a] (μL/mg protein ± SD)	k_p ($min^{-1} \times 10^3$ ± SD)	$t_{1/2}$ (min)
sucrose	7.2 ± 1.1	0.45 ± 0.05[a]	1540
mannitol	7.9 ± 0.8	0.85 ± 0.27[a]	815
urea	5.6 ± 0.3	453 ± 55[a] 373 ± 13[b] ($n = 6$)	1.6
glycerol	N/D	155 ± 7[b] ($n = 2$)	4.5
acetamide	N/D	645 ± 347[b] ($n = 3$)	1.1
zidovudine	7.9 ± 0.7	1175 ± 268[a]	0.59

[a] Parameters determined from computer fits of the uptake versus time profiles to eq 3. [b] Parameters determined from computer fits of initial uptake rates to eq 4.

Intercepts in these plots reflect the residual percentage of permeant in cells at zero time due to extracellular or cell-surface-bound permeant remaining after the wash procedure. This residual percentage was <5% in all cases except for mannitol, where it was 18.5%. However, in every case, including that of mannitol, the residual percentage was not significantly different from zero as judged by the 95% confidence range.

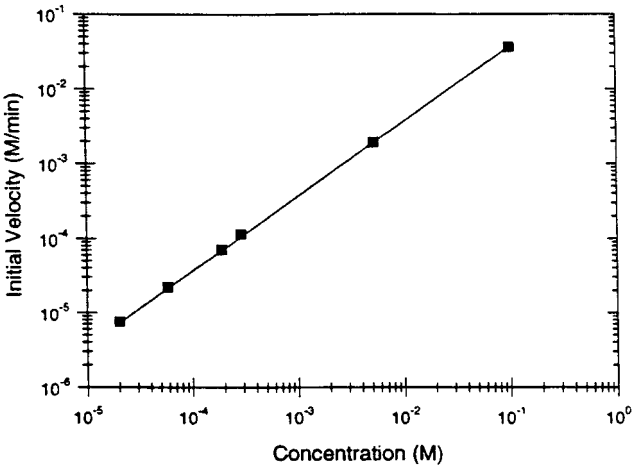

Figure 4—Dependence of initial rate of urea uptake into brain capillary endothelial cell monolayers on urea concentration. The solid line represents the fit using eq 4.

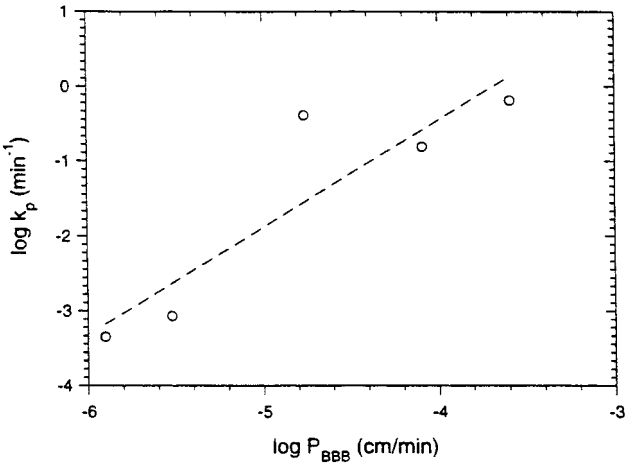

Figure 5—Relationship between log k_p for uptake into brain capillary endothelial cell monolayers to log P_{BBB} from published in vivo data.

As evident in Figure 3a,b, concentrations of permeant in the monolayer appeared to reach equilibrium at distinctly different times. Zidovudine and urea attained apparent equilibrium within approximately 4 and 10 min, respectively, whereas the more hydrophilic molecules mannitol and sucrose took >24 h to approach a constant intracellular concentration. Indeed, the monolayer accumulation of sucrose had not yet achieved a steady-state concentration after 48 h when the study was terminated. In contrast to the similar $P_{monolayer}$ values obtained in transmonolayer experiments, calculated values of k_p for each permeant obtained from these plots (Table 2) vary by >3 orders-of-magnitude from the slowest (sucrose) to the most rapidly permeating compound (zidovudine).

In addition to the % uptake versus time profiles in Figure 3a,b, initial rates of uptake were determined for urea over a concentration range of 2×10^{-5} to 0.1 M. Initial velocities were obtained from the slopes of plots of urea concentration in monolayers versus time as described by eq 4. These velocities, plotted versus urea concentration in Figure 4, demonstrate a linear relationship between rate of uptake and urea concentration consistent with uptake via passive (nonsaturable) diffusion. The first-order rate constant for urea uptake obtained from these data (Table 2) compared favorably with that obtained from the % uptake versus time profile in Figure 3b, thus validating the initial rate method for obtaining k_p values.

The initial rate method was employed to obtain k_p values for glycerol and acetamide after preliminary experiments suggested intracellular metabolism was occurring. Linear uptake kinetics were observed in the initial rate region for both permeants, consistent with eq 4, allowing the k_p values listed in Table 2 to be determined from linear least-squares regression analysis. The mean value for glycerol reflects initial rate studies conducted at concentrations of 2.9×10^{-7} and 1.0×10^{-3} M, which yielded k_p values of 0.16 and 0.15 min^{-1}, indicating that uptake of glycerol was concentration-independent over this range.

All of the above results are consistent with a passive diffusion uptake mechanism. The adherence of the uptake curves in Figure 3a,b to a passive uptake model, the absence of concentration dependence in the initial rates of uptake of glycerol and urea, and the dramatic differences in k_p values, which qualitatively appear to be sensitive to permeant size and lipophilicity, support a passive diffusion mechanism. Estimates of monolayer volume were independent of the permeant employed to obtain the estimate for nonmetabolizable compounds, again consistent with passive diffusion.

The k_p values for monolayer uptake are related to the membrane permeability coefficient of each permeant ($k_p = P_m A_{monolayer}/V_{monolayer}$). Therefore, these values would be expected to correlate with in vivo BBB permeability coefficients, provided that brain uptake in vivo is also passive for these permeants. Figure 5 displays the log k_p values from this study plotted versus the average log P_{BBB} values determined in vivo. The in vivo results for sucrose, mannitol, and urea were obtained from a compilation by Fenstermacher;[6] the glycerol value was the average of data from publications by Fenstermacher and Rapoport[18] and Takasato et al.;[30] and the acetamide literature value was from Rapoport et al.[19] Zidovudine was not included in this comparison because carrier-mediated processes have been implicated in its in vivo brain uptake/efflux.[20,21,31] The dashed line in Figure 5 represents the least-squares fit to the data, which yielded a slope not significantly different from one and an excellent correlation (slope = 1.4 ± 0.4; r = 0.90). There appears to be some size-dependent permeability behavior manifested more strongly in monolayer uptake than in vivo, as evident in the deviation of the k_p for urea, the smallest permeant examined, from the regression line. Why a larger size dependence would exist in the endothelial cell monolayers than in the cerebrovascular system in vivo is not known, if indeed it is the size of urea that accounts for the difference.

In conclusion, transmonolayer flux measurements appear to be poor predictors of blood−brain barrier passage in vivo for polar, small molecule permeants (log $PC_{octanol/water}$ < 0), as transmonolayer permeability coefficients lack the sensitivity to permeant lipophilicity that is observed in vivo. This reflects the predominantly paracellular passage of polar permeants across brain endothelial cell monolayers. However, monolayer uptake kinetics of several polar permeants were found to be highly dependent on permeant lipophilicity and well correlated with in vivo BBB permeability coefficients, with a slope in the plot of log k_p versus log P_{BBB} near one. This preliminary investigation suggests that uptake studies into cerebral capillary endothelial cell monolayers may be superior to transmonolayer flux measurements for probing the role of simple passive diffusion in the passage of polar permeants across the blood−brain barrier. Additional studies are underway to assess the utility of the monolayer uptake method for predicting the in vivo BBB permeability of dideoxynucleoside anti-HIV agents which may also undergo intracellular metabolism during their passage across the BBB.[15]

References and Notes

1. Audus, K. L.; Borchardt, R. T. Characterization of an in vitro blood−brain barrier model system for studying drug transport and metabolism. *Pharm. Res.* **1986**, *3*, 81−87.
2. Miller, D. W.; Audus, K. L.; Borchardt, R. T. Application of cultured endothelial cells of the brain microvasculature in the study of the blood−brain barrier. *J. Tissue Cult. Methods* **1992**, *14*, 217−224.
3. van Bree, J. B. M. M.; de Boer, A. G.; Danhof, M.; Ginsel, L. A.; Breimer, D. D. Characterization of an "in vitro" blood−brain barrier: Effects of molecular size and lipophilicity on cerebrovascular endothelial transport of drugs. *J. Pharmacol. Exp. Ther.* **1988**, *247*, 1233−1239.
4. Pardridge, W. M.; Triguero, D.; Yang, J.; Cancilla, P. A. Comparison of in vitro and in vivo models of drug transcytosis through the blood−brain barrier. *J. Pharmacol. Exp. Ther.* **1990**, *253*, 884−891.
5. Shah, M. V.; Audus, K. L.; Borchardt, R. T. The application of bovine brain microvessel endothelial-cell monolayers grown onto polycarbonate membranes in vitro to estimate the potential permeability of solutes through the blood−brain barrier. *Pharm. Res.* **1989**, *6*, 624−627.
6. Fenstermacher, J. D. Pharmacology of the Blood-Brain Barrier. In *Implications of the Blood-Brain Barrier and Its Manipulation*; Neuwelt, E. A., Ed.; Plenum: New York, 1989; Vol. 1, pp 137−155.
7. Macklis, J. D.; Sidman, R. L.; Shine, H. D. Cross-linked collagen surface for cell culture that is stable, uniform, and optically superior to conventional surfaces. *In Vitro Cell. Dev. Biol.* **1985**, *21*, 189−194.
8. Lowry, O. H.; Rosebrough, N. J.; Farr, A. L.; Randall, R. J. Protein measurement with the folin phenol reagent. *J. Biol. Chem.* **1951**, *193*, 265−275.
9. Takakura, Y.; Audus, K. L.; Borchardt, R. T. Blood-brain barrier: Transport studies in isolated brain capillaries and in cultured brain endothelial cells. In *Advances in Pharmacology*; Academic Press: New York, 1991; Vol. 22, pp 137−165.
10. Audus, K. L.; Bartel, R. L.; Hidalgo, I. J.; Borchardt, R. T. The use of cultured epithelial and endothelial cells for drug transport and metabolism studies. *Pharm. Res.* **1990**, *7*, 435−451.
11. Joo, F. The blood-brain barrier in vitro: The second decade. *Neurochem. Int.* **1993**, *23*, 499−521.
12. Joo, F. The cerebral microvessels in culture, an update. *J. Neurochem.* **1992**, *58*, 1−17.
13. Bowman, P. D.; Betz, A. L.; Ar, D.; Wolinsky, J. S.; Penney, J. B.; Shivers, R. R.; Goldstein, G. W. Primary culture of capillary endothelium from rat brain. *In Vitro* **1981**, *17*, 353−362.
14. Williams, S. T.; Gillis, J. F.; Matthews, M. A.; Wagner, R. C.; Bitensky, M. W. Isolation and characterization of brain endothelial cells: morphology and enzyme activity. *J. Neurochem.* **1980**, *32*, 374−381.
15. Johnson, M. D.; Anderson, B. D. Localization of purine metabolizing enzymes in bovine brain microvessel endothelial cells: an enzymatic blood−brain barrier for dideoxynucleosides? *Pharm. Res.* **1996**, *13*, 1881−1886.
16. Pardridge, W. M. Brain metabolism: A perspective from the blood−brain barrier. *Physiol. Rev.* **1983**, *63*, 1481−1535.
17. Eddy, E. P.; Maleef, B. E.; Hart, T. K.; Smith, P. L. In vitro models to predict blood−brain barrier permeability. *Adv. Drug Delivery Rev.* **1997**, *23*, 185−198.
18. Fenstermacher, J. D.; Rapoport, S. I. Blood-brain barrier. In *Handbook of Physiology. Section 2: The Cardiovascular System. Vol IV: Microcirculation.*; Renkin, E. M., Michel, C. C., Eds.; American Physiological Society: Washington, DC, 1984; Vol. IV, pp 969−1000.
19. Rapoport, S. I.; Ohno, K.; Pettigrew, K. D. Drug entry into the brain. *Brain Res.* **1979**, *172*, 354−359.
20. Masereeuw, R.; Jaehde, U.; Langemeijer, M. W. E.; de Boer, A. G.; Breimer, D. D. In vitro and in vivo transport of zidovudine (AZT) across the blood−brain barrier and the effect of transport inhibitors. *Pharm. Res.* **1994**, *11*, 324−330.
21. Galinsky, R. E.; Hoesterey, B. L.; Anderson, B. D. Brain and cerebrospinal fluid uptake of zidovudine (AZT) in rats after intravenous injection. *Life Sci.* **1990**, *47*, 781−788.
22. Collins, J. M.; Klecker, R. W., Jr.; Kelley, J. A.; Roth, J. S.; McCully, C. L.; Balis, F. M.; Poplack, D. G. Pyrimidine dideoxyribonucleosides: Selectivity of penetration into cerebrospinal fluid. *J. Pharmacol. Exp. Ther.* **1988**, *245*, 466−470.
23. Sawchuk, R. J.; Heydaya, M. A. Modeling the enhanced uptake of zidovudine (AZT) into the cerebrospinal fluid. 1. Effect of probenecid. *Pharm. Res.* **1990**, *7*, 332−338.
24. Glynn, S. L.; Yazdanian, M. In vitro blood−brain barrier permeability of nevirapine compared to other HIV antiretroviral agents. *J. Pharm. Sci.* **1998**, *87*, 306−310.
25. Dehouck, M. P.; Jolliet-Riant, P.; Bree, F.; Fruchart, J. C.; Cecchelli, R.; Tillement, J. P. Drug transfer across the blood−brain barrier: correlation between in vitro and in vivo models. *J. Neurochem.* **1992**, *58*, 1790−1797.
26. Dehouck, M.-P.; Meresse, S.; Delorme, P.; Fruchart, J.-C.; Cecchelli, R. An easier, reproducible, and mass-production method to study the blood−brain barrier in vitro. *J. Neurochem.* **1990**, *54*, 1798−1801.
27. Raub, T. J. Signal transduction and glial cell modulation of cultured brain microvessel endothelial cell tight junctions. *Am. J. Physiol.* **1996**, *271*, C495−C503.
28. Rubin, L. L.; Hall, D. E.; Porter, S.; Barbu, K.; Cannon, C.; Horner, H. C.; Janatpour, M.; Liaw, C. W.; Manning, K.; Morales, J.; Tanner, L. I.; Tomaselli, K. J.; Bard, F. A cell culture model of the blood−brain barrier. *J. Cell Biol.* **1991**, *115*, 1725−1735.
29. Chesne, C.; Dehouck, M. P.; Jolliet-Riant, P.; Bree, F.; Tillement, J. P.; Dehouck, B.; Fruchart, J. C.; Cecchelli, R. Drug transfer across the blood−brain barrier: comparison of in vitro and in vivo models. In *Frontiers in Cerebral Vascular Biology: Transport and Its Regulation*; Drewes, L. R., Betz, A. L., Eds.; Plenum Press: New York, 1993; pp 113−115.
30. Takasato, Y.; Rapoport, S. L.; Smith, Q. R. An in situ brain perfusion technique to study cerebrovascular transport in the rat. *Am. J. Physiol.* **1984**, *247*, H484−H493.
31. Takasawa, K.; Terasaki, T.; Suzuki, H.; Oooie, T.; Sugiyama, Y. Distributed model analysis of 3′-azido-3′-deoxythymidine and 2′,3′-dideoxyinosine distribution in brain tissue and cerebrospinal fluid. *J. Pharmacol. Exp. Ther.* **1997**, *282*, 1509−1517.
32. Levin, V. A. Relationship of octanol/water partition coefficient and molecular weight to rat brain capillary permeability. *J. Med. Chem.* **1980**, *23*, 682−684.
33. Barry, B. W.; Bennett, S. L. Effect of penetration enhancers on the permeation of mannitol, hydrocortisone and progesterone through human skin. *J. Pharm. Pharmacol.* **1987**, *39*, 535−546.
34. Wolosin, J. M.; Ginsburg, H.; Lieb, W. R.; Stein, W. D. Diffusion within egg lecithin bilayers resembles that within soft polymers. *J. Gen. Physiol.* **1978**, *71*, 93−100.
35. Barchi, J. J., Jr.; Marquez, V. E.; Driscoll, J. S.; Ford, H., Jr.; Mitsuya, H.; Shirasaka, T.; Aoki, S.; Kelley, J. A. Potential anti-AIDS drugs. Lipophilic, adenosine deaminase-activated prodrugs. *J. Med. Chem.* **1991**, *34*, 1647−1655.

Acknowledgments

Support for these studies was provided by NIH Grant AI34133. Mark Johnson also received support as a recipient of an Advanced Predoctoral Fellowship in Pharmaceutics from the Pharmaceutical Research and Manufacturers of America Foundation.

JS9803149

Thermodynamic Analysis of the Binding of a Hepatoprotectant Drug, Thioctic Acid, by β-Cyclodextrin

ELENA JUNQUERA AND EMILIO AICART*

Contribution from *Departamento de Química Fisica I, Facultad de Ciencias Químicas, Universidad Complutense de Madrid, 28040 Madrid, Spain.*

Received November 30, 1998. Accepted for publication March 29, 1999.

Abstract □ Spectroscopic and thermodynamic studies of the binding of a hepatoprotectant drug, thioctic acid, by β-cyclodextrin (β-CD) have been carried out using UV–vis and pH potentiometric measurements. The UV–vis spectra and the pH of the aqueous solutions of the drug were measured (i) as a function of total drug concentration in the absence of cyclodextrin, and (ii) as a function of cyclodextrin concentration at constant drug concentration. The spectroscopic study was done at pH = 7 and 25 °C, while the potentiometric study was performed at several temperatures ranging from 15 to 40 °C. From the spectroscopic data, the molar absorption coefficient, ϵ, for the pure drug in aqueous media and the stoichiometry of the inclusion complex with β-CD were determined. The dissociation constant, K_a, of the pure drug (which is a weak acid), and the association constants of the complexes formed by β-cyclodextrin and both the nonionized (HTIO) and ionized (TIO^-) forms of the drug, have been simultaneously determined at several temperatures from the pH data, without the necessity of working with buffered solutions. The nonionic forms are complexed by the β-CD with higher affinity than their ionic counterparts. From the dependency of the association constants on temperature (van't Hoff analysis), the inclusion complexes formed by HTIO or TIO^- and the β-CD were found to be enthalpy driven, with a favorable enthalpic term dominant over an unfavorable entropic term. Both contributions were found to show a possible dependence with temperature ($\Delta C_p^0 \neq 0$). This pattern may reveal the contribution of van der Waals interactions, hydrophobic effect, and solvent reorganization as the main driving forces promoting the complexation.

Introduction

The use of cyclodextrins as a new family of pharmaceutical excipients and drug carriers[1−6] has become an increasingly successful method to improve the general bioavailability of drugs. Particularly, it is known[7−10] that CD formulations of some drugs show a better tolerance since they cause fewer adverse side effects, this effect being more acute as the duration of the treatment increases. The parent cyclodextrins (CD's) are well-known nontoxic macrocyclic sugars, with doughnut-shaped structure, consisting of α(1→4) joined glucopyranose units. As a result of their hydrophobic inner surface, CD's are the most important simple organic compounds, capable of forming noncovalently bonded inclusion complexes with a variety of drug molecules in aqueous solution.

Thioctic acid, the oxidized form of α-lipoic acid (see Scheme 1), is hepatoprotectant drug used in the treatment of liver disease and as an antidote to poisonous mushrooms. It is expected that the formulation of this drug as a CD:

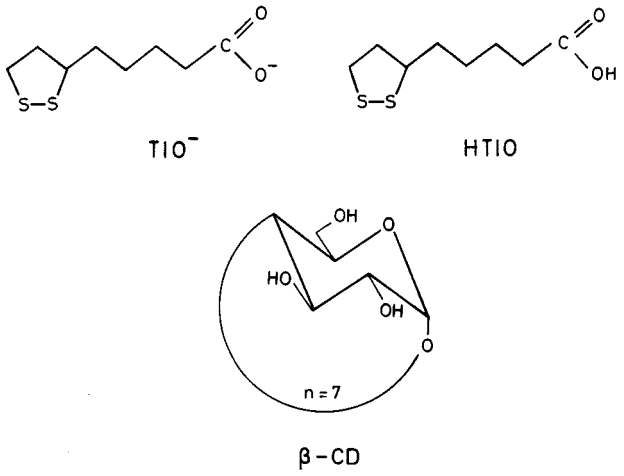

Scheme 1

Drug inclusion complex may help to avoid the undesirable side effects which the administration of the drug alone may provoke, thus improving its therapeutic usefulness. Structural information, such as the stoichiometry and geometry of the complex, and thermodynamic information, such as the association constant ($K_{CD:DRUG}$) and the change on the enthalpy ($\Delta H°$), entropy ($\Delta S°$), and heat capacity ($\Delta C_p°$) of binding, are necessary to draw a complete picture of the driving forces governing the CD−drug interaction. It is generally accepted[11−15] that a balance between van der Waals contacts and hydrophobic and solvent effects is mainly responsible for the overall stability of the complex.

Our group has examined the encapsulation of antiinflammatory and analgesic agents[14−18] by a series of β-cyclodextrins. These drug molecules and thioctic acid have a common characteristic: the presence of an acidic functional group. Thus, in aqueous solution both the ionized and the nonionized forms of the drug can be encapsulated by the cyclodextrin. There are two possible methods for studying the associations of these species with the CD: (i) follow the change in a physicochemical property (i.e., solubility, absorbance, fluorescence intensity, etc.) as a function of cyclodextrin concentration, but fixing the pH of the aqueous drug solution under conditions where only one of the two species is present; or (ii) directly monitor the pH of the aqueous unbuffered solution of the drug as the CD is added. In this work, we study the encapsulation of thioctic acid by β-cyclodextrin[19] in aqueous media by both methods: examination of the buffered drug solution (pH = 7) by UV−vis spectroscopy, and determination of pH of the unbuffered drug solutions in the absence and in the presence of β-CD by potentiometry. The spectroscopic study was performed at 25 °C, while the potentiometric experiments were carried out at temperatures from 15 °C to well above the temperature of human body (40 °C). We expect that the results of this work will show the strength of the potentiometric

* Corresponding author. Phone: 34-91-3944208. Fax: 34-91-3944135. E-mail: aicart@eucmax.sim.ucm.es. http://www-quifi.quim.ucm.es/qf_home/ea/ea_home.html.

10.1021/js980458n CCC: $18.00
Published on Web 05/05/1999

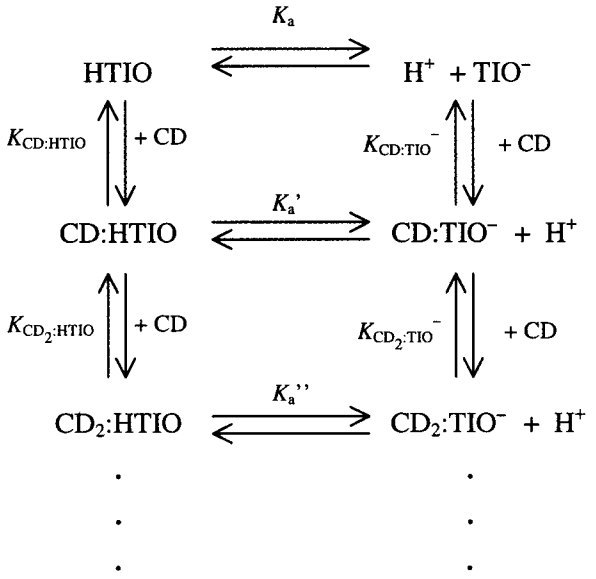

Scheme 2

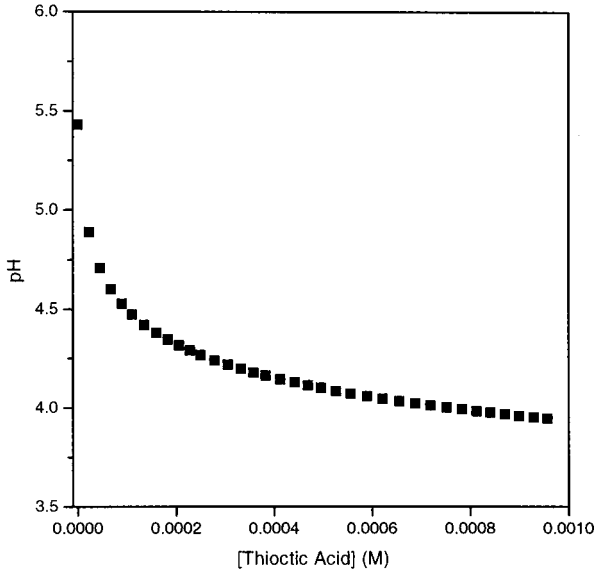

Figure 1—Plot of pH vs total thioctic acid concentration in the absence of β-CD, at 25 °C.

method for characterizing the inclusion complexes formed by CD and the nonionized and ionized forms of an acid/base pair.

Experimental Section

Materials—DL-1,2-Dithiolane-3-pentanoic acid, named as DL-6,8-thioctic acid, and β-cyclodextrin, with purities higher than 99%, were purchased from Sigma and used without further purification. β-Cyclodextrin has been found through a thermogravimetric analysis to consist of 11% of mass water content, which was considered in the calculations of solute concentrations. All the solutions were prepared with distilled and deionized water (taken from a Millipore Super-Q System, with a conductivity lower than 18 $\mu\Omega^{-1}$ cm^{-1}). The initial solutions were brought to homogeneity by sonicating them for 3 h in an ultrasonic bath. The buffer at pH = 7, used in the UV−vis experiment, was a standard Metrohm NaH_2PO_4/Na_2HPO_4 buffer solution.

UV−vis Measurements—The UV−vis spectra of aqueous buffered solutions (pH = 7) of thioctic acid, in the absence and in the presence of β-CD, were recorded at 25 °C with a Varian Cary 5G double beam UV−vis−NIR spectrophotometer from 260 to 500 nm with 1 nm intervals. The equipment was connected to a PC Pentium via a IEEE-Bus interface. Data acquisition and analysis of UV−vis spectra were performed with the software supported by the manufacturer. Two 10 mm, stoppered, rectangular silica UV cells (sample and reference cells) were placed in a stirred cuvette holder, whose temperature was kept constant at 25.00 ± 0.05 °C with a recirculating water bath. The scan rate was selected in all the cases as 300 nm/min. On the experiments with the drug−water binary systems, the thioctic acid concentration was varied from 0.0 to 5.8 mM, while for the CD−drug−water ternary systems, the thioctic acid concentration was kept constant at 4 mM, and β-CD concentration was varied from 0.0 to 4.5 mM, both in the sample and in the reference cells.

pH Potentiometric Measurements—Potentiometric data were collected with a Metrohm 713 Ion Meter (sensitivity of ± 0.001 units), using a combined glass electrode containing 3 M KCl as reference electrolyte solution. The adjustment of both the asymmetry potential and the Nernst slope of the combined glass electrode was made by daily calibration of the electrode with three Metrohm buffer solutions of pH = 1, 4, and 7, at each working temperature. The equipment and the fully computerized experimental procedure used on the pH determination were described previously.[14] The accuracy on the molarity of the solutions is better than 0.1%, and the temperature is held constant within ±0.001 K. The statistical average of 250 pH measurements for each concentration allow us to improve the reproducibility of the pH data by up to 60%, with respect to that reported by the manufacturer. In these experimental conditions, the pH measurements were made (i) as a function of thioctic acid concentration, in the absence of β-CD; and (ii) as a function of cyclodextrin concentration, keeping the drug concentration at 1 mM. The cyclodextrin concentration ranges were chosen to cover at least 80% of the saturation curve in order to guarantee a proper binding constant determination.[20]

Results and Discussion

An aqueous solution of thioctic acid in the presence of cyclodextrin may include the equilibria shown in Scheme 2, where K_a is the dissociation constant of HTIO, and $K_{CD:HTIO}$, $K_{CD_2:HTIO}$, $K_{CD:TIO^-}$ and $K_{CD_2:TIO^-}$ are the association constants of the 1:1 and 2:1 inclusion complexes formed by the β-CD and the acid and base forms of thioctic acid, respectively. From geometrical considerations and also from previous studies[2−5] of similar systems, 1:2, 2:2, and/or even CD:drug complexes with higher stoichiometries are not expected.

The equilibrium constants can be expressed as a function of the activities of the species, as follows:

$$K_a = (a_{H^+}a_{TIO^-})/(a_{HTIO}) \quad (1)$$

$$K_{CD:HTIO} = (a_{CD:HTIO})/(a_{CD}a_{HTIO}) \quad (2)$$

$$K_{CD:TIO^-} = (a_{CD:TIO^-})/(a_{CD}a_{TIO^-}) \quad (3)$$

$$K_{CD_2:HTIO} = (a_{CD_2:HTIO})/(a_{CD:HTIO}\, a_{CD}) \quad (4)$$

$$K_{CD_2:TIO^-} = (a_{CD_2:TIO^-})/(a_{CD:TIO^-}\, a_{CD}) \quad (5)$$

The constants K_a' and K_a'' are related to the others through simple expressions. The study reported in this work focuses on the determination of these equilibrium constants.

Thioctic Acid−Water System—It is of crucial importance, when studying the association of an acid/base pair with CD's, to measure the pK_a of the acid in order to know at which pH the presence of one of the two possible species in solution is negligible. For that purpose, the pH of the aqueous solutions of thioctic acid was measured as a function of drug concentration at 25 °C (Figure 1). From a nonlinear regression analysis (NLR)[14] of these pH data, which works with eq 1, the value of K_a for thioctic acid is 1.51×10^{-5} at 25 °C (pK_a = 4.82). Thus, in agreement with

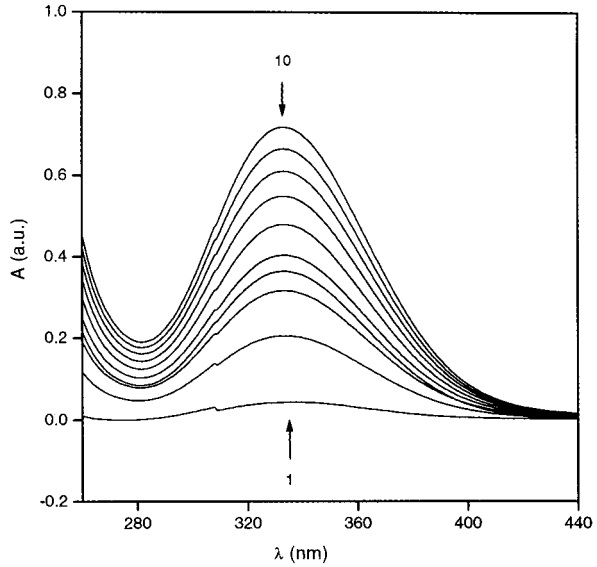

Figure 2—UV–vis spectra of aqueous solutions of thioctic acid at different concentrations, in the absence of cyclodextrin, at 25 °C and pH = 7: **1**, 0.39 mM; **2**, 1.23 mM; **3**, 2.23 mM; **4**, 2.90 mM; **5**, 3.03 mM; **6**, 3.70 mM; **7**, 4.30 mM; **8**, 4.84 mM; **9**, 5.32 mM; **10**, 5.76 mM.

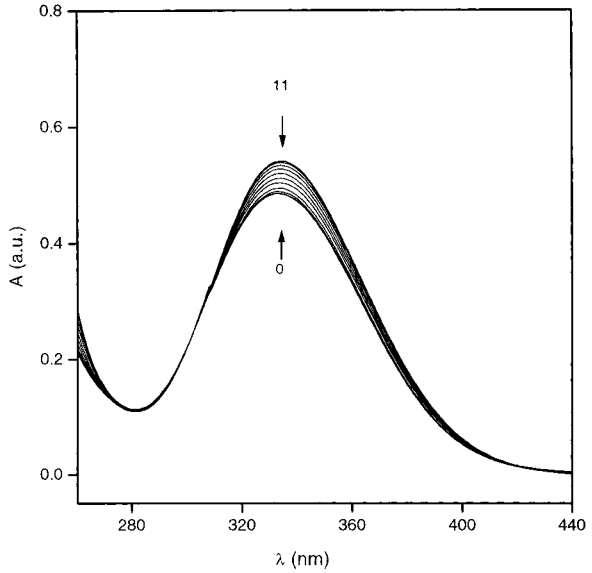

Figure 3—UV–vis spectra of an aqueous solution of thioctic acid at constant concentration (4 mM), 25 °C and pH = 7, in the absence and presence of different concentrations of β-CD: **0**, 0.00 mM; **1**, 0.12 mM; **2**, 0.35 mM; **3**, 0.77 mM; **4**, 1.34 mM; **5**, 1.94 mM; **6**, 2.52 mM; **7**, 3.10 mM; **8**, 3.62 mM; **9**, 4.10 mM; **10**, 4.53 mM.

what we have previously demonstrated,[17] the contribution of the nonprotonated (TIO^-) and protonated (HTIO) species of thioctic acid is negligible at only at pH $\leq$ 2.8 and pH $\geq$ 6.8, respectively. With this conclusion in mind, the UV–vis spectra of aqueous solutions of thioctic acid, buffered at pH = 7, were recorded at 25 °C for different drug concentrations, ranging from 0.0 to 5.8 mM (Figure 2). It can be observed that the spectra show a peak centered at λ_{max} = 333 nm, with absorbance values increasing with drug concentration, following a typical Lambert–Beer behavior. From the linear regression of the A vs [drug] values, the molar absorption coefficient, ϵ, was determined at different wavelengths. At λ_{max} = 333 nm, ϵ = 125 M^{-1} cm^{-1} (fit correlation = 0.99997), in concordance with literature values.[21,22] The experiment at pH = 1, where the nonionized form of the drug (HTIO) is the unique species in solution, was not performed since the absorbance values recorded at λ_{max} were extremely low (A < 0.1 within the whole concentration range).

Thioctic Acid-β-CD-Water System—*UV–vis Results*—Figure 3 shows the UV–vis spectra of a buffered solution of thioctic acid (pH = 7) at a constant concentration of 4.0 mM and 25 °C, at various β-CD concentrations ranging from 0.0 to 4.5 mM. As can be seen in the figure, the spectra show a peak centered at λ_{max} = 333 nm, with two isosbestic points at 300 and 420 nm, which indicate a 1:1 stoichiometry of the β-CD:TIO^- inclusion complex.[23] Although the spectroscopic characteristics of a system are known to be affected by the pH of the media, the geometry of the complex is not expected to change. Thus, once the 1:1 stoichiometry was found at pH = 7, it was assumed at pH = 1 as well. The addition of β-CD results in an increase in the absorbance intensity of the peak at 333 nm, but does not cause a shift in λ_{max}. However, the maximum change in A (ΔA_{max} = 0.06) was so small that the association constant $K_{CD:TIO^-}$ could not be determined accurately by fitting the experimental data to the well-known UV binding isotherm.[23] This feature, often found for other CD:substrate systems,[24,25] reveals that UV spectroscopy is not sensitive enough to study the β-CD–thioctic system, or any other system where the presence of cyclodextrin does not result in a clear change in the spectroscopic properties of the drug.

pH Results—Since H^+ is one of the species involved in the equilibria shown in Scheme 2, variation of pH of an aqueous drug solution, at constant concentration, as a function of β-CD concentration can be used as an indication of the shift in the equilibria, depending on the magnitude of the association constants of eqs 1–5. Figure 4 shows the plot of the ΔpH (= pH–pH_0) values, taken as the difference between the pH of the CD–drug–water system and that of the initial drug–water system (pH_0), as a function of β-CD concentration at different temperatures ranging from 15 to 40 °C. Equations 1–5, together with the following charge and mass balances for the CD and the drug:

$$[H^+] = [TIO^-] + [CD{:}TIO^-] + [CD_2{:}TIO^-] + [OH^-] \quad (6)$$

$$[drug]_{total} = [HTIO] + [TIO^-] + [CD{:}HTIO] + [CD{:}TIO^-] + [CD_2{:}HTIO] + [CD_2{:}TIO^-] \quad (7)$$

$$[CD]_{total} = [CD] + [CD{:}HTIO] + [CD{:}TIO^-] + 2\,[CD_2{:}HTIO] + 2\,[CD_2{:}TIO^-] \quad (8)$$

permit us to obtain the equilibrium constants from the pH (= $-\log a_{H^+}$) experimental data. The fitting procedure is a NLR (nonlinear regression) method based on a Newton–Raphson and a Marquardt algorithm, widely explained elsewhere.[14] The activities in eqs 1–5 are related to the concentrations shown in eqs 6–8 through the activity coefficients, determined with the extended Debye–Hückel theory. The coefficients of the fit are the equilibrium constants we are interested in, whose values for thioctic acid are reported in Table 1 at various temperatures. The data in Table 1 lead us to some general conclusions: (i) The dissociation constant, K_a, of thioctic acid is (1.5 ± 0.1) × 10^{-5}, in excellent agreement with the value obtained from the experiment done with the thioctic–water binary system, thus confirming the appropriateness of the model. It can be observed as well that K_a does not depend on the temperature within the range of temperatures studied herein. (ii) None of the equilibrium constants of Scheme 2 are fixed to zero during the fitting procedure. The inclusion complexes formed by β-CD and HTIO or TIO^- show 1:1 stoichiometries, in agreement with UV–vis results, since $K_{CD_2:HTIO}$ and $K_{CD_2:TIO^-}$ have been found to be negligible and

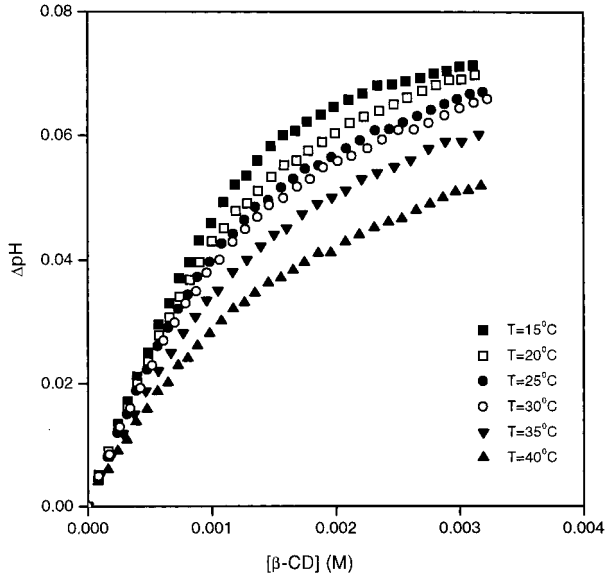

Figure 4—Plot of ΔpH vs β-CD concentration for aqueous solutions of thioctic acid at constant concentration (1 mM), at different temperatures ranging from 15 to 40 °C.

Table 1—Values of the Dissociation Constant K_a of Thioctic Acid, the Association Constants of the 1:1 Inclusion Complexes Formed by β-Cyclodextrin and the Acid and Base Forms of This Drug, $K_{CD:HTIO}$ and $K_{CD:TIO^-}$, Respectively, and the Saturation Degree Covered, f, as a Function of Temperature

T, °C	$10^5 K_a$	$K_{CD:HTIO}$, M^{-1}	$K_{CD:TIO^-}$, M^{-1}	$K_{CD:HTIO}/K_{CD:TIO^-}$	f range, %
15	1.5 ± 0.1	5790 ± 300	4060 ± 200	1.43	20–80
20	1.6 ± 0.1	3640 ± 150	2480 ± 150	1.47	18–79
25	1.6 ± 0.1	3410 ± 140	2390 ± 150	1.43	18–78
30	1.6 ± 0.1	2560 ± 130	1850 ± 100	1.40	21–80
35	1.4 ± 0.1	1650 ± 100	1140 ± 70	1.45	19–80
40	1.5 ± 0.1	1050 ± 90	740 ± 50	1.42	21–75

always below the uncertainty of the fits. This 1:1 stoichiometry is usually found for a wide variety of drug molecules upon binding β-CD or β-CD derivatives.[2–8] (iii) The affinity of β-CD by the protonated form ($K_{CD:HTIO}$) of the drug is around 1.4 times higher at all temperatures than that of the nonprotonated form ($K_{CD:TIO^-}$). This behavior, previously reported[14–17,26–29] for other carboxylic derivatives, has been attributed to either the random character of the inclusion,[27] or the repulsive interaction between the negative charge on the ionic species and the negatively charged end of the CD dipole,[29] or the differences in the entropic balance upon binding related to the structure-breaking character of the carboxylate anions.[14] However, it is worth noting that the ratio $K_{CD:HTIO}/K_{CD:TIO^-}$ found for this system is lower than that obtained for other CD:drug systems previously studied by us,[14–17] thus justifying the lower ΔpH observed for the system reported here in, compared with that observed for the other systems. This ratio implies that the therapeutic effects of β-CD as an excipient for thioctic acid are not much affected by the pH of the medium, the % of free drug being similar either in an acid medium, for example in the stomach, or in other biological media, with higher pH. Anyway, the values of $K_{CD:HTIO}$ and $K_{CD:TIO^-}$ at body temperature fall in the range of 1700−1000 M^{-1}, which can be considered optimum values regarding the use of CD's as effective drug carriers. The confirmation of all these estimations in vivo, although out of the scope of this work, would be welcomed.

It can be observed as well in Table 1 that as the temperature increases, the affinity of the cyclodextrin for

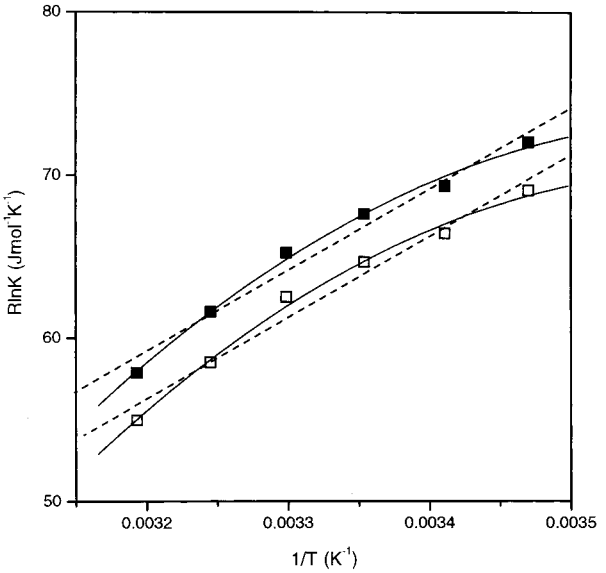

Figure 5—van't Hoff plots for the associations of β-CD with HTIO and TIO^-. Dash lines for linear fits and solid lines for nonlinear fits of eq 11.

both ionized and nonionized forms of the drug decreases. Figure 5 shows the van't Hoff plots of both association processes. A linear relationship of the R ln K vs $1/T$ data indicates the independence of $\Delta H°$ and $\Delta S°$ on T ($\Delta C_p^o \sim 0$), while the absence of such linear behavior reveals that $\Delta H°$ and $\Delta S°$ are temperature dependent, pointing to an association process with $\Delta C_p^o \neq 0$. If we assume that ΔC_p^o is temperature independent and that the dependence on temperature for ΔH and ΔS can be expressed by,

$$\Delta H = \Delta H° + \Delta C_p^o\,(T - 298.15) \quad (9)$$

$$\Delta S = \Delta S° + \Delta C_p^o \ln(T/298.15) \quad (10)$$

where 298.15 K has been taken as the reference temperature, and the thermodynamic quantities $\Delta H°$, $\Delta S°$, and ΔC_p^o at 25 °C are related to R ln K through the van't Hoff equation:

$$R \ln K = -[\Delta H° + (T - 298.15)\Delta C_p^o]/T + \Delta C_p^o \ln(T/298.15) + \Delta S^o \quad (11)$$

Equation 11 explains either the linearity or the curvature of the plots in Figure 5. When $\Delta C_p^o = 0$, eq 11 is simplified to the well-known linear relation (R ln $K = -\Delta H°/T + \Delta S°$), where $\Delta H°$ and $\Delta S°$ can be estimated from the slope and intercept of the fit, respectively. On the contrary, when $\Delta C_p^o \neq 0$, $\Delta H°$, $\Delta S°$, and ΔC_p^o can be determined by using a nonlinear regression of the experimental K values at various temperatures. We have performed both the linear and the nonlinear van't Hoff analysis of the experimental data, and both are drawn on the van't Hoff plots of Figure 5. Table 2 reports the results obtained for $\Delta H°$ and $\Delta S°$ in both cases, and for ΔC_p^o in the case of the nonlinear fit. Although the uncertainty in these results is high (up to 30%) in both the linear and the nonlinear fits, as usual for van't Hoff analysis, it can be observed in the table that both HTIO and TIO^- species bind to β-CD with a favorable enthalpic term ($\Delta H° < 0$) and an unfavorable entropic term ($\Delta S° < 0$). Both processes are exothermic and enthalpy driven ($|\Delta H°| > T\,|\Delta S°|$), as usually found[11–15,31–33] for associations between small guest molecules and an apolar cavity in water. A combination of hydrophobic effect ($\Delta H° \sim 0$; $\Delta S° > 0$), van der Waals forces

Table 2—Values of $\Delta H°$, $\Delta S°$, and $\Delta C_p°$ for the Association of HTIO and TIO^- with β-CD, Obtained with Eq 11 in Both the Linear and Nonlinear Forms

system		$\Delta H°$, kJ mol^{-1}	$\Delta S°$, J mol^{-1} K^{-1}	$\Delta C_p°$, J mol^{-1} K^{-1}	std dev
β-CD + HTIO	linear	–50	–99	—	0.93
	nonlinear	–45[a]	–84[a]	–1980[a]	0.35
β-CD + TIO^-	linear	–50	–102	—	0.98
	nonlinear	–45[a]	–87[a]	–2000[a]	0.41

[a] Obtained at a reference temperature of 298.15 K.

($\Delta H° < 0$; $\Delta S° < 0$), and solvent reorganization could account for such a thermodynamic pattern. It appears that the contribution of van der Waals interactions and hydrophobic effect could be similar in both inclusion processes, while the contribution of solvent reorganization could be the factor which makes the binding of β-CD and HTIO energetically more favorable than that of β-CD and TIO^-. Furthermore, although the use of the nonlinear form of the van't Hoff equation may be risky, given the uncertainty on K values, it is clear that the van't Hoff plots of Figure 5 are not straight lines, as indicated by the standard deviations of the fits. Thus, we would conclude that, within the uncertainty of the fits, a dependence of $\Delta H°$ and $\Delta S°$ on T, i.e., $\Delta C_p° \neq 0$, is an appropriate conclusion. From our data, we may say that $\Delta C_p°$ is negative, as usually found for the inclusion of apolar solutes by cyclodextrins[12,15,31] and cyclophanes,[11] and for carbohydrate association with lectins[33] in aqueous solution. Particularly, $\Delta C_p°$ values of around -2000 J mol^{-1} K^{-1} are typical of biological associations and recognition processes where hydrogen bonds and/or polar groups are present.[31−33] Assigning a value to $\Delta C_p°$, however, given the high error associated with this magnitude, would be just a speculation. Direct calorimetric results would be necessary to confirm these conclusions.

It has been demonstrated that the pH potentiometric technique, together with the model previously reported by us to determine association constants,[14] show clear advantages over the UV−vis technique for the examination of CD's complexing with ionizable guests. The advantages of this method include the following: (i) one pH−potentiometric experiment at each temperature, without buffering the solution, gives a complete thermodynamic description of the system, i.e., dissociation constant of the drug, association constants of both ionic and nonionic species of the drug with the CD, and the stoichiometry of the complex; (ii) the characterization of the CD:HTIO and CD:TIO^- complexes, not available through UV−vis measurements, may be studied from the pH−potentiometric experiments; (iii) the potentiometric technique accurately allows for the study of CD−drug systems for which the experimental properties of the drug in aqueous solution (such as the absorbance or the pH) are not very much affected by the presence or the absence of the CD. The only requirement of this method is that the association constants of the complexes formed by the CD and the nonionized and ionized forms of the guest must be neither very similar, nor very different. In the first case, the experimental ΔpH would be quite small, while in the second case the uncertainty in the highest binding constant would mask the value of the lowest binding constant.

References and Notes

1. Szejtli, J. Medicinal Applications of Cyclodextrins. *Med. Res. Rev.* **1994**, *14*, 353−386.
2. Szejtli, J.; Osa, T. *Comprehensive Supramolecular Chemistry, Vol. 3, Cyclodextrins*; Elsevier: Oxford, 1996.
3. Rajewski, R. A.; Stella, V. J. Pharmaceutical Applications of Cyclodextrins. 2. *In Vivo* Drug Delivery. *J. Pharm. Sci.* **1996**, *85*, 1142−1169.
4. D'Souza, V. T.; Lipkowitz K. B. Cyclodextrins. *Chem. Rev.* **1998**, *98*, 1741−2076.
5. Thompson, D. O. Cyclodextrins-Enabling Excipients: Their Present and Future Use in Pharmaceuticals. *Crit. Rev. Ther. Drug Carrier Syst.* **1997**, *14*, 1−104.
6. Santucci, L.; Fiorucci, S.; Chiucchiu, S.; Sicilia, A.; Bufalino, L.; Morelli, A. Placebo-Controlled Comparison of Piroxicam-β-Cyclodextrin, Piroxicam, and Indomethacin on Gastric Potential Difference and Mucosal Injury in Humans. *Digest. Dis. Sci.* **1992**, *37*, 1825−1832.
7. Warrington, S.; Debbas, N.; Farthing, M.; Horton, M.; Umile, A. Piroxicam-β-Cyclodextrin: Effects on Gastrointestinal Blood Loss and Gastric Mucosal Appearance in Healthy Men. *Int. J. Tissue React.* **1991**, *13*, 243−248.
8. Pitha, J.; Milecki, J.; Fales, H.; Pannel, L.; Uekama, K. Hydroxypropyl-β-cyclodextrin: Preparation and Characterization, Effects on Solubility of Drugs. *Int. J. Pharm.* **1986**, *29*, 73−82.
9. Jarho, P.; Urtti, A.; Jarvinen, T. Hydroxypropyl-β-Cyclodextrin Increases the Aqueous Solubility and Stability of Pilocarpine Prodrugs. *Pharm. Res.* **1995**, *12*, 1371−1375.
10. Loftsson, T.; Fridriksdóttir, H.; Olafsdóttir, B. J. Solubilization and Stabilization of Drugs through Cyclodextrin Complexation. *Acta Pharm. Nord.* **1991**, *3*, 215−217.
11. Inoue, Y.; Liu, Y.; Tong, L.-H.; Shen, B.-J.; Jin, D.-S. Calorimetric Titration of Inclusion Complexation with Modified β-Cyclodextrins.[1] Enthalpy−Entropy Compensation in Host−Guest Complexation: From Ionophore to Cyclodextrin and Cyclophane. *J. Am. Chem. Soc.* **1993**, *115*, 10637−10644.
12. Rekharsky, M. V.; Schwarz, F. P.; Tewari, Y. B.; Goldberg, R. N.; Tanaka, M.; Yamashoji, Y. Thermodynamic and NMR Study of the Interactions of Cyclodextrins with Cyclohexane Derivatives. *J. Phys. Chem.* **1994**, *98*, 4098−4103.
13. Bertrand, G. L.; Faulkner, J. R.; Han, S. M.; Armstrong, D. W. Substituent Effects on the Binding of Phenols to Cyclodextrins in Aqueous Solution. *J. Phys. Chem.* **1989**, *93*, 6863−6867.
14. Junquera, E.; Aicart, E. Potentiometric Study of the Encapsulation of Ketoprophen by Hydroxypropyl-β-cyclodextrin. Temperature, Solvent and Salt Effects. *J. Phys. Chem. B* **1997**, *101*, 7163−7171.
15. Junquera, E.; Martín-Pastor, M.; Aicart, E. Molecular Encapsulation of Flurbiprophen and/or Ibuprophen by Hydroxypropyl-β-cyclodextrin in Aqueous Solution. Potentiometric and Molecular Modeling Studies. *J. Org. Chem.* **1998**, *63*, 4349−4358.
16. Junquera, E.; Aicart, E. A Fluorimetric, Potentiometric and Conductometric Study of the Aqueous Solutions of Naproxen and its Association with Hydroxypropyl-β-Cyclodextrin. *Int. J. Pharm.* **1998**, *176*, 169.
17. Junquera, E.; Aicart, E. Effect of pH on the Encapsulation of the Salicylic Acid/Salicylate System by Hydroxypropyl-β-cyclodextrin at 25 °C. A Fluorescence Enhancement Study in Aqueous Solutions. *J. Incl. Phenom.* **1997**, *29*, 119−136.
18. Junquera, E.; Peña, L.; Aicart, E. Binding of Sodium Salicylate by β-Cyclodextrin or 2,6-di-*O*-methyl-β-cyclodextrin in Aqueous Solution. *J. Pharm. Sci.* **1998**, *87*, 86−90.
19. The β-CD:thioctic acid complex has been patented by Hetthe Helmuth, ref. DE 4338508 Al, 1995; *Chem. Abstr.* **1995** *123*, 266098.
20. Deranleau, D. A. Theory of Measurement of Weak Molecular Complexes. I. General Considerations. *J. Am. Chem. Soc.* **1969**, *91*, 4044−4049.
21. Budavari, S. *The Merck Index. An Encyclopedia of Chemicals, Drugs and Biologicals*; Merck & Co. Inc.: Whitehouse Station, NJ, 1996.
22. Ungnade, H. E. *Organic Electronic Spectral Data*, Interscience Pub. Inc.: New York, 1960.
23. Connors, K. A. *Binding Constants: The Measurement of Molecular Complex Stability*; John Wiley & Sons: New York, 1987.
24. Kano, K.; Tamiya, Y.; Hashimoto, S. Binding Forces in Complexation of p-Alkylphenols with β-Cyclodextrin and Methylated β-Cyclodextrins. *J. Incl. Phenom.* **1992**, *13*, 287−293.
25. Cotta-Ramusino, M.; Rufini, L.; Mustazza, C. UV Spectroscopic Study of the Interaction Between α-, β-, and γ-Cyclodextrins and Pyridine Derivatives. *J. Incl. Phenom.* **1993**, *15*, 359−368.
26. Gelb, R. I.; Schwartz, L. M.; Johnson, R. F.; Laufer, D. A. The Complexation Chemistry of Cyclohexaamyloses. 4. Reactions of Cyclohexaamylose with Formic, Acetic, and Benzoic Acids and Their Conjugate Bases. *J. Am. Chem. Soc.* **1979**, *101*, 1869−1874.
27. Bergeron, R. J.; Channing, M. A.; McGovern, K. A. Dependence of Cycloamylose-Substrate Binding on Charge. *J. Am. Chem. Soc.* **1978**, *100*, 2878−2883.

28. Cromwell, W. C.; Byström, K.; Eftink, M. R. Cyclodextrin-Adamantanecarboxylate Inclusion Complexes: Studies of the Variation in Cavity Size. *J. Phys. Chem*. **1985**, *89*, 326−332.
29. Martin-Davies, D.; Savage, J. R. Cyclodextrin Complexes of Substituted Perbenzoic and Benzoic Acids and Their Conjugate Bases: Free Energy Relationships Show the Interaction of Polar and Steric Factors. *J. Chem. Soc., Perkin Trans. 2* **1994**, 1525−1530.
30. Eftink, M. R.; Andy, M. L.; Byström, K.; Perlmutter, H. D.; Kristol, D. S. Cyclodextrin Inclusion Complexes: Studies of the Variation in the Size of Alicyclic Guests. *J. Am. Chem. Soc*. **1989**, *111*, 6765−6772.
31. Diederich, F.; Smithrud, D. B.; Sanford, E. M.; Wyman, T. B.; Ferguson, S. B.; Carcanague, D. R.; Chao, Y.; Houk, K. N. Solvent Effects in Molecular Recognition. *Acta Chem. Scandinava* **1992**, *46*, 205−215.
32. Stauffer, D. A.; Barrans, R. E., Jr.; Dougherty, D. A. Concerning the Thermodynamics of Molecular Recognition in Aqueous and Organic Media. Evidence for Significant Heat Capacity Effects. *J. Org. Chem*. **1990**, *55*, 2762−2767.
33. Chevernak, M. C.; Toone, E. J. Structure and Energetics of Protein-Carbohydrate Complexes. *Biochemistry* **1995**, *34*, 5686−5695.

Acknowledgments

Authors are grateful to Ministerio de Educación y Ciencia of Spain through DGES Project No. PB95-0356 for financial support. Authors also thank Dr. S. Holmgrem for his help.

JS980458N

Effects of *Taraxacum mongolicum* on the Bioavailability and Disposition of Ciprofloxacin in Rats

MIN ZHU, PRUDENCE Y. WONG, AND RONALD C. LI*

Contribution from *Department of Pharmacy, The Chinese University of Hong Kong, Shatin, N.T. Hong Kong.*

Received September 14, 1998. Final revised manuscript received January 14, 1999.
Accepted for publication March 24, 1999.

Abstract □ *Taraxacum mongolicum* (TM), also known as dandelion, is a herb widely used in the East for its antibacterial activity. The high mineral content of TM presents a potential problem for the absorption of quinolone antibiotics. This study was undertaken to discern the significance of a drug–drug interaction between TM and ciprofloxacin. Two groups of Sprague Dawley rats (220–250 g) were employed; one received a single oral dose of ciprofloxacin (20 mg/kg) with concomitant oral administration of an aqueous TM extract (2 g crude drug/kg) while the control group received oral ciprofloxacin (20 mg/kg) only. Ciprofloxacin in plasma and urine, collected over 6 and 24 h, respectively, was determined by HPLC. Noncompartment analysis was employed for pharmacokinetic parameter estimation. Results indicated that, as compared to control, maximum plasma concentration (C_{max}) of ciprofloxacin was significantly lowered by 73% in rats receiving concurrent TM dosing. Oral TM also caused a 3-fold increase in both apparent drug distribution volume ($V_{d,\lambda z}/F$: 92.0 vs 30.8 L/kg) and terminal elimination half-life ($t_{1/2,\lambda z}$; 5.71 vs 1.96 h). Partly due to the changes in drug distribution and elimination, relative bioavailability of ciprofloxacin, as assessed by $AUC_{0\rightarrow\infty}$, remained similar for both dosing groups. These findings suggest the possibility of a multifactorial drug–drug interaction between TM and ciprofloxacin. Thus, the implications of concomitant dosing of the two agents should not be overlooked.

Introduction

Ciprofloxacin is a fluoroquinolone-type antibiotic with excellent activity against Gram positive and negative bacteria as well as Mycobacteria. Its oral absorption, however, has been shown to be drastically impaired by concomitant administration of agents containing metal cations.[1,2] This phenomenon has been extensively studied for antacids, mineral supplements, and milk products.[3] Information on such an interaction is currently unavailable for herbal medicines and health foods.

The possibility of a drug−drug interaction between ciprofloxacin and a mineral rich antiinflammatory/antibacterial herbal medicine, *Taraxacum mongolicum* Hand-Mazz. (Compositae), was investigated in this study. Traditionally, the dried whole plant of *T. mongolicum* (TM) is used for the treatment of boils, sores, mastitis, lymphadenitis, inflammation of the eye, sore throat, lung and breast abscess, acute appendictis, jaundice, and urinary tract infections.[4,5] In addition, this herb has been shown to exert a bactericidal effect on numerous pathogens showing ranges of MIC from 1:10 to 1:640 with its aqueous extract.[4] In addition, in vitro antifungal, antileptospiral, and antiviral effects of the herb have also been documented.[4] Chemical investigation of TM indicates the presence of triterpenoids (e.g., taraxasterol, taraxacin, taraxarol), inulin, pectin, asparagin, and phenolic compounds.[4,6] To collect more definitive information, the content of metal cations in dried TM was independently measured. A full pharmacokinetic evaluation was conducted in the rat to elucidate the potential of a drug−drug interaction, if any, between TM and ciprofloxacin.

Experimental Section

Plant Materials—The whole dried plant of *T. mongolicum* (TM) was purchased from a local herbal shop and was authenticated by macroscopic examination and microscopic identification in the Pharmacognosy Laboratory, Department of Pharmacy, The Chinese University of Hong Kong, where the voucher specimen (TM01) was deposited. For the preparation of the aqueous TM extract used in animal studies, the powdered crude plant material (5 g) was treated with boiling deionized and distilled water (50 mL) for 1 h, and the extract was evaporated to a concentration equivalent to 0.5 g crude drug/mL.

Chemical Reagents and Apparatus—Ciprofloxacin hydrochloride was kindly provided as a gift by Bayer AG (Leverkusen, Germany). The internal standard, enoxacin, was purchased from Sigma Chemical Co. (St. Louis, MO). Acetonitrile (HPLC grade, Mallinckrodt-Baker, Inc., Phillipsburg, NJ), triethylamine (Riedel-de Haen AG, Germany), and other chemical reagents were acquired commercially.

An HPLC system (Hewelett Packard series 1050) consisting of an UV-detector, an autosampler, a reversed-phase ODS column (4.6 mm i.d. × 250 mm; particle size: 5 μm, Phenomenex), and a guard column (Novapak C_{18}, Waters) was employed for the quantitation of ciprofloxacin in plasma and urine smaples. For the assessment of the content of various cations in the TM extract, an inductive plasma emission spectrometer (Shimadzu ICPQ-1012) was used.

Assessment of Cation Content in *T. mongolicum* Extract—The TM extract was digested with an acid mixture consisting of HNO_3:$HClO_4$ (9:1). A plant-free acid control was also prepared for comparison. The content of Zn, Fe, Cu, Ca, Mn, Mg, Sr, Cr, Pb, and Ni was determined by plasma emission spectrometry.

Pharmacokinetic Studies—Male Sprague−Dawley rats (220−240 g) were housed under a controlled condition (23−25 °C, 55% relative humidity and 12 h light/dark light cycle) and were allowed free access to food and water before experiments. Under anesthetization with an ip injection of 80 mg/kg of ketamine and 10 mg/kg of xylazine, a cannula was surgically inserted into the right jugular of each animal. All study rats were fasted overnight prior to the scheduled blood sampling postdosing on the next day. In the test group, rats (n = 5) were dosed orally with the aqueous TM extract (2 g crude drug/kg) immediately followed by a single oral dose of ciprofloxacin (20 mg/kg). Rats (n = 5) that received a single oral dose of ciprofloxacin (20 mg/kg) alone were used as controls. Blood (0.6 mL) was withdrawn via the cannular just prior to ciprofloxacin dosing (t = 0) and at 5, 30, 60, 90, 120, 150, 180, 240, 300, and 360 min postdosing. Plasma was immediately separated by centrifugation at 10000g for 5 min. Urine samples were collected over 0−2, 2−4, 4−6, and 6−24 h intervals, and the total volume within each interval was recorded. Both plasma and urine samples were stored at −80 °C until assayed.

* Corresponding author. Tel: 978 247 1884; Fax: 978 247 1389; e-mail:rcli@genetics.com.

10.1021/js980367q CCC: $18.00
Published on Web 05/01/1999

HPLC Assay for Ciprofloxacin—The HPLC assay developed by Nix et al.[7] was utilized in the present study with minor modifications. For the quantitation of ciprofloxacin in plasma, acetonitrile (200 μL) was added to the plasma sample (0.3 mL) for protein precipitation and was followed by the addition of enoxacin (internal standard, final concentration: 1.0 ng/μL). The mixture was centrifuged at 10000*g* for 5 min, and 200 μL of the supernatant was tried using a Concentrivap Concentrator (Labconco, Kansas City, MO) at 35 °C. The residue was reconstituted in 70 μL of mobile phase, and a 50 μL aliquot of which was injected onto the HPLC. As for the urine assay, the sample was first diluted with deionized–distilled water containing 10 ng/mL internal standard. The dilution factor was 1:50 for samples collected over the 0–2, 2–4, 4–6 h intervals and 1:10 for the sample collected over the 6–24 h interval. The diluted samples were then centrifuged at 10000*g* for 5 min, and the supernatant (50 μL) was submitted to the HPLC assay.

The HPLC mobile phase consisted of 16% acetonitrile, 1% methanol, and 83% aqueous buffer (pH 3.0) which was comprised of sodium dihydrogen phosphate monohydrate (0.1 M), glacial acetic acid (1% v/v), and triethylamine (0.5% v/v). The flow rate was set at 1.1 mL/min, and detection was preformed at 278 nm. Complete separation of ciprofloxacin and enoxacin (internal standard) was achieved with retention times at 9.0 and 7.0 min, respectively. The calibration curves were linear over the range from 0 to 3 μg/mL and from 1.0 to 10 μg/mL for the respective plasma and urine assays with correlation coefficients >0.999 for both biomatrixes. The lower limit of quantitation of ciprofloxacin was 25 ng/mL for both assays. Adequacy of this analytical methodology was supported by the <9.3% coefficient of variations for the interday assay variability obtained from quality control samples.

Analysis of Pharmacokinetic Parameters of Ciprofloxacin—The plasma concentration–time data of ciprofloxacin were assessed by noncompartmental analysis. The maximum plasma concentration (C_{max}) and the time achieving C_{max} (T_{max}) were directly observed from the individual concentration vs time profiles. Least-squares regression analysis was employed on the terminal elimination phase for estimation of elimination rate constant (λ_z). Elimination half-life ($t_{1/2,\lambda z}$) was computed as 0.693/λ_z, and the area under curve from time zero to infinity ($AUC_{0\to\infty}$) was estimated by trapezoidal integration as:

$$AUC_{0\to\infty} = AUC_{0\to t} + C_t/\lambda_z$$

where $AUC_{0\to t}$ is the AUC from time zero to time t and C_t is the plasma ciprofloxacin concentration at time t. Other parameter estimates including oral clearance (CL/F), renal clearance (CL_r), and apparent volume of distribution ($V_{d,\lambda z}/F$) were estimated by standard procedures.[8] The relative bioavailability (F') of ciprofloxacin was estimated as the ratio of the mean $AUC_{0\to\infty}$ values for the animals receiving both ciprofloxacin and TM to that of ciprofloxacin alone. Statistical significant differences in the derived pharmacokinetic parameter estimates between the groups were assessed by Student-t-test with the level of statistical significance (α) set at 0.05.

Results

Assessment of Cation Content in *T. mongolicum*—Concentrations of the 10 metal cations contained in the aqueous TM extract were determined to be 5760, 4941, 2311, 111.3, 62.4, 31.4, 16.1, 15.3, 6.0, and 1.5 μg/g for Mg, Ca, Fe, Mn, Zn, Sr, Cr, Cu, Ni, and Pb, respectively.

Pharmacokinetics of Ciprofloxacin in Rats—Data obtained from the control group revealed that ciprofloxacin, administered as a single oral dose (20 mg/kg), was rapidly absorbed with C_{max} (1.31 ± 0.49 μg/mL) achieved at 0.42 ± 0.17 h. Distribution of the drug was extensive with $V_{d,\lambda z}/F$ estimated to be 30.8 ± 11.1 L/kg and is approximately 50-fold of total body water. Though affected by F, this large distribution volume suggests a significant degree of tissue penetration and uptake. Oral clearance (CL/F) of the antibiotic was estimated to be 10.8 ± 2.7 L/h/kg and a mean ± SD $t_{1/2,\lambda z}$ of 1.96 ± 0.43 h was observed. Urinary recovery (X_u) of the antibiotic represented approximately 20% of the oral dose administered. All pertinent paramacokinetic parameter estimates are listed in Table 1.

Table 1—Mean (±SD) Pharmacokinetic Parameter Estimates[a] (n = 5) of Ciprofloxacin after a Single Oral Dosing (20 mg/kg) with or without Aqueous Preparation of *T. Mongolicum* (TM, 2 g crude drug/kg) Coadministration

PK parameter estimates	ciprofloxacin	ciprofloxacin + TM
C_{max} (mg L^{-1})	1.31 ± 0.49	0.35 ± 0.04***
T_{max} (h)	0.42 ± 0.17	0.50 ± 0
$t_{1/2,\lambda z}$ (h)	1.96 ± 0.43	5.71 ± 0.91***
λ_z (h^{-1})	0.37 ± 0.07	0.12 ± 0.02***
$AUC_{0\to\infty}$ (mg L^{-1} h)	1.97 ± 0.51	1.90 ± 0.55
$V_{d,\lambda z}/F$ (L kg^{-1})	30.8 ± 11.1	92.0 ± 20.8**
CL/F (L h^{-1} kg^{-1})	10.8 ± 2.7	11.1 ± 2.6
CL_r (L h^{-1} kg^{-1})	2.36 ± 0.45	1.93 ± 0.32
X_u (% dose)	22.9 ± 5.3	18.3 ± 4.4

[a] Significance levels: * $p < 0.05$, ** $p < 0.01$, *** $p < 0.005$.

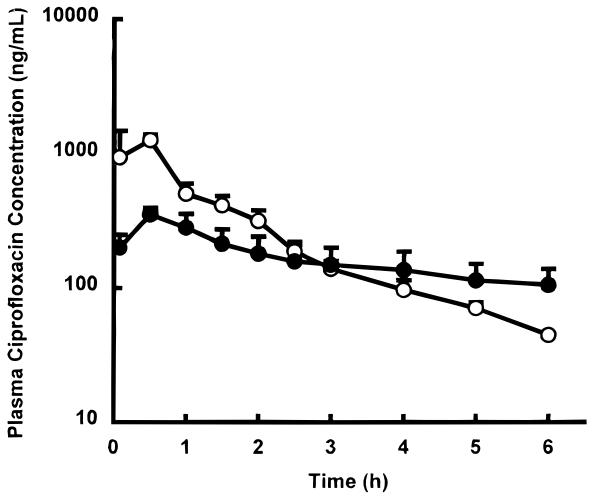

Figure 1—The plasma versus concentration time profiles of ciprofloaxcin. concentration (mean ± SD) measured for oral ciprofloxacin only (20 mg/kg) and oral ciprofloxacin (20 mg/kg) plus TM (2 g crude drug/kg) are depicted by ○ and ●, respectively.

Pharmacokinetics of Ciprofloxacin: Impact of *T. mongolicum* Coadministration—The mean plasma concentration–time profiles of ciprofloxacin for the control group and that with concomitant oral administration of TM are shown in Figure 1. The derived pharmacokinetic estimates for this study group are also available in Table 1. In comparison to the control group, significant alterations in certain pharmacokinetic estimates of ciprofloxacin were observed with concurrent TM administration. In particular, C_{max} of ciprofloxacin was lowered by 73% ($p < 0.005$) with T_{max} slightly prolonged by 16% ($p > 0.05$) (Table 1). Despite the reduction in C_{max}, the $AUC_{0\to\infty}$ estimate for ciprofloxacin remained similar (Figure 1). Although not statistically significant ($p = 0.2$), mean urinary ciprofloaxcin recovery in the TM group showed a 20% decrease. The mean $V_{d,\lambda z}/F$ estimate significantly increased (3-fold) with TM dosing (92.0 vs 30.8 L/kg, $p < 0.01$). In line with this, the average $t_{1/2,\lambda z}$ value was 3 times longer than that observed in the control group (5.71 vs 1.96 h, $p < 0.005$). However, the CL/F estimates were not significantly different between the two groups (Table 1). As a result, the relative bioavailability (F') of ciprofloxacin in the TM group as compared to control was estimated to be 0.96.

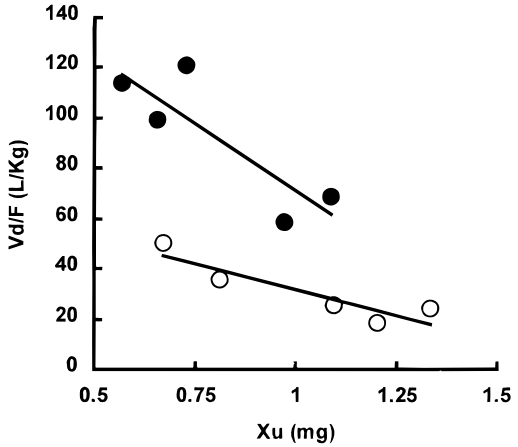

Figure 2—The relationship between apparent tissue distribution ($V_{d,\lambda z}/F$) and urinary drug recovery; equations describing the regression are $y = -40.9x + 72.6$, $p < 0.05$ for oral ciprofloxacin only (20 mg/kg) (○), and $y = -106.7x + 177.7$, $0.05 < p < 0.1$ for oral ciprofloxacin (20 mg/kg) plus TM (2 g crude drug/kg) (●).

Discussion

Ciprofloxacin is one of the newer fluoroquinolones that shows good oral absorption; however, the presence of cation-containing agents can impair oral absorption of this antibiotic.[1,9] In this study, coadministration of TM significantly decreased the C_{max} of ciprofloxacin by 73% with T_{max} essentially unaltered (Table 1). These observations suggest a reduction in oral ciprofloxacin absorption when TM was given concurrently. Independently, the TM extract was shown to contain a large amount of magnesium (5.8 mg/g,) calcium (4.9 mg/g), iron (2.3 mg/g), manganese (0.1 mg/g), zinc (0.06 mg/g), and copper (0.02 mg/g). Since the cation content of the TM extract, i.e., 5−6 mg of total cations received by the study rats, was high relative to the 4−5 mg of oral ciprofloaxcin, the lower ciprofloxacin absorption observed is not unexpected. It has been shown that chelation of quinolones generally requires ligands possessing positive charges and suitable molecular sizes.[1] Therefore, triterpenoids and inulin, the major components of TM reported,[4] should induce a minimal effect on the absorption of this antibiotic because they do not meet the structural requirements for chelation.

A 3-fold increase in the mean $V_{d,\lambda z}/F$ estimate for ciprofloxacin was observed in the rats concomitantly dosed with TM. Such alteration can be a result of an increase in tissue distribution ($V_{d,\lambda z}$) and/or a reduction in F. To further delineate the contribution of these two factors, plots of $V_{d,\lambda z}/F$ vs urinary recovery were constructed with individual data collected for the two animal groups (Figure 2). As anticipated for the control animals, $V_{d,\lambda z}/F$ decreased as the amount of ciprofloxacin excreted into the urine was larger. Interestingly, the regression line derived from the data of the TM group shifted higher and leftward with a steeper slope indicating that, in addition to the decrease in F, an increase in $V_{d,\lambda z}$ is also evident.

The magnitude of the change observed for $V_{d,\lambda z}$ appears to correspond to that of drug elimination (Table 1). The exact reason of this association is unclear but it may be a result of chelate formation in the systemic circulation when both ciprofloxacin and cations existed simultaneously following their independent absorption. Although not statistically significant ($p > 0.05$), the presence of TM caused a lowering of CL_r (Table 1). Interestingly, the pharmacokinetic perturbations observed for ciprofloaxcin in this study were also evident in a number of recent studies with another herb, *Sanquisorba officinalis*,[10] and also with ferrous sulfate when the antibiotic was given intravenously.[11] Although the data were not as vigorously scrutinized, prolongation of elimination half-life for a number of oral quinolones was also noticed in a human study as a result of iron supplementation.[2] All the pharmacokinetic perturbations observed for ciprofloxacin, i.e., lower C_{max}, wider tissue distribution, and slower elimination induced by TM, might be a direct result of an increase in molecular size and thus lipophilicity of metal-ciprofloxacin chelates. Therefore, the factor affecting drug absorption, in this case, may also play a role in the changes observed for drug distribution and elimination.

The relative bioavailability of ciprofloxacin, assessed using $AUC_{0\to\infty}$ estimates obtained for the concomitant TM dosing group relative to control, was 0.96. The similar $AUC_{0\to\infty}$ estimate observed in the TM group is a mixed result of lower drug absorption, wider distribution, and slower elimination. From a pharmacokinetic prospective, comparison of relative bioavailability of a drug under different testing conditions is based on the assumption of a stationary pharmacokinetic system. The secondary effects on drug distribution and elimination induced by TM may have complicated the use of $AUC_{0\to\infty}$ as an estimator for bioavailability. Because CL/F was derived from $AUC_{0\to\infty}$, this estimate should also be interpreted with caution.

The *Taraxacum* species, commonly known as dandelion, can be found in most parts of the globe. In addition to its claimed therapeutic activities, dandelion is also consumed as food and even as beverages in the form of a coffee substitute.[6] Regardless of its intended use, the high mineral content of this herb greatly increases the chance of drug−drug interactions with the conventional medicines that are sensitive to cations. Findings in the present study suggest that coadministration of TM may have clinical implications on the dosing of ciprofloxacin or other quinolone antibiotics.

References and Notes

1. Frost, R. W.; Lasseter, K. C.; Noe, A. J.; Shamblen, E. C.; Lettieri, J. T. Effects of aluminum hydroxide and calcium carbonate antacids on the bioavailability of ciprofloxacin. *Antimicrob. Agents Chemother.* **1992**, *36*, 830−832.
2. Lehto, P.; Kivisto, K. T.; Neuvonen, P. J. The effect of ferrous sulphate on the absorption of norfloxacin, ciprofloxacin and ofloxacine. *Br. J. Clin. Pharmcol.* **1994**, *37*, 82−85.
3. Kuhlmann, J.; Schaefer, H. G.; Beermann, D. Clinical Pharmacology. In *Quinolone Antibacterials*, Kuhlmann, J., Galhoff, A., Zeiler, H. J., Eds.; Springer: Berlin, 1998; pp 359−361.
4. Li, G. X. *Pharmacology, Toxicity and Clinic of Traditional Chinese Medicine*; Tianjin Science and Technique Translation Publishing House: Tianjin, 1992; pp 207−208.
5. Ou, M.; Li, Y. W. *The Traditional Chinese Drug and its Usage*; Hai Feng Press: Hong Kong, 1994; pp 49−51.
6. Newall, C. A.; Anderson, L. A.; Phillipson, J. D. *Herbal Medicines*; The Pharmaceutical Press: London, 1996; pp 96−97.
7. Nix, D. E.; De-Vito, J. M.; Schentag, J. J. Liquid chromatographic determination of ciprofloxacin in serum and urine. *Clin. Chem.* **1989**, *31*, 684−686.
8. Gibaldi, M.; Perrier, D. Noncompartmental analysis based on statistical moment theory. In: Swarbrick, J. ed. *Pharmacokinetics*, 2nd ed.; Swarbrick, J., Ed.; New York: Marcel Dekker: 1982, pp 409−416.
9. Li, R. C.; Nix, D. E.; Schentag, J. J. Interaction between ciprofloxacin and metal cations: its influence on physiochemical characteristics and antibacterial activity. *Pharm. Res.* **1994**, *11*, 917−920.
10. Zhu, M.; Wong, P. Y. K.; Li, R. C. Influence of *Sanquisorba officinalis*, a mineral rich plant drug, on the pharmacokinetics of ciprofloxacin in the rat. *J. Antimicrob. Chemother.* **1999**, in press.
11. Li, R. C.; Wong, P. Y. K.; Zhu, M. Effects of oral ferrous sulfate on the pharmacokinetics and pharmacodynamics of intravenous ciprofloxacin. *Antimicrob. Agents Chemother.* **1998**, submitted.

JS980367Q

Characterization of the Effects of Drug Addition on the Structure of Glyceryl Monoolein/Water Gel Systems Using Low Frequency Dielectric Spectroscopy

RENREN HE AND DUNCAN Q. M. CRAIG*

Contribution from *Centre for Material Science, School of Pharmacy, University of London, 29-39 Brunswick Square, London WC1N 1AX.*

Received June 17, 1998. Accepted for publication January 25, 1999.

Abstract □ The influence of propantheline bromide incorporation on the phase structure of glyceryl monoolein/water systems has been investigated using low-frequency dielectric spectroscopy over a frequency range of 10^{-2} to 10^{6} Hz at 20 °C. The responses of glyceryl monoolein systems composed of 10% and 30% w/w were measured and the spectra modeled using an equivalent circuit based on the Maxwell–Wagner theory.[1,2] Marked changes in the dielectric responses of the systems were noted on addition of the propantheline bromide at concentrations up to 10% w/w. For the lamellar (10% w/w water) glyceryl monoolein systems, an increase in the imaginary permittivity was seen, corresponding to an increase in conductivity due to the presence of additional ionic species within the system. Evidence was also obtained for the incorporation of the drug directly into the lipid bilayers, particularly at higher concentrations (10% drug) at which dielectric behavior corresponding to bilayer disruption was seen. Incorporation of 3% and 5% w/w drug into the cubic phase systems (30% w/w water) resulted in a change to the lamellar phase. However, circuit modeling indicated that the system formed structures which showed features of both the lamellar and cubic phases at 3% w/w drug loadings. The study has therefore demonstrated that dielectric analysis may provide a novel means of studying the effects of drug incorporation on the phase behavior of complex gel systems.

Introduction

Glyceryl monoolein has attracted interest as a pharmaceutical excipient, particularly for controlled drug delivery and bioadhesive systems.[3−7] This material is known to form four mesophases depending on the water content and temperature, namely the reverse micellar (L_2), lamellar (L_α), cubic (C), and reverse hexagonal (H_{II}) phases. Among these, the lamellar and cubic systems have received particular attention within the drug delivery field. The lamellar phase is a semifluid liquid crystalline system consisting of lipid bilayers alternating with water layers, while the cubic system is a highly viscous, ordered, bicontinuous structure with curved lipid bilayers extending in three dimensions separated by water channels.

The multilayer structure and/or high viscosity of the liquid crystalline phases results in the generation of diffusional barriers; hence, there has been interest in studying drug incorporation and release from these systems. The amphiphilic nature of the lipid allows incorporation of a range of drugs of varying lipophilicity; indeed, it has been suggested that hydrophobic drugs may be trapped within the lipophilic bilayers, and hydrophilic drugs are located in the aqueous channels, while amphiphilic drugs may partition into the lipid bilayer−water interface.[8] One would therefore expect the release pattern to depend on the microstructure and physicochemical properties of the liquid crystalline phases. To date, the majority of work in the field has focused on the examination of drug diffusion and release from the liquid crystalline systems. However, it is also necessary to consider the effects of drug addition on the formation and structure of the various phases. Previous studies using polarized light microscopy have reported induced phase changes at high levels of incorporated drugs.[4−6] The study of the effects of drug incorporation has arguably been limited by the difficulties associated with effectively characterizing the physical structure of these complex systems; hence, while drug-induced phase changes are a recognized phenomena, comparatively little is known regarding the mechanisms involved.

The work presented here describes an investigation into the influence of propantheline bromide loading on the phase structure of monoolein/water systems using low-frequency dielectric spectroscopy, with a view to developing the technique as a potential means of characterizing complex pharmaceutical materials. Propantheline bromide is an antimuscarinic agent which has been previously investigated as a means of treating urinary incontinence via vaginal delivery in a monoolein/water gel system.[5] This drug is itself surface active[9] and undergoes self-association in aqueous solution via an open aggregation process, whereby no discontinuity is seen in light-scattering intensity with concentration.[10] Geraghty et al.[5] reported that monoolein/water systems with a water content of less than 15% w/w retained their lamellar structure when an increasing quantity of propantheline bromide was added. However, systems that formed a cubic phase gel in the absence of drug could only maintain their structure up to propantheline bromide loadings of less than 5% w/w. At or above this drug loading, the gels were formed in the lamellar phase. Our previous work on glyceryl monoolein/water systems[1,2] showed that low-frequency dielectric spectroscopy may be used to identify and characterize the liquid crystalline phases. Furthermore, by modeling the dielectric data in terms of an equivalent circuit, it is possible to interpret the response in terms of specific structural features of the samples. The objectives of this study are therefore to develop the use of the dielectric approach by examining a system for which the basic behavior is already known and second to gain more specific information on the effects of propantheline bromide incorporation on the phase structure of glyceryl monoolein.

Materials and Methods

A single batch of Myverol 18-99 (Eastman Chemical Co.), a distilled monoglyceride with 60.9% glyceryl monoolein content, was

* Corresponding author. Present address: School of Pharmacy, The Queens University of Belfast, 97 Lisburn Road, Belfast BT9 7BL, UK. tel/fax: (44) 171 753 5863. E-mail: duncan.craig@qub.ac.uk.

10.1021/js980251u CCC: $18.00
Published on Web 05/04/1999

used throughout the study. Propantheline bromide (Sigma Co.) was used as supplied. All mixes were prepared using water with a resistivity greater than 18 MΩ/cm, obtained from an ultrahigh quality water purification system (Elga Co.). Two sets of gel samples containing 10% and 30% w/w water and 1%, 3%, 5%, and 10% propantheline bromide were prepared. The drug was added to Myverol 18-99 at 60 °C and mixed for 2 min, followed by the addition of water at the same temperature to produce the desired (% w/w) gel composition. The mix was stirred at 2000 rpm using a Heidolph RXR50 mixer. The resulting samples were centrifuged at a speed of 3000 rpm for 20 min and then stored in sealed containers at room temperature for 7 days before use to allow equilibration of the samples, following the recommendation of Geraghty et al.[5]

The dielectric measurements were carried out using a BDC-N broad band dielectric converter (Novocontrol GmbH) and a frequency response analyzer (SI 1255, Solatron-Schlumberger) linked to a Quatro temperature control system (Novocontrol GmbH). The technique involves the application of an oscillating electrical field to a sample and the subsequent measurement of the real and imaginary components of the response over a range of frequencies (ω). This response may be expressed in terms of the complex permittivity $\epsilon^*(\omega)$, where

$$\epsilon^*(\omega) = \epsilon'(\omega) - i\,\epsilon''(\omega) \quad (1)$$

with $\epsilon'(\omega)$ and $\epsilon''(\omega)$ being the real and imaginary components at frequency ω and i being the square root of -1. These components may be measured in terms of the extrinsic parameters $C(\omega)$ and $G(\omega)/\omega$, where $C(\omega)$ is the capacitance and $G(\omega)/\omega$ is the dielectric loss, $G(\omega)$ being the conductance (representing the sum of the a.c. and d.c. contributions). The relationship between the real permittivity and the capacitance is given by

$$\epsilon'(\omega) = \frac{C(\omega)\,d}{\epsilon_0 A} \quad (2)$$

where ϵ_0 is the permittivity of free space, and d and A are the interelectrode distance and electrode area, respectively. Similarly, the imaginary permittivity is related to the dielectric loss via

$$\epsilon''(\omega) = \frac{G(\omega)\,d}{\omega\epsilon_0 A} \quad (3)$$

During a measurement, the sample was placed in a circular dielectric cell designed for liquid and semisolid samples with diameter of 20 mm and an interelectrode distance of 0.5 mm. The dielectric responses were obtained at 20 °C over a frequency range of 10^{-2} to 10^{6} Hz. At least four samples for each concentration were examined, with at least two repeat measurements being made for each sample; excellent reproducibility was found between spectra. The fitting of the data was carried out by employing a modified generalized Maxwell–Wagner equivalent circuit with dispersive RC elements, and using Winfit 2.0 program supplied by Novocontrol GmbH. The main feature of Winfit 2.0 is nonlinear curve fitting of the measured data in the frequency domain, with both real and imaginary components being fitted simultaneously. In general impedance mode, the software supports up to four single fit terms which may hold several combinations of resistance, inductance, and capacitance elements and will also incorporate power law functions for these circuit features. Microscopic observations were obtained under polarized light using an Olympus differential interference contrast (DIC) microscope at room temperature.

Results and Discussion

Two sets of Myverol 18-99/water systems with waters content of 10% w/w and 30% w/w and propantheline bromide concentration of 1% w/w, 3% w/w, 5% w/w, and 10% w/w were investigated. According to the phase diagram determined by Geraghty et al.,[5] the 10% w/w water system is expected to be lamellar phase, while the 30% w/w water system is predicted to be cubic phase at 20 °C in the absence of drug.

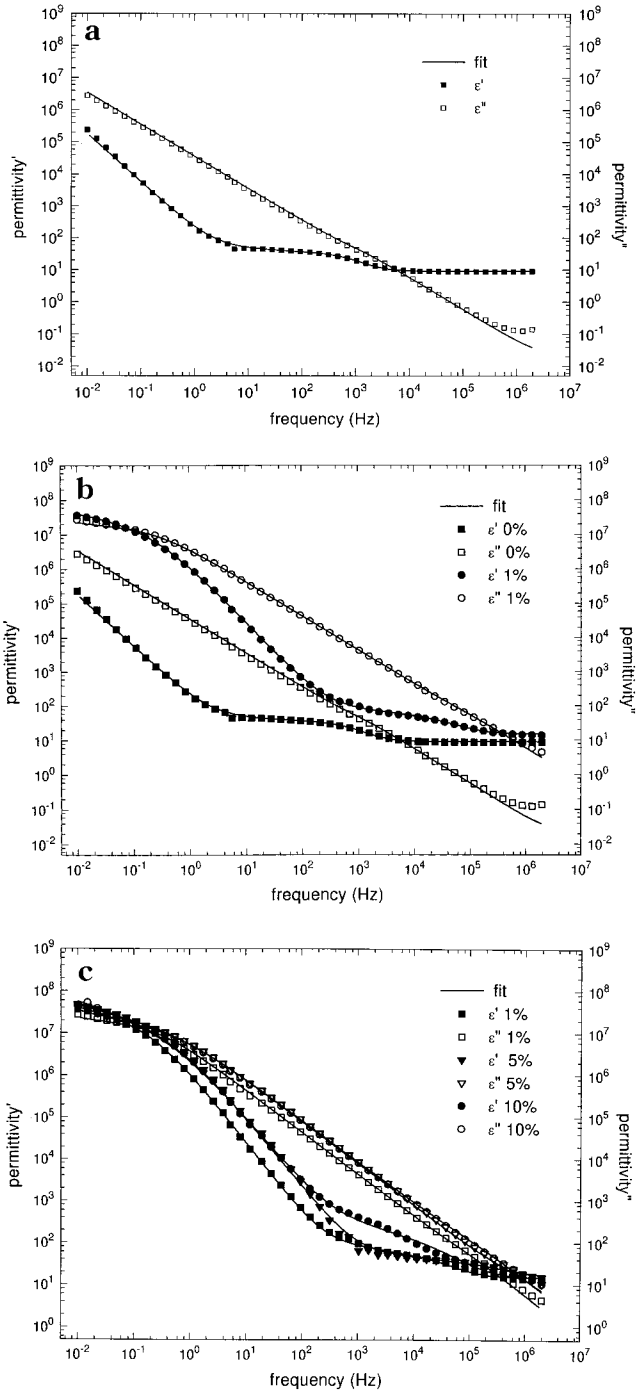

Figure 1—Low-frequency dielectric spectra of Myverol 18-99/water/propantheline bromide systems containing 10% w/w water with propantheline bromide concentration of (a) 0%, (b) comparison of 0% and 1%, and (c) comparison of 1%, 5%, and 10%. Solid lines indicate curve-fitted data.

Influence of Drug Loading on Lamellar Phase System—Both microscopy observations and dielectric spectroscopy measurements confirmed that the monoolein/water system containing 10% w/w water without addition of propantheline bromide was lamellar phase at 20 °C. The dielectric response, as shown in Figure 1a, exhibited the expected lamellar phase spectrum[1] with three principle dielectric processes: a high frequency process, corresponding to the bulk response, which is seen as a frequency independent real permittivity value of approximately 8, together with an inverse frequency dependent imaginary component, $\epsilon'' \propto (\omega)^{-1}$, reflecting a frequency independent value of $G(\omega)$ (see eq 3). A relaxation process in the Hz

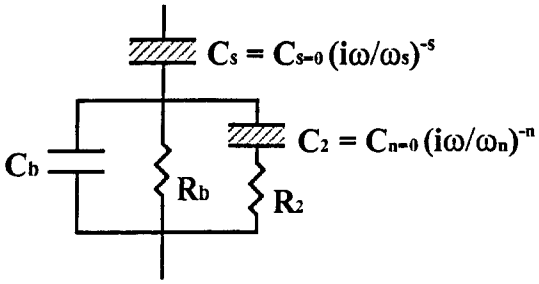

Figure 2—Modified generalized Maxwell–Wagner equivalent circuit employed to model the dielectric responses.

range was indicated by a discontinuity in the real component between frequencies of 5 Hz and 5 kHz which is thought to be caused by the relaxation of weakly bound dipoles and charge transport processes which are partially impeded by the lamellar network.[1,2] In the sub-Hz frequency range, the values of both the real and imaginary components increased, indicating the presence of a low-frequency dispersion caused by adsorbed barrier layers on the electrodes. Such layers have been described in a number of previous studies (e.g.,[11,12,13]) and are discussed in more detail in the context of these systems in a previous publication.[1]

On adding 1%, 5%, and 10% propantheline bromide to the 10% water sample, the systems remained in the lamellar phase, as indicated by the low viscosity and "oil streak" seen using microscopy.[5] The polarized light microscopy studies were unable to unequivocally distinguish between the various drug-containing systems, although the viscosity of the 10% w/w drug systems was visibly lower. However, the dielectric spectra for these systems exhibited marked differences in terms of both shape and magnitude. In comparison to the dielectric response for the 10% w/w gel system alone, the inclusion of 1% w/w drug resulted in a marked increase in imaginary permittivity of approximately 2 orders of magnitude over the frequency range of 10^{-1} to 10^{6} Hz, while the crossover frequency shifted from approximately 5 kHz to 400 kHz (Figure 1b). This crossover frequency (ω_τ) represents the inverse bulk relaxation time ($1/\tau$) of the system at $\epsilon' = \epsilon''$, given by

$$\omega_\tau = G(\omega)/C(\omega) = 1/\tau \qquad (4)$$

Therefore, the bulk relaxation time of the 1% sample decreased by approximately 2 orders of magnitude. The second relaxation process seen in the real component which is characteristic of the lamellar phase was, however, retained and shifted from a frequency of approximately 400 Hz to 400 kHz.

The responses of the 5% and 10% w/w drug systems are shown in Figure 1c in comparison to the 1% response. The spectrum of 5% drug sample showed a further slight increase in overall magnitude, but the change in spectral shape was less marked, indicating the system remained as a lamellar structure with only a slight increase of conductance. The response of the 10% drug sample had similar values of real and imaginary permittivity as the 5% material over the majority of the spectrum, although a marked increase in the magnitude of the real permittivity for the second relaxation process was seen in over a frequency range of 200 Hz to 50 kHz.

The above spectra were modeled in terms of a modified generalized Maxwell−Wagner equivalent circuit which was developed for these systems in a previous study[1] based on work by Hill and Pickup[14] (Figure 2). The circuit consists of a fractional power law dispersive capacitor, C_s, representing a layer formed at the electrode surface, in series with a parallel RC circuit (C_b and R_b), corresponding to the principal bulk processes; these are long range phenomena which are dispersed spatially in a uniform manner throughout the system. A series connection (C_2 and R_2) was employed to model the additional bulk polarization behavior, which represents the effect of the substructure within the sample. Previous studies[1,2] have related this circuit feature to the structure of the lamellar network within the system. The C_2 element is a dispersive capacitor showing power law behavior described by

$$C_2 = C_{n=0}(i\omega/\omega_n)^{-n} = C_{n=0}(\omega/\omega_n)^{-n}[\cos(n\pi/2) - i\sin(n\pi/2)] \qquad (5)$$

where $C_{n=0}$ is the capacitance when $n = 0$ and ω_n is a characteristic frequency. The exponent n is related to the extent of cooperativity between the relaxing dipoles and the immediate environment and is therefore a reflection of the degree of ordering of the system. When $n = 0$, C_2 is frequency independent and the dipoles may be considered to be totally coupled to their surroundings, while when $0 < n < 1$, the dipoles are uncoupled and the value of $C_2(\omega)$ is complex. More details of the physical significance of the exponent n may be found in a number of texts (e.g.,[14,15]).

The fitted parameters for the 10% water content samples with 0, 1%, 5%, and 10% propantheline bromide are given in Table 1. Without drug incorporation, the monoolein/water gel exhibited relatively high resistance values for both R_b and R_2, low values for the bulk capacitance C_b and the frequency dependent C_2, and a value for the exponent n of approximately 0.1. By adding 1% propantheline bromide, the resistance R_b and R_2 decreased by approximately 2 orders of magnitude which may be at least partially interpreted in terms of the increase in drug and counterion concentration. However, in addition to this effect a 10-fold increase in the $C_{n=0}$ value and a 2-fold increase in the value of n were observed, both indicating that the presence of the drug is causing disruption of the lamellar bilayer. Consequently, in addition to charge addition effects the observed decrease in bulk resistance may be a function of changes to the structure of the lipid lamellae. As the drug concentration increased to 5%, the R_b and R_2 values further decreased, while at the highest drug concentration of 10% the resistances R_b and R_2 showed only small decreases compared to the 5% value. However, at this drug concentration marked changes in $C_{n=0}$ and n were seen, indicating that the drug may be causing further alterations to the substructure of the system.

Overall, therefore, the incorporation of the drug appears to maintain the system within the lamellar phase but increases the conductance of the gel, probably due to a combination of ion addition effects and lamellar disruption. However, the increase of the conductance with increase of drug loading was nonlinear, with considerably less marked changes seen for the 5% and 10% drug systems. This could be a consequence of the surface active properties of the drug, with a decreased change in conductance seen due to the formation of assemblies which make a relatively small contribution to the charge-carrying properties of the system as a whole. In addition to this effect, however, the drug also appears to alter the substructure of the gel in a concentration dependent manner. At 1% and 5% levels, the changes in $C_{n=0}$ and n provide evidence for the presence of the drug within the lamellar bilayers themselves, while at 10% w/w the drug appears to cause substantial changes to the bilayers, with the marked increase in the exponent n reflecting disruption of the uniformity of the charge transport path. Taken together with the observation that the 10% drug systems were visibly less viscous than the

Table 1—Values of the Fitted Equivalent Circuit Parameters Derived from the Experimental Data Obtained for Myverol-80/Water/Propantheline Bromide Systems Containing 10% w/w Water Using the Model Circuit Given in Figure 2

drug concn, %	R_b (Ω)	C_b (p)	R_2 (Ω)	$C_{n=0}$ (*F*)	*n*	$C_{s=0}$ (F)	*s*
0	7.1×10^5	5.1×10^{-11}	1.2×10^6	3.1×10^{-10}	0.101	8.7×10^{-5}	0.478
1	5.9×10^3	8.5×10^{-11}	1.5×10^4	2.1×10^{-9}	0.194	1.3×10^{-4}	0.277
5	3.2×10^3	8.9×10^{-11}	2.6×10^3	1.5×10^{-9}	0.191	1.3×10^{-4}	0.349
10	3.3×10^3	8.4×10^{-11}	5.1×10^3	3.0×10^{-8}	0.321	1.4×10^{-4}	0.387

lower concentration drug samples, the data indicate that the drug is incorporated into the bilayer, causing disruption which in turn alters the viscous properties of the gels.

Influence of Drug Loading on Cubic Phase System—The monoolein/water system containing 30% water formed an optically isotropic cubic phase. The dielectric response of this phase, as shown in Figure 3a, consisted of a high-frequency bulk process with greater magnitudes for the imaginary component (i.e. a higher conductance) than for the lamellar phase, and a sub-Hz barrier process caused by an adsorbed layer at electrode. The high conductivity and lack of substructure relaxation processes reflect the homogeneity and bicontinuous structure of the system.[1]

On incorporating 1% drug into the system, the gel still had the appearance of the cubic phase (both visually and using microscopy), while the low frequency dielectric response still showed the same basic shape as the system with no added drug. An increase in imaginary permittivity of approximately 2 orders of magnitude was seen, which again may be attributed to the ionization of the propantheline bromide within the aqueous phase. However, the addition of further propantheline bromide was shown to promote the formation of the lamellar phase. The samples containing 3% and 5% drug concentrations were clearly of lower viscosity, and, under polarized light microscopy, exhibited similar "oily streak" textures. Examination of the dielectric responses (Figures 3b and 3c) revealed marked differences between the two higher concentration systems. The spectrum for the 3% gel showed a second relaxation process which was seen in the real component of the permittivity over a frequency range of 10^5 to 10^6 Hz, while the imaginary component of permittivity maintained similar values to that of the 1% drug sample. Consequently, the system showed features characteristic of the lamellar phase but did not exhibit the decrease in imaginary permittivity associated with the change from the cubic to lamellar phases. The dielectric spectrum of the 5% drug sample, however, showed typical lamellar behavior with the three dielectric processes outlined earlier. In addition, the values of the imaginary permittivity were 1−2 orders of magnitude lower than for the 1% and 3% drug systems over the majority of the response.

The values of the parameters obtained from fitting to the circuit model shown in Figure 2 for the 30% water samples with 0, 1%, 3%, and 5% propantheline bromide are given in Table 2. The cubic structure of the pure monoolein/water system was characterized by a low bulk resistance R_b (2 orders of magnitude lower than the bulk resistance of pure lamellar gel). The R_2 value was also low, while C_2 was frequency independent ($n = 0$) and showed similar values to that of the bulk capacitance, C_b. These features reflect the homogeneous structure of the cubic phase and are in good agreement with findings from the earlier studies.[1,2]

For the sample containing 1% drug, the bulk resistance R_b decreased approximately 30-fold, almost certainly as a result of ionization of the drug, while C_b and R_2 showed little change, implying that the system was still in the cubic phase. However, the 10-fold increase in $C_{n=0}$ and a change of the value of the exponent *n* from 0 to 0.14 reflect the effect of incorporation of drug molecules on interfaces leading to local inhomogeneity. For the 3% drug sample,

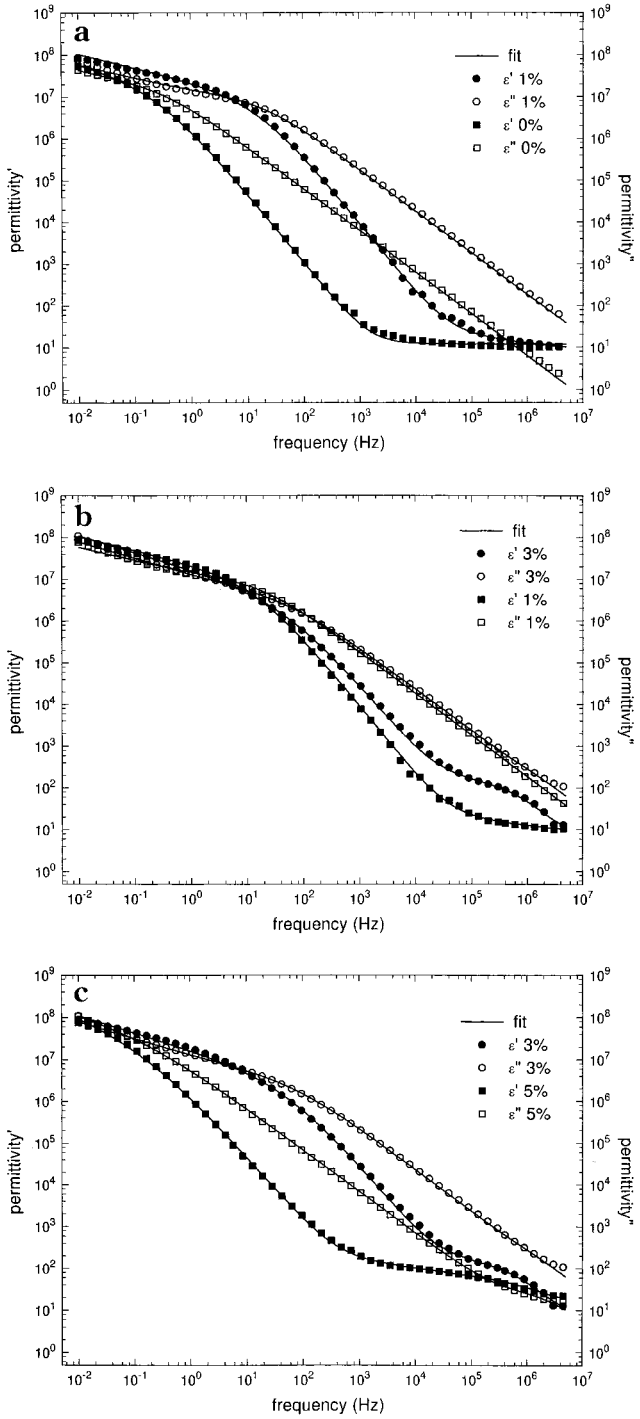

Figure 3—Low-frequency dielectric spectra of Myverol 18-99/water/propantheline bromide systems containing 30% w/w water with propantheline bromide concentration of (a) 0 and 1%, (b) 1% and 3%, and (c) 3% and 5%. Solid lines indicate curve fitted data.

Table 2—Values of the Fitted Equivalent Circuit Parameters Derived from the Experimental Data Obtained for GMOrphic-80/Water/Propantheline Bromide Systems Containing 30% w/w Water Using the Model Circuit Given in Figure 2

drug concn, %	R_b (Ω)	C_b (p)	R_2 (Ω)	$C_{n=0}$ (F)	n	$C_{s=0}$ (F)	s
0	4.5×10^3	3.2×10^{-11}	<10	3.5×10^{-11}	0	1.4×10^{-4}	0.347
1	1.6×10^2	3.5×10^{-11}	<10	3.4×10^{-10}	0.140	2.7×10^{-4}	0.320
3	1.1×10^2	4.3×10^{-11}	2.6×10^2	1.0×10^{-8}	0.180	2.5×10^{-4}	0.394
5	4.1×10^3	8.9×10^{-11}	4.8×10^2	4.8×10^{-9}	0.203	2.6×10^{-4}	0.450

the values of the substructure elements R_2 and $C_{n=0}$ showed marked increases while the bulk resistance R_b and capacitance C_b remained largely unchanged compared to the 1% systems. As the drug concentration increased up to 5%, all bulk and substructure elements R_b, C_b, R_2, and $C_{n=0}$ exhibited similar values for lamellar systems shown in Table 1.

These data indicate that the incorporation of propantheline bromide causes the system to change from the cubic to the lamellar phase at 20 °C, as reported by Geraghty et al.[5] However, the dielectric study has allowed further information to be obtained regarding the transformation. In particular, while the systems containing 0 and 5% drug show spectra typical of the cubic and lamellar phases, respectively, the gels containing 1% and 3% drug show features of both systems which indicate that these systems have structures which appear to be intermediate between the two phases.

Conclusions

The objectives of this study were to explore the use of dielectric analysis as a means of characterizing glyceryl monoolein gel systems containing a model drug and to gain further information on the effects of that drug on the phase behavior of the gel systems. The technique has been shown to be capable of detecting the phase behavior of the gels by matching the spectra of drug-containing systems to those of the cubic and lamellar phases, yielding trends which are in good agreement with those previously reported.[5] However, in addition to gross identification of the phases present the technique also appears to allow a more sophisticated analysis of the effects of incorporated drug than has been previously possible. In particular, the circuit modeling has yielded information on the location of the drug within the gel as well as identifying structures which are intermediate between the lamellar and cubic phases. Such findings may have important implications for understanding not only the drug release properties of these gels but also their mechanical and bioadhesive behavior.

Acknowledgments

The authors thank the EPSRC for provision of financial support for Dr. Renren He. Many of the ideas underpinning this work arose as a result of discussions with Drs. Geraghty and Collett, and the authors gratefully acknowledge their contribution.

References and Notes

1. He, R.; Craig, D. Q. M. Low-frequency dielectric investigations into the phase behaviour of glyceryl monoolein/water systems. *J. Phys. Chem*. **1998**, *102*, 1781−1786.
2. He, R.; Craig, D. Q. M. Identification of thermotropic phase transitions of glyceryl monoolein/water systems by low-frequency dielectric spectroscopy. *Int. J. Pharm*. **1998**, *169*, 131−141.
3. Engstrom, S. Cubic and other lipid-water phases as drug delivery systems. *Lipid Technol*. **1990**, *2*, 42−45.
4. Engstrom, S.; Engstrom, L. Phase behaviour of the lidocaine-monoolein-water system. *Int. J. Pharm*. **1992**, *79*, 113−122.
5. Geraghty, P. B., Attwood, D., Collett, J. H.; Dandiker, Y. The in vitro release of some antimuscarinic drugs from monoolein/water lyotropic liquid crystalline gels. *Pharm. Res.* **1996**, *13*, 1265−1271.
6. Chang, C. M.; Bodmeier, R. Bending of drugs to monoglyceride-based drug delivery systems. *Int. J. Pharm*. **1997**, *147*, 135−142.
7. Chang, C. M.; Bodmeier, R. Swelling of and drug release from monoglyceride-based drug delivery systems. *J. Pharm. Sci.* **1997,** *86(6)*, 747−752.
8. Lawrence, M. J. Surfactant systems: their use in drug delivery. *Chem. Soc. Rev*. **1994**, *23*, 417−424.
9. Attwood, D. Micellar and nonmicellarb association of anti-acetylcholine drugs in aqueous solution. *J. Phys. Chem*. **1976**, *80*, 1984−1987.
10. Attwood, D. The mode of association of amphiphilic drugs in aqueous solution. *Adv. Coll. Interface Sci.* **1995**, *55*, 271−303.
11. Hill, R. M.; Pickup, C., Barrier effects in dispersive media. *J. Mater. Sci*. **1985**, *20*, 4431−4444.
12. Binns, J.; Craig, D.Q. M.; Hill, R.M.; Davies, M.; Melia, C.; Newton, J. M. Dielectric characterisation of sodium alginate gels. *J. Mater. Chem*. **1992**, *2*(5), 545−549.
13. Barker, S.A., Craig, D.Q. M., Taylor, K.M. G.; Hill, R.M. An investigation into the low-frequency dielectric response of liposomes *J. Coll. Interface Sci.* **1994**, *166*, 66−72.
14. Hill, R. M.; Jonscher, A. K. The dielectric behaviour of condensed materials and its many-body interpretation. *Contemp. Phys*. **1983**, *24*, 75−110.
15. Craig, D. Q. M. Dielectric analysis of pharmaceutical systems. Taylor and Francis Ltd.: Basingstoke, 1995.

JS980251U

Encapsulation of Lysozyme in a Biodegradable Polymer by Precipitation with a Vapor-over-Liquid Antisolvent

TIMOTHY J. YOUNG, KEITH P. JOHNSTON,* KENJI MISHIMA, AND HIROYUKI TANAKA

Contribution from *Department of Chemical Engineering, University of Texas, Austin, Texas 78712.*

Received May 31, 1998. Accepted for publication March 10, 1999.

Abstract □ Lysozyme was encapsulated in biodegradable polymer microspheres which were precipitated from an organic solution by spraying the solution into carbon dioxide. The polymer, either poly(*l*-lactide) (*l*-PLA) or poly(DL-lactide-*co*-glycolide) (PGLA), in dichloromethane solution with suspended lysozyme was sprayed into a CO_2 vapor phase through a capillary nozzle to form droplets which solidified after falling into a CO_2 liquid phase. By delaying precipitation in the vapor phase, the primary particles became sufficiently large, from 5 to 70 μm, such that they could encapsulate the lysozyme. At an optimal temperature of −20 °C, the polymer solution mixed rapidly with CO_2, and the precipitated primary particles were sufficiently hard such that agglomeration was markedly reduced compared with higher temperatures. More uniform particles were formed by flowing CO_2 at high velocity in a coaxial nozzle to mix the droplets at the CO_2 vapor–liquid interface. This process offers a means to produce encapsulated proteins in poly(DL-lactide-*co*-glycolide) microspheres without earlier limitations of massive polymer agglomeration and limited protein solubility in organic solvents.

Introduction

Microencapsulation of pharmaceutical compounds in biodegradable polymer particles is of great interest for controlled-release in oral, inhalation, or injection methods of delivery. Typical methods of microencapsulation include emulsion−solvent-extraction, spray-drying, and phase-separation techniques.[1−7] Potential drawbacks associated with these techniques include the use of toxic organic solvents for solubility, residual solvent in the microspheres, low encapsulation efficiencies due to partitioning of the pharmaceutical compound between two immiscible phases, and denaturation. The biodegradable homopolymers poly(*l*-lactic acid), poly(DL-lactic acid), poly(glycolic acid), and copolymers of these have been of particular interest as carrier substances.[8−13]

Several supercritical fluid processes have been utilized to form microparticles of polymers and pharmaceutical compounds. To manipulate particle morphology, the solvent power of compressed CO_2 can be changed by adjusting the temperature and pressure.[14,15] The critical conditions of CO_2 are easily attainable, i.e., T_c = 31 °C and P_c = 73.8 bar. This environmentally benign solvent is essentially nontoxic, nonflammable, and inexpensive. Phase separation techniques based upon supercritical fluids include rapid expansion from supercritical solution (RESS),[13,16−27] gas antisolvent recrystallization (GAS),[27−30] and precipitation with a compressed fluid antisolvent (PCA),[31−43] also known as aerosol solvent extraction system (ASES)[44−47] or supercritical antisolvent technique (SAS).[44] RESS is useful for materials which are soluble in CO_2. Unfortunately, CO_2, with no dipole moment and a very low polarizability, is a very weak solvent and dissolves very few polymers.[48,49] RESS of a highly soluble polymer, poly(1,1,2,2-tetrahydroperfluorodecyl acrylate),[24] from CO_2 produced submicron particles and fibers.

Recently, microparticles have been formed by precipitation with compressed CO_2 in the liquid and supercritical fluid states.[31−47] The PCA process consists of atomizing a solution into compressed liquid or supercritical fluid CO_2. The atomization process may be accomplished by spraying at high velocities through a small nozzle (typically 100 μm) or by sonication[43] through a larger nozzle. The organic solvent diffuses rapidly into the bulk CO_2 phase, while CO_2 diffuses into the droplets, thereby precipitating the polymer. The rate of diffusion in both directions and thus the degree of supersaturation are higher than in the case of conventional liquid antisolvents, often resulting in submicron to micron-sized particles. More viscous polymer solutions at higher polymer concentrations lead to fibers with micron-sized features.[33,37] Several studies have shown very low concentrations of residual solvent in the product materials, especially after a CO_2 extraction step upon completion of the spray.[29,50−52]

Microspheres may be formed for semicrystalline polymers such as poly(*l*-lactic acid) (*l*-PLA) without flocculation and agglomeration at 40 °C.[29,30,38,41,43,45,46] Amorphous polymers, on the other hand, such as polystyrene (PS),[32,39,41] poly(methyl methacrylate) (PMMA),[39] and poly(DL-lactide-*co*-glycolide) (PGLA)[38] often flocculate and agglomerate. The loss of individual particles is a result of plasticization of the polymer by CO_2, which can be further influenced by residual solvent in CO_2. CO_2 can depress the T_g of PMMA by 100 °C below the normal value of 105 °C.[39,53] Upon exposure of PS to CO_2, the temperature at which stationary particles agglomerate corresponds closely with the depressed T_g.[34] For PGLA, agglomeration was present from 0 to 23 °C.[38] Severe agglomeration can occur when poly(d,l-lactide) microspheres precipitate from toluene solution by addition of 2-propanol as the phase-separating agent.[54] However, at temperatures between −40 °C and −100 °C the microspheres become sufficiently firm to avoid agglomeration.

A novel variation of the PCA process was used to form hollow spheres (microballoons) of polystyrene from polystyrene in toluene solutions with concentrations above 6 wt %.[38] In this case the cell was filled only partially with liquid CO_2, with its equilibrium vapor phase above it. The solution was atomized in the vapor phase, and the droplets subsequently fell into the liquid phase where they solidified. By delaying precipitation in the vapor phase, hollow microspheres were formed. The microballoons were slightly larger than the diameter of the nozzle, and it is conceivable that they could be used to encapsulate a pharmaceutical compound.

A key challenge in the PCA process is to maintain the biological activity of proteins, peptides, and enzymes.[35] The dissolution of insulin, lysozyme, and trypsin into a typical solvent for PCA, like DMSO, denatures these proteins, probably due to a change in conformation.[55] Each of these materials remained denatured after processing via PCA. The bioactivity of certain proteins such as insulin and lysozyme recover upon redissolution into an aqueous

10.1021/js980237h CCC: $18.00
Published on Web 04/24/1999

environment, suggesting the interactions causing denaturation can be partially reversible.[44,56] A recent study also suggests that long-term storage of proteins which have been denatured by supercritical fluid processing, such as lysozyme, does not severely alter the stability and ability to recover bioactivity.[57]

The objective of this study was to encapsulate chicken egg-white lysozyme into uniform 50−100 μm poly(DL-lactide-*co*-glycolide) (PGLA) spheres. Smaller particles would be too small to encapsulate a significant number of 5−10 μm protein particles for controlled-release purposes. Larger particles would be undesirable for certain administration methods; for example, parenteral administration requires particles <100 μm in diameter.[58] The first part of this study examines the particle morphology for PGLA particles formed by PCA without any protein present. To produce larger primary particles than the 1−5 μm particles typically produced by PCA in liquid or supercritical CO_2,[31,32,35,36,38−42,44,45,59] we chose to delay precipitation by spraying into a CO_2 vapor phase above a CO_2 liquid phase. Another goal was to achieve high enough local concentrations of polymer in the droplets striking the CO_2 liquid phase to allow significant particle growth, while avoiding agglomeration. To attempt to minimize agglomeration caused by plasticization of the polymer by CO_2, the temperature was varied from 23 to −40 °C. The effects of nozzle diameter, solution flowrate, CO_2 flowrate, and solution concentration were also evaluated. In the second part, we address microencapsulation of chicken egg-white lysozyme into the polymer particles. Lysozyme was suspended in dichloromethane, in contrast with earlier studies where a protein was dissolved in an organic solvent.[27,30,38,43,46] Suspensions may be formed for a broad range of peptides and proteins, many of which are insoluble in organic solvents. Suspension of a protein in an organic solvent typically produces less denaturation than dissolution. The knowledge gained from the study of PGLA particle formation in the first part was utilized to encapsulate lysozyme in nonagglomerated particles with diameters in the 50−100 μm range as desired. In both parts of this study, separate sections are presented to delineate between experiments in static (nonflowing) and flowing CO_2.

Experimental Section

Materials—Semicrystalline poly(*l*-lactic acid) (*l*-PLA) (MEDISORBTM 100L, Stolle-Dupont Co. Cincinnati, OH) had a M_w of 94100 and a M_w/M_n of 1.85. Poly(DL-lactide-*co*-glycolide) (PGLA) was purchased from Birmingham Polymers, Inc. (Birmingham, AL) and had a M_w of 30000. Chicken egg-white lysozyme (Sigma, St. Louis, MO) was spray-dried from aqueous solution to form 1−10 μm particles. Ruthenium tetroxide (Electron Microscopy Sciences, Fort Washington, PA), reagent grade dichloromethane, and bone dry grade CO_2 were used as received.

Apparatus—The apparatus for precipitation with compressed CO_2, shown in Figure 1, is based upon earlier designs.[35,40] The solutions were sprayed into a 1.27 cm. i.d. sapphire tube with a volume of 13 mL. This tube allowed visual observation of skin formation in falling droplets, jet dynamics, and polymer precipitation. Visual observations proved invaluable in optimizing the PCA process. A thermostated water bath was utilized for experiments performed above 0 °C, while a dry ice−ethanol bath was used for subzero temperatures. For all experiments, the CO_2 level inside the cell was maintained 1 cm below the tip of the spray nozzle. The CO_2 inlet line (30 feet long, 0.030 in. i.d. by 1/16 in. o.d.) was immersed in the bath to equilibrate the CO_2 temperature prior to introduction into the cell.

A cylindrical tube (1 in. o.d. by 11/16 in. i.d. by 8 in. long, Autoclave Engineers, model CNLX 1608−316) rated up to 689 bar equipped with a piston was used to pressurize the polymer solution. This tube was pressurized with dichloromethane by using a computer-controlled syringe pump (ISCO, model 260D). The

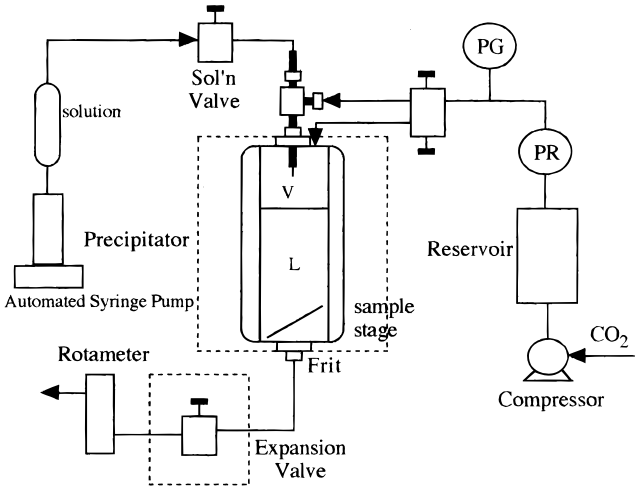

Figure 1—Schematic of the apparatus for precipitation with a vapor-over-liquid compressed fluid antisolvent.

polymer solution was sprayed into the cell via a 100 μm i.d. fused silica capillary tube or a 0.030 in. i.d. stainless steel tube. In all cases, the nozzle length was 6.5 in. Nozzles smaller than 100 μm could not be used because they were plugged by the suspended lysozyme particles. To ensure smoothness, the capillary tips were inspected with a microscope. The lysozyme was suspended in the polymer solution by using an ultrasonic bath.

To collect particles, two small rectangular glass plates (1 in. by 1/4 in.), slanted at an angle of 60°, were stacked in the bottom of the cell with approximately 5 mm between them. These glass plates were partially covered with double-sided carbon conductive tape. Also, a 1/4 in. diameter 0.5 μm filter was placed in the CO_2 effluent line at the base of the precipitation cell.

The solution flow rate was controlled with the automated syringe pump, and in most cases the solution was dripped into the cell at 0.1−1.0 mL/min. The solution was injected into a vapor CO_2 phase residing above a liquid CO_2 phase. In some cases, the solution flowrate was increased to ~1.8 mL/min where the solution no longer dripped, but instead streamed into the cell. This stream subsequently broke up into smaller droplets upon contacting the CO_2 liquid surface. For most cases, the CO_2 was not flowing. In experiments with flowing CO_2, the CO_2 entered the cell either through a port in the top of the cell or through an annular region in a coaxial nozzle, described in detail elsewhere.[41] The CO_2 flow rate was controlled by a needle valve (Whitey, SS-21RS4) in the effluent line and measured by a rotameter (Omega, model FLT-40ST). To prevent freezing due to CO_2 expansion, the valve was heated in a water bath to greater than 50 °C. Upon completion of solution injection, the cell was filled with liquid CO_2 to a pressure of 103 bar. Liquid CO_2 was swept through the cell for 10 min to remove the dichloromethane and further dry the particles. After drying, the cell depressurized over a 15 min span.

Characterization—Scanning electron microscopy (SEM) (JEOL JSM-35C) was used to analyze the morphology of the polymer particles. The glass slides were mounted on a SEM stage and coated to an approximate thickness of 200 Å (Pelco Model 3 Sputter Coater).

To detect lysozyme within the particles, two techniques were used. In the first method, the lysozyme was stained by ruthenium tetroxide prior to suspension in the polymer solution, and the product was observed with an optical microscope (Olympus VANOX-T or Olympus C-35AD-2)) and compared with SEM images of the same particles. Energy dispersive spectroscopy (EDS) was used as the second method (Kevex Analyst 8000 Microanalyzer). Two of the amino acids present in lysozyme, cysteine and methionine, contain sulfur, which is not present in the polymer, and can be detected by this technique.

Results and Discussion

Effect of CO_2−Dichloromethane Mixtures on Morphology of Polymers—For the CO_2 antisolvent process to be successful, the polymer must be highly insoluble in

Table 1—Morphology of Particles Produced by Dripping Homogeneous Solutions of Amorphous Poly(DL-lactide-*co*-glycolide) and Semicrystalline Poly(*l*-lactide) in Dichloromethane into Vapor-over-liquid Carbon Dioxide

polymer	C_{soln} (wt %)	temp (°C)	Q_{soln} (mL/min)	Q_{CO_2} (mL/min)	spray time (min)	particle size (μm)	comments
PGLA	1.0	–20	0.22	0.0	0.35	0.5–5	particles
	5.0	–20	0.22	0.0	0.17	5–70	particles
	5.0	1	0.10	0.0	1.37	10–50	some 500 μm agglomerates
	5.0	5	0.10	0.0	0.35	5–15	some 500 μm agglomerates
	10.0	–20	4.0	0.0	0.33	—	1000 μm agglomerates
	1.0	–30	0.21	0.0	0.36	—	1000 μm agglomerates
	5.0[a]	–20	0.13	0.0	4.66	—	1000 μm agglomerates
	5.0[b]	–18	0.5	17.5	1.68	3–25	particles
	5.0[b,c]	0	0.5	35	0.35	10–50	some 500 μm agglomerates
l-PLA	1.0	20	0.5	0.0	0.45	1–4	particles
	5.0[c]	24	0.5	0.0	0.58	250–500	particles

[a] 750 μm i.d. nozzle. [b] CO_2 flow through coaxial nozzle. [c] 0.5 wt % lysozyme also present.

the CO_2–organic solvent mixture, and this mixture must not cause too much agglomeration of the polymer. Previously, it was shown that lower molecular weight *l*-PLA is only slightly soluble in CO_2–cosolvent mixtures.[18] CO_2 does not cause *l*-PLA particles to agglomerate, since they are semicrystalline.[38] *l*-PLA has a melting temperature (T_m) of 173–178 °C and a glass transition temperature (T_g) of 60–65 °C (manufacturer's data). The amorphous biodegradable polymer poly(DL-lactide-*co*-glycolide) (PGLA), however, is highly plasticized by CO_2. PGLA has a T_g of 45–50 °C.

Experiments were performed to determine if CO_2 causes PGLA particles to agglomerate. PGLA, as a powder, and in some cases dichloromethane, as a liquid, were fed into a high-pressure cell equipped with a sapphire window which has been described previously.[60] The cell was sealed, and then liquid CO_2 was injected slowly into the cell. From ambient temperature down to 0 °C, PGLA powder quickly gels into a viscous mass when in the presence of liquid CO_2 for concentrations from 0.01 to 1.0 wt %. At these concentrations, very little polymer dissolved, even with up to 5 wt % CH_2Cl_2 as a potential cosolvent. The cosolvent concentrations were chosen to mimic conditions used in the PCA process. Upon depressurization, the polymer foamed. At −20 °C, the polymer powder occasionally stuck to the wall of the cell, but was also partially suspended throughout the cell. At temperatures below −40 °C the polymer remained as a free-flowing, nonsticky powder. Since CO_2 acts as a plasticizer, it can lower the T_g of the polymer. The T_g of PGLA containing dissolved CO_2 could easily be as low as −40 °C, or even lower, based upon other systems mentioned previously.[34,39,53,54]

Organic Solvent–CO_2 Miscibility and Mixing—Dichloromethane is highly miscible with CO_2 at ambient temperature and pressures above 61 bar. In our investigations, concentrations as high as 73 wt % CH_2Cl_2 were miscible with liquid CO_2 at temperatures from 23 °C down to −46 °C. The mixing behavior of CH_2Cl_2 and CO_2 was observed inside the sapphire cell. The cell was filled partially with liquid CO_2 and equilibrated at the desired temperature and pressure. Pure dichloromethane was then injected into the cell through the 100 μm i.d. capillary nozzle. For conditions where the cell was only partially filled with liquid CO_2, i.e., vapor and liquid CO_2 phases were both present, the solvent was injected at flow rates of 0.5 mL/min or slower. This flow rate range prevented the solvent stream from atomizing and allowed the solvent to drip into the liquid phase. At temperatures ranging from ambient to −20 °C, the drops quickly dispersed into the liquid CO_2 phase upon contact. At colder temperatures (−30 °C and below) however, the drops were seen to fall about 1 cm through the liquid CO_2 phase before breaking up. Operating at temperatures at or below −30 °C therefore may be expected to delay precipitation of the polymer and/or lead to agglomeration due to insufficient mixing between the drop and liquid phases. While the solvent is still miscible with CO_2 at low temperatures, the rate of mixing decreases significantly.

Polymer Particles Formed in Static Vapor-over-Liquid CO_2—As shown in Table 1, the concentration of the polymer solution, temperature, solution flow rate, and CO_2 flow rate were manipulated to observe the effect on particle formation. In this section, the CO_2 was static (nonflowing). Since both a vapor and a liquid phase are present in each experiment, the initial pressure was simply the vapor pressure of CO_2 at a given temperature. At 0 °C the pressure was 35 bar, and at −20 °C it was 20 bar. As the solution was injected, the pressure decreased slightly, corresponding to the pressure of the CO_2/CH_2Cl_2 mixture. The liquid CO_2 level was maintained at 1 cm below the tip of the nozzle to allow droplet formation and release from the tip before contact with the liquid phase. With the low flow rate and low shear through the vapor phase, ~200 μm drops were formed at a frequency of approximately one per second.

l-PLA is a semicrystalline polymer which has been used many times in PCA to form microparticles without agglomeration.[13,29,38,41,43,45,46] Therefore, we first present results for *l*-PLA to serve as a basis for understanding the more challenging experiments with amorphous PGLA. When a 1.0% solution of *l*-PLA in dichloromethane was dripped into vapor-over-liquid CO_2 at 0.5 mL/min and 20 °C, the result was microspheres 1–4 μm in diameter, as shown in Figure 2 (top) and Table 2. On the basis of visual observation, it appeared that little precipitation occurred before each droplet contacted the liquid phase. After the droplet fell into the liquid CO_2 phase, rapid mass transfer led to intense nucleation resulting in the small microspheres. This result indicates atomization does not play as important a role in achieving small particles as suggested previously.[41] The particles formed a free-flowing powder and could be sprayed for several minutes with no agglomeration even as solvent accumulated inside the cell.

Figure 3 is a schematic of a ternary phase diagram consisting of a polymer, organic solvent, and compressed CO_2.[32] The mass transfer pathways are shown only for the lower liquid CO_2 phase. Two of the binary systems are completely miscible at most conditions in this study, but the polymer–CO_2 binary system is only slightly miscible. The binodal (coexistence) curve separates the one-phase and two-phase regions in the ternary system. Between the binodal and spinodal curves is the metastable region. The system is stable to small concentration fluctuations in this region, and phase separation will be by nucleation and growth. Upon crossing the binodal curve for dilute polymer

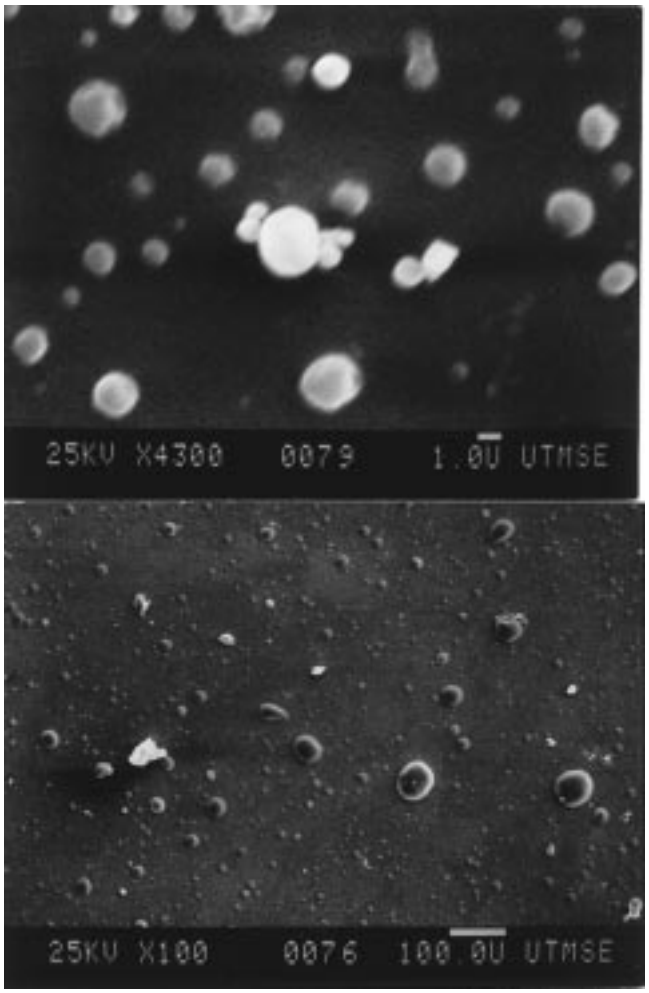

Figure 2—SEM micrographs of *l*-PLA microspheres (top) formed by spraying a 1.0 wt % *l*-PLA in dichloromethane (CH_2Cl_2) solution at 0.5 mL/min at 20 °C and PGLA microspheres (bottom) formed by spraying a 5.0 wt % PGLA in CH_2Cl_2 solution at 0.22 mL/min (T= –20 °C), both through a 100 μm capillary nozzle into static CO_2.

solutions, a polymer-rich phase will nucleate and grow within a solvent-rich continuous phase.

For a 5.0% solution of *l*-PLA sprayed at similar conditions, we observed skin formation on the backlit droplet while it was in the vapor-phase, and the resulting particles were 250−500 μm in diameter. It was easy to observe that the liquid droplet became opaque as it fell through the CO_2 vapor. A viscous skin appeared to form on the surface of the drop, and the drop did not break up upon contact with the liquid CO_2. This observation of skin formation is entirely consistent with SEM micrographs, which indicated that the particles were the same size as the droplets. In other experiments, at lower concentrations, where a skin did not form, a clear transparent droplet fell through the vapor. With the higher polymer concentration, the dissolution of CO_2 into the droplet forms a skin on the droplet while it is still in the vapor phase. At this concentration for *l*-PLA, the mass transfer pathway on the phase diagram in Figure 3 passes above the critical point on the binodal curve (curve B), thus a solvent-rich phase nucleates and grows within a polymer-rich phase causing skin formation. The polymer entanglement and viscosity in the skin are sufficient to maintain the integrity of the droplet as it solidifies in the liquid CO_2, as was observed in a similar system, as shown in Figures 4−10 of ref 34.[34] Here, the final particle size produced in each droplet is larger than the nozzle diameter, 100 μm, which was also the case for PS in toluene solutions sprayed into vapor-over-liquid CO_2.[34]

In vapor-over-liquid PCA when drops fall through vapor and atomization is not present, mass transfer is still fast enough in dilute solutions and is fast enough to produce 1−4 μm *l*-PLA particles, apparently following mass transfer pathway A in Figure 3. However, in a previous study with intense atomization into liquid CO_2 at a high density of 0.96 g/mL, the primary particle sizes were even smaller, from 0.1 to 1 μm.[41] Not only was atomization more intense producing smaller droplets, but the phase boundary was reached more quickly from the faster mass transfer. In addition, the polymer solidified more rapidly leading to smaller particles. Dilute solutions were not studied in the past for V/L CO_2, as, for example, the concentration was 6 wt % or higher for PS solutions and particles were larger than 100 μm.[34]

For PGLA, the solution concentration was varied from 1.0 to 10.0 wt %. To prevent agglomeration, most experiments were performed at −20 °C to raise the polymer solution viscosity sufficiently, while maintaining high enough rates of CO_2−organic solvent mixing (on the basis of the above visual observations of mixing). Also, spray times were generally kept short, <30 s, to avoid accumulating large concentrations of dichloromethane in the static CO_2, which causes agglomeration. As the polymer concentration and thus the solution viscosity increased, it became necessary to raise the solution flow rate to maintain a constant droplet size. The size was chosen to be slightly larger than the nozzle's inner diameter. At 1.0 wt % and −20 °C, small 0.5−5 μm particles were formed by dripping the solution at a flow rate of 0.22 mL/min into CO_2. These nonagglomerated particles were similar to the *l*-PLA microspheres shown in Figure 2 (top). The same experiment conducted at 0 °C and above produced some small (0.5−5 μm) primary particles but mostly large (>500 μm) solid agglomerates. Therefore, the polymer particles are significantly more viscous and less susceptible to agglomeration at −20 °C.

As shown in Figure 2 (bottom), a 5.0 wt % solution resulted in 5−70 μm microspheres. At this higher concentration, larger particles may be expected because of the higher solution viscosity. When the large droplet strikes the liquid surface, the more viscous solution mixes more slowly with the surrounding liquid CO_2 and mass transfer rates are slower. With slower mixing and mass transfer, the degree of supersaturation is lower than with less viscous solutions (lower concentrations), resulting in fewer nuclei per weight of polymer. Because most of the nuclei tend to be formed in a small volume where the droplet falls, coalescence of primary particles is more prevalent than for the experiments with lower polymer concentrations, where faster mixing occurs. With the reduction in nucleation rate and higher polymer concentrations (which produces faster agglomeration), especially in a local volume where the drop falls, larger particles are formed.

Unlike previous studies for polystyrene with the same vapor-over-liquid technique, these particles are much smaller than the initial droplet size, which was ~200 μm. For 6 wt % polystyrene (200000 MW) in toluene solutions, 300 μm diameter microballoons are formed with a 151 μm nozzle.[34] A skin, about 20 μm thick, forms on the droplet while still in the vapor phase which then hardens upon contact with the liquid phase. The polymer entanglement and viscosity in the skin are sufficient to maintain the integrity of the droplet as it solidifies in the liquid CO_2. The PGLA in this study has a much lower molecular weight (~30000), and the solutions are much less viscous. Also, the miscible region in the phase diagram in Figure 3 is

Table 2—Morphology of Particles Produced by Dripping Homogeneous Solutions of Amorphous Poly(DL-lactide-*co*-glycolide) and Semicrystalline Poly(*l*-lactide) in Dichloromethane Containing Suspended Lysozyme into Vapor-over-Liquid Carbon Dioxide

polymer	C_{soln} (wt %)	temp (°C)	Q_{soln} (mL/min)	Q_{CO_2} (mL/min)	spray time (min)	particle size (μm)	encapsulation
PGLA/lysozyme	1.0 /0.1[a]	–23	0.1	0.0	0.48	0.5–5	no
	5.0/0.5	–20	0.1	0.0	1.28	10–60	yes
	5.0/0.5	–20	0.5	0.0	0.63	10–50	yes
	5.0/0.5	–20	1.5	0.0	0.28	5–50	yes
	5.0 /0.5[b]	–20	1.8	0.0	0.18	5–60	yes
	5.0 /0.5[c]	–20	0.5	25	0.42	5–30	yes
	5.0 /0.5[d]	–21	0.5	35	0.82	>1000[e]	no
l-PLA/lysozyme	1.0/0.1	20	0.1	0.0	3.23	0.5–2.5	no
	5.0/0.5	24	0.5	0.0	0.58	250–500	yes

[a] 1.0 wt % PGLA, 0.1 wt % lysozyme. [b] Onset of streaming due to high Q_{soln}. [c] CO_2 flow through coaxial nozzle. [d] CO_2 flow enters from top of cell. [e] Agglomerates.

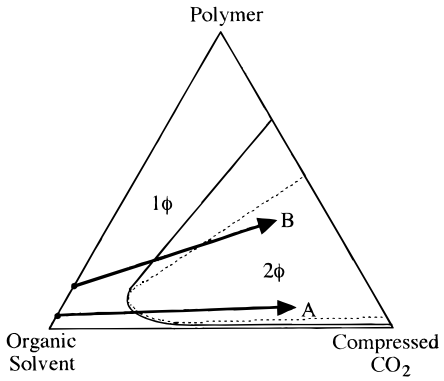

Figure 3—Schematic ternary phase diagram comparing mass transfer pathways for precipitation with a compressed fluid antisolvent: (—) binodal curve, (---) spinodal curve.

larger for PGLA−dichloromethane−CO_2 than for PS−toluene−CO_2 because of the lower molecular weight for PGLA versus PS and the lower solubility parameter of dichloromethane versus toluene. Consequently, it will take longer for PGLA to precipitate on the mass transfer pathway on the phase diagram (Figure 3), delaying skin formation.[34] Without any visual indication of skin formation in the vapor phase, smaller particles are produced, as the droplet breaks up on contact with the liquid phase.

At dilute concentrations, PGLA does not appear to form a skin when contacting CO_2 vapor, and the particles do not form until the large droplet has begun to disperse in the liquid CO_2 phase. When the solution concentration is increased to 10 wt %, the solution becomes extremely viscous and individual particles are not formed, only large agglomerates, >1000 μm. Here, a thin skin is visible on the droplets while they are being formed in the vapor phase, although the microscopic structure of the skin could not observed with the naked eye. The formation of a skin was confirmed by examination of the samples with SEM (not shown). Skin formation is favored by the higher solution viscosity and high concentration, which may shift the mass transfer pathway above the critical point (see Figure 3). This shift would cause solvent-rich domains to nucleate and grow within a polymer-rich domain.[34,37] The thin skin is weak, since it contains a high concentration of dissolved CO_2, and it was easy to observe visually that the skin immediately ruptures upon hitting the CO_2 liquid surface. The ruptured skin appeared as large agglomerates or films when examined by SEM (not shown). The mixing and diffusion of solvent away from the droplet are very slow due to the high polymer concentration and viscosity, resulting in severe agglomeration.

When a polymer solution is sprayed at 1.0 mL/min into flowing liquid CO_2 (without a CO_2 vapor phase), we found that fibers are produced for PGLA concentrations above 1.0 wt %. Fibers are formed from the jet due to the rapid nucleation, high solution concentration, high solution viscosity (to prevent atomization) and skin formation.[33] In experiments with vapor-over-liquid CO_2, the large droplets are formed instead of a jet (at the same flow rate) due to much higher interfacial tension because of the low CO_2 density. The precipitation in the droplets is slower than in the case of a jet due to the larger dimensions of the solution phase and lower miscibility between the phases for CO_2 vapor compared with CO_2 liquid. As a result, fibers are not formed.

The opposing effects of temperature on particle growth, coalescence, and mixing between the phases must be properly balanced to produce large nonagglomerated particles. As temperature is decreased the polymer solution becomes more viscous, which will cause coalescence to be less prevalent. Some coalescence, however, will aid the formation of the desired 50−100 μm particles rather than the typical 1−5 μm particles. As mentioned earlier, decreasing the temperature below −20 °C slows the mixing between the solvent and CO_2 phases. When a 1.0% solution of PGLA in dichloromethane was dripped into liquid CO_2 at −30 °C, no distinct particles were formed, only large agglomerates, due to the slow mixing. When the solution droplets fell, they initially formed a pool at the liquid surface and then penetrated the surface. The polymer began to precipitate at the interface, forming a film, and occasionally droplets fell through the film and agglomerated. Previously, we showed that PGLA particles exposed to CO_2 do not tend to agglomerate at −40 °C, indicating hard particles or even a glassy state. Unfortunately, the rate of mixing between the organic solvent and the liquid CO_2 is too slow at −30 °C and −40 °C to disperse the polymer.

At temperatures higher than 0 °C, agglomeration also occurred readily. As seen in Figure 4 (top), a 5.0 wt % solution dripped into liquid CO_2 at 1 °C yielded some distinct particles in the 10−50 μm range, but the polymer was partially agglomerated. This occurred for every experiment at 0 °C or above since the polymer is excessively swollen by CO_2 and the viscosity is too low at these temperatures.

A 0.030 in. i.d. (~750 μm) stainless steel nozzle was used to form larger initial droplets in order to attempt to produce the desired particle size. For PGLA concentrations of 1.0 and 5.0 wt %, and temperatures from −20 °C to 4 °C, the particles were always severely agglomerated with few, if any, distinct particles. The large drops formed more slowly, providing more time for precipitation to occur which allowed a thin skin to form on the large droplets while in the vapor phase. On the basis of visual observation, this skin was weak and ruptured upon impact with the liquid

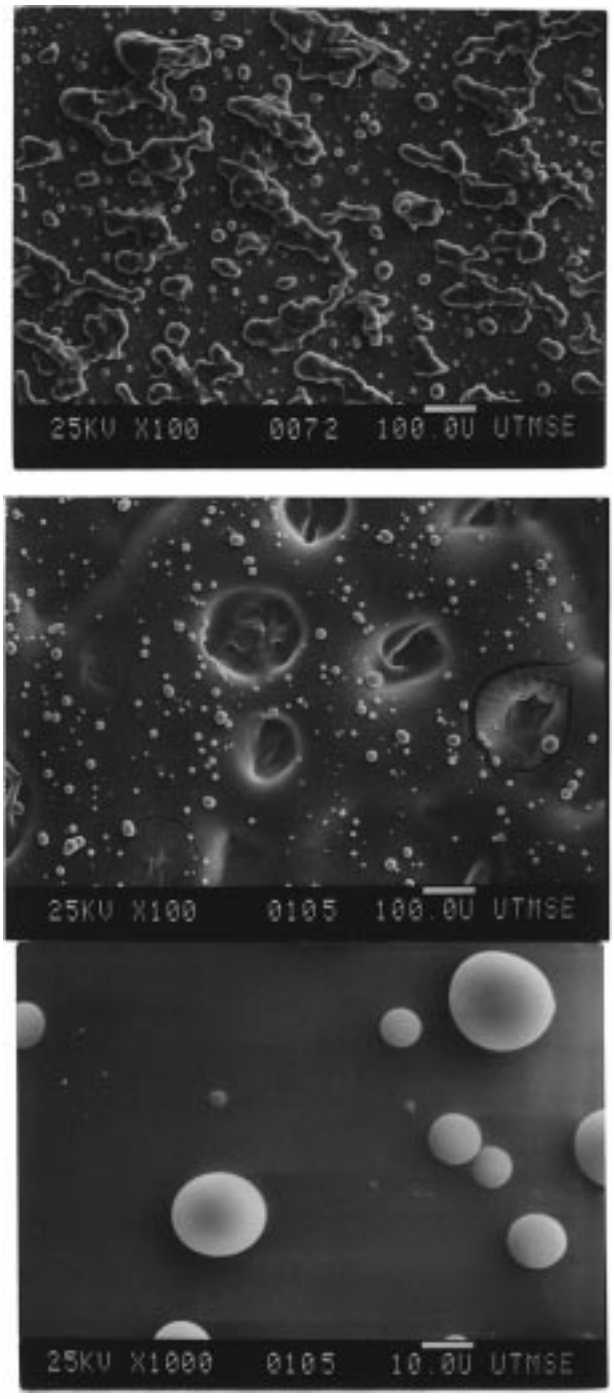

Figure 4—SEM micrographs of PGLA microspheres formed by spraying a 5.0 wt % PGLA in CH_2Cl_2 solution at 0.1 mL/min ($T = 1$ °C) into static CO_2 (top) and at 0.5 mL/min into CO_2 flowing at 17.5 mL/min at –20 °C (middle and bottom) through a 100 μm capillary.

CO_2 surface. The larger droplet size produced a larger local concentration of polymer and solvent which caused severe agglomeration of the polymer.

Polymer Particles Formed in Flowing Vapor-over-Liquid CO_2—Experiments were performed with flowing CO_2 to minimize CH_2Cl_2 accumulation. CO_2 was passed through the annular region of a coaxial nozzle, described previously,[41] at high velocity (69−138 cm/s) to agitate the surface of the liquid phase to enhance mixing. Figure 4 (middle and bottom) shows PGLA particles formed by spraying a 5.0 wt % solution at 0.5 mL/min into the cell through a 100 μm capillary nozzle with CO_2 flowing at 17.5 mL/min and at −20 °C. Vigorous mixing was observed at

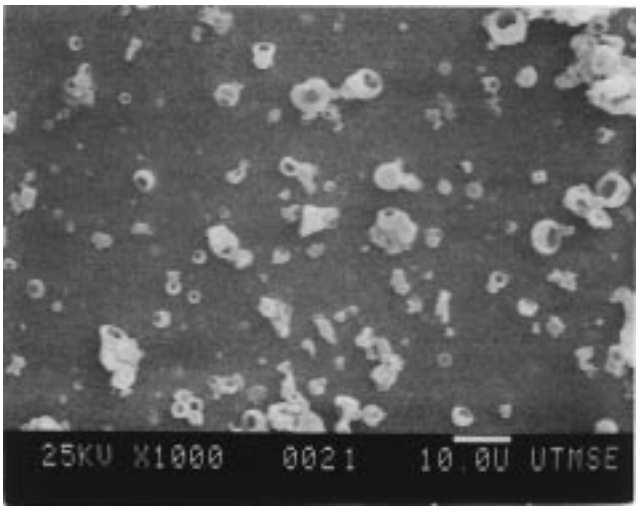

Figure 5—SEM micrograph of spray-dried lysozyme particles.

the interface, such that particles nucleated and grew throughout the liquid-phase rather than in a local region where the droplets fell. The resulting spherical particles ranged in size from 3 to 25 μm in diameter with no agglomeration even after almost 2 min of spraying. The difference in results was dramatic compared to the case for static CO_2. The particles were suspended throughout the cell, but plugging of the frit in the effluent line at the bottom of the cell limited spray times. This problem could be reduced in the future with a larger filter. The increased mixing causes a higher degree of supersaturation, more nucleation, faster solvent removal and quenching, and less time for growth. The result was far less coalescence and agglomeration when compared to the case with static CO_2. Experiments were also run at higher temperatures to determine if the increased mixing was enough to prevent agglomeration. For all cases where the temperature was 0 °C or higher, some 10−50 μm particles were formed, but mostly large (>500 μm) agglomerates were formed. The particles were not sufficiently hard at the higher temperatures to prevent coalescence.

Encapsulation of Lysozyme into PGLA with Static CO_2—In control experiments, lysozyme suspensions in CH_2Cl_2 were sprayed into CO_2 through a 100 μm capillary nozzle at temperatures from 23 to 0 °C. The lysozyme suspensions were formed with an ultrasonic bath and were stable for hours. The suspension flowed smoothly through the capillary, and the particle size (1−10 μm) and morphology of the product were identical to those of the original lysozyme, which is shown in Figure 5. The original spray-dried lysozyme particles and those removed after spraying into CO_2 were "bowl-shaped" when examined by SEM. Since the polymer particles discussed previously were spheres, it is easy to distinguish between polymer and protein particles.

Table 2 summarizes results of encapsulating lysozyme into PGLA. Again, the temperature was chosen as −20 °C to strike a balance between mixing favored at high temperatures and formation of hard, nonsticky particles in CO_2 which is favored at low temperatures. An initial loading of 10:1 by weight of polymer to protein was maintained in each case. Figure 6 (top) shows the result of spraying a 1.0 wt % solution of PGLA with lysozyme into static CO_2. The primary particle size was 0.5−5 μm in diameter with very little encapsulation of the similarly sized protein particles. The solution was too dilute for polymer particles to encapsulate a significant fraction of the protein particles. This result was anticipated, since it was shown above that small 0.5−5 μm PGLA particles are formed by precipitation

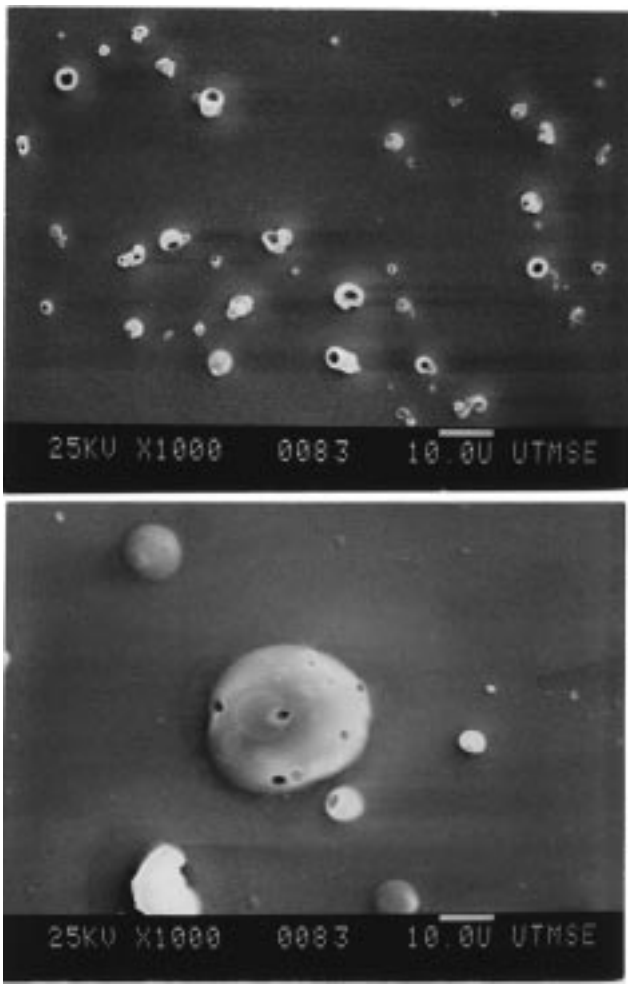

Figure 6—SEM micrographs of PGLA microspheres formed by spraying a 1.0/0.1 wt % (top) and a 5.0/0.5 wt % (bottom) PGLA/lysozyme suspension at 0.1 mL/min in CH_2Cl_2 through a 100 μm capillary nozzle into static CO_2 at –20 °C.

from a 1.0 wt % solution, which are too small to coat the lysozyme particles.

For a PGLA concentration of 5.0 wt %, the particles are in the 5−60 μm diameter range, and the encapsulation efficiency is substantial, as demonstrated in Figure 6 (bottom). Here, the magnification is high enough to examine a single particle. The craters or holes in the polymer particle represent protein particles for the following reasons. In identical experiments without protein, the craters were never present. Also, the size of the craters match those of the pure protein particles. Further evidence that the craters represent protein particles is given below in the subsection on experiments with flowing CO_2.

At lower magnifications, the particles looked similar to those shown in Figure 2 (bottom). Apparently, the presence of the small encapsulated protein particles does not have a significant influence on the polymer particle size. The polymer particles are much larger than in the case of a 1.0 wt % solution and are large enough to encapsulate multiple protein particles. Also, since the solution is more concentrated, the probability of a polymer particle nucleating and growing next to a lysozyme particle is enhanced. Also, the protein has the potential to act as a nucleating agent for the polymer. The large droplets formed in the CO_2 vapor phase lead to relatively slow mixing when the droplets strike the liquid CO_2 phase. The high local concentrations of the sticky CO_2-swollen polymer and protein lead to a large amount of growth.

A desirable feature of this spray geometry is that a polymer-rich phase nucleates in the presence of the protein in the confined space of the droplets, which occupy a small volume fraction compared to the total volume. Such nucleation may be expected to produce higher encapsulation efficiencies than if the polymer nucleated throughout the total cell volume. This advantage of compartmentalization of polymer and protein is not present in the GAS process cited above where CO_2 is added to a liquid solution. A disadvantage of the V/L PCA process is that the primary mass transfer takes place at the vapor−liquid surface rather than throughout the entire volume, which can lower the production rate.

Varying the size of the droplets leaving the nozzle could potentially lead to a change in size of the polymer particles. As the flow rate of the polymer solution increased, it was observed that the droplet size decreased. However, no significant change in particle morphology occurred when the solution flow rate was increased from 0.1 to 1.5 mL/min for a 5.0 wt % solution at −20 °C. In each case, the particles appeared as those shown in Figure 6 (bottom). A complication of extremely slow flow rates is plugging of the nozzle, which occurred very often at 0.1 mL/min, but infrequently at 0.5 mL/min or higher. This plugging is likely a result of precipitation inside the nozzle, caused by CO_2 diffusing upward into the nozzle and/or entrapment of the solid protein particles.

The degree of agglomeration of the polymer product is dependent upon the solution flow rate and spray time. When conducting the spray, at a certain time large particles could easily be seen with the naked eye. When analyzed by SEM, these large particles were agglomerates and not simply large flocculates of small primary particles. At a solution flow rate of only 0.1 mL/min, the experiment could be run for 1 min before agglomeration began to occur. For higher flow rates, the observed time where large particles appeared decreased accordingly to 40 and 20 s at flow rates of 0.5 and 1.5 mL/min, respectively. This agglomeration could potentially be avoided by either flowing CO_2 continuously through the cell as described in the next section or by spraying into a larger volume cell. At 1.8 mL/min, streaming of the solution begins to occur rather than dripping. Here, the range of particle sizes did not change, but there was a higher percentage of large particles compared to the previous cases at lower flow rates. Due to the large amount of solution flowing into the cell, agglomeration began to occur after only 10 s.

Encapsulation of Lysozyme into PGLA with Flowing CO_2—Figure 7 compares an optical micrograph and a SEM micrograph of polymer particles with protein particles visible on the surface. These particles were formed by spraying a 5.0 wt % PGLA solution with suspended lysozyme at 0.5 mL/min along with CO_2 flowing in the annulus at a velocity of 138 cm/s. The SEM image (top) shows particles with craters or holes in their surfaces, which may be identified as the "bowl"-shaped spray-dried lysozyme particles. The micrograph taken with the optical microscope (bottom) shows the same polymer particle with encapsulated stained protein particles. The stained protein directly corresponds to the craters observed in the SEM micrograph. This correspondence between optical and SEM photomicrographs was always observed where we compared images of particles formed by the vapor/liquid PCA process. Figure 8 (top) shows 40−70 μm particles with encapsulated lysozyme formed at the same conditions as Figure 7, except at a higher CO_2 flow rate. By varying the focal plane throughout the depth of the particle (not shown), we observed in the optical microscope that the protein particles were encapsulated throughout the PGLA particles and were not just on the surface. While there did

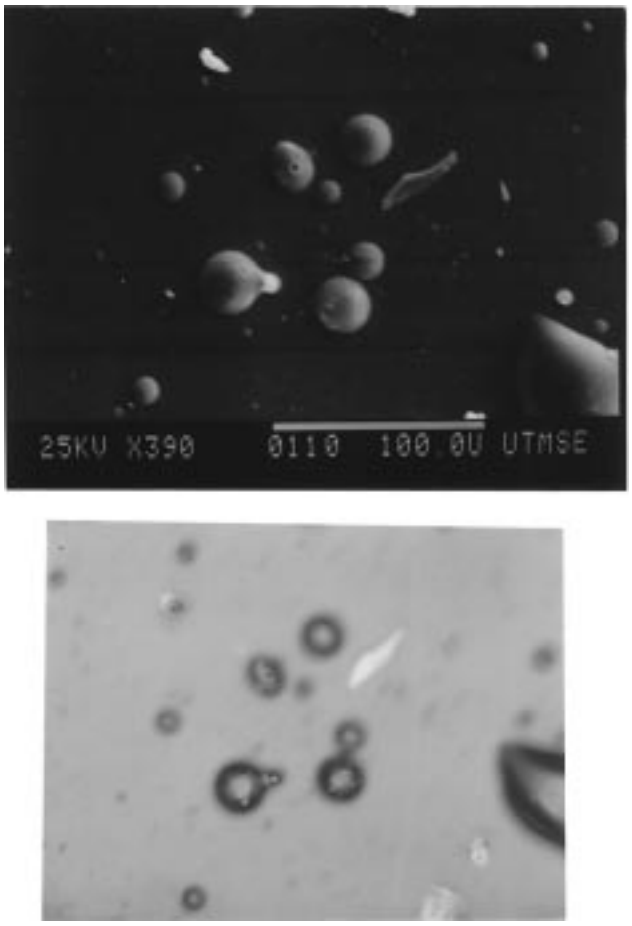

Figure 7—SEM micrograph (top) and optical micrograph (bottom) of PGLA microspheres formed by spraying a 5.0/0.5 wt % suspension of PGLA/lysozyme in CH_2Cl_2 at 0.5 mL/min through a 100 μm capillary nozzle into CO_2 flowing at 15 mL/min at –20 °C.

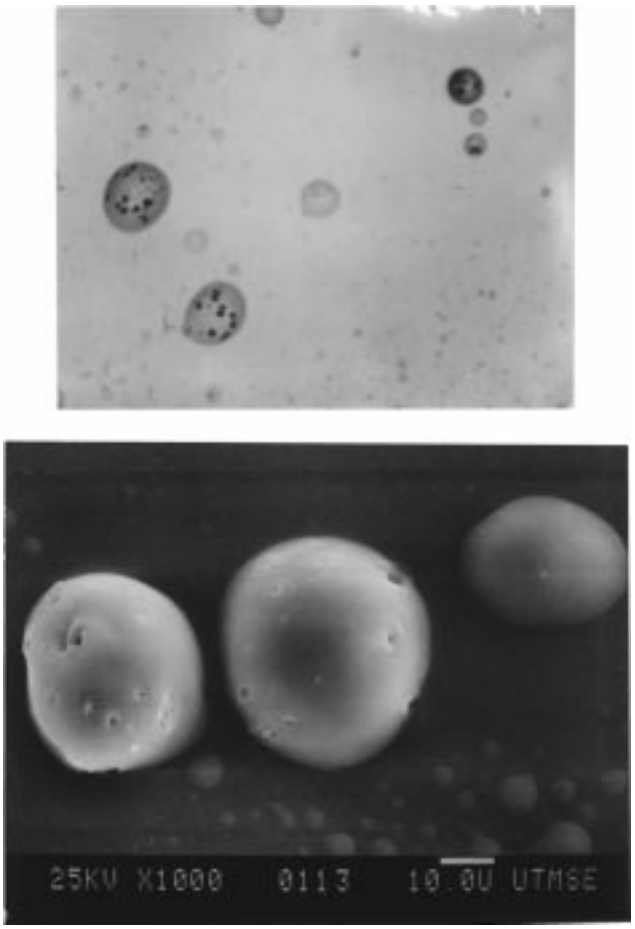

Figure 8—SEM micrograph (bottom) and optical micrograph (top) of PGLA microspheres formed by spraying at 0.5 mL/min a 5.0/0.5 wt %PGLA/lysozyme suspension in CH_2Cl_2 through a 100 μm capillary nozzle into CO_2 flowing at 25 mL/min at –20 °C.

not appear to be any protein particles which were not encapsulated, polymer particles without encapsulated protein were present.

Flowing CO_2 at high velocity during the spray delayed the time at which large particles were observed visually in the tube. This time corresponded to the time where agglomeration was observed in the SEM micrographs. Flowing CO_2 through the annular region surrounding the nozzle at high velocity caused a large amount of mixing at the vapor/liquid interface and suspended the precipitated particles throughout the cell, yielding spherical, nonagglomerated particles. Spraying a 5.0%/0.5% PGLA/lysozyme solution at 0.5 mL/min into the cell at −20 °C with CO_2 flowing at 25 mL/min yielded spherical particles 5−30 μm in diameter, with encapsulation of the protein as seen in Figure 8 (bottom). These particles are more uniform in size and shape than those formed in static CO_2 and appear like those in Figure 4 (middle). The particle sizes are more uniform in this case due to better mixing at the vapor−liquid interface.

In another type of experiment, CO_2 was introduced into the cell through a large opening located in the top of the cell 1 cm above the tip of the nozzle. Here, the CO_2 velocity was relatively low and turbulence from the CO_2 did not have much effect on the solution stream nor on the CO_2 vapor/liquid interface. The purpose of flowing CO_2 was to reduce the accumulation of solvent in the cell. Spraying a 5.0%/0.5% PGLA/lysozyme solution at 0.5 mL/min into CO_2 flowing at 35 mL/min at −21 °C yielded little change in particles size and failed to delay the onset of agglomeration, compared to the case with static CO_2. The same was true for higher CO_2 flow rates up to 52 mL/min. With this cell configuration, the CO_2 stream does not cause significant turbulence or mixing inside the cell. Since agglomeration occurred at the same time as in static CO_2 experiments, most of the agglomeration occurs immediately after precipitation and not after solvent buildup in the cell. In this case the particles were concentrated at the liquid−vapor interface and were not suspended throughout the liquid phase.

Elemental analysis via energy dispersive spectroscopy (EDS) was also used to confirm the presence of lysozyme in the polymer particles. Lysozyme has 2 amino acid constituents containing sulfur, cysteine, and methionine, which can be detected via EDS. Chicken egg white lysozyme is reported to contain eight cysteine molecules and two methionine molecules per protein chain.[61,62] Both of these amino acids have one sulfur atom per molecule, resulting in 10 per lysozyme molecule. EDS scans of the pure protein (top) and particles with encapsulated protein (bottom) are shown in Figure 9. The analysis of the pure lysozyme shows peaks corresponding to the presence of phosphorus, chlorine, and potassium impurities as well as the sulfur. Analysis of the peaks is only qualitative, unfortunately, due to multiple scattering of the X-rays. Particles formed by spraying a 5.0% PGLA solution with suspended lysozyme were analyzed as shown in Figure 9 (bottom). The lower curve represents a polymer particle with no protein present, while the upper curve corresponds to a single polymer particle with entrapped lysozyme. The particles were collected on a section of a glass slide, thus explaining the presence of the silicon impurity peak. The presence of the

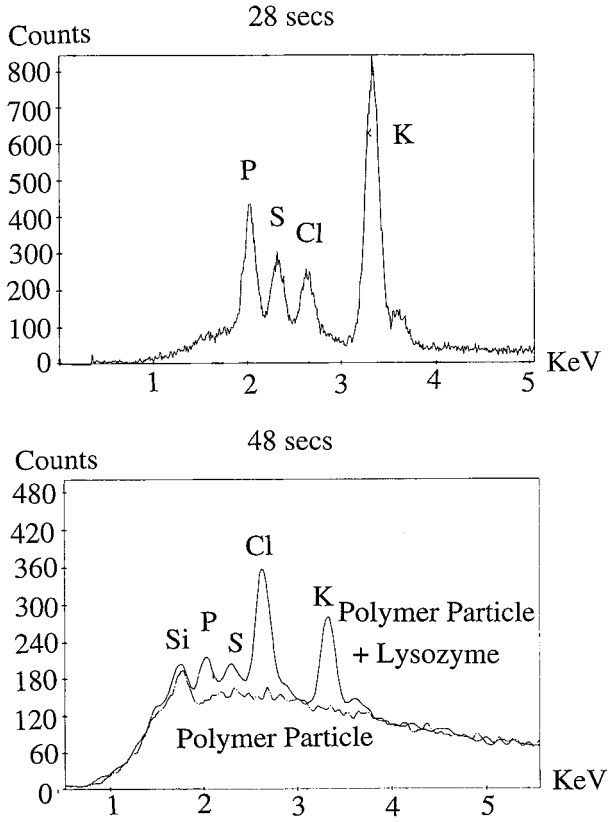

Figure 9—EDS scans of spray-dried lysozyme (top) and PGLA microspheres (bottom) formed by spraying a 5.0/0.5 wt % suspension of PGLA/lysozyme at 0.5 mL/min in CH_2Cl_2 through a 100 μm capillary nozzle into CO_2 flowing at 15 mL/min at –20 °C.

other peaks, excluding silicon, indicates that lysozyme was encapsulated within the polymer particle examined.

Encapsulation of Lysozyme into *l*-PLA—When polymer particles are similar in size to the protein particles, little or no encapsulation is expected to occur. Figure 10 (top) shows particles formed by spraying a 1.0% *l*-PLA solution with suspended lysozyme at 0.1 mL/min and 20 °C. As shown, the 1−4 μm polymer particles do not tend to encapsulate the lysozyme particles. Therefore, the polymer precipitation occurs without requiring the protein as a nucleation site. Solutions with higher polymer concentrations will tend to form larger particles as evidenced earlier for PGLA. Spraying a 5.0% *l*-PLA solution at 0.5 mL/min and 24 °C resulted in particles 250−500 μm in diameter, Figure 10 (bottom). This polymer precipitates very rapidly, and a polymer skin quickly forms on the droplet while still in the CO_2 vapor phase. The high solution viscosity caused the drop size to be larger than the nozzle inner diameter, and the resultant particle diameter was the same as the initial drop size. In this case the large polymer particles appeared to encapsulate all of the protein particles, as no individual protein particles were found on the sample slides.

Conclusions

Several major challenges for the PCA process were overcome in order to encapsulate a protein into PGLA. The PGLA particles were large enough to encapsulate the protein and did not agglomerate. In contrast, the primary particles (0.5 to 5 μm) were too small for encapsulation when the solution was sprayed into liquid or supercritical CO_2; furthermore, the particles were highly agglomerated. By delaying precipitation in a vapor CO_2 phase over a

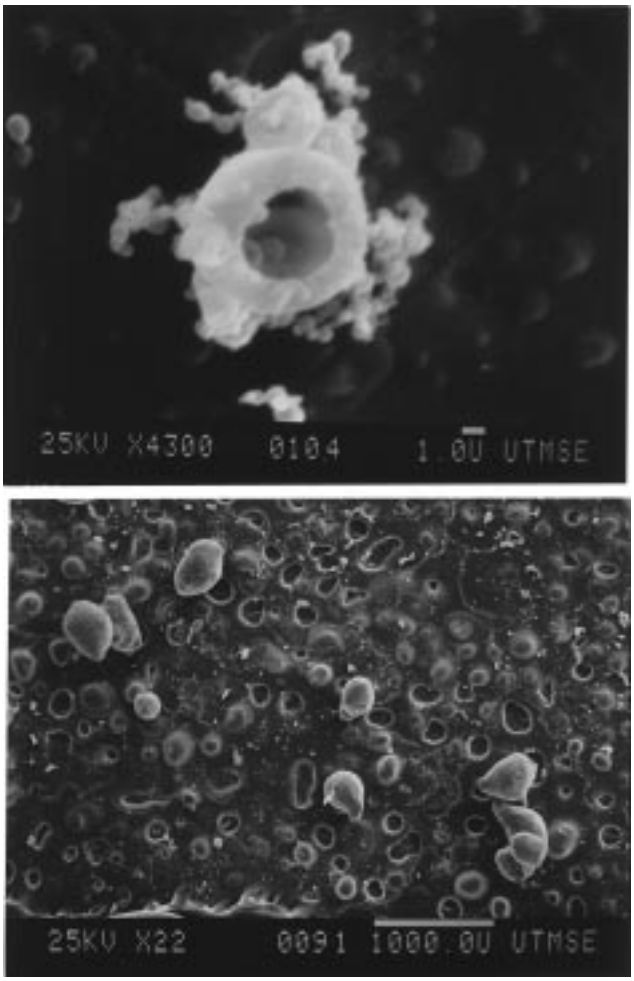

Figure 10—SEM micrographs of *l*-PLA microspheres formed by spraying a 1.0/0.1 wt % *l*-PLA/lysozyme suspension at 0.1 mL/min at 20 °C (top) and a 5.0/0.5 wt % *l*-PLA/lysozyme suspension at 0.5 mL/min at 24 °C (bottom) through a 100 μm capillary nozzle into static CO_2.

liquid CO_2 phase, much larger primary particles were formed, from 5 to 70 μm. At an optimal temperature of −20 °C, the polymer solution mixed rapidly with CO_2, and agglomeration of primary particles was minimal due to harder particles than at higher temperatures.

The amorphous polymer PGLA is highly plasticized by CO_2. Dissolution of CO_2 into PGLA depresses the T_g from the normal value of 45 °C to approximately −40 °C at 276 bar, based upon observation of particle agglomeration. Below −40 °C, the polymer remains as a nonsticky, free-flowing powder in the presence of CO_2 at 276 bar. Below −30 °C, the rate of mixing between CH_2Cl_2 and liquid CO_2 decreases appreciably. At an optimal temperature of −20 °C, the highly viscous PGLA microspheres do not agglomerate, yet the temperature is high enough to achieve adequate mixing between liquid CO_2 and the organic solution. An additional benefit of operating at colder temperatures is the relatively low pressure. At −20 °C, the saturation pressure of CO_2 is 19.7 bar, compared to 61.4 bar at 23 °C.

The vapor-over-liquid PCA process forms microspheres in the 5−70 μm range when a 5.0% solution of PGLA in dichloromethane is sprayed at 0.22 mL/min through a 100 μm diameter nozzle into static CO_2 at −20 °C. Experimental temperatures of 0 °C or above or below −30 °C yielded only large (>1000 μm) agglomerates. At high temperatures the particles are too sticky due to dissolved CO_2, and at low temperatures, the organic solution and CO_2 mix too slowly. Lower concentrations yielded smaller primary

particles whereas highly viscous concentrated solutions above 10.0 wt % led to skin formation in the vapor phase and subsequent agglomeration in the liquid CO_2 phase. The thin skin is weak due to low molecular weight and dissolved CO_2, and hence rupturing occurs upon impact at the liquid interface leading to agglomeration. Particle sizes did not change appreciably with solution flow rate in the "dripping" regime. At the onset of streaming flow, there was a higher percentage of large particles, while the particle size range remained the same. The most spherical and uniform particles ranging in size from 3 to 25 μm in diameter were produced by flowing CO_2 at high velocity through an annular region in a coaxial nozzle to provide mixing at the interface.

Encapsulation of 1−10 μm lysozyme particles proved successful for the 5−70 μm PGLA microspheres for a 1:10 ratio by weight of protein to polymer and a 5 wt % polymer solution. The presence of lysozyme in the particles was demonstrated by SEM analysis, optical microscopy, and EDS. A high encapsulation efficiency for this process is favored by the fact that the protein and polymer precipitate together in small droplets. The use of protein suspensions extends the applicability of the PCA process substantially, since many proteins are insoluble in organic solvents and are less likely to be denatured when suspended.

References and Notes

1. Mathiowitz, E.; Jacob, J. S.; Jong, Y. S.; Carino, G. P.; Chickering, D. E.; Chaturvedi, P.; Santos, C. A.; Vijayaraghavan, K.; Montgomery, S.; Bassett, M.; Morrell, C. Biologically Erodable Microspheres as Potential Oral Drug Delivery Systems. *Nature* **1997**, *386*, 410−4.
2. Cavalier, M.; Benoit, J. P.; Thies, C. The Formation and Characterization of Hydrocortisone-Loaded Poly((±)-Lactide) Microspheres. *J. Pharm. Pharmacol.* **1986**, *38*, 249−53.
3. Leelarasamee, N.; Howard, S. A.; Malanga, C. J.; Ma, J. K. H. A Method for the Preparation of Polylactic Acid Microcapsules of Controlled Particle Size and Drug Loading. *J. Microencapsulation* **1988**, *5*, 147−57.
4. Spenlehauer, G.; Veillard, M.; Benoit, J. P. Formation and Characterization of Cisplatin Loaded Poly(d,l-Lactide) Microspheres for Chemoembolization. *J. Pharm. Sci.* **1986**, *75*, 750−5.
5. Park, T. G.; Alonso, M. J.; Langer, R. Controlled Release of Proteins from Poly(L-Lactic acid) Coated Polyisobutylcyanoacrylate Microcapsules. *J. Appl. Polym. Sci.* **1994**, *52*, 1797−1807.
6. Thanoo, B. C.; Doll, W. J.; Mehta, R. C.; Digenis, G. A.; DeLuca, P. P. Biodegradable Indium-111 Labeled Microspheres for in Vivo Evaluation of Distribution and Elimination. *Pharm. Res.* **1995**, *12*, 2060−4.
7. Fong, J. W. Processes for Preparation of Microspheres; U.S. Patent 4384975, 1983.
8. Domb, A. J.; Amselem, S.; Maniar, M. Biodegradable Polymers as Drug Carrier Systems. In *Polymeric Biomaterials*; Dumitrius, S., Ed.; Marcel Dekker: New York, 1994; pp 399−433.
9. Puisieux, F.; Barratt, G.; Couarraze, G.; Couvreur, P.; Devissaguet, J. P.; Dubernet, C.; Fattal, E.; Fessi, H.; Vauthier, C.; Benita, S. Polymeric Micro- and Nanoparticles as Drug Carriers. In *Polymeric Biomaterials*; Dumitrius, S., Ed.; Marcel Dekker: New York, 1994; pp 749−94.
10. Langer, R. Polymeric Delivery Systems for Controlled Drug Release. *Chem. Eng. Commun.* **1980**, *6*, 1−48.
11. Lewis, D. H. Controlled Release of Bioactive Agents from Lactide/Glycolide Polymers. In *Biodegradable Polymers as Drug Delivery Systems*; M. Chasin, M., Langer, R., Eds.; Marcel Dekker: New York, 1990; Vol. 45, pp 1−41.
12. Alonso, M. J. Nanoparticulate Drug Carrier Technology. In *Microparticulate Systems for the Delivery of Proteins and Vaccines*; Cohen, S., Bernstein, H., Eds.; Marcel Dekker: New York, 1996; Vol. 77, pp 203−242.
13. Knutson, B. L.; Debenedetti, P. G.; Tom, J. W. Preparation of Microparticulates Using Supercritical Fluids. In *Microparticulate Systems for the Delivery of Proteins and Vaccines*; Cohen, S., Bernstein, H., Eds.; Marcel Dekker: New York, 1996; pp 89−125.
14. Johnston, K. P.; Kim, S.; Combes, J. Spectroscopic Determination of Solvent Strength and Structure in Supercritical Fluid Mixtures. *Am. Chem. Soc. Symp. Ser.* **1989**, *406*, 52−71.
15. McHugh, M. A.; Krukonis, V. J. *Supercritical Fluid Extraction Principles and Practice*, 2nd ed.; Butterworth: Stoneham, MA, 1994.
16. Matson, D. W.; Petersen, R. C.; Smith, R. D. Production of Powders and Films by the Rapid Expansion of Supercritical Solutions. *J. Mater. Sci.* **1987**, *22*, 1919−1928.
17. Matson, D. W.; Fulton, J. L.; Peterson, R. C.; Smith, R. D. Rapid Expansion of Supercritical Fluid Solutions: Solute Formation of Powders, Thin Films and Fibers. *Ind. Eng. Chem. Res.* **1987**, *26*, 2298−2306.
18. Tom, J. W.; Debenedetti, P. G. Formation of Bioerodible Microspheres and Microparticles by Rapid Expansion of Supercritical Solutions. *Biotechnol. Prog.* **1991**, *7*, 403−411.
19. Tom, J. W.; Debenedetti, P. G. Particle Formation with Supercritical Fluids − a Review. *J. Aerosol Sci.* **1991**, *22*, 555−584.
20. Phillips, E. M.; Stella, V. J. Rapid Expansion from Supercritical Solutions: Application to Pharmaceutical Processes. *Int. J. Pharm.* **1992**, 1−10.
21. Boen, S. N.; Bruch, M. D.; Lele, A. K.; Shine, A. D. Quick Quenching of Polymer Blends. In *Polymer Solutions, Blends, and Interfaces*; Noda, I., Rubingh, D. N., Eds.; Elsevier Science Publishers B. V.: Amsterdam, 1992; pp 151−172.
22. Lele, A. K.; Shine, A. D. Morphology of Polymers Precipitated From a Supercritical Solvent. *AICHE J.* **1992**, *38*, 742−752.
23. Lele, A. K.; Shine, A. D. Effect of RESS Dynamics on Polymer Morphology. *Ind. Eng. Chem. Res.* **1994**, *33*, 1476−1485.
24. Mawson, S.; Johnston, K. P.; Combes, J. R.; DeSimone, J. M. Formation of Poly(1,1,2,2-tetrahydroperfuorodecyl acrylate) Submicron Fibers and Particles from Supercritical Carbon Dioxide Solutions. *Macromolecules* **1995**, *28*, 3182−3191.
25. Alessi, P.; Cortesi, A.; Kikic, I.; Foster, N. R.; Macnaughton, S. J.; Colombo, I. Particle Production of Steroid Drugs Using Supercritical Fluid Processing. *Ind. Eng. Chem. Res.* **1996**, *35*, 4718−4726.
26. Kim, J. H.; Paxton, T. E.; Tomasko, D. L. Microencapsulation of Naproxen Using Rapid Expansion of Supercritical Solutions. *Biotechnol. Prog.* **1996**, *12*, 650−61.
27. Debenedetti, P. G.; Tom, J. W.; Yeo, S. D.; Lim, G. B. Application of Supercritical Fluids for the Production of Sustained Delivery Devices. *J. Controlled Release* **1993**, *24*, 27−44.
28. Gallagher, P. M.; Coffey, M. P.; Krukonis, V. J.; Klasuts, N. Gas Antisolvent Recrystallization: New Process To Recrystallize Compounds Insoluble in Supercritical Fluids. In *Supercritical Fluid Science and Technology*; K. P. Johnston, K. P., Penninger, J. M. L., Ed.; American Chemical Society: Washington, D. C., 1989; Vol. 406, pp 334−354.
29. Randolph, T. W.; Randolph, A. J.; Mebes, M.; Yeung, S. Sub-Micrometer-Sized Biodegradable Particles of Poly(L-Lactic Acid) via the Gas Antisovent Precipitation Process. *Biotechnol. Prog.* **1993**, *9*, 429−435.
30. Chou, Y. H.; Tomasko, D. L. GAS Crystallization of Polymer-Pharmaceutical Composite Particles. In *The 4th International Symposium on Supercritical Fluids*; International Society for the Advancement of Supercritical Fluids: Sendai, Japan, 1997; pp 55−7.
31. Dixon, D. J. Formation of Polymer Materials by Precipitation with a Compressed Fluid Antisolvent. Thesis, University of Texas at Austin, 1992.
32. Dixon, D. J.; Johnston, K. P.; Bodmeier, R. P. Polymeric Materials Formed by Precipitation with a Compressed Fluid Antisolvent. *AIChE J.* **1993**, *39*, 127−139.
33. Dixon, D. J.; Johnston, K. P. Formation of Microporous Polymer Fibers and Oriented Fibrils by Precipitation with a Compressed Fluid Antisolvent. *J. Appl. Polym. Sci.* **1993**, *50*, 1929−1942.
34. Dixon, D. J.; Luna-Barcenas, G.; Johnston, K. P. Microcellular Microspheres and Microballoons by Precipitation with a Vapour-Liquid Compressed Fluid Antisolvent. *Polymer* **1994**, *35*, 3998−4005.
35. Yeo, S. D.; Lim, G. B.; Debenedetti, P. G.; Bernstein, H. Formation of Microparticulate Protein Powders Using a Supercritical Fluid Antisolvent. *Biotechnol. Bioeng.* **1993**, *41*, 341−346.
36. Yeo, S.-D.; Debenedetti, P. G.; Radosz, M.; Schmidt, H.-W. Supercritical Antisolvent Process for Substituted Para-Linked Aromatic Polyamides: Phase Equilibrium and Morphology Study. *Macromolecules* **1993**, *26*, 6207−6210.
37. Luna-Barcenas, G.; Kanakia, S. K.; Sanchez, I. C.; Johnston, K. P. Semicrystalline Microfibrils and Hollow Fibres by Precipitation with a Compressed-Fluid Antisolvent. *Polymer* **1995**, *36*, 3173−3182.

38. Bodmeier, R. P.; Wang, H.; Dixon, D. J.; Mawson, S.; Johnston, K. P. Polymeric Microspheres Prepared by Spraying into Compressed Carbon Dioxide. *Pharm. Res.* **1995**, *12*, 1211−1217.
39. Mawson, S.; Johnston, K. P.; Betts, D. E.; McClain, J. B.; DeSimone, J. M. Stabilized Polymer Microparticles by Precipitation with a Compressed Fluid Antisolvent I. Polyfluoroacrylate Based Surfactants. *Macromolecules* **1997**, *30*, 71−77.
40. Mawson, S. The Formation and Characterization of Polymeric Materials Precipitated by CO_2-Based Spray Processes. Thesis, University of Texas at Austin, 1996.
41. Mawson, S.; Kanakia, S.; Johnston, K. P. Coaxial Nozzle for Control of Particle Morphology in Precipitation with a Compressed Fluid Antisolvent. *J. Appl. Polym. Sci.* **1997**, *64*, 2105−2118.
42. Mawson, S.; Kanakia, S.; Johnston, K. P. Metastable Polymer Blends by Precipitation with a Compressed Fluid Antisolvent. *Polymer* **1997**, *38*, 2957−2967.
43. Falk, R.; Randolph, T.; Meyer, J. D.; Kelly, R. M.; Manning, M. C. Controlled Release of Ionic Pharmaceuticals from Poly-(L-Lactide) Microspheres Produced by Precipitation with a Compressed Antisolvent. *J. Controlled Release* **1997**, *44*, 77−85.
44. Winters, M. A.; Knutson, B. L.; Debenedetti, P. B.; Sparks, H. G.; Przybycien, T. M.; Stevenson, C. L.; Prestrelski, S. J. Precipitation of Proteins in Supercritical Carbon Dioxide. *J. Pharm. Sci.* **1996**, *85*, 586−594.
45. Bleich, J.; Kleinebudde, P.; Müller, B. W. Influence of Gas Density and Pressure on Microparticles Produced with the ASES Process. *Int. J. Pharm.* **1994**, *106*, 77−84.
46. Bleich, J.; Müller, B. W. Production of Drug Loaded Microparicles by the Use of Supercritical Gases with the Aerosol Solvent Extraction System (ASES) Process. *J. Microencapsulation* **1996**, *13*, 131−9.
47. Fischer, W.; Müller, B. W. Method and Apparatus for the Manufacture of a Product Having a Substance Embedded in a Carrier; U.S. Patent 5043280, 1991.
48. McHugh, M. A.; Krukonis, V. Supercritical Fluids. In *Encyclopedia of Polymer Science and Engineering*, 2nd ed.; Mark, H. F., Bikales, N. M., Overberger, C. G., Menges, G., Eds.; John Wiley: New York, 1988; Vol. 16.
49. McHugh, M. A. Polymers in Supercritical Fluids. In *The 4th International Symposium on Supercritical Fluids*; International Society for the Advancement of Supercritical Fluids: Sendai, Japan, 1997; pp 785−8.
50. Ruchatz, F.; Kleinebudde, P.; Müller, B. W. Residual Solvents in Biodegradable Microparticles. Influence of Process Parameters on the Residual Solvent in Microparticles Produced by the Aerosol Solvent Extraction System (ASES) Process. *J. Pharm. Sci.* **1997**, *86*, 101−5.
51. Steckel, H.; Thies, J.; Müller, B. W. Micronizing of steroids for pulmonary delivery by supercritical carbon dioxide. *Int. J. Pharm.* **1997**, *152*, 99−110.
52. Falk, R. F.; Randolph, T. W. Process Variable Implications for Residual Solvent Removal and Polymer Morphology in the Formation of Gentamycin-Loaded Poly(L-lactide) Microparticles. *Pharm. Res.* **1998**, *15*, 1233−7.
53. Condo, P. D.; Paul, D. R.; Johnston, K. P. Glass Transitions of Polymers with Compressed Fluid Diluents: Type II and III Behavior. *Macromolecules* **1994**, *27*, 365−371.
54. Fong, J. W. *Processes for Preparation of Microspheres*; U.S. Patent 4166800, 1979.
55. Schwendeman, S. P.; Cardamone, M.; Klibanov, A.; Langer, R.; Brandon, M. R. Stability of Proteins and Their Delivery from Biodegradable Polymer Microspheres. In *Microparticulate Systems for the Delivery of Proteins and Vaccines*; Cohen, S., Bernstein, H., Eds.; Marcel Dekker: New York, 1996; Vol. 77, pp 1−49.
56. Yeo, S. D.; Debenedetti, P. G.; Patro, S. Y.; Przybycien, T. M. Secondary Structure Characterization of Microparticulate Insulin Powders. *J. Pharm. Sci.* **1994**, *83*, 1651−1656.
57. Winters, M. A.; Debenedetti, P. G.; Barey, J.; Sparks, H. G.; Sane, S. U.; Przybycien, T. M. Long-term and high-temperature storage of supercritically processed microparticulate protein powders. *Pharm. Res.* **1997**, *14*, 1370−8.
58. Kissel, T.; Koneberg, R. Injectable Biodegradable Microspheres for Vaccine Delivery. In *Microparticulate Systems for the Delivery of Proteins and Vaccines*; Cohen, S., Bernstein, H., Eds.; Marcel Dekker: New York, 1996; Vol. 77, pp 51−87.
59. Bleich, J.; Müller, B. W.; Wabmus, W. Aerosol solvent extraction system − a new microparticle production technique. *Int. Pharm.* **1993**, *97*, 111−7.
60. Lemert, R. M.; Fuller, R. A.; Johnston, K. P. Reverse Micelles in Supercritical Fluids. 3. Amino Acid Solubilization in Ethane and Propane. *J. Phys. Chem.* **1990**, *94*, 6021−28.
61. Bailey, P. D. *An Introduction To Peptide Chemistry*; John Wiley & Sons: New York, 1990; p 232.
62. Hamaguchi, K.; Hayashi, K. Lysozyme. In *Proteins: Structure and Function*; Funatsu, M., Hiromi, K., Imahori, K., Murachi, T., Narita, K., Eds.; John Wiley & Sons: New York, 1972; Vol. 1, pp 85−222.

Acknowledgments

We acknowledge support from NSF (CTS-9626828), DOE (DE-FG03-96ER14664), the Separations Research Program at the University of Texas at Austin, and the Texas Advanced Technology Program. We thank ISCO Corporation for the donation of the high-pressure syringe pump, and Alza for supplying the poly(DL-lactide-*co*-glycolide) and lysozyme samples.

JS980237H

A publication of the American Pharmaceutical Association and the American Chemical Society

JOURNAL OF Pharmaceutical Sciences

July 1999
Volume 88, Number 7

MINIREVIEW

Significance of Controlling Crystallization Mechanisms and Kinetics in Pharmaceutical Systems

NAÍR RODRÍGUEZ-HORNEDO*,† AND DENETTE MURPHY‡

Contribution from *College of Pharmacy, University of Michigan, Ann Arbor, Michigan 48109-1065 and Dupont Pharmaceuticals, P.O. Box 80400, Wilmington, Delaware 19880-0400.*

Received December 23, 1998. Final revised manuscript received April 8, 1999.
Accepted for publication April 12, 1999.

Introduction

Metastable thermodynamic states are frequently encountered in pharmaceutical systems, in the intentional or unintentional creation of supersaturation, in the crystallization of desired solid-state modifications, and in the control of solid-phase conversions during isolation, manufacturing, storage, and dissolution.[1−4] Some examples in which metastable states are encountered include solid solutions, freeze-concentrated solutions, solutions of weak acids or bases exposed to a pH change, solutions prepared by dissolving a solid-state modification with a higher solubility (higher free energy), and residual solutions during filtration, granulation, and drying. Because crystallization provides a way of reducing the free energy of metastable thermodynamic states, the extent to which metastable states can be maintained is determined by the crystallization mechanisms and kinetics.[5−16] What is surprising, however, is that despite the important role that crystallization has in process control and in determining solid-phase outcomes, crystallization phenomena are often neglected in the pharmaceutical industry until a problem is encountered.

While emphasis is often given to the knowledge of equilibrium phase diagrams with the purpose of identifying the concentration and temperature regions of thermodynamic stability of solid phases, information on crystallization processes can only be obtained by combining studies of thermodynamic properties with kinetic measurements. Cases of unwanted or previously unknown nucleation events abound. Dunitz and Bernstein[17] documented cases of "disappearing or elusive polymorphs" that provide evidence for the consequences of poor process control in crystallization of polymorphic systems. The recent shortage in the supply of capsules of the HIV protease inhibitor Norvir (indinavir), due to the sudden formation of a crystalline structure different from the one harvested for months,[18] illustrates the decisive role that nucleation mechanisms and kinetics have on crystallization. Nichols and Frampton[19] have reported considerable efforts that failed to crystallize the metastable polymorph of paracetamol as described in the initial publication of the crystal structure.[20] The critical role of crystallization kinetics in determining the appearance of crystalline modifications is also recognized by the FDA and described in the guidelines for the manufacture of drug substances:[21] "Appropriate manufacturing and control procedures (including in-process testing when needed) should be established for the production of the desired solid-state form(s). It should be emphasized that the manufacturing process (or storage condition) is responsible for producing particular polymorphs or solvates; the control methods merely determine the outcome."

Even when the parameters that regulate crystallization phenomena are neglected, the illusion of process control is motivated by a crystallization process that yields the desired product—solid phase modification, shape, or size distribution—and by the robust analytical methods used for solid state characterization. This situation is greatly complicated by the recent emphasis on an exclusively

* Corresponding author. Tel: 734-763-0101. Fax: 734-763-2022. e-mail: nrh@umich.edu.
† University of Michigan.
‡ Dupont Pharmaceuticals.

10.1021/js980490h CCC: $18.00
Published on Web 05/19/1999

structural approach due to the availability of commercial software for the prediction of crystal structure from molecular structure (ab initio predictions) while kinetic processes are scarcely investigated. Desiraju[22–24] and Gavezzotti[25–29] have discussed the various methods for crystal structure and polymorphism prediction and the capabilities and shortcomings of the various computer simulation techniques. The main challenge lies in determining the relationships between the molecular aggregation pathways that cause some nuclei to grow and the structure and thermodynamics of the crystalline solids. Recent work from various groups[14,30–40] highlight the importance of combining computer simulations with experimental methods to investigate the molecular events that lead to crystallization.

The purpose of this review is to describe ways in which crystal structure, morphology, and crystallization kinetics can be utilized to reproducibly maintain metastable states and control solid-state outcomes. Experimental methods that can be employed to investigate the factors that regulate crystallization from solution will be presented.

Crystallization

A crystalline phase is created as a consequence of molecular aggregation processes in solution that lead to the formation of nuclei (with a configuration compatible with the crystal structure), which achieve a certain size for a sufficient time to enable growth into macroscopic crystals. The rate and mechanisms by which crystals are formed in liquid solutions is determined by the solubility, supersaturation, rate at which supersaturation is created, diffusivity, temperature, and the reactivity of surfaces toward nucleation.[41–45]

Transferability of crystallization microtechniques to larger scale processes that are reproducible requires identification of crystallization mechanisms and kinetics. While operationally useful variables that describe crystallization methods are often related to crystallization outcomes, this approach lacks meaningful information for developing a process that yields reliable outcomes, since the factors that determine the crystallization kinetics and outcomes are not explicitly considered. For instance, compare the following two approaches to describe the processes for the selective crystallization of polymorphs: (1) form I obtained by cooling, form II obtained by evaporation, and (2) form I obtained at a supersaturation x, temperature y, and time z at which crystals were harvested after crystallization onset; form II obtained at supersaturation x', etc. While the former approach is at best anecdotal, the latter employs the causative factors and leads to relationships between the crystallization kinetic parameters and the outcomes.

Control of the processes of nucleation and crystal growth is possible as long as the required information is available. Dunitz and Bernstein[17] have explained the mystery of disappearing polymorphs by considering various examples and the relevant questions that were left unanswered. They state that "once a particular polymorph has been obtained, it is always possible to obtain it again; it is only a matter of finding the right experimental conditions."

Supersaturation

Knowledge of the driving force for crystallization is essential, not only to characterize the kinetics, but also to relate the crystallization outcomes to the parameters that regulate crystallization. The number of molecules necessary to achieve an effective nucleating cluster is inversely proportional to the supersaturation. Therefore, as the supersaturation is increased the probability of nucleation increases. However, nucleation is energetically more demanding than crystal growth, and there are supersaturation regions in which crystal growth proceeds while nucleation is suppressed.[41,42,44]

The driving force for nucleation and growth is the difference in chemical potential of the solute in a supersaturated solution, μ_1, and in a saturated solution, μ_{eq}:

$$\Delta\mu = (\mu_1 - \mu_{eq}) \tag{1}$$

Since $\mu = \mu^\circ + RT \ln a$, then

$$\Delta\mu = \mathrm{RT} \ln (\mathrm{a}_1/\mathrm{a}_{eq}) = \mathrm{RT} \ln (\gamma_1 \mathrm{c}_1/\gamma_{eq}\mathrm{c}_{eq}) \tag{2}$$

and the supersaturation is

$$\sigma = \Delta\mu/\mathrm{RT} = \ln (\mathrm{a}_1/\mathrm{a}_{eq}) = \ln (\gamma_1 \mathrm{c}_1/\gamma_{eq}\mathrm{c}_{eq}) \tag{3}$$

If the activity coefficient, γ, is independent of concentration, in the given concentration regime, then $\gamma_1 = \gamma_{eq}$ and the supersaturation becomes

$$\sigma = \ln (c_1/c_{eq}) = \ln (c/s) \tag{4}$$

where c is the concentration of the crystallizing substance in the supersaturated solution and s is the solubility. (This notation is adopted to avoid the use of subscripts.) A frequently used definition for the supersaturation is

$$\sigma \equiv (c - s)/s \tag{5}$$

For c/s values smaller than 1.15,

$$\sigma = \ln (c/s) \approx (c - s)/s \tag{6}$$

Supersaturation may be created by various methods that regulate the solute activity (concentration) or activity product. These include (a) solvent removal (evaporation or freezing), (b) addition of indifferent salts with ions that participate in precipitation, and (c) dissolution of metastable solid phases. Supersaturation can also be created by methods that regulate the solute solubility, such as temperature change, pH change, and addition of a solvent that lowers the solubility of the solute.

Nucleation

Nucleation is often the decisive step in the crystallization process and is of practical importance in pharmaceutical systems. For instance, questions regarding the concentration threshold above which crystallization is observed at times shorter than the desired product shelf life, or dilution rates and concentrations above which precipitation occurs upon injection, are related to the kinetic stability of supersaturated solutions and are regulated by the nucleation mechanisms and kinetics. Nucleation phenomena are equally important in the control of micromeritic properties and in the selective crystallization of a particular polymorph.

In general, nucleation mechanisms can be divided into two main categories: homogeneous and surface or interface catalyzed.[42–44,46] Homogeneous nucleation rarely occurs in large volumes (greater than 100 μl) since solutions contain random impurities which may induce nucleation.[47,48] This type of nucleation is referred to as heterogeneous. A surface or an interface of different composition than the crystallizing solute may serve as a nucleation substrate, by decreasing the energy barrier for the formation of nuclei that can grow into mature crystals. Nucleation that is promoted by crystals of the crystallizing solute is known

as secondary nucleation. These mechanisms are thoroughly discussed by Mullin,[42] Myerson,[44] and Zettlemoyer.[46]

Homogeneous Nucleation—Thermodynamic considerations for nucleation are based on the work of Gibbs,[49] Volmer [50] and others, where the free energy change for an aggregate undergoing a phase transition ΔG is given by

$$\Delta G = \Delta G_v + \Delta G_s \tag{7}$$

where ΔG_s is the surface free energy change associated with the formation of the aggregate (a positive quantity), and ΔG_v is the volume free energy change associated with the phase transition (a negative quantity). For homogeneous or heterogeneous nucleation

$$\Delta G_v = -\alpha l^3 v k_B T \ln\left(\frac{c}{s}\right) \tag{8}$$

where α is the volume-shape factor, l is the characteristic length, v is the molecular volume of the crystallizing solute, k_B is Boltzmann's constant, and T is temperature. For homogeneous nucleation

$$\Delta G_s = \beta l^2 \gamma_{12} \tag{9}$$

where β is the area shape factor and γ is the interfacial energy per unit area between the crystallization medium, 1, and the nucleating cluster, 2. Consequently, the overall free energy change for nucleation is decreased by a large supersaturation ratio (c/s) and by a low interfacial energy.

The factors that regulate nucleation are best appreciated by considering the equation for the rate of homogeneous nucleation from solutions:

$$J = N_o \nu \exp\left(\frac{-\Delta G^*}{k_B T}\right) = N_o \nu \exp\left(\frac{-4\beta^3 v^2 \gamma_{12}^3}{27\alpha^2 (k_B T)^3 \left(\ln\left(\frac{c}{s}\right)\right)^2}\right) \tag{10}$$

J is the number of nuclei formed per unit time per unit volume, N_o is the number of molecules of the crystallizing phase in a unit volume, ν is the frequency of atomic or molecular transport at the nucleus–liquid interface, and ΔG^* is the maximum in the Gibbs free energy change for the formation of clusters, at a certain critical size, l^*. The nucleation rate was initially derived for condensation in vapors by Becker and Döring,[51] where the preexponential factor is related to the gas kinetic collision frequency. In the case of nucleation from condensed phases, the frequency factor is related to the diffusion process.[52] The value of l^* can be obtained by minimizing the free energy function with respect to the characteristic length

$$l^* = \frac{2\beta v \gamma_{12}}{3\alpha k_B T \ln\left(\frac{c}{s}\right)} \tag{11}$$

For spherical clusters, $\alpha = 4\pi/3$ and $\beta = 4\pi$ based on the cluster radius. Therefore,

$$r^* = \frac{2v\gamma_{12}}{k_B T \ln\left(\frac{c}{s}\right)} \tag{12}$$

Considering these geometric factors, the rate for homogeneous nucleation of spherical clusters is

$$J = N_o \nu \exp\left(\frac{-16\pi v^2 \gamma_{12}^3}{3(k_B T)^3 \left(\ln\left(\frac{c}{s}\right)\right)^2}\right) \tag{13}$$

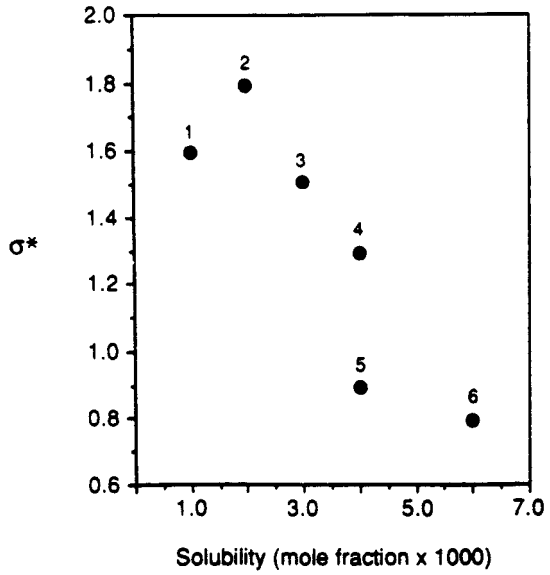

Figure 1—Dependence of the critical supersaturation for nucleation on solubility of nitrofurantoin in (1) formic acid, (2) formic acid:water (4:1), (3) formic acid:ethanol (2:1), (4) formic acid:dioxane (2:1), (5) formic acid:methanol (2:1), (6) formic acid:water (2:1). Data from ref 55.

While the classical theory of nucleation is limited by the implicit assumptions in its derivation (described in detail in ref 41) it successfully predicts the nucleation behavior of a system.[42–44,46,53] Inspection of the equation above clearly suggests that the nucleation rate can be experimentally controlled by the following parameters: molecular or ionic transport, viscosity, supersaturation, solubility, solid–liquid interfacial tension, and temperature.

Nucleation kinetics are experimentally determined from measurements of nucleation rates, induction times and metastability zone widths (the supersaturation or undercooling necessary for spontaneous nucleation) as a function of initial supersaturation.[41–43,54] The nucleation rate will increase by increasing the supersaturation while all other variables are constant. However, at constant supersaturation the nucleation rate will increase with increasing solubility. Solubility affects the pre-exponential factor and the probability of intermolecular collisions. Furthermore, when changes in solvent or solution composition lead to increases in solubility, the interfacial energy decreases since the affinity between crystallizing medium and crystal increases.[41] Consequently, the supersaturation required for spontaneous nucleation decreases with increasing solubility,[55] as shown in Figure 1.

The dependence of nucleation rate on solubility is also consistent with Ostwald's law of stages[56] regarding the preferential formation of a metastable solid phase, that states the following: "when leaving an unstable state, a system does not seek out the most stable state, rather the nearest metastable state which can be reached with loss of free energy". This indicates that if the unstable solid-state modification (the system with highest solubility) precipitates before more thermodinamically stable solid phases, it must have higher nucleation and growth rates than solid states of lower solubility. However, Ostwald's law of stages is not universally valid because the appearance and evolution of solid phases are determined by the kinetics of nucleation and growth under the specific experimental conditions.[5,6,13]

Accounts of nucleation inhibition in the pharmaceutical literature are sometimes confusing because the dependence of the nucleation event (nucleation rate, metastability zone width, or induction time) on supersaturation is not considered. In search for additives that inhibit nucleation,

Table 1—Comparison of Crystallization Behavior of Disodium Phosphate during Far-from-Equilibrium Freezing of Buffer Solutions

crystallization behavior of $Na_2HPO_4 \cdot 12H_2O$		$C_{Na_2HPO_4}$[a] (mM)
reference	observation	
Murase and Franks[63,64]	crystallization begins to decrease	≤200
	does not crystallize	≤10
Cavatur and Suryanarayanan[65]	readily crystallizes	190
	crystallization is inhibited by $C_{NaH_2PO_4}$[b] ≥ 730 mM	190
Gómez[66]	crystallization begins to decrease	≤15
	crystallization readily occurs	≥0.3
	crystallization is not inhibited at $C_{NaH_2PO_4}$ ≤ 94 mM	6

[a] $C_{Na_2HPO_4}$ = initial disodium phosphate concentration in solution at 25 °C. [b] $C_{NaH_2PO_4}$ = initial monosodium phosphate concentration in solution at 25 °C.

induction times are often measured as a function of additive concentration while the dependence of the nucleation event on supersaturation is neglected. Results from such studies possibly lead to the erroneous conclusion that the additive inhibited nucleation[57,58] when indeed the additive decreased the supersaturation, and frequently led to an undersaturated state. Hence, the system is under *thermodynamic* control instead of *kinetic* control.

An important factor contributing to the nucleation mechanism and kinetics is the volume of solution in which nucleation occurs. The dispersal of a bulk liquid into a collection of small droplets has been shown to be an effective way of achieving large supersaturations or undercoolings.[47,48] Precipitation and solidification in small volumes (droplets) involving emulsions have been used to study homogeneous nucleation processes,[59] and to control purity, particle size, and morphology.[60,61] Dispersing a solution into small volumes isolates heterogeneous nucleants within a fraction of the drops and makes nucleation more difficult. Consequently, larger supersaturations need to be reached for nucleation to occur. The boundaries of possible outcomes are represented by the following scenarios: (1) crystals of very small size (even in the nanometer range) are formed as a result of the high nucleation rates,[60,61] or (2) a glass or amorphous solid is formed due to the low diffusion rates of molecules that inhibit the evolution of clusters to crystals within the time scale of the experiment.[62]

Nucleation outcomes from solutions with initially the *same composition* may vary as a consequence of impurities, rates at which supersaturation was created, thermal histories, experimental techniques employed to detect precipitation, and solution volumes in which nucleation occurred. An important factor contributing to the changes in pH during freezing of buffer solutions is the selective crystallization of buffer components.[63–66] The salt and buffer concentrations for precipitation of disodium phosphate during freezing of sodium phosphate buffer solutions among various laboratories are shown in Table 1. Murase et al.[63,64] report higher initial buffer and disodium phosphate concentrations for the precipitation of disodium phosphate, compared to results from our laboratory.[66] The fraction of disodium phosphate precipitated was observed to decrease with decreasing the initial buffer concentration below 500 mM, at 200 mM disodium phosphate concentration, versus an initial buffer concentration below 8 mM, at 0.3 mM disodium phosphate concentration in our studies;[66] furthermore, disodium phosphate did not precipitate at initial disodium salt concentrations below 10 mM[63,64]

Table 2—Experimental Conditions and Methods of Measuring Progress of Sodium Phosphate Crystallization during Freezing

reference	vol of solution (μL)	cooling rate (°C/min)	temp (°C)	method
Murase and Franks[63,64]	2–5	0.62	–52	DSC, SEM
Cavatur and Suryanarayanan[65]	300[a]	15	–40	XRPD
Gómez[66]	25×10^3	0.3–0.5	–10	pH

[a] Personal communication.

while our studies show that precipitation occurs at salt concentrations as low as 0.3 mM.[66] Inspection of the experimental conditions under which these studies were done (Table 2) shows a trend toward slower salt precipitation rates with decreasing volume of solutions from 25 mL to 3 μl and increasing rates of cooling to lower temperatures.

Neglecting the factors that regulate nucleation leads to misleading generalizations when developing guidelines to control precipitation by the addition of noncrystallizing additives. Consider, for example, the conflicting interpretation of additive effects on nucleation when these are expressed in terms of concentration ratios (additive to crystallizing solute) while ignoring other parameters. Data in Table 1 indicates that disodium phosphate precipitation is inhibited at ($H_2PO_4^-/HPO_4^{2-}$) = 4 (0.73 M/0.19 M)[65] while it is not inhibited at ($H_2PO_4^-/HPO_4^{2-}$) = 16 (0.094 M/0.006 M).[66] Compared to the systems we studied,[66] the buffers studied by Cavatur and Suryanarayana[65] have much higher concentrations of monosodium phosphate (which increase the viscosity of solutions), smaller solution volumes, and faster rates of cooling to lower temperatures. All these factors contribute to delaying salt precipitation.

The effect of the viscosity of the crystallization medium on the nucleation rate has been described by Turnbull and Fisher.[52] The frequency of atomic or molecular transport at the nucleus–liquid interface can be related to the bulk viscosity, η, with the Stokes–Einstein relation:

$$\nu \approx \frac{kT}{3\pi a_o^3 \eta(T)} \tag{14}$$

where a_o is the mean effective diameter of the diffusing species. If the viscosity dependence on temperature is described by Arrhenius behavior, then

$$J = \frac{K}{\eta_o} \exp\left(\frac{-\Delta G^* - \Delta G_a}{k_B T}\right) \tag{15}$$

where ΔG_a is the activation energy for transport across the nucleus–liquid interface. Thus, the nucleation rate may go through a maximum when an increase in undercooling or supersaturation is accompanied by an increase in viscosity. This behavior has been observed in the nucleation of citric acid in aqueous solutions,[67] and the crystallization of ice.[68]

Heterogeneous Nucleation—Heterogeneous nucleation processes are of fundamental and practical importance in pharmaceutical systems since unintentionally or intentionally added surfaces or interfaces may promote nucleation. The reactivity of crystals surfaces as heterogeneous nucleants has significant consequences in the isolation of the desired solid-state modification and in the control of conversions between these modifications, since the free energy required for the formation of two-dimensional nuclei is lowered by the presence of an appropriate substrate. Quantitatively this is described by the following equation:[69,70]

$$\Delta G_s = \gamma_{12}A_{12} + (\gamma_{23} - \gamma_{13})A_{23} \quad (16)$$

where γ is the interaction energy per area, A is the surface area of the interfaces, and the subscript 3 represents the substrate. The total change in surface free energy will be lowered by favorable surface interactions between the aggregate and the substrate and unfavorable interactions between the crystallization medium and the substrate, due to the negative value of the second term in eq 16. Consequently, nucleation will be enhanced by increasing the surface area of the substrate.

The effectiveness of crystal seeding in controlling crystallization outcomes relies on the potential of crystal surfaces to promote heterogeneous or secondary nucleation,[42,43] while avoiding heterogeneous nucleation mediated by unknown contaminants. A review by Ward[71] on the structure, properties, and reactivity of organic crystal surfaces is recommended to develop strategies for the choice of surfaces that promote nucleation. Various studies[8,72−75] have demonstrated the influence of substrate topography, lattice parameters, crystallographic symmetry and intermolecular interactions on surface-directed nucleation.

Heterogeneous nucleation mechanisms can significantly affect dissolution of metastable solid phases, because this form of nucleation can occur at low driving forces. While the choice of a metastable solid phase with a solubility higher than other crystalline modifications is motivated by the expectation of faster dissolution rates, achievement of faster dissolution rates and higher concentrations in solutions is jeopardized by surface-mediated nucleation events. We have reported[8] that the surface of the metastable phase of theophylline promoted the nucleation of the stable monohydrate crystals. The observed oriented growth of monohydrate crystals on the anhydrous surface is consistent with a close lattice match between the *b* and *c* crystallographic axes.[8] Other studies on the dissolution of metastable solids such as anhydrous theophylline[76] and anhydrous carbamazepine[77−79] have shown that crystallization of the stable phase occurs during dissolution, Figure 2. It is unfortunate that in view of the important influence that nucleation mechanisms have on dissolution of metastable solid phases, very seldom are studies carried out to identify the potential of substrate-mediated nucleation by the metastable modification. The information gained from this type of study can be used in the design of methods to regulate crystallization during dissolution as well as during isolation of the desired solid form.

Carter and Ward[70] have identified a surface-mediated nucleation mechanism that involves a geometric shape match between planes of a ledge site on the substrate and planes of prenucleation aggregates. They have applied these concepts to the directed nucleation of polymorphs.[72,74] This work provides us with the attractive possibility that "a library of organic seeds can be used to control polymorphism, or to search for unknown polymorphs".[71] Molecular interpretations based on this approach are experimentally more accessible than those based on solvent-selective polymorph crystallization.

Experimental and Computational Strategies—While nucleation phenomena have their origin at the molecular level, they are often described in terms of macroscopic properties due to the scarcity of experimental techniques that allow for monitoring events at the molecular level. Nevertheless, information about molecular association processes in supersaturated systems obtained by laser Raman spectroscopy and laser light scattering has been used to identify prenucleation clusters and growth units under well-defined experimental conditions. Methods that measure cluster size distributions are more appropriate for studying crystallization of macromolecules[80−84] due to the large sizes of prenucleation clusters, while Raman and fluorescence spectroscopic techniques are capable of providing information about the solution structure or the species present in solution.[85−88] The implications for crystallization pathways are examined by comparing the solution and crystal structures at a molecular level, and by combining information obtained from macroscopic analysis with results from molecular simulations.[14,31−40]

Figure 2—Nucleation and growth of dihydrate carbamazepine on crystal faces of anhydrous monoclinic carbamazepine in aqueous solutions of sodium lauryl sulfate (17.3 mM, 0.5%), supersaturation ratio of 1.15 at 25 °C. From ref 79.

Desiraju[22−24] and Gavezzotti[26−29] have described crystal engineering strategies to understand the molecular aggregation processes involved in crystallization and to elucidate the supramolecular motifs in organic crystals. In this context, crystals are viewed as solid-state supermolecules assembled by intermolecular interactions, with the basic approach of establishing a relation between molecular interactions and supramolecular structure. Recent studies by Gavezzotti[29] show how molecular dynamics calculations allow for simulation of solvent and kinetic effects on molecular aggregation.

The supramolecular assembly process can be controlled so that the precursor nuclei in solution adopt a structure that resembles the structure of the desired crystalline modification.[29,89,90] This concept has been used in the design of nucleation inhibitors to prevent growth of the stable polymorph and enhance the growth of the metastable polymorph.[13,15,16] Davey et al.[14] have explained the solvent-dependent polymorph appearance of sulfathiazole by analyzing the intermolecular interactions in the various polymorphic structures and comparing them with the supramolecular assemblies that could exist in the different solvents. In this case, however, the solvent-dependent selective crystallization of a polymorph was not correlated with solubility.[14,91]

Strategies used for the rational choice of additives to selectively inhibit nucleation or growth of the thermody-

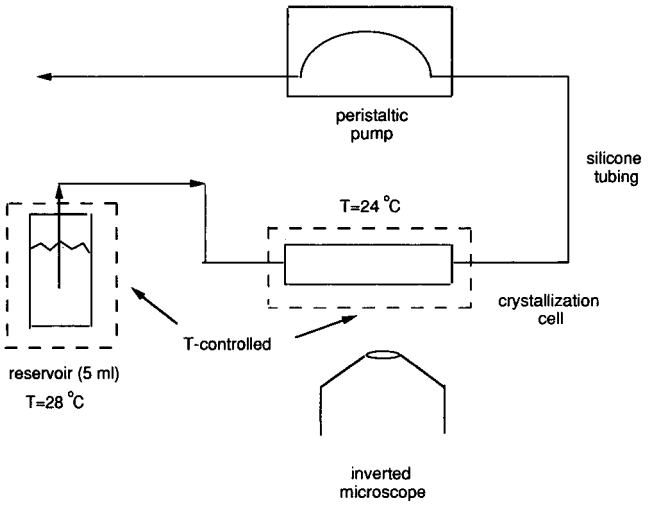

Figure 3—Schematic diagram of a flow system used to measure growth rates of crystal faces. The volume of the crystallization cell is 300 to 500 μL.

namically stable modification are based on the work of Davey,[12–14,92] Leiserowitz,[15,16] and others.[40,93,94] The main features of these strategies are as follows:

(1) identification of the fastest growing faces of the stable crystalline modification,
(2) characterization of intermolecular interactions along the crystallographic direction with fastest growth,
(3) selection of additives that can be incorporated in the crystalline structure along this direction, and
(4) development of experimental methods to investigate the effectiveness of the additive to kinetically stabilize the metastable modification.

The selection of additives can be guided by molecular visualizations of the crystal structure based on geometric fits[13,95] or binding energy calculations.[36,96]

Growth Mechanisms and Kinetics

Once the nucleation step has been overcome, nuclei grow into macroscopic crystals. This stage of the crystallization process is known as crystal growth. The nucleation and growth processes compete for solute in terms of their respective dependence on supersaturation, and their relative rates will determine the crystal size distribution.

Crystal growth is governed by both internal and external factors. Internal factors such as the three-dimensional crystal structure and crystal defects will determine the nature and strength of the intermolecular interactions between the crystal surface and the solution, whereas external factors such as temperature, supersaturation, solvent, and the presence of impurities will affect the type of interactions at the solid–liquid interface.

Depending on the objectives and applications of growth rate measurements, the growth rate may be expressed as (1) overall linear growth rate which is the rate of change of the volume equivalent diameter with time, (2) linear growth rate of a face which is the rate of displacement of a crystal face in a direction perpendicular to the face, and (3) velocity, height, and spacing of growth steps spreading across a crystal surface. The linear growth rate of a face can be expressed in terms of the step velocity, the step height, and the step spacing. Techniques used for in-situ measurement of crystal growth rates as a function of supersaturation include (1) monitoring the crystal population by methods that measure particle size and number,[97,98] (2) monitoring the growth rates of individual crystal faces by optical microscopy with the use of a flow cell system shown in Figure 3,[39,95,99–101] and (3) monitoring the development of surface morphology at the molecular level by atomic force microscopy (AFM)[101–105] and interferometric microscopy.[37,38]

The external shape or morphology of a crystal is a consequence of the relative growth rates of the faces and reveals the molecular events occurring at the crystal face–liquid interfaces during growth. Even when morphology does not play a significant role in quality control, studying it is essential to understand the kinetics of crystallization.[106] The morphological importance of a face (surface area) is inversely related to its growth rate. Based on these concepts, one of the standard methods used for identifying solvents or dissolved additives that influence nucleation and growth is to investigate the relation between crystal morphology and growth conditions.[13,95,107] A common approach is to compare the experimentally observed morphology with the theoretical morphology and to interpret differences on the basis of experimental growth parameters and assumptions of molecular modeling techniques.[37–39]

Batch-to-batch differences in crystal morphology may result from small but significant changes in growth conditions during the crystallization process. For instance, the presence of a small amount of impurity can have a significant effect on the crystal habit. The most potent inhibitors of growth are impurities which are structurally similar to the host molecule (i.e., tailor-made additives and synthetic impurities). For example, the growth of L-alanine in the presence of hydrophobic L-amino acids at concentrations as low as 0.02 m (0.3 g additive/100 g solvent or 0.18 g additive/100 g L-alanine) results in a change in crystal morphology from prismatic to needle-shaped.[95,101] The supersaturation at which crystal growth occurs can also significantly affect growth rates along different crystallographic axes and crystal habit. Growth of phenytoin crystals along the *a* crystallographic axis has a stronger dependence on supersaturation than growth along the *c* axis.[39]

The process of crystal growth consists of several stages through which growth units pass. These include (a) transport from the bulk solution to a site at the crystal surface, (b) adsorption of the growth unit onto the impingement site, or (c) diffusion from the impingement site to a growth site, and (d) incorporation into the crystal lattice. Desolvation can take place in steps b–d; however, the solvent has the possibility of being adsorbed.

Any one of the above steps may be rate-limiting depending on the growth conditions, such as the supersaturation, temperature, additives or solvent, and hydrodynamics of the system. Consequently, crystal growth mechanisms fall into two main categories:[41–44] volume diffusion control and surface integration control, and the goals of crystal growth theories are to determine the source of steps and the rate-controlling step for crystal growth.

As a crystal grows from a supersaturated solution, the solute concentration is depleted in the region of the crystal–solution interface. If diffusion of solute from the bulk solution to the crystal surface is rate limiting, growth is *volume-diffusion controlled*. A diffusion-controlled process is not applicable if there is no dependence of growth rate on hydrodynamic conditions such as flow rate or stirring rate. In practice it is difficult to completely eliminate volume diffusion resistance, and experimental growth kinetics can be misinterpreted as being purely surface-integration controlled when in fact diffusive resistance is still present. Garside has defined an effectiveness factor that is a measure of the relative importance of diffusion and surface integration as the rate-controlling factors for crystal growth.[108]

If incorporation into a crystal lattice is the slowest process, growth is *surface-integration controlled*. Many

crystallization studies involving proteins, small organic electrolytes, and nonelectrolytes have reported growth controlled by surface integration.[37−39,95,99−105] Depending on the roughness of the crystal surface, layer growth or continuous growth may result. If the crystal−solution interface at the molecular level is rough, there are many potential kink (growth) sites. In this case, *continuous or normal growth* models apply. Growth proceeds isotropically resulting in nonfaceted crystals and responds to very small gradients in the growth driving chemical potential (temperature, concentration, etc.). If the interface is smooth, growth proceeds through a *layer growth* model. Kink sites are only found on the edges of two-dimensional nuclei or steps; hence, surface diffusion and surface topography become more important.

Layer growth models describe the formation of steps by two mechanisms: screw dislocation and two-dimensional nucleation. Details of the derivation of these models can be found in the literature.[42,44,109−111]

The spiral growth mechanism or screw dislocation model was first described by Burton, Cabrera, and Frank (BCF).[112] Bennema[111,113,114] modified this theory for crystals growing from aqueous solution. Flat crystal surfaces have a high energy barrier for nucleation at low supersaturations, and the presence of screw dislocations provides a source of steps for the addition of growth units in an infinite sequence of equidistant and parallel steps. In the simplest case, these steps will develop as a spiral which rotates about its axis during growth.

Two-dimensional nucleation requires the formation of clusters above a critical size for growth of layers. The same concepts discussed in the nucleation section apply to the nucleation of a two-dimensional cluster above a critical size. This model accounts for crystal growth at high supersaturations. These models were developed by Volmer[115] and Stranski.[116] Variations in the mode that nuclei spread after being formed lead to the various two-dimensional nucleation models: mononuclear, polynuclear, and birth and spread.

Each crystal growth model describes the growth rate dependence on supersaturation, temperature, and face area. Although the various models can be used to identify the growth mechanism by fitting the various equations to the experimentally measured face-growth rate dependence on supersaturation, it may be difficult to discriminate between models.[39,101,117] This approach is often combined with observations of surface topography to confirm the growth mechanism.

Surface microtopographic observations can reveal growth mechanisms of crystal faces under different growth conditions, as shown for human insulin crystals in Figure 4. Monitoring the development of surface topography and transport processes during crystal growth will reveal events that are not evident from morphology studies. Interactions of growth units and additives with different crystal planes exposed on a surface may be deduced from the shape of two-dimensional nuclei, and the kinetic anisotropy of the growth steps along crystallographic directions. These techniques have been successfully applied for identifying the crystal growth mechanisms and kinetics of small molecules[37,38,101] and proteins.[102−105,118]

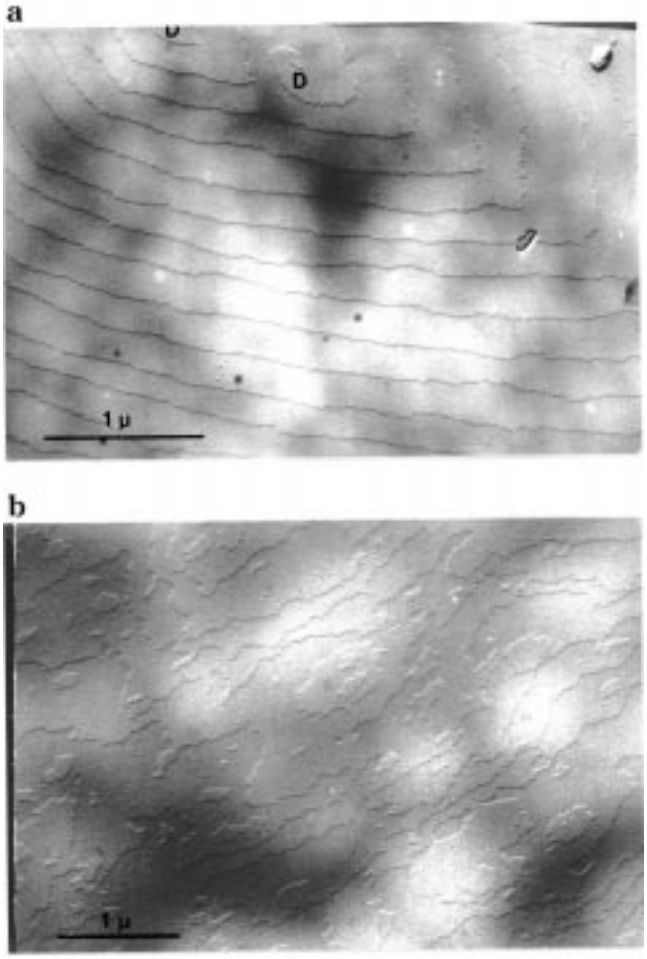

Figure 4—Micrographs of human insulin crystals showing that steps arise by different mechanisms depending on supersaturation. (a) At low supersaturation, steps are created by screw dislocations, D. (b) At high supersaturation, c/s >10, steps occur at the edges of islands as a consequence of two-dimensional nucleation.

Solution-Mediated Transformations

Knowledge of the propensity of a metastable solid phase to dissolve in a liquid phase from which a stable solid phase nucleates and grows is crucial in many stages of pharmaceutical development, because pharmaceutical solids are designed to be dissolved and to come in contact with solvents since the early stages of development (isolated by crystallization from solution) and during processing (wet granulation, spray-drying, freeze-drying, etc.). Given that the sudden disappearance or appearance of a crystalline modification can threaten process development, characterization of the kinetics and mechanisms of solvent-mediated transformations is of practical importance. It will provide answers to questions such as the following: What is the relation between processing conditions and the solid-state modification manufactured? Is there a correlation between dissolution conditions, solid phase(s) dissolving, and concentration of drug dissolved?

The importance of phase transition kinetics, molecular interpretations, and process implications are emphasized by several investigators.[5−9,12−14,119] Cardew and Davey[5] developed a theoretical framework to investigate solvent-mediated transformations in terms of dissolution kinetics of one phase and growth of a second phase. The model represents the time development of the supersaturation with respect to the stable phase, or solute concentration in solution, and solid phase composition during the transformation. The experimental approach involves saturating the solution with respect to the metastable phase under consideration and to monitor both solution concentration and solid phase composition in the presence of the metastable phase, under constant external conditions. More useful information is obtained from the concentration or supersaturation profiles than from the solid phase composition profiles with time. Since the former is related to the

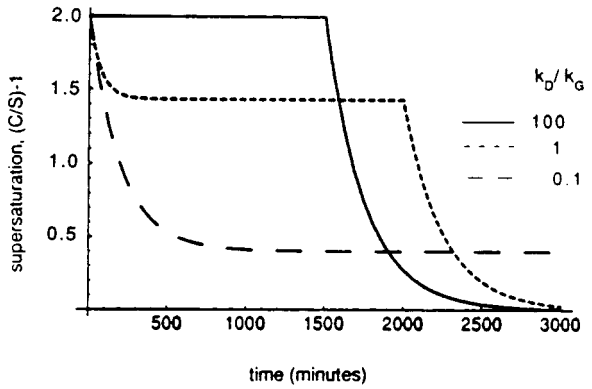

Figure 5—Numerical simulation of the supersaturation–time profiles, as a function of the relative rates of dissolution and crystallization during a solution-mediated transformation. Generated from a kinetic model developed by Cardew and Davey,[5] assuming that both dissolution and growth rates are linearly dependent on their respective driving forces.

Table 3—Information on Crystallization Kinetics and Mechanisms Provided by Various Experimental Techniques

techniques	information
optical microscopy (inverted microscope)	- study crystallization processes *in situ* - monitor transformations in suspensions - determine transformation times - screen and characterize additive/solvent interactions with specific crystal faces - identify nucleation mechanisms - measure crystal growth rates
electron microscopy	- characterize additive/solvent interactions with specific crystal faces - identify nucleation and growth mechanisms - measure crystal growth rates
atomic force microscopy	- study crystallization processes *in situ*
interferometric microscopy	- examine surface topography - identify nucleation and growth mechanisms - measure crystal growth rates
Raman spectroscopy	- monitor molecular association processes that direct nucleation and crystal growth
spectrophotometry chromatography	- monitor concentration of solute in solution and supersaturation
diffraction calorimetry spectroscopy	- monitor solid phase composition

driving forces that regulate the transformation rate and can be used to identify the rate-controlling process: dissolution or growth. A calculated supersaturation profile with growth-limited and dissolution-limited regimes is shown in Figure 5, for the case in which dissolution and growth are linearly dependent on supersaturation.[5,6] Experimental studies of the phase transitions of organic crystals have shown this model to be applicable to explain the solution-mediated transformation kinetics of polymorphs[5,6,119] and solvates,[8] and to be applicable to process development.[119] Some useful experimental techniques for studying small and large scale crystallization and solution-mediated transformations are summarized in Table 3.

Summary

In this review we have presented the significance of crystallization mechanisms and kinetics in directing crystallization pathways. Given the recent advances in computational and analytical techniques that provide access to the molecular events that direct nucleation and crystal growth, there is no reason for the development of ill-defined crystallization processes even when the desired product is obtained. Understanding the thermodynamic and kinetic behavior of the system is vital for the design of reliable processes; thus, at least a holistic approach that identifies the relevant experimental parameters is required. While the objectives of formulation or process development may not explicitly include interpretations at the molecular level, the information concealed in the interfaces present during the process, the structure of the solution, and the solids harvested (crystal structure, morphology, particle size and number) can be significant in the identification of nucleation and growth mechanisms, and will reveal molecular events associated with crystallization. Although the significance of crystallization mechanisms and kinetics has been underestimated in the pharmaceutical industry, we hope that the recent developments in crystallization engineering and techniques will inspire interest in the application of this field to pharmaceutical systems.

References and Notes

1. Marshall, P. V.; York, P. Crystallization Solvent Induced Solid State and Particulate Modifications of Nitrofurantoin. *Int. J. Pharm.* **1989**, *55*, 257−263.
2. Ludlambrown, I.; York, P. The Crystalline Modification of Succinic Acid by Variations in Crystallization Conditions. *J. Phys. D: Appl. Phys.* **1993**, *26*, B60−B65.
3. Byrn, S. R.; Pfeiffer, R. R.; Stephenson, G.; Grant, D. J. W.; Gleason, W. B. Solid-State Pharmaceutical Chemistry. *Chem. Mater.* **1994**, *6*, 1148−1158.
4. Byrn, S.; Pfeiffer, R.; Ganey, M.; Hoiberg, C.; Poochikian, G. Pharmaceutical Solids: A Strategic Approach to Regulatory Considerations. *Pharm. Res.* **1995**, *12*, 945−954.
5. Cardew, P. T.; Davey, R. J. The Kinetics of Solvent-Mediated Phase Transformations. *Proc. R. Soc. London* **1985**, *A 398*, 415−428.
6. Davey, R. J.; Cardew, P. T.; Mcewan, D.; Sadler, D. E. Rate Controlling Processes in Solvent-Mediated Phase Transformations. *J. Cryst. Growth* **1986**, *79*, 648−653.
7. Boylan, J. C.; Swarbrick, J. *Crystallization and the Properties of Crystals*; Rodríguez-Hornedo, N., Ed.; Marcel Dekker Inc.: New York, 1991; Vol. 3, pp pp 399−434.
8. Rodríguez-Hornedo, N.; Lechuga-Ballesteros, D.; Wu, H. J. Phase Transition and Heterogeneous Epitaxial Nucleation of Hydrated and Anhydrous Theophylline Crystals. *Int. J. Pharm.* **1992**, *85*, 149−162.
9. Boylan, J. C.; Swarbrick, J. *Hydrates*; Morris, K., Rodríguez-Hornedo, N., Eds.; 1993; Vol. 7, pp 393−440.
10. Zhu, H. J.; Grant, D. J. W. Influence of Water Activity in Organic Solvent Plus Water Mixtures on the Nature of the Crystallizing Drug Phase. 2. Ampicillin. *Int. J. Pharm.* **1996**, *139*, 33−43.
11. Zhu, H. J.; Yuen, C. M.; Grant, D. J. W. Influence of Water Activity in Organic Solvent Plus Water Mixtures on the Nature of the Crystallizing Drug Phase. 1. Theophylline. *Int. J. Pharm.* **1996**, *135*, 151−160.
12. Davey, R. J.; Black, S. N.; Goodwin, A. D.; Mackerron, D.; Maginn, S. J.; Miller, E. J. Crystallisation in Polymer Films: Control of Morphology and Kinetics of an Organic Dye in a Polysilicone Matrix. *J. Mater. Chem.* **1997**, *7*, 237−241.
13. Davey, R. J.; Blagden, N.; Potts, G. D.; Docherty, R. Polymorphism in Molecular Crystals: Stabilization of a Metastable Form by Conformational Mimicry. *J. Am. Chem. Soc.* **1997**, *119*, 1767−1772.
14. Blagden, N.; Davey, R. J.; Lieberman, H. F.; Williams, L.; Payne, R.; Roberts, R.; Rowe, R.; Docherty, R. Crystal Chemistry and Solvent Effects in Polymorphic Systems −Sulfathiazole. *J. Chem. Soc., Faraday Trans.* **1998**, *94*, 1035−1044.
15. Weissbuch, I.; Leisorowitz, L.; Lahav, M. Tailor-Made and Charge-Transfer Auxiliaries for the Control of the Crystal Polymorphism of Glycine. *Adv. Mat.* **1994**, *6*, 952−956.
16. Weissbuch, I.; Zbaida, D.; Addadi, L.; Leiserowitz, L.; Lahav, M. Design of Polymeric Inhibitors for the Control of Crystal Polymorphism − Induced Enantiomeric Resolution of Racemic Histidine by Crystallization at 25 °C. *J. Am. Chem. Soc.* **1987**, *109*, 1869−1871.
17. Dunitz, J. D.; Bernstein, J. Disappearing Polymorphs. *Acc. Chem. Res.* **1995**, *28*, 193−200.

18. Abbott Laboratories. Letter to health care providers. July 1998. http://www.fda.gov/medwatch/safety/1998/norvir.htm, accessed March 1999.
19. Nichols, G.; Frampton, C. S. Physicochemical Characterization of the Orthorhombic Polymorph of Paracetamol Crystallized From Solution. *J. Pharm. Sci.* **1998**, *87*, 684−692.
20. Haisa, M.; Kashino, S.; Maeda, H. The Orthorhombic Form of P-Hydroxyacetanilide. *Acta Crystallogr.* **1974**, *B30*, 2510−2512.
21. *Food and Drug Administration Guideline for Submitting Supporting Documentation in Drug Applications for the Manufacture of Drug Substances*; FDA Center for Drug Evaluation and Research: Office of Drug Evaluation: Rockville, MD, 1987.
22. Desiraju, G. R. Supramolecular Synthons in Crystal Engineering − A New Organic-Synthesis. *Angew. Chem., Int. Ed. Engl.* **1995**, *34*, 2311−2327.
23. Desiraju, G. R. Crystal Gazing: Structure Prediction and Polymorphism. *Science* **1997**, *278*, 404−405.
24. Desiraju, G. R. Designer Crystals: Intermolecular Interactions, Network Structures and Supramolecular Synthons. *Chem. Commun.* **1997**, 1475−1482.
25. Gavezzotti, A. Are Crystal Structures Predictable. *Acc. Chem. Res.* **1994**, *27*, 309−314.
26. Gavezzotti, A. Computer Simulations of Organic Solids and Their Liquid-State Precursors. *Faraday Discuss.* **1997**, *106*, 63−77.
27. Gavezzotti, A.; Filippini, G. Polymorphic Forms of Organic Crystals at Room Conditions −Thermodynamic and Structural Implications. *J. Am. Chem. Soc.* **1995**, *117*, 12299−12305.
28. Gavezzotti, A.; Filippini, G. Computer Prediction of Organic Crystal Structures Using Partial X-ray Diffraction Data. *J. Am. Chem. Soc.* **1996**, *118*, 7153−7157.
29. Gavezzotti, A.; Filippini, G. Self-Organization of Small Organic Molecules in Liquids, Solutions and Crystals: Static and Dynamic Calculations. *Chem. Commun.* **1998**, 287−294.
30. Blagden, N.; Davey, R. J.; Lieberman, H. F.; Williams, L.; Payne, R.; Roberts, R.; Rowe, R.; Docherty, R. Crystal Chemistry and Solvent Effects in Polymorphic Systems: Sulfathiazole. *J. Chem. Soc., Faraday Trans.* **1998**, *94*, 1919−1919.
31. Weissbuch, I.; Popovitzbiro, R.; Lahav, M.; Leiserowitz, L. Understanding and Control of Nucleation, Growth, Habit, Dissolution and Structure of 2-Dimensional and 3-Dimensional Crystals Using Tailor-Made Auxiliaries. *Acta Crystallogr., Sect. B: Struct. Sci.* **1995**, *51*, 115−148.
32. Leiserowitz, L.; Addadi, L.; Lahav, M. Macroscopic Phenomena in Crystals and Molecular Shape. *J. Mol. Graph.* **1989**, *7*, 95−95.
33. Weissbuch, I.; Addadi, L.; Lahav, M.; Leiserowitz, L. Molecular Recognition at Crystal Interfaces. *Science* **1991**, *253*, 637−645.
34. Gallagher, H. G.; Roberts, K. J.; Sherwood, J. N.; Smith, L. A. A Theoretical Examination of the Molecular Packing, Intermolecular Bonding and Crystal Morphology of 2,4,6-Trinitrotoluene in Relation to Polymorphic Structural Stability. *J. Mater. Chem.* **1997**, *7*, 229−235.
35. Clydesdale, G.; Roberts, K. J.; Telfer, G. B.; Grant, D. J. W. Modeling the Crystal Morphology of Alpha-Llactose Monohydrate. *J. Pharm. Sci.* **1997**, *86*, 135−141.
36. Hendriksen, B. A.; Grant, D. J. W.; Meenan, P.; Green, D. A. Crystallisation of Paracetamol (Acetaminophen) in the Presence of Structurally Related Substances. *J. Cryst. Growth* **1998**, *183*, 629−640.
37. Shekunov, B. Y.; Latham, R. Growth Anisotropy of *N*-Methylurea Crystals in Methanol. *J. Phys. Chem. A* **1996**, *100*, 5464−5469.
38. Shekunov, B. Y.; Grant, D. J. W. In Situ Optical Interferometric Studies of the Growth and Dissolution Behavior of Paracetamol (Acetaminophen) 0.1. Growth Kinetics. *J. Phys. Chem. B* **1997**, *101*, 3973−3979.
39. Zipp, G. L.; Rodríguez-Hornedo, N. Growth Mechanism and Morphology of Phenytoin and Their Relationship With Crystallographic Structure. *J. Phys. D: Appl. Phys.* **1993**, *26*, B48−B55.
40. Khoshkhoo, S.; Anwar, J. Study of the Effect of Solvent on the Morphology of Crystals Using Molecular Simulation: Application to Alpha-Resorcinol and N−N−Octyl-D-Gluconamide. *J. Chem. Soc., Faraday Trans.* **1996**, *92*, 1023−1025.
41. Nyvlt, J.; Söhnel, O.; Matuchová, M.; Broul, M. *The Kinetics of Industrial Crystallization*; Elsevier: New York, 1985.
42. Mullin, J. W. *Crystallization*; Butterworth-Heinemann Ltd.: Oxford, 1993.
43. Söhnel, O.; Garside, J. *Precipitation: Basic Principles and Industrial Applications*; Butterworth-Heinemann Ltd: Oxford, 1992.
44. Myerson, A. S. *Handbook of Industrial Crystallization*; Butterworth-Heinemann Ltd: Oxford, 1993.
45. Mersmann, A. *Crystallization Technology Handbook*; M. Dekker: New York, 1995.
46. Zettlemoyer, A. C. *Nucleation*; Marcel Dekker: New York, 1969.
47. Perepezko, J. H. Nucleation Reactions In Undercooled Liquids. *Mater. Sci. Eng. A* **1994**, *178*, 105−111.
48. Perepezko, J. H. Kinetic Processes in Undercooled Melts. *Mater. Sci. Eng. A* **1997**, *226*, 374−382.
49. Gibbs, J. W. *Collected Works, Vol. I, Thermodynamics*; Yale University Press: New Haven, 1948.
50. Volmer, M. *Kinetic Der Phasenbildung*; Steinkopff, Leipzig: 1939.
51. Becker, R.; Döring, W. Kinetische Behandlung Der Keimbildung in Übersättigen Dämpfen. *Ann. Physik (Leipzig)* **1935**, *24*, 719−752.
52. Turnbull, D.; Fisher, J. C. Rate of Nucleation in Condensed Systems. *J. Chem. Phys.* **1949**, *17*, 71−73.
53. Boistelle, R.; Astier, J. P. Crystallization Mechanisms in Solution. *J. Cryst. Growth* **1988**, *90*, 14−30.
54. Hendriksen, B. A.; Grant, D. J. W. The Effect of Structurally Related Substances on the Nucleation Kinetics of Paracetamol (Acetaminophen). *J. Cryst. Growth* **1995**, *156*, 252−260.
55. Garti, N.; Tibika, F. Habit Modifications of Nitrofurantoin Crystallized From Formic Acid Mixtures. *Drug Dev. Ind. Pharm.* **1980**, *6*, 379−398.
56. Ostwald, W. Studien Über Die Bildung Und Umwandlung Fester Körper. *Zieitschrigt Für Physikalische Chemie* **1897**, *22*, 289−330.
57. Pellett, M. A.; Castellano, S.; Hadgraft, J.; Davis, A. F. The Penetration of Supersaturated Solutions of Piroxicam Across Silicone Membranes and Human Skin in Vitro. *J. Controlled Release* **1997**, *46*, 205−214.
58. Katzhendler, I.; Azoury, R.; Friedman, M. Crystalline Properties of Carbamazepine in Sustained Release Hydrophilic Matrix Tablets Based on Hydroxypropylmethylcellulose. *J. Controlled Release* **1998**, *54*, 69−85.
59. Davey, R. J.; Hilton, A. M.; Garside, J. Crystallization From Oil in Water Emulsions: Particle Synthesis and Purification of Molecular Materials. *Chem. Eng. Res. Des.* **1997**, *75*, 245−251.
60. Davey, R. J.; Garside, J.; Hilton, A. M.; Mcewan, D.; Morrison, J. W. Purification of Molecular Mixtures Below the Eutectic by Emulsion Crystallization. *Nature* **1995**, *375*, 664−666.
61. Davey, R. J.; Garside, J.; Hilton, A. M.; Mcewan, D.; Morrison, J. W. Emulsion Solidification of Meta-Chloronitrobenzene: Purification and Crystallisation. *J. Cryst. Growth* **1996**, *166*, 971−975.
62. Turnbull, D. Under What Conditions Can a Glass Be Formed? *Contemp. Phys.* **1969**, *10*, 473−488.
63. Murase, N.; Franks, F. Salt Precipitation During the Freeze-Concentration of Phosphate Buffer Solutions. *Biophys. Chem.* **1989**, *34*, 293−300.
64. Murase, N.; Echlin, P.; Franks, F. The Structural States of Freeze-Concentrated and Freeze-Dried Phosphates Studied by Scanning Electron-Microscopy and Differential Scanning Calorimetry. *Cryobiology* **1991**, *28*, 364−375.
65. Cavatur, R. K.; Suryanarayanan, R. Characterization of Frozen Aqueous Solutions by Low-Temperature X-ray Powder Diffractometry. *Pharm. Res.* **1998**, *15*, 194−199.
66. Gómez, G. *Crystallization-Related pH Changes During Freezing of Sodium Phosphate Buffer Solutions*; Ph.D. Thesis, University of Michigan, Ann Arbor, MI, 1995.
67. Mullin, J. W.; Leci, C. L. Some Nucleation Characteristics of Aqueous Citric Acid Solutions. *J. Cryst. Growth* **1969**, *5*, 75−76.
68. Franks, F.; Mathias, S. F.; Trafford, K. The Nucleation of Ice in Undercooled Water and Aqueous Polymer Solutions. *Colloids Surfaces* **1984**, *11*, 275−285.
69. Fletcher, N. H. Nucleation by Crystalline Particles. *J. Chem. Phys.* **1963**, *38*, 237−240.
70. Carter, P. W.; Ward, M. D. Topographically Directed Nucleation of Organic-Crystals on Molecular Single-Crystal Substrates. *J. Am. Chem. Soc.* **1993**, *115*, 11521−11535.
71. Ward, M. D. Organic Crystal Surfaces: Structure, Properties and Reactivity. *Curr. Opin. Colloid Interface Sci.* **1997**, *2*, 51−64.
72. Carter, P. W.; Ward, M. D. Directing Polymorph Selectivity During Nucleation of Anthranilic Acid on Molecular Substrates. *J. Am. Chem. Soc.* **1994**, *116*, 769−770.
73. Black, S. N.; Bromley, L. A.; Cottier, D.; Davey, R. J.; Dobbs, B.; Rout, J. E. Interactions at the Organic Inorganic Interface − Binding Motifs for Phosphonates at the Surface of Barite Crystals. *J. Chem. Soc., Faraday Trans.* **1991**, *87*, 3409−3414.

74. Bonafede, S. J.; Ward, M. D. Selective Nucleation and Growth of an Organic Polymorph by Ledge-Directed Epitaxy on a Molecular-Crystal Substrate. *J. Am. Chem. Soc.* **1995**, *117*, 7853−7861.
75. Davey, R. J.; Maginn, S. J.; Andrews, S. J.; Black, S. N.; Buckley, A. M.; Cottier, D.; Dempsey, P.; Plowman, R.; Rout, J. E.; Stanley, D. R.; Taylor, A. Morphology and Polymorphism of Terephthalic Acid. *Mol. Cryst. Liq. Cryst. Sci. Technol., Sect. A: Crystals And Liquid Crystals* **1994**, *242*, 79−90.
76. De Smidt, J. G.; Fokkens, J. G.; Grijseels, H.; Crommelin, D. J. A. Dissolution of Theophylline Monohydrate and Anhydrous Theophyline in Buffer Solutions. *J. Pharm. Sci.* **1986**, *75*, 497−501.
77. Luhtala, S.; Kahela, P.; Kristoffersson E. Effect of Benzalkonium Chloride on Crystal Growth and Aqueous Solubility of Carbamazepine. *Acta Pharm. Fenn.* **1990**, *99*, 59−68.
78. Luhtala, S. Effect of Sodium Lauryl Sulfate and Polysorbate 80 on Crystal Growth and Aqueous Solubility of Carbamazepine. *Acta Pharm. Nord.* **1992**, *4*, 85−90.
79. Murphy, D. *The Solvent-Mediated Phase Transformation of Carbamazepine and the Influence of Surfactants on the Nucleation Mechanism and Crystal Morphology*; Ph.D. Thesis, University of Michigan, Ann Arbor, MI, 1997.
80. Kadima, W.; McPherson, A.; Dunn, M. F.; Jurnak, F. Precrystallization Aggregation of Insulin by Dynamic Light-Scattering and Comparison With Canavalin. *J. Cryst. Growth* **1991**, *110*, 188−194.
81. Georgalis, Y.; Umbach, P.; Raptis, J.; Saenger, W. Lysozyme Aggregation Studied by Light Scattering 0.1. Influence of Concentration and Nature of Electrolytes. *Acta Crystallogr., Sect. D: Biol. Crystallogr.* **1997**, *53*, 691−702.
82. Georgalis, Y.; Umbach, P.; Raptis, J.; Saenger, W. Lysozyme Aggregation Studied by Light Scattering. 2. Variations of Protein Concentration. *Acta Crystallogr., Sect. D: Biol. Crystallogr.* **1997**, *53*, 703−712.
83. Peters, R.; Georgalis, Y.; Saenger, W. Accessing Lysozyme Nucleation With a Novel Dynamic Light Scattering Detector. *Acta Crystallogr., Sect. D: Biol. Crystallogr.* **1998**, *54*, 873−877.
84. Rosenberger, F.; Vekilov, P. G.; Muschol, M.; Thomas, B. R. Nucleation and Crystallization of Globular Proteins − What We Know and What Is Missing. *J. Cryst. Growth* **1996**, *168*, 1−27.
85. Cerreta, M. K.; Berglund, K. A. The Structure of Aqueous-Solutions of Some Dihydrogen Ortho-Phosphates by Laser Raman-Spectroscopy. *J. Cryst. Growth* **1987**, *84*, 577−588.
86. Yedur, S. K.; Berglund, K. A. Use of Fluorescence Spectroscopy in Concentration and Supersaturation Measurements in Citric Acid Solutions. *Appl. Spectrosc.* **1996**, *50*, 866−870.
87. Rasimas, J. P.; Berglund, K. A.; Blanchard, G. J. A Molecular Lock and Key Approach to Detecting Solution Phase Self-Assembly. A Fluorescence and Absorption Study of Carminic Acid in Aqueous Glucose Solutions. *J. Phys. Chem.* **1996**, *100*, 7220−7229.
88. Dunuwila, D. D.; Berglund, K. A. Identification of Infrared Spectral Features Related to Solution Structure for Utilization in Solubility and Supersaturation Measurements. *Org. Proc. Res. Dev.* **1997**, *1*, 350−354.
89. Boistelle, R.; López-Valero, I. Growth Units and Nucleation: the Case of Calcium Phosphates. *J. Cryst. Growth* **1990**, *102*, 609−617.
90. Gidalevitz, D.; Feidenhansl, R.; Matlis, S.; Smilgies, D. M.; Christensen, M. J.; Leiserowitz, L. Monitoring In Situ Growth and Dissolution of Molecular Crystals: Towards Determination of the Growth Units. *Angew. Chem., Int. Ed. Engl.* **1997**, *36*, 955−959.
91. Khoshkhoo, S.; Anwar, J. Crystallization of Polymorphs − The Effect of Solvent. *J. Phys. D: Appl. Phys.* **1993**, *26*, B90−B93.
92. Black, S. N.; Davey, R. J.; Halcrow, M. The Kinetics of Crystal-Crowth in the Presence of Tailor-Made Additives. *J. Cryst. Growth* **1986**, *79*, 765−774.
93. Chen, B. D.; Garside, J.; Davey, R. J.; Maginn, S. J.; Matsuoka, M. Growth of M-Chloronitrobenzene Crystals in the Presence of Tailor-Made Additives − Assignment of the Polar Axes From Morphological Calculations. *J. Phys. Chem.* **1994**, *98*, 3215−3221.
94. Garti, N.; Zour, H. The Effect of Surfactants on the Crystallization and Polymorphic Transformation of Glutamic Acid. *J. Cryst. Growth* **1997**, *172*, 486−498.
95. Lechuga-Ballesteros, D.; Rodríguez-Hornedo, N. Effects of Molecular Structure and Growth Kinetics on the Morphology of L-Alanine Crystals. *Int. J. Pharm.* **1995**, *115*, 151−160.
96. Etter, M. C. Hydrogen-Bonds As Design Elements in Organic Chemistry. *J. Phys. Chem.* **1991**, *95*, 4601−4610.
97. Zipp, G. L.; Rodríguez-Hornedo, N. Phenytoin Crystal Growth Rates in the Presence of Phosphate and Chloride Ions. *J. Cryst. Growth* **1992**, *123*, 247−254.
98. Lechuga-Ballesteros, D.; Rodríguez-Hornedo, N. The Relation Between Adsorption of Additives and Crystal Growth Rate of L-Alanine. *J. Colloid Interface Sci.* **1993**, *157*, 147−153.
99. Li, L.; Rodríguez-Hornedo, N. Growth Kinetics and Mechanisms of Glycine Crystals. *J. Cryst. Growth* **1992**, *121*, 33−38.
100. Zipp, G. L.; Rodríguez-Hornedo, N. The Mechanism of Phenytoin Crystal-Growth. *Int. J. Pharm.* **1993**, *98*, 189−201.
101. Lechuga-Ballesteros, D.; Rodríguez-Hornedo, N. The Influence of Additives on the Growth Kinetics and Mechanism of L-Alanine Crystals. *Int. J. Pharm.* **1995**, *115*, 139−149.
102. Yip, C. M.; Ward, M. D. Atomic Force Microscopy of Insulin Single Crystals: Direct Visualization of Molecules and Crystal Growth. *Biophys. J.* **1996**, *71*, 1071−1078.
103. Malkin, A. J.; Kuznetsov, Y. G.; Glantz, W.; McPherson, A. Atomic Force Microscopy Studies of Surface Morphology and Growth Kinetics in Thaumatin Crystallization. *J. Phys. Chem.* **1996**, *100*, 11736−11743.
104. Yip, C. M.; Brader, M. L.; Defelippis, M. R.; Ward, M. D. Atomic Force Microscopy of Crystalline Insulins: The Influence of Sequence Variation on Crystallization and Interfacial Structure. *Biophys. J.* **1998**, *74*, 2199−2209.
105. Kuznetsov, Y. G.; Malkin, A. J.; McPherson, A. Atomic Force Microscopy Studies of Phase Separations in Macromolecular Systems. *Phys. Rev. B: Condens. Matter* **1998**, *58*, 6097−6103.
106. Sunagawa, I. *Morphology of Crystals*; Terra Scientific Publishing Company: Tokyo, Japan, 1987.
107. Li, L.; Lechuga-Ballesteros, D.; Szkudlarek, B. A.; Rodríguez-Hornedo, N. The Effect of Additives on Glycine Crystal Growth Kinetics. *J. Colloid Interface Sci.* **1994**, *168*, 8−14.
108. Garside, J. The Concept of Effectiveness Factors in Crystal Growth From Solution. *Chem. Eng. Sci.* **1971**, *26*, 1425−1431.
109. Chernov, A. A. Formation of Crystals in Solution. *Contemp. Phys.* **1989**, *30*, 251−276.
110. Chernov, A. A. *Modern Crystallography III: Crystal Growth*; Springer-Verlag: Berlin, 1980.
111. Bennema, P. Spiral Growth and Surface Roughening: Development Since Burton, Cabrera and Frank. *J. Cryst. Growth* **1984**, *69*, 182−197.
112. Burton, W. K.; Cabrera, N.; Frank, F. C. The Growth of Crystals and the Equilibrium Structure of Their Surfaces. *Philos. Trans.* **1951**, *A243*, 299−358.
113. Bennema, P. Analysis of Crystal Growth Models for Slightly Supersaturated Solutions. *J. Cryst. Growth* **1967**, *1*, 225−232.
114. Bennema, P. Interpretation of the Relation of the Rate of Crystal Growth and Low Supersaturation. *J. Cryst. Growth* **1967**, *1*, 278−287.
115. Volmer, M. Crystal Growth. *Z. Physik.* **1922**, *9*, 193.
116. Stranski, I. N. Zur Theorie Der Kristallwachstums. *Z. Phys. Chem.* **1928**, *136*, 259−278.
117. Garside, J.; Janssen-Van Rosmalen, R.; Bennema, P. Verification of Crystal Growth Rate Equations. *J. Cryst. Growth* **1975**, *29*, 353−366.
118. Durbin, S. D.; Feher, G. Studies of Crystal Growth Mechanisms of Proteins by Electron Microscopy. *J. Mol. Biol.* **1990**, *212*, 763−774.
119. Nass, K. K. Process Implications of Polymorphism in Organic Compounds. *AIChE* **1991**, *284*, 72−81.

Acknowledgments

The authors acknowledge financial support from the National Science Foundation, Valteich Research Award from the University of Michigan College of Pharmacy, Elli Lilly and Company, and Dupont Pharma.

JS980490H

An Investigation into the Supramolecular Structure of Ternary Gel Systems Using Oscillatory Rheometry, Microscopy, and Low Frequency Dielectric Spectroscopy

PAUL L. GOGGIN, RENREN HE,[†] DUNCAN Q. M. CRAIG,*[,†] AND DON P. GREGORY[‡]

Contribution from *Centre for Materials Science, School of Pharmacy, University of London, 29-39 Brunswick Square, London WC1N 1AX, UK.*

Received February 18, 1999. Accepted for publication April 7, 1999.

Abstract □ A series of ternary gel systems based on cetostearyl alcohol (CSA) and cetomacrogol 1000 or sodium lauryl sulfate have been studied using oscillatory rheology, differential interference contrast (DIC) microscopy, cryoscanning electron microscopy (cryo-SEM), and low-frequency dielectric analysis in order to elucidate the nature of the lamellar structures formed in relation to composition. The effects of altering the concentration of CSA (0.25% to 8% w/w) for 1% and 2% w/v cetomacrogol 1000 and 0.5% and 1% w/v sodium lauryl sulfate systems have been investigated, with marked increases in the storage and loss moduli seen on increasing the concentration of CSA for both surfactants. DIC microscopy indicated that at low CSA concentrations, needlelike structures were seen which, on increasing the concentration, were observed to congregate into nuclei. At concentrations of 4% CSA and above, neospherical structures were also observed. Cryo-SEM revealed that the needlelike objects were sheet structures ascribed to lamellar gel phases, while the nuclei were folded "rosettes" formed by those sheets, with the spherical structures being ascribed to cetostearyl alcohol. It was also noted that the lamellae were more tightly folded at 8% w/w CSA, which may be associated with the higher rheological moduli for these systems. Low-frequency dielectric analysis was performed over a frequency range of 10^4 Hz to 10^{-2} Hz. A decrease in both the dielectric loss and capacitance was observed as the concentration of cetostearyl alcohol was increased. The dielectric data were described in terms of an equivalent circuit model based on a modified Maxwell–Wagner response. A good correlation was found between the fitted and experimental data and the effect of altering the gel composition on specific features of the equivalent circuit are discussed.

Introduction

Despite the widespread use of semisolid emulsions for topical application, the physical characterization of these systems remains a persistent difficulty. This problem may be ascribed to the physical complexity of creams as the emulsifying agents, which are present in excess of the quantities required to form interfacial monolayers between the oil and aqueous phases, form a range of structures within the continuous phase, resulting in the system exhibiting viscoelastic behavior. Several authors (e.g., refs 1−6) have emphasized the importance of interdroplet liquid gel network formation in determining the rheological properties and physical stability of creams. For example, Barry and Saunders[7] have demonstrated that the influence of alkyltrimethylammonium bromide chain length on the rheological properties of liquid paraffin creams may be attributed to differences in smectic structure formation with cetostearyl alcohol, while Eccleston[8] has correlated changes in the rheological properties of cetrimide creams to alterations in the physical structure of the continuous phase formed via the interaction of cetrimide and fatty alcohols in water.

A number of techniques have been used for the evaluation of creams, including rheology (e.g., refs 1−3), microscopy,[9,10] and thermal analysis.[5,11,12] In addition, a limited number of studies using low-frequency dielectric spectroscopy have also been described.[13−16] This method involves the application of an oscillating electric field to a sample and the measurement of the response in terms of the real and imaginary components of the complex capacitance C^* at frequency ω, with

$$C^*(\omega) = C'(\omega) - iC''(\omega) = \frac{A\epsilon_0}{d}[\epsilon'(\omega) - i\epsilon''(\omega)] \quad (1)$$

where C' and C'' are the real and imaginary capacitances, i is the square root of -1, A is the electrode area, d is the sample thickness, ϵ_0 is the permittivity of free space and ϵ' and ϵ'' are the real and imaginary permittivities. The term C' is synonymous with the measured (real) capacitance while C'' is also referred to as the dielectric loss G/ω where G is the conductance. The dielectric loss incorporates both a.c. and d.c. conductance processes. More details of the approach are available from a number of texts.[17−19] A facet of the approach is to develop a circuit model which gives an equivalent response to that of the sample, thereby facilitating assignment of circuit elements to specific structures within the system. This approach has been adopted in a recent study[16] in which the response of Aqueous Cream BP was successfully modeled in terms of a modified Maxwell−Wagner response, thereby presenting the possibility of relating specific features of the cream to components of the circuit. With further development, this approach has clear potential as a means of characterizing complex semisolid materials.

It is now well established that the interaction between the surfactant and long chain alcohol (and the chemical

* Corresponding author. Tel and fax: 44 (0)1232 272129. E-mail duncan.craig@qub.ac uk.
[†] Current address: The School of Pharmacy, Queens University of Belfast, 97 Lisburn Road, Belfast BT9 7BL.
[‡] Unilever Research, Port Sunlight Laboratory, Quarry Road East, Bebington, Wirral, UK.

10.1021/js990054a CCC: $18.00 Published on Web 05/21/1999

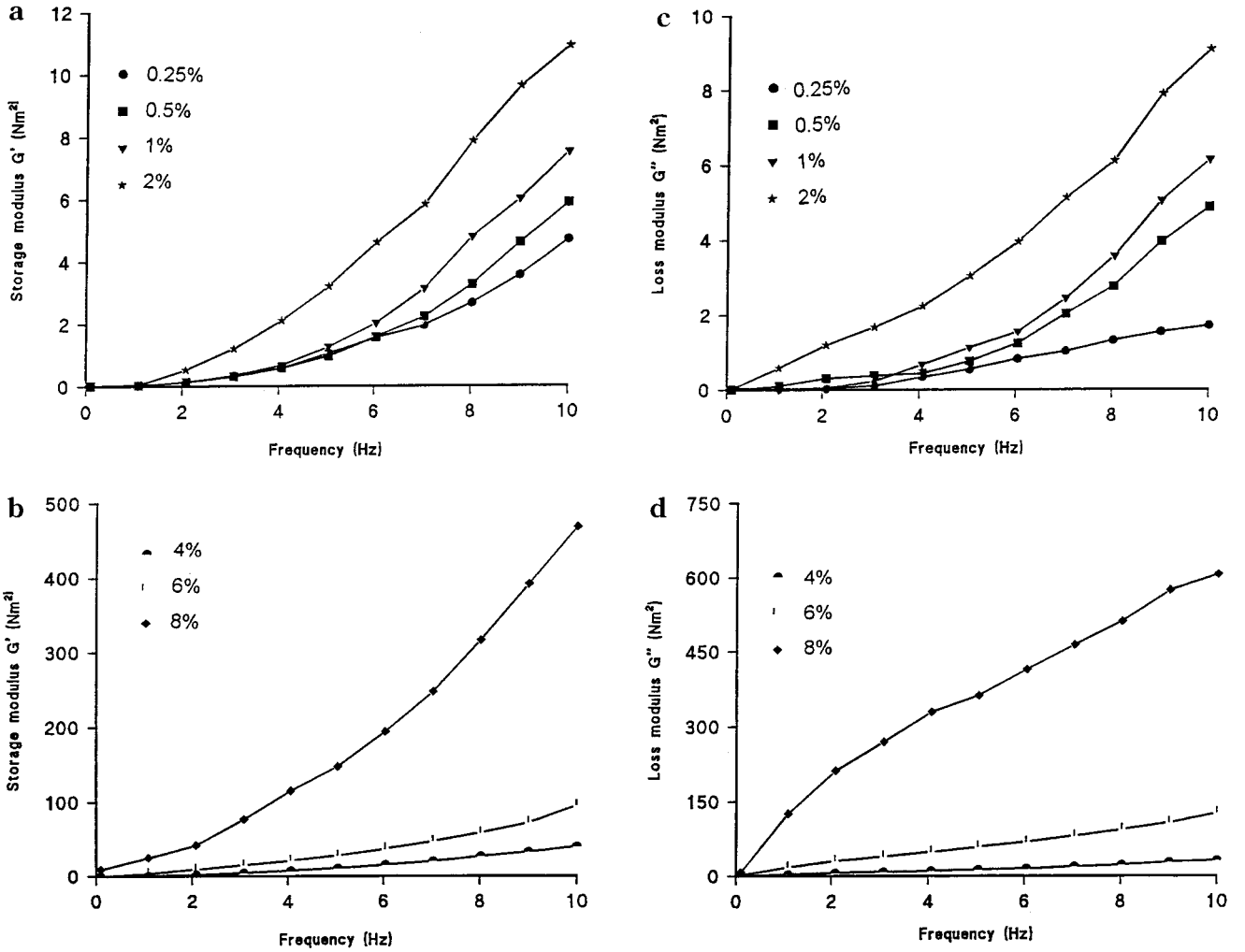

Figure 1—Rheological storage moduli (a, b) and loss moduli (c, d) for ternary systems containing 1% cetomacrogol 1000, water, and cetostearyl alcohol (concentrations as indicated) at 298 K.

compositions of both components) is a key factor in determining the rheological properties of the cream. In addition, it is also accepted that the basic structure of o/w creams consists of hydrated lamellae composed of the alcohol and surfactant, bulk aqueous and oil phases, and, depending on composition, precipitated hydrates of the long chain alcohol. However, considerably less is known regarding the distribution of components on a supramolecular level and how this distribution may be related to product performance. In this investigation, a series of ternary gels (systems containing surfactant, alcohol and water) have been prepared using a range of compositions in order to systematically study the development of structure within the gels. Such systems have been previously used as model creams (e.g., refs 20–22), as these gels may contain all the components of the cream except for the oil phase, thereby simplifying analysis and aiding understanding of the nature of the lamellar phases formed. The rheological behavior of each system has been characterized using oscillatory rheometry and the appearance of the gels noted using differential interference contrast (DIC) microscopy, an optical technique which allows high contrast imaging of unstained samples, and cryo-SEM. In addition, the use of low-frequency dielectric spectroscopy as a means of cream characterization has been further developed via examination of these relatively simple controlled systems. Particular emphasis has been placed on monitoring the cetostearyl alcohol concentration dependence on structure formation in relation to viscoelastic properties. The influence of this ratio on the rheological behavior has not been extensively studied; hence, there is a clear relevance of such knowledge to cream formulation. In addition, the study of systems containing varying ratios facilitates examination of the formation of macroscopic structures, thereby aiding understanding cream structure.

Materials and Methods

Materials—Cetostearyl alcohol was supplied by Unilever Research, Port Sunlight, Wirral; commercial grades of this material contain 50–70% stearyl alcohol and 20–35% cetyl alcohol, with smaller quantities of other alcohols such as myristyl alcohol present. Cetomacrogol 1000 was also supplied by Unilever Research, Port Sunlight, Wirral and is based on the formula $CH_3(CH_2)_m(OCH_2CH_2)_nOH$, where m is 15–17 and n is 20–24. Sodium lauryl sulfate was obtained from BDH. Deionized water was used throughout the study.

Composition and Manufacture of Ternary Systems—Systems were prepared containing 1% w/v and 2% w/v cetomacrogol 1000 and 0.5% and 1% w/v sodium lauryl sulfate with up to 8% cetostearyl alcohol. The water phase was heated in a jacketed and baffled mixing vessel to 70 °C, after which the surfactant was dissolved and the cetostearyl alcohol added and allowed to liquefy. The mixture was then mixed at 10000 rpm using a Heidolph Diax 600 homogenizer disperser mixer for 15 min. The heater was then turned off, and the system was mixed to ambient temperature at 500 rpm. All systems were stored for 14 days prior to testing in order to allow time for the microstructure to develop.

Rheological and Microscopic Measurements—Oscillatory rheological determinations were carried out using a Carrimed CSL

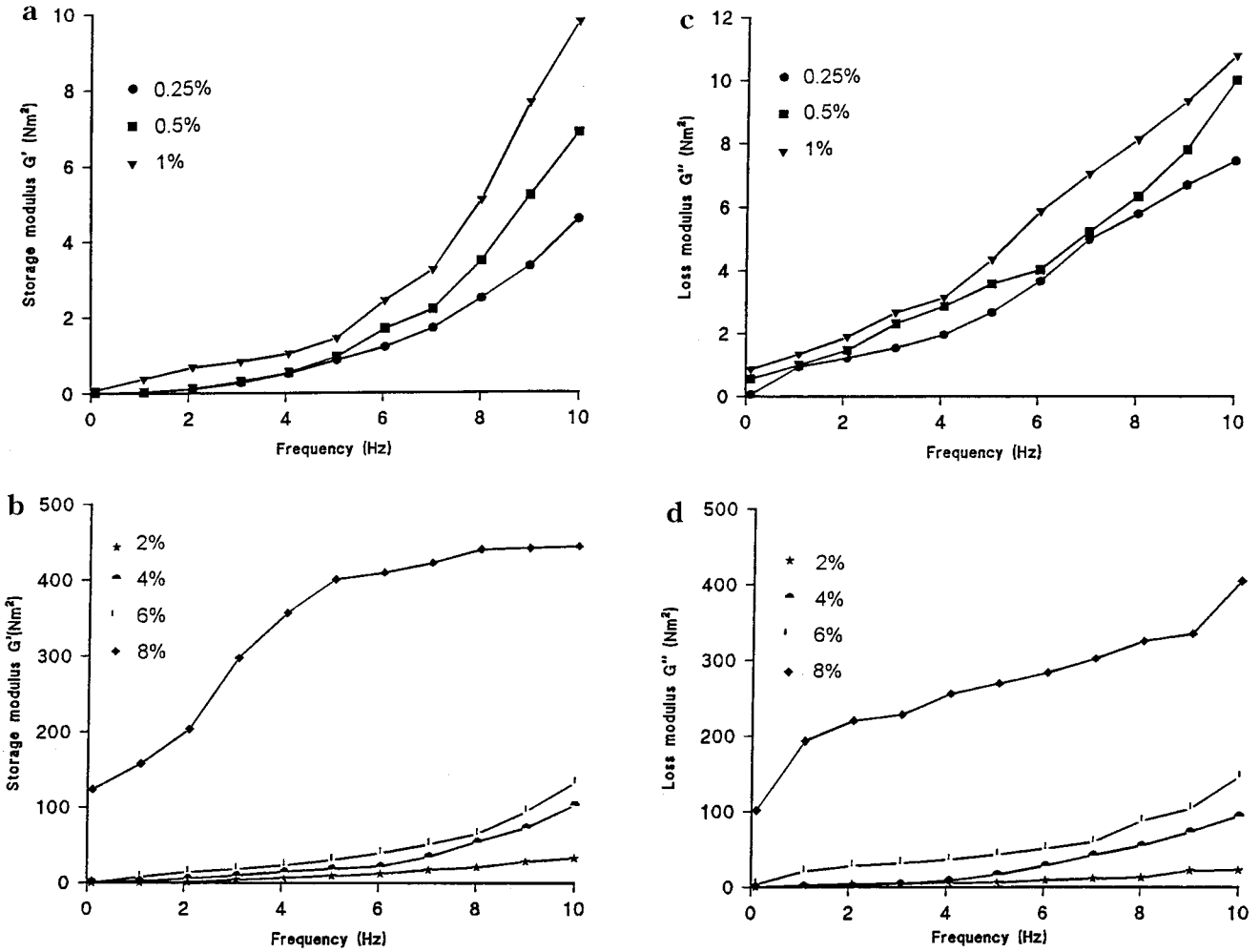

Figure 2—Rheological storage moduli (a, b) and loss moduli (c, d) for ternary systems containing 0.5% sodium lauryl sulfate, water, and cetostearyl alcohol (concentrations as indicated) at 298 K.

500 controlled stress rheometer (TA Instruments Ltd., Surrey, UK), used in cone and plate mode. An oscillating stress of 0.1−10 Hz was applied to each sample at 298 K. The torque used was 200 μN which was established by torque sweep to be within the linear viscoelastic range. Samples were run at least three times to ensure reproducibility, with the values having a coefficient of variation within 5%. The plate and cone were cleaned thoroughly between runs.

Differential interference contrast microscopy was carried out using an Olympus BX50 microscope. A Nikon fully automatic single lens reflex camera was employed for the photographic work. The scanning electron microscopy studies were carried out using a Cambridge Scientific S360 instrument fitted with an Oxford Instruments cold stage. Undiluted samples were placed on the sample holder which was immersed in liquid nitrogen (−196 °C). The material was then loaded into the microscope fracture chamber, also at −196 °C, and fractured. The sample was subsequently transferred to the vacuum chamber (−196 °C), the vacuum applied, and the surface water sublimed. After removal from the vacuum chamber, the sample was electroplated with gold under an argon atmosphere.

Dielectric Analysis—Dielectric studies were conducted using a low-frequency dielectric spectrometer (Dielectric Instrumentation Ltd., Worcs.) which measures between the limits of 10^6 to 10^{-4} Hz. Measurements were conducted in a stainless steel cell comprising two circular parallel plates (area 12.6 cm^2, electrode separation distance 1 mm), as described in a previous study.[16] Three measurements are taken at each frequency, with averaged results being within a coefficient of variation of 2%. Samples were measured over a frequency range of 10^5−10^{-2} Hz at 25 °C using a field of 0.1 V rms. Empty cell runs were performed between runs to ensure cell cleanliness; repeat runs of each sample showed the spectra to be superimposable. Equivalent circuit analysis was performed based on the model proposed by Hill and Pickup[23] using the Winfit 2.0 computer program supplied by Novocontrol GmbH, as described in previous studies.[16,24]

Results

Rheological Studies—The frequency-dependent rheological responses of the nonionic systems containing 1% cetomacrogol 1000 are shown in Figures 1a−d in terms of the storage and loss moduli. A marked increase in both storage and loss were noted on increasing the concentration of cetostearyl alcohol, with a similar trend being noted for the 2% w/v cetomacrogol 1000 systems. Likewise, Figure 2a−d shows the responses of the ionic systems containing 0.5% sodium lauryl sulfate, with an increase in storage and loss again being noted as the concentration of CSA increases. However, it was noted that in this case a more marked increase in both components was seen between 6% and 8% w/v CSA. A similar trend was seen for the 1% w/v SLS systems, although the increase in moduli at higher CSA concentrations was considerably more marked. The relationship between the loss modulus at 10 Hz and cetostearyl alcohol composition is summarized in Figure 3 for the four surfactant systems. The same general trend of a nonlinear increase in loss moduli was observed in all cases, although clearly the 1% ionic gels gave the highest responses, particularly at higher CSA contents.

Microscopy Studies—Representative DIC photomicrographs for the 1% cetomacrogol 1000 systems are shown

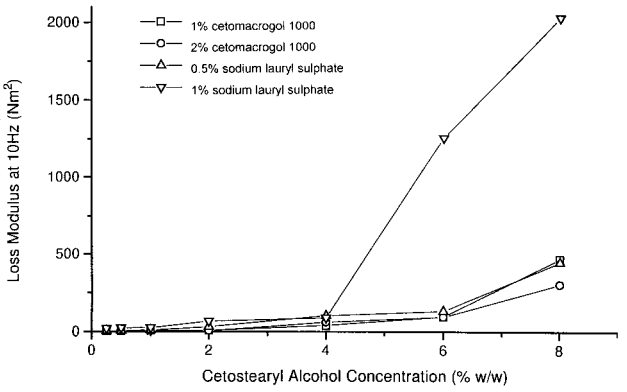

Figure 3—The effect of cetostearyl alcohol concentration on the rheological loss moduli (10 Hz) of ternary systems containing cetomacrogol 1000 or sodium lauryl sulfate.

in Figure 4a–d. At low concentrations of CSA (0.25% w/w, Figure 4a), needlelike structures are seen, while as the concentration increases to 1% (Figure 4b), nuclei are seen in the center of clusters of the needle structures. This effect is further enhanced at 4% w/w CSA (Figure 4c), with a number of small (<5 μm) spherical structures seen. At 8% w/w CSA, a preponderance of these spherical structures is seen (Figure 4d). Similar trends were seen for the 2% cetomacrogol systems, with a representative photomicrograph being shown in Figure 4e. The appearance of the ionic creams was similar, with a representative photomicrograph being given in Figure 4f. However, it is interesting to note that for equivalent CSA concentrations (8% w/w), the ionic creams showed a lower density of the spherical structures than was seen for the cetomacrogol 1000 systems; the significance of this will be discussed in a subsequent section.

Figure 5a,b shows representative cryo-SEM images of the 2% w/w and 8% w/w CSA for the 2% cetomacrogol 1000 systems. Figure 5a shows rosette-type structures which correspond in size and appearance to the nuclei seen in Figure 4b; the SEM images indicate that these nuclei are in fact concentric layers rather than continuous structures. The highest concentration CSA systems (Figure 5b) showed a highly folded structure in which neospherulitic objects were distributed. The size range of these spheres (approximately 5–10 μm) corresponds reasonably well to that the spherical objects seen at the equivalent concentration using DIC microscopy (Figure 4).

Dielectric Analysis—The dielectric responses of the ternary systems containing 1% and 2% cetomacrogol 1000 and a concentration range of 0.25 to 8% cetostearyl alcohol are shown in Figure 6a,b. The real and imaginary relative permittivities are expressed in terms of the capacitance $C(\omega)$ and dielectric loss $G(\omega)/\omega$, where $G(\omega)$ is the conductance, which are related to the former parameters via

$$\epsilon'(\omega) = \frac{C(\omega)d}{A\epsilon_o} \tag{2}$$

and

$$\epsilon''(\omega) = \frac{G(\omega)}{\omega}\frac{d}{A\epsilon_o} \tag{3}$$

where d and A are the interelectrode distance and electrode area, respectively. An increase in the cetostearyl alcohol concentration led to a fall in both the capacitance and loss components of the sample over the majority of the frequency range under study, with a marked decrease seen between 0.5% and 2%. Similar trends were seen for systems containing 2% cetomacrogol 1000. Furthermore, the responses of systems comprising 0.5% and 1% sodium lauryl sulfate and varying quantities of cetostearyl alcohol showed similar concentration dependence, as shown in Figure 7a,b. The capacitance of some of these systems became noisy at frequencies between 10^3 and 10^4 Hz due to the instrument approaching the limits of measuring capability; hence, these data have not been included. Clearly, however, the real and imaginary permittivities show a general trend of a decrease with CSA concentration. Such observations are of interest but somewhat limited in applicability in the absence of more sophisticated structural analysis; hence, the responses have been studied in terms of an equivalent circuit model.

Circuit Analysis of the Response—The circuit model which was developed for this study is based on earlier studies on related systems[16–18] and our own studies on complex semisolid systems.[19,24,25] The diagram which was found to yield the optimum fit is shown in Figure 8. The circuit corresponds to a modified Maxwell–Wagner response,[23] comprising a dispersive (frequency dependent) capacitor C_s in series with a parallel RC circuit, these two main features corresponding to a barrier (electrode surface) and a bulk response, respectively. The barrier response corresponds to a thin layer adsorbed onto the electrode surfaces and may be described by

$$C_s = C_{s=0}\,(i\omega/\omega_s)^{-s} \tag{4}$$

where s is the power law index which indicates the frequency dependence of C_s and $C_{s=0}$ is the capacitance when $s = 0$ and ω_s is a characteristic frequency. It is essential to incorporate the response of such electrode barrier layers when modeling dielectric data of liquid and semisolid systems, particularly in the low-frequency region, as such features may result in high real and imaginary C values in the sub-Hz range. The nondispersive parallel RC circuit R_1C_1 represents the bulk resistance (inverse conductivity) and capacitance of the sample, while the series element R_2C_2 comprises a nondispersive resistance in series with a dispersive capacitor given by

$$C_2 = C_{n=0}(i\omega/\omega_n)^{-n} \tag{5}$$

which is identical in form to eq 4, the index n indicating the power law behavior of the capacitance element. The fitted data are shown as continuous lines in Figures 6 and 7 and the circuit element values for the various systems given in Table 1. While minor changes in capacitance and resistance values may not be regarded as significant due to the inevitable approximations involved in the modeling, changes of 1 order of magnitude or more represent differences which are greater than those expected from the errors arising from the modeling process. The values of C_1 did not show a marked sensitivity to changes in formulation; this value can be considered to be equivalent to the dielectric constant of the sample which, given the high content of water in all the creams, may not be expected to vary greatly with comparatively small changes in the concentration of the minor components. It was noted, however, that the 2% cetomacrogol systems appeared to have higher C_1 values, the reasons for this being unclear at present. The values of R_1 increased on raising the CSA composition, reflecting the greater tortuosity of charge movement through these systems. It is also noted that the R_1 values for the ionic creams were lower than the nonionic by approximately 1 order of magnitude. The values of R_2 and $C_{n=0}$ have been associated with the behavior of thin layers within samples,[19,24] as indicated by the high values of capacitance compared to C_1. Indeed it has been argued

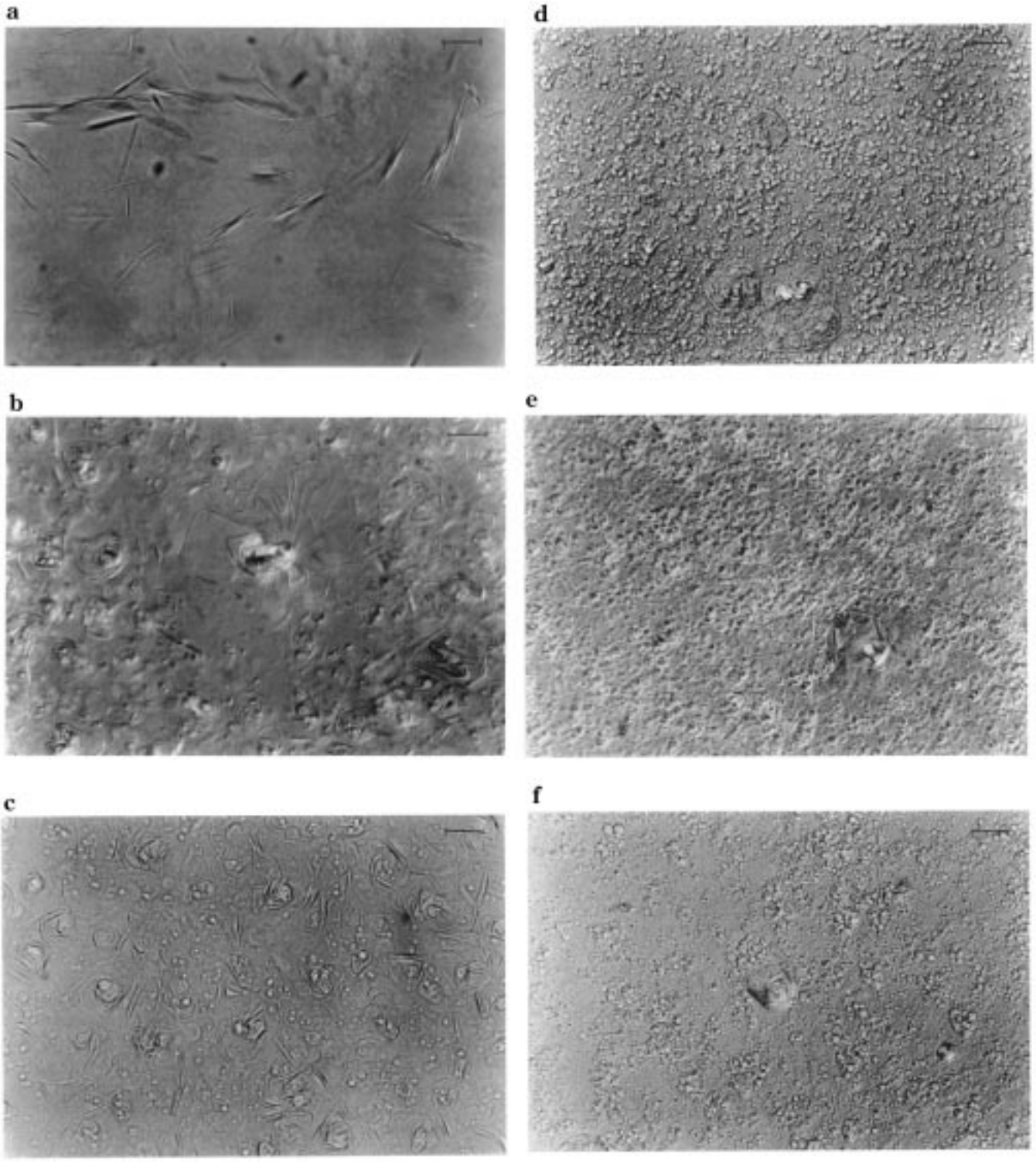

Figure 4—DIC images of ternary systems containing water and (a) 1% cetomacrogol 1000, 0.25% w/w CSA; (b) 1% cetomacrogol 1000, 1% CSA; (c) 1% cetomacrogol 1000, 4% CSA; (d) 1% cetomacrogol 1000, 8% CSA; (e) 2% cetomacrogol 1000, 8% CSA; (f) 0.5% sodium lauryl sulfate, 8% CSA. Bar = 25 μm.

that examination of these values may yield insights into the lamellar structure of creams.[19]

Discussion

The study has demonstrated clear compositional dependence of the supramolecular structure and behavior of ternary gel systems. Such changes must be considered in the context of the existing knowledge base associated with cream formation and structure. During the preparation of creams (or ternary systems), heat is applied which results in the melting of the fatty alcohol which, on dispersion, interacts with the aqueous surfactant to form smectic liquid crystals.[26] Barry and Shotton[27] have suggested that these liquid crystalline phases are elongated into lamellar ("threadlike") structures via turbulence effects. These lamellae form hydrated networks on cooling to the gel phase, this network being largely responsible for the viscoelastic properties of the cream. Interestingly, on the

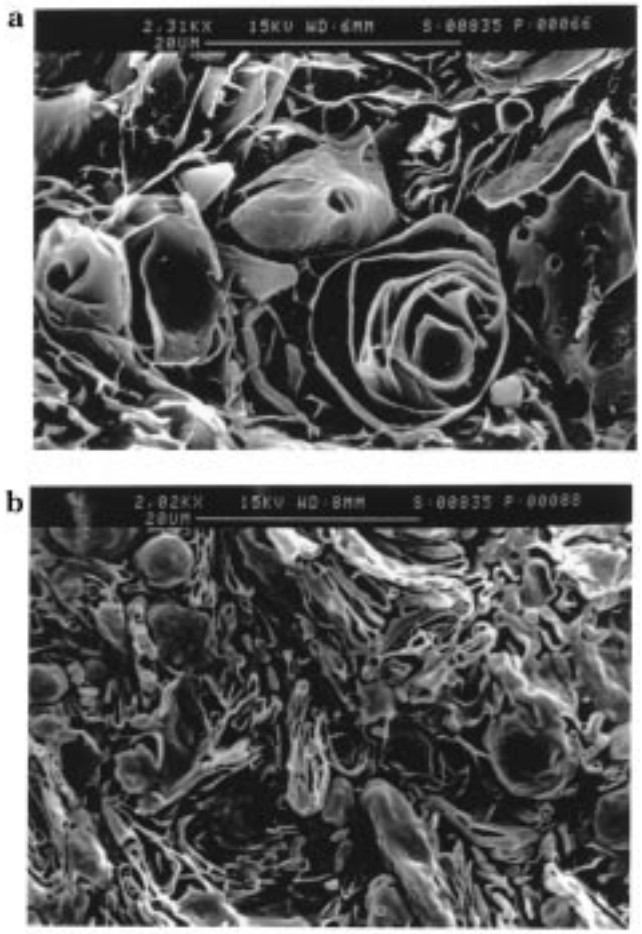

Figure 5—Cryo-SEM images of ternary systems containing 2% cetomacrogol 1000, water and (a) 2% w/w CSA (b) 8% CSA.

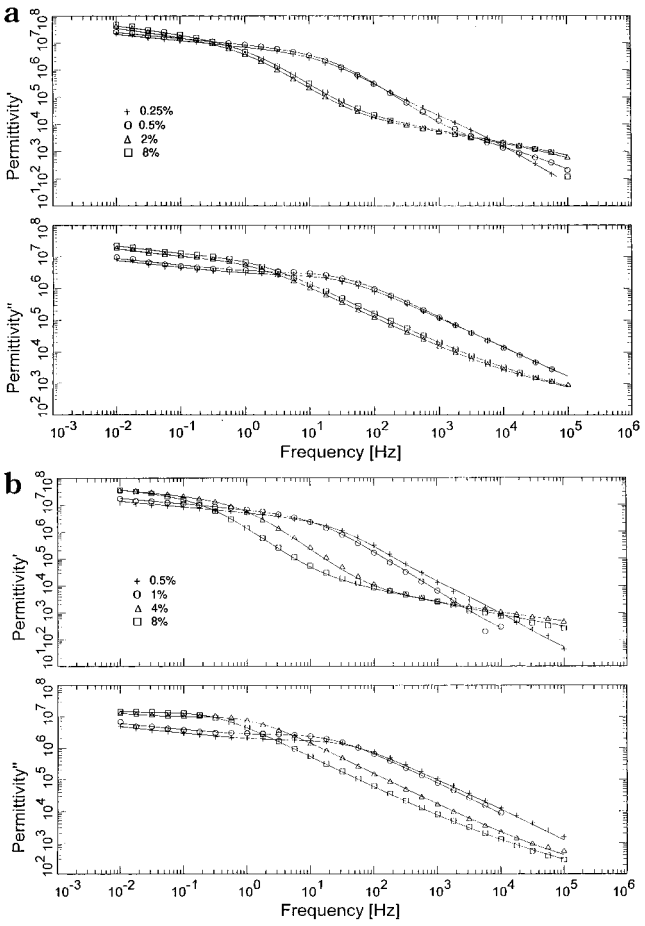

Figure 6—Real and imaginary permittivies of ternary systems containing (a) 1% cetomacrogol 1000 and (b) 2% cetomacrogol 1000, water and cetostearyl alcohol (concentration as indicated) at 298K. Solid lines indicate fitting according to circuit diagram shown in Figure 9.

basis of optical microscopic observations, these authors also suggested the formation of spherulites composed of the liquid crystal/gel phases. The remaining cetostearyl alcohol solidifies either as one of a number of polymorphs or as a hydrate due to the ability of this material to undergo limited swelling in water.

The majority of studies which have examined the rheological properties of creams and ternary systems have used the standard ratios of 9:1 (ionic) and 4:1 (nonionic) alcohol to surfactant; hence, the influence of the ratio used has not been extensively studied. Indeed, Barry and Saunders[28] have reported that the ratio may not be a critical factor in determining the rheological properties of creams. The data presented here do not directly contradict this statement in that the earlier study used a fixed concentration of emulsifier, while the present investigation involved increasing absolute concentrations. Nevertheless, the clear observed dependence of the storage and loss moduli on composition is of interest in terms of controlling the rheological properties of creams and complements earlier studies which have examined the effects of varying the total emulsifier concentration.[26]

The comparison between ternary systems containing nonionic and ionic surfactants is of interest in that the behavior of the two sets of systems is comparable at low CSA contents. However, at 1% SLS a marked increase in storage and loss moduli is observed at high CSA contents. Earlier studies have suggested that the rate of interaction between ionic surfactants and CSA is far greater than for nonionics, leading to formation of a kinetically stable system over a shorter time period when using the former.[26,28] As the samples under examination here were tested at comparable time periods after manufacture, one would expect higher moduli for the ionic systems. In fact, such effects were only observed for the higher CSA content systems, implying that the nature of the surfactant only becomes critical when the structure formed between 4% and 6% CSA is present.

The rheological studies allow characterization of the macroscopic behavior of the sample but in themselves yield little information on the specific structural origin of the observed effects. In this respect the microscopic studies (both using optical and electron beam techniques) are of considerable use. DIC microscopy is particularly well suited to the study of such systems as it allows high contrast images to be obtained in complex samples containing materials of similar refractive index. At low CSA concentrations, the DIC microscopy indicated threadlike structures which almost certainly correspond to those described by Barry and Shotton.[27] On raising the concentration of CSA, spherical structures are observed which may again correspond to the observations of Barry and Shotton.[27] However, the cryo-SEM studies indicated that these "nuclei" are in fact folded lamellae rather than continuous structures; hence, their formation may be related to the quantity and degree of curvature of the lamellae. Similarly, as the CSA content was raised to 4%, further spherical structures were seen which, again in the light of cryo-SEM studies, appears to correspond to solid-phase CSA; similar observations using cryo-SEM with regard to the presence of excess CSA have been reported by Rowe and Bray.[10] It is also interesting to note the considerably more extensive

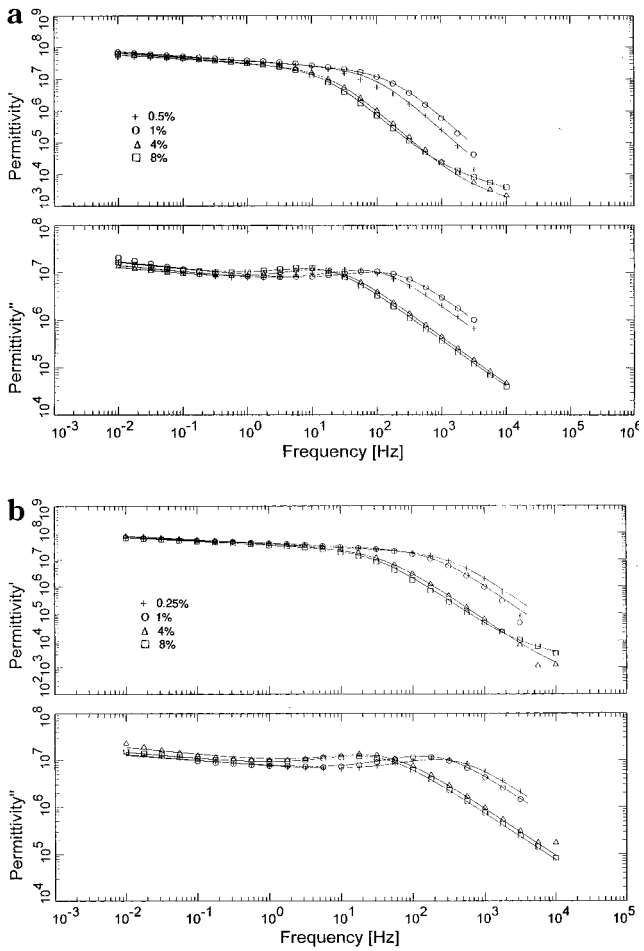

Figure 7—Real and imaginary permittivies of ternary systems containing (a) 0.5% sodium lauryl sulfate and (b) 1% sodium lauryl sulfate, water and cetostearyl alcohol (concentration as indicated) at 298K. Solid lines indicate fitting according to circuit diagram shown in Figure 8.

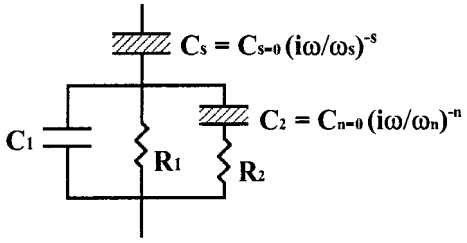

Figure 8—Equivalent circuit diagram for the dielectric responses shown in Figures 6 and 7. For explanation of notation see text.

folded lamellar network observed for the 8% systems shown in Figure 5b. Overall, the data presented here indicate that the observed rheological effects may be due to a combination of factors, including the nature of the lamellar material in terms of bilayer composition and water entrapment, the quantity of such material, and the supramolecular organization of the lamellae (e.g., presence as nuclei as opposed to folded lamellae, nature of the folding). The study suggests that this supramolecular structure may be an important consideration in terms of the understanding of the rheology of creams and ternary systems which has yet to be fully explored.

It is noteworthy that the DIC photomicrographs of the ionic ternary systems indicated a smaller quantity of solid-phase CSA compared to the equivalent nonionic systems, suggesting greater integration of the CSA into the lamellar phase (similar observations in a different context have been made by Eccleston[2]). This may in turn result in more extensive structuring and hence higher viscoelastic moduli. The microscopic observations also serve to explain the concentration dependence of the difference between ionic and nonionic systems, as at low CSA concentrations the quantity of both ionic and nonionic surfactant may be sufficient to allow efficient incorporation of the CSA into the bilayers. As the concentration of CSA is raised, however, the differing penetration properties of the two surfactants becomes a critical factor in determining lamellar formation.

The dielectric data indicated that the bulk resistances of the gels increase with increasing CSA concentration, which may be attributed to more extensive lamellar structuring, as discussed previously.[16] Given the now reasonably well-established link between the bulk resistance and lamellar formation,[16,24,25] it is of interest to compare the dielectric and rheological data, as while the overall trends between the two are comparable, there are also a number of differences. For example, there is no marked change in resistance for 1% SLS systems at high concentrations of CSA, as there was in the rheological responses. The resistance will be a function of the nature of the charge carriers present and the tortuosity of the conduction path within the system. Increasing the content of insoluble CSA is unlikely to result in significant increases in the number and nature of charge carriers present (further evidenced by the increase in resistance with added CSA); hence, the observed effects are almost certainly due to changes in tortuosity of the system. If, however, no parallel trends with the rheology of systems with high CSA content are seen for the ionic systems, then the logical conclusion to be drawn is that the tortuosity (i.e., quantity and folding of the lamellae) is not the determining factor. Instead, the rigidity of the lamellae may be greater for the ionic systems at high CSA contents. As previously stated, the relative importance of the lamellar nature, quantity, and folding in determining the rheological moduli have not yet been fully deconvoluted; hence, it is not yet possible to ascertain these roles with certainty. The data presented here, however, suggest that dielectric analysis may have a role to play in making such determinations. In addition, the circuit model used in the present study appears to allow an excellent fit to a wide range of experimental data. The use of the technique to quantify the bulk resistance has been clearly demonstrated. However, values such as $C_{n=0}$, which have been previously associated with lamellar structure,[19] and which here show a decrease with increasing CSA content, may also provide useful information with regard to the structure of these systems. On a crude level, one can, with reference to eq 1, suggest that the observed decrease may be due to greater thickness of the lamellae, although clearly further studies are required before such direct correlations can be made. Nevertheless, the development of this modeling approach will depend first on being able to provide satisfactory fits with a range of experimental data and second with the fitting parameters to be at least intuitively compatible with the observed behavior of the system. In both these respects, the study described here has proved satisfactory.

Conclusions

The study has provided insights into both the supramolecular structures formed in ternary systems and the use of low-frequency dielectric analysis as an analytical tool, with particular emphasis on circuit modeling. With respect to the former, increasing the CSA content leads to an increase in rheological moduli which may be associated with the formation of a range of supramolecular structures, including previously unreported folded "rosette" systems,

Table 1—Fitted Parameters Corresponding to the Dielectric Responses of Ternary Systems Containing Cetostearyl Alcohol (CSA), Water, and Either Sodium Lauryl Sulfate (SLS) or Cetomacrogol 1000 (Cmac), Using the Circuit Diagram Shown in Figure 8

sample	C_1 (F)	R_1 (Ω)	R_2 (Ω)	$C_{n=0}$ (F)	n	$C_{s=0}$ (F)	s
0.25% A	1.04×10^{-10}	1.41×10^{2}	2.21×10^{2}	1.61×10^{-5}	0.429	1.29×10^{-4}	0.226
0.5% A	1.00×10^{-10}	1.13×10^{2}	1.64×10^{2}	2.84×10^{-6}	0.425	1.56×10^{-4}	0.222
1% A	2.31×10^{-10}	3.53×10^{2}	4.06×10^{1}	1.37×10^{-4}	0.630	2.02×10^{-4}	0.239
2% A	1.00×10^{-10}	1.22×10^{3}	4.81×10^{1}	2.21×10^{-6}	0.391	1.95×10^{-4}	0.292
4% A	1.15×10^{-10}	7.82×10^{2}	1.92×10^{1}	2.25×10^{-6}	0.415	1.75×10^{-4}	0.351
6% A	1.00×10^{-10}	1.65×10^{3}	4.00×10^{1}	1.10×10^{-6}	0.368	1.51×10^{-4}	0.385
8% A	1.00×10^{-10}	9.20×10^{2}	1.76×10^{1}	3.20×10^{-6}	0.419	2.42×10^{-4}	0.292
0.25% B	6.05×10^{-9}	9.01×10^{1}	1.83×10^{2}	1.25×10^{-5}	0.478	2.12×10^{-4}	0.189
0.5% B	1.98×10^{-10}	1.62×10^{2}	3.79×10^{2}	1.13×10^{-5}	0.442	9.01×10^{-5}	0.213
1% B	1.10×10^{-9}	2.07×10^{2}	9.80×10^{2}	1.05×10^{-5}	0.385	1.18×10^{-4}	0.209
2% B	1.16×10^{-9}	4.59×10^{2}	1.36×10^{1}	3.89×10^{-6}	0.474	2.85×10^{-4}	0.179
4% B	2.27×10^{-9}	9.43×10^{2}	3.27×10^{1}	1.42×10^{-6}	0.430	2.43×10^{-4}	0.203
6% B	9.02×10^{-10}	1.42×10^{3}	3.35×10^{1}	1.91×10^{-6}	0.461	2.51×10^{-4}	0.213
8% B	1.10×10^{-9}	2.74×10^{3}	3.27×10^{1}	2.55×10^{-6}	0.486	2.49×10^{-4}	0.207
0.25% C	1.00×10^{-10}	5.47×10^{0}	2.06×10^{2}	1.24×10^{-5}	0.490	2.90×10^{-4}	0.109
0.5% C	1.00×10^{-10}	7.09×10^{0}	3.71×10^{2}	1.00×10^{-5}	0.420	5.35×10^{-4}	0.130
1% C	1.00×10^{-10}	4.35×10^{0}	4.83×10^{2}	4.56×10^{-5}	0.420	5.66×10^{-4}	0.144
2% C	1.00×10^{-10}	2.05×10^{1}	6.97×10^{2}	5.15×10^{-6}	0.442	5.29×10^{-4}	0.156
4% C	1.00×10^{-10}	3.19×10^{1}	5.48×10^{1}	3.30×10^{-6}	0.433	4.58×10^{-4}	0.136
6% C	1.00×10^{-10}	4.99×10^{1}	5.64×10^{1}	6.01×10^{-6}	0.422	4.60×10^{-4}	0.173
8% C	1.00×10^{-10}	3.81×10^{1}	6.10×10^{1}	6.83×10^{-6}	0.417	4.90×10^{-4}	0.153
0.25% D	1.00×10^{-10}	2.13×10^{0}	4.69×10^{2}	1.09×10^{-5}	0.417	5.45×10^{-4}	0.122
0.5% D	1.00×10^{-10}	1.28×10^{0}	1.16×10^{2}	2.86×10^{-5}	0.414	5.62×10^{-4}	0.115
1% D	1.00×10^{-10}	2.98×10^{0}	3.91×10^{1}	5.37×10^{-6}	0.424	5.77×10^{-4}	0.114
4% D	1.00×10^{-10}	1.53×10^{1}	1.54×10^{1}	1.29×10^{-6}	0.441	5.89×10^{-4}	0.149
6% D	1.00×10^{-10}	1.45×10^{1}	1.43×10^{1}	1.03×10^{-6}	0.444	5.32×10^{-4}	0.122
8% D	1.00×10^{-10}	1.95×10^{1}	2.41×10^{1}	4.80×10^{-6}	0.413	5.20×10^{-4}	0.138

[a] A = 1% cetomacrogol 1000; B = 2% cetomacrogol 1000; C = 0.5% sodium lauryl sulfate; D = 1% sodium lauryl sulfate. % Values in table refer to % CSA.

although the relative roles of the nature, quantity, and arrangement of the lamellae in determining the rheological properties is still not fully understood. The dielectric data showed a clear decrease in imaginary permittivity with CSA content which, via circuit modeling, could be related to an increase in bulk resistance which was associated with the tortuosity of charge movement through the system. Further dielectric parameters were derived which, with further development and correlation using supportive technique, may yield further insights into the structure of these complex systems. Despite the considerable number of cream and gel products on the market, there are still numerous difficulties associated with these systems, including the predictability of viscoelastic properties, issues associated with physical stability, and a poor understanding of the effects of added drugs on both consistency and release. It is hoped that by understanding the macro- and microscopic structure in greater detail using techniques such as those described here these problems may be overcome on a rational basis.

References and Notes

1. Barry, B. W. *In* Bean, H. S., Beckett, A. H., Carless, J. E., Eds. *Advances in pharmaceutical science*; Academic Press: London, 1974; Vol. 4, pp 1−72.
2. Eccleston, G. M. Structure and rheology of cetomacrogol creams: the influence of alcohol chain length and homologue composition. *J. Pharm. Pharmacol*. **1997**, *29*, 157−162.
3. Lashmar, U. T.; Beesley, J. Correlation of rheological properties of an oil in water emulsion with manufacturing procedures and stability. *Int. J. Pharm*. **1993**, *91*, 59−67.
4. Junginger, H. E. Colloidal structure of o/w creams. *Pharmaceutisch Weekblad Scientific Ed*. **1984**, *6*, 141−149.
5. Eccleston, G. M. Phase transitions in ternary systems and oil-in-water emulsions containing cetrimide and fatty alcohols. *Int. J. Pharm*. **1985**, *27*, 311−323.
6. Rowe, R. C.; Patel, H. K. Reflectance measurements on gels and emulsions containing cetrimide and cetostearyl alcohol − a preliminary investigation. *J. Pharm. Pharmacol*. **1985**, *37*, 222−225.
7. Barry, B. W.; Saunders, G. M. The self-bodying action of alkyltrimethylammonium bromides/cetostearyl alcohol mixed emulsifiers; influence of quaternary chain length. *J. Colloid Interface Sci*. **1971**, *35*, 689−705.
8. Eccleston, G. M. Phase transitions in ternary systems and oil-in-water emulsions containing cetrimide and fatty alcohols. *Int. J. Pharm*. **1985**, *27*, 311−323.
9. Junginger, H.; Heering, W. Darstellung kolloider Strukturen von Salben, Cremes, Emulsionen and Mikroemulsionen mittels Gefrierbruch-Atztechnik und TEM. *Acta Pharm. Technol*. **1983**, *29*, 85−96.
10. Rowe, R. C.; Bray, D. Water distribution in creams prepared using cetostearyl alcohol and cetrimide. *J. Pharm. Pharmacol*. **1987**, *39*, 642−643.
11. Junginger, H. Differential thermal analysis of o/w creams. *J. Therm. Anal*. **1980**, *2*, 541−545.
12. Peramal, V. L.; Tamburic S.; Craig, D. Q. M. Characterisation of the variation in the physical properties of commercial creams using thermogravimetric analysis and rheology. *Int. J. Pharm*. **1997**, *155*, 91−98.
13. Dissado, L. A.; Rowe, R. C.; Haidar, A.; Hill, R. M. The characterization of heterogeneous gels by means of a dielectric technique. 1. Theory and preliminary evaluation. *J. Colloid Interface Sci*. **1987**, *117*, 310−324.
14. Rowe, R. C.; Dissado, L. A.; Zaidi, S. H.; Hill, R. M. The characterization of heterogeneous gels by means of a dielectric technique. 2. Formulation and structural considerations. *J. Colloid Interface Sci*. **1988**, *122*, 354−366.
15. Cooper, J.; Hill, R. M. Dielectirc spectroscopy of liquid lamellar phases. *J. Colloid Interface Sci*. **1996**, *180*, 27−35.
16. Goggin, P. L.; He, R.; Craig, D. Q. M.; Gregory, D. An investigation into cream characterisation using low-frequency dielectric spectroscopy. *J. Pharm. Sci*. **1997**, *87*, 559−564.
17. Jonscher, A. K. *Universal Relaxation Law*; Chelsea Dielectrics Press: London, 1996.
18. Hill, R. M.; Jonscher, A. K. The dielectric behaviour of condensed materials and its many-body interpretation. *Contemp. Phys*. **1983**, *24*, 75−110.
19. Craig, D. Q. M. *Dielectric analysis of pharmaceutical systems*, Taylor and Francis: London, 1995.
20. Barry, B. W.; Saunders, G. M. Kinetics of structure build-up in self-bodied emulsions stabilized by mixed emulsifiers. *J. Colloid Interface Sci*. **1972**, *41*, 331−342.
21. Barry, B. W.; Shotton, E. Structure and rheology of sodium dodecyl sulphate-cetyl alcohol-water: continuous shear experiments. *J. Pharm. Pharmacol*. **1967**, *19*, 110S−120S.

22. Eccleston, G. M.; Beattie, L. Microstructural changes during the storage of systems containing cetostearyl alcohol/polyoxyethylene alkyl ether surfactants. *Drug Dev. Ind. Pharm.* **1988**, *14*, 2499−2518.
23. Hill, R. M.; Pickup, C. Barrier effects in dispersive media. *J. Mater. Sci.* **1985**, *20*, 4431−4444.
24. He, R.; Craig, D. Q. M. Low-frequency dielectric investigations into the phase behaviour of glyceryl monoolein/water systems *J. Phys. Chem.* **1998**, *102*, 1781−1786.
25. He, R.; Craig, D. Q. M. Characterisation of the effects of drug addition on the structure of glyceryl monoolein/water gel systems using low-frequency dielectric spectroscopy. *J. Pharm. Sci.* **1999**, *88*, 635−639.
26. Eccleston, G. M. Properties of fatty alcohol mixed emulsifiers and emulsifying waxes. In *Materials Used in Pharmaceutical Formulation*; Florence, A. T., Ed.; Blackwell Publications: Oxford, 1984.
27. Barry, B. W.; Shotton, E. Structure and rheology of sodium dodecyl sulphate-cetyl alcohol-water; continuous shear experiments. *J. Pharm. Pharmacol.* **1967**, *19*, 110S−120S.
28. Barry, B. W.; Saunders, G. M. Rheology of systems containing cetomacrogol 1000-cetostearyl alcohol. 1. Self-bodying action. *J. Colloid Interface Sci.* **1972**, *38*, 616−625.

Acknowledgments

The assistance of Mr. Jaz Lichy, Unilever Research, Port Sunlight, in performing the SEM studies is gratefully acknowledged. We thank the EPSRC for financial support for Dr. He.

JS990054A

Correlation and Estimation of Gas–Chloroform and Water–Chloroform Partition Coefficients by a Linear Free Energy Relationship Method

MICHAEL H. ABRAHAM,*,† JAMES A. PLATTS,† ANNE HERSEY,‡ ALBERT J. LEO,§ AND ROBERT W. TAFT||

Contribution from *Department of Chemistry, University College London, 20 Gordon Street, London WC1H OAJ, U.K.; Science Development Group, GlaxoWellcome Research and Development, Park Road, Ware SG12 0DP, U.K.; Seaver Chemistry Laboratory, Pomona College, Claremont, California 91711; and Department of Chemistry, University of California, Irvine, California 92717.*

Received January 11, 1999. Accepted for publication April 7, 1999.

Abstract □ A linear free energy relationship, LFER, has been used to correlate 150 values of gas–chloroform partition coefficients, as log L^{chl} with a standard deviation, sd, of 0.23 log units, a correlation coefficient r^2 of 0.985, and an *F*-statistic of 1919. The equation reveals that bulk chloroform is dipolar/polarizable, of little hydrogen-bond basicity, but as strong a hydrogen-bond acid as bulk methanol or bulk ethanol. However, the main influence on gaseous solubility in chloroform is due to solute–solvent London dispersion interactions. A slightly modified LFER has been used to correlate 302 values of water–chloroform partition coefficients, as log P_{chl}. The correlation equation predicts log P_{chl} for a further 34 compounds not used in the equation with sd = 0.17 log units. When the LFER is applied to all 335 log P_{chl} values, the resulting equation has sd = 0.25, $r^2 = 0.971$, and F = 2218.

Introduction

The partition coefficient of a solute, as log *P*, has widespread applications in such diverse areas as environmental chemistry, biochemistry, pharmaceutical chemistry, toxicology, and chemical engineering.[1] Following the work of Hansch and Leo,[2] the water−octanol partition coefficient, as log P_{oct}, has become a standard parameter in quantitative structure−activity relationships (QSARs), and in the definition of solute lipophilicity.[3] However, other water−solvent systems have been used, especially as models for biochemical proceses;[3,4] indeed the first such system used in this way was water−olive oil.[4]

The water−chloroform system has been used to estimate solute lipophilicity, as log P_{chl},[5] and both the water−cyclohexane and water−chloroform systems have been used to examine the hydrophobicities of nucleic acid bases.[6] The later system has been put forward as one of a "critical quartet" of water−solvent systems that encapsulates most of the information contained in water−solvent systems, in general.[7] Comparisons of water−solvent log *P* values, including log P_{chl}, have been made,[8] but only recently have attempts been made to compute log P_{chl} values. Some of these computations refer to relative partition coefficients,[9,10] but others to absolute values;[11−14] we comment only on these latter calculations.

All the reported computations of log P_{chl} involve the separate calculation of gas−water partition coefficients, L^w, and gas-chloroform partition coefficients, L^{chl}. Various standard states can be used to define *L*, or the related Gibbs free energy change, $\Delta G° = -RT \ln L$. We prefer to work with equilibrium constants[15] and define *L* as a dimensionless quantity via eq 1.

$$L = \text{concn (M) solute in solvent/concn (M) solute in gas phase} \quad (1)$$

Then log P_{chl} is given by eq 2. As we shall see, eq 2 is valuable, not only in the calculation of log P_{chl}, but also as one method of experimental determination of log P_{chl}.

$$\log P_{chl} = \log L^{chl} - \log L^w \quad (2)$$

A GB/SA continuum model together with the OPLS all atom force field was used by Reynolds[11] to compute log L^w, log L^{chl}, and hence log P_{chl} for 30 diverse, but monofunctional, compounds. The standard deviation, sd, between the 30 calculated and observed log P_{chl} values was 0.87 log units with sd defined as $[(Y_{calcd} - Y_{obsd})^2/(n-V-1)]^{1/2}$; n is the number of data points and V the number of variables (zero in the present case). The average deviation, $(Y_{calcd} - Y_{obsd})/n$ was only 0.01 log units, but it was suggested that systematic deviations at low log P_{chl} and high log P_{chl} values occurred. A plot of observed vs calculated log P_{chl} values indeed yielded a smaller standard deviation; see eq 3. In eq 3 and elsewhere *r* is the correlation coefficient and *F* is the Fischer *F*-statistic.

$$\log P_{chl}(obsd) = 0.055 + 0.732 \log P_{chl}(calcd) \quad (3)$$

$$n = 30,\ sd = 0.51,\ r^2 = 0.919,\ F = 318$$

Various other computations of log L^{chl} have been made[12−14] on data sets that vary from only 16 compounds to 88 compounds; see Table 1. In general, the computations summarized in Table 1 lead to log L^{chl} values with an sd of 0.3 to 0.7 log units and to log P_{chl} values with a much larger sd of 0.5−1.0 log units, even when trained on experimental values. The larger error in log P_{chl} is expected, because this will include errors in both log L^{chl} and in log L^w. Additionally, any experimental errors in log P_{chl} will also contribute to the overall sd value, and it is not easy to assess this contribution, especially for small data sets. In general, the more compounds in a data set, the larger will be the sd value, because of the more varied and more complicated structures in the data set.

The method of multiple linear regression analysis (MLRA) has been applied to the correlation of log P_{chl} values, using various physicochemical parameters as descriptors.[1,6,18−20] A summary of results is in Table 1. Only one, preliminary MLRA of log L^{chl} has been reported,[19] as shown in Table 1 also. The disadvantage of the MLRA method, as compared

* Corresponding author.
† University College London.
‡ GlaxoWellcome.
§ Pomona College.
|| University of California (deceased).

10.1021/js990008a CCC: $18.00
Published on Web 05/27/1999

Table 1—Computations and Calculations of log P_{chl} and log L^{chl}

reference	untrained set		trained set			
	n	sd	*n*	sd	r^2	*F*
		A. log P_{chl}				
Reynolds[11]	30	0.87	30	0.51	0.919	318
Cramer (SM5.4A)[13]			26	0.93		
Cramer (SM5.4P)[13]			26	0.96		
Jorgensen[14]			16	0.67		
Marcus (MLRA)[18]			66	0.16	0.994	2973
Taylor (MLRA)[7a]			33	0.11	0.993	610
Maurer (MLRA)[1d]			50	0.12		
Testa (MLRA)[19b]			60	0.29	0.950	369
Abraham (MLRA)[19a]			112	0.11	0.994	3785
this work (MLRA)			335	0.25	0.971	2218
		B. log L^{chl}				
Luque (6-31G)[12]	27	0.28				
Luque (AM1)[12]	27	0.30				
Luque (MNDO)[12]	27	0.28				
Luque (PM£)[12]	27	0.30				
Cramer (OSM5.4A)[13]	88					
Cramer (OSM5.4P)[13]	88					
Cramer (SM5.4A)[13]			88	0.53		
Cramer (SM5.4P)[13]			88	0.67		
Jorgensen[14]	16	0.69	16	0.52	*a*	272
Abraham (MLRA)[19a]			35	0.15	0.994	754
this work			150	0.23	0.985	1919

[a] See note 17.

with computational methods, is that it requires experimental values to use as a training set. However, the untrained computations reported in Table 1 lead to very considerable errors, and if computations have to be trained on experimental data in order to reduce errors to reasonable values, much of the computational advantage disappears. In the event, the trained MLRA method seems capable of leading to rather smaller sd values than do the trained computational methods reported to date. Hence the aim of this work is to determine further log P_{chl} values in order to extend the experimental database and then to apply MLRA methods to a very much enlarged database. Not only will this provide very general correlations, but it will overcome difficulties inherent in the use of small data sets.

There are several problems with the use of small data sets. First, the data set might not be representative. Indeed, a very small data set cannot be representative, in that it will not contain examples of many types of compound that could be included in a full data set. For example, neither the 30 compound data set[11] nor the 16 compound data set[14] contain any compound with a sulfur or with an iodine atom. Second, it is very difficult to assess the effect of possible experimental error when using a small data set. It was suggested that large values of (calculated − observed) log P_{chl} for trimethylamine (1.68) and dimethylamine (1.29) in the 16 compound data set and for diethylamine (1.24) in the 30 compound set were possibly due to experimental errors arising from protonation of the amine in the aqueous layer, but the large differences could also be due to a systematic computational error for aliphatic amines. Third, we know from our own experience in the measurement of log P_{chl} values, that experimental errors, especially with large values of log P_{chl}, can be much greater than expected from measurement of log P_{oct}, for example. A very erroneous experimental value in a small training set might bias a correlation so that the error becomes undetected (and the correlation becomes incorrect), whereas this is much less likely to occur with a large training set.

Methodology

A number of sources of data were used to compile the log P_{chl} and log L^{chl} values. Most of the log P_{chl} values were taken from the MedChem database,[21] and others were measured by the usual shake-flask method. For compounds that are gaseous at room temperature, log P_{chl} could often be obtained from experimental values of log L^{chl} and log L^{w} through eq 2. Directly determined log L^{chl} values were available[22] for the rare gases, hydrogen, oxygen, nitrogen, nitrous oxide, carbon monoxide, and a few organic solutes. Other log L^{chl} values could be obtained from known infinite dilution activity coefficients of solutes in chloroform together with known vapor pressures,[23] through $K^{H} = \gamma^{\infty} p^{o}$ where K^{H} is Henry's constant; L is the inverse of K^{H} with due regard to units. A large number of log L^{chl} values were deduced from log P_{chl} and known[24,25] values of log L^{w} through eq 2. We finally assembled 335 values of log P_{chl} and 150 values of log L^{chl} to use in our correlative equations, as set out in Table 2.

The MLR equation we use to correlate log L^{chl} is the linear free energy relationship (LFER)[26] shown as eq 4.

$$\log SP = c + rR_2 + s\pi_2^{H} + a\Sigma\alpha_2^{H} + b\Sigma\beta_2^{H} + l \log L^{16} \quad (4)$$

Here, SP is a set of solute properties in a given system, for example L^{chl} values, and the independent variables are solute descriptors as follows.[26] R_2 is an excess molar refraction, π_2^{H} is the dipolarity/polarizability, $\Sigma\alpha_2^{H}$ is the overall hydrogen-bond acidity, $\Sigma\beta_2^{H}$ is the overall hydrogen-bond basicity, and L^{16} is the gas−liquid partition coefficient on hexadecane at 298 K.[28]

The coefficients in eq 4 are found by MLRA. They are not just fitting constants, but contain information on the properties of the system under investigation; in particular they refer to chemical properties of the solvent phase. The *r*-coefficient reflects the interaction of the phase with solute π- and σ-lone pairs, the *s*-coefficient is a measure of the phase dipolarity/polarizability, the *a*-coefficient is a measure of the phase hydrogen-bond basicity, the *b*-coefficient is a measure of the phase hydrogen-bond acidity, and the *l*-coefficient is a measure of the phase hydrophobicity. Equation 4 has been applied to numerous sets of gas−liquid chromatographic data,[26,27] to gas−solid adsorption,[28] to the solubility of gases and vapors in water,[24] organic solvents,[20] biological systems,[29] polymers,[30] and petroleum oils,[31] to the characterization of phases for chemical sensors,[32] to the characterization of fullerene,[33] and in the analysis of the effect of gases and vapors in nasal pungency[34] and eye irritation.[35]

A very similar equation to eq 4 is used[26] to correlate processes within condensed phase; it differs only in that the final descriptor is the McGowan[36] characteristic volume, V_X, in (mL mol^{-1})/100. The interpretation of eq 5 follows closely that of eq 4, but now the coefficients refer to the difference of properties of the (two) condensed phases. Equation 5 is also a well-tested equation and has been applied to the solubility of gases and vapors in water,[24] to numerous water−solvent partition systems,[19] to HPLC systems,[37] to thin-layer chromatography,[38] to microemulsion electrokinetic chromatography,[39] to water−micelle partitions,[40] to micellar electrokinetic chromatography,[41] to aqueous anesthesia,[42] to blood−brain distribution,[43] to brain perfusion,[44] and to skin permeation.[45]

$$\log SP = c + rR_2 + s\pi_2^{H} + a\Sigma\alpha_2^{H} + b\Sigma\beta_2^{H} + vV_X \quad (5)$$

Results

The values of log L^{chl} and log P_{chl} that were used in the regression equations are in Table 2. There are far fewer

Table 2—Values of log L^{chl} and log P_{chl} Used in the Regressions

compound name	log L^{Wa}	log L^{chlb} obsd	log L^{chlb} calcd	log P_{chl}^{c} obsd	log P_{chl}^{c} calcd
krypton	–1.21	0.01[d]	–0.039	1.22[e]	1.358
xenon	–0.97	0.53[d]	0.539	1.50[e]	1.706
radon	–0.65	1.12[d]	1.029	1.72[e]	1.936
hydrogen	–1.72	–1.18[d]	–1.01	0.54[e]	0.782
nitrogen	–1.80	–0.87[d]	–0.792	0.93[e]	1.258
nitrous oxide	–0.23	0.71[d]	0.865	0.94[e]	1.035
carbon monoxide	–1.63	–0.71[d]	–0.598	0.92[e]	1.12
hexane	–1.82	2.87[f]	2.786	4.69[e]	4.325
octane	–2.11	3.90[g]	3.777	6.01[e]	5.506
cyclohexane	–0.90	3.26	3.021	4.16	3.879
chloromethane	0.40	1.82[h]	1.811	1.42[e]	1.481
dichloromethane	0.96	2.69[i]	2.731	2.00[e]	1.745
trichloromethane	0.79	3.07[j]	3.034	2.28[e]	2.239
tetrachloromethane	–0.06	3.25[l]	3.143	3.31[e]	3.348
1,1-dichloroethane	0.62	3.01[l]	3.029	2.39[e]	2.185
1,2-dichloroethane	1.31	3.44[l]	3.428	2.13[e]	2.107
1,1,1-trichloroethane	0.14	3.24[l]	3.269	3.10[e]	3.09
1,1,2-trichloroethane	1.46	3.87[l]	4.168	2.41[e]	2.453
1-chloropropane	0.24	2.66[h]	2.84	2.46[e]	2.6
bromoethane	0.54	2.78[f]	2.697	2.24[e]	2.185
iodomethane	0.65	2.78[k]	2.55	2.13[e]	1.946
1,1,2-trifluorotrichloroethane	–1.30	2.54[i]	2.494	3.84[e]	3.675
diethyl ether	1.17	3.05	3.051	1.88	1.752
diisopropyl ether	0.39	2.77	3.404	2.38[l]	3.088
tetrahydrofuran	2.55	3.86[f]	3.893	1.31[e]	1.127
tetrahydropyran	2.29	4.28	4.348	1.99	1.77
1,4-dioxane	3.71	4.44[g]	4.629	0.73[e]	0.74
propanone	2.79	3.29	3.287	0.50	0.562
butanone	2.72	3.87	3.891	1.15	1.209
diethyl carbonate				3.22	2.216
propylene carbonate				0.60	0.589
δ-pentanolactone				0.95	0.928
methyl acetate	2.30	3.46	3.379	1.16	1.091
ethyl acetate	2.16	3.98	3.771	1.82	1.683
propyl acetate	2.05	4.61	4.25	2.56	2.28
butyl acetate	1.94	4.99	4.786	3.05	2.867
pentyl acetate	1.84	5.44	5.27	3.60	3.457
methyl propanoate	2.15	4.02	3.847	1.87	1.695
methyl pentanoate	1.88	4.89	4.802	3.01	2.873
methyl hexanoate	1.83	5.31	5.292	3.48	3.459
ethyl acetoacetate				1.49	1.566
ethyl trifluoroacetate				2.00	1.942
ethyl trichloroacetate				3.47	3.537
acetonitrile	2.85	3.25	3.321	0.40	0.383
ammonia	3.15	1.77	1.699	–1.38	–1.366
methylamine	3.34	2.32	2.574	–1.02	–0.811
ethylamine	3.30	2.95	2.993	–0.35	–0.326
propylamine	3.22	3.47	3.455	0.25	0.263
butylamine	3.11	3.86	3.924	0.75	0.854
dimethylamine	3.15	2.71	2.929	–0.44	–0.23
diethylamine	2.99	3.78	3.771	0.79	0.843
diisopropylamine	2.36	3.97	4.299	1.61	1.894
trimethylamine	2.35	2.86	2.843	0.51	0.613
triethylamine	2.36	4.22	4.362	1.86	1.986
nitromethane	2.95	3.39[g]	3.473	0.44[e]	0.523
acetamide	7.12	5.15		–1.97	–2.049
proprionamide	6.88	5.48		–1.40	–1.494
N,*N*-dimethylacetamide				–0.13	0.484
2,2,2-trichloroacetamide				0.31	0.427
ethyl carbamate				0.12	–0.32
formic acid				–2.12	–2.044
acetic acid	4.91	3.45	3.317	–1.46	–1.397
propanoic acid	4.74	3.88	3.877	–0.86	–0.814
butanoic acid	4.66	4.39	4.383	–0.27	–0.215
2-methylpropanoic acid				–0.26	–0.334
pentanoic acid	4.52	4.84	4.901	0.32	0.383
3-methylbutanoic acid	4.47	4.66	4.699	0.19	0.253
hexanoic acid	4.56	5.58	5.449	1.02	0.968
2-methylpentanoic acid				0.90	0.843
octanoic acid	4.44[m]	6.61	6.524	2.17	2.146
2-methylpropenoic acid				0.00	–0.291
chloroacetic acid				–1.65	–1.176
trichloroacetic acid				–1.11	–0.608
succinic acid				–1.92	–1.824
water	4.64	1.54	1.697	–3.10	–2.968
methanol	3.74	2.41	2.271	–1.33	–1.497
ethanol	3.67	2.80	2.767	–0.87	–0.747
propan-1-ol	3.56	3.26	3.309	–0.30	–0.158
propan-2-ol	3.48	3.13	3.084	–0.35	–0.286
butan-1-ol	3.46	3.88	3.876	0.42	0.431
2-methylpropan-1-ol	3.30	3.64	3.658	0.34	0.441
butan-2-ol	3.39	3.69	3.645	0.30	0.306
2-methylpropan-2-ol	3.28	3.26	3.273	–0.02	0.25
pentan-1-ol	3.35	4.40	4.374	1.05	1.02
hexan-1-ol	3.23	4.92	4.874	1.69	1.61
heptan-1-ol	3.09	5.50	5.369	2.41	2.2
cyclohexanol	4.01	5.13	5.131	1.12	0.997
prop-2-en-1-ol	3.69	3.18	3.22	–0.51	–0.369
2-chloroethanol				–0.40	–0.902
3-chloropropan-1-ol				–0.03	0.035
propan-1,3-diol				–2.90	–2.626
diethyl sulfide	1.07	4.71	3.908	3.64	2.64
dimethyl sulfoxide	7.41	6.56[n]	6.642	–0.85[e]	–0.729
thiourea				–3.14	–2.922
tributylphosphine oxide				3.08	2.856
trimethyl phosphate	6.52[m]	7.28		0.76	0.546
triethyl phosphate	5.53	7.81	7.537	2.28	2.133
tripropyl phosphate				3.67	3.587
benzene	0.63	3.39	3.384	2.76	2.741
toluene	0.65	4.06	3.918	3.41[l]	3.33
ethylbenzene	0.58	4.28	4.357	3.70	3.892
o-xylene	0.66	4.57	4.561	3.91	3.846
m-xylene	0.61	4.29	4.437	3.68	3.855
biphenyl	1.95	6.62	6.86	4.67	4.81
naphthalene	1.73	5.78	5.865	4.05	4.039
phenanthrene	2.80	7.86	8.452	5.06	5.244
fluorobenzene	0.59	3.13	3.473	2.54	2.912
chlorobenzene	0.82	4.22	4.242	3.40	3.46
1,3-dichlorobenzene	0.72	4.59	4.936	3.87	4.134
1,4-dichlorobenzene	0.74	4.63	4.999	3.89	4.123
2-chloronaphthalene				4.56	4.754
bromobenzene	1.07	4.70	4.649	3.63	3.606
iodobenzene	1.28	4.85	5.073	3.57	3.865
methyl phenyl ether	1.80	4.92	4.903	3.12	2.987
ethyl phenyl ether	1.63	5.25	5.243	3.62	3.49
benzaldehyde	2.95	5.20	5.403	2.25	2.383
2-methoxybenzaldehyde				2.53	2.807
phenylacetaldehyde				2.07	2.222
acetophenone	3.36	6.15	6.024	2.79	2.66
benzyl methyl ketone				3.53[l]	2.664
9-fluorenone				3.95	3.772
methyl benzoate	2.88	5.68	6.046	2.80	3.024
phenyl acetate				2.33	2.628
dimethyl phthalate				3.09	3.003
diethyl phthalate				3.69	4.107
benzonitrile	3.09	5.75	5.536	2.66	2.526
phenylacetonitrile				2.25	2.69
1,2-dicyanobenzene				2.60[l]	2.421
1,3-dicyanobenzene				2.12	2.147
1,4-dicyanobenzene				2.60	2.304
aniline	4.30[o]	5.65	5.3	1.35	1.283
o-toluidine	4.06	6.02	5.788	1.96	1.85
p-toluidine	4.09	6.04	5.861	1.95	1.831
4-ethylaniline				2.28	2.44
4-propylaniline				2.99	2.928
4-isopropylaniline				2.51	2.768
4-butylaniline				3.37	3.521
4-chloroaniline	4.33	6.42	6.263	2.09	1.964
2-nitroaniline	5.41	7.24	7.285	1.83	1.933
3-nitroaniline	6.49	8.09	7.963	1.60	1.518
4-nitroaniline	7.54	8.80	8.703	1.26	1.276
3-aminoacetophenone				1.73	1.67
4-aminopropriophenone				2.13	1.972
2,4-dimethylaniline				2.27	2.384
N-methylaniline	3.44	5.84	5.765	2.40	2.115
N,*N*-dimethylaniline	2.53	6.01	5.791	3.48	3.353
N,*N*-diethylaniline				4.26	4.538
1-naphthylamine	5.34	7.94	7.962	2.60	2.466
2-naphthylamine	5.48	8.18	8.014	2.70	2.463
4-aminobiphenyl				3.14	3.483
benzylamine				1.18	1.33
1-amino-2-phenylethane				1.37	1.222
nitrobenzene	3.02	5.71	5.899	2.69	2.8
2-nitrotoluene	2.63	6.02	6.217	3.39[l]	3.389
3-nitrotoluene	2.53	5.98	6.374	3.45	3.498
4-nitrotoluene				3.31	3.39

Table 2—(Continued)

compound name	log L^{Wa}	log L^{chlb} obsd	log L^{chlb} calcd	log $P_{chl}{}^{c}$ obsd	log $P_{chl}{}^{c}$ calcd	compound name	log L^{Wa}	log L^{chlb} obsd	log L^{chlb} calcd	log $P_{chl}{}^{c}$ obsd	log $P_{chl}{}^{c}$ calcd
4-nitroanisole				3.18	3.169	methyl phenyl sulfoxide				1.41	1.193
1,2-dinitrobenzene				2.64	3.002	diphenyl sulfoxide				3.36	3.111
1,3-dinitrobenzene				2.63	2.729	methyl phenyl sulfone				1.93	1.931
1,4-dinitrobenzene				2.62	2.748	phenylthiourea				0.56	0.541
benzamide	8.07	8.19	8.177	0.12	0.106	benzenesulfonamide				–0.24	–0.009
N-methylbenzamide				0.95	0.844	*N*-methylbenzenesulfonamide				1.31	1.326
N-ethylbenzamide				1.54	1.432	*N*,*N*-dimethylbenzenesulfonamide				2.69	2.736
N,*N*-dimethylbenzamide				1.75	1.819	3-methylbenzenesulfonamide				0.32	0.405
acetanilide	7.01[o]	7.81		0.80	0.76	4-methylbenzenesulfonamide				0.33	0.337
phthalimide				1.46	1.253	pyridine	3.44	4.73	4.525	1.29	1.14
benzoic acid				0.60	0.737	2-methylpyridine	3.40	5.12	4.907	1.72	1.555
2-methylbenzoic acid				1.76	1.502	3-methylpyridine	3.50	5.39	5.113	1.89	1.674
4-methylbenzoic acid				1.36	1.295	4-methylpyridine	3.62	5.50	5.135	1.88	1.67
4-ethylbenzoic acid				1.85	1.856	2-ethylpyridine	3.18	5.44	5.275	2.26	2.129
4-butylbenzoic acid				2.86	3.067	2-chloropyridine	3.22	5.22	5.345	2.00	2.077
2-chlorobenzoic acid				0.90	0.945	2-bromopyridine				2.22	2.383
4-chlorobenzoic acid				1.72	1.585	3-bromopyridine				1.65	2.375
2-bromobenzoic acid				0.91	0.95	2-methoxypyridine	2.96[m]	5.17	4.96	2.21	2.182
3-bromobenzoic acid				2.04	1.713	2-acetylpyridine				1.93	1.856
2-iodobenzoic acid				1.09	1.067	2-cyanopyridine				1.42	1.605
2-methoxybenzoic acid				1.65	2.32	3-cyanopyridine	4.95	6.29	6.239	1.34	1.3
4-methoxybenzoic acid				1.19	1.369	4-cyanopyridine	4.42	5.71	6.007	1.29	1.422
2-nitrobenzoic acid				–0.08	0.312	4-aminopyridine				–0.71	–0.656
3-nitrobenzoic acid				0.48	0.482	2-(*N*,*N*-dimethylamino)pyridine				2.45	2.389
4-nitrobenzoic acid				0.67	0.864	nicotine				1.89	2.552
4-aminobenzoic acid				–0.92	–0.901	piperidine	3.75	4.67	4.705	0.92	0.832
phenylacetic acid				0.49	0.546	*N*-methylpiperidine	2.77	4.21	4.66	1.44	1.731
3-phenylpropanoic acid				1.20	1.15	atropine				2.44	2.534
4-phenylbutanoic acid				1.78	1.9	*N*-methyl-2-pyridone				0.26	0.762
phenol	4.85	5.17	5.081	0.32	0.408	quinoline	4.20	7.34	6.726	3.14	2.668
2-methylphenol	4.31	5.54	5.444	1.23	1.271	isoquinoline				2.98	2.647
3-methylphenol	4.60[o]	5.49		0.89	0.963	pyrrole				0.91	0.252
4-methylphenol	4.50	5.56	5.588	1.06	1.07	indole				2.95	1.882
2,4-dimethylphenol	4.41	5.91	6.035	1.50	1.544	3-methylindole				2.24	2.496
2,5-dimethylphenol	4.34	5.93	6.003	1.59	1.585	carbazole				3.75	3.592
3,5-dimethylphenol	4.60	6.20	6.153	1.60	1.5	imidazole				–0.83	–1.667
2-ethylphenol				1.73	1.627	*N*-methylimidazole				0.29	0.137
3-ethylphenol	4.59	6.00	6.142	1.41	1.501	benzimidazole				–0.02	–0.096
4-ethylphenol	4.50	5.97	6.118	1.47	1.538	2-cyanopyrazine				1.03	1.012
2-isopropyl-5-methylphenol				2.80	2.586	pyrazine	4.18[o]	4.77	4.688	0.59	0.616
2-fluorophenol	3.88	4.45	4.557	0.57	0.643	2-methylpyrazine	4.04	5.08	5.007	1.04	1.088
2-chlorophenol	3.34	4.70	5.38	1.36	1.792	2,3-dimethylpyrazine				1.46	1.435
3-chlorophenol	4.85	5.87	6.041	1.02	1.099	2,6-dimethylpyrazine				1.54	1.465
4-chlorophenol	5.16	6.23	6.127	1.07	0.984	trimethylpyrazine				1.93	1.82
2-bromophenol				1.64	1.937	tetramethylpyrazine				2.32	2.145
4-bromophenol	5.23	6.30	6.495	1.07	1.195	2-ethylpyrazine	4.00	5.66		1.66	1.642
2-iodophenol	4.55	6.52	6.077	1.97	2.001	2,3-diethylpyrazine				2.47	2.413
4-iodophenol				1.56	1.54	2-methyl-3-isobutylpyrazine				2.85	2.935
2,4-dichlorophenol				2.09	2.079	2-fluoropyrazine				1.07	1.087
2-methoxyphenol	4.09	5.79	5.953	1.70[l]	1.698	2-chloropyrazine				1.59	1.698
3-methoxyphenol	5.62	6.39	6.527	0.77	0.869	2-methoxypyrazine				1.71	1.701
4-methoxyphenol				0.46	0.627	2-ethoxypyrazine				2.25	2.23
2-hydroxybenzaldehyde				2.21	2.516	2-propoxypyrazine				2.89	2.761
4-hydroxybenzaldehyde	7.68	7.54	7.356	–0.14	–0.196	methyl 2-pyrazinecarboxylate				1.36[l]	1.289
4-hydroxyacetophenone				0.08	0.109	ethyl 2-pyrazinecarboxylate				1.88	1.789
2-nitrophenol	3.36	5.89	6.075	2.53	2.623	2-acetylpyrazine				1.42	1.342
3-nitrophenol	7.06	7.56	7.637	0.50	0.545	2-(dimethylamino)pyrimidine				1.99	1.905
4-nitrophenol	7.81	8.01	8.043	0.20	0.29	5-(dimethylamino)pyrimidine				1.33	1.272
2,4-dinitrophenol				2.25	2.428	2-cyanopyrimidine				0.84	0.801
2-hydroxybenzoic acid				0.58	0.637	2-thiomethoxypyrimidine				1.93	1.836
resorcinol				–1.34	–1.919	pyrimidine				0.32	0.455
methyl 4-hydroxybenzoate				1.23	0.925	2-methylpyrimidine				0.67	0.873
ethyl 4-hydroxybenzoate				1.78	1.517	5-methylpyrimidine				0.95	0.941
methyl 2-hydroxybenzoate				3.15	3.165	2-fluoropyrimidine				0.85	0.865
ethyl 2-hydroxybenzoate				3.91	3.812	5-fluoropyrimidine				0.89	0.891
2-hydroxybenzamide				0.62	0.538	2-chloropyrimidine				1.16	1.197
4-hydroxy-3-methoxybenzaldehyde				1.42	1.501	5-chloropyrimidine				1.43	1.398
4-hydroxypropriophenone				0.71	0.692	2-bromopyrimidine				1.35	1.328
4-hydroxyacetanilide				–1.60	–1.552	5-bromopyrimidine				1.65[l]	1.586
1-naphthol	5.63	7.13	7.272	1.50	1.764	2-methoxypyrimidine				1.28	1.173
2-naphthol	5.95	7.69	7.423	1.74	1.617	2-ethoxypyrimidine				1.77	1.68
benzyl alcohol	4.86	5.82	5.801	0.96	0.783	5-ethoxypyrimidine				1.59	1.513
4-methylbenzyl alcohol				1.83	1.233	methyl 2-pyrimidinecarboxylate				0.73	0.638
2-hydroxybenzyl alcohol				–0.51	–0.378	methyl 5-pyrimidinecarboxylate				1.55	1.419
2-phenylethanol	4.98	6.29	6.33	1.31	1.371	ethyl 2-pyrimidinecarboxylate				1.13	1.038
ephidrine				1.10	1.346	antipyrine				1.45[l]	1.358
thiophenol	1.87	5.58	4.855	3.71	3.022	*N*,*N*-dimethylpiperazine				–0.20[l]	0.525
phenyl methyl sulfide	2.00	4.38		2.38	3.38	1,2,4-triazole				–2.42[l]	–2.295

Table 2—(Continued)

compound name	log L^{Wa}	log L^{chlb} obsd	log L^{chlb} calcd	log $P_{chl}{}^{c}$ obsd	log $P_{chl}{}^{c}$ calcd	compound name	log L^{Wa}	log L^{chlb} obsd	log L^{chlb} calcd	log $P_{chl}{}^{c}$ obsd	log $P_{chl}{}^{c}$ calcd
purine				–1.95	–1.858	thiophene	1.04	4.22	3.447	3.18	2.383
adenine				–2.48	–2.363	thiazole				1.03	1.116
morpholine	5.26	4.93	5.393	–0.33	–0.207	digitoxin				2.40	2.481
N-methylmorpholine	4.64	5.10	5.341	0.46	0.614	phenylurea				–0.68	–0.655
scopolamine				1.64	1.734	1-phenyl-3,3-dimethylurea				1.29[l]	1.138
uracil				–1.70	–1.628	barbituric acid				–2.10	–2.026
1,3-dimethyluracil				0.52[l]	0.442	5-methyl-5-ethylbarbituric acid				–0.72	–0.325
theophylline				–0.48[l]	–1.269	5,5-diethylbarbituric acid				–0.15[l]	0.246
theobromine				–0.43[l]	–1.279	5-ethyl-5-propylbarbituric acid				0.30	0.836
caffeine				1.23	1.079	5-ethyl-5-(2-pentyl)barbital				1.59	1.857
guanine				–3.25	–3.122	5-allyl-5-ethylbarbital				0.64	0.302
codeine				2.20	1.918	5-ethyl-5-phenylbarbital				0.65	0.721

[a] Observed values from refs 24 and 25 unless otherwise shown. Calculated values on eq 6. [b] Observed values obtained from log L^{W} and log P_{chl} unless otherwise shown. Calculated values on eq 9. [c] Directly determined values from ref 21 unless otherwise shown. [d] Solubility Data Project Series. [e] From log L^{chl} and log L^{W}. [f] Thomas, E. R., Newman, B. A., Nicolaider, G. L., Eckert, C. A. *J. Chem. Eng. Data* **1982**, *27*, 233. [g] Park, J. H., Hussam, A., Cousanon, P., Fritz, D., Carr, P. W. *Anal. Chem.* **1987**, *59*, 1970. [h] Gerrard, W. *J. Appl. Chem. Biotechnol.* **1972**, *22*, 623. [i] Dohnal, V., Vrbka, P. *Fluid Phase Equilib.* **1990**, *54*, 121. [j] Taking $\gamma^{inf} = 1$. [k] *Trans. Faraday Soc.* **1957**, *53*, 607. [l] This work. [m] See footnote c. [n] Phillippe, R., Jose, J., Clechet, P. *Bull. Soc. Chim. Fr.* **1971**, 2866. [o] Abraham, M. H. Unpublished results.

Table 3—Descriptors for Some Solutes

solute	*R*	π	α	β	V_x
9-fluorenone	1.37	0.91	0.00	0.63	1.3722
acetanilide	0.87	1.36	0.46	0.69	1.1137
phthalimide	1.18	2.09	0.40	0.42	1.0208
ephidrine	0.92	0.65	0.20	1.24	1.4385
atropine	1.19	1.94	0.36	1.64	2.2820
1,2,4-triazole	0.72	0.98	0.60	0.77	0.4952
scopoloamine	1.07	1.45	0.28	0.71	2.2321
caffeine	1.50	1.60	0.00	1.33	1.3632
codeine	1.78	1.95	0.33	1.78	2.2057
digitoxin	4.50	5.60	1.47	4.52	5.6938

log L^{chl} values, because the values of log L^{w} required in order to obtain log L^{chl} from log P_{chl} via eq 2 were unavailable. Descriptors for most of the compounds have been published before,[19,20,24,26–45] but some new values are in Table 3.

Analysis of log L^{chl}—The 150 values of log L^{chl} in Table 2 cover quite a good range of compound type, from inorganic gases such as hydrogen to organic molecules such as triethyl phosphate and benzamide, with a total range of 9.4 log units in log L^{chl}. When regressed according to eq 4, the 150 log L^{chl} values yielded the statistically very good eq 6, considering that the experimental uncertainty in log L^{chl} must be not less than 0.1 log units. The calculated log L^{chl} values from eq 6 are given in Table 2.

$$\log L^{chl} = \underset{3.19}{0.168} - \underset{-6.46}{0.595} R_2 + \underset{14.13}{1.256}\pi_2^{H} + \underset{3.45}{0.280}\Sigma\alpha_2^{H} + \underset{14.39}{1.370}\Sigma\beta_2^{H} + \underset{41.82}{0.981}\log L^{16} \quad (6)$$

$$n = 150,\ \mathrm{sd} = 0.23,\ r^2 = 0.985,\ r^2_{cv} = 0.984,\ F = 1919$$

In eq 6, r^2_{cv} is the cross-validated squared correlation coefficient; the *t*-ratio for each coefficient is given below the coefficient. The correlation matrix in r^2 is given below,

	R_2	π_2^{H}	$\Sigma\alpha_2^{H}$	$\Sigma\beta_2^{H}$
π_2^{H}	0.591			
$\Sigma\alpha_2^{H}$	0.051	0.108		
$\Sigma\beta_2^{H}$	0.005	0.042	0.006	
log L^{16}	0.677	0.599	0.077	0.019

There are three pairs of coefficients that have rather high cross-correlations, but it must be stressed that we have not designed the data set; we have had to use the available data. The sd value of only 0.23 log units suggests that eq 6 could be useful for the estimation of further values of log L^{chl}. However, the importance of eq 6 lies also in the information that can be extracted from the coefficients in the equation. As outlined above, these coefficients are related to definite chemical properties of the condensed solvent phase. To put these coefficients in context, especially the *b*-coefficient, we summarize in Table 4 the corresponding coefficients for some other solvent phases.[24,43–45] The *r*-coefficient in eq 6 is not exceptional and seems to be related, at least in part, to lone pair–lone pair repulsion. The *s*-coefficient is a measure of the solvent dipolarity/polarizability; the rather large coefficient for chloroform is clearly due to polarizability effects, just as for 1,2-dichloroethane. The *a*-coefficient, a measure of solvent hydrogen-bond basicity, is very low, as expected, but the *b*-coefficient indicates that bulk chloroform can act as a hydrogen-bond acid. However, the magnitude of the *b*-coefficient (1.37) is of the same order as that for methanol (1.43)[46] and ethanol (1.31)[47] solvents, so that to external solutes chloroform is as strong a hydrogen-bond acid as are the alcohols. We give in Table 5 some previous measures of the hydrogen-bond acidity of bulk chloroform; the acceptor number (AN),[49] the solvatochromic α-value,[50,51] and the enthalpic $\Delta_{acid}H$ scale.[51] None of these scales ranks

Table 4—Coefficients in Eq 4 for the Solubility of Gases and Vapors in Solvents, as log *L* Values at 298 K

solvent	*c*	*r*	*s*	*a*	*b*	*l*
chloroform	0.17	–0.60	1.26	0.28	1.37	0.981
water[24]	–1.27	0.82	3.74	3.90	4.80	–2.13
methanol[46]	0.00	–0.22	1.17	3.70	1.43	0.769
ethanol[47]	0.01	–0.21	0.79	3.63	1.31	0.853
1,2-dichloroethane[48]	0.01	–0.15	1.44	0.65	0.74	0.936
benzene[48]	0.11	–0.31	1.05	0.47	0.17	1.020
hexadecane	0.00	0.00	0.00	0.00	0.00	1.000

Table 5—Some Measures of the Hydrogen-Bond Acidity of Solvents

solvent	AN[49]	α^{49}	α^{50}	α^{51}	$\Delta_{acid}H^{51}$	*b*[a]
water	54.8	1.17	1.17	1.16	–10.60	4.81
methanol	41.3			1.09	–11.15	1.43
ethanol	37.1	0.86	0.83	0.88	–9.14	1.31
chloroform	23.1	0.20	0.44		–5.60	1.37
cyclohexane	0.0	0.00	0.00	0.00	2.10	0.00

[a] The *b*-coefficient in eq 4.

Table 6—Factors That Influence the Solubility of Gases and Vapors in Chloroform and in Water at 298 K

solute	rR_2	$s\pi_2^H$	$a\Sigma\alpha_2^H$	$b\Sigma\beta_2^H$	l log L^{16} cav	disp	total[a]
			Solvent Chloroform				
methane	0.00	0.00	0.00	0.00	–2.38	2.06	–0.15
ethanol	–0.15	0.53	0.10	0.66	–3.31	4.77	2.77
butanone	–0.10	0.88	0.00	0.70	–4.19	6.43	3.89
hexane	0.00	0.00	0.00	0.00	–4.85	7.47	2.79
			Solvent Water				
methane	0.00	0.00	0.00	0.00	–4.04	4.11	–1.34
ethanol	0.20	1.15	1.44	2.31	–5.81	5.49	3.51
butanone	0.14	1.92	0.00	2.46	–7.50	7.01	2.76
hexane	0.00	0.00	0.00	0.00	–8.78	8.21	–1.84

[a] This includes the constant 0.168 in eq 6 and –1.271 in eq 7. Observed values are in chloroform 2.80 (ethanol), 3.87 (butanone) and 2.87 (hexane) and in water –1.46 (methane), 3.67 (ethanol), 2.72 (butanone), and –1.82 (hexane).

chloroform as acidic as alcohols, although it must be noted that only the $\Delta_{acid}H$ scale is based on a thermodynamic property, the enthalpy, in contrast to the *b*-coefficient that is related to Gibbs energy. The *l*-coefficient in eq 4 can be regarded as a measure of the solvent hydrophobicity; chloroform is not exceptional, with an *l*-coefficient close to those for benzene or hexadecane.

From the coefficients of eq 6 and solute descriptors, it is possible to dissect the observed log L^{chl} value for any given solute into contributions from the various terms in eq 6. However, the l log L^{16} term includes two opposing effects: (i) an endoergic cavity term that arises through disruption of solvent−solvent interactions, and which will make a negative contribution to l log L,[16] and (ii) an exoergic term due to London dispersion solute−solvent interactions, and which will make a positive contribution to l log L.[16] Indeed, as we have pointed out,[24,32,52] the London interaction term is nearly always larger than any specific solute−solvent interaction involving nonionic solutes.

We can make some headway by calculating the cavity term using scaled particle theory (SPT),[53] and then obtaining the London dispersion term by difference. Even an approximate estimation will suffice to show general trends, and as noted before,[13] there may be a number of possible divisions of experimental log L values into various contributions. To apply SPT we need to know the solvent hard-sphere diameter, σ_1, and Lennard−Jones potential, ϵ_1/k. We calculated these from log L^{chl} for nonpolar solutes, as indicated before,[54] and obtained values of 4.80 Å and 320 K, respectively. Then taking σ_2 as 3.82 (methane), 6.03 (hexane), 4.75 (ethanol), and 5.51 (butanone) for representative solutes, we can calculate the cavity term (Cav) and deduce the dispersion term (Disp) as [Disp = l log L^{16} − Cav]. For comparison, we have done the same for solvent water using eq 7,[24] with σ_1 taken as 2.77 Å.[53] Results are in Table 6. Note that our calculation refers to the separation of cavity and dispersion effects in the l log L^{16} term only. The constant term, which is appreciably more negative for solvent water than for any nonaqueous solvent, may also contain some cavity/dispersion contribution.

$$\log L^{w} = -1.271 + 0.822R_2 + 2.743\pi_2^H + 3.904\Sigma\alpha_2^H + 4.814\Sigma\beta_2^H - 0.213 \log L^{16} \quad (7)$$

In chloroform, the solute−solvent dispersion term, that increases with increase in solute size, outweighs the various specific interaction terms. This is not unique to chloroform solvent, but is the case for all the nonaqueous solvents we have investigated. The specific interaction terms merely discriminate between solutes of about the same size and hence of about the same cavity/dispersion effect. Thus butanone is more soluble than hexane, even though it is somewhat smaller. In any homologous series, with a constant functionality, log L^{chl} increases with carbon number because the positive dispersion effect increases faster than the negative cavity effect. However log L^{w} decreases along any homologous series because the positive dispersion effect now increases slower than the cavity effect.

In summary, application of the MLR eq 4 to the 150 log L^{chl} values yields eq 6 that can be used for the prediction of further values and can be used to quantify the various solute and solvent factors that influence the magnitude of log L^{chl}.

Analysis of log P_{chl}—Table 2 contains 335 values of log P_{chl}, enough to divide into a training set and a test set for the purpose of assessing the predictive capability of any MLR equation. We arbitrarily removed 10% of all the log P_{chl} values to leave 302 as a training set. Application of eq 5 to this set yielded eq 8, where again the *t*-scores are given below the coefficients.

$$\log P_{chl} = \underset{5.87}{0.321} + \underset{2.59}{0.168}R_2 - \underset{-5.94}{0.379}\pi_2^H - \underset{-52.04}{3.170}\Sigma\alpha_2^H - \underset{-52.00}{3.409}\Sigma\beta_2^H + \underset{59.10}{4.149}V_X \quad (8)$$

$$n = 301,\ \text{sd} = 0.28,\ r^2 = 0.965,\ r^2_{cv} = 0.963,\ F = 1635$$

The correlation matrix for eq 8 is,

	R_2	π_2^H	$\Sigma\alpha_2^H$	$\Sigma\beta_2^H$
π_2^H	0.539			
$\Sigma\alpha_2^H$	0.077	0.067		
$\Sigma\beta_2^H$	0.075	0.234	0.004	
V_X	0.312	0.278	0.010	0.251

The statistics of eq 8 are not as good as those for many other water−solvent partitions,[19] but we have already referred to the difficulty of the experimental measurement of log P_{chl} values. The predictive capability of eq 8 can be assessed by the calculation of log P_{chl} for the 34 compounds left out as a test set. These are in Table 7 together with the predicted and observed values of log P_{chl}. Over a range of 6 log units in log P_{chl} the sd between predicted and observed values is only 0.17 log unit; the average unsigned error is 0.13 log unit, and the average signed error is −0.03 log unit. As shown in Figure 1, there are no systematic deviations. None of the other computational or calculational methods summarized in Table 1 employed a test set of compounds to estimate predictive power, so that comparisons are not possible.

Once the predictive power of eq 8 is established, we can use all the available data to construct eq 9. The differences between eq 8 and eq 9 are marginal, but the latter equation is preferred since it covers more compounds, with log P_{chl} covering a range of over nine log units, from −3.25 (guanine) to 6.01 (octane). The calculated values of log P_{chl} on eq 9 are given in Table 2.

$$\log P_{chl} = \underset{8.57}{0.327} + \underset{2.86}{0.157}R_2 - \underset{-7.17}{0.391}\pi_2^H - \underset{-61.93}{3.191}\Sigma\alpha_2^H - \underset{-61.23}{3.437}\Sigma\beta_2^H + \underset{72.40}{4.191}V_X \quad (9)$$

$$n = 335,\ \text{sd} = 0.25,\ r^2 = 0.971,\ r^2_{cv} = 0.970,\ F = 2223$$

The correlation matrix of eq 9 is very similar to that of eq 8. The interpretation of eq 9 follows closely that of eq 6,

Table 7—Predicted Values from Eq 8 and Observed Values of log P_{chl} for the 33 Compound Test Set

compound	predicted	observed
cyclohexane	3.87	4.16
bromoethane	2.18	2.24
propyl acetate	2.28	2.56
ethyl trifluoroacetate	1.94	2.00
diethylamine	0.85	0.79
formic acid	–2.03	–2.12
hexanoic acid	0.98	1.02
2-methylpropan-2-ol	0.26	–0.02
propane-1,3-diol	–2.60	–2.90
triethyl phosphate	2.14	2.28
fluorobenzene	2.90	2.54
benzaldehyde	2.38	2.25
dimethyl phthalate	2.86	3.09
aniline	1.28	1.35
1-naphthylamine	2.46	2.60
4-nitroanisole	3.16	3.18
phthalimide	1.25	1.46
2-bromobenzoic acid	0.96	0.91
4-aminobenzoic acid	–0.88	–0.92
3-phenylpropanoic acid	1.16	1.20
2-ethylphenol	1.63	1.73
2-iodophenol	2.00	1.97
2-nitrophenol	2.62	2.53
methyl 2-hydroxybenzoate	3.16	3.15
benzyl alcohol	0.79	0.96
methyl phenyl sulfone	1.93	1.93
3-methylbenzenesulfonamide	0.42	0.32
2-bromopyridine	2.37	2.22
quinoline	2.66	3.14
pyrazine	0.62	0.59
2-(dimethylamino)pyrimidine	1.91	1.99
5-chloropyrimidine	1.39	1.43
antipyrine	1.37	1.45
digitoxin	2.56	2.40

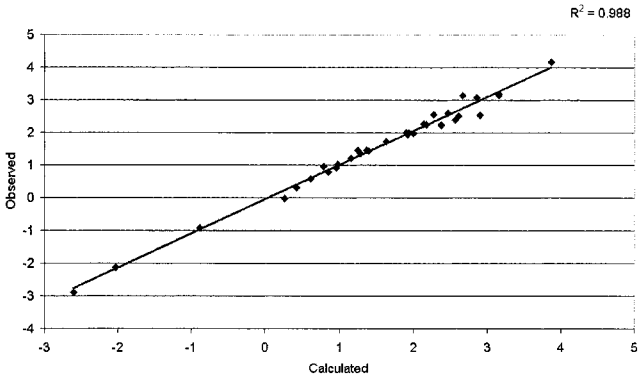

Figure 1—A plot of observed log P_{chl} vs predicted log P_{chl} values on eq 8.

except that now the coefficients refer to differences in properties of chloroform and water. A comparison with coefficients for other water–solvent partitions[19,20] is in Table 8. The *c*- and *r*-coefficients are not exceptional. The *s*-coefficient refers to the difference in dipolarity/polarizability of chloroform and water; a value of −0.39 places chloroform between CCl_4 (−1.15) and 1,2-dichloroethane (0.00) or dichloromethane (0.02). The hydrogen-bond basicity of bulk chloroform, as indicated by eq 6, is very small; hence, the *a*-coefficient in eq 9 is very negative (−3.19) and approaches that for the systems with nonbasic solvents such as hexadecane, cyclohexane, and CCl_4. In view of our discussion, above, on the hydrogen-bond acidity of chloroform, the *b*-coefficient in eq 9 is of some interest. A value of −3.43 places chloroform as acidic as wet octanol (−3.46), exactly in line with the *b*-coefficients in Table 4, and much more acidic than dichloromethane ($b = -4.14$) or 1,2-dichloroethane ($b = -4.29$). The *v*-coefficient in eq 5, just as the *l*-coefficient in eq 4, can be regarded as a measure of the solvent hydrophobicity. Chloroform is no different to most non-hydroxylic solvents which have *v*-coefficients between 4.2 and 4.6 units.

Table 8—Coefficients in Eq 5 for Water–Solvent Partitions

solvent	*c*	*r*	*s*	*a*	*b*	*v*
hexadecane[a]	0.09	0.67	–1.62	–3.59	–4.87	4.43
cyclohexane[a]	0.13	0.82	–1.73	–3.78	–4.90	4.65
benzene[b]	0.02	0.49	–0.60	–3.01	–4.63	4.59
nitrobenzene[b]	–0.18	0.58	0.00	–2.36	–4.42	4.26
decanol, wet[c]	0.01	0.48	–0.97	0.02	–3.80	3.95
octanol, wet[a]	0.09	0.56	–1.05	0.03	–3.46	3.81
isobutanol, wet[c]	0.23	0.51	–0.69	0.02	–2.26	2.78
olive oil[d]	0.01	0.58	–0.80	–1.47	–4.92	4.17
dibutyl ether[d]	0.18	0.82	–1.50	–0.83	–5.09	4.69
CCl_4[b]	0.22	0.56	–1.15	–3.51	–4.54	4.50
1,2-dichloroethane[b]	0.16	0.12	0.00	–3.05	–4.29	4.30
dichloromethane	0.31	0.00	0.02	–3.24	–4.14	4.26
chloroform	0.32	0.16	–0.39	–3.19	–3.43	4.19

[a] Reference 43. [b] Reference 19a. [c] Reference 48. [d] Reference 20.

Table 9—Calculated and Observed log P_{chl} Values for Some Solutes Previously Studied

solute	calcd[11a]	calcd[11b]	calcd[14]	calcd[13c]	calcd[d]	obsd[e]
$MeNH_2$	–0.56	–0.35	–0.33	–1.2	–0.88	–1.02
Me_2NH			0.85		–0.27	–0.44
Me_3N			2.25		0.61	0.51
Et_2NH	2.79	2.09		1.4	0.86	0.79
benzene	4.30	3.20	2.71	2.8	2.78	2.76
MeOAc			0.33		1.08	1.16
4-hexylpyridine	5.38	3.99		4.7	4.47[f]	5.00[g]

[a] Untrained computations. [b] Trained computations. [c] SM5.4P; the SM5.4A results are very similar. [d] On eq 9, this work. [e] Table 2. [f] Not part of the 335 data set. [g] Not corrected for salting-out; see text.

Table 10—Calculated and Observed log P_{chl} Values for Solutes Not Included in Eq 9

solute	calcd[a]	calcd[b]	obsd
hydroquinone	–2.18	–1.54	0.23
cocaine	4.26	6.67	1.21
hydrocortisone	2.21	3.67	0.81

[a] This work. [b] As in ref 13 (see text).

It is possible to analyze eq 9 term-by-term in order to quantify the particular interactions leading to log P_{chl} values for a given solute, just as we have done for log L^{chl} in Table 6, but the arithmetic is trivial. We conclude by examining a number of solutes for which log P_{chl} has not been well calculated by previous methods or by eq 9. The experimental values of log P_{chl} for aliphatic amines have been questioned[11,14] on the grounds that protonation in the aqueous phase could lead to erroneously low values. In Table 9 we collect observed and calculated log P_{chl} values for the aliphatic amines noted before. Values calculated through eq 9 are in good agreement with the observed values, and in our view the experimental log P_{chl} values must be substantially correct. Other workers[13] also calculate values reasonably close to those observed. Values of log P_{chl} for benzene[11] and methyl acetate[14] are also poorly computed, Table 9, but again our procedure suggests that the observed values are correct. We did find that there were three log P_{chl} values that were considerable outliers to eq 9, and which we omitted in the regression analysis; these outliers are shown in Table 10.

We can check our descriptors for hydroquinone, because values of log *P* are available[21] for many water–solvent partition systems for which we have[19] the coefficients in

Table 11—Water-Solvent Partitions (*P*) and HPLC Capacity Factors (*k′*) for Hydroquinone

solvent	log *P* or log *k′* obsd	calcd[a]	calcd[b]
octanol (*P*)	0.59	0.77	0.58
isobutanol (*P*)	0.82	0.99	0.88
hexanol (*P*)	0.74	1.00	0.81
cyclohexane (*P*)	–3.97[c]	–4.19	–4.11
toluene (*P*)	–2.15	–2.61	–2.37
heptane (*P*)	–4.26[d]	–4.07	–4.00
diethyl ether (*P*)	0.39[e]	0.34	0.18
dibutyl ether (*P*)	–0.77	–0.55	–0.73
diisopropyl ether (*P*)	0.02[f]	0.15	–0.03
ethyl acetate (*P*)	0.79	0.88	0.61
butyl acetate (*P*)	0.66[g]	0.88	0.85
1,2-dichloroethane (*P*)	–1.61[h]	–2.00	–1.64
tetrachloromethane (*P*)	–3.30[i]	–3.38	–3.21
ref 67, 50% methanol (*k′*)	–0.84	–0.43	–0.55
ref 67, 75% methanol (*k′*)	–1.42	–1.03	–1.09
ref 68, 60% methanol (*k′*)	–1.11	–0.94	–0.99
ref 68, 75% methanol (*k′*)	–1.46	–1.28	–1.31
ref 68, 90% methanol (*k′*)	–1.81	–1.42	–1.52
ref 69, Column B (*k′*)	–1.10	–1.15	–1.09
ref 70, Column A (*k′*)	–0.60	–0.56	–0.55
ref 70, Column B (*k′*)	–0.62	–0.60	–0.58
ref 70, Column C (*k′*)	–0.77	–0.72	–0.71
ref 46a, 40% methanol (*k′*)	–0.51	–0.38	–0.47
ref 46a, 50% methanol (*k′*)	–0.57	–0.54	–0.60
ref 46a, 60% methanol (*k′*)	–0.70	–0.66	–0.73
ref 46a, 60% methanol (*k′*)	–0.75	–0.79	–0.85
ref 46a, 80% methanol (*k′*)	–0.75	–0.87	–0.92
ref 46a, 30% acetonitrile (*k′*)	–0.46	–0.45	–0.47
ref 46a, 40% acetonitrile (*k′*)	–0.37	–0.50	–0.52
ref 46a, 50% acetonitrile (*k′*)	–0.46	–0.62	–0.63
ref 46a, 60% acetonitrile (*k′*)	–0.60	–0.69	–0.71
ref 46a, 70% acetonitrile (*k′*)	–0.69	–0.79	–0.80
ref 46a, 80% acetonitrile (*k′*)	–0.85	–0.85	–0.87
sd ($n = 33$):		0.20	0.15
benzene (*P*)	0.15		
benzene (*P*)	–1.85	–2.58	–2.29
benzene (*P*)	–2.16		
chloroform	0.23	–2.18	–1.84

[a] With original descriptors: $R_2 = 1.063$, $V_x = 0.8338$, $\pi_2^H = 1.00$, $\Sigma\alpha_2^H = 1.16$, and $\Sigma\beta_2^H = 0.60$. [b] With "best value" descriptors: $R_2 = 1.063$, $V_x = 0.8338$, $\pi_2^H = 1.25$, $\Sigma\alpha_2^H = 1.05$, and $\Sigma\beta_2^H = 0.58$. [c] Average of –3.89 and –4.04. [d] Average of –4.24 and –4.28; another value is 0.05. [e] Average of 0.36, 0.37, 0.38, and 0.46. [f] Average of –0.13, 0.01, 0.01, and 0.20. [h] Another value is 0.32. [i] Another value is 0.04.

eq 5 (log SP = log *P*). In addition, values of the HPLC capacity factor, *k′*, are known for hydroquinone in systems for which we have again the coefficients in eq 5 (logSP = log *k′*), see Table 11.[37a,57–59] Our original descriptors for hydroquinone reproduce the log *P* and log *k′* values for 33 systems with an sd of 0.20 units. We can calculate the set of descriptors that best reproduces the 33 log *P* and log *k′* values, with an sd value of only 0.15 units, but there is not much difference between the two sets of descriptors, Table 11. In either case, the calculated log P_{chl} value (−2.18 and −1.84) is over two log units smaller than the observed value (0.23). We have to conclude that the experimental value is in error. Such discrepancies are not uncommon, thus log *P* for hydroquinone in water−benzene is given[21] as −2.16, −1.85, and 0.15, and log *P* in water−heptane is given as −4.28, −4.24, and 0.05!

In the case of cocaine, only six log *P* values are available[21] as a check. Our present descriptors reproduce these with an sd value of 0.45 units, and the best fit we can obtain still results in an sd value of 0.38 units, see Table 12. However, either set of descriptors leads to a calculated log

Table 12—Water–Solvent Partitions for Cocaine

solvent	log *P* obsd	calcd[a]	calcd[b]
octanol	2.30	2.40	2.43
diethyl ether	1.52[c]	1.54	1.80
diisopropyl ether	1.19	1.50	1.68
olive oil	2.33	1.44	1.85
ethyl acetate	2.00	2.07	1.97
hexane	0.91	0.60	0.54
sd		0.45	0.38
chloroform	1.21[d]	4.26	4.63

[a] With original descriptors: $R_2 = 1.355$, $V_x = 2.2977$, $\pi_2^H = 1.92$, $\Sigma\alpha_2^H = 0.00$, and $\Sigma\beta_2^H = 1.50$. [b] With "best value" descriptors: $R_2 = 1.355$, $V_x = 2.2977$, $\pi_2^H = 2.44$, $\Sigma\alpha_2^H = 0.00$, and $\Sigma\beta_2^H = 1.33$. [c] Average of values 1.15, 1.28, and 2.14. [d] Average of values 1.04 and 1.38.

Table 13—Water–Solvent Partitions (*P*) and HPLC Capacity Factors (*k′*) for Hydrocortisone

solvent	log *P* or log *k′* obs	calc[a]	calc[b]
octanol (*P*)	1.68[c]	1.67	1.60
isobutanol (*P*)	1.74	2.33	2.24
diethyl ether (*P*)	0.16[d]	0.35	–0.06
ethyl acetate (*P*)	1.09	0.98	1.06
benzene (*P*)	–0.49	0.61	–0.46
ref 67 50% methanol (*k′*)	0.69	0.57	0.60
ref 67 75% methanol (*k′*)	–0.31	–0.49	–0.48
ref 71 IAM column (*k′*)	0.94	1.05	0.99
sd		0.49	0.22
hexadecane (*P*)	–2.04	–3.60	–4.09
chloroform (*P*)	0.81	2.21	1.27

[a] With original descriptors: $R_2 = 2.03$, $V_x = 2.7976$, $\pi_2^H = 3.49$, $\Sigma\alpha_2^H = 0.71$, and $\Sigma\beta_2^H = 1.90$. [b] With "best value" descriptors: $R_2 = 2.03$, $V_x = 2.7976$, $\pi_2^H = 2.77$, $\Sigma\alpha_2^H = 0.85$, and $\Sigma\beta_2^H = 2.13$. [c] Average of 1.53 and 1.81. [d] Average of 0.11, 0.15, 0.18, and 0.21.

P_{chl} value over 3 log units greater than that recorded.[21] We have no explanation other than that the experimental value is in error. It is worth noting that lipophilic strong bases are very difficult to study by the "shake-flask" method.

The number of water−solvent log *P* values for hydrocortisone is surprisingly small, but a few log *k′* values are available in calibrated HPLC systems,[57,60] see Table 13. Our usual descriptors lead to an sd value of 0.49 units, rather large but not unreasonable, and to a discrepancy of 1.4 log units in log P_{chl}. We can define a set of descriptors that leads to an sd value of 0.22 for the same eight systems and to a smaller discrepancy of only 0.45 log units in log P_{chl}. It is thus possible that in the case of hydrocortisone there is some error in the experimental log P_{chl} value combined with errors in our assigned descriptors.

In an attempt to resolve these problems, Dr. Cramer kindly calculated log P_{chl} for the three outliers using his computational method.[13] Results are in Table 10. They seem to confirm our suggestion that the three experimental values are in error.

Finally, we can find no evidence for the suggestion[14] that water-saturated chloroform may behave differently to dry chloroform as a partitioning medium. Other workers[13] also regard water-saturated and dry chloroform to be essentially the same as solvating media.

Care must be taken over experimental values, however. A case in point is 4-hexylpyridine with a calculated value of log P_{chl} as 3.99 with a trained computation,[11] as compared to an observed value of 5.00 log units. This latter value does not refer to water−chloroform partition, but to partition between 1 M sodium chloride and chloroform. Correction for the salting-out effect would lower the value

by 0.15 to 0.55, leading to an "experimental" value of 4.85 to 4.45, more in line with the computational value of 3.99,[11] and in good agreement with another computational value[13] of 4.7 and our calculated value of 4.47 through eq 9.

Our data set of 335 compounds therefore leads to a MLR eq 9 that from a training set of 301 compounds seems capable of predicting further log P_{chl} values with sd = 0.17. Equation 9 can also be used to analyze the solute and solvent interactions that affect log P_{chl}, with results almost identical to those obtained by an analysis of log L^{chl} through eq 6. The importance of these results lies in the recent use of the water−chloroform system as a measure of solute lipophilicity,[5,6,11,12] and of recent calculations of the transfer of nucleic acids from water to chloroform.[9,61] The nucleic acid transfers have been analyzed in terms of functional group contributions,[61] but a breakdown into contributions due to dipolarity/polarizability, hydrogen-bond acidity, etc., through eq 9, leads to more information as to the exact solute influences on the water−chloroform partitions.

Furthermore, if the water−chloroform system is to be generally used as a measure of solute lipophilicity in drug design, it will be of very considerable help to have a predictive procedure available. We have shown, see Table 1, that the MLRA method is capable of correlating log P_{chl} values rather better than computational methods, although the present MLRA method suffers from the possible lack of availability of the required descriptors. Recently, we have remedied this deficiency through a simple method (ABSOLVE) for the calculation of descriptors from structure.[62] Together with eq 6 and eq 9 the ABSOLVE method will enable log L_{chl} and log P^{chl} to be predicted from structure.

References and Notes

1. (a) Hansch, C. A Quantitative Approach to Biochemical Structure−Activity Relationships. *Acc. Chem. Res.* **1969**, *2*, 232−239. (b) Hansch, C. Quantitative Structure−Activity-Relationships and the Unnamed Science. *Acc. Chem. Res.* **1993**, *20*, 147−153. (c) Meyer, P.; Maurer, G. Correlation and Prediction of Partition Coefficients of Organic Solvents between Water and an Organic Solvent with a Generalized Form of the Linear Solvation Energy Relationship. *Ind. Eng. Chem. Res.* **1995**, *34*, 373−381.
2. (a) Hansch, C.; Maloney, P. P.; Fujita, T.; Muir, R. M. Correlation of Biological Activity of Phenoxyacetic Acids with Hammett Substituent Constants and Partition Coefficients. *Nature (London)* **1962**, *194*, 178−180. (b) Leo, A. Calculating log *P*(oct) from Structures. *Chem. Rev.* **1993**, *30*, 1283−1306.
3. *Lipophilicity in Drug Action and Toxicology*; Pliska, V., Testa, B., van de Waterbeemd, H., Eds.; VCH: Weinheim, 1996.
4. (a) Overton, E. *Studien uber die Narkose*; Fischer: Jena, Germany, 1901. (b) Macy, R. Partition Coefficients of Fifty Compounds between Olive Oil and Water at 20 °C. *J. Indust. Hygiene Toxicol.* **1948**, *30*, 140−143. (c) Ren, S.; Das, A.; Lien, E.J. QSAR Analysis of Membrane Permeability to Organic Compounds. *J. Drug Targeting* **1996**, *4*, 103.
5. Caron, G.; Carrupt, P.-A.; Testa, B.; Ermondi, G.; Gasco, A. Insight Into the Lipophilicity of the Aromatic *N*-Oxide Moeity. *Pharm. Res.* **1996**, *13*, 1186−1190.
6. Shih, P.; Pedersen, L. G.; Gibbs, P. R.; Wolfenden, R. Hydrophobicities of the Nucleic Acid Bases: Distribution Coefficients from Water to Cyclohexane. *J. Mol. Biol.* **1998**, *280*, 421−430.
7. (a) Leahy, D. E.; Morris, J. J.; Taylor, P. J.; Wait, A. R. Model Solvent Systems for QSAR. 3. An LSER Analysis of the Critical Quartet − New Light on Hydrogen Bond Strength and Directionality. *J. Chem. Soc. Perkin Trans. 2* **1992**, 705−722. (b) Leahy, D. E.; Morris, J. J.; Taylor, P. J.; Wait, A. R. Model Solvent Systems for QSAR. 2. Fragment Values for the Critical Quartet. *J. Chem. Soc., Perkin Trans. 2* **1992**, 723−731.
8. Dunn, W. J., III.; Koehler, M. G.; Grigoras, S. The Role of Solvent-Accessible Surface-Area in Determining Partition Coefficients, *J. Med. Chem.* **1987**, *30*, 1121−1126.
9. Orozco, M.; Colominas, C.; Luque, F. J. Theoretical Determination of the Solvation Free Energy in Water and Chloroform of the Nucleic Acid Bases. *Chem. Phys.* **1996**, *209*, 19−29.
10. Jorgensen, W. L.; Briggs, J. M.; Contreras, M. L. Relative Partition Coefficients for Organic Solutes from Fluid Simulations. *J. Phys. Chem.*, **1990**, *94*, 1683−1686.
11. Reynolds, C. H. Estimating Lipophilicity Using the GB/SA Continuum Solvation Model − a Direct Method for Computing Partition Coefficients. *J. Chem. Inf. Comput. Sci.* **1995**, *35*, 738−742.
12. Luque, F. J.; Zhang, Y.; Aleman, C.; Bachs, M.; Gao, J.; Orozco, M. Solvent Effects in Chloroform Solution: Parametrization of the MST/SCRF Continuum Model. *J. Phys. Chem.* **1996**, *100*, 4269−4276.
13. Giesen, D. J.; Chambers, C. C.; Cramer, C. J.; Truhlar, D. G. Solvation Model for Chloroform Based on Class IV Atomic Charges. *J. Phys. Chem. B* **1997**, *101*, 2061−2069.
14. McDonald, N. A.; Carlson, H. A.; Jorgensen, W. J. Free Energies of Solvation in Chloroform and Water from a Linear Response Approach. *J. Phys. Org. Chem.* **1997**, *10*, 563−576.
15. Solvation Gibbs energies are often calculated and then transformed into log P_{chl} values. For consistency we have converted Gibbs energies into values of log *L*, and all the errors and all the equations that we list refer to log *L* and log *P*.
16. Aqvist, J.; Mowbray, S. L. Sugar Recognition by a Glucose/Galactose Receptor − Evaluation of Binding Energetics from Molecular Dynamics Simulations. *J. Biol. Chem.* **1995**, *270*, 9978−9981.
17. The regression equation was forced through the origin, and hence the regression correlation coefficient has no meaning.
18. Marcus, Y. Linear Solvation Energy Relationships. Correlation and Prediction of the Distribution of Organic Solutes between Water and Immiscible Organic Liquids. *J. Phys. Chem.* **1991**, *95*, 8886−8891.
19. Abraham, M. H.; Chadha, H. S. In *Lipophilicity in Drug Action and Toxicology*; Pliska, V., Testa, B., van de Waterbeemb, H., Eds.; VCH: Weinheim, 1996; p 311.
20. Pagliara, A.; Caron, G.; Lisa, G.; Fan, W.; Gaillard, P.; Carrupt, P.-A.; Testa, B.; Abraham, M.H. Solvatochromic Analysis of di-*n*-Butyl Ether/Water Partition Coefficients as Compared to other Solvent Systems. *J. Chem. Soc., Perkin Trans. 2*, **1997**, 2639−2643.
21. MedChem Software, BioByte Corp., P. O.517, Claremont, CA 91711-0157.
22. (a) Solubility Data Project. (b) Park, J. H.; Hussam, A.; Cousanon, P.; Fritz, D.; Carr, P. W. Experimental Reexamination of Partition Coefficients from Rohrschneider Data Set. *Anal. Chem.* **1987**, *59*, 1970−1976.
23. (a) Thomas, E. R.; Newman, B. A.; Nicolaides, G. L.; Eckert, C. A. Limiting Activity Coefficients from Differential Ebulliometry. *J. Chem. Eng. Data* **1982**, *27*, 233−240. (b) Gerrard, W. Solubility of Hydrogen Sulphide, Dimethyl Ether, Methyl Chloride, and Sulfur Dioxide in Liquids. The Prediction of Solubility of All Gases. *J. Appl. Chem. Biotechnol.* **1972**, *22*, 623−650. (c) Dohnal, V.; Vrbka, P. Infinite-Dilution Activity-Coefficients by Comparitive Ebulliometry − Binary Systems of Chloromethanes, Chloroethanes and Freon-113. *Fluid Phase Equilib.* **1990**, *54*, 121−131.
24. Abraham, M. H.; Andonian-Haftvan, J.; Whiting, G. S.; Leo, A; Taft, R. W. Hydrogen Bonding 34. The Factors that Influence the Solubility of Gases and Vapours in Water at 298K, and a New Method for its Determination. *J. Chem. Soc., Perkin Trans. 2* **1994**, 1777−1791.
25. Cabani, S.; Gianni, P.; Mollica, V.; Lepori, L. Group Contributions to the Thermodynamic Properties of Non-Ionic Organic Solutes in Dilute Aqueous Solution. *J. Soln. Chem.* **1981**, *10*, 563−595.
26. Abraham, M. H. Scales of Solute Hydrogen Bonding − Their Construction and Application to Physicochemical and Biochemical Processes. *Chem. Soc. Rev.* **1993**, *22*, 73−83.
27. Abraham, M. H. Characterization of Some GLC Chiral Stationary Phases: LFER Analysis. *Anal. Chem.* **1997**, *69*, 613−617.
28. Abraham, M. H.; Walsh, D. P. Hydrogen Bonding 23. Application of the New Solvation Equation to logV(g) Values for Solvents on Carbonaceous Adsorbents. *J. Chromatogr.* **1992**, *627*, 294−299.
29. Abraham, M. H.; Weathersby, P. K. Hydrogen Bonding 30. Solubility of Gases and Vapours in Biological Liquids and Tissues. *J. Pharm. Sci.* **1994**, *83*, 1450−1456.
30. Abraham, M. H.; Whiting, G. S.; Doherty, R. M.; Shuely, W. J. Hydrogen Bonding 20. An Analysis of Polymer Probe Interactions in Some Hydrocarbon Polymers Using a new Solvation Equation. *Polymer* **1992**, *33*, 2162−2167.
31. Burg, Ph.; Selves, J.-L.; Colin, J. P. Numerical Simulation of Crude Oil Behaviour from Chromatographic Data, *Anal. Chim. Acta*, **1995**, *317*, 107−125.
32. Abraham, M. H.; Andonian-Haftvan, J.; Du, C. M.; Diart, V.; Whiting, G. S.; Grate, J. W.; McGill, R. A. Hydrogen Bonding 29. Characterization of 14 Sorbent Coatings for

Chemical Microsensors Using a New Solvation Equation. *J. Chem. Soc., Perkin Trans. 2* **1995**, 369−378.
33. Grate, J. W.; Abraham, M. H.; Du, C. M.; McGill, R. A.; Shuely, W. S. Examination of Vapor Sorption by Fullerene, Fullerene-Coated Surface-Acoustic-Wave Sensors, Graphite, and Low-Polarity Polymers Using Linear Solvation Energy Relationships. *Langmuir* **1995**, *11*, 2125−2130.
34. Abraham, M. H.; Kumarsingh, R.; Cometto-Muniz, J. E.; Cain, W. S. An Algorithm for Nasal Pungency Thresholds in Man. *Arch. Toxicol.* **1998**, *72*, 227−232.
35. Abraham, M. H.; Kumarsingh, R.; Cometto-Muniz, J. E.; Cain, W. S. Draize Eye Scores and Eye Irritation Thresholds in Man Combined into One Quantitative Structure−Activity Relationship. *Toxicol. In Vitro* **1998**, *12*, 403−408.
36. Abraham, M. H.; McGowan, J. C. The Use of Characteristic Volumes to Measure Cavity Terms in Reversed-Phase Liquid-Chromatography. *Chromatographia* **1987**, *23*, 243−246.
37. (a) Abraham, M. H.; Chadha, H. S.; Leo, A. J. Hydrogen Bonding 35. Relationship between High-Performance Liquid-Chromatography Capacity Factors and Water-Octanol Partition Coefficients. *J. Chromatogr.* **1994**, *685*, 203−211. (b) Jackson, P.T.; Schure, M.R.; Weber, T.P.; Carr, P.W. Intermolecular Interactions Involved in Solute Retention on Carbon Media in Reversed-Phase High-Performace Liquid-Chromatography. *Anal. Chem.* **1997**, *69*, 416−425.
38. Abraham, M. H.; Poole, C. F.; Poole, S. K. Solute Effects on Reversed-Phase Thin-Layer Chromatography: A Linear Free Energy Relationship Analysis. *J. Chromatogr. A* **1996**, *749*, 201−209.
39. Abraham, M. H.; Treiner, C.; Roses, M.; Rafols, C.; Ishihama, Y. Linear Free Energy Relationship Analysis of Microemulsion Electrokinetic Chromatographic Determination of Lipophilicity. *J. Chromatogr.* **1996**, *752*, 243−249.
40. Abraham, M. H.; Chadha, H. S.; Dixon, J. P.; Rafols, C.; Treiner, C. Hydrogen Bonding. Part 40. Factors that Influence the Distribution of Solutes between Water and Sodium dodecysulfate Micelles. *J. Chem. Soc., Perkin Trans. 2* **1995**, 887−894.
41. Poole, C. F.; Poole, S. K. Interphase Model for Retention and Selectivity in Micellar Electrokinetic Chromatography. *J. Chromatogr. A* **1997**, *792*, 89−104.
42. Abraham, M. H.; Rafols, C. Factors that Affect Tadpole Narcosis − an LFER Analysis. *J. Chem. Soc., Perkin Trans. 2* **1995**, 1843−1851.
43. Abraham, M. H.; Chadha, H. S.; Whiting, G. S.; Mitchell, R. C. Hydrogen Bonding 32. An Analysis of Water-Octanol and Water-Alkane Partitioning and the Δlog *P* Parameter of Seiler. *J. Pharm. Sci.* **1994**, *83*, 1085−1110.
44. Gratton, J. A.; Abraham, M. H.; Bradbury, M. W.; Chadha, H. S. Molecular Factors Influencing Drug Transfer Across the Blood-Brain Barrier. *J. Pharm. Pharmacol.* **1997**, *49*, 1211−1216.
45. Abraham, M. H.; Martins, F.; Mitchell, R. C. Algorithms for Skin Permeability Using Hydrogen Bond Descriptors: the Problem of Steroids. *J. Pharm. Pharmacol.* **1997**, *49*, 858−865.
46. Abraham, M. H.; Whiting, G. S.; Carr, P. W.; Ouyang, H. Hydrogen Bonding 45. The Solubility of Gases and Vapours in Methanol at 298K: an LFER Analysis. *J. Chem. Soc., Perkin Trans. 2* **1998**, 1385−1390.
47. Abraham, M. H.; Whiting, G. S.; Shuely, W. J.; Doherty, R. M. The Solubility of Gases and Vapours in Ethanol − the Connection between Gaseous Solubility and Water−Solvent Partition. *Canad. J. Chem.* **1998**, *76*, 703−709.
48. Abraham, M. H. Unpublished work.
49. Mayer, U. A Semiempirical Model for the Description of Solvent Effects on Chemical Reactions. *Pure Appl. Chem.* **1979**, *51*, 1697−1712.
50. Kamlet, M. J.; Abboud, J.-L. M.; Abraham, M. H.; Taft, R. W. Linear solvation Energy Relationships 23. A Comprehensive Collection of the Solvatochromic Parameters π^*, α, and β, and Some Methods for Simplifying the Generalized Solvation Equation. *J. Org. Chem.* **1983**, *48*, 2877−2887.
51. Catalan, J.; Gomez, J.; Saiz, J. L.; Couto, A.; Ferraris, M.; Laynez, J. Calorimetric Quantification of the Hydrogen Bond Acidity of Solvents and its Relationship with Solvent Polarity. *J. Chem. Soc., Perkin Trans. 2* **1995**, 2301−2305.
52. Abraham, M. H.; Whiting, G. S.; Shuely, W. J.; Doherty, R. M. Hydrogen Bonding 14. The Characterization of Some N-Substituted Amides as Solvents − Comparison with Gas−Liquid Stationary Phases. *J. Chem. Soc., Perkin Trans. 2* **1990**, 1851−1857.
53. Pierotti, R.A. A Scaled Particle Theory of Aqueous and Non-Aqueous Solvents. *Chem. Rev.* **1976**, *76*, 717−726.
54. Wilhelm, E.; Battino, R. Estimation of Lennard-Jones (6, 12) Pair Potential Parameters from Gas Solubility Data. *J. Chem. Phys.* **1971**, *55*, 4012−4017.
55. Hafkenschied, T. L.; Tomlinson, E. Isocratic Chromatographic Retention Data for Estimating Aqueous Solubilities of Acidic, Basic and Neutral drugs. *Int. J. Pharm.* **1983**, *17*, 1−21.
56. Hafkenshied, T.L. Influence of Mobile Phase Methanol Content and Solute Character on Relationships between Reversed-Phase Liquid-Chromatographic Retention and Hydrophobic-Lipophilic Parameters of Aromatic Compounds. *J. Chromatogr. Sci.* **1986**, *24*, 307−316.
57. Sugii, A.; Harada, K. Evaluation of Vinylpyridine and Vinylpyridinium Polymers as Column Packings for High-Performance Liquid-Chromatography. *J. Chromatogr.* **1991**, *544*, 219−232.
58. Szabo, G.; Csato, E.; Offenmuller, K.; Devai, M.; Borbely-Kuszmann, A.; Liptai, Gy. Preparation and Retention Characteristics of Different Phenyl Phases for Reversed-Phase Liquid-Chromatography. *Chromatographia* **1988**, *26*, 255−258.
59. Abraham, M. H.; Chadha, H. S.; Leitao, R.; Mitchell, R. C.; Lambert, W. J.; Kaliszan, R.; Nasal, A.; Haber, P. Determination of Solute Lipophilicity, as log *P*(octanol) and log *P*(alkane) Using poly(styrene-divinylbenzene) and Immobilised Artificial Membrane Stationary Phases in Reversed-Phase High-Performance Liquid-Chromatography. *J. Chromatogr. A* **1997**, *766*, 35−47.
60. Yeh, K. C.; Higuchi, W. I. Oil−Water Distribution of p-Alkylpyridines. *J. Pharm. Sci.* **1976**, *65*, 80−86.
61. Giesen, D. J.; Chambers, C. C.; Cramer, C. J.; Truhlar, D. G. *J. Phys. Chem. B* **1997**, *101*, 5084−5088.
62. Platts, J. A.; Butina, D.; Abraham, M. H.; Hersey, A. *J. Chem. Inf. Comput. Sci.*, in press.

Acknowledgments

This paper is dedicated to the memory of Robert W. Taft, a friend and colleague, who made outstanding contributions in physical organic chemistry, and who, with Mortimer J. Kamlet, pioneered the study of linear solvation energy relationships. One of us (J.A.P.) is grateful to Glaxo Wellcome for a postdoctoral fellowship, and we thank Dr. Christopher J. Cramer for his computations of log P_{chl}, and Dr. Cramer and Dr. Donald G. Truhlar for their interest in this work.

JS990008A

Saturable Transport of H_2-Antagonists Ranitidine and Famotidine Across Caco-2 Cell Monolayers

KIHO LEE AND DHIREN R. THAKKER*

Contribution from *Division of Drug Delivery and Disposition, School of Pharmacy, CB# 7360, Beard Hall, The University of North Carolina at Chapel Hill, Chapel Hill, North Carolina 27599-7360.*

Received December 9, 1998. Final revised manuscript received April 7, 1999.
Accepted for publication April 16, 1999.

Abstract □ The purpose of this study was to investigate the mechanism by which the H_2-antagonists ranitidine and famotidine interacted with the paracellular space during their transport across Caco-2 cell monolayers. Transport experiments with ranitidine and famotidine across Caco-2 cell monolayers were performed to determine the apical-to-basolateral flux at various concentrations. Kinetic analysis of the transport data showed that ranitidine and famotidine were transported by both saturable and nonsaturable processes. Na^+,K^+-ATPase inhibitor ouabain and metabolic inhibitors sodium azide + 2-deoxy-D-glucose did not affect ranitidine transport, suggesting that the active transport was not involved. Famotidine and some other guanidine-containing compounds, e.g., guanethidine, Arg-Gly, L-arginine methyl ester, and L-argininamide, inhibited the transport of ranitidine, whereas other guanidine-containing compounds with an additional negative charge, e.g., L-arginine, did not. 2,4,6-Triaminopyrimidine (TAP), an inhibitor of paracelluar cationic conductance, also inhibited the transport of both ranitidine and famotidine. On the basis of these results, it is proposed that the saturable transport of ranitidine and famotidine across Caco-2 cell monolayers appears to be via a facilitated diffusion process mediated by the paracellular anionic sites. This mechanism is consistent with the observation that ranitidine and famotidine caused a concentration-dependent increase in transepithelial electrical resistance (TEER) across Caco-2 cell monolayers, presumably by blocking the paracellular anionic sites and thus inhibiting the flux of cations (e.g., Na^+).

Introduction

Intestinal epithelium presents a major barrier to orally administered drugs.[1,2] The drug molecules have to traverse this barrier by entering the epithelial cells from the apical (or luminal) side and exiting from the basolateral (or serosal) side (i.e., the transcellular transport), or by passing through the intercellular space (i.e., the paracellular transport). The transcellular transport occurs either via a passive diffusion process or via a carrier-mediated process, involving one of many carrier proteins (i.e., carrier for amino acids, di/tri peptides, glucose, bile acids, etc.).[3] The paracellular transport, involving passive diffusion of compounds in aqueous solution, is less efficient than the transcellular process because of the much lower surface area available to the compounds entering the intercellular space. In addition, presence of the highly specialized structure in the intercellular space restricts the free passage of compounds traversing the intestinal epithelium via the paracellular process.[4−7] Hence, only hydrophilic compounds of low molecular weight (e.g., mannitol) cross the intestinal epithelium predominantly via the paracellular route.

The H_2-antagonist ranitidine appears to be absorbed predominantly via the paracellular pathway based on the studies with Caco-2 cell monolayers as in vitro model of intestinal mucosa.[8] This conclusion was based on the observation that the permeability coefficient (P_{app}) of ranitidine across Caco-2 cell monolayers increased by 15−20-fold when Ca^{2+} was removed from the transport medium, thereby compromising the integrity of the tight junctions.[8] This was further confirmed by the observation that the uptake of ranitidine into Caco-2 cells was minimal.[8] The paracellular transport of ranitidine is consistent with the report that absorption of ranitidine in humans after oral administration is incomplete and that its bioavailability is ∼50% despite little or no first pass metabolism.[9] During the investigation of the mechanism of transport of ranitidine it was uncovered that H_2-antagonists—ranitidine, famotidine, cimetidine, and nizatidine—appeared to affect the tight junctions in Caco-2 cell monolayers as evidenced by a concentration-dependent increase in the transepithelial electrical resistance (TEER) across Caco-2 cell monolayers,[10] which is an indicator of paracellular ionic permeability.[11−13] The increase in TEER was accompanied by a decrease in their own permeability across Caco-2 cell monolayers.[10] These results suggest that H_2-antagonists may affect their own absorption by a mechanism that is related to the mechanism by which they cause an increase in TEER. An inverse relationship between the ability of the four H_2-antagonists to cause an increase in TEER across Caco-2 cell monolayers and their human bioavailability[9,10,14] provides support to this hypothesis.

In light of these observations, we have investigated the mechanism by which the H_2-antagonists cause an increase in TEER and affect their own transport across Caco-2 cell monolayers. Our results suggest that H_2-antagonists cause an increase in TEER by binding to the anionic centers in the paracellular space and thereby decreasing the cationic conductance across the cell monolayers. During our investigation, we have found that ranitidine and famotidine traverse the Caco-2 cell monolayers by a combination of saturable and nonsaturable mechanisms. In this report we have characterized the saturable transport of ranitidine and famotidine and proposed a mechanism of transport for these compounds that is consistent with the saturable transport kinetics as well as their ability to cause an increase in TEER across Caco-2 cell monolayers.

Materials and Methods

Materials—Eagle's minimum essential medium (with Earle's salts and L-glutamate), fetal bovine serum (FBS), nonessential amino acids (NEAA, ×100), and 0.05% trypsin-EDTA solution were obtained from Gibco Laboratories, Grand Island, NY. Hank's balanced salt solution (HBSS, ×1), ranitidine hydrochloride,

* Corresponding author. Tel: (919) 962-0092. Fax: (919) 966-0197. E-mail: dhiren_thakker@unc.edu.

10.1021/js980474k CCC: $18.00
Published on Web 05/25/1999

famotidine, 2,4,6-triaminopyrimidine (TAP), guanethidine monosulfate, Arg-Gly hydrochloride, Gly-Gly, L-arginine hydrochloride, L-argininamide dihydrochloride, L-arginine methyl ester dihydrochloride, glycylsarcosine (Gly-Sar), mannitol, ouabain, sodium azide, 2-deoxy-D-glucose, 2,4-dinitrophenol, antibiotic antimycotic solution (×100), 2-(*N*-morpholino)ethanesulfonic acid (MES), and D-(+)-glucose were purchased from Sigma Chemical Co., St. Louis, MO. *N*-Hydroxyethylpiperazine-*N*′-2-ethanesulfonate (HEPES, 1 M) was purchased from Lineberger Comprehensive Cancer Center, the University of North Carolina, Chapel Hill, NC. Lucifer yellow CH was purchased from Molecular Probes, Eugene, OR. [^{14}C]-Mannitol (51.5 mCi/mmol) and [^{14}C]PEG-4000 (11.0 mCi/g) were obtained from NEN Research Products, Boston, MA. [^{3}H]Gly-Sar (30 Ci/mmol) was purchased from American Radiolabeled Chemicals Inc., St. Louis, MO.

Cell Culture—The Caco-2 cell line was obtained from Glaxo-Wellcome, Inc., Research Triangle Park, NC, and cultured as described previously.[10] Briefly, Caco-2 cells were cultured at 37 °C in minimum essential medium, supplemented with 10% FBS, 1% NEAA, 100 U/mL penicillin, 100 μg/mL streptomycin, and 0.25 μg/mL amphotericin B in an atmosphere of 5% CO_2 and 90% relative humidity. The cells were passaged every 4−6 days at a split ratio of 1:20 at about 90% confluency, using trypsin−EDTA. Caco-2 cells (passage 50∼55) were seeded at a density of 60 000 cells/cm^2 on polycarbonate membranes of Transwells (12 mm i.d., 3.0 μm pore size, Costar, Cambridge, MA). Medium was changed the day after seeding and every other day thereafter (apical volume 0.5 mL, basolateral volume 1.5 mL). The cell monolayers were used 20−25 days postseeding. TEER was measured as described later. TEER and apical-to-basolateral flux for [^{14}C]mannitol, a paracellular transport marker, were used to ensure cell monolayer integrity. Monolayers having TEER values above 300 Ω·cm^2 and the mannitol flux < 0.5%/h were used in the studies.

Measurement of TEER—EVOM Epithelial Tissue Voltohmmeter (World Precision Instruments, Sarasota, FL) and Endohm-12 electrode (World Precision Instruments, Sarasota, FL) were used to measure TEER across the Caco-2 cell monolayers.[10] The cell monolayers were preincubated for 1 h at 37 °C with transport buffer (HBSS supplemented with 25 mM D-glucose and 10 mM HEPES, pH 7.2), and TEER was measured. The experiments were initiated by replacing the apical buffer with the compound of interest dissolved in an appropriate transport buffer (HBSS supplemented with 25 mM D-glucose and 10 mM HEPES, pH 7.2 or HBSS supplemented with 25 mM D-glucose and 10 mM MES, pH 6.0). The cell monolayers were incubated at 37 °C, and TEER was measured at selected times. All the experiments were performed in triplicate.

Transport Studies—Transport experiments were performed as described previously.[10] Briefly, cell monolayers were incubated for 1 h at 37 °C with the transport buffer (pH 7.2), and TEER was measured. Transport experiments were initiated by replacing the apical buffer with 0.4 mL of the transport buffer (pH 7.2 or 6.0) containing the compound being investigated. The inserts were transferred at selected times to a 12-well cell culture cluster (Costar, Cambridge, MA) containing fresh transport buffer (pH 7.2). The temperature was maintained at 37 °C during the transport experiments. TEER was measured after the experiments. No treatment caused a significant decrease in TEER compared to the control monolayers. The amount of drugs in the receiver side was determined as a function of time (see Figure 3A) to calculate the flux (J) across the cell monolayers. All transport experiments were carried out under sink conditions as the concentrations of drugs in the basolateral side remained at least 100-fold lower than those in the apical side. The amount of radiolabeled compounds was measured by using liquid scintillation counter (Tri-Carb 4000, Packard, Downers Grove, IL). The amount of ranitidine or famotidine was quantified by HPLC (1100 series, Hewlett-Packard, Waldbronn, Germany) using an ODS-AQ C18 column (250 × 4.6 (i.d.) mm, YMC Inc., Wilmington, NC) of 5 μm packing and 120 Å pore size and an isocratic mobile phase (65% 50 mM phosphate buffer, pH 6.0 and 35% methanol for ranitidine, and 80% 50 mM phosphate buffer, pH 6.0 and 20% methanol for famotidine).[8,10] The flow rate was 1.0 mL/min. Ranitidine and famotidine were detected by UV at 320 and 280 nm, respectively. Under these conditions, the retention times for ranitidine and famotidine were 5.6 and 9.6 min, respectively, and no other peaks were detected after the transport experiments.

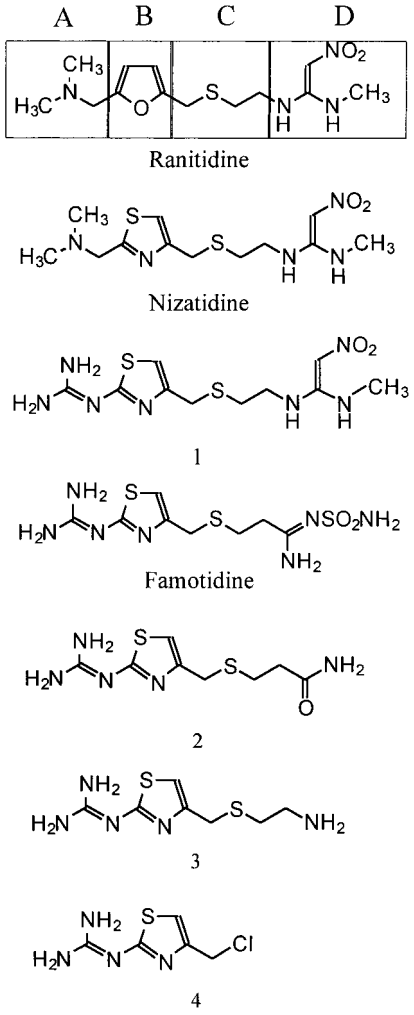

Figure 1—Structures of H_2-antagonists and their derivatives.

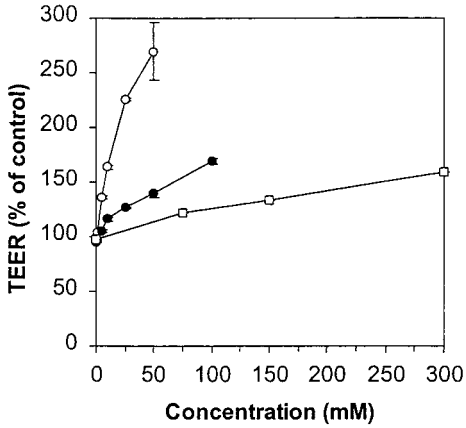

Figure 2—Effect of ranitidine and famotidine on TEER across Caco-2 cell monolayers. Effect of mannitol on TEER was evaluated to demonstrate that the effect of ranitidine and famotidine was selective and not just due to the change in osmolality. TEER was measured 15 min after incubating the cell monolayers with various concentrations of drugs on the apical side (pH 7.2). Percent change of the TEER values was calculated relative to the value at time zero (303 ∼ 419 Ω·cm^2). ○, Famotidine; ●, ranitidine; □, mannitol. Values are the mean of three measurements ± sd. The pH of the famotidine solutions above 10 mM was 6.5 (instead of 7.2); however, the change in pH alone did not contribute to the increase in TEER.

Inhibition of Active Transport—For all the studies described in this section, cell monolayers were preincubated for 30 min at 37 °C with the transport buffer (pH 7.2) and TEER was measured. For the inhibition of Na^+,K^+-ATPase,[15] cell monolayers were

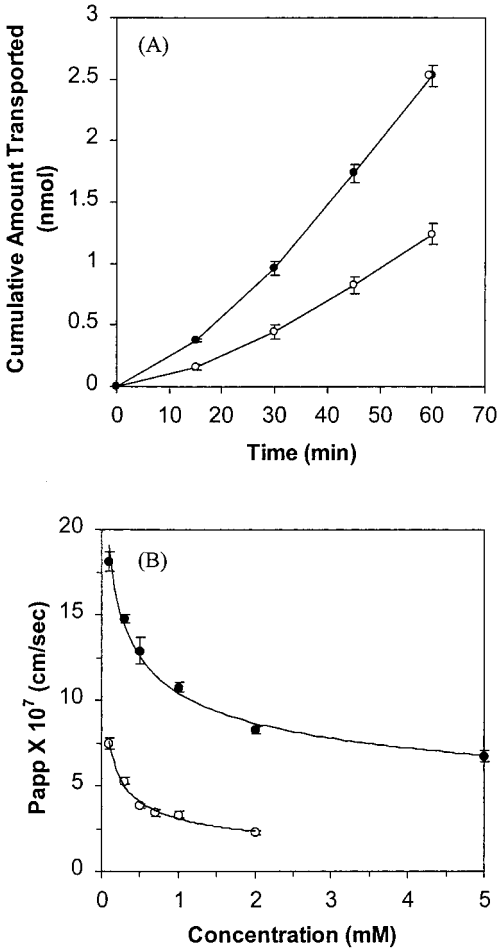

Figure 3—(A) Time course of apical-to-basolateral transport of ranitidine (0.5 mM) and famotidine (0.5 mM) across Caco-2 cell monolayers; (B) permeability of ranitidine and famotidine across Caco-2 cell monolayers as a function of concentration. P_{app} values were calculated from the apical-to-basolateral flux (J) determined in a linear transport region (30–60 min) at various concentrations. The pH of both apical and basolateral sides was 7.2. ●, Ranitidine; ○, Famotidine. Values are the mean of three measurements ± sd.

further incubated for 30 min at 37 °C with ouabain (5 mM) dissolved in the transport buffer (pH 7.2) on both apical and basolateral sides. Ranitidine (0.1 mM) in the transport buffer (pH 7.2) containing ouabain (5 mM) was then added to the apical side. For metabolic inhibition,[15] cell monolayers were incubated for 30 min at 37 °C with sodium azide (1 mM) and 2-deoxy-D-glucose (50 mM), or 2,4-dinitrophenol (1 mM), dissolved in the transport buffer (pH 7.2) on both apical and basolateral sides. Ranitidine (0.1 mM) in the transport buffer (pH 7.2) containing metabolic inhibitors was then added to the apical side. The transport experiments were conducted for 1 h. For control studies, a mixture of [^{3}H]Gly-Sar (0.1 mM, 0.5 μCi/ml) and [^{14}C]mannitol (0.1 mM, 1.0 μCi/ml) in the transport buffer (pH 6.0) was applied to the apical side after incubating the cell monolayers with active transport inhibitors.[16] The pH of the apical solution was adjusted to 6.0 for the control experiments since Gly-Sar (positive control) is a substrate of H^+-coupled dipeptide transporter.[16]

Data Analysis—Apparent permeability coefficients (P_{app}, cm/s) were calculated using eq 1.[10]

$$P_{app} = \frac{1}{AC_o}\frac{dQ}{dt} \quad (1)$$

where dQ/dt is the flux (J) across the monolayer (nmol/s) determined experimentally by measuring the amount of the compounds transported as a function of time (e.g., see Figure 3A for measurement of ranitidine and famotidine flux), A is the surface area of the porous membrane (cm^2), and C_o is the initial concentration (nmol/mL) in the donor side. Kinetic parameters for the transport

Table 1—Effect of Famotidine Derivatives on TEER across Caco-2 Cell Monolayers

compound[a]	TEER[b] (% of control)
1	217 ± 7
2	201 ± 1
3	158 ± 17
4	235 ± 11
ranitidine	127 ± 0.3
nizatidine	117 ± 3[c]
famotidine	193 ± 22

[a] The concentration of nizatidine was 50 mM while others were 25 mM. [b] Measured 15 min after incubating the cell monolayers with a compound in the apical side. Percent change of the TEER values was calculated relative to the value at time zero (366–442 Ω·cm^2). Values are the mean of three measurements ± sd. [c] Taken from ref 10.

of ranitidine and famotidine were calculated by fitting the data to eq 2 using nonlinear regression analysis (WINNONLIN 1.1, Scientific Consulting Inc., Apex, NC):[17,18]

$$J' = \frac{J'_{max}S}{K_m(app) + S} + K_dS \quad (2)$$

where J' (pmol·min^{-1}·cm^{-2}) is the flux (J) normalized to unit surface area, K_m(app) (mM) is a constant equivalent to a Michaelis–Menten constant, J'_{max} is the maximal flux for the saturable term (pmol·min^{-1}·cm^{-2}), K_d is the constant for the nonsaturable term (nL·min^{-1}·cm^{-2}), and S is the concentration in the donor side (mM). The statistical significance of differences between treatments was evaluated using Student's t tests, with a significance level of $p < 0.05$.

Synthesis of Famotidine Derivatives—Famotidine derivatives used in this study (cf. Figure 1) were prepared as described in the literature.[19,20]

Results

Effect of H_2-Antagonists on TEER—Ranitidine and famotidine caused a concentration-dependent but saturable increase in TEER when applied to the apical side of Caco-2 monolayers (Figure 2), as reported previously.[10] A much smaller increase was observed when the monolayers were treated with mannitol solutions of similar osmolality (Figure 2). These results indicated that the increase in TEER caused by ranitidine and famotidine did not simply result from the hyperosmolality of the drug solutions. The specificity of this effect was further evidenced by the fact that famotidine was much more potent than ranitidine in causing the TEER increase across Caco-2 cell monolayers (Figure 2).

Structural Requirements for the Effect of H_2-antagonists on TEER—A systematic study was undertaken to define the structural requirements for the effect of H_2-antagonists and related compounds on TEER. The role of the four key moieties in the H_2-antagonists (Figure 1) in causing an increase in TEER was investigated by comparison of the potencies of appropriate pairs of compounds (Table 1). The heteroaromatic ring (part B) does not seem to play a significant role, as indicated by the marginal difference in the potency between ranitidine and nizatidine (see Figure 1 and Table 1 for all comparisons). The thioether linker (part C) is not a primary determinant of the effect since the potency varies dramatically among compounds which share this moiety. Substitution of the *N*-sulfamoylamidine moiety of famotidine by 1-nitro-2-(methylamino)-2-aminoethylene group (compound **1**) caused no significant change in the potency, indicating that part D is also not a primary determinant of the activity. This was confirmed by the observation that the potency was maintained when part D was replaced with various func-

Table 2—Effect of Famotidine on the Transport of Paracellular Markers

Paracellular Markers	net charge	mol wt	% of control[a]
[^{14}C]mannitol (100 μM, 20 μCi/μmol)	0	182	114 ± 9
[^{14}C]PEG-4000 (100 μM, 5 μCi/μmol)	0	4000	97 ± 2
lucifer yellow CH (250 μM)	–2	457	79 ± 13
ranitidine (100 μM)	+1	314	22 ± 0.2[b]

[a] Determined by measuring the apical-to-basolateral transport of compounds for 1 h across Caco-2 cell monolayers in the absence (control) or presence of famotidine (5 mM) on the apical side (pH 7.2). Values are the mean of three measurements ± sd. [b] $p < 0.05$ compared to control.

tional groups such as amide (compound **2**), amine (compound **3**). Similarly, potency was maintained when part (C + D) was replaced with a chloromethyl group (compound **4**). The basic side chain represented in part A appears to be the essential moiety for the effect since a dramatic increase in the potency was observed when the dimethylaminomethyl group of nizatidine was substituted with guanidine group (compound **1**). This observation also indicates that the potent effect of famotidine may be due to the presence of the guanidine group.

Effect of Famotidine on the Transport of Paracellular Markers—The effect of famotidine on paracellular permeability was examined by measuring the permeability (P_{app}) of various paracellular markers across Caco-2 cell monolayers in the presence of famotidine (Table 2). This was done to determine if the increase in TEER by H_2-antagonists was caused by tightening of the paracellular space. Famotidine did not cause a significant decrease in the permeability of neutral ([^{14}C]mannitol, and [^{14}C]PEG-4000) or anionic (Lucifer Yellow) paracellular markers. In contrast, famotidine inhibited the transport of ranitidine, a cationic compound that is transported via the paracellular route.[8] These results suggest that the increase in TEER caused by famotidine (and other H_2-antagonists) is not due to tightening of the tight junctions in the paracellular space; rather, famotidine appears to inhibit the transport of only positively charged entities through the paracellular space. Thus, the increase in TEER caused by famotidine (and other H_2-antagonists) is likely to be due to inhibition of the cation-selective ionic conductance, i.e., Na^+ transport, mediated by the anionic centers in the paracellular space.[21–23] This mechanism is consistent with our earlier finding that guanidine group, which is positively charged at neutral pH, is essential for causing an increase in TEER across Caco-2 cells by famotidine and its derivatives (Table 1).

Transport of Ranitidine and Famotidine—Consistent with above observations, the apical-to-basolateral permeability of both ranitidine and famotidine through Caco-2 cell monolayers was found to be dependent on concentration (Figure 3B). The P_{app} values decreased exponentially with concentration, but appeared to reach plateau above 2 mM for ranitidine and 0.7 mM for famotidine (Figure 3B). The decrease in P_{app} as a function of concentration suggests that both ranitidine and famotidine inhibit their own transport (Figure 3B). These results also indicate that ranitidine and famotidine are transported by a process other than simple passive diffusion, because the P_{app} values should remain constant over the entire concentration range (under sink condition) if passive diffusion is the major transport mechanism. We have previously reported a concentration-dependent decrease in P_{app} values for ranitidine and famotidine;[10] however, those studies were conducted at concentrations ≥ 5 mM. At these high

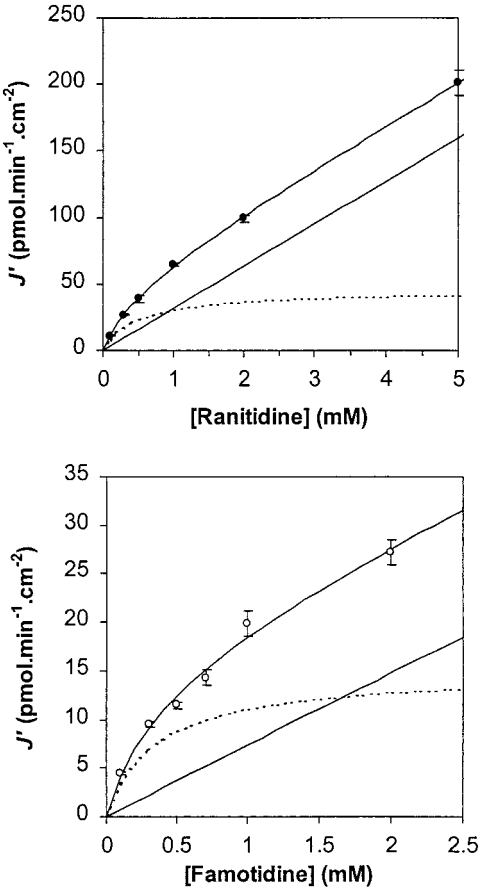

Figure 4—Transport of ranitidine and famotidine across Caco-2 cell monolayers as a function of concentration. Apical-to-basolateral flux (J') (same data used in Figure 3) was plotted as a function of concentration. The straight lines represent the calculated nonsaturable transport and the dotted curves represent the calculated saturable transport (see eq 2). ●, Ranitidine; ○, Famotidine. Values are the mean of three measurements ± sd.

concentrations, the decrease in P_{app} could be due to multiple effects, i.e., saturation of the anionic sites, osmotic effects, and a decrease in pH (famotidine only) necessary to keep the drug in solution. To obtain a better insight into the transport process for these compounds, their flux (J') was plotted as a function of concentration on the donor side (Figure 4). Under sink conditions (as is the case here, see Materials and Methods and Figure 3A), the flux (J') should increase linearly as a function of concentration in the donor side if the compounds are transported by the passive diffusion process. The flux (J') of ranitidine and famotidine increased nonlinearly with concentration (hyperbolic relationship) at relatively low concentrations (<1 mM) and then increased linearly at higher concentration. These results suggested that the apical-to-basolateral transport of ranitidine and famotidine was mediated by both saturable and nonsaturable processes.[17,18] This was also indicated by an excellent fit of the data to the curves obtained from nonlinear regression analysis with an equation consisting of both saturable and nonsaturable terms (Figure 4 and eq 2).[17,18] The calculated equivalent to Michaelis–Menten constant (K_m(app)) and the maximal flux for the saturable process (J'_{max}) for ranitidine were 0.48 mM and 45.6 pmol·min^{-1}·cm^{-2}. The corresponding values for famotidine were 0.36 mM and 15.0 pmol·min^{-1}·cm^{-2}, respectively.

Effect of Inhibitors of Active Transport on the Transport of Ranitidine—Gan et al.[8] have shown that ranitidine is transported predominantly via the paracellular pathway across Caco-2 cell monolayers. This was

Table 3—Effect of Active Transport Inhibitors on the Transport of Ranitidine

inhibitor (mM)	amount transported (%)[a]		
	ranitidine	[^{3}H]Gly-Sar	[^{14}C]mannitol
control	2.60 ± 0.08	4.52 ± 0.25	0.23 ± 0.01
ouabain (5)	2.68 ± 0.05	2.55 ± 0.11[b]	0.28 ± 0.07
sodium azide (1) + 2-deoxy-D-glucose (50)	2.49 ± 0.21	2.91 ± 0.11[b]	0.25 ± 0.002
2,4-dinitrophenol (1)	1.40 ± 0.06[b]	0.76 ± 0.16[b]	0.32 ± 0.10

[a] Determined by measuring the apical-to-basolateral transport across Caco-2 cell monolayers for 1 h in the absence (control) or presence of active transport inhibitors. The monolayers were first incubated with an inhibitor for 30 min, and ranitidine (0.1 mM) or control compound (0.1 mM) was added to the apical side to initiate the experiment (see Materials and Methods for details). [b] $p < 0.05$ compared to control. Values are the mean of three measurements ± sd.

evidenced by a dramatic increase in ranitidine transport by Ca^{2+} depletion, and by relatively low cellular uptake of ranitidine compared to that of lipophilic compounds such as testosterone and ondansetron.[8] Therefore, it is unlikely that transcellular saturable mechanisms are significantly involved in the transport of ranitidine.

It is difficult to conceive an active transport process to explain the saturable transport of ranitidine and famotidine in the absence of a significant transcellular component associated with the transport of these compounds across Caco-2 cell monolayers. However, the transport of ranitidine across Caco-2 cell monolayers was examined in the presence of Na^+,K^+-ATPase inhibitor ouabain, or metabolic inhibitors such as sodium azide + 2-deoxy-D-glucose, and 2,4-dinitrophenol, to determine if the saturable component of the transport is an active transport process.[3,15,17] In our control experiments, the active transport inhibitors significantly inhibited the apical-to-basolateral transport of [^{3}H]Gly-Sar (positive control)[16] without affecting that of [^{14}C]mannitol (negative control) at concentrations that were reported to be inhibitory to active transport processes (Table 3).[3,15,17] Ouabain and sodium azide (+ 2-deoxy-D-glucose), however, did not affect the apical-to-basolateral transport of ranitidine across Caco-2 cell monolayers (Table 3), suggesting that ranitidine is not a substrate for active transport systems (e.g. amino acids, di/tri peptides, glucose, bile acids, etc.) in Caco-2 cells. Interestingly, 2,4-dinitrophenol significantly decreased the transport of ranitidine (Table 3). The inhibitory effect of 2,4-dinitrophenol on the transport of ranitidine may argue for an active transport mechanism; however, there is no precedent for an active transport process that is inhibited by 2,4-dinitrophenol, but is insensitive to sodium azide or ouabain.

Inhibition of Ranitidine Transport by Guanidine Derivatives—To determine if the saturable transport of ranitidine and famotidine occurred via a common mechanism, the permeability (P_{app}) of ranitidine was measured in the presence of famotidine. Indeed the apical-to-basolateral transport of ranitidine (0.5 mM) was significantly inhibited by famotidine (10 mM) (Figure 5). Interestingly, other guanidine-containing compounds such as guanethidine, L-arginine methyl ester, and L-argininamide also significantly inhibited the transport of ranitidine (Figure 5). Arg-Gly, a guanidine-containing dipeptide, significantly inhibited ranitidine transport whereas Gly-Gly, a non-guanidine-containing dipeptide had little effect (Figure 5). The common structural feature shared by all these compounds that inhibited the transport of ranitidine across Caco-2 cell monolayers is the presence of a cationic center. It has been shown that the cell surface, including that making up the paracellular space, has net negative charge.[5–7] These results suggest that the saturable transport of ranitidine and famotidine may involve binding to the anionic cellular components via their basic side chains (dimethylamino group or guanidine group). Taking the predominantly paracellular transport of ranitidine[8] into consideration, it seems likely that the saturable transport of ranitidine and famotidine is mediated by the anionic sites in the paracellular space. This mechanism is consistent with our proposed mechanism for the TEER increase by ranitidine and famotidine. Interestingly, L-arginine did not cause a significant effect on the transport of ranitidine (Figure 5). However, L-arginine methyl ester and L-argininamide (in which the carboxylate group is blocked) effectively inhibited ranitidine transport, suggesting that the negative charge of the carboxylate group in L-arginine interferes with its ability to bind to the anionic sites in the paracellular space. The fact that structural components other than the cationic groups are involved in the interactions of these compounds with the anionic sites is also evident from the observation that tetramethylammonium ion does not inhibit the transport of ranitidine across Caco-2 cells (data not shown).

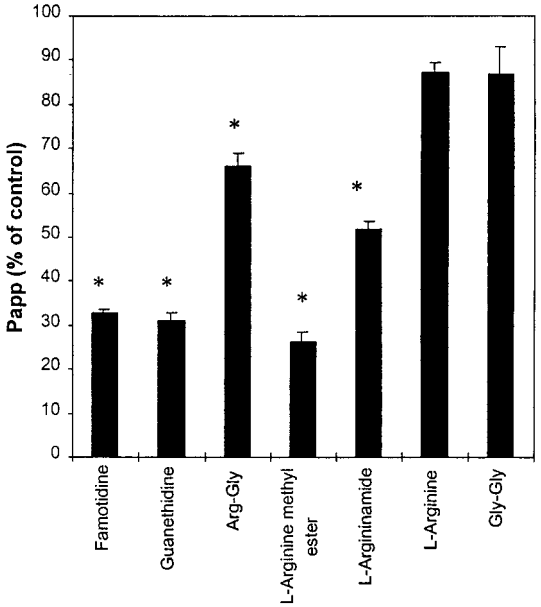

Figure 5—Effect of famotidine and other guanidine-containing compounds on the transport of ranitidine across Caco-2 cell monolayers. P_{app} values were calculated from the apical-to-basolateral flux (J) of ranitidine (0.5 mM) determined in the linear transport region (30–60 min) in the presence or absence of a guanidine-containing compound (10 mM) on the apical side (pH 7.2). The control P_{app} value was $(1.1 \pm 0.04) \times 10^{-6}$ cm/s. Values are the mean of three measurements ± sd. *, $p < 0.05$ compared to control.

Discussion

We have recently reported that ranitidine and other H_2-antagonists cause an increase in TEER across Caco-2 cell monolayers.[10] In the present study we have further characterized this effect and showed that the increase in TEER does not cause any decrease in the permeability of paracellularly transported compounds that are either neutral of anionic in nature. In contrast, paracellular transport of cationic compounds (including their own transport) is inhibited by ranitidine and famotidine. Thus, the effect of ranitidine and famotidine on TEER is clearly not due to tightening of the tight junctions as is the case for protamine.[24] We propose that H_2-antagonists cause an increase in TEER by binding to the anionic sites such as carboxylate and phosphate groups[5–7] on the cell surface in the paracellular space and inhibiting cation-selective ionic conduc-

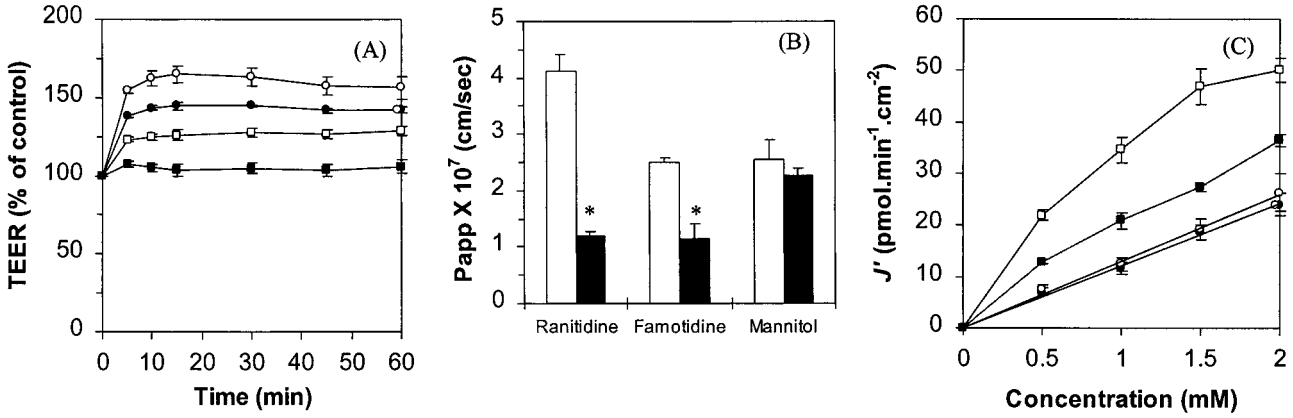

Figure 6—Effect of TAP on TEER and the transport of ranitidine and famotidine across Caco-2 cell monolayers. (A) TEER was measured at selected times after initiating the incubation of the cell monolayers with various concentrations of TAP on the apical side. Percent change of the TEER values was calculated relative to the value at time zero (370–417 $\Omega \cdot cm^2$). ■, Control; □, 5 mM; ●,10 mM; ○, 20 mM TAP. (B) P_{app} values for ranitidine, famotidine (both 1 mM) and [^{14}C]mannitol (1 mM; 2.0 μCi/ml) were calculated from the apical-to-basolateral flux (J) determined in a linear transport region (30–60 min) in the absence or presence of TAP (10 mM) on the apical side; open bars, control (– TAP); solid bars, + TAP (10 mM). (C) ●, Ranitidine and ○, famotidine flux determined in the presence of 10 mM TAP; □, ranitidine and ■, famotidine flux determined in the absence of TAP. All experiments were done at apical pH 6.0/basolaterlal pH 7.2 because TAP (pK_a = 6.72) caused an increase in TEER only in the protonated form.[21] Values are the mean of three measurements ± sd. *, $p < 0.05$ compared to control.

tance,[21–23] and not by tightening of the tight junctions as was previously suspected.[10] Such interactions between cationic compounds and paracellular anionic functionality are not without precedent. 2,4,6-Triaminopyrimidine (TAP) has been shown to inhibit paracellular cation permeation across frog gall bladder and several other epithelia with concomitant increase in TEER.[21–23] In our study, TAP caused a concentration-dependent increase in TEER across Caco-2 cell monolayers (Figure 6A). TAP also caused a significant decrease in the permeability of both ranitidine and famotidine across Caco-2 monolayers without affecting that of [^{14}C]mannitol (Figure 6B). Partial inhibition of the transport of ranitidine (1 mM) and famotidine (1 mM) by TAP is consistent with the fact that at these concentrations both the compounds traverse the cell monolayers via a combination of saturable and nonsaturable mechanisms.

The investigation of the effect of H_2-antagonists on TEER has led to the hypothesis that these compounds not only interact with anionic sites on the cell surface in the paracellular space, but that this interaction may contribute to a saturable transport mechanism. This saturable mechanism is characterized by the hyperbolic relationship between flux and the concentration in the donor side. As expected, certain cationic compounds (e.g., TAP) inhibit the transport of ranitidine and famotidine (cf., Figure 6B). In fact, in the presence of TAP the saturable component of the paracellular transport of ranitidine and famotidine is completely inhibited, such that the flux is linear with concentrations (Figure 6C).

Because TAP can also block Na^+ channels,[25] it can be argued that the increase in TEER caused by TAP as well as by ranitidine and famotidine is due to their effect on these Na^+ channels on the apical surface of Caco-2 cells. However, inhibition of ranitidine and famotidine transport, coupled with virtual elimination of the saturable component of their transport by TAP cannot be explained by its effect on the Na^+ channels because these compounds are not likely to be transported across the cell membrane through these channels.

The saturable transport of ranitidine and famotidine does not appear to be an active transport process as it is unaffected by known active transport inhibitors, i.e., Na^+,K^+-ATPase inhibitor ouabain and metabolic inhibitor sodium azide (+ 2-deoxy-D-glucose). However, the active transport cannot be completely ruled out as a possible mechanism for the saturable transport of ranitidine and famotidine, since ranitidine transport was significantly inhibited by a different metabolic inhibitor 2,4-dinitrophenol. The reason for this is unknown at this stage.

It is clear that some of the well-accepted approaches to evaluate the involvement of an active transport process (e.g., metabolic inhibition) cannot provide clearly interpretable results regarding the involvement of an active transport process for the transport of ranitidine and famotidine. However, if we take into consideration (i) the evidence for predominantly paracellular transport of ranitidine,[8] and (ii) the lack of any effect of some inhibitors of active transport (Table 3), then it is reasonable to conclude that an active transport is not likely to be involved in the translocation of ranitidine or famotidine across Caco-2 cell monolayers.

We propose a mechanism for the transport of H_2-antagonists, ranitidine and famotidine, across Caco-2 cell monolayers to explain the increase in TEER[10] caused by these compounds as well as their saturable (plus nonsaturable) transport kinetics (Figure 7). As depicted in Figure 7, ranitidine and famotidine can interact with anionic sites present on the cell surface in the paracellular space,[5–7] and thus compete with Na^+ ions (and other cations) for these binding sites resulting in decreased ionic transport and increased TEER across the cell monolayers. A similar mechanism has been proposed to explain an increase in TEER caused by the cationic hydrophilic compound TAP across frog gall bladder and several other epithelia.[21,22] The fact that ranitidine affects TEER only when it is applied from the apical side[10] of the Caco-2 cell monolayers suggests that the anionic sites are asymmetrically disposed in the paracellular space, either in the junctional complexes or to the apical side of the junctional complexes. It is conceivable that the effect of ranitidine and famotidine on TEER is due to a mechanism unrelated to their proposed binding to the paracellular anionic sites, i.e., via blocking of the Na^+ channels on the apical surface of the cells. Extensive electrophysiological studies will be necessary to determine the relative contribution of the two mechanisms in causing an increase in TEER.

As shown in Figure 7, these interactions of ranitidine (and famotidine) with anionic sites can also explain how the translocation of these compounds through the paracellular space can occur by a combination of saturable and nonsaturable processes. Their interaction with the anionic sites can assist in their translocation across the cell

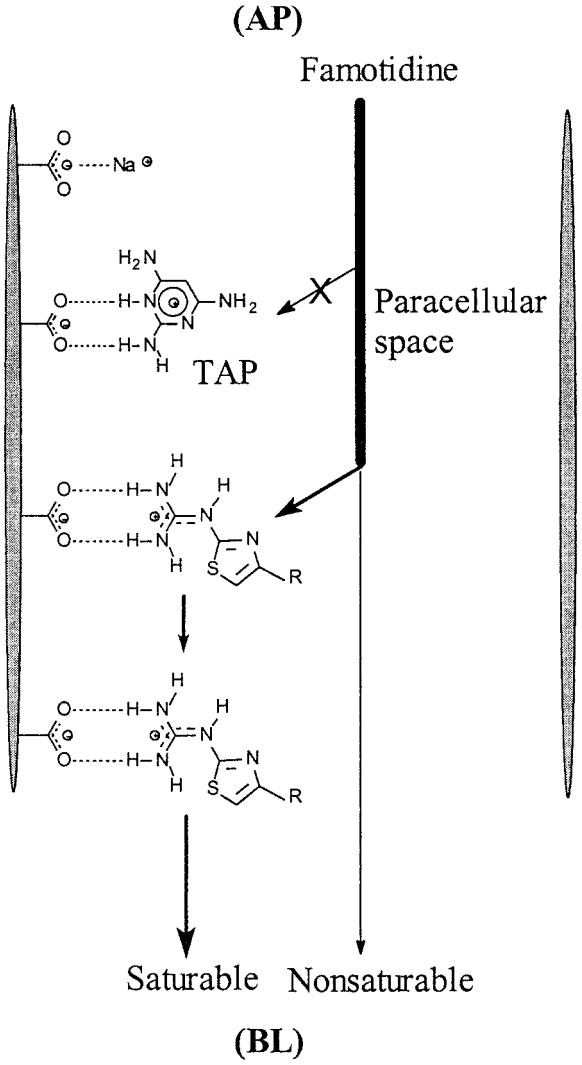

Figure 7—Model for the proposed transport mechanism of H_2-antagonists as exemplified by that for the transport of famotidine. Ionic interaction between Na^+ ions δ and the negatively charged group (as exemplified by carboxylate group here) in the paracellular space mediates cation-selective ion transport.[21] Likewise, the positively charged species of famotidine is transported by facilitated diffusion through interaction with the negatively charged group in the paracellular space (saturable transport). Famotidine can also traverse the paracellular space by simple diffusion (nonsaturable transport). This figure also shows how a cationic compound such as 2,4,6-triaminopyrimidine (TAP) can compete for the anionic site and inhibit the transport of famotidine (or ranitidine).

monolayers in the same way the transport of Na^+ ions is assisted by interactions with the anionic sites. Our results show that this process is not likely to be an active transport process; rather it can be characterized as facilitated diffusion. A population of ranitidine (and famotidine) molecules that do not interact with the anionic sites would traverse the paracellular space by a passive diffusion process (Figure 7). The overall transport of these compounds is thus a sum of the saturable facilitated diffusion process and nonsaturable passive diffusion process. The proposed mechanism is consistent with the observed transport kinetics for ranitidine and famotidine, inhibition of their own transport at high concentration, and inhibition of their transport by cationic compounds such as TAP. The possible involvement of the paracellular anionic sites in the drug transport has been also suggested in some recent reports[26–28] based on the higher paracellular permeability of cationic compounds compared to that of anionic compounds. However, this is the first report in which saturable transport of cationic hydrophilic compounds across epithelial cells has been described that can be explained by a (proposed) molecular mechanism involving their interactions with the anionic sites in the paracellular space. We want to emphasize that other mechanisms can be proposed to explain the observed saturable kinetics for the transport of ranitidine and famotidine across Caco-2 cell monoalyers; however, the mechanism proposed here serves as a good working model to help design further studies[29] that can provide greater insights into the mechanism of intestinal transport for hydrophilic cationic compounds such as ranitidine and famotidine.

The results presented here and the proposed mechanism for transport of ranitidine and famotidine raise an interesting possibility of potential drug interactions and food effects, because the oral absorption of cationic hydrophilic compounds is likely to be affected by coadministered drugs with similar structural characteristics and by hydrophilic cationic peptides generated from hydrolytic digestion of proteins in the diet.[30]

References and Notes

1. Hayton, W. L. Rate-Limiting Barriers to Intestinal Drug Absorption: a Review. *J. Pharmacokinet. Biopharm*. **1980**, *8*, 321–334.
2. Jackson, M. J. Drug Transport across Gastrointestinal Epithelia. In *Physiology of the Gastrointestinal Tract*, 2nd ed.; Johnson, L. R., Ed.; Raven Press: New York, 1987; pp 1597–1621.
3. Tsuji, A.; Takami, I. Carrier-Mediated Intestinal Transport of Drugs. *Pharm. Res*. **1996**, *13*, 963–977.
4. Gumbiner, B. Structure, Biochemistry, and Assembly of Epithelial Tight Junctions. *Am. J. Physiol*. **1987**, *253*, C749–C758.
5. Ballard, S. T.; Hunter, J. H.; Taylor A. E. Regulation of Tight-Junction Permeability during Nutrient Absorption across the Intestinal Epithelium. *Annu. Rev. Nutr*. **1995**, *15*, 35–55.
6. Schneeberger, E. E.; Lynch, R. D. Tight Junctions. Their Structure, Composition, and Function. *Circ. Res*. **1984**, *55*, 723–733.
7. Lutz, K. L.; Siahaan, T. J. Molecular Structure of the Apical Junction Complex and its Contribution to the Paracellular Barrier. *J. Pharm. Sci*. **1997**, *86*, 977–984.
8. Gan, L.-S.; Hsyu, P.-H.; Pritchard, J. F.; Thakker, D. R. Mechanism of Intestinal Absorption of Ranitidine and Ondansetron Transport across Caco-2 cell Monolayers. *Pharm. Res*. **1993**, *10*, 1722–1725.
9. Lin, J. H. Pharmacokinetic and Pharmacodynamic Properties of Histamine H_2-Receptor Antagonists. *Clin. Pharmacokinet*. **1991**, *20*, 218–236.
10. Gan, L.-S.; Yanni, S.; Thakker, D. R. Modulation of the Tight Junctions of the Caco-2 Cell Monolayers by H_2-Antagonists. *Pharm. Res*. **1998**, *15*, 53–57.
11. Graf, J. H.; Cross, S.; Peterlik, M. Vitamin D Increases Tight-Junction Conductance and Paracellular Ca^{2+} Transport in Caco-2 Cell Culture. *Am. J. Physiol*. **1998**, *274*, G389–G396.
12. McRoberts, J. A.; Aranda, R.; Riley, N.; Kang, H. Insulin Regulates the Paracellular Permeability of Cultured Intestinal Epithelial Cell Monolayers. *J. Clin. Invest*. **1990**, *85*, 1127–1134.
13. Grasset, E.; Pinto, M.; Dussaulx, E.; Zweibaum, A.; Desjeux, J.-F. Epithelial Properties of Human Colonic Carcinoma Cell Line Caco-2: Electrical Properties. *Am. J. Physiol*. **1984**, *247*, C260–C267.
14. The oral bioavailability for famotidine (40–49%), ranitidine (51–60%), cimetidine (58–66%), and nizatidine (84–112%) was determined at the oral doses of 40, 100, 300, and 150 mg, respectively; see refs 9, 10, and references therein.
15. Hu, M.; Borchardt, R. T. Transport of a Large Neutral Amino Acid in a Human Intestinal Epithelial Cell Line (Caco-2): Uptake and Efflux of Phenylalanine. *Biochim. Biophys. Acta* **1992**, *1135*, 233–244.
16. Thwaites, D. T.; Brown, C. D. A.; Hirst, B. H.; Simmons, N. L. H^+-Coupled Dipeptide (Glycylsarcosine) Transport across Apical and Basal Borders of Human Intestinal Caco-2 Cell Monolayers Displays Distinctive Characteristics. *Biochim. Biophys. Acta* **1993**, *1151*, 237–245.
17. Dantzig, A. H.; Tabas, L. B.; Bergin, L. Cefaclor Uptake by the Proton-Dependent Dipeptide Transport Carrier of Hu-

man Intestinal Caco-2 Cells and Comparison to Cephalexin Uptake. *Biochim. Biophys. Acta* **1992**, *1112*, 167−173.
18. Wright, S. H.; Wunz, T. M. Succinate and Citrate Transport in Renal Basolateral and Brush-Border Membranes. *Am. J. Physiol.* **1987**, *253*, F432−F439.
19. Yanagisawa, I.; Hirata, Y.; Ishio, Y. Studies on Histamine H_2-Receptor Antagonists. 2. Synthesis and Pharmacological Activities of N-Sulfamoyl and N-Sulfonyl Amidine Derivatives. *J. Med. Chem.* **1987**, *30*, 1787−1793.
20. Gilman, D. J.; Wardleworth, J. M.; Yellin, O. Guanidine Derivatives of Imidazoles and Thiazoles. U.S. Patent 4,165,-378, **1979**.
21. Moreno, J. H. Blockage of Cation Permeability across the Tight Junctions of Gallbladder and Other Leaky Epithelia. *Nature* **1974**, *251*, 150−151.
22. Moreno, J. H. Blockage of Gallbladder Tight Junction Cation-Selective Channels by 2,4,6-Triaminopyrimidinium (TAP). *J. Gen. Physiol.* **1975**, *66*, 97−115.
23. Moreno, J. H.; Diamond J. M. Discrimination of Monovalent Inorganic Cations by "Tight" Junctions of Gallbladder Epithelium. *J. Membr. Biol.* **1974**, *15*, 277−318.
24. Bentzel, C. J.; Fromm, M.; Palant, C. E.; Hegel, U. Protamine Alters Structure and Conductance of *Necturus* Gallbladder Tight Junctions Without Major Electrical Effects on the Apical Cell Membrane. *J. Membr. Biol.* **1987**, *95*, 9−20.
25. Li, J. H.-Y.; Lindemann, B. Competitive Blocking of Epithelial Sodium Channels by Organic Cations: The Relationship between Macroscopic and Microscopic Inhibition Constants. *J. Membr. Biol.* **1983**, *76*, 235−251.
26. Pade, V.; Stavchansky, S. Estimation of the Relative Contribution of the Transcellular and Paracellular Pathways to the Transport of Passively Absorbed Drugs in the Caco-2 Cell Culture Model. *Pharm. Res.* **1997**, *14*, 1210−1215.
27. Knipp, G. T.; Ho, N. F. H.; Barsuhn, C. L.; Borchardt, R. T. Paracellular Diffusion in Caco-2 Cell Monolayers: Effect of Perturbation on the Transport of Hydrophilic Compounds that Vary in Charge and Size. *J. Pharm. Sci.* **1997**, *86*, 1105−1110.
28. Adison, A.;. Raub, T. J.; Burton, P. S.; Barsuhn, C. L.; Hilgers, A. R.; Audus, K. L.; Ho, N. F. H. Quantitative Approaches to Delineate Paracellular Diffusion in Cultured Epithelial Cell Monlayers. *J. Pharm. Sci.* **1994**, *83*, 1529−1536.
29. Lee, K.; Thakker, D. R. Photoaffinity Labeling of the Anionic Cellular Components Mediating Paracellular Transport of Cations Across Caco-2 Cell Monolayers. *PharmSci* **1998**, *1*, S-452.
30. Lee, K.; Thakker, D. R. Potential for Drug-Drug Interactions in the Absorption of Cationic Compounds Across Intestinal Epithelium. *PharmSci* **1998**, *1*, S-453.

Acknowledgments

Financial support from GlaxoWellcome Inc. is gratefully acknowledged.

JS980474K

Lyophilization of Protein Formulations in Vials: Investigation of the Relationship between Resistance to Vapor Flow during Primary Drying and Small-Scale Product Collapse

DAVID E. OVERCASHIER,* THOMAS W. PATAPOFF, AND CHUNG C. HSU

Contribution from *Department of Pharmaceutical Research and Development, Genentech, Inc., 1 DNA Way, South San Francisco, California 94080.*

Received November 17, 1998. Accepted for publication April 28, 1999.

Abstract □ During the lyophilization process, formulations containing protein, bulking agent, or lyoprotectant form a dry product layer that can affect the transport of sublimed water vapor. We carried out an investigation of the primary drying segment of lyophilization to evaluate the relationship between the resistance to water vapor flow through the dried layer and the microstructure of the dried cake. Recombinant humanized antibody HER2 (rhuMAb HER2) formulated in trehalose was studied, as were protein-free formulations containing trehalose and sucrose. Sublimation rate and product temperature data were used to compute the resistance to mass transfer. Dried cake structure was examined by scanning electron microscopy and a novel fluorescence microscopy method. Collapse temperatures were determined by freeze-drying microscopy. Mass transfer resistance was found to decrease with increases in temperature for each material. Resistance also depended on composition, decreasing in the formulation series, rhuMAb HER2, trehalose, sucrose. The lyophilized material consisted of porous cakes, with a distinct denser region at the top. Formulation and temperature affected the microstructure of the dried cakes. The formulated trehalose and sucrose were seen, by both microscopy techniques, to possess small (2–20 μm) holes in their platelike structures after lyophilization. The quantity of holes was higher for material dried at higher temperature. The collapse temperature (T_c) of a material appeared to play a role in the process, as lower T_c was correlated with lower resistance and a greater extent of holes. Our results are consistent with the theory that lower resistance to water vapor flow in the primary drying stage of lyophilization may be due to small-scale product collapse.

Introduction

Lyophilization is commonly used to prepare protein pharmaceuticals in dry form to extend shelf life. Operating cycles may be several days in length and typically involve three process segments: freezing, primary drying, and secondary drying. Freezing transforms the protein−excipient solution in a vial into two or more phases, usually crystalline ice and an amorphous freeze-concentrate containing the protein, lyoprotectant, and water. Additional phases may also form if the excipient precipitates or crystallizes out during freezing. Primary drying is the sublimation of ice from the frozen vial content under vacuum. Secondary drying, also under vacuum, involves the removal of water from the freeze-concentrate, reducing the residual moisture content to a level (e.g. ≤ 3 wt %/wt) suitable for long-term storage.[1]

* Corresponding author. Tel: (650) 225-3205; fax: (650) 225-3191; e-mail: overcashier.david@gene.com.

In the lyophilization of protein pharmaceuticals, the longest process segment is usually the sublimation of ice from frozen vials. The rate of ice removal is a function of the lyophilizer shelf temperature and chamber pressure.[2−6] The product temperature, which is also dependent on the shelf temperature and the pressure, is often 20−30 °C below that of the shelf as a result of the energy consumed by the transformation of ice to water vapor. The product temperature during primary drying is critical, because too high a temperature can result in product meltback or collapse[7] (potentially degradative events), whereas too low a temperature will result in lengthy lyophilization cycles. The product temperature accompanying a given temperature−pressure combination may vary between formulations.

A key parameter governing the relationship between the independent variables (the lyophilizer's shelf temperature and chamber pressure) and the dependent variables (ice sublimation rate and product temperature) is the resistance to water vapor flow exhibited by the growing dry layer. This layer is composed of the freeze-concentrated protein/excipient solid solution and the voids left after the ice crystals have sublimed. Pikal et al. determined the resistance to vapor flow for potassium chloride, povidone, mannitol, and dobutamine hydrochloride−mannitol solutions using a microbalance with capillary tubes and a method involving pressure measurement inside the vial to characterize vial freeze-drying.[7,8] They demonstrated that the resistance increases with increasing thickness of the dried layer, in a nonlinear fashion. They also reported that the resistance decreases with increasing temperature, a phenomenon ascribed to "hydrodynamic surface flow" of the sublimed water through the pores.

Milton et al. later proposed a different mechanism for the observed temperature dependence of resistance to mass transfer, involving product collapse on a microscopic scale.[9] In that study, the investigators determined the resistance to water vapor flow based on the time-dependent chamber pressure increase during brief interruptions of the flow from the chamber to condenser (by closing a valve between the two). For mannitol, lactose, and potassium chloride solutions, they reported that under some conditions, the resistance to vapor flow increased with thickness of the dried layer, as described above. However, at product temperature values near a material's collapse temperature, the resistance was not affected by increases in thickness. This constant-resistance phenomenon was hypothesized to be due to "microcollapse," the development of additional pathways for vapor flow in the form of holes in the dried material, a proposition supported by SEM photomicrographs of freeze-dried lactose.

Further research on the relationship between temperature, pressure, and sublimation rate was described by Chang and Fischer in their study of lyophilization cycle

10.1021/js980445+ CCC: $18.00
Published on Web 06/09/1999

development for rhIL-1ra formulated at 100 mg/mL.[6] In that study, the authors gave a comprehensive description of product temperatures and sublimation rates resulting from 35 different combinations of shelf temperature and chamber pressure. Unlike the reports described above, they observed the resistance to vapor flow to be independent of product temperature, over a wide range of temperatures (−32 to −14 °C).

This report describes our investigation of primary drying in lyophilization of recombinant humanized antibody HER2 (rhuMAb HER2) formulated in a trehalose−histidine−polysorbate system. This lyophilized product has recently received regulatory approval for breast cancer therapy (based on its capacity to inhibit growth of human breast carcinoma cells[10]). rhuMAb HER2 is formulated at high concentration (relative to other Genentech products), and we believe that the results of our investigation will be useful to others in the field. In this study, we measured sublimation rates and product temperatures for formulated rhuMAb HER2, for a range of lyophilization conditions, and determined mass transfer resistances. In addition, protein-free formulations containing either trehalose or sucrose were studied. Sucrose and trehalose have been shown to stabilize proteins in the dried state,[11−14] i.e., function as "lyoprotectants." The structure of materials after drying was examined by scanning electron microscopy and a newly developed fluorescence microscopy method. This study provided a better understanding of the relationship between resistance to vapor flow and small-scale product collapse in protein lyophilization.

Experimental Section

Materials—rhuMAb HER2, molecular mass approximately 160 kD, was produced at Genentech, Inc. by Chinese hamster ovary cells. It is a glycoprotein of 1328 amino acid residues. The bulk was formulated to contain 25 mg/mL rhuMAb HER2, 20 mg/mL trehalose, 0.1 mg/mL polysorbate 20, and 5 mM histidine, pH 6.0. Two excipient formulations also were tested: 45 mg/mL trehalose, 0.1 mg/mL polysorbate 20, and 5 mM histidine, pH 6.0; and 45 mg/mL sucrose, 0.1 mg/mL polysorbate 20, and 5 mM histidine, pH 6.0. Solutions were prepared in distilled water and 0.2-μm filtered. All components used were reagent grade or better.

Sublimation Rate and Product Temperature Measurement in Vial Freeze-Drying—The sublimation of ice in the formulations of interest was evaluated by carrying out primary drying in Leybold−Heraeus GT20 lyophilizers at constant shelf temperature and chamber pressure. Formulations were filled at 5.0 mL in 10-mL Wheaton tubing glass vials (inner diameter 2.37 cm) with 20-mm neck finish. Vials were stoppered for lyophilization using West gray butyl rubber stoppers. Vials were cooled to −50 °C at 20 °C/h and held for 5 h before proceeding with drying. After the chamber was evacuated to the pressure set point, the lyophilizer shelf was warmed to the temperature set point over a 2-h period. Ice sublimation was allowed to proceed, with constant temperature and pressure set points. Such primary drying tests were conducted at various conditions with the shelf temperatures in the range −20 to +25 °C and the chamber pressure at 100 mTorr (regulated with nitrogen gas). Tests also were carried out at −30 and −35 °C under 50 to 75 mTorr and 25 °C under 200 and 300 mTorr.

The temperature of the vial contents was measured by a 30-gauge Type T thermocouple sensor placed vertically through the vial opening, the tip positioned 1−4 mm above the vial base. For each formulation lyophilized in a run, the product temperature stated is the mean of two to four sensors.

At selected time points throughout primary drying, three preweighed vials of each formulation were stoppered in the chamber using a thief arm installed in the dryer. After lyophilization, the stoppered vials were reweighed to determine the water loss. The sublimation rate was determined from the mean water loss determined at four to six timepoints. It has been reported that a vial adjacent to an empty vial or the edge of the shelf shows a sublimation rate increase of 5% or 20%, respectively, relative to a vial in the middle of an array of subliming vials, presumably due to radiation from the shelf and chamber wall.[3] Thus, in this study only those vials adjacent to equivalent filled vials were sampled for temperature or rate determination.

Determination of Mass Transfer Resistance—The resistance to vapor flow through the dried layer in the vial was determined using a method adapted from the work of Pikal et al.[3,8] In our method, the sublimation rate (essentially time-invariant) and the time-dependent product temperature data were used in order to estimate the product temperature (and the corresponding ice vapor pressure) at the ice sublimation front and the overall mass transfer resistance exhibited by the dried product layer. A brief summary of the pertinent equations is given below.

The overall dried product resistance, $\hat{R}_p$, describes the proportionality between the specific sublimation rate, $\dot{m}/A_p$, and the pressure driving force, $P_o - P_v$:

$$\frac{\dot{m}}{A_p} = \frac{1}{\hat{R}_p} \times (P_o - P_v) \tag{1}$$

where $\dot{m}$ is sublimation rate (g/h), A_p is cross-sectional area of product in the vial (cm^2), $\hat{R}_p$ is normalized dried product resistance (cm^2 mTorr h g^{-1}), P_o is equilibrium vapor pressure of ice at the temperature of the subliming ice (mTorr), and P_v is pressure in the vial (assumed equal to chamber pressure P_c) (mTorr).

In our analysis, we assume that the cross-sectional area of product in the vial, A_p, is equal to the internal area of the vial. Recent work suggests that in certain lyophilization cases this may not be true.[15] The investigators provided some evidence that the sublimation front may be nonplanar (concave down) due to faster drying along the vial wall, following cake shrinkage; for further consideration see the Results and Discussion.

In our application of eq 1, we estimate the pressure in the vial to be approximately equal to the chamber pressure. The substitution of P_c for P_v means that the resistance quantity we determine is the sum, $\hat{R}_p + \hat{R}_s$ (where $\hat{R}_s$ is the resistance to vapor flow exhibited by the stopper). Previous investigators, using modified vials for direct measurement of P_v, reported that the contribution of $\hat{R}_s$ (20-mm stoppers) to the sum ($\hat{R}_p + \hat{R}_s$) was less than 4%[3], supporting our approximation.

The temperature dependence of the ice vapor pressure P_o (mTorr) is given by:[16]

$$P_o = 2.7 \times 10^{13} \times \exp[-6145/(T_i + 273.15)] \tag{2}$$

where T_i is the temperature (°C) of the subliming ice interface.

Inserting the vapor pressure expression (eq 2) in the mass transfer equation (eq 1) and substituting P_c for P_v, we obtain:

$$\frac{\dot{m}}{A_p} = \frac{1}{\hat{R}_p} \times (2.7 \times 10^{13} \times \exp[-6145/(T_i + 273.15)] - P_c) \tag{3}$$

During ice sublimation, heat is supplied by the shelf to the bottom of the vial and is consumed at the sublimation front. The temperature gradient in the ice/solute matrix can be estimated by the Fourier heat conduction model and shown to have the axial length dependence described in eq 4:

$$\frac{dT}{dx} = -\frac{\Delta H_s \times \dot{m}}{A_v \times K_I} \tag{4}$$

where x is the axial position relative to bottom of vial (cm), ΔH_s is the heat of sublimation (cal/g), A_v is the cross-sectional area of vial base (cm^2), and K_I is the thermal conductivity of the product (estimated as the area-weighted sum of thermal conductivities of glass (Wheaton) and ice,[17] as described previously[3]).

By integration of eq 4, we obtain an estimation of the temperature at the subliming ice interface in terms of the measured product temperature (eq 5). The interface can be seen to have the lowest temperature in the vial.

$$T_i = T_p - \frac{\Delta H_s \times \dot{m}}{A_v \times K_I} \times (L - l) \tag{5}$$

where T_p is the product temperature (°C) at the temperature sensor, L is the thickness of product, from temperature sensor to initial fill height (cm), and l is the thickness of dried layer (cm), determined from the interpolated weight loss data, with the assumption that the sublimation front is planar, by the formula $l = (\dot{m} \times t + m_0)/(\rho \times A_v)$, where t is the elapsed time, measured from the time at which the shelf temperature reaches the set point, m_0 is the weight loss at $t = 0$, and ρ is the frozen matrix density.

Uncertainty in the sublimation front temperature, as estimated by eq 5, could result from several sources, including the thermal conductivity of the frozen product in the vial, the relative quantities of radial and axial heat flow, the measured product temperature, the vial geometry, and the shape of the subliming interface. In our experiments, the effect of uncertainty in the thermal conductivity of the frozen product in the vial may be low, due to the use of solutions of constant solute concentration (4.6% w/v) for all tests. The effect of radial heat flow was minimized by surrounding all thermocouple and sublimation rate vials with filled, subliming vials.

The act of measuring product temperature may influence the sublimation process: thermocouple vials may nucleate before "normal" vials, resulting in a different microstructure and, possibly, faster sublimation.[18] In our experiments, the potential effect of thermocouples on microstructure would be constant, independent of drying temperature or formulation composition. Uncertainty in the measured product temperature and in the vial geometry were reduced by using replicate measurements (2−4) for each condition.

We obtain our final equation by substituting eq 5 for the interface temperature term in eq 3 and rearranging:

$$\hat{R}_p = \frac{A_p}{\dot{m}} \times \left(2.7 \times 10^{13} \times \exp\left[\frac{-6145}{T_p - \frac{\Delta H_s \times \dot{m}}{A_v \times K_I} \times (L - l) + 273.15} \right] - P_c \right) \quad (6)$$

Equation 6 allows us to estimate the resistance to mass transfer as a function of the dried layer thickness using the measurable quantities sublimation rate, product temperature, and vial dimensions.

Examination of Dried Cake Structure—The microscopic structure of lyophilized material was evaluated by two methods, scanning electron microscopy (SEM) and a novel fluorescence microscopy technique. Samples to be analyzed were prepared by lyophilization using one of two primary drying conditions, 10 °C, 100 mTorr for 30 h or −30 °C, 70 mTorr for 90 h. Following an increase (at 5 °C/h) in the shelf temperature, secondary drying was conducted at 20 °C, with the pressure unchanged, for 8 h. Vials were stoppered under 720 Torr ± 40 Torr nitrogen and then transferred to a desiccator for further drying. Desiccation over phosphorus pentoxide was initiated at <25 Torr pressure and carried out at 20−25 °C for 7−14 d. Samples for SEM were prepared in a nitrogen-purged glovebox under low (<10%) relative humidity by removing the dried cakes from the vials, sectioning vertically by hand using a single-edge razor blade, mounting to a sample stub, and coating under vacuum with a 10 nm gold−palladium layer. Images were obtained by SEM (Philips model 525M; acceleration 5 kV).

Dried cake structure was also evaluated using a second technique, the fluorescence microscopy of rhodamine-containing "cakes" embedded in wax. To selected vials, rhodamine B aqueous solution (20 μL at 0.5 mg/mL) was added before lyophilization. Solutions were lyophilized and desiccated as described in the previous paragraph. These cakes were then placed under vacuum and heated to 60 °C in the presence of low melting paraffin (The Hygenic Corp., Akron, OH) in which Sudan Black B was dissolved. The melted paraffin was allowed to fill the vial until the entire cake was covered by several millimeters. The vacuum was released, and the vials were cooled to room temperature. The vials were broken carefully and the intact paraffin plugs removed. The paraffin plugs containing the lyophilized cakes were sliced vertically as described above. Images of sections were acquired with a Nikon Optiphot-2 microscope using the filter cube for rhodamine (excitation 510−560 nm, emission > 610 nm). Thermal analysis of the dried material was carried out by differential scanning calorimetry (DSC; Seiko model 120 with model SSC/5200H data station). Samples of approximately 12−20 mg were sealed in Al containers, equilibrated to room temperature, and warmed at 5 °C min^{-1} to 200 °C.

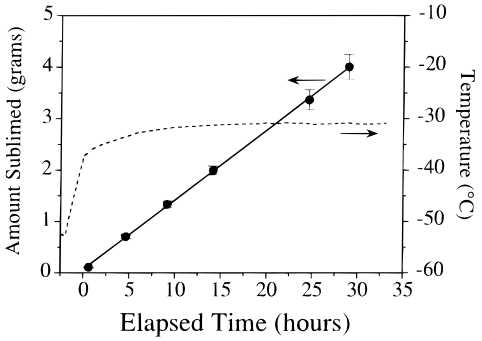

Figure 1—Weight loss (●) and product temperature (- - -) measurements during primary drying of rhuMAb HER2 formulation at –20 °C shelf temperature; 100 mTorr chamber pressure. Note the linearity of the weight loss data.

Collapse Temperature Assessment Using Freeze-Drying Microscope—The presence or absence of collapse during freeze-drying of the rhuMAb HER2, trehalose, and sucrose formulations at various temperatures was investigated using a freeze-drying microscope. This technique was reported by MacKenzie to be useful in identifying structural changes occurring during ice sublimation.[19] In the present study we used a microscope system that includes a compact freeze-drying chamber and a thermoelectric heat pump for cooling. Details of the system were reported previously.[20] The sample to be investigated is held between two glass cover slips on the cooling stage, cooled to approximately −45 °C, and lyophilized as desired.

In our tests, sample freezing was executed in a manner described below to form larger ice crystals for ease of viewing and for faster ice sublimation. A sample aliquot, approximately 4 μL, was cooled to −1.5 °C and held for 1 min to allow for temperature equilibration. The chamber cover was briefly removed, and a dry ice pellet was held against the top glass cover slip for about 5 s to nucleate ice crystals in the sample (at a location away from the microscope viewing area). The sample was held at −1.5 °C for about 2 min and then at −3.5 °C before cooling at 10 °C/min to −45 °C. After a 15-min hold, the chamber was evacuated to approximately 100 mTorr and the stage temperature was increased at 5 °C/min and held at the temperature of interest. It has been shown that the stage temperature and sample temperature are equivalent in this system.[20] The temperature was increased stepwise from −40 °C to −15 °C, in 2−5 °C steps, for each formulation. At the location of the sublimation front, the degree to which the structure of the glassy matrix was retained was evaluated visually. Collapse temperature of the frozen sample was identified as the stage temperature at which the structure was observed to distort or flow. The identification of a collapse temperature is an estimate, since collapse (unlike melting) does not occur at a sharply defined temperature.

Thermal analysis of the frozen aqueous material was carried out using the DSC described above, fitted with a cooling head (mod. CA-5) for controlled cooling by liquid nitrogen. Samples of approximately 15 mg were sealed in Al containers, equilibrated to 5 °C, and cooled at 5 °C min^{-1} to −90 °C. Following equilibration, the sample was warmed at 5 °C min^{-1} to 20 °C.

Results and Discussion

Sublimation Rate and Product Temperature in Vial Freeze-Drying—At a given lyophilizer shelf temperature and pressure, the amount of ice sublimed from vials was approximately linear with respect to time; see Figure 1, depicting rhuMAb HER2 subliming on a −20 °C shelf. Table 1 shows that the sublimation rate was found to increase with higher temperature and pressure set points, as expected. This trend is similar to that reported by

Table 1—Sublimation Rate and Product Temperature for rhuMAb HER2, Trehalose, and Sucrose Formulations (see text) as Functions of Lyophilizer Shelf Temperature and Chamber Pressure

shelf temp (°C)	pressure (mTorr)	specific sublimation rate(g h^{-1} cm^{-2})			product temperature (°C)		
		rhuMAb HER2	trehalose	sucrose	rhuMAb HER2	trehalose	sucrose
25	300	0.19			–20		
25	200	0.16	0.15		–21	–28	
25	100	0.11	0.13		–26	–30	
10	100	0.084	0.083	0.098	–26	–30	–34
–20	100	0.031	0.031	0.035	–31	–36	–37
–30	70			0.019			–37
–30	50	0.014	0.015		–37	–37	
–35	75		0.011	0.012		–37	–37

others.[2–6] The data also indicate that under the same shelf temperature and chamber pressure conditions, sublimation rates for all formulations were approximately equal, except for two conditions at which sucrose rates were slightly higher. The rates reported in Table 1 have coefficients of variation (defined as the standard error divided by the mean) of 1.2 to 3.4%.

During each run, the product temperature was observed to increase as the shelf temperature was ramped from −50 °C to the primary drying shelf temperature set point, then level off (Figure 1). The product temperature was sensitive to shelf temperature, chamber pressure, and formulation (Table 1; data correspond to the middle portion of the sublimation process, at which time the product temperature was approximately constant). The product temperatures during primary drying followed the formulation series, rhuMAb HER2 > trehalose > sucrose, at most process conditions. It might be expected that product temperature and sublimation rate are connected, yet under some process conditions we observed differences in product temperatures between formulations, even though the sublimation rates were approximately equivalent. This situation may be due to differences between formulations in resistance to vapor flow, as is discussed below.

Determination of Mass Transfer Resistance—The measured resistance to mass transfer was seen to increase with increased dry layer thickness (Figure 2; rhuMAb HER2, −20 °C temperature), as expected. The thickness dependence gave a good fit to the nonlinear model proposed by Pikal et al.[8] and shown in eq 7:

$$\hat{R}_p = \frac{A_0 + A_1 l}{1 + A_2 l} \qquad (7)$$

where A_0, A_1, A_2 are constants determined from fitting of data. Figure 2 also illustrates the increase in resistance to vapor flow per unit thickness ($d\hat{R}_p/dl$). As reported previously,[8] the derivative function was high at low values of dried layer thickness and low at higher thicknesses, suggesting that a denser layer was present at the top of the vial.

Figure 3 shows the resistance to mass transfer determined for ice sublimation in the rhuMAb HER2 formulation at several temperature and pressure set points. The mass transfer resistance was sensitive to the shelf temperature, with higher resistance values shown by material processed at lower temperatures. This functionality was reported previously,[8,9] as described above.

Mass transfer resistance was also determined for formulated trehalose (Figure 4) and sucrose (Figure 5). These materials showed similar effects of thickness and shelf temperature on resistance as those seen with rhuMAb HER2. However, the resistance to mass transfer was lower, under most conditions, for trehalose than for rhuMAb HER2, and the resistance for the sucrose-containing material was lower still. Only at lower shelf temperatures (−30 and −35 °C) did the three materials appear equivalent.

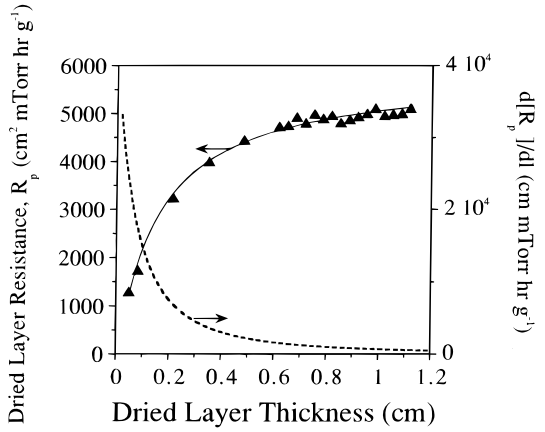

Figure 2—Resistance to mass transfer, $\hat{R}_p$, as a function of dried layer thickness for rhuMAb HER2 at –20 °C, 100 mTorr (▲). The equation for the $\hat{R}_p$ curve fit (solid line) is described in the text (eq 7). Also shown is the derivative (dotted line) of the curve fit, representing the increase in resistance as a function of the increase in dried layer thickness. The derivative curve shows that the upper layer of the dried cake contributes more to the resistance than does the lower portion, suggesting a nonuniformity in the dried layer with respect to vertical position.

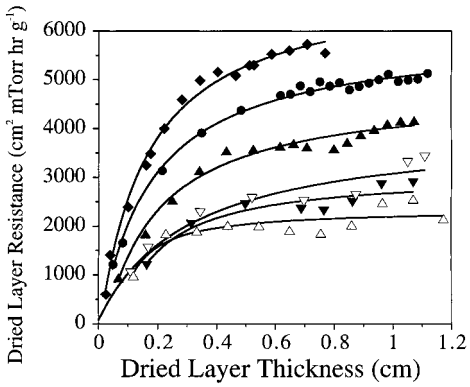

Figure 3—Resistance to mass transfer as a function of dried layer thickness for rhuMAb HER2 at a variety of processing conditions (pressure = 100 mTorr unless noted): –30 °C/50 mTorr (◆), –20 °C (●), 10 °C (▲), 25 °C (▼), 25 °C/200 mTorr (▽), 25 °C/300 mTorr (△). Higher temperature and pressure were observed to result in lower resistance.

The relationships between vapor transfer resistance and temperature at the ice−dry layer interface, determined at the dry layer thickness $l = 0.8$ cm, are summarized for the three formulations in Figure 6. These measurements yield "snapshots" of the ice sublimation processes at points at which approximately 70% of the material had sublimed, enabling the examination of mass transfer resistance as functions of formulation and temperature. The resistance followed the series rhuMAb HER2 > trehalose > sucrose,

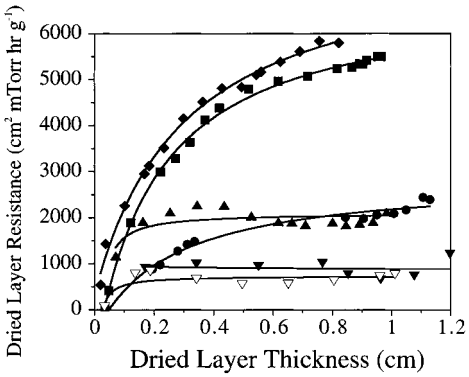

Figure 4—Resistance to mass transfer as a function of dried layer thickness for formulated trehalose at a variety of processing conditions (pressure = 100 mTorr unless noted): –35 °C/75 mTorr (■), –30 °C/50 mTorr (◆), –20 °C (●), 10 °C (▲), 25 °C (▼), 25 °C/200 mTorr (▽). Resistance generally decreased with increased temperature and pressure and was lower at most conditions than that observed for formulated rhuMAb HER2 (Figure 3).

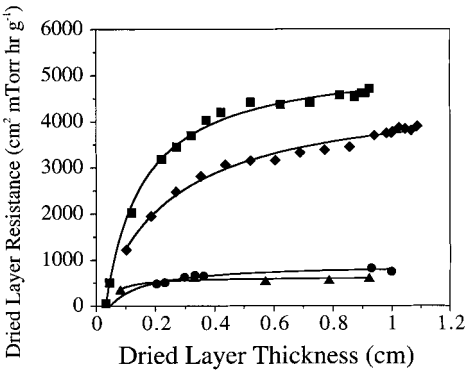

Figure 5—Resistance to mass transfer as a function of dried layer thickness for formulated sucrose at a variety of processing conditions (pressure = 100 mTorr unless noted): –35 °C, 75 mTorr (■), –30 °C, 70 mTorr (◆), –20 °C (●), 10 °C (▲). Resistance decreased with increased temperature and pressure and was lower than that observed for the rhuMAb HER2 (Figure 3) and trehalose (Figure 4) formulations.

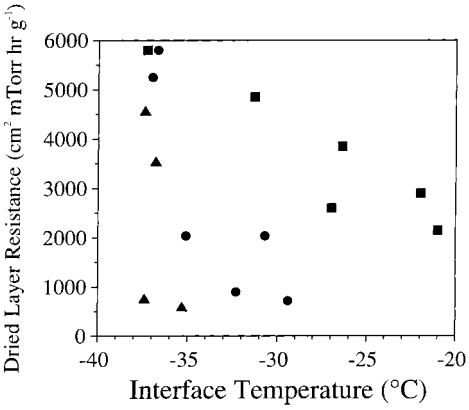

Figure 6—Mass transfer resistance for formulated rhuMAb HER2 (■), trehalose (●), and sucrose (▲) vs interface temperature. Data shown represent values at a dried layer thickness of 0.8 cm. Resistance followed the series rhuMAb HER2 > trehalose > sucrose and decreased with increased interface temperature.

except at interface temperatures below −36 °C, for which the resistances were approximately equal. Figure 6 also illustrates the decrease in resistance with increased temperature. The temperature sensitivity of resistance was highest for sucrose and lowest for rhuMAb HER2.

It is interesting to note that, even under operation conditions which showed large differences between formulations in mass transfer resistance (e.g., 45−80%), the differences in sublimation rate were moderate (8−17%). Limitations in the transfer of heat from the lyophilizer shelf to the vial may be responsible for this phenomenon, although its study was beyond the scope of this work.

As described above, some investigators have hypothesized that when cake shrinkage occurs in lyophilization, the sublimation front may be nonplanar (the magnitude of deviation from a planar sublimation front is not described).[15] In our study, slight shrinkage was observed, so the mass transfer resistance values we determined may be affected by the hypothesized nonplanar nature of the subliming interface. One might expect that the impact of a nonplanar interface would be minimized by the study of relatively thin, flat sections of material. In our study, we monitored the sublimation of 0.8 to 1.0 cm material (average thickness) in vials of diameter 2.4 cm. The effect of nonplanarity, therefore, may have been small. The formulations evaluated in this study exhibited similar cake shrinkage during lyophilization, so the shape of the subliming interface (if not planar) may have been independent of the formulation and drying conditions which we compared.

Overall, uncertainty in the mass transfer resistance results from variability in the measured parameters. In our study, the highest observed uncertainty in sublimation rate (C.V.) was 3.4%; the variation between replicate product temperature values (standard deviation) was 0.1 to 0.8 °C. Analysis of eq 6 shows that "worst-case" errors in rate and temperature have the following effects: An error of ±10% in the sublimation rate gives rise to a variation in mass transfer resistance of ±10%; uncertainty in product temperature of 1 °C induces a variation in resistance of ±20%. These errors in the calculated resistance, while not insignificant, are less than the magnitude of differences between temperatures and formulations shown.

Examination of Dried Cake Structure—The dried material produced by the two lyophilization cycles tested formed white, porous cakes showing slight shrinkage; no large-scale collapse was observed. The morphology of lyophilized material was observed using two techniques, fluorescence microscopy of wax embedded cakes and SEM. The fluorescence images revealed the dried material to have a microporous structure, with a distinct denser layer at the top of the cake (Figure 7A; rhuMAb HER2 dried with a 10 °C primary drying shelf temperature). Examination of this layer at higher magnification (not shown) revealed the layer to have fewer, smaller channels relative to the rest of the dried cake. The layer may contribute to the high $d\hat{R}_p/dl$ corresponding to low dry layer thicknesses, as described above.

At a smaller scale, SEM showed that lyophilization of formulated rhuMAb HER2 using a 10 °C primary drying shelf temperature produced a smooth, platelike structure built around the pores left by the sublimed ice (Figure 7B). The fluorescence microscopy method also illustrated a structure composed of smooth plates and channels (Figure 7C). Formulated rhuMAb HER2 prepared by a −30 °C primary drying shelf temperature was seen, by both methods, to have a similar appearance (not shown).

Lyophilization of formulated trehalose gave a structure which, like rhuMAb HER2, was composed of plates but also contained holes approximately 2−8 μm in diameter. These holes are illustrated by SEM for the 10 °C (Figure 8A) and −30 °C (Figure 8B) primary drying conditions, with lower temperature giving smaller and fewer holes. Holes were also detected by the fluorescence microscopy technique (Figure 8C; 10 °C). As with SEM, fluorescence microscopy detected fewer holes for the −30 °C process (not shown) than for the 10 °C version. Holes of this size range were also reported by others in the lyophilization of lactose.[9]

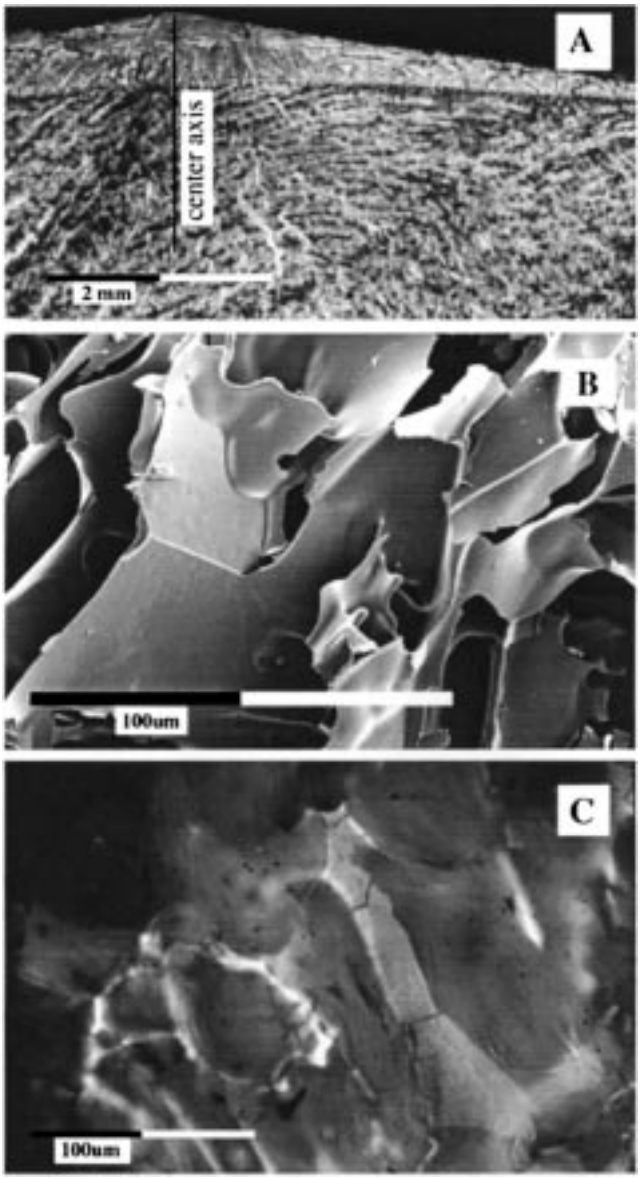

Figure 7—Structure of lyophilized rhuMAb HER2 formulation (10 °C primary drying shelf temperature). (A) Note the denser layer present at the top. The denser layer may be responsible for the higher resistance per unit thickness corresponding to low dried layer thicknesses (Figures 2–5). Fluorescence microscopy, 8X magnification. (B) Note the smooth, plate-like features, separated by open pores. SEM, 270X magnification. (C) Note the smooth structure. Fluorescence microscopy, 150X magnification.

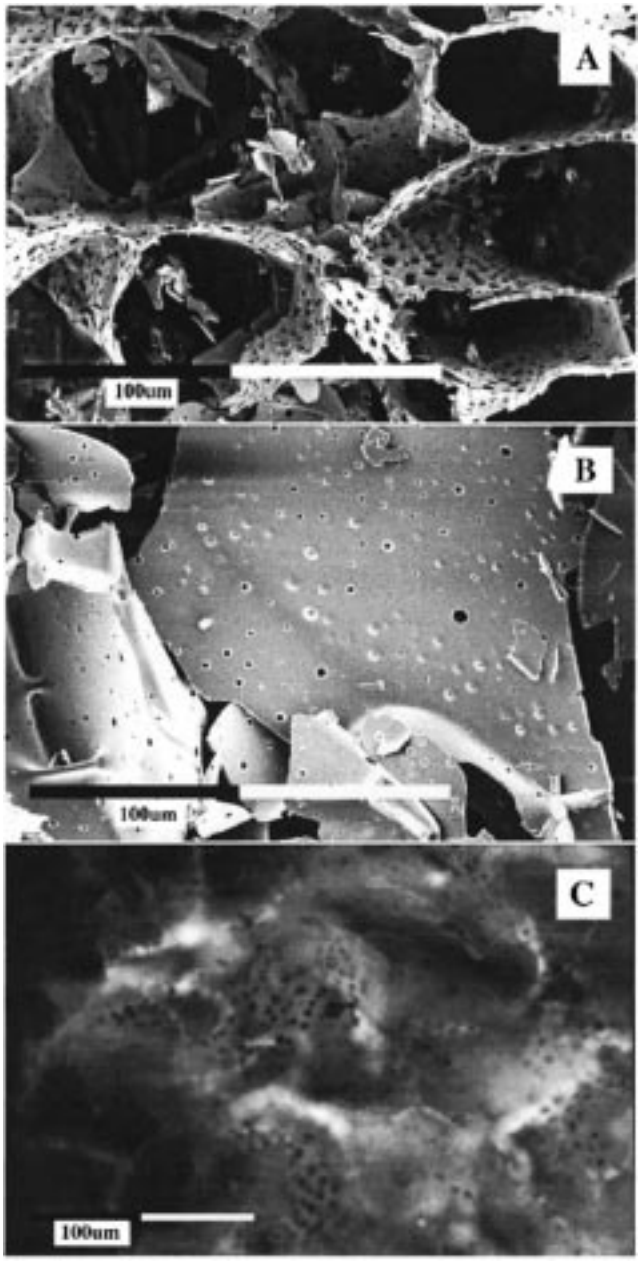

Figure 8—Structure of lyophilized trehalose formulation. Note the appearance of small holes (diameter ~2–8 μm) in the "plates." (A) 10 °C shelf: The large pores (diameter ~100 μm) are thought to be established when the ice crystals grew into the freeze-concentrate. SEM, 270X magnification. (B) –30 °C shelf: The holes are smaller and fewer than those observed in formulated trehalose prepared at the 10 °C shelf temperature. SEM, 270X magnification. (C) 10 °C shelf: Fluorescence microscopy, 150X magnification.

Interestingly, Figure 8A illustrates the pores, approximately 100 μm in diameter, formed by the ice crystals and providing the main avenue for vapor flow through the dried product layer.

The sucrose formulation was seen by SEM to possess holes in the dried structure, both for the 10 °C (Figure 9) and −30 °C process conditions. In addition, the sucrose structures were more "rounded" than the other formulations, with an appearance (Figure 9) suggesting viscous flow of the freeze-concentrate. As with the trehalose formulation, the lower temperature process gave fewer, smaller holes (not shown). Fluorescence microscopy also detected holes in the lyophilized sucrose from both the 10 °C and −30 °C processes (not shown).

The images acquired using the two microscopy techniques indicate that the structure of dried material is sensitive to composition and to the drying process used. Microscopy indicates that the formulated rhuMAb HER2 dries into intact plates, whereas the trehalose and sucrose formulations develop holes in the structure. These holes are more prevalent in material dried by the higher primary drying shelf temperature, so it is likely that they are produced during primary drying. The extent of holes observed in the structure of dried material, increasing with temperature and also in the formulation sequence rhuMAb HER2−trehalose−sucrose, is correlated with lower mass transfer resistance. This agreement suggests that the holes can be an important contributor to the conductance of water vapor through the dried layer. The gradual decrease in mass transfer resistance as a function of temperature seen for rhuMAb HER2 (in the absence of observed holes) suggests that other factors may also play a role.

DSC analysis of the material prepared for microscopic evaluation showed glass transition temperatures (T_g) of 76

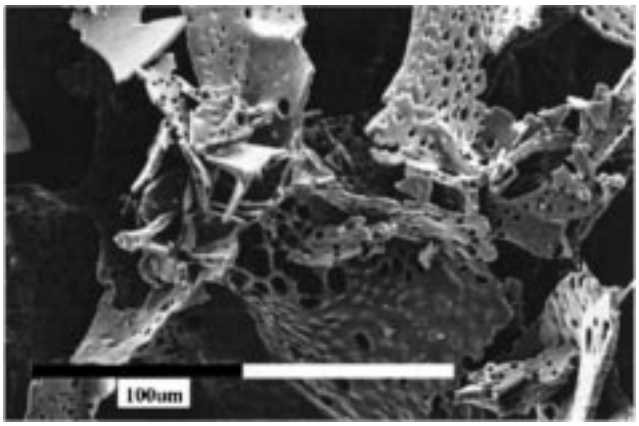

Figure 9—Structure of lyophilized sucrose formulation (10 °C shelf). Note the appearance of small holes (diameter 2–20 μm) in the "plates." Larger holes and smoothed structure suggests increased material flow over that seen in the rhuMAb HER2 and trehalose formulations. SEM, 270X magnification.

Table 2—Transition Temperatures for Frozen Aqueous Formulations Determined by Freeze-Drying Microscopy and DSC

	freeze-drying microscope		DSC: phase transition temp (°C)
formulation[a]	collapse temp (°C)	comment	
rhuMAb HER2	–20	"liquid" phase very viscous	–22
trehalose	–34		–38, –30
sucrose	–40	"liquid" phase flows readily	–43, –33

[a] The composition of each formulation is described in the text.

°C for the sucrose formulation and over 110 °C for the rhuMAb HER2 and trehalose formulations (data not shown). The high T_g values suggest that the materials were thermally stable at the conditions used in the sample preparation and microscopic analysis. In addition, similar structural characteristics were observed by the two methods of microscopy, suggesting that the structures observed were not induced by the evaluation methods. Although the resolution of the fluorescence microscopy technique is lower than that of SEM, it is sufficient to show the presence or absence of holes in the cake structure. In addition, the wax embedment involved in the fluorescence microscopy technique may be useful in protecting samples from atmospheric moisture. This method is under investigation in other freeze-drying studies.

Collapse Temperature Assessment Using Freeze-Drying Microscope—The frozen sample, as observed in the freeze-drying microscope, was composed of branched ice crystals separated by thinner freeze-concentrate regions. Ice crystal growth during cooling was generally from the nucleation site at the center of the stage toward the edges of the sample. Upon evacuation of the chamber, ice sublimation was observed to take place from the edge toward the center of the sample. For each formulation, the structure of the freeze-concentrate was retained at the ice sublimation front at lower stage temperatures but was lost at higher temperatures, as the freeze-concentrated material achieved greater mobility.

The approximate collapse temperature (T_c) and phase transition temperatures (obtained by DSC) for formulated rhuMAb HER2, trehalose, and sucrose are given in Table 2. The formulated rhuMAb HER2 gave the highest T_c, while the sucrose formulation gave the lowest T_c. In our tests, a solution of neat sucrose gave a collapse temperature of −31 to −32 °C, which matches the value reported previously by MacKenzie, −32 °C.[19] For the two protein-free formulations, DSC showed two transitions, possibly corresponding to the glass transition and collapse phenomena. The DSC phase transition temperatures are similar to the T_c data and show the same formulation dependence; we emphasize the T_c results because of their connection to ice sublimation.

For the formulations tested, lower T_c was correlated with lower mass transfer resistance (Figure 6). The data in Table 2 and Figure 6 also suggest that there may be a relationship, for each formulation, between T_c and the temperature dependence of resistance.

The mass transfer resistance data, structure observed by the two microscopy techniques, and collapse temperature results provide a consistent description of ice sublimation and water vapor transport through the dried layer. Increased product temperature during primary drying resulted in lower resistance to vapor flow and, in some cases, the formation of the holes in the dried cake. Between formulations, lower collapse temperature was correlated with lower resistance and more holes. These observations support the theory, set forth by Milton et al. and supported with data for lactose lyophilization,[9] that the alteration in material structure accompanying small-scale collapse results in decreased resistance to water vapor flow in primary drying.

Conclusions

The resistance to water vapor flow through the dried cake layer, as determined from ice sublimation rate and product temperature data, was observed to decrease with increases in temperature. Resistance was also found to depend on formulation, with values following the series: rhuMAb HER2 > trehalose > sucrose. At many process conditions, different formulations were observed to have similar sublimation rates but differing product temperatures. Mass transfer resistance variation between formulations appears to account for these differences. The structure of the dried cake was evaluated by SEM as well as with a newly developed fluorescence microscopy technique. The presence of a dense layer at the top of the dried cake, which may be responsible for the higher resistance determined for this region, was observed. Temperature and formulation affected the microstructure of the cakes. Some of the formulations tested were found to possess small (2−20 μm) holes in their structure after lyophilization. The extent of the holes was observed to increase with the processing temperature, as well as in the formulation series, rhuMAb HER2−trehalose−sucrose. The collapse temperature (T_c), determined by freeze-drying microscopy, was found to decrease over the same formulation series. For the materials studied, lower resistance was correlated with a greater extent of holes and lower T_c. The data obtained in this study support the view that lower resistance to water vapor flow in the primary drying stage of lyophilization may be the result of small-scale product collapse.

References and Notes

1. Pikal, M. J.; Dellerman, K.; Roy, M. L. Formulation and Stability of Freeze-dried Proteins: Effects of Moisture and Oxygen on the Stability of Freeze-dried Formulations of Human Growth Hormone. In *International Symposium on Biological Product Freeze-Drying and Formulation*; May, J. C., Brown, F., Eds.; Karger: Basel, 1991; Vol. 74, pp 21−38.
2. Nail, S. L. The Effect of Chamber Pressure on Heat Transfer in the Freeze-Drying of Parenteral Solutions. *J. Parenter. Drug Assoc.* **1980**, *34*, 358−368.
3. Pikal, M. J.; Roy, M. L.; Shah, S. Mass and Heat Transfer in Vial Freeze-Drying of Pharmaceuticals: Role of the Vial. *J. Pharm. Sci.* **1984**, *73*, 1224−1237.
4. Livesey, R. G.; Rowe, T. W. G. A Discussion of the Effect of Chamber Pressure on Heat and Mass Transfer in Freeze-Drying. *J. Parenter. Sci. Technol.* **1987**, *41*, 169−171.

5. Pikal, M. J.; Shah, S. The Collapse Temperature in Freeze-Drying: Dependence on Measurement Methodology and Rate of Water Removal from the Glassy Phase. *Int. J. Pharm.* **1990**, *62*, 165−186.
6. Chang, B. S.; Fischer, N. L. Development of an Efficient Single-Step Freeze-Drying Cycle for Protein Formulations. *Pharm. Res.* **1995**, *12*, 831−837.
7. Pikal, M. J. Use of Laboratory Data in Freeze-Drying Process Design: Heat and Mass Transfer Coefficients and the Computer Simulation of Freeze-Drying. *J. Parenter. Sci. Technol.* **1985**, *39*, 115−139.
8. Pikal, M. J.; Shah, S.; Senior, D.; Lang, J. E. Physical Chemistry of Freeze-Drying: Measurement of Sublimation Rates for Frozen Aqueous Solutions by a Microbalance Technique. *J. Pharm. Sci.* **1983**, *72*, 635−650.
9. Milton, N.; Pikal, M. J.; Roy, M. L.; Nail, S. L. Evaluation of Manometric Temperature Measurement as a Method of Monitoring Product Temperature During Lyophilization. *PDA J. Pharm. Sci. Technol.* **1997**, *51*, 7−16.
10. Fendly, B. M.; Winget, M.; Hudziak, R. M.; Lipari, M. T.; Napier, M. A.; Ullrich, A. Characterization of Murine Monoclonal Antibodies Reactive to Either the Human Epidermal Growth Factor Receptor or HER2/neu Gene Product. *Cancer Res.* **1990**, *50*, 1550−1558.
11. Townsend, M. W.; DeLuca, P. P. Use of Lyoprotectants in the Freeze-Drying of a Model Protein, Ribonuclease A. *J. Parenter. Sci. Technol.* **1988**, *42*, 190−199.
12. Carpenter, J. F.; Crowe, J. H. An Infrared Spectroscopic Study of the Interactions of Carbohydrates with Dried Proteins. *Biochemistry* **1989**, *28*, 3916−3922.
13. Prestrelski, S. J.; Pikal, K. A.; Arakawa, T. Optimization of Lyophilization Conditions for Recombinant Human Interleukin-2 by Dried-State Conformational Analysis Using Fourier Transform Infrared Spectroscopy. *Pharm. Res.* **1995**, *12*, 1250−1259.
14. Crowe, L. M.; Reid, D. S.; Crowe, J. H. Is Trehalose Special for Preserving Dry Biomaterials? *Biophys. J.* **1996**, *71*, 2087−2093.
15. Pikal, M. J.; Shah, S. Intravial Distribution of Moisture During the Secondary Drying Stage of Freeze-Drying. *PDA J. Pharm. Sci. Technol.* **1997**, *51*, 17−24.
16. Jansco, G.; Pupezin, J.; Van Hook, W. A. The Vapor Pressure of Ice Between 0.01 and −100 °C. *J. Phys. Chem.* **1970**, *74*, 2984−2989.
17. Fletcher, N. H. *The Chemical Physics of Ice*; Cambridge University Press: London, 1970, p 143.
18. Roy, M. L.; Pikal, M. J. Process Control in Freeze-Drying: Determination of the End Point of Sublimation Drying by an Electronic Moisture Sensor. *J. Parenter. Sci. Technol.* **1989**, *43*, 60−66.
19. MacKenzie, A. P. Collapse During Freeze-Drying − Qualitative and Quantitative Aspects. In *Freeze-Drying and Advanced Food Technology*; Goldblith, S. A., Rey, L., and Rothmayr, W. W., Eds.; Academic Press: London, 1975; pp 277−307.
20. Hsu, C. C.; Walsh, A. J.; Nguyen, H. M.; Overcashier, D. E.; Koning-Bastiaan, H.; Bailey, R. C.; Nail, S. L. Design and Application of a Low-Temperature Peltier-Cooling Microscope Stage. *J. Pharm. Sci.* **1996**, *85*, 70−74.

Acknowledgments

We thank Kin Sit, Mary Cromwell, Jamie Moore, Phuong-Anh Nguyen, Al Stern, and Janet Curley for technical assistance and Dr. Tue Nguyen for support of this study.

JS980445+

Selection of Solid Dosage Form Composition through Drug–Excipient Compatibility Testing

ABU T. M. SERAJUDDIN,* AJIT B. THAKUR, RABIN N. GHOSHAL, MICHAEL G. FAKES, SUNANDA A. RANADIVE, KENNETH R. MORRIS,† AND SAILESH A. VARIA

Contribution from *Pharmaceutics R&D Department, Bristol-Myers Squibb Pharmaceutical Research Institute, New Brunswick, New Jersey 08903.*

Received November 6, 1998. Accepted for publication April 16, 1999.

Abstract □ A drug–excipient compatibility screening model was developed by which potential stability problems due to interactions of drug substances with excipients in solid dosage forms can be predicted. The model involved storing drug–excipient blends with 20% added water in closed glass vials at 50 °C and analyzing them after 1 and 3 weeks for chemical and physical stability. The total weight of drug–excipient blend in a vial was usually kept at about 200 mg. The amount of drug substance in a blend was determined on the basis of the expected drug-to-excipient ratio in the final formulation. Potential roles of several key factors, such as the chemical nature of the excipient, drug-to-excipient ratio, moisture, microenvironmental pH of the drug–excipient mixture, temperature, and light, on dosage form stability could be identified by using the model. Certain physical changes, such as polymorphic conversion or change from crystalline to amorphous form, that could occur in drug–excipient mixtures were also studied. Selection of dosage form composition by using this model at the outset of a drug development program would lead to reduction of "surprise" problems during long-term stability testing of drug products.

Introduction

Excipients are integral components of almost all pharmaceutical dosage forms. What emerges from a drug discovery program is only a new chemical entity or drug substance. It becomes a drug product after formulation and processing with excipients. However, the general principles of selecting suitable excipients for dosage forms are not well-defined, and excipients are often selected without systematic drug−excipient compatibility testing.

Acceleration of drug development and optimization of dosage form stability are two major goals of any drug development program. Identification of dosage form composition at the outset of a drug developmental program, especially during the design of Phase I clinical formulations, based on thorough drug−excipient compatibility testing is a key step in accelerating drug development. This is because subsequent changes in formulation during Phases II and III as a result of unexpected stability problems usually lead to increases in time and cost of drug development. In addition, the stability of a formulation can be maximized and "surprise" problems during its formal stability testing for regulatory submissions can be minimized through drug−excipient compatibility testing.

Despite the importance of drug−excipient compatibility testing, no generally accepted method is available for this purpose. Most of the methods reported in the literature have poor predictive values.[1] They are labor-intensive and time-consuming, and the number of variables studied are limited. As a result of frustration over this situation, Monkhouse and Maderich[1,2] suggested that one should do away with drug−excipient compatibility testing and, instead, select excipients on the basis of physical and chemical characteristics of drug substances and literature data on excipients. They recommended that the final composition should be selected on the basis of accelerated stability testing of one or more target formulations at high temperature and high humidity. This latter approach may, however, have the disadvantage that it could prolong the time necessary for selecting dosage form compositions. Development of various target formulations for the purpose of screening different drug−excipient combinations is time-consuming and may require larger quantities of bulk drug substances than are generally available early in drug development. Additionally, meaningful differences in stability of different target formulations of a particular drug stored at high temperature and humidity (for example, 40 °C/75% RH) may not be observed within a short period of time, unless the compound degrades very rapidly in these formulations. Therefore, a rapid method for selection of excipients for dosage form design is essential for a practical drug−excipient compatibility screening method.

In this paper, we report a method that was used successfully to identify relative influences of different excipients on drug stability. The primary objective of developing this method was to identify in a short period of time excipients that would have low potential for adverse effects on chemical and physical stability of drug substances.

Materials and Methods

Materials—All drug substances used in this study were synthesized by Bristol-Myers Squibb, and their chemical structures are given in Table 1. The excipients, procured from commercial sources, were released by Bristol-Myers Squibb for use in drug manufacturing.

Preparation of Samples—The basic model used in the present study consists of multicomponent blends of drug substances with excipients, which were mixed with 20% added water and stored in closed vials at 50 °C for specific periods of time. Samples were analyzed for chemical and physical (appearance, color, etc.) stability after 1 and 3 weeks of storage.

Only a general method of preparation of samples is described here, because it evolved over the long time during which the studies reported in this paper were conducted. Accurately weighed amounts of drug substances were placed in 4-mL glass vials, each vial was labeled with the amount of drug to determine mass balance during chemical analysis, and weighed amounts of excipients were then added to the vials. The total weight of drug−excipient blend in a vial was usually kept at about 200 mg. The

* Corresponding author. Present address: Pharmaceutical Development Department, Novartis, 50 Route 10, East Hanover, NJ 07936.
† Present address: Department of Industrial and Physical Pharmacy, School of Pharmacy, Purdue University, West Lafayette, Indiana 47907.

10.1021/js980434g CCC: $18.00
Published on Web 05/20/1999

Table 1—Names and Chemical Structures of Drugs Used

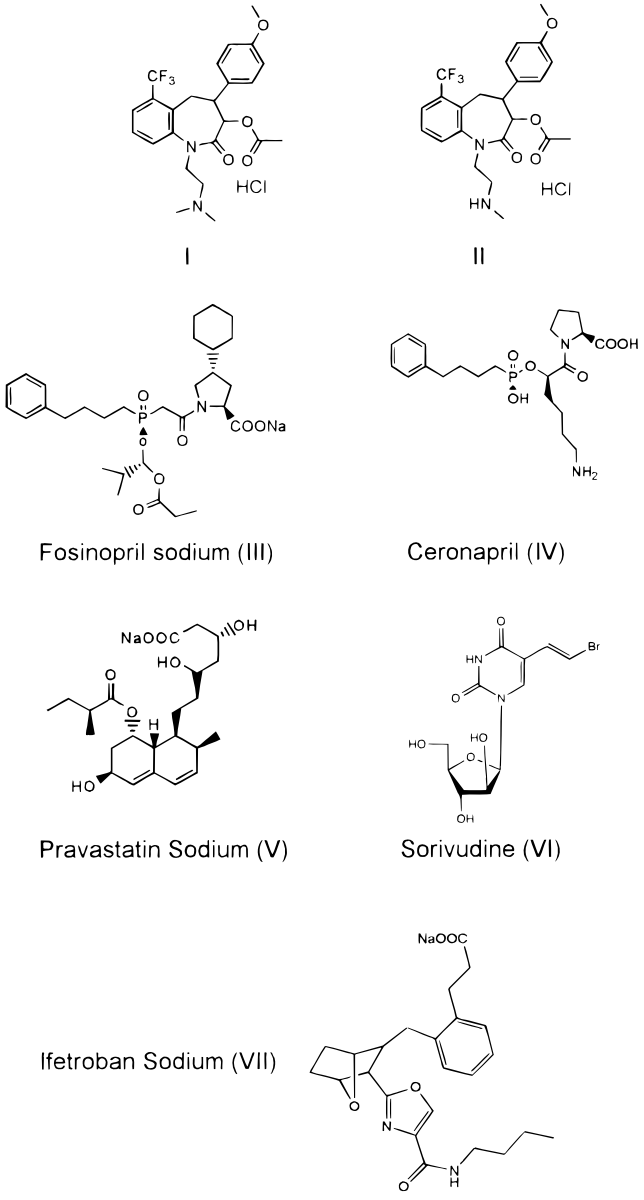

amount of drug substance in a blend was determined on the basis of the expected drug-to-excipient ratio in the final formulation. The highest expected drug-to-excipient ratio was usually used. Both the highest and the lowest drug-to-excipient ratios were occasionally used to bracket drug concentrations in a formulation. The amount of the drug–excipient blend per vial sometimes differed as a result of practical reasons; a smaller amount was used when the drug supply was limited. The powder in each vial was mixed with the tip of a disposable Pasteur pipet or a thin glass rod and 20% water (40 μL per 200 mg blend) was then added using a microsyringe. The blend was further mixed, and to prevent any loss of material, the tip of the stirrer (Pasteur pipet) was usually broken and left inside the vial. Each vial was sealed tightly using a Teflon-lined screw cap.

The total number of drug–excipient blends for each study may be selected by statistical design. However, because it might be necessary to screen many diluents, lubricants, binders, disintegrants, coloring agents, coating agents, and so forth for a particular formulation, the number of blends selected this way becomes very high. To limit the number of samples, the drug–excipient compatibility testing may be conducted in two phases. In the first phase, the compatibility of drug with diluents and lubricants is tested, and on the basis of the results, one primary diluent and one primary lubricant are selected. Table 2 provides the design of such a study for one of the compounds (**I**) tested in the present investigation. Using one drug–diluent–lubricant mixture selected in the first phase, the compatibility of other excipients, such as binders and disintegrants, may then be tested in the second phase. Because capsule formulations, which do not require coating agents and coloring agents, are generally used during initial clinical studies, compatibility testing of such agents may be conducted later with the drug–excipient blend used in capsules.

Storage and Analysis of Samples—Closed vials containing drug–excipient blends with added water were stored in ovens at 50 °C. In some cases, samples were also stored as unwetted powders in closed vials at 50 °C or in open vials at 50 °C/75% RH for comparison with those stored in closed vials with added water. Drug–excipient blends without added water stored in a refrigerator or at room temperature served as controls for samples stored at 50 °C with added water or at 50 °C/75% RH. When the drug was photodegradable, clear glass vials containing certain drug–excipient–water mixtures, especially those with coloring agents, were also exposed to light (room light or high-intensity fluorescent light). In this case, identical vials wrapped in aluminum foil and stored side by side with exposed vials served as controls for light stability.

Duplicate samples of drug–excipient blends were analyzed after 1 and 3 weeks by using HPLC methods. Because the drug–excipient compatibility testing was conducted at an early drug developmental stage when fully validated HPLC methods were generally not available, it was not uncommon to use more than one isocratic HPLC method or a gradient HPLC method to distinguish as many degradation products as possible. The HPLC conditions used are recorded under tables and figures in the Results and Discussions section. Whenever feasible, the degradation products were identified by mass spectral, NMR, and other relevant analytical techniques.

To investigate physical changes in drug substances, for example, polymorphic transition or formation of an amorphous phase due to dissolution of the drug in granulating fluids and subsequent drying, drug–excipient–water mixtures stored in closed vials at 50 °C for a suitable period of time were dried overnight at 40 °C and then analyzed by powder X-ray diffraction, solid-state NMR, FTIR, and other appropriate methods. The techniques were described earlier.[3] To maximize the detection of possible physical changes in drug substances during analyses by these techniques, drug concentrations in the mixtures were usually kept at 25% or higher. It was also advantageous to limit the excipient to one that would have the least interference with the analysis of drug substances. Identical blends stored refrigerated or at room temperature without the addition of water served as controls.

Estimation of Microenvironmental pH—The microenvironmental pH of a drug–excipient blend was estimated by adding 1 mL of water to 200 mg of blend in a vial, mixing the suspension with a vortex mixer, and then recording the pH with a pH meter. It was necessary that the solid remained in equilibrium with the liquid phase; variation in pH was observed if filtered solutions were used.

Results and Discussion

Model—Some factors which may have critical influences on the stability of drug substances in the presence of excipients are the chemical nature of the excipient, drug-to-excipient ratio, moisture, microenvironmental pH of the drug–excipient mixture, temperature, and light. The model allowed identification of the potential roles of all of these factors on dosage form stability. Additionally, certain physical changes, for example, polymorphic conversion and the change from crystalline to amorphous form due to dissolution of drug by the sorption of water or during wet granulation and subsequent drying, that could occur in drug–excipient mixtures were also studied.

One important feature of the model is the incorporation of water in the drug–excipient mixture. Although purely solid-state degradation of drug substances is feasible, such instances are rare, and most drug degradation reactions in solid dosage forms involve moisture.[4,5] The presence of moisture is, therefore, essential in establishing the compat-

Table 2—Compositions of Drug–Excipient Blends Used for I and Assay Results after 3 Weeks of Storage at 50 °C in Closed Vials with 20% Added Water; Weights of All Ingredients Are in Milligrams

	experiment																
	1	2	3	4	5	6	7	8	9	10	11	12	13	14	15	16	17
drug substance (**I**)	200	25	25	25	25	25	25	25	25	25	25	25	25	25	25	25	25
lactose		175				170				170				170			
mannitol			175				170				170				170		
microcrystalline cellulose				175				170				170				170	
dibasic calcium phosphate dihydrate					175				170				170				170
magnesium stearate						5	5	5	5								
sodium stearyl fumarate										5	5	5	5				
stearic acid														5	5	5	5
potency remaining[a] (% initial)	96.4	95.7	95.8	93.9	85.0	64.3	65.4	65.3	68.1	77.9	81.9	77.6	81.8	90.0	92.9	88.1	78.3
hydrolysis product formed[b]	3.3	4.1	4.0	5.8	16.7	37.0	36.7	36.3	33.7	21.8	15.4	20.1	15.3	9.7	6.9	11.7	21.6

[a] Average of two samples. [b] Expressed as percentage of parent drug (**I**). Because in a separate study the molar extinction coefficients of the parent compound and the hydrolysis product were earlier determined to be the same, the hydrolysis product was quantitated directly from its AUC values in the chromatograms.

ibility of drugs with excipients. Although the moisture may be incorporated in the system by exposing samples to high humidity, it has been our experience that the drug–excipient interaction at high humidity conditions always depends on the amount of free moisture present and on relative hygroscopicities of drug substances and/or excipients. Variability in degradation of drugs as a result of differences in the hygroscopicity of excipients has been reported in the literature.[6] Addition of a predetermined amount of water removes this unpredictability from the system. It facilitates intimate mixing of drug substances with excipients and establishes around undissolved drug particles aqueous layers saturated with drugs, excipients, and any impurities that may be present in the system. Such saturation layers also provide a microenvironmental pH to the system. The use of 20% water ensured that a sufficient amount of water would still remain in contact with the drug–excipient blend after evaporation of a certain fraction of added water to saturate the headspace inside the 4-cc vial. The model also works efficiently with lower or higher than 20% water; addition of water ranging from 5% to 20% was reported in the literature.[7–9]

Another important aspect of the model is that the dissolution of drugs and excipients in the added water facilitates the formation of their disordered or amorphous phases. Zografi and co-workers[10] demonstrated that water absorbed in such amorphous phases accelerates drug degradation. Any possible drug–excipient interaction would therefore be facilitated in the amorphous phase as a result of the presence of water and the intimate mixing of drug with excipients. However, it might be argued that the amount of water used in the protocol (20%) might be in excess of what is required to change the glass transition temperature of an amorphous phase and may indeed dissolve the drug in an aqueous solution, thereby increasing its degradation rate. Although this is a possibility for highly water-soluble drugs, most drugs are relatively water-insoluble and amounts dissolved in the added water are usually very small. Also, in the presence of certain excipients, such as cellulose- and starch-derived excipients[11] and poly(vinylpyrrolidone),[12] a large part of the water may be tightly or partially bound with excipients and thus unavailable to dissolve the drug. Even for highly water-soluble drugs, the model is capable of determining relative influences of different excipients of a particular class on the drug degradation. It has been our experience that the absence of a drug–excipient interaction in the present model leads to drug products with long shelf lives. However, if an interaction is observed and no suitable alternative excipient is available, additional studies are needed to determine the impact of such an interaction on the product shelf life and to ascertain whether any restrictive manufacturing and packaging conditions to increase the stability of the drug product would be necessary.

Case Histories—Case histories of the interaction of selected drug molecules with excipient and how such interactions influenced dosage form design decisions are given below.

*Calcium Channel Blockers (**I** and **II**)*—Compounds **I** and **II** are the hydrochloride salts of two calcium channel blockers of the benzazepine series discovered by Bristol-Myers Squibb.[13] They are structurally similar, except for the side chains with amine groups: **I** is a tertiary amine, whereas **II** is a secondary amine. Each compound contains an O-acetyl group that undergoes hydrolysis in aqueous media, forming one degradation product. No degradation product other than the hydrolysis product was observed in aqueous solutions. The formation of hydrolysis products was, therefore, studied during the drug–excipient compatibility testing. Additionally, possible interactions of the compounds with lactose were considered because it has been reported in the literature that amine drugs react with lactose.[14] However, most published reports were for compounds containing primary amines, and it was important to determine how tertiary and secondary amines would behave in the presence of lactose.

The 3-week results of the compatibility screening of **I** with the four diluents and the three lubricants used are shown in Table 2. Since the hydrolysis product **VIII** was the only degradation product formed and there was a good mass balance in all the samples, the results are expressed as the intact drug remaining and the amount of the hydrolysis product formed. As shown in Table 2 and also represented by the chromatograms in Figure 1, the degradation of **I** in the neat drug and in drug–lactose and drug–mannitol mixtures was low and practically similar, indicating that there was no significant interaction of **I** with lactose and mannitol. The degradation of **I**, however, increased in the presence of microcrystalline cellulose (Avicel, FMC) and dicalcium phosphate (DCP, DiTab, Rhone-Poulenc). Among the three lubricants used, stearic acid had the least influence on the degradation of **I**, followed by sodium stearyl fumarate and magnesium stearate in the increasing order of degradation. The HPLC chromatograms of drug–diluent–magnesium stearate mixtures are shown in Figure 2 to indicate that the hydrolysis product **VIII** was the only product formed even when the degradation was high. In a separate study, the compound was observed to have the maximum stability in solution at pH 4, and the stability decreased with an increase or decrease in pH. The maximum stability of **I** in the presence of stearic acid may, in part, be explained by the microenvironmental pH of the systems. The microenvironmental pH of drug–lactose and drug–mannitol mixtures in the

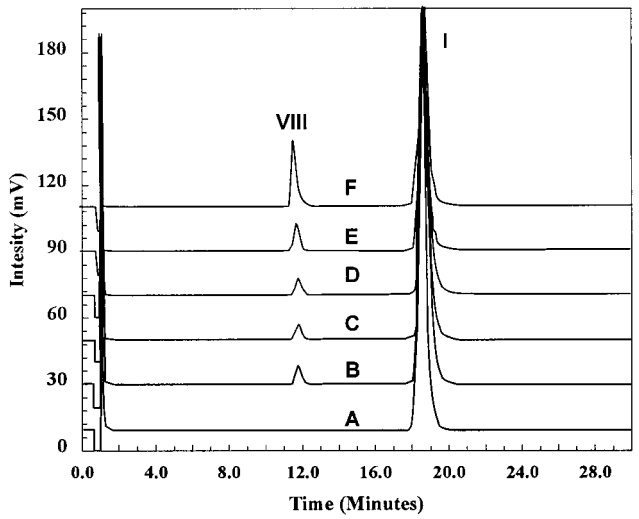

Figure 1—HPLC chromatograms of compound **I**–excipient mixtures (1:7) exposed to 50 °C for 3 weeks with 20% added water. Key: A, reference standard; B, neat drug without excipient; C, drug–lactose mixture; D, drug–mannitol mixture; E, drug–microcrystalline cellulose mixture; and F, drug–dicalcium phosphate dihydrate mixture. Chromatograms were recorded using a 15 cm Novapak C_{18} column and a mobile phase containing 55% aqueous solution (sodium acetate, 14 g/L, and sodium hexane sulfonate, 1.98 g/L) and 45% acetonitrile (flow rate, 1.0 mL/min; UV detection wavelength, 229 nm).

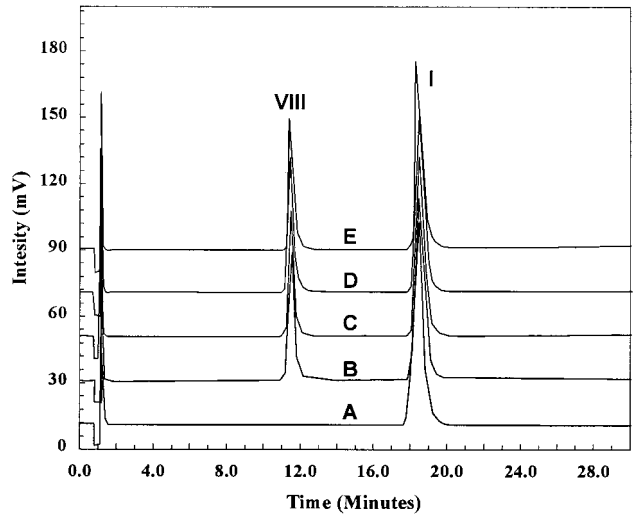

Figure 2—HPLC chromatograms of compound **I**–diluent–magnesium stearate mixtures (25:170:5) exposed to 50 °C for 3 weeks with 20% added water. Key: A, reference standard; B, neat drug without excipient; C, drug–lactose–magnesium stearate mixture; D, drug–mannitol–magnesium stearate mixture; and E, drug–microcrystalline cellulose–magnesium stearate mixture. Chromatographic conditions are the same as in Figure 1.

presence of stearic acid was 3.8, whereas sodium stearyl fumarate and magnesium stearate raised the microenvironmental pH to ~5.5. Mixtures of **I** with DCP gave an initial pH of 6.2−6.5. Additionally, its surface acidity[15] and propensity for forming H_3PO_4 upon its hydrolysis in the presence of water would contribute to the acid-catalyzed degradation of the ester bond in **I**. Thus, there appears to be a good agreement between the microenvironmental pH of the excipient blends and the hydrolysis of the drug. From this phase of the study, it was concluded that mixtures of **I** with either lactose or mannitol as the diluent and stearic acid as the lubricant would provide maximum stability of the drug. The microcrystalline cellulose was also considered to be an acceptable diluent because the extent of drug degradation in its presence was not much higher.

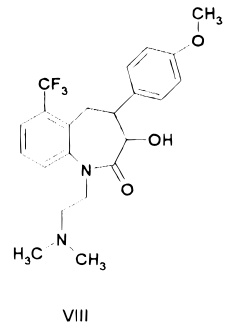

VIII

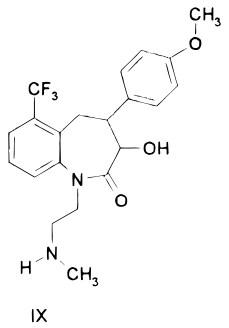

IX

During compatibility screening of the hydrochloride salt of the secondary amine, **II**, it was observed that the drug did not have any significant interaction with lactose and mannitol in binary mixtures (Figure 3). The only significant degradation product formed was the hydrolysis product **IX**. As in the case of **I**, the influence of stearic acid on the compatibility of **II** with lactose and mannitol was minimal; the chromatograms remained similar to those in Figure 3, with hydrolysis being the only drug degradation product. In contrast, both sodium stearyl fumarate and magnesium stearate adversely influenced the drug stability. Figure 4 shows that the hydrolysis product, **IX**, was the major degradation product in the presence of both sodium stearyl fumarate and magnesium stearate. As with **I**, the hydrolysis of **II** was higher with magnesium stearate. Additional peaks at the elution times of 2−3 min were obtained when lactose was present in the mixture, possibly a result of the interaction of lactose with the secondary amine groups of **II** and the hydrolysis product, **IX** (Figure 4, chromatograms B and C). Unidentified degradation products with the elution time of ~1 min were also observed in the presence of magnesium stearate (Figure 4, chromatograms B and D).

The tertiary amine is expected to be nonreactive toward lactose, because the product of such a reaction would lead to unstable ionic species that would revert back to reactants, and for this reason, compound **I** was compatible with lactose. In the case of a secondary amine, a glycosylamine would be formed:

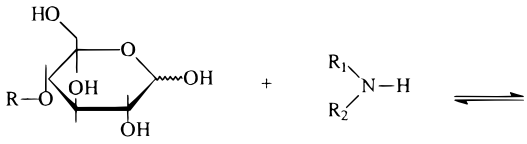

Lactose

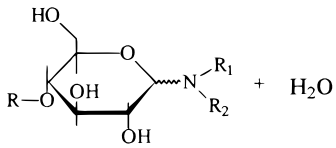

Glycosylamine

For the above reaction to occur in the solid state, optimal microenvironmental conditions of humidity and pH would be required. Under acidic conditions, the reactivity was reduced as a result of the protonation of the amine and the consequent decrease in its nucleophilicity. The observed lack of interaction of the hydrochloride salt of **II** and lactose could thus be rationalized. However, in the presence of magnesium stearate and sodium stearyl fumarate, the microenvironmental pH of the system was expected to rise because of the basicity of the excipients. This would liberate the nucleophilic free base of the drug from the salt to react

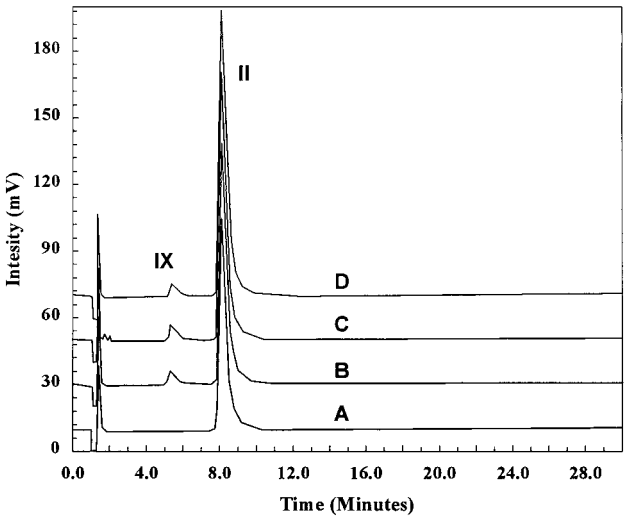

Figure 3—HPLC chromatograms of compound **II**–diluent–stearic acid mixtures (25:170:5) exposed to 50 °C for 3 weeks with 20% added water. Key: A, reference standard; B, neat drug without excipient; C, drug–lactose–stearic acid mixture; and D, drug–mannitol–stearic acid mixture. Chromatographic conditions are the same as in Figure 1.

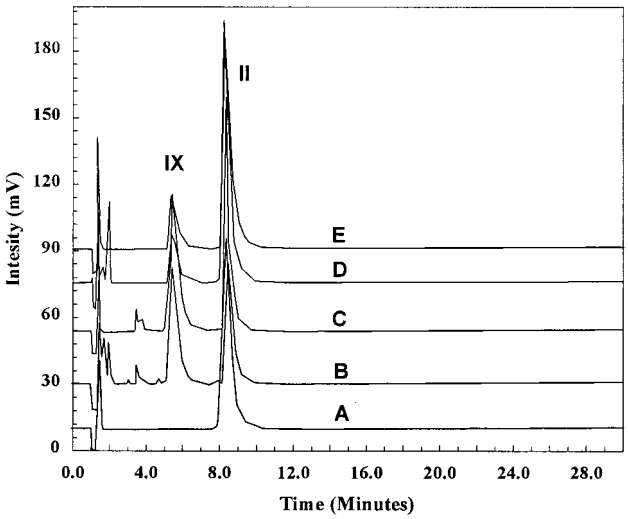

Figure 4—HPLC chromatograms of compound **II**–diluent–lubricant mixtures (25:170:5) exposed to 50 °C for 3 weeks with 20% added water. Key: A, reference standard; B, drug–lactose–magnesium stearate mixture; C, drug–lactose–sodium stearyl fumarate mixture; D, drug–mannitol–magnesium stearate mixture; and E, drug–mannitol–sodium stearyl fumarate mixture. Chromatographic conditions are the same as in Figure 1.

with lactose and form an adduct. A second adduct due to the interaction between the hydrolysis product, **IX**, and lactose could also be formed. A similar reaction between a secondary amine and lactose, which was catalyzed by magnesium stearate, was reported in the literature.[16] The lack of interaction with lactose in the presence of stearic acid is also consistent with this explanation. As shown in the scheme above, the equilibrium of the interaction will be dependent on the moisture content of the system. In the absence of moisture, very little glycosylamine formation would occur because the reaction is postulated to occur in the sorbed layer of water between excipient and drug. In an excess of water, however, the equilibrium will be shifted to the left. Thus, the proposed model attempts to optimize conditions for the observation of the potential interaction between lactose and amine drugs in a relatively short period of time.

On the basis of the above studies, drug−lactose−stearic acid and drug−mannitol−stearic acid mixtures were selected for the solid dosage forms of **I** and **II**, respectively. The compatibility of these mixtures with various binders and disintegrants were studied in the second phase of the screening, in which the compatibility of povidone, crospovidone, and pregelatinized starch with the drugs was established. Because these studies also indicated that the stability of both drugs was susceptible to moisture, their exposure to moisture during processing and storage was minimized to ensure prolonged stability of the solid dosage forms.

*Fosinopril Sodium (**III**)*—Compound **III** is the prodrug form of an angiotensin-converting enzyme inhibitor which produces in vivo the active moiety fosinoprilat (**X**) by hydrolysis of the phosphinic acid ester side chain. Compound **X** was the only degradation product observed in aqueous media during preformulation testing, indicating that the compound would require protection from moisture during processing and storage. In drug−excipient compatibility testing using 20% added water, **X** was also the only degradation product observed, except in the case of interaction with magnesium stearate. Interaction with magnesium stearate not only accelerated the formation of **X**, it also produced two other major degradation products, **XI** and **XII** (Scheme 1). This is shown with the HPLC chromatograms in Figure 5, which indicate that ~90% of the drug degraded in 1 week when tested according to the model. Although the conditions of the model may appear to be very drastic with such a rapid degradation of **III**, it was by this model that the unexpected interaction with magnesium stearate could be discovered within such a short period of time. The mechanism of this magnesium-mediated reaction was later elucidated.[17]

In a separate study, when a 1:1 mixture of **III** and magnesium stearate was exposed to 75% RH at 50 °C, the degradation of **III** after 3 weeks was less than 1% (Figure 6). This is because both **III** and magnesium stearate were nonhygroscopic, although the interaction between them is mediated by water. This, however, would not be the case in capsules and tablets where other formulation components, such as microcrystalline cellulose, starch, gelatin shell, and so forth, would result in moisture sorption. Therefore, a model in which a limited amount of water is added to a system is often more predictive of drug−excipient compatibility because it does not depend on the hygroscopicity of individual components.

From the above study, it was concluded not only that **III** requires protection from moisture in dosage forms, but also that magnesium stearate should be excluded from formulations. This was later confirmed by accelerated stability testing of the tablet formulation of **III**, where **XI** and **XII** were detected only in a formulation lubricated with magnesium stearate.[17] Thus, the elimination of magnesium stearate from a formulation through drug−excipient compatibility screening maximized product stability and eliminated the necessity of monitoring the formation of two extra degradation products during stability testing.

*Ceronapril (**IV**)*—Compound **IV** is an ACE inhibitor with a primary amine group in its structure. Its interaction with lactose was, therefore, expected. What was unexpected was an interaction with DCP. Figure 7 shows representative HPLC chromatograms of the mixtures of **IV** with three diluents, lactose, DCP, and mannitol. In 3 weeks, **IV** degraded 8.4% and 2.5% in the presence of lactose and DCP, respectively, whereas no degradation was observed in the presence of mannitol or any other excipient. By LC-MS and LC-MS-MS studies, the degradation products formed in the presence of lactose and DCP were identified to be **XIII** and **XIV**, respectively. The formation of **XIV** was oxidative in nature, which could not be predicted on the basis of initial preformulation testing. The model served

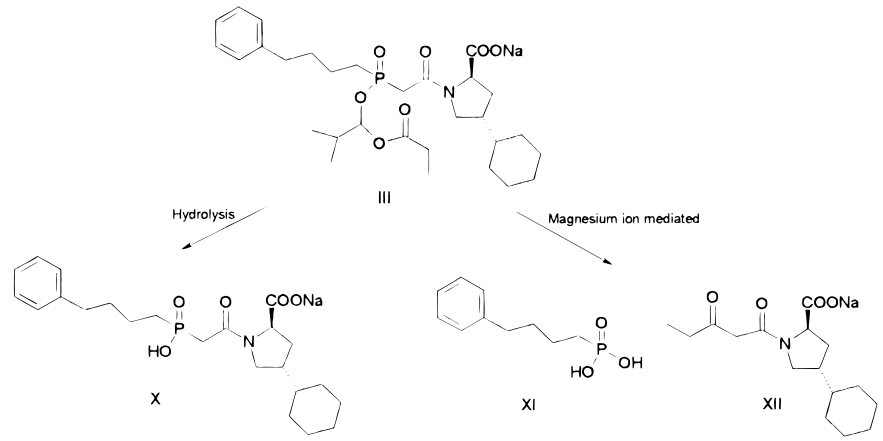

Scheme 1

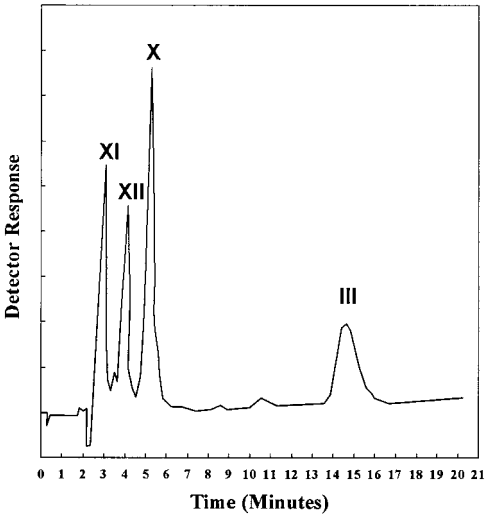

Figure 5—HPLC chromatogram of a fosinopril sodium **(III)**–lactose–magnesium stearate mixture (40:150:10) containing 20% added water stored at 50 °C for 1 week. Compounds **X**, **XI**, and **XII** were the major degradation products formed. A phenyl column (Type C-402, 4.6 mm × 30 cm, 10 μm packing, Column Resolution, Inc., San Jose, CA) using a mixture of methanol and aqueous 0.2% phosphoric acid (72:28) as the mobile phase was utilized (flow rate, 1.5 mL/min; UV detection wavelength, 220 nm).

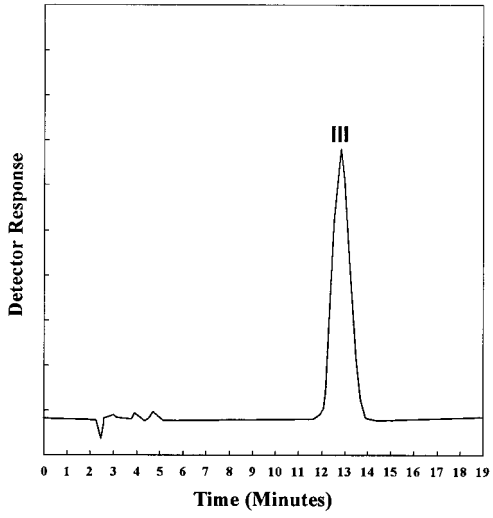

Figure 6—HPLC chromatogram of fosinopril sodium **(III)**–magnesium stearate (1:1) mixture stored at 50 °C under 75% RH for 3 weeks. Chromatographic conditions are the same as in Figure 5.

as a powerful tool in identifying this interaction between **IV** and DCP.

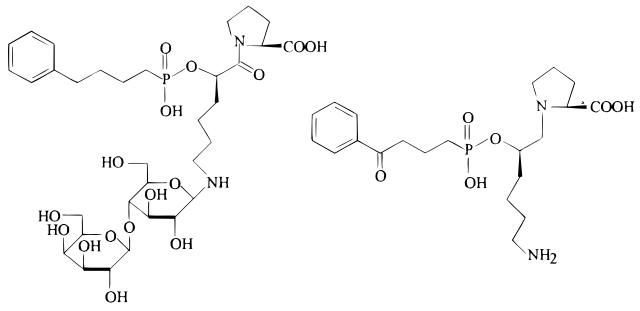

On the basis of the above results, lactose and DCP were excluded from the primary tablet formulation of **IV**. However, because DCP is a commonly used excipient for the direct compression of tablets and the degradation of **IV** in its presence was relatively low, a back-up formulation containing this excipient was also prepared and subjected to accelerated stability testing. For a 20-mg potency tablet with the total weight of 200 mg, the extent of degradation of **IV** upon exposure to 40 °C and 75% RH in an open container for 1, 4 and, 6 months was <1%, 2%, and 5%, respectively. The compound **XIV** was the principal degradation product. These findings indicate that an interaction between **IV** and DCP would possibly have been overlooked if, instead of using the model described in this paper, the drug–excipient blends or miniformulations were exposed to high temperature and humidity for up to 1 month. In closed vials stored at 25 °C, it took about 6 months for the concentration of **XIV** in DCP-based tablets to reach the threshold level of 0.1%. Although such a low concentration of a degradation product may be acceptable in a formulation, it is important that all potential degradation products are detected by drug–excipient compatibility testing prior to dosage form design instead of "discovering" them during formal long-term stability testing. Decisions regarding the potential liability of the presence of any degradation product in a formulation must be made during the dosage form design.

*Pravastatin Sodium (**V**)*—The model described in this paper was also used to study the effects of different excipients on the degradation pattern of **V** in solid dosage forms. An optimal degradation product profile was then selected on the basis of such studies. Figure 8 shows the relative amounts of degradation products formed in two blends of pravastatin sodium containing microcrystalline cellulose, lactose, and magnesium stearate; compositions

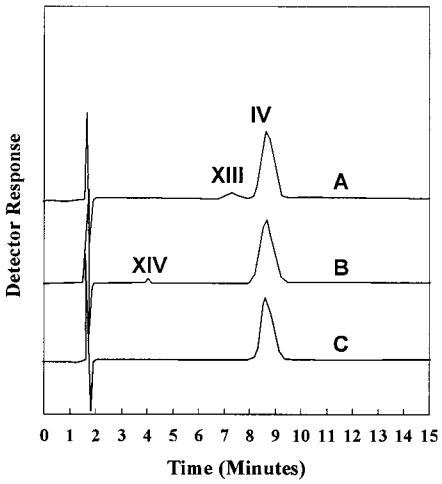

Figure 7—HPLC chromatograms of ceronapril (**IV**)–diluent–magnesium stearate mixtures (40:150:10) containing 20% added water stored at 50 °C for 3 weeks. Diluents used were (A) lactose, (B) dicalcium phosphate dihydrate, and (C) mannitol. Compounds **XIII** and **XIV** are the degradation products formed in mixtures with lactose and dicalcium phosphate dihydrate, respectively. Waters Novapak C_{18} column heated to 30 °C was used. A mixture of acetonitrile and aqueous 0.1% phosphoric acid (19:81) at a flow rate of 1.3 mL/min was used as the mobile phase (detection wavelength: 210 nm).

of the two blends were identical, except for the presence of 3.3% magnesium oxide in Blend 2. The difference in microenvironmental pH values of the two blends (6.5 for Blend 1 vs 9.9 for Blend 2) was responsible for the difference in degradation product profiles; the lower pH favored the formation of **XV** and **XVI**, whereas the higher pH favored the formation of **XVII**. Long-term stability testing of the dosage forms of **V** containing magnesium oxide was in agreement with these results. Thus, by selecting the excipient to adjust microenvironmental pH, the solid dosage form composition of pravastatin sodium was optimized.[18]

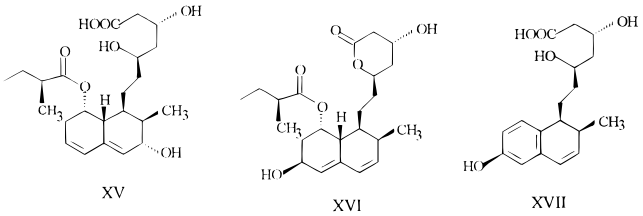

*Sorivudine (**VI**)*—Drug–excipient compatibility testing led to the stabilization of **VI**, an antiviral drug, against photodegradation. When exposed to light, the compound forms its Z-isomer (**XVIII**). The initial compatibility testing

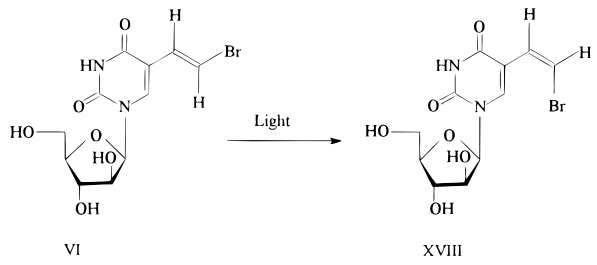

with excipients was, therefore, conducted by protecting samples from exposure to light. This and other preformulation studies suggested that a tablet formulation of the compound would require opaque film coating to protect it from photodegradation. In a later drug–excipient screening study to select coloring agents for the tablet, it was noticed

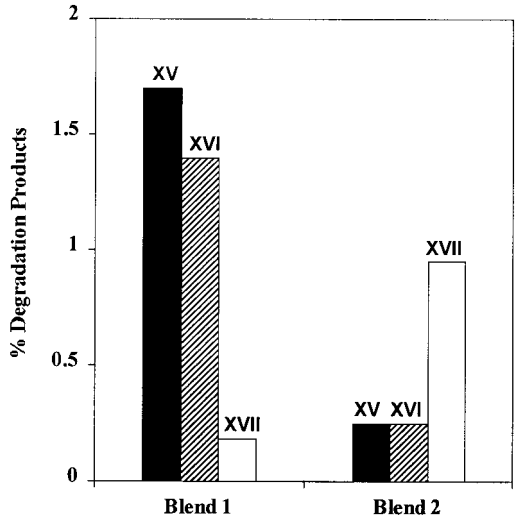

Figure 8—Amounts of degradation products **XV**, **XVI**, and **XVII** formed when pravastatin sodium formulations without magnesium oxide (Blend 1) and with 3.3% magnesium oxide (Blend 2) containing 20% added water were stored at 50 °C for 3 weeks. Products were extracted with a 1:1 mixture of methanol and pH 5.5 aqueous phosphate buffer and analyzed by HPLC using a Waters μ-Bondapak column. A 500:500:1:1 mixture of methanol, water, triethylamine, and acetic acid was used as the mobile phase (flow rate, 1.3 mL/min; UV detection wavelength, 238 nm).

Table 3—Conversion of Sorivudine (VI) to its Z-isomer (XVIII) upon Exposure of Dry and Wet Drug–Excipient Blends Containing Iron Oxides to 900 ft-c Light for 7 Days

	% Z-isomer (**XVIII**) formed[b]	
composition[a]	dry blend	wet blend
no coloring agent	21.1	9.0
red iron oxide	3.4	0.7
yellow iron oxide	2.6	0.7
black iron oxide	2.6	1.3

[a] A 100 mg portion of each blend containing 12.5 mg of drug, 5 mg of iron oxide, and 82.5 mg of other excipients (87.5 mg when no coloring agent was present) was sealed in a 4-mL clear borosilicate glass vial. Each wet blend contained 20 μL of water. The vials were exposed to light from the side by placing them flat. [b] Assayed by HPLC using a 5 μm Lichrosorb RP-18 column (250 mm × 4 mm) using a 15:5:80 mixture of acetonitrile, triethyl ammonium acetate aqueous solution (14% v/v, pH adjusted to 7.0 with acetic acid), and water as the mobile phase (flow rate, 1 mL/min; detection wavelength, 250 nm).

that the formation of **XVIII** was relatively low when drug–excipient blends containing iron oxide dyes were exposed to light. A systematic compatibility testing with iron oxides was therefore conducted by exposing the samples to light, and the results, as shown in Table 3, indicated that iron oxides can greatly reduce the formation of photodegradation product. On the basis of this study, a tablet formulation of **VI** was developed in which iron oxides were admixed with the drug and other excipients to provide color. The tablet did not require any film coating; its stability upon exposure to light was as good as a film-coated tablet which did not contain any iron oxide.[19]

Other Physicochemical Changes—The applications of the model described in this paper are not limited to the testing of the chemical interaction between drugs and excipient. We have used it for many other purposes, including the investigation of (a) dissolution instability of drugs in dosage forms due to conversion of salts to free acid or base forms, (b) changes in crystal forms, such as polymorphic conversion, the formation of an amorphous phase due to dissolution of the drug in granulating fluids and subsequent drying, and so forth, and (c) relative stability of various salt forms during the final form selec-

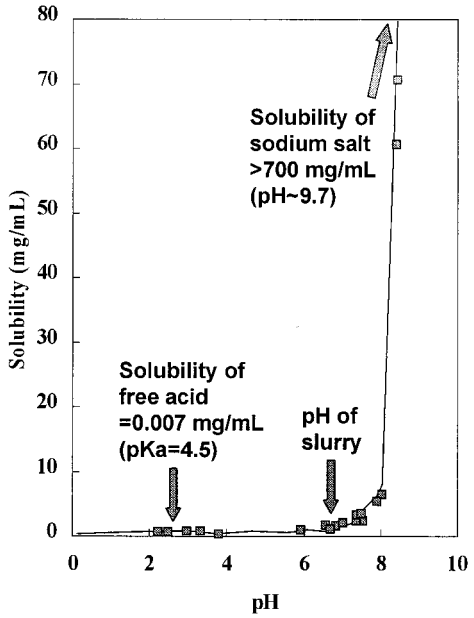

Figure 9—Partial pH-solubility profile of ifetroban sodium (**VII**) at 23 °C. Drug was analyzed by HPLC using a Zorbax Stablebond Cyano column heated to 40 °C. A 35:65 mixture of acetonitrile and 0.005 M KH_2PO_4 aqueous solution, pH adjusted to 3.0 with H_3PO_4, was used as the mobile phase (flow rate, 1.5 mL/min; UV detection wavelength, 215 nm).

$$CaHPO_4.2H_2O \rightarrow\rightarrow Ca_5(OH)(PO_4)_3 + H_3PO_4 + H_2O$$

(Dibasic calcium phosphate dihydrate) (Hydroxyapatite)

$$R\text{-}COO^-Na^+ + H_3PO_4 \rightarrow R\text{-}COOH + NaH_2PO_4$$

(Drug, sodium salt) Water-soluble (Drug, free acid) Water-insoluble

Scheme 2

tion of a drug. Brief descriptions of some of these studies are given below.

Dissolution Instability—During drug–excipient compatibility testing, ifetroban sodium **(VII)** showed excellent chemical stability in the presence of all excipients tested. However, its capsule formulations exhibited a decrease in dissolution rate during accelerated stability testing.[20] This was most pronounced in formulations containing DCP. When the drug–excipient compatibility testing was repeated, the microenvironmental pH values of various dosage form compositions were observed to be between 6.2 and 6.6, where the sodium salt form of the drug could convert to the insoluble free acid form. This is apparent from the pH-solubility profile of the compound as shown in Figure 9. When a mixture of **VII** and DCP containing 20% water was stored at 50 °C for 1 week, almost complete conversion of the sodium salt to free acid was observed.[21] Liberation of H_3PO_4 from DCP at high temperature[22,23] served as the source of hydrogen ions for the salt-to-acid conversion. Indeed, it was observed that the microenvironmental pH of the mixture decreased with time. The conversion of **VII** to the water-insoluble free acid form in a formulation containing DCP is described by Scheme 2.

It is now a common practice in our laboratory to measure the microenvironmental pH values of drug–excipient blends initially and after exposure to 50 °C, with 20% added water, for various intervals of time. If salt forms of drugs are used, any propensity for their conversion to free acid or base forms can be ascertained from such studies. Adjustment of microenvironmental pH with an appropriate excipient can eliminate any such conversion and the consequent drug dissolution problem. For **VII**, alkalizing agents were added to formulations to keep microenvironmental pH above 9, where the compound has high solubility and would not convert to the free acid form.[23]

Crystal Form Changes—Polymorphic and other crystal form changes may lead to dissolution instability of drugs, especially for compounds with low aqueous solubilities. They also cause various physical stability problems in solid dosage forms, including changes in appearance, hardness, disintegration time, and so forth.[24]

Any propensity for polymorphic change was investigated by recording powder X-ray diffraction patterns and solid-state ^{13}C NMR spectra of drug–excipient mixtures initially and after subjecting them to 50 °C with added water for up to 1 week. The wet samples were dried before analysis. If there is any potential for polymorphic conversion, it would be facilitated by the "pressure cooker" effect of the experimental condition and the presence of excipients that could serve as nuclei for recrystallization. In the absence of any chemical degradation, significant change in powder X-ray diffraction patterns or solid-state NMR spectra would indicate polymorphic transformation.

If the drug substance is water-soluble, instead of a polymorphic conversion the drug substance may convert partially or completely to an amorphous form due to wet granulation with the excipient and subsequent drying. This may affect dosage form stability because an amorphous form may be less stable than a crystalline one. The amorphous form thus produced may, in turn, recrystallize into the original or a different crystal form,[25] leading to dissolution or other physical instability problems if this occurs during stability testing of dosage forms. We have studied such changes by recording powder X-ray diffraction patterns of a drug–excipient blend initially and after mixing with water and drying.[3]

Salt Selection—The model was also applied to determine the relative stability of different salt forms of a compound.[26] Inorganic and organic acids and bases used to prepare salts may interact with drug molecules. The tromethamine salt of ketorolac was found to partially convert to the 1-keto analogue and an amide on exposure to high humidity and temperature.[27] Schildcrout et al.[28] reported 1,4-Michael adduct formation between seproxetine and maleic acid in a maleate salt, and Stahl[29] reported the covalent addition of a secondary amine to fumaric acid in a fumarate salt. Different counterions used in salt formation may also provide different microenvironmental pH values to a compound. When the stability of a compound is sensitive to a change in pH, the stability of salts may differ as a result of such a difference. The salt form of a compound with optimal chemical stability may be selected in less than 1 month by stress stability testing according to the model.

Conclusions

In the present health care economic climate, acceleration of the drug development process and optimization of dosage form stability are two major goals of any drug development program. One key step in achieving these goals is the identification of optimal dosage form compositions at the outset of a drug developmental program, which is generally during the design of Phase I clinical formulations. Subsequent changes in formulation during Phases II and III usually lead to increases in time and cost of drug development. In this paper, a practical drug–excipient compatibility screening model to identify potential chemical and physical stability problems with a drug substance in the presence of different excipients has been presented. Case histories described in the paper demonstrate that the

stability of drug products can be optimized by selecting the excipient according to this model. Selection of dosage form composition based on such drug−excipient compatibility testing reduces "surprise" problems during long-term stability testing of drug products.

References and Notes

1. Monkhouse, D. C.; Maderich, A. Whither compatibility testing? *Drug Dev. Ind. Pharm.* **1989**, *15*, 2115−2130.
2. Monkhouse. D. C. Excipient compatibility possibilities and limitations in stability prediction. In *Stability Testing in the EC, Japan and the USA: Scientific and Regulatory Requirements*; Grimm, W., Krummen, A., Eds.; Wissenschaftliche Verlagsgesellschaft: Stuttgart, 1993; pp 67−74.
3. Morris, K. R.; Newman, A. W.; Bugay, D. E.; Singh, A. K.; Ranadive, S. A.; Szyper, M.; Varia, S. A.; Brittain, H. G.; Serajuddin, A. T. M. Characterization of humidity-dependent changes in crystal properties of a new HMG-CoA reductase inhibitor in support of its dosage form development. *Int. J. Pharm.* **1994**, *108*, 195−206.
4. Carstensen, J. T. *Drug Stability: Principles and Practices*; Marcel Dekker: New York, 1990; pp 129−207.
5. Carstensen, J. T.; Gerhardt, A.; Morris, T.; Nikfar, F. Effect of moisture on solid dosage forms. Can the Arrhenius equation be used as a predictor? *Drug Dev. Ind. Pharm.* **1990**, *16*, 2267−2281.
6. Patel, N. K.; Patel, I. J.; Cutie, A. J.; Wadke, D. A.; Monkhouse, D. C.; Reier, G. E. The effect of selected direct compression excipient on the stability of aspirin as a model hydrolyzable drug. *Drug Dev. Ind. Pharm.* **1998**, *14*, 77−98.
7. Carstensen, J. T.; Johnson, J. B.; Valentine, W.; Vance, J. J. Extrapolation of appearance of tablets and powders from accelerated storage tests. *J. Pharm. Sci.* **1964**, *53*, 1050−1054.
8. van Dooren, A. A. Design for drug−excipient interaction studies. *Drug Dev. Ind. Pharm.* **1983**, *9*, 43−55.
9. Gu, L.; Strickley, R. G.; Chi, L. H.; Chowhan, Z. T. Drug−excipient incompatibility studies of the dipeptide angiotensin-converting enzyme inhibitor, moexipril hydrochloride: dry powder vs wet granulation. *Pharm. Res.* **1990**, *7*, 379−383.
10. Shalaev, E. Y.; Zografi, G.; How does residual water affect the solid-state degradation of drugs in the amorphous state? *J. Pharm. Sci.* **1996**, *85*, 1137−1141.
11. Zografi, G.; Kontny, M. J. The interactions of water with cellulose- and starch-derived pharmaceutical excipients. *Pharm. Res.* **1986**, *3*, 187−194.
12. Oksanen, C. A.; Zografi, G. Molecular mobility in mixtures of absorbed water and solid poly(vinylpyrrolidone). *Pharm. Res.* **1993**, *10*, 791−799.
13. Atwal, K. S.; Bergey, J. L.; Hedberg, A.; Moreland, S. Synthesis and biological activity of novel calcium channel blockers: 2,5-dihydro-4-methyl-2-phenyl-1,5-benzothiazepine-3-carboxylic acid esters and 2,5-dihydro-4-methyl-2-phenyl-1,5-benzodiazepine-3-carboxylic acid esters. *J. Med. Chem.* **1987**, *30*, 635−640.
14. Goodhart, F.; Middleton, K. R.; Chowhan, Z.; Jones, T. M. Lactose. In *Handbook of Pharmaceutical Excipients*; American Pharmaceutical Association: Washington, DC, 1986; pp 153−162.
15. Globitza, B. W.; Oelkrug, D.; Schmidt, P. C. Surface acidity of solid pharmaceutical excipients.1: determination of surface acidity. *Eur. J. Pharm. Biopharm.* **1994**, *40*(5), 289−293.
16. Wirth, D. D.; Baertschi, S. W.; Johnson, R. A.; Maple, S. R.; Miller, M. S.; Hallenbeck, D. K.; Gregg, S. M. Maillard reaction of lactose and fluoxetine hydrochloride, a secondary amine. *J. Pharm. Sci.* **1998**, *87*, 31−39.
17. Thakur, A. B.; Morris, K.; Grosso, J. A.; Himes, K.; Thottathil, J. K.; Jerzewski, R. L.; Wadke, D. A.; Carstensen, J. T. Mechanism and kinetics of metal ion-mediated degradation of fosinopril sodium. *Pharm. Res.* **1993**, *10*, 800−809.
18. Joshi, Y. M.; Chiesa, P.; Jain, N. B. Pravastatin pharmaceutical composition having good stability. U. S. Patent 5,180,-589, January 19, 1993.
19. Desai, D. S.; Abdelnasser, M. A.; Rubitski, B. A.; Varia, S. A. Photostabilization of uncoated tablets of sorivudine and nifedipine by incorporating synthetic iron oxides. *Int. J. Pharm.* **1994**, *103*, 69−76.
20. Nikfar, F.; Ku, C.; Jerzewski, R.; Jain, N. Formulation development of BMS-180291-02: Effect of microenvironmental pH. *Pharm. Res.* **1994**, *11* (Suppl.), S-166.
21. Thakur, A. B.; Chen, X.; Bugay, D. E.; Serajuddin, A. T. M. Solid state incompatibility of dicalcium phosphate dihydrate with the sodium salt of a poorly water-soluble drug. *Pharm. Res.* **1994**, *11* (Suppl.), S-166.
22. Carstensen, J. T. *Drug Stability: Principles and Practices*. Marcel Dekker: New York, 1990; p 202.
23. Nikfar, F.; Serajuddin, A. T. M.; Jerzewski, R.; Jain, N. B. Pharmaceutical compositions having good dissolution properties. U.S. and European patents filed.
24. Wadke, D. A.; Serajuddin, A. T. M.; Jacobson, H. Preformulation testing. In *Pharmaceutical Dosage Forms: Tablets;* Lieberman, H. A., Lachman, L., Schwartz, J. B., Eds.; Marcel Dekker: New York, 1989; pp 1−73.
25. Hancock, B. C.; Zografi, G. Characteristics and significance of the amorphous state in pharmaceutical systems. *J. Pharm. Sci.* **1997**, *86*, 1−12.
26. Morris, K. R.; Fakes, M. G.; Thakur, A. B.; Newman, A. W.; Singh, A. K.; Venit, J. J.; Spagnuolo, C. J.; Serajuddin, A. T. M. An integrated approach to the selection of optimal salt form for a new drug candidate. *Int. J. Pharm.* **1994**, *105*, 209−217.
27. Brandl, M.; Magill, A.; Rudraraju, V.; Gordon, M. S. Approaches for improving the stability of ketorolac in powder blends. *J. Pharm. Sci.* **1995**, *84*, 1151−1153.
28. Schildcrout, S. A.; Risley, D. S.; Kleemann, R. L. Drug−excipient interactions of seproxetine maleate hemihydrate: Isothermal stress methods. *Drug Dev. Ind. Pharm.* **1993**, *19*, 1113−1130.
29. Stahl, P. H. Characterization and improvement of the stability behavior of drug substances. In *Stability Testing in the EC, Japan and the USA: Scientific and Regulatory Requirements*; Grimm, W., Krummen, K., Eds.; Wissenschaftliche Verlagsgesellschaft: Stuttgart, 1993; pp 45−65.

JS980434G

Isolation and Identification of a Major Metabolite of PNU-107859, an MMP Inhibitor from the Biliary Fluid of Rats

MING-SHANG KUO,* DAVID A. YUREK, STEVE A. MIZSAK, MARK D. PRAIRIE, SALLY J. MATTERN, AND THOMAS F. DEKONING

Contribution from *Discovery Technologies, Structural, Analytical, and Medicinal Chemistry, and Transgenic Therapeutic in Vivo Core Group, Pharmacia and Upjohn, Kalamazoo, Michigan 49001.*

Received October 28, 1998. Final revised manuscript received March 9, 1999.
Accepted for publication March 24, 1999.

Abstract □ PNU-107859, an important representative structure in a novel class of matrix metalloproteinases (MMP) inhibitors known as thiadiazoles, was found to be quickly eliminated from rats. A major metabolite (approximately 10% of total dose) was found to be present in the bile of rats. The metabolite in question was isolated and purified from the bile fluids collected from six cannulated rats. From a total of approximately 75 mg of PNU-107859 administered to rats, 3.3 mg of the metabolite was recovered. The NMR and mass spectrometry results indicated that the metabolite is a glucuronide conjugate (1-deoxy-1β-substituted D-glucopyranosiduronic acid) of the intact drug. Furthermore, the UV, MS, and NMR data established that the conjugate is located at the nitrogen α to the thiocarbonyl of the thiadiazole ring.

Introduction

The matrix metalloproteinases (MMPs) are a family of zinc endopeptidases which are capable of degrading the extracellular matrix of connective tissues and basement membranes.[1] Overactivation or increased synthesis of the MMPs has been implicated in several disease pathologies, including arthritis, cancer progression, and related connective tissue disorders[2], periodontal disease,[3] atherosclerotic plaque rupturing,[4] and aortic aneurysms.[5] There are currently at least 18 members of this family of proteinases which can be roughly associated into three groups depending on their native substrates. Thus, the gelatinases are effective proteinases of Type IV collagen, the collagenases degrade interstitial collagen, and the stromelysins are effective as protoglycanases. The discovery and characterization of the MMPs is summarized in several recent reports. Recently several research groups have shown that related metalloproteinases are also involved in the conversion of inactive tumor necrosis factor-I (TNF-I) into active TNF.[6,7] Usually this inflammatory cytokine plays a beneficial role in physiological defense responses; however, overproduction of TNF-I can lead to systemic toxicity. Therefore, MMP inhibitors may be indirectly involved in diseases for which TNF-I has been implicated, such as Crohn's disease, MS, cachexia, sepsis, and rheumatoid arthritis.[8] PNU-107859[9] is a member of a novel class of MMP inhibitors known as thiadiazoles. During a preliminary pharmacokinetic study of PNU-107859, it was observed that this experimental drug has rather short half-life (≅40 min) in rats. To investigate the nature of the unfavorable pharmacokinetics, the bile samples from rats treated with this drug were collected and found to contain the intact drug and a metabolite as the only other major thiadiazole-containing component. It was estimated that this putative metabolite represented about 10% of the total drug 3 h after iv administration. A study was therefore initiated to isolate enough metabolite for spectroscopy experiments to elucidate its structure unambiguously.

Experimental Section

Materials—PNU-107859 was synthesized by Pharmacia and Upjohn. All other chemicals were analytical or HPLC grade.

Dosing and Collection of Bile—The jugular veins of six male Sprague−Dawley rats were cannulated using a variation of the Week's chronic jugular vein cannulation technique. The same animals were anesthetized after eight or 9 days and the bile ducts cannulated using PE-10 polyethylene tubing. The free end of the tubing was placed in a test tube to collect draining bile. Animals (230−290 g) were given a 50 mg/kg dose of PNU-107859 (50 mg/mL in a 50% PEG/50% saline vehicle) iv via the chronic jugular vein cannula. The cannulas were flushed with 100 μL of 50% PEG/50% saline followed by 300 μL of 100% saline. Bile was collected hourly for 3 h postdosing. After pooling samples from all animals, a total of 15 mL of bile was collected.

Cation Exchange Methods—One milliliter of pooled bile was passed over one Varian Bondelut SCX cartridge (1 mL) to remove impurities with a UV absorption maximum at 270 nm. The metabolite was not retained by this resin. The resin was washed with water until HPLC showed no presence of the metabolite in the eluent. Fractions containing the metabolite were collected and used directly for prep-HPLC.

Preparative HPLC Methods—The cation-exchange-purified samples were divided into six samples, and each of these was purified by preparative HPLC employing a Waters μBondapak cartridge (2.5 × 10 cm). Elution at 15 mL/min for 5 min at 10/90 ACN/H_2O plus 0.1% TFA was followed by a 15 min gradient to 25/75. These conditions were maintained for 5 min, followed by an elution at 90/10 to wash the column. Detection was at 220 nm. Fractions were collected with a Foxy collector in the peak detect mode. A second run using the same conditions was performed on the pooled fractions from the six initial runs.

Analytical HPLC Methods—Sample was injected onto a Zorbax Rx-C8 column (4.6 × 250 mm) and eluted isocratically with 25/75 ACN/H_2O plus 0.1% TFA at 1 mL/min with detection performed by a Varian 9065 diode array detector at 311 or 220 nm.

FAB-MS Method—The low resolution positive ion fast atom bombardment (FAB) mass spectrum of the glucuronic acid product isolate was obtained on a VG70-SE Nier-Johnson double-focusing mass spectrometer equipped with an OPUS-2 data system. A cesium ion gun operating at 25 kV was used as the source of the ionizing beam, while the instrument was operated at 8 kV accelerating voltage. The instrument was calibrated at selected masses using a mixture of CsI and NaI. A small portion of the isolate as a methanol solution was mixed with the 2-hydroxyethanol disulfide (2-HED) matrix and introduced into the ion source on a stainless steel tip via a direct insertion probe. The sample

* Corresponding author. Tel: (616) 833-7802. Fax: (616)-833−2225. E-mail: MTKUO@am.pnu.com.

10.1021/js980427s CCC: $18.00
Published on Web 05/13/1999

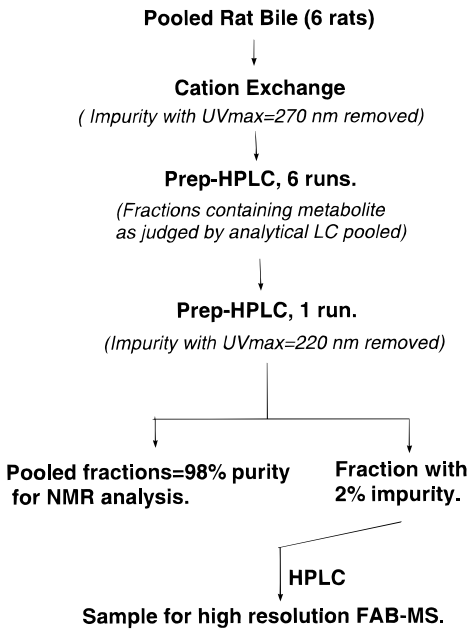

Scheme 1—Purification steps.

spectrum was recorded by scanning the magnetic field from *m*/*z* 2500 to *m*/*z* 15. The results were further analyzed using the mass spectral processing software on the Harris Nighthawk computer system.

The accurate mass of the isolate, as the protonated adduct ([M + H]$^+$), was determined by the peak matching technique relative to the known matrix adduct ion mass of 2-HED at *m*/*z* 463.0445. The mass spectrometer was operating at a mass resolution of approximately 4000 (m/Dm, 10% valley definition).

NMR Methods—^{1}H NMR spectra were recorded at 400.13 MHz using a Bruker ARX-400 spectrometer. Data were processed on an SGI Indy computer using Bruker UXNMR software. Samples were dissolved in 500 μL of DMSO-d_6 in a 5-mm NMR tube. Spectra were recorded at a temperature of 300K (27 °C). One-dimensional proton spectra were recorded as free induction decays of 32K complex points with a spectrum width of 6024 Hz. Four dummy scans were used. The receiver gain and the number of pulses were optimized for each sample. Free induction decays were Fourier transformed with no zero-filling after application of a resolution-enhancing Gaussian window function (LB = −1, GB = 0.2). Two-dimensional homonuclear COSY spectra were recorded in the magnitude mode using 1K × 1K data table (after transformation), with 256 increments in F1 and no zero filling in F2. Unshifted sinebell windows were applied before transformation.

^{13}C NMR spectra were obtained on a Varian XL-300 spectrometer operating at 75.43 MHz. The spectral window was 17391 Hz, and 32K data points were used with an acquisition time of 0.942 s and a pulse delay of 1.00 s. The free induction decays were Fourier transformed using standard sensitivity enhancement parameters.

Heteronuclear Multiple Bond Correlation (HMBC)—NMR spectra were recorded on a Bruker ARX-400 Spectrometer equipped with a 9.4 T magnet, operating at 400.13 MHz for ^{1}H and 100.62 MHz for ^{13}C. A Bruker 5 mm broadband inverse gradient probe was used for these experiments. HMBC data was acquired using the a gradient pulse sequence. 2D transformations were accomplished using Bruker UXNMR software on an SGI Indy computer. Spectra were recorded in the magnitude mode using a 1K by 512 data table with 160 pulses per 256 increments in F1 domain and no zero-filling in F2 domain. All spectra were acquired at 300K. Relaxation delays typically were 1.1 s.

Results

A brief outline of the purification methods is summarized in Scheme 1. Briefly, cation exchange procedures were used to remove some impurities. The pooled fractions containing the metabolite were then processed by preparatory reverse-phase HPLC. Fractions containing the metabolite were dried and redissolved in perdeuterated methanol or DMSO to obtain structural information by NMR. The HMR spectra also revealed a peptidic impurity partially coeluted with the metabolite. This was confirmed by reanalyzing the fractions by HPLC with detection at 220 nm. This peptide has a slightly longer retention time than the metabolite peak. The fractions containing the metabolite were therefore combined and rechromatographed using the same HPLC conditions. The final preparation was judged to be pure by HPLC analysis employing a diode array detector and by HMR spectroscopy. A total of 3.3 mg of the pure metabolite was obtained. Since approximately 70 mg of PNU-107859 was administered to rats and the average conversion rate was 10%, a recovery of nearly 50% of the metabolite present in bile was obtained.

The purified metabolite was then subjected to NMR, FAB-MS, and UV studies. The 1D NMR chemical shift data are summarized in Table 1. The 2D NMR results are summarized graphically in Figure 2. The FAB-MS results are summarized graphically in Scheme 2.

Table 1—NMR Data of U-107859 and Its Metabolite[a]

	U-107859		metabolite	
position	δ_H	δ_C	δ_H	δ_C
1	7.20	126.8 (d)	7.20	126.6 (d)
2	7.29	128.5 (d)	7.29	128.3 (d)
3	7.12	129.6 (d)	7.12	129.4 (d)
4	—	137.3 (s)	—	136.9 (s)
5	2.83, 3.00	38.8 (t)	2.85, 2.99	38.5 (t)
6	4.42	54.6 (d)	4.42	54.4 (d)
7	—	153.1 (s)	—	153.0 (s)
8	—	154.0 (s)	—	150.8 (s)
9	—	183.6 (s)	—	185.0 (s)
10	—	171.0 (s)	—	170.6 (s)
11	2.62	25.9 (q)	2.60	25.6 (q)
6 N–H	6.81	—	6.89	—
7 N–H	10.71	—	10.95	—
9 N–H	13.8	—	—	—
10 N–H	8.15	—	8.15	—
1′	—	—	5.80	84.3 (d)
2′	—	—	3.70	71.1 (d)
3′	—	—	3.40	76.3 (d)
4′	—	—	3.41	71.4 (d)
5′	—	—	3.80	78.0 (d)
6′	—	—	12.9	169.7 (s)

[a] All spectra were collected in DMSO-d_6 solutions and are reported as chemical shift downfield (ppm) from TMS.

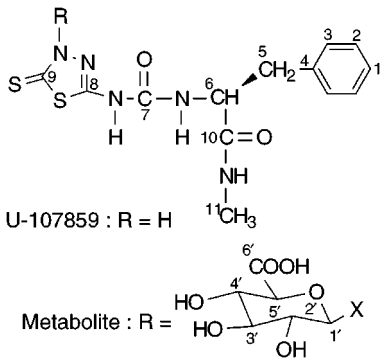

Figure 1—Structure of U-107859 and its metabolite.

Discussion

1. The Nature of the Conjugate—The main features of the HMR spectra of the metabolite collected during the purification stage were the extra resonance signals ob-

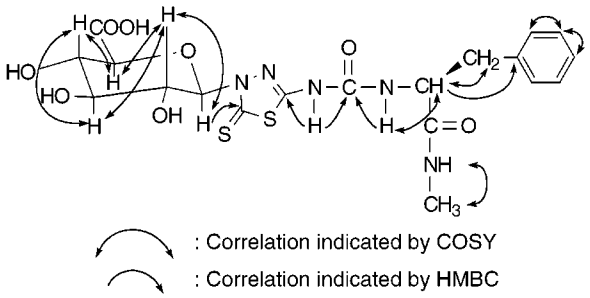

Figure 2—2D NMR results of U-107859 metabolite.

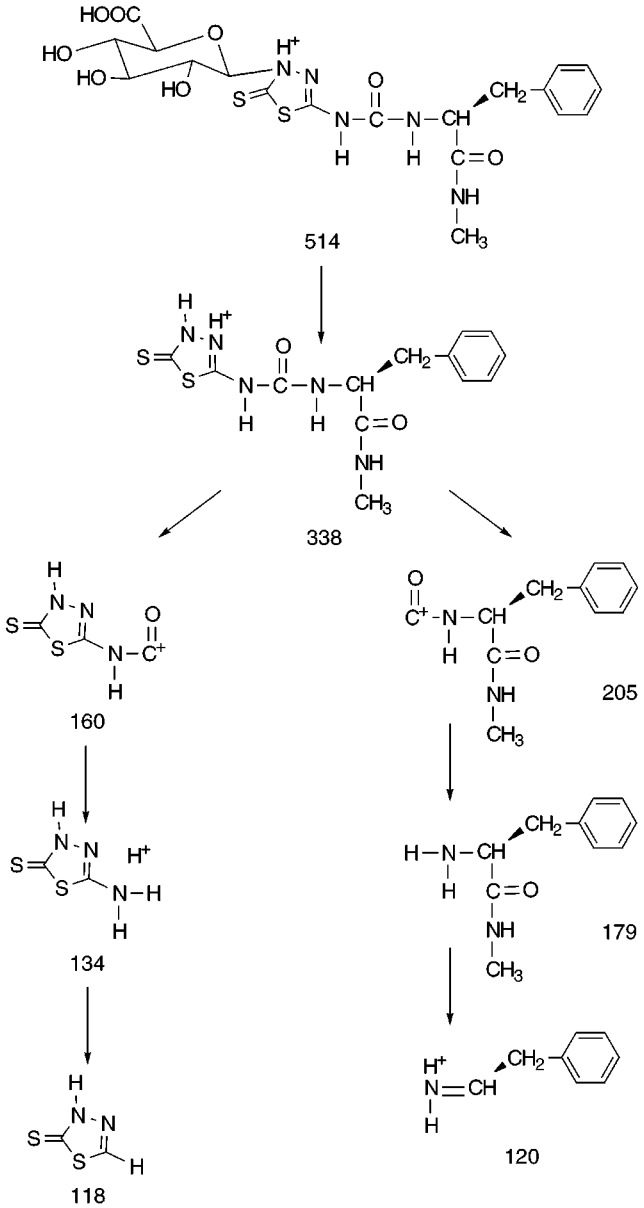

Scheme 2—Major ions observed by FAB-MS.

served between 3 and 6 ppm, suggesting the presence of carbinols, when compared to the parent drug. Integration of these extra signals resulted in a total of five nonexchangeable protons. However, two of the five protons were not resolved in methanol. Resolution of these five signals was attempted with a number of solvents. It was found that DMSO-d_6 provided the best resolution for those five protons. All following experiments, including $^1H-^1H$, $^1H-^{13}C$ COSY, CMR, and $^1H-^{13}C$ HMBC were therefore conducted in DMSO solution. The results are summarized in Table 1 and Figure 2 and discussed below.

The assignments of NMR signals of PNU-107859 are based on various 2D NMR experiments and will not be discussed in this report. Comparison of chemical shift values listed in Table 1 revealed that the major differences were the extra signals (vide infra) obtained for the metabolite when compared to the parent compound. Another important observation was that the conjugate most likely contained a carboxylic acid functional group, as evidenced by the new broad peak at 12.9 ppm and a new carbon signal at 169.7 ppm in the CMR spectrum. The 2D COSY spectrum, the size of $^1H-^1H$ coupling constants (9 Hz), and the HMBC spectrum indicated that the conjugate was a 1-deoxy-1β-aminated-glucopyranuronate. Specifically, the 2D COSY spectrum sequentially linked the five carbinols and connected each of them to an exchangeable hydroxyl proton. The fact that all the carbinols had 9 Hz coupling constants dictated that they adopted a diaxial relationship with their coupled neighbors. Assuming the bulky hydroxyl groups are at the equatorial positions leads to the conclusion that the conjugate is a modified β-D-glucopyranose. Analysis of the HMBC spectrum further connected the 12.9 ppm proton of the pyranoglucoside to the carboxyl carbon, establishing that the conjugate is a glucopyranuronate. Finally, the chemical shift value of the anomeric carbon (84.3 ppm) strongly implied that the conjugate is a 1-deoxy-1β-aminated-D-glucopyranuronate.[10]

2. The Site of Conjugation—There are five possible nitrogens, two on the thiadiazole ring and three on the backbone, that could be linked to the pyranose. Comparison of chemical shift values listed in Table 1 revealed that the 9 N−H signal is missing in the metabolite, suggesting that this position is the site of conjugation. Also, the HMBC spectrum gave a cross-peak between the anomeric proton and the carbon of the thiocarbonyl. Since this experiment will only detect C−H couplings with 2 or 3 bond linkages, the attachment must be on the nitrogen adjacent to the thiocarbonyl. Supporting this conclusion is the observed 3 ppm upfield shift of the C-8 carbon signal caused by the γ gauche effect. Other supporting evidences are the almost identical chemical shift values and the almost identical UV absorption for the metabolite and its parent.

3. Confirmation by Mass Spectrometry—The purified metabolite was subjected to low and high-resolution FAB-mass spectrometry studies. The low resolution FAB-MS results produced the expected molecular ions at 514 $(M + H)^+$ and 536 $(M + Na)^+$ for the glucuronic conjugate. Subsequent high resolution FAB-MS studies unambiguously identified the molecular formula of the metabolite as $C_{19}H_{23}N_5O_8S_2$. The major fragment ions can be rationalized as in Scheme 2. Thus, the FAB-MS results are in total agreement with the conclusions reached by NMR.

Glucuronidation is the most common pathway of conjugation in mammalian metabolism and excretion of xenobiotics.[11] It can be classified as O-, S-, N-, and C-glucuronidation on the basis of the type of atoms to which the glucuronic acid moiety is transferred by a group of inducible UDP-glucuronosyltransferases.[12] We have clearly demonstrated in this study that PNU-107859 is partially cleared by N-glucuronidation. Although N-glucuronidation is a much less commonly observed and a not well understood pathway compared to O-glucuronidation, its participation in the metabolic transformation of xenobiotics has gained increasing recognition in recent years. Examples reported in the literature are of wide structural classes of nitrogen-bearing aglycones, including primary through tertiary amines, and various classes of heterocycles, such as imidazole, hydantoin, pyrimidine, piperidine, tetrahydroiso-

quinoline, triazine, and tetrazole.[13−17] Our result extends this list to include thiadiazole.

References and Notes

1. Docherty, A. J. P.; Murphy, G. The tissue metalloproteinase family and the inhibitor TIMP: A study using cDNAs and recombinant proteins. *Ann. Rheum. Dis.* **1990**, *49*, 469−479.
2. Henderson, B.; Docherty, A. J. P.; Beeley, N. R. A. Design of inhibitors of articular cartilage destruction. *Drugs Future* **1990**, *15*, 495−508.
3. Overall, C. M.; Wiebkin, O. W.; Thonard, J. C. Demonstration of tissue collagenase activity in vivo and its relationship to inflammation severity in human gingiva. *J. Periodontal Res.* **1987**, *22*, 81−88.
4. Henney, A. M.; Wakeley, P. R.; Davies, M. J.; Foster, K.; Hembry, R.; Murphy, G.; Humphries, S. Localization of stromelysin gene expression in atherosclerotic plaques by in situ hybridization. *Proc. Natl. Acad. Sci. U.S.A.* **1991**, *88*, 8154−8158.
5. Vine, N.; Powell, J. T. Metalloproteinases in degenerative aortic diseases. *Clin. Sci.* **1991**, *81*, 233−239.
6. Gearing, A. J. H.; Beckett, P.; Christodoulou, M.; Churchill, M.; Clements, J.; Davidson, A. H.; Drummond, A. H.; Galloway, W. A.; Gilbert, R.; Gordon, J. L.; Leber, T. M.; Mangan, M.; Miller, K.; Nayee, P.; Owen, K.; Patel, S.; Thomas, W.; Wells, G.; Wood, L. M.; Woolley, K. Processing of tumor necrosis factor-I precursor by metalloproteinases. *Nature* **1994**, *370*, 555−557.
7. Mohler, K. M.; Sleath, P. R.; Fitzner, J. N.; Cerretti, D. P.; Alderson, M.; Kerwar, S. S.; Torrance, D. S.; Otten-Evans, C.; Greenstreet, T.; Weerawarna, K.; Kronheim, S. R.; Petersen, M.; Gerhart, M.; Kozlosky, C. J.; March, C. J.; Black, R. A. Protection against a lethal dose of endotoxin by an inhibitor of tumor necrosis factor processing. *Nature* **1994**, *370*, 218−220.
8. Vilcek, J.; Lee, T. H. Tumor necrosis factor. New insights into the molecular mechanisms of its multiple actions. *J. Biol. Chem.* **1991**, *266*, 7313−7316.
9. Jacobsen, E. J.; Mitchell, M. A.; Hendges, S. J.; Belonga, K. L.; Skaletzky, L. L.; Stelzer, L. S.; Lindberg, T. J.; Fritzen, E. L.; Schostarez, H. J.; O′Sullivan, T. J.; Maggiora, L. L.; Stuchly, C. W.; Laborde, A. L.; Kubicek, M. F.; Poorman, R. A.; Beck, J. M.; Miller, H. R.; Petzold, G. L.; Scott, P. S.; Truesdell, S. E.; Wallace, T. L.; Wilks, J. W.; Fisher, C.; Goodman, L. V.; Kaytes, P. S.; Ledbetter, S. R.; Powers, E. A.; Vogeli, G.; Mott, J. E.; Trepod, C. M.; Staples, D. J.; Baldwin, E. T.; Finzel, B. C. Synthesis of a Series of Stromelysin-Selective Thiadiazole Urea Matrix Metalloproteinase Inhibitors. *J. Med. Chem.*, submitted.
10. Nohara, A.; Kuriki, H.; Ishiguro, T.; Saijo, T.; Ukawa, K.; Maki, Y.; and Sanno. Y. Studies on Antianaphlactic Agents. 6. Synthesis of Some Metabolites of 6-Ethyl-3-(1H-tetrazol-5-yl) Chromone and their Analogues; *J. Med. Chem.* **1979**, *22*, 290−295.
11. Dutton, G. J. *Glucuronides of drugs and other compounds*; CRC Press: Boca Raton, 1980.
12. Mulder, G. B.; Coughtrie, M. W. H.; Burchell, B.; Mulder, G. L.; Eds. Glucuronidation in Conjugation Reactions in Drug Metabolism. Taylor and Francis, Ltd.: London, 1990; pp 51−105.
13. Shaefer, W. H. Formation of a Carbamoyl Glucuronide Conjugate of Carvedilol in Vitro using Dog and Rat Liver Microsomes. *Drug Metab. Dispos.* **1992**, *20*, 130−133.
14. Mutlib, A. E.; Nelson, W. L. Synthesis and Identification of the N-glucuronides of Norgallopamil and Norverapamil, Unusual Metabolites of Gallopamil and Verapamil**.** *J. Pharmacol. Exp. Ther.* **1990**, *252*, 593−599.
15. Macrae, P. V.; Kinns, M.; Pullen, F. S.; Tarbit, M. H. Characterization of a Quaternary N-glucuronide Metabolite of the Imidazole Antifungal Tioconazole**.** *Drug Metab. Dispos.* **1990**, *18*, 1100−1102.
16. Mohri, K.; Uesugi, T.; Kamisaka, K. Bucolome N-glucuronide: Purification and Identification of a Major Metabolite of Bucolome in Rat Bile. *Xenobiotica* **1985**, *15*, 615−622.
17. Kuo, G. Y.; Hwang,; B. Y−H.; Staiger, D. B. Structural Assignment of an N-glucuronide Metabolite of the Phenylethanolamine *N*-methyltransferase (PNMT) Inhibitor 1,2,3,4-tetrahydroisoquinoline-7-sulfonamide by ^{15}N NMR. *Biochem. Pharmacol.* **1986**, *35*, 1613−1615.

JS980427S

Preparation of a Complex of Dexamethasone Palmitate–Low Density Lipoprotein and Its Effect on Foam Cell Formation of Murine Peritoneal Macrophages†

YOSHIHIKO TAUCHI,* MASASHI TAKASE, IICHI ZUSHIDA, SUMIO CHONO, JUICHI SATO, KEIJI ITO, AND KAZUHIRO MORIMOTO

Contribution from *Department of Pharmaceutics, Hokkaido College of Pharmacy, Otaru-city, Hokkaido 047-0264, Japan*

Received October 23, 1998. Final revised manuscript received April 16, 1999.
Accepted for publication April 16, 1999.

Abstract □ In the early progression of atherosclerosis, LDL migrates in the subendothelial space of the artery and plays an important role in foam cell formations of macrophages. LDL may serve as a carrier of site-specific delivery of drugs to atherosclerotic lesions. In this exploratory study, dexamethasone palmitate (DP) was incorporated in LDL, and an inhibitory effect of this complex on foam cell formations was examined. LDL was isolated from human plasma, and the DP–LDL complex was prepared by incubation in the presence of Celite 545. No degradation nor modification of LDL was observed. The DP/LDL molar ratio of the complex was 35-50:1. Foam cell formations of murine macrophages were induced by incubation with oxidized LDL. When macrophages were pretreated with the DP–LDL complex, accumulation of cholesterol ester in the macrophages induced by oxidized LDL, i.e., an index of foam cell formation, was decreased. These findings indicated that the DP–LDL complex showed similar characteristics to LDL, and the DP–LDL complex inhibited foam cell formations of macrophages in vitro. This study provides the basis for further study of the DP–LDL complex as a drug–carrier complex for treatment of atherosclerosis.

Introduction

In an early stage of progression of atherosclerosis, atherosclerotic plaques are developed by accumulation of foam cells derived from macrophages or fibroblasts.[1] Recent studies indicate that LDL migrates under the epithelium of the vascular smooth muscle and is modified to be incorporated into macrophages in early atherosclerotic lesions.[2−4] In fact, macrophages can be converted to foam cells containing large amounts of cholesterol esters when incubated with modified LDL, mainly oxidized, in vitro.[5,6] Modified LDL and macrophages interact to form foam cell formations at atherosclerotic lesions. Prevention of foam cell formations of macrophages by reducing cholesterol esters accumulated in the foam cells is thought to be antiatherogenic.

It is well known that the process of plaque formation in atherosclerotic lesions possesses a number of features in common with inflammation.[7] Several studies have reported that anti-inflammatory drugs suppress the development of atherosclerosis in New Zealand White rabbits and Watanabe heritable hyperlipidemic rabbits.[8−11] Asai et al. reported that dexamethasone inhibits the formation of foam cells in atherosclerotic lesions.[12]

Plasma lipoproteins are a carrier of not only water-insoluble lipids but also lipophilic compounds such as certain vitamins, hormones, toxins, and others in the circulatory system. Recently, it has been demonstrated that lipoproteins, especially LDL, can be used as a carrier to deliver drugs to specific sites in the body.[13,14] In most studies, LDL is used as a carrier to deliver antineoplastic drugs to cancer cell.[15,16]

In the present study, to assess the feasibility of LDL as a drug delivery system for atherosclerosis, we prepared a complex of dexamethasone palmitate (DP), a steroidal anti-inflammatory drug, and LDL and examined its inhibitory effects on cholesterol ester accumulation in macrophages induced by oxidized LDL.

Materials and Methods

Animal—Male ICR mice were obtained from Japan SLC, Inc. (Hamamatsu, Japan) and used for experiments at 6−8 weeks of age.

Materials—Dexamethasone palmitate (DP) and dexamethasone nonadecanoate were supplied by Green Cross Co. (Osaka, Japan). Celite 545 was purchased from Kanto Chemical Co. Inc. (Tokyo, Japan), dexamethasone and FAT RED 7B from Sigma Chemical Co. (St. Louis, MO), and cholesterol esterase, oxidase, and peroxidase from Toyobo Co. (Tokyo, Japan). All other chemicals were of analytical grade.

Isolation of LDL—LDL (d = 1.019−1.063 g/mL) was isolated by sequential ultracentrifugation (100 000g) from normolipidemic human plasma.[17] The LDL fraction was dialyzed sufficiently against phosphate-buffered saline (PBS, pH 7.4) and then filtered through a MILLEX-HV filter (pore size; 0.45 μm, Millipore Co., Bedford, MA). The LDL fraction was stored at 4 °C under the darkness and used for experiments within a week.

Preparation of the Drug−LDL Complex—The DP−LDL complex was prepared by the method of Seki et al.[18] with minor modification. Briefly, Celite 545 (100 mg) and 1 mL of DP solution (1 mg/mL in MeOH) were agitated by a vortex mixer. The mixture was evaporated under the vacuum for 30 min, and then the residues were pulverized adequately. The residue and 2 mL of LDL suspension (300−400 μg protein/mL) were mixed gently and packed with N_2 gas. The mixture was incubated for 20 h with shaking at 37 °C. After incubation, the mixture was centrifuged at 2000g for 10 min, and the supernatant was dialyzed with PBS. The complex obtained was passed through a MILLEX-HV filter and stored at 4 °C until experiments were performed (<1 week).

Oxidation of LDL and the DP−LDL Complex—Each LDL and DP−LDL complex was diluted to 100 μg protein/mL with PBS and incubated with 5 μM $CuSO_4$ at 37 °C for 20 h. The oxidized LDL (ox-LDL) and the oxidized DP−LDL complex (ox-DP complex) suspensions were dialyzed against PBS. Confirmations of oxidation were obtained by electrophoresis.

* Corresponding author. Tel: 81-134-62-1851. Fax: 81-134-62-5161. E-mail: tauchiyo@hucc.hokudai.ac.jp.

† Abbreviations: LDL, low density lipoprotein; PBS, phosphate buffered saline; T-ch, total cholesterol; F-ch, free cholesterol; CE, cholesterol ester, DP, dexamethasone palmitate; ox-LDL, oxidized LDL; ox-DP complex, oxidized DP−LDL complex.

10.1021/js980422v CCC: $18.00
Published on Web 06/12/1999

Preparation of Macrophage—Peritoneal cells from unstimulated ICR mice were washed with PBS by centrifugation (800*g*). The cells were suspended to 10^6 cells/mL in RPMI1640 medium (Gibco BRL, Life Technologies, Rockville, MD) supplemented with 10% fetal bovine serum (Gibco BRL), 50 μM 2-mercaptoethanol, and 10 μg/mL of gentamicin. The cell suspensions were distributed (1 mL each) to wells of a 24-well culture plate (Becton Dickinson, Lincoln Park, NJ), and the plate was incubated for 90 min at 37 °C in a CO_2 incubator. After incubation, nonadherent cells were removed by washing with RPMI 1640 medium, and then the macrophage monolayers were placed in fresh RPMI 1640 medium for 20 h at 37 °C in a CO_2 incubator.

Cholesterol Accumulation Assay in Macrophages—Cholesterol accumulation in macrophages was assayed according to the methods of Miyazaki et al.[19] Macrophage monolayers were incubated with ox-LDL or ox-DP complexes for the periods indicated at 37 °C in a CO_2 incubator. After incubation, the macrophage monolayers were washed twice with RPMI 1640 medium and then PBS. Lipids and proteins were extracted directly from the macrophage monolayers. Briefly, 1 mL of a hexane/2-propanol (3:2) mixture was added to macrophage monolayers in the wells, and the macrophage monolayers were incubated for 30 min at room temperature. The solvent of the mixture was collected and extracted again. The extracts were combined, evaporated under the vacuum, dissolved in 500 μL of EtOH, and used for cholesterol measurements. After lipid extraction, 500 μL of a 0.1 M NaOH solution was added into each well and incubated for 15 min at 37 °C. The extracts were collected, and the extraction was repeated. The combined extracts were used for determination of cell protein.

Measurement of Cellular Cholesterol—The cellular concentration of cholesterol was measured by a fluorometric enzymatic method.[20] Briefly, 200 μL of cellular lipid extract and 2.5 mg of Triton X-100 were mixed and evaporated under the vacuum. The residue was suspended with 200 μL of the enzyme mixture and incubated for 30 min at 37 °C. The enzyme mixture for free cholesterol (F-ch) contained 0.12 units/mL of cholesterol oxidase, 45 units/mL of peroxidase, 0.5 mg/mL of homovanillic acid (Wako Pure Chemical Industries Ltd.), and 2 mg/mL of Triton X-100 in 100 mM sodium phosphate buffer (pH 7.0). The enzyme mixture for total cholesterol (T-ch) contained 0.36 units/mL of cholesterol esterase in the enzyme mixture for F-ch. Following incubation, 2.8 mL of a 0.1 M NaOH was added to stop the reaction, and each fluorescence intensity was measured with excitation at 323 nm and emission at 420 nm using a spectrofluorophotometer (Model FP-770, JASCO, Tokyo, Japan). Cellular cholesterol ester (CE) was determined by subtracting F-ch from T-ch.

Electrophoresis—The electrophoretic mobilities of LDL and DP−LDL complexes were determined by the Pol-E-Film System (Ciba-corning Diagnostics Co., Palo Alto, CA). The samples were loaded at 4.0 μg/well of agarose gel film (Universal Gel/8, Ciba-Corning) and run at 90 V for 40 min. After drying, the gels were stained with FAT RED 7B (Sigma) to visualize lipoprotein bands.

Measurement of LDL and Complex Particle Size—Particle size of LDL and DP−LDL complexes was determined by photon correlation spectroscopy using Coulter N4 plus a submicron particle analyzer (Coulter Co., Miami, FL). All samples were suspended with PBS to 100 μg protein/mL, filtered through an HLC disk (pore size 0.2 μm, Kanto Chemical), and then measured at 20 °C.

HPLC Analysis—DP concentration in the complexes was measured by HPLC as follows: a mixture of samples of the complexes (50 μL) and dexamethasone nonadecanoate (as an internal standard, 50 μL) was extracted by dichloromethane (4 mL). A part of the organic fraction (3 mL) was evaporated under the vacuum at 30 °C. The residue was dissolved in 120 μL of acetonitrile−water (95:5), and a 50 μL of aliqot was injected into the HPLC system (Shimadzu Co., Kyoto, Japan) possessing a 7-μm LiChrosorb RP-18 column (4 × 250 mm, Cica-Merck, Kanto Chemical). The mobile phase was acetonitrile−water (95:5), and flow rate was 2.0 mL/min. The eluate was monitored at 236 nm and quantified on a model C-R6A chromatopac integrator (Shimadzu). The concentrations were determined with resect to a standard curve of DP.

Other Determinations—Proteins were measured by Coomassie Protein Assay Reagent (Pierce Chemical Company, Rockford, IL)[21] using bovine serum albumin as a standard. Each level of cholesterol in LDL or DP−LDL complex suspensions was measured by using commercial kits (Wako Pure Chemical).

Statistical Analysis—Data are expressed as means only or means and SDs ($n = 3$). Statistical analysis was done using nonpaired Student's *t*-test or Fisher's PLSD test. A p value of 0.05 or less was considered a significant difference between the sets of data.

Table 1—Lipids and Proteins Compositions in LDL and the DP–LDL Complex[a]

	LDL	DP–LDL complex
T-ch[b] (mg/100 mL)	103.7 ± 4.18	83.39 ± 2.56*
F-ch[c] (mg/100 mL)	29.84 ± 0.50	23.42 ± 1.02*
CE[d] (mg/100 mL)	73.86 ± 3.71	59.97 ± 2.06*
protein (mg/100 mL)	34.89 ± 1.25	25.99 ± 0.33*
F-ch/T-ch	0.29 ± 0.01	0.28 ± 0.01
T-ch/protein	2.97 ± 0.09	3.21 ± 0.13

[a] Values were mean ± SD ($n = 3$), *: significant difference from LDL, $p < 0.001$. [b] Total cholesterol. [c] Free cholesterol. [d] Cholesterol ester.

Table 2—Particle Size and DP Concentration of the DP–LDL Complex[a]

	particle size (nm)	DP concentration (μg/mL)
LDL	22.43 ± 0.65	–
DP–LDL complex	23.67 ± 0.25	14.19 ± 0.75 [47.60 ± 1.92]

[a] Values were mean ± SD ($n = 3$). Bracketed/values indicate the DP contained in the DP–LDL complex (mol of DP/mol of LDL).

Results

Characteristics of LDL and the DP−LDL Complex—Table 1 shows the concentrations of cholesterols and protein in LDL and the DP−LDL complexes. The T-ch, F-ch, and CE concentrations in the complexes were 83.39, 23.42, and 59.97 mg/100 mL, respectively, and the protein concentration in the DP−LDL complexes was 25.99 mg/100 mL. These values of the DP−LDL complexes were about 75−80% of the corresponding values of LDL, and these percentages were indicated as the yields after the complex preparation. However, the ratios of F-ch/T-ch and T-ch/protein in the DP−LDL complexes were similar to those of LDL (0.28 and 3.21 in the DP−LDL complexes, and 0.29 and 2.97 in LDL, respectively). Furthermore, in the case of oxidized LDL and DP−LDL complexes, these ratios were not different between ox-LDL and ox-DP complexes (data are not shown).

Particle size and DP concentration in the DP−LDL complexes are shown in Table 2. Although several studies have reported that particle size of the drug-LDL complexes is larger than that of LDL,[22,23] the particle size of the DP−LDL complexes in this study (23.67 nm) was not significantly different from that of LDL (22.43 nm). The DP concentration in the DP−LDL complexes was 14.19 μg/mL, and DP contained in the DP−LDL complex was 47.6 mol of DP/mol of LDL (LDL molecular weight of 5.5×10^5 based on protein concentration). The DP concentrations in the complex and those in the LDL particle were not altered by oxidation or dialysis with PBS. DP was not detected in a preparation which was prepared with PBS instead of LDL suspension (data are not shown). Neither aggregation of the DP−LDL complexes nor decrease in DP contained in the DP−LDL complex was recognized after 4 weeks of storage at 4 °C.

LDL is unstable in a buffer after isolation and easily modified by negative ions, air, and other stimuli. To examine whether LDL could be modified by the addition of DP, electrophoresis of the DP−LDL complexes was compared with that of LDL. As shown in Figure 1, electorophoretic mobility and the lipid band of the com-

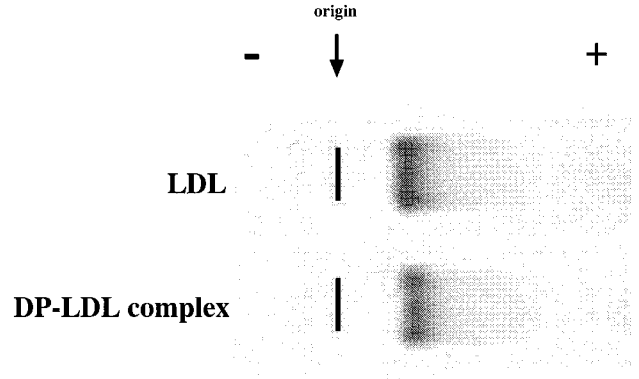

Figure 1—Electrophoretic mobilities of LDL and the DP–LDL complexes. Samples were loaded on agarose gel film at 2 μg/well and run at 90 V for 40 min. The agarose gel film was dried and stained with Fat red 7B.

plexes were similar to those of LDL. Moreover, the concentration of apo-B protein, which is the main protein in the LDL, was over 90% of the total protein concentration in the DP−LDL complexes, and the value was not different from that in LDL (data are not shown). These findings indicate that DP−LDL complexes can be prepared without any transposition and modification.

Cholesterol Accumulation in Macrophages during Incubation with ox-LDL or ox-DP Complex—It is well known that the macrophages are converted to foam cells with lipid droplets consisted of cholesterols during incubation with ox-LDL.

The T-ch and F-ch concentrations in macrophages were increased by incubation with ox-LDL about 2.9- and 2.3-fold of the control value (without ox-LDL), respectively (Figure 2A). The CE concentration in macrophages after incubation with ox-LDL was also increased markedly from 9.2 to 82.4 μg/mg cell protein (Figure 2 B). This increase in CE was associated with conversion of macrophages to foam cells during incubation with ox-LDL. On the other hand, when the macrophages were incubated with ox-DP complexes, CE concentration increased slightly as compared with that with ox-LDL (Figure 2B), while either T-ch or F-ch concentration was increased to the same extent as those in ox-LDL-treated macrophages (Figure 2A).

Effects of the ox-DP Complex on CE Accumulation in Macrophages—Figure 3 shows the changes in cholesterol concentrations in macrophages incubated with ox-LDL alone or ox-LDL together with ox-DP complexes. The concentrations of T-ch, F-ch, and CE in macrophages were increased predominantly by the incubation with ox-LDL alone at 100 μg protein/well rather than those at 50 μg protein/well. The increases in T-ch, F-ch, and CE in macrophages incubated with ox-LDL and ox-DP complexes (total ox-LDL concentration should be 100 μg protein/well) were significantly attenuated as compared with those with ox-LDL alone at 100 μg protein/well. However, the smaller concentration of ox-DP complexes (5 μg protein/well) showed no effects on the increased concentrations of cholesterols in macrophages incubated with ox-LDL at 50 μg protein/well.

Figure 4 shows the changes in cholesterol concentrations in macrophages preincubated with ox-DP complexes at 5 μg protein/well and then incubated with ox-LDL after removing of the ox-DP complexes. Preincubation with ox-DP complexes inhibited the accumulation of T-ch and F-ch in macrophages induced by incubation with ox-LDL. The CE concentration in macrophages preincubated with ox-DP complexes and then incubated with ox-LDL (50.37 μg/mg cell protein) was significantly lower than that in macrophages incubated with ox-LDL alone (83.23 μg/mg cell protein).

Figure 5 shows the changes in cholesterol concentrations in macrophages preincubated with dexamethasone at 0.4 μM in medium and then incubated with ox-LDL after removing of dexamethasone. The CE concentration in macrophages incubated with ox-LDL alone was 62.5 μg/mg cell protein, and the CE concentration in macrophages preincubated with dexamethasone and then incubated with ox-LDL was 39.5 μg/mg cell protein. Therefore, similar to that of the ox-DP complexes, preincubation with dexamethasone inhibited the CE accumulation in macrophages induced by incubation with ox-LDL.

Discussion

Recently, drug−LDL complexes have been examined for use as carriers in site-specific delivery systems.[13−16,22,23] Anticancer drugs have been examined in this drug delivery system. In this study, to study the feasibility of site-specific drug delivery for use in atherosclerosis, the DP−LDL complexes were prepared, and effects of the DP−LDL com-

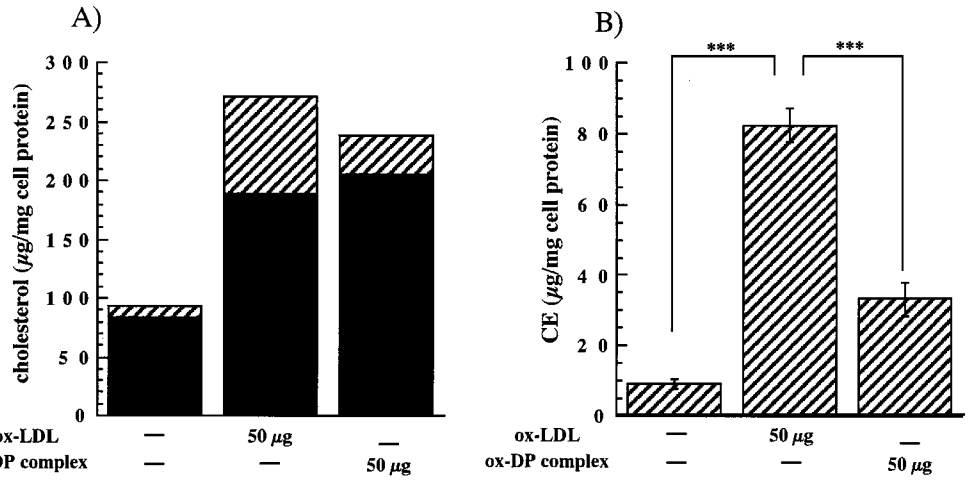

Figure 2—Cholesterol accumulations in macrophages caused by incubation with ox-LDL and the ox-DP complex. Macrophage monolayers were incubated with either ox-LDL or the ox-DP complex (50 μg protein/well, respectively) for 6 h at 37 °C. Final DP concentration in the ox-DP complex medium was 4 μM. After incubation, lipids and protein were extracted, and those levels were measured. In panel A, closed columns and slushed columns are F-ch and CE values, respectively (n = 3), and combined columns' heights indicate T-ch values. In panel B, slushed columns show CE values (mean ± SD, n = 3). The amount of ox-LDL or the ox-DP complex is indicated under the column as protein contents, and "–" indicates the addition of PBS instead of ox-LDL or the ox-DP complexes. Significant differences between groups were determined using a Fisher's PLSD test and are indicated as *** $p < 0.0001$.

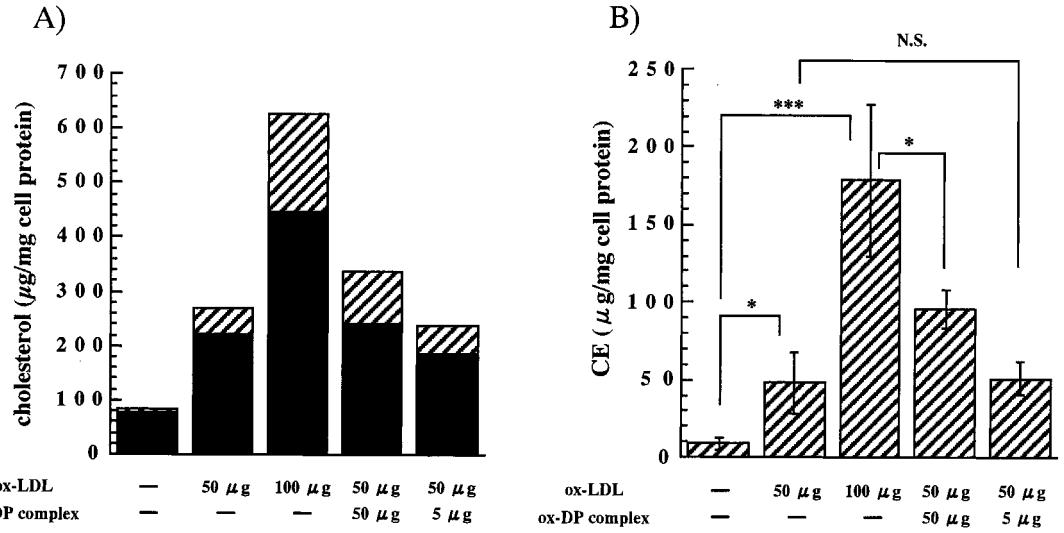

Figure 3—Effect of the ox-DP complex on cholesterol accumulation in macrophages caused by incubation with ox-LDL. Macrophages were incubated with ox-LDL (50 or 100 μg protein/well), or with ox-LDL (50 μg protein/well) and ox-DP complexes (5 or 50 μg protein/well) for 6 h. Final DP concentration in the ox-DP complex medium (5 or 50 μg protein/well) was 0.4 or 4 μM, respectively. Other details are the same as those in Figure 2. *** $p < 0.0001$; * $p < 0.01$. N.S. indicates a difference that is not significant.

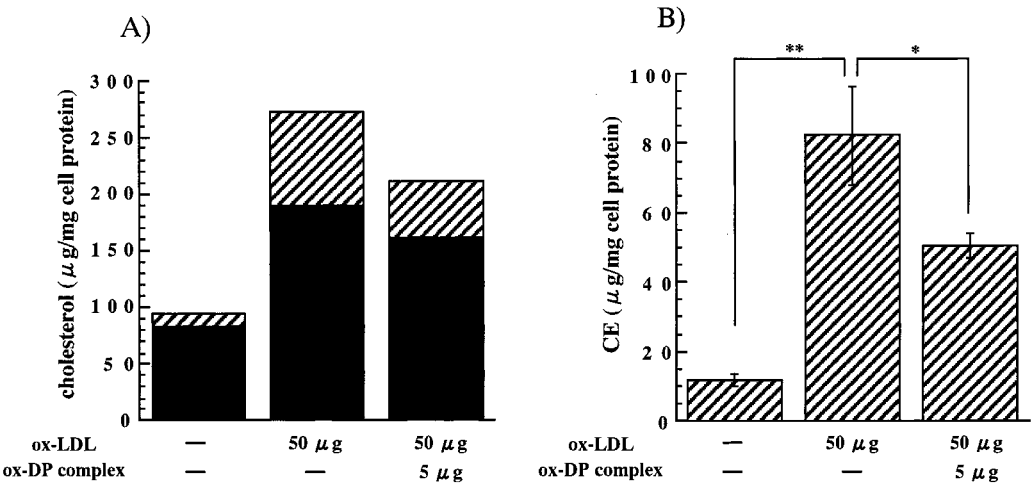

Figure 4—Effect of preincubation with the ox-DP complex on cholesterol accumulation in macrophages caused by incubation with ox-LDL. Macrophages were preincubated with ox-DP complex (5 μg protein/well) for 6 h and then washed with warm medium three times to remove the ox-DP complex. These macrophages were incubated with ox-LDL (50 μg protein/well) for 6 h. Other details are the same as those in Figure 2. ** $p < 0.001$; * $p < 0.01$.

plexes on CE accumulation in macrophages induced by ox-LDL were examined. Because LDL is unstable and easily modified, it was most important to prevent degradation and oxidation of LDL while preparing the DP−LDL complexes. Physiological characteristics and electrophoretic mobilities of the DP−LDL complexes were similar to those of LDL (Table 1 and Figure 1), indicating that the DP−LDL complex can be prepared without degradation, oxidation, and other modifications.

Eley et al.[22] have reported that the particle size (105 nm) of the complex of prednimustine, a steroidal anticancer drug, and LDL is 4 times larger than that of LDL (24.7 nm), and the prednimustine/LDL molar ratio of the complex is 163:1. Lundberg[23] has also demonstrated that the particle size of the prednimustine−LDL complexes is proportional to the concentration of a drug contained in the complex. In this study, however, no significant difference in particle size was observed between the DP−LDL complexes and LDL (Table 2). The reasons for this may be the lower drug concentration contained in our complexes (35−50 mol of DP/mol of LDL) and that the method for complex preparation in our studies was different from that in other studies, in which Celite 545 was not used.

Incubation of macrophages with ox-LDL markedly increased T-ch, F-ch, and especially CE in the cells (Figure 2). Because the accumulation of CE is a good indicator of conversion of macrophages to foam cells,[5,6] the macrophages treated with ox-LDL in this study may be susceptible to foam cell conversion. The accumulation of CE in the macrophages caused by incubation with ox-LDL, however, was significantly attenuated when the macrophages were incubated with ox-LDL containing DP (ox-DP complex). The reduction of CE accumulation may be due to inhibition of CE synthesis or enhancement of CE hydrolysis by DP itself or dexamethasone derived from DP. Asai et al.[12] have reported that dexamethasone can suppress foam cell formations of murine peritoneal macrophages by inhibiting uptake and degradation of lipoproteins.

The T-ch value of macrophages treated with ox-DP complexes was similar to that treated with ox-LDL (Figure 2). This result suggested that ox-DP complexes were incorporated into macrophages by scavenger receptors. Therefore, it is likely that the ox-DP complex can be incorporated into macrophages as well as ox-LDL, and then dexamethasone derived from DP inhibits CE synthesis or enhances CE hydrolysis in macrophages.

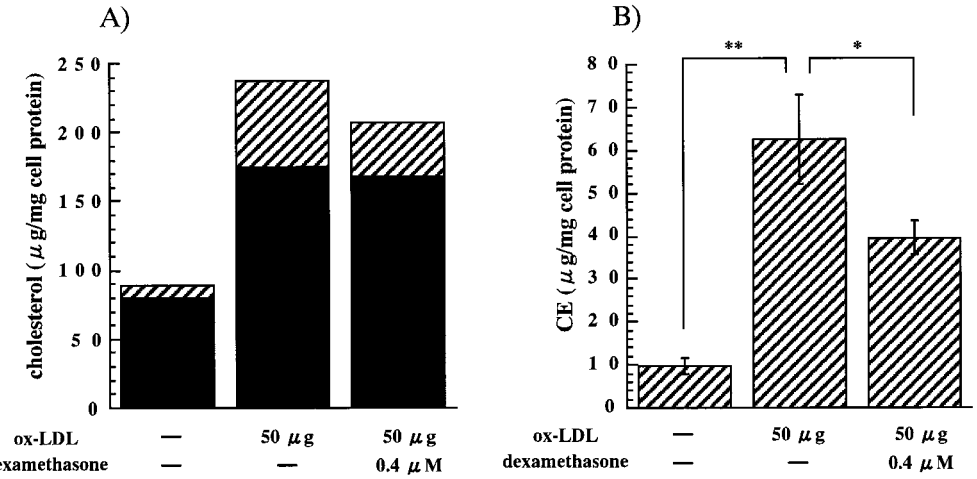

Figure 5—Effect of preincubation with dexamethasone on cholesterol accumulation in macrophages caused by incubation with ox-LDL. Macrophages were preincubated with dexamethasone (0.4 μM) for 6 h and then washed with warm medium three times to remove dexamethasone. These macrophages were incubated with ox-LDL (50 μg protein/well) for 6 h. The amount of ox-LDL (as protein content) or dexamethasone concentration in the well is indicated under the column, respectively. Other details are the same as those in Figure 2. ** $p < 0.001$; * $p < 0.01$.

To confirm the effect of the DP−LDL complex on ox-LDL-induced CE accumulation in macrophages, the cells were incubated with ox-DP complexes together with ox-LDL (Figure 3). Both T-ch and CE contents in macrophages significantly decreased when incubated with 50 μg protein/well of ox-LDL and 50 μg protein/well of ox-DP complexes as compared with those incubated with 100 μg protein/well of ox-LDL alone. This finding indicates that DP or dexamethasone released from ox-DP complexes can reduce the CE accumulation even when the ox-LDL exists simultaneously. However, the lower concentration of ox-DP complexes (5 μg protein/well) showed no effect on the CE accumulation in macrophages incubated with 50 μg protein/well of ox-LDL alone. We considered in this series of experiments that the presence of ox-LDL in 5 μg protein/well of ox-DP complexes is negligible. As shown in Figure 4, we detected a significant attenuation of ox-LDL-induced CE accumulation in macrophages even at 5 μg protein/well (0.4 μM of DP in medium) of the ox-DP complexes, when the cells were incubated with the ox-DP complexes prior to incubation with ox-LDL. Because steroid hormones require a certain period of time to express their effects, the macrophages should be incubated with the ox-DP complexes before incubation with ox-LDL when the concentration of the ox-DP complexes is small. In addition, we examined the effect of free dexamethasone on the CE accumulation in the macrophages induced by ox-LDL. Because free DP was not dissolved in the medium, we used free dexamethasone. The CE accumulation in macrophages incubated with 50 μg protein/well of ox-LDL was significantly inhibited by the pretreatment of the free dexamethasone at 0.4 μM in medium that is the same concentration as that of DP in the ox-DP complexes (Figure 5).

The inhibitory effect of free dexamethasone on the foam cell formation was the same extent as that of the ox-DP complex in the in vitro experiment. This result indicates that ox-DP complexes as well as free dexamethasone can exert a beneficial effect on atherogenic response in vitro. If the DP−LDL complex delivers DP to the atherosclerotic lesions, this complex acts more effectively than free dexamethasone in vivo.

In conclusion, the DP−LDL complex can be prepared by incubation of DP and LDL in the presence of Celite 545, and this complex shows the same lipid composition and electrophoretic mobility as that of LDL. Although this complex is easily oxidized like LDL, the ox-DP complex inhibits CE accumulation in macrophages induced by the ox-LDL. These findings indicate that the DP−LDL complex can be potentially useful as a drug−carrier to atherosclerotic lesions, and reduce foam cell formation in patients with atherosclerosis.

References and Notes

1. Ross, R. The pathogenesis of atherosclerosis:a perspective for the 1990s. *Nature* **1993**, *362*, 801−808.
2. Palinski, W.; Rosenfeld, M. E.; Yla-Herttuala, S.; Guatner, G. C.; Socher, S. S.; Butler, S. W.; Parthasarathy, S.; Carew, T. E.; Steinberg, D.; Witztum, J. L. Low density lipoprotein undergoes oxidative modification in vivo. *Proc. Natl. Acad. Sci. U.S.A.* **1989**, *86*, 1372−1376.
3. Yla-Herttuala, S.; Palinski, W.; Rosenfeld, M. E.; Parthasarathy, S.; Carew, T. E.; Butler, S.; Witztum, J. L.; Steinberg, D. Evidence for the presence of oxidatively modified low density lipoprotein in atherosclerotic lesions of rabbit and man. *J. Clin. Invest.* **1989**, *84*, 1086−1095.
4. Witztum, J. L.; Steinberg, D. Role of oxidized low density lipoprotein in atherosclerosis. *J. Clin. Invest.* **1991**, *88*, 1785−1792.
5. Brown, M. S.; Goldstein, J. L.; Krieger, M.; Ho, Y. K.; Anderson, R. G. W. Reversible accumulation of cholesteryl esters in macrophages incubated with acetylated lipoproteins. *J. Cell Biol.* **1979**, *82*, 597−613.
6. Ryu, B. H.; Mao, F. W.; Lou, P.; Gutman, R. L.; Greenspan, P. Cholesteryl ester accumulation in macrophages treated with oxidized low density lipoprotein. *Biosci. Biotech. Biochem.* **1995**, *59*, 1619−1622.
7. Tedgui, A.; Bernard, C. Cytokines, immuno-inflammatory response and atherosclerosis. *Eur. Cytokine Network* **1994**, *5*, 263−270.
8. Bailey, J. M.; Butler, J. Anti-inflammatory drugs in experimental atherosclerosis: 1. Relative potencies for inhibiting plaque formation. *Atherosclerosis* **1979**, *17*, 515−522.
9. Bailey, J. M.; Makheja, A. N.; Butler, J.; Salata, K. Anti-inflammatory drugs in experimental atherosclerosis: 4. Inhibition of atherosclerosis in vivo and thromboxane synthesis and platelet aggregation in vitro. *Atherosclerosis* **1979**, *32*, 195−203.
10. Naito, M.; Yasue, M.; Asai, K.; Yamada, K.; Hayashi, T.; Kuzuya, M.; Funai, C.; Yoshimine, N.; Kuzuya, F. Effects of dexamethasone on experimental atherosclerosis in cholesterol-fed rabbits. *J. Nutr. Sci. Vitaminol.* **1992**, *38*, 255−264.
11. Makheja, A. N.; Bloom, S.; Muesing, R.; Simon, T. M.; Bailey, J. Anti-inflammatory drugs in experimental atherosclerosis: 7. Spontaneous atherosclerosis in WHHL rabbits and inhibition by cortisone acetate. *Atherosclerosis* **1989**, *76*, 155−161.
12. Asai, K.; Funai, C.; Hayashi, T.; Yamada, K.; Naito, M.; Kuzuya, M.; Yoshida, F.; Yoshimine, N.; Kuzuya, F. Dexamethasone-induces suppression of aortic atherosclerosis in cholesterol-fed rabbits. *Arterioscler. Thromb.* **1993**, *13*, 892−899.

13. Tokui, T.; Kuroiwa, C.; Muramatsu, S.; Tokui, Y.; Sasagawa, K.; Ikeda, T.; Komai, T. Plasma lipoproteins as targeting carriers to tumour tissues after administration of a lipophilic agent to mice. *Biopharm. Drug Dispos.* **1995**, *16*, 91−103.
14. Vitols, S.; Soderberg-Reid, K.; Masquelier, M.; Sjostrom, B.; Peterson, C. Low density lipoprotein for delivery of a water-insoluble alkylating agent to malignant cells. *In vivo* and *in vitro* studies of a drug-lipoprotein complex. *Br. J. Cancer* **1990**, *62*, 724−729.
15. Iwanik, M. J.; Shaw, K. V.; Ledwith, B. J.; Yanovich, S.; Shaw, J. M. Preparation and interaction of a Low-Density lipoprotein:Daunomycin complex with P388 leukenic cells. *Cancer Res.* **1984**, *44*, 1206−1215.
16. Shaw, J. M.; Futch, W. S. J.; Schook, L. B. Induction of macrophages anti tumor activity by acetylated low density lipoprotein containing lipophilic muramyl tripeptide. *Proc. Natl. Acad. Sci. U.S.A.* **1988**, *85*, 6112−6116.
17. Hatch, F.; Lees, R. S. Practical methods for plasma lipoprotein analysis. *Adv. Lipid Res.* **1968**, *6*, 2−63.
18. Seki, J.; Okita, A.; Watanabe, M.; Nakagawa, T.; Honda, K.; Tatewaki, N.; Sugiyama, M. Plasma lipoproteins as drug carriers: Pharmacological activity and disposition of the complex of β-sitosteryl-β-D-glucopyranoside with plasma lipoproteins. *J. Pharm. Sci.* **1985**, *74*, 1259−1264.
19. Miyazaki, A.; Rahim, A. T. M. A.; Ohta, T.; Morino, Y.; Horiuchi, S. High density lipoprotein mediates selective reduction in cholesterol esters from macrophages foam cells. *Biochem. Biophys. Acta* **1992**, *1126*, 73−80.
20. Kunitomo, M.; Yamaguchi, Y.; Matsushima, K.; Bando, Y. Microanalysis of tissue cholesterol using a fluorometric enzymatic methods. *Jpn. J. Clin. Chem.* **1983**, *12*, 117−124.
21. Bradford, M. M. A rapid and sensitive method for the quantitation of microgram quantities of protein utilizing the principle of protein-dye binding. *Anal. Biochem.* **1976**, *72*, 248−254.
22. Eley, J. G.; Halbert, G. W.; Florence, A. T. Incorporation of prednimustine into low density lipoprotein:activity against P388 cells in tissue culture. *Int. J. Pharm.* **1990**, *65*, 219−224.
23. Lundberg, B. B. Evaluation of methods for complexing prednimustine to low density lipoprotein. *Int. J. Pharm.* **1993**, *99*, 275−283.

JS980422V

Tripeptide Discriminations Using Circular Dichroism Detection

NEIL PURDIE,* DENNIS W. PROVINCE, AND ERIN A. JOHNSON

Contribution from *Department of Chemistry, Oklahoma State University, Stillwater, Oklahoma 74078-0447.*

Received September 30, 1998. Accepted for publication April 19, 1999.

Abstract □ A general spectroscopic method is described that might be applied to validating amino acid sequences in peptides and protein fragments with a view to it becoming a routine procedure with which to characterize biotechnology drug products. The tripeptides are the L-enantiomers of GGA, GGH, GGI, GGL, GGF, GHG, LGG, and YGG. The simple procedure calls for their complexation with Cu(II) ion in strong aqueous base. Binding the first three residues in the sequence, beginning at the amine terminus, completes the coordination sphere of the Cu(II) ion, so duplication of the initial sequence from peptide to peptide could be an important limiting factor in determining the extent of differentiation that is possible. The analytical focus is the selectivity associated with the chirality properties of the peptides. Detection is by circular dichroism operating in the visible range. The eight analytes were chosen as representative of a series where the sequences are most similar and therefore potentially the most difficult to discriminate spectroscopically. All have just one chiral center. Using ellipticity data at all ($n = 1500$) wavelengths in the measured spectra, and two novel data reduction procedures, total discrimination among all eight analytes is achieved. The method has considerable potential for use in quality control of peptide and protein biotechnological drug forms, especially their enantiomeric purities.

Introduction

Modern pharmaceutical and biotechnology conglomerates are committed to the production of chiral drug substances.[1,2] Manufacturers have the option to prepare chiral drugs either as pure single substances (enantiomers) or as racemic mixtures. While racemates are easier to make, many good reasons exist for choosing to manufacture enantiomerically pure forms, not the least of which are considerations of the relative therapeutic values and relative toxicity levels of each enantiomer either by itself or as half of a racemate. All of this means that there is a need for simple routine analytical methods that are adaptable to all chiral drug forms which can be used for regulatory control of their chemical and enantiomeric purities (EP), whether it is done by the manufacturer or by a federal agency.

Analytical options currently applied to these tests generally involve simultaneous derivatization of both enantiomers in a partial racemic mixture to their corresponding diastereoisomers by selective reactions with a third chiral species. Unlike enantiomers, diastereoisomers can be differentiated by physical properties other than just the direction of rotation of linearly polarized light.[3] Chiral chromatography is a major player in the development of these methods. The chiral third party is introduced either in the mobile phase or immobilized on the stationary phase.[4,5] Since diastereomers elute after different retention times, achiral detectors, e.g., absorbance, electrochemical, and mass spectrometry, are sufficient to effect quantitative distinctions, within the limit of the detection capabilities of the chosen methods.

If the experimental preference is to determine chemical purities without a prior separation step, spectroscopic procedures generally call for the use of two detectors, one of which is a chiral detector such as polarimetry or circular dichroism (CD).[6−8] By combining CD with absorbance detection, measuring spectral differences or spectral ratios are different strategies that can be applied to handling the data. Generally speaking most of these methods are based on single wavelength detection data.

By combining multiple wavelength detection with modern chemometric methods for data analysis, a third alternative procedure was described.[9,10] The procedure exploits the best characteristics of both of the other methods, namely a single chiral detector, bulk in situ derivatizations, and no separations. Results obtained for the determinations of chemical and enantiomeric impurities using visible CD detection for binary mixtures of the four ephedrine stereoisomers complexed to Cu(II) ion were an improvement over what was capable at that time by either the chiral chromatographic or two-detector methods.

A major new frontier in the pharmaceutical industry is the focus on the therapeutic properties of peptide and protein drug forms. Because the number of chiral centers has virtually no limit, the magnitude of the chirality regulatory control problem is increased almost exponentially. Since derivatizations will not produce a single diastereoisomer, even the very best chiral chromatographic methods face what are probably insurmountable challenges unless the peptides are first cleaved enzymatically.

Problems that are associated with chirality detection also increase. The total CD signal for a metal−peptide complex is not determined by just the number and sequence of chiral centers in the primary peptide structure. It also includes contributions from longer range chiral interactions between side-chain substituents that modify the ternary structure when peptides are coordinated to metal ions. Experimental conditions must be very carefully controlled, otherwise these very pH-sensitive structural modifications would give false information about the analyte to the detector. On the other hand the simple accumulation of these additive chiral properties could conceivably produce a level of analytical selectivity that is unmatched by other detectors and might even approach specificity. Enzymatic cleavage followed by CD detection is also an option. What chirality detection contributes that the others do not is a direct look at the enantiomeric form. This ability will increase in value as long as manufacturers continue to use D- for L-enantiomeric substitutions as a strategy in peptide drug design.

Eight tripeptides were chosen for the study. Common to all eight are two glycine residues which occupy positions 1,2-, 1,3-, and 2,3- in the sequence. The remaining residues are L-enantiomers of aliphatic and aromatic amino acids. The tripeptides have no stable ternary structure to speak of, so variability in the sequence is really the only parameter affecting the chiral response of the CD detector. The order of residues in short peptides is crucial to the extension of the study to peptides and proteins as a whole because coordination of the latter to Cu(II) involves the first

10.1021/js980393o CCC: $18.00
Published on Web 05/20/1999

three amino acids from the amine terminus. If there is no CD selectivity associated with changes in the initial sequence, the method has no value in the study of oligopeptides and proteins where too frequently the same initial sequence is common to several potential analytes.

The experimental procedure is a combination of the methods that were used to discriminate among related dipeptides[11] and insulins[12] and to measure EP's for glycyl-L-alanine and ephedrine mixtures.[9−11] Data reduction and spectral differentiations are done using variations on standardized mathematical algorithms and principal component analysis (PCA).

Experimental Section

Chemicals—Tripeptides used in the study were glycylglycyl-L-alanine (GGA), glycylglycyl-L-histidine (GGH), glycylglycyl-L-isoleucine (GGI), glycylglycyl-L-leucine (GGL), glycylglycyl-L-phenylalanine (GGF), glycyl-L-histidylglycine (GHG) and its D-enantiomer (GhG), l-leucyl-glycylglycine (LGG) and its D-enantiomer (lGG), and L-tyrosylglycylglycine (YGG) and its D-enantiomer (yGG). All eight L-enantiomers were supplied by Sigma Chemical Co. which reported an EP in excess of 99.8%. The D-enantiomers GhG, lGG, and yGG of GHG, LGG, and YGG were prepared by Multiple Peptide Systems (MPS), San Diego, CA. Certificates of Analysis described them as unpurified off white powders. Percent purities as determined by RP-HPLC analyses were reported as 86.57, 99.10, and 97.86, respectively. The low value for GhG is explained as being due to two elution peaks that correspond to the same compound. The percentage is based on the relative area of the first peak which corresponds with most of the material eluting with the void volume peak. The second peak is related to the hydrophobicity of the molecule that causes it to stick to the column to be eluted later. D-Histidine was also a Sigma Chemical Co. product with an EP reported at better than 99.8%. Reagent grade $CuSO_4 \cdot 5H_2O$ was obtained from Fisher Scientific.

Solution Preparations—The chemistry of the derivatization reaction is a simple chiral variation of the classical biuret "color reaction" for the determination of total serum proteins in which the reagent is a solution of [Cu(II)] = 2.0 mM and [tartrate] = 8.0 mM in 0.1 M NaOH. Racemic NaK-tartrate is the solubilizing ligand for Cu(II) and is completely exchanged by protein in the test. The chemistry for the reaction is well understood and relatively uncomplicated.[13] Determinations were done based upon absorbance spectrophotometric detection. Being relatively insensitive and not sufficiently selective, the biuret reaction is no longer the method of choice for serum proteins.

In this instance, aqueous stock solutions at pH 13 were prepared for Cu(II)−D-histidine and each of the Cu(II)−L-tripeptide complexes in which the Cu^{2+} concentration was always 0.020 M. Ligands were present at 0.080 M concentrations, a 4:1 excess over the Cu(II) ion. KI at a concentration of 0.03 M was added as a stabilizer.[9,10] Spectra were measured for working solutions prepared by diluting stocks by a factor of 10 with 0.10 M NaOH. Spectra for the working solutions are the bases for testing the extent of the qualitative analytical selectivity accessible to CD detection.

Quantitation tests were done on two kinds of mixtures. For the first kind, GGA was arbitrarily selected as an enantiomerically pure "reference" material. Aliquots from the stock were spiked with "chemical impurities", i.e., smaller volume aliquots of the other L-tripeptide stocks to cover the impurity range from 1 to 10%, prior to dilution with NaOH. For the second, "enantiomeric purity" tests, aliquots of YGG, LGG, and GHG stocks were spiked with smaller volume aliquots of the corresponding D-enantiomer stocks, yGG, lGG, and GhG, over the same 1−10% impurity range.

Measurements—CD spectra were measured using a Jasco 500-A automatic recording spectropolarimeter coupled to an IBM-compatible PC through a Jasco IF-500 II serial interface and data processing software. Experimental parameters: wavelength range 400−700 nm; sensitivity 100 mdeg/cm; time constant 0.25 s; scan rate 200 nm/min; path length 5.0 cm; ambient temperature.

Calibration of the day to day reproduciblity of the system was done by measuring the CD spectrum for the Cu(II)−D-histidine complex. Statistical data for reproducibilities of the maximum ellipticities measured at wavelengths 487 nm and 682 nm were 7.42 ± 0.07 mdeg and −214 ± 0.60 mdeg, respectively.

Results and Discussion

Cu(II)−Peptide and D-Histidine Complexes—The local microsymmetry of the Cu(II) ion in aqueous solution is essentially square-planar due to axial elongation of the typical octahedral symmetry, assumed by most first row transition metal ions, by Jahn−Teller distortion.[14] Complexation serves to keep the Cu(II) ion in solution at high pH conditions. At pH 13, D-histidine and the amide-nitrogen protons are fully ionized,[15] which essentially eliminates competitive complex formation equilibria when partially protonated anions are present in solution at lower pH.

D-Histidine, the ligand used for instrument calibration, binds via the amine N-atom, the carboxylate functional group, and a pyrimidine N-atom in an equatorial three-coordinate arrangement. Stoichiometry for the complex is 1:1.[15] Complexing a peptide to Cu(II) at pH > 12 involves first attachment through the N-atom of the terminal amine followed by ring closure(s) through bonding with the N-atoms of successive amide bonds until maximum thermodynamic stability is achieved.[15] Side chain substituents on the amino acid residues lie out of the coordinate plane and are factors only in inter- and intramolecular interactions within the inner coordination sphere, unless a potential Lewis base is present, e.g., a histidine residue. Axial positions might be occupied by hydroxide ions which is the only feature that might complicate the stoichiometry of the generic metal−peptide, $(MP)_n$, equilibrium.[16]

By analogy with the Cu(II)−D-histidine equilibrium reaction, the stoichiometry of the Cu(II)−tripeptide complexes is also believed to be 1:1. If the only purpose of the study were to develop analytical selectivity, the question of the stoichiometry of the metal−tripeptide complexes is not relevant. If the stoichiometry were to change from one ligand to another, the analytical selectivity might very well be enhanced. It is only when making an analytical determination by conventional mathematical procedures that knowledge of the stoichiometry is a prerequisite.

CD activity in the visible range for chiral Cu(II) complexes is a result of disymmetric perturbations of ground and excited state ligand field orbitals by the chiral ligands. Bands in the UV range, attributable to only the chirality in the ligands, bound and unbound, are typically very intense but quite insensitive to the environment of the coordinating metal ion. The lack of selectivity is the major reason for not exploiting the obvious analytical sensitivity that is inherent in the intense UV bands.

Visible CD Spectra for Cu(II)−Tripeptide Complexes—Spectra for all eight copper−L-tripeptide complexes, in which [Cu(II)] = 2.0 mM and ligand concentrations are 8.0 mM, are shown in Figure 1. Only GGH, GHG, LGG, and YGG are uniquely differentiable by their zero order CD spectra. Spectra for the histidyl-containing ligand complexes, GGH and GHG, are blue shifted compared with the Cu(II)-D-histidine complex itself which has an intense negative band with a maximum at 689 nm and a weaker positive maximum at 570 nm. The magnitude of the shift is greatly dependent upon the position occupied by the histidyl residue. The sensitivity of the CD spectral response to the histidine position is a significant first result in the context of possibly sequencing short peptides by this spectroscopic method.

Of the five GGX peptides, only the spectrum for GGH is unique, which might be attributable to a special involvement of the pyrimidine N-atom in binding to Cu(II). The remaining four have but one broad negative band that

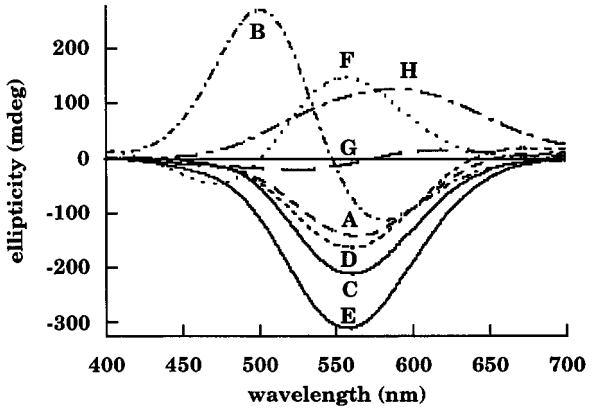

Figure 1—Visible CD spectra for the Cu(II) complexes of (A) GGA, (B) GGH, (C) GGI, (D) GGL, (E) GGF, (F) GHG, (G) LGG, and (H) YGG. Similarities are greatest for the GGA, GGI, GGL, and GGF complexes over the entire wavelength range.

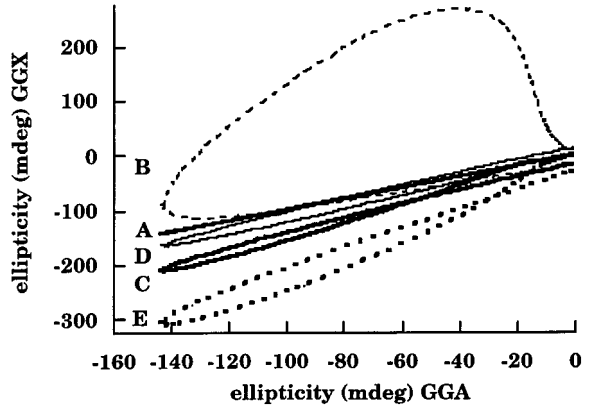

Figure 2—Correlation plots of ellipticity for the Cu(II)GGA complex versus the ellipticities for the analogous complexes with equimolar amounts of (A) GGA, (B) GGH, (C) GGI, (D) GGL, and (E) GGF.

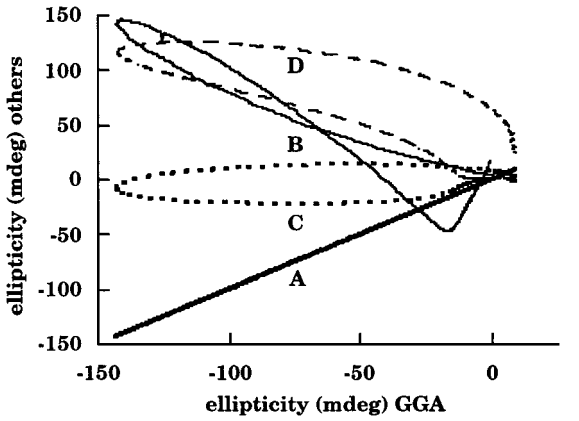

Figure 3—Correlation plots of ellipticity for the Cu(II)GGA complex versus the ellipticities for the analogous complexes with equimolar amounts of (A) GGA, (B) GHG, (C) LGG, and (D) YGG.

maximizes around 550 nm. Aromaticity in the side chain may (YGG) or may not (GGF) induce a spectral change, which with further developments, might be exploited for short range sequencing. There is ambiguity in differentiating among GGA, GGI, GGL, and GGF unless the solution concentrations are carefully controlled.

The L-leucine structural isomers can ostensibly be differentiated in a quality control context. The lack of band intensity for the LGG is a potential problem in quantitation. Although the glycyl residue is achiral, the relative positions that it occupies affect the CD spectra quite

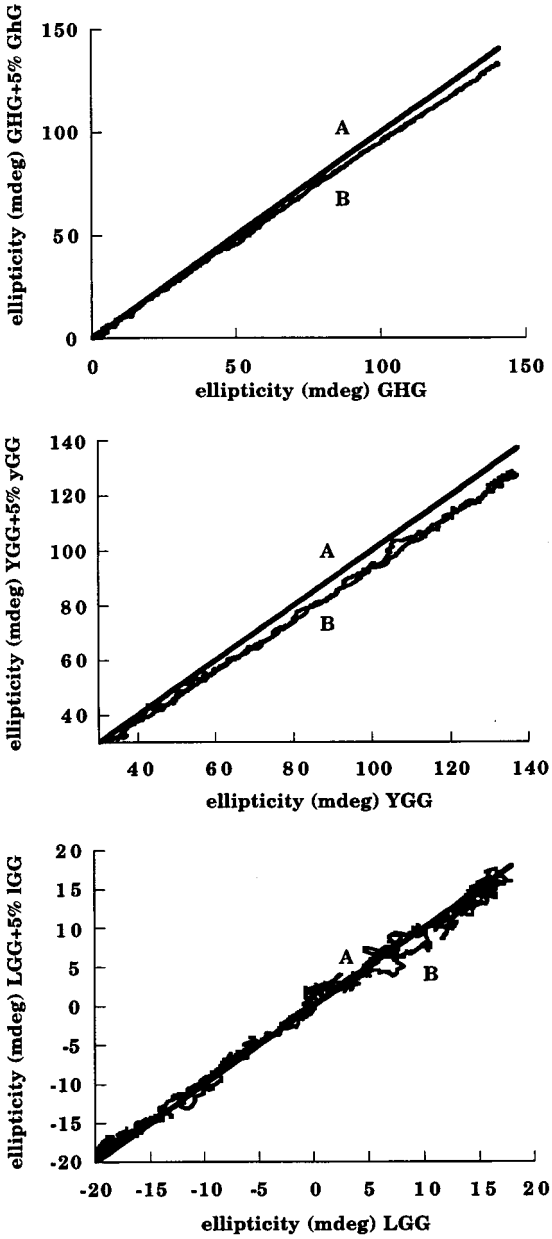

Figure 4—Correlation plots of ellipticities for the Cu complexes of L-GHG, L-YGG, and L-LGG versus ellipticities for 5% racemic mixtures with GhG, yGG, and lGG. In each case line A is for the L-enantiomer against itself and line B is for the L-enantiomer against the mixture.

dramatically, which is good reason to believe that specific interligand interactions occur within the first coordination sphere of the complex.

It is quite clear at this point that total differentiation among all eight analytes is not possible.

Alternative Algorithms for Data Reduction and Enhancing Selectivity—Conventional algorithms typically deal with data measured at just the wavelength of the maximum signal; unless a chemometrics approach is employed.[17] The intent of the algorithms described here was to start with ellipticity data measured at all 1500 wavelengths and, using novel mathematical procedures, reduce the data to a single variable (or factor) upon which selectivity decisions are made. Having a simple numerical means for making selectivity judgments is superior to relying upon subjective graphical superpositions of the CD spectra. Furthermore, if that same numerical factor were to correlate linearly with ligand concentration, then quantitative differentiations might also be accomplished. As a

Table 1—Determination of Enantiomeric Purities for Prepared Binary Mixtures of GHG/GhG, LGG/lGG, and YGG/yGG

% L-form in prepared solution	regression slope (enantiomeric excess)	regression coefficient
	GHG/GhG	
99	0.9919	0.9998
97	0.9685	0.9998
95	0.9503	0.9999
90	0.8973	0.9999
	LGG/lGG	
99	0.9974	0.9951
97	0.9723	0.9957
95	0.9455	0.9946
90	0.8819	0.9932
	YGG/yGG	
99	0.9924	0.9996
97	0.9675	0.9996
95	0.9359	0.9996
90	0.8854	0.9995

final consequence, resultant analytical determinations will be more accurate since experimental uncertainties are significantly reduced when 1500 data points are used rather than only one.

A 2-D Data Reduction Algorithm for Enhancing Selectivity—To illustrate this data reduction procedure, GGA is arbitrarily assigned the status of an enantiomerically pure standard reference material. In a pharmaceutical context, GGA might represent a commercial drug product. The others fill the roles of potential "chemical" and "enantiomeric" impurities.

The simple concept is to plot the 1500 data points for the 8.0 mM GGA spectrum (on the *x*-axis) against analogous data for 8.0 mM solutions for each of the others (on the *y*-axis). To get a baseline reference check for the absolute enantiomeric purity of GGA, its CD spectrum is plotted on both axes. The correlation is a straight line of unit slope and zero intercept. Spectra for the remaining seven tripeptide complexes are plotted against GGA in Figure 2 for the GGX subseries and in Figure 3 for the other sequences.

Plots are decidedly nonlinear and individually distinct from one another. The ellipsoidal shapes for GGI and GGL might appear similar but the best-fit lines do have different slopes. On enlargement, however, the ellipse for GGI is seen to "fold over" on itself in a partial figure 8, implying a latent three-dimensional property in these plots. The same phenomenon can be seen more clearly for the plot of the GGH analogue vs GGA in Figure 3. Differentiation among enantiomerically pure forms of the tripeptides has apparently been achieved at least when the number of possibilities is limited to a small closed set, as they are here. It should be emphasized that in order to reproduce these curves exactly the concentrations must be carefully controlled.

The only other possible correlation line of unit slope (but opposite in sign) and zero intercept is the plot of GGA vs the D-enantiomer, GGa, if their purities are equivalent. This is a consequence of their being chemically identical. The feature that is common to all cases where spectra for chemically dissimilar compounds are correlated is splitting of the correlation line relative to the ideal reference line. Some splittings are extreme, Figures 2 and 3. Conversely, if the correlation plot of the CD spectrum for a newly manufactured lot of GGA vs the reference is linear with a slope less than one, and shows no evidence of splitting, this

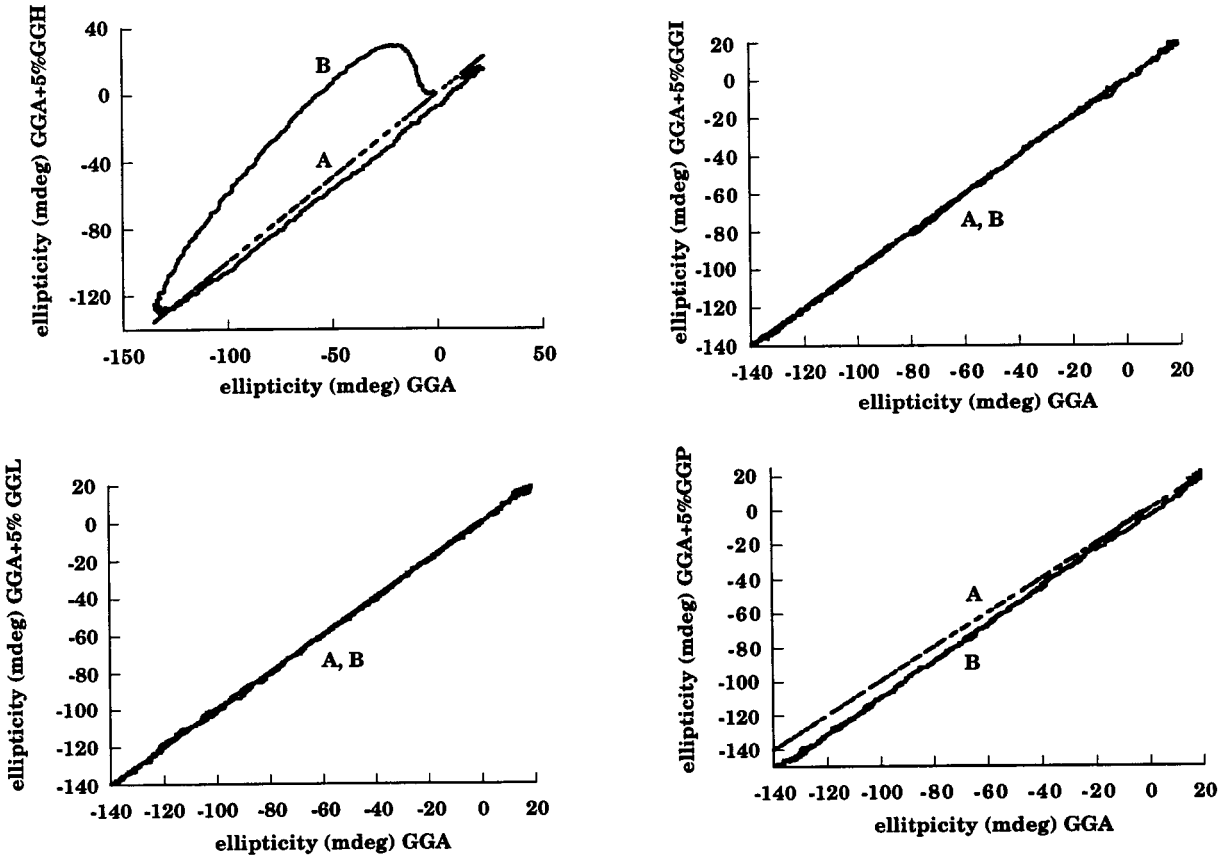

Figure 5—Correlation plots of ellipticity for the Cu(II)–(GGA) complex versus ellipticities for 5% chemical mixtures with GGH, GGI, GGL, and GGF. In each case line A is for GGA against itself and line B is for GGA against the mixture.

is evidence for the presence of the enantiomer. Splitting is instant evidence for the presence of a chemical impurity.

Nonlinear plots, typical of Figures 2 and 3 do not yield easily to quantitation of the "chemical impurities".

(a) Quantitation of Enantiomeric Mixtures—Enantiomeric purity tests were made on three analyte pairs, GHG/GhG, LGG/lGG, and YGG/yGG. As the D-enantiomers were added in increasing amounts, over the range 1, 3, 5, 10% of the L-enantiomer concentration, the slopes of the correlation lines decreased. Data are shown for 5% "impurity" levels only, Figure 4.

Judging by the regression coefficient of 0.9998 for the GHG vs GhG plot, there is no significant loss of linearity compared to the reference baseline, meaning that the EP of GhG is equivalent to that of GHG. The explanation given in the Experimental Section for the low percent purity for GhG, as described in the MPS Certificate of Analysis, is apparently vindicated by the results of this spectroscopic method. Splitting of the YGG/yGG correlation line is consistent with the MPS reported purity level of 97.86% or total impurity of 2.14%. Noise on the LGG/lGG correlation line conceals whether there is splitting of the line or not. A poor S/N ratio is expected since the CD spectral intensity for LGG is the weakest, Figure 1,being approximately one-tenth of the band intensities for the other tripeptides.

Enantiomeric excess, defined for example as:

$$\{[Cu(II)(GHG)] - [Cu(II)(GhG)_x]\}/\{[Cu(II)(GHG)] + [Cu(II)(GhG)_x]\}$$

is given by the correlation slope for each mixture. Calculated values for spiked GHG solutions are in excellent agreement with the measured values for prepared mixtures, Table 1. Imprecisions based on data from three to five repeat measurements are an improvement by almost a factor of 10 over results obtained from the analyses of binary ephedrine mixtures in which a chemometric analysis method was applied to data at five wavelengths.[9] Despite the splitting of the YGG/yGG and the noise in the LGG/lGG plots, by using best-fit correlation lines, the agreements between calculated and measured EP's are still very good. The method is quantitatively valid over the full range of enantiomeric ratios from 100% L to 100% D.

(b) GGA +"Chemical Impurity" Levels for All Other Tripeptides—The question with respect to "chemical impurities" that needs to be addressed is not how great the differences are between the curve for an 8.0 mM solution of GGA and curves for the other tripeptides at equimolar concentrations, Figures 2 and 3, but rather, are the differences sufficient enough to identify and quantitate anonymous chiral "chemical impurities" when these amount to only a few percent of the total composition of a binary mixture? The answer to the question lies in how sensitive the CD detector is in discovering splitting of the correlation line when spectra for "impure" samples are plotted against the spectrum for the primary reference standard.

Spectra were measured for mixtures in which GGA solutions were spiked with small volumes of the other L-tripeptides at levels of 1, 3, 5, and 10%. Data for only the 5% mixtures are plotted in Figure 5 for the GGX subseries and in Figure 6 for GHG, LGG, and YGG. Splittings range from being very small, where they are barely discernible, e.g., for GGI, GGL, and GGF, to extreme, for GGH, GHG, and LGG. Where they are small, the best-fit lines, determined by simple linear regression, are seen to deviate from the unit slope of the reference line. Because of the "absence" of splitting at the lowest concentrations, the plots fail to confirm the presence of GGI, GGL, or GGF at a level of 5% or less, Figure 5. In general the extreme nonlinearity of the split correlations associated with chemical impurities makes it very difficult to determine the amount of impurity.

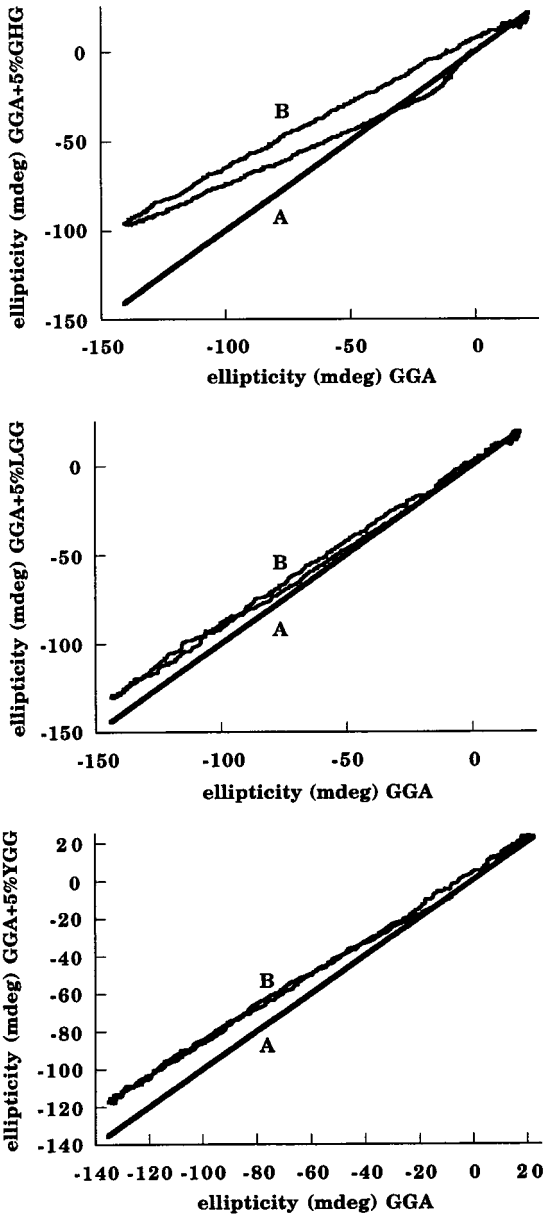

Figure 6—Correlation plots of ellipticity for the Cu(II)–(GGA) complex versus ellipticities for 5% chemical mixtures with GHG, LGG, and YGG. In each case line A is for GGA against itself and line B is for GGA against the mixture.

Briefly recapping the results, the 2-D algorithm has effectively reduced the 1500 spectral data points to one number (the correlation slope), from which EP's can be determined with excellent accuracy over the complete range. Recognition that a potential "chemical impurity" is present is elementary for a limited number of cases, but its analytical determination is not easily done.

A 3-D Data Reduction Algorithm for Enhancing Selectivity—The objectives that relate to this second data reduction algorithm were to discover if the GGA, GGI, GGL, and GGF series can be completely differentiated both qualitatively and quantitatively. The same objectives were achieved when the 3-D algorithm was applied to a series of dipeptides all of which had just one chiral center.[11]

In the 2-D presentations of Figures 2, 3, 5, and 6, wavelength is an implied variable. For the evolution of the 3-D algorithm, wavelength is the third dimension. Since

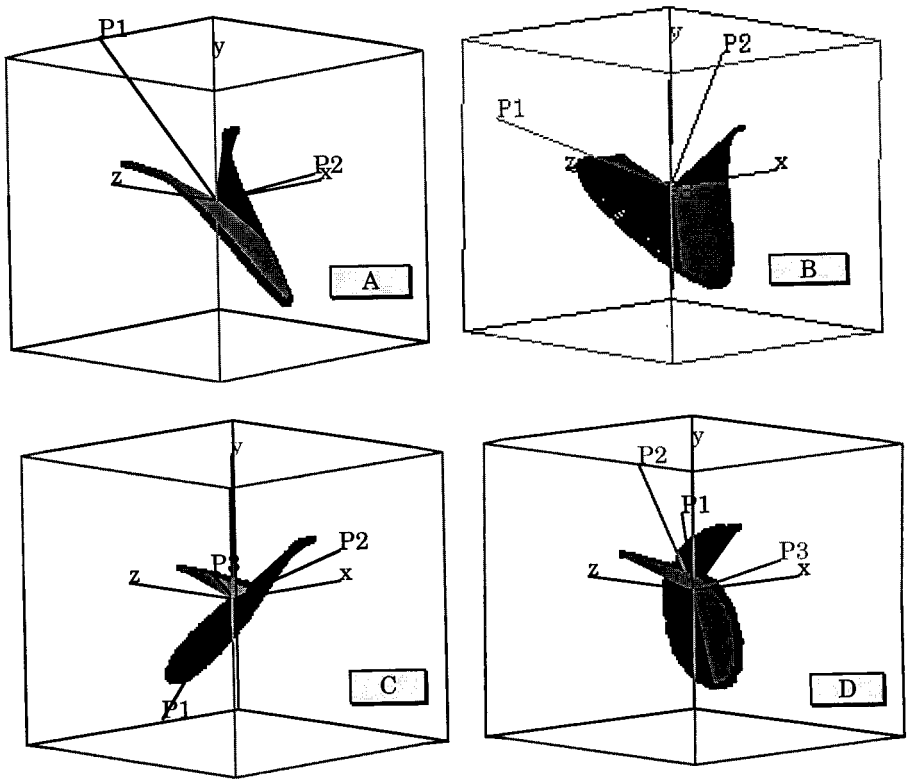

Figure 7—Spinning Plots for the presentation of wavelength (*x*-coordinate), spectral data for the GGA complex (*y*-coordinate), and spectral data for (A) GGA, (B) GGH, (C) GHG, and (D) LGG complexes. The lines P1, P2, and P3 are the principal component axes from the PCA solutions. Dark and light areas distinguish the front four quandrants of the cube from the rear four quadrants.

the experimental parameter measured in CD detection is an absorbance difference, observed signals are positive, negative, and zero. When two CD spectra are plotted against each other, four sign combinations are possible at any wavelength. Repeats of coordinate points, e.g., zero crossover points, can occur at wavelength values that are not adjacent to one another in the spectra. When that occurs, 2-D plots "wrap around" and become three-dimensional. In retrospect what are observed as 2-D plots are simple projections of the 3-D plots on to the $x-y$ coordinate plane, which explains why some of the plots in Figures 2 and 3 appear to have a 3-D character. The added value of the third dimension is that there should be an increase in the overall analytical selectivity.

The algorithm used for the visual presentation of the three-parameter plot was Spinning Plot[18] which is an integral part of a number of commercially available statistical analyses software packages. The software used for these calculations was JMP 3.1 produced by SAS Institute Inc. Four 3-D plots of wavelength (nm) vs ellipticity data for GGA vs ellipticity data for GGA, GGH, GHG, and LGG are shown in Figure 7. By analogy with the 2-D algorithm procedure, GGA plotted against itself is included to provide a baseline for comparison. Front and back quadrants are distinguished by dark and light shading to enhance the 3-D presentation. Discriminations are clearly more evident than they were in Figures 5 and 6.

Factor Analyses of Spinning Plot Data—To derive a quantitative mathematical algorithm, data reduction was done using a Principal Component Analysis (PCA) procedure on the Spinning Plot data.[18] Eigenvalues and eigenvectors for the three principal components, P1, P2, and P3, calculated for the GGA/GGH combination plot are given in Table 2. Spatial projections of these same principal components are superimposed on the coordinate axes of Figure 7.

Table 2—**Principal Components Calculated for the GGA versus GGH System**

		P1	P2	P3
eigenvalues		+1.9603	+0.9798	+0.0599
eigenvectors	nm	+0.19154	+0.97273	–0.13080
	GGA	–0.68522	**+0.22794**	+0.69175
	GHG	+0.70270	–0.04287	+0.71019

Of the twelve resultant eigenfactors, the one that is most sensitive to variations in the identity of the analyte is P22, highlighted in bold type in Table 2. The 22 tag indicates the entry is in the second row of the second column of the eigenvector matrix. Comparative P22 values for all combinations with GGA are as follows: 0.04519 (vs GGA); 0.88194 (vs GGH); 0.13171 (vs GGI); − 0.01932 (vs GGL); 0.10312 (vs GGF); 0.22794 (vs GHG); 0.89248 (vs LGG); 0.57491 (vs YGG). Standard deviations in P22 determined for data from three to five independent repeat measurements are ±0.002, meaning that total analytical selectivity is accomplished. The 3-D algorithm effectively reduced the 1500 original spectral data points to a single discretionary number, P22. The test sets up well in a quality control environment for proving that a chiral substance is or is not a single chemical.

The remaining question is whether the test has the potential to be quantitative. If P22 values were to correlate linearly with the amount of "chemical impurity", then EP's can be determined by difference. Representative plots of P22 vs percent impurity for solutions of GGA spiked with GGH, GGF, LGG, and YGG are shown in Figure 8. The plots cease to be linear when the impurity concentration approaches 2.0 mM, the concentration of the Cu(II) ion. Differences in the slopes of these lines assist in the identification of the chiral impurity. With the exceptions of GGI and GGL, correlation slopes are greater than two

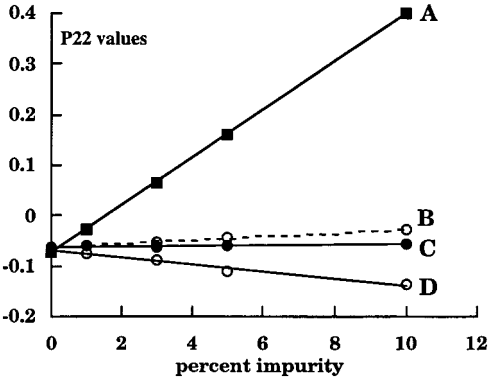

Figure 8—Linear plots of the percent chemical impurity versus the eigenvector P22 for the Cu complex of GGA at a concentration of 8.0 mM spiked with increasing amounts of (A) GGH, (B) GGF, (C) LGG, and (D) YGG.

times the ±0.002 SD in the mean for P22 values, which means that impurity levels as little as 1−3% can be measured with confidence provided the impurity is a single chiral substance. Analytical sensitivities are at least 10 times more accurate than analogous plots in which maximum ellipticity values measured at a single wavelength are plotted against concentration. Why this is so is easily understood when one sees changes in maximum ellipticity values at a single wavelength over the 1−10% impurity range that are less than the best resolution of ± 2.0 mdeg for the CD instrumentation used in this study. The additional accuracy comes from the ability to conveniently include data at 1500 wavelengths.

Where the 2-D method succeeded in providing a means to get accurate values for EP's, the 3-D method provides a way to get a quantitative measure of nonenantiomeric chiral impurities.

Summary and Application of the Method

By the simple chiral modification of the biuret reagent, combined with two novel data reduction algorithms for the handling of visible CD data, a potentially useful QC regulatory procedure for peptides, oligopeptides, and proteins has been developed.

A typical procedure begins with the measurement of the visible CD spectrum for the Cu(II) complex of the chromatographically purest available form of the substance being regulated. Data are archived in a computer file onboard the spectrometer and are updated each time the reference material is measured. Spectra for aliquots taken from each newly manufactured product lot are plotted against the standard and successive on-screen visual comparisons are made.

Deviation from a slope of 1.0 in the 2-D test is an instant indication that the purity is less than that of the reference standard. If the value of the regression coefficient indicates an enantiomeric "impurity", the EP is readily calculated from the regression slope. Splitting of the correlation line for the standard reference material gives instant recognition that a "chemical impurity" is present whose identity may be confirmed by the P22 value calculated from the Spinning Plot algorithm. The percent impurity is calculated from the correlation slope of the P22 vs impurity line.

The two algorithms are complementary in the sense that whereas the 2-D model is capable of measuring EP's with excellent accuracy but only capable of differentiating qualitatively among the eight tripeptides, the 3-D model was capable of quantitatively measuring the compositions of binary mixtures of dissimilar compounds, but incapable of measuring EP's. The latter was not discussed in detail, but is a consequence of the fact the P22 values for an enantiomeric pair are invariant with concentration.

The method is quick, rugged, uses stable inexpensive reagents, requires no specific precautions, and a minimum of technical expertise for a potential operator. Derivatization reactions are instantaneous and data collection is done in a matter of minutes. Spectral data are stored on an onboard computer that is programmed to perform all the mathematical comparisons and quantitative analyses in situ.

All of these advantages point to a very satisfactory and very competitive routine alternative to chromatographic and mass spectrometry methods for the quality control of small peptides. Its successful applications to oligopeptides and proteins[12] are the subjects of subsequent articles.

References and Notes

1. Collins, A. N.; Sheldrake, G. N.; Crosby, J., Eds. *Chirality in Industry, The Commercial Manufacture and Applications of Optically Active Compounds*; Wiley: New York, 1994.
2. DeCamp, W. H. The FDA Perspective on the Development of Stereoisomers. *Chirality* **1989**, *1*, 2−6.
3. Charney, E. *The Molecular Basis of Optical Activity: Optical Rotatory Dispersion and Circular Dichroism*; Wiley: New York, 1960.
4. Zief, M., Crane, L. J., Eds. *Chromatographic Chiral Separations*, *Chromatographic Science Series*; Marcel Dekker: New York, 1988; Vol. 40.
5. Souter, R. W. *Chromatographic Separations of Stereoisomers*; CRC Press: Boca Raton, FL, 1985.
6. Purdie, N. Analytical applications of CD to the forensic, pharmaceutical, clinical, and food sciences. In *Analytical Applications of Circular Dichroism*, *Techniques and Instrumentation in Analytical Chemistry*; Purdie, N., Brittain, H. G., Eds.; Elsevier Scientific: Amsterdam, 1994; Vol. 14, pp 241−278.
7. Gergely, A. The use of circular dichroism as a liquid chromatographic detector. In *Analytical Applications of Circular Dichroism*, *Techniques and Instrumentation in Analytical Chemistry*; Purdie, N., Brittain, H. G., Eds.; Elsevier Scientific: Amsterdam, 1994; Vol. 14, pp 279−292.
8. Horvath, P.; Gergely, A.; Noszal, B. Determination of enantiomeric purity by simultaneous dual circular dichroism and ultraviolet spectroscopy. *Talanta* **1997**, *44*, 1479−85.
9. Engle, A. R.; Purdie, N. Determination of enantiomeric purities using CD/CD detection. *Anal. Chim. Acta* **1994**, *298*, 175−182.
10. Engle, A. R.; Lucas, E. A.; Purdie, N. Determination of enantiomers in ephedrine mixtures by polarimetry. *J. Pharm. Sci.* **1994**, *83*, 1310−14.
11. Purdie, N.; Province, D. W. Algorithms for the quantitative validation of chiral properties of peptides. *Chirality*, in press.
12. Purdie, N.; Province, D. W.; Layloff, T. P.; Nasr, M. M. Algorithms for validating chiral properties of insulins. *Anal. Chem.*, submitted.
13. Tietz, N. W. *Fundamentals of Clinical Chemistry*, 3rd ed.; Saunders: Philadelphia, 1987.
14. Cotton, F. A.; Wilkinson, G. *Advanced Inorganic Chemistry. A Comprehensive Text*, 4th ed.; Wiley-Interscience, New York, 1980.
15. Sigel, H.; Martin, R. B. Coordinating properties of the amide bond. Stability and structure of metal ion complexes of peptides and related ligands. *Chem. Rev.* **1982**, *82*, 384−426.
16. Martell, A. E.; Sillen, L. G. *Stability Constants*; Special Publication No. 17, The Chemical Society: London, 1964.
17. Martens, H.; Naes, T. *Multivariate Calibration*; Wiley: New York, 1989.
18. Kaiser, H. F. The varimax criterion for analytic rotation in factor analysis. *Psychometrika* **1985**, *23*, 187−200.

Acknowledgments

We are very grateful to Dr. Sylvie Blondelle of the Torrey Pines Institute for Molecular Studies, La Jolla, CA, for her collaborative efforts to help the completion of this work and to Multiple Peptide Systems, San Diego, CA, for the synthesis and analyses of the D-enantiomeric forms needed for the enantiomeric purity determinations.

JS980393O

Predicting the Total Entropy of Melting: Application to Pharmaceuticals and Environmentally Relevant Compounds

ROSE-MARIE DANNENFELSER*† AND SAMUEL H. YALKOWSKY‡

Contribution from *Novartis Pharmaceutical Corporation, 59 Route 10, East Hanover, New Jersey 07936, and College of Pharmacy, University of Arizona, Tucson, Arizona 85721.*

Received August 31, 1998. Accepted for publication April 21, 1999.

Abstract □ Experimental entropy of melting values for physical property estimation schemes, such as solubility and vapor pressure, are not readily available. In this study a semiempirical equation, which contains two molecular parameters, is used to estimate the total entropy of melting for a variety of pharmaceutically and environmentally relevant compounds. A database of experimental entropy values consisting of over 370 different compounds was compiled from literature. A molecular rotational symmetry number and a molecular flexibility number for each compound were defined. The simple equation does very well in predicting the total entropy of melting for the complex set of molecules with an average error of 21%.

Introduction

The physicochemical properties of compounds are important in many fields, including the pharmaceutical and environmental sciences. Property estimations can help to minimize time and cost in drug formulation development. They are also useful in assessing exposure limits for new chemical entities. Aqueous solubility and vapor pressure are among the most important of these properties. These properties can be estimated by the rearrangement of the Clausius−Clapeyron equation. For instance, the following equation can be used to predict the ideal mole fractional solubility:[1]

$$\log X_i = [-\Delta H_m(T_m - T)/(2.3RT_mT)] - \Delta C_p/R[\Delta H_m (T_m - T)/(2.3T) + \log(T_m/T)] \quad (1)$$

where ΔH_m is the enthalpy of melting, ΔC_p is the heat capacity difference between the crystalline and the molten form, R is the gas constant, T and T_m are temperature and the melting point in Kelvin. This equation can be simplified to:

$$\log X_i = -\Delta S_m(T_m - T)/(2.3RT) \quad (2)$$

by replacing $\Delta H_m/T_m$ with ΔS_m, the entropy of melting, and assuming that ΔS_m is large compared to ΔC_p.

As can be seen from eqs 1 and 2, the melting point and either the enthalpy of melting or the entropy of melting are required. Unfortunately, the values of the two latter parameters are usually not readily available. The entropy of melting can either be assumed to be a constant (by Walden's rule or Richard's rule) or estimated from structure. Walden's rule is based on aromatic hydrocarbons while Richard's rule is applicable to small, spherical molecules. There are two types of structure-based estimation schemes found in the literature: group contribution methods such as those of Chickos and co-workers[2,3] and Domalski and Hearing,[4] and the semiempirical equation of Yalkowsky and co-workers.[5−8] The group contribution methods which employ tables of values for each group or fragment are cumbersome to use and some times have missing group fragments, whereas the semiempirical equation which uses two nonadditive molecular descriptors is easy to use and can be employed for all nonelectrolytes.

The following semiempirical equation was shown to work quite well in estimating the total entropy of melting for nonelectrolytes:[5,8]

$$\Delta S_m^{tot} = 50 - R \ln \sigma + R \ln \phi \ J/deg{\cdot}mol \quad (3)$$

where R is the gas constant in J/deg·mol, and σ and ϕ are the molecular symmetry and flexibility numbers which are defined below. The total entropy of melting includes entropies associated with solid−solid transitions, as well as the solid−liquid transition. In this paper the above equation is applied to a complex set of data for a wide range of pharmaceutical and environmental compounds.

Methods

Data—Experimental entropy of melting data, including the transitional entropies when reported, for pharmaceutically and environmentally relevant compounds are compiled from literature[9−11] and entered into a database using dBASE IV. The database contains 413 entropy of melting values for 376 different compounds.

The database contains multiple entropy of melting values for some compounds. Since these values are reported by different authors they are treated as individual data points and are not averaged. Entropy of melting values that are less than 9 J/K·mol are considered to be unreasonably low and therefore omitted from the average calculations. Only five compounds consisting of six entropy of melting values have been omitted from the database based on this criteria.

The error associated with the prediction of the entropy melting in this paper is calculated by:

$$\text{error} = (|\Delta S_m^{obsd} - \Delta S_m^{pred}|)/\Delta S_m^{obsd} \times 100 \quad (4)$$

where ΔS_m^{obsd} and ΔS_m^{pred} are the observed and predicted entropies of melting.

There is some overlap between the data set used in the earlier studies[5,6] and the present data set. Only 48 of the 371 different compounds in the present data set were used in the previous studies. They are included here because of their biological relevance.

Molecular Flexibility Number—Increasing molecular flexibility increases the total entropy of melting. To account

* To whom all correspondence should be addressed. Phone: (973) 781-2069. Fax: (973) 781-8487. E-mail: rosemary.dannenfelser@novartis.com.
† Novartis Pharmaceutical Corp.
‡ University of Arizona.

10.1021/js9803609 CCC: $18.00
Published on Web 05/27/1999

Table 1—Examples of Molecular Flexibility for Some Pharmaceutical and Environmental Compounds

name	SP2	SP3	RING	ln ϕ
cinnamic acid	3	0	1	1.0
butanoic acid	1	2	0	1.6
simazine	0	4	1	3.7
heptylcyclohexane	0	6	1	5.8
triacetin	3	6	0	6.8
decane	0	8	0	7.3
glycerol tristearate	3	54	0	57.1

for the effects of flexibility on entropy of melting Dannenfelser and co-workers[5,8] have defined a molecular flexibility number, ϕ, for flexible molecules. A flexible molecule contains at least one twist angle, which consists of a string of four non-hydrogen atoms that are not rotationally restricted. The number of twist angles can be calculated by subtracting 1 from the total number of chain atoms present in the molecule. Radially symmetrical end groups such as halogens and carbonyl oxygens are not counted as chain atoms because their rotation does not contribute to the molecule's flexibility. Methyl, primary amine, and hydroxy groups are assumed to be freely rotating and effectively radially symmetrical.

In calculating the molecular flexibility number, sp^2 and sp^3 chain atoms are assigned values of 0.5 and 1.0, respectively. Since the bonds between sp chain atoms do not contribute to flexibility, these atoms are assigned a value of zero. Ring systems, whether single or fused, are counted as a single group and assigned a value of 0.5 per system.

The molecular flexibility number for all molecules is given by:

$$\phi = 2.85^{[SP3 + 0.5SP2 + 0.5RING - 1]} \quad (5)$$

where SP3 is the number of sp^3 chain atoms, SP2 is the number of sp^2 chain atoms, and RING is the number of single or fused ring systems. It is important to note that the exponent is never less than zero. An exponent of zero indicates a rigid, nonflexible molecule so that ϕ equals unity and ln ϕ equals zero, i.e.,

$$\ln 2.85° = 0 \quad (6)$$

Examples of some molecular flexibility numbers (shown as ln ϕ) for some pharmaceutical and environmental compounds are listed in Table 1 along with the values for the SP3, SP2, and RING designations.

Molecular Rotational Symmetry Number—Highly symmetrical molecules are known to have a lower entropy of melting than unsymmetrical molecules. Yalkowsky and co-workers[6,7] have accounted for the effects of symmetry on entropy by defining a molecular symmetry number, σ. The following describes how these numbers are defined for individual molecules.

Since there are many ways in which a molecule can be oriented, one of these ways is arbitrarily chosen as the reference orientation. The number of orientations that are identical to the reference that are produced by rigid rotation, up to 360° about its center of mass, in both of the two spherical angles is defined as the molecular rotational symmetry number or σ. In assigning a value to σ, some groups, such as the halogens, carbonyl oxygen, and cyano, are assumed to be radially symmetrical. Again hydrogens are assumed to be freely rotating and not to contribute to molecular symmetry. Thus methyl, hydroxyl, mercapto, and primary amine groups are treated the same as halogens. Since every molecule has at least one identical

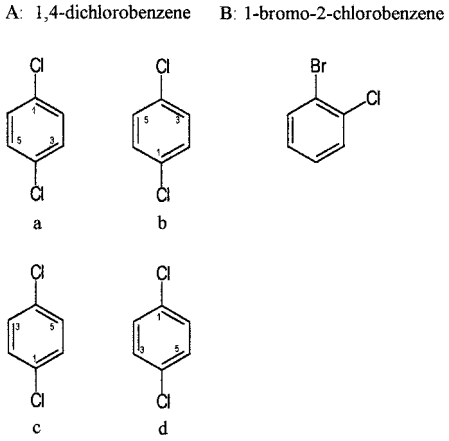

Figure 1—Examples of defining molecular symmetry numbers.

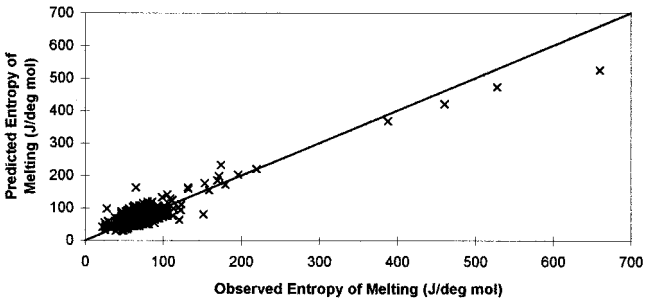

Figure 2—

orientation (produced by a 360° rotation about any axis), the molecular symmetry number is never less than unity (i.e., $\sigma \geq 1$). Thus flexible molecules are assigned a symmetry number of unity.

Molecules with one infinite rotational axis (i.e., cones and cylinders) and molecules with an infinite number of infinite rotational axes (i.e., spheres) have been empirically assigned effective symmetry numbers of 10 and 100, respectively.

Figure 1 shows how 1,4-dichlorobenzene and 1,2-bromochlorobenzene are assigned σ values. Assuming that "a" in Figure 1A is the reference orientation, three other orientations are identical to "a". These can be achieved by rotating "a" 180° about its horizontal axis to obtain "b" and by a 180° clockwise rotation of "a" and "b" to obtain orientations "c" and "d", respectively. Thus 1,4-dichlorobenzene has a molecular symmetry number of four ($\sigma = 4$). As shown in Figure 1B, 1-bromo-2-chlorobenzene, an unsymmetrical molecule, has a molecular symmetry number of unity ($\sigma = 1$) since only a 360° rotation about any axis results in an identical image.

Results and Discussion

The current model to predict the entropy of melting is limited to nonelectrolytes and assumes that the molecules do not self-associate to form dimers or other small aggregates. Only molecular symmetry and flexibility are accounted for in this model. Other factors can effect the entropy of melting, such as eccentricity.

Equation 3 with the molecular parameters, σ and ϕ, was used to predict the total entropy of melting for each compound. No additional parameters or coefficients are used. Figure 2 shows the observed versus predicted entropies of melting. Perfect fit is represented as the solid line with a slope of unity in the graph. As can be seen from the graph, eq 3 does well in predicting the total entropy of

Table 2—Total Entropy of Melting for Highly Flexible Compounds: Walden's Rule versus Eq 3

name	$\Delta S_m^{obsd}/\Delta S_m^{calcd}$ (Walden)	$\Delta S_m^{obsd}/\Delta S_m^{calcd}$ (eq 3)
tridecanoic acid	1.87	0.75
myristyl alcohol	2.82	1.03
pentadecanoic acid	2.34	0.83
hexadecane (cetane)	2.34	0.81
hexadecanol (cetyl alcohol)	3.19	1.05
margaric acid	2.71	0.87
stearic acid	3.00	0.92
fenbutatin oxide	3.04	0.87
ethyl stearate	3.47	0.97
ethyl arachidate	3.89	1.00
chloramphenicol palmitate	3.08	0.75
glyceryl trilaurate	6.87	1.06
glyceryl trimyristate	8.15	1.10
glyceryl tripalmitate	9.35	1.12
tristearin (glyceryl tristearate)	11.68	126
average ratio	4.52	0.96

melting for the complex set of compounds. The average error in predicting the entropy of melting is 21%. This is well within experimental error seen in the reported entropy of melting data. Experimental errors associated with measuring entropy of melting are reflected in the error of the calculated entropy of melting which are based on the measured values. Whenever possible, experimental values are preferred to calculated values.

A constant to estimate the total entropy of melting cannot be utilized well for those compounds that lie at extremes, i.e., molecules that are small and spherical and those that are highly flexible. Richard's rule was based on small, spherical molecules with an average entropy of melting of 10.5 J/deg mol. While Walden's rule, 56.5 J/deg mol, is an average of 17 entropies of melting for petroleum byproducts or aromatic hydrocarbons. All compounds of interest would have the same estimated entropy of melting when one of the constants are used. Since most pharmaceutical and environmental compounds are not small and spherical, Walden's rule would be chosen to predict the entropy of melting. To see the effect of using eq 3 versus a constant, the ratio of the observed over the predicted entropy of melting values are given in Table 2. A ratio of 1 indicates that the prediction is the same or very close to the observed value. Since the average ratio for eq 3 is close to 1, it predicts the total entropy of melting better than using Walden's rule, which has an average ratio of 4.5. The difference between eq 3 and Walden's rule is more dramatic for molecules with a high degree of flexibility.

Conclusion

Equation 3 which uses only two molecular parameters, σ and ϕ, does very well in predicting the total entropy of melting for more than 370 complex pharmaceutical and environmental compounds. This equation results in an average error of 21% for 407 data points.

References and Notes

1. Yalkowsky, S. H. Solubility and Solubilization of Nonelectrolytes. In *Techniques of Solubilization of Drugs*; Yalkowsky, S. H., Ed.; Marcel Dekker: New York, 1981; pp 1−14.
2. Chickos, J. S.; Hesse, D. G.; Liebman, J. F. Estimating Entropies and Enthalpies of Fusion of Hydrocarbons. *J. Org. Chem.* **1990**, *55*, 3833−3840.
3. Chickos, J. S.; Braton, C. M.; Hesse, D. G.; Liebman, J. F. Estimating Entropies and Enthalpies of Fusion of Organic Compounds. *J. Org. Chem.* **1991**, *56*, 927−938.
4. Domalski, E. S.; Hearing, E. D. Estimation of the Thermodynamic Properties of Hydrocarbons at 298.15K. *J. Phys. Chem. Ref. Data* **1988**, *17*, 1637−1647.
5. Dannenfelser, R.-M.; Yalkowsky, S. H. Estimation of Entropy of Melting from Molecular Structure: A Non-Group Contribution Method. *Ind., Eng. Chem. Res.* **1996**, *35*, 1483−1486.
6. Dannenfelser, R.-M.; Surendren, N.; Yalkowsky, S. H. Molecular Symmetry and Related Properties. *SAR QSAR Environ. Res.* **1993**, *1*, 273−292.
7. Abramowitz, R.; Yalkowsky, S. H. Melting Point, Boiling Point, and Symmetry. *Pharm. Res.* **1990**, *7*, 942−947.
8. Dannenfelser, R.-M. Estimating the Entropy of Melting from Structure. Ph. D. Dissertation, University of Arizona, 1997.
9. Plato, C.; Glasgow, A. R., Jr. Differential Scanning Calorimetry as a General Method for Determining the Purity and Heat of Fusion of High-Purity Organic Chemicals. Application to 95 Compounds. *Anal. Chem.* **1969**, *41*, 330−336.
10. Burger, A.; Ramberger, R. On the Polymorphism of Pharmaceuticals and Other Molecular Crystals. II. Applicability of Thermodynamic Rules. *Mikrochim. Acta (Weinheim)* **1979**, *2*, 273−316.
11. Donnelly, J. R.; Drewes, L. A.; Johnson, R. L.; Munslow, W. D.; Knapp, K. K.; Sovocool, G. W. Purity and Heat of Fusion Data for Environmental Standards as Determined by Differential Scanning Calorimetry. *Thermochim. Acta* **1990**, *167*, 155−187.

Acknowledgments

This work was supported by a grant from the Environmental Protection Agency (R-817475).

JS9803609

Effects of True Density, Compacted Mass, Compression Speed, and Punch Deformation on the Mean Yield Pressure

CÉCILE M. D. GABAUDE,[†] MICAEL GUILLOT,[‡] JEAN-CLAUDE GAUTIER,[†] PHILIPPE SAUDEMON,[†] AND DOMINIQUE CHULIA*[,§]

Contribution from *Sanofi Recherche, 371, rue du Professeur Blayac, 34184 Montpellier Cedex 04, France, Sanofi Pharmaceuticals Inc., 9 Great Valley Parkway, P.O. Box 3026, Malvern, Pennsylvania 19355, and GEFSOD, Groupe d'Etude sur la Fonctionnalisation des Solides Divisés, Laboratoire de Pharmacie Galénique, Faculté de Pharmacie, 2 rue du Docteur Marcland, 87025 Limoges, France.*

Received July 28, 1998. Accepted for publication April 9, 1999.

Abstract □ Compressibility properties of pharmaceutical materials are widely characterized by measuring the volume reduction of a powder column under pressure. Experimental data are commonly analyzed using the Heckel model from which powder deformation mechanisms are determined using mean yield pressure (P_y). Several studies from the literature have shown the effects of operating conditions on the determination of P_y and have pointed out the limitations of this model. The Heckel model requires true density and compacted mass values to determine P_y from force-displacement data. It is likely that experimental errors will be introduced when measuring the true density and compacted mass. This study investigates the effects of true density and compacted mass on P_y. Materials having different particle deformation mechanisms are studied. Punch displacement and applied pressure are measured for each material at two compression speeds. For each material, three different true density and compacted mass values are utilized to evaluate their effect on P_y. The calculated variation of P_y reaches 20%. This study demonstrates that the errors in measuring true density and compacted mass have a greater effect on P_y than the errors incurred from not correcting the displacement measurements due to punch elasticity.

Introduction and Background

At the present time and for the foreseeable future, most pharmaceutical forms are oral dosage forms, mainly tablets. The measurement of volume reduction of the particle bed under pressure is one of the most commonly used methods to evaluate particle deformation mechanisms. The powder and granule consolidation is often studied on cylindrical compacts, and the measurement of the compact height is an indication of particle bed volume reduction. This method, currently used for ceramic or metal powders, has been applied to pharmaceutical materials since the 1970s.

There are two methods to obtain density−pressure profiles: the "in-die" and "out-die" (or "ejected tablets") methods.[1,2] The "out-die" method calculates the compact volume by measuring its dimensions when it is ejected from the die after compression at pressure P_a. The "in-die" method measures the compacts dimensions in the die, by evaluating punch displacement(s). The "in-die" method is commonly used because it is quicker to operate and consumes less material than the "out-die" method which requires a new compact for each compression pressure of interest. The "in-die" density measurements contain an elastic component leading to falsely low mean yield pressure which is a disadvantage when using the information for tablet formulation.[3]

Several attempts have been made to fit experimental data from powder or granule bed deformation under load to a universal mathematical model. A large number of empirical models have been developed[4] (Kawakita and Lüdde, Cooper and Eaton, Heckel...) and are based on the compact relative density under pressure.

New models are being developed[5] based on physical assumptions and chemical models. The models studied in the literature to date are not a good representation of particle deformation under pressure. The most universally accepted model used to describe the volume reduction of a particle bed is the Heckel model:[6]

$$\ln\left(\frac{1}{1-\rho_r}\right) = KP_a + A \qquad (1)$$

where, ρ_r is the relative density of the compact and the constants K and A are determined by the slope and intercept of the extrapolated region.

Heckel considered the volume reduction of a plastically deforming particle bed as a first-order kinetics phenomenon, where the pores are the reactant. This is not the case for organic powders, especially pharmaceutical materials, when subjected to low pressure (B zone) (Figure 1). However, converting force-displacement data points into a relative density−pressure relationship shows that most pharmaceutical powders exhibit a linear region (C zone) between two intermediate pressures (Figure 1). The linear part (C zone) is generally accepted to be representative of particle plastic deformation. Heckel[7] suggested that the slope of the linear part of the curve is equal to the reciprocal of $3Y$, Y being the yield strength of the material, and that constant A is a function of the initial volume of the particle bed. Hersey and Rees[8] demonstrated that the mean yield pressure of a material is equal to $1/K$. It is well accepted that the slope, K, of the linear region of the Heckel model is the reciprocal of the mean yield pressure P_y and is a measure of its ability to deform plastically. Since 1961, the Heckel representation has been widely used to interpret the consolidation mechanism. It is not a surprise given the number of different techniques used to measure the compression event that discrepancies in results and disagreements between researcher's conclusions have appeared in the literature. Several parameters influence the calculation of P_y, especially operating conditions:[9] type of compression (a uniaxial press, a rotary press, an alternative press, a compaction simulator...), compression speed,[10,11]

* Corresponding author. Phone: 00-33-5-55-43-58-52. Fax: 00-33-5-55-43-59-10. E-mail: chulia@unilim.fr.
[†] Sanofi Recherche.
[‡] Sanofi Pharmaceuticals Inc.
[§] GEFSOD.

10.1021/js9803050 CCC: $18.00
Published on Web 06/05/1999

Table 1—Parameters of the Simulation

run no.	$P_{y(i)}$	run type
0	$P_{y(0)}$	$D_v = D_{v_0}$ $W = W_0$
1	$P_{y(1)}$	$D_v = D_{v_{min}}$ $W = W_0$
2	$P_{y(2)}$	$D_v = D_{v_{max}}$ $W = W_0$
3	$P_{y(3)}$	$D_v = D_{v_0}$ $W = W_{min}$
4	$P_{y(4)}$	$D_v = D_{v_0}$ $W = W_{max}$

contact time, type and amount of lubricant,[12,13] punch diameter,[14] maximum compression pressure, amount of powder tested and filling method (manual, automatic, constant mass or volume),[15] accuracy of the measurement of displacement for the "in-die" method, accuracy of the measurement of the compact volume after ejection for the "out-die" method, accuracy of the strain gauges or piezoelectric transducers for pressure measurements, initial particle size, type of particle being compressed (powder, granules, mixed powder or granules,[16] true density measurement[17]...).

Researchers traditionally agree that the curvature at very low pressure (B zone) is due to particle packing, rearrangement, and fragmentation in the die while some disagreement occurs when considering the curvature at very high pressure (D zone). For example, negative relative density values can be calculated toward high compression pressures when using the "in-die" method. Some researchers suggested that an increase in the true density value (i.e., polymorphic transformation[18,19]), during compression could explain the abnormal negative values. Small errors in punch displacements or true density measurements may lead to large variations in the calculation of relative density. Therefore, one should be careful when interpreting relative density data and also when comparing results which are obtained under different operating conditions.

The objective of this study is to demonstrate the effects of true density and compacted mass on the mean yield pressure (P_y). In addition, other contributing factors such as compression speed, pressure, and correction of punch displacement for elastic deformation are identified. This study was approached in three steps. In the first step, one set of force and displacement data was collected for each material at two compression speeds. In the second step, Heckel plots were generated following eq 1 using the software provided and a fixed true density and compacted mass value. P_y was then calculated from the Heckel plots. For each set of experimental data measured in the first step, five values of P_y are calculated using different true density and compacted mass values (see Table 1). The third step involved comparing the errors in the P_y values obtained by varying true density, compacted mass, and compression speed with the errors in the P_y values obtained for which no correction for elastic deformation of the punches was made.

Material and Methods

Five materials were used in this study. Three materials are classical pharmaceutical excipients: Avicel PH 102 (filler and dry binder supplied by FMC); Starch 1500 (Disintegrant supplied by Colorcon); Pharmatose DCL 21 (filler supplied by DMW). The other two materials consisted of a drug substance (DS) and its formulated drug product (DP). The DS and DP were supplied by the Pharmaceutical Sciences Department of Sanofi Recherche (patented products).

Table 2—True Density Measured with an Helium Pycnometer and Bulk Density

	starch	avicel	lactose	DS	DP
D_{v_0} (g/cm^3)	1.506	1.594	1.576	1.500	1.526
$n = 3$ (deviation)	(0.003)	(0.001)	(0.002)	(0.001)	(0.000)
D_{bulk} (g/cm^3)	0.643	0.341	0.645	0.270	0.722
$n = 3$ (deviation)	(0.001)	(0.004)	(0.008)	(0.012)	(0.003)

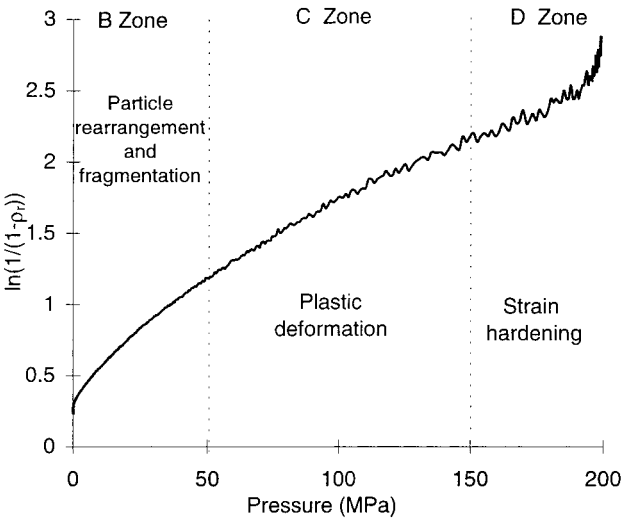

Figure 1—Determination of the linear part in the Heckel treatment.

The true density was measured with a helium pycnometer (Micromeritics, Accupyc 1330), which is accurate to within 0.03% of reading values. Powders were weighed on a Mettler Toledo balance (model AG204), accurate to the nearest 0.1 mg.

The bulk density was measured in a volumenometer following European Pharmacopoeia recommendations (3rd edition, 2.9−15, "Volume apparent"). However, DS had a very low density which did not allow 100 g of powder to be placed in a 250 mL cylinder. The amount of material used for each measurement and each material was 50 g to allow a comparison between products. The measurements were done in triplicate.

Compression experiments were performed on an ESH compaction simulator at two compression speeds (16 and 166 mm·s^{-1}) using linear displacement profiles and a dwell time of zero. The amount of material required to fill a 1 cm^3 die (1 cm^2 × 1 cm) (Table 2) was calculated based on its bulk density (D_{bulk}). The die was manually lubricated with magnesium stearate. The elastic component of the punches was measured. The punch displacements were calibrated and data corrected using polynomial fitting (Figure 2, parts a and b). The punch displacements were measured by Linear Variable Displacement Transducer (LVDT), directly connected to the punches. LVDTs were a RDP Group, type D5/500/392. The accuracy of the upper punch LVDT was 99.91% while the accuracy of the lower punch LVDT was 99.98%. The load cells used to measure force were made by Veccer (U.K.), type s.1333 with a range of 0 to 50 kN. The maximum error of the upper load cell is 0.7% while the maximum error of the lower load cell is 0.2%.

The software allowed for data to be corrected or not corrected for elastic deformation of the punches. Force-displacement data were analyzed using the software provided with the ESH compaction simulator and required the true density and mass of material compacted. The software calculated the mean yield pressure (P_y) using the Heckel model (eq 1). P_y is the inverse of the slope of the C zone shown in Figure 1.

This software was used to generate Heckel plots using three different true density values and three different compacted mass values in order to estimate the effect of true density and compacted mass errors on the mean yield pressure. Experimental errors related to compression itself (i.e., filling the die, measurement of punch displacements and upper punch pressure) were not included.

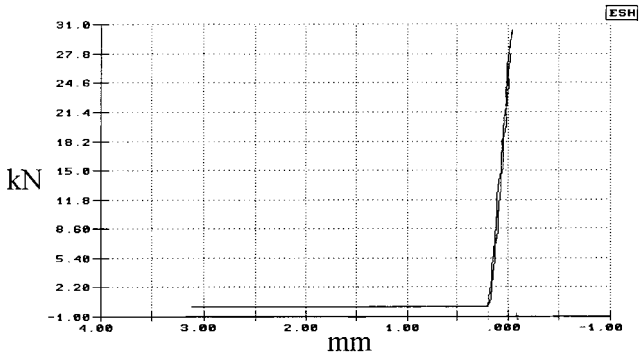

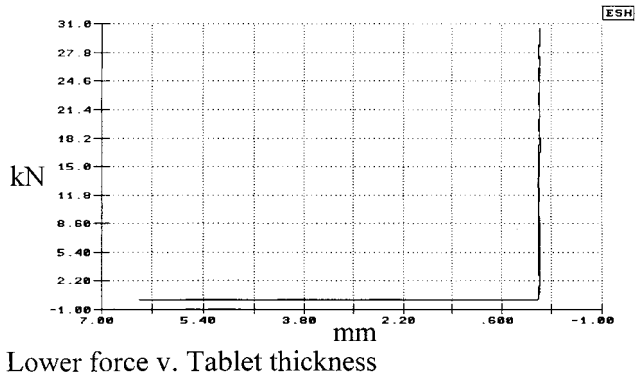

Figure 2—(a) Uncorrected data for punch displacements only. (b) Corrected data for punch displacements only.

Results and Discussion

There are three methods commonly utilized to measure the true density of a material: helium pycnometry, mercury porosimeter, and air pycnometry. True density values will differ according to the measurement method used. In this study, helium pycnometry was utilized because it is the method of choice. Helium pycnometry uses helium atoms which are smaller than both mercury and the atoms composing air. Therefore, helium atoms are able to penetrate pores and interstitial spaces more readily. One of the disadvantages of helium pycnometry is that volatile impurities or adsorbed water may cause a scatter in the measurement. We have found this variation to be up to 3%.

Even when filling material into the die is carried out manually at constant weight and not considering flow properties of materials, a significant source of error can be made on the compacted mass measurement. The amount of material weighed before compressing may differ from the real compressed value because of material losses due to poor flowability, static electricity, sticking, etc. The weight of the compact obtained after ejection may differ from the real weight of the product compacted because of sticking to punches and die walls, capping, lubrication of the die (which will smear onto the tablet and add weight), etc. For some materials such as drug substances which may be very difficult to handle, the error may be up to 10 mg (that is up to 4%, depending on the filling weight). However, for products which are more easily compressed like drug products and direct compression excipients, the weight error may be lower. The difference between the weight of the material before compression and the weight of the compact after ejection is an identification of the error made in the experimental measure. The accuracy of the balance has to be taken into account even though the experimental error made at this stage is negligible.

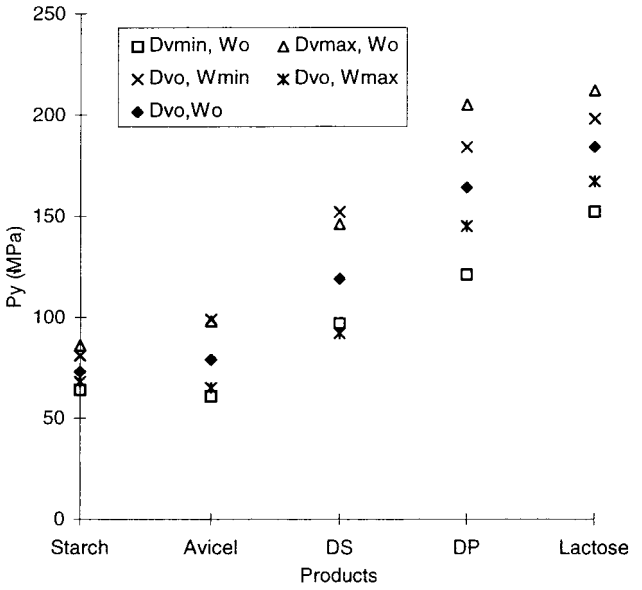

Figure 3—Error due to D_{v_i} and W_i on the mean yield pressure values (P_y, MPa) at V_c = 16.6 mm/s.

For this study, we calculated the mean yield pressure using three different values for the true density (D_{v_0}, $D_{v_{min}}$, and $D_{v_{max}}$) and three different weights for the compacted particles (W_0, W_{min}, and W_{max}) where:

$$D_{v_{min}} = 0.97D_{v_0} \quad \text{and} \quad D_{v_{max}} = 1.03D_{v_0} \qquad (1)$$

$$W_{min} = W_0 - 10\ (\text{mg}) \quad \text{and} \quad W_{max} = W_0 + 10\ (\text{mg}) \qquad (2)$$

The slope of the zone C in Figure 1 has been determined at each simulation test with a good correlation (the correlation coefficient r^2 of the linear regression is greater than 0.99) and the linear zone has been considered to be in the same pressure range [$P_1 - P_2$] for each product.

The value given by the helium pycnometer is assumed to be the best approximation of the true density (designated D_{v_0}, Table 2), and the weight of the compact after ejection (designated W_0) the closest value from the real weight of compacted particles.

Values (D_{v_i}, w_i) used for the mathematical simulations are shown in Table 1.

Figure 3 details the P_y values obtained by varying the true density by ±3% and the compacted mass by ±10 mg for the materials in this study at a compression speed of 16.6 mm·s^{-1}. Materials have been classified according to their increasing $P_{y(0)}$ value. Figure 3 demonstrates that true density exhibits a larger effect on P_y than does weight variation, except for DS. This is because DS has a low bulk density (0.270 g/cm^3). Besides, mean yield pressure decreases when the true density decreases and when the compacted weight increases. The mean yield pressure is calculated in order to determine the particle deformation mechanism(s) of a new product to help understand its compression behavior and to aid in formulation development. How do we characterize a product in such terms if the accuracy of the measurements is not adequate? Considering drug substance and drug product, the mean yield pressure varies at its maximum from 90 to 150 MPa and from 120 to 200 MPa, respectively. Therefore, according to the material deformation classification scheme presented by Roberts and Rowe's[11] (presuming the operating conditions are identical), it is difficult to classify products as plastic or brittle deforming materials.

If the true density varies from ±3% or if the mass of particles compacted varies from approximately ±10 mg, the

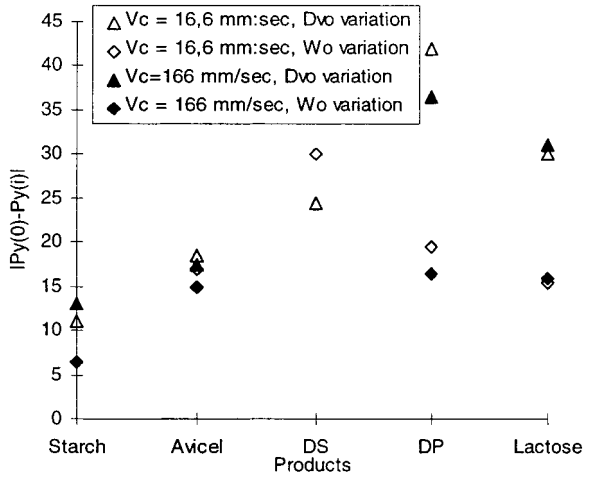

Figure 4—Influence of compression speed on the mean yield pressure variation (MPa).

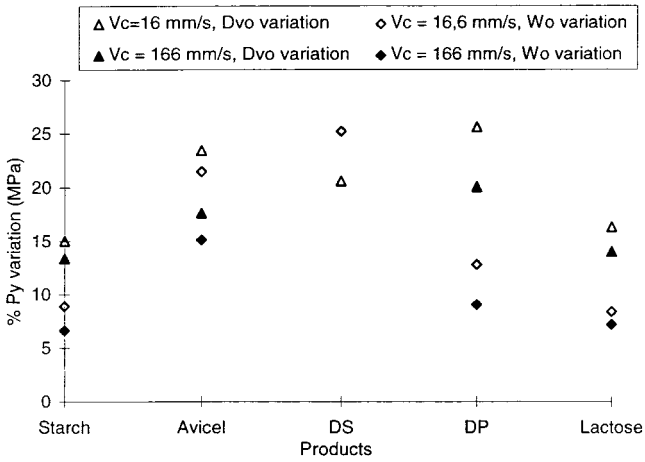

Figure 5—Influence of compression speed on the mean yield pressure relative variation (%).

mean yield pressure differs by approximately the same amount. The P_y variation can be expressed in both directions (either positive or negative) as the absolute value of the difference between $P_{y(0)}$ and $P_{y(i)}$. Figure 4 details the mean yield pressure difference $|P_{y(0)} - P_{y(i)}|$ for the materials in this study from which the effects of compression speed can be observed. Considering the small range of compression speed studied, P_y variation depends on the products and less on the compression speed: the effect of the compression speed is larger for DP than for any of the other products. However, the compression speed consequence is not studied on DS mean yield pressure variation: compacts can be produced at 16.6 mm·s^{-1} but not at 166 mm·s^{-1}. Although production of compacts is not necessary to measure the mean yield pressure, this high speed has not been studied for DS.

The mean yield pressure relative variation $\%P_y$ is defined as the percentage of the yield pressure variation relative to $P_{y(0)}$:

$$\%P_y = \frac{|P_{y(0)} - P_{y(i)}|}{P_{y(0)}} \quad (3)$$

Figure 5 details the $\%P_y$ variation for the materials in this study from which the effects of compression speed can be observed. At the lowest speed, the mean yield pressure relative variation reaches a maximum of 25% for DS and DP. When speed increases, $\%P_y$ decreases. In general, it is well-known from literature that the mean yield pressure of materials increases with increasing compression speed[10,11] (except for brittle deforming materials). Figure 4 shows compression speed does not have a considerable effect on $|P_{y(0)} - P_{y(i)}|$. On the other hand, $P_{y(0)}$ increases with compression speed. Therefore, $\%P_y$ decreases with increasing speed. The variation of the true density value and the compacted mass value has a relatively lower effect on $\%P_y$ when materials are compacted at higher speeds.

Even with the experimental errors introduced by true density and compacted mass measurements, it is possible to deduce the deformation mechanism of new pharmaceutical materials by including reference materials of well-known excipients that are measured at the same operating conditions (including an equivalent accurate measure of the true density and weight of particles compacted). Consequently, complete information about the true density measurement and accuracy of the method should be given with the Heckel model results in order for comparisons to be made.

We can estimate the error on the mean yield pressure when there is a subsequent error on the true density or compacted mass measurements by using the same upper punch force and punch displacements values for one material (also considering the linear part to be in the same pressure range $[P_1 - P_2]$).

The compact height is calculated from the punch displacement data, and depending on the true density of the material and weight of the compacted material, the relative density (ρ_i) is calculated at a pressure P_i:

$$\ln(\rho_i) = \ln\left(1 - \frac{w}{S h_i D_v}\right) \quad (4)$$

where S is the compact surface area, h_i the compact height at pressure P_i, w the compact weight, and D_v the true density of the compacted material.

Since the coefficient of regression r^2 is greater than 0.99, the slope of the linear part of the plot $-\ln(\rho_i)$ versus P (MPa) in the pressure range $[P_1 - P_2]$ can be estimated as follows:

$$K = \frac{-\ln(\rho_2) - [-\ln(\rho_1)]}{P_2 - P_1} \quad (5)$$

and the mean yield pressure can be expressed as:

$$P_y = -\frac{P_2 - P_1}{\ln(\rho_2) - \ln(\rho_1)} \quad (6)$$

From eq 6 we can calculate the error made on the mean yield pressure:

$$\Delta P_y = \frac{P_2 - P_1}{[\ln(\rho_2) - \ln(\rho_1)]^2}\left(\frac{\Delta\rho_2}{\rho_2} - \frac{\Delta\rho_1}{\rho_1}\right) \quad (7)$$

where ρ_i is dependent on the weight and true density value.

Therefore, for a weight variation Δw_0:

$$\Delta P_y = \frac{-\Delta w}{S D_v [\ln(\rho_2) - \ln(\rho_1)]^2}\left[\frac{1}{h_2\rho_2} - \frac{1}{h_1\rho_1}\right] \quad (8)$$

and for a true density variation ΔD_{v_0}:

$$\Delta P_y = \frac{w\Delta D_v}{S(D_v)^2 [\ln(\rho_2) - \ln(\rho_1)]^2}\left[\frac{1}{h_2\rho_2} - \frac{1}{h_1\rho_1}\right] \quad (9)$$

Equation 8 indicates that an underestimation of the compacted material mass ($\Delta W_0 < 0$) increases the mean

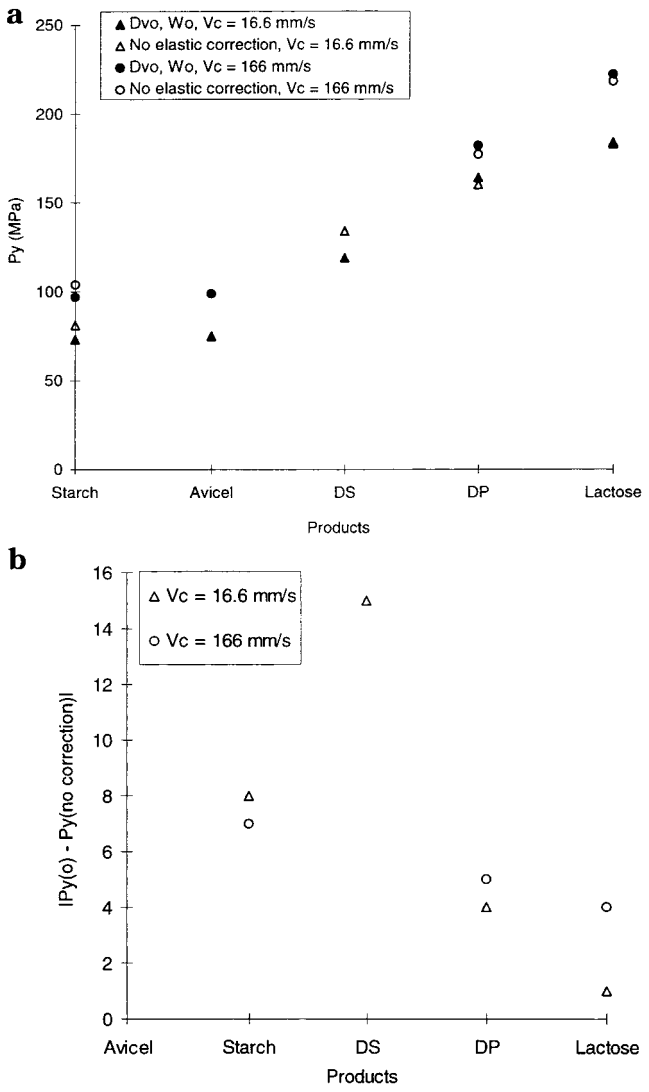

Figure 6—Impact of elastic correction on the mean yield value.

yield pressure value and overestimates the ability of the material to deform by a brittle mechanism. Similarly, eq 9 points out that an underestimation of the true density value ($\Delta D_{v_0} < 0$, which is often the case when it is not measured with a helium pycnometer) decreases P_y value and overestimates the plastic behavior. This reflects the measured variation of mean yield pressure. The two experimental values we studied could have either a complementary effect, i.e., the P_y value error is minimized, or a contradictory effect, i.e., the P_y value error is maximized. Therefore, two extreme cases may appear; if the true density value is minimized and the compacted mass maximized, or, on the other hand, if the true density value is maximized and the compacted mass minimized, the error made on the mean yield pressure would be maximized.

Figure 2, parts a and b, details force versus displacement data for uncorrected (Figure 2a) and corrected (Figure 2b) punch deformation. Most researchers point out that calibration is a significant step for obtaining correct force-displacement profiles.[17,20] The software allows analysis of force-displacement data with or without correction for elastic deformation of the punches. This is useful for comparing the effect elastic deformation of the punches has on P_y while varying the true density or compacted mass values. Figure 6a details P_y for the materials studied for corrected and uncorrected elastic punch deformation at two compression speeds. Figure 6b shows the effect of correction of elastic movement of punches and indicates it is lower than the effect of the true density variation, whatever the compression rate. No calculation of the mean yield pressure without elastic correction of punches has been obtained for microcrystalline cellulose. The greater consequence on P_y variation of the correction of the punches is obtained for DS for which the difference between the two mean yield pressures is 16 MPa. This value is the minimum difference obtained when studying the effect of the true density. The correction of elastic deformation of punches is necessary to improve the accuracy of force-displacement profiles but the consequence on the mean yield pressure is lower than the one which appears when errors occur while measuring true density or compacted mass.

The pressure range used for the Heckel analysis should be as large as possible. Since particle rearrangement and fragmentation often occurs up to 30−50 MPa, it is necessary to compress at least up to 150−200 MPa to increase the accuracy of the mean yield pressure measurement. If the strain-hardening zone[6,7] (D zone in Figure 1) exists when generating the relative porosity of the material column, the maximum amount of data can be used to describe the plastic deformation phase. Then, the mean yield pressure is calculated over a maximum pressure range.

Conclusion

This study showed that the experimental error due to punch displacement accuracy has less effect on the mean yield pressure than the error introduced when measuring the true density or the compacted mass.

Measurements of the force-displacement profiles are quite difficult to interpret according to the literature: Heckel model results are very dependent on the operating conditions. Therefore, it is suggested to analyze well-known pharmaceutical materials with well-known deformation mechanisms such as starch, microcrystalline cellulose, and/or lactose in order to interpret the deformation mechanism of new drug substances and new drug products. To compare the results of P_y between materials, it is important that the operating conditions and measurements methods be extremely accurate and well-defined.

References and Notes

1. Monedero Perales, M. D.; Munoz-Ruiz, A.; Velasco Antequera, M. V.; Jimenez-Castellanos Ballesteros, M. R. Study of the compaction mechanisms of lactose-based direct compression excipients using indentation hardness and Heckel plots. *J. Pharm. Pharmacol.* **1994**, *46*, 177−181.
2. Paronen, P. Heckel plots as indicators of elastic properties of pharmaceuticals. *Drug Dev. Ind. Pharm.* **1986**, *12*, 1903−1912.
3. Krycer, I.; Pope, D. G. The interpretation of powder compaction data − A critical review. *Drug Dev. Ind. Pharm.* **1982**, *8*, 307−342.
4. Celik, M. Overview of compaction data analysis techniques. *Drug Dev. Ind. Pharm.* **1992**, *18*, 767−810.
5. Masteau, J. C.; Thomas, G. Modélisation de l'évolution de la porosité des poudres pharmaceutiques comprimées. *J. Chim. Phys.* **1997**, *97*, 598−619.
6. Heckel, R. W. Density−pressure relationships in powder compaction. *Trans. Met. Soc., AIME.* **1961a**, *221*, 671−675.
7. Heckel, R. W. *Trans. Met. Soc., AIME* **1961b**, *221*, 1000.
8. Hersey, J. A.; Rees, J. E. *Particle Size Analysis Conference.* **1970**, Bradford, England.
9. Rue, P. J.; Rees, J. E. Limitations of the Heckel relation for predicting powder compaction mechanisms. *J. Pharm. Pharmacol.* **1978**, *30*, 642−643.
10. Roberts, R. J.; Rowe, R. C. The effect of the relationship between punch velocity and particle size on the compaction behavior of materials with varying deformation mechanisms. *J. Pharm. Pharmacol.* **1986**, *38*, 567−571.

11. Roberts, R. J.; Rowe, R. C. The effect of punch velocity on the compaction of a variety of materials. *J. Pharm. Pharmacol.* **1985**, *37*, 377−384.
12. DeBoer, H.; Bolhuis, G. K.; Lerk, C. F. Bonding characteristics by scanning electron microscopy of powders mixed with magnesium stearate. *Powder Technol.* **1978**, *20*, 75−82.
13. Ragnarsson G.; Sjogren, J. The influence of die wall friction on the tablet porosity: compaction load relationship. *Acta Pharm. Suec.* **1984**, *21*, 141−144.
14. York, P. A consideration of experimental variables in the analysis of powder compaction behavior. *J. Pharm. Pharmacol.* **1979**, *31*, 244−246.
15. Danjo, K.; Ertell, C.; Carstensen, J. T. Effect of compaction speed and die diameter on Athy-Heckel and hardness parameters of compressed tablets. *Drug Dev. Ind. Pharm.* **1989**, *15 (1)*, 1−10.
16. Ilkka, J.; Paronen, P. Prediction of the compression behavior of powder mixtures by the Heckel equation. *Int. J. Pharm.* **1993**, *94*, 181−187.
17. Paronen, P.; Ilkka, J. Porosity -pressure functions. In *Pharmaceutical Powder Compaction Technology*; Alderborn, G., Nyström, C., Eds.; Marcel Dekker: New York, 1996; pp 55−75.
18. Chan, H. K.; Doelker, E. Polymorphic transformation of some drugs under compression. *Drug Dev. Ind. Pharm.* **1985**, *11 (2&3)*, 315−332.
19. Pedersen, S.; Kristensen, H. G. Change in crystal density of acetylsalicylic acid during compaction. *S. T. P. Pharma Sci.* **1994**, *4 (3)*, 201−206.
20. Doelker, E. Assessment of powder compaction. In *Handbook of Powder Technology*; Chulia, D., Deleuil, M., Pourcelot, Y., Eds.; Elsevier: Amsterdam, 1993; pp 403−471.

Acknowledgments

We are grateful to J. McGurk and S. Laughlin, Sanofi Pharmaceutical Inc., for allowing this work to be carried out in the Pharmaceutical Sciences Department and ELF AQUITAINE for financial support and to Sanofi Recherche for technical assistance.

JS9803050

General Solution for Diffusion-Controlled Dissolution of Spherical Particles. 1. Theory

JIANZHUO WANG AND DOUGLAS R. FLANAGAN*

Contribution from *Division of Pharmaceutics, College of Pharmacy, The University of Iowa, Iowa City, Iowa 52242.*

Received June 2, 1998. Final revised manuscript received January 20, 1999.
Accepted for publication March 9, 1999.

Abstract □ Three classical particle dissolution rate expressions are commonly used to interpret particle dissolution rate phenomena. Our analysis shows that an assumption used in the derivation of the traditional cube-root law may not be accurate under all conditions for diffusion-controlled particle dissolution. Mathematical analysis shows that the three classical particle dissolution rate expressions are approximate solutions to a general diffusion layer model. The cube-root law is most appropriate when particle size is much larger than the diffusion layer thickness, the two-thirds-root expression applies when the particle size is much smaller than the diffusion layer thickness. The square-root expression is intermediate between these two models. A general solution to the diffusion layer model for monodispersed spherical particles dissolution was derived for sink and nonsink conditions. Constant diffusion layer thickness was assumed in the derivation. Simulated dissolution data showed that the ratio between particle size and diffusion layer thickness (a_0/h) is an important factor in controlling the shape of particle dissolution profiles. A new semiempirical general particle dissolution equation is also discussed which encompasses the three classical particle dissolution expressions. The success of the general equation in explaining limitations of traditional particle dissolution expressions demonstrates the usefulness of the general diffusion layer model.

Dissolution phenomena have been studied in a quantitative manner for more than a century. The dissolution of solid particles is more complicated than that of constant surface area tablets because of surface area and/or shape changes during dissolution. Though particle dissolution models have been developed, discrepancies between theory and experimental data are present. It has not been shown whether these discrepancies are due to experimental factors or limitations of the mathematical models.

Two steps are involved in solid particle dissolution: the first step is the detachment of molecules from the solid surface to form hydrated molecules at the solid−liquid interface; the second step is the mass transport from this interface to the bulk solution. Most dissolution processes are controlled by the second step which is diffusion−convection-controlled. The basic diffusion-controlled model for solid dissolution was developed by Noyes and Whitney[1] and later modified by Nernst[2] and Brunner.[3] This model assumes that rapid equilibrium (i.e., saturation) is achieved at the solid−liquid interface and then diffusion occurs across a thin layer of solution, called the diffusion layer, into the bulk solution. Diffusion across this diffusion layer is rate-controlling in most cases, which effectively converts the heterogeneous process of dissolution to a homogeneous process of liquid-phase diffusion. Nernst and Brunner's concept of a diffusion layer being a stagnant or unstirred layer of liquid adhering to the solid surface is naive but allows complex dissolution processes to be analyzed in a tractable fashion. However, as pointed out by King,[4] this layer need not be stagnant and can be a hydrodynamic boundary which has a velocity as well as a concentration gradient.

Three diffusion-controlled models have been reported for single spherical particle dissolution under sink conditions, as shown below:

$$w^{1/3} = w_0^{1/3} - k_{1/3}t \qquad k_{1/3} = \left(\frac{4\pi\rho}{3}\right)^{1/3} \frac{DC_S}{\rho h} \quad \text{(eq 1)}$$

$$w^{1/2} = w_0^{1/2} - k_{1/2}t \qquad k_{1/2} = \left(\frac{3\pi\rho}{2}\right)^{1/2} \frac{DC_S}{k'\rho} \quad \text{(eq 2)}$$

$$w^{2/3} = w_0^{2/3} - k_{2/3}t \qquad k_{2/3} = \left(\frac{4\pi\rho}{3}\right)^{2/3} \frac{2DC_S}{\rho} \quad \text{(eq 3)}$$

where w is particle weight at time t, w_0 is initial particle weight, $k_{1/3}$, $k_{1/2}$, and $k_{2/3}$ are composite rate constants, ρ is the density of the particle, D is diffusion coefficient, C_S is solubility, h is diffusion layer thickness, and k' is a constant. Equation 1 was derived by Hixson and Crowell[5] and is known as the "cube-root law". Equation 2 is the semiempirical expression reported by Niebergall et al.[6] and has a square-root dependency on weight. Equation 3 was derived by Higuchi and Hiestand[7] and has a two-thirds-root dependency on weight. Each of the above equations gives satisfactory fits to certain experimental dissolution data.[6,8,9] These three expressions are still the basis for particle dissolution theories in contemporary dissolution testing.[10] However, the choice of the model to fit experimental data is still somewhat arbitrary. Though they appear different in form, the three equations are difficult to distinguish when applied to experimental data. A particular dissolution profile can often be fitted by at least two of these equations almost equally well.[11] Thus, it seems that dissolution behavior of simple spherical particles is still not theoretically well defined.

Among the three equations, the most commonly used is the "cube-root law". The cube-root law was first derived by assuming that dissolution rate is proportional to particle surface area. Though Hixson and Crowell did not specifically use the diffusion layer model to derive their equation, the cube-root law can also be derived from a simple diffusion layer model. Our further analysis shows that the cube-root law is only an approximate solution to the diffusion layer model, because an assumption used may not be accurate under all conditions for diffusion-controlled particle dissolution.

Below are dissolution rate expressions for the diffusion layer model:

$$\frac{dQ}{dt} = \frac{DA}{h}(C_S - C_b) \quad \text{(eq 4)}$$

$$\frac{dQ}{dt} = -DA\left.\frac{\partial C}{\partial r}\right|_{r=a} \quad \text{(eq 5)}$$

* Corresponding author. Ph: 319-335-8827. Fax: 319-335-9349. E-mail: douglas-flanagan@uiowa.edu.

10.1021/js980236p CCC: $18.00
Published on Web 06/16/1999

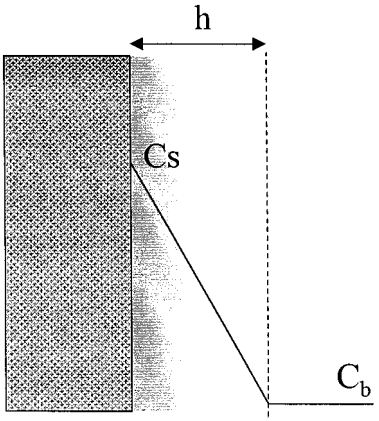

Figure 1—Steady-state concentration gradient around a planar surface.

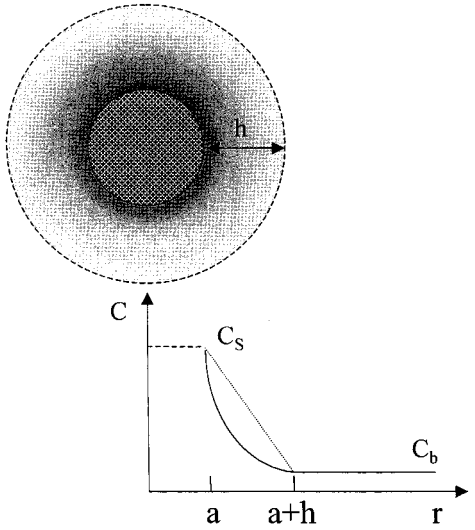

Figure 2—Pseudo-steady-state concentration gradient around a spherical particle (radius = *a*).

where dQ/dt is the rate of dissolution, A is particle surface area, h is the thickness of the diffusion layer, C_b is bulk solution concentration, r is the distance from the center of the particle, and a is particle radius. Equation 4 is exact for planar surface dissolution under sink conditions, because the concentration gradient in the diffusion layer is linear at steady-state (Figure 1). However, for a curved surface, eq 4 is not accurate because the concentration gradient around a spherical particle is not linear under pseudo-steady-state conditions (Figure 2). Particle dissolution rate expressions based on eq 4 will not give accurate solutions to the diffusion layer model for spherical particles. For more accurate results, the derivation should start from eq 5 which is Fick's first law expression for spherical geometry.

For particle dissolution, changing bulk solution concentration complicates the mathematical analysis. Most researchers use sink conditions to make the treatment of experimental data easier. The three traditional particle dissolution expressions are such examples, which is what we emphasize here. A general (and more exact) solution to the diffusion layer model for spherical particle dissolution under sink conditions will be derived, and the relationship between the general solution and the classical expressions will be discussed. A general solution for spherical particle dissolution under nonsink conditions is also included and briefly discussed. Understanding the limitations of the three classical particle dissolution expressions will make it easier to use them appropriately. The availability of the general solution will provide a sound basis for determining whether diffusion layer thickness is dependent upon particle size, which has been a point of discussion.[6,10,12–14] It also provides a sound basis for the investigation of polydispersity effects on particle dissolution.

Theory

The diffusion layer model for single spherical particle dissolution under sink conditions is based on the following assumptions:

(a) The particle is spherical and dissolves isotropically.

(b) The particle is in a well-stirred solution and there exists a boundary layer around the particle of constant thickness (h).

(c) During dissolution, a pseudo-steady-state is established with only minimal solid dissolution, after which the overall mass transport rates across the inner and outer spherical surfaces (at $r = a$ and $a + h$) of the diffusion layer are assumed to be equal.[15]

(d) The concentration at the interface between the solid and the solution is saturated (C_S), and solubility is independent of particle size.

(e) The bulk solution concentration (C_b) is assumed to be zero, and the diffusion coefficient (D) is a constant throughout the diffusion layer.

Since the concentration gradient around a spherical particle is not linear at pseudo-steady-state, it is a function of distance from the center of the particle. The function $G(R)$ can be defined as the concentration gradient at a distance R from the center of the particle and is given by:

$$G(R) \equiv \left.\frac{\partial C}{\partial r}\right|_{r=R}$$

With this definition, eq 5 becomes:

$$\frac{dQ}{dt} = -DAG(a) \qquad \text{(eq 6)}$$

The surface area of a sphere is $4\pi r^2$ and applying the pseudo-steady-state assumption c gives:

$$4\pi a^2 G(a) = 4\pi r^2 G(r) \qquad a \le r \le a + h \quad \text{(eq 7)}$$

and

$$G(r) = \frac{a^2}{r^2} G(a) \qquad \text{(eq 8)}$$

Using assumptions d and e, the total concentration difference across the diffusion layer is C_S, which leads to:

$$\int_a^{a+h} -G(r)dr = C_S \qquad \text{(eq 9)}$$

Substituting eq 8 into eq 9 gives:

$$\int_a^{a+h} -\frac{a^2}{r^2} G(a)dr = C_S \qquad \text{(eq 10)}$$

Integrating eq 10 gives:

$$G(a) = -C_S\left(\frac{1}{a} + \frac{1}{h}\right) \qquad \text{(eq 11)}$$

Substituting eq 11 into eq 6 gives:

$$\frac{dQ}{dt} = DAC_S\left(\frac{1}{a} + \frac{1}{h}\right) \qquad \text{(eq 12)}$$

Using $4\pi a^2$ for area (A) in eq 12 gives:

$$\frac{dQ}{dt} = 4\pi a^2 DC_S\left(\frac{1}{a} + \frac{1}{h}\right) \quad \text{(eq 13)}$$

Considering the change of particle radius during dissolution, the mass balance expression for a dissolving spherical particle is:

$$\frac{dQ}{dt} = -4\pi a^2 \rho \frac{da}{dt} \quad \text{(eq 14)}$$

where ρ is the solid density. Equation 14 is independent from eq 13. Equating eqs 13 and 14 gives:

$$4\pi a^2 DC_S\left(\frac{1}{a} + \frac{1}{h}\right) = -4\pi a^2 \rho \frac{da}{dt} \quad \text{(eq 15)}$$

Rearranging eq 15 gives:

$$\frac{DC_S}{\rho h} dt = \left(-1 + \frac{h}{a+h}\right) da \quad \text{(eq 16)}$$

The integral form of eq 16 is:

$$\int_0^t \frac{DC_S}{\rho h} dt = \int_{a_0}^{a} \left(-1 + \frac{h}{a+h}\right) da \quad \text{(eq 17)}$$

Integrating both sides of eq 17 gives:

$$\frac{DC_S}{\rho h} t = a_0 - a - h \ln \frac{h + a_0}{h + a} \quad \text{(eq 18)}$$

where a_0 is the initial particle radius.

Equation 18 is the general solution (in terms of particle radius) of the diffusion layer model for single spherical particle dissolution under sink conditions. The relationship between particle weight and particle radius is given by:

$$w = \frac{4}{3}\pi a^3 \rho \quad \text{(eq 19)}$$

where w is particle weight and w_0 is initial particle weight.

Substituting eq 19 into eq 18 gives an expression for the change of particle weight with time:

$$\frac{DC_S}{\rho h} t = \left(\frac{3w_0}{4\pi\rho}\right)^{1/3} - \left(\frac{3w}{4\pi\rho}\right)^{1/3} - h \ln \frac{h + \left(\frac{3w_0}{4\pi\rho}\right)^{1/3}}{h + \left(\frac{3w}{4\pi\rho}\right)^{1/3}} \quad \text{(eq 20)}$$

For N monodispersed particles, the total weight (W) of particles is Nw. Using this expression in eq 20 gives eq 21 which describes the dissolution process for N monodispersed particles under sink conditions with total initial weight, W_0.

$$\frac{DC_S}{\rho h} t = \left(\frac{3W_0}{4N\pi\rho}\right)^{1/3} - \left(\frac{3W}{4N\pi\rho}\right)^{1/3} - h \ln \frac{h + \left(\frac{3W_0}{4N\pi\rho}\right)^{1/3}}{h + \left(\frac{3W}{4N\pi\rho}\right)^{1/3}} \quad \text{(eq 21)}$$

Under nonsink conditions, the general dissolution equation can be derived in a similar manner (see appendix II) and is summarized below.

For N monodispersed spherical particles, the general solution in terms of particle size (a) with time is:

$$\frac{D}{\rho h V} t = \frac{1}{\beta - \alpha h^3}\{X + Y + Z\} \quad \text{(eq 22)}$$

$$X = h \ln \frac{a + h}{a_0 + h} - \frac{h}{3} \ln \frac{\alpha a^3 + \beta}{\alpha a_0^3 + \beta}$$

$$Y = \frac{h^2}{\gamma}\left[\frac{1}{2} \ln \frac{(\alpha a^3 + \beta)(\gamma + a_0)^3}{(\gamma + a)^3(\alpha a_0^3 + \beta)} + \sqrt{3} \tan^{-1}\left(\frac{2a - \gamma}{\sqrt{3}\gamma}\right) - \sqrt{3} \tan^{-1}\left(\frac{2a_0 - \gamma}{\sqrt{3}\gamma}\right)\right]$$

$$Z = \frac{\gamma}{3}\left[\frac{1}{2} \ln \frac{(\alpha a^3 + \beta)(\gamma + a_0)^3}{(\gamma + a)^3(\alpha a_0^3 + \beta)} - \sqrt{3} \tan^{-1}\left(\frac{2a - \gamma}{\sqrt{3}\gamma}\right) + \sqrt{3} \tan^{-1}\left(\frac{2a_0 - \gamma}{\sqrt{3}\gamma}\right)\right]$$

where α, β and γ are constants: $\alpha = {}^4/_3\pi\rho N$, $\beta = C_S V - {}^4/_3\pi a_0^3 \rho N$, $\gamma = (\beta/\alpha)^{1/3}$. The above general equation is not applicable when $\beta = 0$ which will lead to an indeterminate condition (i.e., division by zero). Such a situation arises when the initial particle weight (W_0) equals the amount necessary to saturate the solution (i.e., $W_0 = C_S V$). The equation for this condition is:

$$\frac{DC_S}{a_0^3 \rho N} t = \frac{1}{a} - \frac{1}{a_0} + \frac{1}{h} \ln \frac{a(a_0 + h)}{a_0(a + h)} \quad \text{(eq 23)}$$

Results and Discussion

1. Three Classical Particle Dissolution Rate Expressions are Special Cases of the General Solution under Sink Conditions—Two special cases of eq 18 are as follows:

(a) When $a_0 \gg h$ and $a \gg h$, eq 18 becomes (see appendix I):

$$\frac{DC_S}{\rho h} t \approx a_0 - a \quad \text{(eq 24)}$$

This leads to the cube-root expression.[5]

(b) When $a_0 \ll h$, eq 18 becomes (see appendix I):

$$\frac{2DC_S}{\rho} t \approx a_0^2 - a^2 \quad \text{(eq 25)}$$

This leads to the two-thirds-root expression.[7]

It is clear that both the cube-root law and the two-thirds-root expression are approximate solutions to the diffusion layer model at opposite extremes of particle size. Theoretically, the cube-root law is accurate only when the particle size is much larger than the thickness of the diffusion layer, and the two-thirds-root expression is accurate when the particle size is much smaller than the thickness of the diffusion layer.[16] The square-root expression is intermediary between these two limits. It is not surprising that it fits some particle dissolution profiles, but may not describe such profiles exactly. When particle size is comparable to the thickness of the diffusion layer, the general equation provides a more accurate mathematical description.

The above conclusion can also be reached in another way. The concentration gradient at the solid–liquid interface (eq 11) can be considered to be two parts: the particle radius term (C_S/a) and diffusion layer thickness term (C_S/h). When particle size is much larger than diffusion layer thickness ($a \gg h$), the particle radius term can be omitted, we obtain $dQ/dt \approx DAC_S/h$ which will lead to the cube-root

law. On the other hand, when the particle size is much smaller than diffusion layer thickness ($a \ll h$), the diffusion layer thickness term can be omitted and we obtain $dQ/dt \approx DAC_S/a$ which leads to the two-thirds-root expression. It is obvious that both of these expressions underestimate the concentration gradient at the solid–liquid interface.

2. The Ratio between Particle Size and Diffusion Layer Thickness (a_0/h) in Controlling the Shape of a Particle Dissolution Profile—Rearranging eq 18 gives:

$$t = \frac{\rho h}{DC_S}[a_0 - a - h\ln(h + a_0) + h\ln(h + a)] \quad \text{(eq 26)}$$

T can be defined as the time needed for complete dissolution (i.e., at $a = 0$) of a particle as shown below:

$$T = \frac{\rho h}{DC_S}[a_0 - h\ln(h + a_0) + h\ln(h)] \quad \text{(eq 27)}$$

Dividing both sides of eq 26 by eq 27 gives:

$$\frac{t}{T} = \frac{a_0 - a - h\ln(h + a_0) + h\ln(h + a)}{a_0 - h\ln(h + a_0) + h\ln(h)} \quad \text{(eq 28)}$$

Rearranging eq 28 gives:

$$\frac{t}{T} = 1 - \frac{a - h\ln(h + a) + h\ln(h)}{a_0 - h\ln(h + a_0) + h\ln(h)} \quad \text{(eq 29)}$$

Further rearrangement of eq 29 gives:

$$\frac{t}{T} = 1 - \frac{a - h\ln\left(1 + \frac{a}{h}\right)}{a_0 - h\ln\left(1 + \frac{a_0}{h}\right)} \quad \text{(eq 30)}$$

and

$$\frac{t}{T} = 1 - \frac{\frac{a}{a_0} - \frac{h}{a_0}\ln\left(1 + \frac{a}{a_0}\frac{a_0}{h}\right)}{1 - \frac{h}{a_0}\ln\left(1 + \frac{a_0}{h}\right)} \quad \text{(eq 31)}$$

Since $a/a_0 = (w/w_0)^{1/3}$, eq 31 becomes:

$$\frac{t}{T} = 1 - \frac{\left(\frac{w}{w_0}\right)^{1/3} - \frac{h}{a_0}\ln\left[1 + \frac{a_0}{h}\left(\frac{w}{w_0}\right)^{1/3}\right]}{1 - \frac{h}{a_0}\ln\left(1 + \frac{a_0}{h}\right)} \quad \text{(eq 32)}$$

Equation 32 is a dimensionless equation for single particle dissolution under sink conditions where t/T and w/w_0 can be viewed as two variables which range from 0 to 1. Plots of w/w_0 vs t/T give dissolution profiles which are independent of solid and dissolution medium used, but are governed by a_0/h. Theoretical comparisons between the general solution and classical particle dissolution expressions can be made by generating simulated particle dissolution data using eq 32 and comparing the simulated data with the traditional expressions.

If a spherical particle dissolution profile follows one of the three traditional particle dissolution expressions, one of the $(w/w_0)^{1/n}$ vs time plots ($n = 3$, 2, or 3/2) should be linear with a slope of 1. By simulating dissolution profiles using the normalized general equation (eq 32) and plotting the resulting dissolution profiles with these three ordinate axis transformations (Figure 3), it can be seen how well the three approximate particle dissolution rate expressions (eqs 1–3) apply. The dissolution data were simulated with different values of a_0/h. It can be seen from Figure 3 that there are deviations from linearity for some a_0/h ratios no matter what ordinate transformation is used.

It should be pointed out that linearity of such plots is not a sensitive criterion to test whether the dissolution profile is consistent with a certain rate expression. Usually dissolution profiles can be reasonably linear on any of the three transformed axes up to ~80% dissolved (i.e., $[w/w_0]^{1/n} = 0.585$, 0.447, 0.342 for $n = 3$, 2, 3/2, respectively).

3. A New Semiempirical Equation for Single Spherical Particle Dissolution under Sink Conditions—Since there are functional simlarities in the three classical particle dissolution rate expressions, a new semiempirical equation (eq 33) is proposed which incorporates the three classical expressions but the exponent, n, is not limited to values 3, 2, and 3/2. The proportionality constant $k_{1/n}$ is a constant with units of mass$^{1/n}$/time.

$$w^{1/n} = w_0^{1/n} - k_{1/n}t \quad \text{(eq 33)}$$

Single particle dissolution profiles generated from the general equation (eq 32) can be fitted by eq 33 where n ranges from 3/2 to 3 but does not have to be a specific value (i.e., 3/2, 2, or 3). If w is normalized by w_0 and t is normalized by T ($T = w_0^{1/n}/k_{1/n}$), a dimensionless expression is obtained:

$$\frac{w}{w_0} = \left(1 - \frac{t}{T}\right)^n \quad \text{(eq 34)}$$

The two parameters, T and n, can be obtained by fitting eq 34 to dissolution data (w/w_0 vs t). Simulation studies were carried out at six representative a_0/h ratios. For convenience, the w/w_0 values were generated by keeping $a/a_0 = 1.0$, 0.95, 0.90, ..., 0.05, 0 for each a_0/h ratio. The corresponding times (t) for these w/w_0 values were then calculated with eq 32. The values of T and n were obtained by fitting eq 34 to the simulated data and the results are given in Table 1. It can be seen that n depends on a_0/h with the smaller ratio giving a smaller value of n. The other fitted parameter, T, deviates slightly from its theoretical value (1.0) for all a_0/h ratios. Theoretically, it is possible to determine a_0/h from the fitted value of n. However, small variations in n can lead to dramatic changes in calculated a_0/h values making it difficult to obtain an accurate estimation of a_0/h from n.

4. Dependence of Surface-Specific Dissolution Rate upon Particle Size under Sink Conditions—According to Fick's first law,

$$J = -D\frac{\partial C}{\partial r} \quad \text{(eq 35)}$$

J is the diffusional flux and is defined as the amount of substance passing per unit time normal to unit surface area. When applied to dissolution, it may also be defined as the surface-specific dissolution rate. Substituting eq 11 into eq 35 gives:

$$J = DC_S\left(\frac{1}{h} + \frac{1}{a}\right) \quad \text{(eq 36)}$$

Equation 36 demonstrates that the surface-specific dissolution rate depends on particle size, with smaller particles having higher surface-specific dissolution rates (Figure 4). Bisrat et al.[13] and Anderberg et al.[14,17] reported a dependence of surface-specific dissolution rates upon particle size. Their results showed the same trend seen in

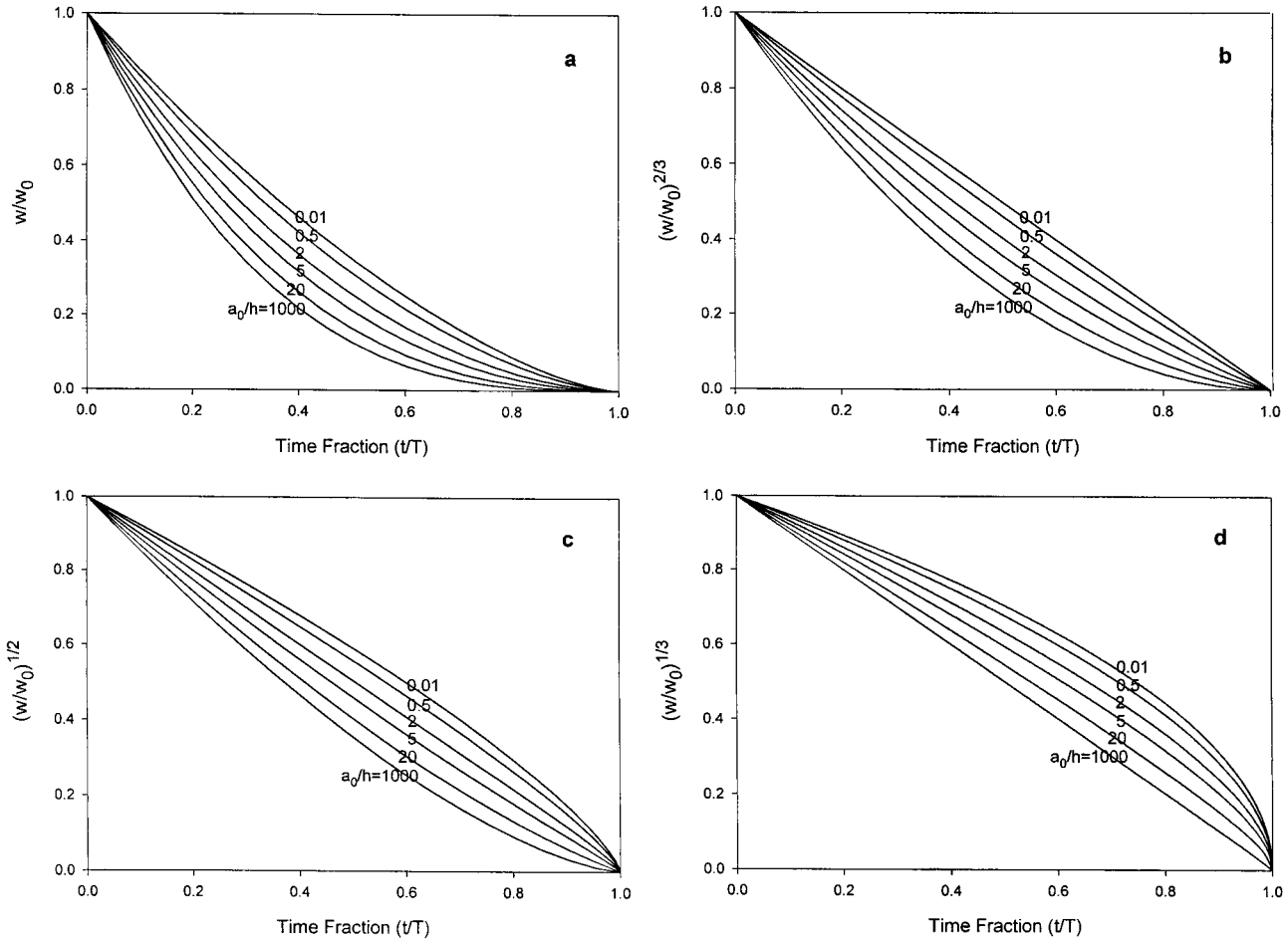

Figure 3—Simulated particle dissolution profiles (eq 32) at representative a_0/h values (0.01, 0.5, 2, 5, 20, 1000) with different $(w/w_0)^{1/n}$ ordinate axes: (a) $n = 1$; (b) $n = 3/2$; (c) $n = 2$; (d) $n = 3$.

Table 1—Fitted Parameters (n, T) for Simulated Data (eq 32) Fitted by eq 34

a_0/h	n	T	r^2
1000	3.00	1.004	1.00000
20	2.80	1.051	1.00000
5	2.43	1.059	0.99999
2	2.09	1.044	0.99998
0.5	1.71	1.016	0.99999
0.01	1.51	1.000	1.00000

Figure 4. The surface-specific dissolution rate increased (after correcting for solubility dependence on particle size) with decreasing particle size. This increase was especially pronounced for particle sizes below ~5 μm.

Harriott similarly reported on mass transfer to particles (i.e., particle growth) for a much wider range of particle sizes.[18] He found that the mass transfer coefficient, k_C (cm/s), was almost independent of particle size for particles larger than 200 μm, but was particle size dependent for smaller particles. Since diffusion layer thicknesses usually range from 10 to 200 μm, it seems that for particles smaller than 200 μm, particle size effects will be significant on particle dissolution.

Equation 36 can be rewritten in a more general form:

$$J = DC_S\left(\frac{1}{h} + \frac{1}{r_c}\right) \qquad \text{(eq 37)}$$

where r_c is the radius of curvature of a dissolving surface and is positive ($r_c > 0$) for a convex surface. For flat surfaces

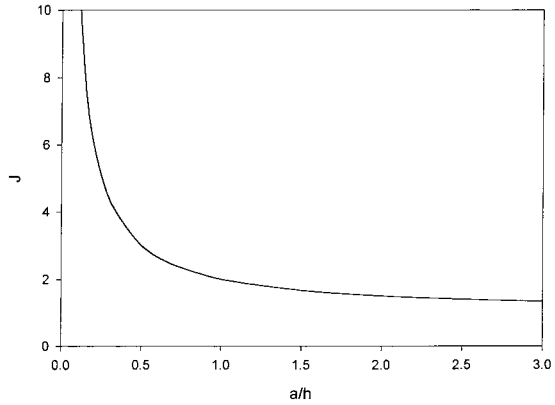

Figure 4—Relative surface-specific dissolution rate dependence (J, $J = 1$ for a flat surface) upon particle radius (a) normalized with diffusion layer thickness (h) using eq 36.

($r_c \rightarrow \infty$), dissolution rate is directly proportional to surface area. However, this simple relationship does not hold for a curved surface. Convex surfaces have larger surface-specific dissolution rates than a flat surface. Hixson and Crowell derived the cube-root law by assuming dissolution rate is proportional to particle surface area. From the above analysis we can see that this assumption is not justified when r_c is comparable to or smaller than h.

5. Particle Dissolution under Nonsink Conditions—The general equation for spherical particle dissolution under nonsink conditions (eq 22) is algebrically complex but can be mathematically simulated. It can also be converted to particle weight (W) which will lead to an

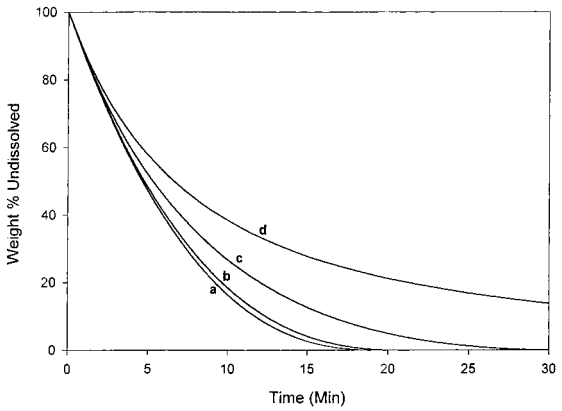

Figure 5—Comparison of particle dissolution under sink conditions (a) and three degrees of saturation: (b) 10%; (c) 50%; (d) 100%.

equally unwieldy equation which we do not show here. The main advantage of such expressions is for dissolution systems in which the drug is quite insoluble where sink conditions are difficult or impossible to maintain.

A simulation was done to compare particle dissolution under sink conditions and different degrees of nonsink conditions using eqs 21−23. Three levels of nonsink conditions were chosen: initial particle weight equal to 10%, 50%, and 100% of the amount necessary to saturate the solution. The initial particle radius was arbitrarily chosen to be 10 times as large as the diffusion layer thickness with $a_0 = 200\ \mu$m, $h = 20\ \mu$m, $D = 1.1 \times 10^{-5}$ cm^2/s, $C_S = 3.4$ mg/mL, $\rho = 1.4$ g/cm^3. A comparison of the dissolution profiles is shown in Figure 5. It can be seen that assuming sink conditions provides good results when initial particle weight is less than 10% of the weight for saturation.

Conclusions

The general solution of the diffusion layer model applied to spherical particle dissolution is derived. The three classical particle dissolution rate expressions, including the cube-root law, are special cases of the general solution to particle dissolution under sink conditions with constant diffusion layer thickness. The ratio between particle radius and diffusion layer thickness (a_0/h) is an important factor in controlling the shape of the dissolution profile. It also controls which classical model can fit a dissolution profile better than the other two models. It is necessary to apply this general equation to typical monodispersed drug powder dissolution data to fit the entire profile. This general equation will be applied to literature and experimental data in future publications.

Nomenclature

a	particle radius
a_0	initial particle radius
A	surface area
C	concentration
C_b	concentration in the bulk solution
C_S	solubility
D	diffusion coefficient
$G(R)$	concentration gradient at distance R from the center of the particle
h	diffusion layer thickness
J	surface-specific dissolution rate, i.e., dissolution rate on unit surface area
$k_{1/3}$	single particle dissolution constant in the cube-root law
$k_{1/2}$	single particle dissolution constant in the square-root expression
$k_{2/3}$	single particle dissolution constant in the two-thirds-root expression
k_n	dissolution rate constant
n	dissolution rate order
N	total number of particles
r	distance from the center of a particle
r_c	radius of curvature
t	time
T	time needed for complete particle dissolution
V	solution volume
w	individual particle weight
w_0	initial individual particle weight
W	total weight of monodispersed particles
W_0	total initial weight of monodispersed particles
ρ	solid density of the particle

Appendix I

The cube-root law and the two-thirds-root expression can be derived from eq 18 using a Taylor series expansion (eq 38).

$$\ln(1+x) = x - \frac{x^2}{2} + \frac{x^3}{3} - \frac{x^4}{4}..... \qquad -1 < x \le 1 \qquad \text{(eq 38)}$$

1. Derivation of the Cube-Root Law from the General Equation (eq 18). Equation 18 can be transformed to:

$$\frac{DC_S}{\rho h}t = a_0 - a + h\ln\left(1 + \frac{a-a_0}{h+a_0}\right) \qquad \text{(eq 39)}$$

To derive the Hixson−Crowell cube-root expression, it is necessary to assume that $h \ll a_0$ and $h \ll a$, so that $|(a - a_0)/(h + a_0)| < 1$. Applying the Taylor series expansion to eq 39 leads to:

$$\frac{DC_S}{\rho h}t = a_0 - a + h\left[\frac{a-a_0}{a_0+h} - \frac{1}{2}\left(\frac{a-a_0}{a_0+h}\right)^2 + \frac{1}{3}\left(\frac{a-a_0}{a_0+h}\right)^3 - \frac{1}{4}\left(\frac{a-a_0}{a_0+h}\right)^4.....\right]$$

$$= a_0 - a + (a-a_0)h\left[\frac{1}{a_0+h} - \frac{1}{2}\frac{(a-a_0)}{(a_0+h)^2} + \frac{1}{3}\frac{(a-a_0)^2}{(a_0+h)^3} - \frac{1}{4}\frac{(a-a_0)^3}{(a_0+h)^4}.....\right]$$

$$= (a_0-a)\left\{1 - \frac{h}{a_0+h}\left[1 - \frac{1}{2}\frac{(a-a_0)}{(a_0+h)} + \frac{1}{3}\frac{(a-a_0)^2}{(a_0+h)^2} - \frac{1}{4}\frac{(a-a_0)^3}{(a_0+h)}.....\right]\right\}$$

$$= (a_0-a)\left\{1 - \frac{h}{a_0+h}\left[1 + \frac{1}{2}\frac{a_0-a}{a_0+h} + \frac{1}{3}\left(\frac{a_0-a}{a_0+h}\right)^2 + \frac{1}{4}\left(\frac{a_0-a}{a_0+h}\right)^3.....\right]\right\} \qquad \text{(eq 40)}$$

Equation 40 can be written as eq 41,

$$\frac{DC_S}{\rho h} = (a_0 - a)(1 - P) \qquad \text{(eq 41)}$$

For the case where $a \geq 0.5a_0$, we have $(a_0 - a)/(a_0 + h) < {}^1/_2$, so,

$$P = \frac{h}{a_0 + h}\left[1 + \frac{1}{2}\frac{(a_0 - a)}{(a_0 + h)} + \frac{1}{3}\left(\frac{a_0 - a}{a_0 + h}\right)^2 + \frac{1}{4}\left(\frac{a_0 - a}{a_0 + h}\right)^3 \ldots\ldots\right]$$

$$< \frac{h}{a_0 + h}\left[1 + \frac{1}{2} \times \frac{1}{2} + \frac{1}{3}\left(\frac{1}{2}\right)^2 + \frac{1}{4}\left(\frac{1}{2}\right)^3 \ldots\ldots\right]$$

$$< \frac{h}{a_0 + h}\left[1 + \frac{1}{2} \times \frac{1}{2} + \frac{1}{2}\left(\frac{1}{2}\right)^2 + \frac{1}{2}\left(\frac{1}{2}\right)^3 \ldots\ldots\right]$$

$$= \frac{3}{2}\frac{h}{a_0 + h} \qquad \text{(eq 42)}$$

Since $a_0 \gg h$, we have $P \ll 1$, so eq 41 can be approximated by:

$$\frac{DC_S}{\rho h} t \approx a_0 - a \qquad \text{(eq 24)}$$

From eq 24, the cube-root law can be derived.

2. Derivation of Two-Thirds-Root Expression from the General Equation (eq 18). Equation 18 can be transformed to:

$$\frac{DC_S}{\rho h} t = a_0 - a - h \ln\left(\frac{h + a_0}{h} \times \frac{h}{h + a}\right) = a_0 - a - h\left[\ln\left(1 + \frac{a_0}{h}\right) - \ln\left(1 + \frac{a}{h}\right)\right] \qquad \text{(eq 43)}$$

In the case of the Higuchi–Hiestand two-thirds-root expression, it is necessary to assume that $h \gg a_0$ which leads to $a_0/h \ll 1$. Applying the Taylor series expansion to eq 43 gives:

$$\frac{DC_S}{\rho h} t = a_0 - a - h\left[\frac{a_0}{h} - \frac{1}{2}\left(\frac{a_0}{h}\right)^2 + \frac{1}{3}\left(\frac{a_0}{h}\right)^3 \ldots\ldots - \frac{a}{h} + \frac{1}{2}\left(\frac{a}{h}\right)^2 - \frac{1}{3}\left(\frac{a}{h}\right)^3 \ldots\ldots\right] \qquad \text{(eq 44)}$$

Since $a_0/h \ll 1$, eq 44 can be approximated by:

$$\frac{DC_S}{\rho h} t \approx a_0 - a - h\left[\frac{a_0}{h} - \frac{1}{2}\left(\frac{a_0}{h}\right)^2 - \frac{a}{h} + \frac{1}{2}\left(\frac{a}{h}\right)^2\right] = \frac{1}{2}\frac{(a_0^2 - a^2)}{h} \qquad \text{(eq 45)}$$

Rearranging eq 45 gives:

$$\frac{2DC_S}{\rho} t \approx a_0^2 - a^2 \qquad \text{(eq 25)}$$

From eq 25 the two-thirds-root expression of Higuchi and Hiestand can be derived.

Appendix II

The general solution for single spherical particle dissolution under nonsink conditions can also be derived in a similar manner as under sink conditions. If the initial bulk concentration is 0 and the solution volume (V) is kept constant, the bulk concentration (C_b) can be described by the following equation for single spherical particle dissolution:

$$C_b = \frac{\frac{4}{3}\pi(a_0^3 - a^3)\rho}{V} \qquad \text{(eq 46)}$$

Under nonsink conditions, eqs 5–8 are still valid, while eq 10 should be modified to give:

$$\int_a^{a+h} -\frac{a^2}{r^2} G(a)\, dr = C_S - C_b \qquad \text{(eq 47)}$$

Integrating eq 47 gives:

$$G(a) = -\left(\frac{1}{a} + \frac{1}{h}\right)(C_S - C_b) \qquad \text{(eq 48)}$$

Substituting eq 48 into eq 6 gives:

$$\frac{dQ}{dt} = 4\pi a^2 D\left(\frac{1}{a} + \frac{1}{h}\right)(C_S - C_b) \qquad \text{(eq 49)}$$

Equating eq 14 and eq 49 and rearranging gives:

$$-\frac{D}{\rho h}\, dt = \frac{a}{(a + h)(C_S - C_b)}\, da \qquad \text{(eq 50)}$$

The integral form of eq 50 is:

$$\int_0^t -\frac{D}{\rho h}\, dt = \int_{a_0}^{a} \frac{a}{(a + h)(C_S - C_b)}\, da \qquad \text{(eq 51)}$$

Substituting eq 46 into eq 51 gives:

$$\int_0^t -\frac{D}{\rho h}\, dt = \int_{a_0}^{a} \frac{a}{(a + h)\left(C_S - \frac{4}{3V}\pi a_0^3 \rho + \frac{4}{3V}\pi a^3 \rho\right)}\, da \qquad \text{(eq 52)}$$

Integrating eq 52 will lead to a relationship between particle radius and time. The integration is complex and only the final form is given below:

$$\frac{D}{\rho h V} t = \frac{1}{\beta - \alpha h^3}\{X + Y + Z\} \qquad \text{(eq 22)}$$

$$X = h \ln \frac{a + h}{a_0 + h} - \frac{h}{3} \ln \frac{\alpha a^3 + \beta}{\alpha a_0^3 + \beta}$$

$$Y = \frac{h^2}{\gamma}\left[\frac{1}{2} \ln \frac{(\alpha a^3 + \beta)(\gamma + a_0)^3}{(\gamma + a)^3(\alpha a_0^3 + \beta)} + \sqrt{3} \tan^{-1}\left(\frac{2a - \gamma}{\sqrt{3}\gamma}\right) - \sqrt{3} \tan^{-1}\left(\frac{2a_0 - \gamma}{\sqrt{3}\gamma}\right)\right]$$

$$Z = \frac{\gamma}{3}\left[\frac{1}{2} \ln \frac{(\alpha a^3 + \beta)(\gamma + a_0)^3}{(\gamma + a)^3(\alpha a_0^3 + \beta)} - \sqrt{3} \tan^{-1}\left(\frac{2a - \gamma}{\sqrt{3}\gamma}\right) + \sqrt{3} \tan^{-1}\left(\frac{2a_0 - \gamma}{\sqrt{3}\gamma}\right)\right]$$

In eq 22, α, β and γ are constants: $\alpha = 4\pi\rho/3$, $\beta = C_S V - 4\pi a_0^3 \rho/3$, $\gamma = (\beta/\alpha)^{1/3}$. For N monodispersed particles, eq

22 is essentially the same except that $C_b = [4\pi(a_0^3 - a^3)\rho N/3]/V$, correspondingly, the values of α and β become $\alpha = {}^4/_3\pi\rho N$, $\beta = C_S V - {}^4/_3\pi a_0^3\rho N$. Weight undissolved ($w$) expressions can be obtained by substituting $a = (3w/4\pi\rho)^{1/3}$ in eq 22.

A special case arises when the initial particle weight (w_0) exactly equals the amount necessary to saturate the solution. In this case, the above equation does not work ($\beta = 0$) and a special equation needs to be derived where:

$$C_S = \frac{4}{3V}\pi a_0^3\rho \qquad \text{(eq 53)}$$

Thus, eq 52 becomes:

$$\int_0^t -\frac{D}{\rho h}\,dt = \int_{a_0}^{a} \frac{1}{\frac{4}{3V}\pi a^2\rho(a+h)}\,da \qquad \text{(eq 54)}$$

Integrating both sides of eq 54 gives:

$$\frac{4D\pi}{3V}\,t = \frac{1}{a} - \frac{1}{a_0} + \frac{1}{h}\ln\frac{a(a_0+h)}{a_0(a+h)} \qquad \text{(eq 55)}$$

Substituting for V using eq 53 into the left-hand side of eq 55 gives:

$$\frac{DC_S}{a_0^3\rho}\,t = \frac{1}{a} - \frac{1}{a_0} + \frac{1}{h}\ln\frac{a(a_0+h)}{a_0(a+h)} \qquad \text{(eq 56)}$$

For N monodispersed particles, $C_S = 4\pi a_0^3\rho N/3V$ and the final equation becomes:

$$\frac{DC_S}{a_0^3\rho N}\,t = \frac{1}{a} - \frac{1}{a_0} + \frac{1}{h}\ln\frac{a(a_0+h)}{a_0(a+h)} \qquad \text{(eq 23)}$$

References and Notes

1. Noyes, A.; Whitney, W. R. The Rate of Solution of Solid Substances in their own Solutions. *J. Am. Chem. Soc.* **1897**, *19*, 930−934.
2. Nernst, W. Theorie der Reaktionsgeschwindigkeit in Heterogenen Systemen. *Z. Physik. Chem.* **1904**, *47*, 52−55.
3. Brunner, E. Reaktionsgeschwindigkeit in Heterogenen Systemen. *Z. Physik. Chem.* **1904**, *47*, 56−102.
4. King, C. V. Reaction Rates at Solid−Liquid Interfaces. *J. Am. Chem. Soc.* **1935**, *57*, 828−831.
5. Hixson, A. W.; Crowell, J. H. Dependence of Reaction Velocity upon Surface and Agitation I − Theoretical Consideration. *Ind. Eng. Chem.* **1931**, *23*, 923−931.
6. Niebergall, P. J.; Milosovich, G.; Goyan, J. E. Dissolution Rate Studies II. Dissolution of Particles Under Conditions of Rapid Agitation. *J. Pharm. Sci.* **1963**, *52*, 236−241.
7. Higuchi, W. I.; Hiestand, E. N. Dissolution Rates of Finely Divided Drug Powders I. Effect of a Distribution of Particle Size in a Diffusion-Controlled Process. *J. Pharm. Sci.* **1963**, *52*, 67−71.
8. Hixson, A. W.; Crowell, J. H. Dependence of Reaction Velocity upon Surface and Agitation II − Experimental Procedure in Study of Surface. *Ind. Eng. Chem.* **1931**, *23*, 1002−1009.
9. Higuchi, W. I.; Rowe, E. L.; Hiestand, E. N. Dissolution Rates of Finely Divided Drug Powders II. Micronized Methylprednisolone. *J. Pharm. Sci.* **1963**, *52*, 163−164.
10. De Almeida, L. P.; Simões, S.; Brito, P.; et al. Modeling Dissolution of Sparingly Soluble Multisized Powders. *J. Pharm. Sci.* **1997**, *86*, 726−732.
11. Pedersen, V. P.; Brown, K. F. Experimental Evaluations of Three Single-Particle Dissolution Models. *J. Pharm. Sci.* **1976**, *65*, 1442−1447.
12. Lu, A. T. K.; Frisella, M. E.; Johnson, K. C. Dissolution Modeling: Factors Affecting the Dissolution Rates of Polydisperse Powders. *Pharm. Res.* **1993**, *10*, 1308−1314
13. Bisrat, M.; Nyström, C. Physicochemical Aspects of Drug Release. VIII. The Relation between Particle Size and Surface-Specific Dissolution Rate in Agitated Suspensions. *Int. J. Pharm.* **1988**, *47*, 223−231.
14. Anderberg, E. K.; Nyström, C. Physicochemical Aspects of Drug Release X. Investigation of the Applicability of the Cube-Root Law for Characterization of the Dissolution Rate of Fine Particulate Materials. *Int. J. Pharm.* **1990**, *62*, 143−151.
15. Steady-state and pseudo-steady-state are important concepts in this paper. Dissolution from a planar surface under sink conditions reaches steady-state when the dissolution rate becomes constant; hence, the concentration gradient in the diffusion layer becomes time-invariant. Dissolution of a spherical surface will not reach steady-state because its surface area decreases with time and the concentration gradient is not time-invariant. However, a pseudo-steady-state may exist in which the following approximation is accurate—the overall mass transport rates across the inner and outer spherical surfaces (at $r = a$ and $a + h$) of the diffusion layer are equal. This assumption requires that within the time for an average molecule to cross the diffusion layer, the change of particle surface area is negligible.
16. In the derivation of the two-thirds-root expression (Higuchi and Hiestand), it was assumed that the fluid is perfectly stagnant and the diffusion equation for spherical geometry was solved. This case is mathematically equivalent to assuming a linear concentration gradient in a diffusion layer of thickness equal to the particle radius. This mathematical identity is just a coincidence and does not have any mechanistic significance.
17. Anderberg, E. K.; Bisrat, M.; Nyström, C. Physicochemical Aspects of Drug Release VII. The Effect of Surfactant Concentration and Drug Particle Size on Solubility and Dissolution Rate of Felodipine, a Sparingly Soluble Drug. *Int. J. Pharm.* **1988**, *47*, 67−77.
18. Harriott, P. Mass Transfer to Particles: Part I. Suspended in Agitated Tanks. *AIChE J.* **1962**, *8*, 93−101.

JS980236P

A publication of the **American Pharmaceutical Association** and the **American Chemical Society**

JOURNAL OF
Pharmaceutical Sciences

August 1999
Volume 88, Number 8

RESEARCH ARTICLES

Metabolic Stability of Glutaraldehyde Cross-Linked Peptide DNA Condensates

ROGER C. ADAMI[†] AND KEVIN G. RICE[*,†,‡]

Contribution from *Divisions of Pharmaceutics and Medicinal Chemistry, College of Pharmacy, University of Michigan, Ann Arbor, Michigan 48109-1065.*

Received February 8, 1999. Accepted for publication May 25, 1999.

Abstract ☐ The stability of peptide DNA condensates was examined after introducing glutaraldehyde to cross-link surface amine groups. A 20 amino acid peptide (CWK_{18}) was used to condense DNA into small (70 nm) condensates. The reaction between glutaraldehyde and peptide DNA condensates was indirectly monitored using a fluorescence-based assay to establish reaction completion in 4–5 h when using glutaraldehyde-to-peptide ratios of 1 to 4 mol equiv. Higher levels of glutaraldehyde cross-linking led to significant increases in particle size. The improved stability imparted by glutaraldehyde cross-linking was demonstrated by the increased resistance of DNA condensates to shear stress induced fragmentation. The cross-linked condensates were also significantly more resistant to in vitro metabolism by serum endonucleases. A decrease in the magnitude of transient gene expression was determined for cross-linked DNA condensates which also resulted in a 10-day steady-state expression when cross-linking with 4 mol equiv of glutaraldehyde. The results suggest that cross-linking DNA condensates may provide a means to alter the time course of transient gene expression by inhibiting DNA metabolism.

Introduction

To achieve optimal and prolonged gene expression, carrier molecules are used to protect plasmid DNA from metabolism while en route, and once inside the target cell. Strategies to enhance nonviral DNA delivery have focused on the use of cationic carriers such as lipids, peptides, and polymers that bind DNA through ionic interaction.[1−5] In each case, ion pairing leads to varying degrees of DNA condensation, resulting in cationic particles that internalize into cells and mediate transient gene expression.[6]

To be effective in delivering DNA, carrier molecules must have low toxicity, exhibit low levels of antigenicity or complement activation, and protect DNA from degradation.[7] Simultaneously addressing each of these has been one of the major impediments to developing highly effective in vivo gene delivery formulations.[1,8]

The stability of DNA condensates in serum is dependent on the nature and affinity of a carrier molecule for binding DNA, the ionic strength, the concentration of endonuclease, and the presence of molecules that compete for carrier binding. Dissociation of the carrier molecule in serum exposes DNA to metabolizing endonuclease leading to premature degradation.[9]

Only a few studies have addressed the issue of DNA metabolism despite its obvious relationship to the level and duration of gene expression.[9−13] Early studies by Wu and co-workers concluded that high molecular weight (HMW) polylysines could protect DNA from rapid metabolism in vitro for up to 1.5 h.[13] Subsequent studies by our group determined that a 20 amino acid peptide (CWK_{18}) was sufficient to stabilize DNA condensates from in vitro metabolism.[14] Despite the ability of HMW polylysines to retard metabolism, the associated toxicity of these polymers has prompted the search for LMW carriers for use in vivo.[15]

An alternative strategy to achieve high affinity using LMW carriers is to provide temporary stability through

* To whom correspondence should be addressed. Tel: 734-763-1032, fax: 734-763-2022, email: krice@umich.edu.
[†] Division of Pharmaceutics.
[‡] Division of Medicinal Chemistry.

10.1021/js990042p CCC: $18.00
Published on Web 07/14/1999

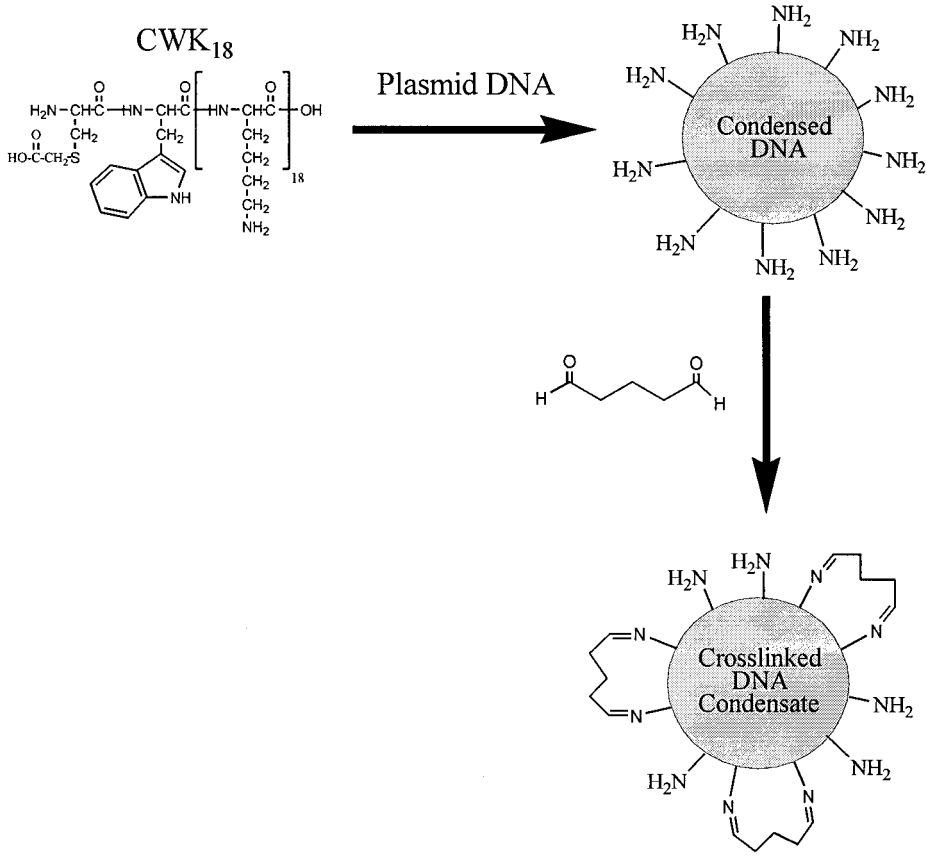

Figure 1—Glutaraldehyde cross-linking DNA condensates. CWK_{18} binds to plasmid DNA to spontaneously form condensed DNA possessing residual surface amines. Glutaraldehdye is reacted with condensed DNA resulting in the formation of two Schiff-bases between neighboring amine groups resulting in cross-linked DNA condensates. The degree of cross-linking is expressed as the mols of glutaraldehyde added relative to mols of CWK_{18}.

molecular cross-linking of carriers on DNA condensates. The unpaired amines on the surface of peptide DNA condensates could potentially be cross-linked with a variety of agents.

Glutaraldehyde is a five-carbon dialdehyde which has long been used as a reagent to increase the tensile strength of transplanted pig heart valves and develop controlled release microspheres for drug delivery.[16−18] The chemical cross-linking of albumin lysines with glutaraldehyde leads to particles which have controlled drug release properties.[19,20] The degree of cross-linking directly affects the particle size, biodegradation, and release properties of drugs encapsulated in glutaraldehyde cross-linked microspheres.[17,18,21]

In the present study, we report the use of glutaraldehyde to cross-link DNA condensates in an attempt to improve their metabolic stability and alter the resulting transient gene expression profiles in vitro. The results indicate that cross-linking can be used to enhance the stability of LMW peptide DNA condensates and leads to steady-state transient gene expression. These attributes may allow the design of nonviral gene delivery carriers that mediate prolonged transient gene expression in vivo.

Materials and Methods

CWK_{18} (alkylated Cys-Trp-Lys_{18}) and dimeric CWK_{18} were synthesized and characterized as described previously.[22] Glutaraldehyde, SDS, ethidium bromide, proteinase K, DNase I (EC 3.1.21.1) from bovine pancreas, and polylysine$_{99}$, polylysine$_{476}$, and polylysine$_{1007}$ were obtained from Sigma. pSEAP (plasmid secreted alkaline phosphatase with SV40 promoter and late polyadenylation sequence) and SEAP chemiluminescent detection kit were obtained from Clontech. pSEAP was grown in *Escherichia coli* and purified using a Qiagen miniprep column (Valencia, CA). TPCK-treated trypsin was obtained from Worthington Biochemicals (Freehold, NJ). Bradford protein assay was obtained from BioRad (Hercules, CA). MEM, fetal calf serum and electrophoresis grade agarose were obtained from Gibco BRL (Gaithersburg, MD). SYBR-Gold was obtained from Molecular Probes (Eugene, OR).

Preparation and Characterization of Cross-Linked DNA Condensates—CWK_{18} DNA condensates were formed by adding 10 μg (100 μL) of pSEAP (4.7 kBp) to 3 nmol of CWK_{18} in 100 μL of 5 mM HEPES, pH 7.4, while vortexing to prepare DNA condensates possessing a calculated charge ratio (amine:phosphate) of 2:1. HMW polylysines$_{99-1007}$ were prepared at 10 mg/mL in HEPES and used to form DNA condensates at a 2:1 amine:phosphate ratio for each.

After 30 min, CWK_{18} DNA condensates were reacted with either 3, 6, 9, or 12 nmol of glutaraldehyde (1 nmol/μL) for 12 h at 4 °C resulting in 1, 2, 3, or 4 mol equiv (mol of glutaraldehyde per mol of CWK_{18}) of cross-linking. The reaction of glutaraldehyde with DNA condensates was studied using a fluorophore exclusion assay. Following the addition of glutaraldehyde, 10 μL aliquots were removed at time intervals ranging from 0 to 5 h and immediately combined with 490 μL of 0.35 M sodium chloride. Prior to measuring fluorescence, 10 μL of SYBR-Gold (diluted 1:200 in DMSO) was added, and the fluorescence intensity (Ex: 495 nm, Em: 537 nm) was measured on a Perkin-Elmer LS-50B fluorimeter.

The particle size of cross-linked DNA condensates was measured using 350 μL of 50 μg/mL DNA condensate in HEPES by quasielastic light scattering (QELS). ζ potential measurements were conducted at the same DNA concentration in HEPES using an average of 10 runs to determine the mean and standard deviation on a Brookhaven ZetaPlus.

Shear Stress Stability of DNA Condensates—Peptide DNA condensates (200 μL) were combined with 0−90 μL of 5 M sodium chloride and normalized with HEPES to a final volume of 300 μL to obtain a final concentration of 0, 0.1, 0.3, 0.5, 0.7, 0.9, 1.2, or 1.5 M sodium chloride. A 100 W Microson XL-2000 ultrasonic

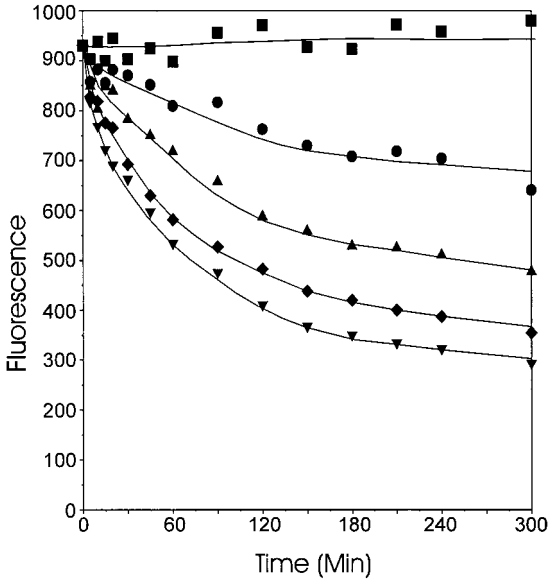

Figure 2—Kinetics of glutaraldehyde cross-linking CWK_{18} DNA condensates. The reaction between glutaraldehyde and condensed DNA was measured indirectly by a fluorescence assay described in Materials and Methods. An inverse relationship between the amount of glutaraldehyde added and fluorescence intensity indicated an increased reaction rate corresponding to increased glutaraldehyde cross-linking. The data represents un-cross-linked (■), 1 mol equiv (●), 2 mol equiv (▲), 3 mol equiv (◆), and 4 mol equiv (▼) cross-linked DNA condensates.

probe homogenizer (Kontes, Vineland, NJ) set at a vibrational amplitude of 5 was used throughout the study. The probe tip was placed $^3/_4$ depth into a 1.5 mL microfuge tube containing 300 μL of sample and then sonicated for 30 s. DNA samples (15 μL) were brought to 1 M sodium chloride by adding 4.6 μL of 5 M sodium chloride and then digested with trypsin (3 μL containing 7 U) for 12 h at 37 °C. The samples were combined with 3 μL of loading buffer, and 18 μL was applied to a 1% agarose gel (50 mL) containing 0.5 μg/mL ethidium bromide. The gel was electrophoresed in TAE buffer at 70 V for 80 min followed by 12 h destaining in deionized water. Transilluminated gels were photographed on polaroid 667 film.

Serum Stability of DNA Condensates—DNA condensates (100 μL) were combined with 100 μL of DNase I augmented mouse serum (0.12 U of DNase I per 100 μL serum) and 3 μL of 5 M sodium chloride to bring the final salt concentration to 150 mM. Samples were incubated at 37 °C for 3 h while withdrawing 20 μL aliquots that were rapidly frozen at time points ranging from 0 to 180 min. Serum samples were processed by adding 3 μL (0.31 U) of proteinase K and then incubated at 37 °C for 30 min to remove endonuclease activity. Sodium chloride was then added (4.6 μL of 5 M) along with trypsin (3 μL containing 7 U) and allowed to digest for 12 h at 37 °C to remove the cross-linked peptide. Samples were applied to a 1% agarose gel containing 0.05% SDS and electrophoresed as described above.

Transient Gene Expression—HepG2 cells (3×10^5) were plated on 6 × 35 mm wells and grown for 48 h to 40% confluence in MEM supplemented with 10% fetal calf serum (FCS). Cross-linked DNA condensates (10 μg of DNA in 200 μL) were transfected in triplicate by dropwise addition to cells in 10% FCS either with or without 80 μM chloroquine followed by 5 h incubation, after which the media was replaced with 2 mL of MEM containing 10% fetal calf serum and allowed to incubate for an additional 19 h. Wells were sampled for 10-days at 24 h intervals by removing and freezing (−20 °C) the media and replacing it with 2 mL of fresh 10% FCS MEM. The amount of heat-stable SEAP in each well was determined using a chemiluminescent kit. Media (50 μL) was combined with 50 μL of dilution buffer followed by incubation at 65 °C for 30 min to denature endogenous alkaline phosphatase. Assay buffer (100 μL) was added and incubated for 10 min at 25 °C followed by the addition of CSPD [(disodium 3-(4-methoxyspiro-{1,2-dioxetane-3,2′-(5′-chloro) tricyclo [3.3.1.1^{3,7}] decan}-4-yl) phenyl phosphate)] substrate in chemiluminescent enhancer. After 30 min, the luminescence was measured with a 10 s integration on a Berthold Lumat LB 9501 luminometer. Light units were converted to μg/mL of SEAP using a standard curve constructed by adding known quantities of SEAP to cell homogenate. Residual endogenous alkaline phosphatase background was determined from a 10-day null control and subtracted from each data set.

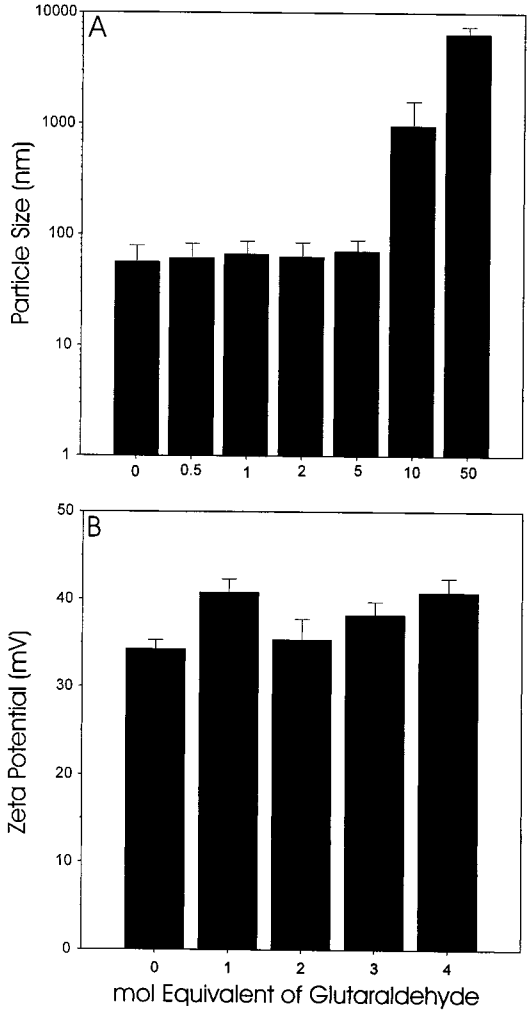

Figure 3—Particle size and ζ potential analysis of cross-linked DNA condensates. CWK_{18} DNA condensates cross-linked with 0–5 mol equiv of glutaraldehyde exhibited particle sizes between 55 and 70 nm as shown in panel A. At concentrations of 10 and 50 mol equiv of glutaraldehyde the particle size increased by 1 and 2 orders of magnitude (panel A). Condensates prepared at 0–4 mol equiv of glutaraldehyde had a ζ potential between +34–41 mV (panel B).

Results

The metabolic stability and transient gene expression was investigated in relationship to the degree of cross-linking applied to peptide DNA condensates. Peptide DNA condensates are colloids that possess primary amines on their surface that can be cross-linked with homobifunctional agents such as glutaraldehyde (Figure 1). The resulting interpeptide cross-links should stabilize condensed DNA from peptide dissociation and from metabolism since it has been previously established that condensed DNA resists endonuclease attack.[13,14]

To establish that glutaraldehyde reacts with DNA condensates to form interpeptide cross-links the time course of the reaction was monitored indirectly using a fluorescent intercalator dye. SYBR-Gold was selected since its intercalation into DNA is not significantly inhibited in sodium chloride up to 1 M. In the absence of sodium

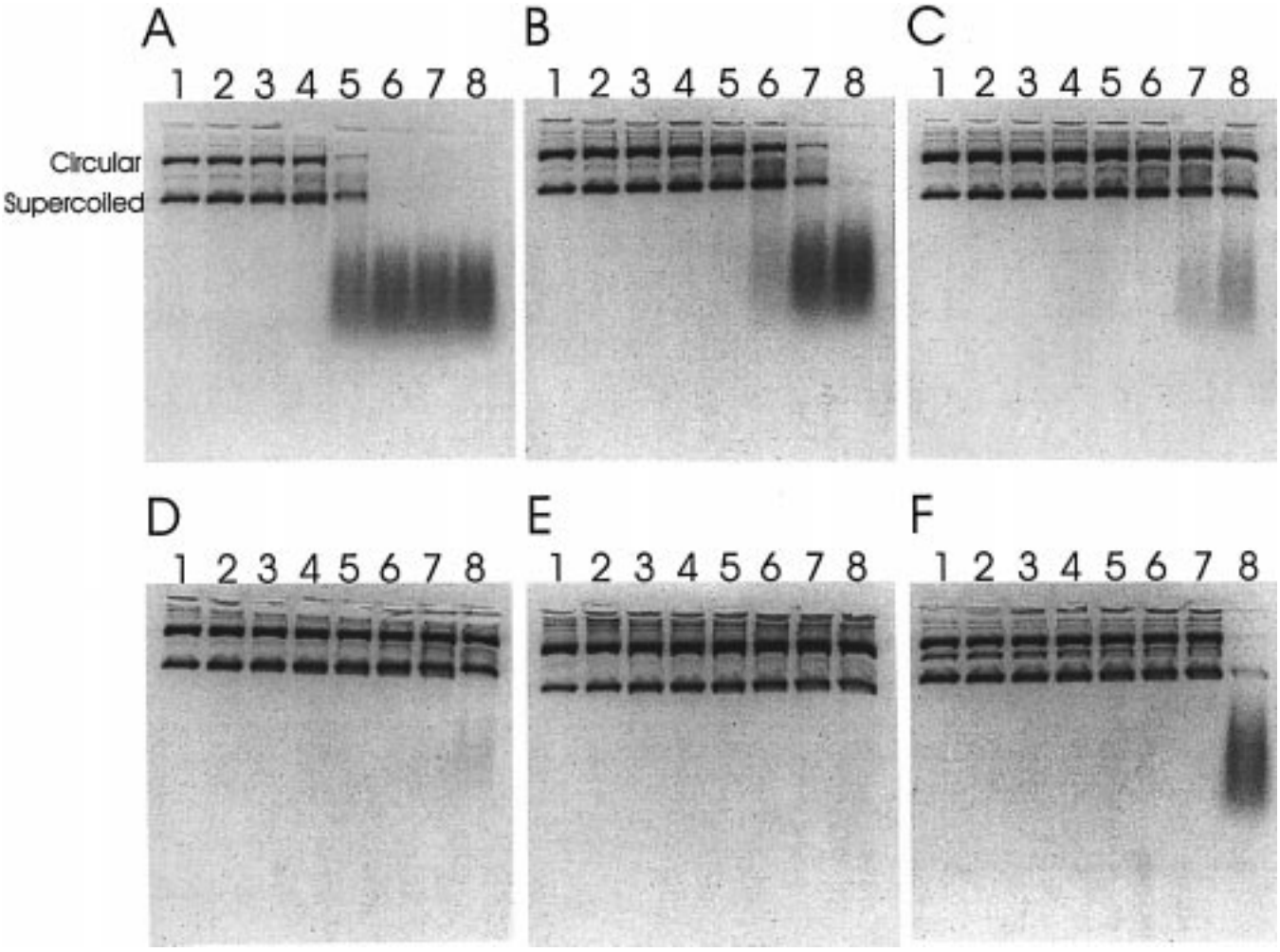

Figure 4—Shear stress stability of cross-linked DNA condensates. The stability of cross-linked DNA condensates was measured by 30 s 100 W sonication in the presence of increasing sodium chloride concentration as described in Methods and Methods. The electrophoretic analysis of CWK_{18} DNA condensates prepared with 0 (A), 1 (B), 2 (C), 3 (D) and 4 (E) mol equiv of glutaraldehyde were compared to $polylysine_{1007}$ DNA condensates (F). Lanes 1 through 8 contain 0, 0.1, 0.3, 0.5, 0.7, 0.9, 1.2, and 1.5 M sodium chloride. The dissociation of CWK_{18} from DNA occurs at 0.7 M sodium chloride (panel A, lane 5) as determined by the formation of fragments during sonication. Alternatively, 1 mol equiv of glutaraldehyde extended the DNA stability to 0.9 M sodium chloride (panel B, lane 6), 2 mol equiv of glutaraldehyde increased the stability to 1.2 M sodium chloride (panel C, lane 7), and 3 and 4 mol equiv of glutaraldehyde resulted in DNA condensates that were stable in 1.5 M sodium chloride (panels D and E). In contrast, $polylysine_{1007}$ DNA condensates dissociate in 1.5 M sodium chloride (panel F, lane 8). Each result was replicated twice.

chloride, the reaction of SYBR-Gold with CWK_{18} DNA condensates produces minimal fluorescence whereas the partial dissociation of condensates that occurred in 0.35 M sodium chloride produced a maximal fluorescence following intercalation (Figure 2). After the addition of glutaraldehyde, the formation of interpeptide cross-links stabilized CWK_{18} DNA condensates from dissociating in 0.35 M sodium chloride, leading to a decrease in the fluorescence intensity as the reaction proceeded over 5 h (Figure 2). Analysis of the reaction profile while varying the stoichiometry of glutaraldehyde from 1 to 4 mol equiv established a progressive decrease in fluorescence intensity that approached reaction completion in 5 h, suggesting that increasing the glutaraldehyde concentration leads to the formation of additional cross-links and further stabilization of DNA condensates (Figure 2).

Since glutaraldehyde could potentially also produce interparticle cross-links leading to larger DNA condensates, the relationship between the degree of cross-linking and the particle size was investigated by QELS analysis. DNA condensates prepared with 1 to 5 mol equiv of glutaraldehyde maintained a particle size of 55−70 nm, whereas stoichiometries of 10 mol equiv or higher caused a significant increase in size suggesting the formation of interparticle cross-links (Figure 3A). At 4 mol equiv of glutaraldehyde or lower, the ζ potential of DNA condensates remained between +34−41 mV, establishing minimal change in the overall charge of DNA condensates (Figure 3B).

The shear stress stability of glutaraldehyde cross-linked DNA condensates was evaluated by gel electrophoresis. CWK_{18} DNA condensates resist fragmentation when subjected to 30 s sonication until the sodium chloride concentration reached 0.7 M or higher, causing dissociation of peptide resulting in DNA fragmentation during sonication (Figure 4A). By comparison, DNA condensates cross-linked with 1 mol equiv of glutaraldehyde resist fragmentation in 0.9 M sodium chloride (Figure 4B). Reaction with 2 mol equiv of glutaraldehyde led to further stabilization resulting in condensates that resist fragmentation in 1.2 M sodium chloride (Figure 4C). Increasing the cross-linking to 3 and 4 mol equiv of glutaraldehyde resulted in DNA condensates that were stable up to 1.5 M sodium chloride (Figure 4D and 4E). Alternatively, $polylysine_{1007}$ DNA condensates were found to be less stable, undergoing fragmentation during sonication in 1.5 M sodium chloride (Figure 4F). These results suggest that the interpeptide cross-links formed with 3 and 4 mol equiv of glutaraldehyde extend the stability of CWK_{18} DNA condensates beyond

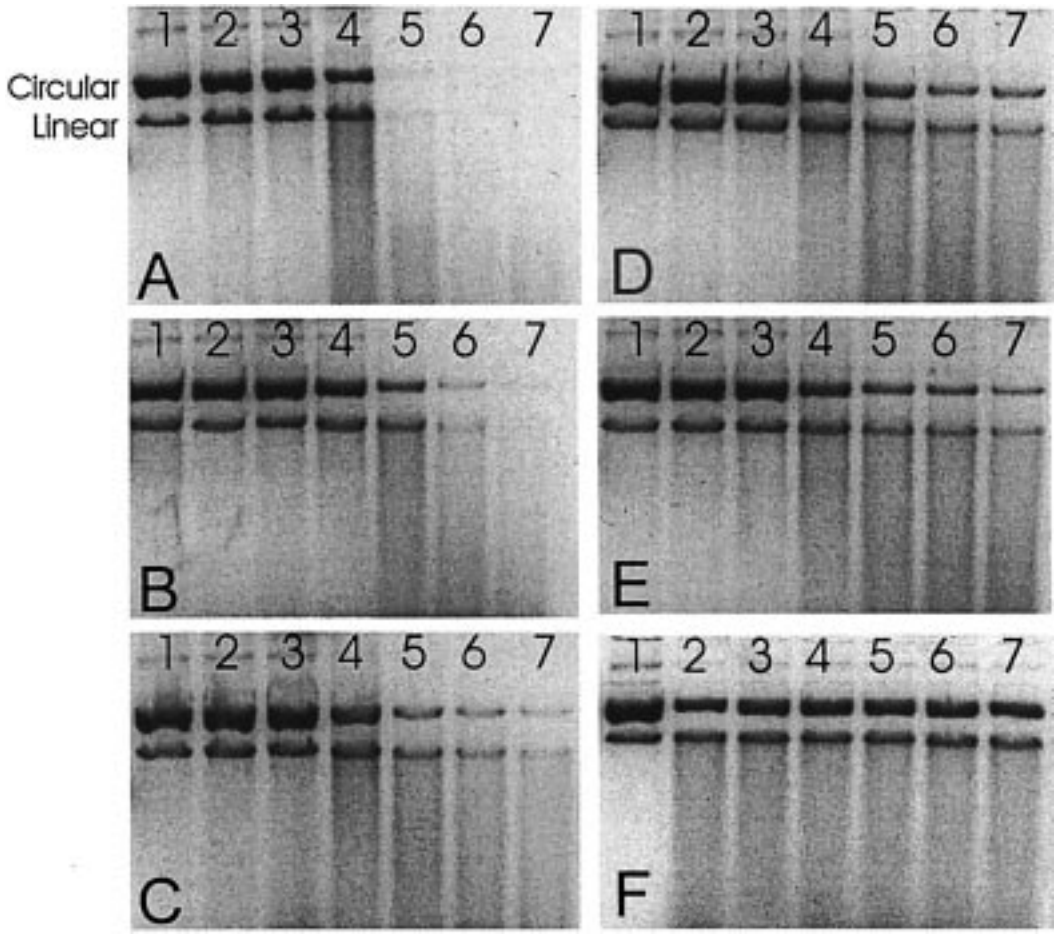

Figure 5—Serum stability of cross-linked condensates. The serum stability of DNA condensates cross-linked with 0 (A), 1 (B), 2 (C), 3 (D) and 4 (E) mol equiv of glutaraldehyde are compared to polylysine$_{1007}$ DNA condensates (F) using gel electrophoresis. Lanes 1 through 7 correspond to 0, 15, 30, 60, 90, 120, and 180 min digestion period. DNA stability was determined by observing a progressive decrease in the intensity of the circular and linear bands during the digestion, ultimately leading to the disappearance of the bands. Metabolism was evident from a decrease in band intensity leading to the complete disappearance of bands after 60 min for un-cross-linked DNA condensates (panel A, lane 4). DNA condensates prepared with 1 mol equiv of glutaraldehyde were delayed in metabolism until 90 min (panel B, lane 5). DNA condensates prepared with 2, 3, and 4 mol equiv of glutaraldehyde were significantly more protected from metabolism during the 180 min digestion, exhibiting only a decrease in the band intensity for circular and linear DNA (panels C–D, lanes 5–7). Polylysine$_{1007}$ was better than cross-linked condensates at protecting DNA throughout the 180 min digestion (panel F). Each results was replicated twice.

that achievable with a HMW polylysine. Control experiments established that plasmid DNA did not change its gel electrophoretic banding pattern when reacted with glutaraldehyde, suggesting that the exocylic amines on plasmid DNA bases are inexcessible to Schiff-base formation.

To be effective in gene delivery, cross-linked DNA condensates should also resist digestion with serum endonucleases. The metabolic stability of DNA was examined by gel electrophoretic analysis of DNA condensates incubated in mouse serum. Since un-cross-linked CWK_{18} DNA condensates proved to be resistant to endogenous serum endonuclease during a 24 h incubation, exogenous DNase I was added to accelerate the metabolism into a 3 h time period. Incubation of CWK_{18} DNA condensates in 50% serum containing 0.12 units of DNase I resulted in metabolism into oligonucleotides after 60 min (Figure 5A, lane 5). A trypsin contaminant produced a single strand nick in the DNA, such that even at time zero only circular and linear forms of DNA were recovered. Cross-linking CWK_{18} DNA condensates with 1−4 mol equiv of glutaraldehyde produced a progressive increase in metabolic stability with even 1 mol equiv of glutaraldehyde extending the stability of DNA condensates from 60 to 90 min (Figure 5B). The addition of 2 to 4 mol equiv extended the stability even further as evidenced by an increase in band intensity at 90 to 180 min (Figure 5C−E). By comparison, polylysine$_{1007}$ DNA condensates demonstrate improved serum stability to that of glutaraldehyde cross-linking at 4 mol equiv (Figure 5F).

The cytotoxicity of both free glutaraldehyde and cross-linked DNA condensates were examined in cell culture. The total protein of cell homogenates harvested 24 h after transfecting cells in the presence of free glutaraldehyde or cross-linked DNA condensates were indistinguishable from control, indicating no toxicity when using 1−4 mol equiv of glutaraldehyde corresponding to 1.5−6 μM.

The ability of cross-linked DNA condensates to release DNA and mediate gene transfer was examined by measuring the alkaline phosphatase secreted from HepG2 cells over a 10-day period. When using chloroquine to augment endosomal escape and increase gene expression, un-cross-linked peptide DNA condensates produced a transient gene expression profile that peaked around day 3−4 and then decreased to near background by day 10 (Figure 6A), with total transgene expression reaching 1.5 μg (Figure 6B). The moderate increase in stability afforded by 1 mol equiv of glutaraldehyde resulted in an expression profile and cumulative SEAP production identical to that afforded by un-cross-linked condensates. Alternatively, cross-linking with 2 mol equiv of glutaraldehyde resulted in a peak expression level that was nearly 2-fold greater than un-cross-linked DNA condensates (Figure 6A). These results are in contrast with those using 3 mol equiv of glutaral-

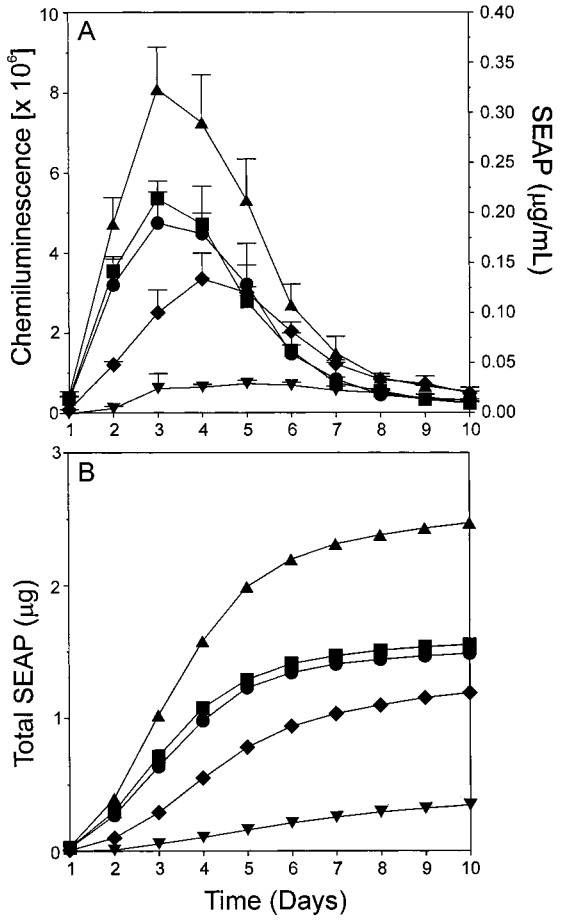

Figure 6—Transient gene expression profiles for cross-linked DNA condensates in the presence of chloroquine. The 10-day HepG2 SEAP expression profiles for cross-linked DNA condensates when including chloroquine in the transfection are shown in panel A. The data represents the mean and standard deviation when using un-cross-linked (■), 1 mol equiv (●), 2 mol equiv (▲), 3 mol equiv (◆), and 4 mol equiv (▼) cross-linked DNA condensates. The cumulative SEAP production for each DNA condensate is plotted in panel B. The slope of the day 7–10 cumulative expression was 28.3 ng/mL ■, 26.8 ng/mL ●, 52.8 ng/mL ▲, and 52.9 ng/mL ◆ with $r^2 \geq 0.965$ for each.

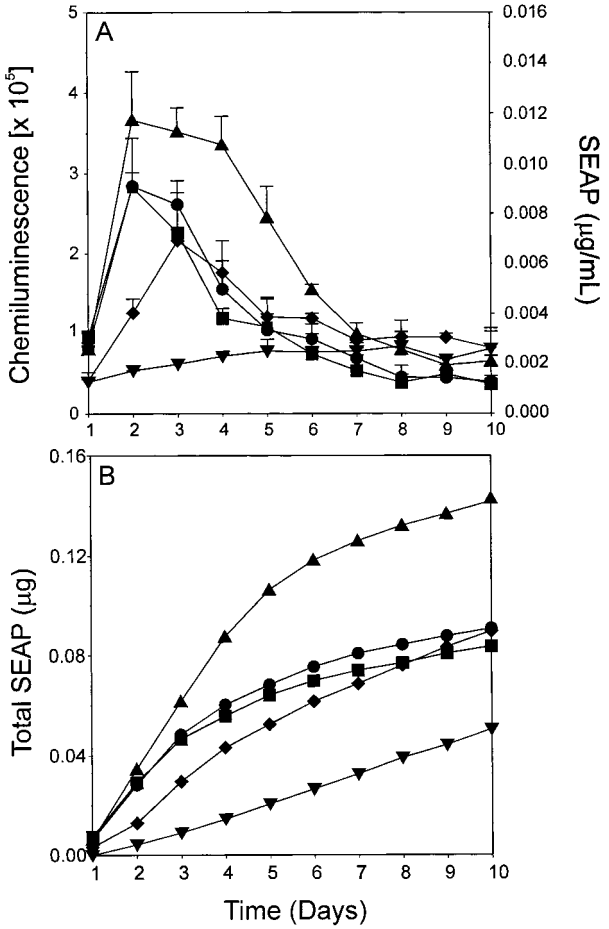

Figure 7—Transient gene expression profiles for cross-linked DNA condensates in the absence of chloroquine. The 10-day HepG2 SEAP expression profile mediated for cross-linked DNA condensates when omitting chloroquine from the transfection are shown in panel A. The data represents the mean and standard deviations when using un-cross-linked (■), 1 mol equiv (●), 2 mol equiv (▲), 3 mol equiv (◆), and 4 mol equiv (▼) cross-linked DNA condensates. The cumulative SEAP production for each DNA condensate is plotted in panel B. The slope of the day 7–10 cumulative expression was 3.3 ng/mL ■, 3.4 ng/mL ●, 5.2 ng/mL ▲, and 7.1 ng/mL ◆ with $r^2 \geq 0.996$ for each.

dehyde which led to a 30% decrease in the maximal expression level. Likewise, the maximal expression determined for 4 mol equiv cross-linked DNA condensate was reduced by approximately 80% compared to CWK_{18} DNA condensates.

Comparison of the cumulative SEAP production for each condensate established a range of 0.3 to 2.2 μg over the 10-day period (Figure 6B). Un-cross-linked condensates and cross-linked condensates possessing 1−3 mol equiv of glutaraldehyde approached a plateau in total SEAP production at day 6. The day 7−10 SEAP production for 2 and 3 mol equiv cross-linked DNA continued at a rate that was 2-fold greater than that of un-cross-linked or 1 mol equiv cross-linked DNA condensates as determined by linear regression of days 7−10. However, the SEAP production mediated by CWK_{18} DNA condensates cross-linked with 4 mol equiv of glutaraldehyde was constant throughout day 1−10 resulting in a linear regression line with a slope of 42 ng/day and $r^2 = 0.986$ (Figure 6B).

When chloroquine was omitted from the assay, the transient gene expression mediated by each peptide DNA condensate was reduced by over 1 order of magnitude (Figure 7A). As was also found for transfection in the presence of chloroquine, the cumulative gene production for 2 and 3 mol equiv cross-linked DNA condensates produced day 7−10 slopes that were 2-fold greater than un-cross-linked or 1 mol equiv cross-linked DNA condensates (Figure 7B). In addition, the cumulative expression for day 1−10 was linear ($r^2 = 0.999$) with a slope of 5.7 ng/day when using 4 mol equiv of glutaraldehyde to cross-link DNA condensates, indicating a steady-state expression of SEAP (Figure 7B).

A possible consequence of glutaraldehyde cross-linking could be the formation of long polylysine chains. To confirm that the expression profiles are not the result of linear polymerization of CWK_{18} the transient gene expression profile was studied using DNA condensates prepared with a panel of HMW polylysines (Figure 8A). The expression of SEAP exhibited a peak intensity correlating directly with the increase in chain length of polylysine, with each peptide DNA condensate mediating a maximum in the gene expression at day 3−4 (Figure 8A). Dimeric CWK_{18} DNA condensates produced approximately 10% more gene product relative to CWK_{18} DNA condensates. $Polylysine_{99}$ resulted in nearly 1.5-fold greater gene expression, whereas the greatest levels of transient gene expression were achieved with $polylysine_{476 \text{ and } 1007}$ DNA condensates which produced 2.1 and 3.2-fold greater gene expression than CWK_{18} DNA condensates (Figure 8B). Likewise, the cumulative SEAP expression for days 7−10 also demon-

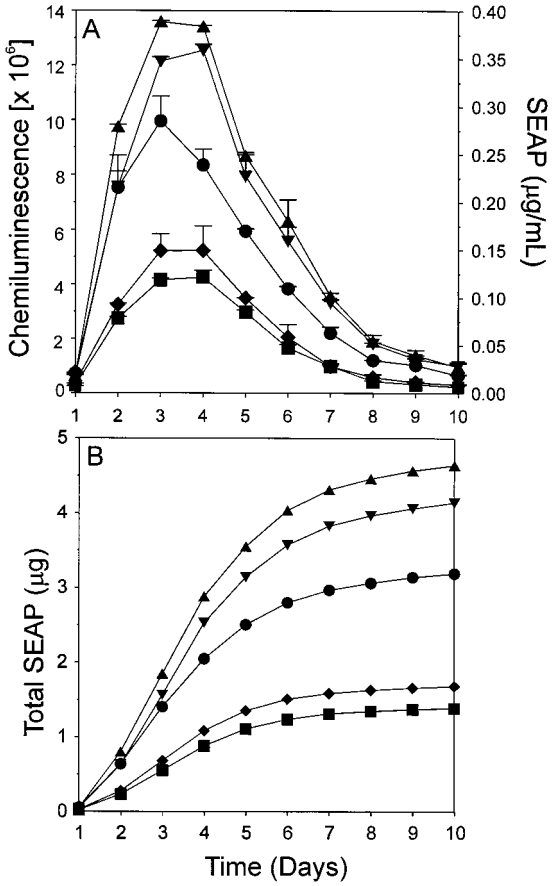

Figure 8—Transient gene expression profiles for HMW polylysine DNA condensates. The 10-day HepG2 SEAP expression profiles are compared for CWK_{18} (■), dimeric-CWK_{18} (◆), polylysine$_{99}$ (●), polylysine$_{476}$ (▼), and polylysine$_{1007}$ (▲) DNA condensates when including chloroquine in the transfection are shown in panel A. The cumulative SEAP production for each DNA condensate is plotted in panel B. The slope of the day 7–10 cumulative expression was 25.5 ng/mL ■, 32.7 ng/mL ◆, 74.7 ng/mL ●, 103.7 ng/mL ▼ and 109.3 ng/mL ▲ with $r^2 \geq 0.978$ for each.

strated a 3-fold increase in slope when comparing CWK_{18} DNA and polylysine$_{1007}$ DNA condensates.

Discussion

The stability of a DNA formulation is fundamental to its successful application in vivo since metabolism results in the generation of fragmented DNA which no longer mediates gene expression.[14] Even though peptide DNA condensates are more resistant to metabolism than naked plasmid DNA[11] or cationic lipid DNA condensates,[10,23] the in vitro stability determined by incubating condensates in serum may not be predictive of the in vivo stability in which the carrier molecules dissociate and are removed during circulation. This is exemplified by earlier studies by Wu and co-workers which showed the prolonged stability of DNA condensates *in vitro*[13] but a more limited stability in vivo.[24]

Even though a short polylysine peptide of 20 amino acids is sufficient to condense DNA into small condensates of approximately 70 nm diameter, HMW polylysines$_{38-1007}$ offer the advantage of binding to DNA with higher affinity, resulting in a greater protection of DNA to metabolism. However, there are also significant drawbacks in using HMW polylysine to create carriers for gene delivery. The polydispersity of HMW polylysine results in batch to batch variation.[25] The derivatization of HMW polylysine with ligands or polyethlene glycol is achieved by random coupling reactions which cannot control the conjugation site along the polylysine chain creating further heterogeneity in the carrier molecule.[26–28] Perhaps most significant, is the known cytotoxicity, complement activation, and inflammation mediated by HMW polylysine.[29] Given these limitations we have focused our efforts on developing LMW DNA carriers that are homogeneous, condense DNA into small condensates, may be selectively derivatized, and are minimal in size to reduce toxicity.

To overcome the limited stability afforded by LMW DNA carriers, we propose to introduce interchain cross-links to preformed DNA condensates to further improve their stability. The advantage of this approach is the ability to vary the degree of cross-linking to create condensates that possess the required stability for different gene therapy applications. Also, a variety of cross-linking agents could potentially be used alone or in combination to create controlled release of the DNA upon hydrolysis and dissociation of the cross-linker and carrier. Control over these events is a prerequisite to achieving delayed or prolonged transgene expression.

The test of this hypothesis was conducted by attempting to cross-link the surface amine groups on CWK_{18} DNA condensates using glutaraldehyde. This cross-linker was chosen because of its prior use in developing cross-linked albumin microspheres for parenteral applications,[20] its safety record when used in a variety of prosthesis,[30] and the Schiff-base that forms is theoretically reversible.[16,31] The results indicate that CWK_{18} DNA condensates undergo cross-linking over a 4–5 h period when very low concentrations of glutaraldehyde (1–4 mol equiv relative to CWK_{18}) are added. This amount of glutaraldehyde is far below the amounts needed to observe toxicity in cells grown in culture. Likewise, the maximum amount of glutaraldehyde used (4 mol equiv) can theoretically cross-link 20% of the amines present, assuming glutaraldehyde distributes equally throughout the DNA condensates. At this low level, the particle size is maintained, the ζ potential of the DNA condensates is unaffected, and trypsin can still be used to enzymatically remove CWK_{18} to quantitatively release the DNA. However, despite numerous attempts, we could not demonstrate the spontaneous reversal of glutaraldehyde cross-linked DNA condensates on prolonged dialysis in the presence of protein.

One measure that establishes the relative stability of peptide DNA condensates is the ability of DNA to resist fragmentation during a 30 s 100 W sonication in a dissociating concentration of sodium chloride. Cross-linked DNA condensates were increasingly stable to sonicative fragmentation at cross-linking levels ranging from 1 to 4 mol equiv of glutaraldehyde and were even found to be more stable than HMW polylysine$_{99-1007}$ DNA condensates. This result suggests that interchain peptide cross-links, and not linear polymerization of CWK_{18}, are responsible for the observed stabilization.

A similar correlation was observed from in vitro metabolism studies that indicated that 4 mol equiv cross-linked DNA condensates were significantly stabilized but still inferior to polylysine$_{1007}$ in their ability to protect DNA from accelerated metabolism. Interestingly, DNA condensates with and without cross-linking appeared to be directly metabolized into fragments without going through the linear form (Figure 5). This is in contrast to the catabolism of naked DNA which is converted completely into linear DNA prior to the formation of fragments.[14] It is also evident that intracellular proteolysis must somehow be involved in the release of DNA from cross-linked condensates since it less likely that the spontaneous reversal of Schiff-base is the major route of DNA release prior to gene expression.

Clearly, the ability of cross-linked DNA condensates to

mediate gene expression is an important measure of their ability to be useful in gene therapy applications. Since cross-linking could delay the release of DNA inside cells, it was important to study the transient gene expression as opposed to a single 24 or 48 h expression level. However, this was also technically challenging due to the doubling rate of cells in culture which slows as they reach confluence. At an optimal seeding density, cell cultures could be maintained for 10 days, and the gene expression occurring each day was determined using secreted alkaline phosphatase. The most significant effect of cross-linking DNA condensates, in addition to stabilization to metabolism, was an apparent flattening of the expression profile such that 4 mol equiv cross-linking of DNA condensates resulted in a low level of steady-state expression over the 10-day transfection which could not be extended in cell culture. Omitting chloroquine more closely models in vivo conditions and further confirmed that cross-linking could produce a steady-state rate of expression.

Analysis of the transient gene expression profile for HMW polylysine$_{38-1007}$ DNA condensates indicated a correlation between the cummulative gene expression and the degree of polymerization. We interpret these results as partial validation of the hypothesis that increasing the DNA condensate stability will result in greater gene expression.

Future studies will examine the influence of cross-linking to prolong the survival of DNA in vivo and to stabilized DNA condensates prepared with more than one LMW carrier to endow the delivery system with specific targeting. The methods developed and used in this study have established the principle of cross-linking DNA condensates using glutaraldehyde and should allow testing of other cross-linkers to stabilize peptide DNA condensates from metabolism leading to prolonged gene expression in vivo.

References and Notes

1. Duguid, J. G.; Li, C.; Shi, M.; Logan, M. J.; Alila, H.; Rolland, A.; Tomlinson, E.; Sparrow, J. T.; Smith, L. C. A Physicochemical Approach for Predicting the Effectiveness of Peptide-Based Gene Delivery Systems for Use in Plasmid-Based Gene Therapy. *Biophysical J*. **1998**, *74*, 2802−2814.
2. Niidome, T.; Ohmori, N.; Ichinose, A.; Wada, A.; Mihara, H.; Hirayama, T.; Aoyagi, H. Binding of Cationic α-Helical Peptides to Plasmid DNA and Their Gene Transfer Abilities into Cells. *J. Biol. Chem*. **1997**, *272*, 15307−15312.
3. Pouton, C. W.; Lucas, P.; Thomas, B. J.; Uduehi, A. N.; Milroy, D. A.; Moss, S. H. Polycation−DNA complexes for gene delivery: a comparison of the biopharmaceutical properties of cationic polypeptides and cationic lipids. *J. Controlled Release* **1998**, *53*, 289−299.
4. Perales, J. C.; Grossmann, G. A.; Molas, M.; Liu, G.; Ferkol, T.; Harpst, J.; Oda, H.; Hanson, R. W. Biochemical and functional characterization of DNA complexes capable of targeting genes to hepatocytes via the asialoglycoprotein receptor. *J. Biol. Chem*. **1997**, *272*, 7398−407.
5. Wagner, E.; Cotten, M.; Mechtler, K.; Kirlappos, H.; Birnstiel, M. L. DNA-binding transferrin conjugates as functional gene-delivery agents: synthesis by linkage of polylysine or ethidium homodimer to the transferrin carbohydrate moiety. *Bioconjugate Chem*. **1991**, *2*, 226−31.
6. Kabanov, A. V.; Kabanov, V. A. DNA complexes with polycations for the delivery of genetic material into cells. *Bioconjugate Chem*. **1995**, *6*, 7−20.
7. Ledley, F. Pharmaceutical Approach to Somatic Gene Therapy. *Pharm. Res*. **1996**, *13*, 1595−1614.
8. Mahato, R. I.; Rolland, A.; Tomlinson, E. Cationic Lipid-Based Gene Delivery Systems: Pharmaceutical Perspectives. *Pharm. Res*. **1997**, *14*, 853−859.
9. Yang, J. P.; Huang, L. Overcoming the inhibitory effect of serum on lipofection by increasing the charge ratio of cationic liposome to DNA. *Gene Ther*. **1997**, *4*, 950−60.
10. Escriou, V.; Ciolina, C.; Lacroix, F.; Byk, G.; Scherman, D.; Wils, P. Cationic lipid-mediated gene transfer: effect of serum on cellular uptake and intracellular fate of lipopolyamine/DNA complexes. *Biochimica et Biophys. Acta* **1998**, *1368*, 276−288.
11. Katayose, S.; Kataoka, K. Remarkable increase in nuclease resistance of plasmid DNA through supramolecular assembly with poly(ethylene glycol)-poly(L-lysine) block copolymer. *J. Pharm. Sci*. **1998**, *87*, 160−163.
12. Liu, F.; Liu, D. Serum independent liposome uptake by mouse liver. *Biochim. Biophys. Acta* **1996**, *1278*, 5−11.
13. Chiou, H. C.; Tangco, M. V.; Levine, S. M.; Robertson, D.; Kormis, K.; Wu, C. H.; Wu, G. Y. Enhanced resistance to nuclease degradation of nucleic acids complexed to asialoglycoprotein-polylysine carriers. *Nucleic Acids Res*. **1994**, *22*, 5439−46.
14. Adami, R. C.; Collard, W. T.; Gupta, S. A.; Kwok, K. Y.; Bonadio, J.; Rice, K. G. Stability of Peptide-Condensed Plasmid DNA Formulations. *J. Pharm. Sci*. **1998**, *87*, 678−683.
15. Gottschalk, S.; Sparrow, J. T.; Hauer, J.; Mims, M. P.; Leland, F. E.; Woo, S. L. C.; Smith, L. C. A novel DNA-peptide complex for efficient gene transfer and expression in mammalian cells. *Gene Ther*. **1996**, *3*, 448−457.
16. Jayakrishnan, A.; Jameela, S. R. Glultaraldehyde as a Fixative in Bioprostheses and Drug Delivery Matrixes. *Biomaterials* **1996**, *17*, 471−484.
17. Jones, C.; Burton, M. A.; Gray, B. N. Albumin microspheres as vehicles for the sustained and controlled release of doxorubicin. *J. Pharm. Pharmacol*. **1989**, *41*, 813−816.
18. Gupta, P. K., and C. T. Hung. Albumin microspheres I: physicochemical characteristics. *J. Microencaps*. **1989**, *6*, 427−462.
19. Lin, W.; Coombes, A. G. A.; Garnett, M. C.; Davies, M. C.; Schact, E.; Davis, S. S.; Illum, L. Preparation of sterically stabilized human serum albumin nanospheres using a novel dextranox-MPEG cross-linking agent. *Pharm. Res*. **1994**, *11*, 1588−1592.
20. Royer, G. P.; Lee, T. K. Entrapment of bioactive compounds within native albumin beads. *J. Parent. Sci. Technol*. **1983**, *37*, 34−37.
21. Leong, K. W.; Mao, H. Q.; Truong-Le, V. L.; Roy, K.; Walsh, S. M.; August, J. T. DNA-polycation nanospheres as nonviral gene delivery vehicles. *J. Controlled Release* **1998**, *53*, 183−193.
22. Wadhwa, M. S.; Collard, W. T.; Adami, R. C.; McKenzie, D. L.; Rice, K. G. Peptide-mediated gene delivery: influence of peptide structure on gene expression. *Bioconjugate Chem*. **1997**, *8*, 81−88.
23. Thierry, A. R.; Rabinovich, P.; Peng, B.; Mahan, L. C.; Bryant, J. L.; Gallo, R. C. Characterization of liposome-mediated gene delivery: expression, stability and pharmacokinetics of plasmid DNA. *Gene Therapy* **1997**, *4*, 226−237.
24. Chowdhury, N. R.; Wu, C. H.; Wu, G. Y.; Yerneni, P. C.; Bommineni, V. R.; Chowdhury, J. R. Fate of DNA targeted to the liver by asialoglycoprotein receptor-mediated endocytosis in vivo. Prolonged persistence in cytoplasmic vesicles after partial hepatectomy. *J. Biol. Chem*. **1993**, *268*, 11265−71.
25. McKenzie, D. L.; Collard, W. T.; Rice, K. G. Comparative gene transfer efficiency of low molecular weight polylysine DNA condensing peptides. *J. Pept. Res*. **1999**, in press.
26. Wagner, E.; Cotten, M.; Foisner, R.; Birnstiel, M. L. Transferrin-polycation−DNA complexes: the effect of polycations on the structure of the complex and DNA delivery to cells. *Proc. Natl. Acad. Sci. U.S.A*. **1991**, *88*, 4255−9.
27. Haensler, J.; Szoka, F. C., Jr. Synthesis and characterization of a trigalactosylated bisacridine compound to target DNA to hepatocytes. *Bioconjugate Chem*. **1993**, *4*, 85−93.
28. Batra, R. K., F. Wang-Johanning, E. Wagner, R. I. Garver, Jr., and D. T. Curiel. Receptor-mediated gene delivery employing lectin-binding specificity. *Gene Ther*. **1994**, *1*, 255−60.
29. Plank, C.; Mechtler, K.; Szoka, F. C., Jr.; Wagner, E. Activation of the complement system by synthetic DNA complexes: a potential barrier for intravenous gene delivery. *Human Gene Ther*. **1996**, *7*, 1437−46.
30. Gratzer, P. F.; Pereira, C. A.; Lee, M. J. Solvent environment modulates effects of glutaraldehyde cross-linking on tissue-derived biomaterials. *J. Biomed. Mater. Res*. **1996**, *31*, 533−543.
31. Ege, S. *Organic Chemistry: Structure and Reactivity*; Heath, D. C., Co.: Lexington, KY, 1994.

Acknowledgments

The authors acknowledge technical support provided by Ron Kelly and financial support provided by NIH grants GM48049, DE13004, NIH predoctoral fellowship (R.C.A.) and support from Selective Genetics Inc.

JS990042P

Application of Oral Bioavailability Surrogates in the Design of Orally Active Inhibitors of Rhinovirus Replication

ROBERT E. STRATFORD, JR.,*,† MICHAEL P. CLAY,† BEVERLY A. HEINZ,‡ MICHAEL T. KUHFELD,§ STACY J. OSBORNE,§ DIANE L. PHILLIPS,† STEPHANIE A. SWEETANA,|| MARK J. TEBBE,⊥ VASU VASUDEVAN,† LARRY L. ZORNES,† AND TERRY D. LINDSTROM†

Contribution from *Lilly Research Laboratories, Division of Eli Lilly and Company, Lilly Corporate Center, Indianapolis, Indiana 46285*

Received February 1, 1999. Final revised manuscript received May 17, 1999.
Accepted for publication May 18, 1999.

Abstract □ Previous studies in rats and humans demonstrated poor oral bioavailability of potent in vitro 2-aminobenzimidazole inhibitors of rhinovirus replication due to significant first-pass elimination and possibly also to poor aqueous solubility. Estimations of aqueous solubility, as well as measurements of caco-2 permeability and NADPH dependent compound loss in rat liver microsomal incubations were employed alongside traditional in vivo experiments in rats to guide subsequent chemistry efforts. Retention of activity upon replacement of the metabolically labile vinyl oxime in the lead molecule with a vinyl carboxamide was a major breakthrough; however, oral bioavailability among the latter compounds was variable. Based on the ability to independently measure solubility, permeability, and metabolic stability of new compounds, variable solubility across the series (ranging from approximately 1 to 10 μg/mL) was identified as the cause of the inconsistent performance. Subsequent efforts to improve solubility led to the discovery of highly soluble (>10 mg/mL) and potent dessulfonyl vinyl carboxamide benzimidazoles. Determination of the metabolic stability of these compounds as a surrogate of the extent of their first-pass elimination supported a prediction of excellent oral bioavailability. In comparison to the sulfonyl-containing vinyl carboxamides, caco-2 permeabilities were reduced 5 to 10-fold; however, these were considered to be in the range of well-absorbed compounds based on comparison to a series of reference compounds of known percentage absorption in humans. Subsequent experiments in the rat verified the oral bioavailability of these *N*-alkyl compounds, with one compound (368177) having an absolute oral bioavailability of 89.4%. The application of solubility and caco-2 permeability as surrogates for oral absorption potential, in conjunction with the use of microsomal incubations as a surrogate for first-pass metabolism, was shown to augment a rational chemistry approach to discover orally bioavailable inhibitors of rhinovirus replication. Future expanded use of these surrogates is planned.

Introduction

The discovery and development of new drugs that are orally bioavailable continues to be a tremendous challenge in the pharmaceutical industry. In the discovery setting, increased reliance on genomics and high throughput screening to identify pharmacologically active lead compounds,[1,2] as well as reliance on combinatorial chemistry to increase molecular diversity and achieve desired activity through structural optimization,[3−6] can result in drug candidates having pharmaceutical properties that are not conducive to oral bioavailability.[7] Realization of this problem has led to a desire for earlier and even parallel consideration in the discovery process of pharmaceutical properties influencing oral bioavailability.[8] In response to the challenge of supplying structure−absorption and structure−metabolism information simultaneous with structure−activity relationships on an increasing supply of new chemical entities, scientists in preclinical drug disposition are increasingly relying on in vitro techniques and more sophisticated analytical methods such as LC-MS and LC-NMR.[9−11] For example, the insightful use of a computational alert approach and turbidimetric solubility measurements to identify compounds with potential for poor oral absorption has recently been employed.[7] With respect to drug transport, caco-2 monolayers have demonstrated potential as a predictive model of human intestinal absorption.[12−15] Coupled with their higher throughput capacity relative to traditional animal experiments, theoretical models of permeability across caco-2 cells show promise to provide additional structure−transport relationship throughput capacity.[16−18] Estimates of drug metabolism using in vitro techniques as a surrogate for first-pass elimination are also being suggested.[19−22]

The objective of the work reported herein was to apply such in vitro approaches to the discovery of orally bioavailable 2-aminobenzimidazoles that inhibit RNA replication in rhinoviruses and enteroviruses.[23] Previous studies demonstrated that, while analogues of this template possessed potent and broad-spectrum inhibition of virus replication in vitro, upon oral administration to both rats and humans these compounds underwent extensive first-pass elimination.[24] An additional objective was to gain experience integrating the results from the various drug absorption and metabolism in vitro techniques, as well as integrating these with in vivo results stemming from traditional bioavailability experiments in animals. This experience could then represent the initial installment of an iterative process to maximize drug discovery and development through parallel potency and bioavailability structural optimization efforts.

Materials and Methods

Materials—2-Aminobenzimidazoles were synthesized and characterized at the Lilly Research Laboratories as previously reported.[25,26]

Culture medium components and reagents for cell culture were obtained from GIBCO Life Technologies, Inc. (Grand Island, NY).

* Corresponding author. Tel: (317) 276-4190. Fax: (317) 276-7040. E-mail: RES@Lilly.com.
† Department of Drug Disposition.
‡ Infectious Diseases Research.
§ Pharmaceutical Sciences.
|| Biopharmaceutical Product Development.
⊥ Discovery Chemistry Research.

10.1021/js990036t CCC: $18.00
Published on Web 07/03/1999

Fetal bovine serum for caco-2 culture was obtained from Hyclone Corp. (Logan, CT). Sulforhodamine 101, used as a marker for caco-2 monolayer integrity,[27] was from Molecular Probes (Eugene, OR). All other reagents were purchased from Sigma Chemical Co. (St. Louis, MO) or Fisher Scientific, Inc. (Fair Lawn, NJ) and were used as received.

Inhibition of Rhinovirus Replication—Human rhinovirus 14 strain 1059 and H-1 HeLa cells were received as a gift from R. Rueckert, University of Wisconsin, Madison. Virus stocks were amplified and diluted as previously described.[23] Plaque reduction assays were conducted by inoculating confluent cell monolayers grown in a 60-mm dish using minimum essential medium, 1% nonessential amino acids, and 10% new born calf serum with 0.2 mL of growth medium containing approximately 150 plaque-forming units of RV14. Following a 30 min attachment period at room temperature, 5 mL of medium containing the desired concentration of an inhibitor was added. Virus-infected cultures were incubated for 48 h at 35 °C, fixed with 10% formalin, and stained with 0.5% crystal violet (which stains only noninfected cells). Results from duplicate flasks at each inhibitor concentration were averaged and compared to nondrug control flasks. The inhibition of plaque formation by 50% (IC_{50}) was calculated from the linear region of the inhibition−concentration curve using the standard method of Reed and Muench as previously described.[23]

Physicochemical Properties—*Solubility*—A rapid throughput solubility screen was implemented to determine if there were gross differences in solubility across the SAR. This assay was based on visual observation 24 h after placing different amounts of compound (0.1, 1, 10, and 100 mg) in 1.0 mL of water. Water was selected as the solvent in this assay because of its fundamental importance in drug solubility for purposes of oral absorption[28] and because of limited compound availability and time in the early stages of an SAR to evaluate the effects of pH, ionic strength, and biological surfactants. In a more detailed evaluation of the solubility of compounds 341908 and 354400, determinations were made in 0.05 M phosphate buffers prepared over the pH range 1.7 to 8.0. Preliminary studies with 341908 indicated that bile salts were unlikely to improve solubility. Namely, the solubility of this compound was not improved in the presence of sodium deoxycholate. Type I flint glass amber vials containing a known quantity of either compound (approximately 5 mg) and 5 mL of buffer were tumbled end-over-end at ambient temperature for up to 7 days. Aliquots of approximately 2 mL were removed on days 3 and 7 and passed through a 0.45 μm Teflon filter. The first 1 mL was discarded and the remaining filtrate assayed by HPLC with UV detection. A Zorbax SB-phenyl column (25 cm × 4.6 mm maintained at 35 °C) was used along with a mobile phase consisting of an equal volume mixture of 0.1% (v/v) trifluoroacetic acid in water and acetonitrile. The flow rate was 1 mL/min and detection was at 244 nm.

Determination of pK_a—Ionization constants were measured using the Sirius PCA 101 Potentiometric System. Compounds were dissolved in various proportions of methanol and 0.15 M KCl, and adjusted to pH 6 or lower. For a given titration, an approximately 0.5 mM solution of each compound was titrated from a low to a high pH. The acid used was 0.5 N HCl, and the base, 0.5 N NaOH. The acid and base were standardized to four decimal places using NIST traceable standards. For a given compound, titrations were performed in triplicate for each of three different proportions of methanol and 0.15 M KCl. These titrations were done under an argon atmosphere at a constant temperature of 25 °C. Estimate of pK_a in 100% water was made using the Yasuda−Shedlovsky method of extrapolation.[29,30]

Caco-2 Permeability—Caco-2 cells were obtained from the Memorial Sloan-Kettering Cancer Center and were cultured at 37 °C in a humidified atmosphere of 5% CO_2 in air. They were grown in DMEM:F12 (3:1) media supplemented with 5% fetal bovine serum and 50 μg/mL tobramycin. Monolayers at 75−90% confluency were either subcultured on a weekly basis using a 1:10 split ratio, or seeded onto Millicell-PCF polycarbonate inserts (30 mm diameter, 0.4 μm pore size; Millipore Corp., Bedford, MA) at a density of 600 000 cells per filter. The culture medium was replaced with fresh medium every other day. For transport studies, cells from passages 43−56 were used at 21−30 days postseeding. Measurement of transepithelial electrical resistance was made immediately prior to an experiment using a Millicell-ERS system (Millipore Corp.). Cells with a net resistance less than 300 $\Omega \cdot cm^2$ were not used.

Measurements of transepithelial flux of the various inhibitors were made at 37 °C using a side-by-side diffusion chamber described previously.[31] This system has now been coupled to a robotics arm to increase throughput capacity.[32] The transport medium consisted of 25 mM HEPES (pH 7.4) or 25 mM MES (pH 6.0) as buffering agents along with 125 mM NaCl, 5.2 mM KCl, 1.2 mM $CaCl_2$, 1.2 mM $MgCl_2$, and 10 mM glucose. To initiate an experiment, a stock solution of an inhibitor in DMSO was added to either the apical or basal side of the monolayer. The final concentration of DMSO was 1.4% (v/v). Samples (200 μL) were taken from the contralateral compartment at various times up to 120 min and replaced with an equal volume of fresh transport buffer. Rates of transport under initial rate conditions (<10% transport) were determined by linear regression analysis; these were divided by the initial donor concentration and filter surface area to calculate the corresponding permeability coefficients. Experiments were conducted in duplicate or triplicate and under limited lighting conditions to minimize light catalyzed *Z*-isomer to *E*-isomer transformation. At the end of an experiment, integrity of each monolayer was assessed by evaluating the percentage transport of sulforhodamine 101 in 30 min. Monolayers with greater than 0.2% transport in this time period were not included in the analysis of permeability (there were never fewer than two monolayers used in the estimation of a given permeability coefficient). Analysis of the various inhibitors via HPLC−UV was conducted as previously described for solubility measurements.

Microsomal-Mediated Metabolism—Using standard techniques,[33] microsomes were prepared from fresh livers obtained from male F344 rats weighing approximately 250 g. Microsomes were diluted to 1 mg protein/mL in 0.1 M sodium phosphate buffer, pH 7.4. Inhibitors were dissolved in either ethanol or acetonitrile to a concentration of 1 mM and spiked into the microsomal suspension such that the final concentration was 10 μM. This concentration was selected based on analytical sensitivity requirements and the desire to keep the concentration in the low micromolar, pharmacologically relevant, range. To start the reaction, either NADPH or, in the case of controls, buffer without NADPH was added. After 30 min, the reaction was stopped with an equal volume of acetonitrile, and the incubation mixture was centrifuged and analyzed for parent compound using HPLC−UV as described previously for measurement of solubility. The integrated peak areas from the HPLC chromatograms were compared for an inhibitor in the presence or absence of NADPH, and the amount of loss of parent compound was calculated.

***In Vivo* Studies**—Pharmacokinetic profiles and absolute oral bioavailability in 24 h fasted male F344 rats weighing approximately 200 to 250 g were determined for select inhibitors in the series. Plasma concentrations of an inhibitor following either an intravenous (iv) dose ($n = 2-3$ rats) or an oral dose ($n = 3$ rats) were quantitated by HPLC−UV analysis as described for solubility measurements. For iv dosing, compounds 341908 and 354400 were prepared in poly(ethylene glycol) PEG-400, ethanol, water mixtures (30%, 30%, 40%; w,v,v), and dosed via the tail vein. Compounds 366094 and 368177 were dissolved in saline and administered similarly. The latter two compounds were also dosed orally as solutions; whereas compounds 341908 and 354400 were dosed orally either as aqueous suspensions (10% acacia/0.5% polysorbate 80) of controlled particle size (5−25 μm), or as solutions (85% PEG-400/0.5% polysorbate 80). Precipitation of formulated solutions of 341908 and 354400 (10 mg/mL) was not observed upon 1:10 dilution with either 0.1 N HCl or 0.1 μ (ionic strength) pH 7.4 buffer. Pharmacokinetic parameters were obtained using model independent methodology. With respect to estimation of $AUC_{0-\infty}$, percent extrapolated areas were never greater than 10%. Percent oral bioavailability was calculated by comparison of dose normalized $AUC_{0-\infty}$ values for iv and oral doses (the equation used is summarized in Table 4B).

Results

In Vitro Potency and Metabolic Stability—Table 1 shows the structures of the compounds evaluated according to structural class. Also included are the potency and metabolic stability of the compounds. Enviroxime, a compound that was tested in Phase II clinical trials in the early 1980s, is included for comparison. Replacing the hydroxyl-

Table 1—Structure, pK_a, Potency, and Metabolic Stability of Vinyl Carboxamide 2-Aminobenzimidazoles

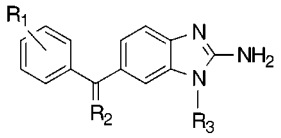

compd no.	R1	R2	R3	structural class	pK_a	potency (mean IC_{50}, μg/mL)[a]	metabolic stability (% loss in 30 min)
enviroxime	all H	oxime	isopropyl sulfonamide	sulfonamide	nd[b]	0.05	39
153186	all H	carboxamide	isopropyl sulfonamide	sulfonamide	nd	0.04	18
341908	3-F	carboxamide	isopropyl sulfonamide	sulfonamide	3.41	0.04	11
354400	2,5-di-F	carboxamide	isopropyl sulfonamide	sulfonamide	3.40	0.08	17
355081	2,5-di-F	*N*-methyl carboxamide	isopropyl sulfonamide	sulfonamide	nd	0.06	28
357132	all H	*N*-methyl carboxamide	isopropyl sulfonamide	sulfonamide	nd	0.07	5
357822	2,3-di-F	*N*-methyl carboxamide	isopropyl sulfonamide	sulfonamide	nd	0.01	22
362546	3-F	*N*-methyl carboxamide	*n*-propyl sulfonamide	sulfonamide	nd	0.04	12
362683	2,3-di-F	carboxamide	isopropyl sulfonamide	sulfonamide	nd	0.01	3
366092	naphthyl	*N*-methyl carboxamide	isopropyl sulfonamide	sulfonamide	nd	0.21	11
366347	2,3,4-tri-F	*N*-methyl carboxamide	isopropyl sulfonamide	sulfonamide	nd	0.01	6
366349	3-F,4-MeO	carboxamide	isopropyl sulfonamide	sulfonamide	nd	0.05	9
366572	3,5-di-F	carboxamide	isopropyl sulfonamide	sulfonamide	nd	0.06	16
366659	2,3,5,6-F	carboxamide	isopropyl sulfonamide	sulfonamide	nd	0.05	4
366799	2-F	carboxamide	isopropyl sulfonamide	sulfonamide	nd	0.03	14
366856	2,3,4-tri-F	carboxamide	isopropyl sulfonamide	sulfonamide	nd	0.02	5
368227	3,4-di-F	carboxamide	isopropyl sulfonamide	sulfonamide	nd	0.05	1
368228	2,4-di-F	carboxamide	isopropyl sulfonamide	sulfonamide	nd	0.05	7
354030	3-F	*N*-methyl carboxamide	*N*,*N*-di-Me sulfonylurea	sulfonylurea	3.41	0.03	19
353462	3-F	carboxamide	*N*,*N*-di-Me sulfonylurea	sulfonylurea	3.41	0.05	13
362898	3-F	*N*-methyl carboxamide	morpholino sulfonylurea	sulfonylurea	3.41	0.05	24
359353	3-F	*N*-methyl carboxamide	pyrrolidino sulfonylurea	sulfonylurea	3.41	0.02	41
368288	3-F	carboxamide	morpholino sulfonylurea	sulfonylurea	3.41	0.08	32
366094	2,3-di-F	*N*-methyl carboxamide	isopropyl	*N*-alkyl	6.69	0.06	7
366853	2,3-di-F	carboxamide	isopropyl	*N*-alkyl	6.70	0.07	4
368177	2-F	*N*-methyl carboxamide	cyclopentyl	*N*-alkyl	6.70	0.03	10

[a] IC_{50}'s are from a plaque reduction assay using Rhinovirus 14. $n = 2$–3. [b] Not determined.

containing oxime in enviroxime at R2, which was extensively conjugated following oral administration of a 10 mg/kg dose in the rat (unpublished results from studies conducted to support enviroxime IND), with a vinylcarboxamide conferred resistance to metabolism by a primary conjugative mechanism. Specifically, incubation of enviroxime and 153186 in rat and human liver microsomes in the presence of UDP-glucuronic acid resulted in a 21% and an 11% loss of enviroxime from rat and human sources, respectively; whereas there was no loss of 153186 from either source. In addition, fluorine substitution at R1, which was a site of aromatic hydroxylation in enviroxime, was expected to provide a further increase in metabolic stability. The percent loss of enviroxime under oxidative conditions was 39% in 30 min. By comparison, the mean percent loss in 30 min of the sulfonamide containing vinylcarboxamides was 11 ± 7.3% (± 1 sd, $n = 17$ compounds). The nonsulfonyl *N*-alkyl compounds were similarly relatively resistant to oxidative metabolism, having a mean percent loss in 30 min of 7 ± 3.0% ($n = 3$ compounds). Importantly, while these structural modifications increased metabolic stability in vitro, they had no effect on antiviral potency relative to enviroxime (Table 1). Mean percentage loss of the sulfonylureas was 26 ± 11.0% ($n = 5$ compounds).

Permeability—Permeability coefficients across caco-2 monolayers relative to several marker compounds of known and varying percentage absorption in humans provided an estimate of the absorption potential of the novel antirhinovirus compounds. These results are shown in Figure 1 according to the three structural classes. The *N*-alkyl compound, 366853, had the lowest permeability ($0.5 \pm 0.05 \times 10^{-5}$ cm/s) while the sulfonamide, 366092, had the highest ($9.3 \pm 0.16 \times 10^{-5}$ cm/s). By comparison to the

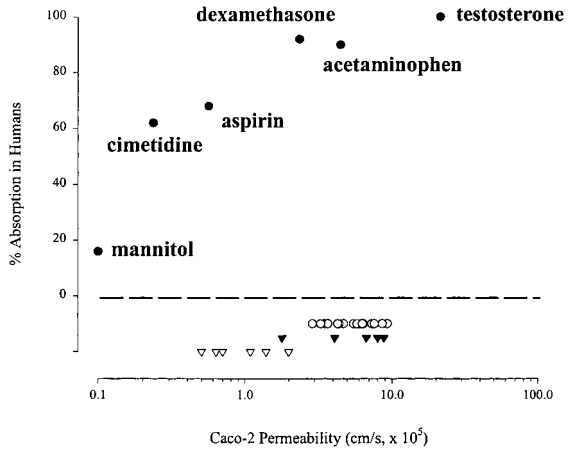

Figure 1—Permeability coefficients of 2-aminobenzimidazoles across caco-2 monolayers in relation to permeability coefficients of reference compounds (●). The three classes of 2-aminobenzimidazoles were sulfonamides, ○; sulfonylureas, ▼; and *N*-alkyls, ▽.

marker compounds, the observed range of permeabilities corresponded to a percentage absorption in humans of approximately 60% to 100%, thus indicating that these compounds should be well absorbed in vivo notwithstanding any potential dissolution or solubility limitations. Since, with a limited set of structurally different compounds, there was no asymmetry with respect to permeability (Table 2), the transport mechanism appeared to be passive. Table 3 indicates the pH dependent permeability of the *N*-alkyl compounds and the lack of pH dependence on the permeability of a sulfonamide. These results were expected due to pK_a differences (Table 1). Indeed, the lower permeability

Table 2—Apical to Basolateral versus Basolateral to Apical Transcellular Permeability of Vinyl Carboxamide 2-Aminobenzimidazoles[a]

compd no.	structural class	donor concentration (μM)	permeability (cm/s $\times 10^5$)[a] apical to basolateral	basolateral to apical
354400	sulfonamide	70	2.9 ± 0.09	2.9 ± 0.15
353462	sulfonylurea	15	6.7 ± 1.20	5.1 ± 0.63
366094	*N*-alkyl	80	1.0 ± 0.06	0.7 ± 0.04

[a] Results are expressed as mean ± one standard deviation; $n = 3$ filters. For the three compounds, $p > 0.05$ based on an unpaired Student's *t*-test, thus indicating no asymmetry with respect to transport direction. pH was 7.4 on both sides.

Table 3—pH-Dependent Permeability of Vinyl Carboxamide 2-Aminobenzimidazoles

compd no.	structural class	permeability (cm/s $\times 10^5$)[a] apical (donor) pH 6.0	apical (donor) pH 7.4
354400	sulfonamide	3.5 ± 0.28	2.9 ± 0.09
366094	*N*-alkyl	0.6 ± 0.01	1.0 ± 0.06[b]
366853	*N*-alkyl	0.5 ± 0.05	0.7 ± 0.03[b]
368177	*N*-alkyl	0.7 ± 0.01	2.0 ± 0.13[b]

[a] Results are expressed as mean ± one standard deviation; $n = 3$ filters. [b] Indicates significantly different from pH 6 result at $p \leq 0.05$ based on an unpaired Student's *t*-test.

of the *N*-alkyl class compared to the sulfonamides and sulfonylureas is attributed to the significant fraction of protonated amine at pH 6.0 for the *N*-alkyl compounds. The fraction present in the ionized form at this pH was estimated to be about 80% for the three *N*-alkyl compounds.

Solubility and Biopharmaceutics of Oral Solution and Suspension Formulations—The equilibrium solubility of enviroxime in water at ambient temperature was approximately 2 μg/mL. The water solubility of compound 341908, one of the earliest compounds in the current SAR, was 1 μg/mL. Based on this finding, there was concern that insufficient solubility in vivo would result in poor bioavailability of the sulfonamide vinyl carboxamide series. These concerns were realized upon administration of compound 341908 to rats. As shown in Figure 2A and summarized in Table 4, systemic exposure from a suspension was substantially lower than from a solution formulation. Interestingly, replacing the fluorine at the 3 position of the phenyl ring at site R1 (compound 341908) with fluorines at positions 2 and 5 (compound 354400), a seemingly minor modification, resulted in a 10-fold enhancement in water solubility (compound 354400 had a solubility of 10 μg/mL in water). As shown in Figure 3, the pH-solubility profiles of these two compounds demonstrate that, over the pH range of 1.75 to 7.9, 354400 solubility in 0.05 M phosphate buffer was consistently 5 to 7 times greater than that of 341908. The cause for this difference may be related more to differences in the interaction of the two compounds with solvent than to crystal lattice energy differences because of the similar melting points of the two compounds, ca. 210 °C. Importantly, as shown in Table 4, the absolute bioavailability of 354400 was similar from both solution and suspension dosage forms and was markedly greater compared to 341908 bioavailability from a suspension. The lower absolute bioavailability of 354400 compared to 341908 bioavailability from solution dosage forms may be due to greater first-pass elimination of 354400. This interpretation is supported by the approximate 6-fold higher systemic clearance of 354400 (Table 4A). While loss in liver microsomes was similar for the two compounds (17% for 354400 versus 11% for 341908, Table 1), as previously indicated, this assay was not scaled to in vivo clearance, nor does it take into account the possibility for conjugative metabolism. The possibility for biliary elimination was also not evaluated. Thus, the cause for the greater clearance of 354400 is not known.

Given the lack of predictability in the solubility properties of the sulfonamides, efforts were made to identify compounds of consistently greater solubility. These efforts led to removal of the sulfonyl group resulting in direct attachment of various alkyl groups to the benzimidazole nitrogen in the R3 position. This modification resulted in conversion of the primary amine to a significantly more basic functional group, as shown by the pK_a values (Table 1). Importantly, this modification had no impact on antiviral potency (Table 1). The water solubility of these so-called *N*-alkyl vinyl carboxamides was consistently greater than 10 mg/mL. As shown in Figure 2C and Table 4, systemic exposure of compound 368177, dosed as neat drug dissolved in water, was excellent, resulting in an absolute bioavailability of 89%.

Discussion

Evaluation of enviroxime disposition in rats demonstrated that glucuronidation of the hydroxyl containing oxime at position R2 was the major metabolic pathway, accounting for 60% to 70% of an oral dose in 24 h and up to 80% in 48 h (unpublished results). Hydroxylation of the phenyl moiety (R1) also significantly contributed to loss of parent. Identification of strategies to obviate these two metabolic pathways while simultaneously preserving or enhancing antiviral potency were the two most important goals of the current structural optimization effort. Discovery of the potent vinyl carboxamide series was a major breakthrough due to the resistance of the acidic primary amide to direct conjugation. Subsequently, attempts to achieve a balance between structural effects on potency and susceptibility to oxidative metabolism became the focus of our optimization work. A 30 min incubation in the presence of rat liver microsomes was used to rank order the compounds with respect to their susceptibility to metabolism, measured as percent loss of parent compound, and was placed after the initial potency screen. No attempt was made to correlate this screen with an in vivo measure of elimination; rather, the intent of the screen was to look for gross effects of structure on susceptibility to metabolism. Although the number of compounds was few, it seemed that the cyclic sulfonylurea compounds 362898, 359353, and 368288 were metabolized to a greater extent than the noncyclic sulfonylureas and sulfonamides. On the basis of loss of parent compound, aromatic fluorine substitution at R1 did not appear to reduce metabolism. However, to conclude that fluorine substitution had no effect is equivocal because metabolites were not identified; also, if fluorine did not have an effect, whether this would translate to the in vivo situation is also not known. Fortunately, fluorine substitution had no effect on antiviral potency.

On the basis of experience with enviroxime, a poor dose to aqueous solubility ratio of the benzimidazoles was considered a potential barrier to achieving adequate and reproducible systemic exposure following oral administration.[34] With a solubility of 2 μg/mL, complete dissolution of a therapeutic dose of enviroxime as low as 10 mg would require 5 L of fluid, which approximates the entire volume consumed and produced by secretions in the human gastrointestinal tract in a 24 h period.[35] The water solubility of compound 341908, one of the earliest vinyl carboxamides made, was 1 μg/mL. Concern that poor solubility of vinyl carboxamide sulfonamides and sulfonylureas would result

Table 4—Summary Single Dose Pharmacokinetics of Vinyl Carboxamide 2-Aminobenzimidazoles in Male F344 Rats

A. Intravenous Bolus Administration

compd no.	structural class	dose (mg/kg)	$AUC_{0-\infty}$[a] (ng·hr/mL)	clearance (L/h/kg)	$T_{1/2}$ (mean ± se) (h)
341908	sulfonamide	3	7703.6	0.37	0.8 ± 0.14
354400	sulfonamide	3	1211.9	2.42	1.8 ± 0.02
366094	*N*-alkyl	5	4042.5	1.18	1.0 ± 0.05
368177	*N*-alkyl	5	6974.7	0.68	1.0 ± 0.09

B. Oral Administration

compd no.	formulation	dose (mg/kg)	$AUC_{0-\infty}$[a] (ng·hr/mL)	C_{max} (mean ± se) (ng/mL)	T_{max} (h)	bioavailability[b] (%)
341908	solution	30	61076.4	10834	0.5	79.3
341908	suspension	30	8971.6	1076	3.0	11.6
354400	solution	6	1175.5	304 ± 51	2.0	48.5
354400	suspension	30	6038.8	1162 ± 361	2.0	49.8
366094	solution	30	8059.3	2128 ± 184	1.0	33.2
368177	solution	30	37404.4	4202 ± 2041	6.0	89.4

[a] Extrapolated areas were less than 10% in all cases. [b] Absolute bioavailability = $(AUC_{0-\infty,po}/AUC_{0-\infty,iv}) \times (dose_{iv}/dose_{po}) \times 100$.

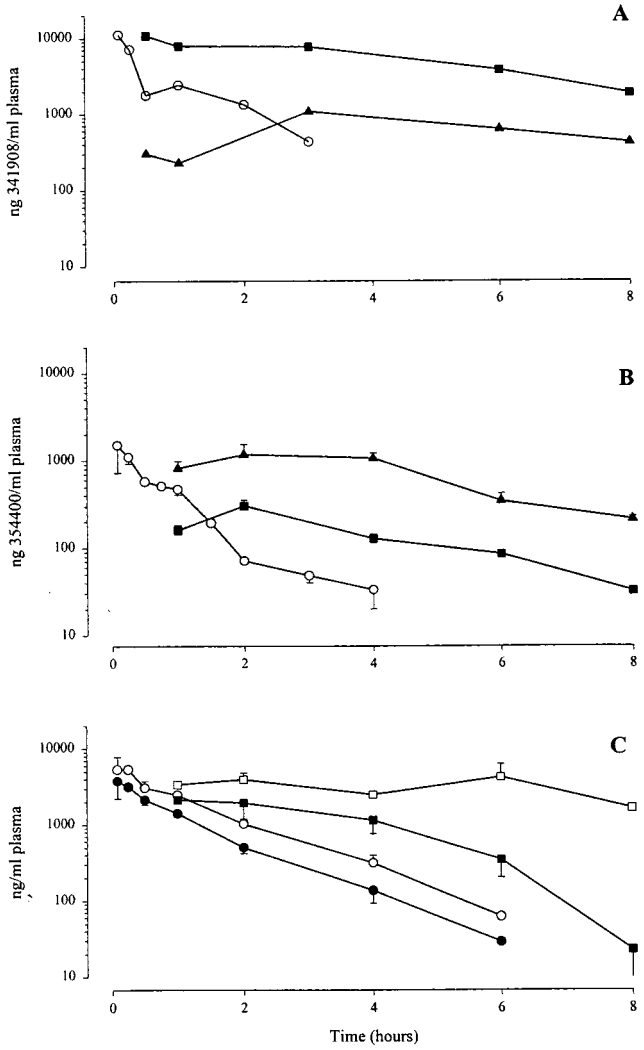

Figure 2—Rat plasma concentration versus time profiles of rhinovirus inhibitors following either intravenous (○ or ●), oral solution (□ or ■), or oral suspension (▲) administration. (A) Compound 341908. (B) Compound 354400. (C) Compounds 366094 (●, ■) and 368177 (○, □). Refer to Table 4 for actual doses administered. For consistency of presentation, 24 h levels following oral administration of compounds 341908, 366094, and 368177 have been omitted; these were <100 ng/mL.

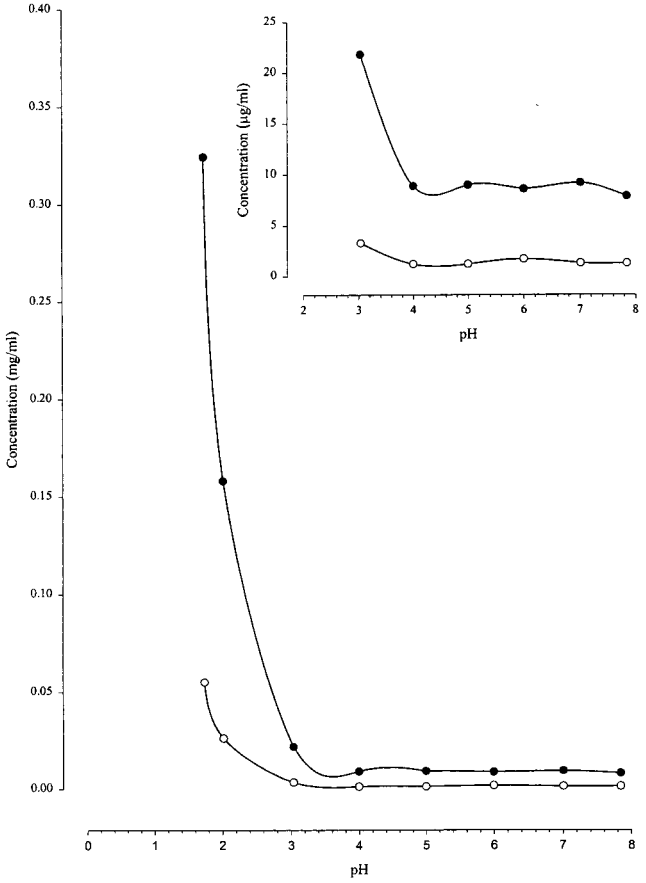

Figure 3—pH versus solubility profiles for compounds 341908 (○) and 354400 (●). Phosphate buffers, 0.05 M, were prepared over the pH range 1.7 to 8.0. Inset graph is of the same results, but expressed in μg/mL over the pH range 3 to 8.

in poor systemic exposure was verified upon oral administration of compound 341908. As shown in Table 4B, absolute bioavailability of this compound when dosed as an aqueous suspension was approximately 10%. In contrast, administration of a solution of 341908 prepared using a mixture of PEG-400, ethanol, and water resulted in a bioavailability of 80%. These results, as well as dose/solubility ratios based on projected human doses and gastrointestinal volumes, indicated that solubility could be problematic in relation to the clinical development of this therapeutic class.

A simplified solubility screen in water was consequently implemented; this was based on visual observation following incubation at room temperature for 24 h. Samples of a given compound were prepared in 10-fold increments of

concentration ranging from 0.1 mg/mL to 100 mg/mL. On the basis of this assay, all compounds tested had a solubility in water less than 0.1 mg/mL (data not shown). Compound 354400 was one of these compounds. HPLC analysis of its pH dependent solubility versus that of compound 341908 indicated a 5- to 7-fold higher solubility throughout the pH range of 1.7 to 7.9 (Figure 3). For the two compounds, an approximate 20-fold increase in solubility was observed at pH 2 relative to pH 4; this is attributed to protonation of the primary amine at the 2 position of the benzimidazole ring, which had a measured pK_a of 3.4 (Table 1). Importantly, the absolute bioavailability of a suspension of 354400 was 49.8%, which was similar to the bioavailability of a solution formulation, 48.5% (Figure 2, Table 4B). On the basis of the physical stability of the solution formulation of 354400 to a 10-fold dilution in either 37 °C 0.1 N HCl, pH 1.2 or pH 7.4 buffer, these results suggested that dissolution of the suspension was sufficient to produce a comparable bioavailability. Furthermore, given the excellent permeabilities of the two compounds (7.3 and 3.5 $\times$ 10^{-5} cm/s, for 341908 and 354400, respectively) and the greater systemic clearance of 354400 (Table 4A), greater solubility of 354400 was the attributed cause of its superior bioavailability from a suspension dosage form. The different effects of the two formulations on the bioavailability of these two compounds suggested that, under the experimental conditions tested, systemic exposure was acutely dependent on solubility and dissolution. Considering the less than 10-fold difference in the solubility of these two compounds, the similar solubilities of the compounds that had thus far been synthesized and the aforementioned unfavorable dose/solubility ratios applicable to human dosing, an effort to identify more soluble compounds was made.

Elimination of the R3 sulfonyl portion of these compounds significantly increased the pK_a of the primary amine at the 2 position of the benzimidazole ring (Table 1). Improvement in aqueous solubility to greater than 10 mg/mL was a consequence of this modification. Importantly, these so-called *N*-alkyl compounds had similar potency and metabolic stability compared to the sulfonamides and sulfonylureas. Given that these compounds had pK_a values in the range of small intestinal pH, it was expected that the *N*-alkyls would have a pH dependent permeability influenced by the ratio of protonated to unprotonated species. As shown in Table 3, *N*-alkyl permeability at pH 7.4 was significantly greater than at pH 6.0. Furthermore, as expected, permeability of compound 354400 was not similarly influenced by pH. It was also expected that the permeability of the *N*-alkyls in general would be less than that of the sulfonylureas and sulfonamides. While this was the case, the permeability of the *N*-alkyls was still in the range of what would be considered moderately well-absorbed compounds (Figure 1). Oral administration of aqueous solutions of compounds 366094 and 368177 to rats resulted in absolute bioavailability estimates of 33.2% and 89.4%, respectively (Table 4B). The approximate 3-fold greater bioavailability of 368177 may be due to either greater absorption, which is consistent with a larger permeability coefficient relative to 366094, or to reduced first-pass elimination, which is supported by the approximate 2-fold lower clearance compared to 366094, or to a combination of these two factors. According to the testing conditions used, both compounds exhibited prolonged absorption behavior, with absorption-rate limited kinetics indicated for compound 368177 (oral terminal half-life was 3.9 h vs 1.0 h following iv administration). The cause of this apparent slow absorption is not known, but may be due to prolonged absorption throughout the rat gastrointestinal tract, possibly including colonic absorption. This possibility is consistent with the known progressive increase in pH along the longitudinal axis of the intestinal tract and the observed increase in permeability of these compounds from pH 6 to 7.4. However, precipitation of drug in the stomach or in the duodenum with subsequent dissolution along the tract cannot be ruled out. The high caco-2 permeability coefficients of these compounds, even at pH 6, are indicative of excellent absorption, but are by no means definitive for novel compounds such as these for which a definitive in vitro/in vivo correlation has not been established.

In conclusion, this work has demonstrated the ability through structural modifications to independently influence potency, solubility, permeability, and metabolism in order to achieve oral bioavailability of potent inhibitors of rhinovirus replication. This positive experience has enabled this laboratory to move forward with a broader implementation of bioavailability surrogates to achieve a more expeditious discovery and development process.

References and Notes

1. Kubinyi, H. Strategies and Recent Technologies in Drug Discovery. *Pharmazie* **1995**, *50*, 647−662.
2. Beeley, L. J.; Duckworth, D. M. The Impact of Genomics on Drug Design. *Drug Discov. Today* **1996**, *1*, 474−480.
3. Moos, W. H.; Green, G. D.; Pavia, M. R. Recent Advances in the Generation of Molecular Diversity. *Annu. Rep. Med. Chem.* **1993**, *28*, 315−324.
4. Baum, R. M. Combinatorial Approaches Provide Fresh Leads for Medicinal Chemistry. *Chem. Eng. News* **1994**, *February 7*, 20−26.
5. Gordon, E. M.; Gallop, M. A.; Patel, D. V. Strategy and Tactics in Combinatorial Organic Synthesis: Applications to Drug Discovery. *Acc. Chem. Res.* **1996**, *29*, 144−154.
6. Patel, D. V.; Gordon, E. M. Applications of Small-Molecule Combinatorial Chemistry to Drug Discovery. *Drug Discov. Today* **1996**, *1*, 134−144.
7. Lipinski, C. A.; Lombardo, F.; Dominy, B. W.; Feeney, P. J. Experimental and Computational Approaches to Estimate Solubility and Permeability in Drug Discovery and Development Settings. *Adv. Drug Deliv. Rev.* **1997**, *23*, 3−25.
8. Rodrigues, A. D. Preclinical Drug Metabolism in the Age of High-Throughput Screening: An Industrial Perspective. *Pharm. Res.* **1997**, *14*, 1504−1510.
9. Lindon, J. C.; Nicholson, J. K.; Sidelmann, U. G.; Wilson, I. D. Directly Coupled HPLC NMR and its Application to Drug Metabolism. *Drug Metab. Rev.* **1997**, *29*, 705−746.
10. Berman, J.; Halm, K.; Adkison, K.; Shaffer, J. Simultaneous Pharmacokinetic Screening of a Mixture of Compounds in Dog Using API LC/MS/MS Analysis for Increased Throughput. *J. Med. Chem.* **1997**, *40*, 827−829.
11. Ehlhardt, W. J.; Woodland, J. M.; Baughman, T. M.; Vandenbranden, M.; Wrighton, S. A.; Kroin, J. S.; Norman, B. H.; Maple, S. R. Liquid Chromatography/Nuclear Magnetic Resonance Spectroscopy and Liquid Chromatography/Mass Spectrometry Identification of Novel Metabolites of the Multidrug Resistance Modulator LY335979 in Rat Bile and Human Liver Microsomal Incubations. *Drug Metab. Dispos.* **1998**, *26*, 42−51.
12. Artursson, P. Epithelial Transport of Drugs in Cell Culture. I: A Model for Studying the Passive Diffusion of Drugs Over Intestinal Absorptive (Caco-2) Cells. *J. Pharm. Sci.* **1990**, *79*, 476−482.
13. Stewart, B. H.; Chan, O. H.; Lu, R. H.; Reyner, E. L.; Schmid, H. L.; Hamilton, H. W.; Steinbaugh, B. A.; Taylor, M. D. Comparison of Intestinal Permeabilities Determined in Multiple In Vitro and In Situ Models: Relationship to Absorption in Humans. *Pharm. Res.* **1995**, *12*, 693−699.
14. Bailey, C. A.; Bryla, P.; Malick, A. W. The Use of the Intestinal Epithelial Cell Culture Model, Caco-2, in Pharmaceutical Development. *Adv. Drug Deliv. Rev.* **1996**, *22*, 85−103.
15. Yamashita, S.; Tanaka, Y.; Dendoh, Y.; Taki, Y.; Sakane, T.; Nadai, T.; Sezaki, H. Analysis of Drug Permeation Across Caco-2 Monolayer: Implication for Predicting in Vivo Drug Absorption. *Pharm. Res.* **1997**, *14*, 486-491.
16. Palm, K.; Luthman, K.; Ungell, A.; Strandlund, G.; Artursson, P. Correlation of Drug Absorption with Molecular Surface Properties. *J. Pharm. Sci.* **1996**, *85*, 32−39.

17. van de Waterbeemd, H.; Camenisch, G.; Folkers, G.; Raevsky, O. A. Estimation of Caco-2 Cell Permeability Using Calculated Molecular Descriptors. *Quant. Struct.-Act. Relat.* **1996**, *15*, 480−490.
18. Norinder, U.; Österberg, T.; Artursson, P. Theoretical Calculation and Prediction of Caco-2 Cell Permeability Using MolSurf Parametrization and PLS Statistics. *Pharm. Res.* **1997**, *14*, 1786−1791.
19. Rodrigues, A. D. Use of in Vitro Human Metabolism Studies in Drug Development: An Industrial Perspective. *Biochem. Pharmacol.* **1994**, *48*, 2147−2156.
20. Iwatsubo, T.; Hirota, N.; Ooie, T.; Suzuki, H.; Shimada, N.; Chiba, K.; Ishizaki, T.; Green, C. E.; Tyson, C. A.; Sugiyama, Y. Prediction of in Vivo Drug Metabolism in the Human Liver from in Vitro Metabolism Data. *Pharmacol. Ther.* **1997**, *73*, 147−171.
21. Bouska, J. J.; Bell, R. L.; Goodfellow, C. L.; Stewart, A. O.; Brooks, C. D. W.; Carter, G. W. Improving the in Vivo Duration of 5-Lipoxygenase Inhibitors: Application of an in vitro Glucuronosyltransferase Assay. *Drug Metab. Dispos.* **1997**, *25*, 1032−1038.
22. Lavé, Th.; Dupin, S.; Schmitt, C.; Vales, B.; Ubeaud, G.; Chou, R. C.; Jaeck, D.; Coassolo, Ph. The Use of Human Hepatocytes to Select Compounds Based on Their Expected Hepatic Extraction Ratios in Humans. *Pharm. Res.* **1997**, *14*, 152−155.
23. Heinz, B. A.; Vance, L. M. The Antiviral Compound Enviroxime Targets the 3A Coding Region of Rhinovirus and Poliovirus. *J. Virol.* **1995**, *69*, 4189−4197.
24. Phillpotts, R. J.; Jones, R. W.; Delong, D. C.; Reed, S. E.; Wallace, J.; Tyrrell, D. A. The Activity of Enviroxime Against Rhinovirus Infection in Man. *Lancet* **1981**, *1*, 1342−1344.
25. Victor, F.; Loncharich, R.; Tang, J.; Spitzer, W. A. Synthesis and Antiviral Activity of C2 Analogues of Enviroxime: An Exploration of the Role of Critical Functionality. *J. Med. Chem.* **1997**, *40*, 3478−3483.
26. Victor, F.; Brown, T. J.; Campanale, K.; Heinz, B. A.; Shipley, L. A.; Su, K. S.; Tang, J.; Vance, L. M.; Spitzer, W. A. Synthesis, Antiviral Activity, and Biological Properties of Vinylacetylene Analogues of Enviroxime. *J. Med. Chem.* **1997**, *40*, 1511−1518.
27. Schasteen, C. S.; Donovan, M. G.; Cogburn, J. N. A Novel In Vitro Screen to Discover Agents which Increase the Absorption of Molecules Across the Intestinal Epithelium. *J. Controlled Release* **1992**, *21*, 49−62.
28. Dressman, J. B.; Amidon, G. L.; Fleisher, D. Absorption Potential: Estimating the Fraction Absorbed for Orally Administered Compounds. *J. Pharm. Sci.* **1985**, *74*, 588−589.
29. Shedlovsky, T.; Kay, R. L. The Behavior of Carboxylic Acids in Mixed Solvents. In *Electrolytes*; Pesce, B., Ed.; Pergamon Press: New York, 1962; pp 146−151.
30. Yasuda, M. Dissociation constants of some Carboxylic Acids in Mixed Aqueous Solvents. *Bull. Chem. Soc. Jpn.* **1959**, *32*, 429−432.
31. Kuhfeld, M. T.; Stratford, R. E. In Vitro Measurement of Drug Transport Using a New Diffusion Chamber Compatible with Millicell Culture supports: Performance with Caco-2 Monolayers. *Int. J. Pharm.* **1996**, *133*, 47−58.
32. Kuhfeld, M. T.; Hinshaw, M. E.; Stratford, R. E.; Zynger, J. An Automated in Vitro Permeability Screen Using Robotics. *Pharm. Res.* **1994**, *11*, S-39.
33. Wrighton, S. A.; Stevens, J. C. The Human Hepatic Cytochromes P450 Involved in Drug Metabolism. *Crit. Rev. Toxicol.* **1992**, *22*, 1−21.
34. Amidon, G. L.; Lennernäs, H.; Shah, V. P.; Crison, J. R. A Theoretical Basis for a Biopharmaceutic Drug Classification: The Correlation of in Vitro Drug Product Dissolution and in Vivo Bioavailability. *Pharm. Res.* **1995**, *12*, 413−420.
35. Horter, D.; Dressman, J. B. Influence of Physicochemical Properties on Dissolution of Drugs in the Gastrointestinal Tract. *Adv. Drug Deliv. Rev.* **1997**, *25*, 3−14.

Acknowledgments

The supply of caco-2 cells by Mr. Tony Gardner and Dr. Don McClure is gratefully appreciated.

JS990036T

Direct Transport of Cocaine from the Nasal Cavity to the Brain Following Intranasal Cocaine Administration in Rats

H.-H. SHERRY CHOW,* ZHI CHEN, AND GREGORY T. MATSUURA

Contribution from *Department of Pharmacy Practice and Science, College of Pharmacy, The University of Arizona, Tucson, Arizona 85721*

Received January 30, 1999. Final revised manuscript received May 4, 1999.
Accepted for publication May 14, 1999.

Abstract □ Individuals who consume cocaine illegally have long since adopted or explored the nasal route of administration. This study was designed to determine in an animal model whether nasally applied cocaine could be transported directly from the nasal cavity to the central nervous system. Male Sprague–Dawley rats were used in the study. The nasal cavity was isolated to prevent drainage of nasally applied dosing solution to nonnasal regions. Cocaine was then administered, either by intranasal (in) administration or by intravenous (iv) injection. At different times post dose, blood and tissues from different regions of the brain were collected. Cocaine concentrations in plasma and tissue samples were analyzed by HPLC. After iv administration, similar cocaine contents in different brain regions were observed. Following in administration, cocaine content in samples collected within 60 min post dose were found to differ considerably in different brain regions. The highest content was observed in the olfactory bulb, followed by the olfactory tract and then the remaining part of the brain. To allow comparison of brain cocaine content after iv and in administration, brain cocaine contents were normalized by plasma cocaine concentrations. The ratios of the area under the cocaine concentration–time curve (AUC) between the olfactory bulb and plasma at early times following in administration were significantly higher than those obtained after the iv dose (13.4 ± 5.56 vs 6.16 ± 0.94, $p < 0.05$, for AUC ratio up to 2 min post dose; 9.39 ± 1.47 vs 7.34 ± 0.59, $p < 0.05$, for AUC ratio up to 4 min post dose). At 1 min post dose, the olfactory bulb-to-plasma cocaine concentration ratios following in administration was three times those obtained after iv administration. After 1 min, the olfactory bulb-to-plasma concentration ratios following in administration were found to be similar to or smaller than those obtained after iv administration. The tissue-to-plasma concentration ratios in other brain regions following in administration were found to be smaller than those obtained following iv dosing. We conclude that nasally administered cocaine was transported directly from the nasal cavity to the brain but that only a very small fraction of the dose was transported via the direct pathway.

Introduction

Over the past decade, the possibility that intranasal drug administration might be useful has received a great deal of attention. Some relevant research efforts have been reviewed comprehensively.[1] The extensive network of blood capillaries under the nasal mucosa seems to facilitate effective systemic absorption and, because venous blood drains directly into the systemic circulation, this route thereby avoids first-pass metabolism of the drug in the gastrointestinal tract and the liver. For a number of drugs, systemic drug exposure following intranasal administration is comparable to that obtained from intravenous or intramuscular injections.[2−4]

Interestingly, individuals who consume cocaine illicitly have either long ago adopted or have explored this route of administration. It often has been noted that a rise in the physiological and behavior effects of cocaine precedes a rise in the plasma cocaine concentration following intranasal "snorting".[5−7] A clockwise hysteresis loop was consistently observed when behavior or physiological responses were plotted against plasma cocaine concentrations. This indicates that the same plasma cocaine concentration corresponds to a higher response at an earlier time after dosing than that at a later time. Development of acute tolerance can be used to explain such a concentration−response relationship. However, there is no evidence that tolerance would develop rapidly following administration of a single dose of cocaine. To exert CNS activity following nasal drug application, it is typically believed that the drug needs to be absorbed into the systemic circulation via the capillary network under the nasal mucosa and subsequently distributed into target regions in the brain. If this is the only pathway of CNS entry, there will be a time delay in the distribution of cocaine to the brain tissues following nasal administration. A rise in the pharmacological response should therefore occur after a rise in the plasma cocaine concentration. Nevertheless, this outcome is not in agreement with the concentration−response relationship observed following intranasal cocaine snorting.

Evidence exists that substances applied nasally may enter the brain directly from the nasal cavity via the olfactory system.[8−10] If nasally applied cocaine can distribute into the brain directly via this alternative CNS entry pathway, an increase in the brain cocaine concentration could occur prior to a rise in the plasma drug levels following nasal application. This hypothesis would be consistent with the clockwise hysteresis loop observed in the plasma concentration−response relationship following nasal cocaine snorting.

In this study, we determined plasma and brain cocaine concentration−time profiles following intravenous and intranasal administration of cocaine in rats in an effort to determine whether cocaine could be transported directly from the nose to the brain following intranasal application.

Materials and Methods

Chemicals and Reagents—Cocaine and tropacocaine were provided by the Research Triangle Institute (Research Triangle Park, NC) through the National Institute on Drug Abuse. All other reagents were of HPLC grade or of the highest grade commercially available.

Animal Experimentation—Male Sprague−Dawley rats (250−350 g) were anesthetized with an ip injection of pentobarbital (50 mg/kg) and kept anesthetized throughout the experiment. The anesthetized animals were placed on a warm pad to maintain

* Corresponding author. Phone: 520-626-4055 Fax: 520-626-7355. E-mail: chow@pharmacy.arizona.edu.

10.1021/js9900295 CCC: $18.00
Published on Web 07/03/1999

normal body temperature. The nasal cavity was isolated from the respiratory and gastrointestinal tracts using a procedure described by Hussain et al.[11] Briefly, an incision was made in the neck, the trachea was severed, and the upper tracheal segment was tied off with a suture. The lower trachea was cannulated with polyethylene tubing (PE 260; o.d.: 2.8 mm, i.d.: 1.77 mm) to provide a patent airway. Another piece of PE 260 tubing with the ends sealed was inserted from the esophagus to the posterior part of the nasal cavity. The nasopalatine opening was closed with cyanoacrylate glue. This surgical procedure was performed to prevent drainage of nasally applied dosing solution to nonnasal regions.

Following nasal cavity isolation, animals received a cocaine dose over 30 s, either by intranasal administration or by intravenous injection. For intranasal administration, 50 μL of cocaine solution (16.7 mg/kg) was injected via a silastic tubing (o.d.: 1.19 mm, i.d.: 0.64 mm) inserted 2 cm into one of the nares toward the roof of the nasal cavity. For intravenous administration, cocaine dosing solution (5 mg/kg) was injected via an indwelling jugular vein cannula. At 1, 2, 4, 8, 15, 60, and 120 min following the end of the 30-s dosing period, a terminal blood sample was collected from the inferior vena cava. Plasma was separated and immediately stored at −70 °C in tubes containing NaF. The blood collection was generally completed within 15 s. Following the completion of blood collection, the skull of the animals was opened and the brain tissues collected in the following order: the whole brain with the exception of the olfactory tract and olfactory bulb (RB), olfactory tract (OT), and olfactory bulb (OB). The collection of all brain tissues was typically completed within 1 min following the blood collection. The tissue samples were weighed and immediately homogenized in 200 mM NaF solution. An aliquot of the homogenate was stored at −70 °C before analysis. The addition of NaF protected cocaine from undergoing hydrolysis during processing and storage. Four or five rats were used at each collection time. The sample collection process always involved two laboratory personnel: one responsible for dosing and sample collection and the other for tracking the time and sample handling.

Analytical Methods—Plasma and brain cocaine concentrations were determined within 48 h of collection by a published HPLC procedure.[12] Briefly, the plasma (200 μL) and brain homogenates (100−200 μL) were mixed with 50 μL of the internal standard (tropacocaine, 1 μg/mL) and 200 μL of 0.5 M carbonate buffer (pH 9.1). The mixture was extracted with 2 mL of ethyl acetate, and the organic phase was back-extracted with 150 μL of 0.05 M HCl. The final acidic aqueous phase was evaporated with a centrifugal evaporator (Savant, Farmingdale, NY) at room temperature. The residue was reconstituted with the mobile phase (see below) and then injected onto a C_8 column (Nova-Pak, 15 cm × 3.9 mm i.d., 4 μm; Waters, Milford, MA). A mobile phase composed of a mixture of 100 mM pentanesulfonic acid and 50 mM monobasic potassium phosphate (pH 6.0) and acetonitrile in an aqueous-to-organic ratio of 76:24 at a flow rate of 1.3 mL/min was used. The UV absorbance of the effluent was monitored (Waters 486 UV detector) at a wavelength of 235 nm.

Data Analysis—The area under the cocaine concentration versus time curve (AUC) was estimated by the trapezoidal rule. The variance for the AUC was estimated by the method of Yuan.[13] The variance (var) for the AUC ratio was approximated using the statistical method described previously,[14]

$$\mathrm{var}\left(\frac{\mathrm{AUC_{in}}}{\mathrm{AUC_{iv}}}\right) \cong \left(\frac{\overline{\mathrm{AUC_{in}}}}{\overline{\mathrm{AUC_{iv}}}}\right)^2 \cdot \left(\frac{\mathrm{var(AUC_{in})}}{(\overline{\mathrm{AUC_{in}}})^2} + \frac{\mathrm{var(AUC_{iv})}}{(\overline{\mathrm{AUC_{iv}}})^2}\right)$$

where $\overline{\mathrm{AUC}}$ denotes the mean AUC value.

A one-way ANOVA followed by a Student−Newman−Keuls test was used to compare the measurements in different brain regions. An unpaired two-sided *t*-test was used to compare the measurements for intravenous and intranasal administration.

Results

Figure 1 illustrates the cocaine concentration versus time profiles in plasma and in different brain regions following intravenous and intranasal administration. Following intravenous administration, plasma and brain cocaine concentrations reached peak levels at 1−2 min after dosing

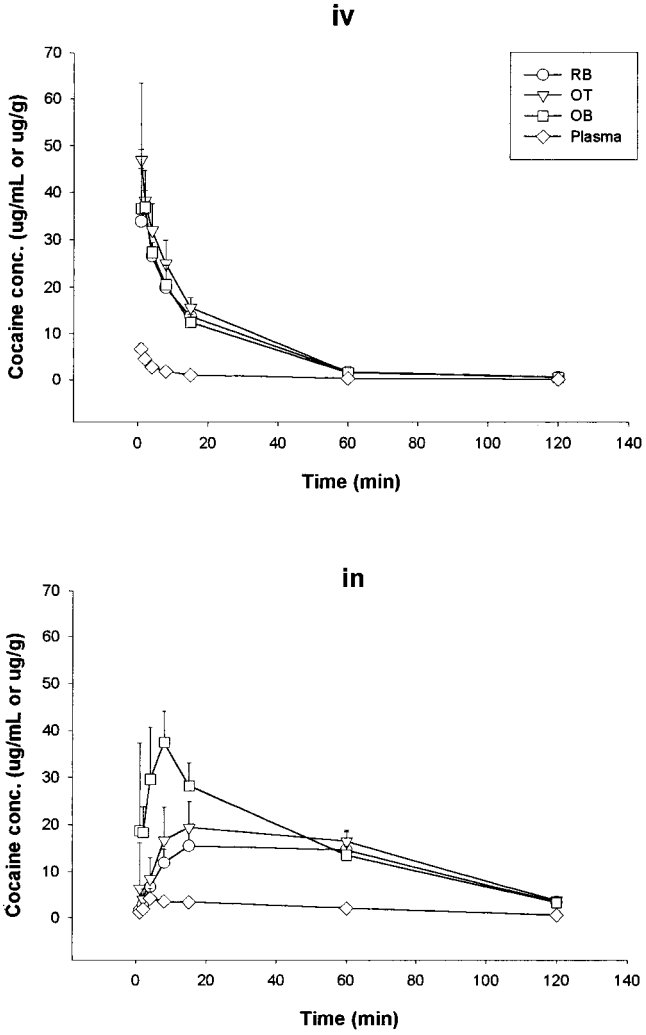

Figure 1—Plasma and brain cocaine concentrations versus time profiles following intravenous (iv) and intranasal (in) administration in rats. Each point represents the average of 4–5 rats and the cross-vertical bars represent one standard deviation of the mean. Key: OT, olfactory tract; OB, olfactory bulb; RB, remaining part of the brain.

and declined exponentially as a function of time. Except for samples collected at 1 min post dose, similar cocaine contents were observed in different brain regions. Following intranasal administration, plasma and brain cocaine concentrations increased gradually to peak levels and started to decline as a function of time. Cocaine contents in samples collected within 60 min post dose were found to differ considerably in different brain regions. The highest content was observed in the olfactory bulb, followed by the olfactory tract and then the remaining part of the brain.

Table 1 summarizes the brain tissue-to-plasma cocaine AUC ratios as a function of time following intravenous and intranasal administration. Following intravenous administration, the tissue-to-plasma AUC ratios in different brain regions increased consistently toward plateau levels as a function of time. Following intranasal dosing, the RB-to-plasma AUC ratios also increased toward plateau levels as a function of time. The OT-to-plasma AUC ratios decreased initially and then started to increase. The OB-to-plasma AUC ratios were high initially and decreased as a function of time. Up to 2 and 4 min following intranasal administration, the cumulative OB-to-plasma AUC ratios were significantly higher than those obtained after the intravenous dose (13.8 ± 6.29 vs 6.06 ± 1.02, $p < 0.05$, for AUC ratio up to 2 min post dose; 9.62 ± 1.77 vs 7.17 ± 0.67, $p < 0.05$, for AUC ratio up to 4 min post dose). At

Table 1—Brain Tissue-to-Plasma Cocaine AUC Ratios as a Function of Time Following Intravenous and Intranasal Administration

	$AUC_{brain\ tissue}/AUC_{plasma}$					
	iv administratio			in administration		
time, min	OB	OT	RB	OB	OT	RB
0–1	5.52 ± 1.09	7.10 ± 1.42	5.11 ± 0.99	16.1 ± 9.30[c,d]	5.52 ± 4.27	1.27 ± 0.73[a]
0–2	6.06 ± 1.02	7.37 ± 1.31	5.73 ± 0.93	13.8 ± 6.29[a,c,d]	4.23 ± 2.91[a]	1.38 ± 0.54[a]
0–4	7.17 ± 0.67	8.28 ± 0.86[b,c]	6.92 ± 0.62	9.62 ± 1.77[a,c,d]	2.67 ± 0.82[a]	1.52 ± 0.24[a]
0–8	8.30 ± 0.50	9.71 ± 0.69[b,c]	8.03 ± 0.47	9.01 ± 1.40[c,d]	3.05 ± 0.54[a]	2.10 ± 0.30[a]
0–15	9.17 ± 0.54	10.91 ± 0.70[b,c]	9.04 ± 0.56	9.27 ± 0.89[c,d]	4.15 ± 0.51[a]	3.04 ± 0.29[a]
0–60	9.94 ± 0.55	12.11 ± 0.69[b,c]	10.42 ± 0.54	8.15 ± 0.56[a,c,d]	5.93 ± 0.48[a]	4.86 ± 0.34[a]
0–120	9.39 ± 0.49	11.41 ± 0.62[b,c]	9.93 ± 0.49	7.61 ± 0.49[a,c,d]	6.50 ± 0.47[a,c]	5.52 ± 0.51[a]

[a] Significantly different from that after intravenous dosing, $p < 0.05$. [b] Significantly different from OB, $p < 0.05$. [c] Significantly different from RB, $p < 0.05$. [d] Significantly different from OT, $p < 0.05$.

later times, the OB-to-plasma cocaine AUC ratios obtained following intranasal administration were similar to or smaller than those obtained after intravenous dosing. The tissue-to-plasma cocaine AUC ratios in other brain regions following intranasal administration were smaller than those obtained after intravenous dosing.

Figure 2 illustrates the brain-to-plasma cocaine concentration ratios following intravenous and intranasal administration as a function of time. There were no significant differences in these ratios among different brain regions following intravenous administration. The tissue-to-plasma ratios of cocaine in OB following intranasal administration were found to be significantly higher than those in other brain regions before 60 min post dose. At 1 min post dose, the tissue-to-plasma ratios in the olfactory bulb following intranasal administration were found to be three times those obtained after intravenous administration (15.0 ± 4.1 vs 5.5 ± 1.1, $p < 0.05$). After 1 min, the olfactory bulb-to-plasma concentration ratios in samples collected following intranasal administration were found to be similar to or smaller than those obtained after intravenous administration. The tissue-to-plasma concentration ratios in other brain regions following intranasal administration were found to be smaller than those obtained following intravenous administration.

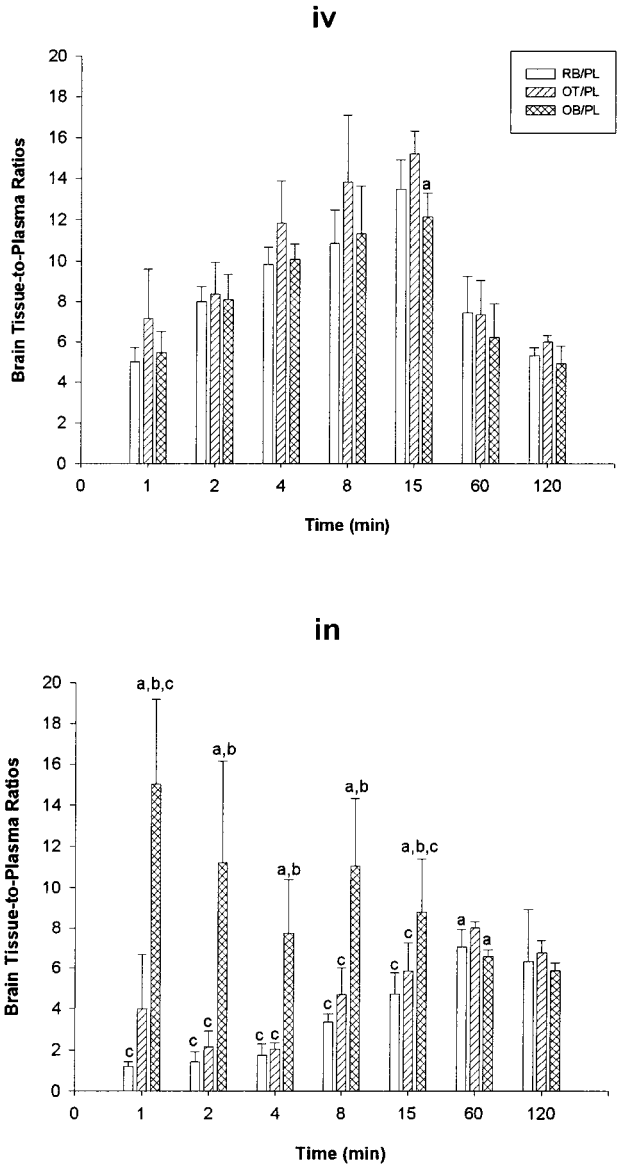

Figure 2—Brain tissue-to-plasma cocaine concentration ratios as a function of time following intravenous (iv) and intranasal (in) administration in rats (mean ± SD, $n = 4–5$ per time point). See legend for Figure 1 for definitions of the abbreviations. a: significantly different from OT/PL cocaine ratio, $p < 0.05$; b: significantly different from RB/PL cocaine ratio, $p < 0.05$; c: significantly different from the corresponding ratios obtained following intravenous administration, $p < 0.05$.

Discussion

Intranasal drug administration has received considerable recent attention, because it is an attractive noninvasive alternative route that can be used for the systemic delivery of compounds with poor oral bioavailability. Individuals who consume cocaine illicitly have long ago adopted and explored this route of administration. Because of the fear of HIV or other types of infection, there has been a recent shift among drug addicts away from intravenous injection to intranasal use. For inexperienced drug users in particular, the intranasal route has been preferred over intravenous injection. Although some evidence exists that substances may enter the brain directly from the nasal cavity, little attention has been paid to addressing the possibility that nasally applied abused substances could be transported directly from the nasal cavity to the central nervous system (CNS). Using a pharmacokinetic study design, we have obtained results suggesting that, when applied intranasally, a small fraction of the cocaine dose can be transported directly from the nasal cavity to the olfactory bulb. Whether the direct entry of nasally applied substances from the nasal cavity to the brain could result in increased abuse potential of nasally applied neurologically active drugs requires further study.

The olfactory system begins peripherally with the olfactory epithelium that is located on the roof of the nasal cavity. The olfactory receptors are bipolar neurons, one end of which is located in the nasal olfactory epithelium and the other end extending through the holes in the cribriform

plate of the ethmoid bone and ending in the olfactory bulb.[15,16] It has been suggested that there is free communication between the nasal submusocal interstitial space and the olfactory perineuronal space, which appears to be continuous with a subarachnoid extension that surrounds the oflactory nerve as it penetrates the cribriform plate.[17,18] Previous studies in mammals have demonstrated transport of protein tracers such as albumin labeled with Evans blue,[19] horseradish peroxidase,[20−22] and conjugated wheat germ agglutinin−horseradish peroxidase[20−22] from the nasal cavity to the olfactory bulb and its connected structures. Studies examining the transport of metals in the olfactory system have reported the movement of colloidal gold,[23] manganese,[24] and cadmium[25,26] within the olfactory system following intranasal administration. A series of recent studies performed by Sakane and co-workers have demonstrated significant increases of drug concentrations in the cerebrospinal fluid following intranasal administration of a variety of model substances, which have been shown to have low permeability to the CNS following systemic administration.[8,27−30] In contrast, enhanced brain delivery of a number of drugs was not always observed when results of nasal administration were compared with those obtained after intravenous dosing.[2,9,31]

One major limitation of the cited work is that brain and CSF drug concentrations usually were determined at a single time following dosing. Depending on the time of sampling, the brain drug concentration obtained following intravenous administration could have passed the maximal level and already have been in the declining phase, while the brain drug concentration obtained following intranasal administration could have been right around the maximal level. One could then incorrectly conclude that enhanced drug exposure in the brain had been observed following intranasal administration, implying the existence of direct nose−brain drug transport. In this research, a more complete pharmacokinetic examination of drug levels in plasma and different regions of the brain in the rat has been used as a tool to determine the existence of the direct nose−brain drug transport of nasally applied cocaine.

Cocaine is known to be a potent vasoconstricting agent commonly used to constrict nasal blood vessels during rhinologic procedures. This unique property of cocaine could prevent or delay its own systemic absorption following local application. Comparison of the dose−normalized plasma data collected from intravenous and intranasal administration indicates that nasally applied cocaine was rapidly and completely absorbed into the systemic circulation. This suggests that because of its high lipophilicity, movement of cocaine from the nasal mucosa to the blood was not limited by the reduction in the nasal blood flow. The detection of cocaine in the brain following intranasal dosing could have been due to the systemic absorption of the drug via the capillary network under the nasal mucosa and the subsequent distribution from the systemic blood into the target regions in the brain. The brain cocaine content was therefore normalized by the plasma cocaine concentration to allow comparisons of data collected following different routes of administration. The brain-to-plasma cocaine AUC or concentration ratios obtained after intravenous administration should represent the distribution of cocaine from systemic circulation into different brain regions (passing through the blood brain barrier). Because nasally applied cocaine does not appear in the systemic circulation instantaneously, the brain-to-plasma cocaine ratios after intranasal dosing should be similar to or smaller than those obtained after intravenous administration if nasally applied cocaine enters the brain only via the systemic blood. In this study, the cumulative OB-to-plasma cocaine AUC ratios obtained up to 4 min following nasal application was 1.5 to 3 times higher than that obtained after intravenous dosing. At 1 min post dose, the OB-to-plasma cocaine concentration ratio following intranasal administration was 3 times those obtained after intravenous dosing. These results support the existence of an alternative brain entry pathway for cocaine. Furthermore, following intravenous administration, no significant differences in cocaine content were observed among different brain regions whereas cocaine content was found to be region specific (olfactory bulb > olfactory tract > the remaining part of the brain) following intranasal administration. If the substance can be transported directly via the olfactory system, the first anatomical brain region of contact is the olfactory bulb. The olfactory tract connects the olfactory bulb to the remaining part of the brain. The brain cocaine content gradient observed following intranasal dosing but not after intravenous dosing further supports the existence of a direct pathway.

Because nasally applied cocaine was extensively and rapidly absorbed into the systemic circulation, the amount available for the direct nose−brain pathway is small. Therefore, the OB-to-plasma cocaine AUC ratios after intranasal administration were higher than those after intravenous administration only at early times after dosing. The distribution of this small amount of cocaine into other brain regions is counteracted by their large masses, thus leading to the insignificant increase in cocaine content in other brain regions. Consequently, the tissue-to-plasma AUC ratios in other brain regions obtained after intranasal administration were not higher than those after intravenous dosing. Similar to the tissue-to-plasma AUC ratios in different brain regions after intravenous dosing, the RB-to-plasma AUC ratios after intranasal administration increased as a function of time. The OT-to-plasma AUC ratios after intranasal dosing were high initially, decreased as a function of time, and subsequently increased as a function of time. The OB-to-plasma AUC ratios after intranasal dosing were high initially and decreased as a function of time. These results suggest that directly transported cocaine also was distributed into the OT regions but, because the amount entered via this pathway was not substantial, the OT-to-plasma AUC ratios after intranasal dosing were not higher than those after intravenous dosing. Similar results were obtained when the data were analyzed in nonaccumulated fashion (brain tissue-to-plasma cocaine concentration ratios).

Mechanisms responsible for the direct nose−brain transport of nasally applied substances are not clear. One suggested anatomical pathway for the direct transport of foreign compounds from the nasal cavity to the brain theorizes that foreign compounds enter into the olfactory sensory neurons by endocytosis or by binding to surface receptors and subsequently undergoing adsorptive endocytosis. The compounds could thereafter be transported within the olfactory sensory neurons by the axoplasmic flow, but whether they could be transported beyond the olfactory system is a question that remains to be answered. Neuronal transport is generally believed to be a slow process and seems to be consistent with the results from studies on heavy metals[23−26] and protein tracers.[19−22] However, this pathway is not likely to explain the observed increase in OB-to-plasma cocaine AUC or concentration ratios within 1−2 min following nasal application.

Another plausible explanation is that foreign substances can diffuse into the nasal submucosa and subsequently travel into the olfactory perineuronal channels because no morphological barrier between the loose submucosal connective tissue and the perineuronal space has been identified.[17,18] Large molecular weight markers injected into the lateral ventricles can be observed to flow down from the

central nervous system and reach the nasal submucosal extracellular space via the open pathway in the perineuronal space.[18] However, an intriguing question to us is the following: How could foreign compounds be transported from the nasal cavity to the brain through this open channel against the direction of flow of the cerebral spinal fluid? More studies are needed to define the exact mechanism(s) responsible for the direct transport of cocaine to the olfactory bulb.

We conclude that nasally administered cocaine can be transported directly from the nasal cavity to the olfactory bulb. Due to rapid and extensive systemic absorption of nasally applied cocaine, only a small fraction was transported to the CNS via the direct pathway. Further studies are necessary to investigate the pharmacological/toxicological consequences of direct nose−brain transport of nasally applied cocaine and other abuse substances.

References and Notes

1. Chien, Y. W.; Su, K. S. E.; Chang, S. F. *Nasal systemic drug delivery*; Marcel Dekker: New York, 1988.
2. Char, H.; Kumar, S.; Patel, S.; Piemontese, D.; Iqbal, K.; Malick, A. W.; Salvador, R. A.; Behl, C. R. Nasal delivery of [^{14}C]dextromethorphan hydrochloride in rats: levels in plasma and brain. *J. Pharm. Sci.* **1992**, *81*, 750−752.
3. Hussain, A. A.; Aungst, B. J. Intranasal absorption of oxymorphone. *J. Pharm. Sci.* **1997**, *86*, 975−976.
4. David, G. F. X.; Puri, C. P.; Kumar, T. C. A. Bioavailability of progesterone enhanced by intranasal spraying. *Experientia* **1981**, *37*, 533−534.
5. Perez-Reyes, M.; Jeffcoat, A. R. Ethanol/cocaine interaction: cocaine and cocaethylene plasma concentrations and their relationship to subjective and cardiovascular effects. *Life Sci.* **1992**, *51*, 553−563.
6. McCance-Katz, E. F.; Price, L. H.; McDougle, C. J.; Kosten, T. R.; Black, E. ; Jatlow. P. I. Concurrent cocaine-ethanol ingestion in humans: pharmacology, physiology, behavior, and the role of cocaethylene. *Psychopharmacology* **1993**, *111*, 39−46.
7. Farre, M.; Torre, R. D. L.; Llorente, M.; Lamas, X.; Ugena, B.; Segura, J.; Cami, J. Alcohol and cocaine interactions in humans. *J. Pharmacol. Exp. Ther.* **1993**, *266*, 1364−1373.
8. Sakane, T.; Yamashita, S.; Nadai, T.; Sezaki, H. Direct drug transport from the nasal cavity to the cerebrospinal fluid: a new strategy for drug delivery to the brain. *S. T. P. Pharm. Sci.* **1997**, *7*, 98−106.
9. Chou, K.-J.; Donovan, M. D. Distribution of antihistamines into the CSF following intranasal delivery. *Biopharm. Drug Dispos.* **1997**, *18*, 335−347.
10. Frey, W. H.; Liu, J.; Chen, X.; Thorne, R. G.; Fawcett, J. R.; Ala, T. A.; Rahman, Y.-E. Delivery of ^{125}I−NGF to the brain via the olfactory route. *Drug Del.* **1997**, *4*, 87−92.
11. Hussain, A. A.; Hirai, S.; Bawarshi, R. Nasal absorption of propranolol from different dosage forms by rats and dogs. *J. Pharm. Sci.* **1980**, *69*, 1411−1413.
12. Sukbuntherng, J.; Walters, A.; Chow, H.; Mayersohn, M. Quantitative determination of cocaine, cocaethylene (ethylcocaine), and metabolites in plasma and urine by high-performance liquid chromatography. *J. Pharm. Sci.* **199**5, *84*, 799−804.
13. Yuan, J. Estimation of variance for AUC in animal studies. *J. Pharm. Sci.* **1993**, *82*, 761−763.
14. *Encyclopedia of statistical sciences*; John Wiley & Sons: New York, 1988; Vol. 8, pp 647.
15. Hilger, O. A. Applied anatomy and physiology of the nose. In *Boies's Fundamentals of Otolaryngology*; Adams, G. L., Boies, L. R., Hilger, P. A., Eds.; W. B. Saunders: Philadelphia, 1989; pp 177−195.
16. Nolte, J. *The human brain*; C. V. Mosby Co.: St. Louis, 1988.
17. Jackson, R. T.; Tigges, J.; Arnold, W. Subarachnoid space of the CNS, nasal mucosa, and lymphatic system. *Arch. Otolaryngol.* **1979**, *105*, 180−184.
18. Erlich, S. S.; McComb, J. G.; Hyman, S.; Weiss, M. H. Ultrastructural morphology of the olfactory pathway for cerebrospinal fluid drainage in the rabbit. *J. Neurosurg.* **1986**, *64*, 466−473.
19. Kristensson, K.; Olsson, Y. Uptake of exogenous proteins in mouse olfactory cells. *Acta Neuropathol.* **1971**, *19*, 145−154.
20. Baker, H.; Spencer, R. F. Transneuronal transport of peroxidase-conjugated wheat germ agglutinin (WGA-HRP) from the olfactory epithelium to the brain of the adult rat. *Exp. Brain Res.* **1986**, *63*, 461−473.
21. Broadwell, R. D.; Dalin, B. J. Endocytic and exocytic pathways of the neuronal secretory process and trans-synaptic transfer of wheat germ agglutinin-horseradish peroxidase in vivo. *J. Comput. Neurol.* **1985**, *242*, 632−650.
22. Balin, B. J.; Broadwell, R. D.; Salcman, M.; El-Kalliny, M. Avenues for entry of peripherally administered protein to the central nervous system in mouse, rat, and squirrel monkey. *J. Comput. Neurol.* **1986**, *251*, 260−280.
23. Czerniawska, A. Experimental investigations on the penetration of ^{198}Au from nasal mucous membrane into cerebrospinal fluid. *Acta Otolaryng.* **1970**, *70*, 58−61.
24. Gianutsos, G.; Morrow, G. R.; Morris, J. B. Accumulation of manganese in rat brain following intranasal administration. *Fundam. Appl. Toxicol.* **1997**, *37*, 102−105.
25. Hastings, L.; Evans, J. E. Olfactory primary neurons as a route of entry for toxic agents into the CNS. *Neurotoxicology* **1991**, *12*, 707−714.
26. Evans, J.; Hastings, L. Accumulation of Cd(II) in the CNS depending on the route of administration: intraperitoneal, intratracheal, or intranasal. *Fundam. Appl. Toxicol.* **1992**, *19*, 275−278.
27. Sakane, T.; Akizuki, M.; Yamashita, S.; Nadai, T.; Hashida, M.; Sezaki, H. The transport of a drug to the cerebrospinal fluid directly from the nasal cavity: the relation to the lipophilicity of the drug. *Chem. Pharm. Bull.* **1991**, *39*, 2456−2458.
28. Sakane, T.; Akizuki, M.; Taki, Y.; Yamashita, S.; Sezaki, H.; Nadai, T. Direct drug transport from the rat nasal cavity to the cerebrospinal fluid: the relation to the molecular weight of drugs. *J. Pharm. Pharmacol.* **1995**, *47*, 379−381.
29. Sakane, T.; Akizuki, M.; Yamashita, S.; Sezaki, H.; Nadai, T. Direct drug transport from the rat nasal cavity to the cerebrospinal fluid: the relation to the dissociation of the drug. *J. Pharm. Pharmacol.* **1993**, *46*, 378−379.
30. Sakane, T.; Akizuki, M.; Yoshida, M.; Yamashita, S.; Nadai, T.; Hashida, M.; Sezaki, H. Transport of cephalexin to the cerebrospinal fluid directly from the nasal cavity. *J. Pharm. Pharmacol.* **1991**, *43*, 449−451.
31. Hussain, M. A.; Rakestraw, D.; Rowe, S.; Aungst, B. J. Nasal administration of a cognition enhancer provides improved bioavailability but not enhanced brain delivery. *J. Pharm. Sci.* **1990**, *79*, 771−772.

Acknowledgments

This work was supported in part by a grant from the National Institute on Drug Abuse (DA12206).

JS9900295

Ultraviolet Spectroscopic Estimation of Microenvironments and Bitter Tastes of Oxyphenonium Bromide in Cyclodextrin Solutions

NORIAKI FUNASAKI,* RYUSAKU KAWAGUCHI, SAKAE HADA, AND SABURO NEYA

Contribution from *Kyoto Pharmaceutical University, 5, Nakauchicho, Misasagi, Yamashina-ku, Kyoto, 607-8414, Japan.*

Received January 28, 1999. Final revised manuscript received April 7, 1999.
Accepted for publication June 2, 1999.

Abstract □ The UV absorbance and bitter taste of oxyphenonium bromide (OB), an antiacetylcholine drug, in cyclodextrin (CD) solutions are measured, and the local environment of the binding site and the reduction of the bitter taste intensity are quantitatively estimated from the UV data. The UV spectrum of OB is changed with the addition of α-, β-, and γ-CD, because the phenyl group of OB is included into the CD cavity. The maximum wavelength, λ_{max}, senses environmental changes of OB best among several spectral characteristics. From comparison of λ_{max} between a CD solution and the reference ethanol–water and dioxane–water systems, the dielectric constant of the binding site is evaluated. This value leads us to estimate the microenvironment and structure of the binding site. The suppression of the bitter taste of 4 mM OB by CDs is in the increasing order α-CD < γ-CD < β-CD. The extent of this suppression can be quantitatively predicted from the UV absorbance by assuming that the free OB molecule alone exhibits the bitter taste, regardless of the kind and concentration of CD. Some implications and limitations of the present approach are discussed.

Introduction

Cyclodextrins (CDs) have homogeneous toroidal structures of different sizes. One side of the torus contains primary hydroxyl groups, whereas the secondary groups are located on the other side. The toroidal structure has a hydrophilic surface resulting from the 2-, 4-, and 6-position hydroxyls, making them water-soluble. The cavity is composed of the glucoside oxygens and methylene hydrogens, giving it a hydrophobic character.[1,2] CDs can give beneficial modifications of guest molecules not otherwise achievable: solubility enhancement, stabilization of labile guests, control of volatility and sublimation, and physical isolation of incompatible compounds. Because they are practically nontoxic, they are added into pharmaceuticals and foods for stabilization of labile compounds and long-term protection of color, odor, and flavor.[2,3] Furthermore, cyclodextrins can mask bitter tastes of drugs,[2,3] e.g., propantheline bromide[4] and oxyphenonium bromide.[5]

The effect of solvents on the ultraviolet (UV) spectra of aromatic molecules, particularly benzene, has been studied extensively. UV spectra are often sensitive to the nature of the local environment in solution.[6] Medium sensitive spectral characteristics can in turn be useful for studying the microenvironments of molecules and, indeed, a great variety of spectroscopic methods in solutions of small molecules and macromolecules as also in micelle and membrane research.[7] Many such studies have the objective of estimating the polarity of the microenvironment by comparison with a number of reference solvents. Many times relatively small changes with CD inclusion can be observed on UV spectra of guest.[2,3] At least an approximate estimation of the polarity of the internal CD cavity enables us to understand the inclusion of the various guests and to predict the type of the potential guests. Various and different estimates have been published. One estimate is based on the fact that the spectral shift shown by the *N*,*N*-diphenylamine (DPA) fluorescence probe depends on the polarity of ethanol−water mixtures. The fluorescence spectra of DPA show that the polarity of β-CD seems to be identical with that of a 40% ethanol/water mixture. Of course, this value cannot be considered to be an absolute one, but probably only as a lower level. The DPA molecule in solution is completely surrounded by solvent molecules, while the extent of penetration of the DPA guest into the CD cavity is probably only a partial inclusion.[3] From measurements of fluorescence quantum yields, Kondo et al. estimated the dielectric constant of 6-*p*-toluidinylnaphthalene-2-sulfonate in the CD cavity.[8]

Sensory tests generally depend on individuals. Some instrumental methods, therefore, are desired for such tests. In this work we develop a UV method for the quantitative estimation of the bitter taste intensity of oxyphenonium bromide (OB, Figure 1), an antiacetylcholine drug, in aqueous solutions of α-, β-, and γ-CDs. The UV absorbance can be used for the determination of the binding constants of OB with the CDs. Those constants enable us to estimate the concentration of the free OB molecule in the CD solutions. Bitter compounds are generally hydrophobic,[9] but their CD complexes are rather hydrophilic, because of the hydrophilicity of CDs.[4] Thus we can expect that the bitter taste of OB in a CD solution is estimated from the free OB concentration alone.[4,5] The other research interest is that OB has two possible hydrophobic groups for CD inclusion, phenyl and cyclohexyl groups. The incorporation of the phenyl group into the CD cavity should result in UV spectral changes, because of the change of its microenvironment. Thus, we can expect to determine which group of OB is entrapped into the CD cavity.

Experimental Section

Materials—A sample of OB was purchased from Sigma Chemical Co. Because this sample was analyzed to be pure by reversed-phase liquid chromatography, it was used without purification. Sodium bromide of analytical grade and α-, β-, and γ-CDs from Nacalai Tesque Co. (Kyoto) were used as received. The ion-exchanged water was used after double distillation.

UV Measurements—All UV spectra were recorded with a Hitachi U-3000 spectrophotometer at 36.5 ± 0.1 °C. The absorbance was determined at an interval of 0.5 nm between 220 and 300 nm and at an interval of 0.1 nm between 240 and 280 nm. The first and second derivative spectra of OB were recorded at an interval of 0.1 nm between 240 and 280 nm. All sample and reference cuvettes contained 154 mM NaBr, unless specified. The sample cuvette contained 4 mM OB and CD, whereas the reference cuvette contained CD of the same concentration as the sample. The difference spectra were obtained by subtracting the spectra of a 4 mM OB solution from those of sample solutions. The maximum wavelength, λ_{max}, was determined from the first deriva-

10.1021/js990026s CCC: $18.00 Published on Web 07/09/1999

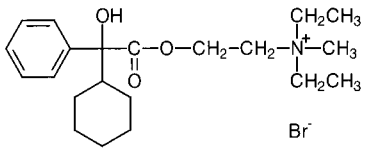

Figure 1—Chemical structure of OB.

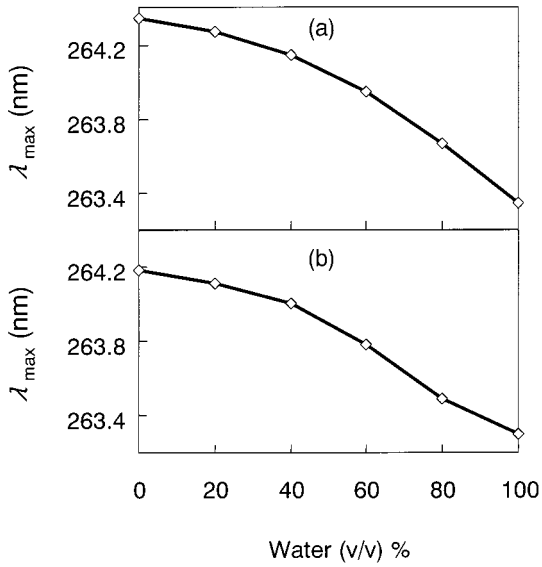

Figure 2—UV maximum wavelength of OB vs volume percent of water in binary mixtures of (a) ethanol and water and (b) dioxane and water. The smooth lines are hand-drawn through the observed data at 36.5 °C.

tive spectrum. The CD concentrations in the sample were changed up to 50 mM, 10 mM, and 50 mM for α-CD, β-CD, and γ-CD, respectively. For each CD system the difference spectra were obtained at about seven concentrations, and those absorbance data were used for the determination of the binding constant of OB and CD.

The effects of ethanol and dioxane on the spectrum of 4 mM OB were investigated at several compositions without NaBr.

Test of Bitter Taste—Five volunteers were involved in the sensory test. These panelists tasted aqueous 154 mM NaBr solutions containing OB alone and a mixture of 4 mM OB and CD. Each volunteer categorized the bitter taste intensity of a solution as one of the following scores: 0 = no bitter taste; 1 = very slightly bitter taste; 2 = slightly bitter taste; 3 = appreciably bitter taste; 4 = very bitter taste; 5 = extremely bitter taste. The bitterness score for the solution was averaged over the five individuals, so that the averaged score of the solution was a continuous variable smaller than 5.

Data Treatments—Absorbance data were transferred to tables in Microsoft Excel 97 to be subject to further analysis. The nonlinear least-squares method available in Microsoft Excel 97 was used.

Results and Discussion

UV Spectra of Oxyphenonium Bromide—The aromatic chromophore absorbs the UV light. The water spectrum of benzene, for example, exhibits a bathochromic shift, a reduction in the peak intensity, and a broadening of the bands.[6] Similar spectral changes were observed for OB in water, dioxane, ethanol, and their mixtures. The maximum wavelength (λ_{max}), minimum wavelength (λ_{min}), and absorbance ratio (A_{max}/A_{min}) at λ_{max} and λ_{min} in original spectra and corresponding spectral parameters in the first and second derivative spectra depend on the solvents. The peak around 263 nm is the most sensitive to the solvent among these spectral parameters. As Figure 2 shows, this band shifts toward the longer wavelength side with the addition of ethanol and dioxane.

Table 1—Absorption Maximum Wavelengths, Dielectric Constants, and Binding Constants of OB in CD Solutions at 309.7 K

CD	λ_{max} (nm)	D_{ETOH}	$D_{ETOHcor}$[a]	D_{DIO}	D_{DIOcor}[a]	K_1 (M^{-1}) UV	K_1 (M^{-1}) emf[b]
none	263.30	74.5	74.5	74.5	74.5	–	–
50 mM α-CD	263.48	66.5	64.7	66.5	64.7	94	58
10 mM β-CD	264.31	<22.7	<22.7	4.5	2.9	7350	8500
50 mM γ-CD	263.98	45.0	40.5	36.5	30.7	140	96

[a] Dielectric constant at full binding. [b] Electromotive force measurements.[5]

As Table 1 shows, the CDs also cause red shifts. This result indicates that OB is bound to these CDs. Comparison between these λ_{max} values and the results of Figure 2 enable us to estimate the local microenvironments of OB in the CDs. The dielectric constants of the water–ethanol[10] and water–dioxane[11] systems at 37 °C are available in the literature. The estimated dielectric constants are shown at columns labeled D_{ETOH} and D_{DIO} in Table 1. The dielectric constant in a 10 mM β-CD solution is smaller than that of ethanol (22.7).[10] These dielectric constant values do not accurately correspond to the true microenvironments of the binding sites, because all of the OB molecules are not incorporated into the CDs under the present conditions. To correct this partial binding, we need the binding constants of OB with the CDs.

Binding Constants of Oxyphenonium Bromide for Cyclodextrins—On the basis of electromotive force data, we have shown that OB (P) does not self-associate below 10 mM and that it forms the 1:1 complexes (PD) alone with α-CD, β-CD, and γ-CD (D).[5] The equilibrium constant of this complexation is defined as

$$K_1 = [PD]/[P][D] \quad (1)$$

The total concentrations of OB and CD are written as

$$C_P = [P] + [PD] \quad (2)$$

$$C_D = [D] + [PD] \quad (3)$$

From eqs 1–3, we can obtain the concentration of free OB:

$$[P] = \{K_1C_P - K_1C_D - 1 + [(K_1C_P - K_1C_D - 1)^2 + 4K_1C_P]^{1/2}\}/2K_1 \quad (4)$$

Figure 3 shows typical difference spectra of OB in solutions of α-CD, β-CD, and γ-CD containing 154 mM NaBr. At a given wavelength the absorbance difference, ΔA, can be expressed as

$$\Delta A = l(\epsilon_{PD} - \epsilon_P)[PD] \quad (5)$$

$$= l(\epsilon_{PD} - \epsilon_P)\{K_1C_P + K_1C_D + 1 - [(K_1C_P - K_1C_D - 1)^2 + 4K_1C_P]^{1/2}\}/2K_1 \quad (6)$$

where ϵ_P and ϵ_{PD} denote the molar absorptivities of OB and the equimolar complex of OB and CD, respectively, and l stands for the optical path length of the cuvette. The ϵ_P value was determined from the spectrum of a 4 mM OB solution.

From eq 6 we can calculate a theoretical absorbance difference value for a given set of C_P and C_D. The values of ϵ_{PD} and K_1 were regarded as adjustable parameters to be best fitted to the observed absorbance difference by nonlinear least-squares method. The best fit binding constants are shown in Table 1. These values are close to those

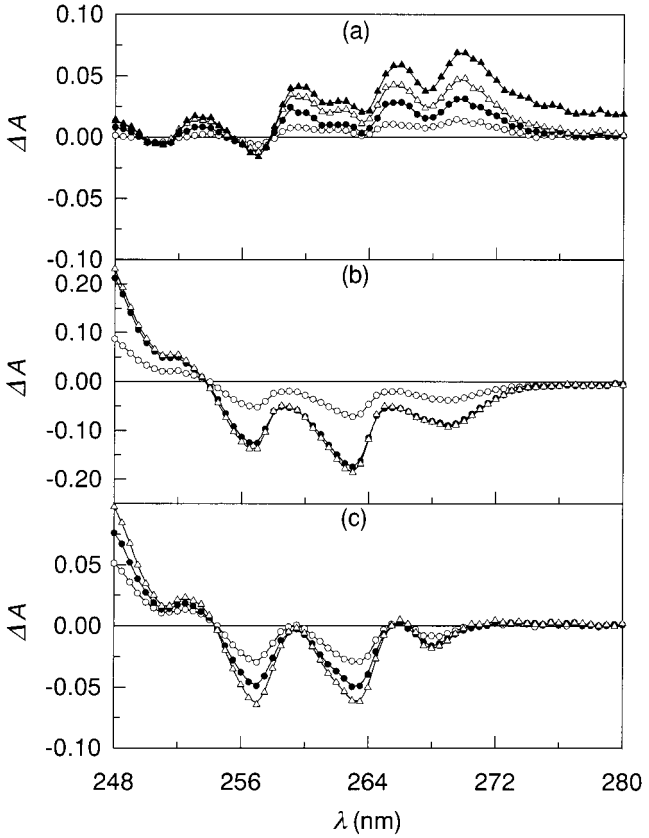

Figure 3—Typical UV difference spectra of 4 mM OB in 154 mM NaBr solutions of (a) α-CD, (b) β-CD, and (c) γ-CD. The CD concentrations (mM) were at 5 (○), 10 (●), 20 (△), and 30 (▲) for α-CD, 1.5 (○), 4.5 (●), and 9.0 (△) for β-CD, and 5 (○), 10 (●), and 15 (△) for γ-CD.

Table 2—Molar Absorptivities (cm^{-1} mM^{-1} at Two Wavelengths) of OB and the Equimolar Complex, the Number of Data, and the SS Value for the OB–CD Systems at 309.7 K

CD	ϵ_P	ϵ_{PD}	λ_1 (nm)	ϵ_P	ϵ_{PD}	λ_2 (nm)	n	SS × 10^4
α-CD	0.1596	0.1752	265.5	0.0821	0.1001	269.5	12	7.79
β-CD	0.2277	0.1945	257.0	0.1886	0.1418	263.0	13	2.49
γ-CD	0.2277	0.2030	257.0	0.1917	0.1669	263.5	13	2.15

determined by electromotive force measurements.[5] For α-CD the observed absorbance differences at 265.5 and 269.5 nm were used simultaneously, because these values exhibited the greatest changes. By the same reasons the wavelengths at 257.0 and 263.0 and at 257.0 and 263.5 nm were employed for β-CD and γ-CD, respectively. The extent of fitting was measured by the SS value defined as

$$SS = \sum^{n} (\Delta A_{obsd} - \Delta A_{calcd})^2 \qquad (7)$$

The number, n, of data and the SS value were shown in Table 2, together with the molar absorptivities for the equimolar complex of OB and CD.

Now we can estimate the dielectric constants at the binding sites of OB in CD by using the binding constants obtained by the UV method. The binding percent of OB is 81.5% for 50 mM α-CD, 97.8% for 10 mM β-CD, and 86.8% for 50 mM γ-CD. We assumed that the estimated dielectric constant is the sum of the free OB and bound OB. Thus, we can estimate the dielectric constants, D_{cor}, at full binding for the ethanol and dioxane systems. As Table 1 shows, these dielectric constants for CD are rather close to one another for the two solvent systems. This fact

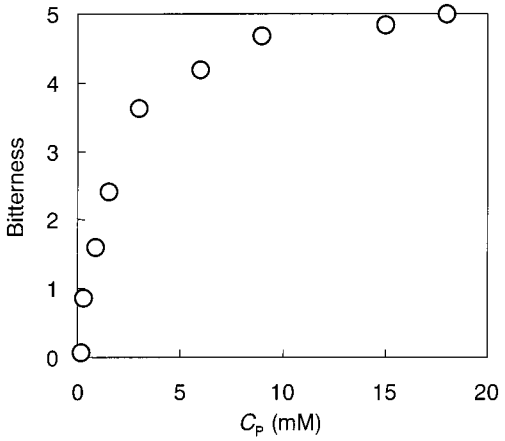

Figure 4—Scores of bitter tastes of aqueous OB solutions plotted against the OB concentrations.

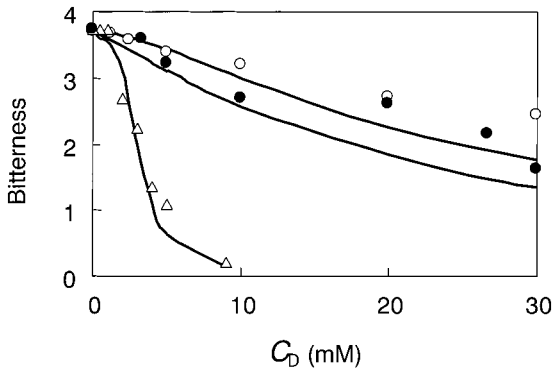

Figure 5—Effects of CDs on the bitter taste intensity of a 4 mM OB solution: α-CD (○), β-CD (△), and γ-CD (●). The solid lines are calculated from eqs 4 and 8 by using the equilibrium binding constants shown in Table 1.

demonstrates the validity of the present estimation. The dielectric constant for α-CD suggests that the phenyl group of OB is outside of the α-CD cavity or is shallowly penetrated into the cavity. The phenyl group of OB will be deeply incorporated into the β-CD cavity, because an estimated dielectric constant of $D_{DIOcor} = 2.9$ is very close to 2.1 of dioxane.[11] Because this group is snugly incorporated in the γ-CD cavity, the cavity has room enough to contain some remaining water molecules. Therefore, OB senses the γ-CD cavity to be a mixture of dioxane and water with $D_{cor} = 30.7$.

Thus, we can estimate the microenvironments of OB in the CDs from the UV spectra.

Effects of Cyclodextrins on the Bitter Taste Intensity of OB—The intensity of bitter taste of an OB solution is shown as a function of OB concentration in Figure 4. As Figure 5 shows, the bitter taste intensity of a 4 mM OB solution is remarkably reduced by the addition of CDs. This reduction by the kind of CD is in the increasing order of α-CD < γ-CD < β-CD, consistent with the magnitude of the binding constant.

Bitter compounds have a variety of chemical structures including alkaloids and terpenes. These compounds, however, are generally hydrophobic and easily absorbed to the receptor of bitter sites.[9] OB tastes bitter, but CD is not a bitter compound, because of its hydrophilicity. We have shown that the complexes of CD with surfactants[12] and propantheline bromide[4] are surface-inactive. Similarly, the complex of OB and CD is rather hydrophilic and would not taste bitter.[4,5] Thus we can assume that the free OB molecule alone exhibits the bitter taste, regardless of its CD complex and CD. On the basis of this assumption, the bitter taste intensity of an aqueous solution of OB and CD

will be determined by the concentration ([P]) of uncomplexed OB in the solution, irrespective of the kind and concentration of CD:

$$\text{bitter taste intensity} = g\{[P]\} \quad (8)$$

Actually we did not attempt to fit any empirical equation to the observed bitter scores shown in Figure 4, but drew a smooth line through these data, albeit not shown therein. This line was used for reading a bitter score at a free concentration of OB and is expected to hold true for all solutions of OB and CD.

To verify this assumption, we calculated a theoretical bitter taste intensity by using eqs 4 and 8 for a solution containing 4 mM OB and CD. Here the binding constant estimated by the UV method was employed in eq 4. The solid curves in Figure 5 show such theoretical values. These values are close to the observed ones. Thus, eq 8 holds true for all solutions containing OB and CDs. This important result enables us to predict the intensity of bitter taste of an OB and CD solution from the observed UV absorbance of their mixed solution.

Implications and Limitations of the Present Work—The present UV approach for estimating the microenvironment of the binding site will apply for CD inclusion of other chromophores. OB exclusively forms the 1:1 complexes with α-, β-, and γ-CD.[5] Other guests often form ternary and quaternary complexes.[12] For such complicated inclusion systems, the present approach will not provide clear information on their microenvironments, though other spectroscopic methods, such as NMR and circular dichroism, can give more detailed information. Such spectroscopic data will generally provide a basis of the present UV method for estimating the binding site.

The UV method for predicting the bitter taste of OB reduced by CDs will apply to other bitter aromatic compounds. This enables us to determine the kind and concentration of CD to suppress the bitter taste of drug from a few and reproducible experiments. The UV method, however, does not apply for the self-associating or multiple complexing systems, because the UV absorbance senses all of the monomer and polymers of guest and its CD complexes. For the same purpose we have proposed the surface tension[4] and electromotive force[5] methods. Many drugs self-associate in aqueous media by hydrophobic interactions,[13] though OB does not self-associate.[5] Guest generally forms multiple complexes with CD.[12,14] The surface tension and electromotive force methods can apply to such self-associating or multiple complexing systems,[4,5] because these methods sense the free drug molecule alone. The UV method, however, has the advantage of convenience over these methods. This method would apply to bitter blockers with characteristics similar to CD. A kind of lipoprotein can specifically inhibit bitter taste by masking the receptor site for bitter substances.[15] The present method will be inapplicable to such masking systems.

References and Notes

1. Bender, M. L.; Komiyama, M. *Cyclodextrin Chemistry*; Springer-Verlag: Berlin, 1978; Chapters 2 and 3.
2. Szejtli, J. *Cyclodextrin Technology*; Kluwer Academic Publishers: Dordrecht, The Netherlands, 1988; Chapters 3 and 7.
3. Frömming, K.-H. Szejtli, J. *Cyclodextrin in Pharmacy*; Kluwer Academic Publishers: Dordrecht, The Netherlands, 1994; Chapters 1 and 4−8.
4. Funasaki, N.; Uemura, Y.; Hada, S.; Neya, S. Reduction of the Bitter Taste Intensity of Propantheline Bromide by Cyclodextrins as Predicted by Surface Tension Measurements. *J. Phys. Chem.* **1996**, *100*, 16298−16301.
5. Funasaki, N.; Kawaguchi, R.; Ishikawa, S.; Hada, S.; Neya, S.; Katsu, T. Quantitative Estimation of the Bitter Taste Intensity of Oxyphenonium Bromide Reduced by Cyclodextrins from Electromotive Force Measurements. *Anal. Chem.* **1999**, *71*, 1733−1736.
6. Cardinal, R.; Mukerjee, P. Solvent Effects on the Ultraviolet Spectra of Benzene Derivatives and Naphthalene. Identification of Polarity Sensitive Spectral Characteristics. *J. Phys. Chem.* **1978**, *82*, 1614−1620 and references therein.
7. Mukerjee, P.; Cardinal, R. Benzene Derivatives and Naphthalene Solubilized in Micelles. Polarity of Microenvironment, Location and Distribution in Micelles, and Correlation with Surface Activity in Hydrocarbon−Water Systems. *J. Phys. Chem.* **1978**, *82*, 1620−1627.
8. Kondo, H.; Nakatani, H.; Hiromi, K. Interaction of Cyclodextrins with Fluorescent Probes and Its Application to Kinetic Studies of Amylase. *J. Biochem.* **1976**, *79*, 393−405.
9. Kurihara, K. *Taste and Smell*; Kagaku Doujin: Kyoto, 1990; Chapter 6.
10. Åkerlöf, G. Dielectric Constants of Some Organic Solvent−Water Mixtures at Various Temperatures. *J. Am. Chem. Soc.* **1932**, *54*, 4125−4139.
11. Åkerlöf, G.; Short, O. A. The Dielectric Constant of Dioxane-Water Mixtures between 0 and 80°. *J. Am. Chem. Soc.* **1936**, *58*, 1241−1243.
12. Funasaki, N.; Yodo, H.; Hada, S.; Neya, S. Stoichiometries and Equilibrium Constants of Cyclodextrin-Surfactant Complexations. *Bull. Chem. Soc. Jpn.* **1992**, *65*, 1323−1330.
13. Funasaki, N. Gel Filtration Chromatographic Study on the Self-Association of Surfactants and Related Compounds. *Adv. Colloid Interface Sci.* **1993**, *43*, 87−136.
14. Connors, K. A. The Stability of Cyclodextrin Complexes in Solution. *Chem. Rev.* **1997**, *97*, 1325−1357.
15. Katsuragi, Y.; Kurihara, K. *Nature* **1993**, *365*, 213-214.

Acknowledgments

Thanks are due to Dr. Seiji Ishikawa for excellent data processing.

JS990026S

Use of Gelatin–Acacia Coacervate Containing Benzocaine in Topical Formulations

ANDREAS M. ICHWAN, MANOUS KARIMI, AND ALEKHA K. DASH*

Contribution from *Department of Pharmaceutical and Administrative Sciences, School of Pharmacy and Allied Health Professions, Creighton University, Omaha, Nebraska 68178.*

Received December 30, 1998. Accepted for publication June 3, 1999.

Abstract □ The in vitro release of a drug from topical formulations depends on the concentration of the drug in the formulation, the solubility of the drug in the base, the diffusion coefficient of the drug in the vehicle, and the partition coefficient of the drug between the vehicle, and the release medium. Incorporation of both complexing agents and cosolvents into such formulations has been used to enhance the in vitro release of a drug from topical formulations. In this investigation, a novel approach to enhance the in vitro release of benzocaine from different ointment formulations has been introduced. In this study, benzocaine was microencapsulated using gelatin–acacia complex coacervation technique. Various weight fractions of the coacervate, 5, 10, and 20% (w/w), were incorporated into both oleaginous and absorption bases. The in vitro release characteristics of benzocaine from the resulting ointments were studied using a modified USP Dissolution Apparatus 2. A plot of the cumulative amount of drug released (7–8%) per unit surface area versus $(\text{time})^{1/2}$ was linear. Microscopic studies of the formulations revealed that the coacervates maintained their integrity in the formulation during the preparation and storage of the dosage form. Differential scanning calorimetric (DSC) studies indicated that the drug existed in the crystalline state in all formulations including those at a low drug load (0.5% w/w). DSC was also used to determine the solubility of the drug in the formulation. The rate and extent of drug release was higher in the absorption base as compared to the oleaginous base.

Introduction

When striving to achieve therapeutic effectiveness in a topical formulation, two important factors are generally considered during the design of such formulations including (i) the rate of drug release from the vehicle used in the formulation and (ii) the ease or difficulty with which the drug will penetrate the skin barrier after its release from the base. Different mathematical models have been utilized in the literature to describe the in vitro release characteristics of a drug from topical dosage forms.[1−3] The rate of drug release from such formulations depends on various physicochemical factors including the solubility of the drug in the vehicle, the concentration of the drug in the formulation, and the diffusion coefficient of the drug in the topical vehicle.[1] However, when two-phase emulsion type topical formulations are utilized, one must consider the type of emulsion used in the formulation of the ointment and also the effect of micellar solubilization on the thermodynamic activity of the drug in various phases.[3−6] When the topical formulation matrix is an emulsion or suspension type, the effective diffusion coefficient of the drug must be used instead of diffusion coefficient.[3] In general, the rate of drug release from topical formulations has been enhanced by increasing the drug load, by changing the diffusivity of the drug in the vehicle, and by changing the drug's solubility in the vehicle. The solubility of a drug in the vehicle has been modified by incorporation of other components into the base, the addition of a cosolvent, changing the pH of the medium, and addition of a complexing agent.[7−9] The diffusivity of the drug has been altered by changing the microscopic viscosity of the vehicle.[1] In essence, the effect of different bases and their composition on the release of benzocaine from topical formulations has been extensively studied.[10−14] The present study attempts to enhance the release rate of a model drug benzocaine from ointments prepared from two different bases using a novel gelatin−acacia coacervation technique.

The gelatin−acacia complex coacervation method has been widely used for the microencapsulation of many hydrophobic drugs.[15−20] During the microencapsulation process, the coacervates formed are usually cross-linked and hardened by the addition of a dehydrating agent.[21] Aldehydes are generally used for this purpose. Cross-linking of the gelatin−acacia coacervate occurs through either a dimethylene ether bridge or methylene bridge.[21] In contrast, this investigation has used gelatin−acacia complex coacervates (without cross-linking) containing benzocaine in topical formulations to modify the release characteristics of this drug. In this study, benzocaine microcapsules prepared using the gelatin−acacia complex coacervation method were incorporated directly into the ointment bases by levigation prior to the hardening process of the microcapsule wall. Therefore, the objectives of this investigation were (i) to modify the release characteristics of benzocaine from various topical formulations by incorporation of the gelatin−acacia coacervate of the drug into base, (ii) to evaluate the effect of various base-types on the release characteristics of the drug, and (iii) to elucidate the mechanism of release from the resulting formulations.

Materials and Methods

Materials—Benzocaine and *n*-butyl PABA (Sigma Chemicals, Milwaukee, WS); gelatin, acacia, chloroform, *n*-octanol, hydrochloric acid (Fisher Scientific, Fairlawn, NJ); white petrolatum (Dayton Hudson, Minneapolis, MN); Aquaphor (Beiersdorf, Norwalk, CT) were used as received.

Preparation of the Benzocaine Microcapsules and the Ointments—Benzocaine (2 g) was dispersed in 100 mL of 1% (w/v) acacia solution in water, and the resulting suspension was then mixed with 1% (w/v) gelatin solution at 40 °C while stirring the solution. The pH of the 1% acacia solution was 4.5 and that of the 1% (w/w) gelatin solution was 4.0. The pH of the gelatin−acacia mixture (50:50 v/v) was 4.3. The pH of this mixture was adjusted to 3.9 with 0.1 N HCl and stirred for an additional 30 min. The coacervates were then centrifuged at 2000 rpm for 5 min in a IEC HN-II model centrifuge (International Equipment Company, Needham Hts, MI), and the supernatant was discarded. Different weight fractions of the coacervate were then incorporated into an oleaginous base (Petrolatum) and an absorption base

* Corresponding author.

10.1021/js9805017 CCC: $18.00 Published on Web 07/03/1999

(Aquaphor). Empty gelatin–acacia coacervates were prepared without benzocaine using the similar procedure described earlier for the benzocaine microcapsules. Physical mixtures of both bases with blank coacervate (microcapsules without drug) were prepared by mixing the coacervates with base by levigation. The resulting mixture will be described as the "physical mixture" in the text, hereafter. Ointments were prepared using the levigation method on an ointment slab. The water content of the coacervate without benzocaine and with benzocaine, prior to incorporation into ointment bases was determined using Karl Fisher titrimetry.

Analysis of Benzocaine—Benzocaine was analyzed by two methods. An HPLC method was used to study the in vitro release kinetics of the drug and its stability in the formulation. A Spherisorb C18, pH stable column (Phase Separations, Norwalk, CT), 15 cm in length was used. The column effluents were monitored at 254 nm (Shimadzu SPD-6A UV detector, Shimadzu. Koyoto, Japan), and the flow rate was maintained at 1 mL/min (Shimadzu LC-6A pump). The mobile phase consisted of methanol: phosphate buffer (58:42 v/v, pH 8.0). A UV/vis spectrophotometer (Perkin-Elmer, Lamda 400, Perkin-Elmer, Norwalk, CT) was operated at a wavelength of 290 nm. This method was used to determine the drug load in the formulation.

Drug Content in the Ointments—A known amount of the ointment was dissolved in chloroform, and the concentration of benzocaine in solution was determined using a calibration curve of the drug in chloroform. Standard curves were linear over the concentration range (0.5–40 μg/mL).

In Vitro Release Studies—The in vitro release of benzocaine from the ointments was carried out in a modified USP Dissolution Apparatus 2 (Hanson Research Corp., Chatsworth, CA). Five hundred milliliters of Sorensen's phosphate buffer pH 7.4 was used as the release medium, and temperature of the medium was maintained at 32 °C. The ointments (3.6–4.0 g) were placed in a specially designed aluminum cell (made in-house) with a diameter of 4.5 cm. The aluminum cells containing the ointments were carefully placed in the bottom of the dissolution medium. The paddles were rotated at 50 rpm. The release of drug from the surface (surface area = 15.90 cm^2) to the bulk of the release medium was studied. At predetermined time intervals, 1 mL of the release medium was collected and replaced with 1 mL of fresh buffer. The concentration of benzocaine in the solution was determined using the HPLC method described earlier. The data presented are the average of three formulations prepared independently.

Phase Contrast Microscopic Studies—The ointment samples were carefully smeared on glass slide and examined under a phase contrast microscope (Olympus, model CK2). This microscope was attached to a camera (OM-10) and used a Kodak Plus-X-Pan film with an ASA 125 automatic exposure.

Differential Scanning Calorimetry—DSC curves were obtained using a Shimadzu (DSC-50) differential scanning calorimeter attached to a Shimadzu (model C-R49) Chromatopac integrator. Samples (2–5 mg) were placed in the aluminum pans and heated at a rate of 10 °C/min with nitrogen purge at a rate of 20 mL/min.

Determination of Solubility of the Drug in the Ointment—The solubility of the drug in the ointment at its melting point was determined by DSC using a method described by Theeuwes et al.[22] The ointment sample (2–5 mg) was crimped into a nonhermatically sealed aluminum pan and heated in a DSC at a controlled rate (10 °C/min) with nitrogen purge. The enthalpy of fusion of the drug was determined and plotted against the known drug load.

Results and Discussion

The phase contrast microscopic studies of the petrolatum base containing benzocaine, empty microcapsules, and microencapsulated benzocaine is shown in Figure 1. Benzocaine crystals were evident in the ointment even at the lowest drug load (0.5% w/w) as shown in Figure 1a. Figure 1b depicts the micrograph of an ointment containing a physical mixture of 20% (w/w) of empty gelatin–acacia coacervate (without benzocaine) and 80% (w/w) of petrolatum after one month of storage in a refrigerator. Figure 1c represents the micrograph of ointment prepared from microencapsulated benzocaine in petrolatum. This study

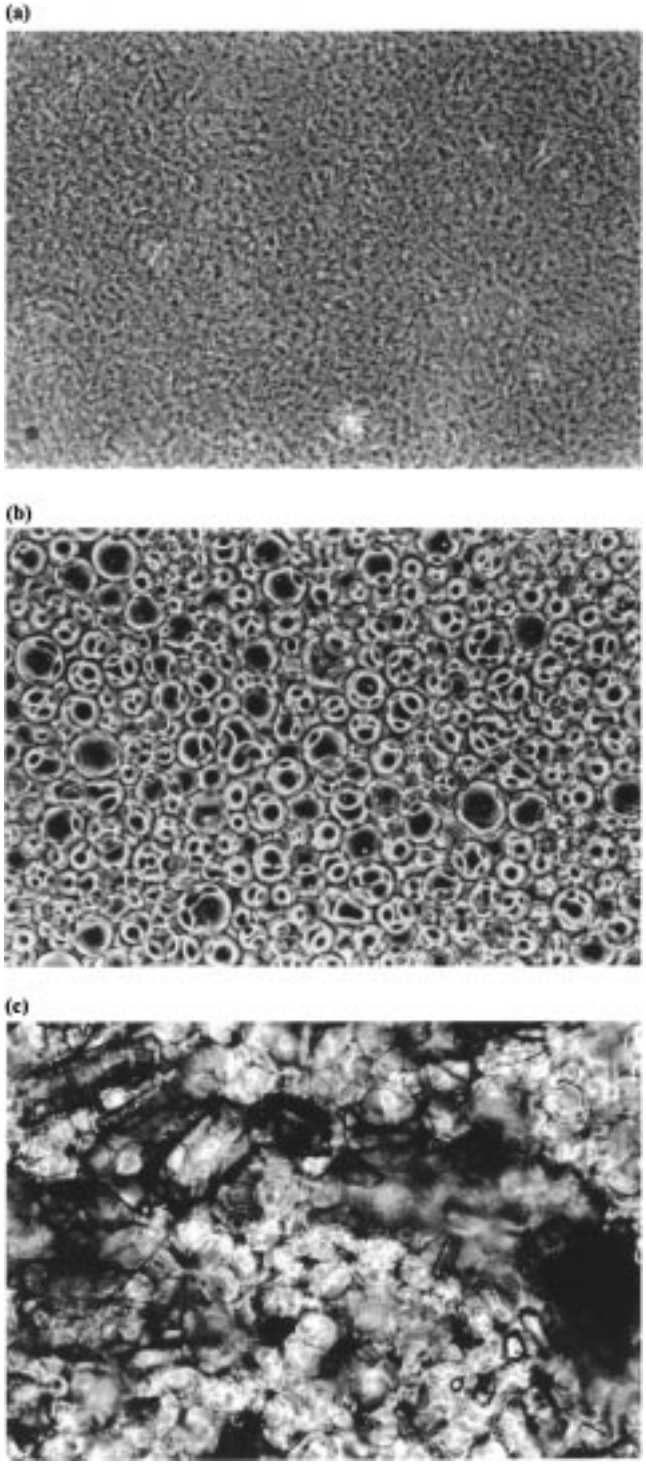

Figure 1—Photomicrographs of (a) benzocaine ointment in Petroatum (0.5% w/w); (b) physical mixture of empty microcapsules 20% (w/w) and Petrolatum 80% (w/w); (c) microencapsulated benzocaine in Petrolatum.

revealed that the coacervate maintains its integrity during preparation of the ointments and storage over a period of at least one month. The physical state of drug in the topical formulation is an important parameter, which in turn affects the drug's release rate from the topical vehicle. The rate of release of a drug from a formulation is always higher if the drug is present in the dissolved state rather than the dispersed state.[3,11] In this investigation, the physical state of the drug was determined by two independent methods. DSC was used to measure the enthalpy of fusion, if any, of the free crystalline drug in the formulation. No melting peak in the formulation indicated the drug was

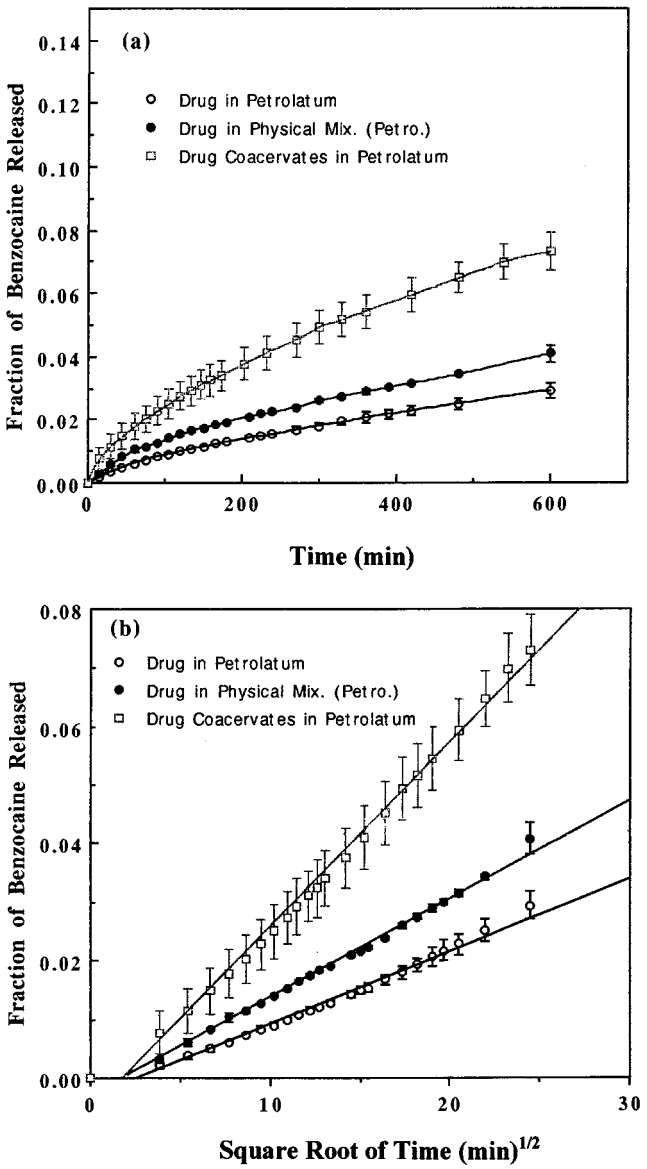

Figure 2—In vitro release of benzocaine from oleaginous (Petrolatum) ointments containing 2.9% (w/w) of benzocaine: (a) plot of cumulative amounts of benzocaine released versus time, and (b) plot of cumulative amounts of benzocaine released versus square root of time.

present in a molecularly dispersed state. The physical state of the drug in the formulation was further confirmed by visual inspection of the free crystalline drug in the formulation under a phase contrast microscope. DSC studies revealed that at even an extremely low drug load (0.5% w/w), an endothermic peak at 88 °C was observed in the DSC thermogram. This endothermic peak was attributed to the melting of benzocaine. Therefore, some of the drug was present in the crystalline state in the formulation at a drug load of 0.5% (w/w).

The fraction of benzocaine released from the ointments prepared from Petrolatum base is shown in Figure 2. In this study, benzocaine was incorporated into the petrolatum base as follows: (i) directly into Petrolatum, (ii) into a physical mixture of the empty microcapsules and Petrolatum (20:80 w/w), and (iii) microencapsulated benzocaine into Petrolatum. The benzocaine load was kept the same in all formulations. The cumulative amount of drug released from ointments containing microencapsulated benzocaine was found to be higher than the physical mixture or Petrolatum alone. A linear relationship was observed when the cumulative amount of drug released was plotted against the square root of time. The results of this study suggest that the release of benzocaine from these formulations occurred by a matrix diffusion control mechanism as described by Higuchi.[1] The slope of the lines (Figure 2b), which is a measure of the rate of drug released from the formulation, was then determined. In the case of the ointment containing coacervated benzocaine in Petrolatum, the release rate was found to be 2.5 times faster than the petrolatum ointment containing benzocaine alone. However, in case of the physical mixture the rate was only 1.4 times higher under similar test conditions.

Also of interest was the determination of the release kinetics of benzocaine from an absorption base. Aquaphor was selected for this study. Three different formulations were prepared in a similar manner as described earlier for Petrolatum. Interestingly, the ointment containing microencapsulated benzocaine also showed a higher rate and extent of benzocaine release. A plot of the cumulative amount of drug released vs the square root of time also showed a linear relationship indicating matrix diffusion control release. The rate of release of benzocaine from Aquaphor containing the coacervated drug was found to be 2.1 times faster than the Aquaphor containing the benzocaine alone. In the case of the physical mixture, the rate of drug release was approximately 1.4 times higher than the base containing benzocaine alone. Comparison of in vitro release profiles of benzocaine from these two bases revealed that in all three types of formulations studied, the release of benzocaine was always higher in Aquaphor than Petrolatum. The in vitro release profiles of benzocaine from Aquaphor and Petrolatum bases containing a similar drug load of benzocaine were then studied. Comparison of the slope of the cumulative amount of benzocaine released versus square root of time for these release profiles revealed that the rate of benzocaine release from the Aquaphor base is approximately 2.6 times higher than that of the Petrolatum base. The increase in drug release from Aquaphor as compared to Petrolatum is possibly explained by the fact that the solubility of the drug in petrolatum is higher than in Aquaphor, thereby held firmly by the vehicle, and the rate of release of drug was slow.[12] The presence of water in the formulation due to the incorporation of the coacervate could also contribute to the rate of release of the drug from these ointments. The water content of the empty coacervates and coacervate containing benzocaine prior to incorporation into the ointments were determined by Karl Fisher Titrimetry and found to be 82.5 and 78.5% w/w, respectively. Therefore, water content of the ointments was approximately 15 to 17% w/w (assuming 20% w/w of the coacervate in the ointment). Presence of water will provide rapid diffusion pathways of drug to get into the dissolution medium. Although benzocaine has very low solubility in water,[23] diffusion through the water pathway or aqueous coacervate pathway would be much faster than through the high viscosity, gellike Petrolatum or Aquaphor. This may explain the increased rate of drug release from ointments containing coacervates or from the physical mixtures.

The solubility of the drug in both bases and the physical mixture was determined by DSC. As mentioned earlier, the solubility of the drug in the matrix is determined by this method at the drug's melting point (approximately 88 °C). As such, the solubility of the drug in the Petrolatum base was determined from the intercept of the line obtained after plotting the drug-load in the formulation versus the heat of fusion. After heating, some samples were allowed to cool to room temperature and again reheated. Melting was observed at the same temperature during reheating indicating the drug was in the same crystalline form. Using this method, the solubility of benzocaine in the Petrolatum

was found to be 0.06 (w/w) (at 88 °C). Unfortunately, the determination of the solubility of benzocaine in Aquaphor, as well as in the physical mixtures, was not possible due to other thermal activity interference near the melting point of the drug from the matrix material.

Conclusions

(1) Gelatin−acacia coacervation method was used in the microencapsulation of benzocaine.

(2) Incorporation of the coacervate (without cross-linking) into Petrolatum or Aquaphor base substantially enhanced the rate of drug release from both bases.

(3) This enhanced release is possibly due to the increased diffusivity of the drug in the base, change in solubility, and the thermodynamic activity of the drug in base by inclusion of coacervates in the formulations.

(4) The release of benzocaine (7−8%, w/w) from all of the formulations occurred via a matrix-controlled diffusion mechanism.

(5) The absorption base showed a higher rate and extent of benzocaine release as compared to the oleaginous base.

References and Notes

1. Higuchi, T. Rate of Release of Medicaments from Ointment Bases Containing Drugs in Suspensions. *J. Pharm. Sci.* **1961**, *50*, 874−875.
2. Higuchi, W. I. Analysis of Data on the Medicament Release from Ointments. *J. Pharm. Sci.* **1962**, *51*, 802−804.
3. Higuchi, W. I. Diffusional Models Useful in Biopharmaceutics: Drug Release Rate Processes. *J. Pharm. Sci.* **1967**, *56*, 315−324.
4. Ong, J. T. H.; Manoukian, E. Release of Lonapalene from Two-Phase Emulsion-Type Ointment Systems. *Pharm. Res.* **1988**, *5*, 16−20.
5. Patel, K. C.; Bankar, G. S.; DeKay, H. G. Study of Anionic and Cationic Surfactants in a Hydrophilic Ointment Base II: The Effect of the Surfactant and its Concentration on Medicament Release. *J. Pharm. Sci.* **1961**, *50*, 300−305.
6. Nyqvist-Mayer, A. A.; Brodin, A. F.; Frank, S. G. Drug Release Studies on an Oil−Water Emulsion Based on a Eutectic Mixture of Lidocaine and Prilocaine as the Dispersed Phase. *J. Pharm. Sci.* **1986**, *75*, 365−373.
7. York, P.; Saleh, A. Z. M. Modification of Diffusion Rate of Benzocaine from Topical Vehicles Using Sodium Salicylate as Complexing Agent. *J. Pharm. Sci.* **1976**, *65*, 493−497.
8. Poulsen, B. J.; Yong, E.; Coquilla, M., Katz. Effect of Topical Vehicle Composition on the In Vitro Release of Fluocinolone Acetonide and its Acetate Ester. *J. Pharm. Sci.* **1968**, *57*, 928−933.
9. Chowhan, Z. T., Pritchard, R. Release of Corticoids from Oleaginous Ointment Bases Containing Drug in Suspension. *J. Pharm. Sci.* **1975**, *64*, 754−759.
10. Malone, T, J. K. Halenblian, Poulsen, B. J., K. H. Burdick. Development and Evaluation of Ointment and Cream Vehicles for a New Topical Steroid, Fluclorolone Acetonide. *Br. J. Dermatol.* **1974**, *90*, 187−195.
11. Osterenga, J., Haleblian, J., Poulsen, B., Ferrell, B., Mueller, N., Subramanium, S. Vehicle Design for a New Topical Steroid, Flucinonide. *J. Invest. Dermatol.* **1971**, *56*, 392−398.
12. Ayrese, J. W., Laskar, P. A. Diffusion of Benzocaine from Ointment Bases. *J. Pharm. Sci.* **1974**, *63*, 1402−1406.
13. Bottari, R., Di Colo, G., Nannipieri, E., Saettone, M. F., Serafini, M. F. Release of Drugs from Ointment Bases II: In vitro Release of Benzocaine from Suspension-Type Aqueous Gels. *J. Pharm. Sci.* **1977**, *66*, 926−931.
14. Lalor, C. B.; Flynn, G. L.; Weiner, N. Formulation Factor Affecting Release of Drug from Topical Formulations. Part 1. Effect of Emulsion Type Upon In Vitro Delivery of Ethyl p-Aminobenzoate. *J. Pharm. Sci.* **1994**, *83*, 1525−1528.
15. Luzzi, L. A.; Gerraughty, R. J. Effects of Selected Variables on the Extractability of Oils from Coacervate Capsules. *J. Pharm. Sci.* **1964**, *53*, 429−431.
16. Luzzi, L. A.; Gerraughty, R. J. Effects of Selected Variables on the Microencapsulation of Solids. *J. Pharm. Sci.* **1967**, *56*, 634−638.
17. Madan, P. L.; Luzzi, L. A.; Price, J. C. Factors Influencing Microencapsulation of a Waxy Solid by Complex Coacervation. *J. Pharm. Sci.* **1972**, *61*, 1586−1588.
18. Nixon, J. R. In Vitro and In Vivo Release of Microencapsulated Chlorothiazide. *J. Pharm. Sci.* **1981**, *70*, 376−378.
19. Takenaka, Y.; Kamashima, Y.; Lin, S. Y. Micromeritic Properties of Sulfamethoxazole Microcapsules Prepared by Gelatin−Acacia Coacervation. *J. Pharm. Sci.* **1980**, *69*, 513−516.
20. Palmieri, A. Microencapsulation and Dissolution Parameters of Undecenvanillylamide: A potential Coyote Deterrent. *J. Pharm. Sci.* **1979**, *68*, 1561−1562.
21. Deasy, P. D. *Microencapsulation and Related Drug Processes*; Marcel Dekker Inc.: New York, 1984; pp 77−80.
22. Theeuwes, F.; Hussain, A.; Higuchi, T. Quantitative Analytical Method for Determination of Drugs Dispersed in Polymers Using Differential Scanning Calorimetry. *J. Pharm. Sci.* **1974**, *63*, 427−428.
23. Richardson, N. E.; Meakin, B. J. The sorption of Benzocaine from Aqueous Solution by Nylon 6 Powder. *J. Pharm. Pharmacol.* **1974**, *26*, 166−174.

Acknowledgments

Financial support from the Health Future Foundation is greatly appreciated.

JS9805017

Multivariate Parameter Evaluation of Pharmaceutically Important Cellulose Ethers

BENGT PERSSON, HANS EVERTSSON,* ROLF BERGMAN,† AND LARS-OLOF SUNDELÖF

Contribution from *Physical Pharmaceutical Chemistry, Uppsala University, Uppsala Biomedical Centre, Box 574, 751 23 Uppsala, Sweden, and SPOC, UF3A1, Pharmacia & Upjohn, 751 82 Uppsala.*

Received February 24, 1998. Accepted for publication April 22, 1999.

Abstract □ A set of nonionic cellulose ethers with varying hydrophobicity and molecular weight has been investigated by principal component analysis (PCA). Several experimental variables such as dynamic surface tension, diffusion coefficient, microviscosity as monitored by a fluorescence probe technique, and intrinsic viscosity are included in the analysis. The experimental variables and observations (polymer fractions) are analyzed in models with good predictive capacities. The apparent equilibrium surface tension correlates to the cloud point and to the critical aggregation concentration in the presence of surfactant. The microviscosity is shown to be a predictive parameter for the degree of hydrophobic substitution. The irreversible process of dynamic surface tension is dependent on the diffusion coefficient but to an even larger degree on the polymer concentration, which is well illustrated by the PCA models.

Introduction

Cellulose ethers of amphiphilic nature such as hydroxypropyl(methyl)cellulose (HPMC) and ethyl(hydroxyethyl)-cellulose (EHEC) are widely used in various pharmaceutical dosage forms. These polymers are used as swelling agents, binders, emulsifiers, rheological stabilizers, and for film coating, etc.[1] Cellulose ethers can be obtained in a variety of fractions (samples) with different physicochemical properties, since the molecular weight and degree of substitution can vary considerably. Furthermore, large batch to batch variations are common which may alter the final pharmaceutical product in which they occur. Interaction between these high molecular weight amphiphiles and low molecular weight active substances, which often are hydrophobic or even amphiphilic in nature,[2] will affect, for example, the release rate of drug from pharmaceutical formulations based on cellulose ethers. The strength of such associative polymer−drug interaction is in turn dependent on the physicochemical properties of the cellulose ether used. Thus, it is of importance to map the influence of the chemical structure of the polymer on its physicochemical properties in aqueous solution.

A set of cellulose ethers differing in hydrophobicity has previously been thoroughly examined in this laboratory by time dependent surface tension determination, viscosity measurements, fluorescence probe techniques, solubilization measurements, light scattering techniques, and size exclusion chromatography. Most of these experimental results have been published elsewhere.[3−5] Some qualitative relationships between the observed variables were seen. However, the interplay between a large number of variables is difficult, if at all possible, to reveal without the aid of mathematical tools capable of handling many, even correlated, variables simultaneously.

Multivariate analysis[6] (MVA) has, over the last couple of decades, become more and more important as the amount of data available on chemical systems increases steadily. This branch of science, today named chemometrics when applied on chemistry, involves a number of multivariate methods[6] and is used in various branches of chemistry and chemical processing[7,8] to find optimum conditions. The present polymer systems have been investigated by principal component analysis[6] (PCA), a method based on linear algebra involving a matrix decomposition. Special emphasis has been put on finding models as simple as possible with which to describe the systems, to find predictive parameters for the physicochemical properties of the polymer fractions (samples). Since the experimental data available on these polymer fractions are quite extensive, the paper also presents a validation of the usefulness of principal component analysis on complex aqueous polymer systems.

Experimental Section

Most of the data used in the analysis are published elsewhere.[3−5] The different polymer samples (observations) are six different ethyl(hydroxyethyl)cellulose (EHEC) fractions, CST-103, DVT-87014, E230G, E411G, PR, OS, varying in molecular weight and degree of substitution, and one fraction each of hydroxypropyl-(methyl)cellulose (HPMC), hydroxypropylcellulose (HPC), hydroxyethylcellulose (HEC), and methylcellulose (MC). All EHEC fractions were obtained from Akzo Nobel AB, Stenungssund, Sweden. HEC and MC were obtained from Aldrich Chemie, Steinham, Germany, HPMC from Colorcon., West Point, PA, and HPC from Hercules Inc., Wilmington, DE. The abbreviations of the variables studied are explained in the Glossary.

The determinations of molecular weight, diffusion coefficient, microviscosity, and the rest of the parameters are presented elsewhere.[3−5] The microviscosity of the mixed sodium dodecyl sulfate−polymer micelles was determined with the fluorescent probe 1,3-di(1-pyrenyl)propane, P3P. The intramolecular excimer formation of P3P is dependent on the local microfluidity around the probe, and the monomer to excimer intensity ratio, I_M/I_E, is a qualitative measure of the microviscosity.[9]

Method

Principal component analysis (PCA) was performed using the SIMCA software package.[10] The data matrix was normalized and centered by an autoscaling procedure, before the principal components (PC:s) were calculated. This is a least-squares method producing principal components which are orthogonal to each other. The first principal component represents the largest variation in the data, and the second component describes the second largest variation orthogonal to the first and so forth. The observations (polymer fractions) are in some sense sum-

* Corresponding author. E-mail: hans.evertsson@farmkemi.uu.se.
† Pharmacia & Upjohn.

10.1021/js9804922 CCC: $18.00
Published on Web 06/05/1999

Table 1—Summary of Some of the Experimental Data Used in the Principal Component Analysis. The Variables Are Explained in the Experimental Section

Polymer	M_w (×10^5 g/mol)	MS_{ao}	DS_{alkyl}	CP (°C)	C1 (mM SDS)	IM/IE-max	[η] (mL/g)	D (×10^{-12} m^2/s)	γ (mN/m)
EHEC Fractions									
CST-103	1.89	0.7	1.5	28	1.5	13.2	455	6.59	37
DVT-87014	1.33	0.9	1.4	28	1.5	8.1	290	7.55	40
E230 G	5.35	0.9	0.9	65	3.9	3.2	410	7.65	48
E411 G	7.85	1.7	1.2	58	3.7	3.2	1000	6.3	52
OS	13.2	1.5	1.6	24	1.5	10.0	1400	–	37
PR	12.4	1.75	1.4	48	2.5	4.0	1500	–	42
Other Cellulose Ethers									
HPMC	3.01	0.4	2	55	3.9	5.2	740	6.48	47
HPC	1.06	0.4	–	42	2.0	6.6	134	12.22	42
MC	1.62	–	2	65	4.1	3.1	400	8.37	47
HEC	1.89	3	–	100	7.0	2.4	237	7.55	63

marized in the score vectors, which are linear combinations of the variables, and the corresponding summary of the variables is named loadings. In other words, the original experimental variables are decomposed into fewer new variables (PC:s) onto which the observations are projected. A multiplication of the score (**T**) and loading (**P′**) matrixes plus a residual (**R**) will regain the original normalized and centered data matrix (**X**) according to

$$\mathbf{X} = \mathbf{T}\cdot\mathbf{P}' + \mathbf{R} \qquad (1)$$

The original, unscaled data matrix is given in Appendix 1. The accuracy of the least squares models is expressed as R^2, the explained variance of the model. R^2 is the comparison between the squared sum of the experimental observations (y_{obsd}) and the squared sum of the values calculated by the model (y_{calcd}) according to

$$R^2 = (\sum y_{obsd}{}^2 - \sum (y_{obsd} - y_{calcd})^2)/\sum y_{obsd}{}^2 \qquad (2)$$

where the sums range from 1 to n observations. R^2 increases with the number of PC:s used in the model since more variation in the experimental data can be explained as the number of "new" variables used increases, and hence the residual decreases. The idea with the PCA, however, is to use as few PC:s as possible in order to get a simpler model. Q^2 describes the relation between the squared sum of observed values and the sum of squares of the values as determined from cross validation (y_{cv}):[8]

$$Q^2 = (\sum y_{obsd}{}^2 - \sum (y_{obsd} - y_{cv})^2)/\sum y_{obsd}{}^2 \qquad (3)$$

Cross validation is a process where the data themselves are used. A few data points are left out at a time of the consecutive model-calculations. Each data point is left out of the calculation once. The closer to 1 that Q^2 is, the better the model. The predictive capacity can never be higher than the explained variance and will reach a maximum when increasing the number of PC:s used. Thus, the optimum model has a high R^2 as well as Q^2 and a small difference between the two. It follows that the model only is valid within the experimental domain. All models presented here contain two principal components. The R^2 value for each component is noted in percent on the axes in the figures. The cumulative R^2 and Q^2 for each model are as follows: Figures 1a and 1b (model 1), 0.882 and 0.536; Figures 2a and 2b (model 2), 0.733 and 0.325; Figures 3a and 3b (model 3), 0.769 and 0.648, respectively. The ellipse in each figure describes the 95% confidence region.[10]

Results and Discussion

The characterization of water soluble polysaccharides is far from trivial, involving a number of physically different methods such as in this case dynamic light scattering, fluorescence probe techniques, and dynamic surface tension. Some, but far from all, qualitative relationships can be deduced just by looking at Table 1 and Appendix 1. Principal component analysis, however, gives a much more objective picture of the complex interplay between the variables. The extensive knowledge of the polymer fractions from this laboratory gives the possibility to construct models containing the appropriate parameters, a critical step in the analysis which is always subjective to some degree. The data set has been divided into two subsets; one containing observations of some of the polymer systems at equilibrium (Figures 1a and 1b (model 1)), and one containing observations describing the irreversible process of dynamic surface tension before equilibrium together with part of the equilibrium responses (Figures 2a and 2b (model 2), Figures 3a and 3b (model 3)). The a-figures give the loading plot (experimental variables in relation to the principal components) of each model, and the b-figures give the score plot (polymer samples in relation to the principal components) of each model.

Equilibrium Parameters—Only the EHEC fractions were chosen for the equilibrium parameter model since complete substituent-information exist for these fractions, and the substituents are of the same types ethyl (hydrophobic) and hydroxyethyl (hydrophilic) groups. This makes the EHEC subgroup straightforward to compare. Figure 1a shows the loadings of the experimental variables for two significant principal components (PC:s, denoted p1 and p2 in the figure) for all EHEC fractions. If a variable is located close to and far along a PC axis, this variable "strongly loads" into that PC. Such an experimental variable then correlates with the new variable, or PC. Original experimental variables lying close to each other correlate in the hyper plane (the two-dimensional window provided by p1 and p2). The model shows four groupings of experimental variables located far along the positive and negative sides on the two principal component axes p1 and p2. The first PC monitors the largest variation in the data. It can be interpreted from the figure that the surface tension γ (measured after 11.7 h on 500 ppm polymer solutions) is strongly correlated to the surfactant concentration corresponding to the onset of polymer–surfactant interaction C1, as well as the cloud point CP, since these variable vectors lie close to and far out on the first principal component axis. Also, these variables are negatively correlated to the microviscosity indices and the surface pressure as these variables are grouped close to and far along the negative side of the first principal component. The negative correlation between the microviscosity and CP/C1/γ is in accord with the earlier reports.[4,5] These correlations can be qualitatively deduced from Table 1. Furthermore, CP, C1, the surface tension, and the micro-

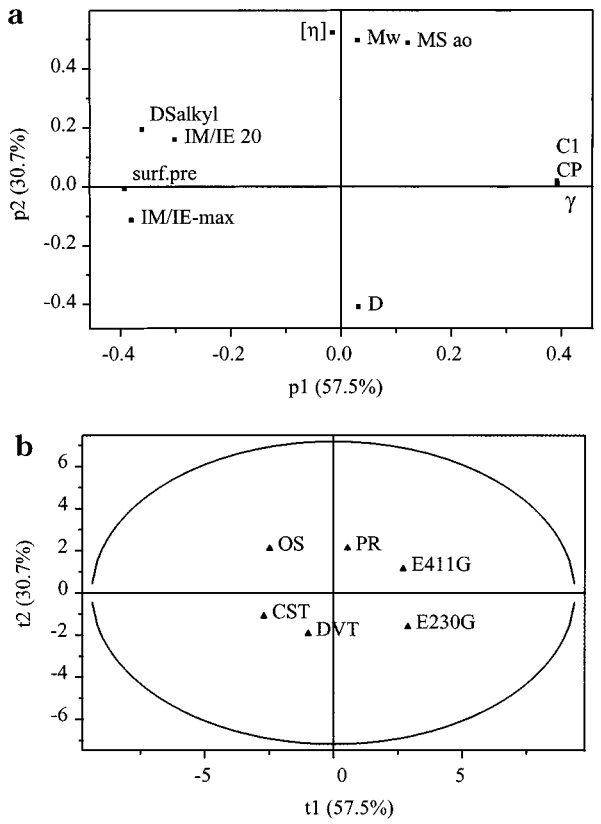

Figure 1—(a) Loading plot of all EHEC fractions of the equilibrium model, showing the first (p1) and second (p2) PC. The cumulative R^2 and Q^2 are 0.882 and 0.536, respectively. (b) The corresponding score plot of all EHEC fractions of the equilibrium model, showing the first (t1) and second (t2) PC.

viscosity are mainly governed by the hydrophobicity of the EHEC fractions, as can be seen by the degree of hydrophobic substitution, DS_{alkyl}, which is located in the group of variables at the negative side of the first principal component axis, and thus correlates with the microviscosity and the surface pressure. A high surface tension, close to that of water, is coupled to a high cloud point as both variables monitor the hydration properties of the polymer. A high surface tension also gives a low surface pressure, or surface activity, since the latter is the difference between the surface tension of water (73 mN/m) and the surface tension of the polymer.

The microviscosity of mixed polymer−surfactant micelles is hence strongly correlated to the hydrophobic substitution of the polymer, as well as the surface activity, which earlier has been discussed[9] in terms of the ability of the polymer to form densely packed mixed polymer−surfactant micelles. This principal component model verifies that the microviscosity of the ternary system EHEC/sodium dodecyl sulfate/water can be used to predict the solubilization properties of the corresponding binary cellulose ether/water system, with the additional information that DS_{alkyl} is the structure-related parameter with the highest influence on the ability to form densely mixed polymer micelles with SDS.

The second PC p2 monitors the second largest variation in data, 30.7%, as compared to the first PC, 57.5%. As expected, the diffusion coefficient D is negatively correlated to the molecular weight and the intrinsic viscosity, which follows directly from the Stokes−Einstein equation $D = kT/(6\pi\eta r)$, where k is the Boltzmann constant, T is the temperature, η is the viscosity of the solvent, and r is the radius of a small hard sphere immersed in the viscous solvent. It should be pointed out that D is obtained by dynamic light scattering, $[\eta]$ from capillary viscometry, and M_w from size exclusion chromatography—that is, from independent methods. The molecular weight correlates as expected with the intrinsic viscosity in accord with the Mark−Houwink equation $[\eta] = KM^a$. These variables, however, do not explain the variation of data along the first PC and hence neither to the surface tension nor to the microviscosity. An interesting feature is that the intrinsic viscosity is correlated to MS_{ao}, the degree of hydrophilic substitution. This is not too surprising since a polymer with a higher hydrophilicity tends to swell in an aqueous solution. MS_{ao} does not occur directly opposite to DS_{alkyl} in the plot. Whereas the degree of hydrophobic substitution has a strong influence on the steady state surface tension and microviscosity, the degree of hydrophilic substitution is important for the intrinsic viscosity. This of course, is not entirely true since DS_{alkyl} and MS_{ao} in combination give the polymer its specific amphiphilic nature. For example, CST-103 is partly self-aggregated in aqueous solution due to the uneven distribution of large hydrophobic substituents,[5,11] a feature originating in the hydrophobic−hydrophilic balance and clearly affecting the hydrodynamics of the polymer. Nonetheless, the degree of hydrophobic substitution DS_{alkyl} seems to affect the microviscosity of polymer/surfactant micelles to a larger extent than the degree of hydrophilic substitution MS_{ao}.

Figure 1b shows the score plot corresponding to the loading plot of Figure 1a. The PC:s are denoted t1 and t2 to signify that the vectors plotted in this space are observables (polymer samples)—not original variables as in the loading plot of Figure 1a, where the PC:s are denoted p1 and p2. The observation vectors in Figure 1b are separated with an even distribution. Such a score plot thus gives a good overview of the observations or polymer samples in relation to the new variables (PC:s), which carry about 88% of the information of the original experimental variables. The two EHEC samples having the highest molecular weight, OS and PR, are located above the others in accord with Figure 1a. The fractions having the higher microviscosities and lower surface tensions, OS and CST-103, are located to the left, also in accord with the loading plot, cf. the original data matrix in Table 1 and Appendix 1. This score plot separates CST from DVT in accord with previous investigations[3−5] even though these two fractions have very similar degree and balance in substitution. The difference is thought to originated in a more separated distribution of substituents and hence longer substituents on the CST fraction, making it effectively more hydrophobic.

The above presented model makes it possible to predict (to 54% using only these six EHEC samples) the solution properties of an unknown EHEC sample by just knowing its DS_{alkyl} and MS_{ao}. If, in addition, some easily measured variable as CP is determined, the other experimental variables can be predicted more precisely and optimum conditions for these determinations might be chosen. Any of the experimental variables along p1 should be useful for the prediction of the strength of amphiphilic polymer−drug interaction, which is important when designing advanced controlled release formulations.

Dynamic Parameters—The irreversible process of surface tension decrease to equilibrium is considered here for all of the cellulose ethers investigated. Figure 2a shows the loadings of the surface tension from time zero to equilibrium at an initial homogeneous polymer concentration of 3 ppm, the lag time, t_{lag}, and the time it takes to reach $(\gamma H_2O - \gamma)/2$, t. t_{lag} is the time from time zero to the point where the surface tension curve shows a negative second derivative. The major variation in data is illustrated along the horizontal first PC axis p1, where the diffusion coefficient is negatively correlated to the surface tension

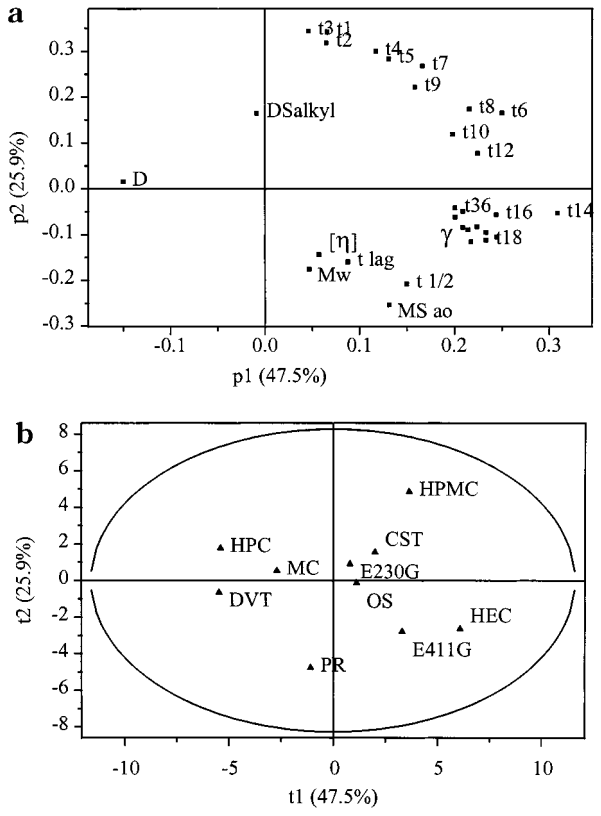

Figure 2—(a) Loading plot of all polymer fractions of the first dynamic model, showing the first (p1) and second (p2) PC. The polymer concentration in the surface tension measurements is 3 ppm. The cumulative R^2 and Q^2 are 0.733 and 0.325, respectively. (b) The corresponding score plot of all polymer fractions of the first dynamic model, showing the first (t1) and second (t2) PC.

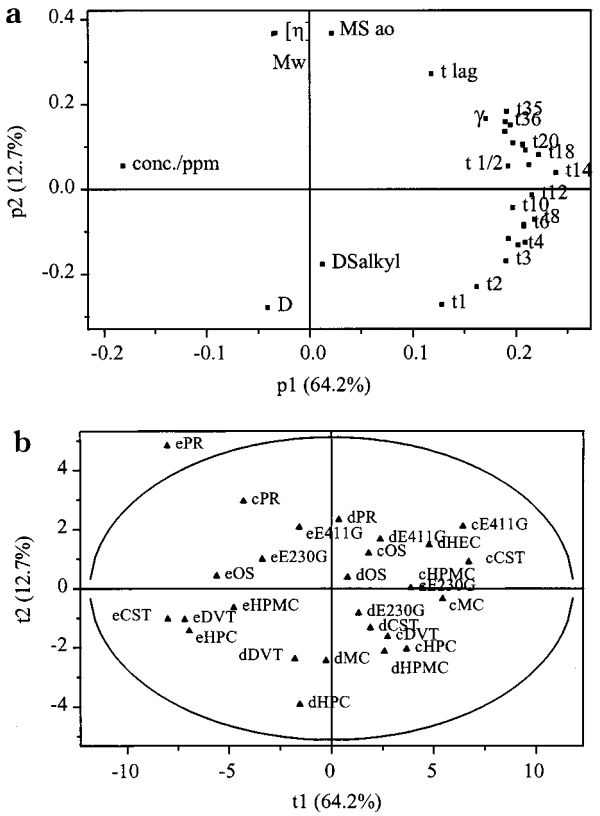

Figure 3—(a) Loading plot of all polymer fractions of the second dynamic model, showing the first (p1) and second (p2) PC. The polymer concentrations in the surface tension measurements are 2, 3, and 10 ppm. The cumulative R^2 and Q^2 are 0.769 and 0.648, respectively. (b) The corresponding score plot of all polymer fractions of the second dynamic model, showing the first (t1) and second (t2) PC. The prefix of each observation corresponds to the polymer concentrations of the surface tension measurements: c = 2 ppm, d = 3 ppm, e = 10 ppm.

at ascending times, meaning that a large diffusion coefficient gives a low surface tension after a certain time. A clear trend within the surface tension variables at ascending times is seen. The early times are located at the top of the plot and a movement downward of the second PC and to the right is seen as the time increases. At very early times the surface tension vectors are totally random due to randomness (a low signal-to-noise ratio) in the measurements, and as time evolves, the discrepancy between the scalars (numerical values) constituting the vectors becomes more stable as the surface tension is lowered by polymer adsorption, which tends to relocate the vectors in the hyper plane (the two-dimensional window provided by p1 and p2). The variable vectors t14 (after about 100 min) to γ (measured at 11.7 h) are located as one cluster indicating they are similar. At these longer times the surface tension has reached the lower plateau of the sigmoidal relationship between the surface tension and time[4] for most of the polymers, and the surface tension does not change very much with time in this time interval. The loading plot thus expresses an excellent overview of the irreversible surface tension build up process.

DS_{alkyl} and MS_{ao} span the second principal component p2 in this model as DS_{alkyl} is located in the upper and MS_{ao} in the lower half of the plot. MS_{ao} is still located quite close to the molecular weight and the intrinsic viscosity in accord with the equilibrium model. The molecular weight and the hydrodynamic volume (proportional to $[\eta]$) are also correlated to the lag time and to some extent to the time it takes to reach $(\gamma H_2O - \gamma)/2$, which seems logical; a long lag time should be coupled to a high molecular weight and to slow diffusion. These times also seem to be dependent on the amount of hydrophilic substitutents in accord with Figure 1a and the discussion above.

The corresponding score plot is given in Figure 2b. The more hydrophilic fractions PR, HEC, and E411 G are located far down in the plot, and the fast-diffusing substances DVT, HPC, and MC to the left, cf., the original data matrix in Appendix 1, and Table 1. The position of each observation in this score plot thus represents a fingerprint of the dynamic behavior of each polymer fraction, since all experimental variables are decomposed into these two principal components t1 and t2.

A conclusion from the dynamic model of Figures 2a and 2b is that the time dependence of the surface tension process is dependent on the molecular weight of the polymer samples to a large extent, which in turn is easily determined from the intrinsic viscosity.

The speed of the irreversible process of dynamic surface tension will, of course, also be dependent on the polymer concentration initially present in the bulk. To determine the effect of the polymer concentration, a second model containing the dynamic parameters is given in Figures 3a and 3b. This model is based on the same data set as above, with time dependent surface tension data at two additional polymer concentrations, 2, 3, and 10 ppm. Hence, the influence of polymer concentration on the irreversible time dependent surface tension process is presented here. In the loading plot of Figure 3a, the main variation in data along the first PC p1 is strongly governed by the polymer concentration. An increase in the polymer concentration results in a decrease in the surface tension after a certain time since the two quantities are negatively correlated. For example: for CST at t2 (100 s after the start of the experiment) the surface tension is 72.55 mN/m at an initial

polymer concentration of 2 ppm, 71.86 mN/m at 3 ppm, and 64.10 mN/m at 10 ppm.

The polymer concentration affects the dynamics to a much larger extent than what the diffusion coefficient does.[12,13] This is logical in the sense that the net mass transport increases to the surface with increasing polymer concentration, assuming a constant diffusion coefficient. According to Fick's first law of diffusion, the mass flux J of a substance per unit area and time is proportional to the diffusion coefficient and to the concentration gradient of the substance, $J = -D\partial c/\partial x$. This implies the amount of the concentration gradient to increase as the polymer concentration increases. It must be remembered though that the process of polymer adsorption to the water/air interface is more complex than free diffusion, involving different states of chemical potential of the polymer in solution compared to the same polymer at the surface, and a negative concentration gradient at longer times.[12,13] The effect however, is a faster lowering of the surface tension if the mass transport to the surface increases.

This second dynamic model of Figures 3a and 3b shows the same general trends concerning the position of the rest of the variable vectors as the dynamic model of Figures 2a and 2b presented above. The second PC p2 in Figure 3a is dominated by the hydrophobicity of the polymer. The apparent equilibrium surface tension γ is located in the upper half of the plot as is the degree of hydrophilic substitution MS_{ao}, in agreement with the discussion above. Furthermore, this model monitors a difference between t and t_{lag}. While the former is governed by the polymer concentration, the latter is more influenced by the hydrophobic balance of the polymer. In the ideal case this is supported by the experimental data, interpreted as follows: An increase in the polymer concentration lowers both the lag time and the time it takes to reach $(\gamma H_2O - \gamma)/2$, but t_{lag} is also in model 3 independently significantly affected by the amphiphilic character of the polymer, with higher lag times for more hydrophilic, slower diffusing polymer fractions. The lag time thus contains valuable structure-information which, in relation to $t_{1/2}$, helps to interpret the hydrodynamics and surface-related thermodynamics of the polymer. The time it takes to lower the surface tension to $t_{1/2}$, on the other hand, is strongly governed by the mass flux J. In conclusion, t_{lag} is more sensitive to the diffusion coefficient which in turn is decided by the hydrodynamic volume, while $t_{1/2}$—governed by the mass flux J—is more sensitive to the polymer concentration.

Turning next to the score plot in Figure 3b, this plot at first looks more "crowded" and complex to deduce. The main variation in data along the first PC t1 due to different polymer concentrations can be seen to be quite structured, however. The prefix of each observation vector corresponds to a certain polymer concentration; c = 2 ppm, d = 3 ppm, and e = 10 ppm. The observations at 10 ppm is located to the left of the figure in accord with the loading plot. CST spans the first PC more than any other polymer fraction, as eCST is located to the far left, and cCST to the far right of the plot. The dynamic surface tension process of CST is in other words more affected by an increase in the polymer concentration than any of the other polymer fractions, e.g., E411 G or DVT. This is most likely due to a more complex adsorption process and reorientation of CST at the surface, which might be attributed to the tendency for self-aggregation.[11] For most of the polymers, the observation with prefix d (= 3 ppm) is located both below the one with prefix c (= 2 ppm) and e (= 10 ppm). This "minimum" in the majority of the observations suggests 3 ppm to be an optimum concentration for the polymer-characterization using dynamic surface tension, since the correlation to the diffusion coefficient and the hydrophobic substitution reaches a maximum—that is, the influence of diffusion on the surface tension process is best described at 3 ppm.

Summary

In summary, the principal component analysis gives an excellent overview of the complex interaction pattern of nonionic cellulose ethers in aqueous solution and verifies the earlier stated qualitative relationships in a more quantitative manner. However, the good models are obtained from the extensive information and knowledge available on these polymer fractions, which enables choice of the appropriate variable settings. The polymer fractions analyzed constitute a heterogeneous group of substances with polydisperse molecular weights ranging from about one hundred thousand to over a million, large differences in the degree of substitution, and documented complex hydrodynamic behavior such as self-aggregation (CST-103[11]) and intermolecular aggregation—formation (E230 G[3]). Despite this and a few missing data, the models obtained have good predictive capacities and manifest the importance of accurate data handling for the characterization of pharmaceutically important polymer fractions. The influence of hydrophobic balance and molecular weight on the experimental variables is clearly illustrated, making the models useful for synthesis of desirable nonionic cellulose ether fractions. For example, the study displays some important differences between the influence of hydrophobic and hydrophilic substitution on the thermo- and hydrodynamics of the polymer samples.

Glossary

DS_{alkyl}	degree of hydrophobic substitution by alkyl groups (the mean number of alkyl groups per anhydroglucose unit of the polymer) as given by the producer. DSalkyl can be 3 at most, as there are three hydroxyl groups on each anhydroglucose unit of cellulose to etherificate
MS_{ao}	degree of hydrophilic substitution (molar substitution) by alkylene oxide groups (the mean number of alkylene oxide groups per anhydroglucose unit of the polymer) as given by the producer. MS_{ao} can theoretically be larger than 3 due to formation of oligo(alkylene oxide) substituents, but is practically only a small number
M_w	molecular weight as determined by size exclusion chromatography with LALLS/RI detection[3]
D	diffusion coefficient as determined from dynamic light scattering[3]
$[\eta]$	intrinsic viscosity as determined from capillary viscometry[3]
γ	apparent equilibrium surface tension as determined by the pendant drop method[4] measured after 11.7 h
surf. press.	the surface tension of water (γH_2O) minus γ
t1—t35	dynamic surface tension before equilibrium at ascending times. The real times in seconds are regained taking (index number × 5)[2], e.g., for t2: $(2 \times 5)2 = 100$ s
t_{lag}	lag time of surface tension, defined as the time it takes to visually detect a negative second derivative of γ

Appendix 1— The Original Data Matrix Used in the Analysis. The Abbreviations of the Experimental Variables and Observations Are Explained in the Experimental Section

batch	concn ppm	CP (°C)	DS_{alkyl}	MS_{ao}	IM/IE -max	IM/IE 20	C1 (mM)	surf. press.	γ (mN/m)	D	$[\eta]$ (mL/g)	t_{lag} (min)	$t_{1/2}$ (min)	mw	t1	t2	t3	t4
cCST	2	28	1.5	0.7	13.2	3.7	1.5	9.1	63.7	6.59	455	60	210	1.89	72.97	72.55	72.95	72.716
cDVT	2	28	1.4	0.9	8.1	1.8	1.5	25.2	47.6	7.55	290	35	249	1.33	73.82		72.44	73.048
cE230G	2	65	0.9	0.9	3.2	2	3.9	7.6	65.2	7.65	410	20	138	5.35	72.36	72.73	71.31	70.95
cE411G	2	58	1.2	1.7	3.2	2.2	3.7	11.9	60.9	6.3	1000	77.5	240	7.85	74.65		72.76	
cOS	2	24	1.6	1.5	10	4	1.5	24.8	48		1400			13.2	72.37	71.69	72.27	70.97
cPR	2	48	1.4	7.75	4	2.2	2.5	17.8	55		1500			12.4	66.9	61.08	58.28	53.52
cHPMC	2	55	2	0.4	5.2	2.2	3.9	18.8	54	6.48	740	84	273.6	3.01	72.05	71.44	71.94	71.878
cHPC	2	42		0.4	6.6	3.9	2	18.5	54.3	12.22	134	40	168	1.06	73.05	72.025	71.97	72.747
cMC	2	65	2		3.1	1.5	4.1	12.8	60	8.37	400	60	234	1.62	73.82	73.483	74.48	72.866
cHEC	2	100		3	2.4	1.5	7			7.55	237			1.89				
dCST	3	28	1.5	0.7	13.2	3.7	1.5	21	51.8	6.59	455	24	63	1.89	72.03	71.86	71.92	70.65
dDVT	3	28	1.4	0.9	8.1	1.8	1.5	30.6	42.2	7.55	290	10	57	1.33	69.81	69.24	69.60	68.10
dE230G	3	65	0.9	0.9	3.2	2	3.9	20.1	52.7	7.65	410	16	89	5.35	72.53		73.33	71.65
dE411G	3	58	1.2	1.7	3.2	2.2	3.7	17.9	54.9	6.3	1000	50	144	7.85	69.31	68.74	68.88	69.21
dOS	3	24	1.6	1.5	10	4	1.5	27.8	45		1400	40	150	13.2	71.698	71.216	71.147	71.913
dPR	3	48	1.4	1.75	4	2.2	2.5	23.8	49		1500	60	180	12.4	67.74	68.07	67.38	67.31
dHPMC	3	55	2	0.4	5.2	2.2	3.9	23	49.8	6.48	740	32	123	3.01	75.39	74.75	75.03	74.324
dHPC	3	42		0.4	6.6	3.9	2	27.3	45.5	12.22	134	7	60	1.06	71.92	71.94	71.68	71.54
dMC	3	65	2		3.1	1.5	4.1	23.8	49	8.37	400	12	56	1.62	71.49	71.745	71.24	70.215
dHEC	3	100		3	2.4	1.5	7	9	63	7.55	237	13		1.89	71.1		70.13	
eCST	10	28	1.5	0.7	13.2	3.7	1.5	37.8	40	6.59	455		30	1.89	69.113	64.104	56.978	52.117
eDVT	10	28	1.4	0.9	8.1	1.8	1.5	30.6	42.2	7.55	290		32	1.33	70.93	66.061	57.94	52.24
eE230G	10	65	0.9	0.9	3.2	2	3.9	22.4	50.4	7.65	410		21	5.35	67.37	63.12	59.65	56.36
eE411G	10	58	1.2	1.7	3.2	2.2	3.7	19	53.8	6.3	1000		24	7.85	71.36	68.043	63.53	57.575
eOS	10	24	1.6	1.5	10	4	1.5	30.3	42.5		1400			13.2	72.54	70.48	66.69	61.52
ePR	10	48	1.4	1.75	4	2.2	2.5	27.8	45		1500			12.4	50.12	48.76	48.74	48.25
eHPMC	10	55	2	0.4	5.2	2.2	3.9	26	46.8	6.48	740		15	3.01	68.98			
eHPC	10	42		0.4	6.6	3.9	2	28.6	44.2	12.22	134		14	1.06	69.01	61.554	52.11	48.358
eMC	10	65	2		3.1	1.5	4.1	21.8	51	8.37	400		35	1.62	71.3		61.59	
eHEC	10	100		3	2.4	1.5	7	9	63	7.55	237		8.4	1.89	70.07		69.22	
gCST	500	28	1.5	0.7	13.2	3.7	1.5	35.8	37	6.59	455			1.89	45.404	45.422	43.663	
gDVT	500	28	1.4	0.9	8.1	1.8	1.5	32.8	40	7.55	290			1.33	43.58		43.01	
gE230G	500	65	0.9	0.9	3.2	2	3.9	24.7	48.1	7.65	410			5.35	52.58	51.552	51.01	50.358
gE411G	500	58	1.2	1.7	3.2	2.2	3.7	21.8	51	6.3	1000			7.85	54.35	53.556	53.59	53.617
gOS	500	24	1.6	1.5	10	4	1.5	35.8	37		1400			13.2	40.76	40.71	40.64	40.25
gPR	500	48	1.4	1.75	4	2.2	2.5	30.8	42		1500			12.4				
gHPMC	500	55	2	0.4	5.2	2.2	3.9	25.4	47.4	6.48	740			3.01	53.9		52.09	
gHPC	500	42		0.4	6.6	3.9	2	31.8	41	12.22	134			1.06	43.43	42.999	42.94	43.13
gMC	500	65	2		3.1	1.5	4.1	27.5	45.3	8.37	400			1.62	55.819	55.164	55.717	
gHEC	500	100		3	2.4	1.5	7	9	63	7.55	237			1.89				

batch	t5	t6	t7	t8	t9	t10	t12	t14	t16	t18	t20	t21	t23	t26	t30	t33	t35	t36
cCST	74.49	72.842	73.18	72.804	73.43	72.911	73.26	71.52	71.52	70.587	70.59	70.341	70.44	67.74	66.37	65.73	65.1	64.45
cDVT	72.13	71.62	71.24	71.324	71.14	71.535	66.84	65.302	64.01	62.405	59.86	58.801	56.6	53.39	50.94		48.83	
cE230G		72.62		72.25	69.8	69.81	68.36	66.58	66.17	66.04	64.17	62.88	60.81	59.55	57.09	57.15	56.89	56.52
cE411G		72.84			72.88		73.97		71.73		69.75		66.8	63.75	62.02	61		60.9
cOS		69.17		69.6		68.33	67.07	64.14	62.97			58.04	54.58	51.61	48.9			
cPR		51.19		50.19		49.022	49.37	48.979	48.69			48.18	47.62	47.54	47.48			
cHPMC	71.537	71.19	71.709	70.491	70.599	70.3	71.342	70.771	68.509	68.241	66.98	67.194	62.96	58.54		54.846	54.301	54.34
cHPC	72.963	71.75	71.593	72.227	70.723	71.47	69.15	68.097		67.121	64.94	63.334	61.42	58.23	56.14	55.372	54.481	54.02

cMC	74.05	72.575	73.23	72.913	72.48	71.481	72.3		70.55	68.383	56.86		64.34	62.28	60.76	60.34	59.3	60.17
cHEC																		
dCST	71.42	71.30	70.78	70.63	70.27		66.95	65.14			60.73		56.64	54.90	52.31	51.56	51.71	51.81
dDVT	68.42	66.10	64.84	64.79	63.44	62.14	59.59			51.53		48.20	46.96	45.04	44.60	44.76	44.14	43.56
dE230G	71.21	71.23	69.16	68.39	66.34	65.18	62.94	60.48	58.92	58.48	56.41	56.69	55.60	53.66	52.52	53.91	52.67	52.67
dE411G		71.00		67.96	68.08		67.23	67.09	63.73	63.57	60.89	59.62	57.91	55.66	55.28	54.28		
dOS		70.516	70.286		69.118		66.275	64.294	62.631	60.496		56.568	53.82	49.137		46.566	46.377	46.189
dPR		66.6		65.32		63.85	62.1	60.67	59.24			54.39	52.2	50.04	49.05			
dHPMC	73.49	74.11	73.705	73.825	72.254	72.21	68.696	65.102	61.725	58.838	56.9	55.045	52.48	51.26	50.38			
dHPC	68.79	67.48	67.33	65.49	63.73	61.77	58.59	53.99	50.81	49.06	47.68	47.25	46.41		45.50	45.57	45.60	45.91
dMC	69.84	67.735	66.66	64.55	63.97	62.259	59.79	57.711	55.57	55.176	53.4	52.752	51.48	50.04	49.21	48.92	48.81	49.05
dHEC	69.32		68.28		65.35		65.05		64.93		65.63		64.29	64.58	64.45	63.07	63.66	62.53
eCST	49.144	47.203	45.089	44.016	43.266	42.451	41.934	41.637	41.314	40.901	40.837	40.591	40.454	40.532	40.059	40.058	39.595	39.983
eDVT	48.76	46.83	45.57	44.55	44	43.694	43.23		42.9	42.895	42.57	42.51	42.23	42.39	42.51	41.843	41.78	41.927
eE230G		54.59	53.41	53.19	52.82		52.51	52.2	51.91	51.95	51.73	51.63	51.34	50.41	50.97	50.03	50.38	50.39
eE411G		57.52	56.641	56.247	55.77		55.45	54.883	54.92	54.637	54.56	53.936	54.73	53.57	53.53	54.258	53.78	53.792
eOS		51.71		46.73		45.22	44.58	44.36	44.16			43.73	43.51	42.96	43.08			
ePR		48.46		47.11		47.42	46.77	46.94	46.76			46.07	45.64	45.81	45.64			
eHPMC	51.03					48.07					47.04		47.51	47.14			46.92	47.2
eHPC	48.91	46.18	46.273		45.36	45.65	45.02			45.15	44.52	44.587	44.68	44.66	44.27	44.16	44.35	44.47
eMC		54.04			50.76		51.13		51.14		50.93		50.87					
eHEC		68.73			67.29		66.07		64.48		66.58		65.36					
gCST	42.618		41.844		41.352		40.878		40.457	40.225	39.668	39.824	39.486	39.346	38./793	38.106	38.289	38.065
gDVT	42.4		42.17		41.82		41.36	41.417	41.37	40.956	40.92	40.662	40.92	40.85	40.07	40.71	40.07	40.29
gE230G	50.51	50.317			50.04		49.68	48.62	48.78	49.523	48.55	48.366	48.58	48.12	58.01	47.98	48.287	48.16
gE411G	53.59		53.25		53.18		52.6	52.311	52.1		52.77	51.826	51.62	52.14	51.9	51.93	51.95	51.7
gOS		40.36		39.96		39.73	39.79	39.83	39.51			39.63	38.96	39.17	38.61			
gPR																		
gHPMC	51.13		50.97		50.22		49.95				49.53		49.05	48.7	48.6	47.75	48.39	48.76
gHPC	42.52	42.203	41.81	41.758	41.67	41.236	41.73		41.37	41.894	41.39	41.762	42.01	41.83	41.34	41.64	41.19	41.84
gMC	55.075		55.042		55.025		55.051	51.075	50.34		47.968	49.494	48.619	47.248	46.557	45.711	45.264	45.42
gHEC																		

$t_{1/2}$	the time it takes to reach ($\gamma H_2O - \gamma$)/2
concn/ppm	the polymer concentration in ppm. Because the low concentrations and measurements carried out at room temperature, 1 ppm = 1×10^{-4} (w/v)%
CP (°C)	the cloud point temperature[3]
C1 (mM)	the surfactant (SDS) concentration at onset of polymer−surfactant interaction[5]
$I_{M/IE-max}$	the maximum monitored value of the microviscosity of polymer−surfactant mixed micelles as monitored by the fluorescent probe P3P[5] in SDS/0.2% polymer/water solutions
$I_{M/IE20}$	an asymptotic value of $I_{M/IE}$ for 20 mM SDS/0.2% polymer/water solutions

References and Notes

1. *Handbook of Pharmaceutical Excipients*; Wade, A., Weller, P. J., Eds.; American Pharmaceutical Association & The Pharmaceutical Press: London, 1994.
2. Attwood, D.; Florence, A. T. *Surfactant Systems*; Chapman & Hall: Bristol, 1983.
3. Nilsson, S.; Sundelöf, L.-O.; Porsch, B. On the Characterization Principles of Some Technically Important Water Soluble Nonionic Cellulose Derivatives. *Carbohydr. Polym.* **1995**, *28*, 265−275.
4. Persson, B.; Nilsson, S.; Sundelöf, L.-O. On the Characterization Principles of Some Technically Important Water Soluble Nonionic Cellulose Derivatives. Part II: Surface Tension and Interaction With a Surfactant. *Carbohydr. Polym.* **1996**, *29*, 119−127.
5. Evertsson, H.; Nilsson, S. Microviscosity in Dilute Aqueous Solutions of SDS and Nonionic Cellulose Derivatives of Different Hydrophobicity: Fluorescence Probe Investigations. *Carbohydr. Polym.* **1998**, *35*, 135−144.
6. Mardia, K. V.; Kent, J. T.; Bibby, J. M. *Multivariate analysis*; Academic Press: Great Yarmouth, 1989.
7. Sjöström, M.; Wold, S.. In *Chemometrics, Theory and Applications;* American Chemical Society Symposium Series 52; Kowalsky, B., Ed.; American Chemical Society: Washington, D.C., 1977.
8. *Anvendelse av kjemometri innen forskning og industri*; Nortvedt, R., Brakstad, F., Kvalheim, O. M., Lundstedt, T., Eds.; Norsk Kjemisk Selskaps & Svenska Kemistsamfundet: Bergen, 1996.
9. Evertsson, H.; Nilsson, S. Microviscosity in Clusters of Ethyl Hydroxyethyl Cellulose and Sodium Dodecyl Sulfate Formed in Dilute Aqueous Solutions As Determined with Fluorescence Probe Techniques. *Macromolecules* **1997**, *30*, 2377−2385.
10. SIMCA, http://www.umetri.se, Umetri, Box 7960, SE 907 19 Umeå, Sweden.
11. Evertsson, H.; Nilsson, S.; Holmberg, C.; Sundelöf, L.-O. Temperature Effects on the Interactions between EHEC and SDS in Dilute Aqueous Solutions. Steady-State Fluorescence Quenching and Equilibrium Dialysis Investigations. *Langmuir* **1996**, *12*, 5781−5789.
12. Ward, A. F. H.; Tordai, L. Time-Dependence of Boundary Tensions of Solutions. *J. Chem. Phys.* **1946**, *14*, 453−461.
13. Chang, S. A.; Gray, D. G. The Surface Tension of Aqueous Hydroxypropyl Cellulose Solutions. *J. Colloid Interface Sci.* **1978**, *67*, 255−265.

Acknowledgments

Dr. Torbjörn Lundstedt is gratefully acknowledged for valuable discussions. This work has been financially supported by the Swedish Natural Science Research Council and the Swedish council for the Engineering Sciences.

JS9804922

Aqueous Solubility and Dissolution Rate Does Not Adequately Predict in Vivo Performance: A Probe Utilizing Some *N*-Acyloxymethyl Phenytoin Prodrugs

VALENTINO J. STELLA,* SUWALDI MARTODIHARDJO,† AND VENKATRAMANA M. RAO

Contribution from *Department of Pharmaceutical Chemistry, The University of Kansas, Lawrence, Kansas 66047.*

Received December 21, 1998. Final revised manuscript received May 19, 1999.
Accepted for publication May 26, 1999.

Abstract □ Some physicochemical properties of *N*-acyloxyalkyl prodrugs of phenytoin were reported previously.[1,2] It was shown that despite their lower aqueous solubilities relative to phenytoin, these lower-melting prodrugs with apparently disrupted crystalline structures gave either comparable or enhanced in vitro solubility and dissolution rate in simulated intestinal media made up of bile salts and lecithin (SIBLM).[2] The current objective was to compare the in vivo behavior of two of these prodrugs to phenytoin in dogs and attempt to correlate the in vitro behavior to their in vivo behavior. The oral bioavailability of phenytoin after administration of phenytoin (**1**) and the selected prodrugs, 3-pentanoyloxymethyl 5,5-diphenylhydantoin (**2**) and 3-octanoyloxymethyl 5,5-diphenylhydantoin (**3**), in fed and fasted beagle dogs were compared to intravenously administered phenytoin. Phenytoin and its prodrugs showed improvement in fed-state phenytoin bioavailability relative to the fasted state indicating that food enhanced the delivery of phenytoin from phenytoin and its prodrugs. The increased bioavailability in the fed state may be due to stimulation of bile release by food and, for the prodrugs, possible catalysis of their dissolution by lipases.[3] In both, fasted and fed states, prodrugs **2** and **3** gave higher AUC values of phenytoin than the parent compound. The enhanced bioavailability of phenytoin after oral administration were more obvious in fed dogs. Although enhanced, AUC values of phenytoin from the prodrugs relative to phenytoin were not statistically different (at 95% confidence level) in fasted state, but were different in fed state. Although the aqueous solubilities and dissolution of both prodrugs were lower than phenytoin, dissolution of **2** and **3** was equivalent and greater, respectively, relative to phenytoin in SIBLM. As expected, the in vivo behavior correlated better with the in vitro SIBLM dissolution behavior. These results indicate that aqueous solubility per se does not adequately predict in vivo behavior.

Introduction

Phenytoin has a high melting point and poor aqueous and lipid solubility resulting in erratic and sometimes incomplete oral availability. The probable cause of this high melting point is strong intermolecular hydrogen bonding between the hydrogen atom on the N_3 of one molecule and a carbonyl oxygen of a neighboring molecule in the crystal packing.

N-Acyloxyalkyl prodrugs of phenytoin were synthesized to lower the melting point and alter the physicochemical properties.[1] Properties such as melting points, solubilities, dissolution rates, and partition coefficient were reported previously.[2] Of all the prodrugs studied, two prodrugs **2** and **3** (Figure 1) showed the most interesting physicochemical properties compared to phenytoin (**1**).[2] It was shown that the solubility and dissolution rate of the prodrugs in a simulated bile−lecithin mixture (SIBLM) was significantly enhanced relative to phenytoin even though their aqueous properties were significantly inferior to phenytoin (Table 1). These properties could not be correlated with the respective values in water, suggesting that water solubility could be a poor predictor of dissolution and bioavailability in vivo. It was therefore hypothesized that this increased solubility and dissolution rate in SIBLM should translate to a significant improvement in bioavailability of the prodrugs over the parent compound, phenytoin. Presented here are the results of an in vivo oral bioavailability study in dogs in both the fasted and fed state.

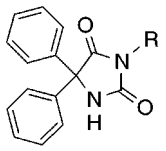

compound	R
1	H
2	$CH_2OCOC_4H_9$
3	$CH_2OCOC_7H_{15}$

Figure 1—The structure of phenytoin (**1**) and selected prodrugs (**2**, **3**).

Experimental Section

Prodrugs **2** and **3** used in this study were prepared by procedures described earlier.[1] All other chemicals were of analytical grade.

Enzymatic Hydrolysis of Prodrugs—The conversion rates of the ester prodrugs to the parent compound, phenytoin, were studied in dog plasma. The plasma was obtained by centrifuging fresh whole blood from a male beagle dog. Sodium ethylenediamine tetraacetate (Na EDTA) was added as an anticoagulant. Centrifugation was carried out in a Dynec I centrifuge (Beckon and Dickinson) for 10 min at 2000 rpm. A stock solution of each prodrug having a concentration of ~2 mg/mL phenytoin equivalent was prepared in acetonitrile. The plasma was equilibrated in a water bath at 37 °C for at least 10 min before the addition of an aliquot of the stock solution. Twenty microliters aliquot of stock solution was added to 2 mL of plasma. All the kinetic studies were followed to completion by monitoring the appearance of phenytoin. At appropriate time intervals 100 μL samples were withdrawn and added to 250 μL of acetonitrile which was then vortexed for 10−15 s. The mixture was then centrifuged at 2000 rpm for 5−10 min, and the supernatant was collected and analyzed by HPLC. No attempt was made to correct for pH drift in plasma samples. Conversion studies of these prodrugs in other animal species and tissues were reported earlier.[1,3]

* To whom correspondence should be addressed. Phone: (785) 864-3755. Fax: (785) 864−5736. E-mail: stella@hbc.ukans.edu.
† Current Address: Faculty of Pharmacy, Gadjahmada University, Sekiputara, Yogyakarta, Indonesia.

10.1021/js980489i CCC: $18.00
Published on Web 07/09/1999

Table 1—Properties of Phenytoin (1) and Its Prodrugs (2 and 3) in Water and SIBLM[a]

compd no.	water solubility ($M \times 10^5$)	SIBLM solubility ($M \times 10^4$)	solubility ratio (SIBLM/water)	dissolution rate[b] in phosphate buffer ($\times 10^{-11}$ mol/cm^2/s)	dissolution rate[b] in SIBLM ($\times 10^{-11}$ mol/cm^2/s)	ratio of dissolution rates
1	8.0	5.5	6.9	10.1	28.7	2.8
2	2.1	4.3	20.5	1.9	28.4	14.9
3	0.03	5.4	1800	0.04[c]	55.9	1379

[a] Data reproduced from previously reported work from our laboratory.[2] [b] All the dissolution rate experiments were conducted at a rotation speed of 200 rpm. [c] The dissolution rates were estimated using the Levich equation.

Intravenous Administration—Four adult male beagle dogs (11−12.8 kg) were used in an iv administration study. The dogs were fasted overnight prior to administration of the drug, but they were allowed water ad libitum during the study. Each dog received a 5.5 and 10 mg/kg phenytoin dose as sodium phenytoin (Dilantin, Parke-Davis), and a two-week washout period was allowed between doses. The drug was injected into the femoral vein over a period of 2−3 min. After dosing, serial venous blood samples of 1.5−2 mL were taken at appropriate time intervals from the alternate femoral vein. The blood samples were then placed into 2 mL Vacutiners (Becton-Dickinson, Ruthford, NJ) containing 3 mg of ethylenediaminetetraacetic acid as the anticoagulant. The samples were shaken and centrifuged for 5 min at 2000 rpm. Two hundred microliters of the separated plasma sample was added to 500 μL of acetonitrile and vortexed for 10−15 s and centrifuged at 2000 rpm for 5−10 min, and the supernatant was collected and analyzed by HPLC.

Oral Administration—A dog model was chosen to study the oral bioavailability of phenytoin, **2** and **3**. The same four adult male beagle dogs used for the iv study were used for a 4 × 6 random crossover study. A two-week washout period was allowed between dosing.

The dogs were fasted overnight prior to drug administration, but were allowed water ad libitum during the study. The prodrugs and phenytoin used in this study were administered without any excipients in hard gelatin capsules which were placed in the back of the mouth cavity. To help ensure particle size homogeneity, the compounds were passed through a 100-mesh sieve and collected on a 200-mesh sieve resulting in a particle size distribution range of 149 to 74 μm.

In the case of the dogs in the fed state, the capsules were given 30 min after feeding the dogs. The food used consisted of 250 g of dry dog food, 5 g of canned-dog food, and 12 mL of water. Once again, the dogs were allowed water ad libitum during the study. After dosing, the same procedures as described under the iv administration section were followed.

HPLC Analysis of Phenytoin—Reverse phase chromatography was used for the quantitative analysis of phenytoin and its prodrugs. A 15 cm long CPS hypersil column (i.d. 4.6 mm, particle size 5 μm) was used. The mobile phase consisted of acetonitrile: phosphate buffer (0.025 M, pH 6.0)/(25:75 v/v), and the samples were detected at 214 nm by Spectroflow 757, Kratos Analytical. The standard reference curve was obtained by spiking blank plasma with phenytoin and then treating the samples as for the plasma samples. Phenytoin concentration in plasma samples obtained from the bioavailability studies were calculated from the peak area by reference to the standard curve.

Statistical Analysis—Statistical comparison of AUC values obtained after oral administration of phenytoin and its prodrugs in both fed and fasted states was performed by analysis of variance method. A posthoc Bonferroni/Dunn test was conducted using STATVIEW 2.0 (Abacus Concepts, Inc., CA) to determine which of the AUC values were significantly different from each other ($p < 0.0033$).

Results and Discussion

Enzymatic Hydrolysis of 2 and 3 to Phenytoin—The enzymatic hydrolysis of the phenytoin prodrugs (**2** and **3**) to phenytoin in dog plasma exhibited pseudo-first-order kinetics. Both the prodrugs completely hydrolyzed to phenytoin presumably by the action of plasma esterases. The hydrolysis of the prodrugs to the parent compound is a two-step reaction. The first step, which is rate-limiting, involves the cleavage of the ester group resulting in the formation of an *N*-hydroxymethyl phenytoin. The second step involving the dehydroxymethylation of *N*-hydroxymethyl phenytoin to phenytoin has been shown to be rapid (half-life < 2 s)[4] at pH 7.4 and 37 °C. The apparent first-order rate constants for compounds **2** and **3** were found to be 7.5×10^{-2} min^{-1} ($t_{1/2}$ = 9.2 min) and 0.9×10^{-2} min^{-1} ($t_{1/2}$ = 74.4 min), respectively. The half-lives of these prodrugs were adequate to ensure that phenytoin would be quantitatively produced from these prodrugs in vivo, and that the enzymatic conversion was probably not a limiting factor.

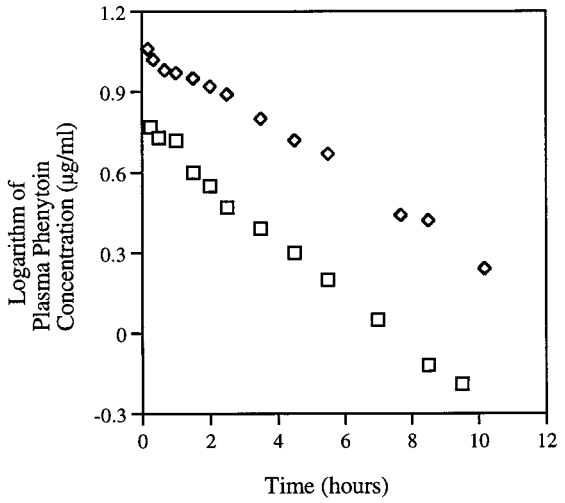

Figure 2—Plots of logarithm of plasma phenytoin concentrations versus time obtained after intravenous administration of 5 mg/kg (□) and 10 mg/kg (◇) of sodium phenytoin to dog no. 4.

Following oral administration, the conversion of the prodrugs to phenytoin could occur in presystemic tissues such as the intestinal lumen, the brush border, the enterocytes, blood, liver, etc.[5] It has also been shown that prodrugs **2** and **3** undergo lipolytic cleavage by pancreatic lipases.[3] Moreover, intact prodrugs were not detected following oral administration of the prodrugs, indicating that the enzymatic conversion is not a limiting factor in the absorption process after oral administration of these prodrugs.

Intravenous Administration of Sodium Phenytoin—Figure 2 is a representative plot of plasma phenytoin concentration versus time curve obtained after intravenous administration of sodium phenytoin (doses 5.5 and 10 mg/kg) to a dog. Phenytoin followed an apparent two-compartment model with a rapid but short distribution phase allowing the overall kinetics to be effectively modeled as a one-compartment model with saturable metabolism since the clearance and the elimination is dose-dependent.[6−8] These findings were in agreement with previously reported studies showing that phenytoin exhibited dose-dependent kinetics in dogs.[6,9] The possible cause for the dose-dependency may be due to the capacity-limited, saturable enzymatic conversion of phenytoin to aromatic hydroxylated metabolites.[10] Such a capacity-limited elimination

Table 2—Pharmacokinetic Properties of Phenytoin after Intravenous Administration of Two Different Doses of Sodium Phenytoin to Four Beagle Dogs

dog	dose[a] (mg/kg)	half-life (h)	AUC (mg·h/mL)	K_m (μg/mL)	V_m (μg/mL/h)	V_d (L/kg)
1	5.5	3.0	24.3	8.17	2.13	1.03
	10	3.3	61.5	8.32	1.44	0.88
2	5.5	2.2	17.7	5.33	2.39	1.03
	10	3.0	52.3	5.72	1.14	1.09
3	5.5	2.0	16.8	5.09	2.35	1.33
	10	2.7	57.4	5.49	1.16	0.84
4	5.5	1.9	15.6	7.33	3.08	1.38
	10	2.7	54.8	7.83	1.44	1.05

[a] Phenytoin dose equivalent.

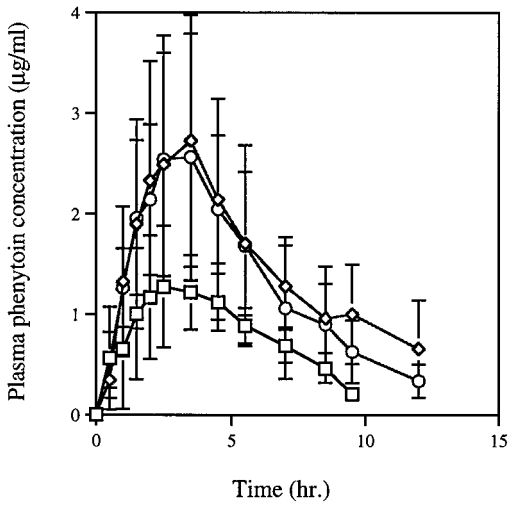

Figure 3—Mean plasma phenytoin concentrations in fasted dogs ($n = 4$) after oral administration of **1** (□), **2** (◇), and **3** (○) at a dose of 10 mg/kg phenytoin dose equivalent. The bars represent standard errors of the mean.

process can be described by the Michaelis Menten equation.

$$\frac{dC}{dt} = -\frac{V_m C}{K_m + C} \quad (1)$$

V_m, theoretical maximum velocity of the capacity-limited process and K_m, Michaelis−Menten constant were calculated using a nonlinear, least-squares iteration of eq 1 as reported previously by Varia et al.[11] The apparent volume of distribution (V_d) was determined as the ratio of dose administered and C_0, obtained by extrapolating the elimination phase of the plot of the logarithm of plasma concentration versus time neglecting the short distribution phase (see Figure 2). The area under the plasma concentration versus time curves $[AUC]^{0\rightarrow\infty}$ were calculated using the trapezoidal rule and the apparent half-lives obtained from the linear, terminal slopes and are given in Table 2 along with apparent K_m and V_m values for each dog. The values obtained for both K_m and V_m were comparable to that obtained by Varia et al.[11]

Oral Administration of Phenytoin—The oral administration of **1**−**3** to the dogs in fasted and fed states was carried out in a 4 × 6 crossover study design. Figures 3 and 4 show plots of the mean plasma concentration versus time following the oral administration of 10 mg/kg phenytoin equivalent dose of **1**−**3** to the four dogs in both the fasted and the fed states, respectively. The AUCs were calculated using the trapezoidal rule. The apparent elimination half-lives of phenytoin and phenytoin from its prodrugs after oral administration were calculated using the linear, terminal slopes of the logarithm of plasma

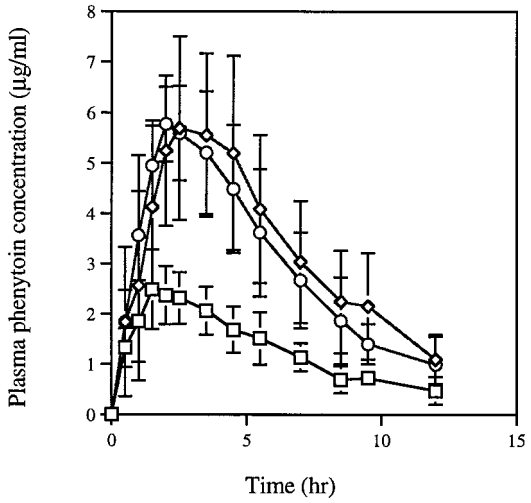

Figure 4—Mean plasma phenytoin concentrations in fed dogs ($n = 4$) after oral administration of **1** (□), **2** (◇), and **3** (○) at a dose of 10 mg/kg phenytoin dose equivalent. The bars represent standard errors of the mean.

Table 3—Apparent Phenytoin Pharmacokinetic Parameters after Oral Administration of Phenytoin (1) and Its Prodrugs 2 and 3 to Fasted and Fed Dogs[a] ($n = 4$)

state	compd	$AUC^{0\rightarrow\infty}$ (μg·h/mL)	apparent elimination half-life (h)	t_{max} (h)
fasted	**1**	8.8 (1.9)	2.5 (0.7)	2.9 (0.7)
	2	20.4 (6.1)	3.1 (0.4)	2.8 (0.8)
	3	17.3 (7.2)	2.9 (0.4)	2.9 (0.8)
fed	**1**	17.1 (4.2)	2.9 (0.4)	2.1 (0.8)
	2	44.8 (11.4)	3.3 (0.4)	3.1 (1.0)
	3	40.9 (10.7)	2.9 (0.3)	2.4 (0.4)

[a] The values shown are the mean values with their standard deviations in parentheses.

phenytoin concentration versus time assuming a simple first-order elimination model. These pharmacokinetic parameters are summarized in Table 3. The in vivo regeneration of phenytoin from its prodrugs appeared to be rapid as intact prodrugs were not detected in the plasma. On the basis of the in vitro half-life of **3** in dog plasma (74 min), one would expect to observe this prodrug with phenytoin in plasma samples. The absence of prodrug in the plasma samples perhaps suggested that the regeneration of phenytoin from **3** was also occurring by the lipase-catalyzed hydrolysis in the lumen or conversion in the brush border, enterocyctes, or liver.[1,3] For example, the half-life for the conversion of **2** and **3** to **1** in rat intestine homogenates was been reported to be less than 2 min.[1]

A two-way ANOVA indicated that both the prodrugs and food had an overall significant effect on phenytoin AUC values. To determine which of the treatments significantly differed from each other, a posthoc Bonferroni/Dunn test was conducted (95% confidence interval, number of comparisons =15, $p < 0.0033$). A portion of the results which are useful for this discussion are presented in the Table 4. In the fasted state, the phenytoin AUC values for phenytoin and its prodrugs were not statistically significant from each other at the 95% confidence level. Qualitative differences were seen, however. The phenyotin AUC values for the dogs in the fed state were significantly different with **2** and **3**, providing higher levels compared to phenytoin per se.

The ratio of $[AUC]^{0\rightarrow\infty}$ after oral dosing to $[AUC]^{0\rightarrow\infty}$ after iv dosing gives an "apparent" absolute bioavailability because the absorption rate and subsequent plasma levels of phenytoin due to the nonlinearities in phenytoin clearance. This can affect bioavailability estimates.[11] Therefore, a correction to the "apparent" absolute bioavailability was

Table 4—Multiple Comparison of AUCs after Oral Administration of Phenytoin (1) and Its Prodrugs 2 and 3 to Fasted and Fed Dogs[a] Using Posthoc Bonferroni/Dunn Test

comparison between treatments	significance[b] (95% confidence, $p < 0.0033$)[c]
1 (fasted), **1** (fed)	NS
2 (fasted), **2** (fed)	S
3 (fasted), **3** (fed)	S
1 (fasted), **2** (fasted)	NS
1 (fasted), **3** (fasted)	NS
1 (fed), **2** (fed)	S
1 (fed), **3** (fed)	S

[a] The values shown are the mean values with their standard deviations in parentheses ($n = 4$). [b] S means significantly different and NS means significantly different. [c] A total of 15 comparisons were conducted at a 95% confidence level making. $p < 0.05/15 = 0.0033$.

needed to obtain a more accurate estimate of the absolute bioavailability. One method of calculating bioavailabilities of drugs possessing dose-dependent elimination due to enzyme saturation was to assume a one-compartment model with a constant (dose-independent) volume of distribution and a capacity-limited pathway of elimination.[11–13] Assuming a rapid conversion of prodrugs to phenytoin, the rate of change of phenytoin concentration in the body after administration of phenytoin or its prodrugs may be written as

$$\frac{dC}{dt} = \frac{k_a F D_{iv} \exp(-k_a t)}{V_d} - \frac{V_m C}{(K_m + C)} \qquad (2)$$

where k_a is the apparent first-order absorption constant, F is the fraction of the total administered dose that is absorbed, D_{iv} is the equivalent iv dose. The true or corrected absolute bioavailability is given as

$$F = \frac{\left(\int_0^\infty \frac{V_m C}{K_m + C}\, dt\right)}{\left(\frac{D_{iv}}{V_d}\right)} \qquad (3)$$

The specific V_m and K_m values for each dog were obtained from the iv data.

The numerator of the above equation was evaluated by applying the trapezoidal rule on $V_m C/(K_m + C)$ versus time curve between time limits $t = 0$ to $t =$ last time point. The contribution of the integral from the last time point to infinity is assumed to be negligible as the concentration at the last time point is small.

Apparent relative bioavailabilities of phenytoin after oral administration of **2** and **3** were calculated as

$$F_{app,rel} = \frac{[AUC]_{prodrug}^{0\to\infty}}{[AUC]_{phenytoin}^{0\to\infty}} \qquad (4)$$

where the AUC are the mean values.

Phenytoin apparent absolute bioavailability, corrected absolute bioavailability and apparent relative bioavailability after oral administration of phenytoin and **2** and **3** are given in Table 5. In the fasted state, the apparent relative bioavailability of prodrugs **2** and **3** was 2.3 and 2 times, respectively, compared to phenytoin. In the fed state, the apparent relative bioavailability of prodrugs **2** and **3** compared to phenytoin were 2.6 and 2.4. The corrected absolute bioavailabilities in the fed state were found to be 84.2 (±16.5)% and 77.5 (± 22.1)%, respectively. These values appear to be close to quantitative suggesting that

Table 5—Calculated Percent Bioavailabilities of Phenytoin after Oral Administration of Phenytoin (1) and Its Prodrugs 2 and 3 to Beagle Dogs[a] ($n = 4$)

state	compd	apparent absolute % bioavailability[b]	apparent relative % bioavailability[c]	corrected absolute % bioavailability[d]
fasted	**1**	15.5 (3.3)	100	21.0 (6.9)
	2	36.5 (11.9)	232	44.2 (16.2)
	3	30.7 (13.5)	197	40.7 (19.8)
fed	**1**	30.4 (4.2)	100	37.8 (9.3)
	2	79.0 (11.4)	262	84.2 (16.5)
	3	73.0 (22.4)	239	77.5 (22.1)

[a] The values shown are mean values with standard deviations in the parentheses. [b] Apparent absolute bioavailability was calculated as $[AUC]^{0\to\infty,oral}/[AUC]^{0\to\infty,iv}$. [c] Equation 4. [d] Equation 3.

when administered in the fed state, **2** and **3** perhaps overcome the dissolution limitations observed with phenytoin.

The accuracy of F depends on the accuracy of the estimates of K_m and V_m. In this study the K_m and V_m values were determined by nonlinear curve fitting of limited iv data (only two doses). A wider range of drug dosage would enable one to determine the Michaelis–Menten constants with more accuracy. The purpose for presenting these "corrected" values was simply to point out that the apparent absolute bioavailabilties based on AUC comparisons alone can lead to undersestimates of the true bioavailability values due to the nonlinear elimination behavior of phenytoin. Note, as pointed earlier, the V_m, K_m, and V_d values obtained here are within the range of values reported for phenytoin in dogs in an earlier study.[11]

Correlation between in Vitro Dissolution Studies and in Vivo Bioavailability—The larger AUC values in the fed state were found to be significantly different from those in fasted state from **2** and **3**. In the fasted state, the AUC values for phenytoin and its prodrugs were not statistically significant from each other at the 95% confidence level. However, the AUC values in the fed state were significantly different.

On the basis of solubility and dissolution characteristics in water alone, **2** and especially **3** were expected to give a lower bioavailability relative to the parent compound.[2] A portion of the results published previously are reproduced in Table 1 for the present discussion. It was obvious from the bioavailability studies that the in vitro dissolution studies in water do not predict the in vivo results. If the dissolution and solubility characteristics in SIBLM were considered, the prodrugs were expected to give higher or equivalent bioavailabilities with respect to the parent compound, phenytoin. In the fed state, the contents of gastrointestinal tract (GIT) will be influenced by the byproducts of food digestion as well as an increased level of bile acids, lecithin, and the lipase/colipase complex. The ratio of dissolution rate of all the compounds in SIBLM to that in water indicates the probable sensitivity of these compounds to changes in the GIT contents. On the basis of the ratio of the dissolution rates in SIBLM to those in water, the bioavailability of phenytoin from **2** and **3** were expected to be much more sensitive to changes in the GIT content than phenytoin itself. This was consistent with the in vivo observation that the bioavailabilities of phenytoin from **2** and **3** were qualitatively superior to phenytoin in the fasted state, and that the differences were quantitatively superior in the fed state animals. When administered in fed state, the prodrugs appeared to have overcome dissolution rate limitations as the corrected absolute bioavailabilities were close to 100%.

The reasons for the altered bioavailability of orally administered drugs in the fed state have been described earlier.[14,15] The most plausible explanation for the effect of food on the bioavailability of phenytoin from phenytoin and phenytoin from its two prodrugs was that the dissolution rates of the drugs may be increased due to the food-induced stimulation of bile flow.[14,16]

This enhanced dissolution rate in the presence of food may be the reason for the improved bioavailability observed after oral administration of several lipophilic drugs such as danazol,[17] itracanazole,[18] phytonadione,[19] 5-methoxypsoralen.[20] The importance of physiologically relevant dissolution media in predicting the effect of food on the oral bioavailability of poorly soluble drugs has been emphasized in a recent review.[21] From the present study, it was clear that the inferior aqueous solubilities of **2** and **3** do not have as great an influence on their in vivo behavior, while their relative behavior in the presence of SIBLM reasonably predicted their in vivo behavior.

Conclusions

Despite possessing poor aqueous solubilities, prodrugs **2** and **3** showed superior qualitative bioavailability of phenytoin relative to phenytoin in the fasted state and a significant enhancement in the fed state. Physicochemical properties such as aqueous dissolution rate or aqueous solubility did not correlate with the in vivo performance in this homologous prodrug series. The in vitro dissolution rates correlated better with the in vivo results when SIBLM was used as the dissolution medium.

References and Notes

1. Yamaoka, Y.; Roberts, R. D.; Stella, V. J. Low-melting phenytoin prodrugs as alternative oral delivery modes for phenytoin: A model for other high-melting sparingly soluble drugs. *J. Pharm. Sci.* **1983**, *72*, 400−405.
2. Stella, V. J., Martodihardjo, S.; Terada, K.; Rao, V. M. Some relationships between the physical properties of various 3-acyloxymethyl prodrugs of phenytoin to structure: potential in vivo performance implications. *J. Pharm. Sci.* **1998**, *87*, 1235.
3. Alvarez, F.; Stella, V. J. Pancreatic lipase-catalyzed hydrolysis of esters of hydroxymethyl phenytoin dissolved in various metabolized vehicles, dispersed in micellar systems, and in aqueous suspensions. *Pharm. Res.* **1989**, *6*, 555−563.
4. Bundgaard, H., Johansen, M. Hydrolysis of N−(alpha-hydroxybenzyl)benzamide and other N−(alpha-hydroxyalkyl)amide derivatives: implications for the design of N-acyloxyalkyl-type prodrugs. *Int. J. Pharm.* **1984**, *22*, 45−56.
5. Krisch, K. In *The Enzyme*, 3rd ed.; Academic Press: New York, 1971; Vol. V, p 43.
6. Frey, H.; Loscher, W. Clinical pharmacokinetics in the dog: a reevaluation. *Am. J. Vet. Res.* **1980**, *41*, 1635.
7. Sanders, J. E.; Yeary, R. A. Serum concentrations of orally administered diphenylhydantoin in dogs. *J. Am. Vet. Med. Assoc.* **1978**, *172*, 153.
8. Arnold, K.; Gerber, N. Rate of decline of diphenylhydantoin in human plasma. *Clin. Pharmacol. Ther.* **1970**, *11*, 121.
9. Dayton, P. G.; Cucinell, S. A.; Weiss, M.; Perel, J. M. Dose-dependence of drug plasma level decline in dogs. *J. Pharmac. Exp. Ther.* **1967**, *158*, 305.
10. Atkinson, A. J.; MacGee, J.; Strong, J.; Garteiz, D.; Gaffney, T. E. Identification of 5-meta-hydroxyphenyl-5-phenylhydantoin as a metabolite of diphenylhydantoin. *Biochem. Pharmacol.* **1970**, *19*, 2483.
11. Varia, S. A.; Stella, V. J. Phenytoin prodrugs V: In vivo evaluation of some water-soluble phenytoin prodrugs in dogs. *J. Pharm. Sci.* **1984**, *73*, 1080−1087.
12. Jusko, W. J.; Koup, J. R.; Alvan, G. Nonlinear assessment of phenytoin bioavailability. *J. Pharmacokinet. Biopharm.* **1976**, *4*, 327.
13. Martis, L., Levy, R. Bioavailability calculations for drugs showing simultaneous first order and capacity limited elimination kinetics. *J. Pharmacokinet. Biopharm.* **1973**, *1*, 283.
14. Charman, W. N.; Porter, C. J. H.; Mithani, S.; Dressman, J. B. Physicochemical mechanisms for the effects of food on drug absorption: the role of lipids and pH. *J. Pharm. Sci.* **1997**, *86*, 269−282.
15. Welling, P. G. Influence of food and diet on gastrointestinal drug absorption: review. *J. Pharmacokinet. Biopharm.* **1977**, *5*, 291−334.
16. Hamaguchi, T.; Shinkuma, D.; Irie, T.; Yamanaka, Y.; Morita, Y.; Iwamoto, B.; Miyoshi, K.; Mizuno, N. Effect of high-fat meal on the bioavailability of phenytoin in a commercial powder with a large particle size. *Int. J. Clin. Pharm., Therapy Toxicol.* **1993**, *31*, 326−330.
17. Charman, W.; Rogge, M. C.; Boddy, A. W.; Berger, B. M. Effect of food and a monoglyceride emulsion formulation on danazol absorption. *J. Clin. Pharmacol.* **1993**, *33*, 381−386.
18. Van Peer, A.; Woestenborghs, R.; Heykants, J.; Gasparini, R.; Gauwenbergh, G. The effects of food and dose on the oral systemic availability of itraconazole in healthy subjects *Eur. J.. Clin. Pharmacol.* **1989**, *36*, 423−426.
19. Tadakazu, T.; Tsushima, Y.; Machida, Y.; Kayano, M.; Nagai, T. Evaluation of bioavailability upon oral administration of phytonadione preparations in beagle dogs. *Biol. Pharm. Bull.* **1993**, *16*, 319−321.
20. Ehrsson, H.; Wallin, I.; Ros, A. M.; Eksborg, S.; Berg, M. Food-induced increase in bioavailability of 5-methoxypsoralen. *Eur. J. Clin. Pharmacol.* **1994**, *46*, 375−377.
21. Dressman, J. B.; Amidon, G. L.; Reppas, C.; Shah, V. P. Dissolution testing as a prognostic tool for oral drug absorption: immediate release dosage forms. *Pharm. Res.* **1998**, *15*, 11−22.

JS980489I

Adsorption of Water by Anhydrous Nedocromil Sodium from 20 to 40 °C

ALISON C. RICHARDS,[†] IAN J. MCCOLM,*[,‡] AND J. BARRIE HARNESS[†]

Contribution from *Department of Industrial Technology, University of Bradford, Bradford, BD7 1DP U.K.*

Received December 18, 1998. Accepted for publication May 25, 1999.

Abstract □ Three different powder preparations of the drug disodium 9-ethyl-4,6-dioxo-10-propyl-4*H*,6*H* pyrano[3,2-*g*]quinoline-2,8-dicarboxylic trihydrate, Nedocromil sodium (trade name Tilade), have been fully dehydrated in a vacuum and their water vapor adsorption characteristics quantitatively assessed at different water vapor pressures over a temperature range 20 to 40 °C. At saturated vapor pressures, 100% RH, rates of adsorption are around 0.1 $s^{-1/2}$. Graphs of square root of time against reduced mass during uptake of water vapor at vapor pressures in the range 20 to 47 mm of Hg, all equivalent to 100% RH, indicate control by a diffusion mechanism with activation energies in the range 8 to 24 kJ mol^{-1}, dependent on the powder preparation method. In two of the powders nonlinear Arrhenius-type plots are interpreted as showing that control of the process is dependent on the surface's ability to hold water molecules at the experimental temperature. The variation in activation energies and the calculated values for diffusivities, around 1×10^{-13} m^2 s^{-1}, are used to explore structural involvement in the overall water adsorption process. The measured values of water vapor diffusivity into the structure have been used to predict the water solubility of nedocromil sodium trihydrate, and the results show good agreement to reported solubilities. This approach to solubility prediction is an alternative to the Noyes and Whitney method where ions leaving the surface are monitored.

Introduction

Some 15 years ago a drug, $C_{19}H_{15}NO_7 \cdot 2Na \cdot 3H_2O$, disodium 9-ethyl-4,6-dioxo-10-propyl-4*H*,6*H* pyrano[3,2-*g*]quinoline-2,8-dicarboxylic trihydrate, was found to have potential for the treatment of asthma.[1] This proved to be the most promising member of a series of salts of nedocromil acid and was simply named as nedocromil sodium (NS), now marketed as Tilade, a registered trade name. NS has been extensively characterized by chemical means[2]. Its behavior has been compared to its acid form[3] and several hydrate forms containing divalent cations.[4] A focus of the investigations has been the relationship between water adsorption and relative humidity of finely powdered crystalline forms of the compounds together with characterization of hydrates using physical techniques. In the case of NS trihydrate a full crystallographic analysis has been achieved[5] which shows the position of water molecules in the trihydrate form. This has led to the description of loosely bound and strongly bound water in the salt.[5] Surprisingly, only limited information exists on rates of water uptake.[4] Most of the experiments involved hydrates and not the anhydrous form. Reaction kinetics, from which activation energies and diffusivites can be found, do not appear to have been studied. This paper reports practical work on the uptake of water vapor by anhydrous NS using thermogravimetric analysis techniques. Restrictions imposed by the fixed water vapor pressure meant that work was done at various relative humidities (RH) in a conventional Cahn balance system. This subsequently led to the development of a sensitive thermobalance housed in a controlled temperature chamber with computer-aided measuring techniques. All work with this system is done at 100% RH from which diffusivities of water in the crystal of anhydrous NS and activation energies of the controlling mechanism have been established.

Table 1—Forms of the Nedocromil Sodium Trihydrate Used in This Work[a]

sample code	form	supplier's code no.[b]	preparation note
A	amorphous A	Bx1909R	atm at 100% RH
B	amorphous B	B-93%RH	atm at 93% RH
C	crystalline	ZBB3W	atm at 100% RH

[a] All samples were of particle size 2.5 ± 0.5 μm except sample C which had a wider spread of ±0.8 μm. [b] The supplier's code number indicates the manufacturer's batch number.

Experimental Procedures

NS was supplied in various forms by Fisons Pharmaceuticals plc., Loughborough, U.K. (prior to various amalgamations), details of which and specimen codes are given in Table 1. The water was double-distilled in glass apparatus in house.

Before the experiments, each sample was dried using a standard procedure: The powders were totally dehydrated by heating to 200 °C in a vacuum to remove both the loosely and tightly bound water in the crystal structure. All samples were cooled in a vacuum of approximately 10^{-4} mm of Hg to room temperature before experiments were performed. The above process was carried out in situ on the balance so that samples were not exposed to air after drying.

Some samples were recycled through several dehydration−hydration−dehydration sequences in order to limit variability from physical features, such as particle size and surface area, and so produce more consistent comparative data. Constant mass changes were a control mechanism to show that the sample was cycling between anhydrous and trihydrate forms. Any variation in this pattern caused the sample to be rejected. As a further control, experiments were performed on repeat samples from the same batch. No differences could be detected in the results whether the NS was recycled several times or fresh samples were used for each temperature point.

Exploratory work was performed using an all-glass system connected to a Cahn microbalance[6,7] with water vapor being delivered via a liquid water reservoir kept at 21 °C, i.e., a water vapor pressure of 18.65 mm of Hg. This constraint meant that RH's were in the range 100 to 39.6% RH. Experiments were timed from opening the water reservoir tap and lasted approximately 4 h. This experimental arrangement produced a fixed water vapor pressure within the system. The sample was heated by a resistance element around the sample holder capable of controlling the temperature to ±1 °C. Results were of limited value due to the range of RH. This led to the development of a new system based on a modified Cahn balance manufactured by Combustion Instrument (CI) which allowed the water reservoir to be thermostatically

* Corresponding author. Tel: 01274 234249. Fax: 01274 391333. E-mail: I.J.McColm@Bradford.ac.uk.
[†] Department of Chemical Engineering, University of Bradford.
[‡] Department of Industrial Technology, University of Bradford.

10.1021/js9804866 CCC: $18.00
Published on Web 07/07/1999

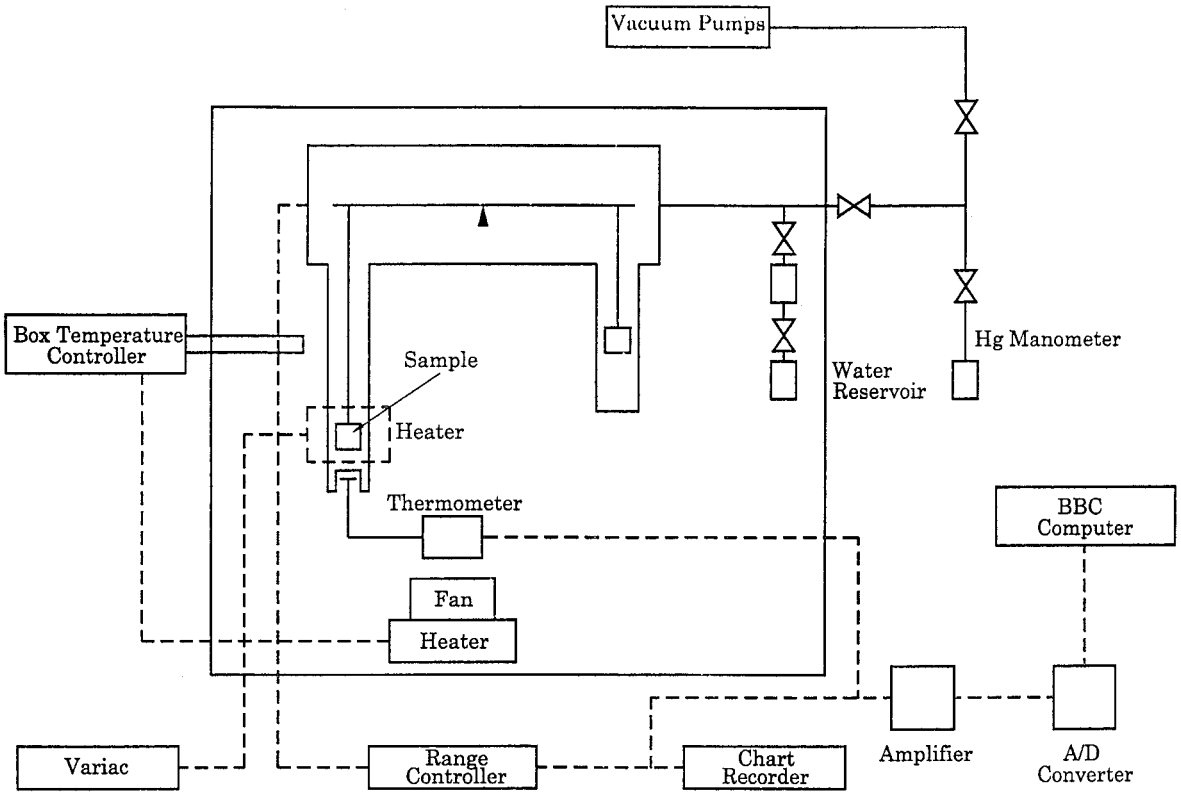

Figure 1—Schematic diagram of Combustion Instrument balance assembly.

controlled along with all itinerant connections. Control of the sample temperature was improved to ±0.1 °C from just above room temperature up to 50 °C. A block diagram is shown in Figure 1. The mass and temperature of the specimens were measured and recorded every 5 s and could be reproduced graphically or the data processed numerically as required.[8] Both balances are sensitive to changes in mass of 1 μg.

Powder X-ray diffraction films were taken from the powders as supplied which confirmed differences in the degree of crystallinity. A sensitive focusing Hägg–Guinier camera was used, capable of high resolution; this showed that samples classed as amorphous were not totally amorphous because some broad, very weak Bragg lines were present.

Results

(a) Reaction at Fixed Water Vapor Pressure, Cahn Balance—The first trial experiments were conducted at a constant water vapor pressure of 18.65 mm of Hg, corresponding to a temperature of 21 °C, on the crystalline sample C, over the temperature range 22 to 40 °C. The crystallinity was qualitatively confirmed by the sharp appearance of the X-ray diffraction lines. The results were obtained graphically as time in minutes against changes in mass in micrograms. The data were represented as square root of time, t, in minutes, against $\Delta W/W_\infty$, the increase in mass at time t divided by the total mass gain. The decision to use the square root function came from the view that the rate most likely would be determined by a diffusion process. Several possible control mechanisms are described and investigated in a theoretical paper in preparation.[9] Changing control processes are indicated as the graphs change from a sigmoidal curve, to linear, to two linear parts and back to sigmoidal curves as the sample temperature was increased. None of the graphs are included because a clearer view of changing control mechanisms is given in Figure 2, where the sample temperature is plotted against total mass gained after 4 h exposed to the constant water vapor pressure. These results are for

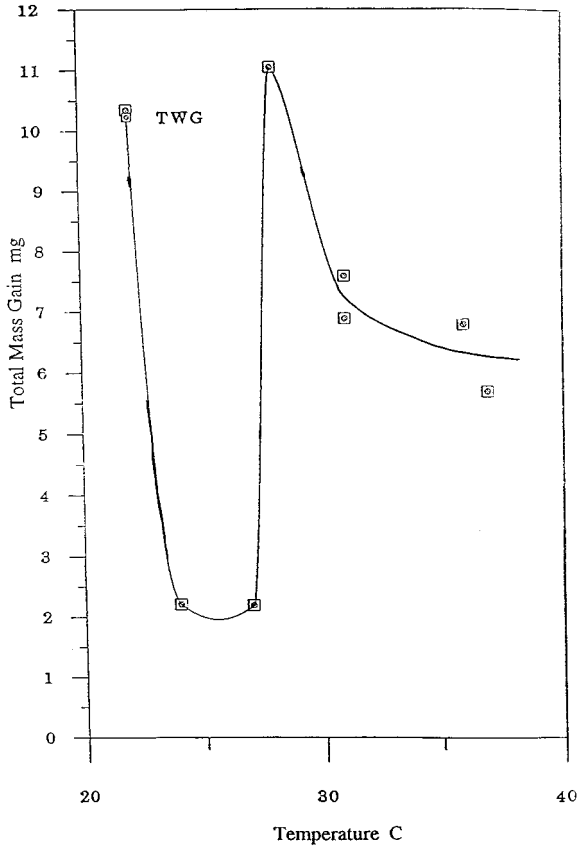

Figure 2—Plot of temperature against total mass gained after 4 h for sample C on the Cahn balance.

the same sample dehydrated by heating to 200 °C under vacuum between each water adsorption experiment. Experiments of this type are useful in delineating temperature intervals where different physicochemical processes

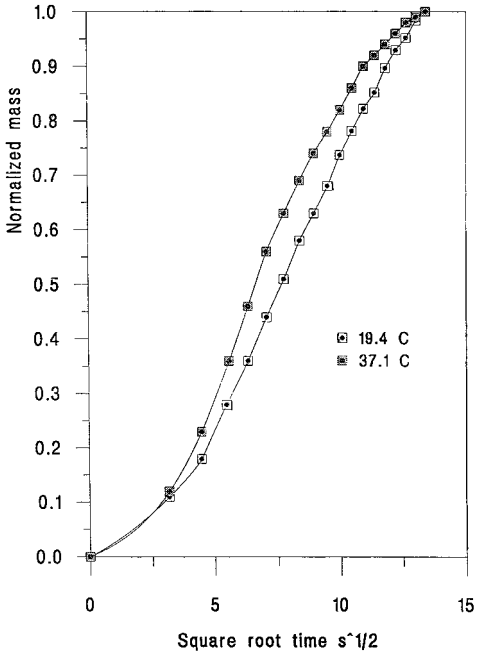

Figure 3—Examples of adsorption curves for sample A on Combustion Instrument balance.

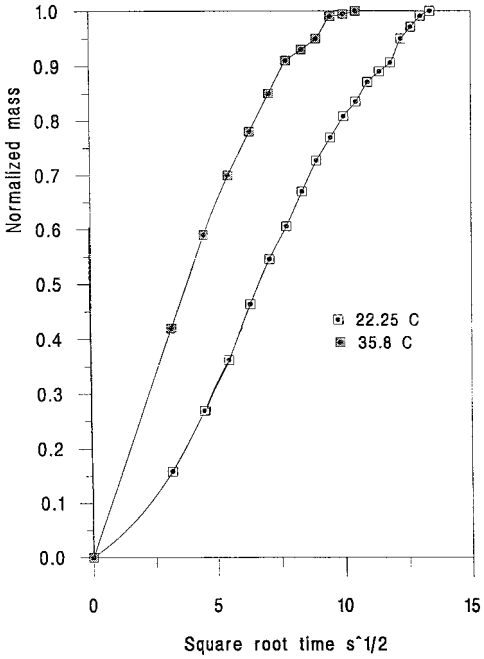

Figure 5—Example of adsorption curves for sample C on Combustion Instrument balance.

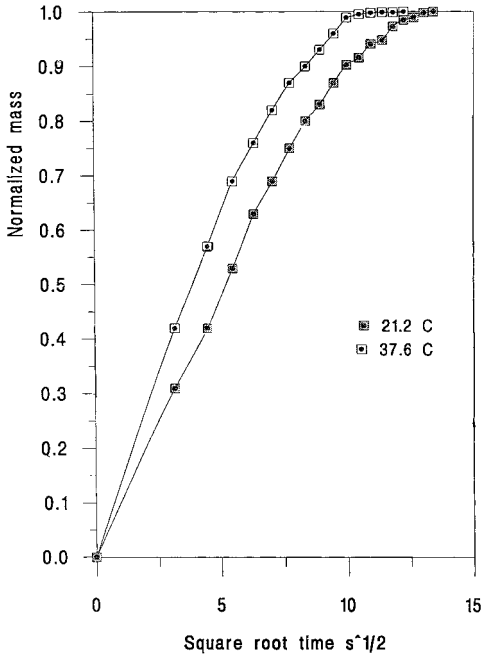

Figure 4—Examples of adsorption curves for sample B on Combustion Instrument balance.

are important and hence where more detailed experiments can be made. It is particularly useful when combined with a theoretical analysis of a model system. More detailed investigations were made at 100% RH for each temperature on the system with improved control and sensitivity.

(b) Experiments at Controlled Water Vapor Pressures, Isothermal Environment—The three samples of NS, A, B, and C, were used in the new thermogravimetric apparatus. Some of the adsorption curves are shown in Figures 3–5, which are plots of square root of time against normalized mass. All the plots are sigmoidal to a greater or lesser degree, and to proceed the rate was determined as the slope of the best fit to a straight line which fitted the experimental points between 0.2 and 0.8 normalized mass. It can be seen that considerable similarities exist between the various forms of the drug. Table 2 contains data for sample C using both balance techniques from which some points can be drawn:

(i) When 100% RH is maintained as the sample temperature is increased (CI system), the time to achieve 60% of the total adsorption decreases with increasing temperature, i.e., the reaction rate increases with temperature throughout the temperature interval studied. These results allow activation energies to be determined.

(ii) When the water vapor was allowed to enter the sample chamber, the balance underwent a brief settling period. Following this period, in the CI system, the square root time function then produced linear adsorption curves up to at least 80% of the total adsorbed mass for all temperatures studied. This supports the view that a diffusion mechanism controls the process in these conditions. The results from the Cahn balance produce a variety of different shaped water uptake curves for a square root time function with only an intermediate temperature range being linear.

(iii) The CI balance results show that when the water vapor pressure was at saturation value the reaction rates were from 4 to 16 times faster than the Cahn balance results obtained with the restricted water vapor pressure. This was true for all the temperatures studied.

Repeat experiments involving all three forms of the drug produced similar curves to those for sample C. Forms A and B showed decreasing rates with increasing temperature over a small range, 26–31 °C. For all the results a reaction rate constant was calculated from the slope of the linear part of the square root time versus the normalized mass plots. This produced much data concerning reaction rate at specific temperatures. A plot of the reciprocal of the absolute temperature against the natural logarithm of the rates was made to extract activation energies. Figures 6–8 are examples of these plots and strongly suggest that even at 100% RH there is a temperature at which a controlling mechanism change occurs for samples A and B. The error bars shown on data points were calculated from the square root time, reduced mass curves by the binomial error expansion technique. Even with the wide uncertainty this produces, it can be seen that two lines

Table 2—Cahn and CI Balance Results for Time to 60% Uptake of Water Vapor for Drug C

Cahn balance[a]			CI system			
temp, °C (% RH)	time, min	shape of curve	temp, °C (% RH)	vapor press. water, mm of Hg	time, min	shape of curve
22 (94.1)	225	linear after 4 min	22.2 (100)	20.2	60	linear after 4 min
24 (83.3)	169	curve	23 (100)	21.1	45	linear
27 (69.7)	240	curve	26.7 (100)	26.3	45	linear after 6.25
28 (65.6)	361	linear after 9 min.	28.2 (100)	28.7	36	linear after 9 min
31 (55.3)	169	linear	31.6 (100)	34.9	35	linear
36 (41.9)	272	curve	35.8 (100)	44.1	20	linear
37 (39.6)	196	curve	37 (100)	47.1	20	linear

[a] Constant water vapor pressure of 18.7 mm of Hg.

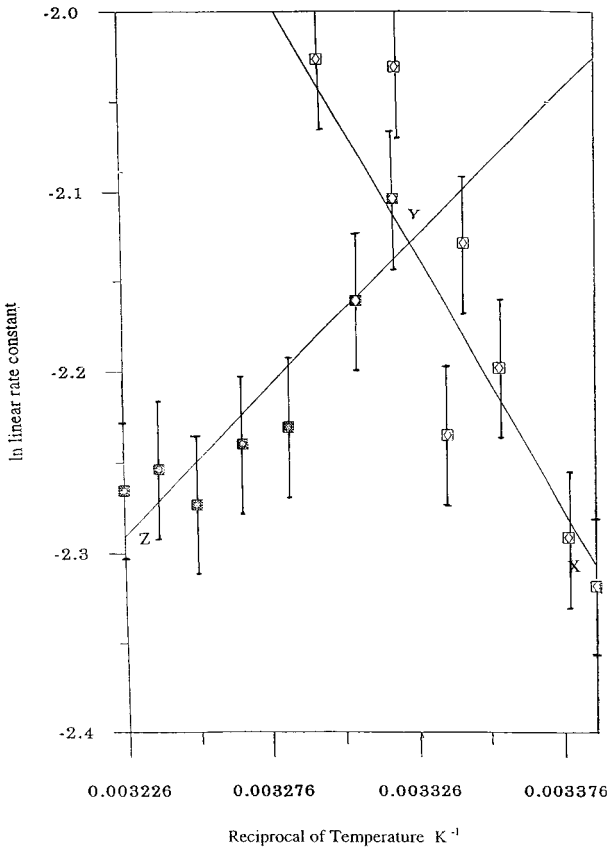

Figure 6—Arrhenius plots of the reciprocal of temperature against natural logarithm of linear rate constant for sample A.

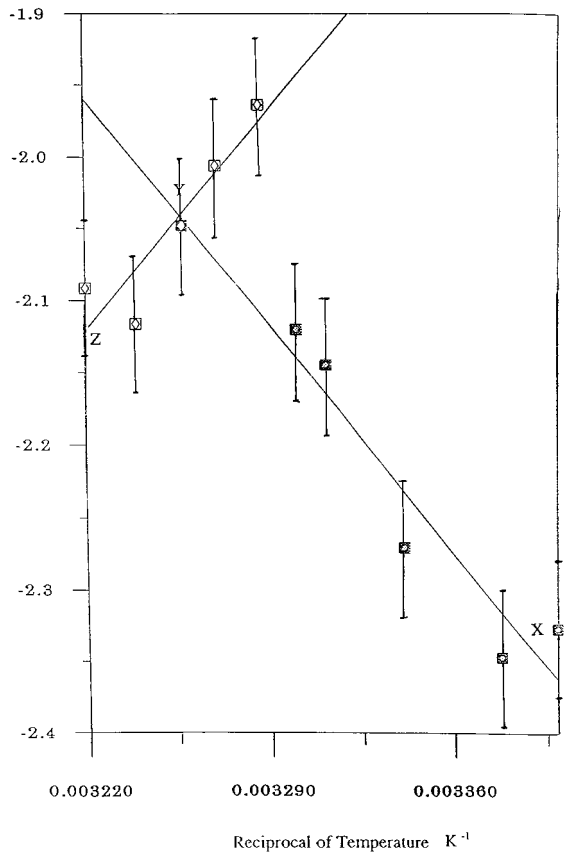

Figure 7—Arrhenius plots of the reciprocal of temperature against natural logarithm of linear rate constant for sample B.

must be drawn through the Arrhenius data, in the cases of samples A and B, while form C gives an almost normal Arrhenius plot throughout the temperature range. This seems to imply a feature of the reaction which involves the physical form of the sample.

From Figure 8, an Arrhenius plot for the crystalline sample C, the line XY corresponds to an activation energy of 8.2 kJ mol^{-1}. The two samples, A and B, show increased activation energies from lines XY in Figures 6 and 7, of 23.6 and 18.7 kJ mol^{-1}, up to temperatures of 26 and 31 °C, respectively. After these temperatures, a negative activation energy is indicated by the lines YZ in Figures 6 and 7. Hence, an interesting feature of the results is the way the form of the drug appears to influence both the activation energy and the temperature at which there is an apparent negative activation energy, see Table 3.

Discussion

The data reported here are supported by earlier indications in the literature as to the rates of water vapor uptake of the anhydrous acid form of nedocromil.[3] Our results for NS show that a second or more elapses before any adsorption is recorded on a sensitive system, and then adsorption rates are modest, around 0.1 $s^{-1/2}$. The literature shows that nedocromil magnesium hydrates also do not appear to absorb water rapidly because Zhu et al.[4] noted that several months in environments saturated with water vapor are needed to increase the crystal water content of the salt to saturation values. In both the acid and magnesium forms of nedocromil, dissolution of the solid into liquid water was reported as a slow process, and this was rationalized using forms of the Noyes–Whitney equation[10] of dissolution kinetics.

Khankari et al.[2] have reported gravimetric experiments performed on anhydrous NS in different relative humidities. The importance of the RH parameter was demonstrated but no indication of the actual time taken to adsorb water at critical relative humidities was given; hence, no conclusions about rates of adsorption can be made from that work.

Why and where the critical temperature for reaction rate changes at 100% RH, seen in this research, occurs need

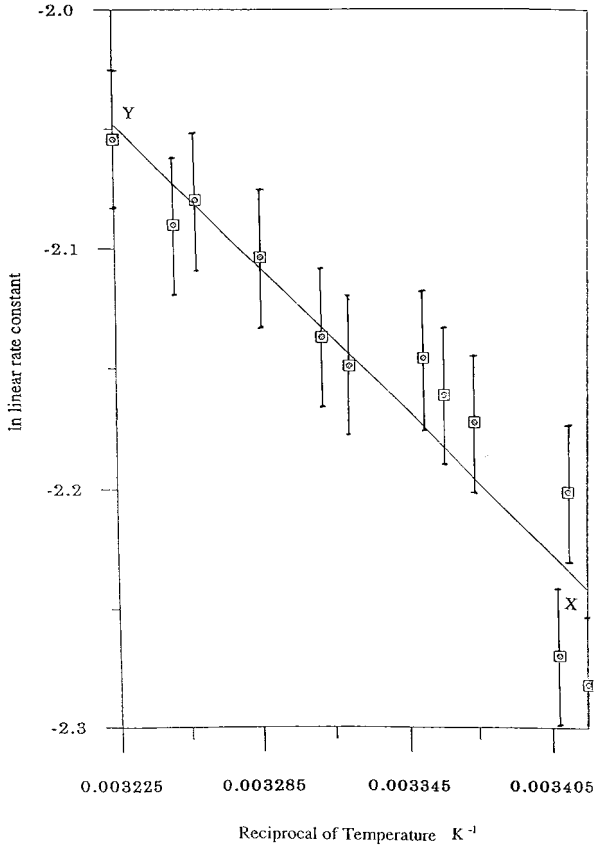

Figure 8—Arrhenius plots of the reciprocal of temperature against natural logarithm of linear rate constant for sample C.

Table 3—Activation Energies Calculated from Thermogravimetric Balance Results[a]

form of drug	balance	temp of process change, °C	activation energy (XY) kJ/mol	activation energy (YZ) kJ/mol
C (crystalline)	Cahn	26	–	–88.4
A (amorphous)	CI	26	23.6	–17.1
B (amorphous)	CI	31	18.7	–18.3
C (crystalline)	CI	–	8.2	–

[a] X, Y, and Z refer to the lines in Figures 6–8.

more detailed investigation using a wider range of techniques. This question is presently being probed using desorption studies from fully hydrated samples as a means to a better understanding of the mechanisms of hydration.

When the humidity is controlled so that vapor phase diffusion is not rate-limiting, diffusion of water in the solid can be the controlling feature, and the mostly linear graphs of square root time against normalized mass suggest that this situation applies here. The rate constants derived from the linear slopes for experiments done at 100% RH allow activation energies to be obtained. The values found here for activation energies, for the adsorption process when availability of water molecules is not limiting, show that the lowest energy barrier is associated with the crystalline form of NS, see Table 3. The answer to questions regarding the activation energy changes might at first seem to be associated with total surface area i.e., the amorphous forms of the drug having a greater surface area, and surface energy and so having the potential to hold more water on the surface. Clearly this is less important than crystal perfection because the crystalline samples have the lowest activation energy values. The Arrehnius-type plots that can be made for the effect temperature has on the absorption rate, Figures 6 and 7, reveal, from the negative activation

Table 4—Diffusivities Calculated from Thermogravimetric Balance Results

sample	temperature, °C	diffusivity $m^2 s^{-1} \times 10^{13}$
A	19.4	9.1
A	37.1	11.0
B	21.2	7.5
B	37.6	7.8
C	22.3	8.1
C	37.0	8.6

energy line, YZ, that two processes at least are involved in water uptake.

The physical form of the salt, whether crystalline or less-so, does affect the activation energy of the hydration process; when well-formed crystals are used, a smaller barrier to the process is encountered, compared to the poorly crystalline or amorphous forms. This suggests that the surface area is of less importance than some other feature in the mechanism, and if diffusion of water molecules into the solid is indeed dominant in controlling the rate of hydration, then the role of the crystal structure must be considered. Freer et al.[9] have published the results of a single-crystal analysis of NS trihydrate, from which, in the structure features of sodium zeolites, can be seen in that sodium ions are accommodated within tunnels formed by cage like molecules. Diffusion as an activated process in such a structure is approached through a logarithmic analysis of the data.[11,12] Given several assumptions, quoted in the references, a standard analysis leads to eq 1:

$$\frac{\Delta W}{W_\infty} = \frac{6(Dt)^{1/2}}{\pi r_c} \tag{1}$$

where D is the intracrystal diffusivity, r_c is the mean particle radius, assuming spherical particles and t is the elapsed time. Equation 1 predicts an essentially linear plot for square root time against $\Delta W/W_\infty$, and since most of the data presented here is linear between 20% and 80% reaction, the importance of diffusion is confirmed. Further analysis gives:

$$D = \frac{(\pi r_c \text{slope})^2}{36} \tag{2}$$

where the slope is that from the linear part of the $t^{1/2}$ against $\Delta W/W_\infty$ graphs and r_c is the average particle radius, taken here to be 2.5 μm, as supplied by the manufacturers.

From eq 2, diffusivities at a range of temperature can be found from all the original experimental results, such as those shown in Figures 3−5. These data are given in Table 4 and show values at the lower end of the range reported for such systems as hydrocarbons diffusing into zeolites,[12] where values range between 10^{-8} to 10^{-13} $m^2 s^{-1}$. This is evidence for a structurally related feature to be critically involved in the water absorption mechanism.

Data from Table 2 in Zhu et al.'s [4] paper on dissolution of nedocromil magnesium enables us to compare both sets of experimental results in the following way:

An equation derived from the Noyes and Whitney's equation[10] of dissolution from a solid surface into a liquid, is given as:

$$J = \frac{k'DS}{h} \tag{3}$$

where J is the intrinsic dissolution rate, S is the solubility, D is the diffusivity into the solution, and h is the diffusion layer thickness.

Using the data for the nedocromil magnesium heptahydrate solubility[4] and the diffusivity values for water vapor into NS crystals found in this work, k' has a value of 20. It is a constant with no units and the value 20 comes from using SI units. Then using this value for k' and a diffusion layer thickness of 1×10^{-6} m, with diffusivity data from Table 4 in this paper, we are able to predict a solubility for nedocromil magnesium decahydrate of 9.6 mol m^{-3}. This compares to 9.77×10^{-3} mol L^{-1}, that is 9.77 mol m^{-3}, measured by Zhu et al.,[4] which is in very close agreement and gives some confidence for the low values for diffusivity we have measured in the NS structure. Furthermore, for dissolution of the solid, it points to a situation where diffusion of water molecules into the crystal structure is as important as the Noyes and Whitney's approach involving diffusion of ions and molecules off the solid surface into the solution. This suggestion is given more credence by using the k' value, already quoted above, with the diffusivity coefficient for 22 °C in Table 4 and applying them to eq 3, using $J = 0.0074$ mol s^{-1}/m^{-2}, derived from data in Khankari et al., to predict the solubility of NS. A value of 3.7×10^3 mol m^{-3} is obtained. This value is in the same order of magnitude as that found experimentally by Khankari et al.; as 1.3×10^3 mol m^{-3}. Furthermore, this model predicts an increased solubility for the anhydrous form of the drug, compared to the hydrates, because diffusivity into the crystal decreases as the degree of hydration increases. This is the order of solubility shown in Khankari et al.'s paper.

References and Notes

1. Cairns, H.; Cox, D.; Gould, K. J.; Ingall, A. H.; Suschitzky, J. L. New anti-allergic pyrano [3,2-g] quinoline-2, 8-dicarboxyllic acids with potential for the topical treatment of asthma. *J. Med. Chem.* **1985**, *28*, 1832−1842.
2. Khankari, R.; Chen, L.; Grant, D. J. W. Physical characterization of nedocromil sodium hydrates. *J. Pharm. Sci.* **1998**, *87*, 1052−1061.
3. Chan, H.-K.; Gonda, I. Physicochemical characterization of a new respirable form of nedocromil. *J. Pharm. Sci.* **1995**, *84*, 692−696.
4. Zhu, H.; Khankrari, R. K.; Padden, B. E.; Munson, E. J.; Gleason, W. B.; Grant, D. J. W. Physicochemical characterization of nedocromil bivalent metal salt hydrates. 1. Nedocromil magnesium. *J. Pharm. Sci.* **1996**, *85*, 1026−1033.
5. Freer, A. A.; Payling, D. W.; Suschitzky, J. L. Structure of nedocromil sodium: a novel anti-asthmatic agent. *Acta Crystallogr.* **1987**, *C43*, 1900−1905.
6. Cahn, L.; Schultz, H. R. Cahn recording gram electrobalance. *Vac. Microbalance Technol.* **1962**, *3*, 29−44.
7. Cahn, L.; Schultz, H. R.; Gaskins, P. New electromagnetic balance with elastic ribbon suspension. *Microchem. J. Symp. Ser.* **1962**, *2*, 1027−1032.
8. Cole, K. Interfacing vapour and pressure and weight monitoring equipment to a BBC microcomputer. MSc. Dissertation, Department of Computing, University of Bradford, 1990.
9. Richards, A. C.; McColm, I. J.; Harness, J. B. The relationship between the rate controlling processes and temperature in the absorption of water vapour by anhydrous nedocromil sodium. Manuscript in preparation.
10. Shefter, E.; Higuchi, T. Dissolution behaviour of crystalline solvated and nonsolvated forms of some pharmaceuticals. *J. Pharm. Sci.* **1963**, *52*, 781−791.
11. Crank, J. *The mathematics of diffusion*. Clarendon Press: Oxford: U.K., 1964.
12. Ruthven, D. M. *Principles of absorption and adsorption processes*; Wiley and Sons: Chichester, 1984.

Acknowledgments

One of us (A.C.R.) would like to thank Fisons for an EPSRC Case Award and one (J.B.H.) would like to thank EPSRC for a Grant Award GRJ68557 to assist in this work.

JS9804866

Resolution of Ephedrine in Supercritical CO_2: A Novel Technique for the Separation of Chiral Drugs

A. KORDIKOWSKI,*,† P. YORK,†,‡ AND D. LATHAM§

Contribution from *Drug Delivery Group, School of Pharmacy, University of Bradford, Bradford, West Yorkshire, BD7 1DP, UK, Bradford Particle Design, 49 Listerhills Science Park, Campus Road, Bradford, West Yorkshire, BD7 1HR, and Medicines Research Centre, Glaxo Wellcome R&D, Gunnels Wood Road, Stevenage, Hertfordshire, SG1 2NY, UK.*

Received November 30, 1998. Accepted for publication May 11, 1999.

Abstract □ Racemic ephedrine has been resolved by diastereomeric salt formation with mandelic acid using supercritical CO_2 as precipitating agent. Crystallizations were performed using the Solution Enhanced Dispersion by Supercritical Fluids (SEDS) technique. Temperature was varied between 35 and 75 °C, and pressures ranged from 100 to 350 bar. Resolution, determined by chiral capillary electrophoresis, is described as a function of temperature and density of the supercritical fluid. A comparison of SEDS-produced material with a conventional resolution method shows that SEDS-crystallized material exhibits identical properties to conventionally crystallized material.

Introduction

Pharmacologically active substances containing chiral centers can exist as pairs of enantiomers, which exhibit the same physical properties but show a different molecular conformation. Since, in general, only one of the enantiomers is biologically active or possesses pharmacological relevance,[1−3] the resolution of enantiomers is of great importance for the pharmaceutical industry.[4−6] Pure enantiomers can be obtained either from chiral starting materials or by asymmetric synthesis.[7] While chiral natural products always exhibit very high enantiomeric purity, only a few natural products show a desired pharmacological activity. By contrast, synthetic drugs are often produced as racemates. It is therefore necessary to have a simple but powerful technique to resolve racemates.

Racemates have been resolved by a variety of methods. If the racemate exists as racemic conglomerate, it will resolve spontaneously when crystallized.[8] In 1850, Pasteur discovered the resolution of sodium ammonium tartrate[9] and was able to separate the enantiomers by sorting them under a microscope. Another method of resolving conglomerates is by seeding a supersaturated solution with crystals of one enantiomer.[10] Additional methods for the resolution of racemates have involved either crystallization by entrainment,[11] or optically active solvents.[12] A detailed description of resolution techniques in terms of thermodynamics is given by Jacques et al.[13]

If the compound of interest is either a carboxylic acid or an organic base, resolution can be achieved by diastereomeric salt formation.[13−16] In many cases a racemate of a chiral carboxylic acid has been resolved using a naturally occurring chiral amine.[17] However, resolution is usually not complete after a single crystallization, and the partially resolved material has to be recrystallized. A classical example is the resolution of racemic ephedrine with (*R*)-mandelic acid, a procedure reported almost 70 years ago.[18] The authors separated diastereomeric (*R*)-mandelates by crystallization from ethanol, but the initial crop had to be recrystallized several times to achieve a pure product.

Conventional crystallization from organic solvents can often lead to solvent inclusion in the crystal. However, it is known that organic substrates crystallized from supercritical CO_2 produce crystals with solvent levels below 25 ppm.[19] Additionally, supercritical CO_2 has been used to produce a variety of materials of defined crystal size.[20,21] Supercritical CO_2 might therefore provide an alternative method for the resolution of racemates. This possibility was briefly investigated by Fogassy et al.,[22] who precipitated diastereomeric mixtures of several similar chiral carboxylic acids onto glass beads and extracted them with supercritical CO_2. Although partial resolution was achieved and both enantiomers were recovered, the degree of resolution was poor. Although resolution was explained in terms of acid−base molecular recognition, no attempt was made to exploit the benefits of the supercritical phase.

We present a simple and reliable method to resolve racemic ephedrine with (*R*)-mandelic acid by crystallization from supercritical CO_2. We show that a high degree of resolution can be achieved within a single crystallization. Furthermore, the product is highly crystalline unlike the conventionally resolved material.

Experimental Section

Chemicals—(1*R*,2*S*)-ephedrine, (1*S*,2*R*)-ephedrine, and (*R*)-mandelic acid had a purity of >99% and were supplied by Aldrich (Gillingham, UK). Methanol was >99.9% and was supplied by BDH Chemicals (Poole, UK). CO_2 was 99.99% and supplied by BOC (Manchester, UK). All chemicals were used without further purification.

Equipment—Experiments were carried out in a SEDS (Solution Enhanced Dispersion by Supercritical Fluids) apparatus for crystallization in supercritical fluids. A scheme of the equipment is given in Figure 1. HPLC pumps P_{1-3} (Jasco, model 880) were used to feed CO_2, solute solution, and additional solvent to the crystallization vessel. Pressure pulses, originating from the pumps, were eliminated by a pulse dampener PD, made from a $^1/_4$ in. stainless steel tube. CO_2 was supplied from a high-pressure cylinder GC, cooled to approximately −10 °C (*T*), and then pumped into the vessel. Simultaneously, solute solution SS was pumped into the crystallization vessel, through a specially designed nozzle N, consisting of two coaxial concentric tubes.[23] The crystallization vessel V (Keystone, 32 mL) was placed inside an oven O (ICI Instruments, TC1900), which controlled the temperature. Pressure was maintained with a backpressure regulator BPR (Jasco, model 880-81). A small additional stream of solvent (0.2 mL·min^{-1}) was introduced at the bottom of the crystallization vessel AS to dissolve material soluble in supercritical CO_2, preventing precipitation in the backpressure regulator. The used solvent was collected SC

* To whom correspondence should be addressed. E-mail: A.Kordikowski@bradford.ac.uk.
† University of Bradford.
‡ Bradford Particle Design.
§ Glaxo Wellcome.

10.1021/js980459f CCC: $18.00 *Published on Web 07/07/1999*

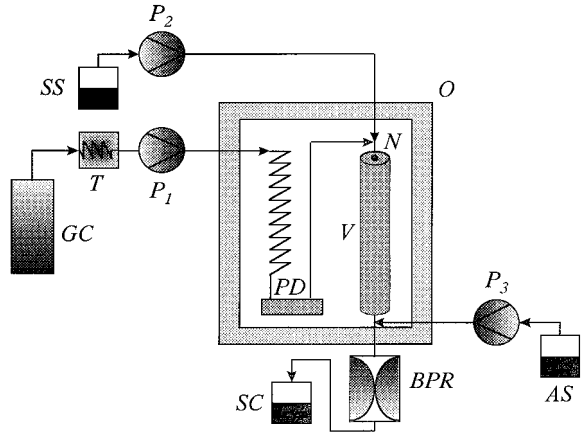

Figure 1—Scheme of the SEDS kit with: pumps P_i, pulse dampener PD, CO_2 cylinder GC, cooler T, solute solution SS, nozzle N, crystallization vessel V, oven O, backpressure regulator BPR, additional solvent AS, solvent collection SC.

after the back pressure regulator BPR. A more detailed description of the equipment and its operating procedure has been given elsewhere.[19,24,25]

Procedure—The general experimental procedure was as follows: 0.261 g (0.79 mmol) of (1*R*,2*S*)-ephedrine, 0.261 g (0.79 mmol) of (1*S*,2*R*)-ephedrine, and 0.239 g of (*R*)-mandelic acid (0.79 mmol) were dissolved in 40 mL of methanol (1.93 w/v%) and the solution was pumped at 0.2 mL·min^{-1} together with 9 mL·min^{-1} CO_2 into the vessel. During the experiment, the solvent dissolved in the supercritical CO_2, leaving the solute behind. The precipitated solid was collected on a filter plate at the bottom of the vessel. After all solute solution had been fed into the vessel, the apparatus was flushed with CO_2 for 15 min. to remove solvent traces present in the vessel. Temperatures for the crystallization ranged from 35 to 75 °C, and pressures varied between 100 and 350 bar. Temperature during the crystallization was constant to ±0.5 °C, and pressure was constant within 1 bar. Densities of CO_2 were obtained from the IUPAC tables.[26] The small variations in temperature and pressure during any experiment result in a small error in density of the supercritical CO_2, which is reflected in the error bars.

Analysis—Samples were analyzed using capillary electrophoresis (CE), using a Beckman P/ACE 2210 system with a fused silica column 27 cm length and an inner diameter of 50 μm. The buffer consisted of a 25 mM solution of dimethyl-β-cyclodextrin in 100 mM triethanolamine at pH 2.5. A voltage of 10 kV was applied producing a current around 50 μA. Separation temperature was 25 °C at a detection wavelength of 200 nm. Sample concentration was typically around 0.1 mg·mL^{-1} in water. Experimental error for the resolution was 0.3 mol %.

Selected samples were investigated by differential scanning calorimetry (DSC) using a Mettler M3 system. A temperature program with a ramp of 2 °C·min^{-1} from 80 to 200 °C was used for all samples. Error in melting point (T_m) was ±0.5 °C. The enthalpy of fusion (ΔH_f) was determined by integration of the melting peak with an error of ±1.5 kJ·mol^{-1}.

Results and Discussion

Pure Diastereomers—The diastereomeric salts (1*S*,2*R*)-ephedrinium-(*R*)-mandelate ((+)-E-(−)-MA) and (1*R*,2*S*)-ephedrinium-(*R*)-mandelate ((−)-E-(−)-MA) were prepared with the SEDS equipment to obtain reference material for the separation. Experimental parameters for the crystallization of the pure diastereomers are summarized in Table 1. From Table 1 it can be seen that (−)-E-(−)-MA was crystallized at the high pressure of 300 bar using methanol as solvent. In contrast, (+)-E-(−)-MA was not obtained under these conditions, due to greater solubility in CO_2 than (−)-E-(−)-MA. For crystallization of (+)-E-(−)-MA, the pressure had to be lowered to 100 bar, and THF used as solvent, because no precipitation occurred in CO_2 with methanol. (+)-E-(−)-MA is less soluble in THF; the same solution concentration is therefore more saturated and precipitates easier when CO_2 is added as an antisolvent.

Table 1—Experimental Parameters for SEDS Crystallizations

	(–)-E-(–)-MA	(+)-E-(–)-MA	racemate
CO_2 flow, mL·min^{-1}	9	9	9
solution flow, mL·min^{-1}	0.2	0.2	0.2
bottom solvent flow, mL·min^{-1}	0.2	0.2	0.2
p, bar	300	100	100–350
T, °C	35	35	35–75
concentration, w/v%	2.5	2.5	1.93
solvent	methanol	tetrahydrofuran	methanol

Table 2—Physicochemical Parameters of Pure Ephedrinium Mandelates

	(–)-E-(–)-MA		(+)-E-(–)-MA	
	SEDS	"classic"[22]	SEDS	"classic"[22]
T_m, °C	169.1	165	108.7	110.8
ΔH_f, kJ·mol^{-1}	40.3	51.9	20.7	27.6

The differences in crystallization between the diastereomers can be explained by their different solubility in CO_2. Solubility of a solid in a liquid can be expressed with the enthalpy of fusion and the isobaric heat capacity. Neglecting the influence of the heat capacity and assuming that in the SEDS process both diastereomers are infinitely diluted, differences in solubility between them can solely be related to their heat of fusion. From the melting points and enthalpies of fusion of both salts shown in Table 2, it can be seen that their T_m differ by more than 50 °C and ΔH_f by 20 kJ·mol^{-1}.[27] The low ΔH_f for (+)-E-(−)-MA explains why it is difficult to crystallize from supercritical CO_2. Table 2 also shows T_m and ΔH_f for the diastereomers produced by SEDS. In comparison to the literature data, the SEDS-produced materials have almost identical melting points. The difference in enthalpy of fusion observed might either be due to small amorphous regions within the SEDS product, or to the minute crystal size of the SEDS material. Supersaturation and subsequent precipitation in the SEDS process occur within milliseconds; therefore, particles can be produced which give rise to the possibility of amorphous regions within the crystal.

SEM photographs were taken as reference of both diastereomeric salts. From the SEM photograph in Figure 2a it can be seen that (−)-E-(−)-MA produced by SEDS is comprised of very thin plates, which were shown to have an average size of 100 × 200 μm. The plates are also translucent, as can be seen from Figure 2b. The SEM photograph in Figure 3a shows the crystal shape of SEDS produced (+)-E-(−)-MA. It is distinctively different to the other diastereomer and consists of needlelike structures with an average length of 300 μm. From Figure 3b, it can be seen that individual needle pieces are "grafted" on top of each other.

Resolution by SEDS—As discussed above, the difference in enthalpy of fusion between the diastereomers results in a large difference in solubility in supercritical CO_2. (−)-E-(−)-MA possesses the higher enthalpy of fusion and should therefore crystallize preferentially making resolution of the racemate in supercritical CO_2 possible. For the separations, racemic ephedrine and (*R*)-mandelic acid were dissolved in methanol, and the solution was pumped into the crystallization vessel simultaneously with the supercritical CO_2. Experimental parameters are sum-

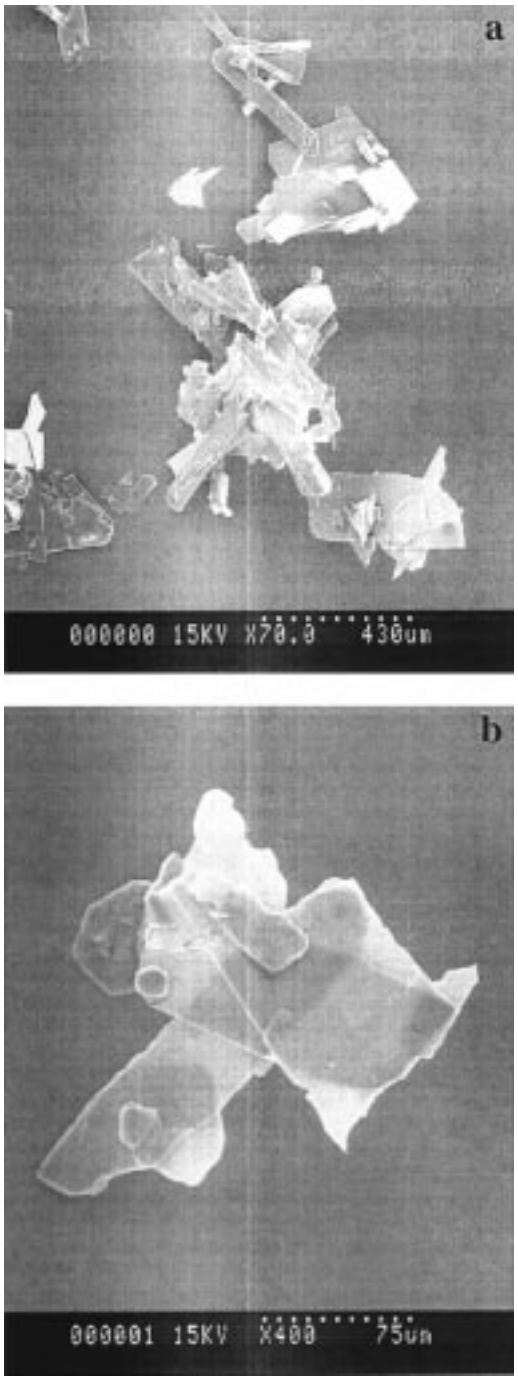

Figure 2—SEM photograph of pure (1*R*,2*S*)-ephedrinium-(*R*)-mandelate crystallized with SEDS from methanol at 35 °C and 300 bar with a CO_2 flow rate of 9 mL·min^{-1} and a solution flow rate of 0.2 mL·min^{-1}.

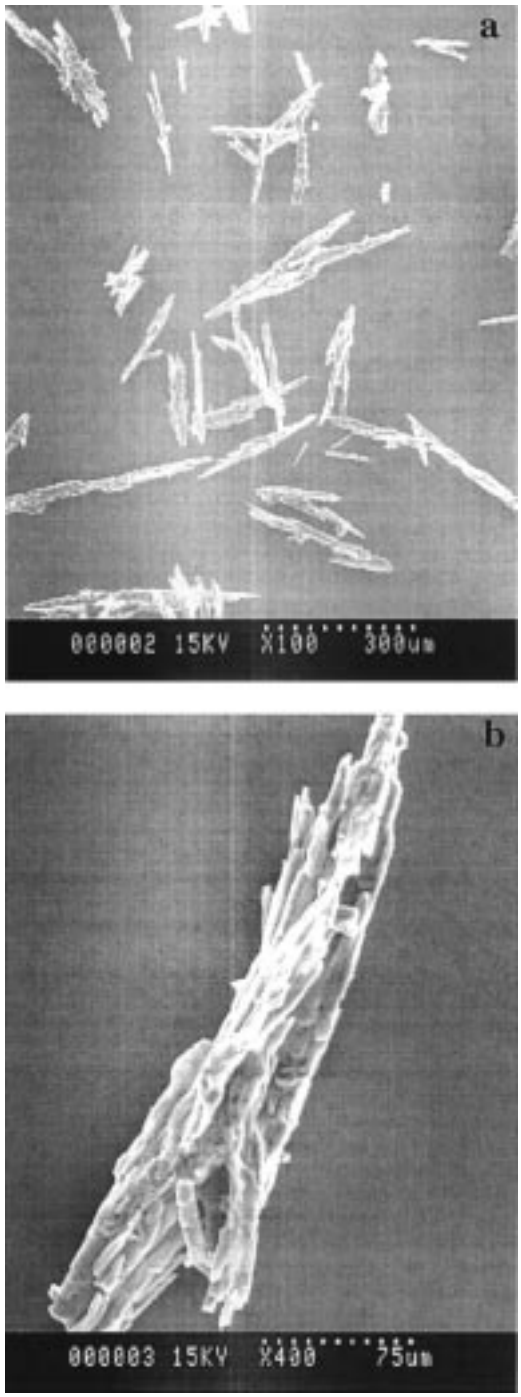

Figure 3—SEM photograph of pure (1*S*,2*R*)-ephedrinium-(*R*)-mandelate crystallized with SEDS from tetrahydrofuran at 35 °C and 100 bar with a CO_2 flow rate of 9 mL·min^{-1} and a solution flow rate of 0.2 mL·min^{-1}.

marized in Table 3. Pressure was varied between 100 and 350 bar at a constant temperature of 35 °C, ensuring that a wide range of densities of CO_2 was covered. Additionally, the temperature was changed between 35 and 75 °C keeping the density of the supercritical CO_2 at a constant value. From Table 3 it can be seen that the achieved resolutions range from 89 to 92%, as expected from the large difference in ΔH_f. In Figure 4, the achieved resolution is plotted against the density of CO_2. Bidirectional error bars are given, reflecting the experimental uncertainties. Within experimental error, a linear relationship between resolution and density of CO_2 can clearly be seen. Resolution rises with increasing density of the supercritical fluid at constant temperature. As explained, (+)-E-(−)-MA is much more soluble in CO_2 than (−)-E-(−)-MA. Thus, at higher pressures the corresponding density of the super-

Table 3—Parameters for Enantiomeric Resolution of (–)-E-(–)-MA with SEDS

p, bar	*T*, °C	ρ_{CO_2}, g·cm^{-3}	resolution$_{(-)-E-(-)-MA}$, %
350	35	0.953	92.7
300	35	0.930	92.3
150	35	0.816	91.3
100	35	0.714	90.5
150	50	0.702	89.5
250	75	0.713	87.8

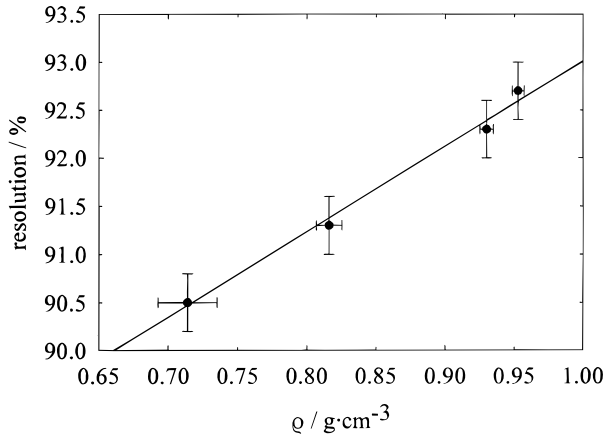

Figure 4—Resolution of SEDS-crystallized ephedrinium-mandelate at a constant density of CO_2 of 0.713 g·cm^{-3}.

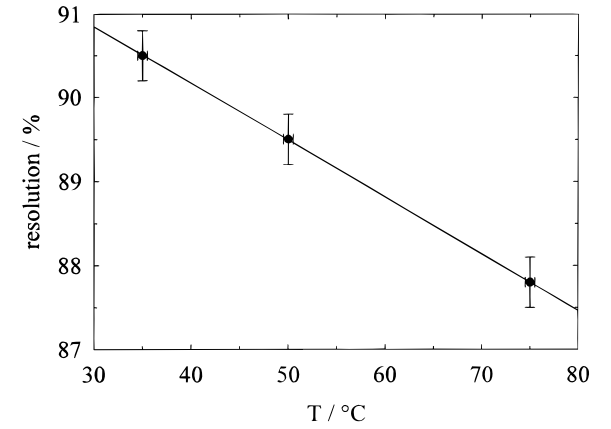

Figure 5—Resolution of SEDS-crystallized ephedrinium-mandelate at a constant temperature of 35 °C.

critical CO_2 is increased supplying more "solvent" in which (+)-E-(−)-MA can be dissolved, resulting in higher enantiomeric excess. As shown, density plays the key role for the resolution, and a higher degree of resolution could therefore be obtained by increasing the density even further. Unfortunately, the density of the supercritical CO_2 rises approximately logarithmically with pressure and, significantly higher densities can only be achieved by applying practically excessive pressures.

As density is an important factor in the resolution of the ephedrinium mandelates, a second series of crystallizations was performed to investigate the temperature dependence of the resolution. In these experiments, the density of the supercritical CO_2 was kept virtually constant (±1.7%) at different temperatures, applying a consecutively higher pressure at elevated temperatures. Results are summarized in Table 3. A linear relationship is obtained in Figure 5 for resolution plotted against temperature with resolution decreased from more than 90% to less than 88% as temperature rises from 35 °C to 75 °C. Bidirectional error bars are included in Figure 5 for the uncertainty in temperature and resolution. The loss in resolution can be explained by changes of ΔH_f with temperature for both diastereomers. Although the difference in ΔH_f between the diastereomers is large, this difference becomes smaller with increasing temperature, causing less efficient resolution. Furthermore, the methanol solution of the solute is less saturated at elevated temperatures, making it more difficult to crystallize the diastereomers. This results in a lower yield in crystalline product at elevated temperatures.

Table 4—Comparison between SEDS and Conventional Resolution

	conventional		
	resolution $_{(-)-E-(-)-MA}$, %	T_m, °C	ΔH_f, kJ·mol^{-1}
crop 1st → 2nd → 3rd	88.0 ± 0.3 → 95.3 ± 0.3 → >99	168.9	46.2
	SEDS		
$p_1 \rightarrow p_2$/bar	resolution $_{(-)-E-(-)-MA}$, %	T_m, °C	ΔH_f, kJ·mol^{-1}
100 → 100	90.5 ± 0.3→ > 99	167.5	41.9
100 → 300	90.5 ± 0.3→ > 99	167.4	42.2
150 → 150	91.3 ± 0.3→ > 99	167.2	38.2
300 → 300	92.3 ± 0.3→ > 99	168.2	42.2

Table 5—ANOVA Table with $K = 4$, $N = 12$, $F(3,8)_{0.05} = 4.07$[26]

	dF	SS	MS	*F*
treatment	3	30.4	10.1	1.46
error	8	55	6.9	
total	11	85.4		

Chiral separations are an extreme case of impurity removal. Considering one of the enantiomers as an impurity, up to 50% has to be removed to obtain an enantiomerically pure product. Yields for each SEDS crystallization lie between 40 and 45%, meaning that 80−90% of the theoretical yield is obtained. Furthermore, highest yields are achieved at low densities of CO_2, because overall solubility of the diastereomeric salts is at a minimum.

SEDS versus "Classic" Resolution—In order, to compare the SEDS products with conventionally obtained enantiomers, a classical resolution of ephedrine with mandelic acid was performed according to the method of Manske and Johnson.[18] For this model resolution, racemic ephedrine and (*R*)-mandelic acid were dissolved in boiling ethanol, and on cooling a diastereomeric salt mixture precipitated. Part of the initial crop was recrystallized twice from boiling ethanol. The first crop had a resolution of 88%, with a yield of 70%. Consecutive recrystallizations with identical yields increased the resolution to 95.3% and finally after another recrystallization to more than 99% with an overall yield of 34%.

SEDS samples produced at 35 °C were recrystallized under identical experimental parameters as for their initial crystallization to determine the efficiency of further purification. The yields for each crystallization was 80% resulting in an overall yield of 64%. Table 4 compares the achieved resolution of the SEDS and classical material and data show that the initial resolution of all SEDS material is higher than for the conventional material. An ANOVA test[28] of the obtained resolutions on a 95% confidence level shows that all samples are significantly different. A summary of the statistical analysis is given in Table 5. Furthermore, after only one recrystallization, the resolution of the SEDS product has risen to more than 99% with no peak of (+)-E-(−)-MA detected by CE. Although the initial resolution of the individual SEDS samples differed by several percent, the recrystallized samples have an identical purity within the error of analysis. Thus it is proposed that also less-resolved material can be resolved to >99% after a recrystallization in supercritical CO_2.

Figure 6 shows a SEM photograph of ephedrinium mandelate that has been crystallized twice from supercritical CO_2. The material exhibits the same very thin plate morphology as pure (−)-E-(−)-MA, as seen in Figure 1. It is known that small amounts of the second enantiomer influence the habit of the crystal[29] and resolution can

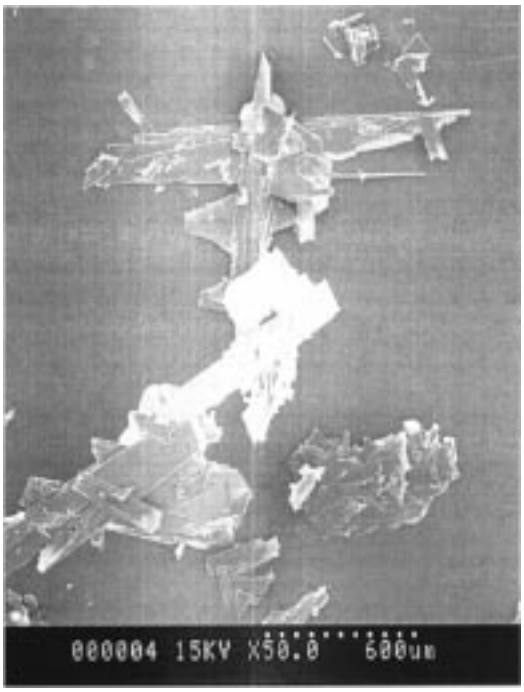

Figure 6—SEM photograph of SEDS-recrystallized ephedrinium-mandelate from methanol at 35 °C and 300 bar with a CO_2 flow rate of 9 mL·min^{-1} and a solution flow rate of 0.2 mL·min^{-1}.

therefore be qualitatively monitored by looking at particle shape. If the crystal habit does not resemble that of the desired diastereomer, it can be assumed that the resolution is not complete. In addition to the crystal shape, T_m and ΔH_f are also almost identical to values for pure (−)-E-(−)-MA. Small differences in T_m and ΔH_f between the individual samples are likely to result from variations in the HPLC-pumps efficiency over the long run periods of the experiment and not from differences in resolution under different conditions. Table 4 also shows that the SEDS-recrystallized samples exhibit T_m comparable to conventionally recrystallized material. The difference in ΔH_f between SEDS and conventional samples is again due to the smaller crystal size, as explained earlier. In contrast to conventionally obtained (−)-E-(−)-MA the material produced by SEDS has the melting point of the pure product after only one recrystallization.

Conclusions

Crystallization by the SEDS process using supercritical CO_2 has been shown to be a versatile method for the resolution of ephedrine racemates via diastereomeric salt and produce material of high enantiomeric purity. Starting from the racemate, crystals with more than 90% resolution can easily be obtained in one crystallization. Resolution has been shown to be a function of density of the supercritical CO_2 and temperature. At constant temperature resolution increased with increasing density of the supercritical CO_2, whereas raising the temperature under isopycnic conditions had a detrimental effect on the degree of resolution. Temperature and density effects were explained by the difference of enthalpy of fusion between enantiomers. After one recrystallization, the SEDS product is indistinguishable from material obtained from enantiomerically pure ephedrine samples. Crystals produced with the SEDS technique exhibit enhanced purity and smoother crystal habits compared to conventionally obtained material. Ease of use and ability to produce highly resolved material make the SEDS process a viable alternative to conventional resolution of chiral compounds.

References and Notes

1. Hegstrom, R. A.,; Kondepudi, D. K. The Handness of the Universe. *Sci. Am.* **1990**, *Jan.*, 108−115.
2. Testa, B.; Trager, W. F. Racemates Versus Enantiomers in Drug Development − Dogmatism or Pragmatism. *Chirality* **1990**, *2*, 129−133.
3. Buser, H. P.; Pugin, B.; Spindler, F.; Sutter, M. Two Enantioselective Syntheses of a Precursor of the Biologically Most Active Isomer of CGA 80000 (Clozylacon). *Tetrahedron* **1991**, *47*, 5709−5716.
4. Gardner, J. C.; DiCicco, R. L. The Growth of Chiral Chemicals. A Higher Value Added Technology. *Specialty Chem.* **1994**, *S9*, July/Aug.
5. Millership, J. S.; Fitzpatrick, A. Commonly used Chiral Drugs: A Survey. *Chirality* **1990**, *5*, 573−576.
6. Midland, M. M.; Nguyen, N. H. Asymmetric Synthesis of γ-Lactones − A Facile Synthesis of the Sex-Pheromone of the Japanese Beetle. *J. Org. Chem.* **1981**, *46*, 4107−4108.
7. Sheldon, R. A. The Industrial Synthesis of Pure Enantiomers. *Drug Inform. J.* **1990**, *24*, 129−139.
8. Collet, A.; Brienne, M. J.; Jacques, J. Studies on Mixtures of Enantiomers XIII. A Further Inventory of Spontaneous Resolution. *Bull. Soc. Chim. Fr.* **1977**, 494−495.
9. Pasteur, L. Recherches Sur les Propriétés Spécifiques des Deux Acides qui Composent L'Acide Racémique. *Ann. Chim. Phys. 3rd Ser.* **1850**, *28*, 56−99.
10. Sato, N.; Uzuki, K. T.; Akashi, T. Direct Resolution of DL-Lysine-3,5-Dinitrobenzoate. *Agric. Biol. Chem.* **1969**, *33*, 1107−1108.
11. Secor, R. M. Resolution of Optical Isomers by Crystallization. *Chem. Rev.* **1963**, *63*, 297−309.
12. Hayes, K. S.; Hounshell, W. D.; Finocchiaro, P.; Mislow, K. Partial Resolution of a Racemic Compound by Crystallization from (+)-α-Pinene: A Novel Use of Inclusion Compounds. *J. Am. Chem. Soc.* **1977**, *99*, 4152−4153.
13. Jacques, J.; Collet, A.; Wilen, S. H. *Enantiomers, Racemates and Resolutions*; John Wiley & Sons: New York, 1981.
14. Bonner, W. A.; Zderic, J. A.; Casaletto, G. A. The Stereochemistry of Raney Nickel. (III). Stereochemical Course of Dehydroxylations in the Benzyl Alcohol Series. *J. Am. Chem. Soc.* **1952**, *74*, 5086−5089.
15. Jacques, J.; Fouquey, C.; Viterbo, R. Reducing the Role of Chance in Spontaneous Resolution Studies. *Tetrahedron Lett.* **1971**, 4617−4621.
16. Wilen, S. H. Resolving Agents and Resolution in Organic Chemistry. *Topics Stereochem.* **1971**, *6*, 107−176.
17. Jacobus, J.; Raban, M.; Mislow, K. The Preparation of (+)-*N*-Methyl-1-(1-naphthyl)ethylamine and the Determination of Its Optical Purity by Nuclear Magnetic Resonance. *J. Org. Chem.* **1968**, *33*, 1142−1145.
18. Manske, R. H. F.; Johnson, T. B. Synthesis of Ephedrine and Structurally Similar Compounds. II. Synthesis of Some Ephedrine Homologues and the Resolution of Ephedrine. *J. Am. Chem. Soc.* **1929**, *51*, 1906−1909.
19. Hanna, M. Novel Approaches for Controlled Particle Formation Using Supercritical Fluid Technology. Ph.D. Thesis, 1995, University of Bradford.
20. Gallagher, P. M.; Coffey, M. P.; Krukonis, V. J.; Klasutis, N. Gas-Antisolvent Recrystallization − New Process to Recrystallize Compounds Insoluble in Supercritical Fluids. *ACS Symp. Ser.* **1989**, *406*, 334−354.
21. Winters, M. A.; Knutson, B. L.; Debenedetti, P. G.; Sparks, H. G.; Przybycien, T. M.; Stevenson, C. L.; Prestrelski, S. J. Precipitation of proteins in supercritical carbon dioxide. *J. Pharm. Sci.* **1996**, *85*, 586−594.
22. Fogassy, E.; Ács, M.; Szili, T.; Simandi, B.; Sawinsky, J. Molecular Chiral Recognition in Supercritical Solvents. *Tetrahedron Lett.* **1994**, *2*, 257−260.
23. Hanna, M.; York, P. U.S. Patent 5851453, 1998. Eur. Patent 0706421B1 and 0767702B1, 1998.
24. Palakodaty, S.; York, P.; Pritchard, J. Supercritical fluid processing of materials from aqueous solutions: The application of SEDS to lactose as a model substance. *Pharm. Res.* **1998**, *15*, 1835−1843.
25. Shekunov, B. Yu.; Hanna, M.; York, P. Crystallization Process in Turbulent Supercritical Flows. *J. Cryst. Growth* **1999**, in press.
26. *Carbon Dioxide International Thermodynamic Tables of the Fluid State-3*; Pergamon Press: New York, 1976.

27. Zingg, S. P.; Arnett, E. M.; McPhail, A. T.; Bothner-By, A. A.; Gilkerson, W. R. Chiral Discrimination in the Structures and Energetics of Association of Stereoisomeric Salts of Mandelic Acid with α-Phenylethylamine, Ephedrine and Pseudoephedrine. *J. Am. Chem. Soc.* **1988**, *110*, 1565−1580.
28. Weiss, N. A., *Elementary Statistics*; 1989, Addison-Wesley Publishing Company: Wokingham, 1989.
29. Li, Z. J.; Grant, D. W, Relationship Between Physical Properties and Crystal Structures of Chiral Drugs. *J. Pharm. Sci.* **1997**, *86*, 1073−1078.

Acknowledgments

The authors thank Glaxo Wellcome R&D for their financial support. We also thank Mrs. H. Cannon of Glaxo Wellcome (PPG) for the DSC analyses, Dr. K. Altria of Glaxo Wellcome (Pharmaceutical Development) for help with the CE analysis, and Mr. G. Townend (Bradford Particle Design) for technical support.

JS980459F

Water Distribution Studies within Cellulose Ethers Using Differential Scanning Calorimetry. 1. Effect of Polymer Molecular Weight and Drug Addition

CONOR B. MCCRYSTAL,† JAMES L. FORD, AND ALI R. RAJABI-SIAHBOOMI*

Contribution from *Pharmaceutical Technology and Drug Delivery Group, School of Pharmacy and Chemistry, John Moores University, Byrom Street, Liverpool L3 3AF, U.K.*

Received October 26, 1998. Accepted for publication May 18, 1999.

Abstract □ Differential scanning calorimetry (DSC) was employed to characterize the distribution of water in gels produced from a series of hydroxypropylmethylcelluloses (HPMC, Methocel K-series) of different molecular weights (i.e., different viscosity grades). The presence of loosely bound water was characterized as pre-endothermic events occurring at temperatures below the main melting endotherm of free water. Both the magnitude and occurrence of these pre-endothermic events were affected by polymer molecular weight and gel storage time. In addition, the amount of water bound to the polymer depended on polymer molecular weight and gel storage time. The temperature at which frozen water melted within the gels was dependent on polymer concentration, with a depression of extrapolated endothermic melting peak onset occurring with an increase in polymer concentration. The addition of propranolol hydrochloride or diclofenac sodium, as model drugs, affected both the occurrence of pre-endothermic events and the distribution of water within the gels.

1. Introduction

Hydrophilic cellulose ether polymers commonly used in controlled release matrices form a gel-like structure when hydrated. Different types of water have been reported to exist within such gel systems.[1] The rate at which water diffuses into hydrophilic matrices and forms a barrier gel layer,[2] followed by water diffusion through this gel layer, both modify the rate at which a drug is released from such systems.[3] Detailed study on the gel layer and more specifically on the types of water which exist is fundamental to the optimization of the use of cellulose ethers in sustained release formulations.

Thermal techniques, including differential scanning calorimetry (DSC) and thermogravimetric analysis (TGA), have been employed to study the states of water within some hydrophilic polymer gel systems.[1] The majority of workers have identified three classes of water within hydrophilic polymer gels which may be defined in terms of their thermal analysis as: (a) free water, i.e., unbound water whose transition temperature enthalpy and peak shape in DSC curves are equal to those of pure (bulk) water;[4] (b) nonfreezing water, i.e., bound water which is attached directly to the polymer and does not undergo a detectable phase transition;[5] (c) freezing bound water, which is characterized as having a phase transition temperature lower than that of bulk water due to a weak interaction with the polymer chain.[6]

There have been many studies comparing drug release from hydroxypropylmethylcelluloses (HPMCs) of different molecular weights with some debate existing within the literature regarding the influence of HPMC viscosity grade on drug release.[7−12]

The presence of a drug in a matrix tablet may influence the way water is bound to or taken up by the cellulose ether. The influence of drugs such as propranolol hydrochloride (a water soluble drug) on the interaction of water with polymer has been studied by DSC[13] and in thermal gelation or cloud-point studies.[14] The presence of free water within the barrier gel layer plays an important part in drug movement across this barrier. Increased availability of free water (i.e., not bound to the polymer) may lead to increased drug diffusion across the gel layer. The effect of diclofenac sodium (a sparingly water soluble drug) on polymer hydration within hydrophilic polymer matrices was studied using cryogenic scanning electron microscopy (SEM) and revealed that internal gel structure was modified by drug addition.[15,16] In addition, it has been reported that diclofenac sodium decreases the hydration of HPMC polymers, causing the polymers to precipitate at elevated temperatures.[2]

The distribution of water within HPMC K15M gels has been characterized.[1,17] Nokhodchi et al.[18] characterized the water distribution in powders of different viscosity grades of the HPMC K-series using DSC and concluded that viscosity grade had no significant effect on the amount of water bound to HPMC polymers.

In this paper, the water distribution within gels of a range of HPMC polymers of different molecular weights but with similar substitution types and levels is characterized using DSC. Furthermore, the influence of drug addition on water distribution within the gel systems is also examined.

2. Experimental Section

2.1 Materials—Hydroxypropylmethylcellulose (HPMC) is a cellulose ether with methoxyl and hydroxypropoxyl substituents on the cellulose backbone. Methocel K-series (22% methoxyl and 8.1% hydroxypropoxyl substitutions) with different viscosity grades, i.e., HPMC K100LV, HPMC K4M, HPMC K15M, and HPMC K100M were obtained from Dow Chemical Co., Midland, MI.

Propranolol hydrochloride and diclofenac sodium were obtained from Becpharm, Harlow, Essex, England and Profarmaco, Milan, Italy, respectively.

2.2 Gel Preparation—HPMC gels (5−25% w/w) (sample size 20 g) were prepared by heating the full quantity of distilled water to ~80 °C and adding in two aliquots to the previously weighed HPMC powder in a mortar and pestle. The mixture was triturated vigorously to ensure thorough wetting before adjusting to weight. Gels containing propranolol hydrochloride (50 mM) or diclofenac sodium (50 mM) were prepared by dissolving the drugs in distilled water by mixing with the aid of gentle heat on a hot plate stirrer (Griffin & George, England) prior to gel preparation. Both drugs

† Present address : Elan Pharmaceutical Technologies, Biotechnology Building, Trinity College, Dublin, Ireland.

* Corresponding author. Tel: ++44 (151) 231 2423. Fax: ++44 (151) 207 1446. e-mail: gamma@livjm.ac.uk.

10.1021/js9804258 CCC: $18.00
Published on Web 06/24/1999

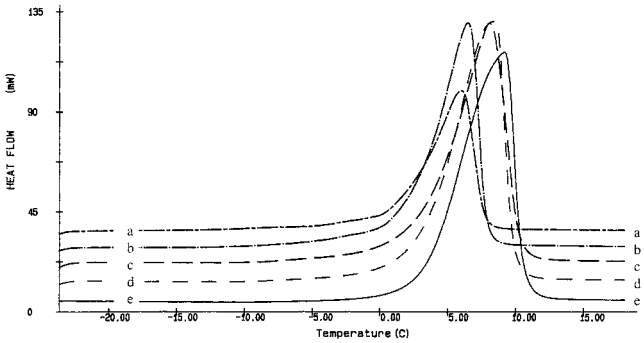

Figure 1—DSC scans of HPMC K15M (5–25% w/w) gels obtained by heating at +10 °C min^{-1} after cooling at –10 °C min^{-1} following storage for 24 h. (a) 5%, (b) 10%, (c) 15%, (d) 20%, (e) 25% (w/w) HPMC K15M.

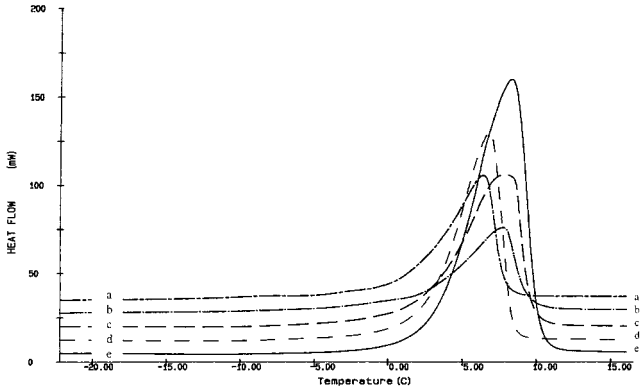

Figure 2—DSC scans of HPMC K15M (5–25% w/w) gels obtained by heating at +10 °C min^{-1} after cooling at –10 °C min^{-1} following storage for 96 h. (a) 5%, (b) 10%, (c) 15%, (d) 20%, (e) 25% (w/w) HPMC K15M.

were fully soluble in warm water at the chosen concentration. Gels were transferred to Pyrex storage vessels which were sealed and stored at 4−6 °C for 24 h before use. Water losses during preparation and storage were taken into account when determining the final polymer concentrations of all gels.

Gel samples >25% w/w were made by preparing gels initially as detailed above in the 10−20% w/w range and storing at 4−6 °C for 24 h. A series of samples (10−16 mg) of the gels were weighed into DSC sample pans (40 μL, Perkin-Elmer) and held at 55 °C in a moisture extraction oven (Townsend & Mercer Ltd., Croydon, England). The samples were removed after defined periods of time to obtain a measurable % weight loss from which the exact polymer:water ratios were calculated.

2.3 Thermal Analysis—A Perkin-Elmer DSC7 (Beaconsfield, UK) with an attached liquid nitrogen based cooling accessory controlled by a Perkin-Elmer TAC-7 was employed. Calibrations with indium (mp onset 156.60 °C) and zinc (mp onset 419.47 °C) were carried out each time the heating rate was changed. Gel samples (5−15 mg) were analyzed in sealed aluminum sample pans (40 μL, Perkin-Elmer, Beaconsfield, UK) by cooling from +20 °C to −35 °C at a cooling rate of −10 °C min^{-1} and then heating from −35 °C to +20 °C at a heating rate of +10 °C min^{-1}.

For gel samples >25% w/w, 5−15 mg of each gel was placed in a DSC pan, sealed, and stored for 24 h at ambient temperature to allow equilibration and uniform water distribution in the gels, before DSC analysis.

3. Results and Discussion

3.1 Characterization of HPMC Gels Using DSC Analysis—Figures 1 and 2 show typical DSC scans for HPMC K15M gels after 24 and 96 h storage time. The exothermic enthalpy (from cooling scans) is the energy released when water within the gels freezes. The endothermic enthalpy (from heating scans) is the energy that is required for melting of frozen water within the gels. Increasing the concentration of HPMC K15M resulted in a decrease in both exothermic (cooling) and endothermic (heating) enthalpies (J/g) after gel storage for both 24 or 96 h (Table 1). Assuming that both exothermic and endothermic peaks are attributable mainly to the crystallization and melting of free water, respectively, it is apparent that there is a decrease in the amount of free water present with an increase in HPMC K15M concentration. As the concentration of the polymer increases, the amount of water required to hydrate the polymer increases and thus less free water is available.

Table 1—Effect of HPMC K15M Concentration (% w/w) on the Extrapolated Exothermic and Endothermic Peak Onsets, the Exothermic and Endothermic Crystallization/Melting Enthalpies (Jg^{-1}) ($n = 3$; ± SD)

HPMC K15M (% w/w)	extrapolated exothermic peak onset (°C)	exothermic enthalpy (J/g)	extrapolated endothermic peak onset (°C)	endothermic enthalpy (J/g)
		After 24 h Storage		
5	–13.4 ± 1.4	259.9 ± 13.9	3.4 ± 0.2	334.7 ± 8.0
10	–16.5 ± 3.0	213.4 ± 21.1	2.9 ± 0.2	289.8 ± 11.3
15	–11.7 ± 2.4	248.2 ± 12.1	2.8 ± 0.3	289.7 ± 14.0
20	–16.0 ± 3.4	208.2 ± 31.7	2.4 ± 0.3	263.6 ± 15.8
25	–13.5 ± 3.4	205.0 ± 18.1	1.8 ± 0.5	228.3 ± 15.4
		After 96 h Storage		
5	–14.2 ± 1.9	218.1 ± 78.3	3.6 ± 0.9	343.3 ± 12.5
10	–15.3 ± 4.7	217.0 ± 33.7	2.8 ± 0.3	304.0 ± 13.9
15	–18.1 ± 0.7	216.7 ± 8.4	2.6 ± 0.2	281.6 ± 15.5
20	–11.3 ± 1.1	209.2 ± 26.8	2.0 ± 0.4	246.3 ± 13.7
25	–14.9 ± 3.8	202.2 ± 9.1	1.5 ± 0.1	231.1 ± 6.6

Increasing HPMC K15M concentration from 5 to 25% (w/w) caused a decrease in the extrapolated endothermic melting peak onset. The extrapolated endothermic melting peak onset is defined as the temperature where the extrapolation of the baseline meets the extrapolation of the ascending melting peak.[19] For example, Table 1 and Figures 1 and 2 show a decrease of extrapolated endothermic melting peak onset from 3.4 ± 0.2 to 1.8 ± 0.5 °C for 5 and 25% w/w gels, respectively, after 24 h hydration, and a decrease from 3.6 ± 0.9 to 1.5 ± 0.1 °C for 5 and 25% w/w gels, respectively, after 96 h hydration. This decrease in the extrapolated endothermic melting peak onset may be related to an increase in the quantity of loosely bound water which melts at a lower temperature than free water due to a stronger interaction with the polymer.[20] This phenomena has previously been reported for HPMC K4M gels.[18] Increasing HPMC K15M concentration has no quantifiable effect on the position of the extrapolated exothermic peak onset (Table 1). This may be because crystallization occurs via nucleation which is an uncontrolled phenomena.[21,22] This lack of control during crystallization was also apparent in HPMC K100LV, HPMC K4M, and HPMC K100M gels (data not shown), where increase in polymer concentration had no effect on the position of the extrapolated exothermic peak onset.

Depression of melting point (extrapolated endothermic peak onset) with increasing concentration of polymer was observed in all HPMC polymers studied here (data not shown). HPMC K100LV (−0.2 ± 0.3 to −2.0 ± 0.1 °C; 5 & 25% w/w gels, respectively, 24 h), HPMC K4M (−2.6 ± 0.1 to −3.4 ± 1.2 °C; 5 & 25% w/w gels respectively, 24 h) and HPMC K100M (−0.2 ± 0.3 to −2.0 ± 0.4 °C; 5 & 25% w/w gels respectively, 24 h), all display this depression in melting point. However, there is no apparent trend between polymer molecular weight and extent of melting point depression with increase in polymer concentration. Similar findings were obtained for HPMC K100LV, HPMC K4M and HPMC K100M gels after 96 h storage.

The presence of endothermic events on low temperature side of the main endotherm for the melting of free water

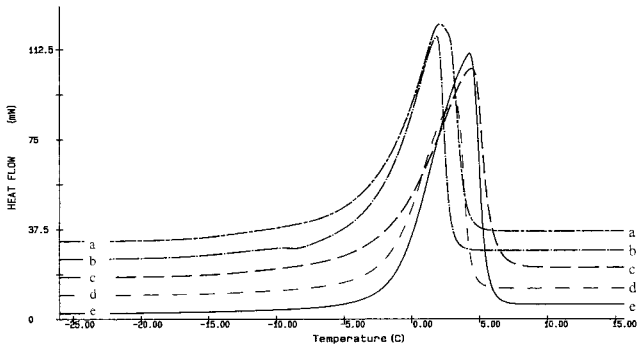

Figure 3—DSC scans of HPMC K100LV (5–25% w/w) gels obtained by heating at +10 °C min^{-1} after cooling at –10 °C min^{-1} following storage for 96 h. (a) 5%, (b) 10%, (c) 15%, (d) 20%, (e) 25% (w/w) HPMC K100LV.

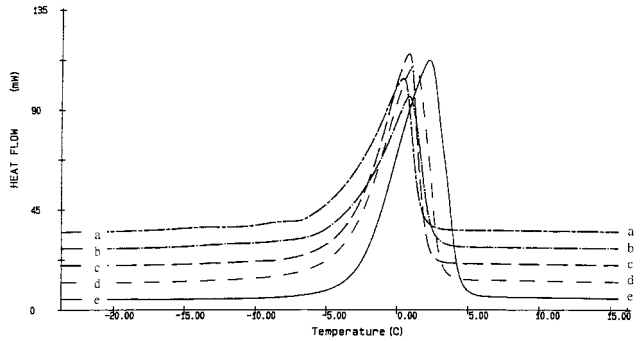

Figure 4—DSC scans of HPMC K4M (5–25% w/w) gels obtained by heating at +10 °C min^{-1} after cooling at –10 °C min^{-1} following storage for 24 h. (a) 5%, (b) 10%, (c) 15%, (d) 20%, (e) 25% (w/w) HPMC K4M.

in DSC scans for HPMC K15M gels was discussed previously.[17] Their occurrence were dependent on polymer concentration, storage time, and scanning rates during DSC analysis. These events were related to the presence of different states of water in the polymer gels. Alternative explanations for similar pre-endothermic events in other systems have been considered in the literature where they were attributed to overlapping ice melting (first-order) and glass transition (second-order) phase transitions.[23] Ratto et al.[24] attributed pre-endothermic events present in water/chitosan systems to cold crystallization. This occurs in systems where only nonfreezing and freezing bound water are present. Upon heating, some of the nonfreezing water becomes mobile, comes into contact with solid freezing bound water, and forms ice. A crystallization exotherm is subsequently visible.

Similar events were also visible prior to the main DSC melting endotherms in gels containing HPMC K100LV, HPMC K4M, or HPMC K100M. Their appearance was dependent on both polymer molecular weight and gel storage time. In HPMC K100LV and HPMC K15M, pre-endothermic events were only visible in 20% w/w and 25% w/w gels after storage for 24 and 96 h (Figures 1−3). In the case of HPMC K15M, pre-endothermic events were more pronounced after 96 h storage.

Gels of HPMC K4M or HPMC K100M showed pre-endothermic events at 15, 20, or 25% w/w polymer content after storage for both 24 and 96 h (Figure 4 and Figure 5). In both these cases, the appearance of such events was unaffected by storage time. It appears that the occurrence of endothermic events varied between HPMCs of different molecular weights.

3.2 Quantitative Analysis of the Effect of Molecular Weight on Water Distribution within Cellulose Ethers—The number of moles of bound (nonfreezing) water per polymer repeating unit (PRU) was calculated for HPMC

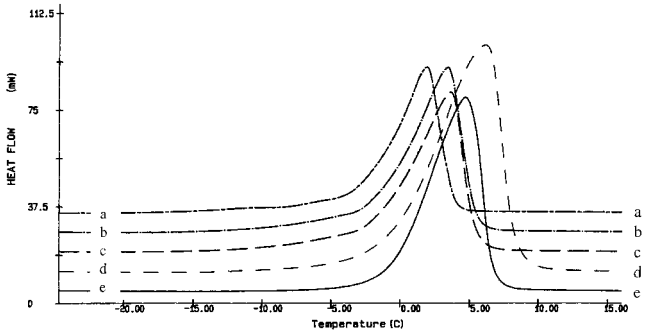

Figure 5—DSC scans of HPMC K100M (5–25% w/w) gels obtained by heating at +10 °C min^{-1} after cooling at –10 °C min^{-1} following storage for 24 h. (a) 5%, (b) 10%, (c) 15%, (d) 20%, (e) 25% (w/w) HPMC K100M.

Table 2—Effect of HPMC Molecular Weight and Equilibration Time on the Bound (nonfreezing) Water (BW) Content per Polymer Repeating Unit (PRU) As Calculated by the Method Proposed by Ford and Mitchell[1]

polymer	viscosity (cP)[a]	PRU value	moles BW per PRU (24 h)	R^2 (24 h)[b]	moles BW per PRU (96 h)	R^2 (96 h)
HPMC K100	93	189	2.4	0.994	4.4	0.973
HPMC K4M	4 196	188	7.1	0.996	4.5	0.973
HPMC K15M	15 825	189	4.5	0.978	6.5	0.934
HPMC K100M	119 768	192	6.0	0.970	6.6	0.963

[a] Values were taken from certificate of analysis provided by the manufacturer of the products. [b] R^2 is the regression coefficient.

K100LV, HPMC K4M, HPMC K15M, and HPMC K100M gels according to the method outlined by Ford and Mitchell[1] and have been reported previously.[17] Enthalpy of fusion of ice (J g^{-1}) was plotted against HPMC concentration (% w/w), and the plots were extrapolated to zero enthalpy through the lines of best fit. The concentration at zero enthalpy was taken as being the minimum ratio of water: HPMC that is required for complete hydration of the polymer. A linear relationship was assumed to exist between enthalpy and polymer concentration. The bound water content was calculated using values for the PRU listed in Table 2 that were calculated for each HPMC viscosity grade based on their % methoxyl and % hydroxypropoxyl substitution on the cellulose ether backbone.

HPMC K4M showed a decrease in bound water content from 24 to 96 h storage, whereas all other polymers showed an increase in their bound water content during this equilibration period (Table 2). The largest change in bound water content occurred in HPMC K100LV (the lowest viscosity grade polymer within the K-series), which shows a 58% increase in the bound water content from 24 to 96 h. Allowing 96 h equilibration, which should be ample time for uniform equilibration in all gel samples, an increase in the bound water content is apparent with an increase in polymer viscosity within the HPMC K-series (Table 2).

3.3 Effect of Drug Addition on Water Distribution in Cellulose Ether Gels—In the absence of a drug, pre-endothermic events were present in 15, 20, and 25% w/w HPMC K4M and HPMC K100M gels and in 20 and 25% w/w HPMC K100LV and HPMC K15M gels after 24 h storage (section 3.2). Incorporation of 50 mM of propranolol hydrochloride did not affect the appearance of such events in HPMC K100LV, HPMC K4M, and HPMC K15M gels. However, in HPMC K100M gels, pre-endothermic events were visible only in 20 and 25% w/w gels after 24 h.

Figure 6 shows the influence of diclofenac sodium on the appearance of pre-endothermic events in 5−25% w/w HPMC K4M gels which is representative of other polymers studied. After 24 h equilibration, pre-endothermic events

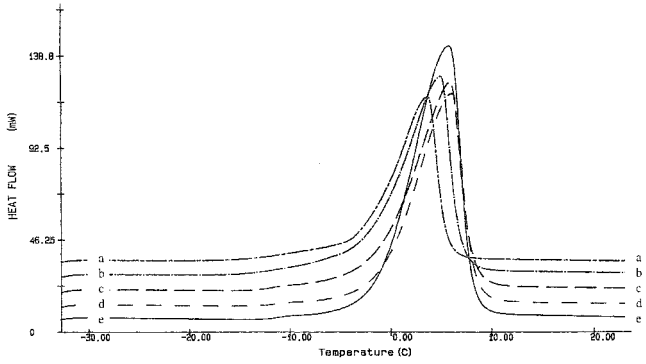

Figure 6—DSC scans of HPMC K4M (5–25% w/w) gels containing 50 mM of diclofenac sodium obtained by heating at +10 °C min^{-1} after cooling at –10 °C min^{-1} following storage for 24 h. (a) 5%, (b) 10%, (c) 15%, (d) 20%, (e) 25% (w/w) HPMC K4M + 50 mM diclofenac sodium.

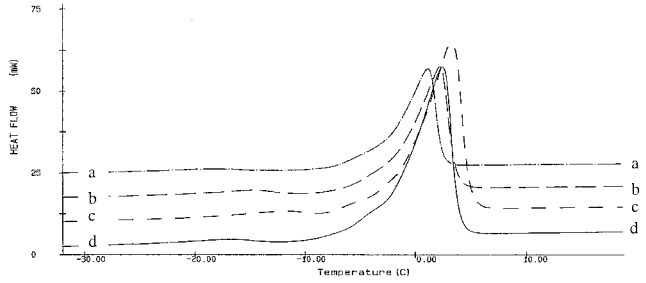

Figure 7—DSC scans of 26.7–32.4% (w/w) HPMC K15M gels in the absence and presence of 50 mM of diclofenac sodium obtained by heating at +10 °C min^{-1} after cooling at –10 °C min^{-1} following storage for 24 h. (a) 26.7% K15M, (b) 30.5% K15M, (c) 29.2% K15M + 50 mM diclofenac sodium, (d) 32.4% (w/w) K15M + 50 mM diclofenac sodium.

were visible in all HPMC K-series studied here, at each concentration (5−25% w/w). It is hypothesized that diclofenac sodium causes the polymer to "salt out", making it less soluble and requiring more water to bind to the polymer to keep it in solution. Therefore, there is more loosely bound water in the system. It is possible that this loosely bound water appears in DSC scans and may explain the appearance of these pre-endothermic events.

Pre-endothermic events in HPMC K15M gels were previously found to be exaggerated in the 25−35% w/w concentration range in comparison to the events observed with 20 and 25% w/w HPMC K15M gels.[17] The influence of each drug on the DSC scans of gels containing 25−40% w/w HPMC K15M was examined.

Following the inclusion of 50 mM of propranolol hydrochloride into HPMC K15M gels, pre-endothermic events were visible at 29.0% w/w but they were not present at the higher concentrations studied (30.7−40.1% w/w). The pre-endothermic events became quite pronounced in the HPMC K15M gels in the 25−35% w/w concentration range when diclofenac sodium (50mM) was added. However, they were not apparent in HPMC K15M gels at concentrations >35% w/w. Figure 7 shows that in 25−33% w/w HPMC K15M gels, secondary events were clearly visible both in the presence and absence of diclofenac sodium.

Increasing HPMC K15M concentration from 5 to 25% w/w caused a decrease in the extrapolated endothermic melting peak onset from 3.4 ± 0.2 to 1.8 ± 0.5 °C after 24 h storage. With the addition of a drug, this depression of melting onset may be expected regardless of polymer molecular weight. For HPMC K15M gels, increasing polymer concentration from 5 to 25% w/w in the presence of 50 mM propranolol hydrochloride caused a depression of the extrapolated endothermic melting peak onset from 3.2 ± 0.7 °C to 0.8 ± 0.2 °C. Similarly, increasing polymer concentration in HPMC K15M gels from 5 to 25% w/w in the presence of 50 mM diclofenac sodium caused a depression of the extrapolated endothermic melting peak onset from 2.9 ± 0.5 °C to 1.3 ± 0.2 °C.

Table 3—The Effect of Addition of 50 mM of Propranolol Hydrochloride or Diclofenac Sodium on the Water Distribution within a Range of Cellulose Ether Gels after 24 h Storage

polymer	viscosity (cP)[a]	polymer (% w/w)	water (% w/w)	R^{2b}	moles bound water per PRU
HPMC K100LV	93	81.2	18.8	0.994	2.4
+ propranolol		80.3	18.3	0.976	2.4
+ diclofenac		70.0	28.5	0.986	4.3
HPMC K4M	4 196	59.6	40.4	0.996	7.1
+ propranolol		79.4	19.2	0.997	2.5
+ diclofenac		65.4	33.1	0.987	5.3
HPMC K15M	15 825	70.2	29.8	0.978	4.5
+ propranolol		76.6	21.9	0.975	3.0
+ diclofenac		71.8	26.8	0.992	3.9
HPMC K100M	119 768	64.1	35.9	0.970	6.0
+ propranolol		81.4	17.2	0.982	2.3
+ diclofenac		65.1	33.4	0.981	5.5

[a] Values were taken from certificate of analysis provided by the manufacturer of the products. [b] R^2 is the regression coefficient.

The number of moles of bound water per PRU (average molecular weight of one polymer repeating unit) were calculated as previously described using the Ford and Mitchell[1] method (section 3.2), and the values chosen for the PRU were as listed in Table 2. In HPMC K4M, HPMC K15M, and HPMC K100M gels, propranolol hydrochloride reduced the amount of water bound to the polymer (Table 3). In effect, less water was required to fully hydrate the polymer, most likely due to the "salting-in" effect of the drug which increases polymer solubility.[25] The ability of propranolol hydrochloride to reduce the amount of water required to fully hydrate HPMC K15M gels has been previously reported.[13]

Addition of propranolol hydrochloride to HPMC K100LV gels did not reduce the amount of bound water. The bound water content initially was very low in these gels. When diclofenac sodium was added to cellulose ether gels, with the exception of HPMC K100LV, the amount of water bound to the polymer was reduced in comparison with that bound in the absence of drug. More water was required to fully hydrate the polymer compared to when propranolol hydrochloride was added. Diclofenac sodium "salts out" cellulose ether polymers making them less soluble. Therefore, more water will be required to hydrate the polymer, and thus the bound water content should increase. For HPMC K100LV, addition of propranolol hydrochloride did not change the bound water content, while addition of diclofenac sodium caused an increase in the amount of water binding to the polymer. Addition of diclofenac sodium would certainly seem to make the polymer less soluble, causing an increase in water required to hydrate the polymer, as reflected in an increase in bound water. In the case of propranolol hydrochloride, the expected reduction in bound water content due to the "salting in" effect of the drug did not occur. It may be that a certain minimum level of water is required to maintain the gel structure and remains tightly bound to the polymer. This amount of tightly bound water cannot be removed even with the addition of a drug like propranolol hydrochloride.

4. Conclusions

The water distribution within cellulose ether polymer gels was found to be dependent on polymer molecular

weight and gel equilibration (or storage) time. The presence of loosely bound water was characterized as pre-endothermic events occurring to the left of the main melting endotherm of free water. The occurrence and magnitude of these pre-endothermic events were affected by polymer molecular weight. The melting of frozen water within the gels, as characterized by the extrapolated endothermic melting peak onset, was dependent on polymer concentration. No apparent trend was found to exist between polymer molecular weight and extent of melting point depression with increase in polymer concentration.

The amount of water tightly bound to the polymer, as calculated by the method proposed by Ford and Mitchell,[1] was dependent on polymer molecular weight. This was further affected by drug addition to the polymer gels. Diclofenac sodium had a marked effect on the appearance of pre-endothermic events in cellulose ether polymer gels; however, a negligible effect was observed with the addition of propranolol hydrochloride.

References and Notes

1. Ford, J. L.; Mitchell, K. Thermal analysis of gels and matrix tablets containing cellulose ethers. *Thermochim. Acta* **1995**, *248*, 329−345.
2. Rajabi-Siahboomi, A. R.; Bowtell, R. W.; Mansfield, P.; Henderson, A.; Davies, M. C.; Melia, C. D. Structure and behaviour in hydrophilic matrix sustained release dosage forms: 2. NMR-imaging studies of dimensional changes in the gel layer and core of HPMC tablets undergoing hydration. *J. Controlled Release* **1994**, *31* (2), 121−128.
3. Rajabi-Siahboomi, A. R.; Bowtell, R. W.; Mansfield, P.; Davies, M. C.; Melia, C. D. Structure and behaviour in hydrophilic matrix sustained release dosage forms: 4. Studies of water mobility and diffusion coefficients in the gel layer of HPMC tablets using NMR Imaging. *Pharm. Res.* **1996**, *13* (3), 376−380.
4. Nakamura, K.; Hatakeyama, T.; Hatakeyama, H. Relationship between hydrogen bonding and bound water in polyhydroxystyrene derivatives. *Polymer* **1983**, *24*, 871−876.
5. Hatakeyama, T.; Yoshida, H.; Hatakeyama, H. A differential scanning calorimetry study of the phase transition of the water−sodium cellulose sulphate system. *Polymer* **1987**, *28*, 1282−1286.
6. Taniguchi, Y.; Horigome, S. The states of water in cellulose acetate membranes. *J. Appl. Polym. Sci.* **1975**, *19*, 2743−2748.
7. Salomon, J. L.; Doelker, E.; Buri, P. Sustained release of a water-soluble drug from hydrophilic compressed dosage forms. *Pharm. Ind.* **1979**, *41* (8), 799−802.
8. Nakano, M.; Ohmori, N.; Ogata, A.; Sugimoto, K.; Tobino, Y.; Iwaoku, R.; Juni, K. Sustained release of theophylline from hydroxypropyl-cellulose tablets. *J. Pharm. Sci.* **1983**, *72*, 378−380.
9. Ford, J. L.; Rubinstein, M. H.; Hogan, J. E. Formulation of sustained release promethazine hydrochloride tablets using hydroxypropylmethylcellulose matrices. *Int. J. Pharm.* **1985**, *24*, 327−338.
10. Ford, J. L.; Rubinstein, M. H.; Hogan, J. E. Propranolol hydrochloride and aminophylline release from matrix tablets containing hydroxypropylmethylcellulose. *Int. J. Pharm.* **1985**, *24*, 339−350.
11. Ford, J. L.; Rubinstein, M. H.; Hogan, J. E. Dissolution of a poorly water soluble drug, Indomethacin, from hydroxypropylmethylcellulose controlled release tablets. *J. Pharm. Pharmacol.* **1985**, *37*, 33P.
12. Liu, C.-H.; Kao, Y.-H.; Chen, S.-C.; Sokoloski, T.-D.; Sheu, M.-T. In-vitro and in-vivo studies of the diclofenac sodium controlled-release matrix tablets. *J. Pharm. Pharmacol.* **1995**, *47*, 360−364.
13. Mitchell, K.; Ford, J. L.; Armstrong, D. J.; Elliott, P. N. C.; Rostron, C.; Hogan, J. E. Differential thermal analysis of HPMC gels: Influence of water content and propranolol HCL. *J. Pharm. Pharmacol.* **1989**, *41*, 59P.
14. Mitchell, K.; Ford, J. L.; Armstrong, D. J.; Elliott, P. N. C.; Rostron, C.; Hogan, J. E. The influence of additives on the cloud point, disintegration and dissolution of HPMC gels and matrix tablets. *Int. J. Pharm.* **1990**, *66*, 233−242.
15. Binns, J. S.; Davies, M. C.; Melia, C. D. A study of polymer hydration and drug distribution within hydrophilic polymer matrices by cryogenic SEM and EDX. *Proc. Int. Symp. Controlled Release Bioact. Mater., Controlled Release Soc., Inc.* **1990**, *17*, 339−340.
16. Melia, C. D.; Binns, J. S.; Davies, M. C. Polymer hydration and drug distribution within the gel layer of hydrophilic matrix devices during drug release. *J. Pharm. Pharmacol.* **1990**, *42*, 125P.
17. McCrystal, C. B.; Ford, J. L.; Rajabi-Siahboomi, A. R. A study on the interaction of water and cellulose ethers using differential scanning calorimetry. *Thermochimica Acta* **1997**, *294*, 91−98.
18. Nokhodchi, A.; Ford, J. L.; Rubinstein, M. H. Studies on the interaction between water and hydroxypropylmethylcellulose. *J. Pharm. Sci.* **1997**, *86* (5), 608−615.
19. Ford, J. L.; Timmins, P. Information derived from thermal analytical data. In *Pharmaceutical Thermal Analysis*; Ford, J. L., Timmins, P., Eds.; Ellis Horwood: Chichester, 1989; pp 25−31.
20. Joshi, H. N.; Wilson, T. D. Calorimetric studies of dissolution of hydroxypropyl methylcellulose E5 (HPMC E5) in water. *J. Pharm. Sci.* **1993**, *82* (10), 1033−1038.
21. Mullin, J. W. In *Crystallization*, 3rd ed.; Mullin, J. W., Ed.; Butterworths: Oxford, 1993.
22. Tanaka, H.; Koga, N.; Galwey, A. K. Thermal dehydration of crystalline hydrates. *J. Chem. Educ.* **1995**, *72* (3), 251−256.
23. Roos, Y.; Karel, M. Water and molecular weight effects on glass transitions in amorphous carbohydrates and carbohydrate solutions. *J. Food Sci.* **1991**, *56* (6), 1676−1681.
24. Ratto, J.; Hatakeyama, T.; Blumstein, R. B. Differential scanning calorimetry investigation of phase transitions in water/chitosan systems. *Polymer* **1995**, *36* (15), 2915−2919.
25. Mitchell, K.; Ford, J. L.; Armstrong, D. J.; Elliott, P. N. C.; Hogan, J. E.; Rostron, C. The influence of drugs on the properties of gels and swelling characteristics of matrices containing methylcellulose or HPMC. *Int. J. Pharm.* **1993**, *100*, 165−173.

JS9804258

Water Distribution Studies within Cellulose Ethers Using Differential Scanning Calorimetry. 2. Effect of Polymer Substitution Type and Drug Addition

CONOR B. MCCRYSTAL,† JAMES L. FORD, AND ALI R. RAJABI-SIAHBOOMI*

Contribution from *Pharmceutical Technology and Drug Delivery Group, School of Pharmacy and Chemistry, John Moores University, Byrom Street, Liverpool L3 3AF, U.K.*

Received October 26, 1998. Accepted for publication May 18, 1999.

Abstract □ The distribution of water within gels composed of a range of cellulose ether polymers of similar molecular weights (viscosity grades of 4000–6000 cP) but varying substitution types and levels was assessed by differential scanning calorimetry (DSC). Water loosely bound to the polymer was detected as one or more events appearing at the low-temperature side of the main endotherm for the melting of free water in DSC scans. Polymer substitution types and levels, and added drugs (50 mM propranolol hydrochloride or 50 mM diclofenac sodium) influenced the appearance of these melting events. Hydroxypropylcellulose (HPC) and hydroxypropylmethylcellulose (HPMC F4M) gels showed behavior different to that of the other polymers studied. It is thought that any water binding to HPC gels is tightly attached and is not visible as pre-endothermic events on DSC scans. The amount of water bound per polymer repeating unit (PRU) was influenced by and related to the degree of hydrophilic and hydrophobic substitution on the polymer backbone and by the inclusion of either drug. HPC gels had the highest bound water content after 96 h and this was probably related to the high percentage of hydrophilic hydroxypropoxyl substitutions in this polymer. In contrast, methylcellulose (MC A4M) had the lowest bound water content after 96 h storage, and this was explained by the lack of hydrophilic hydroxypropoxyl substitutions in the polymer.

1. Introduction

The formation of a barrier gel layer in hydrophilic controlled release matrices containing cellulose ethers, and the subsequent water diffusion through this gel layer determine the rate and mechanism of drug release.[1] Different polymer properties have been reported to be responsible for the rate of polymer hydration including polymer viscosity grade,[2−4] polymer particle size,[5−8] polymer concentration,[2] and polymer substitution type.[5]

It was initially proposed by Alderman[5] that cellulose ethers of different substitution levels hydrate at different rates, and this factor may be used to optimize the formulation of sustained release matrices. However, Mitchell et al.,[9] using a combination of differential scanning calorimetry (DSC) and dissolution studies, have shown that the differences in drug release rates from HPMCs with different substitution levels are not due to differences in their hydration rates. Further studies using thermomechanical analysis[9] have shown that gel layer thickness (which will affect the diffusional path length) is similar in HPMCs of different substitution levels. Using NMR imaging, Rajabi-Siahboomi et al.[10] showed that gel layer development in HPMC tablets occurred to the same extent in both axial and radial directions and was similar in HPMCs with different substitution levels.

Differences in drug release patterns between the three HPMC substitution types (Methocels K, E, and F) were found in matrices containing low quantities of the polymers.[11] In addition, Bonferoni et al.[12] reported differences in drug release profiles from HPMC E4M and the other two substitution levels (HPMC K4M and HPMC F4M) at low polymer concentrations. Rajabi-Siahboomi et al.,[1] using NMR imaging, showed that water mobility in the gel layer of hydrated HPMC tablets varied with substitution levels. They found that the lowest value for water mobility was for HPMC K4M. Although no specific reason was given for the differences in water mobility, this differential water mobility may explain the different drug release profiles observed from their matrices.[1] In this article, the water distribution within a range of polymer gels containing cellulose ethers with different substitution types and levels but similar molecular weights are characterized using differential scanning calorimetry (DSC). The influence of drug addition on the distribution of water within these gel systems is also characterized.

2. Experimental Section

2.1 Materials—Methocel cellulose ethers, HPMC K4M, HPMC E4M, HPMC F4M, and methylcellulose (MC) A4M, were obtained from Dow Chemical Co., Midland, MI. Hydroxypropylcellulose (HPC) was obtained from Hercules Limited, Aqualon Division, U.K.

Propranolol hydrochloride and diclofenac sodium were obtained from Becpharm, Harlow, Essex, England, and Profarmaco, Milan, Italy, respectively.

2.2 Gel Preparation—HPMC gels of 5−25% w/w (sample size 20 g) were prepared as described previously[13] and stored for 24 or 96 h before use. Gels containing propranolol hydrochloride (50 mM) or diclofenac sodium (50 mM) were prepared by dissolving the drugs in distilled water by mixing with the aid of gentle heat on a hot plate stirrer (Griffin and George, England) prior to gel preparation. Gel samples greater than 25% w/w were made by preparing gels initially as above, followed by moisture extraction from the gels as described previously.[13]

2.3 Thermal Analysis—A Perkin-Elmer DSC7 (Beaconsfield, UK) with an attached liquid nitrogen based cooling accessory controlled by a Perkin-Elmer TAC-7 was employed as described previously.[13] For gel samples >25% w/w, 5−15 mg of each gel was placed in a DSC pan, sealed and stored for 24 h at ambient temperature to allow equilibration and uniform water distribution in the gels, before DSC analysis.

* Corresponding author: Dr. Ali R. Rajabi-Siahboomi Pharmceutical Technology and Drug Delivery Group, School of Pharmacy and Chemistry, John Moores University, Byrom Street, Liverpool L3 3AF, U.K. Tel: (0151) 231 2423. Fax: (0151) 207 1446. e-mail: gamma@livjm.ac.uk.

† Present address: Elan Pharmaceutical Technologies, Biotechnology Building, Trinity College, Dublin, Ireland.

10.1021/js9804260 CCC: $18.00 Published on Web 06/30/1999

Table 1—The Substitution Levels of Methocels Used in This Study

Methocels	methoxyl (%)	hydroxypropoxyl (%)
HPMC A	30	0
HPMC E	29	8.5
HPMC F	28	5.0
HPMC K	22	8.1

Table 2—Effect of HPC Concentration (% w/w) on the Extrapolated Endothermic Peak Onset, Endothermic Peak, and the Endothermic Melting Enthalpy (Jg^{-1}) ($n = 3$; ±SD) after 24 h Storage

HPC concn (% w/w)	extrapolated endothermic peak onset (°C)	endothermic peak (°C)	endothermic enthalpy (J/g)
	After 24 h Storage		
5	−2.8 ± 0.5	5.4 ± 1.4	303.7 ± 0.9
10	−4.2 ± 0.1	1.4 ± 0.4	274.4 ± 3.9
15	−4.3 ± 0.3	1.8 ± 1.2	251.8 ± 7.4
20	−5.1 ± 0.1	0.6 ± 0.6	218.1 ± 6.7
25	−5.0 ± 0.2	0.0 ± 0.7	208.5 ± 8.4
	After 96 h Storage		
5	−1.5 ± 0.6	5.7 ± 1.9	294.6 ± 13.9
10	−1.8 ± 0.7	5.6 ± 1.8	270.9 ± 2.7
15	−2.1 ± 0.1	4.9 ± 1.0	255.3 ± 14.7
20	−3.1 ± 0.1	3.1 ± 0.7	220.5 ± 9.6
25	−3.7 ± 0.5	2.2 ± 0.9	195.6 ± 8.3

3. Results and Discussion

3.1 Effect of Polymer Substitution Type on the Nature of Water Distribution within Cellulose Ethers—Cellulose ether polymers of varying substitution types and levels possess different degrees of hydrophilic and hydrophobic substituents (Table 1). HPMC E4M and HPMC F4M both have a higher percentage of hydrophobic methoxyl substituents (about 29%) compared to HPMC K4M (22.2%). HPMC E4M has a similar percentage of hydrophilic hydroxypropoxyl substituents to HPMC K4M (about 8%), unlike HPMC F4M which has a lower hydroxypropoxyl percentage content (6%). Methylcellulose (MC A4M) possesses no hydrophilic hydroxypropoxyl substituents whereas hydroxypropylcellulose (HPC) possesses no methoxyl substituents. Therefore, it may be anticipated that water distribution within cellulose ether polymers would be dependent on substitution types and levels.

Table 2 shows the DSC data for HPC gels stored for 24 and 96 h respectively, and they are representative of the data seen for HPMC E4M, HPMC F4M, HPMC K4M, and MC A4M gels. In all cases, as seen in HPMC K-series,[13] increasing the concentration of the polymer from 5 to 25% w/w resulted in a decrease in the temperature of the extrapolated endothermic peak onset. For example, HPMC E4M (−2.1 ± 0.3 to −3.8 ± 0.3 °C; 5 and 25% w/w gels, respectively, 96 h), HPMC F4M (−3.1 ± 0.6 to −5.5 ± 0.3 °C; 5 and 25% w/w gels, respectively, 96 h), HPMC K4M (−2.7 ± 0.2 to −4.2 ± 0.3 °C; 5 and 25% w/w gels, respectively, 96 h), MC A4M (−2.0 ± 0.5 to −4.2 ± 0.4 °C; 5 and 25% w/w gels, respectively, 96 h) and HPC (−1.5 ± 0.6 to −3.7 ± 0.5 °C; 5 and 25% w/w gels, respectively, 96 h) all show a decrease in the temperature of the extrapolated endothermic peak onset. In addition, a decrease in temperature of the endothermic peak and a decrease in the endothermic melting enthalpy with increasing polymer concentration were observed.

There was no specific trend between polymer substitution type and the extent of melting peak depression with increase in polymer concentration.

The existence of events present at the low-temperature side of the main endotherm for the melting of free water

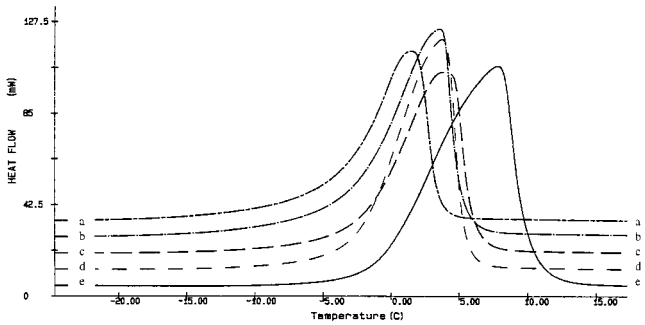

Figure 1—DSC scans of HPC (5–25% w/w) gels obtained by heating at +10 °C min^{-1} after cooling at –10 °C min^{-1} following storage for 96 h: (a) 5%, (b) 10%, (c) 15%, (d) 20%, (e) 25% (w/w) HPC.

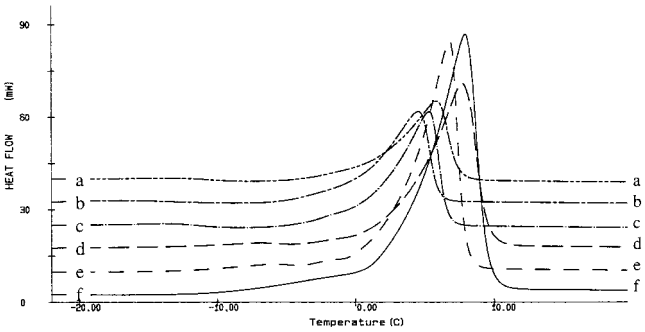

Figure 2—DSC scans of HPMC F4M (19.10–37.80% w/w) gels obtained by heating at +10 °C min^{-1} after cooling at –10 °C min^{-1} following storage for 24 h: (a) 19.10%, (b) 22.49%, (c) 27.14%, (d) 31.71%, (e) 34.07%, (f) 37.80% (w/w) HPMC F4M.

in DSC scans for HPMC K − series gels was discussed previously.[13,14] Such events were related to the presence of different types of water bound to varying degrees to the hydrophilic HPMC polymer and were dependent on polymer molecular weight.[13] Such events were barely visible in HPMC F4M gels, after 24 h storage, but became more pronounced in 20 and 25% w/w gels after 96 h storage. In HPMC E4M, pre-endothermic events were visible in both 20 and 25% w/w gels after 24 and 96 h storage. In the case of methylcellulose, these events were visible in both 20 and 25% w/w gels after 24 h storage, however, they were only visible in 25% w/w gels after 96 h storage. Finally, in all HPC gels, there were no pre-endothermic events visible after either 24 or 96 h (Figure 1). These results indicate that the nature of water distribution within these polymer gels is dependent on substitution types and levels.

Previously, the pre-endothermic events in HPMC K15M gels were found to be exaggerated by an increase in polymer concentration.[14] Therefore, the presence of these events was examined in gels containing higher concentrations of HPC and HPMC F4M.

A series of HPMC F4M 19.10−37.8% w/w and HPC 27.3−48.2% w/w gels were prepared, and their DSC scans were recorded after 24 h storage. Pre-endothermic events were visible in HPMC F4M gels at the higher concentrations studied of >25% w/w (Figure 2). In contrast, in HPC gels, only a small secondary event became visible at concentrations >30% w/w (Figure 3).

Hydroxypropylcellulose gels clearly behaved differently in comparison to the HPMC and MC gels. HPC contains a high percentage of hydrophilic hydroypropoxyl groups and therefore it may be expected to have a larger amount of bound water which is not visible as pre-endothermic events on DSC scans. It is possible that after 96 h storage, the water is tightly attached to the polymer and does not freeze upon cooling. This would explain the nonappearance of pre-endothermic events which have been attributed to loosly

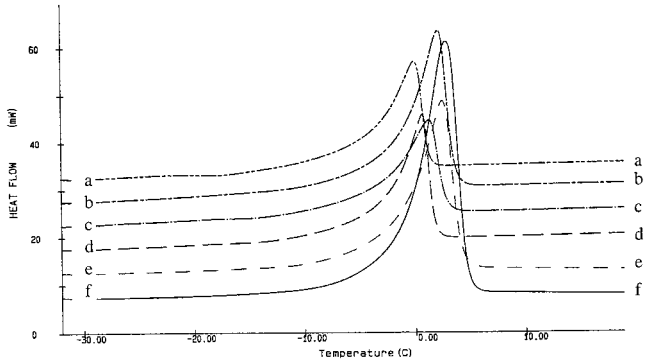

Figure 3—DSC scans of HPC (27.3–35.5% w/w) gels obtained by heating at +10 °C min^{-1} after cooling at –10 °C min^{-1} following storage for 24 h: (a) 27.3%, (b) 29.2%, (c) 30.1%, (d) 31.3%, (e) 32.9%, (f) 35.5% (w/w) HPC.

Table 3—Effect of Polymer Substitution Type and Equilibration Time on the Bound (nonfreezing) Water (BW) Content per Polymer Repeating Unit (PRU) As Calculated by the Method Proposed by Ford and Mitchell[15]

polymer	viscosity (cP)[a]	PRU value	moles BW per PRU (24 h)	R^2 [b] (24 h)	moles BW per PRU (96 h)	R^2 [b] (96 h)
HPMC K4M	4196	188	7.1	0.996	4.5	0.973
HPMC F4M	5218	187	3.2	0.968	5.4	0.993
HPMC E4M	3970	190	6.2	0.974	5.6	0.966
MC A4M	3811	177	5.3	0.999	3.8	0.988
HPC	5950	171	5.5	0.983	6.1	0.990

[a] Values were taken from certificate of analysis provided by the manufacturer of the products. [b] Regression coefficient.

bound water. If this theory is indeed correct, the amount of nonfreezing bound water in HPC gels would be quite high.

3.2 Quantitative Analysis of the Effect of Substitution Type on Water Distribution within Cellulose Ethers—The number of moles of bound (nonfreezing) water per polymer repeating unit (PRU) was calculated for HPMC K4M, HPMC E4M, HPMC F4M, MC A4M, and HPC according to the method outlined by Ford and Mitchell.[15] The PRU value for each polymer was calculated as previously decribed,[13] and they are in Table 3 along with the values for bound water after both 24 and 96 h storage.

HPMC K4M, HPMC E4M, and MC A4M all showed a decrease in their bound water content from 24 to 96 h storage, whereas HPMC F4M and HPC showed an increase in their bound water content during this equilibration period. Considering the bound water content after 96 h to be the equilibrium of the water distribution within these gels, MC A4M has the lowest bound water content compared to other substitution types. This may be due to the fact that MC A4M contains a high hydrophobic methoxyl (29.9%) with no hydrophilic hydroxypropoxyl substitution. A high methoxyl substituent content will not favor large amounts of water binding to the polymer. Previous studies have shown that methoxyl substituent levels are the major factor in causing an apparent decrease in cellulose ether solubility and causing precipitation of the polymer in cloud-point studies.[9]

After 96 h equilibration time, HPC had a high bound water content. HPC contains only hydroxypropoxyl substituents, and a large value for bound water content after equilibration would be expected. This was thought to be the reason for the nonappearance of pre-endothermic events in the DSC scans of HPC gels (Figure 3), indicating that only tightly bound water was present which were not detectable by DSC.

It is reported that HPMC K4M, having a similar hydroxypropoxyl constituent to HPMC E4M, but with smaller

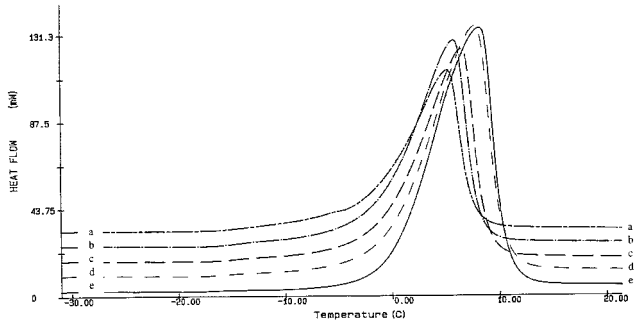

Figure 4—DSC scans of HPMC F4M (5–25% w/w) gels containing 50 mM of propranolol hydrochloride obtained by heating at +10 °C min^{-1} after cooling at –10 °C min^{-1} following storage for 24 h: (a) 5%, (b) 10%, (c) 15%, (d) 20%, (e) 25% (w/w) HPMC F4M + 50 mM propranolol hydrochloride.

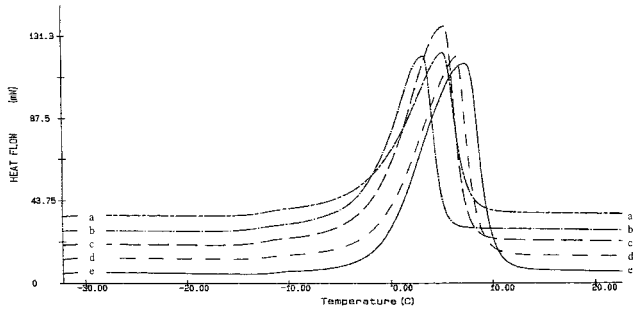

Figure 5—DSC scans of MC A4M (5–25% w/w) gels containing 50 mM of diclofenac sodium obtained by heating at +10 °C min^{-1} after cooling at –10 °C min^{-1} following storage for 24 h: (a) 5%, (b) 10%, (c) 15%, (d) 20%, (e) 25% (w/w) MC A4M + 50 mM diclofenac sodium.

methoxyl substituent levels than HPMC E4M, HPMC F4M, or MC A4M, is more water soluble[5] and undergoes precipitation at higher temperatures than polymers of other substitution types.[9] This may explain the high value for bound water content (7 mol BW per PRU) for HPMC K4M after 24 h storage. However, this high bound water content is not reflected after 96 h storage.

3.3 Effect of Drug Addition on Water Distribution in Cellulose Ether Polymer Gels—In the absence of drug, pre-endothermic events were very slight or not visible in 5−25% w/w HPMC F4M and HPC gels after 24 h equilibration (section 3.2). Figure 4 shows that incorporation of propranolol hydrochloride (50 mM) resulted in the appearance of such events in HPMC F4M gels at concentrations of 15, 20, and 25% w/w. However, no pre-endothermic events were visible in 5−25% w/w HPC gels after incorporation of propranolol hydrochloride (50 mM).

Propranolol hydrochloride addition had no effect on pre-endothermic events in HPMC K4M, HPMC E4M and MC A4M gels after 24 h equilibration with such events being visible in 20 and 25% w/w gels both in the absence or presence of the drug.

Figure 5 illustrates how incorporation of diclofenac sodium into gels resulted in the appearance of pre-endothermic events in 5−25% w/w MC A4M gels. Pre-endothermic events were visible in 5−25% w/w HPMC K4M, HPMC E4M and HPMC F4M gels at all concentrations studied. In HPC gels, however, no pre-endothermic events were visible after addition of diclofenac sodium at any gel concentrations between 5 and 25% w/w.

DSC analysis of 27.3−48.2% w/w HPC gels (with no drug addition) revealed that, even at high concentrations, only a small secondary event was visible at concentrations greater than 30% w/w (section 3.1). In addition, in HPC gels greater than 25% w/w, containing 50 mM of propranolol hydrochloride, pre-endothermic events were barely visible and were similar to the events observed in HPC gels

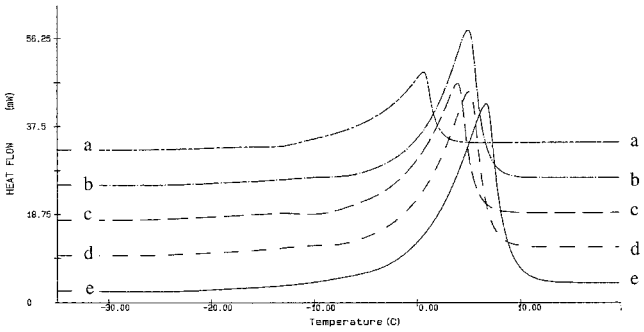

Figure 6—DSC scans of HPC (23.1–32.8% w/w) gels containing 50 mM of diclofenac sodium obtained by heating at +10 °C min^{-1} after cooling at −10 °C min^{-1} following storage for 24 h: (a) 23.1%, (b) 24.9%, (c) 25.3%, (d) 30.0%, (e) 32.8% (w/w) HPC + 50 mM diclofenac sodium.

Table 4—The Effect of Addition of 50 mM of Propranolol Hydrochloride or Diclofenac Sodium on the Water Distribution within a Range of Cellulose Ether Gels after 24 h Equilibration

polymer	viscosity grade (cP)	polymer (% w/w)	water (% w/w)	regression coefficient (R^2)	moles bound water per PRU
HPMC K4M	4196	59.6	40.4	0.996	7.1
+ propranolol		79.4	19.2	0.997	2.5
+ diclofenac		65.4	33.1	0.987	5.3
HPMC F4M	5218	76.4	23.6	0.968	3.2
+ propranolol		76.3	22.2	0.986	3.0
+ diclofenac		83.3	15.3	0.992	1.9
HPMC E4M	3970	63.1	36.9	0.974	6.2
+ propranolol		71.3	27.2	0.951	4.0
+ diclofenac		67.9	30.6	0.958	4.8
MC A4M	3811	65.1	34.9	0.999	5.3
+ propranolol		77.4	21.2	0.995	2.7
+ diclofenac		71.8	26.8	0.998	3.7
HPC	5950	61.6	38.4	0.983	5.5
+ propranolol		67.4	31.1	0.981	4.4
+ diclofenac		63.4	35.2	0.984	5.3

in the absence of drug over a similar concentration range. In contrast, Figure 6 shows that pre-endothermic events are clearly visible in HPC gels containing diclofenac sodium in the 25−35% w/w concentration range. These pre-endothermic events may indicate the presence of loosely bound water which has resulted from the "salting-out" effect of diclofenac sodium.

The number of moles of bound water per PRU were calculated as previously described using the Ford and Mitchell[15] method, and the values chosen for the PRU are as listed in Table 3. In all cases, propranolol hydrochloride reduced the amount of water bound to the polymer (Table 4), i.e., less water was required to fully hydrate the polymer, most likely due to its "salting in" effect. No particular trend was apparent in the extent to which the amount of bound water was reduced by propranolol hydrochloride among the polymers studied. In contrast, diclofenac sodium has a "salting out" effect on cellulose ether polymers. With the exception of HPMC F4M, more water was required to fully hydrate the polymer compared to when propranolol hydrochloride was added.

Differences in the bound water content of polymer gels of different substitution types were previously explained by the degree of substitution of hydrophilic and hydrophobic substituents on the polymer backbone (section 3.2). The bound water content of HPMC F4M in the absence or presence of drug did not follow the pattern shown by other polymer gels studied here. HPMC F4M would be expected to have a fairly low bound water content on the basis that it has a high methoxyl substitution level (28.9%) combined with a low hydroxypropoxyl substitution level (6.1%). This is found to be the case; however, while propranolol hydrochloride exhibits its "salting in" effect, diclofenac sodium does not show its "salting out" properties as in other polymers. A different mechanism may be operating in this case which requires further exploration.

4. Conclusions

Polymer substitution type is an important factor in the distribution of water within cellulose ether polymer gel systems. Polymers of different substitution types possess different degrees of hydrophilic and hydrophobic substitution, and it is thought that these substituents influence the way water attaches itself to the polymer. Pre-endothermic events occurring to the left of the main melting endotherm for the melting of free water in DSC scans, thought to be due to the melting of water loosely bound to the polymer, were dependent on polymer substitution type. HPC gels behaved differently in comparison to the HPMC and MC polymers studied.

The amount of water tightly bound to the polymer, as calculated by the Ford and Mitchell[15] method, was dependent on polymer substitution type. Drug addition influenced both the amount of water bound to the polymer and the appearance of pre-endothermic melting events.

References and Notes

1. Rajabi-Siahboomi, A. R.; Bowtell, R. W.; Mansfield, P.; Davies, M. C.; Melia, C. D. Structure and behaviour in hydrophilic matrix sustained release dosage forms: 4. Studies of water mobility and diffusion coefficients in the gel layer of HPMC tablets using NMR Imaging. *Pharm. Res.* **1996**, *13* (3), 376−380.
2. Ford, J. L.; Rubinstein, M. H.; Hogan, J. E. Formulation of sustained release promethazine hydrochloride tablets using hydroxypropylmethylcellulose matrices. *Int. J. Pharm.* **1985a**, *24*, 327−338.
3. Ford, J. L.; Rubinstein, M. H.; Hogan, J. E. Propranolol hydrochloride and aminophylline release from matrix tablets containing hydroxypropylmethylcellulose. *Int. J. Pharm.* **1985b**, *24*, 339−350.
4. Ford, J. L.; Rubinstein, M. H.; Hogan, J. E. Dissolution of a poorly water soluble drug, Indomethacin, from hydroxypropylmethylcellulose controlled release tablets. *J. Pharm. Pharmacol.* **1985c**, *37*, 33P.
5. Alderman, D. A. A review of cellulose ethers in hydrophilic matrices for oral controlled-release dosage forms, *Int. J. Pharm. Technol. Prod. Manuf.* **1984**, *5* (3), 1−9.
6. Mitchell, K.; Ford, J. L.; Armstrong, D. J.; Elliott, P. N. C.; Hogan, J. E.; Rostron, C. The influence of the particle size of hydroxypropylmethylcellulose K15M on its hydration and performance in matrix tablets. *Int. J. Pharm.* **1993**, *100*, 175−179.
7. Malamataris, S.; Karidas, T. Effect of particle size and sorbed moisture on the tensile strength of some tableted hydroxypropylmethylcellulose (HPMC) polymers. *Int. J. Pharm.* **1994a**, *104*, 115−123.
8. Malamataris, S.; Karidas, T.; Goidas, P. Effect of particle size and sorbed moisture on the compression behaviour of some hydroxypropylmethylcelluose (HPMC) polymers. *Int. J. Pharm.* **1994b**, *103*, 205−215.
9. Mitchell, K.; Ford, J. L.; Armstrong, D.; Elliott, P.; Rostron, C.; Hogan, J. The influence of substitution type on the performance of methylcellulose and hydoxypropylmethylcellulose in gels and matrices. *Int. J. Pharm.* **1993a**, *100*, 143−154.
10. Rajabi-Siahboomi, A. R.; Bowtell, R. W.; Mansfield, P.; Henderson, A.; Davies, M. C.; Melia, C. D. Structure and behaviour in hydrophilic matrix sustained release dosage forms: 2. NMR-imaging studies of dimensional changes in the gel layer and core of HPMC tablets undergoing hydration. *J. Controlled Release* **1994**, *31* (2), 121−128.
11. Mitchell, K.; Ford, J. L.; Armstrong, D. J.; Elliott, P. N. C.; Hogan, J. E.; Rostron, C. The influence of the particle size of hydroxypropylmethylcellulose K15M on its hydration and performance in matrix tablets. *Int. J. Pharm.* **1993b**, *100*, 175−179.

12. Bonferoni, M. C.; Rossi, S.; Ferrari, F.; Bertoni, M.; Caramella, C. A study of three hydroxypropylmethylcellulose substitution types: effect of particle size and shape on hydrophilic matrix performances. *S.T.P. Pharma Sci.* **1996**, *6* (4), 277−284.
13. McCrystal, C. B.; Ford, J. L.; Rajabi-Siahboomi, A.-R. Water distribution studies within cellulose ether polymers commonly employed in hydrophilic matrix controlled release systems using thermal analysis. 1. Effect of polymer molecular weight and drug addition. *J. Pharm. Sci.* **1999**, *88*, 792−796.
14. McCrystal, C. B.; Ford, J. L.; Rajabi-Siahboomi, A.-R. A study on the interaction of water and cellulose ethers using differential scanning calorimetry. *Thermochim. Acta* **1997**, *294*, 91−98.
15. Ford, J. L.; Mitchell, K. Thermal analysis of gels and matrix tablets containing cellulose ethers. *Thermochim. Acta* **1995**, *248*, 329−345.

JS9804260

Determination of Liposome Partitioning of Ionizable Drugs by Titration

KARSTEN BALON,[†] BERND U. RIEBESEHL,*[,†] AND BERND W. MÜLLER[‡]

Contribution from *Lilly Forschung GmbH, Pharmaceutical Product Development, Wiesingerweg 25, D-20253 Hamburg, Germany, and Department of Pharmaceutics and Biopharmaceutics, Christian-Albrecht-University, Gutenbergstrasse 76, D-24118 Kiel, Germany.*

Received October 23, 1998. Final revised manuscript received May 3, 1999.
Accepted for publication May 7, 1999.

Abstract □ Drug partitioning to liposomes has been suggested as a model for partitioning to biomembranes but has been lacking a rapid analytical assay useful for drug screening. A fast pH-metric titration method for the determination of liposome partitioning of ionizable drugs using small unilamellar phosphatidylcholine vesicles prepared by sonic homogenization has been successfully developed, enabling the use of high lipid-to-drug ratios. Liposome–water partition coefficients of diclofenac and propranolol were determined to study the impact of varying titration parameters, temperature, equilibration time, lipid, and liposome types on the partitioning. To validate this method, the results were compared to literature values generated with different techniques and to pH-metric titration results with large unilamellar vesicles. The rapid pH-metric assay gave liposome partitioning data for the two model compounds which were consistent with other analytical techniques and liposome types.

Introduction

Partitioning between phospholipid bilayer vesicles and water has been suggested as a better model for predicting the passive diffusion of drug molecules through biomembranes than partitioning between organic bulk solvents and water.[1−4] In contrast to octanol and other water-immiscible solvents no bulk phase separation between aqueous and organic component occurs in liposome systems. Therefore, standard spectrophotometric techniques cannot be routinely applied to measure drug partitioning in liposomes. The combination of equilibrium dialysis with radiotracer assays has been successfully used to measure partitioning at drug concentrations far below saturation of the lipid and can therefore be regarded as a gold standard for the determination of liposome partitioning.[5] However, this method fails to be useful as a routine method.

Approximately 75% of all drugs are bases, 20% are acids, and less than 5% are nonionic.[6]

The Sirius semiautomated pH-metric logP titration equipment offers a less cumbersome means of generating liposome partitioning data on a routine basis.[7] The impact of titration variables on pH-metric partitioning results with liposomes has been largely unknown and is studied here (e.g., temperature, titration direction, equilibrium time, pH-range). The liposomes are tested for titratable impurities as could, for example, be generated by hydrolysis of phospholipids.

The choice of lipid is studied together with the impact of different liposome preparation techniques and resulting vesicle sizes.

* Corresponding author. Phone: +4940−4909−4089. Fax: +4940−4909−5853. E-mail: riebesehl_bernd@lilly.com.
[†] Lilly Forschung GmbH.
[‡] Christian-Albrecht-University.

The major components of biomembranes such as intestinal brush border membranes are phospholipids, neutral lipids, and proteins. The bilayer has been suggested to be the primary barrier to passive transcellular drug absorption. A contribution of membrane-based proteins to this mode of absorption has not been reported. The molar ratio of rabbit brush border membrane lipids is reported to be 1:1:1 (neutral:phospholipid:glycolipid).[8] The distinct bilayer configuration of the zwitterionic phosphatidylcholine in vesicles appears to mimic the interfacial character as well as the ionic, H-bond, dipole−dipole, and hydrophobic interactions which may define partitioning in real biomembranes. The impact of cholesterol, the most important neutral membrane lipid, is discussed later on.

Small unilamellar vesicles are prepared by sonication, allowing for particularly high lipid concentrations (e.g., 100 mg phospholipid/mL) and consequently for high molar phospholipid/drug ratios (above 100), avoiding saturation of phospholipid with drug. The minimal vesicle size should provide for a maximum surface area, allowing for minimal partitioning equilibrium times. Also, this type of liposome can be prepared with simple lab equipment in sufficient quality and in short time. pH-metric partitioning data from sonicated small unilamellar vesicles (S-SUV) are compared to reference values from small unilamellar vesicles as prepared by equilibrium dialysis (ED-SUV) and other published data. Furthermore, they are compared with other partitioning data obtained by the Sirius pH-metric technique with large unilamellar vesicles prepared by a freeze and thaw technique (FAT-LUV).

Experimental Section

Materials—Diclofenac sodium and propranolol hydrochloride were obtained from Sigma. Cholesterol was obtained from Fluka (Sigma Chemie Vertriebs GmbH Deisenhofen, Germany). Epikuron200 (Soy-PC: >92% glycerophosphocholine esters with various mainly unsaturated fatty acids, <3% lyso-phosphatidylcholine, <2% other phospholipids, <0.8% water, <2% oil, and <0.2% α-tocopherol) was provided by Lucas Meyer GmbH (Hamburg, Germany). Linoleic acid was the predominant fatty acid of the 70−80% of unsaturated fatty acids. Lipoid PC 18:1; 18:1 containing 98.5% dioleoylphosphatidylcholine (DOPC) was obtained from Lipoid GmbH (Ludwigshafen, Germany). Potassium chloride, HCl−Titrisol, and KOH−Titrisol were purchased from Merck KGaA (Darmstadt, Germany).

Liposome Preparation—S-SUV Liposomes were prepared as follows: 1.6 g of phospholipid was dissolved in a small amount of methanol in a 200 mL round-bottom flask. A solid phospholipid film was formed by vacuum evaporation of methanol at 50 °C using a rotary evaporator. As determined by thermogravimetry, the resulting film contained less than 5% volatiles after 30 min of vacuum drying. The phospholipid film was dispersed with 14.4 mL of a 0.15 M potassium chloride solution resulting in a phospholipid concentration of 100 mg/mL. A 15 mL aliquot of this phospholipid dispersion was sonicated for 20 min in a Sirius-titrator vial using a Bandelin Sonopuls HD70 sonifier equipped

10.1021/js9804213 CCC: $18.00
Published on Web 06/16/1999

Table 1—Lipid Ratios Used for Investigations on the Impact of Assay Variations on S-SUV Partitioning Results

[lipid]:[drug][a]	lipid (g)	0.15 M KCl (mL)	"lipid/water"[b]
3	0.025	20	0.0013
10	0.1	15	0.0067
40	0.2	8	0.0250
100	1	20	0.0500

[a] [lipid]:[drug]: molar ratio of lipid to drug. [b] "lipid/water": lipid to water volume ratio as calculated based on partial densities for the aqueous and phospholipid moiety at 1.0 g/mL.

Table 2—Lipid Ratios Used for Investigations on the Effect of Vesicle and Lipid Types on Partitioning

[lipid]:[drug][a]	lipid (g)	0.15 M KCl (mL)	"lipid/water"[b]
1.5	0.005	15	0.0003
3.0	0.025	20	0.0013
10	0.1	15	0.0067
30	0.2	8	0.0250

[a] [lipid]:[drug]: molar ratio of lipid to drug. "lipid/water": lipid to water volume ratio as calculated based on partial densities for the aqueous and phospholipid moiety at 1.0 g/mL.

with a TT13 sonotrode (Bandelin Electronic GmbH, Berlin, Germany) at 50% amplitude setting with argon purge and cooling with ice−water.

Vesicle Size—The size of the SUV liposomes was measured by photon correlation spectroscopy with a Coulter N4 Plus at 90° angle and 600 s sample time. The evaluation of the results could be limited to a range from 5 to 500 nm. Samples were diluted with 0.2 μm filtered 0.15 M KCl solution to reach 10^5 to 10^6 counts per second. Liposomes were not filtered to avoid artifacts.

Determination of Partition Coefficients—Titrations were performed on PCA101 and GLPKA automatic titrators (Sirius Analytical Instruments Ltd., Forest Row, UK). All titrations were carried out in the pH range between 3.5 and 10.5. Alkalimetric titrations from pH 3.5 to 10.5 were called "up-assay", and acidimetric titrations from pH 10.5 to 3.5 were called "down-assays" and differed only with respect to titration direction. In this pH range drug concentrations >0.4 mM were required. After sonication, the liposome dispersion was added manually to the weighed diclofenac sodium or propranolol hydrochloride samples in 20 mL vials. Different volume ratios of lipid dispersion and water were adjusted according to the scheme in Table 1 by automatic addition of 0.15 M KCl solution. A partial density of 1.0 g/mL for aqueous KCl solution and for the phospholipid[9] in the liquid-crystalline state was used for the calculation of the lipid to water volume ratio. For the comparison of S-SUV and FAT-LUV vesicles, the mixtures were constituted according to Table 2. Samples were stirred until complete dissolution of the drug. The resulting diclofenac−liposome solutions had a pH of 7, and the propranolol−liposome solutions a pH between 5.6 and 6.6. Then the pH was adjusted automatically to the start pH of the titration at pH 10.5 or 3.5. The maximum titrant volume increment for one titration step was limited to 0.01 mL. The pH change per titrant addition was limited to 0.2 pH units. Typically, more than 30 pH readings were collected from each titration. The pH values were recorded when the pH-drift was lower than 0.01 pH per minute. The titration time was between 20 and 60 min for low and high lipid concentrations, respectively. Argon purge was applied to all titrations. Processing of titration data was carried out using the PKALOGP version 5.01 software (Sirius Analytical Instruments Ltd., Forest Row, UK). Final partitioning results log $P_{neutral}$ and log P_{ion} were calculated from titrations at different lipid concentrations including at least the two extremes of the lipid-to-drug ratio. A detailed description of the pH-metric log P method can be found elsewhere.[7,10,11]

Results and Discussion

The impact of assay conditions on drug partitioning into small unilamellar soybean phospholipid bilayer vesicles was studied in detail and is discussed in the following paragraphs. Table 3 shows the impact of different assay parameters on the partitioning of neutral and anionic diclofenac and neutral and cationic propranolol. Table 4 shows the results of a study on titratable lipid impurities measurable at the assay conditions. Table 5 shows the comparison of results as generated with the preferred titrimetric assay conditions (see line 2) with results of different liposome and lipid types and analytical techniques. Table 6 shows the results of a reproducibility study.The chemical structures and pK_a values of the neutral species of the two model drugs are shown in Figure 1.

Direction of Titration—The neutral species of diclofenac and propranolol showed no significantly different partitioning for down-titrations. The partitioning of the propranolol cation was found to be reduced by 0.5 log units for the down-titration while no different partitioning was found for the diclofenac anion (see Table 3, columns 1 and 2). The data quality of the results obtained from the down assays was generally better and resulted in smaller errors for the calculated partition coefficients. For this reason the down-assay was selected for routine measurements.

Lipid−Drug Ratio—Columns 2−4 of Table 3 show the differences of partitioning results when calculated based on four titrations covering lipid−drug ratios from 3 to100 or based on three titrations at lipid−drug ratios 3−40 or 10−100. We found no significant differences in the final results when ratios as small as 3 were used together with high ratios.

Temperature—The application of the pH-metric technique to liposome partitioning did not show any evidence for analytical problems or critical liposome instabilities at 37 °C so that this physiologic temperature can be used for routine application. Also, the higher temperature should accelerate the adjustment of the partitioning equilibrium. No significant partitioning differences were found for the different ionic species of the two model drugs at standard laboratory temperature 25 °C and physiologic temperature 37 °C (see Table 3, columns 2 and 5). The pK_a of propranolol was shifted to a significantly lower basicity at the higher temperature, which is typical for many bases, and points out the necessity to evaluate the partitioning and pK_a at the same temperature (see Figure 1).

Equilibration Time—The results of titrations with 3 h extra equilibration time before starting the titration are shown in Table 3. The partitioning of the propranolol species remained unchanged. The partition coefficients of diclofenac acid and anion rose by 0.4 and 0.5 log units, respectively. Another assay variation included a 2-min delay time after each titration step. The additional equilibration time during the assay led to nonsignificant changes of partitioning results. The minimal impact of the additional delay time suggests such a prolongation of the assay is not necessary for a rapid and continuous titration.

Titration pH-Range—The usable pH-range for titrations with phospholipids is limited by ionizable functions in the liposomes and degradation of phospholipids at extreme pH-values. It was found that the ionization of the lipid phosphate disturbs the assay at a pH lower than 3.5. The upper limit of the titration pH-range is defined by increasing hydrolytic degradation of phosphatidylcholine to titratable free fatty acids. Typically, the pH of the sample dissolved in liposome dispersion is approximately neutral. The automatic titration program quickly approaches the acidic or alkaline start pH and approaches the neutral region again after 10 to 30 min depending on the lipid and sample concentration. Consequently, the liposome stressing conditions at extreme pH-values prevail only shortly. With start pH-values not higher than 10.5, assays could be evaluated without major disturbance by generated degradation products or other artifacts.

Table 3—Impact of Assay Variations on S–SUV Partitioning Results[a]

temperature (°C)	25	25	25	25	37	25	25	25
direction of titration	up	down	down	down	down	down	down	down
lipid	Soy-PC	Soy-PC	Soy-PC	Soy-PC	Soy-PC	Soy-PC	Soy-PC	Soy-PC/cholesterol 1:1 (molar)
equilibrium time before assay	0	0	0	0	0	0	3 h	0
equilibrium time after titrant addition	0	0	0	0	0	2 min delay	0	0
range [lipid]:[drug]	3-100	3-100	3-40	10-100	3-100	3-100	3-100	3-100
				log P_{S-SUV}				
diclofenac neutral	4.7	4.5	4.3	-	4.3	4.6	4.9	3.8
diclofenac ion	2.9	3.0	2.9	-	2.9	3.0	3.5	2.7
Δ (neutral–ion)	1.8	1.5	1.4	-	1.4	1.6	1.4	1.1
propranolol neutral	3.5	3.4	3.3	3.3	3.2	3.3	3.4	3.0
propranolol ion	3.1	2.6	2.6	2.5	2.5	2.4	2.8	2.2
Δ (neutral–ion)	0.4	0.8	0.7	0.8	0.7	0.9	0.6	0.8

[a] The pH-titration was performed either from pH 3.5 to 10.5 "up" or in the opposite direction "down". "Range [lipid]:[drug]" gives the range of lipid ratios of Table 1 which were used for the multiset calculation of final log *P* results as listed in the lower section of the table.

Table 4—Titratable Impurities[a]

lipid (g)	total volume (mL)	approx pK_a of impurity	concn (mM)	mol % (impurity/total lipids)
0.025	20	6.4	0.042	2
0.1	15	6.8	0.074	1
0.2	8	6.7	0.192	0.6
1.0	20	6.8	0.185	0.3

[a] The molar fraction of titratable impurity was calculated as oleic acid (mw 282).

Titratable Impurities—An impurity, probably a fatty acid with an apparent pK_a at 6.8,[12] could be detected in blank titrations containing only the phospholipid vesicles without any drug compound. Blank titrations were carried out at 37 °C as down-assays (see Table 4). The calculated concentrations of impurity for the assays with high phospholipid concentrations were more reliable than those at lower phospholipid concentrations since concentrations of impurities below 0.1 mM were likely to be too low to be determined exactly. Partitioning of drugs into phospholipid bilayers has been reported to be influenced by concentrations of free fatty acids above 10%.[13] The direct influence of acidic impurities on the titration curves can be corrected by the refinement of data. Although the start of the titrations at pH 10.5 may increase the formation of these hydrolysis products, the measured free fatty concentration was still below the concentration reported for biological membranes.[8] High free fatty acid values should be interpreted carefully as membrane preparation techniques could also lead to phospholipid decomposition. Generally nonsaturated phospholipids such as soybean phospholipids are susceptible to autoxidation and might form peroxides. For minimizing oxidation, the sonication was carried out under argon at low temperature, and the titration was performed under argon. The titration of an aged liposome dispersion (8 h at 25 °C) did not show additional titratable impurities so that oxidation of the phospholipid is regarded to be insignificant.

Lipid Selection—The liposomes in this study were prepared from a purified soybean phosphatidylcholine so that titratable biomembrane constituents such as free fatty acids, phosphatidylethanolamine, and phosphatidylserine were minimized. The pattern of predominantly unsaturated fatty acids in soy-phospholipids provides for a fluid bilayer structure at 25 °C or higher temperatures. Compared to pure, chemically defined phospholipids such as dioleoylphosphatidylcholine (DOPC), which consists of >98.5% DOPC, phospholipids of natural origin have the advantages of a fatty acyl chain composition similar to biomembranes and low price. No significant differences were found for the partitioning of neutral propranolol and diclofenac to Soy-PC and DOPC liposomes. In contrast, the difference (Soy-PC-DOPC) was up to 0.8 for the diclofenac anion and 0.5 for the propranolol cation. However, the partitioning results for propranolol in Soy-PC/S−SUV were found to be closer to the reference results based on Egg-PC/ED-SUV than those based on DOPC/S−SUV or DOPC/FAT-LUV.

Influence of Cholesterol—Small unilamellar vesicles with cholesterol were made from a 1:1 molar mixture of Soy-PC and cholesterol.[14] The presence of cholesterol in liposomes decreased partitioning for all species, but the decrease for the diclofenac anion may not be significant (see below). The difference between log $P_{neutral}$ and log P_{ion} (Δ (neutral−ion)) was not significantly changed compared to cholesterol-free liposomes (see Table 3). A similarly significant decrease of partitioning with raising cholesterol concentrations in a bilayer was reported for nimodipine by Mason et al.[15] The titrimetric measurement of partitioning to cholesterol containing vesicles appears to be viable and may lead to further refined assay procedures.

Effect of Vesicle-Size—The size determination of the Soy-PC-S-SUV liposomes yielded a mean diameter of 32 ± 2 nm resulting in a vesicle surface area of approximately 35 m^2 per 100 mg of lipid. In contrast, the FAT-LUV technique leads to larger liposomes with a diameter of approximately 100 nm.[7] For the neutral species, no significant changes in partitioning were observed for different vesicles sizes (see Table 5). The diclofenac anion partitioning was decreased in small vesicles by 0.4 log units in DOPC and Soy-PC. The propranolol cation partitioning was decreased by. 0.5 log units in DOPC. The decrease of ion partitioning with lower vesicle size was found to be slightly smaller for Soy-PC based vesicles compared to DOPC. Small vesicles with their stronger curvature have been regarded as a less celllike membrane model than larger liposomes. On the other hand, the measurement in highly concentrated small vesicle dispersions allows for measuring at higher lipid concentrations, higher lipid/drug ratios, and maximum interfacial surface area. This benefit may outweigh the impact of higher artificial curvature.

Reproducibility—The reproducibility of titrimetric liposome partitioning results was assessed at 25 °C based on down-titration results at four different lipid concentrations according to Table 1 which were generated by three operators in two different labs. The results of each four-titration set were fitted to obtain one weighted average partition coefficient for the different ionic species of the two test compounds as listed in Table 6. The high reproducibility of the partitioning results could be achieved despite some differences in equipment, e.g., new versus old sonifier. The standard deviation (SD) was highest for the neutral diclofenac and minimal for its anionic species. We estimate that partitioning differences between two datasets as

Table 5—Effect of Vesicle and Lipid Types and Analytical Techniques on Partitioning

vesicle[a]	size (nm)	lipid	detection	T (°C)	diclofenac		propranolol	
					log $P_{neutral}$	log P_{ion}	log $P_{neutral}$	log P_{ion}
S–SUV	32	Soy-PC	pH-metric	25	4.5	3.0	3.4	2.6
S–SUV	32	Soy-PC	pH-metric	37	4.3	2.9	3.2	2.5
S–SUV	25	DOPC	pH-metric	25	4.3	2.2	3.4	2.1
FAT-LUV	–	Soy-PC	pH-metric	25	4.4	3.3	3.5	2.8
FAT-LUV[7]	100	DOPC	pH-metric	25	4.5	2.6	3.5	2.6
ED-SUV[5]	70	Egg-PC	radiotracer	37	–	–	3.2	2.8
MLV[17]	–	Egg-PC	centrifugation, UV	37	–	–	–	2.4
–	–	octanol	pH-metric	25	4.5	0.7	3.5	0.8

[a] MLV: multilamellar vesicles.

Table 6—Reproducibility

lab	operator	diclofenac		propranolol	
		log $P_{neutral}$	log P_{ion}	log $P_{neutral}$	log P_{ion}
1	1	4.52	3.00	3.40	2.60
2	2	4.49	2.96	3.32	2.53
2	3	4.19	2.94	3.17	2.41
mean		4.40	2.97	3.30	2.51
SD[a]		0.18	0.03	0.12	0.10

[a] SD: standard deviation.

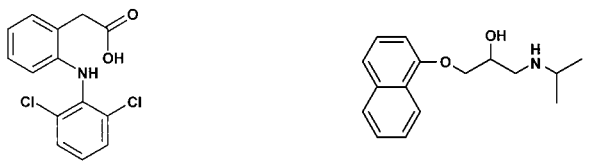

Diclofenac
pK_a (25°C): 3.99
pK_a (37°C): 4.01

Propranolol
pK_a (25°C): 9.53
pK_a (37°C): 9.14

Figure 1—Structure and pK_a of diclofenac and propranolol.

calculated from four titrations at different lipid concentrations may not be significant if they do not exceed ±0.3 log units.

Comparison with Available Partitioning Data—The results obtained with the S-SUV in potentiometric titrations were in good agreement with literature results of membrane partitioning. Equilibrium dialysis results for propranolol liposome partitioning were used as the reference of the first choice. Good agreement could be achieved at 37 °C without any extra equilibrium time (see lines 2 and 6, Table 5). For these experimental conditions, the same partition coefficient was determined for the neutral species of propranolol. The partition coefficient of the cation determined by titration was 0.3 log units lower compared to the equilibrium dialysis result which may not be significant. In ref 16, partitioning results were given for pH 7.4 where propranolol is almost completely present in the cationic form. In the octanol–water partitioning system, drastically smaller partition coefficients have been determined for the ionic species of diclofenac and propranolol.

Conclusions

The use of sonicated small unilamellar vesicles made of soybean-PC as a biomembrane partition model in a pH-metric titration assay was studied with various assay settings. The titrimetric results for the partitioning of propranolol to sonicated small vesicles were in good agreement with results generated with an equilibrium dialysis/radiotracer method at a high lipid-to-drug ratio. Titrimetric partition results measured with S-SUV were also comparable to those obtained with large unilamellar vesicles made by an extrusion technique.

Small unilamellar vesicles made by sonication combine several advantages for its use as a rapid partitioning assay. The production process allows testing at lipid concentrations as high as 100 mg/mL. Therefore partitioning assays can be run at high lipid-to-drug ratios to avoid saturation of lipid with drug. They can also be prepared with simple lab equipment in a short time. Furthermore, partitioning to small vesicles of soybean-PC differed only slightly for minimally from large vesicles despite their more pronounced curvature. The use of pure DOPC instead of soybean-PC did not lead to more relevant partitioning results or other advantages. Since soybean-PC consists of a mixture of acyl-glycerophosphocholines, it should be closer to the composition of biological membranes than pure DOPC. On the basis of the results discussed above, partitioning data to small unilamellar soybean-PC vesicles can be utilized as a potential membrane model and may have advantages over other vesicles. Higher possible lipid concentrations, simple preparation, and low cost of phospholipid make this method attractive as a standard screening procedure. Data generated by this titrimetric assay have been successfully utilized for a correlation of intestinal drug absorption with dose, solubility, and liposome partitioning.[16]

Glossary

S-SUV	Small unilamellar vesicles generated by sonication
ED-SUV	Small unilamellar vesicles generated by equilibrium dialysis
FAT-LUV	Large unilamellar vesicles generated by equilibrium dialysis
Soy-PC	Soybean phosphatidylcholine, purified
MLV	Multilamellar vesicles
DOPC	Dioleoylphosphatidylcholine

References and Notes

1. Barton, P.; Davis, A. M.; McCarthy, D. J.; Webborn, P. J. H. Drug-Phospholipid interactions. 2. Predicting the sites of drug distribution using *n*-octanol/water and membrane/water distribution coefficients. *J. Pharm. Sci.* **1997**, *86*, 1034–1039.
2. Alcorn, C. J.; Simpson, R. J.; Leahy, D.; Peters, T. H. Determination of partition and distribution coefficients with brush border membrane vesicles. *Biochem. Pharmacol.* **1991**, *42*, 2259–2264.
3. Alcorn, C. J.; Simpson, R. J.; Leahy, D. E.; Peters, T. J. Partition and distribution coefficients of solutes and drugs in brush border membrane vesicles. *Biochem. Pharmacol.* **1993**, *45*, 1775–1782.
4. Austin, R. P.; Davis, A. M.; Manners, C. N. Partitioning of ionizing molecules between aqueous buffers and phospholipid vesicles. *J. Pharm. Sci.* **1995**, *84*, 1180–1183.

5. Pauletti, G. M.; Wunderli-Allenspach, H. Partition coefficients in vitro: artificial membranes as a standardized distribution model. *Eur. J. Pharm. Sci.* **1994**, *1*, 273−282.
6. *Pharmaceutical Preformulation*, 1st ed.; Wells, J. I., Ed., Ellis Horwood Ltd.: London, 1988; p 25.
7. Avdeef, A.; Box, K. J.; Comer, J. E. A.; Hibbert, C.; Tam., K. Y. pH − metric logP 10: Determination of vesicle membrane − water partition coefficients of ionisable drugs. *Pharm. Res.* **1998**, *15*, 209−215.
8. Hauser, H.; Howell, K.; Dawson, R. M. C.; Bowyer, D. E. Rabbit small intestinal brush border membrane preparation and lipid composition. *Biochim. Biophys. Acta* **1980**, *602*, 567−577.
9. Small, D. M. The physical chemistry of lipids: From alkanes to phospholipids. In *Handbook of Lipid Research*; Plenum Press: New York, 1986; Vol. 4, p 512.
10. Avdeef, A. pH-Metric logP. Part 1: Difference plots for determining ion-pair octanol−water partition coefficients of multiprotic substances. *Quant. Struct.-Act. Relat.* **1992**, *11*, 510−517.
11. Avdeef, A. pH-metric logP − 2. Refinement of partition coefficients and ionisation constants of multiprotic substances. *J. Pharm. Sci.* **1993**, 82, 183−190.
12. Krämer, S. D.; Wunderli-Allenspach, H. The pH dependence in the partitioning behaviour of (RS)-[3H]Propranolol between MDCK cell lipid vesicles and buffer. *Pharm. Res.* **1996,** 13, 1851−1855.
13. Kraemer, S. D.; Jakits-Deiser, C.; Wunderli-Allenspach, H. Free fatty acids cause pH-dependent changes in drug-lipid membrane interactions around physiological pH. *Pharm. Res.* **1997**, *14*, 827−832.
14. Green, N. M. Membrane Stucture. In *The Encyclopedia of Molecular Biology*; Kendrew, J., Ed.; Blackwell Science Ltd.: Oxford, 1994; p 619.
15. Mason, R. P.; Rhodes D. G.; Herbette, L. G. Reevaluating Eqilibrium and Kinetic Binding Parameters for Lipophlilic Drugs Based on a Structural Model for Drug Interaction with Biological Membranes. *J. Med. Chem.* **1991**, *34*, 869−877.
16. Balon, K.; Riebesehl, B. U.; Müller, B. W. Prediction of passive intestinal drug absorption using liposome partitioning data. Presented at the 2nd World Meeting on Pharmaceutics, Biopharmaceutics, and Pharmaceutical Technology, Paris, France, May 25−28, 1998.
17. Surewicz, W. K.; Leyko, W. Interaction of propranolol with model phospholipid membranes. *Biochim. Biophys. Acta*, **1988**, *643*, 387−397.

Acknowledgments

The authors acknowledge the support and contributions of Dr. M. Sanchez-Felix and Mr. C. White of Lilly Research Laboratories, Windlesham, UK, and Mr. K. Box of Sirius Analytical Instruments, Forest Row, UK, to the present investigation.

JS9804213

Rapid Calculation of Polar Molecular Surface Area and Its Application to the Prediction of Transport Phenomena. 1. Prediction of Intestinal Absorption

DAVID E. CLARK*

Contribution from *Rhône-Poulenc Rorer, Dagenham Research Centre, Rainham Road South, Dagenham, Essex, RM10 7XS, United Kingdom.*

Received October 7, 1998. Final revised manuscript received April 22, 1999.
Accepted for publication April 30, 1999.

Abstract □ A method for the rapid computation of polar molecular surface area (PSA) is described. It is shown that consideration of only a single conformer when computing PSA gives an excellent correlation with intestinal absorption data—as good as previously reported methods employing multiple conformers. Circumventing a time-consuming conformational analysis opens the possibility of computationally screening large numbers of compounds for problems relating to absorption prior to synthesis. The robustness of the criterion for identifying poorly absorbed compounds (PSA $\geq$ 140 Å^2) is illustrated through its application to a diverse test set of 74 drugs. The PSA-based method is also compared to an experimental method for absorption prediction recently described in the literature.

Introduction

In recent years, the pharmaceutical industry has come under increasing pressure to reduce the time that is required for the discovery and development of novel therapeutics. The advent of combinatorial chemistry and high-throughput screening methodologies has brought with it the ability to synthesize and evaluate orders of magnitude more compounds than has been possible using traditional means. However, these new high-throughput techniques alone do not provide the means to faster drug discovery. Increasingly, researchers have become aware that it is not merely the *number* of compounds made and tested that is important; the *nature* of those compounds is just as vital.

In particular, the focus of drug discovery is now not simply on achieving the best possible potency against the biological target of interest, but also on seeking favorable ADME (absorption, distribution, metabolism, and excretion) properties and performing these two tasks in parallel, rather than in sequence.[1−4] The emphasis is now on "failing fast", i.e., weeding out compounds with poor physicochemical properties early in the drug discovery phase, thereby saving both time and expense.

To this end, a battery of in vitro experimental methods has arisen to help screen candidate molecules for their ADME characteristics.[1,5] Of particular note are Caco-2 monolayers for predicting in vivo intestinal absorption[6,7] and systems for the evaluation of metabolic susceptibility employing human liver microsomes, hepatocytes, or recombinant P450 isozymes.[8] The use of artificial membranes for evaluating absorption processes has also been recently reported.[9] More rapid in vivo tests are also being developed such as "cassette" dosing protocols in which multiple compounds are administered in a single dose to a single animal.[10] However, all these techniques require the synthesis of the compounds to be tested. Even more time and effort could be saved if it were possible for computational techniques to assess reliably compounds for ADME properties prior to synthesis and to identify those likely to be problematic. Such problem compounds could then be rejected or assigned a reduced priority for synthesis. For this reason, several groups have developed computational screening methods seeking to distinguish between druglike and nondruglike compounds in a general sense.[11−13]

For most drugs, the preferred route of administration is by oral ingestion. Researchers have therefore sought to delineate the physicochemical properties that favor intestinal absorption[14,15] and to develop computational methods for its prediction. The so-called "rule-of-5" has proved very popular as a rapid, if approximate, screen for compounds likely to be poorly absorbed.[16] This rule states that if a compound satisfies any *two* of the following rules, it is likely to exhibit poor intestinal absorption:

- Molecular weight > 500
- Number of hydrogen bond donors > 5 (a donor being any O−H or N−H group)
- Number of hydrogen bond acceptors > 10 (an acceptor being any O or N including those in donor groups)
- Calculated log P > 5.0 (if ClogP[17] is used) or > 4.15 (if MlogP[18] is used)

Wessel et al.[19] recently reported the generation of a QSPR (quantitative structure−property relationship) model from a training set of 76 compounds with human fractional absorption (%FA) data using a genetic algorithm with a neural network scoring function. The errors (RMSE) in prediction from this model were 9.4% for the training set and 16.0% for the test set of 10 compounds. Another regression-based approach was described by Hirono et al.;[20] however, their work used oral bioavailability data which may include metabolism effects and so cannot be compared directly to intestinal absorption.

Polar Surface Area

The use of molecular surface areas in the modeling of solvation and partitioning processes has a long history.[21,22] More recently, approaches to absorption prediction have been developed that involve a quantity derived from the molecular surface known as the *polar surface area* (PSA). The PSA of a molecule is defined as the area of its van der Waals surface that arises from oxygen or nitrogen atoms or hydrogen atoms attached to oxygen or nitrogen atoms. As such, it is clearly related to the capacity of a compound to form hydrogen bonds. One study relating PSA to

* Corresponding author. Phone: +44 181 919 3353. Fax: +44 181 919 2029. E-mail: david-e.clark@rp-rorer.co.uk.

10.1021/js9804011 CCC: $18.00
Published on Web 06/22/1999

intestinal absorption was that of van de Waterbeemd et al.,[23] in which a quantitative structure−absorption relationship was derived for the passage of 17 compounds across a Caco-2 monolayer:

$$\log P_{app} = 0.008(\pm 0.002)\mathrm{MW} - 0.043(\pm 0.008)\mathrm{PSA} - 5.165(\pm 0.605) \quad (1)$$

where $\log P_{app}$ is the logarithm of the apparent permeability through the monolayer (in cm/s), and MW is the molecular weight of the compounds. The standard errors of the regression coefficients are given in parentheses. The correlation coefficient for this equation was $r = 0.833$ ($r^2 = 0.694$).

The method used by van de Waterbeemd et al.[23] to calculate PSA considered only a single conformation of the molecules concerned. By contrast, Palm and co-workers employed a measure termed the "dynamic" PSA (PSA_d), which is a Boltzmann-weighted average value computed from an ensemble of low-energy conformers obtained by a detailed conformational search.[24] This kind of Boltzmann averaging of molecular surface areas seems to have been used first by Hermann in the modeling of hydrocarbon solubility[21] and has been applied more recently by Lipkowitz et al.[25] in a study of weakly bound diastereomeric complexes. In their work, Palm et al. showed that PSA_d correlated well with intestinal absorption, in terms of both measurements of Caco-2 monolayer permeability[24] and the fraction absorbed (%FA) in humans.[26] In the former case, the correlation between PSA_d values and Caco-2 absorption was $r^2 = 0.99$. In the latter study on 20 carefully selected drugs, a sigmoidal fit with an $r^2 = 0.94$ (RMSE = 9.2%) was obtained. From this sigmoidal curve, Palm et al.[26] suggested that molecules with a PSA_d of ≥ 140 Å^2 should exhibit a %FA of < 10% and that this PSA_d value could therefore be used to identify poorly absorbed compounds prior to synthesis. Conversely, completely absorbed molecules (%FA > 90%) exhibited PSA_d values of ≤ 60 Å^2.

Palm et al.[24] argued that their PSA_d measure, by taking account of multiple low-energy conformations, should give a better description of molecular surface properties than methods that consider only a single conformer. A similar argument has been advanced recently by Krarup and co-workers[27] who developed a PSA_d measure similar to that described by Palm et al.,[24] but using the solvent-accessible, rather than the van der Waals, molecular surface. The difficulty with these "dynamic" methods from a practical point of view is that they are very computationally expensive. To carry out a conformational search with energy minimization for even a moderately flexible small molecule can take several hours of CPU time on a modern workstation. Clearly, a dynamic PSA calculation becomes impractical if one wants to consider more than just a few molecules on a routine basis. Furthermore, from a theoretical viewpoint, the use of gas-phase conformational energies to calculate the Boltzmann-averaged PSA_d value might be questioned on the grounds that, in solution, solvation effects could significantly alter the relative energies of the conformers. To counter this latter argument, it should be noted that a recent paper by Palm et al.[28] showed that, for most of the set of nine beta-blockers studied, the simulation environment (gas phase, water, or chloroform) had only a small effect on the value of PSA_d.

Despite being advocates of a "dynamic" approach, it is noteworthy that both Palm et al.[24] and Krarup et al.[27] concede that good correlations with absorption can be obtained by just considering a single conformation. To quote from the former: "Surprisingly, the correlations between the surface properties of the global minimum conformations and the permeability were *only slightly poorer* [my italics] than the correlations obtained with the dynamic properties".[24] In the work of the latter group,[27] an excellent correlation ($r^2 = 0.98$) with absorption was discovered using just the (extended) starting conformation for the molecular dynamics simulation. These observations accord with earlier work by Pearlman[22] who demonstrated that single conformation-based surface areas could be as effective as the Boltzmann-averaged areas described by Hermann[21] for the modeling of the free energy of cavity formation. These results encouraged us to investigate in more detail the use of calculations of PSA, from just a single conformer, for the prediction of intestinal absorption. If reliable predictions could be made on this basis, it would open the way for the rapid prescreening of large compound collections or combinatorial libraries to eliminate molecules likely to show poor absorption characteristics. These compound sets might already be in existence, perhaps being considered for purchase from an external source, or they could be *virtual*, i.e., not yet synthesized but represented in a computer-readable form. In either case, a computational procedure for assessing absorption in a reasonable time scale would be of great utility in the drug discovery process.

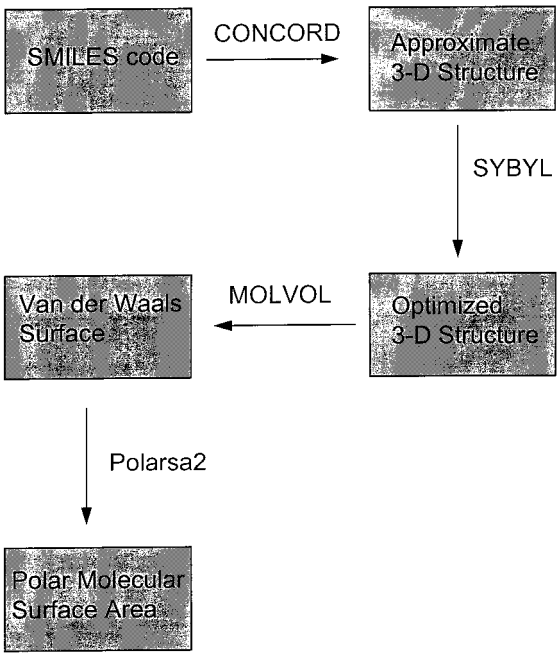

Figure 1—Flowchart of computational procedures.

In the remainder of this paper, the computational methods we have developed will be detailed. Following that, we shall demonstrate their performance first on the training set used by Palm et al.[26] and then on a larger test set drawn from the work of Wessel et al.[19] We shall also compare the results of our method with those of the experimental system developed by Kansy and co-workers.[9] After a discussion of the results obtained to date, some future directions for research in this area will be postulated. The paper immediately following this one will describe the further use of PSA calculations for the prediction of blood-brain partitioning.

Computational Methods

A flowchart of the computational processes employed in this work is given in Figure 1. In detail, the steps are as follows:

1. The molecule is encoded as its neutral species in SMILES[29] format with appropriate stereochemical designations where the stereochemistry is known.

Table 1—Data for the Set of Compounds from Palm et al[26]

compound	PSA/Å^2	PSA$_d$/Å^2	%FA	rule-of-5 status
metoprolol	57.2	53.1	100	pass
nordiazepam	47.5	45.1	99	pass
diazepam	34.5	33.0	97	pass
oxprenolol	53.2	46.8	97	pass
phenazone	28.0	27.1	97	pass
oxazepam	55.6	66.9	97	pass
alprenolol	41.8	37.1	96	pass
practolol	77.2	73.4	95	pass
pindolol	60.9	56.5	92	pass
ciprofloxacin	80.1	78.7	69	pass
metolazone	95.9	94.5	64	pass
tranexamic acid	71.5	69.2	55	pass
atenolol	93.3	90.9	54	pass
sulpiride	101.4	100.2	36	pass
mannitol	129.6	116.6	26	pass
foscarnet	117.3	115.3	17	pass
sulfasalazine	148.6	141.9	12	pass
olsalazine	147.0	141.0	2.3	pass
lactulose	197.8	177.2	0.6	warning
raffinose	266.8	242.1	0.3	warning

2. The program CONCORD[30,31] is used to convert the SMILES representation into an approximate 3-D structure.

3. This conformation is then energy-minimized to relieve any close steric contacts using the maximin2 minimizer in SYBYL.[32] Minimization is terminated after either 1000 iterations or when a gradient of less than 0.05 kcal/(mol.Å) is attained.

4. The minimized conformation is passed to the MOLVOL program developed by Dodd and Theodorou.[33] MOLVOL computes the van der Waals molecular surface area for the conformation and outputs the contributions of the individual atoms to the surface area.

5. Finally, an in-house Fortran program, Polarsa2, sums the contributions of the polar atoms (N, O, and H attached to N or O) and outputs the PSA value.

It should be noted that this procedure is entirely automated by means of a C-shell script and so large numbers of molecules can be processed in batch. An intranet-based interface is also available for medicinal chemists to calculate PSA-based predictions of absorption and blood-brain barrier penetration on single molecules. Typically, the CPU time required to process a compound is of the order of 10−15 CPU seconds (SGI R10000 workstation), most of this time being required for the energy minimization step (which can be curtailed if very large numbers of molecules are to be processed). This efficiency of calculation enables the processing of large sets of compounds, particular virtual combinatorial libraries, in a realistic time frame.

Results

Training Set—The 20 drug molecules studied by Palm et al.[26] were encoded as SMILES and processed in batch using the procedure described above. The CPU time required for this was 138 s (SGI R10000 processor). The resulting PSA values are shown in Table 1, along with the PSA$_d$ and %FA values taken from Palm et al.[26] and the status of the compounds according to the rule-of-5. The fit of the single conformer PSA values to the %FA data using a Boltzmann sigmoidal curve[34] is shown in Figure 2. The statistics for this fit ($r^2 = 0.94$, RMSE = 9.1%) are almost identical to those quoted by Palm et al.[26] ($r^2 = 0.94$, RMSE = 9.2%). Reading from the curve, the PSA value corresponding to a fractional absorption of 10% is 139.4 Å^2 and for 90% absorption, the value is 61 Å^2. Again, these figures are almost identical to those quoted by Palm et al.[26] The correlation coefficient between the values of PSA and PSA$_d$ presented in Table 1 is $r = 0.996$. As might be expected, the agreement in absolute terms is worse for the more-flexible, more-polar compounds such as mannitol, lactulose, and raffinose. Of the more rigid compounds, oxazepam also shows quite a large absolute difference between PSA and PSA$_d$. This difference probably reflects an instance where the use of different computational methods between this work and that of Palm et al.[26] (e.g., for 3-D structure generation and molecular mechanics optimization) has a significant effect on the results.

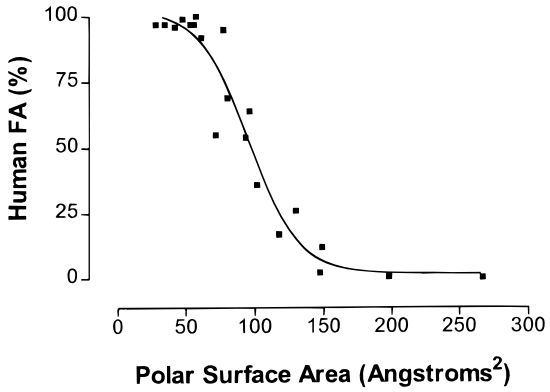

Figure 2—Boltzmann sigmoidal fit of single conformer PSA values to human %FA data for Palm et al.[26] compounds.

From these results, we concluded that, for this set at least, the use of a rapid, single-conformer-based calculation of PSA is sufficient for determining molecules likely to exhibit poor intestinal absorption. It is important to note that all the compounds in the Palm set were chosen on the basis of their being absorbed primarily by passive processes. Thus, the PSA criterion cannot be expected to apply to compounds that are substrates for active transporters.

Applying the value of 140 Å^2 to this set picks out four compounds as being poorly absorbed: sulfasalazine, olsalazine, lactulose, and raffinose. These all show %FA of ≤ 13%. The rule-of-5 only generates warnings for the latter two compounds, suggesting that the PSA value may be a better discriminator of poorly absorbed molecules.

Test Set—To test further the PSA ≥ 140 Å^2 criterion for poor absorption, a further set of compounds was compiled from a recent publication.[19] After removing compounds that are also in the Palm et al. set,[26] 74 compounds remained. PSA values were computed for these compounds and are presented in Table 2 (plotted as a graph in Figure 3) together with the predicted classification of the molecules as "good" (PSA ≤ 61 Å^2), "poor" (PSA ≥ 140 Å^2) or "OK" (140 Å^2 > PSA > 61 Å^2). The rule-of-5 status of each compound is also included, and the %FA values are taken from Wessel et al.[19]

From a practical point of view, when testing this measure, we were most concerned about any *false negative* predictions that might arise from the application of the PSA ≥ 140 Å^2 criterion, i.e., compounds which are predicted to be poorly absorbed but which in fact are well absorbed. False negatives are worrisome because, were the compounds to be discarded on the basis of the prediction, their true absorption would never be discovered. On the other hand, false positive predictions would always be discovered and, while wasteful, would not be serious in the long term. The seven apparent false negatives are highlighted in Table 2 and shown as crosses (×) in Figure 3. Each of these compounds is commented on below.

• Methotrexate has a very high PSA value (225 Å^2), and yet it is still reported as being 100% absorbed. The reason for this is that it is absorbed by a carrier-mediated process which is responsible for folate absorption.[35,36]

• Zidovudine (AZT) just transgresses the PSA limit (142.9 Å^2) while exhibiting 100% absorption. Again, this absorption is made possible by active transport, the carrier in

Table 2—Data for the Set of Compounds from Wessel et al[19]

compound	PSA/Å^2	PSA rating	%FA	rule-of-5 status
acetylsalicylic acid	69.4	OK	100	pass
bumetanide	120.8	OK	100	pass
caffeine	59.2	good	100	pass
corticosterone	75.9	OK	100	pass
desipramine	16.5	good	100	pass
dexamethasone	90.7	OK	100	pass
felodipine	65.2	OK	100	pass
fluvastatin	88.2	OK	100	pass
ibuprofen	42	good	100	pass
ketoprofen	60.9	good	100	pass
loracarbef	117.9	OK	100	pass
lormetazepam	55.9	good	100	pass
methotrexate	**225**	**poor**	**100**	**warning**
ondansetron	38	good	100	pass
prazosin	103.6	OK	100	pass
salicylic acid	62.5	OK	100	pass
testosterone	43.4	good	100	pass
valproic acid	44.2	good	100	pass
zidovudine	**142.9**	**poor**	**100**	**pass**
naproxen	53.8	good	99	pass
prednisolone	98.3	OK	98.8	pass
cephalexin	115.5	OK	98	pass
warfarin	62.8	OK	98	pass
trimethoprim	110.6	OK	97	pass
clonidine	39.5	good	95	pass
fluconazole	75.8	OK	95	pass
imipramine	6	good	95	pass
labetalol	100.6	OK	95	pass
sotalol	90.3	OK	95	pass
amoxicillin	**143.4**	**poor**	**93.5**	**pass**
hydrocortisone	93.7	OK	91	pass
progesterone	41.2	good	91	pass
terazosin	102.3	OK	91	pass
betaxolol	56.3	good	90	pass
chloramphenicol	118.3	OK	90	pass
phenytoin	66.3	OK	90	pass
scopolamine	61.6	OK	90	pass
tenidap	81.9	OK	90	pass
timolol maleate	82.1	OK	90	pass
acebutolol	89.8	OK	89.5	pass
acrivastine	60.2	good	88	pass
trovafloxacin	101	OK	88	pass
bupropion	26.2	good	87	pass
cimetidine	92.1	OK	85	pass
bromazepam	57.4	good	84	pass
methylprednisolone	98.3	OK	82	pass
sorivudine	131.8	OK	82	pass
acetaminophen	58.5	good	80	pass
quinidine	48.6	good	80	pass
cefatrizine	**188.4**	**poor**	**76**	**warning**
guanabenz	72.9	OK	75	pass
propylthiouracil	48.9	good	75	pass
sumatriptan	75	OK	75	pass
lamotrigine	96.4	OK	70	pass
captopril	61.8	OK	67	pass
hydrochlorothiazide	135.2	OK	67	pass
furosemide	127.7	OK	61	pass
ziprasidone	60.5	good	60	pass
etoposide	**183.3**	**poor**	**50**	**warning**
gabapentin	63.4	OK	50	pass
ranitidine	86.7	OK	50	pass
phenoxymethyl penicillinic acid	107.6	OK	45	pass
cefuroxime axetil	**188.6**	**poor**	**36**	**warning**
norfloxacin	81.1	OK	35	pass
nadolol	85.5	OK	34.5	pass
pravastatin	123.9	OK	34	pass
lisinopril	**142.4**	**poor**	**25**	**pass**
chlorothiazide	134.3	OK	13	pass
enalaprilat	115.1	OK	10	pass
cefuroxime	176.8	poor	5	pass
doxorubicin	199.5	poor	5	warning
ganciclovir	151.8	poor	3.8	pass
cromolyn	184.6	poor	0.5	pass
gentamicin	174.4	poor	0	warning

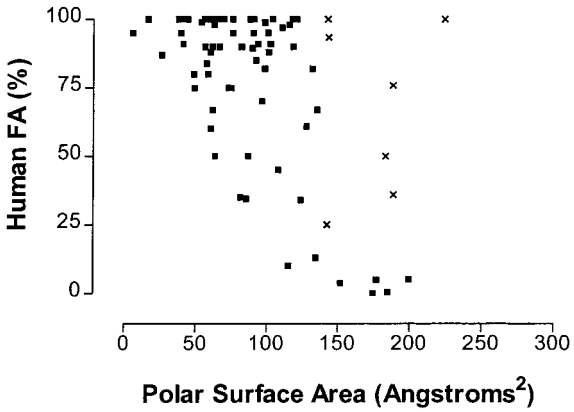

Figure 3—Plot of single conformer PSA values to %FA data for 74 compounds from Wessel et al.[19] set. Seven compounds apparently violating the PSA ≥ 140 Å^2 criterion for poor absorption are shown as crosses (×).

question being a recombinant nucleoside transporter which is responsible for the absorption of pyrimidine nucleosides.[37]

• Amoxicillin and cefatrizine are both amino-β-lactam antibiotics that show good intestinal absorption despite high PSA values. The explanation for this behavior is that both are absorbed via dipeptide carriers.[38,39]

• Cefuroxime axetil shows moderate absorption (36%)—more than would be predicted from its PSA value of 188.6 Å^2. It appears that absorption of this compound takes place by a specialized transport mechanism that obeys Michaelis−Menten kinetics.[40]

• Like zidovudine, lisinopril is a little over the PSA limit and shows a greater than expected absorption. In common with other dipeptide ACE inhibitors, lisinopril is absorbed in a nonpassive process via the dipeptide carrier system.[41]

Thus, all the above compounds are actively transported by one means or another and so are not true false negatives within the scope of the PSA predictions, which only apply to passively transported molecules. The remaining compound, etoposide, is more problematic. To our knowledge, there is no evidence in the literature for any active processes being involved in its intestinal absorption although a recent paper[42] suggests that etoposide distribution into the brain is partly controlled by an active transport process. In any case, etoposide does show very erratic oral bioavailability which has been attributed to low aqueous solubility, slow intrinsic dissolution rate, and chemical instability at pH 1.3[43] and attempts to improve its bioavailability have been unsuccessful.[44] Etoposide, therefore, while apparently a false negative, is not an ideal representative of small molecule oral drugs.

If the above compounds are ignored, the distribution of the remaining points in Figure 3 is roughly sigmoidal; however, there is considerably more scatter than in Figure 2. The reason for this is most likely that the compounds in the Wessel et al. set[19] were not chosen so carefully as those in the Palm et al. set,[26] particularly with regard to the mode of absorption. Even after eliminating the seven "problem" compounds, it is likely that the set contains compounds that are absorbed at least partially by active processes (e.g., acyclovir, cephalexin), and these will tend to add noise to the data.

Nevertheless, the (non)absorption of the remaining 67 compounds is successfully predicted when the PSA value of 140 Å^2 is used to partition the set. These results bolster our confidence that, when passive absorption processes are being considered, the criterion of PSA ≥ 140 Å^2 is a reliable predictor of poorly absorbed compounds and certainly more reliable than the rule-of-5, which only identifies two out of the five compounds showing <10% absorption in this set.

Table 3—Data for the Set of Compounds from Kansy et al[9]

compound	%FA	absorption classification: expt	PAMPA	PSA	PSA/Å²	rule-of-5 status
acetylsalicylic acid	100	h	m	**h**	73.4	pass
alprenolol	93	h	**h**	**h**	41.8	pass
atenolol	54	m	**m**	**m**	93.3	pass
ceftriaxone	1	l	**l**	**l**	220.4	warning
chloramphenicol	90	h	**h**	l	118.4	pass
corticosterone	100	h	**h**	**h**	75.9	pass
coumarin	100	h	**h**	**h**	33.9	pass
dexamethasone	100	h	**h**	m	87.8	pass
diltiazem	92	h	**h**	**h**	60.0	pass
guanabenz	75	h	**h**	**h**	72.9	pass
hydrocortisone	89	h	**h**	m	93.7	pass
imipramine	99	h	m	**h**	6.0	pass
metoprolol	95	h	**h**	**h**	57.2	pass
olsalazine	2	l	**l**	**l**	147.0	pass
propranolol	90	h	**h**	**h**	42.7	pass
salicylic acid	100	h	m	**h**	62.5	pass
sulfasalazine	13	l	**l**	**l**	148.6	pass
sulpiride	35	m	**m**	**m**	102.2	pass
terbutaline	73	h	m	**h**	82.8	pass
testosterone	98	h	**h**	**h**	43.4	pass
theophylline	98	h	m	**h**	74.7	pass
tiacrilast	99	h	m	**h**	79.4	pass
verapamil	95	h	**h**	**h**	73.5	pass
warfarin	93	h	**h**	**h**	62.9	pass

Comparison with a High-Throughput Experimental Method—Recently, Kansy et al.[9] reported the application of a system (called PAMPA − Parallel Artificial Membrane Permeation Assay) for the prediction of passive absorption. PAMPA estimates absorption by measuring the "flux" of a compound through an artificial membrane and is capable of processing large numbers of compounds in parallel by means of 96-well plates. Using the PAMPA system, Kansy et al. classified each member of a set of 25 compounds as being either:

- Highly absorbed (h): %FA ≥ 70, PAMPA flux > 25%
- Moderately absorbed (m): <30 %FA < 70, PAMPA flux 5−25%
- Poorly absorbed (l): %FA ≤ 30, PAMPA flux < 5%

From the curve in Figure 2, the PSA values corresponding to %FA values of 70 and 30 can be determined to be 83 Å² and 112 Å², respectively. Using these limits, it was decided to compare the classification of the compounds based upon PSA values to that arising from the experimental PAMPA system. Of the 25 compounds comprising the test set for the PAMPA, one (cephalexin) was excluded as it is known to be actively transported (for this reason it was poorly predicted by the PAMPA system). PSA values and rule-of-5 status were calculated for the remaining 24 compounds, and the compounds were classified according to their PSA values. The results are shown in Table 3 where the classifications of the compounds from experiment (human %FA), the PAMPA system, and PSA are collated.

The instances where the PAMPA or PSA predictions are correct are highlighted. From this, it can be seen that the PAMPA makes six classification errors, particularly underestimating compounds likely to be transported by a paracellular route, e.g., theophylline and salicylic acid.[9] The PSA classification system makes only three errors, although one of these (chloramphenicol) is a serious one: the compound being predicted to be in the low absorption class, but in fact having a high absorption (i.e., a false negative). The two other errors in the PSA classification are both steroids (dexamethasone and hydrocortisone) which are predicted to have moderate absorption but which are actually well-absorbed. If the original criterion for poor absorption of 140 Å² is applied, all three poor compounds are correctly identified (although two of these are present in the original training set of Palm et al.[26]) and no false negatives are predicted.

Discussion

The results presented above suggest that using single conformer-based calculations to identify compounds with a PSA of ≥ 140 Å² provides a rapid and reliable means of eliminating candidates that are likely to be poorly absorbed in the human intestine. This criterion would seem to be more discriminating than the popular rule-of-5[16] and of similar predictive ability to a high-throughput experimental system.[9] The speed of the method makes it suitable for screening large compound sets, and the fact that it does not require the synthesis of the compounds being assessed means it is especially applicable in the design of combinatorial libraries. For example, we are already using PSA values as an additional constraint in our programs for product-based reagent selection.[45]

Our method is rather different in philosophy from the QSPR-type approach adopted by Wessel et al.,[19] inasmuch as we seek simply a rough classification of compounds whereas their model seeks to predict accurate values across the whole range of absorption. While the results of Wessel et al. seem quite reasonable (RMSEs in predicted %FA: training set 9.4%, cross-validation set 19.7%, and external prediction set 16.0%), there are a number of questions about their work, in particular concerning the data set employed. First, as the authors concede, the data set is heavily skewed toward well-absorbed compounds—only 15 of the 86 compounds have %FA values of less than 50. This bias tends to cause their model to be less accurate in predicting %FA values for less-well-absorbed compounds. For instance, enalaprilat is predicted to have %FA of 47.68, whereas its real value is 10%; conversely, lisinopril is predicted to have a %FA of 0, whereas its true value is 25%. Second, and more fundamentally, we would question the constitution of the data set used by Wessel et al. because it contains compounds that are absorbed by active transport processes as well as passively absorbed compounds. To our minds, it seems unrealistic to expect to find a single model that will accurately predict such different physical processes: passive absorption being diffusion controlled while each active transport mechanism requires more specific molecular recognition.[46] It is for this reason that other workers have striven to use only passively absorbed compounds in their studies.[26] Finally, some of the descriptors used in the model require the use of semiempirical molecular orbital (MO) calculations to generate partial charge information, and these can be moderately time-consuming. A more high-throughput model not including the MO-based descriptors was developed for processing combinatorial libraries, but this was found to give less accurate predictions.[19] Nonetheless, it is interesting to examine the six descriptors used in the model described by Wessel et al. Three seem to code for size, flexibility, and shape while the remainder could be related to PSA: SAAA-2 (surface area of hydrogen bond acceptor atoms), SCAA-2 (surface area × charge of hydrogen bond acceptor atoms), and CHDH-1 (charge on donatable hydrogen atoms). This would seem to provide additional evidence of the validity of polar surface measures in the prediction of absorption.

This begs the question: why should PSA be a useful predictor of passive absorption? Two of the key physicochemical determinants of passive absorption are lipophilicity and hydrogen bonding potential,[47] so it would seem

Table 4—Atomic Radii Used in Molecular Surface Calculations

atom	radius/Å
C	1.9
O	1.74
N	1.82
H	1.5
H attached to O	1.1
H attached to N	1.125
S	2.11
P	2.05
F	1.65
Cl	2.03
Br	2.18
I	2.32

likely that PSA describes one of these in some way. However, PSA is not simply related to lipophilicity. This can be clearly shown by considering, for instance, a homologous series of monoalcohols: MeOH, EtOH, PrOH, etc. In this series, the PSA is constant, while the lipophilicity increases with increasing carbon chain length. More generally, for the 86 compounds in the Wessel et al. set,[19] there is only a poor correlation between PSA and ClogP ($r = 0.56$). PSA is more closely related to hydrogen bonding potential as shown by Palm et al.[25] who found a correlation of $r = 0.92$ between PSA_d and a count of the total number of hydrogen bonds capable of being formed by a molecule (H_t). However, PSA is a more subtle descriptor of hydrogen bonding potential than H_t because it can account for 3D effects such as shielding or burial of polar groups by other parts of a molecule, perhaps because of internal hydrogen bonding. Given that calculations of lipophilicity, at least for neutral species, are readily available,[48] combining these with PSA predictions should help to guide drug design toward orally available compounds.

There are a number of factors affecting the PSA value for any given compound. First, it is incontrovertible that PSA will vary with conformation as shown by Palm et al.[24] However, for the large range of compounds studied here, it seems that using a single low-energy conformer as a representative of the ensemble of conformers likely to be present in vivo is a reasonable approximation. While this approximation will tend to hold best for more rigid compounds, more flexible compounds also pose problems to a "dynamic" approach in terms of the increased CPU time required for a thorough conformational search. Second, for compounds with more than one stereocenter, the choice of absolute configuration can also affect the PSA value although, in general, unless the stereochemistry is complex, this is only a minor effect. Finally, the atomic radii and algorithm used for the molecular surface calculation will also have an effect, as will the method of generating the 3-D structure and the particular force field used for any geometry optimization. In this work, we have used the same radii as Palm et al.,[26] with the exception of not distinguishing between sp^2 and sp^3 carbon atoms. The radii used in this work are given in Table 4.[49]

While the PSA criterion for poor absorption seems robust in avoiding false negative predictions, it is not immune from making false positive assessments. A good example of this is pyridostigmine (**1**, Figure 4), which has a very low PSA value but is poorly absorbed. This indicates that a PSA of <140 Å^2 is a necessary, but not sufficient, criterion for absorption. In the case of pyridostigmine, the cause of the poor absorption is the presence of the positively charged quaternary nitrogen which inhibits partitioning into the intestinal membranes. Likewise, the pK_a of a compound is also a key determinant of its absorption; a point well

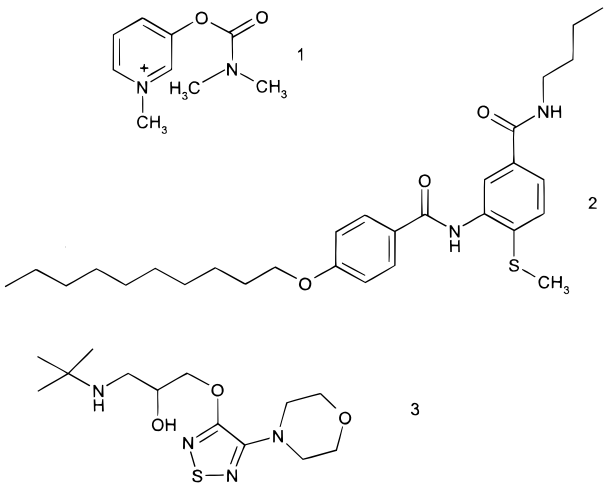

Figure 4—Pyridostigmine (**1**), RP64477 (**2**), and timolol (**3**).

illustrated by a recent publication on 5-HT_{1D} agonists.[50] As indicated above, the lipophilicity of a compound must also be considered. For instance, RP64477 (**2**, Figure 4) has a PSA value of 67.9 Å^2 and on this basis would be expected to be well-absorbed. The fact that it is, in fact, poorly orally available has been attributed to its high log *D* (5.2 at pH 7.4).[51] Finally, aqueous solubility also affects absorption and should be an additional consideration early in compound design.[16] In summary, it is important not to use PSA naively as a guide to absorption but to couple it to existing medicinal chemistry knowledge and intuition. Future work will seek to incorporate some of these factors in an attempt to reduce the number of false positive predictions while avoiding false negatives. Other workers are also exploring these avenues: in a recent article, Winiwarter and coworkers showed that, in addition to PSA, a count of hydrogen bond number and log *D* (octanol/water, pH 5.5 or pH 6.5) were helpful in accurately predicting drug permeability across the human jejunum.[52] Stenberg et al.[53] have also shown recently in a study of a set of peptides that consideration of the nonpolar, as well as the polar, surface area can lead to improved predictions of permeability.

Another interesting avenue of future research is the investigation of refinements to the definition of what constitutes the polar surface area of a molecule. For instance, Krarup et al.[27] reported that for timolol (**3**, Figure 4) and its ester prodrug, a correction was needed to the definition of the polar surface in order to obtain the excellent reported correlation with Caco-2 permeability. The correction was to omit the two nitrogens in the thiadiazole ring from the definition of the polar surface, on the grounds that they are only weak acceptors. When this was done, the correlation between the predicted and actual log P_{app} values improved significantly. The idea of refining the polar surface area so that it takes account of the strength of the hydrogen bonds formed by the groups that comprise it is intriguing. Certainly, the reported improvement in the predictions for timolol and its ester is striking. However, if Krarup et al. were to be consistent, they should also have omitted the non-carbonyl ester oxygen from the polar surface of the timolol prodrug as such oxygens are also known to be extremely infrequent hydrogen-bond acceptors from crystal structure surveys and ab initio calculations.[54–56] The effect of this modification upon their correlation has not yet been investigated. Nonetheless, this idea is certainly worthy of further investigation to see if it helps to improve the accuracy of PSA-based predictions of absorption.

Conclusion

A method for the rapid computation of polar surface area has been described. It has been shown that excellent correlation between polar surface area and intestinal absorption can be obtained without the time-consuming procedure of examining multiple conformations.[57] The use of such rapid calculations in conjunction with the criterion for poor absorption of PSA ≥ 140 Å^2 appears to be an efficient and robust method of computationally screening large numbers of compounds prior to synthesis. It should thus be a valuable tool in both lead generation and optimization.

References and Notes

1. Lloyd, A. W. Can We Relieve the Drug Development Bottleneck? *Pharm. Sci. Technol. Today* **1998**, *1*, 45−46.
2. Rodrigues, A. D. Preclinical Drug Metabolism in the Age of High-Throughput Screening: An Industrial Perspective. *Pharm. Res.* **1997**, *14*, 1504−1510.
3. Lin, J. H.; Lu, A. Y. H. Role of Pharmacokinetics and Metabolism in Drug Discovery and Development. *Pharmacol. Rev.* **1997**, *49*, 403−449.
4. Smith, D. A.; Jones, B. C.; Walker, D. K. Design of Drugs Involving the Concepts and Theories of Drug Metabolism and Pharmacokinetics. *Med. Res. Rev.* **1996**, *16*, 243−266.
5. Tarbit, M. H.; Berman, J. High-throughput Approaches for Evaluating Absorption, Distribution, Metabolism and Excretion Properties of Lead Compounds. *Curr. Opin. Chem. Biol.* **1998**, *2*, 411−416.
6. Artursson, P.; Palm, K.; Luthman, K. Caco-2 Monolayers in Experimental and Theoretical Predictions of Drug Transport. *Adv. Drug Deliv. Rev.* **1996**, *22*, 67−84.
7. Artursson, P.; Borchardt, R. Intestinal Drug Absorption and Metabolism in Cell Cultures: Caco-2 and Beyond. *Pharm. Res.* **1997**, *14*, 1655−1658.
8. Ito, K.; Iwatsubo, T.; Kanamitsu, S.; Nakajima, Y.; Sugiyama, Y. Quantitative Prediction of In Vivo Drug Clearance and Drug Interactions from In Vitro Data on Metabolism, together with Binding and Transport. *Annu. Rev. Pharmacol. Toxicol.* **1998**, *38*, 461−499.
9. Kansy, M.; Senner, F.; Gubernator, K. Physicochemical High Throughput Screening: Parallel Artificial Membrane Permeation Assay in the Description of Passive Absorption Processes. *J. Med. Chem.* **1998**, *41*, 1007−1010.
10. Berman, J.; Halm, K.; Adkison, K.; Shaffer, J. Simultaneous Pharmacokinetic Screening of a Mixture of Compounds in the Dog using API LC/MS/MS Analysis for Increased Throughput. *J. Med. Chem.* **1997**, *40*, 827−829.
11. Gillet, V. J.; Willett, P.; Bradshaw, J. Identification of Biological Activity Profiles Using Substructural Analysis and Genetic Algorithms. *J. Chem. Inf. Comput. Sci.* **1998**, *38*, 165−179.
12. Ajay; Walters, W. P.; Murcko, M. A. Can We Learn to Distinguish Between Drug-like and Non-Drug-Like Molecules? *J. Med. Chem.* **1998**, *41*, 3314−3324.
13. Sadowski, J.; Kubinyi, H. A Scoring Scheme for Discriminating between Drugs and Nondrugs. *J. Med. Chem.* **1998**, *41*, 3325−3329.
14. Navia, M. A.; Chaturvedi, P. R. Design Principles for Orally Bioavailable Drugs. *Drug Discov. Today* **1996**, *1*, 179−189.
15. Chan, O. H.; Stewart, B. H. Physicochemical and Drug-Delivery Considerations for Oral Drug Bioavailability. *Drug Discov. Today* **1996**, *1*, 461−473.
16. Lipinski, C. A.; Lombardo, F.; Dominy, B. W.; Feeney, P. J. Experimental and Computational Approaches to Estimate Solubility and Permeability in Drug Discovery and Development Settings. *Adv. Drug Deliv. Rev.* **1997**, *23*, 3−25.
17. ClogP. Daylight Chemical Information Software, version 4.51. Daylight Chemical Information Inc.: 27401 Los Altos, Suite #370, Mission Viejo, CA 92691.
18. Moriguchi, I.; Hirono, S.; Liu, Q.; Nakagome, I.; Matsushita, Y. Simple Method of Calculating Octanol/Water Partition Coefficient. *Chem. Pharm. Bull.* **1992**, *40*, 127−130.
19. Wessel, M. D.; Jurs, P. C.; Tolan, J. W.; Muskal, S. M. Prediction of Human Intestinal Absorption of Drug Compounds From Molecular Structure. *J. Chem. Inf. Comput. Sci.* **1998**, *38*, 726−735.
20. Hirono, S.; Nakagome, I.; Hirano, H.; Matsushita, Y.; Yoshii, F.; Moriguchi, I. Noncongeneric Structure-Pharmacokinetic Property Correlation Studies Using Fuzzy Adaptive Least-Squares: Oral Bioavailability. *Biol. Pharm. Bull.* **1994**, *17*, 306−309.
21. Hermann, R. B. Theory of Hydrophobic Bonding. II. Correlation of Hydrocarbon Solubility in Water with Solvent Cavity Surface Area. *J. Phys. Chem.* **1972**, *76*, 2754−2759.
22. Pearlman, R. S. Molecular Surface Areas and Volumes and their Use in Structure−Activity Relationships. In *Physical Chemical Properties of Drugs*; Medicinal Research Series Vol. 10; Yalkowsky, S. H., Sinkula, A. A., Valvani, S. C., Eds.; Marcel Dekker: New York, 1980; pp 321−347.
23. van de Waterbeemd, H.; Camenisch, G.; Folkers, G.; Raevsky, O. A. Estimation of Caco-2 Cell Permeability using Calculated Molecular Descriptors. *Quant. Struct.-Act. Relat.* **1996**, *15*, 480−490.
24. Palm, K.; Luthman, K.; Ungell, A.-L.; Strandlund, G.; Artursson, P. Correlation of Drug Absorption with Molecular Surface Properties. *J. Pharm. Sci.* **1996**, *85*, 32−39.
25. Lipkowitz, K. B.; Baker, B.; Larter, R. Dynamic Molecular Surface Areas. *J. Am. Chem. Soc.* **1989**, *111*, 7750−7753.
26. Palm, K.; Stenberg, P.; Luthman, K.; Artursson, P. Polar Molecular Surface Properties Predict the Intestinal Absorption of Drugs in Humans. *Pharm. Res.* **1997**, *14*, 568−571.
27. Krarup, L. H.; Christensen, I. T.; Hovgaard, L.; Frokjaer, S. Predicting Drug Absorption from Molecular Surface Properties Based on Molecular Dynamics Simulations. *Pharm. Res.* **1998**, *15*, 972−978.
28. Palm, K.; Luthman, K.; Ungell, A.-L.; Strandlund, G.; Beigi, F.; Lundahl, P.; Artursson, P. Evaluation of Dynamic Polar Molecular Surface Area as Predictor of Drug Absorption: Comparison with Other Computational and Experimental Predictors. *J. Med. Chem.* **1998**, *41*, 5382−5392.
29. Weininger, D. SMILES, a Chemical Language and Information System. 1. Introduction to Methodology and Encoding Rules. *J. Chem. Inf. Comput. Sci.* **1988**, *28*, 31−36.
30. Pearlman, R. S. Rapid Generation of High Quality Approximate 3D Molecular Structures. *Chem. Des. Auto. News* **1987**, *2*, 1−7.
31. CONCORD v4.02. Balducci, R.; McGarity, C. M.; Rusinko, A., III; Skell, J.; Smith, K.; Pearlman, R. S (University of Texas at Austin). Distributed by Tripos, Inc., 1699 S. Hanley Rd., Suite 303, St. Louis, MO 63144-2913.
32. SYBYL 6.4.2. Tripos, Inc., 1699 S. Hanley Rd., Suite 303, St. Louis, MO 63144-2913.
33. Dodd, L. R.; Theodorou, D. N. Analytical Treatment of the Volume and Surface Area of Molecules Formed by an Arbitrary Collection of Unequal Spheres Intersected by Planes. *Mol. Phys.* **1991**, *72*, 1313−1345.
34. A Boltzmann sigmoidal curve follows the equation: $y =$ bottom + (top − bottom)/(1 + exp (($x_{50} - x$)/slope)). In this instance, $y =$ %FA, $x =$ PSA, and x_{50} is the PSA value at which %FA = 50. Bottom and top refer to the minimum and maximum values of %FA, respectively.
35. Chungi, V. S.; Bourne, D. W. A.; Dittert, L. W. Competitive Inhibition between Folic Acid and Methotrexate for Transport Carrier in the Rat Small Intestine. *J. Pharm. Sci.* **1979**, *68*, 1552−1553.
36. Dudeja, P. K.; Torania, S. A.; Said, H. M. Evidence for the Existence of Carrier-Mediated Folate Uptake Mechanism in Human Colonic Luminal Membranes. *Am. J. Physiol.* **1997**, *272*, G1408−G1415.
37. Yao, S. Y.; Cass, C. E.; Young, J. D. Transport of the Antiviral Nucleoside Analogues 3′-azido-3′-deoxythymine and 2′,3′-dideoxycytidine by a Recombinant Nucleoside Transporter (rCNT) Expressed in Xenopus Laevis Oocytes. *Mol. Pharmacol.* **1996**, *50*, 388−393.
38. Westphal, J. F.; Deslandes, A.; Brogard, J. M.; Carbon, C. Reappraisal of Amoxycillin Absorption Kinetics. *J. Antimicrob. Chemother.* **1991**, *27*, 647−654.
39. Reigner, B. G.; Couet, W.; Guedes, J. P.; Fourtillan, J. B.; Tozer, T. N. Saturable Rate of Cefatrizine Absorption after Oral Administration in Humans. *J. Pharmacokinet. Biopharm.* **1990**, *18*, 17−34.
40. Ruiz-Balaguer, N.; Nacher, A.; Casabo, V. G.; Merino, M. Nonlinear Intestinal Absorption Kinetics of Cefuroxime Axetil in Rats. *Antimicrob. Agents Chemother.* **1997**, *41*, 445−448.
41. Friedman, D. I.; Amidon, G. L. Intestinal Absorption Mechanism of Dipeptide Angiotensin Converting Enzyme Inhibitors of the Lysyl-Prolyl Type: Lisinopril and SQ 29, 852. *J. Pharm. Sci.* **1989**, *78*, 995−998.
42. Burgio, D. E.; Gosl, M. P.; McNamara, P. J. Effects of P-glycoprotein Modulators on Etoposide Elimination and Central Nervous System Distribution. *J. Pharmacol. Exp. Ther.* **1998**, *287*, 911−917.

43. Shah, J. C.; Chen, J. R.; Chow, D. Preformulation Study of Etoposide: Identification of Physicochemical Characteristics Responsible for the Low and Erratic Oral Bioavailability of Etoposide. *Pharm. Res.* **1989**, *6*, 408−412.
44. Joel, S. P.; Clark, P. I.; Heap, L.; Webster, L.; Robbins, S.; Craft, H.; Slevin, M. L. Pharmacological Attempts to Improve the Bioavailability of Oral Etoposide. *Cancer Chemother. Pharmacol.* **1995**, *37*, 125−133.
45. Good, A. C.; Lewis, R. A. New Methodology for Profiling Combinatorial Libraries and Screening Sets: Cleaning Up the Design Process with HARPick. *J. Med. Chem.* **1997**, *40*, 3926−3936.
46. Doring, F.; Will, J.; Amasheh, S.; Clauss, W.; Ahlbrecht, H.; Daniel, H. Minimal Molecular Determinants of Substrates for Recognition by the Intestinal Peptide Transporter. *J. Biol. Chem.* **1998**, *273*, 23211−23218.
47. Conradi, R. A.; Burton, P. S.; Borchardt, R. T. Physicochemical and Biological Factors that Influence a Drug's Cellular Permeability by Passive Diffusion. In *Lipophilicity in Drug Action and Toxicology*; Pliška, V., Testa, B., van de Waterbeemd, H., Eds.; VCH: Weinheim, 1996; pp 233−252.
48. Carrupt, P.-A.; Testa, B.; Gaillard, P. Computational Approaches to Lipophilicity: Methods and Applications. In *Reviews in Computational Chemistry*; Lipkowitz, K. B., Boyd, D. B., Eds.; Wiley-VCH: New York, 1997; Vol. 11, pp 241−315.
49. Luthman, K. Private communication, 1998.
50. Castro, J. L.; Collins, I.; Russell, M. G. N.; Watt, A. P.; Sohal, B.; Rathbone, D.; Beer, M. S.; Stanton, J. A. Enhancement of Oral Absorption in Selective 5-HT_{1D} Receptor Agonists: Fluorinated 3-[3-(Piperidin-1-yl)propyl]indoles. *J. Med. Chem.* **1998**, *41*, 2667−2670.
51. Wils, P.; Warnery, A.; Phung-Ba, V.; Legrain, S.; Scherman, D. High Lipophilicity Decreases Drug Transport Across Intestinal Epithelial Cells. *J. Pharmacol. Exp. Ther.* **1994**, *269*, 654−658.
52. Winiwarter, S.; Bonham, N. M.; Ax, F.; Hallberg, A.; Lennernäs, H.; Karlén, A. Correlation of Human Jejunal Permeability (in Vivo) of Drugs with Experimentally and Theoretically Derived Parameters. A Multivariate Data Analysis Approach. *J. Med. Chem.* **1998**, *41*, 4939−4949.
53. Stenberg, P.; Luthman, K.; Artursson, P. Prediction of Membrane Permeability to Peptides from Calculated Dynamic Molecular Surface Properties. *Pharm. Res.* **1999**, *16*, 205−212.
54. Böhm, H.-J.; Brode, S.; Hesse, U.; Klebe, G. Oxygen and Nitrogen in Competitive Situations: Which is the Hydrogen-Bond Acceptor? *Chem. Eur. J.* **1996**, *2*, 1509−1513.
55. Bruno, I. J.; Cole, J. C.; Lommerse, J. P. M.; Rowland, R. S.; Taylor, R.; Verdonk, M. L. Isostar: A Library of Information about Nonbonded Interactions. *J. Comput.-Aided Mol. Des.* **1997**, *11*, 525−537.
56. Rablen, P. R.; Lockman, J. W.; Jorgensen, W. L. Ab Initio Study of Hydrogen-Bonded Complexes of Small Organic Molecules with Water. *J. Phys. Chem. A* **1998**, *102*, 3782−3797.
57. During the revision of this paper, van de Waterbeemd et al. published a paper describing the use of single conformation PSA values in the classification of drug compounds as CNS active or CNS inactive: van de Waterbeemd, H.; Camenisch, G.; Folkers, G.; Chretien, J. R.; Raevsky, O. A. Estimation of Blood-Brain Barrier Crossing of Drugs Using Molecular Size and Shape, and H-bonding Descriptors. *J. Drug Target.* **1998**, *6*, 151−165. In their experience, the conformational effect in low molecular weight molecules represents a variation of about ±10% in the polar surface area which they do not consider as critical when making first estimates of BBB uptake.

Acknowledgments

I am indebted to my colleagues from Rhône-Poulenc Rorer for many helpful discussions during the work described in this paper. In particular, Drs. Stephen Pickett, Andrew Ratcliffe, and Christopher Newton gave much encouragement and made constructive comments upon the manuscript while it was in preparation. Drs. Nicola Wilsher, Martin Barrett, and Ken Page gave advice on matters relating to absorption while Drs. Richard Lewis (now Eli Lilly, UK) and Paul Bamborough (now GlaxoWellcome, UK) helped in the development of the intranet interface to the calculations. I am grateful to Drs. Kristina Luthman (University of Tromsø, Norway) and Larry Dodd (Polytechnic University, New York) for the kind provision of values for atomic radii (Table 4) and the MOLVOL program, respectively. Prof. Peter Jurs (Pennsylvania State University) and Dr. Inge Christensen (Royal Danish School of Pharmacy) are thanked for providing preprints of refs 19 and 27, respectively. Finally, the comments and suggestions of the anonymous referees were greatly appreciated; particularly regarding the history of the use of molecular surface areas in modeling of transport and partitioning processes (refs 21 and 22) and issues concerning Boltzmann averaging of molecular surface areas.

JS9804011

Rapid Calculation of Polar Molecular Surface Area and Its Application to the Prediction of Transport Phenomena. 2. Prediction of Blood–Brain Barrier Penetration

DAVID E. CLARK*

Contribution from *Rhône-Poulenc Rorer, Dagenham Research Centre, Rainham Road South, Dagenham, Essex, RM10 7XS, United Kingdom.*

Received October 7, 1998. Final revised manuscript received February 9, 1999.
Accepted for publication April 30, 1999.

Abstract □ This paper describes the derivation of a simple QSAR model for the prediction of log BB from a set of 55 diverse organic compounds. The model contains two variables: polar surface area (PSA) and calculated logP, both of which can be rapidly computed. It therefore permits the prediction of log BB for large compound sets, such as virtual combinatorial libraries. The performance of this QSAR on two test sets taken from the literature is illustrated and compared with results from other reported computational approaches to log BB prediction.

Introduction

The blood−brain barrier (BBB) is a complex cellular system whose purpose is to maintain the homeostasis of the central nervous system (CNS) by separating the brain from the systemic blood circulation.[1] In drug discovery, it is important to determine whether a candidate molecule is capable of penetrating the BBB. For drugs targeted at the CNS, BBB penetration is a necessity (unless invasive or intranasal delivery routes are being considered[2]), whereas for drugs aimed at other sites of action, passage through the BBB may lead to unwanted side-effects.

A common measure of the degree of BBB penetration is the ratio of the steady-state concentrations of the drug molecule in the brain and in the blood, usually expressed as $\log(C_{brain}/C_{blood})$ or, more simply, log BB. Experimental values of log BB published to date cover the range about −2.00 to +1.00. Within this range, compounds with log BB > 0.3 cross the BBB readily, while compounds with log BB < −1.0 are only poorly distributed to the brain.[3] The determination of log BB is difficult and time-consuming, requiring animal experiments and the synthesis (sometimes in radiolabeled form) of the compounds to be tested. Although *in vitro*[4] and artificial membrane-based methods[5] for studying BBB penetration are being developed, it would be desirable if log BB could be predicted computationally with enough accuracy to allow the early rejection of unsuitable candidates.

In this paper, we review existing computational approaches for the prediction of log BB and then describe the derivation and validation of a novel, simple QSAR (quantitative structure−activity relationship) model allowing the rapid and accurate prediction of blood-brain barrier penetration.

QSAR Models for log BB Prediction—The first purely computational approach to log BB prediction was that of Kansy and van de Waterbeemd[6] who developed the following QSAR from a set of 20 compounds taken from the work of Young et al.:[7]

$$\log BB = -0.021(\pm 0.003)PSA - 0.003(\pm 0.001)Mol\_Vol + 1.643(\pm 0.465) \quad (1)$$
$$n = 20,\ r = 0.835,\ s = 0.448,\ F = 19.5$$

where PSA is the polar surface area, Mol_Vol is the molecular volume, n is the number of compounds, r is the correlation coefficient, s is the standard error, and F is the Fisher value, a measure of the statistical significance of the equation. The standard errors of the correlation coefficients are given in parentheses.

However, subsequent application of this equation to compounds outside its training set showed it to be poorly predictive,[8] suggesting that the 20 compound training set was insufficient to derive a generally applicable QSAR for predicting log BB.[9] Thus, Abraham and co-workers[9] constructed a larger training set of 65 compounds from which (after the removal of various outliers) they derived the following two models which they denoted ACM-II and log Pplus, respectively:[10]

$$\log BB = -0.038(\pm 0.064) + 0.198(\pm 0.100)R_2 - 0.687(\pm 0.125)\pi_2^H - 0.715(\pm 0.334)\Sigma\alpha_2^H - 0.698(\pm 0.107)\Sigma\beta_2^H + 0.995(\pm 0.096)V_x \quad (2)$$
$$n = 57,\ r = 0.952,\ s = 0.197,\ F = 99.2$$

$$\log BB = +0.055 + 0.023 \log P_{oct} - 0.507\Sigma\alpha_2^H - 0.500\Sigma\beta_2^H \quad (3)$$
$$n = 49,\ r = 0.949,\ s = 0.201,\ F = 136.1$$

No standard errors of the correlation coefficients were given for eq 3.[10] In both of these equations, the various parameters (excepting the experimental quantity, log P_{oct}) are solute descriptors, specifically: R_2 is an excess molar refraction, π_2^H is a dipolarity/polarizability parameter, $\Sigma\alpha_2^H$ and $\Sigma\beta_2^H$ are the solute hydrogen-bond acidity and basicity, respectively, and V_x is the characteristic volume of McGowan.[11]

There are a number of difficulties when applying either of these equations to more than a handful of compounds. First, to estimate log BB using either of these equations, it is necessary to calculate a value for each of the descriptors for the compound in question. The descriptor values in turn are calculated by summing the contributions from the molecule's constituent fragments. While research is ongoing to automate this process, at present, manual calculations require several minutes (at least) to make an

† Corresponding author. Phone: +44 181 919 3353. Fax: +44 181 919 2029. E-mail: david-e.clark@rp-rorer.co.uk.

10.1021/js980402t CCC: $18.00
Published on Web 06/24/1999

appropriate dissection of the molecule under study and retrieve the relevant fragment values. If values for a particular fragment cannot be found, they must be calculated. Equation 3, while more compact, requires experimental values for the partition coefficient log P_{oct}, although it is conceivable that computed estimates of log *P* could be substituted for this quantity. Finally, a close examination of the descriptor values used to construct eq 2 reveals that a number of the descriptors are very highly correlated (the pairs R_2 and π_2^H, R_2 and $\Sigma\beta_2^H$, R_2 and V_x, π_2^H and $\Sigma\beta_2^H$, and π_2^H and V_x are all correlated with $r > 0.9$). Such collinearity among the descriptors may cause the regression coefficients to become unreliable.[12] For these reasons, although the above equations appear statistically impressive, other approaches have been sought.

Lombardo et al.[13] started with a set of 57 compounds drawn from the Abraham training set[9] mentioned above. Detailed conformational analyses and semiempirical calculations were used to arrive at this simple model, denoted here as LBC, which omits two outliers from the original set of 57 compounds:

$$\log BB = 0.054(\pm 0.005)\Delta G^{o}_{W} + 0.43(\pm 0.07) \quad (4)$$
$$n = 55,\ r = 0.82,\ s = 0.41,\ F = 108.3$$

where ΔG^{o}_{W} is the computed free energy of solvation of a compound in water. As described by Lombardo et al., the determination of this quantity is rather computationally expensive, making this approach unsuitable for screening large numbers of compounds. However, recent work has led to faster methods for the calculation of solvation free energies.[14]

Most recently, Norinder and co-workers[15] have developed models for log BB prediction using their computed MolSurf parameters together with statistical analysis by the Partial Least Squares to Latent Structures (PLS) method. The model from their work with the largest training set (56 compounds − model 2 in ref 15, denoted here as NSO) contained three significant PLS components with the following statistics: $n = 56$, $r = 0.913$, $s = 0.312$, $F = 86.95$. Here again, however, the computational methods employed required conformational analysis and computationally intensive semiempirical and ab initio calculations which render the approach too slow for high-throughput applications.

In what follows, we describe the derivation of a simple QSAR model for the prediction of log BB that is automatic and rapid to calculate and therefore applicable to the screening of large compound sets, such as virtual combinatorial libraries. The performance of this QSAR on two test sets taken from the literature will be illustrated and compared with the methods above where such results are available.

Computational Methods—*Training Set*—A set of 57 compounds previously studied by Lombardo et al.[13] was used as a training set. These compounds are illustrated in Figure 1 and listed in Table 1 along with experimental log BB values taken from ref 13.

Test Set 1—This set consists of the seven compounds (shown in Figure 2) used as a test set by Abraham et al.[10] The experimental log BB values listed in Table 2 for these compounds were taken from ref 10 as were the predicted log BB values from eqs 2 and 3.

Test Set 2—This test set was used by Lombardo et al.[13] and also by Norinder et al.[15] It comprises six compounds whose structures are shown in Figure 3. Table 3 shows the log BB values from the various equations and experiment.

Polar Surface Area Calculations—PSA values for the molecules under study were calculated using the methods described in the previous paper.[16]

Calculations of log *P*—Two computational methods for logP prediction were used. ClogP was calculated using the Daylight software.[17] MlogP values were computed using an implementation of the method developed by Moriguchi et al.[18] encoded in the Sybyl Programming Language and executed within the Sybyl Molecular Modeling package.[19]

Regression Analysis—All multiple linear regressions were carried out within the Tsar program.[20]

Results

Training Set—Despite the limitations found with the Kansy and van de Waterbeemd approach,[6] we decided to investigate the possibility of using PSA values to derive a generally applicable QSAR for log BB. Starting from the 57 compounds used by Lombardo et al.,[13] we first tried correlating PSA with log BB and obtained the following equation:

$$\log BB = -0.016(\pm 0.001)PSA + 0.547(\pm 0.050) \quad (5)$$
$$n = 57,\ r = 0.819,\ s = 0.455,\ F = 112.4$$

This initial result was encouraging and, incidentally, suggested a relationship between PSA and ΔG^{o}_{W}. An investigation showed the two quantities were indeed closely correlated ($r = 0.962$). However, a purely PSA-based model failed to distinguish the varying BBB-penetrating abilities of nonpolar compounds. For example, benzene and 3-methylpentane have log BB values of −0.69 and 2.01 respectively, but both have a PSA of zero. Thus, we began to search for an additional descriptor that would differentiate between the nonpolar compounds in the set. Molecular weight, molecular volume, and nonpolar surface area were tried, but none led to a significant improvement in the model.[21] Finally, calculated logP values were tried with more success generating a model we denote DEC-I:

$$\log BB = -0.0148(\pm 0.001)PSA + 0.152(\pm 0.036)ClogP + 0.139(\pm 0.073) \quad (6)$$
$$n = 55,\ r = 0.887,\ s = 0.354,\ F = 95.8$$

where ClogP is the calculated logP.[17] The two compounds omitted from the original set of 57 were N_2, for which ClogP cannot calculate an accurate value, and compound 12 which, if included in the model, shows an error of 1.5 log units in the prediction of its experimental log BB value (data not shown). Compound 12 has also been found to be an outlier by other groups.[13,15] One difficulty with using ClogP values is that there are compounds for which it cannot generate accurate values. For this reason, some workers[22] have proposed the use of the MlogP[18] approach in such circumstances. If MlogP values are substituted for ClogP values, the following model (DEC-II) is generated:

$$\log BB = -0.0145(\pm 0.001)PSA + 0.172(\pm 0.022)MlogP + 0.131(\pm 0.033) \quad (7)$$
$$n = 55,\ r = 0.876,\ s = 0.369,\ F = 86.0$$

To allow a direct comparison of these two equations with a purely PSA-based model, eq 5 was rederived based on the same 55 compounds as were used in the derivation of eqs 6 and 7 giving:

$$\log BB = -0.0156(\pm 0.001)PSA + 0.548(\pm 0.048) \quad (8)$$
$$n = 55,\ r = 0.841,\ s = 0.410,\ F = 128.4$$

When the statistics are compared, eqs 6 and 7 show superior *r* and *s* values to eq 8, and the *F* values for the three equations indicate that all are significant at the 95%

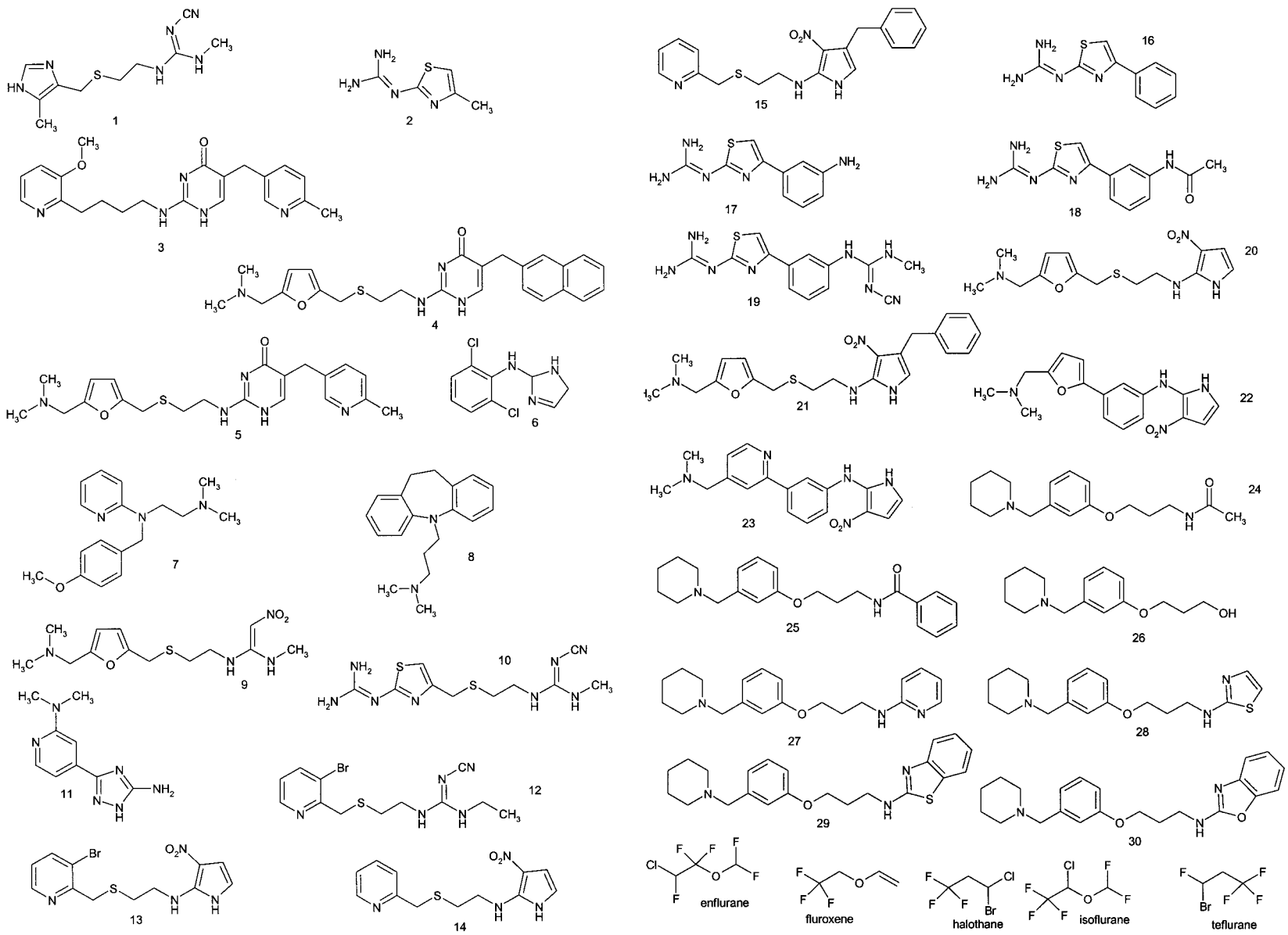

Figure 1—Compounds **1**–**30** and less familiar compounds from the training set.

Table 1—Data and Results for Training Set

compound	PSA/Å^2	ClogP	MlogP	expt log BB	DEC-I log BB	DEC-II log BB
1	92.1	0.351	0.821	–1.42	–1.17	–1.07
2	78.9	0.952	0.786	–0.04	–0.88	–0.88
3	94.0	2.297	2.300	–2.00	–0.90	–0.84
4	73.5	4.046	3.569	–1.30	–0.33	–0.32
5	87.0	1.874	2.107	–1.06	–0.86	–0.77
6	39.0	0.743	3.066	0.11	–0.32	0.09
7	26.8	2.787	2.575	0.49	0.17	0.18
8	6.0	4.413	3.876	0.83	0.72	0.71
9	84.5	1.327	0.659	–1.23	–0.91	–0.98
10	139.2	0.844	1.258	–0.82	–1.79	–1.67
11	88.8	0.911	2.592	–1.17	–1.03	–0.71
12	73.5	2.282	1.940	–2.15	n.d.[a]	n.d.[a]
13	83.9	2.747	1.642	–0.67	–0.68	–0.81
14	84.0	1.800	0.969	–0.66	–0.83	–0.92
15	78.0	3.637	2.484	–0.12	–0.46	–0.58
16	76.6	2.781	2.480	–0.18	–0.57	–0.56
17	104.4	1.784	1.960	–1.15	–1.13	–1.05
18	108.8	1.977	2.087	–1.57	–1.17	–1.09
19	135.8	1.880	2.400	–1.54	–1.58	–1.43
20	85.5	2.287	0.832	–1.12	–0.78	–0.97
21	79.5	4.124	2.253	–0.73	–0.41	–0.64
22	82.7	3.849	1.868	–0.27	–0.50	–0.75
23	85.7	3.234	1.760	–0.28	–0.64	–0.81
24	47.9	2.065	2.069	–0.46	–0.25	–0.21
25	45.2	4.004	3.228	–0.24	0.08	0.03
26	38.5	2.379	2.069	–0.02	–0.07	–0.07
27	39.1	4.259	3.272	0.69	0.21	0.12
28	40.0	4.165	2.627	0.44	0.18	0.00
29	39.2	5.759	3.902	0.14	0.43	0.23
30	54.9	5.029	4.332	0.22	0.09	0.08
butanone	22.7	0.834	0.655	–0.08	–0.07	–0.09
benzene	0.0	2.142	2.255	0.37	0.46	0.52
3-methylpentane	0.0	3.738	3.516	1.01	0.71	0.73
3-methylhexane	0.0	4.267	3.869	0.90	0.79	0.80
2-propanol	23.4	0.074	0.347	–0.15	–0.20	–0.15
2-methylpropanol	22.6	0.693	0.800	–0.17	–0.09	–0.06
2-methylpentane	0.0	3.738	3.516	0.97	0.71	0.73
2,2-dimethylbutane	0.0	3.608	3.516	1.04	0.69	0.73
1,1,1-trifluoro-2-chloroethane	0.0	1.714	2.081	0.08	0.40	0.49
1,1,1-trichloroethane	0.0	2.481	2.226	0.40	0.52	0.51
diethyl ether	11.3	0.870	0.800	0.00	0.10	0.10
enflurane	11.6	2.459	1.766	0.24	0.34	0.27
ethanol	24.4	–0.235	0.172	–0.16	–0.26	–0.19
fluroxene	10.7	1.765	1.257	0.13	0.25	0.19
halothane	0.0	2.447	2.604	0.35	0.51	0.58
heptane	0.0	4.397	3.869	0.81	0.81	0.80
hexane	0.0	3.868	3.516	0.80	0.73	0.73
isoflurane	11.0	2.999	1.766	0.42	0.43	0.27
methane	0.0	1.103	1.115	0.04	0.31	0.32
methylcyclopentane	0.0	3.314	3.124	0.93	0.64	0.67
nitrogen	54.2	n.d.[b]	–2.272	0.03	n.d.[a]	n.d.[a]
pentane	0.0	3.339	3.138	0.76	0.65	0.67
propanol	24.4	0.294	0.347	–0.16	–0.18	–0.16
propanone	22.7	0.305	0.202	–0.15	–0.15	–0.16
teflurane	0.0	2.007	2.419	0.27	0.44	0.55
toluene	0.0	2.641	2.608	0.37	0.54	0.59
trichloroethene	0.0	2.627	2.081	0.34	0.54	0.49

[a] Compounds not included in final training set for eqs 6 and 7. [b] ClogP could not calculate an accurate value for this compound. DEC-I is the predicted set of values using eq 6 and DEC-II is the predicted set of values using eq 7.

confidence level. It is apparent that the inclusion of a calculated log *P* value has improved the model for log BB prediction. Thus, eqs 6 and 7 were preferred for log BB prediction over the simple PSA-based model of eq 8.

The quantities comprising eqs 6 and 7 are rapidly calculable, and, furthermore, the descriptors involved are not significantly correlated with one another: the correlation coefficient *r* being 0.15 for PSA and ClogP, and 0.23 for PSA and MlogP. The predicted log BB values from eqs 6 and 7 are tabulated in Table 1, and plots of computed versus experimental values are shown in Figure 4. However, the real test of any QSAR equation is how well it predicts values for compounds outside its training set. Accordingly, we have applied our equations to two test sets that are available in the literature.

Test Set 1—Looking at Table 2, if all seven compounds are considered, the mean absolute errors in the log BB predictions are: ACM-II: 0.30, log Pplus: 0.54, DEC-I: 0.37 and DEC-II: 0.40. However, it can be seen that all the models overpredict log BB for compounds Y-G19 and Y-G20. This is in accord with the findings of Abraham et al.[10] who considered them as outliers. They suggested that

Table 2—Data and Results from Test Set 1[a]

compound	PSA/Å^2	ClogP	MlogP	expt log BB	ACM-II log BB	log Pplus log BB	DEC-I log BB	DEC-II log BB
Y-G14	29.3	–0.068	0.652	–0.30	–0.31	–0.47	–0.30	–0.18
Y-G15	18.8	–0.338	0.969	–0.06	–0.01	–0.34	–0.09	0.02
Y-G16	43.1	–0.603	–0.316	–0.42	–0.41	–0.50	–0.59	–0.55
Y-G19	40.6	1.495	1.656	–1.30	–0.14	–0.15	–0.24	–0.17
Y-G20	46.7	0.110	0.855	–1.40	–0.57	–0.15	–0.53	–0.40
SKF89124	67.5	2.666	2.634	–0.43	–0.44	–0.91	–0.56	–0.40
SKF101468	44.1	1.999	2.605	0.25	0.24	–0.13	–0.11	–0.06

[a] ACM-II is the predicted set of values from eq 2, log Pplus is the predicted set of values from eq 3, DEC-I and DEC-II are the predicted set of values from eq 6 and eq 7, respectively.

Table 3—Data and Results from Test Set 2[a]

compound	PSA/Å^2	ClogP	MlogP	expt log BB	LBC log BB	NSO log BB	DEC-I log BB	DEC-II log BB
31	46.7	1.980	3.139	0.00	–0.14	–0.58	–0.25	–0.01
32	62.7	0.260	2.408	–0.34	–0.28	–1.11	–0.75	–0.37
33	76.1	1.907	3.446	–0.30	–0.46	–0.75	–0.70	–0.38
34	98.5	0.380	2.698	–1.34	–0.64	–0.99	–1.26	–0.83
35	120.4	–0.932	1.959	–1.82	–0.82	–1.35	–1.77	–1.28
36	5.4	4.641	4.369	0.76–0.98	0.28	1.03	0.76	0.80

[a] LBC is the predicted set of values from eq 4, NSO is the predicted set of values from model 2 of Norinder et al.,[15] DEC-I and DEC-II are the predicted set of values from eq 6 and eq 7, respectively.

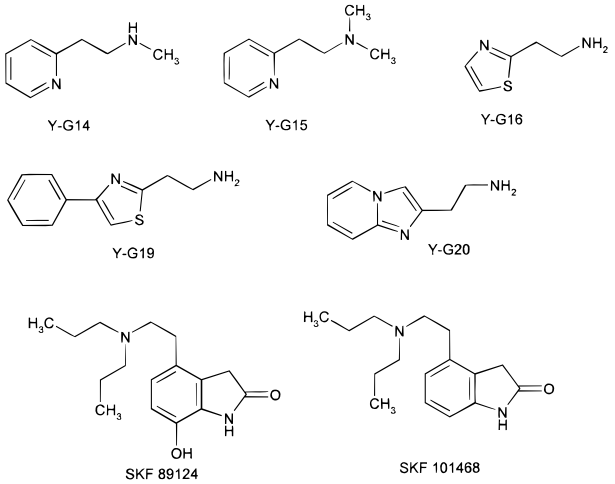

Figure 2—Structures for test set 1.

such outliers might be caused by factors such as inaccurate data due to experimental difficulties or metabolic effects not accounted for in log BB measurements.[10] The fact that our independently derived models also find large deviations for these compounds, while treating the remainder quite well, adds some weight to the argument to consider Y-G19 and Y-G20 as outliers. If this is done, for the remaining five compounds, the mean absolute errors in the log BB predictions are as follows: ACM-II: 0.02, log Pplus: 0.28, DEC-I: 0.14, and DEC-II: 0.13. Thus, whether the outliers are included or excluded, ACM-II is the best predictor for this set, and DEC-I and DEC-II perform about as well as each other and better than log Pplus.

Test Set 2—Considering the results in Table 3, it can be seen that compound **36** (amitryptyline) has a large uncertainty in its experimental log BB value; however, DEC-I and DEC-II predict log BB values within the given range. In so doing, they perform better than LBC, which underpredicts log BB, and NSO which predicts too high a value. Calculating the mean absolute errors over compounds **31**–**35**, we obtain: LBC: 0.41; NSO: 0.52; DEC-I: 0.24; DEC-II: 0.23.

In this case, the equations based on PSA and calculated log *P* perform substantially better than the more computationally expensive methods of Lombardo et al.[13] and Norinder et al.[15]

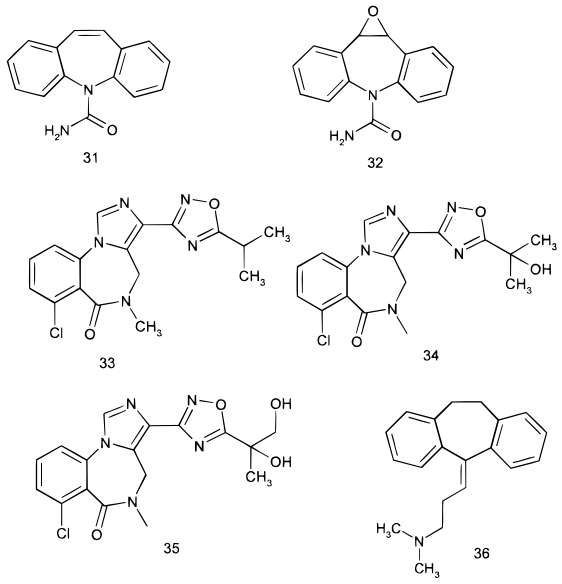

Figure 3—Structures for test set 2.

Discussion

It has been suggested by Lennernäs[23] that purely passive diffusion is universal for membranes with different physiological functions and physicochemical properties. Thus, the factors that determine a compound's intestinal absorption should also, to some extent, model its BBB permeability. Therefore, it is not surprising that PSA, which has been found to be useful in modeling intestinal absorption (see the preceding paper[16] and references therein), together with a direct estimate of lipophilicity, widely acknowledged as an important factor in transport across membranes,[24] should yield a predictive model for log BB. It would seem from our results that, with this set of compounds, quantities such as molecular weight, molecular volume, or nonpolar surface area do not correlate strongly enough with

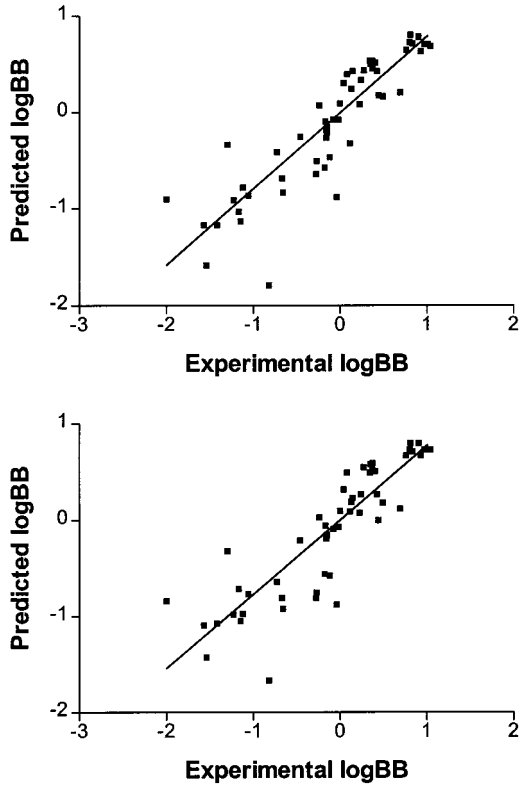

Figure 4—(a) Plot of computed (DEC-I) versus experimental log BB values. (b) Plot of computed (DEC-II) versus experimental log BB values.

lipophilicity to be useful (when combined with PSA) for modeling BBB penetration. An analysis of the 55 compounds used in the training set in this paper bears this out. The correlation coefficients, *r*, for the relationships between ClogP and molecular weight, molecular volume, and nonpolar surface area are 0.386, 0.468, and 0.599, respectively.

It is interesting to note the similarity between the models derived in this paper (DEC-I and DEC-II) and the log Pplus equation of Abraham et al.[10] In the latter (eq 3), the two parameters, $\Sigma\alpha_2^H$ and $\Sigma\beta_2^H$, denote the solute hydrogen-bond acidity and basicity, respectively. The fact that these have negative coefficients while log *P* has a positive coefficient accords with the expectation that membrane permeation will be more facile for compounds that form fewer (and weaker) hydrogen bonds with solvent and with the observation that the brain is more lipophilic than the blood, making lipophilic compounds more likely to penetrate the brain. Similar findings were reported by Norinder et al.[15] who reported that high brain/blood partitioning was favored by an absence of atoms capable of hydrogen bonding together with high lipophilicity. The same may be said for DEC-I and DEC-II, where better brain penetration is predicted for compounds with high calculated log *P* and low PSA (the polar surface area being an indication of a compound's capacity to form hydrogen bonds). In addition, van de Waterbeemd et al.[25] recently showed that, of a set of 125 drugs, all those showing CNS activity could be found within the ranges: $0 \le \text{PSA} \le 90$; $-1 \le \log D$ (pH 7.5) ≤ 4 with the likelihood of CNS activity appearing to increase with decreasing PSA and increasing log *D*. Thus, the models derived in this paper would seem to be sensible from a physiological point of view and are also in agreement with insights from other models into the factors facilitating blood−brain barrier penetration.

As with the model for intestinal absorption described previously (see the preceding paper[16] and references therein), it is likely that the simple model described here is only valid for passive diffusion processes across the BBB. There are active transport systems for both influx and efflux in the brain and compounds which are affected by these are not likely to be well-predicted. Another factor influencing BBB transport is the binding of drugs by plasma proteins.[26] This too is not directly accounted for in the PSA/calculated log P-based model, although plasma binding within a given series may be correlated with log *P*.[27]

Finally, other experimental measures of blood−brain barrier permeability are now becoming available. Eddy et al.[4] have reviewed various in vitro models, and Lombardo et al.[13] showed that, for a small set of 10 compounds, it was possible to correlate permeability across a monolayer composed of endothelial cells from bovine brain microvessels with free energy of solvation. Gratton et al.[28] have reported permeability−surface area measurements (denoted log PS) using a short-duration vascular perfusion method for 18 compounds and correlated the values with Abraham's solute descriptors. A relatively new technique for measuring brain penetration in vivo is microdialysis.[29] This offers the potential for observing drug disposition between the extracellular and intracellular space in the brain, something not possible with traditional log BB measurements.[30] As more data emerge from these various novel techniques, it will be interesting to see how well computational techniques can adapt to predict new measures of blood−brain barrier penetration.

Conclusion

In summary, the equations (DEC-I and DEC-II) described in this paper for log BB prediction show a good predictive ability. Their utility is enhanced by the fact that they comprise only two simple, noncorrelated variables, values for which may be rapidly computed for almost any structure. (As described in the preceding paper,[16] PSA values can be computed in about 10−15 s on a modern workstation, and ClogP and MlogP calculations are very fast.) The procedure for log BB estimation is fully automated, allowing the prescreening of virtual libraries and other compound sets prior to synthesis or purchase. For this reason, it should be of use in drug discovery projects where blood−brain barrier penetration is an issue.

References and Notes

1. De Vries, H. E.; Kuiper, J.; De Boer, A. G.; Van Berkel, T. J. C.; Breimer, D. D. The Blood-Brain Barrier in Neuroinflammatory Diseases. *Pharmacol. Rev.* **1997**, *49*, 143−155.
2. Pardridge, W. M. CNS Drug Design Based on Principles of Blood-Brain Barrier Transport. *J. Neurochem.* **1998**, *70*, 1781−1792.
3. Abraham, M. H.; Takacs-Novak, K.; Mitchell, R. C. On the Partition of Ampholytes: Application to Blood-Brain Distribution. *J. Pharm. Sci.* **1997**, *86*, 310−315.
4. Eddy, E. P.; Maleef, B. E.; Hart, T. K.; Smith, P. L. In Vitro Models to Predict Blood-Brain Barrier Permeability. *Adv. Drug Deliv. Rev.* **1997**, *23*, 185−198.
5. Reichel, A.; Begley, D. J. Potential of Immobilized Artificial Membranes for Predicting Drug Penetration Across the Blood-Brain Barrier. *Pharm. Res.* **1998**, *15*, 1270−1274.
6. Kansy, M.; van de Waterbeemd, H. Hydrogen-Bonding Capacity and Brain Penetration. *Chimia* **1992**, *46*, 299−303.
7. Young, R. C.; Mitchell, R. C.; Brown, T. H.; Ganellin, C. R.; Griffiths, R.; Jones, M.; Rana, K. K.; Saunders: D.; Smith, I. R.; Sore, N. E.; Wilks, T. J. Development of a New Physicochemical Model for Brain Penetration and Application to the Design of Centrally Acting H2 Receptor Histamine Antagonists. *J. Med. Chem.* **1988**, *31*, 656−671.
8. Calder, J. A.; Ganellin, C. R. Predicting the Brain-Penetrating Capability of Histaminergic Compounds. *Drug Des. Discov.* **1994**, *11*, 259−268.
9. Abraham, M. H.; Chadha, H. S.; Mitchell, R. C. Hydrogen Bonding. 33. Factors that Influence the Distribution of

Solutes Between Blood and Brain. *J. Pharm. Sci.* **1994**, *83*, 1257−1268.
10. Abraham, M. H.; Chadha, H. S.; Mitchell, R. C. Hydrogen Bonding. Part 36. Determination of Blood Brain Distribution Using Octanol−Water Partition Coefficients. *Drug Des. Discov.* **1995**, *13*, 123−131.
11. Abraham, M. H.; McGowan, J. C. The Use of Characteristic Volumes to Measure Cavity Terms in Reversed Phase Liquid Chromatography. *Chromatographia* **1987**, *23*, 243−246.
12. Livingstone, D. *Data Analysis for Chemists*. Oxford University Press: Oxford, 1995; pp 126−127.
13. Lombardo, F.; Blake, J. F.; Curatolo, W. J. Computation of Brain−Blood Partitioning of Organic Solutes via Free Energy Calculations. *J. Med. Chem.* **1996**, *39*, 4750−4755.
14. Hawkins, G. D.; Liotard, D. A.; Cramer, C. J.; Truhlar, D. G. OMNISOL: Fast Prediction of Free Energies of Solvation and Partition Coefficients. *J. Org. Chem.* **1998**, *63*, 4305−4313.
15. Norinder, U.; Sjöberg, P.; Österberg, T. Theoretical Calculation and Prediction of Brain−Blood Partitioning of Organic Solutes Using MolSurf Parametrization and PLS Statistics. *J. Pharm. Sci.* **1998**, *87*, 952−959.
16. Clark, D. E. Rapid Calculation of Polar Molecular Surface Area and its Application to the Prediction of Transport Phenomena. 1. Prediction of Intestinal Absorption. *J. Pharm. Sci.*, **1999**, *88*, 807−814.
17. ClogP. Daylight Chemical Information Software, version 4.51. Daylight Chemical Information Inc.: 27401 Los Altos, Suite #370, Mission Viejo, CA 92691.
18. Moriguchi, I.; Hirono, S.; Liu, Q.; Nakagome, I.; Matsushita, Y. Simple Method of Calculating Octanol/Water Partition Coefficient. *Chem. Pharm. Bull.* **1992**, *40*, 127−130.
19. Sybyl 6.4.2. Tripos, Inc., 1699 S. Hanley Rd., Suite 303, St. Louis, MO 63144-2913. The SPL script was originally developed by Dr. James Blake (Pfizer, US) and has been subsequently modified by Dr. Jon Swanson (Tripos Inc.) to accommodate changes in the Tripos Sybyl Line Notation (SLN) description of substructure queries.
20. Tsar 3.1. Oxford Molecular Ltd., The Medawar Centre, Oxford Science Park, Sandford-on-Thames, Oxford, OX4 4GA, England.
21. To allow comparison with eqs 6−8, the statistics for the equations involving these quantities are PSA and molecular weight: $n = 55$, $r = 0.845$, $s = 0.410$, $F = 64.8$; PSA and molecular volume: $n = 55$, $r = 0.849$, $s = 0.405$, $F = 66.9$; PSA and nonpolar surface area: $n = 55$, $r = 0.848$, $s = 0.406$, $F = 66.6$.
22. Lipinski, C. A.; Lombardo, F.; Dominy, B. W.; Feeney, P. J. Experimental and Computational Approaches to Estimate Solubility and Permeability in Drug Discovery and Development Settings. *Adv. Drug Deliv. Rev.* **1997**, *23*, 3−25.
23. Lennernäs, H. Human Jejunal Effective Permeability and its Correlation with Preclinical Drug Absorption Models. *J. Pharm. Pharmacol.* **1997**, *49*, 627−638.
24. Conradi, R. A.; Burton, P. S.; Borchardt, R. T. Physicochemical and Biological Factors that Influence a Drug's Cellular Permeability by Passive Diffusion. In *Lipophilicity in Drug Action and Toxicology*; Pliška, V., Testa, B., van de Waterbeemd, H., Eds.; VCH: Weinheim, 1996; pp 233−252.
25. van de Waterbeemd, H.; Camenisch, G.; Folkers, G.; Chretien, J. R.; Raevsky, O. A. Estimation of Blood-Brain Barrier Crossing of Drugs Using Molecular Size and Shape, and H-bonding Descriptors. *J. Drug Target.* **1998**, *6*, 151−165.
26. Olson, R. E.; Christ, D. D. Plasma Protein Binding of Drugs. In *Annual Reports in Medicinal Chemistry*; Bristol, J. A., Ed.; Academic Press: San Diego, 1996; Vol. 33, pp 327−336.
27. Rowley, M.; Kulagowski, J. J.; Watt, A. P.; Rathbone, D.; Stevenson, G. I.; Carling, R. W.; Baker, R.; Marshall, G. R.; Kemp, J. A.; Foster, A. C.; Grimwood, S.; Hargreaves, R.; Hurley, C.; Saywell, K. L.; Tricklebank, M. D.; Leeson, P. D. Effect of Plasma Protein Binding on in Vivo Activity and Brain Penetration of Glycine/NMDA Receptor Antagonists. *J. Med. Chem.* **1997**, *40*, 4053−4068.
28. Gratton, J. A.; Abraham, M. H.; Bradbury, M. W.; Chadha, H. S. Molecular Factors Influencing Drug Transfer Across the Blood-Brain Barrier. *J. Pharm. Pharmacol.* **1997**, *49*, 1211−1216.
29. Elmquist, W. F.; Sawchuk, R. J. Application of Microdialysis in Pharmacokinetic Studies. *Pharm. Res.* **1997**, *14*, 267−288.
30. Evrard, P. A.; Ragusi, C.; Boschi, G.; Verbeeck, R. K.; Scherrmann, J.-M. Simultaneous Microdialysis in Brain and Blood of the Mouse: Extracellular and Intracellular Brain Colchicine Disposition. *Brain Res.* **1998**, *786*, 122−127.

Acknowledgments

I am very grateful to my colleagues at RPR for many helpful discussions and invaluable advice. I would especially like to thank Dr. Iain McLay for proposing the investigation of PSA values in log BB prediction and Dr. Stephen Pickett for suggesting the inclusion of ClogP as a variable in eq 6. Dr. Ulf Norinder kindly supplied a preprint of ref 15. Dr. James Blake (Pfizer, US) is thanked for making his SPL script for MlogP calculations available and the technical support of Drs. Jon Swanson and Gareth Wilden (Tripos, Inc.) in relation to this code is acknowledged.

JS980402T

Measurement of Drug Distribution in Vascular Tissue Using Quantitative Fluorescence Microscopy

WADE K. WAN,[†,‡] MARK A. LOVICH,[†] CHAO-WEI HWANG,[†] AND ELAZER R. EDELMAN*[,†,§]

Contribution from *Harvard–MIT Division of Health Sciences and Technology, and Department of Electrical Engineering and Computer Science, Massachusetts Institute of Technology, Cambridge, Massachusetts 02139, Cardiovascular Division, Department of Medicine, Brigham and Women's Hospital, Harvard Medical School, Boston, Massachusetts 02115.*

Received September 23, 1998. Final revised manuscript received May 25, 1999.
Accepted for publication June 1, 1999.

Abstract □ Quantitative tools to assess vascular macromolecular distributions have been limited by low signal-to-noise ratios, reduced spatial resolution, postexperimental motion artifact, and the inability to provide multidimensional drug distribution profiles. Fluorescence microscopy offers the potential of identifying exogenous compounds within intact tissue by reducing autofluorescence, the process by which endogenous compounds emit energy at the same wavelength as fluorescent labels. A new technique combining fluorescence microscopy with digital postprocessing has been developed to address these limitations and is now described in detail. As a demonstration, histologic cross-sections of calf carotid arteries that had been loaded endovascularly with FITC-Dextran (20 kD) ex vivo were imaged at two different locations of the electromagnetic spectrum, one exciting only autofluorescent structures and the other exciting both autofluorescent elements and exogenous fluorescent labels. The former image was used to estimate the autofluorescence in the latter. Subtraction of the estimated autofluorescence resulted in an autofluorescence-corrected image. A standard curve, constructed from arteries that were incubated until equilibrium in different bulk phase concentrations of FITC-Dextran, was used to convert fluorescent intensities to tissue concentrations. This resulted in a concentration map with spatial resolution superior to many of the previous methods used to quantify macromolecular distributions. The transvascular concentration profiles measured by quantitative fluorescence microscopy compared favorably with those generated from the proven *en face* serial sectioning technique, validating the former. In addition, the fluorescence method demonstrated markedly increased spatial resolution. This new technique may well prove to be a valuable tool for elucidating the mechanisms of macromolecular transport, and for the rational design of drug delivery systems.

Introduction

The appeal of local pharmaceutical administration is that specific tissues and organs can be targeted for therapy without adverse systemic effects.[1−4] Yet, implementation of local delivery strategies has been limited by a whole new set of pharmacologic issues.[5] Local delivery systems impart large dynamic concentration gradients across tissues that can be difficult to identify, characterize, and control.[6] Because drug levels are not uniform, the concept of dosing takes on another level of complexity.[5] For example, cells near the point of release experience a very different concentration of drug in their extracellular milieu than do cells far away, and these levels are not static in time. The dose a cell sees depends on both time and space as well as administered drug mass. Thus, the successful implementation of local drug delivery systems requires accurate, high resolution techniques to assess drug deposition, and as proof that therapeutic levels are achieved rapidly and persist long enough for biologic effect to emerge. These very issues are especially important in considering the potential of local vascular drug therapy. The scale of the blood vessel wall dimensions, the importance and prevalence of vascular diseases, and the promise of increasingly novel vasoactive compounds make for quantification of local administration all the more essential.

We now describe the development of a new method for visualizing and quantifying drug distribution in vascular tissue. This technique utilizes fluorescence microscopy with digital postprocessing[7−10] and avoids the experimental hazards and disposal costs associated with radiolabeled compounds, while providing spatial resolution superior to conventional radioactive techniques. A nonaqueous method is used to immobilize drug and prevent postexperimental diffusion of soluble molecules. Vessel cross-sections are imaged with fluorescence microscopy, and digital postprocessing algorithms are used to reduce autofluorescence, a prior obstacle to quantitative interpretation. Autofluorescence compensation is accomplished by acquiring images at two different excitation wavelengths, one consisting of only nonspecific autofluorescence and the other containing both the specific fluorescence of markers and autofluorescence.[8,9] The former image is then used to estimate the autofluorescence in the latter image. This estimated autofluorescence could then be subtracted from the latter image to yield an autofluorescence-free image containing only the signal from the fluorescent tags. Fluorescent intensities are then converted to tissue concentrations, yielding a high-resolution map of macromolecular distribution. As a demonstration, the transvascular concentration gradient of an endovascularly applied model drug, 20 kD FITC-dextrans, is measured in the calf carotid artery. This compound was chosen for its inert properties, relative availability, and similarity in size to several vasoactive growth factors. High-resolution transvascular concentration profiles provided by this technique will yield improved understanding of macromolecular transport and deposition in vascular tissue and insight into the special pharmacologic issues raised by local delivery systems.

Experimental Protocol

Calibration Standards—Calf carotid arteries were obtained from a slaughterhouse and stored on ice for no more than 2 h. The arteries were submerged in phosphate-buffered saline with

* Corresponding author. Phone: (617) 253-1569. Fax: (617) 253-2514. E-mail: eedelman@mit.edu.
† Harvard−MIT Division of Health Sciences and Technology, MIT.
‡ Department of Electrical Engineering and Computer Science, MIT.
§ Harvard Medical School.

10.1021/js9803858 CCC: $18.00
Published on Web 07/08/1999

calcium and magnesium (PBS^{2+}; Sigma PBS Catalog no. 1000-3, 0.01 M phosphate buffer salts, 0.120 M NaCl, 0.0027 M KCl with 0.01 M $CaCl_2$ and 0.01 M $MgCl_2$ added) throughout the preparation process to prevent dehydration and maintain tissue viability. Excess fascia and fat were gently teased away using forceps and scissors prior to sectioning vessels into cylindrical segments, 8−12 mm long and 4−8 mm in diameter. These segments were placed into separate vials containing 10 mL of 20 kD dextrans labeled with fluorescein isothiocyanate (FITC-Dx, 0.006−0.007 mol FITC per mol glucose, Sigma) in PBS^{2+} at 0, 0.02, 0.05, 0.1, 0.15, 0.2, 0.25, 0.5, 1, 2, and 2.5 mg/mL. Specimens that were incubated without any FITC-Dx will be referred to as unloaded arteries. The arteries were incubated in the dark, to prevent photobleaching, for 24 h at 4 °C. This duration was determined to be sufficient for FITC-Dx to achieve chemical equilibrium between the tissue and the bulk phase by incubating arterial segments in a single bulk phase and measuring the resulting tissue concentrations after different incubation periods. The data suggest that the tissues were fully saturated in less than 24 h, supporting the claim that 24 h is sufficient to fully load arterial segments with FITC-Dx. Incubation also did not result in any tissue swelling which would cause the calibration standards to not accurately reflect the tissue specimens. In pilot studies, the thickness of the arterial media was measured from histologic cryosections prepared both on arrival from the slaughterhouse and after incubation in PBS^{2+} for 65 h. There was no statistical difference in medial thickness at time zero (459 ± 17 μm) and at 65 h (477 ± 23 μm, $n = 3$, avg ± sd), suggesting that the tissues did not swell significantly.

Drug Immobilization and Tissue Sectioning—To immobilize drug within the tissue and limit diffusion during storage and handling, tissues were snap frozen in embedding medium (OCT, Tissue-Tek) with liquid nitrogen. Specimen blocks were stored at −20 °C prior to being cut into 20-μm-thick axial cross-sections using a precooled cryostat (CM 3050, Leica). Section thickness was previously measured to vary by less than 0.5 μm between slices. Three histologic sections were taken from each tissue standard. Frozen OCT around the tissue was gently removed to facilitate mounting onto glass slides (Superfrost Plus, VWR Scientific). The histologic sections were freeze-dried in the dark at −50 °C in a lyophilizer (Labconco) for 24 h, and stored at room temperature in a dark, dry environment prior to imaging. Freeze-drying of the tissue sections ensured that the FITC-Dx was immobilized throughout subsequent storage and processing.

Image Acquisition System—The histologic sections were imaged without any mounting medium or cover slip. Diffusion of drug from its location within the blood vessel wall was significantly reduced by snap freezing, which does not require applying a liquid phase to the tissue. 24-bit color images were acquired using a CCD video camera system (Optronics) attached to a fluorescence microscope (Optiphot-2, Nikon). The system resided on a pneumatic optical table (Technical Manufacturing Corporation) to minimize vibrations. Video images were captured on a computer (Power Computing) via a frame grabber (LG-3, Scion) using a commercial imaging software package (IPLab Spectrum, Signal Analytics). The frame grabber was calibrated by displaying a test image consisting of color bars generated from the video camera system. The gain and offset of the frame grabber were adjusted to match its dynamic range (0 to 255 units for the red, green, and blue channels) to the dynamic range of the video camera system. Magnification was provided by a 10× ocular and a 10× objective, resulting in 640 by 480 pixel images with pixel dimensions of 1.326 μm by 1.326 μm. Illumination was provided by a super high-pressure mercury lamp (Nikon) which was allowed to warm for at least 2 h prior to imaging for consistent illumination. This duration was previously determined to adequately stabilize the imaging system. Ultraviolet (UV) and FITC filter sets were used to examine tissue specimens. The UV filter set consisted of an excitation filter of 330−380 nm, a dichroic filter (beam splitter) of 400 nm, and a barrier filter of 420 nm. The FITC filter set consisted of an excitation filter of 465−495 nm, a dichroic filter of 505 nm, and a barrier filter of 515−555 nm. Images of each histologic section were acquired at 0.25, 0.5, 1.0, and 2.0 s exposure times for both UV and FITC filters. The image with the maximal signal that did not contain any saturated pixels was used. In this way each section was exposed to less than 4 s at each wavelength. In pilot studies, the impact of photobleachning was found to be negligible by continuously exposing a histologic section with drug signal to the excitation beam and acquiring sequential images. No reduction in intensities was found over one minute.

Hence forth, UV and FITC images refer to images taken with the UV and FITC filter sets, respectively. The fluorescent tag used in these experiments, FITC, is maximally excited around 490 nm so UV images contain only autofluorescence and FITC images contain both autofluorescence and specific signal from the fluorescent labels.

Initial Processing—Images were acquired using 8-bit RGB (red, green, and blue) color components and converted to the HSI (hue, saturation, and intensity) color model.[11] The HSI color model decouples luminance and chrominance in an image, with the intensity image representing the luminance information, and the hue and saturation images representing the chrominance information. Both UV and FITC images were decoupled in this manner, and the hue and saturation images were discarded leaving only the intensity image (Figure 1). Intensities in these images range from 0 (absolute black) to 255 (absolute white).

Autofluorescence Compensation—Since UV images contain only autofluorescence and FITC images contain both autofluorescence and the specific signal of interest, each pixel in a UV image can be used to estimate the autofluorescence present in the corresponding pixel in the counterpart FITC image.[8,9] A 50 pixel wide region that spanned the media but excluded the adventitia and intima was defined on both the UV and FITC images of an unloaded artery. Corresponding pixels from this region of the UV and FITC images were correlated, which allows estimation of the autofluorescence component in each pixel of this region in a FITC image, using the corresponding pixel in the counterpart UV image (Figure 1). The estimated autofluorescence was subtracted from the original FITC image yielding an autofluorescence compensated FITC image that contains only the signal from fluorescent markers (Figure 1).

Conversion of Fluorescent Intensities to Tissue Concentrations—Fluorescent intensities were converted to tissue concentrations using a standard calibration curve obtained from tissue standards incubated until equilibrium in known concentrations of FITC-Dx in PBS^{2+}. A 50 pixel wide region that spanned the media, but excluded adventitia and intima, was selected from each autofluorescence corrected FITC image (three histologic sections each with one image per standard). The average fluorescent signal in this region was correlated with the bulk phase concentration of FITC-Dx that the tissue standard was incubated in.

Whereas in bulk solutions dextrans are free to access an entire unit of volume, compounds in tissue are excluded from areas by steric interactions. Thus, the fractional accessible space in which hydrophilic drugs can distribute in tissue (ϵ) must be less than one.[6] Drug in the accessible space in a tissue is in chemical equilibrium with the bulk phase, and therefore the concentration in the accessible space is known for each tissue standard. This definition of accessible space is dependent not only on the tissue examined, but also on the specific compound of interest. The fluorescent microscopy image, however, contains contributions from both accessible and nonaccessible spaces, and concentrations are detected on a per tissue volume basis. The bulk phase concentrations of tissue standards can be converted to tissue concentration by multiplying the former by the fractional space (ϵ),[12−14]

$$c_T = \epsilon c_{Bulk} \quad (1)$$

which was measured independently (see below).

Measurement of Fractional Space Available for Distribution—To measure the fractional space available for distribution in arterial media, 1 cm long segments of calf carotid arteries were incubated for 24 h to equilibrium in 10 mL of 20 kD FITC-Dx in PBS^{2+} at concentrations (c_{Bulk}) of 0.1, 0.5, 1, and 3 mg/mL. Four arteries were incubated at each concentration. Tissue concentrations in "isolated" arterial media were measured after the intima and adventitia were removed by an *en face* cryosectioning technique (see below).[15,16] The fractional space was determined from the correlation between the bulk phase and the tissue concentrations (eq 1).

En Face Cryosectioning—Carotid artery segments were removed from incubation and cut longitudinally, unfolded, placed on a microscopy slide with the intima face down and covered in OCT. A second slide was placed on top of the specimen with two 1-mm

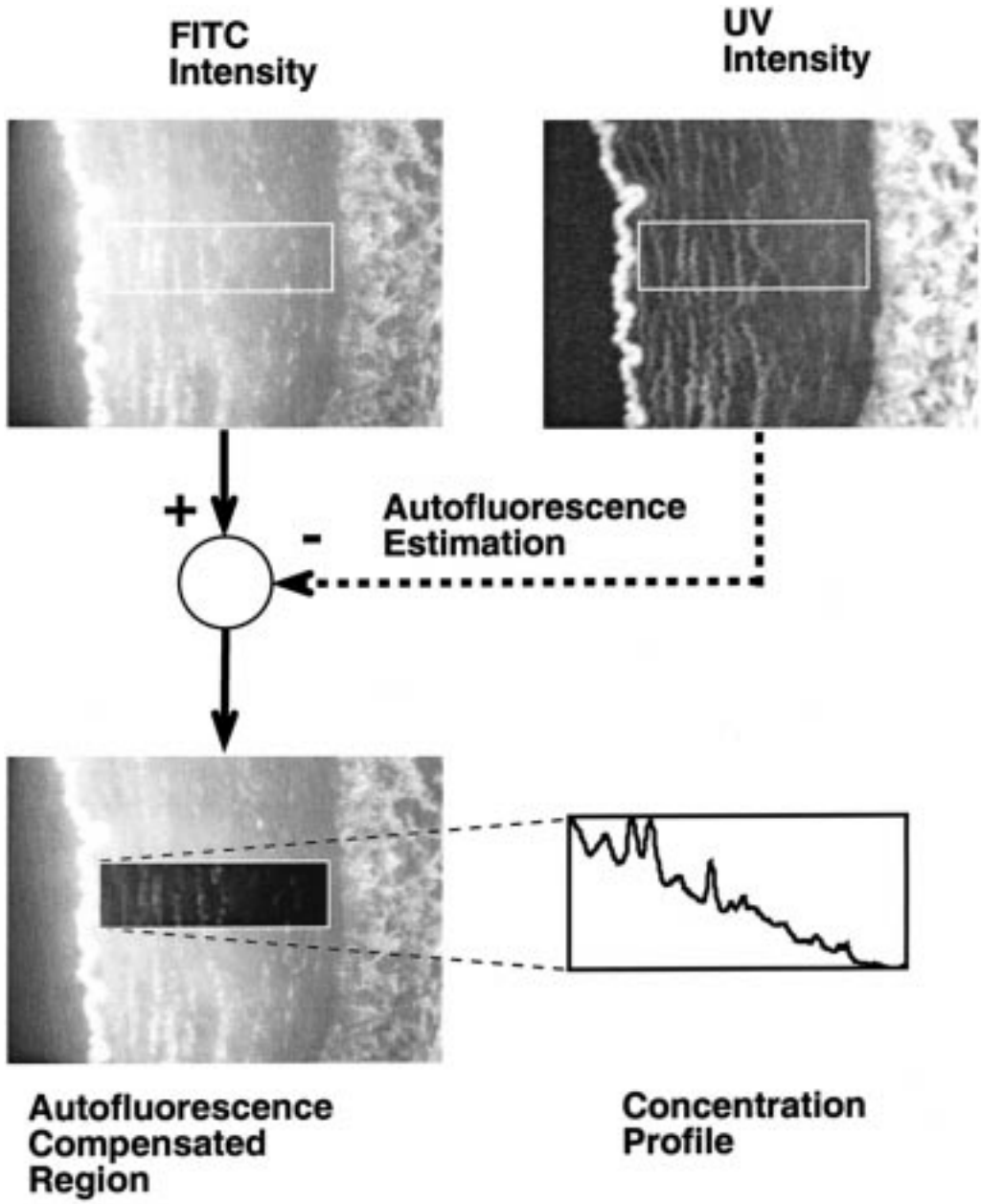

Figure 1—Image processing algorithm to compute concentration profiles. A cross-section of a calf carotid artery is imaged with the FITC and UV filter sets. A 50-pixel wide region corresponding to the media is defined from each intensity subimage. The UV region is used to estimate autofluorescence in the medial region. Pixel intensities are converted to tissue concentrations using a calibration curve. This example shows the transmedial concentration profile of fluorescent-labeled compound 2 h after endovascular application ex vivo.

spacers placed around the specimen. The glass slides were clamped together to ensure that sectioning was parallel to the intimal surface, and the tissue was snap frozen with a freezing aerosol (Cytocool II, Stephens Scientific). The frozen specimen was wrapped in aluminum foil and stored at −20° C prior to sectioning. A frozen block of OCT was mounted in the cryostat to serve as a chuck for the specimens, and was cut until the resulting surface was parallel to the blade. The cryostat was retracted so that the artery could be mounted. Arteries were separated from the slides by gently rubbing a lightly heated spatula against the slide until the specimen easily slid off. The specimens were mounted flat onto the chuck with the intima toward the blade and then trimmed into a rectangle with a razor blade. The length and width of the rectangle were measured so that the volume of each 20-μm-thick slice (V_{Slice}) could be calculated. Additional OCT was frozen around the specimen for support during sectioning.

The artery was sectioned from the intima toward the adventitia. Eighteen slices corresponding to the carotid media were pooled and reincubated in 24 mL of fresh PBS^{2+} for 48 h. This time has been shown to be more than sufficient to release more than 96% of the FITC-Dx from whole arteries. The reincubation bath volume (V_{Bath}) was more than 1000-fold greater than the volume of all the combined tissue slices, permitting the small amount of residual drug in the tissue at the end of reincubation to be neglected. The concentration of the reincubation bath was measured with a spectrofluorimeter (Fluorolog 1681, SPEX), using a standard curve of known concentrations of FITC-Dx in PBS^{2+}. This reincubation concentration ($c_{Release}$) was used to calculate the original tissue concentration of FITC-Dx in PBS^{2+} (c_T) with the following formula:

$$c_T \approx \frac{c_{Release} V_{Bath}}{n V_{Slice}} = \frac{\text{mass of released drug}}{\text{volume of tissue slices}} \qquad (2)$$

where n is the number of tissue slices in each reincubation bath. Thus, the tissue concentration was measured, and the slope between the tissue and bulk phase concentrations was taken to be the fractional space of the media.[12−14] This method of measuring the fractional space assumes that binding between the compound and the tissue is insignificant.

Quantitative Fluorescence Microscopy vs *en Face* Cryosectioning—To demonstrate the validity of this technique, FITC-Dx was applied to the endovascular aspect of an artery, and the resulting transmural concentration profile was determined both through the proposed quantitative fluorescence microscopy technique and the standard method of *en face* serial cryosectioning.[15–18] Calf carotid arteries were obtained and cleaned of adventitia as described above. Arterial segments about 1.5 cm long without visible branches were cannulated at both ends and tested for leaks by visually inspecting the vessel after connecting one end to an elevated bag of Ringer's solution and closing off the other end. The intact artery was then placed in an in vitro perfusion apparatus that has been described elsewhere.[19,20] Briefly, the apparatus recirculates PBS^{2+} through the artery, simulating plasma flow, and allows control of the drug concentration in both the endovascular and perivascular compartments, which are separated by the arterial wall. 20 kD FITC-Dx (5 mg/mL) was applied to the endovascular compartment, and the continuously stirred perivascular compartment contained PBS^{2+}. Throughout this study, the hydrostatic head was set to zero, so that the transarterial pressure gradient and subsequent convective effects on molecular transport were eliminated.

Three arteries were perfused for 2 h and were then removed from the apparatus and cut in longitudinal segments, one for analysis with quantitative fluorescence microscopy, and the other with *en face* cryosectioning. Specimens for quantitative fluorescence microscopy were immediately snap frozen, sectioned onto histologic slides, freeze-dried, and imaged, as described above. Snap freezing and freeze-drying deprives the drug of an aqueous phase to diffuse and therefore significantly reduces post experimental motion artifacts. The image was autofluorescence corrected, and a 50 pixel wide region was defined which spanned the arterial media (Figure 1). The intensity values were averaged across the 50-pixel width to reduce the circumferential variance of drug distribution and were converted to FITC-Dx concentration in tissue using the standard calibration curve. Eight such transmedial regions were defined around the circumference of the artery, and their resulting transmural concentration profiles were averaged.

Specimens for *en face* cryosectioning were splayed open and frozen between two glass slides, stored, mounted, and trimmed as described above. The length and width of the opened and trimmed artery was measured with a ruler so that the volume of each 20-μm slice (V_{Slice}) could be calculated. The slices were transferred in groups of three into a 4 mL PBS^{2+} bath (V_{Bath}) and stored in the dark at 4° C for 48 h to allow drug to diffuse into the bulk phase. Three slices were used in each bath to increase the fluorescent signal into the dynamic range of the spectrofluorimeter, which was used to measure the concentration of drug in the reincubation bath ($c_{Release}$). The tissue concentration (c_T) was determined through eq 2.

Results

Autofluorescence Compensation—UV and FITC images of an unloaded artery were examined to determine the correlation between the autofluorescence with the UV and FITC filter sets. A 50-pixel wide region that spanned the arterial media was defined. The pixel intensities in this region of an UV image were linearly correlated to the corresponding intensities in the FITC image (Figure 2):

$$FITC_{autofluorescence} = 0.073UV_{total} + 44.9 \qquad (R^2 = 0.629) \quad (3)$$

The 50% confidence intervals (dashed lines) for the linear regression of eq 3 (solid line) are shown. The gray scale shading reflects the number of times data appears at the same pair of specific UV and FITC intensity values. The range of FITC values that correspond to specific UV intensities are shown in two sample histograms, which indicate limited scatter about the fitted value. This linear relationship allows the estimation of the autofluorescence component in one pixel of a FITC image using the corresponding pixel in the counterpart UV image. Assuming that the autofluorescence and specific fluorescence from the markers add linearly, the estimated autofluorescence can then be subtracted from the original FITC image yielding only the specific signal of fluorescent markers:

$$FITC_{specific} = FITC_{total} - FITC_{autofluorescence} \quad (4)$$
$$= FITC_{total} - (0.073UV_{total} + 44.9)$$

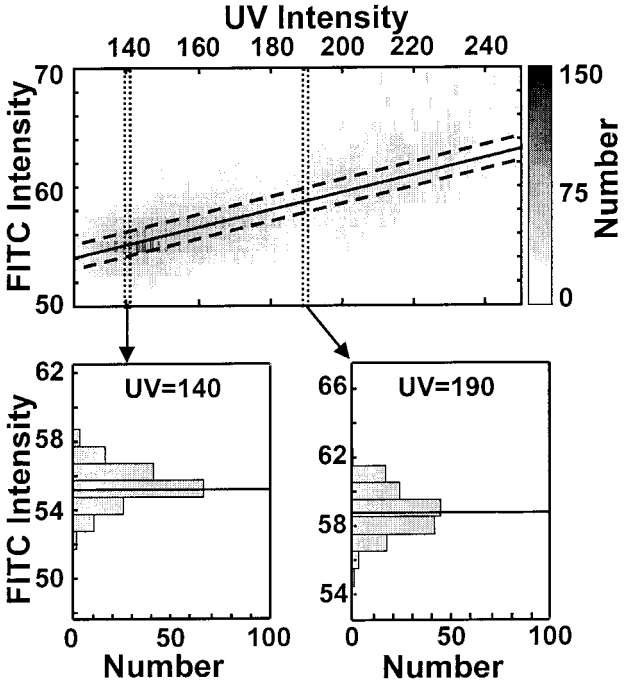

Figure 2—Correlation between autofluorescence with the UV and FITC filter sets. The media of an unloaded artery (devoid of FITC-Dx) was extracted after being imaged with the UV and FITC filter sets. Pixel intensities in the FITC image are plotted as a function of the intensity of the corresponding pixel in the counterpart UV image ($n = 9990$). The gray scale shading reflects the number of times data appears at the same pair of specific UV and FITC intensity values. The linear fit (solid line) can be used to estimate the autofluorescence in a FITC image from the corresponding UV image. The 50% confidence intervals are shown surrounding the linear fit (dashed line). Histograms are shown at two sample UV intensities and demonstrate limited scatter of FITC intensity about the fitted value.

The correlation between UV and FITC autofluorescence (eq 3) was verified by examining three other unloaded arteries subjected to the same processing. When eq 4 was used to subtract autofluorescence in histologic sections of these arteries, the resulting signal in the media hovers close to zero intensity (data not shown).

Conversion of Fluorescent Intensities to Tissue Concentrations—The conversion of fluorescent intensities to tissue concentrations requires two relations. Fluorescent intensities must first be converted to the bulk phase concentrations of tissue standards (c_{Bulk}). Three histologic axial sections were prepared and autofluorescence corrected. Regions were defined that were 50-pixel wide regions and spanned the arterial media. The mean intensity of each of these regions was fit to its corresponding bulk phase incubation concentration using a power relation (Figure 3):

$$\text{mean intensity} = 93.7c_{bulk}^{0.732} \qquad (R^2 = 0.966) \quad (5)$$

The range of this mapping is bounded by two factors. The lower concentration bound of 0.02 mg/mL is determined by the sensitivity of the image acquisition system, and low fluorescent emissions from dilute concentrations

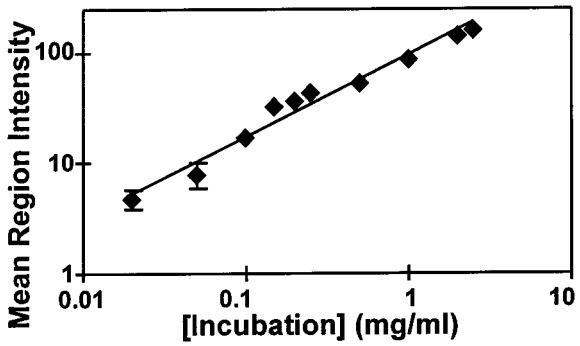

Figure 3—Fluorescent intensity as a function of incubation concentration (mean of three histologic sections from one artery ± standard deviation, $n = 3$). Tissue standards were created by incubating arteries in varying concentrations of FITC-Dx in PBS^{2+} until chemical equilibrium, and the mean intensity of a 50-pixel wide transmedial region in autofluorescence compensated images were calculated.

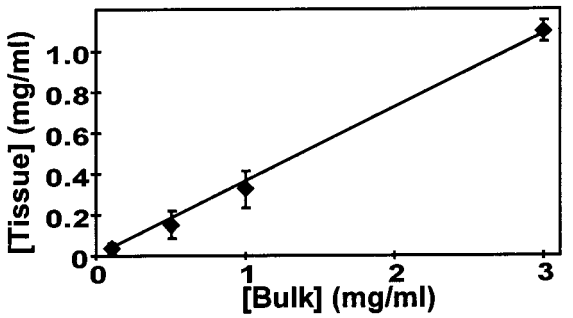

Figure 4—Tissue concentration as a function of bulk phase concentration (mean ± standard deviation, $n = 4$). Arterial segments were incubated to equilibrium in varying concentrations of FITC-Dx in PBS^{2+} until chemical equilibrium. The adventitia and intima were removed through *en face* cryosectioning, and the amount of drug in the remaining arterial media was extracted and quantified to yield the tissue concentration. The slope of the linear fit is a measure of the fractional space available for distribution in the tissue (ϵ).

of the fluorescent marker. The upper concentration bound (2.5 mg/mL) is determined by saturation of the image acquisition system. The bulk phase concentrations and the average tissue concentrations of arteries incubated to equilibrium were fit to a linear equation passing through the origin (eq 1). The slope of this line is an estimate of the fractional space accessible to the drug (ϵ). The data shows that 36.1% ($R^2 = 0.996$) of a unit volume is available for FITC-Dx distribution in the tissue (Figure 4). Equation 5 can then be rearranged and combined with eq 1:

$$c_T = \epsilon(\text{mean intensity}/93.7)^{1.37} \qquad (6)$$

This relationship was used to convert medial regions of autofluorescence corrected images from intensity to tissue concentration.

Comparison of Quantitative Fluorescence Microscopy with *en Face* Cryosectioning—Transvascular concentration profiles were obtained with the new quantitative fluorescence microscopy technique and the established method of *en face* cryosectioning (Figure 5). Three calf carotid arteries were perfused for 2 h with an endovascular bath concentration of 5 mg/mL of 20 kD FITC-Dx, a perivascular bath concentration of 0, and no transvascular pressure gradient. Each artery was cut transversely into two halves, one-half for quantitative fluorescence microscopy, the other for *en face* cryosectioning. The latter measures the average concentration in 60-μm-thick transmural divisions and this curve is depicted as a step function for one of the three arteries (Figure 5). Similar transmural

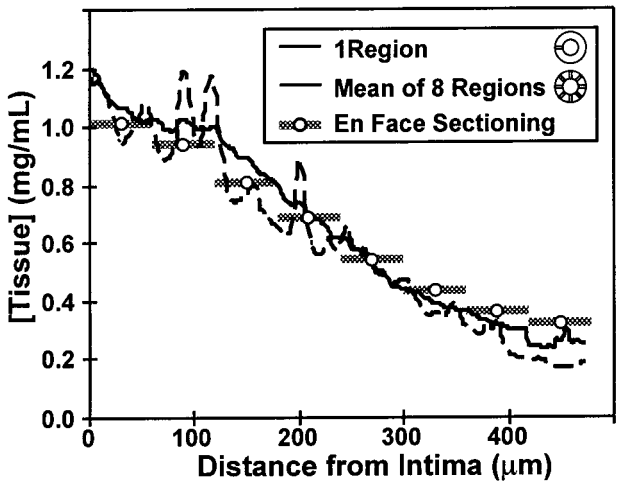

Figure 5—Transvascular concentration profiles obtained with quantitative fluorescence microscopy and *en face* cryosectioning techniques. The transmural concentration profile was obtained from a 50-pixel wide transmedial region. At each transmural location the concentration was averaged across the 50 pixels (dashed line). Another smoother transmural profile was the mean from 8 such regions, approximately equidistant around the circumference of the artery (solid line).

concentration profiles were measured for the other perfused arteries. Superimposing the profiles obtained with the two techniques demonstrates that the quantitative fluorescence microscopy technique provides higher resolution data in the form of measurements between neighboring points obtained with *en face* cryosectioning (Figure 5). For example, the quantitative fluorescence microscopy method shows peaks and valleys superimposed on a gradual transmural profile, whereas *en face* cryosectioning neglects these fine details and loses this potentially important data. Furthermore, the fluorescence technique shows a profile at a specific location about the artery and does not average the signal about the entire circumference. When transmural profiles from eight locations about the circumference of the artery are averaged, the agreement between these two methods increases (Figure 5).

Discussion

A new technique has been developed to obtain arterial concentration profiles combining fluorescence microscopy and digital image processing. Fluorescence microscopy offers several advantages over other techniques (such as higher spatial resolution and smaller marker size) that have been developed to quantify arterial concentrations of compounds, but also introduces additional limitations such as autofluorescence and the difficulty in converting fluorescent intensities to physical concentrations.

Comparison with Other Techniques—Vascular deposition studies have utilized radioactive nucleotides, which minimally change the physical structure of a compound and its transport properties, but these experiments often have limited spatial resolution and are fraught with experimental hazards and disposal costs. Early studies measured the radioactivity in grossly dissected sections providing low detection limits, but questionable repeatability as well as limited spatial resolution.[21] Measuring radioactivity in *en face* serial sections parallel to the intimal surface provides resolution down to 10 μm, but can only assess the macromolecular distribution in one direction and by necessity provides only an average concentration in the plane of sectioning.[15,16,18] The radiolabeled drug content in a specimen can also be visualized by allowing the emitted energy to expose specially prepared photographic film or a silver

emulsion applied to a histologic section.[12,22–24] Silver grain counting or optical densitometry methods can then quantify the density of exposed silver grains. These autoradiographic techniques offer increased resolution (down to ~2 μm), but may be hampered by inaccurate localization, inconsistent background radiation, and postexperimental diffusion of soluble macromolecules in the emulsion.[12,22–24] In addition, the exposure time of the film or emulsion may take months.

Nonisotopic techniques, including biochemical and fluorescent labels, offer higher spatial resolution and avoid the hazards of radioactivity, but may be limited by marker size. Large labels can affect the physicochemical and transport properties of the macromolecules under investigation. For example, the transport of horseradish peroxidase (HRP) has been quantified in arteries using a colored reaction product.[13,17,25,26] Specimens were examined with a light microscope which provided HRP concentration profiles with spatial resolution superior to radioactive techniques. Similar studies could be adapted for study of local delivery systems, however, the large size of HRP (40 kD) prevents its utility as a molecular tag on much smaller drugs. In addition, the aqueous tissue processing required to fix and embed the tissues, and to create the colored reaction product, may also allow for postexperiment diffusion of smaller or more soluble molecules. Fluorescent labels such as FITC and rhodamine isothiocyanate are smaller (~400 D), permitting their use in studies on smaller compounds. Though fluorescence microscopy offers the advantages of high spatial resolution, as in HRP studies, and smaller label size, quantitative studies have been complicated by autofluorescence and the proper application of calibration standards. This digital image processing technique seeks to address these limitations.

Autofluorescence Compensation—Constituent arterial components, such as elastin, fibronectin, and lipofuscin, exhibit autofluorescence, the emission of energy at the same wavelength as exogenous fluorescent labels.[8] The fluorescence spectra of these compounds are often very broad and autofluorescence cannot be avoided by selecting a probe with excitation and emission spectra outside their range. While uniform autofluorescence with small variability has been effectively corrected for by subtracting a constant intensity,[7,10] autofluorescent structures are often distributed inhomogeneously throughout the tissue, resulting in nonuniform artifact that is difficult to compensate for. In addition, autofluorescence may be very intense, masking the fluorescent signals of interest. Counterstaining tissue sections with solutions derived from flow cytometry such as crystal violet[27] or pontamine sky blue[28] to eliminate background autofluorescence may be impractical as aqueous processing can produce postexperimental drug diffusion. Time-resolved fluorometry, which utilizes the different decay times between autofluorescent molecules and fluorescent tags, has also been used to compensate for autofluorescence,[29,30] but utilizes a sophisticated fluorescence microscopy system and lengthy excitation times. In addition, this technique may require special fluorescent tags such as lanthanide chelates,[31] which may not be readily available individually or conjugated to compounds of interest.

Fluorescent labels have narrower excitation and emission spectra than constituent molecules of the arterial wall. Digital image processing methods have been developed that take advantage of this principle and have reduced autofluorescence, in flow cytometry studies[32] and in histologic preparations.[8,9] Images are captured at two wavelengths with one image consisting only of autofluorescence and the other image possessing both autofluorescence and the specific fluorescence signal of interest. The former image is then used to estimate the autofluorescence in the latter image. Assuming that autofluorescence and the fluorescence from the labels are simply additive, the estimated autofluorescence can be subtracted from the latter image to yield an autofluorescence-compensated image. These concepts form the basis of our quantitative fluorescence microscopy method.

Conversion of Fluorescent Intensities to Tissue Concentrations—Fluorescence microscopy is usually used as a binary tool to determine the presence or absence of a compound by qualitatively assessing the fluorescence from markers. The relation between the fluorescent intensity and tissue concentration of the tagged compound is rarely measured in histologic sections. Quantitative analysis requires the development of a reliable calibration curve to convert fluorescent intensities to physical tissue concentrations. Calibration curves have been constructed by measuring the intensity of various concentrations of FITC solution in a hemocytometer[33,34] or capillary tubes.[35] The photoabsorptive properties of solutions, however, may be very different from those of tissues. In addition, the difference in thickness of a section of tissue compared to a hemocytometer or capillary tube may cause calculated tissue concentrations to not accurately represent the actual tissue concentration.[36] Thus, calibration standards for fluorescent compounds should be created from the same substrates and conditions used in experiments and mimic the experimental samples as closely as possible to obtain reliable calibration data. In this study, this was accomplished by incubating calf carotid arteries in different concentrations until equilibrium. The transmural concentration profiles were measured in identical arteries. These calibration standards were then used to construct a relationship between fluorescent intensity and bulk phase concentration. The corresponding tissue concentration of each standard was determined through the fractional volume accessible to the compound, measured in separate experiments.

Comparison of Quantitative Fluorescence Microscopy and *en Face* Cryosectioning—The quantitative fluorescence microscopy technique described in this paper was compared to the established *en face* serial cryosectioning method (Figure 5).[15,16] This new technique performed well at predicting the complex drug distribution pattern imparted by an in vitro perfusion apparatus. Transvascular concentration profiles obtained with quantitative fluorescence microscopy have higher resolution than those obtained with *en face* cryosectioning. The resolution of the former technique is that of the light microscope, about 0.5 μm. The peaks and valleys exhibited using the technique described could not have been appreciated with en *face* cryosectioning.

The high spatial resolution of this quantitative fluorescence microscopy technique provides insights into the mechanisms of drug deposition and distribution. For example, the peaks in the tissue concentration may indicate binding or sequestration to specific arterial elements such as thin connective tissue layers. The height of these peaks are greatest in regions of increased tissue concentration and lowest away from the endovascular source of dextran, suggestive of a small degree of binding that is proportional to the local drug concentration and hence likely to be of first-order kinetics. Recent data has shown that FITC-dextran binds weakly to isolated elastin networks (data not shown). Thus, the high resolution of the quantitative fluorescence microscopy method offers insights into vascular drug deposition and distribution that could not be appreciated by traditional means.

The normalized mean square error (NMSE) between *en face* cryosectioning and the new quantitative fluorescence

microscopy technique was computed to demonstrate the statistical agreement between these two methods. The resolution of the profile from the quantitative fluorescence microscopy technique was first reduced to that of the cryosectioning profile. Data points from the profile generated with the quantitative fluorescence microscopy technique were grouped in sequential sets of 60 μm and then averaged for comparison with the cryosectioning profile. The NMSE was then computed as the sum of the squared differences between every pair of data points over the sum of the squared magnitude of every point in the cryosectioning profile. The NMSE was normalized to the cryosectioning data since cryosectioning is the standard that the new technique is being compared to. The NMSE was equal to 0.0109 for the profile obtained with one region and 0.0060 for the profile obtained by averaging across eight regions. The low NMSE demonstrates the validity and accuracy of the new fluorescence method and is not surprising given the visual similarity of the profiles in Figure 5.

There are significant differences between the transmural concentration profiles generated by quantitative fluorescence microscopy and *en face* cryosectioning (Figure 5). However, when eight concentration profiles from different locations about the circumference of a single artery generated with quantitative fluorescence microscopy were averaged, the agreement between these two methods was greatly increased. This example demonstrates that techniques such as *en face* cryosectioning, which inherently average about the circumference, gloss over important subtleties in the deposition of compounds that quantitative fluorescence microscopy can detect. Furthermore, although the potency of the fluorescence microscopy technique has been illustrated with a one-dimensional transmural concentration profile, it examines histologic sections and therefore is capable of examining drug concentration gradients in any two dimensions within a plane in which a tissue is sectioned.

Summary

This work describes a fluorescence microscopy technique to visualize and quantify drug deposition. It consists of laboratory techniques that immobilize drug in its postexperimental position, digital postprocessing to eliminate autofluorescence, and the appropriate calibration standards to convert fluorescent intensities to drug concentrations. This technique offers spatial resolution superior to conventional radioactive techniques and is adaptable to many compounds and tissues. The complex and dynamic drug deposition patterns imparted by local drug delivery systems might be defined in this manner and may ultimately allow for their rational design.

Nomenclature

c_T	Concentration of drug in a volume of tissue
c_{Bulk}	Bulk phase concentration of drug in first incubation bath
$c_{Release}$	Concentration of drug released from tissue into reincubation bath
ϵ	Fractional space in which drug can distribute through a tissue
V_{Bath}	Volume of the reincubation bath
n	Number of slices of tissue in a reincubation bath
V_{Slice}	Volume of each slice of tissue
$FITC_{Autofluorescence}$	Autofluorescence intensity of tissue imaged under FITC filter set
UV_{Total}	Autofluorescence intensity imaged under UV filter set
$FITC_{Total}$	Total intensity imaged under FITC filter set
$FITC_{Specific}$	Autofluorescence-compensated intensity under FITC filter set
FITC	Fluorescein isothiocyanate
UV	Ultraviolet

References and Notes

1. Lincoff, A. M.; Topol, E. J.; Ellis, S. G. Local Drug Delivery for the prevention of restenosis: Fact, fancy and future. *Circulation* **1994**, *90*, 2070−2084.
2. Wolinsky, H. Local Delivery: Let's keep our eyes on the wall. *J. Am. Coll. Cardiol.* **1994**, *24*, 825−827.
3. Okada, T.; Bark, D. H.; Mayberg, M. R. Local anticoagulation without systemic effect using a polymer heparin delivery system. *Stroke* **1988**, *19*, 1470−1476.
4. Edelman, E. R.; Adams, D. A.; Karnovsky, M. J. Effect of controlled adventitial heparin delivery on smooth muscle cell proliferation following endothelial injury. *Proc. Natl. Acad. Sci.* **1990**, *87*, 3773−3777.
5. Edelman, E. R.; Lovich, M. A. Drug delivery models transported to a new level. *Nature Biotechnol.* **1998**, *16*, 136−137.
6. Lovich, M. A.; Edelman, E. R. Computational simulations of local vascular heparin deposition and distribution. *Am. J. Physiol.* **1996**, *271*, H2014−H2024.
7. Sebkhi, A.; Weinberg, P. D. Effect of age on the pattern of short-term albumin uptake by the rabbit aortic wall near intercoastal branch Ostia. *Arterioscler. Thromb. Vasc. Biol.* **1996**, *16*, 317−327.
8. van de Lest, C. H. A.; Versteg, E. M. M.; Veerkamp, J. H.; van Kuppevelt, T. H. Elimination of Autofluorescence in Immunofluorescence Microscopy with Digital Image Processing. *J. Histochem. Cytochem.* **1995**, *43*, 727−730.
9. Szöllösi, J.; Lockett, S. J.; Balázs, M.; Waldman, F. M. Autofluorescence Correction for Fluorescence In Situ Hybridization. *Cytometry* **1995**, *20*, 356−361.
10. Weinberg, P. D.; Winlove, C. P.; Parker, K. H. Measurement of absolute tracer concentrations in tissue sections by using digital imaging fluorescence microscopy. Application to the study of plasma protein uptake by the arterial wall. *J. Microsc.* **1994**, *173*, 127−141.
11. Gonzalez, R. C.; Woods, R. E. *Digital Image Processing;* Addison-Wesley Publishing Company Inc.: Reading, MA, 1992; pp 229−237.
12. Fry, D. L.; Mahley, R. W.; Oh, S. Y.; Lewis, S. J.; Plowman, F.; Swyt, C. R. Quantitative microautoradiography of arteries: comparison of radioactivity to silver. *Am. J. Physiol.* **1980**, *239*, H289−H295.
13. Penn, M. S.; Saidel, G. M.; Chisolm, G. M. Vascular injury by endotoxin: changes in macromolecular transport parameters in rat aortas in vivo. *Am. J. Physiol.* **1992**, *262*, H1563−H1571.
14. Saidel, G. M.; Morris, E. D.; Chisolm, G. M. Transport of Macromolecules in Arterial Wall In Vivo: A Mathematical Model and Analytical Solutions. *Bull. Math. Biol.* **1987**, *49*, 153−169.
15. Bratzler, R. L.; Chisolm, G. M.; Colton, C. K.; Smith, K. A.; Zilversmit, D. B.; Lees, R. L. The Distribution of Labeled Albumin across the Rabbit Thoracic Aorta in Vivo. *Circ. Res.* **1977**, *40*, 182−190.
16. Bratzler, R. L.; Chisolm, G. M.; Colton, C. K.; Smith, K. A.; Lees, R. S. The Distribution of Labeled Low-Density Lipoproteins Across the Rabbit Thoracic Aorta in Vivo. *Atherosclerosis* **1977**, *28*, 289−307.
17. Penn, M. S.; Koelle, M. R.; Schwartz, S. M.; Chisolm, G. M. Visualization and Quantification of Transmural Concentration Profiles of Macromolecules Across the Arterial Wall. *Circ. Res.* **1990**, *67*, 11−22.
18. Ramirez, C.; Colton, C.; Smith, K.; Stemerman, M.; Lees, R. Transport of ^{125}I−Albumin Across Normal and Deendothelialized Rabbit Thoracic Aorta In Vivo. *Arteriosclerosis* **1984**, *4*, 283−291.
19. Lovich, M. A.; Edelman, E. R. Mechanisms of Transmural Heparin Transport in the Rat Abdominal Aorta After Local Vascular Delivery. *Circ. Res.* **1995**, *77*, 1143−1150.

20. Lovich, M. A.; Philbrook, M.; Sawyer, S.; Weselcouch, E.; Edelman, E. R. Arterial heparin deposition: role of diffusiion, convection, and extravascular space. *Am. J. Physiol.* **1998**, *275*, H2236−H2242.
21. Duncan, L. E.; Buck, K.; Lynch, A. Lipoprotein Movement through Canine Aortic Wall. *Science* **1963**, *142*, 972−973.
22. Aitken, W. M.; Wright, E.; Gray, H. S. Autoradiography of Water-Diffusible Substances in Sections of Whole Baby Rats. *Stain Technol.* **1968**, *43*, 1−7.
23. Schnitzer, J. J.; Morrel, E. M.; Colton, C. K.; Smith, K. A.; Stemerman, M. B. Absolute Quantitative Autoradiography of Low Concentrations of [^{125}I]-Labeled Proteins in Arterial Tissue. *J. Histochem. Cytochem.* **1987**, *35*, 1439−1450.
24. Tompkins, R. G.; Yarmush, M. L.; Schnitzer, J. J.; Colton, C. K.; Smith, K. A.; Stemerman, M. B. Low-density lipoprotein transport in blood vessel walls of squirrel monkeys. *Am. J. Physiol.* **1989**, *257*, H452−H464.
25. Penn, M. S.; Chisolm, G. M. Relation Between Lipopolysaccharide-Induced Endothelial Cell Injury and Entry of Macromolecules Into the Rat Aorta In Vivo. *Circ. Res.* **1991**, *68*, 1259−1269.
26. Penn, M. S.; Saidel, G. M.; Chisolm, G. M. Relative Significance of Endothelium and Internal Elastic Lamina in Regulating the Entry of Macromolecules Into Arteries In Vivo. *Circ. Res.* **1994**, *74*, 74−82.
27. Halldén, G.; Sköld, C. M.; Eklund, A.; Forslid, J.; Hed, J. Quenching of intracellular autofluorescence in alveolar macrophages permits analysis of fluorochrome labeled surface antigens by flow cytofluorometry. *J. Immunol. Methods* **1991**, *142*, 207−214.
28. Cowen, T.; Haven, A. J.; Burnstock, G. Pontamine sky blue: A counterstain for background autofluorescence in fluorescence and immunofluorescence histochemistry. *Histochemistry* **1985**, *82*, 205−208.
29. Koppel, D. E.; Carlson, C.; Smilowitz, H. Analysis of heterogeneous fluorescence photobleaching by video kinetics imaging: the method of cumulants. *J. Microsc.* **1989**, *155*, 199−206.
30. Marriott, G.; Clegg, R. M.; Arndt-Jovin, D. J.; Jovin, T. M. Time-resolved imaging microscopy: Phosphorescence and delayed fluorescence imaging. *Biophys. J.* **1991**, *60*, 1374−1387.
31. Seveus, L.; Väisälä, M.; Syrjänen, S.; Sandberg, M.; Kuusisto, A.; Harju, R.; Salo, J.; Hemmilä, I.; Kojola, H.; Soini, E. Time-Resolved Fluorescence Imaging of Europium Chelate Label in Immunohistochemistry and In Situ Hybridization. *Cytometry* **1992**, *13*, 329−338.
32. Steinkamp, J. A.; Stewart, C. C. Dual-Laser, Differential Fluorescence Correction Method for Reducing Cellular Background Autofluorescence. *Cytometry* **1986**, *7*, 566−574.
33. Nakamura, Y.; Wayland, H. Macromolecular Transport in the Cat Mesentery. *Microvasc. Res.* **1975**, *9*, 1−21.
34. Fox, J. R.; Wayland, H. Interstitial Diffusion of Macromolecules in the Rat Mesentery. *Microvasc. Res.* **1979**, *18*, 255−276.
35. Nugent, L. J.; Jain, R. K. Plasma pharmacokinetics and interstitial diffusion of macromolecules in a capillary bed. *Am. J. Physiol.* **1984**, *246*, H129−H137.
36. Armenante, P. M.; Kim, D.; Duran, W. N. Experimental Determination of the Linear Correlation between in Vivo TV Fluorescence Intensity and Vascular and Tissue FITC-DX Concentrations. *Microvasc. Res.* **1991**, *42*, 198−208.

Acknowledgments

This study is supported in part by grants from the National Institutes of Health (GM/HL 49039), the Burroughs-Welcome Fund in Experimental Therapeutics, and the Whitaker Foundation in Biomedical Engineering. Elazer R. Edelman is an Established Investigator of the American Heart Association. The authors acknowledge the technical assistance of Lily Y. Chen and expert advice of Philip Seifert and Dr. David Ettenson.

JS9803858

Carrier-Mediated Transport Systems for Glucose in Mucosal Cells of the Human Oral Cavity

YUJIRO OYAMA, HITOSHI YAMANO, AKIKO OHKUMA, KEN-ICHI OGAWARA, KAZUTAKA HIGAKI, AND TOSHIKIRO KIMURA*

Contribution from *Department of Pharmaceutics, Faculty of Pharmaceutical Sciences, Okayama University, 1-1-1 Tsushima-naka, Okayama 700-8530, Japan.*

Received July 22, 1998. Final revised manuscript received January 8, 1999.
Accepted for publication May 27, 1999.

Abstract □ The in vitro uptake study was performed using the isolated cells of human oral mucosa, buccal and the dorsum of the tongue, to investigate the mechanisms of glucose uptake. The uptake of D-glucose was much larger in cells of the dorsum of the tongue than in buccal cells and was inhibited more extensively by 2-deoxy-D-glucose, a substrate of facilitative glucose transporters, than by α-methyl-D-glucoside, a specific substrate of SGLT1, suggesting the larger contribution of a facilitative transporter than Na^+/glucose cotransporter. Furthermore, from the results of inhibition studies by several sugar analogues including maltose and D-mannose, GLUT1 and/or GLUT3 were suggested to take part in the glucose uptake by oral mucosa. Therefore, we have attempted to confirm the expression of glucose transporters on the oral mucosa by employing Western blotting. As a result, it was suggested that SGLT1, GLUT1, GLUT2, and GLUT3 are expressed in the epithelial cells of human oral mucosa.

Introduction

Oral mucosa has been used as a site for drug delivery, because the drug thus administered reaches systemic circulation circumventing both intra-alimentary canal and hepatic first-pass eliminations.[1−3] Generally, the mechanism of drug absorption from the oral cavity is passive diffusion.[4,5] On the other hand, not only some nutrients, D-glucose,[6] amino acid,[7] glutathione,[8] thiamine,[9] and nicotinic acid,[10] but also an aminocephalosporin antibiotic cefadroxil[11] were reported to be absorbed by specialized transport mechanisms from the human oral cavity, using a buccal absorption test method.[4] Recently, we developed perfusion cells, which can be applied on five regions in the human oral cavity, the dorsum of the tongue, ventral surface of the tongue, labial mucosa, floor of mouth, and buccal mucosa,[12] and could show the presence of the specialized transport system for D-glucose in the dorsum of the human tongue.[13] D-Glucose is transported into the enterocytes across the brush border membrane by a Na^+/glucose cotransporter (SGLT1), and then the hexose is transported out across the basolateral membrane by a facilitative sugar transporter (GLUT2).[14,15] Furthermore, some glucose transporters have been found in mammalian tissues.[16] However, details of sugar transporters present in oral epithelial cells have not been clarified.

In the present study, the mechanism of D-glucose uptake by epithelial cells isolated from human buccal mucosa and the dorsum of the tongue was examined to clarify the glucose transport system in the human oral cavity.

* Corresponding author. Tel (+81)-86-251-7948. Fax (+81)-86-251-7926. E-mail: kimura@pheasant.pharm.okayama-u.ac.jp.

Materials and Methods

Materials—^{3}H-D-Glucose, ^{14}C-L-glucose, and ^{14}C-2-deoxy-D-glucose were purchased from Amersham International (Buckinghamshire, England). A liquid scintillator, Clear-Sol I, was purchased from Nacalai Tesque (Kyoto, Japan). D-Glucose (Ishizu Pharmaceutical Co., Osaka, Japan), L-glucose (Tokyo Kasei Kogyo Co., Tokyo, Japan), 2-deoxy-D-glucose, and fluorescein isothiocyanate dextran (FITC-dextran, MW 35600, Sigma Chemical Co., St. Louis, MO) were used as supplied. Iatro-Chrom GLU-L_Q and Glucose-Test Wako were purchased from Iatron Laboratories, Inc. (Tokyo) and Wako Pure Chemical Industries (Osaka), respectively. Rabbit anti-SGLT-1, rabbit anti-GLUT-1, rabbit anti-GLUT-2, and rabbit anti-GLUT-3 were obtained from Chemicon International (Temecula, CA). Prestained molecular weight markers for SDS-polyacrylamide gel electrophoresis (PAGE) used in this study were phosphorylase (102 kDa), bovine serum albumin (BSA) (78 kDa), ovalbumin (49.5 kDa), carbonic anhydrase (34.2 kDa), soybean trypsin inhibitor (28.3 kDa), and lysozyme (19.9 kDa) (Bio-Rad Laboratories, Hercules, CA). All other chemicals were regent grade and commercially available.

Subjects—Ten healthy volunteers, aged 22−25 years, participated in this study. Written informed consent, in accordance with the principles of the Declaration of Helsinki, was obtained from each volunteer prior to the study.

Preparation of Oral Mucosal Cells—Epithelial cells were isolated from the buccal mucosa or the dorsum of the tongue of volunteers using a mouthwash technique.[17] Briefly, mucosal cells were obtained on the morning of assay. Subjects swirled high-purity water around their mouth for a short period of time in conjunction with molar scraping action for buccal mucosa or the dorsum of the tongue. This procedure was repeated several times. The pooled expectorate containing mucosal cells was filtered through three layers of 250 μm nylon mesh, centrifuged at 3000 rpm for 10 min, and gently resuspended in the incubation buffer. The composition of the incubation buffer was 100 mM mannitol, 80 mM NaCl, 20 mM Tris-HCl (pH 7.4), 3 mM K_2HPO_4, 1 mM $MgCl_2$, 1 mM $CaCl_2$ and 1 mg/mL bovine serum albumin (BSA). The cell suspension was centrifuged again at 3000 rpm for 10 min and resuspended in the incubation buffer at the concentration of 1×10^6 cells/mL.

Uptake Experiments—The uptake of the substrate was determined by a rapid filtration technique.[18] Uptake studies were initiated by the addition of 0.4 mL of a buffer solution containing a labeled substrate to 0.1 mL of the cell suspension, which was preincubated at 37 °C for 30 min. At the desired times, 4 mL of ice-cold stop solution (100 mM mannitol, 100 mM $MgCl_2$, 8 mM HEPES, 4 mM Tris and 1 mM NaCl, pH 7.4) was added to the mixture. The resulting mixtures were immediately filtered through prewetted 0.45 μm filters (Fuji Photo Film, Tokyo). The filters were quickly rinsed with 4 mL of the ice-cold stop solution three times and transferred into a counting vial for the determination. Background value or nonspecific adsorption to the filter was determined by using the incubation buffer without mucosal cells. This value was subtracted from the uptake data.

Absorption Experiments (Buccal Absorption Test)—The experiments were carried out according to the method of Kurosaki et al.[11] which was originated by Beckett and Triggs.[4] Briefly, a 2-deoxy-D-glucose solution (10 mL) containing an unabsorbable marker, FITC-dextran (1 μM), was placed in the mouth. The

10.1021/js980298f CCC: $18.00
Published on Web 07/03/1999

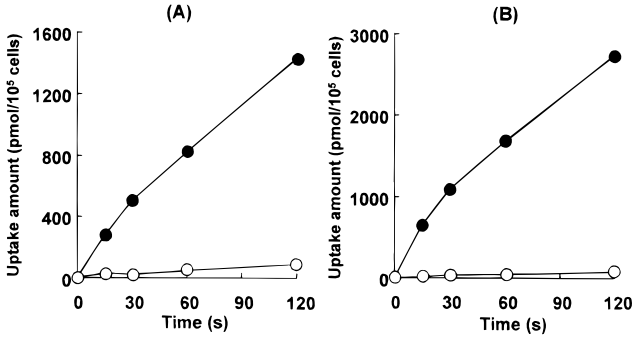

Figure 1—Uptake of D- and L-glucose by isolated cells of human buccal mucosa (A) and dorsum of tongue (B). Initial concentration of glucose was 0.1 mM. Key: ●, D-glucose; ○, L-glucose. Results are expressed as the mean with a vertical bar showing the SE of four experiments. The bars are hidden behind symbols.

solution in the mouth was vigorously agitated using the cheeks and tongue for 5 min, and then the solution was expelled as completely as possible. The subject quickly rinsed his mouth three times with the same buffer solution (total volume, 20 mL) and expelled the rinsing. The expelled solutions were combined and were adjusted to 50 mL with the buffer solution. From the values of the initial and final concentrations of 2-deoxy-D-glucose and the marker, percentage of 2-deoxy-D-glucose absorbed during a period of 5 min was calculated.

Analytical Methods—For uptake studies, radioactivity was measured by a Beckman LS-232 liquid scintillation counter. For absorption studies, D-glucose and 2-deoxy-D-glucose were determined using commercially available assay kits, Iatro-Chrom GLU-L_Q (glucose oxidase method). L-Glucose was determined using commercially available assay kits, Glucose-Test Wako (*o*-toluidine-boric acid method). FITC-dextran was determined spectrofluorometrically (ex 495 nm, em 514 nm).

SDS–Polyacrylamide Gel Electrophoresis and Western Blot Analysis—SDS–PAGE was performed using a 12% polyacrylamide gel for protein separation. Cells suspended in 10 mM Tris-HCl buffer (pH 7.4) containing 1 mM EDTA and 1 μM aprotinin were disrupted by Ultrasonic Generator US300 (Nissei, Tokyo) for 30 min, and the suspension was centrifuged at 200*g* for 30 min. The supernatant fraction was centrifuged at 27000*g* for 1 h. The precipitate was resuspended in 10 mM Tris-HCl buffer (pH 7.4) containing 2% SDS, 2% Triton X-100, and 2 mM EDTA to dissolve membrane proteins. The protein samples were loaded on top of a 4.5% stacking gel. After electrophoresis, proteins were transferred onto nitrocellulose membranes. Remaining active sites on the nitrocellulose membranes were blocked with 5% nonfat dry milk in phosphate-buffered saline for 1 h at room temperature on a flat bed shaker. Membranes were incubated overnight at 4 °C with rabbit anti-human antibodies against SGLT1, GLUT1, GLUT2, or GLUT3 under constant agitation, and then incubated further for 1 h at room temperature with horseradish peroxidase-conjugated goat anti-rabbit immunoglobulin G. Horseradish peroxidase activity was revealed using ECL Western blotting detection reagents (Amersham International).

Statistical Analysis—Statistical significance was evaluated using Student's *t*-test or analysis of variance. Results are expressed as mean ± SE of more than three experiments.

Results

Isolated Mucosal Cells—The photomicroscopic observation of the mucosal cells stained with hematoxylin–eosin revealed that cells isolated from the dorsum of the tongue contain cornified cells, but cells from buccal mucosa do not. The specific character of both sites was observed. The viability of the cells was maintained as 80–90% even 3 h after the isolation.

Uptake of Glucose by Isolated Mucosal Cells—Figure 1 shows the time course of glucose uptake by the cells isolated from buccal mucosa (A) and the dorsum of the tongue (B). As is evident from the figure, the uptake

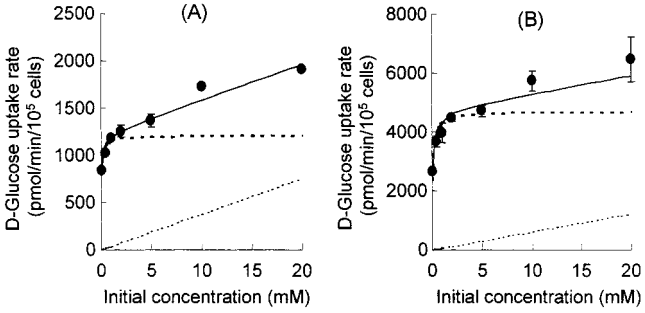

Figure 2—Concentration dependency of D-glucose uptake by isolated cells of human buccal mucosa (A) and dorsum of tongue (B). Results are expressed as the mean with a vertical bar showing the SE of three experiments. —, fitting curve; ••••, uptake via carrier-mediated system; ----, uptake via passive diffusion (uptake rate of L-glucose).

of D-glucose was much greater than that of L-glucose in both cells, and stereospecificity was observed. Furthermore, the uptake by cells from the dorsum of the tongue was greater than that from buccal mucosa.

Figure 2 shows the concentration dependency of the initial rate (in 1 min) of D-glucose uptake by the cells isolated from buccal mucosa (A) and the dorsum of the tongue (B). The kinetic parameters for D-glucose uptake were calculated by fitting these data to the eq 1.

$$v = V_{max}C/(K_m + C) + k_dC \qquad (1)$$

where v is the initial uptake rate at the concentration C, V_{max} and K_m are the maximum uptake rate and Michaelis constant for the specialized transport system, respectively, and k_d is the first-order rate constant for the uptake by simple diffusion. The initial uptake rate constants for L-glucose were used as k_d values: they were 37.7 ± 6.7 nL/min/10^5 cells for cells of buccal mucosa and 61.8 ± 7.8 nL/min/10^5 cells for cells from the dorsum of the tongue. The kinetic parameters for D-glucose uptake thus obtained were as follows: V_{max} and K_m values for cells of buccal mucosa are 1207.4 ± 124.2 pmol/min/10^5 cells and 51.2 ± 47.8 μM, respectively; on the other hand, those for cells from the dorsum of the tongue are 4696.3 ± 132.0 pmol/min/10^5 cells and 97.7 ± 19.8 μM, respectively. The statistical analysis by ANOVA clarified that V_{max} and k_d values in the two cells are significantly different while K_m values are not.

To investigate the characteristics of the glucose transport system, the effect of some transport inhibitors and specific conditions on the uptake by isolated oral mucosal cells were examined, and the results are shown in Table 1. In both mucosal cells, D-glucose uptake at the concentration of 0.05 mM was markedly reduced in the ice-cold condition or by 0.5 mM *p*-chloromercuribenzoic acid (PCMB), suggesting that the uptake is a carrier-mediated process. Since D-glucose uptake was significantly reduced in the Na^+-free condition, it is suggested that a part of this uptake system is Na^+-dependent. The significant inhibition by 1 mM 2,4-dinitrophenol and the slight inhibition, but not statistically significant, by 1 mM phlorizin were observed. These results suggest that a Na^+-dependent D-glucose transport system is operating, at least partly, in the uptake process. To further clarify the carrier system, the effect of various sugars (50 mM) on D-glucose uptake (1 mM) was examined, and the results are also shown in Table 1. α-Methyl-D-glucoside, a specific substrate of SGLT1, significantly inhibited the D-glucose uptake in both mucosal cells. The uptake of D-glucose was inhibited more extensively by substrates of facilitative transporters, 2-deoxy-D-glucose, D-mannose, and maltose. Figure 3 shows the comparison of the inhibitory effects on D-glucose uptake by isolated mucosal cells between α-methyl-D-glucoside and 2-deoxy-

Table 1—Effect of Special Conditions, Transport Inhibitors, and Sugar Analogues on D-Glucose Uptake by Cells Isolated from Human Buccal Mucosa and Dorsum of Tongue[a]

condition or additive	uptake rate (% of control)	
	buccal	dorsum of tongue
control	100.0 ± 4.1	100.0 ± 1.7
ice-cold	6.9 ± 1.4***	3.7 ± 0.5***
Na^+-free	77.4 ± 4.3**	87.3 ± 2.2***
with 0.5 mM *p*-chloromercuribenzoic acid	45.8 ± 0.6***	47.2 ± 2.6***
with 1 mM 2,4-dinitrophenol	78.5 ± 2.1**	80.3 ± 2.3***
with 1 mM phlorizin	86.2 ± 2.5	72.4 ± 2.4***
with 50 mM mannitol	100.0 ± 2.7	100.3 ± 2.9
with 50 mM α-methyl-D-glucoside	40.3 ± 1.4***	34.3 ± 2.3***
with 50 mM 2-deoxy-D-glucose	7.4 ± 0.8***	7.0 ± 0.5***
with 50 mM D-mannose	11.1 ± 0.2***	22.8 ± 3.8***
with 50 mM maltose	6.0 ± 0.9***	5.6 ± 0.4***

[a] Concentration of D-glucose was 0.05 mM. Control values for buccal cells and cells of dorsum of the tongue were 121.3 ± 5.0 and 250.2 ± 4.3 pmol/min/10^5 cells, respectively. Results are expressed as the mean± SE of 3–8 experiments. * $p < 0.05$; ** $p < 0.01$; *** $p < 0.001$, compared with each control value.

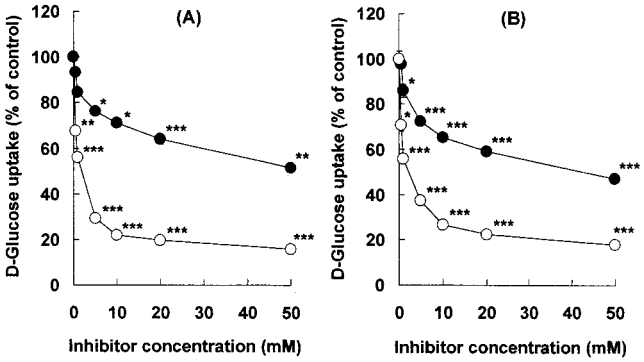

Figure 3—Effect of specific sugars on D-glucose uptake by isolated cells of human buccal mucosa (A) and dorsum of tongue (B). Initial concentration of D-glucose was 0.1 mM. Key: ●, with α-methyl-D-glucoside; ○, with 2-deoxy-D-glucose. Results are expressed as the mean with a vertical bar showing the SE of four experiments. The bars are hidden behind symbols. *** $p < 0.001$; ** $p < 0.01$; * $p < 0.05$, compared with the control.

D-glucose. As is evident from the figure, the inhibitory effect of 2-deoxy-D-glucose is greater than that of α-methyl-D-glucoside, suggesting that the contribution of the facilitative glucose transporters to D-glucose uptake by oral mucosal cells is larger than that of active Na^+/glucose cotransporter.

To further analyze the facilitative glucose transport system, similar uptake studies by isolated cells from buccal mucosa and the dorsum of the tongue were performed for 2-deoxy-D-glucose. Figure 4 shows the concentration dependency of the initial rate of 2-deoxy-D-glucose. Kinetic parameters for 2-deoxy-D-glucose were similarly calculated using the eq 1 shown above, and the results are as follows: V_{max}, K_m, and k_d values for cells of buccal mucosa are 417.9 ± 167.8 pmol/min/10^5 cells, 0.555 ± 0.705 mM, and 29.3 ± 11.2 nL/min/10^5 cells, respectively; on the other hand, those for cells from the dorsum of the tongue are 965.0 ± 115.7 pmol/min/10^5 cells, 0.619 ± 0.263 mM, and 69.1 ± 4.6 nL/min/10^5 cells, respectively. The k_d values thus obtained were similar to the initial uptake rate constants of L-glucose, which were shown above, in both cells. The statistical analysis by ANOVA clarified that both V_{max} and k_d values are significantly different between the two cells, while the difference of K_m value was not statistically significant. Table 2 shows the effect of ice-cold conditions, PCMB, or other sugars on 2-deoxy-D-glucose uptake by oral

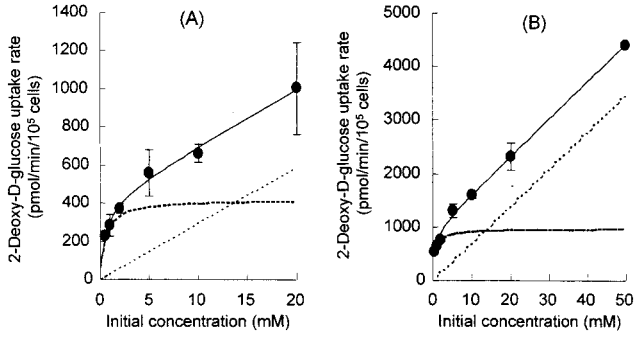

Figure 4—Concentration dependency of 2-deoxy-D-glucose uptake by isolated cells of human buccal mucosa (A) and dorsum of tongue (B). Results are expressed as the mean with a vertical bar showing the SE of three experiments. —, fitting curve; ••••, uptake via carrier-mediated system; ----, uptake via passive diffusion.

Table 2—Effect of Special Conditions, Transport Inhibitors, and Sugar Analogues on 2-Deoxy-D-glucose Uptake by Cells Isolated from Human Buccal Mucosa and Dorsum of Tongue

condition or additive	uptake rate (% of control)	
	buccal	dorsum of tongue
control	100.0 ± 1.0	100.0 ± 1.1
ice-cold	2.6 ± 0.3***	3.8 ± 1.0***
with 0.5 mM *p*-chloromercuribenzoic acid	2.3 ± 0.5***	4.3 ± 0.7***
with 10 mM mannitol	94.8 ± 2.9	97.5 ± 3.0
with 10 mM 2-deoxy-D-glucose	1.6 ± 1.2***	5.2 ± 1.2***
with 10 mM D-mannose	11.1 ± 1.5***	26.2 ± 1.8***
with 10 mM maltose	16.8 ± 1.0***	66.5 ± 0.7***
with 10 mM D-allose	35.5 ± 2.9***	43.1 ± 4.2***

[a] Concentration of 2-deoxy-D-glucose was 0.1 mM. Control values for buccal cells and cells of dorsum of tongue were 152.5 ± 1.8 and 211.8 ± 2.2 pmol/min/10^5 cells, respectively. Results are expressed as the mean± SE of three experiments. *** $p < 0.001$, compared with each control value.

mucosal cells. In both mucosal cells, 2-deoxy-D-glucose uptake at the concentration of 0.1 mM was markedly reduced in ice-cold conditions or by 0.5 mM PCMB. D-Mannose, maltose, and D-allose, sugars transported by the facilitative transporters, inhibited the uptake of 2-deoxy-D-glucose, suggesting that this sugar can be transported by multiple facilitative transporters.

2-Deoxy-D-Glucose Absorption from Oral Cavity—Oral mucosal epithelium is a stratified squamous epithelium with the polarity. In our previous study, we showed that D-glucose is absorbed from oral cavity by carrier-mediated mechanism, a part of which is Na^+-dependent.[13] To investigate whether the facilitative transport system operates on the apical surface of the mucosal cell or not, the absorption of 2-deoxy-D-glucose was examined by buccal absorption test. At the concentration of 1 mM, the absorption rates for 2-deoxy-D-glucose, D-glucose, and L-glucose were 630.9 ± 122.0, 3026.1 ± 91.3, and 198.9 ± 28.4 nmol/5 min, respectively. Although the absorption rate of 2-deoxy-D-glucose is lower than that of D-glucose, the inhibition by D-allose was observed: the absorption rate of 2-deoxy-D-glucose at 0.5 mM (443.2 ± 56.4 nmol/5 min) was inhibited to 267.7 ± 30.6 nmol/5 min ($p < 0.05$) by 5 mM D-allose. Although it was difficult to determine the kinetic parameters for 2-deoxy-D-glucose due to very low absorption (%) of this sugar at the high initial concentration, the expression of the facilitative transporter for D-glucose on the apical surface of the oral mucosal cells was suggested.

Western Blot Analysis of Glucose Transporters Present in Oral Mucosal Membrane—To identify glucose transporters present in oral mucosal membrane, Western blot analysis of the membrane protein was per-

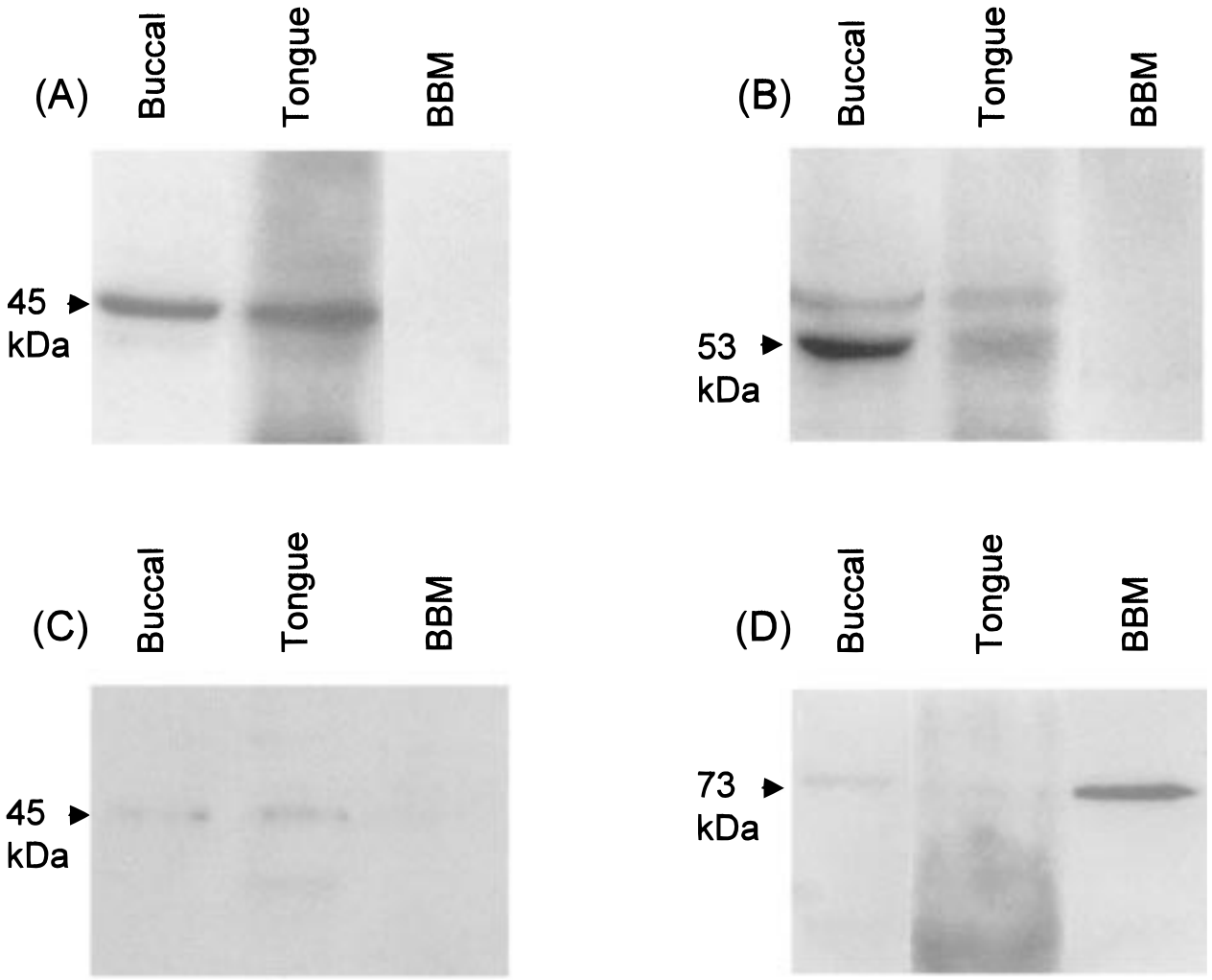

Figure 5—Western blot analysis of glucose transporters in isolated cells of human buccal mucosa, dorsum of the tongue, and brush border membranes of rat small intestine. Protein samples (20–50 μg) were electrophoresed through a SDS–PAGE gel, transferred to a nitrocellulose membrane and incubated with rabbit anti-human antibodies against GLUT1 (A), GLUT2 (B), GLUT3 (C), and SGLT1 (D). The membranes were incubated further with horseradish peroxidase-conjugated goat anti-rabbit immunoglobulin G. Horseradish peroxidase activity was revealed using ECL Western blotting detection reagents.

formed. The brush border membrane prepared from rat small intestine (BBM) was used as the positive control of SGLT1. The results are shown in Figure 5. Although there are some unidentified bands, not only the band for GLUT1 (45kDa[19]) but also the bands for GLUT2 (53kDa[15]), GLUT3 (45kDa[20]) and SGLT1 (73kDa[15]) are found in both buccal mucosal cells and cells of the dorsum of the tongue.

Discussion

D-Glucose is one of the nutrients that can be absorbed from oral cavity by the carrier-mediated mechanism.[6,13] In our previous study, we showed using perfusion cells for human oral mucosa that the carrier-mediated absorption of D-glucose is predominant in the dorsum of tongue.[13] However, details of glucose transporters present in the oral mucosal cells were remaining to be clarified. In the present study, oral mucosal cells were isolated from human buccal mucosa and the dorsum of tongue using a mouth-wash technique[16] and glucose transport systems present in these cells were examined. Lee et al. reported that buccal cells thus obtained containing superficial, intermediate and prickle cells, but not basal cells, are osmotically very stable and did not undergo any discernible swelling.[17] We confirmed that the viability of oral mucosal cells thus prepared was maintained as 80−90% over 3 h after the isolation.

As shown in Figures 1 and 2, stereospecific uptake of D-glucose was observed in both buccal mucosal cells and cells of the dorsum of the tongue. In the perfusion cell study described previously, we could not find the specialized transport mechanism for D-glucose in the buccal mucosa.[13] However, this isolated cell study could clarify that the specialized transport system for D-glucose is present not only in the dorsum of the tongue but also in the buccal epithelium. This discrepancy may be caused by difference in the surface area; that is, the large surface area of isolated mucosal cells could enable them to take up D-glucose more efficiently via the specialized transport mechanism. The result of the inhibition study (Table 1) suggested that, in addition to Na^+/glucose cotransporter, the facilitative glucose transporter is expressed in the oral epithelial cells. Furthermore, it was shown that the contribution of the facilitative transport mechanism to overall D-glucose transport in the oral mucosal cells is more predominant than Na^+-dependent active transport mechanism. The facilitative transport system present in the oral mucosal cells was suggested by the 2-deoxy-D-glucose uptake study (Figure 4, Table 2). D-Mannose, maltose, and D-allose inhibited the uptake of 2-deoxy-D-glucose. D-Mannose is transported by GLUTs1−4.[21,22] Maltose is an inhibitor of glucose transport by GLUT3, but not by GLUT2 or 4.[22] On the other hand, D-allose is an effective inhibitor

of glucose transport by GLUT2, but not by GLUT1, 3, or 4.[22] Thus, multiple facilitative transporters are suggested to be present in the oral mucosal cells. In addition, it was clarified by the buccal absorption test of 2-deoxy-D-glucose that the facilitative transport system is expressed on the apical surface of the stratified squamous epithelium. It has been reported that GLUT1, but not GLUT4, is expressed in human oral mucosa.[23,24] Finally, the result of the Western blot analysis suggested that GLUT1, GLUT2, GLUT3, and SGLT1 are expressed in the oral epithelial membrane (Figure 5). Further studies are necessary to elucidate how the active and facilitative transporters are operating in the stratified squamous epithelium of oral cavity.

As to the kinetic parameters for D-glucose uptake by isolated oral mucosal cells, V_{max} value for the dorsum of the tongue was 2.5 times larger than that for buccal mucosa, while K_m values for both cells were not significantly different. Although these values are pooled parameters of parallel Michaelis−Menten equations, the larger V_{max} value in the dorsum of the tongue suggests that transporters for D-glucose are more abundant in this site. The parameters obtained by 2-deoxy-D-glucose uptake experiments are also pooled values for multiple facilitative glucose transporters, but the larger transport capacity of the facilitative transport system in the dorsum of tongue than in the buccal is suggested, while K_m values in both cells were not significantly different. The reduction of D-glucose uptake rate in the Na^+-free medium and the inhibition of D-glucose uptake by α-methyl-D-glucoside were similar in degree in both mucosal cells, suggesting that Na^+/glucose cotransporter is also expressed more predominantly in the dorsum of tongue than in the buccal.

In conclusion, the in vitro uptake study using the isolated cells of human oral mucosa, buccal and the dorsum of the tongue, revealed that not only the Na^+/glucose cotransporter but also facilitative glucose transporters are expressed in the oral mucosal cells and that the transport system is more abundant in the dorsum of tongue than in the buccal. The glucose transporters were confirmed by the Western blot analysis.

References and Notes

1. Bell, M. D. D.; Muray, G. R.; Mishra, P.; Calvey, T. N.; Weldon, B. D.; Williams, N. E. Buccal morphine − A new route for analgesia? *Lancet* **1985**, *1*, 71−73.
2. Hussain, M. A.; Aungst, B. J.; Kearney, A.; Shefter, E. Buccal and oral availability of naloxone and naltrexone in rats. *Int. J. Pharm.* **1987**, *36*, 127−130.
3. Kurosaki, Y.; Takatori, T.; Kitayama, M.; Nakayama, T.; Kimura, T. Application of propranolol to the keratinized oral mucosa: Avoidance of first-pass elimination and the use of 1-dodecylazacycloheptan-2-one (Azone) as an absorption enhancer of bioadhesive film-dosage form. *J. Phamacobio-Dyn.* **1988**, *11*, 824−832.
4. Beckett A. H.; Triggs, E. J. Buccal absorption of basic drugs and its application as an in vivo model of passive drug transfer through lipid membranes. *J. Pharm. Pharmacol.* **1967**, *19*, 31s−41s.
5. Kurosaki, Y.; Aya, N.; Okada, Y.; Nakayama, T.; Kimura, T. Studies on drug absorption from oral cavity. I. Physicochemical factors affecting absorption from hamster cheek pouch. *J. Pharmacobio-Dyn.* **1986**, *9*, 287−296.
6. Manning, A. S.; Evered, D. F. The absorption of sugars from the human oral cavity. *Clin. Sci. Mol. Med.* **1976**, *51*, 127−132.
7. Evered, D. F.; Vadgama, J. V. Absorption of amino acid from the human buccal cavity. *Biochem. Soc. Trans.* **1981**, *9*, 132−133.
8. Hunjen, M. K.; Evered, D. F. Absorption of glutathione from the gastro-intestinal tract. *Biochim. Biophys. Acta* **1985**, *815*, 184−188.
9. Evered, D. F.; Mallet, C. Thiamine absorption across human buccal mucosa in vivo. *Life Sci.* **1983**, *32*, 1355−1358 1983.
10. Evered, D. F.; Sadoogh-Abasian, F.; Patel, P. D. Absorption of nicotinic acid and nicotinamide across human buccal mucosa in vivo. *Life Sci.* **1980**, *27*, 1649−1651.
11. Kurosaki, Y.; Nishimura, H.; Terao, K.; Nakayama, T.; Kimura, T. Existence of specialized absorption mechanism for cefadroxil, an aminocephalosporin antibiotic, in human oral cavity. *Int. J. Pharm.* **1992**, *82*, 165−169.
12. Kurosaki, Y.; Yano, K.; Kimura, T. Perfusion cells for studying regional variation in oral mucosal permeability in humans (I): Kinetic aspects in oral mucosal absorption of alkylparabens. *Pharm. Res.* **1997**, *14*, 1241−1245.
13. Kurosaki, Y.; Yano, K.; Kimura, T. Perfusion cells for studying regional variation in oral mucosal permeability in humans. 2. A specialized transport mechanism in D-glucose absorption exists in dorsum of tongue. *J. Pharm. Sci.* **1998**, *87*, 613−615.
14. Tamai, I.; Tsuji, A. Carrier-mediated approaches for oral drug delivery. *Adv. Drug Delivery Rev.* **1996**, *20*, 5−32.
15. Wright, E. M.; Hirayama, B. A.; Loo, D. D. F.; Turk, E.; Hager, K. Intestinal sugar transport. In *Physiology of the Gastrointestinal Tract*, 3rd ed.; Johnson, J. R., Alpers, D. H., Christensen, J., Jacobson, E. D., Walsh, J. H., Eds.; Raven Press: New York, 1994; pp 1751−1772.
16. Burant, C. F.; Sivitz, W. I.; Fukumoto, H.; Kayano, T.; Nagamatsu, S.; Seino, S.; Pessin, J. E.; Bell, G. I. Mammalian glucose transporters: Structure and molecular regulation. *Recent Prog. Hormone Res.* **1991**, *47*, 349−387.
17. Lee, E. J.; Patten, G. S.; Burbard, S. L.; McMurchie, E. J. Osmotic and other properties of isolated human cheek epithelial cells. *Am. J. Physiol.* **1994**, *267*, C75−C83.
18. Hopfer, U.; Nelson, K.; Perrotto, J.; Isselbacher, K. J. Glucose transport in isolated brush border membrane from rat small intestine. *J. Biol. Chem.* **1973**, *248*, 25−32.
19. Hsu, H. C.; Molday, R. S. Glycolytic enzymes and a GLUT-1 glucose transporter in the outer segments of rod and cone photoreceptor cells. *J. Biol. Chem.* **1991**, *266*, 21745−21752.
20. Gerhart, D. Z.; Broderius, M. A.; Borson, N. D.; Drewes, L. R. Neurons and microvessels express the brain glucose transporter protein GLUT3. *Proc. Nat. Acad. Sci. U.S.A.* **1992**, *89*, 733−737.
21. Gould, G. W.; Thomas, H. M.; Jess, T. J.; Bell, G. I. Expression of human glucose transporters in Xenopus oocytes: kinetic characterization and substrate specificities of the erythrocyte, liver, and brain isoforms. *Biochemistry* **1991**, *30*, 5139−5145.
22. Colville, C. A.; Seatter, M. J.; Gould, G. W. Analysis of the structural requirements of sugar binding to the liver, brain and insulin-responsive glucose transporters expressed in oocytes. *Biochem. J.* **1993**, *294*, 753−760.
23. Gherzi, R.; Melioli, G.; De Luca, M.; D'Agostino, A.; Guastella, M.; Traverso, V.; D'Anna, F.; Franzi, A. T.; Cancedda, R. High expression levels of the "erythroid/brain" type glucose transporter (GLUT1) in the basal cells of human eye conjunctiva and oral mucosa reconstituted in culture. *Exp. Cell Res.* **1991**, *195*, 230−236.
24. Voldstedlund, M.; Dabelsteen, E. Expression of GLUT1 in stratified squamous epithelia and oral carcinoma from humans and rats. *Acta Pathol. Microbiol. Immunol. Scand.* **1997**, *105*, 537−545.

Acknowledgments

The authors are grateful to Professor T. Tsuchiya and Dr. T. Kuroda, Gene Research Center, Okayama University, for their helpful guidance with respect to the Western blot analysis. This work was supported in part by a Grant-in-Aid for Scientific Research from the Ministry of Education, Science, Sports and Culture in Japan.

JS980298F

Reproducible Fentanyl Doses Delivered Intermittently at Different Time Intervals from an Electrotransport System

SUNEEL K. GUPTA,*,† GAYATRI SATHYAN,† BRAD PHIPPS,† MARK KLAUSNER,‡ AND MARY SOUTHAM†

Contribution from *ALZA Corporation, 950 Page Mill Road, Palo Alto, California 94303, and Janssen Pharmaceutica, 11225 Trenton Harbourton Rd., Titusville, New Jersey 08560.*

Received June 19, 1998. Final revised manuscript received March 18, 1999.
Accepted for publication May 28, 1999.

Abstract □ The electrotransport transdermal fentanyl system (ET [fentanyl]), uses a small electrical current to enhance delivery of fentanyl to systemic circulation. Intermittent doses can be administered by periodic application of the current. The purpose of this study was to compare the effects of the frequency of intermittent drug delivery by ET (fentanyl) and compare the drug delivery to systemic circulation by ET (fentanyl) with intravenous administration. The topical safety was also determined for the ET (fentanyl) system. Nine adult male volunteers completed this three-treatment, randomized, 24-h, crossover study. ET (fentanyl) treatments with 200 μA direct current applied for 30 min at frequent (hourly) or infrequent (4-hourly) intervals over a 24-h period were compared. Also, the drug delivery to systemic circulation from ET (fentanyl) was compared with intravenous fentanyl 75 μg infused over 30 min every 4 h over a 24-hour period. The mean serum fentanyl concentration achieved with the hourly ET (fentanyl) regimen was higher than that for the 4-hourly ET (fentanyl) regimen as expected from the higher frequency of drug doses. The amount of fentanyl delivered estimated per dose from the ET (fentanyl) system using the iv fentanyl treatment as the reference was similar for the two ET regimens throughout the dosing period. This indicates consistent drug delivery regardless of the frequency of ET dosing. The majority of subjects reported either no, or barely perceptible, erythema 24 h after removal of the system.

Introduction

Fentanyl is a short-acting synthetic opioid analgesic. When administered by a passive transdermal system (Duragesic [U.S.]/Durogesic [outside U.S.]), fentanyl is effective for the treatment of moderate to severe chronic pain.[3] Compared to intravenous or oral routes for delivering analgesia, the passive transdermal system has the advantages of being a noninvasive, nonoral route that maintains adequate serum concentrations for the duration of application (for Duragesic, a patch has to be applied every 72 h).[4,5] The fentanyl passive transdermal system has proven effective for control of chronic pain; however, it is not suitable for managing postoperative pain and other acute or intermittent pain conditions.[4]

Analgesic delivery systems that are controlled by the patient (patient-controlled analgesia or PCA) provide better pain control than standard modes of delivery because they allow continuous patient access to pain medication within predetermined limits.[1] Such PCA systems are both efficacious and well accepted. The PCA systems are fully computerized portable syringe pumps with a reservoir for the drug solution. The pump delivers the drug into an intravenous access site on the patient via microbore tubing.

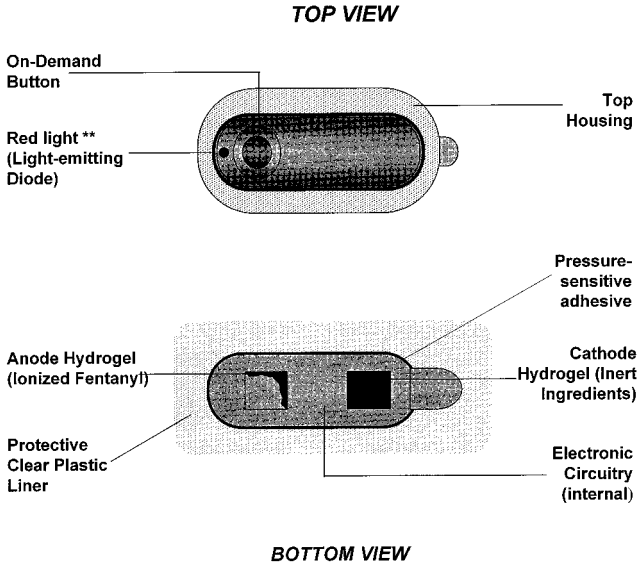

Figure 1—Schematic diagram of ET (fentanyl) system (**indicates when a dose is being delivered, as well as the approximate number of doses the patient has received since application of the particular system).

These pumps have visual displays providing information on patients drug consumption minute by minute. From the PCA systems, the drug can be either administered as a bolus injection, continuous infusion over a period of time, or continuous background infusion plus bolus whenever needed.[2] The economic advantages of PCA include lower cost due to the decreased need for medical intervention and, potentially, earlier release from the medical facility. Unfortunately, PCA equipment is costly, cumbersome, and invasive, and it requires maintenance and sterilization.

An electrotransport (ET) transdermal system for fentanyl has been developed which combines the advantages offered by PCA and the passive transdermal system. The ET system enhances the delivery of drug by means of an electrical current. Application of an electrical field facilitates the transport of charged compounds across the skin. A number of comprehensive reviews on the subject of electrotransport or iontophoresis have been written.[6–8] The pathways of molecular transport through the skin during iontophoresis have also been extensively studied.[19,20] The commercial ET system is a lightweight, self-contained system, worn on the patient's upper outer arm or chest. The system contains internal electronic circuitry, a battery, anode and cathode hydrogels, and an external button to activate delivery of fentanyl. The system is backed with a pressure-sensitive adhesive which allows it to stick to the skin (Figure 1). As with PCA, the drug delivery rate can be set by adjusting the current; as the current is increased, the rate of drug delivery is increased.[9] Intermittent doses

* Corresponding author.
† ALZA Corp.
‡ Janssen Pharmaceutica.

10.1021/js980258b CCC: $18.00
Published on Web 07/07/1999

can be administered by switching the current on for a predetermined period of time (dosing period). This system can, therefore, effectively manage acute or intermittent pain conditions.

The purpose of this randomized crossover study was to compare fentanyl delivery to systemic circulation from frequent intermittent doses administered hourly to infrequent doses administered every 4-hours by an ET (fentanyl) system. An additional objective was to compare serum concentrations achieved from ET (fentanyl) treatments with the reference intravenous (iv) treatment, and estimate the fentanyl dose delivered to systemic circulation from ET (fentanyl) treatments using this reference treatment. The study also evaluated the topical safety of fentanyl delivered by ET (fentanyl) system.

Materials and Methods

The study enrolled 10 healthy adult male volunteers (all Caucasian, aged 20−37 years [mean 27.3, SD 4.8]) to ensure that nine subjects would complete the study. Subjects were within 10% of ideal weight, nonsmokers with no history of drug or alcohol abuse, and they had abstained from recreational drug use within the past 30 days. Subjects also agreed to abstain from alcohol from 48 h before the study started until the end of the study. Exclusion criteria included active skin disease that precluded application of the system; a history of CO_2 retention, asthma or other lung disease; other clinically significant medical problems or organ abnormalities; hemoglobin <13 g/dL; or a history of allergic reaction to fentanyl, other opioids, or naltrexone. The subjects were also screened for physical dependence on opioids by Narcan (Naloxone hydrochloride: Endo Pharmaceuticals, Wilmington, DE) challenge test.[10] The protocol and consent form were reviewed and approved by the Institutional Review Board of Inveresk Clinical Research Ltd. (Edinburgh, Scotland) before the study started.

This was a randomized, open-label, three-treatment, three-period, crossover study. Each subject received three 24-h fentanyl treatments separated by 6-day washout periods. The ET (fentanyl) system (E-TRANS [fentanyl], ALZA Corporation, Palo Alto, CA), using direct current at 200 μA over a 30-min interval, was compared with 75 μg of fentanyl iv delivered over the same interval. The prototype ET (fentanyl) system used in this study consisted of a custom-built current source (Medtronic Model 6443) attached to the wrist and connected by a cable to a patchlike drug unit. The drug unit was composed of two poly(vinyl alcohol) hydrogels: one contacting a silver anode (2 cm^2) and containing fentanyl hydrochloride (10 mg) with polymeric buffer, the other contacting a silver chloride cathode (6.5 cm^2) and containing a biocompatible buffered electrolyte. The hydrogels and electrodes were housed in a medical-grade polyethylene foam with a peripheral acrylic adhesive. The ET (fentanyl) application site (upper arm) was wiped with an alcohol swab as is normally done for cleansing purposes and then either wiped dry or allowed to air-dry. The drug unit was placed on the upper arm after the peel-off protective liner was removed from the adhesive layer.

Fentanyl was delivered for the first 30 min of each hour (regimen A) or for the first 30 min of every fourth hour (regimen B). Fentanyl solution (50 μg/mL) was administered intravenously by a portable, battery-operated, syringe driver pump (Model MS2000; Graseby Medical Ltd., Watford, Hertfordshire, UK) at a rate of 1.5 mL (75 μg) over the first 30 min of every fourth hour (total dose over 24 h, 525 μg; regimen C). To minimize the opioid effects of fentanyl, five doses of naltrexone 50 mg were administered at 12-h intervals, starting 14 h before the first fentanyl dose.

Blood samples were drawn immediately before the initial fentanyl administration and periodically throughout the treatment: 10, 20, 30, 45, 60 min post 0, 12, and 24 h dosing, and also at 25, 26, 28, 32, 36 and 48 h posttreatment initiation. Serum samples were assayed for fentanyl at Janssen Research Foundation (Beerse, Belgium) using a radioimmunoassay method with a quantification limit of 0.1 ng/mL.[11]

Pharmacokinetic Analysis—The average maximum serum fentanyl concentration (C_{max} in ng/mL) and corresponding time (T_{max} in hours) observed during the entire 24-h treatment regimen were calculated. Serum fentanyl elimination rate constants (k) were estimated by linear regression of log-transformed (natural log) serum fentanyl concentrations during the terminal log-linear phase of the data after system removal. Apparent half-life ($t_{1/2}$) values were calculated as 0.693/k.

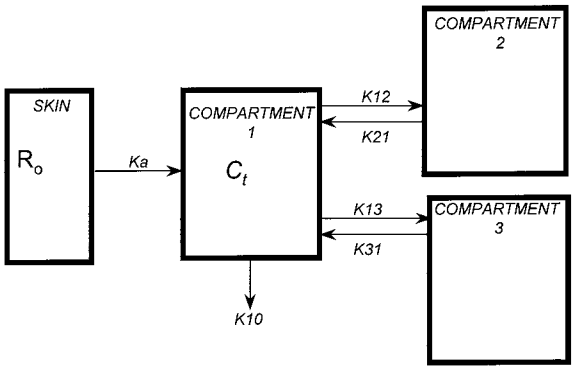

Figure 2—Three-compartment model for fentanyl administered by ET (fentanyl) system and by intravenous infusion (C_p = serum fentanyl concentrations).

For all three regimens, the area under the fentanyl concentration−time curve [$AUC_{(n-n+1)}$] was calculated by the linear trapezoidal method for doses administered during hours 0−1, 12−13, and 24−25, when frequent blood sampling was performed. For the two 4 h regimens (ET and iv), the $AUC_{(24-28)}$ (AUC for one dosing interval) was also estimated.

Statistical Analysis—An analysis of variance (ANOVA) was used to (i) compare $AUC_{(0-1)}$ among the three treatments and (ii) compare steady-state AUC over one dosing interval after the last dose ($AUC_{(24-25)}$ for the hourly regimen and $AUC_{(24-28)}$ for the 4 hly regimen) among the three treatments.

Compartmental Modeling—A three-compartment open distribution model was used to describe the observed fentanyl concentration−time profile after iv infusion. Equation 1 defines the three-compartment disposition model for administration of a single dose by iv infusion.[12] For fentanyl administration by the ET system, absorption was described by first-order kinetics (Figure 2).

$$C(_{t'}) = \frac{R_{iv}\,(1 - e^{\alpha\theta})(k_{21} - \alpha)(k_{31} - \alpha)e^{-\alpha t'}}{-V_1\alpha(\beta - \alpha)(\gamma - \alpha)} + \frac{R_{iv}\,(1 - e^{\beta\theta})(k_{21} - \beta)(k_{31} - \beta)e^{-\beta t'}}{-V_1\beta(\alpha - \beta)(\gamma - \beta)} + \frac{R_{iv}(1 - e^{\gamma\theta})(k_{21} - \gamma)(k_{31} - \gamma)e^{-\gamma t'}}{-V_1\gamma(\beta - \gamma)(\alpha - \gamma)} \quad (1)$$

Equation 2 describes the three-compartment disposition model for a single intermittent dose from an ET (fentanyl) system.[12] The absorption rate constant in this equation defines absorption due to both electrotransport and passive diffusion if any from the ET (fentanyl) system. In a previous study[13] the passive delivery of fentanyl from an ET (fentanyl) system was shown to be negligible. Four models for the ET (fentanyl) treatments were evaluated as described below. Model selection was based on residual sum of squares (RSS) and the Akaike information criterion (AIC).[14] A model with lower RSS and AIC values is preferred.

$$C_{(t')} = \frac{R_t k_a(1 - e^{\alpha\theta})(k_{21} - \alpha)(k_{31} - \alpha)e^{-\alpha t'}}{-V_1\alpha(\beta - \alpha)(\gamma - \alpha)(k_a - \alpha)} + \frac{R_t k_a(1 - e^{\beta\theta})(k_{21} - \beta)(k_{31} - \beta)e^{-\beta t'}}{-V_1\beta(\alpha - \beta)(\gamma - \beta)(k_a - \beta)} + \frac{R_t k_a(1 - e^{\gamma\theta})(k_{21} - \gamma)(k_{31} - \gamma)e^{-\gamma t'}}{-V_1\gamma(\beta - \gamma)(\alpha - \gamma)(k_a - \gamma)} + \frac{R_t k_a(1 - e^{k_a\theta})(k_{21} - k_a)(k_{31} - k_a)e^{-k_a t'}}{-V_1 k_a(\alpha - k_a)(\beta - k_a)(\gamma - k_a)} \quad (2)$$

where

t = Time since initiation of the treatment

$C_{(t')}$ = Concentration at time t′

t' = Time since initiation of the last input

α = First disposition rate constant

β = Second disposition rate constant

γ = Third disposition rate constant

k_{21} = Rate constant for transfer from second compartment to the central compartment

k_{31} = Rate constant for transfer from third compartment to the central compartment

V_1 = Volume of distribution of the central compartment

k_a = Transdermal absorption rate constant

R_{iv} = Rate of intravenous infusion (150 μg/h over 0.5 h)

R_o = Rate of fentanyl input after ET system dose at initiation and throughout for model 1

R_t = Rate of fentanyl input after ET system dose at time t:

= R_o (from 0−12 h); R_1 (from 12−24 h); R_2 (from 24−25 h) [stepwise increase in rate of fentanyl input such that $R_o < R_1 < R_2$; model 2

= R_o + st [linear increase in rate of fentanyl input; model 3]

= R_o (2-e^{-st}) [exponential increase in rate of fentanyl input; model 4]

s = Slope constant to account for increase in the input rate

CL = Clearance = $V_1\alpha\beta\gamma/k_{21}k_{31}$

θ = t' when $t' \leq 0.5$ or 0.5 when $t' > 0.5$

The profiles for multiple dose applications were then obtained by superposition of the profile associated with each administration given before t:

$$C_{(t)} = \sum_{j=1}^{M} C^{j}_{(t-(j-1)\tau)} \qquad (3)$$

where

$C_{(t)}$ = Concentration at time t

j = jth administration before t

M = Total number of administrations

τ = Dosing interval

These equations were simultaneously fitted to the all plasma concentration from each subject following all three treatments. Models were fitted to only those serum fentanyl concentration values above the quantification limit (concentrations below limit of quantification were set to missing). Pharmacokinetic disposition parameters and absorption parameters (both amount and absorption rate constants) were estimated by nonlinear regression, using the PROC NLIN procedure in SAS 6.04, with the "power model" weighting function.[15]

Safety Analysis—Safety was evaluated by analysis of pre- and poststudy blood chemistry, hematology, and urinalysis data, as well as physical examination results and electrocardiograms. During each 24-h administration period, and for 24 h after the end of each administration period, vital signs (heart rate, blood pressure, and respiratory rate) were recorded periodically. At 1, 6, and 24 h after system removal, the skin occluded by the system was evaluated visually, and any evidence of local reaction was scored as follows:

Erythema: 0 = none; 1 = barely perceptible redness; 2 = definite redness; 3 = beet redness.

Edema: Extent of erythema, papules, pustules: 0 = none; 1 = <50% occluded area; 2 = >50% occluded area.

Itching: 0 = none; 1 = mild; 2 = moderate; 3 = severe.

Results and Discussion

Ten healthy Caucasian males, aged 20−37 years (mean 27.3, SD 4.8), entered the study, and nine subjects completed. One subject discontinued study participation for a non-drug-related (personal) reason after completing the first regimen (fentanyl delivered by the ET system for 30 min/h). Data from the nine subjects who completed the study are included in the pharmacokinetic analysis, and data from all 10 subjects enrolled are included in the safety analysis. None of the subjects showed any signs or symptoms of withdrawal after administration of the Narcan challenge.

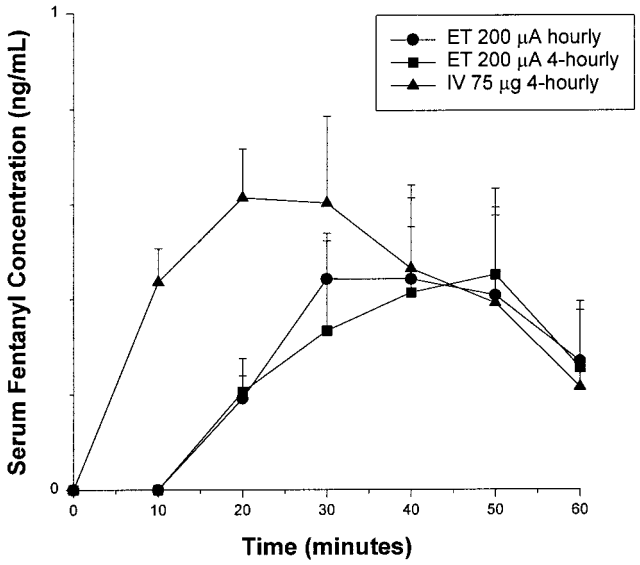

Figure 3—Mean (±SD) serum fentanyl concentrations for the first hour of the three 24-hour fentanyl regimens (n = 9). (Note: Concentrations below limit of quantification are set to zero value).

For three subjects, the duration of fentanyl administration in regimen A (30 min/h) deviated from the approved protocol. One subject received fentanyl for 1 h instead of 30 min, from hour 14 to hour 15 (half-hourly administration was restarted at hour 16). Two subjects received fentanyl for only 20 min during hour 5. The actual duration of drug administration was accounted for in the compartmental analysis.

Fentanyl Pharmacokinetics—Mean serum fentanyl concentrations increased after the first set of intermittent doses at hour 0 for both ET (fentanyl) regimens. However, the rate of increase with the ET (fentanyl) regimens was slower than that of the iv regimen (Figure 3) and serum fentanyl concentration 10 min after the dose was not detectable. Also, the mean serum fentanyl concentration declined rapidly upon termination of the iv infusion at hour 0.5, but when the ET (fentanyl) dosing interval ended, serum fentanyl concentrations did not decline for approximately 10 min (Figure 3). Similar observations were made following intermittent dosing at hours 12 and 24. These observations suggest that the barrier effect of the skin moderates both the rise and fall of serum fentanyl concentrations with ET (fentanyl) administration. Serum concentration profiles for the three regimens are shown in Figure 4. Following the hour 24 dose, the mean serum fentanyl concentration for the ET (fentanyl) hourly regimen was approximately 4-fold higher than that for the ET (fentanyl) 4-hourly regimen, which, in turn, was about twice as high as that for the iv 4-hourly regimen.

The mean fentanyl pharmacokinetic parameters are listed in Table 1. The mean C_{max} value for the ET (fentanyl) hourly regimen (2.6 ng/mL) was higher than those for the ET (fentanyl) 4-hourly or iv 4-hourly regimens (1.3 and 0.9 ng/mL, respectively). The T_{max} values for most subjects were between 24 and 25 h, with median values of 25 h after ET (fentanyl) administration and 24 h after iv administration.

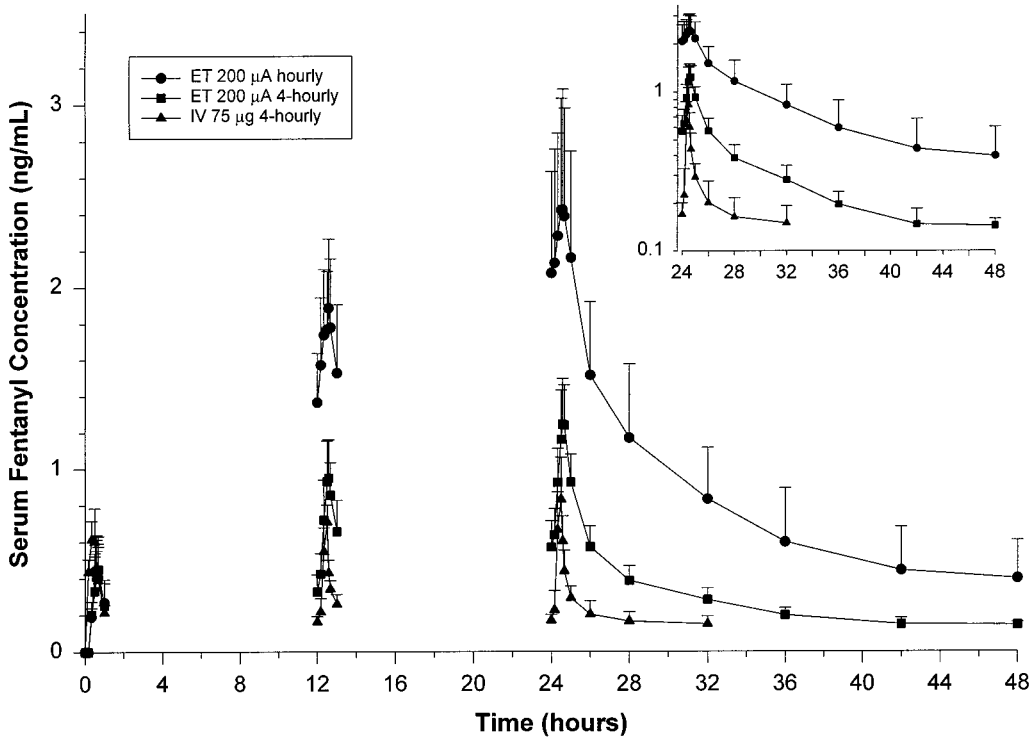

Figure 4—Mean (±SD) serum fentanyl concentrations for the three 24-hour fentanyl regimens ($n = 9$). Serum fentanyl concentrations were measured during hours 0–1, 12–13, and 24–25.

Table 1—Mean (± SD) Fentanyl Pharmacokinetic Parameters in Nine Healthy Volunteers[a]

		regimen		
parameter	units	A ET (fentanyl) hourly	B ET (fentanyl) 4-hourly	C iv 4-hourly
C_{max}	ng/mL	2.6 ± 0.7	1.3 ± 0.3	0.9 ± 0.2
T_{max}[b]	h	23.3 ± 4.0	23.3 ± 4.0	15.2 ± 11.6
K	h^{-1}	0.053 ± 0.029	0.083 ± 0.031	0.308 ± 0.257
$t_{1/2}$	h	22.0 ± 21.0	10.0 ± 5.6	3.4 ± 1.7
$AUC_{(0-1)}$	ng·h/mL	0.25 ± 0.11*	0.24 ± 0.13*	0.39 ± 0.08**
$AUC_{(12-13)}$	ng·h/mL	1.67 ± 0.35	0.75 ± 0.17	0.36 ± 0.04
$AUC_{(24-25)}$ for hourly regimen $AUC_{(24-28)}$ for 4-hourly regimen	ng·h/mL	2.23 ± 0.59*	2.66 ± 0.45*	1.00 ± 0.33**

[a] Abbreviations: C_{max}, peak serum concentration; T_{max}, time to peak concentration; k, apparent elimination rate constant; $t_{1/2}$, apparent half-life; AUC, area under the serum concentration–time curve. [b] The mean value for intravenous administration was skewed downward by three outlying values of <1 h. Median values for the three treatments were 25 h (regimens A and B) and 24 h (regimen C). Note: C_{max} and T_{max} are over the entire treatment period. *Parameters with the same number of asterisks are not significantly different ($p<0.05$).

A polyexponential decline of serum fentanyl concentrations occurred after the last dose in all three regimens (Figure 4). The mean apparent half-life values varied widely among the three regimens; half-lives were longer for the two ET (fentanyl) regimens (regimen A = 22.0 h; regimen B = 10.0 h) than for the iv regimen (regimen C = 3.4 h). Due to the assay sensitivity (0.1 ng/mL), the serum concentrations for all subjects could be quantified to hour 26 for the iv treatment, to hour 32 for the ET (fentanyl) 4-hourly regimen, and to a much longer duration of up to hour 48 for the ET (fentanyl) hourly regimen. This suggests that only the distribution phase, rather than the terminal elimination phase, was observed after the 4-hourly ET (fentanyl) and iv regimens. This probably was the reason for apparent half-life values for these two regimens to be shorter than it would be if the terminal elimination phase could have been quantified. This explanation is further supported by the previously reported terminal elimination half-life of 8 h following iv fentanyl adminsitration.[16] Alternatively, the long mean apparent half-life of the hourly ET (fentanyl) regimen (which was due mainly to two subjects with long apparent half-life values of 49.5 and 65.8 h) may indicate some contribution of the skin to the apparent terminal phase of the ET (fentanyl) regimens. However, if the long apparent terminal half-life observed after ET (fentanyl) administration was the electrotransport absorption half-life value, then the increase in serum fentanyl concentrations after a supplemental fentanyl dose would have been much more delayed than that observed. It appears that for ET fentanyl the depot or the reservoir effect is not as pronounced as seen with the transdermal system. With passive fentanyl transdermal system (Duragesic), the terminal half-life is severalfolds higher than that observed with intravenous fentanyl.[17] In the passive transdermal system, ethanol is incorporated to enhance drug solubility in the system and to enhance drug flux through the skin. Thus, fentanyl flux depends on the ethanol concentration being delivered. Ethanol flux is about 500 times greater than fentanyl flux.[18] After the system is removed, the ethanol in the skin is absorbed into systemic circulation much faster than fentanyl. This causes the rate of fentanyl appearing in systemic circulation to decrease

Table 2—Estimated Pharmacokinetic Parameters by Fitting the Three-Compartment Model to Serum Fentanyl Concentration Following Intravenous Administration and ET (fentanyl) Application (model 4) in Nine Healthy Volunteers[a]

subject no.	α, h^{-1}	β, h^{-1}	γ, h^{-1}	k_{21}, h^{-1}	k_{31}, h^{-1}	V_1, L	k_a, h^{-1}	S_a, h^{-1}	S_b, h^{-1}	ET rate (μg/h)	k_{10}, h^{-1}	k_{13}, h^{-1}	k_{12}, h^{-1}	CL, L/h
101	3.90	0.057	0.162	0.602	0.095	68.5	5.13	0.027	0.074	137.9	0.625	0.205	2.59	42.8
102	3.54	0.051	0.322	0.633	0.103	68.0	5.45	0.210	0.120	118.4	0.900	0.714	1.57	61.2
104	6.62	0.630	0.061	1.383	0.118	52.4	0.90	0.033	0.246	177.2	1.572	1.259	2.98	82.5
105	6.02	0.367	0.045	1.104	0.125	55.0	2.80	0.076	0.068	178.5	0.730	0.927	3.54	40.1
106	6.43	0.240	0.068	0.723	0.105	48.9	2.57	0.025	0.041	261.8	1.387	0.487	4.04	67.8
107	5.57	0.363	0.027	1.237	0.044	54.9	5.72	0.076	0.098	156.7	1.016	0.557	3.10	55.8
108	6.44	0.254	0.066	0.867	0.094	48.3	2.78	0.028	0.148	202.3	1.326	0.388	4.08	64.0
109	2.64	0.567	0.065	1.129	0.145	88.9	6.43	0.089	0.165	165.3	0.598	0.590	0.81	53.2
110	6.90	0.433	0.097	1.418	0.209	48.6	4.69	0.455	0.089	117.2	0.978	0.666	4.16	47.5
mean	5.34	0.329	0.102	1.012	0.115	59.3	4.05	0.113	0.117	168.4	1.015	0.644	2.99	57.2
SD	1.56	0.202	0.091	0.315	0.045	13.6	1.85	0.141	0.625	45.1	0.348	0.308	1.17	13.3
SE	0.52	0.067	0.030	0.105	0.015	4.52	0.62	0.047	0.021	15.0	0.116	0.103	0.39	4.44
Gmean	5.09	0.249	0.079	0.964	0.107	58.1	3.54	0.068	0.103	163.4	0.962	0.577	2.69	55.9
max.	6.90	0.630	0.322	1.418	0.209	88.9	6.43	0.455	0.246	261.8	1.572	1.259	4.16	82.5
min	2.64	0.051	0.027	0.602	0.044	48.3	0.90	0.025	0.041	117.2	0.598	0.205	0.81	40.1

[a] α = First disposition rate constant. β = Second disposition rate constant. γ = Third disposition rate constant compartment. k_{21} = Rate constant for transfer from the second compartment to the central compartment. k_{31} = Rate constant for transfer from the third compartment to the central compartment. k_{10} = Elimination rate constant from the central compartment to out. k_{13} = Elimination rate constant from the central compartment to the third. k_{12} = Elimination rate constant from the central compartment to the second compartment. k_a = Transdermal absorption rate constant. CL = Clearance = $(V_1\alpha\beta\gamma/k_{21}k_{31})$. V_1 = Volume of distribution of the central compartment. S_a = Slope constant to account for increase in the input rate for treatment A. S_b = Slope constant to account for increase in the input rate for treatment B.

(forms a reservoir in the skin) and the terminal half-life is longer than that observed with intravenous administration.[18]

The $AUC_{(0-1)}$ values for the ET (fentanyl) regimens were similar (0.25 and 0.24 ng·h/mL) and were significantly lower ($p < 0.05$), approximately 60% of the value for the iv regimen (0.39 ng·h/mL). However, a direct comparison of the $AUC_{(0-1)}$ values may not be an exact reflection of the dose delivered to the systemic circulation because the profiles for the ET (fentanyl) regimens are shifted to the right of the iv regimen profile, and the concentrations at hour 1 for the ET (fentanyl) regimens are approximately 10% to 15% higher than that for the iv regimen. In contrast, the steady-state AUC after the last dose − mean $AUC_{(24-25)}$ for the ET (fentanyl) hourly regimen and $AUC_{(24-28)}$ for the ET (fentanyl) 4-hourly regimen were significantly more (2-fold) than that of $AUC_{(24-28)}$ for the iv administration. This is discussed further in the Compartmental Modeling section below.

Compartmental Modeling—Compartmental modeling was used to determine the exact amount of fentanyl delivered by the ET (fentanyl) treatments using iv regimen as the reference. Since the serum fentanyl concentrations declined polyexponentially (Figure 4), a model with first-order absorption and triexponential disposition was fitted to the data for the ET (fentanyl) regimens, and a triexponential disposition model was fitted to the data for the iv regimen (eq 1). This model (model 1) was able describe the iv data well. However, for the ET (fentanyl) treatments, with this model (model 1), the observations near hour 24 were underestimated and those near hour 0 were overestimated, suggesting that the amount of fentanyl delivered to the systemic circulation with the ET system increased with time. Three other models (allowing different amounts of fentanyl input at each dose interval) which were modifications of model 1 were investigated. Model 2 allowed stepwise increase in the input rate in eq 2; results from this model showed that the mean rate of input at hour 24 was nearly twice that for input at hour 0. However, since the input rate change is probably a gradual and continuous change rather than a step function, the model was further modified so that the input increased linearly (model 3) or exponentially (model 4) with time (eq 2). For most subjects, the RSS and AIC values with model 4 were less than model

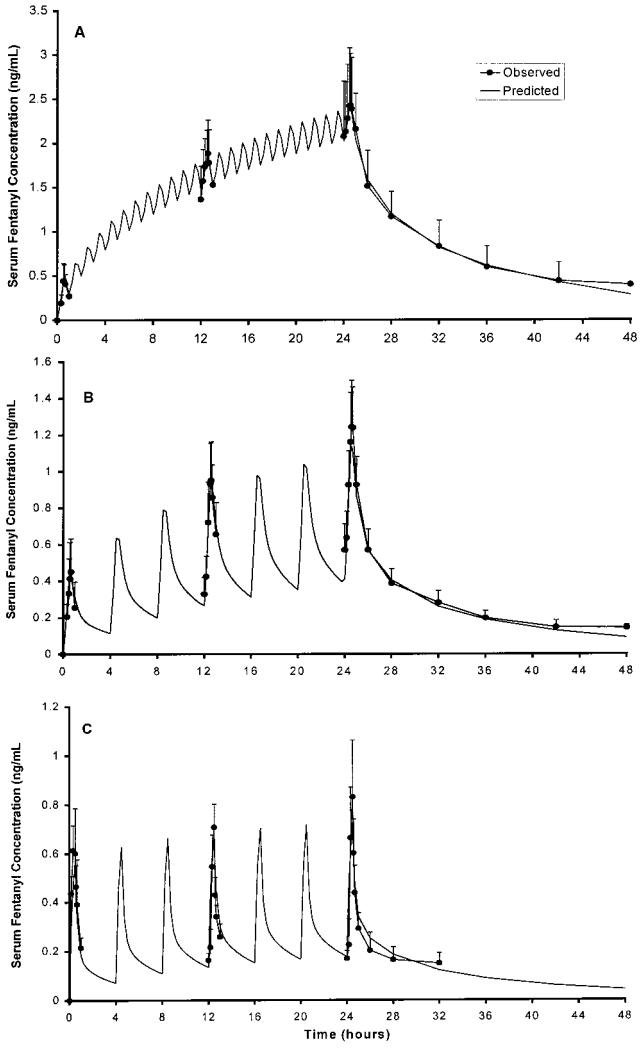

Figure 5—Model predicted and observed (mean ± SD) serum fentanyl concentrations for the three 24-hour fentanyl regimens (n = 9). A = ET (fentanyl) hourly regimen; B = ET (fentanyl) 4-hourly regimen; C = iv (fentanyl) 4-hourly regimen.

Table 3—Summary of Skin Site Reactions 1, 6, and 24 Hours after System Removal

	number of subjects					
	A ET (fentanyl) hourly ($n = 10$)			B ET (fentanyl) 4-hourly ($n = 9$)		
	1 h	6 h	24 h	1 h	6 h	24 h
erythema						
None	0	0	1	0	0	0
Barely Perceptible Redness	2	7	4	1	7	6
Definite Redness	6	2	4	8	2	3
Beet Redness	2	1	1	0	0	0
edema						
None	9	10	10	8	8	8
<50% Occluded Area	1	0	0	1	1	1
<50% Occluded Area	0	0	0	0	0	0
papules						
None	10	10	10	9	8	8
<50% Occluded Area	0	0	0	0	1	1
<50% Occluded Area	0	0	0	0	0	0
itching						
None	10	10	9	8	6	7
Mild	0	0	1	1	3	1
Moderate	0	0	0	0	0	1
Severe	0	0	0	0	0	0

3. Figure 5 shows good agreement between the model predicted concentration and the observed concentration. The rate constants for model 4 are shown in Table 2. Using model 4 parameters, the estimated amounts of fentanyl delivered to the systemic circulation at hours 0, 12, and 24 for the ET (fentanyl) hourly regimen and the ET (fentanyl) 4-hourly regimen were determined ($R_t = R_o[2 - e^{-st}]$; eq 2). The estimated amount of fentanyl delivered in 30 min at 0, 12, and 24 h were 84, 126, and 142 μg, respectively, for the hourly treatment, and 84, 142, and 157 μg, respectively, for the 4-hourly treatment. The increase in the amount of fentanyl delivered at the 24 h time point may be due to skin (depot effect, permeability changes, etc.) equilibrating with the delivery system (current, occlusion, etc). However, any conclusion regarding a time-dependent fentanyl input rate phenomenon should be considered tentative because it is highly dependent on the plasma concentration data from the first intermittent delivery period; these concentrations are low and cluster around the detection limit of the assay. Regardless, the mean amount of fentanyl delivered initially and the rate of increase were of similar magnitude irrespective of the frequency of transdermal dosing (i.e., hourly or 4-hourly).

Safety and Tolerability—All subjects received naltrexone to minimize the opioid effects of fentanyl. One subject reported nausea with the ET (fentanyl) hourly regimen. Three subjects reported adverse events during the ET (fentanyl) 4-hourly regimen (two reports of headache, and one each of abdominal pain and dizziness). Five subjects reported adverse effects during iv administration (one each of abdominal pain, constipation, nausea, asthenia, somnolence, erythema, and pruritus). No clinically significant alterations in vital signs were noted.

All the observed topical reactions 1, 6, and 24 h after system removal are summarized in Table 3. Erythema at the active gel site persisting at 24 h after system removal was comparable for both ET (fentanyl) regimens: no, or barely perceptible, erythema was evident for five subjects in the hourly regimen and six subjects in the 4-hourly regimen, while definite erythema was evident for four and three subjects, respectively. "Beet" redness was evident for one subject in the hourly regimen. No erythema was noted at the inactive gel site 24 h after system removal. The active gel site reactions are likely due to both drug and current.

Conclusion

The amount of fentanyl delivered to the systemic circulation per delivery period by the ET (fentanyl) system was estimated to be similar regardless of whether intermittent delivery was hourly or 4-hourly. About half the subjects reported either no, or barely perceptible, erythema at 24 h after system removal. Therefore, electronically controlled fentanyl delivery from the ET (fentanyl) system provided consistent drug delivery with either frequent or infrequent intermittent dosing. The skin reactions were tolerable, although, a larger study would be needed to assess them.

References and Notes

1. Lehmann, K. A. New developments in patient-controlled postoperative analgesia. *Ann. Med*. **1995**, *27*, 271−282.
2. Carolyn, S. J. Patient controlled analgesia: Drug options, infusion schedules, and other considerations. *Hosp. Formul*. **1991**, *26*, 98−206.
3. Miser, A.; Narang, P.; Dothage, J.; Young, R.; Sindelar, W.; Miser, J. Transdermal fentanyl for pain control in patients with cancer. *Pain* **1989**, *37*, 15−21.
4. Yee, Y.; Lopez, J. R. Transdermal fentanyl. *Ann. Pharmacother*. **1992**, *26*, 1393−1399.
5. Portnoy, R.; Southam, M.; Gupta, S.; Lapin, J.; Layman, M.; Inturrisi, C. Transdermal fentanyl for cancer pain. *Anesthesiology* **1993**, *78*, 36−43.
6. Burnette, R. Iontophoresis. In *Transdermal Drug Delivery: Developmental issues and research Initiatives;* Hadgraft, J., Guy, R., Eds.; Marcel Dekker: New York, 1989; pp 247−291.
7. Chien, Y. W.; Siddiqui, O.; Sun, Y.; Shi, W. M.; Liu, J. C. Transdermal Iontophoretic Delivery of Therapeutic Peptides/Proteins (I) Insulin. In *Biological Approaches to the Controlled Delivery of Drugs;* Juliana, R. L., Ed.; New York Academy of Sciences: New York, 1989; pp 32−51.
8. Singh, J.; Roberts, M. S. Transdermal Delivery of Drugs by Iontophoresis: A Review. *Drug Des. Delivery* **1989**, *4*, 1−12.
9. Haak, R.; Gupta, S. K. Pulsatile drug delivery from electrotransporttherapeutic systems. In *Pulsatile Drug Delivery: Current Applications and Future Trends*; Gurny, R., Junginger, H. E., Peppas, N. A., Eds.; Wissenschaftliche Verlagsgesellschaft mbH.: Stuttgart, Germany; 1993; pp 99−112.
10. Narcan. *Physicians Desk Reference*; Medical Economics Company: Montvale, NJ, 1999; pp 979−981.
11. Woestenborghs, J. H.; Stanski, D. R.; Scott, J. C.; Heykants, J. J. P. Assay methods for fentanyl in serum: gas−liquid chromatography versus radioimmunoassay. *Anesthesiology* **1987**, *67*, 85−90.
12. Gibaldi, M.; Perrier, D. *Pharmacokinetics*; Marcel Dekker: New York, 1982; pp 45−111, p 426.
13. Dunn, C. Touch of button delivers transdermal fentanyl. *Inpharma* **1997**, *1087*, 19−20.
14. Yamaoka, K.; Nakagawa, T.; Uno, T. Application of Akaike's information criterion (AIC) in the evaluation of linear pharmacokinetic equations. *J. Pharmacokinet. Biopharm*. **1978**, *6*, 165−175.
15. Peck, C.; Sheiner, L. B.; Nicholas, A. I. The problem of choosing weights in nonlinear regression analysis of the pharmacokinetic data. *Drug Metab. Rev*. **1984**, *15*, 133−148.
16. Shafer, A.; Varvel, J. R.; Aziz, N.; Scott, J. C. The pharmacokinetics of fentanyl administered by a computer controlled infusion pump. *Anaesthesiology* **1990**, *73*, 66−72.
17. Duragesic. Physicians Desk Reference; Medical Economics Company: Montvale, NJ, 1999; p 1418.
18. Gupta, S. K.; Sathyan, G.; Hwang, S. S. Clinical assessment of transdermal drug delivery systems. In *Transdermal and Topical Drug Delivery Systems*; Ghosh, T. K., Pfister, W. R., Eds.; Interpharm Press: Buffalo Grove, IL; 1997; pp 215−248.
19. Scott, E. R.; Phipps, J. B.; White, H. S. Direct imaging of molecular transport through skin. *J. Invest. Dermatol*. **1995**, *104*, 142−145.

20. Cullander, C. What are the pathways of iontophoretic current flow through mammalian skin? *Adv. Drug. Delivery Rev.* **1992**, *9*, 119−135.

Acknowledgments

The authors thank R. Woestenborghs (Janssen Research Foundation, Belgium) for analysis of fentanyl plasma samples. The authors also thank Dr. Walter Nimmo and his staff (Inveresk Clinical Research Ltd., Edinburgh, Scotland) for support in conducting the study. Financial support for this research was provided by ALZA Corporation and Janssen Pharmaceutica.

JS980258B

A publication of the American Pharmaceutical Association and the American Chemical Society

JOURNAL OF Pharmaceutical Sciences

September 1999
Volume 88, Number 9

MINIREVIEW

Unconventional Dissolution Methodologies

VINESS PILLAY AND REZA FASSIHI*

Contribution from *Temple University, School of Pharmacy, Department of Pharmaceutical Sciences, 3307 North Broad Street, Philadelphia, Pennsylvania 19140.*

Received April 28, 1999. Final revised manuscript received June 30, 1999.
Accepted for publication July 1, 1999.

Introduction

In line with the key focus of recent publications[1−3] emerging from the labs of Dressman, Amidon, and Shah, and in conjunction with the aims of both the FDA and US Pharmacopoeial Convention to improve and possibly develop alternative dissolution testing procedures as well as techniques for data analysis, this work considers an overview of the constantly changing areas of in vitro dissolution research in the evaluation of novel oral drug delivery systems. Over the years, dissolution testing has been employed as a quality control procedure in pharmaceutical production, in product development to assist in selection of a candidate formulation, in research to detect the influence of critical manufacturing variables such as binder effect,[4] mixing effect,[5,6] granulation procedure,[7] coating parameters,[8,9] excipient type,[10] and/or in comparative studies of different formulations,[11] in in vitro−in vivo correlations,[12−15] and possibly as an in vivo surrogate under strictly defined conditions.[16,17] It therefore becomes apparent that sensitive and reproducible dissolution data derived from physicochemically and hydrodynamically defined conditions are necessary in order to compare various in vitro dissolution data and be able to use such results as a surrogate for possible in vivo bioavailability, bioequivalence testing, and in vitro−in vivo correlations (IVIVC). However, the influence of technological differences and process variables involved during manufacturing on dissolution rate often complicates the decision making process in selection of the appropriate dissolution method and subsequent data interpretation technique. Moreover, Skoug and co-workers[18] stressed that this consequence is the reason dissolution studies and the defined specifications so often generate strong interest during regulatory review of solid oral dosage forms. As a result, the Center for Drug Evaluation and Research (CDER) at the Food and Drug Administration (FDA) has recently released guidelines called Scale-Up and Post Approval Changes, commonly referred to as SUPAC[19] and Extended Release Solid Oral Dosage Forms: Development, Evaluation and Application of In vitro/In vivo Correlations, commonly known as IVIVC,[20] to be used by the pharmaceutical sponsor in quality assurance and specific postapproval changes and to demonstrate that the "dissolution profiles of prechange product and postchange product are similar". The impact of the process and establishment of an in vitro and in vivo performance (IVIVR) as a critical stage in development of oral controlled release products has been further highlighted in the recent work of Devane and Butler.[21]

The current sophistication in formulation of new modified release drug delivery systems and associated diversity in dosage form design necessitates the development of new procedures or appropriate modification to the existing apparatus as an alternative for dissolution measurements.[22,23] More recently, it has been shown that the complex hydrodynamics and three-dimensional fluid flow pattern produced by the USP paddle[24] within different regions of the dissolution vessel varies significantly with a relatively more stagnant region at the bottom portion of the vessel.[25,26] Consequently, to mimic and more closely reflect the possible in vivo dosage form surface exposure, have reliable dissolution data, and be able to discriminate between release behavior of various modified release formulations, it becomes apparent that a better understanding of the role of hydrodynamics in relation to delivery

* Corresponding author. Tel. 215-707-7670. Fax 215-707-3678. e-mail. afassihi@vm.temple.edu.

10.1021/js990139b CCC: $18.00
Published on Web 07/31/1999

system and release mechanisms are necessary for the development of alternative dissolution methods.[22,23]

In general, the design of alternative dissolution methods may be approached in one of two ways or a combination. First, the method might consider the establishment of in vitro testing conditions similar to an actual in vivo setting. This approach may encompass instrumental developments mimicking gastrointestinal peristaltic motion with combination of flow-through methods for ensuring sink condition maintenance. All media used in testing of dosage forms should also be very similar to fluids comprising the gastrointestinal compartment particularly with respect to composition. Furthermore, other technical considerations may incorporate fabrication materials that are in contact with the dosage to possibly behave as pliable, flexible gastrointestinal tissue. Irrespective of the extent to which the ideal testing conditions are achieved, this approach becomes a mammoth task flawed by numerous inconsistencies. The second and more amenable approach is to establish in vitro dissolution conditions that may provide drug release profiles very similar to deconvoluted (i.e., fraction absorbed) blood plasma profiles through different levels of correlation as described in the USP. This entails an establishment of in vitro–in vivo correlation through manipulation of process variables such as selection of appropriate dissolution media systems taking into consideration sink condition maintenance and/or manipulation of fluid flow hydrodynamics by use of additional devices within the standard dissolution vessel. A useful example of the latter suggestion is the reported ring/mesh assembly used for the in vitro enhancement of dosage form positioning and surface area exposure in order to simulate hydrodynamically comparable conditions to that of in vivo.[27,28]

Generally reviews, theoretical papers, and research publications on the subject of dissolution have focused on standardizing, expanding, and developing useful mathematical and physical models principally due to apparent unresolved mechanistic complexities in the thermodynamic sense.[29–34] On the basis of such past in-depth analyses, researchers may presently use those concepts in experimental design of alternative dissolution methods. Therefore, to consolidate the principles governing the dissolution process, this article will attempt to provide a brief theoretical perspective of dissolution theory and associated concepts used in drug release from oral dosage forms. In keeping with the significant research activities with hydrophilic swellable matrixes, priority will be given to the optimization of dissolution studies pertaining to modified/controlled release drug delivery from such systems. A summary of attempts to improve the currently recommended USP, 23 dissolution methodologies for swellable sticking and swellable floatable delivery systems is provided, and the approaches recently used to overcome the associated difficulties are referred to in the text.[27] In addition, aspects relating to the lack of an official in vitro dissolution test method for lipid-filled capsules and the strategy used to solve this dilemma is discussed.[28] A critical review on the advantages and limitations of commonly used mathematical and statistical parameters for comparison of dissolution data, including the newly developed FDA-recommended f_2 similarity factor and f_1 difference factor, also follows. The use of "chemical stabilizers" in dissolution testing of drugs (such as ascorbic acid), normally susceptible to rapid decomposition in solution, is discussed for a gel-based controlled release product. We also briefly examine the problems associated with non-UV responsive drugs and the implications of colorimetric adaptation for the evaluation of release characteristics of both soluble and insoluble active substances.

Fundamental Dissolution Theories

Dissolution of a solute is a multistep process involving heterogeneous reactions/interactions between the phases of the solute–solute, solute–solvent, solvent–solvent, and at the solute–solvent interface. As one of the most commonly known mass transfer rate processes, the component heterogeneous reactions may broadly be categorized into (i) diffusion or convective transport of the solute from the interface to the bulk phase; and (ii) the rate of solute liberation and transport from and across the interfacial boundaries.

Various researchers in the field have developed theories to define the dissolution process and these have been comprehensively reported.[35–37] As three of the pioneering theories in the field, this review will not be complete without a brief description of the diffusion layer model, surface renewal theory, and limited solvation theory.

Table 1 concisely depicts the principal mathematical equations associated with the theories and highlights key points regarding the theory. Selected information is derived from the text of Abdou[35] for diffusion layer and surface renewal theories. The limited solvation theory is presented from the original work of Goldberg and co-workers.[38]

In the diffusion layer theory, the simplest model used to describe dissolution makes use of a single crystal in a nonreactive environment. The initial step in solution of the solid (solute or crystal) at the interface is usually very rapid and results in the formation of a saturated stagnant layer around the particle. This is contrasted by the second diffusion step that is slow and becomes the rate-limiting step in the dissolution process. In particular, the Noyes–Whitney equation (eq 3) illustrates that one of the main factors determining the rate of dissolution is drug solubility.[37] From this it is understood that in vivo the dissolution process may become the rate-limiting step if the rate of solution is much slower than the rate of absorption. This may be the case when the drug in question has a very low solubility at both gastric and intestinal pH.

The surface renewal theory assumes an equilibrium at the solute–solution interface is attained and that the rate-limiting step in the dissolution process is mass transport. The model is thought of as being continually exposed to fresh dissolution medium. The agitating medium consists of numerous eddies or packets into which the solute diffuses and is carried to the bulk medium. Due to the turbulence at the surface of the solute, there is no boundary layer and therefore no stagnant film layer. In other words the surface is continually being replaced with fresh medium.

The limited solvation theory[38] predicts that a crystal undergoes dissolution through an interfacial process in the dissolving medium. The true surface area of the crystal must be considered since each face of the crystal may have a different interfacial barrier. Hence each surface may provide a different contribution to the dissolution process.

Basic Theories of Dissolution Profile Analysis

Table 2 in summary depicts four prominent theories used in dissolution profile analysis, namely Wagner's,[39] Kitazawa's,[40–42] El-Yazigi's,[43] and Carstensen's.[44]

Wagner's theory[39] for the interpretation of percent dissolved–time plots of tablets and capsules relates the apparent first-order kinetics under sink conditions to the fact that a percent dissolved value at a certain time may be equivalent to the percent surface area generated at the same time. Kitazawa's theory[40–42] showed that the biphasic straight lines were obtained from plots of $\ln c_s/(c_s - c)$ vs t. The first segment was due to tablet disintegration or

Table 1—Summary of Fundamental Dissolution Theories[a]

theory[b]	equations		associated characteristics
diffusion layer[35]			
Fick's First Law	$J_{ix} = -D_i (\partial c_i/\partial x)$	(1)	Considers diffusion only under steady-state conditions.
Fick's Second Law	$\partial c/\partial t = D (\partial^2 c/\partial x^2)$	(2)	Used when drug concentration decreases with time; hence, considers non-steady state conditions.
Noyes and Whitney	$dc/dt = K (c_s - c_t)$	(3)	Description of drug dissolution based on constant surface area.
Brunner and Tolloczko	$dc/dt = kS (c_s - c_t)$	(4)	Manipulation of Noyes–Whitney's eq 3 by incorporation of surface area term S. Proposed the formation of a stagnant layer around the dissolving particle, a layer through which solute diffuses through into the bulk.
Nernst	-		
Brunner	$dc/dt = kDS/vh (c_s - c_t)$	(5)	Manipulation of Fick's first law and expansion of eq 4 by incorporation of a diffusion coefficient D, stagnant layer thickness h, and volume of dissolution medium v.
	If $c_t \ll c_s$ (i.e. <10%) $\Rightarrow dc/dt = kDS/vhc_s$	(6)	
	If v and S are constant $\Rightarrow dc/dt = K$	(7)	
Hixson and Crowell Cube Root	$w_0^{1/3} - w^{1/3} = (4\pi\rho\eta/3)^{1/3} (Dc_s/h\rho)t$	(8)	Originally developed for single particles but has been extended to use in multiparticulate systems.
	or $w_0^{1/3} - w^{1/3} = Kt$	(9)	
surface renewal[35]	$Vdc/dt = dW/dt = S(\gamma D)^{1/2} (c_s - c_t)$	(10)	Assumes solid–solution equilibrium is achieved at the interface and that mass transport is the rate-limiting step in the dissolution process.
limited solvation[38]	$G = k_i(c_s - c_t)$	(11)	An intermediate drug concentration less than saturation may exist at the interfacial barrier between the solid surface and solvent. Different faces of a crystal may have different interfacial barriers and therefore make different contributions to the dissolution process.

[a] Key to symbols and abbreviations: J_{ix}: flux (mg/cm^2 s^{-1}); D_i: diffusion coefficient; $\partial c_i/\partial x$: concentration gradient; $\partial c/\partial t$ or dc/dt: drug dissolution rate; K: first-order dissolution constant; c_s: equilibrium drug concentration; c_t: drug concentration at time t; k: dissolution constant; S: surface area; v: volume of dissolution medium; h: thickness of stagnant layer; w_0: initial powder weight; w: powder weight at time t; ρ: particle density; η: viscosity; h: thickness of diffusion layer; γ: interfacial tension; G: dissolution rate per unit area; k_i: effective interfacial transport constant. [b] Superscript numbers in first column denote references.

Table 2—Summary of Basic Theories of Dissolution Profile Analysis[a]

theory[b]	equations		associated characteristics
Wagner[39]	$\log(w^\infty - w) = \log M - k_s/2.303 (t - t^\circ)$	(12)	Relates apparent first-order kinetics under sink conditions to the distribution of available surface area and not dissolution per se. In case of exponential decrease in surface area with time, then first-order kinetics could be related to dissolution data.
	where $M = K/k_sC_sS^\circ$	(13)	
Kitazawa[40−42]	$\ln w^\infty/(w^\infty - w) = K't$	(14)	Assumes constant surface as long as sink is maintained. Under these conditions C^∞ is not always equal to C_s. A plot of $\ln w^\infty/(w^\infty - w)$ vs t yields a straight line with slope as the dissolution rate constant K'.
El-Yazigi[43]	$(100 - f_s) = 100k_d/(k_d - k_s)e^{-k_st} - 100k_s/(k_d - k_s)e^{-k_dt}$	(15)	Disintegration and dissolution are consecutive first-order processes. Because disintegration is usually much faster than dissolution, the semilog plot of $(100 - f_s)$ vs t yields a biexponential curve.
Carstensen[44]	If q is small and $F/q \ll 1$		Considered that the dissolution process in the USP basket proceeds in three steps: some disintegration but particles not dislodged from basket; more disintegration and particles move out of basket; more disintegration and first particles have completely dissolved. These three phases have to be mathematically explained to calculate the mass of solute undissolved at time $t = 0$.
	$\Rightarrow \ln m = -q\theta + \ln m_0$	(16)	
	If q is large		
	$\Rightarrow \ln m = -q\theta + q\theta_2 + \ln m_0\, 6(F/q)^3$	(17)	

[a] Key to symbols and abbreviations: w^∞: amount of drug in solution at infinite time; $(w^\infty - w)$: amount of undissolved drug; K: dissolution constant; k_s: dissolution rate constant; t: time in question; t°: time $t = 0$; C_s: aqueous solubility of drug; S°: surface area at time t°; K': dissolution constant; f_s: cumulative percentage of drug dissolved at time t; k_d: disintegration rate constant; k_s: dissolution rate constant; q: erosion constant; m: mass of undissolved solute; θ: experimentally observed time; F: factor as a function of the intrinsic dissolution rate (either in basket or vessel), drug solubility, and particle density. [b] Superscript numbers in first column denote references.

disruption of the capsule shell, while the second segment was obtained from this point onward to the end of the dissolution. Through multiplication by volume the concentration terms were changed to weight as depicted in eq 14. This theory was seriously criticized because it assumed a sudden increase in surface area rather than a continuous change, as proposed by Wagner. The major difference between the approach of El-Yazigi[43] and Kitazawa is that the former treats disintegration and dissolution as two kinetically distinct processes. The application of the eqs 16 and 17 in Carstensen's approach[44] generated curves that had skewed S shapes and followed Weibull or log-normal distributions when the percent dissolved was plotted against time. This may be attributed to the initial lag phase in the dissolution process (also expected from the proposed theory in terms of the time-dependent phases of disintegration, escape of particles through the basket, and dissolution of initial particles).

Currently Recommended USP 23 Methods

The currently available USP-23 has been one of the most valuable references to pharmaceutical scientists involved in the area of dissolution studies. The available dissolution methods within individual drug monographs with respect to solid oral dosage forms have been divided, where appropriate, into immediate and controlled or extended release products. Irrespective of this division and prominence given to differences in specifications such as tolerance (Q) values between immediate and controlled release products, there are no substantial differences in the methodologies used to test these products. Expected differences in dissolution test methods may include variation in the pH of the buffer medium depending on where the designed controlled release product is to deliver the drug or depending on the drug release rate, drug solubility, and absorption window. In most cases, the monographs are not up to date and the necessary refinements reflecting the recent advances in research findings with respect to both changes in media and methods are not included. With the recent tendencies toward application of hydrophilic floatable and/or sticking materials, new impetus has taken over in drug delivery systems design. Another unspoken reason for this shift in scientific momentum has been due to the "sudden" expiration of drug product patents and concurrent

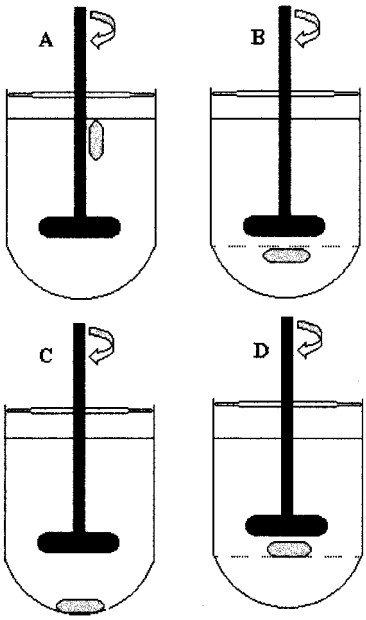

Figure 1—Schematic of drug delivery system positioning within a dissolution vessel: (A) floatable system close to the paddle shaft; (B) floatable system under the ring/mesh assembly; (C) sticking system adhering to bottom of dissolution vessel; (D) sticking system placed over the ring/mesh assembly. (Modified from Pillay and Fassihi[27]).

progress and expansion of "generic" industries. The application of new polymeric materials to enhance drug delivery, particularly in certain aspects of controlled release, has from our experience led to the recognition of limitations in the versatility of the currently recommended USP-23 dissolution methods.[24] This aspect has been adequately demonstrated in the recent publications showing the benefits of alternative dissolution approaches to the currently recommended USP-23 methods applied to swellable sticking and swellable floatable delivery systems, the summary of which is presented in the following sections.

Alternative Dissolution Methods and Examples

(i) Application of Ring/Mesh Assembly for Determination of Release Profiles from Swellable Low- and High-Density Matrices—As pointed out above, new modified release formulation technologies and diversity in dosage form design necessitates the development of new procedures or appropriate modification to the existing apparatus as alternative dissolution measurement methods.[22,23,27,28] For example, in dissolution studies of low-density swellable, floatable controlled release drug delivery systems, often position of the dosage form appears to be close to the paddle shaft and liquid surface as illustrated in Figure 1A (i.e., in schematic). On the other hand, when a sinker such as the USP-recommended[24] "wire helix" is wound around the delivery system, position of the dosage form will vary within the vessel (inconsistent hydrodynamics), and its free three-dimensional swelling process would be adversely affected and difficult to control.[45] Furthermore, and contrary to floatable dosage forms, many drug delivery systems having high density tend to adhere (stick) to the bottom of the dissolution vessel as illustrated in Figure 1C. This problem of sticking is accentuated with the use of swellable polymers such as hydroxypropylmethylcellulose, hydroxypropylcellulose, and poly(ethylene oxide). Under these conditions, the lower surface of the dosage form is not exposed to the dissolution medium, and drug release is limited to the exposed surfaces only. Similar phenomena are unlikely to occur in the human gastrointestinal tract. Furthermore, it may be anticipated that the USP 23 Apparatus 1 (rotating basket method) may be used to surmount this problem by allowing complete immersion of the dosage form and full surface area exposure. However, the early work of Withey and Bowker[46] on fluid flow dynamics clearly show that the rotating basket produces nonreproducible flow patterns with least fluid flow in the axial plane directly above and below the basket as well as within the basket. In addition, our experience has shown that some swellable delivery systems tend to expand greater than the diameter of the basket and often float against the flat base of the rotating shaft. These events will result in restriction of swelling and erosion processes, as well as limited surface exposure to dissolution medium. More recently, it has been shown that the complex hydrodynamics and three-dimensional fluid flow pattern produced by the USP paddle within different regions of the dissolution vessel varies significantly with a relatively more stagnant region at the bottom portion of the vessel.[25,26] Consequently, to mimic and more closely reflect the possible in vivo dosage form surface exposure, have reliable dissolution data, and be able to discriminate between release behavior of various modified release formulations, a better understanding of the role of hydrodynamics, delivery system, and release mechanisms together with the development of alternative dissolution methods is apparent.[22,23]

Recently Pillay and Fassihi[27] have used a new device (ring/mesh assembly) in conjunction with the paddle method to study the influence of the position of various dosage forms on release behavior and evaluated the release profiles obtained with such modification with those derived under standard dissolution conditions including the USP 23- recommended helical wire sinker used for swellable floatable delivery systems (see schematic Figure 1). Model drugs used included theophylline (0.85% water soluble at 25 °C) and diltiazem hydrochloride (>50% water soluble at 25 °C). It was shown that for a low water-soluble drug such as theophylline, full surface exposure was necessary in order to accomplish complete drug release from the delivery system (Figure 2a). This was accomplished by placing the delivery system over the ring/mesh assembly as depicted in Figure 1. This surface area exposure phenomenon was also applicable to a floatable theophylline system. Application of the USP-recommended helical wire sinker to the swellable floatable theophylline delivery system appeared to inhibit the three-dimensional swelling process of the dosage form and consequently suppressed drug release from the formulation (Figure 2b). Such a limitation was alleviated by positioning the delivery system below the ring/mesh assembly (Figure 1). In the case of diltiazem hydrochloride (solubility in water >50% at 25 °C) similar release differences as in the case of theophylline ($p < 0.05$) were also observed when the sticking delivery system was placed either in the vessel as recommended by the USP 23 standard method or when it was positioned over the ring/mesh assembly (Figure 2c). However, in the case of a swellable floatable system containing the highly soluble drug diltiazem hydrochloride, no differences in release were found by employing the helical wire sinker, placing the dosage form in the vessel as such or when the delivery system was fully submerged under the ring/mesh assembly (see Figure 2d). Hence, the nature of drug release behavior from swellable floatable systems depended both on full surface exposure and unhindered swelling as well as drug solubility.

(ii) Evaluation of Drug Release from Lipid-Filled Hardshell or Softgel Capsules—Considerable interest has been shown in the formulation of lipid-filled capsules for the enhancement of either in vivo dissolution rates or

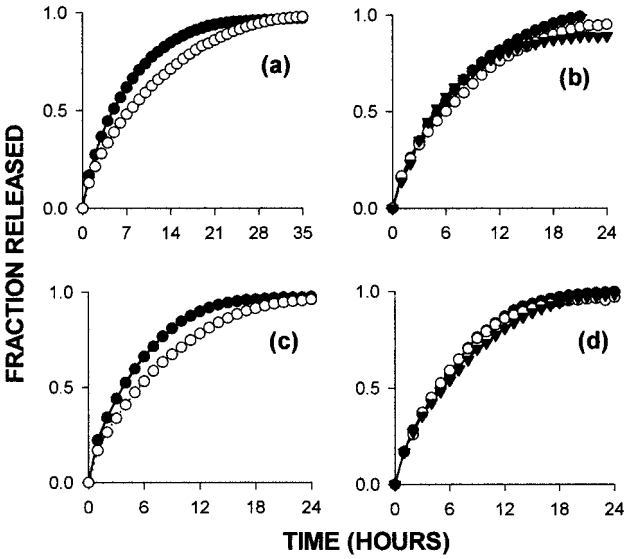

Figure 2—(a) Theophylline release from a swellable sticking drug delivery system. Key: ●, delivery system placed over the ring/mesh assembly for full surface exposure to the dissolution medium; ○, delivery system dropped into the vessel with one surface sticking to the bottom of the vessel. (b) Theophylline release from a swellable floatable drug delivery system. Key: ○, delivery system placed under the ring/mesh assembly to prevent flotation to the surface of the dissolution medium; ●, delivery system dropped into the vessel and allowed to float at the surface of the dissolution medium; ▼, delivery system enclosed within a helical wire sinker to prevent flotation to the surface of the dissolution medium. (c) Diltiazem hydrochloride release from a swellable sticking drug delivery system. Key: ●, delivery system placed over the ring/mesh assembly for full surface exposure to the dissolution medium; ○, delivery system dropped into the vessel with one surface sticking to the bottom of the vessel. (d) Diltiazem hydrochloride release from a swellable floatable drug delivery system. Key: ○, delivery system placed under the ring/mesh assembly to prevent flotation to the surface of the dissolution medium; ●, delivery system dropped into the vessel and allowed to float at the surface of the dissolution medium; ▼, delivery system enclosed within a helical wire sinker to prevent flotation to the surface of the dissolution medium. ($N = 3$ in all of the above cases; standard deviations are not shown because they are smaller than the symbol size; modified from Pillay and Fassihi[27]).

bioavailability of bioactive agents.[28,47,48] To ascertain that drug is completely delivered from its formulation over an appropriate time period and is able to reach and cross the gut wall, an aqueous environment similar to the gut luminal fluid and a sink resembling the lipoidal nature of the gastrointestinal mucosa becomes a necessary condition for the development of a prognostic in vitro test method. Both softgel and hard shell capsules filled with vehicles which are capable of self-emulsification (due to their ability to form fine oil-in-water emulsions) offer great potential for the oral delivery of insoluble hydrophobic and poorly absorbable drugs. However, in vitro evaluation of such dosage forms have thus far been problematic, since no official dissolution method for lipid-based formulations as yet has been established. This may be due to the relative difficulties associated with the evaluation methodology of lipid-based formulations. A greater challenge is presented when poorly soluble drugs in a lipid-based vehicle are presented as lipid-filled capsules for enhancement of solubility. Such matrixes, however, are not soluble in commonly used aqueous dissolution media. With some conventional dissolution methods, the use of surfactants[48–50] or hydro-alcoholic media[47,50] have been recommended. However, it is speculated that exposure of the gelatin shell to such media may induce physical and/or chemical changes, arising either through complex formation or cross-linking reactions. Typically, sodium lauryl sulfate (SLS), an anionic surfactant, is often employed in dissolution media; however, many researchers fail to recognize that SLS will bind to cationic charges of gelatin at pH values equivalent to

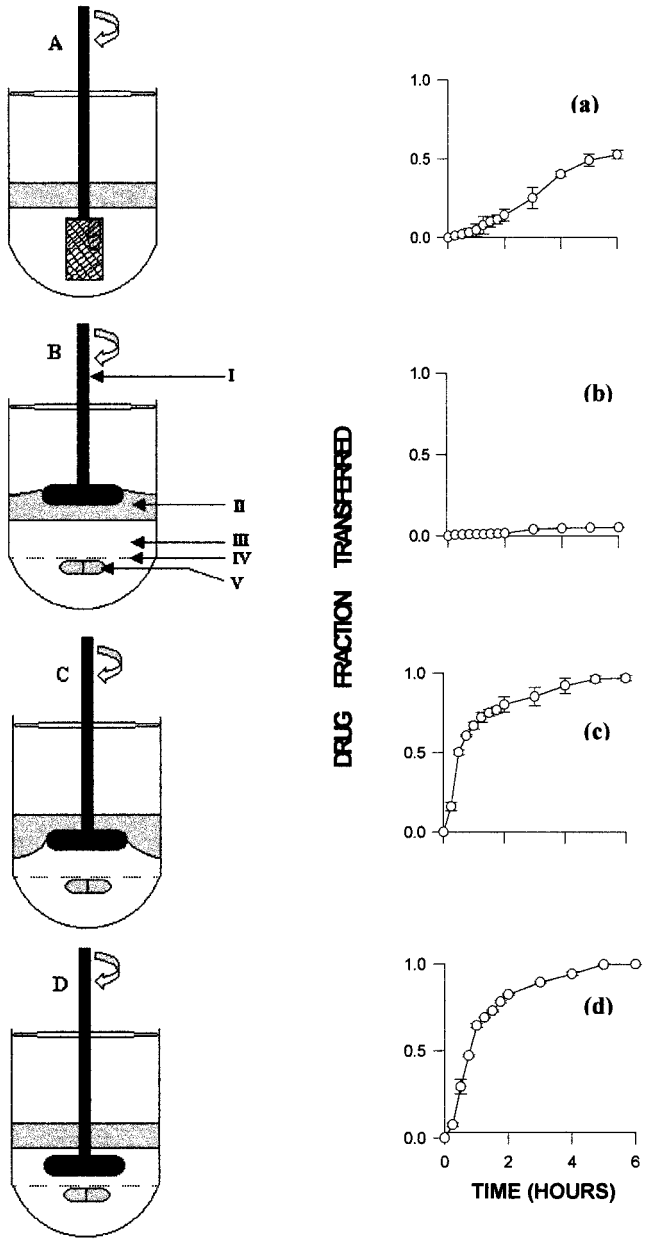

Figure 3—A comparative illustration of the four dissolution designs employed for the induction of different hydrodynamic conditions. Left panel: Key: I = Position of either rotating basket or paddle with hydrodynamic arrangements as follows. Design A: Centrally positioned in aqueous phase between boundaries of organic phase and bottom of vessel. Design B: Halfway at air/organic phase interface. Design C: Halfway at organic/aqueous phase interface. Design D: Centrally positioned in aqueous phase between boundaries of organic phase and ring/mesh assembly. Stirring rate of 75 rpm was used in all designs with exception of design D where in addition 100 rpm was also tested. II = organic phase, i.e., 100 mL 1-octanol. III = aqueous phase i.e., phosphate buffer: 400 mL for design A, 200 mL for designs B and C, 300 mL for design D. Note that 400 and 300 mL of phosphate buffer were employed in designs A and D to ensure that basket and paddle are fully immersed in aqueous phase. IV = ring/mesh assembly. V = Position of capsule either within basket or below ring/mesh assembly. Right panel: Transfer profile of lipid-based nifedipine capsule preparation derived under different hydrodynamic conditions and designs as described above ($N = 3$). (a) Profile obtained using the USP 23 rotating basket method at 75 rpm (dissolution design A). (b) Profile obtained using paddle over ring/mesh assembly halfway at air/organic interface at 75 rpm (dissolution design B). (c) Profile obtained using paddle over ring/mesh assembly halfway at organic/aqueous interface at 75 rpm (dissolution design C). (d) Profile obtained using paddle over ring/mesh assembly in aqueous phase at 100 rpm (dissolution design D). (Modified from Pillay and Fassihi[28]).

gastric pH. These interactions may influence the solubility and disintegration time of the shell and/ or true release potential of the product. Therefore, difficulties that may be experienced include, but are not limited to, exposure of gelatin shell to the organic phase, separation of poorly soluble drugs as metastable liquid crystals, lack of reproducibility in dissolution data, dosage form and lipid flotation in the dissolution vessel, etc.

In a recent report[28,51] a method which encompasses the development, design, and use of a modified two-phase dissolution media system by a novel approach for testing of either soft or hard shell lipid-filled gelatin capsules was proposed. Nifedipine was chosen as the model compound due to its water-insoluble nature (<10 μg/mL at 25 °C) and high octanol–water partition coefficient (10000:1). The experimental design takes advantage of the inherent immiscibility of aqueous phosphate buffer and 1-octanol, as well as the ability to modulate dissolution hydrodynamics and position of the formulation in the aqueous phase within the vessel (see Figure 3, i.e., schematic in left panel). Furthermore, the organic phase will act as a sink for drug removal from the aqueous phase in the dissolution vessels, a concept also recognized and pointed out in the early work of Gibaldi and Feldman[52] on the establishment of in vitro sink conditions in dissolution rate analysis and the merits of using a two-phase dissolution media system.

With USP-23 Apparatus I, it was demonstrated that the standard dissolution basket pores (mesh no. 40) and lack of appropriate hydrodynamic conditions within the basket have a significant limiting effect on drug release from the oleaginous formulation; hence, incomplete release was achieved (maximum of 50% released in 7 h; see profile in Figure 3a in right panel). As depicted in Figure 3, different hydrodynamics and various positionings of the rotating paddle was attempted to afford complete drug transfer to the upper organic 1-octanol phase from the lower aqueous phosphate buffer phase. Note that each design is accompanied by its appropriate release profile as depicted in Figures 3a–d in the right panel. With design C, induction of fluid dilatation at the organic/aqueous interface proved to be effective in encouraging rapid dissolution of the capsule shell and subsequent self-emulsification of the formulation. This essentially enabled complete drug transfer in 6 h (96.84%) (see profile in Figure 3c in right panel). Manipulation of the hydrodynamic conditions in the case of design D proved crucial in determining the rate of drug transfer and reproducibility of such a process (see profile in Figure 3d in right panel).

(iii) Determination of Dissolution Profile under Nitrogen Blanket for Oxidizable or Unstable Substances—A typical example of such substance evaluated in our laboratory will be given below. Ascorbic acid displays very poor stability characteristics in aqueous media in the presence of oxygen. As a result during the release process of ascorbic acid in a typical dissolution study, significant degradation products are simultaneously formed. To suppress the degradation process initially, the dissolution media can be purged with nitrogen gas while the gas flow would continue throughout the dissolution study. To generate a blanket of nitrogen gas over the medium within the vessel, individual vessels were sealed with the exception of allowing enough tolerance for shaft rotation. A typical profile obtained under such conditions is shown in Figure 4. Therefore full stability considerations and utilization of appropriate analytical techniques for determination of degradation and other byproducts is essential.

(iv) Glucosamine Release Study from Swellable Hydrophilic Matrix System—Typically in any dissolution study, UV spectrophotometry measurements are more preferable in terms of simplicity and cost saving. When

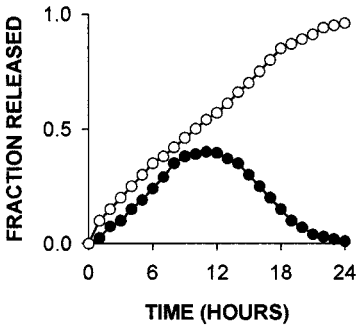

Figure 4—Typical profile for release of ascorbic acid in aqueous medium from a hydrophilic gel-based system ($N = 3$) under standard dissolution conditions showing significant degradation (●) and under modified conditions using a constant nitrogen purge (○). (From Fassihi, unpublished data).

substances do not absorb UV light often derivatization or complexation by addition of specific reagents may be adapted. Glucosamine as such does not absorb UV light. To measure the amount of glucosamine released, sufficient quantity of ninhydrin was added to the dissolution medium and color reduction as a result of glucosamine–ninhydrin complex formation could have been measured. This, however, resulted in the medium penetration into the swellable hydrophilic matrix causing significant peripheral stiffening of the matrix as a result of intragel complexation and suppression of release rate. As a result it was decided to remove samples of glucosamine solution periodically from the medium, adding to standard ninhydrin solution and measuring the color changes spectrophotometrically. Under these conditions, the rate constant of complex formation has to be optimized.

(v) Use of Reverse-Binding Technique for Evaluation of DMP 504, a Water-Insoluble Bile Acid Sequestrant—DMP 504 is a water-insoluble, cross-linked polymeric bile acid used as a nonsystemic cholesterol lowering agent, since it has the ability to bind bile salts with a slow dissociation rate. A film-coated DMP 504 tablet formulation was recently developed.[53] To evaluate the release characteristics of this dosage form, a new dissolution test method was proposed,[53] since direct measurement of drug concentration in the dissolution medium cannot be accomplished due to the water-insoluble nature and the fact that it has a binding function. A sodium cholate–phosphate buffer solution was selected as a dissolution medium. The amount of drug released from the tablet was calculated from the amount of cholate bound by the released drug at various time points using a binding calibration curve. By HPLC analysis, the bound cholate was calculated from the free cholate remaining in the dissolution medium at different time intervals. Through this approach it was determined that DMP 504 was completely released from the film-coated tablets within 15 min. Furthermore, from recovery testing on the bile salt, it was established that the reverse binding technique is robust, and values obtained were representative of complete release/binding.

Elementary and Supac-Based Dissolution Data Analysis

In the past decade many approaches have been proposed for the comparison of dissolution profiles.[54–57] In spite of the development of complicated approaches employing multivariate analysis, time series models, and mathematical models, the main problem persisting in the comparison process was the inability to define an exact measure of quantification, a point strongly acknowledged by Shah et

al. in their recent work on dissolution profile analysis.[2] Over the years, scientists have given much consideration to use of the Weibull function,[58,59] a model-dependent approach, as depicted in eq 18:

$$m = 1 - \exp[-(t - T_1)^{b/a}] \quad (18)$$

where m is the percent dissolved at time t, a is the time scale parameter, b is the shape factor, and T_1 is the location parameter. The shape factor, b, qualitatively defines the curve, i.e., when $b = 1$, the curve becomes a simple first-order exponential. If $b > 1$, the drug release rate is slow initially followed by an increase in release rate. The shape factor also provides qualitative information on diffusion and disintegration processes. The effective surface area for dissolution will be maximum after a certain time at the outset when $b > 1$, while when $b \leq 1$ no disintegration occurs at all, and the rate of dissolution will decrease steadily. The scale factor, a, provides a quantitative evaluation by differentiating the curves along the time axis. As pointed out by Polli and co-workers,[60] the Weibull model becomes fraught with an element of subjectivity because the judgment of the researcher is used in devising criteria for an adequate model fit. This further introduces a lack of metric sensitivity since as with all model-dependent approaches, no acceptance limits have been set as standard. In addition, the success of this approach relies on linearizing the dissolution data. However, a considerable curvature may be found in the upper region of the plot if the accumulated fraction of drug dissolved is not 1.0. In addition, the location parameter, which represents the lag time before the actual onset of the dissolution process, has to be estimated indirectly by a least-squares analysis or a graphical trial and error technique.

Therefore, it may be useful to consider a second category of analyses, i.e., model-independent treatment of dissolution data in order to determine the release profile similarity and concomitant dissimilarity where applicable. In this work we will focus on two classes of model-independency, namely time point or ratio test approaches and pairwise models. Model-independency, previously described by Rescigno,[61] in general would generate results for which the values do not depend on the selection of the specific parameter for fitting the data, but are dependent on the sampling times t_1, t_2,..., t_n and on an appropriate coefficient w_j representing the weight that the sampling time t_j has in the determination of the specific fitted functions.

In the time point/ratio test approach the $t_{50\%}$, $t_{70\%}$, and $t_{90\%}$ values as well as the mean dissolution times ($MDT_{50\%}$, $MDT_{70\%}$, $MDT_{90\%}$) are calculated for each formulation in each of the replicate dissolution measurements. Application of MDT provides more accurate drug release rate as compared to the $t_{x\%}$ approach and is determined as the sum of the individual periods of time during which a specific fraction of the total dose is released.[62]

The following equation (eq 19) may be used to calculate the MDT for each percentage point:

$$\mathrm{MDT} = \sum_{i=1}^{n} \hat{t}_i \frac{M_t}{M\infty} \quad (19)$$

where M_t is the fraction of dose released in time $\hat{t}_i = (t_i + t_{i-1})/2$, and M_∞ corresponds to the loading dose.

In the pairwise approach, determination of a "difference factor, f_1"[63] and "similarity factor, f_2"[19,20,63] (as outlined in the SUPAC and IVIVC guidelines) using the mean percentage released values can be performed by using eqs 20 and 21. To validate the acceptance of the f_1 and f_2 fit factors, calculations should be performed on the individual dissolution data of each formulation, which should reflect no statistical difference ($p > 0.05$) to the mean dissolution values.

The recent guidelines by the CDER at the FDA[20] describes the necessary criteria for granting biowaivers for specific changes in drug product manufacturing such as formulation changes or even changes in manufacturing site. To this end, the guidelines and specific published work[63] on extended release solid oral dosage forms describe the mathematical treatment of dissolution data derived from the pre- and postapproval changes by comparing their release profiles using the "similarity factor, f_2" which may be defined as follows:

$$f_2 = 50 \log\left\{\left[1 + \frac{1}{n}\sum_{t=1}^{n} w_t(R_t - T_i)^2\right]^{-0.5} \times 100\right\} \quad (20)$$

where n is the number of dissolution time points, w_t is an optional weight factor, R_t is the reference assay at time point t, and T_t is the test assay at time point t. Note that the "reference" and "test" products may be identical formulations. Optimization of release profiles may be achieved by the appropriate adoption of standard or alternative dissolution methods. The f_2 value between 50 and 100 suggests that the dissolution profiles are similar. The f_2 value of 100 suggests that the test and reference release profiles are identical, and as the value becomes smaller, the dissimilarity between release profiles increases. Equation 20 is a logarithmic transformation of the sum of squared error. It takes the average sums of squares of the difference between test and reference profiles and fits the result between 0 and 100. It is important to note that eq 20 is for the comparison of dissolution curves in which the average difference between R_t and T_t is <100. The use of the weight factor allows some values to be more important than other values, where w_t will be >1. If all values are treated equally, then $w_t = 1.0$.

In addition, Moore and Flanner[63] in their recent work also describe an f_1 fit factor or "difference factor" as follows:

$$f_1 = \left\{\frac{\sum_{t=1}^{n}|R_t - T_t|}{\sum_{t=1}^{n} R_t}\right\} \times 100\% \quad (21)$$

where f_1 describes the relative error between two dissolution profiles. "It approximates the percent error between two curves. The percent error is zero when the test and reference profiles are identical and increases proportionally with the dissimilarity between the two profiles".

Advantages and Limitations Associated with the Time Point/Ratio Test and Pairwise Approaches Used in Dissolution Data Treatment

The time point approach ($t_{x\%}$) for the interpretation of dissolution data appears to be inadequate for complete characterization of the profiles, since comparison of profiles not following a single path or void of crossover are not uncommon. Consequently, the choice of single data points for the calculation of meaningful dissolution values are questionable in the case of such issues revolving around product bioequivalence. Similarly, the choice of $MDT_{50\%}$, $MDT_{70\%}$, and $MDT_{90\%}$ may not always provide accurate information when profile crossover is too close. In the case of immediate release products such crossover in drug

release profiles may not present a major problem since the time scale of the release event is very short, often in the range of a few minutes to hours. On the contrary, such occurrences with controlled release products may have a significant impact on both quality assurance during product development and establishment of in vitro−in vivo correlations. Therefore, in the characterization of such dissolution profiles, a more in-depth analysis of data could provide a better description of the overall release profile.

Polli and co-workers[60] recently undertook an extensive study to mathematically and statistically evaluate various methods for the comparison of dissolution profiles of conventional metoprolol tartrate dosage forms for the demonstration of IVIVC. One of the selected methods included the application of the "similarity factor, f_2". In this work[60] as well as in studies from our lab,[27,28] it is shown that the similarity factor, f_2" is useful in providing an overall basis for dissolution profile comparisons. In addition, the fit factors evaluate curves that cross without a canceling effect. This effect may be unavoidable when the $t_{x\%}$ and $MDT_{x\%}$ models are used. While the method appears accurate, one of the main difficulties experienced is the "dependence of metric value on length of dissolution profile". When the "similarity−difference factor approach" is employed in data treatment (pairwise procedure), it becomes apparent that the selection and determination of the number of dissolution time points play a critical role in the calculation of the similarity factor value and the subsequent decision as to whether the test and reference profiles resemble each other or not. This observation is in agreement with the latest addition to the CDER document on the dissolution guidance for immediate release products.[64] However, it should be noted that as yet no limit on the selection of the dissolution time points has been released in the case of modified release dosage forms. For example, in the case of the high-density sticking formulation of theophylline (Figure 2a), f_2 values of 49.85 and 51.30 are obtained when time points (i.e., the *n* value) up to 30.5 and 35 h are respectively selected. This is also the case for the high-density sticking system of diltiazem hydrochloride (Figure 2c), i.e., f_2 values of 47.57 and 52.09 are obtained when time points up to 15 and 25 h are selected. Therefore, marginal differences observed in the comparison of dissolution data between the "test" and "reference" products may result in rejection of the test product as it is currently stipulated in the guidelines.

Conclusions

Historically, the theories applied to dissolution have remained unchanged, though to date their application and basic understanding is essential for design and development of sound alternative dissolution methodologies as well as for deriving complementary statistical and mathematical techniques for unbiased dissolution profile comparison. The various approaches described in this review, including intervention with the ring/mesh assembly, application of two-phase dissolution media systems, use of reverse binding technique, chemical stabilization via constant nitrogen gas purge into aqueous dissolution media, and chemical complexation/interaction outside the dissolution vessel as a colorimetric tool for analytical measurements, emphasize the potential of new or alternative methods for both qualitative and quantitative in vitro dissolution analysis. In particular, and as defined by dissolution theories, strict control of sink conditions by possibly mimicking the role played by the lipoidal nature of the gastrointestinal tissue in drug dissolution and absorption is primarily an absolute necessity prior to validating any in vitro−in vivo comparison. Various model-dependent and independent techniques have been used to characterize dissolution profiles for the primary purpose of comparison. With the advent of international harmonization of scientific protocols and implementation of SUPAC guidelines including site-to-site manufacturing conditions, such process comparisons have important regulatory implications. Although not infallible, the most statistically viable approach at this stage appears to be the use of f_2 similarity factor and f_1 difference factor. As outlined earlier, one of the distinct features of these two model-independent statistical measures surpassing all other techniques for profile comparison is their unique ability for complete profile characterization. However, more data on their utility in conjunction with similarity of in vivo drug absorption profiles will provide the ultimate measure of their discerning potential.

References and Notes

1. Dressman, J. B.; Amidon, G. L.; Reppas, C.; Shah, V. P. Dissolution Testing as a Prognostic Tool for Oral Drug Absorption: Immediate Release Dosage Forms. *Pharm. Res.* **1998**, *15*, 11−22.
2. Shah, V. P.; Tsong, Y.; Sathe, P.; Liu, J.-P. In Vitro Dissolution Profile Comparison − Statistics and Analysis of the Similarity Factor, f_2. *Pharm. Res.* **1998**, *15*, 889−896.
3. Galia, E.; Nicolaides, E.; Horter, D.; Lobenberg, R.; Reppas, C.; Dressman, J. B. Evaluation of Various Dissolution Media Performance of Class I and II Drugs. *Pharm. Res.* **1998**, *15*, 698−705.
4. Omelczuk, M. O.; McGinity, J. W. The Influence of Thermal Treatment on the Physical-Mechanical and Dissolution Properties of Tablets Containing Poly (DL-lactic acid). *Pharm. Res.* **1993**, *10*, 542−548.
5. Wang, Z.; Horikawa, T.; Hirayama, F.; Uekama, K. Design and In vitro Evaluation of a Modified Release Oral Dosage Form of Nifedipine by Hybridization of Hydroxypropyl-beta-cyclodextrin and Hydroxypropylcellulose. *J. Pharm. Pharmacol.* **1993**, *45*, 942−946.
6. De Villiers, M. M.; Van der Watt, J. G. The Measurement of Mixture Homogeneity and Dissolution to Predict the Degree of Drug Agglomerate Breakdown Achieved through Powder-Mixing. *Pharm. Res.* **1994**, *11*, 1557−1561.
7. Gordon, M. S.; Rudraraju, V. S.; Dani, K.; Chowan, Z. T. Effect of the Mode of Super Disintegrant Incorporation on Dissolution in Wet Granulated Tablets. *J. Pharm. Sci.* **1993**, *82*, 220−226.
8. Rekhi, G. S.; Jambhekar, S. S. Bioavailability and *In vitro/In vivo* Correlation for Propranolol Hydrochloride Extended Release Bead Products Prepared Using Aqueous Polymeric Dispersions. *J. Pharm. Pharmacol.* **1996**, *48*, 1276−1284.
9. Fassihi, R. A.; Munday, D. L. Dissolution of Theophylline from Film-coated Slow Release Mini-tablets in Various Dissolution Media. *J. Pharm. Pharmacol.* **1989**, *41*, 369−372.
10. Gouldson, M. P.; Deasy, P. B. Use of Cellulose Ether Containing Excipients withMicrocrystalline Cellulose for the Production of Pellets Containing Metformin Hydrochloride bythe Process of Extrusion-spheronization. *J. Microencaps.* **1997**, *14*, 137−153.
11. Naylor, L. J.; Bakatselou, V.; Dressman, J. B. Comparison of the Mechanism of Dissolution ofHydrocortisone in Simple and Mixed Micelle Systems. *Pharm. Res.* **1993**, *10*, 865−870.
12. Williams, R. L.; Upton, R. A.; Ball, L.; Braun, R. L. Lin, E. T.; Liang-Gee, W.; Leeson, L. J. Development of a New Controlled Release Formulation of Chlorpheniramine Maleate Using In vitro-In vivo Correlations. *J. Pharm. Sci.* **1991**, *80*, 22−25.
13. Fassihi, R. A.; Ritschel, W. A. Multiple-Layer, Direct-Compression, Controlled Release System: *In vitro and In vivo* Evaluation. *J. Pharm. Sci.* **1993**, *82*, 750−754.
14. Munday, D. L.; Fassihi, R. A. *In vitro/In vivo* Correlation Studies on Novel Controlled ReleaseTheophylline Delivery System and on Theo-Dur Tablets. *Int. J. Pharm.* **1995**, *118*, 251−255.
15. Grundy, J. S.; Anderson, K. E.; Rogers, J. A.; Foster, R. T. Studies on Dissolution Testing of the Nifedipine Gastrointestinal Therapeutic System. II Improved In vitro−In vivo Correlation Using a Two-Phase Dissolution Test. *J. Controlled Release* **1997**, *48*, 9−17.
16. Yu, Z.; Schwartz, J. B.; Sugita, E. T. Theophylline Controlled Release Formulations: In vitro−In vivo Correlations. *Biopharm. Drug Dispos.* **1996**, *17*, 259−272.

17. Elkoshi, Z. Dissolution Specifications Based on Release Rates. *J. Pharm. Sci.* **1999**, *88*, 434−444.
18. Skoug, J. W.; Halstead, G. W.; Theis, D. L.; Freeman, J. E.; Fagan, D. T.; Rohrs, B. R. Strategy for the Development and Validation of Dissolution Tests for Solid Oral Dosage Forms. *Pharm. Tech.* **1996**, *20*, 59−72.
19. *SUPAC*; Center for Drug Evaluation and Research (CDER) at the Food and Drug Administration (FDA): Washington, D.C., 1995.
20. *IVIVC*; Center for Drug Evaluation and Research (CDER) at the Food and Drug Administration (FDA): Washington, D.C., 1996.
21. Devane, J.; Butler, J. The Impact of In vitro−In vivo Relationships on Product Development. *Pharm Tech.* **1997**, *21*, 146−159.
22. Cohen, J. L.; Hubert, B. B.; Leeson, L. J.; Rhodes, C. T.; Robinson, J. R.; Roseman, J. T.; Shefter, E. The Development of USP Dissolution and Drug Release Standards. *Pharm. Res.* **1990**, *7*, 983−987.
23. AAPS/USP Workshop on Dissolution Calibration and Testing: Workshop Report *Pharm. Res.* **1996**, *13*, 6−9.
24. *USP 23-NF18*; United States Pharmacopoeial Convention, Inc.: Rockville, MD, 1995.
25. Bocanegra, L. M.; Morris, G. J.; Jurewicz, J. T.; Mauger, J. W. Fluid and Particle Laser Doppler Velocity Measurements and Mass Transfer Predictions for the USP Paddle Method Dissolution Apparatus. *Drug Dev. Ind. Pharm.* **1990**, *16*, 1441−1464.
26. Khoury, N.; Mauger, J. W.; Stephen, H. Dissolution Rate Studies from a Stationary Disk/Rotating Fluid System. *Pharm. Res.* **1988**, *5*, 495−500.
27. Pillay, V.; Fassihi, R. Evaluation and Comparison of Dissolution Data Derived from Different Modified Release Dosage Forms: An Alternative Methodol. *J. Controlled Release* **1998**, *55*, 45−55.
28. Pillay, V.; Fassihi, R. A New Method for Dissolution Studies of Lipid-filled Capsules Employing Nifedipine as the Model Drug. *Pharm. Res.* **1999**, *15*, 333−337.
29. Nelson, K. G.; Shah, A. C. Convective Diffusion Model for a Transport-Controlled Dissolution Rate Process. *J. Pharm. Sci.* **1975**, *64*, 610−614.
30. Shah, A. C.; Nelson, K. G. Evaluation of a Convective Diffusion Drug Dissolution Rate Model. *J. Pharm. Sci.* **1975**, *64*, 1518−1520.
31. Patel, M.; Carstensen, J. T. Nonsink Dissolution Rate Equations. *J. Pharm. Sci.* **1975**, *64*, 1651−1656.
32. Kitamori, N.; Iga, K. Dissolution Profiles of Drugs from Tablets. *J. Pharm. Sci.* **1978**, *67*, 1436−1439.
33. Melia, C. D.; Davis, S. S. Review Article: Mechanisms of Drug Release from Tablets and Capsules. I Disintegration. *Alim. Pharmacol. Ther.* **1989**, *3*, 223−232.
34. Melia, C. D.; Davis, S. S. Review Article: Mechanisms of Drug Release from Tablets and Capsules. I Dissolution. *Alim. Pharmacol. Ther.* **1989**, *3*, 513−525.
35. Abdou, H. M. Theory of dissolution and Theoretical concepts for the release of a drug from a dosage form. In *Dissolution, Bioavailability and Bioequivalence*, Gennaro, A., Migdalof, B., Hassert, G. L., Medwick, T., Eds.; Mack Publishing Company: Easton, PA, 1989; pp 11−52.
36. Gibaldi, M. Gastrointestinal absorption − Physicochemical considerations. In *Biopharmaceutics and Clinical Pharmacokinetics*, 4th ed.; Gibaldi, M., Lea and Febiger: Malvern, PA, 1991; pp 40−60.
37. Florence, A. T.; Attwood, D. Properties of the solid state. In *Physicochemical Principles of Pharmacy*, 2nd ed.; Florence, A. T., Attwood, D., Eds.; Macmillan Press: Basingstoke, Hants., England, 1988; pp 21−46.
38. Goldberg, A. H.; Higuchi, W. I.; Ho., N. F.; Zographi, G. Mechanisms of interphase transport. I. Theoretical considerations of diffusion and interfacial barriers in transport of solubilized systems. *J. Pharm. Sci.* **1967**, *56*, 1432−1437.
39. Wagner, J. G. Interpretation of percent dissolved-time plots derived from *in vitro* testing of conventional tablets and capsules. *J. Pharm. Sci.* **1969**, *58*, 1253−1257.
40. Kitazawa, S.; Sakai, K.; Murosaki, H. Effect of pharmaceutical adjuvant on absorption of drugs. Effect of Magnesium aluminosilicate on absorption of aspirin in man (authors translation form Japanese). *Yakugaku Zassihi* **1974**, *94*, 1353−1357.
41. Kitazawa, S.; Johno, I.; Ito, Y.; Teramura, S.; Okada, J. Effects of hardness on the disintegration time and the dissolution rate of uncoated caffeine tablets. *J. Pharm. Pharmacol.* **1975**, *27*, 765−770.
42. Kitazawa, S.; Johno, I.; Minouchi, T.; Okada, J. Interpretation of dissolution rate data from in vitro testing of compressed tablets. *J. Pharm. Pharmacol.* **1977**, *29*, 453−459.
43. El-Yazigi, A. Disintegration-dissolution analysis of percent dissolved-time data. *J. Pharm. Sci.* **1981**, *70*, 535−537.
44. Carstensen, J. T.; Wright, J. L.; Blessel, K. W.; Sheridan, J. *J. Pharm. Sci.* **1978**, *67*, 48−50.
45. Soltero, R. A.; Hoover, J. M.; Jones, T. F.; Standish, M. Effects of Sinker Shapes on Dissolution Profiles. *J. Pharm. Sci.* **1989**, *78*, 35−40.
46. Withey, R. J.; Bowker, A. J. *J. Pharm. Pharmacol.* **1972**, *24*, 345−351.
47. Serajuddin, A. T. M.; Sheen, P.-C.; Mufson, D.; Bernstein D. F.; Augustine, M. A. Effect of Vehicle Amphiphilicity on the Dissolution and Bioavailability of a Poorly Water Soluble Drug from Solid Dispersions. *J. Pharm. Sci.* **1988**, *77*, 414−417.
48. Sheen, P.-C.; Kim, S.-I.; Petillo J. J.; Serajuddin, A. T. M. Bioavailability of a Poorly Water Soluble Drug from Tablet and Solid Dispersion in Humans. *J. Pharm. Sci.* **1991**, *80*, 712−714.
49. Shah, N. H.; Carjaval, M. T.; Patel, C. I.; Infeld M. H.; Malick, A. W. Self-Emulsifying Drug Delivery Systems (SEDDS) for Improving In Vitro Dissolution and Oral Absorption of Lipophilic Drugs. *Bull. Technol. Gattefosse.* **1992**−**1993**, *85*, 45−54.
50. Crison, J. R.; Weiner N. D.; Amidon, G. L. Dissolution Media for In Vitro Testing of Water Soluble Drugs: Effect of Surfactant Purity on In Vitro Dissolution of Carbamazepine in Aqueous Solutions of Sodium Lauryl Sulfate. *J. Pharm. Sci.* **1997**, *87*, 384−388.
51. Grundy, J. S.; Anderson, K. E.; Rogers J. A.; Foster, R. T. Studies on Dissolution Testing of the Nifedipine Gastrointestinal Therapeutic System. I Description of a Two-Phase In Vitro Dissolution Test. *J. Controlled Release* **1997**, *48*, 1−8.
52. Gibaldi, M.; Feldman, S. Establishment of Sink Conditions in Dissolution Rate Determinations. *J. Pharm. Sci.* **1967**, *56*, 1238−1242.
53. Wu, L.-S.; McCormick, T. J.; Chang, R.-K.; Pang, J.; McCummings, T.; Ramos, M.; Hussain, M. A. Development of an Unconventional In Vitro Drug Release Test Method for a Bile Acid Sequestrant, DMP 504, Tablet. *Pharm. Res.* **1999**, in press.
54. Shah, V. P.; Yamamoto, L. A.; Shuirmann, D.; Elkins, J.; Skelly, J. P. Analysis of In Vitro Dissolution of Whole Versus Half Controlled Release Tablets. *Pharm. Res.* **1987**, *4*, 416−419.
55. Chow, S. C.; Ki, F. Y. C. Statistical Comparison between Dissolution Profiles of Drug Products. *J. Biopharm. Stat.* **1997**, *7*, 241−258.
56. Sathe, P.; Tsong, Y.; Shah, V. P. In Vitro Dissolution Profile Comparison: Statistics and Analysis, Model Dependent Approach. *Pharm. Res.* **1996**, *13*, 1799−1803.
57. Tsong, Y.; Hammerstrom, T.; Sathe, P.; Shah, V. P. Statistical Assessment of Mean Difference between Two Dissolution Data Sets. *Drug Inf. J.* **1996**, *30*, 1105−1112.
58. Altaf, S. A.; Yu, K.; Parasrampuria, J.; Friend, D. R. Guar Gum-Based Sustained Release Diltiazem. *Pharm. Res.* **1998**, *15*, 1196−1201.
59. Langenbucher, F. Parametric Representation of Dissolution-Rate Curves by the RRBSW Distribution. *Pharm. Ind.* **1976**, *38*, 472−477.
60. Polli, J. E.; Rekhi, G. S.; Augsburger, L. L.; Shah, V. P. Methods to Compare Dissolution Profiles and Rationale for Wide Dissolution Specifications for Metoprolol Tartrate Tablets. *J. Pharm Sci.* **1997**, *86*, 690−700.
61. Rescigno, A. Bioequivalence. *Pharm Res.* **1992**, *9*, 925−928.
62. Linder, W. D.; Lippold, B. C. Drug Release from Hydrocolloid Embeddings with High or Low Susceptibility to Hydrodynamic Stress. *Pharm. Res.* **1995**, *12*, 1781−1785.
63. Moore, J. W.; Flanner, H. H. Mathematical Comparison of Dissolution Profiles. *Pharm. Tech.* **1996**, *20*, 64−74.
64. *Guidance for Industry: Dissolution Testing of Immediate Release Solid Oral Dosage Forms*; U.S. Department of Health and Human Services, Food and Drug Administration, Center for Drug Evaluation and Research: August, 1997.

Acknowledgments

The National Research Foundation (South Africa) is acknowledged for awarding the Doctoral Fellowship to Viness Pillay. The authors wish to thank Dr. Munir Hussain (DuPont Pharmaceutical Company, DE) for reviewing this article. References have been made in the text with regard to work of Lei-Shu Wu et al. (DuPont Pharmaceutical Company, DE) on reverse binding methodology. Mr. William D. ST. John (Nutraceutix, Inc., Redmond, WA) is acknowledged for supporting projects on vitamin C and glucosamine products.

JS990139B

UPPER III: Unified Physical Property Estimation Relationships. Application to Non-Hydrogen Bonding Aromatic Compounds

NEERA JAIN AND SAMUEL H. YALKOWSKY*

Contribution from *Department of Pharmaceutical Sciences, College of Pharmacy, 1703 E. Mabel Street, The University of Arizona, Tucson, Arizona 85721.*

Received April 9, 1999. Accepted for publication June 28, 1999.

Abstract □ The UPPER scheme uses four additive and two nonadditive parameters and several well-known equations to calculate 21 physical properties of organic compounds strictly from molecular structure. The scheme allows reasonable estimations of melting and boiling points, aqueous and octanol solubilities, air–octanol, air–water, and octanol–water partition coefficients, vapor pressure, and other properties. In this report non-hydrogen bonding aromatic compounds are used to evaluate a portion of the UPPER scheme.

Introduction

A number of group contribution methods of calculating various physical properties of compounds such as melting point, boiling point, aqueous solubility, octanol solubility, partition coefficients, and vapor pressure have been reported. Some of these have been reviewed by Lyman et al.[1]. The most commonly used schemes for each property are independent of one another and are based on different models and assumptions for the molecule. Two notable exceptions have been presented by Bondi[2] and Joback and Reid.[3] These each use a single molecular fragmentation scheme for the calculation of several physical properties. Recently computational approaches have been used by several groups.[4−12] Unlike most existing schemes, the UPPER (unified physical property estimation relationships) scheme[13,14] uses calculations that are simple, straightforward, and can be performed without a computer. They are also based upon well-known physicochemical relationships. The molecular descriptors used in the UPPER scheme are well defined and highly intuitive. The UPPER scheme is unique in its use of a combination of additive group contribution values and simple nonadditive molecular parameters that account for the effects of the overall molecular geometry.

The UPPER scheme has many applications in the fields of pharmaceutical, environmental, and material sciences. Estimations of the above physical properties can provide important insight regarding the pharmaceutical efficacy, environmental fate, and industrial utility of a compound.

In this study estimated values for eight physical properties calculated by UPPER are compared to experimental values obtained from the literature. Aromatic compounds (benzenes, naphthalenes, anthracenes, phenanthrenes, and biphenyls) substituted with non-hydrogen bonding groups (i.e., methyl, fluoro, chloro, bromo, iodo, nitro) are used for this evaluation.

* To whom correspondence should be addressed. Tel: (520) 626-1289, fax: (520) 626-4063, e-mail: yalkowsk@pharmacy.arizona.edu.

Theoretical Background

UPPER is used to calculate a number of physical properties directly from molecular structure. Four sets of group contribution values are used to calculate four additive physical properties: heat of boiling, heat of melting, molar volume, and the aqueous activity coefficient. The breakdown of the molecule into its constitutive groups is both simple and uniform for all the calculations. Additionally, two nonadditive molecular descriptors that account for molecular symmetry and flexibility are used to estimate transition entropies. These six parameters are then used to calculate several fundamental physical properties via well-accepted equations.

Additive Molecular Parameters—the change in enthalpy that accompanies a phase transition is the result of the total intermolecular interactions of the molecule. It can be assumed that a group (for example an aromatic CH_3) will make a nearly constant contribution to the molar enthalpy change. On this basis the enthalpies of boiling and melting can each be considered as the summation of group contributions from constituent groups. Thus the contribution of each group toward the molar heat of boiling and melting can be quantitated as the sum of b_i and m_i values, respectively. Simamora et al.[15] and Krzyzaniak et al.[16] used multiple linear regression to generate b_i and m_i values from literature data for thousands of aliphatic and aromatic compounds. The b_i and m_i values[15] used in this study are shown in Table 1.

The molar volume of a liquid is the ratio of the molecular weight to the density. Each group occupies a nearly constant volume in a molecule that is designated as its v_i value. A number of group contribution schemes have been used to estimate the molar volume. In this study the values developed by Fedors[17] are used and are shown in Table 1.

Myrdal et al.[18−20] presented the AQUAFAC (aqueous functional activity coefficients) scheme that considers the group aqueous activity coefficient as an additive property. The AQUAFAC model is based on an extensive database (AQUASOL) of reported solubilities. The q_i values[18−22] that are given in Table 1 are group contributions to the aqueous activity coefficient of the solute.

Nonadditive Molecular Parameters—The two nonadditive molecular descriptors that account for the geometry of the molecule are the symmetry and flexibility numbers. Dannenfelser et al.[23] and Simamora et al.[24] have

10.1021/js990117p CCC: $18.00
Published on Web 07/31/1999

Table 1—Additive Parameters

group	description	b_i	m_i	v_i	q_i
CAR	substituted aromatic carbon	–704	97	–3.9	0.525
CHAR	unsubstituted aromatic carbon	5670	1940	15.1	0.321
CBR	CAR involved in the bridging of two rings	–704	97	–1.4	0.525
CBIP	CAR involved in a biphenyl linkage	–4890	–2140	–4.1	0.525
YCH3	methyl group attached to an aromatic ring	8040	2600	33.5	0.204
YF	fluorine attached to an aromatic ring	5890	1950	18.0	–0.141
YCl	chlorine attached to an aromatic ring	9330	3400	28.0	0.409
YBr	bromine attached to an aromatic ring	10960	3900	34.0	0.645
YI	iodine attached to an aromatic ring	13630	4440	35.5	0.887
YNO2	nitro group attached to an aromatic ring	13110	5072[a]	32.0	0.082
OBIP	correction for ortho substituents in a biphenyl	–1630	–1190	0.0	–0.123

[a] Note: This value is a misprint in ref 15.

Table 2—Molecular Symmetry Numbers (σ) of Some Compounds

σ	Examples
1	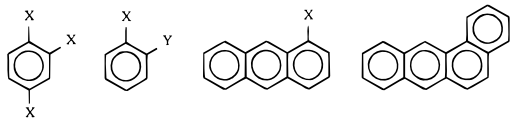
2	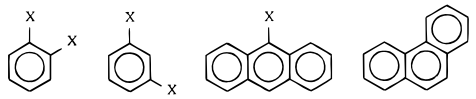
2	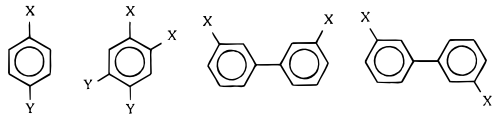
3	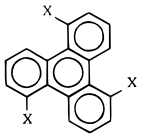
4	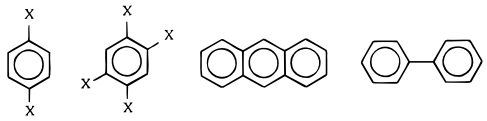
6	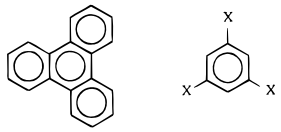
12	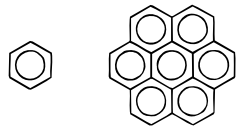

described these parameters in detail. The external rotational symmetry number (σ) is a measure of the rotational degeneracy of the molecule. It is equal to the number of orientations of a molecule that are identical with some reference orientation. The assignment of molecular symmetry number is illustrated in Table 2. The flexibility (ϕ) of a molecule is a measure of the number of stable torsional conformations that it can assume. Since the molecules of this study are considered rigid, they are all assigned a flexibility number of unity. Note, biphenyls can assume more than one conformation; therefore, the entropy of fusion is approximated using the most stable conformation. The ortho substituents on the biphenyl can result in noncoplanarity of the molecule and therefore a correction factor, OBIP, is used as shown in Table 1.

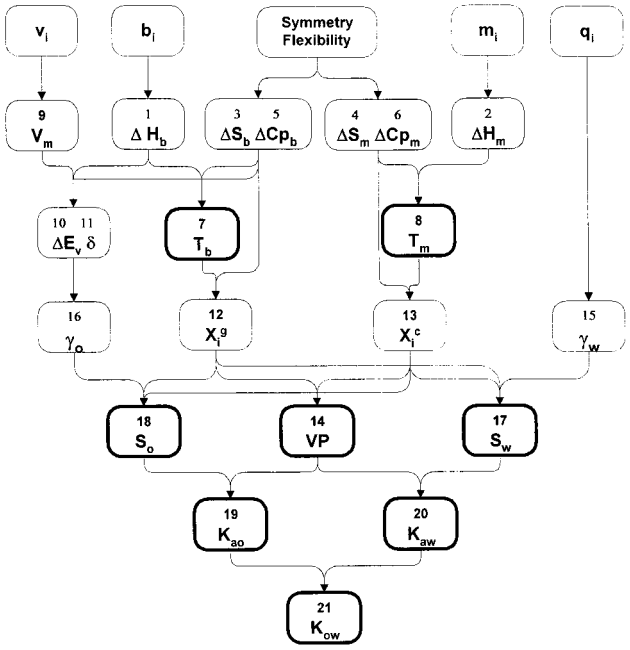

Figure 1—Schematic representation of UPPER.

Calculation of the Physical Properties—The logic of the UPPER scheme is illustrated in Figure 1. Twenty-one physical properties are each calculated from other properties by the use of simple, well-established relationships described below. The eight properties considered in this study are outlined in bold in Figure 1. The numbers in the following brief summary of the UPPER scheme correspond to the numbers in Figure 1.

1. Heat of Boiling (ΔH_b)—The heat of boiling, or the enthalpy of vaporization at the normal boiling temperature (J/mol), is calculated as the summation of the b_i values for the constitutive groups of the molecule. Therefore,

$$\Delta H_b = \sum(n_i b_i) \qquad (1)$$

where n_i is the number of times the group b_i appears in the molecule.

2. Heat of Melting (ΔH_m)—The heat of melting, or the enthalpy of fusion (J/mol) is analogously calculated as the summation of the m_i values for the constitutive groups of the molecule, so that

$$\Delta H_m = \sum(n_i m_i) \quad (2)$$

3. Entropy of Boiling (ΔS_b)—The entropy of boiling, or the entropy of vaporization at the normal boiling point (J/K-mol) is calculated by Trouton's rule, which is applicable to coal tar derivatives, including non-hydrogen bonding aromatic compounds. Trouton's rule states that

$$\Delta S_b = 88 \quad (3)$$

4. Entropy of Melting (ΔS_m)—The entropy of melting, or the entropy of fusion (J/K-mol) is calculated by the Dannenfelser and Yalkowsky equation[23] that accounts for the effects of symmetry (σ) and flexibility (ϕ) upon the probability of a molecule being properly oriented and conformed for incorporation into the crystal lattice. The equation states:

$$\Delta S_m = 56.5 - 19.1 \log \sigma + 19.1 \log \phi \quad (4)$$

For the rigid molecules of this study $\phi = 1$ and eq 4 reduces to

$$\Delta S_m = 56.5 - 19.1 \log \sigma \quad (4a)$$

(Note that for most organic compounds the value of σ is either 1 or 2, and only 2% of compounds have σ exceeding 4.)

5. Heat Capacity Changes on Boiling (ΔC_{p_b})—Myrdal et al.[25] estimated that the heat capacity change on boiling (J/K-mol) is related to the flexibility of the molecule as:

$$\Delta C_{p_b} = -90 - 6.8 \log \phi \quad (5)$$

For the rigid molecules of this study $\phi = 1$, and the above eq 5 reduces to

$$\Delta C_{p_b} = -90 \quad (5a)$$

6. Heat Capacity Changes on Melting (ΔC_{p_m})—Mackay[26] and Yalkowsky and Mishra[27] have shown that the heat capacity change on melting can be approximated to be zero for rigid molecules, i.e.,

$$\Delta C_{p_m} = 0 \quad (6)$$

7. Boiling Point (T_b)—The boiling point (K) is calculated as the ratio of the enthalpy of boiling (from eq 1) to the entropy of boiling (from eq 3). Thus

$$T_b = \frac{\Delta H_b}{\Delta S_b} = \frac{\sum n_i b_i}{88} \quad (7)$$

8. Melting Point (T_m)—The melting point (K) is calculated as the ratio of the enthalpy of melting (from eq 2) to the entropy of melting (from eq 4a).

$$T_m = \frac{\Delta H_m}{\Delta S_m} = \frac{\sum n_i m_i}{56.5 - 19.1 \log \sigma} \quad (8)$$

9. Molar Volume (V_m)—The molar volume (cm^3/mol) is calculated as the summation of the v_i values.

$$V = \sum n_i v_i \quad (9)$$

10. Energy of Vaporization (ΔE_v)—According to the second law of thermodynamics

$$\Delta E_b = \Delta H_b - RT \quad (10)$$

where ΔE_b is the change in energy of boiling at the boiling point. The energy of vaporization, ΔE_v (J/mol) at any temperature is related to its value at the boiling point by

$$\Delta E_v = \Delta E_b - (T_b - T)\Delta C_{p_b} \quad (10a)$$

where ΔH_b, ΔC_{p_b}, and T_b are obtained from eqs 1, 5a, and 7, respectively, R is the gas constant, and T is 298 K. Combining eqs 10 and 10a gives

$$\Delta E_v = \Delta H_b - (T_b - T)\Delta C_{p_b} - RT \quad (10b)$$

11. Solubility Parameter (δ)—The solubility parameter (J/cm^3)$^{0.5}$ is an expression of the cohesion between like molecules. It is calculated from the energy of vaporization (from eq 10b) and the molar volume (from eq 9) by

$$\delta = \sqrt{\frac{\Delta E_v}{V}} \quad (11)$$

12. Ideal Solubility of a Gas (X_i^g)—The ideal mole fractional solubility of a gas is the solubility that it would have in a perfect solvent. It is calculated using the integrated form of the Clausius–Clapyeron equation as

$$\log X_i^g = \frac{\Delta S_b(T_b - T)}{2.3RT} - \frac{\Delta C_{p_b}(T_b - T)}{2.3RT} + \frac{\Delta C_{p_b}}{2.3R} \ln \frac{T_b}{T} \quad (12)$$

where ΔS_b, C_{pb}, and T_b are calculated from eqs 3, 5a, and 7, respectively.

13. Ideal Solubility of a Crystal (X_i^c)—The ideal mole fractional solubility of a crystalline solid is similarly calculated from the van't Hoff equation

$$\log X_i^c = -\frac{\Delta S_m(T_m - T)}{2.3RT} - \frac{\Delta C_{p_m}(T_m - T)}{2.3RT} + \frac{\Delta C_{p_m}}{2.3R} \ln \frac{T_m}{T} \quad (13)$$

According to eq 6, $\Delta C_{p_m} = 0$; therefore, eq 13 can be simplified to

$$\log X_i^c = -\frac{\Delta S_m(T_m - T)}{2.3RT} \quad (13a)$$

where ΔS_m and T_m are calculated from eqs 4a and 8, respectively. Note that when the melting point of a compound is less than 298 K, the logarithm of the ideal solubility of the crystal is zero or in other words it is completely miscible. Also note that for solids of low symmetry the above eq 13a is approximately

$$\log X_i^c = -0.01(T_m - T) \quad (13b)$$

14. Vapor Pressure (VP)—Yalkowsky and Mishra[28] showed that the vapor pressure (atm) can be calculated from the integrated form of the Clausius–Clapeyron equation

$$\log VP = -\frac{\Delta S_m(T_m - T)}{2.3RT} - \frac{\Delta C_{p_m}(T_m - T)}{2.3RT} + \frac{\Delta C_{p_m}}{2.3RT} \ln \frac{T_m}{T} - \frac{\Delta S_b(T_b - T)}{2.3RT} + \frac{\Delta C_{p_b}(T_m - T)}{2.3RT} - \frac{\Delta C_{p_b}}{2.3RT} \ln \frac{T_b}{T} \quad (14)$$

By incorporating eqs 12 and 13 the above equation can be written as

$$\log VP = \log X_i^c - \log X_i^g \quad (14a)$$

If the compound is a liquid, eq 14a is reduced to eq 14b as the crystal term drops out.

$$\log VP = -\log X_i^g \quad (14b)$$

15. Activity Coefficient in Water (γ_w)—The logarithm of the aqueous activity coefficient (mol/L) is equal to the summation of the AQUAFAC substituent group activity coefficients.

$$\log \gamma_w = \sum n_i q_i \quad (15)$$

16. Activity Coefficient in Octanol (γ_o)—The octanol activity coefficient (mol/L) is calculated by applying the Scatchard–Hildebrand relationship to octanol. This gives

$$\log \gamma_o = \frac{V_u(\delta_{oct} - \delta_u)^2 \phi_{oct}{}^2}{2.3RT} \quad (16)$$

where V_u and δ_u are the molar volume and solubility parameter of the solute calculated using eqs 9 and 11, respectively, and ϕ_{oct} is the volume fraction of the solvent, octanol. Using the solubility parameter for octanol as the solvent, eq 16 becomes

$$\log \gamma_{oct} = \frac{V_u(21.1 - \delta_u)^2 \phi_{oct}{}^2}{2.3RT} \quad (16a)$$

Hildebrand and Scott[29] showed that the critical temperature, T_c, at which two liquids are completely miscible, is

$$T_c = \frac{V(\delta_v - \delta_u)^2}{2R} \quad (16b)$$

where V is the arithmetic of the molar volumes of octanol and the solute. If we assume the molar volume of the solute is nearly same as octanol, 138 cm^3/mol, i.e.,

$$V = \frac{V_{oct} + V_u}{2} \approx 138 \quad (16c)$$

then complete miscibility will be achieved if

$$|21.1 - \delta_u| < \sqrt{\frac{2RT}{138}} \quad (16d)$$

which corresponds to $15.1 < \delta_u < 27.1$ in (J/cm^3)$^{0.5}$ at 298 K or higher temperature. As most organic compounds have solubility parameters in this range, they are completely miscible with octanol.

17. Solubility in Water (S_w)—The aqueous solubility (mol/L) for solids is calculated as the ratio of the ideal solubility of the solute to its aqueous activity coefficient. In logarithmic terms this is

$$\log S_w = \log X_i^c - \log \gamma_w \quad (17)$$

where $\log X_i^c$ and $\log \gamma_w$ are calculated from eqs 13a and 15, respectively. For liquids X_i^c is set equal to unity and thus eq 17 reduces to

$$\log S_w = -\log \gamma_w \quad (17a)$$

18. Solubility in Octanol (S_o)—Likewise the octanol solubility (mol/L) is calculated as the ratio of the ideal solubility of the solute to its octanol activity coefficient. For a solid solute this is

$$\log S_o = \log X_i^c - \log \gamma_o \quad (18)$$

where $\log X_i^c$, and $\log \gamma_o$ are calculated from eqs 13a and 16, respectively.

19. Air–Octanol Partition Coefficient (K_{ao})—The air–octanol partition coefficient (atm-L/mol) is calculated as the ratio of the vapor pressure to the octanol solubility.

$$\log K_{ao} = \log VP - \log S_o \quad (19)$$

where $\log VP$, and $\log S_o$ are calculated from eqs 14a and 18, respectively.

Air–Water Partition Coefficient or Henry's Law Constant (K_{aw})—The air–water partition coefficient (atm-L/mol) is calculated as the ratio vapor pressure coefficient to the aqueous solubility.

$$\log K_{aw} = \log VP - \log S_w \quad (20)$$

where $\log VP$ and $\log S_w$ are calculated from eqs 14a and 17, respectively.

21. Octanol–Water Partition Coefficient (K_{ow})—The octanol–water partition coefficient is calculated as the ratio of the aqueous activity coefficient to the octanol activity coefficient.

$$\log K_{ow} = \log \gamma_w - \log \gamma_o \quad (21)$$

where $\log \gamma_w$ and $\log \gamma_o$ are calculated from eqs 15 and 16, respectively. Alternatively $\log K_{ow}$ can be calculated either by

$$\log K_{ow} = \log S_o - \log S_w \quad (21a)$$

$$\log K_{ow} = \log K_{aw} - \log K_{ao} \quad (21b)$$

where $\log S_w$, $\log S_o$, $\log K_{ao}$, and $\log K_{aw}$ are calculated from eqs 17, 18, 19, and 20, respectively.

Data Collection

Four hundred and five rigid, non-hydrogen bonding aromatic compounds including benzenes, naphthalenes, anthracenes, phenanthrenes, and biphenyls substituted with methyl, fluoro, chloro, bromo, iodo, and nitro groups were used in this study. Data for melting and boiling points,[30–33] aqueous,[31,33–37] and octanol[38] solubilities, air–water,[33] air-octanol,[42] and octanol–water[33,43] partition coefficients, and vapor pressure[31,33,39–41] were taken from the literature.

Additive Parameters—Simamora et al.,[15] Fedors,[17] Myrdal et al.,[18,19] and Lee et al.[21] reported the values of the additive parameters used in this study. These are shown in Table 1.

Nonadditive Parameters—Symmetry numbers as described by Dannenfelser et al.[23] and illustrated in Table 2 were assigned to each compound. Since the substituted aromatics considered are rigid molecules ϕ is equal to unity for all compounds.

Results and Discussion

Boiling Point—The observed and predicted boiling points are in good agreement as evidenced by the fit of the data to the line of identity in Figure 2. The average

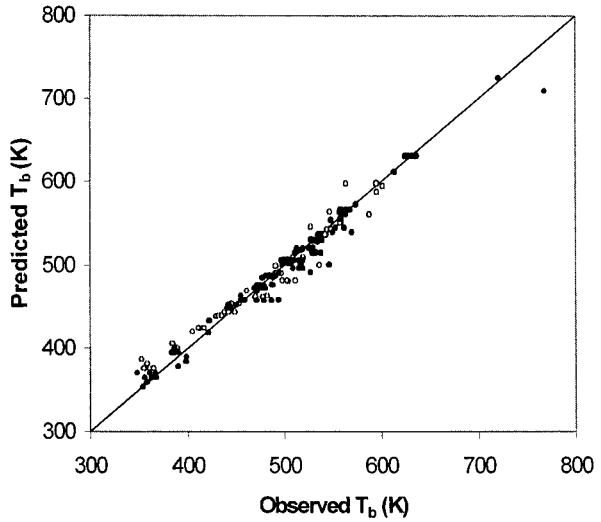

Figure 2—Observed vs predicted boiling point (K). (○) Compounds used in the training set to generate b_i values. (●) Compounds not used in the training set.

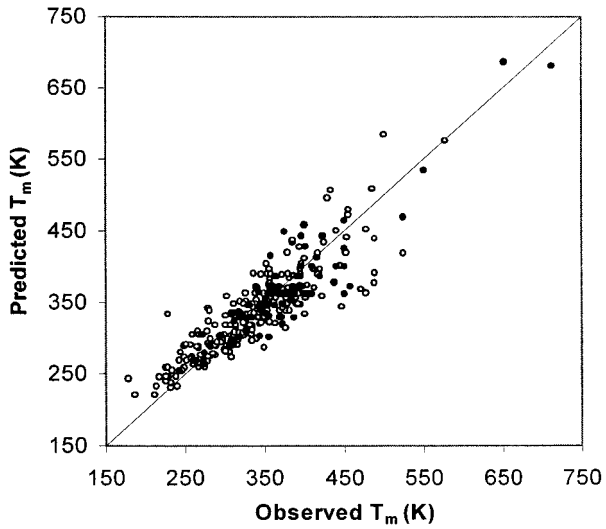

Figure 3—Observed vs predicted melting point (K). (○) Compounds used in the training set to generate m_i values. (●) compounds not used in the training set.

absolute error is 8.67 K for 191 compounds. Only 68 of the 191 compounds were used by Simamora et al.[15] to generate the b_i values. These are denoted by open circles. The remainder of the compounds are a true test and are denoted by filled circles in Figure 2.

Melting Point—The observed and predicted melting points are shown in Figure 3. The average absolute error is 23 K for 338 compounds. Over 85 of these compounds were not used by Simamora et al.[15] to generate m_i values. These compounds are represented by filled circles and are a true test set for the relationship.

As melting point is dependent upon the arrangement of the molecules in the crystal lattice as well as upon the strength of the pairwise group interactions, it is more difficult to predict than boiling point. The importance of incorporating a nonadditive parameter along with the group contributions is evident from the fact that the calculation of the melting points without a symmetry term yields a average absolute error of 30 K. The calculation of the melting point by group contributions alone leads to the same estimated melting point for constitutional isomers while using the symmetry number distinguishes them effectively.

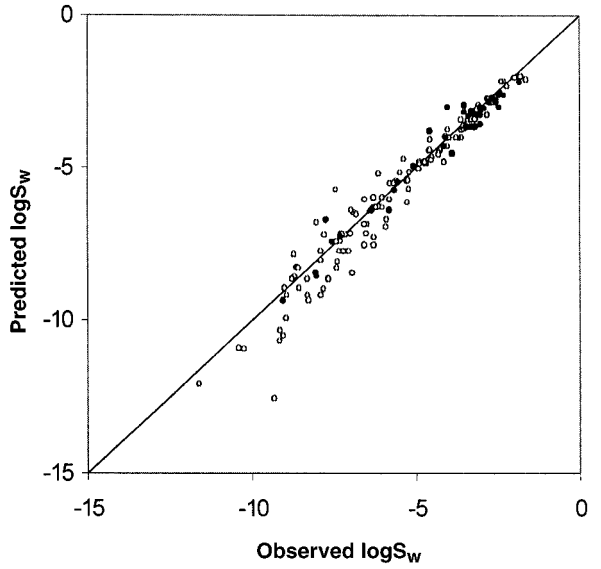

Figure 4—Observed vs predicted logarithm of molar aqueous solubility. (○) Compounds used in the training set to generate q_i values. (●) Compounds not used in the training set.

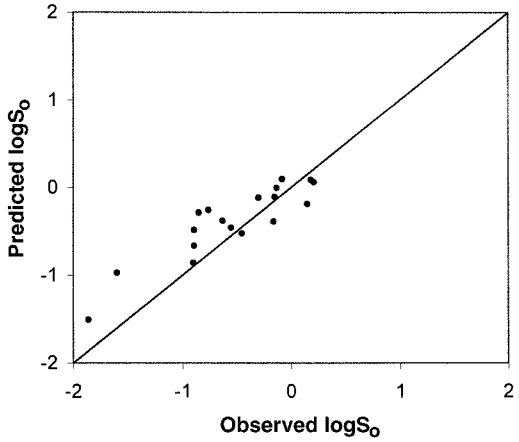

Figure 5—Observed vs predicted logarithm of molar octanol solubility.

Aqueous Solubility—The calculated solubility values agree very well with the experimental data as shown in Figure 4. The average absolute error of 0.38 log units for 165 compounds varying over 10 orders of of magnitude is slightly less than a factor of 2.5. This is well within experimental error of the reported data. One hundred and thirty six compounds were used to generate q_i values by Myrdal et al.[18,19] and Lee et al.[21] using the true melting points. It should be noted that in this study the aqueous solubility was calculated using the calculated melting points. Therefore the filled circles in Figure 4 represent a true test set of melting point in determining solubility.

Octanol Solubility—Although not much data is available for octanol solubility, UPPER appears to be applicable to its prediction. The 22 reported octanol solubilities are in reasonable agreement with the calculated values as shown in Figure 5. The average absolute error is 0.40 log units (or a factor of 2.5) for the 22 compounds. Note that since no values were generated from octanol solubility data, the whole data set represents a true test for eq 18.

Vapor Pressure—Although no vapor pressure data has been used in the generation of the m_i or b_i coefficients in Table 1, the calculated vapor pressures are in very good agreement with the reported values as evident from Figure 6. Of the compounds shown, 27 were used by Myrdal et al.[25] to generate the value of ΔC_{p_b}, the heat capacity change

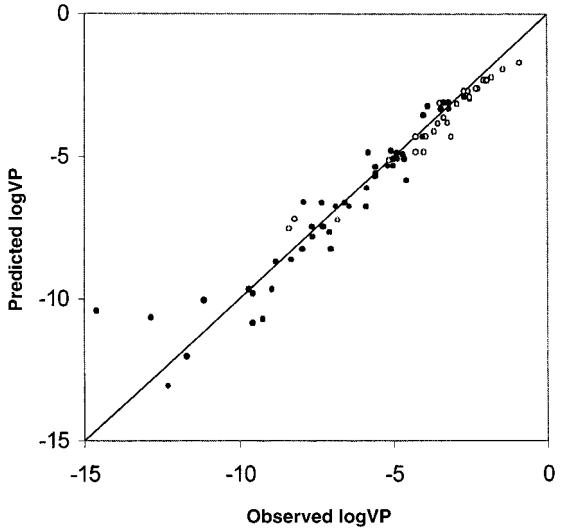

Figure 6—Observed vs predicted logarithm of vapor pressure (atm). (○) Compounds used in the training set to generate ΔC_{p_b}. (●) Compounds not used in the training set.

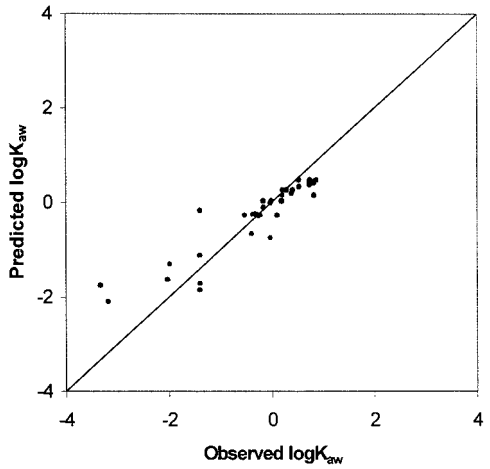

Figure 7—Observed vs predicted logarithm of Henry's Law Constant (atm-L/mol).

on boiling. The average absolute error is 0.38 log units for 73 compounds with vapor pressures covering 11 orders of magnitude. This is well within the error associated with vapor pressure measurements.

Air–Water Partition Coefficient or Henry's Law Constant—Most of the predicted values of the Henry's law constants for 37 compounds show good agreement with the experimentally determined values. However, the error for four compounds is unacceptably large. Because of these points the average absolute error for total test set is 0.49 log units. The data are plotted in Figure 7.

Air–Octanol Partition Coeffficient—The calculated air–water partition coefficients of 25 compounds are in reasonable agreement with the experimental data reported[42] with an average absolute error of 0.45 as shown in Figure 8.

Octanol–Water Partition Coefficient—The agreement between measured and estimated partition coefficients is shown in Figure 9. The average absolute error of 0.40 is primarily due to over estimation of partition coefficients greater than five. The good agreement between the observed and the predicted partition coefficient values below 10^5 (average absolute error of 0.25) is noteworthy since none of the parameters used for the estimations are based upon partitioning data. A note should be made that

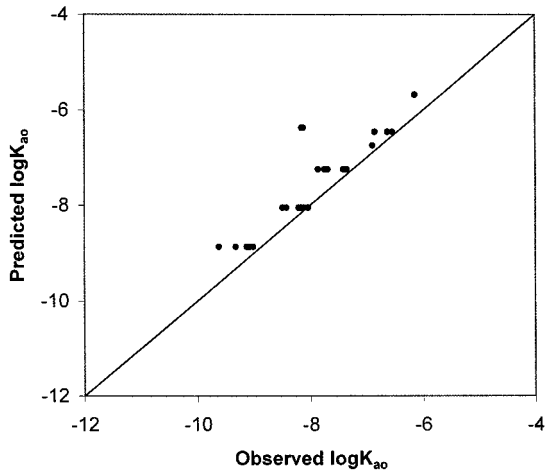

Figure 8—Observed vs predicted logarithm of air–octanol partition coefficient (atm-L/mol).

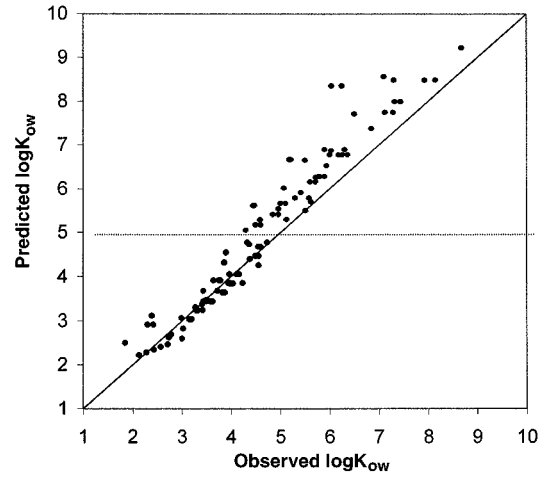

Figure 9—Observed vs predicted logarithm of the octanol–water partition coefficient.

Table 3—Summary of Physical Property Estimation Results

property	*n*	average absolute error	range	
			min	max
T_b	191	8.67	348.00	636.00
T_m	338	23.12	178.00	651.00
log S_w	165	0.38	–11.62	–1.64
log S_o	22	0.40	–2.77	0.21
log *VP*	73	0.38	–12.30	–0.91
log K_{aw}	37	0.49	–1.40	0.88
log K_{ao}	25	0.42	–9.62	–6.14
log K_{ow}	128	0.40	1.85	11.46
log K_{ow} (<10^5)	84	0.25	1.85	5.00

the octanol–water partition coefficient calculated using eq 21 does not take into account the mutual solubilities of octanol and water. This is probably one of the reasons for the overestimations that are especially pronounced with high partition coefficients.

Conclusion

Table 3 summarizes the results of estimating the eight properties considered in this report. For each property it gives the number of compounds studied and the average absolute error of the estimate along with the range of the experimental values. The average absolute error of all the

Table 4—Observed and Predicted Properties for 66 Compounds

name	obsd T_m	pred T_m	obsd T_b	pred T_b	obsd log VP	pred log VP	obsd log S_w	pred log S_w	obsd log K_{ow}	pred log K_{ow}	obsd log K_{aw}	pred log K_{aw}	obsd log S_o	pred log S_o	obsd log K_{ao}	pred log K_{ao}
benzene	279	324	353	387	–0.91	–1.71	–1.64	–2.09	2.13	2.23	0.74	0.38		0.13		
toluenelene	178	244	384	406	–1.43	–1.91	–2.21	–2.33	2.73	2.63	0.83	0.42		0.30		
1,2-dimethylbenzene	248	259	417	424	–2.06	–2.29	–2.80	–2.74	3.15	3.04	0.75	0.46		0.30		
1,3-dimethylbenzene	225	259	412	424	–1.96	–2.29	–2.82	–2.74	3.20	3.04	0.85	0.46		0.30		
1,4-dimethylbenzene	286	292	411	424	–1.94	–2.29	–2.77	–2.74	3.18	3.04	0.76	0.46		0.30		
1,2,3,-trimethylbenzene	248	274	449	443	–2.70	–2.67	–3.20	–3.15	3.59	3.45	0.53	0.48		0.30		
1,2,4-trimethylbenzene	229	246	442	443	–2.57	–2.67	–3.31	–3.15	3.63	3.45	0.75	0.48		0.30		
1,3,5-trimethylbenzene	228	334	438	443	–2.50	–2.94	–3.40	–3.41	3.58	3.45	0.88	0.48		0.04		
1,2,4,5-tetramethylbenzene	353	326	470	462	–3.18	–3.29	–4.59	–3.78	4.00	3.86	1.40	0.49		0.08		
pentamethylbenzene	323	304	504	481	–4.03	–3.52	–4.00	–4.02	4.56	4.27		0.50		0.25		
chlorobenzene	228	260	405	420	–1.79	–2.20	–2.41	–2.54	3.02	2.84	0.54	0.34		0.30		
1,2-dichlorobenzene	256	291	453	454	–2.68	–2.89	–3.02	–3.15	3.44	3.45	0.22	0.26		0.30		
1,3-dichlorobenzene	249	291	445	454	–2.52	–2.89	–3.07	–3.15	3.49	3.45	0.41	0.26		0.30		
1,4-dichlorobenzene	327	328	446	454	–2.92	–3.12	–3.31	–3.39	3.44	3.45	0.30	0.26	0.21	0.06		
1,2,3,-trichlorobenzene	326	321	491	487	–3.42	–3.81	–4.10	–3.97	4.11	4.07	0.22	0.16		0.09		
1,2,4-trichlorobenzene	289	289	487	487	–3.36	–3.60	–3.61	–3.77	3.97	4.07	0.22	0.16		0.30		
pentachlorobenzene	357	383	548	555	–4.58	–5.85	–5.66	–5.75	5.12	5.29	–0.15	–0.10	–0.55	–0.45		
hexachlorobenzene	500	585	596	588	–7.07	–7.67	–7.56	–7.41	5.41	5.90	–0.24	–0.26	–1.86	–1.51		
fluorobenzene	231	231	358	381		–1.44	–1.80	–1.99	2.28	2.29		0.55		0.30		
1,2,3,5-tetrafluorobenzene		238	356	365		–1.13	–2.31	–2.18	2.71	2.48		1.05		0.30		
1,2,4,5-tetrafluorobenzene	277	268	363	365		–1.13	–2.38	–2.18	2.71	2.48		1.05		0.30		
bromobenzene	242	270	429	439	–2.26	–2.57	–2.55	–2.78	2.99	3.08	0.39	0.20		0.30		
1,2-dibromobenzene	277	310	497	491		–3.79	–3.50	–3.73	3.64	3.92		–0.05		0.19		
1,3-dibromobenzene	266	310	491	491	–3.24	–3.79	–3.54	–3.73	3.75	3.92		–0.05		0.19		
iodobenzene	244	281	461	469	–3.88	–3.21	–3.04	–3.02	3.27	3.32		–0.19		0.30		
1,4-diiodobenzene	404	374	558	552		–5.62	–5.37	–4.71	4.39	4.41			–0.91			
nitrobenzene	278	293	483	463		–3.08	–1.83	–2.21	1.85	2.51		–0.87		0.30		
1,2-dinitrobenzene	390	357		540		–5.28	–4.04	–3.02	1.69	2.80		–2.26		–0.22		
1,3-dinitrobenzene	363	357	570	540		–5.28	–2.46	–3.02	1.49	2.80		–2.26		–0.22		
1,4-dinitrobenzene	445	402		540		–5.58	–3.38	–3.32	1.47	2.80		–2.26		–0.52		
o-chlorotoluene	238	247	432	439	–2.30	–2.58	–3.52	–2.95	3.42	3.25		0.36		0.30		
m-chlorotoluene	225	247	435	439		–2.58	–3.52	–2.95	3.28	3.25		0.36		0.30		
o-fluorotoluene	211	221	386	400		–1.80		–2.40	2.78	2.70		0.60		0.30		
m-fluorotoluene	186	221	388	400		–1.80		–2.40	2.78	2.70		0.60		0.30		
m-bromotoluene	233	256	457	458		–2.97	–3.52	–3.18	3.50	3.48		0.22		0.30		
o-nitrotoluene	269	277	498	482		–3.49	–2.31	–2.62	2.30	2.92		–0.87		0.30		
m-nitrotoluene	288	277	503	482		–3.49	–2.46	–2.62	2.42	2.92		–0.87		0.30		
1-chloro-4-nitrobenzene	356	324	515	497		–4.03	–2.92	–3.05	2.39	3.13		–0.98		0.07		
2-bromochlorobenzene	261	270	477	472		–3.28	–3.19	–3.39	3.44	3.69		0.11		0.30		
3-bromochlorobenzene	252	270	469	472		–3.28	–3.21	–3.39	3.72	3.69		0.11		0.30		
1-fluoro-4-iodobenzene	300	283	455	464		–3.09	–3.13	–3.08	3.41	3.38		–0.01		0.30		
1-methylnaphthalene	251	292	513	518	–4.29	–4.28	–3.70	–4.03	3.87	4.33	–0.35	–0.25		0.30		
2-methylnaphthalene	307	292	514	518	–4.05	–4.28	–3.77	–4.03	3.86	4.33	–0.29	–0.25		0.30		
1,4-dimethylnaphthalene	281	339	535	537	–4.65	–5.07	–4.14	–4.80	4.37	4.73	–0.51	–0.27		–0.07		
anthracene	489	440	613	612	–8.40	–7.55	–6.39	–6.43	4.45	5.61	–1.40	–1.12	–1.91	–0.82		
9-methylanthracene	352	405		631	–7.63	–7.83	–5.89	–6.67	5.07	6.02		–1.16		–0.65		
phenanthrene	372	390	613	612	–8.40	–7.25	–5.26	–6.13	4.47	5.61	–1.49	–1.12	–0.45	–0.52		
biphenyl	344	336	527	531	–4.89	–4.86	–4.31	–4.56	3.90	4.56	–1.54	–0.30	–0.13	0.00		
o-chlorobiphenyl	307	274	527	546	–4.69	–4.90	–4.54	–4.75	4.30	5.05		–0.15		0.30		
m-chlorobiphenyl	290	295	547	565	–5.00	–5.32	–4.88	–4.87	4.60	5.17		–0.45		0.30		
p-chlorobiphenyl	348	329	557	565	–5.57	–5.60	–5.20	–5.15	4.50	5.17		–0.45		0.03		
4,4′-dichlorobiphenyl	422	359	564	598	–7.32	–6.65	–6.56	–6.03	5.30	5.79		–0.62		–0.25		
2,2′-dichlorobiphenyl	334	312	588	561	–5.58	–5.37	–5.27	–5.37	4.90	5.54		–0.01		0.17		
3,3′-dichlorobiphenyl	302	359		598	–6.57	–6.65	–5.80	–6.03	5.30	5.79		–0.62		–0.25		
2,2′,3,3′,4,4′,6-heptachlorobiphenyl	395	397		711	–9.56	–9.79	–8.30	–9.17	6.70	8.48		–0.62		–0.68		
2,2′,3,3′,5,5′,6,6′-octachlorobiphenyl	434	507		726	–9.58	–10.83	–9.15	–10.32		8.97		–0.50		–1.35		
2,2′,3,3′,4,4′,5,5′,6-nonachlorobiphenyl	478	452		778	–11.71	–12.01	–10.26	–10.94		9.71		–1.07		–1.23		
2,2′,3,3′,4,4′,5,5′,6,6′-decachlorobiphenyl	578	576		793	–12.30	–13.06	–11.62	–12.10		10.20		–0.96	–2.77	–1.90		
p-bromobiphenyl		338		583		–6.11	–5.55	–5.47	4.96	5.41		–0.64		–0.06		
2,4,6-tribromobiphenyl	339	373		650		–8.00	–7.30	–7.23	6.03	6.86		–0.77		–0.36		
fluoranthene	383	354		596	–7.91	–6.61	–5.92	–6.91	5.22	6.66	–0.76	–0.25	–0.76	–0.25	–8.12	–6.35
pyrene	423	444		596	–8.22	–7.21	–6.18	–7.51	5.18	6.66	–0.90	–0.85	–0.90	–0.85	–8.15	–6.35
chrysene	525	470	721	725	–9.24	–10.69		–8.54		7.30	–2.60	–1.23	–2.60	–1.23		
perylene	551	535		709	–12.85	–10.63	–8.79	–9.92	6.25	8.35	–2.52	–1.57	–2.52	–1.57		
benzo[*a*]pyrene	451	426	768	709	–11.15	–10.03	–7.82	–9.32	6.04	8.35	–1.60	–0.97	–1.60	–0.97		
coronene	715	681			–14.60	–10.39	–9.33	–12.56		10.45	–2.37	–2.11	–2.37	–2.11		

logarithmic terms are generally of the same magnitude as the error associated with the experimental measurements. On the other hand the errors in estimation of the transition temperatures exceed the accuracy of their measurement. However, these errors are less than those produced by any other predictive method and correspond to relatively small

errors in those logarithmic terms that are dependent upon the melting point. Therefore, since none of the average absolute errors exceeds half an order of magnitude, UPPER can be expected to consistently provide reasonable (order of magnitude) estimations of these properties.

The success of UPPER is due to three factors: its use of well-established physicochemical relationships, its use of a uniform breakdown of molecules into substituents, and its use of nonadditive parameters. Because all property values are calculated strictly from thermodynamically sound relationships, UPPER itself is thermodynamically sound. The use of mathematical relationships, which relate one parameter to another, minimizes the need for approximations and eliminates the need to utilize multiple structural breakdown schemes.

The use of nonadditive parameters to account for those molecular properties that are not simply the sum of group values is the most unique feature of UPPER. In the present study the use of molecular symmetry improves the estimation of melting point and enables the distinction of constitutional isomers. Consequently, it improves the estimation of solubility and vapor pressure which are both calculated from the melting point. Note that although a 30 K error in melting point corresponds to a 0.3 log unit error (i.e., a factor of 2) in either solubility or vapor pressure. An error in the estimation of the melting point has no effect on either air−liquid or liquid−liquid partition coefficients.

There were no new fitted parameters generated or used in this study. About one-third of the data set used in this study is a true test of the group contribution values previously determined by Simamora,[15] Myrdal et al.,[18,19] and Lee et al.[21] A total of 119 boiling points, 86 melting points, 29 aqueous solubilities, and 40 vapor pressures were calculated strictly from the molecular structure as they were not used in generating the group contributions previously. Note that in this study the aqueous solubility and vapor pressure were calculated from the calculated melting and boiling points while both AQUAFAC coefficients and the heat capacity change on boiling were generated using the true melting and boiling temperatures. The excellent agreement of the aqueous solubility and vapor pressure values spanning almost 10 orders of magnitude is noteworthy and suggests that UPPER can be used to estimate values before actual costly experimentation. Even higher accuracy can be achieved with the use of the true melting point, an easily measurable property. For example, the use of the true melting point gives an absolute average error of 0.30.

The agreement of both the calculated air−water and octanol−water partition coefficients reflects the strength of the UPPER scheme as no partitioning data were used in the generation of the group contribution values of Table 1.

Thus the overall UPPER scheme does remarkably well as validated using 974 values for 8 biologically and environmentally relevant properties of 405 rigid, nonhydrogen bonding aromatic compounds. The logarithmic values in Table 3 have average absolute errors that correspond to less than a factor of 3 for all the properties and less than a factor of 2 for most of the properties.

A representative set of 66 compounds is presented in Table 4. All the data for 405 compounds are provided in Supporting Information.

Supporting Information Available— Table of obseved and predicted properties. This material is available free of charge via the Internet at http://pubs.acs.org.

References and Notes

1. Lyman, W. J.; Reehl, W.; Rosenbalt, D. H. *Handbook of Chemical Property Estimations*; McGraw-Hill Book Co.: New York, 1982.
2. Bondi, A. *Physical Properties of Molecular Crystals, Liquids, and Glasses*; John Wiley and Sons: New York, 1968.
3. Joback, K. G. *A Unified Approach to Physical Property Estimation Using Multivariate Statistical Techniques*. Ph.D. Thesis. Massachusetts Institute of Technology, Boston, 1984.
4. Todeschini, R.; Gramatica, P.; Provenzani, R.; Marengo, E. Weighted holistic molecular descriptors. Part 2. Theory development and applications on modeling physicochemical properties of polyaromatic hydrocarbons. *Chemom. Intell. Lab. Syst.* **1995**, *27*, 221−229.
5. Mitchell, B. E.; Jurs, P. C. Prediction of Aqueous Solubility of Organic Compounds from Molecular Structure. *J. Chem. Inf. Comput. Sci.* **1998**, *38*, 489−496.
6. Mitchell, B. E.; Jurs, P. C. Prediction of Infinite Dilution Activity Coefficients of Organic Compounds in aqueous Solutions from Molecular Structure. *J. Chem. Inf. Comput. Sci.* **1998**, *38*, 200−209.
7. Katritzky, A. R.; Lobanov, V.S.; Karelson, M. Normal Boiling Points for Organic Compounds: Correlation and Prediction by a Quantitative Structure−Property Relationship. *J. Chem. Inf. Comput. Sci.* **1998**, *38*, 28−41.
8. Huibers, P. D. T.; Katritzky, A. R. Correlation of Hydrocarbons and Halogenated Hydrocarbons with Molecular Structure. *J. Chem. Inf. Comput. Sci.* **1998**, *38*, 283−292.
9. Katritzky, A. R.; Wang, Y.; Sild, S.; Tamm, t. QSPR Studies on Vapor Pressure, Aqueous Solubility, and the prediction of Water−Air Partition Coefficients. *J. Chem. Inf. Comput. Sci.* **1998**, 38, 720−725.
10. Karickhoff, S. W.; Careirra, L. A.; Hilal, S. H. Prediction of Pollutant Physical Properties by Computer (SPARC). *Abstracts of Papers, Part 1*, 210th National Meeting of the American Chemical Society, Chicago, IL, Aug 20−24, 1995; American Chemical Society: Washington, DC, 1995; ENVR 19.
11. Hilal, S.H.; Carreira, L. A.; Karickhoff, S. W. Vapor pressure, Boiling Point and Activity Coefficient Calculation by SPARC. *Abstracts of Papers, Part 1*, 212th National Meeting of the American Chemical Society, Orlando, FL, Aug 25−29, 1996; American Chemical Society: Washington, DC, 1996; COMP 114.
12. Pearlman, R. S.; Smith, K. M. Novel algorithms for the design of diverse and focused combinatorial libraries. *Abstracts of Papers, Part 1*, 217th National Meeting of the American Chemical Society, Anaheim, GA, Mar 21−25, 1999; American Chemical Society: Washington, DC, 1999; U2698.
13. Yalkowsky, S. H.; Dannenfelser, R. M.; Myrdal, P.; Simamora, P. Unified Physical Property Estimation Relationships (UPPER). *Chemosphere* **1994**, *28*, 1657−1673.
14. Yalkowsky, S. H.; Myrdal, P.; Dannenfelser, R. M.; Simamora, P. UPPER II: Calculation of Physical Properties of the Chlorobenzenes. *Chemoshpere* **1994**, *28*, 1675−1688.
15. Simamora, P.; Yalkowsky, S. H. Group Contribution Methods for Predicting the Melting Points and Boiling Points of Aromatic Compounds. *Ind. Eng. Chem.* Res. **1994**, *33*, 1405−1409.
16. Krzyzaniak, J. F.; Myrdal, P. B.; Simamora, P.; Yalkowsky, S. H. Boiling Point and Melting Point Prediction for Non-Hydrogen Bonding Compounds. *Ind. Eng. Chem. Res.* **1995**, *34*, 2531−2535.
17. Fedors, R. F. A Method for estimating Both the Solubility Parameters and Molar Volumes of Liquids. Polym. Eng. Sci. **1974**, *14*, 147−154.
18. Myrdal, P.; Ward, G. H.; Dannenfelser, R. M.; Mishra, D.; Yalkowsky, S. H. AQUAFAC 1: Aqueous Functional Group Activity Coefficients; Application to Hydrocarbons. *Chemosphere* **1992**, *24*, 1047−1061.
19. Myrdal, P.; Ward, G. H.; Simamora, P.; Yalkowsky, S. H. AQUAFAC: Aqueous Functional Group Activity Coefficients. *SAR QSAR Environ. Res.* **1993**, *1*, 53−61.
20. Myrdal, P.; Manka, A. M.; Yalkowsky, S. H. AQUAFAC 3: Aqueous Functional Group Activity Coefficients; Application to the Estimation of Aqueous Solubility. *Chemosphere* **1995**, *30*, 1619−1637.
21. Lee, Y. C.; Myrdal, P.; Yalkowsky, S. H. Aqueous Functional Group Activity Coefficients (AQUAFAC 4): Application to Complex Organic Compounds. *Chemosphere* **1996**, *33*, 2129−2144.
22. Pinsuwan, S.; Myrdal, P.; Lee, Y.C.; Yalkowsky, S. H. AQUAFAC 5: Aqueous Functional Group Activity Coefficients; Application to Alcohols and Acids. *Chemosphere* **1997**, *35*, 2503−2513.

23. Dannenfelser, R. M.; Yalkowsky, S. H. Estimation of Entropy of Melting from Molecular Structure: A Non-Group Contribution Methodol. *Ind. Eng. Chem. Res.* **1996**, *35*, 1483−1486.
24. Simamora, P.; Miller, A. H.; Yalkowsky, S. H. Melting Point and Normal Boiling Point Correlations: Applications to Rigid Aromatic Compounds. *J. Chem. Inf. Comput. Sci.* **1993**, *33*, 437−440.
25. Myrdal, P. B.; Yalkowsky, S. H. Estimating Pure Component Vapor Pressures of Complex Organic Molecules. *Ind. Eng. Chem. Res.* **1997**, *36*, 2494−2499.
26. Mackay, D.; Bobra, A.; Chan, D. W.; Shiu, W. Y. Vapor Pressure Correlations for Low-Volatility Environmental Compounds. *Environ. Sci. Technol.* **1982**, *16*, 645−649.
27. Yalkowsky, S. H.; Mishra, D. S. Ideal Solubility of a Solid Solute: Effect of Heat Capacity Assumptions *Pharm. Res.* **1992**, *9*, 958−959.
28. Yalkowsky, S. H.; Mishra, D. S. Estimation of Vapor Pressure of Some Organic Compounds. *Ind. Eng. Chem. Res.* **1991**, *30*, 1609−1612.
29. Hildebrand, J. H.; Scott, R. L. *The Solubility of Nonelectrolytes*; Reinhold Publishing Corporation: New York, 1950.
30. Lide, D. R., Ed. *Handbook of Chemistry and Physics*, 72nd ed.; CRC Press: Boca Raton, FL, 1991−1992.
31. Gross, W.; Keilhorn, J.; Melber, C. *Polybrominated Biphenyls*; World Health Organization: Geneva, 1994.
32. *Aldrich Catalog of Fine Chemicals*; Aldrich Chemical Co.: Milwaukee, WI, 1998−1999.
33. Mackay, D.; Shiu, W. Y.; Ma, K. C. *Illustrated Handbook of Physical-Chemical Properties and Environmental Fate for Organic Chemicals*; Lewis Publishers: Ann Arbor, MI, 1992.
34. Horvath, A. L. *Halogenated Hydrocarbons Solubility-Miscibility with Water*; Marcel Dekker: New York, 1982.
35. Yalkowsky, S. H.; Dannenfelser, R. M. *Arizona Database*, 5th ed.; College of Pharmacy, University of Arizona: Tuscon, AZ, 1990.
36. Ishihara, Y.; Takano, J.; Yasuoka, T.; Mitsuzawa, S. The Solubilities of Aromatic Nitro Compounds in Pure water. *J. Chem. Soc. Jpn.* **1996**, *11*, 987−990.
37. Baum, E. J. *Chemical Property Estimation Theory and Application;* Lewis Publishers: Boca Raton, FL, 1998.
38. Pinsuwan, S.; Li, A.; Yalkowsky, S. H. Correlation of Octanol/Water Solubility Ratios and Partition Coefficients. *J. Chem. Eng. Data* **1995**, *40*, 623−626.
39. Verschueren, K. *Handbook of Environmental Data on Organic Chemicals*; Van Nostrand Reinhold Co.: New York, 1977.
40. Myrdal, P. B. A Simple Scheme for Estimating Environmentally Relevant Physical Properties of Organic Compounds. Ph.D. Thesis. Department of Pharm. Sci., College of Pharmacy, University of Arizona, Tuscon, AZ, 1994.
41. Sacan, M. T.; Balcioglu, I. A. Estimation of Liquid Vapor Pressures for Low Volatility Chemicals. Chemosphere **1998**, *36*, 451−460.
42. Harner, T.; Bidleman, T. F. Measurement of Octanol-Air Partition Coefficients for Polycyclic Aromatic Hydrocarbons and Polychlorinated Naphthalenes. *J. Chem. Eng. Data* **1998**, *43*, 40−46.
43. Heekman, D. ClogP for Windowsversion 2.0.0b, 1995−1997, Biobyte Corp., Claremount, CA.

JS990117P

Preparation of a Microcrystalline Suspension Formulation of $Lys^{B28}Pro^{B29}$-Human Insulin with Ultralente Properties

JANE P. RICHARDS,[†,||] MARY P. STICKELMEYER,[†] BRUCE H. FRANK,[†] SUSAN PYE,[‡] MICHELLE BARBEAU,[‡] JERRY RADZIUK,[‡] G. DAVID SMITH,[§] AND MICHAEL R. DEFELIPPIS*[,†]

Contribution from *Lilly Research Laboratories, Eli Lilly and Company, Indianapolis, Indiana 46285, Diabetes and Metabolism Research Unit, Ottawa Civic Hospital, Ottawa, Ontario, Canada K1Y 4E9, Hauptman-Woodward Medical Research Institute, Inc., 73 High Street, Buffalo, New York 14203, and Roswell Park Cancer Institute, Elm and Carlton Streets, Buffalo, New York 14263.*

Received April 7, 1999. Accepted for publication June 28, 1999.

Abstract □ The monomeric analogue, $Lys^{B28}Pro^{B29}$-human insulin (LysPro), has been crystallized using similar conditions employed to prepare extended-acting insulin ultralente formulations. In the presence of zinc ions, sodium acetate and sodium chloride, but without phenolic preservative, LysPro surprisingly forms small rhombohedral crystals with similar morphology to human insulin ultralente crystals with a mean particle size of 20 ± 1 μm. X-ray powder diffraction studies on the LysPro crystals prior to dilution in ultralente vehicle ([NaCl] = 1.2 M) revealed the presence of $T_3R_3^f$ hexamers. Consistent with human insulin ultralente preparations, LysPro crystals formulated as an ultralente suspension ([NaCl] = 0.12 M) contain T_6 hexamers indicating that a conformational change occurs in the hexamer units of the crystals upon dilution of the salt concentration. The pharmacological properties of subcutaneously administered ultralente LysPro (ULP) were compared to ultralente human insulin (UHI) using a conscious dog model ($n = 5$) with glucose levels clamped at basal. There were no statistically significant differences between the kinetic and dynamic responses of ULP compared to UHI [C_{max} (ng/mL): 3.58 ± 0.76, ULP and 3.61 ± 0.66, UHI; T_{max} (min): 226 ± 30, ULP and 185 ± 42, UHI; R_{max} (mg/kg min): 11.2 ± 1.9, ULP and 13.3 ± 2.0, UHI; and T_{Rmax} (min): 336 ± 11, ULP and 285 ± 57, UHI]. Although the Pro to Lys sequence inversion destabilizes insulin self-assembly and greatly alters the time action of soluble LysPro preparations, this modification has now been found neither to prevent the formation of ultralente crystals in the absence of phenolics nor to compromise the protracted activity of the insulin analogue suspension.

Introduction

Extended-acting insulin preparations are microcrystalline suspensions that provide their protracted effect by slow dissolution of the crystals and gradual release of insulin into the blood stream. There are several approaches to formulating extended-acting insulin preparations. One example, ultralente human insulin (UHI),[1] is a zinc−insulin suspension composed predominantly of small rhombohedral crystals and characterized by an intermediate to long time−action profile. Ultralente is one of a series of insulin−zinc suspensions (lente insulins) that were developed by Hallas-Møller and colleagues who determined that the addition of zinc ions in preparations that had neutral pH and no zinc-binding ions (i.e., no phosphate or citrate) led to insulin formulations with protracted effects.[2,3] This series of zinc−insulin suspension formulations includes ultralente (crystalline insulin particles), semilente (amorphous insulin particles), and lente (a mixture of amorphous and crystalline insulin particles). A second approach to making protracted insulin preparations is to depress insulin solubility by adding basic peptides. This approach is exemplified by the product Neutral Protamine Hagedorn insulin (NPH). NPH is an intermediate-acting formulation prepared by cocrystallization of insulin with the basic peptide protamine.[4,5]

A recent study showed that the monomeric insulin analogue, $Lys^{B28}Pro^{B29}$-human insulin (LysPro), can be cocrystallized with the basic peptide protamine to form a microcrystalline suspension having a time action nearly identical to human insulin NPH.[6] The cocrystallization of LysPro with protamine requires the presence of both zinc ions and phenolic preservatives. In other work, the X-ray crystal structure of LysPro was reported.[7] The crystals were grown in the presence of both zinc ions and phenol, and LysPro was found to crystallize as $T_3R_3^f$ hexamers. The quaternary structure of LysPro was described using the T, R^f, and R nomenclature[7,8] for insulin hexamers whereby monomer subunits are named according to the conformation of the first eight amino acid residues of the B-chain. In this notation, T refers to an extended conformation, R to an α-helical conformation, and R^f to an extended conformation for the first three residues and α-helical for the remainder. These recent examples of LysPro crystal forms have demonstrated an apparent requirement for the presence of both zinc ions and phenolic preservatives to initiate crystallization, presumably due to the ability of these ligands to promote self-association. Indeed, numerous studies exploring the solution properties of LysPro have confirmed that the addition of zinc ions and phenolic preservatives overcomes the otherwise destabilizing effect on hexamer self-assembly caused by the sequence modification in the region required for dimer formation.[9−11]

The role of ligand binding and its influence on insulin self-assembly and crystallization is well-known for porcine and human insulin species.[12−16] One notable difference between these insulin species and LysPro is their ability to form discrete hexamers in the presence of zinc ions alone. For example, crystals of porcine insulin grown in the presence of zinc ions but without phenolic preservative have been shown by X-ray crystallography to be composed of T_6 hexamers.[16] Although high-resolution structural analysis of ultralente crystals has been thwarted by poor crystal diffraction characteristics and dimensions, atomic force microscopy studies confirmed the presence of insulin

* Corresponding author: Phone: 317-276-6027, fax: 317-277-0833, e-mail: defelippis_michael_r@lilly.com.
[†] Lilly Research Laboratories.
[‡] Ottawa Civic Hospital.
[§] Hauptman-Woodward Medical Research Institute and Roswell Park Cancer Institute.
[||] Current address: Baxter Hemoglobin Therapeutics, Inc., Boulder, CO 80301.

10.1021/js990107o CCC: $18.00 Published on Web 08/07/1999

hexamers in the crystal lattice.[17] Hexamers comprising ultralente crystals likely adopt T_6 or T_3R_3 conformations since these crystallizations are conducted in the presence of both zinc ions and sodium chloride, but in the absence of phenolic preservatives, as this additive will not produce the desired crystal form.[18]

The requirement for zinc ions and phenolic preservatives to induce crystal formation of LysPro offers a unique challenge to preparing an ultralente-type suspension of this analogue. Such a preparation may have a more desirable time−action profile compared to currently available extended-acting insulin suspensions, thus providing the impetus for undertaking the present study to explore the feasibility of producing ultralente LysPro (ULP). A variety of physicochemical techniques were used to characterize the solid material comprising the resulting ULP suspension to determine how the properties compare to authentic UHI. Pharmacological properties of ULP obtained using a conscious dog model are also reported.

Experimental Section

Chemicals—LysPro was manufactured by Eli Lilly and Company using recombinant DNA technology. All chemicals were pharmaceutical grade and were obtained from various suppliers. Humulin U (40 U/mL) (Eli Lilly and Company) was used as a comparator.

Preparation of Crystals and Formulation—A stock solution was prepared containing approximately 22 mg/mL LysPro. The endogenous level of zinc in the LysPro solid was supplemented by the addition of appropriate volumes of an acidic zinc oxide solution (10 mg/mL) to achieve a final zinc ion concentration of 0.24 mg/mL. The pH was lowered to 2.5−3.0 with 10% hydrochloric acid to aid dissolution of the LysPro solid. A separate buffer solution was prepared containing 21.3 mg/mL sodium acetate and 186.7 mg/mL sodium chloride. The pH of the buffer solution was adjusted empirically with 10% sodium hydroxide such that the combination of 62.5% of the LysPro solution and 37.5% of the buffer solution afforded a crystallization mixture having pH 5.5. Combination of the two solutions in the ratio indicated resulted in the immediate formation of a white, flocculent precipitate. The final crystallization mixture contained 14 mg/mL LysPro, 0.15 mg/mL zinc ions, 8.0 mg/mL sodium acetate, and 70 mg/mL sodium chloride. The glass, conical flask containing the crystallization mixture was mounted in a mixing apparatus and stirred continuously with a stainless steel paddle at 100 rpm. A small amount (<1% v/v) of human insulin seed crystals (Eli Lilly and Company) was added to the crystallization mixture shortly after combination. Small, rhombohedral crystals were visible by microscopy within 24 h. Crystallizations were allowed to proceed for 24−96 h at room temperature.

The ultralente LysPro (ULP) preparations used for animal testing were formulated to contain final concentrations of 1.4 mg/mL (40 U/mL) LysPro, 0.084 mg/mL zinc ions, 1.6 mg/mL sodium acetate, 7.0 mg/mL sodium chloride, and 1.0 mg/mL methylparaben at pH 7.3. To make the formulation, a stock diluent solution was prepared containing 1.11 mg/mL methylparaben, 0.89 mg/mL sodium acetate, and 0.077 mg/mL zinc ions. The diluent solution was mixed with the 400 U/mL ultralente LysPro concentrated suspension (ULP C/S) described above in a 9:1 ratio and adjusted to the final pH with 10% hydrochloric acid and/or 10% sodium hydroxide.

Optimization of Crystallization Conditions—The effects of four variables (zinc ion concentration, sodium acetate concentration, sodium chloride concentration, and pH) on ULP crystallization were evaluated using a full-factorial experimental design. All possible combinations of high and low values for each variable were tested, and a total of 16 trials and 4 centerpoints were performed in a randomly assigned order. The high/low concentrations for the four variables in the crystallization were 0.20 versus 0.29 mg/mL zinc ion, 4.0 versus 12.0 mg/mL sodium acetate, 40 versus 100 mg/mL sodium chloride, and pH 5.0 versus pH 6.0. Crystal morphology and time at which crystals formed were used as endpoints.

Analytical Methods—The concentration of LysPro in the solid and solution phases of the suspension was determined by HPLC. An aliquot of suspension was centrifuged and the supernatant decanted and retained for analysis. Distilled water, equal to the original volume of the suspension, was added to wash the pellet. The pellet was suspended and centrifuged, and the supernatant from the wash was discarded. This water wash procedure was repeated three times. After the final wash, the pellet was dissolved in a volume of 0.01 N hydrochloric acid equal to the volume of the original sample and 3 μL of 9.6 N hydrochloric acid per milliliter of solution. The dissolved pellet and supernatant fraction were analyzed with a reversed phase gradient method using a mobile phase of sulfate buffer and acetonitrile (pH 2.3), a C18 column (Spherisorb ODSII, 10 cm × 4.6 mm) temperature controlled at 40 °C and UV detection at 214 nm.

Microscopy and Particle Size Determinations—Crystal morphology was evaluated using a Zeiss Axioskop microscope equipped with a differential phase-contrast accessory. Approximately 5 μL of a resuspended sample was placed on a glass microscope slide and covered with a cover slip. Photographs were taken at 400× magnification. Edge dimensions were estimated with the aid of an ocular micrometer scale graticule subdivided into 10 μm divisions.

Particle size distributions were performed using a Coulter Multisizer and sampling stand (Miami, FL). The aperture tube orifice size was 100 μm. A 0.20 mL aliquot of resuspended sample was pipetted into 100 mL of a solution containing ISOTON II (Miami, FL). Particle size data were collected for 50 s and are reported as volume percent mean diameter ($D_{4,3}$).

Powder Diffraction—Samples were loaded into a 0.8 mm glass capillary along with mother liquor. The capillaries were then centrifuged in order to pack the microcrystals into a pellet at the bottom of the mother liquor, excess mother liquor was removed, and the capillaries were then sealed. Each capillary was placed on a Rigaku R-AXIS II-C image plate system and RU-200 rotating anode generator with graphite monochromated Cu Kα radiation (λ = 1.54178 Å) at 290 K. Following a 10- to 15-h exposure, the plot of intensity versus 2θ of the powder diffraction image was generated with the X12B software.[19] Backgrounds were subtracted from the peaks, and relative intensities were calculated for each diffraction peak. This procedure was employed for the ULP C/S prior to dilution to prepare the ULP preparation, ULP suspension (40 U/mL), and human insulin ultralente (40 U/mL).

Large, single crystals of T_6 human insulin were grown according to published procedures,[16] and a preliminary refinement of single-crystal diffraction data measured from these crystals showed the structure to be identical to that of the published structure.[16] A sample of the single crystals was ground into a fine powder in the presence of mother liquor, and the procedure described above was repeated.

As no powder diffraction data are available for the various $T_3R_3^f$ and R_6 forms of human insulin whose structures have been published,[13−15,20,21] powder patterns were simulated from the single crystal intensity data. Because of the 3-fold symmetry axis in space group *R*3, two or more general and independent reflections will make a contribution to each powder diffraction peak. Since single crystal data from protein crystals frequently have missing data, particularly at very low values of sin θ/λ, multiple sets of data for T_6 porcine[16] and human (unpublished results) insulin, $T_3R_3^f$ human insulin (chloride,[14] 4′-hydroxyacetanilide,[20] p-hydroxybenzamide[21]), and $T_3R_3^f$ LysPro[7] and a second unpublished set of data were merged using SORTAV from the DREAR suite of data reduction program package[22] to minimize missing data. Although the resulting merged data were carefully checked to ensure that there were no missing data which would alter the intensity patterns of the resulting simulated powder diffraction patterns, one strong reflection was absent from the $T_3R_3^f$ human insulin data. The merged squares of the structure factor amplitudes (F^2) were multiplied by the Lorentz and polarization factors ($Lp = (1 + \cos^2 2\theta)/(\sin^2 \theta \cos \theta)$) to give intensities corresponding to powder data. The resulting intensities were plotted as a function of 2θ after applying a broadening function to simulate the powder diffraction pattern as obtained from the R-AXIS image plate system.

$$I_{2\theta} = \sum I_{hkl} \exp - [8.66 \times (2\theta_{hkl} - 2\theta)]^2 \qquad (1)$$

Particular care must be taken in applying the correct unit cell constants in powder patterns from single-crystal intensities. Due to the relationship between the Miller indices (hkl) and the cell constants, small differences in cell constants

$$Q_{hkl} = h^2a^{*2} + k^2b^{*2} + l^2c^{*2} + 2klb^*c^*\cos\alpha^* + 2lhc^*a^*\cos\beta^* + 2hka^*b^*\cos\gamma^* \quad (2)$$

where a^*, b^*, c^*, a^*, β^*, and γ^* are the reciprocal lattice constants and

$$d = 1.0/(Q_{hkl})^{1/2} \quad (3)$$

will displace the position of the powder diffraction peak relative to nearby peaks altering the appearance of the simulated powder diffraction pattern. While single-crystal data are available for $T_3R_3^f$ LysPro human insulin,[7] no data are available for the T_6 form. As a result of the T → R conformational transition in human insulin, the a-dimension in the unit cell decreases from 81.91 to 80.83 Å while the c-dimension increases from 34.13 to 37.76 Å. It should also be noted that due to the sequence inversion in LysPro, the a-dimension in the $T_3R_3^f$ form decreases by 2.29 Å relative to that of human insulin. To a first approximation, it is possible to calculate the expected cell dimensions for T_6 LysPro based upon the observed changes in cell dimensions of human insulin.

$$a(T_6\ \text{LysPro}) = a(T_3R_3^{\,f}\ \text{LysPro}) \times [a(T_6\ \text{human})/a(T_3R_3^{\,f}\ \text{human})] \quad (4)$$

$$c(T_6\ \text{LysPro}) = c(T_3R_3^{\,f}\ \text{LysPro}) \times [c(T_6\ \text{human})/c(T_3R_3^{\,f}\ \text{human})] \quad (5)$$

In this way, a simulated powder pattern can be calculated for T_6 LysPro using expected T_6 cell constants for LysPro and intensities from human insulin.

Pharmacology—The pharmacokinetic and pharmacodynamic properties of UHI and ULP were assessed following previously described procedures.[6] Briefly, five normal conditioned mongrel dogs weighing 15−25 kg each underwent one study with ULP and one with UHI. For each animal, an 18 h fast was followed by three basal samples, a somatostatin infusion (0.3 μg/kg min), and, after a 10 min interval, a 0.5 IU/kg subcutaneous dose of either ULP or UHI. Plasma glucose was monitored at approximately 5 min intervals, and 20% glucose was infused continuously and at a variable rate to maintain near basal fasting glycemia. Additional samples were collected approximately every 5 min for 45 min, every 10 min for 40 min, every 15 min for 30 min, every 20 min for 40 min, every 25 min for 150 min, and then every 30 min until 840 min. Plasma insulin was determined by radioimmunoassay and glucose using the glucose oxidase method.

Interpolated plasma insulin and glucose profiles were compared using analysis of variance with time as a repeated measure. An overall comparison was made between the two groups (ULP and UHI), as well as of the interaction between group and time. Kinetic and pharmacodynamic parameters were compared using paired t-tests. The following parameters were evaluated for the interpolated insulin curves: C_{max}, the maximal insulin or LysPro concentration reached following its subcutaneous injection during the clamp study; T_{max}, the time at which C_{max} was attained; insulin area, the area under the insulin or LysPro curve, deemed to be representative of the total amount of exogenous insulin or LysPro which is absorbed during the course of the study; R_{max}, the maximal rate of glucose infusion which was achieved during the course of the clamp and T_{Rmax}, the time at which R_{max} was achieved. The cumulative rate of glucose infusion was also calculated. All data are reported as means ± SEM.

Results

Preparation and Characterization of ULP—The ULP preparation was prepared following a similar method used to produce ultralente (bovine, human, or porcine) insulin suspensions.[18] The procedure essentially involves preparing two solutions: an acidic protein solution containing excess zinc, and a separate precipitation solution containing sodium acetate and sodium chloride. The precipitation solution pH was appropriately adjusted to achieve crystallization conditions around the isoelectric point of LysPro (pI = 5.5). Upon combination of the protein and precipitation solutions, a flocculated, white precipitate immediately formed. Evaluation of the crystallization mixture by microscopy indicated that small rhombohedral crystals formed within 24 h; however, crystal growth was allowed to continue for up to 96 h to completely transform any remaining amorphous material. Although ULP crystals were observed to form in the absence of seed crystals (data not shown), a small amount of human insulin seed crystals (<1% v/v) were added to the crystallization reaction to improve the uniformity of the crystallization.[23] The addition of seed crystals was also noted to decrease the time required for complete crystallization.

Crystallization was routinely halted after 96 h by diluting the crystallization mixture into a diluent solution containing methylparaben. A dilution to 40 U/mL was prepared to match the concentration of the comparator UHI sample. The size and morphology of the ULP crystals comprising the suspension were evaluated by microscopy and found to be very similar to those contained in the UHI sample (data not shown). The ULP crystals were estimated to have edge lengths of approximately 5−15 μm. Mean particle size for the crystals was determined to be 20 ± 1 μm as measured by the Coulter particle size technique (data not shown). This result is in good agreement with the mean particle size of the commercial UHI sample. The completeness of crystallization in the final formulated preparation was assessed by comparing the amounts of LysPro in the solid and solution phases. Reversed-phase HPLC analysis revealed that the solid phase contained approximately 40 U/mL of LysPro whereas less than 0.05 U/mL of LysPro was found in the soluble fraction.

The conditions for preparing ULP crystals were further evaluated using a standard four-variable, full-factorial experimental design. The effects of zinc concentration, sodium acetate concentration, sodium chloride concentration, and pH were studied, and the results are summarized as follows: (i) pH had a very pronounced effect on ULP crystallization with pH 5.5 being optimal; (ii) no crystals formed at pH 5.0, regardless of the other conditions, and although some crystallization occurred at pH 6.0, these crystals were typically small, slow-growing and of poor quality compared to the crystals grown at pH 5.5; (iii) sodium acetate concentrations had little effect on crystallization within the parameters of the current experiments; (iv) an interaction between zinc and sodium chloride concentration was observed; that is, the effect of zinc concentration on crystallization depends on the sodium chloride concentration; (v) the centerpoint conditions (i.e., those closely matching the procedure for preparing UHI) reproducibly formed the highest quality crystals characterized by rhombohedral morphology with uniform size and well-defined edges forming within 24−48 h.

To characterize further the ULP suspension and possibly identify the nature of the LysPro hexamers comprising the crystals, powder diffraction studies were performed. X-ray powder diffraction has been used for many years as a means of identifying organic and inorganic microcrystalline samples. The d-spacing and intensity can be calculated for each diffraction line, and the resulting information provides an accurate and reproducible fingerprint of the material in question. This method can also be used to distinguish between different crystalline polymorphs of the same compound. While powder diffraction has rarely been applied to proteins due to lack of sufficient microcrystalline material and the requirement that the protein remain

Table 1—2θ and Relative Intensity Data Derived from Powder Diffraction Patterns[a]

ULP	UHI	T_6KP	T_6	T_6HI	$T_3R_3^f$KP	$T_3R_3^f$HI	ULP C/S	R_6R	R_6M
								b	2.10(19)
2.25(100)	2.24(81)	2.18(81)	2.17(67)	2.16(86)	2.22(100)	2.18(3)	2.25(63)		
									2.48(28)
					2.66(18)	2.66(15)	2.71(27)		
c	2.92(3)b	2.88(3)	2.88(3)b	2.88(3)					
									3.24(69)s
					3.46(50)	3.44(60)	3.50(48)		3.46(97)
3.63(13)	3.67(58)	3.78(36)a	3.68(36)	3.70(43)	3.84(5)	3.78(22)	3.85(8)		
					4.12(11)	4.08(22)	4.12(12)	4.02(11)	
4.28(17)s	4.32(52)	4.24(12)	4.19(13)	4.22(14)					4.20(46)
4.44(23)					4.44(4)	4.38(8)	4.40(4)	4.43(19)	
					4.87(3)s				4.88(46)
5.29(76)	5.22(100)	5.24(73)	5.15(82)	5.18(77)	5.18(60)	5.12(73)	5.18(62)	5.10(100)	5.14(64)
								5.54(51)	
5.77(32)	5.71(86)	5.78(60)	5.65(58)	5.70(66)	5.82(42)	5.76(90)a	5.80(87)		5.70(99)
6.12(47)	6.10(66)	6.13(41)	5.98(30)a	6.08(36)				5.94(63)	
								6.36(82)	6.26(87)a
					6.58(66)	*d*	6.60(100)	6.61(30)s	
6.88(44)	6.88(77)	6.90(100)	6.82(100)a	6.86(100)a		6.76(13)s			6.74(27)
7.26(11)		7.18(28)s			7.22(24)	7.10(38)	7.16(35)	7.08(27)	
7.60(13)	7.48(19)	7.56(15)	7.44(13)	7.48(16)		7.58(46)	7.66(40)	7.64(50)	7.46(100)a
	7.81(49)		7.71(27)	7.78(30)	7.70(24)				
8.02(20)	8.05(16)s	7.90(27)	8.02(13)	8.06(19)	8.00(44)	7.92(80)	8.01(85)a	7.98(78)	
		8.14(18)s			8.28(21)s	8.31(38)		8.36(32)	8.20(96)
8.53(3)s	8.67(32)		8.58(32)	8.64(37)	8.54(14)				
8.80(18)		8.74(34)						8.88(65)	8.74(61)
			9.09(23)	9.16(30)	9.14(35)	9.06(70)	9.14(54)		9.08(71)
9.33(24)	9.23(47)	9.26(30)	9.30(30)	9.40(31)				9.46(62)a	9.36(56)
	9.40(45)								
9.66(29)	9.71(27)	9.56(31)a	9.61(27)	9.66(27)	9.66(47)	9.54(100)	9.62(81)		
			9.80(22)s	9.90(23)					9.72(75)a
10.21(6)	10.14(19)	10.07(24)a	10.07(15)	10.12(20)	10.17(11)	10.02(26)	10.18(17)s	10.15(64)	10.22(75)a
			10.39(5)	10.44(8)b	10.40(12)	10.34(23)s	10.45(25)s		
	10.50(9)	10.66(9)	10.71(8)		10.73(13)	10.58(37)	10.66(29)	10.68(14)	
10.81(4)				10.80(9)					
						10.97(13)s			
			11.14(8)	11.24(12)s	11.29(8)a	11.07(13)s		11.06(9)	11.25(27)
				11.45(16)			11.44(19)	11.34(12)	
	11.34(12)b	11.39(12)	11.36(2)			11.33(24)			
11.68(4)		11.58(16)						11.72(16)	11.66(22)
					11.95(11)	11.82(20)	11.92(13)		
12.33(5)	12.17(23)	12.33(19)	12.04(13)	12.15(20)		12.24(25)	12.33(19)	12.08(17)	12.20(22)

[a] 2θ (degrees) and relative intensities (in parentheses) for the four measured powder diffraction patterns and the six simulated powder diffraction patterns. Codes are as follows: **ULP**, observed powder pattern for LysPro Ultralente in the presence of 7 mg/mL NaCl; **UHI**, observed powder pattern for human insulin Ultralente in the presence of 7 mg/mL NaCl; **T_6KP**, simulated powder pattern for T_6 LysPro; **T_6**, observed powder pattern for T_6 human insulin; **T_6HI**, simulated powder pattern for T_6 human insulin; **$T_3R_3^f$KP,** simulated powder pattern for $T_3R_3^f$ LysPro; **$T_3R_3^f$HI**, simulated powder pattern for $T_3R_3^f$ human insulin; **ULP C/S**, observed powder pattern for LysPro Ultralente in the presence of 70 mg/mL NaCl; **R_6R**, simulated powder pattern for the rhombohedral R_6 human insulin; and **R_6M**, simulated powder pattern for the monoclinic R_6 human insulin. A broad peak is designated by the letter b following the intensity; a shoulder on a larger peak by s; and an asymmetric peak by a. [b] Low angle data were not measured for the rhombohedral R_6 human insulin structure. [c] There is a very small broad peak at this value of 2θ, but its intensity is too small to estimate. [d] The (–3,4,2) reflection which comprises 99% of the intensity of this peak was not measured in the human insulin data.

immersed in its mother liquor, it is certainly capable of identifying various polymorphs by changes in *d*-spacings and intensities of the resulting powder pattern. In the case of crystals of hexameric insulin, the low resolution powder lines ($0° < 2\theta < 12°$) provide a definitive way in which to identify the hexamer type within a crystal due to significant differences in the unit cell constants of the three different hexamer types, T_6, $T_3R_3^f$, and R_6.

The powder diffraction results are summarized in Table 1 where the 2θ values and relative intensities are listed for the measured and simulated powder patterns obtained for the various insulin forms. An examination of the simulated powder patterns for the rhombohedral or monoclinic R_6 forms shows no similarity to that of the observed powder patterns for UHI, either of the ULP samples (concentrated or diluted) or T_6 human insulin. Neither is there any similarity of the R_6 forms to the simulated powder patterns for T_6 or $T_3R_3^f$ LysPro or human insulin. Therefore, it is clear that neither of the ultralente forms possess R_6 hexamers in either rhombohedral or monoclinic unit cells.

A comparison of the simulated and observed powder patterns for T_6 human insulin showed that they are in quite good agreement in both 2θ and intensities for each peak, suggesting that preferred orientation is not a serious problem. As noted earlier, some care must be taken in comparing the powder patterns from human insulin to that of LysPro, since the small changes in unit cell constants are sufficient to alter the 2θ values of certain diffraction peaks.

With one exception, a very strong diffraction peak is observed at a 2θ value of approximately 2.20° for all T_6 or $T_3R_3^f$ samples. This strong peak has Miller indices of (−2,1,0) and is a consequence of rows of insulin hexamers spaced 40.2 Å apart and perpendicular to the *a*- and *b*-axes. The presence of this strong peak in the unknown ultralente diffraction patterns is indicative of the presence of hexam-

ers in the crystals. The one exception is that of $T_3R_3^f$ human insulin, but in this case, due to the very low value of θ, a portion of the peak was obscured by the beam stop during the measurement of the data.

While there are similarities in the 2θ values for the crystals containing either T_6 or $T_3R_3^f$ hexamers, there are several peaks which are quite characteristic of one or the other forms. For example, peaks at average 2θ values of 2.66, 3.45, 4.10, and 6.58° are only observed in the simulated powder patterns for $T_3R_3^f$ human insulin or $T_3R_3^f$ LysPro. Likewise, peaks at 2.88, 4.22, 6.06, and 9.32° are only observed in the simulated powder patterns for T_6 human insulin. Therefore, these peaks can be used as a very sensitive indicator of the conformation of the hexamer present in the unknown ultralente samples.

An examination of the observed powder pattern for ULP C/S grown in the presence of 70 mg/mL sodium chloride shows that it contains peaks at 2.71, 3.50, 4.12, and 6.60°, but none at 2.88, 4.22, 6.06, and 9.32° 2θ. Thus, the powder diffraction pattern clearly identifies this sample to be made up of $T_3R_3^f$ hexamers. In contrast, the observed powder patterns for ULP and UHI having sodium chloride concentrations of 7 mg/mL contain peaks at 2.92, 4.30, 6.11, and 9.28°, but none at 2.66, 3.45 or 4.10, or 6.58° 2θ, which is completely consistent with the presence of a T_6 hexamer in the crystal structure.

Pharmacological Characterization—ULP was compared to UHI with respect to both its plasma concentration and glucose requirements following subcutaneous injection. During the study, glucose concentrations were monitored, and its intravenous infusion was adjusted to maintain near-basal concentrations (a clamp procedure). The rate of glucose infusion, in turn, defines the action of insulin administered. For UHI, the basal (fasting, preexperimental) glucose concentration was 109 ± 3 mg/dL. Hourly glucose concentrations thereafter were 116 ± 5, 118 ± 8, 120 ± 7, 117 ± 2, 110 ± 2, 117 ± 4, 112 ± 3, 112 ± 2, 117 ± 3, 115 ± 4, 111 ± 1, 118 ± 3, and 111 ± 5 mg/dL. For ULP, the basal glucose concentration was 105 ± 2 mg/dL with hourly concentrations of 113 ± 6, 110 ± 5, 110 ± 6, 111 ± 5, 105 ± 6, 116 ± 6, 113 ± 6, 113 ± 4, 111 ± 6, 114 ± 5, 114 ± 5, 113 ± 6, and 111 ± 3 mg/dL. There was no difference between the two groups ($F = 0.47$ and $p = 0.51$) or any divergence between them in time ($F = 0.80$ and $p = 0.55$). The stability of the clamp procedure was indicated by the absence of change in the glucose level over time ($F = 1.78$ and $p = 0.15$).

Figure 1 shows the insulin and LysPro concentrations following the subcutaneous injection of the UHI and ULP preparations. The profile of the two curves is similar, and the LysPro concentrations appear to be slightly higher. Analysis of variance, however, indicates that the two curves are not distinguishable ($F = 0.94$ and $p = 0.36$), nor do they diverge in time ($F = 0.31$ and $p = 0.77$). Within the limits of the current study, there are no discernible differences between the responses of the two preparations. The concentration profiles were found to decrease to between 20 and 40% of peak values by the end of the study (14 h after injection). As shown in Table 2, the average maximal concentration (C_{max}) of human or LysPro achieved in these studies is similar (approximately 3.6 ng/mL). The time at which these peaks occur is also not different (approximately 200 min), and the area under the curves remains analogous at ~1500 ng-min/mL. Within the bounds of this comparison, there are no differences in the kinetic parameters examined.

The rate of glucose infusion necessary to maintain fasting glycemia is shown in Figure 2. Inspection of the data reveals an almost identical pattern of glucose infusion over the course of the study. On the basis of statistical

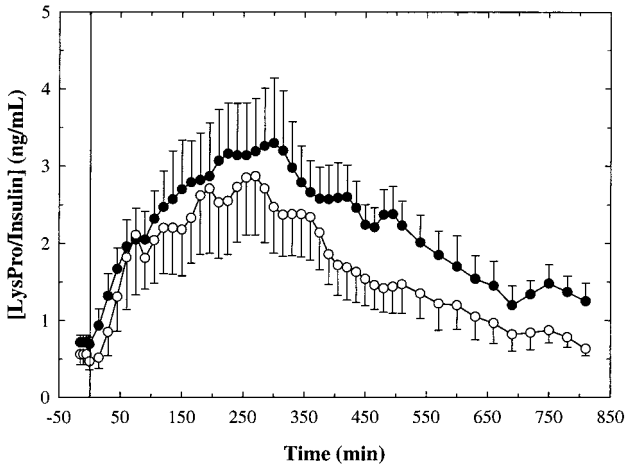

Figure 1—Plasma human insulin or LysPro concentrations following administration of subcutaneous injections of either commercial UHI (○) or ULP suspension (●) at time zero. The dose used was 0.5 U/kg. Concentrations were measured using radioimmunoassays. Error bars represent the average of five test animals.

Table 2—Pharmacokinetic and Pharmacodynamic Parameters Following Subcutaneous Administration of UHI and ULP (means ± SEM)

parameter	UHI	ULP	*T*	*p*
C_{max} (ng/mL)	3.61 ± 0.66	3.58 ± 0.76	0.074	0.94
T_{max} (min)	185 ± 42	226 ± 30	–0.97	0.39
insulin area (ng-min/mL)	1340 ± 257	1760 ± 305	–1.38	0.24
R_{max} (mg/kg-min)	13.3 ± 2.0	11.2 ± 1.9	1.06	0.35
T_{Rmax} (min)	285 ± 57	336 ± 11	–0.94	0.40
total glucose infused[a] (g/kg)	4.95 ± 0.70	4.20 ± 0.70	1.086	0.34

[a] Total glucose infused until $t = 840$ min.

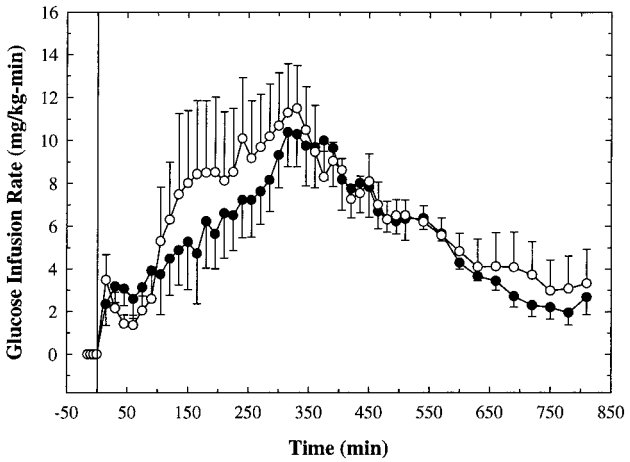

Figure 2—Rates of glucose infusion necessary to maintain fasting glycemia during the glucose clamp imposed following subcutaneous injection of either commercial UHI (○) or ULP suspension (●). The dose used was 0.5 U/kg. Plasma glucose concentrations were measured using a glucose oxidase method. Error bars represent the average of five test animals.

analysis, there is no indication of either an overall group difference or any divergence of the behavior of the groups in time (analysis of variance results: group, $F = 1.77$ and $p = 0.24$; time, $F = 3.81$ and $p = 0.06$; group *x* time, $F = 0.94$ and $p = 0.42$). Both preparations yield very similar peaks approximately 5 h after injection and decrease thereafter until 14 h. The profiles are therefore essentially identical. A plot of the cumulative amount of glucose infused following subcutaneous administration is shown in Figure 3. This cumulative amount is obtained by integrating the glucose infusion curves. Inspection of these data

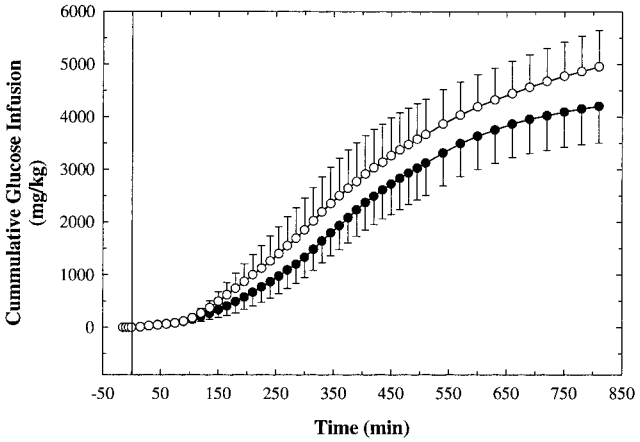

Figure 3—Cumulative glucose infusion following subcutaneous injection of either commercial UHI (○) or ULP suspension (●). Results are based on the integration of the curves shown in Figure 2. Error bars represent the average of five test animals.

show the consistent result that the ultralente preparations of human insulin and LysPro require very similar amounts of glucose to cover their subcutaneous injections. The pharmacodynamic parameters calculated were the maximum rate of glucose infusion (R_{max}), the time at which this was achieved (T_{Rmax}), and the total amount of glucose infused over 14 h and are shown in Table 2. Corroborating the comparison of the curves of glucose infusion, these parameters are all statistically equivalent. Maximal glucose infusion rates are ~12 mg/kg-min and are reached at approximately 5 h after injection of either preparation. A total of about 4.5 g/kg of glucose is infused in each case.

Discussion

LysPro Crystallizes in the Absence of Phenolic Preservatives—On the basis of the wealth of X-ray crystallographic data on wild-type insulins (bovine, human, and porcine), it is clear that the crystals are composed of precisely oriented hexamer units. Studies on the precrystallization stage of 2Zn-porcine insulin further demonstrated that crystal growth proceeds by the addition of hexamers, indicating the importance of solution state self-association to crystallization.[24] Because the wild-type insulin species are known to self-associate into well-defined hexamers in the presence of zinc ions alone, the preparation of ultralente suspensions is straightforward. In contrast, LysPro aggregates nonspecifically in the presence of zinc ions, producing high molecular weight species[11] suggesting that crystallization is unlikely to proceed without modification to the ultralente procedure. We hypothesized that the inclusion of a phenolic preservative in the crystallization media might be necessary, as it is known that LysPro will form well-defined hexamers in the presence of both this ligand and zinc ions.[9,11] Indeed, previous studies describing the preparation of NPH crystals of LysPro demonstrated the necessary requirement of producing LysPro hexamers by the addition of both zinc ions and phenol prior to initiating crystallization.[6]

Contrary to the expected outcome, ultralente crystals of LysPro did form in the absence of phenolic preservative with a procedure similar to that used for wild-type insulins. The fact that LysPro forms crystals with morphology and dimensions indistinguishable from human insulin ultralente crystals suggests that the concentrations of zinc and halide ions override the destabilizing effects of the Pro,Lys amino acid inversion driving the formation of LysPro hexamers. The high sodium chloride concentration (1.2 M) used in the crystallization media may also serve to inhibit nonspecific high-order aggregation by an electrostatic effect.

Evidence for a $T_3R_3^f \rightarrow T_6$ Structural Transformation—Powder diffraction studies revealed that both the ULP and UHI formulations are composed of crystals containing T_6 hexamers. While $T_3R_3^f$ crystals of LysPro have been previously prepared, this is the first report demonstrating the crystallization of LysPro as T_6 hexamers. Furthermore, our studies provide definitive data on the nature of the crystals comprising UHI suspensions. Such information has heretofore been inaccessible due to the poor diffraction quality of the crystals. We also note that the presence of methylparaben in either the ULP or UHI formulations does not affect hexamer conformation (i.e., inducing the T → R transition). In contrast to the T_6 hexamer conformation identified in the ultralente formulations, the ULP C/S sample was found to contain $T_3R_3^f$ hexamers.

While it may appear that the differences between the two LysPro ultralente samples present an anomaly, since one is T_6 and the other $T_3R_3^f$, there is a simple explanation for this behavior. Diffraction quality single crystals of insulin have been transformed from T_6 to $T_3R_3^f$ by reducing the sodium chloride content to less than 0.3 M,[25,26] and a similar transformation can be effected from R_6 to $T_3R_3^f$ by reducing the phenol concentration (unpublished results). Single crystals treated in such a fashion still retain their diffraction properties despite the occurrence of the R → T transition in the crystal structure. In this study, the dilution of the sodium chloride concentration from 1.2 to 0.12 M as formulated for animal testing is sufficient to induce the R → T transition, resulting in a crystalline powder sample made up of T_6 hexamers. Thus, the original ULP C/S crystals grown at 1.2 M sodium chloride contain $T_3R_3^f$ hexamers, and the dilution to 0.12 M sodium chloride transforms these crystals to T_6. These results also show that despite differences in a formulated insulin preparation as compared to the crystallizing media used to prepare diffraction quality single crystals, the formulated microcrystals possess a structure nearly identical to that obtained from single-crystal diffraction studies.

Pharmaceutical Relevance—The primary motivation for exploring the feasibility of preparing a LysPro ultralente formulation was to compare the time–action profile to that of wild-type insulin preparations. A study comparing the activity of bovine, human, and porcine ultralente showed that all preparations evaluated displayed a duration of activity in excess of 30 h.[27] However, bovine ultralente displayed a flat, essentially peakless profile although it was noted that a consistent peak was not evident due to the wide variability between subjects. The authors also concluded that any one of the ultralente formulations is suitable to provide basal insulinemia in clinical practice. Nevertheless, a peakless profile with a time–action greater than 24 h is considered highly desirable in certain diabetes treatment regimens.

Atomic force microscopy studies have provided evidence that the difference in time action between bovine ultralente compared to either human or porcine ultralente may be related to packing and orientation of insulin hexamers at the crystal–solution interface.[17] In bovine ultralente crystals, the hexamers on the predominant faces [(010) and (110)] are oriented "edge-on" to the aqueous medium, limiting solvent penetration into the crystals and consequently further retarding dissolution. Conversely, the predominant exposed crystal surface of human and porcine ultralente crystals is the (001) crystal plane. Hexamer orientation on this face allows for easier penetration of solvent through the crystal surface, contributing to more rapid dissolution. Given this diversity in ultralente crystal

morphology, it is reasonable to evaluate the pharmacological properties of insulin analogue suspensions especially in light of the inherent immunological issues associated with bovine insulin preparations.[28] The pharmacological data collected on ULP indicate that it has a time−action profile that is more consistent with human rather than bovine insulin ultralente. This result is nonetheless interesting considering the perturbed self-association properties of LysPro. Despite the "monomeric" nature of LysPro, crystallization as an ultralente form did not result in any significant decrease in duration of activity compared to UHI.

References and Notes

1. The following abbreviations are used: C_{max}, maximal insulin/LysPro concentration; LysPro, [Lys^{B28},Pro^{B29}]-human insulin analogue; NPH, Neutral Protamine Hagedorn; R_6, insulin hexamers in which the B-chain residues B1−B8 of all monomer subunits are α-helical resulting in a continuous α-helix from B1−B19; R_{max}, maximal rate of glucose infusion; T_3R_3, insulin hexamers in which three of the monomer subunits contain an extended conformation for B-chain residues B1−B8 and B9−B19 are α-helical while the other three monomers contain B-chain residues B1−B8 that are α-helical resulting in a continuous α-helix from B1−B19; $T_3R_3^f$, insulin hexamers in which three of the monomer subunits contain an extended conformation for B-chain residues B1−B8 and B9−B19 are α-helical while the other three monomers have a "frayed" α-helix in which the B-chain residues B1−B3 are extended and only B4−B19 are α-helical; T_6, insulin hexamers in which the B-chain residues B1−B8 of all monomer subunits are in an extended conformation and B9−B19 are α-helical; T_{max}, time at which C_{max} is attained; T_{Rmax}, time at which R_{max} is attained; (UHI), ultralente human insulin; ULP, ultralente LysPro; ULP C/S, ultralente LysPro concentrated suspension.
2. Hallas-Møller, K.; Petersen, K.; Schlichtkrull, J. Crystalline and Amorphous Insulin-Zinc Compounds with Prolonged Action. *Science* **1952**, *116*, 394−398.
3. Hallas-Møller, K. The Lente Insulins. *Diabetes* **1956**, *5*, 7−14.
4. Hagedorn H. C.; Jensen, B. N.; Krarup, N. B.; Wodstrup, I. Protamine Insulinate. *J. Am. Med. Assoc.* **1936**, *106*, 177−180.
5. Krayenbühl, C.; Rosenberg, T. Crystalline Protamine Insulin. *Rep. Steno Mem. Hosp. Nord. Insulinlab* **1946**, *1*, 60−73.
6. DeFelippis, M. R.; Bakaysa, D. L.; Bell, M. A.; Heady, M. A.; Li, S.; Pye, S.; Youngman, K. M.; Radziuk, J.; Frank, B. H. Preparation and Characterization of a Cocrystalline Suspension of [Lys^{B28},Pro^{B29}]-Human Insulin Analogue. *J. Pharm. Sci.* **1998**, *87*, 170−176.
7. Ciszak, E.; Beals, J. M.; Frank, B. H.; Baker, J. C.; Carter, N. D.; Smith, G. D. Role of C-terminal B-chain Residues in Insulin Assembly: The Structure of Hexameric Lys^{B28}-Pro^{B29}−Human Insulin. *Structure* **1995**, *3*, 615−622.
8. Kaarsholm, N. C., Ko, H.-C., Dunn, M. F. Comparison of Solution Structural Flexibility and Zinc Binding Domains for Insulin, Proinsulin, and Miniproinsulin. *Biochemistry* **1989**, *28*, 4427−4435.
9. Bakaysa, D. L.; Radziuk, J.; Havel, H. A.; Brader, M. L.; Li, S.; Dodd, S. W.; Beals, J. M.; Pekar, A. H.; Brems, D. N. Physicochemical Basis for the Rapid Time-action of Lys^{B28}-Pro^{B29}-Insulin: Dissociation of a Protein−Ligand Complex. *Protein Sci.* **1996**, *5*, 2521−2531.
10. Birnbaum, D. T.; Kilcomons, M. A.; DeFelippis, M. R.; Beals, J. M. Assembly and Dissociation of Human Insulin and $Lys^{B28}Pro^{B29}$-Insulin Hexamers: A Comparison Study. *Pharm. Res.* **1997**, *14*, 25−36.
11. Richards, J. P.; Stickelmeyer, M. P.; Flora, D. B.; Chance, R. E.; Frank, B. H.; DeFelippis, M. R. Self-Association Properties of Monomeric Insulin Analogues Under Formulation Conditions. *Pharm. Res.* **1998**, *15*, 1434−1441.
12. Derewenda, U.; Derewenda, Z.; Dodson, E. J.; Dodson, G. G.; Reynolds, C. D.; Smith, G. D.; Sparks, C.; Swenson, D. Phenol Stabilizes More Helix in a New Symmetrical Zinc Insulin Hexamer. *Nature* **1989**, *338*, 594−596.
13. Smith, G. D.; Dodson, G. G. Structure of a Rhombohedral R_6 Insulin/Phenol Complex. *Proteins, Struct. Funct. Genet.* **1992**, *14*, 401−408.
14. Ciszak, E.; Smith, G. D. Crystallographic Evidence for Dual Coordination around Zinc in the T_3R_3 Human Insulin Hexamer. *Biochemistry* **1994**, *33*, 1512−1517.
15. Smith, G. D.; Swenson, D. C.; Dodson, E. J.; Dodson, G. G.; Reynolds. C. D. Structural Stability in the 4-Zinc Human Insulin Hexamer. *Proc. Natl. Acad. Sci. U.S.A.* **1984**, *81*, 7093−7097.
16. Baker, E. N.; Blundell, T. L.; Cutfield, J. F.; Cutfield, S. M.; Dodson, E. J.; Dodson, G. G.; Crowfoot Hodgkin, D. M.; Hubbard, R. E.; Isaacs, N. W.; Reynolds, C. D.; Sakabe, K.; Sakabe, N.; Vijayan, N. M. The Structure of 2Zn Pig Insulin Crystals at 1.5 Å Resolution. *Philos. Trans. R. Soc. London B* **1988**, *319*, 369−456.
17. Yip, C. M.; DeFelippis, M. R.; Frank, B. H.; Brader, M. L.; Ward, M. D. Structural and Morphological Characterization of Ultralente Insulin Crystals by Atomic Force Microscopy: Evidence of Hydrophobically Driven Assembly. *Biophys. J.* **1998**, *75*, 1172−1179.
18. Brange, J.; Skelbaek-Pedersen, B.; Langkjaer, L.; Damgaard, U.; Ege, H.; Havelund, S.; Heding, L. G.; Jørgensen, K. H.; Lykkeberg, J.; Markussen, J.; Pingel, M.; Rasmussen, E. *Galenics of Insulin. The Physicochemical and Pharmaceutical Aspects of Insulin and Insulin Preparations*; Springer-Verlag: Berlin, Heidelberg, 1987.
19. Capel, M. **1998**, X12B Software, http://crim12b.nsls.bnl.gov/x12b_downloads.html.
20. Smith, G. D.; Ciszak, E. The Structure of a Complex of Hexameric Insulin and 4′-Hydroxyacetanilide. *Proc. Natl. Acad. Sci. U.S.A.* **1994**, *91*, 8851−8855.
21. Smith, G. D.; Ciszak, E.; Pangborn, W. A Novel Complex of a Phenolic Derivative with Insulin: Structural Features Related to the T → R Transition. *Protein Sci.* **1996**, *5*, 1502−1511.
22. Blessing, R. H. Data Reduction and Error Analysis for Accurate Single-Crystal Diffraction Intensities. *Crystallogr. Rev.* **1987**, *1*, 3−58.
23. Schlichtkrull, J. Insulin Crystals IV. The Preparation of Nuclei, Seeds and Monodisperse Insulin Crystal Suspensions. *Acta Chem. Scand.* **1957**, *11*, 299−302.
24. Kadima, W.; McPherson, A; Dunn M. F.; Jurnak, F. Precrystallization Aggregation of Insulin by Dynamic Light Scattering and Comparison with Canavalin. *J. Cryst. Growth* **1991**, *110*, 188−194.
25. Bentley G.; Dodson G.; Lewitova, A. Rhombohedral Insulin Crystal Transformations. *J. Mol. Biol.* **1978**, *126*, 871−875.
26. Reynolds, C. D.; Stowell, B.; Joshi, K. K.; Harding, M. M.; Maginn, S. J.; Dodson G. G. Preliminary Study of a Phase Transformation in Insulin Crystals Using Synchrotron-Radiation Laue Diffraction. *Acta Crystallogr.* **1988**, *B44*, 512−515.
27. Seigler, D. E.; Olsson, G. M.; Agramonte, R. F.; Lohman, V. L.; Ashby, M. H.; Reeves, M. L.; Skyler, J. S. Pharmacokinetics of Long-acting (Ultralente) Insulin Preparations. *Diab. Nutr. Metab.* **1991**, *4*, 267−273.
28. Schernthaner, G. Immunogenicity and Allergenic Potential of Animal and Human Insulins. *Diabetes Care* **1993**, *16*, 155−165.

Acknowledgments

We thank Maureen Bell of Eli Lilly and Company for assistance with the Coulter particle size determinations and Quovadis McKenzie (Eli Lilly and Company summer intern) for help in performing the ultralente crystallizations. Dr. Walter A. Pangborn of the Hauptman-Woodward Medical Research Institute is thanked for assistance in measuring the observed powder patterns. The authors also thank Dr. Ron Chance for critical review of the manuscript.

JS990107O

The Correlation and Prediction of the Solubility of Compounds in Water Using an Amended Solvation Energy Relationship

MICHAEL H. ABRAHAM* AND JOELLE LE

Contribution from *Department of Chemistry, University College London, 20 Gordon Street, London, United Kingdom WC1H OAJ.*

Received March 30, 1999. Accepted for publication June 7, 1999.

Abstract □ The aqueous solubility of liquids and solids, as log S_W, has been correlated with an amended solvation equation that incorporates a term in $\Sigma\alpha_2^H \times \Sigma\beta_2^H$, where the latter are the hydrogen bond acidity and basicity of the solutes, respectively. Application to a training set of 594 compounds led to a correlation equation with a standard deviation, SD, of 0.56 log units. For a test set of 65 compounds, the SD was 0.50 log units, and for a combined correlation equation for 659 compounds, the SD was 0.56 log units. The correlation equations enable the factors that influence aqueous solubility to be revealed. The hydrogen-bond propensity of a compound always leads to an increase in solubility, even though the $\Sigma\alpha_2^H \times \Sigma\beta_2^H$ term opposes solubility due to interactions in the liquid or solid. Increase in solute dipolarity/polarizability increases solubility, whereas an increase in solute excess molar refraction, and especially, volume decrease solubility. The solubility of Bronsted acids and bases is discussed, and corrections for the fraction of neutral species in the saturated solution are graphically presented.

Introduction

The solubility of liquids and solids in water is a very important molecular property that influences the release, transport, and extent of absorption of drugs in the body and that is a key determinant of the environmental fate of agrochemicals and pollutants in the environment. Not surprisingly, numerous methods for the prediction of aqueous solubilities have been suggested. We restrict our discussion primarily to methods that include solid solutes because methods that predict only liquid solubilities are of limited use.

One of the first predictive methods for aqueous solubilities was that of Irmann,[1] who set up a group contribution scheme for liquid hydrocarbons and halocompounds. For solids, Irmann used an additional term, $\Delta S_m(T_m - T)/1364$, where ΔS_m is the entropy of fusion (melting) at the melting point T_m. A value of 13 cal deg^{-1} mol^{-1} was taken for ΔS_m, leading to the following simplified correction term

$$-0.0095(\text{mp} - 25) \qquad (1)$$

In eq 1, mp is the melting point in °C; for liquids, the term (mp − 25) is taken as zero. Irmann[1] gave no statistical analysis, but we have used Irmann's original data, excluding compounds for which the observed solubility was given as approximate, and give details in Table 1. Several other group contribution schemes have been constructed,[2−5] some of which[2] do not require any mp correction term.

The UNIFAC and UNIQUAT methods are also group contribution schemes and have been used to estimate aqueous solubilities.[6,7] Because the reference state for solutes in these methods is the pure liquid, they require a knowledge of the solute enthalpy of fusion or an approximate mp correction term for solids. Another type of group contribution scheme is used in the AQUAFAC program,[8−13] which was applied to 970 compounds.[10] Again, either the entropy of fusion or the mp is needed for solid solutes.

A number of correlations are based on theoretically calculated descriptors.[14−18] None of these require any mp correction term for solids and therefore are capable of predicting aqueous solubilities from structure. Interestingly, there is no discussion[14−18] on why it is not necessary to include a correction for solids.

Quite different types of calculation were initiated by Hansch and co-workers,[19] who showed that there was a relationship (eq 2) between log S_W (the solubility in mol dm^{-3}) and the water−octanol partition coefficient (log P_{oct}) for a training set of 156 liquids

$$\log S_W = -1.339 \log P_{oct} + 0.978$$
$$n = 156,\ \text{SD} = 0.472,\ r^2 = 0.874 \qquad (2)$$

Yalkowsky and Valvani[20] extended the applicability of this relationship by incorporation of similar terms to those used by Irmann[1] for solids. They showed that the entropy of fusion could be estimated and that the entropy of fusion term could be replaced by a mp correction term as in eq 3 (compare eq 1). Several related equations were put forward:[10,21,22]

$$\log S_W = -1.05 \log P_{oct} - 0.012(\text{mp} - 25) + 0.87$$
$$n = 155,\ \text{SD} = 0.308,\ r^2 = 0.979 \qquad (3)$$

$$\log S_W = -1.00 \log P_{oct} - \Delta S_m(\text{mp} - 25)/1364 + 0.87$$
$$n = 873 \qquad (4)$$

$$\Delta S_m = 13.5 - 4.6(\log \sigma) \qquad (5)$$

In eq 3, and elsewhere, n is the number of data points, SD is the standard deviation, r is the correlation coefficient and F is the F-statistic. Values of log P_{oct} in eq 4 were not experimental ones but were calculated by the CLOGP program. The entropies of fusion were a combination of experimental and calculated values, using eq 5 where σ is the rotational symmetry number. However, the compound mp is still needed to apply eq 4, so log S_W values cannot be calculated from structure.

Mobile Order Theory[23−25] has recently been applied to the estimation of aqueous solubility with impressive results.[24] However, the method requires not only the entropy of fusion of solid solutes (or a mp correction term), but also a modified nonspecific solute cohesion parameter. The latter is obtained either from experimental solubilities in hydrocarbon solvents or is "...deduced by analogy to similar compounds."[24]

10.1021/js9901007 CCC: $18.00
Published on Web 08/17/1999

Table 1—Models for the Correlation and Prediction of Aqueous Solubility (log S_W) that Require Additional Data (ΔS_f, mp, δ')

training set			test set			
N	SD	outliers	*N*	SD	outliers	ref
168	0.31[a] AAE (0.17)	none				1
694	AAE (0.38)	none				4
68	0.61[b] AAE (0.45)	none				7
167	0.24	none				20
205	0.40[c]	none	none			24
873	0.56[d]	none	97	0.56[d] AAE (0.41)	none	10
873	0.80[e]	none	97	0.80[e] AAE(0.61)	none	10

[a] Calculated in this work. The AAE is given by AAE = $\sum$(|log $S_W$obs – log $S_W$calc|)/n. [b] Calculated in this work from data in Tables 2 and 3 in ref 7. [c] Calculated in this work. Note that the value in ref 24 at the foot of Table 4 is incorrect. [d] Aquasolve method. The SD value for the test set has been calculated in this work, and we have taken the SD value for the training set to be the same. [e] Equation 4. The SD value for the test set has been calculated in this work, and we have taken the SD value for the training set to be the same.

Table 2—Models for the Correlation and Prediction of Aqueous Solubility (log S_W) that Do Not Require Additional Data

training set			test set			
N	SD	outliers	*N*	SD	outliers	ref
469[a]	0.46	none	25	0.50	none	3
			12	0.37	1	
483[b]	0.53	none	25	0.55	none	3
			19	0.86	2	
123[c]	0.22	4	13	0.23	none	17
123[d]	0.28	4	13	0.28	none	17
258	0.37	42				16
411	0.57	none				18
331	0.30	none	17	0.34	none	15

[a] Model I, that is not too general. A later analysis[4] gives AAE = 0.50 for 694 compounds. [b] Model II, that is very general. A later analysis[4] gives AAE = 0.56 for 614 compounds. [c] Using a neural network with nine descriptors. [d] Using a linear model with nine descriptors.

In Tables 1 and 2 we summarize the methods that have been applied more generally; that is, to large sets of structurally diverse compounds. It is not always easy to compare different methods because some have been constructed using only a training set, others have used both a training set and a test set. In addition, various statistics have been used to describe the goodness of fit between observed and calculated log S_W values in a training set and between observed and predicted log S_W values in a test set. We prefer the SD, given by SD = $\sqrt{[\sum(\log S_W\text{obs} - \log S_W\text{calc})^2/(n - 1 - p)]}$ (where p is the number of parameters), but the average absolute error (AAE) is sometimes used. Defined as AAE = $\sum$(|log $S_W$obs − log $S_W$calc|)/n, the AAE is always much smaller than the corresponding SD value. In addition, some workers list outliers but other workers do not. Because the number of outliers can be very large (42 out of 300 for the general case in ref 16), care has to be taken in judging one model against another. Wherever possible in Tables 1 and 2, we have calculated the SD, as already described, to provide a uniform basis of comparison. Even then, comparisons of the various models is difficult. Bodor and Huang[15] obtain a very low SD value of 0.30 log units for a 331 compound data set, using 18 theoretically calculated descriptors, and Sutter and Jurs[17] find even lower SD values of 0.27 and 0.22 for a 123 compound data set. Myrdal and co-workers,[10] however, find a much larger SD of 0.56 for an 873 compound training set using the AQUASOLVE model. However, the 331 training set[15] includes very few complicated molecules and the 123 compound data set[17] no complicated molecules at all, whereas the 873 training set[10] is much more diverse.

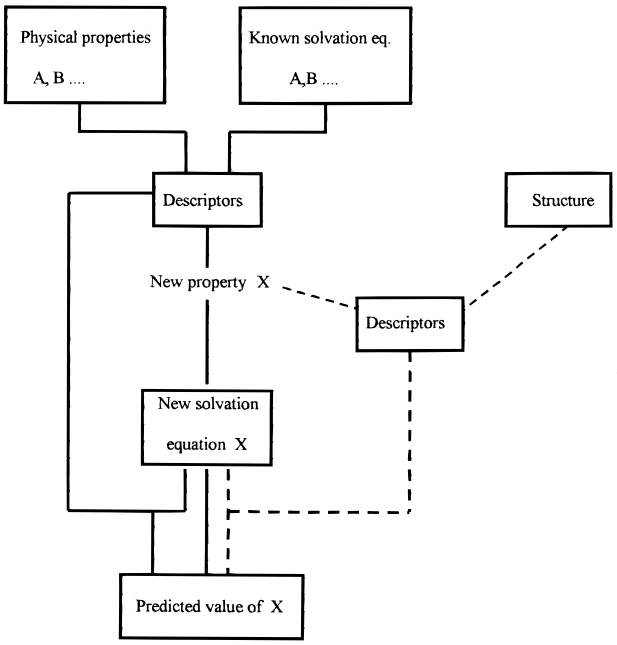

Figure 1—The application of the solvation equation. Full lines show the pathway using experimental descriptors and broken lines show the pathway using calculated descriptors.

Our conclusion is that for training sets that do not contain compounds of complicated structure, SD values as low as 0.30 log units may be obtained, but that for training sets that contain more varied compounds, SD values will not be lower than ~0.50 log units. Myrdal and co-workers[10] point out that the experimental solubilities themselves are a source of considerable error and note that recorded log S_W values for anthracene differ by 1.85 log units, and for fluoranthene by 1.15 log units. Hence, for training sets that contain a reasonable proportion of complicated structures, for many of which only one solubility determination has been made, experimental error probably precludes SD values less than around ~0.50 log units. What is also evident from Tables 1 and 2 is that there is no advantage, as regards SD values, of methods that require additional solute properties. Because there are very considerable advantages in methods that calculate log S_W from structure, especially in view of the importance of high throughput screening, our eventual aim is indeed to calculate aqueous solubility from structure.

Methodology

Our method starts with the following general solvation equation,[26]

$$\log SP = c + rR_2 + s\pi_2^H + a\Sigma\alpha_2^H + b\Sigma\beta_2^H + vV_x \qquad (6)$$

Here, the dependent variable, log SP, is a property of a series of solutes in a given system, such as log P_{oct} or log S_W, and the independent variables are solute descriptors as follows:[26] R_2 is an excess molar refraction in units of (cm^3 mol^{-1})/10, π_2^H is the dipolarity/polarizability, $\Sigma\alpha_2^H$ is the overall or summation hydrogen-bond acidity, $\Sigma\beta_2^H$ is the overall or summation hydrogen-bond basicity, and V_x is the McGowan characteristic volume[27] in units of (cm^3 mol^{-1})/100. The coefficients in eq 6 are found by multiple linear regression analysis, using a set of solutes for which the descriptors are known. There are numerous applications of eq 6 to physicochemical properties, both by ourselves[28–47] and by other workers,[48–59] so that eq 6 can be regarded as a well-established general equation.

Table 3—Test Set of Compounds

compound	log S_W exp	log S_W calc	error	compound	log S_W exp	log S_W calc	error
2,2-dimethylbutane	–3.550	–3.293	0.257	diphenylmethane	–4.080	–4.347	–0.267
3-methylheptane	–5.160	–4.416	0.744	2,3-dimethylnaphthalene	–4.720	–4.790	–0.070
hexadecane	–8.400	–8.909	–0.509	anthracene	–6.350	–5.361	0.989
cycloheptane	–3.510	–3.697	–0.187	pyrene	–6.176	–6.108	0.068
2-methylbut-1-ene	–2.730	–2.324	0.406	benzo[*j*]fluoranthene	–8.000	–7.513	0.487
buta-1,3-diene	–1.870	–1.547	0.323	1,4-difluorobenzene	–1.970	–1.972	–0.002
ethyne	0.290	–0.122	–0.412	1,2,3,5-tetrachlorobenzene	–4.630	–4.789	–0.159
trichloromethane	–1.170	–1.591	–0.421	3-chlorobiphenyl	–4.880	–4.951	–0.071
hexachloroethane	–3.670	–4.237	–0.567	2-bromonaphthalene	–4.400	–4.609	–0.209
1-chlorohexane	–3.120	–3.242	–0.122	4-chloroiodobenzene	–4.030	–4.417	–0.387
tribromomethane	–1.910	–2.478	–0.568	anthraquinone	–5.190	–3.709	1.481
1-bromoheptane	–4.430	–4.074	0.356	3-methylaniline	–0.850	–1.470	–0.620
bromodichloromethane	–1.540	–1.835	–0.295	*N*-ethylaniline	–1.700	–2.222	–0.522
methyl butyl ether	–0.990	–0.965	0.025	3-nitrotoluene	–2.440	–2.552	–0.112
tetrahydrofuran	1.150	0.167	–0.983	2,4-dinitrotoluene	–2.820	–2.200	0.620
2-ethylhexan-2-al	–2.460	–2.052	0.408	lidocaine	–1.710	–2.431	–0.721
heptan-2-one	–1.450	–1.354	0.096	2-methylbenzoic acid	–2.060	–1.761	0.299
propyl formate	–0.490	–0.497	–0.007	2-aminobenzoic acid	–1.520	–1.021	0.499
pentyl acetate	–1.890	–1.847	0.043	3,5-dimethylphenol	–1.400	–1.823	–0.423
ethyl heptylate	–2.740	–2.946	–0.206	2,4-dichlorophenol	–1.550	–2.266	–0.716
acetonitrile	0.260	0.803	0.543	2,3,4,6-tetrachlorophenol	–3.100	–3.506	–0.406
diethylamine	1.030	0.395	–0.635	4-hydroxybenzoic acid	–1.410	–1.110	0.300
acetamide	1.580	1.850	0.270	1-phenylethanol	–0.920	–1.087	–0.167
trichloroacetic acid	0.600	–0.023	–0.623	2,4-dimethylpyridine	0.380	–0.696	–1.076
pentan-2-ol	–0.290	–0.442	–0.152	morpholine	1.965	1.587	–0.378
2-methylpentan-1-ol	–1.110	–1.221	–0.111	codeine	–1.520	–2.318	–0.798
3,3-dimethylbutan-1-ol	–0.500	–1.222	–0.722	17*a*-methyltestosterone	–3.999	–4.318	–0.319
2,4-dimethylpentan-2-ol	–0.920	–1.483	–0.563	5-ethyl-5-(3-methylbutyl)barbital	–2.658	–2.580	0.078
decan-1-ol	–3.630	–3.423	0.207	5-allyl-5-phenylbarbital	–2.369	–3.309	–0.940
pent-4-ene-1-ol	–0.150	–0.315	–0.165	carbofuran	–2.800	–3.102	–0.302
diethyl disulfide	–2.420	–2.593	–0.173	fenoxycarb	–4.700	–4.821	–0.121
isopropylbenzene	–3.270	–3.576	–0.306	propoxur	–2.050	–1.631	0.419
1,4-diethylbenzene	–3.750	–4.090	–0.340				

The application of eq 6 is summarized in Figure 1 (full lines). Various sets of physical properties, already calibrated through known solvation equations, can be used to assign descriptors, exactly as detailed before.[60] In this way, a database of descriptors for some 3500 compounds has been established. If a new property, X, is to be investigated, the experimental database is used to obtain a correlation equation for the new property, through eq 6. Thus we have recently constructed[47] an equation for water–chloroform partition coefficients, log P_{chl}, for solutes as neutral species.

Once such an equation has been set up, more values of the dependent variable can be predicted from the experimental database of descriptors, as shown by the full lines in Figure 1. However, a further step is to calculate descriptors from structure, so that values of property X may be predicted from structure. This prediction is essential for any fast throughput screening of drugs, agrochemicals, etc. We have just completed a computer program, ABSOLVE, for the calculation of descriptors from structure;[61] this is then tantamount to a method for the prediction from structure of any property, X, for which we have solvation equations, as shown by the broken lines in Figure 1.

The aim of the present work is to obtain an equation for the correlation of log S_W values, without the need for a mp correction, using a large training set and also a reasonably large test set of compounds. Together with the program ABSOLVE, we will then be in a position to predict solubilities from structure.

Results and Discussion

Construction of an Equation for log S_W—We have used a number of databases to set out values of log S_W for 664 solids and liquids. We excluded five compounds from the 664 data set (cyclopropyl-5-spirobarbituric acid, uracil, chlorpheniramine, fentanyl, and adenine) because a preliminary analysis showed that these four were large outliers to all the equations we constructed. In addition we have not included any dicarboxylic acids, such as phthalic acid and succinic acid, partly because we have not yet finalised descriptors for these and partly because preliminary analyses suggest that calculated values of log S_W are always too positive. A total of 659 compounds were left for the final analysis. Every tenth compound in a random order was selected to form a test set, to give 594 compounds as a training set and 65 compounds as a test set. The total set of 664 compounds is given in the Appendix. The smaller test set of 65 compounds is in Table 3. Application of eq 6 to the 594 training set yielded eqs 7 and 8, with SD values of 0.56 and 0.63 log units, respectively; note that fewer compounds were used in eq 7, because of lack of mps. These SD values are not far short of the SD values obtained for models that have been applied to large data sets[3,18] (see Tables 1 and 2).

$$\log S_W = 0.579 - 0.576R_2 + 0.980\pi_2^H + 1.233\Sigma\alpha_2^H + 3.389\Sigma\beta_2^H - 4.079V_x - 0.010(\mathrm{mp} - 25)$$

$$n = 411,\ \mathrm{SD} = 0.564,\ r^2 = 0.915,\ F = 724,\ \mathrm{AAE} = 0.389 \quad (7)$$

$$\log S_W = 0.849 - 1.061R_2 + 0.851\pi_2^H + 0.646\Sigma\alpha_2^H + 3.279\Sigma\beta_2^H - 4.050V_x$$

$$n = 594,\ \mathrm{SD} = 0.630,\ r^2 = 0.895,\ F = 1004,\ \mathrm{AAE} = 0.470 \quad (8)$$

It is somewhat surprising that eq 6 has led to the reasonable eqs 7 and 8, because eq 6 was not set up at all to

Table 4—Correlation Equations Without Compounds of Low and High Solubilities[a]

coefficients							statistics				
r	*s*	*a*	*b*	*k*	*v*	*c*	r^2	SD	*n*	AAE	condition[b]
–1.025	0.799	2.026	4.003	–2.953	–3.900	0.450	0.912	0.539	610	0.402	1
–0.891	0.693	2.160	4.231	–3.459	–3.913	0.451	0.901	0.534	636	0.388	2
–0.912	0.713	2.015	3.965	–3.047	–3.781	0.348	0.884	0.512	587	0.385	3
–1.020	0.813	2.124	4.187	–3.337	–3.986	0.510	0.918	0.562	594	0.409	4
–1.004	0.771	2.168	4.238	–3.362	–3.987	0.518	0.920	0.557	659	0.408	5

[a] All equations are without any mp correction term. [b] (1) Omit very soluble compounds; (2) omit very insoluble compounds; (3) omit both very soluble and very insoluble compounds; (4) eq 10; (5) eq 11.

correlate quantities such as log S_W. There is a fundamental difference between processes such as water−solvent partitions, to which eq 6 has previously been applied, and solubility in water. In the former processes, the thermodynamic standard states are those of unit molar concentration and unit activity in both the aqueous and the solvent phase. For solubility in water, the standard states are unit molar concentration and unit activity in the aqueous phase, but the pure liquid or solid (as the other phase). As pointed out before,[62] the standard state of pure liquid or pure solid is equivalent to a different standard state for each compound. Now eq 6 is constructed for processes in which different solutes have the same standard state in each phase. In chemical terms, this means that a solute in a given phase is surrounded by the phase molecules, whereas for the standard state of pure liquid or solid, the solute is surrounded by itself. Difficulties in application to aqueous solubility of equations similar to eq 6 have previously been encountered; for example, aliphatic and aromatic compounds give rise to quite different correlation equations.[63]

We can amend eq 6 to incorporate terms that reflect interactions in the pure liquid or solid. A term in $\Sigma\alpha_2^H \times \Sigma\beta_2^H$ will deal with hydrogen-bond interactions between acid and basic sites in the solid or liquid, and a term in $\pi_2^H \times \pi_2^H$ with dipole/dipole interactions. The best equations constructed on these lines are

$$\log S_W = 0.403 - 0.484R_2 + 0.814\pi_2^H + 1.956\Sigma\alpha_2^H + 4.018\Sigma\beta_2^H - 1.130\Sigma\alpha_2^H \times \Sigma\beta_2^H - 4.067V_x - 0.010(\text{mp} - 25)$$

$$n = 411,\ \text{SD} = 0.496,\ r^2 = 0.934,\ F = 819,\ \text{AAE} = 0.245 \quad (9)$$

$$\log S_W = 0.510 - 1.020R_2 + 0.813\pi_2^H + 2.124\Sigma\alpha_2^H + 4.187\Sigma\beta_2^H - 3.337\Sigma\alpha_2^H \times \Sigma\beta_2^H - 3.986V_x$$

$$n = 594,\ \text{SD} = 0.562,\ r^2 = 0.918,\ F = 1089,\ \text{AAE} = 0.409 \quad (10)$$

Inspection of eqs 7−10 shows that there is little to be gained by inclusion of the mp correction term (compare Tables 1 and 2). The equations with the cross-term are significantly better than those without this term, and eq 9 is better than eq 10. However, the practical advantages of eq 10 quite outweigh the better fit of eq 9; in any case, eq 10 compares well with the equations listed in Table 2 that cover a wide range of compound type.

We can probe the predictive capability of eq 10 through the test set of 65 compounds given in Table 3, where the observed and calculated log S_W values for eq 10 are given. The SD value for the 65 compound test set is 0.496 log units, AAE = 0.397, and av error = −0.122, which we can take as an estimate of the predictive power of eq 10. Finally, we can combine the training set and test set and obtain eq 11 for the total of 659 compounds.

$$\log S_W = 0.518 - 1.004R_2 + 0.771\pi_2^H + 2.168\Sigma\alpha_2^H + 4.238\Sigma\beta_2^H - 3.362\Sigma\alpha_2^H\Sigma\beta_2^H - 3.987V_x$$

$$n = 659,\ \text{SD} = 0.557,\ r^2 = 0.920,\ F = 1256,\ \text{AAE} = 0.408 \quad (11)$$

We consider eq 11 to be the best equation we have constructed from the general solvation descriptors, and conclude that an amended version of eq 6, containing the extra $\Sigma\alpha_2^H \times \Sigma\beta_2^H$ term, can correlate and predict log S_W values to ~0.56 log units. The calculated values of log S_W from eq 11 are included in the Appendix.

There are particular experimental difficulties with regard to compounds that have very low solubilities. To ascertain if such compounds were exerting any undue influence on the regression, we re-ran the correlation leaving out the very insoluble compounds. We also left out separately the very soluble compounds, and finally omitted both the very insoluble and very soluble compounds. A summary of the resulting equations is given in Table 4, where the coefficient of the product term $\Sigma\alpha_2^H \times \Sigma\beta_2^H$ is denoted as '*k*'. By comparison with eqs 10 and 11, changes in the regression coefficients are not very pronounced and so there is little disrupting effect of compounds with very low or very high solubilities.

More important effects probably arise when the solid in equilibrium with the saturated solution is a hydrate, because the solubility of the hydrate will not be the same as the unhydrated solid, to which all the correlation equations refer. In addition, solubilities may depend on the physical form of a solid, for example whether it is amorphous or crystalline.

The Factors that Influence Aqueous Solubility—Unlike most regression equations for log S_W, eqs 10 and 11 can be interpreted to show the physicochemical properties of the compound that influence aqueous solubility. We have already noted that most studies of aqueous solubility in which correlations are constructed without any correction term for solids do not discuss why a correction term is unnecessary. Neither eq 10 nor eq 11 include a solid correction term, and it seems obligatory to comment on this. The two main properties that lead to an increase in solubility are hydrogen-bond acidity and hydrogen-bond basicity; these properties no doubt reflect the strong hydrogen-bond basicity and strong hydrogen-bond acidity of water as a bulk solvent.[28,29] However, if the compound is itself both a hydrogen-bond acid and a hydrogen-bond base, then intermolecular hydrogen-bond interactions will lead to an increase in mp and to a decrease in solubility. Thus, the product term, $\Sigma\alpha_2^H \times \Sigma\beta_2^H$, takes the place (at least partly) of a solid correction term.

Table 5—Hydrogen-Bond Effects on Solubility (log S_W)

compound	2.124 $\Sigma\alpha_2^H$	4.187 $\Sigma\beta_2^H$	−3.337 $\Sigma\alpha_2^H \times \Sigma\beta_2^H$	resultant
acetic acid	1.30	1.84	−0.90	2.24
trichloroacetic acid	2.02	1.17	−0.89	2.30
benzoic acid	1.25	1.67	−0.79	2.14
phenol	1.27	1.26	−0.60	1.93
4-nitrophenol	1.75	1.09	−0.71	2.12
ethanol	0.79	2.01	−0.59	2.20
2,2,2-trifluoroethanol	1.21	1.05	−0.48	1.78
estratriol	2.97	5.11	−5.70	2.38
aniline	0.55	1.72	−0.36	1.91
benzamide	1.04	2.81	−1.10	2.75
pyrazole	1.15	1.88	−0.81	2.22
morpholine	0.13	3.81	−0.18	3.76
progesterone	0.00	4.77	0.00	4.77
trichloromethane	0.32	0.08	−0.01	0.39

Now all hydrogen-bond acids, with the exception of carbon acids, are also hydrogen-bond bases, so that the effect of hydrogen-bonding on solubility will be a resultant of the two single terms and the product term, as shown in Table 5 for some representative acids. It is quite clear that the net result of the presence of hydrogen-bond acid and hydrogen-bond base groups will increase solubility. The intermolecular acid−base interaction in a solid or liquid, given by the $\Sigma\alpha_2^H \times \Sigma\beta_2^H$ term, reduces the hydrogen-bond effect but still leaves a negative resultant. For the large number of compounds that are hydrogen-bond bases, but not acids, there is a straightforward effect of increased solubility (also shown in Table 5). As already mentioned, there are but few compounds that are hydrogen-bond acids and yet have no or very little hydrogen-bond basicity. Again, there will be virtually no cross-term, and all the effect of hydrogen-bond acidity will be toward an increase in solubility, as shown for trichloromethane. The single terms in the descriptors $\Sigma\alpha_2^H$ and $\Sigma\beta_2^H$ both lead to an increase in solubility. The other 'polar' term in eq 10 is $s.\pi_2^H$ that leads also to an increase in solubility. It might be expected that intermolecular interactions, such as dipole/dipole or dipole/induced dipole would lead to an increase in mp and, again, a decrease in solubility. However, the product term $\pi_2^H \times \pi_2^H$ is not significant, no doubt because it is very well correlated with π_2^H which leads to an increase in solubility. However the coefficient of π_2^H in eq 10 is very much less than for the solubility of gases and vapors, so that dipolar effects within the solid or liquid counteract to some extent the solute/water effects that lead to increased solubility.

Two other terms in eq 10, rR_2 and vV_x, both result in a decrease in solubility; the r and v coefficients in eq 10 are markedly more negative than in the solvation equation for gaseous solubility. The R_2 descriptor refers to the propensity of a solute to interact with surrounding σ and π electrons, the negative r coefficient suggesting that such interaction within the solid or liquid is much larger than the corresponding interaction between the solute and bulk water. Although the V_x descriptor refers to the size of the solute, the vV_x term for the solubility of gaseous solutes will be the resultant of two opposing effects, (i) a cavity effect that arises from the disruption of solvent−solvent interactions and leads to a negative coefficient, and (ii) a general solute−solvent dispersion interaction that leads to a positive coefficient. For the solubility of gaseous solutes in water, the v coefficient is negative (−0.869) so that the unfavorable cavity effect dominates.[29] In solids and liquids, part of the cohesive forces will be general dispersion interactions that help to hold the solid or liquid together. These interactions within the solid or liquid will lead to an increase in mp, to a decrease in solubility, and to a much more negative v coefficient in eq 10, as observed (−3.986).

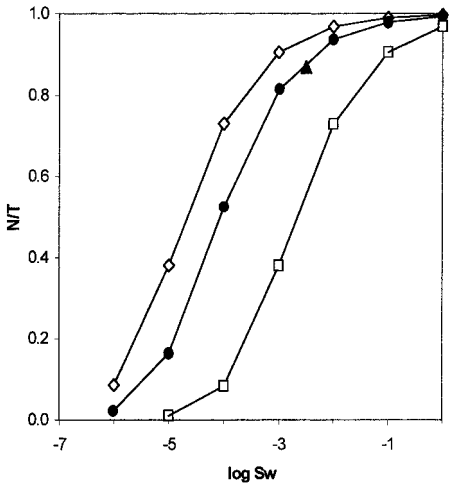

Figure 2—Values of N/T for Bronsted acids as a function of the total solubility, log S_W. Acids pK_a values are 3 (□), 4.37 (●), and 5 (◇), determined value (▲) for *p*-toluic acid.

Thus, the sign and magnitude of the coefficients in eq 10 can be interpreted in terms of known chemical interactions, both between the compound and water, and between molecules of the compound itself. Such interpretation, in turn, leads to information about the physicochemical factors that influence the aqueous solubility of solids and liquids.

We note that in Mobile Order Theory[23−25] the terms in solute volume are interpreted as originating from a balance of entropic effects. The negative dependence of solubility on solute volume arises[24] from the mobile order entropy decrease of the hydrogen-bonded water molecules on introduction of the solute. We have used a cavity theory to interpret volume and other effects because we have used[29] this type of theory (i.e., scaled particle theory[64]) previously to obtain quantitative estimates of cavity terms for solution of gases and vapors in water.

The Solubility of Bronsted Acids and Bases—Grant and Higuchi[65] have noted the effect of pH on the solubility of Bronsted acids and bases and have given equations for the variation of solubility with pH.[65] Most studies on the correlation and prediction of solubility ignore this pH dependency; none of the studies in Tables 1 and 2 mention this problem at all.

If a Bronsted acid, such as a carboxylic acid, is dissolved in water, the pH of the resulting solution will depend both on the acid pK_a and on the total concentration of the acid in solution. For a given acid, the greater the concentration, the lower will be the pH and the larger will be the proportion of the neutral species. Hence, for acids with the same pK_a, the pH of the saturated solution will decrease as the solubility increases. For acids that are quite soluble, the proportion of neutral species will therefore be larger than for acids that are sparingly soluble. Our eq 11 and, indeed, all the other correlation equations in Tables 1 and 2, refer to the solubility of the neutral species, N, so that the predicted (neutral) solubility will be less than the observed solubility, T or S_W, with the difference depending on the acid pK_a value and the actual solubility.

In Figure 2 we give the calculated values of N/T, the fraction of the neutral species, for a series of acids of pK_a 3, 4.37, and 5 as a function of the observed total solubility, log S_W (log T). For an acid with a pK_a of 4.37 or 5, N/T is

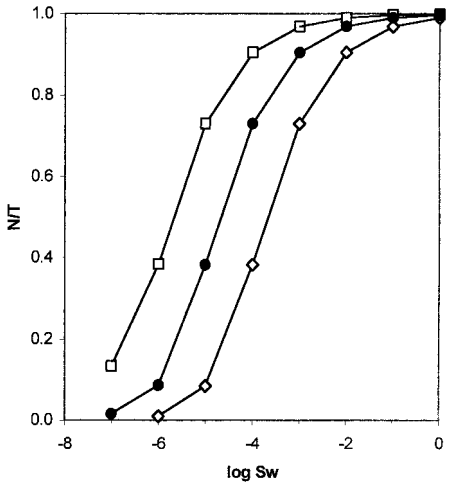

Figure 3—Values of *N*/*T* for Bronsted bases as a function of the total solubility, log S_W; pK_a values are 8 (□), 9 (●), and 10 (◇).

Table 6—Observed and Calculated log S_W Values for Strong Bronsted Acids (pK_a < 4)

acid	obs	calc	obs – calc	pK_a
trichloroacetic acid	0.600	–0.023	0.623	0.65
o-aminobenzoic acid	–1.520	–1.021	–0.499	2.11
chloroacetic acid	1.810	0.858	0.952	2.82
m-bromobenzoic acid	–2.276	–1.771	–0.505	2.85
o-chlorobenzoic acid	–1.890	–1.544	–0.346	2.94
salicylic acid	–1.820	–1.515	–0.305	2.98
p-nitrobenzoic acid	–2.800	–1.577	–1.223	3.42
m-nitrobenzoic acid	–1.680	–1.557	–0.123	3.49
m-chlorobenzoic acid	–2.590	–1.790	–0.800	3.87
o-toluic acid	–2.060	–1.761	–0.299	3.95
p-bromobenzoic acid	–3.539	–2.171	–1.368	3.97
p-chlorobenzoic acid	–3.310	–1.863	–1.447	3.98

larger than ∼0.5 even down to log S_W values of −4. Now an error of a factor of 0.5 (or 2.0) corresponds to an error of 0.3 log units and is not very important in the context of SD values of 0.5 log units. However, for very insoluble acids, with log S_W of −5 or −6, errors of one or two log units will arise if no consideration is given to ionization of Bronsted acids. For stronger acids with pK_a = 3, large errors will arise at log S_W values less than around −3.5 units.

We have chosen one of our pK_a values as 4.37 because this is the pK_a of *p*-toluic acid, studied in considerable detail by Strong and co-workers.[66] Their determined *N*/*T* value for *p*-toluic acid in the saturated solution at 25 °C is shown in Figure 2, and our calculated value is in excellent agreement.

A similar ionization phenomenon occurs in the solubility of Bronsted bases. Many drug molecules, of course, are strong Bronsted bases, with pK_a values of the conjugate acid ranging from 8 to 10. We give in Figure 3 plots of our calculated *N*/*T* values for three series of bases with pK_a = 8, 9, and 10 as a function of the observed solubility, log S_W. If we consider substantial errors in predicted values to arise when *N*/*T* is less than ∼0.5, these errors will be the case for bases with log S_W < −4 (pK_a 10), < −5 (pK_a 9) and < −6 (pK_a 8).

We can compare observed solubilities with those calculated from eq 10 for the neutral species for Bronsted acids and bases in our data set. In Table 6 are given values for strong Bronsted acids, that is, acids with pK_a values <4. Only in the case of trichloroacetic acid is the value of *N*/*T* <0.5 (0.480) for the saturated solution. The observed solubility would therefore be ∼0.32 log units more than the calculated solubility. For all the other acids in Table 6, the difference will be even less. Inspection of Table 6 shows that for three acids, the observed − calculated log S_W values are −1.2 to −1.5 units, so that other interfering factors are far more important than ionization, at least for the acids in Table 6.

Table 7—Observed and Calculated log S_W Values for Strong Bronsted Bases (pK_a > 10)

base	obs	calc	obs – calc	pK_a
octylamine	–1.460	–2.151	0.691	10.57
hexylamine	–0.250	–1.038	0.788	10.64
butylamine	0.960	0.057	0.903	10.66
pentylamine	0.270	–0.491	0.761	10.64
heptylamine	–0.900	–1.600	0.700	10.66
propylamine	1.520	0.618	0.902	10.69
ethylamine	2.060	1.169	0.891	10.70
triethylamine	–0.140	–0.363	0.223	10.85
diethylamine	1.030	0.395	0.635	11.04
dibutylamine	–1.440	–1.804	0.364	11.25

A similar table can be constructed for the strong bases, those with pK_a > 10 (see Table 7). There is a general trend, with (observed − calculated) log S_W values always positive by ∼0.7 log units, on average. However, this trend cannot be accounted for by ionization; even the value of 0.80 for *N*/*T* for dibutylamine would make a difference of only 0.1 log units.

It seems, therefore, that only for very insoluble strong Bronsted acids and Bronsted bases will ionization lead to significant errors in calculation. However, it is worth pointing out that solubilities calculated with eqs 10 or 11, or by the methods summarized in Tables 1 and 2, refer to the solubility of the neutral species. For Bronsted acids and bases this will be the solubility in solutions of pH near to the compound pK_a (see Figures 2 and 3). The observed solubility is that at the pH of the saturated solution. This observed solubility does not refer to any specific pH, but to a pH that has to be calculated from the observed (total) solubility and the compound pK_a. If the solubility of a Bronsted acid or base is required at a given pH of 7 or 7.4, for example, then Figures 2 and 3 can be used to obtain the correction factor *N*/*T*, at least if the difference in pH between the saturated solution and the given pH is not too large.

Conclusions

An amended solvation equation can satisfactorily correlate and predict log S_W values to 0.56 log units.The descriptors used in the correlation equations are either calculated from structure (R_2 and V_x) or are obtained from experimental data (π_2^H, $\Sigma\alpha_2^H$, $\Sigma\beta_2^H$) as shown by the full lines in Figure 1. Now that the ABSOLVE program for the calculation of π_2^H, $\Sigma\alpha_2^H$, and $\Sigma\beta_2^H$ is in place, the correlation equations set up in this work will enable log S_W values to be predicted from structure in a high throughput manner, as shown by the broken lines in Figure 1. Although the correlation equations are for neutral species, corrections for Bronsted acids and Bronsted bases can be made from the predicted log S_W value and a (predicted) pK_a value.

Appendix—Observed and Calculated Aqueous Solubilities (mol dm^{-3}) as log S_w

ref	compound	log S_W obs	log S_W calc (eq 11)	ref	compound	log S_W obs	log S_W calc (eq 11)
62	methane	–0.900	–0.477	16	propyne	–0.410	–0.451
62	ethane	–1.360	–1.038	78	1-butyne	–1.240	–1.161
62	propane	–1.940	–1.600	4	1-pentyne	–1.640	–1.656
62	butane	–2.570	–2.162	4	1-hexyne	–2.360	–2.254
67	2-methylpropane	–2.550	–2.162	78	3-hexyne	–1.990	–2.300
4	pentane	–3.180	–2.723	78	1-heptyne	–3.010	–2.906
78	2-methylbutane	–3.180	–2.723	4	1-octyne	–3.660	–3.463
4	hexane	–3.840	–3.285	4	1-nonyne	–4.240	–4.020
4	2-methylpentane	–3.740	–3.285	78	dichloromethane	–0.630	–0.990
4	3-methylpentane	–3.680	–3.285	4	trichloromethane	–1.170	–1.590
4	2,2-dimethylbutane	–3.550	–3.285	4	tetrachloromethane	–2.310	–2.595
78	2,3-dimethylbutane	–3.650	–3.285	78	chloroethane	–1.060	–1.022
4	heptane	–4.530	–3.847	4	1,1-dichloroethane	–1.290	–1.353
78	2,2-dimethylpentane	–4.360	–3.847	4	1,2-dichloroethane	–1.060	–1.293
78	2,3-dimethylpentane	–4.280	–3.847	4	1,1,1-trichloroethane	–2.000	–2.175
78	2,4-dimethylpentane	–4.260	–3.847	4	1,1,2-trichloroethane	–1.480	–1.703
78	3,3-dimethylpentane	–4.230	–3.847	4	1,1,2,2-tetrachloroethane	–1.740	–2.211
78	2,2,3-trimethylbutane	–4.360	–3.847	4	1,1,1,2-tetrachloroethane	–2.180	–2.520
4	octane	–5.240	–4.408	78	pentachloroethane	–2.600	–3.032
78	2-methylheptane	–5.080	–4.408	4	hexachloroethane	–3.670	–4.225
78	3-methylheptane	–5.160	–4.408	4	1-chloropropane	–1.470	–1.573
78	4-methyloctane	–6.050	–4.408	4	2-chloropropane	–1.410	–1.487
4	2,2,4-trimethylpentane	–4.740	–4.408	78	1,2-dichloropropane	–1.600	–1.808
78	2,3,4-trimethylpentane	–4.800	–4.408	4	1,3-dichloropropane	–1.620	–1.839
78	nonane	–5.880	–4.970	4	1-chlorobutane	–2.030	–2.128
78	2,2,5-trimethylhexane	–5.050	–4.970	78	1-chloro-2-methylpropane	–2.000	–2.048
78	decane	–6.980	–5.532	4	2-chlorobutane	–1.960	–2.061
78	undecane	–7.590	–6.094	4	1-chloropentane	–2.730	–2.688
78	dodecane	–7.670	–6.655	4	2-chloro-2-methylbutane	–2.510	–2.851
78	tetradecane	–7.960	–7.779	78	1-chlorohexane	–3.120	–3.243
78	hexadecane	–8.400	–8.902	67	1-chloroheptane	–4.000	–3.797
4	cyclopentane	–2.640	–2.477	14	chloroethylene	–1.750	–1.109
4	methylcyclopentane	–3.300	–3.001	4	1,1-dichloroethylene	–1.640	–1.732
78	propylcyclopentane	–4.740	–4.124	4	*cis*-1,2-dichloroethylene	–1.300	–1.379
78	pentylcyclopentane	–6.080	–5.243	4	trichloroethylene	–1.960	–2.279
4	cyclohexane	–3.100	–3.081	4	tetrachloroethylene	–2.540	–3.121
4	methylcyclohexane	–3.850	–3.613	4	hexachloro-1,3-butadiene	–4.920	–5.116
78	*cis*-1,2-dimethylcyclohexane	–4.300	–4.181	78	bromomethane	–0.790	–0.820
78	*trans*-1,4-dimethylcyclohexane	–4.470	–4.096	4	dibromomethane	–1.170	–1.563
78	ethylcyclohexane	–4.250	–4.163	4	tribromomethane	–1.910	–2.474
78	cycloheptane	–3.510	–3.688	4	tetrabromomethane	–3.140	–3.738
78	cyclooctane	–4.150	–4.313	4	bromoethane	–1.090	–1.287
78	decalin	–5.190	–4.981	4	1,2-dibromoethane	–1.680	–1.716
62	ethylene	–0.400	–0.601	4	1-bromopropane	–1.730	–1.848
62	propylene	–1.080	–1.174	4	2-bromopropane	–1.590	–1.768
62	1-butene	–1.940	–1.732	4	1-bromobutane	–2.370	–2.404
15	2-methylpropene	–2.330	–1.732	4	1-bromo-2-methylpropane	–2.430	–2.404
4	1-pentene	–2.680	–2.287	67	1-bromopentane	–3.080	–2.962
67	*cis*-2-pentene	–2.540	–2.335	67	1-bromohexane	–3.810	–3.516
4	*trans*-2-pentene	–2.540	–2.320	67	1-bromoheptane	–4.430	–4.072
78	2-methyl-1-butene	–2.730	–2.314	67	1-bromooctane	–5.060	–4.630
78	3-methyl-1-butene	–2.730	–2.257	4	iodomethane	–1.000	–1.303
78	2-methy-2-butene	–2.560	–2.353	67	diiodomethane	–2.340	–2.419
4	1-hexene	–3.230	–2.834	78	iodoethane	–1.600	–1.766
78	2-methyl-1-pentene	–3.030	–2.846	4	1-iodopropane	–2.290	–2.322
4	1-heptene	–3.730	–3.409	4	2-iodopropane	–2.090	–2.264
4	*trans*-2-heptene	–3.820	–3.437	4	1-iodobutane	–2.960	–2.878
4	1-octene	–4.440	–3.973	67	1-iodoheptane	–4.810	–4.543
4	1-nonene	–5.050	–4.531	4	bromochloromethane	–0.890	–1.315
78	1-decene	–5.510	–5.096	4	bromodichloromethane	–1.540	–1.841
78	1,3-butadiene	–1.870	–1.539	4	chlorodibromethane	–1.900	–2.119
4	2-methyl-1,3-butadiene	–2.030	–2.094	4	1-chloro-2-bromoethane	–1.320	–1.691
78	2,3-dimethyl-1,3-butadiene	–2.400	–2.525	4	1,1,2-trichlorotrifluoroethane	–3.040	–2.624
4	1,4-pentadiene	–2.090	–1.988	78	1,2-dichlorotetrafluoroethane	–2.740	–2.410
4	1,5-hexadiene	–2.680	–2.556	4	diethyl ether	–0.090	–0.337
4	cyclopentene	–2.100	–1.874	4	dipropyl ether	–1.100	–1.427
78	cyclohexene	–2.590	–2.499	4	diisopropyl ether	–1.100	–1.635
4	1-methylcyclohexene	–3.270	–3.073	4	dibutyl ether	–1.850	–2.543
78	cycloheptene	–3.180	–3.065	4	methyl propyl ether	–0.390	–0.441
78	1,4-cyclohexadiene	–2.060	–2.022	4	methyl butyl ether	–0.990	–0.945
16	ethyne	0.290	–0.132	4	methyl *tert*-butyl ether	–0.240	–0.228

Appendix (continued)

ref	compound	log S_W obs	log S_W calc (eq 11)	ref	compound	log S_W obs	log S_W calc (eq 11)
4	ethyl propyl ether	–0.660	–0.859	4	methyl acrylate	–0.220	–0.253
4	propyl isopropyl ether	–1.340	–1.444	4	glyceryl triacetate	–0.600	0.726
4	ethyl vinyl ether	–0.850	–0.391	4	malonic acid diethyl ester	–0.820	–0.534
4	dimethoxymethane	0.480	0.787	4	acetonitrile	0.260	0.795
4	1,1-diethoxyethane	–0.430	0.589	4	propionitrile	0.280	0.421
4	1,2-diethoxyethane	–0.770	0.149	4	acrylonitrile	0.150	0.347
4	1,2-propylene oxide	–0.590	0.701	14	ethylamine	2.060	1.200
68	tetrahydrofuran	0.490	0.182	14	propylamine	1.520	0.650
4	2-methyltetrahydrofuran	0.110	–0.151	14	butylamine	0.960	0.089
4	tetrahydropyran	–0.030	–0.369	14	pentylamine	0.270	–0.460
4	propionaldehyde	0.580	0.549	14	hexylamine	–0.250	–1.007
4	butyraldehyde	–0.010	–0.004	14	heptylamine	–0.900	–1.569
4	valeraldehyde	–0.850	–0.542	14	octylamine	–1.460	–2.121
4	caproaldehyde	–1.300	–1.086	14	diethylamine	1.030	0.429
14	2-ethylbutanal	–1.520	–1.103	4	dipropylamine	–0.460	–0.665
14	2-ethylhexanal	–2.130	–2.237	14	dibutylamine	–1.440	–1.771
4	*tert*-crotonaldehyde	0.320	0.294	14	trimethylamine	1.320	0.855
14	2-ethyl-2-hexanal	–2.460	–2.043	4	triethylamine	–0.140	–0.321
4	2-butanone	0.520	0.310	11	tripropylamine	–2.282	–1.853
4	2-pentanone	–0.190	–0.244	4	nitromethane	0.260	0.628
67	3-pentanone	–0.280	–0.271	4	nitroethane	–0.220	0.148
15	3-methyl-2-butanone	–0.120	–0.259	4	1-nitropropane	–0.800	–0.492
4	2-hexanone	–0.800	–0.799	4	2-nitropropane	–0.620	–0.404
15	3-hexanone	–0.830	–0.814	4	chloropicrin	–2.000	–2.069
15	3-methyl-2-pentanone	–0.670	–0.797	4	acetamide	1.580	1.859
4	4-methyl-2-pentanone	–0.740	–0.797	4	*N*,*N*-dimethylacetamide	1.110	1.344
15	3,3-dimethyl-2-butanone	–0.720	–0.815	4	urea	0.960	2.317
67	2-heptanone	–1.450	–1.348	4	*o*-ethyl carbamate	0.850	0.787
4	4-heptanone	–1.300	–1.353	4	acetic acid	2.000	1.184
15	2,4-dimethyl-3-pentanone	–1.300	–1.358	4	hexanoic acid	–1.060	–0.994
67	2-octanone	–2.050	–1.894	4	decanoic acid	–3.440	–3.191
4	2-nonanone	–2.580	–2.467	4	methacrylic acid	0.000	0.047
15	5-nonanone	–2.580	–2.466	4	chloroacetic acid	1.810	0.870
67	2-decanone	–3.300	–3.018	4	trichloroacetic acid	0.600	–0.014
4	cyclohexanone	–0.600	–0.284	15	methanol	1.560	1.594
24	carvone	–2.060	–2.704	15	ethanol	1.100	1.043
24	camphor	–1.960	–2.152	15	1-propanol	0.620	0.492
24	menthone	–2.350	–2.626	4	2-propanol	0.430	0.698
4	methyl formate	0.580	0.607	4	1-butanol	0.000	–0.058
4	ethyl formate	0.150	0.076	67	2-methylpropan-1-ol	0.100	–0.074
4	propyl formate	–0.490	–0.495	16	butan-2-ol	0.470	–0.074
15	isopropyl formate	–0.630	–0.392	4	1-pentanol	–0.600	–0.615
15	butyl acetate	–1.370	–1.046	4	2-pentanol	–0.290	–0.409
4	isobutyl formate	–1.010	–0.958	4	3-pentanol	–0.240	–0.432
15	isopentyl formate	–1.520	–1.517	4	2-methylbutanol	–0.470	–0.638
15	methyl acetate	0.460	0.361	16	3-methylbutan-1-ol	–0.510	–0.611
4	ethyl acetate	–0.040	–0.180	16	2-methylbutan-2-ol	0.150	–0.332
4	propyl acetate	–0.720	–0.743	69	3-methyl-2-butanol	–0.180	–0.431
4	isopropyl acetate	–0.550	–0.644	4	2,2-dimethylpropanol	–0.400	–0.512
4	isobutyl acetate	–1.210	–1.203	4	1-hexanol	–1.240	–1.167
4	pentyl acetate	–1.890	–1.841	4	2-hexanol	–0.890	–0.962
4	isopentyl acetate	–1.920	–1.764	4	3-hexanol	–0.800	–0.975
4	methyl propionate	–0.140	–0.217	69	2-methylpentanol	–1.110	–1.191
4	ethyl propionate	–0.660	–0.753	4	3-methyl-2-pentanol	–0.720	–1.191
4	methyl butyrate	–0.820	–0.757	69	4-methylpentanol	–1.140	–1.176
4	ethyl butyrate	–1.280	–1.296	69	2-methyl-2-pentanol	–0.490	–0.868
4	propyl butyrate	–1.920	–1.855	69	3-methyl-2-pentanol	–0.710	–0.968
4	methyl pentanoate	–1.360	–1.321	4	4-methyl-2-pentanol	–0.800	–0.965
4	ethyl pentanoate	–1.750	–1.839	4	2-methyl-3-pentanol	–0.700	–1.005
62	propyl propanoate	–1.340	–1.299	69	3-methyl-3-pentanol	–0.360	–0.910
62	pentyl propanoate	–2.250	–2.417	4	2-ethyl-1-butanol	–1.170	–1.211
62	methyl hexanoate	–1.870	–1.854	69	2,2-dimethyl-1-butanol	–1.040	–1.229
62	ethyl hexanoate	–2.350	–2.394	4	3,3-dimethyl-1-butanol	–0.500	–1.191
62	ethyl heptanoate	–2.740	–2.940	4	3,3-dimethyl-2-butanol	–0.620	–1.015
62	methyl octanoate	–3.170	–2.963	4	1-heptanol	–1.810	–1.730
62	ethyl octanoate	–3.390	–3.499	4	2-heptanol	–1.550	–1.525
62	methyl nonanoate	–3.380	–3.515	4	3-heptanol	–1.470	–1.515
62	ethyl nonanoate	–3.800	–4.058	4	4-heptanol	–1.400	–1.517
62	methyl decanoate	–4.690	–4.074	69	2-methyl-2-hexanol	–1.080	–1.424
62	ethyl decanoate	–4.100	–4.611	69	3-methyl-3-hexanol	–0.980	–1.458

Appendix (continued)

ref	compound	log S_W obs	log S_W calc (eq 11)	ref	compound	log S_W obs	log S_W calc (eq 11)
4	3-ethyl-3-pentanol	–0.850	–1.495	4	2,3-dimethylnaphthalene	–4.720	–4.790
69	2,2-dimethylpentanol	–1.520	–1.785	4	2,6-dimethylnaphthalene	–4.890	–4.718
4	2,4-dimethyl-2-pentanol	–0.920	–1.445	4	1-ethylnaphthalene	–4.170	–4.784
4	2,4-dimethyl-3-pentanol	–1.220	–1.591	4	2-ethylnaphthalene	–4.290	–4.728
4	1-octanol	–2.390	–2.282	78	1,2,3,4-tetrahydronaphthalene	–4.370	–3.825
4	2-octanol	–2.090	–2.059	4	indan	–3.040	–3.309
69	3-octanol	–1.980	–2.077	4	acenaphthene	–4.630	–4.369
4	2-methyl-2-heptanol	–1.720	–1.994	4	acenaphthylene	–3.960	–4.105
4	3-methyl-3-heptanol	–1.600	–2.014	4	fluorene	–5.000	–4.608
4	2-ethyl-1-hexanol	–2.110	–2.315	4	1-methylfluorene	–5.220	–5.170
67	1-nonanol	–3.010	–2.835	4	anthracene	–6.350	–5.361
69	2-nonanol	–2.740	–2.628	4	2-methylanthracene	–6.960	–5.826
69	1-decanol	–3.630	–3.395	4	9-methylanthracene	–5.890	–5.869
69	2-undecanol	–2.940	–3.745	4	9,10-dimethylanthracene	–6.570	–6.345
69	1-dodecanol	–4.800	–4.502	4	phenanthrene	–5.260	–5.121
69	1-tetradecanol	–5.840	–5.614	78	1-methylphenanthrene	–5.850	–5.713
69	1-pentadecanol	–6.350	–6.170	78	2-methylphenanthrene	–5.840	–5.713
69	1-hexadecanol	–7.000	–6.726	4	fluoranthene	–6.000	–5.975
69	1-octadecanol	–8.400	–7.842	4	benzo[*a*]fluorene	–6.680	–6.794
4	cyclohexanol	–0.440	–0.636	4	benzo[*b*]fluorene	–8.040	–6.767
69	cycloheptanol	–0.880	–1.219	67	pyrene	–6.176	–6.115
69	cyclooctanol	–1.290	–1.834	4	7,12-dimethylbenz[*a*]anthracene	–7.020	–8.125
69	4-pentene-1-ol	–0.150	–0.284	4	naphthacene	–8.600	–7.071
69	1-hexene-3-ol	–0.590	–0.879	67	chrysene	–8.057	–6.932
4	2-butoxyethanol	–0.420	–0.239	78	5-methylchrysene	–6.590	–7.494
4	ethanethiol	–0.600	–0.797	78	6-methylchrysene	–6.570	–7.494
4	butanethiol	–2.180	–1.910	78	5,6-dimethylchrysene	–7.010	–8.056
70	dimethyl sulfide	–0.450	–0.574	67	triphenylene	–6.726	–6.666
70	diethyl sulfide	–1.340	–1.539	67	perylene	–8.804	–7.404
70	di-*n*-propyl sulfide	–2.580	–2.647	4	benzo[*b*]fluoranthene	–8.230	–7.380
70	diisopropyl sulfide	–2.240	–2.452	4	benzo[*j*]fluoranthene	–8.000	–7.519
70	dimethyl disulfide	–1.440	–1.514	4	benzo[*k*]fluoranthene	–8.490	–7.604
70	diethyl disulfide	–2.420	–2.581	78	cholanthrene	–7.850	–7.453
4	thiourea	0.320	1.139	4	3-methylcholanthrene	–7.920	–8.037
4	triethyl phosphate	0.430	0.226	71	benzo[*a*]pyrene	–8.699	–7.832
4	benzene	–1.640	–1.956	4	benzo[*e*]pyrene	–7.800	–7.917
4	toluene	–2.210	–2.509	67	benzo[*ghi*]perylene	–9.018	–8.509
4	ethylbenzene	–2.770	–3.048	78	picene	–7.870	–8.803
4	*o*-xylene	–2.800	–3.018	4	fluorobenzene	–1.800	–2.024
4	*m*-xylene	–2.820	–3.008	78	1,3-difluorobenzene	–2.000	–2.153
4	*p*-xylene	–2.770	–2.998	78	1,4-difluorobenzene	–1.970	–1.978
4	propylbenzene	–3.370	–3.609	78	benzyl trifluoride	–2.510	–2.500
4	isopropylbenzene	–3.270	–3.572	4	chlorobenzene	–2.380	–2.749
4	1,2,3-trimethylbenzene	–3.200	–3.479	4	1,2-dichlorobenzene	–3.050	–3.419
78	1,2,4-trimethylbenzene	–3.310	–3.466	4	1,3-dichlorobenzene	–3.040	–3.517
4	1,3,5-trimethylbenzene	–3.400	–3.469	4	1,4-dichlorobenzene	–3.270	–3.480
78	2-ethyltoluene	–3.210	–3.519	4	1,2,3-trichlorobenzene	–4.000	–4.173
78	4-ethyltoluene	–3.110	–3.500	78	1,2,4-trichlorobenzene	–3.590	–4.162
4	butylbenzene	–4.060	–4.159	4	1,3,5-trichlorobenzene	–4.480	–4.223
4	isobutylbenzene	–4.120	–4.169	4	1,2,3,4-tetrachlorobenzene	–4.570	–4.766
4	*tert*-butylbenzene	–3.660	–4.066	4	1,2,3,5-tetrachlorobenzene	–4.630	–4.800
78	1,2-diethylbenzene	–3.280	–4.097	4	1,2,4,5-tetrachlorobenzene	–5.560	–4.792
4	1,4-diethylbenzene	–3.750	–4.084	4	pentachlorobenzene	–5.650	–5.374
78	1,2,4,5-tetramethylbenzene	–4.590	–4.059	4	hexachlorobenzene	–7.680	–5.999
78	2-isopropyltoluene	–3.760	–4.043	78	2-chlorotoluene	–3.520	–3.355
78	4-isopropyltoluene	–3.770	–4.012	78	4-chlorotoluene	–3.080	–3.313
4	pentylbenzene	–4.640	–4.714	78	benzyl chloride	–2.390	–2.182
4	*tert*-pentylbenzene	–4.150	–4.713	4	1-chloronaphthalene	–3.930	–4.360
4	pentamethylbenzene	–4.000	–4.602	4	2-chloronaphthalene	–4.140	–4.363
4	hexylbenzene	–5.210	–5.281	69	2-chlorobiphenyl	–4.540	–4.991
78	hexamethylbenzene	–5.230	–4.921	69	3-chlorobiphenyl	–4.880	–4.960
4	styrene	–2.820	–2.964	4	bromobenzene	–2.550	–2.977
78	diphenylmethane	–4.080	–4.348	78	1,2-dibromobenzene	–3.500	–4.019
4	bibenzyl	–4.620	–4.910	78	1,3-dibromobenzene	–3.540	–4.061
67	biphenyl	–4.345	–4.262	4	1,4-dibromobenzene	–4.070	–4.056
78	4-methylbiphenyl	–4.620	–4.831	4	1,3,5-tribromobenzene	–5.600	–5.132
4	naphthalene	–3.600	–3.598	4	1,2,4,5-tetrabromobenzene	–6.980	–5.880
4	1-methylnaphthalene	–3.700	–4.164	78	2-bromotoluene	–2.230	–3.587
78	2-methylnaphthalene	–3.770	–4.124	78	4-bromotoluene	–3.190	–3.527
4	1,3-dimethylnaphthalene	–4.290	–4.769	78	1-bromonaphthalene	–4.350	–4.690
4	1,4-dimethylnaphthalene	–4.140	–4.790	4	2-bromonaphthalene	–4.400	–4.617
67	1,5-dimethylnaphthalene	–4.679	–4.789	67	iodobenzene	–3.010	–3.420

Appendix (continued)

ref	compound	log S_W obs	log S_W calc (eq 11)	ref	compound	log S_W obs	log S_W calc (eq 11)
78	1-iodonaphthalene	–4.550	–5.156	24	*p*-fluoroacetanilide	–1.780	–1.113
14	*o*-fluorobromobenzene	–2.700	–3.285	24	*p*-chloroacetanilide	–2.843	–1.808
14	*m*-fluorobromobenzene	–2.670	–3.245	24	*p*-bromoacetanilide	–3.083	–2.085
20	*o*-chlorobromobenzene	–3.190	–3.898	11	4-nitroacetanilide	–2.692	–1.831
20	*m*-chlorobromobenzene	–3.210	–3.919	71	phenacetin	–2.350	–1.741
20	*p*-chlorobromobenzene	–3.630	–3.883	24	lidocaine	–1.710	–2.405
20	*o*-chloroiodobenzene	–3.540	–4.425	4	benzoic acid	–1.550	–1.055
20	*m*-chloroiodobenzene	–3.550	–4.417	4	*o*-toluic acid	–2.060	–1.742
20	*p*-chloroiodobenzene	–4.030	–4.427	4	*m*-toluic acid	–2.140	–1.662
14	*p*-bromoiodobenzene	–4.560	–4.639	4	*p*-toluic acid	–2.600	–1.609
4	anisole	–1.850	–2.038	4	*o*-chlorobenzoic acid	–1.890	–1.517
78	2-chloroanisole	–2.460	–2.916	4	*m*-chlorobenzoic acid	–2.590	–1.771
72	3-chloroanisole	–2.780	–2.896	4	*p*-chlorobenzoic acid	–3.310	–1.848
72	4-chloroanisole	–2.780	–2.782	67	2-bromobenzoic acid	–2.276	–1.739
4	diphenyl ether	–3.960	–4.579	67	4-bromobenzoic acid	–3.539	–2.157
4	benzaldehyde	–1.190	–1.362	4	*m*-nitrobenzoic acid	–1.680	–1.530
4	*p*-methoxybenzaldehyde	–1.490	–1.527	4	*p*-nitrobenzoic acid	–2.800	–1.554
4	acetophenone	–1.280	–1.533	4	*o*-aminobenzoic acid	–1.520	–1.020
4	benzophenone	–3.120	–3.564	4	aspirin	–1.720	–1.132
4	anthraquinone	–5.190	–3.728	4	phenylacetic acid	–0.890	–1.088
4	methyl benzoate	–1.850	–1.890	71	ibuprofen	–3.760	–3.927
4	ethyl benzoate	–2.320	–2.407	71	naproxen	–4.202	–3.892
4	dimethyl phthalate	–1.660	–1.315	4	phenol	0.000	–0.728
4	diethyl phthalate	–2.350	–2.310	4	2-methylphenol	–0.620	–1.440
4	di(2-ethylhexyl)phthalate	–6.960	–8.942	4	3-methylphenol	–0.680	–1.256
4	benzonitrile	–1.000	–1.446	67	*p*-cresol	–0.730	–1.331
4	phthalonitrile	–2.380	–1.103	4	2,4-dimethylphenol	–1.190	–1.819
4	aniline	–0.410	–1.012	67	2,6-dimethylphenol	–1.290	–1.963
4	*o*-toluidine	–2.210	–1.501	67	3,4-dimethylphenol	–1.380	–1.734
4	*m*-methylaniline	–0.850	–1.458	4	3,5-dimethylphenol	–1.400	–1.800
4	*p*-methylaniline	–1.210	–1.435	67	2,4,6-trimethylphenol	–2.050	–2.393
4	*o*-chloroaniline	–1.520	–1.959	4	*p*-*tert*-butylphenol	–2.410	–2.767
4	*m*-chloroaniline	–1.370	–1.816	4	thymol	–2.220	–2.813
4	*p*-chloroaniline	–1.660	–1.768	4	*p*-phenylphenol	–3.480	–3.182
4	*o*-nitroaniline	–1.960	–1.747	4	2-chlorophenol	–1.060	–1.564
4	*m*-nitroaniline	–2.190	–1.438	4	3-chlorophenol	–0.700	–1.372
4	*p*-nitroaniline	–2.370	–1.234	4	4-chlorophenol	–0.700	–1.297
4	ethyl-*p*-aminobenzoate	–2.100	–2.031	4	4-bromophenol	–1.090	–1.603
24	risocaine	–2.452	–2.598	67	2,3-dichlorophenol	–1.300	–2.222
24	butamben	–3.082	–3.173	4	2,4-dichlorophenol	–1.550	–2.249
4	*N*-methylaniline	–1.280	–1.611	67	2,6-dichlorophenol	–1.790	–2.224
4	*N*-ethylaniline	–1.700	–2.208	67	3,4-dichlorophenol	–1.250	–1.810
4	*N*,*N*-dimethylaniline	–1.920	–2.459	67	3,5-dichlorophenol	–1.340	–1.829
4	*N*,*N*-diethylaniline	–3.030	–3.586	67	2,3,4-trichlorophenol	–2.670	–2.570
4	1-naphthylamine	–1.920	–2.446	67	2,3,5-trichlorophenol	–2.670	–2.600
4	*p*,*p*′-biphenyldiamine	–2.700	–2.744	67	2,3,6-trichlorophenol	–2.640	–2.705
4	benzylamine	–1.540	–0.426	4	2,4,5-trichlorophenol	–2.210	–2.641
24	procaine	–1.780	–2.226	4	2,4,6-trichlorophenol	–2.340	–2.667
71	diphenylamine	–3.504	–3.632	67	2,3,4,5-tetrachlorophenol	–3.150	–3.258
4	azobenzene	–2.750	–4.283	67	2,3,4,6-tetrachlorophenol	–3.100	–3.491
4	nitrobenzene	–1.800	–1.865	67	2,3,5,6-tetrachlorophenol	–3.370	–3.387
4	*o*-nitrotoluene	–2.330	–2.422	4	pentachlorophenol	–4.280	–3.475
4	*m*-nitrotoluene	–2.440	–2.565	4	*o*-methoxyphenol	–1.960	–1.211
4	*p*-nitrotoluene	–2.490	–2.426	4	*p*-hydroxybenzaldehyde	–0.960	–0.671
4	*o*-chloronitrobenzene	–2.550	–2.614	4	*o*-aminophenol	–0.720	–0.471
4	*m*-chloronitrobenzene	–2.770	–2.587	4	*p*-aminophenol	–0.800	–0.129
4	*p*-chloronitrobenzene	–2.920	–2.748	4	*o*-nitrophenol	–1.740	–1.862
4	*o*-nitroanisole	–1.960	–2.157	4	*m*-nitrophenol	–1.010	–1.035
4	*p*-nitroanisole	–2.410	–2.113	4	*p*-nitrophenol	–0.740	–0.853
4	1,2-dinitrobenzene	–3.100	–1.981	4	salicylic acid	–1.820	–1.479
4	1,3-dinitrobenzene	–2.290	–1.657	4	*p*-hydroxybenzoic acid	–1.410	–1.074
4	1,4-dinitrobenzene	–3.390	–1.656	4	1,2-benzenediol	0.620	–0.424
4	2,4-dinitrotoluene	–2.820	–2.219	4	1,3-benzenediol	0.810	–0.274
4	2,6-dinitrotoluene	–3.000	–2.303	4	1,4-benzenediol	–0.170	–0.322
4	2,4,6-trinitrotoluene	–3.220	–2.116	24	methylparaben	–1.827	–1.481
4	1,3,5-trinitrobenzene	–2.890	–1.554	4	ethyl-*p*-hydroxybenzoate	–2.350	–2.018
4	1-nitronaphthalene	–3.540	–3.718	4	*o*-hydroxybenzamide	–1.820	–1.109
4	2,3-dichloronitrobenzene	–3.480	–3.374	4	*p*-hydroxyacetanilide	–1.030	–1.022
4	3,4-dichloronitrobenzene	–3.200	–3.436	4	1-naphthol	–2.220	–2.638
4	benzamide	–0.960	–0.401	4	2-naphthol	–2.280	–2.540
4	acetanilide	–1.330	–0.893	4	phenylmethanol	–0.400	–0.785

Appendix (continued)

ref	compound	log S_W obs	log S_W calc (eq 11)	ref	compound	log S_W obs	log S_W calc (eq 11)
4	1-phenylethanol	–0.920	–1.062	75	5-ethyl-5-isopropylbarbituric acid	–2.148	–1.492
4	2-phenoxyethanol	–0.700	–0.882	76	butabarbital	–2.390	–1.974
24	ephedrine	–0.470	–0.781	76	pentobarbital	–2.390	–2.536
4	thiophenol	–2.120	–2.553	75	5-ethyl-5-(3-methylbutyl)barbital	–2.658	–2.536
4	phenylthiourea	–1.770	–1.023	75	5,5-diisopropylbarbital	–2.766	–1.997
4	*p*-toluenesulfonamide	–1.740	–1.057	75	5-allyl-5-methylbarbital	–1.160	–0.679
4	furane	–0.820	–1.031	75	5-allyl-5-ethylbarbital	–1.614	–1.241
4	furfural	–0.100	–0.148	75	5-allyl-5-isopropylbarbital	–1.708	–1.696
4	dibenzofurane	–4.600	–4.469	76	secobarbital	–2.356	–2.821
4	pyridine	0.760	0.043	75	5,5-diallylbarbital	–2.077	–1.733
4	2,3-dimethylpyridine	0.380	–0.737	75	5-(3-methyl-2-butenyl)-5-ethylbarbital	–2.253	–2.335
4	2,4-dimethylpyridine	0.380	–0.679	75	5-(3-methyl-2-butenyl)-5-isoprbarbital	–2.593	–2.868
4	2,6-dimethylpyridine	0.450	–0.698	75	5-ethyl-5-phenylbarbital	–2.322	–2.875
4	3,4-dimethylpyridine	0.360	–0.694	75	5-allyl-5-phenylbarbital	–2.369	–3.283
4	3,5-dimethylpyridine	0.380	–0.808	75	cyclobutyl-5-spirobarbituric acid	–1.655	–0.123
4	2-ethyl pyridine	0.510	–0.866	75	cyclopentyl-5-spirobarbituric acid	–2.349	–0.726
4	4-ethyl pyridine	0.830	–0.902	75	cyclohexyl-5-spirobarbituric acid	–3.060	–1.330
73	cocaine	–2.253	–2.167	75	cycloheptyl-5-spirobarbituric acid	–3.168	–1.937
74	atropine	–2.119	–2.532	75	cyclooctyl-5-spirobarbituric acid	–2.982	–2.562
63	quinoline	–1.300	–1.883	77	amitrole	0.522	0.864
63	isoquinoline	–1.450	–1.802	77	carbaryl	–3.224	–2.744
4	carbazole	–5.270	–3.871	77	carbofuran	–2.800	–1.774
4	antipyrene	0.720	0.440	13	chlorfenac	–3.078	–3.097
67	morpholine	1.965	1.615	77	coumatetralyl	–2.837	–4.767
4	theophylline	–1.390	–0.212	77	2,4-DB	–3.734	–3.602
67	caffeine	–0.876	0.446	4	DDT	–7.150	–7.457
4	morphine	–3.280	–2.382	77	desmedipham	–4.632	–5.103
4	codeine	–1.520	–2.278	77	dichlorophen	–3.953	–4.582
70	thiophene	–1.330	–1.653	77	dichlorprop	–2.827	–3.350
24	imipramine	–4.190	–4.153	4	diuron	–3.049	–2.975
4	progesterone	–4.420	–4.022	77	DNOC	–1.456	–2.397
4	testosterone	–4.020	–4.075	77	etofenprox	–8.600	–7.836
72	deoxycorticosterone	–3.450	–3.979	77	fenoxycarb	–4.700	–4.816
13	hydroxyprogesterone-17*a*	–3.817	–4.240	4	fenuron	–1.600	–1.637
72	corticosterone	–3.240	–4.043	4	fluometuron	–3.430	–2.111
4	cortisone	–3.110	–3.293	77	isoprocarb	–2.863	–2.213
4	hydrocortisone	–3.090	–4.929	11	isoproturon	–3.536	–3.000
13	17*a*-methyltestosterone	–3.999	–4.336	77	linuron	–3.592	–3.387
72	prednisolone	–3.180	–5.202	77	methyldymron	–3.350	–3.739
24	hydrocortisone 21-acetate	–4.880	–4.690	77	metolcarb	–1.803	–1.571
74	estrone	–3.955	–4.068	11	metoxuron	–2.564	–2.175
24	estradiol	–5.030	–4.389	4	monolinuron	–2.570	–2.358
72	dexamethasone	–3.590	–5.347	4	propoxur	–2.050	–1.617
75	5,5-dimethylbarbituric acid	–1.742	0.204	77	warfarin	–4.259	–4.074
75	5-methyl-5-ethylbarbituric acid	–1.228	–0.357	77	XMC	–2.581	–2.084
76	barbital	–2.400	–0.960				
				Outliers			
75	cyclopropyl-5-spirobarbituric acid	–1.886	0.358	74	fentanyl	–1.129	–4.224
4	uracil	–1.490	1.191	74	adenine	–2.432	0.185
74	chlorpheniramine	–0.235	–3.056				

References and Notes

1. Irmann, F. Eine einfache korrelation zwischen wasserloslichkeit und strukture von kohlenwasserstoffen und halogenkohlenwasserstoffen. *Chem. Ing. Tech.* **1965**, *37*, 789−798.
2. Wakita, K.; Yoshimoto, M.; Miyamoto, S.; Watanabe, H. A method for calculation of aqueous solubility of organic compounds using new fragment solubility constants. *Chem. Pharm. Bull.* **1986**, *34*, 4663−4681.
3. Klopman, G.; Wang, S.; Balthasar, D. M. Estimation of aqueous solubility of organic molecules by the group contribution approach. *J. Chem. Inf. Comput. Sci.* **1992**, *32*, 474−482.
4. Kuhne, R.; Ebert, R.-U.; Kleint, F.; Schmidt, G.; Schuurmann, G. Group contribution methods to estimate water solubility of organic compounds. *Chemosphere* **1995**, *30*, 2061−2077.
5. Nirmalakhanden, N. N.; Speece, R. E. Prediction of aqueous solubility of organic compounds based on molecular structure. 2. Application to PNAs, PCBs, PCDDs, etc. *Environ. Sci. Technol.* **1989**, *23*, 708−713.
6. Banerjee, S. Calculation of water solubility of organic compounds with UNIFAC-derived parameters. *Environ. Sci. Technol.* **1985**, *19*, 369−370.
7. Kan, A. T.; Tomson, M. B. UNIFAC prediction of aqueous solubilities of chemicals of environmental interest. *Environ. Sci. Technol.* **1996**, *30*, 1369−1376.
8. Myrdal, P. B.; Ward, G. H.; Dannenfelser, R.-M.; Mishra, D.; Yalkowsky, S. H. Aquafac 1: aqueous functional group activity coefficients; application to hydrocarbons. *Chemosphere* **1992**, *24*, 1047−1061.
9. Myrdal, P. B.; Ward, G. H.; Simamora, P.; Yalkowsky, S. H. Aquafac: aqueous functional group activity coefficients. *SAR QSAR Environ. Res.* **1993**, *1*, 53−61.
10. Myrdal, P. B.; Manka, A. M.; Yalkowsky, S. H. Aquafac 3: Aqueous functional group activity coefficients; application to the estimation of aqueous solubility. *Chemosphere* **1995**, *30*, 1619−1637.
11. Lee, Y.-C.; Myrdal, P. B.; Yalkowsky, S. M. Aqueous functional group activity coefficients (Aquafac) 4: applications to complex organic compounds. *Chemosphere* **1996**, *33*, 2129−2144.

12. Lee, Y.-C.; Pinsuwan, S.; Yalkowsky, S. M. A comparison of AQUAFAC group q-values to the corresponding CLOGP f-values. *Chemosphere* **1997**, *35*, 775−782.
13. Pinsuwan, S.; Myrdal, P. B.; Lee, Y.-C.; Yalkowsky, S. H. AQUAFAC 5: aqueous functional group activity coefficients; application to alcohols and acids. *Chemosphere* **1997**, *35*, 2503−2513.
14. Bodor, N.; Harget, A.; Huang, M.-J. Neural network studies. 1. Estimation of the aqueous solubility of organic compounds. *J. Am. Chem. Soc.* **1991**, *113*, 9480−9483.
15. Bodor, N.; Huang, M.-J. A new method for the estimation of aqueous solubility of organic compounds. *J. Pharm. Sci.* **1992**, *81*, 954−960.
16. Nelson, T. M.; Jurs, P. C. Prediction of aqueous solubility of organic compounds. *J. Chem. Inf. Comput. Sci.* **1994**, *34*, 601−609.
17. Sutter, J. M.; Jurs, P. C. Prediction of aqueous solubility for a diverse set of hereroatom- containing compounds using a quantitative structure−property relationship. *J. Chem. Inf. Comput. Sci.* **1996**, *36*, 100−107.
18. Katritzky, A. R.; Wang, Y.; Sild, S.; Tamm, T.; Karelson, M. QSPR studies on vapor pressure, aqueous solubility and the prediction of water−air partition coefficients. *J. Chem. Inf. Comput. Sci.* **1998**, *38*, 720−725.
19. Hansch, C.; Quinlan, J. E.; Lawrence, G. L. The linear free energy relationship between partition coefficients and the aqueous solubility of organic liquids. *J. Org. Chem.* 1**968**, *33*, 347−350.
20. Yalkowsky, S. H.; Valvani, S. C. Solubility and partitioning. I: solubility of nonelectrolytes in water. *J. Pharm. Sci.* **1980**, *69*, 912−922.
21. Valvani, S. C.; Yalkowsky, S. H.; Roseman, T. J. Solubility and partitioning IV: solubility and octanol−water partition coefficients of liquid nonelectrolytes. *J. Pharm. Sci.* **1981**, *70*, 502−507.
22. Yalkowsky, S. H.; Valvani, S. C.; Roseman, T. J. Solubility and partitioning VI: octanol solubility and octanol−water partition coefficients. *J. Pharm. Sci.* **1983**, *72*, 866−870.
23. Ruelle, P.; Kesselring, U. W. The hydrophobic effect. 1. A consequence of the mobile order in H-bonded liquids. *J. Pharm. Sci.* **1998**, *87*, 987−997.
24. Ruelle, P.; Kesselring, U. W. The hydrophobic effect. 2. Relative importance of the hydrophobic effect on the solubility of hydrophobes and pharmaceuticals in H-bonded solvents. *J. Pharm. Sci.* **1998**, *87*, 998−1014.
25. Ruelle, P.; Kesselring, U. W. The hydrophobic effect. 3. A key ingredient in predicting n- octanol−water partition coefficients. *J. Pharm. Sci.* **1998**, *87*, 1015−1024.
26. Abraham, M. H. Scales of solute hydrogen-bonding: their construction and application to physicochemical and biochemical processes. *Chem. Soc. Rev.* **1993**, *22*, 73−83.
27. Abraham, M. H.; McGowan, J. C. The use of characteristic volumes to measure cavity effects in reversed phase liquid chromatography. *Chromatographia* **1987**, *23*, 243−246.
28. Abraham, M. H.; Chadha, H. S.; Whiting, G. S.; Mitchell, R. C. Hydrogen bonding. 32. An analysis of water-octanol and water-alkane partitioning and the ΔlogP parameter of Seiler. *J. Pharm. Sci.* **1994,** *83*, 1085−1100.
29. Abraham, M. H.; Andonian-Haftvan, J.; Whiting, G. S.; Leo, A.; Taft, R. W. Hydrogen bonding. Part 34: the factors that influence the solubility of gases and vapours in water at 298 K, and a new method for its determination. *J. Chem. Soc., Perkin Trans. 2* **1994**, 1777−1791.
30. Abraham, M. H.; Chadha, H. S.; Leo, A. J. Hydrogen bonding. 35. Relationship between high performance liquid chromatography capacity factors and water-octanol partition coefficients. *J. Chromatogr. A* **1994**, *685*, 203−211.
31. Abraham, M. H.; Roses, M. Hydrogen bonding. 38. Effect of solute structure and mobile phase on reversed phase high performance liquid chromatography capacity factors. *J. Phys. Org. Chem.* **1994**, *7*, 672−684.
32. Abraham, M. H.; Chadha, H. S.; Dixon, J. P.; Leo, A. J. Hydrogen bonding. 39. The partition of solutes between water and various alcohols. *J. Phys. Org. Chem.* **1994**, *7*, 712−716.
33. Abraham, M. H.; Chadha, H. S.; Dixon, J. P.; Rafols, C.; Treiner, C. Hydrogen bonding. Part 40. Factors that influence the distribution of solutes between water and sodium dodecyl sulfate micelles. *J. Chem. Soc., Perkin Trans. 2* **1995**, 887−894.
34. Abraham, M. H.; Treiner, C.; Roses, M.; Rafols, C.; Ishihama, Y. Linear free energy relationship analysis of microemulsion electrokinetic chromatographic determination of lipophilicity. *J. Chromatogr. A* **1996,** *752*, 243−249.
35. Siebert, D. S.; Poole, C. F.; Abraham, M. H. Retention properties of a spacer-bonded propanediol sorbent for reversed-phase liquid chromatography and solid-phase extraction. *Analyst* **1996**, *121*, 511−520.
36. Tan, L. C.; Carr, P. W.; Abraham, M. H. Study of retention in reversed phase liquid chromatography using linear solvation energy relationships. I. The stationary phase. *J. Chromatogr. A* **1996**, *752*, 1−18.
37. Abraham, M. H.; Poole, C. F.; Poole, S. K. Solute effects on reversed phase thin-layer chromatography, *J. Chromatogr. A* **1996**, *749*, 201−209.
38. Nasal, A.; Haber, P.; Kaliszan, R.; Forgacs, E.; Cserhati, T.; Abraham, M. H. Polyethylene coated silica and zirconia stationary phases in view of quantitative structure-retention relationships. *Chromatographia* **1996**, *43*, 484−490.
39. Abraham, M. H.; Chadha, H. S.; Dixon, J. P.; Rafols, C.; Treiner, C. Hydrogen bonding. 41. Factors that influence the distribution of solutes between water and hexadecylpyridinium chloride micelles. *J. Chem. Soc., Perkin Trans. 2* **1997,** 19−24.
40. Abraham, M. H.; Roses, M.; Poole, C. F.; Poole, S. K. Hydrogen bonding. 42. Characterization of reversed-phase high-performance liquid chromatographic C18 stationary phases. *J. Phys. Org. Chem.* **1997**, *10*, 358−368.
41. Abraham, M. H.; Chadha, H. S.; Leitao, R. A. E.; Mitchell, R. C.; Lambert, W. J.; Kaliszan, R.; Nasal, A.; Haber, P. Determination of solute lipophilicity as logP(octanol) and logP(alkane) using poly(styrene-divinylbenzene) and immobilised artificial membrane stationary phases in reversed-phase high-performance chromatography. *J. Chromatogr. A* **1997**, *766*, 35−47.
42. Pagliara, A.; Caron, G.; Lisa, G.; Fan, W.; Gaillard, P.; Carrupt, P.-A.; Testa, B.; Abraham, M. H. Solvatochromic analysis of di-*n*-butyl ether/water partition coefficients as compared to other systems. *J. Chem. Soc., Perkin Trans. 2* **1997**, 2639−2643.
43. Valko, K.; Plass, M.; Bevan, C.; Reynolds, D.; Abraham, M. H. Relationships between the chromatographic hydrophobicity indices and solute descriptors obtained by using several reversed phase diol, nitrile, cyclodextrin and immobilised artificial membrane-bonded high performance liquid chromatographic columns. *J. Chromatogr. A* **1998**, *797*, 41−55.
44. Plass, M.; Valko, K.; Abraham, M. H. Determination of descriptors of tripeptide derivatives based on high-throughput gradient high-performance liquid chromatographic retention data. *J. Chromatogr. A* **1998**, *803*, 51−60.
45. Du, C. M.; Valko, K.; Bevan, C.; Reynolds, D.; Abraham, M. H. Rapid gradient RP-HPLC method for lipophilicity determination: a solvation equation based comparison with isocratic methods. *Anal. Chem.* **1998**, *70*, 4228−4234.
46. Abraham, M. H.; Martins, F.; Mitchell, R. C.; Salter, C. J. Hydrogen bonding. 47. Characterization of the ethylene glycol−heptane partition system; hydrogen bond acidity and basicity of peptides. *J. Pharm. Sci.* **1999**, *88*, 241−247.
47. Abraham, M. H.: Platts, J. A.; Hersey, A.; Leo, A.; Taft, R. W. The correlation and estimation of gas-chloroform and water-chloroform partition coefficients by an LFER method. submitted for publication *J. Pharm. Sci.*, in press.
48. Seibert, D. S.; Poole, C. F. Retention properties of a cyanopropylsiloxane-bonded silica based sorbent for solid-phase extraction. *J. High Resol. Chromatogr.* **1995**, *18*, 226−230.
49. Poole, C. F.; Poole, S. K.; Seibert, D.; Chapman, C. M. Determination of kinetic and retention properties of cartridge and disk devices for solid-phase extraction. *J. Chromatogr. B* **1997**, *689*, 245−259.
50. Boillet, D.; Poole, C. F. Influence of solvent effects on retention for a porous polymer sorbent in reversed phase liquid chromatography. *Chromatographia* **1997**, *46*, 381−398.
51. Poole, C. F.; Poole, S. K. Interphase model for retention and selectivity in micellar electrokinetic chromatography. *J. Chromatogr. A* **1997**, *792*, 89−104.
52. Poole, S. K.; Poole, C. F. Retention of neutral organic compounds from solution on carbon adsorbents. *Anal. Comm.* **1997**, *34*, 247−251.
53. Boillet, D.; Poole, C. F. Influence of temperature on retention and selectivity in reversed phase liquid chromatography. *Analyst* **1998**, *123*, 295−299.
54. Kiridena, W.; Poole, C. F. Structure-driven retention model for solvent selection and optimization in reversed-phase thin-layer chromatography. *J. Chromatogr. A* **1998**, *802*, 335−347.
55. Kiridena, W.; Poole, C. F. Influence of solute size and site-specific surface interactions on the prediction of retention in liquid chromatography using the solvation parameter model. *Analyst* **1998**, *123*, 1265−1270.
56. Poole, C. F. Relationship between liquid−liquid distribution and liquid-micelle distribution systems. *J. Chromatogr. A* **1998**, *807*, 307−310.
57. Bolliet, D.; Poole, C. F.; Roses, M. Conjoint prediction of the retention of neutral and ionic compounds (phenols) in reversed-phase liquid chromatography using the solvation

parameter model. *Anal. Chim. Acta* **1998**, *368*, 129−140. Li, J.; Carr, P. W. Characterization of polybutadiene-coated zirconia and comparison to conventional bonded phases by use of linear solvation energy relationships. *Anal. Chim. Acta* **1996**, *334*, 239−250.
58. Jackson, P. T.; Schure, M. R.; Weber, T. P.; Carr, P. W. Intermolecular interactions involved in solute retention on carbon media in reversed-phase high-performance liquid chromatography. *Anal. Chem.* **1997**, *69*, 416−425.
59. Tan, L. C.; Carr, P. W. Study of retention in reversed-phase liquid chromatography using linear solvation energy relationships. *J. Chromatogr. A* **1998**, *799*, 1−19.
60. Abraham, M. H.; Kumarsingh, R.; Cometto-Muniz, J. E.; Cain, W. S.; Roses, M.; Bosch, E.; Diaz, M. L. The determination of solvation descriptors for terpenes, and the prediction of nasal pungency thresholds. *J. Chem. Soc., Perkin Trans. 2* **1998**, 2405−2411.
61. Platts, J. A.; Abraham, M. H.; Butina, D.; Hersey, A. *J. Chem. Inf. Comput. Sci.*, in press.
62. Abraham, M. H. Thermodynamics of solution of homologous series of solutes in water. *J. Chem. Soc., Faraday Trans. 1* **1984**, *80*, 153−181.
63. Kamlet, M. J.; Doherty, R. M.; Abraham, M. H.; Carr, P. W.; Doherty, R. F.; Taft, R. W. Linear solvation energy relationships. 41. Important differences between aqueous solubility relationships for aliphatic and aromatic solutes. *J. Phys. Chem.* **1987**, *91*, 1996−2004.
64. Pierotti, R. A. A scaled particle theory of aqueous and nonaqueous solutions. *Chem. Rev.* **1976**, *76*, 717−726,
65. Grant, D. G. W.; Higuchi, T. *Solubility Behaviour of Organic Compounds*; John Wiley & Sons: New York, 1990; pp 486−488.
66. Strong, L. E.; Neff, R. M.; Whitesel, I. Thermodynamics of dissolving and solvation for benzoic acid and the toluic acids in aqueous solution. *J. Soln. Chem.* **1989**, *18*, 101−114.
67. Brunas, J. P. The aqueous solubility of drugs and other compounds. University College London. Third Year Project, 1995.
68. Calculated from the gas−water partition coefficient and the saturated vapor concentration, this work.
69. Ruelle, P.; Kesselring, W. The hydrophobic propensity of water toward amphiprotic solutes: prediction and molecular origin of the aqueous solubility of aliphatic alcohols. *J. Pharm. Sci.* **1997**, *86*, 179−186.
70. Schwarzenbach, R. P.; Gschwend, P. M.; Imboden, D. M. *Environmental Organic Chemistry*; John Wiley-Interscience: New York, 1993; pp 618−625.
71. Pinsuwan, S.; Li, A.; Yalkowsky, S. Correlation of octanol/water solubility ratios and partition coefficients. *J. Chem. Eng. Data* **1995**, *40*, 623−626.
72. Huuskonen, J.; Salo, M.; Taskinen, J. Neural network modelling for estimation of the aqueous solubility of structurally related drugs. *J. Pharm. Sci.* **1997**, *86*, 450−454.
73. Siedell, A. *Solubilities of organic compounds: A compilation of quantitative solubility data from the periodical literature*, 3rd ed. (4th printing); D. Van Nostrand Company: 1941; Vol. 2, p 777.
74. *The Merck Index: An encyclopedia of chemicals, drugs, and biologicals*, 11th ed.; Merck & Company: Rahway, NJ, 1989.
75. Prankerd, R. J.; McKeown, R. H. Physico-chemical properties of barbituric acid derivatives: IV. Solubilities of 5,5-disubstituted barbituric acids in water. *Int. J. Pharm.* **1994**, *112*, 1−15.
76. Vaution, C.; Treiner, C.; Puisieux, F.; Cartensen, J. T. Solubility behaviour of barbituric acids in aqueous solution of sodium alkyl sulfonate as a function of concentration and temperature. *J. Pharm. Sci.* **1981**, *70*, 1238−1242.
77. *The Pesticide Manual*, 11th ed.; Tomlin, C. D. S., Ed.; British Crop Protection Council, 1997.
78. Ruelle, P.; Kesselring, W. Aqueous solubility prediction of environmentally important chemicals from the mobile order thermodynamics. *Chemosphere* **1997**, *34*, 275−298.

Acknowledgments

We are very grateful to Roche Products Ltd, for a research studentship (to J.L.). We thank Jean-Paul Brunas for help with preliminary work, and Dr. Derek Reynolds, Dr. Brad Sherbourne, Dr. Gordon Beck, and Dr. Ian Cooper for help and advice.

JS9901007

Solubility of Recombinant Human Tissue Factor Pathway Inhibitor

BAO-LU CHEN,* XIAORONG WU, SUSAN J. BABUKA, AND MANINDER HORA

Contribution from *Department of Formulation Development, Chiron Corporation, 4560 Horton Street, Emeryville, California 94608-2916.*

Received March 4, 1999. Accepted for publication June 8, 1999.

Abstract □ Study of recombinant human tissue factor pathway inhibitor (rhTFPI) solubility shows (1) an inverted bell-shaped pH–solubility profile with a broad solubility minimum between pH 5 and 10 such that the solubility minimum midpoint is 2–3 pH units away from its isoelectric point; (2) a negative temperature–solubility coefficient; (3) a strong dependence of solubility on the valence of electrolytes, with both multivalent cations and anions enhancing this effect; and (4) a significant increase of solubility in the presence of charged polymers. At pH 6–7, rhTFPI solubility–salt profiles display typical salting-in and salting-out biphasic effects. At a slightly lower pH (pH 5), a third phase in addition to the salting-in and salting-out phases was observed at low ionic strength conditions (5 to 50 mM) where rhTFPI solubility increased as salt concentration decreased. The salting-out constant for rhTFPI in NaCl is 1.04 M^{-1} and is independent of the pH of the solution. Resolubilization of rhTFPI precipitates revealed that "insolubility precipitates" (seen during buffer exchanges) resulted from protein solute saturation and could be redissolved by "native" solvent conditions. On the other hand, "instability precipitates" (typically seen after exposure to elevated temperatures or extended storage periods) were caused by insoluble protein aggregate formation and required strongly denaturing conditions to redissolve.

Introduction

Tissue factor pathway inhibitor (TFPI), formerly known as lipoprotein associated coagulation inhibitor (LACI)[1] or extrinsic pathway inhibitor (EPI),[2] is an endogenous inhibitor of tissue factor-mediated blood coagulation. It forms a quaternary complex with tissue factor, factor VIIa, and factor Xa. This complex prevents factor Xa from participating in the formation of prothrombinase complex, thus blocking the generation of thrombin from prothrombin.[3]

Recombinant human tissue factor pathway inhibitor (rhTFPI) expressed from *Escherichia coli* is a pharmaceutically important protein. In animal studies, rhTFPI has been shown to be effective in preventing thrombosis in a rabbit model of vascular trauma.[4] In a baboon sepsis model and a rabbit focus-of-infection model, rhTFPI was associated with a marked improvement in survival rate compared with that of the placebo.[5,6]

The *E. coli*-derived rhTFPI lacks glycosylation and is sparingly soluble in physiological media (approximate solubility in aqueous media under physiological pH conditions is 0.2 mg/mL). Chaotropic agents (e.g., urea) have been employed to maintain its solubility during the purification process.[7] The low solubility of rhTFPI poses a significant challenge during process and formulation development, product manufacturing, and clinical administration of this molecule.

* To whom correspondence should be addressed. Phone: (510) 923-4294. Fax: (510) 923-4116. E-mail: bao-lu_chen@cc.chiron.com.

Protein solubility has recently been reviewed in a number of publications.[8−10] Although it is known that pH and salt conditions can have a modulatory effect, strategies for enhancing the solubility of proteins at or near physiological conditions are usually derived through trial and error, and differ considerably from one protein to the other. Low solubility is often thought to result from a combination of electrostatic and hydrophobic interactions between protein−solvent and protein−protein molecules.[11] The solubility of a protein apparently depends on subtle solvent disturbances in the distribution of charged, polar, and hydrophobic residues on the protein surface. However, because the key interactions dictating the mechanisms of insolubility and precipitation are not fully understood, an empirical approach is often taken when attempting to increase the solubility of a protein.

The solubility properties of rhTFPI are unique in being significantly influenced by the distribution of both positively and negatively charged residues in clustered domains on the polypeptide chain. The rhTFPI molecule consists of an acidic amino-terminal region, three Kunitz-type domains in tandem, and a basic carboxyl-terminal region (Figure 1).[7,12] Inter- and intramolecular electrostatic interactions between the two charged termini may confer poor solubility characteristics on the protein under physiological conditions. One goal of the present investigation was to understand the solubility behavior of rhTFPI under various pH, salt, and formulation conditions to aid in developing robust manufacturing processes and an appropriate formulation for this protein.

A second goal of this study was to understand precipitation phenomena in pharmaceutical proteins using rhTFPI as an example. Protein precipitation resulting from changes in protein solubility is a common occurrence during purification and formulation processes. It is often not differentiated from the formation of insoluble protein aggregates caused by protein instability resulting from exposure to stress conditions encountered during production processes or extended storage. For example, a temperature change during processing could either alter protein solubility, resulting in protein precipitation, or affect protein stability, leading to protein aggregation and precipitation. In this article, we have designated a protein precipitate originating from an excess amount in a saturated solution as an "insolubility precipitate". In contrast, a protein precipitate attributable to changes in stability has been labeled as an "instability precipitate". Because the mechanisms of creation of the two precipitates are different, it was hoped that the characterization of these precipitate types would aid in developing approaches to prevent their formation during processing and storage of the protein.

Materials and Methods

Materials—Recombinant human TFPI was expressed in *E. coli* and purified by a series of chromatographic, diafiltration, and associated procedures described previously.[7,12,13] The purified

10.1021/js9900708 CCC: $18.00
Published on Web 07/27/1999

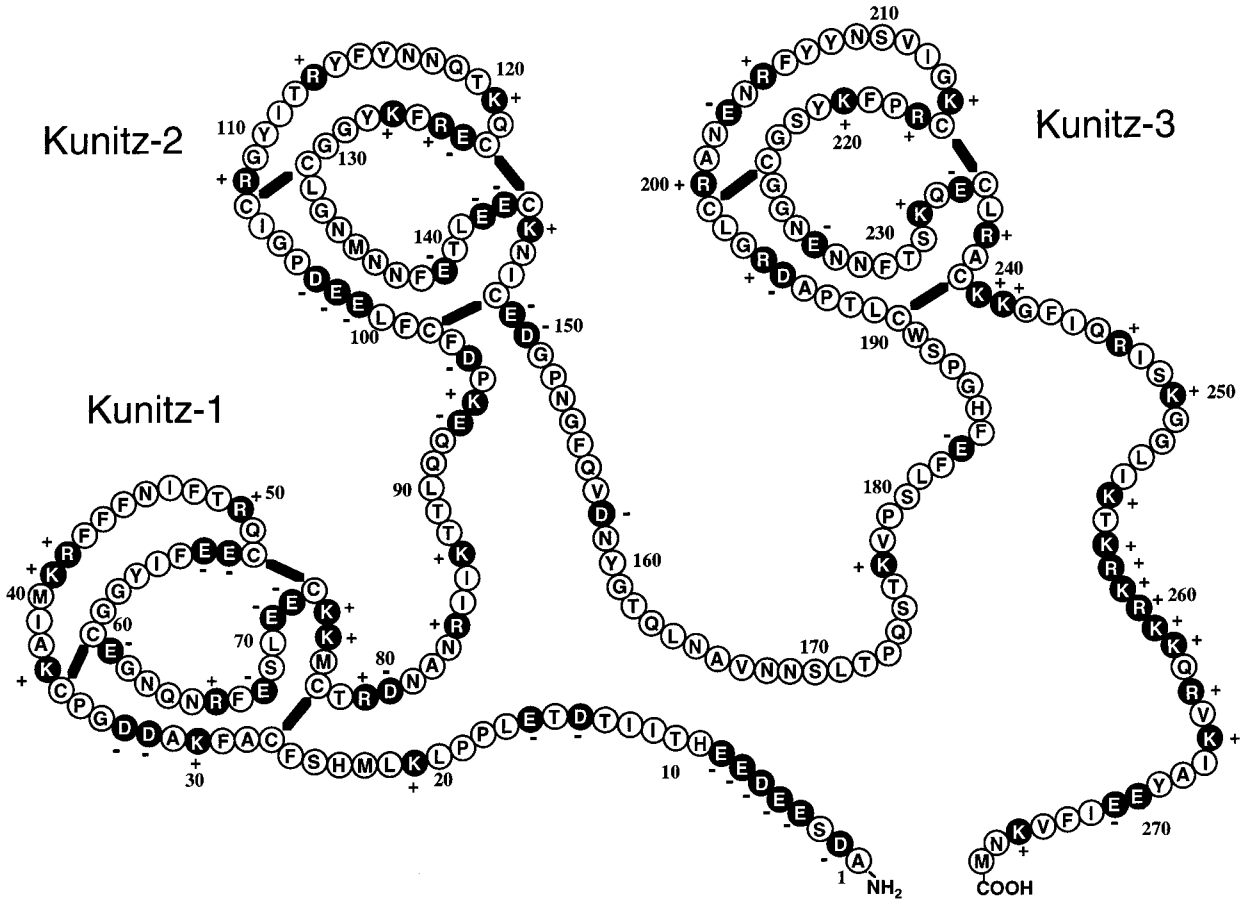

Figure 1—Structure of rhTFPI with the charged amino acid side chains marked. The three Kunitz-type domains are also shown.

protein, 10 mg/mL in a solution containing 150 mM NaCl and 2 M urea buffered with 20 mM sodium phosphate at pH 7, was stored at −70 °C as a frozen bulk. This protein was used as the starting material for all solubility studies. Dextran (MW 10 000), dextran sulfate (MW 10 000), poly-L-arginine hydrochloride (MW 11 800), poly-L-glutamine (MW 10 100), and poly-L-glutamic acid sodium salt (MW 1000) were purchased from Sigma Chemical Co. Poly(acrylic acid) (MW 10 000) was purchased from Polysciences, Inc. All buffer solutions for solubility screening and resolubilization experiments were prepared by Chiron Media Service Groups using reagent grade chemicals.

Solubility Screening—A dialysis method was used for the solubility screening experiments. Approximately 2−3 mL of rhTFPI bulk was loaded into a dialysis tubing (Spectra/Por 7 from Spectrum Inc., MWCO 3500) and dialyzed against 50- to 100-fold excess buffer solution (three exchanges per run) at either 4 °C or ambient temperature for 12 to 24 h. The dialysate was filtered through a 0.2-μm filter (Spin-X centrifuge tube filters from Corning Costar Corp.) to remove visible precipitate, and the resulting clear protein solution was analyzed for concentration of remaining soluble rhTFPI by ultraviolet (UV) absorbance and/or one of two high-performance liquid chromatography (HPLC) methods. Bioactivity, based on the anticoagulation role of TFPI, was assessed by measuring in vitro prothrombin time.

UV Absorbance Measurement—UV absorbance of protein solutions was measured using a Hewlett-Packard Diode Array spectrometer (Model 8452). Absorbance at 278 and 400 nm for protein solutions (P_{278} and P_{400}) and buffer solutions (B_{278} and B_{400}) was recorded using a 1.0-cm path length quartz cuvette. The concentration of rhTFPI in mg/mL was calculated using an extinction coefficient of 0.68 $(mg/mL)^{-1}cm^{-1}$ according to the following expression:

$$[(P_{278} - P_{400}) - (B_{278} - B_{400})]/0.68 \quad (1)$$

High-Performance Liquid Chromatography (HPLC)—Cation-exchange HPLC (CEX-HPLC) was performed on a Pharmacia Mono-S HR 5/5 glass column using a Waters 626 LC system with a 717 heater/cooler autosampler. The column was equilibrated with 80% mobile phase A (70:30 v/v, 20 mM sodium acetate: acetonitrile at pH 5.4) and 20% mobile phase B (70:30 v/v, 20 mM sodium acetate and 1 M ammonium chloride:acetonitrile at pH 5.4). After injection, the protein was eluted by increasing mobile phase B to 85% in 21 min at a flow rate of 0.7 mL/min. The rhTFPI eluted at ~16.5 min as a single peak and was detected by UV absorbance at 280 nm with a Waters 486 absorbance detector. Data acquisition and processing were performed on a Perkin-Elmer Turbochrom system. Protein concentration was estimated by integrating the peak area and comparing it with a standard curve generated from samples of known concentrations.

Reversed-phase HPLC (RP-HPLC) was performed on a Rainin Microsorb-MVC8 column (5 cm × 4.6 mm, 5 μm, 300 Å) using a Waters 626 LC system with a 717 heater/cooler autosampler. The column was equilibrated with 86% mobile phase A (30% acetonitrile/0.45% TFA) and 14% mobile phase B (60% acetonitrile/0.45% TFA). After injection, the protein was eluted by increasing mobile phase B to 20% in 6.5 min, then to 68% in 15.5 min, and finally to 100% in 17 min at a flow rate of 1 mL/min. Eluted protein was detected by UV absorbance at 280 nm with a Waters 486 absorbance detector. Data acquisition and processing were performed on a Perkin-Elmer Turbochrom system.

The Prothrombin Time Bioassay—The in vitro Prothrombin Time bioassay (PT assay) was performed on a Coag-A-Mate RA4 instrument (Organon, Teknika). Samples were first diluted to 150 μg/mL with a urea buffer (2 M urea, 20 mM sodium phosphate, 250 mM NaCl, pH 7.2) and then to 30 μg/mL with a Tris buffer (50 mM Tris, 100 mM NaCl, 1 mg/mL bovine serum albumin, pH 7.5). Finally, standards of known rhTFPI concentrations were diluted to 18, 15, 12 and 9 μg/mL and test samples to ~15 and 12 μg/mL by the Tris buffer. A 10-μL aliquot of diluted sample was first mixed with 90 μL of Verify I (Organon Teknika) in a plastic test tray (Organon Teknika) and the tray was then placed into the Coag-A-Mate instrument. A 200-μL aliquot of Simplastin Excel (Organon Teknika) was added to each well to initiate the clotting process. The clotting times for test samples and standards were recorded. The clotting time for the test sample was converted to

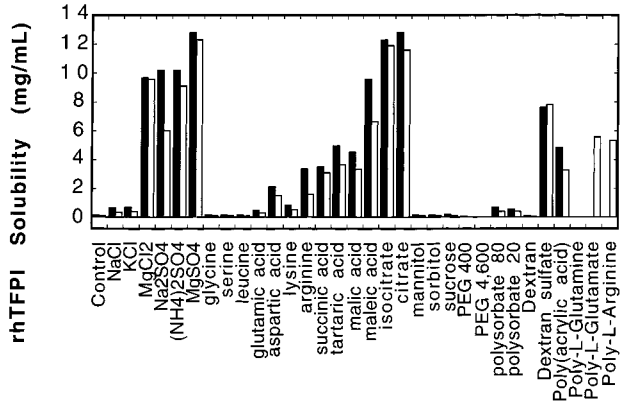

Figure 2—rhTFPI solubility in various solvent systems at 4 °C (shaded) and ambient temperature (open). All solutions were buffered at pH 7 by 10 mM sodium phosphate, which is also shown as the control. Concentrations of tested compounds were 150 mM for salts and amino acids, 5% (w/v) for mannitol and sorbitol, 9% (w/v) for sucrose, 0.1% (w/v) for polysorbates, 0.5% (w/v) for dextran, dextran sulfate, and poly(acrylic acid), 0.75 mM for poly-L-glutamine, and 1 mM for poly-L-glutamic acid and poly-L-arginine. Poly-L-glutamine, poly-L-glutamic acid, and poly-L-arginine show only ambient temperature solubility data.

rhTFPI potency by interpolation on the standard curve, which plotted the natural log of the clotting time versus rhTFPI concentration.

Circular Dichroism (CD) Measurement—Far UV CD spectra of rhTFPI samples were obtained with a JASCO-710 spectropolarimeter (Jasco Inc., Easton, MD) using a 0.2-mm path length cylindrical quartz cell.

Results

Solubility Screening Studies—The solubility of rhTFPI in 10 mM sodium phosphate at pH 7 is <0.5 mg/mL. Known amounts of a number of solubilizing solutes were added to this buffer to enhance the aqueous solubility of rhTFPI, and the data are shown in Figure 2. We have divided the tested solutes into three classes: minor, moderate, or good solubilizing agents. Minor solubilizers were defined as compounds that enhanced rhTFPI solubility by several fold to a concentration not exceeding 1 mg/mL; these include NaCl, KCl, mannitol, sorbitol, sucrose, glycine, leucine, glutamic acid, polysorbate 20, polysorbate 80, dextran, and poly-L-glutamine. Moderate solubilizers were defined as those compounds that increase rhTFPI solubility into the range of 1 to 5 mg/mL; these include lysine, arginine, aspartic acid, succinic acid, malic acid, and tartaric acid. Finally, good solubilizers were those that increased rhTFPI solubility to concentrations >5 mg/mL. These include $MgCl_2$, Na_2SO_4, $(NH_4)_2SO_4$, maleic acid, citric acid, poly-L-glutamic acid, poly-L-arginine, dextran sulfate, and poly(acrylic acid). The classification reveals a clear pattern. Neutral compounds, polymers, and monovalent ions have a marginal effect on rhTFPI solubility, whereas multivalent electrolytes and ionic polymers exhibit a more marked effect.

There was a modest temperature effect on rhTFPI solubility. Solubility of rhTFPI at 4 °C was slightly higher than that measured at ambient temperature. This was independent of the type of solvent tested. Thus, rhTFPI has a negative temperature coefficient for solubility.

Effect of pH on Solubility—The solubility of rhTFPI as a function of pH was investigated in the pH range 3−11 buffered by either 20 mM sodium acetate, sodium glutamate, sodium succinate, sodium phosphate, or glycine. Because the pH profile of a protein may depend on the ionic strength,[14] we included 150 mM NaCl in the buffer systems to minimize the difference in ionic strength for these

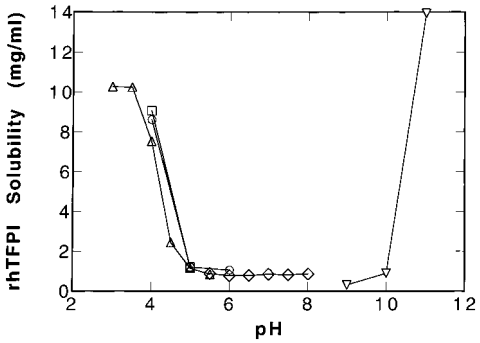

Figure 3—Dependence of rhTFPI solubility on pH in 150 mM NaCl and 20 mM buffer of sodium acetate (triangle), sodium phosphate (diamond), glycine (inverted triangle), sodium L-glutamate (square), and sodium succinate (circle).

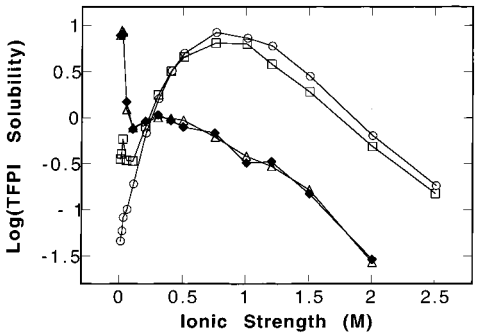

Figure 4—Dependence of logarithm rhTFPI solubility on the ionic strength in sodium chloride solutions buffered with 5 mM sodium acetate at pH 5 (filled diamond) and sodium phosphate at pH 5 (open triangle), pH 6 (open square), and pH 7 (open circle).

buffers. The function appeared as an inverted bell-shaped curve (Figure 3) with a minimum solubility trough between pH 5 and pH 10. The lowest solubility was ~0.5−1 mg/mL centered near pH 7, which is 2−3 pH units away from the isoelectric point of rhTFPI (9.2). Below pH 4.5 and above pH 10.5, rhTFPI solubility rose sharply and eventually exceeded 10 mg/mL.

Effect of Ionic Strength on Solubility—We investigated the dependence of rhTFPI solubility on ionic strength in NaCl solutions buffered by sodium phosphate at pH 5, 6, and 7 and by sodium acetate at pH 5. Figure 4 shows the logarithm of rhTFPI solubility as a function of the ionic strength at the three pH conditions. The ionic strength, I, was defined as

$$I = 1/2 \, \Sigma \, C_i \, Z_i^2 \qquad (2)$$

where C_i is the concentration of the i^{th} ion and Z_i is the charge on the i^{th} ion. At pH 6 and 7, rhTFPI solubility shows typical "salting-in" and "salting-out" biphasic curves. The solubility initially increased with ionic strength to ~1 M and then decreased at subsequent, higher ionic strengths. The entire solubility curve at pH 6 was lower than that at pH 7. At pH 5, buffered by either phosphate or acetate, a triphasic solubility curve was observed. At this pH, the rhTFPI solubility curve in the normal salting-in and salting-out regions was lower than the curve at pH 6. In contrast to the behavior at pH 6 and 7, a large part of the salting-in phase was diminished. Instead, a third phase at low ionic strength conditions was observed in which rhTFPI solubility increased as the ionic strength decreased.

The salting-out part of the solubility curves at pH 5 (0.5−2 M ionic strength), 6, and 7 (1−2.5 M ionic strength) exhibited a linear dependence of the logarithm of the solubility value on ionic strength. This part of the solubility

Table 1—Salting-Out Parameters for rhTFPI in Sodium Chloride Solutions Buffered by Either Acetate or Phosphate to pH 5, 6, and 7[a]

pH (buffer species)	β	K_s (M^{-1})
5 (sodium acetate)	0.51	0.95
5 (sodium phosphate)	0.56	0.99
6 (sodium phosphate)	1.90	1.09
7 (sodium phosphate)	2.07	1.12

[a] The salting-out parameters were calculated by linear fitting salting-out part of the solubility curves from 0.5 to 2 M ionic strength for pH 5 and from 1 to 2.5 M ionic strength for pH 6 and 7.

curve was analyzed by the following empirical equation:[8]

$$\log S = \beta - K_s I \quad (3)$$

where S is protein solubility, β is a constant, K_s is the salting-out constant, and I is the ionic strength. The two salting-out parameters, β and K_s, were calculated (Table 1). Results in Table 1 show the parameter β (solubility extrapolates to zero salt concentration without considering the salting-in effect) depended on pH, whereas the salting-out constant K_s did not and was averaged to be 1.04 M^{-1}. These results are consistent with similar data for other proteins.[15]

Resolubilization of Insolubility Precipitates—Protein precipitates are usually formed from one of two distinct mechanisms. (1) exceeding the solubility limit of the protein in the medium leads to an "insolubility precipitate"; and (2) a partial or complete unfolding of the protein resulting in aggregation that eventually gives rise to an "instability precipitate". The latter is so-called because this type of precipitate is usually seen as a result of prolonged storage of the protein. Experiments were designed to understand these processes by examining the resolubilization behavior of the two types of precipitates in selected media.

A double-dialysis approach was employed for investigation of the insolubility precipitate. In the first step of this experiment, insolubility precipitates were generated within dialysis bags. A bulk solution of rhTFPI was dialyzed against phosphate-buffered saline (PBS) because of its rather limited solubility in this medium. One bag containing the precipitate was removed, and the amount of soluble protein was measured to obtain a control solubility value for each experiment. In a subsequent step, the remaining dialysis bags containing precipitate were transferred into resolubilizing media such as sodium citrate, arginine, or urea, and further dialyzed against those media. After completion of this second dialysis step, the amount of soluble protein in the bag was measured. We compared the amount of rhTFPI resolubilized by a given medium with the control solubility in PBS obtained from the first step to evaluate the effect of the resolubilization condition. We also measured the in vitro bioactivity of the resolubilized rhTFPI to assess its conformational state.

The resolubilization results are shown in Table 2. The control sample (dialyzed against PBS only) showed that 0.69 mg of the initial 10 mg of rhTFPI present per mL in the bag remained soluble after the first dialysis step; that is, >90% of the protein precipitated. In the second dialysis for resolubilization, 0.15 M arginine was able to convert approximately one-fourth to one-third of the precipitated amount into soluble protein, and 0.15 M sodium citrate converted almost the entire precipitate into soluble protein. Urea proved to be another good resolubilization agent, with 2 M urea converting half and 8 M urea converting all of the precipitated rhTFPI into soluble protein. A slightly higher recovery in 8 M urea than the starting concentration was probably caused by concentration due to osmotic pressure produced during dialysis.

Table 2—Resolubilization of rhTFPI Solubility Precipitate[a]

resolubilization buffer	soluble rhTFPI (mg/mL)	specific bioactivity
control (PBS)	0.69	1.10
PBS + 2 M urea	5.52	0.82
PBS + 8 M urea	12.2	1.04
PBS + 2 M urea + 0.1 M DTT	0.01	0.10
PBS + 8 M urea + 0.1 M DTT	11.4	0.11
0.15 M L-arginine	3.01	0.92
0.15 M sodium citrate	9.44	1.01

[a] The concentration of soluble rhTFPI was measured by the RP-HPLC method regardless of peak shift for samples containing DTT. Specific bioactivity was estimated from the PT assay results versus the protein concentration measured by the RP-HPLC.

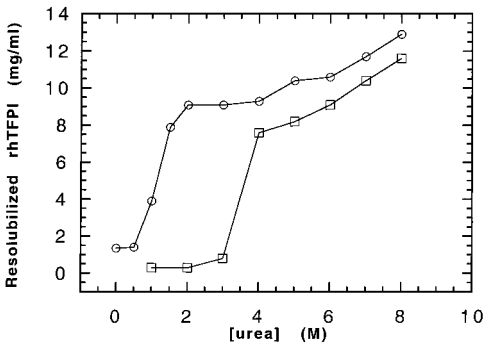

Figure 5—Resolubilization of rhTFPI "insolubility precipitate" in urea solvents in the absence (circle) and presence (square) of 0.1 M DTT.

The addition of 0.1 M dithiothreitol (DTT) to the two different concentrations of urea produced dissimilar effects. In 2 M urea containing 0.1 M DTT, almost no soluble rhTFPI was detected after the second dialysis step, showing that the presence of DTT had an adverse effect on resolubilization in the more dilute urea solution. In contrast, 0.1 M DTT in 8 M urea had little effect on the resolubilization of rhTFPI. Regardless of its effect on resolubilization, DTT evidently produced conformational changes in the rhTFPI molecule. The bioactivity data in Table 2 indicate that resolubilized rhTFPI remained fully active (within the ±20% variation of the assay) except when DTT was present in the resolubilization medium.

To understand the role of DTT in the resolubilization studies more clearly, the urea/DTT resolubilization experiment was repeated using a broader urea concentration range (Figure 5). When the amount of rhTFPI resolubilized in the second dialysis step was plotted as a function of the urea concentration in the dialysis medium, an initial low phase was followed by a transition phase and a high recovery phase regardless of the presence of DTT. However, the transition occurred at a much lower urea concentration (~1.5 M) in the absence of DTT. In 1.5 M urea, rhTFPI was still biologically active, as determined by the PT assay. Measurements by CD or fluorescence showed that the molecule retained its native conformation (data not shown). With DTT present in the resolubilization medium, the transition was shifted to a higher urea concentration (~3.5 M). Because disulfide bonds have been shown to play a critical role in folding and conformational stability of Kunitz-domain-containing proteins,[16] it is thought that reduction of these bonds by DTT may have resulted in the exposure of hydrophobic regions to the aqueous medium, leading subsequently to rhTFPI denaturation. Thus, stronger denaturing conditions were needed to resolubilize the precipitated protein when DTT was present in the medium.

To test this hypothesis further, we analyzed rhTFPI in 8 M urea with and without DTT by CD and a RP-HPLC procedure. As shown in Figure 6, the far UV CD spectrum

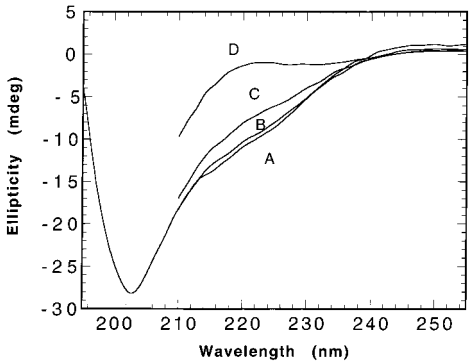

Figure 6—Far UV CD spectra of four rhTFPI samples. These four samples are (A) 0.48 mg/mL rhTFPI in PBS; (B) 0.94 mg/mL rhTFPI in 2 M urea and PBS; (C) 1.24 mg/mL rhTFPI in 8 M urea and PBS; (D) and 1.27 mg/mL rhTFPI in 0.1 M DTT, 8 M urea, and PBS (D). The CD signals were normalized to the 0.48 mg/mL rhTFPI sample for comparison.

Table 3—Percent Remaining Soluble Protein in rhTFPI Samples after Incubation at 40 °C for 0, 3, and 13 Days and after Resolubilization[a]

samples	soluble protein in stability samples with no resolubilization, %	total soluble protein in resolubilized stability samples by the following solvents, %		
		0.1 M citrate	2 M urea	8 M urea
t = 0	100	–	100	–
t = 3 days	73	–	73	110
t = 13 days	44	51	54	96

[a] Resolubilization by 0.1 M sodium citrate (only for $t = 13$ days stability sample), 2 M urea (all three stability samples), and 8 M urea (only for $t = 3$ and 13 days stability samples). All values were normalized to the $t = 0$ stability sample.

of rhTFPI in 8 M urea resembles the spectra in both 2 M urea and PBS, but with a slight loss of conformation, whereas addition of 0.1 M DTT in 8 M urea results in a significant loss of secondary structure. Similarly, RP-HPLC chromatograms showed that the rhTFPI peak eluted at 13 min in both a control sample without urea and an 8 M urea sample. With the addition of 0.1 M DTT in the 8 M urea solution, the rhTFPI peak shifted to 17.5 min, indicating increased hydrophobicity of the protein under this condition. These observations support the conclusion that reduction of disulfide bonds by DTT unfolds the protein, thus exposing hydrophobic regions at the surface.

Resolubilization of Instability Precipitates—Instability precipitates of rhTFPI were generated by incubating a 0.4 mg/mL rhTFPI solution in 10 mM sodium phosphate at pH 7, 150 mM NaCl, and 0.005% polysorbate 80 at 40 °C for various periods of time. Under these conditions, the major degradation pathway of the protein has been determined to be protein aggregation that eventually results in formation of a visible precipitate over time. Stability samples at $t = 0$, 3, and 13 days were withdrawn and were analyzed for remaining soluble protein after removal of the visible precipitate by filtration. Samples containing precipitate (i.e., without filtration) were also dialyzed against 0.1 M sodium citrate, 2 M urea, and 8 M urea in attempts to resolubilize the precipitated protein.

Table 3 displays the remaining soluble protein in stability samples and the total amount of soluble rhTFPI in the stability samples after resolubilization. Upon incubation at 40 °C for 3 and 13 days, the amount of soluble protein decreased to 73 and 44% of the initial value, respectively. When the stability samples containing the soluble and precipitated protein were dialyzed into citrate and urea resolubilizing media, only small fractions of the precipitated protein could be resolubilized using 0.1 M sodium citrate or 2 M urea solutions (7−10% resolubilized from the 13-day stability sample containing 56% rhTFPI as a precipitate). On the other hand, resolubilization by an 8 M urea solution afforded a quantitative recovery of the instability precipitate. These data indicate that the precipitated protein in stability samples was not resolubilized by native or near-native media (such as 0.1 M sodium citrate or 2 M urea) but needed strong denaturing conditions for resolubilization.

Discussion

Adequate solubility of a protein in aqueous media is a critical requirement for development of commercial manufacturing processes and stable formulations for clinical application. Determination of protein solubility often requires preparation of a saturated solution in the given medium. Common techniques include dialysis, ultrafiltration, dissolution of a dried protein powder, or precipitation with poly(ethylene glycol).[10,17,18] We have used a dialysis method to study rhTFPI solubility. The dialysis approach is simple and allows rapid screening of a large number of potential solvents. If the protein concentration in the starting material is sufficiently high and precipitation is observed during dialysis, the soluble fraction of the protein measured within the dialysis membrane represents its saturated solubility in the selected medium. If protein solubility in a particular solvent exceeds the protein concentration in the starting material, further concentration of the dialyzed solution by ultrafiltration may be necessary to obtain the true maximum solubility. In this paper, we used the dialysis approach not only for obtaining the solubility value for a protein but also for performing further studies to elucidate solubility mechanisms.

Attractive Ionic Interaction Limits rhTFPI Solubility—Proteins with poor aqueous solubility are often considered to be "hydrophobic".[9] We have reason to believe that the insolubility of rhTFPI's may originate from attractive electrostatic interaction between the termini of the protein. The rhTFPI molecule consists of a single polypeptide chain of 277 amino acid residues. It has a total of 11 aspartate, 25 glutamate, 17 arginine, and 25 lysine residues. (The histidine residue is not included because the pK_a of its side chain is close to neutral pH, making its protonation state difficult to predict.) These ionizable residues in the protein are randomly distributed within the polypeptide structure, including the three Kunitz domains, except at the two termini where they are present in clusters (Figure 1). The N-terminus contains 3 aspartate and 5 glutamate residues that are located between residues 2 to 16. Similarly, 10 lysine, 4 arginine, and 2 glutamate residues are located between residues 240 to 275 at the C-terminus. At neutral pH, the N-terminus (containing 8 negatively charged residues) behaves as an anionic polymer and the C-terminus (containing 14 positively charged residues) behaves as a cationic polymer. Such uneven charge distribution may result in a large dipole moment on the protein molecule. Thus, electrostatic attractive forces between the two termini and dipole−dipole interaction between two protein molecules may cause both intra- or intermolecular interactions, resulting in reduction of protein solubility.[19]

The hypothesis that insolubility of rhTFPI is attributable to the electrostatic interaction of its two charged termini is supported by the following facts: (1) The rhTFPI pH−solubility curve shows an unusually broad solubility minimum trough around neutral pH (Figure 3). This trough is probably caused by the strong ionic interaction of positively charged lysine and arginine residues with negatively charged aspartate and glutamate residues. In the trough

pH region, these residues are all strongly charged. (2) The C-terminal truncation analogues of rhTFPI exhibit a much greater aqueous solubility than the full-length rhTFPI. For example, an analogue containing the N-terminus and the first two Kunitz domains (analogue 1−160) and missing the positively charged C-terminus, has an aqueous solubility >15 mg/mL (Gustafson, M. E., personal communication). This solubility is almost 2 orders of magnitude higher than the submilligram solubility of the full-length protein. (3) Both cationic (e.g., poly-L-arginine) and anionic polymers (e.g., dextran sulfate, poly-L-glutamate, and poly(acrylic acid)) have remarkable solubilizing effects on rhTFPI. Presumably, ionic polymers can bind to the termini clustered with oppositely charged residues. Such binding shields charges on one terminus, preventing it from interacting with the other terminus. (4) Compounds likely to affect hydrophobic properties of proteins have no effect on rhTFPI solubility. For instance, hydrophobic and neutral amino acids have little effect on rhTFPI solubility (Figure 2). In addition, polysorbate surfactants and poly(ethylene glycol) also did not enhance the protein solubility. Therefore, it is unlikely that hydrophobic interactions play a critical role in rhTFPI insolubility. (5) The solubility of rhTFPI shows a negative temperature coefficient. Because most of the tested conditions are within the salting-in region, where the electrostatic interaction dominates the solubility, the negative temperature effect is probably due to the decreased dielectric constant instead of the increase in the hydrophobic interaction at high temperatures. Decrease in dielectric constant strengthens the electrostatic interaction between the protein termini, thus reducing the solubility. Taken together, these observations strongly suggest that poor aqueous solubility of rhTFPI is a result of ionic interaction of the two charged termini.

Unbalanced Charge Distribution on the Two Termini Shifts the Solubility Minimum Away from the p*I*—Many proteins show an inverted bell-shaped pH−solubility curve with a solubility minimum at or close to the isoelectric point.[20,21] The net zero charge on the protein surface at its p*I* decreases the repulsive forces between protein molecules and makes the protein prone to precipitation. Solubility rises as net charge increases at lower pH due to the protonation of negatively charged residues, and at higher pH, because of deprotonation of positively charged residues. The p*I* of rhTFPI is 9.2 and its solubility minimum is centered around pH 7. The considerable deviation of the solubility minimum from its p*I* may be attributed to the nature of the charge distribution on the polypeptide chain. As already mentioned, the N-terminus contains 8 negatively charged residues and the C-terminus contains 14 positively charged residues. Because the number of positively charged residues on the C-terminus is greater than the number of negatively charged residues on the N-terminus, the interaction between the two termini may not reach a maximum at its p*I* but at neutral pH where all the anionic and cationic residues are fully charged. Therefore, the minimum solubility of rhTFPI is shifted to the neutral pH region.

Salting-In, Salting-Out, and the Third Solubility Phase at Low Ionic Strength—When salt is gradually added to a protein solution, the solubility of the protein usually exhibits two macroscopic processes. First, protein solubility increases, reaching a maximum when the salt concentration produces low to moderate ionic strength conditions. Then, protein solubility decreases as the salt concentration further increases the ionic strength of the solution. These two macroscopic processes are known as "salting-in" and "salting-out" effects. The salting-in effect can be readily explained using the Debye−Hückel screening through nonspecific electrostatic interactions between a charged protein macro-ion and surrounding small ions.[20,22] This theory assumes protein molecules are approximately spherical macro-ions with uniformly distributed charges. Interaction with small counterions stabilizes protein macro-ions and decreases their activity coefficients, resulting in an increase in solubility. At low ionic strengths where the salting-in effect predominates, protein solubility is usually a function of the ionic strength and independent of the ion type.

At higher concentrations of salt, the solute molecules compete with protein molecules for water molecules to attain hydration. An increase in salt concentration promotes hydrophobic interactions between protein molecules, decreasing protein solubility. In contrast to the salting-in effect, protein salting-out depends strongly on the ion type. The effectiveness of a salt for this phenomenon follows the lyotropic or Hofmeister series.[23]

At pH 5, in addition to the expected salting-in and salting-out, a new phase was observed for rhTFPI at low ionic strength conditions (5 to 50 mM). Addition of salt resulted in an effect opposite to the salting-in effect, as protein solubility decreased with increase in salt concentration. The origin of this phase is not clear to the authors at the present time. However, we speculate that increased electrostatic repulsive forces between protein molecules at low ionic strength may increase its solubility. At pH 5, positively charged residues, such as arginine and lysine, are fully charged, whereas negatively charged residues, such as glutamate and aspartate, are only partially charged. Under low ionic strength conditions, an overwhelming population of positively charged residues on rhTFPI may yield a repulsive force strong enough to prevent it from precipitating. The addition of salt to such a solution would increase the dielectric constant of the solution, resulting in a weakening of the electrostatic interactions, thus decreasing solubility.

In addition to the third phase observed at the low ionic strength conditions at pH 5, we also noticed that rhTFPI solubility became somewhat pH independent around an ionic strength of 0.25 M under the tested pH range. Further work is needed to explore this effect.

The salting-in effect explains quite well the solubility effectiveness of the salts we examined in Figure 2. Compared with the relatively poor solubilizing salts NaCl and KCl, the good solubilizing salts $MgCl_2$, Na_2SO_4, $(NH_4)_2SO_4$, and $MgSO_4$ all affect the ionic strength to a much greater extent and are, therefore, believed to be more effective in solubilizing rhTFPI. In contrast, the polyelectrolytes showing good solubilizing effect on rhTFPI act by binding to the basic C-terminus or the acidic N-terminus but not by merely increasing the ionic strength. For example, 0.75 mM poly-L-arginine (MW 11 800 daltons) and 1 mM poly-L-glutamate (MW 1000 daltons) both solubilized rhTFPI to the same extent (Figure 2) despite having widely different effects on the solution ionic strength because of the approximately 10-fold variance in the number of charges they are carrying.

Insolubility Precipitates and Instability Precipitates—As shown in Table 2, rhTFPI insolubility precipitate can be redissolved in media containing sodium citrate, arginine, or low concentrations of urea. These media do not denature the protein and are good solubilizers for native rhTFPI. This result indicates that the interactions responsible for formation of insolubility precipitates are weak and probably nativelike. Therefore, insolubility precipitates are most likely formed from native rhTFPI molecules. The following reaction scheme is indicated:

$$N \leftrightarrow \text{Insolubility Precipitates}$$

In contrast, instability precipitates formed as a result of a thermal treatment or on addition of DTT require media with high concentrations (4 M) of urea for resolubilization (Figure 5). The interactions between precipitated protein molecules are strong in these cases and require denaturing conditions to break them down, suggesting that instability precipitates must be formed from denatured (or partially denatured) protein molecules. The reaction scheme can be described as follows:

$$N \leftrightarrow U \rightarrow \text{Instability Precipitates}$$

Although it is possible that instability precipitates may be converted from insolubility precipitates as shown in the following mechanism, we do not believe this mechanism fits our data on rhTFPI:

$$N \leftrightarrow \text{Insolubility Precipitates} \rightarrow \text{Instability Precipitates}$$

The small temperature coefficient for rhTFPI solubility is unlikely to limit its solubility at 40 °C to create an insolubility precipitate. Further, addition of 2 M urea failed to recover any instability precipitates for the $t = 3$ days stability sample (Table 3), demonstrating an absence of the insolubility precipitates. Finally, the slow kinetics of rhTFPI degradation at 40 °C also ruled out the possibility of a quick conversion from insolubility precipitates to instability precipitates.

The kinetics of formation of insolubility precipitates differ from those for instability precipitates. The amorphous precipitation caused by protein insolubility is often a much faster event than the aggregation and precipitation resulting from protein instability. In rhTFPI, the insolubility precipitate is formed immediately upon buffer exchange, and the turbidity of the solution develops within minutes. On the other hand, rhTFPI instability precipitates are formed over much longer periods of time (weeks to months at high temperatures). For example, loss of soluble rhTFPI (increase of precipitated protein) at 40 °C was estimated to have a half-life of ~12 days, based on the data in Table 3. The kinetics of formation of an insolubility precipitate often contains a lag phase (nucleation) and a rapid growth phase (polymerization),[10] whereas instability precipitate formation may be governed by its unimolecular unfolding as the rate-limiting step that is then followed by a rapid polymerization process.[24]

Conclusions

In conclusion, our studies to determine the solubility of rhTFPI under various solvent conditions showed that rhTFPI solubility is predominantly affected by the charge distribution on the protein molecule itself as well as on the solvent ions present in the surrounding medium. Considering these interactions, the limited solubility of the protein under physiological conditions could be explained and solutes were identified to enhance rhTFPI solubility in aqueous media. Detailed examinations of protein−salt interactions have revealed a third solubilizing phase for rhTFPI at pH 5 under low ionic strength condition that is different from the normal salting-in and salting-out phases of the protein. Finally, by comparing the dissolving power of nondenaturing and denaturing solvent conditions, we have shown that rhTFPI precipitates formed due to the limited protein solubility are different from those resulting from protein instability. Whereas insolubility precipitates can be resolubilized by nondenaturing solvent conditions, such as citrate, arginine, and low concentrations of urea, strong denaturing conditions, such as >4 M concentrations of urea, are required for resolubilization of instability precipitates. These observations are expected to be useful in designing purification processes and formulations needing high aqueous solubility of rhTFPI for further development of the molecule as a therapeutic agent.

Acknowledgments

We appreciate Dr. David Reifsnyder for providing the drawing for Figure 1 and Dr. Heatherbell Fong for excellent text editing of the manuscript.

References and Notes

1. Broze, G. J., Jr.; Warren, L. A.; Novotny, W. F.; Higuchi, D. A.; Girard, J. J.; Miletich. J. P. The Lipoprotein-associated Coagulation Inhibitor That Inhibits the Factor VII-tissue Factor Complex also Inhibits Factor Xa: Insight into Its Possible Mechanism of Action. *Blood* **1988**, *71*, 335−343.
2. Rao, L. V. M.; Rapaport, S. I. Studies of Mechanism Inhibiting the Initiation of the Extrinsic Pathway of Coagulation. *Blood* **1987**, *69*, 645−651.
3. Rapaport, S. I. Inhibition of Factor VIIa/tissue Factor-induced Blood Coagulation: with Particular Emphasis upon a Factor Xa-dependent Inhibitory Mechanism. *Blood* **1989**, *73*, 359−365.
4. Khouri, R. K.; Koudsi, B.; Kaiding, F.; Ornberg, R. L.; Wun, T.-C. Prevention of Thrombosis by Topical Application of Tissue Factor Pathway Inhibitor in a Rabbit Model of Vascular Trauma. *Ann. Plastic Surg.* **1993**, *30*, 398−404.
5. Creasey, A. A.; Chang, A. C. K.; Feigen, L.; Wun, T.-C.; Taylor, F. B., Jr.; Hinshaw, L. B. Tissue Factor Pathway Inhibitor Reduces Mortality from *Escherichia coli* Septic Shock. *J. Clin. Invest.* **1993**, *91*, 2850−2856.
6. Carr, C.; Bild, G. S.; Chang, A. C. K.; Peer, G. T.; Palmier, M. O.; Frazier, R. B.; Gustafson, M. E.; Wun, T. C.; Creasey, A. A.; Hinshaw, L. B.; Taylor, F. B., Jr.; Galluppi, G. R. Recombinant E. coli-derived Tissue Factor Pathway Inhibitor Reduces Coagulopathic and Lethal Effects in the Baboon Gram-Negative Model of Septic Shock. *Circ. Shock* **1995**, *44*, 126−137.
7. Gustafson, M. E.; Junger, K. D.; Wun, T.-C.; Foy, B. A.; Diaz-Collier, J. A.; Welsch, D. J.; Obukowicz, M. G.; Bishop, B. F.; Bild, G. S.; Leimgruber, R. M.; Palmier, M. O.; Matthews, B. K.; Joy, W. D.; Frazier, R. B.; Galluppi, G. R.; Grabner, R. W. Renaturation and Purification of Human Tissue Factor Pathway Inhibitor Expressed in Recombinant E. coli. *Protein Exp. Purif.* **1994**, *5*, 233−241.
8. Arakawa, T.; Timasheff, S. N. Theory of Protein Solubility. *Meth. Enzymol.* **1985**, *114*, 49−77.
9. Schein, C. H. Solubility as a Function of Protein Structure and Solvent Components. *Bio/Technology* **1990**, *8*, 308−317.
10. Middaugh, C. R.; Volkin, D. B. Protein Solubility. In *Stability of Protein Pharmaceuticals, Part A: Chemical and Physical Pathways of Protein Degradation*; Ahern, T. J., Manning, M. C., Eds.; Plenum: New York, 1992; pp 109−134.
11. van Oss, C. J.; Good, R. J.; Chaudhury, M. K. Solubility of Proteins. *J. Protein Chem.* **1986**, *5*, 385−405.
12. Wun, T.-C.; Kretzmer, K. K.; Girard, T. J.; Miletich, J. P.; Broze, G. J., Jr. Cloning and Characterization of a cDNA Coding for the Lipoprotein-associated Coagulation Inhibitor Shows that It Consists of Three Tandem Kunitz-type Inhibitory Domains. *J. Biol. Chem.* **1988**, *263*, 6001−6004.
13. Daiz-Collier, J. A.; Palmier, M. O.; Kretzmer, K. K.; Bishop, B. F.; Combs, R. G.; Obukowicz, M. G.; Frazier, R. B.; Bild, G. S.; Joy, W. D.; Hill, S. R.; Duffin, K. L.; Gustafson, M. E.; Junger, K. D.; Grabner, R. W.; Galluppi, G. R.; Wun, T.-C. Refold and Characterization of Recombinant Tissue Factor Pathway Inhibitor Expressed in *Escherichia coli*. *Thromb. Haemost.* **1994**, *71*, 339−346.
14. Davio, S. R.; Hageman, M. J. Characterization and Formulation Considerations for Recombinantly Derived Bovine Somatotropin. In *Stability and Characterization of Protein and Peptide Drugs: Case Histories*; Wang, Y. J., Pearlman, R., Eds.; Plenum: New York, 1993; pp 59−89.
15. Shih, Y.-C.; Prausnitz, J. M.; Blanch, H. W. Some Characteristics of Protein Precipitation by Salts. *Biotechnol. Bioeng.* **1992**, *40*, 1155−1164.
16. Ma, L.-C.; Anderson, S. Correlation between Disulfide Reduction and Conformational Unfolding in Bovine Pancreatic Trypsin Inhibitor. *Biochemistry* **1997**, *36*, 3728−3736.
17. Pohl, T. Concentration of Proteins and Removal of Solutes. *Meth. Enzymol.* **1990**, *182*, 68−83.

18. Stevenson, C. L.; Hageman, M. J. Estimation of Recombinant Bovine Somatotropin Solubility by Excluded-volume Interaction with Polyethylene Glycols. *Pharm. Res.* **1995**, *12*, 1671−1676.
19. Arakawa, T.; Timasheff, S. N. Abnormal Solubility Behavior of β-Lactoglobulin: Salting-In by Glycine and NaCl. *Biochemistry* **1987**, *26*, 5147−5153.
20. Cohn, E. J.; Edsall, J. T. *Proteins, Amino Acids and Peptides as Ions and Dipolar Ions*; Reinhold Publishing: New York, 1943; pp 569−585.
21. Rupley, J. A. Comparison of Protein Structure in the Crystal and in Solution, IV. Protein Solubility. *J. Mol. Biol.* **1968**, *35*, 455−476.
22. Tanford, C. *Physical Chemistry of Macromolecules*, John Wiley & Sons: New York, 1961; pp 180−274.
23. von Hippel, P. H.; Schleich, T. The Effects of Neutral Salts on the Structure and Conformational Stability of Macromolecules in Solution. In *Structure and Stability of Biological Macromolecules*, Timasheff, S. N.; Fasman, G. D., Eds.; Marcel Dekker: New York, 1969; pp 417−574.
24. Chen, B.-L.; Arakawa, T.; Morris, C. F.; Kenney, W. C.; Wells, C. M.; Pitt, C. G. Aggregation Pathway of Recombinant Human Keratinocyte Growth Factor and Its Stabilization. *Pharm. Res.* **1994**, *11*, 1581−1587.

JS9900708

Improvement in Solubility and Dissolution Rate of 1,2-Dithiole-3-thiones upon Complexation with β-Cyclodextrin and Its Hydroxypropyl and Sulfobutyl Ether-7 Derivatives

GILLES DOLLO,*,† PASCAL LE CORRE,† MARYLÈNE CHOLLET,‡ FRANÇOIS CHEVANNE,† MARCEL BERTAULT,§ JEAN-LOUIS BURGOT,‡ AND ROGER LE VERGE†

Contribution from *Laboratoire de Pharmacie Galénique et Biopharmacie and Laboratoire de Chimie Analytique, Faculté des Sciences Pharmaceutiques et Biologiques, Université de Rennes I, 35043 Rennes Cedex, France, and Groupe Matière Condensée et Matériaux, UMR 6626 au CNRS, Université de Rennes I, Campus de Beaulieu, 35042 Rennes Cedex, France.*

Received February 26, 1999. Accepted for publication June 22, 1999.

Abstract □ Inclusion complexes between β-cyclodextrin derivatives and 1,2-dithione-3-thiones were studied in aqueous solution and in the solid state. Phase solubility study was used to evaluate the complexation in solution, at 37 °C, of three cyclodextrins, i.e., β-cyclodextrin (βCD), hydroxypropyl-β-cyclodextrin (HPβCD), sulfobutyl ether-7-β-cyclodextrin (SBE7βCD), and four 1,2-dithiole-3-thiones, i.e., the parent compound dithiolethione (DTT), dimethyldithiolethione (DMDTT), 5-phenyldithiolethione (5PDTT), and anetholetrithione (ATT). Stability constants of the DTT complexes with HPβCD and SBE7βCD were also determined spectrophotometrically using a nonlinear least-squares methodology. Differential scanning calorimetry (DSC) and scanning electronic microscopy (SEM) were used to characterize spray-dried complexes formed between 5PDTT and SBE7βCD, ATT and SBE7βCD. Dissolution studies using the USP paddle method were carried out in water at 37 °C for both ATT and 5PDTT binary systems with HPβCD and SBE7βCD. Solubility enhancements were much greater with the more lipophilic ATT and 5PDTT compared to DTT and DMDTT, whatever the cyclodextrin used, in the rank order SBE7βCD > HPβCD ≫ βCD. Stability constants obtained (between 120 and 12800 mol^{-1}) were also the highest for the more lipophilic drugs and in the same rank order SBE7βCD > HPβCD ≫ βCD. Results obtained by UV spectrophotometry were in good agreement with those obtained by phase-solubility study. DSC thermograms of spray-dried complexes of ATT and 5PDTT with HPβCD and SBE7βCD lacked the endothermal peak of pure drug peak which was found for the physical mixtures (107 °C and 125 °C for ATT and 5PDTT, respectively). Finally, dissolution profiles of spray-dried inclusion complexes studied displayed a faster dissolution rate compared to physical mixtures and pure drugs. The present study showed that complexation of 1,2-dithiole-3-thiones with β-cyclodextrin derivatives resulted in an increase in solubility, allowing intravenous formulation for bioavailability and metabolism studies and an increase in the dissolution rate of the drugs, which shoud be of interest for oral absorption of these lipophilic compounds.

Introduction

1,2-Dithiole-3-thiones are sulfur heterocyclic compounds naturally found in cruciferous vegetables.[1] Among these compounds of pharmaceutical interest, anetholetrithione (ATT) has been marketed since 1947[2] and is prescribed for its choleretic and sialagogue properties. In the last 15 years, it has been shown that these molecules were able to inhibit carcinogenesis by increasing the activity of electrophile detoxification enzymes (phase II enzymes conjugating with carcinogens favoring their elimination)[3] and by increasing intracellular glutathione levels (increasing protection against free radicals, oxidants...). For that reason the pharmaceutical interest of 1,2-dithiole-3-thiones is growing since they may be useful for cancer chemoprevention in humans.[4−6] An oral formulation allowing a chronic administration of these compounds would be highly desirable.

Since 1,2-dithiole-3-thiones are highly lipophilic compounds,[7−8] and since too high a lipophilicity can result in low permeability,[9] there is a need from a biopharmaceutical standpoint to increase the poor aqueous solubility of these nonionizable molecules (around 0.001 mg/mL) in order to circumvent the low and highly variable absorption generally seen with such products.[10] To reach that goal, we used cyclodextrins, since preliminary solubilization studies with cosolvents such as DMSO or PEG resulted in drug precipitation upon dilution. The β-cyclodextrins (βCD) are α-1,4-linked cyclic oligosaccharides composed of seven D-glucopyranose units with a relatively hydrophobic central cavity and an hydrophilic outer surface.[11] These products are able to entrap poorly soluble drug molecules of appropriate size and polarity in their cavities to form reversible noncovalent inclusion complexes. This may improve physical and chemical properties of the incorporated guest molecule allowing, for example, the improvement of stability, solubility,[12] in vivo drug delivery, and bioavailability.[13−14] βCD has been studied extensively despite a very low aqueous solubility but some derivatives such as 2-hydroxypropyl-β-cyclodextrin (HPβCD) and more recently an anionically charged derivative with an average degree of substitution of 7, sulfobutyl ether-7-β-cyclodextrin (SBE7βCD) have attracted growing interest due to their greater intrinsic solubilities allowing improved complexing abilities.[12,15] SBE7βCD and HPβCD appear to be parenterally safer materials, compared to the parent β-cyclodextrin.[16]

The objectives of this work were (i) to examine the potential of βCD, HPβCD, and SBE7βCD as solubilizing agents for four 1,2-dithione-3-thiones, the parent compound dithiolethione (DTT), dimethyldithiolethione (DMDTT), 5-phenyldithiolethione (5PDTT), and anetholetrithione (ATT), using the phase-solubility technique and UV−visible spectrophotometry, (ii) to characterize the complexes formed by differential scanning calorimetry (DSC) and by scanning electronic microscopy (SEM), and (iii) to evaluate the rate of drug dissolution when complexed or not with cyclodextrins according to the USP paddle method.

* Corresponding author. Tel: (33) 2-99-33-62-65. Fax: (33) 2-99-33-68-91. e-mail: Gilles.Dollo@univ-rennes1.fr.
† Laboratoire de Pharmacie Galénique et Biopharmacie.
‡ Laboratoire de Chimie Analytique.
§ Groupe Matière Condensée et Matériaux.

10.1021/js990067o CCC: $18.00
Published on Web 08/17/1999

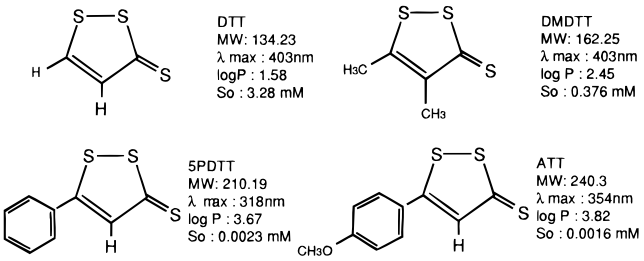

Figure 1—Chemical structures of 1,2-dithiole-3-thiones studied, their molecular weights (MW), λ_{max}, log *P*, and intrinsic water solubility (S_0) values.

Experimental Section

Materials—βCD (KLEPTOSE, MW = 1135 g/mol) and HPβCD (ref 615446, D. S. (degree of substitution) = 5.88; MW = 1476 g/mole) were kindly provided by Roquette (Lestrem, France) and SBE7βCD (CAPTISOL, cat. ref no. 7585−39−9; D. S. = 6.4; MW = 2163 g/mole) by CyDex (Overland Park, KS).

All 1,2-dithiole-3-thiones studied (Figure 1) were synthesized by our team, except that ATT was supplied by Solvay Pharma (Laboratoire de Thérapeutique Moderne, Suresnes, France).

All other reagents and solvents (E. Merck, Darmstadt, Germany) were of analytical grade, and freshly prepared distilled water was used throughout the study.

Phase-Solubility Study—Solubility measurements were determined according to the method of Higuchi and Connors.[17] Excess amounts of 1,2 dithiole-3-thione (10 mg) were weighted into 1 mL screw-cap polypropylene tubes to which were added aqueous solutions containing increasing concentrations of CDs, ranging from 0% to 10% (w/v) for HPβCD and SBE7βCD, 0% to 2% (w/v) for βCD. The suspensions formed were then rotated on a top to bottom shaker, thermostatically controlled at 37 ± 0.1 °C. After one week of agitation (equilibrium and absence of drug degradation were confirmed in preliminary studies), the suspensions were centrifugated (20000*g* for 10 min) and appropriately diluted with the mobile phase, and the total concentration of 1,2-dithiole-3-thione in the filtrate was analyzed by a reversed phase HPLC system according to Lefeuvre et al.[18] It consisted of a Waters Model 6000A pump (Waters Assoc., Milford, MA) equipped with a Waters Model WISP 710 B automatic injector, an LDC Milton Roy Model Spectromonitor 3100 variable-wavelength UV detector (LDC Milton Roy, Riviera Beach, FL), and a Delsi Model Enica 21 integrator (Delsi, Suresnes, France). The analytical chromatography column was a Lichrospher RP−SelectB (Interchim, Montluçon, France) (125 × 3 mm i.d.; particle size 5 μm). The chromatographic conditions were as follows: injection volume, 20 μL; column temperature, 30 °C; mobile phase, mixture of acetonitrile and water (50:50, v/v); flow rate, 0.5 mL/min; detector operated at 318 and 354 nm for 5PDTT and ATT, respectively.

The experiment was carried out in triplicate, and the stability constant of each drug-cyclodextrin system (K_s) was then calculated from the linear portion of the phase solubility diagrams (reporting drug concentration vs cyclodextrin concentration), assuming that a 1:1 stoichiometric ratio complex was formed at the initial step (slope smaller than 1) according to eq 1.[17]

$$K_s = \text{slope}/s_o(1 - \text{slope}) \quad (1)$$

where s_o is the drug solubility in water.

UV−Visible Spectrophotometry—The determination of the stability constants (K_s) of the parent compound DTT with the cyclodextrins HPβCD and SBE7βCD was also realized in solution by UV−visible spectrophotometry ultraviolet (UV) absorption changes of DTT (5×10^{-5} M) in the presence of aqueous solutions of HPβCD or SBE7βCD (various concentrations of 5×10^{-5} M, 10^{-4} M, 2.5×10^{-4} M, 5×10^{-4} M, 10^{-3} M, 2.5×10^{-3} M, 5×10^{-3} M, 10^{-2} M, 2.5×10^{-2} M and 5×10^{-2} M) were recorded from 200 to 500 nm with a Uvikon model 922 UV−visible spectrophotometer (Bio-Tek Kontron instruments, Saint Quentin en Yvelines, France). Absorbance data were treated by a nonlinear least-squares methodology. The stability constants were obtained together with the molar absorptivity coefficient of the DTT−CD complex studied which could not be experimentally determined since the complex could not stand alone in solution owing to the dilution effects. The mathematical model allowing the calculation of absorbances to be compared to the experimental ones according to the nonlinear least-squares methodology, issued from the basic equations:

$$K_s = [\text{DTT−CD}]/[\text{DTT}][\text{CD}] \quad (2)$$

$$[\text{DTT}] + [\text{DTT−CD}] = c_2 \quad (3)$$

$$[\text{CD}] + [\text{DTT−CD}] = c_3 \quad (4)$$

where [DTT], [CD], [DTT−CD] are free equilibrium concentrations of DTT, CD, and complex, respectively; c_2 and c_3 are the analytical concentrations of DTT and cyclodextrin, respectively. The above system of three equations reduced to the second-order equation in [DTT-CD]:

$$K_s[\text{DTT−CD}]^2 - [K_s(c_2 + c_3) + 1][\text{DTT−CD}] + K_s c_2 c_3 = 0 \quad (5)$$

The absorbances were calculated for each of the relative concentrations used according to the Beer−Lambert Law:

$$A^{\text{calc}} = \epsilon_{\text{DTT}}[c_2 - (\text{DTT−CD})] + \epsilon_{\text{DTT−CD}}[\text{DTT−CD}] \quad (6)$$

where ϵ_{DTT} and $\epsilon_{\text{DTT−CD}}$ are the molar extinction coefficients of the pure drug and from the complex, respectively. The minimization of the least-squares function $U = \sum(A^{\text{calc}} - A^{\text{exp}})^2$, calculated over the 10 concentration ratios mentioned above, was achieved by an algorithm developed in our department.[19,20]

Preparation of Solid Complexes—Solid complexes of 1,2-dithiole-3-thiones and cyclodextrins were obtained by spray-drying of stoechiometric amounts of drug (ATT or 5PDTT) and cyclodextrin (HPβCD or SBE7βCD) (1:1 or 1:2 drug−cyclodextrin mole ratio). A solution containing the drug (500 mg in 500 mL 95% ethanol) to which was added 250 mL of an aqueous solution of the cyclodextrin was spray-dried in a Büchi Mini Spray-drier B-191 apparatus (Büchi, Switzerland) under the following conditions: flow rate of the solution, 10 mL/min; drying air flow rate, 600 L/h; air inlet temperature, 100 °C; air outlet temperature, 65 °C; aspirator capacity, 35 m^3/h. The yield of the spray-drying process was about 60% in the receiving vessel.

Physical mixtures of 1,2-dithiole-3-thione−cyclodextrin systems were prepared by gently mixing the drug and the cyclodextrin in a mortar, in the same 1:1 or 1:2 molar ratio.

Particle Size Measurements—Size distribution of pure materials, physical mixtures, and spray-dried products was determined by laser diffractometry using a Mastersizer S (Malvern Instruments, Orsay, France) particle size analyzer. All results were expressed as the median volumetric diameter *d*(v,0.5) which is the diameter that divides the volume distribution curve of the sample analyzed in two equal parts.

Differential Scanning Calorimetry—DSC was used to characterize the interactions between both lipophilic 1,2-dithiole-3-thiones, 5PDTT and ATT, with SBE7βCD. The calorimetric measurements of raw materials as well as 1:1 physical mixtures and 1:1 and 1:2 spray-dried complexes were performed with a Perkin-Elmer DSC-7 differential scanning microcalorimeter (Perkin-Elmer, Norwalk, CT) connected to a DEC 425 calculator. The measurement head was flushed with pure nitrogen gas, and its temperature was stabilized by circulating cold water−ethanol from a thermostatic bath controlled at 7 ± 0.1 °C. Temperatures were calibrated using the melting points of *p*-nitrotoluene (99.99%, mp = 51.5 °C, Carlo Erba, Milan, Italy) and indium (99.99%, mp = 156.6 °C, Perkin-Elmer, Norwalk, CT). Energy was calibrated from the melting enthalpy of indium (28.45 J/g). Samples weighting from 0.1 to 0.2 mg (for pure compounds 5PDTT and ATT allowing precise determination of the fusion point) to 10−20 mg (for physical mixtures and spray-dried complexes with SBE7βCD) were carefully encapsulated in aluminum pans with a crimped cap into which was made a needle hole, allowing water evaporation. Only heat flow measurements were made on all samples at a scanning heating rate of 10 °C/min in the 85−130 °C temperature range.

Scanning Electronic Microscopy—Morphological features of the raw materials were compared with a 1:1 physical mixture and 1:1 and 1:2 spray-dried complexes for the binary system (ATT, SBE7βCD), after examination by SEM (JEOL model JSM-6400, Tokyo, Japan). The samples were fixed on a brass stub using

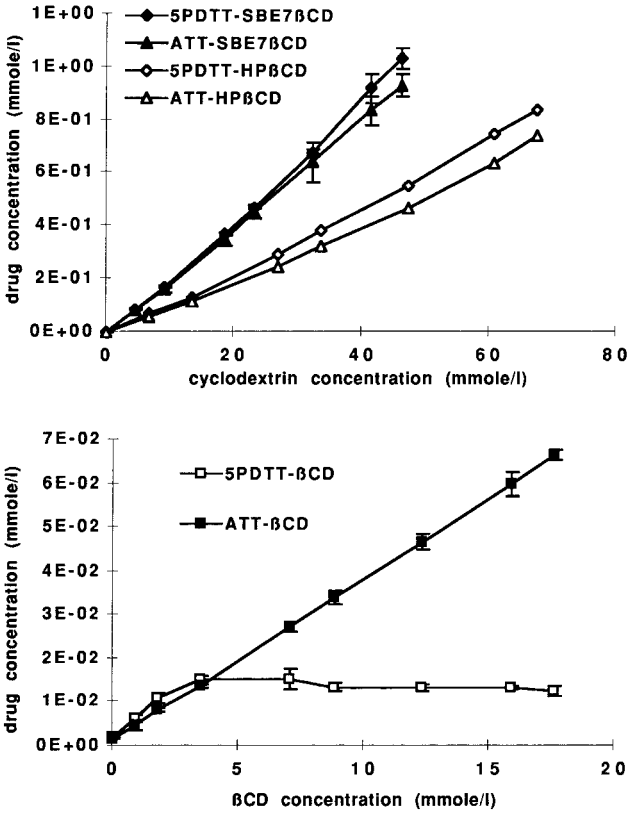

Figure 2—Phase-solubility diagrams of ATT– and 5PDTT–cyclodextrin systems. Top: SBE7βCD and HPβCD; bottom: βCD. Each point is the mean (±SD) of three determinations.

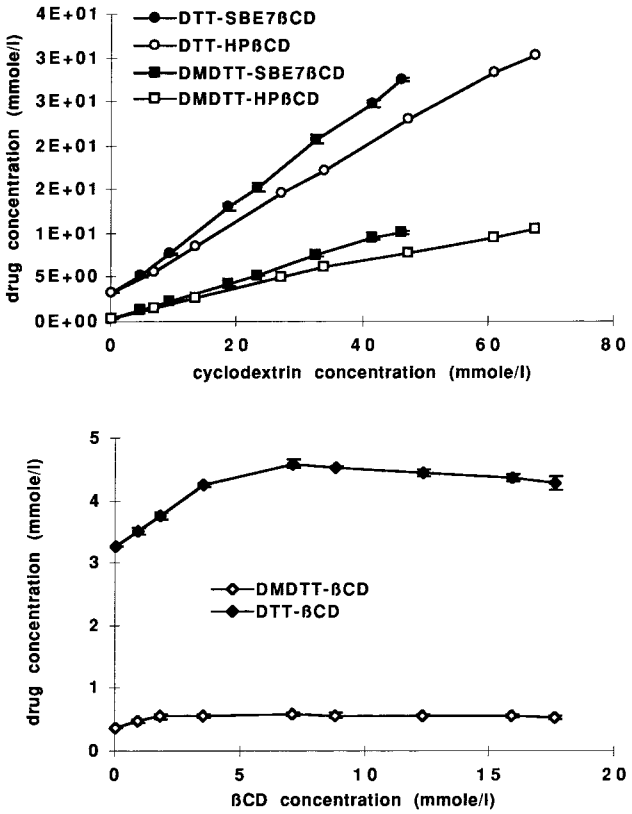

Figure 3—Phase-solubility diagrams of DTT– and DMDTT–cyclodextrin systems. Top: SBE7βCD and HPβCD; bottom: βCD. Each point is the mean (±SD) of three determinations.

double-sided tape and then made electrically conductive by coating in a vacuum with a thin layer of gold/palladium.

Dissolution Study—USP XX Type 2 apparatus (rotating paddle method) was employed to obtain all the dissolution profiles of pure drugs, 1:1 and 1:2 physical mixtures, and spray-dried complexes of ATT and 5PDTT with HPβCD and SBE7βCD. Due to the poor aqueous solubility of these nonionizable compounds, sink conditions (less than 20% of saturation concentration) could not be maintained during the tests. Each powdered sample contained 5 mg of 1,2-dithiole-3-thione. The dissolution medium consisted of 1000 mL of distilled water thermostated at 37 ± 0.1 °C, and the paddle speed was 100 rpm. Concentration of dissolved drug was measured continuously (every 15 min for drugs and physical mixtures, every 30 s for complexes at a wavelength of 318 and 354 nm for 5PDTT and ATT, respectively) using a UV spectrophotometer (Spectronic 1201 Milton, LDC Milton Roy, Riviera Beach, FL). Each experiment was carried out in triplicate.

Results and Discussion

Phase-Solubility Analysis—Phase-solubility diagrams for ATT and 5PDTT, DTT and DMDTT are shown in Figure 2 and Figure 3, respectively. Data obtained from these diagrams are presented in Table 1. Phase solubility diagrams obtained with HPβCD and SBE7βCD showed a linear relationship between the amount of 1,2-dithiole-3-thione solubilized and the concentration of cyclodextrin in solution (*Al* type diagram) for less lipophilic drugs DTT and DMDTT (log P = 1.59 and 2.45, respectively) (Figure 3). According to Higuchi and Connors theory,[17] this may be ascribed to the formation of soluble 1:1 (1,2-dithiole-3-thione–cyclodextrin) inclusion complexes. For more lipophlilic ATT and 5PDTT (log P = 3.82 and 3.67, respectively), the diagrams were of the *Ap* type (Figure 2), the positive curvatures indicating the existence of soluble complexes with an order greater than 1 in cyclodextrin. βCD, however, exhibited *Al* type diagrams according to Higuchi and Connors classification only with the more lipophilic ATT, while *Bs* type diagrams were observed with DTT, DMDTT, and 5PDTT, with an initial rising portion followed by a plateau and/or a very slight decrease in total drug concentration in the filtrate due to solid complex precipitation.

Table 1: Data Obtained from the Phase-Solubility Analysis for Each (1,2-dithiole-3-thione–cyclodextrin) Binary System: Type and Slope of the Diagrams, Apparent Stability Constant (K_s), and Solubility Increase with 2% βCD, 10% HPβCD, and 10% SBE7βCD

1,2-dithiole-3-thione	cyclodextrin	type of curve	slope of curve	stability constant[a] (M^{-1})	solubility increase[a]
ATT	βCD	Al	0.004	2841	41.3
	HPβCD	Ap	0.009	6227	458
	SBE7βCD	Ap	0.020	12834	576
5PDTT	βCD	Bs	0.049	2322	7.05
	HPβCD	Ap	0.009	2863	391
	SBE7βCD	Ap	0.022	10705	482
DMDTT	βCD	Bs	0.109	408	1.57
	HPβCD	Al	0.175	654	28.3
	SBE7βCD	Al	0.214	764	27.1
DTT	βCD	Bs	0.280	119	1.4
	HPβCD	Al	0.424	225	9.2
	SBE7βCD	Al	0.544	364	8.4

[a] Mean of three determinations.

Solubility enhancements obtained with the three cyclodextrin solutions, i.e. βCD (2% w/v), HPβCD (10% w/v), and SBE7βCD (10% w/v), were much greater with the more lipophilic 1,2-dithiole-3-thiones than with less lipophilic drugs, in the rank order SBE7βCD > HPβCD ≫ βCD (Table 1). The values obtained were near 480 times the intrinsic solubility for 5PDTT (which is 0.0023 mmol/L or 0.48 mg/L) and near 580 times the intrinsic solubility for ATT (0.0016 mmol/L or 0.39 mg/L) while they only reached 9 times the intrinsic solubility for DTT (3.28 mmol/L or 441 mg/L) and 28 times the intrinsic solubility for DMDTT

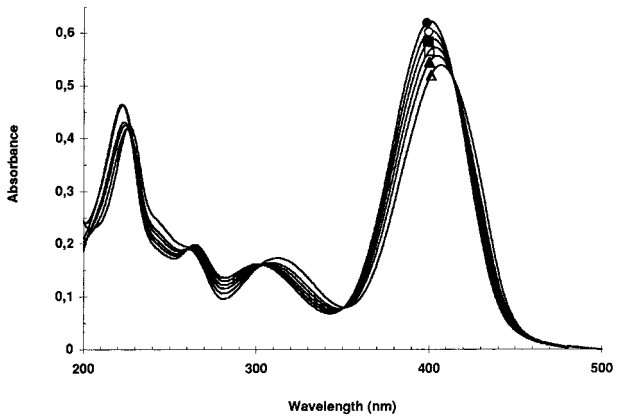

Figure 4—Effect of different concentrations of HPβCD (●: 0 mM; ○: 2.5×10^{-4} mM; ■: 10^{-3} mM; □: 5×10^{-3} mM; ▲: 10^{-2} mM; Δ: 5×10^{-2} mM) on the UV spectrum of DTT (5×10^{-2} mM).

Table 2: Data Obtained from UV Spectroscopy Study of the Complexation between DTT and the Cyclodextrins HPβCD and SBE7βCD: Stability Constants (K_s), Calculated (calcd) and Experimental (exp) Molar Absorptivities of Free (ϵ_{DTT}) and complexed (ϵ_{DTT-CD}) DTT

	K_s (M^{-1})	$(\epsilon_{DTT})^{calc}$ ($cm^{-1}\,M^{-1}$)	$(\epsilon_{DTT})^{exp}$ ($cm^{-1}\,M^{-1}$)	$(\epsilon_{DTT-CD})^{calc}$ ($cm^{-1}\,M^{-1}$)
DTT-HPβCD	178	12441	12458	9982
DTT-SBE7βCD	184	12376	12350	9831

(0.376 mmol/L or 61 mg/L). Apparent 1:1 stability constants (K_s) were obtained from the slopes of the linear portion of each diagram (slopes always lower than 1); the values, ranging from 119 to 12834 mol^{-1}, were also the highest for the more lipophilic drugs (exhibiting *Ap* type diagrams), in the same rank order SBE7βCD > HPβCD ≫ βCD (Table 1). Such results, showing the highest complexing ability of the SBE7βCD compared to HPβCD were also reported by Okimoto et al.[21] for binding constants of several neutral (uncharged) drugs with SBE7βCD and HPβCD, when studing the effect of charge on complexation.

UV−Visible Spectrophotometry—The stability constants (K_s) between the parent compound (DTT) and the cyclodextrins HPβCD and SBE7βCD could also be determined by UV−visible spectrophotometry taking into account the fact that the complex formation gave a bathochromic shift of the maximum located near 403 nm. Figure 4 shows the effect of different concentrations of HPβCD on the UV spectrum of DTT, for example; only 6 of 11 spectra are shown for clarity. The absorption maximum at 403 nm was shifted to higher wavelength with a concomitant decrease in the molar extinction coefficient (Table 2). The complexation of DTT with both cyclodextrins may be related to the high electron density inside the CD cavity on one hand,[22] and to the positive charge of the DTT

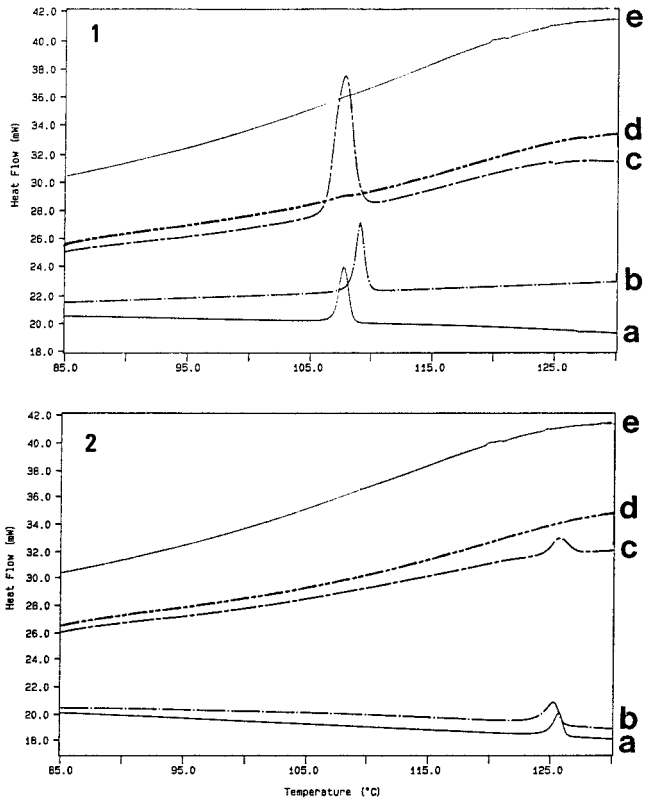

Figure 5—DSC thermograms of (1,2-dithiole-3-thiones, SBE7βCD) binary systems: Figure 5.1 (ATT,SBE7βCD) and Figure 5.2 (5PDTT,SBE7βCD). (a) 1:1 physical mixture (drug + SBE7βCD); (b) drug alone; (c) spray-dried complex obtained with a 1:1 initial mole ratio (drug–SBE7βCD); (d) spray-dried complex obtained with a 1:2 initial molar ratio (drug–SBE7βCD); (e) SBE7βCD alone.

nucleus on the other hand. Indeed, a lot of chemical and physical data indicate that the structure of 1,2-dithiole-3-thiones must be considered to be an hybrid resonance according to the following scheme:[23]

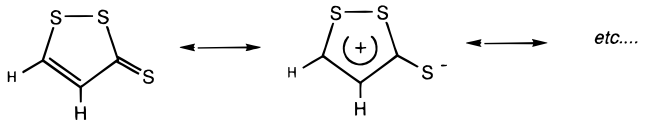

where the two mentioned structures have approximatively the same weight. The partially positive charge brought by the DTT nucleus may explain also on an electrostatic ground, the systematically enhanced stability for the complexes formed with the anionic SBE7βCD compared to those formed with neutral HPβCD, in agreement with Okimoto et al.,[21] i.e., a driving force for complexation being a combination of Coulombic and hydrophobic forces with regard to the binding of charged drugs to

Table 3: Data Obtained from DCS (sample weight, endothermic peak onset, ΔH, complexation efficiency) and Drug Content Determined by HPLC for 1:1 Physical Mixtures (1:1 PM), 1:1 Mole Ratio Spray-Dried Products (1:1 SD), and 1:2 Mole Ratio Spray-Dried Products (1:2 SD) for Each (1,2-dithiole-3-thione, cyclodextrin) Binary System Studied

binary system	product	sample (mg)	drug content (%)	onset (°C)	ΔH (J/g)	drug complexed (%)
ATT–SBE7βCD	ATT alone	0.19		109.0	101.50	
	1:1 PM	1.91	9.99	107.0	8.10	20.0
	1:1 SD	15.24	9.36	106.3	3.45	63.7
	1:2 SD	17.73	4.41	106.1	0.056	98.7
5PDTT–SBE7βCD	5PDTT alone	0.096		124.8	125.00	
	1:1 PM	1.70	8.86	123.8	10.25	7.4
	1:1 SD	18.41	5.44	124.3	0.70	89.7
	1:2 SD	20.13	4.55	none	none	100.0

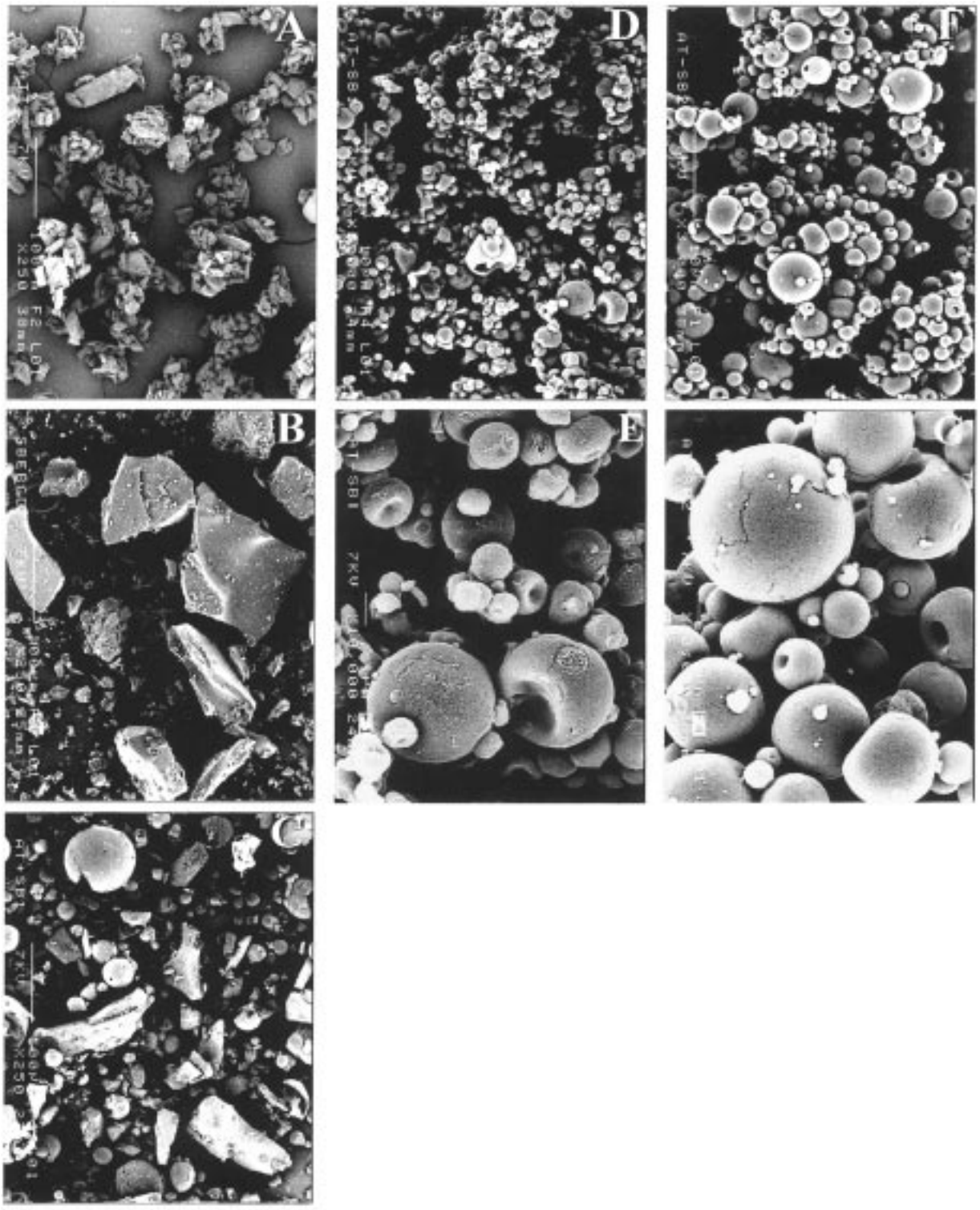

Figure 6—SEM micrographs of of binary system (ATT–SBE7βCD): (A) ATT alone; (B) SBE7βCD alone; (C): 1:1 physical mixture (ATT + SBE7βCD); (D and E) ATT–SBE7βCD spray-dried complex complex obtained with a 1:1 initial molar ratio (ATT–SBE7βCD1), × 3000 and × 10000, respectively; (F and G) ATT–SBE7βCD spray-dried complex complex obtained with a 1:2 initial molar ratio (ATT–SBE7βCD2), × 3000 and × 10000, respectively.

charged cyclodextrins. The occurrence of five isosbestic points at 227, 260, 303, 352, and 414 nm warranted the existence of only one equilibrium between the three species, i.e., the free DTT, the complexed DTT, and the cyclodextrin. This suggests that the model chosen (1:1 complexation) is appropriate and agrees well with the *Al*-type phase-solubility diagrams obtained with both cyclodextrins. Stability constants were extracted from the absorbance data obtained with the different relative concentrations of cyclodextrins and DTT, by a nonlinear least-squares methodology (see Experimental Section). Care was taken to ensure that equilibria were reached before determination of the absorbances. Results, which are given in Table 2, are in satisfactory agreement with those obtained by phase-solubility measurements (Table 1). It is interesting to note that another treatment of the experimental data performed by considering also the molar absorptivity coefficient of the pure DTT as unknown gave the same value for that

grandeur than that determined experimentally (Table 2). This is a strong argument to validate the accuracy of both the chemical model, i.e., the model with one equilibrium, and the experimental data.

Differential Scanning Calorimetry—DSC revealed some information on solid-state interactions between both 1,2-dithiole-3-thiones ATT and 5PDTT and cyclodextrin SBE7βCD. DSC thermograms are presented in Figure 5.1 and 5.2. Table 3 sums up all the data obtained from DSC. The DSC scan of SBE7βCD showed a typical broad endothermic peak between 85 and 150 °C (only the range 85−130 °C is shown) corresponding to its dehydration. DSC thermograms of pure drugs exhibited a sharp endothermic peak corresponding to their melting point, at 109 °C (ΔH = 101.5 J/g) and 124.8 °C (ΔH = 125 J/g) for ATT and 5PDTT, respectively. Both characteristic peaks (due to cyclodextrin water loss and drug melting) were also clearly visible in the physical mixtures of ATT and 5PDTT with SBE7βCD, even if the melting endotherms were slightly shifted to 107 and 123.8 °C for ATT and 5PDTT, respectively. This may be due to an interaction between the two species occurring during their mixing. From the ΔH values obtained (8.1 and 10.25 J/g for ATT and 5PDTT, respectively) it was easy to obtain the percentage of free drug, from the following equation:

$$\% \text{ free drug} = [\Delta H_{DTT,CD} \times 100]/[\Delta H_{DTT} \times (DC)/100)] \quad (7)$$

where ΔH_{DTT} and $\Delta H_{DTT,CD}$ are the enthalpy values of pure drug and of drug from each system with cyclodextrins (physical mixture or spray-dried complex), respectively, and DC is the drug content (%) of each system. From eq 7, we could estimate that the percentage of complexed drug (100 − % free drug) concerned 20 and 7.45% of the drug present in the mixture, for ATT and 5PDTT, respectively. Concerning the spray-dried products obtained with both drugs, increasing the initial concentration of the complexing agent led to a more complete or a total dissappearance of the drug characteristic melting endotherm and also to a higher complexation efficiency (Table 3 and Figure 5). The endothermic peak of pure 1,2-dithiole-3-thione was found for each 1:1 mole ratio spray-dried product with ΔH values of 3.45 and 0.70 J/g, for ATT and 5PDTT, respectively, indicating the presence of 36.3 and 10.3% free drug, respectively. In fact, only DSC thermograms of 1:2 drug−cyclodextrin mole ratio products lacked the melting peak (corresponding to 98.7 and 100% of complexed drug, for ATT and 5PDTT, respectively). As the disappearance of an endothermic peak may be attributed to an amorphous state and/or to an inclusion complexation,[24] these results suggest that only 1:2 spray-dried products can be considered as true and complete inclusion complexes, differing from simple physical mixtures.

Scanning Electronic Microscopy—From SEM (Figure 6) we can see the particle morphology of pure compounds ATT and SBE7βCD (micrographs A and B, respectively), both irregular three-dimensional particles with parallelogram shape. The physical mixture (micrograph C) showed particles of SBE7βCD embedded with ATT particles and a comparable morphology with pure compounds taken separately, revealing no apparent interaction between both species. In contrast, a drastic change in the morphology and shape of particles was observed in 1:1 (micrographs D and E) and 1:2 (micrographs F and G) spray-dried products, revealing an apparent interaction in the solid state. Spherical microparticles obtained also showed a reduction in size due to the spray-drying process, confirmed by laser diffractometry where the median volume diameters d(v,0.5) obtained, i.e., 39.87 μm, 11.54 μm, and 63.53 μm for SBE7βCD, ATT, and their physical mixture, respectively, decreased to 4.13 μm and 3.85 μm for a 1:1 and 1:2 mole ratio of spray-dried products, respectively.

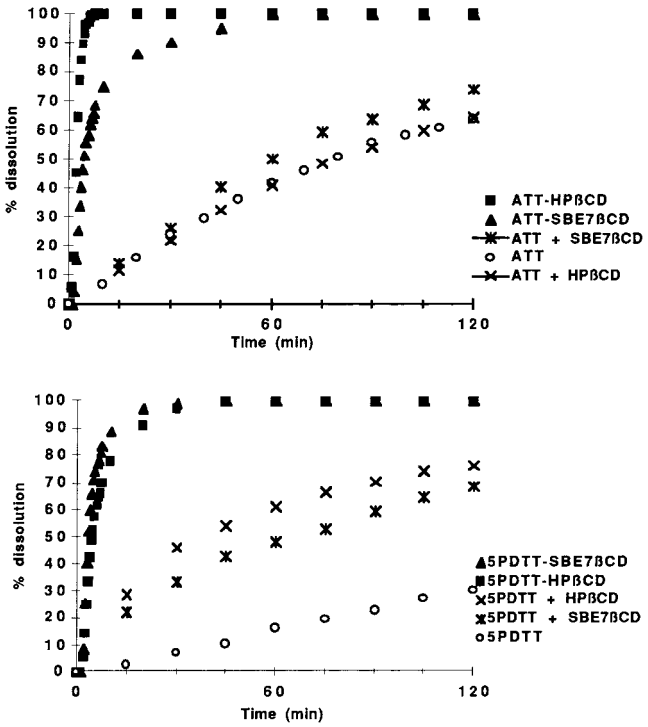

Figure 7—Dissolution rate profiles for ATT (top) and 5PDTT (bottom) systems with SBE7βCD or HPβCD. (○) 1,2-dithiole-3-thione alone; (*) physical mixture with SBE7βCD; (×) physical mixture with HPβCD; (▲) spray-dried complex with SBE7βCD; (■) spray-dried complex with HPβCD.

Dissolution Study—Dissolution profiles of pure ATT and 5PDTT, their 1:1 mole ratio physical mixtures, and spray-dried inclusion complexes with HPβCD and SBE7βCD are presented in Figure 7. From these curves we can see that all binary systems displayed an increase in drug dissolution rate with respect to pure drug. However, the dissolution enhancements of the drugs from the physical mixtures were not as marked, as they were from the spray-dried products (especially for ATT, the more lipophilic drug) and may be explained by mean of greater solubility of the drug in aqueous solution of cyclodextrins because of the hydrophilic environment surrounding the drug in the early stages of dissolution process, resulting in a better wettability of the drug. Concerning the significant enhancement of the dissolution rate that occurred with all spray-dried products, this may be attributed to an increase of solubility upon complexation, to the amorphous state generally occurring during spray-drying (i.e. a decrease in cristallinity), and to the reduction in the particle size resulting in an increase of the surface area of the drug, according to the Noyes−Whitney equation:[25]

$$dC/dt = D/h \times S\,(C_s - C_t) \quad (8)$$

where dC/dt is the dissolution rate, D is the diffusion coefficient of the drug, h is the thickness of the diffusion layer, S is the surface area of the dissolving solid, C_s and C_t are the aqueous solubility and the concentration of the drug in the aqueous medium at time t, respectively.

Conclusion

The present study showed that 1,2-dithiole-3-thiones could form inclusion complexes with β-cyclodextrin deriva-

tives, in solution as well as in the solid state, allowing an increase in solubility, a possible intravenous administration without using cosolvents, and also an increase in the dissolution rate of the drugs. These data shoud be of interest for improving oral absorption of these lipophilic compounds, allowing bioavailability and metabolism studies. An oral formulation allowing a chronic administration of these compounds for cancer chemoprevention is under investigation.

References and Notes

1. Jirousek, L.; Starka, L. Über das vorkommen von trithionen (1,2-dithiocyclopent-4-en- -3-thione) in brassica pflanzen. *Nature* **1958**, *45*, 386−387.
2. Laboratoire de Thérapeutique Moderne: Suresnes, France.
3. Ansher, S. S.; Dolan, P.; Bueding, E. Biochemical effects of dithiolethiones. *Food Chem. Toxicol.* **1986**, *24*, 405−415.
4. Egner, P. A.; Kensler, T. W.; Prestare, T.; Talalay, P.; Libby, A. H.; Joyner, H. H.; Curphey, T. J. Regulation of phase II enzyme induction by oltipraz and other dithiolethiones. *Carcinogenesis* **1994**, *15*, 177−181.
5. Gupta, E.; Olopade, O. I.; Ratain, M. J.; Mick, R.; Baker, T. M.; Berezin, F. K.; Benson, A. B.; Dolan, M. E. Pharmacokinetics and pharmacodynamics of oltipraz as a chemopreventive agent. *Clin. Cancer Res.* **1995**, *1*, 1133−1138.
6. Crowell, J. A.; Page, J. G.; Rodman, L. E.; Heath, J. E.; Goldenthal, E. I.; Hall, L. B.; Kelloff, E. I. Chronic toxicity studies of 5-(2-pyrazinyl)-4-methyl-1,2-dithiole-3-thione, a potential chemopreventive agent. *Fundam. Appl. Toxicol.* **1997**, *35*, 9−21.
7. Bona, M.; Boudeville, P.; Zekri, O.; Christen, M. O.; Burgot, J.-L. Water/*n*-octanol partition coefficients of 1,2-dithiole-3-thiones. *J. Pharm. Sci.* **1995**, *84*, 1107−1112.
8. Boudeville, P.; Bona, M.; Burgot, J.-L. Correlations between *n*-octanol/water partition coefficients and RP-HPLC capacity factors of 1,2-dithiole-3-thiones and 1,2-dithiol-3-ones. *J. Pharm. Sci.* **1996**, *85*, 990−998.
9. Wils, P.; Warnery, A.; Phung-Ba, V.; Legrain, S.; Scherman, D. High lipophilicity decreases drug transport across intestinal epithelial cells. *J. Pharmacol. Exp. Ther.* **1994**, *269*, 654−658.
10. Amidon, G. L.; Lennernäs, H.; Shah, V. P.; Crison, J. R. A. Theoretical basis for a biopharmaceutics drug classification: the correlation of in vitro drug product dissolution and in vivo bioavailability. *Pharm. Res.* **1995**, *12*, 413−420.
11. Duchêne, D. *Cyclodextrins and their industrial uses*; Editions de Santé: Paris, 1987.
12. Loftsson, T.; Brewster, M. E. Pharmaceutical applications of cyclodextrins. 1. Drug solubilization and stabilization. *J. Pharm. Sci.* **1996**, *85*, 1017−1025.
13. Hirayama, F.; Uekama, K. *Cyclodextrins and their industrial uses*; Editions de Santé: Paris, 1987.
14. Rajewski, R. A.; Stella, V. J. Pharmaceutical application of cyclodextrins. 2. In vivo drug delivery. *J. Pharm. Sci.* **1996**, *85*, 1142−1169.
15. Müller, B. W.; Brauns, U. Solubilization of drug by modified β-cyclodextrins. *Int. J. Pharm.* **1985**, *26*, 77−88.
16. Rajewski, R. A.; Traiger, G.; Bresnahan, J.; Jaberaboansari, P.; Stella, V. J.; Thompson, D. O. Preliminary safety evaluation of parenterally administered sulfoalkyl ether β-cyclodextrin derivatives. *J. Pharm. Sci.* **1995**, *84*, 927−932.
17. Higuchi, T.; Connors, K. A. Phase-solubility techniques. *Adv. Anal. Chem. Instr.* **1965**, *4*, 117−212.
18. Lefeuvre, C.; Le Corre, P.; Dollo, G.; Chevanne, F.; Burgot, J.-L.; Le Verge, R. Biopharmaceutics and pharmacokinetics of potential cancer chemopreventive agent 5-phenyl-1,2-dithiole-3-thione complexed with sulfobutyl ether-7-β-cyclodextrin in rabbits. *J. Pharm. Sci.*, in press.
19. Boudeville, P.; Burgot, J.-L. A new pH-metric methodology for the determination of thermodynamic inclusion constants of guest/cyclodextrin complexes. *J. Pharm. Sci.* **1995**, *84*, 1083−1089.
20. Chollet, M.; Legouin, B.; Burgot, J.-L. Assessment of the substituent constants of the 3-thioxo-1,2-dithiol-4- and -5-yl groups through pK_a values measurements of 4 and 5-(hydroxy- or amino-phenyl)-1,2-dithiole-3-thiones in water at 298 K. *J. Chem. Soc., Perkin Trans. 2* **1998**, 2227−2231.
21. Okimoto, K.; Rajewski, R. A.; Uekama, K.; Jona, J. A.;.Stella, V. J. The interaction of charged and uncharged drugs with neutral (HPβCD) and anionically charged (SBEβCD) β-cyclodextrins. *Pharm. Res.* **1996**, *13*, 256−264.
22. Green, A. R.; Guillory, J. K. Heptakis(2,6-di-*O*-methyl)-β-cyclodextrin complexation with the antitumor agent chlorambucil. *J. Pharm. Sci.* **1989**, *78*, 427−431.
23. Pedersen, K. Th. 1,2-dithiole-3-thiones and 1,2-dithiol-3-ones. *Sulfur Rep.* **1995**, *16*, 173−221.
24. Kurozumi, M.; Nambu, N.; Nagai, T. Inclusion compounds of non steroidal antiinflammatory and other slightly water soluble drugs with α and β-cyclodextrins in powered form. *Chem. Pharm. Bull.* **1975**, *23*, 3062−3068.
25. Noyes, A. A.; Whitney, W. R. The rate of solution of solid substances in their own solutions. *J. Am. Chem. Soc.* **1897**, *19*, 930.

JS990067O

O-Ethylphosphatidylcholine: A Metabolizable Cationic Phospholipid Which Is a Serum-Compatible DNA Transfection Agent

ROBERT C. MACDONALD,* VERA A. RAKHMANOVA, KENNETH L. CHOI, HOWARD S. ROSENZWEIG,† AND MARC K. LAHIRI

Contribution from *Department of Biochemistry, Molecular Biology and Cell Biology, Northwestern University, Evanston, Illinois 60208*

Received January 8, 1999. Final revised manuscript received April 26, 1999.
Accepted for publication June 12, 1999.

Abstract □ 1,2-Dioleoyl-*sn*-glycero-3-ethylphosphocholine was prepared in a one-step reaction from phosphatidylcholine by reaction with ethyl trifluoromethanesulfonate. This and related *O*-alkyl phosphatidylcholines constitute the first chemically stable triesters of biological lipid structures and the first cationic derivatives of phospholipids consisting entirely of biological metabolites linked with ester bonds. The complex of cationic phospholipid and plasmid DNA transfected cells with high efficiency. Maximum efficiency of transfection was obtained with complexes in which the positive charge was a few percent in excess over the negative charge. Modest stimulation of transfection of common cell lines was obtained by continuous culture in the presence of 10% serum. Incubation of the phospholipid complex for at least 2 h at 37 °C in nearly pure serum had no deleterious effects on transfection efficiency. The lipid has low toxicity; BHK cells tolerated amounts of 2 mg/2 × 10^6 cells at concentrations of 1 mg/mL. The lipid is biodegradable; it was hydrolyzed by phospholipase A_2 in vitro and was metabolized with a half-life of a few days in cells in culture. The synthetic route to cationic phospholipids is well suited to the preparation of derivatives that are tailor-made to have a wide variety of different properties.

Introduction

Since the demonstration that membrane lipids and other amphipaths of similar structure form closed, membrane-bounded vesicles or liposomes,[1] these structures have been used in many applications.[2] Most recently, dispersions of cationic amphipaths have been used to deliver DNA to cells,[3,4] an application that could become important clinically. Although cationic liposomes were reported to be potential cellular delivery vehicles many years ago,[5−8] it was not until their efficiency in DNA delivery was recognized[9,10] that they have been widely used for that purpose. Cationic lipids are particularly effective in packaging DNA because interactions with the positive surfaces lead to formation of a rather compact particle with a high content of DNA, now frequently termed a "lipoplex".[11] In addition to their uses as DNA delivery agents for gene therapy,[12] cationic lipids may find important applications in the delivery of antisense oligonucleotides.[13] Proteins and small molecules can also be delivered to cells as cationic complexes.[14−17]

The mode of delivery of DNA to the nucleus by cationic lipids remains to be elucidated, although endocytosis is generally accepted as the major route of cellular uptake. For in vitro applications, the cationic lipids are often combined with 1,2-dioleoyl-*sn*-glycero-3-phosphoethanolamine (DOPE), without which activity is frequently low; however, in vivo[18] or in vitro in the presence of serum,[19] cholesterol is a much more effective helper lipid. The need for DOPE has been rationalized on the basis of the tendency of this lipid to destabilize lamellar phase lipids, and it could be such an activity that facilitates escape from endosomal compartments.[20] However, some form of neutralization, perhaps by cellular lipids[21] or other cellular molecules of the cationic lipid must occur for the DNA to be released from the complex.

The correlation between in vivo and in vitro activity is generally very poor, in part because many barriers are presented to the delivery vehicle by the whole organism that do not exist in the in vitro situation. One set of such factors is due to serum, which contains, among others, proteins that can bind to the surface of the complex, lipids that can mix with or extract the lipid, and nucleases that can degrade the DNA. One test of whether the lipoplex can survive exposure to serum is to measure transfection of cultured cells in the presence of 10% serum. Even at this dilution, serum inactivates many lipoplexes, however, methods have been devised to modify the formulation of some lipoplexes so that their resistance to interference by serum is greatly enhanced.[19,22−25] Recent evidence is beginning to suggest that the complex may remain intact in serum and that the main effect of serum is to reduce cellular uptake.[19,26]

With few exceptions,[27] most cationic "lipids" are synthetic compounds that are physically similar but chemically different from natural polar lipids. The compound described here is an ethyl ester of the common cellular lipid phosphatidycholine, and hence consists of only normal cellular metabolites linked with ester bonds. It exhibits low toxicity and, given its resistance to serum, may be well suited for clinical applications involving gene and drug therapy. A closely related cationic lipid has, in fact, been found to be an efficient gene delivery agent in vivo.[28]

Materials and Methods

Synthetic Methods—1,2-Dioleoyl-*sn*-glycero-3-phosphocholine (DOPC) in $CHCl_3$ was treated at room temperature with 3 (typically) mole equivalents of ethyl triflate (ethyl trifluoromethanesulfonate, Aldrich), and the mixture was allowed to react for several hours under dry argon. In some cases, 0.5−1 mol equivalent of the hindered base, 4-methyl-2,6-di-*tert*-butylpyridine, was included to ensure more complete reaction. The reaction mixture was applied to a silica gel column that was washed with $CHCl_3$, and the product was eluted with $CHCl_3$:MeOH (9:1). Purity and identity of the product were verified by thin-layer chromatography (TLC) and mass spectral (MS) analysis, respectively.

* Corresponding author, E-mail: macd@nwu.edu. Tel: 847 491-5062. Fax: 847 467-1380.
† Current address: Wesley Jessen, Inc., Des Plaines, IL.

10.1021/js990006q CCC: $18.00
Published on Web 08/03/1999

This reaction was also used to convert 1-oleoyl-2-[12-[(7-nitro-2-1,3-benzoxadiazol-4-yl)amino]dodecanoyl]-*sn*-glycero-3-phosphocholine (Avanti), 1,2-dipyrenbutanoyl-*sn*-glycero-3-phosphocholine (DPYPC), and 1-alkyl-2-pyrenebutanoyl-*sn*-glycero-3-phosphocholine to the corresponding fluorescent cationic phospholipids, 1-oleoyl-2-[12-[(7-nitro-2-1,3-benzoxadiazol-4-yl)amino]dodecanoyl]-*sn*-glycero-3-ethylphosphocholine (ENBDPC), 1,2-dipyrenbutanoyl-*sn*-glycero-3-ethylphosphocholine (EDPYPC), and 1-alkyl-2-pyrenebutanoyl-*sn*-glycero-3-ethylphosphocholine, respectively. The latter two compounds were prepared by standard methods. The dipyrene compound was prepared by diacylation of glycerophosphorylcholine[29] and the monopyrene compound was prepared by monoacylation of alkyl lysophosphatidylcholine,[30] both with pyrenebutanoic anhydride that was synthesized from pyrene butanoic acid (Aldrich) according to Selinger and Lapidot.[31]

Lipid Dispersions—Lipids were stored at −20 °C in chloroform. Solvent was removed with a stream of argon followed by high vacuum for at least 30 min. The appropriate aqueous solution was then added, and the tube was vortexed. When used for transfection, normally the aqueous phase was Dulbecco's phosphate-buffered saline (D-PBS; containing calcium and magnesium) and the lipid concentration was 1 mg/mL. The molecular weight of EDOPC triflate is 964 g/mol, so that a 1 mg/mL dispersion is very close to 1 mM.

Enzyme-Catalyzed Hydrolysis—*Activity of Known Phospholipases*—To examine the enzymatic hydrolysis of a cationic phospholipid, ENBDPC, dispersed as liposomes, was incubated with partially purified enzymes,[32] and the reaction was followed by TLC. The enzymes examined were: phospholipase A_2 from *Naja naja* venom, phospholipase C from *Clostridium perfringens*, and phospholipase D from *Streptomyces chromofuscus*, Savoy cabbage, peanuts, and Brussels sprouts. All enzymes were from Sigma except the last, which was prepared according to Christie.[32]

Phospholipase A_2 Activity In Vitro—The procedure used is standard.[33] In brief, 5 mg of lipid in 100 μL of ethyl ether was combined with 10 μL of borate buffer containing 250 μg of calcium acetate and 6 units of phospholipase A_2 from either snake venom (Naja naja) or bee venom (*Apis mellifera*). The mixture was incubated at 37 °C, and samples were removed at desired intervals and analyzed by TLC on silica gel plates developed in chloroform: methanol:water (65:25:4). Reaction products were visualized by iodine staining, fluorescence quenching of fluor incorporated in the plates, or by intrinsic fluorescence of the compound itself.

The rate of hydrolysis of EDPYPC by phospholipase A_2 was quantified with a fluorescence assay,[34] modified to include detergent.[35] The hydrolysis of 0.6 μM EDPYPC in 0.1 M NaCl, 5 mM $CaCl_2$, 5 mM Tris (pH 7) buffer containing 10 mM cholate by phospholipase A_2 from *Apis mellifera* bee venom (Sigma) was measured with a Farrand spectrofluorometer with 5-nm slit widths. Various amounts of enzyme, up to 160 units, were used. At an excitation wavelength of 350 nm, emission spectra were recorded to encompass the monomer (400 nm) and excimer (480 nm) emission peaks, as well as sufficient additional lower wavelength portions of the emission spectrum to allow subtraction of the background from the peak values for the monomer. Enzyme activity was determined from changes in fluorescence intensity using 4-(1-pyrenyl) butyric acid as a standard. Porcine pancreas lipase gave measurable, but lower activity than bee venom. Triton X-100 was also tested as a detergent in this assay and found to be inferior to cholate.

Phospholipase Activity in Cells—To test for degradation of the cationic phospholipid in cultured cells, 50 μg of fluorescent ENBDPC combined with 50 μg of 1,2-dioleoyl-*sn*-glycero-3-ethylphosphocholine (EDOPC) was incubated with BHK cells in 25-cm^2 culture dishes. A second set of experiments was done using lipid complexed 3:1 by weight with DNA (COT-1 DNA from Life Technologies). The lipid or lipid−DNA complexes were incubated with cells for 6 h in the presence of serum-free medium, following which bovine serum was added to 10%. After 1, 3, and 7 days, the cells and the medium (separately) were extracted to isolate total lipids. After removing the medium, the cells were washed with 2.5 mL of D-PBS and then removed from the dish by scraping with a rubber policeman. Then 2.5 mL of chloroform−methanol (2:1) were added to both the medium and cell suspensions. The lower chloroform phase was removed, and the aqueous phase was re-extracted with 3.0 mL of chloroform−methanol−water (2:1:0.8). The chloroform phases were combined, the solvent removed under an argon steam, and the residue dissolved in a known volume of chloroform.[33] The lipids were analyzed by TLC and visualized using long-wave ultraviolet (uv) light. Cells treated and grown under the same conditions were also examined by fluorescence microscopy to determine the distribution of the fluorescent cationic lipid. Similar experiments were done with L-cells.

To verify that the degradation observed was not limited to the NBD derivative, the procedure just described was also carried out with two other fluorescent derivatives of a generic cationic phospholipid (PC+), EDPYPC, and 1-alkyl-2-pyrenebutanoyl-*sn*-glycero-3-ethylphosphocholine.

Transfection Mediated by Cationic Phospholipids—*Standard Procedure*—BHK cells were transfected with plasmid coding for green fluorescent protein (pGreen Lantern-1, Life Technologies) or with plasmid carrying the β-galactosidase gene (pCMV-βgal; Life Technologies). Complete medium was Glasgow minimal Eagle's medium (GMEM) containing 10% fetal bovine serum, 2 mM glutamine, 2% tryptose phosphate, and 50 mg/L of Gentamycin. The cells were seeded at densities to give ∼70% confluence at the time of transfection and incubated at 37 °C under 5% CO_2. Normally, the lipids were suspended in D-PBS at 1 mg/mL and added to the plasmid DNA at 0.1 mg/mL in D-PBS, except as stated otherwise, and incubated at room temperature for 20−30 min. The DNA−lipid complex was added to the cells that were either in medium with 10% fetal bovine serum or in medium lacking serum (total volume bathing cells was 100 μL). In the latter case, 1/10 volume of bovine serum was added to each well after 4−6 h in the incubator. Then, 20−24 h after treatment with the DNA−lipid complex, the cells were assayed for expression of the reporter gene. Expression of green fluorescent protein was monitored by fluorescence microscopy. Measurement of β-galactosidase level in transfected cells was performed by a microplate fluorimetric assay.[36] To date, optimum conditions yield 10−15 milliunits of enzyme activity per well of a 96-well plate. The X-gal (5-bromo-4-chloro-3-indolyl β-galactopyranoside) procedure was used to determine the number of tranfected cells histochemically.[37] Viability of cells after treatment by cationic lipids and lipid−DNA complexes was assessed by staining cells with trypan blue and counting them in a hemacytometer.

For comparison of toxicity and transfection efficiency in the same experiment, replicates of four were used. Twenty hours after transfection, the cells of two replicates were trypsinized for viability determination. The cells from two other replicates were assayed for β-galactosidase activity.

Incubation of Transfection Complexes in Serum—First, 1.2 μL of cationic lipid suspension (10 mg/mL) was added to 4 μL of plasmid solution (1 mg/mL). After 20 min at room temperature, the complex was incubated in 100 μL of fetal bovine serum (not heat inactivated) from 30 min to 2 h at 37 °C. Each cell sample of a 96-well plate was transfected with lipid−DNA complex containing 1.5 μg of cationic lipid and 0.5 μg of plasmid DNA (i.e., 13 μL of the serum−lipid−DNA incubation mixture). The measurement of transfection efficiency was performed as usual.

Assay for Protection of DNA in Transfection Complexes from DNase—A suspension of lipid−DNA complex (3:1, wt/wt) was prepared from EDOPC (10 mg/mL) and plasmid DNA (1 mg/mL) as already described. The EDOPC−DNA complex was then diluted in fetal bovine serum (not heat inactivated) or in D-PBS at a 1:20 ratio and incubated for 2 hs at 37 °C. As a control, plasmid DNA alone was incubated under identical conditions. The incubations were stopped by dilution into gel-loading buffer containing 0.25% bromophenol blue, 0.25% xylene cyanol FF, and 30% glycerol and by addition of sodium dodecyl sulfate to a final concentration of 1%, which also released the DNA from the cationic lipid. Afterward, the samples were electrophoresed through a 1% agarose gel and visualized by ethidium bromide staining.

To test the sensitivity of the complex to restriction endonuclease, plasmid DNA or EDOPC−DNA complex containing the same amount of DNA (4 mg) was treated with 12 units of Eco RI in a total volume of 6 μL of high salt restriction enzyme buffer. The samples were incubated for 2 h at 37 °C and diluted with D-PBS to a final volume of 100 μL. After addition of gel-loading buffer and sodium dodecyl sulfate, they were analyzed by electrophoresis on a 1% agarose gel as already described.

Fluorescence Microscopy of Lipid and DNA Uptake by Cells—BHK cells were grown in 35-mm culture dishes according to conditions already described. To generate fluorescent lipid mixtures, *N*-lissamine-rhodamine-B-phosphatidylethanolamine (RhPE) or ENBDPC was mixed with EDOPC in chloroform,

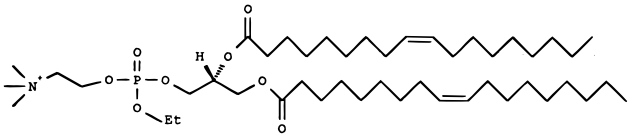

Figure 1—Structure of the cationic phospholipid EDOPC.

usually at 2.5−5 mol % fluorescent lipid. Mouse COT-1 DNA (50−300 bp) was used as is at 1 mg/mL in water or labeled with one of the high-affinity intercalating dyes, YOYO-1 or ethidium homodimer, at a ratio of 2 nanomol of dye per 10 μg of DNA. To verify that the pattern of DNA fluorescence seen in cells was not unique to COT-1 DNA labeled with an intercalating dye, we did additional experiments of this type using the standard plasmid DNA (pCMV-βgal) that was covalently labeled with Alexa maleimide dye with the FastTag Reagent (Vector Laboratories). For these experiments the lipid label was reduced to 0.5 mol % of RhPE to avoid dissimilar intensities of lipid and nucleic acid fluorescence.

Results

***O*-Alkylation of Phospholipids with Alkyl Trifluoromethanesulfonates (Triflates)**—Triflates react with phospholipids (e.g., DOPC) to generate *O*-alkyl derivatives (Figure 1). The reaction was complete in a few hours or less at room temperature, with yields up to 90%. The alkylated product migrates on silica gel plates with a R_f of 0.56 and was well separated from the reactant, which migrates with a R_f of 0.32 in a developing solvent of chloroform−methanol−water, 65:25:4. The structure of the product was verified by proton nuclear magnetic resonance (NMR) and MS analysis. The characteristic new absorption for the *O*-ethyl compound is a double quartet (one quartet for each molecule of the diastereomeric pair) at ~4.2 ppm. It may be mentioned that the reaction with ethyl triflate is not unique, and the reaction of phosphatidylcholines with other alkyl triflates having chain lengths as long as C_{18} (prepared from the corresponding alcohol and triflic anhydride[38]) has also been found to proceed smoothly.[39]

Cationic Phospholipid Stability and Metabolism—Although the experiments reported here were mostly done using material that was synthesized within the previous year, material was on hand from some early syntheses, having been stored in chloroform at −20° for nearly 5 years. Using current conditions for transfection, this material was found to have retained its ability to mediate transfection of DNA. According to TLC results, there was no detectable breakdown over that time period. As an aqueous dispersion, EDOPC can be stored for at least 3 months in the freezer without significant loss in transfection efficiency. This lipid is thus more than adequately stable for a wide variety of applications as a gene transfer agent.

Although stable to hydrolysis in the absence of a catalyst, cationic phospholipids are degraded by some purified phospholipases. ENBDPC was treated with purified phospholipases from various sources by standard procedures. Hydrolysis was established by TLC of the reaction mixture. Reaction in the presence of phospholipase C (Clostridium) was too slow to be detected under our conditions. Phospholipase D (cabbage) produced slow degradation of ENBDPC. The product of this reaction has not been unambiguously identified, but based on its R_f, phosphatidylethanol appears to be the only possibility. Phospholipase A_2 (cobra and bee venom) catalyzed the release of the NBD fatty acid. This reaction was also investigated with EDPYPC, the reaction of which could be monitored in the fluorimeter.

Figure 2 shows the extent of phospholipase A_2-catalyzed hydrolysis of EDPYPC (*O*-ethyl cationic phospholipid with two pyrene butanoic acyl substituents in place of fatty acyl chains) as a function of time. The intact molecule exhibits

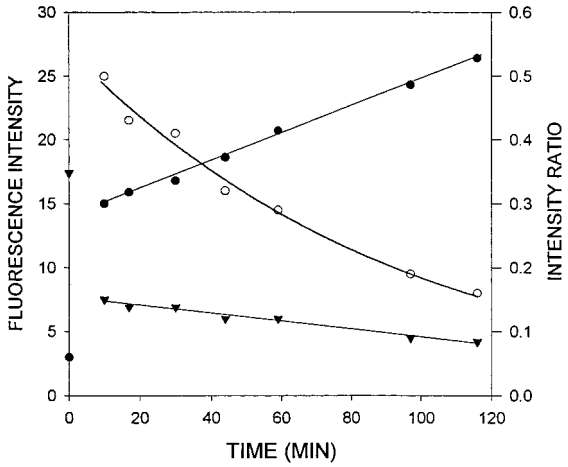

Figure 2—Time course of hydrolysis of dipyrenbutanoyl cationic phospholipid by phospholipase A_2. Hydrolysis of the pyrene-labeled fluorogenic phospholipase substrate is indicated by the increase in monomer emission (solid circles) and decrease in the excimer emission (triangles) as one of the pyrenebutanoic acid moieties is removed from the phospholipid. The substrate was dispersed in Tris buffer containing cholate, calcium ion and phospholipase A_2. The ratio of monomer to excimer emission intensity is given by the open circles.

excimer emission at 480 nm, whereas pyrene moieties that are not in contact with each other emit at 400 nm. Thus, hydrolysis can be quantified according to the rate of decrease in eximer emission and increase in monomer emission. The fluorescence intensity of the monomer (closed circles) increases markedly, but that of the excimer (triangles) falls modestly, as does the ratio of the former to the latter (open circles). This pattern shows that one of the pyrene acyl chains was removed from the molecule, for as hydrolysis occurs, the pyrene butanoic acid becomes diluted into detergent such that its emission as a monomer increases and concomitantly the excimer dissociates, leading to a reduction of its emission. Because there was initially little monomer and much excimer, the fractional change in monomer emission was large and that of the excimer was small.

The generation of product was linear for 2 h, as shown in Figure 2, however, abrupt changes in both monomer and excimer intensities are seen at very early times. This result could be due either to hydrolysis of the first molecules that bind to the enzyme followed by a steady-state rate dictated by a slower dissociation of the product from the enzyme or by a change in the conformation of the substrate—and thus in the probability of excimer formation—as the substrate binds to the enzyme (or perhaps other proteins in the solution). The average hydrolysis rate catalyzed by amounts of enzyme ranging from 40 to 160 units, as measured in experiments such as that of Figure 2, was 66 pmol/h/mg.

Comparison of the rate of hydrolysis of dipyrenebutanoylphosphatidylcholine with that of the cationic compound of Figure 2 showed that the cationic lipid was hydrolyzed at a rate ~40 X slower than that of the zwitterionic compound.

Using TLC, we determined the approximate relative rates of hydrolysis of dioleoylphosphatidylcholine and dipyrenebutanoylphosphatidylcholine. The procedure involved reducing the amount of enzyme used with the former substrate until the amount of product generated in a convenient reaction time (few hours) was approximately the same as that generated from the latter substrate. Based on this experiment, we estimate that pyrene butanoic acid was removed from phosphatidylcholine 1−2 orders of magnitude more slowly than was oleic acid. This result is not surprising, because others who have used the pyrene excimer assay have reported that when the pyrene group

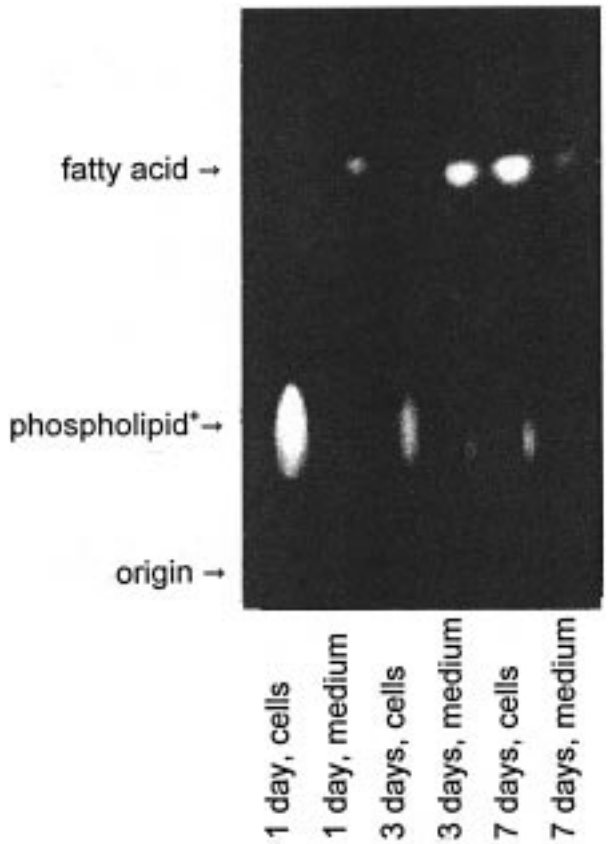

Figure 3—Cationic phospholipid degradation by cells. BHK cells were treated with a DNA–lipid complex in which the lipid was fluorescent (one acyl chain was NBD-dodecanoyl) and incubated with cells. Cells and medium were extracted with chloroform–methanol after 1, 3, and 7 days. The extracts were chromatographed, yielding the thin layer chromatogram shown, which was imaged under fluorescence illumination. Extent of degradation is indicated by growth of the upper spot and diminution of the lower spot.

is close to the ester bond, it reduces reactivity by about one order of magnitude.[40]

In addition to being susceptible to hydrolysis by isolated enzymes, PC+ is degraded by cells, as shown in Figure 3, which is the image of a TLC plate of extracts of ENBDPC that had been combined with DNA (1:1, by charge) and incubated with BHK cells for up to 7 days. Hydrolysis of ENBDPC (lower spot) to NBD−dodecanoic acid (upper spot) and lysoPC+ (not fluorescent) was detectable in the medium after 1 day, in cells after 3 days, and was very extensive in both cells and medium after 7 days. The amount of PC+ in the cells decreased drastically, whereas the fatty acid concentration in the cells rose considerably. In the same way, we also examined the hydrolysis of ENBDPC that had been presented to cells in the absence of DNA. Although there were some perceptible differences in the TLC pattern, essentially the same result was obtained, namely, the cationic phospholipid was largely metabolized within a week under culture conditions. To verify that hydrolysis of the cationic lipid was not limited to the NBD derivative, experiments identical to those of Figure 3 were done with EDPYPC and with 1-alkyl-2-pyrenebutanoyl-*sn*-glycero-3-ethylphosphocholine. These compounds were degraded to essentially the same extent as was the NBD-containing substrate. Furthermore, using the same methods, we found mouse L-cells also hydrolyze ENBDPC.

Transfection of DNA Mediated by EDOPC—To assess transfection efficiency of EDOPC, β-galactosidase and, to a lesser extent, green fluorescent protein were used as reporter genes. Cells used for routine assays were BHK,

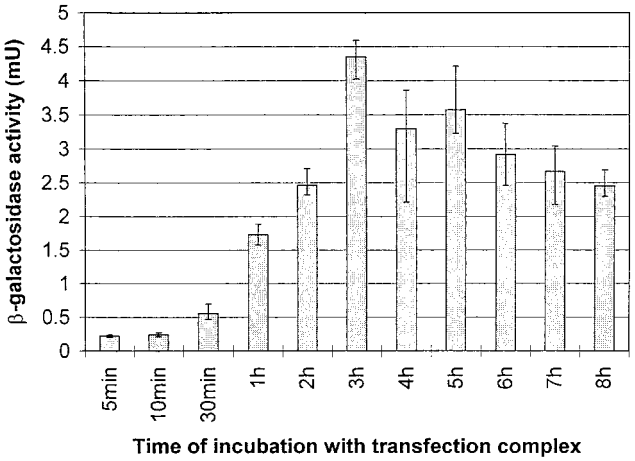

Figure 4—Time course of expression of β-galactosidase following delivery of EDOPC–DNA complex to BHK cells. EDOPC–DNA in amounts of 1.5 μg of EDOPC and 0.5 μg of DNA per well was incubated with BHK cells for various times (5 min to 8 h) as shown in the figure. The total volume of medium in each well was 100 μL. The medium with transfection complex was then aspirated and replaced with medium containing 10% fetal bovine serum. The efficiency of transfection was determined by the standard method. Bars show high and low values of three replicates.

but we also carefully examined the response of CHO cells and did less extensive examination of several other common cell lines. Transfected cells were visualized for expression of green fluorescent protein by fluorescence microscopy. For histochemical detection of β-galactosidase, the X-gal substrate was used. A large proportion of cells—up to 50% of the total—expressed β-galactosidase.

The quantitative assay for β-galactosidase used most frequently was microplate fluorimetry of fluorescein di-β-galactoside as the substrate. As shown in Figure 4, a 3−5 h incubation with EDOPC−β-galDNA complexes was sufficient for maximum expression of β-galactosidase in BHK cells. With both CHO and BHK cells, we found EDOPC gave slightly more transfection than did Lipofectamine at optimal dose and lipid−DNA ratio, although the optimal dose for EDOPC was typically somewhat larger than that for Lipofectamine. Transfection efficiency of EDOPC was rather weakly dependent on the ratio of cationic amphipath to DNA and on the total amount of complex added to cells. For a 3:1 ratio of lipid to DNA (3% excess positive charge), the activity was maximal at 3 and 1.5 μg of lipid per well. With increasing lipid-to-DNA ratio, the transfection efficiency gradually decreased. The underivatized DOPC was devoid of cell transfection activity; β-galactosidase expression in BHK cells treated with DOPC−DNA complexes was the same as background (data not shown).

Figure 5 depicts the relationship between dose of complex and transfection efficiency as well as cell viability, both in the presence and absence of serum. When the cells were cultured in the presence of serum for the entire time (upper panel), expression was higher than when serum was absent for the first 4 h of contact with the transfection complex, except at the lowest doses. This effect seems to be largely due to the better growth of cells in the presence of serum during the entire growth period, as is shown by the cell number data in Figure 5. The points connected by lines in the figure represent the number of live (trypan blue-excluding) BHK cells in wells that were treated with the same amount of transfection complex as those that were assayed for β-galactosidase. As the dose of lipid−DNA complex was increased beyond 1.5−3 μg/well (15−30 μg/mL of lipid or 5−10 μg/mL of DNA), enzyme expression tended to be maintained, even though there was some reduction in cell number, indicating a higher expression per cell.

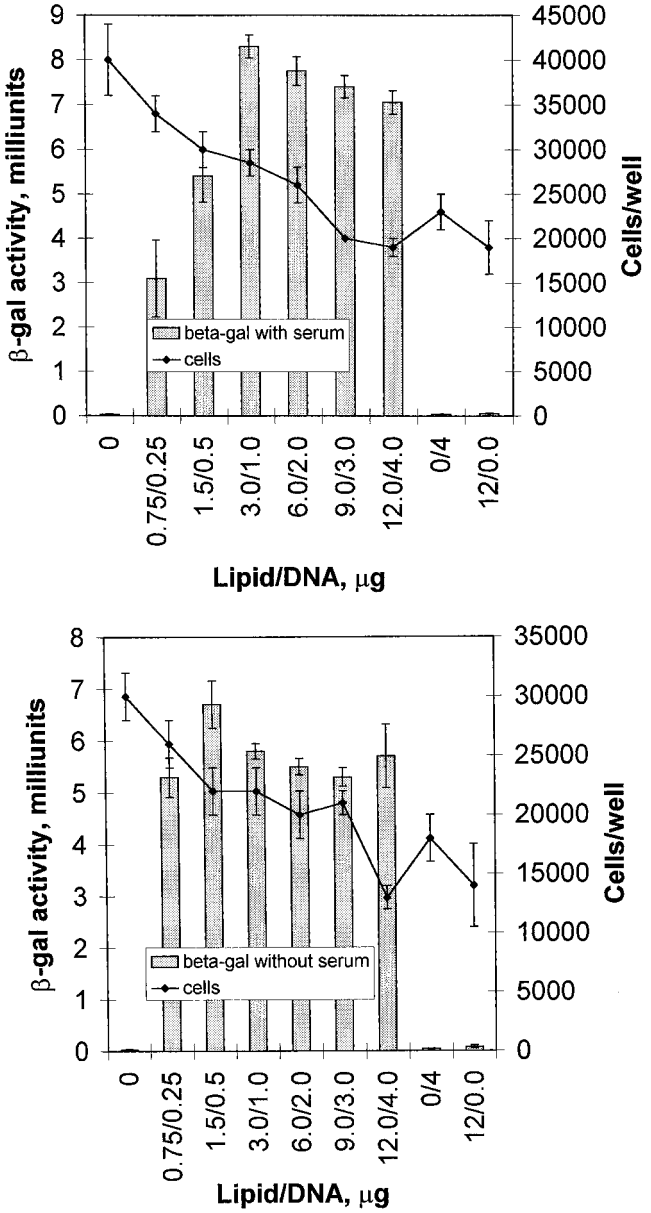

Figure 5—Transfection activity and toxicity of cationic phospholipid as a function of dose, with and without 10% serum. The figures show the level of expression of β-galactosidase (bars) and viable cells (line) for different amounts of lipid–DNA complex (in μg as shown on the horizontal axis) incubated with BHK cells in 96-well plates. The lipid:DNA ratio was 3:1 by weight in all cases, corresponding to a 3% excess of positive charge, except in the case of the control experiments corresponding to the last two bars. Volume per well was 100 μL. Upper panel: Serum present during entire incubation. Lower panel: Serum not present during first 4 h of incubation. Bars show high and low values of three replicates.

The cell number data of Figure 5 indicate that EDOPC has low toxicity because, although the number of viable cells was reduced to about half the initial number at doses of ~10 μg/well, this is a large dose, corresponding to ~2.5 mg of lipid in a 10-cm^2 Petri dish. By this test, EDOPC is ~30 times less toxic than Lipofectamine. The cell number counts in Figure 5 represent a lower limit, because it appears that cationic lipids reduce cell adhesion and some live cells are lost in washing procedures. The effects on cell viability of EDOPC and DNA separately were also examined and found not to differ greatly from that of the complex (two bars on far right of figure).

Addition of DOPE and cholesterol to EDOPC, in amounts >10 mol % at a constant ratio of EDOPC to DNA, reduced transfection. The lack of stimulation by DOPE was surprising given that most cationic amphipaths are nearly inactive in the absence of DOPE, [20,41,42] although at 1:1, DOPE had the smallest inhibitory effect (25−50%) relative to higher or lower amounts.

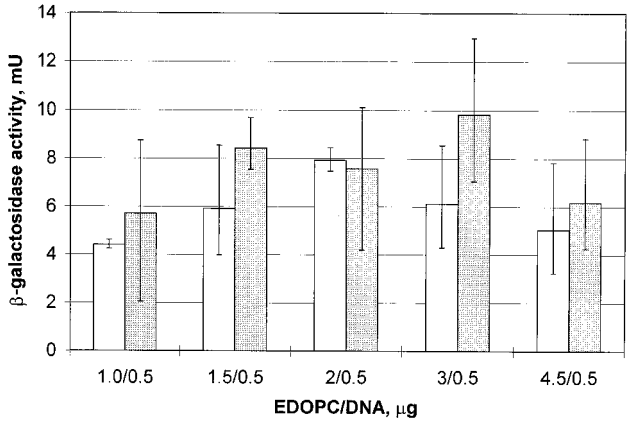

Figure 6—Effect of 10% serum on transfection efficiency as a function of the EDOPC:DNA ratio. EDOPC–DNA complexes were prepared according to the standard protocol using different lipid:DNA ratios. Transfection complexes with 2:1, 3:1, 4:1, 6:1, and 9:1 EDOPC:DNA weight ratios were then applied to BHK cells in medium without supplements (□) and to the cells in medium with 10% fetal bovine serum (■). Volume per well was 100 μL. Bars show high and low values of three replicates.

The EDOPC−DNA complex could be kept in the freezer or at room temperature for at least 3 days without loss of transfection efficiency. The ionic strength of the medium in which the complex was formed could be varied from the lowest value that was easily accessible, namely water, to a physiological value, namely D-PBS; however, this change in conditions had no significant effect on the transfection efficiency of the resultant complex.

Although not described in detail here, the phase state of the lipid appears to be important for transfection. We have examined EDPPC (the *O*-ethyl derivative of dipalmitoylphosphatidylcholine), a derivative that has a chain-melting phase transition temperature of ~40 °C. It was clear from the very low transfection efficiency of EDPPC that the phospholipid must be in the liquid phase to form an effective transfection complex.[43] In addition, extending the alkyl chain to a decyl group, which generates a lipid that resides in the hexagonal lyotropic phase, markedly altered the conditions for formation of transfection complexes with optimal activity.[39]

Another parameter likely to affect transfection efficiency is particle size. Based on dynamic light scattering, the number average particle size of the complex made under standard conditions is ~300 nm. The particle structure, according to both X-ray scattering and electron microscopy, is lamellar, consisting of DNA strands interspersed between lipid bilayers,[43] as are other complexes with low or no proportions of DOPE.[44,45]

To determine if DNA delivery to the nucleus by cationic phospholipid complexes depends on endocytosis and normal vesicle movement in the cell, we performed transfection with compounds that affect intracellular vesicle traffic. Preincubation of cells with chloroquine (60 μM), monensin (3 μM), or nocodazole (20 μM) inhibited transfection activity of EDOPC by >95%. A 2-h exposure to deoxyglucose (50 mM) reduced transfection by ~65%.

Stability of Transfection Complexes in Bovine Serum—Transfection efficiency usually improved in the presence of 10% serum over a wide range of EDOPC−DNA ratios (Figure 6). Given these data, it appeared possible that the EDOPC−DNA complex would survive incubation in a higher concentration of serum. To test for gross structural effects on the complex, which would be reflected

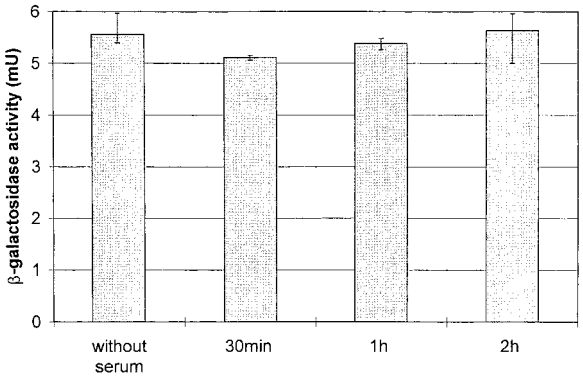

Figure 7—Transfection activity of cationic phospholipid is not affected by incubation with 95% serum. EDOPC–DNA complex was prepared from EDOPC and DNA at concentrations 10 times greater than usual (see *Methods, Standard Transfection Procedure*). The complex was incubated at a ratio of 1:20 with fetal bovine serum for 30 min and 1 and 2 h at 37 °C, and then used for transfection of BHK cells in 96-well plates in amounts corresponding to 1.5 μg of EDOPC and 0.5 μg of DNA in a total volume of 100 μL per well. Bars show high and low values of three replicates.

in the amount of light scattered by the complex, we measured the apparent absorbance of EDOPC−DNA particles at the wavelength of 450 nm (where there is no significant true absorbance) over the course of a 2-h incubation in serum at 37 °C. The compositions of the complexes were 3:1 and 6:1 by weight, prepared by mixing lipid at 1 mg/mL with DNA at 0.1 mg/mL. One volume of serum ($A_{450} = 0.32$) was mixed with one volume of complex dispersion (A_{450} were 0.62 and 0.72 for 3:1 and 6:1 weight ratio EDOPC−DNA complexes, respectively). Immediately after mixing, the absorbance was slightly higher than the sum of the absorbances of the components measured separately. We presume this difference is due to a small amount of aggregation occurring immediately, which amounted to 8% for the EDOPC−DNA complex at a 3:1 weight ratio and ~21% for the complex at a 6:1 weight ratio. Subsequently, there was a slight increase in absorbance with time: 8%/h for the complex with a 3:1 EDOPC−DNA weight ratio and 5.5%/h for the complex with a 6:1 weight ratio.

Given this indication of stability, we therefore examined the effect on transfection of 95% (the highest we could conveniently use) serum. Transfection of BHK cells was performed with lipid−DNA complexes preincubated in fetal bovine serum for 30 min, or 1 or 2 h (Figure 7). For this experiment, EDOPC and DNA were used at concentrations 10 times more than usual, which allowed us to add serum and transfection complex simultaneously to cells. As seen from the figure, the EDOPC−DNA complex retained its transfection efficiency during incubation in serum.

The effect of serum on DNA in the EDOPC−DNA complex was examined using a gel-electrophoresis-based protection assay. Figure 8 shows that after a short incubation of naked DNA in serum, the supercoiled form of plasmid was converted to linear and open circular forms. Although significant conversion to linear form also occurred in the EDOPC−DNA complex, the lipid clearly afforded a considerable amount of protection against nuclease activity. Similar results were obtained after treatment of DNA and EDOPC−DNA complex with the restriction enzyme Eco RI. In that case, the supercoiled plasmid, as well as all of the open circular plasmid present in the preparation, was completely converted to linear form. Again, EDOPC partially protected DNA from the action of restriction enzyme; that is, ~50% of the DNA remained supercoiled over the time course of the experiment.

Uptake by Cultured Cells of Cationic Phospholipids and Their DNA Complexes—Intracellular transport of transfection particles was investigated using separate labels for EDOPC and DNA. Figure 9 shows BHK cells that had been treated with EDOPC doped with RhPE, alone or in combination with DNA. When examined the next day, the pattern of labeling was quite dramatic and differed quite significantly, depending on whether DNA was delivered simultaneously with the lipid. When treated with lipid alone (upper panel), most cells exhibit localized fluorescence in large compartments adjacent to the nuclei. Although not definitively identified, the latter compartments are very similar to those labeled when cells are exposed to FITC−dextran and examined a day later, hence are suspected to be lysosomes.[46] Labeling of cellular membranes outside the perinuclear region was usually relatively weak. When cells were treated with lipid−DNA complexes, the typical lipid fluorescence pattern was significantly different (lower panel). Some fluorescence was seen around the nucleus, but the bulk of it was distributed throughout the cell in a punctate pattern, with extensive labeling of the surface and internal membranes.

When the DNA of the complex contained the tightly bound fluorophore, YOYO-1, the cytoplasm and the nuclei (with the exception of the nucleoli) of some of the cells were also fluorescent with the green fluorescence of intercalated YOYO-1. Our images of cells treated with lipid plus DNA were similar to those of CHO cells obtained by Hui et al.,[47] who introduced this combination of dyes in an earlier study of the transfection agent, 1,2-dioleoyl-3-(trimethylammonio)propane (DOTAP). We obtained the same results when plasmid DNA was covalently labeled with Alexa 488 C_5 maleimide dye as when we used the intercalating dye YOYO-1, indicating that the fluorescence observed was not due to migration of the YOYO-1 from delivered DNA to cellular DNA.

Discussion

We found that it is straightforward to change a zwitterionic phospholipid to a cationic phospholipid that is a highly effective transfection agent. The reaction is one step, involves readily available precursors, and purification is straightforward. The combination of efficacy and low toxicity makes the cationic phospholipids attractive candidates for agents to deliver nucleic acids and other pharmacological and physiological agents[17] to cells. Because the precursors are readily available and inexpensive, these compounds should also be cost-effective options for such applications.

Transfection Activity of Cationic Phospholipids—EDOPC exhibits transfection activity that is similar to that of other available agents, like Lipofectamine. Cationic phospholipids are, however, unaffected by serum, a property that distinguishes them from a number of common cationic amphipaths that are significantly inhibited by even 10% serum. Because it is not completely understood why those compounds are inhibited by serum, we cannot be sure why the cationic phospholipid escapes that fate. Current evidence points to interactions with serum proteins as an important cause for inhibition,[26] and it was found that inhibition could be avoided by changing the ratio of lipid to DNA,[23] the size of the complex,[22] or the concentrations at which it was formed.[25] In the case of EDOPC, because resistance to serum was observed over a wide range of PC+:DNA ratios (Figure 6), it is unlikely that the stability of the complex can be attributed to a particular surface charge density of the particle surface. It therefore would seem to be a property of the complex itself and evidently depends on a characteristic of the cationic phospholipids. The results of protection assays showed that when incubated in serum, supercoiled plasmid DNA complexed with

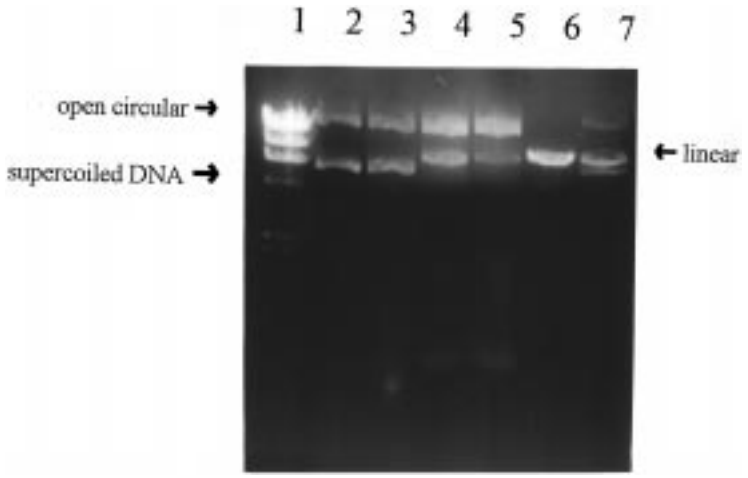

Figure 8—Agarose gel electrophoresis. DNA protection assay. EDOPC–DNA complexes were formed at concentrations 10 times higher than usual and incubated in fetal bovine serum or with the restriction endonuclease EcoRI (see *Methods* for additional details): Lane 1, in λ\HindIII; lane 2, DNA in D-PBS; lane 3, EDOPC–DNA in D-PBS; lane 4, DNA in serum; lane 5, EDOPC–DNA in serum; lane 6, DNA after treatment with EcoRI; lane 7, EDOPC–DNA after treatment with EcoRI.

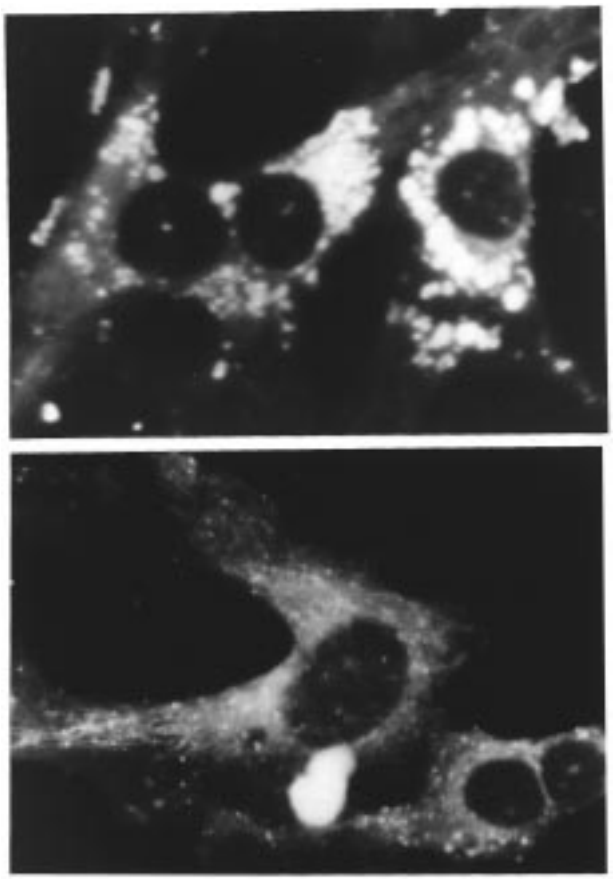

Figure 9—Cell uptake of cationic lipids and DNA–cationic lipid complexes. BHK cell cultures were treated with EDOPC containing 2.5 mol % RhPE either alone (upper panel) or complexed with DNA (lower panel). After incubation for 6 h in serum-free medium and an additional 14–18 h in serum-containing medium, the cells were fixed, mounted, and subsequently photographed. When lipid alone was added to the cells, it accumulated in large cellular vesicles in the region of the nucleus. When cells were treated with lipid–DNA complex, the surface and intracellular membranes often became fluorescent. Punctate fluorescence is also seen in these cells, but is usually distributed throughout the cell in much smaller vesicles than those seen in cells treated with lipid alone. The dark ovals outlined by surrounding fluorescence are the nuclei.

EDOPC was converted mainly to the open circular form instead of the linear form. This protection characteristic of EDOPC could be due to the structure of the polar group region, or to the fact that there is a single type of lipid present (which would exclude the possibility that even small incompatibilities between the two components could lead to some form of disproportionation under the influence of serum). Whether or not this means that cationic phospholipid complexes with DNA bind appreciably less serum protein than other transfection complexes remains to be determined. In any case, the ability to withstand extended contact with serum is an essential characteristic of a transfection complex if it is to be useful in gene therapy, and it is hence a potentially important characteristic of cationic phospholipids.

The cationic phospholipid exhibits relatively low toxicity to cells in culture, for which two possible explanations are apparent. One possibility is simply that the compounds may be sufficiently similar to cellular lipids that they have less disruptive effects on normal membrane function. A second possibility is that the lipids are degraded by cells to species that may either diffuse out of cells or be metabolized further. The rate of degradation was low, with a half time of days for the fluorescent substrates we tested, but if the intracellular phospholipase A_2(s) is similar to the venom enzymes we tested in the test tube, the unlabeled lipid could be degraded an order of magnitude faster. We doubt, however, that this potential advantage is realized under cellular conditions. Rather, we suspect that lipid degradation is limited by accessibility; the very mass of the lipid—both in the lipid by itself and the lipid–DNA complex—is likely to present a significant barrier to access by intracellular lipases. This interpretation is strongly supported by the punctate disposition of fluorescent lipids in the cell; large fluorescent masses appear within cells shortly after administration of lipid or complex and they remain sizable for at least a day.

Unlike many amphipathic cations used as transfection agents, EDOPC does not require DOPE for effectiveness.[41,42] We found that no mixtures of DOPE and EDOPC were as effective as pure EDOPC; however, the 1:1 mixture (the common ratio used with other cationic lipidic transfection agents) was nearly as effective as pure EDOPC. (We do not yet know what phase these mixtures reside in, and we will publish more extensive transfection results on DOPE-containing complexes when their phase structures have been determined.) It has been suggested that DOPE—a hexagonal phase-preferring lipid—may destabilize the endosomal membrane to facilitate escape of the DNA.[21] It may be that this adjunct activity is not required by PC+

because PC+ possesses membrane-destabilizing characteristics on its own; we have observed that cationic phospholipid vesicles fuse with anionic lipid vesicles,[48] EDOPC−DNA particles fuse with the bilayer of phosphatidylglycerol vesicles,[49] and mixtures of EDOPC and dioleoylphosphatidylglycerol form a bicontinuous cubic phase.[50]

Differential Uptake of Lipid and Lipid−DNA Complex by Cells—In the absence of DNA, the lipid fluorophore that was presented to cells accumulated in the perinuclear region. Presented in complex with DNA, the fluorophore was distributed in many small compartments throughout the cell. There are two obvious differences in the physical properties of the lipid and the lipid−DNA complex. One is buffer capacity. The complex could accept protons, because the DNA is present in the complex as a salt. The cationic phospholipid, being a quaternary amine, has no buffer capacity. Endosomal compartments may thus become more slowly acidified if DNA is present along with cationic phospholipid. The lipid is, in fact, delivered to compartments that resemble lysosomes morphologically, as would be expected if there were no significant interference with the normal acidification sequence in cellular vesicle traffic patterns. These results are also consistent with the cell fractionation results reported by Wattiaux et al. for liver cells treated with cationic amphipaths, in which the compounds accumulated in lysosomes.[51] Others have argued that cationic transfection agents function in part by neutralizing endosomal acid, with the result that lysosomal nucleases are inhibited.[52] If this result is true, then perhaps the reason we have noticed a difference between delivery of the lipid and that of the complex is because in our case only the complex would have buffer capacity.

The other obvious difference between the lipid and the complex is in osmolarity. The lipid has an osmolarity that is nearly the same as the concentration of its counteranions. The complex, in contrast, has an osmolarity that is essentially zero, for at the most effective composition for transfection, the charges on both lipid and DNA are almost completely neutralized. But the complex does have a latent high osmolarity, for if the DNA becomes protonated or if hydrophobic cellular anions diffuse into the complex, the complex is no longer a single particle in the osmotic sense. Thus, residence in an endosome could lead to changes in the lipid−DNA complex that could both buffer the endosome and lead to osmotic swelling of the compartment, both of which would delay transit to lysosomes. Generally attention has been focused on the cationic component as instrumental for DNA delivery, but it should not be overlooked that DNA, in complex with a cationic amphipath, acquires new properties that could play a role in its own delivery to the nucleus.

A number of cell lines were transfected by EDOPC, including CHO, mouse 3T3, Niemann-Pick, Rcho-1, L, K562 (erythroleukemia), and quail fibroblasts, although conditions were not optimized except for the first and second of these. Human vascular endothelial cells, primary cells of umbilical cord origin, are also efficiently transfected by EDOPC, however, in this case, not in the presence of serum.[53] In the case of CHO and 3T3 cells, the optimal conditions were not greatly different from those for BHK. Even without optimization, however, it was clear that EDOPC is effective with a wide variety of cells. An important advantage of the relatively low toxicity of EDOPC is that high doses may be used with recalcitrant cell lines. It remains to be determined to what extent cationic amphipaths will acquire clinical importance as gene therapy agents; however, because cationic phospholipids can be synthesized with a considerable variation in structure, there is reason to believe that a variety of these molecules could be constructed as effective delivery agents with minimal toxic effects.

References and Notes

1. Bangham, A. D.; Standish, M. M.; Watkins, J. C. Diffusion of univalent ions across the lamellae of swollen phospholipids. *J. Mol. Biol.* **1965**, *13*, 238−252.
2. Gregoriadis, G. Engineering liposomes for drug delivery: Progress and problems. *Trends Biotechnol.* **1995**, *13*, 527−537.
3. Felgner, P. L. The evolving role of the liposome in gene delivery. *J. Liposome Res.* **1995**, *5*, 725−734.
4. Farhood, H.; Gao, X.; Son, K.; Yang, Y. Y.; Lazo, J. S.; Huang, L.; Barsoum, J.; Bottega, R.; Epand, R. M. Cationic liposomes for direct gene transfer in therapy of cancer and other diseases. *Ann. N. Y. Acad. Sci.* **1994**, *716*, 23−34; discussion 34−35.
5. Straub, S. X.; Garry, R. F.; Magee, W. E. Interferon induction by poly (I): poly (C) enclosed in phospholipid particles. *Infect. Immun.* **1974**, *10*, 783−792.
6. Magee, W. E.; Talcott, M. L.; Straub, S. X.; Vriend, C. Y. A comparison of negatively and positively charged liposomes containing entrapped polyinosinic-polycytidylic acid for interferon induction in mice. *Biochim. Biophys. Acta* **1976**, *451*, 610−618.
7. Martin, F. J.; MacDonald, R. C. Lipid vesicle-cell interactions. III. Introduction of a new antigenic determinant into erythrocyte membranes. *J. Cell. Biol.* **1976**, *70*, 515−526.
8. Martin, F.; MacDonald, R. Liposomes can mimic virus membranes. *Nature* **1974**, *252*, 161−163.
9. Rodicio, M. R.; Chater, K. F. Small DNA-free liposomes stimulate transfection of streptomyces protoplasts. *J. Bacteriol.* **1982**, *151*, 1078−1085.
10. Felgner, P. L.; Gadek, T. R.; Holm, M.; Roman, R.; Chan, H. W.; Wenz, M.; Northrop, J. P.; Ringold, G. M.; Danielsen, M. Lipofection: a highly efficient, lipid-mediated DNA-transfection procedure. *Proc. Natl. Acad. Sci. U.S.A.* **1987**, *84*, 7413−7417.
11. Felgner, P. L.; Barenholz, Y.; Behr, J. P.; Cheng, S. H.; Cullis, P.; Huang, L.; Jessee, J. A.; Seymour, L.; Szoka, F.; Thierry, A. R., et al. Nomenclature for synthetic gene delivery systems. *Hum. Gene Ther.* **1997**, *8*, 511−512.
12. Morgan, R. A.; Anderson, W. F. Human gene therapy. *Annu. Rev. Biochem.* **1993**, *62*, 191−217.
13. Bennett, C. F.; Chiang, M. Y.; Chan, H.; Shoemaker, J. E.; Mirabelli, C. K. Cationic lipids enhance cellular uptake and activity of phosphorothioate antisense oligonucleotides. *Mol. Pharm.* **1992**, *41*, 1023−1033.
14. Zhou, F.; Huang, L. Liposome-mediated cytoplasmic delivery of proteins: an effective means of accessing the MHC class I-restricted antigen presentation pathway. *Immunomethods* **1994**, *4*, 229−235.
15. Debs, R. J.; Freedman, L. P.; Edmunds, S.; Gaensler, K. L.; Duzgunes, N.; Yamamoto; K. R. Regulation of gene expression in vivo by liposome-mediated delivery of a purified transcription factor. *J. Biol. Chem.* **1990**, *265*, 10189−10192.
16. Huang, L.; Farhood, H.; Serbina, N.; Teepe, A. G.; Barsoum, J. Endosomolytic activity of cationic liposomes enhances the delivery of human immunodeficiency virus-1 trans-activator protein (TAT) to mammalian cells. *Biochem. Biophys. Res. Commun.* **1995**, *217*, 761−768.
17. Barber, K.; Mala, R. R.; Lambert, M. P.; Qiu, R.; MacDonald, R. C.; Klein, W. L. Delivery of membrane-impermeant fluorescent probes into living neural cell populations by lipotransfer. *Neurosci. Lett.* **1996**, *207*, 17−20.
18. Hong, K.; Zheng, W.; Baker, A.; Papahadjopoulos, D. Stabilization of cationic liposome-plasmid DNA complexes by polyamines and poly(ethylene glycol)-phospholipid conjugates for efficient in vivo gene delivery. *FEBS Lett.* **1997**, *400*, 233−237.
19. Crook, K.; Stevenson, B. J.; Dubouchet, M.; Porteous, D. J. Inclusion of cholesterol in DOTAP transfection complexes increases the delivery of DNA to cells in vitro in the presence of serum. *Gene Ther.* **1998**, *5*, 137−43.
20. Farhood, H.; Serbina, N.; Huang, L. The role of dioleoyl phosphatidylethanolamine in cationic liposome mediated gene transfer. *Biochim. Biophys. Acta* **1995**, *1235*, 289−295.
21. Xu, Y.; Szoka, F., Jr. Mechanism of DNA release from cationic liposome/DNA complexes used in cell transfection. *Biochemistry* **1996**, *35*, 5616−5623.
22. Escriou, V.; Ciolina, C.; Lacroix, F.; Byk, G.; Scherman, D.; Wils, P. Cationic lipid-mediated gene transfer: Effect of serum on cellular uptake and intracellular fate of lipopolyamine/DNA complexes. *Biochim. Biophys. Acta* **1998**, *1368*, 276−288.

23. Yang, J. P.; Huang, L. Overcoming the inhibitory effect of serum on lipofection by increasing the charge ratio of cationic liposome to DNA. *Gene Ther.* **1997**, *4*, 950−960.
24. Boukhnikachvili, T.; Aguerre-Chariol, O.; Airiau, M.; Lesieur, S.; Ollivon, M.; Vacus, J. Structure of in-serum transfecting DNA-cationic lipid complexes. *FEBS Lett.* **1997**, *409*, 188−194.
25. Hofland, H. E.; Nagy, D.; Liu, J. J.; Spratt, K.; Lee, Y. L.; Danos, O.; Sullivan, S. M. In vivo gene transfer by intravenous administration of stable cationic lipid/DNA complex. *Pharm. Res.* **1997**, *14*, 742−749.
26. Zelphati, O.; Uyechi, L. S.; Barron, L. G.; Szoka, F. C., Jr. Effect of serum components on the physicochemical properties of cationic lipid/oligonucleotide complexes and on their interactions with cells. *Biochim. Biophys. Acta* **1998**, *1390*, 119−133.
27. Gao, X.; Huang, L. A novel cationic liposome reagent for efficient transfection of mammalian cells. *Biochem. Biophys. Res. Commun.* **1991**, *179*, 280−285.
28. Gorman, C. M.; Aikawa, M.; Fox, B.; Fox, E.; Lapuz, C.; Michaud, B.; Nguyen, H.; Roche, E.; Sawa, T.; Wiener-Kronish, J. P. Efficient in vivo delivery of DNA to pulmonary cells using the novel lipid EDMPC. *Gene Ther.* **1997**, *4*, 983−992.
29. Mason, J. T.; Broccoli, A. V.; Huang, C. A method for the synthesis of isomerically pure saturated mixed-chain phosphatidylcholines. *Anal. Biochem.* **1981**, *113*, 96−101.
30. Gupta, C. M.; Radhakrishnan, R.; Khorana, H. G. Glycerophospholipid synthesis: improved general method and new analogues containing photoactivable groups. *Proc. Natl. Acad. Sci. U.S.A.* **1977**, *74*, 4315−4319.
31. Selinger, Z.; Lapidot, Y. Synthesis of fatty acid anhydrides by reaction with dicyclohexylcarbodiimide. *J. Lipid Res.* **1966**, *7*, 174−175.
32. Christie, W. W. *Lipid Analysis*; Pergammon: Oxford, 1982; p 161.
33. Kates, M. *Techniques for Lipidology: Isolation, Analysis and Identification of Lipids*; American Elsevier: New York; 1972; Chapters 3 and 7.
34. Hendrickson, H. S.; Rauk, P. N. Continuous fluorometric assay of phospholipase A_2 with pyrene-labeled lecithin as a substrate. *Anal. Biochem.* **1981**, *116*, 553−538.
35. Thuren, T. A model for the molecular mechanism of interfacial activation of phospholipase A_2 supporting the substrate theory. *FEBS Lett.* **1988**, *229*, 95−99.
36. Rakhmanova, V. A.; MacDonald, R. C. A microplate fluorimetric assay for transfection of the β-galactosidase reporter gene. *Anal. Biochem.* **1998**, *257*, 234−237.
37. Sanes, J. R.; Rubenstein, J. L.; Nicolas, J.-F. Use of a recombinant retrovirus to study post-implantation cell lineage in mouse embryos. *EMBO J.* **1986**, *5*, 3133−3142.
38. Stang, P. F.; Hanack, M.; Subramanian, L. R. Perfluoroalkanesulfonic esters: Methods of preparation and applications in organic chemistry. *Synthesis* **1982**, 85−126.
39. Rosenzweig, H., et al., unpublished work.
40. Lusa, S.; Myllarniemi, M.; Volmonen, K.; Vauhkonen, M.; Somerharju, P. Degradation of pyrene-labeled phospholipids by lysosomal phospholipases in vitro. Dependence of degradation on the length and position of the labeled and unlabeled acyl chains. *Biochem. J.* **1996**, *315*, 947−952.
41. Leventis, R.; Silvius, J. R. Interactions of mammalian cells with lipid dispersions containing novel metabolizable cationic amphiphiles. *Biochim. Biophys. Acta* **1990**, *1023*, 124−132.
42. Felgner, J. H.; Kumar, R.; Sridhar, C. N.; Wheeler, C. J.; Tsai, Y. J.; Border, R.; Ramsey, P.; Martin, M.; Felgner, P. L. Enhanced gene delivery and mechanism studies with a novel series of cationic lipid formulations. *J. Biol. Chem.* **1994**, *269*, 2550−2561.
43. MacDonald, R. C. et al. *Biophys. J.*, submitted for publication.
44. Radler, J. O.; Koltover, I.; Salditt, T.; Safinya, C. R. Structure of DNA-cationic liposome complexes: DNA intercalation in multilamellar membranes in distinct interhelical packing regimes. *Science* **1997**, *275*, 810−814.
45. Lasic, D. D.; Strey, H.; Stuart, M. C. A.; Podgornik, R.; Frederik, P. M. The structure of DNA-liposome complexes. *J. Am. Chem. Soc.* **1997**, *119*, 832−833.
46. Kennedy, M. T.; MacDonald, R. C., unpublished observations.
47. Hui, S. W.; Langner, M.; Zhao, Y. L.; Ross, P.; Hurley, E.; Chan, K. The role of helper lipids in cationic liposomes as a vector for gene transfer. *Biophys. J.* **1996**, *71*, 590−599.
48. Pantazatos, D. P.; MacDonald, R. C. *J. Membrane Biol.*, in press.
49. MacDonald, R. C., et al., unpublished work.
50. MacDonald, R. C., et al., manuscript in preparation.
51. Wattiaux, R.; Jadot, M.; Dubois, F.; Misquith, S.; Wattiaux-De Coninck, S. Uptake of exogenous DNA by rat liver: Effect of cationic lipids. *Biochem. Biophys. Res. Commun.* **1995**, *213*, 81−87.
52. Boussif, O.; Lezoualc'h, F.; Zanta, M. A.; Mergny, M. D.; Scherman, D.; Demeneix, B.; Behr, J. P. A versatile vector for gene and oligonucleotide transfer into cells in culture and in vivo: polyethylenimine. *Proc. Natl. Acad. Sci. U.S.A.* **1995**, *92*, 7297−7301.
53. Matsumura, J.; Shively, V., personal communication.

Acknowledgments

We are grateful to Michael Kennedy for measuring the size of the EDOPC−DNA complex and to Ruby MacDonald for reviewing the manuscript. This work was supported by NIH GM 52329 and Avanti Polar Lipids.

JS990006Q

Hydroxypropyl-β-cyclodextrin Inhibits Spray-Drying-Induced Inactivation Of β-Galactosidase

SÉBASTIEN BRANCHU, ROBERT T. FORBES,* PETER YORK, SVEN PETRÉN,† HÅKAN NYQVIST,† AND OLA CAMBER‡

Contribution from *Drug Delivery Group, The School of Pharmacy, University of Bradford, Bradford, BD7 1DP, UK.*

Received December 17, 1998. Accepted for publication June 21, 1999.

Abstract □ The single-step, fast spray-drying process may represent a valuable alternative to the multistep, time-consuming freeze-drying process in the area of formulation and processing of biopharmaceuticals. In this study, we tested the use of sucrose and hydroxypropyl-β-cyclodextrin (HP-β-CD) as stabilizing excipients in the spray-drying of a model protein, β-galactosidase. The solutions were processed using a Büchi 190 cocurrent Mini Spray Dryer at an outlet temperature of 61 ± 2 °C. The powders were redissolved and analyzed for catalytic activity, aggregation, chemical decomposition, and thermal susceptibility as observed by high-resolution calorimetry. Spray-drying significantly inactivated β-galactosidase. Spray-drying β-galactosidase in the presence of sucrose did not prevent inactivation. However, after spray-drying β-galactosidase in the presence of HP-β-CD, or HP-β-CD and sucrose, full catalytic activity was exhibited on reconstitution. Furthermore, the reconstituted product was unchanged in terms of molecular weight, charge, and thermal stability. These findings are consistent with a hypothesis that the change responsible for inactivation of β-galactosidase was mainly a monomolecular, noncovalent change, i.e., the formation of incorrect structures, that arose from surface denaturation. This study clearly demonstrates that cyclodextrins can be useful stabilizing excipients in the preparation of spray-dried protein pharmaceuticals.

With the advent of new drug therapies and the increasing commercial availability of biotechnology-derived proteins, great expectations have arisen from the development of biopharmaceuticals.[1] However, a significant technical challenge lies in the formulation of these drugs. Compounds such as proteins are often physicochemically fragile and readily degrade,[2] the most common degradation pathways being aggregation, fragmentation, deamidation, and oxidation, which influence critical pharmaceutical properties including biological activity, metabolic half-life, and immunogenicity.[3] Freeze-drying has in general been the method of choice for stabilizing labile biopharmaceuticals, while spray-drying has been used for the stabilization of various heat-sensitive biological (enzymes), food (milk and egg products), and pharmaceutical (antibiotics and vaccines) products.[4] Despite the relatively high temperatures involved in the use of a hot airstream as a drying medium, the droplets in a spray-dryer do not attain a high temperature. Additionally, the low water content of the product that leaves the drying chamber allows the labile compound to withstand the effect of heat. Thus, spray-drying has been used under certain conditions to produce fully biologically active proteins.[5,6] The controllable particle size and shape characteristics of spray-dried powders make this process suited to the formulation of pharmaceuticals for inhalation.[7] Thus, the single-step, fast spray-drying process may represent a valuable alternative to the multistep, time-consuming freeze-drying process in the area of formulation and processing of biopharmaceuticals.

Nonetheless, the physical stress of the drying process on proteins may cause degradation,[3,8,9] which necessitates the use of stabilizing excipients when preparing dried biopharmaceuticals. Sugars and other polyols have been used as protein stabilizers because of their preferential interaction behavior in solution.[10] During spray-drying, polyols have been observed to reduce the rate constant of protein inactivation and improve recovered enzyme activity.[11,12] In contrast, cyclic oligosaccharides, or cyclodextrins (CDs), favor protein thermal denaturation in solution.[13] However, cyclodextrins have been reported to stabilize proteins against other protein degradation pathways, such as aggregation[14] and precipitation,[15] and as a result improve protein folding reversibility.[16] Cyclodextrins have also been shown to protect proteins from freeze-drying-induced inactivation[17] and maintain the native structure in elevated temperature stability studies.[3] Cyclodextrins are thought to have an impact on protein behavior through weak interactions between the oligosaccharide hydrophobic core and nonpolar protein groups when these are exposed.

Since polyols and cyclodextrins affect different protein degradation pathways, we wished to probe the influence of a combination of these two types of cosolvents on protein integrity during spray-drying and observe whether the two excipients would have additive, antagonistic, or synergistic effects, to compare these effects to those occurring in solution.[18] In this study, we tested the use of sucrose and hydroxypropyl-β-cyclodextrin (HP-β-CD) as stabilizing agents in the spray-drying of a model enzyme, β-galactosidase derived from *Aspergillus oryzae*. A monomeric glycoprotein, *Aspergillus oryzae* β-galactosidase is a multidomain, 105 kDa, 4.5 pI enzyme.[19,20] In contrast to small, single-domain proteins, β-galactosidase may follow a two-step folding mechanism involving successively fast domain folding and slow domain pairing.[21] Unlike natural cyclodextrins, HP-β-CD is surface active;[22] it was chosen as a model cyclodextrin for its high aqueous solubility and its pharmaceutical relevance as a potential excipient for parenteral and oral routes.[23] Sucrose was chosen because of its good glass-forming abilities and its widespread use as a protein stabilizer. Powder samples were dissolved and analyzed for catalytic activity, aggregation, and chemical change. Further, high-sensitivity differential scanning calorimetry (HSDSC) was used to measure the susceptibility of the reconstituted enzyme to thermal denaturation. This technique measures directly the forces stabilizing the globular structure and has a potential predictive capability of long-term stability of proteins.[24]

* Corresponding author e-mail: R.T.Forbes@Bradford.ac.uk, fax +44 1274 234769, tel +44 1274 234653.

† Pharmaceutical Analysis, Analytical and Pharmaceutical R&D, Astra Arcus AB, S-151 85, Sodertalje, Sweden.

‡ Licensing Department, Astra Arcus AB, S-151 85, Sodertalje, Sweden.

10.1021/js9804819 CCC: $18.00
Published on Web 08/14/1999

Experimental Section

Chemicals—β-Galactosidase (EC 3.2.1.23) derived from *Aspergillus oryzae* (lot 115H1179), *o*-nitrophenyl-β-D-galactoside (ONPG, lot 105H5017), and anhydrous sucrose (lot 70H-018715) were obtained from Sigma-Aldrich Ltd, Poole, UK. Hydroxypropyl-β-cyclodextrin (HP-β-CD, degree of substitution 0.6, batch 07B-271/1) was supplied by Janssen Biotech N. V., Olen, Belgium.

Spray-Drying—Each solution to be processed was prepared by dispersing 4 g of protein in 100 mL of deionized double-distilled water, with or without excipient, and centrifuged for 10 min at 13000 rpm. The concentration level was 1% w/v for each excipient, so that the sucrose:cyclodextrin:protein ratio was 0.25:0.25:1 in terms of mass and 76.8:19.0:1 in molar terms. A silicone tubing of inner diameter 4 mm and a peristaltic pump were used to feed the solutions to the nozzle of a Type B, Büchi 190 co-current Mini Spray Dryer (Büchi Labortechnik AG, Flawil, Switzerland). This dryer has a two-fluid, pneumatic nozzle 0.5 mm in diameter. Cooling water was continuously run through the nozzle to prevent protein degradation in the nozzle. The solution feed rate was 0.36 $\pm$ 0.06 L h^{-1}, the air spray flow consumption 750 $\pm$ 50 L h^{-1}, and the aspirator vacuum level 10 (approximately 30000 L h^{-1}). The inlet and outlet temperatures were set to 190 $\pm$ 2 °C and 61 $\pm$ 2 °C respectively, because these temperatures were expected to cause some inactivation of *Aspergillus oryzae* β-galactosidase.[12]

Catalytic Assay—the samples were reconstituted in 100 mM sodium acetate buffer, pH 4.5, at an approximate protein concentration of 1 mg mL^{-1}, and yielded clear solutions. One hundred microliter aliquots of this solution were added to 3 mL of 4.93 mg.mL^{-1} ONPG substrate solution. The rate of increase in absorbance at λ = 420 nm and 37 °C, caused by the enzyme-catalyzed hydrolysis of ONPG to *o*-nitrophenol, was monitored for 1 to 2 min.[12] The relative standard deviation of this method is 5%. Protein determination was carried out by the Bradford (Coomassie blue) method at λ = 590 nm, as described by Stoscheck.[25]

High-Sensitivity Differential Scanning Calorimetry (HSDSC)—Powders were dissolved in deionized double-distilled water to a protein concentration of 2−3 mg mL^{-1}. The solutions exhibited no turbidity and had a measured pH of 6.5, indicating that none of the excipients used affected the pH significantly. Thermal denaturation profiles for β-galactosidase were generated over the temperature range 20−100 °C using a Micro Calorimetry System high-sensitivity differential scanning calorimeter (MCS DSC, MicroCal Inc., Northampton, MA) controlled by the MicroCal Origin software. The instrument was calibrated for heat capacity using electrical pulses of known power and for temperature using sealed paraffin hydrocarbon standards of known melting points (28.2 °C and 75.9 °C for *n*-octadecane and n-hexatriacontane, respectively). Typically, this instrument has a noise level of 0.3 μW, a reproducibility on refilling the cells of 0.13 mJ K^{-1}, and a relative error in the heat capacity determination of 0.005%.[26]

The accuracy for the temperature measurement was 0.2 °C. All solutions were degassed for 2 min under vacuum before being loaded into the calorimeter, and were held under 2 bar nitrogen excess pressure to avoid bubble formation at higher temperatures. For each sample, a reference profile, obtained from water samples, was subtracted from the protein thermal data, and the excess heat capacity function was normalized for protein concentration. Since several processed samples contained sucrose or/and HP-β-CD, controls made of unprocessed protein and sucrose and/or HP-β-CD (in the same proportions as for processed samples) were prepared and analyzed in the same conditions. Thus, any change occurring both in the processed samples and in the controls would result from an excipient effect during the analysis and not during the spray-drying process.

High-Performance Size-Exclusion Liquid Chromatography (HPSEC)—For the chromatographic and electrophoretical experiments, the water used for reconstitution was deionized and filtered in a Milli-Q system (Millipore), and the samples were reconstituted in 0.1% aqueous acetic acid. Size-exclusion fractionation was performed in 50 mM phosphate buffer saline pH 7 at 40 °C using a TSKgel Super SW3000 column from TosoHaas GmbH (Stuttgart, Germany) made of 4 μm silica particles. This column was setup on a Merck-Hitachi HPLC chromatograph comprising an AS-2000 autosampler, a L-7100 pump, a LiChrograph L-6000 A HPLC pump, a D-6000 A interface, an L-5025 column thermostat, an L-4250 UV−vis detector set to λ = 214 nm, and a water-circulated, temperature-controlled rack at 8 °C for the sample vials. Typically, duplicate samples (5 μL) were analyzed at a concentration of 1 mg/mL and using a flow rate of 0.35 mL/min. The calibration kit from BioRad contained thyroglobulin (670 kDa), bovine γ-globulin (158 kDa), chicken ovalbumin (44 kDa), equine myoglobin (17 kDa), and vitamin B-12 (1.35 kDa). The data were analyzed using the Merck-Hitachi D-7000 HSM Chromatography Data Station Software.

Table 1—Enzymatic Activity of Redissolved Spray-Dried β-Galactosidase Samples Relative to the As-Received, Commercial Protein[a]

	relative activity (%)
no excipient	75.0
sucrose[b]	71.5
HP-β-CD[b]	98.3
HP-β-CD:sucrose[b]	90.0

[a] Reconstituted at a concentration of 1 mg mL^{-1} in 100 mM sodium acetate buffer, pH 4.5. [b] One gram of each excipient was added to the 4% w/v protein solution (100 mL) prior to spray-drying.

Sodium Dodecyl Sulfate Polyacrylamide Gel Electrophoresis (SDS−PAGE) and Isoelectric Focusing (IEF)—All materials were obtained from Amersham Pharmacia Biotech, Uppsala, Sweden, unless specified. Electrophoretical experiments were performed at 10 °C on a Multiphor II unit, with a thermostatic circulating water bath. SDS−PAGE runs were controlled by a BioRad 1000/500 power supply, and IEF ones by an Electrophoresis Power Supply EPS 3500 XL. The samples (run in quadruplicate) were separated according to molecular weight in both reducing and nonreducing conditions on ExcelGel SDS Homogeneous 12.5% containing 120 mM Tris, 120 mM acetate, 1 g L^{-1} SDS, pH 6.4, and using ExcelGel SDS buffer strips at the anode and cathode made of 450 mM Tris-acetate, 4 g L^{-1} SDS, pH 6.6, and 80 mM Tris, 800 mM Tricine, 6 g L^{-1} SDS, pH 7.1, respectively. A high molecular weight calibration kit was used, for the range 36 kDa (beef heart lactate dehydrogenase subunit) up to 330 kDa (hog thyroid thyroglobulin subunit). After fixing, the gels were stained using a Coomassie, PhastGel Blue R solution. IEF experiments were carried out in the pH range 2.5−8.0, with prior rehydration of CleanGel in a mixture of 700 μL of Pharmalyte carrier ampholytes in the pH range 2.5−5.0 and 700 μL Pharmalyte pH 5.0−8.0. The IEF calibration kit covered the pH range 2.80 (pepsinogen) to 6.55 (human carbonic anhydrase B). The gels were stained with a 1 g L^{-1} silver solution. All staining was done with an automated gel stainer (Hoefer Pharmacia Biotech Inc., San Francisco, CA).

Results and Discussion

Catalytic Data—The enzymatic activity data measured for the reconstituted samples are given in Table 1. As expected from the choice of the processing conditions, and in particular the outlet temperature which is the main factor influencing recovered protein activity,[27,28] the reconstituted spray-dried *Aspergillus oryzae* β-galactosidase had a significantly lower catalytic activity (75%) than the as-received, commercial protein. Interestingly, the addition of 1% w/v sucrose in the feed protein solution did not significantly alter the activity of the reconstituted product. Broadhead et al.[12] have found sucrose to stabilize β-galactosidase during spray-drying. A noticeable difference in the conditions, though, was the sucrose:protein mass ratio, which was more than or equal to 1.67 in Broadhead et al.'s study, but as low as 0.25 in our work. In terms of inactivation kinetics, a level as low as 1% w/v sucrose would not slow the spray-drying-induced deterioration of glucose oxidase.[29] However, sucrose concentrations as low as that used here (0.03 M) have been found to stabilize oxyhemoglobin on spray-drying.[6] In contrast, our results show that the use of 1% w/v HP-β-CD fully protected β-galactosidase against inactivation. This is interesting as high concentrations (10 to 20%)[3] of this cyclodextrin are usually needed

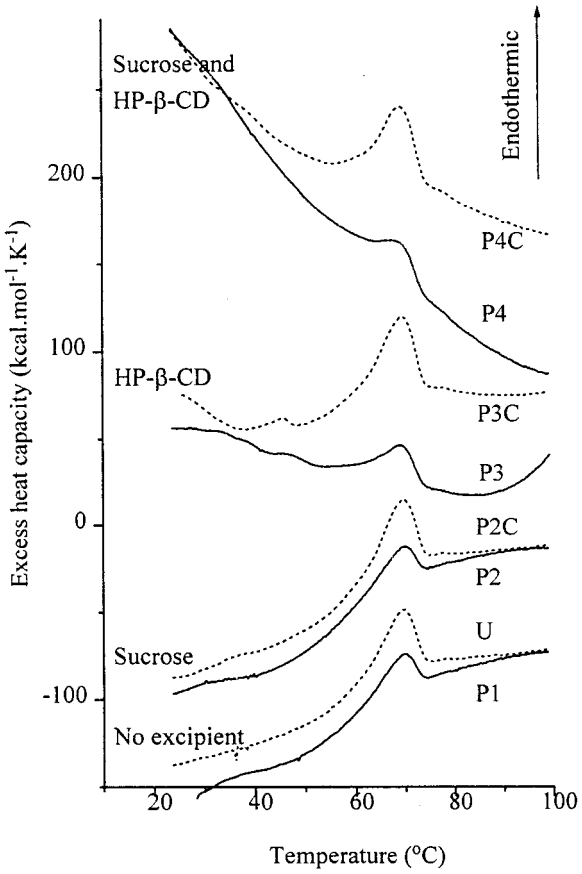

Figure 1—Thermal denaturation profiles for unprocessed (broken lines) and spray-dried (solid lines) β-galactosidase samples reconstituted in water at 2–3 mg mL^{-1} protein concentration, pH 6.5. U: excipient-free, unprocessed; P1: excipient-free, processed; P2: sucrose-containing, processed; P2C: control for P2 (unprocessed enzyme to which sucrose was added); P3: HP-β-CD-containing, processed; P3C: control for P3; P4: sucrose- and HP-β-CD-containing, processed; P4C: control for P4. The excipient composition was matched for each pair of unprocessed/processed samples, as explained in the Experimental Section.

to affect protein stability. The recovered activity (90%) obtained through the use of a combination of both excipients did not differ significantly from that measured for the cyclodextrin-containing sample. Since these carbohydrates at such levels do not interfere with the measurement of enzyme kinetics,[18] it appears that the cyclodextrin used prevented spray-drying-induced inactivation of β-galactosidase, whereas sucrose did not provide any protection. This inactivation process and the excipient effects were further investigated with thermal and biochemical measurements.

Thermal Denaturation Data—The calorimetric profiles and derived thermodynamic parameters are given in Figures 1 and 2 and Tables 2 and 3. The calorimetric profile for commercial β-galactosidase displayed a single endotherm with a transition temperature, T_m, of 69.7 °C. All samples exhibited a similar profile and T_m values were in the range 68.4−70.0 °C. The differences in slope were presumably due to excipient effects, as seen from the control data, and caused the small variations seen in T_m. Differences in transition enthalpies were ascribed to differences in concentrations of the reconstituted samples. All profiles were explained by a similar three-transition, non-two-state model. Differences were found in the relative intensities of the fitted transitions, but no trend appeared. The van't Hoff enthalpy, calculated for each fitted transition under the two-state approximation, yielded calorimetric-to-van't Hoff enthalpy ratios, which can be valuable for

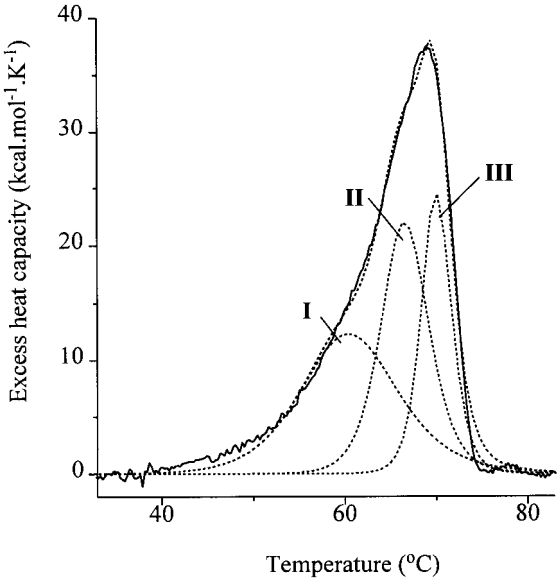

Figure 2—Three-transition, non-two-state model fitted to the calorimetric profile for reconstituted unprocessed β-galactosidase.

Table 2—Observed Denaturation Temperatures (T_m) for Redissolved Unprocessed and Spray-dried β-galactosidase Samples[a]

	denaturation temperatures, T_m (°C)	
	unprocessed	spray-dried
no excipient	69.7	70.0
Sucrose[b]	69.7	69.9
HP-β-CD[b]	69.5	69.1
HP-β-CD:sucrose[b]	69.0	68.4

[a] The excipient:protein mass ratio was 0.25 for each excipient in all preparations. [b] One gram of each excipient was added to the 4% w/v protein solution (100 mL) prior to spray-drying.

estimating the number of cooperative units. Transition I generally exhibited ratios much larger than 1, except for the HP-β-CD sample (P3). Transition II yielded ratios in the interval 0.6−1.1. Transition III showed ratios significantly less than 1, except for the unprocessed sample (U). However, because of the number of factors (e.g., baseline determination, exothermic processes, transition reversibility) that may bias the apparent enthalpies, no conclusions could be drawn from the observed calorimetric-to-van't Hoff enthalpy ratios.

Chromatographic and Electrophoretical Profiles—A representative size-exclusion HPLC trace is shown in Figure 3, with estimated parameters for all samples listed in Table 4. Electrophoretical fractions and estimates, respectively, are given in Figures 4 and 5 and Table 5. Fractionation by HPLC indicated the presence of five separated species, although not fully resolved. They were ascribed to the monomer (143 kDa), two fragments (53 and 42 kDa), a dimer (292 kDa), and a higher-MW aggregate (509 kDa). The peaks at 4.9 and 11.7 min were a high-molecular weight species eluting outside the size limits of the column and the buffer acetate anion, respectively. No effect of the spray-drying process or excipients on the retention times of these fractions was detected, although the relative intensity of the 9.0 min fragment peak was slightly larger for the sucrose sample (P2). Separation with SDS−PAGE of commercial β-galactosidase gave estimates for the main species of 105 kDa in nonreducing conditions and 119 kDa in the presence of mercaptoethanol. This band was attributed to the monomer. Additionally, three main bands appeared with MW estimates of 70, 64, and 40 kDa, which were probably responsible for the 8.7 min and 9.0

Table 3—Calorimetrically Derived Thermodynamic Parameters for Redissolved Unprocessed and Spray-Dried β-Galactosidase Samples[a]

sample	transition	T_m,[b] °C	ΔH_{cal},[c,f] kcal mol^{-1}	$\Delta T_{1/2}$,[d] °C	ΔH_{vH},[e,f] kcal mol^{-1}	$\Delta H_{cal}/\Delta H_{vH}$
U	I	60.3	172	12.2	72	2.38
U	II	66.4	153	6.1	150	1.02
U	III	68.6	192	6.1	152	1.26
P1	I	60.1	121	11.2	79	1.54
P1	II	66.5	98	6.0	153	0.64
P1	III	70.1	57	3.6	260	0.22
P2	I	59.5	134	12.5	70	1.91
P2	II	66.2	98	6.3	146	0.67
P2	III	69.8	59	4.0	232	0.25
P2C	I	61.9	183	11.5	77	2.36
P2C	II	67.7	168	5.3	175	0.96
P2C	III	70.6	84	3.4	279	0.30
P3	I	60.7	88	8.3	107	0.82
P3	II	66.6	103	5.9	156	0.66
P3	III	70.0	79	4.2	225	0.35
P3C	I	62.1	148	9.7	92	1.61
P3C	II	67.3	188	5.7	162	1.16
P3C	III	70.6	103	3.7	257	0.40
P4	I	60.9	170	11.3	78	2.17
P4	II	67.0	134	6.1	150	0.90
P4	III	70.3	63	4.3	221	0.29
P4C	I	62.4	203	10.1	88	2.29
P4C	II	67.7	194	5.3	175	1.11
P4C	III	70.7	90	3.5	267	0.34

[a] Abbreviations as in Figure 1. [b] Temperature of the maximum of the heat capacity function for each fitted transition. [c] Enthalpy change upon denaturation measured by integrating each transition. [d] Temperature width of the transition at half-height. [e] Van't Hoff enthalpy change calculated as $\Delta H_{vH} = 4RT_m^2/\Delta T_{1/2}$. [f] 1 cal = 4.184 J.

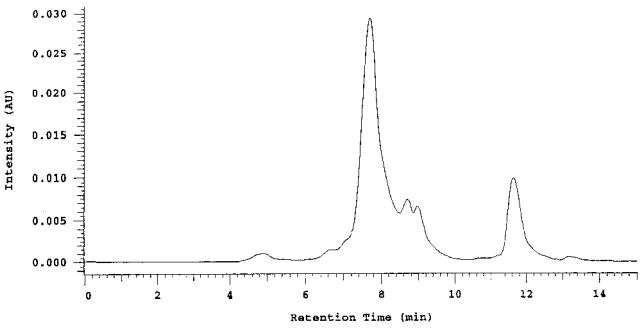

Figure 3—Size-exclusion HPLC profile observed for all unprocessed and spray-dried β-galactosidase samples reconstituted at 1–2 mg mL^{-1} protein concentration in 0.1% aqueous acetic acid.

min HPLC peaks. The use of the surfactant SDS for gel electrophoresis allowed the nature of the aggregates detected with HPLC to be tested. The absence of electrophoretical band above the monomer-size band indicated that the high-molecular weight chromatographic fractions reflected noncovalent aggregates. Faint SDS−PAGE bands appeared in the range 29−35 kDa in reducing conditions, indicative of the presence of multichain species held by disulfides in nonreducing conditions. No spray-drying- or excipient-induced change in the molecular weight or relative amount of protein fractions was found. Isoelectric focusing of unprocessed β-galactosidase revealed a number of bands, of which the two main bands were in the 4.5 and 3.5 pI regions, consistent with the expected value. Neither the process nor the excipients altered the isoelectric profiles.

Nature of the Inactivation Process and Cosolvent Effects—Thus, spray-drying significantly inactivated β-galactosidase as observed by the level of recovered enzyme kinetic activity. The addition of HP-β-CD stabilized the enzyme against inactivation, as did the combination of both

Table 4—Measured Retention Times (RT), Estimated Molecular Weights (MW), and Relative Areas for the Size-Exclusion HPLC Fractions of Unprocessed and Spray-Dried β-Galactosidase Samples[a]

	retention time, RT (min)						relative area (%)		
sample	peak 1	peak 2	peak 3	peak 4	peak 5	sample	peak 3	peak 4	peak 5
U	ca. 6.7	ca. 7.1	7.69	8.70	8.97	U	94.3	2.6	3.1
P1	ca. 6.7	ca. 7.1	7.69	8.69	8.97	P1	95.4	1.3	3.2
P2	ca. 6.7	ca. 7.1	7.69	8.71	8.99	P2	94.0	1.9	4.1
P4	ca. 6.7	ca. 7.1	7.69	8.70	8.98	P4	95.3	1.5	3.2
P3	ca. 6.7	ca. 7.1	7.69	8.70	8.98	P3	95.6	1.4	3.1
P2C	ca. 6.7	ca. 7.1	7.69	8.70	8.97	P2C	95.2	1.6	3.2
P4C	ca. 6.7	ca. 7.1	7.69	8.69	8.97	P4C	95.4	1.4	3.2
P3C	ca. 6.7	ca. 7.1	7.69	8.69	8.97	P3C	95.3	1.5	3.3
MW	509	292	143	53	42				

[a] Abbreviations as in Figure 1. Relative areas were calculated without taking into account the 4.9 and 11.7 min peaks, which are a higher-molecular weight species eluting outside the size limits of the column, and the buffer acetate anion, respectively. Peaks 1 and 2 were too poorly resolved for meaningful integration.

HP-β-CD and sucrose, but not sucrose alone. These results demonstrate that cyclodextrins can be useful stabilizers in the preparation of spray-dried protein pharmaceuticals. Further experiments indicated that the spray-dried enzyme was unchanged in terms of thermal stability, size-exclusion HPLC, SDS−PAGE, and IEF patterns. These findings highlight the relevance of functional probes for the detection of certain changes in multidomain proteins that involve interactions between distant sites which remain undetected by physical probes.[21] The reduction in the activity that was observed may reflect either an almost complete loss of activity affecting only a fraction of the population of molecules, or a conformational alteration inducing less activity in most of the molecules.[30] Our data indicate that the structural change causing inactivation was subtle; it is likely that this change was not the formation of covalent or noncovalent aggregates, fragmentation, or deamidation. Since the droplets of a solution atomized in a cocurrent spray-drier usually reach a maximum temperature which is approximately 15 °C below the outlet temperature for 5 to 30 s,[11,31] β-galactosidase was only briefly exposed to temperatures approaching 45 °C, thus undergoing only small and reversible thermal denaturation as inferred from the calorimetric data. Temperatures in this region for a formulation at a pH close to neutral also mean that the inactivation process involved no change in primary structure.[32] Therefore, it is hypothesized that the change responsible for partial inactivation of β-galactosidase was mainly a monomolecular, noncovalent change, i.e., the formation of incorrect structures, and did not affect the thermal susceptibility of the protein but weakened its kinetic properties, i.e., interferred with its active site.

Furthermore, it is known that protein adsorption to surfaces can be a source of destabilization,[33] inducing, for example, inactivation of *Escherichia coli* β-galactosidase.[34] In our study, denaturation at the air−liquid interface was a probable explanation for inactivation because it was consistent with three relevant factors: the consistency between the absence of effect of sucrose and the expected large droplet surface coverage of the protein; indeed, it has been found that for a protein:lactose ratio of 1/99, the protein can dominate the droplet surface due to its higher surface activity than the sugar;[35] the reduction of inactivation in the presence of surface-active cyclodextrin, which may compete with protein molecules at the droplet surface; and the results of atomization studies indicating surface denaturation at the air−liquid interface of droplets in a spray and reduction of this instability by addition of

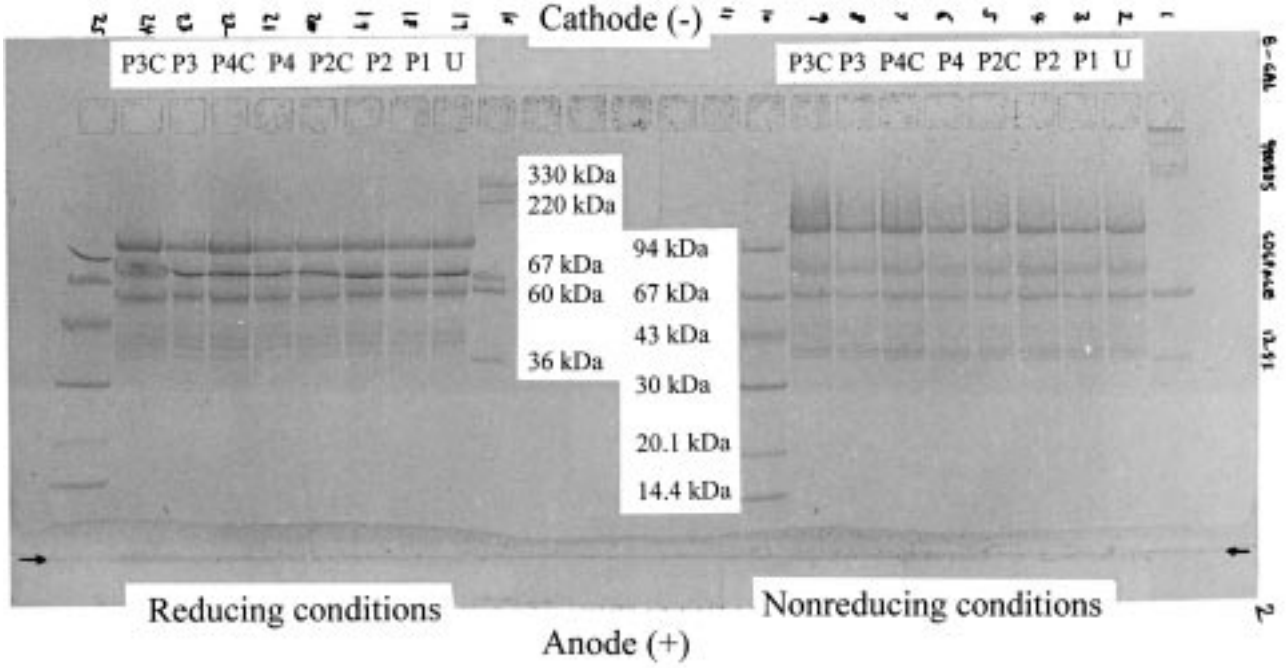

Figure 4—SDS–PAGE profile for unprocessed and spray-dried β-galactosidase samples. Same reconstitution conditions as in Figure 3. Reducing (left) and nonreducing conditions (right). Abbreviations as in Figure 1.

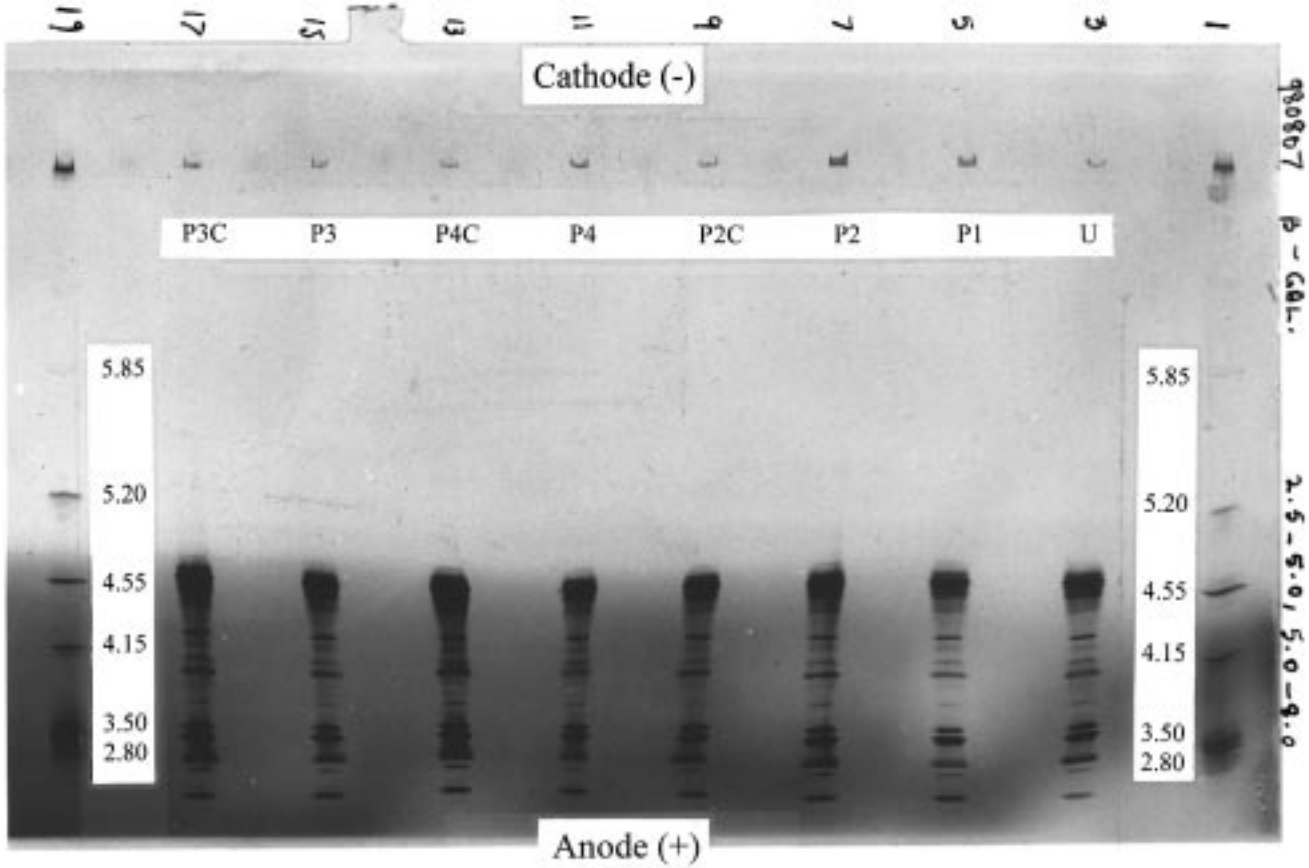

Figure 5—Isoelectric focusing (IEF) profile of unprocessed and spray-dried β-galactosidase samples. Same reconstitution conditions as in Figure 3. Abbreviations as in Figure 1.

surfactants.[5] Foaming that has been observed to result from the shear forces occurring during atomization[36] is another phenomenon that could explain the inactivation of β-galactosidase.

Thus, we propose that, in the particular formulation and processing conditions examined, i.e., at low outlet temperatures and low excipient:protein ratios, thermal degradation was small, and the usual thermodynamic stabilization provided by sucrose[29] did not occur to a significant extent; rather, it was primarily surface denaturation that caused inactivation, and HP-β-CD inhibited this instability pathway. It is further proposed that HP-β-CD may impact

Table 5. —Estimated Molecular Weights (MW) and Isolectric Points of the Observed SDS–PAGE and IEF Fractions, Respectively, for Unprocessed and Processed β-Galactosidase Samples[a]

molecular weight (kDa)		
nonreduced[b]	reduced[c]	isoelectric point
105	119	4.62
78	89	4.47
63	64	4.25
42	38	4.05
41	35	3.95
	32	3.55
	29	3.40
		< 2.80

[a] No connection was established between molecular weights and isoelectric points of the fractions. [b] Nonreducing conditions. [c] In the presence of mercaptoethanol.

protein stability during spray-drying (i) by weak hydrophobic interaction between the oligosaccharide core and the protein nonpolar groups exposed by instability, hence inhibiting undesirable protein−protein and protein-interface interactions and (ii) by changing water properties since HP-β-CD is surface-active. The first of these mechanisms is partly cyclodextrin-specific, and may occur with nonderivatized cyclodextrins of different core dimensions, such as α-cyclodextrin,[13] but is also nonspecific, since any additives masking exposed nonpolar regions should prevent protein−interface interactions.

We believe that, depending on the processing conditions, spray-drying of proteins gives rise to a delicate balance between two instability pathways: thermal degradation and surface denaturation. Thermal degradation occurs in the interior of droplets due to the high water content in this region, but less at the droplet surface where there is less water.[37] It is consistent with the finding that thermal degradation is lower with smaller droplet size.[38] However, for surface denaturation at the droplet−air interface, it may be the opposite: it takes place at the surface and not in the interior, and it increases as droplet size decreases. That is why the ideal spray-dried formulation may necessitate a combination of differents excipients, such as a preferentially excluded stabilizer against thermal denaturation, and a surfactant against interfacial denaturation. Because of the number of effects involved, a multifactorial approach using factorial and/or composite designs[12,18] seems adequate.

In this study, oxidation was initially expected to be another possible degradation pathway.[29] This was not directly tested, e.g., through the use of dithiothreitol. However, the full enzymatic activity found for the cyclodextrin-containing formulation showed that if any oxidation was occurring, it did not affect the activity level of the formulation.

Besides the spray-drying process, the reconstitution step has to be considered explicitly. Aggregation is often observed to take place when dried proteins are reconstituted. It has been found that there may be differences in amount of aggregation based on additives in the initial solution as well as in the reconstitution medium.[39] In our study, the positive cyclodextrin effect might result from the ability of this excipient to prevent aggregation during the redissolution step. Additionally, if refolding occurred on reconstitution, then the presence of cyclodextrin would favor refolding because it would inhibit the off-pathway of aggregation. Overall, cyclodextrins may behave like naturally occurring chaperones that have similar functions in vivo.[40] From this viewpoint, the fast spray-drying process is attractive because, unlike freeze-drying, it occurs at nonequilibrium conditions, thus making less likely the achievement of a thermodynamically stable denatured state.[3] Therefore, on reconstitution, aggregation may not occur before refolding. In any case, our fractionation data suggested no aggregation, hence suggesting that the cyclodextrin effect took place during the process and not on reconstitution.

Conclusions

We used sucrose and hydroxypropyl-β-cyclodextrin (HP-β-CD) as stabilizing agents in the spray-drying of a model enzyme, β-galactosidase. Spray-drying without stabilizing agents significantly inactivated β-galactosidase. The reconstituted samples containing HP-β-CD exhibited full catalytic activity, but not those containing sucrose as the sole stabilizing agent. All samples exhibited similar thermal profiles and transition temperatures. No general effect of the spray-drying process or excipients was detected on the retention times of the protein chromatographic fractions, although the relative intensity of the 9.0 min fragment peak was slightly larger for the sucrose-containing sample. No spray-drying- or excipient-induced change in the molecular weight or relative amount of protein electrophoretical fractions was found. These findings are consistent with a hypothesis that the change responsible for inactivation of β-galactosidase was a subtle monomolecular, noncovalent change, i.e., the formation of incorrect structures, which arose from surface denaturation and weakened the catalytic properties of the protein, i.e., interfered with its active site. The data suggest that the cyclodextrin inhibited protein denaturation by preventing adsorption at the droplet−air interface. This stabilization mechanism occurred mainly during the process rather than on redissolution. Sucrose did not provide any stabilization, presumably because of the nonthermal nature of the stress.

References and Notes

1. Thayer, A. M. Great Expectations. Biopharmaceutical Industry Expects Success From New Drug Therapies and a Full Product Development Pipeline. *Chem. Eng. News* **1998**, *76*, 19−31.
2. Manning, M. C.; Patel, K.; Borchardt, R. T. Stability of Protein Pharmaceuticals. *Pharm. Res.* **1989**, *6*, 903−918.
3. Cleland, J. L.; Powell, M. F.; Shire, S. J. The Development of Stable Protein Formulations. A Close Look at Protein Aggregation, Deamidation, and Oxidation. *Crit. Rev. Ther. Drug Carrier Syst.* **1993**, *10*, 307−377.
4. Masters, K. Spray-drying. *An Introduction to Principles, Operational Practice, and Applications*; Leonard Hill Books: London, 1972.
5. Mumenthaler, M.; Hsu, C. C.; Pearlman, R. Feasibility Study on Spray-Drying Protein Pharmaceuticals. Recombinant Human Growth Hormone and Tissue-Type Plasminogen Activator. *Pharm. Res.* **1994**, *11*, 12−20.
6. Labrude, P.; Rasolomanana, M.; Vigneron, C.; Thirion, C.; Chaillot, B. Protective Effect of Sucrose on Spray Drying of Oxyhemoglobin. *J. Pharm. Sci.* **1989**, *78*, 223−229.
7. Forbes, R. T.; Davis, K. G.; Hindle, M.; Clarke, J. G.; Maas, J. Water Vapor Sorption Studies on the Physical Stability of a Series of Spray-Dried Protein/Sugar Powders for Inhalation. *J. Pharm. Sci.* **1998**, *87*, 1316−1321.
8. Prestrelski, S. J.; Tedeschi, N.; Arakawa, T.; Carpenter, J. F. Dehydration-induced Conformational Transitions in Proteins and Their Inhibition by Stabilizers. *Biophys. J.* **1993**, *65*, 661−671.
9. Tzannis, S. T.; Meyer, J. D.; Prestrelski, S. J. Secondary Structure Considerations During Protein Spray-Drying. *Abstracts of Papers*, 213th National Meeting of the American Chemical Society, San Francisco, CA, April 13−17, 1997; American Chemical Society: Washington, DC, 1997; 297-BIOT.
10. Arakawa, T.; Timasheff, S. N. Stabilization of Protein Structure by Sugars. *Biochemistry* **1982**, *21*, 6536−6544.
11. Broadhead, J.; Edmond Rouan, S. K.; Rhodes, C. T. The Spray Drying of Pharmaceuticals. *Drug Dev. Ind. Pharm.* **1992**, *18*, 1169−1206.

12. Broadhead, J.; Edmond Rouan, S. K.; Hau, I.; Rhodes, C. T. The Effect of Process and Formulation Variables on the Properties of Spray-dried β-Galactosidase. *J. Pharm. Pharmacol.* **1994**, *46*, 458−467.
13. Cooper, A.; McAuley-Hecht, K. E. Microcalorimetry and the Molecular Recognition of Peptides and Proteins. *Philos. Trans. R. Soc. London A* **1993**, *345*, 23−35.
14. Katakam, M.; Banga, A. K. Aggregation of Proteins and Its Prevention by Carbohydrate Excipients. Albumins and γ-Globulin. *J. Pharm. Pharmacol.* **1995**, *47*, 103−107.
15. Charman, S. A.; Mason, K. L.; Charman, W. N. Techniques for Assessing the Effects of Pharmaceutical Excipients on the Aggregation of Porcine Growth Hormone. *Pharm. Res.* **1993**, *10*, 954−962.
16. Branchu, S.; Forbes, R. T.; Nyqvist H., and York P. Hydroxypropyl-β-Cyclodextrin Improves the Folding Reversibility of Aggregating Lysozyme. *J. Pharm. Pharmacol.* **1997**, *49*, S-86.
17. Hora, M. S.; Rana, R. K.; Smith, F. W. Lyophilized Formulations of Recombinant Tumor Necrosis Factor. *Pharm. Res.* **1992**, *9*, 33−36.
18. Branchu, S.; Forbes, R. T.; York, P.; Nyqvist, H. A central composite design to investigate the thermal stabilisation of lysozyme. *Pharm. Res.* **1999**, *16*, 702−708.
19. Tanaka, Y.; Kagamiishi, A.; Kiuchi, A.; Horiuchi, T. Purification and Properties of β-Galactosidase from *Aspergillus oryzae*. *J. Biochem.* **1975**, *77*, 241−247.
20. Ogushi, S.; Yoshimotot, T.; Tsuru, D. Purification and Comparison of Two Types of β-Galactosidase from *Aspergillus oryzae*. *J. Ferment. Technol.* **1980**, *58*, 115−122.
21. Garel, J.-R. Folding of Large Proteins. Multidomain and Multisubunit Proteins. In *Protein Folding*; Creighton T. E., Ed.; W. H. Freeman and Company: New York, 1992; pp 405−454.
22. Izutsu, K.-I.; Yoshioka, S.; Terao, T. Stabilization of β-Galactosidase by Amphiphilic Additives During Freeze-Drying. *Int. J. Pharm.* **1993**, *90*, 187−194.
23. Irie, T.; Uekama, K. Pharmaceutical Applications of Cyclodextrins. III. Toxicological Issues and Safety Evaluation. *J. Pharm. Sci.* **1997**, *86*, 147−162.
24. Remmele, R. L., Jr.; Nightlinger, N. S.; Srinivasan, S.; Gombotz, W. R. Interleukin-1 Receptor (IL-1R) Liquid Formulation Development Using Differential Scanning Calorimetry. *Pharm. Res.* **1998**, *15*, 200−208.
25. Stoscheck, C. M. Quantitation of Protein. In *Guide to Protein Purification*; Deutscher M. P., Ed.; Academic Press Ltd: London, 1990; pp 50−68.
26. Privalov, P. L.; Potekhin, S. A. Scanning Microcalorimetry in Studying temperature-Induced Changes in Proteins. In *Methods in Enzymology. Enzyme Structure*; Hirs, C. H. W., Timasheff, S. N., Eds.; Academic Press: London, 1986; Vol. 131, pp 4−51.
27. Shah, V. D. The Spray-Drying of Enzyme Rennin. Ph.D. Thesis, University of Wisconsin, 1963.
28. Daemen, A. L. H.; Van Der Stege, H. J. The Destruction of Enzymes and Bacteria During the Spray Drying of Milk and Whey. 2. The Effect of Drying Conditions. *Neth. Milk Dairy J.* **1982**, *36*, 211−229.
29. Yamamoto, S.; Agawa, M.; Nakano, H.; Sano, Y. Enzyme Inactivation During Drying of a Single Droplet. In *Proceedings of the Fourth International Drying Symposium*, Kyoto, Japan; Society of Chemical Engineers: Japan, Tokyo, 1984; pp 328−355.
30. Fatouros, A.; Österberg, T.; Mikaelsson, M. Recombinant Factor VIII SQ—Influence of Oxygen, Metal Ions, pH and Ionic Strength on its Stability in Aqueous Solution. *Int. J. Pharm.* **1997**, *155*, 121−131.
31. Deasy P. B. Spray Drying, Spray Congealing, Spray Embedding, and Spray Polycondensation. In *Microencapsulation and Related Drug Processes*; Swarbrick, J., Ed.; Dekker: New York and Basel, 1984; pp 181−193.
32. Klibanov, A. M. Stabilization of Enzymes against Thermal Inactivation. *Adv. Appl. Microbiol.* **1983**, *29*, 1−28.
33. Steadman, B. L.; Thompson K. C.; Middaugh, C. R.; Matsuno, K.; Vrona, S.; Lawson, E. Q.; Lewis, R. V. The Effects of Surface Adsorption on the Thermal Stability of Proteins. *Biotech. Bioeng.* **1992**, *40*, 8−15.
34. Edwards, R. A.; Huber, R. E. Surface Denaturation of Proteins. The Thermal Inactivation of β-Galactosidase (*Escherichia coli*) on wall-liquid surfaces. *Biochem. Cell Biol.* **1992**, *70*, 63−69.
35. Fäldt, P.; Bergenståhl, B. The Surface Composition of Spray-Dried Protein Lactose Powders. *Colloids and Surf. A − Physicochem. Eng. Asp.* **1994**, *90*, 183−190.
36. Hill, W. M.; Cotterill, O. J.; Funk, E. M.; Baldwin, R. E. Spray-Drying Egg White at Various pH Levels. *Poultry Sci.* **1965**, *44*, 1155−1163.
37. Wijlhuizen, A. E.; Kerkhof P. J. A. M.; Bruin, S. Theoretical Study of the Inactivation of Phosphatase During Spray-Drying of Skim-Milk. *Chem. Eng. Sci.* **1979**, *34*, 651−660.
38. Yamamoto, S.; Sano, Y. Drying of Enzymes. Enzyme Retention During Drying of a Single Droplet. *Chem. Eng. Sci.* **1992**, *47*, 177−183.
39. Webb, S.; Randolph, T. W.; Carpenter, J. F.; Cleland, J. L. An Investigation Into Reconstitution of Lyophilized Recombinant Human Interferon-γ. *PharmSci* **1998**, *1*, S-542.
40. Cooper, A.; Lovatt, M.; Nutley M. A. Energetics of Protein-Cyclodextrin Interactions. *J. Incl. Phenom. Mol. Recog. Chem.* **1996**, *25*, 85−88.

Acknowledgments

The authors and S.B. in particular thank Astra Arcus AB for the provision of studentship to support this project. Dr Sven Jacobsson, from Astra Arcus AB, is acknowledged for laboratory support.

JS9804819

Biopharmaceutics of Boronated Radiosensitizers: Liposomal Formulation of MnBOPP (Manganese Chelate of 2,4-(α,β-Dihydroxyethyl) Deuterioporphyrin IX) and Comparative Toxicity in Mice

RONG ZHOU,[†,‡] SATHYAMANGALAM V. BALASUBRAMANIAN,[§] STEPHEN B. KAHL,[¶] AND ROBERT M. STRAUBINGER*[,§]

Contribution from *The Department of Pharmaceutics, 539 Cooke Hall, University at Buffalo State University of New York, Amherst, New York 14260-1200, The Department of Molecular and Cellular Biophysics, Roswell Park Cancer Institute, Elm and Carlson Streets, Buffalo, New York 14263, and The Department of Pharmaceutical Chemistry, University of California at San Francisco, San Francisco, California 94143-0446.*

Received November 30, 1998. Final revised manuscript received April 26, 1999.
Accepted for publication June 9, 1999.

Abstract □ Binary treatment modalities such as photodynamic therapy (PDT) and neutron capture therapy (NCT) combine low-toxicity electromagnetic irradiation with an appropriate radiation sensitizer to enhance selectivity for tumor targets. The porphyrin derivative tetrakiscarborane carboxylate ester of 2,4-(α,β-dihydroxyethyl) deuterioporphyrin IX (BOPP) shows tumor-selective uptake and is active in both treatment modalities. BOPP also chelates paramagnetic ions such as Mn^{2+}, and therefore its tissue accumulation and selectivity can be detected noninvasively by using magnetic resonance imaging. However, local and systemic toxicity appears elevated for the Mn^{2+} chelate (MnBOPP), but is poorly characterized. Here we have developed a liposomal formulation of MnBOPP and compared its toxicity with that of MnBOPP administered to mice in saline. The optimal liposome composition and maximal capacity to accommodate MnBOPP were investigated by differential scanning calorimetry and by encapsulation efficiency. MnBOPP was encapsulated quantitatively at up to 12 mol % (drug:lipid) in liposomes of varying composition, and remained incorporated during extended dialysis. Phase separation of drug- and lipid-rich domains was observed above 12% drug. MnBOPP in buffered saline was lethal to animals at 90 μmol/kg, and caused severe necrosis at the injection site at dose levels of 60 μmol/kg or greater. In contrast, MnBOPP formulated in liposomes was well tolerated at the highest tested dose of 135 μmol/kg, with the elimination of local toxicity.

Introduction

The combination of treatment modalities to achieve greater therapeutic effect and lower side effects is a frequent objective in the development of new cancer therapies. In such approaches as photodynamic therapy (PDT)[1,2] or neutron capture therapy (NCT),[3,4] electromagnetic radiation of comparatively low toxicity interacts with a sensitizer compound of low toxicity, and their combination results in a high cell-kill effect. In both cases, confining the irradiation to the disease field and confining the sensitizer to the tumor cells are essential for maximal selectivity of effect.

In NCT, selective uptake of boronated radiosensitizer compounds into tumor tissues is an important factor that determines the effectiveness of therapy.[3,5] A boronated porphyrin, the tetrakiscarborane carboxylate ester of 2,4-bis-(α,β-dihydroxyethyl) deuterioporphyrin IX (BOPP),[6] has shown selective tumor deposition in mice bearing C-6 murine glioma, and the ratio of BOPP taken up in brain tumor versus normal brain was 400:1.[7] An additional advantage of metalloporphyrins such as BOPP is that the porphyrin nucleus can chelate paramagnetic ions, such as manganese, while retaining their tumor-localizing property, so that the pharmacokinetics and selectivity of uptake can be monitored by noninvasive methods such as magnetic resonance imaging (MRI).[8,9] Therefore, the manganese chelate of BOPP (MnBOPP) is an agent of dual functions: that of a radiation sensitizer in boron NCT and that of a contrast agent for enhancement of tumors in MRI. In this dual-functional agent, boron serves as the key element for therapy and Mn serves as the key element for MRI contrast enhancement. By combining an imaging function with a therapeutic function, therapy could be individualized both to patients and to the disease state, and irradiation could be applied at the time of peak tumor selectivity or effect.

Previously we demonstrated that MnBOPP is selectively localized in intracranial 9L brain tumors in rats,[10] a tumor model that bears many similarities to *Glioblastoma multiforme*, a lethal human brain tumor.[11] In MRIs, the uptake of MnBOPP significantly enhanced the contrast between tumor and normal brain. Preliminary results in our laboratory also suggested that high doses of MnBOPP administered in saline had acute systemic toxicity and delayed chronic toxicity, and that drug encapsulated in liposomes was better tolerated by animals at high doses (≥100 μmol/kg, unpublished data). Moreover, the magnitude of brain tumor contrast enhancement in MRIs suggested that there was comparable tumor-selective uptake of MnBOPP for both the saline and liposomal forms. Peak contrast enhancement was observed at ~24 and 70 h after administration of free and liposomal MnBOPP, respectively.[12] Because liposomes offer the possibility for high-dose administration of MnBOPP with reduced toxicity, we have investigated the optimal conditions for liposomal encapsulation of MnBOPP and compared the in vivo toxic effects of liposomal MnBOPP with that of drug administered in buffered saline.

Experimental Procedures

Materials—Egg phosphatidylcholine (EPC), dipalmitoylphosphatidylcholine (DPPC), distearoylphosphatidylcholine (DSPC), and poly(ethylene glycol) (PEG) 1900 conjugated to distearoylphos-

* Corresponding author. Telephone: (716) 645-2844 × 243. Fax: (716) 645-3693. E-mail: rms@Buffalo.edu.
† The Department of Molecular and Cellular Biophysics.
‡ Current address: B1 Stellar-Chance Laboratories, 422 Currie Boulevard, Department of Radiology, University of Pennsylvania, Philadelphia, Pennsylvania 19104.
§ The Department of Pharmaceutics.
¶ The Department of Pharmaceutical Chemistry.

10.1021/js980454i CCC: $18.00
Published on Web 08/07/1999

phatidylethanolamine (DSPE) were purchased from Avanti Polar Lipids (Alabaster, AL). Cholesterol (CHOL) was from Sigma Chemicals (St. Louis, MO) and was recrystallized three times from methanol prior to use. MnBOPP (molecular weight 1485) was synthesized as described previously.[6] Female BALB/C mice (6 weeks, 20−25 g) were purchased from Harlan Sprague Dawley (Indianapolis, IN).

Preparation of Liposomes—Liposomes were prepared by a reversed-phase evaporation (REV) procedure.[13] Typically, 10 μmol of phospholipid in chloroform were mixed at defined ratios with MnBOPP dissolved in methanol (4−5 mM), and the solvents were removed with a rotary evaporator. The dried film of drug and lipid was then resuspended in 0.5−1.0 mL of isopropyl ether, emulsified by brief (15 s) sonication after the addition of 350 μL of saline/HEPES buffer (140 mM NaCl, 20 mM *N*-2-hydroxyethyl-piperazine-*N*′-[2 ethanesulfonic acid], pH 7.4, osmolality 290 mOsm/kg), and converted into a liposome suspension by removal of ether under reduced pressure. Liposome preparations were extruded to a final diameter of ~0.08−0.10 μM by passing three times each under high pressure (~1250 kPa or 185 psi) through double-stacked polycarbonate membranes of decreasing pore size (1, 0.4, 0.2, and 0.08 μm) with a gas extruder (Mico Instrument, Middleton, WI). Extruded liposomes were then dialyzed free of residual drug with a membrane tubing having a molecular weight cutoff of 12 000−14 000 Da (Spectrapor Medical Industries, Los Angeles, CA). Dialysis was performed overnight at 4 °C against three changes of a 400-fold excess of saline/HEPES buffer.

Analytical Methods—The drug concentration in liposome samples before and after processing was determined spectrophotometrically after extraction from liposomes using methanol. The visible absorption spectrum of MnBOPP dissolved in methanol has peaks at 367 and 460 nm. A calibration curve was constructed for optical density at 460 nm as a function of MnBOPP concentration in methanol. Phospholipid concentrations were determined by phosphorus assay.[14] The results were expressed as "encapsulation efficiency", which is defined as the drug:lipid ratio after dialysis divided by the initial drug:lipid ratio (i.e., before extrusion or other processing).

Differential scanning calorimetry (DSC) was performed on a Perkin-Elmer DSC-2C instrument with samples sealed in aluminum pans. Thermograms were acquired and recorded on chart paper using a scan speed of 2.5 K/min, a sensitivity setting of 1 mCal/s, a temperature range of 20−60 °C, and a chart speed of 40 mm/min. After acquisition, the data were input into a computer (Macintosh, Apple Inc., Cupertino, CA) using a digital scanner and DataThief (National Institute for Nuclear Physics and High Energy Physics (NIKHEF), Amsterdam, The Netherlands), a program that extracts scanned data into a digital form. The DSC instrument was calibrated over a wide range of temperatures using various standard samples provided by the manufacturer. Each sample contained 14 μL of liposomes at a phospholipid concentration of 55 mM, and the drug:lipid molar ratios investigated were 0, 3, 7, 11, and 15% (moles of drug per 100 mol phospholipid). Thermograms were also obtained for MnBOPP dissolved in saline/HEPES buffer. All samples were maintained at the initial temperature (295 K) for 15 min to ensure temperature equilibration.

Experiments In Vivo—MnBOPP was administered to mice in saline/HEPES buffer at doses of 45, 60, 75, and 90 μmol drug per kilogram of body weight. The dose range for liposomal drug was 75, 90, 110, and 135 μmol/kg. Six mice per group were treated at each dose level, and the drug was injected via tail vein. The injection volume was <0.3 mL/20 gm body weight. After injection, the mice were observed for mortality and weighed regularly for 6 weeks. The maximum tolerated dose (MTD) is defined as the dose at which animals survived but had ~10% weight loss.

Results

Optimization of the Liposome Formulation—Preliminary experiments raised concern over potential local and systemic toxicity of the Mn^{2+} chelate of BOPP (data not shown), and liposomes were investigated for mitigation of the toxicity. Although MnBOPP is moderately water soluble, it appeared also to be incorporated quantitatively in liposomes, which suggested localization of the drug in the liposome membrane phase (data not shown). Therefore,

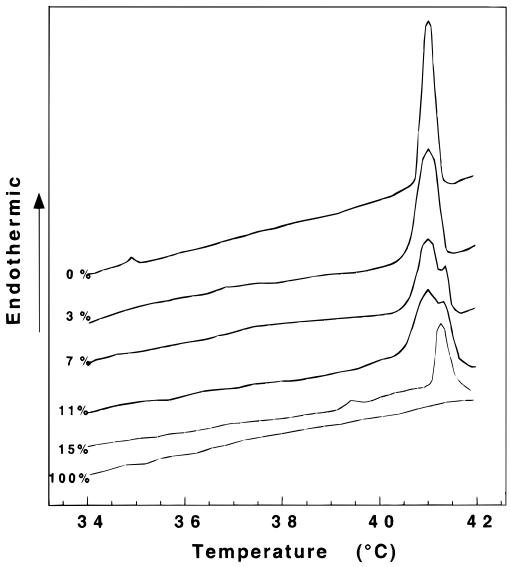

Figure 1—Incorporation of MnBOPP in lipid bilayers. DSC thermograms of DPPC liposomes containing various molar ratios of MnBOPP. Liposomes composed of DPPC and the indicated amount of drug were made, processed, and analyzed by DSC as described in Experimental Procedures. The drug:lipid ratios varied from 0% (no drug) to 100% (no phospholipids). The ratio is calculated as the number of moles of drug per 100 mol of phospholipid; the phospholipid concentration was not adjusted, i.e., the total moles of drug and phospholipid do not sum to 100%.

the interactions between MnBOPP and liposome membrane constituents were investigated in greater detail. The drug:lipid ratio was varied, and the effect on membrane structure was investigated by DSC. DPPC was used as the predominant phospholipid because of its highly cooperative and well-defined phase transition at 41.3 °C. DPPC liposomes without drug showed a large, sharp transition at ~41 °C (Figure 1). MnBOPP alone did not undergo a distinct phase transition, as indicated in Figure 1 by the thermogram for 100% MnBOPP.

Inclusion of 3 mol % MnBOPP in DPPC bilayers (3 mol drug in 100 mol phospholipid) resulted in broadening of the main transition. The transition width at half-height increased from 0.3 to 0.46 °C. At 7 mol % MnBOPP, the main transition peak was further broadened and a shoulder appeared on the high-temperature side, suggesting the formation of a new phase that was possibly enriched in MnBOPP. Because this phase melts at higher temperature, lipid packing in the new phase may be different from, and tighter than, the lipid-rich domain. This new phase became more prominent at 11 mol % MnBOPP, and at 15 mol % MnBOPP, the predominant transition occurred at the temperature characteristic of the new MnBOPP-rich phase. Concomitantly, the transition endotherm characteristic of pure DPPC disappeared. The new phase apparently resulted from interactions between MnBOPP and DPPC; MnBOPP itself does not undergo a thermal transition in this temperature range, and DPPC undergoes a thermal transition at a lower temperature. Based on the DSC results, 10−12 mol % was hypothesized as the maximum capacity for DPPC bilayers to accommodate MnBOPP.

MnBOPP incorporation into DPPC membranes was investigated quantitatively as a function of the initial drug:lipid ratio. Ratios were included that were above and below the optimal suggested by DSC experiments (Figure 1). Following preparation of the liposomes, extrusion through controlled-pore membranes was performed to remove unincorporated drug that had precipitated.[15] Liposomes pass through the membrane pores, and are extruded to a diameter that approximately equals the pore size of the filter.[16] Because extrusion would not remove unencapsu-

Table 1—Encapsulation Efficiency of MnBOPP in DPPC Liposomes[a]

initial drug:lipid ratio, %[b]	drug:lipid ratio after extrusion, %[b]	drug:lipid ratio after dialysis, %[b]	encapsulation efficiency, %[c]
4	3.8 ± 0.46	3.6 ± 0.47	91 ± 11
8	7.6 ± 0.25	7.1 ± 1.5	89 ± 2
12	11.6 ± 0.36	11.0 ± 0.25	91 ± 3
20	11.6 ± 0.46	11.5 ± 0.68	57 ± 5

[a] Data are expressed as mean ± standard deviation from at least 3 experiments. [b] Drug:lipid ratio is the molar ratio between MnBOPP and DPPC phospholipid. [c] Encapsulation efficiency is defined as the ratio between the final (after dialysis) and initial drug/lipid ratio.

lated drug molecules that are in soluble monomer or micellar form, dialysis was performed after extrusion, and the drug:lipid ratio was determined before and after each processing step.

At drug:lipid ratios of ≤10 mol % (MnBOPP:DPPC), incorporation of drug was quantitative (Table 1), which is a characteristic of lipophilic agents located within the membrane bilayer. Neither extrusion nor dialysis reduced the drug:lipid ratio significantly (Table 1), suggesting a lack of substantial precipitated MnBOPP or unincorporated drug in monomer or micellar form. Dialysis was prolonged, and MnBOPP retention in the liposome further suggested stable incorporation of the drug in the bilayer.

For drug:lipid ratios ≥10 mol %, a plateau value of ~12 mol % (MnBOPP:DPPC) incorporation was observed after extrusion. This ratio was determined to be the maximal drug:lipid ratio achievable in DPPC membranes.

The membrane physical state can have major impact on both liposome performance in vivo and on the incorporation of lipophilic molecules. Therefore, encapsulation efficiency was investigated for a selection of liposome compositions that represent a broad range of physical or in vivo performance properties. This selection of compositions (Table 2) included low- and high-transition temperature phospholipids, charged and neutral (zwitterionic) compositions, cholesterol-containing formulations, and polymer-coated liposomes with extended circulation times in vivo.[17] Table 2 shows the effect of lipid composition on the incorporation of MnBOPP. Three phosphatidylcholines (EPC, DPPC, and DSPC) were tested individually, with or without cholesterol, at initial drug:lipid ratios of ~8%. For EPC liposomes, in which the bilayer is in a fluid state, the drug:lipid ratio achieved was ~7% following extrusion, and subsequent dialysis had little effect on the incorporation of MnBOPP. The addition of CHOL had little effect on the encapsulation efficiency in EPC liposomes.

For DPPC liposomes, in which the bilayer exists in the gel phase, encapsulation efficiency was similarly high. The addition of CHOL to DPPC liposomes did not alter MnBOPP incorporation.

In contrast, the drug:lipid ratio achieved for DSPC liposomes prepared with an 8 mol % drug:lipid ratio, the MnBOPP incorporation was ~3.4 mol % after extrusion; overall, only 40% of the initial drug was incorporated. Like DPPC liposomes, DSPC liposomes exist in the gel phase at room temperature. However, the DSPC acyl chain length is greater. The addition of CHOL, which broadens the phase transition and imparts a fluidizing effect, did not increase MnBOPP incorporation markedly.

Liposomes bearing hydrophilic polymer headgroups, such as PEG, and consisting of high-transition temperature phospholipids show greatly extended circulation times in vivo[17,18] as well as intratumor deposition.[18,19] MnBOPP incorporation into PEG-bearing liposomes was investigated for both fluid (EPC) and gel-phase (DPPC) lipids. MnBOPP was incorporated nearly quantitatively in either composition, and the maximal mole ratio achieved was 12% (Table 2).

Comparative Toxicity of MnBOPP Formulations—Free or liposomal MnBOPP was administered to healthy mice at various dose levels to determine the effect of formulation on the maximum tolerated dose (MTD) of the drug. Body weight and vital signs (respiration, heart rate) of the animals were monitored after bolus injection. Preliminary experiments using 2 mice per group showed that 100% (2 of 2) of the animals died following administration of free MnBOPP at a dose of 100 μmol/kg, whereas all survived at 80 μmol/kg (data not shown). A more comprehensive experiment with 6 mice per group showed that 90 μmol/kg free MnBOPP was lethal, resulting in 80% death (5 of 6 animals) within 48 h after injection. For all other doses tested, all animals survived the treatment (data not shown).

Figure 2 shows the percent body weight change following injection of free MnBOPP. MnBOPP at 75 μmol/kg mediated 11% weight loss, which did not recover until 30 days after injection. Local necrosis was observed at the injection site 24 h after injection in animals treated with ≥60 μmol/kg of free drug. Doses of 45 μmol/kg caused ~4% weight loss that recovered within 10 days after injection. Based on body weight changes, the MTD of free MnBOPP appeared to be ~75 μmol/kg.

Two liposome compositions incorporating MnBOPP, PEG−DSPE:EPC:CHOL (1:10:5) and PEG−DSPE:DPPC:CHOL (1:10:5), were tested in preliminary dose-ranging experiments using small numbers of animals. The two liposome formulations appeared to cause similar weight change profiles in mice (data not shown); therefore, only the PEG−DSPE:DPPC:CHOL (1:10:5) liposome formulation was selected for investigation with a larger number of animals. All animals survived injection of MnBOPP at doses up to 135 μmol/kg, and no necrosis was observed at the injection site. Observation of the animals was continued for 3 months. The maximal weight loss (~8%) occurred at the 135 μmol/kg dose level, and the body weight did not recover until day 40 after injection (Figure 3). However,

Table 2—Effect of Lipid Composition on Drug:Lipid Molar Ratios Achieved[a]

lipid composition	initial drug:lipid ratio, %[b]	drug:lipid ratio after extrusion, %[b]	drug:lipid ratio after dialysis, %[b]	encapsulation efficiency, %[c]
EPC	8.0 ± 0.3	7.0 ± 0.4	6.9 ± 0.2	87 ± 5
EPC/CHOL (2:1)	8.0 ± 0.5	6.4 ± 0.9	6.4 ± 1.2	80 ± 15
DPPC	8.0 ± 0.5	7.6 ± 0.5	7.3 ± 0.2	92 ± 4
DPPC/CHOL (2:1)	8.0 ± 0.2	7.4 ± 0.2	7.5 ± 0.5	94 ± 5
DSPC	8.0 ± 1.7	3.4 ± 0.8	3.1 ± 0.1	40 ± 9
DSPC/CHOL (2:1)	8.0 ± 1.0	4.3 ± 0.3	3.9 ± 0.7	50 ± 6
PEG–DSPE/EPC/CHOL (1:10:5)	12.3 ± 0.6	11.8 ± 1.1	11.0 ± 1.8	89 ± 11
PEG–DSPE/DPPC/CHOL (1:10:5)	12.3 ± 0.8	11.9 ± 1.3	10.5 ± 0.9	94 ± 3

[a] Data are expressed as mean ± standard deviation from at least 3 experiments. [b] Drug:lipid ratio is the molar ratio between MnBOPP and DPPC phospholipid. The ratio is calculated as the number of moles of drug per 100 mol of phospholipid. [c] Encapsulation efficiency is defined as the ratio between the final (after dialysis) and initial drug/lipid ratio.

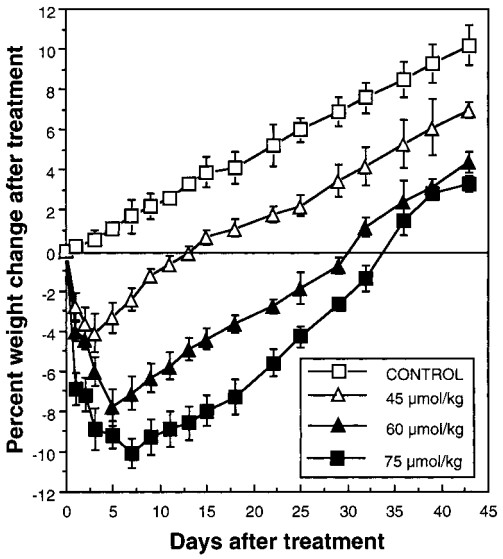

Figure 2—Toxicity of MnBOPP in saline. Body weight changes of mice were recorded after injection of MnBOPP dissolved in buffered saline. The concentration of MnBOPP was 10 mM in saline/HEPES buffer (140 mM, 20 mM, pH 7.4, osmolality 290 mOsm), and the volume of one injection was <0.3 mL/20 gm body weight. The weight change of each animal was normalized to its weight before injection, and each point represents the mean ± standard deviation for each group ($n = 6$).

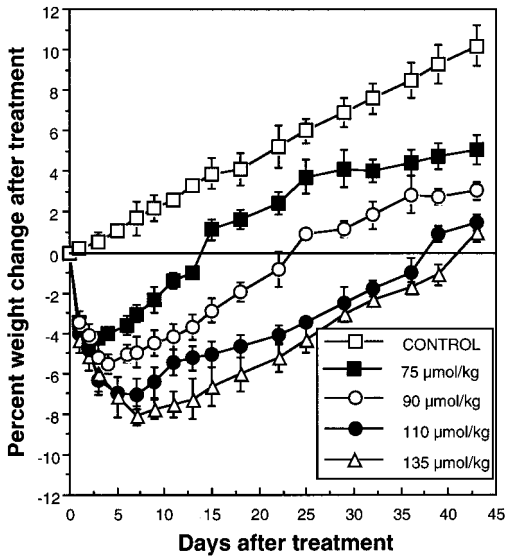

Figure 3—Toxicity of liposomal MnBOPP. Body weight changes of mice were recorded after injection of MnBOPP encapsulated in liposomes. MnBOPP was incorporated at a molar ratio of 12% (with respect to phospholipid) in liposomes composed of PEG–DSPE:DPPC:CHOL (1:10:5). The drug concentration was ~8 mM. If the volume required for a specific dose was >0.3 mL/20 gm body weight, it was split into two injections with an interval of ~10 min. The weight change of each animal was normalized to its weight before injection, and each point represents the mean ± standard deviation for each group ($n = 6$).

the MTD, defined as a 10% loss in body weight, was not observed in the dose range tested for either PEG−DSPE:EPC:CHOL (1:10:5) or PEG−DSPE:DPPC:CHOL (1:10:5) liposomes containing MnBOPP, even though the highest dose tested (135 μmol/kg) was nearly twice the tolerated dose of free drug (75 μmol/kg).

Discussion

Selective delivery of a sufficient quantity of boron (^{10}B) compound to the tumor site via the systemic route is a key requirement for the success of boron NCT as a tumoricidal modality.[3,4] In addition, the selective deposition of MnBOPP in tumor tissues may facilitate its application in diagnosis as an MRI contrast-enhancing agent.[10]

Here we established that the MTD of MnBOPP in saline was ~75 μmol/kg, as judged by body weight loss of animals. However, even at that dose, considerable injection-site toxicity was noted. The MTD determined here for the manganese chelate of BOPP is significantly lower than the MTD of ~200 mg/kg (147 μmol/kg) determined previously for the nonmetalated compound in mice.[7] Thus, free MnBOPP is roughly twice as toxic as BOPP. From the standpoint of dose-limiting systemic toxicity and local injection-site toxicity, mitigation of these effects using liposomes may aid in clinical application of the promising Mn-containing compound.

Liposomes have been shown to reduce the systemic toxicity of encapsulated drugs, and liposomes of small size bearing PEG moieties on the surface have shown enhanced tumor uptake.[17,18,20] Because of the beneficial effects of encapsulation on toxicity and selectivity of deposition, liposomes hold considerable promise for the delivery of boronated compounds in NCT.[21−24] With the reduction in toxicity observed here, dose escalation and possibly increased tumor uptake of MnBOPP may be achievable via liposome encapsulation. However, liposomal formulation of lipophilic compounds involves optimization of the large number of parameters that affect stability;[25−27] these parameters include the preferred membrane physical state, determined by the phase transition temperature (T_m) of the predominant lipid constituent, the lipid acyl chain composition, and the CHOL content, which both modifies T_m and has the effect of stabilizing liposomes in vivo. Additional parameters having impact on drug incorporation include the liposome membrane charge and the presence of surface-localized hydrophilic polymers.

To approach this problem of multiparameter optimization, a prototype liposome formulation was chosen; DPPC, a phospholipid with a defined phase transition, was used as a probe for membrane interaction of the drug. A maximal drug:lipid ratio was determined qualitatively by DSC. In the case of MnBOPP, exceeding the maximal capacity of the bilayer to accommodate the drug was manifested by the appearance of a new, higher-melting drug:lipid phase. This behavior contrasts with other cases,[15,28] in which exceeding the maximum drug:lipid ratio may be marked by an abrupt reappearance of the original T_m of the pure phospholipid component when catastrophic destabilization results in precipitation of drug outside of the membrane environment. An additional advantage of the use of DSC is that the progressive, MnBOPP-dependent changes observed in the T_m confirmed interaction of the drug with the bilayer of the membrane as well as suggested the existence of an unusual, higher-melting drug:lipid complex involving a specific lamellar phase state of the lipid. This unusual phase may be worthy of future study because it suggests the possibility for developing drug-rich particles that may be structurally distinct from liposomes (cf. ref 29).

The qualitative overview of bilayer maximal capacity for drug provided by DSC was investigated in greater detail using simple methodology to quantify the drug:lipid ratio; this investigation involved manipulations to resolve precipitated and weakly associated drug. Extrusion of liposomes through controlled-pore filters[16] not only redefines the mean diameter to a size that circulates more readily in the blood, but also allows the separation of liposomes from precipitated drug.[15] The subsequent dialysis step was performed to eliminate micellar or monomer drug because it would not be removed from liposomes during the extrusion step. Overnight dialysis had little effect on MnBOPP

incorporation, suggesting reasonably stable incorporation of the drug in the membrane.

Once the approximate bilayer capacity for MnBOPP was established using a prototype phospholipid, a small number of liposome compositions were chosen for further investigation, and these represented broad differences in membrane properties and in vivo performance. We observed quantitative incorporation of MnBOPP in most of these formulations, suggesting considerable latitude in selecting liposome constituents. A lack of such latitude could limit the ability to overcome possible future challenges posed as specific in vivo performance objectives are pursued.

The membrane physical state, governed largely by the T_m of the predominant lipid constituent, is a major parameter that affects the performance of liposomes in vivo.[30−32] In this study, liposomes encapsulating MnBOPP were formed from each of three phospatidylcholines (egg PC, DPPC, and DSPC) having increasing T_m. EPC (T_m, −5 to −17 °C) exists in the liquid crystalline state at room temperature, whereas DPPC (T_m, 41.3 °C) and DSPC (T_m, 55.8 °C) exist in the gel state. At room temperature or body temperature, membrane fluidity is decreased in the order EPC > DPPC > DSPC, as indicated by the T_m (EPC < DPPC < DSPC). Both fluid- (EPC) and gel-phase (DPPC) liposomes incorporated MnBOPP quantitatively. Interestingly, the nature of the gel-phase lipid had a major effect on drug incorporation; DSPC, which also forms gel-phase liposomes, had the lowest MnBOPP incorporation capacity (Table 2). This observation may be explained by the highly ordered, cooperative packing of lipid molecules in the gel phase. More fluid membranes, such as DPPC and EPC, may better accommodate bulky, lipid-soluble drugs such as MnBOPP within the bilayers because these lipid bilayers tend to have more disordered hydrocarbon domains.

Cholesterol was tested as a constituent in several formulations. Cholesterol increases the packing density of the phospholipid bilayer by inserting itself between the lipid molecules, resulting in decreased permeability of phospholipid bilayer to small polar molecules and preventing plasma proteins from penetrating.[26,33] Physical stability of liposomes often is enhanced by incorporation of CHOL in the bilayer.[26] Cholesterol also increases the disorder within bilayer, resulting in broadening or elimination of the T_m.[30−32] In this study, the addition of CHOL in EPC- or DPPC-containing liposomes did not change the drug: lipid ratio significantly (Table 2) at a molar ratio of 1:2 (CHOL:phospholipid), suggesting that CHOL did not alter significantly the interaction between EPC or DPPC and MnBOPP molecules. Interestingly, CHOL did not increase the incorporation of MnBOPP in DSPC liposomes, despite the broadening effect of CHOL on the T_m.[31,32]

The PEG headgroup of the PEG−DSPE lipid provides a hydrated coating on the surface of liposome and can hinder the access of plasma proteins to the liposome surface; such "sterically stabilized liposomes" (SSLs)[34] have shown a 5-fold increase in circulation time compared with liposomes without the surface coating.[18] The altered pharmacokinetics may allow increased extravasation of liposomes into tumors, resulting in the enhanced antitumor effect seen in various preclinical and clinical trials.[17] Here, PEG-containing liposomes of both fluid- and gel-phase lipids incorporated MnBOPP as efficiently as the optimal non-PEG formulations.

MnBOPP encapsulated in liposomes was much better tolerated than the free drug. The MTD of free MnBOPP in mice was ~75 μmol/kg, whereas that of the liposomal drug exceeded 135 μmol/kg for the PEG−DSPE-containing formulations that included either EPC or DPPC as the predominant lipid constituent. We observed previously[12] that tumor accumulation of MnBOPP administered in a prototype liposomal form was roughly comparable to that observed for free MnBOPP. The high incorporation of MnBOPP in the diverse liposome compositions defined here provides the opportunity to optimize further the tumor deposition in vivo and shows clearly the potential to increase the dose intensity of MnBOPP, with the aim of further enhancement in tumor delivery.

The amount of phospholipid required to administer the highest dose of MnBOPP (135 μmol/kg) was ~28 μmol lipid per animal. Although this concentration of lipid is high, we have previously administered comparable doses of liposomes to mice[35] up to 9 times in 3 weeks. Although those liposomes contained high concentrations of paclitaxel, a cytotoxic agent, all animals administered a dose of 30 μmol lipid per injection survived the entire 9-course treatment. Caution must be exercised in using these previous experiments to interpret the present results because different lipid compositions were used, and the liposomes contained a potent cytotoxic agent. However, the compositions used here would be cleared less rapidly to the lung, liver, and spleen than those used previously, and thus should have relatively less impact on the overall health of the animal. Thus, liposomal encapsulation appears to provide a means to administer higher doses of MnBOPP with reduced toxicity.

References and Notes

1. Dougherty, T. J.; Gomer, C. J.; Henderson, B. W.; Jori, G.; Kessel, D.; Korbelik, M.; Moan, J.; Peng, Q. Photodynamic therapy. *J. Natl. Cancer Inst.* **1998**, *90*, 889−905.
2. Popovic, E. A.; Kaye, A. H.; Hill, J. S. Photodynamic therapy of brain tumors. *J. Clin. Laser Med. Surg.* **1996**, *14*, 251−261.
3. Barth, R. F.; Soloway, A. H.; Fairchild, R. D.; Brugger, R. M. Boron neutron capture therapy for cancer. Realities and prospects. *Cancer* **1992**, *70*, 2995−3007.
4. Hawthorne, M. F. The role of chemistry in the development of boron neutron capture therapy of cancer. *Angew. Chem., Int. Ed. Engl.* **1993**, *32*, 950−984.
5. Fairchild, R. G.; Kahl, S. B.; Laster, B. H.; Kalef, E. J.; Popenoe, E. A. In vitro determination of uptake, retention, distribution, biological efficacy, and toxicity of boronated compounds for neutron capture therapy: a comparison of porphyrins with sulfhydryl boron hydrides. *Cancer Res.* **1990**, *50*, 4860−4865.
6. Kahl, S. B.; Koo, M. Synthesis of tetrakis-carborane-carboxylate ester of 2,4-bis-(a,b-dihydroxyethyl) deuterioporphyrin IX. *J. Chem. Soc., Chem. Commun.* **1990**, *24*, 1769−1771.
7. Hill, J. S.; Kahl, S. B.; Kaye, A. H.; Stylli, S. S.; Koo, M.; Gonzales, M. F.; Vardaxis, N. J.; Johnson, C. I. Selective tumor uptake of a boronated porphyrin in an animal model of cerebral glioma. *Proc. Natl. Acad. Sci. U.S.A.* **1992**, *89*, 1785−1789.
8. Chen, C. W.; Cohen, J. S.; Myers, C. E.; Sohn, M. Paramagnetic metalloporphyrins as potential contrast agents in NMR imaging. *FEBS Lett.* **1984**, *168*, 70−74.
9. Lyon, R. C.; Faustino, P. J.; Cohen, J. S. Tissue distribution and stability of metalloporphyrin MRI contrast agents. *Magn. Reson. Med.* **1987**, *4*, 24−33.
10. Huang, L.; Straubinger, R.; Kahl, S.; Koo, M.; Alletto, J.; Mazurchuk, R.; Chau, R.; Thamer, S.; Fiel, R. Boronated metalloporphyrins: a novel approach to the diagnosis and treatment of cancer using contrast-enhanced MR imaging and neutron capture therapy. *J. Magn. Reson. Imaging* **1993**, *3*, 351−356.
11. Weizsaecker, M.; Deen, D. F.; Rosenblum, M. L.; Hoshino, T.; Gutin, P. H.; Barker, M. The 9L rat brain tumor: description and application of an animal model. *J. Neurol.* **1981**, *224*, 183−192.
12. Huang, L. R. Magnetic resonance imaging: contrast enhancement of brain tumor pathology through chemical intervention. State University of New York at Buffalo, Ph.D. Dissertation, 1994.
13. Szoka, F. C., Jr.; Papahadjopoulos, D. Procedure for preparation of liposomes with large internal aqueous space and high capture by reverse-phase evaporation. *Proc. Natl. Acad. Sci. U.S.A.* **1978**, *75*, 4194−4198.
14. Bartlett, G. R. Phosphorus assay in column chromatography. *J. Biol. Chem.* **1959**, *234*, 466−468.

15. Sharma, A.; Straubinger, R. M. Novel taxol formulations: preparation and characterization of taxol-containing liposomes. *Pharm. Res.* **1994**, *11*, 889−896.
16. Szoka, F. C., Jr.; Olson, F.; Heath, T.; Vail, W.; Mayhew, E.; Papahadjopoulos, D. Preparation of unilamellar liposomes of intermediate size (0.1−0.2 μm) by a combination of reverse phase evaporation and extrusion through polycarbonate membranes. *Biochim. Biophys. Acta* **1980**, *601*, 559−571.
17. Gabizon, A.; Papahadjopoulos, D. Liposome formulations with prolonged circulation time in blood and enhanced uptake by tumors. *Proc. Natl. Acad. Sci. U.S.A.* **1988**, *85*, 6949−6953.
18. Papahadjopoulos, D.; Allen, T. M.; Gabizon, A.; Mayhew, E.; Matthay, K.; Huang, S. K.; Lee, K.-D.; Woodle, M. C.; Lasic, D. D.; Redemann, C.; Martin, F. J. Sterically stabilized liposomes: improvements in pharmacokinetics and antitumor therapeutic efficacy. *Proc. Natl. Acad. Sci. U.S.A.* **1991**, *88*, 11460−11464.
19. Sharma, U. S.; Sharma, A.; Chau, R. I.; Straubinger, R. M. Liposome-mediated therapy of intracranial brain tumors in a rat model. *Pharm. Res.* **1997**, *14*, 992−998.
20. Allen, T. M.; Chonn, A. Large unilamellar liposomes with low uptake into the reticuloendothelial system. *FEBS Lett.* **1987**, *223*, 42−46.
21. Hawthorne, M. F.; Shelly, K. Liposomes as drug delivery vehicles for boron agents. *J. Neur. Oncol.* **1997**, *33*, 53−58.
22. Feakes, D. A.; Shelly, K.; Hawthorne, M. F. Selective boron delivery to murine tumors by lipophilic species incorporated in the membranes of unilamellar liposomes. *Proc. Natl. Acad. Sci. U.S.A.* **1995**, *92*, 1367−1370.
23. Feakes, D. A.; Shelly, K.; Knobler, C. B.; Hawthorne, M. F. $Na_3[B_{20}H_{17}NH_3]$: synthesis and liposomal delivery to murine tumors. *Proc. Natl. Acad. Sci. U.S.A.* **1994**, *91*, 3029−3033.
24. Yanagie, H.; Tomita, T.; Kobayashi, H.; Fujii, Y.; Nonaka, Y.; Saegusa, Y.; Hasumi, K.; Eriguchi, M.; Kobayashi, T.; Ono, K. Inhibition of human pancreatic cancer growth in nude mice by boron neutron capture therapy. *Br. J. Cancer* **1997**, *75*, 660−665.
25. Mayhew, E.; Rustum, Y. M.; Szoka, F.; Papahadjopoulos, D. Role of cholesterol in enhancing the antitumor activity of cytosine arabinoside entrapped in liposomes. *Cancer Treat. Rep.* **1979**, *63*, 1923−1928.
26. Senior, J.; Gregoriadis, G. Stability of small unilamellar vesicles in serum and clearance from the circulation: the effect of the phospholipid and cholesterol components. *Life Sci.* **1982**, *30*, 2123−2136.
27. Hunt, C. A. Liposome disposition in vivo. V. Liposome stability in plasma and implications for drug carrier function. *Biochim. Biophys. Acta* **1982**, *719*, 450−463.
28. Balasubramanian, S. V.; Straubinger, R. M. Taxol-lipid interactions: taxol-dependent effects on the physical properties of model membranes. *Biochemistry* **1994**, *33*, 8941−8947.
29. Janoff, A. S.; Boni, L. T.; Popescu, M. C.; Minchey, S. R.; Cullis, P. R.; Madden, T. D.; Taraschi, T.; Gruner, S. M.; Shyamsunder, E.; Tate, M. W.; Mendelsohn, R.; Bonner, D. Unusual lipid structures selectively reduce the toxicity of amphotericin B. *Proc. Natl. Acad. Sci. U.S.A.* **1988**, *85*, 6122−6126.
30. Szoka, F. C., Jr.; Papahadjopoulos, D. Comparative properties and methods of preparation of lipid vesicles (liposomes). *Annu. Rev. Biophys. Bioeng.* **1980**, *9*, 467−508.
31. Sankaram, M. B.; Thompson, T. E. Modulation of phospholipid acyl chain order by cholesterol. A solid-state ^2H NMR study. *Biochemistry* **1990**, *29*, 10676−10684.
32. Sankaram, M. B.; Thompson, T. E. Cholesterol-induced fluid phase immiscibility in membranes. *Proc. Natl. Acad. Sci. U.S.A.* **1991**, *88*, 8686−8690.
33. Semple, S. C.; Chonn, A.; Cullis, P. R. Influence of cholesterol on the association of plasma proteins with liposomes. *Biochemistry* **1996**, *35*, 2521−2525.
34. Lasic, D.; Martin, F.; Gabizon, A.; Huang, S.; Papahadjopoulos, D. Sterically stabilized liposomes: a hypothesis on the molecular origin of the extended circulation times. *Biochim. Biophys. Acta* **1991**, *1070*, 187−192.
35. Sharma, A.; Mayhew, E.; Straubinger, R. M. Antitumor effect of taxol-containing liposomes in a taxol-resistant murine tumor model. *Cancer Res.* **1993**, *53*, 5877−5881.

Acknowledgments

We thank Dr. Frank Szoka, University of California at San Francisco, for advice on the encapsulation of MnBOPP, Dr. Myoung-Seo Koo for preparation of the MnBOPP, and the Pharmaceutical Sciences Instrumentation Facility (UB) for data acquisition. Support for this work was provided in part by research grants from the National Institutes of Health, United States Public Health Service (CA55251 to R.M.S. and CA37961 to S.B.K.) and from the Association for Research of Childhood Cancer (to R.M.S.).

JS980454I

Pharmacokinetics of Fluphenazine, a Highly Lipophilic Drug, Estimated from a Pulse Dose of a Stable Isotopomer in Dogs at Steady State

JOHN W. HUBBARD,* SALIM HADAD, JIANG-PING LUO, GORDON MCKAY, AND KAMAL K. MIDHA

Contribution from *College of Pharmacy & Nutrition, University of Saskatchewan, Saskatoon, Saskatchewan, Canada, S7N 5C9.*

Received November 10, 1998. Final revised manuscript received March 30, 1999.
Accepted for publication June 7, 1999.

Abstract □ The potential utility of a pulse dose of a deuterium-labeled isotopomer (FLU-D_4) in elucidating the pharmacokinetics of fluphenazine (FLU) at steady state was investigated in dogs. The single-dose oral pharmacokinetics of FLU in dogs were established. After resting the dogs for 3 weeks, the animals were dosed to steady state with oral FLU administered at 12-h intervals. Following 15 doses, one dose of FLU was replaced by a pulse dose of FLU-D_4, after which dosing with FLU was resumed. FLU and FLU-D_4 plasma concentrations were determined by tandem mass spectrometry. Comparable estimates of apparent oral clearance were calculated from (i) a single dose of FLU, (ii) a pulse dose of FLU-D_4, and (iii) over a dosing interval at steady state. Average steady-state plasma concentrations were reliably predictable from a pulse dose of FLU-D_4.

Introduction

A difficult task facing the psychiatrist is the determination of the optimal dose of neuroleptic for an individual patient in the acute phase of a psychosis because therapeutic effects of treatment with classical neuroleptics generally require 2−4 weeks to become optimal. Aggressive dosing in the early stages of treatment, however, may lead to the establishment of unnecessarily high maintenance doses.[1] Dysken and co-workers[2] suggested that a therapeutic window of 0.2 to 2.8 ng/mL trough concentrations of fluphenazine (FLU) in plasma was appropriate for schizophrenic patients. These early studies, however, gave no indication of the extent to which aberrantly high plasma levels are associated with inferior antipsychotic response.[3] A more recent and more sophisticated study by Van Putten and colleagues[4,5] employed logistic regression and survival analysis to examine relationships between plasma concentrations of FLU, estimated probability of improvement, and estimated probability of disabling side effects. Disabling side effects were defined as "side effects that significantly interfered with patients' functioning" or "side effects that outweigh therapeutic effects." The study showed that the probability of improvement increased as plasma FLU concentrations approached 4.0 ng/mL, but so did the probability of disabling side effects. It was found that the maximum probability of improvement without disabling side effects occurred at a plasma FLU concentration of 0.7 ng/mL.[5] Thus, patients who tolerate the drug well may benefit from plasma concentrations >1.0 ng/mL, whereas poorly responding patients with plasma levels of 4.0 ng/mL and above may benefit from a reduction in dosage. These data have provided a more rational basis for the use of plasma concentration data in FLU posology.

The acquisition of pharmacokinetic data from floridly psychotic acute schizophrenics, however, is difficult or impossible because these patients are usually too ill to be able to cooperate by providing samples of body fluids. It is certainly not appropriate to interrupt therapy to obtain single-dose pharmacokinetic data. In this situation, therefore, individualized pharmacokinetic information must be acquired after the clinical condition of the patient has been stabilized by treatment with a neuroleptic drug such as FLU. The use of a pulse dose of a stable isotopomer to assess the pharmacokinetics of a single dose of the drug while at steady state[6] is an appealing technique for two reasons: (i) there is no need to interrupt therapy or to disturb the steady state of active drug; and (ii) stabilized schizophrenic out-patients under maintenance therapy with oral FLU often take their medication at uneven time intervals, which renders uncertain any attempt to estimate pharmacokinetic parameters from plasma concentrations of unlabeled drug at steady state.

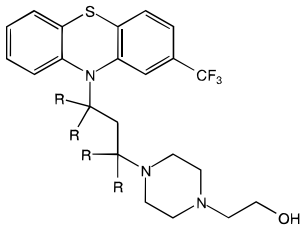

Figure 1—Structures FLU (R = H) and tetradeuterated FLU (R = ^{2}H).

FLU is a lipophilic drug that exhibits after intravenous dosing in humans (Midha et al., unpublished data), a very large apparent volume of distribution (398 ± 202 L), a relatively short half-life (13.1 ± 4.1 h), and a systemic clearance (23.0 ± 12.3 L/h) of ∼25% of liver blood flow. Similar results were obtained after beagle dogs were dosed intravenously with FLU:[7] a large volume of distribution (51.0 ± 17.8 L), a relatively short half-life (6.0 ± 1.5 h), and a systemic clearance (5.8 ± 1.0 L/h) of ∼40% of liver blood flow. These data suggest that FLU undergoes extensive tissue distribution/binding in both humans and dogs. The present exploratory study in dogs was designed to test the hypothesis that exchange of isotopomer with unlabeled drug in tissue compartments would not impede the utility of the technique in practical terms. A tetradeuterated isotopomer (FLU-D_4, Figure 1) to be used in such studies was prepared in these laboratories[8] and was shown to be free of any isotopic metabolic effects in either humans[9] or dogs.[10]

Materials and Methods

Chemicals and Reagents—FLU dihydrochloride was purchased from Sigma-Aldrich Canada, Ltd. (Ontario, Canada). FLU-D_4 was synthesized in our laboratories as described previously.[8] The isotopic purity of FLU-D_4 was >99%. Oral solutions containing FLU dihydrochloride equivalent to 1 mg/mL FLU base in distilled water were prepared daily. Oral solutions of the FLU-D_4 were

* To whom correspondence should be addressed. E-mail: Hubbard@duke.usask.ca.

10.1021/js980440c CCC: $18.00
Published on Web 08/14/1999

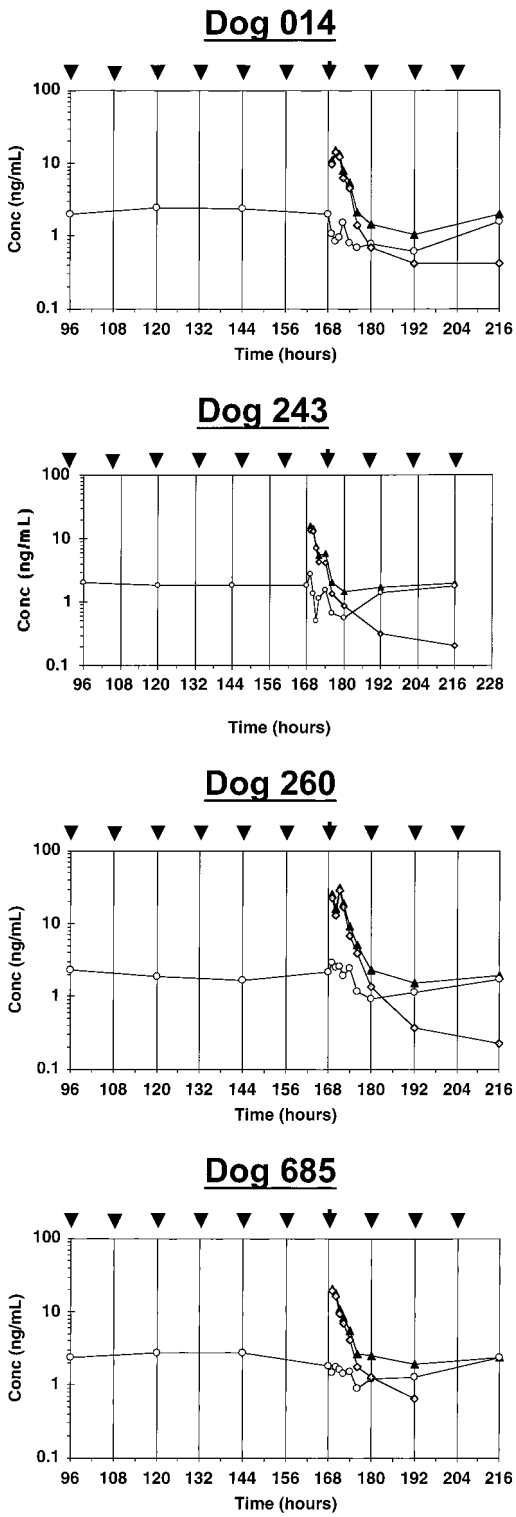

Figure 2—Steady-state trough plasma concentrations over the interval 96–216 h after the initial dose for FLU (circles), FLU-D_4 (diamonds), and total (FLU plus FLU-D_4, triangles) in four dogs. In each panel, black darts represent doses of FLU at 12-h intervals and the gray dart represents the pulse dose of FLU-D_4.

prepared in the same manner. Solvents and other chemicals were of analytical grade and were used without further purification.

Animals and Study Design—The study protocol was approved by the University of Saskatchewan Animal Care Committee. The experiments were carried out according to the Principles of Laboratory Animal Care (NIH Publication #85-23, revised 1985) and under conditions specified by the Canadian Council on Animal Care. Four pure bred female beagle dogs (ID nos. 014, 243, 260, and 685), ranging in weight (initially) from 7.0 to 9.5 kg (mean 8.1 ± 1.1 kg), were used. For each dose, the oral solution (2 mL, containing FLU or FLU-D_4 hydrochloride equivalent to 2 mg of the corresponding base) was trickled from a syringe (3 mL) into the right side of the dog's mouth over a period of 2−3 min. Immediately after administration of the oral solution, the right side of the mouth was slowly irrigated with 5 mL of distilled water. The oral pharmacokinetics of unlabeled FLU were determined from serial blood samples (5 mL) drawn via an indwelling jugular catheter at 0 (predose) and 0.25, 0.5, 1, 2, 4, 6, 8, 12, 24, 36, and 48 h after a single oral dose. The animals were rested for 3 weeks, after which they were dosed to steady state with unlabeled FLU administered at 12-h intervals (09:00 and 21:00 h). After administration of 15 doses of FLU (168 h after the initial dose), the dogs were re-weighed and a pulse dose of FLU-D_4 was given in place of a regular dose of FLU. Blood samples (5 mL) were harvested immediately prior to administration of FLU-D_4 and at 1, 2, 3, 4, 6, 8, 12, 24, 36, and 48 h post FLU-D_4. (Unfortunately the blood samples at 36 h were lost because of a technical error). Administration of unlabeled drug was resumed for a total of three doses post FLU-D_4, as shown in Figure 2. Trough steady-state plasma concentrations were established as the arithmetic mean of minimum concentrations (C_{min}) of FLU plasma concentrations harvested at 72, 96, 120, 144, and 168 h after the initial dose and of total (FLU+FLU-D_4) C_{min} plasma concentrations at 180, 192, and 216 h post initial dose. After collection of each sample, plasma was separated by centrifugation within 0.5 h and frozen (−20 °C) until analysis. Concentrations of FLU and FLU-D_4 in plasma were monitored by means of a validated tandem mass spectrometry technique[11] with a lower limit of detection of 25 pg/mL for both FLU and FLU-D_4, and overall coefficients of variation of 4.82% for FLU and 4.72% for FLU-D_4.

Pharmacokinetic Analysis—The plasma concentrations versus time data for both FLU-D_4 and FLU were analyzed by noncompartmental methods (WinNonlin Version 1.1). Steady-state trough plasma concentrations were estimated as the mean of eight measurements, five taken before administration of the pulse dose of FLU-D_4 and three taken post pulse dose. The accumulation index (R_{ac})[12] was estimated according to eq 1:

$$R_{ac} = \frac{\mathbf{1}}{(\mathbf{1} - e^{-k\tau})} \tag{1}$$

where τ is the dosing interval, and k is an estimated apparent terminal elimination rate constant following a single oral dose. The average plasma concentration of drug at steady state ($Cpss_{av}$) was calculated according to eq 2:

$$Cpss_{av} = \frac{AUC_\tau}{\tau} \tag{2}$$

where AUC_τ was estimated from the total plasma concentration (FLU plus FLU-D_4). Apparent oral clearances (CL_O) were estimated variously as (i) dose/AUC_∞ from a single dose of FLU, (ii) dose/AUC_∞ from a pulse dose of FLU-D_4, and (iii) dose/AUC_τ calculated from the sum of FLU and FLU-D_4 plasma concentrations in dogs at steady state. Apparent volumes of distribution (V_d) were estimated as the quotient of CL_o and k.

A relationship between CL_o and $Cpss_{av}$ was established as follows:[12]

$$Cpss_{av} \propto A$$

$$Cpss_{av} \times V_d = A$$

$$Cpss_{av} \times CL = A \times k = \frac{F \times \text{Dose}}{\tau}$$

$$Cpss_{av} = \frac{F \times \text{Dose}}{CL \times \tau} = \frac{\text{Dose}}{CL_o \times \tau} \tag{3}$$

where A is the amount of drug in the body.

Results and Discussion

FLU and FLU-D_4 (Figure 1) were shown previously to give virtually identical plasma concentration versus time

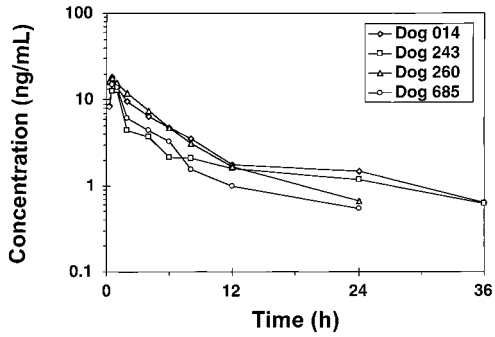

Figure 3—Plasma concentration versus time curves after single oral doses of FLU in four dogs.

profiles in schizophrenic patients[9] and in beagle dogs.[10] It was thereby concluded that the isotopomer was devoid of any isotopic metabolic effects in either humans or dogs.

After a single oral dose, plasma concentrations of FLU were measurable up to 24 h in two dogs and up to 36 h in the remaining two (Figure 3). The very short t_{max} (0.25 h in 1/4 dogs and 0.5 h in 3/4 dogs) may have been attributable to rapid absorption through the buccal mucosae. This method of administration was chosen for two reasons. Earlier (unpublished) experiments had shown that oral administration of the drug in gelatin capsules to dogs led to erratic absorption characteristics. Administration of an oral solution was clearly desirable but it was not practicable to inflict gastric intubation on the animals twice a day for 1.5 weeks. Thus, the irrigated oral solution was the best compromise to give minimal variability. The apparent elimination half-life of FLU after the single oral dose was 12.75 ± 3.25 h, which is comparable to that obtained[13] after a single oral dose in humans, but at variance with an earlier study from our laboratories[7] in which the reported half-life was 6.0 ± 1.5 h after intravenous administration of FLU in four different beagle dogs (ID nos. 236, 244, 341, 960).

Once dosing to steady state with a lipophilic drug has commenced, drug from each successive dose undergoes exchange with drug from earlier doses sequestered in deep compartments. In the present study, dosing at 12-h intervals with unlabeled drug was continued until the dogs had received 15 doses, which in clinical terms would be a minimum number of doses after which rational dosage adjustments might be attempted. Moreover, it is possible that the deep compartments were fully loaded at this point. Individual plasma concentration versus time plots rather than averaged data are shown in Figure 2 to give an impression of (i) the steady state, (ii) the profile of the pulse dose of FLU-D_4, and (iii) the behavior of unlabeled FLU after the administration of the pulse dose of isotopomer.

Figure 2 shows a segment from 96 through 216 h of the steady state achieved by regular 12-h doses of 2 mg of FLU. At 168 h, one dose of FLU was replaced by a pulse dose of FLU-D_4 after which the mass spectrometer discriminated between FLU-D_4 (diamonds) and FLU (circles). Arithmetic mean trough steady-state plasma concentrations (mean ng/mL ± SD) were as follows: dog 014, 2.06 ± 0.29; dog 243, 1.77 ± 0.23; dog 260, 1.98 ± 0.29; and dog 685, 2.24 ± 0.47. In each case, the geometric mean steady-state concentration was close to the corresponding arithmetic mean (ng/mL): dog 014, 2.04; dog 243, 1.75; dog 260, 1.96; and dog 685, 2.19. The accumulation index (eq 1) was relatively low (mean ± SD = 2.089 ± 0.377).

It was possible to monitor FLU-D_4 for 48 h post pulse dose in 3 of the 4 dogs. Each animal showed undulations in the plasma concentrations of FLU after the pulse dose of FLU-D_4, suggesting that FLU arising from earlier doses of unlabeled drug appeared to rebound. Observation of this phenomenon indicates the presence of saturable distribution and/or tissue binding because rebound would not be expected to occur if distribution and/or tissue binding processes were linear. Saturable tissue binding has no effect on CL_o but does affect V_d and therefore the apparent elimination rate constant. As anticipated, therefore, estimates of apparent volume of distribution after a pulse dose of FLU-D_4 at steady state tended to be smaller than those estimated from the single dose (Table 1) because the latter was beginning the process of loading deep compartments. Maximum change in apparent volume of distribution should occur when the deep compartments are fully loaded. Failure to reach statistical significance (ANOVA) was probably due to low statistical power in this pilot study. The effects of saturable tissue binding, however, might explain why the terminal portions of the plasma concentration versus time curves of FLU-D_4 do not appear to be log linear (Figure 2). Consequently the data points at 48 h post FLU-D_4 were not used in estimates of apparent elimination rate constants. The weight-corrected apparent oral clearances estimated from the pulse dose were very similar to those estimated by dose/AUC_τ or from the single oral dose in each dog (Table 1).

Table 1— Comparison of Apparent Oral Clearance and Volume of Distribution after a Single Oral Dose of Fluphenazine or a Pulse Dose of Isotopomer in Dogs at Steady State on Fluphenazine

	CL_o(L/kg/h)			V_d(L/kg)	
dog	single dose[a]	pulse dose[a]	steady state[b]	single dose[c]	pulse dose[c]
014	1.81	2.86	2.92	44.67	42.15
243	2.82	3.60	3.45	52.73	40.05
260	2.12	2.17	2.02	28.81	15.75
685	2.77	2.83	3.02	45.84	46.59
mean ± SD	2.38 ± 0.50	2.86 ± 0.59	2.86 ± 0.60	43.01 ± 10.11	36.14 ± 13.86

[a] Dose/AUC∞. [b] Dose/AUCτ (where AUCτ estimated from total FLU + FLU-D4 over a dosing interval). [c] CL_o/k (where CL_o estimated as dose/AUC∞).

Table 2— Comparison of Observed $Cpss_{av}$ (ng/mL) at Steady State with Values Calculated from Single Dose Data and from a Pulse Dose of Isotopomer

		predicted steady state	
dog	observed steady state[a]	single dose[b]	pulse dose[b]
014	6.0	10.0	6.1
243	5.7	6.9	6.5
260	11.8	8.5	11.0
685	7.4	5.6	7.9
mean ± SD	8.9 ± 2.2	7.7 ± 1.9	8.4 ± 2.4

[a] AUCτ/τ (where AUCτ estimated from total FLU + FLU-D4 over a dosing interval). [b] Dose/CL_o*τ (where CL_o estimated as dose/AUC∞).

$Cpss_{av}$, however, is not affected by saturable tissue binding. One would therefore expect predictions of $Cpss_{av}$ from a single dose of FLU calculated by eq 3 to be similar to those estimated from a pulse dose of FLU-D_4 at steady state (eq 2). Table 2 shows good within-dog agreement between $Cpss_{av}$ values estimated from the pulse dose and those observed in the steady state. Pharmacokinetic parameters calculated from the steady state, however, may not be of value for patients in whom the dosing interval may vary, whereas a pharmacokinetic parameters calculated from a pulse dose of the isotopomer should be applicable in such patients.

Conclusions

The results from this study suggest that the oral pharmacokinetics estimated from a pulse dose of FLU-D_4 would

be a viable method applicable to patients at steady state on oral FLU. The technique is potentially useful in schizophrenic patients who respond to treatment with potent neuroleptics but are sensitive to side effects and therefore require doses at the low end of the therapeutic range.

References and Notes

1. Tupin, J. Focal neuroleptization: An approach to optimal dosing for initial and continuing therapy. *J. Clin. Psychopharmacol.* **1985**, *5*, 15S−21S.
2. Dysken, M. W.; Javaid, J. I.; Chang, S. S.; Schaffer, C.; Shahid, A.; Davis, J. M. Fluphenazine Pharmacokinetics and Therapeutic Response. *Psychopharmacology* **1981**, *73*, 205−210.
3. Van Putten, T.; Marder, S. R.; Wirshing, W. C.; Aravagiri, M.; Chabert, N. Neuroleptic plasma levels. *Schizophr. Bull.* **1991**, *17*, 197−216.
4. Van Putten, T.; Aravagiri, M.; Marder, S. R.; Wirshing, W. C.; Mintz, J.; Chabert, N. Plasma fluphenazine levels and clinical response in newly admitted schizophrenic patients. *Psychopharmacol. Bull.* **1991**, *27*, 91−96.
5. Midha, K. K.; Hubbard, J. W.; Marder, S. R.; Marshall, B. D.; Van Putten, T. Impact of clinical pharmacokinetics on neuroleptic therapy in patients with schizophrenia. *J. Psychiatr. Neurosci.* **1994**, *19*, 254−264.
6. Eichelbaum, M.; von Unruh, G.; Somogyi, A. Application of stable labeled drugs in clinical pharmacokinetic investigations. *Clin. Pharmacokinet.* **1982**, *7*, 490−507.
7. Luo, J.-P.; Hubbard, J.; Midha, K. Studies on the mechanism of absorption of depot neuroleptics: fluphenazine decanoate in sesame oil. *Pharmaceut. Res.* **1997**, *14*, 1079−1084.
8. Sardessai, M. S.; Brander, M. J.; Midha, K. K.; Hawes, E. M. Synthesis of deuterium labeled fluphenazine utilizing borane reduction. *J. Labelled Compd. Radiopharm.* **1986**, *23*, 317−327.
9. Hadad, S.; Hubbard, J. W.; McKay, G.; Hawes, E. M.; Shrikhande, S.; Midha, K. K. Evidence for the lack of a human metabolic isotope effect of a deuterium analogue of fluphenazine. *Pharmaceu. Res.* **1995**, *12*, 1388−1390.
10. Edom, R.; McKay, G.; Hawes, E.; Midha, K. In *Proceedings of the 37th ASMS Conference on Mass Spectrometry and Alled Topics*; Miami Beach, Florida, 1989; pp 684−685.
11. Hadad, S.; Edom, R.; McKay, G.; Hawes, E. M.; Midha, K. K. Simultaneous measurement of fluphenazine and [H-2(4)]-fluphenazine in plasma using solids probe tandem mass spectrometry. *J. Mass Spectrom.* **1995**, *30*, 849−856.
12. Rowland, M.; Tozer, T. *Clin. Pharmacokinet. Concepts Applications*, 2nd ed.; Lea & Febiger: Philadelphia and London, 1989.
13. Midha, K. K.; Hawes, E. M.; Hubbard, J. W.; Korchinski, E. D.; McKay, G. Variation in the single dose pharmacokinetics of fluphenazine in psychiatric patients. *Psychopharmacology* **1988**, *96*, 206−211.

JS980440C

A Novel Prodrug Approach for Tertiary Amines. 2. Physicochemical and in Vitro Enzymatic Evaluation of Selected *N*-Phosphonooxymethyl Prodrugs

JEFFREY P. KRISE, SHINJI NARISAWA,† AND VALENTINO J. STELLA*

Contribution from *Department of Pharmaceutical Chemistry, The University of Kansas, 2095 Constant Avenue, Lawrence, Kansas 66047.*

Received September 21, 1998. Final revised manuscript received May 21, 1999.
Accepted for publication May 26, 1999.

Abstract □ Quaternary amine prodrugs resulting from *N*-phosphonooxymethyl derivatization of the tertiary amine functionality of drugs represents a novel approach for improving their water solubility. Separate reports have demonstrated the synthetic feasibility and rapid and quantitative prodrug to parent drug conversion in rats and dogs. This work is a preliminary evaluation of the physicochemical and in vitro enzymatic reversion properties of selected prodrugs. The loxapine prodrug had over a 15 000-fold increase in aqueous solubility relative to loxapine free base at pH 7.4. The loxapine prodrug was also shown to be quite stable at neutral pH values. The time for degradation product (parent drug) precipitation from an aqueous prodrug formulation would be expected to dictate the shelf life. Using this assumption, together with solubility and elevated temperature chemical stability studies, the shelf life of a parenteral formulation of the loxapine prodrug was projected to be close to 2 years at pH 7.4 and 25 °C. In addition, the prodrugs of cinnarizine and loxapine have been shown to be substrates for alkaline phosphatase, an enzyme found throughout the human body, and revert to the parent compound in its presence. The results from these evaluations demonstrate that the derivatives examined have many of the ideal properties required for potential clinical application.

Introduction

In separate reports, the synthesis and biological evaluation of a novel prodrug approach for improving the water solubility of tertiary amine containing drugs was described.[1,2] A representation of the prodrug strategy is shown in Scheme 1. The parent tertiary amine containing drug **1** is chemically modified to produce the quaternary, water-soluble, prodrug **2**. The prodrug releases the parent tertiary amine in vivo through a two-step bioreversion process. The first step (k_1, rate determining step) in this bioreversion involves a dephosphorylation (phosphatase-catalyzed) to give the resultant hydroxymethyl quaternary ammonium intermediate **4** and inorganic phosphate (**3**). This intermediate **4** is highly unstable at neutral pH and spontaneously breaks down (k_2) to give the parent tertiary amine **1** plus formaldehyde (**5**).

Drugs are most often identified by their ability to interact with target receptors, and their physicochemical properties are initially of secondary concern. With a drug exhibiting poor aqueous solubility, the safe and efficient delivery to the site of action may be an obstacle.[3,4] The solubility behavior of weakly basic drugs such as tertiary amine

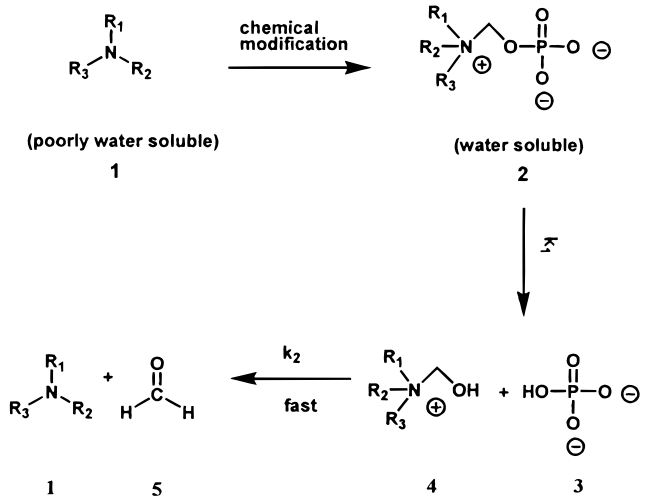

Scheme 1—Illustration of the Novel Prodrug Strategy.

containing drugs is dependent upon individual molecular properties and the environment in which the drug finds itself. Generally, an ionized molecule is more water-soluble than an un-ionized form, and aqueous formulations are sometimes designed at low pH to utilize the greater solubility of the ionized species.[5] With weakly basic amines (low pK_a), the pH necessary for acceptable solubility may be too acidic to be of practical use. In addition, the intrinsic solubility of the amine salt may be low. This being the case, other means for improving the solubility are often used, such as the addition of cosolvents[6] or complexing agents.[7] Whether using pH extremes and/or organic solvents to improve the solubility, the risk of drug precipitation at the injection site is high for parenterally administered drug.[8,9] This is due to pH changes and/or dilution of cosolvent.

Producing quaternary ammonium prodrugs (of tertiary amine containing drugs) to improve the solubility has been attempted.[10−13] The toxic nature of many quaternary amines[14−16] along with the superior chemical stability of derivatives resulting from simple *N*-alkylation may be responsible for the lack of favorable results.

The shelf life of fosphenytoin (**9-P**), a water soluble prodrug of phenytoin, has been shown to be dictated by the time it takes for phenytoin to precipitate from the aqueous formulation at neutral pH.[17] Likewise, the stability-limiting factor for a formulation containing *N*-phosphonooxymethyl prodrugs would be expected to be the same and not simply be the time for some percentage (i.e., 10%) loss of prodrug.

This report also serves to confirm the in vitro enzymatic lability of selected prodrugs in the presence of alkaline

* To whom correspondence should be addressed. Phone: (785) 864-3755. FAX: (785) 749-7393. Email: stella@hbc.ukans.edu.
† Current address: Tanabe Seiyaku Co., Ltd., Japan.

10.1021/js9803813 CCC: $18.00
Published on Web 07/09/1999

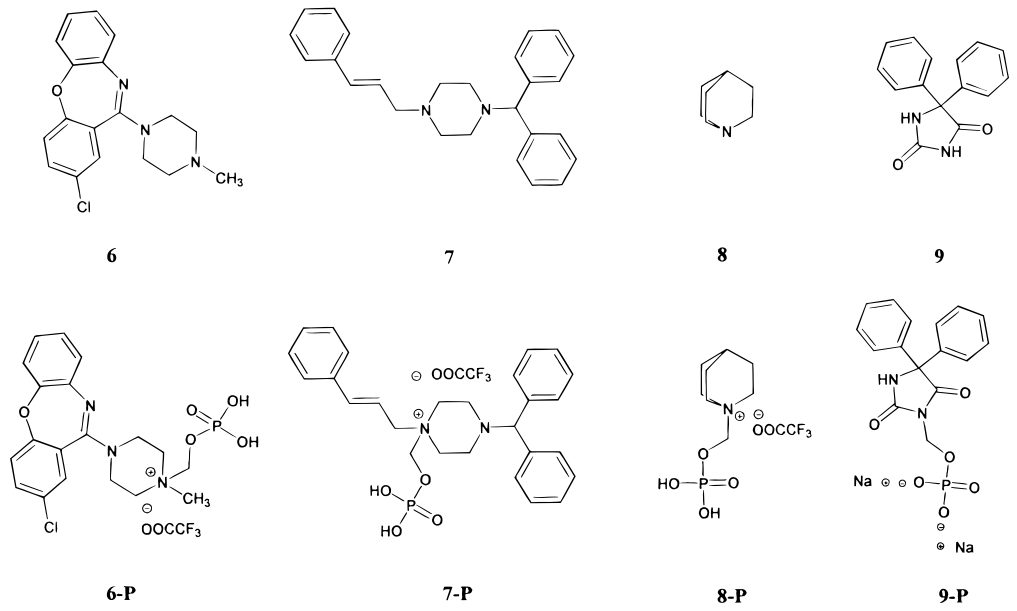

Figure 1—Structures of loxapine (**6**), *N*-phosphonooxymethyl loxapinium trifluoroacetate (**6-P**), cinnarizine (**7**), *N*-phosphonooxymethyl cinnarizinium trifluoroacetate (**7-P**), quinuclidine (**8**), *N*-phosphonooxymethyl quinuclidinium trifluoroacetate (**8-P**), phenytoin (**9**), and fosphenytoin (**9-P**).

phosphatase. Alkaline phosphatase is found throughout the body and is mainly associated with membranes of the intestine, placenta, bone, liver, and kidney in high concentration.[18,19] As mentioned, these prodrugs are designed to be substrates for phosphatases in vivo, which would trigger a rapid chemical breakdown releasing the parent tertiary amine.

Structures of the compounds examined in this work are depicted in Figure 1.

Experimental Section

Materials—**6-P**, **7-P**, and **8-P** were synthesized from a previously described synthetic procedure.[1] Loxapine succinate was obtained from Research Biochemicals Incorporated (Natick, MA). **9-P** was obtained from Parke-Davis Pharmaceuticals (Ann Arbor, MI). Human placental alkaline phosphatase, Type XVII (4.4 units/mg) was obtained from Sigma Chemical Company (St. Louis, MO). All other chemicals were obtained from conventional sources and were used without further purification.

pK_a Determination (Potentiometric)—A 0.01 M quinuclidine prodrug aqueous solution (dihydrogen phosphate form) was titrated using a buret containing a 0.1 N sodium hydroxide volumetric standard solution. The pH was recorded with a calibrated Corning pH/ion analyzer (Corning Incorporated, Corning, NY) after each 0.25 mL addition of NaOH. This experiment was conducted at 25 °C, and all solutions were purged with dry nitrogen gas. The pK_a was calculated from the titration data according to the method of Albert and Seargent.[20]

pK_a Determination (^{31}P NMR)—A 0.25 mmol quantity of the prodrug was dissolved in a 10% v/v D_2O in H_2O solution to prepare a stock solution of 10 mL total volume. Samples spanning the expected pK_a were made by adding minute volumes of a 0.1 N NaOH aqueous solution and recording the pH. Aliquots (0.5 mL) were withdrawn from the stock solution after each pH measurement, transferred to NMR tubes, capped, and frozen at −20 °C until analysis at 25 °C. Spectra were recorded from a Bruker AM 500 MHz NMR spectrophotometer that was tuned to the ^{31}P nucleus. The change in chemical shift was recorded as a function of pH. An insert tube, containing 30% H_3PO_4, was inserted into each NMR tube prior to analysis to serve as an internal reference for the ^{31}P chemical shift of the prodrugs.

The equilibrium for the second ionization of the prodrugs' phosphate monoester (K_{a2}) is represented in Scheme 2. Ignoring the first ionization (K_{a1}), the fraction of prodrug in the zwitterionic form (f_Z) and the fraction in the net anionic form (f_A) are expressed

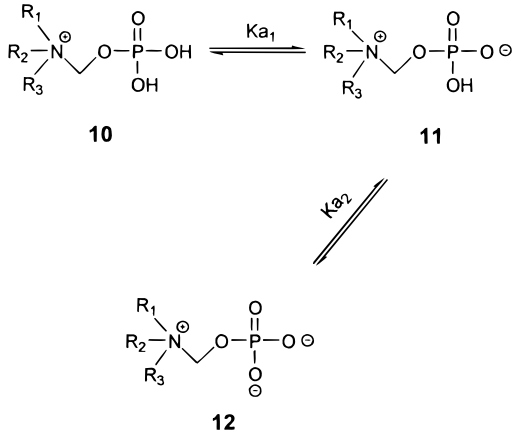

Scheme 2—Possible Ionic Species of the *N*-phosphonooxymethyl Prodrugs.

in eqs 1 and 2, respectively, where $[H^+]$ represents hydronium ion

$$f_Z = \frac{[H^+]}{[H^+] + K_{a2}} \quad (1)$$

$$f_A = \frac{K_{a_2}}{[H^+] + K_{a2}} \quad (2)$$

molar concentration. The observed chemical shift (δ_{obs}) of the ^{31}P signal is expressed in eq 3, where δ_Z and δ_A represent the chemical

$$\delta_{obs} = f_Z\delta_Z + f_A\delta_A \quad (3)$$

shift for the zwitterionic and net anionic prodrug, respectively. Substituting eqs 1 and 2 into eq 3 gives eq 4. The experimental

$$\delta_{obs} = \frac{[H^+]\delta_Z + K_a\delta_A}{[H^+] + K_a} \quad (4)$$

data was fit to eq 4 using SigmaPlot graphics software (SPSS Inc., Chicago, IL) to estimate values for K_{a2}.

Solubility Determinations—Loxapine succinate was converted to the free base before conducting experiments. All experimental solutions contained 0.05 M buffer and were adjusted to

an ionic strength of 0.2 with NaCl. The pH values with each buffer composition are listed: pH 3.24, HCl/CH_3COONa; pH 3.96 and 4.96, CH_3COOH/CH_3COONa; pH 5.82−7.94, NaH_2PO_4/Na_2HPO_4; pH 8.95 and 9.98, H_3BO_3/NaOH. To glass containers were added 0.2 mL of buffer for the **6-P** samples and 2 mL for the samples of **6**. Each buffered solution was saturated with **6** or **6-P**. The vials were then capped, sonicated, and vortexed prior to submersion in a constant temperature shaking water bath at 25 °C. The samples were shaken at a rate of 100 shakes/min for 24 h. The samples were then centrifuged, and the clear supernatants were diluted and analyzed by HPLC for **6**/**6-P**.

Chemical Stability Evaluations—All experimental solutions contained 0.05 M buffer and were adjusted to an ionic strength of 0.2 with NaCl. The pH values along with their buffer composition are listed: pH 2.05, HCl; pH 3.27, HCl/CH_3COONa; pH 3.94 and 4.95, CH_3COOH/CH_3COONa; pH 5.82−7.94, 8.36, NaH_2PO_4/Na_2HPO_4. Stock solutions for each pH were prepared by dissolving approximately 0.2 mg of **6-P** in 10 mL of buffer. The solution was then assayed for initial prodrug concentration. One-milliliter aliquots were taken and separated into nine glass ampules and sealed. The samples were then submerged in a constant temperature water bath at 65, 75, or 85 °C until analysis. At predetermined times the ampules was opened and mixed with 0.5 mL of acetonitrile to dissolve any precipitate. Each solution was then assayed for prodrug content by HPLC. Individual estimations of k_{obs} were obtained in triplicate by curve-fitting the experimental data to eq 5 (SigmaPlot, SPSS Inc., Chicago, IL), where A is the

$$A = A_0\, e^{-k_{obs}t} \tag{5}$$

prodrug concentration, A_0 is the initial prodrug concentration, k_{obs} is the first-order rate constant for loss of prodrug, and t is time. The loss of prodrug was followed for at least one half-life for all determinations.

In Vitro Enzymatic Lability Evaluations—All experiments involving alkaline phosphatase were performed in a pH 10.4 glycine buffer at 37 °C. The buffer solution contained 1 mM $ZnCl_2$, 1 mM $MgCl_2$, and 0.1 M glycine. The final pH of the buffer was adjusted to pH 10.4 with additions of 2 N NaOH.

For the Michaelis−Menten kinetic evaluation, an alkaline phosphatase stock solution was prepared at a concentration of 149.1 μg/mL (656.0 units/L) in glycine buffer. Four stock solutions of **6-P** (815.3, 163.0, 81.5, and 16.3 μM) were prepared in glycine buffer. To 200 μL of each **6-P** stock solution in a shaking water bath maintained at 37 °C was added 120 μL of the alkaline phosphatase stock solution (at 37 °C). The final concentration of alkaline phosphatase was 245.9 units/L, and the final concentrations of **6-P** were 509.5, 101.9, 51.0, and 10.2 μM. Each reaction was quenched and diluted with addition of 192 μL of a 0.2 N acetic acid solution, 250 μL of acetonitrile, and 232 μL of HPLC mobile phase at predetermined time points (t = 0, 5, 15, and 20 min). Each solution was then vortexed for 30 s, injected into the HPLC, and assayed for **6**.

The initial linear appearance of loxapine was plotted as a function of time for each initial loxapine prodrug concentration following alkaline phosphatase addition. The slope of each was recorded as the initial rate of the reaction. The calculation of Michaelis−Menten parameters was done through plotting the data according to the Lineweaver−Burke equation (eq 6), where V is

$$\frac{1}{V} = \frac{K_m}{V_{max}}\frac{1}{S} + \frac{1}{V_{max}} \tag{6}$$

the initial rate of the reaction, S is the initial concentration of the prodrug, K_m is the Michaelis−Menten constant, and V_{max} is the maximum velocity of the reaction. The slope of this linear plot is equivalent to K_m/V_{max}, and the y-intercept is equal to $1/V_{max}$. From these two relationships the K_m and V_{max} were calculated.

For the enzymatic lability comparisons, stock solutions of alkaline phosphatase (588.7 units/ml), **7-P** (815.9 μM), **6-P** (815.3 μM), and **9-P** (803.6 μM) were prepared in glycine buffer. To 200 μL of prodrug stock solution in a shaking water bath maintained at 37 °C was added 120 μL of the alkaline phosphatase stock solution (at 37 °C). The final concentration of alkaline phosphatase was 220.1 units/L and the final **7-P**, **6-P** and **9-P** concentrations were 509.9, 509.5, and 502.3 μM, respectively. The reaction was quenched and diluted with 100 μL of a 0.4 N acetic acid solution and 200 μL of acetonitrile at predetermined time points (t = 0, 10, 20, 30, 40, and 60 min.). After quenching, each solution was vortexed for 30 s, injected into the HPLC, and assayed for prodrug.

HPLC Conditions—The HPLC system hardware used for all compounds consisted of a Shimadzu LC-6A pump (Kyoto, Japan), a Shimadzu RF-535 fluorescence detector, a Shimadzu SPD-6A UV spectrophotometer, a Shimadzu CR-601 integrator, and Rheodyne 7125 injector (Cotati, CA).

For the analysis of **6**/**6-P**, the mobile phase consisted of acetonitrile (32% v/v) and a 25 mM ammonium phosphate monobasic buffer solution adjusted to pH 3.8 with phosphoric acid (68% v/v). This was pumped at a flow rate of 0.9 mL/min. The injection volume was 20 μL, and the detection was performed by absorbance at 254 nm. The column used for analysis was a Waters Symmetry C-18 150 mm × 4.6 mm with 5 μm particle size (Milford, MA). The retention times were 3.5 and 4.5 min for **6-P** and **6**, respectively.

For the analysis of **7-P**, the mobile phase consisted of acetonitrile (40% v/v) and a 25 mM potassium phosphate monobasic buffer solution adjusted to pH 3.8 with phosphoric acid (60% v/v). The entire mobile phase contained 0.5 mM tetrabutylammonium dihydrogen phosphate (0.5 mM). This was pumped at a flow rate of 1 mL/min. The injection volume was 20 μL, and the detection was by absorbance at 254 nm. The column used for analysis was a Chemco Nucleosil C-18 150 mm × 4.6 mm with 5 μm particle size (Osaka, Japan). The retention time of **7-P** was 4 min.

For the analysis of **9-P**, the mobile phase consisted of acetonitrile (35% v/v) and a 25 mM potassium phosphate monobasic buffer solution adjusted to pH 3.8 with phosphoric acid (65% v/v). This was pumped at a flow rate of 1.1 mL/min. The injection volume was 50 μL, and detection was by fluorescence using an excitation wavelength of 260 nm and an emission wavelength of 315 nm. The column used for analysis was a C18 ODS Hypersil 15 cm × 4.6 mm with 5 μM particle size. The retention time of **9-P** was 4 min.

Results and Discussion

Solubility Evaluation—For the *N*-phosphonooxymethyl prodrugs to be useful for parenteral delivery, they must have sufficient water solubility at the desired formulation pH, preferably in the physiologically acceptable pH range. Limited quantities of prodrug materials prevented us from fully elucidating the pH solubility behavior of the prodrugs. Some limited estimates and predictions were made, however.

The prodrugs have a quaternary center that bears a cationic charge at all pH values, and the phosphate monoester has an ionization scheme depicted in Scheme 2. The phosphate ester exists in equilibrium between the diacidic **10**, monobasic **11**, and the dibasic species **12**, and the fraction of each species present in solution is a function of the pK_a values and the pH of the solution. The overall net charge of the prodrug will be zero when the phosphate ester is predominantly monobasic **11**. Accordingly, at this pH, the water-solubility of this prodrug species would be expected to be the least. Lowering or raising the pH several units from this pH should increase the solubility of the prodrug, as the net charge of the prodrug will become plus one and minus one, respectively.

The pK_{a_2} of the phosphate ester is important considering its potential influence on the solubility, chemical stability, and effectiveness as an enzymatic substrate in the physiological pH range. The pK_{a1} is expected to be less than one and of little physiological importance, except that it is quite acidic. The pK_{a2} was determined by ^{31}P NMR and was found to be 4.7 and 4.9 for **6-P** and **8-P**, respectively. A plot of the ^{31}P NMR chemical shift as a function of pH for **8-P** is shown in Figure 2. The pK_{a2} for **8-P** was 5.0 by potentiometric titration, which was in close agreement with the value determined by ^{31}P NMR.

The measured solubility of **6-P** at pH 3 was 290.5 ± 2.9 mg/mL, which is expected to be a reasonable estimate of

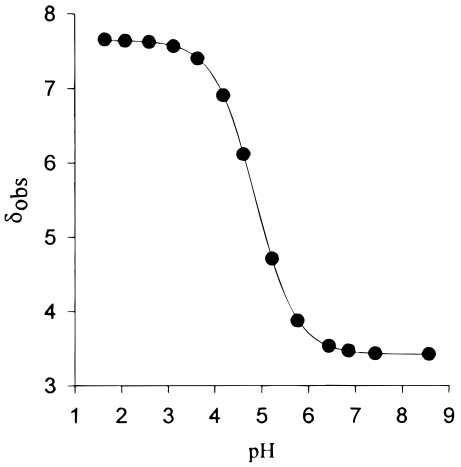

Figure 2—Plot of the observed chemical shift of the ^{31}P NMR signal from **8-P** as a function of pH. The solid line is the curve fit to the experimental data.

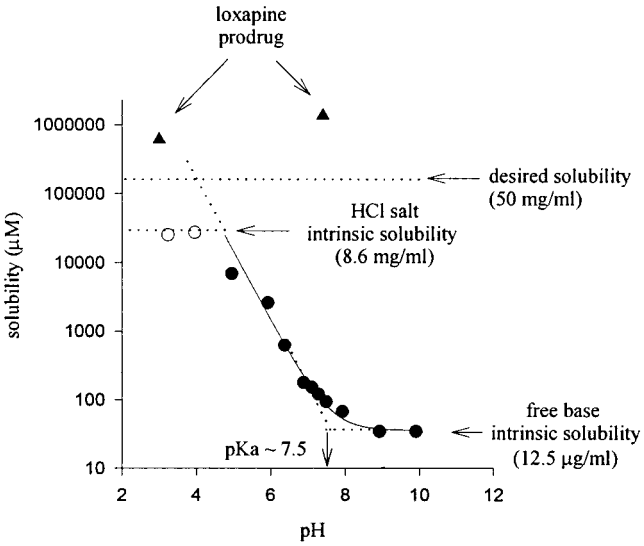

Figure 3—Plot of the water solubility of **6** (●, ○) and **6-P** (▲) as a function of pH.

the solubility of **6-P** in the least soluble zwitterionic form. When the pH was raised to 7.4, the solubility of the prodrug more than doubled (648.2 ± 0.6 mg/mL). Figure 3 compares the solubility behavior of **6-P** relative to **6** as a function of pH. The solid points represent the experimentally determined solubilities for **6** as a function of pH. The line through these points is a theoretical plot of the solubility profile obtained through curve fitting the experimental data to eq 7, where S_t is the total measured solubility of **6**,

$$\log S_t = \log\left(\frac{[H^+]}{K_a} + 1\right) + \log S_o \qquad (7)$$

$[H^+]$ is the hydrogen ion molar concentration, K_a is the acid dissociation constant for the protonated amine, and S_o is the intrinsic solubility of the free base. Estimates of S_o and pK_a were obtained through curve fitting and were found to be 12.6 μg/mL and 7.5, respectively.

Lowering the pH is a common method used for improving the solubility of weakly basic drugs through ionization. Even at pH 3.2, however, the solubility of **6** only reaches 8.2 mg/mL, which is still distant from the desired formulation concentration of 50 mg/mL. **6-P** offers over a 15 000-fold increase in solubility compared to the free base at pH 7.4. This translates to prodrug solubilities that are over

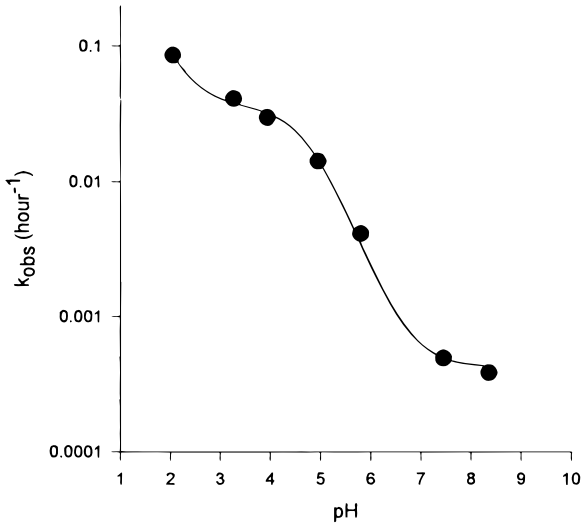

Figure 4—Plot of the observed rate constant (k_{obs}) for loss of **6-P** as a function of pH at 65 °C. The solid line is the curve fit to the experimental data.

nine times higher than those used in the im formulation without the need for cosolvents.

Chemical Stability Evaluation—The prodrugs must have adequate chemical stability in any formulation, especially in ready-to-use parenteral dosage forms. The pH rate profile for **6-P** at 65 °C is shown in Figure 4. The pH of maximum stability occurs in the neutral pH range, which is ideal for formulation from a physiological viewpoint.

The prodrug can exist in three distinct ionic species (see Scheme 2). Because each of these is potentially reactive, several mechanistic pathways for the degradation are possible. A theoretical profile, in reasonable agreement with the observed profile, was constructed according to eq 8, where k_{obs} is the observed rate constant for loss of

$$k_{obs} = \frac{k_o[H^+]^2 + k'_oK_{a1}[H^+] + k''_oK_{a1}K_{a2}}{[H^+]^2 + [H^+]K_{a1} + K_{a1}K_{a2}} \qquad (8)$$

prodrug while K_{a1} and K_{a2} are the first and second acid dissociation constants for the phosphate ester. The k_o, k'_o, and k''_o variables represent the rate constants for water-catalyzed or spontaneous hydrolysis of the diacidic **10**, monobasic **11**, and dibasic **12** phosphate species of the prodrug, respectively. Values for k_o, k'_o, k''_o, and K_{a2} were estimated through curve fitting while the value for K_{a1} was fixed at 0.4 (estimated value). The parameters used to generate the theoretical profile in Figure 4 were as follows: $k_o = 2.32 \pm 0.21$ h^{-1}; $k'_o = (3.62 \pm 0.24) \times 10^{-2}$ h^{-1}; $k''_o = (4.24 \pm 1.95) \times 10^{-4}$ h^{-1}; $K_{a1} = 0.4$; $K_{a2} = (1.73 \pm 0.36) \times 10^{-5}$. The kinetically determined pK_{a2} value of 4.76 ± 0.08 at 65 °C was in good agreement with the value of 4.7 ± 0.01 determined by ^{31}P NMR at 25 °C, especially considering the temperature differences.

The shape of this profile is consistent with other phosphate monoesters for which the increased rate of hydrolysis at low pH is consistent with the higher reactivity of the monobasic phosphate species.[21−26]

A concentrated parenteral formulation of a water-soluble prodrug (of a sparingly soluble drug) might produce sparingly soluble products following degradation. The stability-limiting factor, therefore, may be parent drug precipitation. The precipitation is expected to occur far in advance to the time for 10% loss of prodrug ($t_{90\%}$) often used as an indicator of shelf life of pharmaceuticals. Figure 5 shows Arrhenius plots for the loss of **6-P** at pH values 5.8, 7.45, and 8.36 at temperatures of 65, 75, and 85 °C. From the slope of these plots, Arrhenius activation energies were calculated to be

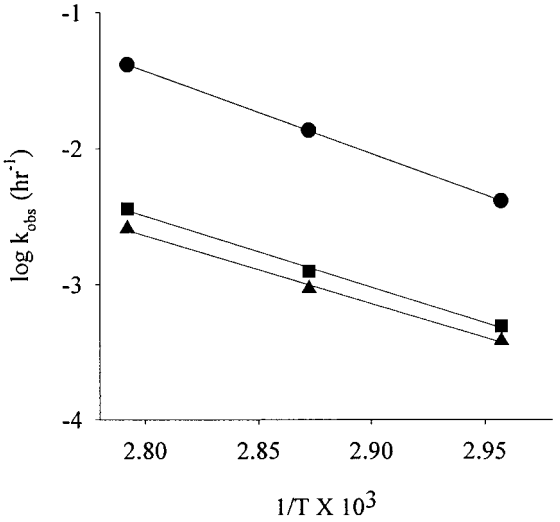

Figure 5—Arrhenius plots for **6-P** degradation at pH values 5.8 (●), 7.4 (▲), and 8.36 (■). The temperatures studied were 65, 75, and 85 °C. Error bars are hidden by the symbols.

Table 1—Arrhenius Plot Extrapolations of the Mean (±SD) k_{obs}, Half-Life, and $t_{90\%}$ for *N*-Phosphonooxymethyl Loxapine Degradation at 25 °C at Several pH Values

pH	k_{obs} (hr^{-1} 10^6)	$t_{1/2}$ (years)	$t_{90\%}$ (years)
5.36	16.2 ± 0.1	4.8 ± 0.1	0.7 ± 0.1
7.45	3.7 ± 0.7	21.1 ± 5.3	3.2 ± 0.8
8.36	3.6 ± 0.7	21.7 ± 5.6	3.3 ± 0.8

27.7 ± 0.2, 23.9 ± 0.8, and 22.9 ± 0.7 kcal/mol at pH values 5.8, 7.4, and 8.3, respectively. These values were then used to predict the $t_{90\%}$, half-life ($t_{1/2}$), and k_{obs} for **6-P** degradation at 25 °C listed in Table 1.

To estimate the shelf life based upon precipitation of **6**, the following example is used. An im formulation of **6-P** at a concentration of 72 mg/mL (equivalent to 50 mg/mL of **6**) at pH 7.4 could only tolerate 0.06% degradation before the solubility of **6** (30 μg/mL) is exceeded. Using the k_{obs} from Table 1 at pH 7.4 to calculate the time for 0.06% degradation ($t_{99.94\%}$) gives a value of 6.7 days, which is drastically shorter than the 3.2 year $t_{90\%}$ estimate from Table 1. This calculation assumes that upon degradation **6-P** is quantitatively converted to **6** and that the solution of **6-P** does not alter the solubility of **6**. Fortunately, a solution of **6-P** at a concentration of 72 mg/mL does in fact improve the solubility of **6**. The intrinsic solubility of **6** at pH 11.8 in a solution containing 72 mg/mL of **6-P** ($n = 1$, as a result of lack of prodrug material) was found to be 2.7 mg/mL. Taking this solubility change into account, a possible shelf life ($t_{94.6\%}$) for **6-P** at pH 7.4 would be about 1.7 years. The solubility of **6** would be expected to be higher than 2.7 mg/mL at pH 7.4 compared to pH 11.8. Therefore, the shelf life of 1.7 years is probably an underestimate.

In Vitro Evaluation—For the derivatives to behave as prodrugs, they must undergo a rapid and quantitative enzymatic bioreversion. The prodrugs are designed to undergo a two-step bioreversion process to give the parent amine, formaldehyde, and inorganic phosphate (Scheme 1). The first step in bioreversion is a rate-determining, enzyme-catalyzed dephosphorylation step ($\mathbf{k_1}$) followed by a fast chemical breakdown ($\mathbf{k_2}$) of the hydroxymethyl derivative (**4**).

In an earlier report, **6-P** and **7-P** were shown to be substrates for alkaline phosphatase. Further evaluation of this enzymatic process can provide information on the kinetics of hydrolysis. The hydrolysis kinetics of **6-P** were

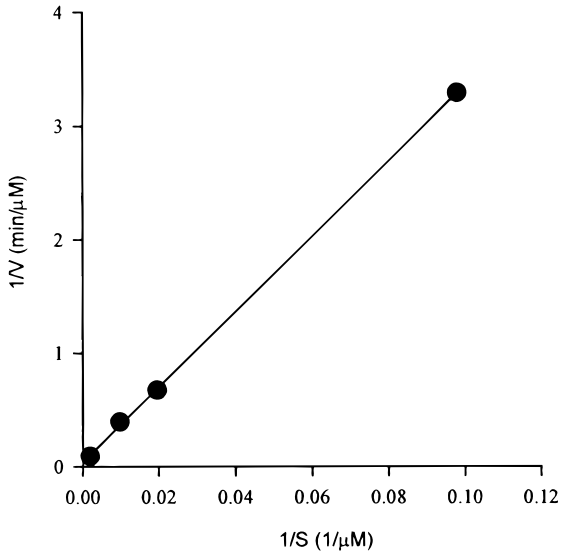

Figure 6—Lineweaver–Burke plot for the enzymatically catalyzed dephosphorylation of **6-P** with alkaline phosphatase at pH 10.4 and 37 °C.

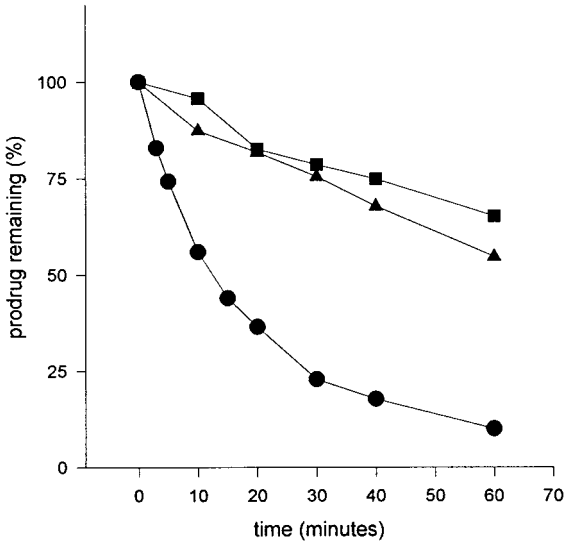

Figure 7—Plot of percent prodrug remaining as a function of time for **9-P** (●), **6-P** (▲), and **7-P** (■) in the presence of alkaline phosphatase.

found to be consistent with a Michaelis–Menten kinetic model similar to other phosphate monoesters reported in the literature.[27,28]

The values for K_m and V_{max} were 872 μM and 26 μM/min obtained from a Lineweaver–Burke plot shown in Figure 6. The value for k_{cat} (0.9 s^{-1}) was obtained by dividing V_{max} by the molar enzyme concentration. The value for k_{cat}/K_m (the second-order rate constant for catalysis) was 1063 M^{-1} s^{-1}. This value is similar to[27] and significantly lower[29] than values others have reported, but comparing these k_{cat}/K_m values may be somewhat meaningless because the enzyme source and experimental conditions of temperature and pH were different.

Fosphenytoin (Cerebyx, **9-P**) is a commercially available phosphate prodrug of phenytoin that requires an in vivo enzyme-catalyzed dephosphorylation step to release phenytoin.[30] Fosphenytoin is rapidly converted to phenytoin in humans with a half-life of approximately 8 min.[31] A comparison of the in vitro labilities of the prodrugs in the presence of isolated alkaline phosphatase would provide some insight as to how the cinnarizine and loxapine prodrugs might behave in vivo. Figure 7 is a plot of % prodrug remaining versus time for **6-P** and **7-P** compared

to fosphenytoin with isolated alkaline phosphatase. Each of the prodrugs was found to be chemically stable under the experimental conditions when the solution was devoid of enzyme. From this plot it appears that enzyme-catalyzed breakdown of **7-P** and **6-P** are similar, and **9-P** appears to be catalyzed at a significantly faster rate. The rapid in vivo conversion of the *N*-phosphonooxymethyl prodrugs in rats and dogs would not have predicted this trend; however, the inability of in vitro trends to predict in vivo results is not uncommon. It also cannot be ruled out that alkaline phosphatase may not exclusively be responsible for the catalytic dephosphorylation; catalytic promiscuity displayed by other enzymes (i.e., esterases) may be responsible for a significant fraction of the in vivo enzymatic reversion.

Conclusion

The *N*-phosphonooxymethyl prodrug approach has been described as a novel method for improving the water solubility of tertiary amine containing drugs. Separate reports have demonstrated the synthetic feasibility and rapid and quantitative prodrug to parent drug conversion in rats and dogs, which are essential characteristics for a clinically useful prodrug. This work has confirmed the prodrugs to have dramatically improved water solubility behavior and very good chemical stability at physiological pH values. The prodrugs have also been shown to be substrates for alkaline phosphatase, which triggered the release of the parent molecule. These results suggest that this approach for improving the water solubility of tertiary amine containing drugs is very promising and deserves further evaluation.

References and Notes

1. Krise, J. P.; Zygmunt, J.; Georg, G.; Stella, V. J. A Novel Prodrug Approach for Tertiary Amines: Synthesis and Preliminary Evaluation of *N*-Phosphonooxymethyl Prodrugs. *J. Med. Chem.* **1999**, in press.
2. Krise, J. P.; Charman, W. N.; Charman, S. A.; Stella, V. J. A Novel Prodrug Approach for Tertiary Amines. 3. In Vivo Evaluation of Two *N*-Phosphonooxymethyl Prodrugs in Rats and Dogs. *J. Pharm. Sci.* **1999**, *88*, 928−932.
3. Yalkowsky, S. H.; Krzyzaniak, J. F.; Ward, G. H. Formulation-Related Problems Associated with Intravenous Drug Delivery. *J. Pharm. Sci.* **1998**, *87*, 787−796.
4. Fleisher D.; Bong, R.; Stewart, B. H. Improved Oral Drug Delivery−Solubility Limitations Overcome by the Use of Prodrugs. *Adv. Drug Del. Rev.* **1996**, *19*, 115−130.
5. Damia, G.; D'Incalci, M. Clinical Pharmacokinetics of Altretamine. *Clin. Pharmacokinet.* **1995**, *28*, 439−448.
6. Singhai, A. K.; Jain, S.; Jain, N. K. Cosolvent Solubilization and Formulation of an Aqueous Formulation of Ketoprofen. *Pharmazie* **1996**, *51*, 737−740.
7. Amdidouche, D.; Darrouzet, H.; Duchêne, D.; Poelman, M. C. Inclusion of Retinoic Acid in β-cyclodextrin. *Int. J. Pharm.*, **1989**, *54*, 175−179.
8. Myrdal, P. B.; Simamora, P.; Surakitbanharn, Y.; Yalkowsky, S. H. Studies in Phlebitis. VII: In Vitro and in Vivo Evaluation of pH-Solubilized Levemopamil. *J. Pharm. Sci.* **1995**, *84*, 849−852.
9. Ward, G. H.; Yalkowsky, S. H. Studies in Phlebitis. VI: Dilution Induced Precipitation of Amiodarone HCl. *J. Parent. Sci. Technol.* **1993**, *47*, 161−165.
10. Vinogradova, N. D.; Kuznetsov, S. G.; Chigareva, S. M. Quaternary Ammonium Salts with Labile N+-C Bonds as Drug Precursors. *Khim.-Farm. Zh.* **1980**, *14*, 41−47.
11. Bogardus, J. B.; Higuchi, T. Kinetics and Mechanism of Hydrolysis of Labile Quaternary Ammonium Derivatives of Tertiary Amines. *J. Pharm. Sci.* **1982**, *71*, 153−159.
12. Tercel, M.; Wilson, W. R.; Denny, W. A. Nitrobenzyl Mustard Quaternary Salts: A New Class of Hypoxia-Selective Cytotoxins Showing Very High In Vitro Selectivity. *J. Med. Chem.* **1993**, *36*, 2578−2579.
13. Davidson, S. K.; Summers, J. B.; Albert, D. H.; Holms, J. H.; Heyman, H. R.; Magcoc, T. J.; Conway, R. G.; Rhein, D. A.; Carter, G. W. *N*-(Acyloxyalkyl) Pyridinium Salts as Soluble Prodrugs of a Potent Platelet Activating Factor Antagonist. *J. Med. Chem.* **1994**, *37*, 4423−4429.
14. Cooper, J. C. Review of the Environmental Toxicity of Quaternary Ammonium Halides. *Ecotoxic. Environ. Safety* **1988**, *16*, 65−71.
15. Dimmock, J. R.; Arora, V. K.; Quail, J. W.; Pugazhenthi, U.; Allen, T. M.; Kao, G. Y.; De Clercq, E. Cytotoxic Evaluation of Some 3,5-Diarylidene-4-piperidones and Various Related Quaternary Ammonium Compounds and Analogues. *J. Pharm. Sci.* **1994**, *83*, 1124−1130.
16. Sanders, J. M.; Griffin, R. J.; Burka, L. T.; Mathews, H. B. Toxicokinetics of the Cholinomimetic Compound Benzyltrimethylammonium Chloride in the Male Rat and Mouse. *Xenobiotica* **1995**, *25*, 303−313.
17. Narisawa, S.; Stella, V. J. Increased Shelf-Life of Fosphenytoin: Solubilization of a Degradant, Phenytoin, Through Complexation with $(SBE)_{7m}$-β-CD. *J. Pharm. Sci.* **1998**, *87*, 926−930.
18. Garattini, E.; Margolis, J.; Heimer, E.; Felix, A.; Udenfriend, S. Human Placental Alkaline Phosphatase in Liver and Intestine. *Proc. Natl. Acad. Sci. U.S.A.*. **1985**, *82*, 6080−6084.
19. Stigbrand, T.; Fishman, W. H. *Human Alkaline Phosphatases*. Alan R. Liss, New York, 1984.
20. Albert, A.; Serjeant, E. P. In *The Determination of Ionization Constants. A Laboratory Manual*. Chapman and Hall: London, 1984.
21. Varia, S. A.; Schuller, S.; Stella, V. J. Phenytoin Prodrugs IV: Hydrolysis of Various 3-(Hydroxymethyl) Phenytoin Esters. *J. Pharm. Sci.* **1984**, *73*, 1074−1079.
22. Kearney, A. S.; Stella, V. J. Hydrolysis of Pharmaceutically Relevant Phosphate Monoester Monoanions: Correlation to an Established Structure−Reactivity Relationship. *J. Pharm. Sci.* **1993**, *82*, 69−72.
23. Flynn, G. L.; Lamb, D. J. Factors Influencing Solvolysis of Corticosteriods-21-Phosphate Esters. *J. Pharm. Sci.* **1970**, *59*, 1433−1438.
24. Bunton, C. A. Hydrolysis of Monosubstituted Orthophosphate Esters. *J. Chem. Educ.* **1968**, *45*, 21−26.
25. Bunton, C. A.; Liewellyn, D. R.; Oldham, K. G.; Vernon, C. A. The Reaction of Organic Phosphates. Part I. The Hydrolysis of Methyl Dihydrogen Phosphate. *J. Chem. Soc.* **1958**, 3574−3594.
26. Kumamoto, J.; Westheimer, F. H. The Hydrolysis of Mono- and Dibenzyl Phosphates. *J. Am. Chem. Soc.* **1955**, *77*, 2515−2518.
27. Kearney, A. S.; Stella, V. J. The In Vitro Enzymatic Labilities of Chemically Distinct Phosphomonoester Prodrugs. *Pharm. Res.* **1992**, *9*, 497−503.
28. Safadi, M.; Oliyai, R.; Stella, V. J. Phosphoryloxymethyl Carbamates and Carbonates−Novel Water Soluble Prodrugs for Amines and Hindered Alcohols. *Pharm. Res.* **1993**, *10*, 1350−1355.
29. Simopoulos, T. T.; Jencks, W. P. Alkaline Phosphatase Is an Almost Perfect Enzyme. *Biochemistry* **1994**, *33*, 10375−10380.
30. Stella, V. J. A Case for Prodrugs: Fosphenytoin. *Adv. Drug Del. Rev.* **1995**, *19*, 311−330.
31. Gerber, N.; Mays, D. C.; Donn, K. H.; Laddu, A.; Guthrie, R. M.; Turlapaty, P.; Quon, C. Y. Safety, Tolerance and Pharmacokinetics of Intraveneous Doses of 3-Hydroxymethyl-5,5-diphenylhydantoin: A New Prodrug of Phenytoin. *J. Clin. Pharmacol.* **1988**, *28*, 1023−1032.

Acknowledgments

The authors thank the American Foundation for Pharmaceutical Education Fellowship and a National Cancer Institute Training Grant for financial support. Additional support was given by the Center for Drug Delivery Research and by Kansas Technology Enterprise Corporation through the Centers of Excellence program.

JS9803813

A Novel Prodrug Approach for Tertiary Amines. 3. In Vivo Evaluation of Two *N*-Phosphonooxymethyl Prodrugs in Rats and Dogs

JEFFREY P. KRISE,[†] WILLIAM N. CHARMAN,[‡] SUSAN A. CHARMAN,[‡] AND VALENTINO J. STELLA*,[†]

Contribution from *the Department of Pharmaceutical Chemistry, The University of Kansas, 2095 Constant Avenue, Lawrence, Kansas 66047, and Department of Pharmaceutics, Victorian College of Pharmacy, Monash University, Parkville, Melbourne 3052, Australia.*

Received September 21, 1998. Final revised manuscript received May 21, 1999.
Accepted for publication May 26, 1999.

Abstract □ *N*-Phosphonooxymethyl derivatives of tertiary amine containing drugs have been identified as a novel prodrug approach for improving aqueous solubility. The in vivo reversion of two prodrugs to the corresponding parent compounds following iv and im administration to rats and dogs was investigated. Equimolar doses of parent drugs (loxapine or cinnarizine) and the corresponding prodrugs were each administered via a rapid iv infusion to rats and dogs. Equimolar doses of loxapine and its prodrug were each administered im to rats only. Blood samples were collected over 12 h, and plasma was assayed for both parent drug and intact prodrug by HPLC. Comparison of the plasma AUC for the parent drugs following administration of the parent drugs and prodrugs allowed estimation of the apparent bioavailability of parent drug from prodrug dosing. Plasma levels of the prodrugs fell below the limit of detection 5 min after iv infusion with an approximate half-life of 1 min. The mean AUCs following iv and im dosing of parent drugs were not statistically different from the parent drug AUCs obtained after prodrug dosing. The results are consistent with rapid and quantitative prodrug to parent drug reversion following administration of the phosphonooxymethyl prodrugs to the rats and dogs. This information, together with previous studies on the synthesis and physicochemical evaluation of the prodrugs, suggests that this novel prodrug strategy is a very promising approach for overcoming solubility limitations seen with many tertiary amine containing drugs at physiological pH values.

Introduction

The synthesis and the physicochemical and in vitro enzymatic evaluation of a novel prodrug approach for improving the water solubility of tertiary amine containing drugs has been described.[1,2] A schematic of this prodrug strategy is shown in Scheme 1. The tertiary amine drug **1** is chemically derivatized to produce the quaternary water-soluble derivative **2**. This derivative was designed to behave as a prodrug and release parent tertiary amine following in vivo administration. This bioreversion process is thought to occur through two steps, the first step being a rate-determining (enzyme-catalyzed) dephosphorylation.

The *N*-phosphonooxymethyl prodrugs of two drugs, cinnarizine[3−7] and loxapine,[8] were selected for the in vivo evaluation of this prodrug strategy. Both drugs are sparingly water soluble. Cinnarizine is not formulated as an injectable, whereas loxapine (formulated for im use) requires a potentially toxic cocktail of propylene glycol and polysorbate 80.[9] Each of the prodrugs can be formulated in pure water at physiological pH, which might eliminate the vehicle-related toxicities encountered with poorly soluble drugs.

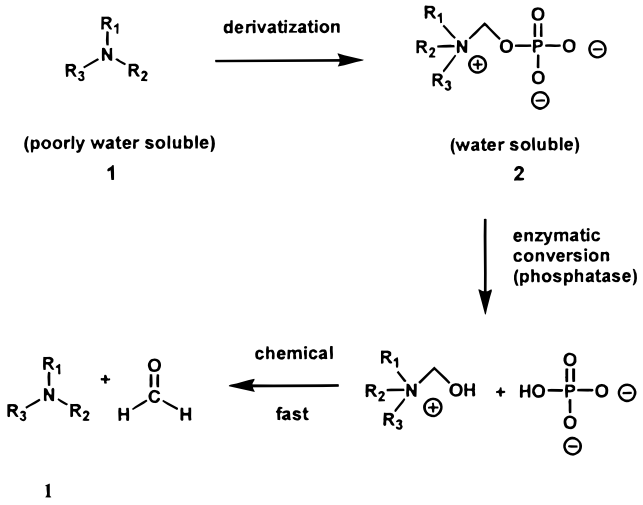

Scheme 1—Illustration of the *N*-Phosphonooxymethyl Prodrug Strategy.

The objective of the work described in this paper was to show that the *N*-phosphonooxymethyl derivatives of loxapine and cinnarizine quickly and quantitatively revert to parent compounds after administration to rats and dogs. To realize quantitative parent drug delivery, the rate of prodrug reversion must be optimal. Assuming that the prodrug does not extensively distribute into tissues, the prodrug can be removed by elimination (k_e) and conversion (k_r) to parent drug. If k_e is fast or even comparable to k_r, then quantitative recovery of parent drug would not occur. If k_r was large relative to k_e, quantitative delivery of parent drug would be realized and the pharmacokinetic profiles would be identical to those resulting from direct delivery of parent compound. Theoretically, a conversion that is too rapid may lead to some complications; however, in most cases a fast k_r is desirable both for quantitatively delivering parent drug and for reducing the risk of a pharmacological effect by the prodrug, if the prodrug is not completely inert.

Materials and Methods

Chemicals—Cinnarizine was obtained from Sigma Chemical Co. (St. Louis, MO). Loxapine succinate was obtained from Research Biochemicals Incorporated (Natick, MA). *N*-Phosphonooxymethyl derivatives of cinnarizine (**7-P**) and loxapine (**6-P**) (Figure 1) were synthesized as previously described.[1] $(SBE)_{7M}$-β-cyclodextrin (Captisol) was obtained from Cydex, Inc. (Overland Park, KS). Methyl *tert*-butyl ether was obtained from EM Science (Gibbstown, NJ). Isoflurane (Forthane) was obtained from Abbott

* To whom correspondence should be addressed. Phone: (785) 864-3755. FAX: (785) 749-7393. Email: stella@hbc.ukans.edu.
[†] University of Kansas.
[‡] Monash University.

10.1021/js980382v CCC: $18.00
Published on Web 07/09/1999

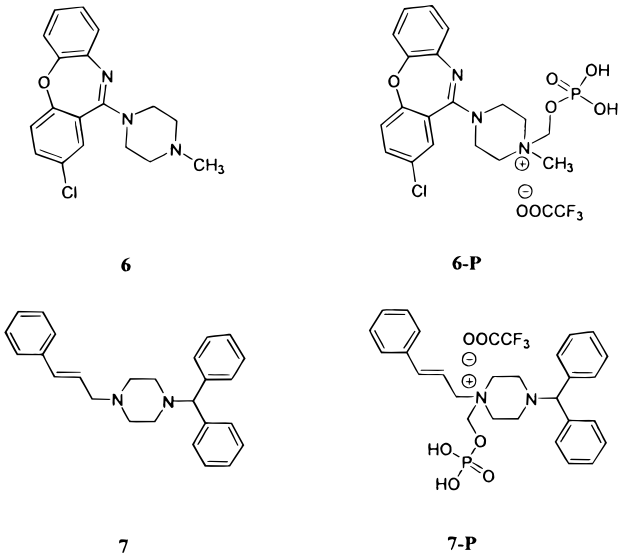

Figure 1—Structures of loxapine (**6**), *N*-phosphonooxymethyl loxapinium trifluoroacetate (**6-P**), cinnarizine (**7**), and *N*-phosphonooxymethyl cinnarizinium trifluoroacetate (**7-P**).

Australasia (Kurnell, Australia). All other chemicals were obtained from conventional sources.

Experimental Procedure, Rat Study—Male Sprague-Dawley rats (weight range 250−300 g) were fasted for 24 h prior to experimentation. The rats were anesthetized with a continuous 2% dose of isoflurane given by inhalation with a 95% O_2, 5% CO_2 carrier gas flowing at 1 L/minute. The rats were implanted with in-dwelling polyethylene cannulae (i.d. 0.58 mm, o.d. 0.965 mm) inserted into the jugular vein and the carotid artery for drug administration and blood sampling, respectively. The cannulae were sutured into position and then exteriorized through a subcutaneous tunnel made from the frontal neck incision to the back of the neck. The rats were then connected to a harness that secured the cannula while allowing the rat free mobility and access to water. The rats awoke 10 min after the cessation of anesthesia and were allowed to recover from the surgical procedure for at least 12 h before dosing. Intravenous doses were administered over 3 min into the jugular cannula, after which the cannula was flushed with 1 mL of normal saline containing 20 units/mL of heparin sodium. Intramuscular doses were administered into the hind leg using a 25 gauge needle. Blood samples (200 μL) for parent drug and prodrug analysis were taken from the carotid cannula before dosing and at predetermined time points following drug/prodrug administration. The sampling times for **6**/**6-P** were 0, 5, 15, and 30 min and 1, 2, 3, and 4 h postinfusion and 1, 5, 15, 30, and 45 min and 1, 2, 4, 6, and 8 h after the im injection. The sampling times for **7**/**7-P** were 0, 5, 10, 20, and 40 min and 1, 2, and 4 h postinfusion. After each blood sample, 200 μL of heparinized saline (20 units/mL) was infused through the carotid cannula. All blood samples were collected in microcentrifuge tubes containing 100 units of heparin sodium (20 μL of a 5000 units/mL solution) and were immediately centrifuged at 3000 rpm for 10 min with a Beckman SG-6R series centrifuge (Fullerton, CA). One hundred microliters of plasma was then separated and stored at −20 °C until analysis.

Experimental Procedure, Dog Study—The study was conducted as a 3 × 3 randomized crossover study in male beagle dogs (weight range 11.8−17.8 kg). The dogs were fasted for 1 day prior to drug/prodrug administration and were given a 1 week washout period between doses. In-dwelling venous catheters were placed in each front leg, one for dosing and the other for sampling. Blood samples (3 mL) for **6** and **6-P** analysis were taken before dosing and at 0, 5, 15, and 30 min and 1, 2, 4, and 6 h postinfusion. All catheters were flushed with 3 mL of heparinized saline (1 unit/mL) after dosing and after each blood sample. Blood samples were collected into 5 mL collection tubes containing EDTA and were immediately centrifuged at 10 000 rpm for 4 min, and 1.5 mL of plasma was separated and stored at −20 °C until extraction.

iv and im Formulations—A solution of **6** for iv infusion was prepared in a cosolvent formulation consisting of 10% (v/v) ethanol, 1.5% (v/v) benzyl alcohol, and 40% (v/v) propylene glycol. This is the commercially used vehicle for iv diazepam[10] and was employed because **6** is not available for iv delivery. A solution of **6** for im delivery was prepared in a cosolvent consisting of 70% (v/v) propylene glycol and 5% (v/v) polysorbate 80 in sterile water for injection, which is the commercially available im injection formulation for loxapine.[11]

A method of formulating **7** for iv infusion was adapted from Järvinen et al.[12] **7** was prepared in a 10 mM sodium phosphate buffer solution containing 37.5 mM of Captisol as a solubilizing excipient. The pH of the solution was lowered to pH 3.5 with addition of 1 M HCl solution. The solution was allowed to stir overnight at room temperature, and the final pH was adjusted to 5.5 with addition of 1 M NaOH.

All prodrugs for all routes of administration were formulated in phosphate buffered saline at pH 6.5 except for **6-P** for im delivery, which was formulated in normal saline. All solutions were passed through a 0.22 μM nylon filter and assayed for drug/prodrug content just prior to administration.

Plasma Extractions of 6, 6-P, 7, and 7-P—One milliliter or 100 μL plasma samples were obtained from the dog or rat blood, respectively, at specified time points. To the plasma following administration of **6**/**6-P** was added 20 μL of H_2O and 20% plasma volume of saturated $ZnSO_4$ (in 0.5 N NaOH). To the plasma following administration of **7**/**7-P** was added 20 μL of acetonitrile−H_2O (50:50) and 20 μL of 10% (w/v) trichloroacetic acid aqueous solution. To the protein-precipitated plasma was added 2 mL of methyl *tert*-butyl ether. Each sample was subsequently vortexed for one minute and centrifuged at 3000 rpm for 10 min. To assay for **6** or **7**, an aliquot of the organic layer (1.7 mL) was taken and evaporated to dryness with a stream of nitrogen gas. The residue was redissolved in 200 μL of HPLC mobile phase, vortexed briefly, and injected onto the HPLC. The efficiencies of the extraction procedure were 88% and 83% for **6** and **7**, respectively. To assay for **6-P** or **7-P**, the remaining aqueous phase from the ether extraction was evaporated to dryness under a stream of nitrogen gas (for rat plasma samples) or lyophilized (for dog plasma samples). To the dried residue was added 2 mL of methanol and 40 or 400 μL of 10% (w/v) trichloroacetic acid aqueous solution for the rat and dog samples, respectively. The mixture was vortexed for 5 min and centrifuged at 3000 rpm for 10 min. An aliquot of the organic layer (1.7 mL) was taken and reduced to dryness under a stream of nitrogen gas. The resulting residue was redissolved in 200 μL of water and vortexed briefly, after which the solution was filtered through a 0.2 μM microcentrifuge filter unit and injected into the HPLC. The efficiencies of the extraction procedure were 47% and 70% for **6-P** and **7-P**, respectively.

Stability of all drugs and prodrugs under the previously described conditions was assessed. Drugs **6** and **7** had complete stability for at least 2 h in whole blood. Prodrugs **6-P** and **7-P**, however, had detectable conversion to **6** and **7** in whole blood that was very temperature-dependent. The extent of this conversion was determined by spiking freshly drawn blood with a known concentration of prodrug and assaying for parent drug and prodrug with the described method. The extent of prodrug to drug conversion was less than 10% for both prodrugs within a 2 h period at room temperature, whereas approximately 50% of **6-P** was converted to **6** at 37 °C in the same amount of time. As a result, all blood samples were chilled on ice and processed as quickly as possible to limit ex vivo conversion.

To evaluate intraday and interday precision of the extraction methods, each procedure was repeated five times in 1 day and on 3 separate days with low, medium, and high plasma drug/prodrug concentrations. The percent standard deviations using either peak height or peak area values were generally less than 10% for both intraday and interday evaluations. Linear standard curves (r^2 > 0.990) resulted by spiking known amounts of drug/prodrug in blank plasma to achieve plasma concentrations in the range of interest for each compound.

HPLC Analysis—The HPLC system for all compounds consisted of a Waters model 510 pump, a Waters 717 autosampler (Milford, MA), a Perkin-Elmer LC240 fluorescence detector (Beaconsfield, Buckinghamshire, England), an LDC Analytical Spectromonitor 3100 variable wavelength detector, a Waters C18 Symmetry column (3.9 × 150 mm, Milford, MA), a Shimadzu CR6A intergrator (Kyoto, Japan), and a column heater (Timberline Instruments Inc., Boulder, CO).

For the analysis of **6**, the mobile phase consisted of acetonitrile (50% v/v) and a 10 mM ammonium dihydrogen phosphate buffer adjusted to pH 7 with ammonium hydroxide (50% v/v). This was pumped at a flow rate of 0.9 mL/min. The injection volume was 150 μL with detection at 251 nm. Under these conditions, the retention time was 11.4 min.

For the analysis of **6-P**, the mobile phase consisted of acetonitrile (25% v/v) and a 10 mM ammonium dihydrogen phosphate buffer adjusted to pH 3 with phosphoric acid (75% v/v). The solvent was pumped at a flow rate of 0.9 mL/min. The injection volume was 150 μL with detection at 251 nm. Under these conditions, the retention time was 12 min.

For the analysis of **7**, the mobile phase consisted of acetonitrile (50% v/v) and a 10 mM ammonium dihydrogen phosphate buffer (50% v/v). This was pumped at a flow rate of 0.9 mL/min. The injection volume was 50 μL with fluorescence detection using an excitation wavelength of 249 nm and an emission wavelength of 311 nm. Under these conditions, the retention time was 7.7 min.

For the analysis of **7-P**, the mobile phase consisted of acetonitrile (30% v/v) and a 10 mM ammonium dihydrogen phosphate buffer (70% v/v). Solvent was pumped at a flow rate of 0.9 mL/min, and the injection volume was 150 μL. Detection was conducted at 253 nm with an observed retention time of 9 min.

AUC and Bioavailability Calculations—After intravenous administration, all concentration versus time profiles were fit to eq 1 using SigmaPlot graphics software (SPSS Inc, Chicago, IL)

$$C = A\,e^{-\alpha t} + B\,e^{-\beta t} \quad (1)$$

with reciprocal concentration weighting. Equation 1 describes the plasma drug concentration as a function of time for a drug that exhibits biexponential pharmacokinetics. The parameters A, α, B, and β generated from the curve fit were used to calculate the AUC_0^∞ values.

After intramuscular administration the AUC_0^t, where t was the last time point, was estimated using the trapezoidal method,[13] and the area under the last point to infinity was estimated by dividing the last point by the apparent elimination rate constant obtained from the curve fit to the iv data. The area under the tail was combined with AUC_0^t to give estimates of AUC_0^∞.

The apparent bioavailability of the parent drug following administration of the prodrug (F_{app}) was calculated by dividing the parent drug AUC following prodrug dosing by that from parent drug dosing as is shown in eq 2. The absolute bioavailability (F_{abs})

$$F_{app} = \frac{\text{Parent Drug AUC (after prodrug dosing)}}{\text{Parent Drug AUC (after parent drug dosing)}} \quad (2)$$

of parent drug following parent and prodrug intramuscular dosing were calculated using eq 3. A one-way ANOVA test was used to

$$F_{abs} = \frac{AUC_0^\infty(\text{im})}{AUC_0^\infty(\text{iv})} \times \frac{\text{Dose(iv)}}{\text{Dose(im)}} \quad (3)$$

compare mean AUCs following drug and prodrug dosing.

Results and Discussion

In all studies, equimolar doses of drug and prodrug were administered and plasma concentrations of both parent drug and prodrug were recorded as a function of time. Doses between different routes of administration did differ. The area under the concentration versus time profile for parent drug following prodrug administration was compared to that following parent drug administration to quantitatively assess the bioreversion. Table 1 summarizes the mean AUCs from each dosing along with the calculated availability, where relevant. Results are discussed in more detail below.

Evaluation of 6-P—Plasma concentration versus time profiles for **6** following equimolar (4.6 μmol/kg) intravenous infusions of **6** and **6-P** to dogs are shown in Figure 2. Plasma concentrations of **6-P** at 0 and 5 min postinfusion

Table 1—Summary of AUC Values and Bioavailabilities of 6 and 7 Resulting from Administration of Parent Drugs (6 and 7) and *N*-Phosphonooxymethyl Prodrugs (6-P and 7-P) to Rats and Dogs

compd	dose (μmol/kg)	route	animal (n)	AUC[a] (ng·hr/mL ± SE)	F_{app}	F_{abs}
6	4.6	iv	dog (3)	663 ± 115		
6-P	4.6	iv	dog (3)	564 ± 75	0.86	
6	21.3	iv	rat (3)	626 ± 193		
6-P	21.3	iv	rat (3)	711 ± 169	1.13	
6	30.5	im	rat (3)	661 ± 181		0.70
6-P	30.5	im	rat (3)	839 ± 323	1.27	0.89
7	6.2	iv	rat (3)	183 ± 98		
7-P	6.2	iv	rat (3)	166 ± 31	0.91	
7-P	18.6	iv	rat (3)	333 ± 60		

[a] AUC is for **6** or **7**.

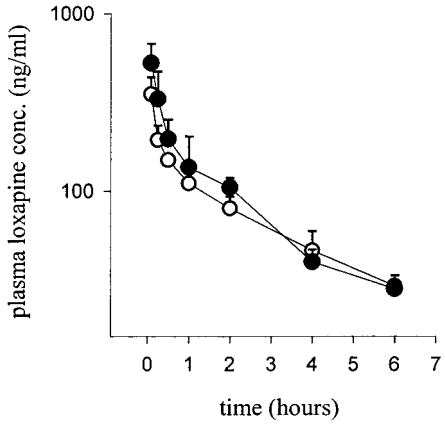

Figure 2—Semilog plot of mean (±SD) plasma concentration versus time profiles of **6** following equimolar (4.6 μmol/kg) 3 min iv infusions of **6** (●) or **6-P** (○) to beagle dogs in a 3 × 3 randomized crossover study.

Table 2—Summary of Plasma Prodrug Levels following Prodrug Administration to Dogs and Rats[a]

compd	dose (μmol/kg)	route	animal (n)	plasma prodrug concn (ng/mL ± SE) 0 min	5 min
6-P	4.6	iv	dog (3)	11,902 ± 983	414 ± 218
6-P	21.3	iv	rat (3)	1605 ± 737	386 ± 145
6-P	30.5	im	rat (3)	0[b]	0[b]
7-P	6.2	iv	rat (3)	1388 ± 615	96 ± 9

[a] After 5 min, prodrug levels were below the limit of detection for all samples collected. [b] Levels were below the limit of detection.

are shown in Table 2. Levels of **6-P** were below the limit of detection (48 ng/mL) following the 5 min sample. The mean AUC values of **6** resulting from dosing of **6-P** and **6** were not significantly different ($\alpha = 0.05$), and the apparent bioavailability of **6** following **6-P** administration was found to be 0.86. Similar results are shown in Figure 3 following equimolar (21.3 μmol/kg) iv infusions of **6** and **6-P** to rats. Again, the prodrug was rapidly cleared from the plasma, and the mean AUCs of **6** resulting from **6** and **6-P** dosing were not statistically different ($\alpha = 0.05$) and gave a calculated bioavailability of **6** following **6-P** administration of 1.13. Rapid disappearance of the prodrug from the plasma along with the virtual superimposability of plasma parent drug profiles following equimolar iv infusions of parent drug and prodrug are consistent with rapid and quantitative reversion, which was evident for all animals tested.

As **6** is currently formulated for intramuscular injection at a concentration of 50 mg/mL in a predominantly nonaqueous cosolvent (70% v/v propylene glycol and 5% v/v

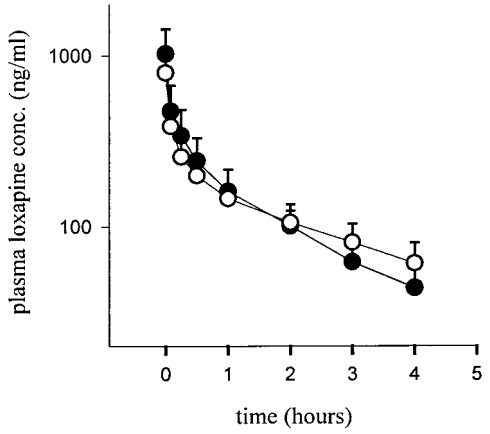

Figure 3—Semilog plot of mean (±SD) plasma concentration versus time profiles of **6** following equimolar (21.3 μmol/kg) 3 min iv infusions of **6** (●) or **6-P** (○) to conscious rats ($n = 3$).

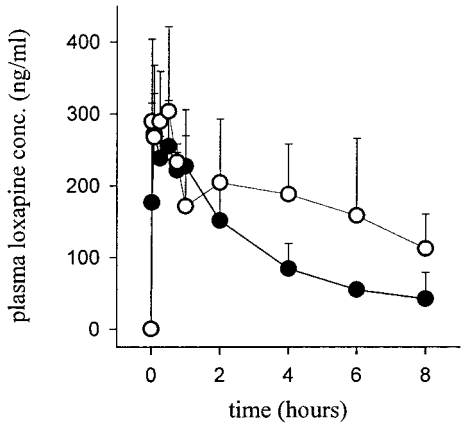

Figure 4—Plot of mean (±SD) plasma concentration versus time profiles of **6** following equimolar (30.5 μmol/kg) im injections of **6** (●) or **6-P** (○) to conscious rats ($n = 3$).

polysorbate 80), the ability of **6-P** to deliver **6** following intramuscular injection in an aqueous vehicle was investigated. Figure 4 illustrates the plasma concentration versus time profile following equimolar (30.5 μmol/kg) intramuscular injections of **6** and **6-P**. The mean AUCs of **6** after dosing with **6** and **6-P** were not significantly different ($\alpha = 0.05$) and the apparent bioavailability of **6** following **6-P** administration was found to be 1.27. Plasma levels of **6-P** were below the limit of detection (80 ng/mL) for all blood samples collected. Following intramuscular injection of **6-P**, a large fraction of the dose was immediately converted to **6**, which led to high plasma levels of **6** within 5 min of dosing. The **6-P** injections also resulted in some apparent elevations in **6** plasma levels 2−6 h postdosing; however, these apparent elevations are not statistically significant. The advantage of intramuscular administration of **6-P** in a purely aqueous formulation relative to **6** in its cosolvent system would be the potential avoidance of the tissue damage that is often associated when injecting organic cosolvents intramuscularly.[9,14]

Evaluation of 7-P—Figure 5 illustrates the plasma level versus time profiles of **7** following equimolar (6.2 μmol/kg) intravenous infusions of **7** and **7-P** to rats. There was no significant difference ($\alpha = 0.05$) between mean AUCs of **7** resulting from dosing with **7** and **7-P**. The apparent bioavailability of **7** following **7-P** administration was found to be 0.91.

To examine the potential for enzyme saturation, a **7-P** iv dose of 18.6 μmol/kg ($n = 3$) was given to the rats and compared to a 6.2 μmol/kg dose. This comparison is shown

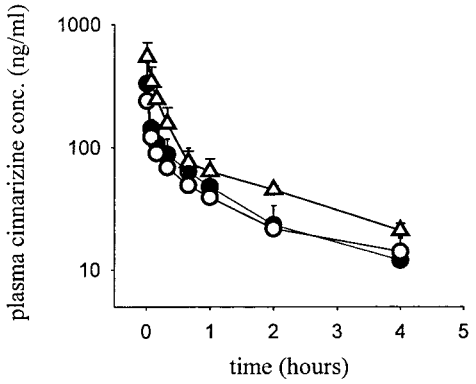

Figure 5—Semilog plot of mean (±SD) plasma concentration versus time profiles of **7** following equimolar (6.2 μmol/kg) 3 min iv infusions of **7** (●) or **7-P** (○) or 18.6 μmol/kg of **7-P** (△) to conscious rats ($n = 3$).

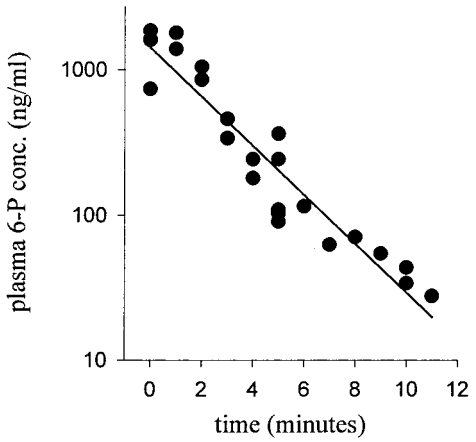

Figure 6—Semilog plot of plasma concentration of **7-P** as a function of time following a 3 min iv infusions of 6.2 μmol/kg of **7-P** (●) to conscious rats ($n = 4$).

in Figure 5. The mean AUC from the 18.6 μmol/kg dose (Table 1) was not statistically different from that for the 6.2 μmol/kg dose after dose correction. Any saturation that may have occurred through tripling of the dose of **7-P** could not be detected through AUC comparisons. As a result of limited quantities of prodrug, this experiment was not repeated with **6-P**.

The concentration versus time profile of **7-P** in plasma is shown in Figure 6. This plot contains data from a rat dosed with 6.2 μmol/kg of **7-P** for which blood samples were taken continuously for the first 10 min postinfusion to obtain a more complete profile. The disappearance of **7-P** from plasma was extremely rapid, and the half-life was estimated to be 2 min.

Conclusion

N-Phosphonooxymethyl derivatives have been evaluated as prodrugs for increasing the aqueous solubility of drugs containing a tertiary amine functional group. Previous reports have demonstrated the synthetic feasibility, improved water solubility, good chemical stability, and ability to revert to parent drug in vitro in the presence of alkaline phosphatase.[1,2] To prepare injectable solutions of cinnarizine and loxapine required additions of complexing agent and cosolvents, respectively. Each of the prodrugs, however, was easily formulated in water near physiological pH. Following iv administration to rats and dogs, the prodrugs were rapidly and quantitatively reverted to parent drug. In addition, the loxapine prodrug was able to deliver parent drug by the im route.

Saturation of the enzyme systems responsible for prodrug to drug reversion was not evident following iv dosing of cinnarizine prodrug to rats when the prodrug dose was tripled from 6.2 to 18.6 μmol/kg. Evaluations of the linearity at higher doses was not possible because of limited prodrug quantities.

The in vivo hydrolysis of the prodrugs was remarkably fast considering the relatively slow in vitro hydrolysis in the prescence of alkaline phosphatase and in blood (see Experimental Section). One could speculate that enzymes contained in blood alone (at their respective concentrations) are not sufficient to explain the rapid hydrolysis found when the prodrugs were administered in vivo. It could be that a significant fraction of the enzymes responsible are membrane-associated and/or organ-specific. Additionally, contribution of enzymes other than alkaline phosphatase may significantly contribute to the in vivo hydrolysis.

As is shown in Scheme 1, prodrug reversion generates a mole equiv of formaldehyde and inorganic phosphate. Although formaldehyde has some known toxicity that may preclude long term, repetitive dosing with these prodrugs, the small amount of formaldehyde released should not present any significant problems. In fact, most drugs that undergo N- or O-demethylation will release formaldehyde as a metabolic product, and many of these drugs are clinically approved and minimally toxic.

In conclusion, the described prodrug approach appears to be a promising technique for safely overcoming the solubility limitations observed with tertiary amine containing drugs.

References and Notes

1. Krise, J. P.; Zygmunt, J.; Georg, G.; Stella, V. J. A Novel Prodrug Approach for Tertiary Amines: Synthesis and Preliminary Evaluation of *N*-Phosphonooxymethyl Prodrugs. *J. Med. Chem*. **1999**, in press.
2. Krise, J. P.; Narisawa, S.; Stella, V. J. A Novel Prodrug Approach for Tertiary Amines. 2. Physicochemical and in Vitro Enzymatic Lability Evaluation of Selected *N*-Phosphonooxymethyl Prodrugs. *J. Pharm. Sci.*, **1999**, *88*, 922−927.
3. Godfraind, T.; Towse, G.; Van Nueten; J. M. Cinnarizine−A Selective Calcium Entry Blocker. *Drugs Today* **1982**, *18*, 27−42.
4. Peeters, J. Determination of Ionization Constants in Mixed Aqueous Solvents of Varying Composition by a Single Titration. *J. Pharm. Sci*. **1978**, *67*, 127−129.
5. Tokumura, T.; Ichikawa, T.; Sugawara, N.; Tatsuishi, K.; Kayano, M.; Machida, Y.; Hoshida, H.; Nagai, T. Kinetics of Degradation of Cinnarizine in Aqueous Solution. *Chem. Pharm. Bull*. **1985**, *33*, 2069−2072.
6. Ogata, H.; Aoyagi, N.; Kaniwa, N.; Ejima, A.; Kitaura, T.; Ohki, T.; Kitamura, K. Evaluation of Beagle Dogs as an Animal Model for Bioavailability Testing of Cinnarizine Capsules. *Int. J. Pharm*. **1986**, *29*, 121−126.
7. Ogata, H.; Aoyagi, N.; Kaniwa, N.; Ejima, A.; Sekine, N.; Kitamura, M.; Inoue, Y. Gastric Acidity Dependent Bioavailability of Cinnarizine from Two Commercial Capsules in Healthy Volunteers. *Int. J. Pharm*. **1986**, *29*, 113−120.
8. Latimer, C. N. Neuropharmacologic Evaluation of Oxilapine, a Potent Psychoactive Agent. *J. Pharmacol. Exp. Ther*. **1969**, *166*, 151−162.
9. Al-Suwayeh, S. A.; Tebett, I. R.; Wielbo, D.; Brazeau, G. A. *In Vitro-In Vivo* Myotoxicity of Intramuscular Liposomal Formulations. *Pharm. Res*. **1996**, *13*, 1384−1388.
10. *Physicians' Desk Reference*, *52nd Edition*. Medical Economics Company, Inc: Montvale, NJ. **1998**; pp 2525−2527.
11. *Physicians' Desk Reference*, 52nd ed.; Medical Economics Company, Inc: Montvale, NJ, 1998; pp 1396−1397.
12. Järvinen, T.; Järvinen, K.; Schwarting, N.; Stella, V. J. β-Cyclodextrin Derivatives, SBE_4-β-CD and HP-β-CD, Increase the Oral Bioavailability of Cinnarizine in Beagle Dogs. *J. Pharm. Sci*. **1995**, *84*, 295−299.
13. Gibaldi, M.; Perrier, D. *Pharmacokinetics*; Dekker: New York, 1981; pp 293−296.
14. Brazeau, G. A.; Fung, H.-L. Physicochemical Properties of Binary Organic Cosolvent−Water Mixtures and Their Relationship to Muscle Damage Following Intramuscular Injection. *J. Parent. Sci. Technol*. **1989**, *43*, 144−149.

Acknowledgments

The authors thank Ms. Toni Bloodworth and Dr. Glenn Edwards for their assistance in these studies, the American Foundation for Pharmaceutical Education Fellowship, and the National Cancer Institute Training Grant for financial support. Additional support was provided by the Takeru Higuchi/Nigel Manning Intersearch program, Kansas University Endowment Association, the Center for Drug Delivery Research, and Kansas Technology Corporation through the Centers of Excellence program.

JS980382V

Oral Delivery of Insulin Using pH-Responsive Complexation Gels

A. M. LOWMAN,[†,‡] M. MORISHITA,[§] M. KAJITA,[§] T. NAGAI,[§] AND N. A. PEPPAS*[,‡]

Contribution from *Biomaterials and Drug Delivery Laboratories, School of Chemical Engineering, Purdue University, West Lafayette, Indiana 47907, and Department of Pharmaceutics, Hoshi University, Tokyo 142, Japan.*

Received August 17, 1998. Accepted for publication June 24, 1999.

Abstract ☐ The goal of oral insulin delivery devices is to protect the sensitive drug from proteolytic degradation in the stomach and upper portion of the small intestine. In this work, we investigate the use of pH-responsive, poly(methacrylic-*g*-ethylene glycol) hydrogels as oral delivery vehicles for insulin. Insulin was loaded into polymeric microspheres and administered orally to healthy and diabetic Wistar rats. In the acidic environment of the stomach, the gels were unswollen due to the formation of intermolecular polymer complexes. The insulin remained in the gel and was protected from proteolytic degradation. In the basic and neutral environments of the intestine, the complexes dissociated which resulted in rapid gel swelling and insulin release. Within 2 h of administration of the insulin-containing polymers, strong dose-dependent hypoglycemic effects were observed in both healthy and diabetic rats. These effects lasted for up to 8 h following administration.

Introduction

Diabetes mellitus affects 20 million people in the U.S. alone.[1] Approximately, 10% of these diabetics are treated using insulin therapy. The most common form of this therapy is twice-daily subcutaneous injections of insulin. This type of treatment is painful and as a result encourages noncompliance by up to half of the diabetics.[2] One way to significantly improve patient compliance would be by developing oral delivery systems for insulin.[3] Oral delivery is the most popular method for drug delivery. However, two problems exist in developing oral delivery systems for insulin. The major problem is the inactivation of insulin by digestive enzymes in the gastrointestinal (GI) system, mainly in the stomach and the proximal regions of the small intestine.[3−10] This can be overcome by designing carriers which can protect the insulin from the harsh environments of the stomach before releasing the drug into more favorable regions of the GI tract, specifically the colon.[4−13] Additionally, researchers have attempted to incorporate protease inhibitors into oral insulin formulations which serve to prevent insulin degradation by the proteolytic enzymes.[4,7−10,12,14]

The other major barrier is the slow transport of insulin across the lining of the colon into the blood stream. Researchers have attempted to bypass this hurdle with the addition of compounds known as absorption enhancers which can facilitate the transport of macromolecules across the lining of the GI tract.[4,7−10]

Several research groups have attempted to use polymeric carriers as oral delivery systems for insulin. Touitou and Rubinstein[11] designed a system consisting of insulin encapsulated by polyacrylates. The coating was designed to dissolve only in the colon. In this work, weak hypoglycemic effects were observed only with very high insulin doses and the addition of absorption enhancers. Saffran[4] developed a system of insulin dispersed in a terpolymer of styrene and hydroxyethyl methacrylate cross-linked with a difunctional azo-containing compound. The azo bond was cleaved by microflora present in the colon, and the polymer degraded allowing for release of insulin into the colon. In this work, a hypoglycemic effect was obtained only with addition of absorption enhancers and protease inhibitors. However, the hypoglycemic effect obtained was not affected by the initial dosing.

Morishita et al.[12] administered insulin contained within Eudragit 100 gels. We observed strong hypoglycemic effects in healthy and diabetic rats after the addition of absorption enhancers. Platé et al.[7] developed a hydrogel system containing immobilized insulin and protease inhibitors that was effective in lowering the blood glucose levels in rabbits. More recently, Mathiowitz et al.[13] have developed insulin containing poly(anhydride) microspheres. These materials adhered to the walls of the small intestine and released insulin based on degradation of the polymeric carrier. They observed a 30−50% decrease in the blood glucose levels of healthy rats.

In this work, we have used a pH-responsive carrier designed to protect the insulin in the harsh, acidic environment of the stomach before releasing the bioactive agent in the small intestine. The delivery system consists of insulin-containing microparticles of cross-linked copolymers of poly(methacrylic acid) which are grafted by ethylene. These new systems glycol (henceforth designated P(MAA-*g*-EG)) function because the structure of the copolymers exhibits pH sensitive swelling behavior due to the reversible formation of interpolymer complexes stabilized by hydrogen bonding between the carboxylic acid protons and the etheric groups on the grafted chains.[15] The complex formation in the insoluble copolymers is sensitive to the nature and pH of the surrounding fluid as well as the copolymer composition and graft chain length.[15]

In the acidic environment of the stomach, the gels are in the complexed state. Under these conditions insulin cannot readily diffuse through the membrane because of the small mesh size, ζ, and is protected from the harsh environment of the stomach.[16] As the particles pass the stomach into the intestine, the environmental pH increases above the transition pH of the gel. The complexes immediately dissociate and the network pore size rapidly increases leading to the release of insulin.[16] Because of their nature, these materials may be ideal for the delivery of drugs at rates specified by the pH of the environmental fluid.[16,17]

Experimental Section

Hydrogel Synthesis—Microparticles of P(MAA-*g*-EG) were prepared[18] by a free-radical bulk, suspension polymerization of methacrylic acid (MAA, Sigma Chemical Co., St. Louis, MO) and

* To whom correspondence should be addressed.
† Current address: Chemical Engineering Department, Drexel University, Philadelphia, PA 19104.
‡ Purdue University.
§ Hoshi University.

10.1021/js980337n CCC: $18.00
Published on Web 08/04/1999

poly(ethylene glycol) (PEG) monomethacrylate (PEGMA, Polysciences Inc., Warrington, PA) with PEG of molecular weight 1000. The MAA was vacuum-distilled prior to use to remove the inhibitor. The PEGMA was used as received.

For the polymerization reaction, the suspending phase, 250 mL of silicon oil, Dow 200 fluid (Dow Chemical Co., Midland, MI) was added to a three-necked flask and heated to 70 °C while being agitated at 250 rpm using an overhead stirrer. A reflux condenser was attached to the flask. The flask was sealed and purged with nitrogen to ensure an inert atmosphere for the reaction vessel.

The monomers were mixed in appropriate molar ratios to yield a 1:1 ratio of MAA:EG units in the gel. Tetraethylene glycol dimethacrylate (TEGDMA, Polysciences Inc., Warrington, PA) was added as a cross-linking agent in the amount of $X = 0.075$ mol of TEGDMA per mole MAA. Following complete dissolution of the monomers, nitrogen was bubbled through the well-mixed solution for 30 min to remove dissolved oxygen, a free radical scavenger, which would act as an inhibitor. 2,2′-Azobis(isobutyronitrile) (AIBN) was added in the amount of 0.5% of the total monomers as the thermal reaction initiator. Poly(dimethyl siloxane-*b*-ethylene oxide) (P(DMS-*b*-EO), Polysciences Inc., Warrington, PA) containing 25% DMS was added in the amount of 1% of total monomers as a surfactant to prevent microparticle aggregation during and after the reaction.

The monomer mixture was added to the oil phase, agitated at 350 rpm, and allowed to react for 3 h at 70 °C. After 3 h, the temperature was increased to 90 °C and allowed to react for an additional 2 h. Following the higher temperature reaction period, the solution was cooled to 37 °C, and the agitation rate was decreased to 250 rpm. Once the temperature reached 37 °C, 20 mL of deionized water was added to the reaction vessel, and the polymer suspension was mixed for an additional 2 h.

The suspension was allowed to settle and the oil was decanted. The reaction flask was filled with deionized water, and the swollen particles were stirred for 24 h at 100 rpm. After 24 h, the particles were filtered and rinsed with fresh deionized water. This process was continued until all of the silicon oil had been removed (approximately one week). Following the washing, the particles were stored in deionized water with the pH adjusted to 8 by the addition of NaOH.

Drug Loading—Drug loading was accomplished by equilibrium partitioning of insulin into the P(MAA-*g*-EG) microparticles. Crystalline porcine insulin (10 mg, 26.9 IU/mg, Shimizu Pharmaceutical Co., Ltd., Shizuoka, Japan) was dissolved in 100 μL of 0.1 N HCl. The insulin solution was diluted with 19.8 mL of phosphate buffer solution (pH = 7.4) and normalized with 100 μL of 0.1 N NaOH. The final pH of the loading solution was 7.4. Loading was accomplished by soaking 140 mg of dried P(MAA-*g*-EG) microparticles for 24 h in the insulin solution. The concentration of insulin in the solution was monitored over time using HPLC.

The particles were then filtered using filter paper with 1 μm pores and washed with 100 mL of 0.1 N HCl solution to collapse the microparticles and exude the remaining buffer solution. The insulin-loaded microspheres were dried under vacuum and stored at 4 °C. The degree of loading was determined from HPLC analysis of the insulin concentrations of the initial solutions and the filtrate from the washings. Using this loading technique, 94 ± 9% of the insulin in the initial solution was entrapped within the polymer.[19] The activity of the insulin loaded in the gels was verified using an Insulin EIA kit (Abbot Laboratories, Chicago, IL).

In Vivo Studies—For these studies, male Wistar rats (200 g) were used. Diabetes was induced[12] in the rats by intraperitoneal injection of streptozotocin (40 mg/kg body weight once daily for three consecutive days) dissolved in citrate buffer at pH = 4.5. The rats were considered diabetic when the fasted glucose levels exceeded 250 mg/dL at 2 weeks following the streptozotocin treatment. The average blood glucose levels of the healthy animals used in the studies was 80 mg/dL while the diabetic animals had average glucose levels of 345 mg/dL.

Prior to administration of the insulin-loaded polymer, the animals were fasted for 48 h. The rats were restrained in the supine position. The insulin-loaded P(MAA-*g*-EG) microparticles and the control solutions were administered via the mouth using a gelatin capsule. The gelatin capsules dissolved readily in the stomach. During the experiment, a 0.2 mL aliquot of blood was collected from the jugular vein at 0.25, 0.5, 1, 2, 4, 6, and 8 h following dosing. The blood serum was separated by centrifugation at 3000 rpm for 3 min and stored in a freezer until analysis. The serum insulin levels were determined by an enzyme immunoassay using an Insulin EIA kit (Abbot Laboratories, Chicago, IL). Serum glucose levels were determined by the glucose oxidase method using a glucose B-test kit.

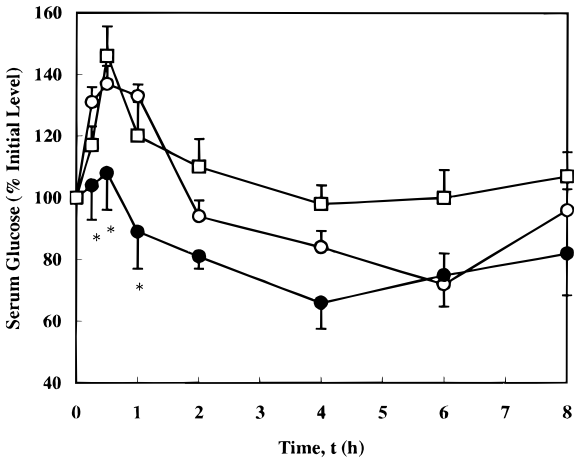

Figure 1—Blood glucose response in healthy male Wistar rats following the oral administration of P(MAA-*g*-EG) microspheres containing insulin doses of (○) 25 IU/kg body weight ($n = 7$) and (●) 50 IU/kg body weight ($n = 5$) and (□) insulin solutions (50 IU/kg body weight, $n = 4$). Comparison calculated between the doses at each point *$p < 0.05$.

To determine the relative efficacy of each formulation, healthy and diabetic rats received sc injections, and the blood glucose levels were monitored over time. Healthy rats received injections of 0.5, 1, and 3 IU/kg, while diabetic rats received injections of 0.25, 0.5, and 1.0 IU/kg. The cumulative area under the curve (AUC) was determined from each dosage, and the following dose dependent AUC relationships were developed for subcutaneous injections:

$$\text{healthy Rats } (n = 4): \ \text{AUC} = 219.29 \log(\text{sc dose}) + 145.96 \quad (1a)$$

$$\text{diabetic Rats } (n = 4): \ \text{AUC} = 512.64 \log(\text{sc dose}) + 319.76 \quad (1b)$$

Results and Discussion

In designing a device for oral delivery of sensitive peptide drugs such as insulin, it was important to protect the drug in the harsh environment of the stomach and upper GI tract and release the drug into the distal portions of the intestine. Therefore, in an effective carrier the release rates must be significantly greater in neutral or basic conditions than acidic conditions. One significant parameter in evaluating the viability of a particular hydrogel for oral delivery of proteins and peptides was the ratio of the diffusion coefficients of the drug in the carrier in the stomach (acid environment) and the intestine (neutral environment). In the P(MAA-*g*-EG) gels, the release rates in neutral or basic conditions were more than 1 order of magnitude greater than the release rates in acidic solutions.[16]

In Vivo Response to Oral Administration of P(MAA-*g*-EG) Microspheres—The blood glucose response of rats following oral administration of insulin doses contained in P(MAA-*g*-EG) microparticles is shown in Figure 1. The rats received insulin doses of 25 IU/kg and 50 IU/kg contained in the polymer microparticles and a control solution (50 IU/kg). Initially, the blood glucose levels rose due to the physical stress on the animals during administration and blood sampling. The initial rise was followed by a decrease back to normal levels due to absorption into the muscle. Because of the nature of these gels, little if any of the insulin was released in the stomach, as the gels were in the collapsed state due to the formation of polymer

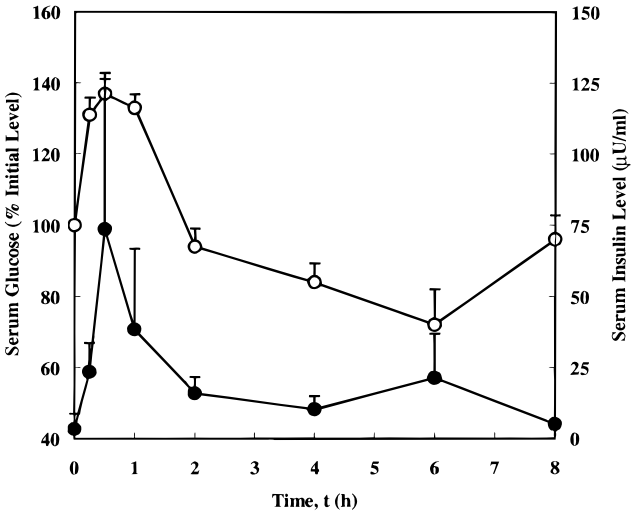

Figure 2—Serum (○) glucose and (●) insulin levels in healthy male Wistar rats following oral administration of insulin-containing P(MAA-g-EG) microspheres (25 IU/kg body weight doses) ($n = 7$).

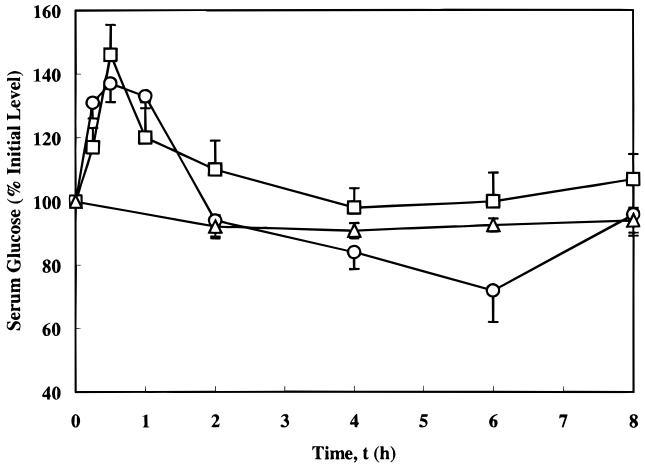

Figure 3—Blood glucose response in healthy male Wistar rats following the oral administration of 25 IU/kg body weight insulin doses contained (○) P(MAA-*g*-EG) microparticles ($n = 5$) and (△) Eudragit microspheres ($n = 10$) and (□) insulin solutions ($n = 4$).

complexes in the acidic environment of the stomach. The insulin was protected inside of the gel from the proteolytic enzymes that were unable to penetrate the gel.

Within 2 h of receiving the polymeric dosage form, a strong hypoglycemic effect or lowering of the blood glucose level was observed in the animals that had received the polymeric dosage forms. This was clear evidence that the insulin was delivered effectively in the biologically active form to the small intestine. Insulin delivery in the small intestine was due to the rapid dissociation of the polymer complexes in the basic environment of the intestine. As the complexes dissociated, the pore size of the gels increased dramatically, and insulin was rapidly released into the intestine. Additionally, the reduction of the blood glucose levels depended strongly on the insulin dose. The reduction in blood sugar was greater in the animals receiving the higher doses of insulin (50 IU/kg). The hypoglycemic effects were present for up to 8 h in these animals.

The serum insulin levels of the rats following oral administration of the dosage forms are shown in Figure 2. Within 1 h of administration, the insulin levels in the rats receiving the insulin containing rose to greater than 20 times their initial levels. The serum insulin levels remained at elevated levels for up to 6 h following administration as the polymer delivered the insulin to the proximal small intestine. As a result, the blood glucose levels were decreased for the period.

One major reason for the effectiveness of this device is the pH-sensitive swelling behavior of the gels. However, such strong effects could not be obtained with the use of another pH-responsive carrier that had been used as oral delivery vehicle for insulin, Eudragit L100. In our previous work,[12] we prepared insulin-containing microspheres of Eudragit L100 to serve as oral insulin delivery systems. A comparison of the hypoglycemic effects following oral administration of 25 IU/kg doses of insulin contained in P(MAA-*g*-EG) and Eudragit L100 microparticles is shown in Figure 3. Clearly, the hypoglycemic effects observed following administration of the complexation gels are much greater than those obtained using the Eudragit carrier.

The P(MAA-*g*-EG) gels are significantly more effective in delivering biologically active insulin than traditional enteric coating-type carriers because of the presence of the PEG-grafts. Such strong hypoglycemic effects were not observed using other oral delivery carriers without the addition of additives such as protease inhibitors or absorption enhancers.[4,7,12,13] The addition of PEG to the gels is critical because the PEG chains participate in the macromolecular complexes, function as a peptide stabilizer, and enhance the mucoadhesive characteristics of the gels. In these gels, the PEG will form interpolymer complexes with the PMAA in acidic media. Not only do the complexes contribute strongly to the pH-dependent changes in the network structure,[15–18] they also serve to stabilize the insulin.[16,20] Additionally, the presence of the PEG grafts helps maintain the biological activity of the insulin by stabilizing the drug and preventing binding to ionizable backbone chain.[16,17,21]

Another important characteristic of these gels is their ability to adhere more strongly to the mucosa of the small intestine than the mucosa of the stomach. This is significant because the major impetus for controlled drug release is to maintain a steady flux of an active agent over an extended period of time. One such means of increasing the residence time would be through the use of a mucoadhesive carrier. The primary goal of such devices is to localize the delivery vehicle within the desired location to enhance the drug absorption process in a site-specific manner.[22–24] Hydrogels of P(MAA-*g*-EG) exhibit excellent mucoadhesive characteristics for delivery of drugs to the small intestine due to the presence of the graft PEG chains which serve as adhesion promoters.[16,17] Adhesion promoters, such as polymer grafts or even linear polymers, function by penetrating the gel/mucosa or gel/gel interface and forming temporary anchors.[25,26]

The mucoadhesive characteristics of P(MAA-*g*-EG) hydrogels are strongly dependent on the pH of the environmental fluid. These gels adhere to the mucosa of the intestine to a much greater extent than the stomach.[16] Therefore, the residence of insulin carriers would be much greater in regions where the insulin could be absorbed, such as the distal regions of the small instestine.

The reduction of blood glucose in healthy animals following oral administration of the insulin-loaded polymers was significant in that it showed the efficacy of P(MAA-*g*-EG) carriers. However, it is more significant if these results can be obtained in diabetic animals. The blood glucose response of diabetic rats following oral administration of insulin containing P(MAA-*g*-EG) microparticles (25 IU/kg doses) is shown in Figure 4. The blood glucose levels of the diabetic rats were lowered by up to 40% for greater than 8 h. The degree to which the glucose levels were suppressed was in fact greater for the diabetic animals

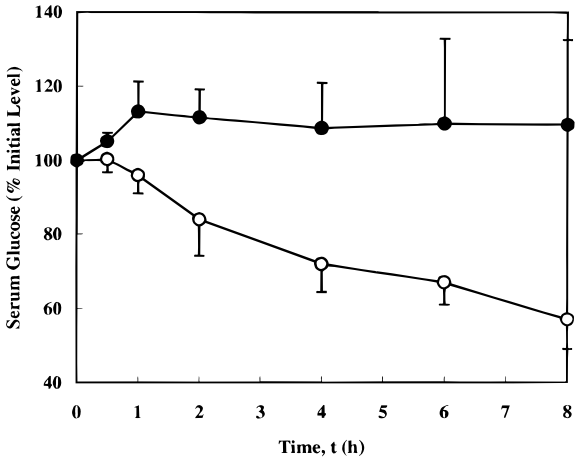

Figure 4—Blood glucose in diabetic, male Wistar rats following oral administration of 25 IU/kg body weight doses contained in (○) P(MAA-*g*-EG) microspheres and (●) insulin solutions ($n = 5$).

Table 1—Efficacy of Oral Administration of Insulin Using Complexation Polymers Relative to iv Injection

dosage form	insulin dose (IU/kg)	bioavailability	
		healthy rats	diabetic rats
P(MAA-g-EG)	25	3.40 ± 1.53	2.44 ± 0.41
	50	4.22 ± 2.09	ND[a]
solution	25	ND	0.88 ± 0.34
	50	0.55 ± 0.08	ND
Eudragit L100[12]	25	0.9 ± 0.3	1.1 ± 0.2

[a] ND: no data collected.

than the healthy animals. Additionally, the strong hypoglycemic effects were observed to last longer in the diabetic animals.

Relative Efficacy of P(MAA-*g*-EG) Carriers to S. C. Injection—The overall efficacy of each of the formulations was determined in comparison to the efficacy of an iv injection. For each dosage form, the AUC was determined. The overall efficacy was determined as the ratio of the AUC for the oral dosage divided by the AUC for a sc injection of the same dose. These data appear in Table 1. When the insulin was administered orally using solutions, the efficacy of the formulation in comparison to sc injection was less than 1%. However, when the insulin was delivered using polymer microparticles, the efficacy was increased significantly. Of all of the samples tested, the greatest efficacy or bioavailibility (4.22%) was observed for the P(MAA-*g*-EG) gels containing 50 IU/kg doses delivered to healthy rats. Significant bioavailibilities were also observed for polymers containing 25 IU/kg doses in both healthy and diabetic animals. All of the P(MAA-*g*-EG) devices were found to be significantly more effective than Eudragit L100 as oral delivery devices for insulin.

Conclusions

Oral insulin delivery systems must be able to protect the sensitive macromolecular drug from the harsh environment of the stomach and deliver biologically active insulin for an extended period of time to more favorable regions for absorption along the GI tract. Because of their nature, complexing P(MAA-*g*-EG) hydrogels are ideal for such an application. P(MAA-*g*-EG) hydrogels were able to effectively deliver biological active insulin via the oral route. Microparticles prepared from these gels were prepared and loaded with insulin. Following administration of insulin-loaded microparticles to healthy and diabetic rats, the blood glucose levels in these animals were decreased significantly for at least 8 h due to the absorption of insulin in the GI tract. The strong hypoglycemic effects were observed without the addition of additives such as absorption enhancers or protease inhibitors and were found to be strongly dependent on the administered dose.

References and Notes

1. Anonymous. Report of the Expert Committee on the Diagnosis and Classification of Diabetes Mellitus. *Diabetes Care* **1997**, *20*, 1183−1197.
2. Campbell, R. K.; White, J. R. *New Opportunitites in Diabetes Management*; Miles Inc.: Terrytown, NY, 1993.
3. Costantino, H. R.; Liauw, S.; Mitragotri, S.; Langer, R.; Klibanov, A. M.; Sluzky, V. The Pharmaceutical Development of Insulin: Historical Perspectives and Future Directions. In *Therapeutic Protein and Peptide Formulation and Delivery*; Shahrokh, Z., Sluzky, V., Cleland, J. L, Shire, S. J., Randolph, T. W., Eds.; American Chemical Society: Washington, D. C., 1997; pp 29−66.
4. Saffran, M.; Sudesh Kumar, G.; Savariar, C.; Burnham, J. C.; Williams, F.; Neckers, D. C. A New Approach to the Oral Administration of Insulin and Other Peptide Drugs. *Science* **1986**, *233*, 1081−1084.
5. Lee, V. H. L.; Dodd-Kashi, S.; Grass, G. M.; Rubas, W. Oral Route of Peptide and Protein Drug Delivery. In *Protein and Peptide Drug Delivery*; Lee, V. H. L., Ed.; Marcel Dekker Inc.: New York, NY, 1991; pp 691−740.
6. Saffran, M. Oral Colon-Specific Drug Delivery With Emphasis on Insulin. In *Oral Colon-Specific Drug Delivery*; Friend, D. R., Ed.; CRC Press: Boca Raton, FL, 1992; pp 115−142.
7. Platé, N. A.; Valuev, L. I.; Starosel'tseva, L. K.; Valueva, T. A.; Vanchugova, L. V.; Ul'yanova, M. V.; Valuev, I. L.; Sytov, G. A.; Ametov, A. S.; Knyazhev V. A. Macromolecular Systems Containing Insulin as Related to the Problem of Diabetes. *Vysokomol. Soedin.* **1994**, *36*, 1876−1879.
8. Fix, J. A. Oral Controlled Release Technology for Peptides: Status and Future Prospects. *Pharm. Res.* **1996**, *13*, 1760−1764.
9. Wang, W. Oral Protein Drug Delivery. *J. Drug Targ.* **1996**, *4*, 195−232.
10. Saffran, M.; Pansky, B.; Budd, G. C.; Williams, F. E. Insulin and the Gastrointestinal Tract. *J. Controlled Release* **1997**, *46*, 89−98.
11. Touitou, E.; Rubinstein, A. Targeted Enteral Delivery of Insulin to Rats. *Int. J. Pharm.* **1986**, *30*, 93−99.
12. Morishita, I.; Morishita, M.; Takayama, K.; Machida, Y.; Nagai, T. Hypoglycemic Effect of Novel Oral Microspheres of Insulin With Protease Inhibitor in Normal and Diabetic Rats. *Int. J. Pharm.* **1992**, *78*, 9−16.
13. Mathiowitz, E.; Jacob, J. S.; Jong, Y. S.; Carino, G. P.; Chickering, D. E.; Chaturvedi, P.; Santos, C. A.; Vijayaraghavan, K.; Montgomery, S.; Bassett, M.; Morrell, C. Biologically Erodible Microspheres as Potential Oral Drug Delivery Systems. *Nature* **1997**, *386*, 410−414.
14. Langguth, P.; Bohner, V.; Heizmann, J.; Merkle, H. P.; Wolframm, S.; Almidon, G. L.; Yamashita, S. The Challenge of Proteolytic Enzymes in Intestinal Peptide Delivery. *J. Controlled Release* **1997**, *46*, 39−57.
15. Lowman, A. M.; Peppas, N. A. Analysis of the Complexation/Decomplexation Phenomena in Polyelectrolyte Networks. *Macromolecules* **1997**, *30*, 4959−4965.
16. Lowman, A. M.; Morishita, M.; Peppas, N. A.; Nagai, T. Novel Bioadhesive Complexation Networks for Oral Protein Drug Delivery. In *Materials for Controlled Release Applications*; McCulloch, I., Shalaby, S. W., Eds.; American Chemical Society: Washington, DC, 1998; pp 156−164.
17. Peppas, N. A.; Lowman, A. M. Protein Delivery from Novel Bioadhesive Complexation Hydrogels. In *Protein and Peptide Drug Research*; Frøkjær, S., Christup, L., Krogsgaard-Larsen, P., Eds.; Munksgaard: Copenhagen, 1998; pp 206−216.
18. Drummond, R. K.; Klier, J.; Alameda, J. A.; Peppas, N. A. Preparation of Poly(methacrylic acid-*g*-ethylene oxide) Microspheres. *Macromolecules* **1989**, *22*, 3816−3818.
19. Lowman, A. M.; Peppas, N. A..; Morishita, M.; Takayama, K.; Nagai, T. Evaluation of the Uptake and Release Behavior of pH-Responsive Complexation Networks. *J. Controlled Release*, submitted.
20. Bektorova, E.; Bimendina, L. Interpolymer Complexes. *Adv. Polym. Sci.* **1981**, *41*, 99−147.

21. Harris, J. M. *Poly(ethylene glycol) Chemistry*; Plenum Press: New York, 1992.
22. Lehr, C. M. Bioadhesion Technologies for the Delivery of Peptide and Protein Drugs to the Gastrointestinal Tract. *Crit. Rev. Ther. Drug Carrier Syst.* **1994**, *11*, 119−160.
23. Peppas, N. A.; Sahlin, J. J. Hydrogels as Mucoadhesive and Bioadhesive Materials: A Review. *Biomaterials* **1996**, *17*, 1553−1561.
24. am Ende, M. T.; Mikos, A. G. Diffusion-Controlled Delivery of Proteins From Hydrogels and Other Hydrophilic Systems. In *Protein Delivery: Physical Systems*; Sanders, L. M., Hendren, R. N., Eds.; Plenum Press: New York, 1997; pp 139−165.
25. Mikos, A. G.; Peppas, N. A. Scaling Concepts and Molecular Theories of Adhesion of Synthetic Polymers to Glycoproteinic Networks. In *Bioadhesive Drug Delivery Systems*; Lenaerts, V., Gurny, R., Eds.; CRC Press: Boca Raton, FL, 1990; pp 25−42.
26. Sahlin, J. J.; Peppas, N. A. Enhanced Hydrogel Adhesion by Polymer Interdiffusion. *J. Biomat. Sci., Polym. Ed.* **1997**, *8*, 421−436.

Acknowledgments

Acknowledgments This work was supported by a grant from the National Institutes of Health (No. GM43331) to N.A.P. and The Nagai Foundation, Tokyo.

JS980337N

Assessment of Complex Peptide Degradation Pathways via Structured Multicompartmental Modeling Approaches: The Metabolism of Dynorphin A1–13 and Related Fragments in Human Plasma

STEFAN MÜLLER,[†,‡] ALAN HUTSON,[§] V. ARYA,[†] AND GÜNTHER HOCHHAUS*[,†]

Contribution from *Department of Pharmaceutics, College of Pharmacy, University of Florida, Gainesville, Florida 32610.*

Received January 26, 1998. Final revised manuscript received May 10, 1999.
Accepted for publication June 21, 1999.

Abstract □ Peptide metabolic pathways in blood or other tissues are often complex because multiple enzyme systems are involved in the degradation of parent drug and its metabolites. Michaelis–Menten-type studies with isolated enzymes have been frequently employed for evaluating the metabolism of peptides. Alternatively, studies with selective enzyme inhibitors or the evaluation of the area under the drug– or metabolite–time profiles have been employed. We tested in this study the usefulness of a multicompartmental pharmacokinetic approach for the assessment of the apparent first-order metabolism of dynorphin A1–13 up to the fourth metabolite generation in human plasma. This multicompartmental kinetic analysis proved instrumental in clarifying ambiguous degradation pathways not easily detectable by the other methods of assessment (enzyme inhibition studies and noncompartmental analysis) because of the lack of specific enzyme inhibitors or specificity problems of the analytical technique employed. The proposed multicompartmental fitting approach was also highly suitable to verify the overall metabolic pathways suggested by the other methods up to the fourth metabolite by testing whether the rate constants obtained by these methods are suitable to describe the overall degradation profile after Dyn A1–13 degradation. Local sensitivity analysis for the degradation of DYNA 1–13 revealed that the model was, however, not able to adequately identify on its own all of the parameters involved in the degradation of dynorphin A1–13. Thus, the method proved beneficial in evaluating and testing the correctness of the overall degradation pathways suggested by other methods.

Introduction

Biologically active peptides often exert their effects via active metabolites. With the use of peptides as therapeutic agents, a detailed understanding of their metabolism is therefore important. The model peptide Dyn A1−13 used in this study is extensively metabolized in plasma.[1] N-terminally intact metabolic fragments of Dyn A1−13 (Dyn A1−12 through Dyn A1−5) retain opioid receptor affinity,[2] while N-terminally truncated dynorphin derivatives such as Dyn A2−13 modulate morphine tolerance via nonopioid pathways, possibly the NMDA-receptor[3,4] and/or melanocortin receptor.[5]

The in-vitro metabolic pathway of Dyn A1−13 in human plasma is complex, as previously assessed up to the fourth metabolic generation by enzyme inhibition studies and a noncompartmental analysis of the metabolic pathway.[1] Enzyme inhibition studies can only assess the contribution of one enzymatic system to the overall metabolic fate of the parent drug or identified metabolites; and they depend on the specificity of the enzyme inhibitors involved. A noncompartmental (AUC-based) approach introduced in these studies[1] compared the area under the concentration−time profiles of a given metabolite during degradation of the parent drug (e.g., Dyn A1−13) with the area observed after direct degradation of the synthesized metabolite. This approach allows simultaneously monitoring of several metabolites and does not depend on the availability of selective enzyme inhibitors but on the high selectivity of the chromatographic system for the determination of parent drug and metabolites. Because of the limitations found for both methods, this study focuses on the applicability of a structured multicompartmental kinetic analysis (nonlinear curve fitting procedures for apparent first-order kinetic processes) for the analysis of complex metabolic events. The results presented here suggest that this mode of analysis has certain advantages over the above methods and that it should be applied in conjunction with the other methods to assess complex metabolic degradation pathways of peptide drugs.

Materials and Methods

Data—Concentration−time profiles of parent compound (generally Dyn A1−13 or shorter fragments such Dyn A1−12 or Dyn A2−12, Dyn A 3−12, Dyn A 4−12, Dyn A 1−10, Dyn A 2−13) and resulting metabolites obtained after incubation of peptides at 37 °C in neat plasma in the presence or absence of specific enzyme inhibitors (GEMSA, bestatin, captopril, leucinetiol) have been previously described.[1] These data were reanalyzed in this study.

Data Analysis—Differential equations describing sequential and parallel pathways of dynorphin metabolism (see Figures 1 and 2, for the metabolic pathways of Dyn A1−13 investigated, see Figure 1 for final pathway) were established.[6] These equations incorporated the overall rate of degradation of a given peptide (degradation rate constant of DynA1−13: k_1; degradation rate of metabolites: $k_2 - k_7$) and the rate of generation of metabolites (k_{12}, k_{16}, k_{23}, k_{63}, k_{27}...). See Figure 1 for explanation of the abbreviations of rate constants used. The Laplace transform of the concentration of a given dynorphin fragment (as,c) was calculated as the product of the input (ins; here the initial amount of peptide spiked into the incubation solution) and the following modified disposition function ($d_{s,c}$).[7]

$$d_{s,c} = \frac{\prod_{i=2}^{N}(s + k_i)}{\prod_{i=1}^{N}(s + k_i) - \sum_{j=2}^{N}[k_{1_j}\prod_{\substack{m=2 \\ m\neq j}}^{N}(s + k_m)]}$$

* Corresponding author. Tel: (352) 846 2727, fax: (352) 392-4447, e-mail: Hochhaus@UFL.EDU.
† University of Florida.
‡ Current address: Mundipharma GmbH, Mundipharmastrasse2, D-65549Limburg/Lahn.
§ Department of Statistics, College of Liberal Arts, Health Science Center, Gainesville, FL 32610.

10.1021/js980036d CCC: $18.00
Published on Web 07/31/1999

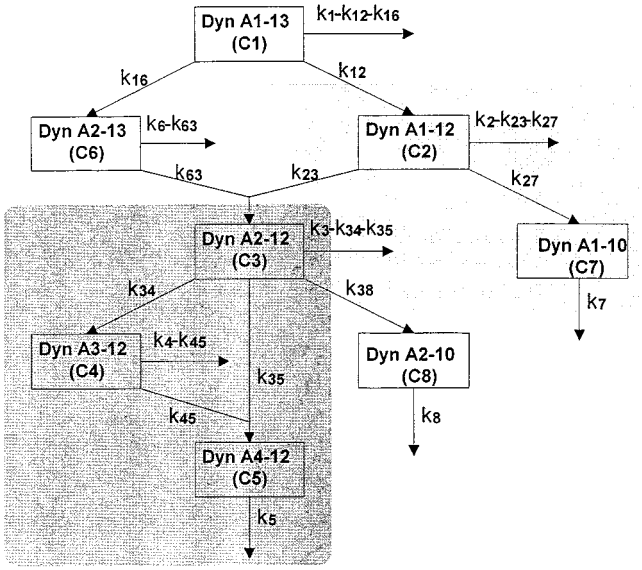

Figure 1—Kinetic model describing the arrangement of metabolite pools in the plasma metabolism of Dyn A 1–13. This model was the basis for compartmental kinetic analysis of Dyn A1–13. Single digit abbreviations (e.g., k_1) are used for degradation rate constants that describe the total outflow of a certain compartment (in this example C1). Rate constants that describe the specific flow from one compartment to another have double digit denominations (e.g., k_{12}) and represent the generation rate constants. The difference between the overall degradation rate constant (e.g., k_1) and relevant generation rate constants (e.g., k_{16} and k_{12}) reflect unknown metabolic events not incorporated into the model. The area in dark gray highlights the metabolic events of Dyn A2–12 under captopril inhibition, the added area in the medium gray shade shows the extension of the model in the metabolic events of Dyn A1–12. The dashed lines signify compartments for which direct data (from HPLC) was not available.

where $d_{s,c}$ is the disposition function for compartment 1 (it is a function of s, the Laplace operator); $\prod$ is the continued product where any term is defined as equal to 1 when the index takes a forbidden value (that is, $i = 1$ in the numerator or $m = j$ in the denominator); $\sum$ is the continued sum where any term is defined as equal to zero when the index takes a forbidden value; k_{1j} is the first-order generation of a metabolite, estimated from relevant generation rate constant; k_i, k_m is the overall degradation rate of a dynorphin fragment, estimated from relevant degradation rate constants; N is the number of the compartments.

The Anti-Laplace of $a_{s,c}$ was obtained by the method of partial fractions.[7] The resulting equations for the final model of Dyn A1−13 (C1) with its metabolites Dyn A1−12 (C2), Dyn A2−12 (C3), Dyn A3−12 (C4), Dyn A2−13 (C6), and Dyn A4−12 (C5) coeluting with Dyn A1−10 (C7) are listed in Appendix 1. The nonlinear curve fitting program Scientist (Micromath, Salt Lake City, Utah) was used to fit the experimental data to the derived equations.

The initial estimates of the degradation rate constants for the parent compound and metabolites (but not generation rate constants) were taken from the estimates obtained from direct incubations of this fragment.[1] Fitting parameters were not allowed to differ from these initial estimates by more than 30% (the maximum variability generally excepted), if not otherwise stated. Initial estimates for the generation rate constant were based on the initial estimates of the degradation rate constants under enzyme inhibition (Table 1). Since some enzyme inhibitors lacked selectivity, these generation rate constants were generally allowed to vary in the curve fitting procedure between 10% and 130% from the initial estimate of the overall rate constant of the relevant metabolic step.

Goodness of fits were evaluated by r^2 and the Model Selection Criterion (MSC), a value based on the Akaike Information Criterion.[8] A local sensitivity analysis was carried out for each of the Dyn derivatives along with some summary measures.[9] The normalized sensitivity coefficient (SC) detailed by Bieniasz and Speiser was calculated for each Dyn derivative (see Appendix 2).[10]

Results and Discussion

Peptides are of importance as therapeutic agents. For a detailed assessment of their therapeutic and clinical properties a detailed knowledge of the metabolic fate of a given peptide is necessary. Approaches employing Michaelis−Menten-type kinetics would depend on the detailed assessment of enzyme kinetics[11] of parent compound and metabolites, as well as the identification and measurement of all relevant (iso-) enzyme concentrations in the investigated biological media. Using Dyn A1−13 as a model compound, we have previously shown that the size of metabolic pools of peptides can be efficiently evaluated over several metabolic generations by noncompartmental analysis (area under the concentration time profiles) and enzyme inhibition studies with parent drug and synthesized metabolites.[1] Within this study, it was also shown that the degradation of Dyn A1−13 and all its metabolites followed apparent first-order kinetics, similar to results for other peptide drugs.[12] It was therefore of interest to test whether a structured compartmental curve fitting approach is helpful for the assessment of complex metabolic events using Dyn A1−13 degradation as an example. Plasma was chosen since it often represents a major metabolic site for peptide drugs given intravenously.[12] In the following, the advantages and disadvantages of such a multicompartmental kinetic analysis are presented in three examples.

Example 1: Identification of the Metabolic Pathways of Peptide Degradation—The following section demonstrates some of the advantages of the multicompartmental modeling approach for the identification of metabolic pathways. As shown in Figure 1, the metabolic fate of Dyn A2−12, one of the main metabolites of Dyn A1−13, produces Dyn A3−12 and Dyn A4−12. To investigate this N-terminal metabolism in more detail, captopril was added to the incubation solution to suppress the C-terminal metabolism of Dyn A2−12 which is dominated by the angiotensin converting enzyme[1] and restricted the metabolic events on the N-terminus. Initial enzyme inhibition studies[1] with the established aminopeptidase inhibitor bestatin were able to fully block the amino-terminal degradation pathway of Dyn A2−12, suggesting a unidirectional degradation from Dyn A2−12 to Dyn A3−12 and subsequently to Dyn A4−12. A comparison of the AUC estimates of Dyn A3−12 obtained from metabolism of Dyn A2−12 under captopril inhibtion with those obtained after direct incubation of Dyn A3−12 contradicted this hypothesis, as the AUC of Dyn A3−12 was smaller than expected for a unidirectional degradation.[1] Quite in agreement, a simulation with the multicompartmental model using rate constants determined from direct degradation of the involved fragments (degradation rate constant under captopril inhibition for Dyn A2−12, Dyn A3−12, Dyn A4−12 using a sequential metabolism from Dyn A2−12 to Dyn A3−12 to Dyn A4−12) failed to describe the data adequately (Figure 2A). Therefore the metabolic pathways differed somewhat from the simple sequential metabolism suggested by bestatin data.

AUC data would support this unidirectional model of metabolic pathways only, if the rate constant of Dyn A3−12 degradation (under captopril: $k_{45} = k_4$) was increased by 10-fold from its initial estimate (obtained from direct degradation of Dyn A3−12). Such an increase in the metabolic rate of Dyn A3−12 could not be fully excluded if the cleavage of Gly2-Gly3 of Dyn A2−12 would facilitate the subsequent cleavage of Gly3-Phe4 of Dyn A3−12 by the same enzyme (the generated Dyn A3−12 would not have to enter the enzymatic pocket for further cleavage). Such cases of "rate enhancement" have been reported in the literature for other peptides.[13] The reference AUC of

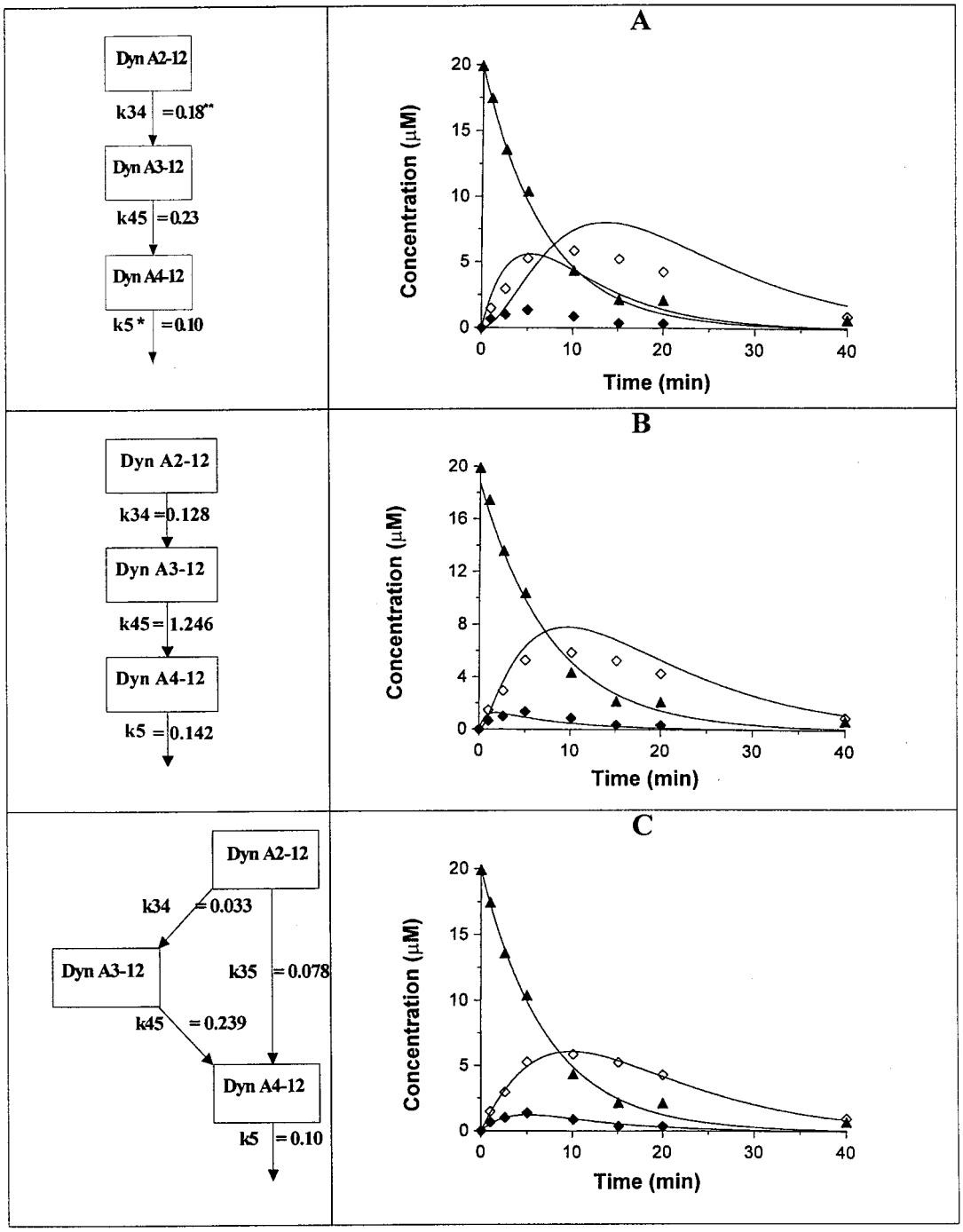

Figure 2—(A) Simulation of concentration–time profiles of Dyn A2–12 (▲) and major metabolites (Dyn A3–12 ◆ and Dyn A4–12 ◇, $r^2 = 0.216$, MSC = –2.781) in human plasma at 37 °C under captopril inhibition using the model of sequential metabolism of Dyn A2–12 into Dyn A3–12 and Dyn A3–12 into Dyn A4–12 with previously obtained rate constants (rate constants under captopril inhibition taken from from Table 1. *k_5 in the presence of captopril was calculated as k_5 (0.17 min^{-1}) minus rate constant associated with captopril sensitive pathway (0.07 min^{-1}): 0.17–0.07 = 0.10 min^{-1} (see Table 1), **k_{34} was based on bestatin enzyme inhibition data ($k_{34} + k_{35}$, see Table 1). (B) Least-squares fit of concentration–time profiles of Dyn A2–12 (▲) and major metabolites (Dyn A3–12 (◆) and Dyn A4–12 (◇), $r^2 = 0.989$, MSC = 3.491) in human plasma at 37 °C under captopril inhibition using model of sequential metabolism of Dyn A2–12 into Dyn A3–12 and increased rate constant k_{45}. k_{34} and k_5 were allowed to float freely (limits for deviation from initial estimates did not apply, see Materials and Methods). (C) Least-squares fit of concentration–time profiles of Dyn A2–12 (▲) and major metabolites (Dyn A3–12 (◆) and Dyn A4–12 (◇), $r^2 = 0.988$, MSC = 5.244) in human plasma at 37 °C under captopril inhibition using the model of simultaneous metabolism of Dyn A2–12 via aminopeptidase and dipeptidylaminopeptidase.

Dyn A3−12 for total conversion from Dyn A2−12 would then be smaller than the AUC observed after direct incubation of Dyn A3−12. For testing this hypothesis with the compartmental model, the rate constant for converting Dyn A3−12 into Dyn A4−12 by the relevant aminopeptidase was assumed to be larger in a series of metabolic events than its estimate obtained from direct degradation of Dyn A3−12. In our data set obtained under captopril inhibition (no C-terminal enzymatic attack), all Dyn A2−12 was then assumed to be converted into Dyn A3−12, and in turn all Dyn A3−12 into Dyn A4−12. However, discrepancies between fitted and observed estimates of Dyn A3−12 or Dyn A4−12 concentration−time profiles were observed in the relevant compartmental model (Figure 2B).

Table 1—Rate Constants of Dynorphin Fragments in Plasma. Listed Is the Overall Rate Constant and the Contribution of Various Enzymatic Systems to the Overall Rate Constant[a]

peptide	*n*	overall rate constant (min^{-1})	rate constant associated with blocked enzyme pathway (min^{-1})			
			GEMSA	bestatin	leucinethiol	captopril
Dyn A1–13	3	0.78 (k_1)	0.61 (k_{12})	0.22 (k_{16})	–	N.T.
Dyn A1–12	3	0.38 (k_2)	N.T.	0.30 (k_{23})	0.28 (k_{23})	0.067 (k_{27})
Dyn A2–13	1	0.99 (k_6)	N.T.	N.T.	N.T.	N.T.
Dyn A2–12	4	0.22 (k_3)	–	0.18 ($k_{34} + k_{35}$)	0.08 (k_{34})	0.07 (k_{38})
Dyn A3–12	2	0.28 (k_4)	N.T.	0.23 (k_{45})	–	0.043
Dyn A4–12	3	0.17 (k_5)	N.T.	0.13	0.09	0.07
Dyn A1–10	1	0.50 (k_7)				

[a] Calculated from ref 1 by transforming half-lives of Table 2 listed in ref 1 into the rate constants associated with the blocked enzyme (associated rate constants of Figure 1 are given in parentheses). NT = not tested; –: no effect.

Table 2—The Formation of Metabolites from Their Parent Compound As Calculated from Multicompartmental Fitting, Enzyme Inhibition Experiments, and Noncompartmental (AUC-based) Analysis[c]

peptide incubated	metabolite formation in % of starting material as calculated by					
	fit	inhibitor	AUC	fit	inhibitor	AUC
Dyn A1–13	79	Dyn A1–12 82	78	10	Dyn A2–13 0 (30[a]	15
Dyn A1–12	78	Dyn A2–12 83 (85)[a]	78	20	Dyn A1–10 19	*b*
Dyn A2–12	15	Dyn A3–12 37 (80)[a]	17	39	Dyn A4–12 28	42

[a] Based on leucinethiol data, bestatin data in brackets. [b] Coeluting with Dyn A4–12. [c] Enzyme inhibition and noncompartmental data taken from ref 1.

These deviations between experimental and modeled concentration−time profile, detected by multicompartmental kinetic analysis, showed the invalidity of the "rate enhanced" unidirectional model.

Finally, a model employing parallel pathways, consequently contradicting the high selectivity of bestatin for aminopeptidase, was investigated using simultaneous least-squares fitting of Dyn A2−12 degradation under ACE inhibition. Rate constants for parallel metabolic pathways were allowed to vary within the limits outlined in the data analysis section. This model adequately described the experimental data (Figure 2C). Thus, the use of the compartmental analysis, suggested the nonspecificity of bestatin, a widely used aminopeptidase inhibitor, very much in agreement with findings by Otero.[14] The consequent use of the more specific inhibitor leucinethiol in the original publication[1] triggered by the results of this fitting procedure supported a smaller involvement of aminopeptidase in the N-terminal metabolism of Dyn A 2−12 (see Table 2). In addition, the analysis suggested a direct degradation of Dyn A2−12 into Dyn A4−12, a pathway which was not revealed by enzyme inhibition studies alone, but in agreement with results of the noncompartmental analysis. These results already argue for one strength of the compartmental approach, namely to incorporate information on the concentration−time relationships in the analysis of complex metabolic events.

Example 2: Detection of Assay Selectivity Problems—Another advantage of simultaneous curve fitting was revealed in the analysis of Dyn A1−12 data. The degradation of Dyn A1−12 under ACE inhibition with captopril using a similar, yet extended, metabolic model described accurately the experimental data (data not shown). Contrary to these results, the concentration−time profile of Dyn A1−12 in naive plasma (no enzyme inhibition) showed a persistent underfit in the profile of Dyn A4−12 in both visual assessment and the correlation statistics on the data set of Dyn A4−12 (Figure 3A).

The hypothesis was that the poor fit might be attributed to the small amounts of generated Dyn A1−10 which was present in the Dyn A1−12 but not in the Dyn A2−12 incubations. Dyn A1−10 and Dyn A4−12 were known to have very similar chromatographic retention profiles in the applied chromatographic system[1] and therefore probably coelute. To investigate the possibility of this peak impurity causing the observed underfit, the concentration−time profile of Dyn A4−12, Dyn A1−10, and their cumulative profile were simulated using the rate constant estimates of k_{27}, k_7, k_2, k_{35}, k_{45}, k_5 from Table 1 (for explanation of abbreviations, see Figure 1) obtained by separate degradation of the relevant dynorphin fragments with or without enzyme inhibitors. The cumulative profile closely resembled the observed data points (Figures 3B and 3C). A fit of Dyn A1−12 degradation in naive plasma taking the impurity into account resulted in a good description of the observed data points (Figure 3C). Although the contributions of Dyn A1−10 to the overall AUC was minor (see relevant degradation rate constants), it illustrates the dependency of noncompartmental kinetic data on chromatographic resolution. Unfortunately, the likelihood of chromatographic impurity increases with the number analytes to be separated; as this was the case for the degradation of Dyn A1−13 for which a total of 17 metabolites were identified. Since all metabolic processes followed apparent first-order kinetics, the multicompartmental modeling approach was instrumental in detecting coelution of chromatographic peaks which none of the other methods would have been able to detect.

Example 3: Application of the Model to Data Sets Describing Entire Degradation Pathways—The above sections showed several advantages of the simultaneous curve fitting procedures in evaluating isolated events in the analysis of complex metabolic systems. In the following the ability to describe and analyze entire degradation pathways is assessed. The applied method, presented so far, incorporated degradation constants based on enzyme inhibition studies into the compartmental analysis to ensure valid initial estimates for the rate constants during the curve fitting procedure. This ensured that the fitting procedure stayed within limits imposed by direct degradation or valid enzyme inhibition experiments of parent drug and metabolites. The same procedure applied to the entire degradation pathway resulted in fits shown in Figure 4 and rate constants observed under rigid limits in Table 3. The agreement between experimentally found and predicted values (Figure 4) strongly supports the validity of the identified metabolic pathway (Figure 1). Table 2 compares the results of the multicompartmental approach, noncompartmental method, and results of the enzyme inhibition studies. Here, the rate constants of degradation or generation obtained from above fitting procedures of Dyn A2−

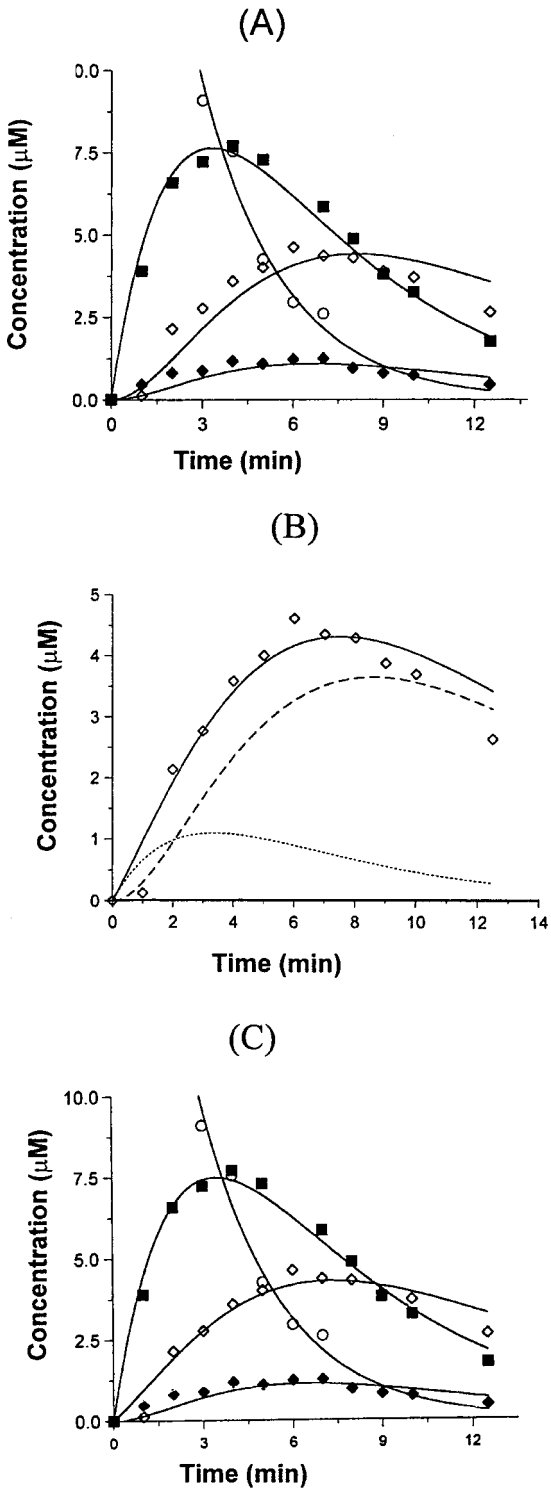

Figure 3—(A) Least-squares fit of concentration–time profiles of Dyn A1–12 (○) and major metabolites (Dyn A2–12 ■, Dyn A3–12 ◆, and assumed Dyn A4–12 (see Figure 3B for more information on "mixed peak") ◇, $r^2 = 0.996$, MSC = 4.81) in human plasma at 37 °C based on the model of Figure 1. (B) Simulation of concentration–time profiles of Dyn A4–12 (- - -) and Dyn A1–10 (•••) after incubation of Dyn A1–12 with overlay of mixed peak (◇). Concentration–time profiles were simulated using unfitted initial estimates of the relevant rate constants (Table 1) or estimates obtained in Figure 2C: $k_7 = 0.5$ min^{-1}, $k_{27} = 0.067$ min^{-1}, $k_{23} = 0.30$ min^{-1}, $k_{34} = 0.008$ min^{-1}, $k_4 = 0.28$ min^{-1}, $k_{45} = 0.239$ min^{-1}, $k_{35} = 0.078$ ($r^2 = 0.987$, MSC = 0.861). (C) Least-squares fit of concentration–time profiles of Dyn A1–12 (○) and major metabolites (Dyn A2–12 ■, Dyn A3–12 ◆, and mixed Dyn A4–12 and Dyn A1–10 ◇, $r^2 = 0.998$, MSC = 5.213) in human plasma at 37 °C based on the model of Figure 1, accounting for coelution of Dyn A4–12 and Dyn A1–10.

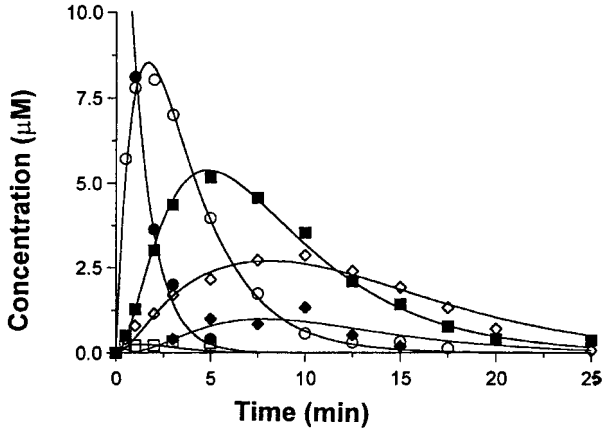

Figure 4—Least-squares fit of concentration–time profiles of Dyn A1–13 (●) and major metabolites (Dyn A1–12 ○, Dyn A2–13 □, Dyn A2–12 ■, Dyn A3–12 ■, and coeluting Dyn A4–12 and Dyn A1–10 ◇, $r^2 = 0.995$, MSC = 4.485) in human plasma at 37 oC accounting for coelution of Dyn A4–12 and Dyn A1–10.

Table 3—Initial Concentration and Rate Constants (min^{-1}) of Dyn A1–13 and Metabolic Fragments in Plasma Fitted to the Model Depicted in Figure 1[a]

parameter	rigid limits*	free-floating parameters**
degradation of A1–13 (k_1)	0.901 ± 0.013	0.892
generation of A2–13 (k_{16})	0.091 ± 0.043	0.015
generation of A1–12 (k_{12})	0.713 ± 0.082	0.702
degradation of A1–12 (k_2)	0.299 ± 0.002	0.384
generation of A2–12 (k_{63})	0.792 ± 0.001	80.9
generation of A1–10 (k_{27})	0.059 ± 0.001	2.2×10^{217}
degradation of A1–10 (k_7)	0.502 ± 0.004	2.1×10^{53}
degradation of A2–13 (k_6)	1.007 ± 0.014	0.178
generation of A2–12 (k_{23})	0.232 ± 0.001	0.266
degradation of A2–12 (k_3)	0.220 ± 0.004	0.197
generation of A3–12 (k_{34})	0.032 ± 0.001	0.119
generation of A4–12 (k_{35})	0.077 ± 0.001	0.227
degradation of A3–12 (k_4)	0.278 ± 0.003	0.536
generation of A4–12 (k_{45})	0.210 ± 0.002	2.53×10^{-16}
degradation of A4–12 (k_5)	0.170 ± 0.004	0.313

[a] Parameters were kept in rigid limits as outlined in the data analysis section or allowed to vary freely ("float") between zero and infinity. *$n = 6$, **$n = 1$.

12, Dyn A1−12, and Dyn A1−13 (Table 3) were used to calculate the % of Dyn A 1−13, Dyn A 1−12, or Dyn A2−12 entering a specific metabolite pool. A good agreement between the compartmental curve fitting approach and the other two methods[1] suggests that one strength of the structured multicompartmental approach is the ability to test the correctness of metabolic pathways suggested by other methods.

Removing the limits of the curve fitting procedure, while retaining the initial estimates for the rate constants, probed how well the compartmental model could stand on its own. After least-squares optimization, the majority of rate constants compared to the rate constants obtained with imposed limits (Table 3). However, minor metabolites, rate constants of metabolites for which no direct data were available and/or fast degradation processes (Dyn A2−13 and Dyn A1−10, Table 3) deviated markedly. This suggests that the unrestricted use of parameter estimates carries the danger of "overfitting" the data (e.g., of minor metabolites) to suit a certain model and the loss of identifiability. Although the resulting fit is good, the predicted rate constants are irrelevant, since they do not possess any practical significance (Table 3) when compared with rate constants obtained from enzyme inhibition studies. Another attempt was made to perform the fitting procedure without

Table 4—Results of Local Sensitivity Analysis

	k_{12}	k_{16}	k_{23}	k_{27}	k_{34}	k_{35}	k_{45}	k_5	k_{63}	k_7
Cl	11.0	1.40	0.00	0.00	0.00	0.00	0.00	0.00	0.00	0.00
C2	0.26	0.12	3.27	0.83	0.00	0.00	0.00	0.00	0.00	0.00
C3	2.82	0.78	0.82	0.28	0.34	0.81	0.00	0.00	3.95	0.00
C4	0.22	0.11	0.59	0.21	0.79	0.51	0.90	0.00	0.07	0.00
C6	7.79	0.87	0.00	0.00	0.00	0.00	0.00	0.00	3.57	0.00
C5 C7	1.21	0.33	2.88	0.76	0.18	0.62	0.00	1.32	0.44	1.43
overall	3.88	0.60	1.89	0.52	0.44	0.65	0.90	1.32	2.65	1.43

good initial estimates for the rate constants (setting all to 0.5 or 1) and without limits. Under these circumstances the data for Dyn A1−13 and its metabolites could not be fitted to the model outlined in Figure 1 (data not shown). More detailed evaluation of the fits described in Figure 4 by local sensitivity analysis identified k_{12} (linked to k_1), k_{63}, and k_{23} as the most sensitive rate constants, while k_{16}, k_{27}, k_{34}, k_{35} represent overall the least sensitive (see Appendix 2 for a more detailed description of the method and Table 4 for a representation of the results of the analysis). Thus, the sensitivity analysis confirmed the presence of general identifiability problems, similar to those indicated by comparing results of rigid and free-floating parameter estimations. The sensitivity analysis reemphasized that the isolated use of such complex models is not feasible. However, the use of experimentally derived estimates of rate constants (e.g., obtained from incubations of synthesized metabolites in the presence or absence of enzyme inhibitors, see Materials and Methods for more detail) in the model is very helpful in probing for the acceptability of a metabolic scheme proposed by the other methods. Thus, structured multicompartmental modeling approaches will be useful in the evaluation of complex peptide degradation pathways when used hand in hand with alternative forms of analysis, such as enzyme inhibition studies and noncompartmental analytical approaches.

In conclusion, the presented apparent first-order multicompartmental approach has several advantages. It is relatively rapid and focuses only on the metabolically relevant processes. The presented model can be extended to include Michaelis−Menten kinetics when necessary. However, such an extension would add several parameters which have to based on further experiments and should only be applied when necessary (i.e., the half-life changes in the experimental concentration range). The application of the compartmental approach in the evaluation of the metabolic fate of Dyn A1−13 and related fragments helped to identify a lack of chromatographic resolution and a low selectivity of one of the enzyme inhibitors employed in the study. It further was able to support the correctness of the proposed metabolic pathways.

Peptide metabolism has been generally evaluated by biochemists with the help of enzyme inhibition studies. The application of pharmacokinetic tools such as noncompartmental approaches have been recently incorporated into such investigations.[1] The results presented in this study suggest distinct advantages of the compartmental analysis for evaluating complex metabolic events. Because of the inherent possible pitfalls of all three methods, the combined use of all approaches might be best suited to assess complex metabolic degradation patterns of peptides in a detailed fashion.

Appendix 1

Equations Employed for the Simultaneous Fitting of Dyn A1−13 and Its Main Metabolites According to Figure 1—*For Dyn A1−13:* $C1 = C0\ \exp((-k_1)t)$

For Dyn A1−12: $C2 = k_{12}C0/(k_1 - k_2)(\exp((-k_2)t) - \exp((-k_1)t))$

For Dyn A2−13: $C6 = k_{16}C0/(k_1 - k_6)(\exp((-k_6)t) - \exp((-k_1)t))$

For Dyn A2−12: $C3 = k_{12}k_{23}C0/((k_2 - k_3)(k_1 - k_3))\exp((-k_3)t) + k_{12}k_{23}C0/((k_3 - k_2)(k_1 - k_2))\exp((-k_2)t) + k_{12}k_{23}C0/((k_3 - k_1)(k_2 - k_1))\exp((-k_1)t) + k_{16}k_{63}C0/((k_6 - k_3)(k_1 - k_3))\exp((-k_3)t) + k_{16}k_{63}C0/((k_3 - k_6)(k_1 - k_6))\exp((-k_6)t) + k_{16}k_{63}C0/((k_3 - k_1)(k_6 - k_1))\exp((-k_1)t)$

For Dyn A3−12: $C4 = k_{12}k_{23}k_{34}C0/((k_3 - k_4)(k_2 - k_4)(k_1 - k_4))\exp((-k_4)t) + k_{12}k_{23}k_{34}C0/((k_4 - k_3)(k_2 - k_3)(k_1 - k_3))\exp((-k_3)t) + k_{12}k_{23}k_{34}C0/((k_4 - k_2)(k_3 - k_2)(k_1 - k_2))\exp((-k_2)t) + k_{12}k_{23}k_{34}C0/((k_4 - k_1)(k_3 - k_1)(k_2 - k_1))\exp((-k_1)t) + k_{16}k_{63}k_{34}C0/((k_3 - k_4)(k_6 - k_4)(k_1 - k_4))\exp((-k_4)t) + k_{16}k_{63}k_{34}C0/((k_4 - k_3)(k_6 - k_3)(k_1 - k_3))\exp((-k_3)t) + k_{16}k_{63}k_{34}C0/((k_4 - k_6)(k_3 - k_6)(k_1 - k_6))\exp((-k_6)t) + k_{16}k_{63}k_{34}C0/((k_4 - k_1)(k_3 - k_1)(k_6 - k_1))\exp((-k_1)t)$

For Coeluting Dyn A4−12 (C5) and Dyn A1−10 (C7): $C5 = k_{12}k_{23}k_{35}C0/((k_3 - k_5)(k_2 - k_5)(k_1 - k_5))\exp((-k_5)t) + k_{12}k_{23}k_{35}C0/((k_5 - k_3)(k_2 - k_3)(k_1 - k_3))\exp((-k_3)t) + k_{12}k_{23}k_{35}C0/((k_5 - k_2)(k_3 - k_2)(k_1 - k_2))\exp((-k_2)t) + k_{12}k_{23}k_{35}C0/((k_5 - k_1)(k_3 - k_1)(k_2 - k_1))\exp((-k_1)t) + k_{16}k_{63}k_{35}C0/((k_3 - k_5)(k_6 - k_5)(k_1 - k_5))\exp((-k_5)t) + k_{16}k_{63}k_{35}C0/((k_5 - k_3)(k_6 - k_3)(k_1 - k_3))\exp((-k_3)t) + k_{16}k_{63}k_{35}C0/((k_5 - k_6)(k_3 - k_6)(k_1 - k_6))\exp((-k_6)t) + k_{16}k_{63}k_{35}C0/((k_5 - k_1)(k_3 - k_1)(k_6 - k_1))\exp((-k_1)t) + k_{12}k_{23}k_{34}k_{45}C0/((k_4 - k_5)(k_3 - k_5)(k_2 - k_5)(k_1 - k_5))\exp((-k_5)t) + k_{12}k_{23}k_{34}k_{45}C0/((k_5 - k_4)(k_3 - k_4)(k_2 - k_4)(k_1 - k_4))\exp((-k_4)t) + k_{12}k_{23}k_{34}k_{45}C0/((k_5 - k_3)(k_4 - k_3)(k_2 - k_3)(k_1 - k_3))\exp((-k_3)t) + k_{12}k_{23}k_{34}k_{45}C0/((k_5 - k_2)(k_4 - k_2)(k_3 - k_2)(k_1 - k_2))\exp((-k_2)t) + k_{12}k_{23}k_{34}k_{45}C0/((k_5 - k_1)(k_4 - k_1)(k_3 - k_1)(k_2 - k_1))\exp((-k_1)t) + k_{16}k_{63}k_{34}k_{45}C0/((k_4 - k_5)(k_3 - k_5)(k_6 - k_5)(k_1 - k_5))\exp((-k_5)t) + k_{16}k_{63}k_{34}k_{45}C0/((k_5 - k_4)(k_3 - k_4)(k_6 - k_4)(k_1 - k_4))\exp((-k_4)t) + k_{16}k_{63}k_{34}k_{45}C0/((k_5 - k_3)(k_4 - k_3)(k_6 - k_3)(k_1 - k_3))\exp((-k_3)t) + k_{16}k_{63}k_{34}k_{45}C0/((k_5 - k_6)(k_4 - k_6)(k_3 - k_6)(k_1 - k_6))\exp((-k_6)t) + k_{16}k_{63}k_{34}k_{45}C0/((k_5 - k_1)(k_4 - k_1)(k_3 - k_1)(k_6 - k_1))\exp((-k_1)t)$

$C7 = k_{12}k_{27}C0/((k_2 - k_7)(k_1 - k_7))\exp((-k_7)t) + k_{12}k_{27}C0/((k_7 - k_2)(k_1 - k_2))\exp((-k_2)t) + k_{12}k_{27}C0/((k_7 - k_1)(k_2 - k_1))\exp((-k_1)t)$

Appendix 2

Calculation of Sensitivity Coefficients—A local sensitivity analysis was carried out for each Dyn along with some summary measures, e.g., see Rabitz for a detailed description.[9] The normalized sensitivity coefficient (SC) detailed in Bieniasz and Speiser was calculated for each Dyn i as[10]

$$SC_{ij}(t) = \frac{\partial \ln C_i(t)}{\partial \ln k_j}\Big|_{k_j = k'_j} \qquad (1.1)$$

where i, $i = 1, 2, 7$, the rate constant j corresponds to the set $j = \{12, 16, 23, 27, 34, 35, 45, 5, 63, 7\}$, and the equations for the C_i's are given in Appendix 1. The values for the k_j are given in Table 3. Furthermore, the SC for C5 and C7 was calculated jointly, since C5 and C7 were considered additive, i.e., the joint SC was given by $SC_{5,j} + SC_{7,j}$. The rate constants k_1, k_2, k_3, k_4, k_6 were linked to the other rate constants through the equations $k_1 = k_{16} + k_{12} + k_{1u}$ or $k_2 = k_{23} + k_{27} + k_{2u}$ or $k_3 = k_{34} + k_{35} + k_{3u}$ or $k_4 = k_{45} + k_{4u}$ or $k_6 = k_{63} + k_{6u}$, where k_{1u}, k_{2u}, k_{3u}, k_{4u}, k_{6u} represents degradation of specific metabolites not included in known metabolic pathways. The absolute magnitude of the SC's were summarized across time as

$$ASC_{i,j} = \sum_{k=1}^{7} |SC_{i,j}(t_k)|, \quad (1.2)$$

where $t_1 = 1$, $t_2 = 2$, $t_3 = 5$, $t_4 = 10$, $t_5 = 20$, $t_6 = 30$, and $t_7 = 40$. The results are given in the body of Table 4. The values were then averaged for each rate constant in order to provide a global measure of sensitivity across time. To calculate the overall mean sensitivity, we did not average in the values of $ASC_{i,j} = 0$.

References and Notes

1. Mueller, S.; Hochhaus, G. Metabolism of dynorphin A1−13 in human blood and plasma. *Pharm. Res.* **1995**, *12*, 1165−1170.
2. Chavkin, C.; Goldstein, A. Specific receptor for the opioid peptide dynorphin: Structure−activity relationship. *Proc. Natl. Acad. Sci. U.S.A.* **1981**, *78*, 6543−6547.
3. Takemori, A. E.; Loh, H. H.; Lee, N. N. Suppression by dynorphin A and [des-Tyr1]dynorphin A peptides of the expression of opiate withdrawal and tolerance in morphine-dependent mice. *J. Pharm. Exp. Ther.* **1993**, *266*, 121−124.
4. Mueller, S.; Chang-Sing-Pang, F. B.; Hochhaus, G. Displacement of [^{3}H]-L-glutamate in Rat Brain Membranes by Metabolic Dynorphin Fragments. *Die Pharmazie* **1998**,
5. Quillan, J. M.; Sadee, W. Dynorphin Peptides; Antagonists of melanocortin receptors. *Pharm. Res.* **1997**, *14*, 713−719.
6. Henriksen, J. H. Kinetics of whole-body and organ degradation. In *Degradation of bioactive substances: Physiology and Pathophysiology*; Henriksen, J. H., Ed.; CRC: Boca Raton, 1991; pp 3−32.
7. Gibaldi, M.; Perrier, D. *Pharmacokinetics*; 2nd ed.; Raven: New York, 1982.
8. *Micromath, Scientist, Mathematical modeling/differential and nonlinear equations*; MicroMath Scientific Software: Salt Lake City, UT, 1993; pp 193−194.
9. Rabitz, H. Systems analysis at the molecular scale. *Science* **1989**, *246*, 221−246.
10. Bieniasz, L. K.; Speiser, B. Use of sensitivity analysis methods in the modelling of electrochemical transients. Part 1. Gaining more insight into the behaviour of kinetic models. *J. Electroanal. Chem.* **1998**, *441*, 221−246.
11. Bausback, H. H.; Ward, P. E. Degradation of low molecular-weight opioid peptides by vascular plasma membrane aminopeptidase M. *Biochim. Biophys. Acta* **1986**, *882*, 437−444.
12. Powell, M. F. Peptide stability in drug development: A comparison of peptide reactivity in different biological media. *J. Pharm. Sci.* **1992**, *81*, 731−735.
13. Walker, R.; Krishnaswamy, S. The activation of prothrombin by the prothrombinase complex. The contribution of the substrate-membrane interaction to catalysis. *J. Biol. Chem.* **1994**, *274*, 41−50.
14. Otero, M. J.; Iglesias, T.; Fuentes, J. A. Hypoalgesic action of bestatin analogues that inhibit central aminopeptidases, but not neutral endopeptidases. *Neuropeptides* **1993**, *25*, 175−182.

Acknowledgments

This study was supported in part by Neurobiological Technologies Incorporated, Richmond, CA. The work of A.H. was supported in part by NIH General Clinical Research Center Grant RR0082.

JS980036D

Solubilization of Flavopiridol by pH Control Combined with Cosolvents, Surfactants, or Complexants

PING LI,† S. ESMAIL TABIBI,‡ AND SAMUEL H. YALKOWSKY*,†

Contribution from *Department of Pharmaceutical Sciences, College of Pharmacy, University of Arizona, Tucson, Arizona 85721, and Pharmaceutical Resources Branch, National Cancer Institute, NIH, Bethesda, Maryland 20892.*

Received March 30, 1999. Accepted for publication June 11, 1999.

Abstract □ This study investigates the roles of both ionized and un-ionized species of flavopiridol in solubilization by complexation, micellization, and cosolvency. Control of pH was used in combination with surfactants (polysorbate 20 and polysorbate 80), cosolvents (ethanol and propylene glycol), as well as uncharged and anionic complexing agents [hydroxypropyl β-cyclodextrin (HPβCD) and sulfobutyl ether β-cyclodextrin (SBEβCD)] to solubilize flavopiridol. These combined techniques increase not only the solubility of the un-ionized flavopiridol but also the solubility of the ionized drug. This study confirms that previously developed equations effectively characterize the roles of pH, pK_a, and either complexation constant, micelle partition coefficient, or cosolvent solubilizing power in determining drug total aqueous solubility.

Introduction

Flavopiridol is a synthetic derivative of rohitukine that is currently undergoing clinical trails by the National Cancer Institute as an antineoplastic agent. This compound is a potent cyclin-dependent enzymes (CDK) inhibitor and promotes apoptosis when combined with other chemotherapeutic agents.[1] It has a water solubility of 0.025 mg/mL, which is 400 times lower than the desired concentration for intravenous (iv) infusion. Although this compound has an apparent pK_a value of 5.86, solubilization by pH control could not produce a stable 10 mg/mL solution that does not precipitate upon injection.[2] Furthermore, other solubilization techniques, such as cosolvency, micellization, and complexation, were ineffective in providing adequate solubilization within a physiologically acceptable vehicle.[2]

In a previous study, we investigated the combined effect of pH control and complexation on drug solubilization.[3] It was shown that the solubility of the complex is proportional to the product of the complexation constant and the solute solubility for both the un-ionized and ionized solutes. Though the ionized solute has a smaller complexation constant, it has greater water solubility compared with that of the un-ionized solute. A change in pH favoring solute ionization will not simply increase the solubility of the solute in water, but it will increase the solubility of the complex because the latter is proportional to solute concentration. Further studies also suggest that under certain circumstances the solubilization of the ionized solute by either cosolvent or surfactant is more important than the solubilization of the un-ionized solute in determining the total solubility.[4] It is of note that the current iv flavopiridol dosage form used for clinical trails is formulated in a 10 mg/mL solution by using pH control in combination with complexation. This formulation does not precipitate upon dilution by isotonic Sorensen's phosphate buffer.[2,5]

This paper compares the role of the ionized flavopiridol species with the role of the un-ionized species in drug solubilization by complexation, micellization, and cosolvency. Control of pH is used in combination with surfactants (polysorbate 20 and polysorbate 80), cosolvents (ethanol and propylene glycol (PG)) as well as the uncharged and anionic complexing ligands [hydroxypropyl β-cyclodextrin (HPβCD) and sulfobutyl ether β-cyclodextrin (SBEβCD)], respectively.

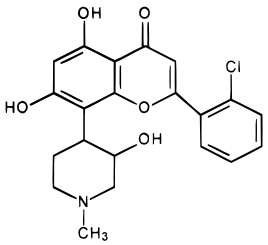

Flavopiridol

Materials

Flavopiridol was provided by the National Cancer Institute and used as received. Hydroxypropyl β-cyclodextrin (HPβCD), with an average molecular weight of 1390 and an average degree of substitution of 4.4, was obtained from Cyclodextrin Technologies Development Inc. (Gainesville, FL). Sulfobutyl ether β-cyclodextrin (SBEβCD), with an average molecular weight of 2162 and an average degree of substitution of 7, was a gift from CyDex, L. C. (Overland Park, KS). All other chemicals were of reagent grade, purchased from Sigma (St. Louis, MO) or Aldrich (St. Louis, MO), and used without further purification. Citrate-phosphate buffers were prepared according to Scientific Tables.[6]

Methods

Solubility Determination. An excess of flavopiridol was added to duplicate vials containing 0.5 mL of the following solutions: HPβCD, SBEβCD, polysorbate 20, polysorbate 80, ethanol, and propylene glycol with concentrations of 0, 2.5, 5, 10, and 20% in citric-phosphate buffers at pH 4.3 and 8.4. The sample vials were then rotated using

* To whom correspondence should be addressed.
† Department of Pharmaceutical Sciences.
‡ Pharmaceutical Resources Branch.

10.1021/js990097r CCC: $18.00
Published on Web 07/31/1999

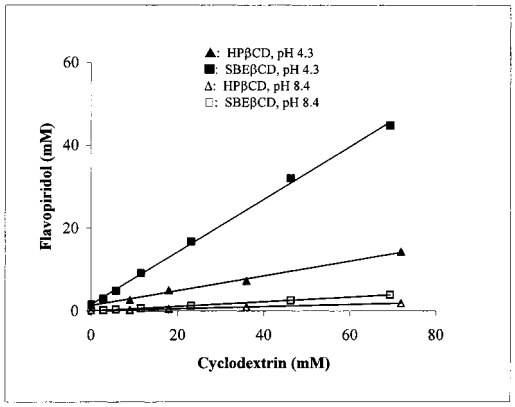

Figure 1—Total experimental aqueous flavopiridol solubilities (symbols) in cyclodextrin solutions at different pHs.

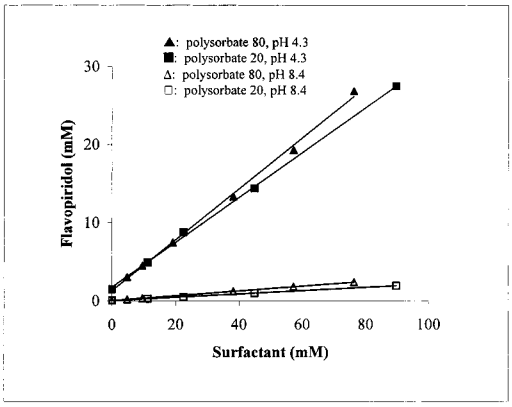

Figure 2—Total experimental aqueous flavopiridol solubilities (symbols) in surfactant solutions at different pHs.

an end-over-end mechanical rotator at 20 rpm (Glas-Col Laboratory Rotator, Terre Haute, IN) at 25 °C for 6 days (preliminary data indicate that flavopiridol is stable for 2 months under these conditions). Samples with drug crystals present were considered to have reached their equilibrium solubility and were removed from the rotator. The samples were filtered through a 0.45-μm filter and the pH at equilibrium was measured before performing the high-performance liquid chromatography (HPLC) analysis.

HPLC Analysis. The HPLC assay was modified from a previous report.[6] Briefly, a Pinnacle octylamine column (150 cm × 4.6 mm, Restek, Bellefonte, PA) was used with a mobile phase composed of 0.1% triethylamine in 50 mM phosphate buffer at pH 2.5 (adjusted by H_3PO_4) and acetonitrile in a ratio of 35: 65. The flow rate was controlled at 1 mL/min (125 Solvent Module, Beckman, Fullerton, CA), and the effluent was detected at 263 nm (168 detector, Beckman, Fullerton, CA). Neither the buffer nor any of the solubilizing agents interfere with the assay.

Results and Discussions

Solubilization by pH Control and Complexation. Figure 1 shows the effect of the complexation agents, HPβCD and SBEβCD, on the solubility of flavopiridol at pH 4.3 and 8.4. The drug solubility in the absence of either HPβCD or SBEβCD is ~0.055 mM at pH 8.4 and ~1.37 mM at pH 4.3. The solubility increases linearly as a function of the concentration of both cyclodextrins at both pH conditions. However, the solubility increase is far more significant at the low pH where the drug is cationic. For example, in the presence of 10% HPβCD, its solubility is 6-fold greater at pH 4.3 than that at pH 8.4. Similarly, when SBEβCD is used, the solubility difference between the two solution pHs is 12-fold.

Li et al.[3] showed that eq 1 describes the dependency of total solubility of a drug on the concentration of complexation ligand at any pH.

$$[D^{tot}] = [D_u] + [D_u]10^{(pK_a - pH)} + K_u[D_u][L] + K_i[D_u]10^{(pK_a - pH)}[L] \quad (1)$$

where $[D_u]$ is the solubility of free un-ionized drug, $[L]$ is the ligand concentration, and K_u and K_i are the complexation constants of the un-ionized and of the ionized species, respectively. The equation describes the total solubility as the sum of four species: free un-ionized drug $[D_u]$, free ionized drug $[D_u]10^{(pK_a - pH)}$, un-ionized drug−ligand complex $K_u[D_u][L]$, and ionized drug−ligand complex $K_i[D_u]10^{(pK_a - pH)}[L]$. The solubility data from Figure 1 were used to calculate the complexation constants of neutral and cationic flavopiridol species with a neutral ligand, HPβCD, or with an anionic ligand, SBEβCD, via eq 1. The values obtained are $K_u = 485\ M^{-1}$ and $K_i = 149\ M^{-1}$ for HPβCD, and $K_u = 991\ M^{-1}$ and $K_i = 421\ M^{-1}$ for SBEβCD.

Although the complexation constant is greater for the uncharged form than for the cation, the latter is often more efficiently solubilized. The solubility of a weak base increases exponentially with a decrease in solution pH below the pK_a. As a result, the ratio of the solubility of the ionized to un-ionized drug often exceeds the ratio of the complexation constant of the un-ionized to ionized drug, that is, $10^{(pK_a - pH)} > K_u/K_i$ (or $[H]/K_a > K_u/K_i$). Accordingly the cationic drug−ligand complex can have a greater solubility than the un-ionized drug−ligand complex. This result is consistent with the results of other studies.[7−9]

Solubilization by pH Control and Micellization. Figure 2 shows the solubility of flavopiridol as a function of both surfactant concentration and pH of the solution. An increase in the concentration of surfactants, either polysorbate 20 or polysorbate 80, produces a linear increase in drug solubility. Again, the solubility increase is much greater at pH 4.3 than that at pH 8.4. This phenomenon can be described by eq 2.[4]

$$[D^{tot}] = [D_u] + [D_u]10^{(pK_a - pH)} + \kappa_u[D_u][C_m] + \kappa_i[D_u]10^{(pK_a - pH)}[C_m] \quad (2)$$

where κ_u and κ_i are micellar partition coefficients for the un-ionized species and the ionized species of drugs, respectively, and $[C_m]$ is micellar concentration. The value of $[C_m]$ is approximately equal to the total surfactant concentration when the critical micellar concentration is small. Note that eq 2 is analogous to eq 1, which characterizes solubilization by combined pH control and complexation.

The solubility data from Figure 2 are incorporated into eq 2 and the micellar partition coefficients are calculated to be $\kappa_u = 375\ M^{-1}$ and $\kappa_i = 194\ M^{-1}$ with polysorbate 20, and $\kappa_u = 551\ M^{-1}$ and $\kappa_i = 214\ M^{-1}$ with polysorbate 80. The lower micellar partition coefficients for the cation is obviously due to its greater affinity to water. According to eq 2, the solubility of drug in micelles is determined by the product of the micellar partition coefficient and drug water solubility, that is, $\kappa_u[D_u]$ for the un-ionized drug and $\kappa_i[D_i]$ for the ionized drug. As in the case of complexation, the solubility of the drug in micelles will be greater for the ionized species than for the un-ionized species if $10^{(pK_a - pH)} > \kappa_u/\kappa_i$. Again, the greater solubility of ionized drug in micelles at pH 4.3 results from its greater solubility in water. The slightly higher solubilization capacity of polysor-

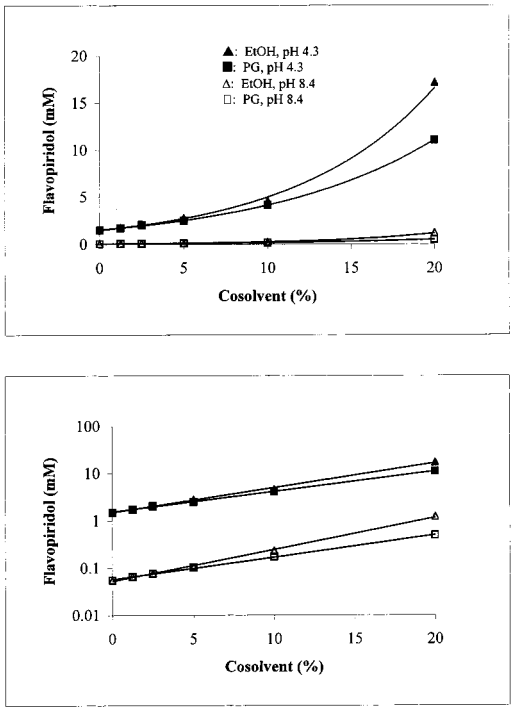

Figure 3—(a) Total experimental aqueous flavopiridol solubilities (symbols) in cosolvent solutions at different pHs. (b) Schematic semilogarithmical plot of the total aqueous solubility of flavopiridol against cosolvent volume fraction.

bate 80 in comparison with polysorbate 20 is because of the larger hydrophobic core produced by its longer alkyl chains.

Solubilization by pH Control and Cosolvency. Figure 3a shows the effects of ethanol and propylene glycol on the total solubility of flavopiridol as a function of pH. Unlike the effects of complexant or surfactant, an increase in the concentration of cosolvents produces an exponential increase in drug solubility. Once more, the drug solubility at pH 4.3 is much higher than that at pH 8.4. In a previous study,[4] the pH related solubilization produced by a cosolvent was described by

$$[D^{tot}] = [D_u]10^{\sigma_u f} + [D_u]10^{(pK_a - pH)}10^{\sigma_i f} \qquad (3)$$

where f is the volume fraction of cosolvents and σ_u and σ_i are the solubilizing powers of the cosolvent for the un-ionized and the ionized species, respectively. Note that because the values of σ_u and σ_i are dependent on the polarity of the solute, σ_u will be greater than σ_i for both cosolvents. If the difference between the drug pK_a and the solution pH is greater than the difference between the cosolvent solubilizing powers for the un-ionized species and for the ionized species (i.e., $pK_a - pH > \sigma_u - \sigma_i$), then the solubilization of the charged species can exceed that of the neutral species.

Figure 3a can be re-plotted semilogarithmically as is seen in Figure 3b, where linear relationships between log-[D^{tot}] and cosolvent volume fraction f are evident at both pHs in both cosolvents. The slopes at pH 4.3 and pH 8.4 show that σ_u and σ_i are only slightly different, with respective values of 0.06 and 0.05 for ethanol, and 0.05 and 0.04 for propylene glycol. Although the un-ionized drug solubility increases by a slightly higher factor than that of the ionized drug (i.e., $\sigma_u > \sigma_i$ for both cosolvents), the amount of drug solubilized is much greater at the lower pH where the drug ionizes because the concentration of cation far exceeds the concentration of the uncharged drug in the solution at pH 4.3. It was also observed that both σ_u and σ_i in ethanol are slightly larger than in propylene glycol. This larger increase in drug solubility results from the fact that ethanol is less polar than propylene glycol.

Conclusions

As described by eqs 1, 2, and 3, pH control can be used in combination with complexation, micellization, or cosolvency, respectively, to improve the ionized drug solubility as well as the un-ionized drug solubility. These equations characterize the effects of un-ionized and particularly ionized species with respect to the pH, pK_a, and either the complexation constant K, micelle partition coefficient κ, or solubilizing power σ. They provide a theoretical background for understanding the dynamics of these combined techniques. The knowledge gained in this study may help in producing physically stable formulations for weakly ionizable drugs.

References and Notes

1. Schwartz, G. K.; Farsi, K.; Danso, D.; Dhuper, S. K.; Kelsen, D.; Spriggs, D. "The protein kinase C (PKC) inhibitors UCN-01 and flavopiridol(Flavo) significantly enhance the cytotoxic effect of chemotherapy by promoting apoptosis in gastric and breast cancer cells. *Proc. ASCO*. **1996**, *15*, 501−504.
2. Dannenfelser, R. M.; Surakitbanharn, Y.; Tabibi, S. E.; Yalkowsky, S. H. Parenteral formulation of flavopiridol (NSC-649890). *PDA J. Pharm. Sci. Technol*. **1995**, *50*, 356−359.
3. Li, P.; Tabibi, S. E.; Yalkowsky, S. H. Combined effect of complexation and pH on solubilization. *J. Pharm. Sci*. **1998**, *87*, 1535−1537.
4. Li, P.; Tabibi, S. E.; Yalkowsky, S. H. Solubilization of ionized and un-ionized flavopiridol by ethanol and polysorbate 20. *J. Pharm. Sci*. **1999**, *88*, 507−509.
5. Li, P.; Patel, H.; Tabibi, S. E.; Vishnuvajjala, R.; Yalkowsky, S. H. Evaluation of intravenous flavopiridol formulations. *PDA J. Pharm. Sci. Technol*. **1999**, *53*, 137−140.
6. Diem, K.; Lentner, C. *Scientific Tables*, seventh edition, Geigy Pharmaceuticals, Ardsley, NY, 1974; pp 280−282.
7. Okimoto, K.; Rajewski, R. A.; Uekama, K.; Jona, J. A.; Stella, V. J. The interaction of charged and uncharged drugs with neutral (HP-βCD) and anionically charged (SBE7-β-CD) β-cyclodextrins. *Pharm. Res*. **1996**, *13*, 256−264.
8. Johnson, M. D.; Hoesterey, B. L.; Anderson, B. D. Solubilization of a tripeptide HIV protease inhibitor using a combination of ionization and complexation with chemically modified cyclodextrins. *J. Pharm. Sci*. **1994**, *83*, 1142−1146.
9. Yalkowsky, S. H. *Solubility and solubilization in aqueous media*; Oxford University Press: Cambridge, 1999.

Acknowledgments

This work was performed under contract No. N01-CM-27757 from the National Cancer Institute.

JS990097R

Blood–Brain Barrier Properties of Human Immunodeficiency Virus Antiretrovirals

MEHRAN YAZDANIAN

Contribution from *Department of Pharmaceutics, Boehringer Ingelheim Pharmaceuticals Inc., 900 Ridgebury Road, P.O. Box 368, Ridgefield, Connecticut 06877.*

Received June 7, 1999. Final revised manuscript received July 14, 1999.
Accepted for publication July 21, 1999.

Introduction

Human immunodeficiency virus (HIV) enters the central nervous system (CNS) early in infection and forms a reservoir in the brain as evidenced by the presence of large quantities of unintegrated viral DNA in the brains of HIV infected individuals.[1,2] The mechanism by which HIV enters the brain is not well understood, however, the resulting infection leads to a number of CNS disorders such as autoimmune deficiency syndrome (AIDS) dementia complex, HIV encephalitis, and peripheral neuropathy.[3,4] Current HIV therapies are focused on reducing the viral load in serum, however, the presence of HIV in sequestered compartments such as the brain significantly limits their efficacy. Hence, the ability of antiretrovirals to enter the brain in therapeutic amounts to treat HIV infection is an essential part of effective HIV therapy. The main barrier for transport of antiretroviral agents to the brain is the blood−brain barrier (BBB). To combat infection and inhibit the replication of HIV in the brain, antiretroviral agents must cross the BBB. Remarkably, there are very few studies that have addressed this issue. This review presents the current understanding of the BBB transport properties of the Food and Drug Administration (FDA)-approved HIV antiretrovirals. Future directions for a better understanding of the BBB permeability of current and upcoming HIV antiretrovirals to treat the devastating neurological and cognitive disorders seen in AIDS patients are also discussed.

Blood–Brain Barrier

The brain is protected by a unique regulatory barrier composed of brain microvessel endothelial cells (BMEC), astroglia, pericytes, perivascular macrophages, and basal lamina, which is collectively known as the BBB. The BMECs provide the functional and morphological basis of the BBB, which acts as a regulatory interface and limits the permeability of the brain to drugs. The selective permeability of the BBB is due to BMECs distinct morphological and enzymatic properties that enable them to form continuous and unfenestrated tight junctions with minimal endocytotic and pinocytotic activity. The presence of tight junctions limits the entry of many blood-borne elements, including small molecules and macromolecules as well as circulating leukocytes, to the brain.[5] The presence of efflux pumps such as P-glycoproteins, which are associated with multidrug resistance (MDR) in BMECs, also limits the transport of drugs across the BBB.

The Effect of HIV on the BBB

HIV infection of the brain is believed to occur through direct and indirect effects on BMECs of the BBB. For example, in vitro studies have shown that HIV readily infects human BMECs to allow its direct entry into the brain.[6] The indirect passage of HIV-infected monocytes or lymphocytes across the BBB via adhesion molecules of BMECs and astrocytes has also been reported.[6] Moreover, HIV entry to the brain may be facilitated by alterations in the BBB permeability due to elevated levels of circulating cytokines, such as TNFα and IL2, in infected patients.[7]

Only indirect methods have been used for determining changes in the integrity of the BBB. These methods include immunostaining for fibrinogen and immunoglobulin G, which are markers of vascular permeability, in postmortem brains, monitoring changes in the magnetic resonance imaging of the brain, and measuring cerebrospinal fluid (CSF) serum protein levels of the HIV-infected individuals. The results of immunostaining for immunoglobulin G and fibrinogen deposition in postmortem brains of AIDS and control patients to detect excess leakage across the BBB due to HIV infection have been inconclusive.[8] Histological, immunocytochemical, and ultrastructural analysis of brain tissues have not shown significant abnormalities either.[7] However, marked accumulations of serum proteins have been seen in the brains of patients with AIDS dementia.[7] Given the limited data and shortcoming of the methods used, the functional integrity of the BBB is thought to remain intact after HIV infection.[9]

HIV Antiretroviral Agents

Currently there are three classes of compounds available for treatment of HIV infection; these are nucleoside reverse transcriptase inhibitors (NRTI), nonnucleoside reverse transcriptase inhibitors (NNRTI), and protease inhibitors. NRTI inhibit HIV replication by blocking reverse transcription of the viral RNA and preventing the formation of DNA as a template for future viral replication. NNRTI inhibit HIV replication by binding through hydrophobic interactions to the reverse transcriptase catalytic sites. Protease inhibitors stop viral replication by inhibiting HIV encoded protease and result in the release of noninfectious immature viral particles. The generic name, brand/common

* To whom all correspondence should be sent. Telephone (203) 798-4685. Fax: (203) 791-6942. E-mail: myazdani@rdg.boehringer-ingelheim.com.

10.1021/js990174i CCC: $18.00
Published on Web 09/15/1999

Table 1—Physicochemical and Protein Binding Properties of HIV Antiretrovirals

generic name	brand/common names	MW	aqueous solubility (mg/mL)[a]	log D_{oct}[b]	% protein binding[a]
		nucleoside-inhibitors			
abacavir	Ziagen	286.3	77	1.20	~50[47]
didanosine	Videx, ddI	236.2	27.3	–0.54	<5
lamivudine	Epivir, 3TC	229.3	70	–0.92	<36
stavudine	Zerit, d4T	224.2	83	–0.72	negligible
zalcitabine	Hivid, ddC	211.3	76.4	–1.10	<4
zidovudine	Retrovir, AZT	267.2	20.1	–0.58	34–38
		non-nucleoside inhibitors			
delavirdine	Rescriptor	516.0	0.003	—	98
efavirenz	Sustiva	315.7	0.008[48]	—	99[26]
nevirapine	viramune	266.3	0.1	1.81	60
		protease inhibitors			
amprenavir	agenerase	505.2	0.04[49]	2.53	90[49]
indinavir	Crixivan	613.8	soluble	2.79	60
nelfinavir	Viracept	567.8	slightly soluble	4.0[50]	>98
ritonavir	Norvir	721.0	insoluble	—	99.3–99.5[51]
saquinavir	Invirase	670.7	insoluble	4.51	98

[a] Solubility in water at room temperature and protein binding as reported in the *Physician's Desk Reference*.[25] [b] Log D_{oct} = logarithm of octanol/phosphate buffered saline (pH 7.4) distribution coefficient.[11]

names, molecular weight, octanol/water distribution coefficients, and plasma protein binding of the approved HIV antiretroviral drugs are listed in Table 1.

The physicochemical properties of the currently marketed HIV antiretrovirals are vastly different. NRTIs are low molecular weight, highly water soluble, and (with the exception of the most recently approved NRTI, abacavir) very hydrophilic drugs. The extent of protein binding of NRTIs ranges from negligible for stavudine to ~50% for abacavir. Among the NNRTIs, nevirapine has significantly higher solubility and lower protein binding than either delavirdine or efavirenz. The latter two are almost completely protein bound. Protease inhibitors have higher molecular weights and are highly lipophilic compared with NRTIs and NNRTIs. Except for indinavir, protease inhibitors are highly protein bound.

Measuring BBB Penetration

In Vitro Studies—Isolation and culture of BMECs from the brain has led to the development of in vitro models for studying a variety of CNS drug delivery issues ranging from passive diffusion, carrier-mediated transport, and metabolism to specific factors affecting the BBB permeability.[10] In these models, BMECs can be grown as monolayers and retain the characteristics of brain endothelial cells in vivo, including the morphology, specific BBB enzyme markers, and tight intercellular junctions. The in vitro bovine BMEC monolayer permeability coefficients, P_{BMEC}, of different classes of HIV antiretroviral agents have recently been reported.[11,12] These agents included four NRTIs (didanosine, stavudine, zalcitabine, and zidovudine), two NNRTIs (nevirapine and delaviridine), and three protease inhibitors (amprenavir, indinavir, and saquinavir). Figure 1 shows P_{BMEC} values for these HIV antiretrovirals as well as for abacavir compared with those of progesterone, a highly permeable transcellular marker, and sucrose, a paracellular marker.[11,12]

The P_{BMEC} value for nevirapine is significantly higher than all the other HIV antireterovirals tested. The P_{BMEC} value for saquinavir is >2 orders of magnitude lower than nevirapine. The values for indinavir, amprenavir, and all

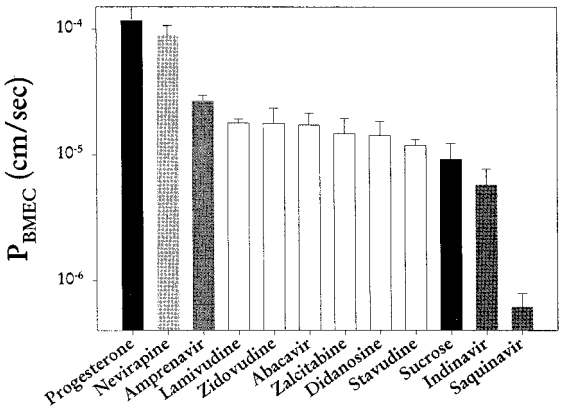

Figure 1—In vitro permeability of HIV antiretrovirals across the BMEC monolayers.[11,12]

NRTIs are also significantly lower than that of nevirapine. Moreover, the P_{BMEC} values for all NRTIs are not significantly different from each other because they have similar molecular weights and, with the exception of abacavir, very similar partitioning values. The low permeability of the protease inhibitors was attributed to their high lipophilicity and large molecular weights as well as higher potential for hydrogen bonding. The order of in vitro BBB permeability is: nevirapine ≫ amprenavir > abacavir, didanosine, stavudine, zalcitabine, and zidovudine > indinavir > saquinavir.[11,12]

In Vivo Studies—The concentration of antiretrovirals necessary to suppress HIV replication in the human brain is not known and naturally cannot be obtained in vivo. Hence, in vivo measurements of the extent of HIV antiretroviral penetration across the BBB in humans are limited to obtaining CSF concentrations from lumbar punctures. Clinical studies show that the presence of HIV antiretrovirals, such as stavudine and zidovudine, in CSF correlates well with improvement of HIV dementia.[13,14] HIV antiretroviral CSF concentrations have been most commonly used in conjunction with plasma concentrations to obtain the so-called CSF-to-plasma concentration ratios as a surrogate marker for the extent of the BBB permeability. These values have been reported with more frequency for the newly approved HIV antiretroviral inhibitors as a measure of their effectiveness in treating the CNS component of HIV infection (Table 2).

The major shortcomings of CSF-to-plasma concentration ratios as potential markers for drug penetration into the brain are the manner in which they are determined and interpreted. Direct comparisons cannot be made because of the varied experimental conditions (e.g., steady state versus non-steady state) under which these values have been obtained. Nor have these values been corrected for possible metabolism or protein binding in the brain. For example, the values for CSF-to-plasma concentration ratios reported for zidovudine are in the range of 0.15 to 1.35 and depend on the route of administration and dose given and hence do not conclusively determine how readily zidovudine crosses the BBB. Moreover, it has been shown that the CSF peak lags behind the plasma peak in concentration curves for zidovudine in plasma and CSF.[15] Hence, CSF-to-plasma concentration ratios are strongly time dependent and one time point measurements of CSF-to-plasma concentration ratios are not reliable. Furthermore, the absence of protein in CSF necessitates comparing CSF concentrations of HIV antiretrovirals to unbound plasma concentrations. Such comparisons are rarely done when CSF-to-plasma concentration ratios are reported.

The use of CSF levels may also be misleading because of differences in permeability of blood–CSF barrier (BCB)

Table 2—Cerebrospinal Fluid-to-Plasma and Brain-to-Plasma Concentration Ratios in Humans and Rat for Various HIV Antiretrovirals

antiretroviral	[CSF]/[plasma] in humans	[brain]/[plasma] in rat
	nucleoside-inhibitors	
abacavir	—	—
didanosine	0.16–0.19[52] not detected in CSF[55]	0.05, 0.007[41 a]
lamivudine	0.06–0.31[24]	—
stavudine	0.16–0.97[54]	0.33[55]
zalcitabine	0.09–0.37[24]	not measurable[56]
zidovudine	0.15–1.35[57]	0.19,[28] 0.23 ± 0.02[58]
	non-nucleoside inhibitors	
delavirdine	0.004[25]	—
efavirenz	0.01[26]	—
nevirapine	0.45[24]	1.0[24]
	protease-inhibitors	
amprenavir	—	—
indinavir	0.16,[28 b] 0.06[29]	0.18[33]
nelfinavir	not detected in CSF[32]	—
ritonavir	negligible[31]	—
saquinavir	negligible[30]	—

[a] Corrected for blood contribution to total brain concentration. [b] Mean CSF-to-plasma concentration ratios.

and the BBB.[9] The BBB is a more restrictive barrier than the BCB and because of its 5000-fold greater surface area, it is the main route of entry for drugs from blood to the brain.[9] Moreover, CSF and brain interstitial fluid are not in equilibrium and therefore the drug concentration in CSF does not necessarily reflect the extent of BBB transport of that drug because it may also include transport through the choroid plexus via the BCB. It then appears that CSF and CSF-to-plasma concentration ratios can only be used as qualitative measures of the ability of HIV antiretrovirals to cross the BBB and cannot be used to rank and order compounds in terms of their BBB permeability.

Due to inherent difficulty and indirect nature of the methods used in obtaining human data, a number of investigators have used laboratory animals to determine brain-to-plasma concentration ratios of HIV antiretrovirals. This parameter is the simplest and most direct measure of the BBB penetration of a given drug. The extent of brain drug uptake can also be presented by brain uptake index (BUI) or blood-to-brain transfer constant values.[16] The BUI is the extraction ratio of a drug relative to highly permeable compounds such as water or butanol. The major shortcomings of all of these values are that they are time dependent, require sacrificing of the animals, and must be corrected for the amount of drug retained in vascular space of the brain.[17] Furthermore, the relevance of these values in predicting the extent of penetration of the BBB in humans by HIV antiretroviral has not yet been established.

The reported in vivo studies of BBB properties of different classes of HIV antiretroviral agents are summarized next.

NRTI—There is no clear correlation between the BBB properties of NRTIs determined from animal studies and measurements of CSF values in humans. Available data on surrogate markers for BBB permeability, such as CSF-to-plasma concentration ratios in humans and brain-to-plasma concentration ratios in rats, suggest that the extent of BBB penetration for NRTIs is low and, in the case of stavudine and zidovudine, highly variable (Table 2). Moreover, clinical studies have shown that the BBB permeability of NRTIs could also be significantly different in humans. For example, in a small study of 16 patients, CSF HIV-1 RNA levels were reduced following zidovudine and not didanosine treatment.[18] Similarly, there were no clinical benefits associated with didanosine treatment suggesting that the extent of its BBB penetration in humans was also low.[19] The BBB permeability of zidovudine in humans is further supported by data suggesting reduction in the risk of developing AIDS dementia as well as improvement in cognitive impairment of AIDS patients after systemic treatment with zidovudine.[20,21] Lamivudine and stavudine also appear to penetrate the BBB in humans as indicated by a recent study where the levels of CSF HIV-1 RNA in 22 patients were reduced following treatment with these NRTIs.[22]

NNRTI—Nevirapine was the first NNRTI approved for treatment of HIV, and its BBB properties have been extensively studied.[11,12,23] The plasma-to-brain concentration ratios of nevirapine in rats and monkeys were shown to be close to 1.[23] In humans, nevirapine has a CSF-to-plasma concentration ratio of 0.45, which is approximately equal to the fraction not bound to plasma protein.[24] Taken together, these data support the contention that nevirapine readily crosses the BBB and enters the brain. In contrast, the penetration of delavirdine into the CNS appears to be low, as evidenced by its low CSF-to-plasma concentration ratio of 0.004.[25] Similarly, the BBB penetration of efavirenz is reported to be low, with a CSF-to-plasma concentration ratio of 0.01.[26]

Protease Inhibitors—In general, the extent of the BBB penetration of protease inhibitors has been reported as being low.[27–31] For example, CSF-to-plasma concentration ratios for indinavir are in the range of 0.06 to 0.16, and only negligible concentrations of ritonavir and saquinavir were present in CSF after oral administration.[27–31] Moreover, nelfinavir was not detected at all in CSF of patients following a variety of oral dosing regimens.[32] Limited BBB permeability of indinavir has also been observed in rats where a brain-to-plasma concentration ratio of 0.18 at steady state was reported.[33]

Combination Therapy—Currently, the recommended approach to HIV treatment is combination therapy with at least one protease inhibitor. Although protease inhibitors do not appear to cross the BBB to the extent of showing significant therapeutic efficacy, combinations of protease inhibitors (indinavir, ritonavir, or saquinavir) with zidovudine have been reported to prevent or reverse the progression of AIDS dementia, as suggested by brain magnetic resonance imaging studies.[34] Similarly, ritonavir and saquinavir, when taken in combination suppressed CSF HIV-1 RNA levels in 9 of 10 nucleoside-experienced patients, suggesting potential increases in the extent of their BBB penetration.[35] The addition of stavudine to this regimen increased the number of patients with undetectable HIV viral loads in serum and CSF to 80%.[36]

The effect of combination therapy on BBB permeability has only been reported in one in vitro study where there were no significant effects on the P_{BMEC} value for nevirapine in combination with amprenavir, delavirdine, didanosine, indinavir, saquinavir, stavudine, zalcitabine, or zidovudine.[11]

The Effect of Partitioning

It is generally accepted that the degree of lipophilicity of compounds is a determinant factor for their BBB permeability. For example, in vitro BBB permeability has been shown to correlate well with octanol/water partitioning and molecular weight for a variety of solutes.[37] The relationship between in vitro P_{BMEC} values and distribution coefficients (D) in pH 7.4 octanol/phosphate buffered solution for a variety of HIV antiretrovirals has been described as being roughly bell shaped.[11,12] Nevirapine appeared to have the optimum distribution coefficient ($\log D_{oct} = 1.81$) to allow for the highest permeability among the HIV

antiretrovirals studied. The permeability of hydrophilic NRTIs and very lipophilic protease inhibitors was significantly less than nevirapine. This relationship was descriptive only for the limited number of antiretroviral agents used in that study and was not meant to establish a general relationship between P_{BMEC} and D for all HIV antiretrovirals.[11]

The Effect of Efflux Pumps

P-Glycoprotein efflux pumps are present ubiquitously in both the BBB and the gastrointestinal tract.[38] A number of recent studies have shown that protease inhibitors, in general, are substrates for P-glycoprotein efflux pumps.[11,12,39,40] For example, it has been shown that indinavir, ritonavir, and saquinavir are substrates for these efflux pumps in BMECs and Caco-2 cells.[11,12,39] It has also been shown that the transports of indinavir, nelfinavir, and saquinavir in P-glycoprotein expressing cell lines L-MDR1 and Caco2 are affected by P-glycoprotein efflux pumps.[12,40] Similarly, the concentration of these protease inhibitors in the brain was shown to increase 7.4-, 10.6-, and 36.3-fold, respectively, in mice in which the MDR1a gene had been disrupted compared with the wild type.[40] This study clearly demonstrates the potetial effect of P-glycoprotein efflux pumps in reducing the BBB permeability of HIV protease inhibitors.

The effect of BBB efflux pumps on the limited distribution of NRTIs in the CNS after systemic administration is not clearly understood.[41−44] For example, microdialysis techniques in rabbits have shown that zidovudine is actively transported across the BBB and the BCB from brain to blood resulting in lower levels of zidovudine in brain and CSF than in plasma after systemic administration.[44] Similarly, it was shown that both zidovudine and didanosine were transported from the brain to the circulating blood across the BBB via saturable, probenicid sensitive efflux transporters.[45,46] However, in vitro transport studies using bovine BMECs could not identify selective efflux transport systems for NRTIs such as zidovudine.[11,12,43]

Future Directions

Understanding the mechanism of transport of HIV antiretrovirals across the BBB is essential for design and implementation of novel strategies for drug delivery to the brain to inhibit viral replication. The effect of HIV infection and the stage of the disease on the BBB properties and CNS uptake of drugs have not been fully understood. Further development of therapeutic strategies with the use of prodrugs, efflux inhibitors, and both in vitro and whole animals to evaluate intrinsic BMEC cellular permeability is needed. Although an HIV antiretroviral that is a substrate for BMEC efflux pumps may be taken alone with no adverse affects, the addition of other drugs that are competitive substrates for these pumps may affect the BBB permeability and efficacy of the first drug. Hence, the role of cellular efflux pumps on permeability of HIV antiretrovirals should be further studied to allow for rational drug delivery approaches for optimum BBB penetration.

This field of research is active and is likely to expand based on the paucity of information on the BBB permeability of currently used HIV antiretrovirals. Moreover, the BBB properties of novel classes of HIV antiretrovirals, such as HIV fusion and integrase inhibitors, need to be evaluated to determine their overall effectiveness in HIV therapy.

References and Notes

1. Davis, L. E.; Hjelle, B. L.; Miller, V. E., Palmer, D. L.; Llewellyn, A. L.; Merlin, T. L.; Young, S. A.; Mills, R. G., Wachsman, W.; Wiley: C. A. Early viral brain invasion in iatrogenic human immunodeficiency virus infection. *Neurology* **1992**, *42*, 1736−1739.
2. Pang, S.; Koyangi, Y.; Miles, S.; Wiley, C.; Harry, V.; Chen, I. High levels of unintegrated HIV-1 DNA in brain tissue of AIDS dementia patients. *Nature* **1990**, *34*, 85−89.
3. Lipton, S. A.; Gendelman, H. E. Dementia associated with the acquired immunodeficiency syndrome. *N. Engl. J. Med.* **1995**, *332*, 934−940.
4. Spencer, D. C.; Price, R. W. Human immunodeficiency virus and the central nervous system. *Annu. Rec. Microbiol.* **1992**, *46*, 655−693.
5. Hurwitz, A. A.; Berman, J. W.; Lyman, W. D.. The role of the blood brain barrier in HIV infection of the central nervous system. *Adv. Neuroimmuno.* **1994**, *4*, 249−256.
6. Moses, A. V.; Nelson, J. A. HIV infection of human brain capillary endothelial cells − implications for AIDS dementia. *Adv. Neuroimmun.* **1994**, *4*, 239−247.
7. Power, C.; Kong, P.-A.; Crawford, T. O.; Wesselingh, S.; Glass, J. D.; McArthur. J. C.; Trapp, B. D. Cerebral white matter changes in acquired immunodeficiency syndrome dementia: alterations of the blood-brain barrier. *Ann. Neutrol.* **1993**, *34*, 339−350.
8. Lenhardt, T. M.; Wiley: C. A. Absence of humorally mediated damage within the central nervous system of AIDS patients. *Neurology* **1989**, *39*, 278−280.
9. Clifford, D. B.; Simpson, D. Targeting HIV therapy for the brain. *HIV*: *Adv. Res. Ther.* **1998**, *8*, 10−17.
10. Audus, K. L.; Borchardt, R. T. Characterization of an in vitro blood-brain barrier model system for studying drug transport and metabolism. *Pharm. Res.* **1986**, *3*, 81−87.
11. Glynn, S. L.; Yazdanian, M. In vitro blood-brain barrier permeability of nevirapine compared to other HIV antiretroviral agents. *J. Pharm. Sci.* **1998**, *87*, 306−310.
12. Yazdanian, M.; Glynn, S. L. Nevirapine has excellent blood brain barrier permeability and absorption properties compared to other HIV antiretrovirals. *Extended Version of Abstracts. Vol. 2. Clinical Sciences*, Geneva, Switzerland, June 28−July 3, 12th World AIDS Conference, 1998; pp 303−307.
13. Sidtis, J. J.; Gatsonis, C.; Price, R. W.; Singer, E. J.; Collier, A. C.; Richman, D. D.; Hirsch, M. S.; Schaerf, F. W.; Fischl, M. A.; Kieburtz, K.; Simpson, D.; Koch, M. A.; Feinberg, J.; Dafni, U. Zidovudine treatment of the AIDS dementia complex: results of a placebo controlled trial. *Ann. Neurol.* **1993**, *33*, 343−349.
14. Arendt, G.; Giessen, H. J.; Jablonowski, H. Stavudine stops neuro-AIDS in AZT-nonresponders. Presented at the 12th World AIDS Conference, Geneva, Switzerland, June 28−July 3, 1998; Abstract 32207.
15. Rollinski, B.; Bogner, J. P.; Sadri, I.; Wintergerst, U.; Goebel, F. D., Absorption and elimination kinetics of zidovudine in the cerebrospinal fluid in HIV-1 infected patients. *J. Acquired Immune Defic. Synd. Hum. Retrovirol.* **1997**, *15*, 192−197.
16. Fenstermacher, J. D., Blasberg, R. G., Patlak, C. S. Methods for quantifying the transport of drugs across brain barrier systems. *Pharmacol. Ther.* **1981**, *14*, 217−248.
17. Groothuis, D. R.; Levy R. M. The entry of antiviral and antiretroviral drugs into the central nervous system. *J. Neurol. Virol.* **1997**, *3*, 387−400.
18. Gisslen, M.; Norkans, G.; Svennerholm, B.; Hagberg, L. The effect on human immunodeficiency virus type 1 RNA levels in cerebrospinal fluid after initiation of zidovudine or didanosine. *J. Infect. Dis.* **1997**, *175*, 434−437.
19. Portegis, P.; Enting, R. H.; De Jong, M. D.; Danner, S. A.; Reiss, P.; Goudamit, J.; Lang, J. M. A. AID dementia complex and didanosine, *Lancet* **1994**, *344*, 759.
20. Baldeweg, T.; Catalan, J.; Lovett, E.; Gruzelier, J.; Riccio, M., Hawkins, D. Long-term zidovudine reduces neurocognitive deficits in HIV-1 infection. *AIDS* **1995**, *9*, 589−596.
21. Portegis, P.; de Gans, J.; Lange, J.; Derix, M. M. A.; Speelman, H.; Bakker, M.; Danner, S. A.; Goudsmit, J. Declining incidence of AIDS dementia complex after introduction of zidovudine treatment. *Br. Med. J.* **1989**, *299*, 819−821.
22. Foudraine, N. A.; Hoetelmans, R. M. W.; Lange, J. M. A., de Wolf, J., van Benthem, H. B., Maas, J. J., Keer, I. P. M., Portegies, P. Cerebrospinal fluid HIV-1 RNA and drug concentrations after treatment with lamivudine plum zidovudine or stavudine. *Lancet* **1998**, *351*, 1547−1551.
23. Silverstein, H.; Riska, P.; Johnstone, J. N.; Richter, I.; Norris, S.; Hattox, S.; Grob. P. Nevirapine, a Nonnucleoside Reverse Transcriptase Inhibitor, Freely Enters the Brain and crosses the Placental Barrier. XI International Conference on AIDS, Vancouver British Columbia, Canada, July 9, 1996, Abstract 2325.
24. *Physicians' Desk Reference*, 52 ed., Medical Economic Company: Montvale, NJ; 1998.

25. Davey, R. T.; Chiatt, D. G.; Reed, G. F.; Freimuth, W. W.; Herpin, B. R.; Metcalf, J. A.; Eastman, P. S.; Fallon, J.; Kovacs, J. A.; Polis, M. A.; Wlaker, R. E.; Masur, H.; Boyle, J. Coleman, S.; Cox, S. R.; Wathen, L.; Daenzer, C. L.; Lane, H. C. Randomized, controlled phase I/II trail of combination therapy with delavirdine (U-910152S) and conventional nucleosides in HIV-1 infected patients. *Antimicrob. Agents Chemother.* **1996**, *40*, 1657−1664.
26. Fiske, W. D.; Nibbelink, D. W.; Brennan, J. M.; Mutlib, A. E.; Ruiz, N. M. DMP 266 Cerebrospinal fluid concentations in after oral administration. 37th Interscience Conference on Antimicrobial Agents and Chemotherapy (ICAAC), Sept. 28 − Oct. 1, 1997; Abstract A-12.
27. Ståhle, L.; Guzenda, E.; Ljungdahle-Ståhle, E. Pharmacokinetics and extracellular distribution to blood, brain, and muscle of alovudine (3′-fluorothymidine) and zidovudine in the rat studied by microdialysis. *J. Accquired Immune Deffic. Syndr.* **1993**, *6*, 435−439.
28. Ståhle, L.; Martin, C.; Svensson, J. O.; Sonnerborg, A. Indinavir in cerebrospinal fluid of HIV-1 infected patients. *Lancet*. **1997**, *350*, 1823.
29. Letendre, S. L.; Caparelli, E.; Ellis, R. J.; Dur, D.; McCutchan, J. A. Levels of serum in cerebrospinal fluid (CSF) indinavir (IDV) and HIV RNA in HIV-infected individuals. 6th Conference on Retroviruses and Opportunistic Infections, Jan 31 − Feb 4, 1999; Abstract 407.
30. Swindells, S. Therapy of HIV-1 infection: a practical guide for providers. In *The Neurology of AIDS*; Gendelman, H. E.; Lipton, S. A.; Epstein, L.; Swindells, S., Eds.; Chapman & Hall, New York, 1998; pp 364−376.
31. Invirase, Saquinavir mesylate, Roche Laboratories Inc.; Package Insert.
32. Aweeka, F.; Jayewardene, A.; Staprans, S.; Beltibas, E.; Kearney, B.; Lizak, P.; Novakovic-Agopian, Price, R. W. Failure to detect nelfinavir in the cerebrospinal fluid of HIV-1 infected patients with and without AIDS dementia. *J. Accquired Immune Deffic. Syndr.* **1999**, *20*, 39−43.
33. Lin, J. H.; Chiba., M.; Balani, S. K.; Chen, I.; Kwei, G. Y. S.; Vastag, K. J.; Nishime, J. A. Species differences in the pharmacokinetics and metabolism of indinavir, a potent human immunodeficiency virus inhibitor. *Drug. Metab. Dispos.* **1996**, *24*, 1111−1120.
34. Scolnick, A. A. Protease inhibitors may reverse AIDS dementia. *JAMA* **1998**, *279*, 419.
35. Farthing, C.; Japour, A.; Cohen, C. J. Cerebrospinal fluid (CSF) and plasma HIV RNA suppression with ritonavir (RIT)-saquinavir (SQV) in protease inhibitor naïve patients. 37th Interscience Conference on Antimicrobial Agents and Chemotherapy (ICAAC), Sept. 28−Oct. 1, 1997; Abstract LB3.
36. Gisolf, G. H.; Portegies, P.; Hoetelmans, R.; Van der Ende, M. E.; Brinkman, K.; de Wolf, F.; Danner, S. A. Effect of ritonavir (RTV)/saquinavir (SQV) versus RTV/SQV/stavudine (d4T) on CSF HIV−RNA levels: Preliminary rerults. 12th World AIDS Conference, June 28−July 3, Geneva, Switzerland; Abstract 32197.
37. Shah, M. V.; Audus, K. A.; Borchardt, R. T. The application of bovine brain microvessel endothelial cell monolayers grown onto polycarbonate membranes in vitro to estimate the potential permeability of solutes through the blood-brain barrier. *Pharm. Res.* **1989**, *6*, 624−627.
38. Barrand, M. A.; Robertson, K. J.; von Wiekersthal, S. F. Comparisons of P-glycoprotein in isolated rat brain microvessels and in primary cultures of endothelial cells derived from microvasculature of rat brain, epididymal fat pad and from aorta. *FEBS Lett.* **1995**, *374*, 179−183.
39. Alsenz, J.; Steffen, H.; Alex, R. Active apical secretory efflux of the HIV protease inhibitors Saquinavir and Ritonavir in Caco-2 cell monolayers. *Pharm Res.* **1998**, *15*, 423−428.
40. Kim, R. B.; Fromm, M. F.; Wandel, C.; Leake, B.; Wood, A. J. J.; Roden, D. M.; Wilkinson, G. R. The drug transporter P-glycoprotein limits oral absorption and brain entry pf HIV-1 protease inhibitors. *J. Clin. Inves.* **1998**, *101*, 289−294.
41. Anderson, B. D.; Hoesterey. B. L.; Baker, D. C.; Galinsky, R. E. Uptake kinetics of 2′. 3′-dideoxyinosine into brain and cerebrospinal fluid of rats: intravenous infusion studies. *J. Pharmacol. Exp. Ther.* **1990**, *253*, 113−118.
42. Galinsky, R. E.; Flaharty, K. K.; Hoesterey, B. L.; Anderson, B. D. Probenicid enhances central nervous system uptake of 2′,3′- dideoxyinosine by inhibiting cerebrospinal fluid efflux. *J. Pharmacol. Exp. Ther.* **1991**, *257*, 972−978.
43. Masereeuw, R.; Jaehde, U.; Langemeijer, M. W. E.; de Boer, A. G.; Breimer,. D. D. In vitro and in vivo transport of zidovudine (AZT) across the blood-brain barrier and the effect of transport inhibitors. *Pharm. Res.* **1994**, *11*, 324−330.
44. Wang, Y.; Sawchuck, R. J. Zidovudine transport in the rabbit brain during intravenous and intracerebroventricular infusion. *J. Pharm. Sci.* **1995**, *84*, 871−876.
45. Wong, S. L.; VanBelle, K.; Sawchuck, R. J. Distributional transport kinetics of zidovudine between plasma and brain extracellular fluid and cerebrospinal fluid in rabbit: investigation of the inhibitory effect of probenicid utilizing micordialysis. *J. Pharmacol. Exp. Ther.* **1993**, *264*, 899−909.
46. Takasawa, K.; Terasaki, T.; Suzuki, H.; Sugiyama, Y. In vivo evidence for carrier-mediated efflux transport of 3′-azido-3′-deoxythymidine and 2′,3′-dideoxyinosine across the blood-brain barrier via a probenicid-sensitive transport system. *J. Pharmacol. Exp. Ther.* **1997**, *281*, 369−375.
47. Ziagen, abacavir, GlaxoWellcome, Package Insert.
48. Rabel, S. R.; Maurin, M. B.; Rowe, S. M.; Hussain, M. Determination of the pK_a and pH-solubility behavior of an ionizable cyclic carbamate, (S)-6-chloro-4-(cyclopropylethynyl)-1,4-dihydro-4-(trifluromethyl)-2H-3,1-benzoxazin-2-one (DMP266). *Pharm. Dev. Technol.* **1996**, *1*, 91−95.
49. Agenerase, Amprenavir, Vertex, Package Insert.
50. Longer, M.; Shetty, B.; Zamansky, I.; Tyle, P. Preformulation studies of a novel HIV protease inhibitor, AG1343. *J. Pharm. Sci.* **1984**, *84*, 1090−1093.
51. Dennisen, J. F.; Grabowski, B. A.; Johnson, M. K.; Buko, A. M.; Kempp, D. J., Thomas, S. B., Surber, B. W. Metabolism and disposition of the HIV-1 protease inhibitor ritonavir (ABT-538) in rats, dogs, and humans. *Drug Metab. Dispos.* **1997**, *25*, 489−501.
52. Shelton, M. J.; O'Donnell, A. M.; Morse, G. D. Didanosine. *Ann. Pharmacother.* **1992**, *26*, 660−670.
53. Ballis, F. M.; Pizzo, P. A.; Butler, K. M.; Hawkins, M. E.; Brouwers, Pim, Husson, R. N.; Jacobson, F.; Blaney, S. M.; Gress, J.; Jarosinski, P.; Polack, D. G. Clinical pharmacology of 2′-3′-didoexyinsoine in human immunodeficiency virus infected children. *J. Infect. Dis.* **1992**, *324*, 137−144.
54. Zerit, Stavudine, Bristol Meyers Squibb. Package Insert.
55. Yang, A.; Brundage, R. C.; Barbhaiya, R. H.; Sawchuck, R. J. Microdialysis studies of the distribution of stavudine into the central nervous system in the freely moving rat. *Pharm. Res.* **1997**, *14*, 865−872.
56. Terasaki, T.; Pardridge, W. M. Restricted transport of 3′-azido-3′-deoxythymidine and dideoxynucleosides through the blood-brain barrier. *J. Infect. Dis.* **1988**, *158*, 630−632.
57. Klecker, R. W.; Collins, J. M.; Yarchoan, R.; Thomas, R.; Jenkins, J. F.; Border, S.; Myers, C. E. Plasma and cerebrospinal fluid pharmacokinetics of 3′-azido-3′-deoxythymidine: A novel pyrimidine analogue with potential applications for the treatment of patients with AIDS and related diseases. *Clin. Pharmacol. Ther.* **1987**, *41*, 407−412.
58. Galinsky, R. E.; Hoesterey, B. L.; Anderson, B. D. Brain and cerebrospinal fluid uptake of zidovudine (AZT) in rats after intravenous injection. *Life Sci.* **1990**, *47*, 781−788.

JS990174I

Transdermal Penetration Enhancers: Applications, Limitations, and Potential

BARRIE C. FINNIN* AND TIMOTHY M. MORGAN

Contribution from *Department of Pharmaceutics, Victorian College of Pharmacy, Monash University, 381 Royal Parade, Parkville, Victoria 3052, Australia.*

Received May 13, 1999. Final revised manuscript received July 19, 1999.
Accepted for publication July 21, 1999.

Introduction

Delivery of drugs via the skin has many attractions, including increased patient acceptability (noninvasiveness) and avoidance of gastrointestinal disturbances[1] and first-pass metabolism of the drug.[2] The fact that this route is not more widely used is because of the inherent barrier properties of the skin.[3] It is generally difficult to get drugs to cross the skin at a sufficient rate to deliver a therapeutic dose even when the drug is potent. Many different approaches have been taken to overcome the barrier presented by the skin, including mechanical disruption,[4,5] electrical disruption,[6,7] and chemical modification[8,9] of the barrier function. This review will focus on the use of chemicals to alter the penetration rate of drugs across the skin.

Agents capable of modifying the barrier to penetration presented by the skin have been called "penetration enhancers". There is usually a distinction drawn between chemicals that have their effect merely by occlusion of the skin leading to hydration of the skin, which in turn leads to increased permeability and those that interact with either the formulation applied or the skin itself. The former are generally not classified as "penetration enhancers".[10] Much research has been performed to identify penetration enhancers with the aid of in vitro screens,[11,12] and literally hundreds of different chemicals with a wide divergence of chemical structure that are able to modify the penetration characteristics of different drugs and marker compounds into the skin have been identified.[13,14] However, only a small number of these agents have been shown to produce useful enhancement in vivo, only a few have actually been incorporated into products and successfully tested in humans, and, other than previously used ingredients of topical preparations, none has yet been successful in the market place. This review is intended to examine why, despite all this work, we seem to have had very little success to date.

Historical and Current Perspectives

The idea of delivering drugs through the skin is old, as far back as the 16th century B.C., the Ebers Papyrus recommended that the husk of the castor oil plant be crushed in water and placed on an aching head and "the head will be cured at once, as though it had never ached." [15] Today transdermal drug delivery (TDD) is a well-accepted means of delivering many drugs to the systemic circulation, and currently transdermal patch devices are used to treat motion sickness, hypertension, angina, female menopause, severe pain states, nicotine dependence, and male hypogonadism.[16] The advantages of TDD are summarized in Table 1.

Despite all these advantages, a timely warning to formulators was issued by Hadgraft and Guy in 1987,[18] "TDD is not a subject which can be approached simplistically without a thorough understanding of the physicochemical and biological parameters of percutaneous absorption. Researchers who attempt TDD without appreciating this fact do so at their peril."

Our knowledge of these processes has been well reviewed in relation to percutaneous penetration by Barry.[19] Some specific issues that are worth singling out are the variability of the skin both within and between individuals,[20] the importance of metabolism in the viable epidermis as a metabolic barrier,[21] and the role of the immune system in limiting the use of some agents on the skin.[22,23]

The factors influencing the suitability of a drug for TDD are as follows:

⇒ potency of the drug − the daily systemic dose should be ≤20 mg
⇒ molecular size − the drug should have a MW of <500 Daltons
⇒ lipophilicity − the log P should be in the range 1−3
⇒ melting point − should be <200 °C
⇒ hydrogen bonding groups—should be ≤2
⇒ irritation − the drug should not be directly irritant to the skin
⇒ immunogenicity − the drug should not stimulate an immune reaction in the skin

A predictive rule of thumb is that the maximum flux of drug through the skin should decrease by a factor of 5 for an increase of 100 Da in MW, and decrease by a factor of 10 for an increase of 100 °C in melting point.[24]

Enhancement of Delivery

In addition to the potential for enhanced TDD to improve transdermal delivery rate control, the main reason that drug delivery across the skin needs to be enhanced is because of the low permeability of most transdermal candidates across the skin.[25] Traditionally, enhanced TDD has been achieved with patch devices that occlude the skin. Occlusion traps the natural transepidermal moisture of the skin, which increases the water content of the horny layer and swells the membrane, thus compromising its barrier function.[10] Prolonged occlusion of this nature can cause a 10−100-fold increase in drug permeability.[26] However, the tradeoff with these occlusive delivery systems is their propensity to cause local skin irritation.[27]

Physical Enhancement

Although many different physical approaches to enhancing percutaneous absorption have been attempted, the most

* Corresponding author. Telephone: (Int +61) 3 9903 9520. Fax: (Int +61) 3 9903 9583. E-mail: barrie.finnin@vcp.monash.edu.au.

10.1021/js990154g CCC: $18.00
Published on Web 09/15/1999

Table 1—Advantages of TDD

- provides constant blood levels in the plasma for drugs with a narrow therapeutic window, thus minimizing the risk of toxic side effects or lack of efficacy
- avoids first-pass metabolism in the gastrointestinal tract and liver, which allows drugs with poor oral bioavailability and/or short biological half-lives to be administered at most, once a day, and which can result in improved patient compliance[17]
- the problems of the gastrointestinal environment, such as chemical degradation of the drug and gastric irritation, are avoided
- removing the transdermal drug reservoir from the stratum corneum can easily terminate drug input
- provides a noninvasive alternative to parenteral, subcutaneous, and intramuscular injections
- suitable for patients who are unconscious or vomiting

notable approaches are iontophoresis,[6] ultrasound (sonophoresis),[4] and electroporation.[7] None of these enhancement methods is passive in that they require the input of energy to achieve their effects. To date, these methods show most promise for TDD systems that incorporate a large drug reservoir on the surface of the skin, and that need to deliver very large molecular weight compounds in the kiloDalton range.[16]

Supersaturation

The thermodynamic activity of a drug can be increased by employing supersaturated systems that give rise to unusually high thermodynamic potentials; this effect was first shown in a volatile:nonvolatile vehicle by Coldman et al.[28] However, topical vehicles relying on supersaturation have the major limitation of formulation instability, both prior to and during application to the skin, unless the formulation can be stabilized with antinucleant and anti-crystal-growth agents.[29]

For example, Kondo et al.[30] used supersaturation to enhance the transdermal delivery of nifedipine in rats. The bulk vehicle was stabilized with polymers and this formulation formed an appreciable mass on the surface of the skin. The vehicle remained on the surface of the skin for a prolonged period (many hours). Therefore, although Kondo et al.[30] advocated the use of a metered spray to deliver these formulations, in reality it would be impossible to obtain a nonocclusive TDD system with a short application time and cosmetic acceptability and still maintain a clinically useful transdermal penetration enhancement.

Metabolic or Biochemical Enhancers

Chemicals that provoke biochemical and metabolic events within the skin can potentially be used to alter skin permeability. For example, these types of enhancers can reduce the barrier properties of the skin by either inhibiting enzymes responsible for the synthesis of specific stratum corneum lipids during stratum corneum repair[31] or by promoting the metabolism of existing skin lipids that are responsible for skin barrier function.[32] Although promising, both of these approaches need to undergo further investigation in vivo of their enhancement effects and their potential to produce skin irritation. It should be noted that chemical penetration enhancers may also provoke unwanted reactionary biochemical and metabolic events within the skin that could alter skin permeability,[16,33] however this is not their aim.

Chemical Penetration Enhancers

Ideally, the goal of dermal penetration enhancement is for the accelerant to reversibly reduce the barrier resistance of the stratum corneum without damaging viable cells.[10,34] The properties proposed for an ideal penetration enhancer are shown in Table 2.

Over the last 15 years, a tremendous amount of work has been directed toward the search for specific chemicals, or combinations of chemicals, that can act as penetration enhancers.[9,35] The bulk of this work has been carried out by pharmaceutical companies that regard the results of their work as proprietary. Consequently, much of the cited literature is found in patents[13] as well as the usual pharmaceutical science literature.[14]

Table 2—Properties of an Ideal Penetration Enhancer[10]

- pharmacologically inert
- nontoxic, nonirritating, and nonallergenic
- rapid onset of action; predictable and suitable duration of action for the drug used
- following removal of the enhancer, the stratum corneum should immediately and fully recover its normal barrier property
- the barrier function of the skin should decrease in one direction only, and efflux of endogenous materials should not occur
- chemically and physically compatible with the delivery system
- readily incorporated into the delivery system
- inexpensive and cosmetically acceptable

Despite the large amount of work performed and the large number of different chemical entities identified, few have made it to the market place because of the following reasons.

1. The Applicability of the Method used to Demonstrate Enhancement—Most of the investigations involve in vitro penetration studies using a variety of membranes.[12,36] The follies of these methods have recently been pointed out by Barry.[37] Although attempts are currently being made to develop a generally accepted standardized methodology for in vitro testing,[11] there is still a large extrapolation to be made from performance in vitro to use in a clinical setting.

2. Incorporation of the Enhancer into a Doseform that is Acceptable to the User While Retaining the Activity of the Enhancer—When developing topical preparations for optimum bioavailability it is necessary to formulate them to ensure that the drug has the maximum tendency to leave the vehicle and partition into the skin. The driving force behind diffusive transport is a gradient in the chemical potential,[38] which is the continuous function (not the concentration) across interfaces. The presence of enhancers, which often will have good solvent properties, can decrease the chemical potential. The formulator needs to balance the solubility, and therefore the ability to use high concentrations of drug in a formulation, with the need to increase the chemical potential. These difficulties were realized early in the evaluation of laurocapram (Azone) where it was shown that incorporation of laurocapram into a commercially available cream containing fluocinolone acetonide did not increase vasoconstrictor activity, whereas simply incorporation of the steroid with 2% laurocapram in ethanol resulted in strong outperformance of the cream.[39]

3. The Need for Delivery of the Enhancer to the Skin and the Maintenance of Skin Concentrations of Enhancer for the Required Time Intervals—Although ethanol can act as a penetration enhancer, and various mechanisms of action have been postulated,[40] in practice its use as a penetration enhancer has relied on the application of a bulk aqueous ethanol vehicle to the skin whereupon the increase in the flux of the drug across the skin is mainly due to a solvent drag effect shown previously.[41] The mechanism of effect relies on the rapid

penetration of the solvent itself and the subsequent drag of the penetrant with it. A necessary corollary of this rapid flux is that the concentrations cannot be prolonged unless there is a reservoir present, thus limiting the applications of this type of enhancer to reservoir-based systems.

Clinical Usefulness

Of all of the potential enhancers identified those that have undergone significant clinical testing are discussed next.

In 1964, Stoughton and Fritsch reported that dimethyl sulfoxide (DMSO) enhanced the percutaneous penetration of various agents.[8] This characteristic was exploited clinically in many different circumstances but it did not lead to significant commercial products partly because of the high concentration needed for an effect and partly because DMSO is unpleasant to use.[42,43] It is interesting to note that after being virtually discarded, DMSO has recently been revived, and topical products containing DMSO with diclofenac are currently undergoing clinical trials.[44]

Laurocapram (Azone) is probably the most widely known chemical enhancer, and it is often used by transdermal research groups because of its good overall enhancing abilities,[45,46] which also makes it a useful basis of comparison for new chemical enhancers. However, because of its potential to irritate the skin,[47−50] laurocapram has failed to gain general clinical acceptance.

Fatty acids and fatty acid esters have been known for some time to enhance penetration. The major attraction of these compounds is that many of these materials are classified as Generally Recognized As Safe (GRAS). For example, Theratech Inc. uses a combination of glyceryl monooleate and lauryl lactate to enhance the diffusion of testosterone across nonscrotal skin in hypogonadal males in the Androderm patch.[51] A major concern is the irritation caused by these agents.[52] In clinical practice, one of the marketers of this product (SmithKline Beecham Pharmaceuticals) suggests the prior application of triamcinolone acetonide to overcome this irritation problem.[53]

There are also attempts to gain regulatory approval for newly synthesized enhancers, such as Macrochem's SEPA enhancer, 2-*n*-nonyl-1,3-dioxolane,[54] and NexMed's NexACT enhancers, alkyl *N*,*N*-dialkyl-substituted amino acetates.[55] Both of these types of agents have already shown good enhancing abilities that are comparable to those of laurocapram.[49, 56−58] Topical gel formulations containing SEPA with ibuprofen or alprostadil are currently in phase II clinical trials in the USA.[59] The NexACT enhancers are undergoing pre-Phase II toxicology studies in the USA, and a Phase III clinical trial in China has been completed for a topical gel formulation of alprostadil.[59] The success of these formulations will probably depend as much on the irritation observed in these trials as on the actual clinical effect.[60]

We have identified some novel GRAS chemical enhancers[61] that are currently used as topical sunscreening agents.[62] The main chemical enhancers in this group are padimate O, octyl salicylate, and octyl methoxycinnamate. As sunscreens, these agents have maximum approved topical concentrations of 8.0, 5.0, and 7.5%, respectively, in the USA, Europe, Japan, and Australia.[62] Over their many years of use as topical sunscreens, these agents have shown a low incidence of local skin reactions.[63]

These compounds have been shown to increase the penetration rate of a range of different drugs across skin from a number of different animal species in vitro.[64−66] We have also shown the enhancing effect of these compounds in vivo using microdialysis in conscious rats to measure the penetration of ibuprofen from topically applied gels.[67] The enhancers in these studies were incorporated into gel formulations suitable for clinical use. The effect of these enhancers in circumstances relevant to clinical use has also been demonstrated in vivo with the hormones estradiol and testosterone applied in the form of a spray to weanling pigs.[68] Significantly higher plasma levels of both of these compounds were found when the enhancer was incorporated into the spray formulations. These enhancers were also used in a small clinical trial in postmenopausal women designed to demonstrate the feasibility of delivery of estradiol via a transdermal spray.[69] The dose form was shown to deliver clinically relevant amounts of estradiol without signs of irritation.

The future will tell whether the enhancers currently under investigation can be formulated into acceptable and nonirritant products. Regardless, the search for new enhancers with ideal properties (Table 2) will continue.

References and Notes

1. Payne, R. Factors influencing quality of life in cancer patients: the role of transdermal fentanyl in the management of pain. *Semin. Oncol.* **1998**, *25*, Suppl 7, 47−53.
2. Crook, D. The metabolic consequences of treating postmenopausal women with nonoral hormone replacement therapy. *Br. J. Obstet. Gynaecol.* **1997**, *104*, Suppl 16, 4−13.
3. Scheuplein, R. J.; Blank, I. H. Permeability of the skin. *Physiol. Rev.* **1971**, *51*, 702−747.
4. Mitragotri, S.; Edwards, D. A.; Blankschtein, D.; Langer, R. A mechanistic study of ultrasonically enhanced transdermal drug delivery. *J. Pharm. Sci.* **1995**, *84*, 697−706.
5. Henry, S.; McAllister, D. V.; Allen, M. G.; Prausnitz, M. R. Microfabricated microneedles: a novel approach to transdermal drug delivery. *J. Pharm. Sci.* **1998**, *87*, 922−925.
6. Guy, R. H. Iontophoresis-recent developments. *J. Pharm. Pharmacol.* **1998**, *50*, 371−374.
7. Weaver, J. C.; Vaughan, T. E.; Chizmadzhev, Y. Theory of electrical creation of aqueous pathways across skin transport barriers. *Adv. Drug Delivery Rev.* **1999**, *35*, 21−39.
8. Stoughton, R. B.; Fritsch, W. Influence of dimethyl sulfoxide on human percutaneous absorption. *Arch. Dermatol.* **1964**, *90*, 512−517.
9. *Pharmaceutical Skin Penetration Enhancement*; Walters, K. A.; Hadgraft, J., Eds.; Marcel Dekker: New York, 1993.
10. Barry, B. W. Vehicle effect: what is an enhancer? In *Topical Drug Bioavailability, Bioequivalence, and Penetration*; Shah, V. P.; Maibach, H. I., Eds.; Plenum: New York, 1993; pp 268−270.
11. Howes, D.; Guy, R.; Hadgraft, J.; Heylings, J.; Hoeck, U.; Kemper, F.; Maibach, H.; Marty, J.-P.; Merk, H.; Parra, J.; Rekkas, D.; Rondelli, I.; Schaefer, H.; Tauber, U.; Verbiese, N. Methods for asssessing percutaneous absorption. *ATLA* **1996**, *24*, 81−106.
12. In *Percutaneous Absorption: Drugs-Cosmetics-Mechanisms-Methodology*, 3rd ed., rev. and expanded.; Bronaugh, R. L.; Maibach, H. I., Eds.; Marcel Dekker: New York, 1999.
13. Santus, G. C.; Baker, R. W. Transdermal enhancer patent literature. *J. Controlled Release* **1993**, *25*, 1−20.
14. Osborne, D. W.; Henke, J. J. Skin penetration enhancers cited in the literature. *Pharm. Technol.* **1997**, *Nov.*, 58−66.
15. Mez-Mangold, L. In *A History of Drugs*; F. Hoffmann-La Roche: Basle, Switzerland, 1971; pp 17−27.
16. Guy, R. H. Current status and future prospects of transdermal drug delivery. *Pharm. Res.* **1996**, *13*, 1765−1769.
17. Burris, J. F.; Papademetriou, V.; Wallin, J. D.; Cook, M. E.; Weidler, D. J. Therapeutic adherence in the elderly: transdermal clonidine compared with oral verapamil for hypertension. *Am. J. Med.* **1991**, *1A*, 22S−28S.
18. Guy, R. H.; Hadgraft, J. Transdermal drug delivery: a perspective. *J. Controlled Release* **1987**, *4*, 237−251.
19. Barry, B. W. In *Dermatological Formulations: Percutaneous Absorption*; Marcel Dekker: New York, 1983.
20. Southwell, D.; Barry, B. W.; Woodford, R. Variations in permeability of human skin within and between specimens. *Int. J. Pharm.* **1984**, *18*, 299−309.
21. Nicolau, G.; Yacobi, A. Skin metabolism. Cutaneous first-pass effect of a transdermally absorbed prostaglandin. In *Topical Drug Bioavailability, Bioequivalence, and Penetration*, Shah, V. P.; Maibach, H. I., Eds.; Plenum: New York, 1993; p 292.
22. Lynch, D. H.; Roberts, L. K.; Daynes, R. A. Skin immunology: The Achilles heal to transdermal drug delivery? *J. Controlled Release* **1987**, *6*, 39−50.
23. Flynn, G. L.; Stewart, B. Percutaneous drug penetration: choosing candidates for transdermal development. *Drug Dev. Res.* **1988**, *13*, 169−185.

24. Berner, B.; Cooper, E. R. Models of skin permeability. In *Transdermal Delivery of Drugs*, Vol. 2; Kydonieus, A. F.; Berner, B., Eds.; CRC: Boca Raton, FL, 1987; p 44.
25. Flynn, G. L. Physicochemical determinants of skin absorption. In *Principles of Route-to-Route Extrapolation for Risk Assessment*, Gerrity, T. R.; Henry, C. J., Eds.; Elsevier: New York, 1990; pp 93−127.
26. Scheuplein, R. J.; Ross, L. W. Mechanism of percutaneous absorption V: percutaneous absorption of solvent deposited solids. *J. Invest. Dermatol.* **1974**, *62*, 353−360.
27. Hogan, D. J.; Maibach, H. I. Adverse dermatologic reactions to transdermal drug delivery systems. *J. Am. Acad. Dermatol.* **1990**, *22*, 811−814.
28. Coldman, M. F.; Poulsen, B. J.; Higuchi, T. Enhancement of percutaneous absorption by the use of volatile: nonvolatile systems as vehicles. *J. Pharm. Sci.* **1969**, *58*, 1098−1102.
29. Davis, A. F.; Hadgraft, J. Supersaturated solutions as topical drug delivery systems. In *Pharmaceutical Skin Penetration Enhancement*; Walters, K. A.; Hadgraft, J., Eds.; Marcel Dekker: New York, 1993; pp 243−267.
30. Kondo, S.; Yamanaka, C.; Sugimoto, I. Enhancement of transdermal delivery by superfluous thermodynamic potential. III. Percutaneous absorption of nifedipine in rats. *J. Pharmacobio-Dyn.* **1987**, *10*, 743−749.
31. Tsai, J.-C.; Guy, R. H.; Thornfeldt, C. R.; Gao, W.; Feingold, K. R.; Elias, P. M. Metabolic approaches to enhance transdermal drug delivery. 1. Effect of lipid synthesis inhibitors. *J. Pharm. Sci.* **1996**, *85*, 643−648.
32. Patil, S.; Singh, P.; Szolar-Platzer, C.; Maibach, H. Epidermal enzymes as penetration enhancers in transdermal drug delivery? *J. Pharm. Sci.* **1996**, *85*, 249−252.
33. Palacio, S.; Schmitt, D.; Viac, J. Contact allergens and sodium lauryl sulphate upregulate vascular endothelial growth factor in normal keratinocytes. *Br. J. Dermatol.* **1997**, *137*, 540−544.
34. Barry, B. W. The LPP theory of skin penetration enhancement. In *In Vitro Percutaneous Absorption: Principles, Fundamentals, and Applications*; Bronaugh, R. L.; Maibach, H. I., Eds.; CRC: Boca Raton, FL, 1991; pp 165−185.
35. *Percutaneous Penetration Enhancers*; Smith, E. W.; Maibach, H. I., Eds.; CRC: Boca Raton, FL, 1995.
36. Schaefer, H.; Redelmeier, T. E. In *Skin Barrier: Principles of Percutaneous Absorption*, Karger: Basel, Switzerland, 1996.
37. Barry, B. W. Reflections on transdermal drug delivery. *PSTT* **1999**, *2*, 41−43.
38. Katchalsky, A.; Curran, P. F. Membrane permeability to nonelectrolytes: discontinuous systems. In *Nonequilibrium Thermodynamics in Biophysics*; Harvard University: Cambridge, MA, 1965; pp 113−132.
39. Stoughton, R. B., McClure, W. O. Azone: A new nontoxic enhancer of cutaneous penetration. *Drug Dev. Ind. Pharm.* **1983**, *9*, 725−744.
40. Manabe, E.; Sugibayashi, K.; Morimoto, Y. Analysis of skin penetration enhancing effect of drugs by ethanol−water mixed systems with hydrodynamic pore theory. *Int. J. Pharm.* **1996**, *129*, 211−221.
41. Berner, B.; Mazzenga, G. C.; Otte, J. H.; Steffens, R. J.; Juang. R.; Ebert, C. D. Ethanol: water mutually enhanced transdermal therapeutic system. II. Skin permeation of ethanol and nitroglycerin. *J. Pharm. Sci.* **1989**, *78*, 402−407.
42. Barry, B. W. Optimizing percutaneous absorption. In *Percutaneous Absorption*, Bronaugh, R. L.; Maibach, H. I., Eds.; Marcel Dekker: New York, 1985; pp 492−494.
43. Schaefer, H.; Zesch, A.; Stuttgen, G. In *Skin Permeability*, Springer-Verlag: Berlin, Germany, 1982; p 654.
44. Hui, X.; Hewitt, P. G.; Poblete, N.; Maibach, H. I.; Shainhouse, J. Z.; Wester, R. C. In vivo bioavailability and metabolism of topical diclofenac lotion in human volunteers. *Pharm. Res.* **1998**, *15*, 1589−1595.
45. Stoughton, R. B. Enhanced percutaneous absorption with 1-dodecylazacycloheptan-2-one (Azone). *Arch. Dermatol.* **1982**, *118*, 474−477.
46. Vaidyanathan, R.; Rajadhyaksha, V. J.; Kim, B. K.; Anisko, J. J. Azone. In *Transdermal Delivery of Drugs*, Vol. 2.; Kyodenius, A. F.; Berner, B., Eds.; CRC: Boca Raton, FL, 1987; pp 63−83.
47. Okamoto, H.; Hasida, M.; Sezaki, H. Structure−activity relationship of 1-alkyl- or 1-alkenylazacycloalkanone derivatives as percutaneous penetration enhancers. *J. Pharm. Sci.* **1988**, *77*, 418−424.
48. Lashmar, U. T.; Hadgraft, J.; Thomas, N. Topical application of penetration enhancers to the skin of nude mice: a histopathological study. *J. Pharm. Pharmacol.* **1989**, *41*, 118−122.
49. Wong, O.; Huntington, J.; Nishihata, T.; Rytting, J. H. New alkyl *N*,*N*-dialkyl-substituted amino acetates as transdermal penetration enhancers. *Pharm. Res.* **1989**, *6*, 286−295.
50. Okabe, H.; Obata, Y.; Takayama, K.; Nagai, T. Percutaneous absorption enhancing effect and skin irritation of monocyclic monoterpenes. *Drug Des. Deliv.* **1990**, *6*, 229−238.
51. Mazer, N. A.; Heiber, W. E.; Moellmer, J. F.; Meikle, A. W.; Stringham, J. D.; Sanders, S. W.; Tolman, K. G.; Odell, W. D. Enhanced transdermal delivery of testosterone: a new physiological approach for androgen replacement in hypogonadal men. *J. Controlled Release* **1992**, *19*, 347−361.
52. Jordan, W. P., Jr.; Atkinson, L. E.; Lai, C. Comparison of the skin irritation potential of two testosterone transdermal systems: an investigational system and a marketed product. *Clin. Ther.* **1998**, *20*, 80−87.
53. Wilson, D. E.; Kaidbey, K.; Boike, S. C.; Jorkasky, D. K. Use of topical corticosteroid pretreatment to reduce the incidence and severity of skin reactions associated with testosterone transdermal therapy. *Clin. Ther.* **1998**, *20*, 299−306.
54. Gyurik, R. J. Chemical skin penetration enhancers − the future. In *Perspectives in Percutaneous Penetration*, Vol. 5a; Brain, K. R.; James, V. J.; Walters, K. A., Eds.; STS: Cardiff, Wales, UK, 1997; p 6.
55. Buyuktimkin, S.; Buyuktimkin, N.; Yeager, J. L.; Rytting, J. H. The utility of biodegradable penetration enhancers: dodecyl 2-(N,N-dimethylamino)-propionate (DDAIP) and 2-(N,N-dimethylamino)-propyl tetradecanoate (DAIPM). In *Symposia Abstracts & Biographies, AAPS Annual Meeting & Exposition*; Boston, MA, Nov. 1997; p 80.
56. Turunen, T. M.; Buyuktimkin, S.; Buyuktimkin, N.; Urtti, A.; Paronen, P.; Rytting, J. H. Enhanced delivery of 5-fluorouracil through shed snake skin by two new transdermal penetration enhancers. *Int. J. Pharm.* **1993**, *92*, 89−95.
57. Walters, K. A. Some novel aspects of transdermal drug delivery. In *Chemical Aspects of Drug Delivery Systems*; The Royal Society of Chemistry: Cambridge, UK, 1996; pp 41−51.
58. Gauthier, E. R.; Gyurik, R. J.; Krauser, S. F.; Pittz, E. P.; Samour, C. M. SEPA absorption enhancement of polar and nonpolar drugs. In *Perspectives in Percutaneous Penetration*, Vol. 5a; Brain, K. R.; James, V. J.; Walters, K. A., Eds.; STS: Cardiff, Wales, UK, 1997; p 79.
59. In *PharmaProjects on CD-Rom*, May update; PJB Publications: Richmond, Surrey, UK, 1999.
60. In *Dermatotoxicology*, 5th ed.; Marzulli, F. N.; Maibach, H. I. Eds.; Taylor & Francis: Washington, DC, 1996.
61. Reed, B. L.; Morgan, T. M.; Finnin, B. C.; Dermal penetration enhancers and drug delivery systems involving same. PCT Int. Appl. PCT/AU97/00091, 1997, 19 Feb.
62. Murphy, E. G.; Janousek, A.; Groves, G. A.; Fukuda, M.; Naganuma, M. Regulatory aspects. In *Sunscreens. Development, Evaluation, and Regulatory Aspects*, 2nd ed.; Lowe, N. J.; Shaath, N. A.; Pathak, M. A., Eds.; Marcel Dekker: New York, 1997; pp 201−260.
63. Funk, J. O.; Dromgoole, S. H.; Maibach, H. I. Sunscreen intolerance. *Dermatol. Clin.* **1995**, *13*, 473−481.
64. Bakalova, M. V.; Morgan, T. M.; Reed, B. L.; Finnin, B. C. The effect of pretreatment with new 'safe' penetration enhancers on the diffusion of NSAIDs across shed snake skin. In *Perspectives in Percutaneous Penetration*, Vol. 5a, Brain, K. R.; James, V. J.; Walters, K. A., Eds.; STS: Cardiff, UK, 1997; p 78.
65. Finnin, B. C.; Morgan, T. M.; Klose, K. T.; Bakalova, M. V.; Taylor, D. A.; Reed, B. L. Enhancement of epidermal penetration of NSAIDs by padimate O, octyl salicylate and octyl methoxycinnamate. AAPS Annual Meeting. *Pharm. Res.* **1997**, *14*, S304.
66. Morgan, T. M.; Reed, B. L.; Finnin, B. C. Enhanced skin permeation of sex hormones with novel topical spray vehicles. *J. Pharm. Sci.* **1998**, *87*, 1213−1218.
67. Klose, K. T.; Taylor, D. A.; Reed, B. L.; Finnin, B. C.; Enhanced percutaneous penetration of ibuprofen determined by microdialysis in conscious rats. In *Perspectives in Percutaneous Penetration*, Vol. 5a, Brain, K. R.; James, V. J.; Walters, K. A., Eds.; STS: Cardiff, UK, 1997; p 77.
68. Morgan, T. M.; Parr, R. A.; Reed, B. L.; Finnin, B. C. Enhanced transdermal delivery of sex hormones in swine with a novel topical aerosol. *J. Pharm. Sci.* **1998**, *87*, 1219−1225.
69. Morgan, T. M.; O'Sullivan, H. M. M.; Reed, B. L.; Finnin, B. C. Transdermal delivery of estradiol in postmenopausal women with a novel topical aerosol. *J. Pharm. Sci.* **1998**, *87*, 1226−1228.

Acknowledgments

The authors thank Professor Barry L. Reed for his valued help in reviewing the manuscript.

JS990154G

Frequency-Domain Photon Migration Measurements for Quantitative Assessment of Powder Absorbance: A Novel Sensor of Blend Homogeneity†

RAJESH R. SHINDE, G. V. BALGI, S. L. NAIL,‡ AND E. M. SEVICK-MURACA*

Contribution from *The Photon Migration Laboratory, School of Chemical Engineering, Purdue University, West Lafayette, Indiana 47907-1283.*

Received March 15, 1999. Accepted for publication August 3, 1999.

Abstract □ The measurement and analysis of frequency-domain photon migration (FDPM) measurements of powder absorbance in pharmaceutical powders is described in the context of other optical techniques. FDPM consists of launching intensity-modulated light into a powder and detecting the phase delay and amplitude modulation of the re-emitted light as a function of the modulation frequency. From analysis of the data using the diffusion approximation to the radiative transport equation, the absorption coefficient can be obtained. Absorption coefficient measurements of riboflavin in lactose mixtures are presented at concentrations of 0.1 to 1% (w/w) at near-infrared wavelengths where solution absorption cross sections are difficult to accurately measure using traditional transmission measurements in nonscattering solutions. FDPM measurements in powders enabled determinations of absorption coefficients that increase linearly with concentration (w/w) according to Beer–Lambert relationship. The extension of FDPM for monitoring absorbance of low-dose and ultralow-dose powder blending operations is presented.

1. Introduction

The blending of powders of differing particle size, density, shape, and surface characteristics can result in demixing and segregation phenomenon that can have a critical impact on pharmaceutical powder blending and tableting processes. Indeed, the complexity of the blending process and the uncertainty in assessment of spatial homogeneity of the active agent in the powder bed within the blender are especially crucial in low dose (<1% w/w) or ultralow-dose (<0.1% w/w) formulations involving high potency pharmaceutical compounds. While much progress has been made toward a better physical understanding of the complexities involved in powder blending, measurements which validate the end point of a mixing process and provide assurance of the blend homogeneity remain as missing tools required to better address the quality assurance issues facing the pharmaceutical industry. In 1993, the "Barr decision" highlighted the litigious nature of incomplete knowledge of powder blending and sampling operations that could impact the uniformity of pharmaceutical tablets. Furthermore, the decision underscored the necessity for a measurement technique that (i) provides assessment of blend homogeneity, (ii) minimizes the error associated with powder sampling, (iii) provides sampling size measurements reflective of no more than three unit dosages and, (iv) enables real time measurements of blend homogeneity during the mixing operation. Currently, the "gold-standard" measurement of blend homogeneity rests with "thief sampling" combined with HPLC or other wet chemistry analysis. The typical sampling "thief" consists of an inner cylinder with sampling compartments along its axis and an outer, rotating, hollow cylinder stamped with apertures that permit flow into the inner sampling chambers when both cylinders are properly aligned. The difficulties associated with thief sampling are (i) the induced variance error associated with uneven flow of differing sized particles into sampling chambers, (ii) the disturbance of powder bed by the insertion of the thief, and (iii) the inability to make in situ, real time variance measurements, σ_m^2, related to actual variance in drug concentrations, σ_d^2, during the blending operation. It should be emphasized that the measured variance, σ_m^2, reflects a contribution from sampling, σ_s^2, analysis, σ_a^2, and drug concentration, σ_d^2, variances, i.e., $\sigma_m^2 = \sigma_s^2 + \sigma_a^2 + \sigma_d^2$. The Barr decision stipulates the largest sample volume for analysis must be less than three times that of a single tablet.

Numerous investigators have sought to develop techniques to assess the blend homogeneity without the need to remove a sample from the powder bed, thereby eliminating the influence of sampling error or variance, σ_s^2. In a system to model blend homogeneity, Muzzio and coworkers[1] have developed a technique to investigate the blending phenomenon that involves solidification of the contents of a mixing vessel and slicing cross sections of the solid mixture for image analysis. The blend homogeneity is then studied by using statistical methods to assess the mixing of differently colored glass beads in the size range of tens of microns. Their technique to assess mixing in a model system is static, and restricted to a specific model system of glass beads, yet provides a means for assessing measured variances independent of σ_s^2, and aids in building process models for validation of powder mixing.

Other investigators have sought optical means to assess blend homogeneity. Diffuse-reflectance fiber optic probes are being investigated extensively for evaluating powder characteristics.[2,3] Using near infrared (NIR) fiber optics reflectance from powders, Cho et al. (1997)[4] measured

* To whom correspondence should be directed. Phone: 765-496-2377. Fax: 765-494-0805. E-mail: sevick@ecn.purdue.edu. http://photon.ecn.purdue.edu/~chepmi/ppml.html.

† Supported by the Purdue NSF I/UCRC in Pharmaceutical Processing.

‡ School of Pharmacy.

10.1021/js990079+ CCC: $18.00
Published on Web 09/08/1999

derivative spectra from backscattered light in the wavelength range between 1100 and 2500 nm to measure blend homogeneity of a lactose, microcrystalline cellulose, and sodium benzoate mixture based on its variance as a function of mixing time. Since the spectra can be measured in situ, the sampling variance arises only from the volume of powders probed in the diffuse backscattered light and is not impacted by the powder flow problems associated with a sampling thief. Their results suggest that backscatter techniques using fiber optics can interrogate 0.154 to 0.858 g of powder with a standard deviation of 0.16 g. Arguing that single doses range from 0.1 to 1.0 g, these investigators contend that the backscatter technique fits the regulatory requirements for probing 0.3 to 3.0 g of total tablet mass. Analysis of diffuse reflectance and backscatter measurements often assumes wavelength-independent scattering so that variance of the derivative spectra is assumed to be a measure of the variance of light-absorbing constituents in the blend. Unfortunately, the assumption of wavelength-independent scattering is not always correct, and monitoring spectral derivatives for blend homogeneity studies may not always be a prudent approach for minimizing artifact.

In this contribution, we introduce the techniques of frequency-domain photon migration for assessment of blend homogeneity and demonstrate its applicability for determination of powder absorbance for pharmaceutical process monitoring. In contrast to diffuse reflectance and backscatter measurement and analysis currently pursued for such applications, FDPM is based upon the *time-dependent diffusive* scattering of light. Owing to the measurement approach, the variance of analysis and measurement are minimized when compared to thief sampling and time-invariant diffuse reflectance or backscatter techniques, respectively. In the following, we briefly review the theory describing light transport in powders and describe the inherent difficulties associated with time-invariant measurement of diffuse reflectance. We describe the physics of FDPM measurements as well as the instrumentation and analysis of measurements and present FDPM absorbance values of riboflavin in lactose powders to demonstrate the feasibility of the technology. Finally, we comment upon the diagnostic ability of FDPM for pharmaceutical monitoring of intermediate and final powder-based products.

2. Light Transport in Powders

Optical techniques for monitoring the absorbance associated with active ingredients in a powder bed are typically based upon diffuse reflectance or backscatter techniques that employ a constant intensity source of broadbeam illumination or a point source illumination via fiber optic coupling. Analysis of backscatter or diffuse reflectance are typically employed using empirically based chemometric analyses or physically based radiative transfer equations and associated assumptions. Since chemometrics is beyond the scope of this contribution, we refer the reader to a treatise on the subject by Muhammad and Kowalski[5] and Adams.[6] Instead, in this contribution we are concerned with extraction of the absorption coefficient, $\mu_a(\lambda)$, at wavelength λ, within the powder bed. Assuming that the absorption coefficient is the sum of different light absorbing species, i.e., $\mu_a(\lambda) = \Sigma_i \epsilon_{\lambda,i}[C_i]$, measurements made at multiple wavelengths enable determination of concentration of the light absorbing components from the simultaneous solution of a series of linear equations. However, as briefly described below, it is difficult and in some approaches impossible to determine absorption coefficients independently from first-principles data analyses of time-invariant, reflected light.

Radiative Transfer of Light in Scattering Media—Light propagation is ubiquitously described by the radiative transfer equation (RTE), that can be solved with proper boundary conditions to predict the radiance, L, [Watts/(m^2 sr)] associated with light traveling in direction of unit vector $\hat{s}$ per unit solid angle.

$$\frac{1}{c}\frac{\partial L(\bar{r},\hat{s},t)}{\partial t} + \bar{\nabla} L(\bar{r},\hat{s},t)\hat{s} = -(\mu_s + \mu_a)L(\bar{r},\hat{s},t) + \mu_s \int_{4\pi} L(\bar{r},\hat{s}',t) f(\hat{s},\hat{s}') d\Omega' + Q(\bar{r},\hat{s},t) \quad (1)$$

Briefly, the first and second terms on the left hand side of eq 1 describe the accumulation of radiance (where c is the speed of light in the medium), and the net rate of increase of radiance associated with light traveling in direction $\hat{s}$, respectively. The first term on the right hand side denotes the loss mechanisms whereby light traveling in direction $\hat{s}$ is lost through absorption and scattering out of direction $\hat{s}$. Here, μ_s and μ_a [1/(length)] are the linear scattering and absorption coefficients, respectively. The second term describes a "gain term" by which light traveling all directions $\hat{s}'$ (or solid angle $\hat{\Omega}'$) is scattered into the preferred direction $\hat{s}$. To properly account for this "inscattering," into direction $\hat{s}$, the phase function, $f(\hat{s}',\hat{s})$ must be known. $f(\hat{s}',\hat{s})$ describes the probability of photons traveling in direction $\hat{s}'$ being scattered into direction $\hat{s}$ and must satisfy the relation:

$$\int_{4\pi} f(\hat{s},\hat{s}') d\Omega' = 1 \quad (2)$$

$Q(\bar{r},\hat{s},t)$ represents the source term for the photons traveling in direction $\hat{s}$.[7−10]

Diffusion Approximation to RTE—The typical powder bed of micron-sized particles scatters light multiple times in all directions. Integration of eq 1 over all possible solid angles, Ω, leads to the equation of continuity shown below.

$$\frac{1}{c}\frac{\partial \phi(\bar{r},t)}{\partial t} + \bar{\nabla}\bar{j}(\bar{r},t) = -\mu_a \phi(\bar{r},t) + S(\bar{r},t) \quad (3)$$

where

$$S(\bar{r},t) \equiv \int_{4\pi} Q(\bar{r},\hat{s},t) d\Omega,$$

$$\phi(\bar{r},t) \equiv \int_{4\pi} L(\bar{r},\hat{s},t) d\Omega$$

and

$$\bar{j}(\bar{r},t) \equiv \int_{4\pi} L(\bar{r},\hat{s},t)\hat{s}\, d\Omega$$

$S(\bar{r},t)$ is an isotropic source term, $\phi(\bar{r},t)$ is the angle-independent fluence rate, and $\bar{j}(\bar{r},t)$ is the photon flux.

The *diffusion approximation*, which assumes weak angular dependence of radiance, $L(\bar{r},\hat{s},t)$, and predominant scattering such that $\mu_a \ll (1 - g)\mu_s$, is typically valid in powders. Specifically, in the standard diffusion approximation, the angular radiance, $L(\bar{r},\hat{s},t)$, is expressed as a sum of the angle independent fluence rate, $\phi(\bar{r},t)/(4\pi)$, and a small directional flux, $3/(4\pi)\hat{s}\cdot\bar{j}(\bar{r},t)$. Details regarding the diffusion approximation as well as higher order approximations to the RTE are available in literature[11,12] and not described here for brevity. Nonetheless, the optical diffusion equation derived from RTE describing the angle-independent fluence of light $\phi(\bar{r},t)$(W/m^2) is written as:

$$D\nabla^2\phi(\bar{r},t) - \mu_a\,\phi(\bar{r},t) = \frac{1}{c}\frac{\partial\phi(\bar{r},t)}{\partial t} - S(\bar{r},t) \qquad (4)$$

where

$$D \equiv \frac{1}{3[(1-g)\mu_s + \mu_a]} \equiv \frac{l_{tr}}{3}.$$

D is the optical diffusion coefficient (cm), g is the average cosine of the scattering angle and the term $(1-g)\mu_s$ is the isotropic scattering coefficient. l_{tr} is the transport mean free path of the diffusing photon. Equation 4 can be solved for different boundary conditions (see section 3). However, the diffusion theory has limitations. The diffusion theory assumes that the radiance is nearly isotropic in its angular dependence and the sources are isotropic. These conditions are satisfied in strongly scattering situations, i.e., $\mu_a \ll (1-g)\mu_s$, and far from the boundaries and sources. The minimum distance from the source and boundaries at which light is detected must be at least greater than $10l_{tr}$ without having to resort to higher order approximations. As described in the section below, the diffusion equation can be solved for incident intensity-modulated light to enable determination of absorption independently of scattering properties and without the need to know scattering phase functions.

3. Frequency Domain Photon Migration

The technique of frequency-domain photon migration depends upon launching intensity modulated, monochromatic light at modulation frequencies ranging from 100's of kHz to 100's of MHz. As the resulting "photon-density wave" propagates through the scattering media, its amplitude is attenuated and it is phase-delayed relative to the incident light. The transport of photons via FDPM in the media can be treated as a diffusive process. The light detected in reflectance or transmittance mode is modulated at the same frequency as that of the incident light. This light is found to be phase-shifted, θ', and its amplitude attenuated by a factor M relative to the incident light. Measurements of θ' and M are acquired at different modulation frequencies, $\omega/2\pi$, of the source. The solution of the diffusion equation (section 2) is used to relate the phase-shift, θ', and amplitude modulation attenuation, M, to the two separate optical properties of the powder, the absorption coefficient, μ_a, and the isotropic scattering coefficient, μ'_s. The advantages of FDPM are twofold: first, these measurements do not require an external calibration, and second, the absorption and isotropic scattering coefficients are obtained as separate parameters rather than as a single product (as determined in continuous wave measurements analyzed with multiflux approximations to the radiative equation).

3.1. Theory of FDPM—The measurements described herein were conducted with the frequency-domain photon migration apparatus illustrated in Figure 1. The light source was a 670 nm laser diode (150 mW) which was sinusoidally modulated at the frequency of interest by modulation of the current input. The light from the laser sources was split so that approximately 10% of the light was collected by a reference photomultiplier tube (Hamamatsu R928, Hamamatsu, Japan) via a 1000 μm optical fiber. The remaining transmitted light was launched into the lactose–riboflavin powder mixture using a 1000 μm source optical fiber positioned flush with the wall of the sample container. The scattered light from the powder was detected by another 1000 μm optical fiber that was mounted at known distances away from the source fiber, also flush

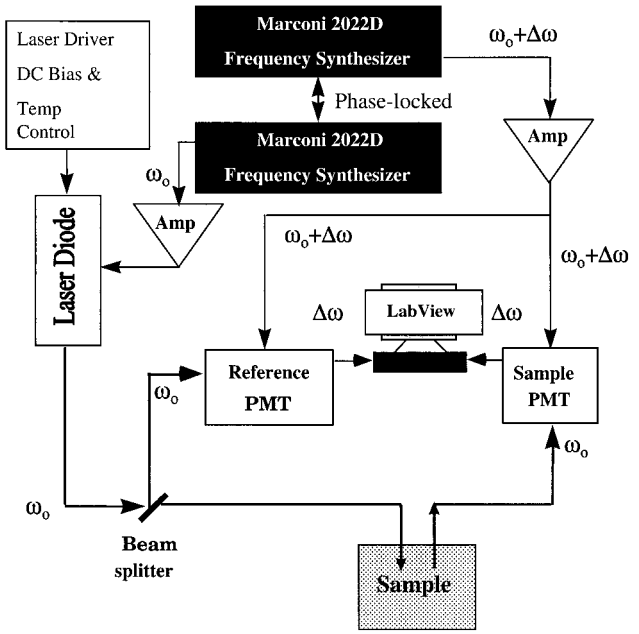

Figure 1—A schematic of an experimental setup of the frequency domain photon migration (FDPM). The light source is a laser diode, but can be substituted with a Ti:sapphire laser.

with the wall of the container. The other end of this detecting optical fiber was directed to a second photomultiplier tube. The source and detector fibers were maintained in a coplanar geometry. Estimates of the isotropic scattering and absorption coefficients using the phase-difference and amplitude modulation data were obtained by regression from analytical solutions to the optical diffusion equation described below. The relative separations between the source and detector fibers were chosen such that the distances between them were at least 10 isotropic scattering mean free paths l^* (or $1/\mu'_s$) to ensure multiple light scattering. The photomultiplier tubes (PMT's) were gain modulated at a modulation frequency, $\omega/2\pi$, of the laser diode plus an offset frequency ($\Delta\omega/2\pi$) of 100 Hz. This standard heterodyne technique yielded a 100 Hz signal at the photomultiplier output from which the phase shift, θ', and modulation, M, could be extracted. A data acquisition software (Labview 4.01, National Instruments) was customized to acquire and process the experimental data.

A pulsed light source was also employed for the frequency-domain studies enabling us to interrogate the samples with a Ti:sapphire system at other wavelengths. The source was a tunable 2 ps pulsed optical train output of a Tsunami picosecond-pulsed titanium–sapphire (Ti:sapphire) laser (Model 3950B, Tsunami, Spectra Physics, CA) pumped by a 10 W argon-ion laser (Beamlok 2060, Spectra Physics). Near infrared wavelengths of 750 and 820 nm were generated using this Ti:sapphire laser. The Ti:sapphire laser pulse train was delivered at a repetition rate of 4 MHz with an average output power level of 20 mW. The light was delivered to the powder mixtures in the same manner as that for the 670 nm laser diode. For the Ti:sapphire light source, PMT gain modulation was achieved at a harmonic of the pulsed laser repetition rate plus the 100 Hz offset frequency. Details of the instrumentation have been discussed elsewhere.[13]

The experimentally measured quantities were the phase lag, θ', at the detector relative to a reference signal as a function of modulation frequency, ω. To nullify instrument responses (i.e., phase delays induced by instrumentation), measurements at multiple detector positions were used to determine relative phase shifts ($\Delta\theta'_{rel}$).

3.2. Prediction of FDPM Measurements—For photon diffusion in an infinite medium, the optical diffusion equation (section 2) has been solved to obtain analytical expressions for different boundary conditions.[11,14] The following solutions for infinite and zero boundary conditions have been obtained by Haskell et al.

Zero Boundary Condition—The zero boundary condition sets the fluence rate, ϕ, to zero at the physical boundary. This condition was found suitable for our experimental setup. The solution for the diffusion equation with this boundary condition leads to the following expression for $\Delta\theta'_{rel}$.

$$\Delta\theta'_{rel}(\lambda) = |d_1 - d_2|k_{imag} - \arctan\left(\frac{k_{imag}}{k_{real} + \frac{1}{|d_1 - d_2|}}\right) \quad (5)$$

where

$$k_{imag} = \sqrt{\frac{3}{2}\mu_a\mu'_s\left(\left(1 + \left(\frac{\omega}{\mu_a c}\right)^2\right)^{1/2} - 1\right)}$$

and

$$k_{real} = \sqrt{\frac{3}{2}\mu_a\mu'_s\left(\left(1 + \left(\frac{\omega}{\mu_a c}\right)^2\right)^{1/2} + 1\right)}$$

$$k = k_{real} + ik_{imag}$$

where d_1 and d_2 are the two source-detector positions, λ is the wavelength of light in vacuum, and c is the speed of light in the continuous medium. k is the wavenumber which has a real component, k_{real}, and an imaginary component, k_{imag}. The experimental data of phase-shift versus modulation frequency was then fit to eq 5 using a Marquardt–Levenberg nonlinear regression algorithm to yield independent parameter estimates of the absorption coefficient, μ_a, and the isotropic scattering coefficient, μ'_s. The measured variance in θ' at different frequencies was less than 1%.

The volume sampled by diffusing light depends upon the absorption and scattering properties of the powder. The average distance traveled by photons into the powder bed from the light source can be calculated from the approach developed by Sevick et al.[15] The fluence of the photons is determined at various points in the powder bed, and the amount of photons detected at various source-detector separations is calculated. The average distance of travel of photons into the powder increases with separation, and then drops off. For example, in these set of measurements at source-detector separations of 0.55 and 1.22 cm, and for a scattering coefficient of 120.0 cm^{-1}, and an absorption coefficient of 0.02 cm^{-1}, the average distance that the photons traveled into the powder bed are 0.44 and 0.50 cm respectively. Assuming a spherical profile of the photons propagating in the powder bed, the volume sampled does not exceed more than 0.5 cm^3. We can see that the volume probed by this technique is not very large, and is well within the sampling volume limit.

4. Experimental Section

Materials—In order to demonstrate the ability to detect small changes in absorbance, we chose to employ riboflavin/lactose powder mixtures as a model system. Lactose monohydrate USP was supplied by Sheffield, Inc. (Norwich, NY), and riboflavin USP was provided by Hoffmann LaRoche Laboratories Inc. (Nutley, NY). Both materials were used as received. In the following, we describe measurements of riboflavin and lactose absorption cross section using conventional attenuation measurements in dilute nonscattering solutions, as well as by FDPM techniques.

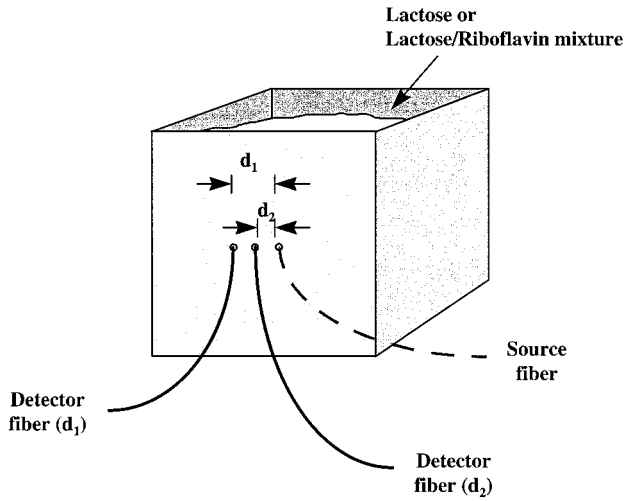

Figure 2—An illustration of the sample box used for making FDPM measurements on lactose–riboflavin mixtures.

4.1. Absorption Coefficient of Riboflavin Solution—The extinction coefficient for riboflavin (molecular weight = 376.4) was measured using a Perkin-Elmer UV-vis spectrophotometer. Riboflavin is sparingly soluble in water; hence, in order to facilitate the dissolution of riboflavin, sodium hydroxide solution was added dropwise until a clear solution was obtained. The solution was centrifuged to remove debris. A stock solution was prepared with riboflavin concentration of 0.014 g/L. The samples were prepared 1 h prior to experiments, because riboflavin is unstable in solution and the instability increased with increasing sodium hydroxide concentrations. The measurements were accomplished on the stock solution and dilutions of the stock solution of 1:2 and 1:5 by deionized water. The absorption spectra was obtained at wavelengths ranging from 200 to 900 nm scanned at a rate of 240 nm/minute. The extinction coefficient of a light-absorbing species in a mixture is determined from the Beer–Lambert's law, $(1/l)\log_{10}(I_o/I) = \mu_a(\lambda) \equiv \epsilon(\lambda)[C]$, where μ_a is the absorption coefficient of the solution, I_o is the incident light, I is the detected light passing through a sample of thickness l. C denotes the concentration of the absorbing species, i.e., riboflavin, in the solution. $\epsilon(\lambda)$ is the extinction coefficient of the species and can be obtained for a particular wavelength by measuring the absorption coefficient (μ_a) at various concentrations. The slope of the straight line fit to the data provides the extinction coefficient.

4.2. Extinction Coefficient of Lactose-Riboflavin Mixtures—The extinction coefficients for various lactose–riboflavin mixtures were obtained for wavelengths ranging from 350 to 470 nm. Riboflavin content in the lactose varied from 0 to 1.0 wt %. The powder samples were dissolved in deionized water, and their absorption coefficient was obtained at different riboflavin concentrations. The slope of the straight line fit gave the extinction coefficient of the total lactose–riboflavin mixture.

4.3. Absorption Coefficients and Extinction Coefficients of Lactose–Riboflavin Powder Mixtures by FDPM—In order to measure the isotropic scattering and absorption coefficient of the powder mixtures, the samples were placed in a rectangular box. Three optical fibers were inserted into one side of the box and the tip of the fibers were flush with the interior side of the box as shown in Figure 2. Such an arrangement prevented movement of the

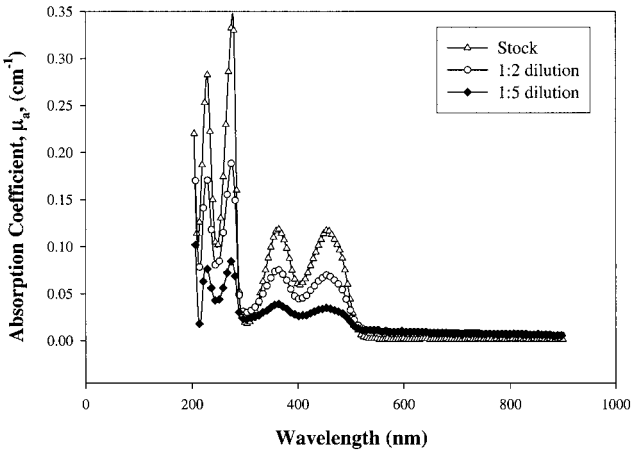

Figure 3—Absorption spectra obtained at three dilutions of a riboflavin stock solution of 0.0372 mM in deionized water. The dilutions were effected in the ratios of (i) 1:1 (0.0186 mM), (ii) 1:2 (0.0124 mM), and (iii) 1:5 (0.0062 mM) with deionized water. The wavelengths scanned were from 200 to 900 nm.

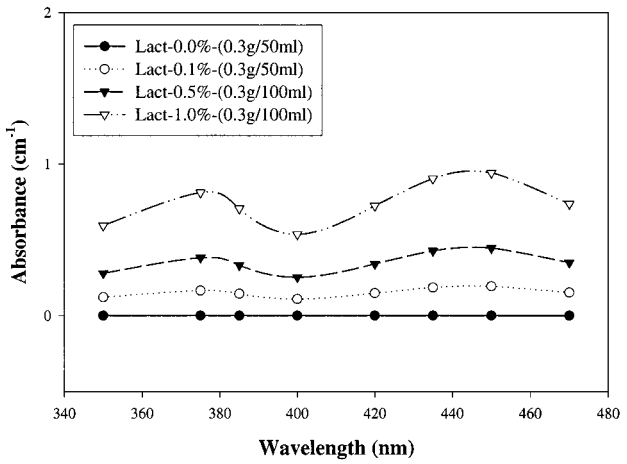

Figure 4—Absorption spectra of four dissolved lactose–riboflavin mixtures. Measurements were accomplished from 350 to 475 nm. Riboflavin concentrations ranged from 0 to 1 wt % for the four powders. The symbols denote the concentrations of the four powder mixtures dissolved in deionized water. Lines are spline fits to the data.

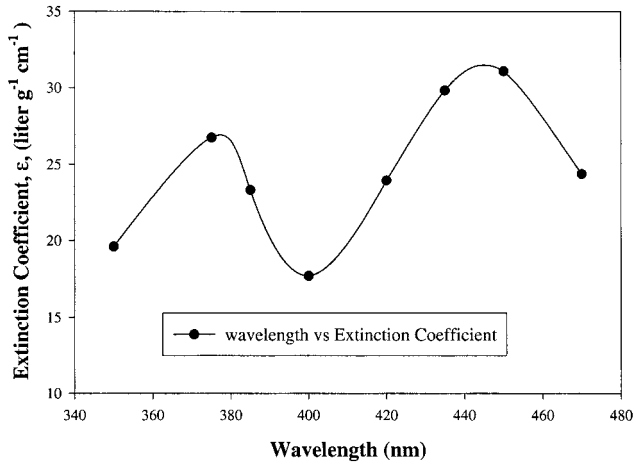

Figure 5—Plot of the extinction coefficients of riboflavin calculated from the experimentally measured absorption coefficients at wavelengths from 350 to 475 nm, using a UV-spectrophotometer. The UV extinction coefficients for lactose were negligible and hence neglected. The symbols represent the calculated extinction coefficients, and the lines are spline fits to the data.

powder arising due to insertion of fibers or probes. One fiber delivers monochromatic light from the laser source, and the scattered light is collected by the other two fibers. All the fibers were of the same length, and the fiber separations were 0.55 and 1.22 cm. In order to eliminate instrumentation errors, the relative phase shifts between the two detector positions were measured by taking the difference of the measured phase shifts for each position d_1 and d_2. The fibers could be used in any combinations as source and detectors. The powder mixtures were poured into the box (5.7 × 7.2 × 7.6cm), and measurements were carried out without any compaction of the powders. The powders were mixed in a V-blender, in batches of 250 g.

FDPM measurements were accomplished on four different powder mixtures. The four mixtures were lactose with 0, 0.1, 0.5, and 1 wt % riboflavin mixed uniformly in a blender. Riboflavin absorbs strongly at 470 nm. Extensive trial runs were carried out to determine the scattering and absorption coefficients of the powder mixtures at different wavelengths. Initially, modulated light at wavelengths of 488 and 515 nm was used. At these wavelengths, a good signal could be detected for the pure lactose powder. However, the lactose powder containing riboflavin tended to absorb a substantial amount of light, causing a significant attenuation of the amplitude and preventing an accurate measurement of the phase-delay, θ'. As a result, FDPM measurements were conducted at wavelengths of 670 nm and higher, away from the absorbance maximum of riboflavin. At these wavelengths and smaller absorption cross sections, absorption by the riboflavin does not predominate and FDPM provided accurate signals for determination of powder optical properties. The two other wavelengths of light used were 750 and 820 nm.

It is noteworthy that the FDPM technique is capable of measuring small changes in the absorbance of the powders, due to the absorption by riboflavin.

5. Results and Discussion

5.1. Absorption Coefficient of Riboflavin Solution—Figure 3 shows a plot of the absorption spectrum of riboflavin in alkaline solution. As can be seen from the figure, there is significant absorption in the UV range from 300 to 500 nm. Two peaks are observed in the spectra at around 360 and 480 nm. The absorption drops to negligible values beyond 500 nm, thus providing only a small window for measuring riboflavin concentrations. Owing to the small absorption cross section of the riboflavin at wavelengths greater than 500 nm, it is not possible to accurately detect solution riboflavin concentrations outside the UV range.

5.2. Extinction Coefficient of Lactose−Riboflavin Mixtures—On the basis of these results, further measurements were made on lactose−riboflavin mixtures in the UV range 350 to 470 nm. The mixtures were dissolved in deionized water in concentrations ranging from 3 to 6 g/L. Lactose dissolves very easily in water and does not show any detectable absorption in the UV range that was studied. Results are presented in Figure 4. It can be seen that as the riboflavin content in the lactose is increased from 0 to 1% (by weight) at constant lactose concentration, the absorption spectra shows two peaks originating at the same wavelength ranges (360 and 480 nm) as those for pure riboflavin (Figure 3). The results from Figure 4 were then utilized to calculate the extinction coefficient of riboflavin in the powder mixtures at different wavelengths. The slope of a straight-line plot of the absorbance for the solutions of the mixtures at different riboflavin concentration gave the extinction coefficient of riboflavin. The extinction coefficients thus determined for riboflavin in the powder mixtures at different wavelengths are plotted in Figure 5.

5.3. Absorption Coefficients and Extinction Coef-

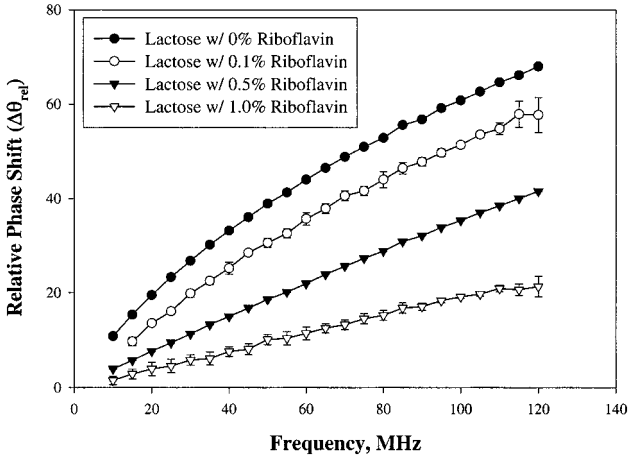

Figure 6—The relative phase shifts of four different lactose–riboflavin powder mixtures plotted at different modulation frequencies. The lactose–riboflavin mixtures are in the same ratios as given in Figure 4 represented by symbols. Measurements were accomplished at 670 nm using a laser diode. Error bars are a result of 10 measurements at each frequency.

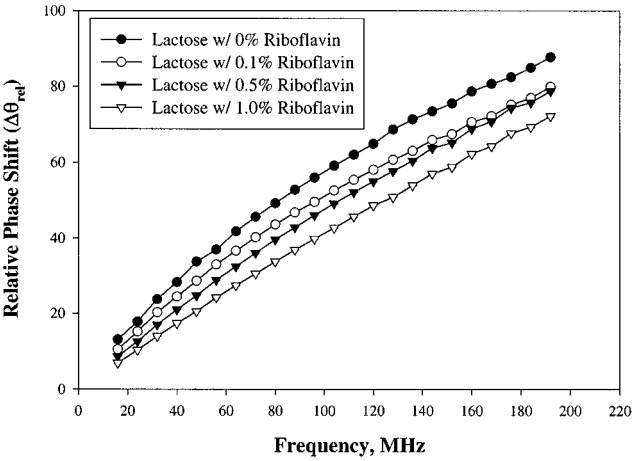

Figure 7—The relative phase shifts of four different lactose–riboflavin powder mixtures plotted at different modulation frequencies. The lactose–riboflavin mixtures are in the same ratios as given in Figure 4 represented by symbols. Measurements were accomplished at 750 nm using a Ti:sapphire laser. Error bars are a result of 10 measurements at each frequency.

ficients of Lactose−Riboflavin Powder Mixtures by FDPM—Again, owing to the sensitivity of FDPM measurements to absorption, measurements at 488 and 515 nm were not possible in the presence of 0.1−1.0% riboflavin. For this reason, we conducted FDPM measurements at a wavelength where riboflavin absorption was small. At these wavelengths, the absorption cross section spectra cannot be accurately measured using conventional attenuation measurements due to low extinction coefficients of the powder mixtures.

Shown in Figure 6 are the relative phase shifts, $\Delta\theta'_{rel}$, for the four different powders at different modulation frequencies measured at 670 nm. Each data point is an average of at least 10 continuous measurements, with the respective error bars as shown in the Figure 6. A steady decrease in the $\Delta\theta'_{rel}$ values is observed at a given modulation frequency with increase in the riboflavin content in lactose. This is expected due to an increase in absorption coefficient by riboflavin. Similar results were obtained for $\Delta\theta'_{rel}$ measurements carried out at 750 and 820 nm as shown in Figures 7 and 8, respectively. A noticeable difference in each of these plots is the magnitude of the change in $\Delta\theta'_{rel}$ as a function of riboflavin content. At higher wavelengths, the change is smaller, indicating lower absorption coefficients of the powder, which can be attributed to lower extinction coefficients for riboflavin. $\Delta\theta'_{rel}$ values at the various frequencies for each wavelength and powder composition were regressed using eqs 5 (reflectance mode) to give the isotropic scattering and absorption coefficients. The absorption coefficients at 670, 750, and 820 nm obtained by regression using eqs 5 are plotted in Figure 9. At 670 nm, the FDPM data for powder mixtures containing 1% riboflavin could not be fit to the solution of the diffusion equation. This may have been due to high absorption levels at this wavelength, which (i) causes significant dampening of the light signal before it can reach the PMT's and (ii) invalidates the diffusion approximation. Nonetheless, for a given wavelength, an increase in the absorption coefficient is observed with increasing riboflavin content in the powder mixtures. Furthermore, the change in absorbance with increasing riboflavin content is greatest at 670 nm, consistent with the largest extinction coefficient value. At longer wavelengths of 750 and 820 nm, the sensitivity drops further, indicating evidence of a reduction of riboflavin extinction coefficients.

If the absorbance due to the lactose constituent is taken to be the *Y*-intercept of the absorbance versus riboflavin content plots, and then its contribution can be subtracted to provide the absorbance owing to riboflavin only. The results plotted in Figure 10 show a linear relationship between the riboflavin absorption coefficient with its concentration in the powder, from which an extinction coefficient can be determined. It is noteworthy that there

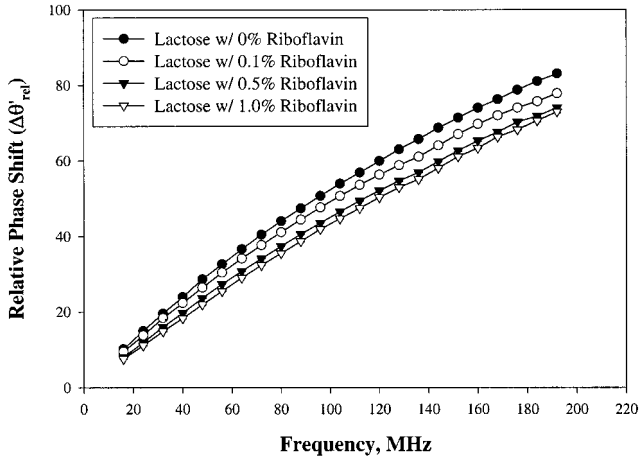

Figure 8—The relative phase shifts of four different lactose–riboflavin powder mixtures plotted at different modulation frequencies. The lactose–riboflavin mixtures are in the same ratios as given in Figure 4 represented by symbols. Measurements were accomplished at 820 nm using a Ti:sapphire laser. Error bars are a result of 10 measurements at each frequency.

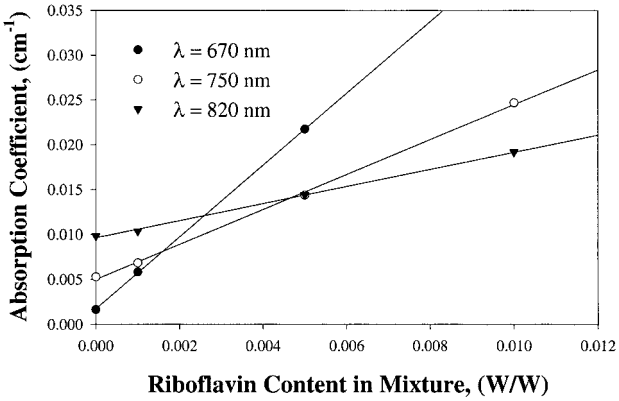

Figure 9—The absorption coefficients for four lactose–riboflavin powder mixtures at three wavelengths, 670, 750, and 820 nm, represented by the three symbols. The absorption coefficients were obtained by regressing the measured relative phase shifts at various frequencies to eq 5.

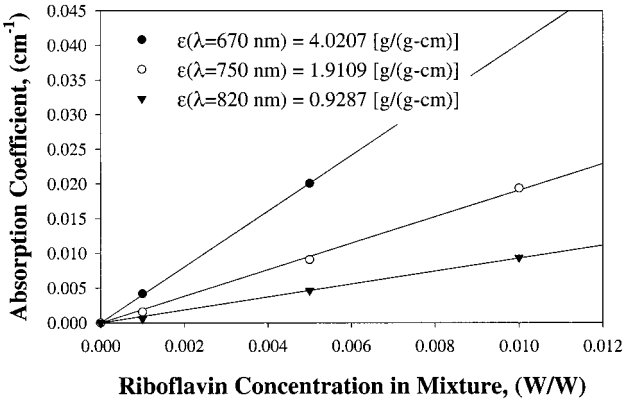

Figure 10—The symbols represent the net absorption coefficients for riboflavin in the four powder mixtures obtained by subtracting the absorption coefficient of pure lactose at each wavelength. The extinction coefficients of riboflavin, shown in the plot, at each wavelength were obtained by regressing the absorption data at the known concentrations using Beer–Lambert's law.

is no significant difference between the extinction coefficients obtained from infinite and reflectance modes of regression of the raw $\Delta\theta'_{rel}$ data. In addition, the riboflavin extinction coefficients are observed to decrease with increasing wavelengths as expected from the UV-spectrophotometer results.

The analysis of the experimental data of the four powder mixtures also yielded the isotropic scattering cross section of the particles. The isotropic scattering coefficients vary from 87 to 123 cm^{-1} for all the four samples at the three wavelengths used, i.e., 670, 750, and 820 nm. The wide range in the measured values may be attributed to the significant polydispersity of the powder mixtures.

6. Conclusions

We have presented FDPM measurements for a simple, two-component powder mixture of riboflavin and lactose. Owing to the sensitivity of FDPM to powder absorbance, we were forced to conduct measurements at wavelengths where riboflavin absorbance did not entirely attenuate the light signal in the powder bed. That is, the measurements were conducted at wavelengths away from the absorbance peaks for the powder mixtures, and the modulated light signal could be detected. At these photon migration wavelengths, the absorbance of riboflavin could not be assessed using conventional attenuation measurements in dilute nonscattering solutions. The results illustrate that for a two-component powder system, the FDPM absorbance increases linearly with riboflavin concentration. The extension to multicomponent mixtures requires additional wavelength sources, but does not require illumination at absorption maxima for maximum sensitivity. Indeed, the ability to detect small absorption cross sections promises applications in low-dose blending operations. Owing to our first principles approach that does not require differential spectroscopy, the variance associated with our analysis should be minimized. Since there is no sampling of powder involved (measurements are made within the powder bed as described herein), there are no sampling variances that need to be assessed. Consequently, the measured variances should be predominantly due to variances associated with the constituents within the powder bed. Finally, since FDPM does not involve *relative* intensity measurements, but rather *absolute* "time-of-flight" phase-delay measurements, there are no measurement errors associated with calibration on an external standard. At the NSF I/UCRC Center in Pharmaceutical Processing at Purdue University we are currently adapting FDPM technology as an in-situ sensor of blend homogeneity.

Nomenclature

Symbols:

c	speed of light in medium (cm/s)
d_1, d_2	source-detector distances (cm)
D	optical diffusion coefficient (cm)
g	average cosine of scattering angles
$\bar{j}(\bar{r},t)$	photon flux (W/m^3)
k	wavenumber (cm^{-1})
k_{real}	real part of k
k_{imag}	imaginary part of k
l^*	isotropic scattering mean free path (cm)
l	thickness of sample (cm)
l_{tr}	transport mean free path of photon (cm)
L	radiance ($W/(m^2\ sr)$)
n	refractive index of the medium
$Q(\bar{r},\hat{s},t)$	photon source term
$\bar{r}$	position vector (cm)
r	radial distance (cm)
$\hat{s},\hat{s}'$	unit vectors in the direction of flux of the photons
$S(\bar{r},t)$	source term

Greek:

$\phi(\bar{r},t)$	isotropic fluence rate (W/m^2)
λ	wavelength of light in media (cm)
μ_a	absorption coefficient (cm^{-1})
μ'_s	isotropic scattering coefficient (cm^{-1})
$\omega/2\pi$	modulation frequency (MHz)
θ'	phase shift angle (radians)
$\Delta\theta'_{rel}$	relative phase-shift (radians)
Ω,Ω'	solid angles of orientation about direction, $\hat{s}$ and $\hat{s}'$ (radians), respectively

References and Notes

1. Muzzio, F. J.; Robinson, P.; Wightman, C.; Brone, D. Sampling Practices in Powder Blending. *Int. J. Pharm.* **1997**, *155*, 153−178.
2. Burger, T.; Kuhn, J.; Caps, R.; Fricke, J. Quantitative Determination of the Scattering and Absorption Coefficients from Diffuse Reflectance and Transmittance Measurements: Applications to Pharmaceutical Powders. *Appl. Spectrosc.* **1997**, *51*, 309−317.
3. Sekulic, S. S.; Ward, H. W.; Brannegan, D. R.; Stanley, E. D.; Evans, C. L.; Sciavolino, S. T.; Hailey, P. A.; Aldridge, P. K. On-line Monitoring of Powder Blend Homogeneity by Near-Infrared Spectroscopy. *Anal. Chem.* **1996**, *68*, 509−513.
4. Cho, J.; Gemperline, P. J.; Aldridge, P. K.; Sekulic, S. S. Effective Mass Sampled by NIR Fiber-Optic Reflectance Probes in Blending Processes. *Anal. Chim. Acta* **1997**, *348*, 303−310.
5. Muhammud, S. A.; Illman, D. L.; Kowalski, B. R. *Chemometrics*; Wiley Publications: New York, 1986.
6. Adams, M. J. *Chemometrics in Analytical Spectroscopy*; Cambridge: England, 1995.
7. Duderstadt, J. J.; Hamilton, L. J. *Nuclear Reactor Analysis*; Wiley Publications: New York, 1976.
8. Davison, B.; Sykes, J. B. *Neutron Transport*; Oxford U. Press: London, 1958.
9. Ishimaru, A. *Wave Propagation and Scattering in Random Media*; Academic Press: New York, 1978, Vol. I.
10. Chandrashekhar, S. *Radiative transfer*; Oxford U. Press: London, 1960.
11. Haskell, R. C.; Svaasand, L. O.; Tsay, T. T.; Feng, T.; McAdams, M. S.; Tromberg, B. J. Boundary Conditions for the Diffusion Equation in Radiative Transfer. *J. Opt. Soc. Am.* **1994**, *11*, 2727−2741.

12. Welch A. J.; van Gemert M. J. C. *Optical-Thermal Response of Laser-irradiated Tissue*; Plenum Publishing Corporation: New York, 1995.
13. Alacala, J. R.; Gratton, E.; Jameson, D. M. A Multifrequency Phase Fluorometer Using the Harmonic Content of a Mode-Locked Laser. *Anal. Instr.* **1985**, *14*, 225−250.
14. Fishkin, J. B.; So, P. T. C.; Cerussi, A. E.; Fantini, S.; Franceschini, M. A.; Gratton, E. Frequency-Domain Method for Measuring Spectral Properties in Multiple-Scattering Media: Methemoglobin Absorption Spectrum in a Tissuelike Phantom. *Appl. Opt.* **1995**, *34*, 1143−1155.
15. Sevick, E. M.; Friscoli, J. K.; Burch, C. L.; Lakowicz, J. R. Localization of Absorbers in Scattering Media by Use of Frequency-Domain Measurements of Time-Dependent Photon Migration. *Appl. Opt.* **1994**, *33*, 3562−3570.

Acknowledgments

The authors are grateful to the NSF I/UCRC Center for Pharmaceutical Processing Research (CPPR) at Purdue University for their material and financial support for conducting this work.

JS990079+

Solubilization of Fluasterone

LUWEI ZHAO, PING LI, AND SAMUEL H. YALKOWSKY*

Contribution from *Department of Pharmaceutical Sciences, College of Pharmacy, The University of Arizona, Tucson, Arizona 85721.*

Received April 30, 1999. Accepted for publication July 30, 1999.

Abstract □ Solubilization of nonpolar drugs constitutes one of the most important tasks in parenteral formulations design. This study investigates and assesses the solubility enhancement of Fluasterone by various techniques including cosolvency, micellization, and complexation. Of the solubilizing agents used, the modified β-cyclodextrins were found to be the most effective. The solubility of Fluasterone is 1.55×10^{-4} mM, 3.13 mM, and 4.04 mM in water, 20% sulfobutyl ether-β-cyclodextrin (SBEβCD), and 20% hydroxypropyl-β-cyclodextrin (HPβCD), respectively.

Introduction

A structural analogue of dehydroepiandrosterone, Fluasterone (16α-fluoro-5-androsten-17-one, see Figure 1) has recently been developed for cancer treatment. The aqueous solubility of Fluasterone is 0.045 μg/mL (1.55×10^{-4} mM) and the desired dose is 1000 μg/mL (3.44 mM). This study evaluates Fluasterone solubilization by various techniques that are commonly encountered in parenteral formulation design.

The major approaches for increasing drug solubility are alteration of the solute or alteration of the solvent. Solvent modification is the most effective means of producing a thermodynamically stable increase in solubility.[1] The four most commonly used types of solubilizing agents are cosolvents, surfactants, complexation ligands, and pH control by buffers. With each technique, there is a maximum in the solubility that can be obtained. The choice of a solubilization technique also depends on many other factors: the physicochemical property of the drug molecule, the desired concentration, the effectiveness of the method, the safety and cost of solubilizing agents, and possible precipitation upon injection.

With Fluasterone of such low aqueous solubility, it is interesting to explore the effect on drug solubilization enhancement by using cosolvents, surfactants, and complexation ligands (cyclodextrins). The control of pH is not covered here since the drug has no ionizable group. The results obtained may provide guidance to the solubility improvement of other highly nonpolar drugs and steroidal compounds in particular.

Experimental Section

Materials—Fluasterone was used as provided by Aeson Therapeutics Inc., Tucson, AZ. Hydroxypropyl-β-cyclodextrin (HPβCD), with an average molecular weight of 1390 and an average degree of substitution of 4.4, was obtained from Cyclodextrin Technologies Development Inc. (Gainesville, FL). Sulfobutyl ether-β-cyclodextrin (SBEβCD), with an average molecular weight of 2162 and an average degree of substitution of 7, was a gift from CyDex, L.C. (Overland Park, KS). All other chemicals were of analytical or HPLC grade, purchased from Sigma and Aldrich.

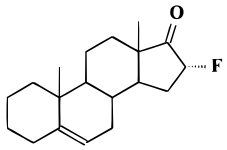

Figure 1—Structure of Fluasterone (MW: 290.42).

Solubility Measurement—The Fluasterone powder was added to vials containing various percentages of a variety of cosolvents, surfactants, or complexation ligands. The duplicate sample vials were prepared for each particular solubilizing agent at its particular concentration and were placed on an end-over-end mechanical rotator at 20 rpm at 25 °C for 6 days. Samples with drug crystals present were considered to have reached equilibrium and were removed from the rotator. The samples were then filtered through a 0.45-μm filter and diluted before injection into HPLC system.

The cosolvents used were ethanol (EtOH), propylene glycol (PG), and poly(ethylene glycol) 400 (PEG400) and glycerin. The surfactants were polyethylene sorbitan monolaurate (Tween 20), polyethylene sorbitan monooleate (Tween 80), and bile salts—sodium cholate, sodium deoxycholate, and sodium taurocholate. The complexation ligands were α-cylcodextrin (αCD), hydroxypropyl-β-cyclodextrin (HPβCD), sulfobutyl ether-β-cyclodextrin (SBEβCD), and hydroxypropyl-γ-cyclodextrin (HPγCD). The concentration ranges were given in Table 1.

HPLC Assay—A Beckman Gold HPLC system equipped with a model no. 168 detector at 220 nm was used for all assays. A Pinnacle octylamine column (150 cm × 4.6 mm, Restek, Bellefonte, PA) was used with a mobile phase composed of 75% acetonitrile in water. The flow rate was controlled at 1.1 mL/min. The retention time of Fluasterone was 6.2 min. The injection volume was 100 μL. The evaluation of the assay was conducted by using Fluasterone standard solutions at concentrations ranging from 0.001 to 0.1 mg/mL, intraday and interday, at the presence of different solubilization agents. The relative standard deviation was 1.05%. None of the solubilization agents interfere with the assay.

Results and Discussion

Cosolvency—Figure 2 shows the exponential increase in Fluasterone solubility with the increasing concentration of cosolvents EtOH, PG, PEG400. The semilogarithmic relationship between total drug solubility (D_{tot}) and cosolvent concentration (C) can be described by eq 1[2,3]

$$\log D_{tot} = \log D_u + \sigma C \qquad (1)$$

where D_u is drug solubility in water and σ is cosolvent solubilization power. The value of σ depends inversely on polarities of both the solute and the cosolvent. Similar solubilization curves were reported for hundreds of nonpolar compounds.[1]

For a single nonpolar solute, the value of σ depends only on cosolvent polarity. Table 1 indicates that Fluasterone solubility enhancement follows the cosolvent order as: EtOH (σ: 5.8) > PEG400 (σ: 4.9) > PG (σ: 4.1) (see Table

* To whom correspondence should be addressed. Tel: 520-626-1289; fax: 520-626-4063, e-mail: yalkowsky@pharmacy.arizona.edu.

10.1021/js9901413 CCC: $18.00
Published on Web 09/03/1999

Table 1—Solubilization Parameters for Fluasterone

excipent	concentration range, %	dependence of D_{tot} on D_u ([C]: excipient concentration[c])
EtOH	0–80 (v/v)	$10^{5.8\,[C]}$
PG	0–80 (v/v)	$10^{4.1\,[C]}$
PEG400	0–80 (v/v)	$10^{4.9\,[C]}$
glycerin	0–20 (v/v)[a]	$10^{1.1\,[C]}$
Tween 20	0–20 (v/v)	32 258 [C]
Tween 80	0–20 (v/v)	43 226 [C]
sodium cholate	0–20 (w/v)	43 871 [C]
sodium deoxycholate	0–20 (w/v)	55 484 [C]
sodium taurocholate	0–10 (w/v)[b]	24 516 [C]
HPβCD	0–20 (w/v)	180 000 [C]
SBEβCD	0–20 (w/v)	216 129 [C]
αCD	0–14 (w/v)[b]	645 [C]
HPγCD	0–20 (w/v)	19 355 [C]

[a] Maximum concentration prepared due to the increased viscosity of cosolvent solution. [b] Maximum concentrations prepared due to the limited solubility of the excipients. [c] The units for *C* are % for cosolvents and mM for surfactants and cyclodextrins.

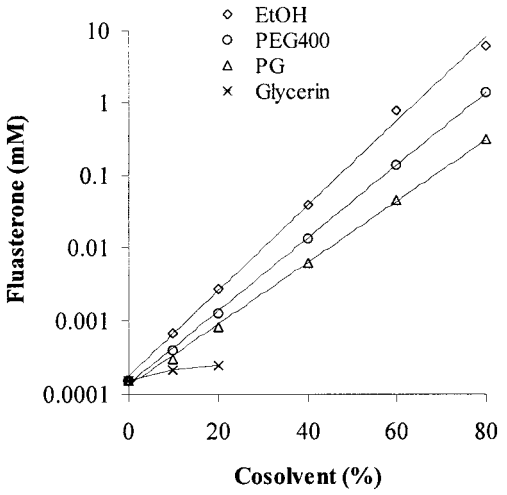

Figure 2—Effects of cosolvents on Fluasterone solubility.

1). Note that the unit for σ is $\%^{-1}$. Glycerin (σ: 1.1), up till 20%, only produces a negligible drug solubility increase, which can be explained by the fact that the glycerin is quite polar. The less polar the cosolvent, the more effective it is at disrupting hydrogen bonding interactions in water molecules. This in turn reduces the ability of the newly formed solvent (aqueous−cosolvent mixture) to squeeze out nonpolar solutes. As a result, nonpolar drugs such as Fluasterone can be solubilized most efficiently by EtOH, the least polar cosolvent.

Micellization—Figure 3 shows the effect of several representative surfactants on Fluasterone solubility. The relationship between the drug solubility and the surfactant micellar concentration is described by eq 2

$$D_{tot} = D_u + \kappa D_u S \qquad (2)$$

where S is the concentration of micellar surfactant (i.e., the total surfactant concentration minus the critical micellar concentration), and κ is the micellar partition coefficient. The product of κ and D_u reflects the number of surfactant molecules required to solubilize a solute molecule. Note that when the critical micellar concentration (CMC) is small, S can be approximated to the total surfactant concentration.

Figure 3 indicates that Fluasterone solubility enhancement is relatively small by Tween 20 or Tween 80 if less than 10% are used. The slightly higher κ value of Tween

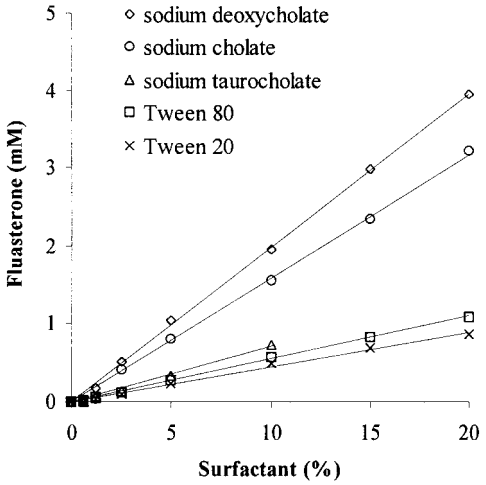

Figure 3—Effects of surfactants on Fluasterone solubility.

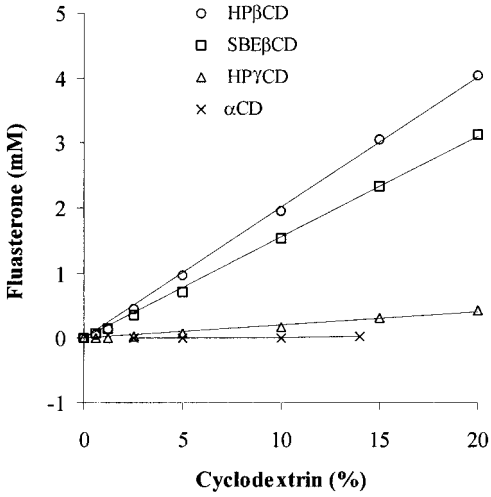

Figure 4—Effects of cyclodextrins on Fluasterone solubility.

80 is likely a result of its longer chains. Interestingly, two bile salts, both sodium cholate and sodium deoxycholate have solubilization capacities that are comparable to those of the polysorbates. These molecules are so arranged that all of the polar moieties are on one side and form a single diffused polar region.[1] As surface-active agents, the bile salts are known for their ability to form aggregates or small micelles in aqueous solutions.[4] Because it has a similar hydrocarbon backbone structure, Fluasterone is likely to fit efficiently into the bile salt micelles, and may even facilitate the formation of these micelles. The reason for the relatively low κ value for sodium taurodeoxycholate (24 516 M^{-1}) is not clear.

Complexation—Figure 4 shows that the effects of various cyclodextrins on Fluasterone solubility can be described by eq 3

$$D_{tot} = D_u + K D_u L \qquad (3)$$

where L is the total ligand concentration, and K is the complexation constant of the drug−ligand complex. As an equilibrium constant, K depends on the polarity and geometry of the solute and the compatibility between the solute and the cyclodextrin cavity. The linear rise in Fluasterone solubility as a function of the ligand concentration indicates that the drug−ligand complex has a one-to-one stoichiometry. This is commonly observed when the ligand concentration is low. Note that higher order complexes may form at relatively high ligand concentrations.

The modified β-cyclodextrins have been widely used and reportedly have higher solubilization capacity than natural βCD for most drugs.[5,6] Figure 4 shows that HPβCD and SBEβCD are better complexation ligands than both αCD and HPγCD, indicating that the 7 Å interior diameter of βCDs' cavity has greater ability to accommodate the Fluasterone molecule, most likely the ring A. The rationale is that the ring A with a 6.5 Å cross-sectional length is more nonpolar than ring D to which both a ketone group and a fluorine group are attached. In fact studies on most steroidal compounds such as testosterone have indicated that the ring A is indeed the part to be complexed into the βCD's cavity due to the matched sizes. Both αCD and HPγCD have the interior cavities that are either too tight (5 Å for αCD) or too loose (9 Å for HPγCD) for efficient incorporation of Fluasterone, which explains the small drug solubility increase by HPγCD and the negligible effect by αCD. It was also found that the solubilization capacity K by SBEβCD (216 129 M^{-1}) is slightly greater than that by HPβCD (180 000 M^{-1}), which is consistent with other reports.[7]

Choice of Technique—Cosolvents are employed in approximately 10% of FDA approved parenteral products.[8] The 10% ethanol−40% propylene glycol cosolvent system is commonly used in iv preparations such as digoxin, diazapam, and phenytoin. In this study the great impact of cosolvents on Fluasterone solubility is clearly shown in Figure 2. For example, the drug solubility is 2.8×10^{-3} mM, 3.96×10^{-2} mM, and 0.77 mM at EtOH concentration 20%, 40%, and 60%, respectively. However, cosolvent use has its clinical limitations: high concentrations often lead to high tonicity, high toxicity, and the precipitation of solubilized drugs upon injection or infusion which are associated with phlebitis.[9,10] Also, EtOH in concentration of greater than 10% may produce significant pain.[1]

Safety is the major concern in using surfactants: though numerous long-chain anionic, cationic, and nonionic surfactants are available as solubilizing agents, only Tween 80 have been used to significant extent in parenteral formulation (0.01−10%; e.g.: 10% in Amiodarone injection), while Tween 20 is much less (0.01−1.7%; e.g; 1.7% in multivitamin injection).[11] This is because surfactants are known to be toxic to blood, which restricts their use in parenteral preparations. With 10% of Tween 80, the drug solubility can be improved to 0.58 mM, but still far below the desired dose, while with 10% sodium cholate and 10% sodium deoxycholate, the drug solubility can be increased to 1.56 and 1.95 mM, respectively. It is of note, though, that the surfactants are very useful for low-dose parenteral preparations.

On the other hand, the complexation ligands HPβCD and SBEβCD provide an effective method for drug solubilization. Fluasterone concentrations of over 3 mM can be obtained with 20% HPβCD or 20% SBEβCD (4.04 mM and 3.13 mM, respectively). This is substantially higher than 60% of any cosolvents or 10% of any surfactants investigated. Clinically, the complexation offers an important benefit: it does not produce precipitation upon injection or upon dilution. Though not employed in any FDA-approved parenteral preparations,[8] cyclodextrins and the modified βCDs in particular have drawn enormous research interest over the past decade. The parent cyclodextrins have their drawbacks: in addition to the limited solubility, they are also found to have toxic effects on the kidney, which is the main organ for the removal of CDs in the proximal convoluted tubule after glomerular filtration. The chemically modified βCDs such as HPβCD and SBEβCD, however, have offered a much increased intrinsic solubility and much reduced renal toxicity.[12] It has been reported that SBEβCD is safe on acute dosing without the nephrotoxicity and membrane-destabilizing properties of parent βCD.[12−14] Currently SBEβCD is undergoing extensive chronic safety assessment.[15]

Conclusion

This study discussed and compared Fluasterone solubility enhancement by cosolvency, micellization, and complexation. It was found that solutions containing 20% of either SBEβCD or HPβCD enable the formulation of 3 mM Fluasterone that will not precipitate upon dilution.

References and Notes

1. Yalkowsky, S. H. *Solubility and solubilization in aqueous media*; Oxford University Press: New York, 1999.
2. Yalkowsky, S. H.; Roseman T. J. *Solubilization of drugs by cosolvents. In Techniques of solubilization of drugs*; Yalkowsky, S. H., Ed; Dekker: New York, 1981.
3. Yalkowsky, S. H.; Rubino, J. T. Solubilization of cosolvents 1: organic solutes in propylene glycol-water mixtures. *J. Pharm. Sci.* **1985**, *74*, 416.
4. Small, D. M. In *The bile acids: chemistry, physiology and metabolism*; Nair, P. P., Kritchevsky, D., Eds.; Plenum: New York, 1971; Vol. 1.
5. Pitha, J.; Milecki, J.; Fales, H.; Pannel, L.; Uekama, K. Hydroxypropyl-β-cyclodextrin: preparation and characterization: effects on solubility of drugs. *Int. J. Pharm.* **1986**, *29*, 73.
6. Uekama, K.; Otagiri, M. Cyclodextrins in therapeutic drug carrier systems. In *CRC Critical reviews in therapeutic drug carrier systems*; CRC Press: Boca Raton, FL, 1987.
7. Rajewski, R. A.; Stella, V. J. Pharmaceutical applications of cyclodextrins. 2. In vivo drug delivery. *J. Pharm. Sci.* **1996**, *85*, 1142.
8. Sweetana, S.; Akers, M. J. Solubility principles and practices for parenteral drug dosage form development. *PDA J. Pharm. Sci., Technol.* **1996**, *5*, 50.
9. Selander, D.; Curelaru, I.; Stefansson, T. Local discomfort and thrombophlebitis following intravenous injection of diazepam. *Acta Anesth. Scand.* **1981**, *25*, 516.
10. Yalkowsky, S. H.; Krzyzaniak, J. F., Ward, G. H. Formulation-related problems associated with intravenous drug delivery. *J. Pharm. Sci.* **1998**, *87*, 787.
11. Powell, M. F.; Nguyen, T.; Baloian, L. Compendium of Excipients for Parenteral Formulations. *PDA J. Pharm. Sci. Technol.* 52, **1998**, *5*, 238.
12. Mesems, J. L.; Putteman, P.; Verheyen, Pharmaceutical applications of 2-hydroxypropyl-β-cyclodextrin. In *New Trends in Cyclodextrins and Derivatives*; Duchene, D., Ed.; Editions de Sante: Paris, 1991.
13. Brewster, M. E.; Simpkins, J. W.; Hora, M. S.; Stern, W. C.; Bodor, N. The potential use of cyclodextrins in parenteral formulations. *J. Parent. Sci. Technol.* **1989**, *43*, 231.
14. Rajewski, R. A.; Traiger, G.; Bresnahan, P.; Jaberaboansari, P.; Stella, V. J.; Thompson, D. O. Preliminary safety evaluation of paraenterally administered sulfoalkyl ether β-cyclodextrin derivatives. *J. Pharm. Sci.* **1995**, *84*, 927.
15. Okomoto, K.; Rajewski, R. A.; Uekama, K.; Jona, J. A.; Stella, V. J. The interaction of charged and uncharged drugs with neutral (HPβCD) and anionically charged (SBE7βCD) β-cyclodextrins. *Pharm. Res.* **1996**, *13*, 256.

JS9901413

Heptakis(2,6-di-*O*-methyl-3-*O*-acetyl)-β-cyclodextrin: A Water-Soluble Cyclodextrin Derivative with Low Hemolytic Activity

FUMITOSHI HIRAYAMA, SHIUHEI MIEDA, YUJI MIYAMOTO, HIDETOSHI ARIMA, AND KANETO UEKAMA*

Contribution from *Kumamoto University, 5-1 Oe-honmachi, Kumamoto 862-0973, Japan.*

Received April 20, 1999. Accepted for publication July 23, 1999.

Abstract □ Acetyl groups were introduced to the hydroxyl groups of heptakis(2,6-di-*O*-methyl)-β-cyclodextrin (DM-β-CyD), and the resulting heptakis(2,6-di-*O*-methyl-3-*O*-acetyl)-β-CyD (DMA-β-CyD) was evaluated for the inclusion property and hemolytic activity. It was confirmed by means of NMR and mass spectroscopies that in the DMA-β-CyD molecule, all seven hydroxyl groups at the 3-position were substituted by acetyl groups. Thus, it has the degree of substitution (DS) of 7, whereas DMA4-β-CyD with the lower substitution (DS 3.8) was a mixture of components with different DS. The aqueous solubility of DMA-β-CyD was higher than those of β-CyD, DM-β-CyD, and heptakis(2,3,6-tri-*O*-methyl)-β-CyD (TM-β-CyD). The hydrophobicity of the whole molecule, assessed from measurements of surface tension, increased in the order of DM-β-CyD < DMA-β-CyD < TM-β-CyD. The half-life of DMA-β-CyD for hydrolysis in pH 9.5 and 60 °C was about 19 h, and there was only slight liberation of acetic acid in rabbit plasma and carboxylesterase (EC 3.1.1.1) at 37 °C. DMA-β-CyD had an inclusion ability similar to that of TM-β-CyD for *p*-hydroxybenzoic acid esters with different alkyl chain lengths and an antiinflammatory drug, flurbiprofen, although it was inferior to that of DM-β-CyD. The hemolytic activity and rabbit muscular irritation of DMA-β-CyDs were much weaker than those of DM-β-CyD: no hemolysis was observed even in the presence of 0.1 M DMA-β-CyD with DS 7. The results suggest that the water-soluble CyD derivative with superior bioadaptability and inclusion ability can be prepared by properly designing substituents at the 3-position and by optimally controlling their degree of substitution.

Introduction

Cyclodextrins (CyDs) are cyclic oligosaccharides usually consisting of six to eight glucose units and are used successfully as drug carriers with improved levels of solubility, stability, and bioavailability, etc.[1−3] Recently, various kinds of CyD have been prepared in order to improve physicochemical properties and inclusion capacities of parent CyDs.[4−6] For example, hydrophilic CyD derivatives such as methylated, hydroxyalkylated, and branched CyDs are useful for the improvement of low solubility, dissolution rate, and bioavailability of poorly water-soluble drugs.[7,8] On the other hand, hydrophobic CyDs such as ethylated and acylated derivatives have potential as sustained release carriers for water-soluble drugs.[9,10] Among these derivatives, heptakis(2,6-di-*O*-methyl)-β-CyD (DM-β-CyD) is of interest because of its powerful solubilizing ability for the majority of lipophilic drugs such as steroid hormones,[11] vitamins A, E, and K,[12,13] cyclosporin A,[14] and long chain fatty acids.[15] However, one of the drawbacks of DM-β-CyD is its membrane toxicity, causing tissue irritation and hemolysis in a concentration-dependent manner.[16] For example, the concentration of DM-β-CyD to induce 50% hemolysis of human erythrocytes is lower than that of the so-called bioadaptable CyD derivatives such as 2-hydroxypropyl-β-CyD, sulfobutyl ether of β-CyD, and maltosyl-β-CyD.[17−23] The hemolytic activity of CyDs is associated with the extraction of membrane components, mainly through inclusion complexation with cholesterol. In this study, we have attempted to reduce the membrane toxicity of DM-β-CyD, through a chemical modification of hydroxyl groups at the 3-position of glucose units of DM-β-CyD. As a first step of the modification, acetyl groups were introduced to the hydroxyl groups, and the resulting heptakis(2,6-di-*O*-methyl-3-*O*-acetyl)-β-CyD (DMA-β-CyD) was evaluated for the inclusion property, the hemolytic activity, and muscular tissue irritation.

Experimental Section

Materials—β-CyD, DM-β-CyD, and heptakis(2,3,6-tri-*O*-methyl)-β-CyD (TM-β-CyD) were supplied by Japan Maize Co. (Tokyo, Japan). Flurbiprofen, 2-(2-fluoro-4-biphenylyl)propionic acid, was donated by Mitsubishi Kasei Co. (Tokyo, Japan), and *p*-hydroxybenzoic acid esters with different alkyl groups were purchased from Tokyo Kasei Co. (Tokyo, Japan). All other chemicals and solvents were of analytical reagent grade, and deionized double-distilled water was used throughout the study.

Apparatus—Nuclear magnetic resonance (NMR) spectra were taken on a JEOL JNM-α 500 instrument (Tokyo, Japan) operating at 500.16 MHz for protons at 25 °C. The concentration of DMA-β-CyDs was 1.0×10^{-2} M in deuterated chloroform ($CDCl_3$), and the chemical shifts were given as parts par million (ppm) downfield from that of tetramethylsilane. Fast atom bombardment mass (FAB-MS) spectra were measured in a negative mode at 25 °C by a JEOL JMS-DX 303 mass spectrometer (Tokyo, Japan) using the matrix (methanol/glycerol/*m*-nitrobenzyl alcohol). Ultraviolet (UV), fluorescence, and circular dichroism (CD) spectra were measured at 25 °C using Hitachi U-2000 UV and F-4010 fluorescence spectrometers (Tokyo, Japan) and a Jasco J-720 polarimeter (Tokyo, Japan), respectively. Surface tension was measured at 25 °C by a Shimadzu duNouy surface tensionmeter (Kyoto, Japan).

Preparation of DMA-β-CyD—Dried DM-β-CyD (10 g, 7.5 mmol) was dissolved in dried pyridine (50 mL), acetic anhydride (10.7 g, 105 mmol) was added dropwise for 2−3 h, and the mixture was stirred at 80 °C for about 24 h. The reaction was terminated by addition of ice−water, and the resulting oil was extracted with chloroform. The organic phase was washed with 2 mM sodium carbonate and in turn with water, dried with anhydrous sodium sulfate, and evaporated under reduced pressure. The residue was subjected to silica gel chromatography (Kieselgel 60, 0.063−0.2 mm, 70−200 mesh) with an eluent of methanol/chloroform increasing the methanol concentration from 0 to 12% v/v. DMA-β-CyD (DS 7) was recrystallized from water and obtained as white crystals (yield 60%). Mp 126 °C; TLC $R_f = 0.3$ (silica gel 60 F_{254}, methanol/chloroform 2:15 v/v); FAB MS (negative mode) *m*/*z* 1777 [M + *m*-nitrobenzyl alcohol (matrix) − H)$^-$; ^{1}H NMR ($CDCl_3$) δ 5.16 (t, 1H, CyD H-3), 5.00 (d, 1H, CyD H-1), 3.91−3.87 (m, 2H, CyD H-5 and H-6b), 3.79 (t, 1H, CyD H-4), 3.54 (d, 1H, CyD H-6a), 3.37 (s, 3H, 6-CH_3), 3.33 (s, 3H, 2-CH_3), 3.21 (dd, 1H, CyD H-2), 2.04 (s, 3H, 3-CH_3). DMA4-β-CyD with a low degree of substitution

* To whom correspondence should be addressed. Telephone and fax: (+81−96)-371−4160. e-mail: uekama@gpo.kumamoto-u.ac.jp.

10.1021/js990128i CCC: $18.00
Published on Web 09/17/1999

(DS) was prepared by using small amounts of the acid anhydride (4.6 g, 45 mmol) versus DM-β-CyD (10 g, 7.5 mmol). The other condition of preparation was identical to that described above, except for the recrystallization due to the fact that it was a mixture of components with different DS. The residue after the extraction and evaporation was subjected to the silica gel chromatography described above, and the factions containing acetylated DM-β-CyDs (TLC $R_f = 0.4-0.5$, silica gel 60 F_{254}, methanol/chloroform 2:15 v/v) were collected and evaporated under reduced pressure. DMA4-β-CyD was obtained as white powder (yield 80%). It was confirmed that DMA4-β-CyD contains neither DM-β-CyD (R_f = 0.7) nor DMA-β-CyD (DS 7, $R_f = 0.3$) by TLC analysis and no solvents such as methanol and chloroform by ^{1}H-MMR spectroscopy. The DS value was determined by a peak ratio of the CyD anomeric or skeleton protons and the methyl proton of acetyl groups in ^{1}H NMR spectra (see Supporting Information), and was 3.8. This value coincided with that (DS = 3.9 ± 0.1) determined by the amount of acetic acid released after alkaline hydrolysis in 2.0 N NaOH solution. Unfortunately, the mass spectroscopic determination of DS was difficult because of the partial degradation of DMA4-β-CyD to DM-β-CyD during the ionization.

Solubility Measurements—The solubility method was carried out according to the method of Higuchi and Connors.[24] The screw-capped vials containing drugs in excess amounts in aqueous CyD solutions at various concentrations ($1.0-5.0 \times 10^{-2}$ M) were shaken at 25 °C. After equilibrium was attained (about 5 days), the solution was centrifuged at 800*g* force for about 5 min, and the supernatant was filtered through a membrane filter (Advantec DISMIC-3CP (TOYO−Roshi), Tokyo, Japan) and analyzed for drugs by high-performance liquid chromatography (HPLC) under the following condition: a Hitachi L-6000 pump and an L-4000 UV detector (Tokyo, Japan) at 256 nm, a YMC AM-312 column (6.0 × 150 mm), flow rate of 1.0 mL/min. The mobile phases for the analysis of flurbiprofen and *p*-hydroxybenzoic acid esters were methanol/0.1 M acetic acid (7:3 v/v) and methanol/water (7:3 v/v), respectively. The stability constants ($K_{1:1}$) of 1:1 complexes were calculated from the slope and intercept of straight line of the phase solubility diagram according to the equation of Higuchi and Connors.[24] In the case of phase solubility diagrams with positive curvature, the diagrams were analyzed according to the method of Kristiansen[25] to obtain the 1:1 and 1:2 ($K_{1:2}$, guest:host) stability constants.

Hydrolysis Studies—Alkaline hydrolysis of DMA-β-CyD (1.0×10^{-2} M) was conducted in 0.1 M phosphate buffers (pH 8.5−11.5) at 60 °C. At timed intervals, the reaction solution (20.0 μL) was sampled and analyzed for the resulting acetic acid by HPLC under the following condition: a YMC AP-303 column (4.6 × 250 mm), a mobile phase of 0.1% phosphoric acid, a flow rate of 1.0 mL/min, a detection of 210 nm. The hydrolysis was monitored by measuring acetic acid at an early stage of the reaction (240 min, 150, 120, and 30 min at pH 8.5, 9.5, 10.5, and 11.5, respectively), because the pH of the solution changed due to the liberation of acetic acid. The rate constant (k) was calculated according to the following equation: $\ln(7C_0 - C) = -kt + \ln 7C_0$, where C_0 and C are the initial concentration of DMA-β-CyD and the concentration of the liberated acetic acid at time t, respectively. The total concentration of acetic acid at infinite time is supposed to be $7C_0$.

Carboxylesterase-catalyzed hydrolysis of DMA-β-CyD was conducted in 0.1 M *N*-(2-hydroxyethyl)piperazine-*N*′-ethanesulfonic acid (HEPES)/NaOH buffer solution (pH 7.4) at 37 °C. The concentrations of DMA-β-CyD and the enzyme (EC 3.1.1.1 obtained from porcine liver, purchased from Sigma Aldrich Japan, Tokyo) were 5.0×10^{-3} M and 0.25 or 25 units/mL, respectively. At timed intervals, an aliquot (20.0 μL) was sampled and analyzed for acetic acid by HPLC under the aforementioned condition.

Hydrolysis of DMA-β-CyD was conducted in 50% and 80% rabbit plasma at 37 °C. Rabbit blood was taken by heparinized injection syringe and centrifuged at 12000*g* for 5 min at 4 °C. DMA-β-CyD solution (1.0 mL, 2.0×10^{-2} M in pH7.4 isotonic phosphate buffer) was added to the plasma (1.0 mL). At appropriate times, an aliquot (0.3 mL) of the reaction solution was ultrafiltered using a membrane filter (Amicon Kit (Tokyo, Japan), a centrifugation of 2000*g* for 15 min at 4 °C), and the filtrate was analyzed for acetic acid by HPLC under the aforementioned condition.

Hemolysis Studies—Erythrocytes were separated by centrifugation of freshly drawn citrated rabbit blood at 1000*g* for 5 min, washed three times with phosphate buffer (0.154 M sodium chloride and 0.01 M phosphate, pH 7.4), and resuspended in the buffer solution to give a hematocrit of 5%. The cell suspension (0.1 mL) was added to the buffer solution (2.0 mL) containing β-CyDs at various concentrations. Each mixture was incubated for 30 min at 37 °C and centrifuged at 1000*g* for 5 min. The release of hemoglobin from the cells was measured spectrophotometrically at 543 nm. Results were expressed as percentages of the total efflux of hemoglobin which was obtained when water was used instead of the buffer solution. The morphological observation of erythrocytes was carried out as follows: the cell suspension (5%, 0.1 mL) was incubated with the buffer solution (2.0 mL) containing β-CyDs at 37 °C for 60 min, and fixed with 2% glutaraldehyde solution (5.0 mL). After standing for 1 h at room temperature, the fixed cells were washed three times with water, dried under reduced pressure for 16 h, coated with gold, and observed by scanning electron microscope (Akashi, MSM4C, Tokyo, Japan).

Determination of cholesterol: the cell suspension (5%, 0.2 mL) was incubated with the buffer solution (4.0 mL, pH 7.4) containing β-CyDs at 37 °C for 30 min. After centrifugation (1000*g*, 5 min), cholesterol in the supernatant (3.0 mL) was extracted with chloroform (5.0 mL), the organic phase was evaporated under reduced pressure, and cholesterol in the residue was determined by the cholesterol oxidase method with using a Cholesterol E-test kit (Wako, Osaka, Japan). Results were expressed as percentages of the total amount of cholesterol which was released when water was used instead of the buffer solution.

Intramuscular Irritation Studies—The intramuscular irritation study was carried out by the method of Shintani et al.[26] β-CyD solutions (100 mg/1.0 mL of normal sterile saline) were injected into *M. vastus lateralis* of three rabbits (2.5−3.0 kg) using a 23-gauge 0.5 in. needle. The rabbits were killed 2 days after the injection, the muscle was exposed and cut longitudinally, and the lesion were scored according to the method of Shintani et al.,[26] that is, score 0, no discernible gross reaction; score 1, slight hyperemia and discoloration; score 2, moderate hyperemia and discoloration; score 3, distinct discoloration in comparison with the color of surrounding area; score 4, brown degeneration with small necrosis; score 5, widespread necrosis.

Results and Discussion

Some Physicochemical Properties of DMA-β-CyD—It was confirmed by means of NMR and mass spectroscopies that in DMA-β-CyD molecule, all seven hydroxyl groups at the 3-position were substituted by acetyl groups, thus having DS 7. DMA4-β-CyD with the lower substitution (DS 3.8) was a mixture of components with different DS. In the following evaluation of physicochemical and inclusion properties, DMA-β-CyD with DS 7 was employed, and the lower DS form was used only for comparative studies of hemolysis and muscular irritation.

The melting point decreased in the order, DM-β-CyD (295−300 °C), the parent β-CyD (280 °C), TM-β-CyD (157 °C), and DMA-β-CyD (126 °C). The aqueous solubility of DMA-β-CyD (>60 g/dL at 25 °C) was much higher than those of the parent β-CyD (1.85 g/dL), DM-β-CyD (57 g/dL), and TM-β-CyD (31 g/dL); however, DMA-β-CyD ≥ 70%w/v gave a viscous solution. DMA-β-CyD exhibited an exothermic dissolution in water in the similar manner as DM- and TM-β-CyDs[27] and thus precipitated at higher temperature. The hydrophobicity of DMA-β-CyD was assessed by measurements of the surface tension, because the oil/water partition method is affected by the inclusion of organic solvents in the CyD cavity. As shown in Figure 1, the surface tension of DMA-, DM-, and TM-β-CyDs decreased as the concentration increased, and the hydrophobicity of the whole molecule increases in the order of DM-β-CyD < DMA-β-CyD < TM-β-CyD. This order was in accordance with that of the π value of the substituents introduced at the hydroxyl groups, that is, −0.67 (OH of DM-β-CyD) < −0.64 (OCOCH$_3$ of DMA-β-CyD) < −0.02 (OCH$_3$ of TM-β-CyD).[28] The hydrolysis of DMA-β-CyD in alkaline solution was studied by monitoring the resulting acetic acid, because it was difficult to determine partially hydrolyzed

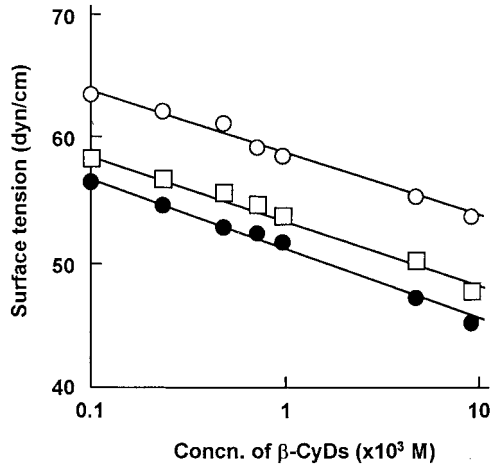

Figure 1—Surface tension of DMA-β-CyD (□), DM-β-CyD (○), and TM-β-CyD (●) in water at 25 °C.

DMA-β-CyDs having various regioisomers by means of HPLC. The hydrolysis was followed at an early stage of the reaction, because pH of the solution changed owing to the liberation of acetic acid. The appearance rates of acetic acid from DMA-β-CyD were 9.0 ($\pm$1.5) $\times$ 10^{-5} min^{-1} (mean ($\pm$SE), n = 3, pH 8.5), 6.2 ($\pm$0.2) $\times$ 10^{-4} min^{-1} (pH 9.5), 2.1 ($\pm$0.1) $\times$ 10^{-3} min^{-1} (pH 10.5), and 1.9 ($\pm$0.1) $\times$ 10^{-2} min^{-1} (pH 11.5) at 60 °C, giving the linear rate−pH profile (correlation coefficient = 0.990) with a slope of 0.75. The carboxylesterase-catalyzed hydrolysis of DMA-β-CyD was conducted at concentrations of 5.0 $\times$ 10^{-3} M of DMA-β-CyD and 0.25 or 25 units/mL of the esterase in HEPES buffer (pH 7.4) at 37 °C. No liberation of acetic acid (less than the detection limit of 3%) in the 0.25 units/mL enzyme solution was observed for 10 h, and the releases even in the 25 units/mL enzyme solution were less than 5% and 15% of the total amounts of acetic acid for 5 and 10 h, respectively. Furthermore, no liberation of acetic acid (less than 3%) was observed in 50% and 80% plasma of rabbits for 12 h, suggesting that DMA-β-CyD is chemically stable in biological fluids such as plasma.

Inclusion Property of DMA-β-CyD—The inclusion property of DMA-β-CyD was compared with those of the parent β-CyD and DM- and TM-β-CyDs. Table 1 shows the results of phase solubility diagrams of β-CyDs with *p*-hydroxybenzoic acid esters with different alkyl chains. The guest molecules with short alkyl chains showed A_L type phase solubility diagrams where the solubility of the guests increased linearly as a function of CyD concentrations (0−0.02 M), indicating the 1:1 complexation.[24] On the other hand, the ester with longer alkyl chains showed A_P type diagrams where the solubility curve deviated positively from a straight line, indicating the 1:2 (guest:host) complexation.[25] The stability constant of the 1:1 complexes increased as the alkyl chain lengthens up to the propyl ester, whereas the butyl ester formed the 1:2 complex with DMA-β-CyD and the hexyl eater formed the 1:2 complex with the three CyDs. The stability constants were generally in the order of DM-β-CyD ≫ TM-β-CyD ≈ DMA-β-CyD.

Table 1—Stability Constants ($K_{1:1}$ and $K_{1:2}$, M^{-1})[a] and Types of Phase Solubility Diagrams for Inclusion Complexes of *p*-Hydroxybenzoic Acid Esters with β-CyDs in Water at 25 °C

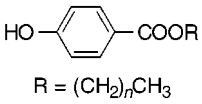

	DM-β-CyD			TM-β-CyD			DMA-β-CyD		
ester	$K_{1:1}$	$K_{1:2}$	type	$K_{1:1}$	$K_{1:2}$	type	$K_{1:1}$	$K_{1:2}$	type
methyl	230	–	A_L	63	–	A_L	35	–	A_L
ethyl	960	–	A_L	120	–	A_L	140	–	A_L
propyl	5600	–	A_L	300	–	A_L	470	–	A_L
butyl	slope > 1[b]	–	A_L	290	–	A_L	46	110	A_P
hexyl	3400	90	A_P	1000	40	A_P	110	120	A_P

[a] Average of the values for duplicate measurements, which coincided with each other within ±5%. [b] Could not be determined due to the slope > 1.

Spectroscopic studies on the interaction of flurbiprofen with DMA-β-CyD was carried out, because the complexation of the drug with DM- and TM-β-CyDs had been investigated in detail.[29] Figure 2 shows the UV, CD, and fluorescence spectra of flurbiprofen in the absence and presence of DM-, TM-, and DMA-β-CyDs in pH 7.0 phosphate buffer. Flurbiprofen gave a UV absorption maximum (λ_{max}) at 246 nm, and by the addition of β-CyDs the intensity decreased with concomitant shifts to longer wavelength. This bathochromic shift was largest with DMA-β-CyD (λ_{max} 251 nm) compared with those of DM-β-CyD (249 nm), TM-β-CyD (249 nm), and β-CyD (247 nm),

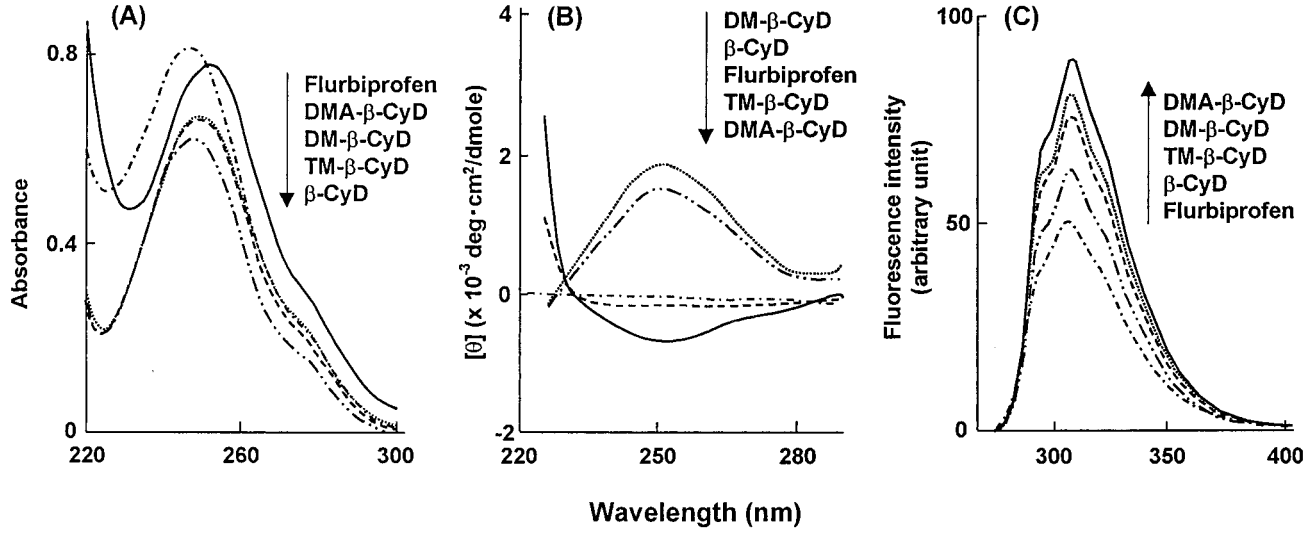

Figure 2—UV (A), CD (B), and fluorescence (C) spectra of flurbiprofen in the absence (–·–) and presence of DMA-β-CyD (—), β-CyD (–··–), DM-β-CyD (····) and TM-β-CyD (---) in 0.1 M phosphate buffer (pH 7.4, I = 0.2) at 25 °C. The concentrations of flurbiprofen and β-CyDs in UV and CD spectroscopic studies were 4.0 $\times$ 10^{-5} M and 4.0 $\times$ 10^{-3} M, respectively, and those in fluorescence spectroscopic studies were 1.0 $\times$ 10^{-6} M and 1.0 $\times$ 10^{-3} M, respectively. The excitation wavelength was 256 nm.

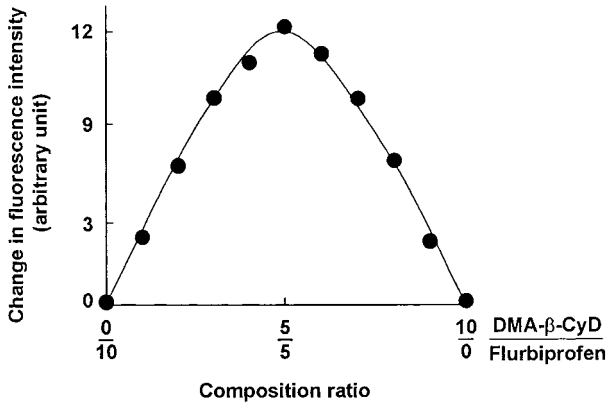

Figure 3—Continuous variation plot for flurbiprofen/DMA-β-CyD system (total concentration of the host and guest molecules = 5.0×10^{-6} M) in 0.1 M phosphate buffer (pH 7.4, $I = 0.2$) at 25 °C.

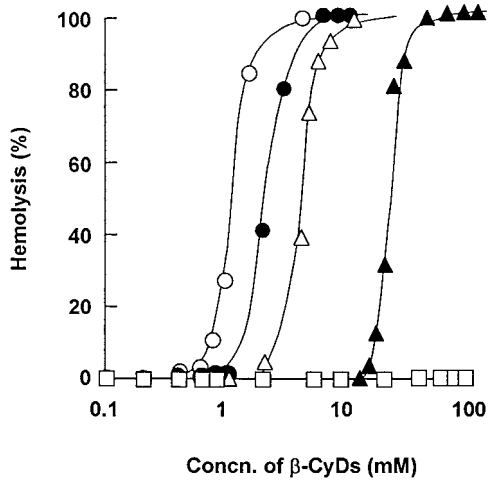

Figure 4—Hemolytic effects of β-CyDs on rabbit erythrocytes in isotonic phosphate buffer (pH 7.4) at 37 °C. Key: (□) DMA-β-CyD; (▲) DMA4-β-CyD; (△) β-CyD; (○) DM-β-CyD; (●) TM-β-CyD.

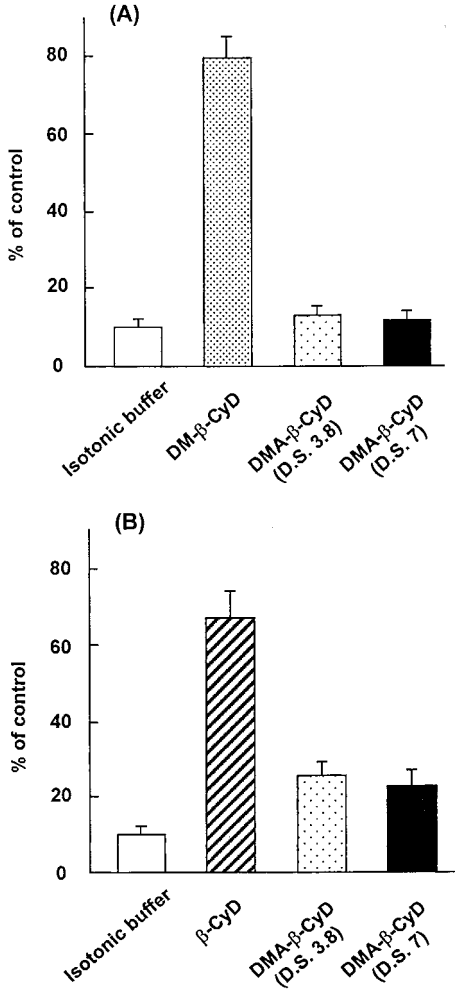

Figure 5—Cholesterol release from intact erythrocytes of rabbits treated with β-CyDs (A, 0.5 mM; B, 3.0 mM) in isotonic phosphate buffer (pH 7.4) at 37 °C. Each value represents the mean ± SE of three experiments.

although the intensity change was small with DMA-β-CyD. In the CD spectra, the optical activity of flurbiprofen was induced positively by the addition of DM-β-CyD and β-CyD, whereas it was induced negatively by DMA-β-CyD and TM-β-CyD where the effect of DMA-β-CyD was larger than that of TM-β-CyD. The sign of CyD-induced CD bands depends on a spatial relationship between the asymmetric center of CyD cavity and the perturbed chromophore of guest molecules. For example, the electronic transition of an included guest with a transition dipole moment, parallel to the z-axis of the CyD cavity, gives a positive CD, and that with a transition dipole moment perpendicular to the z-axis gives a negative CD.[30] Our crystallographic studies indicated that flurbiprofen is included in such a manner that the long molecular axis of the drug is parallel to the z-axis of the β-CyD cavity, that is, an axial inclusion, whereas the long axis of the drug is inclined in the TM-β-CyD cavity.[31,32] These dispositions of flurbiprofen in CyD cavities were reflected in the sign of induced CD bands, giving a positive CD with β-CyD and a small negative CD with TM-β-CyD. DMA-β-CyD gave a larger negative CD band than TM-β-CyD, suggesting that the drug is more inclined in the former cavity than in the latter cavity. The fluorescence intensity of flurbiprofen at 315 nm was markedly increased in the order of β-CyD < TM-β-CyD < DM-β-CyD < DMA-β-CyD. Since the fluorescence of the drug is known to be increased significantly in organic solvents such as ethanol, the CyD-induced fluorescence change suggested that the drug is included within the hydrophobic CyD cavity. The largest enhancement of the fluorescence by DMA-β-CyD may be attributable to the increase in hydrophobicity of the cavity, although the hydrophobicity of the whole molecule of DMA-β-CyD was lower than that of TM-β-CyD as is apparent from the surface tension. The methyl moieties of acetyl groups in the DMA-β-CyD molecule seem to be directed inside the cavity, while the carbonyl moieties are directed outside the cavity, providing a more hydrophobic environment of the cavity. On the other hand, TM-β-CyD is known to have the distorted macrocyclic ring in which the secondary rim is wider whereas the primary rim is narrower,[33] thus allowing water molecules easily to access the inside of the cavity. This may be a reason the fluorescence enhancement of TM-β-CyD was smaller than DMA-β-CyD, despite the higher hydrophobicity of TM-β-CyD as a whole molecule. Figure 3 shows a continuous variation plot of the fluorescence intensity at 310 nm of the flurbiprofen/DMA-β-CyD system. The plot gave a maximum at 0.5, indicating the 1:1 stoichiometry which was the same as that of β-CyD, DM-β-CyD, and TM-β-CyD complexes.[29] Therefore, the fluorescence change as a function of concentrations of the four β-CyDs was analyzed quantitatively by the Scott equation[34] to obtain the stability constant ($K_{1:1}$) of the 1:1 complexes. The $K_{1:1}$ values in pH 7.0 phosphate buffer at 25 °C were 3610 (±120) M^{-1} (mean (± SE), $n = 3$), 8060 (±600) M^{-1}, 1660 (±80) M^{-1}, and 1410 (±80) M^{-1} for the complexes with β-CyD, DM-β-CyD, TM-β-CyD, and DMA-β-CyD, respectively. Furthermore, the phase solubility diagram of flur-

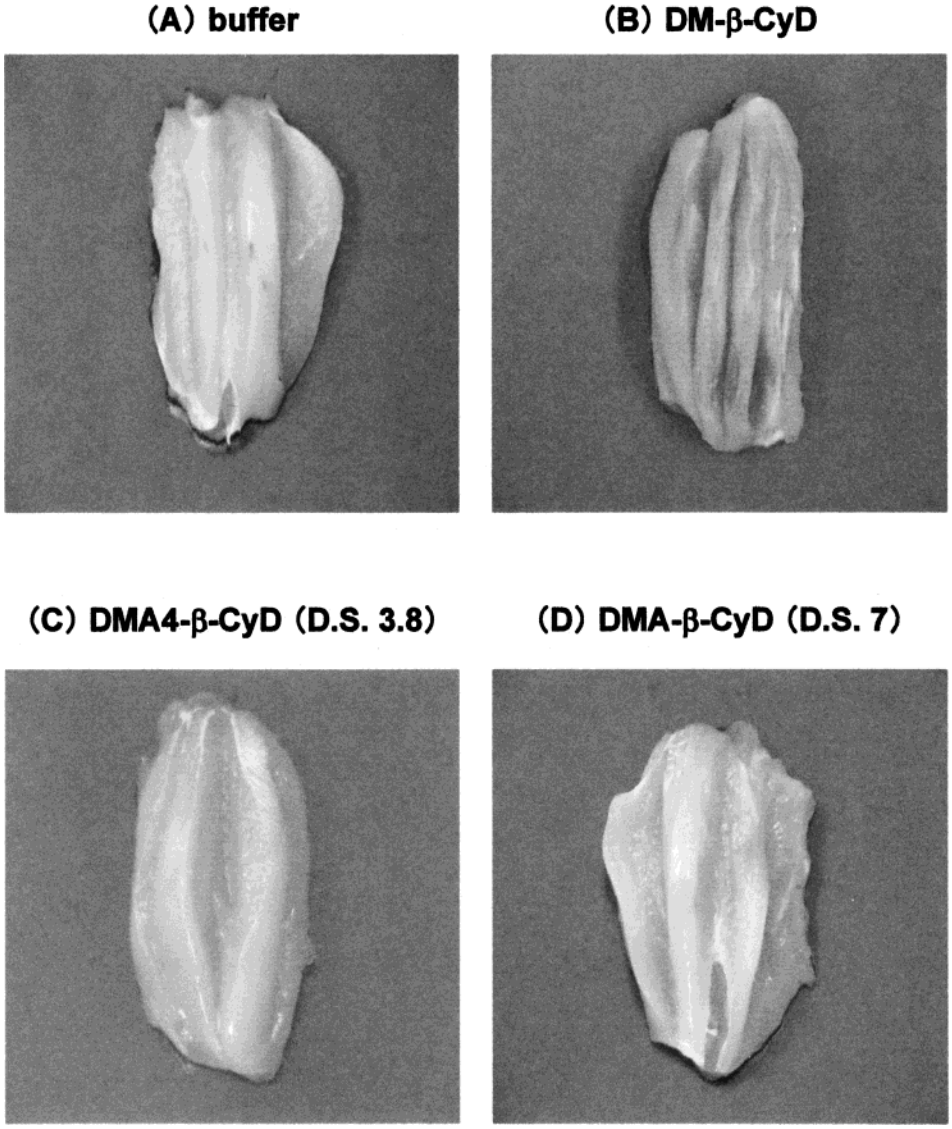

Figure 6—Macrographs of *M. vastus lateralis* after intramuscular injections of β-CyDs (100 mg/site, 1.0 mL) to rabbits. (A) Isotonic buffer; (B) DM-β-CyD; (C) DMA4-β-CyD; (D) DMA-β-CyD.

biprofen with DMA-β-CyD ($0.0-5.0 \times 10^{-2}$ M) in water at 25 °C showed the A_L type and gave the stability constant of 2020 ($\pm$90) M^{-1}. This value was the same as that (2200 ($\pm$110) M^{-1}) of the TM-β-CyD complex, but was smaller than that (14700 ($\pm$900) M^{-1}) of the DM-β-CyD complexes determined under the same conditions. The stability constants determined by the fluorescence method in pH 7.0 phosphate buffer were smaller than those determined by the solubility method in water, which may be due to the acid-ionization of flurbiprofen (pK_a 3.8). These results suggested that DMA-β-CyD has the same inclusion ability as TM-β-CyD, although it is inferior to that of DM-β-CyD, and the hydrophobicity of the DMA-β-CyD cavity is higher than that of TM-β-CyD.

Hemolysis and Muscular Irritation of DMA-β-CyD—Hemolytic activity of DMA-β-CyDs was compared with that of other CyD derivatives in order to estimate its local irritation. Figure 4 shows hemolysis profiles of β-CyD, DM-β-CyD, TM-β-CyD, and DMA-β-CyDs with different DS (7 and 3.8), measured under the same conditions. It is apparent that the hemolytic activity of DMA-β-CyDs was weaker than those of β-CyD, DM-β-CyD, and TM-β-CyD. For example, the hemolysis began at about 2 mM, 0.5 mM, and 1 mM, and the concentrations to induce 50% hemolysis were about 4 mM, 1 mM, and 2 mM for β-CyD, DM-β-CyD, and TM-β-CyD, respectively. On the other hand, the hemolysis of DMA4-β-CyD with DS 3.8 began at about 12 mM, and its 50% hemolysis concentration was about 22 mM. In the case of DMA-β-CyD with DS 7, no hemolysis was observed up to 100 mM. Scanning electron micrographic studies indicated no change in the shape of erythrocytes even at a concentration of 100 mM DMA-β-CyD, that is, they maintained the discocyte shape same as that in the buffer control (Supporting Information). One of the causes of CyD-induced hemolysis is known to be extractions of cholesterol and phospholipids from erythrocytes through the inclusion complex formation.[16] Therefore, the cholesterol release behavior from rabbit erythrocytes by the addition of DMA-β-CyDs was investigated and compared with those of β-CyD and DM-β-CyD. Figure 5 shows the released amounts of cholesterol from the intact erythrocytes of rabbits treated with β-CyDs in 0.1 M phosphate buffer (pH 7.4) at 37 °C. DM-β-CyD induced about 80% release of cholesterol at a concentration of 0.5 mM at which the hemolysis only slightly occurred (see Figure 4). On the other hand, DMA-β-CyDs induced only 10% release of cholesterol at the same concentration, and this release was the same as that of the control experiment conducted in isotonic buffer. Similarly, the 3 mM parent β-CyD solution induced 65% release of cholesterol, whereas

DMA-β-CyDs induced only about 20−25% release of cholesterol. These results indicated that the hemolytic activity of DMA-β-CyDs, particularly the DS 7 derivative, is much weaker than those of the parent β-CyD and the methylated β-CyDs.

Figure 6 shows macrographs of *M. vastus lateralis* of rabbit dissected 2 days after the single injection of DM-β-CyD and DMA-β-CyDs with DS 7 and 3.8 at a dose of 100 mg/site. In the case of DM-β-CyD, a discoloration of the muscle with hemorrhage was observed, and the irritation score according to Shintani et al.[26] was 4.0 ± 1.0. On the other hand, both DMA- and DMA4-β-CyD gave negligible damage to the muscle, giving the irritation score of 0.3 ± 0.7 which was the same as that of the saline injection.

In conclusion, the hemolytic activity and the muscular tissue irritation of DM-β-CyD were significantly reduced by acetylating hydroxyl groups at the 3-position of the glucose units, and the inclusion ability of DMA-β-CyD was comparable to that of TM-β-CyD. These results suggest that water-soluble CyD derivatives with superior bioadaptability and inclusion ability can be prepared by pertinently designing substituents at the 3-position and by optimally controlling their degree of substitution.

References and Notes

1. Duchêne, D., Ed. *Cyclodextrin and Their Industrial Uses*; Editions de Santé: Paris, 1987.
2. Uekama, K.; Otagiri, M. Cyclodextrins in drug carrier systems. *CRC Crit. Rev. Ther. Drug Carrier Syst.* **1987**, *3*, 1−40.
3. Szejtli, J., Ed. *Cyclodextrin Technology*; Kluwer: Dordrecht, 1988.
4. Loftsson, T.; Brewster, M. E. Pharmaceutical applications of cyclodextrins. Drug solubilization and stabilization. *J. Pharm. Sci.* **1996**, *85*, 1017−1025.
5. Stella, V. J.; Rajewski, R. A. Cyclodextrins: Their future in drug formulation and delivery. *Pharm. Res.* **1997**, *14*, 556−567
6. Uekama, K.; Hirayama, F.; Irie, T. Cyclodextrin drug carrier systems. *Chem. Rev.* **1998**, *98*, 2045−2076.
7. Pitha, J.; Szente, L.; Szejtli, J. Molecular encapsulation of drugs by cyclodextrins and congeners. In *Controlled Drug Delivery*; Bruck, S. D., Ed.; CRC: Boca Raton, FL, 1983; pp 125−148.
8. Albers, E.; Müller, B. W. Cyclodextrin derivatives in pharmaceutics. *CRC Crit. Rev. Ther. Drug Carrier Syst.* **1995**, *12*, 311−337.
9. Duchêne, D.; Ponchel, G.; Wouessidjewe, D. Cyclodextrins in targeting. Application to nanoparticles. *Adv. Drug Delivery Rev.* **1999**, *36*, 29−40.
10. Hirayama, F.; Uekama, K. Cyclodextrin-based controlled drug release. *Adv. Drug Delivery Rev.* **1999**, *36*, 125−141.
11. Hermens, W. A. J. J.; Deurloo, M. J. M.; Romeyn, S. G.; Verhoef, J. C.; Merkus, F. W. H. M. Nasal absorption enhancement of 17β-estradiol by diemthyl-β-cyclodextrin in rabbits and rats. *Pharm. Res.* **1990**, *7*, 500−503.
12. Pitha, J. Enhanced water solubility of vitamins A, D, E, and K by substituted cycloamyloses. *Life Sci.* **1981**, *29*, 307−311.
13. Uekama, K.; Horiuchi, Y.; Kikuchi, M.; Hirayama, F. Enhanced dissolution and oral bioavailability of α-tocopheryl esters by dimethyl-β-cyclodextrin complexation. *J. Incl. Phenom.* **1988**, *6*, 167−174.
14. Miyake, K.; Hirayama, F.; Uekama, K. Solubility and mass and nuclear magnetic resonance spectroscopic studies on interaction of cyclosporin A with dimethyl-α- and -β-cyclodextrins in aqueous solution. *J. Pharm. Sci.* **1999**, *88*, 39−45.
15. L.-Nicolas, J. M.; Bru, R.; S.-Ferrer, A.; G.-Carmona, F. Use of soluble lipids for biochemical processes: Linoleic acid-cyclodextrin inclusion complexes in aqueous solutions. *Biochem. J.* **1995**, *308*, 151−154.
16. Irie, T.; Uekama, K. Pharmaceutical applications of cyclodextrins. III. Toxicological issues and safety evaluation. *J. Pharm. Sci.* **1997**, *86*, 147−162.
17. Frank, D. W.; Gray, J. E.; Weaver, R. N. Cyclodextrin nephrosis in the rat. *Am. J. Pathol.* **1976**, *83*, 367−382.
18. Gerlóczy, A.; Fónagy, A.; Keresztes, P.; Perlaky, L.; Szejtli, J. Absorption, distribution, excretion and metabolism of orally administered ^{14}C-β-cyclodextrin in rat. *Arzneim. −Forsch.* **1985**, *35*, 1042−1047.
19. Yamamoto, N.; Yoshida, A.; Hirayama, F.; Uekama, K. Some physicochemical properties of branched β-cyclodextrins and their inclusion characteristics. *Int. J. Pharm.* **1989**, *49*, 163−171.
20. Brewster, M. E.; Estes, K. S.; Bodor, N. An intravenous toxicity study of 2-hydroxypropyl-β-cyclodextrin, a useful drug solubilizer, in rats and monkeys. *Int. J. Pharm.* **1990**, *59*, 231−243.
21. Frijlink, H. W.; Visser, J.; Hefting, N. R.; Oosting, R.; Meijer, D. K. F.; Lerk, C. F. The pharmacokinetics of β-cyclodextrin and hydroxypropyl-β-cyclodextrin in the rat. *Pharm. Res.* **1990**, *7*, 1248−1252.
22. Shiotani, K.; Uehata, K.; Irie, T.; Uekama, K.; Thompson, D. O.; Stella, V. J. Differential effects of sulfate and sulfobutyl ether of β-cyclodextrin on erythrocyte membranes in vitro. *Pharm. Res.* **1995**, *12*, 78−84.
23. Thompson, D. O. Cyclodextrins − Enabling excipients: Their present and future use in pharmaceuticals. *CRC Crit. Rev. Ther. Drug Carrier Syst.* **1997**, *14*, 1−104.
24. Higuchi, T.; Connors, K. A. Phase-solubility techniques. *Adv. Anal. Chem. Instr.* **1965**, *4*, 117−212.
25. Higuchi, T.; Kristiansen, H. Binding specificity between small organic solutes in aqueous solution: Classification of some solutes into two groups according to binding tendencies. *J. Pharm. Sci.* **1970**, *59*, 1601−1608.
26. Shintani, S.; Yamasaki, M.; Nakamura, M.; Nakayama, I. A new method to determine the irritation of drugs after intramuscular injection in rabbits. *Toxicol. Appl. Pharmacol.* **1967**, *11*, 293−301.
27. Imai, T.; Irie, T.; Otagiri, M.; Uekama, K. Comparative study on inclusion complexations of antiinflammatory drug flurbiprofen with β-cyclodextrin and methylated β-cyclodextrins. *J. Incl. Phenom.* **1984**, *2*, 597−604.
28. Hansch, C.; Leo, A.; Unger, S. H.; Kim, K. H.; Nikaitani, D.; Lien, E. J. Aromatic substituent constants for structure−activity correlations. *J. Med. Chem.* **1973**, *16*, 1207−1216.
29. Uekama, K.; Imai, T.; Maeda, T.; Irie, T.; Hirayama, F.; Otagiri, M. Improvement of dissolution and suppository release characteristics of flurbiprofen by inclusion complexation with heptakis(2,6-di-*O*-methyl)-β-cyclodextrin. *J. Pharm. Sci.* **1985**, *74*, 841−845.
30. Harata, K. Induced circular dichroism of cycloamylose complexes with *meta*- and *para*-disubstituted benzenes. *Bioorg. Chem.* **1984**, *10*, 255−265.
31. Uekama, K.; Hirayama, F.; Imai, T.; Otagiri, M.; Harata, K. Crystal and molecular structure of 2: 2 (±)flurbiprofen-β-cyclodextrin complex. *Chem. Pharm. Bull.* **1983**, *31*, 3363−3365.
32. Harata, K.; Uekama, K.; Otagiri, M.; Hirayama, F. Conformation of permethylated cyclodextrins and the host−guest geometry of their inclusion complexes. *J. Incl. Phenom.* **1984**, *1*, 279−293.
33. Harata, K. Structural aspects of stereodifferentiation in the solid state. *Chem. Rev.* **1998**, *98*, 1803−1827.
34. Scott, R. L. Some comments on Benesi-Hildebrand equation-.*Rec. Trav. Chim.* **1956**, *75*, 787−789.

Supporting Information Available—Three figures of ^{1}H-NMR and FAB mass spectra of DMA-β-CyD and SEM of erythrocytes. This material is available free of charge via the Internet at http://pubs.acs.org.

JS990128I

Modulation of Sulfate Renal Transport by Alterations in Cell Membrane Fluidity

HWA JEONG LEE,[†] SATHYAMANGALAM V. BALASUBRAMANIAN,[†] HEINI MURER,[‡] JÜRG BIBER,[‡] AND MARILYN E. MORRIS*,[†]

Contribution from *Department of Pharmaceutics, School of Pharmacy, State University of New York at Buffalo, Amherst, New York 14260, and Institute of Physiology, University of Zürich, CH-8057 Zürich, Switzerland.*

Received April 12, 1999. Final revised manuscript received June 28, 1999.
Accepted for publication July 14, 1999.

Abstract □ Changes in membrane fluidity have been shown to alter the sodium-dependent renal transport of glucose and phosphate; however, this has not been examined for sodium/sulfate cotransport in the renal proximal tubule. Sodium/sulfate cotransport regulates the homeostasis of sulfate in mammals. The objective of this study was to investigate the influence of alterations of membrane fluidity on sodium-coupled sulfate transport in the Madin–Darby canine kidney cells, which have been stably transfected with sodium/sulfate cotransporter (NaSi-1) cDNA (MDCK-Si). Preincubation of cells with 0.2 mM cholesterol significantly decreased the V_{max} for sodium/sulfate cotransport (13.69 ± 1.11 vs 10.15 ± 1.17 nmol/mg protein/5 min, mean ± SD, $n = 4$, $p < 0.01$) with no significant alteration in K_m. The addition of benzyl alcohol (20 mM) to cells increased the V_{max} of sulfate uptake by 20% (11.97 ± 0.91 vs 14.35 ± 0.56 nmol/mg protein/5 min, mean ± SD, $n = 3$, $p < 0.05$) with no significant change in K_m. Membrane fluidity, as measured by the fluorescence polarization of 1,6-diphenyl 1,3,5-hexatriene (DPH), was significantly increased in MDCK-Si cells treated with 20 mM benzyl alcohol and decreased in the cells preincubated with 0.2 mM cholesterol, compared with control cells. Our results suggest that alterations in membrane fluidity that may occur as a result of disease states, aging, and pregnancy may play an important role in the modulation of renal sodium/sulfate cotransport.

Introduction

Membrane fluidity (membrane motional order or lipid packing order) affects the activity and kinetics of membrane-bound enzymes and transport carriers, accessibility of membrane receptors, and passive permeability properties of membranes.[1] Membrane fluidity can be determined by two factors: environmental factors, such as temperature, and intrinsic factors, such as membrane composition. Alterations in fluidity have been reported in a variety of physiological/pathological conditions such as aging, organ maturation, ischemia, low phosphate diet, vitamin D-induced hypercalcemia, succinylacetone-induced Fanconi syndrome, streptozotocin-induced diabetes mellitus, and liver disease produced by biliary obstruction.[2−4] Drug treatment including treatment with estrogens, gentamicin, anesthetic alcohols (pentanol, hexanol and heptanol), and salicylic acid can also alter membrane fluidity.[2,5,6]

Cholesterol is an essential constituent of the membranes of mammalian cells and is involved in normal cell growth and function. It is mainly located in the cell plasma membrane and acts as the main lipid rigidifier in natural membranes under physiological conditions.[7] The increase in brush border membrane (BBM) cholesterol content and decrease in BBM fluidity in aged rats are associated with a decrease in the V_{max} of sodium-dependent transport of phosphate in renal BBM.[8] Furthermore, Levi et al.[9] have reported that cholesterol directly modulates renal BBM Na^+/phosphate cotransport activity without affecting Na^+/glucose and Na^+/proline cotransport.

Numerous investigations have used the local anesthetic, benzyl alcohol, to alter the physical properties of membranes by increasing their motional order or fluidity. The increase in renal BBM fluidity produced by benzyl alcohol treatment reduced sodium-dependent glucose transport and stimulated Na^+/phosphate cotranport with no change in the affinities of glucose and phosphate for their transport proteins.[2] Friedlander et al.[10] have also confirmed that the increase in apical membrane fluidity achieved by benzyl alcohol produces an increase in phosphate uptake and a decrease of glucose uptake in renal epithelial cells.

Inorganic sulfate, a physiological anion involved in conjugation reactions involving both endogenous and exogenous substrates, is predominantly reabsorbed in the proximal tubule of the mammalian kidney by a sodium-dependent mechanism at the BBM.[11,12] The sodium/sulfate cotransporter is distinct from sodium-dependent phosphate, amino acid, and glucose transport proteins,[13] and the NaSi-1 cDNA identified by Markovich et al.[14] is involved in renal sodium-dependent sulfate transport at the BBM. Unlike other renal sodium-coupled solute transport systems, the effect of membrane fluidity on sodium/sulfate cotransport has not been studied. The objective of the present investigation was, therefore, to examine whether the alterations in membrane fluidity produced by preincubation with cholesterol or by benzyl alcohol treatment affect the activity of the apically located sodium-dependent sulfate transport protein in Madin−Darby canine kidney cells (MDCK) which have been stably transfected by NaSi-1 cDNA (MDCK-Si).[15]

Materials and Methods

Materials—$^{35}SO_4^{2-}$ (as Na_2SO_4, 1050−1600 Ci/mmol) was obtained from New England Nuclear Research Products (DuPont Company, Boston, MA). Biodegradable counting scintillant was purchased from Amersham Co. (Arlington Heights, IL). Commassie blue dye reagent concentrate and bovine plasma γ-globulin protein standard were supplied from Bio-Rad (Richmond, CA). Dulbecco's modified Eagle's medium, fetal bovine serum, and trypsin were obtained from Gibco BRL (Buffalo, NY). All other chemicals were obtained from Sigma Chemical Co. (St. Louis, MO) or J. T. Baker (Phillipsberg, NJ).

Cell Culture Conditions—MDCK cells which had been stably transfected with NaSi-1 cDNA (MDCK-Si)[15] were maintained in Dulbecco's modified Eagle's medium, which contained 22 mM $NaHCO_3$, 2 mM L-glutamine, 50 IU/mL penicillin, 50 μg/mL

* Corresponding author. Tel: (716 645-2842 ext 230. Fax: 716 645-3693. e-mail: memorris@acsu.buffalo.edu.

10.1021/js990114c CCC: $18.00
Published on Web 08/25/1999

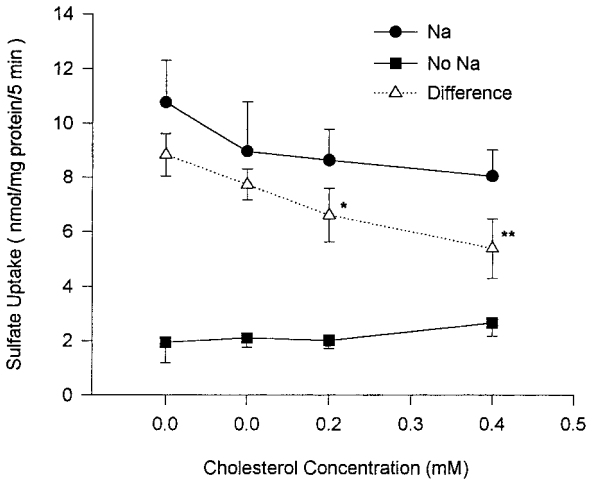

Figure 1—Concentration-dependent effect of cholesterol on sulfate uptake in MDCK-Si cells. Uptake rates were determined at 5 min in the presence of NaCl or of *N*-methyl-D-glucamine. Each data point is the mean ± SD of three separate experiments in which triplicate determinations were obtained. * $p <$ 0.01 compared with control (0 mM cholesterol), ** $p < 0.001$ compared with control.

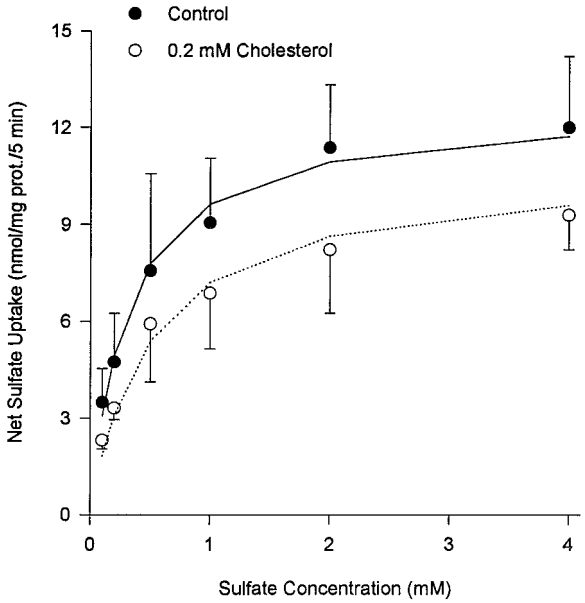

Figure 2—Concentration-dependent sulfate uptake in 0.2 mM cholesterol-preincubated MDCK-Si cells. Sodium-dependent sulfate uptake was calculated as the difference between sulfate uptake rates determined with and without sodium. Each data point is the mean ± SD from four separate preparations, with triplicate determinations of uptake in each preparation. The data were fitted to the Michaelis–Menten equation using nonlinear regression analysis, and the lines represent the fitted lines for the mean data.

streptomycin, 1% nonessential amino acids, and 10% fetal bovine serum, under an atmosphere of 95% air/5% CO_2 at 37 °C. MDCK-Si cells were used up to 15 passages and induced by an incubation with 10^{-6} M dexamethasone for 16 h before sulfate uptake studies.[15]

Sulfate Uptake Studies—The uptake of inorganic sulfate was determined in MDCK-Si cells grown to confluency on culture dishes (35 mm), as described by Hansch et al.[16] Uptake studies were performed at room temperature in a buffered solution which consisted of 137 mM NaCl, 5.4 mM KCl, 2.8 mM $CaCl_2$, 1.2 mM $MgCl_2$, 10 mM HEPES/Tris (pH 7.4) containing K_2SO_4 and tracer amounts of radiolabeled sulfate (2 μCi/mL). At the end of incubation, the uptake was stopped by washing the cells three times with ice-cold stop solution (137 mM NaCl, 10 mM Tris/HCl, pH 7.4). Cells were then solubilized with 1% Triton X-100, and radioactivity and protein concentrations of aliquots were determined by liquid scintillation counting and the Coomassie blue binding method[17] using bovine plasma γ-globulin as the protein standard, respectively.

For estimation of transport kinetic parameters, V_{max} and K_m, for sulfate BBM transport, sulfate uptake into MDCK-Si cells was determined at 5 min at various concentrations of sulfate (0.1−6 mM) in the presence and absence of NaCl. For studies done in the absence of sodium, NaCl was replaced by an equimolar amount of *N*-methyl-D-glucamine/HCl. The difference between the uptake rates at the same sulfate concentrations with and without sodium represents the sodium-dependent transport process. Preliminary studies have demonstrated that the 5 min uptake value provides an estimate of the linear uptake of sulfate in MDCK-Si cells. Cells were preincubated with cholesterol at 37 °C for 2 h for the experiments with cholesterol, whereas benzyl alcohol was added to the uptake solution in studies examining the effect of benzyl alcohol on sulfate uptake.

Membrane Fluidity Measurements—The membrane fluidity of intact MDCK-Si cells which were treated with 20 mM benzyl alcohol or preincubated with 0.2 mM cholesterol was examined by measuring the fluorescence polarization of 1,6-diphenyl-1,3,5-hexatriene (DPH). MDCK-Si cells were diluted with 2 mL of phosphate-buffered saline solution (PBS, pH 7.4), and 5 μL of 1 mg/mL DPH in tetrahydrofuran was added. One potential problem of measuring fluorescence polarization using the DPH probe in intact cells is the larger particle size of the intact cells which causes depolarization. This problem was partly alleviated by diluting the cells with 2 mL of PBS. Further, the depolarization due to light scattering was corrected by conducting appropriate control experiments as described previously.[18] The binding of the probe to cell components and restricting motions of the probe were evaluated by using various probe-to-cell ratios, produced by serial dilution of the cell suspension.

Fluorescence polarization measurements were performed using a SLM Aminco (SLM Aminco, Urbana, IL) 8000 spectrofluorometer with film polarizers (FP110) at temperatures of 25 °C and 37 °C with the excitation wavelength of 355 nm and the emission wavelength of 430 nm.[6] The temperature equilibration was established by maintaining the chamber at appropriate temperatures for 15 min prior to the measurements using a Neslab (RTE 110) water bath.

Data Analysis—The Michaelis−Menten equation was used to fit the data representing linear sulfate uptake (5 min determinations) over a wide range of concentrations using nonlinear regression analysis (PCNONLIN, Statistical Consultants Inc., Lexington, KY) with a weighting factor, 1/variance, to obtain estimates of the V_{max} and K_m values for sodium/sulfate cotransport.[19] The uptake values were determined in triplicate in any one experiment, and the data from each experiment were fitted to the Michaelis−Menten equation. Three or four experiments were performed, and the mean ± SD for these parameter estimates are reported.

The measured polarization and anisotropy values were used to calculate the lipid order parameter S, using the formula $S^2 = [(4r/3) - 0.1]/r_0$ where r_0 is the maximal fluorescence anisotropy value in the absence of any rotational motion (0.40), and r is the steady state anisotropy value. The lipid order parameter was used to estimate the membrane fluidity, as they are inversely related. The static and dynamic components of S were analyzed as described by Pottel et al.[20]

Statistical Analysis—All results were reported as the mean ± SD, unless stated otherwise. The data were compared by unpaired Student's *t*-test between two groups and by ANOVA followed by a Tukey's test among more than two groups. The differences were considered to be statistically significant when $p < 0.05$.

Results

Time Course of Sulfate Uptake—Sodium-dependent sulfate uptake into MDCK-Si cells was examined at various times and increased linearly with time, up to 20 min of incubation. The uptake of sulfate in cells reached a plateau after 60 min, indicating equilibrium (data not shown).

Effect of Cholesterol on Sulfate Uptake—In all studies, sulfate uptake in MDCK-Si cells was significantly increased in the presence of sodium compared with that in the absence of sodium, indicating the sodium dependence

Table 1—Transport Parameter Estimates for Sodium-Dependent Sulfate Uptake into Cholesterol-Preincubated MDCK-Si Cells[a]

	V_{max} (nmol/mg prot/5 min)	K_m (μM)
control	13.69 ± 1.11	435.5 ± 142.8
0.2 mM cholesterol	10.15 ± 1.17[b]	416.7 ± 153.9

[a] Values are presented as mean ± SD of four separate experiments. The estimate for V_{max} was significantly different in control and cholesterol-preincubated cells ($p < 0.01$) with no significant change in the K_m value. [b] $p < 0.01$.

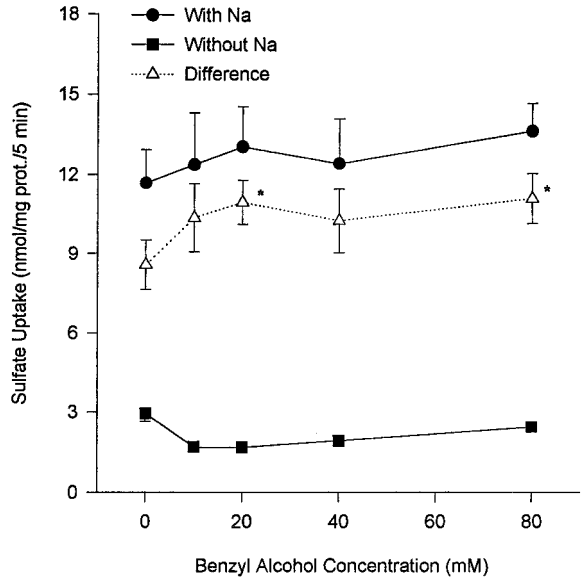

Figure 3—Concentration-dependent effect of benzyl alcohol on sulfate uptake in MDCK-Si cells. Sulfate uptake rates at 5 min were examined in the presence and absence of sodium. Each data point is the mean ± SD of four separate preparations in which triplicate determinations were obtained. * $p < 0.05$ compared with control (0 mM benzyl alcohol).

Table 2—Transport Parameter Estimates for Sodium-Dependent Sulfate Uptake into Benzyl Alcohol-Treated MDCK-Si Cells[a]

	V_{max} (nmol/mg prot./5 min)	K_m (μM)
control	11.97 ± 0.91	464.1 ± 55.9
20 mM benzyl alcohol	14.35 ± 0.56[b]	406.9 ± 174.7

[a] Values are reported as mean ± SD of three separate experiments. The V_{max} value was statistically different in control and benzyl alcohol-treated cells ($p < 0.05$) with no significant difference in the K_m estimate. [b] $p < 0.05$.

of the transport process (Figure 1). Increasing concentrations of cholesterol reduced sulfate uptake in a dose-dependent manner with no significant influence on the sodium-independent component of sulfate transport (Figure 1). The concentration-dependent sulfate uptake in MDCK-Si cells preincubated with 0.2 mM cholesterol is presented in Figure 2. Over a wide range of sulfate concentrations, sodium-dependent sulfate uptake in cholesterol-preincubated cells was decreased compared with the control group. The V_{max} estimate for sodium/sulfate cotransport in cholesterol-enriched cells was significantly lower than that in control cells, while the K_m value was not significantly altered (Table 1).

Effect of Benzyl Alcohol on Sulfate Uptake—Benzyl alcohol increased sodium/sulfate cotransport activity in MDCK-Si cells (Figure 3). As shown in Table 2, the increase of sodium-dependent sulfate uptake in the presence of 20 mM benzyl alcohol (Figure 4) resulted from a increase in the V_{max} estimate of this transport process with no significant change in the K_m value.

Membrane Fluidity—The steady-state fluorescence polarization of DPH represents membrane motional order

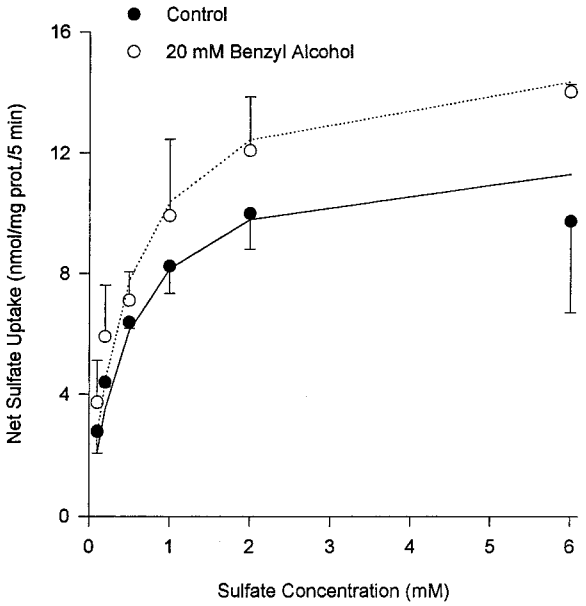

Figure 4—Concentration-dependent sulfate uptake in 20 mM benzyl alcohol-treated MDCK-Si cells. Sodium-dependent sulfate uptake was determined from the difference between uptake rates at 5 min measured in the presence of NaCl or of *N*-methyl-D-glucamine. Each data point is the mean ± SD from three separate experiments, with triplicate determinations of uptake in each preparation. The data were fitted to the Michaelis–Menten equation using nonlinear regression analysis, and the lines represent the fitted lines for the mean data.

Table 3—Lipid Order Parameter and Fluorescence Polarization of DPH in MDCK-Si Cells[a]

temperature	sample	polarization	anisotropy	lipid order parameter (*S*)
25 °C	control	0.396 ± 0.008	0.3041	0.8738
	benzyl alcohol	0.351 ± 0.002[b]	0.2650	0.7958
	cholesterol	0.419 ± 0.009[b]	0.3246	0.9121
37 °C	control	0.292 ± 0.014	0.2156	0.6845
	benzyl alcohol	0.212 ± 0.010[b]	0.1520	0.5066
	cholesterol	0.365 ± 0.011[b]	0.2770	0.8205

[a] Values for fluorescence polarization are expressed as mean ± SD from five measurements. The fluorescence polarization of DPH as a function of temperature was determined in MDCK-Si cells treated with 20 mM benzyl alcohol and preincubated with 0.2 mM cholesterol as well as in control cells. Benzyl alcohol treatment significantly decreases and cholesterol treatment significantly increases the fluorescence polarization of DPH in intact MDCK-Si cells at both temperatures, compared with the value in control cells. The data were compared by ANOVA followed by a Tukey's test among three groups at same temperature. [b] $p < 0.001$.

in the hydrophobic core of the membrane lipid bilayer and is inversely related to membrane fluidity.[6] The calculated lipid order parameter *S* is a measure of lipid packing of the bilayer and can be defined as fluidity. The observed changes in *S* indicate that benzyl alcohol treatment resulted in the fluidization of the membrane, and cholesterol treatment produced a more rigid membrane. The membrane fluidity of MDCK-Si cells treated with 20 mM benzyl alcohol was significantly higher than that of control cells at 25 °C and 37 °C. Cholesterol, at a concentration of 0.2 mM, significantly reduced the membrane fluidity of the cells at both temperatures, compared with controls (Table 3).

Discussion

Changes in membrane fluidity and/or membrane composition have been reported in various physiological and

pathological conditions. Devi et al.[21] have reported an age-dependent increase in membrane cholesterol content and a gradual decrease in membrane fluidity during the prenatal period of liver development in humans. Schwarz et al.[22] have also shown that there are age-dependent increases in total cholesterol and the cholesterol/phospholipid molar ratio, as well as a significant reduction in fluidity in basolateral membranes from rabbit proximal colon throughout postnatal maturation. In rat liver plasma membrane, the cholesterol content increases and the extent of unsaturated fatty acids as well as membrane fluidity decrease during aging.[23] In diabetic rats, the fluidity of renal BBM and BLM is reduced due to changes in the composition of fatty acids esterified in membrane phospholipids.[3] Reversible ischemia increases renal BBM fluidity while a decrease in renal BBM fluidity has been observed in hypercalcemia[25] and liver disease.[4]

Previously, we reported that sodium-dependent sulfate transport in renal BBM was increased in young and pregnant guinea pigs.[24] We also observed that the fluorescence polarization of DPH was decreased in BBM isolated from the kidney cortex of young and pregnant animals, indicating an increased fluidity in the hydrophobic core of the membrane. These results suggested that the increase in BBM fluidity may represent one possible mechanism for the observed changes in sodium/sulfate cotransport during development and pregnancy. The purpose of this study was to investigate whether the modulations of apical membrane fluidity affect sodium/sulfate cotransport in MDCK-Si cells. The present investigation represents the first examination of the effects of membrane fluidity on sodium-dependent sulfate transport.

Preincubation of MDCK-Si cells with 0.2 mM cholesterol significantly decreased the membrane fluidity of the cells. This is consistent with the decreased membrane fluidity in the presence of an increased membrane cholesterol content reported in a number of cell lines including akata cells (lymphoid cell line), human umbilical vein endothelial cells, rat aortic smooth cells, guinea pig keratinocytes, human renal carcinoma cells, and rat prostatic epithelial cells.[7,25–30] In the present studies, the increase in cholesterol concentration produced a reduction of sodium-dependent sulfate uptake in cells in a concentration-dependent manner due to a reduction in the V_{max} of sodium/sulfate cotransport in MDCK cells transfected with NaSi-1. Levi et al.[8] also reported a decreased V_{max} for sodium/phosphate cotransport with no change in K_m in the BBM isolated from aged rats which exhibit a decrease in BBM fluidity and an increase in BBM cholesterol content. In addition, the adaptive increases in the V_{max} of BBM sodium-dependent phosphate transport and BBM fluidity as a result of a low phosphate diet were completely reversed by the increase of cholesterol content in BBM.[9] In vitro enrichment of renal BBM with cholesterol decreases sodium/phosphate transport but has no effect on Na^+/H^+ exchange, sodium/glucose, or sodium/proline cotransport activities which suggests the presence of different lipidic environments (microdomains) for different transport carriers and the absence of an effect on the sodium gradient.[2,9]

Addition of 20 mM benzyl alcohol to the uptake buffer significantly increased the membrane fluidity of the MDCK-Si cells at 25 °C and 37 °C in the present investigation. Friedlander et al.[31] have reported that treatment of MDCK cells with increasing concentrations of benzyl alcohol decreases the steady-state anisotropy of propionyl-diphenylhexatriene and trimethylammonium-diphenylhexatriene, which are located in the hydrophilic surface of the lipid bilayer, suggesting an increased cell plasma membrane fluidity. Our results demonstrated a significantly increased sodium-dependent sulfate uptake in MDCK-Si cells in the presence of 20 mM and 80 mM concentrations of benzyl alcohol. The treatment of cells with 20 mM benzyl alcohol produced an increase in the V_{max} of sodium/sulfate cotransport activity with no change in K_m value. We have also found that benzyl alcohol, at 5 mM and 20 mM concentrations, significantly stimulates the sodium-dependent sulfate uptake at 10 s (linear uptake) in BBM vesicles isolated from the kidney cortex of rats (M. E. Morris, unpublished data). These results are consistent with our previous finding that the increase in sodium/sulfate BBM cotransport was associated with an increased BBM fluidity in young and pregnant guinea pigs.[24] Unlike the effect of benzyl alcohol on sodium/sulfate cotransport, the increase in membrane fluidity by benzyl alcohol altered sodium-dependent phosphate uptake in renal epithelial cells in a bimodal manner: a moderate increase in fluidity (benzyl alcohol concentration less than 20 mM) enhanced phosphate uptake while larger increases reduced it markedly. This biphasic phenomenon for modulation in membrane fluidity by local anesthetics or aliphatic alcohols was also shown for the activity of Na^+,K^+-ATPase,[32,33] whereas fluidization of isolated renal BBM[34] and intact LLC-PK_1 cells[10] decreased the V_{max} of sodium/glucose cotransport in a concentration-dependent manner. Benzyl alcohol concentrations greater than 30 mM also resulted in an increased affinity for glucose for the transporter in kidney BBM vesicles.[34] Therefore, membrane fluidity may influence not only the V_{max} but also the K_m of the substrate for a transporter. The different alterations in the activities of the apically located transporters involved in the sodium-dependent uptake of phosphate, glucose, and sulfate, following the same modification of membrane fluidity, suggest that the lipidic domain around each carrier may be different and the sodium-dependent sulfate transport protein is distinct from sodium/phosphate and sodium/glucose cotransporters.[2,13] Additionally, the different alterations observed for these sodium-dependent transport processes suggest that a change in the driving force (sodium gradient) is not responsible for changes in the observed transport.[2]

Based on the fluidity measurements, we speculate that membrane fluidity changes alter the sulfate transport through altered domain dynamics (altered lipid mobility within a domain). Even though DPH may not be a suitable probe to investigate the lamellar domain properties, due to their fluorescence lifetime alterations (thus polarization), DPH can provide qualitative information regarding the dynamics of lamellar domains. In studies carried out using DPH-labeled artificial membranes, the probe showed higher fluorescence polarization values for the gel phase and reduced polarization values as the fraction of liquid crystalline phase increased.[6,35] This is due to the changes in the fluorescence lifetime of the probe as a result of altered molecular motions. The fluorescence lifetime values decrease from 10.5 to 7.5 ns, as the bilayer transfers from a solid gel phase to a more fluid liquid crystalline phase.[35] Thus, polarization values provide qualitative information regarding the domain formation. In the present study we observed that benzyl alcohol-treated cell membranes are more fluid (decrease in polarization values) as a result of an increase in the fraction of liquid crystalline domains. This alteration in the domain size and dynamics may alter the lipid mobility in the lamellar plane in which the protein is embedded. A secondary effect of this change in lipid dynamics is that the percolation of lipids at the protein–lipid interface and in lipid–protein domains may be altered.

In conclusion, the decrease in fluidity of apical membranes of MDCK-Si cells produced by preincubation with cholesterol resulted in a reduction of sodium/sulfate cotrans-

port whereas the increase in apical membrane fluidity of the cells treated with benzyl alcohol produced an increase in sodium-dependent sulfate uptake. These results suggest that membrane fluidity may play an important role in the regulation of sulfate renal reabsorption in physiological/pathological conditions, including aging and pregnancy.

References and Notes

1. Shinitzky, M. Membrane fluidity and cellular functions. In *Physiology of Membrane Fluidity*; Shinitzky, M., Ed.; CRC Press: Boca Raton, FL, 1984; pp 1−52.
2. LeGrimellec, C.; Friedlander, G.; Yandouzi, E. H. E.; Zlatkine, P.; Giocondi, M.-C. Membrane fluidity and transport properties in epithelia. *Kidney Int.* **1992**, *42*, 825−836.
3. Ramsammy, L. S.; Boos, C.; Josepovitz, C.; Kaloyanides, G. J. Biophysical and biochemical alterations of renal cortical membrane in diabetic rat. *Biochim. Biophys. Acta* **1993**, *1146*, 1−8.
4. Imai, Y.; Scoble, J. E.; McIntyre, N.; Owen, J. S. Increased Na^+-dependent D-glucose transport and altered lipid composition in renal cortical brush-border membrane vesicles from bile duct-ligated rats. *J. Lipid Res.* **1992**, *33*, 473−483.
5. Kutchai, H.; Chandler, L. H.; Geddis, L. M. Effects of anesthetic alcohols on membrane transport processes in human erythrocytes. *Biochim. Biophys. Acta* **1980**, *600*, 870−881.
6. Balasubramanian, S. V.; Straubinger, R. M.; Morris, M. E. Salicylic acid induces changes in the physical properties of model and native kidney membranes. *J. Pharm. Sci.* **1997**, *86*, 199−204.
7. Yeagle, P. L. *The Membranes of Cells*, 2nd ed.; Academic Press: San Diego, CA, 1993; pp 139−165.
8. Levi, M.; Jameson, D. M.; van der Meer, B. W. Role of BBM lipid composition and fluidity in impaired renal Pi transport in aged rat. *Am. J. Physiol.* **1989**, *256*, F85−F94.
9. Levi, M.; Baird, B. M.; Wilson, P. V. Cholesterol modulates rat renal brush border membrane phosphate transport. *J. Clin. Invest.* **1990**, *85*, 231−237.
10. Friedlander, G.; Shahedi, M.; LeGrimellec, C.; Amiel, C. Increase in membrane fluidity and opening of tight junctions have similar effects on sodium-coupled uptakes in renal epithelial cells. *J. Biol. Chem.* **1988**, *263*, 11183−11188.
11. Lücke, H.; Stange, G.; Murer, H. Sulphate-ion/sodium-ion cotransport by brush-border membrane vesicles isolated from rat kidney cortex. *Biochem. J.* **1979**, *182*, 223−229.
12. Schneider, E. G.; Durham, J. C.; Sacktor, B. Sodium-dependent transport of inorganic sulfate by rabbit renal brush border membrane vesicles. *J. Biol. Chem.* **1984**, *259*, 14591−14599.
13. Tenenhouse, H. S.; Lee, J.; Harvey, N. Renal brush-border membrane Na^+-sulfate cotransport: Stimulation by thyroid hormone. *Am. J. Physiol.* **1991**, *261*, F420−F426.
14. Markovich, D.; Forgo, J.; Stange, G.; Biber, J.; Murer, H. Expression cloning of rat renal $Na^+/SO_4$2- cotransport. *Proc. Natl. Acad. Sci. U.S.A.* **1993**, *90*, 8073−8077.
15. Quabius, E. S.; Murer, H.; Biber, J. Expression of proximal tubular Na−Pi and Na−SO_4 cotransporters in MDCK and LLC−PK_1 cells by transfection. *Am. J. Physiol.* **1996**, *39*, F220−F228.
16. Hansch, E.; Forgo, J.; Murer, H.; Biber, J. Role of microtubules in the adaptive response of Na−Pi cotransport to low phosphate in OK cells. *Pflügers Arch.* **1993**, *422*, 516−522.
17. Bradford, M. M. A rapid and sensitive method for the quantitation of microgram quantities of protein utilizing the principle of protein-dye binding. *Anal. Biochem.* **1976**, *72*, 248−254.
18. Shinitzky, M.; Barenholz, Y. Fluidity parameters of lipid regions determined by fluorescence polarization. *Biochim. Biophys. Acta* **1978**, *525*, 367−394.
19. Darling, I. M.; Mammarella, M. L.; Chen, Q.; Morris, M. E. Salicylate inhibits the renal transport of inorganic sulfate in rat membrane vesicle preparations. *Drug Metab. Dispos.* **1994**, *22*, 318−323.
20. Pottel, H.; van der Meer, W.; Herreman, W. Correlation between the order parameter and the steady-state fluorescence anisotropy of 1,6-diphenyl-1,3,5-hexatriene and an evalation of membrane fluidity. *Biochim. Biophys. Acta* **1983**, *730*, 181−186.
21. Devi, B. G.; Gupta, P. D.; Habeebullah, C. M. Changes in membrane fluidity during human liver development. *Biochem. Int.* **1992**, *28*, 41−49.
22. Schwarz, S. M.; Lambert, A. S.; Medow, M. S. Ontogeny of proximal colon basolateral membrane lipid composition and fluidity in the rabbit. *Biochim. Biophys. Acta* **1992**, *1107*, 70−76.
23. Hegner, D. Age-dependence of molecular and functional changes in biological membrane properties. *Mech. Aging Dev.* **1980**, *14*, 101−108.
24. Lee, H.-J.; Balasubramanian, S. V.; Morris, M. E. Effect of pregnancy, postnatal growth and gender on renal sulfate transport. *Proc. Soc. Exp. Biol. Med.*, in press.
25. Pozzi, D.; Lisi, A.; Grimaldi, S. Role of Akata cell membrane fluidity in susceptibility to Epstein−Barr virus infection. *Virology* **1995**, *146*, 301−305.
26. Pritchard, J., K. A.; Schwarz, S. M.; Medow, M. S.; Sterman, M. B. Effect of low-density lipoprotein on endothelial cells membrane fluidity and mononuclear cell attachment. *Am. J. Physiol.* **1991**, *260*, C43−C49.
27. Sachinidis, A.; Liu, M.; Weber, A.-A.; Seul, C.; Harth, V.; Seewald, S.; Ko, Y.; Vetter, H. Cholesterol enhances platelet-derived growth factor-BB-induced $(Ca^{2+})_i$ and DNA synthesis in rat aortic smooth muscles cells. *Hypertension* **1997**, *29*, 326−333.
28. Callaghan, T. M.; Metezeau, P.; Gachelin, H.; Redziniak, G.; Milner, Y.; Goldberg, M. E. Modulation of the binding and endocytosis of concanavalin A by guinea pig keratinocytes: reversible antagonistic effects of cholesterol and phospholipid-liposomes. *J. Invest. Dermatol.* **1990**, *94*, 58−64.
29. Ludes, B.; Staedel, C.; Jacqmin, D.; Cremel, G.; Hubert, P.; Bollack, C.; Beck, J.-P. Increased immunogenicity of human renal carcinoma cells following treatment with cholesterol derivatives. *Eur. Urol.* **1990**, *17*, 166−172.
30. Prieto, J. C.; Hueso, C.; Carmena, M. J. Modulation of the beta-adrenergic stimulation of cyclic AMP accumulation in rat prostatic epithelial cells by membrane fluidity. *Gen. Pharmacol.* **1990**, *21*, 931−933.
31. Friedlander, G.; LeGrimellec, C.; Giocondi, M.-C.; Amiel, C. Benzyl alcohol increases membrane fluidity and modulates cyclic AMP synthesis in intact renal epithelial cells. *Biochim. Biophys. Acta* **1987**, *903*, 341−348.
32. Grisham, C. M.; Barnett, R. E. The effect of long-chain alcohols on membrane lipids and the (Na^++ K^+)-ATPase. *Biochim. Biophys. Acta* **1973**, *311*, 417−422.
33. Sweet, W. D.; Schroeder, F. Charged anesthetics alter LM-fibroblast plasma-membrane enzymes by selective fluidization of inner or outer membrane leaflets. *Biochem. J.* **1986**, *239*, 301−310.
34. Carriere, B.; LeGrimellec, C. Effects of benzyl alcohol on enzyme activities and D-glucose transport in kidney brush border membranes. *Biochim. Biophys. Acta* **1986**, *857*, 131−138.
35. Parasassi, T.; De Stasio, G.; Ravagnan, G.; Rusch, R. M.; Gratton, E. Quantitation of lipid phases in phospholipid vesicles by the generalized polarization of Laurdan fluorescence. *Biophys. J.* **1991**, *60*, 179−189.

Acknowledgments

This work was supported by NSF grant IBN 9629470 and grants from the Western New York Kidney Foundation/Upstate Transplant Services and the Kapoor Charitable Foundation at SUNY at Buffalo (for M.E.M.). Additional support was provided by the Swiss National Science Foundation (for H.M.).

JS990114C

Physicochemistry, Pharmacokinetics, and Pharmacodynamics of *S*-Nitrosocaptopril Crystals, a New Nitric Oxide Donor†

LEE JIA,*,‡ XINPING YOUNG, AND WENHU GUO§

Contribution from *Chinese Academy of Medical Sciences, Beijing 100730, China, Division of Clinical Pharmacology, East Hospital, Fuzhou, 350004 China, and University of California, San Diego School of Medicine, VAMC (151H), San Diego, California 92161.*

Received April 7, 1999. Final revised manuscript received June 18, 1999.
Accepted for publication July 21, 1999.

Abstract □ S-nitrosocaptopril (CapNO) has been proposed as a compound possessing capacities of both a nitric oxide (NO) donor and an inhibitor of angiotensin converting enzyme (ACE). In the present study, we characterized the physicochemical, pharmacokinetic, and pharmacological properties of the crystalline CapNO. The novel stable crystals are in a red flake form. Spectroscopic analyses of CapNO revealed its UV/visible λ_{max} and the corresponding extinction coefficients, and characteristic infrared frequencies for the N═O and S–N stretch. The NMR signals corresponding to the protons attached to the carbon (C–S) and the carbon itself were remarkably shifted downfield upon S-nitrosylation. Mass and HPLC analyses, solubility, and melting point of CapNO were determined. Simultaneous on-line analyses of pharmacodynamic and pharmacokinetic profiles of CapNO in catheterized awake rats of spontaneous hypertension (SHR) showed acute decreases in mean arterial pressure (MAP), concomitant with the corresponding increases in plasma levels of CapNO after po or iv administration. The pharmacokinetic parameters for CapNO, i.e., $t_{1/2}$, T_{max}, C_{max}, V_d, AUC, and oral bioavailability were analyzed to understand the dose-dependent potency and effective period of CapNO. The highest concentrations of oral CapNO distributed in tissues were found in kidney, liver, lung, and small intestine. CapNO was excreted predominantly via urine, and second via feces in the detectable forms of thiols and nitrogen oxide although a small portion of CapNO was found in bile. The results provide the evidence of in vivo cleavage of the S–N bond and biotransformation of CapNO.

Introduction

The endothelium-derived relaxing factor, known as EDRF,[1] is generally considered to be a labile NO-containing precursor. Evidence has accumulated implicating that reduced generation of NO has been involved in several diseases.[2,14] Thus, there is a great demand for exogenous, potent NO donors to treat NO-deficient diseases. However, it is difficult to reliably introduce NO into most biological systems for therapeutic purposes without premature decomposition. Due to a growing appreciation for NO-related responses that are not mediated directly by NO itself, there is an increasing interest in compounds which generate NO, mimic its biological function, and might have pharmacological effects in a controlled manner.

Water-soluble RSNOs, where R can be any one of a large range of chemical entities, might meet these major requirements as possible storage and transport forms for the otherwise highly reactive NO molecule.[3−5] Many efforts have been made to prepare a solid powder of RSNOs; however, most RSNOs are reported to be too unstable to isolate as pure solids. It has long been known that RSNOs decompose to yield NO and the corresponding disulfide RSSR;[7−9] the latter could then be reduced by either an intracellular spontaneous recovery mechanism[10] or a general protein disulfide reductase.[11] Therefore, an RSNO composed of an NO group and another pharmacological active component RSH would have considerable theoretical and practical significance. CapNO may be the best candidate due to its dual role as an ACE inhibitor and an NO carrier.[3,6,12,13]

We have recently developed a facile synthesis of CapNO in a good yield. The first synthesized red crystals, after being dried, could be stored in the dark at about 25 °C for at least two months and 4 °C for at least one year without a significant decay. The stability of the red crystals provides us with an opportunity to characterize the authentic physicochemical properties of the novel crystalline CapNO in the present report. Although numerous reports concerning the cardiovascular pharmacology of RSNOs have been published,[3−6,11−13] none of them has addressed the pharmacokinetic profiles and oral bioavailability of RSNOs. The exemplary CapNO, that nonenzymetically releases NO in a manner similar to most of RSNOs,[8,15] is certainly a very useful tool for exploring pilot information regarding in vivo biotransformation and functional significance of RSNOs. Therefore, we investigated the overall pharmacokinetical profiles and antihypertensive effects of CapNO simultaneously and evaluated the drug's tissue distribution and elimination.

Experimental Section

Spectral Analyses—The preparation of crystalline CapNO was accomplished via a S-nitrosylation reaction of captopril (Cap) as described in detail.[12] The resulting red crystals were dissolved in distilled water at a final concentration of 1 mM. Five different spectrometers (Perkin-Elmer Lambda 2S, Hewlett-Packard 8452 A, Beckman DU-7, Shimadzu UV 2101PC, Shimadza UV 160) were calibrated with 0.5 mM of $K_2Cr_2O_7$ (Aldrich, Milwaukee, WI) before experiments. These spectrometers were then used to determine the peak wavelengths and the corresponding extinction coefficients of CapNO. Infrared spectra were analyzed using Nicolet Impact 400 Fourier Transform IR spectrometer (Nicolet Instruments, Inc., WI). The polyethylene film (KBr) was used to calibrate the full scale and features of the spectrometer. The purified CapNO in an NMR tube was dissolved in $CDCl_3$ for ^1H NMR analysis with a Varian 300 MHz NMR system (Oxford Instruments, Osney Mead, Oxford), or dissolved in D_2O for ^{13}C NMR analysis with a Unity 500 MHz system, respectively. Chemical shifts were recorded as parts per million relative to tetramethylsilane (TMS) as the internal standard (for ^1H NMR) and to $CDCl_3$ as the external

* Corresponding author.
† Abbreviations: CapNO, *S*-nitrosocaptopril; Cap, Captopril; RSNOs, *S*-nitrosothiols; ACE, angiotensin converting enzyme; MAP, mean arterial pressure; NO, nitric oxide.
‡ Present address: 11283 Carmel Creek Rd., San Diego, CA 92130. Tel.: 619-597-5563. Fax: 619-794-6865. e-mail: Lee.jia@ljpc.com.
§ East Hospital.

10.1021/js990108g CCC: $18.00 Published on Web 09/03/1999

standard (for ^{13}C NMR). Mass spectral analysis was carried out with VG 70-SE analyzer (VG Analytical, Manchester, England) equipped with an electron-impact ionization source and a data-processing system.

Chromatographic Analyses—Thin-layer chromatography (TLC) was performed on Analtech silica gel F_{254} plates (0.25 mm thick). A 5-μL of CapNO (1 mM in H_2O) was spotted on the origin of the plates, which were developed a distance of 6 cm in a solvent-developing system consisting of isopropyl alcohol−acetic acid−water (4:1:1, by volume). CapNO, its parent compound Cap, and the corresponding disulfide were analyzed using a reversed phase HPLC system (Shimadzu, Kyoto, Japan) consisting of a LC-10A liquid delivery module, a SPD-10A ultraviolet detector, a CTO-10A column oven, and a Shim-pack CLC-ODS column (150 mm × 6.0 mm i.d., 5 μm particle size). The system was controlled with an SCL-10A system controller under the following conditions: flow rate, 1.0 mL/min; column temperature, 25 °C; UV detection wavelength, 220 nm. A 5-μL aliquot of CapNO, Cap, or its corresponding disulfide was injected into the injection loop, respectively, and chromatographed using the C_{18} (octadecylsilane) column eluted isocratically with a mobile phase of 50% methanol and 50% phosphoric acid (0.1%). The area under each peak was calibrated with a Shimadzu data processor. The detection limits were 1 μg/ mL on the basis of peak:noise ratio at 3:1. All samples were diluted with 0.1 N HCl immediately before injection.

Simultaneous Measurement of CapNO Plasma Level and Effect Relationship in Awake SHR—Male SHR rats, weighing 365 ± 32 g, were anesthetized with sodium thiopentone (50 mg/kg, ip) and underwent cannulation of the left femoral artery (PE 50), which was used for periodic blood sampling and monitoring of the MAP with a transducer. After recovery from general anesthesia, the catheterized SHR rats were placed in individual restraining cages with free access to food and drinking water. For intravenous administration, the femoral vein was used for the drug injection. For oral administration, the rats were fasted for 4 h before CapNO was given by gavage. CapNO solutions (50 mg/mL) were prepared using saline (for iv) or water (for po) immediately before administration. Serial blood samples (0.2 mL) were collected each time with heparinized 1 mL syringes and replaced with 0.2 mL of normal saline at 0, 1, 5, 30, 60, 120, and 240 min after each iv injection, or 0, 10, 20, 30, 60, 120, 240, and 480 min after the oral dosing. Between samplings, the arterial cannula was connected to a pressure transducer for measurement of MAP. Blood samples were immediately centrifuged at 10000*g* for 5 min. The plasma was prepared and diluted with ice-cold Milli Q water in order to observe the appropriate area of signals. The diluted plasma was collected in airtight syringes and introduced via a HPLC pump (Shimadzu, Kyoto, Japan) into a photolysis−chemiluminescence system at a fixed flow rate of 1 mL/min, where the homolytic cleavage of NO from CapNO was completed. The CapNO concentration is directly proportional to detected signal area, which could be converted to the plasma level of CapNO by using the peak−concentration standardization curve of CapNO. The pharmacokinetic study was performed in each individual rat with the PharmK kinetic software.[16] Pharmacokinetic parameters for individual plasma concentration−time data were determined by a nonlinear least-squares regression program of the PharmK, using a one-compartment open model for single oral dosing, and a two-compartment model for single bolus iv dosing (Table 1). The goodness of fit was assessed from the distribution of residuals. The bioavailability was calculated using the values of area under the concentration−time curve (po versus iv).

Six calibration standard concentrations ranging from 2.5 to 500 ng/mL of CapNO were prepared by spiking blank plasma with CapNO working standards. To determine sensitivity and specificity of the assay prior to the initiation of the study, CapNO and its major contaminants, $NaNO_2$, the starting compound Cap, and the corresponding disulfide, were detected in Milli Q water or rat blank plasma. The diluted rat blank plasma itself gave no signal peaks, indicating no interfering materials present. The detection limit for CapNO was approximately 2.5 ng/mL, which was sensitive enough to measure the predicted plasma levels of CapNO for at least three $t_{1/2}$ periods after single oral dose (5 mg/kg). However, the detection limit for $NaNO_2$ was 2.5 μg/mL with the retention time remarkably shifted, and the system did not respond to the parent Cap and its disulfide, indicating the assay specificity for plasma CapNO. To assess accuracy, precision, and reproducibility, five sets of quality control samples were analyzed together with the diluted plasma and urine samples, or kidney homogenates. The mean predicted quality control concentrations were within 3.6% of the nominal values. The within-day and between-day coefficients of variation were determined for triplicate spiked samples of CapNO at 12.5, 25, and 250 ng/mL and resulted in values of 4.1−8.4%. The recovery of CapNO spiked to rat plasma, urine, bile, and various tissue homogenates was >89%. The relationship between peak areas and CapNO concentrations (2.5, 12.5, 25, 62.5,125, and 500 ng/mL) in rat plasma, urine, bile, and tissue homogenates was linear with correlation coefficients > 0.99.

Table 1—Pharmacokinetic Data for CapNO after Dosing to SHR

route	parameter	dose 5 mg/kg	dose 10 mg/kg	dose 50 mg/kg
iv	$t_{1/2(\alpha)}$ (min)	1.9 ± 0.5	1.9 ± 0.3	5.3 ± 0.4
	$t_{1/2(\beta)}$ (min)	24.6 ± 3.5	19.7 ± 5.9	26.2 ± 5.9
	K_{12} (min^{-1})	0.17 ± 0.03	0.12 ± 0.03	0.05 ± 0.01
	K_{21} (min^{-1})	0.24 ± 0.03	0.28 ± 0.05	0.31 ± 0.03
	K_{10} (min^{-1})	0.07 ± 0.02	0.06 ± 0.01	0.04 ± 0.01
	V_d (L/kg)	0.09 ± 0.01	0.11 ± 0.01	0.21 ± 0.02
	$CL_{(T)}$ (mL/min/kg)	16.0 ± 0.7	22.4 ± 3.2	25.0 ± 1.7
	AUC (μg/mL·min)	247 ± 13	408 ± 25	1122 ± 165
po	K (min^{-1} 10^{-3})	12.3 ± 2.1	13.3 ± 1.0	8.9 ± 0.5
	$K\alpha$ (min^{-1} 10^{-3})	54.9 ± 10.9	62.5 ± 12.1	67.7 ± 18.4
	$t_{1/2}$ (min)	64.4 ± 12.3	70.6 ± 10.0	78.8 ± 5.0
	$CL_{(T)}$ (mL/min/kg)	15.8 ± 0.7	16.4 ± 0.7	23.6 ± 1.8
	V_d/F (mL/kg)	52.7 ± 2.1	56.4 ± 2.2	106.5 ± 8.5
	T_{max} (min)	45.3 ± 2.6	41.8 ± 5.2	37.7 ± 4.4
	C_{max} (μg/ mL)	393 ± 81	606 ± 40	1199 ± 105
	AUC (μg/mL·min)	60 ± 5	89 ± 24	277 ± 29
	bioavailability (%)	24.3	21.8	24.7

For iv route, $t_{1/2(\alpha)}$ and $t_{1/2(\beta)}$ were the half-life of distribution and elimination, respectively. K_{12} was the rate constant for the movement of drug from central to tissue compartment; K_{21}, rate constant for the movement of drug from tissue to central compartment; K_{10}, elimination rate constant. For po route, K was elimination rate constant, and $K\alpha$, absorption rate constants. $t_{1/2}$ was elimination half-life. $CL_{(T)}$, systemic clearance; V_d, apparent volume of distribution; F, bioavailability; T_{max}, time to attain maximum plasma concentration; C_{max}, maximum plasma concentration. AUC, the total area under plasma concentration-time curve from 0 to 4 h.

Tissue Preparation for CapNO Distribution Studies—CD-1 mice, 25 ± 6 g, eight males and seven females were used. Mice were fasted overnight with water available ad libitum. Tissues were excised following ether anesthesia at 0.5, 1, and 5 h after oral administration of CapNO. The intestine was cut opened and rinsed with cold saline to remove the contents. Tissues were washed three times with cold saline, weighed, and minced with scissors. Homogenization of each tissue (0.2 g) was performed in five volumes by tissue weight of ice-cold 10 mM potassium phosphate buffer (pH 7.4) for 5 min. The homogenates were then centrifuged at 14000*g* for 15 min (0−4 °C). The supernatants were removed and diluted with 10-fold excess of Milli Q water. An aliquot of 100-μL diluted supernatants was assayed for CapNO by the photolysis−chemiluminescence method described above. CapNO concentrations in the various tissue samples were determined with standardization curves ranging from 2.5 to 500 ng/mL prepared in the corresponding tissue samples.

Urine, Feces, and Bile Collection—SD rats individually resided in stainless steel metabolism cages, where urine and feces were separated by a cone-shaped device. Pooled urine and feces were collected overnight prior to drug administration and then at 5, 10, 24, and 48 h after a single oral dose. Feces were homogenized in a mortar in two volumes by fecal weight of cold water. Both fecal homogenates and urine were centrifuged at 14000*g* at 0 °C for 15 min. The supernatants of urine and feces were diluted with 10^3−10^4 fold excess of Milli Q water, and the diluted supernatants were analyzed by Ellman test[17] for SH groups, and by Griess assay[18] for nitrite determination. Rats were anesthetized with sodium thiopentone (50 mg/kg, ip), and the peritoneal cavity was opened by an incision along the bloodless midabdominal line. The common bile duct was cannulated with tubing PE50 toward the liver. The abdominal wall was then closed by suturing to prevent hypothermia and dehydration. The open end of the tubing was kept in a sample tube for bile collection before and at 20, 30, 60, 120, 240, and 360 min after oral administration of CapNO (50 mg/

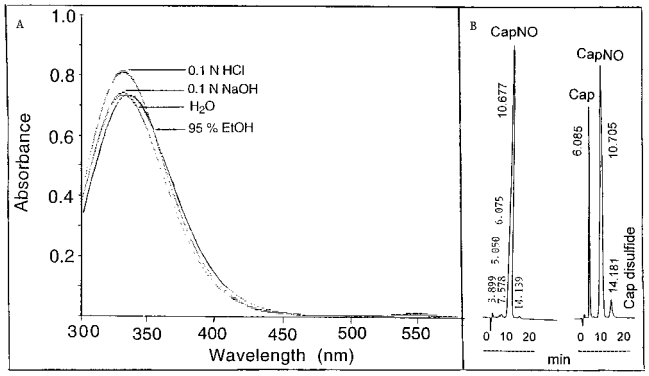

Figure 1—UV-visible spectroscopic and chromatographic characterization of CapNO. A. UV–visible absorption spectra revealed the presence of two maxima at 332 and 546 nm when CapNO was prepared in Milli Q water. HCl caused a hyperchromic shift, and ethanol resulted in a bathochromic shift, whereas NaOH did not have significant effects on the absorption maxima. B. Representative HPLC analysis using UV detection at 220 nm revealed that CapNO solution (50 mM) prepared with its flake crystals in 0.1 N HCl showed only one peak at t_R = 10.6 min without the corresponding monosulfide and disulfide (left tracing), whereas a mixture solution consisting of CapNO, its monosulfide, and its disulfide exhibited three peaks at different retention times (right tracing).

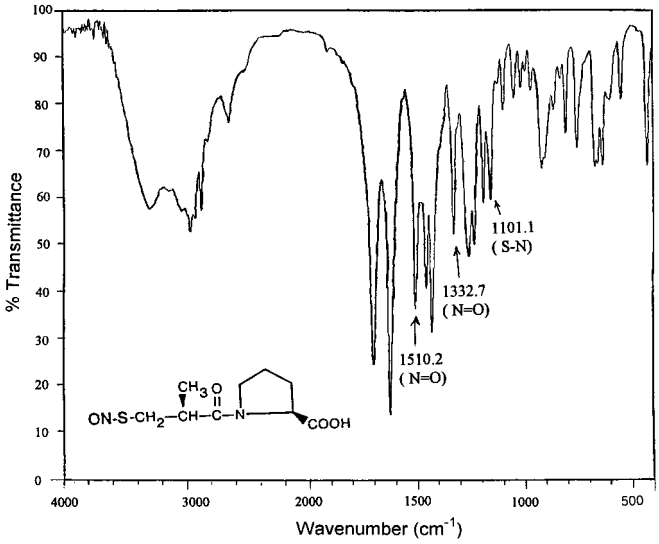

Figure 2—Infrared spectra observed in CapNO molecules showed the most important frequencies at 1332 and 1510 cm^{-1} corresponding to the functional group N═O; 1101 cm^{-1} was assigned to the S–N stretch.

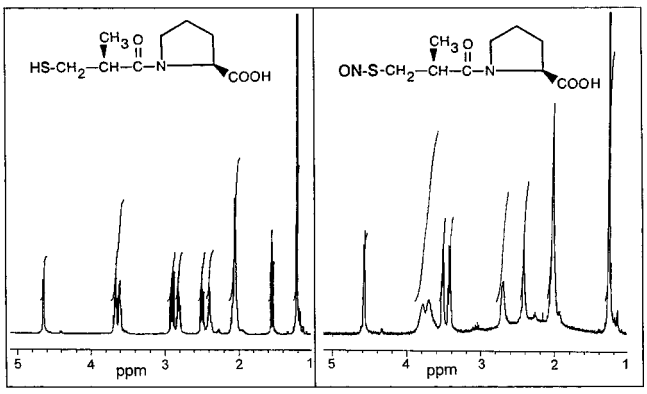

Figure 3—Representative ^1H NMR spectra of CapNO crystals (right) and its starting compound Cap (left). The substitution of SH group with SNO was confirmed by an electron-withdrawing effect of the SNO group, which shifted the signals of the methylenic protons (SCH_2) from δ 2.8–2.9 (in Cap) to δ 3.4–3.5 (in CapNO). In addition, the peak at about 1.5 ppm corresponding to the HS proton disappeared.

kg). CapNO levels in rat bile were determined by the photolysis–chemiluminescence method using the corresponding standardization curve.

Statistical Analyses—Unless otherwise noted, all results are presented as mean ± SE. In some figures, only one SE is shown either above or below the mean to improve clarity. Differences were analyzed by Student's *t* test, a $p < 0.05$ was accepted as significant.

Results

Physicochemical Properties of CapNO—The red flake crystals of CapNO were not hygroscopic, and the stability of the crystals was significantly improved after purification. The red flake crystals were freely soluble in ethanol, chloroform, acetone, and ether and soluble in H_2O, NaOH (0.1 N), and HCl (0.1 N). The melting point of CapNO was found in the range of 49–52 °C, which was determined in open capillary tubes with a melting point apparatus. After being heated over the melting point, the red crystals instantaneously decomposed to an off-white color, which was demonstrated to be captopril disulfide according to the disulfide's retention time of HPLC. The off-white material exhibited a beehive-like appearance when the temperature passed through 104 °C.

Spectral Analyses of CapNO—Scanning by the five UV–visible spectrometers at every ±0.5 nm around the two maxima revealed the peak wavelengths for CapNO at 332 and 546 nm with a molar extinction coefficient (mol^{-1} m^2) of 874.8 ± 12.1 and 15.5 ± 0.2, respectively. Solvent effects on the absorption maxima of CapNO were compared (Figure 1A). TLC spots were detected with UV light (254 nm) or visualized with iodine vapors. TLC showed Cap and CapNO with R_f values of 0.90 and 0.72, respectively (not shown). From the HPLC study (Figure 1B), in each case a single major peak was observed, indicating that the crystalline CapNO has a purity of >99% without detectable monosulfide and disulfide Cap residues. Retention time ranged from 10.6 min for CapNO to 6.1 min for the starting compound Cap to 14.1 min for the major metabolite Cap disulfide. The HPLC analysis revealed that the peak area generated was linear over a range of 1.64 μg/mL to 1.64 mg/mL ($r = 0.99$).

The presence of a S–NO group in CapNO can be readily determined from the strong IR band at 1332 and 1510 cm^{-1}, which corresponds to the stretching vibration of the N═O bond. An absorption band at 1101 cm^{-1} is characteristic of the vibration of the S–N bond. The other absorption bands were identical by IR (KBr) to the bands found in the starting compound Cap although the frequency associated with a particular group varies slightly owing to the influence of the molecular environment. These bands appeared at 1626 cm^{-1} for the amide C–N, 2962, 2930, 2883, and 1460 cm^{-1} for the stretching vibration of the C–H bond, and 3400, 1703, 1433, and 922 cm^{-1} corresponding to the COOH group (Figure 2).

The ^1H NMR spectrum of CapNO is shown in Figure 3. Upon completion of S-nitrosylation of Cap, the signals corresponding to the methylenic protons (SCH_2) of the side chain of Cap were shifted downfield from δ 2.8–2.9 to δ 3.4–3.5. This shift is expected because a thiol is transformed into a more electron-withdrawing nitrosothiol group. The disappearance of the triplet signals of the sulfur proton of Cap at δ 1.53 is indicative of the conversion of Cap to CapNO as well. Reported below are the ^1H NMR data for the CapNO: δ 1.25 (3H,d, CH_3), 2.01(3H, m, 3,4-CH_2CH in proline), 2.42 (1H, q, 4-CH in proline), 2.70 (1H, m, CH), 3.50 (2H, m, SCH_2 in side chain), 3.75 (2H, t, CH_2 in side chain), 4.58 (1H, t, 5-CH in proline). The replacement of SH with S–NO induced the ^{13}C NMR signals of

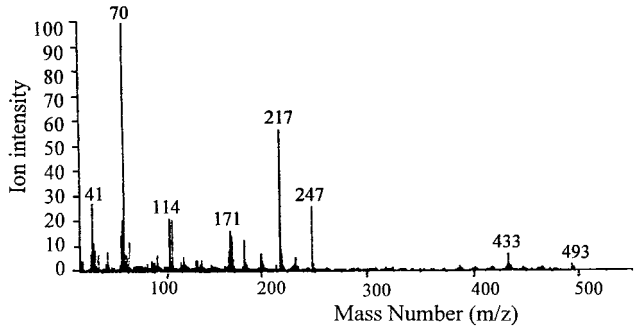

Figure 4—Mass analysis of CapNO crystals using fast atom bombardment mass spectrum analysis of CapNO. The analysis revealed *m/z* 247 and 493, which corresponds to CapNO and a dimer of Cap, respectively. The ion intensity is expressed in an arbitrary unit by taking the height of the base peak at *m/z* 70 as 100.

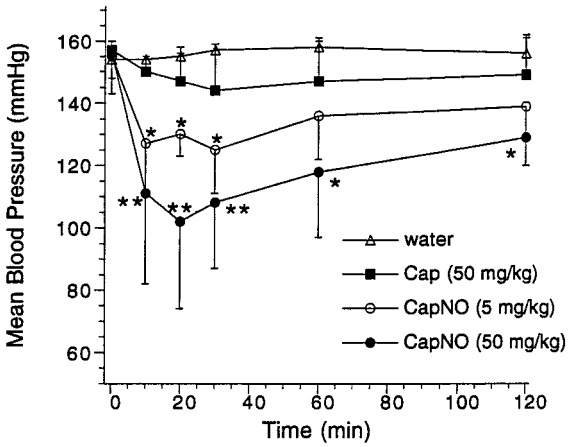

Figure 5—Time course of mean arterial pressure after oral administration of water, Cap, and CapNO to SHR rats. Points and vertical bars represent the mean ± SD (n = 4–6). *p < 0.05, **p < 0.01, compared with water group.

the methylenic carbon (S−CH_2) to shift from δ 42.437 to δ 37.801 (data not shown).

Mass analysis indicated an apparent molecular ion of *m/z* 217 and *m/z* 247, both of which provided valuable diagnostic evidence for the proposed structure of CapNO. First, the base peak of molecular ion at *m/z* 30 (NO) and the largest *m/z* 217 (Cap) strongly suggested the homolysis of the S−NO bond in the CapNO after electron-impact ionization. Second, analysis of the molecular weight of CapNO by fast atom bombardment mass spectrometry (Figure 4) yielded values of *m/z* 247 and 493 $[M + H]^+$, which correspond to CapNO and a dimer of Captopril, respectively. Third, high-resolution mass spectrum analysis of CapNO using glycerol as the reference indicated that the ion at *m/z* 247 (calculated 247.07525) represented a $C_9H_{15}O_4N_2S$ formula for the tested compound.

Pharmacodynamics and Pharmacokinetics of CapNO—After collection of blank blood samples, CapNO was administered (po or iv) to the conscious SHR (n = 6, each group). CapNO (iv) immediately resulted in hypotensive responses in awake SHR. MAP fell to the nadir within 2 min. At doses of 5 and 50 mg/kg, CapNO decreased MAP from 160 ± 7 to 102 ± 8 mmHg (p < 0.01), and 154 ± 5 to 82 ± 9 mmHg (p < 0.001), respectively. The hypotensive effects lasted for more than 4 h. The plasma concentrations of CapNO at 1 min after injections reached the peak of 35.9 ± 1.3 μg/mL (5 mg/kg), 64.4 ± 1.4 μg/mL (10 mg/kg), 219.6 ± 18.8 μg/mL (50 mg/kg); thereafter, the drug concentrations declined with time (Figure 6). Oral administration of CapNO to catheterized awake SHR produced reduction in MAP from 153 ± 10 to 126 ± 18 mmHg (p < 0.05, 5 mg/kg), from 151 ± 5 to 130 ± 5 mmHg (p < 0.05,

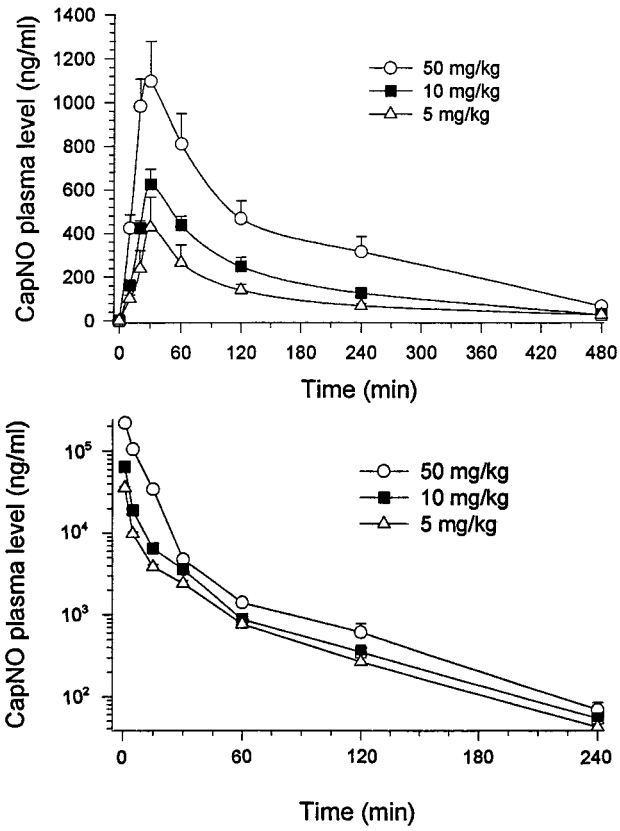

Figure 6—Plasma concentration–time course of CapNO after oral (upper) or intravenous (lower) administration to awake SHR rats (n = 6).

10 mg/kg). As shown in Figure 5, CapNO 50 mg/kg (po) produced a marked and sustained hypotension. In contrast, both vehicle (H_2O) and Cap (50 mg/kg) did not produce significant hypotensive effects in SHR rats (Figure 5).

The plasma concentration−time curves for CapNO after po and iv administration are shown in Figure 6. Concomitant with this decrease in blood pressure, CapNO level in plasma reached 425 ± 62 ng/mL at 10 min and 1092 ± 183 ng/mL at 30 min after oral administration. The time course of decreases in blood pressure and increases in CapNO plasma levels paced almost simultaneously. Peak effect and peak plasma level were noted synchronously by 30 min intervals (Figures 5 and 6). The relationship between single oral CapNO doses (5, 10, and 50 mg/kg) and the area under the plasma concentration−time curves was linear. The pharmacokinetic parameters of CapNO after po and iv dosing are listed in Table 1. The bioavailability of oral CapNO, as determined by the ratio of oral AUC to intravenous AUC, ranged from 22 to 25% (Table 1). The results suggest that CapNO is subject to either incomplete absorption or hepatic first-pass metabolism when administered orally.

CapNO Tissue Distribution and Excretion—Tissue levels of CapNO were shown in Table 2. The kidney, liver, lungs, and small intestine were found to contain the highest levels of CapNO, while brain and fat tissues contained almost no CapNO. The urinary levels of CapNO were not detectable 5 h after dosing with 50 (data not shown) and 500 mg/kg of CapNO by using either the photolysis−chemiluminescence or Saville assay[4] to quantify the *S*-nitroso content of CapNO. This result reflected the in vivo biotransformation of CapNO caused by the cleavage of the S−NO bond. However, the major CapNO metabolites such as NO_2^- and thiols, were detected in the pooled urine and feces by the Griess and Ellman assays (Table 3). The data indicate that CapNO was subjected to extensive

Table 2—Tissue Distribution of CapNO (50 mg/kg) after Oral Administration to Mice

time (h)	*n*	kidney	liver	lungs	small intestine	heart	spleen	skeletal muscle	brain	fat
0.5	5	389 ± 165	366 ± 24	317 ± 65	619 ± 76	189 ± 49	112 ± 69	27 ± 9	26 ± 18	ND[a]
1	5	211 ± 109	279 ± 45	192 ± 73	238 ± 109	178 ± 42	80 ± 30	19 ± 9	25 ± 15	ND[a]
5	5	43 ± 23	34 ± 29	49 ± 34	10 ± 23	23 ± 20	35 ± 23	8 ± 2	5 ± 6	ND[a]

[a] Not detected. Results are the mean ± SD (ng/g) for five experiments.

Table 3—Cumulative Excretion (% of dose) of Thiols and NO_2^- in Pooled Rat Urine and Feces after Oral Dosing of CapNO (500 mg/kg, $n = 5$)

time after dosing (h)	SH compounds[a]		NO_2^- [b]	
	urine	feces	urine	feces
0–5	3.54 ± 0.43		15.42 ± 2.93	
0–10	6.80 ± 0.92		25.37 ± 4.72	
0–24	7.52 ± 1.08	3.04 ± 0.74	40.17 ± 5.62	18.25 ± 2.13
0–48	7.91 ± 1.03	3.18 ± 0.91	40.60 ± 5.78	19.42 ± 3.16

[a] Determined by Ellman assay. [b] Determined by Griess assay.

Table 4—Excretion Rate and Recovery of CapNO (50 mg/kg) in Rat Bile after Oral Dosing

time after dosing (min)	excretion rate (ng/mL/h)	recovery of dose ($\times 10^{-5}$)
0–20	912 ± 81	1.38 ± 0.12
20–30	1461 ± 546	0.54 ± 0.21
30–60	511 ± 73	0.93 ± 0.13
60–120	262 ± 10	1.78 ± 0.06
120–240	75 ± 10	2.95 ± 0.19
240–360	26 ± 7	0.45 ± 0.05
0–360		8.03[a]

[a] Total recovery of the dose in the 0–360 min excreta.

metabolism. CapNO excretion via the rat bile within 6 h after a single dose was shown in Table 4.

Discussion

This is the first report systematically characterizing physicochemistry of the novel crystalline CapNO by spectral UV−visible, IR, MS, and NMR. The two absorption maxima at 332 nm (UV, assigned to B band) and 546 nm (visible) are indicative of S-nitrosylation. The λ_{max} of CapNO solution at 546 nm indicates that the solution absorbs a green light, and thus the solution color looks like pink, which is complementary to the color of green. The formation of CapNO could be conveniently monitored by the visible pink and quantified at 332 and 546 nm. Neither such maxima nor the pink color could be observed when the S-nitrosylation reactions were carried out using equimolar concentrations of $NaNO_2$ and disulfides (either Cap disulfide or glutathione disulfide dimer) under the same conditions of reaction. This indicates a specific replacement of SH with SNO.

Infrared and NMR spectra of crystalline CapNO are excellent probes for the nitrosation of thiols in structural determinations. Chemical shifts of CapNO are significantly different from those of the parent Cap. The greater electronegativity of the *S*-nitroso group has a deshielding effect, which is readily identified by downfield shifts of resonance of the α-protons and α-carbon atom attached to the SNO group. The characteristic infrared frequencies assigned to the stretching vibration of the N=O bond are indicative of the presence of S-nitrosylation (Figure 2).

Single oral doses of CapNO are capable of reducing blood pressure in the awake SHR and causing the quick onset of hypotension (approximately 32% reduction in MAP), whereas Cap possesses no such quick activity. It is likely that the variation in the extent of hypotension between the two compounds arises from the NO moiety since only the crystalline CapNO produces immediate vasodilation in vitro[12] and an acute antihypertensive effect in vivo. Very importantly, the concomitant measurement of CapNO plasma concentration and efficacy in the awake SHR has been incorporated to establish the relationships between pharmacokinetics and pharmacodynamics for CapNO in the present studies. The potency and duration of action of CapNO were clearly dose-dependent and were paralleled to the plasma levels of CapNO (Figures 5 and 6). The mean time courses for decreases in blood pressure and increases in CapNO plasma concentration were parallel and concurrent (Figures 5 and 6). Also the oral plasma T_{max} of CapNO (Figure 6, Table 1) was close to the peak time of efficacy (Figure 5). The pharmacokinetic analyses for single doses showed that CapNO displayed a linear pharmacokinetic relationship between doses and dose-normalized AUC values (data not shown). The oral bioavailability of CapNO in the SHR was assessed 22−25% on the basis of the ratio of oral AUC to intravenous AUC. Consistent with these results was the comparison of antihypertensive effects produced by oral and intravenous administration of CapNO (both 5 mg/ kg). The oral effect was about 30% as potent as the intravenous effect calculated by dividing the area under the oral effect-time tracings by the intravenous ones. The differences in bioavailability determined by plasma data and pharmacological effects may be attributed to the additive effects caused by CapNO metabolites, which might not be detectable in plasma by the photolysis−chemiluminescence.

Distribution of CapNO in awake animals reached a peak at 30 min in tissues, where blood flow is relatively rapid. CapNO was eliminated 5 h after oral administration. The results indicate a rapid equilibrium of CapNO between the central and peripheral compartments. The negligible amounts of CapNO found in brain and fat tissues reflects the compound's poor penetration into brain and fat tissues owing most likely to the hydrophilic properties of CapNO. After oral administration, CapNO is excreted as its metabolites, i.e., reduced thiol and NO_2, predominantly in the urine and to a lesser extent in the feces (Table 3). The cumulative urinary recovery of CapNO within 48 h accounted for about 40% of the dose in the form of nitrogen dioxide, and to a minor portion in the form of thiols (Table 3). The relatively less elimination of thiols might be explained by the formation of disulfide dimers after dosing. Failure to detect the vulnerable S−NO bond of CapNO in the pooled urine and feces indicates the extensive metabolism due to the cleavage of S−NO bond when CapNO was eliminated out of the body. It is unlikely that the bile is a major excretion route for CapNO. We only recovered 8×10^{-5} of total CapNO from rat bile (Table 4) within 6 h although the CapNO bile excretion rate was fairly high within 1 h after oral dosing. The hepatic metabolism of RSNOs is worthy to be further investigated.

The mechanism by which CapNO reduced blood pressure in SHR may have involved the ability of CapNO to deliver NO to the blood vessels within a short period, and inhibit ACE[6,19] in vivo for a longer period. A more likely explanation of the antihypertensive action of CapNO can be divided into two phases: an early phase and a late phase. The early

phase involves a direct action of CapNO as an exogenous NO donor to restore the impaired intrinsic NO-mediated vasodilation and directly counteract the vasoconstrictive influences of angiotensin II and other vasoconstrictors that ACE inhibitors may not directly antagonize. The early phase represents a potent hypotensive effect of exogenous NO donors. The time course of this phase is described in Figure 6. The late phase displays a moderate antihypertensive effect produced by a number of bioactive metabolites of CapNO after homolytic cleavage of the S−N bond in CapNO. The metabolites may include Cap disulfides, Cap-cysteine, and Cap-glutathione disulfides.[20] Indirect evidence from the early studies of Cap suggests that these disulfides may play a role in the maintenance of the antihypertensive action of Cap.[21] Compounds containing S−NO group usually have a biotransnitrosylation effect, which involves conjugation with endogenous thiol-containing amino acids to form mixed S-nitrosothiol-thiols.[22] Hence, these potential effects produced by S-nitrosothiol-cysteine, -glutathione, and -serum albumin cannot be excluded from antihypertensive action of CapNO.

It has been known that the photolysis−chemiluminescence method is superior to others in accuracy, reproducibility, and convenience for determining NO and RSNOs.[4] Photolysis homolytically releases NO, and cold traps remove all nonvolatile parent compounds or derivatives. Therefore, the plasma, urine, and other biological samples do not need to be pre-prepared before measurement. This ensures our obtaining more accurate data without facing the problems such as sample processing and thermal and chemical decomposition of the target compound. The NO group exchange between a biochemical active thiol and a RSNO has been reported.[22−24] Because S-nitrosothiol-thiol exchange may produce a detectable signal in the photolysis−chemiluminescence, we cannot be absolutely certain of the nature of the derivative, especially when samples were obtained hours after CapNO was administered. Although it cannot unequivocally distinguish among different RSNOs, this methodology is valuable for studies of CapNO pharmacokinetics when coupled with pharmacodynamic studies.

Unlike glyceryl trinitrate, CapNO is not subject to tolerance,[25] and has no cross-tolerance with glyceryl trinitrate in vivo in dogs.[26] Our preliminary data proved that chronic oral administration of CapNO showed a potent effect in the SHR and SS/Jr hypertensive models (unpublished observation). CapNO is among the most advantageous of the known NO donor drugs from the therapeutic and toxicological point of view. The studies described herein is valuable in predicting effects of the related RSNOs in animals and planning clinical studies of CapNO.

References and Notes

1. Furchgott, R. F.; Zawadski, J. V. The Obligatory Role of Endothelial Cells in the Relaxation of Arterial Smooth Muscle of Acetylcholine. *Nature (London)* **1980**, *288*, 373−376.
2. Moncada, S.; Higgs, E. A. Molecular Mechanisms and Therapeutic Strategies Related to Nitric Oxide. *FASEB J.* **1995**, *9*, 1319−1330.
3. Jia, L.; Blantz, R. C. The Effects of S-nitrosocaptopril on Renal Filtration and Blood Pressure in Rats. *Eur. J. Pharmacol.* **1998**, *354*, 33−41.
4. Jia, L.; Bonaventura, C.; Bonavenura, J.; Stamler, J. S. S-nitrosoheamoglobin: A Dynamic Activity of Blood Involved in Vascular Control. *Nature (London)* **1996**, *380*, 221−226.
5. Jia, L.; Stamler, J. S. Dual Actions of S-nitrosylated Derivative of Vasoactive Intestinal Peptide as a Vasoactive Intestinal Peptide-like Mediator and a Nitric Oxide Carrier. *Eur. J. Pharmacol.* **1999**, *366*, 79−96.
6. Loscalzo, J.; Smick, D.; Andon, N.; Cooke, J. S-nitrosocaptopril: I. Molecular Characterization and Effect on the Vasculature and on Platelets. *J. Pharmacol. Exp. Ther.* **1989**, *249*, 726−729.
7. Roy, B.; d'Hardemare, A,; Fontecave, M. New Thionitrites: Synthesis, Stability, and Nitric Oxide Generation. *J. Org. Chem.* **1994**, *59*, 7019−7026.
8. Singh, R. J.; Hogg, N.; Joseph, J.; Kalyanaraman, B. Mechanism of Nitric Oxide Release from S-nitrosothiols. *J. Biol. Chem.* **1996**, *271*, 18596−18603.
9. Mathews, W. R.; Kerr, S. W. Biological Acitivity of S-nitrosothiols: the Role of Nitric Oxide. *J. Pharmacol. Exp. Ther.* **1993**, *267*, 1529−1537.
10. Clancy, R. M.; Levartovsky, D.; Leszczynskapiziak, J.; Yegudin.; Abramson, S. B. Nitric Oxide Reacts with Intracellular Glutathione and Activates the Hexose Monophosphate Shunt in Human Neutrophils: Evidence for S-nitrosoglutathione as a Bioactive Intermediary. *Proc. Natl. Acad. Sci. U.S.A.* **1994**, *91*, 3680−3684.
11. Nikitovic, D.; Holmgrent, A. S-nitrosoglutathione is Cleaved by the Thioredoxin System with Liberation of Glutathione and Redox Regulating Nitric Oxide. *J. Biol. Chem.* **1996**, *271*, 19180−19185.
12. Lin, M.; Young, X.; Wang, J.; Jia, B. J.; Jia, L. Inhibitory Effects of S-nitrosocaptopril on Vasomotor Tone. *Acta Pharmacol. Sin.* **1998**, *19*, 485−488.
13. Amano, M.; Takahashi, M.; Kosaka, T.; Kinoshita, M. Differential Inhibition of Platelet Aggregation and Calcium Mobilization by Nitroglycerin and Stabilized Nitric Oxide. *J Cardiovasc. Pharmacol.* **1994**, *24*, 860−866.
14. Benjamin, N.; Vane, J. Nitric Oxide and Hypertension. *Circulation* **1996**, *94*, 1197−1198.
15. Jansen, A.; Drazen, J.; Osborne, J. A.; Brown, R.; Loscalzo, J.; Stamler, J. S. The Relaxant Properties in Guinea Pig Airways of S-nitrosothiols. *Pharmacol. Exp. Ther.* **1992**, *261*, 154−161.
16. Lu, D. R.; Mao, F. An Interactive Program for Pharmacokinetic Modeling. *J. Pharm. Sci.* **1993**, *82*, 537−542.
17. Ellman, G. L. Tissue Sulfhydryl Groups *Arch. Biochem. Biophys.* **1959**, *82*, 70−77.
18. Phizackerley, P. J. R.; Al-Dabbagh, S. A. The Estimation of Nitrate and Nitrite in Saliva and Urine. *Anal. Biochem.* **1983**, *131*, 242−245.
19. Park, J. W. Duel Role of S-nitrosocaptopril as an Inhibitor of Angiotensin-converting Enzyme and a Nitroso Group Carrier. *Biochem. Biophys. Res. Commun.* **1992**, *189*, 206−210.
20. Migdalof, B.; Antonaccio, M.; McKinstry, D. N.; Singhvi, S. M.; Lan, S. J.; Egli, P.; Kripalani, K. J. Captopril: Pharmacology, Metabolism, and Disposition. *Drug Metab. Rev.* **1984**, *15*, 841−869.
21. Drummer, O. H.; Jarrott, B. Captopril Disulfide Conjugates May Act as Prodrugs: Disposition of the Disulfide Dimer of Captopril in the Rat. *Biochem. Pharmacol.* **1984**, *33*, 3567−3571.
22. Meyer, D. J.; Kramer, H.; Ozer, N.; Coles, B.; Ketterer, B. Kinetics and Equilibria of S-nitrosothiol-thiol Exchange Between Glutathione, Cysteine, Penicillamines and Serum Albumin. *FEBS* **1994**, *345*, 177−180.
23. Stamler, J. S.; Jia, L.; McMahon, T. J.; Demchenko, I. T.; Bonaventura, J.; Gernert, K.; Piantadosi, C. A. Blood Flow Regulation by S-nitrosohemoglobin in the Physiological Oxygen Gradient. *Science* **1997**, *276*, 2034−2037.
24. Williams, D. L. H. S-nitrosothiols and Role of Metal Ions in Decomposition to Nitric Oxide. *Methods Enzymol.* **1996**, *268*, 299−308.
25. Matsumoto, T.; Takahashi, M.; Nakae, I.; Kinoshita, M. Vasorelaxing Effect of S-nitrosocaptopril on Dog Coronary Arteries: No Cross-tolerance with Nitroglycerin. *J. Pharmacol. Exp. Ther.* **1995**, *275*, 1247−1253.
26. Takaoka, A.; Nakae, I.; Takahashi, M.; Matsumoto, T.; Liu, Q.; Mitsunami, K.; Kinoshita, M. No Cross-tolerance between S-nitrosocaptopril and Nitroglycerin in Dog Coronary Arteries in vivo. *J. Cardiovasc. Pharmacol.* **1998**, *31*, 231−239.

JS990108G

Role of Baseline Parameters in Determining Indirect Pharmacodynamic Responses

YU-NIEN SUN† AND WILLIAM J. JUSKO*

Contribution from *Department of Pharmaceutics, School of Pharmacy, State University of New Your at Buffalo, Buffalo, New York 14260.*

Received April 7, 1999. Final revised manuscript received July 27, 1999.
Accepted for publication July 30, 1999.

Abstract □ Indirect Response Models account for the pharmacodynamics of numerous drugs which inhibit or stimulate the production (k_{in}) or loss (k_{out}) of the response variable (R). The dose and pharmacokinetics, capacity (S_{max}, I_{max}), and potency (SC_{50}, IC_{50}) factors of the Hill function incorporated in these models are the primary determinants of overall responsiveness. However, the initial or baseline value for the response ($R_0 = k_{in}/k_{out}$) should also be considered as an important factor for the net response. Using Indirect Response Model III (stimulation of input) as an example, the net area under the effect curve ($AUEC_{NET}$) can be proportional to the R_0 values. Such a feature is demonstrated in this report by computer simulations, by examination of the integral of the simulated response vs time profiles, and with examples from the literature. Also shown is an adjustment of R_0 when the therapeutic agent is an endogenous substance. These analyses show that the role of R_0 and k_{in} should not be overlooked as determinants of indirect responses and source of variation among subjects or patient groups.

Introduction

The role of the initial or baseline value of a pharmacological response is often overlooked in considering factors which control pharmacodynamics. For indirect responses where drugs alter the production or loss of the response, the initial or baseline value (R_0) is a dependent variable which is usually described as the ratio of k_{in} (zero-order formation rate constant) ÷ k_{out} (first-order elimination rate constant).[1] The k_{in} is under the direct control of many drugs and subject to physiological and pathophysiologic alterations. Many biotech products produce their pharmacodynamic effects in a similar fashion: Interleukin-10 (IL-10) increases the blood monocyte and neutrophil counts,[2] growth hormone (GH) stimulates the formation for insulin-like growth factor I (IGF-I),[3] interferon α-2a (INF α-2a) induces the production of MX protein,[4] and erythropoeitin stimulates reticulocyte/red blood cell production,[5] and soluble transferrin receptor.[6] Drugs with actions according to Indirect Response Models,[1] especially Model III which accounts for stimulation of k_{in} when k_{out} remains unchanged, can exhibit variable responses in patients when there are marked interindividual differences in R_0 and k_{in} values.[4,6] This report provides simulations to demonstrate how differences in R_0 and k_{in} among patients or different groups will affect net responses to pharmacological agents and points out how this is of particular concern for the drugs which are intended to stimulate natural physiologic processes.

* To whom correspondence should be addressed. e-mail: wjjusko@acsu.buffalo.edu.
† Current address: Department of Pharmacokinetics and Metabolism, Genentech Inc., South San Francisco, CA 94080.

Experimental Section

Methods—Computer simulations were performed using the ADAPT II program.[7] The pharmacokinetic/pharmacodynamic (PK/PD) relationships for a hypothetical drug concentration (C) and the induction of the response (R) were simulated.

Pharmacokinetics—The pharmacokinetics were described by the Bateman Function with a baseline value (C_{BL}):

$$C_p = C_{BL} + \frac{k_a \text{dose}}{V(k_a - k_{el})}(e^{-k_{el}t} - e^{-k_a t}) \quad (1)$$

The assigned PK parameter values were as follows: dose = 250, 500, 1000, and 2000 μg; absorption rate constant $k_a = 0.693\ h^{-1}$; elimination rate constant $k_{el} = 4\ h^{-1}$; CL = 10 L/h; volume V = 2.5 L. Simulations were performed with both $C_{BL} = 0$ and 1 ng/mL.

Pharmacodynamics—Assuming that the drug stimulates the formation rate of R, Indirect Response Model III (1) was applied:

$$\frac{dR}{dt} = k_{in}(1 + S(t)) - k_{out}R \quad (2a)$$

where

$$S(t) = \frac{S_{max}C_p}{SC_{50} + C_p} \quad (2b)$$

and

$$k_{in} = k_{out}R_0 \quad (3a)$$

where S_{max} is the maximum effect and SC_{50} is the drug concentration which can produce 50% of the maximum stimulation of the formation rate.

When the therapeutic agent is an endogenous substance, the basal response occurs when $C_p = C_{BL}$. As a result, the relationships between k_{in}, k_{out}, and R_0 should be defined as follows:[3]

$$k_{in} = \frac{k_{out}R_0}{(1 + S(BL))} \quad (3b)$$

where

$$S(BL) = \frac{S_{max}C_{BL}}{SC_{50} + C_{BL}} \quad (3c)$$

The assigned PD parameter values for the simulations were $R_0 = 25$, 50, 100, or 200 ng/mL; $k_{out} = 0.4\ h^{-1}$; $S_{max} = 5$; $SC_{50} = 4$ ng/mL.

If the baseline level (C_{BL}) = 0, then $k_{in} = k_{out}R_0 = 10$, 20, 40, or 80 ng/mL/h.

If $C_{BL} = 1$ ng/mL, then

$$k_{in} = \frac{k_{out}R_0}{(1 + S(BL))} = \frac{k_{out}R_0}{2} = 5, 10, 20, \text{or } 40 \text{ ng/mL/h}$$

10.1021/js9901155 CCC: $18.00
Published on Web 09/14/1999

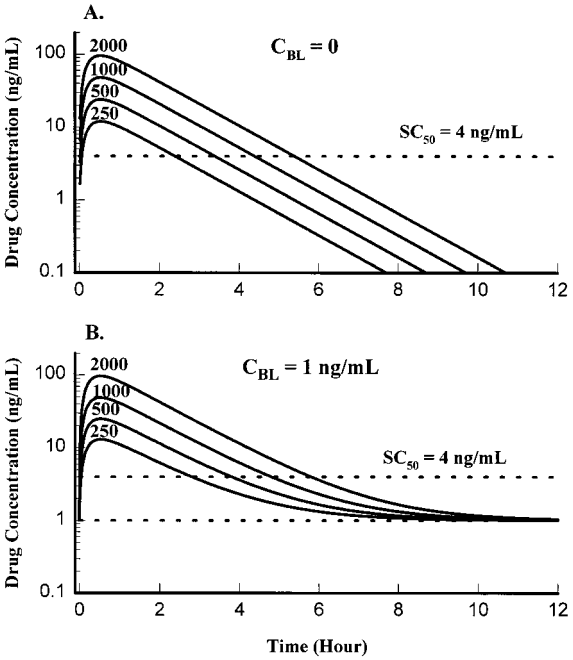

Figure 1—Simulated values for the pharmacokinetic profile of a hypothetical drug at doses of 250, 500, 1000, and 2000 μg. Top (Figure 1A): $C_{BL} = 0$ when the baseline value is negligible. Bottom (Figure 1B): $C_{BL} = 1.0$ ng/mL when the drug is an endogenous substance with a constant baseline value.

Area Analysis—The total areas under the response curves ($AUEC_{total}$) from time 0 to 20 h after drug dosing were obtained by integrating eq 2 in the ADAPT II program.[7] The net AUEC values ($AUEC_{NET}$) = $AUEC_{total} - AUEC_{base}$, where $AUEC_{base} = R_0(20\ h)$.

Results

Pharmacokinetics—Simulations for drug concentration vs time profiles after four different doses are shown in Figures 1a ($C_{BL} = 0$) and 1B ($C_{BL} = 1$ ng/mL). The curves show an expected up-curve, a C_{max} proportional to dose, a t_{max} at 0.5 h, and monoexponential decline. The presence of the baseline adds curvature to the lower profiles.

Pharmacodynamics—*No Baseline*—Simulations for the response vs time profiles are shown in Figure 2. When R_0 (or k_{in}) is a constant, the maximum response as well as the time to reach the maximum response increases when the dose increases. These are the basic characteristics of Indirect Response Model III.[8] As shown in Figure 2, R_0 (or k_{in}) has a profound effect on the magnitude of the overall response. When the dose is constant, the maximum response is proportional to R_0 (or k_{in}).

Presence of Baseline—Simulations for the response vs time profile are shown in Figure 3. Since R_0 is now regulated by the endogenous drug concentration (C_{BL}), the k_{in} value is a fraction of $k_{out}R_0$ as defined in eq 3b. In this particular case, $(1 + S(BL)) = 2$. These response profiles are similar to the results shown in Figure 2. However, the magnitudes of the responses are approximately one-half of those with $C_{BL} = 0$ owing to the lower k_{in} values.

Area Analysis—$AUEC_{NET}$ vs log dose profiles are shown in Figures 4a ($C_{BL} = 0$) and 4b ($C_{BL} = 1$ ng/mL). Within the dose range of 250 to 2000 μg, all curves show linear relationships ($r^2 = 0.9991-0.9997$). The slopes obtained by linear regression are listed in the figure legend.

As shown in Figure 4, the slope coefficients are proportional to R_0 (or k_{in}) values. Krzyzanski and Jusko[9] provided an exact solution for the $AUEC_{NET}$ based on Indirect Response Model III:

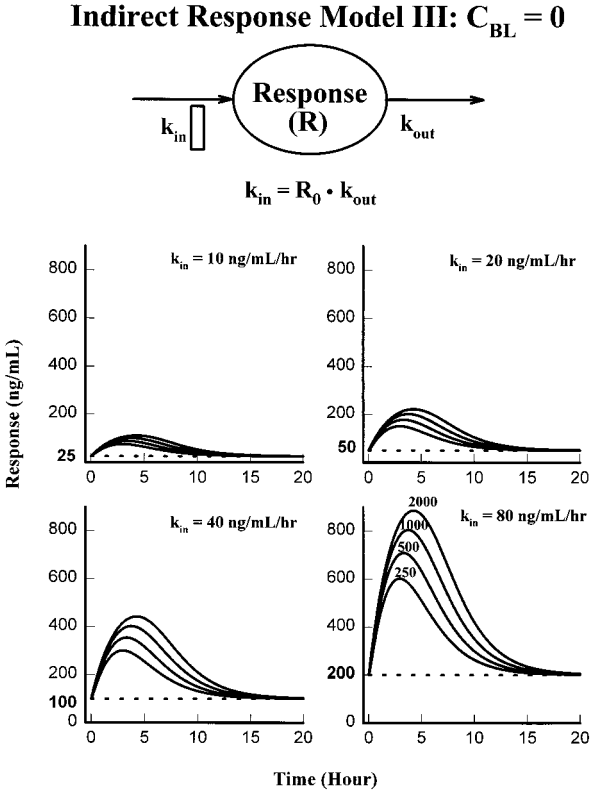

Figure 2—Simulations for drug effects on the production of responses based on the principles of Indirect Response Model III. Four dose levels were simulated: 250, 500, 1000, and 2000 μg. Assuming the baseline is negligible ($C_{BL} = 0$), four different R_0 values were utilized in the simulation: 25 (top, left), 50 (top, right), 100 (bottom, left), and 200 ng/mL (bottom, right). Based on the relationship described by eq 3a, the k_{in} values are 10, 20, 40, and 80 ng/mL/h, respectively.

$$AUEC_{NET} = R_0 \frac{S_{max}}{k_{el}} \ln\left(1 + \frac{dose/V}{SC_{50}}\right) \quad (4)$$

where k_{el} is the elimination rate constant for the function $C(t) = dose(e^{-k_{el}t})/V$. When doses are large, then

$$AUEC_{NET} \sim R_0 \frac{S_{max}}{k_{el}} \ln(Dose) \sim 2.3 R_0 \frac{S_{max}}{k_{el}} \log(Dose) \quad (5)$$

Therefore, the slope coefficient is approximately equal to $(2.3R_0S_{max}/k_{el})$. The k_{el} should be replaced by k_a when flip-flop kinetics occurs in eq 1. The estimates of slopes based on eq 5 for $R_0 = 25$, 50, 100, and 200 ng/mL are 415, 831, 1661, and 3323. These values are close to the results from linear regression for AUEC analysis, although they are slightly overestimated owing to the approximation and use of the Bateman Function.

The $AUEC_{NET}$ vs log dose profiles and the results for linear regression when $C_{BL} = 1.0$ ng/mL are shown in Figure 4B. The slope coefficients are also proportional to R_0 values. When the same R_0 values are compared, the slope coefficients are less than 50% of the estimates for which $C_{BL} = 0$. This disproportionality is due to the alteration of the definition for k_{in} (between eq 3a and 3b), and the different ratios of the stimulation factor, $S(t)$.

Application—The stimulating effects of a single sc dose of Interleukin-10 (IL-10) on monocytes in blood were characterized in normal volunteers[2] using Indirect Response Model III. Figure 5 shows the mean plasma concentrations of IL-10 and the time-course of monocyte numbers. The SC_{50} of IL-10 averaged 0.66 ± 0.70 ng/mL while the S_{max} was predetermined to be 1.5. The relation-

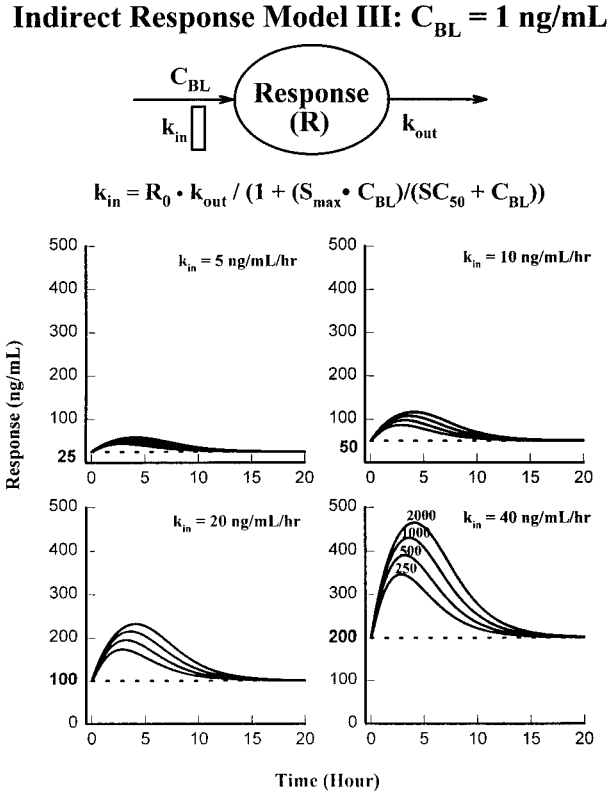

Figure 3—Simulations for drug effects on the production of responses based on the principles of Indirect Response Model III and eq 3b assuming that the drug is an endogenous substance with a constant baseline (C_{BL} = 1.0 ng/mL). Other conditions and simulations are the same as in Figure 2.

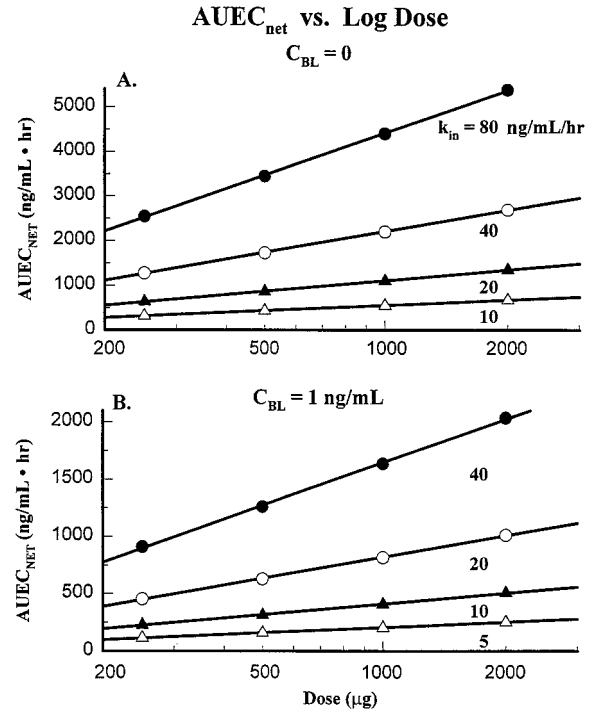

Figure 4—$AUEC_{NET}$ vs log dose for the response profiles in Figures 2 and 3. Top (Figure 4A): baseline is negligible (C_{BL} = 0). Slopes are 394, 787, 1574, and 3148. Bottom (Figure 4B): the drug is an endogenous substance with a constant baseline value (C_{BL} = 1 ng/mL). Slopes are 155, 310, 620, and 1248.

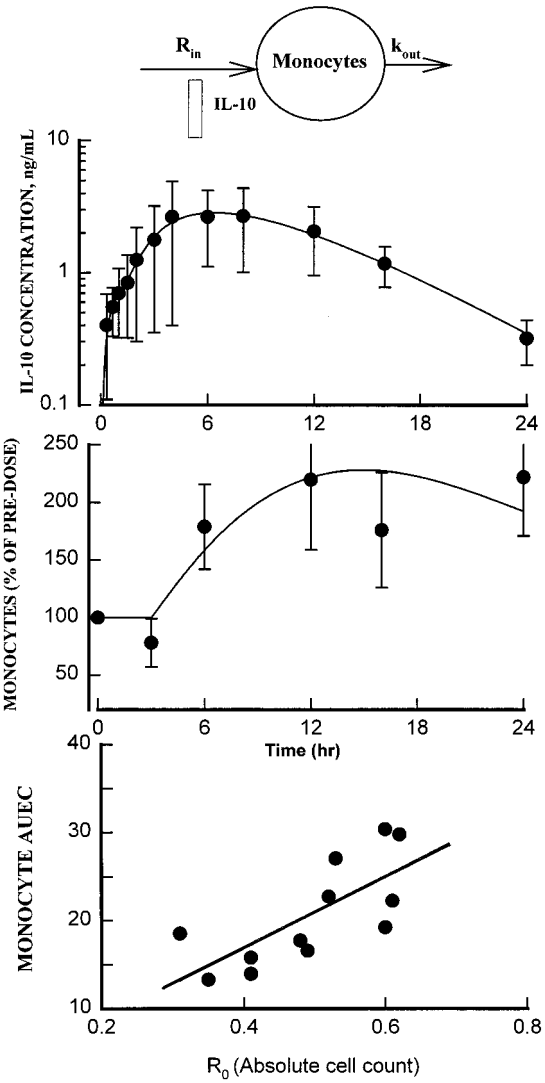

Figure 5—Pharmacokinetics of Interleukin-10 (IL-10) in normal volunteers (top), time course of stimulation of monocytes in blood (middle), and relationship of AUEC of monocytes to initial cell number in blood (R_0) (bottom). Adapted from ref 2.

ship between AUEC and R_0 was found to correlate strongly and indicated that R_0 was a major determinant of the net response.

Discussion

Our simulations show that the baseline value of the pharmacodynamic response (R_0) may play an important role in affecting the extent of the response if its PK/PD relationship can be described by Indirect Response Model III. When other factors remain unchanged (such as S_{max}, SC_{50}, k_{out}), the R_0 which intrinsically reflects the k_{in}/k_{out} ratio dictates the overall magnitude of the response. The same principles apply for drugs which inhibit k_{in} (Indirect Response Model I). The extent of the observed response is also jointly determined by k_{in} and the Hill Function,[1,8,9] and an equation analogous to eq 4 exists.[9] The net response ($AUEC_{NET}$) is also proportional to R_0 in a more complex fashion for drugs which inhibit or stimulate k_{out}.[9] However, such equations also indicate that the present simulations are generally applicable to all drugs with indirect mechanisms of action.

Many protein therapeutic agents stimulate natural physiological processes. For example, IL-10 increases the

blood monocyte and neutrophil counts.[2] GH stimulates the formation of IGF-I, which is a mediator for the growth effect and is often used as a surrogate measurement.[3] IFN α-2a induces the production of MX protein which exerts various antiviral activities.[4] EPO stimulates soluble transferrin receptor.[6] The PK/PD relationships for these biotech products were characterized by Indirect Response Model III.[2−4,6] The relationship between k_{in}, k_{out}, and R_0 can be adjusted accordingly using eq 3B when the pharmacodynamic effect is produced by an endogenous substance which is present at the time of dosing.[3]

Disease states, physiological conditions, medication history (treated vs naive patients, drug interactions, etc.), and other factors may affect the R_0 values of the response. Even for well-controlled studies, interindividual variation in R_0 values is often noticeable. For example, about a 2-fold difference of MX protein baseline values were observed among healthy subjects in a study where IFN α-2a effects were measured.[4] As a result, marked interindividual variation for MX protein production was found. For the effect of EPO on the increase of soluble transferrin receptors (sTfr) in athletes, interindividual variation in sTfr baseline values may be one reason there were large differences in responses observed among the subjects.[6]

These simulations show that the $AUEC_{NET}$ values are well correlated with log(dose) and R_0. The relationship is linear-log and predictable especially when $C_{BL} = 0$, and doses are relatively large.[6] Further investigations of the role of noticeable C_{BL} values on the response profiles are needed. These results suggest that dosages may have to be adjusted according to individual R_0 values. For example, a patient with a lower R_0 value may require higher doses compared to another patient with a higher R_0 value in order to produce similar overall responses. If pathophysiologic alterations of R_0 occur, dosage regimens designed for patients should not solely depend on the response profile obtained from healthy subjects. Finally, when indirect response models are applied to agents which are endogenous substances, the equations for the models will require utilization of eq 3b in order to account for the role of the naturally present active substance. In conclusion, for those therapeutic agents stimulating (or inhibiting) the production rate (or k_{out}) of the response, the R_0 and k_{in} are important determinants of the extent of the response and adjustment of model equations for baseline effects may be needed.

References and Notes

1. Dayneka, N. L.; Garg, V.; Jusko, W. J. Comparison of four basic models of indirect pharmacodynamic responses. *J. Pharmacokin. Biopharm.* **1993**, *21*, 457−478.
2. Chakraborty, A.; Blum, R. A.; Cutler, D. L.; Jusko, W. J. Pharmacoimmunodynamic interactions of interleukin-10 and prednisone in healthy volunteers. *Clin. Pharmacol. Ther.* **1999**, *65*, 304−318.
3. Sun, Y.-N.; Lee, H. J.; Almon, R. R.; Jusko, W. J. A pharmacokinetic/pharmcodynamic model for recombinant human growth hormone effects on induction of insulin-like growth factor I in monkeys. *J. Pharmacol. Exp. Ther.* **1999**, *289*, 1523−1532.
4. Nieforth, K. A.; Nadeau, R.; Patel, I. H.; Mould, D. Use of an indirect pharmacodynamic stimulation model of MX protein induction to compare in vivo activity of interferon alfa-2a and a polyethylene glycol-modified derivative in healthy subjects. *Clin. Pharmacol. Ther.* **1996**, *59*, 636−648.
5. Koury, M. J.; Bondurant, M. C. The molecular mechanism of erythropoietin action. *Eur. J. Biochem.* **1992**, *210*, 649−663.
6. Bressolle, F.; Audran, M.; Gareau, R.; Pham. T.-N.; Gomeni, R. Comparison of a direct and indirect population pharmacodynamic model: application to recombinant human erythropoietin in athletes. *J. Pharmacokin. Biopharm.* **1997**, *25*, 263−275.
7. D'Argenio, D. Z.; Schumitzky, A. *ADAPT II User's Guide: Pharmacokinetic/Pharmacodynamic Systems Analysis Software*; Biomedical Simulations Resource: Los Angeles, CA, 1997.
8. Sharma, A.; Jusko, W. J. Characterization of four basic models of indirect pharmacodynamic responses. *J. Pharmacokin. Biopharm.* **1996**, *24*, 611−635.
9. Krzyzanski, W.; Jusko, W. J. Integrated functions for four basic models of indirect pharmacodynamic responses. *J. Pharm. Sci.* **1998**, *87*, 67−72.

Acknowledgments

This work was supported by Grant No. GM 57980 from the National Institute of General Medical Sciences, National Institutes of Health.

JS9901155

Pharmacokinetic and Glucodynamic Comparisons of Recombinant and Animal-Source Glucagon after IV, IM, and SC Injection in Healthy Volunteers

CASEY J. GRAF, JAMES R. WOODWORTH,* MARY E. SEGER, JOHN H. HOLCOMBE, RONALD R. BOWSHER, AND RENEE LYNCH

Contribution from *Lilly Research Laboratories, Eli Lilly and Company, Lilly Corporate Center, Indianapolis, Indiana.*

Received March 9, 1999. Final revised manuscript received July 14, 1999.
Accepted for publication July 23, 1999.

Abstract □ The structure of the hormone glucagon is identical among humans and several species of other mammals. Equivalence of recombinant glucagon (rG) to animal-source glucagon (aG) was assessed in this two-part, open-label, randomized study. Part I was a four-way crossover intravenous dose-ranging study of rG (pH 2.8) involving 12 subjects. Part II was a six-way crossover study of 29 subjects comparing rG (diluent pH 2.0 and 2.8) with aG administered subcutaneously (sc) and intramuscularly (im). Maximum glucagon plasma concentrations (C_{max}) and area under the glucagon concentration curve (AUC) were calculated. Additionally, maximum blood glucose concentrations (BG_{max}), maximum absolute BG excursion (MAE), and area under the glucose concentration curve from time of dosing to return to baseline (AUC_{rtb}) were calculated. The primary focus was equivalence of the formulation intended for marketing (rG pH 2.0) to aG. Administration of rG pH 2.0 through the im route demonstrated equivalence to aG for all pharmacokinetic and glucodynamic comparisons. Subcutaneous administration of rG pH 2.0 demonstrated standard bioequivalence for AUC (5.87 versus 6.63 ng·h/mL; NS) and near equivalence for C_{max} (7.94 versus 9.12 ng/mL; $p < 0.05$). rG pH 2.0 showed glucodynamic equivalence to aG (BG_{max}, 136 versus 133 mg/dL; MAE, 50.0 versus 47.4 mg/dL, respectively) and statistically greater AUC_{rtb} values (151 versus 126 mg·h/dL, $p < 0.05$). rG and aG were equally safe and well tolerated. In conclusion, rG provides equivalent safety and efficacy to aG.

Introduction

Glucagon is a naturally occurring protein hormone secreted from the α cells of the pancreas. The primary sequence of glucagon is highly conserved in mammals and is identical in man, cattle, pigs, dogs, and rats. The principal function of glucagon is to maintain glucose production, through both glycogenolysis and gluconeogenesis, at a rate sufficient to meet glucose requirements. In man, approximately 75% of net glucose production is mediated through glucagon.[1]

Glucagon is used therapeutically to treat severe hypoglycemia, particularly in patients with diabetes when intravenous glucose is unavailable.[2,3] Glucagon is also used intravenously to relax the intestinal tract to facilitate radiographic examination of the upper and lower gastrointestinal tract.[3,4] Although glucagon is used to treat diabetic hypoglycemia, it may induce hyperglycemia in patients with diabetes when used for radiologic purposes if the patients are in good metabolic control. However, glucagon can induce gut immobilization at lower doses than 1 mg. Lower doses of glucagon may provide necessary gut immobilization while inducing lesser amounts of hyperglycemia and therefore achieving greater safety in patients with diabetes.

Historically in the United States, commercial glucagon has been produced through an extraction process of beef and pork pancreas glands, followed by a high degree of purification. With a trend away from the manufacturing of beef and pork insulins, the availability of quality animal pancreas glands has diminished. Recent advances in recombinant deoxyribonucleic acid (DNA) technology have provided a reliable and efficient source of purified glucagon, recombinant glucagon (rG), with an amino acid sequence identical to that of animal glucagon. The purpose of this study was to compare the pharmacokinetic and pharmacodynamic parameters of rG and animal-source glucagon (aG).

Methods

Patient Population—Forty-one healthy volunteers (24 males, 18 females) between the ages of 23 and 60 years and who were within 15% of normal body weight for their height and frame size (Metropolitan Life Insurance standards) were enrolled in Part I ($n = 12$) or in Part II ($n = 29$) of this study. Subjects participated in only one part of the study. Each subject had a complete medical history, physical examination, complete blood count, urinalysis, a fasting chemistry panel, and chest X-ray prior to enrollment.

For this study, the primary study drug was rG, and the comparator study drug was aG. Each was supplied by Eli Lilly and Company (Indianapolis, IN). The study drug was supplied as a lyophilized powder and reconstituted at the time of injection to a concentration of 1 mg/mL. The diluting solutions were pH 2.0 and 2.8 for rG and pH 2.8 for aG. The Institutional Review Board of the participating institution approved the study, and each subject gave written informed consent for the study.

Study Design—Part I was a randomized, open-label, four-way crossover study that assessed the pharmacokinetics, glucodynamics, dose proportionality, and safety of rG after intravenous (iv) administration. Each healthy volunteer received four doses (0.25, 0.5, 1.0, and 2.0 mg) of rG pH 2.8 as an iv bolus injection with a 7−10 day interval between each dose.

Part II was a randomized, open-label, six-way crossover study that assessed the bioequivalence of rG pH 2.0 and pH 2.8 with aG pH 2.8 after intramuscular (im) and subcutaneous (sc) administration. Two separate pH values were used, since the pH used currently (2.8, for aG) occasionally results in a gel formation. Reduction of the pH to 2.0 reduces the occurrence of this phenomenon. Each subject was scheduled to receive all six possible dose combinations: (1) aG sc, (2) rG pH 2.8 sc, (3) rG pH 2.0 sc, (4) aG im, (5) rG pH 2.8 im, and (6) rG pH 2.0 im. Each dose (sc or im, aG or rG) was 1 mg and was separated by a 7−10 day interval. Administrations were given sc in the lower abdomen and im in the upper deltoid muscle.

* Corresponding author. Telephone: (317) 276-1304. Fax (317) 276-5495. e-mail: WOODWORTH_JAMES_R@lilly.com.

10.1021/js990077p CCC: $18.00
Published on Web 08/27/1999

Table 1—Pharmacokinetic and Glucodynamic Parameters, Intravenous Administrations[a]

	C_{max}, ng/mL	$AUC_{(0-t)}$, ng·h/mL	$AUC_{(0-inf)}$, ng·h/mL	CL, L/h	V_{ext}, L	V_{ss}, L	$t_{1/2}$, h	BG_{max}, mg/dL	TBG_{max}, h	$AUC_{(0-rtb)}$, mg·h/dL
recombinant 0.25 mg (A)	37.4 ± 9.24	4.07 ± 0.631	4.08 ± 0.632	62.5 ± 9.0	11.9 ± 6.6	4.2 ± 2.0	0.13 ± 0.06	131 ± 17.5	0.34 ± 0.1	137 ± 96.2
recombinant 0.5 mg (B)	77.6 ± 20.7	8.47 ± 1.83	8.48 ± 1.84	61.1 ± 11.3	12.7 ± 6.9	4.6 ± 2.2	0.15 ± 0.09	138 ± 16.8	0.35 ± 0.1	129 ± 61.7
recombinant 1.0 mg (C)	171 ± 67.3	17.9 ± 4.04	17.9 ± 4.04	58.4 ± 13.3	18.5 ± 10.7	3.8 ± 2.0	0.22 ± 0.12	132 ± 21.0	0.36 ± 0.2	101 ± 52.9
recombinant 2.0 mg (D)	368 ± 117	37.7 ± 6.98	37.7 ± 6.97	54.6 ± 10.1	23.8 ± 9.2	3.5 ± 2.1	0.30 ± 0.09	129 ± 23.1	0.35 ± 0.2	123 ± 103
p-value[b]	NS	NS	NS	nc	nc	nc	<0.001	NS	NS	NS

[a] All data are reported as mean (±SD). NS = not significant ($p > 0.05$). nc = not compared. [b] From the ANOVA comparing treatment means.

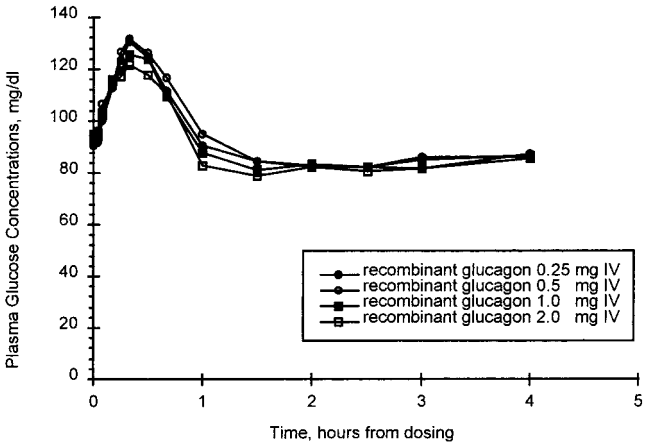

Figure 1—Mean blood glucose concentration versus time curves, all intravenous treatments (part I). $n = 10$. ● = 0.25 mg, ○ = 0.5 mg, ■ = 1.0 mg, □ = 2.0 mg.

For Part I and II, patients received doses of glucagon after an overnight fast, and they remained fasting during the test. Serum samples were collected over a 4-h period after each injection for measurement of glucose and glucagon concentrations. For Part I, samples were collected at 0, 2, 5, 10, 15, 20, 30, 40, 60, 90, 120, 150, 180, and 240 min after administration. For Part II, samples were collected at 0, 5, 10, 15, 20, 25, 40, 60, 90, 120, 150, 180, and 240 min after administration. Serum glucagon concentrations were measured at a central laboratory (Pharmaco International, Richmond, VA) using radioimmunoassay (RIA) techniques. A modified commercial glucacon RIA kit (LINCO, St. Louis, MO) was used for measurement of rG. The modification consisted of replacing the kit calibration standards with standards prepared with rG in the kit's ligand-free matrix. Test samples, standards, and QC samples were analyzed after extracting all samples with four volumes of methanol, evaporation of the extracts, and reconstitution in assay buffer. Although the primary sequence of aG is highly conserved in mammals (the 29-amino acid sequence is identical for man, cattle, pigs, dogs, and rats), aG was cross-validated within this assay, showing equivalent potency, parallel dilution, and nearly identical recovery. The lowest quantifiable concentration for the assay was 40 pg/mL.

Additionally, blood glucose concentrations were determined using a glucose hexokinase method (Clinical Laboratory of MDS Harris, Lincoln, NE).

Pharmacokinetic Measurements—Pharmacokinetic parameters were estimated by noncompartmental pharmacokinetic methods. Maximum glucagon concentration (C_{max}), the time at which C_{max} was observed relative to drug administration (t_{max}), area under the glucagon concentration versus time curve from time 0 to infinity ($AUC_{(0-inf)}$), and apparent terminal elimination phase half-life ($t_{1/2}$) for glucagon plasma concentrations derived from Parts I and II were calculated. Additional parameters, including total systemic clearance (CL), the volume of distribution at steady-state (V_{ss}), and the extrapolated volume of distribution (V_{ext}) were calculated from the iv bolus data (Part I).

Glucodynamic Measurements—Several glucodynamic measurements were derived from the blood glucose concentrations, including the following: maximum blood glucose concentration (BG_{max}), time to BG_{max} (TBG_{max}), area under the glucose versus time curve from time 0 to the time of return to baseline ($AUC_{(0-rtb)}$), area under the glucose excursion versus time curve from 0 to return to baseline (AUC_{ex}), maximum absolute BG excursion (MAE), and earliest recorded time of the MAE (TBG_{ex}). "Baseline" is defined as the blood glucose concentration reported just prior to injection. "Return to baseline" is the achievement of that baseline concentration after blood glucose peaked. If necessary, $AUC_{(0-rtb)}$ and AUC_{ex} values were interpolated. The excursion values (AUC_{ex}, MAE, TBG_{ex}) reflect a subtraction of the baseline value from all measured concentrations and calculations in a fashion similar to the nonadjusted values. All AUC measurements were calculated using the trapezoidal rule.

Statistical Methods—For Part I, a parametric (normal theory) general linear model was applied to the pharmacokinetic and glucodynamic parameters using the SAS GLM procedure. The analysis of variance (ANOVA) model included sequence, period, and treatment as fixed effects and subject within sequence as a random effect. Differences between the treatments with respect to any given parameter were further assessed using pairwise multiple *t*-tests (Bonferroni method). Dose linearity was assessed by linear regression of the dose-normalized parameters with respect to dose. Dose linearity with respect to a parameter was concluded if the slope was not significantly different from 0 ($\alpha = 0.05$). For Part II, a similar ANOVA was performed comparing the pharmacokinetic and glucodynamic parameters and the log-transformed values of C_{max}, $AUC_{(0-t)}$, $AUC_{(0-inf)}$, BG_{max}, $AUC_{(0-rtb)}$, AUC_{ex}, and MAE. The two one-sided hypotheses (Schuirmann two one-sided tests procedure) were tested at the 5% level for the parameters by constructing 90% confidence intervals for the ratio of the test and reference means. The 90% confidence intervals were obtained from the antilogs of the lower and upper bounds of the 90% confidence intervals for the difference in the means of the log-transformed data. Bioequivalence was concluded if the 90% confidence intervals for the variables C_{max}, $AUC_{(0-t)}$, $AUC_{(0-inf)}$, BG_{max}, $AUC_{(0-rtb)}$, AUC_{ex}, and MAE were contained within the range of 80% to 125%.

Results

Part I—For Part I, 10 out of the 12 subjects successfully completed the study. Two subjects withdrew from the study for reasons unrelated to the study. All adverse events in Part I occurred within 24 h following dosing and were mild in severity. The most common adverse events were dizziness and nausea.

Pharmacokinetics—The pharmacokinetic parameters are shown in Table 1. rG pH 2.8 exhibited dose proportionality for C_{max} ($p = 0.186$ for the test of 0 slope), $AUC_{(0-t)}$ ($p = 0.099$), and $AUC_{(0-inf)}$ ($p = 0.104$) when administered intravenously over the 0.25 to 2.0 mg dose range. Mean maximal plasma glucagon concentrations ranging from 37 to 368 ng/mL occurred within 0.05 h following the iv bolus dose. Glucagon was rapidly eliminated, with mean half-lives ranging from 0.13 to 0.30 h. Half-life appeared to increase with increasing dose. This could be an effect of the appearance of a second compartment that only becomes apparent with higher glucagon doses. The mean clearance was similar between the treatments (≈59 L/h). The volume of distribution (V_{ext}), which is affected by changes in the rate of elimination, increased with increasing doses.

Glucodynamics—Glucodynamic parameters are shown in Table 1. Mean maximal blood glucose concentrations were similar for each treatment (129 to 136 mg/dL) and occurred within 0.36 h after the iv bolus dose of glucagon. This finding indicates that even at the lowest glucagon dose, a

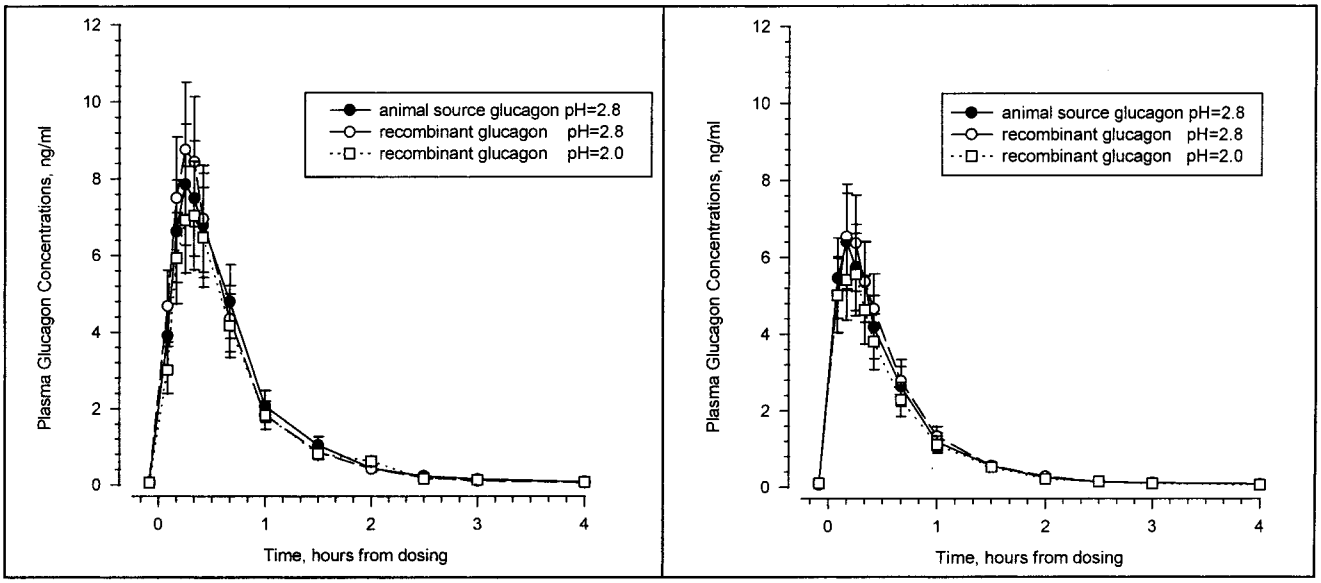

Figure 2—Mean plasma glucagon concentration versus time curves, all treatments (part II). All glucagon doses were 1.0 mg. Left panel shows subcutaneous (sc) administrations; right panel shows intramuscular (im) administrations. Bars indicate standard errors. $n = 25$. ● = animal-source glucagon pH 2.8, ○ = recombinant glucagon pH 2.8, □ = recombinant glucagon pH 2.0.

Table 2—Pharmacokinetic Parameters and Bioequivalence Assessments, Subcutaneous Administrations[a]

	$t_{1/2}$, h	C_{max}, ng/mL	t_{max}, h	$AUC_{(0-t)}$, ng·h/mL	$AUC_{(0-inf)}$, ng·h/mL
animal-source pH = 2.8 (A)	0.488 ± 0.166	9.12 ± 5.11	0.33 ± 0.10	6.57 ± 2.29	6.63 ± 2.30
recombinant pH = 2.8 (B)	0.451 ± 0.146	10.0 ± 3.65	0.27 ± 0.11	6.43 ± 2.15	6.47 ± 2.15
recombinant pH = 2.0 (C)	0.461 ± 0.166	7.94 ± 3.83	0.35 ± 0.098	5.82 ± 1.61	5.87 ± 1.62
		90% CI		90% CI	90% CI
B vs A[b]		102–126		91.4–109	91.2–109
C vs A[b]		79.1–97.8		82.4–98.2	82.4–98.1

[a] All data are reported as mean (±SD). All glucagon doses were 1.0 mg. [b] Comparisons reflect bioequivalence assessments based on log-transformed parameters. The specified range for any given parameter is the 90% confidence interval (90% CI) of the comparative ratios. If the interval falls between a range of 80% to 125%, it meets the standard bioequivalence criteria.

Table 3—Pharmacokinetic Parameters and Bioequivalence Assessments, Intramuscular Administrations[a]

	$t_{1/2}$, h	C_{max}, ng/mL	t_{max}, h	$AUC_{(0-t)}$, ng·h/mL	$AUC_{(0-inf)}$, ng·h/mL
animal-source pH = 2.8 (D)	0.414 ± 0.147	7.36 ± 2.51	0.22 ± 0.10	4.31 ± 1.36	4.36 ± 1.38
recombinant pH = 2.8 (E)	0.382 ± 0.100	7.81 ± 3.57	0.21 ± 0.11	4.62 ± 1.86	4.67 ± 1.87
recombinant pH = 2.0 (F)	0.364 ± 0.141	6.90 ± 2.64	0.22 ± 0.095	3.92 ± 1.48	3.97 ± 1.49
		90% CI		90% CI	90% CI
D vs E[b]		93.6–115		97.1–115	97.4–116
D vs F[b]		85.2–105		83.6–99.5	83.8–99.6

[a] All data are reported as mean (± SD). All glucagon doses were 1.0 mg. [b] Comparisons reflect bioequivalence assessments based on log-transformed parameters. The specified range for any given parameter is the 90% confidence interval (90% CI) of the comparative ratios. If the interval falls between a range of 80% to 125%, it meets the standard bioequivalence criteria.

maximum glucodynamic effect was present. Blood glucose returned to baseline value by 1 h in most subjects (Figure 1). There were no statistically significant differences among the four glucagon doses with respect to any glucodynamic parameters.

Part II—For Part II, 25 out of the 29 subjects successfully completed the study. Three subjects withdrew from the study for reasons unrelated to the study, and one patient withdrew due to difficult venipuncture. One subject was removed from the study due to nausea, dizziness, and pallor after a 1 mg dose of aG. rG and aG appeared to be equally safe and well tolerated. The most common adverse events reported were nausea, dizziness, and headache, occurring throughout treatment with both aG and rG.

Pharmacokinetics—Visual inspection of the mean glucagon concentration−time plots suggests that the profiles have similar absorption and elimination when comparing the glucagon formulations (aG, rG pH 2.8, and rG pH 2.0) for either route of administration (Figure 2). Slight differences in glucagon concentrations were noted between the injection routes with higher plasma concentrations occurring after sc administration. The absorption was rapid by either route, with maximum concentrations attained approximately 0.21 to 0.35 h after dosing.

A summary of the pharmacokinetic parameters is given in Table 2 and Table 3 for the sc and im routes of administration, respectively. rG pH 2.0 and pH 2.8 administered sc met the standard criteria for bioequivalence to aG with respect to $AUC_{(0-t)}$ and $AUC_{(0-inf)}$ and was nearly equivalent with respect to C_{max} comparisons. Following im administration, both rG formulations met standard bioequiv-

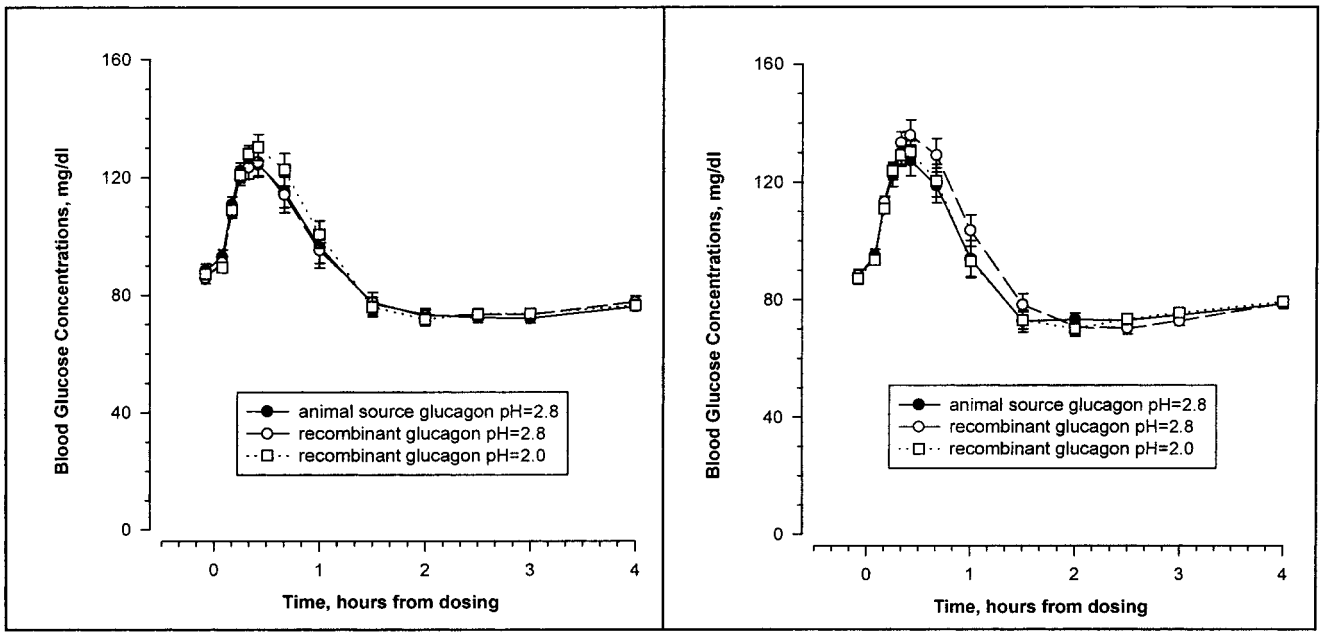

Figure 3—Mean blood glucose concentration versus time curves, all treatments (part II). All glucagon doses were 1.0 mg. Left panel shows subcutaneous (sc) administrations; right panel shows intramuscular (im) administrations. Bars indicate standard errors. $n = 25$. ● = animal-source glucagon pH 2.8, ○ = recombinant glucagon pH 2.8, □ = recombinant glucagon pH 2.0.

Table 4—Glucodynamic Parameters and Glucodynamic Equivalence Assessments, Subcutaneous Administrations[a]

	BG_{max}, mg/dL	TBG_{max}, h	$AUC_{(0-rtb)}$, mg·h/dL	MAE, mg/dL	TBG_{ex}, h	AUC_{ex}, mg·h/dL
animal-source pH = 2.8 (A)	133 ± 20.6	0.49 ± 0.46	126 ± 65.3	47.4 ± 19.2	0.60 ± 0.55	29.0 ± 25.7
recombinant pH = 2.8 (B)	132 ± 19.0	0.43 ± 0.18	130 ± 68.1	48.0 ± 13.6	0.60 ± 0.45	30.5 ± 21.4
recombinant pH = 2.0 (C)	136 ± 19.8	0.52 ± 0.54	151 ± 61.5	50.0 ± 18.5	0.59 ± 0.57	35.0 ± 20.5
	90% CI		90% CI	90% CI		90% CI
B vs A[b]	96.2–103		86.5–109	95.8–113		87.0–125
C vs A[b]	99.2–106		111–139	98.1–116		119–171

[a] All data are reported as mean (±SD). All glucagon doses were 1.0 mg. [b] Comparisons reflect bioequivalence assessments based on log-transformed parameters. The specified range for any given parameter is the 90% confidence interval (90% CI) of the comparative ratios. If the interval falls between a range of 80% to 125%, it meets the standard bioequivalence criteria.

Table 5—Glucodynamic Parameters and Glucodynamic Equivalence Assessments, Intramuscular Administrations[a]

	BG_{max}, mg/dL	TBG_{max}, h	$AUC_{(0-rtb)}$, mg·h/dL	MAE, mg/dL	TBG_{ex}, h	AUC_{ex}, mg·h/dL
animal-source pH = 2.8 (D)	137 ± 22.3	0.37 ± 0.14	136 ± 77.7	51.7 ± 17.4	0.59 ± 0.52	32.2 ± 25.9
recombinant pH = 2.8 (E)	143 ± 20.6	0.43 ± 0.15	147 ± 72.7	56.4 ± 16.8	0.61 ± 0.57	39.7 ± 29.4
recombinant pH = 2.0 (F)	138 ± 16.5	0.45 ± 0.16	129 ± 60.4	50.6 ± 16.3	0.67 ± 0.62	32.1 ± 22.8
	90% CI		90% CI	90% CI		90% CI
E vs D[b]	101–108		98.9–124	101–119		99.6–143
F vs D[b]	96.7–103		85.7–108	88.1–104		87.0–125

[a] All data are reported as mean (±SD). All glucagon doses were 1.0 mg. [b] Comparisons reflect bioequivalence assessments based on log-transformed parameters. The specified range for any given parameter is the 90% confidence interval (90% CI) of the comparative ratios. If the interval falls between a range of 80% to 125%, it meets the standard bioequivalence criteria.

alence criteria to aG with respect to all pharmacokinetic parameters.

The mean absolute bioavailability for the subcutaneous administrations of aG, rG pH 2.0, and rG pH 2.8 were 0.39, 0.35, and 0.38, respectively, using mean $AUC_{(0-inf)}$ measurements from the intravenous administrations as an index. Similar absolute bioavailability calculations for im administrations showed values of 0.25, 0.23, and 0.27 for of aG, rG pH 2.0, and rG pH 2.8, respectively.

Glucodynamics—All glucagon formulations produced nearly identical glucose response curves after sc or im administration (Figure 3). A summary of the glucodynamic parameters is given in Table 4 and Table 5 for the sc and im administrations, respectively. Comparison of glucodynamic response following sc administration showed that both rG formulations had equivalent BG_{max} and MAE values when compared to aG. Furthermore, aG and rG pH 2.8 were equivalent with respect to $AUC_{(0-rtb)}$ and glucose excursion AUC_{ex}. Compared with aG, rG pH 2.0 had a statistically greater $AUC_{(0-rtb)}$ and AUC_{ex}. All im administrations had statistically equivalent $AUC_{(0-rtb)}$ values. The rG pH 2.8 formulation showed greater BG_{max} and MAE values. However, since maximum activity appears to be achieved with low intravenous doses, this "greater" activity is likely a type I statistical error. Additionally, the AUC_{ex} of rG pH 2.0 was glucodynamically equivalent to that of aG.

Discussion

Historically, commercial glucagon has been produced through an extraction of beef and pork glands. However, recombinant DNA technology has led to an efficient process for producing pure glucagon. Moreover, the Food and Drug Administration has recently approved for marketing glucagon manufactured by that technology. The present study was designed to compare the pharmacokinetic and pharmacodynamic parameters of recombinant glucagon and animal-source glucagon. Since the sequence of animal-source glucagon is identical to that of recombinant glucagon, no difference in biological effect was expected when comparing the two formulations.

Part I of the study provided a dose-ranging assessment of rG given intravenously. Our analysis showed that rG exhibits linear disposition, with AUC and C_{max} increasing in a dose-proportional fashion. The half-life was short, with relatively high clearance (approximately 1 L/h) and small volume of distribution. The small volume of distribution is typical with proteins with their large molecular weight and polarity.

No dose−response was found with rG between the various intravenous doses. A maximum response was achieved by even the lowest dose tested, suggesting that the use of even small doses may induce hyperglycemia in patients with diabetes who use rG for radiologic procedures.

Part II of the present study demonstrated that both rG formulations administered sc were glucodynamically equivalent with respect to BG_{max} and MAE values when compared to aG. Furthermore, rG pH 2.8 was equivalent with respect to $AUC_{(0-rtb)}$ and glucose excursion AUC_{ex} when compared to aG. However, rG pH 2.0 induced higher glucose-related areas than aG following sc administration. When calculating $AUC_{(0-rtb)}$ and AUC_{ex}, it is necessary to assume that baseline glucose concentrations are stable within subject. In reality, fluctuations can occur in a subject's baseline, which can cause high intersubject variability in $AUC_{(0-rtb)}$ (41% to 53%) and AUC_{ex} (29% to 89%) and broad confidence intervals. For these reasons, the glucose-related areas may not be the most robust pharmacoynamic parameters for comparing the glucagon formulation.

TBG_{max} was observed to be greater than t_{max} after administration of glucagon by any route, although the discrepancy is smallest for sc and largest for iv. The size of this hysteresis and relative delay appears to be inversely related to the rate of appearance in the bloodstream (rate of absorption for sc and im routes) and is typical for a compound which exerts an effect in a tissue distant to where it is being measured. Nonetheless, the onset can still be considered rapid with the peak effects from the slowest absorption (sc) averaging approximately 30 min after dosing.

A review of the literature yielded a single study that investigated the pharmacokinetics and glucodynamics of a recombinant glucagon. Urae and colleagues[5] measured the pharmacokinetics and glucodynamics of a 1 mg dose of recombinant glucagon administered iv and sc (upper arm). Unlike the present study, recombinant glucagon was not compared to animal-source glucagon to determine bioequivalence. Minor differences in pharmacokinetic and glucodynamic parameters for rG pH 2.0 were noted compared to those determined by Urae et al. The glucodynamic parameter of $AUC_{(0-rtb)}$ for both iv and sc administrations was lower than those reported by Urae et al.[5] One possible explanation for this difference is the duration of blood sampling. In the Urae study, blood samples were collected over 720 min,[5] while in the present study blood samples were collected for only 240 min. Although we cannot verify the calculations of the Urae study, it appears that calculations were performed to the end of collection rather than the return to baseline. Both studies show rapid absorption of glucagon following sc administration (TBG_{max}, 0.34 ± 0.083 h and 0.52 ± 0.54 h, respectively). However, the mean BG_{max} was slightly lower in the present study when compared to the values determined by Urae et al.[5] (136 ± 19.8 mg/dL versus 160.4 ± 26.5 mg/dL, respectively). In general, mean values of pharmacokinetic parameters in the current study tended to be higher than those determined by Urae et al.[5] The minor discrepancies that were noted may be related to differences in assays, injection sites, and methods of injection.

In conclusion, we have demonstrated that glucagon produced through recombinant DNA technology demonstrates equivalent activity to the currently marketed animal-source glucagon following im and sc administration. Additionally, we have provided evidence of the pharmacokinetic equivalence between rG and aG when given by the im and sc routes. We have also shown the pharmacokinetic dose-proportionality of glucagon and that the glucose response appears to be saturated with even low doses of glucagon. Nonetheless, it is best to ensure the achievement of a maximum glucose response in emergency situations, with a clinical dose of 1 mg recommended.

References and Notes

1. Unger R. H.; Orci L. Glucagon. In *Joslin's Diabetes Mellitus*; Kahn C. R., Weir G. C., Eds.; Lea & Febiger: Philadelphia, 1994; p 170.
2. Marks V. Glucagon in the diagnosis and treatment of hypoglycemia. In *Glucagon II*; Lefebvre P. J., Ed.; Springer-Verlag: New York, 1983; pp 646−649.
3. Khan C. R.; Shechter Y. Insulin, oral hypoglycemic agents. In *The Pharmacological Basis of Therapeutics*, 8th ed.; Gilman A. G., Rall T. W., Nies A. S., Taylor P., Eds.; Pergamon Press: New York, 1990; pp 1488−1489.
4. Diamant B.; Picazo J. Spasmolytic action and clinical use of glucagon. In *Glucagon II*; Lefebvre P. J., Ed.; Springer-Verlag: New York, 1983; pp 611−634.
5. Urae A.; Irie S.; Makino K.; Amamoto T.; Morise H.; Sakata Y.; Urae R. Phase I study of glucagon (GL-G) produced by genetic engineering technology. *Jpn. J. Clin. Pharmacol. Ther.* **1991**, *22*, 451−458.

Acknowledgments

This work was sponsored by Eli Lilly and Company (Indianapolis, IN) and has been presented in part at the American Diabetes Association (ADA) 58th Scientific Sessions in Chicago, IL, 1998.

JS990077P

Formulation of Highly Soluble Poly(ethylene glycol)-Peptide DNA Condensates

KAI Y. KWOK, DONALD L. MCKENZIE, DAVID L. EVERS, AND KEVIN G. RICE*

Contribution from *Divisions of Pharmaceutics and Medicinal Chemistry, College of Pharmacy, University of Michigan, Ann Arbor, Michigan 48109-1065.*

Received March 4, 1999. Accepted for publication July 19, 1999.

Abstract □ Two poly(ethylene glycol) (PEG)-peptides were synthesized and tested for their ability to bind to plasmid DNA and form soluble DNA condensates with reduced spontaneous gene expression. PEG-vinyl sulfone or PEG-orthopyridyl disulfide were reacted with the sulfhydryl of Cys-Trp-Lys$_{18}$ (CWK$_{18}$) resulting in the formation of nonreducible (PEG-VS-CWK$_{18}$) and reducible (PEG-SS-CWK$_{18}$) PEG-peptides. Both PEG-peptides were prepared on a micromole scale, purified by RP-HPLC in >80% yield, and characterized by ^{1}H NMR and MALDI-TOF. PEG-peptides bound to plasmid DNA with an apparent affinity that was equivalent to alkylated (Alk)CWK$_{18}$, resulting in DNA condensates with a mean diameter of 80–90 nm and ζ (zeta) potential of +10 mV. The particle size of PEG-peptide DNA condensates was constant throughout the DNA concentration range of 0.05–2 mg/mL, indicating these to be approximately 20-fold more soluble than AlkCWK$_{18}$ DNA condensates. The spontaneous gene transfer to HepG2 cells mediated by PEG-VS-CWK$_{18}$ DNA condensates was over two orders of magnitude lower than PEG-SS-CWK$_{18}$ DNA condensates and three orders of magnitude lower than AlkCWK$_{18}$ DNA condensates. PEG-VS-CWK$_{18}$ efficiently blocked in vitro gene transfer by reducing cell uptake. The results indicate that a high loading density of PEG on DNA is necessary to achieve highly soluble DNA condensates that reduce spontaneous in vitro gene transfer by blocking nonspecific uptake by HepG2 cells. These two properties are important for developing targeted gene delivery systems to be used in vivo.

Introduction

A variety of macromolecules including cationic lipids,[1] polylysine,[2] polyethylenimine,[3] and dendrimers[4] have been used as carriers to bind to negatively charged plasmid DNA and facilitate spontaneous gene transfer in cell culture as a result of charge interaction between the DNA carrier complex and the cell surface. Unfortunately, the performance of these nonviral gene delivery carriers are far less efficient in vivo due in part to the rapid pharmacokinetics and clearance of DNA complexes.[5,6] This relates to both the particle size and surface charge of the delivery system.[7] For example, cationic lipids form large DNA complexes that are trapped in the capillary beds of the lung[5] whereas smaller (<100 nm) peptide DNA condensates are scavenged by mononuclear phagocytic system (MPS) cells of the liver,[6] limiting the development of DNA delivery systems that target peripheral tissues.

The intravenous dosing of most colloids leads to opsonization and MPS cell uptake in the lung, liver, and spleen.[8] In the case of liposomes, this limitation has been largely overcome by simultaneously reducing the particle size to <100 nm and modifying the surface with PEG[9] since this polymer possesses the ideal hydration and flexibility to create a steric layer that allows liposomes to avoid opsonization and detection by MPS cells.[10]

Several studies have described the synthesis of PEG-containing polymers designed to create a steric layer on the surface of DNA condensates,[7,11−17] with the aim of improving their solubility and in vivo performance. An early study by Wolfert et al. described the synthesis of grafted copolymers of PEG (5 or 12 kDa) and polylysine$_{100}$ prepared by carbodiimide coupling 5−10 mol % of succinylated-PEG onto the side chains of polylysine.[11,12] The resulting PEG-peptides were less toxic to cells in culture compared to polylysine$_{100}$, formed DNA condensates possessing a reduced effective surface charge, and had slightly improved solubility over control polylysine DNA condensates but surprisingly were unable to reduce spontaneous gene transfer in HepG2 cells[12] in vitro, suggesting that they would not be able to block nonspecific interactions with cells in vivo.

Subsequently, Choi et al. derivatized the side chains of polylysine$_{120}$ with 5−25 mol % low molecular weight PEG of 550 Da.[13] The resulting PEG-peptide DNA condensates were also less toxic to cells than polylysine$_{120}$ DNA condensates but were similar to Wolfert's PEG-peptides in their inability to reduce spontaneous gene transfer in HepG2 cells, indicating that low molecular weight PEG was no more effective than high molecular weight PEG. Using a similar approach, PEG polylysine dendrimer copolymers were recently reported by the same group and used to form DNA condensates that were more nuclease resistant than polylysine DNA condensates but which were not examined for gene transfer.[14]

In addition, Katayose et al. synthesized PEG-polylysine block copolymers to incorporate 5 kDa PEG into polylysine by random polymerization of *N*-carboxyanhydride ϵ-(benzyloxycarbonyl)-lysine with amino-PEG, resulting in a polymer with a lysine to PEG ratio of approximately 18:1[15,16] representing approximately 5 mol % PEG. These PEG-polylysine DNA condensates were also reportedly much more resistant to endonuclease than uncondensed DNA but were not examined for solubility or gene transfer.[16,17]

To date, there are no reports of a PEG-peptide DNA condensing agents that significantly increase the solubility of the DNA condensates and/or reduce spontaneous gene transfer to HepG2 cells. These are both significant problems since the poor solubility of peptide DNA condensates of approximately 50−100 μg/mL limits the dosing volume and precludes dose escalation during in vivo gene transfer. Likewise, reducing the level of spontaneous gene transfer in vitro is a first step toward developing DNA formulations that avoid nonspecific gene transfer to cells in vivo and may allow the development of DNA formulations that target to peripheral sites. Here we describe the synthesis and formulation properties of two PEG-peptides, both of which

* To whom correspondence should be addressed. Tel: 734-763-1032. Fax: 734-763-2022. E-mail: krice@umich.edu.

10.1021/js990072s CCC: $18.00
Published on Web 08/27/1999

significantly improve DNA condensate solubility and one of which dramatically reduces spontaneous gene transfer of DNA condensates in vitro. The results suggest that these two properties are closely linked to the loading level of PEG on peptide DNA condensates.

Materials and Methods

PEG-orthopyridyl disulfide (PEG-OPSS, 5 kDa) and PEG-vinyl sulfone (PEG-VS, 5 kDa) were purchased from Shearwater Inc. (Huntsville, AL) and Fluka (Ronkonkoma, NY), respectively. Fetal calf serum and LipofectAce were obtained from Gibco BRL (Gaithersburg, MD). Minimum essential media (MEM) and CM Sephadex C50 were purchased from Sigma (St. Louis, MO). TCEP (tris(2-carboxyethyl)phosphine hydrochloride) was purchased from Aldrich, (Milwaukee, WI). D-Luciferin and luciferase from *Photinus pyralis* were from Boehringer Mannheim (Indianapolis, IN). The 5.6 kb plasmid (pCMVL) encoding the reporter gene luciferase under the control of the cytomegalovirus promoter was a gift from Dr. M. A. Hickman at the University of California, Davis.[18] pCMVL was produced in *E. coli* and purified using a Qiagen Ultrapure-100 kit (Santa Clarita, CA). Bradford reagent was purchased from Bio-Rad (Hercules, CA). Preparative and analytical C18 reverse phase HPLC columns were purchased from Vydac (Hesperia, CA). HPLC was performed using a computer-interfaced HPLC and fraction collector from ISCO (Lincoln, NE).

Synthesis of PEG-VS-CWK$_{18}$ and PEG-SS-CWK$_{18}$—CWK$_{18}$ (Cys-Trp-Lys$_{18}$) and dimeric-CWK$_{18}$ were synthesized and characterized as described previously.[19] The Cys residue on CWK$_{18}$ was alkylated with iodoacetic acid resulting in AlkCWK$_{18}$ as reported.[19] The synthesis of PEG-VS-CWK$_{18}$ utilized dimeric-CWK$_{18}$ (0.5 μmol) which was reduced to form 1 μmol of CWK$_{18}$ by reaction with 25 μmol of TCEP[20] in 0.5 mL of 0.1 M sodium phosphate pH 7 for 4 h at room temperature. PEG-VS-CWK$_{18}$ was formed by reacting 1 μmol of reduced CWK$_{18}$ with 30 μmol of PEG-VS in a total volume of 1.2 mL of 0.1 M sodium phosphate pH 7 at room temperature for 12 h. The progress of the reaction was monitored by analytical RP-HPLC eluted at 1 mL/min with 0.1% TFA and a gradient of acetonitrile (5−65% over 30 min) while detecting by A_{280nm}. The reaction mixture was applied to a CM Sephadex C50 cation-exchange column (0.7 × 15 cm) eluted with 60 mL of water to remove free PEG-VS as the unbound fraction and then with 15 mL of 1.5 M sodium chloride while collecting 5 mL fractions. PEG-VS-CWK$_{18}$ and CWK$_{18}$ were detected by A_{280nm} and were pooled and desalted by 5 h dialysis against 4 L of water in 1000 MWCO tubing and then freeze-dried. PEG-VS-CWK$_{18}$ was resolved from CWK$_{18}$ by injecting 0.5 μmol onto a semipreparative C18 RP-HPLC column (2 × 25 cm) eluted at 10 mL/min with 0.1% TFA and a gradient of acetonitrile (5 to 65% over 30 min) while detecting by A_{280nm}. The peak eluting at 25 min yielded 0.8 μmol of PEG-VS-CWK$_{18}$ (80%) based on tryptophan absorbance (ϵ_{280nm} = 5600 M^{-1} cm^{-1}).

A disulfide bond exchange reaction was used to prepare PEG-SS-CWK$_{18}$. Prior to conjugation of PEG-OPSS, dimeric-CWK$_{18}$ was reduced and then purified by RP-HPLC eluted as described above. Reduced CWK$_{18}$ (1 μmol) was reacted with 4 μmols of PEG-OPSS in 1 mL of 0.1 M sodium phosphate pH 7 at room temperature for 30 min. The reaction was monitored by analytical RP-HPLC which detected a single new product peak eluting at 25 min. PEG-SS-CWK$_{18}$ was purified by injecting 0.5 μmol portions onto semi-preparative RP-HPLC eluted as described above resulting in an isolated yield of 95%.

PEG-VS-CWK$_{18}$ and PEG-SS-CWK$_{18}$ (1 μmol) were prepared for ^{1}H NMR by D_2O exchange followed by dissolving the sample in 0.5 mL of D_2O (99.96%) containing acetone as an internal standard. ^{1}H NMR spectra were generated on a Bruker 500 MHz spectrometer operated at 23 °C. PEG-peptides were prepared for MALDI-TOF by dissolving 5 nmol in 20 μL of water. These (0.5 μL) were combined with 0.5 μL of saturated α-cyano-4-hydroxycinnamic acid in 50 v/v % acetonitrile and 0.3% trifluoroacetic acid and then analyzed on a Vestec LaserTec MS (PerSeptive Biosystems, Framingham, MA) operated in the linear mode at 20 kV.

Formulation of Peptide DNA Condensates—Peptide DNA condensates were formed by adding 75 μg of DNA (pCMVL in 750 μL of 5 mM Hepes pH 7.4) to varying amounts of peptide (7.5 to 90 nmol in 750 μL of Hepes) while vortexing, followed by equilibration at room temperature for 1 h. Peptide binding to DNA was monitored by a fluorescent dye displacement assay.[19] A 1 μg aliquot of the peptide DNA condensate was diluted to 1 mL in Hepes containing 0.1 μM thiazole orange. The fluorescence of the intercalated dye was measured on an LS50B fluorometer (Perkin-Elmer, UK) in a microcuvette by exciting at 500 nm while monitoring emission at 530 nm.

The particle size of peptide DNA condensates were analyzed at a DNA concentration of 50 μg/mL in Hepes by quasielastic light scattering (QELS). The particle surface charge was determined by ζ (zeta) potential analysis using a Brookhaven ZetaPlus (Brookhaven Instruments). The solubility of peptide DNA condensates were determined by measuring particle size as a function of DNA concentration (50 μg/mL to 2 mg/mL) at a constant peptide: DNA stoichiometry of 0.4 nmol of peptide per μg of DNA corresponding to a charge ratio (NH_4^+:PO_4^-) of 2.3:1.

DNA cocondensates were prepared by add-mixing AlkCWK$_{18}$ and PEG-VS-CWK$_{18}$ in ratios ranging from 0 to 100 mol % and condensing DNA at a charge ratio of 2.3:1 as described above. To establish the mol ratio of peptides bound to DNA, condensates were dialyzed in a fixed volume (0.5 mL) dialyzer for 75 h against water using a 100 000 MWCO membrane. Peptide DNA condensates in the retentate (0.5 mL) were dissociated by adding 50 μL of 5 M sodium chloride in 0.1% TFA. AlkCWK$_{18}$ and PEG-VS-CWK$_{18}$ were quantified by injecting 1 nmol of peptide (100 μL) onto analytical RP-HPLC eluted with 0.1% TFA and a gradient of acetonitrile (5 to 65% over 30 min) while detecting tryptophan by fluorescence ($\lambda_{ex280nm}$, $\lambda_{em350nm}$). The peak integration areas were used to quantify AlkCWK$_{18}$ and PEG-VS-CWK$_{18}$ with reference to standard curves developed for each peptide.

In Vitro Gene Expression and Cell Binding—HepG2 cells were plated at 1.5 × 10^5 cells per 35 mm well and grown to 40−70% confluence in MEM supplemented with 10% fetal calf serum (FCS). Peptide DNA condensates (10 μg of DNA) were added dropwise to triplicate sets of cells in 2% FCS containing 80 μM chloroquine. After 5 h incubation at 37 °C, the media was replaced with MEM supplemented with 10% FCS, and luciferase expression was determined at 24 h. Cells were washed twice with ice-cold phosphate-buffered saline (calcium and magnesium free) and then treated with 0.5 mL of ice-cold lysis buffer (25 mM Tris hydrochloride pH 7.8, 1 mM EDTA, 8 mM magnesium chloride, 1% Triton X-100, 1 mM DTT) for 10 min. The cell lysate was scraped, transferred to 1.5 mL microcentrifuge tubes, and centrifuged for 7 min at 13 000g at 4 °C to pellet debris. Lysis buffer (300 μL), sodium-ATP (4 μL of a 180 mM solution, pH 7, 4 °C), and cell lysate (100 μL, 4 °C) were combined in a test tube, briefly mixed, and immediately placed in the luminometer. Luciferase relative light units (RLU) were recorded on a Lumat LB 9501 (Berthold Systems, Germany) with 10 s integration after automatic injection of 100 μL of 0.5 mM D-luciferin (prepared fresh in lysis buffer without DTT). The expression level of luciferase was normalized for protein using the Bradford assay,[21] and the relative light units were converted to fmol of luciferase/mg of protein using a standard curve developed by adding luciferase to cell supernatant. Each experimental result represents the mean and standard deviation derived from a triplicate set of transfections.

LipofectAce (Gibco BRL, 1:2.5 w/w dimethyl dioctadecylammonium bromide and dioleoylphosphatidylethanolamine) was optimized for use to mediate gene transfection in HepG2 cells according to the manufacturer's instructions. DNA/LipofectAce complexes were prepared by combining 10 μg of DNA in 100 μL of serum free media (SFM) with 60 μL of LipofectAce prepared in 150 μL of SFM. The LipofectAce DNA complex was then diluted with 1.7 mL of SFM and used to transfect HepG2 cells for 5 h followed by replacement of the transfecting media with MEM supplemented with 10% FBS. The cells were incubated for a total of 24 h, harvested, and then analyzed for luciferase as described above.

Iodinated plasmid DNA was prepared with specific activity of 300 nCi per μg of DNA as described previously.[22] Prior to forming DNA condensates, the specific activity of the ^{125}I DNA was adjusted to 4.5 nCi per μg of DNA by combining with unlabeled plasmid. DNA condensates were prepared using AlkCWK$_{18}$, PEG-SS-CWK$_{18}$, or PEG-VS-CWK$_{18}$ as described above. Peptide ^{125}I-DNA condensates (10 μg) were used to transfect HepG2 cells for 5 h according to the procedure described above. The radioactive media was removed, cells were washed with phosphate-buffered saline, harvested with lysis buffer, and the cell-associated radioactivity was quantified by gamma counting.

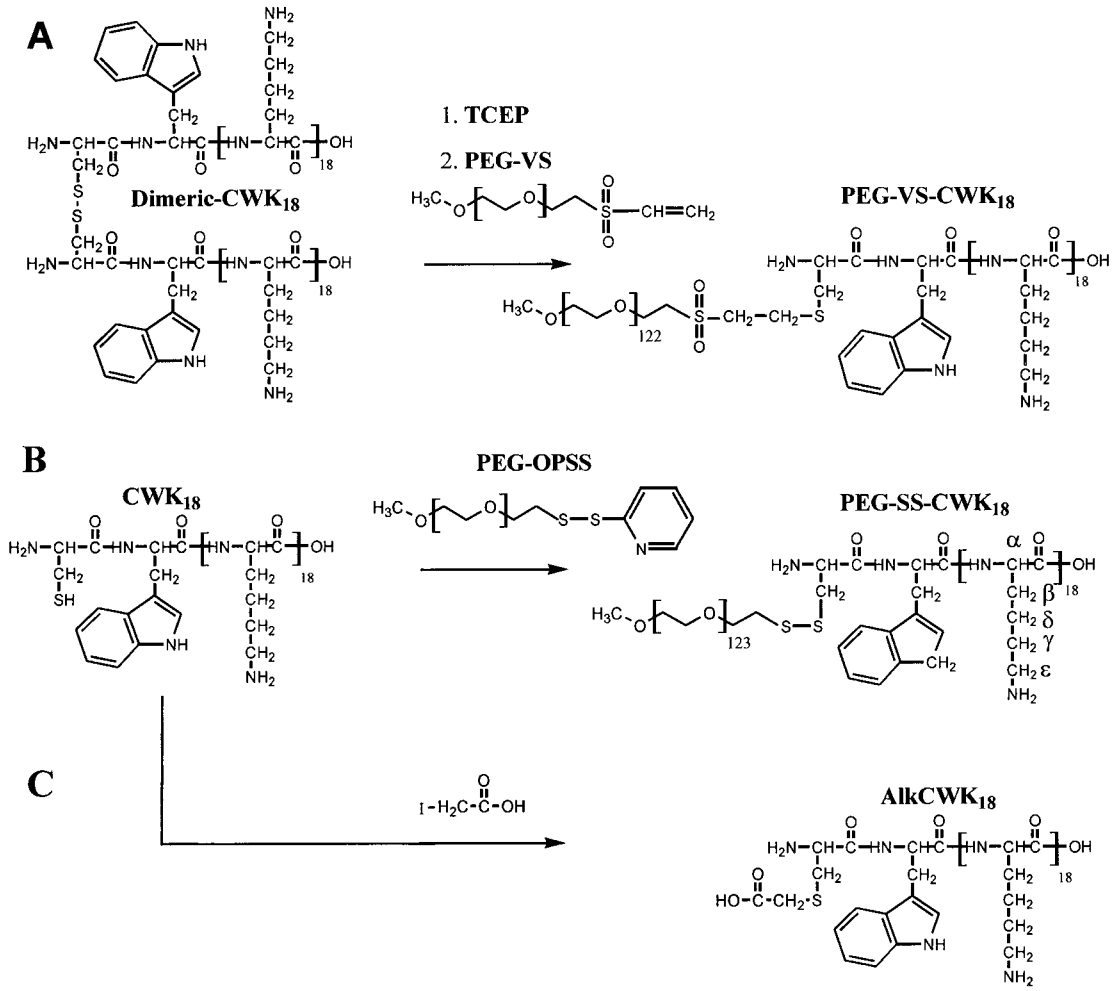

Figure 1—Reaction schemes for the synthesis of PEG-CWK_{18} conjugates. (A) TCEP was used to reduce dimeric-CWK_{18} to generate CWK_{18}. This was reacted in situ with PEG-VS to form PEG-VS-CWK_{18}. (B) Alternatively, the reaction of CWK_{18} with PEG-OPSS formed PEG-SS-CWK_{18}. (C) AlkCWK_{18} was produced by reacting CWK_{18} with iodoacetic acid. The α, β, γ, δ, and ϵ protons of Lys of PEG-SS-CWK_{18} illustrate the nomenclature used for assigning PEG-peptides in Figure 3.

Results

PEG-Peptide Synthesis—PEG was covalently attached to the Cys residue of a 20 amino acid synthetic peptide (CWK_{18}) to prepare two PEG-peptides possessing either a reversible (PEG-SS-CWK_{18}) or irreversible (PEG-VS-CWK_{18}) covalent linkage (Figure 1). Each reaction was optimized by systematically changing the pH and the stoichiometry of peptide to PEG while monitoring the product formation by analytical RP-HPLC. Since the reaction of CWK_{18} with PEG-VS at pH 7 was slow (12 h), TCEP was added to reduce dimeric-CWK_{18} and also inhibit its re-formation during conjugation with PEG-VS. At pH 7, a mol ratio of PEG-VS:CWK_{18} of 30:1 resulted in optimal conjugation to form PEG-VS-CWK_{18}. At suboptimal stoichiometries or lower pH the reaction was incomplete whereas at a higher pH, dimeric-CWK_{18} re-formed as the major product.

In contrast to the synthesis of PEG-VS-CWK_{18}, the optimal reaction conditions to prepare PEG-SS-CWK_{18} only required a 4 mol excess of PEG-OPSS over CWK_{18} at pH 7. In this case, attempts to block the formation of dimeric-CWK_{18} with TCEP led to the reduction of PEG-OPSS, completely inhibiting the desired reaction. Instead, reduced CWK_{18} was prepared and found to react rapidly (30 min) with PEG-OPSS with minimal formation of dimeric-CWK_{18}.

RP-HPLC analysis of the crude reaction product of PEG-VS-CWK_{18} demonstrated a nearly complete disappearance of CWK_{18} with the formation of a new peak eluting at 25 min (Figure 2B). Despite the apparent complete resolution of the desired product, careful examination revealed that PEG-VS coeluted with PEG-VS-CWK_{18}. This was evident from NMR analysis which determined a 10-fold excess of PEG relative to CWK_{18} in the HPLC purified product (data not shown). Consequently, PEG-VS-CWK_{18} was purified using cation exchange to remove excess PEG-VS and then by RP-HPLC to remove unreacted CWK_{18} resulting in a product that rechromatographed as a single peak on RP-HPLC (Figure 2D). Proton NMR analysis identified resonances assigned to the α, β, γ, δ, and ϵ protons of the Lys residues as well as the Trp aromatic resonances (Figure 3A). Integration of protons at 3.67 ppm (PEG) relative to the signal at 2.97 ppm (Lys ϵ) produced a peak area ratio of 13.5:1 corresponding to a 1:1 conjugate of PEG_{122} and CWK_{18}.

RP-HPLC analysis of the crude reaction product of PEG-OPSS and CWK_{18} identified a product peak eluting at 25 min, a PEG-OPSS reagent peak at 28 min, a thiol pyridine (TP) byproduct peak at 5 min, and a trace of dimeric-CWK_{18} eluting at 15 min (Figure 2C). PEG-SS-CWK_{18} was isolated in a single step by semipreparative RP-HPLC, rechromatographed as a single peak on analytical HPLC (Figure 2E), and produced an NMR spectrum with an integration ratio of PEG:Lys also establishing a 1:1 conjugate of PEG_{123} and CWK_{18} (Figure 3B).

MALDI-TOF analysis of PEG-VS-CWK_{18} and PEG-SS-CWK_{18} produced a broad peak centered at 8433 and 8297

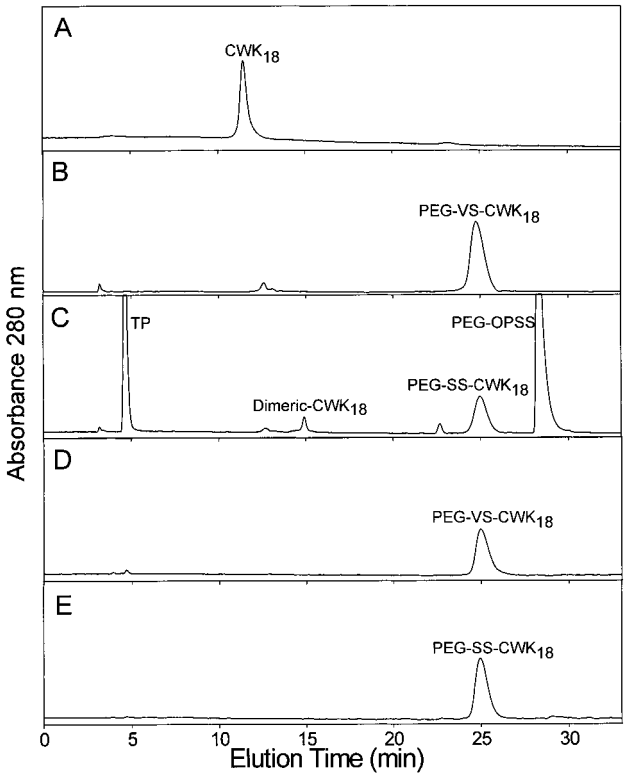

Figure 2—Analytical RP-HPLC analysis of PEG-CWK_{18} conjugates. The reaction of dimeric-CWK_{18} with TCEP and PEG-VS formed a single major product as shown in panel B. Alternatively, reduced CWK_{18} (panel A) reacted with PEG-OPSS to produce PEG-SS-CWK_{18}, dimeric-CWK_{18}, thiol-pyridine (TP), and unreacted PEG-OPSS as shown in panel C. Purified PEG-VS-CWK_{18} and PEG-SS-CWK_{18} both eluted as a single peak as shown in panels D and E, respectively.

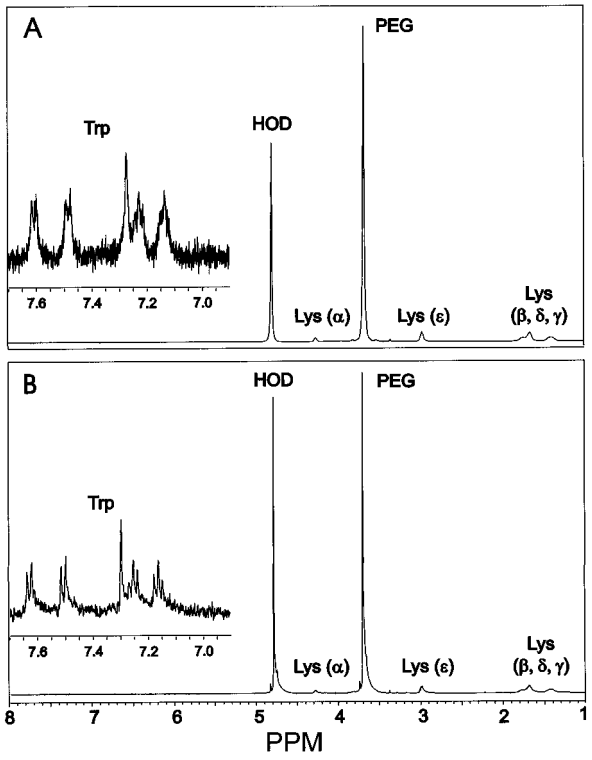

Figure 3—^{1}H NMR analysis of PEG-CWK_{18} conjugates. The 500 MHz ^{1}H NMR spectrum of PEG-VS-CWK_{18} (panel A) and PEG-SS-CWK_{18} (panel B) are illustrated with the key signals of the Lys, Trp and PEG identified according to Figure 1. The integration of the ϵ protons of Lys relative to the PEG protons established a degree of polymerization of 122 for PEG-VS-CWK_{18} and 123 for PEG-SS-CWK_{18}.

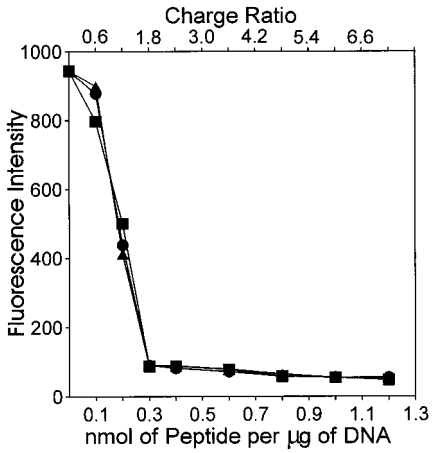

Figure 4—Relative binding affinity of PEG-CWK_{18} conjugates to DNA. The fluorescence intensity resulting from the titration of AlkCWK_{18} (●), PEG-SS-CWK_{18} (■), and PEG-VS-CWK_{18} (▲) to compete for intercalator dye binding to DNA is shown. An asymptote at 0.3 nmol of each peptide per μg of DNA established that each peptide binds to DNA with equivalent affinity.

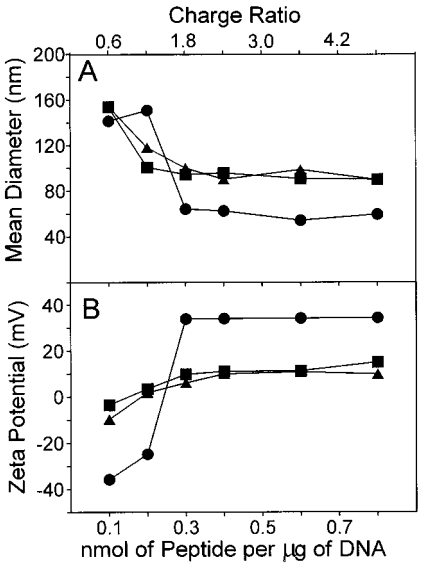

Figure 5—QELS particle size and ζ potential analysis of PEG-CWK_{18} DNA condensates. The mean particle size of AlkCWK_{18} (●), PEG-SS-CWK_{18} (■), and PEG-VS-CWK_{18} (▲) DNA condensates is plotted as a function of peptide:DNA stoichiometry in panel A. The mean ζ potential for each DNA condensate is plotted in panel B. An indistinguishable particle size and ζ potential was determined for each PEG-CWK_{18} conjugate. However, a significant decrease in the ζ potential for PEG-CWK_{18} DNA condensates (+10 mV) versus AlkCWK_{18} DNA condensates (+35 mV) provided evidence of the formation of a steric barrier.

m/z, respectively. These results were consistent with the formation of conjugates of CWK_{18} (2648 amu) and polydisperse PEG of approximately 5800 Da.

PEG-Peptide DNA Condensate Formulation—The DNA binding affinity of AlkCWK_{18}, PEG-VS-CWK_{18}, and PEG-SS-CWK_{18} were compared using a fluorescent dye displacement assay. A coincident titration curve for each peptide with an asymptote at 0.3 nmol per μg of DNA corresponding to a charge ratio of 1.8:1 suggested that both PEG-peptides bind to DNA with equivalent affinity as AlkCWK_{18} (Figure 4).

The particle size and ζ potential of DNA condensates prepared with AlkCWK_{18}, PEG-VS-CWK_{18}, and PEG-SS-CWK_{18} were examined as a function of peptide:DNA stoichiometry (Figure 5). The mean diameter for both PEG-peptide DNA condensates was 90 nm at a charge ratio of 1.8:1 or higher whereas the mean diameter for AlkCWK_{18}

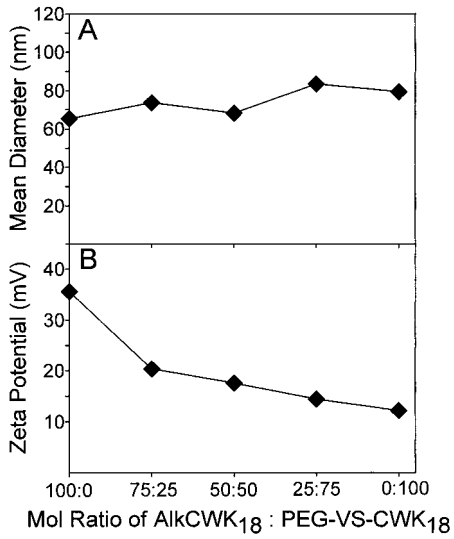

Figure 6—QELS particle size and ζ potential analysis of peptide DNA cocondensates. Particle size analysis was used to characterize peptide DNA cocondensates prepared at 50 μg/mL of DNA and varying mol % of $AlkCWK_{18}$ and PEG-VS-CWK_{18} as shown in panel A. The ζ potential of DNA cocondensates is shown in panel B. The mean particle size changes from 65 to 80 nm whereas the ζ potential of DNA cocondensates decreases from +35 to +10 mV with increasing mol % of PEG-VS-CWK_{18}.

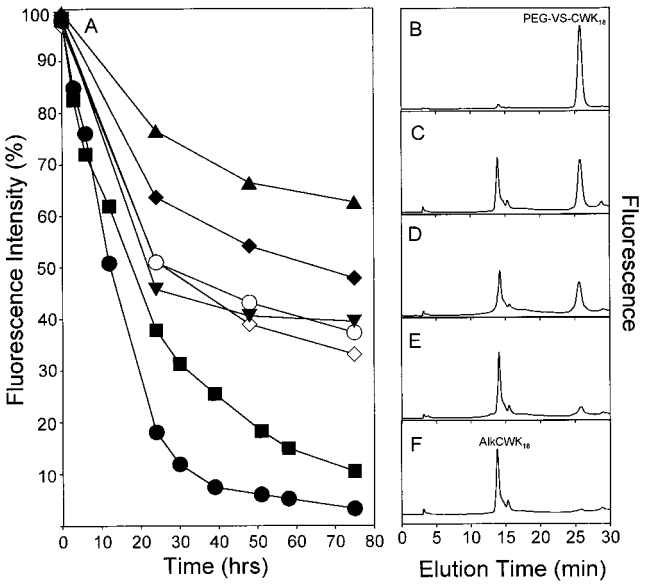

Figure 7—RP-HPLC analysis of peptide DNA cocondensates. The time course of dialysis of free $AlkCWK_{18}$ (●), free PEG-VS-CWK_{18} (■), $AlkCWK_{18}$ DNA condensates (▼), PEG-VS-CWK_{18} DNA (▲), and cocondensates of 25:75 (◆), 50:50 (○), 75:25 (◇) mol % of $AlkCWK_{18}$:PEG-VS-CWK_{18} bound to DNA was determined by tryptophan fluorescence of the retentate (panel A). After 75 h of dialysis, peptide DNA condensates in the retentate were dissociated with sodium chloride and directly chromatographed on RP-HPLC. Panels B–F illustrate chromatograms resulting from 100 mol % PEG-VS-CWK_{18} DNA condensates (panel B), DNA cocondensates prepared with 75:25 (panel C), 50:50 (panel D), 25:75 (panel E) PEG-VS-CWK_{18}:$AlkCWK_{18}$, and 100 mol % $AlkCWK_{18}$ DNA condensates (panel F).

DNA condensates was 60 nm (Figure 5A). In contrast, a large decrease in ζ potential of +25 mV was identified for PEG-peptide DNA condensates at a charge ratio of 1.8:1 compared to $AlkCWK_{18}$ DNA condensates (Figure 5B).

Since PEG-VS-CWK_{18} and $AlkCWK_{18}$ possess equivalent DNA binding affinity, add-mixtures of the two peptides were used to prepare DNA cocondensates. The average particle size increased from 65 to 80 nm using add-mixtures of $AlkCWK_{18}$ and PEG-VS-CWK_{18} varying from 0 to 100 mol % while keeping the charge ratio constant at 2.3:1

Table 1—Quantitative Analysis of DNA Cocondensates

input add-mixture (mol % $AlkCWK_{18}$: mol % PEG-VS-CWK_{18})	recovery ratio[a] (mol % $AlkCWK_{18}$: mol % PEG-VS-CWK_{18})
0:100	0:100
25:75	41:59
50:50	59:41
75:25	82:18
100:0	100:0

[a] Based on HPLC standard curves developed for $AlkCWK_{18}$ and PEG-VS-CWK_{18}.

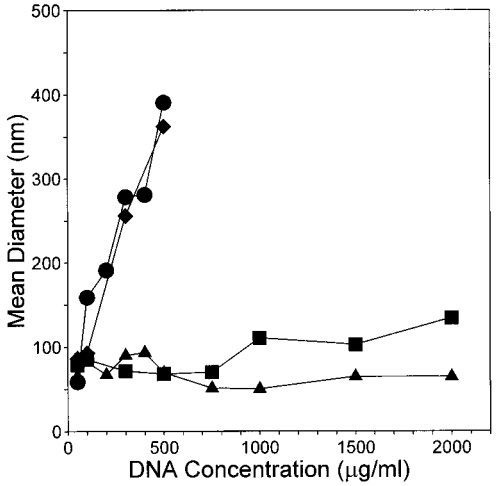

Figure 8—Solubility of peptide DNA condensates. Particle size analysis was performed as a function of DNA concentration using 100 mol % $AlkCWK_{18}$ (●) and 100 mol % PEG-VS-CWK_{18} (▲) DNA condensates and using $AlkCWK_{18}$:PEG-VS-CWK_{18} DNA cocondensates prepared with 50 (◆) and 90 (■) mol % PEG-VS-CWK_{18}. The particle size increased to >400 nm above 500 μg/mL for $AlkCWK_{18}$ DNA condensates but remained at <100 nm for PEG-VS-CWK_{18} DNA condensates throughout concentrations up to 2 mg/mL.

(Figure 6A). Likewise, the ζ potential decreased from +35 mV to +10 mV as the stoichiometry of PEG-VS-CWK_{18} increased (Figure 6B), suggesting the formation of DNA cocondensates with intermediate PEG loading.

To further confirm the formation of DNA cocondensates, unbound peptides were removed by microdialysis and the ratio of peptides bound to DNA was determined by HPLC. Control experiments established the nearly complete removal (>90%) of free $AlkCWK_{18}$ or PEG-VS-CWK_{18} from the retentate after 75 h of dialysis (Figure 7A). However, the dialysis of DNA cocondensates prepared at charge ratios of 2.3:1 resulted in the removal of unbound peptide and retention of >35% of the tryptophan fluorescence. Dissociation and RP-HPLC analysis of the retained peptide (Figure 7B–F) allowed recovery of $AlkCWK_{18}$ and PEG-VS-CWK_{18} at ratios that agreed to within 16% of the input ratio for each DNA cocondensate (Table 1) in which the loss of PEG-VS-CWK_{18} was greater than that of $AlkCWK_{18}$.

DNA condensate solubility was evaluated by examining the particle size of concentrated solutions. $AlkCWK_{18}$ DNA condensates increased in particle size from 60 to 400 nm when increasing DNA concentration from 50 to 500 μg/mL and then formed visible flocculates at higher concentrations. Alternatively, PEG-VS-CWK_{18} DNA condensates maintained a mean diameter of <100 nm throughout concentrations ranging from 0.05 to 2 mg/mL and showed no sign of increasing in size (Figure 8). Likewise, substitution of PEG-SS-CWK_{18} for PEG-VS-CWK_{18} resulted in the formation of DNA condensates with 88 nm mean diameter at 2 mg/mL.

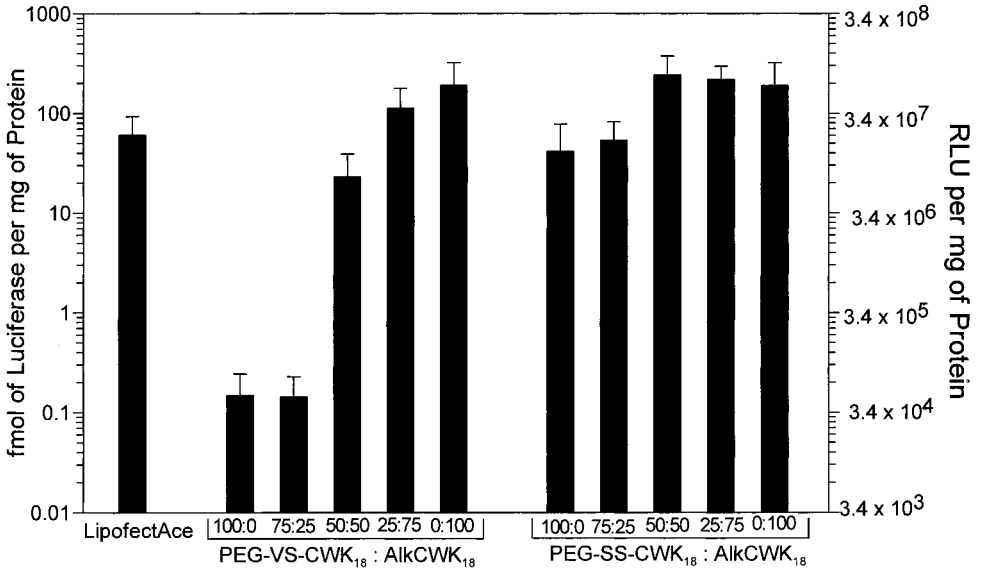

Figure 9—In vitro gene transfer efficiency of PEG-CWK_{18} DNA condensates. The in vitro expression of luciferase in HepG2 cells is compared for PEG-VS-CWK_{18} and PEG-SS-CWK_{18} as well as cocondensates prepared with $AlkCWK_{18}$ at the ratios indicated. LipofectAce is included as a control gene transfer agent.

DNA cocondensates containing 50 mol % PEG-VS-CWK_{18} and $AlkCWK_{18}$ possessed similar poor solubility properties to that of 100 mol % $AlkCWK_{18}$ DNA condensates. However, DNA cocondensates composed of 90 mol % PEG-VS-CWK_{18} and 10 mol % $AlkCWK_{18}$ also maintained a particle size of <100 nm up to 750 μg/mL and then formed larger particles (>100 nm) at DNA concentrations of 1 mg/mL or higher (Figure 8).

DNA condensates prepared with PEG-VS-CWK_{18}, PEG-SS-CWK_{18}, $AlkCWK_{18}$, and add-mixtures of $AlkCWK_{18}$ and PEG-peptides were compared by measuring luciferase expression in HepG2 cells 24 h post-transfection (Figure 9). PEG-VS-CWK_{18} DNA condensates reduced spontaneous gene transfer by three orders of magnitude compared to $AlkCWK_{18}$ DNA condensates. The reduction was only 10-fold when transfecting with DNA cocondensates prepared with 50 mol % PEG-VS-CWK_{18} and only 2-fold using cocondensates composed of 25 mol % PEG-VS-CWK_{18} (Figure 9).

The gene transfer properties of PEG-SS-CWK_{18} DNA condensates were significantly different than PEG-VS-CWK_{18} DNA condensates. DNA condensates prepared with 100 or 75 mol % PEG-SS-CWK_{18} reduced spontaneous gene transfer by 5-fold relative to $AlkCWK_{18}$ DNA condensates while DNA cocondensates prepared with 50 or 25 mol % of PEG-SS-CWK_{18} were equivalent to $AlkCWK_{18}$ DNA condensates (Figure 9).

The cell binding of ^{125}I-DNA was compared for $AlkCWK_{18}$, PEG-VS-CWK_{18}, and PEG-SS-CWK_{18} DNA condensates during a 5 h transfection. Approximately 14% of the radioactivity was cell-associated for $AlkCWK_{18}$ DNA condensates whereas only 6.8% and 0.2% were cell-associated when using PEG-SS-CWK_{18} and PEG-VS-CWK_{18} as DNA condensing agents, respectively (Figure 10). These results correlated well with the observed gene transfer efficiency for each peptide DNA condensate, suggesting differences in the uptake of these condensates was the main cause of their difference in gene expression.

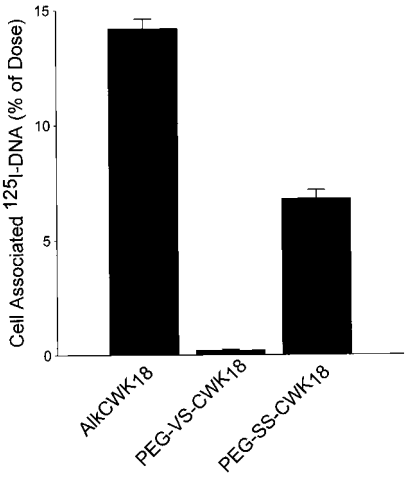

Figure 10—HepG2 cell binding of peptide DNA condensates. HepG2 cells were transfected for 5 h with 45 nCi (10 μg) of ^{125}I-DNA condensates prepared with either $AlkCWK_{18}$, PEG-VS-CWK_{18}, or PEG-SS-CWK_{18}. The cell associated DNA recovered is expressed as the percent of ^{125}I-DNA dosed onto cells. The results represent the mean ± SD for three determinations.

Discussion

The targeting of DNA to specific cells in vivo for the purpose of mediating therapeutically relevant levels of gene expression will require systematic optimization of the drug delivery system.[23] The design of such delivery systems must attempt to minimize the carrier's toxicity and antigenicity, increase the DNA's metabolic stability, control the particle size and charge, and increase the DNA condensate solubility as well as provide a means to target DNA to the nucleus of the cell. Thus far, PEG-peptides have been reported to decrease toxicity,[11–13] increase DNA stability,[14,17] and improve DNA solubility.[12] In the present study we report the synthesis of two PEG-peptides that simultaneously create very soluble DNA condensates and significantly inhibit spontaneous gene transfer of peptide DNA condensates in vitro. A major finding is that both of these properties are influenced to different degrees by the load level of PEG on DNA condensates.

The directed synthesis of the low molecular weight PEG-peptides reported here is a major distinction of this work compared to others. The conjugation of PEG (5000 Da) to a single cysteine of CWK_{18} afforded highly purified PEG-peptides that controlled the PEG attachment site and allowed comparison of reducible and nonreducible linkages. Notably, the apparent binding affinity of both PEG-peptides for DNA were equivalent to $AlkCWK_{18}$ as determined by the intercalator exclusion assay (Figure 4),

indicating that conjugates of CWK_{18} retain their ability to bind and condense DNA. Due to the homogeneity of the peptide portion of PEG-VS-CWK_{18} and PEG-SS-CWK_{18}, DNA condensates formed at charge ratios of 1.8:1 or higher achieved a constant particle size and ζ potential, establishing both the absence of interfering peptides and that excess PEG-peptide does not bind to fully condensed DNA.

ζ potential measurements revealed evidence that PEG-peptides altered the surface properties of DNA condensate. The ζ potential of PEG-VS-CWK_{18} and PEG-SS-CWK_{18} DNA condensates were indistinguishable and reached a minimum of +10 mV at a calculated charge ratio of 1.8:1 (Figure 5B). The decrease in ζ potential resulted from the covalent attachment of PEG since the addition of equivalent amounts of free PEG to AlkCWK_{18} DNA condensates did not influence its ζ potential (data not shown). Likewise, analysis of DNA cocondensates established a correlation between the ζ potential and the mol % of PEG-VS-CWK_{18} incorporated into the cocondensate (Figure 6B). The recovery of the approximate input ratio of AlkCWK_{18} and PEG-VS-CWK_{18} following prolonged dialysis confirmed the formation of DNA cocondensates. This allowed add-mixing of two condensing peptides (AlkCWK_{18} and PEG-VS-CWK_{18}) to systematically alter both physical and biological properties of peptide DNA condensates.

The formation of a steric layer is highly dependent on the amount PEG loaded onto DNA condensates.[10,12] This is most evident with DNA cocondensates possessing between 0 and 25 mol % PEG-peptide where the ζ potential decreased sharply to +20 mV and then only declined gradually to reach +10 mV at 25−100 mol % PEG-peptide. Even though the ζ potential only changed by +10 mV when titrating between 25 and 100 mol % of PEG-peptide (Figure 6B), these DNA condensates were most altered in solubility and gene transfer efficiency.

The solubility achieved for 100 mol % PEG-peptide DNA condensates (2 mg/mL) is far greater than the solubility reported (60 μg/mL) for other PEG-peptides DNA condensates.[12] This physical property appears to be very dependent on the loading density of PEG since cocondensates prepared with 50 mol % PEG-VS-CWK_{18} were not improved in solubility relative to AlkCWK_{18} DNA condensates. Even cocondensates formed with as much as 90 mol % PEG-VS-CWK_{18} demonstrated an increase in particle size at concentrations greater than 750 μg/mL, indicating that even slightly less PEG on the DNA condensate will result in lower solubility.

Earlier studies demonstrated that the in vitro gene transfer efficiency for peptide DNA condensates was dependent on the charge ratio.[19,24] The expression reached a maximum when AlkCWK_{18} DNA condensates were formed at charge ratio of 1.8:1 or higher, suggesting that the positive charge on DNA condensates contributes to their spontaneous transfection in cell culture. In support of this hypothesis, fully condensed PEG-VS-CWK_{18} DNA condensates prepared at a charge ratio of 2.3:1 possess a lower ζ potential of +10 mV and reduced spontaneous gene transfer by 1000-fold compared to AlkCWK_{18} DNA condensates. Likewise, DNA cocondensates possessing intermediate ζ potential partially reduced gene transfer, further demonstrating a correlation between DNA condensate charge and the level of spontaneous gene transfer. However, these data also established that the PEG load level needed to block spontaneous gene transfer in vitro is much lower than that required to create soluble PEG-peptide DNA condensates.

Even though PEG-VS-CWK_{18} and PEG-SS-CWK_{18} DNA condensates were equivalent in their physical properties, they proved to be unequivalent in their ability to reduce spontaneous gene transfer (Figure 9). Since the two peptides only differ in their linkage between PEG and peptide, a possible explanation was the reduction of PEG-SS-CWK_{18} either outside or inside the cell to form CWK_{18} DNA condensates during the time of transfection. To test this hypothesis, radioiodinated DNA condensates were used to determine the percent cell associated after a 5 h transfection (Figure 10). PEG-VS-CWK_{18} DNA condensates did not significantly bind to cells, with only 0.2% of the dose being cell associated. In contrast, 14% of AlkCWK_{18} DNA condensates and 6.8% of PEG-SS-CWK_{18} DNA condensates dose were cell-associated following 5 h transfection, supporting the hypothesis that differences in cell uptake are responsible for the 2 orders of magnitude difference in gene expression mediated by PEG-SS-CWK_{18} and PEG-VS-CWK_{18} DNA condensates. To determine if PEG-SS-CWK_{18} underwent reduction during gene transfer, its stability was analyzed while incubating in cell culture media containing 2% FCS. This led to its partial reduction over time (data not shown), suggesting that the removal of PEG by disulfide bond scission results in the formation of CWK_{18} DNA condensates in situ and is a likely explanation of the difference between PEG-SS-CWK_{18} and PEG-VS-CWK_{18} DNA condensates.

Therefore, the utility of PEG-SS-CWK_{18} may be in generating soluble DNA condensates that can be formulated within a gene-activated matrix intended for implantation in which targeting is not necessary and spontaneous transfection of infiltrating cells is desired.[25] Alternatively, the greater stability of PEG-VS-CWK_{18} may result in its utility in modifying the surface of DNA condensates used during intravenous gene delivery.

Future studies will demonstrate the utility of PEG-peptides in gene activated matrixes and in altering the biodistribution of DNA condensates in vivo. The ability to form DNA cocondensates that incorporate both PEG and targeting ligands attached to CWK_{18} may provide a unique approach to systematically optimize gene delivery formulations for maximum efficacy in vivo.

References and Notes

1. Zhang, Y. P.; Reimer, D. L.; Zhang, G.; Lee, P. H.; Bally, M. B. Self-Assembling DNA-Lipid Particles for Gene Transfer. *Pharm. Res.* **1997**, *14*, 190−196.
2. Wu, G. Y.; Wu, C. H. Evidence for Targeted Gene Delivery to HepG2 Hepatoma Cells in Vitro. *Biochemistry* **1988**, *27*, 887−892.
3. Ogris, M.; Steinlein, P.; Kursa, M.; Mechtler, K.; Kircheis, R.; Wagner, E. The Size of DNA/Transferrin-PEI complexes is an Important Factor for Gene Expression in Cultured Cells. *Gene Ther.* **1998**, *5*, 1425−1433.
4. Tang, M. X.; Redemann, C. T.; Szoka, F. C., Jr. In Vitro Gene Delivery by Degraded Polyamidoamine Dendrimers. *Bioconjugate Chem.* **1996**, *7*, 703−714.
5. Niven, R.; Pearlman, T.; Wedeking, T.; Mackeigan, J.; Noker, P.; Simpson-Herren, L.; Smith, J. G. Biodistribution of Radiolabeled Lipid-DNA Complexes and DNA in Mice. *J. Pharm. Sci.* **1996**, *87*, 1292−1299.
6. Nishikawa, M.; Takemura, S.; Takakura, Y.; Hashida, M. Targeted Delivery of Plasmid DNA to Hepatocytes In Vivo: Optimization of the Pharmacokinetics of Plasmid DNA/Galactosylated Poly (L-Lysine) Complexes by Controlling their Physicochemical Properties. *J. Pharm. Exp. Ther.* **1998**, *287*, 408−415.
7. Kwoh, D. Y.; Coffin, C. C.; Lollo, C. P.; Jovenal, J.; Bananszczyk, M. G.; Mullen, P.; Phillips, A.; Amini, A.; Fabriycki, J.; Bartholomew, R. M.; Brostoff, S. W.; Carlo, D. J. Stabilization of Poly-L-Lysine/DNA Polyplexes for In Vivo Gene Delivery to the Liver. *Biochim. Biophys. Acta* **1999**, *1444*, 171−190.
8. Woodle, M. C. Controlling Liposome Blood Clearance by Surface-Grafted Polymers. *Adv. Drug Delivery Rev.* **1998**, *32*, 139−152.
9. Torchilin, V.; Omelyanenko, V. G.; Papisov, M. I.; Bogdanov, A. A.; Trubetskoy, V. S.; Herron, J. N.; Gentry, C. A. Poly(ethylene glycol) on the Liposome Surface: On the Mechanism of Polymer-Coated Liposome Longevity. *Biochim. Biophys. Acta* **1994**, *1195*, 11−20.

10. Torchilin, V. P. Polymer-Coated Long-Circulating Microparticulate Pharmaceuticals. *J. Microencaps.* **1998**, *15* (1), 1−19.
11. Wolfert, M. A.; Schacht, E. H.; Toncheva, V.; Ulbrick, K.; Nazarova, O.; Seymour, L. W. Characterization of Vectors for Gene Therapy Formed by Self-Assembly of DNA with Synthetic Block Co-Polymers. *Human Gene Ther.* **1996**, *7*, 2123−2133.
12. Toncheva, V.; Wolfert, M. A.; Dash, P. R.; Oupicky, D.; Ulbrich, K.; Seymour, L. W.; Schacht, E. H. Novel Vectors for Gene Delivery Formed by Self-Assembly of DNA with Poly(L-lysine) Grafted with Hydrophobic Polymers. *Biochim. Biophys. Acta* **1998**, *1380*, 354−368.
13. Choi, Y. H.; Liu, F.; Kim, J. K.; Choi, Y. K.; Park, J. S.; Kim, S. W. Polyethylene Glycol-Grafted Poly-L-Lysine as Polymeric Gene Carrier. *J. Controlled Release* **1998**, *54*, 39−48.
14. Choi, J. S.; Lee, E. J.; Choi, Y. H.; Jeong, J. Y.; Park, J. S. Poly(ethylene glycol)-*block*-poly(L-lysine) Dendrimer: Novel Linear Polymer/Dendrimer Block Copolymer Forming a Spherical Water-Soluble Polyionic Complex with DNA. *Bioconjugate Chem.* **1999**, *10*, 62−65.
15. Harada, A.; Kataoka, K. Formation of Polyion Complex Micelles in an Aqueous Milieu from a Pair of Oppositely-Charged Block Copolymers with Poly(ethylene glycol) Segments. *Macromolecules* **1995**, *28*, 5294−5299.
16. Katayose, S.; Kataoka, K. Water-Soluble Polyion Complex Associates of DNA and Poly(ethylene glycol)-Poly(L-lysine) Block Copolymers. *Bioconjugate Chem.* **1997**, *8*, 702−707.
17. Katayose, S.; Kataoka, K. Remarkable Increase in Nuclease Resistance of Plasmid Supramolecular Assembly with Poly-(ethylene glycol)-Poly(L-lysine) Block Copolymer. *J. Pharm. Sci.* **1998**, *87*, 160−163.
18. Plank, C.; Zatloukal, K.; Cotten, M.; Mechtler, K.; Wagner, E. Gene Transfer into Hepatocytes Using Asialoglycoprotein Receptor Mediated Endocytosis of DNA Complexed with an Artificial Tetraantennary Galactose Ligand. *Bioconjugate Chem.* **1992**, *3*, 533−539.
19. Wadhwa, M. S.; Collard, W. T.; Adami, R. C.; McKenzie, D. L.; Rice, K. G. Peptide-Mediated Gene Delivery: Influence of Peptide Structure on Gene Expression. *Bioconjugate Chem.* **1997**, *8*, 81−88.
20. Burns, J. A.; Butler, J. C.; Moran, J.; Whitesides, G. M. Selective Reduction of Disulfides by Tris-(2-carboxyethyl)-phosphine. *J. Org. Chem.* **1991**, *56*, 2648−2650.
21. Bradford, M. M. A Rapid and Sensitive Method for the Quantitation of Microgram Quantities of Protein Utilizing the Principle of Protein-Dye Binding. *Anal. Biochem.* **1976**, *72*, 248−254.
22. Teribesi, J.; Kwok, K. Y.; Rice, K. G. Iodinated Plasmid DNA as a Tool for Studying Gene Delivery. *Anal. Biochem.* **1998**, *263*, 120−123.
23. Pouton, C. W.; Seymour, L. W. Key Issues in Non-Viral Gene Delivery. *Adv. Drug Delivery Rev.* **1998**, *34*, 3−19.
24. Wadhwa, M. S.; Knoell, D.; Young, T.; Rice, K. G. Targeted Gene Delivery with a Low Molecular Weight Glycopeptide. *Bioconjugate Chem.* **1995**, *6*, 283−291.
25. Fang, J.; Zhu, Y. Y.; Smiley, E.; Bonadio, J.; Rouleau, J.; Goldstein, S. A.; McCauley, L. K.; Davidson, B. L.; Roessler, B. J. Stimulation of New Bone Formation by Direct Transfer of Osteogenic Plasmid Genes. *Proc. Natl. Acad. Sci.* **1996**, *93*, 5753−5758.

Acknowledgments

The authors acknowledge financial support provided by NIH grants GM48049, DE13004 and support from Selective Genetics, Inc.

JS990072S

Rapidly Disintegrating Tablets Prepared by the Wet Compression Method: Mechanism and Optimization

YUNXIA BI,* YORINOBU YONEZAWA, AND HISAKAZU SUNADA

Contribution from *Faculty of Pharmacy, Meijo University, 150 Yagotoyama, Tempaku-ku, Nagoya, Aichi 468-8503, Japan.*

Received February 22, 1999. Accepted for publication July 12, 1999.

Abstract □ To make rapidly disintegrating tablets with sufficient mechanical integrity, tablets were prepared by compressing wet granules under low compression force and then drying the resulting wet mass in a circulating-air oven (wet compression method). Lactose with various particle sizes was used as the excipient, and water was used as a wetting agent. The effect of drying time, compression force, size of lactose particles, and moisture content of wet granules on tablet properties indicated that the formation and disintegration time of tablets were related to the effect of the formation of solid bridges between lactose particles. By optimizing compression force, size of lactose particles, and moisture content of the granules, tablets meeting tensile strength greater than 0.5 MPa and disintegration time shorter than 15 s were obtained by the wet compression method.

Introduction

Due to a decline in swallowing ability with age, a great many elderly patients complain that it is difficult for them to take some currently used dosage forms such as tablets, capsules, or powders.[1] For this reason, tablets which can rapidly dissolve or disintegrate in the oral cavity have attracted a great deal of attention. Rapidly dissolving or disintegrating tablets are not only indicated for people who have swallowing difficulties, but also are ideal for active people.

Commercially available rapidly dissolving or disintegrating tablets are obtained by various methods.[2−4] Fast disintegrating tablets were developed using wet powders containing drugs. Such tablets were produced by two methods, compression[4] and molding.[5] The preparation processes are usually as follows: after blending the excipient with the drug, the powder mixture is moistened with solvent. The resultant wet powder will then be molded or compressed under low compression force, and after drying in ambient air or an oven, the desired tablets will be obtained. The most commonly used solvent is aqueous alcohol, although other volatile solvents such as acetone and hydrocarbons have also been used. To increase the hardness and reduce erosion of the edges of the tablets during handling, binding agents such as glucose, sucrose, acacia, or povidone are usually added to the solvent mixture.

As volatile solvents are often used, it is difficult to protect the wet mass from solvent evaporation. Therefore, the moisture content of the wet mass is prone to become uneven, which will result in poor uniformity of the tablets. The binding agent must also be added with care, since if used in excessive amounts such agents can markedly decrease the rate of disintegration of the tablets.

* Corresponding author. Tel: 81-52-8321781 (ext 272). Fax: 81-52-8328904. E-mail: d5971101@meijo-u.ac.jp.

Table 1—Physical Properties of Excipient

	lactose 450M	lactose 200M	lactose 80M
particle size (μm)[a]	13.2	23.9	61.4
SF = (A/ML)4π[b]	0.52	0.52	0.56
particle density (g/cm^3)	1.52	1.52	1.52

[a] Heywood diameter (n = 500). [b] Shape factor (SF) represents sphericity of particles (when particle is spherical, SF = 1). ML: maximum length of particle, A: projection area of particle (n = 500).

Previously, we developed rapidly disintegrating tablets by a direct compression method.[6−8] In the present study, we prepared rapidly disintegrating tablets by the wet compression method using lactose as the excipient. The objective of the study was to delineate the mechanism of formation and rapid disintegration of the tablets prepared by the wet compression method.

Experimental Section

Excipient and Its Physical Properties—α-Lactose monohydrate with various particle sizes (Pharmatose 80M, 200M, and 450M, DMV Co., Holland) was used as the excipient. Its particle density was measured with a helium−air pycnometer (Model 1302, Micromeritics Instrument Co., Norcross, GA). Heywood diameter and shape factor, SF, were determined with an image analyzer (Luzex 500, Nireco Co., Japan). Data are listed in Table 1.

Preparation of Tablets—Kneading was performed in a multipurpose powder handling mill (MECHANOMiLL, Okada Seiko, Co., Ltd., Japan) with the rotation speed of the paddles fixed at 2000 rpm. Distilled water was added to 50 g of lactose powder in milliliter increments, and then the powder was agitated for 60 s. To ensure moisture homogeneity of the mixture, water addition and agitation processes were conducted alternately until the moisture content of the powder mass reached a predetermined value.

The wet powder mass was then extruded through a sieve with a pore size of 710 μm into a container which was then covered with a wet paper towel. The wall of the container was high enough to prevent the wet granules coming into direct contact with wet paper towel. Wet granules were then compressed into flat-faced tablets 10 mm in diameter using a hydraulic press (O. J. Shop, press model 10, Osaka Jack MFG. Co., Japan). The necessary weight of wet granules was calculated from the true density of dry powder and the moisture content of the wet mass to make tablets with a dry weight of 300 mg. The wet tablets were dried in a circulating-air oven at 60 °C. After drying, the tablets were kept in a desiccator for 12 h at room temperature before testing of tablet properties.

Moisture Evaporation of Wet Granules—Wet lactose (450M) granules with a moisture content of 10% were placed in desiccators at 25 °C, each containing a different saturated solution of inorganic salt.[9] The samples were weighed every 10 min, and the moisture loss at each relative humidity (RH) was calculated. The moisture loss of wet granules kept in a container covered with a wet paper towel (our manufacturing humidity conditions) was measured by the same method.

Differential Scanning Calorimetry (DSC)—Samples (10 mg) were analyzed in crimped vented aluminum pans using a MAC Science 3100 type differential scanning calorimeter. Thermographs were recorded over a temperature range of 30−200 °C, with a scanning rate of 10 °C min^{-1}.

10.1021/js990061z CCC: $18.00
Published on Web 09/10/1999

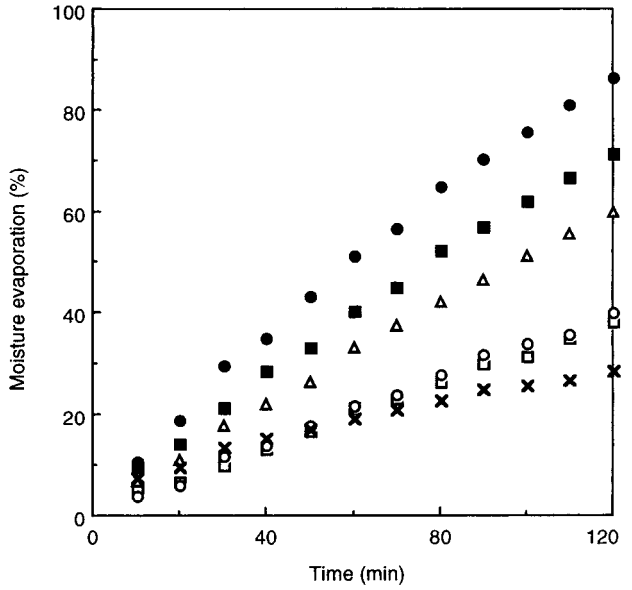

Figure 1—Water evaporation curves of lactose wet granules under various humidity conditions. Relative humidity: □ 100%, ○ 93%, △ 84%, ■ 75%, ● 61.8%, × water evaporation under our manufacturing humidity conditions.

Measurement of Tablet Tensile Strength—The tablet crushing load, which is the force required to break a tablet into halves by compression in the diametral direction, was measured using a tablet hardness tester (TS-50N, Okada Seiko Co., Ltd., Japan). The plunger was driven down at a speed of 20 mm/min. Tensile strength for crushing (T) was calculated using the following equation:

$$T = 2F/(\pi d h) \quad (1)$$

where F is the crushing load, and d and h denote the diameter and thickness of the tablet, respectively.

Measurement of Tablet Porosity—Tablet porosity ϵ was calculated as follows:

$$\epsilon = 1 - m/(\rho_t V) \quad (2)$$

where ρ_t is the true density and m and V are the weight and volume of the tablet, respectively.

Measurement of Disintegration Time—The disintegration test was performed using a JP 13 disintegration apparatus, using distilled water at 37 ± 1 °C.

All tablet property values are shown as averages of five determinations.

Results

Moisture Evaporation of Wet Lactose Granules under Various Humidity Conditions—The moisture content of wet granules markedly affected the properties of the resultant tablets (discussed later). Thus, it is necessary to regulate the ambient humidity to protect the wet granules from moisture evaporation during the tableting process. In our experiments, a wet paper towel covering on the container of wet granules was used for this purpose. Figure 1 shows the evaporation curves of wet granules under various humidity conditions.

The evaporation data of wet granules under our manufacturing humidity conditions are shown as crosses. Moisture evaporation percentage under such conditions was a little larger than that at 93% RH within 40 min, but after 50 min the moisture loss showed values even smaller than that at 100% RH. In our experiments, the tableting process finished within 20 min, during which time less than 10% of the moisture would be lost. In contrast, the moisture loss of wet granules at 61.8% RH was twice as fast as that under our manufacturing humidity conditions. The tablet

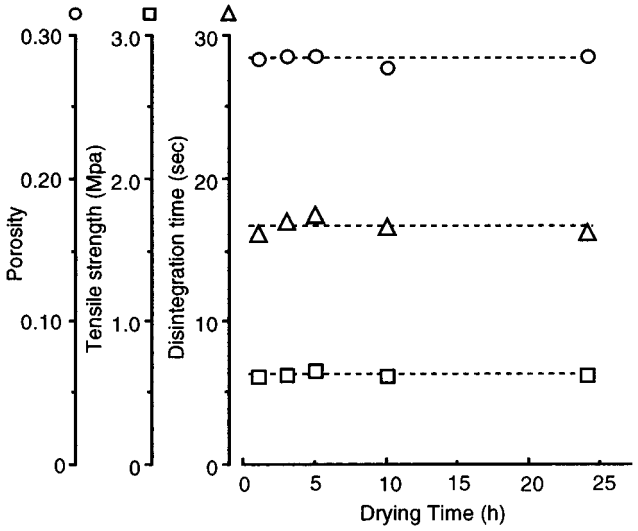

Figure 2—Effects of drying time in tablet properties. ○ Porosity, □ tensile strength (MPa), △ disintegration time (s) lactose: 450M, moisture content of wet granules: 8.56%, compression force: 500 kN.

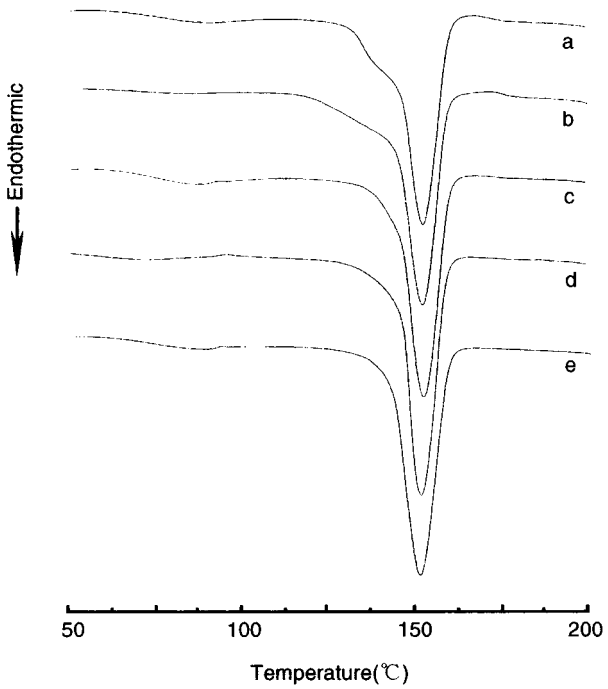

Figure 3—DSC thermograms of α-lactose monohydrate powder and lactose tablets. (a) α-lactose monohydrate powder (450M), (b) tablet being dried for 1 h, (c) tablet being dried for 3 h, (d) tablet being dried for 10 h, (e) tablet being dried for 24 h. Tablets used were the same as those described in Figure 2.

properties determined in our experiments showed small relative standard deviation (RSD) values, which confirmed that although a very simple procedure, covering the container with a wet paper towel is an effective method to slow the moisture evaporation rate.

Effects of Drying Time on the Properties of Tablets—The effects of drying time on porosity, tensile strength, and disintegration time of tablets were evaluated, and the results are shown in Figure 2. No obvious changes in tablet properties were found with increases in drying time.

DSC curves of α-lactose monohydrate raw powder and tablets dried for 1, 3, 10, and 24 h are shown in Figure 3. All samples showed an endothermic peak at about 152 °C, corresponding to the dehydration (elimination of crystal water) of α-lactose monohydrate crystals. Lactose raw

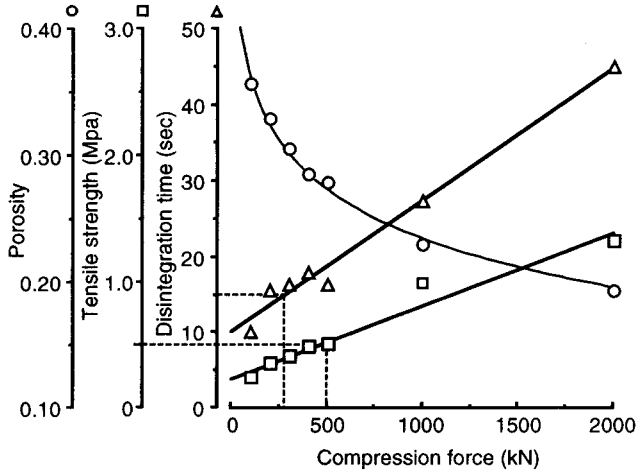

Figure 4—Effects of compression force in tablet porosity. Lactose: 450M; moisture content of wet granules: 8.56%. Dotted lines showed the compression forces corresponding to the tensile strength of 0.5 MPa and disintegration time of 15 s.

powder and tablets with a drying time of 1 h showed a shoulder peak before the endothermic peak of crystal water, suggesting that the two samples contained absorbed water. The DSC results were in agreement with the report of Lerk.[10] According to this report, an unstable anhydrous product was formed when α-lactose monohydrate crystals were heated at temperatures of 100−130 °C. When heated at temperatures below 100 °C, α-lactose monohydrate crystals do not undergo any change. The drying temperature (60 °C) was far lower than 100 °C, and hence drying time had almost no effect on the crystal water of α-lactose monohydrate. Although absorbed water was present in 1 h dried tablets, its amount was too little to affect the properties of the tablets (Figure 2).

The changes in tablet weight with drying time were also measured. After drying for 3 h, tablet weight became constant. Hence, in the following experiments, all tablets were dried at 60 °C for 3 h.

Effects of Compression Force in Tablet Properties—Properties of tablets compressed at 100−2000 kN were investigated. With the increase in compression force, a decrease in porosity and increases in tensile strength and disintegration time were observed (Figure 4). Furthermore, both tensile strength and disintegration time showed linear relationships with the logarithm of tablet porosity (Figure 5).

Compression forces corresponding to our requirements for rapidly disintegrating tablets, i.e., tensile strength greater than 0.5 MPa and disintegration time shorter than 15 s, were found (Figure 4). The results were >500 kN and <280 kN, respectively; i.e., no conditions meeting the requirements were found. Although compression force is a very important factor regulating tablet properties, it is not the only such factor. To obtain tablets with desirable properties, the effects of other factors on tablet properties were investigated. Here, because tablets prepared under 500 kN had a disintegration time of shorter than 20 s, which is close to the requirement, in the following section tablets were prepared under 500 kN.

Effects of Moisture Content and Particle Size on the Properties of Tablets and Optimization of the Two Factors—Besides compression force, many factors affect properties of wet compressed tablets. Among these, particle size and shape of raw materials and moisture content of wet granules are supposed to be the most important. Consequently, lactoses with various particle sizes were used. Wet granules with various moisture contents were made into 14 kinds of tablets to evaluate the effects of factors other than compression force on tablet properties. The shapes of the lactose particles with various sizes were almost the same (see Table 1). Therefore, particle size of lactose and moisture content of wet granules were selected as controlling factors, tablet tensile strength and disintegration time were selected as response variables, and a polynomial regression algorithm was used to relate the controlling factors to the response variables.

The values of 14 groups of controlling factors and response variables are listed in Table 2, and the resultant multiple regression equations are as follows:

$$T_s = -0.1426x + 0.1540y - 0.0312xy + 0.5736 \quad (3)$$

$$N = 14 \quad R^2 = 0.968 \quad T < 0.05 \quad F(3,10) = 10.4842$$

$$\mathrm{Dis} = -10.328x + 15.625y + 18.683 \quad (4)$$

$$N = 14 \quad R^2 = 0.563 \quad T < 0.05 \quad F(2,11) = 7.093$$

Where T_s is tablet tensile strength (MPa), Dis is the disintegration time (s). x and y stand for the transformed

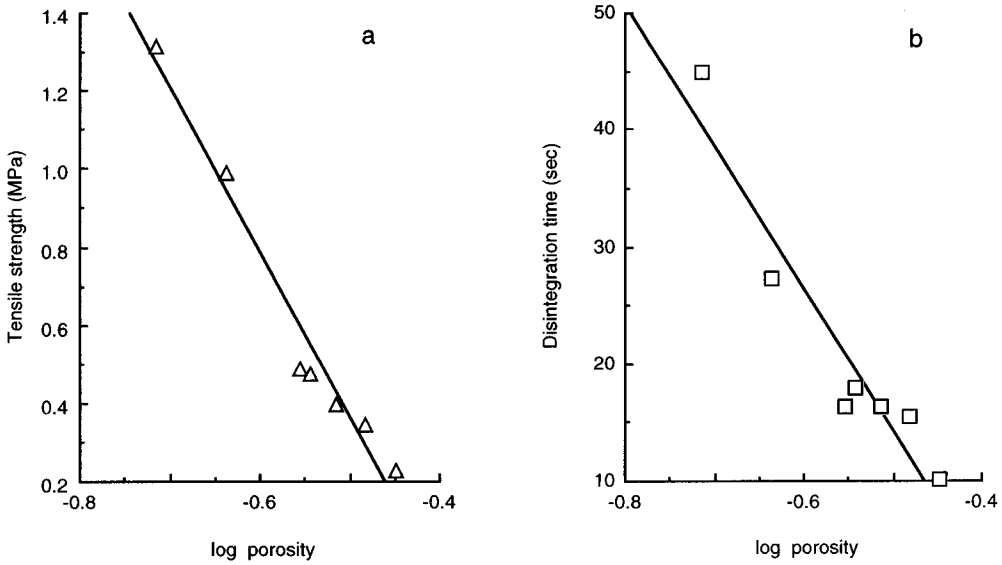

Figure 5—Relationship between common logarithm of porosity and tensile strength and disintegration time of tablets. (a) Tensile strength, (b) disintegration time. Lactose: 450M; moisture content of wet granules: 8.56%.

Table 2—Experimental Values of Controlling Factors and Response Variables

formulation number	particle size (μm)	x	moisture content (%)	y	tensile strength (MPa)	disintegration time (s)	porosity
1	13.18	–1.00	4.70	–1.00	0.503	16.23	0.279
2	13.18	–1.00	8.56	–0.45	0.667	19.97	0.275
3	13.18	–1.00	14.20	0.35	0.809	31.06	0.261
4	13.18	–1.00	18.80	1.00	0.836	82.45	0.275
5	23.90	–0.55	4.70	–1.00	0.454	9.55	0.261
6	23.90	–0.55	7.56	–0.59	0.563	11.02	0.265
7	23.90	–0.55	10.20	–0.22	0.608	11.23	0.272
8	23.90	–0.55	14.20	0.35	0.755	16.12	0.256
9	23.90	–0.55	18.80	1.00	0.843	21.47	0.263
10	61.35	1.00	4.70	–1.00	0.326	2.86	0.285
11	61.35	1.00	8.56	–0.45	0.358	4.89	0.274
12	61.35	1.00	10.20	–0.22	0.382	6.20	0.273
13	61.35	1.00	14.20	0.35	0.505	10.85	0.280
14	61.35	1.00	18.56	0.97	0.531	21.47	0.270

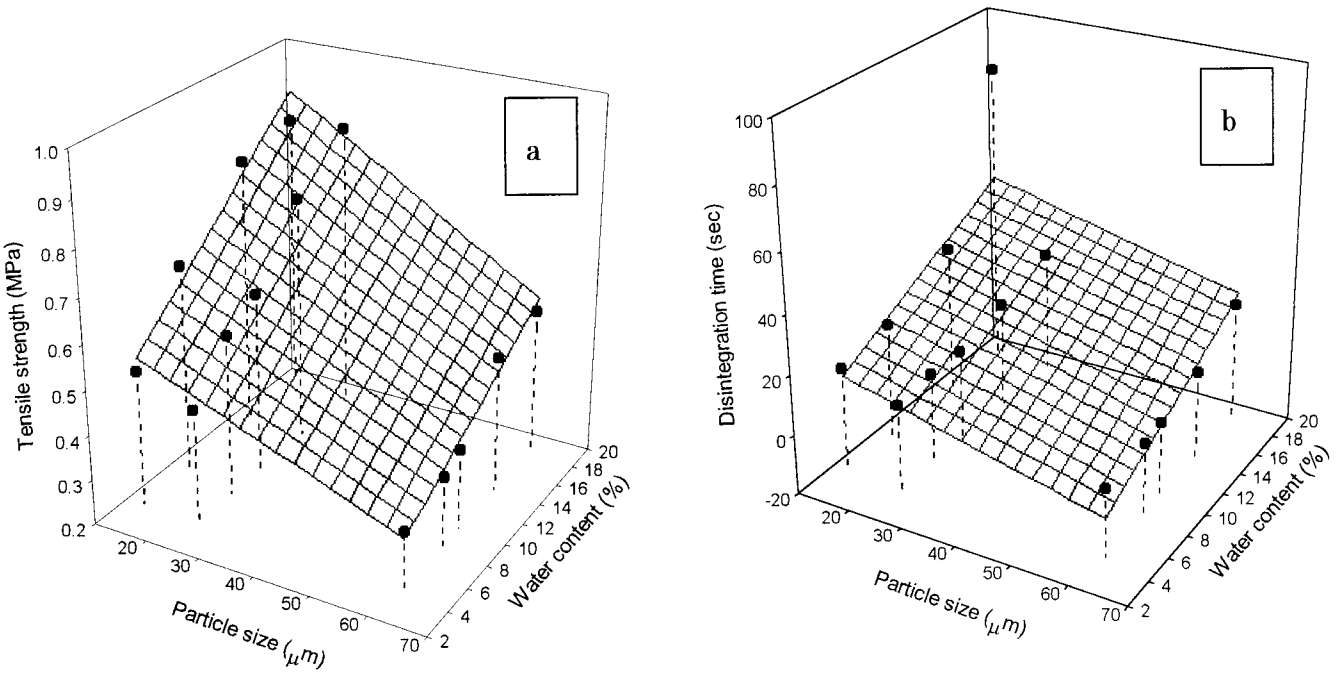

Figure 6—Response surfaces of tablet tensile strength and disintegration time obtained by multiple regression analysis as a function of particle size and moisture content. (a) Tensile strength, (b) disintegration time. Black dots stand for the experimental data.

particle size and moisture content, respectively, and the transformation was processed using the method described in our previous report.[7] N is the number of samples, and R is the multiple correlation coefficient. T denotes the P value determined by Student's t-test, and F, that obtained by F-test. Student's t-test showed that coefficients for all the components on the right side of eqs 3 and 4 were highly significant ($P < 0.05$).

In the multiple regression equation of disintegration time, the multiple correlation coefficient R was not very large. Therefore, an artificial neural network (ANN) was also constructed by Takayama's method to relate the controlling factors to the response variables.[11–13] Three-dimensional surface plots based on multiple regression and ANN are shown in Figures 6 and 7, respectively. The surface plots of tensile strength obtained by multiple regression analysis and ANN were almost the same. In detail, tensile strength increased with increases in moisture content. When moisture content was constant, tablets made of small lactose particles showed higher tensile strength. Disintegration time increased with increases in moisture content and decreases in particle size, which is analogous to the tendency of tensile strength. Although the tendencies of disintegration plots obtained by the two methods were similar, the disintegration plot obtained by ANN method more accurately reflected the experimental data.

Disintegration time showed a similar tendency to tensile strength with the changes in particle size and moisture content. However, the requirements of tensile strength and disintegration time of rapidly disintegrating tablets are the converse of this tendency. A rapidly disintegrating tablet should disintegrate rapidly in the mouth, while having sufficient structural integrity to withstand handling without substantial breakage. To find suitable tableting conditions under which desired tablets could be obtained, contour plots response to surface plots in Figure 7a,b were also constructed and are shown in Figure 8a,b. With 0.5 MPa as the minimum expected tensile strength, and 15 s as the maximum expected disintegration time, we superimposed the contour plots and obtained the optimum particle size and moisture content combination (the region marked with horizontal lines in Figure 8c). More desirable particle size and moisture content combination could be obtained by changing the target tablet property values. For example, tablets with tensile strength greater than 0.75 MPa and disintegration time shorter than 15 s can be found in the region marked with both horizontal and vertical lines in Figure 8c.

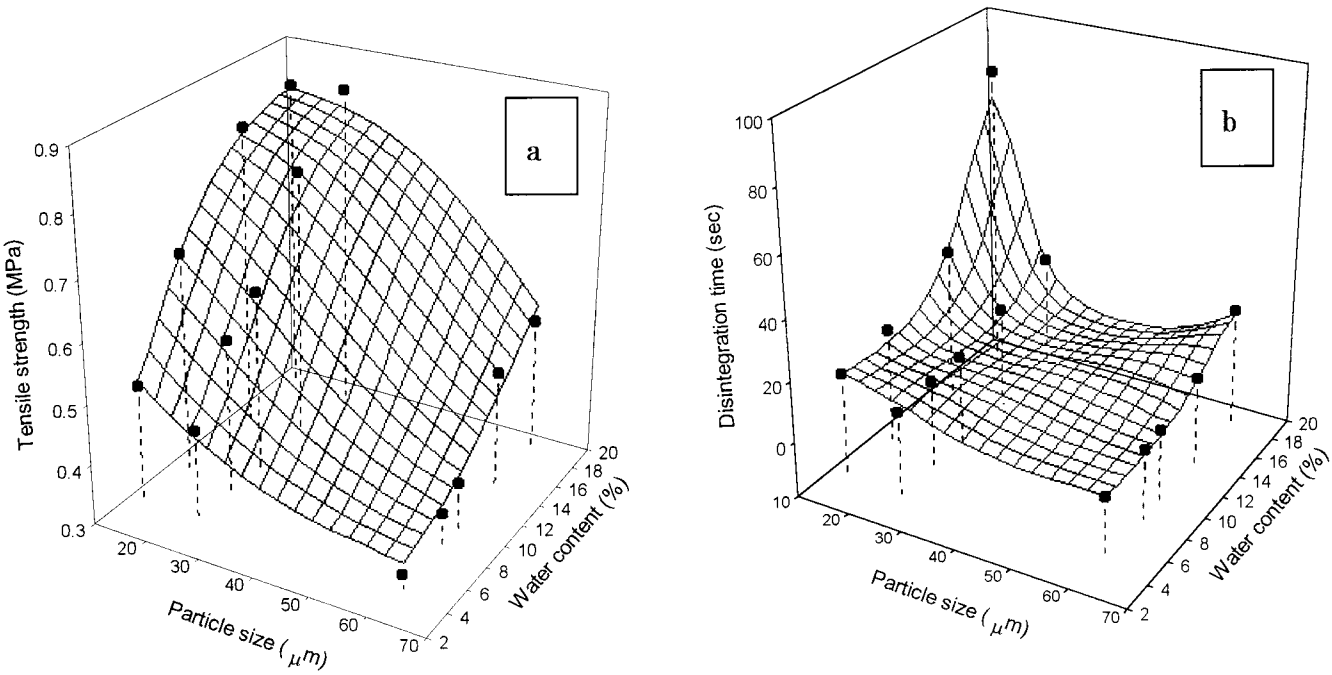

Figure 7—Response surfaces of tablet tensile strength and disintegration time obtained by ANN using particle size and moisture content as input factors. (a) Tensile strength, (b) disintegration time. Parameters of ANN: input layer unit: 2, output layer unit: 2, hidden layer unit: 3, reconstruction: 0, sigmoid curve: 2, training times: 1000, mean error: <0.03, neuron weight: 12. Black dots stand for the experimental data.

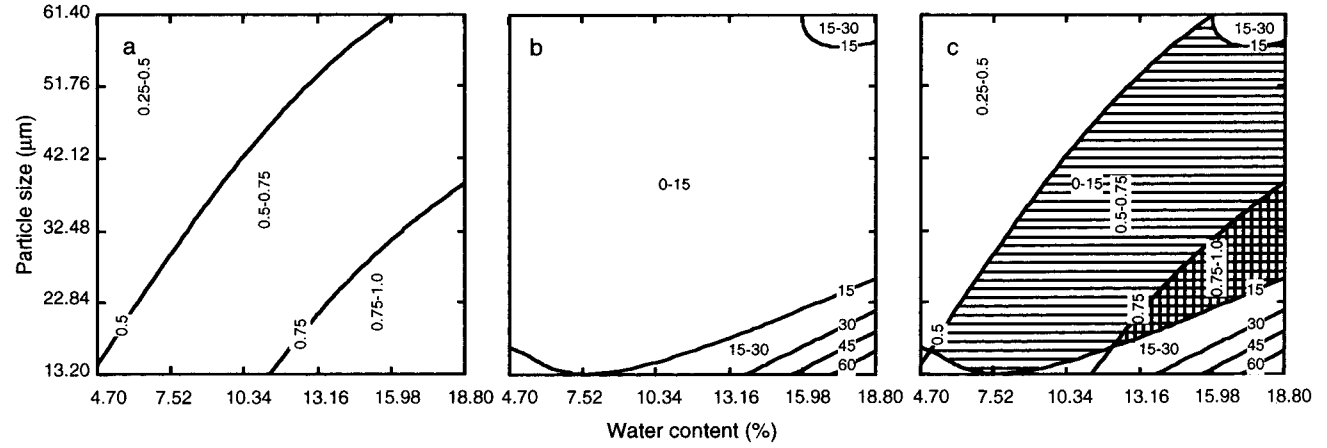

Figure 8—Contour plots of tablet tensile strength and disintegration time obtained by ANN using particle size and moisture content as input factors. (a) Tensile strength, (b) disintegration time, (c) superimposition of plots a and b. The values marked vertically within plots refer to tensile strength (MPa), while values marked horizontally refer to disintegration time (s).

Discussion

Preliminary experiments indicated that for lactose tablets with the same porosity (0.31), the tensile strength of tablets made by the wet compression method (0.4 MPa) is 10-fold greater than that of tablets prepared by the common compression methods (0.035 MPa). Such results suggested that the mechanisms of formation of the two tablets are different.

Discussion of tablet formation must necessarily start with a consideration of the particle–particle bonding mechanism involving adhesion and cohesion of particles. Several forces that can act between small neighboring particles have been identified. Among these, although van der Waals forces are not very large (1kal/mol), they can act over distances up to 1000 Å and must be considered capable of forming interparticle bonds. This intermolecular force plays the most important role in the formation of common compressed tablets. Lactose has many hydroxyl groups, and therefore hydrogen bonding is also an important interparticle force that cannot be neglected. The formation of lactose tablets prepared by the common compression method was thought to be mainly due to the above two forces. In contrast, for tablets prepared by the wet compression method, the solvent (water in this study) plays a key role in the tableting process. The postulated mechanism of formation of wet compressed tablets is shown in Figure 9. After mixing with water, the surface of lactose particles will be wetted and dissolve in water, and the particles will be coated with a layer of lactose solution. During the drying process, interparticle bonds, the so-called solid bridges, will result from recrystallization of lactose. It is these solid bridges which endow wet compression tablets with greater tensile strength, while maintaining relatively high porosity. This mechanism of formation of wet compressed tablets is similar to that of powder metallurgy, which is quite different from that of common compressed tablets.

For common compressed tablets, the number of contact points between particles is another factor which plays an

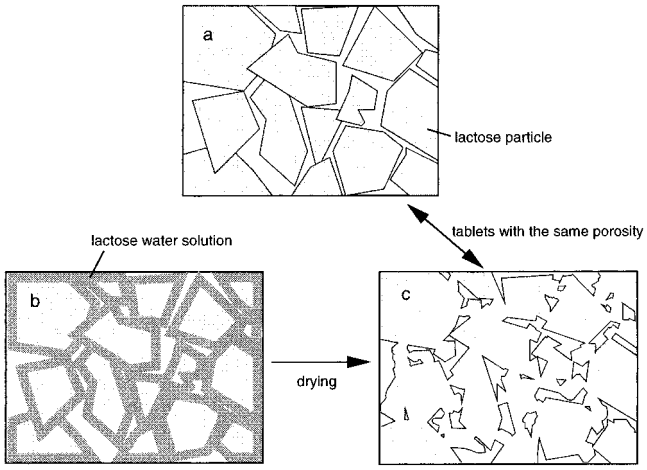

Figure 9—Hypothesized mechanism of formation of wet compressed tablets. (a) Tablets prepared by common compression method. (b) Wet compressed tablets before drying. (c) Wet compressed tablets after drying.

important role in tablet tensile strength.[14] With decreases in tablet porosity, the number of contact points increases, and tensile strength of the tablets shows a higher value. For wet compressed tablets, with increase in compression force, tablet porosity decreases, and the distances between particles become small. Thus, more solid bridges can be formed between particles. As a result, the tensile strength of wet compressed tablets increases linearly with the logarithm of porosity (Figure 5a).

Disintegration time showed a similar tendency to tensile strength with changes in tablet porosity (Figure 5b). Our previous studies indicated that porosity, hydrophilicity (solubility if the tablet constituents are water-soluble), swelling ability of the particles, and interparticle force are important factors for tablet disintegration.[6] Lactose is not a swellable material, and thus for lactose tablets the most important factors for disintegration are tablet porosity and interparticle force. With increases in compression force, tablet porosity decreases. Consequently, water penetration into the tablets would slow with decreases in porosity.[15] This is one reason disintegration time was prolonged with decreases in tablet porosity. When porosity decreases, more solid bridges are formed, which would make the annihilation of interparticle force more difficult. For such reasons, the effect of tablet porosity on disintegration time is similar to that on tensile strength.

Tensile strength and disintegration time of wet compressed tablets were markedly affected by tablet porosity, which can be easily controlled by compression force. In this study, size of lactose particles and moisture content of wet granules showed little effect on tablet porosity (see Table 2, porosity values of all tablets were around 0.3). However, they were shown to be the other two factors which are very important for determining tensile strength and disintegration time of wet compressed tablets (Figures 6 and 7).

As mentioned above, the number of contact points is one of the key factors regulating the integrity of tablets. When tablet porosity and the shape of the constituent particles of tablets are the same, the number of contact points per unit cross-sectional area of the fracture plane of a tablet is mainly dominated by particle size of tablet constituents. Smaller particle size is accompanied by a large number of contact points, as confirmed by SEM (Figure 10a–c). With

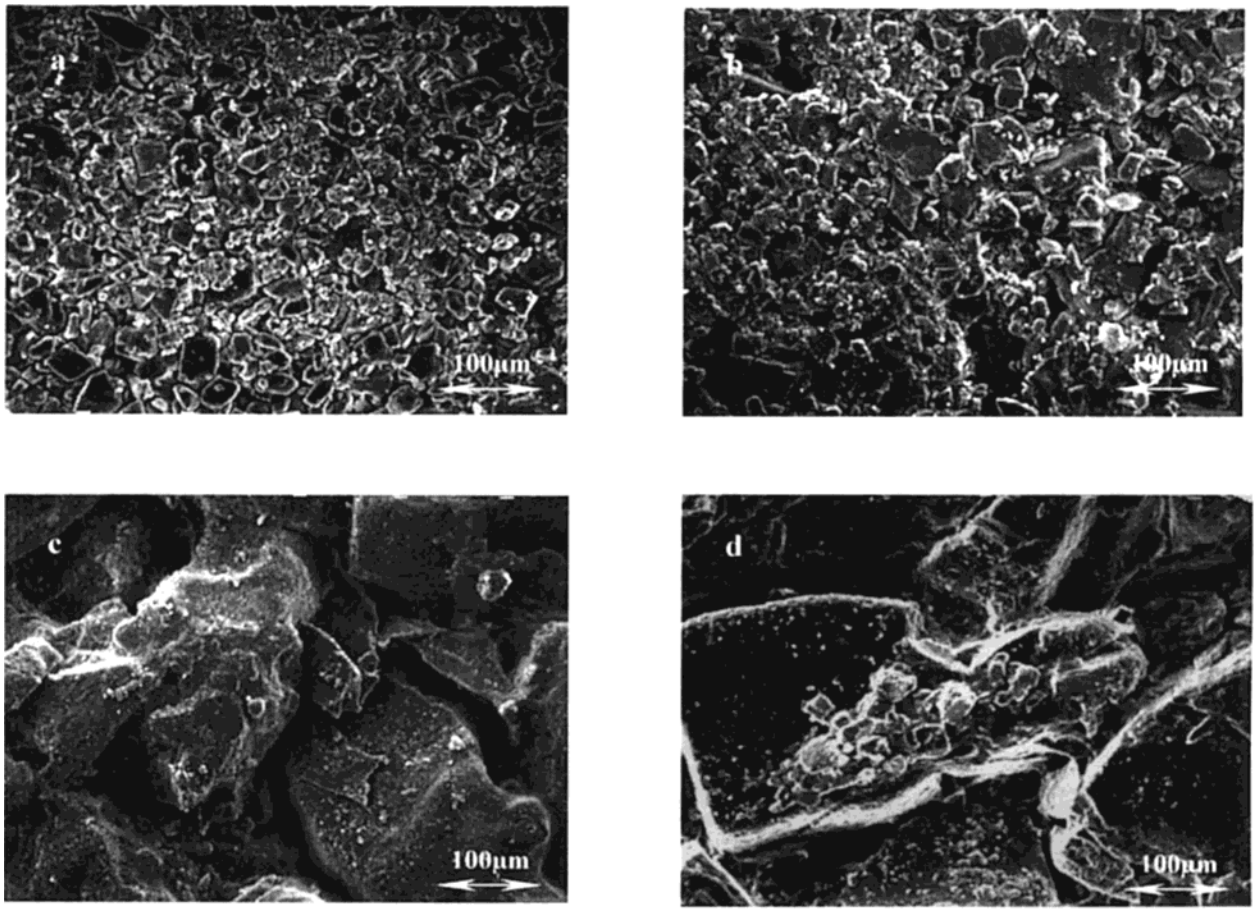

Figure 10—Scanning electron microscopic analysis of wet compressed lactose tablets. (a) Lactose: 450M; moisture content of wet granules: 8.56%. (b) Lactose: 200M; moisture content of wet granules: 8.56%. (c) Lactose: 80M; moisture content of wet granules: 8.56%. (d) Lactose: 80M; moisture content of wet granules: 18.80%.

increases in lactose particle size, the cracks and pores between particles became larger and the number of contact points decreased. This may explain why tensile strength increased with decreases in lactose particle size.

The effect of moisture content on tablet tensile strength can also be readily explained by the hypothesized mechanism of formation mentioned above. When more water is added in the kneading process, more lactose will dissolve in water, and then more small lactose crystals will recrystallize between the existing lactose particles, and stronger tablets will be formed. When moisture content of wet granules was 8.56%, the cracks between particles could be distinguished clearly, while when moisture content was increased to 18.8%, so many small lactose crystals recrystallized that the large cracks almost disappeared (Figure 10c,d).

Disintegration time showed the same tendency as tensile strength for the reasons mentioned above (Figures 6b and 7b). As the porosity values of these tablets were almost the same, disintegration time was only affected by interparticle force.

All our experimental results can be explained by the hypothesized mechanism of formation of wet compressed tablets.

Conclusions

In this study, we proposed a mechanism of formation of wet compressed tablets which was then confirmed by experimental results.

Tensile strength and disintegration of wet compressed tablets are closely related to the formation and annihilation of the solid bridges formed between lactose particles. The intensity and number of the solid bridges are influenced by compression force, moisture content, and size of lactose particles.

With increases in compression force and moisture content, and the decreases in particle size, the distances between constituent particles will become shorter, more lactose will dissolve and recrystallize, and the number of contact points between particles will increase. Consequently, the resulting tablets will become harder and disintegrate less readily.

By optimization of compression force, moisture content of wet granules, and particle size, rapidly disintegrating lactose tablets meeting our design specifications were obtained by the wet compression method.

References and Notes

1. Sugihara, M. New Dosage Forms and Packages Developed for the Elderly Patients. *Farumashia* **1994**, *30* (12), 1396−1400.
2. Kearney, P.; Yarwood, R. J. The Zydis Fast Dissolving Oral Dosage Form. *Pharm Tech Jpn*. **1993**, *9* (6), 713−719.
3. Masaki, K. Orally Disintegrating Famotidine Tablet. *The collected papers of the 22nd Conference on Pharmaceutical Technology*; Academy of Pharmaceutical Science and Technology, Japan, July 1997; pp 79−84.
4. Tsushima, Y. Tablets Easily to be Taken- - -Dosage Form Developed for the Elderly Patients. *Farumashia* **1997**, *33* (10), 1119−1123.
5. Lieberman, H. A.; Lachman, L. *Pharmaceutical Dosage Form*; Marcel Dekker: New York and Basel, 1980; Volume 1, p 265.
6. Bi, Y.; Sunada, H.; Yonezawa, Y. et al. Preparation and Evaluation of a Compressed Tablet Rapidly Disintegrating in the Oral Cavity. *Chem. Pharm. Bull.* **1996**, *44* (11), 2121−2127.
7. Bi, Y.; Sunada, H.; Yonezawa, Y.; Danjo, K. Evaluation of Rapidly Disintegrating Tablets Prepared by a Direct Compression Methodology *Drug Dev. Ind. Pharm*. **1999**, *25* (5), 573−583.
8. Bi, Y.; Sunada, H. Preparation and Evaluation of Directly Compressed Tablets Rapidly Disintegrating in the Oral Cavity. *Pharm Tech Jpn*. **1998**, *14* (11), 1723−1733.
9. Callahan, J. C.; Cleary, G. W.; Elefant, M.; Kaplan, G.; Kensler, T.; Nash, R. A. Equilibrium Moisture Content of Pharmaceutical Excipients. *Drug Dev. Ind. Pharm*. **1982**, *18*, 355.
10. Lerk, C. F. Consolidation and Compaction of Lactose. *Drug Dev. Ind. Pharm*. **1993**, *19*, 2359−2398.
11. Takayama, K.; Nagai, T. Simultaneous Optimization for Several Characteristics Concerning Percutaneous Absorption and Skin Damage of Keloprofen Hydrogels Containing d-limonene. *Int. J. Pharm*. **1991**, *74*, 115−126.
12. Takahara, J.; Takayama, K.; Nagai, T. Multi-objective Simultaneous Optimization Technique Based on an Artificial Neural Network in Sustained Release Formulation. *J. Controlled Release* **1997**, *49*, 11−20.
13. Takahara, J.; Takayama, K.; Nagai, T. Multi-objective Simultaneous Optimization Based on Artificial Neural Network in a Ketoprofen Hydrogel Formula Containing O-ethylmenthol as a Percutaneous Absorption Enhancer. *Int. J. Pharm*. **1997**, *158*, 203−210.
14. Nystrom, C.; Alderborn, G.; Duberg, M.; Karehill, P. G. Bonding Surface Area and Bonding Mechanism − Two Important Factors for the Understanding of Power Compactibility. *Drug Dev. Ind. Pharm*. **1993**, *19* (17, 18), 2143−2196.
15. Washburn, E. W. The Dynamics of Capillary Flow. *Phys. Rev.* **1921**, *17*, 273−281.

Acknowledgments

The authors are grateful to Dr. Kadzumi Danjo and Dr. Hirokadzu Okamoto for many helpful suggestions.

JS990061Z

Development and Evaluation of Microbicidal Hydrogels Containing Monoglyceride as the Active Ingredient

THÓRDÍS KRISTMUNDSDÓTTIR,*,† SIGRÍDUR G. ÁRNADÓTTIR,† GUDMUNDUR BERGSSON,‡ AND HALLDÓR THORMAR‡

Contribution from *Department of Pharmacy and Institute of Biology, University of Iceland, Reykjavik, Iceland.*

Received February 4, 1999. Final revised manuscript received May 20, 1999.
Accepted for publication June 25, 1999.

Abstract □ A number of medium-chain saturated and long-chain unsaturated fatty acids and their monoglycerides were tested against herpes simplex virus (HSV-1) to determine which lipids were most active during a short incubation time. The aim was to find which lipid would be preferable as the active ingredient in a virucidal hydrogel formulation for the purpose of preventing transmission of pathogens to mucosal membranes, particularly sexually transmitted viruses, such as herpes simplex virus and human immunodeficiency virus (HIV), and bacteria, such as *Chlamydia trachomatis* and *Neisseria gonorrheae.* The main strategy was that the formulations would be fast-acting, killing large numbers of virus or bacteria on contact in a short time, preferably causing at least a 10000-fold reduction in virus/bacteria titer in 1–5 min. Monocaprin, the 1-monoglyceride of capric acid, and lauric acid were found to be most active of all the lipids tested, causing a greater than 100000-fold reduction in virus titer in 1 min at a concentration of 20 mM. When tested at a concentration of 10 mM for 1 min, monocaprin was still fully active whereas lauric acid had no or neglible activity. It was concluded that monocaprin was most suitable as the active ingredient in a fast-acting virucidal gel formulation, and several hydrogel formulations containing monocaprin were tested. Formulations where the monoglyceride was dissolved in glycofurol were found to be active against HSV-1. The hydrogel formulations containing 20 mM monocaprin were highly virucidal in vitro and caused a greater than 100000-fold (HSV-1) inactivation of virus in human semen in 1 min. Formulations in dilution 1:10 were cytotoxic in monolayers of CV-1 cells, but they were 10–100 fold less cytotoxic than a commercial product which contains 2% nonoxynol-9.

Introduction

There are several published reports on antiviral and antibacterial activities of lipids.[1−5] Research has shown that enveloped viruses, such as herpes simplex virus type 1 (HSV-1), vesicular stomatitis virus (VSV), and visna virus are inactivated by long-chain unsaturated and medium-chain saturated fatty acids, whereas long-chain saturated and short-chain fatty acids have no or only a minor virucidal effect at the highest concentrations tested. Electron microscopy studies of VSV suggest that fatty acids disrupt the lipid envelope of the virus, but the mechanism is not known.[4]

It has been proposed that fatty acids and monoglycerides may be used as intravaginal microbicides for protection against sexually transmitted diseases.[6] To prevent infection by a sexually transmitted pathogen it is important that the micobicide is fast acting and kills the infectious agent before it has time to infect cells of the genital mucosa. It is also important that the microbicide be solubilized in a pharmaceutical formulation which can be easily and effectively applied to mucosa or skin areas which can serve as entry sites for infectious agents. The objective of the work was the development of hydrogels which could be used as vehicles for microbicidal lipids for the purpose of preventing transmission of pathogens to mucosal membranes, particularly sexually transmitted viruses, such as HSV and HIV, and bacteria, such as *Chlamydia trachomatis* and *Neisseria gonorrheae.* The main strategy was to design fast-acting formulations which kill large numbers of virus or bacteria on contact in a short time, preferably causing at least a 10000-fold reduction in virus/bacteria titer in 1−5 min. The effectiveness of the hydrogel formulations was tested against HSV-1 as a model.

Materials and Methods

Materials—Fatty acids and monoglycerides as well as sodium carboxymethylcellulose (NaCMC) and poly(vinylpyrrolidone) (PVP) were purchased from Sigma Chemical Co., St. Louis, MO. Carbomer (Carbopol 934) was obtained from Nomeco, Copenhagen, Denmark, and hydroxypropylmethylcellulose (HPMC) was from Aldrich Chemical Co. Inc., Milwaukee, WI. All other chemicals were of reagent grade.

Hydrogel Formulations—Hydrogels containing either 10 or 20 mM monocaprin were formulated using as gel-forming agents either NaCMC and PVP (series 1A−M) or carbomer and HPMC (series 2A−D). The concentration of gel-forming agents was such that the viscosity of the gels was comparable. One of the following compounds was used to bring the monoglyceride into solution: glycofurol 75, Tween 80, Chremophor PH40, Chremophor EL, 2-hydroxypropyl-β-cyclodextrin.

Formulations based on 2% w/v NaCMC and 1% w/v PVP were produced by adding 1.0 g of NaCMC and 0.5 g of PVP to a solution of monocaprin. The pH of gel formulation 1A is 7 but for formulations 1B−M the pH is adjusted to 5.0 by the dropwise addition of a lactic acid solution. Finally, purified water is added, bringing the solution to a final weight of 50 g. Immediately after the addition of water, the solution is stirred continuously until a hydrogel is produced. The hydrogel is centrifuged at high speed (>8000 rpm) for 60 min in order to remove air bubbles.

Hydrogels based on 0.5% w/v carbomer and 1% w/v HPMC are produced by dispersing 0.5 g of HPMC in 10 mL of hot (80−90 °C) purified water in a glass beaker. The solution is allowed to cool to about 30−35 °C under continuous stirring at room temperature and then chilled in a refrigerator at about 4 °C for at least 1 h. A 0.25 g amount of carbomer is suspended in 5 mL of purified water at room temperature under vigorous stirring to prevent lumping. The carbomer solution is mixed with the HPMC solution, and then a solution of monocaprin is added. Gelling of the carbomer polymer is induced by raising the pH to approximately 5.5 with the dropwise addition of a 2 w/v % sodium hydroxide solution. The hydrogel is brought to its final weight (50 g) with purified water. Finally, the hydrogel is centrifuged at high speed (>8000 rpm) for 60 min to remove air bubbles.

Cell Cultures and Media—CV-1 cells (African green monkey kidney cell line) were grown in Dulbecco's Modified Eagle Medium

* Corresponding author. Phone: 354-525-4370, fax: 354-525-4071, e-mail: thordisk@hi.is.
† Department of Pharmacy, University of Iceland.
‡ Institute of Biology, University of Iceland.

10.1021/js9900396 CCC: $18.00
Published on Web 10/01/1999

(D-MEM) with 2 mM L-glutamine, 20 μg/mL of gentamicin, and 10% heat-inactivated fetal bovine serum (FBS). The maintenance medium (MM) for CV-1 cell monolayers was D-MEM with 2% FBS. All media were obtained from GIBCO, Paisley, Scotland.

Virus and Virus Titration—HSV-1 strain MacIntyre was obtained from the American Type Culture Collection, Rockville, MD, and grown in CV-1 cells. Virus stocks with an infectivity titer of $10^{6.5}$–$10^{7.5}$ $CCID_{50}$ (50% cell culture infective dose) per 100 μL were used in the experiments. Virus was titrated by inoculation of 10-fold dilutions in MM into monolayers of CV-1 cells in 96-well microtiter tissue culture plates (Nunc, Roskilde, Denmark). One hundred microliters of each virus dilution were inoculated into quadruplicate wells. The plates were incubated at 37° C in a humidified incubator with 5% CO_2 in air and examined for cytopathic effect daily for 5 days. All virus titers were calculated by the method of Reed and Muench.[7]

Assay of Virucidal Activity of Fatty Acids and 1-Monoglycerides in Medium—The stock lipid solutions were diluted to the desired concentration in MM by vortexing at the highest speed for 10 min. The lipids were thoroughly mixed with equal volumes (200 μL) of HSV-1 in 12 × 75 mm polystyrene round-bottom tubes (Falcon) and incubated for 1 min at room temperature. The action of the lipid was then stopped by immediately diluting the mixture 100-fold in medium. Virus mixed with MM alone and with 2% ethanol in MM served as controls. The virus titers of the mixtures were determined by inoculation of 10-fold dilutions into cell cultures as previously described. The lowest inoculated dilution was 10^{-2} because of toxic effect of the lipids on cells. In such lipid–virus mixtures where no cytopathic effect was detectable in the 10^{-2} dilution the titer was assumed to be $\leq 10^{1.5}$ $CCID_{50}$ per 100 μL. The titer (log_{10}) of a lipid–virus mixture was subtracted from the titer (log_{10}) of the control mixture and the difference, i.e., the reduction in viral infectivity, was used as a measure of the virucidal activity of the lipid.

Assay of Virucidal Activity of Hydrogel Formulations—A hydrogel (200 μL) was placed in a 35 mm tissue culture dish (Nunc), and equal volume of HSV-1 in medium was added. The hydrogel was thoroughly mixed with the virus at room temperature for 1, 5, or 10 min. The mixtures were then immediately diluted 100-fold in medium and titrated in 10-fold dilutions. Virus mixed with medium instead of hydrogel was used as a control. The activity of the hydrogels was calculated as in the experiments with lipid solutions. Virucidal activity against HSV-1 in semen was tested in the same way except that the virus was first concentrated 10-fold by centrifugation in a Sorvall ultracentrifuge at 100000*g* for 90 min and then diluted 1:10 in fresh (<2 h) liquefied human semen. Virus-spiked semen mixed with medium was used as a control.

Evaluation of Toxic Effects of Gel Preparations in Monolayers of CV-1 Cells—Tenfold dilutions of hydrogel formulas were added to monolayers of CV-1 cells, 4 wells per dilution, and the cell layers were examined for lysis or other toxic effects after 1 and 24 h.

HPLC Assay of Monocaprin—The monoglyceride content was determined using a high-performance liquid chromatography (HPLC) component system consisting of a Thermo Separations Products Spectra Series P200 HPLC solvent delivery system, a μBondapak C18 125A 10μm (3.9 × 300 mm) column, a Waters Intelligent Sample Processor (WISP) Model 710B, a Thermo Separations Products SP4400 Integrator, and a Thermo Separations Products Spectra Series UV150 detector. The wavelength was 218 nm, and the mobile phase consisted of acetonitrile, water, and tetrahydrofuran (57:42:1) with the retention time being 2.1 min at 1.25 mL/min flow rate.

Drug Release from Hydrogels—Release of monoglyceride was investigated using a membraneless diffusion cell at 37 °C. Phosphate buffer (pH = 4.5) containing 0.1% 2-hydroxypropyl-β-cyclodextrin was used as the receiver phase. Samples were taken from the receiver phase at regular intervals and filtered through a 0.22 μm membrane filter. After each sampling, the volume was replaced. The amount of monoglyceride released was determined by HPLC using a calibration curve of the monoglyceride in the receiver phase. Each experiment was carried out in triplicate.

Results

Anti-HSV-1 Activity of Fatty Acids and 1-Monoglycerides in MM—In a previous study[4] medium-chain saturated and long-chain unsaturated fatty acids were found to inactivate HSV-1 in 30 min at 37 °C, and 1-monoglycerides were found to be more active than the corresponding fatty acids. In the present study caprylic acid (8:0), capric acid (10:0), lauric acid (12:0), myristic acid (14:0), palmitoleic acid (16:1), and oleic acid (18:1) and their 1-monoglycerides were tested against HSV-1 for 1 min at room temperature. In addition, undecylenic acid (11:0) was tested. The purpose of this experiment was to determine which of these compounds would be preferable as the active ingredients in a fast-acting virucidal gel formulation, i.e., would inactivate an enveloped virus such as HSV-1 within 1 min. In the first experiment all of the lipids were tested at a concentration of 20 mM. The results are shown in Figure 1. Of the fatty acids only lauric acid (12:0) and palmitoleic acid (16:1) caused a 100000-fold reduction of virus titer in 1 min. All the other fatty acids had no or a very small effect. Of the monoglycerides, monocaprin (10:0) was the most active, but monolaurin also had considerable activity and caused a 100000-fold reduction in virus titer. The most active compounds were tested further in concentrations of 2.5 mM, 5 mM and 10 mM. The results are shown in Tables 1 and 2. Both lauric and palmitoleic acid lost most of their activity at 10 mM or lower concentrations, whereas the activity of monolaurin was unchanged. Monocaprin had by far the highest activity and caused a greater than 700000-fold reduction of virus titer in 1 min at a concentration of 5 mM (Table 2). The virucidal activities of less active compounds were additive if two or more were mixed together (results not shown).

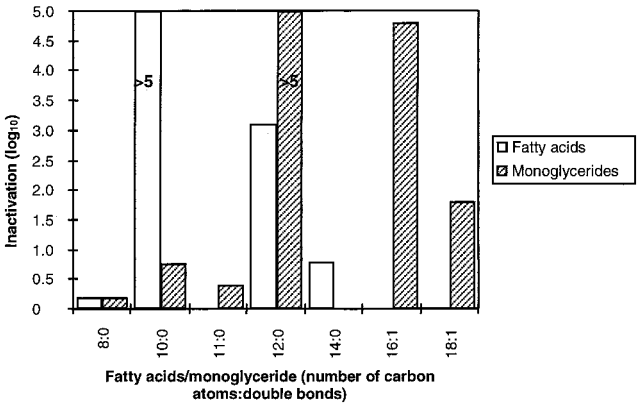

Figure 1—Inactivation of HSV-1 by incubation with an equal volume of 20 mM fatty acid or monoglyceride at room temperature for 1 min. Fatty acids and monoglycerides are indicated by the number of carbon atoms and double bonds. Inactivation is expressed as log reduction of virus titer. The data are the means of at least three experiments.

Table 1—Inactivation of HSV-1 by Incubation with an Equal Volume of Fatty Acid at Room Temperature for 1 min

fatty acid	concn, mM	reduction of virus titer (log_{10})[a]
lauric acid (12:0)[b]	20	≥5.8
	10	0
palmitoleic acid (16:1)	20	4.9
	10	1.6
	5	0
oleic acid (18:1)	20	1.7
	10	0

[a] The data are the means of three experiments. [b] Numbers of carbon atoms: double bonds.

Anti-HSV-1 Activity of Different Hydrogel Formulations Containing Monocaprin—Since monocaprin had the highest virucidal activity against HSV-1 as shown in Tables 1 and 2, this monoglyceride was selected as the active ingredients in hydrogel formulations. The gel-forming agents used were carbomer (series 2A–D) and

Table 2—Inactivation of HSV-1 by Incubation with an Equal Volume of 1-Monoglycerides at Room Temperature for 1 min

monoglyceride	concn, mM	reduction of virus titer (log_{10})[a]
monocaprin (10:0)[b]	20	≥5.8
	10	≥5.5
	5	≥5.5
	2.5	2.2
monolaurin (12:0)	20	3.0
	10	3.4
	5	3.0

[a] The data are the means of three experiments. [b] Numbers of carbon atoms: double bonds.

Table 3—Inactivation of HSV-1 by Incubation at Room Temperature for 1 min with Various Hydrogel Formulations. Series 1A–M Formulations Containing NaCMC and PVP and Series 2A–D Formulations Containing Carbomer and HPMC

gel	method of dissolving monocaprin	monocaprin concn, mM	reduction of virus titer (log_{10})[a]
1A	Glycofurol 75 (pH adjusted to 7)	0	0
		10	2.9
		20	≥5.5
1B	Glycofurol 75 (pH adjusted to 5)	0	0
		0	2.8
		20	≥5.5
1D	Glycofurol 75 and PEG200	0	0.2
		10	2.0
1H	Tween 80	0	0.2
		20	<1.0
1I	Chremophor PH40	0	0.1
		20	<0.8
1L	Chremophor EL	0	0.3
		10	<0.8
1M	2-hydroxypropyl-β-cyclodextrin	0	0
		10	<0.8
2A	Glycofurol 75	0	0
		10	3.2
		20	≥5.5
2B	Propylene glycol	0	0.2
		10	2.2
		20	≥4.2
2D	2-hydroxypropyl-β-cyclodextrin	0	0
		10	<0.8

[a] The data are the means of three experiments.

NaCMC (series 1A−M), both compounds that have good bioadhesive properties and have been used for the formulation of vaginal dosage forms.[8,9] As monocaprin is not soluble in water the hydrogels were formulated in such a way that the monoglyceride was solubilized in the dosage form. It was attempted to use a surface active agent (Tween 80, Cremophor RH40, Cremophor EL) to solubilize the compound, and complex formation with a cyclodextrin (2-hydroxypropy-β-cyclodextrin) was also attempted. Solvents were used to dissolve the monoglyceride (propylene glycol, glycofurol 75) as well as a combination of solvents and surfactants. Table 3 shows the inactivation of HSV-1 by incubation at room temperature for 1 min with hydrogels, with or without monocaprin. The results indicate that both propylene glycol and glycofurol 75 are suitable solvents for monocaprin in hydrogels with either Carbopol or NaCMC as carrier. Addition of surfactants or complex-forming compounds such as 2-HPβCD inhibits the activity of monocaprin in the hydrogels. As propylene glycol can cause irritation of mucosal membranes it was decided to continue the work using hydrogels formulated with glycofurol 75.

Hydrogel formulations 1A, 1B, and 2A were further tested for activity against HSV-1. The hydrogels were mixed with equal volumes of HSV-1, incubated at room temperature for 1 or 10 min, and then titrated as described in Materials and Methods. The results are shown in Table 4. Control hydrogels without monocaprin had an insignificant effect on the virus except hydrogel 2A after incubation for 10 min. In all the hydrogels, monocaprin at 5 mM or higher concentration inactivated the virus more than 100000-fold (>5 log) in 1 min. Monocaprin concentration of 2.5 mM was less active.

Table 4—Inactivation of HSV-1 Mixed with an Equal Volume of Gels 1A, 1B, or 2A without Active Ingredient or with Various Concentrations of Monocaprin and Incubated at Room Temperature for 1 and 10 min

gel	monocaprin concn, mM[a]	incubation, min	reduction of virus titer (log_{10})[b]
1A	0	1	0.4
	0	10	0.6
	2.5	1	<0.8
	2.5	10	2.3
	5	1	≥5.2
	10	1	≥5.2
	20	1	≥5.2
1B	0	1	0.2
	0	10	0.3
	2.5	1	1.0
	2.5	10	2.0
	5	1	≥5.2
	10	1	≥5.2
	20	1	≥5.2
2A	0	1	0.2
	0	10	2.3
	2.5	1	3.3
	2.5	10	≥4.8
	5	1	≥5.2
	10	1	≥5.2
	20	1	≥5.2

[a] The concentration is reduced by half in the final mixture. [b] The data are the means of three experiments.

Table 5—Inactivation of HSV-1 Diluted 1:10 in Semen and Mixed with an Equal Volume of Gels 1A, 1B, and 2A. Incubation Was at Room Temperature for 1, 5, or 10 min[a]

gel	monocaprin concn, mM	incubation, min	reduction of virus titer (log_{10})
1A	0	10	0
	5	10	2.3
	10	1	2.9
	10	5	4.2
	10	10	≥5.0
	20	1	≥5.5
1B	0	10	0
	5	10	1.0
	10	1	2.8
	10	5	4.4
	10	10	≥5.0
	20	1	≥5.5
2A	0	10	0
	5	10	1.6
	10	1	3.2
	10	5	≥5.0
	10	10	≥5.5
	20	1	≥5.5

[a] The data are the means of three experiments.

The virucidal activity of the hydrogels was further tested against HSV-1 suspended in semen rather than in maintenance medium. The results are shown in Table 5. The virucidal activity was considerably less in semen with only the 20 mM concentration causing greater than 100000-fold inactivation in 1 min.

In Vitro Study of Drug Release—The drug release profiles from the different hydrogels are shown in Figure 2. Drug release profile from the 1B hydrogels, containing

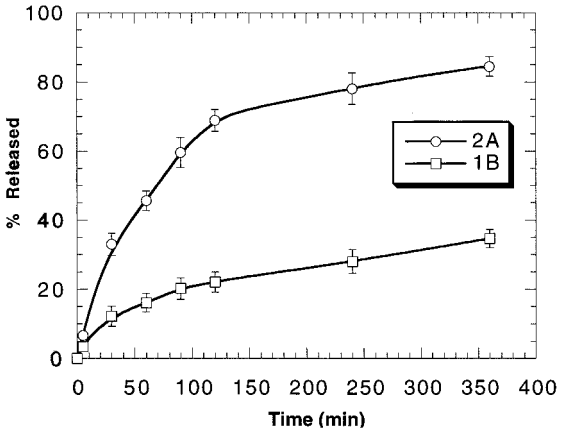

Figure 2—Release of monocaprin from hydrogel formulations 1B (containing NaCMC) and 2A (containing carbomer and HPMC).

Table 6—Cytotoxic Effects of Hydrogel Formulations 1A and 2A,with or without Monocaprin, in Monolayers of CV-1 Cells

		cytotoxic dilution	
gel	monocaprin concn, mM	1 h	24 h
1A	0	$(10^{-1})^a$	10^{-1}
	10	10^{-1b}	10^{-1}
	20	10^{-1}	10^{-1}
2A	0	(10^{-1})	10^{-1}
	10	10^{-1}	10^{-1}
	20	10^{-1}	10^{-1}
Gynol-plus[c]		10^{-2}	10^{-3}

[a] In parentheses: round cells, not lysed. [b] Without parentheses: complete lysis of cells. [c] A commercial (Cilag AG, Schaffhausen,Switzerland) spermicidal gel containing 2% nonoxynol-9 in Povidone K30 and propylene glycol.

NaCMC and PVP as the gelling agents, show a burst effect phenomenon during the first 30 min. Comparison of the release from the two hydrogel bases reveals that the monoglyceride release rate is appreciably higher from the hydrogel 2A containing carbomer and HPMC. This could be due to a less dense gel structure or a different release mechanism in the two hydrogel structures. These results indicate that the release of monocaprin is suitable for prolonged spermicidal and virucidal activity.

Cytotoxic Effect of Hydrogel Formulations in Monolayers of CV-1 cells—Hydrogels containing 10 or 20 mM of monocaprin were found to be cytotoxic in dilution 10^{-1} in virus titrations. Hydrogels 1A and 2A without monocaprin and with 10 or 20 mM monocaprin were inoculated in dilution 10^{-1} onto cell monolayers. The cells were then examined microscopically for cytotoxic effect after 1 and 24 h. Gynol-plus, a commercial contraceptive containing nonoxynol-9, was tested in the same way for comparison. The results are shown in Table 6. Both hydrogel formulations without monocaprin showed some toxic effect after 1 h and complete lysis after 24 h. Hydrogels with monocaprin were more cytotoxic and lysed all the cells in 1 h. No visible toxic effect was seen in 10^{-2} or higher dilutions even after incubation for 4 days (results not shown). A vaginal gel (Gynol-plus) which contains 2% nonoxynol-9, caused a complete cell lysis in 1 h in dilution 10^{-2} and in 24 h in dilution 10^{-3}. It was therefore 10- to 100-fold more toxic to the cell layers than formulations 1A and 2A containing 20 mM (0.5%) monocaprin.

Discussion

In this paper we report novel pharmaceutical formulations in the form of hydrogels of various compositions, which contain a simple lipid, i.e., monocaprin, as the microbicidal ingredient. Monocaprin was selected after a comparison of the virucidal activity of several fatty acids and monoglycerides. In addition to monocaprin, some of these lipids showed considerable activity when suspended in maintenance medium, particularly lauric and palmitoleic acid (Figure 1). However their activities in hydrogel formulations have not yet been studied.

Hydrogels containing monocaprin in concentrations of 5−20 mM are highly active against HSV-1, which was used as a test virus, and cause greater than 100000-fold inactivation of the virus in 1 min. Since some viruses are transmitted by semen, we tested the activity of the hydrogels against HSV-1 suspended in semen and found that a monocaprin concentration of 20 mM was needed for maximum efficacy of the gels. A lower activity of monocaprin in a biological fluid like semen could be expected because previous studies have shown that as much as 10-fold higher lipid concentrations are required for inactivation of virus in human blood than in culture medium.[6] Several enveloped viruses, such as HSV-1, VSV, measles virus, respiratory syncytal virus, cytomegalovirus, visna virus, and HIV-1 have been found to be equally susceptible to lipids.[1,10−12] It was therefore considered appropriate to use HSV-1 as a model in the present experiments to study the rapid microbicidal effect of various lipids. Recent studies on the effect of fatty acids and monoglycerides on *Chlamydia trachomatis*[13] have shown that monocaprin is also the most active in killing this bacterium in a short time and that hydrogel formulations 1A, 1B, and 2A containing 10 mM monocaprin kill *Chlamydis trachomatis* and *Neisseria gonorrheae* at high titers in 5 and 1 min, respectively.[14]

The hydrogel formulations in 10^{-1} dilution were found to be toxic to monolayers of CV-1 cells, but they were 10- to 100-fold less cytotoxic than a commercial spermicidal product containing 2% nonoxynol-9. However, such a comparison must also be carried out in vivo. A preliminary experiment with hydrogel fomulation 1A in mice showed no adverse effect on their vaginal mucosa.[14] Testing of the hydrogel formulations 1A and 2A by the standard rabbit vaginal irritation test showed no irritation of the vaginal mucosa after daily application for 10 days.[14] A comparison of the toxicity of the hydrogels and a vaginal contraceptive gel which contains 4% nonoxynol-9 is now in preparation.

Conclusions

The hydrogel formulations containing 20 mM monocaprin are highly virucidal in vitro and cause a greater than 100000-fold inactivation of virus (HSV-1) in 1 min, even in the presence of semen which considerably reduces the activity at a concentration of 10 mM. Formulations in dilution 1:10 are cytotoxic in monolayers of CV-1 cells, but they are 10- to 100-fold less cytotoxic than a commercial product which contains 2% nonoxynol-9.

References and Notes

1. Isaacs, C. E.; Litov, R. E.; Thormar, H. Antimicrobial activity of lipids added to human milk, infant formula, and bovine milk. *Nutr. Biochem.* **1995**, *6*, 362−366.
2. Kabara, J. J. Fatty acids and derivatives as antimicrobial agents. In: *The pharmacological effect of lipids*.; Kabara, J. J., Ed.; The American Oil Chemists Society: St. Louis, 1978; pp 1−13.
3. Shibasaki, I.; Kato, N. Combined effects on antibacterial activity of fatty acids and their esters against gram-negative bacteria, In *The Pharmacological Effect of Lipids*; Kabara, J. J., Ed.; The American Oil Chemists Society; St. Louis, 1978; pp 15−24.
4. Thormar, H.; Isaacs, C. E.; Brown, H. R.; Barshatzky, M. R.; Pessolano, T. Inactivation of enveloped viruses and killing

of cells by fatty acids and monoglycerides. *Antimicrob. Agents Chemother.* **1987**, *31*, 27−31.
5. Welsh, J. K.; Arsenakis, M.; Coelen, R. J.; May, J. T. Effect of antiviral lipids, heat and freezing on the activity of viruses in human milk. *J. Infect. Dis.* **1979**, *140*, 322−328.
6. Isaacs, C. E.; Kim, K. S.; Thormar, H. Inactivation of enveloped viruses in human bodily fluids by purified lipids, *Ann. N.Y. Acad. Sci.* **1994**, *724*, 457−464.
7. Reed, L. J.; Muench, M. A simple method of estimating 50% end points. *Am. J. Hyg.* **1938**, *27*, 493−497.
8. Knuth, K.; Amiji, M.; Robinson, J. R. Hydrogel delivery systems for vaginal and oral applications. *Adv. Drug Delivery Rev.* **1993**, *11*, 137−167.
9. Park, H.; Robinson, J. R., Mechanism of mucoadhesion af poly(acrylic acid) hydrogels. *Pharm. Res.* **1987**, *4*, 457−465.
10. Isaacs, C. E.; Thormar, H. The role of milk-derived antimicrobial lipids as antiviral and antibacterial agents. In *Immunology of Milk and the Neonate*; Mestecky, J., Plenum Press: New York, 1991; pp 159−165.
11. Thormar, H.; Isaacs, C. E.; Kim, K. S.; Brown, H. R. Inactivation of visna virus and other enveloped viruses by free fatty acids and monoglycerides. *Ann. N.Y. Acad. Sci.* **1994**, *724*, 465−471.
12. Isaacs, C. E.; Thormar, H.; Pessolano, T. Membrane disruptive effect of human milk: Inactivation of enveloped viruses. *J. Infect. Dis.* **1986**, *154*, 966−971.
13. Bergsson, G.; Arnfinnsson, J.; Karlsson, S. M.; Steingrímsson, Ó.; Thormar, H. In vitro inactivation of *Chlamydia trachomatis* by fatty acids and monoglycerides. *Antimicro. Agents Chemother.* **1998**, *42*, 2290−2294.
14. Thormar, H.; Bergsson, G.; Gunnarsson, E.; Georgsson, G,; Witvrouw, M.; Steingrímsson, Ó.; De Clercq, E.; Kristmundsdóttir, T. Hydrogels containing monocaprin have potent microbicidal activities against sexually transmitted viruses and bacteria in vitro. *Sex. Transm. Inf.* **1999**, *75*, 181−185.

Acknowledgments

This work was supported by the Icelandic Research Council and the Research Fund of the University of Iceland.

JS9900396

Biopharmaceutics and Pharmacokinetics of 5-Phenyl-1,2-dithiole-3-thione Complexed with Sulfobutyl Ether-7-β-cyclodextrin in Rabbits

CLAUDIA LEFEUVRE,[†] PASCAL LE CORRE,*[,†] GILLES DOLLO,[†] FRANÇOIS CHEVANNE,[†] JEAN LOUIS BURGOT,[‡] AND ROGER LE VERGE[†]

Contribution from *Laboratoire de Pharmacie Galénique, Biopharmacie et Pharmacie Clinique, and Laboratoire de Chimie Analytique, Faculté des Sciences Pharmaceutiques et Biologiques, Université de Rennes 1, 35043 Rennes Cedex, France*

Received January 27, 1999. Final revised manuscript received July 20, 1999.
Accepted for publication July 26, 1999.

Abstract ☐ The biopharmaceutics and pharmacokinetics of 5-phenyl-1,2-dithiole-3-thione (5PDTT) were investigated in rabbits, after administration as a complex with sulfobutyl-ether-7-β-cyclodextrin (SBE7-β-CD) by intravenous and oral routes and as a micronized powder by oral route. 5PDTT had a rapid and large red blood cell partitioning that was not dependent on drug concentration either in vitro or ex vivo. The blood clearance was very high (354 ± 131 mL/min) suggesting extrahepatic metabolism and/or nonrenal elimination and a significant volume of distribution (67 ± 76 L). The renal clearance was 0.17% of total clearance. 5-phenyl-1,2-dithiol-3-one (5PDTO) was identified as a metabolite in blood and urine. The bioavailability of 5PDTT following administration of 5PDTT/SBE7-β-CD complex was estimated to 41% while it was close to zero when 5PDTT was given as a micronized powder.

Introduction

Some chemical agents can inhibit carcinogenesis at different stages and could be used in cancer chemoprevention. Epidemiological studies suggest that consumption of cruciferous vegetables such as brussel sprouts, broccoli, or cabbage, which are probably sources of 1,2-dithiole-3-thiones,[1] results in decreased cancer risk in humans in various localizations.[2,3] In vitro and animal studies suggest that the cruciferous vegetables and 1,2-dithiole-3-thiones protect against carcinogens by an increase in the activities of electrophile detoxification Phase II enzymes, in conjunction with an increase of intracellular glutathione level.[4] The Phase II enzymes, such as glutathione-S-transferase and quinone reductase can conjugate potential carcinogens with glutathione favoring their elimination. Glutathione is a cellular thiol, which is very important for the cellular integrity by protection against free radicals, oxidants, and electrophilic intermediates of various compounds. Animals studies have shown an inhibition of experimental carcinogenesis in liver, bladder, breast colon, lung, and skin cancer after administration of dithiolethiones such as anetholtrithione and oltipraz.[5−7] On the basis of these data, dithiolethiones appear to be promising chemopreventive agents. 5PDTT was chosen among 1,2-dithiole-3-thiones because derivatives substituted on the carbon-5 by an aryl moiety have exhibited the most interesting antioxidant properties.[8,9] Furthermore, oltipraz and anetholtrithion, which are known for their cancer chemoprevention properties, are also substituted on the carbon-5 by such a moiety.

Biopharmaceutic and pharmacokinetic studies have only been conducted with two dithiolethiones: anetholtrithione used for its scialogogue and choleretic properties, and oltipraz which has been developed for its antischistosomal activity.[10] These studies have been conducted only after oral administration in animals[11] and in humans.[5,12−14]

The goal of the current work was to study the pharmacokinetics and biopharmaceutics of 5-phenyl-1,2-dithiole-3-thione (5PDTT) after administration by intravenous and oral routes in rabbits. To study this un-ionized and highly lipophilic compound (log $P = 3.67$, intrinsic solubility 0.48 mg/L),[15] we used sulfobutyl-ether-7-β-cyclodextrin (SBE7-β-CD) that has been shown to significantly increase 5PDTT aqueous solubility[16] (480 times the intrinsic solubility at a 10% SBE7-β-CD concentration).

Materials and Methods

Materials—5-Phenyl-1,2-dithiole-3-thione and 5-phenyl-1,2-dithiol-3-one were synthesized according to A. Thuillier and J. Vialle.[17] Their chemical structure is presented in Figure 1.

The sulfobutyl-ether-7-β-cyclodextrin was supplied by Cydex L. C. (Overland Park, KS). Heptane and acetonitrile (Merck, Darmstadt, FR, Germany), ethyl acetate (Carlo Erba Reagenti, Milano, Italy), and diethylene glycol monoethyl ether (Sigma Chemical, St Louis, MO) were of analytical grade.

Analytical Method—Analysis of 5PDTT and 5PDTO was carried out by a one-step extraction procedure. 5PDTT was quantified in plasma, blood, red blood cells, and urine samples, and 5PDTO was quantified in blood and urine.

One milliliter of biological sample (plasma, red blood cells, or blood) was extracted with 2 mL of a 80:20 (v/v) mixture of heptane and ethyl acetate. Extraction was performed by mixing for 5 min (horizontal shaker, model Agitelec SL 200). Then, the vials were centrifuged at 2000*g* for 5 min. The supernatant (≈1.5 mL) was poured into a polypropylene tube, containing 50 μL of a solution of diethylene glycol monoethyl ether (5 μL) and heptane-ethyl acetate (80:20, v/v, 45 μL). Diethylene glycol monoethyl ether (bp = 194 °C) was necessary to avoid the adsorption of 5PDTT and 5PDTO onto the polypropylene tubes. Then, the volatile organic phase was evaporated at room temperature under a nitrogen stream. The residue was diluted in acetonitrile (50 μL) and then stored at 4 °C until analysis.

For urine sample extraction, the volume of the samples was 5 mL, the extraction was performed by mixing for 15 min (rotary shaker Bioblock), and the vials were centrifuged at 4500*g* for 15 min.

The samples were analyzed using a HPLC system, consisting of a Waters Model 6000 A pump (Waters Assoc., Millford, MA) equipped with a Waters 717 Autosampler (Waters Assoc., Millford, MA), and a Delsi integrator, model Enica 21 (Delsi, Suresnes, France). Chromatography was performed using a Lichrospher RP-

* Corresponding author: Tel: 33 2 99 33 6861. Fax: 33 2 99 33 6891. e-mail: Pascal.Le-corre@univ-rennes1.fr.
[†] Laboratoire de Pharmacie Galénique, Biopharmacie et Pharmacie Clinique.
[‡] Laboratoire de Chimie Analytique.

10.1021/js9900248 CCC: $18.00
Published on Web 09/10/1999

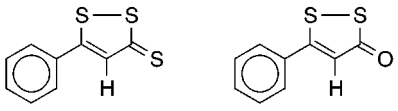

Figure 1—Chemical structure of 5-phenyl-1,2-dithiole-3-thione (left) and of 5-phenyl-1,2-dithiol-3-one (right).

SelectB column maintained at 30 °C (5 μm, 125 × 3 mm; Interchim, Montluçon, France) with a water−acetonitrile (50:50, v/v) mobile phase at a flow-rate of 0.5 mL/min.

The detection was set at 318 nm (λ_{max} of 5PDTT: 318 nm and λ_{max} of 5PDTO: 288 nm) using a Milton Roy model Spectromonitor 3100 (LDC Milton Roy, Riviera Beach, FL).

The yields of extraction of 5PDTT from whole blood and urine were 88.5 ± 2.6% and 91.0 ± 5.5%, respectively. The yields of extraction of 5PDTO from whole blood and urine were 95.5 ± 1.5% and 94.6 ± 8.3%, respectively. The selectivity factor (α) for the separation of 5PDTT and 5PDTO was 1.6. The linearity was established for concentrations up to 1000 ng/mL. The limits of quantification of 5PDTT and 5PDTO in blood were 1.3 ng/mL and 2.4 ng/mL, respectively. The limits of quantification of 5PDTT and 5PDTO in urine were 0.3 ng/mL and 0.5 ng/mL, respectively. The within-day reproducibilities, checked at a blood concentration of 200 ng/mL, were 7.8% and 4.5% for 5PDTT and 5PDTO, respectively. The within-day reproducibilities, checked at a urine concentration of 20 ng/mL, were 5.6% and 6.6% for 5PDTT and 5PDTO, respectively.

Red Blood Cell Partitioning—Red blood cell (RBC) partitioning of 5PDTT was evaluated in vitro and ex vivo in rabbits. In the in vitro experiment, the kinetics of partitioning (incubation time of 1, 5, 15, and 30 min at a blood concentration of 500 ng/mL, n = 3) and the influence of the 5PDTT concentration (blood concentration of 200, 500, and 1000 ng/mL at the incubation time of 30 min, n = 2) were investigated at 37 °C. A 30 mL blood sample maintained under gentle agitation was spiked with 20 μL of a solution of 5PDTT/SBE7-β-CD complex.

In the ex vivo experiment, the influence of 5PDTT concentration on the RBCs partitioning was checked in blood samples drawn at 1, 5, 15, and 30 min following an iv administration of a solution of 5PDTT/SBE7-β-CD complex (2 mg in 10 mL).

Blood samples (2 mL) were immediately centrifuged (9800 g for 1 min), and RBCs were lysed by freezing at −20 °C. 5PDTT concentrations in RBCs and plasma were determined as described above.

The extent of RBCs partitioning ($K_{e/p}$) was determined according to Hinderling[18] as follows:

$$K_{e/p} = C_e/C_p$$

where C_e and C_p are the concentration in the RBCs and plasma, respectively.

The whole blood-to-plasma concentration ratio ($K_{b/p}$) represents an additional drug distribution parameter of interest depending on the hematocrit (H_c). $K_{b/p}$ was determined according to Hinderling[18] as follows:

$$K_{b/p} = K_{e/p} \cdot H_c + (1 - H_c)$$

Study Formulations—*Pure Drug*—5PDTT was micronized using a rotomill SRM 100 apparatus (Beckman, Nyon, Switzerland). The mean diameter, expressed by D[4,3] (Mastersizer, Malvern, Orsay, France), was 29 μm. 5PDTT was administered as a capsule containing 20 mg of the drug.

Inclusion Complex—An ethanolic solution of 5PDTT (20 mg in 10 mL) was diluted in an aqueous solution of SBE7-β-CD (11.88 g in 80 mL) to obtain a 1/10 molar ratio and a final ethanol concentration of 25%. The resulting solution was concentrated under vacuum at 60 °C using a rotavapor apparatus until elimination of ethanol. The solution was then diluted with water to obtain a 5PDTT concentration of 1 mg/mL and 0.2 mg/mL for oral and iv dosing, respectively. The solutions were checked for 5PDTT concentration by HPLC and stored protected from light at ambient temperature.

Experimental Protocol—New Zealand adult males rabbits (n = 15, mean weight 3.2 kg) were housed individually in standard cages, and were provided free access to food and water. They were fasted 12 h before each experiment. The study was approved by the Local Committee of Laboratory Animal Care in accordance with the rules and guidelines concerning the care and use of laboratory animals.

Six rabbits received 5PDTT as a complex at a dose of 2 mg (10 mL) as an iv bolus injection via the marginal ear vein. Blood samples (1.5 mL) were collected from the controlateral marginal ear vein before drug administration and at 0.5, 1, 2, 5,10,15, 20, 30, 60, 90, 120, 180, 240, 300, 360, 420, and 480 min. The samples were immediately frozen at −20 °C.

Six rabbits received 5PDTT as a complex at a dose of 20 mg (20 mL) by oral route with a gastric catheter which was subsequently flushed with water (10 mL). Three rabbits received 5PDTT as a capsule of pure drug (20 mg) and then received water (30 mL) with a syringe. Blood samples were collected before drug administration and at 15, 25, 30, 40, 45, 60, 90, 120, 180, 240, 300, 360, 420, and 480 min. The samples were immediately frozen at −20 °C.

To obtain a regular urine flow throughout the experiments, the rabbits were hydrated by a sc infusion of normal saline (250 mL over 30 min) the day before and within the hour preceding the drug administration. During the study, the animals received iterative iv infusions 20% mannitol (20 mL/h for the first hour and then for 30 min every 2 h) and normal saline (60 mL/h between the administration of mannitol). Urine was collected by miction. Samples (5 mL) were kept frozen until analysis.

Pharmacokinetic Analysis—After iv dosing, a model with two-exponential or three-exponential functions and first-order elimination from the central compartment was fitted to the individual 5PDTT blood concentrations, using weighted nonlinear least-squares regression analysis with the reciprocal of squared concentration as a weighting factor (WinNonlin version 1.5, Scientific Consulting Inc., Apex, NC). The choice between the models was judged by the distribution of residuals and comparison of the sum of squared deviations.[19] Standard methods were used to calculate the following parameters: total body clearance (CL), renal clearance (CL_r), apparent volume of distribution of the central compartment (V_c), apparent volume of distribution at steady-state (V_{ss}), distribution rate constants (K_{12}, K_{13}, K_{21}, and K_{31}), elimination rate constant (K_{10}), and apparent distribution and elimination half-lives ($t_{1/2}\,\alpha$, $t_{1/2}\,\beta$, and $t_{1/2}\,\gamma$). The extrapolated area was calculated as the ratio of the last measured whole blood concentration (C_{last}) and the slope of the terminal phase.

After oral dosing, individual 5PDTT and 5PDTO blood concentration data were analyzed using noncompartmental analysis assuming a first-order elimination from the central compartment with the software package WinNonlin. Peak plasma concentration (C_{max}) and corresponding time to peak concentration (T_{max}) were derived from raw data. The area under the whole blood curve from zero to the last sampling point (AUC_{0-last}) and from zero to infinity (AU_{0-inf}) were calculated by linear trapezoidal method from experimental data. The extrapolated area was calculated as the ratio of the last measured whole blood concentration (C_{last}) and the slope of the terminal phase. Standard methods were used to calculate the following parameters for 5PDTT: total body clearance (CL/F), renal clearance (CL_r/F), apparent volume of distribution at pseudodistribution equilibrium (V_z/F), and apparent elimination half-lives ($t_{1/2}\,\lambda z$). Pharmacokinetic parameters were corrected by the average bioavailability (F).

Q_u is the cumulative amount of 5PDTT or 5PDTO recovered in urine during 480 min.

The average absolute bioavailability of 5PDTT (F) was determined according to: F = (mean $AUC_{0-inf(oral)}$/oral dose)/(mean $AUC_{0-inf(iv)}$/iv dose).

Statistical Analysis—All data are presented as the mean ±SD Student's t-test was used to compare individual means. A p value less than 0.05 was considered as statistically significant.

Results and Discussion

Red Blood Cell Partitioning—Most pharmacokinetic studies are derived from drug concentrations measured in plasma or in serum. To investigate 5PDTT pharmacokinetics, quantitation in whole blood has to be considered owing to the high lipophilicity of the drug.[15] Among the cellular constituents of blood, RBCs represent the largest population and drugs may bind to their membrane, to

Table 1—In Vitro and Ex Vivo Red Blood Cell Partitioning of 5PDTT[a]

	theoretical C_b (ng/mL)	duration of incubation (min)	H_c (%)	C_b (ng/mL)	C_e (ng/mL)	C_p (ng/mL)	$K_{e/p}$	$K_{b/p}$
				In Vitro Experiment				
($n = 3$)	500	30	38	512 ± 17	642 ± 30	431 ± 42	1.5 ± 0.2	1.2 ± 0.1
	200	30	35	175	266	126	2.1	1.4
	500	1	35	455	578	389	1.5	1.2
	500	5	35	462	632	369	1.7	1.3
($n = 2$)	500	15	35	482	592	422	1.4	1.1
	500	30	35	509	609	455	1.3	1.1
	1000	30	35	941	1279	759	1.7	1.4
				Ex Vivo Experiment				
	nd	1	35	1136	1380	974	2.1	1.4
	nd	5	35	332	389	301	1.5	1.2
($n = 2$)	nd	15	35	157	220	123	1.7	1.3
	nd	30	35	92	128	73	1.4	1.1

[a] n = no. of experiments.

hemoglobin, and to proteins in the cytosol. The determination of concentrations in whole blood or erythrocytes rather than in plasma should be more suitable for studying the drug disposition of lipophilic drugs that usually have a high hepatic extraction (flow-rate-limited clearance). Moreover, in case of a significant RBC distribution, measuring blood concentrations increases the sensitivity of an analytical method allowing a follow-up of the drug elimination for at least one additional half-life.[18]

The results of the in vitro and ex vivo experiments are presented in Table 1. The extent of RBC partitioning of 5PDTT, estimated by $K_{e/p}$ and $K_{b/p}$, was significant (around 50% of the drug in the RBCs). The RBC partitioning was not dependent on the concentration ex vivo in a blood concentration range from 92 to 1136 ng/mL and in vitro in a blood concentration range from 200 to 1000 ng/mL. The distribution equilibrium was obtained rapidly, 95% of the maximum RBC concentration being reached in 1 min in the in vitro experiment. The high lipophilicity of 5PDTT may account for this rapid distribution in RBCs. On the basis of these data, we choose to study the blood pharmacokinetics of this lipophilic compound.

Although RBCs contain drug-metabolizing enzymes,[20] 5PDTT was not apparently metabolized in vitro in RBCs since the recovery of the drug in RBCs and in plasma aliquots were close to the initial blood loading. Moreover, 5-phenyl-1,2-dithiol-3-one (5PDTO), which is a metabolite of 5PDTT measured in plasma and urine, was not detected in the in vitro experiments.

Biopharmaceutics and Pharmacokinetics—The mean concentration−time profiles of blood 5PDTT and 5PDTO in rabbits following iv and oral dosing of 5PDTT are presented in Figure 2. The pharmacokinetic parameters of 5PDTT after iv and oral dosing are listed in Tables 2 and 3, respectively.

The 5PDTT blood concentration−time curves following iv administration were best described using a tricompartmental model. The extrapolated area averaged 7.2 ± 5.4% indicating that the sampling schedule was suitable.

Due to its high lipophilicity and significant RBC partitioning, 5PDTT was expected to have a high tissue distribution. The volume of distribution (V_{ss}(iv)) was high, suggesting a large distribution. However, the volume of distribution was highly variable compared to other pharmacokinetic parameters. Considering the respective values of the distribution rate constants (K_{12} plus K_{13}) compared to the elimination rate constant (K_{10}), 5PDTT has, from a statistical point of view, more chance to be distributed in tissues than to be eliminated, even though the systemic clearance of 5PDTT was high. The tissue affinity of 5PDTT

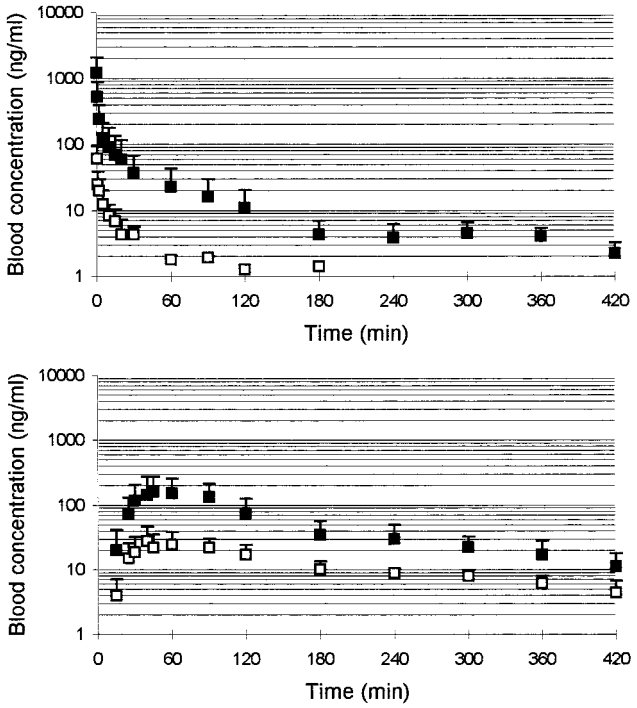

Figure 2—Mean (±SD) whole blood concentrations of 5PDTT and 5PDTO after administration of 5PDTT as a complex with SBE7-β-CD at a dose of 2 mg by intravenous route (top) and at a dose of 20 mg by oral route (bottom) in rabbits. 5PDTT (filled square); 5PDTO (empty square).

can be illustrated by the rapid distribution half-lives. Moreover, the values of the redistribution rate constants (K_{21} and K_{31}) were on average five to six times lower than the corresponding distribution rate constants (K_{12} and K_{13}), also suggesting the affinity of 5PDTT for tissue components. It should be noticed that a very slow redistribution back into the central compartment cannot be ruled out. However, the LOQ of our assay precluded such investigation.

The total blood clearance was three times higher than the hepatic blood flow described in rabbits (around 120 mL/min),[21] suggesting a significant extrahepatic metabolism and/or extrarenal excretion. However, the omission of a very slow redistribution might have led to an underestimation the AUC, leading to an overestimation of the clearance. Considering this assumption, a terminal half-life of around 35 h will lead to a clearance close to the liver blood flow.

The contribution of the renal clearance to the overall clearance was very low, 0.2% of the administered dose

Table 2—Pharmacokinetic Parameters of 5PDTT after Intravenous Administration as a Complex with SBE7-β-CD at a Dose of 2 mg in Rabbits

	$AUC_{0-inf(iv)}$ (ng·min/mL)	CL (mL/min)	Q_u (μg)	CL_r (mL/min)	V_c (L)	V_{ss} (L)	K_{12} (min^{-1})	K_{21} (min^{-1})	K_{13} (min^{-1})	K_{31} (min^{-1})	K_{10} (min^{-1})	$T_{1/2}$ α (min)	$T_{1/2}$ β (min)	$T_{1/2}$ γ (min)
R1	3834	522	3.3	0.9	5.5	200	0.414	0.185	0.106	0.032	0.095	0.9	13.6	472
R2	4899	408	0.4	0.1	0.3	8	1.030	0.162	0.305	0.017	1.230	0.3	7.2	51
R3	5915	338	1.8	0.3	1.5	50	1.195	0.209	0.264	0.210	0.228	0.4	11.5	165
R4	4867	411	4.3	0.9	1.1	11.4	0.586	0.169	0.635	0.006	0.386	0.4	6.6	301
R5	15123	132	8.1	0.5	0.3	5	1.020	0.246	0.428	0.048	0.393	0.4	5.7	36
R6	6437	311	5.0	0.8	0.7	26	1.671	0.184	0.351	0.013	0.440	0.3	11.4	102
mean	6846	354	3.8	0.6	1.6	67	0.986	0.193	0.348	0.054	0.462	0.4	9.3	188
SD	4155	131	2.7	0.3	2.0	76	0.448	0.031	0.177	0.078	0.398	0.2	3.2	169

Table 3—Biopharmaceutic and Pharmacokinetic Parameters of 5PDTT after Oral Administration as a Complex with SBE7-β-CD at a Dose of 20 mg in Rabbits

	C_{max} (ng/mL)	T_{max} (min)	$AUC_{0-inf(po)}$ (ng·min/mL)	CL (mL/min)	Q_u (μg)	CL_r (mL/min)	V_z (L)	$T_{1/2}$ λ-z (min)
R7	200	45	17586	466	9.3	0.2	177	263
R8	46	90	7153	1146	10.2	0.6	255	154
R9	119	90	33703	243	16.1	0.2	236	672
R10	299	60	39026	210	15.2	0.2	51	169
R11	261	60	46164	177	26.6	0.2	42	163
R12	333	40	25114	326	114.3	1.9	57	122
mean	210	64	28124	428	31.9	0.5	136	257
SD	110	22	14390	367	40.8	0.7	98	209

being excreted in urine. The high RBC partitioning may account for such a low contribution. A low renal excretion (less than 1% of the dose) has also been shown for oltipraz after oral administration in mouse, rat, monkey, and humans.[11,14]

The use of cyclodextrins to solubilize drug administered by the iv route raises the problem of a potential alteration of the drug pharmacokinetics by an incomplete or a delayed release of the drug from the cyclodextrin.[22] This problem should be considered for 5PDTT given the magnitude of the stability constant obtained with SBE7-β-CD (10 705 M^{-1}).[16] The answer to this problem would be given by a comparative pharmacokinetic study of the drug with a control formulation providing that the excipient(s) used (e.g., organic solvent, surfactant in case of lipophilic drugs) are themselves devoid of any effect on drug kinetics. The influence of complexation on 5PDTT pharmacokinetics cannot be ruled out in the current study since we did not compare the drug disposition to that obtained with a control formulation. However, 5PDTT can be expected to be quickly released from its complex as a result of (i) the dilution of the study formulation in the blood circulation, (ii) the rapid and significant distribution of 5PDTT in RBCs, and (iii) the extensive distribution of 5PDTT that further dilutes the complex. Furthermore, competitive displacement of the drug from its complex by lipophilic plasma components may also favor the drug release. Moreover, in an in vitro study comparing the RBC partitioning from a solution of SBE7-β-CD complex to that of obtained from an ethanol−DMSO solution of 5PDTT, it appeared that the RBC partitioning were similar. The RBC and plasma concentrations of 5PDTT (687 ± 11 ng/mL and 374 ± 31 ng/mL, respectively) were close to those obtained with the SBE7-β-CD complex (Table 1), suggesting that the complexation between 5PDTT and SBE7-β-CD was not a limiting factor for 5PDTT partitioning and should not be a limiting factor for 5PDTT disposition.

5PDTO was identified as a metabolite of 5PDTT. The urinary excretion of this metabolite represented around 0.025% of the dose of 5PDTT administered. A metabolic investigation is in progress to identify other metabolites, the structures of which are not so far determined. Following iv administration of 5PDTT, it was not possible to delineate the metabolite kinetics since 5PDTO blood concentrations were below the LOQ in five of the six animals after 90 min postdosing. However, following oral administration, 5PDTO blood concentrations were measured until 420 min with a C_{max} (209 ± 110 ng/mL) and a T_{max} (64 ± 22 min) being close to those of the parent drug. The apparent terminal elimination half-life of 5PDTO ($T_{1/2}$ λ-z = 190 ± 89 min) was close to that of 5PDTT, suggesting a formation rate-limited metabolite kinetics.

Given that dithiolethiones have a chemopreventive potential against solid tumors,[7] a more precise investigation of the distribution of 5PDTT should be performed to specify if the drug has a selective distribution in particular organs and tissues. In this respect, the evaluation of the distribution in the colon, breast, skin, bladder, and lung should be investigated. In an autoradiographic study in mice, ^{14}C-anetholtrithione given orally displayed high concentrations in intestine, liver, gall-bladder, kidney, and urinary bladder.[23] The study of the organ and tissue distribution of ^{14}C-oltipraz orally administered in mice showed that, during the 6 h postdosing, the highest levels were found, in a decreasing order, in stomach and intestine contents, in gall-bladder, in bladder, and at a lower level in brown fat, liver, and kidney.[11]

Individual concentration−time profiles of complex 5PDTT-SBE7-β-CD following oral dosing displayed a distribution-nose, indicating the multicompartmental pharmacokinetic pattern of 5PDTT. However, concentration−time profiles could not be suitably fitted according to a pharmacokinetic model so that a noncompartmental analysis was performed. With the exception of one animal, whose concentration−time profile was rather unusual and displayed some scattering, the extrapolated area averages 10.3 ± 3.0%, indicating that the sampling schedule was suitable. T_{max} was much smaller and less variable that described for oltipraz in humans[13] (mean 2.8 h, range: 0.5 to 8 h). Following oral administration, the volume of distribution (V_z/F) also indicated a large distribution but the difference was less pronounced than after bolus regimen. The apparent elimination half-life of 5PDTT was slightly higher than that observed following iv dosing ($p = 0.54$) and lower than

that described for oltipraz in humans (4.2 to 11.1 h with increase in dose). The contribution of the renal clearance to the overall clearance of oral 5PDTT was very low, 0.16% of the administered dose being recovered in urine.

In two of three rabbits receiving 5PDTT as a micronized powder, 5PDTT was not detectable during the study period (until 8 h). In the third animal, 5PDTT was detected only at 7 h (100 ng/mL). These data suggest that the absorption of 5PDTT given as a powder did not occur, highlighting the need of a particular oral formulation for such lipophilic drugs. The optimization of the formulation of the complex between 5PDTT and SBE7-β-CD is currently in progress in order to reduce the amount of cyclodextrin (11.88 g of cyclodextrin by 20 mg of 5PDTT in the formulation studied) and to obtain a solid-state complex.[16]

Biopharmaceutic data on dithiolethiones are scarce and have only be obtained for oltipraz following oral dosing in animals[11] and humans.[5,12−14] These studies have shown that the pharmacokinetics of oltipraz was dose-dependent, suggesting a increased oral bioavailability with increasing doses that may result from a saturable first-pass effect.[5,10,11] Since 5PDTT was not administered by iv and oral routes in the same animals, the oral bioavailability could not be determined individually. The average absolute oral bioavailability of 5PDTT complexed with SBE7-β-CD was estimated to 41% while its was close to zero when administered as a micronized powder.

The current study has shown that 5PDTT had a rapid and significant red blood cell partitioning. After administration by intravenous and oral routes in rabbits, 5PDTT had a very high clearance, suggesting extrahepatic metabolism and/or nonrenal elimination, and a large volume of distribution. 5PDTO was identified as a metabolite of 5PDTT in plasma and urine. The bioavailability of 5PDTT after administration as complex 5PDTT/SBE7-β-CD was estimated to 41% while it was close to zero when it was given as a micronized powder.

References and Notes

1. Jirousek, L.; Starka, L. Über das vorkommen von trithionen (1,2-dithiocyclopent-4-en-3thione) brassicapflanzen. *Die Naturwissen*. **1958**, *45*, 386−387.
2. Wattenberg, L. W. Chemoprevention of cancer. *Cancer Res.* **1985**, *45*, 1−8.
3. Steinmetz, K. A.; Potter, J. D.. Vegetables, fruit, and cancer prevention: a review. *J. Am. Diet. Assoc.* **1996**, *96*, 1027−1039.
4. Ansher, S. S.; Dolan, P.; Bueding, E. Biochemicals effects of Dithiolthiones. *Food Chem. Toxicol.* **1986**, *24*, (5), 405−415.
5. Benson, A. B., III. Oltipraz: a laboratory and clinical review. *J. Cell. Biochem.* **1993**, *Suppl. 17F*, 278−291.
6. Kensler, T. W.; Egner, P. A.; Trush, M. A.; Modification of aflatoxin B1 binding to DNA in vivo in rats fed phenolic antioxidants, ethoxyquin and a dithiolethione. *Carcinogenesis* **1985**, *6*, 759−763.
7. Steele, V. C.; Moon, R. C.; Lubet, R. A.; Grubbs, C. J.; Reddy, B. S.; Wargovich, M.; McCormick, D. L.; Pereira, M. A.; Crowell, J. A.; Bagheri, D.; Sigman, C. C.; Boone, C. W.; Kelloff, G. J. Preclinical efficacy evaluation of potential chemopreventive agents in animal carcinogenesis models: methods and results from the NCI chemoprevention drug development program. *J. Cell. Biochem.* **1994**, *20*, 32−54.
8. Burgot, J. L.; Martin, C.; Bertrand, H. O.; Warnet, J. M.; Christen, M. O. Structure-antilipoperoxidative activity relationship in the 1,2-dithiole-3-thione series. International Symposium on Natural Antioxidants: Molecular mechanisms and health effects. Pekin, June 1995.
9. European Patent 0 641 792 A1, 1995, Mitsui Toatsu Chemicals Inc.
10. Bueding, E.; Dolan, P.; Leroy, J. P. The antishistosomal activity of Oltipraz. *Res. Commun. Chem. Pathol. Pharmacol.* **1982**, *37*, 293−303.
11. Heusse, D.; Malard, M.; Bredenbac, J.; Decouvelaere, B.; Leroy, J. P.; Bieder, A.; Jumeau, H. Disposition of ^{14}C-oltipraz in animals. *Drug Res.* **1985**, *9*, 1431−1436.
12. Dimitrov, N. V.; Bennett, J. L.; McMillan, J.; Perloff, M.; Leece, C. M.; Malone, W. Clinical pharmacology studies of Oltipraz − a potential chemopreventive agent. *Invest. New Drugs* **1992**, *10*, 289−298.
13. Gupta, E.; Olopade, O. I.; Ratain, M. J.; Mick, R.; Baker, T. M.; Berezin, F. K.; Benson, A. B., III; Dolan, M. E. Pharmacokinetics and pharmacodynamics of Oltipraz as a chemopreventive agent. *Clin. Cancer Res.* **1995**, *1*, 1133−1138.
14. Bieder, A.; Decouveleare, B.; Caillard, C.; Depaire, H.; Heusse, D.; Ledoux, C.; Lemar, M.; Leroy, J. P.; Raynaud, L.; Snozzi, C.; Gregoire, J. Comparison of the metabolism of oltipraz in the mouse, rat and monkey and in man. *Drug Res.* **1983**, *33*, 1289−1297.
15. Bona, M.; Boudeville, P.; Zekri, O.; Christen, M. O.; Burgot, J. L. Water/*n*-octanol partition coefficients of 1,2-dithiole-3-thiones. *J. Pharm. Sci.* **1995**, *84*, 1107−1112.
16. Dollo, G.; Le Corre, P.; Chollet, M.; Chevanne, F.; Bertault, M.; Burgot, J. L.; Le Verge, R. *J. Pharm. Sci.*, in press.
17. Thuillier, A.; Vialle, J. Composés organiques soufrés. I. Sur une nouvelle méthode de préparation des aryl-5-dithiole-1,2-thiones-3. *Bull. Soc. Chim. Fr.* **1959**, 1298−1501.
18. Hinderling, P. H. Red blood cells: a neglected compartment in pharmacokinetics and pharmacodynamics. *Pharmacol. Rev.* **1997**, *49*, 279−295.
19. Boxenbaum H. G.; Riegelman, S.; Elashoff, R. M. Statistical estimation in pharmacokinetics. *J. Pharmacokinet. Biopharm.* **1974**, *2*, 123−148.
20. Cossum, P. A. Role of the red blood cell in drug metabolism. *Biopharm. Drug Dispos.* **1988**, *9*, 321−336.
21. Neutze, J. M.; Wyler, F.; Rudolph, A. M. Use of radioactive microspheres to assess distribution of cardiac output in rabbits. *Am. J. Physiol.* **1968**, *215*, 486-495.
22. Rajesky, R. A., Stella, V. L. Pharmaceutical applications of cyclodextrins. 2. In vivo drug delivery. *J. Pharm. Sci.* **1996**, *85*, 1142−1169.
23. Isacsson, G.; Singer, P. Studies on the whole-body distribution of 14C-trithioparamethoxyphenylpropene in mice. *Scand. J. Dent. Res.* **1985**, *93*, 249−252.

JS9900248

Dehydration Behavior of Eprosartan Mesylate Dihydrate

JIE SHENG,[†,‡] GOPADI M. VENKATESH,[§,||] SARMA P. DUDDU,[§,⊥] AND DAVID J. W. GRANT*[,†]

Contribution from *Department of Pharmaceutics, College of Pharmacy, University of Minnesota, Weaver-Densford Hall, 308 Harvard Street SE., Minneapolis, Minnesota 55455-0343 and SmithKline Beecham Pharmaceuticals R&D, Pharmaceutical Development Maildrop UP 1230, 1250 S. Collegeville Road, Collegeville, Pennsylvania 19426-0949.*

Received January 27, 1999. Final revised manuscript received July 7, 1999.
Accepted for publication July 19, 1999.

Abstract □ Eprosartan mesylate (SKF 108566-J; EM) is an antihypertensive agent approved for marketing in the USA. EM dihydrate was prepared by three methods, one of which included suspending the anhydrous drug in an aqueous solution of 1.0 M methanesulfonic acid to form a slurry, followed by filtration. The dehydration kinetics of EM dihydrate were derived by analyzing the fit of the isothermal thermogravimetric analytical (TGA) data to numerous kinetic models. EM dihydrate undergoes dehydration in two distinct steps, each involving the loss of 1 mol of water at 25–70 °C and 70–120 °C, respectively. Recrystallization of EM occurs at ~120–140 °C after dehydration to the anhydrous phase. This explanation is supported by variable temperature powder X-ray diffractometry. The mechanism of the dehydration reaction is complex, the dependence of the reaction rate on temperature varying as a function of the particles size. For the dihydrate of sieve fraction <125 μm, the kinetics of the first and second dehydration steps are consistent with the Avrami–Erofeev equation (A3, $n = 1/3$) over the temperature range studied, corresponding to three-dimensional growth of nuclei. In contrast, for the 125–180-μm and 180–250-μm sieve fractions, the kinetics are best described by the two-dimensional phase boundary reaction (R2) at a lower dehydration temperature (i.e., 28.3 °C), and by the Avrami–Erofeev equation (A3, $n = 1/3$) at a higher dehydration temperature (i.e., 93.7 °C). The activation energies (15–40 kcal/mol) and frequency factors of the dehydration of EM dihydrate were determined both by Arrhenius plots of the isothermal rates determined by TGA and by Kissinger plots of the nonisothermal differential scanning calorimetric data. Hot stage microscopy of single crystals of EM dihydrate showed random nucleation at the surface and dehydration with the growth of microcrystals along the needle *a* axis. Cerius^{2TM} molecular modeling software showed the existence of water channels along the *a* axis and enabled the observed dehydration behavior of EM dihydrate crystals to be explained in terms of the bonding environment of water molecules in the crystal structure.

Introduction

The presence of water of hydration is common in molecular crystals of both organic and inorganic compounds. Numerous pharmaceuticals exist in both hydrated and anhydrous forms.[1,2] More than 90 hydrates are listed in the *United States Pharmacopoeia*,[3] and at least one-third of the solid crystalline substances of the *European Pharmacopoeia*[4] are reported to form hydrates. The stability and behavior of hydrates can vary widely,[5−7] and hydrate formation and dehydration may occur during processing or storage of pharmaceuticals. Knowledge of the hydration and dehydration behavior of drug substances is essential in the development of stable formulations because the physicochemical, mechanical, processing, and biological properties of hydrates can differ significantly from those of the corresponding anhydrate; these differences are ascribed to differences in crystal structure[7−14] brought about by the presence of lattice water. In general, water molecules in hydrates are almost always involved in hydrogen bonds that usually contribute to the coherence of the crystal structure. Shefter and Higuchi[13] found that the apparent dissolution rate and solubility of the anhydrous form of several drugs are greater than those of the hydrate, which crystallizes from water at the same temperature as in the dissolution experiments (e.g., theophylline, caffeine, and glutethimide). Poole et al.[14] showed that the enhanced bioavailability of ampicillin correlated positively with the greater aqueous solubility and dissolution rate of anhydrous ampicillin compared with that of the trihydrate form. Lerk et al. reported that the binding capacity and flowability of α-lactose monohydrate[15] and of α-D-glucose[16] increased after dehydration because of a difference in pore size distribution. Because the phase transition on hydration or dehydration is accompanied by a change in the physicochemical properties, it is important to understand the mechanisms of these transitions, the experimental and environmental conditions under which they take place, and their rates under various conditions.

Classic dehydration kinetics is treated as a solid-state reaction, as shown in eq 1.[7,17]

$$A{\cdot}H_2O\ (s) \rightarrow A\ (s) + H_2O\ (g) \qquad (1)$$

Usually, reactions involving solids start from the surface and proceed inward as the reactant−product boundary layer contracts.[18] The initial generation of small product crystallites at the reactant−product interface is termed nucleation.[19] Such nucleation is most likely to occur at surfaces, where the molecules are usually more energetic than in the bulk of the crystal.[20] For a reaction such as desolvation, which involves a single solid, nucleation may occur rapidly over all surfaces or at the points of initial contact between the constituents of a mixture of solids. Two general points should be taken into consideration for solid-state reactions. First, the reactivity of a solid substance is often dependent on the total concentrations of highly deformed, or defective, regions of the lattice. Damaged external surfaces, superficial lattice imperfections, and scratches are often chemically more reactive than more perfect crystal faces. Second, the kinetics of a solid-state reaction may be controlled by the surface area, which is related to the mean particle size and to the particle size

* Corresponding author. Telephone: (612) 624-3956. Facsimile: (612) 625−0609. E-mail: grant001@tc.umn.edu.
† Department of Pharmaceutics.
§ SmithKline Beecham Pharmaceuticals R&D.
‡ Present address: Lilly Research Laboratories, A Division of Eli Lilly and Company, Drop Code GL36, 2001 West Main Street, P.O. Box 708, Greenfield, Indiana 46140.
|| Eurand, 845 Center Drive, Vandalia, Ohio.
⊥ Inhale Therapeutic Systems, San Carlos, California 94070.

10.1021/js9900250 CCC: $18.00
Published on Web 09/11/1999

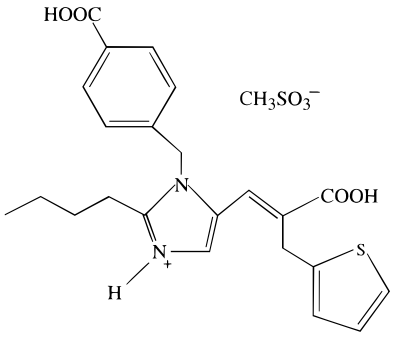

Scheme 1—The Molecular Structure of Eprosartan Mesylate (EM)

distribution. Because of the intrinsic heterogeneity of solid phases, the dehydration reaction is also sensitive to the environmental and reactant conditions, such as temperature, water vapor pressure, sample pre-history, sample weight,[21,22] and the geometry of the solid particles.[23]

Growth of nuclei in three dimensions has been observed during the decomposition of several compounds, but is not general because experimental observations for other substances have shown that the growth of nuclei under other conditions may be confined to particular lattice planes (i.e., along one or two dimensions).[19] Numerous methods have been used to study the dehydration process, including thermomicroscopy (hot stage microscopy, HSM), differential scanning calorimetry (DSC), thermogravimetric analysis (TGA), X-ray crystallography (powder X-ray diffractometry, PXRD), and analysis of the evolved gases.[7] The experimental dehydrated fraction, x, at different times, t, is plotted against t according to the kinetic models of the reaction mechanisms that are capable of operating in the solid-state decomposition.[18,24,25] The goodness of the fit to each kinetic equation was derived by examining the scatter of the residuals, s_e, about the mean, the standard deviation of the regression, S, and the determination coefficient, R^2, with less emphasis on the latter. Davis and Pryor[26] and Brown and Galwey[27] have criticized the use of R^2 alone as the sole determinant of the kinetic equation of best fit, especially when it has similar values for closely related equations. Random s_e without a trend and relatively small values of S of the regression are required for demonstrating a good fit to any reasonable kinetic model.[21,26] However, a good fit to a particular equation does not necessarily imply that the corresponding mechanism is correct.

Eprosartan mesylate (EM, Scheme 1) is used in the treatment of hypertension and exists as a dihydrate and anhydrate.[28,29] EM dihydrate can be prepared under a variety of conditions, for examples, by exposing the anhydrous drug substance to 98% RH for >15 days, by suspending the drug in an aqueous solution of 1.0 M methanesulfonic acid to form a slurry, and by granulating the drug in the presence of 3% corn starch. Little work has been done to study the dehydration behavior and kinetics of EM dihydrate, which is the basic information required for predicting the stability and other physicochemical properties of EM tablets. The purpose of this paper is to elucidate the dehydration kinetics of EM dihydrate, especially the effects of the particle size and temperature. Variable temperature PXRD and HSM should help to justify a mechanistic interpretation of the data. Cerius^{2TM} molecular modeling was used to visualize the crystal packing and to provide insight into the dehydration process at the molecular level. Preliminary reports of this work have been presented at the 1997 Annual Meeting of the American Association of Pharmaceutical Scientists.[30,31]

Experimental Section

Materials—Eprosartan mesylate (EM) anhydrate was supplied by SmithKline Beecham Pharmaceuticals, King of Prussia, PA. Methanesulfonic acid used for the preparation of EM dihydrate was supplied by Aldrich Chemical Company, Milwaukee, WI.

Preparation of EM Dihydrate—EM dihydrate was prepared by suspending 1.6 g of the anhydrous drug in 40 mL of 1.0 M aqueous methanesulfonic acid (to prevent the formation of eprosartan free base and to reduce the solubility of the salt, EM dihydrate, by the common ion effect) at 22.5 °C (room temperature). The suspension was sonicated for 2 min at 22.5 °C, and was then stirred for 2 h. The solid phase was collected by filtration, thoroughly washed with distilled water at 0 °C, and dried for 48 h at 22.5 °C in a 58% RH chamber. EM dihydrate was also prepared by exposing the anhydrous drug to 98% RH at 45 °C for 15 days or longer and by granulating the anhydrous drug in the presence of 3% (w/w) corn starch and 10% (w/w) distilled water. The experimental techniques for solid-state characterization, described later, show that the materials prepared by each of the three methods (slurry process, exposure to 98% RH, or granulation with 3% (w/w) corn starch) are indeed the same phase of EM dihydrate. The crystals, prepared by each method, were fractionated using USP standard sieves into the following three particle size ranges: <125 μm, 125−180 μm, and 180−250 μm.

Differential Scanning Calorimetry (DSC)—A DuPont differential scanning calorimeter (model 910, TA Instruments, New Castle, DE) equipped with a data station (Thermal Analyst 2000, TA Instruments) was used for the nonisothermal DSC studies. The temperature axis and cell constant of the DSC cell were calibrated with indium. The sample (2.05 ± 0.02 mg) was heated in open pans at heating rates of 5, 10, 15, 20, 25, 30, and 35 °C/min under 300−400 mL/min nitrogen purge. The activation energy of each dehydration step was determined by Kissinger's method[32] in which the heating rate, ϕ in °C/min, and the temperature at peak maximum, T_m in degrees Kelvin, are plotted according to the eq 2. This equation is derived with the assumption that the rate of reaction is maximal at the temperature at which the endothermic peak reaches a maximum. The activation energy was calculated from the slopes of the plots of $\ln(\phi/T_m^2)$ versus $1/T_m$.

$$\mathrm{d}\ln(\phi/T_m^2)/\mathrm{d}(1/T_m) = -E_a/R \qquad (2)$$

Thermogravimetric Analysis (TGA)—A DuPont thermogravimetric analyzer (model 951, TA Instruments, New Castle, DE) linked to a data station (Thermal Analyst 2000, TA Instruments) was used for the isothermal dehydration studies. The weight loss, expressed as fraction dehydrated, x, at time t, was fitted to the known solid-state kinetic equations.[7,18,25] The activation energy and the frequency factor for the dehydration of EM dihydrate were calculated from the slope and the intercept, respectively, of the Arrhenius plots of the logarithm of the rate constants versus reciprocal absolute temperature. For the first dehydration step, corresponding to the formation of the monohydrate, isothermal scans of x versus t were obtained at fixed temperatures covering the range of 28 to 35 °C. The fraction dehydrated was calculated as the ratio, weight of water lost/maximum possible weight loss of water, in dehydrating EM dihydrate to the monohydrate. Therefore, 100% fraction dehydrated ($x = 1$) corresponds to the loss of 1 mol of water of hydration. For the second dehydration step, corresponding to the formation of the anhydrate from the monohydrate, the samples were heated in advance to 40 °C to allow completion of the first dehydration step. Analogous isothermal x versus t plots were obtained at fixed temperatures from 75 to 95 °C. Therefore, 100% fraction dehydrated ($x = 1$) corresponds the loss of 1 mol of water from EM monohydrate leading to the anhydrate. Prior to each isothermal scan, the sample (10.00 ± 0.02 mg) was rapidly heated to the set temperature at a rate of 150 °C/min and maintained at that temperature until the each dehydration step was completed. Nitrogen purge at a constant rate (300−400 mL/min) was maintained during each run.

Variable Temperature Powder X-ray Diffraction (PXRD)—Variable temperature PXRD of EM dihydrate was carried out at ambient temperature and atmosphere using a diffractometer (Scintag 2000, Sunnyvale, CA) with a hot stage attachment, with Cu Kα radiation (40 mA, 45 kV). Samples were packed in a copper

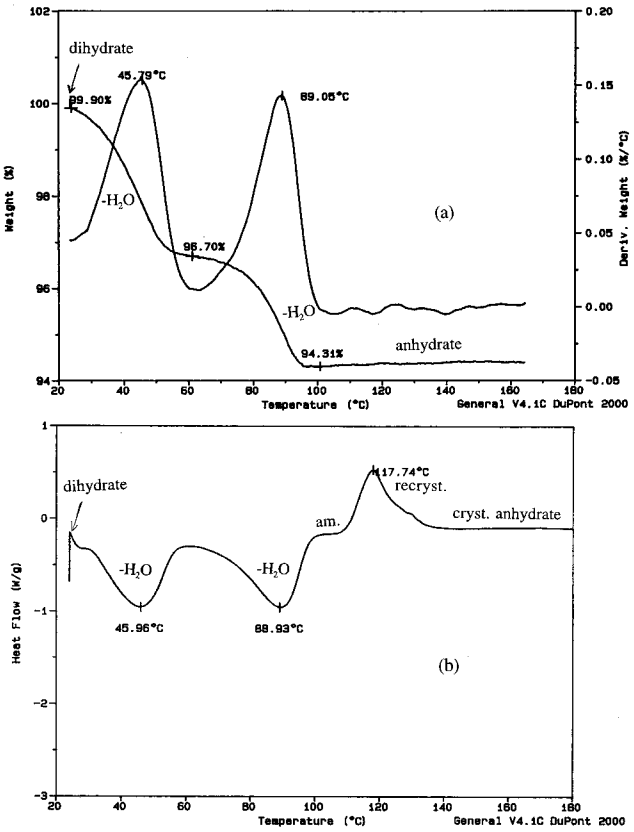

Figure 1—Typical curves for (a) thermogravimetric analysis (TGA), derivative thermogravimetric analysis (dTGA), and (b) differential scanning calorimetry (DSC) of eprosartan mesylate (EM) dihydrate.

holder and heated at the rate of 10 °C/min to the set temperature. The diffraction angle, 2θ, was scanned from 5° to 15° and increased at a rate of 3°/min with a counting time of 1 s.

Polarized Light Microscopy—EM dihydrate and the solid phase remaining after dehydration were observed under an optical microscope equipped with polarized light accessories (M3J, Wild Heerbrugg, Heerbrugg, Switzerland).

Hot Stage Microscopy (HSM)—The thermal events were observed on a hot stage (FP80, Mettler Instrument Corp., Highstown, NJ) under a microscope (M3J, Wild Heerbrugg, Heerbrugg, Switzerland). The EM dihydrate crystals were heated at a constant rate of 5 °C/min up to the melting point of anhydrous EM at ~250 °C.

Molecular Modeling—All molecular modeling calculations were performed using Cerius^{2TM} software, program version 3.5 (Molecular Simulations, San Diego, CA), running on the commercial workstations (Silicon Graphics, Personal Iris 4D/20, Power Series 2×R3000 and Indigo R4000).

Results and Discussions

Identification of Dehydration Steps—EM dihydrate exhibits two successive dehydration steps at 25−70 °C and 70−120 °C in open-pan TGA (Figure 1a), each corresponding to the loss of 1 mol of water. When EM dihydrate samples were subjected to DSC in an open pan under experimental conditions similar to those for TGA, the peak maximum temperatures in the DSC curve (46 °C and 89 °C in Figure 1b) agreed well with those in derivative TGA (dTGA) (46 °C and 89 °C in Figure 1a) for both dehydration steps. In addition, the DSC curve showed an exotherm with a peak maximum at 118 °C, suggesting recrystallization of EM anhydrate from the amorphous phase that was presumably formed immediately after the second dehydration step. These results were confirmed by variable temperature PXRD (Figure 2), despite the low signal-to-noise

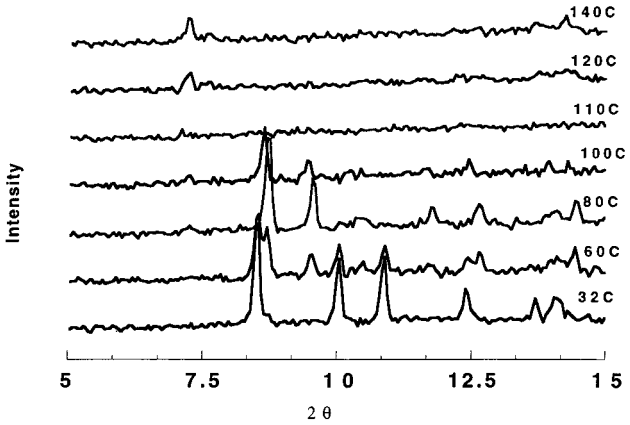

Figure 2—Variable temperature powder X-ray diffraction patterns for eprosartan mesylate (EM) dihydrate.

ratio, which is attributed to the small sample size and to the narrow range of scan angles. At 32 °C, EM dihydrate remains as its original form, as indicated by the PXRD pattern, which is similar to that of EM dihydrate (Figure 3a). As the temperature increases from 32 to 100 °C, the EM dihydrate gradually loses 1 mol of water to yield a mixture of the original dihydrate and a new phase, presumably the monohydrate, at 60 and 80 °C, and the monohydrate alone at 100 °C. Above 100 °C, the EM monohydrate gradually loses the final 1 mol of water and to form an amorphous phase, presumably that of EM anhydrate at 110 °C. At 150 °C, the PXRD pattern shows a new solid phase with low intensity peaks corresponding to a phase of low crystallinity, presumably the EM anhydrate that crystallized at ~118 °C in DSC (Figure 1b). Unlike the amorphous anhydrate, the partially crystalline anhydrate appeared birefringent under polarized light microscopy (Figure 4f). The phase changes of EM dihydrate on heating are summarized as follows:

first step dehydration:

$$EM{\cdot}2H_2O\ (crystal) \xrightarrow{25-70\ ^\circ C} EM{\cdot}H_2O\ (crystal) + H_2O\ (g)$$

second step dehydration:

$$EM{\cdot}H_2O\ (crystal) \xrightarrow{70-120\ ^\circ C} EM\ (amorphous) + H_2O\ (g)$$

recrystallization:

$$EM\ (amorphous) \xrightarrow{120-140\ ^\circ C} EM\ (crystal)$$

melting:

$$EM\ (crystal) \xrightarrow{\sim 250\ ^\circ C} EM\ (liquid)$$

The single-crystal structure of EM dihydrate[33] has four water molecules per asymmetric unit, with the following two types of intermolecular hydrogen bond interactions, as shown in Table 1: (a) each oxygen atom in each water molecule forms a hydrogen bond with the hydrogen atom on the carboxyl group of the same asymmetric unit; and (b) each hydrogen atom in each water molecule forms a hydrogen bond with the oxygen atom on the mesylate anion either within the same or in the neighboring unit cell. Each of the four different water molecules forms two or three hydrogen bonds. The hydrogen bond lengths and angles for each water molecule were calculated using Cerius^{2TM} molecular modeling software and are summarized in Table 1. The $H_2O(3)$ molecule is probably more loosely bound than the other water molecules because it forms only two hydrogen bonds, whereas the other three water molecules

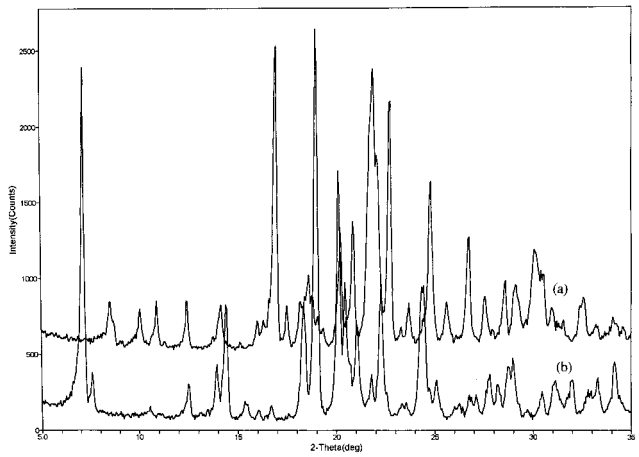

Figure 3—Typical powder X-ray diffraction patterns for eprosartan mesylate (EM): (a) dihydrate and (b) anhydrate.

form three hydrogen bonds. The $H_2O(4)$ molecule may also be more loosely bound than the $H_2O(1)$ and $H_2O(2)$ molecules because of its slightly greater hydrogen bond lengths and smaller hydrogen bond angles. Therefore, $H_2O(3)$ or $H_2O(4)$ may be included in the 1 mol of water that escapes during the first dehydration step at 25−70 °C in open-pan TGA (Figure 1a), whereas $H_2O(1)$ and $H_2O(2)$ may correspond to the second mole of water released during the second dehydration step at 70−120 °C.

Isothermal Dehydration Studies—Typical isothermal dehydration curves are shown in Figure 5 for the <125-μm sieve fraction of EM dihydrate; Figure 5a depicts the first step dehydration and Figure 5b depicts the second step dehydration. The isothermal dehydration curves for the other sieve fractions show similar features; namely, sigmoidal profiles and dehydration rates that increase with increasing temperature. The sigmoidal curves are characterized by an induction period at low x values, a growth period with an inflection at intermediate values of x, and a deceleratory period at high x values. The sigmoid-shaped curves usually result from reactions that occur at a reactant−product interface. The interface is initially established as a limited number of points on the surface of the reactant crystal by the formation of microcrystals (nuclei) of the product. Reaction thereafter proceeds within the strained contact area at the reactant−product interface. At the start of the reaction, the area of such an interface is small and limited to a number of surface sites so that the reaction is slow. At a later stage of the reaction, some nuclei have grown to a significant size and other nuclei are being formed. The reaction rate is greater than that during the initial formation of nuclei because of the increase of the reactant−product interfacial area. On continued growth of such nuclei, a point is reached at which the reactant−product interfaces from different nuclei begin to overlap so that the rate of expansion of the interface and the rate of reaction decrease.[19]

For the <125-μm fraction and for both the first and second dehydration steps, Table 2 shows that the Avrami−Erofeev equation (A3, $n = 1/3$) gave the smallest S, whereas the s_e values were randomly distributed without a trend and R^2 was largest. Thus, the successive dehydrations of the <125-μm fraction of EM dihydrate best fit the Avrami−Erofeev equation ($n = 1/3$) for which Figures 6a and 6b are the representative plots.

For the 125−180-μm and 180−250-μm fractions of EM dihydrate, the statistical parameters (S and R^2) and the dehydration equations of best fit are summarized in Tables 3 and 4, respectively. These isothermal dehydration studies were carried out between 28.3 and 93.7 °C. Up to 90.8 °C, for the first and second dehydration steps of the 125−180-μm fraction, the dehydration kinetics are best represented by the equations for a phase boundary reaction, in particular R2, the two-dimensional cylindrical symmetry reaction. At 91.2 °C, corresponding to the second dehydration step, the equation of best fit is the three-dimensional nucleation-controlled equation, A3, suggesting the dominance of nucleation and growth processes at this higher temperature. Similar dehydration kinetics were observed for the 180−250-μm fraction. At temperatures <90.7 °C for the first and second dehydration steps of the 180−250-μm fraction, the dehydration kinetics are best described by R2, the two-dimensional cylindrical phase boundary reaction. At 90.7 and 93.7 °C for the second step dehydration of the 180−250-μm sieve fraction, the equation of best fit is A3. The best fitting kinetic equations for dehydration of various sieve fractions of EM dihydrate, and the s_e values (i.e., the experimental x − the predicted x), are shown in Table 5.

The previous paragraph (Table 5) shows that the dehydration kinetics of the relatively large particles (125−180-μm and 180−250-μm fractions) up to 90.7 °C most closely follows the two-dimensional phase boundary equation (R2). Indeed, visual observation of the larger crystals under HSM (Figure 4) supports this mechanism. Direct microscopic observations of single crystals of EM dihydrate showed that tiny ruptures first appeared at a few random positions on the crystal surface, indicating initial formation of the reactant−product interface. The appearance and growth of the microcrystals proceeded along the needle axis of the crystals. The growth rate of these centers perpendicular to the needle-axis was slower than that along the needle-axis, indicating that the water molecules escape along this long axis during dehydration. The needle shape of the crystals was retained even after completion of the dehydration at the higher temperatures. This observation suggests that the dehydration reaction is confined to two-dimensions rather than to three-dimensions, which was indicated by fragmentation of the larger crystals upon dehydration.

Molecular modeling simulation (Cerius^{2TM} software) was used to visualize the crystal packing and to interpret the dehydration behavior of EM dihydrate under HSM, and revealed the existence of a water channel at the molecular level. Figures 7a and 7b show the crystal packing pattern of EM dihydrate. In general, the structure of EM dihydrate, when viewed in the direction of the a axis, is composed of alternate layers of hydrophobic regions, containing aromatic rings and hydrocarbon chains, and hydrophilic regions, containing polar functional groups and water molecules that form the hydrogen-bonded networks. A discrete hydrogen-bonding tunnel lies parallel to the a crystallographic axis as presented in Figures 7a and 7b, indicating that the water channel is also parallel to the a axis. The water molecules can leave the EM dihydrate crystal along these water channels with the smallest resistance. Dehydration along other crystallographic directions (i.e., along the b and c axes) would require the water molecules to penetrate the somewhat closely packed layers of nonpolar groups along these directions, which is unlikely. Suzuki et al.[34] and Gerdil et al.[35] applied microscopic observations and crystallographic data to the dehydration of caffeine 4/5-hydrate. Scanning electron micrographs showed that the needle-shaped crystals of the anhydrous dehydrated phase of caffeine are oriented parallel to the long axis forming channel-like cavities. This arrangement is consistent with crystallographic studies that show the chains of water molecules arranged along this axis. Byrn[7] reported that the tunnels of water molecules in thymine hydrate are oriented along the c crystallographic axis, and that rapid dehydration is consistent with the preferential exit of water molecules through these tunnels. We note that

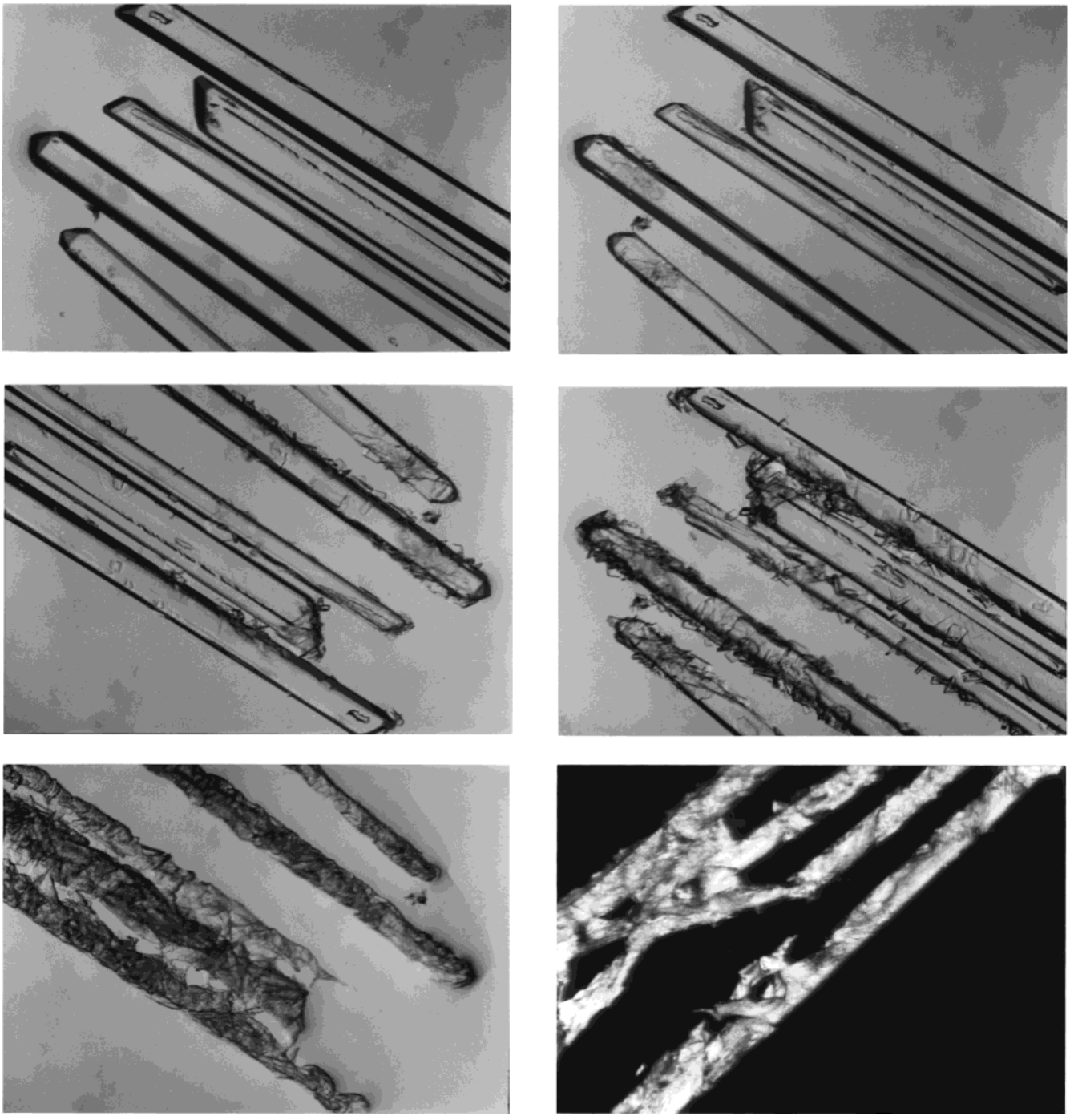

Figure 4—Photomicrographs of eprosartan mesylate (EM) dihydrate crystals while heating on the hot stage microscope at (a) 25 °C, (b) 61.0 °C, (c) 63.5 °C, (d) 65.5 °C, (e) 80.0 °C, and (f) 150 °C under polarized light.

Table 1—The Hydrogen Bond Lengths and Angles of the Four Water Molecules in the Asymmetric Unit of Eprosartan Mesylate (EM) Dihydrate

molecule	$H_2O^a\cdots H–OCO$ (Å)	bond angle (°)	$HO–H^b\cdots OSO_2CH_3$ (Å)	bond angle (°)	$HO–H^b\cdots OSO_2CH_3$ (Å)	bond angle (°)
$H_2O(1)$	2.588(9)	168.212(7)	2.823(2)	166.451(3)	2.887(3)	178.051(8)
$H_2O(2)$	2.575(0)	168.213(8)	2.878(0)	168.259(0)	2.963(2)	159.609(5)
$H_2O(3)$	2.635(3)	167.434(1)	2.783(8)	137.460(9)	—[c]	—[d]
$H_2O(4)$	2.616(6)	160.932(4)	2.802(7)	162.035(4)	2.749(7)	150.544(9)

[a] and [b] represent two different hydrogen bonds within one water molecule. [c] Distance is >4.0 Å, suggesting insignificant hydrogen bonding. [d] Bond angle is <90.0°, suggesting insignificant hydrogen bonding.

many of these hydrates crystallize with the long crystal axis parallel to the water tunnels and nearly perpendicular to the aromatic rings.

The kinetic equations of best fit for the first and second isothermal dehydration steps of three sieve fractions of EM dihydrate differ somewhat at different temperatures (Table 5). For the <125-μm fraction, the A3 equation (three-dimensional growth of nuclei) may arise from the greater total surface area or from the greater surface-to-volume ratio of these smaller crystals because nucleation is fre-

Table 2—Statistical Parameters for Fitting the First and Second Isothermal Dehydration Steps of Eprosartan Mesylate (EM) Dihydrate (<125-μm Sieve Fraction) to Eleven Solid-State Reaction Equations[a]

temperature (°C)	range of *x*		P1	A2	A3	F1	R1	R2	R3	D1	D2	D3	D4
					first dehydration step								
28.2	0.0621–	R^2	0.9856	0.9946	**0.9985**[b]	0.9225	0.9456	0.9942	0.9931	0.9716	0.9757	0.9081	0.9656
	0.9845	*S*	0.3637	0.2284	**0.2070**[b]	0.8455	0.7919	0.2305	0.2520	0.5114	0.4727	0.9210	0.5630
30.7	0.0569–	R^2	0.9813	0.9870	**0.9962**	0.8997	0.9477	0.9954	0.9864	0.9760	0.9693	0.8799	0.9517
	0.9900	*S*	0.3365	0.2610	**0.1555**	0.7800	0.5631	0.1666	0.2867	0.3811	0.4312	0.8537	0.5412
32.6	0.0292–	R^2	0.9680	0.9807	**0.9950**	0.8675	0.9656	0.9958	0.9742	0.9710	0.9501	0.8403	0.9253
	0.9968	*S*	0.3371	0.2620	**0.1368**	0.7924	0.4032	0.1982	0.3492	0.3705	0.4860	0.8699	0.5947
33.4	0.0419–	R^2	0.9941	0.9967	**0.9993**	0.9276	0.9735	0.9977	0.9852	0.9791	0.9551	0.8689	0.9327
	0.9940	*S*	0.1448	0.1279	**0.1489**	0.5854	0.3542	0.1443	0.2640	0.3146	0.4610	0.7880	0.5646
					second dehydration step								
75.7	0.0913–	R^2	0.9363	0.9933	**0.9983**[b]	0.9251	0.9653	0.9985	0.9889	0.9816	0.9535	0.9364	0.9479
	0.9848	*S*	0.5203	0.4006	**0.2929**[b]	1.3485	0.9173	0.2031	0.0906	0.3791	0.4510	0.5271	0.4770
83.8	0.0341–	R^2	0.9364	0.9655	**0.9901**	0.8161	0.9917	0.9744	0.9422	0.9531	0.8520	0.8282	0.8440
	0.9900	*S*	0.3177	0.0333	**0.1879**	0.2211	0.1719	0.1769	0.1916	0.3723	0.4022	0.4334	0.4129
88.9	0.0536–	R^2	0.9765	0.9840	**0.9979**	0.8811	0.9940	0.9729	0.9507	0.9418	0.8896	0.7842	0.8570
	0.9500	*S*	0.0827	0.1321	**0.0475**	0.3605	0.0808	0.1719	0.2320	0.2520	0.3473	0.4857	0.3953
95.0	0.0347–	R^2	0.9503	0.9623	**0.9922**	0.8222	0.9844	0.9567	0.9257	0.9249	0.8753	0.7508	0.8400
	0.9861	*S*	0.08264	0.1284	**0.0622**	0.2786	0.0823	0.1375	0.1416	0.1812	0.2335	0.3301	0.2645

[a] Garner[18] and Sharp et al.[25] [b] The statistical parameters for the best fitting kinectic equation are in bold.

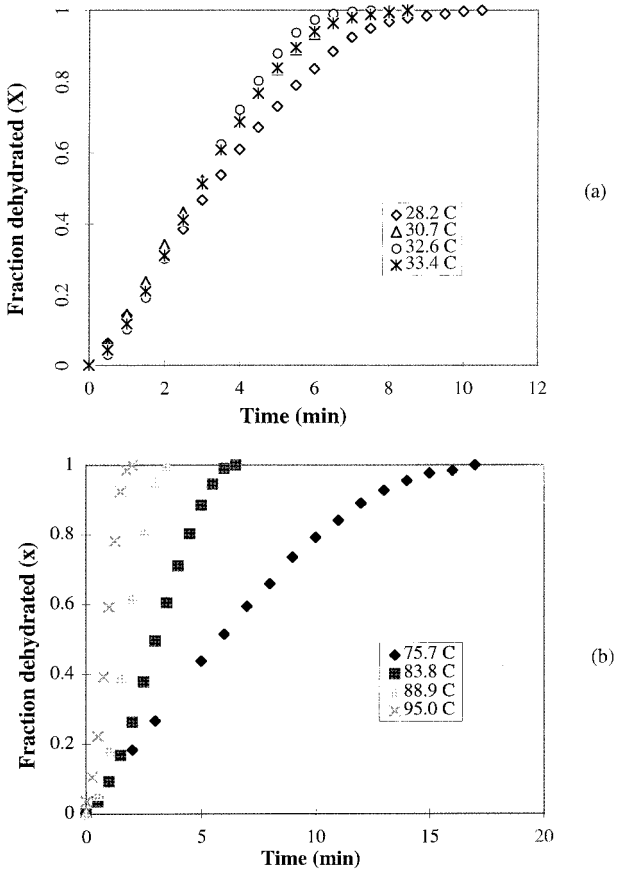

Figure 5—Representative isothermal dehydration progress curves for < 125-μm sieve fraction of eprosartan mesylate (EM) dihydrate powder during (a) the first dehydration step and (b) the second dehydration step.

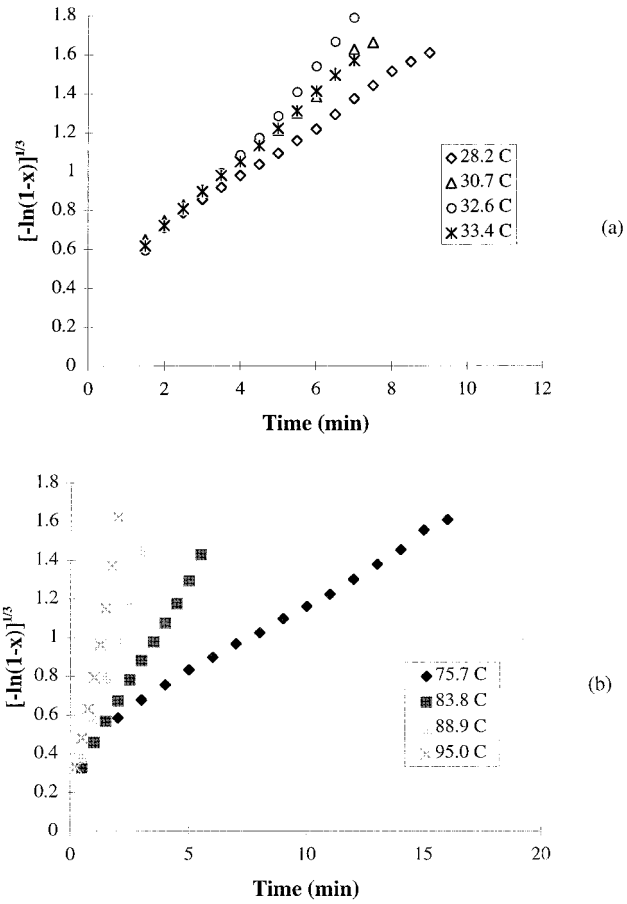

Figure 6—Representative plots for the best-fitting kinetic equation for the dehydration of eprosartan mesylate (EM) dihydrate powder (<125-μm sieve fraction) during (a) the first dehydration step and (b) the second dehydration step.

quently initiated at the crystal surfaces. The A3 equation may also arise from the greater fraction of the more reactive zones of the smaller particles (i.e., the crystal faces, edges, corners, and cracks). The smaller crystals usually have more lattice imperfections on their surfaces, which are believed to be more reactive chemically than the more perfect crystalline faces of the larger crystals. The initial generation of the small product nuclei may be a difficult process that can occur only at a limited number of the reactive sites on the crystal surface. Reaction may thereafter proceed with greater facility at the reactant−product interface. Griesser and Burger[36] reported that the dehydration of caffeine 4/5-hydrate is controlled by nucleation and growth for the smaller crystals but by diffusion for the larger crystals. In the dehydration of the larger EM dihydrate crystals (125−180 μm and 180−250 μm) at lower temperatures, the escape of water molecules from the crystal lattice follows the R2 equation (two-dimensional

Table 3—Statistical Parameters for Fitting the Isothermal Dehydration Steps of Eprosartan Mesylate (EM) Dihydrate (125–180-μm Sieve Fraction) to Eleven Solid-State Reaction Equations[a]

temperature (°C)	range of x		P1	A2	A3	F1	R1	R2	R3	D1	D2	D3	D4
first dehydration step													
28.3	0.1156–	R^2	0.9857	0.9958	0.9957	0.9541	0.9854	**0.9980**[b]	0.9922	0.9899	0.9600	0.8837	0.9381
	0.9827	S	0.2929	0.1524	0.2082	0.5664	0.3192	**0.1421**[b]	0.0976	0.2649	0.5290	0.9021	0.6580
30.8	0.0561–	R^2	0.8837	0.9716	0.9902	0.8602	0.9631	**0.9972**	0.9793	0.9441	0.9201	0.8888	0.9100
	0.9971	S	0.2376	0.0508	0.1368	0.1864	0.0395	**0.1220**	0.0905	0.3127	0.3737	0.4409	0.3968
33.2	0.1540–	R^2	0.9364	0.9876	0.9957	0.9136	0.9629	**0.9974**	0.9852	0.9559	0.9267	0.8833	0.9129
	0.9811	S	0.2525	0.0586	0.1054	0.2094	0.5135	**0.0818**	0.0909	0.2778	0.3581	0.4518	0.3903
34.8	0.1038–	R^2	0.9572	0.9890	0.9926	0.9213	0.9581	**0.9937**	0.9845	0.9435	0.9141	0.8702	0.9002
	0.9937	S	0.3397	0.1698	0.1536	0.2375	0.1707	**0.1502**	0.1964	0.3141	0.3877	0.4765	0.4179
second dehydration step													
75.4	0.0647–	R^2	0.8871	0.9748	0.9906	0.8751	0.9711	**0.9967**[b]	0.9780	0.9912	0.9717	0.8507	0.9438
	0.9935	S	0.9240	0.7283	0.4778	1.7416	0.8376	**0.2845**[b]	0.7304	0.4610	0.8293	1.9039	1.1678
81.7	0.1634–	R^2	0.8488	0.9594	0.9831	0.8325	0.9724	**0.9938**	0.09659	0.9836	0.9547	0.8140	0.9218
	0.9967	S	0.5248	0.4385	0.2833	0.9498	0.3501	**0.1716**	0.4287	0.2966	0.4939	1.0006	0.6491
90.8	0.3101–	R^2	0.7993	0.9318	0.9610	0.8104	0.9796	**0.9905**	0.9513	0.8586	0.8643	0.8067	0.8251
	0.9968	S	0.2351	0.1918	0.1444	0.3187	0.1045	**0.0712**	0.1305	0.2224	0.2408	0.2601	0.2474
93.6	0.0671–	R^2	0.9570	0.9755	**0.9971**[b]	0.9597	0.9753	0.9440	0.9246	0.9929	0.9928	0.8938	0.9937
	0.9840	S	0.0706	0.1928	**0.0578**[b]	0.1298	0.6692	0.0733	0.9208	0.9921	0.9901	0.0818	0.9934

[a] Garner[18] and Sharp et al.[25] [b] The statistical parameters for the best fitting kinectic equation are in bold.

Table 4—Statistical Parameters for Fitting the Isothermal Dehydration Steps of Eprosartan Mesylate (EM) Dihydrate (180–250-μm Sieve Fraction) to Eleven Solid-State Reaction Equations[a]

temperature (°C)	range of x		P1	A2	A3	F1	R1	R2	R3	D1	D2	D3	D4
first dehydration step													
28.3	0.0427–	R^2	0.8910	0.9774	0.9901	0.8581	0.9663	**0.9971**[b]	0.9791	0.9837	0.9644	0.8388	0.9375
	0.9970	S	0.5816	0.4569	0.3019	1.1447	0.5583	**0.1633**[b]	0.4395	0.3885	0.5731	1.2201	0.7596
30.8	0.0372–	R^2	0.9344	0.9928	0.9979	0.9055	0.9659	**0.9990**	0.9913	0.9867	0.9836	0.8996	0.9669
	0.9907	S	0.3341	0.2212	0.1060	0.8016	0.4810	**0.0689**	0.2161	0.2676	0.2976	0.7354	0.4216
32.4	0.1032–	R^2	0.8609	0.9614	0.9839	0.8273	0.9715	**0.9956**	0.9714	0.9882	0.9660	0.8198	0.9347
	0.9968	S	0.4886	0.3898	0.2735	0.8452	0.3436	**0.1354**	0.3440	0.2211	0.3749	0.8634	0.5197
34.9	0.0856–	R^2	0.9477	0.9935	0.9971	0.9276	0.9761	**0.9961**	0.9829	0.9851	0.9596	0.8629	0.9346
	0.9939	S	0.3749	0.1692	0.1022	0.5501	0.2925	**0.1181**	0.2471	0.2310	0.3799	0.7001	0.4837
second dehydration step													
76.5	0.0854–	R^2	0.8423	0.9602	0.9821	0.8454	0.9687	**0.9962**[b]	0.9743	0.9923	0.9758	0.8453	0.9480
	0.9968	S	1.1447	0.9258	0.6204	1.8247	0.8207	**0.2853**[b]	0.4219	0.4081	0.7212	1.8254	1.058
83.2	0.0521–	R^2	0.8538	0.9588	0.9836	0.8294	0.9744	**0.9937**	0.9686	0.9869	0.9639	0.8223	0.9329
	0.9967	S	0.4546	0.3839	0.2419	0.7810	0.3024	**0.1499**	0.3350	0.2164	0.3588	0.7971	0.4898
90.7	0.0444–	R^2	0.8868	0.9922	**0.9979**[b]	0.9307	0.9600	0.9902	0.9829	0.9732	0.9616	0.8929	0.9457
	0.9905	S	0.0777	0.0836	**0.0432**[b]	0.2488	0.3206	0.0936	0.1234	0.2514	0.2164	0.2863	0.2167
93.7	0.0477–	R^2	0.9496	0.9834	**0.9952**	0.9043	0.9800	0.9867	0.9651	0.9346	0.9319	0.8946	0.9255
	0.9809	S	0.0573	0.0762	**0.0456**	0.1830	0.0837	0.0756	0.1501	0.2054	0.2095	0.2606	0.2191

[a] Garner,[18] and Sharp etal.[25] [b] The statistical data for the best fitting kinectic equation are in bold.

Table 5—The Best-Fitting Kinetic Equations at Various Temperatures for the First and Second Isothermal Dehydrations of All the Eprosartan Mesylate (EM) Dihydrate Samples

	< 125 μm			125–180 μm			180–250 μm		
dehydration	temperature (°C)	equation[a]	residual plots[b]	temperature (°C)	equation[a]	residual plots[b]	temperature (°C)	equation[a]	residual plots[b]
first	28.2	A3	no trend	28.3	R2	no trend	28.3	R2	no trend
	30.7	A3	no trend	30.8	R2	no trend	30.8	R2	no trend
	32.6	A3	no trend	33.2	R2	no trend	32.4	R2	no trend
	33.4	A3	no trend	34.8	R2	no trend	34.9	R2	no trend
second	75.6	A3	no trend	75.4	R2	no trend	76.5	R2	no trend
	83.8	A3	no trend	81.7	R2	no trend	83.2	R2	no trend
	88.9	A3	no trend	90.8	R2	no trend	90.7	A3	no trend
	95.0	A3	no trend	93.6	A3	no trend	93.7	A3	no trend

[a] Garner[18] and Sharp et al.[25] [b] The residual plots of the residuals, s_e (i.e., the experimental x – the predicted x), versus the predicted x at different dehydration times, t.

phase boundary reaction). The explanation offered is that the escape of the loosely bound water molecules in the crystal lattice produces a vacancy on the surface of the EM dihydrate crystals. This intermediate structure is unstable, so recrystallization to the anhydrous phase occurs. In this way, a phase boundary is formed that is preferentially oriented along the a axis inside the crystal. At higher temperatures, the large EM dihydrate particles can presumably break up to produce smaller crystals. A large number of reactive crystal defects, which are the initial sites for the nucleation, are presumably produced by the fragmentation of the larger particles into smaller ones.

Table 6—The Activation Energy (E_a, kcal/Mol) and Frequency Factors (A, min) from Arrhenius Plots for the Dehydration of Eprosartan Mesylate (EM) Dihydrate Samples of various particle size ranges

	< 125 μm		125–180 μm		180–250 μm	
parameter	first dehydration	second dehydration	first dehydration	second dehydration	first dehydration	second dehydration
E_a (kcal/mol)	18.9 (0.2)[a]	31.9 (0.6)[a]	19.2 (0.5)	31.1 (0.5)	19.1 (0.6)	35.1 (0.5)
ln A (min)	29.5	43.4	29.8	42.1	29.8	48.2

[a] The standard deviations are given in parentheses.

Table 7—The Activation Energy (E_a, kcal/mol) and Frequency Factors (A, min) from Kissinger Plots for the First and Second Dehydrations of Eprosartan Mesylate (EM) Dihydrate Samples of Various Particle Sizes and from Various Preparation Methods[a]

	preparation methods						
	98% RH		slurry process			with 3% corn starch	
dehydration step	< 125 μm	125–180 μm	< 125 μm	125–180 μm	180–250 μm	125–180 μm	180–250 μm
first, E_a (kcal/mol)	18.5(0.6)	19.6(0.8)	12.0(0.2)	11.8 (0.1)	12.3(0.3)	13.6(0.3)	14.5(0.5)
second, E_a (kcal/mol)	33.9(1.1)	31.4(0.8)	20.9(0.8)	18.7(0.5)	23.4(0.6)	38.9(0.9)	29.6(0.3)
first, ln A (min)	30.0	32.2	18.9	18.4	19.2	20.8	23.0
second, ln A (min)	43.0	43.8	28.9	25.8	32.5	53.4	39.7

[a] The standard deviations are given in parentheses.

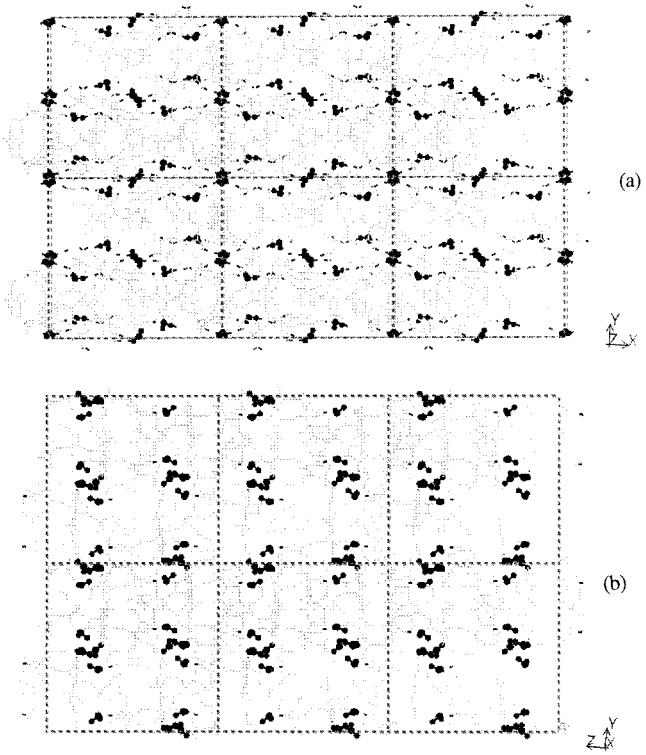

Figure 7—Packing diagrams of eprosartan mesylate (EM) dihydrate, where the dotted lines between the atoms indicate the hydrogen bonds along (a) the *a* axis and (b) the *c* axis.

Hence, for the larger crystals, the dominant dehydration process (two-dimensional phase boundary, R2, cylindrical symmetry) at low temperatures is replaced by three-dimensional nucleation-controlled (A3) dehydration at high temperatures because of the creation of increased surface area and crystal defects at high temperatures, which are the reactive sites for the formation of nuclei.

For the first and second dehydration steps of EM dihydrate, the activation energies, E_a, obtained from Arrhenius plots (Figure 8) and the frequency factors according to the best-fitting mechanism are presented in Table 6. In all cases, E_a for the second dehydration step (~32 kcal/mol) is higher than that for the first step (~19 kcal/mol), which indicates that the second mole of escaping water molecules is more tightly bound. This conclusion agrees

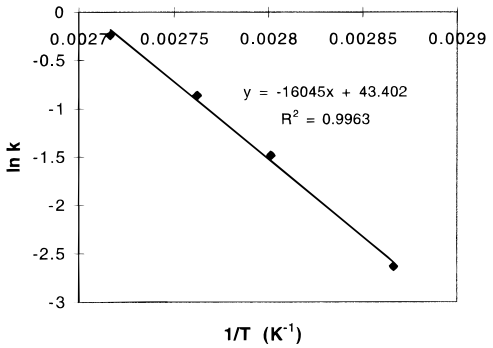

Figure 8—Arrhenius plot from the best-fitting dehydration mechanism for the second dehydration step of eprosartan mesylate (EM) dihydrate samples (<125-μm sieve fraction).

with that from the study of the bonding environment of water molecules in EM dihydrate, already discussed. Neither the activation energy nor the frequency factor depend significantly on the particle size. However, Agbada and York[21] and Van Dooren[37] reported the tendency toward lower activation energy with decreasing particle size for the dehydration of theophylline monohydrate and sodium citrate.

Nonisothermal Dehydration Studies—For the EM dihydrate samples prepared by different methods, the activation energies and the frequency factors of the first and second dehydration steps were calculated from the Kissinger plots of DSC data and are listed in Table 7. The activation energies for dehydration of the EM dihydrate samples depend on the method of preparation and increase in the following order: slurry process < 98% RH < in the presence of 3% corn starch. The dependence of the activation energy of dehydration on the manufacturing process suggests the influence of variables, such as crystals defects, sample geometry, and surface characteristics, on the properties of the crystals. Similarly, Agbada and York[21] noted that the sample history plays a critical role in the dehydration reactions of theophylline monohydrate.

Conclusions

The two consecutive dehydration reactions of EM dihydrate are complex and represent different kinetic processes that are greatly dependent on the particle size and tem-

perature. Both three-dimensional growth of nuclei and two-dimensional phase boundary equations are postulated to represent the predominant processes in the dehydration kinetics of EM dihydrate. Such information is essential for understanding and improving the stability of EM dihydrate, which may be compromised during the processes of manufacture and storage. In addition, the activation energies for the two consecutive dehydration processes of EM dihydrate depend on the sample preparation history. HSM and variable temperature PXRD are valuable complementary tools for the interpretation of dehydration behavior, whereas molecular modeling provides structural insight into the dehydration mechanisms.

Acknowledgments

We thank the following: Dr. Victor G. Young, Jr., for solving the crystal structure of eprosartan mesylate dihydrate (ref 33) on which Figure 7 and associated discussion is based; Geoff G. Z. Zhang and Linna R. Chen for helpful discussions; SmithKline Beecham Pharmaceuticals, King of Prussia, PA, for financial support and for supplying eprosartan mesylate; and the Supercomputing Institute of the University of Minnesota for financially supporting our use of the Medicinal Chemistry/Supercomputing Institute Visualization−Workstation Laboratory.

References and Notes

1. Khankari, R. H.; Grant, D. J. W. Pharmaceutical hydrates. *Thermochim. Acta*. **1995**, *248*, 61−79.
2. Haleblian, J. Characterization of habits and crystalline modification of solids and their pharmaceutical applications. *J. Pharm. Sci.* **1975**, *64*, 1269−1288.
3. *The United State Pharmacopeia, The National Formulary*; United States Pharmacopeial Convention, Inc.: Rockville, MD; 1995.
4. *European Pharmacopoeia*. 3rd ed., Council of Europe: Strasbourg, France, 1996.
5. Burger, A. Das Auflösungsverhalten von Sulfanilamid in Wasser. *Pharm. Ind*. **1973**, *35*, 626−633.
6. Burger, A.; Griesser, U. J. Physical stability, hygroscopicity and solubility of succinyl-sulfathiazole. *Eur. J. Pharm. Biopharm*. **1991**, *37*, 118−124.
7. Byrn, S. R. *Solid-State Chemistry of Drugs*, Academic: New York, 1982; pp 59−74, 149−186.
8. Ando, H.; Ohwaki, T.; Ishii, M.; Watanabe, S.; Miyake, Y. Crystallization of theophylline in tablets. *Int. J. Pharm*. **1986**, *34*, 153−156.
9. Chowhan, Z. T. Physical paths of instability. *Pharm. Technol.* **1982**, *6*, 47−48.
10. Brittain, H. G.; Bugay, D. E.; Bogdanowich, S. J.; DeVincentis, J. Spectral methods for determination of water. *Drug. Dev. Ind. Pharm*. **1988**, *14*, 2029−2046.
11. Giron, D. Thermal analysis and calorimetric methods in the characterization of polymorphs and solvates. *Thermochim. Acta* **1995**, *248*, 1−59.
12. Jaffé, J.; Foss, N. E. Compression of crystalline substances. *J. Am. Pharm. Assoc. Sci. Ed.* **1959**, *48*, 26−29.
13. Shefter, E.; Higuchi, T. Dissolution behaviour of crystalline solvated and nonsolvated forms of some pharmaceuticals. *J. Pharm. Sci.* **1963**, *52*, 781−791.
14. Poole, J. W.; Owen, G.; Silverio, J.; Freyholf, J. N.; Rosenman, S. B. Physicochemical factors influencing the absorption of anhydrous and trihydrate forms of ampicillin. *Curr. Ther. Res*. **1968**, *10*, 292−303.
15. Lerk, C. F.; Andreae, A. C.; Bolhuis, G. K.; Zuurman, K.; Hoog, P.; Kussendrager, K.; Leverink, J. V. Increased binding capacity and flowability of α-lactose monohydrate after dehydration. *J. Pharm. Pharmacol.* **1983**, *35*, 747−748.
16. Lerk, C. F.; Zuurman, K.; Kussendrager, K. Effect of dehydration on the binding capacity of particulate hydrates. *J. Pharm. Pharmacol.* **1984**, *36*, 399.
17. Otsuka, M.; Kaneniwa, N. Dehydration of cephalexin hydrates. *Chem. Pharm. Bull.* **1983**, *31*, 1021−1029.
18. *Chemistry of the Solid State*; Garner, W. E., Ed.; Academic: New York, NY, 1955; pp 232−253.
19. Galwey, A. K. *Chemistry of Solids*. Chapman and Hall: London, UK, 1967; pp 163−195.
20. Carstensen, J. T. *Drug Stability*: *Principles and Practice*, 2nd ed.; Marcel Dekker: New York, 1995; pp 230−280.
21. Agbada, C. O.; York, P. Dehydration of theophylline monohydrate powder—effects of particle size and sample weight. *Int. J. Pharm*. **1994**, *106*, 33−40.
22. Chen, L.; Grant, D. J. W. *Dehydration of Nedocromil Sodium Trihydrate*, College of Pharmacy, University of Minnesota, Minneapolis, MN, Personal Communication, 1996.
23. Monkhouse, D. C.; Campen, L. V. Solid-state reactions—theoretical and experimental aspects. *Drug. Dev. Ind. Pharm*. **1984**, *10*, 1175−1276.
24. Criado, J. M.; Morales, J.; Rivers, V. Computer kinetic analysis of simultaneously obtained TG and DTG curves. *J. Therm. Anal.* **1978**, *14*, 221−228.
25. Sharp, J. H.; Brindley, G. W.; Achar, B. N. N. Numerical data for some commonly used solid-state reaction equations. *J. Am. Ceram. Soc.* **1966**, *49*, 379−382.
26. Davis, W. H. J.; Pryor, W. A. Measures of goodness of fit in linear free energy relationships. *J. Chem. Educ.* **1976**, *53*, 285−287.
27. Brown, M. E.; Galwey, A. K. The distinguishability of selected kinetic models for isothermal solid-state reactions. *Thermochim. Acta* **1979**, *29*, 129−146.
28. Duddu, S. P.; Venkatesh, G. M.; Palepu, N. R. *Effect of excipients on the solid-state conversion of SK&F 108566-J into its hydrated form in the presence of water.* SmithKline Beecham Pharmaceuticals, King of Prussia, PA; *Report*, 1996.
29. Venkatesh, G. M. *SK&F 108566-J: Hydrate Formation − Further Studies*. SmithKline Beecham Pharmaceuticals, King of Prussia, PA; *Report*, 1996.
30. Sheng, J.; Duddu, S. P.; Venkatesh, G. M.; Palepu, N. R.; Zell, M. T.; Munson, E. J.; Grant, D. J. W. Dehydration behavior of eprosartan mesylate dihydrate. *Pharm. Res. Suppl.* **1997**, *14*, S-493, 3092.
31. Sheng, J.; Zhang, G.; Young, V. G.; Duddu, S. P.; Venkatesh, G. M.; Palepu, N. R.; Grant, D. J. W. Phase transformation and the single-crystal structure of SKF 108566-J dihydrate. *Pharm. Res. Suppl.* **1997**, *14*, S-492, 3091.
32. Kissinger, H. E. Reaction kinetics in differential thermal analysis. *Anal. Chem*. **1957**, *29*, 1702−1706.
33. Sheng, J.; Young, V. G., Jr.; Haltwanger, R. C.; Eggleston, D. S.; Grant, D. J. W. Crystal structure of eprosartan mesylate dihydrate and its comparison with that of eprosartan mesylate anhydrate, manuscript in preparation.
34. Suzuki, E.; Shirotani, K.; Tsuda, Y.; Sekiguchi, K. Studies on methods of particle size reduction of medicinal compounds: XXII. Water content and dehydration behaviour of crystalline caffiene hydrate. *Chem. Pharm. Bull.* **1985**, *33*, 5028−5035.
35. Gerdil, R.; Marsh, R. E. On the arrangement of water molecules in the crystal structure of caffeine. *Acta Crystallogr.* **1960**, *13*, 166−167.
36. Griesser, U. J.; Burger, A. The effect of water vapor pressure on desolvation kinetics of caffeine 4/5-hydrate. *Int. J. Pharm*. **1995**, *120*, 83−93.
37. Van Dooren, A. A. *Effect of operational factors on kinetic parameters determined with DSC*. Proc. 7th. Int. Conf. on Thermal Analysis; Wiley: Chichester, UK, 1982; pp 80−84.

JS9900250

Effect of Transdermal Iontophoresis Codelivery of Hydrocortisone on Metoclopramide Pharmacokinetics and Skin-Induced Reactions in Human Subjects

MICHEL CORMIER,*,† STELLA T. CHAO,†,‡ SUNEEL K. GUPTA,† AND RON HAAK†

Contribution from *ALZA Corporation, 950 Page Mill Road, P.O. Box 10950, Palo Alto, California 94303-0802.*

Received December 24, 1998. Final revised manuscript received June 14, 1999.
Accepted for publication August 2, 1999.

Abstract □ The effects of transdermal iontophoresis (IP) codelivery of hydrocortisone (HC) on metoclopramide hydrochloride (MCP) pharmacokinetics and on skin-induced reactions were evaluated in a randomized, crossover clinical study. MCP, an antiemetic, low molecular weight, cationic drug intended for systemic delivery, was delivered from the anode of IP systems at a constant current of 100 μA/cm^2. HC, a neutral endogenous antiinflammatory agent, was codelivered from the same electrode, primarily by electroosmotic processes. Each subject ($n = 7$) wore two identical IP systems (MCP alone or MCP plus HC), each supplying 500 μA, one on each upper arm for 4 h. One week later, each subject repeated the procedure with the alternate type of MCP system. HC did not change the pharmacokinetics of MCP: There were no statistically significant differences in MCP plasma concentrations, half-life, area under the curve (AUC), or rate of absorption between the two treatment groups. However, HC significantly decreased erythema and edema scores produced by the IP of MCP. In both groups, a steady-state MCP flux of about 100 μg/(cm^2 × h) was achieved after only 1 h of transport, and input rate dropped dramatically immediately after removal of the system. In vitro, HC flux through human epidermis from an MCP plus HC formulation was 2.8 ± 1.1 μg/(cm^2 × h) after 4 h transport at 100 μA/cm^2, suggesting negligible systemic exposure to hydrocortisone. These data indicate that MCP input rate and its clearance from the skin are unaltered by HC and that the codelivery of HC by IP is an effective strategy for inhibition of local reactions resulting from the transdermal delivery of drugs.

Introduction

Transdermal drug delivery was introduced as a means to deliver drugs intended for systemic therapy more than 20 years ago. Typically, transdermal systems deliver a drug in a zero-order fashion over several days.[1] This mode of delivery is particularly desirable for drugs with a low therapeutic index.[2] For these agents, zero-order delivery may result in reduction of systemic side effects. Unfortunately, local delivery results in high drug concentrations in the delivery site that can result in irritation and sensitization to the drug being delivered.[3] Several clinically available transdermal systems have been reported to produce local irritation or sensitization.[4−6] In addition, reports indicate that many potential candidates for transdermal delivery may be too irritating or sensitizing for development.[7,8] Various strategies have been developed to minimize these local side effects.[9−14] One of the most promising strategies consists of pretreating the skin with a glucocorticoid (GC) or codelivering it with the drug.[15] This pretreatment strategy has been applied to several transdermal systems already on the market.[4,16] To date, there are no commercialized combination products. One of the potential problems associated with the use of the topical delivery of GCs results from their local vasoconstrictive effect.[17] This pharmacological effect is directly dependent on the potency and the flux of the GC[18] and may possibly affect the pharmacokinetics of the drug being delivered.

Surprisingly, there are only a few reports of the effect of GCs on the pharmacokinetics of a drug being delivered transcutaneously. Ito and O′Connor reported that pretreatment with a 0.5% HC cream did not affect the pharmacokinetics of clonidine delivered from Catapres-TTS applied to the same skin site.[16] Unfortunately, this study did not address HC delivery through the skin—in particular if HC was codelivered efficiently during the 7-day patch application. Finally, the effectiveness of HC in reducing the clonidine-induced skin reaction could not be accurately evaluated because the subjects were not previously sensitized to clonidine.

IP offers a means to deliver drugs through the skin with a minimum lag time and an optimal control of drug flux.[19] IP delivery of MCP, an antiemetic drug intended for systemic delivery, was previously found to result in moderate skin irritation at the site of delivery (unpublished data). We decided to use the IP technology to demonstrate that hydrocortisone can be used in transdermal delivery to minimize skin reactions caused by the transdermal delivery of drugs without significant alteration of drug flux and drug clearance from the skin.

Materials and Methods

In Vitro Studies—For in vitro studies, human skin from cadavers was used. The epidermis was separated from the dermis after incubating the skin for about 1 min in water heated to 60 °C. The separated epidermis was mounted in custom-made IP cells (two compartment cells) with the stratum corneum facing the donor compartment. IP cells were assembled with a silver foil anode in the drug donor compartment and a silver/silver chloride cathode in the receptor compartment. The donors were filled with 2 mL of saturated HC (USP clinical grade, Diosynth, Chicago, IL) aqueous solution in Dulbecco's phosphate-buffered saline or 10% (w/w) MCP (USP clinical grade, Lee Lab, Arlington, VA) aqueous solution saturated with HC. The receptors were filled with 1.8 mL of Dulbecco's phosphate-buffered saline. The permeation cells were thermostated at 32 °C. Experiments were run without current or under constant current set at 0.1 mA/cm^2 for 18 h with samples taken every 4 h. Both HC and MCP were assayed by high-performance liquid chromatographic (HPLC) methods.[20,21]

Clinical Study—Electrically assisted delivery of MCP was accomplished with custom-built IP systems. The IP systems had

* Corresponding author. ALZA Corporation, 1010 Joaquin Rd., P.O. Box 7210, Mountain View, CA 94039-7210. Phone: (650) 237-2708. Fax: (650) 237-2700. e-mail: michel.cormier@alza.com.
† ALZA Corporation.
‡ Present address: Elan Pharmaceuticals, 3760 Haven Ave., Menlo Park, CA 94025-1012.

10.1021/js980491+ CCC: $18.00
Published on Web 09/01/1999

a silver anode (donor) and an anodic reservoir gel containing a 10% (w/w) aqueous solution of MCP with or without a 0.5% (w/w) saturated aqueous solution of HC and 3% (w/w) hydroxy ethyl cellulose (HEC, Aqualon, Wilmington, DE) to form a gel. The IP systems also had a silver chloride cathode (counter electrode) and a cathodic reservoir containing a buffered saline gel. The reservoir gels (i.e., both the anodic and cathodic gels) each had a volume of approximately 600 μL and a skin-contacting surface area of about 5 cm^2. The electrodes were connected to a DC power source that supplied a constant level of electric current of 500 μA or 100 μA/cm^2. The study was undertaken in volunteers after approval by the Medical Review Board at ALZA, which, at the time the study was performed, met FDA criteria, and in accordance with the principles of the Declaration of Helsinki. Each study volunteer met all of the following inclusion criteria: male, 18−50 years old; medical history, physical examination demonstrating no clinically relevant abnormalities, SMA 17 blood profile tests (glucose, blood-urea-nitrogen, uric acid, calcium, phosphorus, total protein, albumin, cholesterol, total bilirubin, alkaline phosphatase, aspartate aminotransferase, alanine aminotransferase, lactate dehydrogenase, sodium, potassium, creatinine, bicarbonate, and chloride), complete blood count, urinalysis, and electrocardiogram; normotensive. Exclusion criteria included dermatological disorders, application sites presenting scar tissue or moles, known hypersensitivity to any component of the IP system, use of antiinflammatory drugs such as steroids, nonsteroidal antiinflammatory drugs, and abnormal clinical laboratory tests. Informed, written consent was obtained from each subject. The IP systems were applied to and removed from the upper arms of subjects by the study investigators. The application site was wiped with 70% isopropyl alcohol pads prior to system application. Each week, each subject wore two identical IP systems simultaneously, one per arm, for 4 h. On the first week, four subjects wore two systems containing MCP and four subjects wore two systems containing MCP plus HC. One week later, each subject repeated the procedure with the alternate type of MCP system. Seven subjects completed this study.

Voltage and current were measured at 0.5, 1, 2, 3, and 4 h after system application. To perform voltage measurements at each individual electrode, an adjacent skin site was lightly abraded using electrocardiogram-grade abrasive tape (One-Step Skin Prep, 3M Canada Inc, London, Ontario). An electrocardiogram electrode (TenderTrace, NDM, Dayton, OH) was immediately applied to this skin site. Voltage was measured between this reference electrode and the anode or cathode of the IP system at each time point. Electrode resistance was extrapolated from current and voltage measurements. Blood samples (10 mL) were drawn at hours 0, 0.5, 1, 2, 3, 4, 4.5, 5, 6, 8, and 20 (systems were removed at hour 4). Blood samples were centrifuged immediately after collection. The plasma was divided into duplicate aliquots and frozen at −20 °C until analysis. MCP analysis was performed by Harris Labs (Lincoln, NE) with a validated HPLC method.[21] The MCP assay quantification limit was 3.0 ng/mL.

Individual plasma concentrations were used for all pharmacokinetic calculations and were summarized by nominal sampling times. Plasma MCP concentrations below the assay quantification limit of 3.0 ng/mL were assigned a value of 0. The maximum observed plasma MCP concentration (C_{max}) and corresponding sampling time (T_{max}), expressed in hours following initial dosing, were determined for each treatment. The plasma MCP apparent elimination rate constant (k) was estimated by linear regression of the log-transformed (natural log) plasma MCP concentrations during the log-linear phase of the data after system removal. Apparent half-life values were calculated as 0.693 divided by k. MCP area under the plasma concentration versus time values (AUC) were determined by the linear trapezoidal method from study hours 0 to 20, and from hour 0 to the last detectable concentration at time t, AUC_t. The AUC value extrapolated to infinity, AUC_{inf}, was determined as the sum of AUC_t plus the area extrapolated to infinity, as calculated by the concentration at time t (C_t) divided by k. The average MCP concentration, C_{avg}, was calculated as $AUC_{(0-20)}$ divided by 20 h. The cumulative amount of metoclopramide absorbed and the rate of MCP absorption was calculated according to the Wagner and Nelson method.[22]

Visual skin inspection following system removal was done to evaluate the presence and extent of erythema, edema, papules, and pustules. Edema, extent of erythema, papules, and pustules were scored using a 0−2 visual scale and rated as follows: 0 = none, 1 = <50% of occluded area, 2 = >50% of occluded area. Scores for erythema: 0 = none, 1 = barely perceptible redness, 2 = definite redness, 3 = beet redness. Subjects were also asked to report any itching. Visual skin site evaluations were conducted by a trained nurse under the supervision of a medical doctor at 0 (within 10 min after system removal), 1, 4, 24, and 48 h following system removal and were continued until skin sites were clear. Skin sites were also evaluated by skin color reflectance using a Chroma meter CR 210 (Minolta, Ramsey, NJ) at 1, 4, 24, and 48 h following system removal.[23] Reflectance measurements were made by taking the mean a^* value of three readings at adjacent untreated sites and subtracting that value from the mean of three readings taken at the treated site.

Table 1—In Vitro Transdermal Flux of HC and MCP 4 Hours after Initiation of Transport. Transdermal Flux Was Evaluated at 32 °C. HC solubility was determined at 25 °C

formulation	current (μA/cm^2)	HC solubility (mg/mL)	flux (μg/(cm^2 h)	
			HC	MCP
HC	0	0.26	0.02 ± 0.00	NA
HC	100	0.26	0.32 ± 0.11	NA
HC + MCP	100	4.0	2.84 ± 1.12	131 ± 27

Table 2—Subject Demographics of the Seven Caucasian Healthy Men Completing the Study

	mean	SEM	range
age (years)	32.3	1.9	25–39
height (cm)	183	3.0	173–198
weight (kg)	76.6	3.7	68–91

Statistical Analysis—All results are presented as the mean with its associated standard error of the mean (SEM). Statistical analysis was performed using the Student's t test. A probability value of $p < 0.05$ was considered statistically significant.

Results

In Vitro Studies—HC flux through human epidermis was found to be 2.8 ± 1.1 μg/(cm^2×h) after 4 h transport at 0.1 mA/cm^2 from a 10% MCP solution saturated with HC. The flux of MCP from the same formulation was 131 ± 27 μg/(cm^2 × h) (Table 1). HC flux from this formulation was almost 1 order of magnitude greater than that from the formulation containing no MCP. A 0.1 mA/cm^2 current increased the passive flux of HC by more than 1 order of magnitude. Under IP conditions, steady-state flux was achieved for both drugs at or before the 4-h time point (data not shown). Solubility of hydrocortisone at 25 °C was increased from 0.26 mg/mL in the solution without MCP to 4 mg/mL in the presence of 10% MCP.

Demographics—Laboratory exams conducted before the study showed that all subjects were healthy. Eight Caucasian men entered the study and seven completed it. One subject dropped out due to an unrelated illness. Subject demographics are summarized in Table 2.

System Functionality—All IP systems reached the desired current setting within 30 min after application. With MCP alone, average current at this time was 470 ± 6 μA, and was not significantly different from 484 ± 3 μA for MCP plus HC. Current remained constant for the remaining application time. At 4 h, current was 478 ± 3 μA for MCP versus 486 ± 5 μA for MCP plus HC. Anode resistance values at the MCP anode 30 min and 4 h after application were 24 ± 3 kΩ × cm^2 and 18 ± 2 kΩ × cm^2, respectively. In the presence of HC, anode resistance values were 21 ± 2 and 14 ± 1 kΩ × cm^2 at the same time points. At 4 h, cathode resistance was 2.0 ± 0.4 kΩ × cm^2 for MCP versus 3.1 ± 1.3 kΩ × cm^2 for MCP plus HC. Resistance

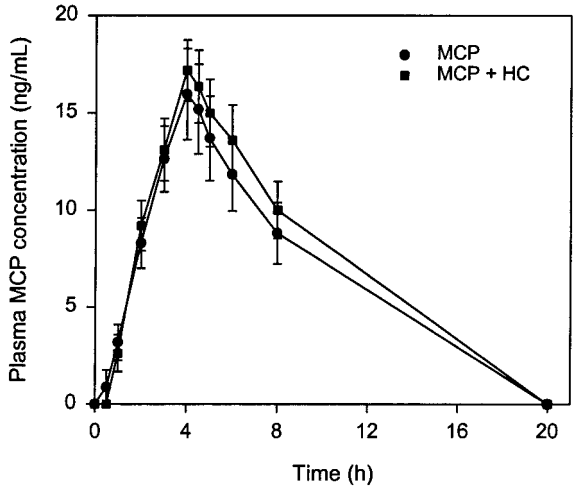

Figure 1—Mean plasma MCP concentrations in subjects receiving IP of MCP or IP of MCP plus HC. Systems were removed at the 4-h time point.

Table 3—Pharmacokinetics Parameters of MCP Delivered by IP from an MCP System or an MCP Plus HC System

	MCP		MCP + HC	
parameter	mean	SEM	mean	SEM
C_{max} (ng/mL)	16.1	2.3	17.3	1.6
T_{max} (h)	4.07	0.07	4.14	0.09
$t_{1/2}$ (h)	4.76	0.38	4.86	0.49
elimination rate constant	0.153	0.015	0.151	0.013
AUC_t (ng × h/mL)	80.1	12.4	86.9	10.6
AUC_{inf} (ng × h/mL)	143	25	163	29
C_{avg} (ng/mL)	4.01	0.62	4.35	0.53

values were not significantly different when MCP alone was compared with MCP with HC.

Plasma MCP Pharmacokinetics—Measurable MCP plasma concentrations were detected in most subjects 1 h after system application. The mean plasma MCP concentrations, with and without HC, are displayed in Figure 1. C_{max} averaged 16 ng/mL for MCP alone, and was not significantly different from the 17 ng/mL C_{max} value for MCP plus HC. T_{max} coincided with the time of system removal in both groups (Table 3). Mean plasma concentrations of MCP, with or without HC, started to drop 0.5 h after system removal (Figure 1). Sixteen hours after system removal, mean plasma drug concentrations were all below the limits of detection. The mean half-life and AUC values of MCP, with and without HC, were equivalent (Table 3). The mean rate of MCP absorption (Figure 2) was not significantly different for the two groups. Steady-state input for MCP of about 100 μg/(cm^2 × h) was achieved by 1 h. Half an hour after removal of the systems, the input rate had dropped by about a factor of 4 to less than 25 μg/(cm^2 × h). The cumulative amount of MCP absorbed per subject is shown in Figure 3. After 4 h IP, about 4 mg MCP had been absorbed, irrespective of the treatment (3.8 ± 0.6 mg for MCP alone versus 4.1 ± 0.7 mg for MCP plus HC). Little absorption was observed following removal of the IP systems.

Topical Effects—all subjects presented some erythema at the anode following system removal. The erythema was homogeneously distributed and limited to the skin-contacting area of the gel (1 h after removal of the system, erythema extent at the anode was 2.0 ± 0.0 versus 1.9 ± 0.1 for MCP and MCP with HC, respectively). Erythema had resolved in all subjects by 72 h. HC significantly decreased erythema scores as assessed visually at all time points except 1 h (Figure 4). Similar results were obtained

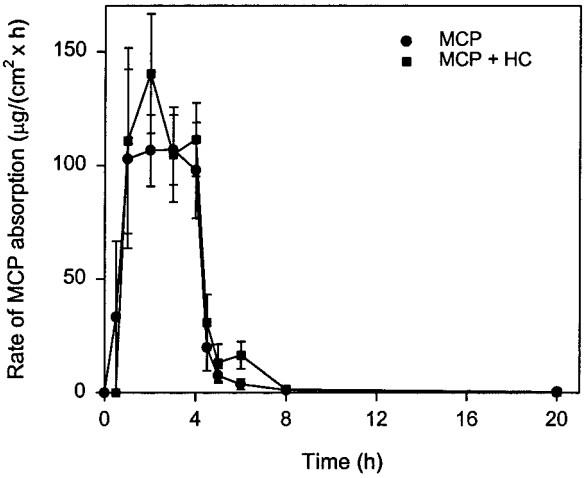

Figure 2—Mean rate of MCP absorption in subjects receiving IP of MCP or IP of MCP plus HC. Systems were removed at the 4-h time point.

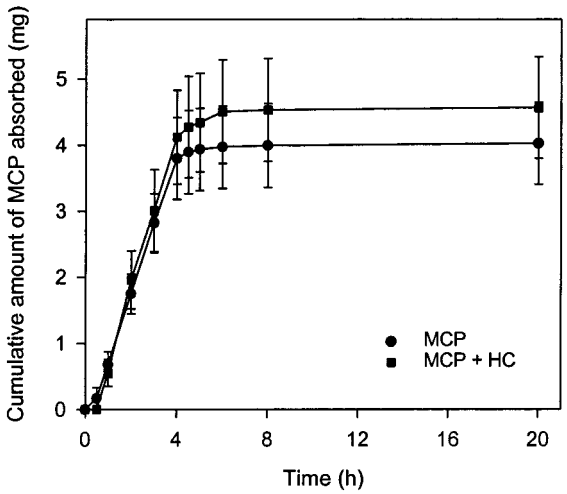

Figure 3—Mean cumulative amount of MCP absorption in subjects receiving IP of MCP or IP of MCP plus HC. Systems were removed at the 4-h time point.

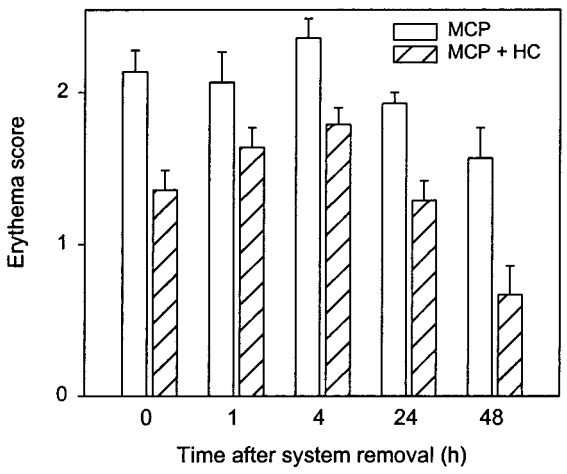

Figure 4—Mean erythema scores at the anode after 4 h IP of MCP or MCP plus HC.

with skin color reflectance measurements: One hour after removal of the system, reflectance values were 2.1 ± 0.3 and 0.8 ± 0.3 for MCP and MCP with HC, respectively. Four hours after removal of the system, reflectance values were 2.7 ± 0.2 and 0.7 ± 0.3 for MCP and MCP with HC, respectively. At 24 and 48 h after removal of the system,

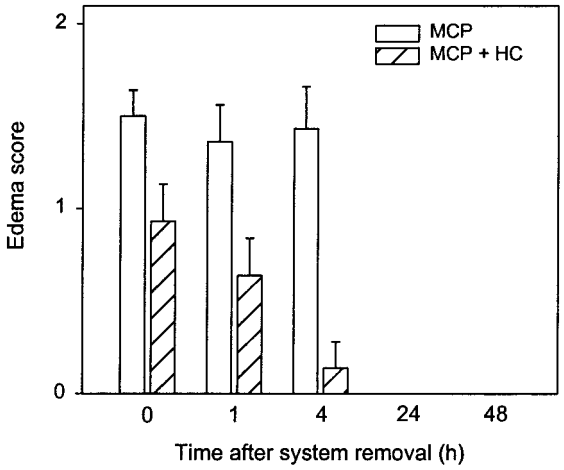

Figure 5—Mean edema scores at the anode after 4 h IP of MCP or MCP plus HC.

reflectance values were below 1 in both groups and were not statistically significant between the two groups.

Edema at the site of system application was observed in most subjects. HC significantly decreased edema score at 0, 1, and 4 h. Four hours after system removal, the mean edema score at the anode delivering MCP was 1.4. HC almost completely inhibited edema at this time point. Edema was resolved in all subjects by 24 h following system removal (Figure 5). There were no papules or pustules observed in any of the subjects and no subjects reported itching.

Discussion

MCP is an antiemetic prescription drug used in the treatment of gastroesophageal reflux and in the prevention of nausea and vomiting. This drug is intended for systemic delivery (iv or oral), and clinical MCP doses range between 10 and 60 mg/d.[24] Subjects in this study wore two 5-cm^2 IP transdermal systems, and input rate was about 1 mg/h at steady state. The cumulative amount of MCP absorbed systemically was about 4 mg after 4 h IP. Steady-state MCP flux of about 100 μg/($cm^2 \times$ h) was achieved after only 1 h of transport, indicating a brief lag time, and input rate dropped dramatically immediately after removal of the systems. The brief lag time observed and the rapid drop in calculated input rate is consistent with a negligible MCP depot or accumulation in the skin. In addition, the calculated MCP half-life is similar to values reported in the literature following iv administration,[24] an outcome also consistent with an absence of skin depot. Collectively, these results indicate that usable MCP therapy could be achieved with an electrode size of about 5 to 30 cm^2.

Although we have demonstrated the feasibility of MCP IP transdermal delivery from an input rate standpoint, local skin irritation has been observed at the delivery site. This local side effect could jeopardize clinical acceptability of this transdermal system. The goal of the present study was to investigate the feasibility of codelivery of HC with MCP and evaluate the inhibitory effect of HC on the skin response. MCP is a low molecular weight, cationic, water-soluble drug salt. Although most MCP transport is accomplished via migration of ionized drug molecules in the electric field, HC transport is mainly the result of passive diffusion and electroosmosis (i.e., migration of nonionized molecules in an electric field).[25] IP through the skin occurs chiefly through aqueous pathways (i.e., sweat glands and hair follicles).[26] As a result, the stratum corneum, which accounts for most of the reservoir effect observed during transdermal steroid delivery,[27] is bypassed; this routing should result in a reduced transport lag time of HC compared with passive delivery. We did not attempt to measure HC flux during this clinical study because theoretical calculations indicated that the resulting HC blood levels would be indistinguishable from endogenous levels. In the in vitro flux experiment, HC steady-state flux was achieved within less than 4 h transport under an anodic current of 0.1 mA/cm^2, indicating that IP effectively bypasses the reservoir effect of the stratum corneum with respect to HC delivery. In addition, we found that HC flux is affected by current and the presence of MCP. A current of 0.1 mA/cm^2 results in a more than 1 order of magnitude increase over the passive flux of HC. This result is consistent with transport of HC by electroosmosis and increased skin permeability resulting from IP, as was demonstrated with other neutral molecules.[28,29] Increase in HC flux in the presence of MCP may be explained by the increase in HC solubility in the presence of MCP. MCP is a very water-soluble drug that does not seem to present significant colloidal properties (in this study, it did not decrease significantly the surface tension of water at up to 0.5 M). Therefore, the observed increase in HC solubility in the presence of MCP cannot be the result of solubilization of hydrocortisone in MCP aggregates as has been observed with surfactants and compounds presenting colloidal properties.[30] Increase in HC solubility is probably the result of a salting-in phenomenon that commonly occurs when organic-substituted ammonium salts are added to aqueous solutions of nonelectrolytes.[31] In any case, the flux of a solute (electrosmotic as well as passive diffusion) has been reported to be directly dependent on its concentration.[28] Consequently, the increase in HC flux observed in the presence of MCP is consistent with the increase in HC solubility.

Neither the plasma concentration profile nor any of the pharmacokinetic parameters of MCP differed when it was delivered by IP, with or without HC, indicating that MCP input rate and its clearance from the skin were unaltered by HC. However, HC inhibited erythema as well as edema resulting from IP delivery of MCP. This result indicates that HC was delivered in vivo at a rate sufficient to exert its local pharmacological effect. Inhibition of erythema was very effective, as assessed visually and by skin color reflectance, and could be the result of the vasoconstrictive effect produced by HC, while the inhibition of edema probably reflects the antiinflammatory action of HC. Vasoconstriction is known to retard drug clearance from the delivery site.[32] Codelivery of HC could therefore impact the pharmacokinetic profile of MCP. No such effect of HC was observed possibly because of the high transport rate of MCP through the skin by IP and saturation of the skin binding sites. Alternatively, this could be explained by the low potency of HC. Indeed, HC is the weakest GC available; stronger GCs could possibly modify the pharmacokinetics of a codelivered drug by increasing local vasoconstriction at the delivery site.

GCs are broad-based antiinflammatory agents; they are expected to exert their activity on any type of inflammation, regardless of the triggering mechanism.[33] As a result, GCs are among the most universal agents for counteracting skin reactions. Using GCs when an inflammation mechanism is unknown or poorly understood provides a definitive advantage compared with using more specific antiinflammatory strategies described in the literature.[9,10,12,13]

The use of topical steroids more potent than HC can be more beneficial from an antiinflammatory standpoint in cases of extreme inflammation.[33,34] However, an increase in potency implies that potential side effects may also be observed. In normal subjects, adrenal suppression did not

occur with high-potency corticosteroid ointment formulations applied to 75% of the body surface once a day for six consecutive days.[35] However, in clinical practice, mild adrenal suppression has been observed after intensive use in patients who required rigorous treatment of their skin disease.[36] This observation indicates that the risk of systemic side effect with high-potency steroids is not completely negligible. Local side effects such as skin thinning resulting from local administration of steroids are also related to potency.[37] The usefulness of high-potency steroids, therefore, may be limited by the potential for systemic and local side effects.

The beneficial effect of HC has been reported only with weak sensitizers or moderate irritants.[15,16] Since IP delivery of MCP results in only moderate inflammation, it is thought that HC is more appropriate than stronger steroids for codelivery with it. The use of HC may be a good alternative to more potent GCs for inhibition of mild to moderate inflammatory responses for three reasons. First, HC is an endogenous compound; the amount needed to produce local antiinflammatory effects is a small fraction of the endogenous production. (In this study, the total calculated flux of HC per subject was about 0.1 mg after 4 h IP delivery, whereas endogenous HC production is reported to be about 10 mg/d.[33] Even if the amount of HC delivered is extrapolated to 24 h, this daily total is still a small fraction of the endogenous HC production. Therefore, systemic activity of HC is probably not responsible for the antiinflammatory effects observed in this study. Second, to the best of our knowledge, local side effects such as skin thinning have never been observed with HC. Finally, water solubility of HC is higher than that of most GCs and, if needed, solubility can be increased by the addition of solvents such as propylene glycol in concentrations compatible with IP delivery.[38] Therefore, the effect observed with MCP can probably be extended to the delivery of other irritating or sensitizing drugs, making this strategy a very powerful tool for achieving safe and acceptable transdermal delivery of drugs.

References and Notes

1. Shaw, J. E. Pharmacokinetics of Nitroglycerin and Clonidine Delivered by the Transdermal Route. *Am. Heart J.* **1984**, *108*, 217−223.
2. Enscore, D. J.; Osborne, J. L.; Shaw J. E. In Vitro/in Vivo Functionality of Catapres-TTS. *Methods Find. Exp. Clin. Pharmacol.* **1989**, *11*, 173−178.
3. Knepp, V. M.; Hadgraft, J.; Guy, R. H. Transdermal Drug Delivery: Problems and Possibilities. *Crit. Rev. Ther. Drug Carrier Syst.* **1987**, *4*, 13−37.
4. Wilson, D. E.; Kaidbey, K.; Boike, S. C.; Jorkaski, D. K. Use of Topical Corticosteroid Pretreatment to Reduce the Incidence and Severity of Skin Reactions Associated with Testosterone Transdermal Therapy. *Clin. Therap.* **1998**, *20*, 299−306.
5. Dick, J. B. C.; Northridge D. B.; Lawson, A. A. H. Skin Reactions to Long-Term Transdermal Clonidine. *Lancet* **1987**, *1*, 516.
6. Patil, S. M.; Hogan, D. J.; Maibach, H. I. Transdermal Drug Delivery Systems: Adverse Dermatologic Reactions. In *Dermatotoxicology Fifth Edition*, Marzuli, F. N., Maibach, H. I., Eds.; Taylor & Francis: Philadelphia, 1996; pp 389−396.
7. Kalish, R. S.; Wood, J. A.; Wille, J. J.; Kydonieus, A. Sensitization of Mice to Topically Applied Drugs: Albuterol, Chlorpheniramine, Clonidine and Nadolol. *Contact Dermatitis* **1996**, *35*, 76−82.
8. Mize N. K.; Johnson J. A.; Hansch C.; Cormier M. Quantitative Structure−activity Relationship and Cytotoxicity. *Curr. Probl. Dermatol.* **1995**, *23*, 224−229.
9. Sharpe, R. J.; Chandrasekar, A.; Arndt, K. A.; Wang, Z. S.; Galli, S. J. Inhibition of Cutaneous Contact Hypersensitivity in the Mouse with Systemic or Topical Spiperone: Topical Application of Spiperone Produces Local Immunosuppression without Inducing Systemic Neuroleptic Effects. *J. Invest. Dermatol.* **1992**, *99*, 594−600.
10. Kalish, R. S.; Wood, J. A.; Kydonieus, A.; Wille, J. J. Prevention of Contact Sensitivity to Topically Applied Drugs by Ethacrynic Acid: Potential Application to Transdermal Drug Delivery. *J. Controlled Release* **1997**, *48*, 79−87.
11. Cormier, M.; Ledger, P. W.; Amkraut A. A. Reduction or Prevention of Skin Irritation or Sensitization during Transdermal Administration of a Irritating or Sensitizing Drug. US Patent 5,451,407, 1995.
12. Cormier, M.; Ledger, P. W.; Amkraut, A. A.; Marty, J. P. Method for Reducing Sensitization or Irritation in Transdermal Drug Delivery and Means Therefor. US Patent 5, 304,379, 1994.
13. Cormier, M.; Ledger, P. W.; Amkraut, A. A.Reduction or prevention of skin irritation by drugs. US Patent 5,130,139, 1992.
14. Mize N.; Buttery M.; Ruis N.; Leung I.; Cormier M.; Daddona P. Antiflammin 1 Peptide Delivered Noninvasively by Iontophoresis Reduces Irritant-induced Inflammation in Vivo. *Exp. Dermatol.* **1997**, *6*, 181−185.
15. Amkraut, A. A.; Jordan, W. P.; Taskovich L. Effect of Coadministration of Corticosteroids on the Development of Contact Sensitization. *J. Am. Acad. Dermatol.* **1996**, *35*, 27−31.
16. Ito, M. K.; O'Connor, D. T. Skin Pretreatment and the Use of Transdermal Clonidine. *Am. J. Med.* **1991**, *91*, 42S−49S.
17. Sommer, A.; Veraart, J.; Neumann, M.; Kessels, A. Evaluation of the Vasoconstrictive Effects of topical steroids by Laser-Doppler-perfusion-imaging. *Acta Derm. Venereol.* **1998**, *78*, 15−18.
18. Stoughton, R., B. The Vasoconstrictor Assay in Bioequivalence Testing: Practical Concerns and Recent Developments. *Int. J. Dermatol.* **1992**, *31s1*, 26−28.
19. Haak, R. H.; Gupta, S. K. Pulsatile Drug Delivery from Electrotransport Therapeutic Systems. In *Pulsatile Drug Delivery. Current Applications and Future Trends*; Gurny, R., Junginger, H. E., Pappas, N. A., Eds.; Wissenschaftliche Verlagsgesellschaft mbH: Stuttgart, 1993; pp 99−112.
20. Scott, N. R.; Dixon, P. F. Determination of Cortisol in Human Plasma by Reversed-phase High-performance Liquid Chromatography. *J. Chromatogr.* **1979**, *164*, 29−34.
21. Buss, D. C.; Hutchings, A. D.; Scott, S.; Routledge, P. A. A Rapid Liquid Chromatographic Method for the Determination of Metoclopramide in Human Plasma. *Ther. Drug Monit.* **1990**, *12*, 293−296.
22. Wagner, J. G.; Nelson, E. Percent Absorbed Time Plots Derived from Blood Level and/or Urinary Excretion Data. *J. Pharm. Sci.* **1963**, *52*, 610−611.
23. Wilhelm, K. P.; Maibach, H. I. Skin Color Reflectance Measurements for Objective Quantification of Erythema in Human Beings. *J. Am. Acad. Dermatol.* **1989**, *21*, 1306−1310.
24. *AHFS 98 Drug Information;* McEvoy, G. K., Ed; American Society of Health-System Pharmacists: Bethesda, MD, 1998; 2438−2445.
25. Lin, R. Y.; Ou, Y. C.; Chen, W. Y. The Role of Electroosmotic Flow on In-vitro Transdermal Iontophoresis. *J. Controlled Release* **1997**, *43*, 23−33.
26. Burnette, R. R.; Ongpipattanakul, B. Characterization of the Pore Transport Properties and Tissue Alteration of Excised Human Skin during Iontophoresis. *J. Pharm. Sci.* **1988**, *77*, 132−137.
27. Foreman, M. I.; Clanachan, I. Steroid Diffusion and Binding in Human Stratum Corneum. *J. Chem. Soc.* **1984**, *80*, 3439−3944.
28. Ruddy, S. B.; Hadzija, B. W. Iontophoretic Permeability of Polyethylene Glycols through Hairless Rat Skin. Application of Hydrodynamic Theory for Hindered Transport through Liquid Filled Pores. *Drug Des. Discovery.* **1992**, *8*, 207−224.
29. Delgado-Charro, M. B.; Guy R. H. Characterization of Convective Solvent Flow During Iontophoresis. *Pharm. Res.* **1994**, *11*, 929−935.
30. Attwood, D.; Florence, A. T. Pharmaceutical Aspects of Solubilization. In *Surfactant Systems. Their Chemistry, Pharmacy and Biology;* Attwood, D, Florence, A. T., Eds.; Chapman and Hall: London, New York, 1983; pp 293−387.
31. Sokoloski, T. D. Solutions and Phase Equilibria. In *Remington's Pharmaceutical Sciences*, 18th ed.; Gennaro A. R., Ed.; Mack Publishing Company: Easton, PA, 1990; pp 207−227.
32. Riviere, J. E.; Monteiro-Riviere, N. A.; Inman, A. O. Determination of Lidocaine Concentrations in Skin after Transdermal Iontophoresis: Effect of Vasoactive Drugs. *Pharm. Res.* **1992**, *9*, 211−214.
33. Schimmer, B. P.; Parker, K. L. Adrenocorticotropic Hormone; Adrenocortical Steroids and their Analogues; Inhibitors of the Synthesis and Actions of Adrenocortical Hormones. In *Goodman & Gilman's The Pharmacological Basis of Therapeutics*, 9th ed.; Hardman, J. G., Limbird, L. E.; Molinoff, P.

B., Ruddon, R. W., Eds.; The McGraw-Hill Companies Inc.: New York, 1996; pp 1465−1485.
34. Burrows, W. M.; Stoughton, R. B. Inhibition of Induction of Human Contact Sensitization by Topical Glucocorticosteroids. *Arch. Dermatol.* **1976**, *112*, 175−178.
35. Novak, E.; Francom, S. F.; Schlagel, C. A. Adrenal Suppression with High-potency Corticosteroid Ointment Formulations in Normal Subjects. *Clin. Ther.* **1983**, *6*, 59−71.
36. Munro, D. D. The Effect of percutaneously Absorbed Steroids on Hypothalamic-pituitary-adrenal Function after Intensive Use in In-patients. *Br. J. Dermatol.* **1976**, *94s12*, 67−76.
37. Lubach, D.; Bensmann, A.; Bornemann, U. Steroid-induced Dermal Atrophy. Investigations on Discontinuous Application. *Dermatologica* **1989**, *179*, 67−72.
38. Ledger, P. W.; Cormier, M.; Campbell, P. Reduction of Skin Irritation during Electrotransport Delivery. US Patent 5, 693,010, 1997.

Acknowledgments

The authors gratefully acknowledge the contribution of their co-workers for expert technical assistance, particularly Pat Campbell, Joe Leonard, Barbara Pruitt, and Jane Yieh.

JS980491+

Development of an in Vitro Dissolution Method Using Microdialysis Sampling Technique for Implantable Drug Delivery Systems

ALEKHA K. DASH,*,† PAUL W. HANEY,† AND MARC J. GARAVALIA†,‡

Contribution from *Department of Pharmaceutical and Administrative Sciences, School of Pharmacy and Allied Health Professions, Creighton University, Omaha, Nebraska 68178.*

Received December 17, 1998. Accepted for publication July 30, 1999.

Abstract □ The major challenge faced during the development of implantable dosage forms for site-specific delivery is monitoring the local concentration of the drug at or around the site of action. The tissue concentration at the site is generally measured by either sacrificing the animal at different points in time or by determining the amount of drug left in the implants at various time intervals. Unfortunately, there are no official in vitro dissolution methods available to study the release characteristics of drugs from this drug delivery system. The objective of this investigation was to develop a simple method using microdialysis sampling technique to serve as an in vitro dissolution method for implantable drug delivery systems. Ciprofloxacin implants were prepared by compressing ciprofloxacin microcapsules in poly(lactic acid) (PLA) and poly(lactic-glycolic acid) (PLGA). A sensitive HPLC method was developed and validated for the assay of Ciprofloxacin. An in vitro dissolution method was developed to study the release characteristics of drug from these implants. The method used a microdialysis sampling technique and a small sample volume of release medium. The various advantages and disadvantages of this method over other USP methods are discussed.

Introduction

In vitro dissolution testing of pharmaceuticals is not a guarantee of therapeutic efficacy, but it is the best available in vitro method that can reveal qualitatively the physiological availability of a drug. Furthermore, the FDA Generic Drugs Advisory Committee has recently recommended the use of dissolution testing as an in vitro surrogate marker for bioavailability and bioequivalence.[1] Unfortunately, no such methods are officially available for implantable dosage forms. An in vitro method which may correlate to the local concentration of drug near the target site(s) will be invaluable for the design and evaluation of implantable dosage forms. Implantable dosage forms are gaining tremendous interest for the treatment of bone cancer, osteomyelitis, and for the delivery of short half-life polypeptides.[2−4] Therefore, a need to develop an in vitro dissolution method for these dosage forms will be an important contribution to the area of pharmaceutical dosage form design and analysis.

Microdialysis is a very useful technique because it permits continuous monitoring of drug concentration in extracellular spaces and has been used extensively in pharmacokinetics and pharmacodynamics studies.[5−7] In vitro microdialysis sampling technique has also been used to determine the protein binding of a drug,[8,9] partition coefficient,[10] and dissolution testing of pharmaceutical formulations.[11,12] The overall goal of this study is to develop an in vitro dissolution method using a microdialysis sampling technique to study the release characteristics of drugs from implantable dosage forms and compare the in vitro release profiles obtained from an established USP dissolution method. The idea of microdialysis is to mimic the passive function of a capillary blood vessel by perfusing a perfusate solution through a thin dialysis tube implanted in the tissue near the site of the implant. Therefore, the objectives of this investigation are to (i) develop and validate a sensitive HPLC method for the assay of ciprofloxacin, (ii) design a biodegradable implant for ciprofloxacin, (iii) design an in vitro dissolution apparatus using microdialysis as the sampling technique to study the release characteristics of ciprofloxacin from the implants, and (iv) compare the in vitro release profiles of drugs obtained from this method with an established USP dissolution method.

Experimental Section

Materials—Ciprofloxacin (Miles Pharmaceutical, West Haven, CT), a broad-spectrum antibiotic of the fluoroquinolone group, was used as a model compound. Poly DL-lactide-*co*-glycolide (PLGA) (50:50) and poly-lactic acid (PLA) (Birmingham Polymer, Birmingham, AL) were used as the biodegradable polymeric matrix materials. Citric acid, sodium phosphate (dibasic), acetonitrile, methanol, perchloric acid, and water (HPLC grade) were used as received (Fisher Scientific, Fair Lawn, NJ).

Preparation of Microcapsules and the Implants—Coacervation-phase separation method was used for the preparation of the microcapsules. The PLGA/PLA polymer (1 g) was dissolved in 30 mL of methylene chloride. Ciprofloxacin hydrochloride powder was dispersed in 600 mL of cyclohexanes. The polymer solution was then added, dropwise, over a period of 5 min to the cyclohexanes containing the dispersion of the drug. Methylene chloride was then evaporated off over a period of 2.5 h. After the microcapsules were formed, the solution was vacuum-filtered and dried overnight. Implants were made by compressing ciprofloxacin microcapsules in a Carver press using stainless steel dies and punches. The compression force used was 1000 psi for 5 s.

Scanning Electron Microscopy (SEM)—Samples were mounted onto the SEM specimen stub using transparent adhesive tabs. They were coated with gold and palladium, for 3 min, using a Polaron (model-E511) sputter coater and examined under a JEOL-JSM840 SEM (JEOL, Tokyo, Japan) operated at 10 kV.

Assay of Ciprofloxacin—The HPLC method developed by Bauer et al. was extensively modified and used for the analysis of the drug.[13] The mobile phase consisted of a citrate buffer: acetonitrile:methanol mixture (85:10:5 v/v/v). The apparent pH of the mobile phase was adjusted to 2.4 with perchloric acid. The citrate buffer (pH 3.8) was prepared by mixing 64.6% (v/v) of 0.1 M citric acid to 35.4% (v/v) 0.2 M Na_2HPO_4 solution. The flow rate was maintained at 1.5 mL/min (Shimadzu LC-6A pump). A Spherisorb C18 pH stable column (Phase Separations, Norwalk, CT), 15 cm in length, was used, and the column effluents were monitored at 280 nm (Shimadzu SPD-6A UV detector, Shimadzu. Koyoto, Japan).

Microdialysis System—This system consisted of a Harvard-22 syringe pump, Hamilton gastight (3.26 mm diameter) 500 μL

* Corresponding author. Phone: (402) 280-3188. Fax: (402) 280-1883. e-mail: adash@creighton.edu.
† Creighton University.
‡ Present address: Abbott Laboratories, North Chicago, IL 60064.

10.1021/js980480g CCC: $18.00
Published on Web 09/03/1999

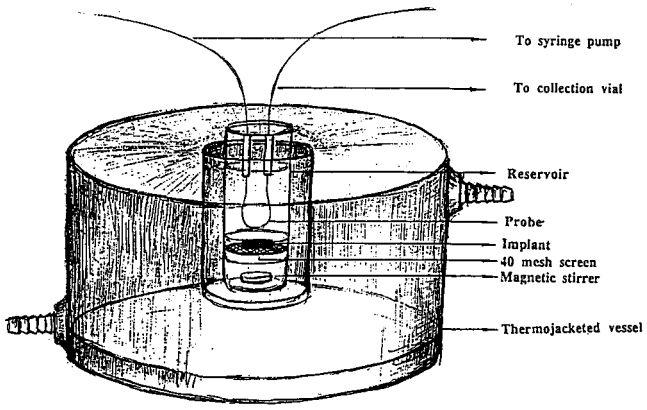

Figure 1—In vitro dissolution apparatus with microdialysis sampling technique designed in our laboratory for implantable drug delivery system.

syringes, and flexible microdialysis probes (made in house).[8] Flow-through loop-type probes were constructed using fused-silica tubing (Polymicro Technologies, Phoenix, AZ) with 75 μm i.d. and 150 μm o.d. Regenerated cellulose Spectro/Pro microdialysis hollow fibers (Spectrum Medical Industries, Los Angeles, CA) with a molecular weight cut-off of 1300 Da and 28−36 mm long were used as the dialysis membrane. The inner diameter of the dialysis fiber was 150 μm with a wall thickness of 9 μm. Probes were connected to the perfusion syringe with fused silica tubing. Initially, the probes were soaked and perfused with 80% (v/v) ethanol in water. Prior to experimentation, all of the probes were soaked and perfused with Sorensen's phosphate buffer (pH 7.4). These experiments were carried out at 37 °C with constant stirring (50 rpm) of the dissolution medium.

In Vitro Dissolution Apparatus with Microdialysis Sampling Technique—An in vitro dissolution apparatus which utilizes a microdialysis sample collection technique was developed in our laboratory and a schematic representation of the apparatus is depicted in Figure 1. The diameter of the reservoir was 15 mm, and its height was 45 mm. A 40 mesh screen was kept at a height of 5 mm from the bottom of the reservoir. The implantable delivery system was placed on the screen, and the microdialysis probe was placed at a fixed distance (10 mm) from the implant. Sorensen's phosphate buffer (pH 7.4) was used as the perfusate and the dissolution medium. The release medium was constantly stirred with the aid of a magnetic stirrer (50 rpm) placed at the bottom of the release medium as shown in Figure 1. The flow rate of the perfusate varied from 0.5 to 1 μL/min. At 25−40 min time intervals, the perfusate samples were collected directly into the HPLC autosampler injection vials with 200 μL inserts. To avoid evaporation, the vials were rapped with Parafilm. After the end of sample collection the Parafilm was immediately replaced with the cap containing the rubber septum. The concentration of the drug in the perfusate was determined using the HPLC method.

Microdialysis Probe Calibration—The in vitro calibration was performed at 37 °C in a Sorensen's phosphate buffer in a special thermojacketed Plexiglass microdialysis chamber containing 8.0 mg/L of ciprofloxacin. Probe recovery was measured before each experiment.

Factors Affecting the in Vitro Microdialysis Recovery—Probe flow rate was validated gravimetrically using preweighed collection vials. The effect of the flow rate and probe length on recovery of the drug during the microdialysis studies were evaluated.

Data Analysis—The in vitro recovery of the probes was calculated as the ratio of the ciprofloxacin concentration in the dialysate to that in the Sorensen's phosphate buffer in the reservoir vial, expressed as the peak height ratio (PHR) of drug to the internal standard (IS), represented by eq 1:

$$\text{recovery}_{\text{in vitro}} = \frac{C_{\text{dial}}}{C_{\text{res}}} = \frac{\text{PHR}_{\text{(drug/IS) dialysate}}}{\text{PHR}_{\text{(drug/IS) reservoir}}} \qquad \text{(eq 1)}$$

USP Dissolution Apparatus 3[14]—Sorensen's phosphate buffer pH 7.4 (150 mL) was used as the dissolution medium and equilibrated to 37 °C. The ciprofloxacin implant was then placed on the plastic wire mesh of the reciprocating tube and dipped at a rate of 20 dips per minute into the dissolution medium. At predetermined time intervals, 1 mL of the sample was collected and an equal volume of fresh phosphate buffer was replaced after each sample collection. The drug content in the release medium was determined by the HPLC method.

Results and Discussion

Formulation of the PLGA Implants Containing Ciprofloxacin—The drug is highly water soluble and has been reported to be stable in solution.[15] The pK_as of ciprofloxacin are 6 and 8.8 with a molecular weight of 385.8 (g/mol). These physicochemical properties indicate that the drug can easily pass through the microdialysis membranes used in this investigation and, therefore, be utilized as the model drug. Initial attempts to make the PLGA/PLA implants by direct compression of the physical mixture of the drug and polymer in a Carver press was unsuccessful. Therefore, the drug was first microencapsulated in the polymer and then compressed into cylindrical implants. The microstructure of the drug both before and after microencapsulation is shown in Figure 2. The scanning electron micrographs indicated that the free drug (Figure 2a) is crystalline and rod-shaped in nature, whereas the microcapsules (Figure 2b) are agglomerates with a different microstructure. Such a change in microstructure was essential for the direct compression of these polymers (PLA and PLGA) and the drug (ciprofloxacin) into implant. The detailed dimensions of the implants made and their composition are provided in Table 1.

HPLC Method Validation—Representative chromatograms of the internal standard (phenacetin), ciprofloxacin, and both the drug and internal standard are shown in Figure 3. No interfering peaks were observed in the chromatograms. The linearity, precision, accuracy, and sensitivity of the assay were determined as indicated below.

Linearity—The standard curves were linear over the concentration range of 0.0−9.5 mg L^{-1}. The equation of the standard curve relating the peak height ratio (P) to the ciprofloxacin hydrochloride concentration (C in mg l^{-1}) in this range was:

$$P = 0.27578C + 0.00147, \qquad r^2 > 0.999$$

Precision—Within-day precision was determined by analysis of four different standard curves on the same day. Day-to-day precision was determined from the standard curves prepared on each seven different days during 60 days. The precision of the assay was determined from the variability in the peak height ratio at each concentration. The RSD for the within-day and day-to-day precision were 0.6−2.6% and 1.9−4.3%, respectively, and are depicted in Table 2.

Accuracy—Known amounts of ciprofloxacin were added to the mobile phase to make the quality control samples. Three quality control samples and the standard solutions were kept at 4 °C for 60 days. These solutions were analyzed seven times during this period, and the accuracy of the assay was determined by comparing the measured concentration to its true value of the drug. The RSD for the accuracy measurement for this method was between 3.8 and 4.7% as shown in Table 3.

Sensitivity—The sensitivity criteria was determined from seven different standard curves using the lowest limit of reliable assay measurement guidelines described by Oppenheimer et al.[16] In this study, the critical level is defined as the assay response above which an observed response is reliably recognized as detectable. The critical level is also considered a threshold value, thus, defining

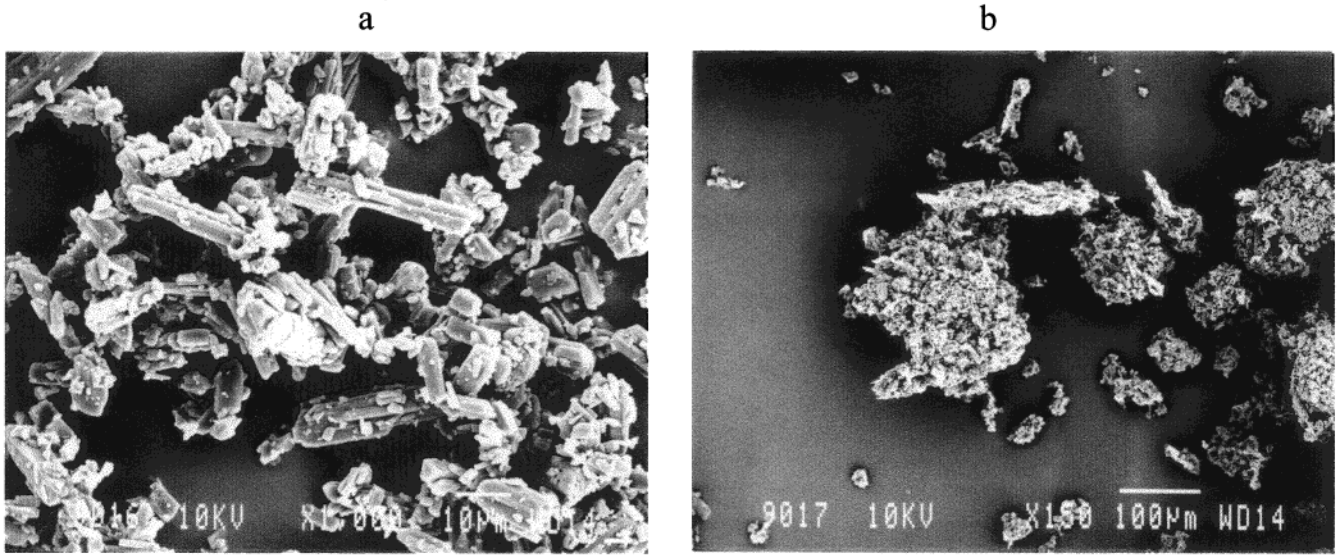

Figure 2—Scanning electron micrographs of (a) Ciprofloxacin powder, and (b) microencapsulated Ciprofloxacin in PLGA.

Table 1—Physical Dimensions and Drug Load of the Implants

implant ID	polymer used	weight of implant (mg)	height of the implant (mm)	diameter (mm)	actual[a] drug load, % (w/w)
A	PLGA	220.0	7.0	6.0	9.4
B		216.4	6.5	6.0	
C		216.7	6.6	6.0	
A	PLA	135.3	3.5	6.0	9.6
B		144.5	4.0	6.0	
C		144.3	4.0	6.0	
A	PLA	152.7	4.0	6.0	16.6
B		153.8	4.0	6.0	
C		154.1	4.0	6.0	

[a] Actual drug load represents the drug load determined by HPLC analysis.

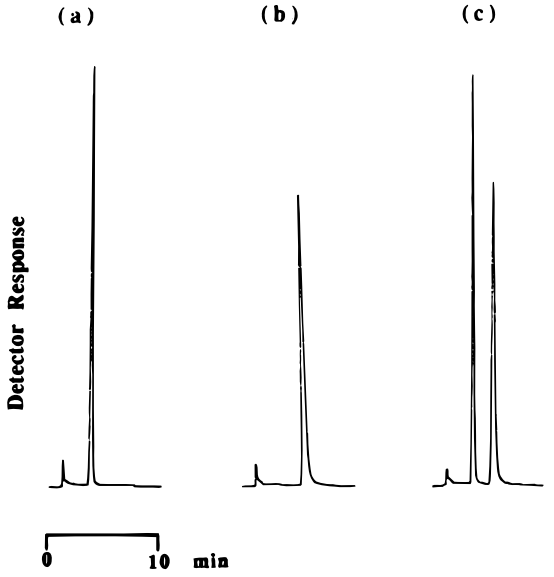

Figure 3—Representative chromatograms obtained following injection of (a) Phenacetin (21.3 mg L^{-1}), (b) Ciprofloxacin (3.9 mg L^{-1}), and (c) Phenacetin (21.3 mg L^{-1}), and Ciprofloxacin (3.9 mg L^{-1}).

detection. Therefore, if the measured response exceeds this value, the presence of an analyte is detected, otherwise, it is not reliably recognized as detectable. In this investigation, the critical value was determined as 0.034 ± 0.007 μg mL^{-1} (mean ± SD).

Table 2—Within-Day and Day-to-Day Analytical Precision of Ciprofloxacin Assay

	within-day[a]		day-to-day[b]	
concn (mg L^{-1})	peak height ratio[c]	RSD (%)	peak height ratio[d]	RSD (%)
0.00	0.000	–	0.000	–
0.19	0.046 ± 0.001	2.6	0.050 ± 0.002	4.3
1.90	0.545 ± 0.008	1.3	0.520 ± 0.010	1.9
2.85	0.734 ± 0.004	0.6	0.780 ± 0.030	3.8
5.7	1.511 ± 0.041	2.7	1.590 ± 0.030	1.9
7.6	1.987 ± 0.048	2.4	2.09 ± 0.070	3.3
9.5	2.579 ± 0.053	2.1	2.620 ± 0.080	3.1
slope	0.267 ± 0.0022	0.81	0.276 ± 0.0072	2.6

[a] Analyzed on the same day. [b] Analyzed on seven different days within a period of 60 days. [c] Mean ± SD; $n = 4$. [d] Mean ± SD; $n = 7$.

Table 3—Accuracy in the Analysis of Ciprofloxacin in Quality Control Samples

actual concentration (mg L^{-1})	accuracy[b]	RSD (%)
0.95	99.82 ± 4.7[a]	4.68
3.80	99.59 ± 3.8	3.78
6.65	100.75 ± 4.5	4.45

[a] Mean ± SD; $n = 7$. [b] Accuracy = (measured concentration/actual concentration) × 100.

In addition to the critical value, another important parameter is the detection level defined as the actual net response, which may, a priori, be expected to lead to detection. This response is defined as the smallest value of the true concentration that is "nearly sure" to produce a measurement value that results in detection.[17] The detection level in this analysis was found to be 0.069 ± 0.013 μg mL^{-1} (mean ± SD).

The determination level is defined as the concentration at which the measurement precision will be satisfactory for quantitative analysis. This level was determined as 0.191 ± 0.035 μg mL^{-1} (mean ± SD) to obtain a 10% RSD level of precision.

Microdialysis Probe Calibration—The recovery of the probes was determined prior to each in vitro release study. The effects of probe length and perfusion flow rate on the in vitro recovery of ciprofloxacin were then determined and shown in Table 4. As expected, decreasing the length of the probe decreased the in vitro recovery of the drug.

Table 4—Effect of Probe Length and Flow Rate on the in Vitro Recovery of Ciprofloxacin

probe length (mm)	flow rate (μL/min)	mean recovery ± SD[a] (%)	RSD (%)
36	0.75	83.47 ± 2.5	1.19
31	0.75	80.64 ± 1.6	1.98
29	0.75	77.42 ± 0.33	0.43
28	1.0	56.52 ± 2.23	3.95
28	0.75	73.64 ± 3.96	5.38
28	0.5	79.98 ± 4.90	6.12

[a] Mean ± SD; $n = 3$.

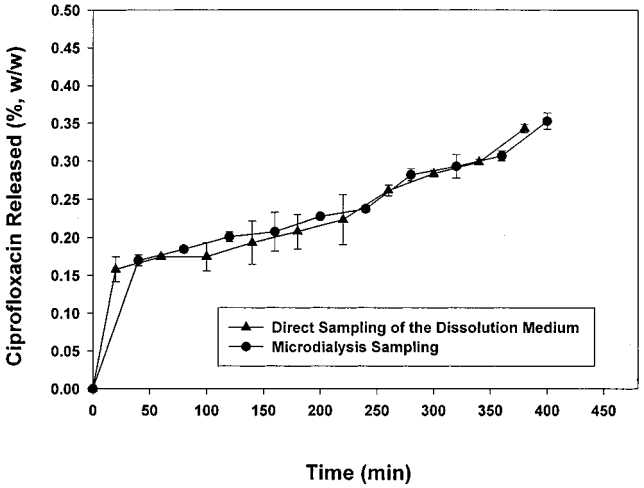

Figure 4—In vitro release profiles of Ciprofloxacin from PLGA implants (9.4% w/w drug load) determined by direct sampling of the dissolution medium and sampling by microdialysis.

However, the perfusate flow rate had an inverse relationship with the in vitro recovery of the drug. Through the analysis of the results of these studies, the optimal perfusate flow rate was determined to be 0.75 μL/min and the length of the microdialysis probe was kept within the range of 30−32 mm for the entire study. Probe flow rate was validated gravimetrically using preweighed collection vials. Within sample precision of the microdialysis sampling was determined in seven microdialysate samples collected using the same probe and same flow rate. The RSD for this precision determination was within 5%.

In Vitro Release of Ciprofloxacin from the Implants—The in vitro release of ciprofloxacin from these implants was then determined by two separate and independent methods. The drug was first analyzed using the method developed in our lab with microdialysis sampling technique and second by utilizing USP dissolution method 3.

Using the dissolution method developed in our lab, the ciprofloxacin concentration in the release medium was determined by two different sampling methods. At appropriate time intervals, 30 μL of the sample was collected directly from the dissolution medium and injected into the HPLC for assay of ciprofloxacin. Simultaneously, 30 μL of fresh phosphate buffer was replaced in the chamber. In the second sampling method, the microdialysis probes were used to monitor the concentration of the drug in the dialysis chamber. Before using the probes for monitoring the in vitro drug concentration, they were calibrated to determine their in vitro recovery. The perfusate (30 μL) was collected every 40 min at a flow rate of 0.75 μL/min, and the concentration of the drug in the microdialysate was determined by HPLC. The drug concentration in the dissolution medium was then calculated using the in vitro recovery of the probe. Figure 4 depicts the in vitro release profiles of

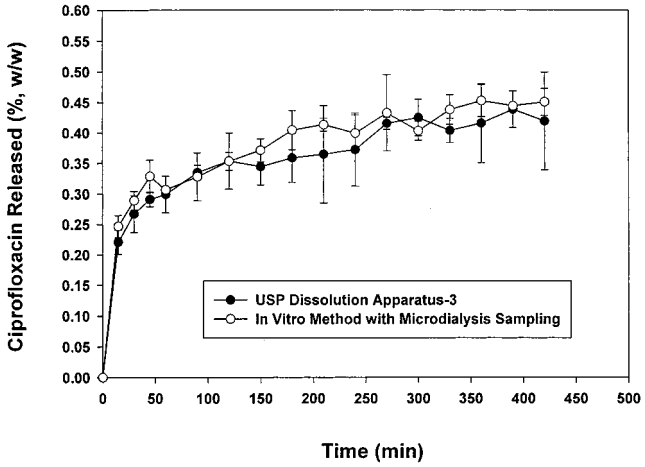

Figure 5—Comparison of the in vitro release profiles of Ciprofloxacin from PLGA implants (9.4% w/w drug load) determined by the use of microdialysis sampling method and the USP dissolution method 3.

Table 5—Comparison of the Extent of Ciprofloxacin Released in 6 h from Various Implants with Similar Drug Load. The in Vitro Release Profiles of PLGA Implants Are Only Shown in Figure 4 and Figure 5

implant type	microdialysis using direct sampling	microdialysis using microdialysis probe	USP apparatus 3
PLA	0.15 ± 0.003[a]	0.15 ± 0.004	0.17 ± 0.02
PLGA	0.40 ± 0.01	0.44 ± 0.05	0.41 ± 0.02

[a] Mean ± SD; $n = 3$.

the drug from a PLGA implant determined by the two sampling techniques. The method by which the samples were collected had no effect on the release profiles of the drug. Therefore, this study clearly indicated that this microdialysis sampling technique could be used to monitor the concentration of various drugs in the release medium if the determination of the in vitro recovery of the probe is correct.

The in vitro release characteristics of ciprofloxacin from the implants were then studied using the two independent methods. We selected the USP dissolution method 3 for the following reasons: (i) a low volume (150 mL) of release medium is required as compared to the 900 mL in the case of USP methods 1 and 2, (ii) low rate of evaporation of the release medium during dissolution studies over a prolonged period of time as compared to the USP methods 1 and 2, and (iii) in our laboratory, we have already compared and reported the in vitro release characteristics of other dosage forms using both USP apparatus 2 and 3 without any significant differences in their release profiles.[18] The in vitro release profiles of the drug from various implants containing similar drug loads were then obtained by both methods and are shown in Figure 5. The rate and extent of drug release determined by both of these methods were in close agreement. The burst effect shown during the in vitro release studies could arise due to the presence of free drug on the surface of the implants. This free drug might have originated during compaction of the microcapsules or due to the presence of uncoated drug in the formulation. Table 4 summarizes and compares the extent of ciprofloxacin released from various implants with similar drug loads in 6 h. This study indicated that the release of ciprofloxacin from the PLGA implants was higher than the PLA implants (release profiles not shown here). Moreover, the preparation of PLGA microcapsules was easier than the PLA microcapsules. The former microcapsules were compact, whereas the latter were fluffy and difficult to handle during compression. Comparison of the in vitro

release profiles of drug from the implants within a batch was found to be in close agreement and independent of the sampling (Figure 4) and dissolution methods (Figure 5) used. However, a slight difference in the release profiles was noticed between batches (Figure 4 and Figure 5) even though the drug load was kept constant in both the batches. This difference in the release profiles could possibly be attributed to batch-to-batch variations.

Conclusions

(1) A sensitive HPLC method was developed and validated for the analysis of ciprofloxacin.

(2) An in vitro dissolution method using a microdialysis sampling technique was developed and used to determine the release characteristics of ciprofloxacin from various implants.

(3) The proposed method has the following advantages: (i) it is simple, (ii) it requires a very small volume of dissolution medium, (iii) on-line analysis of the drug is possible, (iv) continuous monitoring of the drug over a prolonged period of time is possible, and (v) this method could be used to determine the local concentrations of the drug near the implant site.

(4) The rate and extent of ciprofloxacin release determined by both methods were in close agreement.

(5) In the future, this method could be used in evaluating the in vitro dissolution characteristics of potent drugs and dosage forms (microcapsules and microspheres of proteins and peptides) requiring a small volume dissolution medium.

References and Notes

1. *AAPS Newsletter;* American Association of Pharmaceutical Scientists: Alexandria, VA, February 1994; Vol. 9, pp 1−3.
2. Dash, A. K.; Suryanarayanan, R. An Implantable Dosage Form for the Treatment of Bone Infections. *Pharm. Res.* **1992**, *9*, 993−1002.
3. Ranade, V. J. Drug Delivery Systems 4. Implants in Drug Delivery. *Clin. Pharm.* **1990**, *30*, 871−889.
4. Dash, A. K.; Cudworth, G. C., II. Therapeutic Applications of Implantable Drug Delivery Systems. *J. Pharm. Tox. Methods* **1998**, *41*, 1−12.
5. Stahle, L. Microdialysis in Pharmacokinetics. *Eur. J. Drug. Metab. Pharmacok.* **1993**, *18*, 89−96.
6. Elmquist, W. F.; Sawchuk, R. J. Application of Microdialysis in Pharmacokinetic Studies. *Pharm. Res.* **1997**, *14*, 267−288.
7. Wang, Y.; Wong, S. L.; Sawchuk, R. J. Comparison of In Vitro and In Vivo Calibration of Microdialysis Probes Using Retrodialysis. *Curr. Sep.* **1991**, *10*, 87.
8. Herrera, A. M.; Scott, D. O.; Lunte, C. E. Microdialysis Sampling for Determination of Plasma Protein Binding of Drugs. *Pharm. Res.* **1990**, *7*, 1077−1081.
9. Yang, H.; Elmquist, W. F. The Binding of Cyclosporine A to Human Plasma: An In Vitro Microdialysis Study. *Pharm. Res.* **1996**, *13*, 622−627.
10. Knaub, S. R.; Chang, M. F.; Lunte, C. E.; Topp, E. M.; Riley, C. M. Automated Analytical Systems for Drug Development Studies. Part 4. Microdialysis System to Study the Partitioning of Lomefloxacin Across an Erythrocyte Membrane In Vitro. *J. Pharm. Biomed. Anal.* **1995**, *14*, 121−129.
11. Shah, K. P.; Chang, M.; Riley, C. M. Automated analytical Systems for Drug Development Studies. II. A System for Dissolution Testing. *J. Pharm. Biomed. Anal.* **1994**, *12*, 1519−1527.
12. Shah, K. P.; Chang, M.; Riley, C. M. Automated analytical Systems for Drug Development Studies. 3. Multi Vessel Dissolution Testing System Based on Microdialysis Sampling. *J. Pharm. Biomed. Anal.* **1995**, *13*, 1235−1245.
13. Bauer, J. F.; Elord, J.; Fornnarino, J. R.; Heathcoate, D. E.; Krough, S. K.; Linton, C. L.; Norris B. J.; Quick, J. E. Determination of Temafloxacin, Sarafloxacin, and Difloxacin in Bulk Drug and Dosage Forms by High-Performance Liquid Chromatography. *Pharm. Res.* **1990**, *7*, 1177−1180.
14. *The United States Pharmacopeia*, XXIII rev; United States Pharmacopeial Convention, Inc.: Rockville, MD, 1995; pp 1793−1795.
15. Ross, D.; Riley, C. M. Aqueous Solubilities of some Variously Substituted Quinolone Antimicrobials. *Int. J. Pharm.* **1990**, *63*, 237−250.
16. Oppenheimer L., Capizzi, T. P., Weppelman, R. M., Meheta. H. Dertermining the lowest limit of reliable assay measurement. *Anal. Chem.* **1983**, *55*, 638−643.
17. Kalman, S. M., Clark, D. R. and Moses, L. E. Limits of detection and quantification, as applied to an assay for digoxin. *Clin. Chem.* **1984**, *30*, 515−517.
18. Ichwan, A. M. and Dash, A. K. In vitro release of valproic acid from coated particles: Comparison of various dissolution methods. *Int. J. Pharm. Adv.* **1995**, *1*, 64−72.

Acknowledgments

The authors thank AAPS (APQ Section) for providing the Undergraduate Research Award to Mr. P. W. Haney. We would also like to thank Dr. W. F. Elmquist, College of Pharmacy, University of Nebraska Medical Center for his valuable suggestions and technical support during the microdialysis studies. The generous gift of Ciprofloxacin from Miles Pharmaceuticals is also greatly appreciated.

JS980480G

A Spin Filter Method for Continuous Evaluation of Hemolysis

FERNANDO ALVAREZ-NÚÑEZ,† DANIELLE A. ROSIN, AND SAMUEL H. YALKOWSKY*

Contribution from *Department of Pharmacy Practice and Science College of Pharmacy The University of Arizona Tucson, Arizona 85721.*

Received December 17, 1998. Final revised manuscript received June 8, 1999.
Accepted for publication July 9, 1999.

Abstract □ A novel method for quantifying hemolysis is described. This method uses a spin filter to separate the free hemoglobin from the red blood cells suspended in the test solution. This procedure enables the use of a closed loop system that continuously measures hemolysis spectrophotometrically. It is shown that hemolysis does not always stop after the solution has been quenched with normal saline. In fact, the process of hemolysis induced by chemicals such as potassium oleate is relatively slow.

1. Introduction

Hemolysis is defined as the destruction of red blood cells in such a manner that hemoglobin is liberated into the medium in which the cells are suspended.[1] Increases in free hemoglobin in the plasma resulting from hemolysis are associated with serious medical conditions such as renal dysfunction, splenomegaly, jaundice and kernicterus.[2]

In 1936, Wokes[3] defined the hemolyzing concentration of a solution as the concentration that will produce a supernatant liquid that is faintly pink after half of an hour of contact time with freshly shed normal human blood. This method for detecting hemolysis does not quantify the amount of hemolysis produced and is not sensitive enough to detect hemolysis that could not be seen by the naked eye. Husa and Adams[4] developed an in vitro method for evaluating hemolysis that became the standard parenteral screening method for many years. This method involves the incubation of red blood cells with a large excess of test solution. In this method the supernatant is measured for absorbance at 540 nm (the absorbance maximum for hemoglobin). The use of a spectrophotometer provides a sensitive method for quantifying the extent of hemolysis. Although the Husa and Adams method is generally quite useful, three main problems have been noted.[5] The first problem with this procedure is that the presence of nonaqueous solvents and metal ions produce changes in the absorbance spectrum of hemoglobin and therefore can give inaccurate results. The second problem with this method is that the formulation:blood ratio of 50 is unrealistically high for modeling intravenous injections. The third problem is that this method used a very long contact time (30 min) of formulation with blood before separation and analysis of hemoglobin. This contact time does not mimic the dilution that occurs naturally after injection of the formulation into the human vein.

In 1985, Reed and Yalkowsky[6] developed a more physiologically realistic model using a formulation:blood ratio of 0.1 and a 2-min contact time of blood with the test solution. However, this contact time is still too long to accurately model hemolysis that occurs after an intravenous injection.[2] Reed and Yalkowsky also addressed the issue of alterations in the absorbance spectrum of hemoglobin caused by the presence of nonaqueous solvents and metal ions that are sometimes present in parenteral injections by washing the red blood cells and ghosts that remained after mixing the test solution with blood. The intact red blood cells were then lysed with water, and the fraction of healthy cells was determined. This procedure, which is analogous to a back-titration, allowed all spectral analysis of hemoglobin to be performed in a purely aqueous medium.

Obeng and Cadwallader[7] were the first to develop a dynamic method that mimics hemolysis occurring in the body following an intravascular injection. Their method utilizes an in vitro flow system that provided a reasonable simulation of the mixing that occurs at the intravenous injection site, taking into consideration tubing diameter, blood flow rate, injection volume, and injection time. In this method, Obeng and Cadwallader injected the formulation into a flowing stream of red blood cells. Then the formulation and blood mixture entered a large volume of saline, which was assumed to quench the hemolytic reaction. The saline mixture was then centrifuged and the supernatant was analyzed with spectrophotometer. Although this method is capable of measuring the effect of contact time, this was not done to any significant extent. Krzyzaniak and coworkers[8] developed a dynamic in vitro method that is able to quantify hemolysis at short contact times (1 s) with a formulation:blood ratio of 0.1. This contact time of 1 s provides a more physiologically realistic model of the injection site.

Both the Reed and Yalkowsky and the Obeng and Cadwallader methods assume that quenching the test solution with saline stops the hemolytic reaction. However, some red blood cells that are slightly damaged could still break some time after the solution has been quenched. This reaction could not be detected by the previous methods because all other methods quantify hemolysis at one point of time after the reaction has been quenched. Another problem with all previous methods is that they determine the degree of hemolysis at a relatively long time after quenching because of a lengthy centrifugation step. They cannot be used to evaluate the very early reaction between red blood cells and the test solution.

The aim of this investigation is to develop a method for quantifying hemolysis that is physiologically realistic and that is able to evaluate the very early reaction between red blood cells and the test solution.

2. Materials and Methods

2.1 Materials—The blood used in this investigation was obtained from the American Red Cross (Tucson, AZ). Sodium lauryl sulfate, (SLS), poly(ethylene glycol) 400 (PEG 400), propylene glycol (PG), and sodium chloride were purchased from Sigma Chemical Company. Tween 80, glycerine, potassium oleate, and

* To whom all correspondence should be sent. Telephone: 520-626 1289. Fax: 520-626 4063. E-mail: yalkowsky@pharmacy.arizona.edu.
† Present address: Market Image, Pharmaceutical Delivery Systems, Parke-Davis, 170 Tabor Rd., Morris Plains, NJ 07950.

10.1021/js980484l CCC: $18.00 Published on Web 09/03/1999

Table 1—Tested Compounds and Their Concentrations

compound	concentration (% w/v in normal saline
potassium oleate	1
sodium lauryl sulfate (SLS)	1
polysorbate 80 (Tween 80)	12
polyethylene glycol 400 (PEG 400)	50
propylene glycol (PG)	50
glycerine	50

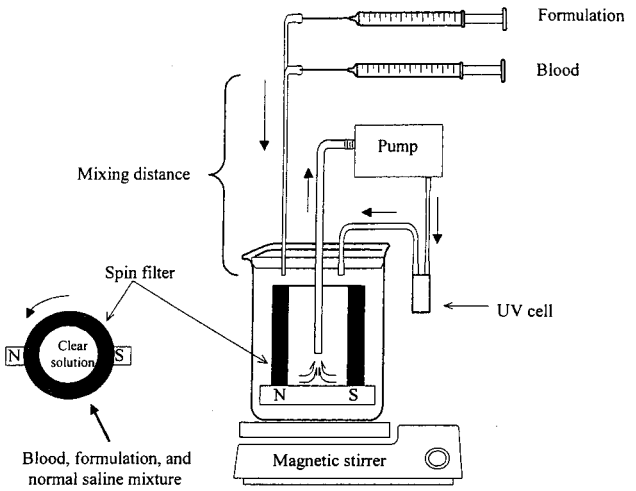

Figure 1—The spin filter apparatus for evaluating hemolysis.

red food color (red dye) were purchased from Biotech, Mallinckrodt, TCI America, and McCormick & Company Inc., respectively. All chemicals were used as received. These compounds were chosen because they are commonly used in pharmaceutical formulations. Each of these were admixed with normal saline to the concentration listed in Table 1.

2.2 Methods—*2.2.1. Spin Filter Method*—Figure 1 illustrates the experimental apparatus. Whole blood was washed three times with normal saline to remove the damaged red blood cells, buffy coat, and free hemoglobin. The washed red blood cells were reconstituted to a 40% hematocrit with Sorensen phosphate buffer (pH 7.4). The intact red blood cells were then pumped through Tygon tubing (1/32 in. i. d.) with a syringe pump. The vehicles were injected into the blood flow with the aid of syringe pump. The formulation-blood mixture at the ratio of 0.1 remained in contact for one second. These formulation:blood ratio and contact time were obtained by a blood flow rate of 6 mL/min, a formulation flow rate of 0.6 mL/min, and a mixing distance of 5 cm in the approximately 1 mm i. d. tubing. The mixture then was diluted with a large amount of normal saline. The normal saline containing the formulation:blood mixture was continuously sampled with a centrifugal filtering system (0.3 μm Whatman, Gamma-12 high efficiency in-line units) as described by Shah.[9] The spin filter allows only the contents of lysed red blood cells mixed with normal saline to enter the spectrophotometer. The spin filter, which rotates at a speed of ~142 rpm, throws off by centrifugal force erythrocytes, ghosts, and other matter that would clog a stationary filter. Using this spin filter apparatus, the supernatant and the cells are rapidly separated without centrifugation. The filtered solution was then allowed to circulate through the spin filter until the hemolytic reaction has terminated. Red dye was used to determine the lag-time in this method. A pump was used to circulate the solution through the spin filter and flow cell in the spectrophotometer. Hemolysis was then calculated with the following formula:

$$\%\text{Hemolysis} = \frac{A_F - A_0}{A_{100} - A_0} \times 100 \qquad (1)$$

where A_F = absorbance of hemoglobin in the filtered solution after injecting test solution, A_0 = absorbance of hemoglobin in the filtered solution after injecting normal saline, and A_{100} = absorbance of hemoglobin in the filtered solution after total cell lysis with water. Because the filtered solution is continuously sampled, a percent hemolysis versus time profile is generated. This profile describes both the extent of hemolysis and the time frame of the hemolytic reaction.

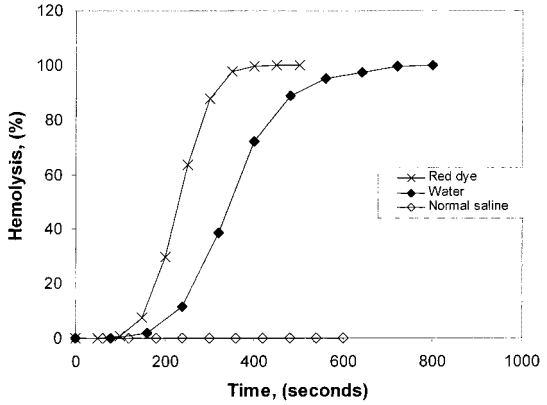

Figure 2—Percent hemolysis versus time profile for the blanks used on the spin filter method; that is, normal saline and water. The Y axis for red dye was obtained considering its absorbance at the plateau as 100% hemolysis and eq 1.

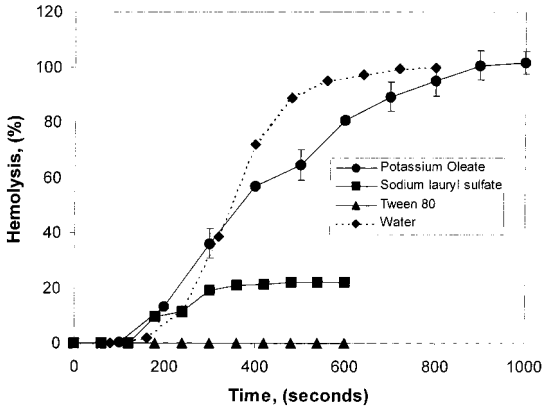

Figure 3—Hemolysis induced by surfactants.

3. Results

Figure 2 shows the percent hemolysis versus time profile for normal saline and water. The Y axis data for the red dye were obtained by the normalization of the absorbance data at 540 nm with the absorbance at t_{100} (A_{100} or absorbance at the plateau) and eq 1. All samples were run in triplicate at room temperature.

The six pharmaceutical vehicles were divided into two categories, surfactants and cosolvents. The first category includes SLS, potassium oleate, and Tween 80. The second category includes PG, PEG 400, and glycerine. The percent hemolysis produced by each vehicle at each time point was measured three times and their mean and standard deviation was determined. A cumulative graph of the percent hemolysis versus time for the surfactants and cosolvents are presented in Figures 3 and 4, respectively.

4. Discussion

Red dye data (Figure 2) indicate that the spin filter method has a lag-time of ~100 s. This figure also shows 0% hemolysis at 600 s for normal saline, indicating that red blood cells are not destroyed during the experiment. Interestingly, this figure shows that the hemolysis produced by water is a time-dependent process. The time to reach 100% hemolysis is ~700 s (almost 2 min longer that

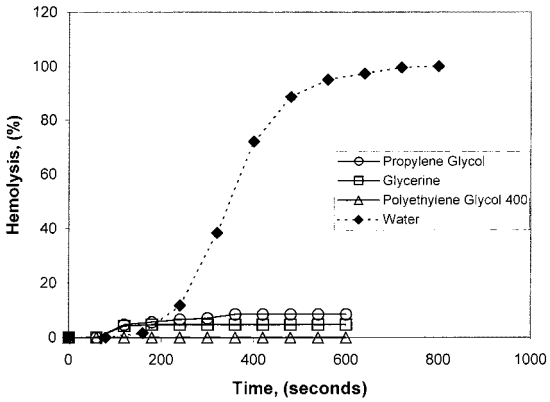

Figure 4—Hemolysis induced by cosolvents.

the red dye). These data indicate that hemolysis is not stopped instantaneously by quenching, and that the spin filter method is able to measure both the extent of hemolysis and the time required for the hemolysis process to occur.

Figures 3 and 4 show that the hemolytic reactions for the cosolvents PG and glycerine are less complete and more rapid than the reactions produced by the surfactants potassium oleate and SLS, at the tested concentrations. Also, these figures indicate that the cosolvent PEG 400 and the surfactant Tween 80 are not hemolytic, at the tested concentrations, which is consistent with the results of previous investigations.[2,10]

Figure 3 shows that the hemolytic reaction produced by potassium oleate is slower than the reaction produced by water. Potassium oleate takes longer to produce complete hemolysis than does water. However, Figure 3 shows that potassium oleate is as hemolytic as water at longer times. In addition, Figure 3 shows that although SLS is less hemolytic than water, it reaches its maximum value in less time than does water.

5. Conclusions

Unlike other methods, the spin filter method for evaluating hemolysis provides a means of assessing hemolysis that occurs after quenching. If it is assumed that the mixture of the blood from an injected vein with blood from other parts of the body is equivalent to quenching of hemolysis, then the spin filter method provides a more realistic simulation of the process of hemolysis, as it would occur in the body following an intravascular injection, than other methods. This method is able to determine not only the extent of hemolysis but also the estimated time frame of the reaction.

References and Notes

1. *Stedman's Medical Dictionary*, 26th ed.; Spraycar M., Ed.; Williams & Wilkins: Baltimore, MD; 1995; p 780.
2. Krzyzaniak, J. F.; Raymond D. M.; Yalkowsky, S. H. Lysis of human red blood cells 2: Effect of contact time on cosolvent induced hemolysis. *Int. J. Pharm*. **1997**, *152*, 193−200.
3. Wokes, F. Isotonic solutions for injection. *Quart. J. Pharm. Pharmacol.* **1986**, *9*, 455−459.
4. Husa, W.; Adams, J. R. Isotonic solutions. II. The permeability of red corpuscles to various substances. *J. Am. Pharm. Assoc.* **1944**, *33*, 329−332.
5. Ward, G. H.; Yalkowsky, S. H. The role of the effective concentration in interpreting hemolysis data. *J. Parenteral Sci. Technol*. **1992**, *46*, 161−162.
6. Reed, K. W.; Yalkowsky, S. H. Lysis of human red blood cells in the presence of various cosolvents. *J. Parenteral Sci. Technol*. **1985**, *39*, 64−68.
7. Obeng, E. K.; Cadwallader, D. E. In vitro dynamic method for evaluating the hemolytic potential of intavenous solutions. *J. Parenteral Sci. Technol*. **1989**, *43*, 167−172.
8. Krzyzaniak, J. F.; Raymond, D. M.; Yalkowsky, S. H. Lysis of human red blood cells 1: Effect of contact time on water induced hemolysis. *PDA J. Pharm. Sci. Technol*. **1996**, *50*, 223−226.
9. Shah, A. C.; Peot, C. B.; Ochs, J. F. Design and evaluation of a rotating filter-stationary basket in vitro dissolution test apparatus I: Fixed fluid volume system. *J. Pharm. Sci.* **1973**, *62*, 671−676.
10. Krzyzaniak, J. F.; Yalkowsky, S. H. Lysis of Human Red Blood Cells 3: Effect of Contact Time on Surfactant-Induced Hemolysis. *PDA J. Pharm. Sci. Technol.* **1998**, *52*, 66−69.

Acknowledgments

We thank The Pharmaceutical Research and Manufactures of America Foundation (PhRMA) for their generous support through the 1997 Undergraduate Research Fellowship. The work of Ms. Mi Jin Kim is appreciated. Also, we thank CONACYT and UNAM of México.

JS980484L

Pore Charge Distribution Considerations in Human Epidermal Membrane Electroosmosis

S. KEVIN LI,* ABDEL-HALIM GHANEM, AND WILLIAM I. HIGUCHI

Contribution from *301 Skaggs Hall, Department of Pharmaceutics and Pharmaceutical Chemistry, University of Utah, Salt Lake City, Utah 84112.*

Received November 10, 1998. Accepted for publication July 13, 1999.

Abstract □ The aim of this study was to assess the extent to which a model with pores having only net negative charges would adequately describe transdermal electroosmosis in human epidermal membrane (HEM) at neutral pH. Such information would enhance the predictive value of the modified Nernst–Planck model for transdermal iontophoresis, in addition to providing insights regarding the likelihood of significant pore charge distribution in HEM. Baseline results (the control) obtained from 0.1 to 0.4 V anodal and cathodal electroosmosis experiments with synthetic polycarbonate membranes (Nuclepore membranes), using radiolabeled urea and mannitol as the model permeants, demonstrated that such a membrane system can be modeled by the electrokinetic (electroosmosis) theory with the assumption of the pores possessing only negative charges. The studies with HEM were carried out at low voltage ($\leq$0.5 V) where alterations in the barrier properties of HEM were minimal and at higher voltages ($\gtrsim$1.0 V) where significant field-induced pore formation in HEM occurred. In both the low and high voltage studies, radiolabeled urea, mannitol, and water were employed as permeants in cathodal and anodal iontophoresis experiments. The results of the low voltage iontophoresis experiments suggest significant pore charge distribution in HEM (a significant deviation between the predictions from the single pore charge type assumption and the experimental data). Under the higher applied voltage conditions ($\gtrsim$1.0 V), results from anodal and cathodal electroosmosis studies were consistent with the model in which the HEM has only pores that are net negatively charged.

Introduction

There has been important progress in our understanding of the mechanisms of transdermal iontophoresis with human epidermal membrane (HEM). The modified Nernst–Planck model (Nernst–Planck equation with corrections for convective solvent flow due to electroosmosis) has been tested with HEM under low voltage iontophoresis conditions,[1,2] and semiquantitative agreement between the experimental results and predictions from the model has been generally observed. In other studies with HEM, the effective sizes of the pores involved in passive permeation and of the pores induced during low to moderate voltage iontophoresis have been deduced from the hindered transport theory and found to be in the range of ~6 to 25 Å.[3,4] More recently, a method based on square-wave alternating current (ac) iontophoresis was developed to study the induction of pores (electroporation) in HEM during iontophoresis at low to moderate voltages without interference from electroosmosis.[5] With this method, direct evidence of new pore induction as an iontophoretic flux enhancing mechanism was presented, and the effective pore sizes of the induced pores were assessed.

* To whom corespondent should be addressed. E-mail: kevin.li@m.cc.utah.edu.

As part of an effort to establish a more comprehensive understanding of the mechanisms of iontophoresis in HEM and to maximize the predictive value of the modified Nernst–Planck model, some independent quantitative assessment of electroosmosis in HEM is necessary. Burnette and Ongpipattanakul[6] previously examined the permselectivity of human cadaver skin at current densities of ~0.08–0.2 mA/cm^2 and showed that skin has an apparent net negative charge at neutral pH. Later studies by Pikal and by Pikal and Shah[7–9] on iontophoretic transport across hairless mouse skin at current densities $\gtrsim$0.3 mA/cm^2 have suggested that negatively charged pores dominate at neutral pH, but the presence of positively charged and neutral pores was also hypothesized. In these hairless mouse skin studies, pore size, pore charge, and their distributions were estimated with a theoretical model using experimental iontophoretic fluxes and electrical resistance measurements made as a function of pH, NaCl concentration, and current density. In an HEM study conducted in our laboratory,[10] the direction of the net electroosmotic convective solvent flow at neutral pH was anode-to-cathode; this direction is consistent with the HEM pores being net negatively charged. However, we have not previously examined the question of the importance of possible positively charged and/or neutral pores in HEM electroosmosis.

The aim of the present study was to examine the extent to which HEM electroosmosis data obtained at neutral pH could be described/predicted by the presence of only negatively charged pores (i.e., that convective solvent flow in the pores would be only in the anode-to-cathode direction). Electroosmotic flux enhancements of urea and mannitol in both anodal and cathodal iontophoresis and iontophoretic water fluxes were determined under different applied voltage conditions (in pH 7.4 and 0.1 M ionic strength phosphate buffered saline) for model analysis. These results were compared with theory predictions assuming a single pore charge (negative), and an assessment was made as to the need to involve positively charged and/or neutral pores in interpreting HEM electroosmosis data. A point of particular interest in this study is the comparison of results obtained with pores newly induced in HEM (induced by applied electric fields) with those from the preexisting pores.

Experimental Section

Materials—[^{14}C]Urea, [^{3}H]mannitol, and [^{3}H]water were obtained from New England Nuclear (Boston, MA) and American Radiolabeled Chemicals (St. Louis, MO). Human epidermal membrane (HEM) was provided by TheraTech, Inc. (Salt Lake City, UT). The epidermal membrane was prepared by heat separation as previously described[10] and immediately frozen for later use. Millipore GVWP filters (0.22 μm pore diameter) were obtained from Millipore Corp. (Bedford, MA). Nuclepore polycarbonate membranes with a nominal pore radius of 7.5 nm and porosity of

10.1021/js980442x CCC: $18.00
Published on Web 09/16/1999

0.001 were purchased from Costar Scientific Corporation (Pleasanton, CA). Phosphate-buffered saline with 0.02% sodium azide (PBS), ionic strength 0.1 M and pH 7.4 (0.077 M NaCl and 0.0074 M phosphate buffer), was prepared from reagent grade chemicals and distilled deionized water.

Theory and Model Analysis—The steady-state iontophoretic flux ($J_{\Delta\psi}$) of a nonionic permeant across a homogeneous porous membrane can be described by the modified Nernst−Planck model:[3]

$$J_{\Delta\psi} = \epsilon\left(-HD\frac{dC}{dx} + W'vC\right) \quad (1)$$

where v is the average velocity of the convective solvent flow (positive v denotes flow from donor to receiver and negative v denotes flow from receiver to donor), ϵ is the combined porosity and tortuosity factor for the membrane; C, x, and D are the concentration, the position in the membrane, and the diffusion coefficient of the permeant, respectively; and H and W' are the hindered transport factors for passive diffusion and for transport due to electroosmosis, respectively. Assuming a single pore size (radius, R_p) and a cylindrical pore geometry in the membrane and when the ratio of solute radius to pore radius (r/R_p) is small (i.e., $r/R_p < 0.4$), the hindrance factor for Brownian diffusion (H) and the hindrance factor for pressure-induced parabolic convective solvent flow (W) can be expressed by:[11]

$$H = (1-\lambda)^2(1 - 2.104\lambda + 2.09\lambda^3 - 0.948\lambda^5) \quad (2)$$

$$W = (1-\lambda)^2(2 - (1-\lambda)^2)(1 - 0.667\lambda^2 - 0.163\lambda^3) \quad (3)$$

where $\lambda = r/R_p$. For convenience, W' is assumed to be equal to W as discussed previously.[3] The diffusion coefficients and Stokes−Einstein radii of the permeants in the present study were taken from literature.[4,12] Integrating eq 1 results in

$$J_{\Delta\psi} = \frac{C_D\epsilon Wv}{1 - \exp[-Wv(\Delta x)/(HD)]} \quad (4)$$

where C_D is the donor concentration and Δx is the effective thickness of the membrane. At the convection limit (electroosmotic transport ≫ passive diffusion), eq 4 reduces to

$$J_{\Delta\psi} = \epsilon WvC_D \quad (5)$$

The total flux enhancement (E_{total}) is defined as the ratio of iontophoretic flux to the passive flux at the same donor concentration:

$$E_{total} = \frac{J_{\Delta\psi}}{J_{passive}} \quad (6)$$

where

$$J_{passive} = \frac{DC_D\epsilon H}{\Delta x} \quad (7)$$

Under an applied potential of ≳1 V, when the electrical resistance of HEM decreases due to pore induction, the total transport enhancement can be expressed by eq 8:

$$E_{total} = E_{\Delta R}E_v \quad (8)$$

where $E_{\Delta R}$ is the enhancement due to pore induction and is defined as the ratio of the porosity-tortuosity factor in iontophoretic transport to the porosity-tortuosity factor in passive transport:

$$E_{\Delta R} = \frac{\epsilon_{ion}}{\epsilon_{pass}} \quad (9)$$

E_v is the transport enhancement due to electroosmosis as described by

$$E_v = \frac{Pe}{1 - \exp\{-Pe\}} \quad (10)$$

where Pe is the Peclet number, which characterizes the contribution of convective transport due to electroosmosis. Pe is expressed as

$$Pe = \frac{Wv\Delta x}{HD} \quad (11)$$

Previous studies[5,13] have demonstrated a proportional relationship between the HEM electrical conductance and HEM permeability under the iontophoresis conditions of a few volts when the sizes of the conducting ions in the solution are comparable to those of the permeants. Thus, the $E_{\Delta R}$ values will be estimated from changes in HEM conductance during iontophoresis in the present study. For the Nuclepore membranes, $E_{\Delta R}$ is equal to unity, and E_{total} equals E_v. Effective pore radii for HEM during iontophoresis and in passive diffusion experiments will be estimated by the flux ratios of the model permeants as described previously,[2−5] with the assumption that the permeant pairs follow the same polar transport pathway in a given run.

In the present study, eq 10 will be used with experimental data obtained from both the anodal and cathodal configurations. The analysis should provide an assessment of the extent to which the model with only negatively charged pores may hold.

Transport Experiments: General Procedure—Transport experiments with HEM and with Nuclepore membranes were conducted using a side-by-side diffusion cell (with a diffusional area of ~0.75 cm^2 and cell volume of 2 or 4 mL) and a four-electrode potentiostat system (JAS Instrument Systems, Inc., Salt Lake City, UT) with Ag-AgCl counter electrodes as described previously.[3] Square-wave ac iontophoresis experiments were carried out with a waveform programmer (JJ 1276, JAS Instrument Systems, Inc., Belmont, NC) with the four-electrode potentiostat setup just described. The electrical resistance of the membranes was calculated with Ohm's law and the current was measured by the potentiostat system in direct current (dc) iontophoresis experiments or with an oscilloscope (Model 2211, Tektronix Inc., Beaverton, OR) in the ac experiments. Transport runs were conducted at 37 °C, which was maintained with a circulation water bath. Before each run, the receiver and donor chambers were filled with PBS and PBS premixed with appropriate amounts (tracer levels) of radiolabeled permeants, respectively. Urea/mannitol and urea/water were the permeant pairs employed. At predetermined time intervals, a 1-mL sample was withdrawn from the receiver chamber and replaced with fresh PBS. At the same time, a 10 μL sample was taken from the donor. The samples were then mixed with 10 mL of scintillation cocktail (Ultima Gold, Packard, Meriden, CT) and assayed in a liquid scintillation counter (1900 TR Liquid Scintillation Analyzer, Packard, Meriden, CT). The permeability coefficients for iontophoretic transport ($P_{\Delta\psi}$) and for passive transport ($P_{passive}$) were calculated by

$$P_{\Delta\psi} \text{ or } P_{passive} = \frac{1}{AC_D}\frac{dQ}{dt} \quad (12)$$

where A is the membrane surface area, t is time, Q is the cumulative amount of permeant transported into the receiver chamber, and

$$P_{\Delta\psi} = J_{\Delta\psi}/C_D \quad (13)$$

$$P_{passive} = J_{passive}/C_D \quad (14)$$

Experiments with Nuclepore Membranes—Nuclepore membranes were presoaked and sonicated in PBS to remove any entrapped air in the membranes. Then, 50 of the membranes were assembled into a single composite membrane in the diffusion cell. The Nuclepore membrane studies were divided into two stages: passive permeation experiments and iontophoresis experiments. Anodal and cathodal iontophoresis experiments were conducted at 0.1, 0.2, 0.4, and/or 0.75 V dc. Passive permeation runs were carried out before and after each iontophoresis run. The same sets of Nuclepore membranes (from the same lot) were used without disassembling to avoid variabilities arising from membrane-to-membrane variations.

Experiments with HEM—HEM was equilibrated in PBS for 12 to 24 h at 37 °C before starting a transport experiment. The

initial electrical resistances were 41 ± 26 kΩ cm^2, average ± SD, $n = 50$. HEM studies were divided into two parts: Studies I and II.

Study I was a baseline study with low applied voltage iontophoresis (0.25 and/or 0.5 V dc) where alterations in the barrier properties of HEM were minimal (generally within 15% of the original HEM electrical resistance). Experiments in Study I were divided into five stages. With each HEM sample, passive permeability coefficients were determined in Stages I, III, and V. Stage II was an iontophoresis run at an applied potential of 0.25 or 0.5 V dc. In Stage IV, the iontophoresis run was carried out with the same applied voltage as in Stage II but with the opposite electrode polarity. Anodal iontophoresis was conducted first (Stage II) with about half of the HEM samples and cathodal iontophoresis was first with the other half.

Study II involved higher applied voltage conditions where significant pore induction occurred in HEM. The initial experimental design in this study was a 4.0 V dc prepulse for 1 min followed by 1.0, 2.0, or 3.0 V dc exposure during which transport experiments were conducted. The 1-min 4.0 V dc prepulse preceding the 1.0, 2.0, or 3.0 V dc iontophoresis run was an attempt (with only variable success) to enhance the extent of pore induction and to minimize differences in the pore conditions between the anodal and cathodal runs. With this experimental protocol, cathodal iontophoresis generally induced a greater extent of pore induction than anodal iontophoresis at the same applied voltage and duration (>3 times in some cases; data not shown). Also, the $E_{\Delta R}$ values in some experiments were <10, suggesting a >10% contribution from preexisting pores to transport in these experiments. Thus, this initial protocol was problematic as we desired simultaneously (a) to compare the anodal and cathodal electroosmotic fluxes under conditions of comparable electroporation and (b) not to have significant flux contributions from preexisting pores compromising data analysis. A new protocol was introduced at this point that was designed to overcome or minimize these problems. This protocol involved superimposing 12.5 Hz square-wave ac onto cathodal or anodal dc iontophoresis with the aim to maintain comparable HEM electrical conductance (pore induction) during the anodal and cathodal electroosmosis runs and to achieve a high extent of pore induction ($E_{\Delta R} > 10$). In this arrangement, 0.5, 1.0 or 2.0 V dc was employed as the driving force for electroosmosis, and the 12.5 Hz square-wave ac with adjustable voltage between 0 and 3 V was used to manually control the extent of pore induction ($E_{\Delta R}$). The outcome of this arrangement was that there was always a >10-fold increase in HEM electrical conductance during iontophoresis (relative to the initial conductance) and a <30% variation in conductance during the combined anodal and cathodal iontophoresis runs. The particular ac frequency of 12.5 Hz was chosen only because of our previous experience with it in the dc/ac superposition iontophoresis.[5]

The experiments of Study II with this new protocol were divided into four stages. Similar to Study I, Stage I was a passive permeation run before the application of the electric field. Stage II was the iontophoresis run superimposing 12.5 Hz square-wave ac (0−3 V) with 0.5, 1.0, or 2.0 V dc for electroosmosis. Stage II was followed by rinsing the receiver chamber two to three times with fresh PBS. In Stage III, the same protocol of superimposing ac and dc was carried out as in Stage II but with opposite electrode polarity. HEM electrical resistance in Stages II and III was regulated by adjusting the ac voltage to obtain a >10-fold increase in electrical conductance (relative to the initial resistance in Stage I) and a <30% variation in resistance throughout the anodal and cathodal iontophoresis runs (Stages II and III). Stage IV was a passive diffusion run after iontophoresis.

Results and Discussion

Analysis of the Urea/Mannitol Dual-Permeant Data—Figure 1 presents the experimental results with the Nuclepore membrane, where the enhancement factor (E_v) for cathodal iontophoresis is plotted against that for anodal iontophoresis. The predictions from the electroosmosis theory (eq 10) with the assumption of a single pore charge are given by the curved line. It is evident that transport data obtained in the experiments with the Nuclepore membrane are consistent with the ideal, single pore charge

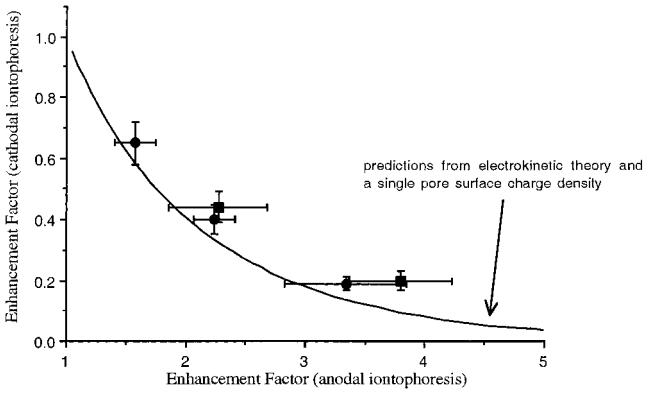

Figure 1—Relationship between cathodal and anodal electroosmotic flux enhancement for Nuclepore membranes at 0.1, 0.2, and 0.4 V dc. The curve represents predictions from electrokinetic theory with the assumption of a single pore surface charge density: E_v for anodal transport is plotted against E_v for cathodal transport (eq 10). Key: (circles) urea; (squares) mannitol. Each data point represents the mean and standard deviation of $n \geq 3$.

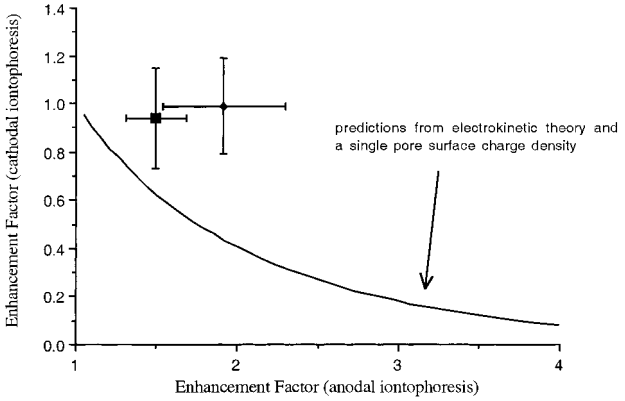

Figure 2—Relationship between cathodal and anodal electroosmotic flux enhancement for urea with HEM at 0.25 and 0.5 V dc. The curve represents predictions from electrokinetic theory with the assumption of a single pore surface charge density. Key: (square) 0.25 V; (diamond) 0.5 V. Each data point represents the mean and 90% confidence interval ($n = 6$).

theory. This result validates the theory and demonstrates that the Nuclepore membrane (a synthetic hydrophilic, poly(vinylpyrrolidone)-coated, polycarbonate membrane) can be modeled accordingly.

Figure 2 presents the low voltage (0.25 and 0.5 V dc) results with HEM (Study I) for urea. The changes in HEM electrical resistance in these low voltage experiments were generally <15% relative to the initial resistance before the iontophoresis runs; thus, these results may be interpreted as being essentially for the preexisting pores of HEM. Significant deviations can be noted between the predictions from electrokinetic theory with a single pore charge type assumption (the curve) and the experimental data with HEM (diamonds and squares). These deviations between the actual transport behavior of HEM and the theory predictions (in the positive direction from the theory) demonstrate that the preexisting pores of HEM, although predominantly negatively charged, may include some positively charged and/or some neutral pores.

Figure 3 summarizes the results of Study II where significant pore induction was involved and when the ac/dc superimposition protocols (0.5, 1.0, and 2.0 V dc plus ac) were employed to control the extent of pore induction ($E_{\Delta R}$) during electroosmosis transport experiments. In Figure 3, the enhancement factors due to electroosmosis (E_v) for urea were calculated from eq 8. An important outcome here is that the experimental results are consistent with theoretical predictions based on a single pore

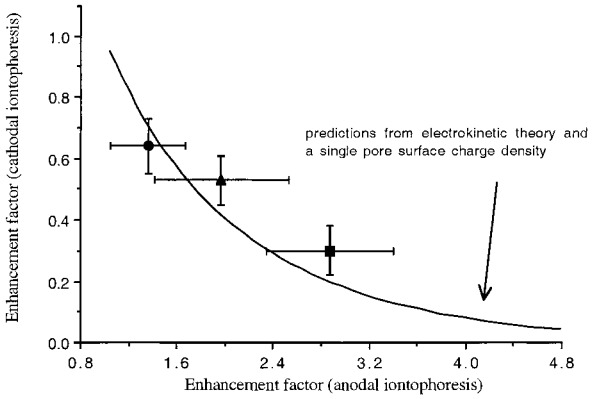

Figure 3—Relationship between transport enhancement due to cathodal and anodal electroosmosis for urea with HEM in 12.5 Hz square-wave ac and dc superposition iontophoresis experiments (Study II). The curve represents predictions from electrokinetic theory with the assumption of a single pore surface charge density. Key: (circle) 0.5 V dc plus 1–3 V ac; (triangle) 1.0 V dc plus 0–3 V ac; (square) 2.0 V dc plus 0–3 V ac. Each data point represents the mean and 90% confidence interval ($n = 7$).

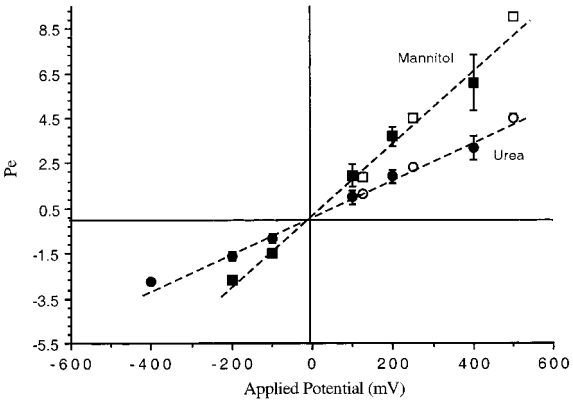

Figure 4—Relationship between the apparent *Pe* and the applied voltage for Nuclepore membranes. Key for closed (present study) and open (data from Peck et al.[2]): (circles) urea; (squares) mannitol. Each data point represents the mean and standard deviation of $n \geq 3$.

(charge) model, suggesting that newly induced pores are essentially all net negatively charged. Although preexisting positive and/or neutral pores may have still been present, the high $E_{\Delta R}$ values in these higher voltage experiments likely reduced their importance during 0.5, 1.0, and 2.0 V electroosmosis to a very small or negligible level.

Figures 4 and 5 present the relationships between the apparent *Pe* and the applied voltage obtained with the Nuclepore membrane and with HEM, respectively. The *Pe* values in Figure 4 were calculated from the urea and mannitol flux data with eq 10. Figure 4 includes data from a previous Nuclepore membrane study.[2] The linear relationship of *Pe* and the applied voltage and the close to zero ordinate intercept in Figure 4 for the Nuclepore membrane system are consistent with what would be expected from electrokinetic theory assuming an effective single pore charge type and density. The greater slope for the mannitol results than for the urea results reflects the smaller diffusion coefficient of mannitol (see eq 11). The *Pe* data in Figure 5 for HEM were determined from the urea flux and HEM electrical resistance data in Studies I and II by eqs 8 and 10. There are likely two separate relationships between *Pe* and the applied voltage in Figure 5. One relationship is for the situation at low voltages (0.25 and 0.5 V dc) where there are predominantly preexisting pores. The second relationship is for the situation at the higher voltages (0.5, 1.0, and 2.0 V dc for electroosmosis plus 0−3 V ac to maintain a high extent of pore induction) where

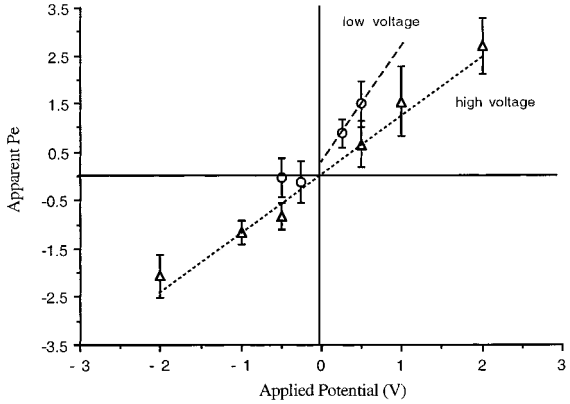

Figure 5—Relationship between the apparent *Pe* for urea as the permeant and the applied voltage with HEM. Key: (circles) low voltage, ≤0.5 V dc; (triangles) high voltages, ≥0.5 V dc plus 0–3 V ac. Each data point represents the mean and 90% confidence interval ($n \geq 6$).

the newly induced pores dominate electroosmosis. The steeper slope under the low voltage anodal conditions (0.25−0.5 V dc) relative to that under the higher voltage anodal and cathodal conditions (−2.0, −1.0, −0.5, 0.5, 1.0, and 2.0 V dc plus ac) is consistent with the interpretation that the effective pore charge density of the negatively charged induced pores is less than that of the preexisting pores. This interpretation is in agreement with the previously observed smaller than expected (based on low voltage studies) electroosmotic enhancement with 2.0 V dc iontophoresis.[3] The approximately linear relationship in Figure 5 for the low voltage anodal electroosmosis without pore induction (0.25−0.5 V dc) is consistent with what will be expected from the electrokinetic theory and the preexisting pores being dominated by negatively charged pores. The deviation from this linear relationship of the data for cathodal iontophoresis (especially at −0.5 V) is a departure, however, from the idea of preexisting pores being only negatively charged (as was also concluded from the data in Figure 2). This low voltage behavior contrasts with the high voltage results (of newly induced pore) that are essentially linear in Figure 5 in both the anodal and cathodal regions and consistent with the induced pores being essentially only negatively charged.

An alternate explanation for the lower slope of the high voltage data in Figure 5 might be based on pore sizes of the newly induced pores being significantly different from those of the preexisting pores. However, electroosmotic flux ratios of urea and mannitol determined as part of the present study at ≥1.0 V have yielded (from the hindered transport theory) pore sizes comparable to those found in similar experiments conducted at low voltages (∼8 Å). Therefore, it appears unlikely that pore size differences can contribute importantly to the slope differences in Figure 5.

Although the results from the higher voltage cathodal/anodal HEM electroosmosis studies are consistent with a model based on only negatively charged pores, one obviously needs to be cautious in making any detailed mechanistic conclusions. Considering the complicated morphology of the stratum corneum, it is only safe to state that HEM electroosmosis behavior under these circumstances is effectively equivalent to that of a membrane with only negatively charged pores. Nonetheless, this information is quite useful in assessing and in correcting for electroosmosis effects in various iontophoretic situations involving HEM.

Analysis of the Water/Urea Dual-Permeant Data—The passive permeability coefficient ratio, tritiated water-to-urea, for the Nuclepore membrane (average ± SD: ratio

$= 2.1 \pm 0.2$, $n = 5$) is consistent with what would be expected (ratio = 1.8) from the urea and water molecular diffusion coefficients with a small correction arising from hindered diffusion effects and with there being no significant difference between the diffusion coefficients (or the effective diffusion coefficients) of ordinary water and tracer tritiated water under the present experimental conditions.[12,14,15] During 0.75 V anodal dc iontophoresis with the Nuclepore membranes, water and urea fluxes were essentially the same at the same donor concentration (permeability coefficients of urea and water $= 1.1 \pm 0.4 \times 10^{-5}$ and $1.2 \pm 0.3 \times 10^{-5}$ cm/s, respectively, average ± SD, $n = 3$), demonstrating that the water velocity was essentially the same as the average velocity for urea and that the electroosmotic transport was at the convection limit.[2]

Tritiated water has been used to study the barrier properties of skin[16–18] and the electroosmosis behavior of skin.[19] The study of water transport across HEM during iontophoresis was expected to provide some independent insights into the mechanism of electroosmosis because liquid water is the carrier in electroosmotic transport. In the present study, the water passive permeability coefficients for HEM (average ± SD: $1.2 \pm 0.3 \times 10^{-6}$ cm/s, $n = 9$; HEM electrical resistance $= 30 \pm 19$ kΩ cm^2, ranging from 12 to 74 kΩ cm^2) are consistent with the permeability coefficients in a previous study.[20] The relatively high passive permeability coefficients of water for HEM compared with that of urea may be due to the accessibility of water to both the pore and the lipoidal pathways of HEM. This hypothesis is supported by present and previous studies: (a) the transport of water across HEM in the present study does not demonstrate an inverse proportionality between HEM permeability (P) and HEM electrical resistance (R) (slope of log P versus log R plot $= -0.26$ with $r^2 = 0.293$) as observed for urea in the present study and literature;[3,5,21] (b) the diffusional activation energy for water transport in HEM was reported to be ~17 kcal/mol,[22] which contrasts with the value of 7 kcal/mol for the transport of polar permeants across HEM[21] and the value (~4 kcal/mol) for unhindered diffusion in an aqueous medium; and (c) transport of water across lipid bilayers has been observed to be much higher than that for polar nonelectrolytes and ions.[23]

No significant difference between the transport rates of water across HEM during 0.25 V dc iontophoresis and during passive diffusion was found [ratios of iontophoretic flux to passive flux during anodal and cathodal iontophoresis (average ± SD) were 1.08 ± 0.05 ($n = 3$) and 1.03 ± 0.07 ($n = 3$), respectively]. This result is direct evidence of the lipoidal pathway being the dominant transport pathway for water in HEM in the absence of pore induction (i.e., low voltage iontophoresis). Under higher voltage conditions (e.g., a prepulse of 4.0 V dc for 1 min followed by 2.0 V dc iontophoresis) when significant pore induction occurred ($E_{\Delta R} > 10$), the pore pathway became dominant for water transport across HEM.

The permeability coefficient of the pore pathway for water in passive diffusion was estimated by the urea passive transport data of each individual HEM sample and eq 7:

$$P^{\text{pore}}_{\text{water,p}} = \frac{H_{\text{water}} D_{\text{water}}}{H_{\text{urea}} D_{\text{urea}}} P_{\text{urea,p}} \qquad (15)$$

The permeability coefficient of the pore pathway in HEM for water during 2.0 V dc iontophoresis was estimated by a parallel pore and lipoidal pathway model:

$$P^{\text{pore}}_{\text{water,i}} = P^{\text{total}}_{\text{water,i}} - (P^{\text{total}}_{\text{water,p}} - P^{\text{pore}}_{\text{water,p}}) \qquad (16)$$

where the subscripts "p" and "i" represent the passive and the iontophoresis experiments, respectively; the superscripts "*total*" and "*pore*" represent the total permeability coefficient and the permeability coefficient of the pore pathway, respectively; and $P_{\text{urea,p}}$ is the experimental permeability coefficient for urea in passive transport. Equations 15 and 16 assume (a) that transport via the lipoidal pathway is the same in passive transport and during iontophoresis, (b) an effective pore radius of 12 Å (the average R_p value deduced in the present passive transport experiments in the *Analysis of the Urea/Mannitol Dual-Permeant Data* section) for the calculation of H_{water} and H_{urea}, and (c) independent lipoidal and pore pathways in HEM. It should be noted that, with eq 16, water transport via the lipoidal pathway was generally small compared with the total iontophoretic flux of water with the application of 2.0 V dc.

With eq 16 and correcting for pore induction with eq 8, the enhancement due to electroosmosis (E_v) for water was estimated to be 2.0 ± 0.7 (average ± SD, $n = 5$) during 2.0 V anodal electroosmosis and 0.4 ± 0.2 (average ± SD, $n = 5$) during cathodal electroosmosis. This result corresponds to water Pe of ~1.6 and −1.5 and apparent water volumetric flow rates (ϵWvA) of $6 \pm 3 \times 10^{-6}$ and $-5 \pm 2 \times 10^{-6}$ cm^3/s across 1 kΩ cm^2 HEM at 2.0 V dc (average ± SD, $n = 5$; calculated using eq 4 and the experimental water P values normalized to 1 kΩ cm^2 HEM) during anodal and cathodal iontophoresis, respectively. These results are consistent with significant convective solvent flow and a net negatively charged HEM under the 2.0 V dc conditions. With the assumption that water and urea follow the same pore pathway in HEM and a R_p value of 8 Å (the average R_p calculated from the present anodal electroosmosis experiments in the *Analysis of the Urea/Mannitol Dual-Permeant Data* section), the water velocity and the velocity of urea convective transport across the pore pathway were compared using eq 4. The ratio of water velocity to that for urea was estimated to be ~1.2. This close-to-unity ratio is direct evidence of water being the carrier for urea during electroosmosis. The slightly higher water velocity than that for urea estimated here (the factor of 1.2) is consistent with differential hindered transport effects if pore radii of ~6 Å is assumed. This 6 Å value is of the same order of magnitude as that deduced from urea/mannitol flux data (i.e., the average R_p of 8 Å). Results from this analysis independently show that water is the carrier in electroosmotic transport during iontophoresis.

Conclusion

By conducting both anodal and cathodal electroosmosis experiments with polar nonionic permeants, the predictivity of a model of pores with a single charge was examined for the preexisting pores and the newly induced pores (due to applied electric fields) in HEM. The electrokinetic model was first checked with a synthetic polycarbonate membrane system, and the experimental results with this model membrane system were consistent with what would be expected of pores possessing only negative charges. Results from experiments with HEM at low voltages (little or no electroporation) showed that although negative pore charges dominate, there were effectively some positive or positive and neutral pores at neutral pH. At higher voltages (>1.0 V), where new pores dominated, there seemed to be contributions only from negatively charged pores at neutral pH. Results from the water transport experiments provide further support that water is the carrier in electroosmotic transport during iontophoresis.

References and Notes

1. Li, S. K.; Peck, K. D.; Ghanem, A.-H.; Higuchi, W. I. Iontophoretic transport across a synthetic membrane and human epidermal membrane: A study of the effects of permeant charge. *J. Pharm. Sci.* **1997**, *86*, 680−689.
2. Peck, K. D.; Srinivasan, V.; Li, S. K.; Higuchi, W. I.; Ghanem, A.-H. A quantitative description of the effect of molecular size upon electro-osmotic flux enhancement during iontophoresis for a synthetic membrane and human epidermal membrane. *J. Pharm. Sci.* **1996**, *85*, 781−788.
3. Li, S. K.; Peck, K. D.; Ghanem, A.-H.; Higuchi, W. I. Characterization of the transport pathways induced during low to moderate voltage iontophoresis in human epidermal membrane. *J. Pharm. Sci.* **1998**, *87*, 40−48.
4. Peck, K. D.; Ghanem, A.-H.; Higuchi, W. I. Hindered diffusion of polar molecules through and effective pore radii estimates of intact and ethanol treated human epidermal membrane. *Pharm. Res.* **1994**, *11*, 1306−1314.
5. Li, S. K.; Ghanem, A.-H.; Peck, K. D.; Higuchi, W. I. Pore induction in human epidermal membrane during low to moderate voltage iontophoresis: a study using AC Iontophoresis. *J. Pharm. Sci.* **1999**, *88*, 419−427.
6. Burnette, R. R.; Ongpipattanakul, B. Characterization of the permselective properties of excised human skin during iontophoresis. *J. Pharm. Sci.* **1987**, *76*, 765−773.
7. Pikal, M. J. Transport mechanisms in iontophoresis. I. A theoretical model for the effect of electroosmotic flow on flux enhancement in transdermal iontophoresis. *Pharm. Res.* **1990**, *7*, 118−126.
8. Pikal, M. J.; Shah, S. Transport mechanisms in iontophoresis. II. Electroosmotic flow and transference number measurements for hairless mouse skin. *Pharm. Res.* **1990**, *7*, 213−221.
9. Pikal, M. J.; Shah, S. Transport mechanisms in iontophoresis. III. An experimental study of the contributions of electroosmotic flow and permeability change in transport of low and high molecular weight solutes. *Pharm. Res.* **1990**, *7*, 222−229.
10. Sims, S. M.; Higuchi, W. I.; Srinivasan, V. Skin alteration and convective solvent flow effects during iontophoresis: I. Neutral solute transport across human skin. *Int. J. Pharm.* **1991**, *69*, 109−121.
11. Deen, W. M. Hindered transport of large molecules in liquid-filled pores. *AIChE J.* **1987**, *33*, 1409−1425.
12. Mills, R. Self-diffusion in normal and heavy water in the range 1−45 °C. *J. Phys. Chem.* **1973**, *77*, 685−688.
13. Inada, H.; Ghanem, A.-H.; Higuchi, W. I. Studies on the effects of applied voltage and duration on human epidermal membrane alteration/recovery and the resultant effects upon iontophoresis. *Pharm. Res.* **1994**, *11*, 687−697.
14. Easteal, A. J.; Edge, V. J.; Woolf, L. A. Tracer diffusion coefficients for $H_2{}^{18}O$ in ordinary water. *J. Phys. Chem.* **1984**, *88*, 6060−6063.
15. Easteal, A. J. Tracer diffusion in aqueous sucrose and urea solutions. *Can. J. Chem.* **1990**, *68*, 1611−1615.
16. Potts, R. O.; Francoeur, M. L. The influence of stratum corneum morphology on water permeability. *J. Invest. Dermatol.* **1991**, *96*, 495−499.
17. Squier, C. A.; Cox, P.; Wertz, P. W. Lipid content and water permeability of skin and oral mucosa. *J. Invest. Dermatol.* **1991**, *96*, 123−126.
18. Dick, I. P.; Scott, R. C. The influence of different strains and age on in vitro rat skin permeability to water and mannitol. *Pharm. Res.* **1992**, *9*, 884−887.
19. Kim, A.; Green, P. G.; Rao, G.; Guy, R. H. Convective solvent flow across the skin during iontophoresis. *Pharm. Res.* **1993**, *10*, 1315−1320.
20. Galey, W. R.; Lonsdale, H. K.; Nacht, S. The in vitro permeability of skin and buccal mucosa to selected drugs and tritiated water. *J. Invest. Dermatol.* **1976**, *67*, 713−717.
21. Peck, K. D.; Ghanem, A.-H.; Higuchi, W. I. The effect of temperature upon the permeation of polar and ionic solutes through human epidermal membrane. *J. Pharm. Sci.* **1995**, *84*, 975−982.
22. Golden, G. M.; Guzek, D. B.; Kennedy, A. H.; McKie, J. E.; Potts, R. O.. Stratum corneum lipid phase transitions and water barrier properties. *Biochemistry* **1987**, *26*, 2382−2388.
23. Stein, W. D. *Transport and Diffusion across Cell Membranes*; Academic: New York, 1986.

Acknowledgments

These studies were supported by NIH Grant GM 43181 and an Advanced Predoctoral Fellowship in Pharmaceutics by the Pharmaceutical Research and Manufacturers of America Foundation. The authors thank TheraTech Inc. (Salt Lake City, UT) for kindly donating us the human epidermal membrane.

JS980442X

Studies of Diffusional Release of a Dispersed Solute from Polymeric Matrixes by Finite Element Method

X. Y. WU* AND Y. ZHOU

Contribution from *Department of Pharmaceutical Sciences, Faculty of Pharmacy, University of Toronto, Toronto, Ontario, Canada M5S 2S2.*

Received November 9, 1998. Final revised manuscript received April 13, 1999.
Accepted for publication July 30, 1999.

Abstract □ This paper presents systematic analyses by the finite element method of release kinetics of a dispersed solute from various matrixes (i.e., slab, sphere, cylinder, and convex tablet), with or without boundary-layer resistance, into a finite or an infinite external volume. In the case of sink conditions, the numerical results agree well with the existing analytical solutions. For the problems of solute release into a finite external volume, where the analytical solutions are not available, this work has provided numerical solutions of the differential equations describing the release kinetics, moving boundaries, and concentration profiles. This work has also revealed the dependence of release kinetics on the initial solute loading, the external volume, and the boundary-layer thickness. The method presented here can describe the entire process of diffusional release before and after the dispersed solute has been dissolved without the pseudo steady-state assumption and it is applicable to both small and large ratio of initial solute loading to the solute solubility in the matrix.

Introduction

The kinetics of diffusional release of a dispersed solute, i.e., the initial solute loading (A) is higher than the solute solubility in the matrix (C_s), has been a subject of practical importance in controlled drug delivery. Drug delivery systems such as pharmaceutical solid dosage forms often contain dispersed biologically active agents, which makes it difficult to solve the differential equations and thus predict the release kinetics of the agents because of a moving boundary of the dispersed solute. The task becomes more complicated when the solute is released from a multidimensional dosage form, such as a convex tablet, with boundary-layer resistance into a finite external medium. So far, no analytical solution has been made available for investigation of such a complex system.

In the past decades, a number of mathematical models have been developed to describe the release kinetics of dispersed solutes[1−17] mainly for one-dimensional release except for ref 6. The majority of the models postulate infinite well-agitated sink, that is, no boundary layer resistance and no solute accumulation in the release medium due to the mathematical complication. A few groups have considered boundary-layer resistance under the sink condition[2,3,11] and in a finite external medium.[12] It must be noted that the analytical or semianalytical solutions of the above models are only applicable to the release process up to the time, t^*, for all the dispersed solute to dissolve,[3,4,17] except for those with a pseudo steady-state assumption.[1,2,6,10,12] This is because the concentration distribution in the matrix at t^* is nonuniform and unknown ahead of time. For a matrix with a small A/C_s ratio, a considerable amount of dissolved solute remains in the matrix at time t^*, whose contribution to the release kinetics is not described by the models without a pseudo steady-state assumption.[3,4,17] To overcome the difficulty, a linear distribution is assumed in the pseudo steady-state approach.[1,2,6,10,12] This approach has been applied extensively for $A \gg C_s$ and sink conditions or near-sink conditions with success especially for planar geometry.[3,4,16] Nevertheless, when the A/C_s ratio is small, for example, when $A/C_s = 2$ or approaches 1, the real concentration distribution deviates from the linear one noticeably. As a consequence, prediction by the pseudo steady-state approach becomes less accurate.[3,4]

In practice, drug release from a dosage form into a finite volume of surrounding medium is often found. In this case, the release rate may be reduced as a consequence of drug accumulation in the medium, deviating from the prediction by the models for sink conditions. Such an effect can be expected when the drug removal from the medium is slow or the drug solubility in the medium is minimal, typified by drug release in the lower gastrointestinal tract where liquid content and absorption rate are relatively low, or from an implant or an insert into a confined cavity such as solid tumors and root canals. Therefore, prediction of release kinetics for these dosage forms in a finite external volume is of more practical importance than that for sink conditions, although both may be governed by the same release mechanism.

The analytical solutions for solute release into a finite volume can be found for one-dimensional release from slab, sphere, and cylinder with a loading, $A \leq C_s$. Nevertheless, there is no analytical solution available for release kinetics of sphere, cylinder, and convex tablet with a boundary layer and $A > C_s$ in a finite volume, except that for a sphere with assumptions of pseudo steady-state and boundary-layer thickness much smaller than the radius of the sphere.[12] This is perhaps because of the above-mentioned difficulty involving the moving boundary of the solute, time-dependent boundary condition, and nonuniform solute concentration in the matrix at t^*. Therefore, numerical methods must be applied in order to solve the differential equations for such systems.

The objective of this work is to study the kinetics of the entire process of diffusional release of an initially dispersed solute from polymeric matrixes into a finite external volume with or without the boundary-layer effect. The finite element method, a computer-aided numerical approach, is employed to solve the differential equations. The release profiles for matrixes of various shapes (i.e., slab, sphere, cylinder, and convex tablet) are presented for different A/C_s ratios and various external volumes ranging from infinite to a small liquid/matrix volume ratio. The evolution of solute concentration in these matrixes and the

* Corresponding author. Tel. (416)978-5272; fax: (416)978-8511; e-mail: xywu@phm.utoronto.ca.

10.1021/js9804361 CCC: $18.00
Published on Web 09/08/1999

effect of boundary-layer resistance are discussed based on the numerical results.

Theoretical Background

It is assumed that dissolution of a dispersed solute is rapid compared with the subsequent depletion of the solute by diffusion. The process of diffusional release of a dispersed solute from a matrix can be physically visualized[18] as a process of solute extraction, i.e., the solution of the dispersed solute followed by the diffusion of the dissolved solute. Initially, the dispersed solute is dissolved and diffuses out from the surface layer; after a certain time, the solute concentration in the surface layer is reduced to the saturated level (C_s), and the extraction of the solute in the next layer is initiated. Between the just-extracted layer and the next layer, there exists a sharp concentration gradient, i.e., the moving boundary of the dispersed solute, and the concentration difference between the two layers is $A - C_s$. The boundary will move inward layer by layer continuously until all the dispersed solute is dissolved.

Since the process is diffusion-controlled, the governing equation of the diffusion is held for the whole process no matter whether the solute is dispersed or dissolved. The general expression of the governing equation for a problem of three-dimensional and homogeneous material with boundary layer resistance in a well-mixed finite external medium is given as follows,

$$\frac{\partial C_i}{\partial t} = \nabla\cdot(D_i \nabla C_i) \qquad i = 1, 2 \tag{1}$$

where ∇ is the differential operator, the suffixes 1 and 2 denote the polymeric matrix and the boundary layer, D_i and C_i are the diffusion coefficient (cm^2/s) and solute concentration (g/cm^3) in these two domains, respectively. Definition of these domains and relevant boundaries for an arbitrary geometry is illustrated in the following schematic diagram:

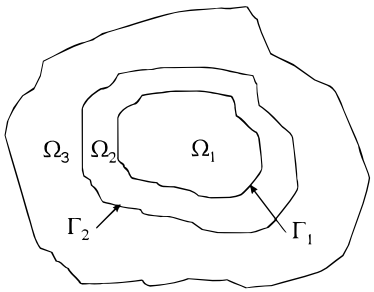

The corresponding initial and boundary conditions are

$$C_1 = A, \text{ in } \Omega_1, t = 0 \tag{2}$$

$$C_2 = C_3 = 0, \text{ in } \Omega_2 \text{ and } \Omega_3, t = 0 \tag{3}$$

$$D_1\frac{\partial C_1}{\partial n} = D_2\frac{\partial C_2}{\partial n}, \text{ on } \Gamma_1, t > 0 \tag{4}$$

$$C_1 = KC_2, \text{ on } \Gamma_1, t > 0 \tag{5}$$

$$(A - C_s)\frac{d\xi}{dt} = D_1|\nabla C_1|, \text{ on } \xi(t), 0 < t < t^* \tag{6}$$

$$C_1 = C_s, \text{ on } \xi(t), 0 < t \le t^* \tag{7}$$

$$V\frac{\partial C_3}{\partial t} = D_2\frac{\partial C_2}{\partial n}S_2, \text{ on } \Gamma_2, t > 0 \tag{8}$$

where A is the initial solute loading (g/cm^3), K is the partition coefficient, $\xi(t)$ is the moving boundary, Ω_1, Ω_2, and Ω_3 are the domains of the matrix, boundary layer, and the finite external medium, respectively. Γ_1 and Γ_2 denote the boundaries of Ω_1 and Ω_2, S_2 is the area of the interface between Ω_2 and Ω_3. V is the volume of the finite external medium, and t^* is the time for all the dispersed solute to dissolve. In eqs 4 and 8,

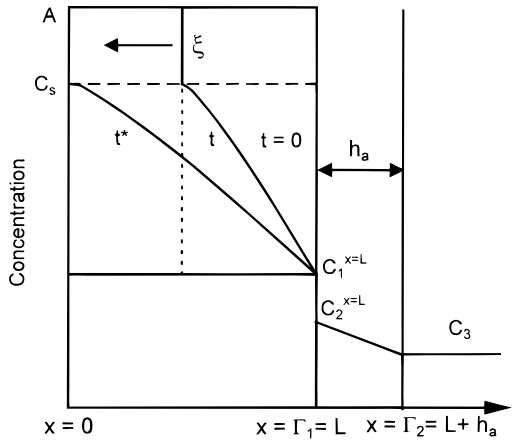

Figure 1—Schematic diagram of moving boundary, boundary layer, and concentration profile for a one-dimensional slab, sphere, and cylinder, where L denotes either the half-thickness of a slab, or radius of a sphere or a cylinder; $x = 0$ stands for the midplane or the center of the matrixes.

$$\frac{\partial C}{\partial n} = n_x\frac{\partial C}{\partial x} + n_y\frac{\partial C}{\partial y} + n_z\frac{\partial C}{\partial z} \tag{9}$$

where n_x, n_y, and n_z are the directional cosines of the outward normal n to the closed boundary Γ_i.

For a sink condition, the boundary condition described by eq 8 is replaced by eq 10,

$$C_3 = 0 \qquad \text{on } \Gamma_2 \qquad t \ge 0 \tag{10}$$

For the matrixes with one-dimensional release such as a sphere, an infinite slab or an infinitely long cylinder, the above equations can be simplified to conventional presentations[2-4] as illustrated in Figure 1, where ξ is the moving boundary of the dispersed solute, x is the distance, L is the half thickness of a slab or the radius of a sphere or a cylinder, h_a is the thickness of the boundary layer, $C_1^{x=L}$ is the concentration in the matrix at x = L, $C_2^{x=L}$ is the concentration in the boundary layer at $x = L$, C_3 is the concentration in the bulk solution. For a system with no boundary-layer resistance, $C_2 = C_3$; a system in a sink with boundary layer, $C_3 = 0$; and a system in a sink without boundary layer, $C_2^{x=L} = C_2 = C_3 = 0$.

As aforementioned, the whole release process is diffusion-controlled. Therefore, the computational procedures of the finite element method developed in the previous work[19-22] for dissolved solute are still applicable to the release of dispersed solute except that eqs 6 and 7 need to be incorporated into the computation. Mathematically these equations represent the instantaneous mass balance at the diffusion moving front. Physically they can be viewed as that, in order for the diffusion front to move a distance δx in a time δt per unit area perpendicular to x, an excess amount of solute, $(A - C_s)\delta x$, must be removed by diffusion. Based on this interpretation, the computational procedures were correspondingly modified to incorporate eqs 6 and 7. The whole matrix domain was divided into many thin layers. The diffusion was initiated from the most outer layer. The solute concentration in the current thin layer was examined at very small time intervals using an iteration checking subroutine. Once the excess amount of

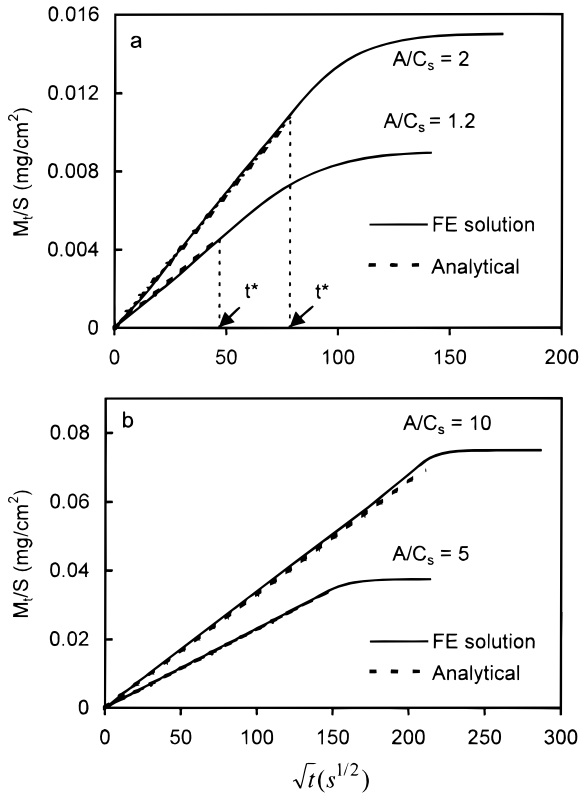

Figure 2—Cumulative amount of a dispersed solute released per unit surface area from a slab into a perfect sink ($L = 0.1$ cm, $D_1 = 1 \times 10^{-6}$ cm^2/s). (a) $A/C_s = 1.2$ and 2; (b) $A/C_s = 5$ and 10.

solute, $(A - C_s)\delta x$, had been depleted, i.e., $C_1 = C_s$ in the current layer, the solute diffusion in the next thin layer was allowed. Otherwise the iteration continued until the saturation level was reached. The amount of solute released (M_t) at time t was obtained by subtracting the amount of solute remained in the matrix from the initial amount of solute. The remaining was calculated by multiplying the solute concentration in each finite element at time t by the volume of the element.

Results and Discussion

To verify the computational procedures and results, release profiles of a dispersed solute from a one-dimensional slab, sphere, and cylinder into a sink were first calculated and compared with the available analytical solutions. Release kinetics for three basic geometries and convex tablet in different external volumes and its dependence on the boundary-layer resistance and initial solute concentration were then studied.

One-Dimensional Release and Verification—*(a) Slab*—Figure 2 depicts the amount of the drug released per unit surface area of a slab as a function of square root of time. Evidently, the results of this work agree well with the analytical solution by Paul and McSpadden[3] at earlier stage, i.e., $t \leq t^*$. At a later stage, i.e., $t > t^*$, the analytical solution is no longer applicable, whereas the finite element solution continuously describes the rest of the release process. When the A/C_s ratio is large, e.g., $A/C_s = 10$ or 5, the analytical solution may be extended to $t > t^*$ with an acceptable error, as only a small portion of the solute remains in the matrix. Nevertheless, the error can be significant when the A/C_s ratio is small. As will be discussed in section d), there is still about 50% of the solute unreleased at t^* for $A/C_s = 1.2$ and 28% for $A/C_s = 2$. This implies that up to 50% of the solute is released by a

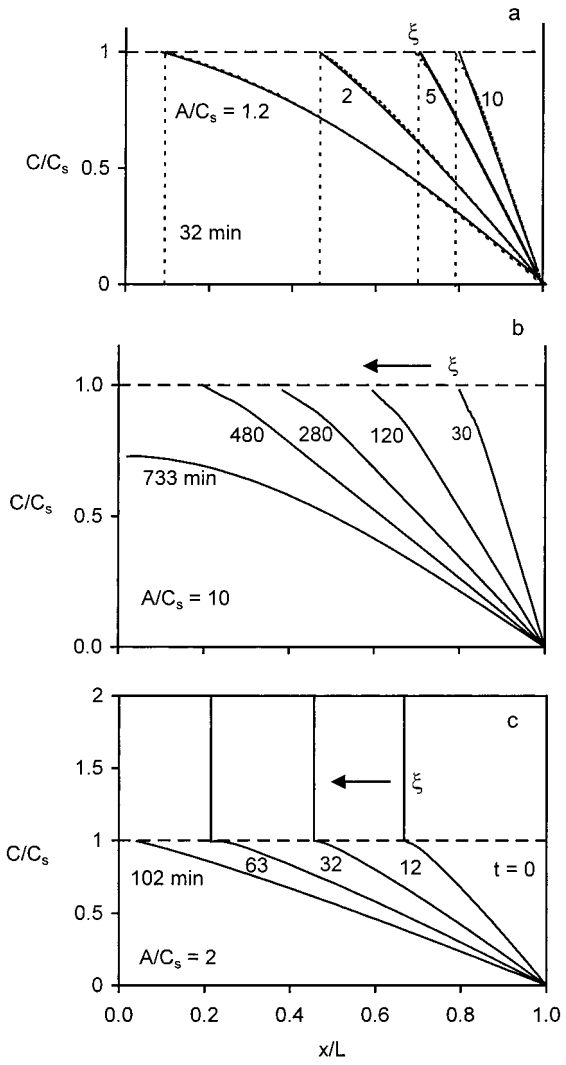

Figure 3—Moving boundary of a solid solute and concentration profile for a sphere with various A/C_s ratios in a perfect sink ($L = 0.1$ cm, $D_1 = 1 \times 10^{-6}$ cm^2/s). (a) Time = 32 min, $A/C_s = 1.2$, 2, 5, and 10, (- - - -) Paul and McSpadeen,[3] (—) FEM; (b and c) $A/C_s = 10$ and 2, respectively, at various time intervals.

different mechanism (i.e., no moving boundary). The release kinetics of this portion of the solute cannot be described by the analytical solution. Therefore, the straight line predicted by the model was linearly extrapolated and linked with the horizontal line of 100% release.[3] The experimental data showed that the release profile is a asymptotic curve approaching to the 100% line,[3] especially for small A/C_s ratios. This experimental observation is predicted by the numerical solutions of this work (Figure 2a).

Figure 3a compares the concentration distribution of a solute in the matrix for different A/C_s ratios at the same time (32 min). A good agreement between this work and the analytical solution[3] is evidenced. Apparently, the smaller the A/C_s ratio, the more advanced the moving boundary of the dispersed solute, due to smaller excess amount of solute to be removed by diffusion. Figures 3b and 3c illustrate the progress of the moving boundary and concentration distribution at different times for $A/C_s = 10$ and 2, respectively. It is noticed that more linear distribution curves are obtained at $A/C_s = 10$ than those at $A/C_s = 2$, supporting Higuchi's pseudo steady-state assumption for $A \gg C_s$.[1]

The amount of solute released into a well-mixed finite medium with the effective volume ratio, $\lambda = V/(V_1K) = 5$,

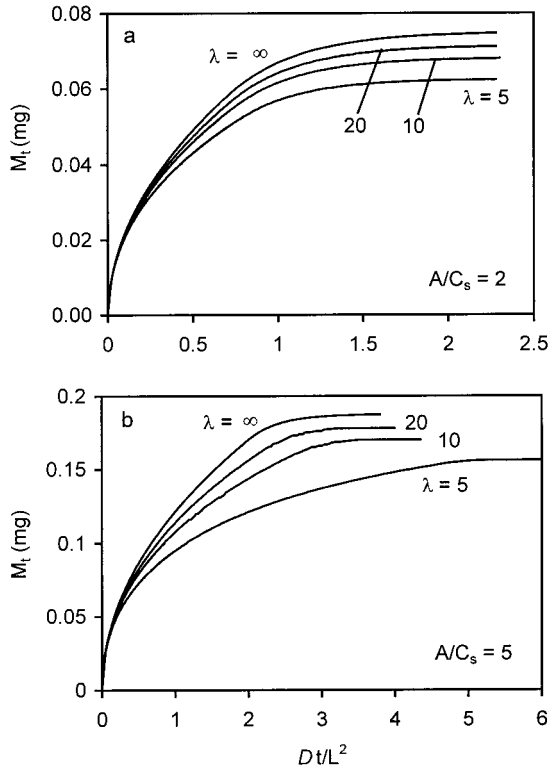

Figure 4—Influence of effective volume ratio on the amount of solute released from a slab into a well-mixed liquid of finite volume ($L = 0.1$ cm, $D_1 = 1 \times 10^{-6}$ cm^2/s, $K = 1$). (a) $A/C_s = 2$ and (b) $A/C_s = 5$. The 100% solute released is indicated by the plateau of the release curve for $\lambda = \infty$.

10, 20, and ∞, is plotted against D_t/L^2 in Figure 4 for (a) $A/C_s = 2$ and (b) $A/C_s = 5$, where $K = 1$, V and V_1 are the volume of the liquid and the matrix, respectively. The influence of the effective volume ratio on the release rate is consistent with previous analytical and experimental results.[19,21] It is shown that the release rate and the final amount of the solute decrease with the decrease in λ value. Given a fixed partition coefficient, this observation can be attributed to quicker concentration build-up and consequently higher diffusional resistance in a smaller volume. Note that at $A/C_s = 5$, the influence of λ becomes more profound as indicated by larger differences among the curves in Figure 4b compared to those in Figure 4a. In addition, more abrupt change in the curves before reaching the plateau is observed for $A/C_s = 5$. This is an indication of inhibition of release by the saturation of the solute in the liquid at higher A/C_s ratios. The analysis can also be carried out in the same way for the effect of K value and for the solute released into a poorly mixed external finite volume.[20]

(b) Sphere—Figure 5 shows the amount of the released solute versus D_t/L^2 for a spherical matrix in a perfect sink by this work compared with the approximate analytical solutions derived by Lee[4] and by Baker and Lonsdale.[5] It is depicted that this work agrees well with Lee's solution at $A/C_s = 2$ and with Baker and Lonsdale at $A/C_s = 5$ and 10. It should be pointed out that the latter, with pseudo steady-state assumption, is restricted to A/C_s ratio > 3 or 4,[16] while the former is suitable for small A/C_s ratios and $t \leq t^*$. In contrast, the numerical method presented in this work, with no restriction, can predict the entire release process for various A/C_s ratios.

As delineated by Figure 6, the progress of the moving boundary is much faster in spheres than that in slabs. Interestingly, due to the spherical geometry, the concentration profiles are considerably nonlinear compared with that in the slab even at a high A/C_s ratio. The distribution curve

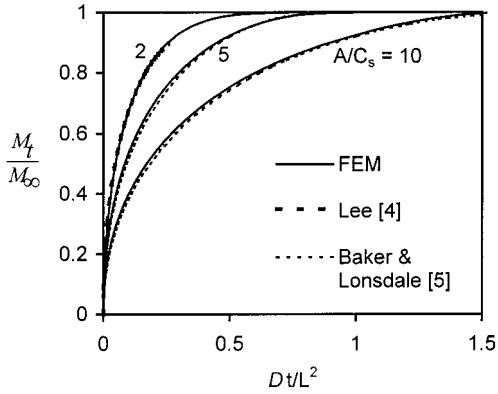

Figure 5—Fractional release of a dispersed solute from a sphere into a perfect sink ($L = 0.1$ cm, $D_1 = 1 \times 10^{-6}$ cm^2/s). Comparison of finite element solution with semianalytical solution from Lee[4] and solution from Baker and Lonsdale with pseudo steady-state assumption.[5]

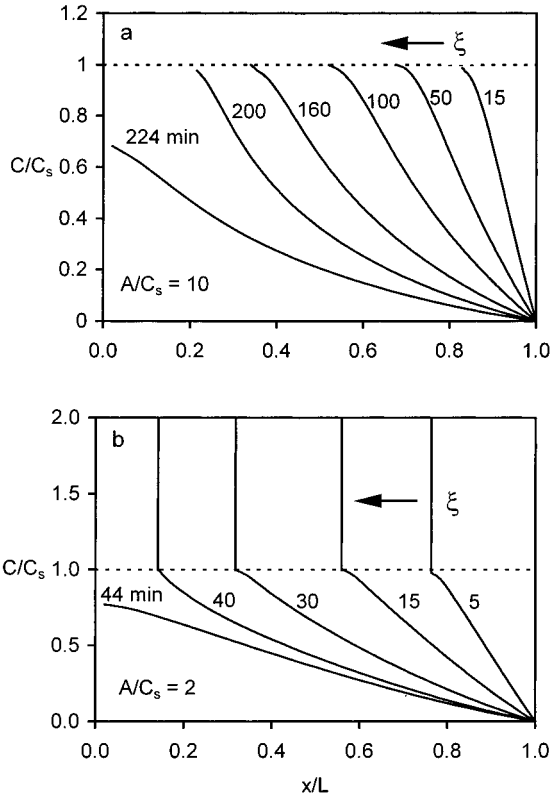

Figure 6—Moving boundary of a solid solute and concentration profile for a sphere in a perfect sink ($L = 0.1$ cm, $D_1 = 1 \times 10^{-6}$ cm^2/s). (a) $A/C_s = 10$ and (b) $A/C_s = 2$.

is gradually changed from convex to concave due to the relative change rate between the surface area of the dispersed solute core and the diffusional distance which is the distance from the moving boundary to the matrix surface.

The amount of the solute released into a well-mixed finite volume with the effective volume ratio, $\lambda = 5$, 10, 20, and the sink condition is presented in Figure 7. The dependence of the release kinetics on the volume ratio and initial loading is similar to that in planar geometry.

(c) Cylinder—The only available analytical solutions for the cylindrical geometry were developed by Crank[23] and Roseman and Higuchi.[2] The former is applicable to $A/C_s \leq 1$ and the latter is an approximate solution and only suitable for $A \gg C_s$ under the sink condition. No analytical solution is available for a cylindrical matrix with a small A/C_s ratio ($A > C_s$) in either a perfect sink or a finite

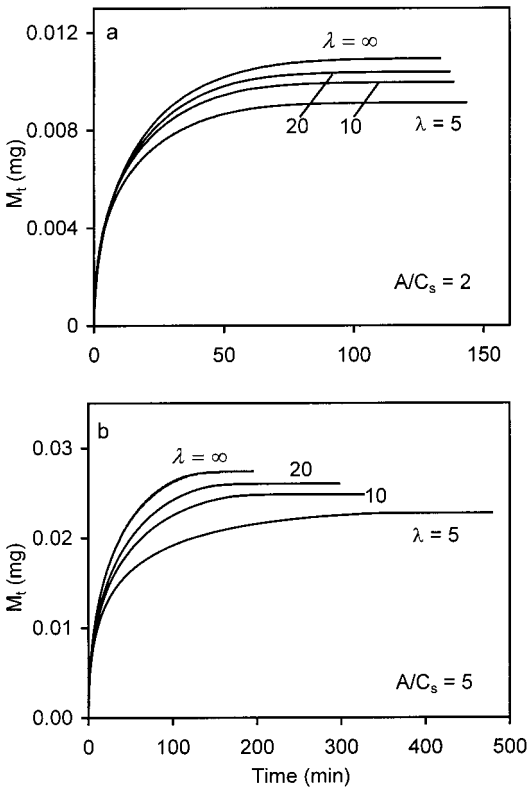

Figure 7—Influence of effective volume ratio on the amount of solute released from a sphere into a well-mixed liquid of finite volume ($L = 0.1$ cm, $D_1 = 1 \times 10^{-6}$ cm^2/s, $K = 1$). (a) $A/C_s = 2$ and (b) $A/C_s = 5$. The 100% solute released is indicated by the plateau of the release curve for $\lambda = \infty$.

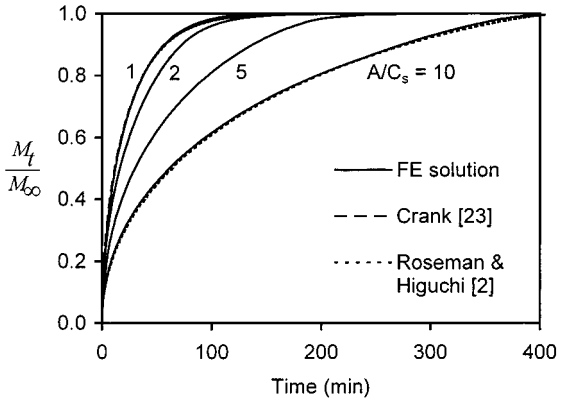

Figure 8—Fractional release of a dispersed solute from a cylinder into a perfect sink ($L = 0.1$ cm, $D_1 = 1 \times 10^{-6}$ cm^2/s, $A/C_s = 1$, 2, 5, and 10).

volume, and there is little knowledge of the concentration distribution in the cylinder. Therefore, Crank's and Roseman and Higuchi's solutions are used here as bounding cases to verify the finite element results. As shown in Figure 8, a very convincing agreement has been obtained between the finite element solutions and the analytical ones in both lower ($A/C_s = 1$) and upper ($A/C_s = 10$) bounding cases. For the A/C_s ratios between these two extremes, where the analytical solutions are not applicable, the solutions of this work have filled the gap. It is expected that the present numerical approach can provide reliable solutions for a broad range of A/C_s ratios from $A/C_s \leq 1$ to $A \gg C_s$.

The progress of the moving front versus time and the concentration distribution in the cylinder for $A/C_s = 2$ and 10 are presented in Figure 9. By comparison of the concentration profiles of slab, sphere, and cylinder, i.e., Figures 3b, 6a, and 9a, some interesting features are

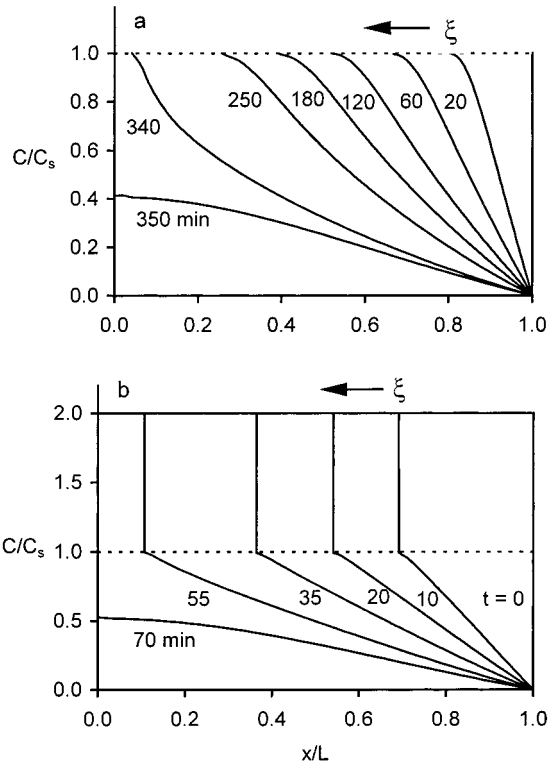

Figure 9—Moving boundary of a solid solute and concentration profile for a cylinder in a perfect sink ($L = 0.1$ cm, $D_1 = 1 \times 10^{-6}$ cm^2/s). (a) $A/C_s = 10$ and (b) $A/C_s = 2$.

noticed. In the slab, the concentration distribution is near linear and always convex. The concentration profile becomes nonlinear and is gradually changed from convex to concave with time in the cylinder. The more nonlinear concentration profile is observed in the sphere with a faster change from convex to concave than in the cylinder. This phenomenon can be ascribed to the inherent difference in the geometry. For diffusional release from matrixes with a dispersed solute, the concentration distribution depends on the relative change rate of the surface area of the solid core and the diffusional distance. The former determines the supply of the solute for diffusion, and the latter determines the time for the solute to leave the matrix. Although surface area and diffusional distance are functions of the moving front in all three geometries, the dependence of the area on the distance is zero for slab, linear for cylinder, and quadratic for sphere. In other words, the relative rate of reduction in the surface area of the undissolved core is the highest in the sphere and the lowest in the slab. Consequently, the change from convex to concave occurs more dramatically in the sphere due to insufficient solute supply for diffusion.

Figure 10 presents the amount of the drug released into different external volumes for cylinders with (a) $A/C_s = 2$ and (b) $A/C_s = 5$. The figures reveal that the influence of volume ratio on the release kinetics for cylinder is similar to that for planar and spherical geometries (Figures 4 and 7). These results are particularly useful for prediction of in vivo release kinetics based on the information of in vitro release.

(d) Correlation of t^* and $(M_r/M_0)^*$ with A/C_s—As aforementioned, the fraction of a solute remaining in the matrix at t^* can be noticeable at small A/C_s. Figure 11 illustrates the remaining fraction at t^*, $(M_r/M_0)^*$, as a function of A/C_s for three geometries, where M_r and M_0 denote the remaining and the initial amount of the solute in the matrix, respectively. $(M_r/M_0)^*$ drops drastically as A/C_s increases from 1 to 2 and then decreases gradually till $A/C_s = 5$,

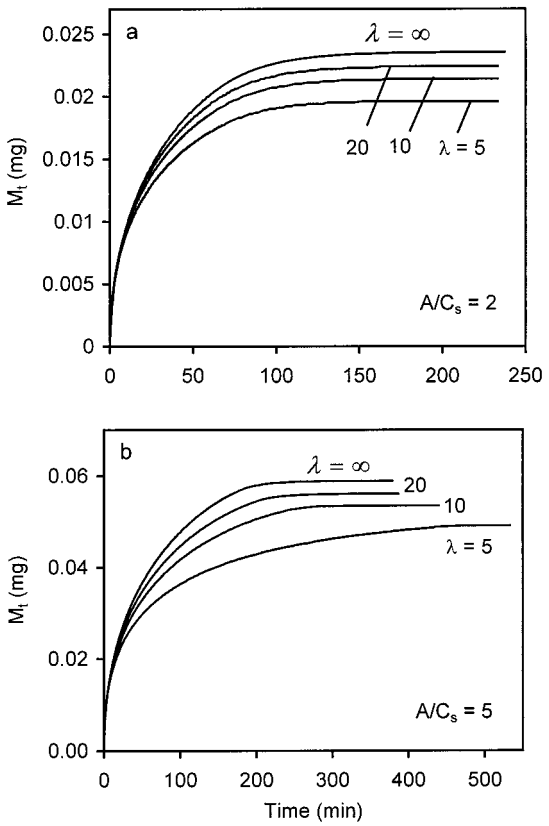

Figure 10—Influence of effective volume ratio on the amount of solute released from a cylinder ($L = 0.1$ cm, $D_1 = 1 \times 10^{-6}$ cm^2/s, $K = 1$). (a) $A/C_s = 2$ and (b) $A/C_s = 5$. The 100% solute released is indicated by the plateau of the release curve for $\lambda = \infty$.

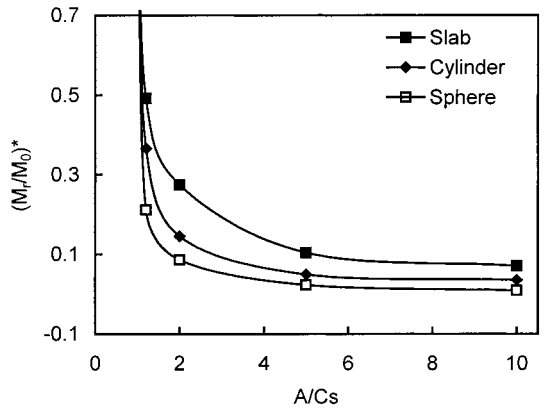

Figure 11—The fraction of a solute remaining in the matrix at t^* for three geometries in a perfect sink ($L = 0.1$ cm, $D_1 = 1 \times 10^{-6}$ cm^2/s).

beyond which the reduction in $(M_r/M_0)^*$ becomes insignificant. The remaining fraction of the solute is the largest for the slab and the smallest for the sphere, suggesting that $(M_r/M_0)^*$ is a function of diffusion rate. One may infer that the remainder could increase as the diffusion coefficient, or the external volume decreases because of the reduced release rate. $(M_r/M_0)^*$ can be correlated with A/C_s by

$$(M_r/M_0)^* = B[A/C_s]^{-\alpha} \qquad (11)$$

where B and α are constants. The values of B and α for three basic geometries were obtained from the nonlinear regression of the data in Figure 11 and are listed in Table 1.

A good linear relationship between the t^* and A/C_s is revealed by Figure 12 for all three geometries. Table 1 summarizes the slope (β) and intercept (γ) of the linear function (eq 12) together with the correlation coefficients of the linear regression.

Table 1—Parameters in Eqs 11 and 12 Evaluated from the Data in Figures 11 and 12 for Three Basic Geometries in a Perfect Sink

geometry	β (slope)	γ (intercept)	r^2 (correlation coefficient)	B	α
slab	75.57	58.69	0.9986	0.7098	1.086
cylinder	36.76	23.72	0.9949	0.5696	1.348
sphere	25.34	14.60	0.9951	0.4678	1.810

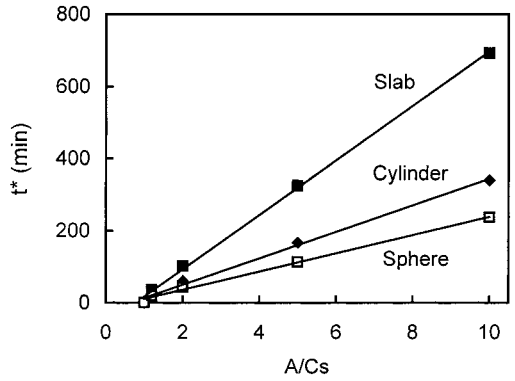

Figure 12—Dependence of t^* on A/C_s for three geometries in a perfect sink ($L = 0.1$ cm, $D_1 = 1 \times 10^{-6}$ cm^2/s).

$$t^* = \beta[A/C_s] - \gamma \qquad (12)$$

Again, the influence of A/C_s on t^* is the greatest for the slab and the least for the sphere, suggesting that, like $(M_r/M_0)^*$, t^* is also dependent on the diffusion rate.

(e) Boundary Layer Effect—It has been demonstrated that the stagnant boundary layer is responsible for the reduced release rate.[2,13] It was intended here to develop a model with consideration of the effect of boundary layer rather than elaborating its mechanism. From the simulation point of view, the boundary layer acts as a thin layer coating. Hence, a thin layer element with corresponding material properties was introduced to the surface of the matrix of interest. The computed release profile was compared with the theoretical solution reported by Roseman and Higuchi[2] for a cylinder in a sink. As depicted in Figure 13a, the finite element solution matches the analytical solution well for a solute with diffusion coefficients in the matrix and in the boundary layer, $D_1 = 1 \times 10^{-6}$ cm^2/s, and $D_2 = 5 \times 10^{-6}$ cm^2/s, respectively, and the thickness of the boundary layer, $h_a = 0.01$ cm. Figure 13b shows that the release rates of a solute from three basic geometries ($L = 0.1$ cm, $A/C_s = 5$) into a finite volume of liquid ($V/V_1 = 10$, $K = 2$) is reduced in the presence of a boundary layer of thickness, $h_a = 0.01$ cm, i.e., $h_a/L = 0.1$. This trend agrees with general observations. The degree of the reduction for the cylinder is slightly greater than the prediction by Roseman & Higuchi's model.[2] For example, at $t = 100$ min, the reduction in the fractional release calculated in this work is ~4% in the presence of a boundary layer, whereas it is ~1% by their model for the same cylinder in a perfect sink. This is likely a result of the difference in the volume of surrounding medium, which is infinite in the analytical solutions and is finite ($V/V_1 = 10$) in the numerical solutions. In a finite volume of liquid, the drug concentration builds up, contributing to a slower release rate and a greater boundary-layer effect.

It is interesting to notice a geometry dependence of the boundary-layer effect. The effect appears the most marked

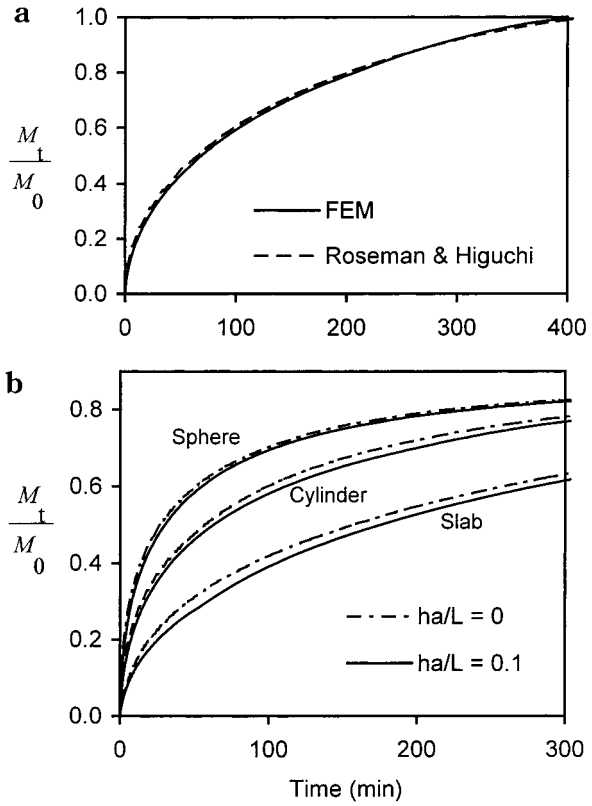

Figure 13—(a) Fractional release of a dispersed solute from a cylinder into a perfect sink with boundary layer resistance ($A/C_s = 10$, $L = 0.1$ cm, $h_a/L = 0.1$, $D_1 = 1 \times 10^{-6}$ cm^2/s, $D_2 = 5 \times 10^{-6}$ cm^2/s, $K = 2$). Comparison of FE solution with the solution from Roseman and Higuchi with pseudo-steady-state assumption.[2] (b) Effect of boundary layer resistance on the release rate of a solute from three geometries in a well-stirred liquid of finite volume ($\lambda = 10$, $A/C_s = 5$, $L = 0.1$ cm, $D_1 = 1 \times 10^{-6}$ cm^2/s, $D_2 = 5 \times 10^{-6}$ cm^2/s, $K = 2$).

for the slab and the least for the sphere. For example, at $t = 100$ min, the reduction in the fractional release in the presence of a boundary layer is 7.2%, 4.1%, and 1.2% for the slab, cylinder, and sphere, respectively. This suggests that the boundary layer effect depends on the relative release rate in the matrix to that in the boundary layer. The solute release from the slab is the slowest and thus is affected most by the boundary layer.

Multidimensional-Release Convex Tablets—The finite element method presented here can model complex matrix dosage forms of virtually any shape. However, the emphasis was placed on matrix tablets here in the hope that the efforts of this work could facilitate the design of this popular controlled-release dosage form for oral administration. For convex tablets with three-dimensional release, dispersed initial drug loading, and the boundary layer resistance, no analytical solution has been reported. This original work provides insight into the release kinetics in relation to design parameters such as A/C_s ratio and environmental conditions. The fractional release, M_t/M_∞, of a drug from convex tablets with different A/C_s ratios into a well-mixed finite volume is depicted in Figure 14, where M_∞ is the amount of drug released at the final stage, $V/V_1 = 10$, $K = 1$, and $D_1 = 1 \times 10^{-6}$ cm^2/s. Clearly, the time for the completion of the release increases with increasing A/C_s ratio, which is consistent with the observation of other geometries.

Figure 15 shows the moving boundary and concentration distribution within a tablet with $A/C_s = 2$ in a well-mixed finite volume ($V/V_1 = 10$, $K = 1$, and $D_1 = 2 \times 10^{-7}$ cm^2/s). The concentration profiles are similar to those in the slab. However, unlike the release into a perfect sink (Figures 3, 6, and 9), the concentration near the surface of the tablet increases with time, reflecting concentration build-up in the bulk solution of a limited volume. Such concentration build-up leads to a smaller driving force for diffusion, i.e., the concentration gradient between the matrix and the medium, and thus lower release rate. This result explains partly why the in vivo release is slower than the in vitro one.

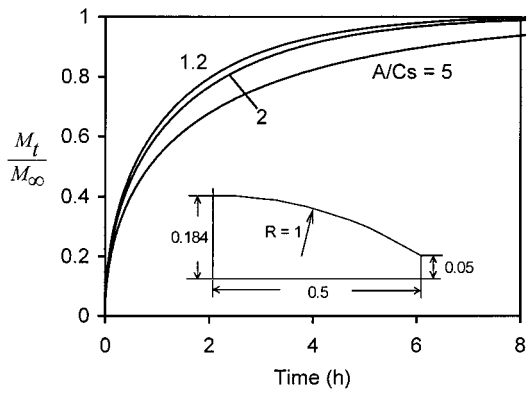

Figure 14—Fractional release of a dispersed drug from a convex tablet with $A/C_s = 1.2$, 2, and 5 into a well-mixed finite volume ($\lambda = 10$, $D_1 = 1 \times 10^{-6}$ cm^2/s, $K = 1$).

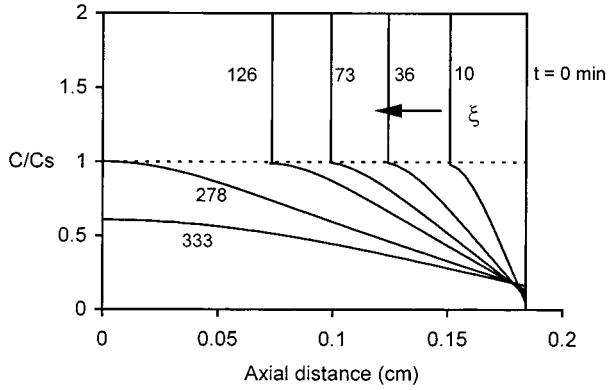

Figure 15—Moving boundary and concentration profile of a dispersed drug for a convex tablet in a well-stirred liquid of finite volume ($\lambda = 10$, $D_1 = 2 \times 10^{-7}$ cm^2/s, $K = 1$).

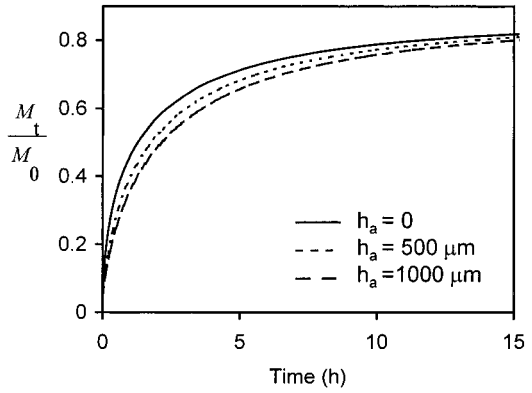

Figure 16—Influence of boundary layer resistance on the fractional release of a dispersed drug from convex tablets into a well-stirred finite volume ($A/C_s = 5$, $\lambda = 10$, $D_1 = 1 \times 10^{-6}$ cm^2/s, $D_2 = 5 \times 10^{-6}$ cm^2/s, $K = 2$).

Another factor that is often associated with the lower in vivo release rate is the diffusion boundary layer. The boundary-layer effect on the fractional release, M_t/M_0, where M_0 is the initial amount of the solute, is illustrated in Figure 16 for a tablet with $A/C_s = 5$ in a well-mixed finite volume ($V/V_1 = 10$, $K = 2$, $D_1 = 1 \times 10^{-6}$ cm^2/s, and $D_2 = 5 \times 10^{-6}$ cm^2/s). As shown by the figure, the release rate

decreases as the boundary-layer thickness increases. It should be indicated that the curves in Figure 16 could only reach ~83% of the initial loading at a much longer time, e.g., 25 h, as a result of saturation of the medium.

In reality, polymeric matrix tablets involve not only the moving boundary of a dispersed drug, but also the moving boundaries of swelling and erosion. The finite element model for matrix tablets with swelling and erosion has been developed by our group for $A/C_s \leq 1$.[22] Further work on incorporation of all three moving boundaries into the model is in progress.

Conclusions

The numerical solutions of differential equations have been obtained by the finite element method for diffusional release of a dispersed solute from slab, sphere, cylinder, and convex tablet into various external volumes. The kinetics of the entire release process have been presented for these matrixes with a broad range of A/C_s ratios and boundary conditions varying from a perfect sink to a finite volume with boundary-layer resistance. The evolution of solute concentration profiles in the matrixes has been revealed. The shape of the concentration profiles depends on the geometry of the matrixes. The nonlinearity of the profiles is found to be sphere > cylinder > slab, in the same order of the release rate. The numerical results for the sink conditions agree well with the existing analytical solutions. The existence of boundary-layer resistance reduces the release rate, and the degree of the reduction increases with increasing thickness.

References and Notes

1. Higuchi, T. Rate of Release of Medicaments from Ointment Bases Containing Drugs in Suspension. *J. Pharm. Sci.* **1961**, *50*, 874−875.
2. Roseman, T. J.; Higuchi, W. I. Release of Medroxyprogesterone Acetate from a Silicone Polymer. *J. Pharm. Sci.* **1970**, *59*, 353−357.
3. Paul, D. R.; McSpadden, S. K. Diffusional Release of a Solute from a Polymer Matrix. *J. Membr. Sci.* **1976**, *1*, 33−48.
4. Lee, P. I. Diffusional Release of a Solute from a Polymeric Matrix-Approximate Analytical Solutions. *J. Membr. Sci.* **1980**, *7*, 255−275.
5. Baker, R. W.; Lonsdale, H. K. Controlled Release: Mechanisms and Rates, In *Controlled Release of Biologically Active Agents*; Tanquary, A. C., Lacey, R. E., Eds.; Plenum Press: New York, 1974, pp 15−71.
6. Cobby, J.; Mayersohn, M.; Walker, G. C. Influence of shape Factors on Kinetics of Drug Release from Matrix Tablets. I: Theoretical, *J. Pharm. Sci.* **1974**, *63*, 725−732.
7. Rhine, W. D.; Hsieh, D. S. T.; Langer, R. Polymers for Sustained Macromolecule Release: Procedures to Fabricate Reproducible Delivery systems and Control Release Kinetics, *J. Pharm. Sci.* **1980**, *69*, 265−270.
8. Rhine, W. D.; Sukhatme, V.; Hsieh, D. S. T.; Langer, R. A New Approach to Achieve Zero-Order Release Kinetics from Diffusion-Controlled Polymer Matrix Systems,. In *Controlled Release of bioactive Materials*; Baker, R., Ed.; Academic Press: New York, 1980; pp 177−187.
9. Brooke, D.; Washkuhn, R. J. Zero-Order Drug Delivery System: Theory and Preliminary Testing, *J. Pharm. Sci.* **1977**, *66*, 159−162.
10. Kuu, W. Y.; Yalkowsar, S. H. Multiple-Hole Approach to Zero-Order Release. *J. Pharm. Sci.* **1985**, *74*, 926−933.
11. Tojo, K. Intrinsic Release Rate from Matrix-Type Drug Delivery Systems, *J. Pharm. Sci.* **1985**, *74*, 685−687.
12. Gupta, D. V. S.; Sparks, R. E. Mathematical Model for Progesterone Release from injectible Poly(Lactic Acid) Microcapsules in vitro. In *controlled Release of Bioactive Materials*; Backer, R., Ed.; Academic Press: New York, 1980; pp 198−212.
13. Ayres, J. W.; Lindstrom, F. T. Diffusion Model for Drug Release from Suspensions. I: Theoretical considerations. *J. Pharm. Sci.* **1977**, *66*, 654−662.
14. Lindstrom, F. T.; Ayres, J. W. Diffusion Model for Drug Release from Suspensions. II: Release to a Perfect Sink. *J. Pharm. Sci.* **1977**, *66*, 662−668.
15. Chandrasekaran, S.; Paul, D. R. Dissolution-Controlled Transport from Dispersed Matrixes. *J. Pharm. Sci.* **1982**, *71*, 1399−1402.
16. Fan, L. T.; Singh, S. K. Controlled Release: A Quantitative Treatment, Springer-Verlag: New York, 1989.
17. Abdekhodaie, M. J.; Cheng, Y.-L. Diffusional Release of a Dispersed Solute From Planar and Spherical Matrixes Into Finite External Volume.. *J. Controlled Relat.* **1997**, *43*, 175−182.
18. Chien, Y. W. Thermodynamics of Controlled Drug Release from Polymeric Delivery Devices. In *Controlled Release Polymeric Formulations*; Paul, D. R., Harris, F. W., Eds.; ACS Symposium Series 33, 1976; pp 53−71.
19. Zhou, Y.; Wu, X. Y. Finite Element Analysis of Diffusional Drug Release from Complex Matrix Systems. I. Complex geometries and composite structures. *J. Controlled Release* **1997**, *49*, 277−288.
20. Wu, X. Y.; Zhou, Y. Finite Element Analysis of Diffusional Drug Release from Complex Matrix Systems. II. Factors Influencing Release Kinetics, *J. Controlled Release* **1998**, *51*, 57−72.
21. Wu, X. Y.; Eshun, G.; Zhou, Y. Effect of Interparticulate Interaction on Kinetics of Drug Release in Microsphere Ensembles. *J. Pharm. Sci.* **1998**, *87*, 586−593.
22. Wu, X. Y.; Zhou, Y. Numerical Analysis of Drug Release from Matrix Tablets with Moving Boundaries. *Proc. Intern. Symp. Controlled Release Bioact. Mater.* **1998**, *25*, 451−452.
23. Crank, J. *The Mathematics of Diffusion*; Oxford University Press: London, 1975.

JS9804361

Solid Dispersion of Poorly Water-Soluble Drugs: Early Promises, Subsequent Problems, and Recent Breakthroughs

ABU T. M. SERAJUDDIN†

Contribution from *Pharmaceutics R & D Department, Bristol-Myers Squibb Pharmaceutical Research Institute, New Brunswick, New Jersey 08903-0191.*

Received October 7, 1998. Accepted for publication July 15, 1999.

Abstract □ Although there was a great interest in solid dispersion systems during the past four decades to increase dissolution rate and bioavailability of poorly water-soluble drugs, their commercial use has been very limited, primarily because of manufacturing difficulties and stability problems. Solid dispersions of drugs were generally produced by melt or solvent evaporation methods. The materials, which were usually semisolid and waxy in nature, were hardened by cooling to very low temperatures. They were then pulverized, sieved, mixed with relatively large amounts of excipients, and encapsulated into hard gelatin capsules or compressed into tablets. These operations were difficult to scale up for the manufacture of dosage forms. The situation has, however, been changing in recent years because of the availability of surface-active and self-emulsifying carriers and the development of technologies to encapsulate solid dispersions directly into hard gelatin capsules as melts. Solid plugs are formed inside the capsules when the melts are cooled to room temperature. Because of surface activity of carriers used, complete dissolution of drug from such solid dispersions can be obtained without the need for pulverization, sieving, mixing with excipients, etc. Equipment is available for large-scale manufacturing of such capsules. Some practical limitations of dosage form development might be the inadequate solubility of drugs in carriers and the instability of drugs and carriers at elevated temperatures necessary to manufacture capsules.

Introduction

The enhancement of oral bioavailability of poorly water-soluble drugs remains one of the most challenging aspects of drug development. Although salt formation, solubilization, and particle size reduction have commonly been used to increase dissolution rate and thereby oral absorption and bioavailability of such drugs,[1] there are practical limitations of these techniques. The salt formation is not feasible for neutral compounds and the synthesis of appropriate salt forms of drugs that are weakly acidic or weakly basic may often not be practical. Even when salts can be prepared, an increased dissolution rate in the gastrointestinal tract may not be achieved in many cases because of the reconversion of salts into aggregates of their respective acid or base forms. The solubilization of drugs in organic solvents or in aqueous media by the use of surfactants and cosolvents leads to liquid formulations that are usually undesirable from the viewpoints of patient acceptability and commercialization. Although particle size reduction is commonly used to increase dissolution rate, there is a practical limit to how much size reduction can be achieved by such commonly used methods as controlled crystallization, grinding, etc. The use of very fine powders in a dosage form may also be problematic because of handling difficulties and poor wettability.

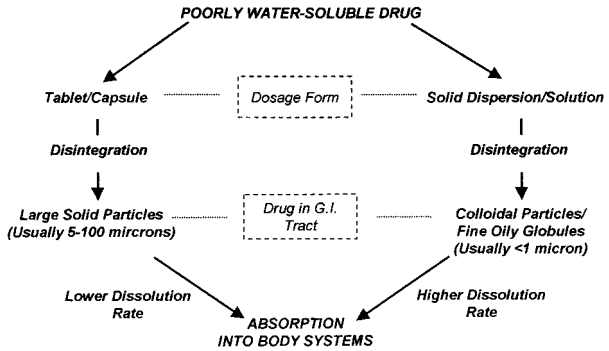

Figure 1—A schematic representation of the bioavailability enhancement of a poorly water-soluble drug by solid dispersion compared with conventional tablet or capsule.

In 1961, Sekiguchi and Obi[2] developed a practical method whereby many of the limitations with the bioavailability enhancement of poorly water-soluble drugs just mentioned can be overcome. This method, which was later termed solid dispersion,[3] involved the formation of eutectic mixtures of drugs with water-soluble carriers by the melting of their physical mixtures. Sekiguchi and Obi[2] suggested that the drug was present in a eutectic mixture in a microcrystalline state. Later, Goldberg et al.[4,5] demonstrated that all the drug in a solid dispersion might not necessarily be present in a microcrystalline state; a certain fraction of the drug might be molecularly dispersed in the matrix, thereby forming a solid solution. In either case, once the solid dispersion was exposed to aqueous media and the carrier dissolved, the drug was released as very fine, colloidal particles. Because of greatly enhanced surface area obtained in this way, the dissolution rate and the bioavailability of poorly water-soluble drugs were expected to be high.

The advantage of solid dispersion, compared with conventional capsule and tablet formulations, is shown schematically in Figure 1.[6] From conventional capsules and tablets, the dissolution rate is limited by the size of the primary particles formed after the disintegration of dosage forms. In this case, an average particle size of 5 μm is usually the lower limit, although higher particle sizes are preferred for ease of handling, formulation, and manufacturing. On the other hand, if a solid dispersion or a solid solution is used, a portion of the drug dissolves immediately to saturate the gastrointestinal fluid, and the excess drug precipitates out as fine colloidal particles or oily globules of submicron size.

Because of such early promises in the bioavailability enhancement of poorly water-soluble drugs, solid dispersion has become one of the most active areas of research in the pharmaceutical field. Numerous papers on various aspects

† Present address: Novartis, 59 Route 10, Building 401, East Hanover, New Jersey 07936.

10.1021/js980403l CCC: $18.00
Published on Web 08/27/1999

of solid dispersion were published since 1961; Chiou and Riegelman[3] and Ford[7] reviewed the early research in this area. Despite an active research interest, the commercial application of solid dispersion in dosage form design has been very limited. Only two products, a griseofulvin-in-poly(ethylene glycol) solid dispersion (Gris-PEG, Novartis) and a nabilone-in-povidone solid dispersion (Cesamet, Lilly) were marketed during three decades following the initial work of Sekiguchi and Obi in 1961. The objectives of the present article are to critically review some of the limitations of solid dispersion that prevented its wider commercial application and to discuss how the situation is now changing because of the availability of new types of vehicles and the development of new manufacturing technologies.

Limitations of Solid Dispersion Systems

Problems limiting the commercial application of solid dispersion involve (a) its method of preparation, (b) reproducibility of its physicochemical properties, (c) its formulation into dosage forms, (d) the scale up of manufacturing processes, and (e) the physical and chemical stability of drug and vehicle. Some of the issues are discussed next.

Method of Preparation—In their pioneering study, Sekiguchi and Obi[2] prepared solid dispersions of sulfathiazole in such carriers as ascorbic acid, acetamide, nicotinamide, nicotinic acid, succinimide, and urea by melting various drug–carrier mixtures. To minimize melting temperatures, eutectic mixtures of the drug with carriers were used. Yet, in all cases, except acetamide, the melting temperatures were >110 °C, which could chemically decompose drugs and carriers.[3] High temperatures (>100 °C) were also utilized by Goldberg et al. in preparing acetaminophen–urea,[4] griseofulvin–succinic acid,[4] and chloramphenicol–urea[8] solid dispersions. After melting, the next difficult step in the preparation of solid dispersions was the hardening of melts so that they could be pulverized for subsequent formulation into powder-filled capsules or compressed tablets. Sekiguchi and Obi[2] cooled the sulfathiazole–urea melt rapidly in an ice bath with vigorous stirring until it solidified. Chiou and Riegelman[9] facilitated hardening of the griseofulvin–PEG 6000 solid dispersion by blowing cold air after spreading it on a stainless steel plate and then storing the material in a desiccator for several days. In preparing primidone–citric acid solid dispersions, Summers and Enever[10] spread the melt on Petri dishes, cooled it by storing the Petri dishes in a desiccator, and finally placed the desiccator at 60 °C for several days. Allen et al.[11] prepared solid dispersions of corticosteroids in galactose, dextrose, and sucrose at 169, 185, and 200 °C, respectively, and then placed them on aluminum boats over dry ice. Timko and Lordi[12] also used blocks of dry ice to cool and solidify phenobarbital–citric acid mixtures that had previously been melted on a frying pan at 170 °C. The fusion method of preparing solid dispersion remained essentially similar over the period of time. More recently, Lin and Cham[13] prepared nifedipine–PEG 6000 solid dispersions by blending physical mixtures of the drug and the carrier in a V-shaped blender and then heating the mixtures on a hot plate at 80–85 °C until they were completely melted. The melts were rapidly cooled by immersion in a freezing mixture of ice and sodium chloride, and the solids were stored for 24 h in a desiccator over silica gel before pulverization and sieving. Mura et al.[14] solidified naproxen–PEG melts in an ice bath and the solids were then stored under reduced pressure in a desiccator for 48 h before they were ground into powders with a mortar and pestle. In another study, Owusu-Ababio et al.[15] prepared a mefenamic acid–PEG solid dispersion by heating the drug–carrier mixture on a hot plate to a temperature above the melting point of mefenamic acid (253 °C) and then cooling the melt to room temperature under a controlled environment.

Another commonly used method of preparing a solid dispersion is the dissolution of drug and carrier in a common organic solvent, followed by the removal of solvent by evaporation.[9,16,17] Because the drug used for solid dispersion is usually hydrophobic and the carrier is hydrophilic, it is often difficult to identify a common solvent to dissolve both components. Large volumes of solvents as well as heating may be necessary to enable complete dissolution of both components. Chiou and Riegelman[9] used 500 mL of ethanol to dissolve 0.5 g of griseofulvin and 4.5 g of PEG 6000. Although in most other reported studies the volumes of solvents necessary to prepare solid dispersions were not specified, it is possible that they were similarly large. To minimize the volume of organic solvent necessary, Usui et al.[18] dissolved a basic drug in a hydro alcoholic mixture of 1 N HCl and methanol, with drug-to-cosolvent ratios ranging from 1:48 to 1:20, because as a protonated species, the drug was more soluble in the acidic cosolvent system than in methanol alone. Some other investigators dissolved only the drug in the organic solvent, and the solutions were then added to the melted carriers. Vera et al.[19] dissolved 1 g of oxodipine per 150 mL of ethanol before mixing the solution with melted PEG 6000. In the preparation of piroxicam–PEG 4000 solid dispersion, Fernandez et al.[20] dissolved the drug in chloroform and then mixed the solution with the melt of PEG 4000 at 70 °C. Many different methods were used for the removal of organic solvents from solid dispersions. Simonelli et al.[16] evaporated ethanolic solvent on a steam bath and the residual solvent was then removed by applying reduced pressure. Chiou and Riegelman[9] dried an ethanolic solution of griseofulvin and PEG 6000 in an oil bath at 115 °C until there was no evolution of ethanol bubbles. The viscous mass was then allowed to solidify by cooling in a stream of cold air. Other investigators used such techniques as vacuum-drying,[20,21] spray-drying,[22–25] spraying on sugar-beads using a fluidized bed-coating system,[26] lyophilization,[27] etc., for the removal of organic solvents from solid dispersions. None of the reports, however, addressed how much residual solvents were present in solid dispersions when different solvents, carriers, or drying techniques were used.

Reproducibility of Physicochemical Properties—In their pioneering studies, Sekiguchi and Obi[2] observed that manufacturing conditions might greatly influence the physicochemical properties of solid dispersions formed. They cooled drug–carrier melts under vigorous stirring conditions to obtain fine and uniform drug particles in solid dispersions. Various investigators observed that heating rate, maximum temperature used, holding time at a high temperature, cooling method and rate, method of pulverization, and particle size may greatly influence the properties of solid dispersions prepared by the melt method. McGinity et al.[28] prepared solid dispersions of tolbutamide in urea and PEG 6000 by flash cooling in a bath of dry ice and acetone or by gradual cooling over a period of several hours by immersion in an oil bath. The powder X-ray diffraction patterns of the tolbutamide–urea solid dispersion differed markedly depending on the cooling rate. The slow-cooled solid dispersion of tolbutamide in urea demonstrated a complete lack of crystallinity for both the drug and urea, whereas the flash-cooled dispersions showed only the absence of drug crystallinity. In the powder X-ray diffraction patterns of tolbutamide–PEG 6000 solid dispersions, peaks for both tolbutamide and PEG 6000 were observed; however, their degree of crystallinity in flash-cooled samples was less than that in the slow-cooled

samples. In another study, a metastable amorphous form of nifedipine was formed in its solid dispersions in PEG 4000 and PEG 6000 when the drug–carrier melts were cooled rapidly, whereas slow cooling of melts or powdering of solidified mass resulted in the crystallization of drug.[29] Ginés et al.[30] studied the effect of fusion temperature on oxazepam–PEG 4000 solid dispersions. Microscopic examination revealed the presence of crystalline oxazepam and the spherulitic form of PEG 4000 in solid dispersions prepared by fusion at 100 °C. In contrast, a fusion temperature of 150 °C produced a solid dispersion with no crystalline form of the drug and the presence of PEG 4000 in a hedritic form. Complete dissolution of drug in the carrier at 150 °C in contrast to 100 °C was reported to be responsible for such a difference in physicochemical properties of the solid dispersions produced. Dordunoo et al.[31] also observed a change of triamterene and temazepam from crystalline to amorphous form in poly(ethylene glycol) solid dispersions when the fusion temperature was increased from 100 to 150 °C. Such changes in physical states of drugs in solid dispersions result into differences in drug dissolution rates in aqueous media.[30] Drug-to-carrier ratio and particle size of solid dispersions were also reported to influence the dissolution rate of drug.[32]

The properties of solid dispersions prepared by the solvent method may also vary depending on manufacturing conditions. The solvent method usually leads to amorphous forms of drugs. However, some crystallinity of drug may be observed depending on the drug-to-carrier ratio used.[33] Although no detailed studies were reported in the literature, it is expected that the nature of solvent used, drug-to-solvent and carrier-to-solvent ratios, drying method, and drying rate may significantly influence the physicochemical properties of solid dispersions formed.

Dosage Form Development—Solid dispersion must be developed into convenient dosage forms, such as capsules and tablets, for their clinical use and successful commercialization. As already mentioned, solid dispersions produced by the melt method are usually hardened at very low temperatures and then pulverized with mortars and pestles. Similarly, solid dispersions produced by the solvent method are also pulverized after solvent removal and hardening. Some of the challenges in the dosage form development of such materials are difficulty of pulverization and sifting of the dispersions, which are usually soft and tacky, poor flow and mixing properties of powders thus prepared, poor compressibility, drug–carrier incompatibility, and poor stability of dosage forms. However, there are very few reports in the literature addressing these important issues.[7] Even the limited number of reports describing any dosage form developmental aspects of solid dispersions only confirm that the task of formulating solid dispersions into capsules or tablets may be a very complex and difficult one. In developing a tablet formulation for the indomethacin–PEG 6000 solid dispersion, Ford and Rubinstein[34] reported that the solid dispersion was not amenable to wet granulation because water could disrupt its physical structure. In addition, the dispersion was soft and tacky. To overcome these problems, the authors adopted an in situ dry granulation method where the excipients (calcium hydrogen phosphate and sodium starch glycolate) were preheated and rotated in a water-jacketed blender at 70 °C, and the indomethacin–PEG 6000 mixture that melted at 100 °C was then added to the moving powder. After mixing, the granules were passed through a 20-mesh sieve and allowed to harden at 25 °C for 12 h. Then, the granules were mixed with a relatively high concentration of magnesium stearate (1%) and compressed into tablets. To process 100 mg of solid dispersion, 506 mg of other excipients were used, thus making the final weight of a 25-mg indomethacin tablet 606 mg. Yet, the tablet did not disintegrate in water despite the use of a large amount of excipients. It dissolved slowly by erosion, and the dissolution rate decreased on aging of the tablet. In another study, the same investigators used an essentially similar in situ dry granulation method for the preparation of tablet dosage forms for a chlorpropamide–urea solid dispersion, where the drug, the carrier, and the excipients were mixed in a rotating flask on a water bath maintained at 100 °C.[35] The properties of these formulations also changed with time, and the authors concluded that aging could "limit their usefulness as prospective dosage forms". During the development of a tablet formulation for a furesemide–poly(vinylpyrrolidone) (PVP) solid dispersion, Akbuga et al.[36] observed that method of preparation, choice of disintegrant and particle size of solid dispersions were critical factors in determining the properties of tablets produced. Despite the use of relatively large amounts of disintegrants, the tablets did not disintegrate. Rather, they dissolved by erosion only, and the erosion rate varied depending on the disintegrant used. In addition, the dissolution rate of tablets prepared by double compression (slugging and recompression of dry granules) was much slower than that of the tablets prepared by single compression. The dissolution rate of tablet was also dependent on the particle size of solid dispersion used; the rate decreased by a factor of 5 when 100-mesh particles were used in place of 80-mesh particles. Also, the compressibility of solid dispersion decreased with a decrease in particle size. In another study, Sjökvist and Nystrom [37] overcame the compression difficulties due to sticking of griseofulvin–xylitol solid dispersions to dies and punches by lubricating die wall and punch faces with 1% (w/w) magnesium stearate suspension before the compression of each tablet. The authors observed that the dissolution rate of tablet was highly sensitive to compression pressure. The sticking of solid dispersion to dies and punches might become so problematic that Kaur et al. [38] resorted to placing small pieces of grease-proof paper between metal surfaces and granules before the compression of tablets.

The lack of disintegration and the slow dissolution of tablets prepared from solid dispersions could be related to the soft and waxy nature of carriers used (e.g., PEG) in many of the reported studies. Such carriers essentially act as strong binders within tablets. During compression, the carriers could plasticize, soften, or melt, filling the pores within tablets and thus making them nondisintegrating. It is also possible that the softened and melted carriers coat the disintegrants and other ingredients used in tablets, and such a coating, along with the reduction of porosity of tablets, make the disintegrants ineffective. Use of a very high ratio of solid dispersion to added excipient might alleviate the problem. In one study,[15] 270 mg of microcrystalline cellulose (Avicel) was used to formulate 30 mg of mefenamic acid–PEG solid dispersion into a tablet with good dissolution. The use of such a high ratio of added excipient would, however, greatly increase the size of tablet and might, therefore, be impractical in most formulations.

Scale Up of Manufacturing Processes—Because very few solid dispersion products prepared by melt or solvent methods have been marketed, there are practically no reports on the scale up of such products. It is apparent from the discussion just presented that the scale up of the methods of preparation of solid dispersions and their dosage forms could be very challenging. In most of the studies reported in the literature, solid dispersions by the melt method were prepared in a small scale by heating drug–carrier mixtures in beakers, frying pans, etc. that were placed on hot plates and then cooling the melts in an ice bath, a dry ice-acetone mixture, etc.[2–5,7–14] Because there could be condensation of moisture over solid disper-

sions during cooling to low temperatures, strict protection from moisture was necessary in all cases. The scale up challenges may be illustrated with the example of the preparation of a phenytoin−PEG 4000 solid dispersion by Yakou et al.[39] The drug−carrier mixture was heated at 250 °C under constant stirring until a clear homogeneous melt was obtained, and the melt was air-cooled by spreading on stainless steel trays. The trays were stored in a desiccator for 3 days to enhance solidification of the solid dispersion. The resulting material was then crushed in a cutter mill, and the powders were sieved to collect a sieve fraction of 105−177-μm particle size for use in the dosage form. The scale up of such a method would be difficult and it might even be impractical in many cases because of possible degradation of both drug and carrier at high temperatures used. The scale up might also necessitate a large capital investment because a chemical plant-like facility, rather than a common pharmaceutical dosage form manufacturing plant, would be required to process and manufacture the products. For scale up of the cooling process, Lefebvre et al.[40] recommended such continuous operation as cooling on the surfaces of moving belts or rotating cylinders, and spray congealing. The practical application of the methods, however, was not demonstrated. Kennedy and Niebergall[41] described a hot-melt fluid bed method whereby nonpareils could be coated with PEGs having molecular weights between 1450 and 4600. A similar method can possibly be used to deposit solid dispersions on nonpareils and might in the future find application in the manufacture and scale up of solid dispersion formulations.

The physicochemical properties and stability of solid dispersions may also be affected by scale up because heating and cooling rates of solid dispersions under large-scale manufacturing conditions may differ greatly from that in small beakers.[28,29] Drug−carrier compatibility at a high temperature also requires careful consideration. Dubois and Ford[42] reported the chain scission of PEG 600 during fusion with disulfiram, furosemide, chlorthiazide, and chlorpropamide.

The scale up of the solvent method of preparing solid dispersions may also be very challenging. A chemical plant environment would be necessary to evaporate hundreds and even thousands of liters of organic solvents necessary to prepare solid dispersions for kilogram quantities of drugs.[17,20] The cost of recovery of these solvents may be very high. Removal of residual amounts of potentially toxic organic solvents such as chloroform and methanol from large masses of material may be difficult because the solid dispersions are usually amorphous and may exist in viscous and waxy forms. Solvates may also be formed with drugs and carriers. Because most dosage form manufacturing facilities are not equipped to handle large volumes of organic solvents, one way to resolve the issue might be the designation of solid dispersion as an active pharmaceutical ingredient or bulk drug substance. In that case, the responsibility of the manufacture of solid dispersion can be shifted to the chemical plant. It would be necessary to conduct all developmental activities using the solid dispersion, so this approach might not be suitable for situations where active pharmaceutical ingredients have multiple uses (e.g., oral and parenteral).

The final step in the manufacturing process, which is the conversion of solid dispersions into stable and marketable dosage forms, may be the most difficult one to scale up, optimize, and validate. Most of the commonly used solid dispersion vehicles are soft and sticky and, as a result, the pulverized forms of solid dispersions produced by such vehicles may not be amenable to processing by high-speed capsule or tablet filling machines.

Stability—The physical instability of solid dispersions due to crystallization of drugs was the subject of most published reports in the literature.[3,7] In a solid dispersion prepared by the melt method, a certain fraction of the drug may remain molecularly dispersed, depending on its solubility in the carrier used, thus forming a solid solution. How the excess drug exists may greatly depend on the method of manufacture of the system; it may, as a whole or in part, form a supersaturated solution, separate out as an amorphous phase, or crystallize out. The supersaturated and amorphous forms may, in turn, crystallize out on aging. Similarly, certain carriers may also exist in thermodynamically unstable states in solid dispersions and undergo changes with time. Chiou[43] reported that griseofulvin precipitated out in an amorphous form in a griseofulvin−PEG 6000 solid dispersion during the time of its preparation. The amorphous material crystallized out on aging, except when the drug concentration in the dispersion was 5% or less. Ford and Rubinstein[44] attributed similar crystallization as the cause for a decrease in dissolution rate of drug from indomethacin−PEG 6000 solid dispersions with time. The decrease in the dissolution rate of indomethacin was also dependent on drug concentration in the solid dispersion. The decrease was greater for a higher drug concentration because a larger fraction of drug crystallized out. In another study, Suzuki and Sunada[45] observed that on exposure of a nifedipine−nicotinamide−hydroxypropylmethylcellulose (HPMC) solid dispersion to 60% RH at 30 °C or 75% RH at 40 °C for 1 month, nifedipine converted from the amorphous to the crystalline state, thus lowering the dissolution rate of nifedipine drastically. No conversion of nifedipine to the crystalline state was observed when the solid dispersion was stored at an elevated temperature in the absence of humidity. Although the presence of HPMC facilitated the conversion of nifedipine to an amorphous state during the cooling of drug−nicotinamide melt to room temperature at the time of manufacturing, it did not prevent the subsequent crystallization of drug under humid conditions. Pronounced decreases in dissolution rates due to drug crystallization were also reported for tablets prepared from solid dispersions.[34,35] No such decrease in dissolution rate on aging was observed by Khalil et al.[46] in corticosteroid−PEG solid dispersions prepared with a drug-to-carrier ratio of 1:99, possibly because most of the drug was molecularly dispersed in the carrier. The corticosteroid, however, exhibited chemical degradation due to oxidation by the peroxides present in PEG. The cooling rate of solid dispersions may also significantly influence their aging behavior. It has been reported that the crystallinity of drug in solid dispersions is less influenced by aging when a slow cooling rate is used because thermodynamically more stable systems are produced during the time of preparation.[47,48]

The conversion of drug to crystalline state is also the primary stability issue with solid dispersions prepared by the solvent method. PVP, which is commonly used as a carrier in such solid dispersions, is amorphous and does not convert to a crystalline state. However, certain other carriers may convert from their amorphous states to crystalline states in solid dispersions. Zografi and coworkers[49,50] extensively studied the physicochemical properties of the amorphous states of drugs and excipients and observed that the crystallization of amorphous materials is facilitated by moisture. This effect is why strict protection from moisture is necessary during the preparation and storage of most solid dispersions. Doherty and York[51] studied the stability of furosemide−PVP solid dispersion in the temperature range of 6 to 45 °C and 40% RH for up to 1 year. They did not observe any crystallization of furosemide and suggested that PVP may indeed act as a

stabilizer in the solid dispersion by retarding crystallization of drug at a relatively low humidity. Rapid crystallization of furosemide in the solid dispersion was, however, evident when the humidity was raised to 75% RH. Similar observations were also made by Guillaume et al.[52] for an oxodipine−PVP solid dispersion where no crystallization of oxodipine was observed in 18 months when samples were stored under 55% RH at various temperatures, but the drug crystallized out at 80% RH. The stabilization of drugs in amorphous forms in solid dispersions is an active area of research in the pharmaceutical field. For an indomethacin−PVP solid dispersion system, Taylor and Zografi[53] suggested that hydrogen bonding between the drug and PVP might offer an explanation for the absence of drug crystallization. Lu and Zografi[54] recently demonstrated that indomethacin forms a completely miscible amorphous mixture with citric acid and PVP when the weight fraction of PVP in the ternary mixture exceeds 0.3 weight fraction. Thus, both the choice of carrier and the drug-to-carrier ratio are important considerations in the stabilization of solid dispersions.

Breakthroughs in Solid Dispersion Technology

Because of the various limitations just mentioned, it is not surprising that the solid dispersion system, despite its many potential advantages, has not been widely used in pharmaceutical dosage forms. Under the present health care economic climate, the goal of any drug development program in the pharmaceutical industry is to rapidly progress a new chemical entity from the discovery stage to clinical testing to determine whether it is safe and clinically effective. The limited supply of the bulk drug substance at the early drug development phase and the accelerated time line would not allow a formulator to address most of the challenges (vide supra) of a solid dispersion formulation. Most importantly, if a compound proves promising in early clinical testing, the scale up of complex manufacturing processes for the development of marketable dosage forms cannot be ensured.

Two recent breakthroughs in the formulation of solid dispersion systems involve (1) the development of technologies to fill solid dispersions directly into hard gelatin capsules and (2) the availability of surface-active and self-emulsifying carriers. As a result, there is renewed interest in such systems for use in commercial development of drug products.[6,55]

Direct Capsule-Filling—Although the filling of semisolid materials into hard gelatin capsules as melts, which solidify at room temperature, was first described by Francois and Jones in 1978,[56] it was not until much later that the potential application of the technique for solid dispersions was fully realized. Chatham[57] reported the possibility of preparing PEG-based solid dispersions by filling drug−PEG melts in hard gelatin capsules. By using PEG with molecular weights ranging from 1000 to 8000, Serajuddin et al.,[58] however, demonstrated that a PEG by itself might not be a suitable carrier for solid dispersion of poorly water-soluble drugs intended for direct filling into hard gelatin capsules. They dissolved a poorly water-soluble drug, REV5901, in molten PEG 1000, PEG 1450, and PEG 8000 and filled the hot solutions into hard gelatin capsules such that each size 0 capsule contained 100 mg of drug and 550 mg of PEG. At room temperature, solid plugs were formed inside the capsules, where the drug remained molecularly dispersed in the carriers. Although a sink condition existed for the dissolution of 100 mg of the weakly basic REV5901 ($pK_a \sim 3.6$) in 900 mL of simulated gastric fluid (drug solubility = 0.7 mg/mL at 37 °C), the dissolution of drug from all PEG-based solid dispersions was incomplete.

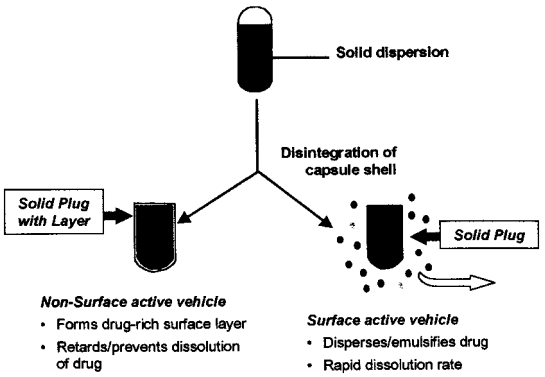

Figure 2—A schematic representation of the comparative dissolution of a poorly water-soluble drug from surface-active versus nonsurface-active vehicles.

Because the water-soluble carrier dissolved more rapidly than the drug, drug-rich layers were formed over the surfaces of dissolving plugs, which prevented further dissolution of drug from solid dispersions. The dissolution was practically zero at pH > 2, where the solubility of drug was low and a drug layer coated the surface of the solid plug as soon as the capsule shell disintegrated. Corrigan[59] also reported the possibility of such a retardation of drug dissolution from solid dispersions.

Surface-Active Carriers—The direct filling of melts into hard gelatin capsules would not be a viable method for the preparation of solid dispersions unless the formation of drug-rich layers on the surfaces of dissolving plugs could be prevented. Serajuddin et al.[58,60] achieved a complete dissolution of drug from solid dispersions by using surface-active or self-emulsifying carriers. The vehicles acted as dispersing or emulsifying agents for the liberated drug, thus preventing the formation of any water-insoluble surface layers. Although the liberated drug remained undissolved in the dissolution medium when its concentration exceeded its saturation solubility, it was dispersed or emulsified in a finely divided state because of surface activity of the dissolved vehicle.[58,60] The high surface area of a drug produced in this way would facilitate its dissolution in the gastrointestinal fluid, especially in the presence of bile salts, lecithin, and lipid digestion mixtures.[61]

The advantage of a surface-active carrier over a nonsurface-active one in the dissolution of drug from a capsule formulation is shown schematically in Figure 2.[6] The physical state of drug in a solid dispersion must, however, be carefully considered in evaluating the advantage of a surface-active vehicle. As mentioned earlier, the drug can be molecularly dispersed in the carrier to form a solid solution or it can be dispersed as particles. It can also be both partially dissolved and partially dispersed in the carrier. The potential for the formation of a continuous drug-rich surface layer is possibly greater if the drug is molecularly dispersed, whereas the drug dispersed as particulates may be more prone to dissociation from the water-soluble matrix. It is, however, rare that the drug is dispersed just as particulates and is not at least partially dissolved in the vehicle. Therefore, a surface-active carrier may be preferable in almost all cases for the solid dispersion of poorly water-soluble drugs.

The interest in surface-active and self-emulsifying carriers for solid dispersion of poorly water-soluble drugs increased greatly in recent years.[58,60,62−67] For ease of manufacturing, the carriers must be amenable to liquid filling into hard gelatin capsules as melts. The melting temperatures of carriers should be such that the solutions do not exceed ~70 °C, which is the maximum acceptable temperature for hard gelatin capsule shells.[68] Some of the manufacturing difficulties mentioned earlier may be en-

countered if solid dispersion products using surface-active carriers are prepared by methods other than direct filling into hard gelatin capsules; for examples, the solvent evaporation method,[69] compaction into tablets from granules,[37] etc.

One surface-active carrier that has commonly been used in solid dispersion for the bioavailability enhancement of drugs is Gelucire 44/14 (Gattefossé Corp., France).[58,62–65,67] It is a mixture of glyceryl and PEG 1500 esters of long-chain fatty acids and is official in the European Pharmacopeia as lauryl macrogolglycerides; the suffixes 44 and 14 in its name refer, respectively, to its melting point and hydrophilic–lipophilic balance (HLB) value. Another surface-active carrier that generated certain interest in recent years is Vitamin E TPGS NF (Eastman, Kingsport, TN),[70] which is prepared by the esterification of the acid group of *d*-α-tocopheryl acid succinate by PEG 1000. The material has an HLB value of 13 and is miscible with water in all parts. Its melting point is, however, relatively low (38 °C) and it may require mixing with other carriers to increase melting temperatures of formulations.

In search of alternative surface-active carriers, Serajuddin and co-workers[60,71] demonstrated that a commonly used surfactant, polysorbate 80, could be used in solid dispersions by mixing it with solid PEG. Although polysorbate 80 is liquid at room temperature, it forms a solid matrix when it is mixed with a PEG because it incorporates within the amorphous regions of PEG solid structure. As high as 50% (w/w) polysorbate 80 could be incorporated in a PEG with a lowering of <6 °C in its melting point. Even when 75% (w/w) polysorbate 80 was incorporated, PEG remained semisolid, and the lowering of the melting temperature of the PEG used was <12 °C.[71] The crystalline structure of solid PEG was minimally affected by polysorbate 80 because the two compounds have low miscibility in each other. Other investigators also reported enhanced dissolution[72] and bioavailability[65] of drugs from PEG–polysorbate carriers. Law et al.[73] reported a >2-fold increase in the dissolution rate of nifedipine from a PEG-based solid dispersion after incorporation of 5% (w/w) phosphatidylcholine. Increased dissolution rate of drug from solid dispersions in PEG containing varying amounts of ionic and nonionic surfactants, including sodium dodecyl sulfate and polysorbate 80, were also reported by Sjökvist et al.[74] The authors, however, pulverized the waxy material instead of filling them into hard gelatin capsules as melts.

Ease of Manufacturing—Cadé and Madt[75] and Shah et al.[76] reviewed various formulation and processing considerations for liquid-filled hard gelatin capsules. Initial formulation development studies can be conducted by filling hot solutions or dispersions into hard gelatin capsule shells manually by using pipets or by using laboratory scale semiautomatic equipment.[77] Equipment is also available to scale up the manufacturing process and for large scale manufacturing.[78] As mentioned earlier, the temperature of solutions during the filling of hard gelatin capsules should not exceed 70 °C.[68] Solutions can also be filled into soft gelatin capsules for which the solution temperature should remain <40 °C.[79] Several hard gelatin[80,81] and soft gelatin[82] capsule products prepared according to these techniques have been marketed in recent years.

Bioavailability Enhancement—The reports on the bioavailability enhancement by solid dispersion in surface-active carriers are promising. The human bioavailability of the poorly soluble REV5901 from a solid dispersion in Gelucire 44/14 under a fasting regimen was much higher than that of a tablet formulation even though the micronized form of drug and a wetting agent were used in the tablet.[83] The bioavailability of ubidecarenone in dogs from solid dispersion in Gelucire 44/14 and the Gelucire 44/14–lecithin mixture were, respectively, two and three times higher than that of commercially available tablet.[63] The bioavailability of another poorly water-soluble drug, RP69698, in dogs was 4.5 times higher (27.6% versus 6%) from its solid dispersion in a PEG 3350–Labrasol–polysorbate 80 system than from an aqueous suspension in 0.5% methylcellulose.[65] Aungst et al.[67] reported that the bioavailability of an HIV protease inhibitor, DMP323, in dogs from a PEG-based formulation decreased from 49.6 to 5.2% when the dose was increased from 100 to 350 mg. No such drastic decrease in bioavailability was observed in a Gelucire 44/14-based formulation of DMP323; the bioavailability values were 68.9 and 49.5% after doses of 85 and 350 mg, respectively. The bioavailability of ritonavir (Norvir, Abbott), another poorly soluble HIV protease inhibitor (solubility <1 μg/mL at pH >2), was enhanced by formulation as a solid dispersion in a mixture of such surface-active carriers as Gelucire 50/13, polysorbate 80 and polyoxyl 35 castor oil.[84]

Special Considerations for Surfactant-Based Solid Dispersions—Solid dispersion in surface-active carriers may not be the answer to all bioavailability problems with poorly water-soluble drugs. One of the limitations of bioavailability enhancement by this method might be the low solubility of drug in available carriers.[64,85] The desired doses of a drug cannot be solubilized and filled into hard gelatin capsules if adequate solubility in a carrier cannot be obtained. Dordunoo et al.[64] reported that the particle size of a drug in a solid dispersion remained unchanged if it is just mixed with the carrier instead of dissolving in it. On the other hand, if the drug is dissolved by heating in excess of its solubility in the carrier under normal storage condition, it may subsequently crystallize out from the solid dispersion. Either situation would defeat the purpose of bioavailability enhancement of poorly water-soluble drugs by solid dispersion, as described in Figure 1.

The crystallization of ritonavir from the supersaturated solution in a solid dispersion system was responsible for the withdrawal of the ritonavir capsule (Norvir, Abbott) from the market.[86] The crystallization of drug adversely influenced the dissolution of the ritonavir capsule, and the product was switched to a thermodynamically stable solution formulation. Aungst et al.[67] also stressed the importance of drug solubility in carriers in the development of capsule formulations. They prepared high-dose formulations of a water-insoluble HIV protease inhibitor by dissolving it in carriers at an elevated temperature only, and the formulations were used for bioavailability testing in dogs within 24 h of preparation when no crystallization occurred. The authors cautioned that precipitation of drug could occur upon storage at room temperature over a longer period of time, and that lowering of drug concentration in the carrier would be necessary to ensure long-term physical stability of the formulation.

To ensure that a drug would not crystallize out of solid dispersion at the desired storage temperature, it is important to screen the drug solubility in different carriers at such a temperature. However, no practical method for determining or estimating drug solubility in a carrier at a relatively low temperature, where the carrier exists in a solid state, has been reported in the literature. The relative solubility of a drug in different carriers may be determined by equilibrating the drug at an elevated temperature where all the carriers exist in a liquid state.[67] If the solubility of a drug in a carrier at an elevated temperature is much higher than the concentration required for solid dispersion, an accurate estimation of solubility at room temperature might not be necessary and a reasonable assumption might be made that the drug would not precipitate out. When a better estimation of solubility is needed, one practical

approach is the determination of solubility−temperature relationship of drug in a chemically related carrier that exists as liquid at a wider range of temperature. For example, for the purpose of estimating the solubility of a drug in a solid PEG at room temperature, the solubility may be determined at an elevated temperature where the PEG exists in a liquid state. Then the solubility of drug at a lower temperature may be estimated from the solubility−temperature relationship in a related vehicle, PEG 400, which remains liquid at a wider range of temperature. This method assumes, however, that similar temperature−solubility relationships for the drug would exist in both PEGs and that the relationship would not change when one of them solidifies. The solubility may also be estimated by microscopic examination of solid solutions with increasing drug concentration for any possible crystallization of drug, assuming that the drug does not exist as a separate amorphous phase and the crystallization occurs in a relatively short period of time. A similar microscopic technique was use for determining the solubility of diazepam in liquid crystalline phases of lecithin.[87]

Another possible limitation of the use of surface-active carrier reported by Aungst et al.[67] is that the bioavailability of a drug may vary depending on the amount of carrier administered along with it. This variation is because different amounts of a surface-active carrier may have different solubilization or dispersion effects on a drug in the gastrointestinal fluid. Serajuddin et al.[58,60] reported a method whereby the rate and efficiency of dispersion of drug in aqueous media from different formulations can be studied.

In addition to the solubility, careful attention must be given to the drug-to-carrier ratio in the successful development of a formulation. When the solubility of a particular drug is relatively low, a high drug-to-carrier ratio is necessary to deliver it in a solubilized state, and, therefore, the dose has to be low if it is desired that the total dose is delivered as a single unit. As mentioned earlier, any attempt to supersaturate the drug in solid dispersion to reduce drug-to-carrier ratio may lead to stability problems and, ultimately, to product failure.

Attention should also be given to optimization and validation of the manufacturing process. It is not only that the physicochemical properties of the drug is affected by the cooling rate, the properties of carriers in a solid dispersion might also be influenced by the solidification rate of the product.[88,89] The implication of this observation on bioavailability and stability of drug product is not known.

Future Prospects

Despite many advantages of solid dispersion, issues related to preparation, reproducibility, formulation, scale up, and stability limited its use in commercial dosage forms for poorly water-soluble drugs. Successful development of solid dispersion systems for preclinical, clinical, and commercial use have been feasible in recent years due to the availability of surface-active and self-emulsifying carriers with relatively low melting points. The preparation of dosage forms involves the dissolving of drugs in melted carriers and the filling of the hot solutions into hard gelatin capsules. Because of the simplicity of manufacturing and scale up processes, the physicochemical properties and, as a result, the bioavailability of solid dispersions are not expected to change significantly during the scale up. For this reason, the popularity of the solid dispersion system to solve difficult bioavailability issues with respect to poorly water-soluble drugs will grow rapidly. Because the dosage form can be developed and prepared using small amounts of drug substances in early stages of the drug development process, the system might have an advantage over such other commonly used bioavailability enhancement techniques as micronization of drugs and soft gelatin encapsulation.

One major focus of future research will be the identification of new surface-active and self-emulsifying carriers for solid dispersions. Only a small number of such carriers are currently available for oral use. Some carriers that are used for topical application of drug only may be qualified for oral use by conducting appropriate toxicological testing. One limitation in the development of solid dispersion systems may the inadequate drug solubility in carriers, so a wider choice of carriers will increase the success of dosage form development. Research should also be directed toward identification of vehicles or excipients that would retard or prevent crystallization of drugs from supersaturated systems. Attention must also be given to any physiological and pharmacological effects of carriers used. Many of the surface-active and self-emulsifying carriers are lipidic in nature, so potential roles of such carriers on drug absorption, especially on their inhibitory effects on CYP3-based drug metabolism and *p*-glycoprotein-mediated drug efflux, will require careful consideration.[90]

In addition to bioavailability enhancement, much recent research on solid dispersion systems was directed toward the development of extended-release dosage forms. Although a review of literature on this aspect of solid dispersion is outside the scope of the present article, it may be pointed out that this area of research has been reinvigorated by the availability of surface-active and self-emulsifying carriers and the development of new capsule-filling processes. Because the formulation of solid dispersion for bioavailability enhancement and extended release of drugs may employ essentially similar processes, except for the use of slower dissolving carriers for the later use,[91] it is expected that the research in these two areas will progress simultaneously and be complementary to each other.

Physical and chemical stability of both the drug and the carrier in a solid dispersion are major developmental issues, as exemplified by the recent withdrawal of ritonavir capsules from the market,[86] so future research needs to be directed to address various stability issues. The semisolid and waxy nature of solid dispersions poses unique stability problems that might not be seen in other types of solid dosage forms. Predictive methods will be necessary for the investigation of any potential crystallization of drugs and its impact on dissolution and bioavailability. Possible drug−carrier interactions must also be investigated.

Although, as mentioned earlier, the direct filling of solid dispersion into hard gelatin capsules is a relatively simple process, there are very limited reports on the scale up of the technology. Further studies on scale up and validation of the process will be essential. Many problems and challenges still remain with solid dispersion systems. Nevertheless, as a result of recent breakthroughs, it will continue to be one of the exciting frontiers of drug development.

References and Notes

1. Wadke, D. A.; Serajuddin, A. T. M.; Jacobson, H. Preformulation testing. In *Pharmaceutical Dosage Forms: Tablets, Vol. 1*; Lieberman, H. A.; Lachman, L.; Schwartz, J. B., Eds.; Marcel Dekker: New York, 1989; pp 1−73.
2. Sekiguchi, K.; Obi, N. Studies on absorption of eutectic mixture. I. A comparison of the behavior of eutectic mixture of sulfathiazole and that of ordinary sulfathiazole in man. *Chem. Pharm. Bull.* **1961**, *9*, 866−872.

3. Chiou, W. L.; Riegelman, S. Pharmaceutical applications of solid dispersion systems. *J. Pharm. Sci.* **1971**, *60*, 1281−1302.
4. Goldberg, A. H.; Gibaldi, M.; Kanig, J. L. Increasing dissolution rates and gastrointestinal absorption of drugs via solid solutions and eutectic mixtures II. Experimental evaluation of eutectic mixture: urea-acetaminophen system. *J. Pharm. Sci.* **1966**, *55*, 482−487.
5. Goldberg, A. H.; Gibaldi, M.; Kanig, J. L. Increasing dissolution rates and gastrointestinal absorption of drugs via solid solutions and eutectic mixtures III. Experimental evaluation of griseofulvin-succinic acid solution. *J. Pharm. Sci.* **1966**, *55*, 487−492.
6. Serajuddin, A. T. M. Bioavailability enhancement of poorly water-soluble drugs by solid dispersion in surface active and self-emulsifying vehicles. *Bull. Technique Gattefossé* **1997**, *90*, 43−50.
7. Ford, J. L. The current status of solid dispersions. *Pharm. Acta Helv.* **1986**, *61*, 69−88.
8. Goldberg, A. H.; Gibaldi, M.; Kanig, J. L.; Mayersohn, M. Increasing dissolution rates and gastrointestinal absorption of drugs via solid dispersion in eutectic mixtures IV. Chloramphenicol-urea system. *J. Pharm. Sci.* **1966**, *55*, 581−583.
9. Chiou, W. L.; Riegelman, S. Preparation and dissolution characteristics of several fast-release solid dispersions of griseofulvin. *J. Pharm. Sci.* **1969**, *58*, 1505−1509.
10. Summers, M. P.; Enever, R. P. Preparation and properties of solid dispersion system containing citric acid and primidone. *J. Pharm. Sci.* **1976**, *65*, 1613−161.
11. Allen, L. V.; Yanchick, V. A.; Maness, D. D. Dissolution rates of corticosteroids utilizing sugar glass dispersions. *J. Pharm. Sci.* **1977**, *66*, 494−497.
12. Timko, R. J.; Lordi, N. G. Thermal characterization of citric acid solid dispersions with benzoic acid and phenobarbital. *J. Pharm. Sci.* **1979**, *68*, 601−605.
13. Lin, C. W.; Cham, T. M. Effect of particle size on the available surface area of nifedipine from nifedipine-poly(ethylene glycol) 6000 solid dispersions. *Int. J. Pharm.* **1996**, *127*, 261−272.
14. Mura, P.; Manderioli, A.; Bramanti, G.; Ceccarelli, L. Properties of solid dispersion of naproxen in various poly(ethylene glycol)s. *Drug Dev. Ind. Pharm.* **1996**, *22*, 909−916.
15. Owusu-Ababio, G.; Ebube, N. K.; Reams, R.; Habib, M. Comparative dissolution studies for mefenamic acid-poly-(ethylene glycol) solid dispersion systems and tablets. *Pharm. Dev. Technol.* **1998**, *3*, 405−412.
16. Simonelli, A. P.; Mehta, S. C.; Higuchi, W. I. Dissolution rates of high energy poly(vinylpyrrolidone)(PVP)-sulfathiazole coprecipitates. *J. Pharm. Sci.* **1969**, *58*, 538−549.
17. Thakkar, A. L.; Hirsch, C. A.; Page, J. G. Solid dispersion approach for overcoming bioavailability problems due to polymorphism of nabilone, a cannabinoid derivative. *J. Pharm. Pharmacol.* **1977**, *29*, 783−784.
18. Usui, F.; Maeda, K.; Kusai, A.; Ikeda, M.; Nishimura, K.; Yamamoto, K. Dissolution improvement of RS-8359 by the solid dispersion prepared by the solvent method. *Int. J. Pharm.* **1998**, *170*, 247−256.
19. Vera, N.; Veiga, M. D.; Cadorniga, R. Solid dispersions of oxodipine/PEG 6000 characterization and dissolution study. *S. T. P. Pharma Sci.* **1991**, *1*, 125−129.
20. Fernandez, M.; Rodriguez, I. C.; Margarit, M. V.; Cerezo, A. Characterization of solid dispersions of piroxicam/poly-(ethylene glycol) 4000. *Int. J. Pharm.* **1992**, *84*, 197−202.
21. Singla, A. K.; Vijan, T. Dissolution of sulfamethoxazole from poly(ethylene glycol) and poly(vinylpyrrolidone) solid dispersions. *Drug Dev. Ind. Pharm.* **1990**, *16*, 875−882.
22. Corrigan, O. I.; Holohan, E. M. Amorphous spray-dried hydroflumethiazide-poly(vinylpyrrolidone) systems: physicochemical properties. *J. Pharm. Pharmacol.* **1984**, *36*, 217−221.
23. Takahashi, Y.; Tsukuda, T.; Izumi, C.; Ikemoto, K.; Kokubun, K.; Yagi, N.; Takada, M. Preparation of solid dispersion systems of disopyramide with poly(vinylpyrrolidone) and γ-cyclodextrin. *Chem. Pharm. Bull.* **1988**, *36*, 2708−2710.
24. Jachowicz, R.; Nürnberg, E.; Hoppe, R. Solid dispersions of oxazepam. *Int. J. Pharm.* **1993**, *99*, 321−325.
25. Kai, T.; Akiyama, Y.; Nomura, S.; Sato, M. Oral absorption improvement of poorly soluble drug using solid dispersion technique. *Chem. Pharm. Bull.* **1996**, *44*, 568−571.
26. Ho, H. O.; Shu, H. L.; Tsai, T.; Sheu, M. T. The preparation and characterization of solid dispersions on pellets using a fluidized bed system. *Int. J. Pharm.* **1996**, *139*, 223−229.
27. Betageri, G. V.; Makarla, K. R. Enhancement of dissolution of glyburide by solid dispersion and lyophilization techniques. *Int. J. Pharm.* **1995**, *126*, 155−160.
28. McGinity, J. W.; Maincent, P.; Steinfink, H. Crystallinity and dissolution rate of tolbutamide solid dispersions prepared by the melt method. *J. Pharm. Sci.* **1984**, *73*, 1441−1444.
29. Save, T.; Venkitachalam, P. Studies on solid dispersions of nifedipine. *Drug Dev. Ind. Pharm.* **1992**, *18*, 1663−1679.
30. Ginés, J. M.; Arias, M. J.; Moyano, J. R.; Sanchez-Soto, P. J. Thermal investigation of crystallization of poly(ethylene glycol)s in solid dispersions containing oxazepam. *Int. J. Pharm.* **1996**, *143*, 247−253.
31. Dordunoo, S. K.; Ford, J. L.; Rubinstein, M. H. Physical stability of solid dispersions containing triamterene or temazepam in poly(ethylene glycol)s. *J. Pharm. Pharmacol.* **1997**, *49*, 390−396.
32. Ford, J. L.; Elliott, P. N. C. The effect of particle size on some in vitro and in vivo properties of indomethacin-poly(ethylene glycol) 6000 solid dispersions. *Drug Dev. Ind. Pharm.* **1985**, *11*, 537−549.
33. Tantishaiyakul, V.; Kaewnopparat, N.; Ingkatawornwong, S. Properties of solid dispersions of piroxicam in poly(vinylpyrrolidone) K-30. *Int. J. Pharm.* **1996,** *143*, 59−66.
34. Ford, J. L.; Rubinstein, M. H. Formulation and aging of tablets prepared from indomethacin-poly(ethylene glycol) 6000 solid dispersions. *Pharm. Acta Helv.* **1980**, *55*, 1−7.
35. Ford, J. L.; Rubinstein, M. H. Preparation, properties and aging of tablets prepared from the chlorpropamide-urea solid dispersion. *Int. J. Pharm.* **1981**, *8*, 311−322.
36. Akbuğa, J.; Gürsoy, A.; Yetimoğlu, F. Preparation and properties of tablets prepared from furosemide-PVP solid dispersion systems. *Drug Dev. Ind. Pharm.* **1988**, *14*, 2091−2108.
37. Sjökvist, E.; Nyström, C. Physicochemical aspects of drug release. XI. Tableting properties of solid dispersions using xylitol as carrier material. *Int. J. Pharm.* **1991**, *67*, 139−153.
38. Kaur, R.; Grant, D. J. W.; Eaves, T. Comparison of poly-(ethylene glycol) and polyoxyethylene stearate as excipients for solid dispersion systems of griseofulvin and tolbutamide II: Dissolution and solubility studies. *J. Pharm. Sci.* **1980**, *69*, 1321−1326.
39. Yakou, S.; Umehara, K.; Sonobe, T.; Nagai, T.; Sughihara, M.; Fukuyama, Y. Particle size dependency of dissolution rate and human bioavailability of phenytoin powders and phenytoin-poly(ethylene glycol) solid dispersions. *Chem. Pharm. Bull.* **1984**, *32*, 4130−4136.
40. Lefebvre, C.; Brazier, M.; Robert, H.; Guyot-Hermann, A. M. Les dispersions solides, pourquoi et comment? Aspect industriel. *S. T. P. Pharma.* **1985**, *1*, 300−322.
41. Kennedy, J. P.; Niebergall, P. J. Development and optimization of a solid dispersion hot-bed fluid bed coating method. *Pharm. Dev. Technol.* **1996**, *1*, 51−62.
42. Dubois, J. L.; Ford, J. L. Similarities in the release rates of different drugs from poly(ethylene glycol) 600 solid dispersions. *J. Pharm. Pharmacol.* **1985**, *37*, 494−496.
43. Chiou, W. L. Pharmaceutical applications of solid dispersion systems: X-ray diffraction and aqueous solubility studies on griseofulvin-poly(ethylene glycol) 6000 systems. *J. Pharm. Sci.* **1977**, *66*, 989−991.
44. Ford, J. L.; Rubinstein, M. H. Aging of indomethacin-poly-(ethylene glycol) 6000 solid dispersion. *Pharm. Acta Helv.* **1979**, *54*, 353−358.
45. Suzuki, H.; Sunada, H. Some factors influencing the dissolution of solid dispersions with nicotinamide and hydroxypropylmethylcellulose as combined carriers. *Chem. Pharm. Bull.* **1998**, *46*, 1015−1020.
46. Khalil, S. A. H.; El-Fattah, S. A.; Mortada, L. M. Stability and dissolution rates of corticosteroids in poly(ethylene glycol) solid dispersions. *Drug Dev. Ind. Pharm.* **1984**, *10*, 771−787.
47. Duclos, R.; Grenet, J.; Saiter, J. M.; Besançon, P.; Orecchioni, A. M. Effect of aging on progesterone-poly(ethylene glycol) 6000 dispersions. X-ray study. *Drug Dev. Ind. Pharm.* **1990**, *16*, 255−265.
48. Saers, E. S.; Nyström, C.; Aldén, M. Physicochemical aspects of drug release. XVI. The effect of storage on drug dissolution from solid dispersions and the influence of cooling rate and incorporation of surfactant. *Int. J. Pharm.* **1993**, *90*, 105−118.
49. Hancock, B. C.; Zografi, G. Characteristics and significance of the amorphous state in pharmaceutical system. *J. Pharm. Sci.* **1997**, *86*, 1−12.
50. Andronis, V.; Yoshioka, M.; Zografi, G. Effects of sorbed water on the crystallization of indomethacin from the amorphous state. *J. Pharm. Sci.* **1997**, *86*, 346−351.
51. Doherty, C.; York, P. Accelerated stability of an X-ray amorphous furesemide-poly(vinylpyrrolidone) solid dispersion. *Drug Dev. Ind. Pharm.* **1989**, *15*, 1969−1987.
52. Guillaume, F.; Guyot-Herman, A. M.; Duclos, R.; Besançon, P.; Orechioni, A. M.; Drache, M.; Conflant, P.; Gadefait, A.; Bécourt, P. Elaboration and physical study of an oxodipine solid dispersion in order to formulate tablets. *Drug Dev. Ind. Pharm.* **1992**, *18*, 811−827.

53. Taylor, L. S.; Zografi, G. Spectroscopic characterization of interactions between PVP and indomethacin in amorphous molecular dispersions. *Pharm. Res.* **1997**, *14*, 1691−1698.
54. Lu, Q.; Zografi, G. Phase behavior of binary and ternary amorphous mixtures containing indomethacin, citric acid, and PVP. *Pharm. Res.* **1998**, *15*, 1202−1206.
55. Serajuddin, A. T. M. Bioavailability enhancement of poorly water-soluble drugs by solid dispersion in surface-active vehicles: A recent breakthrough. *La Gazette de l'ApGI* (France) **1997**, *14*, 144−145.
56. Francois, D.; Jones, B. E. The hard capsule with the soft center. *European Capsule Technology Symposium*, Constance, October 11−13, 1978; pp 55−61.
57. Chatham, S. M. The use of bases in SSM formulations. *S. T. P. Pharma.* **1987**, *3*, 575−582.
58. Serajuddin, A. T. M.; Sheen, P. C.; Mufson, D.; Bernstein, D. F.; Augustine, M. A. Effect of vehicle amphiphilicity on the dissolution and bioavailability of a poorly water-soluble drug from solid dispersions. *J. Pharm. Sci.* **1988**, *77*, 414−417.
59. Corrigan, O. E. Mechanism of dissolution of fast release solid dispersions. *Drug Dev. Ind. Pharm.* **1985**, *11*, 697−724.
60. Serajuddin, A. T. M.; Sheen, P. C.; Augustine, M. A. Improved dissolution of a poorly water-soluble drug from solid dispersions in poly(ethylene glycol):polysorbate 80 mixtures. *J. Pharm. Sci.* **1990**, *79*, 463−464.
61. Serajuddin, A. T. M.; Sheen, P. C.; Mufson, D.; Bernstein, D. F.; Augustine, M. A. Physicochemical basis of increased bioavailability of a poorly water-soluble drug following oral administration as organic solutions. *J. Pharm. Sci.* **1988**, *77*, 325−329.
62. Dennis, A. B.; Farr, S. J.; Kellaway, I. W.; Taylor, G.; Davidson, R. In vivo evaluation of rapid release and sustained release Gelucire capsule formulations. *Int. J. Pharm.* **1990**, *65*, 85−100.
63. Pozzi, F.; Longo, A.; Lazzarini, C.; Carenzi, A. Formulations of ubidecarenone with improved bioavailability. *Eur. J. Pharm. Biopharm.* **1991**, *37*, 243−246.
64. Dordunoo, S. K.; Ford, J. L.; Rubinstein, M. H. Preformulation studies on solid dispersions containing triamterene or temazepam in polyethylene glycols or Gelucire 44/14 for liquid filling of hard gelatin capsules. *Drug Dev. Ind. Pharm.* **1991**, *17*, 1685−1713.
65. Sheen, P. C.; Khetarpal, V. K.; Cariola, C. M.; Rowlings, C. E. Formulation studies of a poorly water-soluble drug in solid dispersions to improve bioavailability. *Int. J. Pharm.* **1995**, *18*, 221−227.
66. Porter, C. J. H.; Charman, S. A.; Williams, R. D.; Bakalova, M. V.; Charman, W. N. Evaluation of emulsifiable glasses for the oral administration of cyclosporin in beagle dogs. *Int. J. Pharm.* **1996**, *141*, 227−237.
67. Aungst, B. J.; Nguyen, N. H.; Rogers, N. J.; Rowe, S. M.; Hussain, M. A.; White, S. J.; Shum, L. Amphiphilic vehicles improve the oral bioavailability of a poorly soluble HIV protease inhibitor at high doses. *Int. J. Pharm.* **1997**, *156*, 79−88.
68. Cole, E. T. Liquid-filled hard gelatin capsules. *Pharm. Technol.* **1989**, *September*, 124−140.
69. Hahn, L.; Sucker, H. Solid Surfactant solutions of active ingredients in sugar esters. *Pharm. Res.* **1989**, *6*, 958−960.
70. Product literature, *Eastman Vitamin E TPGS NF properties and applications*; Eastman, Kingsport, TN; 1998.
71. Morris, K. R.; Knipp, G. T.; Serajuddin, A. T. M. Structural properties of poly(ethylene glycol)-polysorbate 80 mixture, a solid dispersion vehicle. *J. Pharm. Sci.* **1992**, *81*, 1185−1188.
72. Veiga, M. D.; Escobar, C.; Bernard, M. J. Dissolution behavior of drugs from binary and ternary systems. *Int. J. Pharm.* **1993**, *93*, 215−220.
73. Law, S. L.; Lo, W. Y.; Lin, F. M.; Chang, C. H. Dissolution and absorption of nifedipine in poly(ethylene glycol) solid dispersion containing phosphatidylcholine. *Int. J. Pharm.* **1992**, *84*, 161−166.
74. Sjökvist, E.; Nyström, C.; Aldén, M.; Caram-Lelham, N. Physicochemical aspects of drug release. XIV. The effects of some ionic and nonionic surfactants on properties of a sparingly soluble drug in solid dispersions. *Int. J. Pharm.* **1992**, *79*, 23−133.
75. Cadé, D.; Madit, N. Liquid filling in hard gelatin capsules − preliminary steps. *Bull. Technique Gattefossé* **1996**, *89*, 15−19.
76. Shah, N. H.; Phuapradit, W.; Ahmed, H. Liquid/semisolid filling in hard gelatin capsules: Formulation and processing considerations. *Bull. Technique Gattefossé* **1996**, *89*, 27−37.
77. Wiley: G. J.; Ullah, I.; Agharkar, S. N. Development of a semiautomatic system for R&D and clinical use for liquid-filled hard gelatin encapsulation. *Pharm. Technol.* **1995**, *May*, 72−76.
78. Cole, E. T. Equipment for filling and sealing liquids in hard gelatin capsules. *Bull. Technique Gattefossé* **1996**, *89*, 87−88.
79. Serajuddin, A. T. M.; Sheen, P. C.; Augustine, M. A. Water migration from soft gelatin capsule shell to fill material and its effect on drug solubility. *J. Pharm. Sci.* **1986**, *75*, 62−64.
80. Maes, P.; Brusselmans, J.; Sereno, A.; Pitti, C.; Sonck, M.; Coffiner, M. In vitro and in vivo behavior of some liquid or semisolid filled hard gelatin capsules. *Bull. Technique Gattefossé* **1996**, *89*, 63−69.
81. Al-Razzak, L. A.; Dias, L.; Kaul, D.; Ghosh, S. Lipid based systems for oral delivery: Physiological, mechanistic, and product development perspectives. *Symposia Abstracts and Biographies*, AAPS Annual Meeting, Boston, 1997; AAPS, Alexandria, VA, 1997; p 18.
82. Zantac Capsules, *Physicians' Desk Reference 1997*, Medical Economics Company: Montvale, NJ.
83. Sheen, P. C.; Kim, S. I.; Petillo, J. J.; Serajuddin, A. T. M. Bioavailability of a poorly water-soluble drug from tablet and solid dispersion in humans. *J. Pharm. Sci.* **1991**, *80*, 712−714.
84. Norvir capsules, *Physician's Desk Reference 1997*; Medical Economics Company: Montvale, NJ.
85. Ginés, J. M.; Veiga, M. D.; Arias, M. J.; Rabasco, A. M. Elaboration and thermal study of interactions between cinnarizine and Gelucire 53/10 physical mixtures and solid dispersions. *Int. J. Pharm.* **1995**, *126*, 287−291.
86. Press release, *Abbott to Substitute Norvir Capsules with Liquid Formulation*, Abbott Laboratories, July 29, 1998.
87. Rosoff, M.; Serajuddin, A. T. M. Solubilization of diazepam in bile salts and in sodium cholate-lecithin-water phases. *Int. J. Pharm.* **1980**, *6*, 137−148.
88. Sutananta, W.; Craig, D. Q. M.; Newton, J. M. An investigation into the effects of preparation conditions and storage on the rate of drug release from pharmaceutical glyceride bases. *J. Pharm. Pharmacol.* **1995**, *47*, 355−359.
89. Dordunoo, S. K.; Ford, J. L.; Rubinstein, M. H. Solidification studies of poly(ethylene glycol)s, Gelucire 44/14 or their dispersions with triamterene or temazepam. *J. Pharm. Pharmacol.* **1996**, *48*, 782−789.
90. Charman, W. N. Lipids and oral bioavailability: Are there yet-to-be realised opportunities? *Bull. Technique Gattefossé* **1998**, *91*, 51−62.
91. Serajuddin, A. T. M.; Fakes, M. G. Sustained release formulation containing captopril and method. U. S. Patent 5,433,951, July 18, 1995, assigned to Bristol-Myers Squibb.

JS980403L

Role of P-Glycoprotein-Mediated Secretion in Absorptive Drug Permeability: An Approach Using Passive Membrane Permeability and Affinity to P-Glycoprotein†

STEPHAN DOPPENSCHMITT,[§,‡] HILDEGARD SPAHN-LANGGUTH,[§] CARL GUNNAR REGÅRDH,[‡] AND PETER LANGGUTH*[,||]

Contribution from *School of Pharmacy, Martin Luther-University Halle-Wittenberg, Wolfgang-Langenbeck-Strasse 4, D-06120 Halle (Saale), Germany, Astra Hässle AB, PKDM, S-431 83 Mölndal, Sweden, and Johannes Gutenberg-University, Staudingerweg 5, D-55099 Mainz, Germany*

Received September 21, 1998. Final revised manuscript received June 24, 1999.
Accepted for publication June 26, 1999.

Abstract □ It has been shown in vivo and in vitro that P-glycoprotein (P-gp) may be able to influence the permeability of its substrates across biological membranes. However, the quantitative contribution of the secretion process mediated by P-gp on the overall permeability of membranes has not been determined yet. In particular, observations need to be clarified in which substrates showing high affinity to P-glycoprotein, e.g., verapamil, apparently do not seem to be greatly influenced by P-gp in their permeability and consequently also with respect to their extent of GI-absorption after oral administration, whereas weaker substrates of P-gp, e.g., talinolol, have clearly shown P-gp-related absorption phenomena such as nonlinear intestinal permeability and bioavailability. Experiments with Caco-2 cell monolayers and mathematical simulations based on a mechanistic permeation model should aid in clarifying the underlying mechanism for these observations and quantifying the influence of passive membrane permeability and affinity to P-gp to the overall transmembrane drug flux. In addition, the concentration range of drug at which P-glycoprotein-mediated transport across the biological membrane is relevant should be examined. The permeability of various drugs in Caco-2 monolayers was determined experimentally and modeled using a combination of passive absorptive membrane permeability and a Michaelis–Menten-type transport process in the secretory direction. The passive permeabilities were experimentally obtained for the apical and basolateral membrane by efflux experiments using Caco-2 monolayers in the presence of a P-gp inhibitor. The Michaelis–Menten parameters were determined by a newly developed radioligand-binding assay for the quantification of drug affinity to P-gp. The model was able to accurately simulate the permeability of P-glycoprotein substrates, with differing passive membrane permeabilities and P-glycoprotein affinities. Using the outlined approach, permeability vs donor–concentration profiles were calculated, and the relative contribution of passive and active transport processes to the overall membrane permeability was evaluated. A model is presented to quantitatively describe and predict direction-dependent drug fluxes in Caco-2 monolayers by knowing the affinity of a compound to the exsorptive transporter P-gp and its passive membrane permeability. It was shown that a combination of high P-gp affinity with good passive membrane permeability, e.g., in the case of verapamil, will readily compensate for the P-gp-mediated reduction of intestinal permeability, resulting in a narrow range in which the permeability depends on the apical drug concentration. On the other hand, the permeability of compounds with low passive membrane permeability (e.g., talinolol) might be affected over a wide concentration range despite low affinity to P-gp.

Introduction

The presence of the exsorptive multidrug transporter P-glycoprotein (P-gp) in the apical membrane of absorptive cells throughout the gastrointestinal tract has been identified as a possible source of low or erratic absorption of drugs after peroral dosing. Furthermore, the possibility for drug–drug and drug–food interaction on this level has been pointed out.[1]

It is known that P-gp is abundant in several tissues under physiological conditions, especially in organs and tissues physiologically involved with excretion or distribution to specific organs, e.g., the liver, kidneys, and the blood–brain barrier.[2] In human tissues P-gp has been shown to be mainly expressed in two isotypes, MDR-1 and MDR-3, with distinct differences in substrate specificity.[3] MDR-3 is likely to be involved in the biliary excretion of phosphatidylcholine,[4] whereas the MDR-1 isoform is expressed in the human gastrointestinal tract and is responsible for interference with the intestinal absorption of a number of drugs.[5]

Recently, a model has been introduced to quantitate the affinity of compounds to human P-gp, based on the radioligand displacement principle.[6,7] Several drugs have been classified by this technique with respect to their affinity toward this secretory carrier. Nevertheless, until today, the relevance of the P-gp affinity for the overall transport rate of a P-gp substrate across a biological membrane remains unresolved.

For example, some authors have concluded from a small secretory P-gp-mediated drug efflux, that the respective compound may be a "noncompetitive" inhibitor or an "inhibitor but not a substrate" to P-gp, neglecting, however, the possibility that the P-gp-mediated, saturable secretory transport could be minimized due to high drug concentrations and/or high passive membrane permeability.[8]

Based on the information available today on P-gp-mediated drug secretion, a transport model can be constructed, which contains the relevant parameters controlling drug flux of P-gp substrates across biological membranes expressing the glycoprotein. The use of such a model should enable us to elucidate the quantitative contribution of the P-gp-mediated secretion to the overall membrane permeability of a P-gp substrate.

A scheme of the transport model is shown in Figure 1. As parameters, the model contains the affinity of a compound to P-gp and its passive permeability across the cell membrane. As a model membrane the human colonic carcinoma cell line (Caco-2) overexpressing P-glycoprotein was used. A general outline which describes the experimental approach applied for obtaining data for *passive drug permeability* (by efflux experiments for each compound) and for the *affinity to P-gp* (by a radioligand-binding assay (RBA)[6,7]) is outlined in Figure 2. In a first step, the passive permeation of the apical and basolateral membranes comprising the Caco-2 monolayer was determined, and the permeability was simulated for compounds exhibiting no affinity to P-gp and for P-gp substrates under permeation conditions, where the P-gp "pump" was inhibited by verapamil. In a second step, the model was extended to include

* Corresponding author. Phone ++49-6131-39 57 49, fax ++49-6131-39 35 21, e-mail langguth@mail.uni-mainz.de.

† Dedicated to Prof. B. C. Lippold on the occasion of his 60th birthday.

‡ Astra Hässle AB.
§ Martin Luther-University Halle-Wittenberg.
|| Johannes Gutenberg-University.

10.1021/js980378j CCC: $18.00
Published on Web 08/27/1999

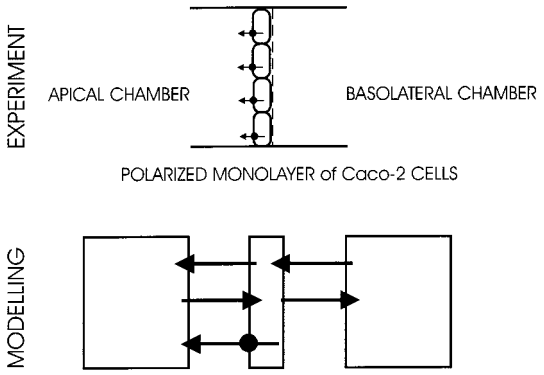

Figure 1—Outline of experimental and modeling approach depicting the compartments as well as passive fluxes and active, P-gp-mediated secretion between the three compartments.

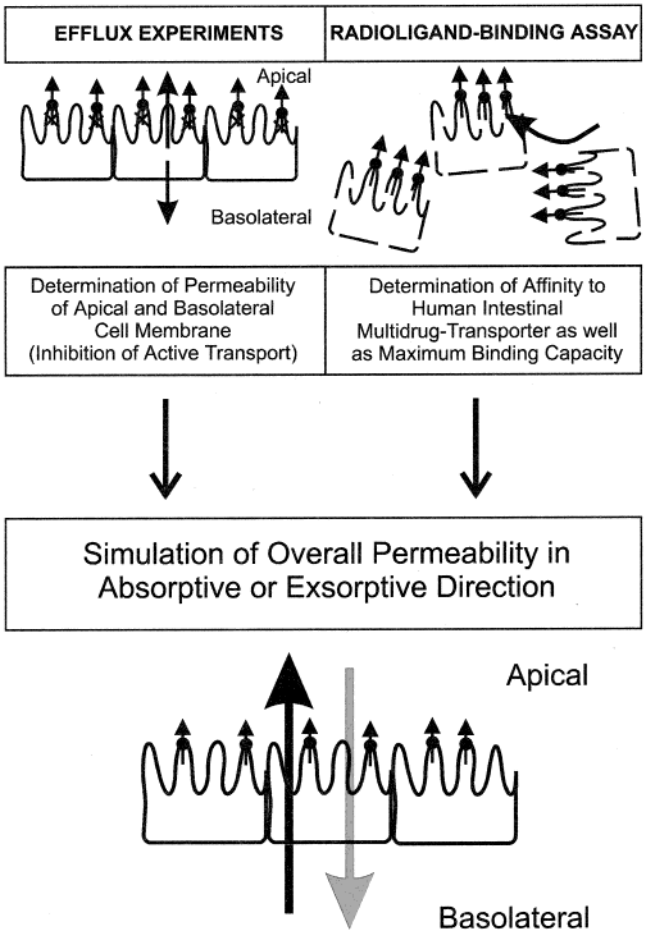

Figure 2—Scheme of experimental approaches used to obtain passive apparent permeablities of apical and basolateral membranes in Caco-2 monolayers by efflux studies as well as affinity to P-gp by radioligand-binding assay.

a saturable, carrier-mediated flux from the intracellular compartment to the apical compartment using affinity data obtained from RBA and estimates of V_{max} obtained from the carrier density and substrate turnover rates. These results were then correlated to data from transport experiments in order to investigate the predictive performance of the model.

Materials and Methods

Cell Culture—Dulbecco's Modified Eagle Medium, fetal calf serum (FCS), L-glutamine 200 mM, penicillin/streptomycin (10000 U/mL, 10 mg/mL), trypsin/EDTA, MEM nonessential amino acids (NEAA), Hanks's Balanced Salt Solution (HBSS), and phosphate-buffered saline (PBS) were from Life Technologies, Paisley, UK. Transwell cell culture inserts used for transport experiments (24 mm, 0.4 μm pore size, polycarbonate membrane) and all other cell culture materials were from Costar, Cambridge, MA. The Caco-2 cells obtained from the American Type Culture Collection (ATCC), Rockville, MD (starting with passage 74), were grown in the presence of 10 nM vinblastine sulfate for induction of P-gp expression. This vinblastine-adapted cell line has been characterized previously with respect to the extent and specificity of P-gp overexpression as well as to growth characteristics of monolayers.[6] For conducting the transport experiments, 90–95% confluent monolayers of vinblastine-induced Caco-2 cells were trypsinized and seeded into Transwell (24 mm, 0.4 μm pore size, polycarbonate membrane) (Costar, Cambridge, UK) cell culture inserts (300000 cells/well) and cultured for 14–17 days. Vinblastine-free medium was provided to the cells 8–16 h before performing binding or transport studies.

Compounds—[^{3}H]Atenolol, [^{3}H]metoprolol, pafenolol, and metoprolol were from Astra Hässle, Mölndal, Sweden. [^{3}H]Verapamil (25 μCi, 84 Ci/mmol) was purchased from New England Nuclear (Boston, MA), and [^{3}H]vinblastine (50 μCi, 16 Ci/mmol) and [^{3}H]-vincristine (50 μCi, 8 Ci/mmol) were from Amersham (Buckinghamshire, UK). Talinolol was a kind gift from Arzneimittelwerk Dresden (Radebeul, Germany). 2-(Morpholino)ethanesulfonic acid (MES) was from Fluka (Gothenburg, Sweden). All other compounds and reagents used were from Sigma (Malmö, Sweden) or BDH (Poole, UK).

Radioligand Binding Assay—The MultiScreen 96-well plate assay system was from Millipore (Eschborn, Germany), MultiScreen 96-well plates with Durapore membrane of 0.22 μm pore size were provided by Millipore (Malmö, Sweden). Liquid scintillation counting was performed by a WinSpectral 1414 counter from Wallac (Turku, Finland), using scintillation fluid Optiphase "Hisafe" 3 from Wallac (Loughborough, UK).

Transport and Efflux Experiments—An Electrical Voltage-Ohm-Meter (EVOM) equipped with "chopstick" electrodes (World Precision Instruments, Sarasota, FL) was used for monitoring transepithelial resistance of Caco-2 monolayers growing in Transwell inserts.

HPLC Analysis—The liquid chromatographic system consisted of a Pharmacia LKB 2150 pump (Uppsala, Sweden), a Perkin-Elmer ISS-100 autoinjector (Allerød, Denmark), a 206 PHD UV-absorbance detector from Linear (Reno, NV), or a Shimadzu RF 350 fluorescence monitor (Kyoto, Japan). Solvents used were of analytical grade and purchased from Skandinaviska Gentech (Kungsbacka, Sweden).

Determination of Affinity to P-gp by Radioligand-Binding Assay—The affinity of the test compounds to P-gp was investigated using a specific and sensitive radioligand binding assay described previously.[7] The displacement of the radioligand [^{3}H]verapamil from the P-gp-preparation by increasing concentrations of the nonlabeled compound of interest was determined. In short, porated cells of the P-gp-overexpressing Caco-2 cell line were incubated in duplicate with 16 different concentrations of each competitor at 37 °C in HBSS buffered with 10 mM MES at pH 7.0 for 30 min in the presence of ATP. Furthermore an ATP-regenerating system consisting of magnesium chloride (10 mM), creatine phosphate (10 mM), and creatine kinase (100 μg/mL) (19 mM) was present in the incubation mixture. The incubation was stopped by removing the liquid, and the filter membranes were washed twice with 100 μL of ice-cold HBSS buffered with 10 mM MES pH 7.0. The filter membranes were incubated with scintillation fluid for 12–16 h, and total radioactivity was determined by liquid scintillation counting.

Transport Experiments in Caco-2 Cell Monolayers—Transport experiments were performed with vinblastine at donor concentrations of 0.1, 1, 10, and 100 μM, with talinolol at 500 μM, and with quinidine at 0.25, 2.5, 25, and 250 μM. Furthermore transport experiments were carried out on atenolol (100 μM), metoprolol (100 μM), pafenolol (1000 μM), vincristine (0.1 μM), and verapamil (0.001 μM). Furthermore, for vinblastine (0.1 μM), vincristine (0.2 μM), talinolol (250 μM), and quinidine (25 μM), transport experiments in the presence of 0.5 mM verapamil were conducted for validation of the passive flux model under exclusion of P-gp-mediated transport. Transepithelial resistance of the vinblastine-induced Caco-2 monolayers (typically around 2500 Ω·

cm^2, for details see ref 6) was monitored prior to and after each transport experiment for verification of the integrity of the cell layer.

Transport experiments were conducted in HBSS buffered with 10 mM MES to pH 6.5 at 37 °C in correspondence to the experimental conditions of the radioligand-binding experiments. Each compound was added to the apical (A) or basolateral (B) compartment, and samples were taken from the corresponding acceptor compartment at predefined times. For vinblastine and vincristine, samples were taken every 30 min for 2.5 h from the acceptor compartments, for talinolol, metoprolol, atenolol, and pafenolol every 15 min for 1 h, and for verapamil and quinidine, samples were taken every 10 min for 1 h. To quantitate the flux across the monolayer, [^{3}H]vinblastine, [^{3}H]vincristine, [^{3}H]metoprolol, [^{3}H]verapamil, and [^{3}H]atenolol were determined by liquid scintillation counting, and talinolol, pafenolol, and quinidine were analyzed using HPLC methods.

Efflux Experiments—The apparent permeabilities of the apical and basolateral membranes of the vinblastine-induced Caco-2 cells were determined in monolayers grown on Transwell filters. The monolayers were loaded (30 min, 37 °C) with a solution of the drug at a concentration of interest in HBSS buffered with 10 mM MES, in the presence of 0.5 mM verapamil, for competitive inhibition of P-gp. When verapamil was studied, 0.5 mM of rhodamine 123 (Molecular Probes, Leiden, Netherlands) was used for competitive inhibition. The monolayers were washed gently with drug-free, ice-cold buffer of the same composition as used for loading of the cells. Efflux over the apical and basolateral membrane was started by placing the drug-loaded monolayer into a fresh six-well plate containing drug-free, prewarmed (37 °C) loading buffer (including verapamil or rhodamine 123) and adding the same buffer to the apical chamber of the Transwell. Samples were taken from the apical and basolateral compartments at 10, 20, and 30 min except for verapamil where samples were taken at 5.0, 7.5, 10.0, 12.5, and 15.0 min.

HPLC Methods—Validation and quality assurance was performed according to international recommendations.[9]

Talinolol and quinidine were determined as described previously.[6] Talinolol was analyzed using a chiral stationary phase (LiChrospher 100 Chiraspher NT, 250 × 4 mm i.d., Merck, Darmstadt, Germany) with ethanol:triethylamine (1000:0.5 [v:v]) and UV-absorbance detection at 245 nm after liquid−liquid extraction into dichlormethane:2-propanol (95:5 [v:v]) and reconstitution with methanol (internal standard pindolol). The method for the quantification of quinidine employed a LiChrospher RP-18 (Merck, Darmstadt, Germany) HPLC analytical column, 150 × 4.6 mm i.d., using methanol:acetonitrile:sulfuric acid (350:100:450 [v:v:v]), containing 10 mM octanesulfonic acid as the mobile phase and fluorescence detection at an excitation wavelength of 350 nm and an emission wavelength of 450 nm.

For the quantification of pafenolol, samples were analyzed by reversed phase HPLC using a LiChrospher RP-18 (Merck, Darmstadt, Germany) stationary phase (150 × 4.6 mm i.d.) and acetonitrile:0.02 M sodium dihydrogen phosphate pH 4.5:triethylamine (400:2000:1.5) as the mobile phase. UV-absorbance at 227 nm was monitored for detection. Pafenolol was determined with a precision and accuracy of 4.1 to 13.4% and −8.2 to 5.4% in the concentration range from 10 to 1000 ng/mL. For details on the analytical validation, see ref 6.

For talinolol, the precision and accuracy in the concentration range of 2.5 to 500 ng/mL per enantiomer was 3.5 to 12.7% and 1.2 to 15.4% ($n = 6$ for each concentration). The analytical method for the determination of quinidine exhibited in the concentration range from 1 to 1000 ng/mL a precision and accuracy of 1.9 to 9.0% and −4.9 to 5.6%.

Data Analysis—*A. Radioligand Binding Assay for P-gp*—A two-affinity model was fitted to the data obtained from competition experiments as described previosly.[6] SigmaPlot 2.01 (SPSS Science Software, Erkrath, Germany) was used for all nonlinear regression analysis.

B. Transport Experiments—The effective permeability (P_{eff}) was determined from the transport data according to

$$P_{eff} = \frac{dC/dt\,V}{AC_D} \tag{1}$$

where dC/dt is the flux across the monolayer, V is the volume of the acceptor chamber (3.0 mL for experiments in the apical to basolateral direction and 1.5 mL for experiments in the reverse direction), A is the apparent surface area of the monolayer used for the transport experiments (4.71 cm^2), and C_D represents the donor concentration of the respective drug. The flux across the monolayer was calculated as the slope of the amount transported vs time.

C. Efflux Experiments—The relationships between the drug efflux and time were adequately described by a monoexponential decay function.[10,11] The apparent permeability, P_{eff}, of the cell membrane was calculated from initial drug flux versus time into the respective compartment and the concentration used for loading of the cell monolayer.[10,11]

Modeling of Transport Experiments Using Efflux Permeabilities and Data from Radioligand Binding Assay—*A. Passive Permeability without P-gp Activity*—For modeling transport experiments of compounds lacking affinity to P-gp (e.g., atenolol), and transport with inhibition of P-gp, the passive drug fluxes for all three compartments depicted in Figure 1 were calculated according to

$$\frac{dM}{dt} = P_{eff,apical/basolateral} A C_{compartment} \tag{2}$$

where $P_{eff,apical/basolateral}$ was the apparent permeability of the apical or basolateral membrane, as determined from efflux experiments, A is the apparent surface area of the monolayer (4.71 cm^2), and $C_{compartment}$ is the concentration of the analyte in the respective compartment, calculated from the amout of drug in the compartment, the compartmental volume (1.5/3.0 cm^3 for the apical/basolateral compartment and 0.0247 cm^3 for the intracellular compartment of a Caco-2 cell monolayer with an area of 4.71 cm^2. The mean cell number of a monolayer amounted to 2.1×10^5 cells per cm^2 and was determined following trypsinization of monolayers grown in Transwells. The cell volume of 25 pL per Caco-2 cell was calculated on the geometrical dimensions of an ashlar with a basal square area of 4.8×10^{-6} cm^2 and a height of of 30 μm). The time interval used for numerical integration was 2−6 s. The concentration in the acceptor compartment was predicted for the various sampling times, and the apparent permeability of the substrate across the Caco-2 monolayer was calculated.

B. Transport Experiments Including Secretion by P-gp—For the transport experiments performed in the presence of functional P-gp, the carrier-mediated secretion of the drug from the cellular compartment was calculated according to

$$\text{carrier-mediated flux} = A_{max}\left(\frac{(1 - F_h)CC}{K_{i_1} + CC} + \frac{F_h CC}{K_{i_2} + CC}\right)t \tag{3}$$

where the maximum capacity of the P-gp pump, A_{max} [mol/s], is calculated from

$$A_{max} = N_{P-gp} A \tag{4}$$

N_{P-gp} is the number of P-gp molecules per cell, as determined by RBA-saturation experiments in P-gp-overexpressing Caco-2 cells as 800000 binding sites per cell,[6] and A is the average ATP-turn over per second (25 s^{-1}).[12] F_h is the fraction of high-affinity binding sites for the respective compound, K_{i_1} and K_{i_2} are the respective equilibrium dissociation constants ("affinity constants") to P-gp, both determined from competition experiments by radioligand-binding assay, CC is the intracellular concentration of the drug, and t is the interval of numerical integration (2−6 s). All simulations were performed using S-PLUS 3.3 (MathSoft, Seattle, WA).

Results

Permeability across Caco-2 Monolayer—*A. Passive Permeation without Involvement of P-gp*—In this first step, the diffusional transport, i.e., transport for nonsubstrates of P-gp or for P-gp substrates in the presence of 0.5 mM verapamil, was determined from the permeability of the apical and basolateral membranes in efflux experiments. The fluxes across the membranes were calculated from the passive permeabilities of the single membranes given in Table 1.

Table 1—Parameters Used for Predicting the Permeability in Caco-2 Monolayers of the Respective Compound. Passive Permeability (P_{apical} and $P_{basolateral}$) of the Apical and Basolateral Membrane of Caco-2 Monolayers as Determined by Efflux Experiments with Inhibition of P-gp, As Well As Affinity Constants (K_i) to P-gp and Fraction of High Affinity Binding Sites (f_H), As Determined by Radioligand Binding Assay

	passive permeability		affinity data		
compound	$P_{apical} \times 10^6$[cm/s]	$P_{basolateral} \times 10^6$ [cm/s]	K_{i_1} [μM]	K_{i_2} [μM]	f_H
atenolol	0.57	0.69	–	–	–
talinolol	1.3	3.6	72	1570	0.20
metoprolol	43	45	200	1750	0.46
pafenolol	0.70	1.3	5.5	3200	0.20
quinidine	75	96	2.6	225	0.21
verapamil	519	330	0.30	3.6	0.42
vinblastine	18	33	0.15	107	0.34
vincristine	0.33	0.29	0.50	150	0.20

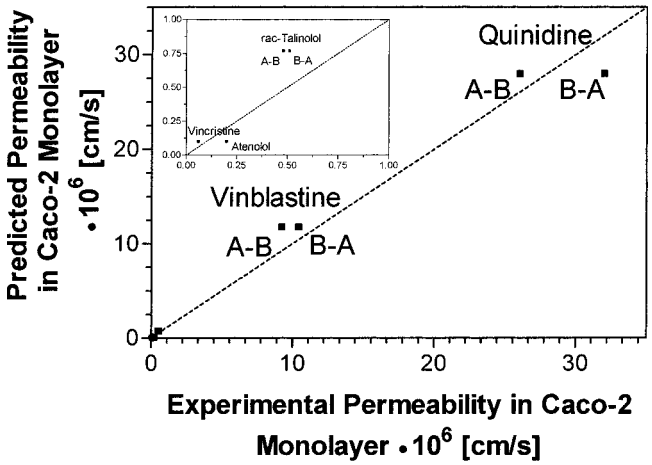

Figure 3—Correlation of experimentally obtained and predicted permeabilities in Caco-2 monolayers for nonsubstrate (atenolol, $C_D = 100$ μM) and different P-gp substrates under inhibition of P-gp (vinblastine, $C_D = 0.1$ μM, vincristine, $C_D = 0.2$ μM, talinolol, $C_D = 250$ μM, quinidine, $C_D = 25$ μM) to evaluate the validity of the passive-flux model used. The hatched line represents the line of identity.

The obtained apparent permeability coefficients were compared with those experimentally determined in transport experiments with Caco-2 monolayers. The results reveal a good correlation between experimental and predicted data, as shown in Figure 3. Thus the passive-flux model was considered an adequate basis for advancing to the next step, the carrier-mediated secretion.

B. Transport Experiments with Functional P-gp in Caco-2 Monolayers—Secretory flux mediated by P-gp was introduced into the permeability model by adding a two-affinity, Michaelis–Menten-type transport process. The values of the affinity constants and the relative proportions of high and low affinity binding sites determined from the radioligand-binding assay are listed in Table 1. The effect of the intracellular drug concentration on the flux mediated by the P-gp pump is shown for verapamil, vinblastine, quinidine, and talinolol in Figure 8. According to these results, the "working range" of P-gp, compared to a classical, single-affinity Michaelis–Menten process is greatly enhanced by the two-affinity mechanism.

The predictive model turned out to satisfactorily describe the permeability of the monolayer for a number of different solutes and permeation conditions, such as various concentrations and permeation directions.

Figures 4 and 5 show the correlations between the observed and predicted results in transport experiments on vinblastine and quinidine. The experiments were performed at four different concentrations covering a 1000-fold difference for both, apical to basolateral and the reverse direction across the P-gp overexpressing Caco-2 monolayers.

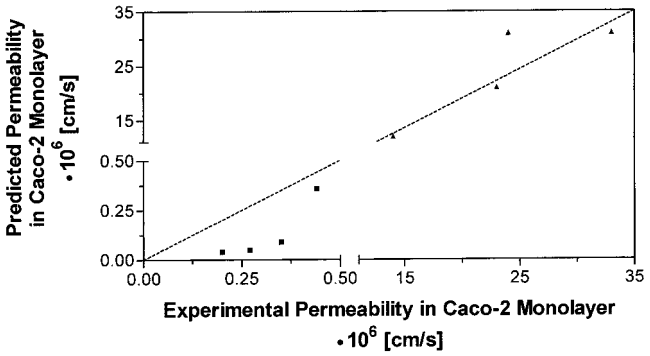

Figure 4—Correlation of experimentally obtained and predicted permeabilities in Caco-2 monolayers for vinblastine in A–B (■) and B–A (▲) direction.

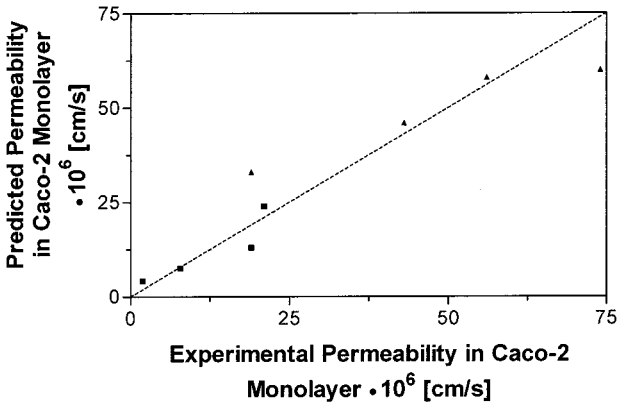

Figure 5—Correlation of experimentally obtained and predicted permeabilities in Caco-2 monolayers for quinidine in A–B (■) and B–A (▲) direction.

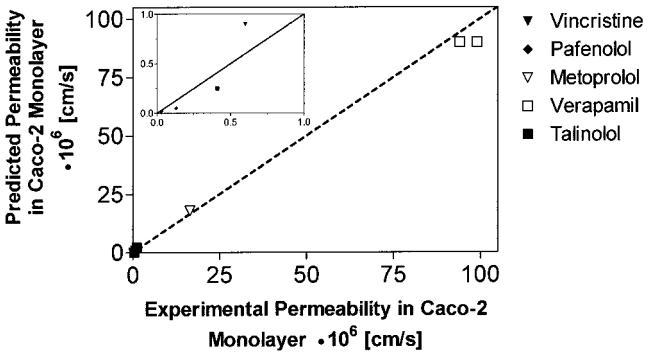

Figure 6—Correlation of experimentally obtained and predicted permeabilities in Caco-2 monolayers for verapamil, vincristine, metoprolol, talinolol, and pafenolol.

Similar results were obtained for various other lipophilic and hydrophilic compounds including examples with both high and low affinity to P-gp, Figure 6.

Dependence of Epithelial Permeability on Apical Drug Concentration—The results of simulations of the transport in the absorptive direction (A–B) in Caco-2 monolayers for four P-gp substrates with varying passive permeabilities and affinities to P-gp at different donor concentrations are given in Figure 7. The dashed line represents the permeability coefficient determined in the absence of P-gp-mediated secretion, in accordance with the fact, that for a diffusive transport process, the permeability is independent of the concentration of the permeating species.

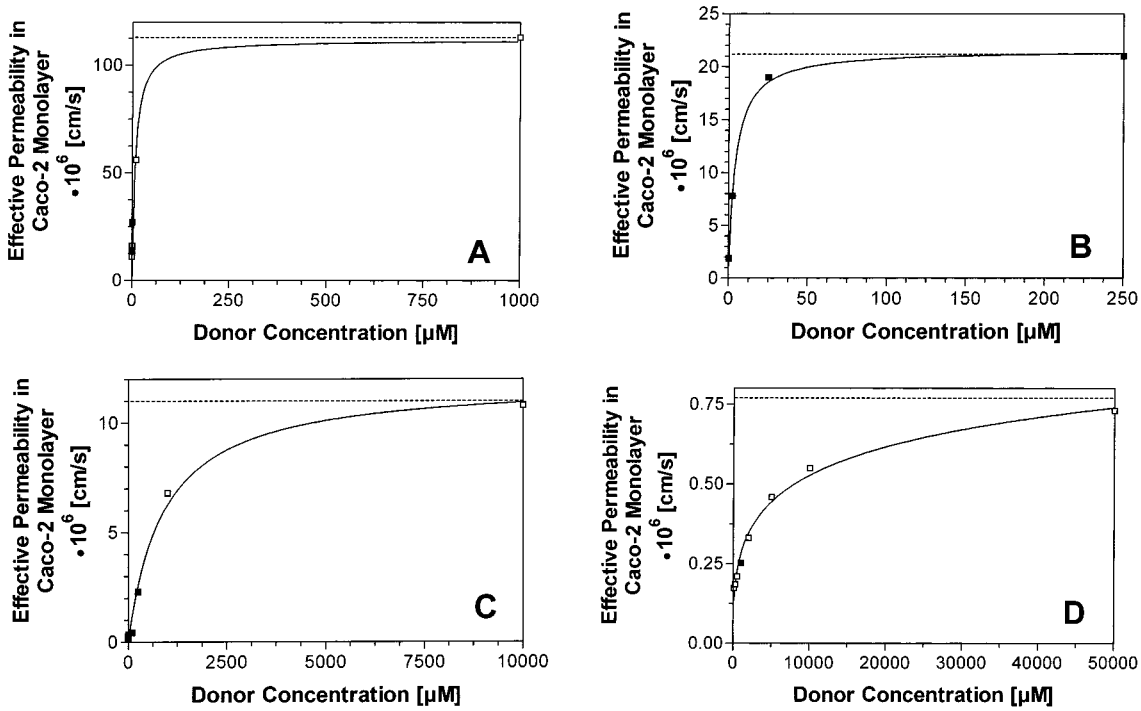

Figure 7—Simulated (□) and experimentally determined (■) effective permeabilities in Caco-2 monolayers (A–B direction) of verapamil (A), quinidine (B), vinblastine (C), and talinolol (D) at different donor concentrations, as well as passive permeability in absence of P-gp (----). The line is drawn according to the Michaelis–Menten equation.

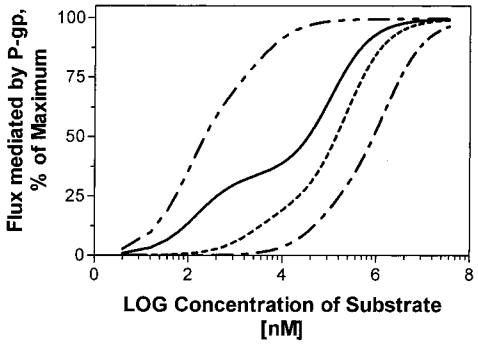

Figure 8—Secretory capacity of P-gp for verapamil (-•••-), vinblastine (—), quinidine (----) and talinolol (-•-•-). Percentage of maximum secretion rate as a function of the respective substrate concentration.

Depending on the drug's affinity to P-gp and its passive membrane permeability, different permeability versus initial donor concentration profiles can be observed:

Verapamil—This drug exhibits very high passive permeability of the cell membrane and high affinity to P-gp (Table 1). This results in a pseudolinear concentration-independent permeability of the Caco-2 cell monolayer. Only at very low donor concentrations, the effect of P-gp is visible, resulting in a systematic trend toward lower permeability values.

Vinblastine and Quinidine—Both compounds are characterized by moderate-to-high passive permeability and moderate-to-high affinity to P-gp, resulting in a strong influence of P-gp on the permeability in the medium and low drug concentration range. For vinblastine this resulted in permeability values comparable to the paracellular flux of small molecules, e.g., mannitol, in Caco-2 monolayers.

Talinolol—This compound possesses moderate-to-low passive permeability and moderate-to-low affinity to P-gp. This results in a clearly visible dependence of P_{eff} on the apical drug concentration over a wide concentration range. Accordingly, the permeability approached that of paracellular flux in the lower concentration range.

Discussion

The results presented here were obtained using the same P-gp-overexpressing cell line for the transport experiments that has also been used for the binding studies. This cell line has been demonstrated to selectively overexpress P-gp and to exhibit expression of other cation transport systems only to a negligible extent. The permeabilites of various P-gp substrates determined in this system were accurately predicted by a model employing the passive drug flux across the apical and basolateral membranes and the P-gp-mediated flux. In the case of vinblastine an overestimation of the influence of P-gp by the model, especially in the low permeability range was obvious. The reason for this might be that only a part of the total P-gp identified in the binding assay is functional, and, e.g., intracellular P-gp may well contribute to substrate binding but not to its transport.[13] Another explanation could be that the model described here does not include paracellular permeation, which might become relevant at the very low permeability range.

The apparent permeability vs donor concentration profiles presented here allow an assessment of the possible compromising influence of P-glycoprotein on the membrane permeability of a drug. The four compounds for which the transport model was applied, verapamil, quinidine, vinblastine, and talinolol, show distinct differences in the quantitative contribution of P-gp-related secretion to the overall membrane permeability. For example, it can be stated that the membrane permeability of verapamil is hardly affected despite the high affinity of verapamil to P-gp. On the other hand, talinolol exhibits a strong influence of P-gp-mediated transport on the permeability over a wide concentration range, despite the fact that it has much lower affinity to P-gp than verapamil.

It can be concluded from the present findings that the passive permeability of a compound in the absence of P-gp-mediated transport equals the maximum possible permeability. Affinity to P-gp determines the shape and concentration range of the observed negative deviation from this

maximum permeability. In addition, this is governed by the intracellular concentration of the compound, being a function of its diffusive permeability of the apical and basolateral membrane.

Assuming 0.25 to 0.5 L of liquid available within the GI tract for dissolution of a perorally administered drug and the dose, an estimate of the local concentration range of a drug in the intestine can be guessed in order to apply the in vitro data to the in vivo situation. For talinolol, nonlinearity in absorption was detected following peroral dosing of four different doses spread over a 16-fold range (25−400 mg of the racemate) in humans.[14] Due to the absence of metabolic degradation, this effect was attributed to saturable intestinal secretion, most probably P-gp. These observations are well in accordance with the results presented here, thus demonstrating the in vivo relevance of this simulation approach. Furthermore, for verapamil, almost complete absorption has been found following p.o. administration of different therapeutic doses.[15,16] This is also in accordance with the predictions of the model presented here. For vinblastine, the bioavailability after peroral administration is negligible at therapeutic doses of 3.5 mg/m^2 body surface in adults, a fact that can also be derived from the P_{eff} vs donor concentration plots provided here.

The findings in this communication can thus be taken as an extension of the hypothesis by Hunter and Hirst[17] with respect to the influence of ATP-dependent efflux on the permeability of physiological barriers. The new findings reveal that relevant deviations from the maximum permeability by simple diffusion requires both affinity to P-glycoprotein as well as appropriate physicochemical properties of the permeating species to reach intracellular drug concentrations in the "working range" of the secretory carrier. Thus the approach chosen here reveals that affinity to P-gp may not necessarily compromise the absorption of a compound, even for a high affinity ligand, as, e.g., shown for verapamil.

In conclusion, high permeability drugs have a much decreased chance that their intestinal permeability is limited by P-glycoprotein activity, whereas low permeability drugs, irrespective of their affinity to P-gp, have a much greater chance of undergoing permability restriction mediated by P-gp at therapeutically applied peroral doses.

References and Notes

1. Spahn-Langguth, H.; Baktir, G.; Radschuweit, A.; Okyar, A.; Terhaag, B.; Ader, P.; Hanafy, A.; Langguth, P. P-Glycoprotein transporters and the gastrointestinal tract: Evaluation of the potential in vivo relevance of in vitro data employing talinolol as model compound. *Int. J. Clin. Pharmacol. Ther.* **1998**, *36*, 16−24.
2. Greenberger, L. M.; Ishikawa, Y. ATP−Binding Cassette Proteins, Common Denominators between Ion Channels, Transporters, and Enzymes. *Trends Cardiovasc. Med.* **1994**, *4*, 193−198.
3. Müller, P. M.; Jansen, P. L. M. Molecular aspects of hepatobiliary transport. *Am. J. Physiol.* **1997**, *272*, G1285−G1303.
4. Smit, J. J. M.; Schinkel, A. H.; Elferink, R. P. J. Homologous disruption of the murine mdr2 P-glycoprotein gene leads to a complete absence of phospholipid in the bile and liver desease. *Cell* **1993**, *75*, 451−462.
5. Wacher, V. J.; Wu, C. Y.; Benet, L. Z. Overlapping substrate specificities and tissues distribution of cytochrome P-450 3A and P-glycoprotein have implications for drug delivery and activity in cancer chemotherapy. *Mol. Carcinogen.* **1995**, *13*, 129−134.
6. Döppenschmitt, S.; Langguth, P.; Regårdh C. G.; Andersson, T. B.; Hilgendorf, C.; Spahn-Langguth, H. Characterization of Binding Properties to Human P-glycoprotein: Development of a 3-H−Verapamil Radioligand-Binding Assay. *J. Pharmacol. Exp. Ther.* **1999**, *288*, 348−357.
7. Döppenschmitt, S.; Spahn-Langguth, H.; Regårdh, C. G.; Langguth, P. Radioligand-Binding Assay Employing P-Glycoprotein-Overexpressing Cells: Testing Drug Affinities to the Secretory Intestinal Multidrug Transporter. *Pharm. Res.* **1998**, *15*, 1001−1006.
8. Ayesh S.; Shao, Y.-M.; Stein, W. D. Cooperative, competitive and noncompetitive interactions between modulators of P-glycoprotein. *Biochim. Biophys. Acta* **1996**, *1316*, 8−18.
9. Shah, V. P.; Midha, K. K.; Dighe, S.; McGilveray, I. J.; Skelly J. P.; Jacobi, A.; Layloff, T.; Viswanathan, C. T.; Cook C. E.; McDowall, R. D.; Pittmann, R. A.; Spector, S. Bioanalytical method validation. *J. Pharm. Sci.* **1992**, *81*, 309−314.
10. Jacquez, J. A. Application of Tracers to the Study of Membrane Transport Processes. In *Physiology of membrane disorders*; Andreoli, T. E., Hoffmann J. F., Fanestil, D. D., Schultz, S. G., Eds.; Plenum: New York, 1986; pp 133−150.
11. Riggs, D. S. Transfer of Substances between Biological Compartments. Simple Diffusion. In *The Mathematical Approach to Physiological Problems*; MIT Press: Cambridge, UK, 1963; pp. 169−192.
12. Stein W. D. Kinetics of the multidrug transporter (P-glycoprotein) and its reversal. *Physiol. Rev.* **1997**, *77*, 545−590.
13. Kim, H.; Barroso, M.; Samanta, R.; Greenberger, L.; Sztul, E. Experimentally induced changes in the endocytic traffic of P-glycoprotein alter drug resistance of cancer cells. *Am. J. Physiol.* **1997**, *63*, C687−C702.
14. Wetterich U.; Spahn-Langguth H.; Mutschler E.; Terhaag B.; Rösch W.; Langguth P. Evidence for Intestinal Secretion as an Additional Clearance Pathway of Talinolol Enantiomers: Concentration- and Dose-dependent Absorption in Vitro and in Vivo. *Pharm. Res.* **1996**, *13*, 514−522.
15. Eichelbaum M.; Echizen H. Clinical Pharmacology of Calcium Antagonists: A Critical Review. *J. Cardiovasc. Pharmacol.* **1984**, *6* (Suppl 7), S963−S967.
16. Hoffmann D. J.; Seifert T.; Borre A.; Nellans H. N. Method to estimate the rate and extent of intestinal absorption in conscious rats using an absorption probe and portal blood sampling. *Pharm. Res.* **1995**, *12*, 889−894.
17. Hunter J.; Hirst, B. H. Intestinal secretion of drugs. The role of P-glycoprotein and related drug efflux systems in limiting oral drug absorption. *Adv. Drug Deliv. Rev.* **1997**, *25*, 129−157.

Acknowledgments

Financial support by Dr. Robert Pfleger-Shiftung, Bamberg, and the Fonds der Chemischen Industrie, Frankfurt (to. H.S.-L. and P.L.), is gratefully acknowledged.

JS980378J

Chemical Stability of Peptides in Polymers. 1. Effect of Water on Peptide Deamidation in Poly(vinyl alcohol) and Poly(vinyl pyrrolidone) Matrixes

MEI C. LAI,[†] MICHAEL J. HAGEMAN,[†,‡] RICHARD L. SCHOWEN,[†] RONALD T. BORCHARDT,[†] AND ELIZABETH M. TOPP*,[†]

Contribution from *Department of Pharmaceutical Chemistry, The University of Kansas, Lawrence, Kansas 66047, and Pharmaceutical Development I, Pharmacia & Upjohn, Inc., Kalamazoo, Michigan 49001.*

Received May 27, 1998. Final revised manuscript received July 21, 1999.
Accepted for publication July 21, 1999.

Abstract □ This paper examines the effect of water content, water activity, and glass transition temperature (T_g) on the deamidation of an asparagine-containing hexapeptide (VYPNGA; Asn-hexapeptide) in lyophilized poly(vinyl alcohol) (PVA) and poly(vinyl pyrrolidone) (PVP) at 50 °C. The rate of Asn-hexapeptide deamidation increases with increasing water content or water activity and, hence, decreasing T_g. The rate of deamidation is more sensitive to changes in these parameters in PVA than in PVP. Deamidation is clearly evident in the glassy state in both formulations. In the glassy state, the peptide is more stable in PVA than in PVP formulations but is less stable in the rubbery state. No single variable (water content, water activity, or T_g) could account for the variation in deamidation rates in PVA and PVP formulations. Deamidation rates were correlated with the degree of plasticization by water (distance of T_g from the dry intrinsic glass transition temperature); coincident curves for the two polymers were obtained with this correlation. Deamidation in PVA and PVP was closely correlated with the extent of water-induced plasticization experienced by the formulation relative to its glass transition at 50 °C, suggesting that the physical state of formulations could be used to predict chemical stability.

Introduction

Many proteins are formulated with polymers to protect against degradation during storage and/or processing or to provide a matrix for controlled release. Moisture content, polymer composition, and temperature can affect the stability of solid protein formulations by influencing the rates of chemical degradation reactions, such as asparagine deamidation.[1−4] Hydration of these solid formulations can easily occur during processing, storage, or after in vivo implantation. However, although the importance of polymer selection and moisture content is recognized, a complete mechanistic understanding of their effects on the chemical stability of proteins has not been developed. This manuscript addresses this mechanistic issue by examining the deamidation of a model hexapeptide (Val-Tyr-Pro-Asn-Gly-Ala, Asn-hexapeptide) in lyophilized poly(vinyl alcohol) (PVA) and poly(vinylpyrrolidone) (PVP) matrixes at various hydration levels at a constant temperature of 50 °C.

Water can affect the chemical stability of solid protein formulations in at least three ways: (1) as a solvent, (2) as a reactant in a reaction such as hydrolysis, and/or (3) as a plasticizer.[1,5] Water as a plasticizer of amorphous solids induces a physical transition from a brittle, dynamically constrained glassy state to a more mobile, less viscous, rubbery state at some temperature T_g, the glass transition temperature.[1] Because many reactions require sufficient mobility of the reactants to proceed, an increase in mobility with water content could promote chemical reactivity.[1,6,7] The decrease in T_g with increasing water content is often cited as an important factor in protein degradation in solids.[1,2,4,8] The effect of water as a plasticizer may be qualitatively described by changes in T_g produced by a given amount of water. The effect of water as a solvent or reactant should be related to its concentration (water content) or chemical potential (water activity). We report here the effects of water on the stability of the Asn-hexapeptide in solid formulations as a function of water content, water activity, and T_g.

Poly(Vinyl Alcohol) (PVA)	Poly(Vinyl Pyrrolidone) (PVP)
2 Molecular Weights	2 Molecular Weights
PVA 103 - 20,000	K12 - 4,000
PVA 125 - 125,000	K17 - 10,000

Scheme 1—Structures of poly(vinyl alcohol) (PVA) and poly(vinyl pyrrolidone) (PVP).

Deamidation at asparagine residues is one of the most prevalent chemical instabilities in proteins and peptides. The Asn-hexapeptide was selected as a model compound because its deamidation kinetics and mechanisms have been well characterized in solution.[9,10] This degree of mechanistic understanding makes the Asn-hexapeptide ideally suited for a study of the effect of water on reaction kinetics and mechanisms in solid polymer matrixes. PVP and PVA were selected as model polymers because they are commonly used pharmaceutical excipients with a simple chemical structure. Both polymers are linear, amorphous, polar, and hydrophilic (Scheme 1). Each consists of a vinyl backbone with pendant functional group (*N*-pyrrolidone for PVP and hydroxyl for PVA) at a 1,3-separation.

This paper examines the effect of water on Asn-hexapeptide deamidation in PVA and PVP at 50 °C. The relationships between water content, water activity, and T_g in these two polymer formulations will first be determined to characterize the effect of water on these polymer matrixes. Then the relationship between deamidation rates and residual moisture will be explored by correlating deamidation rates with formulation water content, water activity,

* To whom correspondence should be addressed. Telephone: (785) 864-3644. Fax: (785) 864-5736. E-mail: topp@ukans.edu.
[†] The University of Kansas.
[‡] Pharmacia & Upjohn, Inc.

10.1021/js980227g CCC: $18.00
Published on Web 09/01/1999

and T_g. The impact of polymer composition on chemical stability is addressed by comparing these correlations in PVA and in PVP.

Experimental Section

Materials—L-Val-L-Tyr-L-Pro-L-Asn-Gly-L-Ala (Asn-hexapeptide) was synthesized by Dr. Madhup Dhaon (Abbott Laboratories, North Chicago, IL). The buffers and salts used in this study, together with organic solvents used in the HPLC mobile phase, were purchased from Mallinckrodt Chemical, Inc. (Paris, Kentucky). The two types of PVA, under the trade names of Airvol 103 and 125 [average MW 20 000 and 125 000], were obtained from Air Products and Chemicals, Inc. (Lehigh Valley, PA). The two types of PVP, under the trade names of Kollidon K12 and K17 [MW 4000 and 10 000], were obtained from BASF Corporation (Parsippany, NJ). Trifluoroacetic acid (TFA) was obtained from Pierce (Rockford, IL). Deionized and distilled water was used throughout.

Preparation of PVA and PVP Formulations—Prior to use in formulations, the polymers were dissolved in water and dialyzed. Spectra/Pro molecular weight cutoff (MWCO) cellulose membranes from Spectrum Medical Industries (Houston, TX) were used to remove low molecular weight impurities. Membranes of MWCO 1000 and 3500 were used for PVP K12 and PVP K17, respectively. PVA 103 and PVA 125 were dialyzed using 10 000 and 50 000 MWCO membranes, respectively. After dialysis, the polymers were lyophilized in a VirTis Unitop 600SL Freeze-Dryer (Gardner, NY).

The polymers were then mixed with 0.01 M potassium phosphate buffer (pH 6.8) to yield 5% w/w polymer solutions. The PVP dissolved readily in buffer. The PVA mixtures were heated at 120 °C for 25 min to dissolve the polymers and then allowed to cool to 25 °C. The Asn-hexapeptide, first dissolved in a small amount of buffer, was added to the polymer solutions to produce a peptide concentration of 1.0−1.5 mg/mL (1.5−2.5 mM), as verified by HPLC. The pH of the resulting solution was measured with a Corning pH/ion Analyzer 350 with a Corning Semi-micro Combination Electrode (Corning, NY) and, if needed, was adjusted to pH 6.8 with NaOH.

The polymer and peptide solutions were placed into individual syringes fitted with 21-gauge needles. The solutions were then dispensed in a dropwise manner into liquid nitrogen to form individual frozen pellets ~2 mm in diameter. The frozen pellets were placed in a FTS Dura-Stop MicroProcessor Freeze-Dryer (FTS Systems, Inc., Stone Ridge, NY) with the shelves precooled to −40 °C. The chamber vacuum was set at 150 mTorr. The shelf temperature was ramped in 10 °C intervals every 3−4 h up to −5 °C. Afterward, shelf temperature was increased in 10 °C intervals every 6−8 h. The final drying was conducted at 25 °C for 17 h. After lyophilization, the resulting white spherical pellets were transferred into containers in a PlasLabs Dry Box (Lansing, MI), which was purged with dry nitrogen, and placed in a desiccator containing $CaSO_4$. The peptide loads for PVP and PVA were 0.017 ± 0.0006 and 0.024 ± 0.001 g/g solid, respectively, based on the maximum amount released. To determine peptide load, both PVA and PVP formulations were immersed in water. The PVP formulations dissolved completely, whereas the PVA pellets released >95% of their theoretical load after 4−8 h. The final composition of the dry formulation (in w/w) was ~2% peptide, 2% buffer, and 96% polymer, with a residual moisture content of <1%.

Characterization of Water Sorption Behavior—Sorption isotherms relating formulation water content to relative humidity (RH, water activity) at 50 °C were generated using a Controlled Atmosphere Microbalance (CAM), which monitored the sample mass at a specified relative humidity. The CAM was built at Pharmacia & Upjohn, Inc., as previously described.[11] The CAM consisted of a Cahn microbalance within an enclosed glass chamber, a nitrogen gas saturator assembly, water baths, and digital interfaces. Data were collected on a 486 PC computer and stored in a Microsoft Excel spreadsheet. Each CAM run was conducted on 5−10 mg of sample over a range of 0 to 85% RH at 5% RH step increases. When equilibrium was achieved, the system would step the chamber humidity to the next level. The criterion for equilibrium was defined as no more than a 0.5 μg change in sample mass over a 20-min interval. Water sorption was rapid, with 95% of the equilibrium mass reached within 20 min. The CAM took, on average, 2−3 h to achieve equilibrium at 5% RH intervals. Water desorption of the PVP and PVA formulations showed little or no hysteresis (data not shown), evidence that equilibrium water content was reached.

Two points on each isotherm were verified independently by thermogravimetric analysis (TGA). Samples from each formulation were stored at two RHs. The water contents were then determined with a DuPont 2050 TGA with a 2200 Data Analysis System from TA Instruments (Newcastle, DE). The water content of each sample was defined as the weight loss during heating from 25 to 120 °C at a heating rate of 10 °C/min.

The water sorption data obtained by the CAM were fitted to the Guggenheim−Anderson−deBoer (GAB) equation (eq 1), which describes the sorption of water by heterogeneous sorbents or solids.[1]

$$W = \frac{W_m C_g K_{GAB}(\rho/\rho_o)}{[1 - K_{GAB}(\rho/\rho_o)][1 - K_{GAB}(\rho/\rho_o) + C_g K_{GAB}(\rho/\rho_o)]} \quad (1)$$

In eq 1, W is the mass (mg) of water vapor adsorbed per mg of dry solid at (ρ/ρ_o), (ρ/ρ_o) is the relative vapor pressure, W_m is generally regarded as the amount of water vapor necessary to saturate the heterogeneous active sorption sites, and C_g and K_{GAB} are dimensionless constants that are related to the thermodynamic parameters for sorption of strongly and weakly interacting water.[12−14] The GAB equation (eq 1) was used because it provides the ability to relate vapor pressure and water content of the systems under investigation. Alternatively, material science-based descriptions for water sorption isotherms of amorphous solids may be more thermodynamically and physically relevant for these systems.[15] However, these alternative models are not necessary to empirically describe the relationship between vapor pressure and water content. All curve fitting of data was carried out with SigmaPlot Version 3.0 (Jandel Corporation, San Rafael, CA).

The relative water vapor pressure (ρ/ρ_o) or humidity was taken to be equal to the activity of water in the systems studied. These systems were assumed to be in equilibrium because the formulations were stored in a closed system (glass chamber) at constant temperature (50 °C) and pressure during the study.

Characterization of Formulation Glass Transition Temperature—A Thermal Analyst Instruments 2920 DSC outfitted with a TA 2200 Data Analysis System (Newcastle, DE) was used to determine T_g values. The DSC was calibrated with indium. A modulated temperature ramping program was used in which the sample temperature was increased at 2 °C/min with a modulation of ±1 °C/min. The DSC was cooled with a liquid nitrogen cooling apparatus. After storage at 50 °C under various RHs for 4 days, ~3−5 mg of each sample was sealed in aluminum DSC pans obtained from TA Instruments (Newcastle, DE). The T_g was defined as the midpoint of the glass transition. The T_g measurements for each formulation at each RH were made in triplicate.

The T_g data were fitted to the Gordon−Taylor equation (eq 2) for two miscible components:

$$T_g = \frac{w_1 T_{g_1} + K_{GT} w_2 T_{g_2}}{w_1 + K_{GT} w_2} \quad (2)$$

where T_g is the glass transition temperature of the mixture, w_1 and w_2 are the weight fractions of the individual components, T_{g1} and T_{g2} are the intrinsic T_gs of each component, and K_{GT} is a constant that can be considered to be a ratio of the free volumes of the two components.[16,17] The T_g for water was set at the estimated value of 135 K.[17]

Stability Study—For the stability study, the solid formulations were transferred to 2-mL glass lyophilization vials, with each vial containing ~5 mg of pellets. The vials were placed in several closed controlled RH chambers, which were maintained at various specified RHs (11−75% RH) using saturated salt solutions.[18] The solid formulations were allowed to equilibrate in chambers at 20 °C for 12 h. Afterward, samples from various RHs chambers were removed and analyzed for Asn-hexapeptide and its degradation products. No degradation products were observed after this initial equilibration period. The samples were then transferred to chambers with similar RHs in a 50 °C room for the stability study. Saturated solutions of LiCl, $MgCl_2$, $Mg(NO_3)_2$, KI, and NaCl were

used to maintain RHs of 11, 30, 45, 64, and 75%, respectively, at 50 °C. $CaSO_4$ was used as the desiccant for the 0% RH condition. Samples were prepared in triplicate. Peptide composition was assayed by HPLC after various storage times to determine degradation kinetics and product distribution. The duration of the study was 6 months.

Peptide Analysis—Analyses of Asn-hexapeptide and its degradation products were performed by reversed-phase HPLC according to an established method.[10] The system consisted of a Varian VISTA 5500 liquid chromatography system with a Varian UV200 detector and a Varian Series 600 Data System (Walnut Creek, CA). Peptide separation was performed with an Alltech Econosphere C18, 5 μm, 250 × 4.6 mm analytical column (Deerfield, IL) in conjunction with a Applied Biosystems Brownlee Spheri-5, C-18, 5 μm, 30 × 4.6 mm guard column (San Jose, CA). A Perkin-Elmer ISS-100 Autoinjector (Norwalk, CT) was used to deliver 50-μL sample injections. An isocratic elution method was used at a flow rate of 0.8 mL/min. The mobile phase consisted of 6% (v/v) acetonitrile and 0.1% (v/v) TFA in 40 mM ammonium acetate at a pH of 4.4, which was adjusted using 1 N HCl. An ultraviolet (UV) detection wavelength of 218 nm was used to detect Asn-hexapeptide and its degradation products, which were identified via co-injection with known standards.

Kinetic Measurements—After a specified time interval, triplicate samples of each formulation at each RH were removed for peptide analysis. A 0.5-mL aliquot of deionized water was added to each vial. The PVP formulations dissolved readily in water. However, PVA was not soluble in water without heating. Therefore, the PVA pellets were immersed in water at 4 °C for 6 h and were shaken periodically. Less than 0.5% peptide decomposition occurred during this extraction ($t_{1/2}$ = 1150 h). More than 90% of the peptide was released in the first 2 h, with >95% released after 6 h. The pH of the resulting solution was ~6.8. The content of Asn-hexapeptide in the resultant solution was assayed by the HPLC method already described.

The observed rate constant (k_{obs}) for the disappearance of Asn-hexapeptide was determined from the slope of the plot of ln(% peptide remaining) versus time. This calculation was based on the pseudo-first-order degradation kinetics previously described for this peptide in solution[10] and solid[8] states according to the following relationship:

$$\ln\frac{A}{A_o} = -k_{obs}t \qquad (3)$$

where A is the amount of peptide at time t, and A_o is the initial peptide concentration. Analysis of kinetic data was handled with Excel Version 5.0 (Microsoft Corporation, Redmond, WA).

Results

Physical Characterization of Formulations—*Physical Appearance*—PVP and PVA formulations stored under desiccated or dry conditions were white, smooth, spherical pellets. The texture for the dry PVP formulation (water content < 0.004 g/g wet solid) was powdery, whereas dry PVA (water content < 0.003 g/g wet solid) had a fibrous, Styrofoam-like texture. As the RH increased, both PVP and PVA pellets decreased in diameter. At lower RHs (11% RH), this decrease in pellet size was the most noticeable change in PVP and PVA. At intermediate RHs (30−45% RH), the PVP pellets were dome shaped and sticky and had a yellowish, melted appearance, whereas the PVA pellets took on a wrinkled appearance and were less foamy in texture. At high RH (65−75% RH), the PVP pellets had become an opaque, viscous fluid, which coated the bottom of the vial. The PVA pellets had collapsed into a hard sphere with a wrinkled surface.

Water Sorption Isotherms—Researchers have reported that residual water in solid formulations can compromise drug stability.[1,19] Therefore, characterizing the hydration behavior of these polymers is important. The water sorption isotherms, which relate formulation water content to relative water vapor pressure or humidity, are shown in Figure 1 for PVA and PVP at 50 °C. The water content of both polymers increases with increasing RH. PVP and PVA formulations have different water sorption behaviors, with PVP being more hygroscopic than PVA. Thus, water activity is greater in PVA than in PVP at a given water content.

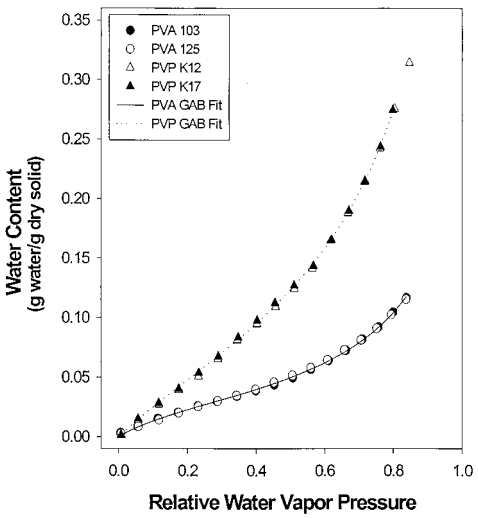

Figure 1—Water sorption isotherms for PVA and PVP formulations at 50 °C. The curved lines are nonlinear least-squares fits of the sorption data to the GAB equation (eq 1).

Table 1—Parameter Values and Standard Errors Derived from Fitting the Water Sorption Data at 50 °C to the GAB Equation (eq 1) for PVA and PVP Formulations

formulation	W_m (g H_2O/g dry solid)	C_g	K_{GAB}
PVA 103	0.0350 ± 0.0010	5.54 ± 0.42	0.861 ± 0.008
PVA 125	0.0378 ± 0.0007	5.00 ± 0.20	0.835 ± 0.006
PVP K12	0.111 ± 0.003	2.61 ± 0.11	0.825 ± 0.007
PVP K17	0.101 ± 0.003	3.13 ± 0.17	0.849 ± 0.009

The curved lines in Figure 1 represent the nonlinear least-squares fit of the water sorption data to the GAB equation (eq 1). The fitted parameter values of the GAB equation are shown in Table 1. Polymer molecular weight did not appear to significantly affect water sorption behavior for either PVA or PVP at 50 °C. The W_m value for PVP was ~3 times greater than for PVA, which is consistent with the greater affinity of PVP for water. The GAB equation, together with these fitted values, was used to relate water content and water activity in the analysis of stability data.

Formulation T_g as a Function of Water Content—Water in amorphous polymers can act as a plasticizer, increasing both the segmental mobility of the polymer chains and the flexional and translational mobility of incoporated low molecular weight solutes.[20] This increased mobility of the peptide in water-plasticized PVA and PVP systems may contribute to reactivity. One way to monitor the plasticizing effect of water is to measure the T_g. Figure 2 shows the effect of water content on formulation T_g. As water content increased, the T_g of PVA and PVP formulations decreased, indicating that water acts to plasticize both polymers. The dry PVP T_g was 80° greater than that of PVA (Table 2). At similar water contents, the PVP T_g was greater than the PVA T_g. Formulations with T_gs above the experimental temperature (T_{exp}= 323 K or 50 °C) were considered to be glassy, whereas those with T_gs of <323 K were assumed to be in the rubbery state.

The solid (PVA 103) and dashed (PVP K17) curves in Figure 2 represent the nonlinear least-squares fits of the

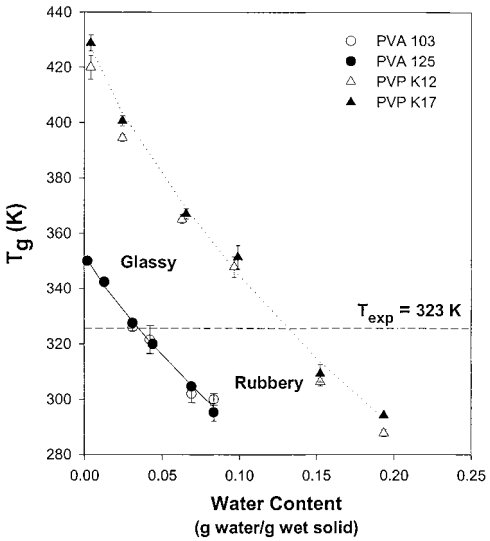

Figure 2—Glass transition temperature (T_g) as a function of water content. The curved lines are nonlinear least-squares fits of the sorption data to the Gordon–Taylor equation (eq 2). The labels "Glassy" and "Rubbery" indicate the physical state of the polymer matrix at the experimental temperature, T_{exp} (dashed line). Matrixes with $T_g > T_{exp}$ are glassy at T_{exp}; matrixes with $T_g < T_{exp}$ are rubbery at T_{exp}. Error bars represent standard deviations ($n = 3$).

Table 2—Glass Transition Data for PVA and PVP[a]

formulation	intrinsic T_g (K)[b]	fitted K_{GT} value	W_g (g H_2O/g wet solid)[c]	A_g[d]
PVA 103	346.3 ± 3.5	0.276 ± 0.04	0.0383	0.40
PVA 125	347.0 ± 1.1	0.266 ± 0.09	0.0384	0.40
PVP K12	421.1 ± 3.8	0.265 ± 0.08	0.127	0.58
PVP K17	429.4 ± 4.4	0.281 ± 0.09	0.135	0.60

[a] The K_{GT} values are from data fitted to the Gordon–Taylor equation (eq 2), and the T_g for water was assumed to be 135 K. [b] T_g value for "dry" formulations (water content < 0.004 g/g dry solid). [c] Amount of water required to reduce T_g to the experimental temperature (323 K). [d] Water activity corresponding to the W_g value.

data to the Gordon−Taylor equation (eq 2). The observed depression of T_g by an increase in water content was well described by the equation, suggesting that the mixing behavior of water with PVA and PVP was ideal.[17] The fitted K_{GT} values (Table 2), which can be considered to be the ratio of free volumes of water and polymer, were similar to the estimated K_{GT} values of 0.29 (PVA) and 0.25 (PVP). The K_{GT} values were estimated based on T_g and density values given for water, PVP, and PVA in the cited references.[17,21]

From the Gordon−Taylor equation (eq 2), the amount of water (W_g) required to induce the glass transition (i.e., to bring T_g into equality with T_{exp}) was calculated for PVA and PVP. The W_g values and the corresponding water activities at T_g (A_g) are listed in Table 2. Three times more water was required to induce the glass transition at 50 °C in PVP than in PVA, in part because of the greater dry T_g of PVP. Correspondingly, the water activity at the glass transition ($T_g = T_{exp}$) was higher in PVP than PVA. Initially, the same amount of water had a greater plasticizing effect on PVP. We will correlate formulation T_g with deamidation rates to evaluate the potential for a relationship between chemical instability and formulation viscosity.

Polymer molecular weight did not significantly affect the T_g values for either PVA or PVP. In general, T_g values are expected to increase with increasing polymer molecular weight up to a limiting or "persistent" T_g value, although both decreases in T_g with molecular weight and molecular-weight-independent T_g values have also been observed.[22]

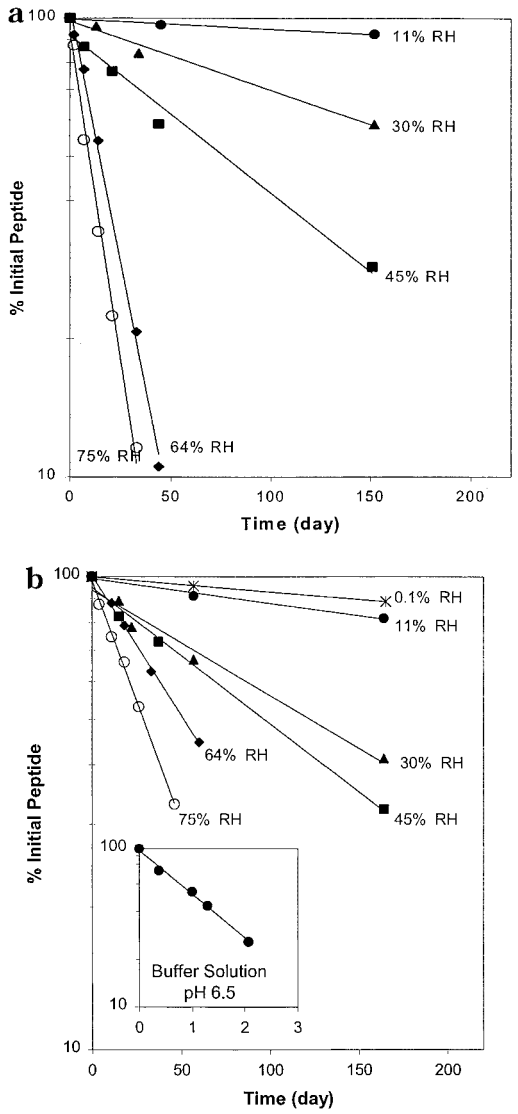

Figure 3—Asn-hexapeptide degradation profiles at various RHs at 50 °C for (a) PVA (Airvol 103) and (b) PVP (Kollidon K12) formulations ($n = 3$). The insert in Figure 3b shows the disappearance of the Asn-hexapeptide in polymer-free phosphate buffer, pH 6.8.

The lack of molecular weight dependence observed here may be due to the narrow range of molecular weights studied (particularly for PVP), to the removal of low molecular weight components during extensive dialysis prior to use, or to unusual intrinsic T_g behavior of the polymers. For our purposes, this result effectively removes polymer molecular weight from the list of independent variables that can be manipulated to control T_g.

Degradation Products—The major degradation products of Asn-hexapeptide deamidation were the isoAsp-hexapeptide (isoAsp), the Asp-hexapeptide (Asp), and the cyclic imide hexapeptide (Asu). Although isoAsp and Asp are commonly observed in solution-state deamidation at neutral pH, the cyclic imide is usually not observed because it is rapidly hydrolyzed to produce the isoAsp and Asp hexapeptides.[9,10] The dominance of isoAsp and Asu suggests that formation of the cyclic imide is the major route of Asn-hexapeptide deamidation in these polymer formulations.[9,10] Oliyai et al. have noted that Asn-hexapeptide deamidation in solid sugar formulations also occurs through a degradation pathway similar to that in solution.[8]

Deamidation Kinetics—Figures 3a and 3b show representative time-dependent disappearances of Asn-hexapeptide in PVA and PVP at different RHs. The disappearance

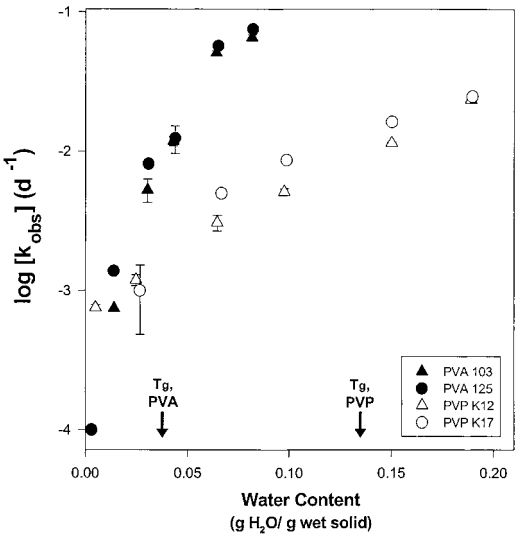

Figure 4—Effect of water content on the observed rate constant of Asn-hexapeptide deamidation (k_{obs}) in PVP and PVA at 50 °C. Error bars represent standard deviations ($n = 3$). The approximate water contents needed to lower the T_g of the PVA and PVP formulations to the experimental temperature are noted with arrows labeled "Tg, PVA" and "Tg, PVP", respectively.

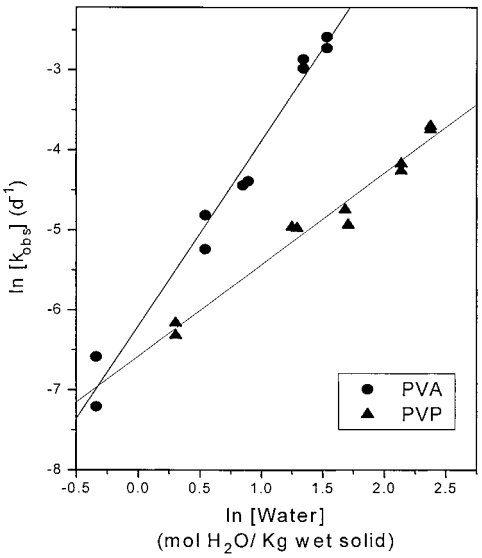

Figure 5—Plot showing the apparent dependence of deamidation rates on water content. Error bars represent standard deviations ($n = 3$).

of Asn-hexapeptide was observed to follow pseudo-first-order kinetics in peptide content at all RHs studied. Deamidation of this peptide in solution is known to exhibit pseudo-first-order kinetics.[9,10] The reaction order in peptide content appears to be similar in the solution and in these solid polymer formulations. As the RH increased, the rate of peptide degradation also increased. The observed rate constants (k_{obs}) were obtained from the slopes of the plots of ln [%Asn-hexapeptide remaining] versus time. Subsequent discussion of Asn-hexapeptide deamidation rates will employ the observed pseudo-first-order degradation rate constant.

Correlation with Water Content—The effect of formulation water content on the deamidation rate of Asn-hexapeptide is shown in Figure 4. At higher water contents ($\cong$ 10% w/w, or 0.10 g H_2O/g wet solid), the rate in PVA is nearly an order of magnitude faster than in PVP. As the water content decreases from 10% to ~2% (w/w), the deamidation rates in the two polymers become nearly equal. At very low water content (<2% w/w), the rate in PVA appears to be approximately an order of magnitude slower than in PVP, but this observation should be regarded as tentative given the limited data in this region. Polymer molecular weight had no apparent effect on peptide reactivity in either polymer. The results are consistent with those of Oliyai et al., who observed an increase in the rate of cyclic imide formation with increasing moisture level in lyophilized sugar formulations.[8]

Peptide reactivity in PVA appeared to be more sensitive to increases in water content than in PVP at water contents >5%. An increase in water content of 0.083 g/g wet solid in the PVA formulation increased the observed deamidation rate constant by almost 3 orders of magnitude [$(1.0 \pm 0.05) \times 10^{-4}$ to $(7.5 \pm 0.4) \times 10^{-2}$ day^{-1}]. In contrast, the deamidation rate in PVP increased by only 1 order of magnitude over a wider range of water contents. Figure 5 shows that there is an apparent first-order dependence of the rate of Asn-hexapeptide deamidation on water content in PVP (slope = 1.15 ± 0.10), but an apparent second-order dependence on water content in PVA (slope = 2.31 ± 0.12), according to the following relationship:

$$k_{obs} = k\,[\text{water content}]^n \qquad (4)$$

where k is a constant and n is the order of the reaction with respect to water content in mol water/kg wet solid. The difference in reaction order between PVP (first order) and PVA (second order) is indicative of differences in reaction mechanism or environmental response, or both, in the two media. Further study will be required to establish the molecular origins of the difference because changes in water content can cause both mechanistic and environmental effects. For example, water may serve as a reactant or catalyst in the conversion of a reactant state to a transition state (a mechanistic effect) or may act as a plasticizer in affecting the ease of molecular motion in the medium (an environmental effect). Even a consideration of mechanistic effects alone is less straightforward than it might appear initially. If the reaction in polymeric media proceeds by the mechanism established in the solution state (Scheme 2), the initial cyclization step will not involve water stoichiometrically, whereas the hydrolysis step in ring opening of the cyclic imide will stoichiometrically require one molecule of water per molecule of cyclic imide. This conclusion might suggest that the higher order in water content observed in PVA is associated with rate-determining ring opening, whereas the lower order observed in PVP is indicative of rate-determining cyclization. However, catalytic involvement of unknown numbers of water molecules in either step of the solid-state reaction would render such a conclusion incorrect.

Correlation with Water Activity—The amount of water present is not always representative of the amount of water available for reaction; chemical potential or water activity may be a better indicator of its possible role as a reactant. In this study, the formulations were assumed to be in equilibrium within the closed RH chambers at constant temperature and pressure. Therefore, it is reasonable to assume that the relative water vapor pressure in the chambers is equal to the formulation water activity. Figure 1 shows that PVA and PVP have different water vapor sorption behavior and thus have different water activities when water content is similar.

Figure 6 correlates the rate of Asn-hexapeptide deamidation in PVA and PVP with water activity or RH. The rate of Asn-hexapeptide deamidation increases with increases in water activity (A_w). Reactivity may be better described by water activity (Figure 6) than by water content (Figure 4) in these systems because the differences between the PVA and PVP curves are reduced in Figure

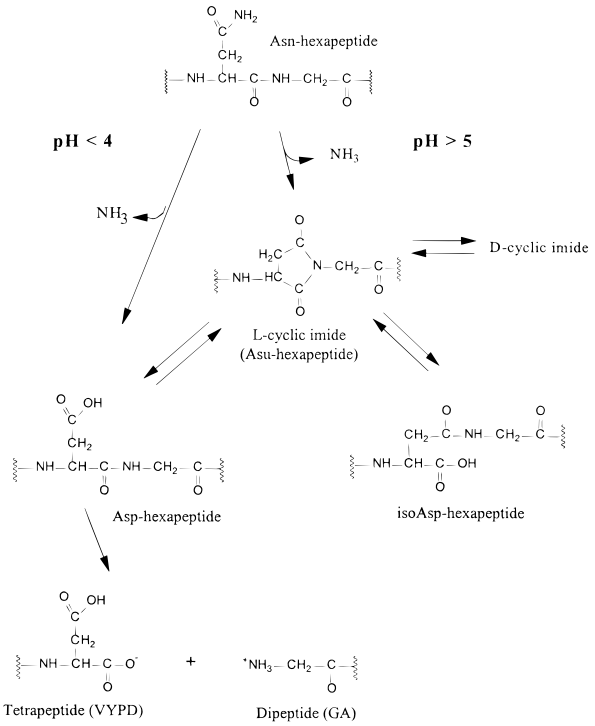

Scheme 2—Solution state degradation pathways of Asn-hexapeptide (adapted from ref 10).

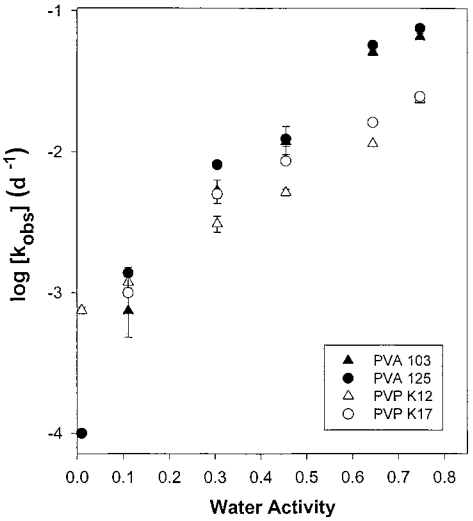

Figure 6—Effect of water activity on the observed rate constant of Asn-hexapeptide deamidation (k_{obs}) in PVP and PVA at 50 °C. Error bars represent standard deviations ($n = 3$).

6. Although the discrepancy in Asn-hexapeptide reactivity between PVA and PVP was less when differences in formulation A_w were taken into account, peptide reactivity at high (>0.6) or low (<0.1) water activity was still markedly different in PVA and PVP. Thus, water activity alone was not adequate to describe peptide reactivity in these different polymer solids, again implying that additional effects of water may be important in these systems.

Correlation with Formulation T_g—The finding that reactivity was not predicted by water content or activity alone suggests that the effect of water on Asn-hexapeptide deamidation in PVA and PVP was not entirely due to its role as a reactant. Another possible role of water is as a plasticizer to facilitate polymer chain mobility and decrease polymer viscosity, along with a decrease in T_g. The T_g was thus taken as a qualitative measure of matrix mobility. If deamidation in the solid state is controlled by reactant mobility, then the degradation rate should be affected by changes in T_g, assuming some degree of coupling between reactant and formulation mobility. It should be noted that because T_g measures a bulk property of the polymer matrix, it is not possible to distinguish the flexional and translational mobilities of the incorporated peptide using T_g.

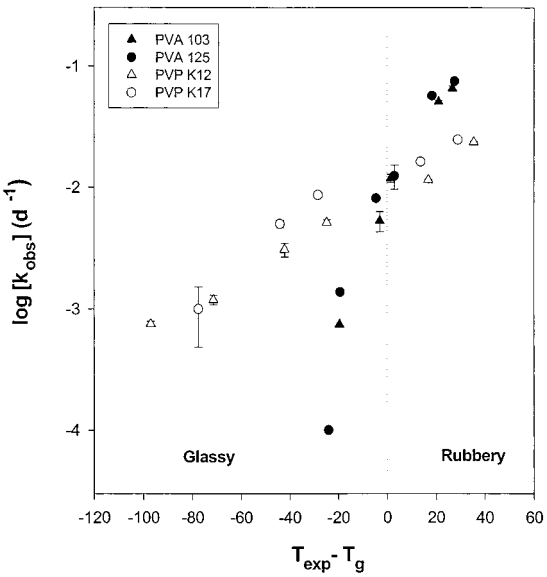

Figure 7—Effect of formulation T_g on the rate of Asn-hexapeptide deamidation in PVA and PVP at 50 °C. Temperatures are in °C. Error bars represent standard deviations ($n = 3$).

Figure 7 correlates the rate of Asn-hexapeptide deamidation to changes in formulation mobility, as expressed by ($T_{exp} - T_g$) based on the Vogel–Tamman–Fulcher and Williams–Landel–Ferry equations.[23–25] The T_{exp} parameter was chosen as the constant reference temperature with T_g as a variable. Negative values on the x axis denote formulations in the glassy state with $T_g > T_{exp}$, whereas positive values represent formulations in the rubbery state with $T_g < T_{exp}$. As the formulation T_g decreased (i.e., as $T_{exp} - T_g$ increased), the rates of deamidation increased in both PVA and PVP. In the glassy state, the rate of Asn-hexapeptide deamidation was greater in PVP than in PVA. However, as the formulations became more rubbery, peptide reactivity in the two polymers was reversed; that is, Asn-hexapeptide deamidation in the rubbery state was more rapid in PVA than in PVP. In going from a glassy to a rubbery state, the deamidation rate in PVA increased by 3 orders of magnitude with a 50 °C decrease in formulation T_g as compared with only 1 order of magnitude increase in PVP over the same range. At the glass transition, the rates of Asn-hexapeptide deamidation were similar in both polymers. The rate of Asn-hexapeptide deamidation seemed to be more sensitive to changes in the T_g of PVA than in PVP. If T_g alone described reactivity in these polymers, the curves for PVA and PVP would be expected to be coincident. That they differ suggests that formulation T_g alone was not adequate in describing Asn-hexapeptide reactivity in the two polymers.

Discussion

The rate of Asn-hexapeptide deamidation increased with increasing water content and water activity and decreasing formulation T_g in PVA and in PVP. However, degradation behavior in the two polymers differed so that chemical reactivity could not be predicted from water content, water activity, or formulation T_g alone. Thus, no single parameter seems to dictate the deamidation rate over the range of water content, water activity, and T_g studied.

Formulation mobility appears to affect the reactivity of the Asn-hexapeptide. All glassy formulations were more stable than rubbery formulations, regardless of water content. This result suggests that limited peptide mobility in the dynamically constrained glassy state may contribute to the greater stability of glassy formulations. This idea is consistent with the likely mechanism of Asn-hexapeptide degradation in these formulations. The degradation product data suggest that the mechanism of deamidation in these polymer solids is similar to that observed in solution. Thus, it is likely that deamidation in these systems proceeds via intramolecular cyclization to form a cyclic imide, a process that requires sufficient peptide mobility to adopt the necessary conformation for cyclization. Local segmental flexibility has been shown to influence the propensity for spontaneous cyclic imide formation from asparagine residues in calmodulin.[26] Yoshioka et al. observed that the γ-globulin aggregation rate was faster in lyophilized PVA than in dextran, although water content was lower in PVA than in dextran (0.098 versus 0.177 g/g of solid).[27] They attributed this lower stability to the lower critical temperature for mobility of PVA and proposed that the greater mobility in PVA accounted for the more rapid aggregation.

Although the less mobile glassy formulations were more stable, chemical reactivity was not negligible in these systems; as shown in Figure 7, deamidation occurred at a measurable rate in glassy matrixes of both PVA and PVP. Hancock et al. have suggested that glassy solids should be expected to experience significant molecular mobility at temperatures up to 50 °C below T_g,[28] which suggests that mobility-dependent reactions may still occur. Notably, the data in Figure 7 demonstrate that the rate of deamidation in glassy PVP matrixes is rapid enough to preclude adequate shelf stability. At an experimental temperature 100 °C below the T_g of the "dry" PVP formulation ($T_{exp} - T_g = -100$ °C, with T_g of the dry formulation = 150 °C), the Asn-hexapeptide was observed to have a half-life of only 2 years, suggesting that significant reactivity may be observed at temperatures far below T_g. Although the dry PVA formulation had a lower T_g (75 °C), the half-life for deamidation was much longer than that observed for the dry PVP formulations (20 versus 2 years). This result suggests that formulation mobility, as measured by T_g, is in itself insufficient to predict deamidation rates in these polymer systems.

An examination of Asn-hexapeptide reactivity and viscosity changes around the glass transition further supports this idea. The transition from a glassy to a rubbery state usually is characterized by a decrease in viscosity of >5 orders of magnitude.[6,24] Around this region ($T_g = T_{exp}$), the rates of deamidation increased by only 3 orders of magnitude in PVA and barely 2 orders of magnitude in PVP. The absence of an increase in rate comparable in magnitude to the decrease in viscosity at the glass transition may suggest incomplete coupling of deamidation rate to matrix mobility.

The inability of T_g alone to predict deamidation rates in PVA and PVP suggests that the level of mobility required for deamidation may be less than the bulk mobility represented by T_g. As already noted, the mechanism of deamidation in these solid polymer systems appears to be similar to that in solution, proceeding via a cyclic imide intermediate. Formation of the cyclic imide requires localized conformational flexibility of the peptide chain, allowing the attack of the backbone NH of the glycine residue on the side-chain amide function of the asparagine. Because T_g measures a bulk property of the system, it may not adequately reflect the localized molecular motions required for deamidation. Thus, although PVA and PVP formulations may have the same T_g, the degree of localized molecular mobility may differ. The characteristic length

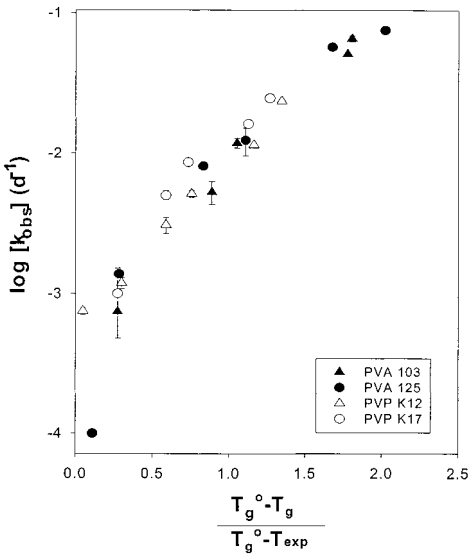

Figure 8—Correlation between deamidation rates and water plasticization in PVA and PVP at 50 °C.

scale for motions associated with the relaxation of the glassy modulus can have different temperature [or water] dependencies and can vary significantly for amorphous polymers.[29] Thus, the discrepancy in deamidation rates in PVA and PVP may be due to differences in polymer properties and structural responses to water, leading to differences in localized molecular mobility changes with increases in water content.

Although mobility affects deamidation, water may affect deamidation also as a solvent and proton-transfer agent. Among the three correlations made between deamidation rates and formulation parameters, water activity appeared to correlate best with Asn-hexapeptide instability in PVA and in PVP. The closer correlation between deamidation rates and water activity in PVA and PVP formulations suggests that some factor related to water activity may be influencing deamidation. In solution, solvent effects have been shown to affect deamidation due to changes in dielectric constant (polarity) and peptide pK_as. Brennan and Clarke have shown that deamidation rates decrease as solvent dielectric constant decreases.[30] Although water contents in these solid systems are low relative to solution, the "solvent" properties of water may still affect chemical reactivity, and changes in deamidation rate may be partially due to "polarity" changes upon hydration. The rate discrepancy in PVA and PVP further suggests that the "solvent" environment may affect deamidation because the PVA and PVP matrixes are serving as the main "solvent" for Asn-hexapeptide.

Water and polymer type both appeared to have an effect on deamidation, indicating that more than one parameter should be required to describe chemical reactivity in these systems. Figure 8 shows the correlation between deamidation rate and the degree of plasticization ($T_g^o - T_g$), normalized for the extent of plasticization required to induce the glass transition at 50 °C ($T_g^o - T_{exp}$). Data for both polymers are described by a single relationship. The expression was derived by making the approximation that the relationship between T_g and water content was linear over the range used in this study (see Figure 2) such that

$$T_g = T_g^o - \alpha W \qquad (5)$$

where α is a constant and W is the weight fraction of water. A similar relationship has been proposed for the more general case of plasticization by any additive.[31] Assuming

that α is constant for each polymer, eq 5 can be expected to hold when $T_g = T_{exp}$ and $W = W_g$ so that

$$\alpha = \frac{T_g^{\circ} - T_{exp}}{W_g} \tag{6}$$

where W_g is the water content needed to induce the glass transition at $T_{exp} = 50$ °C. Substituting this value for α (i.e., the slope) into eq 5 yields:

$$\frac{T_g^{\circ} - T_g}{T_g^{\circ} - T_{exp}} = \frac{W}{W_g} \tag{7}$$

This equation states that the degree of plasticization needed to induce a glass transition is related to water content, the experimental temperature, and the dry intrinsic T_g° of the polymer. A convergence of the deamidation rates in PVA and PVP was also observed when the rate constant (k_{obs}) was plotted against W/W_g. Although this parameter $[(T - T_g)/(T_g^{\circ} - T_{exp})]$ may be useful in correlating reaction rates in other systems, its utility in these studies (Figure 8) may be due to the near linear relationship between T_g and water content observed for PVA and PVP under these experimental conditions (Figure 2).

The results of this study suggest that several factors, including water content and mobility, may affect the chemical reactivity of Asn-hexapeptide in lyophilized polymer formulations. Isolating a single dominant mechanism driving deamidation is difficult because water content, water activity, and T_g are coupled. Future studies will attempt to vary T_g and water content independently with the use of a separate plasticizer to deconvolute their effects on deamidation in the solid state.

References and Notes

1. Hageman, M. J. Water sorption and solid-state stability of proteins. In *Stability of Protein Pharmaceuticals, Part A: Chemical and Physical Pathways of Protein Degradation*; Ahern, T. J.; Manning, M. C., Eds.; Plenum: New York, 1992; pp 273−309.
2. Roy, M. L.; Pikal, M. J.; Rickard, E. C.; Maloney, A. M. The effects of formulation and moisture on the stability of a freeze-dried monoclonal antibody-vinca conjugate: A test of the WLF glass transition theory. *Dev. Biol. Standard.* **1992**, *74*, 323−340.
3. Constantino, H. R.; Langer, R.; Klibanov, A. M. Moisture-induced aggregation of lyophilized insulin. *Pharm. Res.* **1994**, *11*, 21−29.
4. Strickley, R. G.; Anderson, B. D. Solid-state stability of human insulin. I. Mechanism and the effect of water on the kinetics of degradation in lyophiles from pH 2−5 solutions. *Pharm. Res.* **1996**, *13*, 1142−1153.
5. Shalaev, E. Y.; Zografi, G. How does residual water affect the solid-state degradation of drugs in the amorphous state? *J. Pharm. Sci.* **1996**, *85*, 1137−1141.
6. Levine, H.; Slade, L. The glassy state phenomenon in food molecules. In *The Glassy State in Foods*; Blanshard, J. M. V.; Lillford, P. J., Eds.; Nottingham: Nottingham, 1993; pp 35−101.
7. Ahlneck, C.; Zografi, G. The molecular basis of moisture effects on the physical and chemical stability of drugs in the solid state. *Int. J. Pharm.* **1990**, *62*, 87−95.
8. Oliyai, C.; Patel, J.; Carr, L.; Borchardt, R. T. Solid-state stability of lyophilized formulations of an asparaginyl residue in a model hexapeptide. *J. Parenteral Sci. Technol.* **1994**, *48*, 167−173.
9. Geiger, T.; Clarke, S. Deamidation, isomerization and racemization at asparaginyl and aspartyl residues in peptides. Succinimide-linked reactions that contribute to protein degradation. *J. Biol. Chem.* **1987**, *262*, 785−794.
10. Patel, K.; Borchardt, R. T. Chemical pathways of peptide degradation. II. Kinetics of deamidation of an asparaginyl residue in a model hexapeptide. *Pharm. Res.* **1990**, *7*, 703−711.
11. Bergren, M. S. An automated controlled atmosphere microbalance for the measurement of moisture sorption. *Int. J. Pharm.* **1994**, *103*, 103−114.
12. Guggenheim, E. A. *Applications of Statistical Mechanics*; Clarendon: Oxford, 1966.
13. Anderson, R. B. Modifications of the Brunauer, Emmett and Teller equation. *J. Am. Chem. Soc.* **1946**, *68*, 686.
14. van den Berg, C.; Bruin, S. Water activity and its estimation in food systems: Theoretical aspects. In *Water Activity: Influences of Food Quality*; Rockland, L. B.; Stewart, G. F., Eds.; Academic: New York, 1981; pp 1−61.
15. Hancock, B. C.; Zografi, G. The use of solution theories for predicting water vapor absorption by amorphous pharmaceutical solids: A test of the Florry-Huggins and Vrentas models. *Pharm. Res.* **1993**, *10*, 1262−1267.
16. Gordon, M.; Taylor, J. S. Ideal copolymers and the second-order transitions of synthetic rubbers. I. Noncrystalline copolymers. *J. Appl. Chem.* **1952**, *2*, 493−500.
17. Hancock, B. C.; Zografi, G. The relationship between the glass transition temperature and the water content of amorphous pharmaceutical solids. *Pharm. Res.* **1994**, *11*, 471−477.
18. Nyquist, H. Saturated salt solutions for maintaining specified relative humidities. *Technol. Prod. Mfr.* **1983**, *4*, 47−48.
19. Connors, K. A.; Amidon, G. L.; Stella, V. J. *Chemical Stability of Pharmaceuticals, 2nd ed.*; John Wiley & Sons: New York, 1986; pp 115−133.
20. Sperling, L. H. *Introduction to Physical Polymer Science*; John Wiley & Sons: New York, 1986; p 278.
21. In *Polyvinyl Alchohol-Developments*; Finch, C. A., Ed.; John Wiley & Sons: New York, 1992; pp xix−xx.
22. Peyser, P. Glass transition temperatures of polymers. In *Polymer Handbook*, 3rd ed.; Brandrup, J.; Immergut, E. H., Eds.; John Wiley & Sons: New York, 1989; p VI-211.
23. Williams, M. L.; Landel, R. F.; Ferry, J. D. The temperature dependence of relaxation mechanisms in amorphous polymers and other glass-forming liquids. *J. Am. Chem. Soc.* **1955**, *77*, 3701−3707.
24. Angell, C. A. Formation of glasses from liquids and biopolymers. *Science* **1995**, *267*, 1924−1935.
25. Hancock, B. C.; Zografi, G. Characteristics and significance of the amorphous state in pharmaceutical systems. *J. Pharm. Sci.* **1997**, *86*, 1−12.
26. Ota, I. M.; Clarke, S. Calcium affects the spontaneous degradation of aspartyl/asparaginyl residues in calmodulin. *Biochemistry* **1989**, *28*, 4020−4027.
27. Yoshioka, S.; Aso, Y.; Nakai, U.; Kojima, S. Effect of high molecular mobility of poly(vinyl alcohol) on protein stability of lyophilized insulin. *J. Pharm. Sci.* **1998**, *87*, 2, 147−151.
28. Hancock, B. C.; Zografi, G. Molecular mobility of amorphous pharmaceutical solids below their glass transition temperatures. *Pharm. Res.* **1995**, *12*, 799−806.
29. Inoue, T.; Cicerone, M. T.; Ediger, M. D. Molecular motions and viscoelasticity of amorphous polymers near Tg. *Macromolecules* **1995**, *28*, 3425−3433.
30. Brennan, T. V.; Clarke, S. Spontaneous degradation of polypeptides of aspartyl and asparaginyl residues: Effect of the solvent dielectric. *Protein Sci.* **1993**, *2*, 331- 338.
31. Boyer, R. E. Effect of plasticizers on some physical properties of polymers. *Tappi* **1951**, *34*, 357−362.

Acknowledgments

M.C.L. thanks Bob Dalga of Pharmacia & Upjohn, Inc. for his help on the CAM and Pharmacia and Upjohn for the opportunity of an industrial externship. This project was supported by the Takeru Higuchi Predoctoral Fellowship (M.C.L.), a NIGMS Biotechnology Training Grant (M.C.L.), Pharmacia & Upjohn, Inc., and by NIH Grant GM-54195.

JS980227G

Chemical Stability of Peptides in Polymers. 2. Discriminating between Solvent and Plasticizing Effects of Water on Peptide Deamidation in Poly(vinylpyrrolidone)

MEI C. LAI,[†,‡] MICHAEL J. HAGEMAN,[†,§] RICHARD L. SCHOWEN,[†] RONALD T. BORCHARDT,[†] BRIAN B. LAIRD,[||] AND ELIZABETH M. TOPP*,[†]

Contribution from *Department of Pharmaceutical Chemistry, The University of Kansas, Lawrence, Kansas 66047, Pharmaceutical Development I, Pharmacia & Upjohn, Inc., Kalamazoo, Michigan 49001, and Department of Chemistry, The University of Kansas, Lawrence, Kansas 66047.*

Received May 27, 1998. Final revised manuscript received June 6, 1999.
Accepted for publication July 9, 1999.

Abstract □ The mechanistic role of water in the deamidation of a model asparagine-containing hexapeptide (Val-Tyr-Pro-Asn-Gly-Ala) in lyophilized formulations containing poly(vinylpyrrolidone) (PVP) and glycerol was investigated. Glycerol was used as a plasticizer to vary formulation glass transition temperature (T_g) without significantly changing water content or activity. Increases in moisture and glycerol contents increased the rate of peptide deamidation. This increase was strongly correlated with T_g at constant water content and activity, suggesting that increased matrix mobility facilitates deamidation. In rubbery systems ($T > T_g$), deamidation rates appeared to be independent of water content and activity in formulations with similar T_gs. However, in glassy formulations with similar T_gs, deamidation increased with water content, suggesting a solvent/medium effect of water on reactivity in this regime. An increase in water content also affected the degradation product distribution; less of the cyclic imide intermediate and more of the hydrolytic products, isoAsp- and Asp-hexapeptides, were observed as water content increased. Thus, residual water appears to facilitate deamidation in these solid PVP formulations both by enhancing molecular mobility and by solvent/medium effects, and also participates as a chemical reactant in the subsequent breakdown of the cyclic imide.

Introduction

Many protein and peptide drugs are formulated as lyophilized or freeze-dried products to prolong shelf life.[1−3] Although the "dried" product is usually more stable than the aqueous formulation, chemical degradation reactions such as deamidation and hydrolysis can still occur.[1−3] Residual water in lyophilized protein formulations is known to promote chemical reactivity, leading to loss of biological activity and a shortened shelf life.[2−6] Although the destabilizing effect of water on proteins is widely acknowledged, the exact mechanistic role of water in facilitating chemical reactivity in the solid state is not well understood. This study will examine the mechanistic role of water in the deamidation of the model asparagine-containing hexapeptide Val-Tyr-Pro-Asn-Gly-Ala (Asn-hexapeptide) in lyophilized formulations containing poly(vinylpyrrolidone) (PVP).

* To whom correspondence should be addressed. telephone:(785) 864-3644. Fax: (785) 864-5736. E-mail: topp@ukans.edu.
† Department of Pharmaceutical Chemistry.
‡ Current address: Bristol-Meyers Squibb, New Brunswick, New Jersey 08903.
§ Pharmaceutical Development I.
|| Department of Chemistry.

Water may affect the solid-state chemical reactivity of polymer-incorporated peptides and proteins through three possible mechanisms: 1) changing the dynamic mobility of the protein or peptide, 2) direct participation as a reactant, or 3) indirect participation as a medium/solvent.[2,7] The mobility mechanism is based on the premise that if chemical reactions require sufficient mobility to proceed, an increase in mobility would result in increased reactivity. In polymer matrixes, water can increase molecular mobility by acting as a plasticizer to increase free volume and decrease viscosity.[8,9] Second, water can increase chemical reactivity directly by acting as a reactant, as in hydrolysis.[2,7] Water may also affect chemical degradation by acting as a medium for the mobilization of reactants or by modifying the reaction environment, as when the effective solvent dielectric or polarity is altered.[2,7]

The plasticizing effect of water on molecular mobility of the matrix may be monitored by measuring the glass transition temperature (T_g), the temperature at which a glassy, brittle, dynamically constrained material becomes rubbery and soft, with increased molecular mobility. Many studies have correlated decreases in T_g with decreases in system viscosity and increases in mobility.[9,10] The Vogel−Tamman−Fulcher (VTF) equation and the Williams−Landel−Ferry (WLF) equation, which is a special case of the VTF, describe the changes in viscosity in terms of $T_{exp} - T_g$ or distance from the glass transition, where T_{exp} is the experimental temperature.[9−12] Thus, we can use T_g as a qualitative measure of the plasticizing effect of water on formulation mobility. Because the effective concentration of a reactant may be expressed in terms of its chemical potential, we can use formulation water activity to measure the role of water as a reactant. Last, water content can probably best describe the medium/solvent effect of water. Thus, we can use water content, water activity, and T_g as indictors of the various mechanistic roles of water.

A technical problem with using these formulation parameters is that they are interdependent; changing water content or water activity will also affect T_g. Unambiguous mechanistic interpretations of the data are therefore difficult to achieve.[13] In a previous study, we demonstrated a dependence of deamidation rate on matrix water content in poly(vinylpyrrolidone) and poly(vinyl alcohol) matrixes, but were unable to distinguish among the more fundamental effects of water as a solvent, reactant, or plasticizer because of this interdependence.[14] To overcome this problem in the present studies, we used glycerol as an additional plasticizer to vary formulation T_g without significantly affecting water content or water activity. We therefore could systematically determine the effect of water activity

10.1021/js9802289 CCC: $18.00
Published on Web 09/01/1999

and content on deamidation kinetics when T_g is constant, as well as the effect of T_g on deamidation under constant water content and activity. Because water content and activity will not vary significantly between formulations, the role of water as a medium cannot be separated from its role as a reactant. In this study, these two roles of water will be combined under the role of solvent effects. Thus, using this strategy, we propose to deconvolute the mechanistic role of water as a plasticizer from its role as a solvent in solid-state deamidation.

Because deamidation is one of the most prevalent chemical degradations found in proteins and peptides,[15,16] we selected the Asn-containing hexapeptide (Val-Tyr-Pro-Asn-Gly-Ala) (Asn-hexapeptide) as the model compound for this study. An advantage of using the Asn-hexapeptide is that its solution-state degradation kinetics and mechanisms are well understood.[16−18] This knowledge will provide a solid mechanistic basis with which we can better interpret the solid-state deamidation kinetic and product distribution data.

In this manuscript, we present our findings on the effect of water on Asn-hexapeptide deamidation in lyophilized PVP formulations. We show that glycerol was successfully used to modify formulation T_g without a significant effect on water content or activity. Then, we correlate the rates of Asn-hexapeptide deamidation with water content/activity and T_g to elucidate the role of water in solid-state deamidation. We also examine the Asn-hexapeptide deamidation product distribution to provide information regarding the mechanism of degradation and the effect of water on product distribution.

Experimental Section

Materials—L-Val-L-Tyr-L-Pro-L-Asn-Gly-L-Ala (Asn-hexapeptide) was synthesized by Dr. Madhup Dhaon (Abbott Laboratories, North Chicago, IL). The buffers and salts used in this study were purchased from Mallinckrodt Chemical, Inc. (Paris, KY). Organic solvents and trifluoroacetic acid were purchased from Fisher Scientific (Fair Lawn, NJ). The poly(vinylpyrrolidone), under the trade name of Kollidon K17 [MW = 10 000], was purchased from BASF Corporation (Parsippany, NJ). Glycerol was obtained from the manufacturing division of Pharmacia & Upjohn, Inc. (Kalamazoo, MI). Deionized and distilled water was used throughout.

Preparation of Formulations—Five formulations were prepared: four solid-state PVP formulations with 0, 10, 20, and 30% glycerol, and a liquid-state formulation in 100% glycerol. The detailed procedure has been described previously.[14] Briefly, the solid PVP formulations were prepared from solutions containing peptide, glycerol, and PVP in phosphate buffer (pH 6.8). The solutions were added in a dropwise manner to liquid nitrogen to form frozen spherical pellets, which were then lyophilized to remove residual moisture. The average peptide load, calculated on the basis of the maximum amount released,[14] was 0.017 g/g dry solid for 100% PVP, 0.022 g/g dry solid for 10% glycerol/PVP, 0.022 g/g dry solid for 20% glycerol/PVP, 0.014 g/g dry solid for 30% glycerol/PVP, and 0.24 g/g glycerol for 100% glycerol, with errors at 5% ($n = 3-5$). The approximate final composition of the formulations was 2% peptide, 2% buffer, and 96% (w/w) PVP and/or glycerol, with a residual water content of <0.1% (w/w).

Characterization of Water Sorption Behavior—Sorption isotherms relating formulation water content to relative humidity (water activity) at 50 °C were generated using a controlled atmosphere microbalance (CAM), according to a method reported previously.[14] As in the previous study, the water sorption data obtained with the CAM were fitted to the Guggenheim−Anderson−deBoer (GAB) equation which describes the sorption of water by heterogeneous sorbents or solids:[2]

$$W = \frac{W_m C_g K_{GAB}(\rho/\rho_o)}{[1 - K_{GAB}(\rho/\rho_o)][1 - K_{GAB}(\rho/\rho_o) + C_g K_{GAB}(\rho/\rho_o)]} \quad (1)$$

where W is the mass (mg) of water vapor adsorbed per mg of dry solid at (ρ/ρ_o), (ρ/ρ_o) is the relative vapor pressure, W_m is generally regarded as the amount of water vapor necessary to saturate the heterogeneous active sorption sites, and C_g and K_{GAB} are dimensionless constants that are related to the thermodynamic measures of sorption for strongly and weakly interacting water.[2,19,20]

Characterization of Formulation Glass Transition Temperature—Glass transition temperatures (T_g) were measured using modulated differential scanning calorimetry (DSC) according to the method described previously.[14] As in that study, the T_g data were fitted to the Gordon−Taylor equation (eq 2), which describes the T_g of two miscible components:

$$T_g = \frac{w_1 T_{g1} + K_{GT} w_2 T_{g2}}{w_1 + K_{GT} w_2} \quad (2)$$

where T_g is the glass transition temperature of the mixture, w_1 and w_2 are the weight fractions of the individual components, T_{g1} and T_{g2} are the intrinsic T_gs of each component, and K_{GT} is a constant of the system describing the true density of the materials and changes in the thermal expansivity.[21,22] In applying the Gordon−Taylor equation, we treated the ternary system PVP/glycerol/water as a binary system, with PVP/glycerol and water as the two components. This simplification is justified because the relative proportions of PVP and glycerol remained unchanged as water content varied in our studies. In fitting the data, we used the experimentally measured values for T_g, w_1 and w_2, and set the T_{g1} value for water to the reported value of 135 K, as in the previous study.[14] Values for T_{g2} (the glass transition temperature of "dry" PVP/glycerol systems) and K_{GT} were determined by regression.

Stability Study—Stability studies were conducted on 4 mg of pellets stored in glass lyophilization vials; details of the method have been reported previously.[14] Before beginning the stability study, the solid Asn-hexapeptide formulations were allowed to equilibrate in chambers at 20 °C for 12 h. After this initial equilibration period, formulations stored at 75% RH were removed and analyzed for Asn-hexapeptide content and integrity prior to beginning the stability study. No significant degradation products were observed. For the stability study, the samples were transferred to controlled relative humidity chambers in a 50 °C room. Samples were prepared in triplicate. Peptide composition was assayed by HPLC after various storage times to determine degradation kinetics and product distribution. At specified time intervals, triplicate samples were removed for peptide analysis, as described previously.[14] Observed rate constants (k_{obs}) for the disappearance of the parent Asn-hexapeptide were determined from the slopes of plots of ln(% peptide remaining) versus time, assuming first-order kinetics as previously observed for this peptide in solution[17] and solid[6,14] states.

Peptide Analysis—The analyses of Asn-hexapeptide and its degradation products were performed by reversed-phase HPLC, using a modification of a method described previously.[14] The HPLC analytical system consisted of a Shimadzu (Shimadzu Corp., California) LC-6A pump, a Shimadzu SPD-6A variable-wavelength UV detector, a Shimadzu CR601 Chromatopac integrator, and a Rheodyne 7161 manual injector outfitted with a 50-μL injection loop. The Asn-hexapeptide and its degradation products were separated on an Alltech Econosphere C-18 reversed-phase column (5 μm resin, 4.6 × 250 mm) by an isocratic method with a mobile phase of 10% (v/v) acetonitrile and 0.1% (v/v) trifluoroacetic acid (TFA) in 40 mM ammonium acetate at a pH of 4.5 and a flow rate of 0.8 mL/min. The detection wavelength was 214 nm. The identification of the degradation products was conducted by co-injection of standards.

Results

Physical Characterization—*Water Sorption Isotherms*—Water sorption isotherms at 50 °C are shown in Figure 1 for PVP formulations with different glycerol contents, and also for liquid glycerol. In all cases, the water content of the formulations increased as relative water vapor pressure increased. The curved lines in Figure 1 represent the nonlinear least-squares fits of the water sorption data to the GAB equation, which adequately described the water

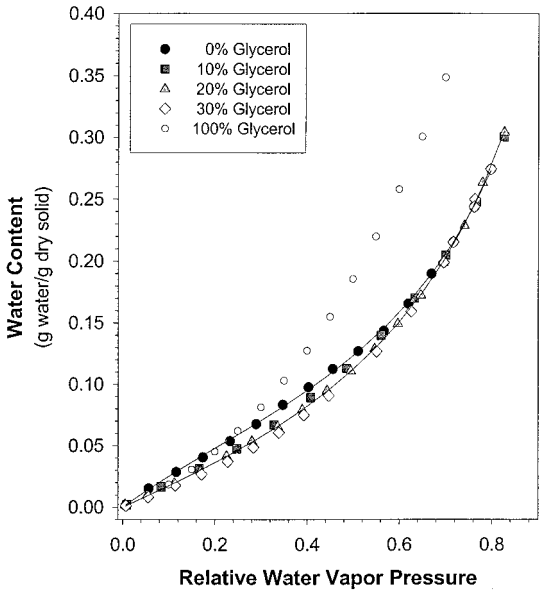

Figure 1—Water sorption isotherms for PVP formulations of various glycerol contents at 50 °C. The curved lines represent nonlinear least-squares fits to the Guggenheim–Anderson–deBoer equation (eq 1) for 0% glycerol–PVP and 20% glycerol–PVP formulations. The 100% glycerol data were taken from the literature.[24]

Table 1—Calculated Parameter Values and Standard Errors from Nonlinear Least Squares Fits of the Water Sorption Data (Figure 1) for PVP–Glycerol Formulations to the GAB Equation (eq 1) at 50 °C

PVP formulation % glycerol	W_m (g/g dry solid)	C_g	K_{GAB}
0	0.101 ± 0.003	3.13 ± 0.17	0.849 ± 0.009
10	0.129 ± 0.005	1.75 ± 0.09	0.809 ± 0.009
20	0.121 ± 0.004	1.65 ± 0.08	0.833 ± 0.008
30	0.129 ± 0.004	1.29 ± 0.05	0.838 ± 0.007

sorption behavior for all formulations. The calculated parameter values (Table 1) in conjunction with the GAB equation were used to describe formulation water content at specific relative humidities.

Figure 1 and the fitted GAB parameters (Table 1) suggest that the water sorption isotherms of the four solid PVP formulations were similar. At three of the four relative humidities studied (0, 11, and 75%), the presence of glycerol did not significantly affect formulation water sorption behavior, because the formulations (0−30% glycerol) have similar water contents. At 30% RH, the three PVP formulations with glycerol had similar water contents but contained 15% less water than the PVP formulation without glycerol. Thus, the maximum difference in water content is ~15%, and will be observed at the intermediate relative humidity (30% RH) for the PVP formulation without glycerol. The 100% glycerol, which was included as a control (freely mobile system), will also exhibit significantly greater water contents than the other formulations, particularly at 30% RH.

Glass Transition Temperature—The addition of plasticizers can decrease the T_g of amorphous polymers.[23] This plasticizing effect of water is evident in Figure 2. Figure 2a shows a representative DSC thermogram, and Figure 2b shows T_g as a function of water content for the different formulations studied. The curved lines in Figure 2b are the nonlinear least-squares fits of the data to the Gordon−Taylor equation, which appears to adequately describe the depression of formulation T_g by the absorbed water. The fitted parameter values are listed in Table 2. The horizontal dotted line in Figure 2 corresponds to the experimental

Table 2—Calculated Parameter Values and Standard Errors from Nonlinear Least Squares Fits of the T_g Data (Figure 2) to the Gordon–Taylor Equation (eq 2)

PVP formulation % glycerol	intrinsic T_g[a] (K)	fitted K_{GT} value
0	428.9 ± 2.9	0.281 ± 0.092
10	368.5 ± 1.4	0.224 ± 0.084
20	336.5 ± 2.0	0.164 ± 0.091
30	311.6 ± 1.3	0.153 ± 0.076

[a] The T_g of the "dry" formulation (water content < 0.004 g/g wet solid).

temperature (50 °C). During these stability studies, formulations with T_g > 50 °C will be in the glassy state, whereas those with T_g < 50 °C will be in the rubbery state. All "dry" PVP−glycerol formulations (water content <0.004 g/g dry solid), except for the one containing 30% glycerol, were in the glassy state at 50 °C.

Glycerol also acted as a plasticizer to lower the T_g of PVP. On a weight basis, water was a stronger plasticizer than glycerol. As shown in Figure 2b, an increase in water content from 0 to 20% (w/w) corresponded to a 120 K decrease in T_g, whereas a comparable change in glycerol content depressed the T_g by only 90 K. As the glycerol content increased, the amount of water required to decrease the formulation T_g to the experimental temperature decreased. With no glycerol added, 0.14 g water/g dry solid was needed to lower the PVP formulation T_g to 50 °C. With the addition of 10% (w/w) glycerol to the PVP formulation, less water (0.05 g water/g wet solid) was needed to achieve the same formulation T_g (50 °C).

By using glycerol to vary T_g, we have obtained PVP formulations with similar T_gs but different water contents. These formulations will allow us to study the effect of water content/water activity on deamidation in formulations with similar T_gs. As shown in Figure 2b, we also have generated PVP formulations with similar water contents or activities but significantly different T_gs. These formulations will help determine the effect of T_g on deamidation at constant water activity and water content. From these two sets of formulations, the dominant role of water in peptide deamidation in solid formulations may be inferred.

Physical Appearance—At 50 °C, the physical appearance of the "dry" PVP formulations (water content < 0.4% w/w) changed as the weight percentage of glycerol increased. Most notable was a decrease in pellet size and a change from a brittle to a soft, sticky texture. Formulations without glycerol were white, dry, powdery pellets. PVP pellets with 10% (w/w) glycerol were similar in appearance to the 0% glycerol formulation, except for a decrease in size. PVP pellets with 20% glycerol were approximately one-third the size of the 0% glycerol PVP pellets and had a shiny, opaque surface and a sticky texture. PVP pellets with 30% glycerol had melted into a sticky, viscous, opaque liquid with a yellowish color.

As the relative humidity and water content increased, the pellet size decreased with a concomitant increase in stickiness. At high relative humidity, the 20 and 30% glycerol formulations became viscous liquids. The changes in the physical appearance of the PVP formulations support the T_g data, which indicate that the formulations are undergoing the transition from a glassy state to a rubbery state with increases in water and glycerol content.

Degradation Profiles—Figures 3a and 3b show the disappearance of the Asn-hexapeptide over time for representative PVP−glycerol formulations at different relative humidities. Peptide degradation exhibited a pseudo-first-order dependence on peptide content in all formulations and at all relative humidities studied. This observation is consistent with previous reports of Asn-hexapeptide dea-

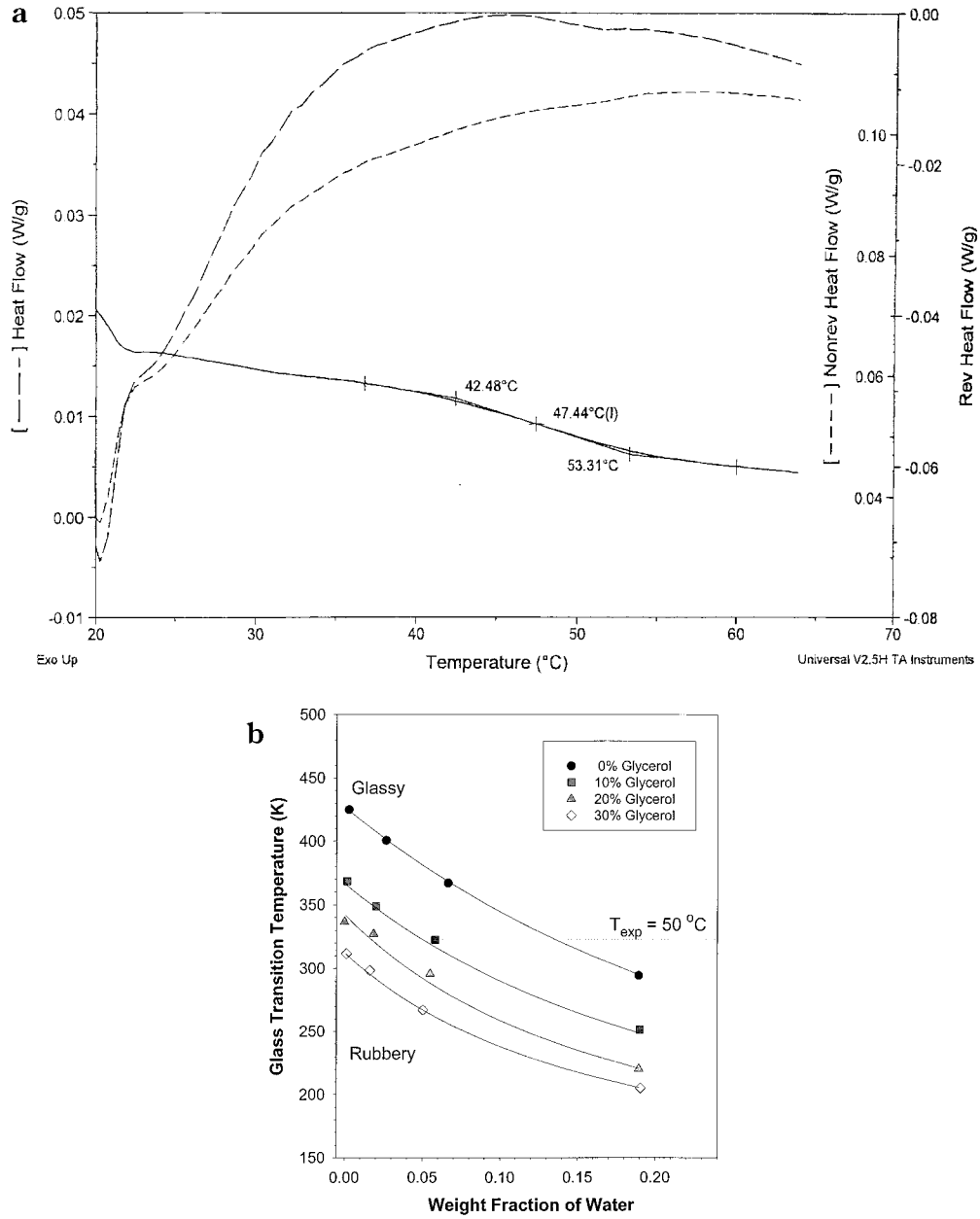

Figure 2—(a) Representative thermogram for a PVP K17 sample (containing 10% glycerol and stored at 30% RH) obtained with a scan rate of 2 °C/min and modulated at ± 1 °C/min. The endothermic T_g at 47.4 °C was calculated using the reversible heat flow curve. (b) Formulation glass transition temperature (T_g) as a function of water content at various glycerol contents ($n = 3$). The dotted line shows the experimental temperature used in the stability studies ($T_{exp} = 50$ °C, 323 K). The curved lines are the nonlinear least-squares fits to the Gordon-Taylor equation (eqn 2).

midation in lyophilized formulations.[6] The reaction order was not affected by glycerol or water. The apparent first-order deamidation rates (k_{obs}) were determined from the slopes of the lines shown in the figure, as described previously.[14]

Deamidation Kinetics—*Effect of Water Content and Activity*—Figure 4 shows the effect of water content on the decomposition of Asn-hexapeptide in lyophilized PVP with different glycerol contents. Because the PVP formulations had similar water sorption behavior (Figure 1), water activity affected deamidation rates in a manner similar to that observed for water content (data not shown). An increase in either water or glycerol content increased the rate of Asn-hexapeptide deamidation (Figure 4). The data suggest that at higher water or glycerol content, increasing the amount of either plasticizer did not affect rate as significantly as at lower levels. Increasing the weight fraction of water from 0 to 1 increased the rate of Asn-hexapeptide deamidation by 3 orders of magnitude in 0% glycerol formulations, by 2 orders of magnitude in PVP formulations with 30% glycerol, and by only 1 order of magnitude in 100% glycerol–0% PVP formulations.

The relatively rapid deamidation in glycerol when little water is present suggests that deamidation may not require water to proceed when the solvent environment allows for sufficient reactant mobility. Deamidation in glycerol was unaffected by increases in water content from <0.006 to 0.09 g/g wet glycerol. In contrast, much greater increases in Asn-hexapeptide reactivity were observed in polymer-containing formulations over the same region.

Effect of Glass Transition Temperature—Water can act as a plasticizer to decrease formulation T_g, with a corresponding decrease in viscosity and increase in molecular mobility.[9] This increase in molecular mobility may be the mechanism by which water promotes deamidation. By correlating deamidation kinetics to formulation T_g at constant water content/activity, we can determine the plasticizing effect of water on deamidation. Figure 5 shows

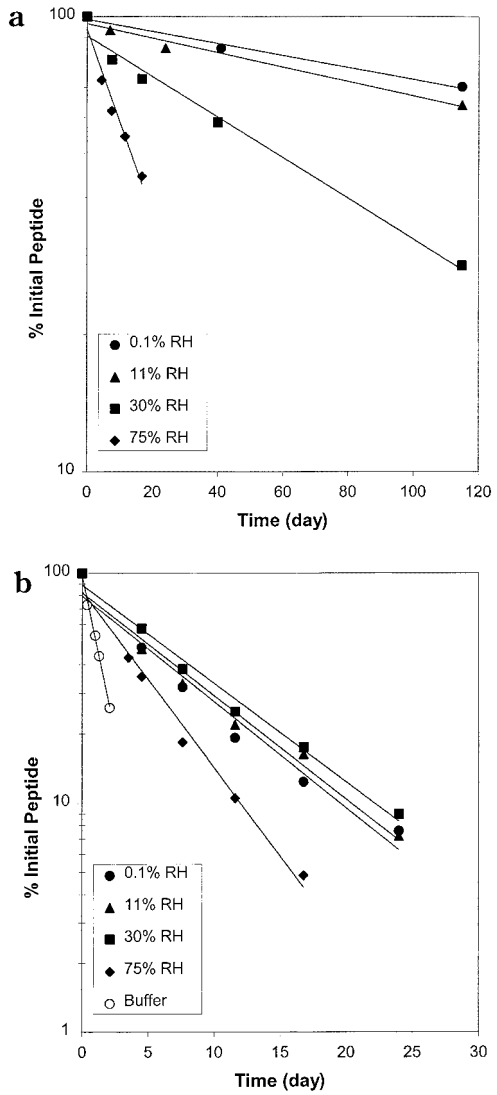

Figure 3—Disappearance of the Asn-hexapeptide as a function of time at 50 °C in (a) 10% glycerol–PVP formulation and (b) 100% glycerol at various relative humidities ($n = 3$).

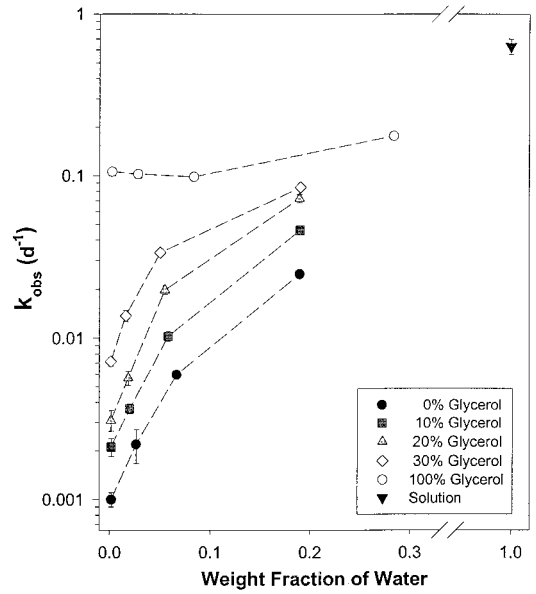

Figure 4—Observed rate constant (k_{obs}) of Asn-hexapeptide degradation at 50 °C as a function of water content in various PVP–glycerol formulations ($n = 3$). Lines have been added to clarify trends and do not represent regression.

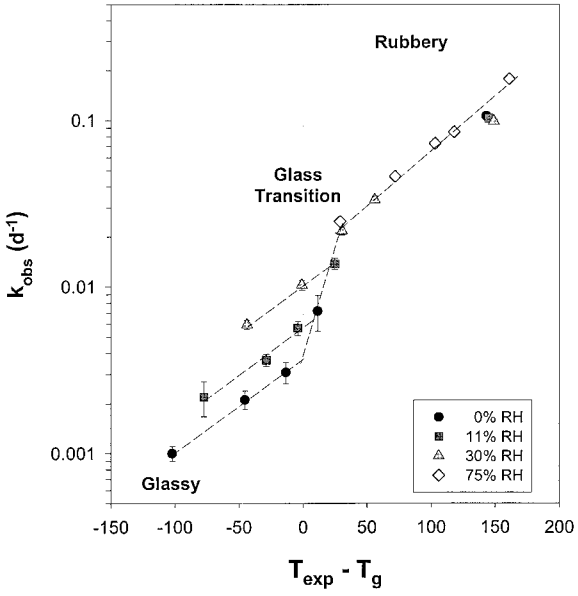

Figure 5—Observed rate constant (k_{obs}) of Asn-hexapeptide degradation as a function of T_g at $T_{exp} = 50$ °C at different relative humidities ($n = 3$). Water content (in g/g wet solid) at 0% RH is <0.004, at 11% RH is 0.02, at 30% RH is 0.06, and at 75% RH is 0.19. At each relative humidity, formulations with increasing ($T_{exp} - T_g$) (i.e., with lower T_g) were generated by adding increasing amounts of glycerol. The dashed lines denote trends in the data and do not represent curve fits to any equation.

the relationship between deamidation kinetics and T_g at different relative humidities for Asn-hexapeptide in 0−30% glycerol−PVP formulations and 100% glycerol.

When water activity was held constant, the rate of deamidation increased with decreasing T_g. For formulations in the rubbery state ($T_{exp} - T_g > 0$), the rate of deamidation appeared to be log linearly related to ($T_{exp} - T_g$), with no observed deviations for formulations with different water activities. This result suggests that the destabilizing effect of water in these formulations may be due to its role as a plasticizer. In the glassy state ($T_{exp} - T_g < 0$), decreases in T_g at constant water activity again resulted in increased deamidation rates. However, increasing water activity or content in formulations with similar T_gs also increased the rate of deamidation, suggesting that the role of water in the glassy state extends beyond that of a plasticizer. These results suggest that water may also facilitate deamidation through its role as a medium or reactant, especially in glassy PVP formulations.

Degradation Products and Their Distribution—In this study, the major degradation products observed for the deamidation of the Asn-hexapeptide in PVP solid formulations were the cyclic imide-hexapeptide (Asu), the isoAsp-hexapeptide (isoAsp), and the Asp-hexapeptide (Asp). In previous studies, these peptides have also been observed to be the products of Asn-hexapeptide deamidation in solution[16,17] and in the solid state.[6] The ratio of isoAsp to Asp was ~3, a value similar to that observed in solution at neutral pH.[16,17]

Figure 6 shows the effect of water on deamidation product distribution for the reaction in 100% glycerol. In this figure, the "% total degradation products" was calculated on the basis of the total area under the chromatographic peaks for the Asn-hexapeptide and its degradation products at each time point. Under low moisture conditions, the dominant degradation product is the cyclic imide-hexapeptide. As water content increases, the product distribution shifts toward increased formation of the isoAsp- and Asp-hexapeptides, with a corresponding de-

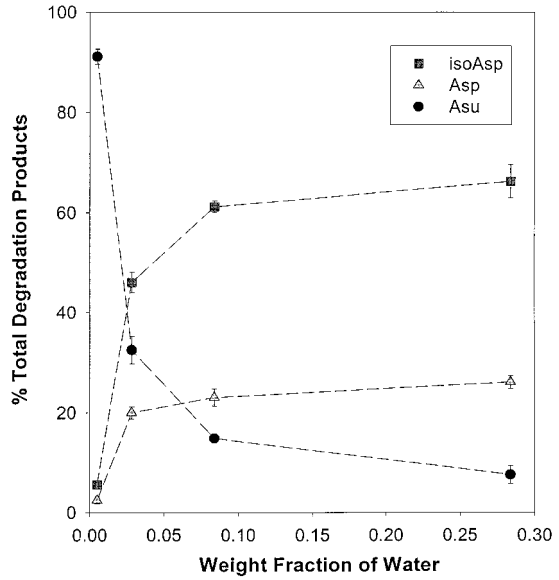

Figure 6—The Asn-hexapeptide degradation product distribution as a function of water content in 100% glycerol after 16 days at 50 °C ($n = 3$). The "% total degradation products" was determined on the basis of the total HPLC peak area at each time point.

crease in the cyclic imide. At higher water contents, isoAsp and Asp are the major degradation products with Asu present in minor quantities. These shifts in product distribution with increasing water content/activity were observed for all formulations (representative plots shown in Figures 7a and 7b, with "% total area" determined as in Figure 6).

When little or no water was present (<0.4% w/w), increasing glycerol content (and therefore decreasing T_g) did not noticeably affect product distribution. However, Figures 6, 7a, and 7b show that formulation mobility may affect the manner in which product distributions shift toward higher levels of isoAsp and Asp, with a reduction in the presence of the cyclic imide as water content increases. For example, at a water content of 0.03 g/g wet solid (water activity = 0.11), the fraction of Asu in the degradation products was lower in PVP formulations with higher glycerol contents. A higher water content was required to obtain the same product distribution in formulations with lower glycerol content and, thus, lower matrix mobility. Because of similar water activities for formulations of similar water content, water activity affected the product distribution (data not shown) in a manner similar to that observed for water content (Figure 6).

Discussion

Residual moisture can decrease the long-term stability of lyophilized protein formulations by promoting chemical degradation reactions such as asparagine deamidation. Numerous mechanistic interpretations for the destabilizing effect of water have been suggested based on relationships between chemical reactivity and formulation parameters such as water content, water activity, and T_g. However, the unambiguous interpretation of experimental results often is difficult because these parameters are interdependent and are affected by temperature.[13,14] To avoid this difficulty, we used glycerol as a plasticizer to change the T_g of the PVP formulation without significantly affecting water content or water activity. In this way, the effects of water content/activity and T_g on the deamidation of the Asn-hexapeptide can be determined independently in solid PVP formulations without a change in temperature.

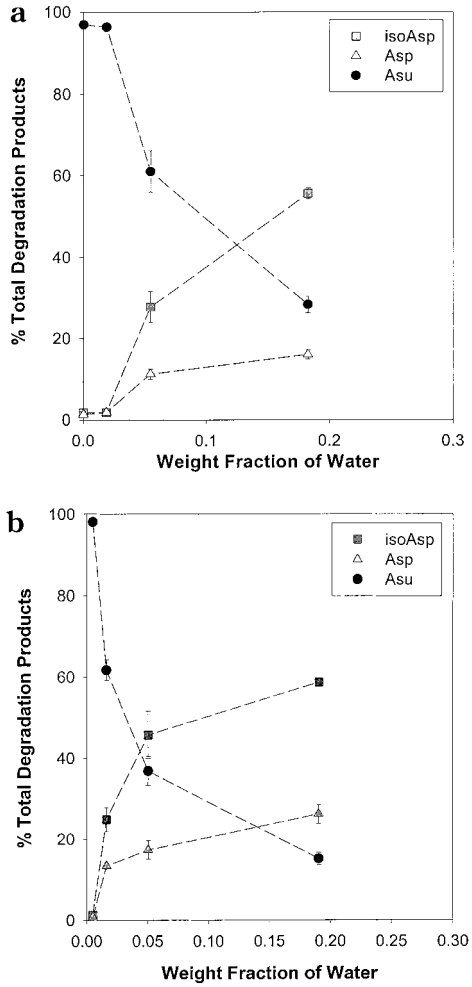

Figure 7—The Asn-hexapeptide degradation product distribution for PVP formulations with (a) 10% and (b) 30% glycerol contents as a function of water content ($n = 3$). The "% total degradation products" was determined on the basis of the total HPLC peak area at each time point.

Mechanism of Deamidation—The major degradation products of Asn-hexapeptide deamidation in PVP solid formulations are the cyclic imide hexapeptide (Asu), the isoAsp-hexapeptide (isoAsp), and the Asp-hexapeptide (Asp). These degradation products are identical to those observed for deamidation in solution, suggesting that the mechanism of deamidation in these polymer solids may be similar to that observed in solution. In solution at neutral pH, the deamidation of the Asn-hexapeptide occurs via intramolecular cyclization, which results from the nucleophilic attack of the succeeding peptide nitrogen onto the side-chain carbonyl of the Asn residue to form the cyclic imide (Scheme 1).[17] The cyclic imide hexapeptide is then rapidly hydrolyzed to form the isoAsp- and Asp-hexapeptides.[16,17] The observed ratio of isoAsp to Asp of ~3 in these solid formulations is also similar to the ratio observed for Asn-hexapeptide deamidation in solution and for the hydrolysis of the cyclic imide.[16,17] In solution, isoAsp is formed only from the hydrolysis of Asu.[16] The presence of this product in these solid formulations suggests its formation from Asu hydrolysis here as well. Taken together, these results support the hypothesis that the deamidation of the Asn-hexapeptide in these PVP–glycerol formulations proceeds via intramolecular cyclization to form the cyclic imide intermediate (Scheme 1), a mechanism similar to that observed in solution.

Other researchers have made similar observations. Oliyai et al. observed that Asn-hexapeptide degradation in lyophilized formulations containing either mannitol or

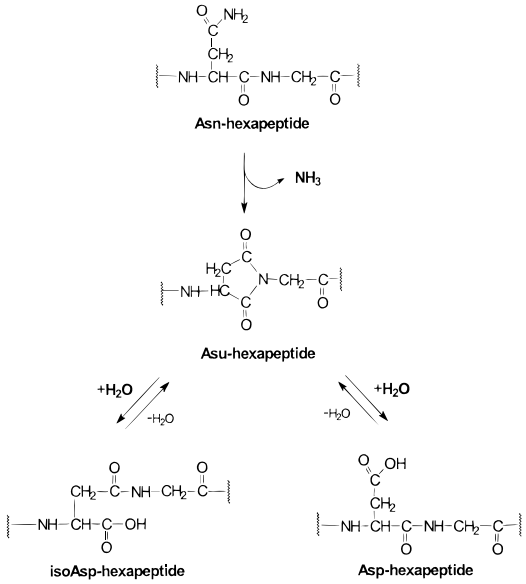

Scheme 1. —Solution-state mechanism for the deamidation of the Asn-hexapeptide at neutral pH (Adapted from Patel et al.[16]).

lactose yielded isoAsp, Asp, and Asu.[6] They concluded that the solid-state deamidation mechanism was similar to that in the solution state. Strickley and Anderson showed that the deamidation of insulin in the solid state was similar to that in the solution state in terms of degradation products, mechanism, and pH−rate profile.[5] The interpretation that the mechanism of Asn-hexapeptide deamidation in these solid systems is via intramolecular cyclization to form a five-membered cyclic imide hexapeptide is consistent with the results of this study and others.

Effect of Water on Deamidation Kinetics—Residual water appears to facilitate deamidation in lyophilized PVP formulations both by enhancing molecular mobility and by medium effects. Figures 4 and 5 show that increased mobility (decreasing T_g) and increased solvation (increased water content/activity) had a destabilizing effect on the Asn-hexapeptide in PVP. When water activity was held constant, the rate of deamidation increased with decreasing T_g, indicating that matrix mobility may be important in determining deamidation kinetics. Notably, water does not appear to act as reactant in the initial loss of the Asn-hexapeptide to form the cyclic imide. The rapid rate of deamidation in 100% glycerol at 0% RH suggests that deamidation can occur when very little water is present (<0.4% w/w). Furthermore, increases in water activity of up to 0.3 in glycerol did not affect the deamidation rate. If water was a reactant, deamidation would not be able to proceed in its absence, and the rate would be expected to vary with water content/activity. Therefore, it is likely that water is not directly affecting deamidation as a reactant. This explanation is also consistent with the deamidation mechanism determined in solution, in which water does not participate directly in the formation of the cyclic imide (Scheme 1).

Many researchers have proposed that increased dynamic mobility in solids leads to increased chemical reactivity.[1,2,7,8] The data in Figure 5 support this hypothesis. That the plasticizing role of water facilitates deamidation in lyophilized PVP formulations by increasing mobility is also consistent with the apparent mechanism of Asn-hexapeptide deamidation. In these polymer formulations, the deamidation of Asn-hexapeptide appears to proceed via intramolecular cyclization to form the cyclic imide hexapeptide. For cyclization to occur, the asparagine side chain and the peptide backbone require sufficient flexibility to assume the correct local conformation. Ota et al. have shown that decreased segmental flexibility decreases the deamidation rate in solution.[24] Because cyclization requires adequate segmental flexibility, deamidation would be expected to be sensitive to changes in formulation molecular mobility.

This explanation is supported by the trends in Figure 5. We observed a sharp increase in deamidation rate with decreasing T_g in the region of the glass transition ($T_g \sim T_{exp}$). This increase in deamidation rate appears to correspond with the sharp decrease in viscosity characteristic of the glass transition. Viscosity can decrease by as much as 4 orders of magnitude at the glass transition, leading to a large increase in matrix mobility.[8,10] The roughly 1 order of magnitude increase in deamidation rate shown in Figure 5 is significantly less than this potential viscosity decrease, which may suggest that deamidation and/or side-chain mobility is not completely coupled to overall matrix viscosity.

Figure 5 shows that the effect of water as a plasticizer and/or solvent on deamidation appears to depend on the physical state of the formulation. In the rubbery state, the strong correlation between reaction rate and T_g, regardless of water activity/content, suggests that water affects deamidation predominantly through its role as a plasticizer. In other words, water or its direct effect on deamidation is not the rate-limiting factor. However, in glassy formulations, water appears to affect deamidation via both mobility and medium/solvent effects. The mobility mechanism is supported by the increase in deamidation rates with decreasing T_g when water activity/content was held constant. In contrast, in formulations with similar T_g, increasing water content/activity increases Asn-hexapeptide reactivity, suggesting that water may also facilitate deamidation in the glassy state through its role as a solvent. If matrix mobility was the only factor dictating Asn-hexapeptide deamidation, then differences in water activity or content would not have affected degradation rates at constant T_g. Alternatively, even in a glassy matrix, the peptide has some degree of mobility. Peptide mobility thus may be influenced by increases in water content in a manner not coupled to matrix mobility.

Interestingly, the relationship between k_{obs} and T_g shown in Figure 5 is linear in both the rubbery and glassy states, with a slightly greater slope in the rubbery region. This relationship is reminiscent of so-called "cooling curves", which show the transition from a liquid to a glassy solid in terms of specific volume (or enthalpy) as a function of temperature, and display families of near parallel curves in the glassy state for materials cooled at different rates.[25] Although this similarity suggests that deamidation rate may be related to matrix specific volume in our studies, this claim must be regarded as speculative on the basis of the current data.

Because of the low amounts present, water technically is not a solvent in these solid systems. However, it is not unreasonable to postulate that water may affect the reaction environment in a manner that facilitates deamidation. The environment to which an asparagine residue is exposed can greatly affect its stability. Studies of deamidation in the solution state reveal that the crucial step for cyclic imide formation is deprotonation of the attacking peptide bond nitrogen to form a charged activated complex in the reaction transition state.[16−18] Brennan and Clarke have shown that deamidation at asparagine residues is markedly reduced in solvents of low dielectric strength because of decreased stability of the anionic peptide bond nitrogen.[26] Deamidation would be expected to be favored in polar environments, which can adequately stabilize the charged transition state during intermolecular cyclization. Although these findings are for the solution

state, water may affect deamidation in glassy formulations by increasing the polarity of the matrix. Water may also facilitate deamidation by serving as a medium for proton transfer during the cyclization process.[5,16]

In addition to having an effect on reactant mobility, matrix mobility may also affect the ability of a solvent to adequately solvate and stabilize charged reaction centers. In the glassy state, the solid polymer solvent may not have sufficient mobility to rearrange itself to "solvate" the charged transition state during Asu formation. Although the polymer may be dynamically constrained, Oksanen and Zografi have shown that water in solid PVP maintains a high degree of mobility relative to the polymer.[27] The more mobile water may be able to facilitate deamidation by "solvating" the charged transition state during Asu formation. In the rubbery state, PVP is more mobile than in the glassy state. With greater mobility, PVP may be more able to solvate and stabilize the development of a charged transition state during deamidation. Thus, matrix mobility may have an impact on chemical reactions beyond influencing reactant mobility.

Because water appears to have a solvent effect on deamidation in these solid systems, glycerol may have had a solvent effect on the reaction rates in addition to a plasticizing effect. We cannot rule out the possibility that the increase in deamidation rates with decreasing T_g (increasing glycerol content) is in part due to a solvent effect (Figure 5).

Effect of Water on Deamidation Product Distribution—Three major degradation products were observed in this study: the cyclic imide hexapeptide (Asu), the isoAsp-hexapeptide (isoAsp), and the Asp-hexapeptide (Asp). In these lyophilized PVP–glycerol systems, the Asn-hexapeptide appears to deamidate through intramolecular cyclization to form Asu, which may degrade to produce isoAsp and Asp. The deamidation product distribution would then depend on Asu formation (deamidation of Asn) and breakdown (hydrolysis to form isoAsp and Asp). In formulations with minimal moisture content (<0.004 g water/g wet solid), Asu is the dominant degradation product with little isoAsp or Asp observed at the sampling time evaluated. As water content increases, the product distribution shifts toward less Asu and greater fractions of isoAsp and Asp. These observations are consistent with the hydrolytic formation of isoAsp and Asp from Asu, as observed in solution (Scheme 1). In solution at neutral pH, Asu undergoes spontaneous hydrolysis to form isoAsp and Asp, where the attack of water or hydroxide ion on the cyclic imide is the rate-limiting step.[16,17,28]

Because the amount of Asu observed depends on the rates of Asn-hexapeptide deamidation and Asu hydrolysis, the decrease in the percentage of Asu among the degradation products with increasing water content suggests that Asu hydrolysis becomes more rapid than Asu formation under these conditions. The shift in product distribution with increasing glycerol content (Figures 6, 7a, and 7b) suggests that mobility may also affect Asu hydrolysis through its role as a plasticizer to increase formulation mobility, although direct evidence for a plasticizing role in this reaction was not obtained in these experiments. These differences in product distribution may be due to differences in the reaction time course. For example, reactions in formulations with higher glycerol contents occur at a faster rate. Therefore, these reactions would be more complete than slower reactions (lower glycerol content) at the time the reactions were sampled.

Conclusion

The mechanistic role of water in the deamidation of an Asn-containing model hexapeptide (Val-Tyr-Pro-Asn-Gly-Ala) in lyophilized formulations containing PVP and glycerol was investigated. Increases in moisture and glycerol contents increased the rate of peptide deamidation. This increase was strongly correlated with T_g at constant water content and activity, suggesting that increased matrix mobility facilitates deamidation. In rubbery systems ($T > T_g$), deamidation rates appeared to be independent of water content and activity in formulations with similar T_gs. However, in glassy formulations with similar T_gs, deamidation increased with water content, suggesting a solvent/medium effect of water on reactivity in this regime. An increase in water content also affected the degradation product distribution; less of the cyclic imide intermediate (Asu) and more of the hydrolytic products, isoAsp and Asp, were observed as water content increased. Under low moisture conditions, the water-catalyzed hydrolysis of the cyclic imide intermediate to produce the isoAsp and Asp is suppressed. Thus, residual water appears to facilitate deamidation in these solid PVP formulations both by enhancing molecular mobility and by solvent/medium effects, and also participates as a chemical reactant in the subsequent breakdown of the cyclic imide.

Acknowledgments

M.C.L. thanks Julie Bauer, John Biermacher, Bob Dalga, and Kate Weaver of Pharmacia & Upjohn for their help in this project, and thanks Pharmacia & Upjohn, Inc. for the opportunity to carry out an industrial externship. This project was supported by the Takeru Higuchi Predoctoral Fellowship (M.C.L.), an NIGMS Biotechnology Training Grant, Pharmacia & Upjohn, Inc., and by NIH grant #GM-54195.

References and Notes

1. Carpenter, J. F.; Pikal, M. J.; Chang, B. S.; Randolph, T. W. Rational design of stable lyophilized protein formulations: Some practical advice. *Pharm. Res.* **1997**, *14*, 969–975.
2. Hageman, M. J. Water sorption and solid-state stability of proteins, In *Stability of Protein Pharmaceuticals, Part A*: *Chemical and Physical Pathways of Protein Degradation*; Ahern, T. J.; Manning, M. C. Eds.; Plenum: New York, 1992; pp 273–309.
3. Pikal, M. J.; Dellerman, K. M.; Roy, M. L.; Riggin, R. M. The effect of formulation variables on the stability of freeze-dried human growth hormone. *Pharm. Res.* **1991**, *8*, 427- 436.
4. Constantino, H. R.; Langer, R.; Klibanov, A. M. Moisture-induced aggregation of lyophilized insulin. *Pharm. Res.* **1994**, *11*, 21–29.
5. Strickley, R. G.; Anderson, B. D. Solid-state stability of human insulin. I. mechanism and the effect of water on the kinetics of degradation in lyophiles from pH 2–5 solutions. *Pharm. Res.* **1996**, *13*, 1142–1153.
6. Oliyai, C.; Patel, J.; Carr, L.; Borchardt, R. T. Solid-state stability of lyophilized formulations of an asparaginyl residue in a model hexapeptide. *J. Parenteral Sci. Technol.* **1994**, *48*, 167–173.
7. Shalaev, E. Y.; Zografi, G. How does residual water affect the solid state degradation of drugs in the amorphous state? *J. Pharm. Sci.* **1996**, *85*, 1137–1141.
8. Levine, H.; Slade, L. The glassy state phenomenon in food molecules. In *The Glassy State in Foods*; Blanshard, J. M. V.; Lillford, P. J., Eds.; Nottingham: Nottingham, U.K. 1993; pp 35–101.
9. Ferry, J. D. *Viscoelastic Properties of Polymers*, 3rd ed.; Wiley & Sons: New York, 1980; pp 486-544.
10. Angell, C. A. Formation of glasses from liquids and biopolymers. *Science* **1995**, *267*, 1924–1935.
11. Williams, M. L.; Landel, R. F.; Ferry, J. D. The temperature dependence of relaxation mechanisms in amorphous polymers and other glass-forming liquids. *J. Am. Chem. Soc.* **1955**, *77*, 3701–3707.
12. Hancock, B. C.; Zografi, G. Characteristics and significance of the amorphous state in pharmaceutical systems. *J. Pharm. Sci.* **1997**, 86, 1–12.
13. Bell, L. N.; Hageman, M. J. Differentiating between the effects of water activity and glass transition dependent mobility on a solid-state chemical reaction: Aspartame degradation. *J. Agric. Food Chem.* **1994**, *42*, 2398–2401.

14. Lai, M. C.; Hageman, M. J.; Schowen, R. L.; Borchardt, R. T.; Topp, E. M. Chemical stability of peptides in polymers. 1. Effect of water on peptide deamidation in poly(vinyl alcohol) and poly(vinylpyrrolidone) matrixes. *J. Pharm. Sci.* **1999**, *88*, 1073−1080.
15. Manning, M. C.; Patel, K.; Borchardt, R. T. Stability of protein pharmaceuticals. *Pharm. Res.* **1989**, *6*, 903−917.
16. Geiger, T.; Clarke, S. Deamidation, isomerization and racemization at asparaginyl and aspartyl residues in peptides. Succinimide-linked reactions that contribute to protein degradation. *J. Biol. Chem.* **1987**, *262*, 785−794.
17. Patel, K.; Borchardt, R. T. Chemical pathways of peptide degradation. II. Kinetics of deamidation of an asparaginyl residue in a model hexapeptide. *Pharm. Res.* **1990**, *7*, 703−711.
18. Capasso, S.; Mazzrella, L.; Sic, F.; Zagari, A.; Salvadori, S. Kinetics and mechanism of succinimide ring formation in the deamidation process of asparagine residues. *J. Chem. Soc., Perkin Trans. 2* **1993**, *2*, 679−682.
19. Guggenheim, E. A. *Applications of Statistical Mechanics*; Clarendon: Oxford, 1966.
20. van den Berg, C.; Bruin, S. Water activity and its estimation in food systems: Theoretical aspects. In *Water Activity: Influences of Food Quality*; Rockland, L. B.; Stewart, G. F., Eds.; Academic: New York, 1981; pp 1−61.
21. Gordon, M.; Taylor, J. S. Ideal copolymers and the second-order transitions of synthetic rubbers. I. Noncrystalline copolymers. *J. Appl. Chem.* **1952**, *2*, 493−500.
22. Hancock, B. C.; Zografi, G. The relationship between the glass transition temperature and the water content of amorphous pharmaceutical solids. *Pharm. Res.* **1994**, *11*, 471−477.
23. Sperling, L. H. *Introduction to Physical Polymer Science*; John Wiley & Sons: New York, 1986; p 278.
24. Ota, I. M.; Clarke, S. Calcium affects the spontaneous degradation of aspartyl/asparaginyl residues in calmodulin. *Biochemistry* **1989**, *28*, 4020−4027.
25. Craig, D. Q. M.; Royall, P. G.; Kett, V. L.; Hopton, M. L. The relevance of the amorphous state to pharmaceutical dosage forms: glassy drugs and freeze-dried systems. *Int. J. Pharm.* **1999**, *179*, 179−207.
26. Brennan, T. V.; Clarke, S. Spontaneous degradation of polypeptides at aspartyl and asparaginyl residues: Effect of the solvent dielectric. *Protein Sci.* **1993**, *2*, 331−338.
27. Oksanen, C. A.; Zografi, G. Molecular mobility in mixtures of absorbed water and solid poly(vinylpyrrolidone). *Pharm. Res.* **1993**, *10*, 791−799.
28. Xie, M.; Vander Velde, D.; Morton, M.; Borchardt, R. T.; Schowen, R. L pH-Induced change in the rate-determining step for the hydrolysis of the Asp/Asn-derived cyclic-imide intermediate in protein degradation. *J. Am. Chem. Soc.* **1996**, *118*, 8955−8956.

JS9802289

Mechanisms of Solvent Evaporation Encapsulation Processes: Prediction of Solvent Evaporation Rate

JUAN WANG AND STEVEN P. SCHWENDEMAN*

Contribution from *Division of Pharmaceutics, College of Pharmacy, The Ohio State University, 500 West 12th Avenue, Columbus, Ohio 43210.*

Received April 17, 1998. Final revised manuscript received September 15, 1998.
Accepted for publication July 15, 1999.

Abstract □ The mechanism of organic solvent evaporation during microencapsulation and its role during microsphere hardening has been investigated. Evaporation and encapsulation studies were carried out in a jacketed beaker, filled with aqueous hardening solution, which was maintained at constant temperature and constant stirring rate in the turbulent regime. Evaporation of dissolved methylene chloride (MC), ethyl acetate (EA), and acetonitrile (ACN) was examined by the decline in organic solvent concentration in the hardening bath, which was monitored by gas chromatography. The evaporation from the bath followed first-order kinetics under dilute conditions (e.g., MC < 3 mg/mL), yielding an overall permeability coefficient, *P*. The value of *P* was theoretically related to the Kolmogorov length-scale of turbulence under conditions that favor liquid-side transport control. According to theory, factors that favored liquid-phase control (as opposed to gas-phase control) were those that favored a high Henry's law constant [i.e., elevated temperature near the normal boiling point (bp) of the organic solvent] and properties of the dissolved organic solvent (i.e., low normal bp and low aqueous solubility). These theoretical hypotheses were confirmed by (1) correlating the experimentally determined *P* with process variables raised to the appropriate power according to theory, $r^2 = 0.95$ (i.e., $P \propto$ rotational speed, $\omega^{3/4}$, impeller diameter, $d^{5/4}$, volume of hardening bath, $V^{-1/4}$, and the product of kinematic viscosity and diffusion coefficient, $\nu^{-5/12}D^{2/3}$), and (2) illustrating that at constant temperature, the tendency of the evaporation system to obey liquid-side transport control follows the same order of increasing Henry's law constant (i.e., MC > EA > ACN). To establish the relationship of evaporation with microsphere hardening, the decline in MC concentration was determined in both the continuous and dispersed polymer phases during microencapsulation. By applying a mass balance with respect to MC in the hardening bath, the cumulative hardening profile of the microspheres was accurately predicted from the interpolating functions of the kinetics of MC loss from the bath with and without polymer added. These results have potential use for microsphere formulation, design of encapsulation apparatus, and scale up of microsphere production.

Introduction

The solvent evaporation encapsulation method has been widely used for preparation of microspheres for the controlled release of drugs. During encapsulation, a single oil-in-water (o/w) emulsion is commonly used for un-ionized and lipophilic drugs, and a double w/o/w emulsion is often used for the encapsulation of hydrophilic or ionized compounds, such as proteins and peptides.[1] Despite the widespread use of this technique, encapsulation methodologies are still largely based on trial and error. More quantitative theory and experiments are required to improve our understanding of how the encapsulation conditions affect the final particle characteristics. Such studies also may help to reduce batch-to-batch variation, organic solvent residual content, and scale up difficulties.

The physical chemical events that take place between emulsion formation to eventual microsphere hardening can be separated into several components; such as diffusion of the organic solvent from the embryonic particles into the aqueous hardening bath, evaporation of the solvent, polymer phase separation at the microsphere surface, particle coalescence, and drug loss into the hardening bath. Among these coupled events, the rate of solvent evaporation will directly influence the organic solvent level in the hardening bath, which in turn will influence the chemical potential gradient of the same species across the particle hardening surface, and consequently, the solvent removal rate. It has been shown that the solvent removal rate can have significant effect on the microsphere properties.[1−5] Therefore, the evaporation rate kinetics was selected as a logical place to begin quantitative evaluation of these coupled physical chemical events during microsphere preparation.

The objectives of this paper were (1) to devise a theory to relate process conditions to organic solvent evaporation rate from a stirred aqueous hardening bath, (2) to test such a theory experimentally by measuring solvent evaporation kinetics, and (3) to use the theoretical model to predict the kinetics of microsphere hardening during encapsulation by simultaneously monitoring the kinetics of organic solvent levels in the continuous phase of the hardening bath.

Theoretical Section

Definition of Permeability Coefficients—Consider a system consisting of a stirred jacketed beaker filled with an aqueous hardening bath maintained at constant temperature, as shown in Figure 1A. An overhead mixer rotates an impeller of type shown in Figure 1B at constant rotational speed sufficient to induce turbulent flow [e.g., the impeller Reynolds number (*Re*) >1000 for the system described in Figure 1].[6] *Re* is defined as

$$Re \equiv \frac{\omega d^2}{\nu} \tag{1}$$

where ω, d, and ν are the rotational speed, impeller diameter, and fluid kinematic viscosity, respectively.

When a volatile organic solvent is introduced in the aqueous hardening bath below its aqueous solubility, the solvent dissolves and begins to evaporate. The solvent either is added directly or accumulates during hardening of the polymer microspheres. Let an overall (or total) permeability coefficient (equivalent to overall mass transfer

* To whom correspondence should be addressed. Telephone: (614)-688-3797. Fax (614)292-7766. E-mail: schwende@dendrite.pharmacy.ohio-state.edu.

10.1021/js980169z CCC: $18.00
Published on Web 09/03/1999

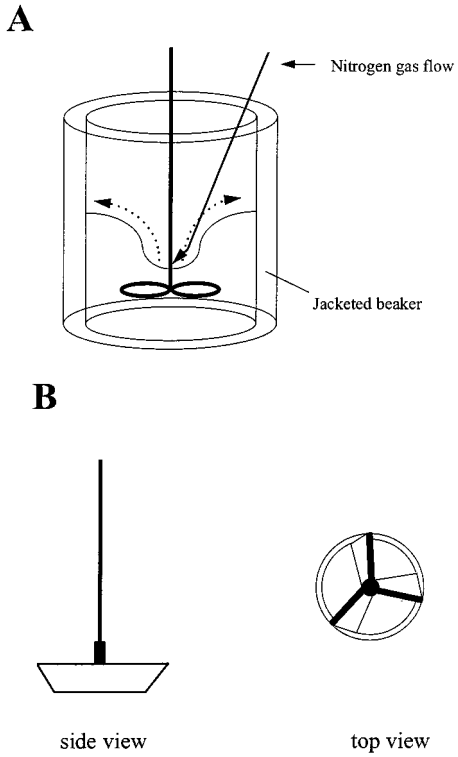

Figure 1—Stirring apparatus used to assess evaporation from the hardening bath. (A) A jacketed beaker was maintained under constant rotational speed and temperature. In some cases, a light flow of N_2 gas was delivered across the air/water interface to disrupt the gas-phase boundary layer. (B) Side and top views of the turbine impeller used to mix the bath.

coefficient) at the air/liquid interface, P, be defined in the usual way from the quotient of mass flux of the evaporating organic solvent, j_s, and the difference in bulk concentration in the bath (continuous phase), C, and some point in space above the bath where the concentration becomes zero; that is

$$P \equiv \frac{j_s}{\Delta C} = \frac{j_s}{C - 0} = \frac{j_s}{C} \tag{2}$$

The P may be separated into contributions of the liquid and gas sides according to eq 3[7]

$$\frac{1}{P} = \frac{1}{P_L} + \frac{1}{H \cdot P_G} \tag{3}$$

where P_L and P_G are the liquid-side and gas-side permeability coefficients, respectively, and H is Henry's law constant.

Organic Solvent Mass Balance in the Hardening Bath—A mass balance with respect to the organic solvent in the continuous phase during hardening of the microspheres yields

$$V\frac{dC}{dt} = R_H - R_E = R_H - PAC \tag{4}$$

where V, R_H, R_E, A, and t are the volume of the fluid, overall rate of organic solvent removal from microspheres (or hardening rate), rate of solvent evaporation, air/water surface area, and time, respectively.

To determine P, let $R_H = 0$ by addition of organic solvent directly (i.e., no microspheres) and the concentration in the solvent bath is monitored. P has been reported to be independent of C,[4,7,8] which results in first-order evaporation kinetics. In this case, integration of eq 4 gives

$$C = C_0\, e^{-P\frac{A}{V}t} \tag{5}$$

where C_0 is the initial organic solvent concentration in the bath. During encapsulation, $R_H > 0$ and integration gives an expression for cumulative mass removed from microspheres, M_H, as follows:

$$M_H \equiv \int_0^t R_H\, dt = V[C(t) - C_0] + A\int_0^t PC\, dt \tag{6}$$

Hence, the cumulative solvent removed may be related to the permeability coefficient and the concentration−time profile in the continuous phase during encapsulation.

Calculation of the Kolmogorov Length-Scale—The size of the characteristic eddy, or Kolmogorov length, δ_K, induced by turbulence originating from the energy input from the impeller, is[9]

$$\delta_K = \left(\frac{\nu^3}{\epsilon}\right)^{1/4} \tag{7}$$

where ϵ is the energy dissipation rate per unit mass of fluid. The Kolmogorov length can be described as the length scale of the smallest eddy at which inertial forces equal viscous forces. In turbulent fluids, large eddies become unstable and cascade into smaller eddies without energy loss until δ_K is reached. At δ_K eddies disappear losing their kinetic energy to thermal energy.

To calculate δ_K, ϵ must be determined. For isotropic turbulence, ϵ is equivalent to the rate of energy loss from the impeller to the fluid, $\dot{Q}$, divided by the mass of fluid (ρV). $\dot{Q}$ is given as[10]

$$\dot{Q} = N_p \rho \omega^3 d^5 \tag{8}$$

where ρ is the density and N_p is the dimensionless power number, which is dependent on the impeller type and thickness, as well as the presence or absence of baffles in the tank.

Thus, in a hardening tank containing a fluid volume, V, by combining eqs 7 and 8, δ_K becomes

$$\delta_K = \left[\frac{\nu^3}{(N_p \rho \omega^3 d^5/\rho V)}\right]^{1/4} = \left[\frac{Vd}{N_p\left(\frac{\omega^3 d^6}{\nu^3}\right)}\right]^{1/4} = \frac{(Vd)^{1/4}}{N_p{}^{1/4} Re^{3/4}} \tag{9}$$

Estimating the Liquid-Side Boundary Layer Thickness, δ_D—The movement of the fluid near an air/liquid interface is somewhat more controversial than near a solid/liquid interface. Near a solid/liquid interface, the turbulence is damped within a viscous sublayer, δ_V, over which the bulk mean velocity is dissipated with the square of position toward the interface.[8] At the interface, the fluid velocity becomes zero in all directions. Near an air/liquid interface, only the velocity component normal to the surface is zero. At a 'clean' interface (i.e., a surface free of contaminants), the vertical mean velocity is dissipated linearly with position toward the interface, and the boundary layer thickness, δ_D ($=D/P_L$), is given as[8]

$$\delta_D \propto \delta_V Re^{*-1/2} Sc^{-1/2} \tag{10}$$

where Re^* is the local Reynolds number, $u_e \cdot \delta_e/\nu$, of approaching eddies (u_e and δ_e are velocity and length scale of the eddy, respectively) to the interface, and Sc is the

Schmidt no. (ν/D), where D is the diffusion coefficient of the volatile species evaporating at the air/liquid interface.

Most surfaces, however, contain contaminants, especially in small-scale laboratory and industrial flows.[8] In this so-called 'dirty' interface category, surface-active substances (e.g., organic solvent molecules and surfactant molecules in the case of encapsulation by solvent evaporation) are present in excess at the surface. The mean vertical velocity component is then dissipated with the square of position (like the solid/gas interface case) and

$$\delta_D \propto \delta_e \cdot Sc^{-1/3} \tag{11}$$

If the characteristic length, δ_e, is assumed to be proportional to the Kolmogorov length-scale, δ_K, then

$$\delta_D \propto \delta_K \cdot Sc^{-1/3} \tag{12}$$

Finally, by assuming a constant impeller type and thickness, and turbulent flow conditions, N_p becomes nearly constant[10] and δ_D may be related to system variables as follows:

$$\delta_D \propto \left(\frac{Vd}{Re^3}\right)^{1/4} Sc^{-1/3} \tag{13}$$

This result also may be given in nondimensional form. The Sherwood number, Sh, is equivalent to Pd/D. Under liquid-side transport control according to the film theory,[7] $P = P_L = D/\delta_D$ and

$$Sh = \frac{d}{\delta_D} \propto Ko \cdot Sc^{1/3} \tag{14}$$

Ko is introduced as the corrected Kolmogorov number as follows:

$$Ko = \left(Re\frac{d}{\sqrt[3]{V}}\right)^{3/4} \tag{15}$$

which is defined as the ratio of the impeller diameter to the Kolmogorov length corrected for $N_p^{1/4}$; that is, $Ko \equiv d/(N_p^{1/4}\delta_K)$.

The relationship in eq 14 can also be written in a manner to test the dependence on individual variables; that is

$$P \propto d^{5/4} V^{-1/4} \omega^{3/4} \nu^{-5/12} D^{2/3} \tag{16}$$

or

$$\delta_D = D/P \propto d^{-5/4} V^{1/4} \omega^{-3/4} \nu^{5/12} D^{1/3} \tag{17}$$

Finally, it is useful to note that the same relationship may be obtained from

$$Sh \propto \left[\frac{d^4(\dot{Q}/V)}{\rho\nu^3}\right]^{1/4} \cdot Sc^{1/3} \tag{18}$$

which has been reported for mass transport at the interface of bubbles or small drops dispersed in a liquid.[7]

Materials and Methods

Chemicals—Methylene chloride (MC) was purchased from Fischer Scientific with gas chromatography (GC) purity of 99.9%. High-performance liquid chromatography (HPLC) grade acetonitrile (ACN), ethyl acetate (EA), and 2-propanol were also obtained from Fisher Scientific. PRA grade chloroform (suitable for pesticide residual analysis) was purchased from Sigma-Aldrich with GC purity of 99.9%. Poly(DL-lactide-*co*-glycolide) (PLGA; 50:50; intrinsic viscosity, 0.65 dL/g in hexafluoro-2-propanol (HFIP) at 30 °C; lot no. 410-27-1A) was obtained from Birmingham Polymers, Inc., and 80% hydrolyzed poly(vinyl alcohol) (PVA; average MW 9000–10 000) was purchased from Aldrich Chemical Company. Triamcinolone acetonide was obtained from Sigma Chemical Company with 99% purity. All chemicals were used as received.

Evaporation of Organic Solvents from Aqueous Solution—Evaporation of organic solvents from aqueous solution was carried out in a jacketed beaker (unbaffled), which was connected with a TYP FS2N water bath (HAAKE Instruments Inc., Saddle Brook, NJ) to maintain constant temperature. Dimensions of the jacketed beaker were 59 mm i.d., 90 mm o.d., and 122 mm height. An overhead stir-tester (G. K. Heller HST 20 series) was purchased from Glas-Col (Terre Haute, IN) and used to maintain a stable rotational speed (100–900 rpm) of an axially mounted turbine impeller (see Figure 1A). Turbine stirrers (45° pitch-blade and ringed, Figure 1B) all had the same thickness (1.2 cm) and were purchased from IKA-WORKS, Inc. (Wilmington, NC; catalog nos. R1311, R1312, and R1313 for stirrers with o.d.'s of 3, 5, and 7 cm, respectively). During the study, a known amount of organic solvent was dissolved in various volumes (150–1000 mL) of double distilled water or 0.3% PVA aqueous solution at a preset temperature and constant rotational speed. Samples were taken at scheduled time intervals and assayed by GC. When examining the large stirrer diameter or large bath volume, a glass cylindrical tank (top open, 166.5 mm i.d., 87.5 mm height) placed directly into the constant temperature bath was used. The constant temperature was confirmed by reading a thermometer inserted directly in the tank.

The volume replacement after each sampling was not carried out for the organic solvent evaporation studies at low temperatures. Control experiments demonstrated that the volume loss due to sampling had little influence on the determination of permeability coefficient (data not shown). However, at relatively high temperatures (T > 40 °C), the volume loss due to evaporation of water became noticeable. Under such conditions, manual water replacement was completed at 10-min intervals at a rate roughly equal to the evaporation rate so that total volume of the bath was kept nearly constant.

Organic Solvent Analysis by Gas Chromatography—Sample analysis was performed on a Varian series 3700 GC with a 5% Carbowax 20M 80/120 Carbopack B-AW analytical column (Supelco). The GC conditions for determination of MC, EA, and ACN in aqueous samples were as follows: N_2 and H_2 carrier gas flow rate, 30 mL/min; air flow rate, 300 mL/min; column oven temperature, 100 °C; and injector and flame ionization detector temperatures, 200 °C. For organic samples where MC was extracted by chloroform, a programmed column temperature gradient with the following settings was used: initial temperature of 100 °C for 2 min, followed by a temperature gradient of 80 °C/min, then a final temperature of 200 °C for 4 min.

Disruption of Gas-Phase Boundary Layer by Blowing N_2 (g) over the Gas/Liquid Interface—The evaporation experiments with nitrogen flow were carried out under identical conditions as the typical evaporation experiments, except that compressed nitrogen gas at room temperature was blown over the liquid/gas interface from a metal ferrule at a fixed gauge pressure (~28 psig; Figure 1A). The distal part of the metal ferrule was deformed to blow directly toward the center of the stirrer shaft to avoid violent disturbance to the surface of the evaporating solution. In this configuration, the gas was presumably forced from the bottom of the vortex outward along the surface of the liquid.

Encapsulation of Triamcinolone Acetonide by the Solvent Evaporation Method—The solvent evaporation encapsulation process was carried out by dissolving 2 × 800 mg of PLGA 50/50 and 2 × 40 mg of triamcinolone acetonide in 2 × 4 mL of MC in two 18 × 150-mm Pyrex glass tubes. A 1% (w/w) PVA aqueous solution (4 mL) was added to each tube, and the system was mixed for 20 s at the highest speed setting on a Vortex Genie 2 (Scientific Industries Inc., Bohemia, NY). The emulsion produced in both tubes was poured into a jacketed beaker (Figure 1A) that contained 142 mL of 0.3% PVA solution (30 °C), and the resulting mixture was stirred at 600 rpm. Samples drawn at specified times were assayed for organic solvent content. After 4 h of agitation, microspheres were collected, centrifuged, washed with double distilled water three times, freeze-dried for 2 days, and stored desiccated in microcentrifuge tubes at 4 °C.

Determination of MC Levels in Dispersed and Continuous Phases during Encapsulation—For MC evaporation without encapsulation, 1-mL aliquots were drawn from the hardening bath at each time point and stored at 4 °C in 1.9-mL Fisherbrand glass vials with a plastic screw cap fitted with a Teflon insert until GC analysis. A 50 μL aliquot of internal standard solution was added to each sample and mixed by vortex.

For determination of MC levels during encapsulation, samples were taken at each scheduled time point, which lasted <1 min/sample. A 0.3% PVA aqueous solution (2 mL) was replenished after each sampling procedure. For determining the MC content of the aqueous continuous phase, 1.4 mL of aqueous dispersion was withdrawn with a 5-mL polypropylene syringe and filtered through a 0.22-μm hydrophilic poly(tetrafluoroethylene) (PTFE) Millex filter unit (SE2M035J5, Millipore Corp.). Triplicate 200-μL aliquots from the filtered solution were mixed with 800 μL of pure water and 50 μL of internal standard and were subjected to GC analysis. Solvent concentrations were calculated by using a standard curve constructed with a filtered 0.3% PVA solution that contained known solvent concentrations processed by the same procedure.

For determination of MC in microspheres, the amount of MC in the dispersion was subtracted from the MC in the continuous phase. To accomplish this, triplicate 0.2-mL aliquots were taken directly from the stirred aqueous dispersion and placed in glass vials containing 0.5 mL of chloroform to prevent fast evaporation of MC. The glass vials were capped immediately. Samples were later mixed by vortex for 5 s and stored overnight at 4 °C to extract MC into chloroform before the GC analysis. The calculation of concentration of MC in the sample was based on the standard curve constructed by equilibrating a series of known amounts of MC in 0.5 mL of chloroform with 0.2 mL of 0.3% PVA aqueous solution, as in the sample preparation case. An impurity in the purchased PRA grade chloroform was used as the internal standard after appropriate validation to correct for variability in injection volume. This compound was stable in chloroform and its polarity was similar to that of MC.

The MC content in the hardening polymer phase (w/w MC/PLGA ratio) during the hardening period was calculated with eq 27, which is described in the *Data Analysis* section. The MC loss during pouring was determined gravimetrically after pouring the emulsion into a tared capped bottle.

Determination of MC Solubility in 0.3% PVA Aqueous Solution—A 5-mL aliquot of MC was added to 10 mL of 0.3% PVA (aq) in 20-mL scintillation vials and mixed. Samples were put on a type 50800 Thermolyne shaker (Bamstead/Thermolyne Corp., Dubugue, IA) under mild agitation in a Precision Economic Incubator (Precision Scientific, Chicago, IL) set at 30 ± 0.5 °C. Samples were taken out every 8 h and vigorously agitated. After 2 days, 200-μL aliquots were removed from the aqueous layer and mixed with 800 μL of pure water and 50 μL of internal standard, and then assayed by GC. Solubility of MC at 30 °C was determined to be 22.6 ± 0.7 mg/mL (mean ± SD, $n = 6$).

Data Analysis—*Calculation of the Surface Area*—Surface area, A, used to determine P was estimated manually for each stirring condition. First, a line was drawn around the outer wall of the stirred beaker, which traced the contour of the air/water surface during the evaporation experiments. After the experiment, a piece of paper was inserted vertically into the beaker and a second line was obtained by projecting the first contour line on the paper. The surface area was calculated by integrating the strips, which were generated by rotating the projected line (which had been segmentally divided) about its center axis.[11]

Determination of Permeability Coefficient P—Below ~3 mg/mL (for MC), the slope of ln C versus t line was constant, and eq 5 is thus satisfied. The value of P was determined from $P = k'V/A$, where k' is the least squares slope of ln C versus t data. The r^2 was invariably >0.99.

Estimation of Diffusion Coefficient and Kinematic Viscosity in the Hardening Bath—The diffusion coefficients for various organic solvents in the aqueous hardening bath under different temperatures were estimated by the Wilke–Chang equation:[12]

$$D = \frac{7.4 \times 10^{-8}(\Phi M_B)^{1/2} T}{\eta_B V_A^{0.6}} \tag{19}$$

where D is the mutual diffusion coefficient of organic solvent at very low concentrations in the aqueous solvent (cm^2/s), M_B is the molecular weight of water, T is the temperature (K), η_B is the viscosity of water (cp), V_A is the molar volume of organic solvent at its normal boiling temperature (cm^3/mol), and Φ is the association factor (2.6 for water). Values of V_A for EA and ACN were taken from literature,[12] whereas the V_A for MC was calculated from the average of estimation methods by Schroeder and Le Bas.[12]

$$\ln \eta_B = k_1 + k_2/T + k_3 T + k_4 T^2 \tag{20}$$

where $k_1 = -0.02471$, $k_2 = 4209$, $k_3 = 0.04527$, and $k_4 = -0.00003376$.

The kinematic viscosity was determined from the ratio of η_B with eq 20 and ρ, which was obtained from literature.[10]

Prediction of Hardening Profile from Microspheres During Encapsulation—According to eq 6, the cumulative organic solvent removed from microspheres, M_H, can be expressed as a function of V, A, C, P, and t. Because V, A, and C can be determined directly during the encapsulation experiment and P can be obtained from pure evaporation experiments carried out under the same conditions as during encapsulation, the hardening profile [i.e., $M_H(t)$ versus t] can be predicted without direct measurement.[13]

However, most encapsulation protocols result in values of C in the range where P is dependent on C. The origin of this dependence is largely determined by the contribution of the derivative of ln(activity coefficient) with respect to ln C.[7] The value of $P(C)$ was determined from a series of pure evaporation experiments ($C_0 \cong C_S$) under the encapsulation conditions of interest (i.e., $V = 150$ mL, $d = 3$ cm, $T = 30$ °C, and $\omega = 600$ rpm). According to eq 4, when $R_H = 0$,

$$V\frac{dC}{dt} = -P(C)\cdot AC \tag{21}$$

which may also be written as

$$P(C) = -\frac{V}{A}\frac{d \ln C}{dt} \tag{22}$$

An n^{th}-order polynomial interpolating function, $p_n(\ln C)$, was fit to the t versus ln C data obtained during evaporation. The $P(C)$ was then determined from the derivative of the $p_n(\ln C)$ with respect to ln C. The interpolating function is

$$t = a_n(\ln C)^n + \ldots + a_1(\ln C)^1 + a_0 = p_n(\ln C) \tag{23}$$

The derivative, d ln C/dt, may be determined from eq 23 by using the chain rule

$$\frac{d(\ln C)}{dt} = \frac{1}{na_n(\ln C)^{n-1} + \ldots + a_1} = \frac{1}{\dfrac{d[p_n(\ln C)]}{d(\ln C)}} = \frac{1}{p_n'(\ln C)} \tag{24}$$

From eqs 22 and 24, $P(C)$ becomes

$$P(C) = -\frac{V}{A}\frac{1}{p_n'(\ln C)} \tag{25}$$

Over the entire concentration range where encapsulation occurs, eq 6 may be rewritten as follows, accounting for concentration-dependent $P(C)$:

$$M_H(t) = \int_0^t R_H dt = V[C(t) - C_0] - V\int_0^t \frac{1}{p_n'(\ln C)} C dt = V\left[q_n(t) - \int_0^t \frac{q_m(t)}{p_n'[\ln q_m(t)]} dt\right] \tag{26}$$

where $C_0 = 0$, and $q_m(t)$ is an mth order polynomial interpolating function for C versus t during encapsulation. From eq 26, the hardening profile M_H was determined numerically by the Runge–Kutta method[14] on a spread sheet (time step size = 0.1 min).

Calculation of Cumulative Amount of MC Removed, M_H, during Encapsulation—The MC content in the dispersed polymer phase was calculated on the basis of the difference of MC in the total aqueous dispersion and in the continuous phase, as follows:

$$C_{DP}(t)(w/w) = \frac{[C_T(t)/\Psi(t) - C(t)]V}{M_P} \quad (27)$$

where C_T, M_P, and Ψ, are the measured MC content in the aqueous dispersion, the overall mass of PLGA in the dispersed system, and the ratio of the volume of the continuous phase to the volume of the entire aqueous dispersion, respectively. The value of Ψ ranged from 0.95 to 1.0 in the experiment and was approximated by

$$\Psi(t) \cong 1 - \frac{C_T(t) - C(t)}{C_T(0)} \quad (28)$$

where $C_T(0)$ is the initial MC content in the aqueous dispersion.

The cumulative amount of MC removed during hardening (or the cumulative hardening profile), M_H, was then calculated according to the following equation:

$$M_H = V[C_{DP}{}^0 - C_{DP}(t)] \quad (29)$$

where $C_{DP}{}^0$ was estimated by the starting weight ratio of the MC to the polymer just before the emulsion was formed and then corrected by the loss of MC into the air during pouring. This loss was determined to be 4.0 ± 0.6% (mean ± SD, $n = 5$).

Results

Organic Solvent Evaporation Kinetics—The kinetics of evaporation in the hardening bath was observed to be first-order under dilute conditions ($C < 3$ mg/mL), as shown for MC evaporation in Figure 2. Also shown in the figure is that increasing either rotational speed or temperature resulted in a faster loss of solvent from the bath (i.e., an increased evaporation rate). The slope of the first-order plots of the type in Figure 2 and the determined air/water surface area (see Experimental Section) allowed the calculation of the P.

Correlation of *P* with Process Variables—To test the correlation in eq 16, four variables were varied independently during the evaporation of MC: temperature (T), liquid volume (V), rotational speed (ω), and diameter of the overhead stirrer (d). Among these variables, V, ω, and d directly appear in the theoretical relationship for P in eq 16. The T influences both kinematic viscosity of water (ν) and the diffusion coefficient of organic solvent in the water (D). The results are shown in Figure 3.

Good linearity between P and process variables, which were raised to their appropriate power according to eq 16, was observed for ω, V, and d under tested conditions. The value of ω was varied from 100 to 900 rpm, that of V from 150 to 1000 mL, and that of d from 3 to 7 cm. The correlation between P and $\nu^{-5/12}D^{2/3}$ [i.e., $f(T)$], however, was not as successful at first glance. A significant deviation from linearity was observed at 5 °C.

Because P_{exp} became nonlinear with respect to the product, $\nu^{-5/12}D^{2/3}$ at the low T, a partial gas-phase control was postulated. According to this postulate, the plotted data from Figure 3 obtained at $T \geq 25$ °C were combined to form a master curve, yielding a proportionality constant a, according to eq 16. Excellent agreement was observed ($r^2 = 0.95$), as shown in Figure 4. This high correlation strongly validates eq 16 for the prediction of P for MC at $T \geq 25$ °C.

Contribution of the Gas-Phase Unstirred Layer to the Overall Mass Transport Resistance—To understand the deviation from eq 16 by the MC data at low T in Figure 3 and to understand the rate-limiting step for mass transport during organic solvent evaporation, the evaporation of two additional solvents, EA and ACN, were studied. In addition, a light flow of nitrogen gas across the air/water interface was included in the experimental procedure to disturb any unstirred layer in the gas phase. It was assumed that by blowing the N_2 (g) over the surface of the liquid, the unstirred layer in the gas phase would be mixed, shifting the rate-determination step (transport control step) to the liquid side. It was also assumed that the light flow of gas would have little effect on the boundary layer in the liquid phase because the N_2 gas flow did not have a direct impact on the gas/liquid interface; that is, the liquid surface contour was not significantly distorted.

Because T appeared to play a role in the transport control of MC in Figure 3, the temperature was varied with and without N_2 flow during the evaporation of the three solvents. As shown in Figure 5, the flow of N_2 gas increased the P in all cases. However, in the two experiments

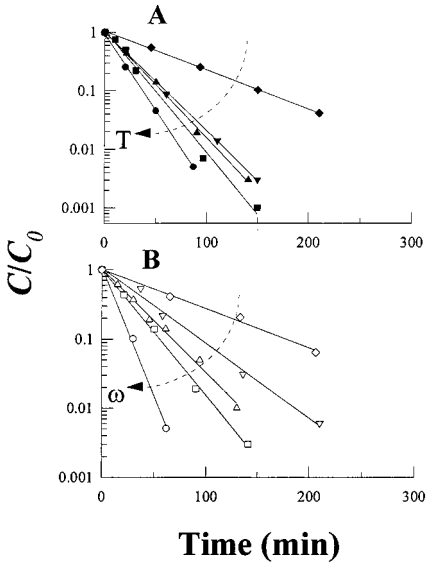

Figure 2—Loss of MC in the hardening bath follows first-order kinetics under dilute condtions. (A) Temperature was varied from 5 (◆), to 25 (▲), to 30 (▼), to 35 (■) and to 40 (●) °C while maintaining ω, V, and d at 600 rpm, 150 mL, and 3 cm, respectively. (B) Rotational speed was varied from 100 (◇), to 300 (▽), to 450 (△), 600 (□), and 900 (○) rpm, while maintaining T, V, and d at 30 °C, 150 mL, and 3 cm, respectively.

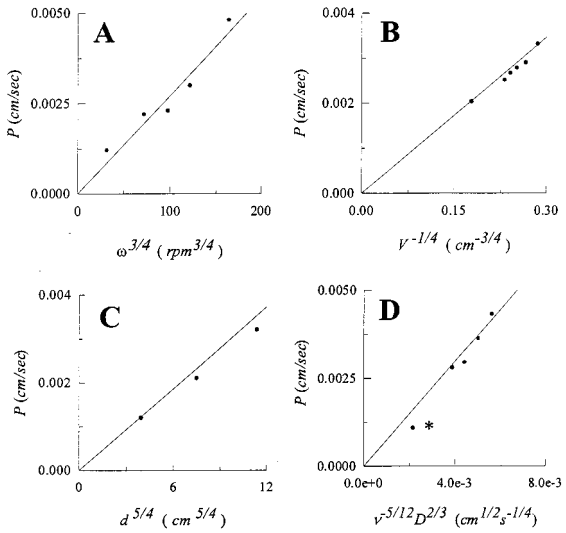

Figure 3—Correlation of process variables with permeability coefficient P. The measured P was correlated with (A) $\omega^{3/4}$ at constant T, V, and d; (B) $V^{-1/4}$ at constant ω, T, and d; (C) $d^{5/4}$ at constant ω, T, and V; and (D) $\nu^{-5/12}D^{2/3}$ (variation of T) at constant ω, ν, and d. The theoretical lines were produced from the master curve in Figure 4. Constant conditions were $T = 30$ °C (303 K), $\omega = 600$ rpm, $V = 150$ mL, and $d = 3$ cm. * The evaporation mechanism at the lowest temperature ($T = 278$ K) was governed by both the gas and liquid phases (see Figure 5).

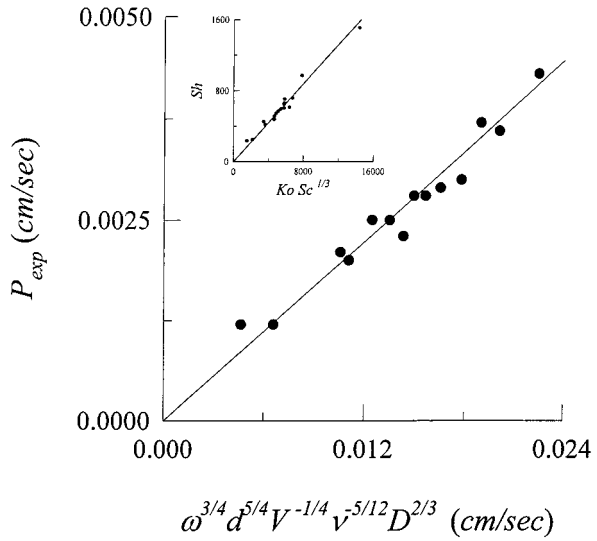

Figure 4—Generation of master curve for evaporation under turbulent flow conditions and liquid-side transport control. The *P* was correlated with the product ($\omega^{3/4}d^{5/4}V^{-1/4}\nu^{-5/12}D^{2/3}$), $r^2 = 0.95$. The data were obtained from evaporation of MC at $T \geq 25$ °C (liquid-side transport control, see Figure 5). The proportionality constant, *a*, was 0.18. Insert: The master curve in dimensionless form: *Sh* is correlated with $Ko \cdot Sc^{1/3}$ ($r^2 = 0.97$) for the same data set.

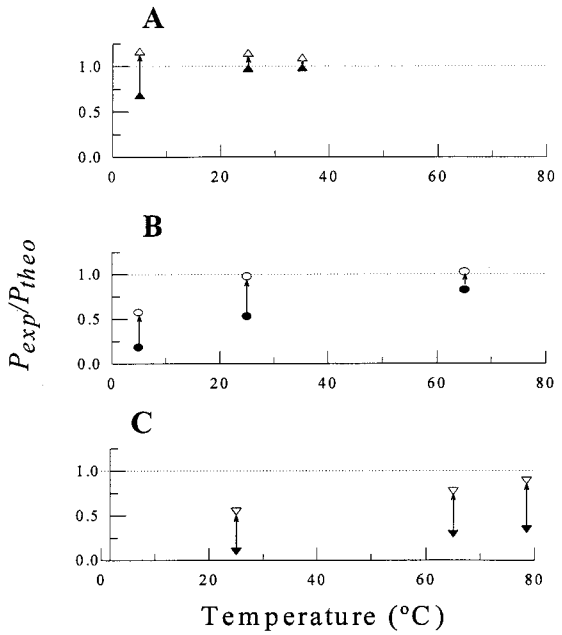

Figure 5—The influence of the gas-phase resistance to solvent evaporation. The gas-phase boundary layer was either unaltered (closed symbols) or disrupted by light N_2(g) flow over the air–water surface (open symbols). The ratio of experimental permeability to that calculated from the master curve obtained in Figure 4 (i.e., P_{exp}/P_{theo}) was determined for (A) methylene chloride, (B) ethyl acetate, and (C) acetonitrile.

included in the master curve (Figure 4; i.e., MC at 25 and 35 °C), the increase was not substantial (<15%). This result indicated that the gas phase had negligible resistance to the transport of MC under these conditions, which is consistent with the assumptions used to arrive at eq 16. In contrast, as *T* was decreased to 5 °C, the presence of N_2 (g) raised the value of P_{exp} near the value expected by liquid-side control as determined with eq 16. This large difference in P_{exp} induced by N_2 flow justifies the exclusion of the 5 °C data in Figure 4.

EA and ACN were selected for evaluation because their Henry's law constants, *H*, favor gas-phase control relative to MC. Because P_L or P_G should not strongly depend on the type of solvent, *H* was used as an indicator of the gas to obey liquid-side transport control at a given temperature according to eq 3. In Table 1, the relative trend of the values of *H* for various solvents at constant *T* is given. Because MC has a low bp (and a high saturated vapor pressure, p^v) and a low solubility in water (C_s), *H* ($\sim p^v/C_s$) must be a relatively high value. Because EA has a higher bp (therefore a lower p^v) and a higher C_s than MC, it must have a lower *H* (i.e., *H* = medium). Finally, because ACN has an equivalent bp to EA but is completely miscible with water, the *H* for ACN must be even lower (i.e., *H* = low). Therefore, it is expected that the trend favoring liquid-side transport control is MC > EA > ACN.

Table 1—Properties of Organic Solvents Examined for Evaporation[a]

organic solvent	bp (°C)[b]	p^v	C_s (w/w)	H ($\sim p^v/C_s$)	observed transport control at 25 °C[f]
MC	40	high	2.0%[c]	high	liquid
EA	77	med	6.92%[d]	med	mixed (gas/liq)
ACN	82	med	miscible[d]	low[e]	gas

[a] Abbreviations: bp normal boiling point; p^v, saturated vapor pressure; C_s, aqueous solubility; *H*, Henry's law constant. [b] Values were taken from ref 15. [c] Values at 25 °C were taken from ref 16. [d] Values at 25 °C were taken from ref 15. [e] $H \sim p^v/C_s$ only applicable to EA and MC. ACN is completely miscible with H_2O resulting in a very low *H*. [f] See Table 2.

As shown in Figures 5B and 5C, as *T* was increased, $P_{exp,\ w/o\ N_2(g)}$ for EA and ACN approached both the $P_{exp,\ w/N_2\ (g)}$ and the P_{theo}, as was the trend for MC just described. Also as expected, the resistance in the gas phase was steadily more difficult to overcome as *H* was decreased (following the trend MC < EA < ACN), indicating the gas-phase resistance increases as *H* decreases. At 25 °C the transport control was in the liquid phase for MC, in both liquid/gas phases for EA, and in the gas phase for ACN (Table 1). These data are consistent with (1) the validity of the correlation in eq 16 to predict *P* under liquid-side transport control conditions, and (2) the presence of significant gas-phase resistance when *H* becomes too low.

Independence of δ_D on *T*—The theoretical boundary layer thickness in the liquid phase varied from ~30 to 170 μm, as shown in Table 2 (which also summarizes the evaporation data). The range of δ_D values determined from theory are consistent with typical values quoted from the literature.[7] A particularly notable trend was the independence of δ_D on *T*. In Table 2, for protocol #1−5, $\delta_D \sim 45\ \mu$m for a temperature range of 5−40 °C. This theoretical result was also confirmed experimentally as indicated by the equivalence of $P_{exp,w/N_2\ gas}$ and P_{theo} for this data set.[25]

Determination of Concentration-Dependent Permeability Coefficient—To make practical use of the evaporation treatment described here, the evaporation was related to the formulation of the microspheres; that is, microsphere hardening kinetics. To illustrate this relationship, the permeability coefficient in the concentration-dependent regime was acquired under the same conditions used during the encapsulation (vide infra). To obtain a reliable permeability coefficient $P(C)$ for the calculation, multiple pure evaporation experiments were performed (three of them from pure water and one of them from 0.3% PVA aqueous solution[17]). After fitting each group of data with a 4th-order polynomial (see eq 11), the data were normalized by plotting ln *C* versus ($t - a_0$), as shown in Figure 6A. This normalization was necessary because MC is so volatile that it is very difficult to start at an exact

Table 2—Summary of Evaporation of Organic Solvents from the Aqueous Hardening Bath

protocol #	solvent	T (K)	$\nu \times 10^{-3}$ (cm^2/s)	$D \times 10^{-5}$ (cm^2/s)	V (cm^3)	d (cm)	ω (rpm)	A_{exp} (cm^2)	$P_{exp} \times 10^{-3}$ (cm/s)	$P_{theo} \times 10^{-3}$ (cm/s)[a]	δ_D (=D/P_{theo}) (μm)	transport control[b]
1	MC	313	6.75	1.84	150	3	600	35.5	4.32	4.15	44.3	liq
2[c]	MC	308	7.42	1.65	150	3	600	35.5	3.63 (4.04)	3.71	44.5	liq
3	MC	303	8.21	1.47	150	3	600	35.5	2.96	3.29	44.6	liq
4[c]	MC	298	9.14	1.29	150	3	600	35.5	2.80 (3.29)	2.90	44.7	liq
5[c]	MC	278	15.0	0.73	150	3	600	35.5	1.08 (1.86)	1.60	45.7	gas/liq
6	MC	303	8.21	1.47	150	3	900	44.5	4.75	4.46	32.9	liq
3	MC	303	8.21	1.47	150	3	600	35.5	2.96	3.29	44.6	liq
7	MC	303	8.21	1.47	150	3	450	33.7	2.43	2.65	55.3	liq
8	MC	303	8.21	1.47	150	3	300	29.9	2.09	1.96	75.0	liq
9	MC	303	8.21	1.47	150	3	100	27.4	1.15	0.86	170.8	liq
3	MC	303	8.21	1.47	150	3	600	35.5	2.96	3.29	44.6	liq
10	MC	303	8.21	1.47	200	3	600	35.5	2.90	3.06	47.9	liq
11	MC	303	8.21	1.47	250	3	600	35.5	2.78	2.90	50.6	liq
12	MC	303	8.21	1.47	300	3	600	35.5	2.67	2.77	53.0	liq
13	MC	303	8.21	1.47	450	3	600	35.5	2.52	2.66	55.1	liq
14[d]	MC	303	8.21	1.47	1000	3	600	224.7	2.04	2.05	71.6	liq
15[d]	MC	303	8.21	1.47	1000	3	300	217.7	1.22	1.22	120.4	liq
16[d]	MC	303	8.21	1.47	1000	5	300	224.2	2.52	2.31	63.6	liq
17[d]	MC	303	8.21	1.47	1000	7	300	246.4	3.69	3.51	41.8	liq
18[c]	EA	338	4.52	2.35	150	3	600	35.5	4.81 (5.99)	5.78	40.7	gas/liq
19[c]	EA	298	9.14	1.01	150	3	600	35.5	1.29 (2.57)	2.45	41.1	gas/liq
20[c]	EA	278	15.0	0.57	150	3	600	35.5	0.25 (0.78)	1.36	41.9	gas
21[c]	ACN	352	3.80	4.23	150	3	600	35.5	3.33 (8.42)	9.19	46.1	gas/liq
22[c]	ACN	338	4.52	3.40	150	3	600	35.5	2.28 (5.84)	7.38	46.0	gas/liq
23[c]	ACN	298	9.14	1.46	150	3	600	35.5	0.35 (0.84)	3.14	46.5	gas

[a] $P_{theo} \equiv a\,\omega^{3/4} d^{5/4} V^{-1/4} \nu^{-5/12} D^{2/3}$ (where a is the regression constant), according to linear regression of master curve in Figure 4. [b] Transport governed by liquid-side (liq), gas-side (gas), or a combination (gas/liq). [c] Blowing of N_2(g) over the air/liquid surface was also performed for this protocol; value of P_{exp} for blowing experiment is given in parentheses. [d] The large glass vessel instead of the jacketed beaker was used to perform the evaporation study.

concentration at a precise designated time. Also shown in the figure, the second-, third-, fourth-, and sixth-order polynomial fit (according to eq 23) for the same group of data all interpolated the data extremely well. To select the optional $p_n(\ln C)$, the slope of each polynomial was compared with the slope of the data as C approaches C_s, as shown in Figure 6B. Among $n = 2$, 3, 4, and 6, the optional fit according to this criterion was between $n = 3$ an 4, so $p_3(\ln C)$ was selected for future use.

Predicting Microsphere Hardening Kinetics—To test the ability to predict the hardening profile, a drug soluble in MC, triamcinolone acetonide, was encapsulated in PLGA microspheres under standard conditions of encapsulation. These data are shown in Figure 7. The normalized MC concentration in the continuous phase (i.e., C/C_s) became essentially saturated ($C^* \sim 1$) for the first 40 min, and then declined sharply until negligible solvent remained by 200 min. The normalized MC concentration in the dispersed phase (i.e., C_{DP}/C_{DP}^0) declined exponentially over this time interval until the particles were dry.

Also shown in Figure 7 is the 6th-order interpolating function of $C(t)$, $q_6(t)$. From $q_6(t)$ and $p_3'(\ln q_6(t))$, the hardening profile $M_H(t)$ was predicted and displayed in Figure 8. The theoretical M_H matched very closely with the experimental value determined from the C_{DP} versus t data shown in Figure 7. Thus, both the concentration-dependent $P(C)$ determined without encapsulation and the experimental procedure to detect C and C_{DP} have been validated.

Distribution of Organic Solvent during Encapsulation—The distribution of MC during encapsulation of triamcinolone acetonide is depicted in Figure 9. Note again, over the first 40 min, the concentration of MC in the continuous phase was nearly saturated. It is important to note that hardening still occurred over this time interval, despite this elevated bath concentration, at a rate very similar to the evaporation rate.[18] Thus, the hardening rate during this interval was limited by evaporation. After this period, the hardening rate declined and the MC amount in the continuous phase began to fall below saturation. The

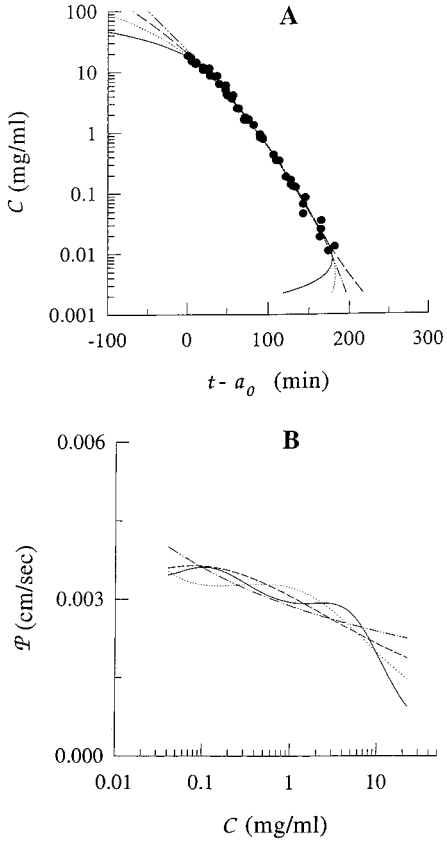

Figure 6—(A) Determination of the interpolating n^{th} order polynomial function to describe the permeability coefficient. The 2nd (–•••–), 3rd (– –), 4th (••••), and 6th (—)-order polynomial functions, $p_n(\ln C)$, were fitted according to eq 21 for the normalized evaporation data ($n = 4$). (B) The dependence of P on C (log-scale), as determined from the derivative of the n^{th} order polynomial interpolating functions with respect to ln C according to eq 25.

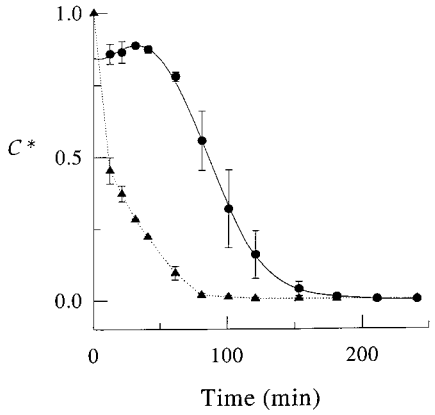

Figure 7—The concentration decline of MC during microencapsulation of triamcinolone acetonide by the solvent evaporation method. The concentration in dispersed (▲) and continuous phases (●) were normalized by the initial MC concentration in the polymer C_{DP}^0 (i.e., $C^* = C_{DP}/C_{DP}^0$) and by the solubility of MC in 0.3% PVA aqueous solution (i.e., $C^* = C/C_s$), respectively. The plotted data are mean ± SD ($n = 2$). (—) is a sixth-order polynomial fit, $q_6(t)$, and (·····) connects data points.

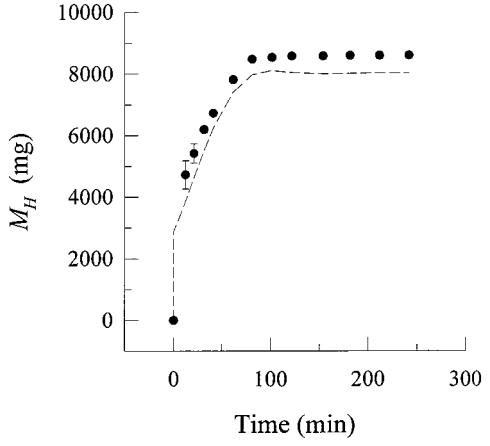

Figure 8—Predicting the hardening profile during microencapsulation of triamcinolone acetonide from $q_6(t)$ and $p_3'(\ln q_6(t))$. The microsphere hardening profile was measured (●) and predicted (– – –). The plotted data are mean ± SD ($n = 2$).

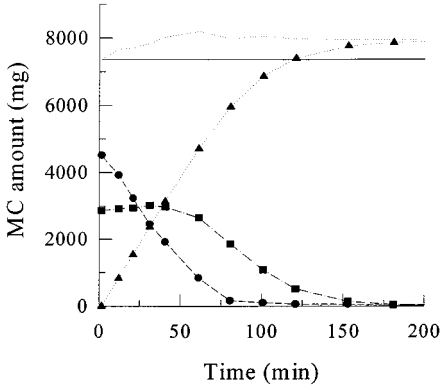

Figure 9—The distribution of MC during microencapsulation of triamcinolone acetonide. The mass of MC was determined in the dispersed phase (●), the continuous phase (■), and the surroundings (evaporated) (▲) during the hardening of the microspheres. The overall mass recovered from the calculation (·····) showed good agreement with the initial MC in the hardening bath (—).

sum of MC mass from experimentally determined C, C_{DP}, and the theoretical loss of MC to surroundings ($\int R_E dt$) accounted for 104−110% of the mass during the entire encapsulation experiment.

For completeness, microspheres thus formed were observed to be spherical under the microscope and had a size distribution of 44 ± 18 (mean ± SD, $n = 100$) by light microscopic size determination. The triamcinolone acetonide loading was 3.9 ± 0.2% (mean ± SD, $n = 6$) as determined by HPLC after dissolution of the polymer in acetonitrile.[19] Control studies also revealed that the controlled-release function of these microspheres was intact; that is, release was slow and continuous for >30 days.

Discussion

Identification of Process Variables that Control Solvent Evaporation—The most efficient method to change the evaporation rate was to adjust ω, d, or T. The effect of V was very weak (−1/4 power dependence). As indicated by the similarity of P_{exp} and P_{theo} in Table 2 (usually <15% error when under liquid phase transport control), the relationship in eq 16 is well validated. This result suggests the potential to accurately affect the hardening rate of microspheres by manipulating the continuous phase concentration, C, during encapsulation. Specific applications of eq 16 will be pursued in a future paper.

Rate-Limiting Step for Mass Transport during Evaporation—As shown in the *Theoretical Section*, the resistance to mass transport in an evaporation system originates from two major sources: the diffusion layers in the liquid and gas phases. Because these two resistance are in series, if one resistance is much greater than the second, the greater of the two will largely determine the overall resistance. If the unstirred layer is relatively thin in the gas phase (or resistance is very small) compared with the liquid phase, the overall mass transport barrier will reside in the liquid phase. Under these conditions, the P of the evaporation system can be predicted by eq 16 with reasonable accuracy (Table 2). If the resistance in the gas phase is not too large to be reduced effectively by N_2 gas flow, the P may still be predicted by eq 16 with acceptable accuracy, as evidenced by the data for MC at 5 °C and for EA at 25 °C (Figure 5).

The analysis in Figure 5 confirms the hypothesis that the Henry's law constant and temperature are the predominant indicators of whether a specific organic solvent evaporates according to gas- or liquid-side transport control. Dissolved gases, such as O_2, with extremely high values of H will always be liquid-side transport limited,[20] and solvents such as ACN that are highly soluble in water with lower vapor pressure (i.e., low H) will be expected to be gas-side transport limited. A particularly notable result was that MC at room temperature is liquid-side transport limited, whereas EA, a frequently used alternative in encapsulation, has a significant resistance in the gas phase at this temperature. This result suggests that blowing N_2 (g), as performed here and elsewhere,[21] may be appropriate for the use of EA at room temperature.

Physical Description of Solvent Evaporation from the Hardening Bath—It was demonstrated that under the most common encapsulation conditions (i.e., MC evaporation at room temperature in turbulent flow), the evaporation largely falls under liquid-phase transport control. Two important concepts underlie the mass transport in the liquid-phase boundary layer. The first concept is turbulence. The nature of the turbulence induced by the impeller controls the size and speed of the smallest eddies that approach the evaporating surface. The eddy of size $\sim\delta_K$ is formed by an energy cascade, which begins with large eddies that are unstable and break up into steadily smaller liquid "packages" of chaotic movement. At the scale where local $Re \sim 1$, the fluid elements lose their kinetic energy to thermal energy. Because δ_K is only dependent on the

kinematic viscosity and the total energy per unit mass (or volume) of fluid according to the assumption of isotropic turbulence, the evaporation rate is somewhat independent of bath geometry after correction for the surface area at the air/water interface. There is, however, a small dependence of P on bath volume because more fluid means more fluid mass available to dissipate the turbulent energy. This dependence as well as the dependence of P on $d^{5/4}$, have obvious scaling implications.

The second concept is the velocity distribution in the viscous sublayer and how it is affected by the approaching eddy to the free air/water surface. The velocity distribution affects the relationship between the diffusion layer thickness and viscous sublayer thickness (by either $Sc^{-1/2}$ or $Sc^{-1/3}$). Because organic solvents are surface active,[22] we must have the equivalent of the 'dirty' surface case, which is similar hydrodynamically to the liquid/solid interface. This hypothesis was confirmed by the validity of eq 16, which would not have been so if a "clean" surface was assumed. The parabolic velocity distribution in the sublayer leads to the well-known variation of δ_D with $Sc^{-1/3}$.[23]

The Role of Solvent Evaporation on Microsphere Hardening during Microencapsulation—Because the microsphere hardening profile was successfully predicted with $P(C)$ and C without directly measuring C_{DP}, it is theoretically possible in the future to continuously monitor the microsphere hardening kinetics by simply measuring C during encapsulation provided that the $P(C)$ is known. It is also reasonable to envision on-line systems to monitor the continuous-phase organic solvent concentration during encapsulation. Because the microsphere hardening kinetics may directly affect the final microsphere quality, the monitored results could potentially be used as quality control criteria for microsphere production.

It is important to note, however, that it is expected that the evaporation will only play a dominant role in the microsphere hardening kinetics if two conditions are satisfied: (1) the extraction capacity of the continuous phase has been saturated; and (2) the diffusion rate of organic solvents from the dispersed phase (DP) to the continuous phase (CP) is fast compared with the solvent evaporation kinetics. The first condition is determined by the organic solvent solubility in continuous aqueous phase and the initial DP/CP volume ratio. The second prerequisite, however, will be much more complicated and influenced by several factors, including the initial organic solvent extraction rate, polymer MW and concentration, and temperature of encapsulation.[24] All these factors are directly related to the microsphere hardening conditions and remain to be investigated in the future.

In closing, the mechanism of evaporation during solvent evaporation encapsulation processes has been elucidated, confirmed experimentally, and used to predict microsphere hardening kinetics. These results have potential use for formulation, design of encapsulation apparatus, and scaling-up of microsphere production.

Nomenclature

A = surface area of air−water interface, cm^2
C = organic solvent concentration in the continuous phase of the bath, mg/mL
C_0 = initial organic solvent concentration in the continuous phase of the bath, mg/mL
C_{DP} = MC content in the dispersed polymer phase, mg/mg PLGA
C_{DP}^0 = initial MC content in the dispersed polymer phase, mg/mg PLGA
C_S = solubility of organic solvent in the continuous phase of the bath, mg/mL
C_T = MC content in the entire aqueous dispersion, mg/mL
C^* = normalized MC content in continuous phase ($C^* = C/C_s$) or in dispersed phase (DP; $C^* = C_{DP}/C_{DP}^0$), unitless
D = diffusion coefficient of the organic solvent in the continuous phase of the bath, cm^2/s
d = impeller diameter, cm
H = Henry's law constant, atm·mL/mg
j_s = organic solvent flux at the air/liquid interface, mg/(cm^2·s)
Ko = corrected Kolmogorov number, $d/(\delta_K \cdot N_p^{1/4})$, unitless
M_B = molecular weight of aqueous solvent in the bath, g/mol
M_H = cumulative mass removed from microspheres, mg
M_P = mass of PLGA in the dispersed aqueous system, mg
N_P = power number, unitless
P = overall permeability coefficient, cm/s
P_G = permeability coefficient in the gas phase, mg/(atm·cm^2·s)
P_L = permeability coefficient in the liquid phase, cm/s
p_n = n^{th}-order polynomial interpolating function for t versus ln C during evaporation, min
$\dot{Q}$ = rate of energy loss from the impeller to the fluid, g·cm^2/s^3
q_m = mth-order polynomial interpolating function for C vs t during encapsulation, mg/mL
R_E = organic solvent evaporation rate, mg/min
R_H = overall rate of organic solvent removal from microspheres (i.e., hardening rate), mg/min
Re = impeller Reynolds number, $\omega\, d^2/\nu$, unitless
Re^* = local Reynolds number, $u_e\delta_e/\nu$, unitless
Sc = Schmidt number, ν/D, unitless
Sh = Sherwood number, Pd/D, unitless
T = temperature, K
t = time, min or s
u_e = velocity of the eddies approaching air−water interface, μm/s
V = volume of fluid in the hardening tank, mL
V_A = molar volume of organic solvent at its boiling temperature, cm^3/mol
δ_e = length scale of the eddies approaching air−water interface, μm
δ_D = diffusion sublayer thickness, μm
δ_K = Kolmogorov length scale, μm
δ_V = viscous sublayer thickness, μm
ϵ = energy dissipation rate per unit mass fluid, cm^2/s^3
ν = kinematic viscosity, cm^2/s
η_B = viscosity of aqueous solution in hardening bath, cp
ω = rotational speed of overhead stirrer, rev/s or rpm
Φ = association factor (for prediction of D), unitless
Ψ = ratio of the volume of the continuous phase to the volume of the entire aqueous dispersion, unitless
ρ = density of aqueous solution in hardening bath, mg/mL

References and Notes

1. Thies, C. Formation of Degradable Drug-Loaded Microparticles by In−Liquid Drying Processes. In *Microcapsules and Nanoparticles in Medicine and Pharmacy*; Donbrow, M., Ed.; CRC: Ann Arbor, MI, 1991; pp 47−71.
2. Arshady, R. Preparation of Biodegradable Microspheres and Microcapsules: 2. Polyactides and Related Polyesters. *J. Controlled Release* **1991**, *17*, 1−22.
3. Crotts, G.; Park, T. G. Preparation of Porous and Nonporous Biodegradable Polymeric Hollow Microspheres. *J. Controlled Release* **1995**, *35*, 91−105.
4. Li, W. I.; Anderson, K. M.; Mehta, R. C.; Deluca, P. P. Prediction of Solvent Removal Profile and Effect on Properties for Peptide-Loaded PLGA Microspheres Prepared by Solvent Extraction/Evaporation Method. *J. Controlled Release* **1995**, *37*, 199−214.
5. Jeyanthi, R., Thanoo, B. C.; Metha, R. C.; Deluca, P. P. Effect of Solvent Removal Technique on the Matrix Characteristics

of Polylactide/Glycolide Microspheres for Peptide Delivery. *J. Controlled Release* **1996**, *38*, 235−244.
6. Oldshire, J. Y. *Fluid Mixing Technology*; Chemical Engineering: New York, 1983; pp 43−71.
7. Cussler, E. L. *Diffusion-Mass Transfer in Fluid Systems*; Cambridge University: New York, 1984; pp 215−248, 172−193.
8. Hunt, J. C. R. Turbulence Structure and Turbulent Diffusion Near Gas−Liquid Interfaces. In *Gas Transfer at Water Surfaces*; Brutsaert, W.; Jirka, G. H., Eds.; D. Reidel Publishing: Dordrecht, Holland, 1984; pp 67−82.
9. Blevins, R. D. Dimensional Analysis. In *Applied Fluid Dynamics Handbook*; Blevins, R. D., Ed.; Van Nostrand Reinhod: New York, 1984; pp 8−18.
10. Perry, R. H.; Green, D. W.; Maloney J. O. *Perry's Chemical Engineers' Handbook*, 6th ed.; McGraw-Hill: New York, 1984; pp 19-(5−14), 3-(75−77).
11. Gillett, P. *Calculus and Analytic Geometry*; D. C. Heath and Company: Lexington, MA, 1981; pp 290−294.
12. Reid, R. C.; Prausnitz, J. M.; Poling B. E. *The Properties of Gases and Liquids*, 4th ed.; Sun, B., Fleck, G. H., Eds.; Mcgraw-Hill: New York, 1987; pp 52−54, 388−485, 577−626.
13. To perform the prediction of M_H with reasonable accuracy, the hardening rate must be of a similar magnitude or greater than the evaporation rate. If $R_H \ll R_E$, then the common problem of taking the difference of two very close large experimental values is encountered.
14. Boyce, W. E.; Diprima, R. C. *Elementary Differential Equations*, 3rd ed.; John Wiley & Sons: New York, 1977; pp 358−361.
15. Smallwood, I. M. *Handbook of Organic Solvent Properties*; John Wiley & Sons: New York, 1996; pp 37, 227, 289.
16. Horvath, A. L. *Halogenated Hydrocarbons Solubility-Miscibility with Water*; Marcel Dekker: New York, 1982; pp 658−660.
17. The presence of PVA had no influence on the experiment described in Figure 6A so the data with and without PVA were combined for the determination of the interpolating function, $p_n(t)$.
18. It was unexpected to observe such a high hardening rate as $C \rightarrow C_s$ because the chemical potential of MC in the DP cannot be greater than the chemical potential in the CP at $C = C_s$. Therefore, the hardening must proceed with a very small chemical driving force (i.e., difference between the chemical potential in the DP and the chemical potential in the continuous phase).
19. Zhou, T. H.; Lewis, H.; Foster, R. E.; Schwendeman, S. P. Development of a Multiple-Drug Delivery Implant for Intraocular Management of Proliferative Vitreoretinopathy. *J. Controlled Release* **1998**, *55*, 281−295.
20. Sherwood, T. K.; Pigford R. L.; Wilke C. R. *Mass Transfer*; Clark, B. J.; Maisel, J. W., Eds.; McGraw-Hill Book Company: New York, 1975; pp 101−196.
21. Cleland, J. L.; Jones, A. J. S. Stable Formulations of Recombinant Human Growth Hormone and Interferon-γ for Microencapsulation in Biodegradable Microspheres. *Pharm. Res.* **1996**, *13(10)*, 1464−1475.
22. Sluzky, V. Insulin Stability and Aggregation in Agitated Aqueous Solutions. Ph.D. Thesis, Massachusetts Institute of Technology, Cambridge, MA, 1992.
23. Levich, V. G. *Physicochemical Hydrodynamics*; Amundson, N. R., Ed.; Prentice-Hall: Englewood Cliffs, NJ, 1962; pp 139−183.
24. Li, Wen-I. Mechanism and mathematical modeling of microsphere formation. Ph.D. Thesis, University of Kentucky, Lexington, KY, 1994.
25. The fascinating independence of δ_D on T stems from the negligible temperature dependence of the product, $\nu^{5/12}D^{1/3}$, in eq 17.

Acknowledgments

This work was supported in part by NIH DE 12183 and an OSU Comprehensive Cancer Center support grant (NIH P30 CA 16058). Support to Juan Wang was also provided by an OSU multiple year university fellowship.

JS980169Z

A publication of the American Pharmaceutical Association and the American Chemical Society

JOURNAL OF Pharmaceutical Sciences

November 1999
Volume 88, Number 11

MINIREVIEW

Allometric Issues in Drug Development†

IFTEKHAR MAHMOOD

Contribution from *Office of Clinical Pharmacology and Biopharmaceutics, Division of Pharmaceutical Evaluation I (HFD-860), Food & Drug Administration, Woodmont Office Center II, Room 4079, 1451 Rockville Pike, Rockville, Maryland 20852.*

Received June 28, 1999. Final revised manuscript received August 5, 1999.
Accepted for publication August 17, 1999.

Abstract ☐ The concept of correlating pharmacokinetic parameters with body weight from different animal species has become a useful tool in drug development. The allometric approach is based on the power function, where the body weight of the species is plotted against the pharmacokinetic parameter(s) of interest. Clearance, volume of distribution, and elimination half-life are the three most frequently extrapolated pharmacokinetic parameters. Over the years, many approaches have been suggested to improve the prediction of these pharmacokinetic parameters in humans from animal data. A literature review indicates that there are different degrees of success with different methods for different drugs. Overall, though interspecies scaling requires refinement and better understanding, the approach has lot of potential during the drug development process.

Introduction

To develop a new therapeutic compound, relevant pharmacological and toxicological studies are initially conducted in small laboratory animals such as mice, rats, rabbits, dogs, or monkeys. These initial studies are helpful in screening the potential therapeutic compounds in the process of drug development. This extrapolation, termed as interspecies scaling, may be helpful in the selection of a suitable dose for first-time administration to humans.

Interspecies scaling is based on the assumption that there are anatomical, physiological, and biochemical similarities between animals.[1,2] Two approaches are generally used for interspecies pharmacokinetic scaling: (i) physiological-based models, and the (ii) allometric method. Though physiological models provide a mechanistic-based evaluation of drug disposition, these models are complex. Many investigators[3−6] have used physiological-based models to predict pharmacokinetic parameters of drugs. Since physiological models are costly, mathematically complex, and time-consuming for their use in drug discovery, and development remains limited.

The anatomical, physiological, and biochemical similarities between animal species can be generalized and expressed mathematically by the allometric equations and have been discussed in detail by Boxenbaum.[7,8] Though the allometric approach is empirical, it is less complicated and easy to use than the physiologically based models. Therefore, this review will only focus on the basic principles, application, and issues of the allometric scaling in pharmacokinetics.

The allometric approach is based on the power function, as the body weight from several species is plotted against the pharmacokinetic parameter of interest. The power function is written as follows:

$$Y = aW^b \tag{1}$$

where Y is the parameter of interest, W is the body weight, and a and b are the coefficient and exponent of the allometric equation, respectively. The log transformation of eq 1 is represented as follows:

$$\log Y = \log a + b \log W \tag{2}$$

where $\log a$ is the y-intercept, and b is the slope.

* Telephone: (301) 594−5575. Fax: (301) 480−3212. e-mail: Mahmoodi@CDER.FDA.GOV.

† The views expressed in this article are those of the author and do not reflect the official policy of the FDA. No official support or endorsement by the FDA is intended or should be inferred.

10.1021/js9902163 CCC: $18.00
Published on Web 09/24/1999

Clearance (CL), volume of distribution (V), and elimination half-life ($t_{1/2}$) are the three most important pharmacokinetic parameters. In the forthcoming sections different allometric approaches to predict these pharmacokinetic parameters from animals to man will be discussed.

Clearance

Both in drug discovery and drug development, clearance is the focus of attention. During drug discovery or the screening process, clearance is important since drugs which are eliminated quickly may have a low bioavailability and may not be suitable for further investigation. Clearance can also play an important role for the selection of the first-time dosing in humans (as inverse of clearance indicates the total exposure (AUC) of a drug). Therefore, over the years, a lot of attention has been focused in order to improve the performance of allometry to predict clearance.

A glance on the literature indicates that clearance cannot be predicted only using the simple allometry (body weight vs clearance).[9,10] Over the years, many different approaches have been suggested to address this issue. Some of the approaches are (i) to predict clearance on the basis of species weight and maximum life-span potential (MLP),[7] (ii) the use of a two-term power equation[11] based on brain weight and body weight to predict intrinsic clearance of drugs, (iii) use of the product of CL × brain weight,[9,10] and (iv) the normalization of in vivo clearance by in vitro clearance versus body weight.[12−14] Unfortunately, these approaches are used indiscriminately without identifying the suitability of a given approach.

In a study, Mahmood and Balian[9] showed that CL × MLP or CL × brain weight estimates the clearance of some antiepileptic drugs more accurately than the simple allometric approach (CL vs body weight). But it is also important to know under what circumstances the simple allometric equation, CL × MLP or CL × brain weight is most suitable. Mahmood and Balian[10] proposed the selection of one of the methods based on the exponents of the simple allometry. The authors demonstrated that there are specific conditions under which only one of the three methods can be used for reasonably accurate prediction (a maximum of 30% error) of clearance: (i) if the exponent of the simple allometry lies between 0.55 and 0.70, simple allometry will predict clearance more accurately than CL × MLP or CL × brain weight; (ii) if the exponent of the simple allometry lies between 0.71 and 1.0, the CL × MLP approach will predict clearance better compared to simple allometry or CL × brain weight; and (iii) if the exponent of the simple allometry is ≥1.0, the product of CL × brain weight is a suitable approach to predict clearance in humans compared to the other two methods. If the exponent of the simple allometry is greater than 1.3, it is possible that the prediction of clearance from animals to man may not be accurate even using the approach of CL × brain weight, and if the exponent of simple allometry is below 0.55, the predicted clearance may be substantially lower than the observed clearance. However, this "rule of exponents" is not rigid, and caution should be applied when the exponents are on the borderline (i.e., 0.69 vs 0.71).

The exponents of allometry have no physiological meaning. As the exponents of the simple allometry get larger, the predicted clearance will be comparatively higher than the observed clearance. Furthermore, the normalization of clearance by MLP or brain weight is a mathematical manipulation which may not be associated with any physiological relevance. The predicted clearance values will be in order of simple allometry > MLP × CL > brain weight × CL. The exponents of a given drug are not universal and will depend on the species used in the allometric scaling. This has been shown for theophylline and antipyrine following iv administration,[10] though this will be true for any given drug.

The concept of using a fixed exponent of 0.75 for the prediction of clearance does not seem to be appropriate. From the data published by Mahmood and Balian,[10] it can be seen that the exponents of allometry range from 0.35 to 1.39. The mean of the exponents is 0.78, which is close to 0.75, but given the wide range of exponents it is obvious that using a fixed exponent of 0.75 will produce serious errors in the prediction of clearance. However, it should be noted that the use of a fixed exponent may be helpful when pharmacokinetic data from only one species are available. This approach may provide a rough estimate of clearance.

Incorporation of in Vitro Data in in Vivo Clearance—Over the years, a lot of interest in using in vitro data in allometric scaling has been developed, and a comprehensive review article has been published by Houston[12] on this topic. Recently, Lave et al.[13] attempted to predict hepatic clearance of 10 extensively metabolized drugs in man by incorporating in vitro data into allometric scaling. The authors concluded that integrating the in vitro data with the allometric approach improved the prediction of clearance in humans as compared to the approach of the simple allometry or the product of clearance and brain weight. In their comparison between simple allometry or the product of clearance and brain weight with the in vitro approach, Lave et al. assumed that clearance of all drugs can be either predicted by simple allometry or by the product of clearance and brain weight. Since this assumption is incorrect, Lave's data[13] were reanalyzed by Mahmood[15] and the results indicated that the normalization of clearance by MLP (as required based on the exponents) could have produced the same results as observed by the in vitro approach. Furthermore, based on the exponents of the simple allometry, it was found that the product of clearance and brain weight was not a suitable approach for the prediction of clearance for these drugs.

In a separate study, Obach et al.[14] used different methods for the prediction of clearance and concluded that the in vitro approach was the best method for the prediction of clearance. In their comparison, the authors also assumed that clearance for all drugs can be predicted by only one method. A comparison between the in vitro approach and the allometry using the "rule of exponents" as suggested by Mahmood and Balian would have provided information whether the in vitro approach is really better than the empirical allometric approach.

There are obvious limitations of the in vitro approach. A definitive disadvantage of the in vitro approach is that one requires to measure the in vitro clearance in at least three species which may be time-consuming. This approach is inappropriate for drugs which are excreted renally as well as for those drugs which are partly metabolized and partly excreted renally.

Extensive work will be needed in this direction before one can clearly establish the advantage and accuracy of the in vitro approach in predicting clearance of drugs over other existing methods. However, it should be kept in mind that the in vitro approach in allometric scaling is one of the many suggested approaches which are attempts to improve the prediction of clearance and should be used as deemed necessary.

Role of Protein Binding in the Prediction of Clearance—Considerable variability in plasma protein binding of drugs have been observed among animal species, resulting in variable distribution and elimination of drugs in different species. The unbound intrinsic clearance of antipyrine,[11] phenytoin,[8] clonazepam,[8] caffeine,[16] and cy-

Table 1—Observed and Total Predicted Clearance (mL/min) of Several Drugs with or without Considering Protein Binding

drug	observed total CL	predicted total CL	predicted total CL
diazepam	26	861	817
tamsulosin	48	814	102
GV150526	5–7	320	5
cyclosporin	273	716	611
quinidine	330	1452	2423

[a] Obtained by multiplying the predicted unbound clearance in humans by free fraction of drug in human plasma. For example, the predicted unbound clearance of tamsulosin in humans was 10218 mL/min and fu was 0.01. Therefore, the predicted total clearance in humans was 10218*0.01 = 102 mL/min.

closporine[17] has been reported in the literature. It is also widely believed that unbound clearance can be predicted with more accuracy than total clearance.[14] However, a systematic study, which compares whether unbound clearance can be predicted better than total clearance, is lacking. Mahmood[18] compared the total and unbound clearance of a wide variety of drugs to determine whether unbound clearance of a drug can be predicted more accurately than total clearance, and if there is any real advantage of predicting unbound clearance. The results of the study indicated that unbound clearance cannot be predicted any better than total clearance. There are drugs whose unbound clearance can be predicted better than total clearance or vice versa. For example, using simple allometry, predicted total clearance of diazepam,[19] tamsulosin,[20] GV 150526,[21] cyclosporin,[17] and quinidine[38–40] was 861, 814, 320, 716, and 1452 mL/min, respectively (Table 1). When the predicted unbound clearance in humans was multiplied by the respective free fraction of drug in human plasma, the predicted total clearances for tamsulosin and GV 150526 were vastly improved, whereas no improvement was observed for diazepam, cyclosporin, and quinidine (Table 1). It is clear from this analysis that protein binding may or may not be helpful for the improved prediction of clearance. At this time it is not possible to determine a priori for which drug unbound or total clearance can be predicted better.

In a separate study, Obach et al.[14] predicted clearance with or without taking protein binding into account. Based on average-fold error (1.91 without protein binding and 1.79 with protein binding), a slightly improved prediction of unbound clearance was noted, though for all practical purposes this difference may not be of any significance.

Prediction of Clearance for Renally Secreted Drugs—Allometry is not always successful in predicting pharmacokinetic parameters. A recent example is the failure of the allometric approach for the prediction of total clearance of renally secreted drugs.[22] Interspecies scaling of drugs for the prediction of clearance may be complicated due to the differences in the mechanism of excretion of drugs in different species. Using 10 renally secreted drugs, it was shown by Mahmood[22] that it is likely that the predicted total and renal clearances for renally secreted drugs may be lower in humans than the observed clearances. The prediction of renal clearance was improved by normalizing the renal clearance by a "correction factor" for animals who exhibited renal secretion. The "correction factor" was obtained by the following equation:

$$\frac{(\text{glomerular filtration rate} \times \text{kidney blood flow})}{(\text{body weight} \times \text{kidney weight})} \quad (3)$$

Though the proposed approach for the prediction of renal clearance for renally secreted drugs worked fairly well on the tested drugs, more work will be needed to validate the approach. Furthermore, a method which can improve the prediction of total clearance for renally secreted drugs requires investigation.

Volume of Distribution—Like clearance, volume of distribution is also an important pharmacokinetic parameter. Volume of distribution of the central compartment (V_c) can play an important role in establishing the safety or toxicity for first-time dosing in humans. Since an administered dose is always known, the predicted V_c can be used to calculate plasma concentration of a drug at time zero (C_0) following intravenous administration. This initial plasma concentration may be an index of safety or toxicity. Furthermore, V_c can also be used to predict half-life, if clearance is known ($t_{1/2} = 0.693V_c/\text{CL}$).

There is a good correlation between body weight and V_c among species. Generally the exponents of volume pivots around 1.0, which indicates that body weight and volume are directly proportional. However, in practice this may not be the case for all drugs; for example, exponents of 0.81, 0.86, 0.58, and 0.76 were observed for topiramate,[9] diazepam,[9] diazepoxide,[23] and ciprofloxacin,[24] respectively. Overall, volume of distribution can be predicted in humans from animals with reasonable accuracy.

Obach et al.[14] used four different methods to predict volume of distribution at steady state (V_{ss}), and on the basis of their geometric mean prediction accuracy they concluded that V_{ss} can be predicted better when protein binding is taken into account.

In the literature one can find that V_{ss} and V_β or V_{area} are also predicted. It has been shown by Mahmood[24] that V_c can be predicted with more accuracy than V_{ss} and V_β. In fact V_{ss} and V_β are of no real significance for the first time dosing in humans and can be estimated from human data.

The concept of a fixed exponent for volume may be acceptable, as in the majority of cases the exponents of volume revolve around 1. Therefore, the use of a fixed exponent of 1 may not produce as much error in predicted volume as clearance and half-life.

Elimination Half-Life—Elimination half-life is difficult to predict across species. Conceptually, it is difficult to establish a relationship between body weight and half-life. In practice, indeed a poor correlation between $t_{1/2}$ and body weight across the species has been found. This poor correlation may be due to the fact that $t_{1/2}$ is not directly related to the physiological function of the body, rather it is a hybrid parameter. Therefore, this poor correlation results in a poor prediction of half-life. To improve the prediction of half-life, some indirect approaches have been suggested by different investigators.

Bachmann,[25] Mahmood and Balian,[9] and Obach et al.[14] used the equation ($t_{1/2} = 0.693V_c/\text{CL}$) to predict the half-lives of many drugs. Though this approach predicted the half-life with reasonable accuracy, to obtain a reasonable prediction of half-life both CL and V_c must be predicted with reasonable accuracy. Another indirect approach was suggested by Mahmood.[24] In this approach, mean residence time (MRT) was predicted, and then predicted MRT was used to predict half-life in humans using the equation ($t_{1/2}$ = MRT/1.44). The results of his study indicated that MRT can be predicted in humans with a fair degree of accuracy from animal data. The predicted half-life from MRT was also reasonably accurate.

Like clearance, the concept of fixed exponent may not be applicable for half-life. From the published work of Mahmood,[24] it can be seen that the exponenmts of half-life varies from −0.066 to 0.547, but the average is 0.19. Therefore, a fixed exponent of 0.25 for the prediction of half-life may also produce serious errors in the prediction of half-life.

Physiological Time or Pharmacokinetic Time Scale—Besides predicting pharmacokinetic parameters, attempts were also made by several investigators to predict plasma concentrations in humans from animal data. The initiative in this direction was taken by Dedrick et al.,[2] and Boxenbaum[7,8] further refined the concept of Dedrick's approach.

In chronological time, heart beat and respiratory rates decrease as the size of the animals increases. On the other hand, on a physiological time scale, all mammals have the same number of heart beats and breaths in their lifetime. The physiological time can be defined as the time required to complete a species independent physiological event. Thus, smaller animals have faster physiological processes and shorter life span. The concept of pharmacokinetic time scale originates from the concept of physiological time which was first described by Brody.[26]

Dedrick et al.[27] were the first to use the concept of physiological time to describe methotrexate disposition in five mammalian species following intravenous administration. They transformed the chronological time to physiological time using the following equation:

$$Y\text{-axis} = \frac{\text{concentration}}{(\text{dose}/W)} \quad (4)$$

$$X\text{-axis} = \frac{\text{time}}{W^{0.25}} \quad (5)$$

where W is the body weight.

By transforming the chronological time to physiological time, the plasma concentrations of methotrexate were superimposable in all species. The authors termed this transformation as "equivalent time". Later, Boxenbaum[7,8] introduced two new units of pharmacokinetic time, kallynochrons and apolysichrons. Kallynochrons and apolysichrons are transformed time units termed as elementry Dedrick plot and complex Dedrick plot, respectively. Boxenbaum also incorporated the concept of MLP in physiological time and termed this new time unit as "dienetichrons".

Though many investigators[28–30] have used the concept of physiological time in their allometric analysis, a direct comparison of allometric approaches with physiological time has not been systematically evaluated. Recently Mahmood and Yuan[31] compared the predicted values of clearance, volume of distribution, and elimination half-life of ethosuximide, cyclosporine, and ciprofloxacine by allometry with physiological time using equivalent time, kallynochron, apolysichron, and dienetichrons. The results of this study indicated that there is no specific advantage of using physiological time over the allometric approach. Almost similar predictions in pharmacokinetic parameters were obtained from both methods. The equivalent time approach based on the assumption that the exponent of half-life is 0.25 was not found to be suitable for the prediction of plasma concentrations or pharmacokinetic parameters. This may be due to the fact that the exponent of elimination half-life of drugs is not always 0.25. Due to the small sample size used in this study, it is difficult to conclude whether the physiological time approach in predicting pharmacokinetic parameters is as good/better as allometric approaches. One advantage of pharmacokinetic time scale approach is that it provides some information about the plasma concentrations of a given drug, though it is not known to what extent the predicted concentrations are reliable?

Prediction of Pharmacokinetic Parameters Using Pharmacokinetic Constants—Swabb and Bonner[32] and Mordenti[33] predicted the plasma concentrations of aztreonam and ceftizoxime, respectively, using an allometric relationship on pharmacokinetic constants (A, B, a, and β). Though the authors successfully used this approach for the prediction of CL, V_c, and $t_{1/2}$, a systematic study of suitability of this approach for prediction of pharmacokinetic parameters was lacking. Mahmood[34] compared the pharmacokinetic parameters of six drugs predicted by pharmacokinetic constants and by the conventional allometric approach.

The following equation representing a two-compartment model following intravenous administration was used to generate plasma concentrations in man from the pharmacokinetic constants predicted from animals.

$$C = Ae^{-\alpha t} + Be-\beta t \quad (6)$$

where A and B are the intercepts on Y-axis of plasma concentration versus time plot. a and β are the rate constants for the distribution and elimination phase, respectively.

Pharmacokinetic constants (A, B, a, and b) were plotted as a function of body weight as described in eq 1. The allometric equation thus generated was used to predict pharmacokinetic constants in man. For the prediction of plasma concentrations in man, the predicted pharmacokinetic constants were used.

The results of the study indicated an inconsistent correlation between body weight and A, B, or a. For some drugs, a good correlation was obtained, whereas a poor correlation was noted for other drugs. Though the prediction of A and B was occasionally reasonable, the predicted a values were manyfold higher or lower than the observed values. Overall it was found that the use of pharmacokinetic constants to predict pharmacokinetic parameters does not necessarily provide an improvement over the conventional allometric approach. Like the pharmacokinetic time scale approach, the pharmacokinetic constant method may provide some information about plasma concentrations of a drug, but the accuracy of the method for the prediction of plasma concentrations in man may not be reliable.

Conclusion

The most important objective of allometric scaling is to select a safe and tolerable dose for the first time administration to humans. Therefore, in recent years, interspecies scaling of pharmacokinetic parameters has drawn enormous attention. Interspecies scaling is not without shortcomings and failures, and over the years, many approaches have been suggested to improve the predictive performance of allometric scaling. These approaches are not perfect, but they may be of considerable importance to understand and refine the concept of allometric scaling. There is no right or wrong approach in interspecies scaling.

There may be anatomical similarities among species, but there are external factors which will affect the allometric scaling. Experimental design, species, analytical errors, and physicochemical properties of drugs such as renal secretion or biliary excretion may have impact on allometric extrapolation. There are drugs such as diazepam,[19] warfarin,[25] valproic acid,[35] tamsulosin,[20] and GV150526[21] whose predicted clearance are manyfold higher than the observed clearance and may be considered as drugs which exhibit vertical allometry. The role and importance of vertical allometry in allometric scaling is unclear. It is also difficult to identify a priori when a drug will exhibit vertical allometry. Extensive work will be needed to classify drugs as vertical allometry and to find a solution to improve the prediction of clearance for such drugs.

There were also attempts to identify the suitability of a particular species for the prediction of clearance in humans. Campbell[36] concluded that the prediction of clearance in humans was best predicted when data from rhesus or cynomolgus monkey were used with the incorporation of MLP. The rat was the next best species for the prediction of human clearance whereas dog appeared to be a poor predictor of clearance in humans. The number of species can also affect the predictive performance of allometry. Mahmood and Balian[37] have shown that three or more species are needed for a reliable prediction of clearance in humans. They also showed that volume of distribution of a compound is predicted equally well using data from two species or more. Therefore, all these methods should be used with caution and proper understanding of allometric scaling.

Besides success, there are numerous failures in interspecies scaling. Such failed studies should also be published so that further investigation can be conducted to find the underlying reasons for failure. Such investigations will be helpful to improve the predictive performance of allometric scaling.

References and Notes

1. Mordenti, J. Man versus beast. *J. Pharm. Sci.* **1986**, *75*, 1028−40.
2. Dedrick, R. L. Animal Scale-up. *J. Pharmacokin. Biopharm.* **1973**, *1*, 435−61.
3. Bischoff, K. B. Some fundamental considerations of the applications of pharmacokinetics to cancer chemotherapy. *Cancer Chemother. Rep.* **1975**, *59*, 777−93.
4. Sugita, O.; Sawada, Y.; Sugiyama. Y.; Iga, T.; Hanano, M. Physiologically based pharmacokinetics of drug-drug interaction: a study of tolbutamide-sulfonamide interaction in rats. *J. Charmacokin. Biopharm.* **1982**, *10*, 297−316.
5. Lin, H.; Sugiyama, Y.; Awazu, S.; Hanano, M. Physiological pharmacokinetics of ethoxybenzamide based on biochemical data obtained in vitro as well as on physiological data. *J. Pharmacokin. Biopharm.* **1982**, *10*, 649−61.
6. King, F. G.; Dedrick, R. L.; Farris, F. F. Physiological pharmacokinetic modeling of cis-dichlorodiammineplatinum (II) (DDP) in several species. *J. Pharmacokin. Biopharm.* **1986**, *14*, 131−55.
7. Boxenbaum, H. Interspecies pharmacokinetic scaling and the evolutionary-comparative paradigm. *Drug. Metab. Rev.* **1984**, *15*, 1071−1121.
8. Boxenbaum, H. Interspecies scaling, allometry, physiological time and the ground plan of pharmacokinetics. *J. Pharmacokin. Biopharm.* **1982**, *10*, 201−27.
9. Mahmood, I.; Balian J. D. Interspecies scaling: Predicting pharmacokinetic parameters of antiepileptic drugs in humans from animals with special emphasis on clearance. *J. Pharm. Sci.* **1996**, *85*, 411−414.
10. Mahmood, I.; Balian J. D. Interspecies scaling: Predicting clearance of drugs in humans. Three different approaches. *Xenobiotica* **1996**, *26*, 887−895.
11. Boxenbaum, H.; Fertig, J. B. Scaling of antipyrine intrinsic clearance of unbound drug in 15 mammalian species. *Eur. J. Drug. Metab. Pharmacokin.* **1984**, *9*, 177−183.
12. Houston, B. Utility of in vitro drug metabolism data in predicting in vivo metabolic clearance. *Biochem. Pharmacol.* **1994**, *47*, 1469−1479.13.
13. Lave, T.; Dupin, S.; Schmitt, C.; Chou, R. C.; Jaeck, D.; Coassolo, P. Integration of in vitro data into allometric scaling to predict hepatic metabolic clearance in man: Application to 10 extensively metabolized drugs. *J. Pharm. Sci.* **1997**, *86*, 584−590.
14. Obach, R. S.; Baxter, J. G.; Liston, T. E.; Silber, B. M.; Jones, C.; Macintyre, F.; Rance, D. J.; Wastall, P. The prediction of human pharmacokinetic parameters from preclinical and in vitro metabolism. *J. Pharmacol. Exp. Ther.* **1997**, *283*, 46−58.
15. Mahmood, I. Integration of in-vitro data and brain weight in allometric scaling to predict clearance in humans: some suggestions. *J. Pharm. Sci.* **1998**, *87*, 527−529.
16. Bonati, M.; Latini, R.; Tognoni, G. Interspecies comparison of in vivo caffeine pharmacokinetics in man, monkey, rabbit, rat, and mouse. *Drug Metab. Rev.* **1984−85**, *15*, 1355−83.
17. Sangalli, L.; Bortollotti, A.; Jiritano, L.; Bonati, M. Cyclosporine pharmacokinetics in rats and interspecies comparison in dogs, rabbits, rats, and humans. *Drug Metab. Dispos.* **1988**, *16*, 749−53.
18. Mahmood, I. Interspecies scaling: A comparative study of unbound vs total clearance. Does unbound clearance improve the predictive performance of allometric scaling? *Pharm. Res.* **1997**, *14*, S-241.
19. Klotz, U.; Antonin, K. H.; Bieck, P. R. Pharmacokinetics and plasma binding of diazepam in man, dog, rabbit, guinea pig and rat. *J. Pharmacol. Exp. Ther.* **1976**, *199*, 67−73.
20. Hoogdalem, E.; Soeish, Y.; Matsushima, H.; Higuchi, S. Disposition of the selective α_{1A}-adrenoceptor antagonist tamsulosin in humans: Comparison with data from interspecies scaling. *J. Pharm. Sci.* **1997**, *86*, 1156−1161.
21. Iavarone, L.; Hoke, J. F.; Bottacini, M.; Barnaby, R.; Preston, G. C. First time in human for GV196771: Interspecies scaling applied on dose selection. *J. Clin. Pharmacol.* **1999**, *39*, 560−566.
22. Mahmood, I. Interspecies scaling of renally secreted drugs. *Life Sci.* **1998**, *63*, 2365−2371.
23. Boxenbaum, H.; Ronfeld, R. Interspecies pharmacokinetic scaling and the Dedrick plots. *Am. J. Physiol.* **1983**, *245*, R768−74.
24. Mahmood, I. Interspecies Scaling: Predicting volumes, mean residence time and elimination half-life. Some suggestions. *J. Pharm. Pharmacol.* **1998**, *50*, 493−499.
25. Bachmann, K. Predicting toxicokinetic parameters in humans from toxicokinetic data acquired from three small mammalian species. *J. Appl. Toxicol.* **1989**, *9*, 331−38.
26. Brody, S. Relativity of physiologic time and physiologic weight. *Growth* **1937**, *1*, 61−67.
27. Dedrick, R. L.; Bischoff, K. B.; Zaharko, D. Z. Interspecies correlation of plasma concentration history of methotrexate (NSC-740). *Cancer Chemother. Rep (Part 1)* **1970**, *54*, 95−101.
28. Hutchaleelaha, A.; Chow, H.; Mayersohn, M. Comparative pharmacokinetics and interspecies scaling of amphotericin B in several mammalian species. *J. Pharm. Pharmacol.* **1997**, *49*, 178−183.
29. Lave, T.; Saner, A.; Coassolo, P.; Brandt, R.; Schmitt-Hoffmann, A. H.; Chou, R. C. Animal pharmacokinetics and interspecies scaling from animals to man of lamifiban, a new platelet aggregation inhibitor. *J. Pharm. Pharmacol.* **1996**, *48*, 573−577.
30. Mehta, S. C.; Lu, D. R.. Interspecies pharmacokinetic scaling of BSH in mice, rats, rabbits, and humans. *Biopharm. Drug. Dispos.* **1995**, *16*, 735−744.
31. Mahmood, I.; Yuan, R. A comparative study of allometric scaling with plasma concentrations predicted by species invariant time methods. *Biopharm. Drug. Dispos.* **1999**, *20*, 137−144.
32. Swab, E.; Bonner, D. Prediction of aztreonam pharmacokinetics in humans based on data from animals. *J. Pharmacokinet. Biopharm.* **1983**, *11*, 215−223.
33. Mordenti, J. Pharmacokinetic scale-up: Accurate prediction of human pharmacokinetic profiles from human data. *J. Pharm. Sci.* **1985**, *74*, 1097−1099.
34. Mahmood, I. Prediction of clearance, volume of distribution and half-life by allometric scaling and by plasma concentrations predicted by pharmacokinetic constants: A comparative study. *J. Pharm. Pharmacol.* **1999**, *51*, 905−910.
35. Loscher, W. Serum protein binding and pharmacokinetics of valproate in man, dog, rat and mouse. *J. Pharmacol. Exp. Ther.* **1978**, *204*, 255−261.

36. Campbell, B. D. Can allometric interspecies scaling be used to predict human kinetics? *Drug. Inform. J.* **1994**, *28*, 235−45.
37. Mahmood, I.; Balian J. D. Interspecies scaling: a comparative study for the prediction of clearance and volume using two or more than two species. *Life Sci.* **1996**, *59*, 579−85.
38. Guentert, T. W.; Huang, J. D.; Qie, S. Disposition of quinidine in the rabbit. *J. Pharm. Sci.* **1982**, *71*, 812−815.
39. Ueda, C. T.; Ballard, B. E.; Rowland, M. Concentration−time effects on quinidine disposition kinetics in rhesus monkeys. *J. Pharmacol. Exp. Ther.* **1977**, *200*, 459−468.
40. Swada, Y.; Hanano, M.; Sugiyama, Y., Iga, T. Prediction of the disposition of nine weakly acidic and six weakly basic drugs in humans from pharmacokinetic parameters in rats. *J. Pharmacokin. Biopharm.* **1985**, *13*, 477−492.

JS9902163

Combined Effect of Cosolvent and Cyclodextrin on Solubilization of Nonpolar Drugs

PING LI, LUWEI ZHAO, AND SAMUEL H. YALKOWSKY*

Contribution from *Department of Pharmacy Practice and Science, College of Pharmacy, University of Arizona, Tucson, Arizona 85721.*

Received May 21, 1999. Accepted for publication August 9, 1999.

Abstract □ Solubility enhancement has broad implications in parenteral formulation design. A simple mathematical model has been developed to describe the combined effect of cosolvency and complexation on nonpolar drug solubilization. The total drug solubility is determined by the summation of three drug species present in the solution: free drug [D], drug–ligand binary complex [DL], and drug–ligand–cosolvent ternary complex [DLC]. The proposed model established the dependencies of these three species upon the intrinsic drug solubility, $[D_u]$, the cosolvent solubilizing power, σ, the binary and ternary intrinsic complexation constants, K_b^{int} and K_t^{int}, and the cosolvent destabilizing powers for the binary and the ternary complexes, ρ_b and ρ_t. A nonpolar solute, Fluasterone, is used to evaluate the newly generated equation. The model explains the decline in drug solubility produced by low cosolvent concentrations as well as the increase in the solubility produced by high cosolvent concentrations that are observed at all cyclodextrin concentrations.

Introduction

Solubility enhancement has broad implications in parenteral formulation design. This is especially true for poorly water-soluble drugs, as it is often necessary to deliver the desired dose in a specified volume of aqueous liquid. Over the years a variety of solubilization techniques have been studied and widely used including pH adjustment, cosolvent addition, surfactant addition, and cyclodextrin addition.[1−5]

Among these techniques, cosolvent and cyclodextrin addition are highly effective for nonpolar solutes. As a water-miscible or partially miscible organic solvent, the cosolvent reduces strong water−water interactions and thereby reduces the ability of water to squeeze out nonpolar solute.[2] Cosolvency is often considered at early stages due to its huge solubilization potential. Because of their safety, cosolvents are employed in approximately 10% of FDA approved parenteral products.[3] Cyclodextrins are cyclic oligomers of dextrose or its derivatives joined by α-1,4-linkages. They increase drug solubility by forming an inclusion complex with the nonpolar region of the drug molecule (guest) being inserted into the cavity of the cyclodextrin molecule (host).[3−6] Such a drug−ligand complex has a rigid structure and a definite stoichiometry, usually one-to-one at low ligand concentrations.[4−6] It is of note, however, that there exist clinical limitations to these aforementioned methods.[2,3] For example, high concentrations of cosolvent have high viscosity and high tonicity, and phlebitis can result from precipitation of the solubilized drug upon iv injection.[7,8] In fact, ethanol in concentrations greater than 10% may well produce significant pain.[7,8] Some cyclodextrins have been reported to have significant renal toxicity.[3,8,9]

Recently, the combined use of cosolvency and complexation has drawn particular interest.[10−14] Zung et al. observed synergistic effects of cosolvency and complexation in solubilizing pyrene by using a series of alcohols.[14] The complexation constants of both pyrene/β-cyclodextrin and pyrene/γ-cyclodextrin were found to be much greater in the presence of an alcohol than in pure water. It was suggested that the cosolvent act as a space-regulating molecule so that the drug molecule can better fit into the cyclodextrin cavity. In other studies, it was found that the presence of cosolvents decreases the formation of drug−ligand complex. Pitha et al. reported that the complexation constant of testosterone with hydroxy propyl-β-cyclodextrin (HPβCD) is 10 000-fold lower in 80% ethanol than in water.[11] They reasoned that the cosolvent may act by competing with the drug for entry into the cyclodextrin cavity or by reducing the solvent polarity. A similar antagonistic cosolvent effect was observed for ibuprofen in a HPβCD−propylene glycol−water system.[10]

Given the fact that both cosolvency and complexation have been well studied and understood, it is of interest to explore the mechanisms of the combined effect of the two techniques on nonpolar drug solubilization and to explore the dynamics among the solute, cosolvent, and the cyclodextrin. The knowledge gained in this study may shed light for possible synergistic effect out of this combined technique and be useful in future parenteral formulation design.

This paper aims at constructing a simple mathematical model to explain the combined effect of cosolvency and complexation on nonpolar drug solubilization. The model will be evaluated by using Fluasterone as nonpolar solute, ethanol (EtOH) as cosolvent, and hydroxy propyl-β-cyclodextrin (HPβCD) as complexing ligand. Fluasterone (16α-fluoro-5-androsten-17-one) is a structural analogue of dehydroepiandosterone that is being developed for cancer chemoprevention.[12]

Theoretical Background

Assumptions—The proposed model is based upon the following assumption: the complex formed is either a drug−ligand (cyclodextrin) binary complex or a drug−

* To whom correspondence should be addressed.

10.1021/js990159d CCC: $18.00
Published on Web 09/23/1999

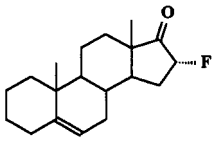

Fluasterone

ligand–cosolvent ternary complex with the stoichiometries assumed as 1:1 and 1:1:1, respectively.

Basics—For a given complexant solution there is an equilibrium between the free drug and the drug–ligand binary complex. When a cosolvent is introduced into the solution, it not only changes the concentration of the free drug [D] and the binary complex [DL], but it also may be involved in the formation of a drug-bearing ternary species, DLC.[14–16] In the presence of a binary 1:1 complex and a ternary 1:1:1 complex, the total solubility of the drug [D^{tot}] is:

$$[D^{tot}] = [D] + [DL] + [DLC] \quad (1)$$

Free Drug—The concentration of free (i.e., uncomplexed) drug [D] is related to intrinsic drug solubility [D_u] and cosolvent concentration [C] by:[2,8,17]

$$[D] = [D_u] \times 10^{\sigma[C]} \quad (2)$$

where σ is the cosolvent solubilizing power. The value of σ depends on the polarity of both the solute and the solvent.[2,8] Here it is assumed that complexation ligand has a negligible effect on the solubilizing power. Similar assumptions have been made in some other studies.[2,8] Equation 2 indicates that the logarithm of solubility in a mixed solvent increases linearly with cosolvent composition, i.e., an increase in [C] will produce an exponential increase in [D]. It has been validated on hundreds of nonpolar solutes in ethanol, propylene glycol, and other cosolvents.[2,8,17]

Binary Complex—The concentration of drug–ligand binary complex [DL] is related to the concentration of free drug [D], the total concentration of ligand [L], and the apparent binary complexation constant, K_b^{app}, by:[18]

$$[DL] = K_b^{app}[D][L] \quad (3)$$

in which K_b^{app} is a function of cosolvent concentration.[11,18,20] The apparent complexation constant, K_b^{app}, in a cosolvent–water solution is empirically related to the cosolvent concentration and the intrinsic complexation constant K_b^{int}, i.e., the complexation constant in water, by:

$$K_b^{app} = K_b^{int} \times 10^{-\rho_b[C]} \quad (4)$$

where ρ_b is the destabilizing power of the cosolvent for the binary complex. The value of ρ_b depends on the polarity deference between the solute and the cosolvent, the steric factors between the solute and the complexing ligand. By incorporating eqs 2 and 4 into eq 3, the binary complex can be expressed as:

$$[DL] = K_b^{int} \times 10^{-\rho_b[C]}[D_u] \times 10^{\sigma[C]}[L] = [D_u][L]K_b^{int} \times 10^{(\sigma - \rho_b)[C]} \quad (5)$$

which shows that [DL] is linearly dependent upon the ligand concentration and exponentially dependent upon the cosolvent concentration. If $\sigma > \rho_b$, an increase in [C] will give rise to an exponential increase in [DL]. If $\sigma < \rho_b$, an increase in [C] will give rise to an exponential decrease in [DL]. If $\sigma = \rho_b$, [C] will have no effect upon [DL].

Ternary Complex—The concentration of the 1:1:1 ternary complex [DLC] is related to the free drug concentration [D], the ligand concentration [L], the cosolvent concentration [C], and apparent ternary complexation constant, K_t^{app}, by:

$$[DLC] = K_t^{app}[D][L][C] \quad (6)$$

By analogy to eq 4, K_t^{app} is related to the cosolvent concentration and the intrinsic ternary complexation constant, K_t^{int}, by:

$$K_t^{app} = K_t^{int} \times 10^{-\rho_t[C]} \quad (7)$$

where ρ_t is the cosolvent destabilizing power for the ternary complex. The value of ρ_t depends on the polarity deference between the solute and the cosolvent, the steric factors between the solute and the complexing ligand. Note that K_t^{app} approaches K_t^{int} as the cosolvent concentration approaches zero. The concentration of the ternary complex can be expressed by inserting eqs 2 and 7 into eq 6. This gives:

$$[DLC] = K_t^{int} \times 10^{-\rho_t[C]}[D_u] \times 10^{\sigma[C]}[L][C] = [D_u][L][C]K_t^{int} \times 10^{(\sigma - \rho_t)[C]} \quad (8)$$

which indicates that [DLC] has a linear dependency upon the ligand concentration and a complex dependency upon the cosolvent concentration. If $\sigma > \rho_t$, an increase in [C] will produce an increase in [DLC]. If $\sigma < \rho_t$, an increase in [C] will increase [DLC] only when $[C] > 10^{(\sigma - \rho_t)[C]}$; when $[C] < 10^{(\sigma - \rho_t)[C]}$, an increase in [C] will decrease [DLC]. If $\alpha = \rho_t$, an increase in [C] will increase [DLC] linearly.

Total Solubility—In the presence of both cosolvent and complexant the drug's total solubility is determined by the summation of three solution components: free drug [D], drug–ligand binary complex [DL], and drug–ligand–cosolvent ternary complex [DLC]. Inserting eqs 2, 5, and 8 into eq 1 gives:

$$[D^{tot}] = [D_u] \times 10^{\sigma[C]} + [D_u]K_b^{int} \times 10^{(\sigma - \rho_b)[C]}[L] + [D_u]K_t^{int} \times 10^{(\sigma - \rho_t)[C]}[L][C] \quad (9)$$

where the total solubility is related to the parameters: [D_u], K_b^{int}, K_t^{int}, σ, ρ_b, and ρ_t, which have been described in the preceding sections. In the following sections, the combined effect of cosolvent and complexation on drug solubilization described by eq 9 is confirmed by solubilization of a very nonpolar compound, Fluasterone, in a water–EtOH–HPβCD system.

Methods

Solubility Determination—Fluasterone was added to vials containing certain percentages of both hydroxy propyl-β-cyclodextrin (HPβCD) and ethanol (EtOH). HPβCD concentration ranges from 0 to 20% and ethanol concentration ranges from 0 to 75% were investigated. The sample vials were rotated using an end-over-end mechanical rotator at 20 rpm (Glas-Col Laboratory Rotator, Terre Haute, IN) at 25 °C for 6 days (preliminary data indicate that Fluasterone is stable for 50 days under these conditions). Samples with drug crystals present were considered to have reached their equilibrium solubility and were removed from the rotator, passed through a 0.45-μm filter, and analyzed by HPLC. All samples were prepared in duplicate.

HPLC Analysis of Fluasterone—A Pinnacle octylamine column (150 cm × 4.6 mm, Restek, Bellefonte, PA) was used with a mobile phase composed of 75% acetonitrile in water. The flow rate was controlled at 1.1 mL/min (125 Solvent Module, Beckman,

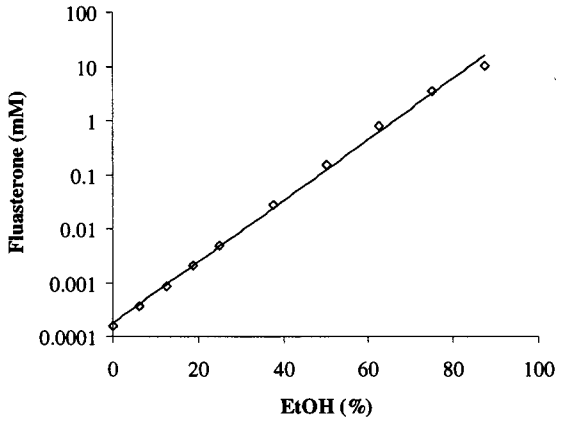

Figure 1—Fluasterone solubility as a function of EtOH concentrations.

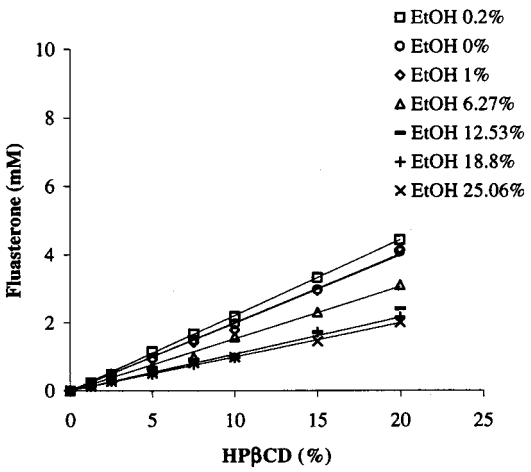

Figure 2—Solubility of Fluasterone as a function of HPβCD and EtOH concentrations.

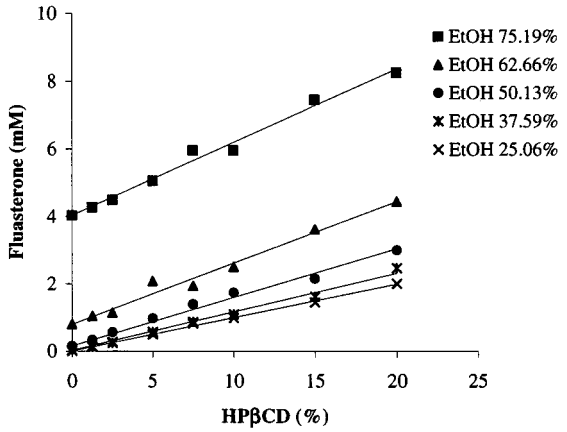

Figure 3—Solubility of Fluasterone as a function of HPβCD and EtOH concentrations.

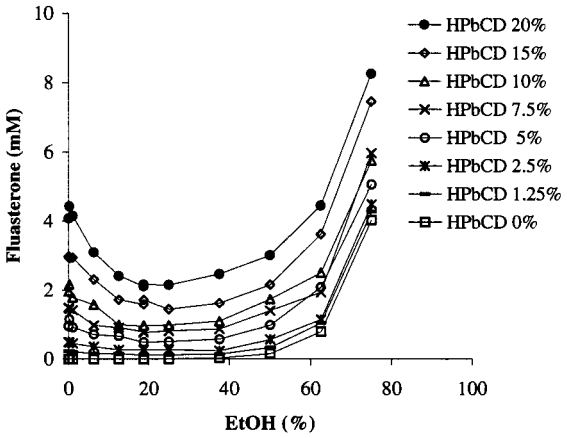

Figure 4—Solubility of Fluasterone as a function of EtOH concentration in different HPβCD concentrations.

Fullerton, CA). The column effluent was monitored at a wavelength of 220 nm (168 detector, Beckman, Fullerton, CA). The retention time of a 100 μL sample was 6.3 min. The evaluation of the assay was made by using Fluasterone standard solutions at concentrations ranging from 0.001 to 0.1 mg/mL, intraday and interday, coupled with different solubilizing agents. The relative standard deviation was 1.05%. None of the solubilizing agents interfere with the assay.

Results and Discussion

Solubilization by Ethanol Alone—The intrinsic solubility [D_u] of Fluasterone was determined to be 0.045 μg/mL (0.000155 mM). Figure 1 shows the dependency of the drug's total solubility [D^{tot}] upon ethanol concentration [C]. The exponential solubility increase is described by eq 2, with a cosolvent solubilizing power (σ) of 0.3401.

Solubilization by HPβCD Alone—The aqueous solubility of Fluasterone increases linearly with HPβCD concentration [L] up to 20% as shown by the open circles in Figure 2. Incorporating the slope into eq 3 indicates the formation of a 1:1 reversible drug−ligand complex with an intrinsic complexation constant (K_b^{int}) of 1.80×10^5 M^{-1}.

Solubilization by Combined Use of Ethanol and HPβCD—Figure 2 shows that at every HPβCD concentration investigated the Fluasterone solubility is slightly higher in the presence of 0.2% ethanol (open squares in Figure 2) than in pure water. An ethanol concentration of 0.2% is not enough to function as a cosolvent to affect drug complexation.[14−16,21] Nevertheless, it produces a consistent increase in drug solubility. This suggests that ethanol must increase Fluasterone solubility by some other mechanism, such as the formation of a complex that contains drug, ligand, and cosolvent. Equation 9 shows that the formation of a ternary complex would be responsible for the increased Fluasterone solubility in the HPβCD solutions containing 0.2% EtOH. Here, as in other studies,[15,16] it is assumed that the ternary species responsible for the increased drug solubility is a 1:1:1 complex. Extrapolation of K_t^{app} ($= K_t^{int} \times 10^{-\rho_t[C]}$) to zero cosolvent concentration by eq 9 gives a K_t^{int} of 1.42×10^4 M^{-1}.

The solubility of Fluasterone increases linearly with HPβCD concentration at all ethanol concentrations. It is interesting to note that the slope of the solubilization curve varies with ethanol concentrations [C]. The slope decreases when [C] increases from 0.2% to 25.06% as shown in Figure 2, but increases when [C] increases from 25.06% to 75.19% as shown in Figure 3. This can be seen more clearly from cross sections of the data of Figures 2 and 3 at equal HPβCD concentrations that are shown in Figure 4. The figure also indicates a minimum total drug concentration at about 25% ethanol. Nearly 60 total solubility [D^{tot}] data points from Figure 4 and known values of [D_u], σ, K_b, K_t, [L], and [C] were used to calculate ρ_b and ρ_t by means of nonlinear regression analysis. Their values were found to be 0.515 and 0.340, respectively. As the cosolvent concentration increases, the magnitude of ρ_b[C] and ρ_t[C] increases, resulting in a greater destabilizing power for both the binary and ternary complexes. This is because the increased cosolvent concentration reduces solvent polarity so that nonpolar molecules are more likely to stay out of the cyclodextrin cavity.

The concentration of binary drug−ligand complex [DL] is proportional to the product of the apparent complexation

Table 1—Estimation of Solubilization Parameters

parameter	symbol	value
intrinsic binary complexation constant	K_b^{int} (M^{-1})	1.80×10^5
intrinsic ternary complexation constant	K_t^{int} (M^{-1})	1.42×10^4
cosolvent solubilizing power	σ	3.40×10^{-1}
cosolvent destabilizing power on binary complex	ρ_b	5.15×10^{-1}
cosolvent destabilizing power on ternary complex	ρ_t	3.40×10^{-1}

constant and the concentration of the free drug, i.e., K_b^{app}-[D], which equals $[D_u]K_b^{int} \times 10^{(\sigma - \rho_b)[C]}$. An increase in the cosolvent concentration simultaneously produces an exponential increase in [D] ($= [D_u] \times 10^{\sigma[C]}$) and an exponential decrease in K_b^{app} ($= K_b^{int} \times 10^{-\rho_b[C]}$). As a result, [DL] is dependent upon the difference between the solubilizing power (σ) and the destabilizing power (ρ_b) of the cosolvent for [DL]. Since $\sigma = 0.340$ and $\rho_b = 0.515$, this difference is negative. An increase in [C] leads to an exponential decrease in [DL], and the concentration of the binary complex becomes negligible when [C] reaches 50%.

The concentration of the ternary complex depends on the cosolvent concentration [C] and the difference between the cosolvent solubilizing power (σ) and the cosolvent destabilizing power (ρ_t) for the ternary complex. Nonlinear regression analysis of the solubility data indicates that the difference between σ and ρ_t for Fluasterone is negligible (see Table 1). Consequently, the exponential term in eq 8 is constant and an increase in ethanol concentration produces a linear increase in the ternary complex concentration [DLC].

With the values of $[D_u]$, K_b^{int}, K_t^{int}, ρ_b, and ρ_t given in the table, we can calculate [D], [DL], [DLC], and $[D^{tot}]$ at any given combination of EtOH and HPβCD concentration by using eqs 2, 5, 8, and 9, respectively. Figure 5a shows the calculated values of [D], [DL], [DLC], and $[D^{tot}]$ at 20% HPβCD under different EtOH concentrations. Both the exponential increase and the exponential decrease can be seen more directly as straight lines on the semilogarithmic scale of Figure 5b. The figure also shows that the calculated $[D^{tot}]$ decreases initially and approaches a minimum where [C] is approximately at 25%. Such a decrease is due to the fact that the decrease in [DL] outweighs the increase in [D] and [DLC] resulting from the addition of ethanol. After 25%, $[D^{tot}]$ starts to increase due to the increase in both [D] and [DLC]. Note that [DLC] is greater than [DL] even though K_b^{int} is approximately 10-fold greater than K_t^{int}. This finding is consistent with testosterone studies[11] in which [DL] was diminished in a solution containing HPβCD and 60% ethanol. However, the solid produced by evaporating the aqueous solvent contained a small amount of ethanol. Since a 1:1:1 testosterone–HPβCD–ethanol complex would contain only 2.7% ethanol, this observation might be explained by the existence of the ternary complex [DLC], such as described above.

Validation of the Proposed Model—Calculated total drug solubilities (solid lines) using eq 9 are compared in Figure 6 with the experimental solubility data (symbols) at different concentrations of HPβCD. The strong agreement between the predicted and the observed solubility data supports the validity of the proposed model. Note that as the cyclodextrin concentration approaches zero, the total solubility approaches the log-linear relationship commonly observed in a simple cosolvent–water system.

Conclusion

An equation is developed to describe the combined effect of ethanol and HPβCD upon Fluasterone solubility. The equation is validated with respect to the intrinsic drug solubility, $[D_u]$, the cosolvent solubilizing power, σ, the binary and ternary intrinsic complexation constants, K_b^{int} and K_t^{int}, and the cosolvent destabilizing powers for the binary and the ternary complexes, ρ_b and ρ_t. This equation can be used to explain the linear dependence of nonpolar solute solubility upon cyclodextrin concentration that is observed at all ethanol concentrations. It also can be used to describe the decline in the solubility produced by low cosolvent concentrations as well as the increase in the solubility produced by high cosolvent concentrations that are observed at all cyclodextrin concentrations. Thus it provides a theoretical background for understanding the dynamics of the combined cosolvent–complexant technique in the solubilization of nonpolar drugs.

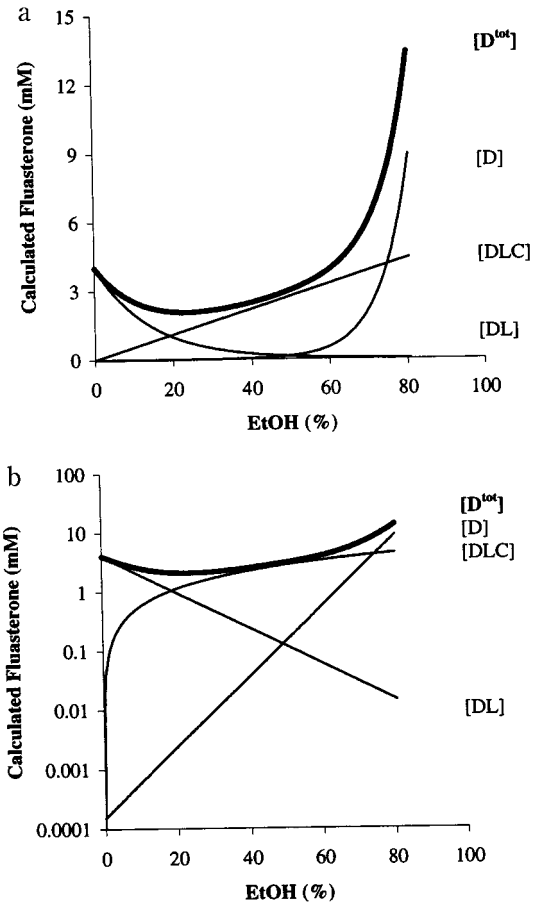

Figure 5—Calculated solubility in 20% HPβCD.

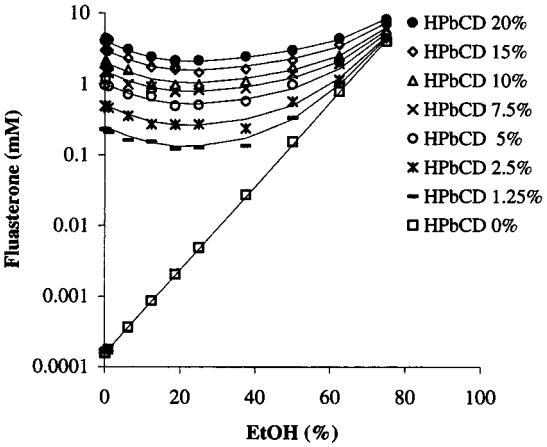

Figure 6—Calculated total drug solubilities (solid lines) versus the experimental solubility data (symbols) at different HPβCD concentrations.

References and Notes

1. Martin, A., et al. *Physical Pharmacy*, 4th ed.; Lea & Febiger: Philadelphia, PA, 1993.
2. Yalkowsky, S. H. *Solubility and Solubilization in Aqueous Media*; American Chemical Society: Washington, DC, 1999; in press.
3. Sweetana, S.; Akers, M. J. Solubility principles and practices for parenteral drug dosage form development. *PDA J. Pharm. Sci. Technol.* **1996**, *50*, 330−342.
4. Loftsson, T.; Brewster, M. Pharmaceutical applications of cyclodextrins. 1. solubilization and stabalization. *J. Pharm. Sci*. **1996**, *85*, 1017−1025.
5. Uekama, K. Pharmaceutical applications of cyclodextrin complexations. *Yukugaku Zusshi.* **1981**, *101*, 857−873.
6. Connors, K. A. The stability of cyclodextrin complex in solution. *Chem. Rev.* **1997**, 1325−1357.
7. Yalkowsky, S. H. et al. Formulation-related problems associated with intraveneous drug delivery. *J. Pharm. Sci.* **1998**, *87*, 787−795.
8. Rubino, J. T. Solubilization of some poorly soluble drugs by cosolvents. Ph.D. Dissertation, The University of Arizona, 1984.
9. Rajewski, R. A.; Stella, A. J. Pharmaceutical Applications of Cyclodextrins. 2. In Vivo Drug Delivery. *J. Pharm. Sci.* **1966**, *85*, 1142−1168.
10. Loftsson, T. et al. Cyclodextrin complexation of NSAIDs: physicochemical characteristics. *Eur. J. Pharm. Sci.* **1993**, *1*, 95−101.
11. Pitha, J.; Hoshino, T. Effect of ethanol on formation of inclusion complexes of hydroxypropylcyclodextrins with testosterone or with methyl orange. *Int. J. Pharm.* **1992**, *80*, 243−251.
12. Kelloff, G. J. et. al. New agents for cancer chemoprevention. *J. Cell. Biochem.* **1996**, *265*, 1−28.
13. Reer, O.; Muller, B. W. Investigation of the influence of cosolvents and surfactants on the complexation of dexamethasone with hydroxypropyl-β-cyclodextrin by use of a simplex lattice design. *Eur. J. Pharm. Biopharm.* **1993**, *39*, 105−111.
14. Zung, J. B. et al. Influence of alcohol addition on the γ-CD: pyrene complex. *J. Phys. Chem.* **1991**, *95*, 6701−6709.
15. Kano, K. et al. Fluorescence quenching of pyrene and naphthalene in aqueous cyclodextrin solutions. Evidence of three-component complex formation. *J. Phys. Chem.* **1982**, *86*, 1833−1838.
16. Hamai, S. Inclusion compounds in the systems of β-cyclodextrin-alcohol-pyrene in aqueous solution. *J. Phys. Chem.* **1989**, *93*, 2074−2078.
17. Li, A.; Yalkowsky, S. H. Solubility of organic solutes in ethanol/water mixtures. *J. Pharm. Sci.* **1994**, *83*, 1735−1740.
18. Harrison J. C.; Eftnk, M. R. Cyclodextrin-adamantanecarboxylate inclusion complexes: a model system for the hydrophobic effect. *Biopolymers* **1982**, *21*, 1153−1166.
19. Li, P.; Tabibi, S. E.; Yalkowsky, S. H. Combined effect of complexation and pH on solubilization. *J. Pharm. Sci.* **1998**, *87*, 1535−1537.
20. Tachibana, M.; Kiba, N. Correlation between inclusion formation constant and distribution coefficient in a liquid−liquid extraction sysytem consisting of hydrocarbon solvents and aqueous dimethyl sulfoxide solutions of β-cyclodextrin. *Analyst* **1997**, *122*, 903−909.
21. Munoz de la Pena et al. Alcohol size as a factor in the ternary complexes formed with pyrene and β-cyclodextrin. *J. Am. Chem. Soc.* **1991**, *113*, 1572−1578.

JS990159D

Optimization of Folate-Conjugated Liposomal Vectors for Folate Receptor-Mediated Gene Therapy

JOSEPH A. REDDY,[†] DAVID DEAN,[‡] MICHAEL D. KENNEDY,[†] AND PHILIP S. LOW*,[†]

Contribution from *Department of Chemistry, 1393 Brown Building, Purdue University, West Lafayette, Indiana 47907-1393 and Department of Microbiology and Immunology, College of Medicine, Medical Sciences Building, University of South Alabama, Mobile, Alabama 36688.*

Received May 29, 1999. Accepted for publication August 23, 1999.

Abstract □ A folate-targeted transfection complex that is internalized by certain cancer cells and displays several properties reminiscent of enveloped viruses has been developed. These liposomal vectors are comprised of a polycation-condensed DNA plasmid associated with a mixture of neutral and anionic lipids supplemented with folate–poly(ethylene glycol)–dioleylphosphatidylethanolamine for tumor cell-specific targeting. *N*-Citraconyl-dioleylphosphatidylethanolamine is also included for pH-dependent release of endosome-entrapped DNA into the cytoplasm, and a novel plasmid containing a 366-bp segment from SV40 DNA has been employed to facilitate transport of the plasmid into the nucleus. Because formation of the DNA core is an important step in the assembly of liposomal vectors, considerable effort was devoted to comparing the transfection efficiencies of various DNA condensing agents. It was found that complexation of plasmid DNA with high molecular weight polymers such as acylated-polylysine and cationic dendrimers leads to higher folate-mediated transfection efficiency than DNA complexed with unmodified polylysine. In contrast, compaction of plasmid DNA with small cationic molecules such as spermine, spermidine, or gramicidin S yields only weakly active folate-targeted liposomal vectors. Compared to analogous liposomal vector preparations lacking an optimally compacted DNA core, a cell-specific targeting ligand, a caged fusogenic lipid, and a nucleotide sequence that facilitates nuclear uptake, these modified liposomal vectors display greatly improved transfection efficiencies and target cell specificity.

Introduction

Gene therapy constitutes an attractive strategy for the treatment of a variety of human genetic disorders.[1−5] Although viral gene therapy can report the greatest successes in animal and human trials to date,[6−10] liposomal vectors have stimulated increased attention due to their low immunogenicity, lack of potential infectivity, and ease of assembly from chemically defined components.[11] Unfortunately, liposomal vectors also suffer from their own set of disadvantages, including generally low efficiencies of transfection and elevated toxicities toward normal cells.[9,12] Work on liposomal vectors has consequently focused on developing formulations that improve transfection efficiency without compromising host cell viability.[13,14]

One reasonable approach for addressing the deficiencies of liposomal vectors has been to identify the features of viral vectors that render them efficient vehicles for gene transfer and then mimic these features in synthetic liposomal constructs. Based on information available to date, the desirable characteristics of the more promising viral vectors would seem to include (i) their ability to efficiently compact and package the genetic material, (ii) their expression of a surface-exposed ligand for stable attachment and endocytosis/delivery of the condensed DNA into the target cell, (iii) their means of releasing their nucleic acid from the endosome into the target cell's cytoplasm, and (iv) their mechanisms for enhancing transport of their genome into the host cell's nucleus. It can be speculated that future liposomal gene therapy vectors will incorporate components that mimic many of these desirable viral functions. Indeed, some progress has already been made toward achievement of these objectives.[2,14−20]

Probably the greatest advance in optimizing liposomal vectors has stemmed from development of cationic liposomes that not only promote DNA compaction and avid cell association, but also enhance delivery of the genetic cargo into the cell's cytoplasm.[21−24] Associated with these desirable features, however, is a significant loss of cell-specific targetability, since strongly cationic complexes indiscriminately bind most cell surfaces and thereby render any ligand-specific interactions largely meaningless. While such generic cell surface affinity can be prevented by eliminating excess cationic charge, the resulting neutral DNA−lipid particles are generally poorly fusogenic, even when delivered into target cells by receptor-mediated endocytosis. Clearly, modification of cationic liposomes for cell specific targeting involves more than simple attachment of a high affinity ligand to the liposome surface.

Our laboratory has been interested in the use of folic acid as a targeting ligand to deliver attached therapeutic and imaging agents to cancer cells that overexpress the receptor for folic acid.[25−31] Because folate-linked cargo's of diameters <150 nm are efficiently bound and internalized by folate receptor (FR)-expressing cells, it seemed reasonable to explore the possibility of using folic acid to facilitate liposomal vector delivery to FR-enriched cells. In this paper we describe our efforts at integrating several desirable features of viral vectors into folate-targeted liposomal vectors. While several excellent publications describing the use of folic acid to deliver genes into cancer cells have already appeared,[29,32−34] a more comprehensive attempt to optimize components that might mimic desirable viral characteristics has not been reported.

Materials and Methods

Materials—All commercially available lipids were purchased from Avanti Polar lipids (Alabaster, AL). Citraconic anhydride, 2,6-lutidine, folic acid, poly-L-lysine hydrobromide (MW ∼ 25.6 kDa), myristoyl chloride, palmitic acid *N*-hydroxysuccinimidyl ester (NHS), oleic acid-NHS, and gramicidin S were purchased from Sigma Chemical Co. (St. Louis, MO). Spermine, spermidine, and chitosan (medium MW, 200−800 cps) were from Aldrich (Milwaukee, WI). Cationic dendrimers were obtained from Dendritech Inc. (Midland, MI) and Aldrich (St. Louis, MO). [^{3}H]-

* To whom correspondence should be addressed. E-mail: lowps@omni.cc.purdue.edu. Phone: (765) 494-5273. Fax: (765) 494-0239.
[†] Purdue University.
[‡] University of South Alabama.

10.1021/js990169e CCC: $18.00 *Published on Web 09/30/1999*

Cholesteryl hexadecyl ester and $Na^{125}I$ were purchased from DuPont. Folate deficient modified Eagle's medium (FDMEM) and other additives were purchased from Life Technologies, Inc. and fetal calf serum was from HyClone Labs (Logan, UT). β-galactosidase assay kits were purchased from Promega (Madison, WI). BCA protein assay reagents were from Pierce (Rockford, IL).

Plasmid Preparation—A 366 bp HindIII−KpnI fragment of SV40 DNA containing the origin and promoter region (SV40 nts 5171 to 294) was amplified by polymerase chain reaction and cloned into the TA cloning vector (Invitrogen, San Diego CA) to create plasmid pTA-DTS. Subsequently, a 384 bp HindIII−SalI fragment was isolated from pTA-DTS and inserted into the corresponding sites of pCMVβgal (Clontech, Palo Alto, CA), downstream of the lacZ gene. Protein-free preparations of plasmids pCMVlacZ and pDTSlacZ were purified following alkaline lysis using Qiagen megaprep columns.

Synthesis of Fatty Acylated Polylysine—Acylated polylysine was synthesized by reaction of polylysine (M_r ~25 700) with activated fatty acids at a fatty acid/lysine ratio of 1:5. Myristoyl chloride, palmitic acid-NHS, or oleic acid-NHS (0.077 mmol) in 1 mL of dry DMF was added to 15 mg of polylysine in 500 μL of dry DMSO, and the mixture was allowed to react for 24 h at room temperature. The solution was then added to a large excess of diethyl ether to precipitate the derivatized polylysine,[35] and the polymer was purified by dialysis against deionized water. The resulting polymer was quantified by trypan blue assay[36] using unmodified polylysine as the standard.

Preparation of Liposome Formulations—*N*-Citraconyl-dioleylphosphatidylethanolamine (C-DOPE) is a caged form of dioleylphosphatidylethanolamine (DOPE) that resists hexagonal phase formation and consequent liposome fusion until the citraconyl moiety is released by acidification at pHs < 6.[37,38] Assuming such low pHs are only experienced following endocytosis by target cells, incorporation of C-DOPE into liposomal vectors should allow acquisition of fusogenic properties only following uptake by transfected cells.

C-DOPE was synthesized by reacting DOPE with citraconic anhydride, and the resulting caged fusogenic lipid was purified as described earlier.[37,38] Liposomes were prepared by mixing chloroform solutions of DOPE, cholesterol, C-DOPE, and folate−poly(ethylene glycol)−dioleylphosphatidylethanolamine (FA-PEG-DOPE, a derivative of dioleylphosphatidylethanolamine linked covalently to folic acid via a poly(ethylene glycol) spacer[28]) or poly-(ethylene glycol)−dioleylphosphatidylethanolamine (PEG-DOPE, the nontargeted control for FA-PEG-DOPE) followed by removal of the chloroform under vacuum to produce a dry lipid film. Hydration of the lipid was then achieved by addition of 1.0 mL of sterile 20 mM HEPES buffer, pH 8.0, followed by vortexing for 1 min and bath sonication to obtain a clear emulsion. The total lipid content in these liposome formulations was ~5 mg/mL.

Preparation of Transfection Competent Complexes—Polylysine, acylated-polylysine, dendrimers, gramicidin S (stock solutions of 10 mg/mL in dimethyl sulfoxide), spermine, spermidine, and chitosan (stock solutions of 10 mg/mL in aqueous 1% acetic acid solution) were diluted to 1 mg/mL in sterile deionized water and stored at 4 °C until use. Polycation−DNA complexes were then generated by vortexing equal volumes (100 μL) of the appropriate polycation solution with 40 μg/mL pCMVlacZ plasmid DNA in serum free medium for 1 min, followed by incubation at room temperature for at least 15 min. Ratios of nucleic acid to polycation charge were estimated from the electrostatic charge present on each component.[32,39−43] The resulting polycation−DNA complexes (200 μL) were then combined with 200 μL of 0.24 mg/mL liposomes suspended in serum free medium by gentle vortexing. The hydrodynamic diameter of the complex was determined by dynamic light scattering (Coulter N4plus Submicron Particle Sizer, Miami, FL).

Cell Culture and Transfection of Cells with Liposomal Vectors—KB cells, a human nasopharyngeal cancer cell that expresses elevated levels of folate receptor were cultured in folate deficient Dulbecco's modified Eagles medium (FDMEM) containing 10% heat-inactivated fetal calf serum (FCS), penicillin (50 units/ml), streptomycin (50 μg/mL), 2 mM L-glutamine, and nonessential amino acids at 37 °C in a 5% CO_2 humidified atmosphere. In a typical experiment, cells were seeded 48 h before transfection in 24-well plates at 15% to 20% confluence. Immediately prior to transfection, the cells were washed with 0.5 mL of serum free FDMEM and then incubated for 4h at 37 °C with DNA/liposome complexes in 400 μL of serum free FDMEM. After incubation, the medium containing any free DNA/liposome complexes was replaced with vector-free medium (FDMEM) containing 10% fetal calf serum. Thirty-six hours after transfection, cells were analyzed for β-galactosidase expression, as described by others.[44]

Evaluation of Liposome Complexation with Condensed DNA—Plasmid DNA was labeled with ^{125}I using the published method of Prensky.[45] Labeled DNA was then separated from free iodine by gel filtration chromatography on a Sephadex G-25 column in 50 mM HEPES (pH 8.0) buffer. A discontinuous sucrose gradient containing layers of 3 mL, 5 mL, and 5 mL of 0%, 20%, and 40% sucrose dissolved in deionized water, respectively, was then constructed. Samples comprised of ^{125}I-labeled DNA/polycation complexes and/or ^{3}H-labeled anionic liposomes were layered on top of the gradient and centrifuged at 24 000 rpm (100 000*g*) in a Beckmann SW28 ultracentrifuge rotor for 45 min. One milliliter fractions were collected sequentially from the top to the bottom of the gradient and analyzed for lipid and DNA content by scintillation and gamma counting, respectively.

Results

In agreement with observations of others,[46−48] we have found that cationic lipid formulations cannot be readily targeted to receptor-bearing cells using cell-specific ligands such as folic acid (data not shown). We, therefore, undertook to integrate features into neutral liposomes that might facilitate uptake and delivery of encapsulated DNA into the nucleus. From previous studies, it was noted that C-DOPE, a caged form of DOPE that converts to the natural fusogenic lipid (i.e., DOPE) upon exposure to acidic pH, could enable pH-dependent release of encapsulated DNA from endosomal compartments.[38] However, because these earlier lipid formulations contained large amounts of unmodified DOPE, they were found to be unstable during storage and hence not viable for eventual clinical applications. Although addition of 40% cholesterol was observed to render these formulations stable for at least a month, the added sterol was simultaneously found to compromise the fusogenicity of the lipid complexes. We, therefore, undertook to reevaluate various lipid formulations for a combination that might be both stable and targetable, yet capable of facilitating efficient transfection of FR-expressing cells. We have used 0.1 mol % FA-PEG-DOPE as the targeting ligand in all such formulations, because we have previously found that this percentage was optimal for targeting vectors to cells expressing folate receptors and since cells lacking such receptors are not detectably transfected by such formulations.[38] Figure 1 shows that lipid envelopes of the composition DOPE/C-DOPE/cholesterol/FA-PEG-DOPE (45.9:10:40:0.1 mol %) are highly efficient in transfecting KB cells with a polylysine-compacted pCMVβgal vector. Importantly, when the FA-PEG-DOPE liposomes are replaced with nontargeted liposomes (FA-PEG-DOPE replaced with PEG-DOPE), the β-galactosidase expression decreases to background levels, indicating the above formulation facilitates ligand selective cell association. Further, when DOPS is substituted for C-DOPE in the targeted formulations, no transfection is observed, demonstrating that the caged lipid's pH dependent fusogenicity rather than its negative charge enables gene expression. Finally, when the optimal formulation is compared with unstable liposomes of the composition DOPE/C-DOPE/FA-PEG-DOPE (97:3:0.1 mol %), the cholesterol-stabilized liposomes are seen to exhibit only 15 to 20% lower transfection activity (data not shown). Since the nonstabilized formulations lose all transfection activity during 3 days of storage, formulations containing 40% cholesterol were employed in all remaining experiments.

Inclusion of C-DOPE in the lipid mixture was found to benefit the vector formulation by a second mechanism.

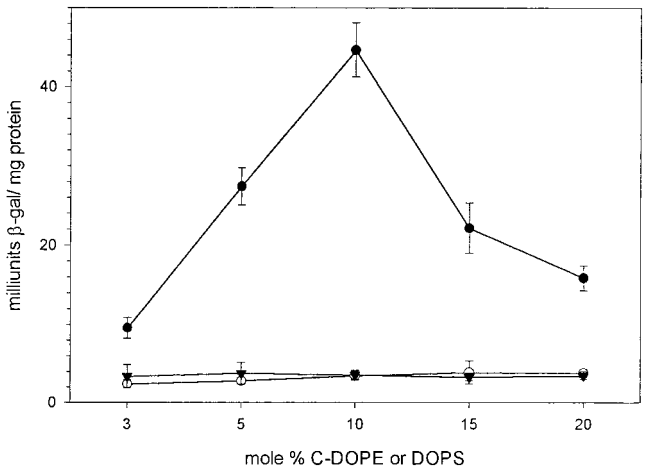

Figure 1—Optimization of C-DOPE content for maximum transfection activity. Liposomal vectors were prepared by mixing pCMVlacZ:polylysine (1:0.75 w/w) complexes with liposomes consisting of 40% cholesterol, 0.1% FA-PEG-DOPE (●,▼) or PEG-DOPE (○), plus the indicated mole % of C-DOPE (●,○) or DOPS (▼). DOPE was then added to raise the lipid total to 100%. Folate receptor bearing KB cells were transfected as described in the Methods section. Assay results are expressed as milliunits of β-galactosidase per mg cell protein. Data are presented as means ± SD where $n = 6$ from two independent experiments. Mean values were compared using one-way analysis of variance (ANOVA) followed by the Student–Newman–Keuls Multiple Comparisons Test (Sigmastat). Significance was set at $p < 0.05$. *P* values for comparison of βgal expression with FA-PEG-DOPE liposomes containing the indicated mole % of C-DOPE are 3% versus 5% < 0.001, 5% versus 10% < 0.001, 10% versus 15% = 0.003 and for 15% versus 20% = 0.002.

Because of its double negative charge at neutral pH, C-DOPE incorporation endowed the derived liposome with a strongly anionic character. Thus, upon mixing with cationic DNA/polycation complexes, a particle spontaneously formed that had a neutral to slightly negative charge (data not shown). In contrast to positively charged particles, this neutral to slightly anionic particle could be readily targeted by attachment of a cell-specific ligand (i.e. folic acid). Thus, the C-DOPE assisted in vector assembly, vector targeting, and pH-dependent vector release into the target cell's cytoplasm.

Since physical characteristics of liposomal vectors can make an important contribution to the transfection efficacy, we measured the sizes of the DNA/polylysine/liposome complexes. All vectors tested were found to have diameters of 170 ± 40 nM, and no statistical variance between the many preparations of control and C-DOPE vectors was detected. We also did not notice any trend in the size of the vectors as C-DOPE content was varied. This is probably because the primary step of DNA condensation is always performed with the same amount of polylysine, and the added C-DOPE containing liposomes simply conform to the size of this particle. Hence, we conclude that a variation in size is not the basis for the differences in transfection efficiency observed at different C-DOPE concentrations.

Effect of Incorporating a DNA Targeting Sequence into the Plasmid—Since most vectors employed for eukaryotic gene therapy must enter the nucleus to function, we next explored whether facilitated nuclear import of the plasmid DNA would enhance the efficiency of gene expression. For this purpose, a novel plasmid (pDTSβgal) was constructed (Figure 2), which is identical to the commercial plasmid (pCMVβgal) except for insertion of a 366 bp SV40 nuclear targeting sequence downstream of the *lacZ* gene and polyadenylation signal. To evaluate the possible contribution of this nuclear targeting sequence, pDTSβgal was compared with the parent pCMVβgal for expression of β-galactosidase in transfected cells. Figure 3 shows that a 1.5−2-fold increase in β-galactosidase activity was measured when pDTSβgal plasmid was substituted for pCMV-βgal in each of the three formulations tested. This nuclear-directed plasmid was therefore employed in the remainder of the studies reported here.

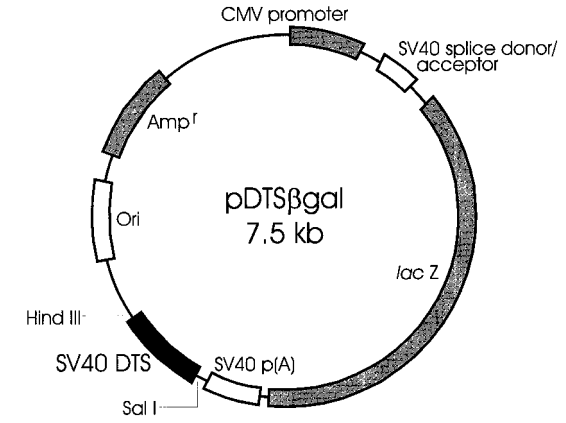

Figure 2—Map of pDTSβgal plasmid. A 384 bp HindIII–SalI fragment (SV40DTS) containing the origin and promoter region (SV40 nts 5171 to 294) from SV40 DNA was inserted into the corresponding sites of pCMVβgal, downstream of the lacZ gene, to facilitate plasmid entry into the nucleus. A cytomegalovirus immediate early gene promoter/enhancer was employed to drive expression of the reporter gene, β-galactosidase (lac Z). SV40 p(A), SV40 polyadenylation signal; Amp^r, β-lactamase gene.

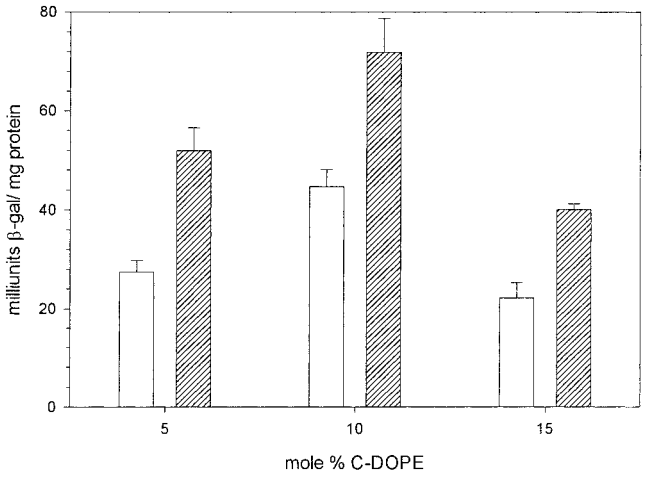

Figure 3—Effect on transfection efficiency of inserting a 366 bp SV40 nuclear targeting sequence into the pCMVlacZ plasmid. Transfection particles were prepared by mixing 4 μg of control plasmid, pCMVβgal (open bar) or 4 μg of plasmid containing a nuclear targeting sequence, pDTSβgal (slashed bar) with 3 μg polylysine, and then incubating the derived complexes with liposomes consisting of 40% cholesterol, 0.1 mol % FA-PEG-DOPE plus the indicated mole % of C-DOPE. Unmodified DOPE was added to bring the total lipid content to 100%. Transfection of KB cells was then assayed as described in the Methods section. Data are expressed as means ± SD where $n = 6$. *P* values comparing βgal expression with pCMVβgal and pDTSβgal are < 0.001 in all three cases.

Identification of Optimal DNA Compacting Polymers—Although a variety of cationic polymers have been exploited as DNA condensing agents, the resulting complexes are thought to differ in degree of compaction, compatibility with different lipid formulations, resistance to cellular nucleases, and extent of DNA unloading following entry into a cell's interior. Since ligand-mediated endocytic pathways might differ considerably from cationic lipid-promoted uptake pathways, it seemed advisable to reevaluate various DNA compaction methods for use with ligand-targeted liposomal vectors.

A panel of polycations including spermine, spermidine, gramicidin S, polyamidoamine dendrimer, polylysine, and chitosan were therefore examined for their abilities to

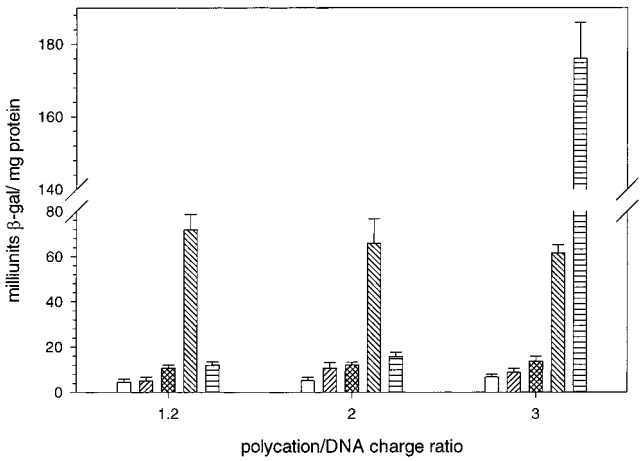

Figure 4—Effect of various oligo- and polycations on the transfection ability of folate-targeted liposomes. Polycation/DNA complexes at the indicated charge ratios were prepared by mixing pDTSlacZ with spermine (open bar), spermidine (left slashed bar), gramicidin S (double slashed bar), polylysine (right slashed bar), or 68 Å polyamidoamine cationic dendrimers (horizontal slashed bar). FA-PEG-liposomes were then prepared and transfection efficiencies compared, as described in the Methods section. The lipid composition of the complexes was 10 mol % C-DOPE, 49.9 mol % DOPE, 40% cholesterol, 0.1 mol % FA-PEG-DOPE. The polycation/DNA charge ratio refers to the charge ratio of the complex before addition of the anionic liposomes. Data are expressed as means ± SD where $n = 6$.

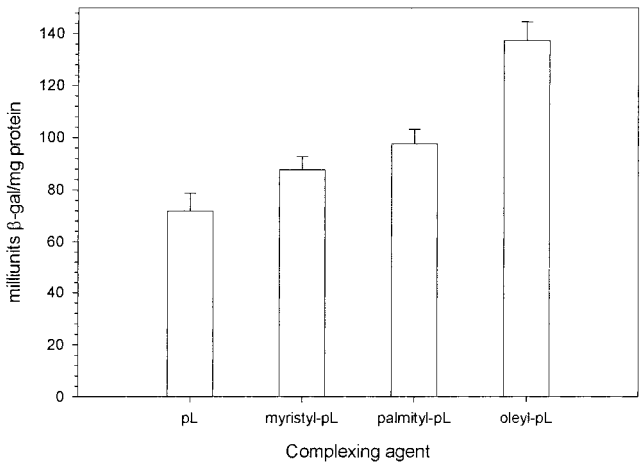

Figure 5—Effect of polylysine acylation on transfection efficiency. pDTSlacZ plasmid was mixed with polylysine (pL) or polylysine derivatized with the indicated acyl chains (see Methods) at a ± charge ratio of 1.2/1. The resulting complexes were then incubated with FA-PEG-liposomes and tested for transfection efficiency on KB cells. The lipid composition of the FA-PEG-liposomes was 10 mol % C-DOPE, 49.9 mol % DOPE, 40 mol % cholesterol, 0.1 mol % FA-PEG-DOPE. Data are expressed as means ± SD where $n = 3$. *P* values for comparison of βgal containing the indicated type of polylysine are pL versus myristyl-pL = 0.032, myristyl-pL versus palmityl-pL = 0.086 and for palmityl-pL versus oleyl-pL = 0.002.

facilitate folate-targeted gene expression. Charge ratios (±) of 1.2/1, 2/1, and 3/1 were chosen so that upon further complexation with anionic lipid mixtures the vectors would remain anionic, neutral, or even slightly cationic to ensure low levels of nontargeted gene transfection. As seen in Figure 4, only the high molecular weight polylysine and polyamidoamine dendritic polymers were highly active. Oligocations such as spermine, spermidine, and gramicidin S, in contrast, yielded low transfection efficiencies at the charge ratios tested. It was also noted that transfections with chitosan-condensed DNA (data not shown) resulted in high mortality, eliminating this complex from further consideration. However, the near absence of toxicity of the polylysine and dendritic polymers qualified them for further exploration, as described below.

Further Examination of Polylysine-Derived DNA Condensing Agents—Encouraged by the potential displayed by polylysine, and motivated by a recent report that partially acylated isoforms of the polycation might enable still better transfection efficiencies,[35] we undertook to compare various acylated polylysines in our folate-targeted KB cell transfection assay. Acylated polylysines were synthesized by N-alkylation of polylysine at a fatty acid-to-lysine ratio of 1:5 under anhydrous coupling conditions. Following purification[35] and determination of residual charge,[36] pDTSβgal plasmid DNA was successively complexed with acylated-polylysine and then DOPE/C-DOPE/cholesterol/FA-PEG-DOPE (45.9:10:40:0.1 mol %) liposomes. As shown in Figure 5, folate-targeted vectors with acylated polylysines showed higher transfection activities (~1.3 to 2-fold) than vectors with nonacylated polylysine. Furthermore, oleic acid-derivatized polylysine displayed higher transfection efficiency than either palmitic acid- or myristic acid-conjugated polylysine.

Optimization of Dendrimer/DNA Complexes for Transfection—To determine the optimal charge ratio of dendrimer/DNA complexes for ligand-targeted gene therapy, KB cells were transfected with dendrimer-compacted DNA (generation 6; 68 Å diameter) complexed with either FA-PEG-DOPE- or PEG-DOPE-containing liposomes. β-Galactosidase expression was then measured as a function of dendrimer/DNA charge ratio, which ranged from 1.2:1 to

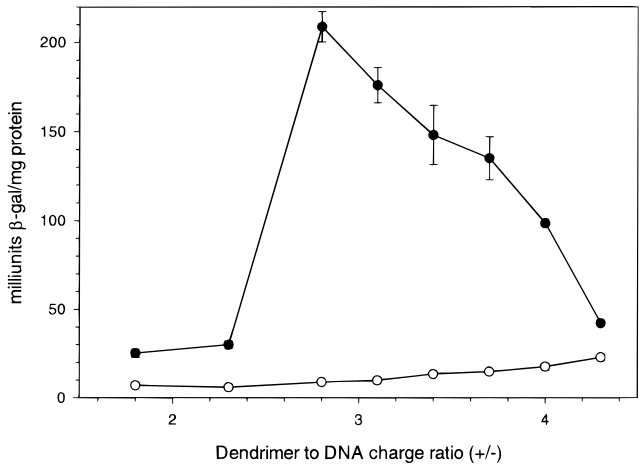

Figure 6—Effect of dendrimer/DNA charge ratio on folate-targeted liposomal vector transfection of KB cells. Complexes were prepared by mixing dendrimer/pDTSlacZ complexes at increasing charge ratios with C-DOPE liposomes consisting of 10 mol % C-DOPE, 49.9 mol % DOPE, 40% cholesterol, and 0.1 mol % FA-PEG-DOPE (●) or PEG-DOPE (○). Transfection competency was then analyzed in KB cells, as described in the Methods. The dendrimer to DNA charge ratio refers to the charge ratio of the complex before addition of the anionic liposomes. Data are expressed as means ± SD where $n = 6$.

4.5:1. As seen in Figure 6, the maximum level of β-galactosidase expression was observed at a charge ratio of 2.8:1, while at none of the examined charge ratios were nontargeted liposomes effective agents for gene delivery. A charge ratio of 2.8:1 was, therefore, used in all further dendrimer-based studies.

The heterogeneous nature of most DNA−polycation complexes makes it difficult to determine which of the diversity of complexes in any suspension is most effective in mediating transfection.[49] In contrast, dendrimers with their uniform shapes and sizes allow quantitative analysis of the influence of vector size on the efficiency of gene transfer. As shown in Figure 7, an increase in transfection efficiency was observed with increasing dendrimer size from 40 to 68 Å, followed by a decrease in activity at 84 Å. Interestingly, expression of β-galactosidase with the optimum (68 Å) dendrimer complexes was 2.5- to 3-fold higher

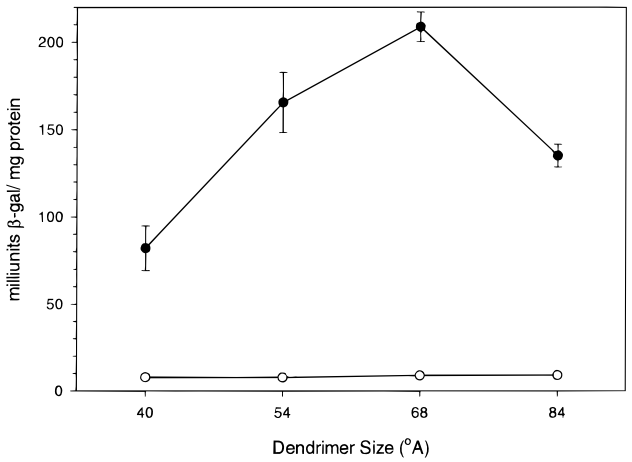

Figure 7—Influence of dendrimer size on gene transfer efficiency. pDTSlacZ plasmid vectors were formulated with dendrimers of the indicated sizes at the optimal dendrimer/DNA charge ratio of 2.8:1. The resulting complexes were then mixed with FA-PEG-liposomes (●) or PEG-liposomes (○) and tested for transfection efficiency on KB cells, as described in Figure 6. Data are expressed as means ± SD where $n = 3$.

than that seen with polylysine complexes (compare with Figure 3). As before, negligible levels of β-galactosidase expression were observed when FA-PEG-DOPE was replaced with equimolar PEG-DOPE in the lipid fraction of all dendrimer complexes tested.

Analysis of the Interaction of Polycation/DNA Complexes with Anionic Liposomes—With any ligand-targeted gene therapy formulation, it is important to determine the fraction of ligand-derivatized empty liposomes that might compete with DNA containing liposomes for cell surface receptors. For this purpose, oleyl-polylysine/DNA or cationic dendrimer (68 Å)/DNA complexes were prepared at their optimal DNA:polycation ratios, and the complexes were incubated with anionic liposomes comprised of DOPE/C-DOPE/cholesterol/FA-PEG-DOPE. The resulting folate-tethered liposomal vectors were then fractionated on a 0%/20%/40% discontinuous sucrose gradient and fractions were analyzed for their DNA and lipid contents. As noted in Figure 8 and elsewhere,[32,39] free DNA and free liposomes remained on top of the gradient, while unprotected polycation/DNA complexes migrated to the bottom (Figure 8A). In contrast, fully assembled polycation/DNA/liposome complexes were of intermediate density and sedimented as a broad band in the middle of the gradient (Figures 8B and 8C). Quantitative evaluation of the distribution of lipid and DNA radiolabels in these gradients revealed that the majority of the DNA complexes were associated with liposomes, and very few empty liposomes remained in the preparations to compete with the DNA-containing liposomes for folate receptors.

Discussion

We have shown that the transfection efficiency of folate-targeted, cholesterol-stabilized liposomal vectors can be significantly enhanced by (i) use of a pH-sensitive fusogenic lipid, (ii) incorporation of a nuclear localization sequence into the encapsulated plasmid, and (iii) selection of the optimal composition, size and charge density of the compacting polycation. Indeed, when compared to polylysine-compacted conventional plasmids, associated with folate-targeted, but pH-insensitive (lacking C-DOPE), liposomes, an increase in gene expression of more than 100-fold is observed. While further improvements in each of these features may be necessary before a clinically useful vector can be assembled, the above exploratory study constitutes

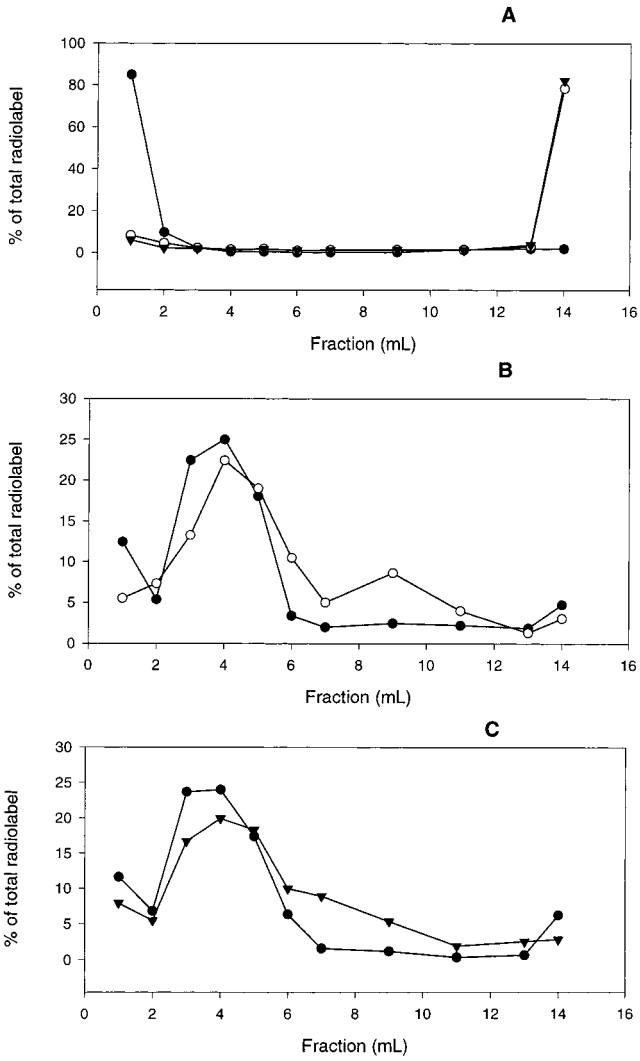

Figure 8—Analysis of polycation–DNA–liposome interactions using sucrose density gradient ultracentrifugation. (A) Oleyl-polylysine/DNA (○) or dendrimer/DNA (▼) complexes containing ^{125}I-labeled DNA (20 μg), and free liposomes containing ^{3}H-labeled lipids (240 μg) (●) were separately fractionated on a 0/20/40% (3/5/5 mL) discontinuous sucrose gradient at 100 000*g* for 45 min. One milliliter fractions were collected starting from the top of each gradient and counted for ^{125}I and ^{3}H radioactivity. After incubating the liposomes with either oleyl-polylysine/DNA (B) or dendrimer/DNA (C) particles, as described in the text, the assembled liposomal vectors were fractionated using the same gradient and counted for radioactivity. The oleyl-polylysine/DNA and the dendrimer/DNA complexes are seen to sediment to the bottom of the gradient, while the anionic liposomes and free DNA remain at the top. Mixed complexes sediment to an intermediate position in the gradient. Data are expressed as means ± SD where $n = 3$.

at least a first step toward development of a liposomal vector that mimics the desirable traits of many viral vectors.

One of the most critical limitations of standard neutral liposomal vectors appears to be their inability to dock with and enter mammalian cells.[50] Cationic liposomes obviously do not share this problem, but they are encumbered with their own set of limitations.[14] Although the advantages of ligand-mediated cell association and internalization were not emphasized in this report, it should be noted that the nontargeted vectors were generally 50 to 100-fold less effective than their folate-targeted counterparts. This differential would suggest that ligand-mediated cell association and uptake is a viral feature that should be mimicked in liposomal vectors whenever possible.

A second characteristic that contributes measurably to the usefulness of viral vectors involves their ability to

promote gene transfer across a target cell's plasma/endosomal membrane into the cell's cytoplasm. In the liposomal vector described here, this capability is accomplished in two steps. First, the cell's natural folate receptor-mediated endocytosis pathway is exploited to carry the therapeutic vector into the target cell's endosome, and then both the citriconylated and unmodified DOPE combine to facilitate escape of the DNA from the endosome into the cytoplasm. According to this strategy, the vector's full fusogenic potential is not realized until the citraconyl group of the C-DOPE is hydrolyzed at low pH. Because the required acidic conditions are not encountered prior to entry into endosomes, incorporation of C-DOPE limits vector unloading prior to intracellular uptake. With the optimized combination of C-DOPE and DOPE employed here, an increase in gene expression over vectors lacking C-DOPE of 40- to 70-fold was observed. Excess C-DOPE presumably reduced transfection efficiency, either because too much C-DOPE had to be hydrolyzed to enable fusion, or because the excess lipid assembled into folate-targeted but plasmid-free liposomes that competed with the plasmid-containing liposomes for cell surface receptors.

Probably the easiest viral trait to mimic in liposomal vector formulations lies in the ability of the viral genome to promote its own nuclear import. Because the DNA sequences involved in this process are located within the origin of replication and promoter regions, the likely mechanism for nuclear import involves binding of specific cellular proteins and their facilitation of genome transfer across the nuclear membrane.[51] While the enhancement accompanying inclusion of this viral sequence into our plasmid vector was only ~2-fold (Figure 3), the benefit to vectors targeted to less actively dividing cells could be considerably greater.[52] Thus, DNA transit across the nuclear membrane only becomes rate-limiting when the nuclear membrane remains intact over long intervals. In rapidly dividing cells such as those used in our study, this membrane is dismantled each time the cell enters M phase.

Viral capsids are able to condense their nucleic acids to a size that can be efficiently packaged and internalized by target cells. Synthetic polycations have been traditionally employed to achieve the same objective with liposomal vectors.[20,53] Indeed, for folate-targeted neutral liposomes, both polylysine and polyamidoamine dendrimers were judged to be acceptable mediators of DNA compaction (Figure 4). Further, when polylysine was partially derivatized with fatty acyl chains of varying length, an additional increase in transfection efficiency was observed. This enhancement in expression activity could conceivably be due to a decrease in electrostatic interaction between the acylated polylysine and DNA, thereby allowing the internalized plasmid to dissociate from the polylysine and enter the nucleus more easily.[35,54] Alternatively, the lipophilicity of the acylated polylysine could enhance association of the DNA/polylysine complex with the anionic liposomes or improve the stability of the folate-targeted vectors. We suggest that incorporation of acylated polycationic condensing agents warrants further examination in any quest for an optimal liposomal vector.

In contrast to the substituted and unmodified polylysines, simple oligocations such as spermine, spermidine, and the cyclic amphipathic peptide, gramicidin S, were only weakly active. Although spermine, spermidine,[40] and gramicidin S[41] are known to condense DNA and facilitate transfection, the spermine/DNA complexes are unfortunately not stable at physiological ionic strength.[39,55] This inherent instability may be responsible for the overall weak transfection activity of these targeted liposomal formulations.

The complex of plasmid DNA and cationic dendrimers was found to display the highest targeted gene expression activity of any formulation tested. Unlike the polycations of low molecular weight, cationic dendrimers have a higher surface charge density and are consequently capable of forming DNA complexes that are stable at a variety of pHs and salt concentrations.[56] With these dendrimers, transfection efficiency was found to depend on the number and size of dendrimers in each complex, with the highest expression obtained using the 68 Å dendrimer at a ± charge ratio prior to liposome addition of 2.8/1. Although stable DNA complexes could be formed at charge ratios greater than 5:1, these complexes were invariably ineffective, even though such vectors had been previously shown to be optimal in the absence of complexation with anionic lipid.[57] Why the more strongly charged complexes were less efficient in our hands is not clear, but an excess of noncomplexed dendrimer could have competed for association with the folate-linked anionic liposomes, thereby reducing the total number of dendrimer/DNA/liposome complexes capable of folate receptor binding on the cell surface.

Conclusions

Although neutral liposomal vectors generally exhibit lower transfection efficiencies than cationic liposomal vectors, they simultaneously display several advantages not shared by their cationic counterparts. Thus, vectors with low surface charge density can be readily targeted to specific cell types, commonly exhibit little or no nonspecific cytotoxicity,[20] and display reduced tendency to activate complement,[58] in contrast to most cationic liposomal vectors.[58] With the development of novel components/strategies to facilitate (i) DNA compaction, (ii) cell surface association and entry, (iii) endosome unloading, and (iv) intranuclear delivery, the prospects for improving the transfection efficiency of neutral liposomal vectors is increasingly bright.

References and Notes

1. Dachs, G. U.; Dougherty, G. J.; Stratford, I. J.; Chaplin, D. J. Targeting gene therapy to cancer: a review. *Oncol. Res.* **1997**, *9*, 313−325.
2. Cristiano, R. J. Targeted, nonviral gene delivery for cancer gene therapy. *Front. Biosci.* **1998**, *3*, D1161−1170.
3. Feldman, L. J.; Tahlil, O.; Steg, G. Perspectives of arterial gene therapy for the prevention of restenosis. *Cardiovasc. Res.* **1996**, *30* (2), 194−207.
4. Colledge, W. H.; Evans, M. J. Cystic fibrosis gene therapy. *Br. Med. Bull.* **1995**, *51*, 82−90.
5. Spear, M. A.; Herrlinger, U.; Rainov, N.; Pechan, P.; Weissleder, R.; Breakefield, X. O. Targeting gene therapy vectors to CNS malignancies. *J. Neurovirol.* **1998**, *4*, 133−147.
6. Ranga, U.; Woffendin, C.; Verma, S.; Xu, L.; June, C. H.; Bishop, D. K.; Nabel, G. J. Enhanced T cell engraftment after retroviral delivery of an antiviral gene in HIV-infected individuals. *Proc. Natl. Acad. Sci. U.S.A.* **1998**, *95*, 1201−1206.
7. Ragot, T.; Opolon, P.; Perricaudet, M. Adenoviral gene delivery. *Methods Cell Biol.* **1997**, *52*, 229−260.
8. Descamps, V.; Duffour, M. T.; Mathieu, M. C.; Fernandez, N.; Cordier, L.; Abina, M. A.; Kremer, E.; Perricaudet, M.; Haddada, H. Strategies for cancer gene therapy using adenoviral vectors. *J. Mol. Med.* **1996**, *74*, 183−189.
9. Robbins, P. D.; Ghivizzani, S. C. Viral vectors for gene therapy. *Pharmacol. Ther.* **1998**, *80*, 35−47.
10. Medin, J. A.; Karlsson, S. Viral vectors for gene therapy of hematopoietic cells. *Immunotechnology* **1997**, *3*, 3−19.
11. Felgner, P. L.; Rhodes, G. Gene therapeutics. *Nature* **1991**, *349*, 351−352.
12. Campain, J. A.; Matassa, A. A.; Felgner, P. L.; Barnhart, K. M.; Curiel, D. T.; Harrison, G. S. Lipid- and adenoviral-mediated gene transfer into AIDS−Kaposi's sarcoma cell lines. *Cancer Gene Ther.* **1998**, *5*, 131−143.
13. Mahato, R. I.; Takakura, Y.; Hashida, M. Nonviral vectors for in vivo gene delivery: physicochemical and pharmacokinetic considerations. *Crit. Rev. Ther. Drug Carrier Syst.* **1997**, *14*, 133−172.

14. Lee, R. J.; Huang, L. Lipidic vector systems for gene transfer. *Crit. Rev. Ther. Drug Carrier Syst.* **1997**, *14*, 173−206.
15. Vile, R. G.; Sunassee, K.; Diaz, R. M. Strategies for achieving multiple layers of selectivity in gene therapy. *Mol. Med. Today* **1998**, *4*, 84−92.
16. Michael, S. I.; Curiel, D. T. Strategies to achieve targeted gene delivery via the receptor-mediated endocytosis pathway. *Gene Ther.* **1994**, *1*, 223−232.
17. Uherek, C.; Fominaya, J.; Wels, W. A modular DNA carrier protein based on the structure of diphtheria toxin mediates target cell-specific gene delivery. *J. Biol. Chem.* **1998**, *273*, 8835−8841.
18. Abe, A.; Miyanohara, A.; Friedmann, T. Enhanced gene transfer with fusogenic liposomes containing vesicular stomatitis virus G glycoprotein. *J. Virol.* **1998**, *72*, 6159−6163.
19. Mahato, R. I.; Rolland, A.; Tomlinson, E. Cationic lipid-based gene delivery systems: pharmaceutical perspectives. *Pharm. Res.* **1997**, *14*, 853−859.
20. Remy, J. S.; Kichler, A.; Mordvinov, V.; Schuber, F.; Behr, J. P. Targeted gene transfer into hepatoma cells with lipopolyamine-condensed DNA particles presenting galactose ligands: a stage toward artificial viruses. *Proc. Natl. Acad. Sci. U.S.A.* **1995**, *92*, 1744−1748.
21. Bloomfield, V. A. DNA condensation. *Curr. Opin. Struct. Biol.* **1996**, *6*, 334−341.
22. Farhood, H.; Gao, X.; Son, K.; Yang, Y. Y.; Lazo, J. S.; Huang, L.; Barsoum, J.; Bottega, R.; Epand, R. M. Cationic liposomes for direct gene transfer in therapy of cancer and other diseases. *Ann. N. Y. Acad. Sci.* **1994**, *716*, 23−34.
23. Felgner, P. L.; Tsai, Y. J.; Sukhu, L.; Wheeler, C. J.; Manthorpe, M.; Marshall, J.; Cheng, S. H. Improved cationic lipid formulations for in vivo gene therapy. *Ann. N. Y. Acad. Sci.* **1995**, *772*, 126−139.
24. Gao, X.; Huang, L. Cationic liposome-mediated gene transfer. *Gene Ther.* **1995**, *2*, 710−722.
25. Reddy, J. A.; Low, P. S. Folate-mediated targeting of therapeutic and imaging agents to cancers. *Crit. Rev. Ther. Drug Carrier Syst.* **1998**, *15*, 587−627.
26. Leamon, C. P.; Pastan, I.; Low, P. S. Cytotoxicity of folate-Pseudomonas exotoxin conjugates toward tumor cells. Contribution of translocation domain. *J. Biol. Chem.* **1993**, *268*, 24847−24854.
27. Mathias, C. J.; Wang, S.; Waters, D. J.; Turek, J. J.; Low, P. S.; Green, M. A. Indium-111-DTPA-folate as a potential folate-receptor-targeted radiopharmaceutical. *J. Nucl. Med.* **1998**, *39*, 1579−1585.
28. Lee, R. J.; Low, P. S. Folate-mediated tumor cell targeting of liposome-entrapped doxorubucin in vitro. *Biochim. Biophys. Acta* **1995**, *1233*, 134−144.
29. Douglas, J. T.; Rogers, B. E.; Rosenfeld, M. E.; Michael, S. I.; Feng, M.; Curiel, D. T. Targeted gene delivery by tropism-modified adenoviral vectors. *Nat. Biotechnol.* **1996**, *14*, 1574−1578.
30. Roy, E. J.; Cho, B. K.; Rund, L. A.; Patrick, T. A.; Kranz, D. M. Targeting T cells against brain tumors with a bispecific ligand- antibody conjugate. *Int. J. Cancer* **1998**, *76*, 761−766.
31. Ladino, C. A.; Chari, R. V.; Bourret, L. A.; Kedersha, N. L.; Goldmacher, V. S. Folate-maytansinoids: target-selective drugs of low molecular weight. *Int. J. Cancer* **1997**, *73*, 859−864.
32. Lee, R. J.; Huang, L. Folate-targeted, anionic liposome-entrapped polylysine-condensed DNA for tumor cell-specific gene transfer. *J. Biol. Chem.* **1996**, *271*, 8481−8487.
33. Gottschalk, S.; Cristiano, R. J.; Smith, L. C.; Woo, S. L. Folate receptor mediated DNA delivery into tumor cells: potosomal disruption results in enhanced gene expression. *Gene Ther.* **1994**, *1*, 185−191.
34. Mislick, K. A.; Baldeschwieler, J. D.; Kayyem, J. F.; Meade, T. J. Transfection of folate-polylysine DNA complexes: evidence for lysosomal delivery. *Bioconjug. Chem.* **1995**, *6*, 512−515.
35. Kim, J.-S.; Maruyama, A.; Akaike, T.; Kim, S. W. In vitro gene expression on smooth muscle cells using a terplex delivery system. *J. Controlled Release* **1997**, *47*, 51−59.
36. Shen, W. C.; Yang, D.; Ryser, H. J. Colorimetric determination of microgram quantities of polylysine by trypan blue precipitation. *Anal. Biochem.* **1984**, *142*, 521−524.
37. Drummond, D. C.; Daleke, D. L. Synthesis and characterization of N-acylated, pH-sensitive 'caged' aminophospholipids. *Chem. Phys. Lipids* **1995**, *75*, 27−41.
38. Reddy, J. A.; Low, P. S. Enhanced folate receptor mediated tumor specific gene delivery with a novel pH-sensitive lipid formulation. *J. Controlled Release* **1999**, in press.
39. Gao, X.; Huang, L. Potentiation of cationic liposome-mediated gene delivery by polycations. *Biochemistry* **1996**, *35* (5), 1027−1036.
40. Ibanez, M.; Gariglio, P.; Chavez, P.; Santiago, R.; Wong, C.; Baeza, I. Spermidine-condensed DNA and cone-shaped lipids improve delivery and expression of exogenous DNA transfer by liposomes. *Biochem. Cell Biol.* **1996**, *74*, 633−643.
41. Legendre, J. Y.; Szoka, F. C., Jr. Cyclic amphipathic peptide-DNA complexes mediate high-efficiency transfection of adherent mammalian cells. *Proc. Natl. Acad. Sci. U.S.A.* **1993**, *90*, 893−897.
42. Kukowska-Latallo, J. F.; Bielinska, A. U.; Johnson, J.; Spindler, R.; Tomalia, D. A.; Baker, J. R., Jr. Efficient transfer of genetic material into mammalian cells using Starburst polyamidoamine dendrimers. *Proc. Natl. Acad. Sci. U.S.A.* **1996**, *93*, 4897−4902.
43. Erbacher, P.; Zou, S.; Bettinger, T.; Steffan, A. M.; Remy, J. S. Chitosan-based vector/DNA complexes for gene delivery: biophysical characteristics and transfection ability. *Pharm. Res.* **1998**, *15*, 1332−1339.
44. Rosenthal, N. Identification of regulatory elements of cloned genes with functional assays. *Methods Enzymol.* **1987**, *152*, 704−720.
45. Prensky, W. The radioiodination of RNA and DNA to high specific activities. *Methods Cell Biol.* **1976**, *13*, 121−152.
46. Zhu, N.; Liggitt, D.; Liu, Y.; Debs, R. Systemic gene expression after intravenous DNA delivery into adult mice. *Science* **1993**, *261*, 209−211.
47. Bandyopadhyay, P.; Kren, B. T.; Ma, X.; Steer, C. J. Enhanced gene transfer into HuH-7 cells and primary rat hepatocytes using targeted liposomes and polyethylenimine. *Biotechniques* **1998**, *25*, 282−284, 286−292.
48. Thierry, A. R.; Rabinovich, P.; Peng, B.; Mahan, L. C.; Bryant, J. L.; Gallo, R. C. Characterization of liposome-mediated gene delivery − expression, stability and pharmacokinetics of plasmid DNA. *Gene Ther.* **1997**, *4*, 226−237.
49. Hofland, H. E.; Shephard, L.; Sullivan, S. M. Formation of stable cationic lipid/DNA complexes for gene transfer. *Proc. Natl. Acad. Sci. U.S.A.* **1996**, *93*, 7305−7309.
50. Bandyopadhyay, P.; Ma, X.; Linehan-Stieers, C.; Kren, B. T.; Steer, C. J. Nucleotide exchange in genomic DNA of rat hepatocytes using RNA/DNA oligonucleotides. Targeted delivery of liposomes and polyethyleneimine to the asialoglycoprotein receptor. *J. Biol. Chem.* **1999**, *274*, 10163−10172.
51. Dean, D. A. Import of plasmid DNA into the nucleus is sequence specific. *Exp. Cell Res.* **1997**, *230*, 293−302.
52. Vacik, J.; Dean, B. S.; Zimmer, W. E.; Dean, D. A. Cell-specific nuclear import of plasmid DNA. *Gene Ther.* **1999**, in press.
53. Kabanov, A. V.; Kabanov, V. A. DNA complexes with polycations for the delivery of genetic material into cells. *Bioconjug. Chem.* **1995**, *6*, 7−20.
54. Erbacher, P.; Roche, A. C.; Monsigny, M.; Midoux, P. The reduction of the positive charges of polylysine by partial gluconylation increases the transfection efficiency of polylysine/DNA complexes. *Biochim. Biophys. Acta* **1997**, *1324*, 27−36.
55. Milson, R. W.; Bloomfield, V. A. Counterion-induced condensation of DNA. A light-scattering study. *Biochemistry* **1979**, *18* (8), 2192−2196.
56. Frechet, J. M. Functional polymers and dendrimers: reactivity, molecular architecture, and interfacial energy. *Science* **1994**, *263*, 1710−1715.
57. Haensler, J.; Szoka, F. C., Jr. Polyamidoamine cascade polymers mediate efficient transfection of cells in culture. *Bioconjug. Chem.* **1993**, *4*, 372−379.
58. Plank, C.; Mechtler, K.; Szoka, F. C., Jr.; Wagner, E. Activation of the complement system by synthetic DNA complexes: a potential barrier for intravenous gene delivery. *Hum. Gene Ther.* **1996**, *7*, 1437−1446.

Acknowledgments

This work was supported in part by a grant from Endocyte, Inc.

JS990169E

Increased Bioavailability of Clomipramine after Sublingual Administration in Rats

SUN DONG YOO,[†] BYUNG MUN YOON,[†] HYE SUK LEE,[‡] AND KANG CHOON LEE*,[†]

Contribution from *College of Pharmacy, SungKyunKwan University, 300 Chonchon-dong, Jangan-ku, Suwon City, 440-746, Korea, and College of Pharmacy, Wonkwang University, 344-2 Shinyong-dong, Iksan, 570-749, Korea.*

Received May 24, 1999. Accepted for publication August 26, 1999.

Abstract □ This study examined the absorption and disposition of clomipramine in rats after sublingual (5 and 50 mg/kg), oral (50 mg/kg), and iv (5 mg/kg) administration. The mean oral bioavailability of clomipramine was 24.8% and 29.7%, respectively, in conscious rats and in rats anesthetized with ketamine/xylazine (30/3 mg/kg). When given sublingually in isotonic saline at a dose of 50 mg/kg, clomipramine was rapidly absorbed, and the mean absolute bioavailability (36.2%) was increased over oral dosing. The mean AUC values of clomipramine were 2258 ± 1762 ng·h/mL and 1891 ± 867 ng·h/mL after oral administration to conscious and anesthetized rats, respectively, and 3303 ± 1576 ng·h/mL after sublingual administration to anesthetized rats. Sublingual administration (5 mg/kg doses) of clomipramine formulated with a permeation enhancer, 2-hydroxypropyl β-cyclodextrin, further increased the sublingual bioavailability to 57.1%. The sublingual route may be an alternative route of administration of clomipramine, providing enhanced bioavailability.

Introduction

Clomipramine is a tricyclic antidepressant widely used for the treatment of depression in a number of countries in Western Europe and Canada. In the United States, it has only recently been approved for the treatment of obsessions and compulsions in patients with obsessive-compulsive disorder.[1] Beneficial effects of clomipramine have also been reported in patients with phobia, panic disorder, chronic pain, premature ejaculation, enuresis, and anorexia nervosa.[2] Despite the widespread use of clomipramine for more than a decade, its pharmacokinetics are less well documented than those of other tricyclic antidepressants.[3,4] There are a few reports on the oral absorption of clomipramine in humans in which the oral bioavailability is approximately 50%.[5−7] To our knowledge, no information is available on the bioavailability of clomipramine after sublingual or buccal administration in humans or laboratory animals. Of the antidepressant drugs available at present, only imipramine has been indirectly shown to be efficiently absorbed across the oral mucosa in humans.[8]

The aim of this study was to determine the extent of absorption of clomipramine in rats after sublingual administration. Clomipramine given sublingually as a solution in isotonic saline was rapidly absorbed and its sublingual bioavailability was increased over oral dosing. The sublingual bioavailability of clomipramine was further enhanced when given with hydroxypropyl β-cyclodextrin as a permeation enhancer.

* Corresponding author. Tel 82-331-290-7704. Fax 82-331-292-8800. E-mail kclee@yurim.skku.ac.kr.
[†] SungKyunKwan University.
[‡] Wonkwang University.

Experimental Section

Chemicals—Clomipramine hydrochloride, imipramine hydrochloride, ketamine, xylazine, and triethylamine were purchased from Sigma Chemical Co. (St. Louis, MO). Methocel MC (methyl cellulose) and 2-hydroxypropyl β-cyclodextrin were obtained from Fluka Chemie AG (Buchs, Switzerland). Sodium hydroxide and phosphoric acid were purchased from Samchun Chemical Co. (Pyungtaek, Korea) and Yakuri Chemical Co. (Osaka, Japan), respectively. Acetonitrile and methanol (all HPLC grades) were obtained from Fisher Scientific (Fair Lawn, NJ) and hexane (HPLC grade) from Mallinckrodt (Paris, KY). Mannitol and heparin were obtained from Choongwae Pharma Co. (Seoul, Korea).

Animals and Surgical Preparation—Male Sprague Dawley rats (7−8 weeks, 240−300 g) were purchased from Jaeil Animals Co. (Ansung, Korea). The rats were placed in plastic rat cages and housed in a temperature-controlled (23 ± 2 °C) animal facility with light/dark cycle of 12/12 h and relative humidity of 50 ± 10%. The animals had free access to standard rat diet (DaeJong Co., Seoul, Korea) and water throughout the study. After at least one week of acclimatization, the rats were anesthetized with im injection of ketamine and xylazine (90/10 mg/kg) and cannulated with PE tubing (0.58 mm i.d. and 0.96 mm o.d., Natume Co., Tokyo, Japan) in the right jugular vein. In animals used in the iv injection study, the right femoral vein was also cannulated with PE tubing. After surgery, at least 2 days of recovery were allowed prior to drug administration.

Intravenous Injection Study—Clomipramine dissolved in isotonic saline (3 mg/mL) was administered iv in rats via the femoral vein at 5 mg/kg doses (n = 4). Serial blood samples of approximately 0.3 mL were collected from the jugular vein at 0, 5, 15, 30, and 45 min and 1, 1.5, 2, 4, 8, 12, and 24 h after drug injection. Equal volumes of drug-free heparinized saline were injected after each sampling. Serum samples were harvested by centrifugation at 2500 rpm for 10 min and were kept at −70 °C until drug analysis.

Oral Dosing—Clomipramine dissolved in isotonic saline was administered po at 50 mg/kg doses in rats (n = 4). A second group of rats (n = 4) was also given clomipramine orally (50 mg/kg) followed by induction of light anesthesia with ketamine/xylazine (30/3 mg/kg). The animals gained consciousness within 10−30 min. Serial blood samples of approximately 0.3 mL were collected from the jugular vein as described above. Equal volumes of drug-free saline were injected after each sampling. Serum samples were harvested by centrifugation at 2500 rpm for 10 min and were kept at −70 °C until drug analysis.

Sublingual Administration—Clomipramine dissolved in isotonic saline (50 mg/kg doses) was applied to the sublingual mucosa of rats (n = 4) under light ketamine/xylazine (30/3 mg/kg) anesthesia. The volume of the drug solution administered was approximately 30 μL applied with an autopipet. Prior to application, the buccal and subligual areas were blotted dry with cotton swabs, and the animals were kept face downward until recovery from anesthesia. The animals gained consciousness within 10−30 min after induction of anesthesia. Separately, clomipramine (5 mg/kg doses) formulated with 2-hydroxypropyl β-cyclodextrin (100 mg/mL), mannitol (50 mg/mL), and Methocel M. C. (20 mg/mL) in isotonic saline was applied to the sublingual mucosa of rats (n = 4) as described above. Serial blood samples of approximately 0.3 mL were collected from the jugular vein at 0, 5, 15, 30, and 45 min and 1, 1.5, 2, 4, 8, 12, and 24 h after application.

10.1021/js990163p CCC: $18.00
Published on Web 10/09/1999

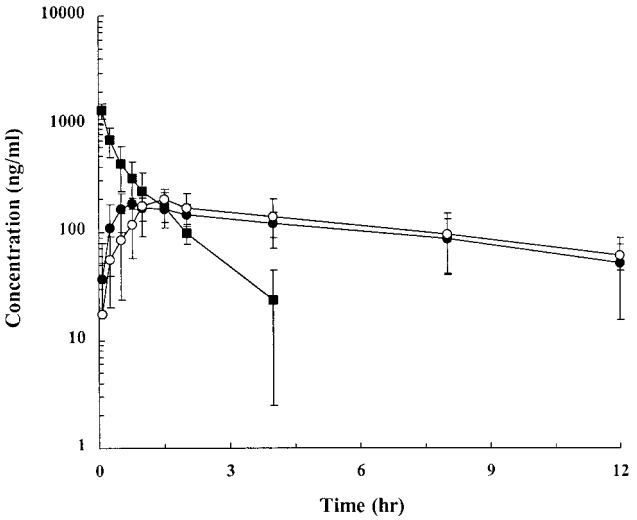

Figure 1—Mean serum concentration vs time curves of clomipramine after iv administration (5 mg/kg doses) to conscious rats (■) and after oral administration (50 mg/kg doses) to conscious (●) and anesthetized (○) rats ($n = 4$ each).

Equal volumes of drug-free saline were injected after each sampling. Serum samples were harvested by centrifugation at 2500 rpm for 10 min and were kept at −70 °C until drug analysis.

Drug Analysis—Drug analysis was performed on a HPLC system consisting of a Gynkoteck Model M480G pump, a Model UVD 340 photodiode array detector and a Model Gina 50 autosampler (Germering, Germany), a degasser (Lab-Quatec Co., Tokyo, Japan), and a Chromeleon Data System integration software (Softran GmbH, Germering, Germany). Chromatographic separations were achieved using a HAISIL HL RP C_{18} analytical column (4.6 mm i.d. × 250 mm, 5 μm) and a guard column (3.2 mm i.d. × 20 mm, 5 μm) (Higgins Analytical Inc., Mountain View, CA). The mobile phase consisted of acetonitrile:0.1% triethylamine in deionized water (50/50, v/v). The mobile phase was adjusted to pH 3.5 by phosphoric acid, passed through a 0.2 μm membrane filter, and degassed prior to use. Clomipramine was extracted by a single liquid−liquid extraction with hexane. Briefly, to an aliquot (100 μL) of the rat serum were added 100 μL of the internal standard solution (imipramine 200 ng/mL) and 100 μL of 5.0 M NaOH, and the mixture was vortexed for 10 s. The mixture was then extracted with 2 mL of hexane on a vortex mixer for 60 s and centrifuged at 2500 rpm for 3 min. The resulting supernatant was transferred into a fresh tube and dried at 35 °C under nitrogen gas. The residue was then reconstituted with 100 μL of the mobile phase on a vortex mixer for 30 s. The reconstituted solution was centrifuged at 2500 rpm for 60 s, and a portion (40 μL) was injected onto the chromatograph. The flow rate of the mobile phase was 1.0 mL/min at ambient temperature, and the effluent was monitored at 253 nm. Clomipramine and imipramine were well-resolved, with retention times of 3.8 and 5.0 min, respectively. Standard curves were linear over the concentration range of 10−1000 ng/mL, with a typical correlation coefficient of $r = 0.9998$. The intra- and interday assay coefficients of variation were <3.2% and <4.7%, respectively, for clomipramine and imipramine over the concentration range studied ($n = 5$ each).

Data Analysis—Serum clomipramine concentration vs time data were analyzed by a compartmental method for the iv injection study and by a noncompartmental method for the oral and sublingual studies. The nonlinear least squares regression program WinNonlin (Scientific Consulting Inc., Cary, NC) was used in the analysis. Statistical differences in pharmacokinetic parameters between conscious and anesthetized rats and between different doses were tested by the unpaired Student t-test. The significance level was set at $p < 0.05$.

Results and Discussion

Figure 1 shows the serum concentration vs time curves of clomipramine in rats obtained after iv injection (5 mg/kg doses) and oral administration (50 mg/kg doses). Following iv injection, the disposition of clomipramine was described by a biexponential curve, with a mean distribution and terminal elimination half-life of 7.8 ± 4.2 min and 63.0 ± 15.6 min, respectively. The elimination half-life of clomipramine in rats was much shorter than in humans (mean range, 24−39 h), primarily due to a higher systemic clearance and lower V_{ss} (96.6 ± 27.3 mL/min/kg and 6.1 ± 1.3 L/kg, respectively) (Table 1) compared to those in humans (10.8 mL/min/kg and 7−20 L/kg, respectively).[5,7,9,10] Clomipramine was administered orally at 50 mg/kg doses so that the maximum serum drug concentrations were within an acceptable therapeutic range of 150−450 ng/mL.[3] Upon oral administration in conscious rats, clomipramine was rapidly absorbed (Figure 1), with an average t_{max} of 0.8 ± 0.2 h and C_{max} of 209.4 ± 44.1 ng/mL (Table 2). The mean C_{max} found in this study (209.4 ng/mL) was higher than those reported after administration of 90 mg/kg po doses (162 ng/mL) or 15 mg/kg i.p. doses (144 ng/mL).[11,12] The oral bioavailability of clomipramine was 24.8% in conscious rats and 29.7% in rats anesthetized with ketamine/xylazine (30/3 mg/kg). There was no significant difference in AUC between the conscious and anesthetized rats (2258 ± 1762 ng·h/mL vs. 1891 ± 867 ng·h/mL). The C_{max} values between the two groups of animals were comparable, although the rate of absorption was lower in the anesthetized rats (Table 2). Therefore, it is unlikely that the light anesthesia induced by ketamine/xylazine (30/3 mg/kg) caused any significant alterations in the extent of drug absorption and elimination. The terminal elimination half-life was prolonged after oral administration (9.2 ± 7.8 h) as compared with iv injection (1.1 ± 0.3 h), suggesting that the drug elimination was rate-limited by the absorption process. These increased elimination half-lives are similar to the half-life of 6 h reported previously in rats after i.p injection.[12] The oral bioavailability of clomipramine in the rat was lower than that found in humans (approximately 50%).[5,6]

When the drug was given sublingually at 50 mg/kg doses, higher C_{max} (414.5 ± 47.0 ng/mL) and AUC (3303 ± 1576 ng·h/mL) were observed compared to those obtained after oral administration (Figure 2). Also, the absolute bioavailability of clomipramine after sublingual administration (36.2%) was higher than after oral administration. Clomipramine is known to be extensively metabolized by the liver in rats and humans via demethylation and hydroxylation.[13,14] Since the rats used in the sublingual study were lightly anesthetized to facilitate drug administration, it may be argued that the increased bioavailability was due to reduced hepatic metabolism caused by anesthesia. However, given no differences in AUC, C_{max} and $t_{1/2,\lambda z}$ between conscious and anesthetized rats after oral administration, it is unlikely that the increased sublingual bioavailability was caused by induction of anesthesia.

Table 1. Pharmacokinetic Parameters of Clomipramine in Rats ($n = 4$) after iv Injection of 5 mg/kg doses[a]

body weight (g)	$t_{1/2,\lambda1}$ (min)	$t_{1/2,\lambda2}$ (min)	AUC (ng·h/mL)	AUMC (ng·h²/mL)	k_{10} (h^{-1})	k_{12} (h^{-1})	k_{21} (h^{-1})	Cl (mL/min/kg)	V_{ss} (L/kg)
295.0 (5.8)	7.8 (4.2)	63.0 (15.6)	912 (234)	1007 (372)	2.35 (1.15)	2.53 (1.73)	2.28 (1.76)	96.6 (27.3)	6.1 (1.3)

[a] Values are expressed as the mean (±1 SD).

Table 2. Pharmacokinetic Parameters (mean ± SD) of Clomipramine after Oral and Sublingual Administration in Rats without and with a Permeation Enhancer ($n = 4$ for each group)

parameter	50 mg/kg oral dose in conscious rats without enhancer	50 mg/kg oral dose in anesthetized rats without enhancer	50 mg/kg sublingual dose in anesthetized rats without enhancer	5 mg/kg sublingual dose in anesthetized rats with enhancer
body weight (g)	270.0 ± 8.2	297.5 ± 5.0	280.0 ± 24.5	272.5 ± 23.6
$t_{1/2,\lambda z}$ (h)	9.2 ± 7.8	6.5 ± 1.6	5.4 ± 1.4	2.2 ± 1.3
t_{max} (h)	0.8 ± 0.2[a]	1.3 ± 0.3	1.5 ± 0.4	1.5 ± 0.0
C_{max} (ng/mL)	209.4 ± 44.1	210.0 ± 55.7	414.4 ± 47.0	135.5 ± 25.1
AUC (ng·h/mL)	2258 ± 1762	1891 ± 867	3303 ± 1576	521 ± 174
V_z/F (L/kg)	284.6 ± 22.5	270.3 ± 81.9	124.2 ± 28.5	29.0 ± 8.6
Cl/*F* (mL/min/kg)	522.1 ± 284.3	500.7 ± 178.4	289.3 ± 116.8	170.6 ± 44.7
F (%)[b]	24.8	29.7	36.2	57.1

[a] Significantly different from anesthetized rats ($p < 0.05$). [b] $F = (AUC_{sublingual} \cdot dose_{iv}) \cdot 100/(AUC_{iv} \cdot dose_{sublingual})$.

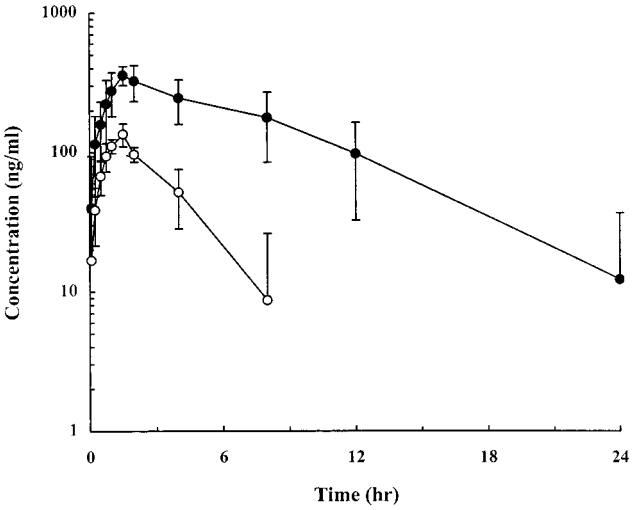

Figure 2—Mean serum concentration vs time curves of clomipramine after sublingual administration to rats with (5 mg/kg, ○) and without (50 mg/kg doses, ●) permeation enhancer ($n = 4$ each).

To further improve the sublingual bioavailability, clomipramine was formulated with a permeation enhancer, 2-hydroxypropyl β-cyclodextrin together with methyl cellulose and mannitol. After administration of this sublingual formulation in rats (5 mg/kg dose), C_{max} and AUC were higher by 3.3- and 1.6-fold, respectively, on a dose-normalized basis, than without permeation enhancer. Whether these increases were caused by the presence of the absorption enhancer, or were a result of a dose-dependent absorption, is unclear at present, although all the C_{max} values obtained in our study were within an acceptable therapeutic range. The terminal elimination half-life (2.2 ± 1.3 h) was shorter than found after oral and sublingual administration of 50 mg/kg doses but was still longer than found after iv injection. Therefore, at 5 mg/kg sublingual doses, the absorption process across the sublingual mucosa still seemed to have governed the elimination of clomipramine from the body. Nonetheless, the bioavailability of clomipramine was significantly increased (57.1%) for the sublingual formulation containing the permeation enhancer, and its relative bioavailability was increased to >192% over oral administration.

In conclusion, the pharmacokinetics of clomipramine showed multicompartment characteristics in rats. The oral bioavailability of clomipramine was low after administration of 50 mg/kg doses in rats. However, when given sublingually, clomipramine was well absorbed and its bioavailability was significantly increased over oral dosing. The sublingual route may be an alternative route of administration for clomipramine, providing enhanced bioavailability.

References and Notes

1. Peters, M. D.; Davis, S. K.; Austin, L. S. Clomipramine: an antiobsessional tricyclic antidepressant. *Clin. Pharm.* **1990**, *9*, 165−178.
2. Timble, M. R. Worldwide use of clomipramine. *J. Clin. Psychiatry* **1990**, *51*, S51− S54.
3. Balant-Gorgia, A. E.; Gex-Fabry, M.; Balant, L. P. Clinical pharmacokinetics of clomipramine. *Clin. Pharmacokin.* **1991**, *20*, 447−462.
4. Sallee, F. R.; Pollock, B. G. Clinical Pharmacokinetics of imipramine and desipramine. *Clin. Pharmacokin.* **1990**, *18*, 346−364.
5. Evans, L. E. J.; Bett, J. H. N.; Cox, J. R.; Dubois, J. P.; van Hees, T. The bioavailability of oral and parenteral clomipramine (Anafranil). *Prog. Neuro-Psychopharmacol.* **1980**, *4*, 293−302.
6. de Cuyper, H. J. A.; van Praag, H. M.; Mulder-Hajonides, W. R. E. M.; Westenberg, H. G. M.; de Zeeuw, R. A. Pharmacokinetics of clomipramine in depressive patients. *Psychol. Res.* **1981**, *4*, 147−156.
7. Müller, F. O.; Schall, R.; Mogilnicka, E. M.; Groenewoud, G.; Hundt, H. K. L.; Luul, H. G.; Middle, M. V.; Swart, K. J.; De Vaal, A. Relative bioavailability of four clomipramine hydrochloride tablet products. *Biopharm. Drug Dispos.* **1996**, *17*, 81−90.
8. Bickel, M. H.; Weder, H. J. Buccal absorption and other properties of pharmacokinetic importance of imipramine and its metabolites. *J. Pharm. Pharmacol.* **1969**, *21*, 160−168.
9. Nagy, A.; Johansson, R. The Demethylation of imipramine and clomipramine as apparent from their plasma kinetics. *Psychopharmacology* **1977**, *54*, 125−131.
10. Dawling, S.; Braithwaithe, R. A.; McAuley, R.; Montgomery, S. A. Single oral dose pharmacokinetics of clomipramine in depressed patients. *Postgrad. Med. J.* **1980**, *56*, S115−S116.
11. Sgaragli, G. P.; Valoti, M.; Palmi, M.; Frosini, M.; Giovannini, M. G.; Bianchi, L.; Corte, L. D. Rat tissue concentrations of clomipramine, chlorpromazine and their N-demethylated metabolites after a single oral dose of the parent compounds. *J. Pharm. Pharmacol.* **1995**, *47*, 782−790.
12. Friedman, E.; Cooper, T. B. Pharmacokinetics of clomipramine and its demethylated metabolite in blood and brain regions of rats treated acutely and chronically with clomipramine. *J. Pharmacol. Exp. Ther.* **1983**, *225*, 387−390.
13. Gex-Febry, M.; Balant-Gorgia, A. E.; Balant, L. P.; Garrone, G. Clomipramine metabolism: model-based analysis of variability factors from drug monitoring Data. *Clin. Pharmacokin.* **1990**, *19*, 241−255.
14. Krüger, R.; Hölzl, G.; Kuss, H. J.; Schefold, L. Comparison of the metabolism of the three antidepressants amitriptyline, imipramine, and chlorimipramine in vitro in rat liver microsomes. *Psychopharmacology* **1986**, *88*, 505−513.

JS990163P

Direct Biophysical Characterization of Human Apolipoprotein A-1 in ISCOMs

HONGMING CHEN* AND GAUTAM SANYAL

Contribution from *AstraZeneca Research and Development Boston, 128 Sidney Street, Cambridge, Massachusetts 02139.*

Received May 19, 1999. Accepted for publication August 9, 1999.

Abstract □ Human apolipoprotein A-1 was formulated in "Immune Stimulating Complexes" (ISCOMs). The structure of the protein in ISCOMs was examined directly using several biophysical techniques including Fourier transform infrared (FTIR) spectroscopy, near UV circular dichroism (CD), and fluorescence spectroscopy. Amide I FTIR data indicate that human apolipoprotein A-1 displays a slightly increased α-helical content after its incorporation into ISCOMs. Near UV CD and tryptophan fluorescence data suggest that association with ISCOMs results in the tryptophan residues of the protein experiencing a relatively hydrophobic environment, motional restriction, and local electrostatic interactions. These observations are consistent with an increased order in the protein structure upon incorporation in ISCOMs. In addition, biomolecular interaction analysis (BIA), based on surface plasmon resonance (SPR) measurements, suggests that the binding affinity of human apolipoprotein A-1 to a monoclonal anti-human apolipoprotein A-1 antibody is moderately decreased (by 20%) after its incorporation into ISCOMs. This study demonstrates that these biophysical techniques can be used to noninvasively monitor integrity of or changes in secondary and tertiary structure of proteins within the ISCOM particles without the need for protein extraction.

Introduction

Monitoring the structure of a protein following its formulation is crucial to the development of a successful formulation. Unfolding or changes in protein structure during formulation may result in loss of the desired biological efficacy. Although a large number of protein and peptide drugs have been formulated in delivery systems, monitoring structural changes after incorporation in these systems remains a challenging task. Most existing techniques require extraction of protein from the delivery systems with an organic solvent or a strong detergent.[1] These harsh extraction methods can be damaging to the secondary and tertiary structures of a protein and, therefore, prevent meaningful examination of any structural perturbations that may have occurred during formulation.[1]

In this study, several noninvasive spectroscopic techniques, including Fourier transform infrared (FTIR), near UV circular dichroism (CD), and fluorescence, were employed to directly examine the structure of a formulated protein. FTIR spectroscopy is a powerful tool for studying protein secondary structure, and it can be applied to samples in different physical states.[2] This technique has recently been applied to directly examine the integrity of recombinant human growth hormone[1,4] (rhGh), bovine serum albumin[3] (BSA), and chicken egg-white lysozyme[3] in poly(lactic-*co*-glycolic acid) (PLGA) microspheres, and in PLGA films.[4] Near UV CD spectroscopy is widely used for monitoring changes in the environments of aromatic amino acids that may result from changes in the protein's tertiary structure.[5] Changes in tryptophan fluorescence spectra usually reflect changes in the local environment of tryptophan residues, which may result either from a global change or a subtle local perturbation in the tertiary structure of a protein.[6] All of these spectroscopic techniques provide direct structural information using intrinsic chromophores or fluorophores of a protein, provided that any background interference from formulation excipients or delivery vehicles is minimal or can be corrected for.

Biomolecular interaction analysis (BIA) is a functional assay that monitors biological interactions at the molecular level. It uses an optical phenomenon called surface plasmon resonance (SPR) and a continuous flow system to monitor biomolecular interactions in real time.[7] Typically, one biomolecule is immobilized on the sensor surface, while a solution containing other biomolecules flows continuously over the sensor surface. As molecules from the solution bind to the immobilized biomolecule, a signal is registered in the form of a sensorgram which is based on the change of refractive index that results from this binding.[7] Real time monitoring of intermolecular interactions in the form of sensorgrams provides kinetic information such as association rate constants and dissociation rate constants as well as equilibrium binding constants.[7]

Human apolipoprotein A-1 was used in this study as a model protein and was incorporated into immune stimulating complexes (ISCOMs), a nanoparticulate delivery system made of a phospholipid, cholesterol, and Quil A.[8] Human apolipoprotein A-1 protein is the major protein component of high-density lipoprotein (HDL) particles. It has a molecular weight of 28 kDa, and its known protein sequence is composed of 243 amino acid residues including four tryptophan residues.[9] In the solution form, it is loosely folded with a high degree of exposure of its nonpolar groups to solvent.[10] Upon interaction with lipids, it undergoes subtle rearrangements in its tertiary structure to accommodate the more nonpolar environment of lipids.[10]

In the study reported here, FTIR, near UV CD and fluorescence spectra of human apolipoprotein A-1 in solution and in ISCOMs were compared. Binding of human apolipoprotein A-1 in ISCOMs to a specific monoclonal anti-human apolipoprotein A-1 antibody was studied using BIAcore (Biacore, Inc.) and compared to binding of the free protein in solution to the same antibody. The data indicate that human apolipoprotein A-1 undergoes subtle changes in secondary and tertiary structures when incorporated into ISCOMs. Furthermore, incorporation in ISCOMs also resulted in a modest alteration in its binding affinity for the anti-human apolipoprotein A-1 antibody. These results are consistent with the reported ability of human apolipoprotein A-1 to change its structure to accommodate lipophilic environments.[10] Our findings suggest that these

* Corresponding author. Tel: 617-234-2557, fax: 617-576-3030, e-mail: hongming.chen@arcb.us.astra.com.

10.1021/js990158l CCC: $18.00
Published on Web 09/21/1999

biophysical techniques can indeed be used to monitor protein structure in ISCOMs without the need for protein extraction.

Experimental Methods

ISCOMs Formation—ISCOMs were formed according to previously published method[11] with slight modifications. Briefly, 10 mg of L-α-phosphatidylcholine dipalmitoyl (Sigma) and 10 mg of cholesterol (Sigma) were dissolved in 1 mL of 20% decanoyl-*N*-methylglucamide (Mega-10, Sigma) in phosphate-buffered saline (PBS, pH 7.4). A 100 μL amount of the lipid mixture was mixed with 200 μL of 20 mg/mL Quil A (Superfos Biosector) and 600 μL of 2 mg/mL human apolipoprotein A-1 in PBS (Calbiochem). When preparing protein-free ISCOMs, PBS alone was used. The final volume was made up to 1 mL with PBS. The mixture was dialyzed against PBS over 48 h to remove the detergent. ISCOMs were formed upon detergent removal.

Sucrose Gradient Ultracentrifugation—Human apolipoprotein A-1 incorporated into ISCOMs was separated from unincorporated protein by ultracentrifugation at 200 000*g* for 18 h at 10 °C through a 10−50% discontinuous sucrose gradient. The gradient was then fractionated into volumes of 1 mL. The fractions were tested for the presence of protein with a colorimetric Lowry assay kit from BioRad, and for the presence of cholesterol with a colorimetric total cholesterol assay kit obtained from Sigma. Fractions containing both protein as well as cholesterol were pooled and washed with PBS to remove sucrose. Final protein concentration in each sample was determined by SDS−PAGE densitometry.

Dynamic Light Scattering—Hydrodynamic size distribution of the ISCOMs was determined using a dynamic light scattering (DLS) apparatus (Model 4700, Malvern Instrument) using the 488 nm line of a 5 W argon ion laser and a detection angle of 90°. The autocorrelation functions obtained from scattering measurements were fitted using the nonnegative least square (NNLS) algorithm to yield the size distribution of the ISCOMs.[12]

Transmission Electron Microscopy—Transmission electron microscopy (TEM) was used to examine the morphology of ISCOMs. Samples were stained with 2% uranyl acetate and examined under a JEOL JEM 1010 microscope.

Fourier Transform Infrared (FTIR) Spectroscopy—FTIR spectra were recorded at 25 °C with a resolution of 4 cm^{-1} on a BOMEM MB-104 FTIR spectrometer (BOMEM, Inc.), continuously purged with nitrogen and equipped with a DTGS detector. For each spectrum, 400 scans were accumulated in the single beam mode. Samples were placed in a sample cell with two CaF_2 windows separated by a 6 μm spacer. Human apolipoprotein A-1 and its ISCOM formulation were concentrated to 5 mg/mL using a 10 000 MWCO ultrafiltration device (Millipore). Proper blank spectra (PBS buffer for protein in solution and protein-free ISCOMs for protein in ISCOMs) and water vapor components were subtracted from the protein spectra using the BOMEM-PROTA (BOMEM, Inc.) software. Second derivatives of the spectra were calculated for peak identification. Secondary structure of the protein was analyzed using factor analysis[13] with the BOMEM-PROTA database[14] (BOMEM, Inc.).

Near UV Circular Dichroism (CD)—Near UV CD (in the wavelength range of 250−350 nm) spectra were obtained using a Jasco J-715 spectropolarimeter. Samples at a protein concentration of 0.3 mg/mL were placed in a rectangular quartz cell of 0.1 or 1 cm path length. The cell holder was maintained at a temperature of 25 °C. A bandwidth of 2 nm and a scan speed of 20 nm/min were used for each spectrum. For each sample, four spectral scans were averaged. Proper background spectra (PBS or protein-free ISCOMs) were recorded and subtracted to obtain background-corrected protein spectra.

Fluorescence Spectroscopy—Steady-state fluorescence spectra were recorded using a Perkin-Elmer LS50B fluorometer. Samples were excited at 295 nm, and tryptophan fluorescence was monitored between 305 and 400 nm using excitation and emission slits of 5 nm. Blank spectra (PBS or protein-free ISCOMs) were subtracted to obtain background-corrected tryptophan fluorescence spectra. Spectra were then corrected for wavelength-dependent monochromator and photomultiplier tube responses.

Biomolecular Interaction Analysis (BIA)—Binding interactions between human apolipoprotein A-1 (in solution or in ISCOMs) and a specific antibody were determined using a BIAcore 3000 biosensor system (Biacore, Inc.). Rabbit anti-mouse antibody (Biacore, Inc.) was immobilized on a research grade CM5 sensor chip in 10 mM sodium acetate, pH 4.5, using the amine-coupling kit (Biacore, Inc.). Mouse monoclonal anti-human apolipoprotein A-1 antibody (Calbiochem) was captured at a concentration of 10 μg/mL. Human apolipoprotein A-1 in solution or in ISCOMs was diluted in HEPES buffer for kinetic binding study. The samples were allowed to flow over the captured antibody for binding. Dissociation of the protein from the antibody was achieved by continuously flowing HEPES buffer over the sensor chip. All measurements were carried out at 25 °C using a flow rate of 20 μL/min. The sensor chip surfaces were regenerated with 20 μL of 10 mM glycine/HCl, pH 2, after each measurement.

The resulting sensorgram data were fitted with the 1:1 Langmuir binding model[7,15] using the BIAevaluation 3.0 software (Biacore, Inc.), yielding values for association and dissociation rate constants (k_a and k_d, respectively). Binding affinities of the antibody for human apolipoprotein A-1 in solution and in ISCOMs were expressed as dissociation constants K_D, where $K_D = k_d/k_a$.

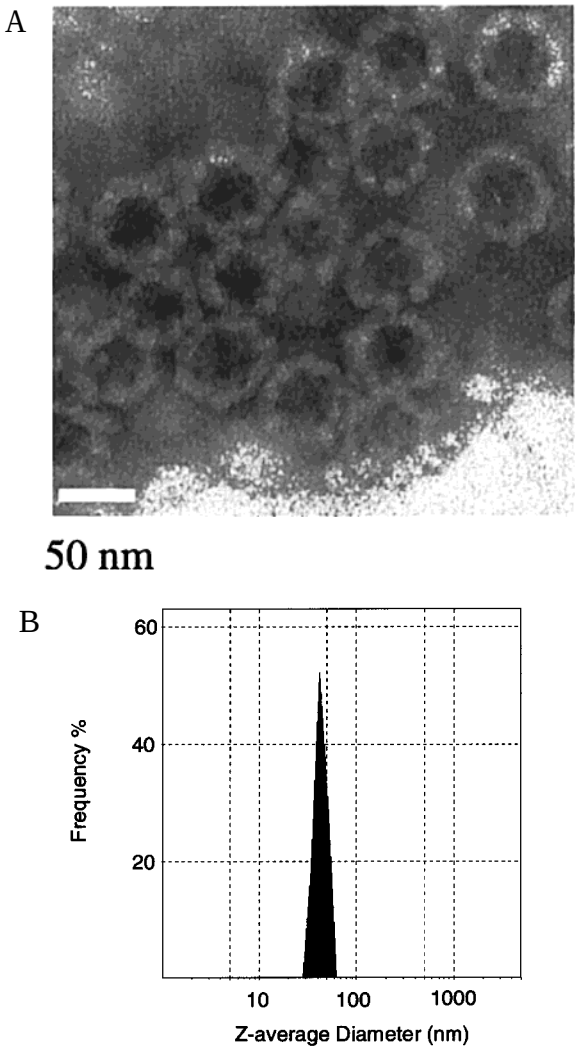

Figure 1—(A) Negatively stained transmission electron micrograph of apolipoprotein A-1 ISCOMs. (B) Size distribution of human apolipoprotein A-1 ISCOMs as measured by dynamic light scattering (DLS).

Results and Discussion

ISCOMs Characterization—*A. Size*—TEM indicated that human apolipoprotein A-1 ISCOMs had the characteristic cagelike appearance[8] (Figure 1A). DLS measurement showed that the ISCOMs had a *z*-average hydrodynamic diameter of 50 nm with a narrow unimodal size

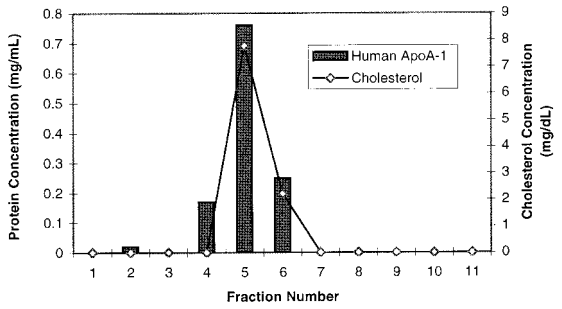

Figure 2—Sucrose gradient centrifugation of human apolipoprotein A-1 in ISCOMs. The gradient was fractionated into 1 mL fractions and each fraction was analyzed for the presence of cholesterol and protein.

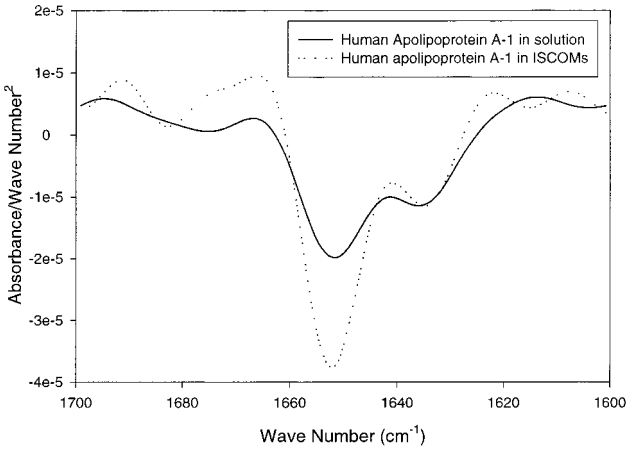

Figure 3—Amide I region of second derivative FTIR spectra of human apolipoprotein A-1 in solution and in ISCOMs. Proper blank spectra have been subtracted as described in the text.

distributions (polydispersity index = 0.08) (Figure 1B). This particle size is consistent with the size estimated from the TEM image shown in Figure 1A.

B. Protein Incorporation—The percentage of human apolipoprotein A-1 incorporated into the ISCOMs was determined using sucrose gradient ultracentrifugation. The ISCOMs showed up as a narrow band on the gradient after ultracentrifugation. Fractionation of the gradient indicated that close to 90% of the protein was associated with cholesterol after ultracentrifugation. Since cholesterol is an essential component of ISCOMs, the data suggested that approximately 90% of the total protein added was incorporated into the ISCOMs (Figure 2).

Direct Estimation of Protein Secondary Structure in ISCOMs by FTIR Spectroscopy—Protein-free ISCOMs gave minimal spectral interference in the region of interest, i.e., the amide I region (1600−1700 cm^{-1}). Figure 3 shows the amide I region of the second derivative FTIR spectra of human apolipoprotein A-1 in solution and in ISCOMs. Human apolipoprotein A-1 is known to contain a high percentage of α-helices.[9,16] This was clearly reflected in the prominent absorption band observed at 1656 cm^{-1} for human apolipoprotein A-1 in solution (Figure 3). The presence of some β-sheets was also seen from the band at 1634 cm^{-1}. The assignments of these amide I IR bands to defined secondary structures are based on a previously published report.[17] For the protein formulated in ISCOMs, an increase in absorption intensity was observed for the 1656 cm^{-1} absorption band. This observation is consistent with previously published findings that human apolipoprotein A-1 displays increased amount of α-helices when it is in HDL particles and bound to lipids, as compared to being in a lipid-free solution environment.[9,16]

Table 1—Secondary Structure Components of Human Apolipoprotein A-1 in Solution or in ISCOMs. Results Are Presented as Mean ± sd of Three Independent FTIR Measurements

	helix (%)	sheet (%)	bend and turn (%)	coil (%)
apolipoprotein A-1 in solution	44 ± 5	16 ± 2	17 ± 2	23 ± 3
apolipoprotein A-1 in ISCOMs	56 ± 5	10 ± 2	15 ± 2	20 ± 2

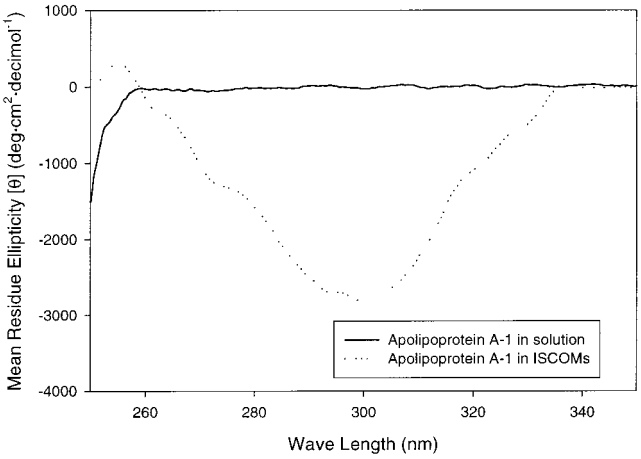

Figure 4—Near UV CD spectra of human apolipoprotein A-1 in solution and human apolipoprotein A-1 in ISCOMs. Proper blank spectra have been subtracted as described in the text.

Factor analysis was used to generate quantitative information on protein secondary structure from the IR absorption spectra.[13,14] This method predicts the secondary structure of an unknown protein using the (BOMEM-PROTA database of proteins with known crystal structures.[13,14] The results for human apolipoprotein A-1 in solution and in ISCOMs obtained from factor analysis are shown in Table 1. These values represent averages of results from three independently measured spectra. A modest increase in the amount of α-helices and a slight decrease in the amount of β-sheets were observed after apolipoprotein A-1 was incorporated into ISCOMs. These estimates are in qualitative agreement with the second derivative spectra in Figure 3.

It should be noted that far UV CD spectroscopy could not be used reliably to estimate secondary structure content of the protein in ISCOMs due to large interferences from the lipids and Quil A in ISCOMs.

Near UV Circular Dichroism—Near UV CD spectra for human apolipoprotein A-1 in solution and human apolipoprotein A-1 in ISCOMs are shown in Figure 4. When free in solution, human apolipoprotein A-1 did not show any near UV CD signal at the concentration of 0.3 mg/mL used, at either 0.1 or 1 cm optical path length, suggesting motional freedom of its aromatic side-chains. When incorporated into ISCOMs, human apolipoprotein A-1 displayed a broad CD signal with the spectral maximum at 300 nm and a shoulder at 295 nm. This indicates that the tryptophan residues experience motional restriction when the protein is in ISCOMs. It should be noted that apolipoprotein A-1 contains four tryptophan residues, and the individual contribution of each to the near UV CD or fluorescence spectrum (below) may or may not be equal. These data, therefore, reflect the environment of one or more, but not necessarily of all, of the tryptophans in the protein.

Fluorescence Spectroscopy—Figure 5 shows the tryptophan fluorescence spectra for human apolipoprotein A-1 in solution and in ISCOMs. The observed fluorescence maximum at 345 nm suggests that, on the average,

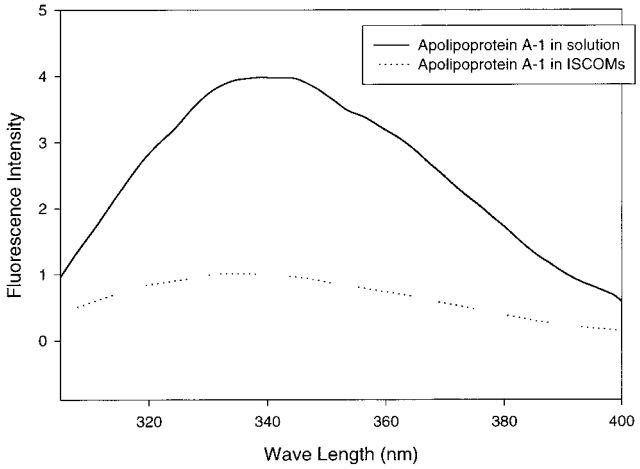

Figure 5—Fluorescence spectra of human apolipoprotein A-1 in solution and human apolipoprotein A-1 in ISCOMs. Proper blank spectra have been subtracted as described in the text.

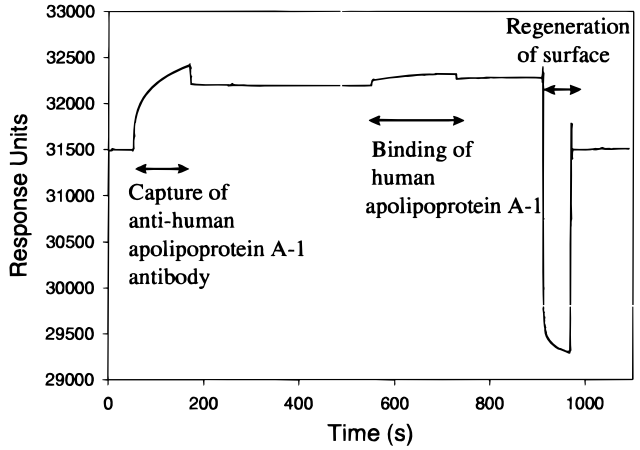

Figure 6—Sensorgram illustrating capture of a monoclonal anti-human apolipoprotein A-1 antibody, binding of human apolipoprotein A-1, and surface regeneration steps in kinetic analysis.

tryptophan residues in the free protein are partially exposed to water. This is consistent with previously published data suggesting that, in solution, human apolipoprotein A-1 has a high degree of exposed nonpolar groups.[10] After incorporation into ISCOMs, a blue-shift of the fluorescence maximum to 335 nm was seen, suggesting that ISCOMs provide a more hydrophobic environment for the tryptophan residues, possibly via interaction with the phospholipid or cholesterol in the ISCOMs. The quenching of fluorescence observed upon incorporation of the protein in ISCOMs may be a result of electrostatic interactions with the lipids or Quil A, which are in close proximity to the contributing tryptophan(s). Alternatively, the protein in ISCOMs may experience sterically allowed neighboring group interactions.

Biomolecular Interaction Analysis (BIA)—The sensorgram in Figure 6 illustrates the BIA data collection process. A mouse monoclonal anti-human apolipoprotein A-1 antibody was immobilized onto the sensor chip surface through binding to the rabbit anti-mouse antibody covalently bound to the chip surface. Human apolipoprotein A-1 in solution or in ISCOMs was then flowed over the chip surface and allowed to bind to the anti-human apolipoprotein A-1 antibody. Finally, the chip surface was regenerated before the next cycle would begin.

Figure 7 shows the antibody binding regions of the sensorgrams for human apolipoprotein A-1 in solution

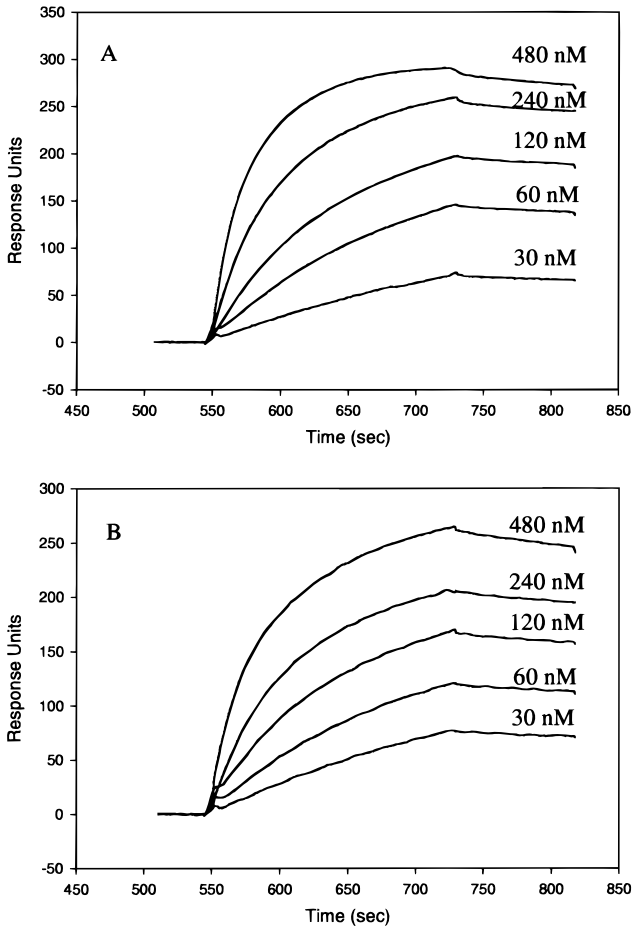

Figure 7—Effects of varying concentrations of human apolipoprotein A-1 on its binding kinetics to immobilized monoclonal antibody. (A) Human apolipoprotein A-1 in solution. (B) Human apolipoprotein A-1 in ISCOMs.

Table 2—Affinity and Rate Constants for Human Apolipoprotein A-1 in Solution and Human Apolipoprotein A-1 in ISCOMs. A Total of Three Measurements Were Made and the Results Are Presented as Mean ± sd

	$k_a \times 10^4$ ($M^{-1}s^{-1}$)	$k_d \times 10^{-4}$ (s^{-1})	K_D (nM)
human apolipoprotein A-1 in solution	11.5 ± 0.1	6.3 ± 0.1	5.7 ± 0.1
human apolipoprotein A-1 in ISCOMs	7.3 ± 0.1	4.8 ± 0.1	6.6 ± 0.1

(Figure 7A) and for human apolipoprotein A-1 in ISCOMs (Figure 7B). Five different protein concentrations were tested in each case. It can be seen that as the protein concentration was increased (either in the case of protein in solution or that of protein in ISCOMs), binding response increased correspondingly. When protein-free ISCOMs were tested, no response was seen (data not shown).

The sensorgram data in Figure 7 were fitted using the BIAevaluation 1:1 Langmuir binding model[7,15] to yield binding affinity and rate constants. A total of three evaluations were made for each sample, and the mean results are summarized in Table 2. After incorporation into ISCOMs, human apolipoprotein A-1 showed a 1.6-fold and a 1.3-fold decrease in k_a and k_d, respectively, for the monoclonal antibody. This translated to a 1.2-fold decrease in the binding affinity (or a 1.2-fold increase in K_D) for this interaction upon incorporation of the protein in ISCOMs. It is not known whether this slightly decreased antibody

affinity is the result of reduced accessibility of the antibody to ISCOM-associated protein compared to the free protein in solution.

Conclusion

FTIR spectroscopy suggests that human apolipoprotein A-1 experiences small changes in its secondary structure content upon incorporation in ISCOMs. Tryptophan fluorescence and near UV CD data indicate the protein's tryptophan residues, on the average, experience a more hydrophobic and motionally restrictive environment in ISCOMs compared to that in aqueous solution. BIA results suggest that the binding affinity of the protein to a monoclonal antibody is slightly reduced upon incorporation into ISCOMs. Results from these measurements suggest that the protein largely maintains its folded structure in ISCOMs, with its side chains engaged in local interactions with components of the ISCOM matrix. We conclude that a combination of biophysical techniques, such as those employed here, can provide complementary information on the secondary and tertiary structures of a protein formulated in ISCOMs. For other delivery systems, problems of interference will need to be carefully evaluated for each technique.

References and Notes

1. Yang, T.; Dong, A.; Meyer, J.; Johnson, O. L.; Cleland, J. L.; Carpenter, J. F. Use of infrared spectroscopy to assess secondary structure of human growth hormone within biodegradable microspheres. *J. Pharm. Sci.* **1999**, *88* (2), 161−165.
2. Middaugh, C. R.; Mach, H.; Ryan, J. A.; Sanyal, G.; Volkin, D. B. Infrared spectroscopy. *Methods Mol. Biol.* **1995**, *40*, 137−56.
3. Fu, K.; Griebenow, K.; Hsieh, L.; Klibanov, A. M.; Langer, R. FTIR characterization of the secondary structure of proteins encapsulated within PLGA microspheres. *J. Controlled Release* **1999**, *58*, 357−366.
4. Carrasquillo, K. G.; Costantino, H. R.; Cordero, R. A.; Hsu, C. C.; Griebenow, K. On the structural preservation of recombinant human growth hormone in a dried film of a synthetic biodegradable polymer. *J. Pharm. Sci.* **1999**, *88* (2), 166−173.
5. Strickland, E. H. Aromatic contributions to circular dichroism spectra of proteins. *CRC Crit. Rev. Biochem.* **1974**, 113−175.
6. Cantor, C. R.; Schimmel, P. R. Biophysical chemistry. Part II. Techniques for the study of biological structure and function. W. H. Freeman and Company: San Francisco, CA, 1980.
7. *BIAtechnology handbook;* Biacore, Inc.: Piscataway, NJ.
8. Morein, B.; Sundquist, B.; Hölglund, S.; Dalsgaard, K.; Osterhaus, A. ISCOMs, a novel structure for antigen presentation of membrane proteins from enveloped viruses. *Nature* **1984**, *308*, 457−460.
9. Gursky, O.; Atkinson, D. Thermal unfolding of human high-density apolipoprotein A-1: Implications for a lipid-free molten globular state. *Proc. Natl. Acad. Sci. U.S.A.* **1996**, *93*, 2991−2995.
10. Osborne, J.; Lee, N.; Powell, G. Solution properties of apolipoproteins. *Methods Enzymol.* **1986**, *128*, 375−387.
11. Kazanji, M.; Laurent, F.; Péry, P. Immune responses and protective effect in mice vaccined orally with surface sporozoite protein of *Eimeria falciformis* in ISCOMs. *Vaccine* **1994**, *12* (9), 798−804.
12. Koppel, D. E. Analysis of macromolecular polydispersity in intensity correlation spectroscopy: The method of cummulants. *J. Chem. Phys.* **1972**, *15*, 4814−4820.
13. Wi, S.; Pancoska, P.; Keiderling, T. A. Predictions of protein secondary structures using factor analysis on Fourier transform infrared spectra: effect of Fourier self-deconvolution of the amide I and amide II bands. *Biospectroscopy* **1998**, *4* (2), 93−106.
14. *Prota FTIR protein analyzer user's guide;* Bomem, Inc.: Quebec, Canada.
15. Hinshelwood, C. N. *The kinetics of chemical change;* Clarendon Press: Oxford, 1940.
16. Atkinson, D.; Small, D. M. Recombinant lipoproteins: Implications for structure and assembly of native lipoproteins. *Annu. Rev. Biophys. Biophys. Chem.* **1986**, *15*, 403−456.
17. Susi, H.; Byler, D. Resolution-enhanced Fourier transform infrared spectroscopy of enzymes. *Methods Enzymol.* **1986**, *130*, 290−311.

JS990158L

Major Metabolites of Substance P Degraded by Spinal Synaptic Membranes Antagonize the Behavioral Response to Substance P in Rats

CHIKAI SAKURADA,*,† CHIZUKO WATANABE,‡ SHINOBU SAKURADA,§ KOICHI TAN-NO,|| AND TSUKASA SAKURADA†

Contribution from *Department of Biochemistry, Daiichi College of Pharmaceutical Sciences, 22-1 Tamagawa-cho, Minami-ku, Fukuoka 815-8511, Japan, and Center for Laboratory Animal Science, Department of Physiology and Anatomy, and Department of Pharmacology, Tohoku Pharmaceutical University, 4-4-1 Komatsushima, Aoba-ku, Sendai 981-0905, Japan.*

Received May 12, 1999. Accepted for publication August 11, 1999.

Abstract □ Substance P (SP) was degraded by synaptic membranes of rat spinal cord. Cleavage products were separated by reversed phase high performance liquid chromatography and identified by amino acid composition analyses. Major products of SP were phenylalanine, SP(1–4), SP(1–6), SP(1–7), SP(10–11), and SP(8–9). Both the degradation of SP and the accumulation of the major cleavage products were strongly inhibited by a metal chelator, *o*-phenanthroline, and also by specific inhibitors of endopeptidase-24.11, thiorphan, and phosphoramidon. Thus, endopeptidase-24.11 plays a major role in SP degradation in the rat spinal cord. N-Terminal fragments, SP(1–7) and SP(1–4), detected after incubation with spinal synaptic membranes were examined in vivo for antagonism against the scratching, biting, and licking response induced by intrathecal (IT) injection of SP (3.0 nmol) in rats. When IT coadministered with SP, SP(1–7) and SP(1–4) produced a significant inhibition of behavioral response to SP with ED_{50} of 135.0 pmol and 6.2 nmol, respectively. These results suggest that the degradation of SP in the spinal cord is not only responsible for inactivation of parent peptide, but may also lead to the formation of N-terminal SP-fragments which are shown to display a novel physiological function.

Introduction

Substance P (SP) is an undecapeptide which is widely distributed in the central nervous system and peripheral tissues.[1] This peptide is thought to function as a neurotransmitter or neuromodulator after secretion into synapse.[2,3] A member of tachykinins, SP is the endogenous ligand for the tachykinin NK_1 receptor, while neurokinin A and neurokinin B are endogenous ligands for NK_2 and NK_3 receptors, respectively.[4,5]

SP is believed to play an important role as an excitatory peptide in the spinal cord. Recently, two groups have reported that mice in which the preprotachykinin A gene was disrupted showed reduced responses to pain stimuli. Zimmer et al.[6] indicated that knockout mice which cannot produce SP and neurokinin A display no significant pain responses following hindpaw formalin injection. In addition, the animals have an increased pain threshold in the hot-plate test. Cao et al.[7] also reported that nociceptive response evoked by a hindpaw injection of capsaicin, an intensely noxious chemical stimulus that directly activated C-fibers, was significantly reduced in the knockout mice. They also found decreased nociceptive response of the knockout mice in the model of acute visceral pain by using the procedure of the acetic acid- and $MgSO_4$-induced writhing assay.

The physiological action of SP is probably terminated by a membrane-bound protease capable of degrading SP in the synaptic region, by analogy with membrane-bound acetylcholinesterase functioning in acetylcholine degradation in the synapse. Several membrane-bound neuropeptidases, endopeptidase-24.11,[8−10] SP-degrading enzyme from human brain,[11] SP-degrading endopeptidase from rat brain,[12] post-proline dipeptidyl-aminopeptidase,[13] and angiotensin-converting enzyme,[10,14−16] have been reported to be involved in the degradation of SP. SP is degraded into N- and C-terminal fragments by endogenous neuropeptidase. However, the physiological function of these neuropeptidases from a membrane fraction of rat spinal cord has still remained obscure. It has been reported that some of C-terminal SP-fragments exert actions within the central nervous system similar to those observed with SP, whereas N-terminal fragments have opposite or antagonizing effects on SP action.[17]

In our previous study,[18] SP(1−7) and SP(1−8) in the low picomole range antagonize the scratching, biting, and licking response induced by IT co-administration of SP in mice. In this study, we examined the degradation of SP by synaptic membranes of rat spinal cord. Additional in vivo experiments were performed to investigate the antagonizing effect of N-terminal SP-metabolites, SP(1−7) and SP-(1−4), on the characteristic behavioral response elicited by IT administration of SP in the rat.

Experimental Section

Animals—Male Wistar rats (Shizuoka Laboratory Center, Japan), weighing 250−300 g at the time of surgery, served as subjects. Animals were housed in a temperature (22 ± 24 °C)- and humidity (60−70%)-controlled room illuminated on a 12-h light and 12-h dark cycle. Food (Clea Japan, Inc., Osaka, Japan) and water were provided ad libitum throughout the course of the study.

Peptides and Chemicals—The commercial drugs used were: SP, phosphoramidon, chymostatin, leupeptin (Peptide Institute, Inc., Osaka, Japan), SP (1−4), SP(1−7), SP(1−9), SP(2−11), SP-(3−11), SP(4−11), SP(5−11), SP(8−11), SP(9−11), SP(6−11), SP-(7−11), *p*-chloromercuribenzenesulfonic acid (PCMBS), thiorphan (Sigma Chemical Co., St. Louis, MO), constant boiling hydrochloric acid (Pierce Chemical Co., Rockford, IL), captopril and phenylmethyl sulfonyl fluoride (PMSF) (Nacalai tesque, INC, Kyoto, Japan). Z-321 was obtained through courtesy of Zeria Pharmaceutical Co., Ltd., Saitama, Japan.

Preparation of Synaptic Membranes from Rat Spinal Cord—Rat spinal cord was washed with 10 mM Tris-HCl (pH 7.5)

* To whom correspondence should be sent. Tel: +81−92−541−0161. Fax: +81−92−553−5698. E-mail: chikai@daiichi-cps.ac.jp.
† Daiichi College of Pharmaceutical Sciences.
‡ Center for Laboratory Animal Science, Tohoku Pharmaceutical University.
§ Department of Physiology and Anatomy, Tohoku Pharmaceutical University.
|| Department of Pharmacology, Tohoku Pharmaceutical University.

10.1021/js990149c CCC: $18.00 Published on Web 10/05/1999

containing 155 mM NaCl, suspended in a 10-fold volume of 10% (w/w) sucrose, and homogenized with a Teflon homogenizer. The homogenate was centrifuged at 800*g* for 20 min and then at 9000*g* for 20 min. The second pellet was suspended in about a 5-fold volume of 5 mM Tris-HCI (pH 8. 1). Then the suspension was incubated at 0 °C for 30 min for lysis of the pellet and subjected to discontinuous sucrose density gradient centrifugation according to the method of Jones and Matus.[19] Particle materials present at the interface between the layer containing 28.5% sucrose and that containing 34% sucrose were taken, diluted with 5 mM Tris-HCI (pH 8.1), and centrifuged at 100 000*g* for 1 h. The resulting pellet was suspended in 10 mM [2-[4-(2-hydroxyethyl)1-piperazinyl]ethanesulfonic acid (HEPES)−NaOH (pH 7.5) containing 155 mM NaCl and stored at −80 °C. Protein was determined by the method of Bradford[20] using bovine serum albumin (Bio-Rad) as a standard.

Degradation of Substance P by Synaptic Membranes of Rat Spinal Cord—The degradation of SP by synaptic membranes of rat spinal cord was carried out at 37 °C in a mixture (0.1 mL) containing of 10 mM HEPES−NaOH (pH 7.4), 80 mM NaCl, 2.5 mM KCl, 2 mM $MgCl_2$, 1 mM $CaCl_2$, 50 μM SP, and 50 μg protein of the membrane. The reaction was terminated by heating at 100 °C for 10 min. The reaction mixture was centrifuged, filtered through a membrane filter (Cosmonice Filter; pore size, 450 nm), and subjected to high performance liquid chromatography (HPLC) on a reversed phase column (4.6 × 150 mm) of SYMMETRYC18 (Waters) which had previously been equilibrated with l % (v/v) acetonitrile in 0.05% (v/v) trifluoroacetic acid (TFA). Elution was carried out at room temperature with a 32 min linear gradient of 1−65% acetonitrile in 0.05% TFA at a flow rate of 1 mL/min. The peptide fragments eluted were detected by monitoring the absorbance at 210 nm.

Identification of Substance P Fragments—The cleavage products separated by HPLC were lyophilized and hydrolyzed with 6 M hydrochloric acid containing 0.1% mercaptoethanol at 150 °C for 1 h. Their amino acid compositions were determined as phenylthiocarbamoyl amino acid derivatives by the reversed phase HPLC.[21]

Intrathecal Injection—To permit application of peptides directly into the spinal subarachnoid space, rats were anesthetized with pentobarbital sodium (50 mg/kg, ip) and chronically implanted with IT catheters.[22,23] Briefly, this involved inserting a length of polyethylene tubing (PE-10) following laminectomy between L3 and L4 and careful placing the catheter tip in the subarachnoid space of L5 and L6. The rats were allowed to recover over 7 days following implantation of the catheter. The catheter was filled with sterile artificial cerebrospinal fluid (CSF) containing (in g/L) NaCl 7.4, KCl 0.19, $MgCl_2$ 0.19, $CaCl_2$ 0.14. Peptides used in the experiments were administered in volumes of 10 μL followed by 15 μL of artificial CSF to ensure that peptides reached the spinal cord. SP(1−7) or SP(1−4) was mixed and coadministered IT with SP such that all doses were delivered in a total volume of 10 μL followed by 15 μL of artificial CSF to flush the catheter.

Behavioral Observation—One hour prior to IT injection, animals were adapted to an individual plastic cage (34 × 30 × 17 cm) which also served as the observation chamber. Immediately following IT injection of SP, each rat was replaced into the transparent cage, and behavioral testing was begun. The total respose time(s) of behaviors was measured for 5 min beginning immediately after IT injection of SP. These behaviors included hindlimb scratching directed toward the flank, biting, or licking of the hindpaw. All these different behaviors were pooled as a single value for each animal. Studies on the behavioral experiments were performed with the approval of the Ethics Committee of Animal Experiment in Tohoku Pharmaceutical University.

Calculations of ED_{50} and Data Analysis—Statistical analyses of the results were performed using the Dunnett's test for multiple comparisons, after analysis of variance (ANOVA). Differences were considered to be significant if $P < 0.05$. All values are expressed as means ±SEM.

Results

Degradation of SP by Synaptic Membranes of Rat Spinal Cord—Degradation of SP by synaptic membranes of rat spinal cord was analyzed by HPLC (Figure 1). About

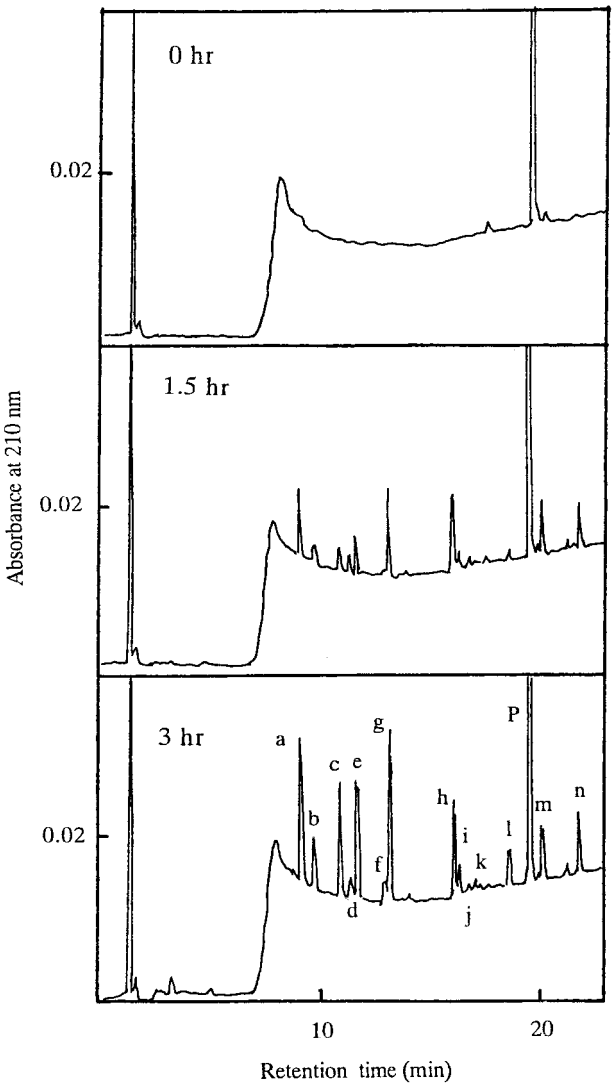

Figure 1—Degradation of substance P by synaptic membranes of rat spinal cord. The reaction mixture (0.5 mL, pH 7.5) containing 150 μg of the membrane preparation was incubated 37 °C for 0, 1.5, and 3.0 h. After heating at 100 °C for 5 min, 30 μL aliquots of the mixture were analyzed by HPLC on a reversed-phase column (4.6 × 150 mm) of SYMMETRYC18, which had been equilibrated with 1% acetonitrile in 0.05% trifluoroacetic acid. Elution was carried out at the room temperature with a 32-min linear gradient of 1–65% acetonitrile in 0.05% trifluoroacetic acid at a flow rate of 1 mL/min. The absorbance at 210 nm was monitored.

14 peaks were separated and named alphabetically from a to n according to the increasing order of their retention times. When only the membrane was incubated in the absence of SP or only SP was incubated, newly formed peaks were not detected at all. The position of peak P was identical to that of the substrate, SP, and the area of this peak decreased as a function of time (i.e., 15% and 32% of SP were degraded 1.5 h and 3 h after incubation, respectively), whereas those of other peaks increased. The results of analyses of amino acid compositions for the cleavage products separated by HPLC allowed their assignment (Table 1). Fragments b, c, g, h, l, m, and n were assignable as SP(1−4), free phenylalanine, SP(1−7), SP(1−9), SP(8−11), SP(3−11), and SP(5−11), respectively, by comparing their retention times in HPLC. The yield of peaks (a to n) was calculated on the basis of SP degraded by using procedure of quantitative amino acid composition analysis. Thus, N-terminal SP-fragments, SP(1−4), SP(1−6), SP(1−7), and SP(1−9), were found as major products in addition to free phenylalanine, SP(8−9), and SP(10−11).

Table 1–Amino Acid Composition of Fragments of SP[a] Produced through the Action of Synaptic Membranes of Rat Spinal Cord

peak	amino acid (mol %)								fragment identified	yield[b] (%)
	Arg	Pro	Lys	Glu	Phe	Gly	Leu	Met		
a	16	32	20	32	0	0	0	0	1–6	13
b	25	48	26	0	0	0	0	0	1–4	11
c	0	0	0	0	100	0	0	0	Phe	45
d	0	0	0	0	0	0	66	32	10–11	15
e	0	0	0	0	52	48	0	0	8–9	38
f	0	12	20	35	29	0	4	0	3–8	3
g	13	24	15	32	15	0	0	0	1–7	18
h	9	19	14	22	25	11	0	0	1–9	5
i	0	7	9	17	44	20	2	0	nd	
j	0	13	13	20	36	6	11	0	3–10	1
k	0	2	3	32	38	20	0	6	5–9	2
l	0	0	0	1	33	27	29	8	8–11	6
m	0	10	14	19	27	12	11	6	3–11	3
n	0	0	0	27	36	16	13	7	5–11	2
P[c]	8	14	11	16	22	10	13	6	complete	

[a] The sequence, Arg-Pro-Lys-Pro-Gln-Gln-Phe-Phe-Gly-Leu-MetNH_2. [b] Yield was determined on the basis of SP degraded. [c] The extent of degradation of SP was 68%. n.d., not determined.

Table 2–Effect of Protease Inhibitors on the Degradation of SP by Synaptic Membranes of Rat Spinal Cord[a]

inhibitor	concentration (mM)	inhibition (%)
o-phenanthroline	1.0	94
phosphoramidon	0.1	78
thiorphan	0.1	80
PCMBS	1.0	18
PMSF	1.0	24
captopril	0.1	0
bestatin	0.1	0
leupeptin	0.1	0
chymostatin	0.1	28
Z-321	0.1	3

[a] The activity was measured on the basis of the disappearance of SP, as detected by HPLC with isocratic elution.

Next, we examined the effects of various protease inhibitors on the degradation of SP by synaptic membranes of rat spinal cord. First, the inhibitory effects on the initial cleavage rate of SP were analyzed by measuring the effects on decrease of the HPLC peak for SP (peak P). The result was shown in Table 2. A metal chelator, *o*-phenanthroline and specific inhibitors for endopeptidase-24.11, phosphoramidon and thiorphan, inhibited SP degradation by synaptic membranes. Other inhibitors, including an angiotensin-converting enzyme inhibitor (captopril), a prolylendopeptidase inhibitor (Z-321),[24] an aminopeptidase inhibitor (bestatin), and inhibitors (PCMBS, PMSF, leupeptin, and chymostatin) for serine and cysteine proteases, had little inhibitory effects on SP degradation.

Second, the inhibitory effects on the generation of cleavage products of SP separated by HPLC were analyzed (Figure 2). The generation of all of the peaks including major peaks of N-terminal SP-fragments was strongly inhibited by the addition of thiorphan. Phosphoramidon and *o*-phenanthroline also showed strong inhibition, while other inhibitors exerted little inhibitory effect on the generation of almost all of the peaks (data not shown).

Effect of SP(1−7) and SP(1−4) on SP-Induced Behavioral Response—IT injections of SP (3.0 nmol) produced an immediate behavioral syndrome characterized by reciprocal hindlimb scratching, caudally directed biting, and licking. The intensity of the behavior peaked at 0−5 min, declined gradually at 5−10 min, and was no longer apparent at 15 min postinjection. In subsequent experiments, therefore, the animals were observed for 10 min following IT administration. In the in vivo experiments, N-terminal SP-fragments were tested for antagonism against the behavioral response induced by IT administration of SP. When coadministered IT with SP, SP(1−7) at doses of 40−400 pmol reduced the SP-induced behavioral response consisting of scratching, biting, and licking in a dose-dependent way (Figure 3). The SP-induced response was also dose-dependently decreased by IT coadministration of SP(1−4) (0.6−38.4 nmol) (Figure 3). The ED_{50} for SP(1−7) and SP(1−4) was 135.0 pmol and 6.2 nmol against SP, respectively. SP(1−7) and SP(1−4) in the dose-range tested did not produce SP-like behavioral response or any other motor disturbance.

Discussion

Although a number of laboratories have demonstrated that SP is extracellularly hydrolyzed by cell-surface endopeptidase, within the central nervous system,[8−16] the concurrent monitoring of SP and its metabolic fragments by synaptic membranes of rat spinal cord have not yet been explored. It is extremely of importance to note metabolic routes of SP in the spinal cord, since spinal dorsal horn is regarded as an important site for the processing of information related to the transmission and/or modulation of sensory signals including pain. The present findings show that SP was readily cleaved into SP(1−7) as a major product when incubated with synaptic membranes of rat spinal cord. Other N-terminal SP-fragments were also found, including SP(1−4), SP(1−6), and SP(1−9). It is, therefore, likely that the C-terminal SP-fragments released through the initial cleavage of SP may be susceptible readily to the action of neuropeptidases, since recoveries of C-terminal fragments were low compared with those of N-terminal fragments. These results are in accordance with our previous data that SP(1−7) is the main metabolite after endogenous cleavage of SP; in the dorsal spinal cord of rats the levels of SP(1−7) were about 20% those of SP, though in most of areas of the CNS the concentrations of SP(1−7) were about 10% those of SP.[25,26] Both the degradation of SP and the accumulation of the major cleavage products were strongly inhibited by a metal chelator, *o*-phenanthroline, and also by specific inhibitors of endopeptidase-24.11, thiorphan and phosphoramidon. Formation of the fragment SP(1−4) was also inhibited by the addition of thiorphan and phosphoramidon to the reaction medium. Since fragment SP(1−4) has not been reported to be formed directly by the action of endopeptidase-24.11 on SP, it may arise from the action of some other protease on the initial cleavage products formed by endopeptidase-24.11. Other peptide fragments were those formed by the cleavage between the Gln^6-Phe^7, Phe^7-Phe^8, Gly^9-Leu^{10} bonds of SP, all of which have been reported to be the sites of cleavage by endopeptidase-24.11 obtained from various synaptic membranes of pig caudate,[8] pig kidney,[9] human kidney,[10] rat substantia nigra,[27] glioma C6 cells,[28] and glial cells cultured from rat fetal brain.[29] In our previous report,[30] we have examined the effect of protease inhibitors on the scratching, biting, and licking response elicited by IT injection of SP in mice. Phosphoramidon simultaneously injected with SP remarkably enhanced and prolonged SP-induced behavioral response in a dose-dependent manner. SP-induced behavioral response was not enhanced by bestatin, an aminopeptidase inhibitor, and captopril, an angiotensin-converting enzyme inhibitor. Taking account of these behavioral observations, the present results suggest that thiorphan-sensitive metalloendopeptidse, probably endopeptidase-24.11, would play a critical role in the initial stage of cleavage of SP by synaptic membranes of rat spinal cord.

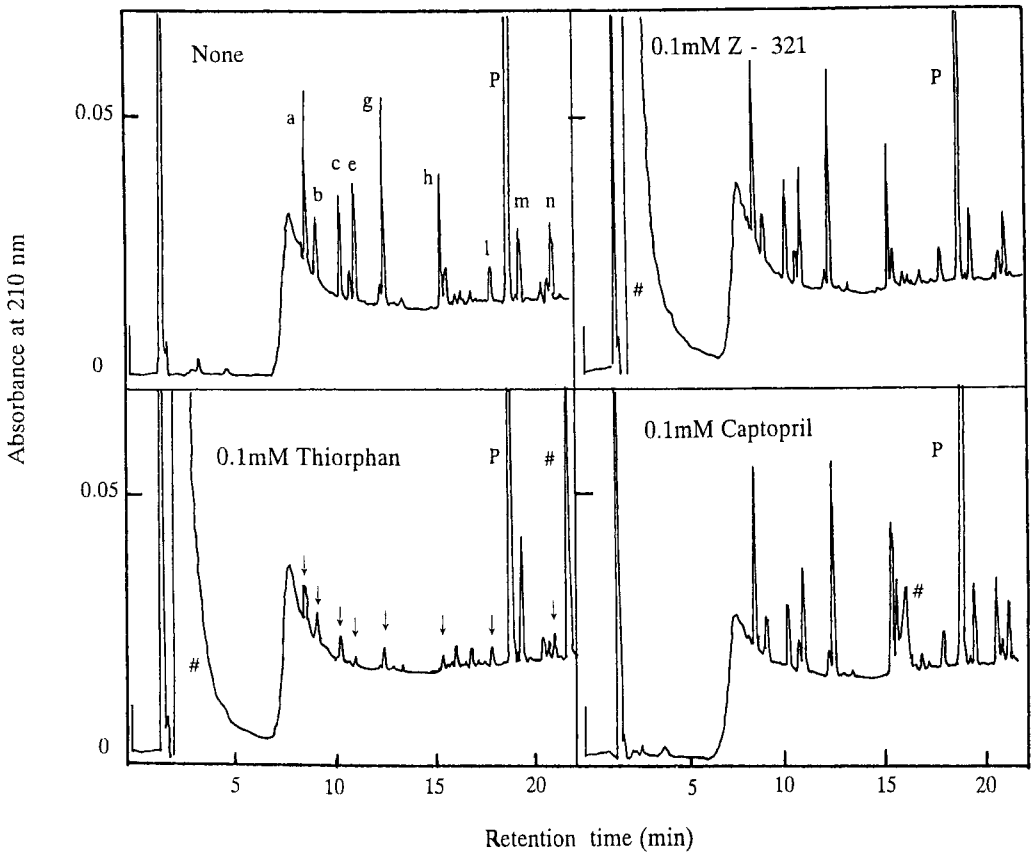

Figure 2—Effect of protease inhibitors on the degradation of substance P by synaptic membranes of rat spinal cord. The reaction mixture (0.5 mL, pH 7.5) containing 50 μg of the membrane preparation was incubated 37 °C for 6 h in the absence or the presence of 0.1 mM thiorpan, 0.1 mM Z-321, or 0.1 mM captopril. After heating at 100 °C for 5 min to stop the reaction, 20 μL aliquots of the sample were analyzed by HPLC as in Figure 1. # indicates the peak derived from the inhibitor added.

There are some reports related to SP degradation in rat spinal cord. Mauborgne et al.[31] have previously examined the effect of peptidase inhibitors on SP-like immunoreactive materials released by K^+-induced depolarization from slices of the rat spinal cord. They indicated that bacitracin was the most potent agent to protect SP-like immunoreactive materials from degradation, and captopril and thiorphan also protected it from degradation. Suzuki et al.[32] have reported the effects of peptidase inhibitors on the enzymatic degradation of SP by synaptic membranes of neonatal rat spinal cord. While they did not analyze and characterize the cleavage products of SP, they have presented that thiorphan, actinonin for an aminopeptidase N inhibitor, and captopril inhibited SP degradation. The inhibition potency of each peptidase inhibitor was lower than that of the mixture. They have also reported in electrophysiological studies that the magnitude of SP-evoked depolarization of a lumbar ventral root in the isolated spinal cord preparation was increased by a mixture of peptidase inhibitors, consisting of actinonin for an aminopeptidase N inhibitor, arphamenine B for an aminopeptidase B inhibitor, bestatin for an aminopeptidase B and M inhibitor, captopril, and thiorphan. These results are inconsistent with our results. Although the reason for this discrepancy remains unknown, in all cases, however, susceptibilities of SP degradation to thiorphan are consistent with each other. Recent biochemical data show that two enzymes with SP-degrading activity from the membrane bound fraction of the rat spinal cord are separated,[33] one enzyme exhibited similarity to endopeptidase-24.11, while the other resembled a substance P converting endopeptidase which has been identified and purified from human cerebrospinal fluid. Accordingly, SP(1−7), SP(1−8), SP(8−11), and SP(9−11) were detected after incubation with both enzyme. The former enzyme preparation also gave SP(1−6) as a major product. It is still unknown whether these enzymes play critical roles in SP degradation in rat spinal cord synapses.

Thus, SP is enzymatically cleaved into several C-terminal and N-terminal fragments, which have biological activity in the CNS sensory system. Some of C-terminal fragments, injected IT into mice, elicit scratching, biting, and licking response similar to that observed with SP, whereas N-terminal fragments have antagonizing effects on SP-induced behavioral response.[34] In addition, central actions of N-terminal fragments have previously been found to produce effects opposite to those of C-terminal fragments in mice. For example, the N-terminal heptapeptide inhibited grooming and increased rearing, whereas the C-terminal hexapeptide had the opposite effect.[17,35] Studies with microinjection into the substantia nigra demonstrate that SP induces dopamine release in the ipsilateral striatum and produces contralateral rotation in a dose-dependent manner.[36] In addition, intranigrally injected SP(1−7) produces an antagonistic action on the SP-induced response. In agreement with these previous findings, SP(1−7), injected into conscious rats produced a dose-dependent antagonizing effect on SP-induced behavioral response. Similar effects were obtained by coadministration of SP-(1−4), though SP(1−4) is approximately 45 times less potent than SP(1−7) in antagonizing the response to SP. These results are in line with our recent data in mice (unpublished data) that SP(1−7) is much more potent than SP(1−4) as assayed by the spinally mediated SP response. Taken together, our biochemical and pharmacological results suggest that endogenously formed SP(1−7) may be a main modulator of SP actions in the rat spinal cord.

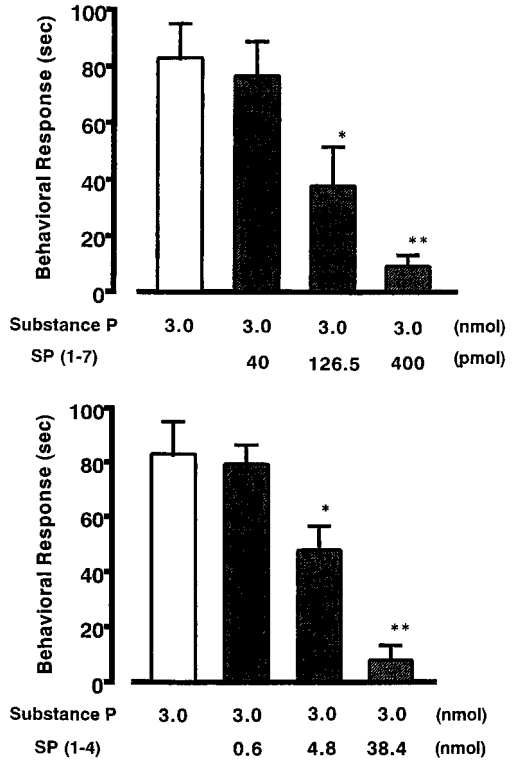

Figure 3—The effectiveness of substance P(1–7) (upper panel) and substance P(1–4) (lower panel) in antagonizing the scratching, biting, and licking behavior induced by substance P in rats. Substance P (3.0 nmol) was coadministered intrathecally with substance P(1–7) or substance P(1–4). The duration of the behavioral response induced by substance P was determined over a 10 min period starting immediately after intrathecal injection. The data are given as means ±SEM of six rats in each group. $^{**}P < 0.01$, $^{*}P < 0.05$ when compared to substance P alone.

Mechanism of spinal actions of N-terminal SP-fragments is still unclear. In the present study, there was no significant difference of potency in the antagonizing effect of SP(1−7) on SP-induced behavioral response between rats and mice, when comparing the ED_{50} value of SP(1−7) (135.0 pmol) against SP (3.0 nmol) in rats with that of SP(1−7) (2.9 pmol) against SP (100 pmol) in mice.[34] These data suggest that SP(1−7) may inhibit binding of [^{3}H]-SP(1−7) to rat and mouse spinal cord membranes with similar potency.[37] It is noteworthy that similar phenomena are seen in affinities of CP-96,345 for tachykinin NK_1 receptor; the nonpeptide tachykinin NK_1 receptor antagonist, CP-96,345, was much less active at NK_1 receptors in rat and mouse than the other mammalian species including human, whereas there was no significant difference in affinity of CP-96,345 for NK_1 receptors between rat and mouse.[38,39]

It is of interest to note that the antagonistic effect of SP-(1−7) on SP-induced behavioral response in mice was inhibited by naloxone, an opioid receptor antagonist, and [D-Pro^2, D-Phe^9] SP(1−7), an inhibitor of [^{3}H]-SP(1−7) binding, but not by selective antagonists of μ-, δ-, and κ-opioid receptors.[40] One could speculate that a physiological action of SP(1−7) in the spinal cord may not be mediated by an action at a typical opioid receptor but by an action at SP(1−7) binding site or its own receptor.

In conclusion, the degradation of SP by endopeptidase-24.11 in the spinal cord is not only responsible for inactivation of SP, but may also lead to the formation of N-terminal fragments which are shown to display a novel physiological function as a result of a shift to receptor specificity.

References and Notes

1. Maggio, J. E.: Tachykinins. *Annu. Rev. Neurosci.* **1988**, *11*, 13−28.
2. Nicoll, R. A.; Schenker, C.; Leeman, S. E.: Substance P as a transmitter candidate. *Annu. Rev. Neurosci.* **1980**, *3*, 227−268.
3. Pernow, B.: Substance P. *Pharmacol. Rev.* **1980,** *35*, 85−141.
4. Maggi, C. A.; Patacchini, R.; Rovero, P.: Giachetti, A.: Tachykinin receptors and tachykinin receptor antagonists. *J. Autonom. Pharmacol.* **1993**, *13*, 23−93.
5. Regoli, D.; Nantel, F.: Pharmacology of neurokinin receptors. *Biopolymers* **1991**, *31*, 777−783.
6. . Zimmer, A.; Zimmer, A. M.; Baffi, J.; Usdin, T.; Reynolds, K.; Konig, M.; Palkovits, M.; Mezey, E.: Hypoalgesia in mice with a targeted deletion of the tachykinin 1 gene. *Proc. Natl. Acad. Sci. U.S.A.* **1998**, *95*, 2630−2635.
7. Cao, Y. Q.; Mantyh, P. W.; Carlson, E. J.; Gillespie, A. M.; Epstein, C. J.; Basbaum, A. I.: Primary afferent tachykinins are required to experience moderate to intense pain. *Nature* **1998**, *392*, 390−394.
8. Matsus, R.; Fulcher, I. S.; Kenny, A. J.; Turner, A. J.: Substance P and [Leu] enkephalin are hydrolyzed by an enzyme in pig caudate synaptic membranes that is identical with the endopeptidase of kidney microvilli. *Proc. Natl. Acad. Sci. U.S.A.* **1983**, *80*, 3111−3115.
9. Matsus, R.; Kenny, A. J.; Turner, A. J.: The metabolism of neuropeptides. The hydrolysis of peptides, including enkephalins, tachykinins and their analogues, by endopeptidase-24.11. *Biochem. J.* **1984**, *223*, 433−440.
10. Skidgel, R. A.; Engelbrecht, S.; Johnson, A. R.; Erdos, E. G.: Hydrolysis of substance P and neurotensin by converting enzyme and neutral endopeptidase. *Peptides* **1984**, *5*, 769−776.
11. Lee, C. M.; Sandberg, B. E. B.; Hanley, M. R.; Iversen, L. L.: Purification and characterization of a membrane-bound substance P-degrading enzyme from human brain. *Eur. J. Biochem.* **1980**, *114*, 315−327.
12. Endo, S.; Yokosawa, H.; Ishii, S.: Purification and characterization of a substance P-degrading endopeptidase from rat brain. *J. Biochem. (Tokyo)* **1988**, *104*, 999−1006.
13. O'Connor, B.; O'Connor, G.: Post-proline dipeptidyl-aminopeptidase from synaptosomal membranes of guinea-pig brain. *Eur. J. Biochem.* **1986**, *154*, 329−335.
14. Hooper, N. M.; Turner, A. J.: Isolation of two differentially glycosylated forms of peptidyl-dipeptidase A (angiotensin-converting enzyme) from pig brain: a reevaluation of their role in neuropeptide metabolism. *Biochem. J.* **1987**, *241*, 625−633.
15. Strittmatter, S. M.; Thiele, E. A.; Kapiloff, M. S.; Snyder, S. H.: A rat brain isozyme of angiotensin-converting enzyme. *J. Biol. Chem.* **1985**, *260*, 9825−9832.
16. Yokosawa, H.; Endo, S.; Ogura, Y.; Ishii, S.: A new feature of angiotensin converting enzyme: hydrolysis of substance P. *Biochem. Biophys. Res. Commun.* **1983**, *116*, 735−742.
17. Hall, M. E.; Stewart, J. M.: Substance P and behavior: Opposite effects of N-terminal and C-terminal fragments. *Peptides* **1983**, *4*, 763−768.
18. Sakurada, T.; Tan-No, K.; Yamada, T.; Sakurada, S.; Kisara, K.; Ohba, M.; Terenius, L.: N-terminal substance P fragments inhibit the spinally induced, NK-1 receptor mediated behavioural responses in mice. *Life Sci.* **1990**, *47*, PL109−PL113.
19. Jones, D. H.; Matus, A. I.: Isolation of synaptic plasma membrane from brain by combined flotation-sedimentation density gradient centrifugation. Biochim. *Biophys. Acta* **1974**, *356*, 276−287.
20. Bradford, M. M.: A rapid and sensitive method for the quantitation of microgram quantities of protein utilizing the principle of protein-dye binding. *Anal. Biochem.* **1976**, *72*, 248−254.
21. Bidlingmeyer, B. A.; Cohen, S. A.; Tarvin, T. L.: Rapid analysis of amino acids using precolumn derivatization. *J. Chromatogr.* **1984**, *336*, 93−104.
22. Kawamura, S.; Sakurada, S.; Sakurada, T.; Kisara, K.; Akutsu, Y.; Sasaki, Y.; Suzuki, K.: Antinociceptive effect of centrally administered cyclo (*N*-methyl-L-Tyr-L-Arg) in the rat. *Eur. J. Pharmacol.* **1983**, *93*, 1−8.
23. Yaksh, T.; Rudy, T. A.: Chronic catheterization of the spinal subarachnoid space. *Physiol. Behav.* **1976**, *17*, 1031−1036.
24. Tanaka, Y.; Yoshinaga, K.; Kizaki, K.; Furuichi, H.; Nakata, N.; Izumi, J.; Miura, N.; Matsumura, T.; Washizumi, M.; Kuwabara, Y.; Ikeda, Y.: Improving effects of Z-321, a new prolyl endopeptidase inhibitor, on the impaired cerebral functions. *Jpn. J. Pharmacol.* **1996**, *71*, Suppl 279P.

25. Sakurada, T.; Le Greves, P.; Terenius, L.: Measurement of substance P metabolites in rat CNS. *J. Neurochem.* **1985**, *44*, 718−722.
26. Sakurada, T.; Le Greves, P.; Terenius, L.: Fragmentation of calcitonin gene-related peptide and substance P in the rat central nervous system. *Neurochem. Int.* **1991**, *19*, 341−347.
27. Oblin, A.; Danse, M. J.; Zivkovic, B.: Metalloendopeptidase (EC 3.4.24.11) but not angiotensin converting enzyme is involved in the inactivation of substance P by synaptic membranes of the rat substantia nigra. *Life Sci.* **1989**, *44*, 1467−1474.
28. Endo, S.; Yokosawa, H.; Ishii, S.: Involvement of endopeptidase- 24.11 in degradation of substance P by glioma cells. *Neuropeptides* **1989**, *14*, 177−184.
29. Endo, S.; Yokosawa, H.; Ishii, S.: Degradation of substance P by neuronal and glial cells cultured from rat fetal brain and their membranes. *Neuropeptides* **1989**, *14*, 31−37.
30. Sakurada, T.; Tan-No, K.; Yamada, T.; Sakurada, S.; Kisara, K.: Phosphoramidon potentiates mammalian tachykinin-induced biting, licking and scratching behaviour in mice. *Pharmacol. Biochem. Behav.* **1990**, *37*, 779−783.
31. Mauborgne, A.; Bourgoin, S.; Benoliel, J. J.; Hamon, M.; Cesselin, F.: Is substance P released from slices of the rat spinal cord inactivated by peptidase(s) distinct from both 'enkephalinase' and 'angiotensin-converting enzyme' *Neurosci. Lett.* **1991**, *123*, 221−225.
32. Suzuki, H.; Yoshioka, K.; Yanagisawa, M.; Urayama, O.; Kurihara, T.; Hosoki, R.; Saito, K.; Otsuka, M.: Involvement of enzymatic degradation in the inactivation of tachykinin neurotransmitters in neonatal rat spinal cord. *Br. J. Pharmacol.* **1994**, *113*, 310−316.
33. Karlsson, K.; Eriksson, U.; Andren, P.; Nyberg, F.: Purification and characterization of substance P endopeptidase activities in the rat spinal cord. *Prep. Biochem. Biotechnol.* **1997**, 27, 59−78.
34. Sakurada, T.; Kuwahara, H.; Takahashi, K.; Sakurada, S.; Kisara, K.; Terenius, L: Substance P (1−7) antagonizes substance P-induced aversive behaviour in mice. *Neurosci. Lett.* **1988**, *95*, 281−285.
35. Hall, M. E.; Grantham, P.; Limoli, J.; Stewart, J. M.: Effects of substance P and neurokinin A (substance K) on motor behavior: unique effect of substance P attributable to its amino-terminal sequence. *Brain Res.* **1987**, *420*, 82−94.
36. Herrera-Marschitz, M.; Terenius, L.; Sakurada, T.; Reid, M. S.; Ungerstedt, U.: The substance P (1−7) fragment is a potent modulator of substance P actions in the brain. *Brain Res.* **1990**, *521*, 316−320.
37. Igwe, O. J.; Kim, D. C.; Seybold, V. S.; Larson, A. A.: Specific binding of substance P aminoterminal heptapeptide [SP(1−7)] to mouse brain and spinal cord membranes. *J. Neurosci.* **1990**, *10*, 3653−3663.
38. Gitter, B. D.; Waters, D. C.; Bruns, R. F.; Mason, N. R.; Nixon, J. A.; Howbert, J. H.: Species differences in affinities of non-peptide antagonists for substance P receptors. *Eur. J. Pharmacol.* **1991**, *197*, 237−238.
39. Beresford, I. J.; Birch, P. J.; Hagan, R. M.; Ireland, S. J.: Investigation into species variants in tachykinin NK_1 receptors by use of the non- peptide antagonist, CP-96, 345. *Br. J. Pharmacol.* **1991**, *104*, 292−293.
40. Mousseau, D. D.; Sun, X.; Larson, A. A.: Identification of a novel receptor mediating substance P-induced behavior in the mouse. *Eur. J. Pharmacol.* **1992**, *271*, 197−201.

Acknowledgments

This work was partly supported by a research grant, No. 08772151, from the Ministry of Education, Science, and Culture of Japan. The authors thank Yoshiko Inoue, Toshiko Kikuta, Hiromi Murakami, and Kaori Sueyoshi for technical assistance.

JS990149C

Physical Characterization of Picotamide Monohydrate and Anhydrous Picotamide

GIAMPIERO BETTINETTI,*,† PAOLA MURA,‡ MILENA SORRENTI,† MARIA T. FAUCCI,‡ AND ALESSANDRA NEGRI†

Contribution from *Dipartimento di Chimica Farmaceutica, Università di Pavia, Viale Taramelli 12, I-27100 Pavia, Italy, and Dipartimento di Scienze Farmaceutiche, Università di Firenze, Via G. Capponi 9, I-50121 Firenze, Italy.*

Received May 12, 1999. Accepted for publication August 2, 1999.

Abstract □ Picotamide is an antiplatelet agent given by mouth as monohydrate (PICOW) (Plactidil) in thrombo-embolic disorders. This study deals with physical characterization of PICOW recrystallized from various solvents and the respective dehydration products using X-ray powder diffractometry (XRD), infrared spectroscopy (IR), and thermal analytical techniques (differential scanning calorimetry, DSC; thermogravimetric analysis, TGA; simultaneous TGA/DSC; hot stage microscopy, HSM). Monophasic and biphasic DSC and TGA profiles of water loss were recorded under open conditions for PICOW samples which showed the same monoclinic crystal structure. Biphasic profiles became monophasic for gently ground samples which were, however, structurally identical to the intact samples. Morphological factors, the various degree of "perfection" of the PICOW crystal lattice, and/or cluster aggregation of PICOW crystals were assumed to be responsible for the differing dehydration patterns. Polymorphism in anhydrous picotamide, i.e., nucleation of crystal forms A, mp 135.5 ± 0.4 °C, and B, mp 152.9 ± 0.3 °C after dehydration of PICOW, was detected by DSC and HSM. The dehydration product of PICOW under isothermal conditions (115 °C, 20 mmHg), PICOA, was mainly composed of the lower melting polymorph A (fusion enthalpy 74.4 ± 2.2 J g^{-1}), which gradually reverted to the starting hydrate by storing in an ambient atmosphere. Dissolution tests of PICOW and PICOA in water at 37 °C as both powders and compressed disks reflected to some extent the higher solubility of the metastable form (by 24% at 37 °C) in terms of both higher dissolution efficiency and percent of active ingredient dissolved (by 28%) and intrinsic dissolution rate (by 32%).

Introduction

Picotamide (4-methoxy-*N*,*N*′-bis(3-pyridinylmethyl)-1,3-benzenedicarboxamide, Figure 1) is an antiplatelet agent sharing a dual anti-thromboxane activity (i.e., inhibition of thromboxane A2 synthase and thromboxane A2 receptor antagonism) which in the second half of the 1990s has been widely studied from the pharmacological and clinical point of views mainly in Italy.[1] Picotamide is given by mouth in thrombo-embolic disorders as monohydrate (PICOW), the active ingredient present in commercial dosage forms (Plactidil). The crystal structure of PICOW has been determined since 1986,[2] but the solid-state properties of this drug[3] and some of its binary systems with pharmaceutical excipients[4,5] have been investigated only recently.

Although all picotamide samples recrystallized by precipitation from various solvents showed the same physicochemical properties as PICOW, different DSC dehydration profiles and dehydration products were obtained depending on the recrystallizing solvent of the tested PICOW sample.[3] The same anhydrous crystal form, hereafter reported as PICOA, was however obtained by dehydration under isothermal conditions (115 °C, 20 mmHg) of PICOW, whatever the recrystallization solvent of the sample.

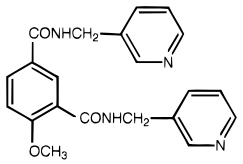

Figure 1—Molecular structure of picotamide.

The thermodynamic differences between a drug hydrate and its anhydrous counterpart necessitate detailed studies on their phase stability. The change in thermodynamic activity of the drug due to hydration/dehydration alters pharmaceutically important properties such as physical and chemical stability, as well as solubility and dissolution rate.[6–8] The effect of mechanical treatments, i.e., grinding, also deserve attention in this respect,[9] particularly because of the possible dependence of the dehydration mechanism on the particle size.[10,11]

The present study deals with the physical characterization of PICOW and PICOA by X-ray powder diffractometry (XRD), mid- and near-infrared (IR) spectroscopy, differential scanning calorimetry (DSC), thermogravimetric analysis (TGA), simultaneous TGA-DSC, and hot-stage microscopy (HSM). Thermal dehydration of intact and ground samples of PICOW from different recrystallization solvents and rehydration of PICOA under controlled conditions of relative humidity (RH) and temperature were investigated. The aqueous solubilities of PICOW and PICOA as a function of temperature (20−45 °C), as well as their dissolution rates in water at 37 °C as both powders and compressed disks, were also determined.

Experimental Section

Materials—Commercially available PICOW (Manetti & Roberts, Firenze, Italy) was used. The product was recrystallized from water−ethanol 8:1 (v/v) and subsequently dried in a desiccator over P_2O_5 at room temperature (see Table 1). PICOA was prepared by drying PICOW from water−ethanol 8:1 (v/v) under reduced pressure (over P_2O_5 in a drying pistol, 20 mmHg) in a hot air oven at 115 °C for 1 h and storing over P_2O_5 in a desiccator (see Table 1). Solvents of analytical reagent grade and bi-distilled water were used.

Preparation of PICOW Samples—Recrystallized samples were prepared by precipitation of PICOW from different recrystallization solvents following the procedures described in ref 3. Ground samples were prepared by manually grinding 500 mg of

* To whom correspondence should be addressed. Tel: 0382-507-368; fax: 0382-507-368; e-mail: betti@chifar.unipv.it.
† Università di Pavia.
‡ Università di Firenze.

10.1021/js990150b CCC: $18.00
Published on Web 09/16/1999

Table 1—Elemental Analysis and Water Content of Picotamide Monohydrate (PICOW) from Water–Ethanol 8:1 (v/v) and Anhydrous Picotamide (PICOA)

sample	elemental analysis (% w/w) found (calcd)	water content (% w/w)[a] KFT[b]	TGA[c]
PICOW	C 63.78(63.95)		
$C_{21}H_{20}N_4O_3 \cdot H_2O$	H 5.69(5.62)	4.96 (0.23)	4.84 (0.21)
	N 14.01(14.20)		
PICOA	C 67.24(67.01)		
$C_{21}H_{20}N_4O_3$	H 5.46(5.36)		
	N 14.81(14.88)		

[a] Calculated for the monohydrate 4.57% (w/w). [b] Karl-Fischer titrimetry, standard deviation in parentheses ($n = 6$). [c] Thermogravimetric analysis in open pans (mass loss over the temperature range of the DSC dehydration endotherm), standard deviation in parentheses ($n = 6$).

material with pestle and mortar. Rehydrated samples were prepared by storing PICOA (≈2 g samples spread on Petri dishes) in a desiccator at room temperature (22 °C) kept at a relative humidity (RH) of 45% or ≈100% by equilibrating over a saturated solution of KNO_2 or pure water, respectively. Samples (5−10 mg) were taken out at appropriate intervals and checked for water content by DSC and TGA (see below).

X-ray Diffractometry (XRD)—Powder X-ray diffraction patterns were taken at ambient temperature and atmosphere with a computer-controlled Philips PW 1800/10 apparatus equipped with a specific PC-APD software. Wavelengths: Cu $K_{\alpha,1} = 1.54060$ Å, Cu $K_{\alpha,2} = 1.54439$ Å. Scan range: 2−50° 2θ. Scan speed: 0.02° 2θ s^{-1}. Monochromator: graphite crystal.

Infrared (IR) Spectroscopy—Mid-IR (400−4000 cm^{-1}) spectra were recorded by the Nujol mull method using a double beam Perkin-Elmer 983 IR spectrophotometer. Near-IR (4500−10000 cm^{-1}) spectra (NIR) were recorded directly on powder samples (75−150 μm sieve granulometric fraction) by using an optical head linked to the NIR reflectance analyzer (Infraprover II Technicon Model No. 450 RP) by optical fibers.

Karl Fischer Titrimetry (KFT)—The amount of water in the PICOW samples was determined with a Mettler DL40GP Memo titrator apparatus. Samples (80−90 mg) were quickly transferred to the titration vessel containing anhydrous methanol and titrated using Hydranal Composite 5 (Riedel-de Haen, Milano, Italy).

Differential Scanning Calorimetry (DSC)—Temperature and enthalpy values were measured with a METTLER STAR^e system equipped with a DSC821^e Module on 3−5 mg (Mettler M3 Microbalance) samples in uncovered aluminum pans under static air. An uncovered empty pan was used as reference. The heating rate was 5 K min^{-1} over the 30−180 °C temperature range.

Thermogravimetric Analysis (TGA)—Mass losses were recorded with a Mettler TA 4000 apparatus equipped with a TG 50 cell at the heating rate of 5 K min^{-1} on 7−10 mg samples in open alumina crucibles in the 30−180 °C temperature range under static air.

Simultaneous TGA-DSC—Simultaneous recording of mass loss and enthalpy change was carried out with a METTLER STAR^e system equipped with a TGA/SDTA851^e Module and calibrated with indium on 2.5−3.5 mg samples in a platinum crucible under nitrogen gas flow (150 mL min^{-1}). The heating rate was 10 K min^{-1} over the 40−200 °C temperature range.

Hot-Stage Microscopy (HSM)—Microscopic observation of the thermal events was carried out under a Reichert polarized light microscope equipped with a Mettler FP82HT/FP80 system at a heating rate of 10 K min^{-1} which was reduced to 5 K min^{-1} in the regions of the DSC peaks. Images were transferred via a Panasonic WV-CP100E CCTV camera to a Panasonic WC-CH110A video monitor.

Solubility Measurements—Excess amounts (50 mg) of PICOW or PICOA powder (75−150 μm sieve granulometric fraction) were added to 30 mL of nonbuffered water (pH ≈ 6) in sealed 50 mL glass containers, which were electromagnetically stirred at a constant temperature (20, 25, 32, 37, 45 °C ± 0.2 °C). At suitable time intervals aliquots were withdrawn, filtered (pore size 0.45 μm), suitably diluted with water, and spectrophotometrically assayed for drug concentration at $\lambda = 254.4$ nm (Perkin-Elmer 552S Spectrophotometer). Residual solid material was identified

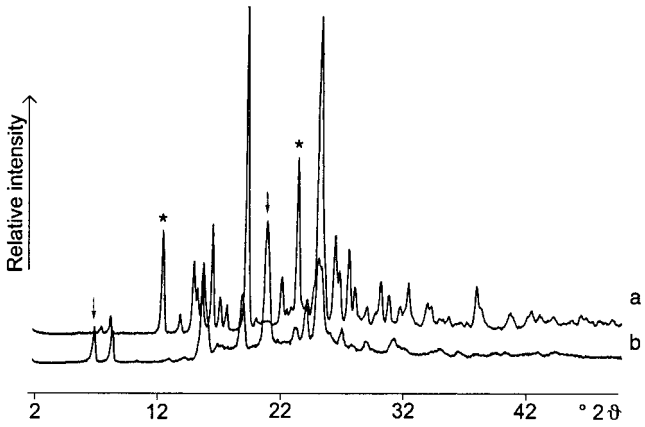

Figure 2—XRD patterns of (a) picotamide monohydrate (PICOW) from water–ethanol 8:1 (v/v) and (b) anhydrous picotamide (PICOA). Characteristic diffraction peaks of PICOW at 12.6° and 23.6° (2θ) (stars) and of PICO A at 7.1° and 21.2° (2θ) (arrows) are indicated.

postequilibrium by DSC and IR analysis. Plateau values of dissolved concentration of the metastable PICOA form, before declining toward the corresponding plateau value of the stable PICOW form, were assumed as the equilibrium solubility. Tests were performed in triplicate and averaged.

Dissolution Tests—Dispersed amount experiments were performed in nonbuffered water (pH ≈ 6) at 37 ± 0.2 °C by adding 45 mg of PICOW or PICOA powder (75−150 μm sieve granulometric fraction) to 75 mL of water in a 150 mL beaker (nonsink conditions). A glass three-blade propeller (19 mm diameter) was immersed in the beaker 25 mm from the bottom and rotated at 100 ± 1 rpm. In the rotating disk method, tablets (1.3 cm in diameter) were prepared by compressing 300 mg of powders using a Perkin-Elmer hydraulic press for KBr disks for IR spectroscopy, at a force of 1.5 t cm^{-2} for 10 min which yielded tablets with a surface area of 1.33 cm^2 which would not disintegrate during the test. No lubricant was used. No detectable PICOW dehydration or PICOA hydration associated with compression was found in the disks by IR, DSC, and TGA analysis of powder samples taken by gently scratching the disk surface with a blade. The tablets were inserted into a stainless steel holder, so that only one face was exposed to the dissolution medium. The holder was then connected to a stirring motor, centrally immersed in a 150 mL beaker containing 100 mL of nonbuffered water (pH ≈ 6) at 37 ± 0.2 °C and rotated at 100 ± 1 rpm. In both methods, suitable aliquots were withdrawn with a filter-syringe (pore size 0.45 μm) at the specified times and assayed for drug content as in Solubility Measurements. A correction was calculated for the cumulative dilution caused by replacement of the sample with equal volume of original medium. Each test was repeated four times (coefficient of variation, CV < 3% and < 7% for dispersed amount and rotating disk experiments, respectively).

Results and Discussion

Physicochemical Properties of the Solid Phases—PICOW and PICOA (see Table 1 for elemental analysis and water stoichiometry) were characterized with data from XRD, IR, conventional and simultaneous DSC and TGA, and HSM. The XRD pattern of PICOW corresponding to the theoretical powder pattern assessed from crystal structure data[3] was obtained using a ground sample (Figure 2). Actually, using an intact sample, a strong enhancement of the diffracted intensities of some peaks probably due to preferred orientation effects[12] was observed.[3] A distinctly different XRD pattern was recorded for PICOA, which shows characteristic reflections at 7.1° and 21.2° (2θ) which are useful for identification purposes and an apparent lower crystallinity than that of the parent hydrate.

The IR spectra of PICOW and PICOA are presented in Figure 3. In the O−H stretching region of PICOW, crystal-

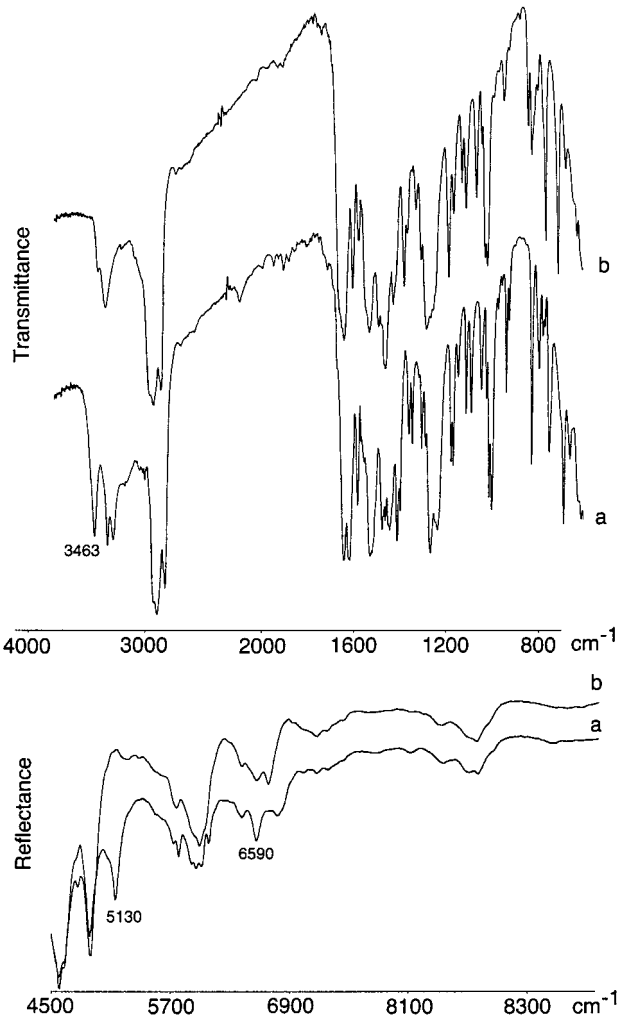

Figure 3—IR spectra of (a) picotamide monohydrate (PICOW) from water–ethanol 8:1 (v/v) and (b) anhydrous picotamide (PICOA) in the 4000–700 and 4500–9900 cm^{-1} range. Characteristic absorption bands of water at 3463 cm^{-1}, 5130 cm^{-1}, and 6590 cm^{-1} are indicated.

line water shows a sharp high-frequency (3463 cm^{-1}) absorption band[13] which suggests the presence of "tightly bound" water in the crystal lattice.[14] The number and strength of hydrogen bonds involving the water molecules regularly arranged through the crystal[2] confirm this hypothesis. Other differences at the level of the 3354−3304 (assignable to the N−H amide stretching) and 1658−1632 cm^{-1} (assignable to the amide carbonyl group) doublets in the anhydrous and hydrated structures can be attributed to the absence and presence of lattice water within the hydrogen bond patterns. The NIR absorption bands at 5130 and 6590 cm^{-1} are also characteristic of crystalline water[15,16] and permit discrimination between the anhydrous and hydrated picotamide forms.

The thermal behavior of PICOW obtained by recrystallization from water−ethanol 8:1 (v/v), ethyl acetate, or benzene and of PICOA is depicted in Figures 4−6. The negative DSC peak for endotherms between 60 and 130 °C (enthalpy change 189 ± 5 J g^{-1}) of the intact PICOW sample from water−ethanol 8:1 (v/v) (Figure 4a) was reflected by the negative derivative TGA peak for mass loss over the same temperature range (Figure 5a). The relevant mass loss of 4.84 ± 0.21% (w/w) was confirmed by simultaneous TGA/DSC (Figure 6) and corresponded to a monohydrate stoichiometry (see Table 1). Moderate grinding did not substantially alter the water content and the dehydration enthalpy of the sample, whereas it decreased (by 3−4

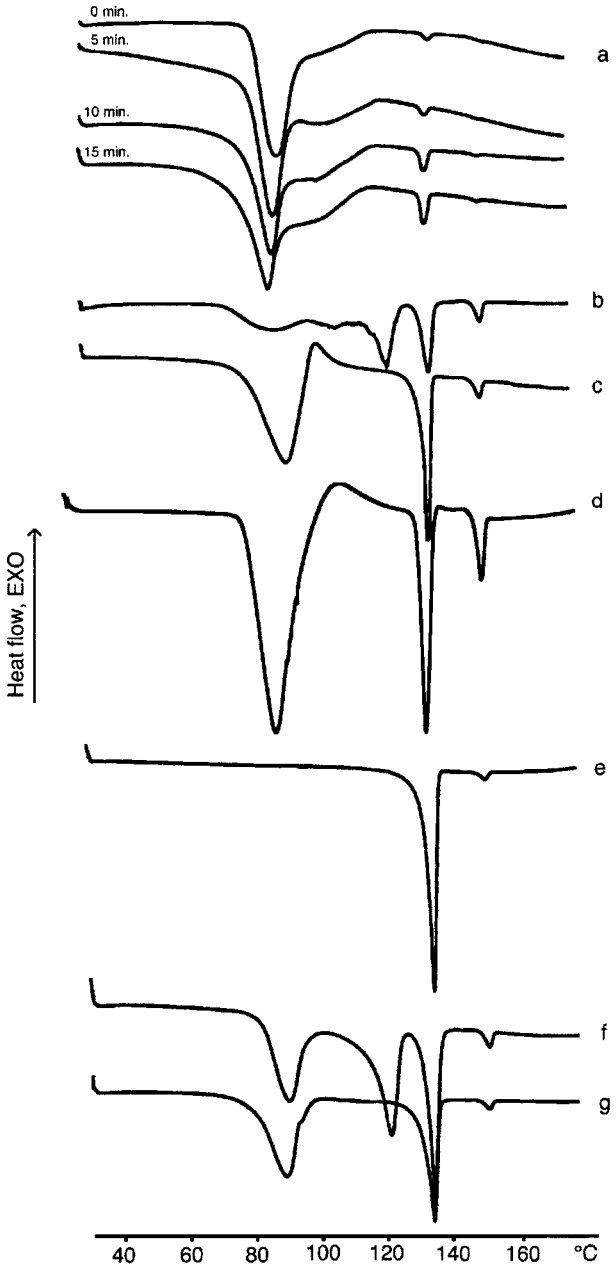

Figure 4—DSC curves of picotamide monohydrate (PICOW) and anhydrous picotamide (PICOA). Key: (a) PICOW from water–ethanol 8:1 (v/v) (grinding time on the curves); (b) PICOW from ethyl acetate, intact sample; (c) PICOW from ethyl acetate, ground sample; (d) PICOW from benzene, intact sample; (e) PICOA by isothermal dehydration (115 °C, 20 mmHg) of an intact sample of PICOW from water-ethanol 8:1 (v/v); (f) PICOW by rehydration of PICOA in an ambient atmosphere (RH ≈ 45%), intact sample; (g) PICOW by rehydration of PICOA at RH ≈ 45%, ground sample.

°C) the onset and peak temperatures of the DSC dehydration endotherm (see Figure 4a) possibly by reducing the particle size and changing the surface feature of the crystals.[17] A parallel increase in the enthalpy change of the small endothermal effect at ≈136 °C was evident. This effect was attributable to melting of the anhydrous crystal form A of picotamide (see later).

A thermal behavior similar to that depicted in Figures 4a and 5a was recorded for PICOW samples recrystallized from water, methanol, ethanol, and *n*-propanol.[3] Different DSC and TGA profiles in both the dehydration and post-dehydration stages were instead observed for PICOW recrystallized from ethyl acetate (Figures 4b and 5b) and from benzene (Figures 4d and 5d). The distinct crystal-

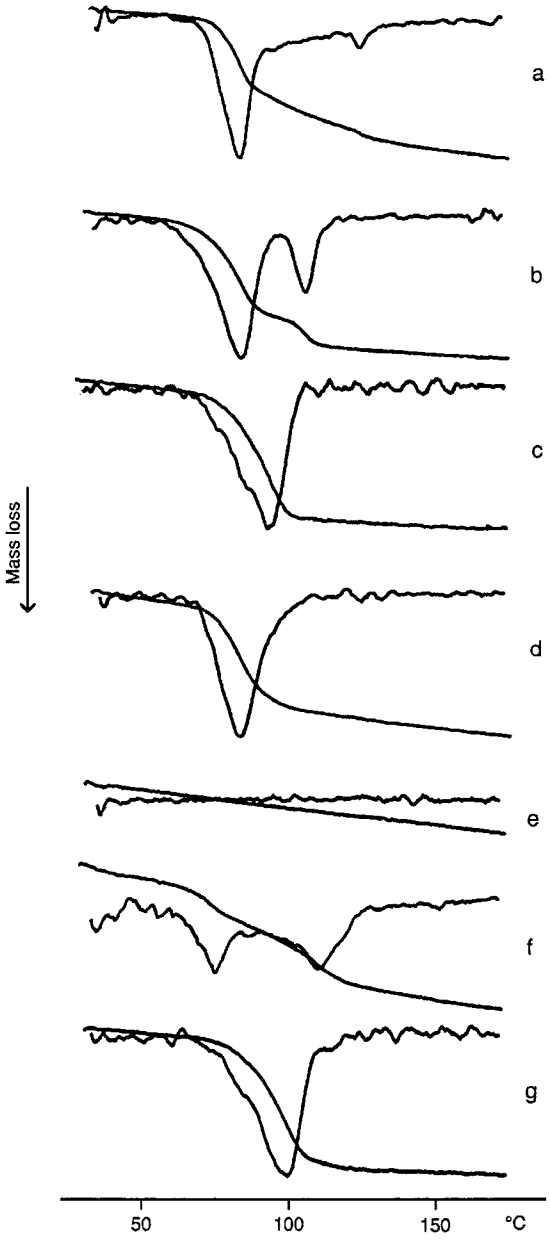

Figure 5—TGA curves of picotamide monohydrate (PICOW) and anhydrous picotamide (PICOA). Key: (a) PICOW from water–ethanol 8:1 (v/v), intact sample; (b) PICOW from ethyl acetate, intact sample; (c) PICOW from ethyl acetate, ground sample; (d) PICOW from benzene, intact sample; (e) PICOA by isothermal dehydration (115 °C, 20 mmHg) of (a); (f) PICOW by rehydration of PICOA in an ambient atmosphere (RH ≈ 45%), intact sample; (g) PICOW by rehydration of PICOA at RH ≈ 45%, ground sample.

lization of the lower-melting crystal form A (mp 135.5 ± 0.4 °C, fusion enthalpy 62 ± 10 J g^{-1}; $n = 8$) and the higher-melting crystal form B (mp 152.9 ± 0.3 °C, fusion enthalpy 14 ± 3 J g^{-1}; $n = 8$) of anydrous picotamide can be seen by the small exothermal effects at 115 °C and 138 °C in the sample recrystallized from benzene (Figure 4d).

The sequence of thermal events in Figure 4d was confirmed by HSM. Upon heating at 10 K min^{-1} from 25 to 100 °C and then reducing the heating rate to 5 K min^{-1} on a microscope stage, water evolution started at 110 °C and the newly formed small prismatic crystals melted at 136 °C. Upon further heating very few needle crystals were formed, which then melted at 153 °C.

XRD patterns of all recrystallized picotamide samples matched the theoretical XRD pattern of the monohydrate,[2,3] indicating that no difference existed in the fundamental

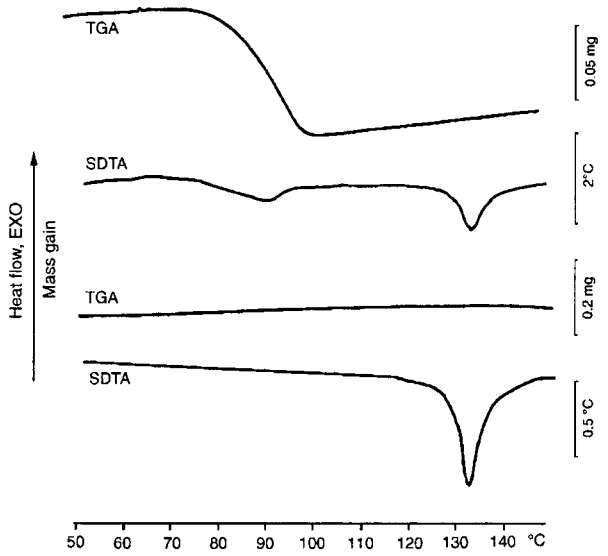

Figure 6—Simultaneous TGA-DSC curves over the 50–150 °C temperature range of picotamide monohydrate (PICOW) from water–ethanol 8:1 (v/v) (upper curves) and anhydrous picotamide (PICOA) (lower curves).

crystal lattice of the PICOW samples examined.[18] IR spectra also show that these samples were structurally identical. Therefore, the biphasic DSC dehydration profile recorded for the intact sample from ethyl acetate (Figure 4b) and reflected by the dTGA curve (Figure 5b) can be attributed to different crystal size and shape or various degrees of "perfection" of a common lattice structure of the tested samples.[19,20] Implications of the morphology of a pharmaceutical solid on the bulk properties of the material have been reported for furosemide,[21] nitrofurantoin,[22] and diclofenac/*N*-(2-hydroxyethyl)pyrrolidine salt.[23] Surface characteristics, adsorbed or occluded impurities and crystal defects which prevent the perfect alignment of molecules in the crystal lattice as well as nuclei of anhydrous polymorphs formed, may also affect the kinetics of solid-state transitions,[23] in particular dehydration. Actually, a highly strained or stressed lattice structure loses water more easily than a regular one. Cluster aggregation of PICOW crystals grown in ethyl acetate solution may also be responsible for the observed thermal behavior. Samples from ethyl acetate, which had been gently ground to ensure homogeneity of the polycrystalline material with no apparent alteration of the XRD pattern of the intact samples, showed indeed a monophasic dehydration pattern in both DSC (Figure 4c) and dTGA (Figure 5c) curves.

As can be seen in Figures 4e and 5e, the product of isothermal dehydration at 115 °C and 20 mmHg of PICOW from water−ethanol 8:1 (v/v) was almost totally composed of the lower-melting crystal form A, with enthalpy of fusion 74.4 ± 2.2 J g^{-1} ($n = 7$). Simultaneous TGA/DSC confirmed that no mass loss was associated with the endothermal effect at ≈136 °C (Figure 6). By storing at a RH of 45% or ≈100% and room temperature (22 °C), PICOA transformed to PICOW, as confirmed by DSC, TGA, and IR spectroscopy. Transformation to monohydrate was rather fast (within 48 h) at ≈100% RH and rather slow (within 3 months) at 45% RH. PICOW samples obtained by rehydration of PICOA in an ambient atmosphere (RH ≈ 45%) show biphasic dehydration patterns similar to those recorded for intact PICOW samples recrystallized from ethyl acetate (see Figures 4b and 5b). The couple of DSC endotherms centered at 91 °C (dehydration enthalpy 56.2 J g^{-1}) and 122 °C (dehydration enthalpy 60.4 J g^{-1}) in Figure 4f was reflected by a two-step TGA mass loss of 1.9% (w/w) and 2.5% (w/w) in Figure 5f. Thermal analysis of gently ground samples of rehydrated PICOA showed that

Table 2—Equilibrium Solubilities of Picotamide Monohydrate (PICOW) from Water–Ethanol 8:1 (v/v) and Anhydrous Picotamide (PICOA) in Water at Various Temperatures

temperature (°C)	equilibrium solubility (μg/mL)[a]	
	PICOW	PICOA
20	88(8)	158(13)
25	123(9)	207(16)
32	172(12)	249(17)
37	234(14)	289(18)
45	328(13)	368(18)

[a] Standard deviation in parentheses ($n = 3$).

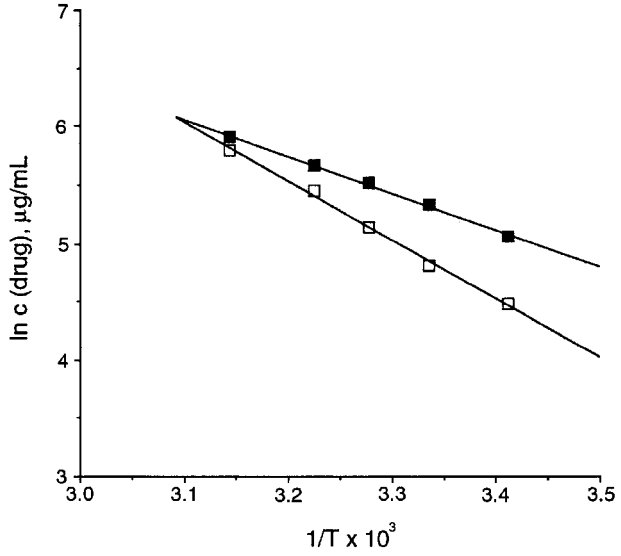

Figure 7—Van't Hoff plot from the solubility data (Table 2) of picotamide monohydrate (PICOW) from water–ethanol 8:1 (v/v) (□) and anhydrous picotamide (PICOA) (■).

the split DSC endotherms and dTGA peaks gathered in a single thermal effect with an associated enthalpy change (121.5 J g^{-1}) and mass loss (4.9% (w/w)) nearly equal to the sum of those of the single effects (Figures 4g and 5g). The monophasic dehydration pattern of ground samples, which show the same XRD pattern (i.e., structural arrangement) as the intact ones, confirms that external factors such as morphology, surface characteristics, cluster aggregation, etc., are responsible for the observed thermal behavior.

Solubility and Dissolution Properties of the Solid Phases—The equilibrium solubilities of PICOW and PICOA in water as a function of temperature are given in Table 2. The solubility of the stable hydrated form was calculated from the plateau value of dissolved concentration at each temperature. The maximum concentrations of dissolved PICOA at each temperature also gave plateau values, which were maintained for about 1 h (at 45 °C) to about 4 h (at 20 °C) before declining toward the corresponding equilibrium solubility values of PICOW due to phase transition. A crystalline anhydrous to hydrate phase change has been reported for theophylline, which is rapidly transformed to monohydrate in contact with water where simultaneous dissolution and hydrate formation occurs.[24,25] At 45 °C the solubility level of PICOW (i.e., complete transformation of the metastable phase, as confirmed by DSC and IR analysis of the residual solid material) was reached in >4 h. This behavior suggested that the maximum dissolved concentration of PICOA can be assumed as its equilibrium solubility.[26] The metastable to stable solubility ratios of 1.1−1.8 over the range of temperatures tested (Table 2) were typical of anhydrous−hydrate drug systems[27] and confirmed this hypothesis. By plotting the solubility data according to the van't Hoff equation,[26] a good linearity was observed (Figure 7). The least squares linear regression gave a slope of $(-4.90 \pm 0.16) \times 10^3$, an intercept of 21.2 ± 0.5 and a coefficient of determination of 0.997 for the stable PICOW form, and a slope of $(-3.0 \pm 0.2) \times 10^3$, an intercept of 15.4 ± 0.6 and a coefficient of determination of 0.988 for the metastable PICOA form. The transition temperature at which PICOW and PICOA have equal solubilities, free energies, and stabilities was 50 ± 6 °C.

Table 3—Dissolution Efficiency (DE),[a] Percent of Active Ingredient Dissolved (DP),[b] and Intrinsic Dissolution Rate Constants (IDR)[c] of Picotamide Monohydrate (PICOW) from Water–Ethanol 8:1 (v/v) and Anhydrous Picotamide (PICOA) in Water at 37 °C (standard deviations in parentheses refer to last decimal digit).[d]

sample	DE			DP			IDR
	10 min	30 min	60 min	10 min	30 min	60 min	
PICOW	12.6(3)	17.3(4)	19.8(5)	17.5(4)	21.5(5)	23.0(4)	1.26(8)
PICOA	15.9(4)	22.4(6)	25.4(7)	22.7(6)	27.6(8)	29.2(8)	1.66(9)

[a] Area under the dissolution curve with $t = 10$, 30, and 60 min (measured using the trapezoidal rule) expressed as a percentage of the area of the rectangle described by 100% dissolution in the same time (see Figure 8). [b] Calculated at $t = 10$, 30, and 60 min. [c] K_i, mg cm^{-2} h^{-1}. [d] Each value is the average of four determinations.

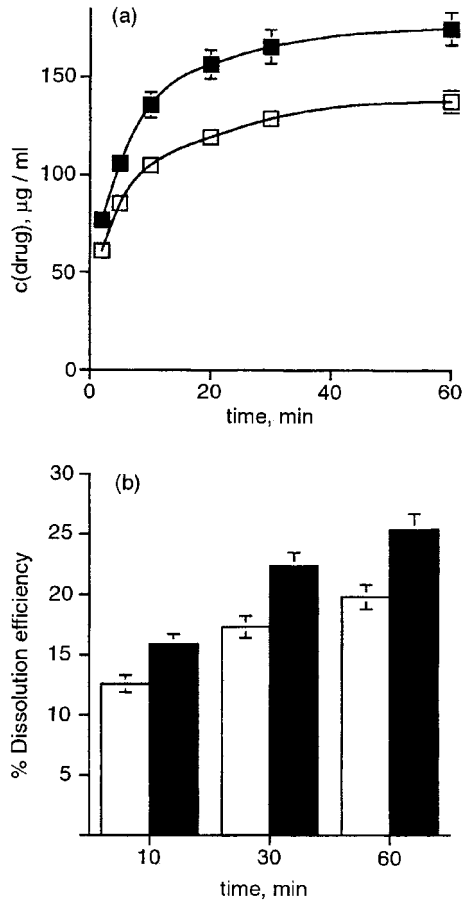

Figure 8—Dispersed amount curves in water at 37 °C (a) and dissolution efficiency (b) of picotamide monohydrate (PICOW) from water–ethanol 8:1 (v/v) (□) and anhydrous picotamide (PICOA) (■). Error bars indicate standard deviation ($n = 4$).

Dispersed amount experiments revealed statistically significant differences ($P < 0.01$) between PICOA and PICOW in terms of both dissolution efficiency at 10, 30, and 60 min and percent of drug dissolved at the same

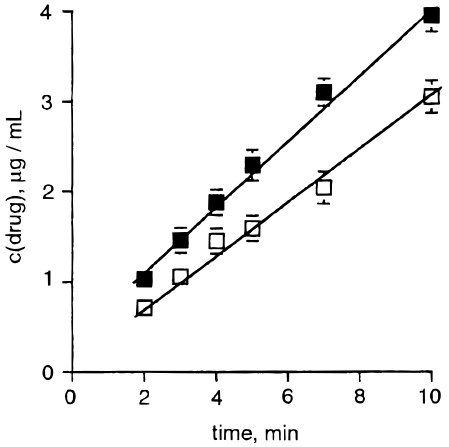

Figure 9—Intrinsic dissolution rates in water at 37 °C of picotamide monohydrate (PICOW) from water-ethanol 8:1 (v/v) (□) and anhydrous picotamide (PICOA) (■). Error bars indicate standard deviation ($n = 4$).

times, in accordance with the solubility data (Table 3 and Figure 8). The metastable to stable dissolution efficiency ratios and percent of drug dissolved ratios (≈1.3 at each time point) reflect to some extent the metastable to stable solubility ratio (1.24 at 37 °C). The higher thermodynamic activity and lower crystallinity (see Figure 2) of PICOA probably concur to its higher dissolution efficiency (by 28%) compared to PICOW. The dissolution rate data in water at 37 °C using nondisintegrating disks of PICOA or PICOW were in agreement with those obtained from powder samples (Table 3 and Figure 9). The metastable anhydrous form shows a better performance also in terms of intrinsic dissolution rate, which results higher than that of the stable hydrated form by 32%.

Conclusions

PICOW, the most stable picotamide form in water and organic solvent as well as under ambient atmosphere, is the raw material of choice for the preparation of commercial tablets (Plactidil). The dehydration of PICOW under open DSC and TGA conditions follows a monophasic or biphasic pattern, depending on the history of the sample (recrystallization solvent, rehydration conditions, intact or ground specimen, etc.). Morphological factors, various degrees of "perfection" of a common lattice structure, and/or cluster aggregation may be responsible for the distinct thermal behavior of the same hydrate phase and for the nature of the dehydration products (amorphous or polymorphic crystal forms A and B).

Total or partial dehydration of PICOW can occur in pharmaceutical processes where aqueous wetting and drying are involved. The subsequent in situ rehydration of PICOA, which depends on numerous factors (temperature, water vapor pressure, excipients in the formulation, etc.), is also possible. The careful characterization of the solid state is necessary so that the behavior of the material can be predictable and reproducible.

PICOA, the metastable picotamide anhydrous form, due to its physical stability in an ambient atmosphere and compatibility with pharmaceutical excipients, could be a promising modification to improve the dissolution rate of the active principle in solid dosage forms because of its higher solubility reached in water before recrystallizing to the less soluble hydrate. A study of possible implications on bioavailability will be the subject of future work.

References and Notes

1. Pulcinelli, F. M.; Pignatelli, P.; Pesciotti, M.; Sebastiani, S.; Parisi, S.; Gazzaniga, P. P. Mechanism of the persisting TxA2 receptor antagonism by picotamide. *Thromb. Res.* **1997**, *85*, 207−215.
2. Foresti, E.; Riva di Sanseverino, L.; Sabatino, P. Structure of an antithrombotic agent and its dimethyl derivative: 4-methoxy-N,N′-bis(3-pyridylmethyl)isophthalamide monohydrate (I) and 4-methoxy-N,N′-dimethyl-N,N′-bis(3-pyridylmethyl)isophthalamide emihydrate (II). *Acta Crystallogr. Sect. C* **1986**, *42*, 224−227.
3. Sorrenti, M.; Negri, A.; Bettinetti, G. P.; Mura, P.; Faucci M. T.; Setti, M. Structural and thermal characterization of hydrated and dehydrated crystal forms of picotamide. *Proceedings of the 2nd World Meeting APGI/APV*, Paris, 1998; APGI: Chatenay Malabry, France, 1998; pp 25−26.
4. Mura, P.; Bettinetti, G. P.; Faucci, M. T.; Manderioli, A.; Parrini, P. L. Differential scanning calorimetry in compatibility testing of picotamide with pharmaceutical excipients. *Thermochim. Acta* **1998**, *321*, 59−65.
5. Mura, P.; Faucci, M. T.; Manderioli, A.; Furlanetto, S.; Pinzauti, S. Thermal analysis as a screening technique in preformulation studies of picotamide solid dosage forms. *Drug Dev. Ind. Pharm.* **1998**, *24*, 747−756.
6. Han, J.; Suryanarayanan, R. Applications of pressure differential scanning calorimetry in the study of pharmaceutical hydrates I. Carbamazepine dihydrate. *Int. J. Pharm.* **1997**, *157*, 209−218.
7. Khankari, R.; Chen, L.; Grant, D. J. Physical characterization of nedocromil sodium hydrates. *J. Pharm. Sci.* **1998**, *87*, 1052−1061.
8. Suzuki, E.; Shimomura, K.; Sekiguchi, K. Thermochemical study of theophylline and its hydrate. *Chem. Pharm. Bull.* **1989**, *37*, 493−497.
9. Ketolainen, J.; Poso, A.; Viitasaari, V.; Gynther, J.; Pirttimaki, J.; Laine, E.; Paronen, P. Changes in solid-state structure of cyclophosphamide monohydrate induced by mechanical treatment and storage. *Pharm. Res.* **1995**, *12*, 299−304.
10. Agbada, C. O.; York, P. Dehydration of theophylline monohydrate powder − effects of particle size and sample weight. *Int. J. Pharm.* **1994**, *106*, 33−40.
11. Otsuka, M.; Kaneniwa, N. The dehydration kinetics of theophylline monohydrate powder and tablets. *Chem. Pharm. Bull.* **1988**, *36*, 4914−4920.
12. Suryanarayanan, R. X-ray Powder Diffractometry. In *Physical characterization of pharmaceutical solids*; Brittain, H. G., Ed.; Marcel Dekker: New York, 1995; p 190.
13. Brittain, H. G. Spectral methods for the characterization of polymorphs and solvates. *J. Pharm. Sci.* **1997**, *86*, 405−412.
14. Zhu, H.; Padden, B. E.; Munson, E. J.; Grant, D. J. W. Physicochemical characterization of nedocromil bivalent metal salt hydrates. 2. Nedocromil zinc. *J. Pharm. Sci.* **1997**, *86*, 418−429.
15. Brittain, H. G.; Bogdanowich, S. J.; Bugay, D. E.; DeVincentis, J.; Lewen, G.; Newman, A. W. Physical characterization of pharmaceutical solids. *Pharm. Res.* **1991**, *8*, 963−973.
16. Bugay, D. E.; Williams, A. C. Vibrational Spectroscopy. In *Physical characterization of pharmaceutical solids*; Brittain, H. G., Ed.; Marcel Dekker: New York, 1995; pp 72−76.
17. Puttipipatkhachorn, S.; Yonemochi, E.; Oguchi, T.; Yamamoto, K.; Nakai, Y. Effect of grinding on dehydration of crystal water of theophylline. *Chem. Pharm. Bull.* **1990**, *38*, 2233−2336.
18. Ghosh, S.; Ojala, W. H.; Gleason, W. B.; Grant, D. J. W. Relationships between crystal structures, thermal properties and solvate stability of dialkylhydroxypyridones and their formic acid solvates. *J. Pharm. Sci.* **1995**, *84*, 1392−1399.
19. Pearson, J. T.; Varney, G. The anomalous behaviour of some oxyclozanide polymorphs. *J. Pharm. Pharmacol.* **1973**, *25S*, 62P−70P.
20. Forbes, R. T.; York, P.; Fawcett, V.; Shields, L. Physicochemical properties of salts of p-aminosalicylic acid. I. Correlation of crystal structure and hydrate stability. *Pharm. Res.* **1992**, *9*, 1428−1435.
21. De Villiers, M. M.; Van der Watt, J. G.; Lotter, A. P.; Liebengerg, W.; Dekker: T. G. Correlation between physicochemical properties and cohesive behavior of furosemide crystal modifications. *Drug Dev. Ind. Pharm.* **1995**, *21*, 1975−1988.
22. Marshall, P. V.; York, P. Crystallisation solvent induced solid-state and particulate modifications of nitrofurantoin. *Int. J. Pharm.* **1989**, *55*, 257−263.

23. Holgado, M. A.; Fernandez-Hervas, M. J.; Rabasco, A. M.; Fini A. Characterization study of a diclofenac salt by means of SEM and fractal analysis. *Int. J. Pharm*. **1995**, *120*, 157−167.
24. De Smidt, J. H.; Fokkens, J. G.; Grijseels, H.; Crommelin, D. J. A. Dissolution of theophylline monohydrate and anhydrous theophylline in buffer solutions. *J. Pharm. Sci.* **1986**, *75*, 497−501.
25. Phadnis, N. V.; Suryanarayanan, R. Polymorphism in anhydrous theophylline − Implications on the dissolution rate of theophylline tablets. *J. Pharm. Sci.* **1997**, *86*, 1256−1263.
26. Shefter, E.; Higuchi, T. Dissolution behavior of crystalline solvated and nonsolvated forms of some pharmaceuticals. *J. Pharm. Sci.* **1963**, *52*, 781−791.
27. Jozwiakowski, M. J.; Nguyen, N.-A. T.; Sisco, J. M.; Spancake, C. W. Solubility behaviour of lamivudine crystal forms in recrystallization solvents. *J. Pharm. Sci.* **1996**, *85*, 193−199.

Acknowledgments

This work was supported by a grant from Istituto Superiore di Sanità − Roma (Progetto proprietà chimico-fisiche dei medicamenti e loro sicurezza d'uso).

JS990150B

Electrolyte-Induced Compositional Heterogeneity: A Novel Approach for Rate-Controlled Oral Drug Delivery

VINESS PILLAY AND REZA FASSIHI*

Contribution from *Temple University, School of Pharmacy, Department of Pharmaceutical Sciences, 3307N Broad Street, Philadelphia, Pennsylvania 19140.*

Received April 2, 1999. Final revised manuscript received July 26, 1999.
Accepted for publication September 9, 1999.

Abstract □ In this work a new approach for in situ interactions between drug and electrolyte(s) is devised to control the release of highly water soluble drugs from oral hydrophilic monolithic systems. The model drug diltiazem hydrochloride (water solubility in excess of 50% at 25 °C), in conjunction with specific electrolytes, was principally employed in the design of swellable tablet formulations comprised of hydrophilic polymers such as hydroxypropylmethlcellulose (HPMC) or poly(ethylene oxide) (PEO). Electrolytes such as sodium bicarbonate or pentasodium tripolyphosphate were used to modulate intragel pH dynamics, swelling kinetics, and gel properties. Through in situ ionic interactions (an intragel matrix system composed of different chemical species that promote competition for water of hydration), a compositionally heterogeneous structure referred to as a "metamorphic scaffold" was established. It is shown that this latter structure results in the inhibition of drug dissolution, induction of a differential swelling rate, and attainment of "matrix stiffening" and axially provides a uniform gel layer. Presence of such phases in matrix structure and its influence on swelling dynamics enabled control of diltiazem hydrochloride release in a zero-order manner in different pH environments over a 24-h period. From kinetic analysis using the power law expressions [$M_t/M_\infty = k_1 t^n$, $M_t/M_\infty = k_1 t^n + k_2 t^{2n}$] and Hopfenberg model [$M_t/M_\infty = 1 - (1 - k_1 t)^n$], it became apparent that the dynamics of matrix relaxation and controlled erosion were major factors involved in the release mechanism, while the composite rate constant k_1 (in Hopfenberg model) decreased by approximately 2-fold in the presence of electrolyte(s). These findings indicated that the dynamics of swelling and gel formation in the presence of ionizable species within hydrophilic matrices provide an attractive alternative for zero-order drug delivery from a simple monolithic system.

Introduction

Controlled release drug delivery systems have received much attention in the past two decades with numerous technologically sophisticated products on the marketplace. Such advancements have come about by the simultaneous convergence of many factors, including the discovery of novel polymers, formulation optimization, better understanding of physiological and pathological constraints, prohibitive cost of developing new drug entities, and the introduction of biopharmaceutics in drug product design. The major benefits of these products lie in the optimization of drug input rate into the systemic circulation in order to achieve an appropriate pharmacodynamic response. This in turn should add to product safety and reduce the extent and incidence of major adverse drug reactions due to a more strict control of blood levels. Furthermore, with less frequent dosing, it is speculated that this should improve patient compliance and possibly maximize drug product efficacy in therapeutics.

Recently numerous hydrophilic polymers have been investigated and are currently used in the design of complex controlled release systems.[1−4] In many cases the formulator depends on the inherent rate-controlling mechanisms of the polymer to provide constant rate drug delivery. Among desirable features, the polymer should possess inherent physicochemical characteristics which provide for the attainment of high gel-state viscosity upon swelling, ability to maintain constant gel layer integrity over a prolonged period of time and hence low erosion rate, and complete dissolution of polymer upon exhaustion of drug release. Alternatively, a programmed system is sought for which swelling and erosion are the key factors in controlling drug liberation. The ideal polymer would permit these processes to operate synchronously, i.e., affording a balance between the principal processes of swelling, erosion, and dissolution. Among the most widely used polymers, such as the nonionic hydroxypropylmethylcellulose (HPMC), hydroxypropylcellulose (HPC), poly(ethylene oxide) (PEO) types, the cationic chitosan types, and anionic alginate types, the attainment of high gel-state viscosity, maintenance of constant gel layer, or synchronous erosion−dissolution in a monolithic sense for linear drug release over a prolonged period of time is not easily achievable and still remains a challenge. Since the various dynamic phases in the rate processes of polymer relaxation, disentanglement, and/or erosion during dissolution are manifested in a nonconstant manner, realization of zero-order drug release from such monolithic devices is difficult.

This limitation of hydrophilic polymers may be circumvented through modification of the physical and chemical infrastructure of the polymeric gel system. In the present work a reliable process has been established for inducing in situ reactions between pharmaceutically acceptable electrolytes/acids and drug which influences the intragel swelling dynamics and relative physical integrity of the swollen matrix structure. Furthermore, this may produce heterogeneous domains within the swollen gel boundary referred to as "metamorphic scaffold" in this work (see Figure 1).

In the past, alkaline compounds or buffers have been included in solid oral formulations of several acidic drugs that undergo dissolution rate-limited absorption.[5−11] The same principle of addition of buffers, osmotically active agents, surfactants, or combinations thereof has also been utilized to control the swelling of hydrophilic polymers with different coating and inclusion techniques.[12] However, no specific strategy has been employed to apply the same principle to design a simple, directly compressible, monolithic, controlled-release system with provision of zero-order kinetics. In general, the application of buffers and ionizable

* Corresponding author. Tel. 215-707-7670, fax. 215-707-3678, e-mail. afassihi@vm.temple.edu.

10.1021/js9901054 CCC: $18.00
Published on Web 10/12/1999

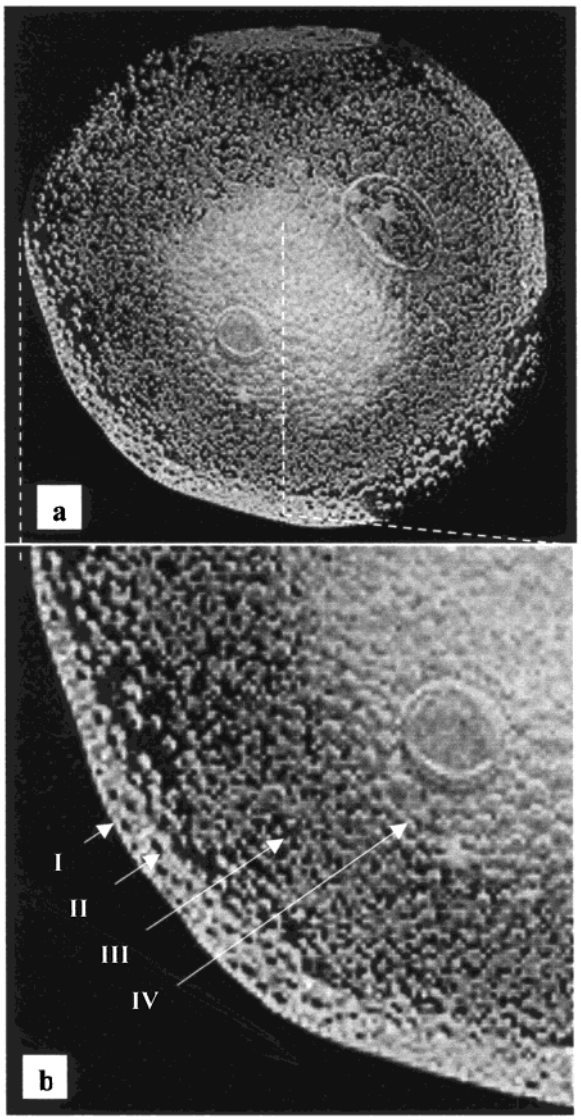

Figure 1—(a) Photomicrograph of swollen matrix (pH 1.5) of HPMC-based tablet containing 100 mg each of sodium bicarbonate and diltiazem hydrochloride, depicting the putative "metamorphic scaffold" and heterogeneous composition (magnification: ×7). (b) Magnified region of above swollen gelled matrix distinctly reflecting the proposed matrix transition phases (magnification: ×14): I) Water saturated diffusion front; II) Peripheral gel layer; III) Swollen infiltrated layer; and IV) Glassy swelling front. (For more detailed explanation see Figure 6c).

compounds in dosage form design has essentially been limited to the minimization of localized gastrointestinal tract adverse effects and the pH-solubility dependency of poorly soluble compounds.[5,6,13,14]

The aim of this work was to provide and expand on a means to design, formulate, and develop a novel oral monolithic, controlled-release tablet dosage form for drugs of various solubility that may be tailored to provide zero-order or quasi-steady-state drug release over a 24-h period.[15] The model drug employed in this work was diltiazem hydrochloride, which has a water solubility in excess of 50% at 25 °C. The rationale behind the mechanisms and dynamics of electrolyte-induced matrix stiffening and modulation of intragel pH changes for the provision of controlled drug release will be elucidated.

Experimental Section

Materials—Hydroxypropylmethylcellulose (HPMC K4M, Dow Chemical Company, Midland, MI) and poly(ethylene oxide) (PEO 4 million molecular weight, Union Carbide, CT) were employed in tablet production. Diltiazem hydrochloride (Seloc AG, Switzerland) was use as a model compound. The following electrolytes/acids used were of analytical grade: sodium bicarbonate (Ruger Chemical Co., NJ), potassium bicarbonate, magnesium carbonate (Fischer Scientific Co., NJ), calcium carbonate (E.M. Science, NJ), dibasic sodium phosphate as the 12-hydrate crystal (J. T. Baker Inc., NJ), sodium carbonate, pentasodium tripolyphosphate, sodium deoxycholate from parent 7-deoxycholic acid, maleic acid, adipic acid, and L-(+)-tartaric acid (Sigma Chemical Co., St. Louis, MO).

Methods—*Preparation of Tablets*—A typical monolithic formulation consisted of polymer, drug, and electrolyte. The ratio of drug:polymer was always maintained at the 1:2 level (i.e., 100 mg:200 mg), while the electrolyte content was varied. For example, a single tablet would be composed of 200 mg of HPMC K4M or PEO 4M, 0−100 mg of electrolyte, and 100 mg of drug. Pure and drug-loaded compacts of polymer were used as control indicators. The powder mixture was blended in a V-blender for 15 min prior to compression at 4000 lbs in an 11.5 mm diameter die using the Carver Press (Model C, Fred S. Carver, IN) and flat-faced punch. To minimize processing variables, all tablets were produced under identical conditions.

Drug Release and Matrix Erosion Studies—Dissolution studies on each formulation were performed in a calibrated six station dissolution test apparatus (VK 7000, Vankel Industries Inc., Edison, NJ) using the USP 23 Apparatus 2 in USP-recommended buffers (pH 1.5, 2.6, 4.1, 5.4, 6, 6.4, 6.8; 900 mL, 37 ± 0.5 °C, 50 rpm). All studies were conducted in triplicate ($N = 3$) using an automated sampling procedure. Drug release was analyzed by ultraviolet spectroscopy (HP Diode Array) at 238 nm.

The erosion properties for the above-described HPMC and PEO tablets were studied in pH 1.5 using Apparatus 2 in order to simulate actual dissolution conditions. At predetermined time intervals, tablets were removed, dried to constant weight under vacuum at 40 °C, and thereafter weighed.

Diltiazem Free Base Formation—Diltiazem hydrochloride (1.5 g) was solubilized in deionized water (10 mL) and transferred to a separatory flask. This solution was alkalinized with sodium bicarbonate (0.5 g) to precipitate the drug as the free base. The free base was extracted with ether (20 mL) and recrystallized on a rotavap (Rotavapo-R, Buchi) at 35 °C over a period of 30 min. The solvent residue was completely removed by drying under vacuum over a further 30-min period through an acetone−dry ice reservoir maintained at −178 °C.

Intragel pH Measurements—Transitions in the intragel pH (i.e., within the tablet gel matrix) were monitored with aid of a flat surface polymer combination electrode having a 5 mm contact area (Accumet, Fischer Scientific). The electrode, attached to a pH meter (Accumet pH meter 25, Fischer Scientific), was used for pH measurements of gel at the periphery and within the swollen matrix in both the axial and radial planes at predetermined time intervals on tablet formulations exposed to dissolution medium pH 1.5. Various inwardly depths were exposed for pH measurements by excisions with a scalpel. Furthermore, a continuous pH measurement of the external matrix interface was performed by having the perforated guard and the flat surface of the pH electrode in constant contact with the tablet during a dissolution study in buffer medium pH 1.5. pH titration methods were also adopted on plain HPMC solutions with and without drug to evaluate the influence of electrolyte content on concurrent pH changes and interaction with drug.

Sample Treatment and Force−Displacement Profiling by Textural Analysis—Textural analysis was performed on different tablet formulations in order to determine the electrolyte-related effects on structural alteration of the gelled scaffold and swelling dynamics. One planar base as well as the entire lateral surface of each tablet was sealed off with an organic coating consisting of 20 g of Eudragit PO in a mixture of 50 mL of acetone and 50 mL of 2-propranol. This coating rendered these surfaces impermeable to penetration by buffer medium. These steps ensured (i) prevention of interfacial deformation of core/gel structure during probe advancement, and (ii) confinement of swelling in the axial direction. When radial measurements were undertaken, both planar surfaces of the tablet were coated. Triplicate samples were then placed in dissolution vessels containing 900 mL of buffer medium pH 1.5 at 37 °C during separate tests. The paddle speed was set at 50 rpm to simulate the actual tablet dissolution process. At

predetermined time intervals individual tablets were removed and subjected to textural analysis in a similar manner described in recently published work.[16]

In summary, the Texture Analyzer instrument (TA XT2*i*, Stable Micro Systems, England) which has the ability to capture stress–strain profiles with a high degree of accuracy was used. Data were captured at a rate of 200 pps via the Texture Expert for Windows software, Version 1.20. A flat-tipped steel probe, 2 mm in diameter, was connected to a force transducer within the analyzer that measured the force of resistance encountered by the probe during advancement into the sample. During a typical test, the probe was advanced at a predetermined velocity into the sample in accordance with the following parameters: Pretest speed = 1 mm/s, test speed and post-test speeds = 0.2 mm/s, maximum compression force = 40 N, and an auto trigger using 0.5*g* as the trigger force.

Furthermore, the influence of stepwise pH changes on matrix structure was also evaluated in Apparatus 2 by periodically moving the tablets into different pH environments (i.e., pH 1.5, 3, 5.4, 6, 6.4, 6.8) and then evaluating their textural properties.

Data Treatment for Analysis of Release Kinetics and Deconvolution of Texture Profiles—To precisely determine the nature of release mechanism in the presence and absence of electrolyte, application of kinetic modeling for analysis of release profiles is necessary. Such analysis was performed on formulations comprised of HPMC K4M in the absence and presence of 100 mg of sodium bicarbonate. The kinetics of drug release (buffer medium pH 1.5) were analyzed using WinNonlin, Version 1.0 (SCI Software). In all least squares analyses, the Gaussian-Newton (Levenberg–Hartley) approach was adopted. The power law expression (eq 1) and its geometry-independent form (eq 2) were considered for data analysis.[17–20] In addition, the Hopfenberg model, a geometry-dependent equation (eq 3), was also employed for determination of release kinetics[21] (see below).

With reference to textural analysis, the predetermined maximum compression force of 40 N was established over a series of tests, such that after deconvolution of raw data, based on computed gradient changes within the matrix, distinct matrix phase transitions could be identified. By running Texture Expert macros, triplicate data from each experimental formulation was used in the calculation of time-related parameters associated with the diffusion layer, peripheral gel phase, swollen infiltrated gel phase, and glassy swelling fronts. These include changes in force, phase thickness, swelling gradients in axial and radial planes (determined from up-curving force–displacement changes), and associated resistance to probe penetration. The rationale behind the establishment of the above-mentioned phases will be discussed.

Results and Discussion

Drug Release Potential as a Function of Electrolyte Content and Release Kinetics—By incorporation of sodium bicarbonate into hydrophilic monolithic tablet matrices, it was possible to progressively reduce the release rate of diltiazem hydrochloride (water solubility in excess of 50% at 25 °C) over a 24-h period. Distinct evidence of this phenomenon is provided with application of a typical nonionic hydrophilic polymeric material such as poly(ethylene oxide), 4 million molecular weight (PEO 4M) (Figure 2a). With an increase in electrolyte concentrations (from 0 to 100 mg), the release rate of diltiazem hydrochloride tended to slow, indicating greater inhibition in release in comparison to the control formulation (i.e., in the absence of electrolyte). This electrolyte-induced, controlled release phenomenon was also observed with other polymeric materials such as HPMC, chitosan, and sodium alginate. To further illustrate the utility of the electrolyte effect typical release profiles for HPMC K4M-based matrix and diltiazem hydrochloride is provided (Figure 2b). The distinctive feature in the case of HPMC formulations is that an increase in the linearity of the release profiles was evident as the electrolyte content increased from 10 mg to 100 mg, with corresponding correlation coefficients of 0.7499 to 0.9836 (Figure 2b). Based upon this latter

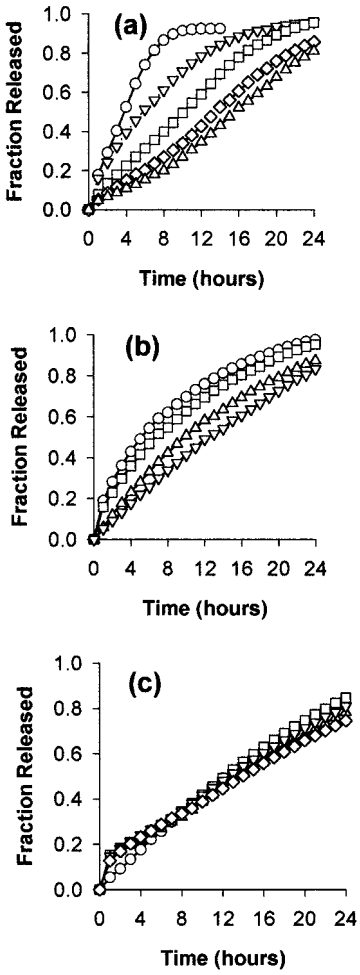

Figure 2—(a) Release of diltiazem hydrochloride from PEO 4 million formulations containing different quantities of sodium bicarbonate in buffer medium pH 1.5: 0 mg (○), 10 mg (▽), 50 mg (□), 75 mg (◇), 100 mg (△). (b) Release of diltiazem hydrochloride from HPMC K4M formulations containing different quantities of sodium bicarbonate in buffer medium pH 1.5: 0 mg (○), 10 mg (□), 50 mg (△), 100 mg (▽). (c) Influence of different bulk pH media on the release of diltiazem hydrochloride (100 mg) from formulation containing 100 mg of sodium bicarbonate: pH 1.5 (○), pH 5.4 (□), pH 6 (△), pH 6.4 (▽), pH 6.8 (◇).

observation, all other testing procedures were conducted on the HPMC-based matrices. In addition, HPMC has good compactibility behavior and is widely used within the pharmaceutical industry. Under the given experimental conditions, the formulation containing 100 mg of sodium bicarbonate was considered optimal. On exposure of this electrolyte-containing HPMC formulation to different pH environments, a minimal burst effect (<10% of total dose) and linear drug release for up to 24 h was achieved (see Figure 2c). It is apparent that the delivery system has potential to function in a relatively pH-independent manner and is able to control the release of a highly soluble drug such as diltiazem hydrochloride (solubility >50% in water at 25 °C).

As an initial test to confirm that the process of electrolyte inclusion within the swelling matrix was not purely a catalyst for free base formation but was also involved in fundamental structural changes in gel boundary, the hydrochloride form of diltiazem was converted into its free base and incorporated into a HPMC-based tablet dosage form in the presence of acidic and basic electrolytes and thereafter evaluated its drug release potential in pH 1.5 and 6.8 buffer media (Figure 3a,b). As expected from pH-solubility theory, the free base displayed a higher solubility

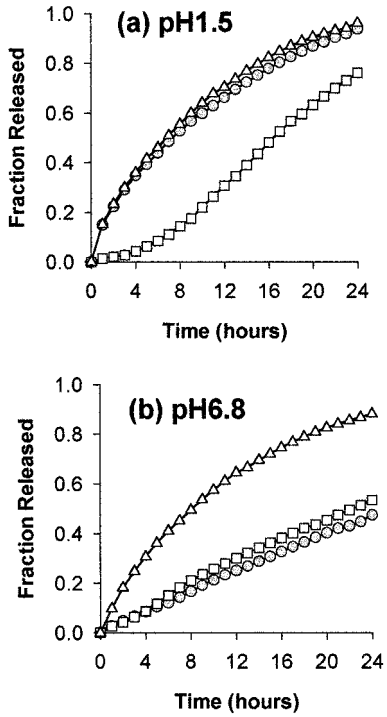

Figure 3—(a) Release of diltiazem free base in pH 1.5 from HPMC-based control (i.e., no electrolyte) and formulations containing sodium bicarbonate (100 mg) or tartaric acid (100 mg): control (gray ○), sodium bicarbonate (□), tartaric acid (△). (b) Release of diltiazem free base in pH 6.8 from control (i.e., no electrolyte) and formulations containing sodium bicarbonate (100 mg) or tartaric acid (100 mg): control (gray ○), sodium bicarbonate (□), tartaric acid (△).

in strongly acidic media (Figure 3a) as opposed to higher pH or weakly acidic media (Figure 3b). However, the overall release profile in this case was significantly different from that of the hydrochloride form shown in Figure 2c. The incorporation of tartaric acid in the free base-containing formulation did not alter drug release in acidic environment such as pH 1.5 (Figure 3a), but release was enhanced at higher pH values such as pH 6.8 (Figure 3b). It appears that the presence of sodium bicarbonate was crucial in controlling the release process (see Figure 3a). Even though the profiles for free base and free base mixed with sodium bicarbonate are comparable in pH 6.8, the extent of release is not acceptable (only 45−50% of drug is released in 24 h, Figure 3b). Therefore it is postulated that the incorporation of electrolyte into the tablet might essentially inhibit the dissolution of diltiazem hydrochloride through intragel pH-control and subsequent induction of textural variations in the swollen matrix. On substitution of sodium bicarbonate by other electrolyte types (e.g., sodium carbonate, calcium carbonate, magnesium carbonate, potassium bicarbonate, pentasodium tripolyphosphate, sodium phosphate (dibasic), or sodium deoxycholate), it appears that electrolyte solubility and formation of a buffer threshold within the matrix plays an essential role in effective interaction with drug and textural changes as shown in Figure 4 and Table 1 (based on extent of constant drug release and corresponding correlation coefficients).

Detailed consideration will be given to the rationale of these postulated mechanisms in following sections.

In general, drug release from simple swellable systems may be described by the power law expression:[17]

$$M_t/M_\infty = k_1 t^n \qquad (1)$$

where M_t and M_∞ are the amounts of drug released at time

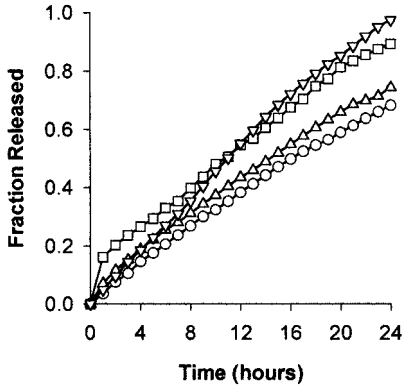

Figure 4—The influence of different electrolytes (100 mg) on the release of diltiazem hydrochloride–HPMC matrices in buffer media pH 1.5 using magnesium carbonate (○), potassium bicarbonate (▽), pentasodium tripolyphosphate (□), sodium carbonate (△).

t and the overall amount released respectively, k_1 is a release constant, and n is a release exponent indicative of the release mechanism. Classically, $n = 0.5$, $0.5 < n < 1$, or $n = 1$ for a slab, is indicative of Fickian release, anomalous transport, or Case II transport kinetics, respectively. However, the n values may change with the matrix geometry. Particularly in the case of a cylinder (as considered in this work), zero-order release is indicated by an n-value of 0.89, instead of 1.

Irrespective of dosage form geometry, various authors[18−20] have reported on the evaluation of contributions provided by Fickian diffusion and matrix relaxation/dissolution through the use of the following equation:

$$M_t/M_\infty = k_1 t^n + k_2 t^{2n} \qquad (2)$$

where k_1 is the Fickian kinetic constant and k_2 is the relaxational/erosion rate constant.

Additionally, release from systems with surface erosion and varying geometries also have been analyzed by Hopfenberg,[21] where a model applicable to a slab, cylinder, or sphere showing heterogeneous erosion is proposed (eq 3):

$$M_t/M_\infty = 1 - (1 - k_1 t)^n \qquad (3)$$

In this equation, k_1 is equal to $k_0/C_0 r_0$, k_0 is the erosion rate constant, C_0 is the uniform initial concentration of drug in the matrix, and r_0 is the initial radius for a sphere or cylinder or the half-thickness for a slab. In eq 3 the n values are as follows: $n = 1$ for a slab, $n = 2$ for a cylinder, and $n = 3$ for a sphere. The model assumes that time-dependent diffusional resistances internal or external to the eroding matrix do not influence the release kinetics. Furthermore, the contribution of the secondary surfaces to the release process is not considered, as discussed by Katzhendler and co-workers.[22]

From model fitting, it was observed that the simple power law expression (eq 1) provided an n-value of 0.837 for the electrolyte-containing formulation, confirming the closeness to attainment of ideal zero order drug release. The control formulation (i.e., without electrolyte) produced an n-value of 0.466, indicating a Fickian release mechanism. However, on the basis of the application of the geometry-independent expression (eq 2), it becomes apparent that through separation of the release constant into Fickian and relaxational components, matrix relaxation is predominant both in the presence and absence of electrolytes (without electrolyte $k_1 = 1.8 \times 10^{-5}$, $k_2 = 0.232$; with electrolyte $k_1 = 1.2 \times 10^{-5}$, $k_2 = 0.059$). Using an n-value of 2 in the Hopfenberg model (eq 3) produces a k_1 of 0.045

Table 1—Physicochemical Properties and Influence of Various Electrolytes on Drug Release

electrolytes	water solubility (wt %)[a]	pK_a[a]	pH of 1% in deionized water $T = 21$ °C	pH of 1% in deionized water $T = 37$ °C	induced intragel pH[b]	release and associated characteristics[d]	R^2 [e]
sodium bicarbonate	9.32[23]	6.37, 10.33[26]	8.159	8.069	7.037	constant throughout (0–24 h)	0.9836
sodium carbonate	23.5[23]	6.37, 10.33[26]	11.298	10.891	9.742	constant throughout (0–24 h)	0.9929
calcium carbonate	3.36×10^{-9} (K_{sp})[23]	6.37, 10.33[26]	10.041	9.561	5.674	constant middle phase (8–16 h)	0.8811
magnesium carbonate	6.82×10^{-6} (K_{sp})[23]	6.37, 10.33[26]	10.297	10.085	6.375	constant throughout (0–24 h)	0.9883
potassium bicarbonate	26.6[23]	6.37, 10.33[26]	7.96	8.132	6.841	burst; constant from 1.5–24 h	0.9235
pentasodium tripolyphosphate	16.67[24]	–	9.142	9.162	6.531	constant throughout (0–24 h)	0.9686
sodium phosphate	48.68[23]	2.12, 7.21, 2.67[26]	9.167	9.072	1.530	curved	0.6932
sodium deoxycholate	24.81[24]	6.58[24]	8.212	7.979	1.448	constant in latter phase (11–24 h)	0.8141
maleic acid	44.1[25]	2, 6.26[26]	1.739	1.638	8.842[c]	induces pH-independent release	0.9328
tartaric acid	58.16[25]	2.98, 4.34[24]	2.258	2.113	7.174[c]	does not assist pH-independent release	–
adipic acid	1.42[24]	4.41, 5.28[24]	2.778	2.522	9.287[c]	effective counterion for sodium deoxycholate	–

[a] Source of solubility data and pK_a values are shown as superscripts. All data reported at 25 °C except for sodium deoxycholate (15 °C), tartaric acid (20 °C), and adipic acid (20 °C). Due to the practically insoluble nature of calcium carbonate and magnesium carbonate in water, the solubility products (K_{sp}) are reported at 25 °C. [b] Measured using approach described in Methods section ($N = 3$, SD < 0.1). [c] Each of maleic acid and tartaric acid were used in combination with sodium carbonate to develop a system with pH-independent release. [d] The phase at which constant release is initiated is in part also an indication of the degree of reactivity of the electrolyte within the matrix and reflects an existence of a pH threshold value for the attainment of constant release. [e] Intercept set to zero.

in the absence of electrolyte while 0.024 in the presence of electrolyte. As k_1 incorporates the erosion rate constant k_0, it is evident that through drug–electrolyte interaction and related mechanisms of textural stiffening, the electrolyte-containing formulation experiences a 2-fold reduction in matrix erosion. On the basis of erosion studies (data not provided here), it became apparent that control formulations (i.e., without electrolyte) demonstrated a linear decrease in matrix weight. In this case 49.19% and 96.27% weight reduction was observed after 16 h for HPMC and PEO, respectively. However, in the case of the electrolyte-containing formulations, matrix weight reduction followed square root of time kinetics with 67.04% and 61.93% weight reduction observed at equivalent time (16 h) for both HPMC and PEO.

Determination of Intragel pH Changes in Swellable Matrices and Drug–Polymer Solutions—Specific physicochemical data extracted from the literature and experimentally determined values with respect to solubility, acid–base dissociation, solution pH, and intragel pH-control by the above-mentioned electrolytes and some acids to be evaluated are presented in Table 1.

pH measurements in the axial and radial planes were performed on swollen tablet formulations with and without sodium bicarbonate. Typically from axial plane pH measurements on control formulations (i.e., without sodium bicarbonate) at different depths, it became evident that the internal matrix essentially maintained a pH value that was the same as that of the surrounding dissolution medium (pH ≈ 1.5). This may be regarded as the baseline pH as shown in Figure 5a (broken line). On the other hand, the formulation containing sodium bicarbonate had the ability to maintain a relatively constant pH level >8 within the swollen matrix at similar depths to that of the control (Figure 5a). In the axial plane, the pH tended to stabilize at a depth of 5 mm. The constant pH value seen in the case of control on the gel surface interface in contact with the flat end of the pH electrode may be attributed to the predominance of the dissolution medium at this interface. Diltiazem hydrochloride has been reported to possess pH-independent solubility when studied with respect to buffer solutions.[27] In addition, when the solubility study was undertaken in our lab using USP-recommended buffers in the range from pH 1.5–10, no significant differences in drug solubility were observed. This may be due to the fact that the ionic strength of the electrolytes in the buffer systems has not reached the required threshold to induce marked changes in diltiazem hydrochloride solubility. Such levels of ionic strength might be achievable within a restricted gel structure. Hence, the ionic strength achieved with sodium bicarbonate within the swollen matrix tablet might be sufficiently high to produce this intragel pH effect on drug solubility.

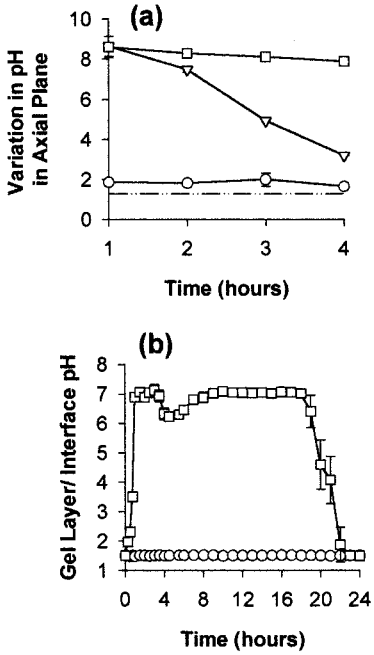

Figure 5—(a) Relationship between time and pH variation obtained by examination of swollen HPMC matrixes with and without sodium bicarbonate (100 mg), after exposure to buffer medium pH 1.5 for different time periods: Axial depth measurements: 0 mm, i.e., surface (○), 2 mm (▽), 5 mm (□). (b) Illustration of time–pH profile for diltiazem hydrochloride–HPMC K4M tablet formulations without (○) and with (□) sodium bicarbonate (100 mg) attached to the pH electrode during a typical dissolution study in buffer medium pH 1.5.

From the investigation on simultaneous transitions in intragel pH and drug release (i.e., tablet attached to electrode), it was found that approximately after 1 h, a maximum surface/gel layer pH of ≈7 was attained in the formulation containing sodium bicarbonate, as opposed to the control tablet formulation which essentially maintained a pH value equivalent to the dissolution medium (Figure 5b). This constant intragel pH was maintained for up to ≈20 h, upon which a rapid decrease in pH was noted possibly due to the exhaustion of sodium bicarbonate and dominance of the penetrated dissolution medium to the matrix core.

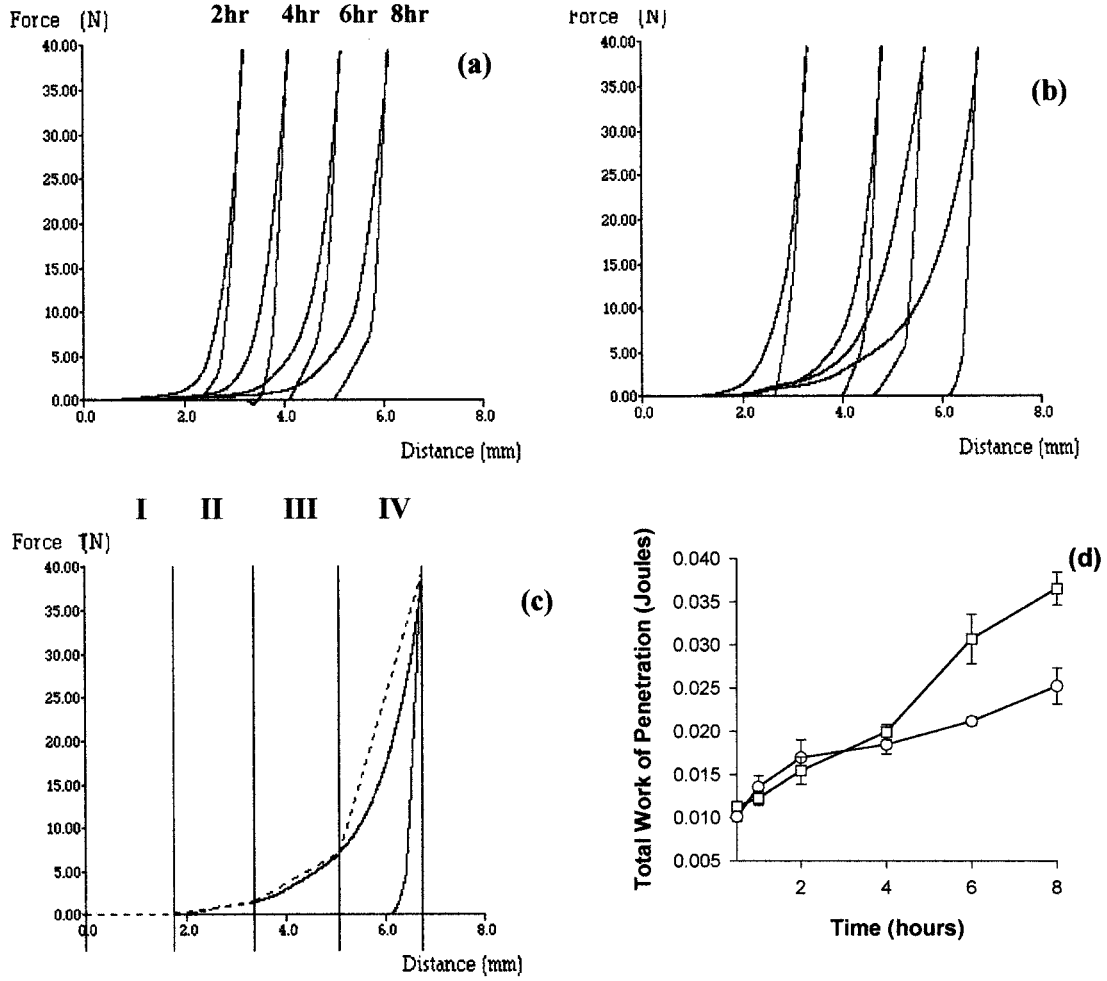

Figure 6—(a) Force–displacement (F–D) profiles for drug-loaded, control HPMC K4M compacts exposed for different time periods to buffer medium pH 1.5. (b) Similar profiles for electrolyte-containing formulation. (c) Details of typical F-D profile for electrolyte containing formulation after 8 h of exposure to buffer medium pH 1.5: (I) water-saturated diffusion front; (II) peripheral gel layer; (III) swollen infiltrated layer; and (IV) glassy swelling front. (d) Profiles depicting compositional heterogeneity within the polymer matrix as manifested through total work of probe penetration.

Through pH-titration studies in the presence and absence of drug-loaded polymeric solutions, it was established that drug−electrolyte interaction is effectively initiated at pH ≈ 6.4. This phenomenon may be used to develop a rationale on which constant release of diltiazem hydrochloride from the swollen gel system might be attainable. Table 1 effectively demonstrates that all electrolytes used in this study are able to maintain a basic pH in solution. However, this does not exclusively apply within the polymeric gel system (i.e., variable water availability), as some electrolytes appear to have a poor buffer threshold when confronted by the acidic penetrant (buffer medium pH 1.5) and hence are unable to maintain basicity, e.g., calcium carbonate (practically water-insoluble, pH-drop from 9.561 to 5.674), sodium phosphate (pH-drop from 9.072 to 1.530), and sodium deoxycholate (pH-drop from 7.979 to 1.448). The other electrolytes such as sodium bicarbonate, sodium carbonate, magnesium carbonate (practically water-insoluble), potassium bicarbonate, and pentasodium tripolyphosphate are able to maintain an intragel pH in excess of ≈6.4, a threshold above which drug−electrolyte interaction is likely to occur. Through this intragel pH-control, significant drug−electrolyte interaction was anticipated, which may lead to variable textural properties in the gel structure and suppression of drug release. Knowing that the pK_a of diltiazem hydrochloride is 7.7,[28] the degree of ionization and hence solubility will be affected in this pH threshold. Such effects may also affect the degree of polymer relaxation and swelling leading to formation of the putative metamorphic scaffold (see Figure 1).

Evaluation of Gel Strength and Time-Dependent Phase Transitions—To measure any transitions in gel matrix structure and alteration in swelling behavior in the presence of electrolytes, textural analysis was undertaken. By application of the texture analyzer instrument, it was possible to obtain the compressive force−displacement profiles for monolithic tablets containing (i) HPMC and drug, and (ii) HPMC, drug, and interacting electrolyte (such as sodium bicarbonate).

Figure 6a illustrates typical force−displacement profiles for compacts comprised of HPMC and drug (e.g., controls) exposed to buffer medium (pH 1.5) up to an 8-h period. The common feature presented in these profiles is a sharp, smooth, up-curving region followed by a rapid decline associated with the probe retraction. The overall features of these profiles reflect the formation of a relatively uniform gel boundary in different stages of hydration. On inclusion of sodium bicarbonate (100 mg) within the matrix system and measuring the profile under identical conditions, there are systematic increases in swelling as well as up-curving force after the initial 2 h of the experiment. Values computed for the maximum increase in matrix swelling (using the control as reference) corresponding to 0.5, 1, 2, 4, 6, and 8 h of exposure to buffer media are typically represented by −4.79%, −25.99%, −4.55%, 6.11%, 5.55%, and 5.34% (negative % indicates the value by which

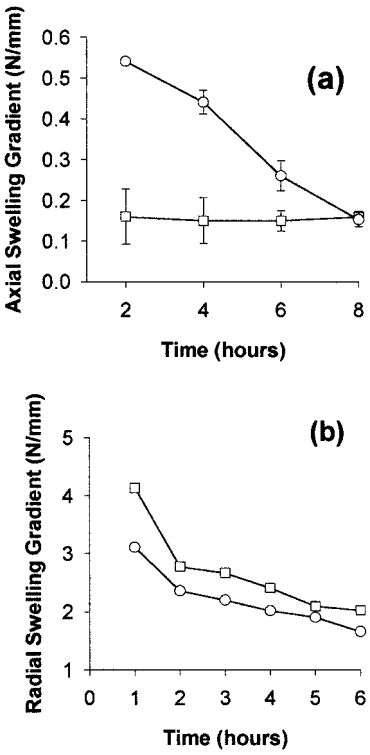

Figure 7—(a) Depiction of the attainment of constant average gradients of axial swelling for diltiazem hydrochloride–HPMC K4M formulations containing 100 mg of sodium bicarbonate (□) and control formulations, i.e., without electrolyte (○) in buffer medium pH 1.5. (b) Changes in the average gradients of radial swelling for HPMC-based formulations containing 100 mg of sodium bicarbonate (□) and control, i.e., without electrolyte (○) in buffer medium pH 1.5.

swelling of the electrolyte-containing formulation is lower than that of the control). In addition, the presence of increased resistance to probe penetration, as seen in the nonlinear rise in the initial stages of force–displacement in Figure 6b, reflects the more heterogeneous nature of the electrolyte-containing matrix. On the basis of the trend that was observed in force–displacement in both controls and in the presence of electrolyte, it was possible to identify and classify four distinct transition phases/regions (see Figure 1 and Figure 6c), namely:

- Phase I: Water saturated diffusion front;
- Phase II: Peripheral gel layer where initial interaction between sodium bicarbonate (or other electrolyte) and diltiazem hydrochloride is observed;
- Phase III: Swollen infiltrated layer where the electrolyte-induced effects are fully manifested; and
- Phase IV: Glassy swelling front.

The sharp increase in the total work associated with probe penetration (Figure 6d) in the case of the electrolyte-containing formulation is indicative of two phenomena, namely higher matrix swelling and greater resistance of the swollen structure to probe penetration, reflecting the heterogeneous structure induced through electrolyte interactions. This is contrasted by the uniform and linear trend in the work changes associated with the control formulation. Further work on this aspect is presently underway.

Differential Swelling Characterization of Matrices—As shown in Figure 7a, the constant peripheral gel phase observed to the depth of 1.5 mm through measurement of the axial gradient developed during matrix swelling of formulations containing sodium bicarbonate in buffer medium pH 1.5 essentially indicates the formation of a constant gel layer thickness, a phenomenon not seen in the absence of electrolyte.

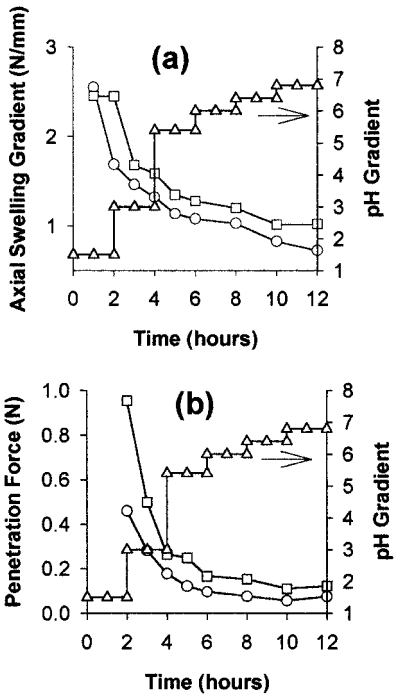

Figure 8—Influence of stepwise pH variation on (a) average gradients of axial swelling, and (b) penetration force in the axial plane for diltiazem hydrochloride–HPMC K4M formulations without (○) and with (□) 100 mg sodium bicarbonate. pH variation follows the order of 1.5, 3, 5.4, 6, 6.4, and 6.8 with both formulations being exposed for 2 h in each environment.

One of the important aspects revealed in this work is that the degree of swelling in the axial direction appears to be greater than that in the radial plane (i.e., for both controls and electrolyte-containing formulations). Apart from actual measurements, this was also apparent from the fact that the lower resistance to penetration in the axial plane (Figure 7a) as opposed to the radial plane (Figure 7b) is indicative of greater matrix infiltration and hence more swollen gel network in the axial plane. For example, from actual measurements on the electrolyte-containing formulation, it was shown that axial expansion occurred up to ≈5.75 mm in 6 h as opposed to ≈2.35 mm in the radial plane during the same time period. This swelling differential represents the nonuniform gel structure, and it is apparent that gel formation is relatively more rigid diametrically (Figure 7b).

Additional investigation conducted under different pH conditions demonstrated the sensitive nature of the electrolyte-containing gel matrix in terms of swelling gradients (determined from up-curving F–D profiles) and resistance to probe penetration (Figure 8a). From Figure 8a it can be seen that in spite of the lack of formation of a constant and uniform peripheral gel layer during stepwise pH changes, it may still be possible to attain constant drug release in these various pH environments (see Figure 2c). It has been postulated that attainment of zero-order drug release in these different pH environments may be attributed to associated textural changes in the swollen matrix, namely, an increase in the stiffness of the gelled structure induced through drug–electrolyte interactions as opposed to formulations without electrolyte (Figure 8b).

Release Modulation and Mechanisms—On the basis of the above data supporting electrolyte-induced compositional heterogeneity in intragel pH-control and proposed metamorphic scaffold structure, the following mechanisms may prevail during the period of drug release in a controlled, constant manner.

As the penetrant enters the periphery of the tablet, there is a rapid electrolyte–water interaction with significant

chemical reactivity through electrolyte solubilization and subsequent events that may lead to both initial suppression and later enhancement of polymer swelling. During this infiltration process, chemical species likely to be present within the gelled boundaries include sodium bicarbonate, sodium chloride formed via the interaction between the former electrolyte and hydrochloride species of the drug, ionized diltiazem, and possibly existence and formation of a free drug base. Diltiazem hydrochloride has a pK_a of 7.7,[28] and since the measured intragel pH is >7 but <pK_a, it is expected that drug species would not entirely exist in a precipitated base form. However, limited formation of the base form of drug may precipitate within the polymeric matrix and may result in hindrance of the relaxation process. Employing a modified concept of Schott,[29] the passive and actively formed electrolyte species within the gelled polymeric HPMC matrix would compete for water species at the outset and hence bind part of the water of the gelling polymer in order to become hydrated. This initial competition for water of hydration "dehydrates" the polymer molecules, leading to suppression of initial swelling, as seen up to 2 h where the formulation containing 100 mg of sodium bicarbonate is maximally inhibited in the range of ≈4−25% in overall swelling when compared to control tablet. However, once sufficient water has been attracted by electrolyte species into the polymer matrix the solubilized species will diffuse out, creating a capillary network for more water penetration after which an enhancement of swelling in comparison to controls is observed. Such possible alterations in physical polymeric configuration are manifested as a textural effect shown by the increased resistance to probe penetration resulting in "matrix stiffening" (see Figures 6d and 7b). The degree of matrix stiffening consistently decreases toward the center of the matrix core in a time-dependent manner over a long period (e.g., 24 h). Through these mechanisms and dynamics of intragel changes, it seems possible to inhibit drug dissolution and enhance polymer swelling to an extent, both of which would significantly contribute to achieving zero-order kinetics. This inhibition in dissolution may also be a time-dependent phenomenon, since as more penetrant enters the gel matrix layer-by-layer (i.e., sequentially), the electrolyte(s) content and their byproducts (such as sodium chloride) are diluted and any drug base may revert to its hydrochloride form and is subsequently released. An additional parameter that requires a more in-depth analysis is the influence of osmotic pressure and its impact on both swelling dynamics and diffusion mechanism.

Electrolyte Effects for Establishment of pH-Independent System—In an attempt to develop a pH-independent system, the sodium bicarbonate was replaced by sodium carbonate since it displays a less vigorous and delayed effervescent reaction in the presence of acidic electrolytes (Figure 9). Furthermore, to counteract the strong interaction between drug and sodium carbonate in higher pH environments, an opposing electrolyte was added to the system, namely maleic acid. Maleic acid essentially served to reduce the intragel pH at higher external pH conditions. PEO 4 million molecular weight was selected as the polymer for its ability to display greater free volume changes than HPMC, hence ensuring drug release in less acidic pH environments. Adipic and tartaric acids were also evaluated, but did not prove successful in providing comparable release in acidic and basic media. This may be due to the relatively lower and higher solubility of each acid within the gel system (see Table 1) and the dynamic structural changes during polymer infiltration and associated swelling conditions.

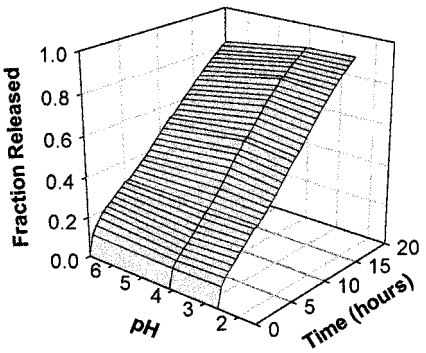

Figure 9—Release plot for diltiazem hydrochloride from a designed pH-independent system containing 100 mg of sodium carbonate and 50 mg of maleic acid in buffer media pH 1.5, 4, and 6.8.

Conclusions

This work has provided a novel simple approach to formulate an oral, swellable, monolithic, controlled-release delivery system designed for delivery of highly soluble, ionizable drugs over a long time period. An important feature of this system is the potential for generating constant drug release, a trend highly desirable for many pharmaceutical agents such as cardiovasculars, antiasthmatics, antihistamines, and narrow therapeutic index drugs. Through careful selection of electrolyte(s) and drug, an *in situ chemical interaction* within the gelled structure may be induced for the alteration of matrix-swelling dynamics and inhibition of drug dissolution. On the basis of textural analysis, peripheral axial front synchronization and greater radial matrix stiffening was observed to occur. This directional discrepancy in operating swelling mechanisms may be related to the fact that the degree of axial expansion of HPMC compacts was greater than radial expansion. In addition, the presence of electrolyte in the formulation clearly contributed to the formation of a more heterogeneous gel structure referred to as "metamorphic scaffold" in this work. The delivery system was also shown to be versatile in that it was neither electrolyte- nor polymer-limited, and specific formulation design can lead to release that is independent of variation in pH.

References and Notes

1. McClelland, G. A.; Sutton, S. C.; Engle, K.; Zentner, G. M. The Solubility-Modulated Osmotic Pump: *In Vitro/in Vivo* Release of Diltiazem Hydrochloride. *Pharm. Res.* **1991**, *8*, 88−92.
2. Hayashida, T.; Kikumaru, K.; Tomoyuki, O. Sustained Release Tablet. U.S. Patent 5,593,694, 1997.
3. Conte, U.; La Manna, A.; Maggi, L. Controlled Release Pharmaceutical Tablet Having Lenticular Form. U.S. Patent 5,626,874, 1997.
4. Fassihi, R.; Yang, L. Controlled Release Drug Delivery System. U.S. Patent 5,783,212, 1998.
5. Ramtoola, Z. Corrigan, O. I. Influence of Buffering Capacity of the Medium on the Dissolution of Drug-Excipient Mixtures. *Drug Devel. Ind. Pharm.* **1989**, *15*, 2359−2374.
6. Doherty, C.; York, P. Microenvironmental pH control of Drug Dissolution. *Int. J. Pharm.* **1989**, *50*, 223−232.
7. Mooney, K. G.; Mintun, M. A.; Himmelstein, K. J.; Stella, V. J. Dissolution Kinetics of Carboxylic Acids II: Effect of Buffers. *J. Pharm. Sci.* **1981**, *70*, 22−32.
8. Michelucci, J. J.; Sherman, D. M. Sustained Release Etodoloc. U.S. Patent 4,966,768, 1996.
9. Chakrabarthi, S.; Southard, M. Z. Control of Poorly Soluble Drug Dissolution in Conditions Simulating the Gastrointestinal Tract Flow 2. Cocompression of Drugs with Buffers. *J. Pharm. Sci.* **1997**, *86*, 465−469.
10. Pagay, S. N. Use of Buffers in Matrix Capsule Formulations. *Drug Devel. Ind. Pharm.* **1988**, *14*, 875−894.
11. Venkatesh, G. M. Development of Controlled Release SK&F 82526-J Buffer Bead Formulations with Tartaric Acid as the Buffer. *Pharm. Devel. Technol.* **1998**, *3*, 477−485.

12. McClelland, G. A.; Zentner, G. M. Swelling Modulated Polymeric Drug Delivery Device. U.S. Patent 5,120,548, 1992.
13. Thoma, K.; Zimmer, T. Retardation of Weakly Basic Drugs with Diffusion Tablets. *Int. J. Pharm.* **1990**, *58*, 197−202.
14. Gabr, K. E. Effect of Organic Acids on the Release Patterns of Weakly Basic Drugs from Inert Sustained Release Matrix Tablets. *Eur. J. Pharm. Biopharm.* **1992**, *38*, 199−202.
15. Pillay, V.; Fassihi, R. Monolithic Tablet for Controlled Drug Release. *U.S. Patent Appl.* 09/037,096, 1998.
16. Yang, L.; Johnson, B.; Fassihi, R. Determination of Continuous Changes in the Gel Layer Thickness of Poly(ethylene oxide) and HPMC Tablets Undergoing Hydration: A Texture Analysis Study. *Pharm. Res.* **1998**, *15*, 1902−1906.
17. Ritger, P. L.; Peppas, N. A. Simple Equation for Description of Solute Release: II Fickian and Anomalous Release from Swellable Devices. *J. Controlled Release* **1987**, *5*, 37−42.
18. Peppas, N. A.; Sahlin, J. J. A Simple Equation for the Description of Solute Release: III Coupling of Diffusion and Relaxation. *Int. J. Pharm.* **1989**, *57*, 169−172.
19. Pillay, V.; Fassihi, R. In vitro Release Modulation from Crosslinked Pellets for Site-specific Drug Delivery to the Gastrointestinal Tract: I Comparison of pH-responsive Drug Release and Associated Kinetics. *J. Controlled Release* **1999**, *59*. 220−242.
20. Durig, T.; Fassihi, R. Mechanistic Evaluation of Binary Effects of Magnesium Stearate and Talc as Dissolution Retardants at 85% Drug Loading in an Experimental Extended Release Formulation. *J. Pharm. Sci.* **1997**, *86*, 1092−1098.
21. Hopfenberg, H. B. In *Controlled Release Polymeric Formulations*; Paul, D. R., Haris, F. W., Eds.; ACS Symposium Series 33; American Chemical Society: Washington, DC, 1976; pp 26−31.
22. Katzhendler, I.; Hoffman, A.; Goldberger, A.; Friedman, M. Modeling of Drug Release from Erodible Tablets. *J. Pharm. Sci.* **1997**, *86*, 110−115.
23. Lide, D. R.; Frederikse, H. P. R. CRC Handbook of Chemistry and Physics: A Ready-Reference Book of Chemical and Physical Data, 78th ed.; CRC Press: New York, 1997.
24. Budaveri, S.; O"Neil, M. J.; Heckelman, P. E.; Kinneary, J. F. *The Merck Index: An Encyclopedia of Chemicals, Drugs and Biologicals*, 12th ed.; Merck and Co., Inc.: Rahway, New Jersey, 1996.
25. Felthouse, T. R.; Burnett, J. C.; Mitchell, S. F.; Mummey, M. J. Maleic Anhydride, Maleic Acid and Fumaric Acid. In *Encyclopedia of Chemical Technology*, 4th ed.; Kroschwitz, J. I., Howe-Grant, M., Vol. 15, Humphreys, L., Aitieri, L., Eds.; John Wiley and Sons: New York, 1995; pp 893−928.
26. Martin, A. *Physical Pharmacy: Physical Chemical Principles in the Pharmaceutical Sciences*, 4th ed.; Lea and Febiger: Philadelphia, 1993; pp 143−168.
27. Bodmeier, R.; Guo, X.; Sarabia, R. E.; Skultety, P. F. The Influence of Buffer Species and Strength on Diltiazem HCl Release from Beads Coated with the Aqueous Cationic Polymer Dispersions, Eudragit RL, RS 30D. *Pharm. Res.* **1996**, *13*, 52−56.
28. Pade, V.; Stavchansky, S. Estimation of the Relative Contribution of the Transcellular and Paracellular Pathway to the Transport of Passively Absorbed Drugs in the Caco-2 Cell Culture Model. *Pharm. Res.* **1997**, *14*, 1210−1215.
29. Schott, H. Colloidal Dispersions. In *Remington: The Science and Practice of Pharmacy*, 19th ed., Gennaro, A. R., Ed.; Mack Publishing Company: Easton, Pennsylvania, 1995; Vol. 1, pp 252−277.

Acknowledgments

The authors thank Dr. Hans Schott (Temple University, School of Pharmacy) for his constructive comments and critical review of this paper. The National Research Foundation (NRF, South Africa) is acknowledged for providing the Doctoral Fellowship to Viness Pillay. We also thank Dr. Daniel Canney (Temple University, School of Pharmacy) for his expertise and guidance in diltiazem-free base formation. Mr. Boine Johnson (Texture Technologies Corp., New York) is acknowledged for providing us with the texture analyzer instrument and his technical expertise in making the texture analysis study possible.

JS9901054

Preferential Distribution of Amphotericin B Lipid Complex into Human HDL_3 Is a Consequence of High Density Lipoprotein Coat Lipid Content

ALLISON L. KENNEDY AND KISHOR M. WASAN*

Contribution from *Division of Pharmaceutics and Biopharmaceutics, Faculty of Pharmaceutical Sciences, The University of British Columbia, Vancouver, British Columbia, Canada.*

Received March 31, 1999. Final revised manuscript received July 8, 1999.
Accepted for publication August 20, 1999.

Abstract □ The purpose of this study was to determine the plasma lipoprotein (LP) distribution of amphotericin B (AmpB) and amphotericin B lipid complex [ABLC; Abelcet composed of dimyristoyl phosphatidylcholine (DMPC) and dimyristoyl phosphatidylglycerol (DMPG)] and define the relationship between LP lipid concentration and composition and the distribution of AmpB and ABLC in human plasma with varying total and lipoprotein cholesterol and triglycerides. AmpB and ABLC at a concentration of 20 μg amphotericin B/mL were incubated in plasma obtained from different human subjects ($n = 7$) for 60 min at 37 °C. Following these incubations plasma samples were separated into their high-density lipoprotein (HDL), triglyceride-rich lipoprotein (TRL; which contains very low-density lipoproteins and chylomicrons), low-density lipoprotein (LDL), and lipoprotein-deficient (LPDP) fractions by density-gradient ultracentrifugation (UC) and each fraction was assayed for AmpB using high-pressure liquid chromatography (HPLC). The HDL fraction was further separated into its HDL_3 and HDL_2 subclasses by UC and assayed for AmpB using HPLC. Separation of HDL into its subclasses was confirmed by gel electrophoresis. To assess the influence of modified lipoprotein concentrations and lipid composition on the plasma distribution of AmpB and ABLC, these compounds were incubated in plasmas from human subjects with varying total and lipoprotein lipid concentrations. In addition, to demonstrate that alterations in HDL lipid composition influence the plasma distribution of ABLC, ABLC (20 μg amphotericin B/mL) was incubated in plasma pretreated with dithionitrobenzoate (DTNB, a compound which inhibits lecithin:cholesterol acyltransferase conversion of HDL_3 free cholesterol to esterified cholesterol) 18 h prior to the experiment or in untreated plasma for 60 min at 37 °C. Total plasma and lipoprotein cholesterol (TC), free cholesterol (fC), esterified cholesterol (CE), triglyceride (TG), phospholipid (PL), and protein (TP) concentrations in each human sample were determined by enzymatic assays. When AmpB was incubated in human plasmas of varying lipid concentrations, the majority of the drug was recovered in the LPDP fraction. However, the majority of AmpB was recovered in the HDL_3 fraction following the incubation of ABLC. Differences in lipid coat content (fC and PL) carried by HDL influenced the distribution of ABLC within plasma of different human subjects. These findings were confirmed by the DTNB treatment experiments. These findings suggest that the association of AmpB with DMPC and DMPG to form drug–lipid complexes modifies the plasma distribution of the AmpB. In addition, the distribution of ABLC among plasma lipoproteins of different human subjects is defined by the HDL lipid coat content and is possibly an important consideration when evaluating the pharmacokinetics, toxicity, and activity of these compounds following administration to humans with differing plasma lipid concentrations.

Introduction

Amphotericin B (AmpB) remains one of the most effective and widely used agents in the treatment of systemic fungal infections including *Candida albicans* and *Histoplasma capsulatum*.[1] The clinical use of AmpB has been limited by dose-dependent nephrotoxicity, which may result in as much as a 60% reduction in the glomerular filtration rate.[1,2] The fungal cytotoxicity of AmpB is related to its amphiphilic structure, which facilitates binding to cell membrane sterols, thereby disrupting membrane integrity, and to its preferential binding to ergosterol in fungal membranes versus cholesterol in mammalian membranes.[3,4] However, when AmpB is formulated into a amphotericin B lipid complex (ABLC) it has been shown to be well-tolerated in doses up to 5 mg/kg of AmpB/kg of body weight and has been effective in patients that failed to respond to conventional AmpB therapy.[5,6]

Plasma lipoproteins are macromolecules of lipid and protein that transport polar and nonpolar lipids through the vascular and extravascular body fluids.[7−9] However, it is well-known that plasma lipoprotein profiles vary considerably between different animal species.[7,8] In addition, disease states can significantly influence plasma lipoprotein profiles, possibly resulting in altered therapeutic outcomes. Current research has shown that lipoprotein association of drug compounds can significantly influence not only the pharmacological and pharmacokinetics of the drug but also the relative toxicity.[7,8]

There is growing evidence that suggests increases in serum cholesterol concentrations increase the renal toxicity of AmpB. Koldin and co-workers demonstrated elevated AmpB-induced nephrotoxicity when AmpB bound to low-density lipoproteins (LDL) was administered to hypercholesterolemic rabbit's compared to AmpB alone.[10] Recent work by our lab suggests that increases in cholesterol, specifically LDL cholesterol levels, modify the disposition and renal toxicity of AmpB alone when administered to hypercholesterolemic rabbits.[11] However, the pharmacokinetics and renal toxicity of ABLC were independent of elevations in total and LDL cholesterol levels.[11] Lopez-Berestein et al. observed that when AmpB was administered to patients with leukemia who exhibited lower serum cholesterol concentrations, AmpB-induced renal toxicity was decreased.[12] Chabot and co-workers observed no measurable renal toxicity when AmpB was administered to cancer patients who exhibited hypocholesterolemia.[13] We have further reported that patients with a higher percentage of AmpB recovered within the serum LDL fraction are more susceptible to AmpB-induced kidney toxicity.[14]

A number of recent studies have suggested that increases in the association of AmpB with serum LDL enhanced the

* Corresponding author. Telephone: 604 822-4889. Fax: 604 822-3035. E-mail: Kwasan@unixg.ubc.ca.

10.1021/js990101z CCC: $18.00
Published on Web 09/28/1999

ability of AmpB to damage cells. Verlut-Doi et al. demonstrated that internalization of AmpB into Chinese hamster ovary cells in the presence of serum occurred by endocytosis.[15] Kreiger further reported that the cellular uptake of AmpB was a result of LDL-receptor mediated endocytosis.[16] We have reported that LDL-bound AmpB was as toxic to kidney cells as unbound AmpB.[17] However, HDL-bound AmpB was less toxic to these cells than either unbound or LDL-bound AmpB.[17] Furthermore, when the number of LDL receptors expressed on these cells were reduced, LDL-bound AmpB was less toxic to these cells than unbound AmpB,[17] suggesting that LDL receptors may play an important role in promoting the renal toxic affects of AmpB. Taken together, these studies[11,17] suggest an alternative hypothesis on how the ABLC formulation may decrease AmpB-induced renal toxicity than simply maintaining drug in the circulation in a complexed form effectively reducing the free concentration available to exert toxicity and/or by the rapid removal of the lipid complex from the circulation, thus reducing kidney tissue exposure.[5,6]

Our laboratory has recently observed that when ABLC was incubated in human plasma for 5−120 min at 37 °C, the majority of drug was recovered in the HDL fraction.[8] These findings are similar to what was observed with liposomal nystatin and annamycin.[8] A rationale for these results may be related to the similar lipid composition of these formulations [i.e., they all contain dimyristoyl phosphatidylcholine (DMPC) and dimyristoyl phosphatidylglycerol (DMPG)]. We have further observed that the DMPG component of these lipid-based formulations predominantly distributes into HDL because of its interaction with the protein components of HDL (apolipoproteins AI and AII).[8] Since ABLC is composed of the same phospholipids as liposomal nystatin and annamycin, the increased distribution of AmpB into the HDL fraction when formulated into these lipid complexes may also be a result of the attraction of DMPG for apolipoproteins AI and AII.[8,18] This rationale is further substantiated by recent findings which demonstrated that as the amount of HDL protein decreased, the percent of nystatin recovered within the HDL fraction proportionally decreased following the incubation of liposomal nystatin.[19]

The studies presented in this paper determine the plasma lipoprotein distribution of AmpB and ABLC following incubation in plasma from different human subjects with varying total and lipoprotein lipid concentrations and address the role of lipoprotein lipid and protein content on the distribution of AmpB to plasma lipoproteins.

Materials and Methods

Chemicals, Lipids, and Plasma—AmpB formulated as a micelle clear liquid (Fungizone; Bristol Myers Squibb, Princeton, NJ) and as a lipid complex, i.e., amphotericin B lipid complex (ABLC; Abelcet; The Liposome Company Inc., Princeton, NJ), were purchased from Vancouver General Hospital, Department of Pharmaceutical Sciences. The British Columbia Red Cross provided human plasma from seven different human volunteers not known to have preexisting hyperlipidemia. Organic solvents (methanol, etc.) were purchased from Fisher Canada. Ultracentrifugation supplies (i.e., centrifuge tubes, density gradient solutions) were purchased from Beckman Canada. Lipid and protein analysis kits were purchased from Sigma Chemical (St. Louis, MO). Free cholesterol and phospholipid analysis kits were purchased from Boehringer Mannheim (Germany).

Heterogeneity of Human Plasma Lipoprotein Profiles—Blood collected from healthy human volunteers (Screened by British Columbia Red Cross) was placed in drug-free glass test tubes, which contained 0.05M EDTA and centrifuged using a tabletop centrifuge for 10 min at 2,000 rpm; plasma was stored at −20 °C until used in the study.

Lipoprotein Separation—*Lipoprotein Separation by Step-Gradient Ultracentrifugation*—For the separation of lipoprotein plasma components by step-gradient ultracentrifugation, sodium bromide density solutions were carefully layered on top of the plasma samples in order of highest to lowest density. The density of the plasma samples was initially altered such that it had the greatest density of all layers in the gradient. The samples were ultracentrifuged overnight, and separation of the lipoprotein fractions was accomplished in a single spin. Each distinct layer was removed and separated for further analysis.

(i) Treatment of Plasma with AmpB or ABLC—To an ultraclear centrifuge tube (Beckman Instruments, Inc., Palo Alto, CA) was added 2.88 or 3 mL of human plasma for sample ($n = 3$ for AmpB and $n = 3$ for ABLC) or standard curve ($n = 6$) purposes, respectively. The contents of all tubes were prewarmed to 37 °C. To the samples tubes was added either 12 μL of an AmpB solution (5 mg/mL) or 12 μL of an ABLC suspension (5 mg/mL). The final concentration of AmpB in human plasma for both AmpB and ABLC formulations was 20 μg/mL. Immediately after the addition of AmpB or ABLC, the samples were returned to 37 °C and incubated for 60 min, whereupon they were removed and cooled on ice for 30 min.

(ii) Separation of Lipoprotein Constituent—Briefly, solutions of all densities (density [δ] = 1.006, 1.063, and 1.21 g/mL) were stored at 4 °C prior to the layering of the gradient. To the previously cooled plasma used for standard curves and the plasma samples was added 1.02 g of accurately weighted sodium bromide (0.34 g of sodium bromide per 1.0 mL of plasma) in order to modify the density of the plasma to approximately 1.25 g/mL.[19] Once the sodium bromide had dissolved into the plasma, 2.8 mL of the highest density sodium bromide ($\delta = 1.21$ g/mL) was carefully layered on top of the plasma. By using the same volume of 2.8 mL, the next highest sodium bromide solution ($\delta = 1.063$ g/mL) was layered on top of the sample, followed by 2.8 mL of the lowest density solution ($\delta = 1.006$ g/mL). The ultracentrifuge tubes were balanced, placed into individual titanium buckets, and capped. The buckets were placed into their respective positions on a SW 41 Ti swinging bucket rotor (Beckman Instruments, Inc.) and centrifuged at 40 000 rpm for 18 h at a temperature of 15 °C in a Beckman L8−80M Ultracentrifuge (Beckman Instruments, Inc.) Upon completion of the run, the ultracentrifuge tubes were carefully removed from the titanium buckets. Each tube showed four visibly distinct regions represented by the triglyceride rich lipoprotein (TRL, which includes very low-density lipoproteins and chylomicrons), LDL, HDL, and lipoprotein-deficient plasma (LPDP) fractions. Subsequently, each of the layers was removed with a Pasteur pipet from the top to the bottom layer, respectively, and the volume of each of the fractions was measured. Fractions removed for standard curve purposes were pooled together. All sample and pooled standard curve fractions were transferred to clean test tubes, covered, and stored at 4 °C until further analysis.

(iii) Control—LPDP was used as the control medium. The LPDP was acquired by the technique of step-gradient ultracentrifugation as described above. The LPDP was dialyzed (molecular weight cutoff 1000) against a 0.9% sodium chloride solution for 24 h at a temperature of 4 °C and was then used as the control medium for the incubation of AmpB or ABLC. Preparation of the samples with AmpB or ABLC as well as separation of the constituents was carried out by techniques identical to those described above for step-gradient ultracentrifugation. After ultracentrifugation, the removal of each "lipoprotein" fraction was estimated by comparison to previously separated lipoprotein fractions (i.e., removal of the layer from where TRL would normally reside was based on previous separation of actual plasma in which the layers were visible). The removal of the nonlipoprotein fractions in the control medium was estimated as being close to the placement of their separated lipoprotein counterparts in plasma.

HDL_2/HDL_3 Separation by Step-Gradient Ultracentrifugation—Plasma was separated into its TRL/LDL, HDL_2, HDL_3, and LPDP fractions by an ultracentrifugation method modified from the published methods of Groot et al.[20]

(i) Treatment of Plasma with AmpB or ABLC—To an ultraclear centrifuge tube (Beckman Instruments, Inc., Palo Alto, CA) was added 1.64 or 1.7 mL of human plasma for sample ($n = 3$ for AmpB and $n = 3$ for ABLC) or standard curve ($n = 6$) purposes, respectively. The contents of all tubes were prewarmed to 37 °C. To the samples tubes was added either 6.4 μL of an AmpB solution (5 mg/mL) or 6.4 μL of an ABLC suspension (5 mg/mL). The final

concentration of AmpB in human plasma for both AmpB and ABLC formulations was 20 μg/mL. Immediately after the addition of AmpB or ABLC, the samples were returned to 37 °C and incubated for 60 min, whereupon they were removed and cooled on ice for 30 min.

(ii) Separation of Lipoprotein Constituent—Briefly, solutions of all densities (δ = 1.00, 1.19, and 1.25 g/mL) were stored at 4 °C prior to the layering of the gradient. To the previously cooled plasma used for standard curves and the plasma samples was added 0.936 g of accurately weighed sodium bromide in order to modify the density of the plasma to approximately 1.40 g/mL.[20] Once the sodium bromide had dissolved into the plasma, 1.70 mL of the highest density sodium bromide (δ = 1.25 g/mL) was carefully layered on top of the plasma. By using the volume of 6.4 mL, the next highest sodium bromide solution (δ = 1.19 g/mL) was layered on top of the sample, followed by 1.70 mL of the lowest-density solution (δ = 1.00 g/mL). The ultracentrifuge tubes were balanced, placed into individual titanium buckets, and capped. The buckets were placed into their respective positions on a SW 41 Ti swinging bucket rotor (Beckman Instruments, Inc.) and centrifuged at 40 000 rpm for 21 h at a temperature of 15 °C in a Beckman L8-80M Ultracentrifuge (Beckman Instruments, Inc.) Upon completion of the run, the ultracentrifuge tubes were carefully removed from the titanium buckets. Each of the layers was removed from the top to the bottom layer with the following volumes; TRL/LDL, 0.5 mL; HDL_2, 2.4 mL; HDL_3, 4.8 mL; and LPDP/bottom, 4.3 mL. Fractions removed for standard curve purposes were pooled together. All sample and pooled standard curve fractions were transferred to clean test tubes, covered, and stored at 4 °C until further analysis.

(iii) Control—LPDP was used as the control medium. The LPDP was acquired by the technique of step-gradient ultracentrifugation as described above for HDL_2/HDL_3. The LPDP was dialyzed as previously described and then used as the control medium for the incubation of AmpB or ABLC. Preparation of the samples with AmpB or ABLC as well as separation of the constituents was carried out by techniques identical to those described above for HDL_2/HDL_3 step-gradient ultracentrifugation.

HDL_2/HDL_3 Separation by Gel Electrophoresis—Polyacrylamide gradient gels with a linear gradient of 4−30% of acrylamide were used in the separation of HDL_2 and HDL_3 as previously described.[21] The electrophoresis buffer contained TRIS base (90 mM), boric acid (80 mM), EDTA (3 mM), and sodium azide (3 mM) at pH 8.35. The gradient gels were preconditioned in electrophoresis buffer for 20 min at 125 V and 10° C in an electrophoresis chamber. Ten microliters of a sample containing HDL and sucrose (40%) and bromphenyl blue (0.05%) was applied to the gel for 20 min at 15 V, 30 min at 70 V, and then 24 h at 125 V at 10 °C. Calibration protein standards containing 2.5 μg of thyroglobulin, ferritin, catalase, lactate dehydrogenase, and bovine serum albumin were applied concurrently to other wells of the gel. Following electrophoresis, gels were stained for 1.5 h with Coomassie G-250 (0.04%) in methanol and acetic acid. The gels were than destained in 10% acetic acid and 30% methanol until the background was clear.

AmpB Quantification—AmpB was extracted from each lipoprotein and lipoprotein-deficient fraction by a liquid−liquid extraction method previously described.[22] Immediately prior to analysis, the residue was reconstituted with methanol and injected onto a high-pressure liquid chromatography (HPLC) column. The drug level was analyzed against external calibration curves by HPLC.

TRL, LDL, and LPDP Standard Curve Preparation—To a series of test tubes labeled 0, 0.039, 0.078, 0.156, 0.3125, 0.626, 1.25, 2.5, 5, 10 μg/mL was added 0.5 mL of pooled standard curve fraction, and to a test tube labeled 20 μg/mL was added 0.96 mL of the same pooled fraction. A 4 μL aliquot of either an AmpB solution (5 mg/mL) or an ABLC suspension (5 mg/mL) was then added to the test tube labeled 20 μg/mL, and the test tube was vortexed for 10 s. From the 20 μg/mL test tube, a 0.5 mL aliquot of this mixture was subsequently transferred to the test tube labeled 10 μg/mL. This procedure of serial dilution was carried out for the remaining tubes used for the standard curve.

(i) HDL Standard Curve Preparation—The procedure for the preparation of a HDL standard curve is the same as described above with one minor adjustment. To all tubes in the standard curve was added 1.0 mL of pooled standard curve fraction. To the tube labeled 20 μg/mL was added 1.92 mL of pooled standard curve fraction. An 8 μL aliquot of either an AmpB solution (5 mg/mL) or an ABLC suspension (5 mg/mL) was then added to the test tube labeled 20 μg/mL, and the procedure was carried out as described above.

(ii) Determination of AmpB Content within the Separated Lipoprotein Fraction: TRL and LDL—To an appropriately labeled test tube was added a 0.5 mL aliquot of sample. To these sample tubes as well as the tubes used for the standard curve was added 3 mL of dichloromethane. The mixture was vortexed for 10 s, and all samples were dried under a steady stream of nitrogen at ambient temperature. Once the sample was dried, the AmpB was extracted from the residue with a single methanol wash. Extraction efficiency was determined to be greater than 90% (data not shown). Briefly, a 3.0 mL aliquot of methanol was added to the residue, and the mixture was vortexed for 20 s before being completely dried under a steady stream of nitrogen at ambient temperature. Immediately prior to analysis, the residue was reconstituted with 0.5 mL of methanol and was injected onto the column.

(iii) Determination of AmpB Content within the Separated Lipoprotein Fraction: HDL—To an appropriately labeled test tube was added a 1.0 mL aliquot of sample. The procedure described above was then followed until the last step, when the residue was reconstituted with 0.250 mL of methanol prior to injection onto the column.

(iv) Determination of AmpB Content within the Separated Lipoprotein Fraction: LPDP—To an appropriately labeled test tube was added a 0.5 mL aliquot of sample. To these sample tubes as well as the tubes used for the standard curve was added 3 mL of dichloromethane. The mixture was vortexed for 10s, and all samples were dried under a steady stream of nitrogen at ambient temperature. Once the sample was dried, the AmpB was extracted from the residue with a series of methanol washes. Briefly, a 3.0 mL aliquot of methanol was added to the residue and the mixture was vortexed for 20 s. All test tubes were then centrifuged at 1200*g* for 2 min at 15 °C. The supernatant was transferred to a clean test tube, and the procedure was repeated an additional two times with 2.0 mL of methanol. The supernatant from each of the three extraction steps was pooled with the previous supernatant to provide a final volume of approximately 7 mL of methanol. This pooled methanol was then dried to completion under a steady stream of nitrogen at ambient temperature. Immediately prior to analysis, the residue was reconstituted with 0.5 mL of methanol and was injected onto the column.

HPLC Apparatus—The HPLC system consisted of a Waters 600 Controller interfaced to a Waters 717_{plus} autosampler and a Waters 486 tunable absorbency detector. The detector was set at an UV absorbency wavelength of 405 nm and an absorbency sensitivity of 0.05 absorbency units-full scale. All results were recorded on a Waters 746 Data Module Integrator (Waters Corp., Milford, MA). Samples (100 μL volume) were injected onto a Zorbax SB-C18 column (4.6 × 150 mm; 5 μm particle size), prefitted with a Zorbax Reliance SB-C18 guard column (4.6 × 12.5 mm; 5 μm particle size) (Rockland Technologies, Inc.). Chromatographic separation was carried out at ambient temperature. The mobile phase employed an isocratic flow and consisted of sodium acetate (10 mM) with acetonitrile (70/30 v/v) at a flow rate of 1.5 mL/min. The sensitivity of this assay was 50 ng/mL with an intraday CV of 5−8% (data not shown).

Lipid and Protein Content Analysis of Lipoprotein and Lipoprotein-Deficient Plasma Fractions—Total plasma and lipoprotein triglycerides, cholesterol (free and cholesteryl ester), phospholipids (phosphatidylcholine), and protein concentrations of the human plasma were determined by enzymatic assays purchased from Sigma Diagnostics (St. Louis, MO) and Boehringer Mannheim (Laval, QUE, Canada).

Experimental Design—To assess the distribution of AmpB and ABLC within human plasma, AmpB and ABLC at 20 μg of drug/mL of plasma were incubated in human plasma obtained from seven different human subjects for 60 min at 37 °C. Following incubation, the plasma samples were placed on ice to prevent redistribution of drug within the plasma samples as previously described.[19,22] The plasma was then partitioned into its lipoprotein and lipoprotein-deficient plasma fractions: TRL, consisting of VLDL and chylomicrons; LDL, consisting of intermediate-density lipoproteins and LDLs; HDL, consisting of all subclasses of HDL; and LPDP, consisting of albumin and α-1-glycoprotein by step-gradient ultracentrifugation. Each lipoprotein fraction was analyzed for cholesterol (total, esterified, and unesterified), triglyc-

Table 1—Total and Lipoprotein Plasma Lipid and Protein Concentrations in Samples from Seven Different Human Subjects[a]

plasma sample	TRL[b]			LDL			HDL			total[c]		
	C	TG	P	C	TG	P	C	TG	P	C	TG	P
patient I	11.6	32.1	7.0	36.8	14.3	19.2	23.3	20.1	128.9	77.6	83.1	4406.5
	(0.1)	(2.4)	(0.9)	(1.1)	(2.1)	(0.3)	(0.7)	(0.4)	(15.9)	(3.0)	(2.4)	(262.5)
patient II	45.5	53.5	25.8	16.9	102.3	79.3	26.5	63.9	318.9	106.4	233.7	4616.6
	(2.6)	(3.0)	(3.7)	(3.7)	(3.0)	(2.1)	(2.9)	(2.4)	(18.0)	(5.7)	(10.1)	(165.0)
patient III	54.7	175.1	39.1	41.6	26.2	34.1	23.0	28.8	305.8	125.9	250.5	4564.2
	(0.9)	(11.9)	(1.6)	(2.4)	(1.7)	(3.9)	(1.0)	(1.1)	(60.5)	(1.9)	(10.8)	(341.7)
patient IV	18.3	20.7	6.0	66.7	18.6	28.2	58.5	51.9	239.7	144.3	114.3	4728.0
	(1.8)	(1.6)	(2.2)	(3.6)	(1.6)	(1.4)	(7.4)	(19.2)	(38.8)	(5.6)	(14.4)	(317.6)
patient V	70.0	157.8	49.1	68.4	34.0	98.1	56.4	24.5	215.9	206.8	227.4	4963.5
	(3.3)	(7.3)	(1.5)	(5.0)	(5.2)	(3.1)	(10.7)	(5.8)	(6.4)	(7.0)	(8.6)	(311.5)
patient VI	39.0	31.3	10.8	94.8	20.6	35.5	65.8	35.0	215.7	211.7	110.3	4750.0
	(1.5)	(1.0)	(1.7)	(4.5)	(1.8)	(5.6)	(4.5)	(3.1)	(24.8)	(13.6)	(8.1)	(506.7)
patient VII	47.1	144.3	74.6	102.2	46.9	55.8	59.7	43.9	175.1	219.6	258.2	4749.2
	(3.5)	(2.8)	(8.9)	(5.4)	(3.9)	(6.7)	(10.1)	(1.6)	(11.3)	(16.2)	(4.3)	(164.4)

[a] Data are expressed as mean ± standard deviations (n=6 replicates). [b] Units in mg/dL. [c] Total values represent all plasma lipoprotein and lipoprotein-deficient fractions (which includes α-1 glycoprotein and albumin). Abbreviations: TRL, triglyceride-rich lipoproteins (including chylomicrons and very low-density lipoproteins); LDL, low-density lipoproteins; HDL, high-density lipoproteins; C, cholesterol (esterified and unesterified); TG, triglycerides; P, protein.

Table 2—Plasma Lipoprotein and Lipoprotein-Deficient Distribution of Amphotericin (AmpB) and Amphotericin B Lipid Complex (ABLC) (20 μG/mL) Following Incubation for 60 min at 37 °C in Samples from Seven Different Human Subjects[a]

plasma sample	TRL[b]		LDL		HDL		LPDP	
	AmpB	ABLC	AmpB	ABLC	AmpB	ABLC	AmpB	ABLC
patient I	12.2	0.9	5.7	2.0	7.0	79.4	66.8	11.6
	(0.8)	(0.1)	(0.2)	(0.04)	(0.1)	(0.2)	(10.2)	(1.2)
patient II	2.3	ND	2.5	1.3	12.3	61.4	72.9	25.0
	(0.3)		(0.8)	(0.04)	(1.5)	(2.2)	(1.6)	(1.7)
patient III	1.5	0.2	1.6	ND	7.0	89.7	89.8	2.7
	(0.2)	(0.2)	(0.2)		(1.0)	(1.8)	(1.0)	(0.2)
patient IV	4.2	ND	4.7	ND	4.5	86.6	80.4	4.5
	(0.5)		(0.7)		(0.2)	(3.9)	(6.6)	(0.2)
patient V	4.0	0.3	1.3	0.5	3.3	73.3	89.5	19.4
	(0.03)	(0.3)	(0.02)	(0.4)	(0.9)	(3.0)	(3.8)	(1.8)
patient VI	0.5	ND	2.2	0.5	7.3	50.0	77.4	42.6
	(0.1)		(0.5)	(0.5)	(1.3)	(8.4)	(8.7)	(4.3)
patient VII	10.6	0.8	1.6	1.0	1.6	71.3	69.1	22.4
	(0.4)	(0.01)	(0.2)	(0.1)	(0.3)	(0.1)	(2.8)	(3.6)

[a] Data are expressed as mean ± standard deviations (n = 3 replicates). [b] Percent of initial AmpB or ABLC concentration incubated. Abbreviations: TRL, triglyceride-rich lipoproteins (including chylomicrons and very low-density lipoproteins); LDL, low-density lipoproteins; HDL, high-density lipoproteins; LPDP, lipoprotein-deficient plasma fraction (which includes α-1, glycoprotein and albumin); AmpB, amphotericin B; ABLC, amphotericin B lipid complex; ND, non detectable. Percent of drug recovery for incubations in all patients ranges from 82.9 to 99.8%.

Table 3—Correlational Analysis Comparing the Amount of AmpB Recovered to Lipid and Protein Contents and Compositions of the Separated Lipoprotein and Lipoprotein-Deficient Plasma Fractions Following the Incubation of ABLC (20 μg/mL) for 60 min at 37 °C in Plasmas from Seven Different Human Subjects[a]

component or ratio	*r* value			
	TRL–AmpB*	LDL–AmpB**	HDL–AmpB	LPDP–AmpB
TC	–0.26	–0.33	–0.37	NA
CE				NA
fC	0.02	0.25	–0.66	NA
TG	0.33	0.57	–0.16	NA
PL	–0.15	–0.17	–0.66	NA
TP	0.01	–0.15	0.04	
Core lipid content (CE + TG)	0.21	–0.14	0.27	NA
Coat lipid content (fC + PL)	–0.12	–0.01	–0.78[c]	NA
TC:TP ratio	–0.62	–0.21	–0.42	NA
TG:TP ratio	0.71	0.21	0.23	NA
PL:TP ratio	–0.60	0.03	0.03	NA
TG:TC ratio	0.75	0.33	–0.04	NA

[a] Calculations are based on the Pearson correlation coefficient values with significance. Abbreviations: ABLC, amphotericin B lipid complex; TRL, triglyceride-rich lipoproteins (which includes very low-density lipoproteins and chylomicrons); LDL, low-density lipoproteins; HDL, high-density lipoproteins; LPDP, lipoprotein-deficient plasma (which includes α-1-glycoprotein and albumin); TC, total cholesterol; CE, cholesteryl ester; fC, free cholesterol; TG, total triglycerides; PL, phospholipid; TP, total protein. [b] NA, not applicable; analysis was not performed due to a lack of sufficient data. [c] $P < 0.05$. *n = 4; three patients had nondetectable AmpB concentrations. **n = 5; two patients had nondetectable AmpB concentrations.

eride, phospholipids, protein, and AmpB concentration. Since the majority of AmpB was not recovered in the HDL fraction following the incubation of free AmpB in plasma (Table 2), all additional experiments pertaining to HDL were done with only ABLC.

To determine which subfractions of HDL AmpB is recovered from, AmpB (as a negative control) and ABLC at 20 μg of drug/mL of plasma were incubated in human plasma for 60 min at 37 °C. Following incubation the plasma was separated into its HDL_2 and HDL_3 fractions by ultracentrifugation and each fraction was assayed for AmpB by HPLC. Separation of HDL into its different subfractions was confirmed by gel electrophoresis (Figure 1).

To further assess the influence of HDL lipid composition and structure on the plasma distribution of ABLC, ABLC at 20 μg of drug/mL of plasma was incubated in human plasma pretreated for 18 h with a lecithin:cholesterol acyltransferase (LCAT) inhibitor, dithionitrobenzoate (DTNB; 15 mM), as previously described[24] for 60 min at 37 °C. Following incubation the plasma was separated into its TRL, LDL, HDL, and LPDP fractions by ultracentrifugation and each fraction was assayed for AmpB by HPLC (Figure 2). DTNB is a sulfhydryl inhibitor that prevents the esterification of cholesterol to cholesteryl ester,[23] resulting in an elevation of HDL_3 coat lipid concentrations (fC + PL) (Table 6). In a second DTNB treatment experiment following the incubation of ABLC in plasma, the plasma was separated into its HDL_2 and HDL_3 fractions by ultracentrifugation and each fraction was assayed for AmpB by HPLC (Table 6).

Data and Statistical Analysis—Correlation coefficients between the amount of AmpB recovered within the TRL, HDL, and LDL plasma fractions and the amount of fC, CE, TC, TG, and TP within these fractions and plasma lipoprotein composition were determined using Pearson's Test (Tables 3 and 4). Differences in plasma distribution of AmpB and ABLC following incubation in plasmas obtained from different human subjects with varying lipid concentrations were determined by two-way analysis of variance without repeated measures (INSTAT; Human Systems Dynamics). Critical differences were assessed by Newman–Keuls and Tukey post hoc tests. A difference was considered significant if the probability of chance explaining the results was reduced to less than 5% ($p < 0.05$). All data were expressed as a mean ± standard deviation.

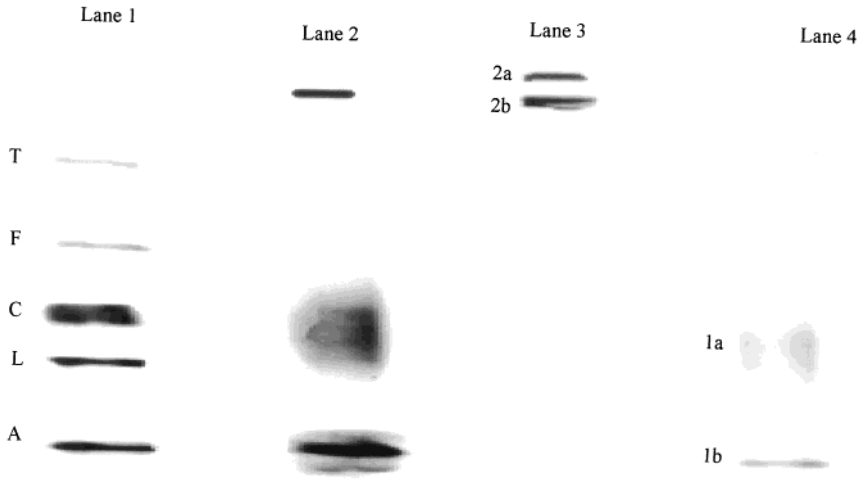

Figure 1—Human plasma samples run on the HDL gel formats. Lane 1 contains the standards: T, thyroglobulin; F, ferritin; C, catalase; L, lactate dehydrogenase; A, bovine serum albumin. Lane 2 is total HDL (including both HDL_3 and HDL_2) separated by ultracentrifugation. Lane 3 is HDL_2 separated by ultracentrifugation, 2a-HDL_{2b}, and 2b-HDL_{2a}. Lane 4 is HDL_3 separated by ultracentrifugation, 1a-HDL_{3a}, and 1b-HDL_{3b}. Lipoproteins and proteins in the standards were stained with Coomassie Brilliant Blue as described in the text (methods section).

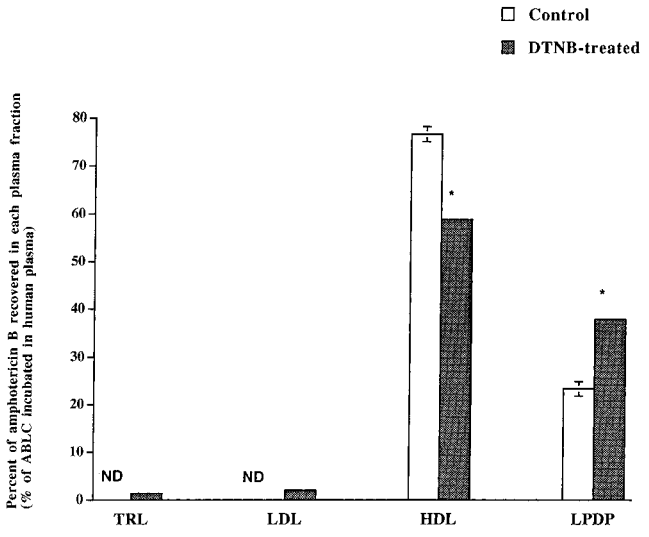

Figure 2—Distribution of amphotericin B lipid complex (ABLC) (20 μg of AmpB/mL of plasma) following incubation within human plasma that has been treated with DTNB (15 mM). ABLC was incubated in plasma pretreated with DTNB 18 h prior to the experiment or in untreated plasma (control) for 60 min at 37 °C. Following incubation the plasma was separated into its triglyceride-rich lipoprotein (TRL), low-density lipoprotein (LDL), high-density lipoprotein (HDL), and lipoprotein-deficient plasma (LPDP) fractions by ultracentrifugation and assayed for AmpB by HPLC. $N = 3$; data are expressed as mean ± standard deviation. *$p < 0.05$ vs control.

Table 4—Correlational Analysis Comparing Amount of AmpB Recovered to Lipid and Protein Contents and Compositions of the Separated Lipoprotein and Lipoprotein-Deficient Plasma Fractions Following the Incubation of AmpB (20 μg/mL) for 60 min at 37 °C in Plasmas from Seven Different Human Subjects[a]

component or ratio	*r* value			
	TRL–AmpB	LDL–AmpB	HDL–AmpB	LPDP–AmpB
TC	–0.44	–0.32	–0.59	NA
CE				NA
fC	–0.10	–0.06	0.47	NA
TG	0.11	0.20	0.22	NA
PL	–0.34	–0.71	–0.20	NA
TP	–0.32	–0.63	0.58	
Core lipid content (CE + TG)	0.10	–0.72	–0.50	NA
Coat lipid content (fC + PL)	–0.30	–0.50	0.02	NA
TC:TP ratio	–0.49	0.39	–0.30	NA
TG:TP ratio	0.70	0.31	0.01	NA
PL:TP ratio	–0.56	0.47	–0.10	NA
TG:TC ratio	0.60	0.11	0.80[c]	NA

[a] Calculations are based on the Pearson correlation coefficient values with significance. Abbreviations: AmpB, amphotericin B; TRL, triglyceride-rich lipoproteins (which includes very low-density lipoproteins and chylomicrons); LDL, low-density lipoproteins; HDL, high-density lipoproteins; LPDP, lipoprotein-deficient plasma (which includes α-1-glycoprotein and albumin); TC, total cholesterol; CE, cholesteryl ester; fC, free cholesterol; TG, total triglycerides; PL, phospholipid; TP, total protein. [b] NA, not applicable; analysis was not performed due to a lack of sufficient data. [c] $P < 0.05$.

Results

Distribution of Amphotericin B (AmpB) and Amphotericin B Lipid Complex (ABLC) following Incubation in Plasma from Human Subjects with Varying Lipid Concentrations—Table 1 reports differences in total plasma and lipoprotein cholesterol (esterified and unesterified), triglyceride, and protein concentrations that were observed for the seven different patient samples measured.

Table 2 reports the human plasma lipoprotein and lipoprotein-deficient fraction distribution of AmpB and ABLC in seven different plasma samples following incubation at 37 °C for 60 min. For plasma incubated with AmpB, 0.5%−12.2% of the original AmpB concentration incubated was recovered in the TRL fraction, 1.3%−5.7% was recovered in the LDL fraction, 1.6%−12.3% was recovered in the HDL fraction, and 66.8%−89.8% was recovered in the LPDP fraction. For plasma incubated with ABLC, nondetectable levels to 0.9% of the original AmpB concentration incubated was recovered in the TRL fraction, nondetectable levels to 2.0% was recovered in the LDL fraction, 50.0%−89.7% was recovered in the HDL fraction, and 2.7%−42.6% was recovered in the LPDP fraction. Similar findings were observed following the incubation of AmpB and ABLC at 1, 5, and 10 μg AmpB/mL of plasma (data not shown).

When AmpB and ABLC were incubated in the LPDP fraction, the majority of the drug (>92%) was recovered in the density fraction from 1.21 to 1.25 g/mL, suggesting that the distribution of AmpB and ABLC is not a function of formulation density (data not shown).

When correlations between the amount of AmpB recovered within the TRL, LDL, HDL, and LPDP fractions following ABLC incubation and the amount of TC, CE, fC,

Table 5—Chemical Composition by Dry Weight of Plasma HDL_2 and HDL_3 and Amphotericin B Concentrations Recovered in HDL_2 and HDL_3 following the Incubation of Amphotericin B or Amphotericin B Lipid Complex (20 μg/mL) in Human Plasma for 60 min at 37 °C

component	units	HDL_2	HDL_3
ABLC	%[a]	ND	98.6 (0.2)*
AmpB	%[a]	ND	6.8 (0.2)* [c]
$M_r \times 10^{-6}$		0.36	0.18
density	g/cm^3	1.09	1.15
protein	%[b]	41	55
phospholipids	%[b]	30	23
triglycerides	%[b]	4.5	4.1
cholesteryl ester	%[b]	16	12
free cholesterol	%[b]	5.4	2.9

[a] Data are presented as mean ± standard deviation (*n = 3 replicates) for the drug distribution work. Abbreviations: ABLC, amphotericin B lipid complex; AmpB, amphotericin B. HDL, high-density lipoproteins; M_r; molecular weight; ND, non detectable concentration. [b] Percent of initial drug incubated. [c] Percent chemical composition by dry weight from ref 26. [d] $P < 0.05$ vs ABLC.

Table 6—Plasma Lipid, Protein and Amphotericin B (AmpB) Concentrations Recovered in HDL_2 and HDL_3 following the Incubation of Amphotericin B Lipid Complex (20 μG/mL) in Human Plasma (control) or Human Plasma Pretreated with Dithionitrobenzoate (DTNB) for 60 min at 37 °C

high-density lipoprotein fraction	coat lipid content (fC + PL) mg/dL	CE, mg/dL	AmpB, (%)[a]
	HDL_3		
control	101	26.0	60.8
	(13)	(1.7)	(6.6)
DTNB-treated	126*	25.2	15.1*
	(10)	(5.3)	(3.6)
	HDL_2		
control	51	30.4	11.6
	(13)	(9.4)	(0.6)
DTNB-treated	39	18.4	8.6*
	(6)	(5.3)	(0.6)

[a] Data are presented as mean ± standard deviation (n = 6 replicates). *$P < 0.05$ vs control. Abbreviations: ABLC, amphotericin B lipid complex; AmpB, amphotericin B. HDL, high-density lipoproteins; TC, total cholesterol; CE, esterified cholesterol; PL, phospholipid. [a]percent of the original ABLC concentration incubated in human plasma.

TG, PL, TP, core lipid content, and coat lipid content within these fractions were calculated for all seven patient plasma samples, only one statistically significant relationship was observed. As HDL coat lipid content (fC + PL) increased, the amount of AmpB recovered in this fraction proportionally decreased (Table 3).

When correlations between AmpB amount recovered in each lipoprotein and lipoprotein-deficient fraction and lipoprotein composition were determined following AmpB incubation, only one statistically significant relationship was observed. As the HDL TG:TC ratio increased, the amount of AmpB recovered in HDL proportionally increased (Table 4).

Amphotericin B (AmpB) and Amphotericin B Lipid Complex (ABLC) Distribution within Plasma HDL_2 and HDL_3 Subfractions—Table 5 shows the human plasma HDL_2 and HDL_3 distribution of AmpB and ABLC in plasma. The distribution of AmpB and ABLC in the HDL_2 and HDL_3 and LPDP fractions of plasma incubated at 37 °C for 60 min showed the following differences. For plasma incubated with AmpB and separated into HDL_2 and HDL_3 subfractions, only 6.8% of the total drug incubated was recovered from the HDL_3 fraction, with the remaining drug being found within the LPDP fraction (Table 5). For plasma incubated with ABLC and separated into HDL_2 and HDL_3 subfractions, >95% of the initial concentration of the drug incubated was recovered from the HDL_3 fraction, with the remaining drug located within the LPDP fraction (data not shown).

When ABLC was incubated in plasma pretreated with DTNB for 18 h, the percentage of AmpB recovered in the HDL fraction was significantly decreased and the percentage recovered in the LPDP fraction was significantly increased compared to controls (Figure 2). Furthermore, the percentage of AmpB recovered in the HDL_3 and HDL_2 fractions was significantly decreased compared to the HDL_3 and HDL_2 fractions in untreated control plasma (Table 6).

Discussion

We have previously observed that AmpB predominantly associates with HDL in human serum when AmpB is incorporated into a lipid complex containing DMPC and DMPG.[16] When annamycin (Ann), an anticancer anthracycline analogue, and Nys were incorporated into liposomes with the same phospholipid composition, the majority of Ann and Nys was recovered in the HDL fraction.[8,18,22] Since HDL and LDL are not found in an equimolar ratio in human plasma but at LDL cholesterol/HDL cholesterol ratios varying from 4:1 to 6:1,[7] these data suggest that a mechanism(s) besides random probability or mass lipoprotein cholesterol levels must drive these drug–liposome complexes toward HDL rather than LDL. One such mechanism appears to be related to liposome composition. We have observed that the DMPG component of ABLC predominantly distributes into HDL because of its interaction with the protein components (apolipoproteins AI and AII) of HDL.[7,19]

In this study, consistent with our previous findings,[7,19] differences in AmpB lipoprotein distribution were observed following the incubation of free AmpB or ABLC in human plasma (Table 2). In particular, independent of plasma lipoprotein lipid and protein concentration, the majority of AmpB was recovered in the LPDP fraction (which contains albumin and α-1-glycoprotein) following the incubation of free AmpB (Table 2). However, the majority of AmpB was recovered in the HDL fraction following the incubation of ABLC (Table 2).

Previous studies with AmpB have suggested that an alteration in plasma lipid concentrations modify this drug's pharmacological behavior. Chavanet and co-workers have demonstrated that an increase in plasma triglyceride concentration led to a reduction in AmpB toxicity in rats.[24] These findings suggested that triglycerides, or their main vehicle in serum, chylomicrons, and VLDL, were involved in the protective effect against AmpB toxicity. Souza and co-workers have further shown that a triglyceride-rich emulsion that behaves in vivo in rats as chylomicrons was able to reduce the in vivo and in vitro toxicity of AmpB.[25] Our laboratory has recently shown enhanced AmpB-induced kidney toxicity within patients who exhibited elevated serum LDL cholesterol concentrations.[14]

In the present study, we have observed differences in the plasma distribution of AmpB when ABLC was incubated in plasmas from seven different human subjects (Table 2). It appears that these differences can be attributed to differences in the lipoprotein lipid and protein concentration profile of the plasmas (Table 1). In particular, increases in HDL coat lipid content (which contains free cholesterol and phospholipid) resulted in less AmpB recovered in this fraction following the incubation of ABLC (Table 3). However, increases in the TG:TP ratio within HDL resulted in more AmpB recovered in this fraction following the incubation of free AmpB (Table 4). These findings suggest that the AmpB lipoprotein distribution following the incubation of free AmpB is regulated by

different plasma HDL components (triglycerides and cholesterol) than following the incubation of ABLC, which appears to be regulated by HDL coat lipid content (free cholesterol and phospholipids).

We further observed that the majority of the AmpB recovered in the HDL fraction following the incubation of ABLC was found in the HDL_3 fraction following experiments in two different human plasmas (Tables 5 and 6). In addition, when the HDL_3 coat lipid content (fC + PL) was artificially elevated by DTNB, the percentage of AmpB recovered in this fraction was significantly decreased compared to controls following the incubation of ABLC (Table 6 and Figure 2). These findings suggest that the compositional and structural differences of HDL_3 as compared to HDL_2 may play an important role in determining the plasma distribution of the drug. In particular, since HDL_3 has a lower percentage by weight coat lipid content (free cholesterol and phospholipids) than does HDL_2[26] (Table 5), the lower percentage of AmpB recovered in the HDL fraction as HDL coat lipid content increased (Table 3) may be a function of the percentage of HDL_3 particles within the HDL fraction. This is supported by our observation that increases in the HDL_3/HDL_2 particle ratio in plasmas from different subjects resulted in a greater percentage of AmpB recovered in the HDL fraction ($r > 0.70$; $P = 0.05$) following the incubation of ABLC (data not shown). Taken together, these findings suggest that HDL coat lipid content (specifically HDL_3) may be an important factor in determining which lipoprotein AmpB associates following the incubation of ABLC.

In conclusion, we have determined that the plasma distribution of AmpB is altered when incorporated into a lipid complex composed of DMPC and DMPG. Furthermore, not only does the relative levels of individual lipoproteins but also the HDL coat lipid content defines the distribution of AmpB among plasma lipoproteins of different human subjects and may be an important consideration when predicting and/or evaluating the pharmacokinetics and toxicity of these compounds following administration to patients with varying lipid profiles.

References and Notes

1. Cipolle, R. J.; Solomkin, J. S. Clinical application of therapeutic drug monitoring. In *Amphotericin B*; Taylor, W. J., Diers Caviness, M. H., Eds.; Diagnostics Division, Abbott Laboratories: Irving, TX, 1986; pp 321−328.
2. Khoo, S. H.; Bond, J.; Denning, D. W. Administering amphotericin B—A practical approach. *J. Antimicrob. Chemother.* **1994**, *33*, 203-213.
3. Schaffner, C. P.; Mechlinski, W. Polyene macrolide derivatives. II. Physical chemical properties of polyene macrolide esters and their water soluble salts. *J. Antibiot.* **1972**, *25*, 259−260.
4. Stevens, N. M.; Eagle, C. A.; Fisher, P. B.; Mechlinski, W.; Schaffner, C. P. In vitro antiherpetic activity of water soluble amphotericin methyl ester. *Arch. Virol.* **1975**, *48*, 391−394.
5. Adedoyin, A.; Bernardo, J. F.; Swenson, C. E.; et al. Pharmacokinetic profile of ABELCET (amphotericin B lipid complex injection): combined experience from phase I and phase II studies. *Antimicrob. Agents Chemother.* **1997**, *41*, 2201−2208.
6. Sharkey, P. K.; Graybill, J. R.; Johnson, E. S.; et al. Amphotericin B lipid complex compared with amphotericin B in the treatment of cryptococcal meningitis in patients with AIDS. *Clin. Infect. Dis.* **1996**, *22*, 315−321.
7. Wasan, K. M. Modifications in plasma lipoprotein concentration and lipid composition regulate the biological activity of hydrophobic drugs. *J. Pharmacol. Toxicol. Methods* **1996**, *36*, 1−11.
8. Wasan, K. M.; Cassidy, S. M. The role of plasma lipoproteins in modifying the biological activity of hydrophobic drugs. *J. Pharm. Sci.* **1998**, *86*, 411−424.
9. Harmony, J. A. K.; Aleson, A. L.; McCarthy, B. M. In A. M. Scanu and A. A. Spector (ed.), Biochemistry and biology of plasma lipoproteins. Marcel Dekker: New York, 1986; Chapter 15, pp 403−430.
10. Koldin, M. H.; Kobayashi, G. S.; Brajtburg, J.; Medoff, G. Effects of elevation of serum cholesterol and administration of amphotericin B complexed to lipoproteins on amphotericin B-induced toxicity to rabbits. *Antimicrob. Agents Chemother.* **1985**, *28*, 144−145.
11. Wasan, K. M.; Kennedy, A. L.; Cassidy, S. M.; Ramaswamy, M.; Holtorf, L.; Chou, J. W. L.; Pritchard, P. H. Pharmacokinetics, Distribution in Serum Lipoprotein and Tissues, and Renal Toxicities of Amphotericin B and Amphotericin B Lipid Complex in a Hypercholesterolemic Rabbit Model: Single Dose Studies. *Antimicrob. Agents Chemother.* **1998,** *42*, 1346−1352.
12. Lopez-Berestein, G. Liposomes as carriers of antifungal drugs. *Ann. N.Y. Acad. Sci.* **1988**, *544*, 590−597.
13. Chabot, G. G.; Pazdur, R.; Valeriote, F. A.; Baker, L. H. Pharmacokinetics and toxicity of continuous infusion of amphotericin B in cancer patients. *J. Pharm. Sci.* **1989**, *78*, 307−310.
14. Wasan, K. M.; Conklin, J. S. Enhanced amphotericin B nephrotoxicity in intensive care patients with elevated levels of low-density lipoprotein cholesterol. *Clin. Infect. Dis.* **1997**, *24*, 78−80.
15. Vertut-Doi, A.; Ohnishi, S. I.; Bolard, J. The endocytic process in CHO cells, a toxic pathway of the polyene antibiotic amphotericin B. *Antimicrob. Agents Chemother.* **1994**, *38*, 2373−2379.
16. Krieger, M. The use of amphotericin B to detect inhibitors of cellular cholesterol biosynthesis. *Anal. Biochem.* **1982**, *135*, 383−391.
17. Wasan, K. M.; Rosenblum, M. G.; Cheung, L.; Lopez-Berestein, G. Influence of lipoproteins on renal cytotoxicity and antifungal activity of amphotericin B. *Antimicrob. Agents Chemother.* **1994**, *38*, 223−227.
18. Wasan, K. M.; Ramaswamy, M.; Cassidy, S. M.; Kazemi, M.; Strobel, F. W.; Thies, R. L. Physical Characteristics and Lipoprotein Distribution of Liposomal Nystatin in Human Plasma. *Antimicrob. Agents Chemother.* **1997**, *41*, 1871−1875.
19. Cassidy, S. M.; Strobel, F. W.; Wasan, K. M. The plasma lipoprotein distribution of liposomal nystatin is influenced by the protein content of high-density lipoproteins. *Antimicrob. Agents Chemother.* **1998**, *42*, 1878−1888.
20. Groot, P. H. E.; Scheek, L. M.; Havekes, L.; et al. A one-step separation of human serum high-density lipoproteins 2 and 3 by rate-zonal density gradient ultracentrifugation in a swinging bucket rotor. *J. Lipid Res.* **1982**, *23*, 1342−1353.
21. Rainmaker, D. L. Electrophoretic separation of LDL and HDL subclasses. In *Methods in Molecular Biology: Lipoprotein Protocols*; Ordovas, J. M., Eds.; Humana Press: Totowa, NJ, 1998; Vol. 110, pp 137−151.
22. Wasan, K. M.; Brazeau, G. A.; Keyhani, A.; Hayman, A. C.; Lopez-Berestein, G. Role of liposome composition and temperature in distribution of amphotericin B in serum lipoproteins. *Antimicrob. Agents Chemother.* **1993**, *37*, 246−250.
23. Wasan, K. M.; Ng, S.; Cassidy, S. M. Modifications in High-Density Lipoprotein Lipid Composition and Structure Alters the Plasma Distribution of Free and Liposomal Annamycin. *J. Pharm. Sci.* **1997**, *86*, 872−875.
24. Chavanet, P.; Joly, V.; Rigaud, D.; Bolard, J.; Carbon, C.; Yeni, P. Influence of diet on experimental toxicity of amphotericin B deoxycholate. *Antimicrob. Agents Chemother.* **1994**, *38*, 963−968.
25. Souza, L. C.; Maranhao, R. C.; Schrier, S.; Campa, A. In vitro and in vivo studies of the decreased of amphotericin B toxicity upon association with a triglyceride-rich emulsion. *J. Antimicrob. Agents.* **1993**, *32*, 123−132.
26. Shen, B. W.; Scanu, A. M.; Kezdy, F. J. Structure of human serum lipoproteins inferred from compositional analysis. *Proc. Natl. Acad. Sci. U.S.A.* **1977**, *74*, 837−841.

Acknowledgments

This work was funded by the Medical Research Council of Canada (Grant #MT-14484).

JS990101Z

In Vitro and in Vivo Study of Water-Soluble Prodrugs of Dexanabinol

EMIL POP,*,†,‡ STANISLAW RACHWAL,†,§ JIRINA VLASAK,†,‡ ANAT BIEGON,|| ALEVTINA ZHARIKOVA,⊥ AND LASZLO PROKAI⊥

Contribution from *Pharmos Corporation and Alchem Laboratories Corporation, 13305 Rachael Boulevard, Alachua, Florida 32615, Pharmos Limited, Kyriat Weizmann Science Park, Rehovot 78326, Israel, and Center for Drug Discovery, College of Pharmacy, University of Florida, Box 100497, Health Science Center, Gainesville, Florida 32610.*

Received March 30, 1999. Final revised manuscript received June 8, 1999.
Accepted for publication July 23, 1999.

Abstract □ Trialkylammonium acetoxymethyl esters of dexanabinol were synthesized and evaluated as water-soluble prodrugs. Syntheses were performed by conventional methods; solubility in water and stability in buffers and human plasma were determined by HPLC, and in vivo tissue distribution studies were performed in a rat model. Most of the new derivatives were soluble in water (~50 mg/mL). They were relatively stable in water, while rapidly hydrolyzed in human plasma. Distribution studies indicated that peak concentrations of drug both in blood (30 μg/mL) and brain (2 μg/mL) were rapidly (5 min) achieved after iv administration of a selected prodrug to rats. The blood concentration decreased faster than brain levels which were detectable even after 24 h. Some of the examined esters could be further developed as water soluble prodrugs of dexanabinol.

Introduction

Dexanabinol (HU-211), [(6a*S-trans*)-6,6-dimethyl-3-(1,1-dimethylheptyl)-1-hydroxy-6a,7,10,10a-tetrahydro-6*H*-dibenzo[*b*,*d*]pyran-9-methanol] (**1**), a synthetic, nonpsychotropic cannabinoid,[1] is a noncompetitive *N*-methyl-D-aspartate (NMDA) receptor antagonist[2] and an effective radical scavenger.[3] The compound is currently in clinical trials as a neuroprotective agent with potential use in the treatment of brain damage associated with stroke, head trauma, and cardiac arrest.[4−6]

An obstacle in the development of dexanabinol as a single-dose neuroprotective agent, considering the intravenous route as the best way of administration, is its very poor solubility in water, which makes formulation in aqueous compositions extremely difficult. The large dimethylheptyl side-chain and potential formation of stable, lipophilic molecular aggregates, such as dimers, mediated by strong hydrogen bonding[7] account for this behavior.

Cosolvent systems containing cremophor EL used in vivo and in phase I and II clinical trials are associated with allergic-type side effects and, accordingly, not unanimously accepted. Other technologies for solubilization of dexanabinol in aqueous compositions, including water-soluble prodrug approaches, have been investigated.

Various polar combinations or combinations bearing permanent charges were synthesized for dexanabinol as esters at either the allylic hydroxyl or phenolic functionalities. They included glycinate and N-substituted glycinates,[8,9] esters of amino acids containing tertiary or quaternary heterocyclic nitrogen,[10] and hemiesters of dicarboxylic acids[8] and phosphates;[11] more than 30 combinations were used in a preliminary screening process in which solubility in water and stability in water and plasma (rat and human) were determined. The results demonstrated that only trialkylammonium glycinate salts possessed properties required by prodrugs: solubility and stability in water and rapid hydrolysis in human plasma.

The in-depth investigation of trialkylammonium moiety containing glycinates, targeting identification of a prodrug of practical use for dexanabinol, has been considered in this work. Syntheses, solubility, and stability determinations, in vivo tissue distribution in a rat model and preliminary formulation experiments of a selected prodrug, are presented herein.[12]

Materials and Methods

Synthesis—Conventional procedures were used for the synthesis of the novel derivatives. Melting points are uncorrected and were determined on an Electro-thermal melting point apparatus (Fisher Scientific). Elemental microcombustion analyses were performed by Atlantic Microlabs, Inc., Atlanta, GA. Proton (^{1}H) and carbon (^{13}C) nuclear magnetic resonance spectra (NMR) were recorded on a Varian XL-300 spectrometer. Samples were dissolved in an appropriated deuterated solvent, and chemical shifts were reported as parts per million (δ) relative to tetramethylsilane (0.00) which served as an internal standard. Coupling constants (J) are reported in hertz. The progress of various reactions were followed by thin-layer chromatography (TLC). TLC was performed on EM Reagents DC aluminum foil plates coated to a thickness of 0.2 mm with silica gel (60 mesh). All solvents and chemicals were of reagent grade. Dexanabinol was synthesized in-house.

(6a*S-trans*)-9-(Chloroacetoxymethyl)-6,6-dimethyl-3-(1,1-dimethylheptyl)-1-hydroxy-6a,7,10,10a-tetrahydro-6*H*-dibenzo[*b*,*d*]pyran—A solution of dexanabinol (4.93 g, 12.7 mmol) and chloroacetic anhydride (2.05 g, 12.0 mmol) in chloroform (20 mL) was stored under argon in a dark room at 22 °C for 4 days. The reaction mixture was poured onto crushed ice (100 g), neutralized with 5% aqueous $NaHCO_3$, and extracted with chloroform (200 mL). The extract was washed with 5% aqueous $NaHCO_3$ (100 mL) and dried over anhydrous $MgSO_4$. The solvent was evaporated, and the residue was purified by column chromatography (silica gel, hexanes:diethyl ether, 9:11) to give 4.73 g (80%) of the product as a sticky oil of 98% purity (HPLC). Anal. Calcd for $C_{27}H_{39}ClO_4$: C, 70.03; H, 8.49; Cl, 7.66. Found: C, 70.28, H, 8.56; Cl, 7.46.

[(6a*S-trans*)-6,6-Dimethyl-3-(1,1-dimethylheptyl)-1-hydroxy-9-(trimethylammonioacetoxymethyl)-6a,7,10,10a-tetrahydro-6*H*-dibenzo[*b*,*d*]pyran] Chloride (**2**)—Anhydrous trimethylamine (0.65 g, 11.0 mmol) was added via a needle to a solution of (chloroacetyl)dexanabinol (1.90 g, 4.1 mmol) in anhydrous toluene (30 mL) and stirred under argon in a flask with a septum at 40 °C for 3 days. The precipitate was filtered, washed with toluene (20 mL), and dried in a vacuum oven (0.5 Torr, 60 °C, 4 h) to give

* Corresponding author: Tel: 904-418-1578. Fax: 904-418-1584. e-mail: emilpop@aol.com. Internet: http://www.alchem.com.
† Pharmos Corp., Alachua, FL.
‡ Present address: Alchem Corp.
§ Present address: Neurogen Corp., 35 Northeast Industrial Park, Branford, CT 06405.
|| Pharmos Limited, Israel.
⊥ University of Florida.

10.1021/js990098j CCC: $18.00
Published on Web 09/16/1999

2.05 g (96%) of product of 98% purity (HPLC); mp 212 °C. Anal. Calcd for $C_{30}H_{48}ClNO_4$: C, 69.01; H, 9.27, Cl, 6.79; N, 2.68. Found: C, 68.93; H, 9.26; Cl, 6.82; N, 2.69.

(6a*S-trans*)-9-(Bromoacetoxymethyl)-6,6-dimethyl-3-(1,1-dimethylheptyl)-1-hydroxy-6a,7,10,10a-tetrahydro-6*H*-dibenzo[*b,d*]pyran—A modified previously described procedure[9] was used, starting from dexanabinol (3.40 g, 8.8 mmol) and bromoacetic anhydride (3.43 g, 13.2 mmol) in anhydrous toluene (20 mL). After stirring 20 h at 22 °C, ethyl ether (20 mL) and 5% aqueous $NaHCO_3$ were added, and the mixture was stirred vigorously for 30 min. The organic phase was dried on $MgSO_4$, the solvent evaporated, and the resulting oil dried in a vacuum oven (0.5 Torr, 80 °C, 6 h). No column chromatography was required, the purity of compound (4.08 g, 91%) being 98% (HPLC peak area). Anal. Calcd for $C_{27}H_{39}BrO_4$: C, 63.90; H, 7.75; Br, 15.74. Found: C, 63.79; H, 7.80; Br, 15.68.

[(6a*S-trans*)-6,6-Dimethyl-3-(1,1-dimethylheptyl)-1-hydroxy-9-(trimethylammonioacetoxymethyl)-6a,7,10,10a-tetrahydro-6*H*-dibenzo[*b,d*]pyran] Bromide (**3**) (reported earlier[9])—A solution of (bromoacetyl)dexanabinol (1.10 g, 2.2 mmol) and anhydrous trimethylamine (0.25 g, 4.3 mmol) in hexanes (20 mL) was kept at − 5 °C for 3 days. The resulting precipitate was filtered, rinsed with hexanes, and dried in a vacuum oven (0.5 Torr, 70 °C, 4 h) to give 1.10 g (90%) of product with 98.6% purity (HPLC); mp 215 °C. Anal. Calcd for $C_{30}H_{48}BrNO_4$: C, 63.59; H, 8.54; N,2.47; Br, 14.01. Found: C, 63.75; H, 8.62; N, 2.45; Br, 14.08.

[(6a*S-trans*)-6,6-Dimethyl-3-(1,1-dimethylheptyl)-1-hydroxy-9-(triethylammonioacetoxymethyl)-6a,7,10,10a-tetrahydro-6*H*-dibenzo[*b,d*]pyran] Bromide (**4**) (reported earlier[9])—A solution of (bromoacetyl)dexanabinol (1.00 g, 1.97 mmol) and triethylamine (0.35 mL, 2.50 mmol) in hexanes (10 mL) was stored under argon in a dark room at 22 °C for 3 days. The deposited crystalline material was separated by decantation, washed with hexanes, and dissolved in hot tetrahydrofuran (1.7 mL). The solution was diluted with diethyl ether (10 mL), filtered through a sintered glass funnel, and stirred at 22 °C for 2 days. The obtained precipitate was filtered, washed with diethyl ether, and dried in a vacuum oven (0.5 Torr, 50 °C, 24 h) to give 404 mg (34%) of product of 98% purity (HLPC); mp 127 °C. Anal. Calcd for $C_{33}H_{54}BrNO_4$: C, 65.11; H, 8.94; Br, 13.13; N, 2.30. Found: C, 65.23; H, 8.80; Br, 13.42, N, 2.42.

[(6a*S-trans*)-6,6-Dimethyl-3-(1,1-dimethylheptyl)-1-hydroxy-9-(*N,N*-dimethyl-*N*-ethylammonioacetoxymethyl)-6a,7,10,-10a-tetrahydro-6*H*-dibenzo[*b,d*]pyran] Bromide (**5**)—A solution of (bromoacetyl)dexanabinol (622 mg, 1.23 mmol) and *N,N*-dimethylethylamine (0.162 mL, 1.50 mmol) in anhydrous diethyl ether (10 mL) was stored under argon at − 5 °C for 4 days. The obtained precipitate was separated by filtration, rinsed with diethyl ether, and dried in a vacuum oven (0.5 Torr, 60 °C, 4 h) to give 0.69 g (97%) of product of 98.6 purity (HPLC); mp 134 °C. Anal. Calcd for $C_{31}H_{50}BrNO_4$: C, 64.12; H, 8.68; Br, 13.76; N, 2.41. Found: C, 63.87; H, 8.69; Br, 13.99; N, 2.37.

[(6a*S-trans*)-6,6-Dimethyl-3-(1,1-dimethylheptyl)-1-hydroxy-9-(*N*-methyl-*N,N*-diethylammonioacetoxymethyl)-6a,7,10,-10a-tetrahydro-6*H*-dibenzo[*b,d*]pyran] Bromide (**6**)—A solution of (bromoacetyl)dexanabinol (622 mg, 1.23 mmol) and *N,N*-diethylmethylamine (0.182 mL, 1.50 mmol) in anhydrous ether (10 mL) was stored at 22 °C for 1 week and then at − 15 °C for an additional week. The resulting precipitate was filtered, rinsed with diethyl ether, and dried in a vacuum oven (0.5 Torr, 50 °C, 2 h) to give 424 mg (59%) product of 91.9% (HPLC) purity; mp 134 °C. Anal. Calcd for $C_{32}H_{52}BrNO_4$: C, 64.63; H, 8.81; Br, 13.44; N, 2.36. Found: C, 64.35; H, 8.81; Br, 13.58; N, 2.42.

[(6a*S-trans*)-6,6-Dimethyl-3-(1,1-dimethylheptyl)-1-hydroxy-9-(triproylammonioacetoxymethyl)-6a,7,10,10a-tetrahydro-6*H*-dibenzo[*b,d*]pyran] Bromide (**7**)—A solution of bromoacetyl dexanabinol (622 mg, 1.23 mmol) and tripropylamine (0.285 mL, 1.50 mmol) in diethyl ether (5 mL) was stored under argon at 22 °C for 10 days. The resulting mixture was triturated with an additional portion of diethyl ether (5 mL). The crystals were filtered, washed with diethyl ether (2 × 5 mL), and dried in a vacuum oven (0.5 Torr, 60 °C, 1 h) to give 720 mg (90%) product of 97.5% purity (HPLC); mp 158 °C. Anal. Calcd for $C_{36}H_{60}BrNO_4$: C, 66.44; H, 9.29; Br, 12.28; N, 2.15. Found: C, 66.52; H, 9.35; Br, 12.41; N, 2.30.

Solubility—The solubility of the novel derivatives in deionized water (pH 5.6−5.7; determined with a Ionalyzer7 model 501, Orion Research pH meter) was determined by preparation of saturated solutions at 21 °C (sonication for 60 min), filtration of the undissolved material, and determination of the concentration of the resulting solutions by HPLC. Calibration solutions of 0.1, 0.25, 0.50, and 1.00 mg/g concentrations were prepared. The four-point calibration had correlation of 0.99991. Average results of three determinations are reported.

Stability—The stability in aqueous buffers and human plasma of selected prodrugs was determined.

Sample Preparation and Incubation Conditions for Stability in Buffers—Stock solutions were prepared by dissolving prodrugs in water (pH 6.1) at concentrations of 50 mg/mL. Work solutions were prepared by diluting stock solutions with buffers of various pHs to final concentrations of 5 mg/mL. Samples were then incubated at 21 °C. Aqueous samples were analyzed by HPLC at various time points (pHs were determined each time both at the beginning and at the end point of determinations and proved to be unchanged). For HPLC determinations 100 μL of work solutions were diluted with 900 μL water to concentration of 0.5 mg/mL. Buffers used were: pH 7.4, Dulbeko's phosphate saline buffer (2.00 g/L KCl; 2.00 g/L KH_2PO_4; 8.00 g/L NaCl; 1.78 g/L Na_2HPO_4); pH 9, 0.05 M solution of tris(hydroxymethyl)aminomethane 5.47 g/L; pH 1.2 (simulated gastric fluid): 1 g of NaCl, 1.6 g of pepsin, 3.5 mL of HCl dissolved in 500 mL solution (according to USP XXII); pH 5.5: 0.1 N citric acid (6.4 g/L) (pH, 2.2) adjusted with 1 N NaOH; pH: 3.0 was prepared from 0.05 M K_2HPO_4 (pH 8.95) by adjusting pH with 0.1 N HCl. Aliquots were analyzed by HPLC, and concentrations of dexanabinol resulting from hydrolysis were determined. Hydrolysis followed first- order kinetics, and half-lives of compounds were calculated by plotting time versus the natural logarithm of peak area. Average values for three experiments were reported.

Sample Preparation and Incubation Conditions for Stability in Blood—Stock solutions were prepared at concentrations of 30 mg prodrug/mL in pH 7.4 buffer (0.05 M, $\mu = 0.15$). Work solutions were obtained by diluting stock solution with freshly collected blood to give 3 mg/mL or 200 μg/mL concentrations. Samples were incubated at 37 °C, and HPLC determinations were performed at various time points by extracting 100 μL samples with acetonitrile (900 μL for higher concentration and 400 μL for the lower concentration), followed by vortexing and immediate centrifugation and analysis.

Assay Method—High performance liquid chromatography (HPLC) (reversed-phase) was used for quantitative determinations. The HPLC consisted of a Spectra-Physics SP 8810 precision isocratic pump, Spectra-Physics SP 4290 system 2 integrator, Spectra-Physics SP 8880 autos ampler, Kratos Spectroflow 757 UV absorbance detector, and a Hewlett-Packard-HP3365, series II, version 3.33 Chemstation. The chromatographic conditions: HPLC columns, Alltima C8, 5 μm, 250 × 4.6 cm; mobile phase: acetonitrile: buffer (5 mL acetic acid and 5 mL triethylamine/L), 75:25 (v/v); flow rate: 1.0 mL/min; UV detection: 230 nm; volume of injection: 10 μL.

In Vivo Tissue Distribution Studies—The tissue distribution of a selected prodrug (**2**) was determined in a rat model. Male Sprague−Dawley rats (250−300 g body weight) were injected via tail vein with an aqueous (deionized water) solution of prodrug at 6.75 mg/kg body weight dose (250 g rats received ~200 μL of solution obtained by dissolving 25 mg prodrug in 3 mL water, the final pH being ~5). Animals were sacrificed by decapitation at 5, 15, 30, 60, 120, 240, 480, and 1440 min, and blood and brain tissues were collected. Three rats were used per time point. The research adhered to the "Principles of Laboratory Animal Care" (NIH publication no. 85-23, revised in 1985).

Sample Preparation—Plasma was obtained from trunk blood by centrifugation (1500 rpm). Brain was removed and rinsed with ice-cold saline. Samples were kept frozen until extraction. Acetonitrile (4 mL) was added to plasma (1 mL) followed by addition of the internal standard, a deuterated dexanabinol, synthesized in-house[13] (0.1 μg dexanabinol-d_5 in DMSO). Brain was weighed and homogenized in 2 mL of deionized water, and then acetonitrile (4 mL) was added, followed by the addition of the internal standard (0.5 μg/g brain). Multistep liquid−liquid extraction was then applied (both for plasma and brain homogenate). After the protein precipitation by acetonitrile, the supernatants were removed and concentrated to ~1 mL. A solution of NaOH (2 N, 2 mL) was added, followed by extraction with hexane/ethyl acetate (9/1, v/v) (4 mL). The organic phase was separated and washed with 0.1 N aqueous HCl solution (4 mL), and the solvent was evaporated under a

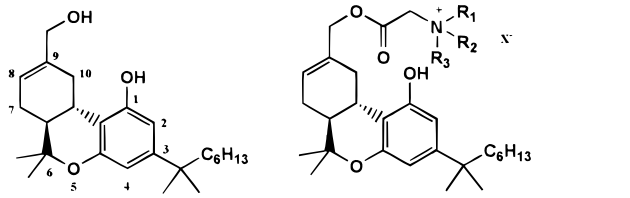

Figure 1—Structures of dexanabinol (**1**) and its prodrugs.

stream of nitrogen gas. Sample reconstitution was done in the HPLC mobile phase (100 μL). Average recovery for **1** was 55–60%.

Analytical Method—LC/MS methods were developed for determination of concentrations of **1** in plasma and brain. HPLC separation was done on a Supelco (Bellefonte, PA) LC–CN (cyanopropylsilica) 3.3 cm × 4.6 mm i.d. analytical column, protected with a Supelguard LC–CN (2 cm × 4.0 mm i.d.) cartridge. The mobile phase was 45% methanol and 55% aqueous acetic acid (1% v/v) at 1.0 mL/min flow rate. The solvent delivery system consisted of a Kratos (Manchester, UK) Spectroflow 400 isocratic pump. A Finnigan MAT (San Jose, CA) LCQ[7] ion-trap mass spectrometer with the manufacturer's APCI source was used. Injection volume was 5 μL. Retention time for analyte and internal standard was 2.70 min. Selected-ion monitoring (SIM) of the protonated molecules *m/z* 387.40 and 392.33 were used for the analyte and internal standard, respectively.

Quantitation was based on calibration by tissue spiked with known amount of analyte (0.1, 10, and 150 μg/mL plasma and 0.1, 1.0, and 5.0 μg/g brain) and the ratio of the area under the peak for the analyte ion (*m/z* 387.40, 1-amu window) to the area under the curve for the ion of the internal standard (*m/z* 392.33, 1-amu window) was used for regression to concentration (linear fitting, with quadratic weighing for concentration).

Results and Discussion

The investigated prodrugs are summarized in Figure 1. The synthetic procedures included acylation of dexanabinol (**1**) with chloroacetic or bromoacetic anhydride, followed by reaction of the resulting haloacetyl dexanabinol with appropriate tertiary amines. The allylic hydroxyl group is chemically more reactive than the sterically hindered and more rigid phenolic group. Accordingly, the acylation was quite specific, resulting in allylic esters without formation of any side products. The bromoacetate of dexanabinol reacted rapidly with trimethylamine, even at low temperature (−5 °C), affording high purity product with good yield. Consecutive substitution of methyl groups with ethyl groups led to slower reactions, lower yields, and products with lower melting points; the isolation of triethylammonium derivative, which proved to be quite lipophilic and soluble in common organic solvents, was difficult. However, this trend was surprisingly reverted to some degree in the case of derivatives containing higher alkyl groups, such as the tripropylammonium derivative.

To determine the influence of the counterion on the solubility of the quaternary derivatives, the chloride of the trimethylammonium acetate was also synthesized.

Attempts to use a similar procedure for the synthesis of trialkylammonium propionate derivatives of dexanabinol failed, because the reaction of bromopropionyl ester with tertiary amines gave predominantly dehydrobromination (elimination of hydrogen bromide) with formation of the acrylic ester, rather than the quaternization. While the dimethylamino derivative could be obtained from acrylate, by reaction with dimethylamine, its quaternization with methyl iodide was not possible since the resulting trimethylammonium derivative easily eliminated hydrogen iodide with formation of the acrylate.[14]

Table 1—Stability (half-lives) of Prodrugs in Buffers[a]

	half-lives ($t_{1/2}$) (days, mean ± SEM) at various pH			
prodrug	1.2	3.0	5.5	7.4
2	114.0 ± 4	52.00 ± 5	26.11 ± 1	14.64 ± 0.5
3	NA	NA	11.96 ± 0.8	3.64 ± 0.4
4	140.3 ± 5	51.30 ± 0.6	27.68 ± 0.9	11.94 ± 0.6
5	NA	NA	14.80 ± 1	10.30 ± 0.8
6	NA	NA	19.90 ± 0.7	10.45 ± 0.9

[a] SEM = standard error means. NA = data not available.

Prodrugs of practical use should have adequate solubility and sufficient stability in water to allow for formulation and storage. On the other hand, they should rapidly convert to the active parent drug within the body, particularly in blood since the administration is performed intravenously.

Solubility studies indicated that all of the investigated prodrugs were soluble in water. The determined solubilities were around 50 mg/mL (53.4, 52.2, 47.5, 47.0 mg/mL for **3**, **2**, **6**, **4**, respectively) except for compound **5** which proved to be less soluble (5 mg/mL) (no data are available for **7**). This spectacular increase in the solubility of the esters, as compared to dexanabinol which is insoluble in water, is a result of two factors: (1) the ionic character of the molecule induced by the permanently charged ammonium moiety, and (2) the prohibition of formation of strong dimers by double hydrogen bonding. It is difficult to explain some anomalies in solubilities in the examined series. While derivatives **2** and **3** were expected to have the best solubility due to smaller, less lipophilic alkyl groups linked to the quaternary nitrogen, the much lower solubility of **5** compared to **4** and **6** is unusual. The counterion, Cl^- or Br^- in **2** and **3**, respectively, does not have much influence, the two otherwise similar esters having almost the same solubility in water.

The esters were relatively stable in aqueous buffers. In each case, the stability was higher at the pH of distilled water (5.5), as compared to physiological pH (7.4) (Table 1).

Stability of selected prodrugs was determined at other pHs as well. At basic pH (9.0), the tested prodrugs were rapidly hydrolyzed (half-lives could not be calculated due to the fast rate of hydrolysis), while at strongly acidic pH (such as at 1.2, the pH of the stomach fluid) their stability increased considerably.

The results indicate that esters of **1** can be easily dissolved in water (buffered or unbuffered), but since the resulting solutions are not stable enough to allow for long time storage, they should be stored in the form of lyophilized powders and reconstituted a short time before their use.

Stability of **2** and **4** in human whole blood and plasma was determined at body temperature (37 °C). At concentration of 200 μg/mL, half-lives were 102 and 114 min (whole blood) and 47 and 90 min (plasma) for **2** and **4**, respectively. At lower concentration, which better reflects the real situation (doses used in clinical trials are in the range of ~100–300 mg dexanabinol/person), **2** hydrolyzed even faster, $t_{1/2}$ in plasma being 26.3 min at 50 μg/mL and very short at 20 μg/mL (70% of prodrug hydrolyzed at time point zero). This difference indicates saturation at higher concentration. As demonstrated during preliminary studies,[8,9] glycinate esters containing quaternary ammonium moieties are substrates for blood esterases and as a result are readily hydrolyzed. There are numerous esters containing

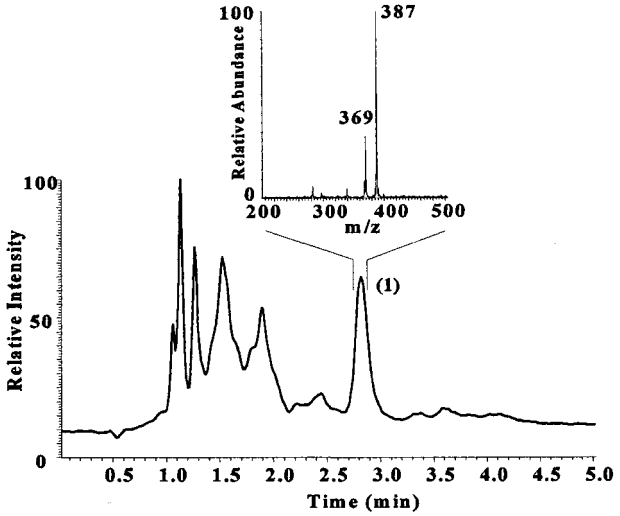

Figure 2—Representative LC-MS total-ion current (TIC) chromatogram of an extract of plasma spiked with 1.5 μg/mL dexanabinol (**1**). Inset: atmospheric pressure chemical ionization (APCI) mass spectrum of the peak indicated.

quaternary ammonium groups which are good substrates for enzymes which possess an anionic site. That includes obviously acetylcholine which is hydrolyzed by acetylcholinesterase present in postsynaptic membranes and also in plasma. Cholinesterases from plasma (pseudocholinesterases) are less specific than those from brain and they, or related esterases, might have a role in the hydrolysis of dexanabinol esters. These results indicate that the quaternary ammonium moiety containing esters can be used as prodrugs since they rapidly release the active **1** after their intravenous administration.

In vivo tissue distribution studies were performed in a rodent model. A selected prodrug (**2**) was administered intravenously to groups of rats, animals were sacrificed at various time points, and blood and brain concentrations of **1** were determined. These studies also addressed analytical method development for LC-MS, which offered an improvement over the gas chromatographic separation developed for compounds with similar structures, where sample derivatization was needed.[15] The HPLC assay developed during this study has benefits over similar methods using alkyl silica bonded phases, because the endogenous lipids extracted from the tissue elute before the analyte upon using cyanopropylsilica bonded phase. The short (3.3-cm), 3-μm particle-size column afforded reduced analysis time (5 min), compared to the 15-cm or 25-cm (5 μm) columns employed previously. A representative total-ion current chromatogram and the APCI mass spectrum of **1** are shown in Figure 2.

The in vivo distribution results are presented in Table 2 and in Figure 3. In agreement with the in vitro experiments performed in rodent blood,[9] a rapid hydrolysis of the prodrug was noticed. At 5 min following the administration, plasma levels of ~30 μg/mL were obtained. At the same time point, brain concentrations of dexanabinol reached a peak concentration of 2 μg/g as well. As the blood concentration of dexanabinol decreased following a typical two-compartment pharmacokinetic model, brain concentrations also became lower. However, the brain/blood concentration ratio increased from 0.07% at 5 and 15 min to 0.13, 0.35, 0.65, 2.48, 2.68, and 3.90 at 30, 60, 120, 240, 480, and 1440 min, respectively. Apparently, the lipophilic compound was retained by the brain tissues, while eliminated from blood. Even after 24 h, detectable levels of dexanabinol were identified in brain. It is important that peak concentrations of drug can be obtained rapidly (5 min) after administration, since the faster the neuroprotectant agent reaches the

Table 2—Plasma and Brain Concentrations of Dexanabinol (1) after iv Administration of 6.75 mg/kg Prodrug (2, equivalent to 5 mg/kg of 1) to Male Sprague–Dawley Rats

	concentrations (average ± SEM)	
time (min)	plasma (μg/mL)[a]	brain (μg/g)
5	29.36 ± 5.86	2.06 ± 0.31
15	10.73 ± 1.19	0.75 ± 0.11
30	4.34 ± 2.54	0.57 ± 0.16
60	1.26 ± 0.47	0.44 ± 0.05
120	0.40 ± 0.12	0.26 ± 0.05
240	0.25 ± 0.07	0.37 ± 0.08
480	0.19 ± 0.09	0.51 ± 0.08
1440	0.12 ± 0.03	0.47 ± 0.16

[a] Area under the curve = 14.51 μg mL^{-1} h, clearance = 0.345 L kg^{-1} h^{-1}, mean residence time = 8.0 h. Two-compartment pharmacokinetic model[16] for plasma concentration of 1, $c = Ae^{-\alpha t} + Be^{-\beta t}$: A = 33.7 μg/mL, B = 0.392 μg/mL, α = 0.066 min^{-1}, β = 0.0011 min^{-1} (nonlinear curve fitting by Scientist for Windows, Version 2.0, MicroMath, Inc., Salt Lake City, UT). k_{el} = 0.0393 min^{-1}, k_{12} = 0.0259 min^{-1}, k_{21} = 0.0019 min^{-1}, volume of the central compartment = 0.147 L kg^{-1}; apparent volume, steady state = 2.201 L kg^{-1}.

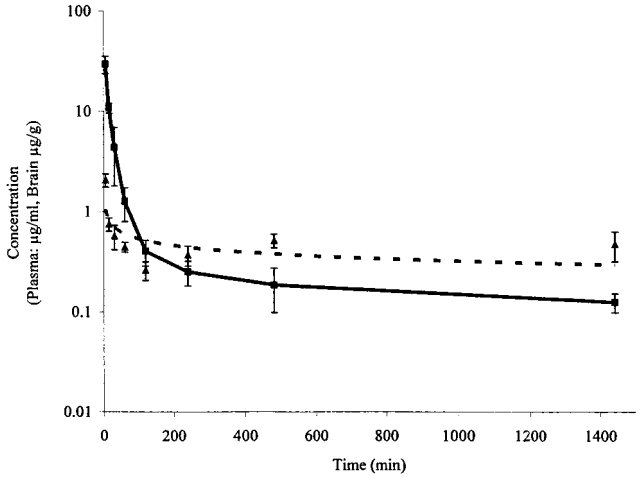

Figure 3—Concentration versus time profile of dexanabinol (**1**) in rat plasma (■, solid line) and brain (▲, dashed line) after iv administration of 6.75 mg/kg of prodrug **2**.

target, the more effective it is. It has to be mentioned that distribution results generated in rodent model might be different in humans, since esterases in mice and rats are much more active than in more evolved mammals. However, the in vitro experiments indicated that the selected combinations are good substrates for human blood esterases as well. It is then safe to affirm that the presented distribution study can be extrapolated to humans. Table 2 also contains some important pharmacokinetic parameters, calculated from the concentration−time profiles, including area under the curve, clearance, mean residence time, etc.

No control experiments, using **1** dissolved in a cosolvent system were performed. Such a study, in which **1** (5 mg/kg) was administered to rats in a cremophor/ethanol vehicle,[17] has been available for comparison and indicated a different tissue distribution profile. For example, the blood levels of dexanabinol were lower (maximum 4.5 μg/mL) and brain concentrations higher (maximum 10 μg/g) as compared to the results of the present study. The comparison of data might be misleading due to a variety of differences induced by solvents, including effects on the permeability of the blood−brain barrier.

Preliminary formulation studies were performed for selected prodrugs. Compounds **2** and **3** were dissolved in pure water (concentrations of ~50 mg/mL), and the resulting solutions were filtered through S&S Nylon-66 mem-

brane (45 μm pore size) and then freeze-dried in a Labconco freeze-dryer, model 77500, equipped with a Sargent-Welch vacuum pump, at a vacuum of 10 mmHg and temperature of − 50 °C for 6 h. The resulting powder was stored in dry conditions in dark, closed containers. The compound was analyzed by HPLC following the lyophilization and at a 1 month interval for 3 months; no degradation was registered, the purity being constantly 98%.

Conclusions

Several quaternary nitrogen-containing glycinate esters of dexanabinol were synthesized and investigated. Most of these combinations possess the required properties to be used as water-soluble prodrugs; they are soluble and fairly stable in water, but rapidly hydrolyze in human blood. In vivo distribution studies performed in a rat model indicated the brain uptake of **1**, when administered intravenously in the form of a prodrug, as a result of the rapid hydrolysis of the water-soluble ester. The prodrugs should be formulated as freeze-dried powders and reconstituted in water prior to their use. Prodrugs might present an advantageous alternative to the currently used formulations of dexanabinol.

References and Notes

1. Mechoulam, R.; Lander, N.; Bauer, A.; Zahalka, J. Synthesis of the individual, pharmacologically distinct, enantiomers of a tetrahydrocannabinol derivative. *Tetrahedron: Asymmetry* **1990**, *1*, 315−318.
2. Feigenbaum, J. J.; Bergmann, F.; Richmond, S. A.; Mechoulam, R.; Nadler, V.; Kloog, Y.; Sokolovsky, M. Nonpsychotropic cannabinoids act as a functional *N*-methyl-D-aspartate receptor blocker. *Proc. Natl. Acad. Sci. U.S.A.* **1989**, *86*, 9584−9587.
3. Eshhar, N.; Striem, S.; Kohen, R.; Tirosh, O.; Biegon., A. Neuroprotective and antioxidant activities of HU-211, a novel NMDA receptor antagonist. *Eur. J. Pharmacol.* **1995**, *283*, 1−3.
4. Shohami, E.; Novikov, M.; Mechoulam, R. A nonpsychotropic cannabinoid, HU-211, has cerebroprotective effects after closed head injury in the rat. *J. Neurotrauma* **1993**, *10*, 109−119.
5. Vered, M.; Bar Joseph, A.; Belyaev, L.; Biegon, A. Anti-ischemia activity of HU-211, a synthetic, nonpsychotropic cannabinoid. *Acta Neurochir.* **1994**, *70* (suppl), 335−337.
6. Brewster, M. E.; Pop, E.; Foltz, R.; Griffith, W.; Amselem, S.; Biegon, A. Clinical Pharmacokinetics of Escalating I. V. Doses of Dexanabinol (HU-211), a Neuroprotectant Agent, in Normal Volunteers, *J. Clin. Pharm. Ther.* **1997**, *35*, 361−365.
7. Pop, E.; Brewster, M. E. Dimerization of Dexanabinol by Hydrogen Bonding Accounts for its Hydrophobic Character. *Int. J. Quantum Chem. Quantum Biol. Symp. 24* **1997**, *65*, 1057−64.
8. Pop, E.; Brewster, M. E.; Liu, Z. Z.; Soti, F.; Rachwal, S.; Dinculescu, A.; Nadler, V.; Barenholz, Y.; Mechoulam, R.; Biegon, A. *A Water Soluble Prodrugs and Congeners of Dexanabinol*. In Proceedings of the 1st World Meeting on Pharmaceutics, Biopharmaceutics and Pharmaceutical Technology, Budapest, 1995; APGI: Châtenay Malabry, France, 1995; pp 127−128.
9. Pop, E.; Liu, Z. Z.; Brewster, M. E.; Barenholz, Y.; Korablyov, V.; Mechoulam, R.; Nadler, V.; Biegon, A. Derivatives of Dexanabinol. I. Water-soluble Salts of Glycinate Esters. *Pharm. Res.* **1996**, *13*, 62−69.
10. Pop, E.; Soti, F.; Brewster, M. E.; Barenholz, Y.; Mechoulam, R.; Nadler, V.; Biegon, A. Derivatives of Dexanabinol. II. Salts of Amino acid Esters Containing Tertiary and Quaternary Cyclic Nitrogen with Increased Water-Solubility. *Pharm. Res.* **1996**, *13*, 469−475.
11. Pop, E.; Soti, F.; Biegon, A.; Brewster, M. E. Allylic and Phenolic Phosphate Esters of Dexanabinol. *Org. Prep. Proced. Int.* **1997**, *29*, 341−347.
12. Partial results presented: Pop, E.; Rachwal, S.; Vlasak, J.; Brewster, M. E.; Prokai L.; Biegon, A. *Quaternary Ammonium Moiety Containing Water Soluble Amino Acid Ester-Type Prodrugs of Dexanabinol.* In Proceedings of the 2nd World Meeting on Pharmaceutics, Biopharmaceutics, and Pharmaceutical Technology, Paris, 1998; APGI: Châtenay Malabry, France, 1998; pp 101−102.
13. Pop, E.; Rachwal, B.; Rachwal S.; Vlasak J.; Prokai L.; Brewster, M. E. Synthesis of Labeled Dexanabinol, a Non-psychotropic Cannabinoid with Neuroprotective Properties. *J. Labeled Comp. Radiopharm.* **1998**, *15*, 885−897.
14. Pop, E.; Rachwal, S. Unpublished results.
15. Nelson, C. C.; Fraser, M. D.; Wilfahrt, J. K.; Folz, R. Gas Chromatography/Tandem Mass Spectrometry Measurement of Δ^9-Tetrahydrocannabinol, Naltrexone, and Their Active Metabolites in Plasma. *Ther. Drug Monit.* **1993**, *15*, 557−562.
16. Gibaldi M.; Perrier, D. *Pharmacokinetics*; Marcel Dekker: New York, 1982; p 48.
17. Biegon, A. Unpublished results.

Acknowledgments

This work was performed at Pharmos Corporation, Alachua, FL, supported by a Small Business Innovation Research grant from the National Institute of Health (NIH), National Institute of Neurological Disorders and Stroke, Division of Stroke and Trauma (1R43NS3582, to E.P.). The LC/MS instrument was available through a grant by the National Center for Research Resources (S10 RR12023, to L.P.)

Supporting Information Available— ^{1}H and ^{13}C NMR data for novel derivatives 9-(chloroacetoxymethyl)dexanabinol, **2**, and **5**−**7**. This material is available free of charge via the Internet at http://pubs.acs.org.

JS990098J

Dodecylphosphocholine-Mediated Enhancement of Paracellular Permeability and Cytotoxicity in Caco-2 Cell Monolayers

DONG-ZHOU LIU,† EDWARD L. LECLUYSE, AND DHIREN R. THAKKER*

Contribution from *Division of Drug Delivery and Disposition, School of Pharmacy, The University of North Carolina at Chapel Hill, Chapel Hill, North Carolina 27599-7360.*

Received March 27, 1999. Accepted for publication August 26, 1999.

Abstract □ The intestinal epithelium is a significant barrier for oral absorption of hydrophilic drugs because they cannot easily traverse the lipid bilayer of the cell membrane and their passage through the intercellular space (paracellular transport) is restricted by the tight junctions. In this report we show that dodecylphosphocholine (DPC) can improve the paracellular permeability of hydrophilic compounds across Caco-2 cell monolayers by modulating the tight junctions. The results show that the alkyl chain as well as the zwitterionic head group of DPC are required for its activity. DPC appears to act by modulating the permeability of tight junctions as evidenced by the fact that treatment of Caco-2 cell monolayers by this agent results in a decreased transepithelial electrical resistance (TEER), increased permeability of paracellular markers (e.g., mannitol) with no change in the permeability of the transcellular marker testosterone, and redistribution of the tight junction-associated protein ZO-1. The effect of DPC on Caco-2 cells (e.g., decrease in TEER) is reversible, and is not caused by gross cytotoxicity (as indicated by the MTT test) or by nonspecific disruption of the cell membrane (as indicated by only slight nuclear staining due to the nonpermeable DNA-specific dye propidium iodide). We propose in the present study a parameter, potency index, that allows comparison of various enhancers of paracellular transport in relation to their cytotoxicity. The potency index is a ratio between the IC_{50} value (concentration at which 50% inhibition of control mitochondrial dehydrogenase activity occurs in the MTT test) and the EC_{50} value (concentration at which TEER drops to 50% of its control (untreated) value). By this parameter, DPC is significantly safer than the commonly used absorption enhancer palmitoyl carnitine (PC), which has the potency index of ~1 (i.e., no separation between effective and toxic concentration).

Introduction

The intestinal epithelium represents a major barrier to absorption of orally administered drugs and nutrients into systemic circulation. The translocation of drug molecules across the intestinal epithelium occurs by passive diffusion via transcellular or paracellular route, or through carrier-mediated active or facilitated transport. The intercellular space of the intestinal epithelium restricts the passage of molecules because of the presence of junctional complexes (tight junctions, intermediate junctions, and desmosomes).[1,2] Hence, the intestinal epithelium is a significant barrier for hydrophilic molecules because they cannot easily traverse the lipid bilayer of the cell membrane, and their passage through the intercellular space is restricted by the tight junctions, i.e., zonula occludens (ZO).

Numerous classes of compounds with diverse chemical properties, including detergents, surfactants, bile salts, Ca^{2+} chelating agents, fatty acids, phospholipids etc., have been reported to enhance the intestinal absorption of not only small drug molecules but also relatively large polypeptides drugs.[3−19] Many of these enhancers act as detergents/surfactants and increase the transcellular transport of drugs by disrupting the structure of the lipid bilayer and rendering the cell membrane more permeable and/or by increasing the solubility of insoluble drugs. Others act as Ca^{2+} chelators, and improve the paracellular transport of hydrophilic drug molecules by disrupting the tight junctions after the removal of extracellular Ca^{2+} from the medium. Several phospholipid-like agents, many of which are lysophosphatidylcholines,[8−12] medium chain fatty acids,[16−18] and acyl carnitines (e.g., palmitoyl carnitine),[3,5,13−15] appear to increase the paracellular permeability of hydrophilic compounds by mechanism(s) other than Ca^{2+} chelation. Although the exact mechanism(s) of action for many of these agents is yet to be determined, at least one mechanism by which they appear to exert their effect on the tight junctions is via upregulation of intracellular Ca^{2+}.[16−18]

A major concern regarding the use of these agents to enhance intestinal absorption is their postulated linkage to the epithelial damage and toxicity associated with the compromised mucosal function and morphology.[6,7] While these compounds are extensively used as absorption/transport enhancers, it is difficult to assess their relative potency and toxicity because of limited data available on concentration vs effect and also because of the use of different agents in different model systems. For example, palmitoyl carnitine (PC) has been used as a transport enhancer at a concentration range of 0.1−0.4 mM[14,15] in Caco-2 cell culture model. In our hands, PC was effective as transport enhancer in Caco-2 cell culture model at concentrations above 0.4 mM (cf., Figures 2, 5).

Our preliminary results have shown that dodecylphosphocholine (DPC), which lacks the glycerol moiety present in lysophoshatidylcholines, enhances the transport of hydrophilic compounds across Caco-2 cell monolayers by modulating the tight junctions (and perhaps other junctional complexes).[20] These results suggest that the activity of LGPC and other lysophosphatidylcholines[9] as enhancers of paracellular permeability is due to the presence of alkyl chain and a zwitterionic group and not due to the glycerol functionality. DPC contains these structural features in the simplest possible configuration. Hence, in this paper we report a systematic evaluation of DPC as an enhancer of paracellular transport of hydrophilic compounds across Caco-2 cell monolayers. Furthermore, we have compared DPC with several absorption enhancers in order to determine its potency as a paracellular transport enhancer and its cytotoxicity relative to the potency and cytotoxicity of other well-established absorption enhancers. While several

* Corresponding author. Tel: (919) 962-0092. Fax: (919) 966-0197. E-mail: dhiren_thakker@unc.edu.

† Current address: Wyeth-Ayerst Research, 401 North Middletown Rd., Pearl River, NY 10965.

10.1021/js990094e CCC: $18.00 Published on Web 10/15/1999

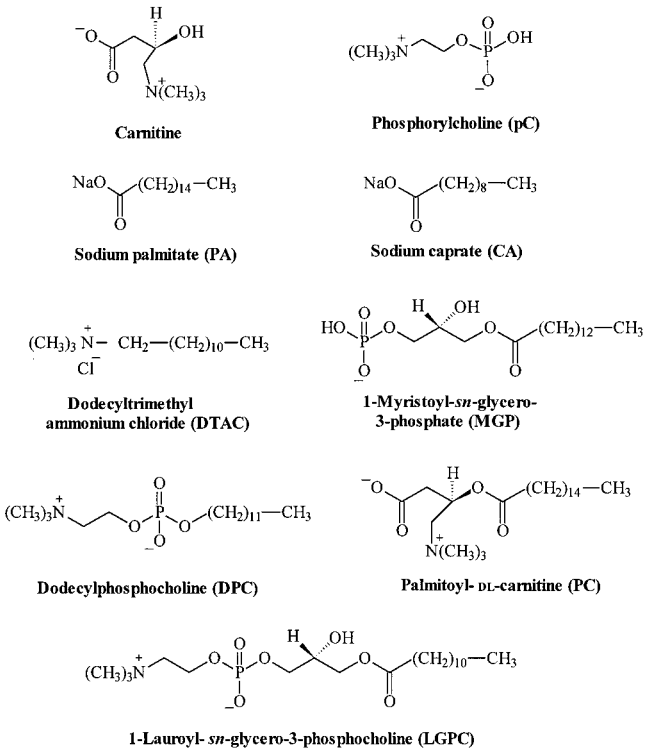

Figure 1—Chemical structures of the compounds evaluated as transport/absorption modulators.

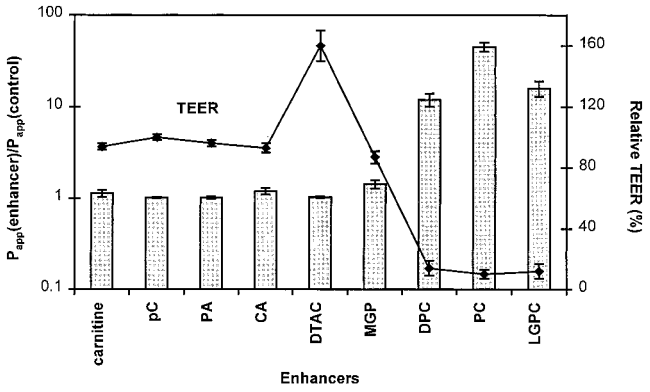

Figure 2—Effect of absorption enhancers and their analogues on TEER across Caco-2 cell monolayers. All the agents (0.75 mM) were applied to the apical compartment of the monolayers for 20 min at room temperature. Mannitol transport was measured (P_{app}) after the treatment by the agents and was compared to the control P_{app} value obtained with the untreated cells. (Abbreviations not used in the text: PA, palmitic acid; CA; sodium caprate). ◆ :P_{app}(treated)/P_{app}(control).

reports of the use of Caco-2 cells to evaluate toxicity of absorption enhancers have appeared recently,[20−24] we propose in the present study a parameter, potency index, that allows comparison of various paracellular transport enhancers in relation to their cytotoxicity.

Materials and Methods

Reagents—Caco-2 cells were purchased from American Type Culture Collection (Rockville, MD). Eagle's Minimum Essential Medium (EMEM), 0.25% trypsin/0.02% ethylenediamine−tetraacetic acid−sodium salt (EDTA-4Na), goat serum, and fetal bovine serum (FBS) were obtained from Gibco (Grand Island, NY). Nonessential amino acids (NEAA), Hank's balanced salt solution (HBSS), 3-(4,5-dimethylthiazol-2-yl)-2,5-diphenyltetrazolium (MTT), palmitoyl-DL-carnitine chloride (PC), sodium caprate (CA), sodium dodecyl sulfate (SDS), palmitic acid (PA), dodecyltrimethylammonium chloride (DTAC), phosphorylcholine (pC), and DL-carnitine hydrochloride were purchased from either Sigma (St. Louis, MO) or Aldrich (Milwaukee, WI). Dodecylphosphocholine (DPC), 1-myristoyl-*sn*-glycero-3-phosphate sodium (MGP), 1-lauroyl-*sn*-glycero-3-phosphocholine (LGPC) were purchased from Avanti Polar Lipids (Alabaster, AL). *N*-(2-Hydroxyethyl)piperazine-*N*′-2-ethanesulfonic acid (HEPES) and penicillin /streptomycin were obtained through the Tissue Culture Facility (UNC at Chapel Hill, NC). Transwell plates and inserts (12 wells/plate, 3.0 μm pore and 1.0 cm^2 area, polycarbonate) were purchased from Corning-Costar (Cambridge, MA). [^{3}H]Mannitol, [^{3}H]-PEG-900, [^{3}H]-PEG-3500, and [^{14}C]testosterone were obtained from DuPont NEN (Boston, MA). Lucifer Yellow (LY) and propidium iodide were obtained from Molecular Probes (Eugene, OR).

Antibodies—Rabbit polyclonal antibody against ZO-1 was purchased from Zymed Laboratory, Inc. (San Francisco, CA). Fluorescein isothiocyanate (FTIC)-labeled Goat anti-Rabbit IgG antibodies were purchased from Sigma (St. Louis, MO).

Caco-2 Cell Culture—Caco-2 cells were maintained in EMEM, containing 10% fetal bovine serum, 1% l-glutamine, 1% NEAA, and antibiotics (100 U/mL of penicillin and 100 μg/mL of streptomycin) in 75 cm^2 culture flasks. The cultures were kept at 37 °C in an atmosphere of 5% CO_2, 95% air, and 90% relative humidity. Cells were passaged after 95% confluency and were seeded with a density of 1.2×10^5 cells/mL onto porous polycarbonate filter membranes with a pore size of 3.0 μm and a surface area of 1.0 cm^2. Cells of passage number 40−55 were used throughout. Media were changed every 2 days after seeding until late confluence (21−23 days). Just before the experiments, the culture medium was replaced with transport buffer (HBSS contained 25 mM HEPES and glucose) and incubated for 1 h at 37 °C.

Preparation of Enhancer Solution—All the compounds being evaluated as transport enhancers were dissolved in a HBSS that contained 25 mM HEPES at pH 7.4. The stock solutions (50 mM) of the test compounds were obtained by dissolving them in HBSS-buffer/ethanol (60:40, v/v) and were stored at −20 °C. Just before the experiments, the enhancer solutions were thawed and diluted to the appropriate concentrations by HBSS buffer and sonicated for 5 min in an ice bath.

Critical Micelle Concentration (CMC)—The CMC of all tested enhancers was determined by measurement of surface tension as a function of concentration of enhancers in HBSS (contained 25 mM glucose and 25 mM HEPES) buffer at room temperature. For this study, a Kruss K10T digital tensionmeter (Hamburg, Germany) was used.

Cell Viability Assay—The cell viability was measured by the MTT test[25] as performed for evaluation of the cytotoxic effects of absorption enhancers to Caco-2 cells.[26] Approximately 3×10^3 cells (in 100 μL of cell culture medium) were seeded into the wells in a 96-well tissue culture plate (Corning-Costar, Cambridge, MA). The cells were then cultured under the same condition as the monolayer preparation for 72−96 h before use. Just prior to the start of each experiment, the medium was removed from the wells, and 100 μL of the enhancer solution in HBSS was added to each well. After exactly 20 min, 20 μL of a 5 mg/mL MTT solution was added to each well, and the cells were incubated for another 90 min. Then 100 μL of 5% SDS in 0.02 M HCl/isobutanol (1:1, v/v) solution was added to stop the reaction and solubilize the reaction products. The absorption was measured at 590 nm with a multiwell scanning spectrophotometer (Bio-Rad, Hercules, CA).

Transepithelial Electrical Resistance (TEER)—The monolayers were treated on the apical side with the absorption enhancers at various concentrations dissolved in 0.5 mL of HBSS. The volume of HBSS on the basolateral side was 1.5 mL. Measurements of the effects of these enhancers on TEER across Caco-2 monolayers were performed using an EVOM Epithelial Tissue Voltohmmeter (World Precision Instruments, Sarasota, FL) at room temperature and 37 °C. The resistance due to the cell monolayers was determined in the presence or absence of the enhancers after subtracting the contribution of the blank filter and the HBSS. The control TEER values were in the range of 500−600 Ω·cm^2.

Cytoplasmic Membrane Permeability—The DNA-intercalating dye, propidium iodide, was used to discern cells with damaged membranes. Caco-2 cells (5.0×10^4 cells/mL) were seeded on to glass coverslips. After 5 days, the completely confluent cell monolayers were used for propidium iodide staining. After expo-

sure by DPC at 0.75 mM, 1.0 mM, and 1.25 mM, the monolayers were rinsed twice with PBS and then incubated with propidium iodide (30 μg/mL PBS) for 3 min. After rinsing twice with PBS, the cells were fixed for 10 min in 3.7% formaldehyde in PBS on ice and then rinsed four more times in PBS. In a separate experiment, the same DPC-exposed monolayer samples, after rinsing with PBS, were incubated in cell culture medium for 8 h and then stained by propidium iodide. Experiments excluding the enhancer were run as controls. The preparations were mounted on glass slides in a 1:1 solution of PBS and glycerol and examined under a fluorescence microscope.

Immunohistochemistry—Caco-2 cell monolayers were prepared as described under "Cell Culture" for transport experiments, and those with TEER values 600−800 O·cm^2 were used for the immunohistochemistry study. The cell monolayers were first treated with 0.75 mM DPC for 20 min. Then the monolayer was washed twice after removal of DPC-containing medium. The cells were fixed in 3.7% paraformaldehyde, rinsed in 1x PBS and permeabilized using 0.25% Triton X-100. After further rinsing, the cell monlayer was blocked with PBS containing 10% FCS, 10% goat serum, and 0.2% Tween 20. The primary antibody (rabbit polyclonal antibody against ZO-1), diluted in PBS containing 10% FCS/10% goat serum/0.2% Tween 20, was applied to the cell monolayers and incubated for 2 h. After several washes with 1x PBS/0.2% Tween 20, the monolayer was blocked again and then incubated for another 2 h with the FITC-labeled goat anti-rabbit IgG antibody that was diluted in PBS containing 10% FCS/10% goat serum/0.2% Tween 20. After rinsing in PBS, the filter was cut out, mounted in glass slides, and examined using Zeiss confocal microscope fitted with 60× objective. ZO-1 staining excluding DPC was run as a control. The final images were stored digitally and transferred to Adobe Photoshop for graphical representation.

Transport Experiments—Transport studies were performed at room temperature on filter-grown Caco-2 monolayers with [^{3}H]-labeled mannitol (80 μM, 0.5 μCi/mL), [PEG-900 (100 μM, 0.5 μCi/mL) and PEG-3500 (100 μM, 0.5 μCi/mL), [^{14}C]testosterone (100 μM, 0.1 μCi/mL), or LY (100 μM). The enhancer solution in HBSS (0.5 mL) was added to the apical side of the cells and 1.5 mL of HBSS was added to the basolateral side. After treatment for 20 min, the enhancer solutions were discarded, and the monolayers were washed once with fresh HBSS. Then 0.5 mL of HBSS solution containing one of the compounds was applied to the apical side. Transport rates were determined by measuring the radioactivity/fluorescence associated with the transported compounds present in the BL side at 20-min intervals. The amount of radioactivity was measured by liquid scintillation counting in a PACKARD 1600 TR analyzer (Downers Grove, IL). Transported LY was quantitated with Perkin-Elmer LS50B Luminescence Spectrometer (Beaconsfield, Buckinghamshire, England).

Data Analysis—All transport experiments were carried out under sink conditions, such that the concentration of the compounds in the receiver compartment was always less than 10% of the concentration in the donor compartment. TEER was measured prior to each experiment to ensure the confluency of the cell monolayer. The apparent permeability coefficient was calculated using the following equation:

$$P_{app} = (dQ/dt)\cdot(1/A)\cdot(1/C_o)$$

where dQ/dt (mol transported/sec) is the flux of the marker compound across Caco-2 cell monolayer, A (cm^2) represents the diffusional area of the inserts, and C_o (M) denotes the initial concentration of marker compound in the donor compartment. All measurements and transports were in triplicate and expressed as mean ± SD values.

Results

Comparative Effect of DPC, PC, and LGPC on TEER and Mannitol Transport Across Caco-2 Cell Monolayers—Because both TEER and mannitol permeability across Caco-2 cells are indicators of tight junction integrity of the cell monolayer, relative effect of compounds on these two indicators reflects their relative ability to modulate tight junctions. PC[15] and lysophosphosphatidylcholines[9] (e.g., LGPC) have been reported as absorption enhancers. The structural features that are common to these very different classes of molecules include a several-carbon-long alkyl chain, an anionic functionality (carboxyl or phosphate group), and a cationic functionality (trimethylaminoalkyl group). We have chosen DPC as a model compound to confirm the role of these structural features in affecting the paracellular permeability. This is because DPC contains all three structural moieties in relatively simple configuration (see Figure 1). In a preliminary study,[20] we have reported that DPC, PC, and LGPC (at 0.75 mM) cause a decrease in TEER to less than 10% of the control value and a significant increase in mannitol permeability across Caco-2 cell monolayers. To elucidate the common structural features that may be responsible for the effect of these compounds on tight junctions, we have evaluated the effect of several other compounds that represent only a partial structure of DPC, PC, or LGPC on TEER and mannitol permeability across Caco-2 cell monolayers at the same concentration (0.75 mM) as that used for the above three compounds (Figures 1 and 2). Interestingly, compounds with an 11- to 15-carbon alkyl chain and either an anionic group or a cationic group (e.g., sodium caprate,[27] palmitate,[27] DTAC, or MGP) did not show any effect on TEER or mannitol transport at the concentration used. Similarly, compounds containing the zwitterionic functionality without the alkyl chains (e.g., carnitine or phosphorylcholine) did not cause any change in TEER or permeability of mannitol. These findings are in agreement with previous findings that the structural components of PC, i.e., carnitine chloride and palmitic acid, had no effect on the transport of paracellular markers across Caco-2 cell monolayers.[15] While DPC, LGPC, and PC appear different structurally, they all contain an alkyl chain and a zwitterionic functionality. All three compounds are quite effective at causing a decrease in TEER and an increase in mannitol permeability across Caco-2 cells. Thus, it is reasonable to conclude that the glycerol functionality of LGPC is not necessary for the activity, and that the minimum structural features contributing to the activity of these compounds include a medium to long alkyl chain and a zwitterionic group. While these results do not show that a zwitterionic compound containing a short alkyl chain is not very effective as an enhancer of paracellular permeability, a previous report[9] clearly suggests that such is the case.

Effect of DPC on TEER as a Function of Time and Concentration—The influence of DPC on TEER across Caco-2 monolayer was monitored as a function of time at several concentrations (Figure 3). At room temperature, monolayers treated with up to 0.5 mM DPC showed very little change in TEER with only 0−20% drop for the first 30 min. However, when the concentration of DPC was increased to 0.75 mM, a rapid decrease in TEER (within 3 min) was observed. The drop in TEER as a function of concentration exhibited a sharp inflection between 0.5 mM and 0.75 mM of DPC. Interestingly, the drop in TEER as a function of concentration is more gradual and uniform at 37 °C (data not shown) than at room temperature. To determine whether the effect of DPC on Caco-2 cell monolayers is reversible, apical HBSS containing DPC was replaced with fresh cell culture medium after 30 min of treatment. In all cases, TEER returned to the control value upon removal of DPC when measured after 10 h. This indicates that DPC treatment does not lead to the disruption of the monolayer or cell lysis (see cytotoxicity of tight junction modulators).

The effect of DPC on TEER was much more pronounced when it was applied to the apical side than to the basolateral side of Caco-2 cell monolayers (Figure 3 insert). Furthermore, the decrease in TEER achieved after baso-

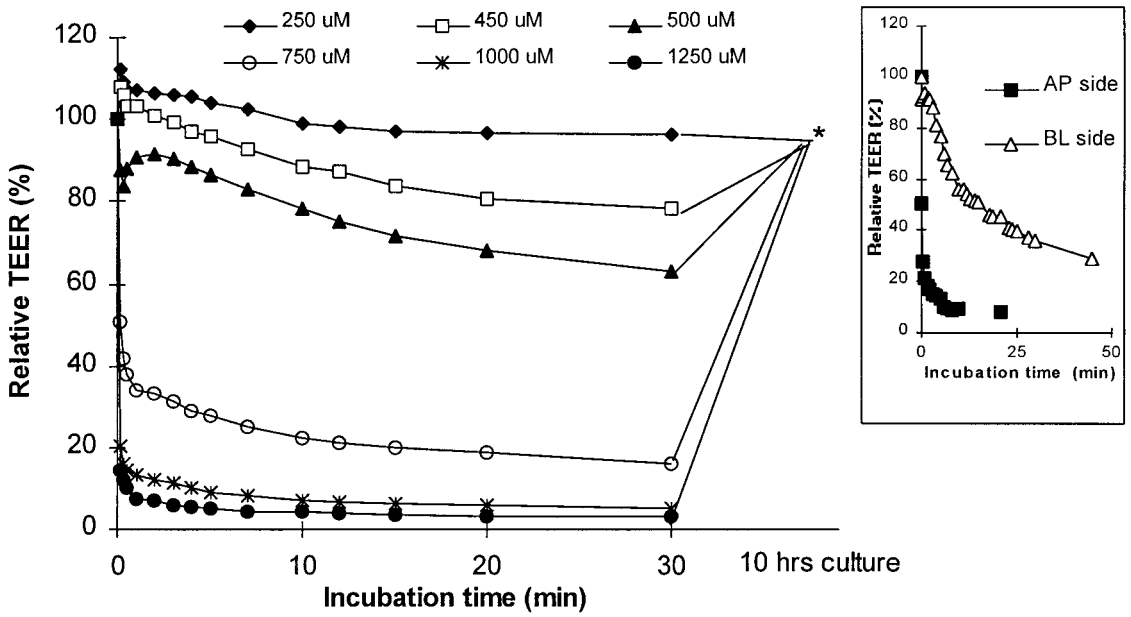

Figure 3—Effect of DPC on TEER (ambient temperature) across Caco-2 cell monolayers as a function of time and DPC concentration. In all cases TEER values returned to the control value when measured 10 h after removal of DPC (after 30 min treatment). The insert displays the effect of 1.0 mM DPC on TEER when it was applied to AP or BL side of the cell monolayers.

lateral application of DPC was much more gradual than that achieved after apical application; in fact, the magnitude of maximum decrease in TEER after basolateral application of DPC never approached that seen with the apical application. We have confirmed that the delayed and decreased effect of DPC when applied on the basolateral side is not due to the polycarbonate membrane, as it does not constitute a significant barrier to the transport of DPC (data not shown). The asymmetry in the effect on TEER suggests that the effect of DPC on TEER or mannitol permeability is not due to its permeation into the cells, followed by an intracellular change. Rather, the effect appears to be due to different interactions with the tight junction components depending on whether DPC is on the apical or the basolateral side. It is also possible that the observed difference in the effect on the decrease in TEER is due to interactions of DPC with cell membrane on the apical versus the basolateral side that lead to different effects on the structure and function of the tight junctions.

Effect of DPC on the Transport of Paracellular Markers—To determine if DPC-induced drop in TEER is accompanied by an increase in the tight junction permeability, we measured transport rates of a few paracellular markers across the Caco-2 cell monolayers. The enhancing effect of DPC pretreatment of the cell monolayers on the transport of hydrophilic paracellular markers was concentration-dependent (Figure 4). At low concentration of DPC (less than 0.5 mM), the permeability of all paracellular molecules was the same as that of the control. In general, DPC-induced decrease in TEER correlated with an increase in transport of the paracellular markers. At 0.75 mM concentration (a nontoxic concentration, see cytotoxicity of tight junction modulators), DPC pretreatment increased the apparent permeability constant (Papp) across Caco-2 cells for mannitol by 12-fold, for LY by 16-fold, and for PEG-900 by 2.2-fold. It caused no significant enhancement in the Papp value for PEG-3500, a large MW paracellular marker. Furthermore, DPC did not affect the transport rate of testosterone, a transcellularly transported marker, indicating that cell membranes were not compromised or disrupted by DPC at 0.75 mM concentration.

The enhancement in permeability of paracellular molecules is treatment-dependent. When DPC was coadministered with the paracellular markers after the initial pretreatment by DPC for 20 min (0.75 mM), further enhancement in the transport rates was observed for these compounds. Especially the transport of PEG-3500, a larger molecular weight marker, could be effectively enhanced with pre- plus cotreatment with DPC (data not shown).

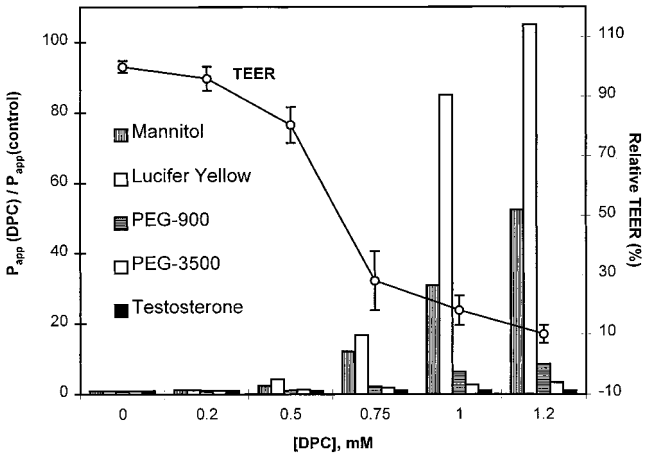

Figure 4—Enhancement of transport of paracellular markers by DPC after 20 min pretreatment. Testosterone was included as control (marker for transcellular transport) to ensure that the cell membrane was not disrupted and that the integrity of the cell monolayer was not compromised. ○: relative TEER (%).

Comparison of Potency of the Tight Junction Modulators—The absorption enhancers are used at different concentrations and in different model systems by different groups. Because of this, it is impossible to establish the concentration at which a given enhancer is effective or to determine (from the literature) relative potencies of different enhancers. Hence, we define the term EC_{50}, the concentration at which an enhancer decreases the TEER of the cell monolayer to 50% of the initial (control) value, and propose that the enhancers should be tested at several concentrations in order to define their effective concentration(s) and their relative potencies. This will allow a more meaningful translation of the results from different groups and comparison of relative potencies of different enhancers. While TEER at a given value may not

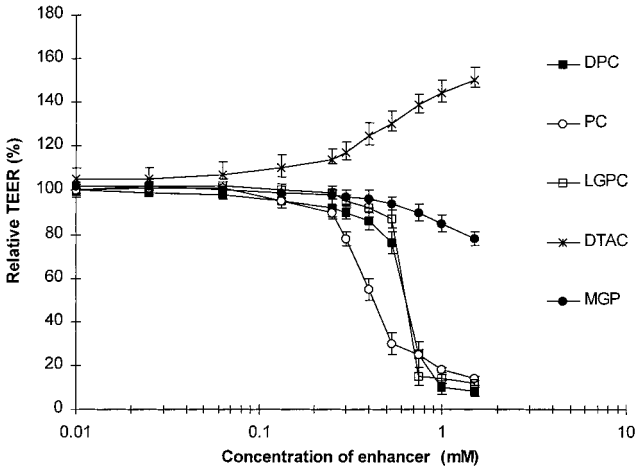

Figure 5—Relationship between concentration of the transport modulators and TEER. The cell monolayers were treated with the compounds for 20 min at ambient temperature. The measurements were made in triplicate and expressed as mean ± SD.

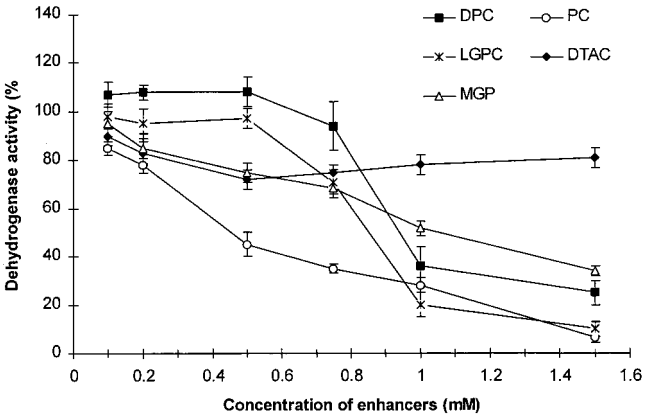

Figure 6—Mitochondrial dehydrogenase activity (MTT) in Caco-2 cells after treatment with transport modulators at various concentrations. All measurements were made in triplicate and expressed as mean ± SD.

be indicative of the paracellular permeability of compounds, the changes in TEER over a range of the enhancer concentrations correspond well with the changes in paracellular permeability.[28] Therefore, the EC_{50} values provide a good indicator of the potency of a given compound in causing an increase in paracellular permeability. Such an approach has been previously used by Anderberg et al.[29] to compare the efficacy of surfactant excipients. The effect of five agents on TEER is compared as a function of concentration in Figure 5. The EC_{50} values for PC (0.42 ± 0.06 mM), LGPC (0.65 ± 0.04 mM), and DPC (0.65 ± 0.05 mM) indicate that DPC and LGPC are equipotent, with PC showing a somewhat higher potency than the other two compounds. Interestingly, the EC_{50} value for DPC increased from 0.65 mM to 0.74 mM when the temperature increased from 20 °C to 37 °C (data not shown). The anionic MGP was significantly less effective as it caused less than 20% drop in TEER at concentration as high as 1.5 mM. The cationic compound DTAC actually caused a concentration-dependent increase in TEER at concentrations above 0.2 mM. Similar increase in TEER by cationic compounds has been observed previously.[30,31]

Cytotoxicity of the Tight Junction Modulators—The reversibility of the effect of DPC on TEER across Caco-2 cell monolayers (Figure 3) suggests that its effect is not secondary to cytotoxicity resulting in disruption of the cell monolayer. To further evaluate the cytotoxicity of these enhancer-related agents toward Caco-2 cells, the viability of the cells was directly measured using the MTT test.[25,26,29] MTT is a tetrazolium salt that is oxidized by mitochondrial dehydrogenases in living cells to give a dark blue formazan product. Damaged or dead cells show reduced or no dehydrogenase activity. Reports of this and other related tests to assess the cytotoxicity of absorption enhancers toward Caco-2 cells have appeared recently.[20–24,26,29] The results depicted in Figure 6 indicate that at 0.1 mM concentration, none of the agents were cytotoxic. However, at higher concentrations (more than 0.2 mM), the toxicity caused by the agents showed significant differences. To quantitatively compare the cytotoxicity of the enhancer-related agents, the IC_{50} values (concentration at which the enhancer produces 50% inhibition of the mitochondrial dehydrogenase activity measured by the MTT method) were determined. DPC (IC_{50} = 0.92 ± 0.03 mM) and LGPC (IC_{50} = 0.84 ± 0.02 mM) were approximately 2-fold less cytotoxic than PC (IC_{50} = 0.45 ± 0.05 mM) toward Caco-2 cells. SDS, used as a positive control, had an IC_{50} value of ~0.2 mM (data not shown). It is interesting to note that for the extensively used absorption enhancer PC there is no separation between its EC_{50} and its IC_{50} value. Both DPC and LGPC are likely to be somewhat better as absorption enhancers than PC, as their IC_{50} values are ~50% greater than their EC_{50} values. It is important to note that the "cytotoxic" effect of DPC (and other agents) reported here may actually be "cytostatic" effect as evidenced by the fact that removal of DPC from the solutions bathing the cell monolayers results in restoration of TEER over several hours.

Effect of DPC on the Apical Cell Membrane Integrity—To ensure that the effect of DPC and related enhancers was predominantly due to modulation of the tight junctions and not due to compromised apical membrane, we have evaluated DPC-induced DNA staining by propidium iodide. This probe fluoresces when it interacts with DNA, but can access DNA only if the cell membrane and the nuclear membrane are compromised, as it does not permeate intact membranes.[32] When Caco-2 cells were treated with different concentrations of DPC prior to propidium iodide staining, fluorescence microscopy showed that the permeability of the cell membrane remained low after 20 min of exposure to 0.75 mM DPC, but increased at 1.0 mM and 1.25 mM DPC exposures (Figure 7). After removal of DPC and incubation in cell culture medium for 8 h, the membrane integrity was restored for 0.75 and 1.0 mM DPC treatment, but not after treatment with 1.25 mM DPC. These results suggest that above 1 mM concentration, DPC causes irreversible damage to the cell membrane and/or the nuclear membrane.

Effect of DPC on ZO-1 Redistribution—ZO-1 is a tight junction-associated protein,[33,34] which is localized on the cytoplasmic surface just beneath the membrane. When Caco-2 cells are treated with a rabbit antibody to ZO-1 (and visualized by treatment with FTIC-labeled goat anti-rabbit IgG antibody), the fluorescence image obtained with a confocal microscope clearly indicates a uniform distribution of ZO-1 at intercellular junctions (Figure 8A). Interestingly, treatment of these cells with DPC (0.75 mM) appears to cause a redistribution of ZO-1 as indicated by discontinuous ZO-1 labeling (Figure 8B). Thus, DPC appears to affect the spatial distribution of ZO-1 in Caco-2 cells by inducing its dissociation from the plasma membrane.

Discussion

To date, numerous compounds have been evaluated and used as absorption enhancers for orally administered drugs.[3–20] These enhancers fall in one of two categories: Ca^{2+} chelators that act by reducing the extracellular Ca^{2+}

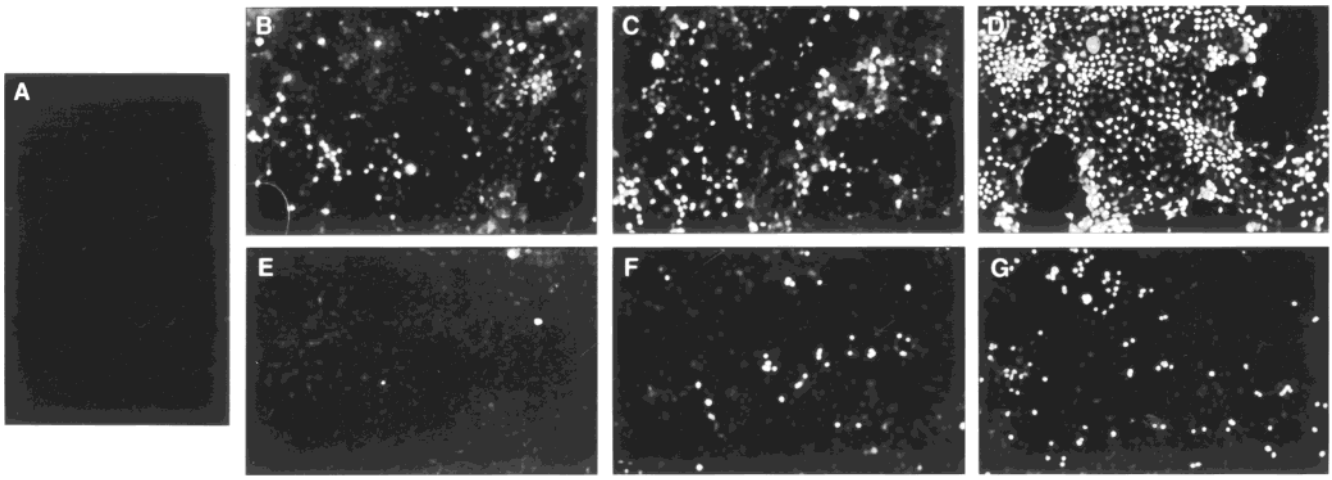

Figure 7—Effect of DPC treatment on the permeability of Caco-2 cells to propidium iodide. Caco-2 cells were treated with propidium iodide; control cells exclude propidium iodide and show no nuclear fluorescence (A). Cells were exposed for 20 min to 0.75 mM (B, E), 1.0 mM (C, F), and 1.5 mM (D, G) DPC. Propidium iodide was applied immediately after DPC treatment (B, C, D) or after DPC was removed and the cells were allowed to recover for 8 h (E, F, G). The frames are photographs of the images obtained by fluorescence microscope using 10x objective.

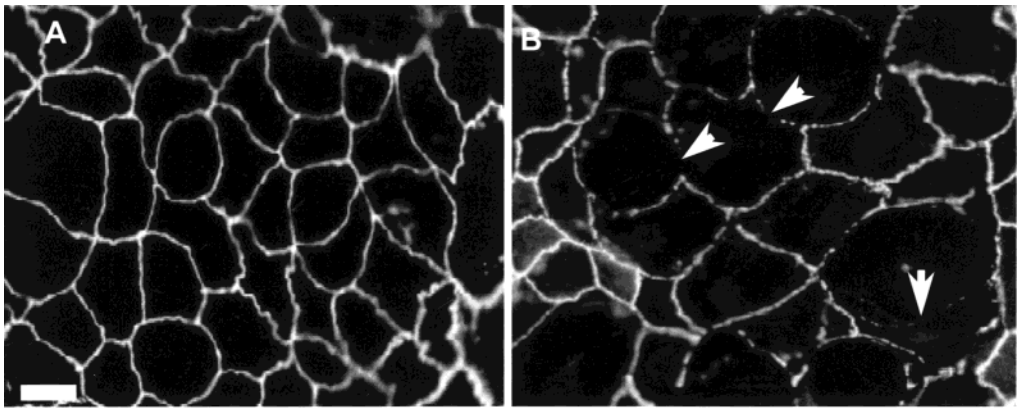

Figure 8—Effect of DPC treatment on the distribution of the tight junction-associated protein ZO-1 in Caco-2 cells. Untreated cells (A) or those treated with 0.75 mM DPC (B) were allowed to react sequentially with ZO-1 antibody and FITC-labeled anti-rabbit IgG as described in the Methods Section, and examined with a fluorescence confocal microscope. Bar = 50 μm.

concentration and thus compromising the integrity of the tight junctions, and detergents/surfactants that may act by causing a perturbation in the lipid bilayer of cell membrane as well as by a variety of intracellular mechanisms.[15–18,22,23] Among the latter class of compounds, PC has been one of the most extensively studied and used absorption enhancers. It appears to function by increasing the intracellular concentration of Ca^{2+} ions; however, the exact mechanism of its action is yet to be understood.[15,17] Also included in the latter class of compounds are phospholipid derivatives such as lysophosphatidylcholines[9,35,36] that appear to increase the permeability of peptides such as human growth hormone and a vassopressin derivative by unknown mechanism(s). These compounds have several features that make them particularly attractive as absorption enhancers. They occur in biological membranes as products of phospholipid metabolism[8,9] and are further metabolized to relatively nontoxic endogenous products. Furthermore, their absorption-promoting effects are spontaneously reversible upon their removal.

In the present study we have demonstrated that DPC, a zwitterionic amphiphile that lacks the glycerol moiety of lysophosphatidylcholine, is equally effective as the lysophosphatidylcholine LGPC in improving the permeability of hydrophilic compounds across Caco-2 cell monolayers. We have further showed that the presence of an (medium to long) alkyl chain and a zwitterionic functionality are essential for its activity. Thus, our studies have defined the minimum structural requirements of the phospholipid derivatives for their activity as absorption enhancers. It is interesting to note that while PC is a member of a different chemical class than phospholipids, its structural features essential for absorption-enhancing activity are quite similar to those for DPC; i.e., presence of an alkyl chain and a zwitterionic functionality (see Figures 1, 2). This is an important finding as the structures of DPC and PC can form the basis of a systematic structure–activity relationship that could lead to a more definitive information regarding the biochemical mechanism underlying their activity as absorption enhancers.

Our studies have shown that DPC, like PC, increases the permeability of the Caco-2 cell monolayers toward hydrophilic compounds predominantly by modulation of the tight junctions and not by disruption of the cell membrane. This was evidenced by a decrease in TEER and an increase in the permeability of paracellular markers (e.g., mannitol, LY, etc.) with no change in the permeability of the transcellular transport marker testosterone. While the cell membrane was rendered somewhat permeable to propidium iodide at high concentration of DPC, it was clear that DPC did not cause extensive damage to the cell membrane at the concentrations that caused significant decease in TEER and an increase in mannitol permeability. Furthermore, our evidence that DPC caused significant redistribution of the tight junction-associated protein ZO-1 (Figure 8) provided confirmation that this compound

increases the permeability of Caco-2 cell monolayers by modulation of the tight junctions.

Our results show that DPC causes a rapid decrease in TEER as has been observed for other agents that act via modulation of tight junctions, such as PC[15] and sodium caprate.[16] The decrease in TEER is more gradual and less extensive when DPC is applied from the basolateral side, suggesting that the effect on the apical side is due to modulation of the tight junctions directly or through perturbation in the apical membrane that is not as accessible from the basolateral side due to the presence of the tight junctions. The decrease in TEER and increase in the permeability of the paracellular markers caused by DPC was concentration dependent, with a sharp inflection occurring (for drop in TEER) between 0.5 and 0.75 mM concentration (Figure 3). The inflection did not correspond to a change in solution properties of DPC; for example, the critical micelle concentration (CMC) for DPC was found to be 0.96 mM. In fact, our results suggested that the effect on TEER was not related to the CMC of these agents, as CMC for PC was more than 1 order of magnitude lower (0.015 mM) than that for DPC despite their somewhat similar potency in causing a decrease in TEER. When the Caco-2 cell monolayers were exposed to DPC, LGPC, and PC at concentrations above CMC for 20 min and then washed, the TEER values rapidly decreased and the transport rates of mannitol were also significantly enhanced compared to the control (data not shown). These results suggest that the monomer and the micelle, at least for these agents, are both active as modulators of the tight junctions.

It has been shown previously[14] that treatment with paracellular enhancers such as EGTA or PC causes a greater enhancement in the permeability of anionic or cationic compounds than of the neutral molecules. Our results confirm this finding in that the permeability of anionic LY was enhanced to a greater extent than that of neutral mannitol by pretreatment of Caco-2 cell monolayers with DPC (Figure 4). As expected, the enhancement in the permeability of the larger neutral molecules (PEG-900 and PEG-3500) is much smaller than that achieved with a smaller neutral molecule like mannitol (Figure 4).

It is important that we are able to compare different absorption enhancers not only in terms of their potency in causing an increased transport of drug molecules, but also in terms of the separation between their potency as enhancers and their potency in causing cellular toxicity. Hence, we propose the use of the parameter PI (potency index) that is a ratio of IC_{50} and EC_{50}, where IC_{50} refers to the concentration that causes a 50% decrease in mitochondrial dehydrogenase activity (an indicator of cytotoxicity in MTT test) and EC_{50} refers to the concentration that causes 50% decrease in TEER with respect to untreated control. We have used TEER as a surrogate for permeability of a paracellular marker because it is an easy measurement and EC_{50} values for TEER relate well to the similar index for permeability of a paracellular marker.[28] While it has been reported frequently that a change in TEER does not parallel a change in the permeability of paracellular markers, when these effects are measured over a concentration range and expressed as relative change they do indeed relate well with each other as has been shown.[28] The potency index for DPC is 1.42; for LGPC, 1.29; for PC, 1.07; for SDS, 1.11; and for MGP, less than 0.22. The larger potency index would mean a better separation between the activity and cytotoxicity of an enhancer, and thus a greater potential for an agent to be useful as an absorption enhancer. DPC possesses better separation between activity (tight junction modulation) and cytotoxicity than all other absorption enhancers evaluated, although less than 2-fold separation is not adequate for safe use of such an agent as an absorption enhancer. Interestingly, for one of the more extensively used agent PC, the potency index is approximately 1, indicative of no separation between toxic and effective concentrations. Clearly, the relationship between such parameters obtained in vitro to the activity and toxicity of such agents in vivo needs be evaluated extensively before the in vitro parameters can be used to compare different enhancers. However, use of such parameters should make the comparison of enhancers more meaningful when they have been evaluated in different groups and in different model systems rather than reporting the activity at one or two arbitrary concentrations. The comparisons of the efficacy of absorption enhancers evaluated by different groups can be made even more meaningful if one of the enhancers is used as a reference compound so that the potencies of the other enhancers can be expressed in relation to the EC_{50} of the reference compound.

References and Notes

1. Anderson, J. M.; Van Italie, C. M. Tight junctions and the molecular basis for regulation of paracellular permeability (review). *Am. J. Physiol.* **1995**, *269*, G467−G475.
2. Lutz, K. L.; Siahaan, T. J. Molecular structure of the apical junction complex and its contribution to the paracellular barrier. *J. Pharm. Sci.* **1997**, *86*, 977−984.
3. Van Hoogdalem, E. J.; De Boer, A. G.; Breimer, D. D. Intestinal drug absorption enhancement: an overview. *Pharmac. Ther.* **1989**, *44*, 407−443.
4. Lee, V. H. L.; Yamamoto, A.; Kompella, U. B. Mucosal penetration enhancers for facilitation of peptide and protein drug absorption. *Crit. Rev. Ther. Drug Carrier Syst.* **1991**, *8* (2), 91−192.
5. LeCluyse, E. L.; Sutton, S. C. In vitro models for selection of development candidates. Permeability studies to define mechanisms of absorption enhancement. *Adv. Drug Deliv. Rev.* **1997**, *23*, 163−183.
6. Swenson, E. C.; Curatolo, W. J. Intestinal permeability enhancement for proteins, peptides and other polar drugs: Mechanisms and potential toxicity. *Adv. Drug Deliv. Rev.* **1992**, *8* (1), 39−92.
7. Van Hoogdalem, E. J.; Wackwitz, A. T. E.; De Boer, A. G.; Breimer, D. D. Topical effects of absorption enhancing agents on the rectal mucosa of rats in vivo. *J. Pharm. Sci.* **1990**, *79* (10), 866−70.
8. Weltzien, H. U. Cytolytic and membrane-perturbing properties of lysophosphatidylcholine. *Biochim. Biophys. Acta* **1979**, *559*, 259−287.
9. Hovgaard, L.; Brondsted, H.; Nielsen, H. M. Drug delivery studies in Caco-2 monolayers. II. Absorption enhancer effects of lysophosphatidylcholine. *Int. J. Pharm.* **1995**, *114*, 141−149.
10. Brondsted, H.; Nielsen, H. M.; Hovgaard, L. Drug delivery studies in Caco-2 monolayers. III. Intestinal transport of various vasopressin analogues in the presence of lysophosphatidylcholine. *Int. J. Pharm.* **1995**, *114*, 115−157.
11. Drejer, K.; Vaag, A.; Bech, K.; Hansen, P.; Sørensen, A. R.; Mygind, N. Intranasal administration of insulin with phospholipids as absorption enhancer: pharmacokinetics in normal subjects. *Diabetic Med.* **1992**, *9*, 335−340.
12. Jacobs, M. A.; Schreuder, R. H.; Jap-A-Joe, K.; Nauta, J. J.; Andersen, P. M.; Heine, R. J. The pharmacodynamics and activity of intranasally administrated insulin in healthy male volunteers. *Diabetes* **1993**, *42*, 1649−1655.
13. Shimazaki, T.; Tomita, M.; Sadahiro, S.; Hayashi, M.; Awazu, S. Absorption-enhancing effects of sodium caprate and palmitoyl carnitine in rat and human colons. *Dig. Dis. Sci.* **1998**, *43* (3), 641−5.
14. Knipp, G. T.; Ho, N. F.; Barsuhn, C. L.; Borchardt, R. T. Paracellular diffusion in Caco-2 cell monolayers: effect of perturbation on the transport of hydrophilic compounds that vary in charge and size. *J. Pharm. Sci.* **1997**, *86* (10), 1105−10.
15. Hochman, J. H.; Fix, J.; LeCluyse, E. L. In vitro and in vivo analysis of the mechanism of absorption enhancement by palmitoyl carnitine. *J. Pharmacol. Exp. Ther.* **1994**, *269* (2), 813−822.
16. Anderberg, E. K.; Lindmark, T.; Artursson, P. Sodium caprate elicits dilatations in human intestinal tight junctions

and enhances drug absorption by paracellular route. *Pharm. Res*. **1993**, *10*, 857−864.
17. Tomita, M.; Hayashi, M.; Awazu, S. Absorption-enhancing mechanism of EDTA, caprate and decanoylcarnitine in Caco-2 cells. *J. Pharm. Sci*. **1996**, *85* (6), 608−611.
18. Lindmark, T.; Kimura, Y.; Artursson, P. Absorption enhancement through intracellular regulation of tight junction permeability by medium chain fatty acids in Caco-2 cells. *J. Pharmacol. Exp. Ther.* **1998**, *284*, 362−369.
19. Gan, L.-S.; Thakker, D. R. Applications of the Caco-2 model in the design and development of orally active drugs: Elucidation of biological and physical barriers posed by the intestinal epithelium. *Adv. Drug Delivery Rev*. **1997**, *23*, 80−100.
20. Liu, D. Z.; Thakker, D. R. Modulation of Caco-2 Cell tight junctions by dodecanoylphosphorylcholine (DPC). *Pharm. Res*. **1997**, *14*, S-23.
21. Sakai, M.; Imai, T.; Ohtake, H.; Azuma, H.; Otagiri, M. Effects of absorption enhancers on cytoskeletal actin filaments in caco-2 cell monolayers. *Life Sci.* **1998**, *63*, 45−54.
22. Sakai, M.; Imai, T.; Ohtake, H.; Otagiri, M. Cytotoxicity of absorption enhancers in caco-2 cell monolayers. *J. Pharm. Pharmacol.* **1998**, *50*, 1101−1108.
23. Duzier, E.; Van Der Wulp, C.; Versantvoort, C. H. M.; Groten, J. P. Absorption enhancement, structural changes in tight junctions and cytotoxicity caused by palmitoyl carnitine in Caco-2 and IEC-18 cells. *J. Pharmacol. Exp. Ther.* **1998**, *287*, 395−402.
24. Quan, Y.-S.; Hattori, K.; Lundboro, W.; Fujita, T.; Murakami, M.; Muranishi, M.; Yamamoto, M. Effectiveness and toxicity screening of various absorption enhancers using caco-2 cell monolayers. *Bio. Pharm. Bull.* **1998**, *21*, 615−620.
25. Mosmann, T. Rapid colorimetric assay for cellular growth and survival: application to proliferation and cytotoxicity assays. *J. Immunol. Methods* **1983**, *65*, 55−63.
26. Anderberg, E. K.; Artursson, P. Epithelial transport of drugs in cell culture: VIII. Effects of the pharmaceutical surfactant sodium dodecyl sulfate on cell membrane and tight junctional permeability in human intestinal epithelial (caco-2) cells. *J. Pharm. Sci.* **1993**, *82*, 392−398.
27. It has been reported that the sodium salts of capric acid (CA) and lauric acid show the absorption-enhancing effects in Caco-2 cell monolayers.[15−17] However, the concentrations used in those studies were much higher than that in this study (10−15 mM versus 0.75−1.0 mM).
28. Liu, D. Z.; Morris-Natschke, S. L.; Kucera, L. S.; Ishaq, K. S.; Thakker, D. R. Structure−activity relationships for enhancement of paracellular permeability by 2-alkyoxy-3-alkylamidopropylphosphocholines across Caco-2 cell monolayers. *J. Pharm. Sci*. **1999**, *88*, 1169−1174.
29. Anderberg E. K.; Nystrom, C.; Artursson, P. Epithelial Transport of Drugs in Cell Culture. VII: Effects of Pharmaceutical Surfactant Excipients and Bile Acids on Transepithelial Permeability in Monolayers of Human Intestinal Epithelial (Caco-2) Cells. *J. Pharm. Sci*. **1992**, *81*, 879−887.
30. Gan, L. S.; Yanni, S.; Thakker, D. R. Modulation of the tight junctions of intestinal epithelia by H2-antagonist. *Pharm. Res*. **1998**, *15*, 53−57.
31. Lee, K.; Thakker, D. R. Saturable Transport of H_2-Antagonists Ranitidine and Famotidine across Caco-2 Cell Monolayers. *J. Pharm. Sci*. **1999**, *88*, 680−687.
32. Haugland, R. P. Nucleic acid stains (8−1). In *Handbook of Fluorescent Probes and Research Chemicals*, 6th ed.; Spence, M. T. Z., Ed., Molecular Probes, Inc.: Oregon, 1996; pp 144−156.
33. Stevenson, B. R.; Siliciano, J. D.; Mooseker, M. S.; Goodenough, D. A. Identification of ZO-1: a high molecular weight polypeptide associated with the tight junction (zonula occludens) in a variety of epithelia. *J. Cell Biol.* **1986**, *103*, 755−766.
34. Anderson, J. M.; Stevenson, B. R.; Jesaitis, L. A.; Goodenough, D. A.; Mooseker, M. S. Characterization of ZO-1: a protein component of the tight junction from mouse liver and Madin-Darby canine kidney cells. *J. Cell Biol.* **1988**, *106*, 1141−1149.
35. Fisher, A. N.; Farraj, N. F.; O′Hagan, D. T.; Gill, I. J.; Johanse, B. R.; Davis, S. S.; Illum, L. Effect of lysophosphatidylcholine on the nasal absorption of human growth hormone in three animal species. *Int. J. Pharm*. **1991**, *74* (2−3), 147−157.
36. Schulze, C.; Smales, C.; Rubin, L. L.; Staddon, J. M. Lysophosphatidic acid increases tight junction permeability in cultured brain endothelial cells. *J. Neurochem*. **1997**, *68* (3), 991−1000.

Acknowledgments

The authors gratefully acknowledge Dr. John LeMaster (UNC) for his help and the use of the core facility for confocal microscopy in the ZO-1 distribution studies, and Mr. Tim Tippin (Glaxo Wellcome and UNC) for a careful review of the manuscript. This study was supported by an unrestricted gift by Glaxo-Wellcome.

JS990094E

Structure–Activity Relationships for Enhancement of Paracellular Permeability by 2-Alkoxy-3-alkylamidopropylphosphocholines across Caco-2 Cell Monolayers

DONG-ZHOU LIU,[†,‡] SUSAN L. MORRIS-NATSCHKE,[§] LOUIS S. KUCERA,[||] KHALID S. ISHAQ,[§] AND DHIREN R. THAKKER*,[†]

Contribution from *Division of Drug Delivery and Disposition, and Division of Medicinal Chemistry and Natural Products, School of Pharmacy, University of North Carolina at Chapel Hill, Chapel Hill, North Carolina 27599-7360, and Department of Microbiology and Immunology, Wake Forest University, School of Medicine, Winston-Salem, North Carolina 27103.*

Received March 27, 1999. Accepted for publication August 26, 1999.

Abstract □ The oral route is the preferred route of delivery for a large number of drug molecules. However, the intestinal epithelium presents a formidable barrier for delivery of drugs into systemic circulation. Phospholipids are among compounds that enhance the absorption of drugs across the intestinal epithelium. In this paper, we describe structure–activity relationships for phospholipid derivatives as enhancers of paracellular permeability across Caco-2 cell monolayers. In a series of 2-alkoxy-3-alkylamidopropylphosphocholine derivatives, compounds with a long chain at C-3 (R_3) and short chain at C-2 (R_2) were potent in causing a decrease in transepithelial electrical resistance (TEER) and an increase in mannitol transport, but also showed significant cytotoxicity. Compounds with 9–11 carbons at C-3 and 6–10 carbons at C-2 provided good separation (up to 2.7-fold) between activity and cytotoxicity. Notably, a good correlation ($r^2 = 0.93$) was observed between EC_{50} (TEER) [concentration that caused a drop in TEER to 50% of its control (untreated) value] and $EC_{10\times}$ (mannitol) [concentration that caused 10-fold increase in mannitol transport over the control (untreated) value], confirming that a decrease in TEER is associated with enhanced permeability of the hydrophilic compounds across Caco-2 cell monolayers. Compounds with *medium to long carbon chains* at C-2 and C-3, *and* the total carbons in the alkyl chains > 20, showed poor activity and no cytotoxicity.

Introduction

The oral route is the preferred route of delivery for a large number of drug molecules. However, the intestinal epithelium presents a formidable barrier for delivery of many drugs into systemic circulation. Lipophilic drug molecules can cross this barrier by diffusion through the cell membranes, whereas small hydrophilic compounds diffuse through the intercellular space via the paracellular route. Some drugs can act as substrates for the carrier proteins present in the intestinal epithelium (e.g., amino acid, di/tripeptide, glucose, etc.), and are absorbed by a carrier-mediated active transport process. For those hydrophilic drugs that are likely to traverse the intestinal epithelium via the paracellular route, the intestinal barrier is particularly formidable because of the presence of the tight junctions that severely restrict the free passage of solutes through the paracellular space.[1,2] Hence, development of absorption enhancers that can improve the absorption of hydrophilic molecules via the paracellular route is an active area of research in many laboratories. To date, a large number of absorption enhancers with diverse chemical structures have been identified. These include bile salts, medium chain fatty acids, phospholipids, acyl carnitines, Ca^{2+} chelators, surfactants, and detergents.[3−23]

Among many compounds that can enhance the intestinal absorption of hydrophilic drug molecules, phospholipid-like agents with medium length fatty acid chains are of special interest, because they are ubiquitous in living organisms and are found in the membranes and membranous organelles of all living matter.[7] In two separate studies, formulations containing dodecanoylphoshatidylcholine achieved ~8−13% bioavailability (with respect to the iv bolus dose) of insulin after intranasal administration to healthy volunteers.[8,9] Lysophosphatidylcholine, containing a mixture of palmitoyl and stearoyl side chains, significantly increased the nasal absorption of human growth hormone in rats, rabbits, and sheep.[10] Palmitoyllysophosphatidylcholine[11] as well as its analogues[12] increased the permeability of poorly permeable vasopressin analogues across Caco-2 cell monolayers by almost 2 orders of magnitude. The increase in the permeability was achieved at concentrations of the enhancer that did not perturb the membrane significantly (trypan blue exclusion).[12] Lysophoshatidic acid caused a decrease in transepithelial electrical resistance (TEER) and an increase in sucrose flux across cultured brain capillary endothelial cells.[13] Our recent studies have shown that dodecylphosphocholine (DPC) can cause an increase in the permeability of hydrophilic compounds and a decrease in TEER across Caco-2 cell monolayers by modulation of the tight junctions.[14]

Very little information is available regarding the mechanism by which the phospholipid derivatives are able to enhance the absorption of drug molecules or the structural requirements for their activity. In vitro studies[11−14] suggest that these agents increase the paracellular permeability of compounds by modulation of the tight junctions. Studies with the brain endothelial capillary cells[13] suggest that such agents may alter the permeability of the tight junctions by intracellular mechanisms such as tyrosine phosphorylation of proteins at focal contact, recruitment of focal adhesion components, and activation of yet undefined signaling pathways. Our studies have shown that DPC displaces some of the tight junction (zonula occludens)-associated protein ZO-1 at a concentration that causes a decrease in TEER and an increase in paracellular perme-

* Corresponding author. Tel: (919) 962-0092. Fax: (919) 966-0197. E-mail: dhiren_thakker@unc.edu.
[†] Division of Drug Delivery and Disposition, School of Pharmacy, The University of North Carolina.
[‡] Current address: Wyeth-Ayerst Research, 401 North Middletown Rd., Pearl River, NY 10965.
[§] Division of Medicinal Chemistry and Natural Products, School of Pharmacy, The University of North Carolina.
[||] Department of Microbiology and Immunology, Wake Forest University.

10.1021/js9900957 CCC: $18.00 Published on Web 10/15/1999

ability across Caco-2 cells.[14] Our studies with DPC[14] have further suggested that the presence of a medium (or long) alkyl chain and a zwitterionic headgroup are essential for the activity of phospholipid-like agents as enhancers of paracellular permeability across Caco-2 cell monolayers. Similar requirements (i.e., alkyl chain and zwitterionic headgroup) for enhancement of paracellular permeability by structurally unrelated acyl carnitines[14,15] suggest the possibility of an emerging structure−activity relationship for enhancement of paracellular permeability across intestinal epithelium by modulation of tight junctions.

In this paper, we describe a more definitive and detailed study to delineate the structure−activity relationship for phospholipid-like agents as enhancers of paracellular permeability across Caco-2 cell monolayers. An excellent group of compounds for such a structure−activity relationship study is a series of 2-alkoxy-3-amidopropylphosphocholine derivatives[22] with varying lengths of alkyl chains at C-2 and C-3 positions. As proposed in our previous study,[14,23] we have applied the concept of potency index in developing the structure−activity relationship. Embedded in the potency index are two parameters—one reflecting the potency of the compounds as modulators of the tight junctions, i.e., transepithelial electrical resistance (TEER), and the other reflecting their potency in causing cytotoxicity by indiscriminate damage to the cell membrane (MTT test). We report here one of the first attempts to delineate the relationship between phospholipid structure and enhancement of paracellular permeability in relation to the cytotoxicity of this class of compounds.

Materials and Methods

Materials—Caco-2 cells were purchased from American Type Culture Collection (Rockville, MD). Eagle's Minimum Essential Medium (EMEM), 0.25% trypsin/0.02% ethylenediaminetetraacetic acid−tetrasodium salt (EDTA-4Na), and fetal bovine serum (FBS) were obtained from Gibco (Grand Island, NY). Nonessential amino acids (NEAA), Hank's balanced salt solution (HBSS), antibiotic antimycotic solution, 3-(4,5-dimethylthiazol-2-yl)-2,5-diphenyltetrazolium bromide (MTT), palmitoyl-DL-carnitine chloride, sodium dodecyl sulfate (SDS), DPC, 1-myristoyl-sn-glycero-3-phosphate sodium (MGP), 1-lauroyl-sn-glycero-3-phosphocholine (LGPC), 3-amino-1,2-propanediol, acyl chlorides, triphenylmethyl chloride, 60% sodium hydride (in oil), alkyl halides, *p*-toluenesulfonic acid monohydrate, and aqueous (40%) trimethylamine were purchased from either Sigma (St. Louis, MO) or Aldrich (Milwaukee, WI). *N*-(2-hydroxyethyl)piperazine-*N*′-2-ethanesulfonic acid (HEPES) was obtained through Tissue Culture Facilities (UNC at Chapel Hill, NC). Transwell plates and inserts (12 wells/plate, 3.0 μm pore and 1.0 cm^2 area, polycarbonate) were purchased from Corning-Costar (Cambridge, MA). [^{3}H]Mannitol was obtained from DuPont NEN (Boston, MA).

Caco-2 Cell Culture—Caco-2 cells were grown in EMEM containing 10% FBS, 1% l-glutamine, 1% NEAA and antibiotics (100 U/mL of penicillin, 100 μg/mL of streptomycin, and 0.25 μg/mL of amphotericin B) in 75 cm^2 culture flasks. The cultures were kept at 37 °C in an atmosphere of 5% CO_2, 95% air, and 90% relative humidity. Cells were passaged after 95% confluency and were seeded with a density of 1.0×10^5 cells/mL on to porous polycarbonate filter membranes with a pore size of 3.0 μm and a surface area of 1.0 cm^2. Cells of passage number 45−55 were used in all the studies. Media were changed every 2 days after seeding until late confluence (20−22 days). Just before the experiments, the culture medium was replaced with HBSS transport buffer (HTB) that contained 1x HBSS, 25 mM HEPES, and 25 mM glucose at pH 7.4 and incubated for 1 h at 37 °C. The cell monolayers with TEER values in the range of 600−800 Ω·cm^2 were used for the experiments.

General Chemical Methods—Compounds **1**−**12** (Table 1) were synthesized as described previously.[24,25] Briefly, 3-amino-1,2-propanediol was reacted with various acyl chlorides to give the corresponding (alkylamido)propanediols. The primary hydroxyl group was selectively protected as the trityl ether with triphenylmethyl chloride in pyridine. Reaction of the secondary hydroxyl with sodium hydride and various alkyl halides gave the C2 alkyl ether. Deprotection of the primary hydroxyl group with *p*-toluenesulfonic acid in CH_2Cl_2/MeOH gave the 3-alkylamido-2-alkoxy-1-propanol. The phosphocholine was formed in two steps: (1) reaction with 2-bromoethyl dichlorophosphate and (2) amination with aqueous trimethylamine in $CHCl_3$/*i*-PrOH/DMF. Confirmation of chemical structure and determination of purity of the compounds have been reported.[26,27]

Table 1—Structures of 2-Alkoxy-3-alkylamidopropylphosphocholines

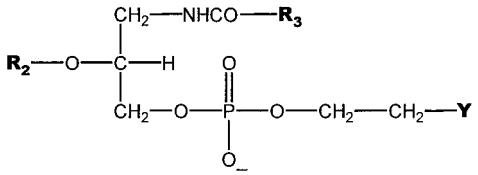

group	enhancers	R_3	R_2	Y
I	**1**	$C_{17}H_{35}$	CH_3	$N(CH_3)_3$
	2	$C_{16}H_{33}$	C_2H_5	$N(CH_3)_3$
	3	$C_{17}H_{35}$	C_2H_5	$N(CH_3)_3$
	4	$C_{19}H_{39}$	C_2H_5	$N(CH_3)_3$
II	**5**	C_9H_{19}	C_6H_{13}	$N(CH_3)_3$
	6	$C_{11}H_{23}$	C_8H_{17}	$N(CH_3)_3$
	7	$C_{11}H_{23}$	C_8H_{17}	$CH_2N(CH_3)_3$
	8	C_9H_{19}	$C_{10}H_{21}$	$N(CH_3)_3$
III	**9**	$C_{17}H_{35}$	C_8H_{17}	$N(CH_3)_3$
	10	$C_{11}H_{23}$	$C_{10}H_{21}$	$N(CH_3)_3$
	11	C_9H_{19}	$C_{12}H_{25}$	$N(CH_3)_3$
	12	$C_{11}H_{23}$	$C_{12}H_{25}$	$N(CH_3)_3$

The stock solutions of phospholipids (80 mM) were obtained by dissolving them in HBSS/ethanol (20:80, v/v) and were stored at −20 °C. Just before the experiments, the phospholipid solutions were thawed and diluted to the appropriate concentrations with HTB (final ethanol concentrated up to 2% v/v) and sonicated for 5 min in an ice bath.

Cytotoxicity Assay—The cell viability was measured by the MTT assay.[26,27] Approximately 3.0×10^3 Caco-2 cells (in 100 μL of cell culture medium) were seeded into each of the wells in a 96-well tissue culture plate (Corning-Costar, Cambridge, MA). The cells were then cultured under the same condition (see Caco-2 Cell Culture) for 96 h, and the culture medium was changed once. Just prior to the start of each experiment, the medium was removed from the wells, and 100 μL of the compound solution in HTB was added to each well. After 20 min, 20 μL of a 5 mg/mL MTT solution was added to each well, and the cells were incubated for another 90 min. Then 100 μL of 10% SDS in 0.02 M HCl/isobutanol (1:1, v/v) solution was added to stop the reaction. The cells without the treatment of any compound were harvested as above and were used as controls. Absorbance was measured at 590 nm (indicative of the formation of the formazan product by mitochondrial dehydrogenase of the viable cells) using a multiwell scanning spectrophotometer (Bio-Rad, Hercules, CA). IC_{50} represented the concentration of the phospholipid derivatives that caused 50% cell death as measured by the mitochondrial dehydrogenase activity.

EC_{50} (TEER) Determination—To measure the effect of the phospholipids on the TEER values of Caco-2 cell monolayers, the test compounds, dissolved in 0.5 mL of HTB at various concentrations, were applied to the apical side. The monolayers were treated for 20 min at room temperature and the TEER measured using an Epithelial Tissue Voltohmmeter (EVOM, World Precision Instruments, Sarasota, FL) and calculated as Ω·cm^2 by multiplying it with the surface area of the monolayer (1.0 cm^2). The resistance due to the cell monolayers was determined after subtracting the contribution of the blank filter and HTB. From the data, EC_{50} for TEER, the concentration at which the phospholipid decreases the TEER of cell monolayer by 50% of the control (untreated) value, was calculated.

Transport Experiments—All transport studies were performed at room temperature on filter-grown Caco-2 monolayers. The transport experiments were carried out under sink conditions such that the concentration of the transported compound in the

receiver compartment was less than 10% of its initial concentration in the donor compartment. Permeability coefficients (P_{app}) were calculated using the following equation:

$$P_{app} = (dQ/dt)\ (1/A)\ (1/C_o)$$

where dQ/dt (mol transported/s) is the flux of the marker compound across the Caco-2 cell monolayer, A (cm^2) represents the diffusional area of the inserts, and C_o (M) denotes the initial concentration of marker compound in the donor compartment. All measurements were in triplicate and expressed as mean ± SD values.

Transport without the Tight Junction Barrier—To evaluate the maximum transport rate of mannitol without the functional barrier of epithelial tight junctions, EDTA was used to open up the tight junction completely.[28] A solution of EDTA at concentration range of 0.001 mM to 15 mM was prepared using HTB without Ca^{2+}/Mg^{2+}. The solution was applied to the apical and basolateral sides of cell monolayer for 30 min. Then the solution was removed, and the cells were washed once with HTB without Ca^{2+}/Mg^{2+}. [^{3}H]-Mannitol (0.5 mL of 0.1 mM, 0.25 μCi) was added to the apical compartment, and the transport rate was determined by measuring the radioactivity (PACKARD 1600 TR liquid scintillation counter, Downers Grove, IL) appearing in the basolateral compartment as a function of time.

Absorption Enhancement—To calculate the compound concentration at which the permeability of mannitol is increased by 10-fold [$EC_{10\times}$ (mannitol)], the compound solution at concentration range of 0.05 to 5.0 mM in HTB (0.5 mL) was added to the apical side of the cells. HTB (1.5 mL) was added to the basolateral side. After treatment for 20 min, the lipid solution was removed and the monolayer was washed once with fresh HTB. Following the measurement of the TEER, 0.5 mL of HTB solution containing 0.1 mM [^{3}H]mannitol (0.25 μCi) was applied to the apical side. Samples from the basolateral side were taken at 10, 20, 40, and 60 min. Transport rates were determined by measuring the radioactivity in the basolateral side by liquid scintillation counter.

Results

Previous studies with two structurally distinct compounds, i.e., DPC and PC, have shown that the minimum structural requirements to cause a decrease in TEER and a corresponding increase in paracellular permeability across Caco-2 cells are (i) the presence of a medium to long alkyl chain and (ii) a zwitterionic group.[14,15] The same structural features may also confer a similar activity to phospholipid derivatives.[7−12,14] Here we report the effect of varying the length of alkyl chains at C-2 and C-3 positions of phospholipid derivatives on TEER, paracellular permeability across Caco-2 cell monolayers, and cytotoxicity to these cells.

Effect of Synthetic Phospholipid Derivatives on TEER and Paracellular (mannitol) Permeability across Caco-2 Cells—The chemical structures of the 2-alkoxy-3-alkylamidopropylphosphocholines studied are shown in Table 1. The effect of these compounds on TEER across Caco-2 cell monolayers was determined by exposing the cells to various concentrations of these agents on the apical side for 20 min prior to the measurement of TEER. The time of exposure was determined based on our studies with DPC which showed that maximal effect on TEER was achieved in 20 min.[14] Under these conditions, the mannitol permeability across Caco-2 cell monolayers was also determined. The typical TEER−concentration profiles as well as mannitol permeability−concentration profiles observed are shown in Figure 1. Based on the TEER/mannitol permeability−concentration profiles, the synthetic ether phospholipids were classified into three groups. Compounds in group I (**1**−**4**, Table 1) caused a precipitous drop in TEER and a steep rise in mannitol permeability with concentration (e.g., compound **2**, Figure 1A). These compounds are

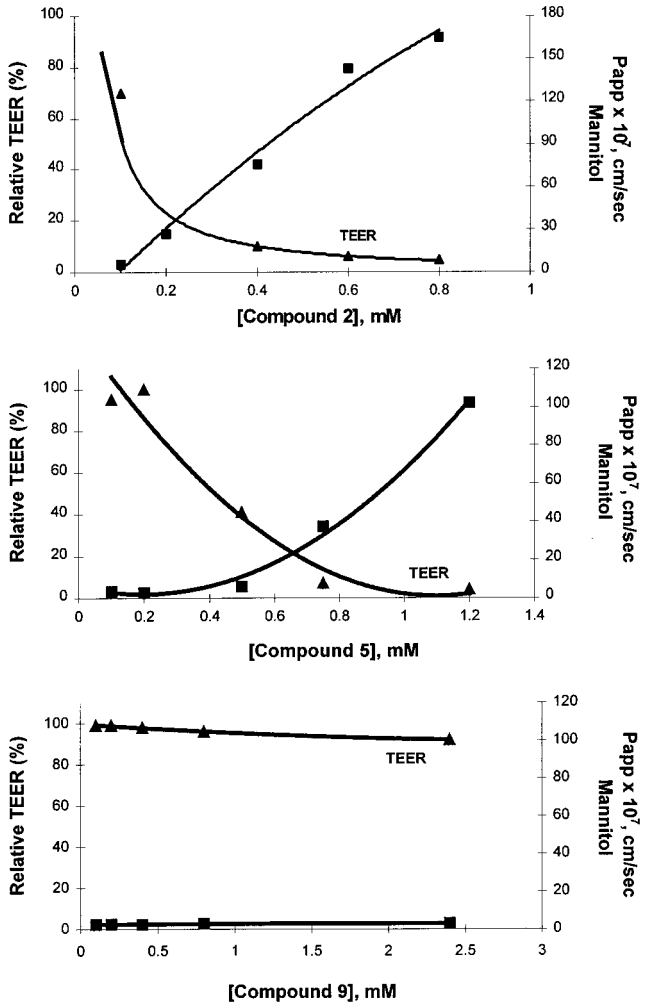

Figure 1—Effect of concentration on TEER and mannitol permeability for 2-alkoxy-3-alkylamidopropylphosphocholines. A, compound **2**; B, compound **5**; C, compound **9**. ■, mannitol permeability; ◆, TEER. Compounds were applied to the apical side of the monolayers for 20 min at room temperature.

characterized by a short alkyl chain (1−2 carbons) as the R_2 substituent and a long alkyl chain (16−19 carbons) as the R_3 substituent. In contrast, compounds in group II (**5**−**8**, Table 1) caused a more gradual decrease in TEER and increase in mannitol permeability with concentration (e.g., compound **5**, Figure 1B). These compounds contain medium length alkyl chains as the R_2 (6−10 carbons) and R_3 (9−11 carbons) substituents, with the total carbons in both the alkyl chains < 20. Compounds in group III (**9**−**12**, Table 1) had little or no effect on TEER or mannitol permeability over the concentration range examined (e.g., compound **9**, Figure 1C). These compounds contain a medium length alkyl chain as the R_2 substituent (8−12 carbons) and a medium to large alkyl chain as the R_3 substituent (9−17 carbons) with the total number of carbons in both alkyl chains > 20.

For comparison, the effect of EDTA, a known modulator of paracellular permeability via tight junction modulation,[28] on TEER and mannitol permeability is shown in Figure 2. The mannitol permeability reached a plateau at high concentrations of EDTA; no such plateau was reached with 2-alkoxy-3-alkylamidopropylphosphocholines (Figures 1 and 2). The compounds in groups I and II appear to be more potent than EDTA in causing a drop in TEER and an increase in the mannitol permeability across Caco-2 cell monolayers.

Comparison of the Effect of Synthetic Phospholipids on TEER and Mannitol Permeability across

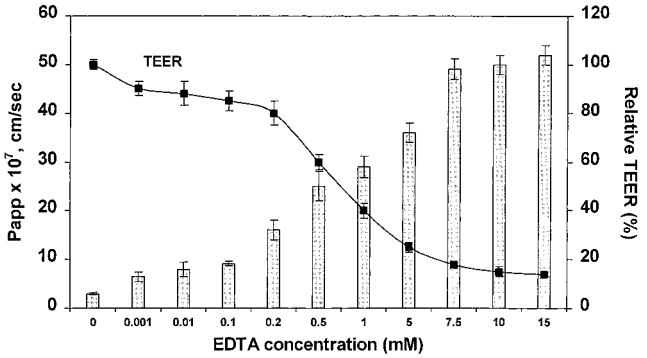

Figure 2—Effect of EDTA concentration on TEER and mannitol permeability. EDTA was applied on both apical and basolateral side of the monolayers for 30 min at room temperature. All measurements were in triplicate and expressed as mean ± SD.

Table 2. Values of EC_{50}, $EC_{10\times}$, IC_{50}, and PI of the Synthetic Phospholipids

group	enhancers	EC_{50} (TEER)[a]	$EC_{10}\times$ (mannitol)[a]	IC_{50} (MTT)[a]	PI[b]
I	1	0.14 (0.02)	0.21 (0.02)	0.16 (0.02)	1.14
	2	0.12 (0.01)	0.20 (0.02)	0.11 (0.01)	0.83
	3	0.16 (0.01)	0.29 (0.02)	0.16 (0.02)	1.02
	4	0.28 (0.02)	0.42 (0.01)	0.25 (0.02)	0.89
II	5	0.42 (0.03)	0.73 (0.05)	1.10 (0.05)	2.62
	6	0.25 (0.02)	0.70 (0.03)	0.68 (0.02)	2.72
	7	0.42 (0.03)	0.73 (0.05)	1.10 (0.10)	2.62
	8	0.80 (0.02)	1.35 (0.12)	1.40 (0.25)	1.75
III	9	no effect	ND[c]	>2.0	–
	10	1.45 (0.02)	ND	1.50 (0.05)	1.03
	11	1.6 (0.1)	ND	2.0 (0.2)	1.25
	12	no effect	ND	no effect	–

[a] Values of EC_{50} (TEER), $EC_{10}\times$ (mannitol) and IC_{50} (MTT) are expressed as mM; the numbers in parentheses indicate SD. [b] PI: the ratio of IC_{50}/EC_{50} based on the data from Caco-2 cells. [c] ND: not detectable because of the insolubility of the lipids at higher concentrations.

Caco-2 Cells—To express the effect of these compounds on TEER and paracellular permeability quantitatively, we have defined the terms EC_{50} (TEER)[14] and $EC_{10\times}$ (mannitol).[22] EC_{50} (TEER) is the concentration of an enhancer at which TEER drops to 50% of its control value (untreated cells), and $EC_{10\times}$ (mannitol) is the concentration at which mannitol permeability is increased by 10-fold over the control value (untreated cells). In case of mannitol permeability, the term $EC_{10\times}$ was defined instead of EC_{50} because the plateau in the mannitol permeability was not always easy to obtain (see Figure 1); hence, a percentage of maximal effect could not always be determined. Furthermore, 10-fold increase in mannitol permeability over the control value ($\sim 2.5 \times 10^{-7}$ cm/s) represented 50% of the maximal mannitol permeability (25×10^{-7} cm/s) obtained by opening up the tight junctions with EDTA (Figure 2). The EC_{50} (TEER) and $EC_{10\times}$ (mannitol) for the synthetic phospholipids are shown in Table 2. By both these parameters, the compounds in group I were the most potent phospholipid derivatives tested, the compounds in group II showed moderate potency, and those in group III were weakly active or inactive.

The relationship between the EC_{50} (TEER) and the EC_{10x} (mannitol) is shown in Figure 3. Clearly, an excellent correlation exists between the EC_{10x} (mannitol) values and the EC_{50} (TEER) values. Hence, EC_{50} (TEER) can serve as a reliable index of the potency of the compounds as enhancers of paracellular permeability if the data on mannitol permeability are not available.

Interestingly, at their EC_{50} concentrations, the changes in TEER and mannitol transport caused by group II compounds were reversible. After removal of the compounds and recovery of the cells in complete cell culture medium (10% fetal calf serum, 1% NEAA in EMEM) for 2 h, the decreased TEER and the enhanced mannitol transport returned to their initial values (approximately 85–95% TEER recovery and 90–95% recovery of mannitol permeability). However, on similar treatment of the cell monolayers with group I compounds, the TEER and mannitol transport values did not recover, indicating that tight junction integrity cannot be restored after exposure of the cells to group I compounds.

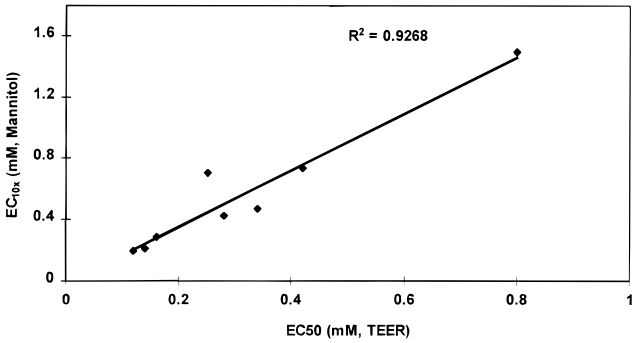

Figure 3—Relationship between EC_{50} (TEER) and EC_{10x} (mannitol) for 2-alkoxy-3-alkylamidopropylphosphocholines. EC_{50} (TEER) and EC_{10x} (mannitol) have been defined in Materials and Methods.

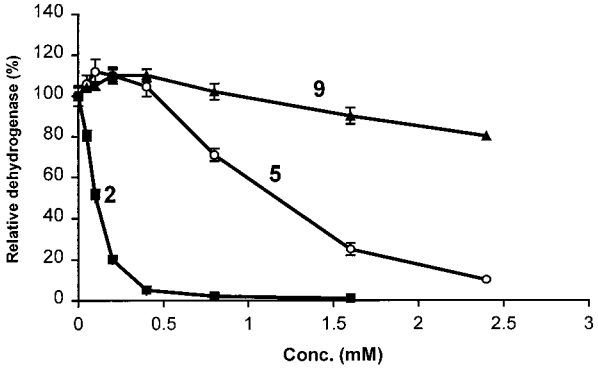

Figure 4—Relationship between concentration and mitochondrial dehydrogenase activity (MTT) for 2-alkoxy-3-alkylamidopropylphosphocholines that are typical of three groups of compounds within this series. All measurements were in triplicate and expressed as mean ± SD.

Cytotoxicity of the Synthetic Phospholipids—To evaluate cytotoxicity of the synthetic phospholipids toward Caco-2 cells, the viability of the cells was evaluated using the MTT method.[26,27] MTT is a tetrazolium salt that is cleaved by mitochondrial dehydrogenase in living cells to give a dark blue formazan product. Damaged or dead cells show reduced or no mitochondrial dehydrogenase activity. Cytotoxicity of compounds **2**, **5**, and **9**, representing the compounds in groups I, II, and III, respectively, as a function of their concentration is shown in Figure 4. The toxicity of these compounds is expressed as IC_{50}, which is defined as the concentration at which the compounds caused 50% decrease in mitochondrial dehydrogenase activity in the MTT test. The IC_{50} values of all the compounds tested are given in Table 2. Among the three compounds shown in Figure 4, compound **2** was most cytotoxic ($IC_{50} = 0.11$ mM), compound **5** showed moderate cytotoxicity (IC50 = 1.1 mM), and compound **9** did not show any toxicity even at the highest concentration (2.5 mM) tested. The cytotoxicity of compounds **2**, **5**, and **9** was representative of the cytotoxicity exhibited by compounds in their respective groups.

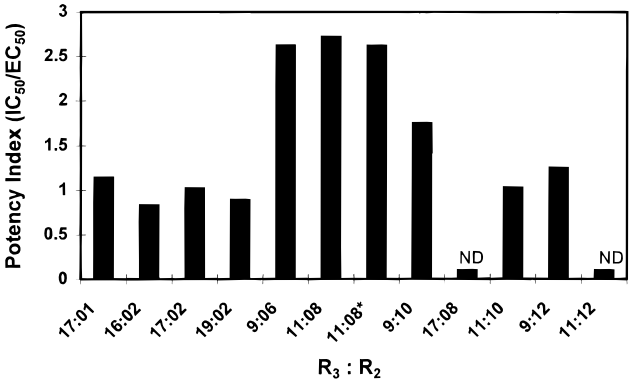

Figure 5—Relationship between R2 and R3 substituents in 2-alkoxy-3-alkylamidopropylphosphocholines and the potency index, PI [IC_{50}/EC_{50}(TEER)]. The compounds are in numerical order (**1** to **12**) from left to right. *The trimethylammonium group is separated from the phosphate group by a three-carbon chain instead of a two-carbon chain

Discussion

A decrease in TEER and an increase in mannitol permeability across Caco-2 cell monolayers caused by 2-alkoxy-3-alkylamidopropylphosphocholines suggest that this class of compounds has the potential to act as absorption enhancers. Their effect on TEER and mannitol permeability suggests that they are acting via modulation of the tight junctions; however, the evidence is entirely circumstantial. In a previous study,[14] we had presented evidence that a long alkyl chain and a zwitterionic functionality are essential for the activity of such compounds as modulators of paracellular permeability. In the present study, we have examined a limited structure−activity relationship (2-alkoxy-3-alkylamidopropylphosphocholines) that provides more insights on the effect of branching of the alkyl chain on the activity (as enhancers of paracellular permeability) and toxicity of phospholipid derivatives. The branching is not achieved with branched alkyl chains, but rather by introducing an ether functionality at C-2 and an amido functionality at C-3 of a propylphosphocholine.

Surprisingly, introduction of a small alkyl group at the C-2 position (R_2) significantly enhanced the potency of phospholipids in causing a decrease in TEER and an increase in mannitol permeability across Caco-2 cell monolayers. For example, the EC_{50} (TEER) value of compound **2** (0.12 mM) was 3.5- to 5-fold lower than the previously reported values for PC (0.42 mM), DPC (0.65 mM), or LGPC (0.65 mM). Unfortunately, this structural feature also caused the phosphocholine derivatives to be more potent cytotoxic agents. Thus the IC_{50} value for compounds **2** (0.11 mM) is much lower than that for PC (0.45 mM), DPC (0.92 mM), and LGPC (0.84 mM).[14] Increasing the length of C-2 alkyl chain to 6−8 carbon atoms while simultaneously decreasing the length of C-3 alkyl chain caused a decrease in the potency of the compounds as modulators of the paracellular permeability with a concurrent decrease in cytotoxicity. Finally, further increase in the length of the C-2 or C-3 alkyl chains rendered the compound inactive.

In developing a structure−activity relationship for paracellular permeation enhancers, the potency of these agents must be addressed in relation to their cytotoxicity. Hence, we have defined the term potency index (PI), which is a ratio of the IC_{50} (MTT) value of a compound to its EC_{50} (TEER) value.[14,22] For the synthetic phospholipid derivatives, the PI values are listed in Table 2 and plotted in Figure 5. Clearly, for all compounds having a short alkyl chain at C-2 (group I), the PI value is ∼1; i.e., the concentration at which they can exhibit enhancement in paracellular permeability is very similar to the concentration at which they are cytotoxic. In contrast, the compounds in group II, with medium length alkyl chains at C-2 and C-3 (total carbons < 20), have PI values in the range of 1.75−2.72 and achieve the best separation of activity as paracellular permeation enhancer and cytotoxicity among all the compounds tested including those tested in our previous study.[14] This PI range is significantly greater than that for the extensively investigated enhancer PC (PI ≅ 1). Compounds **6** and **7** exhibit comparable PI values despite the fact that their cationic and anionic centers are separated by two and three carbons, respectively. Thus a small change in the distance between the cationic and the anionic centers does not lead to any change in activity or toxicity. Some compounds in group III (medium to long alkyl chains at C-2 and C-3 *and* total carbons > 20) have PI values of approximately 1, whereas others are too inactive to determine either the EC_{50} or the IC_{50} value.

In conclusion, with this limited series of compounds, we have been able to demonstrate that the structure−activity (modulation of paracellular permeability) relationship for synthetic phospholipid derivatives is distinct from the structure−toxicity relationship. Interestingly, the separation of activity and toxicity is most pronounced (>2.5-fold) for moderately active compounds, while the activity and the toxicity appear to converge among the more potent compounds. Hence, further assessment of the structure−activity relationships should focus on phospholipid derivatives with medium-size alkyl substituents at C-2 and C-3. The relationship between relative position and distance of the anionic and cationic centers and the activity/toxicity should be further explored.

References and Notes

1. Van Hoogdalem, E. J., De Boer, A. G., Breimer, D. D. Intestinal drug absorption enhancement: an overview. *Pharmacol. Ther.* **1989,** *44*, 407−443.
2. Lutz, K. L.; Siahaan, T. J. Molecular structure of the apical junction complex and its contribution to the paracellular barrier. *J. Pharm. Sci.* **1997**, *86*, 977−984.
3. Lee, V. H. L.; Yamamoto, A.; Kompella, U. B. Mucosal penetration enhancers for facilitation of peptide and protein drug absorption. *Crit. Rev. Ther. Drug Carrier Syst.* **1991**, *8* (2), 91−192.
4. LeCluyse, E. L.; Sutton, S. C. In vitro models for selection of development candidates. Permeability studies to define mechanisms of absorption enhancement. *Adv. Drug Delivery Rev.* **1997**, *23*, 163−183.
5. Swenson, E. C.; Curatolo, W. J. Intestinal permeability enhancement for proteins, peptides and other polar drugs: Mechanisms and potential toxicity. *Adv. Drug Delivery Rev.* **1992**, *8* (1), 39−92.
6. Van Hoogdalem, E. J.; Wackwitz, A. T. E.; De Boer, A. G.; Breimer, D. D. Topical effects of absorption enhancing agents on the rectal mucosa of rats in vivo. *J. Pharm. Sci.* **1990**, *79* (10), 866−70.
7. Weltzien, H. U. Cytolytic and membrane-perturbing properties of lysophosphatidylcholine. *Biochim. Biophys. Acta* **1979**, *559*, 259−287.
8. Drejer, K.; Vaag, A.; Bech, K.; Hansen, P.; Sørensen, A. R.; Mygind, N. Intranasal administration of insulin with phospholipids as absorption enhancer: pharmacokinetics in normal subjects. *Diabetic Med.* **1992**, *9*, 335−340.
9. Jacobs, M. A.; Schreuder, R. H.; Jap-A-Joe, K.; Nauta, J. J.; Andersen, P. M.; Heine, R. J. The pharmacodynamics and activity of intranasally administered insulin in healthy male volunteers. *Diabetes* **1993**, *42*, 1649−1655.
10. Fisher, A. N.; Farraj, N. F.; O'Hagan, D. T.; Jabbal-Gill, I.; Johnsen, B. R.; Davis, S. S.; Illum, L. Effect of L-α-lysophosphatidylcholine on the nasal absorption of human growth hormone in three animal species. *Int. J. Pharm.* **1991**, *74*, 147−156.
11. Brondsted, H.; Nielsen, H. M.; Hovgaard, L. Drug delivery studies in Caco-2 monolayers. III. Intestinal transport of various vasopressin analogues in the presence of lysophosphatidylcholine. *Intl. J. Pharm.* **1995**, *114*, 115−157.

12. Hovgaard, L.; Bronsted, H.; Nielsen, H. M. Drug delivery studies in Caco-2 monolayers. II. Absorption enhancer effects of lysophosphatidylcholine. *Int. J. Pharm*. **1995**, *114*, 141−149.
13. Schulze, C.; Smales, C.; Rubin, L. L.; Staddon, J. M. Lysophosphatidic acid increases tight junction permeability in cultured brain endothelial cells. *J. Neurochem*. **1997**, *68*, 991−1000.
14. Liu, D.-Z.; LeCluyse, E. L.; Thakker, D. R. Dodecylphosphocholine-mediated enhancement of paracellular permeability and cytotoxicity in Caco-2 cell monolayers. *J. Pharm. Sci*. **1999**, *88*, 1161−1168.
15. Hochman, J. H.; Fix, J.; LeCluyse, E. L. In vitro and in vivo analysis of the mechanism of absorption enhancement by palmitoyl carnitine. *J. Pharmacol. Exp. Ther*. **1994**, *269* (2), 813−822.
16. Shimazaki, T.; Tomita, M.; Sadahiro, S.; Hayashi, M.; Awazu, S. Absorption-enhancing effects of sodium caprate and palmitoyl carnitine in rat and human colons. *Dig. Dis. Sci*. **1998**, *43*, 641−645.
17. Knipp, G. T.; Ho, N. F.; Barsuhn, C. L.; Borchardt, R. T. Paracellular diffusion in Caco-2 cell monolayers: effect of perturbation on the transport of hydrophilic compounds that vary in charge and size. *J. Pharm. Sci*. **1997**, *86* (10), 1105−10.
18. Anderberg, E. K.; Lindmark, T.; Artursson, P. Sodium caprate elicits dilatations in human intestinal tight junctions and enhances drug absorption by paracellular route. *Pharm. Res*. **1993**, *10*, 857−864.
19. Tomita, M.; Hayashi, M.; Awazu, S. Absorption-enhancing mechanism of EDTA, caprate and decanoylcarnitine in Caco-2 cells. *J. Pharm. Sci*. **1996**, *85* (6), 608−611.
20. Lindmark, T.; Kimura, Y.; Artursson, P. Absorption enhancement through intracellular regulation of tight junction permeability by medium chain fatty acids in Caco-2 cells. *J. Pharmacol. Exp. Ther*. **1998**, *284*, 362−369.
21. Gan, L.-S.; Thakker, D. R. Applications of the Caco-2 model in the design and development of orally active drugs: Elucidation of biological and physical barriers posed by the intestinal epithelium. *Adv. Drug Delivery Rev*. **1997**, *23*, 80−100.
22. Liu, D. Z.; Morris-Natschke, S. L. Ishaq, K. S.; Thakker, D. R. Structural requirements for synthetic phospholipids that modulate tight junction permeability across Caco-2 cells. *PharmSci* **1998**, *1* (1), S-453.
23. Liu, D. Z.; Thakker, D. R. Modulation of Caco-2 cell tight junctions by dodecanoylphosphorylcholine (DPC). *Pharm. Res*. **1997**, *14*, S-23.
24. Meyer, K. L.; Marasco, C. J.; Morris-Natschke, S. L.; Ishaq, K, S.; Piantadosi, C.; Kucera, L. S. In vitro evaluation of phosphocholine and quaternary ammonium containing lipids as novel anti-HIV agents. *J. Med. Chem*. **1991**, *34* (4), 1377−83.
25. Surles, J. R.; Morris-Natschke, S.; Marx, M. H.; Piantadosi, C. Multigram synthesis of 1-alkylamido phospholipids. *Lipids* **1993**, *28* (1), 55−57.
26. Mosmann, T. Rapid colorimetric assay for cellular growth and survival: application to proliferation and cytotoxicity assays. *J. Immunol. Methods* **1983**, *65*, 55−63.
27. Andenberg, E. K.; Artursson, P. Epithelial transport of drugs in cell culture: VIII. Effects of the pharmaceutical surfactant sodium dodecyl sulfate on cell membrane and tight junctional permeability in human intestinal epithelial (caco-2) cells. *J. Pharm. Sci.* **1993**, *82*, 392−398.
28. Artursson, P.; Magnusson, C. Epithelial transport of drugs in cell culture. II. Effect of extracellular calcium concentration on the paracellular transport of drugs of different lipophilicities across monolayers of intestinal epithelial (Caco-2) cells. *J. Pharm. Sci*. **1990**, *79*, 595−600.

Acknowledgments

The authors gratefully acknowledge Mr. Tim Tippin (Glaxo Wellcome and UNC) for a careful review of the manuscript and suggestions.

JS9900957

Amphiphilic Association of Ibuprofen and Two Nonionic Cellulose Derivatives in Aqueous Solution

ANNIKA RIDELL, HANS EVERTSSON,* STEFAN NILSSON, AND LARS-OLOF SUNDELÖF

Contribution from *Physical Pharmaceutical Chemistry, Uppsala University, Uppsala Biomedical Centre, Box 574, S-751 23, Uppsala, Sweden.*

Received March 26, 1999. Final revised manuscript received June 14, 1999.
Accepted for publication August 10, 1999.

Abstract □ The aqueous interaction of the sodium salt of ibuprofen with the cellulose ethers ethyl hydroxyethyl cellulose, EHEC, and hydroxypropyl methyl cellulose, HPMC, has been investigated in the concentration range 0–500 mM ibuprofen and 0.1–1% (w/w) polymer, by cloud point, capillary viscometry, equilibrium dialysis, and fluorescence probe techniques. Ibuprofen forms micelles in pure water, with the critical micelle concentration, cmc, at 180 mM. A combination of time-resolved and static fluorescence quenching shows that micelle-like ibuprofen aggregates are formed in the solution. The average aggregation number of pure ibuprofen micelles in water is about 40. In the presence of EHEC or HPMC the aggregation numbers decrease. The interaction of ibuprofen with cellulose ethers is similar to the normally accepted model for polymer–surfactant interaction, although more complex. Ibuprofen adsorbs to the polymer in the form of mixed polymer–drug micelles, noncooperatively up to cmc and cooperatively when cmc is passed. The interaction starts below 50 mM ibuprofen as monitored by the fluorescent probes pyrene and 1,3-di(1-pyrenyl)-propane, P3P, with a maximum in microviscosity below cmc, corresponding to polymer-dense mixed micelles. The study illustrates the importance of a precise apprehension of the aggregation behavior as a background for transport studies in drug–polymer systems.

Introduction

Amphiphilic molecules are characterized by the presence of both polar and nonpolar regions of the same molecule. This dual nature is responsible for the surface activity of these substances leading to accumulation at hydrophobic interfaces and formation of aggregates. Many types of drug molecules, such as antihistamines, antidepressants, tranquilizers, local anesthetics, and nonsteroidal antiinflammatory drugs (NSAIDs) are known to be amphiphilic in character and to form ordinary micelles or micelle-like associations[1] above a critical concentration value. Although the self-association of surface active drugs usually occurs at concentrations well above average therapeutic levels, the local concentration can reach, under certain circumstances, high values, for instance when the drug is instantaneously released from a tablet or accumulated at a membrane.

Cellulose derivatives play an important role in many technical applications and especially in the pharmaceutical field[2,3] where they have several uses such as to regulate the rheology of a system and to control the release of the drug. These polymers have an amphiphilic structure with mixed hydrophilic/hydrophobic segments, thus leading to an apparent surface activity the magnitude of which depends on type and degree of substitution.[4]

* Corresponding author. Tel: +46 18 4714370, fax: +46 18 4714377, e-mail: Hans.Evertsson@farmkemi.uu.se.

The interaction between polymers and surfactants in aqueous solution has attracted great interest during the last 20−30 years, and the topic has recently been reviewed.[5] As a prerequisite for a better understanding of polymer−drug interaction there has in this laboratory been a specific focus on the interaction of nonionic cellulose derivatives and the common anionic surfactant sodium dodecyl sulfate, SDS, in dilute aqueous solutions.[6−8] It has been shown that the surfactant forms interaction complexes with the polymer in a cooperative manner, giving rise to formation of a three-dimensional polymer network where mixed micelles of surfactant and polymer act as connecting tie points.

Since a surface active drug can form micelles by itself or bind hydrophobically to membranes, proteins, or other biological macromolecules as well as associate with hydrophobic excipients present in pharmaceutical formulations, all these types of associations may affect the release of the drug and alter the therapeutic effect.

The present paper deals with the general problem of the aqueous association of surface active drugs and polymers. The sodium salt of ibuprofen is an NSAID which is surface active[9] and was chosen as model substance, due to its, contrary to normal surfactants, high critical micelle concentration (180 mM) and hence a wider molar concentration interval of interest for the buildup of the interaction. Previous studies of NSAIDs have reported on dissolution properties,[10−12] solubility behavior,[13] release,[14] and other thermodynamic properties[12,15] of the drugs. In this work we have studied the association behavior in aqueous solutions between ibuprofen and two nonionic cellulose derivatives ethyl hydroxyethyl cellulose, EHEC, and hydroxypropyl methyl cellulose, HPMC. These two cellulose ethers are well-characterized materials[16] and represent polymers of different hydrophobicity. Both macroscopic and microscopic system properties are presented. The results will furthermore be discussed and compared in close relation to previous knowledge about the features of the corresponding polymer/SDS complexes.

Materials

The ethyl hydroxyethyl cellulose (EHEC) fraction CST-103, $DS_{ethyl} = 1.5$, $MS_{ethylene\ oxide} = 0.7$, was obtained from Akzo Nobel AB, Stenungssund, Sweden. The hydroxypropyl methyl cellulose (HPMC) fraction Methocel E4MCR was obtained from Pharmacia and Upjohn, Stockholm, Sweden. The sodium salt of ibuprofen (α-methyl-4-[isobutyl]phenylacetic acid), 9-methylanthracene, 98% (9-MA), and tris(2,2′-bipyridyl)ruthenium(II) chloride ($Ru(bipy)_3^{2+}$) were bought from Sigma-Aldrich Chemie, Steinheim, Germany, and used as supplied. Pyrene (+98%), Janssen Chimica, Geel, Belgium, was recrystallized twice from absolute ethanol prior to use. 1,3-Bis-(1-pyrenyl)propane (P3P) was bought from Molecular Probes, Eugene, OR, and used as supplied. Analytical grade NaCl was obtained from Merck, Darmstadt, Germany. The standard

10.1021/js990092u CCC: $18.00 Published on Web 09/18/1999

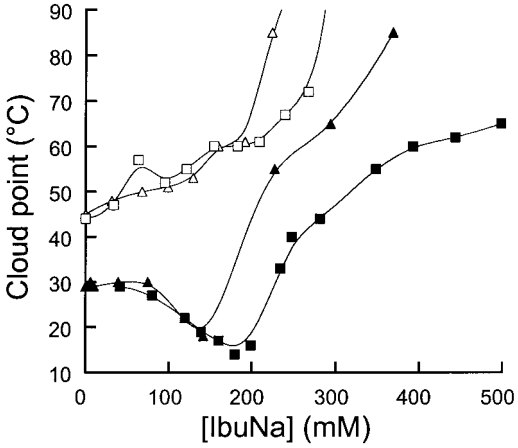

Figure 1—Cloud point, CP, as a function of the concentration of ibuprofen, [IbuNa], for different polymer concentrations; ▲ 0.1% and ■ 0.5%. Filled symbols are EHEC and open symbols are HPMC.

procedure for producing an EHEC or HPMC stock solution is presented elsewhere.[6] After preparation, the stock solutions were rinsed from low molecular weight material and salts using a Spectra/Por tube dialysis membrane, Spectrum Medical Ind., Houston, TX, with molecular weight cut off at 12 000−14 000. Dialysis was performed against Milli Q water (Millipore) during 1 week, and then the stock solutions were centrifugated at 20 000 rpm. The polymer concentrations of these stock solutions were determined gravimetrically by drying samples to constant weight at 105 °C. All polymer/ibuprofen solutions were prepared using Milli Q water as solvent. The pH of all solutions containing ibuprofen was close to 7.0. The pK_a of the corresponding acid of ibuprofen is about 4.6. It is thus taken that the sodium salt of ibuprofen is quantitatively ionized. To achieve appropriate concentrations of the very hydrophobic substances P3P and 9-MA, these substances were dissolved in absolute acetone of which aliquots were dissolved in the solutions to be measured by fluorescence.

Experimental Section

Cloud Point—The cloud point of polymer/ibuprofen solutions was determined visually in glass tubes and taken as the temperature when the last visible sign of clouding in the solution disappeared upon cooling.

Capillary Viscometry—The viscosity measurements were performed in ordinary Ostwald viscometers with a water flow time of approximately 100 s at 20 °C. The samples were thermostated in a Lauda CD 20 water bath for 15 min prior to measurements. Corrections for capillary and end effects were considered unnecessary.

Equilibrium Dialysis—The equilibrium dialysis experiments were performed in order to determine the adsorption isotherm of ibuprofen onto the cellulose ethers. The dialysis cell used consists of two compartments of 2 mL volume each, separated by a dialysis membrane (Spectra/Por with a M_w-cutoff of 12 000−14 000) according to the principle developed by Fischman and Eirich.[17] The polymer solution was placed on one side of the dialysis membrane, and a water solution on the other side, both sides with equal ibuprofen concentrations at the start. The cells were maintained at 20 °C for one week, and the ibuprofen concentrations on both sides of the membrane were determined spectrofotometrically at 273 nm ($\epsilon = 256.5\ M^{-1}\ cm^{-1}$). Kinetic studies showed that 6 days were needed to reach equilibrium. Since the ternary system EHEC (CST-103)/ibuprofen/water shows phase separation at 20 °C in the ibuprofen concentration range ≈120−200 mM, cf., Figure 1, dialysis experiments on this system were also performed at 10 °C in order to confirm the adsorption isotherm to be correct. The equilibrium ibuprofen concentration not bound to the polymer ($[ibu]_{eq}$), the amount of ibuprofen bound to the polymer (y, in mmol/g polymer), and the total ibuprofen concentration ($[ibu]_{tot}$) can then be calculated. Since the system studied is salt-free, a correction for the Donnan effect has been made as described previously.[6] The mass balance equation then becomes

$$[ibu]_{tot} = [ibu]_{eq} + c_p y \quad (1)$$

where c_p is the polymer concentration in grams per liter. This methodology has been utilized in several recent investigations of interactions in aqueous mixtures of the surfactant sodium dodecyl sulfate and nonionic cellulose ethers.[6,7,18−22]

Steady-State Fluorescence Measurements—All steady-state fluorescence measurements were performed at room temperature on a SPEX Fluorolog 2 model FL1T2 spectrometer operated in the "s" mode with 1.88 nm excitation and 0.85 nm emission bandwiths. All fluorescence measurements including time-resolved were run in duplicates, and the error was ±5% or less. The fluorescent probe concentrations were about 10^{-6} M. The concentration of the quencher 9-MA was ≤ 10^{-4} M.

Emission spectra were recorded for pyrene excitation at $\lambda = 334$ nm. The first (I_1, $\lambda = 374$ nm) to third (I_3, $\lambda = 388$ nm) emission intensity peak height ratio (I_1/I_3, the micropolarity index) of the vibrational emission spectrum of pyrene is a qualitative measure of the micropolarity at the probe solubilization site.[23] The micropolarity index is at most 2.0 in pure water and 1.0 in hydrophobic solvents such as toluene. It has been shown[23] that I_1/I_3 suddenly drops when the critical micelle concentration (cmc) is passed since pyrene quantitatively distributes to the more hydrophobic micellar phase if present. Micropolarity measurements with pyrene have been utilized in several papers from this laboratory on ternary surfactant/cellulose ether/water systems.[7,8,22,24]

P3P consists of two pyrene molecules connected by a propane chain, making this fluorescent probe capable of forming intramolecular excimers. Emission spectra were recorded between $\lambda = 350$ nm and $\lambda = 500$ nm for P3P excitation at $\lambda = 348$ nm. The extent of intramolecular excimer formation of P3P is dependent on the local friction of the probe imposed by its surroundings.[25] Hence, the monomer (I_M, $\lambda = 377$ nm) to excimer (I_E, $\lambda = 485$ nm) emission intensity peak ratio, I_M/I_E, is a qualitative index of the microviscosity at the probe solubilization site. P3P have been used in this laboratory to measure the microviscosity in polymer−surfactant systems,[8,24,26] and the method has been validated by NMR relaxation measurements.[27]

Time-Resolved Fluorescence Measurements—Time-resolved fluorescence measurements were recorded on a Photon Technology International model C-72 apparatus, equipped with a pulsed GL 3300 nitrogen laser/GL 320 dye laser as light source. Time-resolved fluorescence quenching, TRFQ, was used here in combination with steady-state fluorescence quenching, SSFQ, to measure the average aggregation number, the average number of ibuprofen monomers per aggregate or micelle, in aqueous solution. $Ru(bipy)_3^{2+}$ was used as probe and 9-MA as quencher. The fluorescence decay or steady-state luminescence of $Ru(bipy)_3^{2+}$ was recorded at $\lambda = 625$ nm for excitation at $\lambda = 450$ nm. In TRFQ experiments the decay was recorded up to 1000 ns. The concentration of 9-MA was determined spectrofotometrically at $\lambda = 388$ nm. Fluorescence decay curves were recorded for each sample both in the presence and absence of quencher. The lifetime of $Ru(bipy)_3^{2+}$ in solutions without quencher, τ_0, was determined by fitting the decay to a single-exponential function. Suggested by Infelta et al.[28] and proved by Tachiya,[29] the time evolution of the quenched fluorescence decay signal $F(t)$ from an ensemble of probe molecules situated in small monodisperse micelles can be expressed by

$$F(t) = A_1 \exp[-A_2 t + A_3\{\exp(-A_4 t) - 1\}] \quad (2)$$

If the probe and quencher can be considered as stationary within the micelle during the time of activation−deactivation, and a Poisson distribution of the quencher among the micelles is assumed, the parameters A_i in eq 2 take the simple forms

$$A_1 = F(0) \quad (2.1)$$

$$A_2 = 1/\tau_0 \quad (2.2)$$

$$A_3 = \langle n \rangle \quad (2.3)$$

$$A_4 = k_q \quad (2.4)$$

where k_q is the quenching rate constant, $F(0)$ the decay intensity signal at time zero, and $\langle n \rangle$ the average number of quencher molecules per micelle. Since the quencher concentration, [Q], is known, the average aggregation number, N, can be calculated by

putting

$$N = \langle n \rangle ([\text{ibu}]_{\text{tot}} - \text{cmc})/[\text{Q}] \quad (3)$$

where $[\text{ibu}]_{\text{tot}} - \text{cmc}$ represents the molar concentration of ibuprofen monomers constituting the aggregates, taken that all ibuprofen exceeding cmc are incorporated in micelles. In SSFQ the micellar concentration in the solution, denoted [micelles], is obtained from the relationship[30]

$$\ln(I^{\circ}/I) = [\text{Q}]/[\text{micelles}] \quad (4)$$

where I° and I are the steady-state luminescence in absence and presence of quencher, respectively. The mean aggregation number is then simply calculated by putting

$$N = ([\text{ibu}]_{\text{tot}} - \text{cmc})/[\text{micelles}] \quad (5)$$

SSFQ works well if there is no migration between probe and quencher and if the quenching is efficient. This is the case if an efficient probe-quencher pair is employed that distributes quantitatively to the micelles, and if the aggregation numbers to be determined are small, ≤ 120.[31] TRFQ showed no sign of migration between probe and quencher for any of the solutions investigated, as the semilogarithmic decay curves with and without added quencher at longer times were parallel, that is, equations 2:1−4 are valid. The quenching rate constant was in all cases larger than 3×10^7 s^{-1}. The use of TRFQ thus monitors the presence of micelle-shaped clusters, or aggregates of finite sizes, which can be considered as zero-dimensional entities as monitored by fluorescence quenching. Since the concentration of micelles in the solutions is high—up to 10 mM—compared to the highest quencher concentration that can be used practically, which is $\leq 5 \times 10^{-4}$ M, the effect of added quencher is quite small. Therefore the aggregation numbers presented here were finally determined by SSFQ since fitting a quenched decay time curve by global analysis only with very low $\langle n \rangle$ available gives a higher error than using steady-state luminescence, which has a very high signal-to-noise ratio.

Results and Discussion

A characteristic feature of nonionic cellulose ether/water systems is the existence of reversible phase separation including a lower critical solubility temperature, LCST, also denoted cloud point, CP, above which the solution becomes "cloudy". At the CP the polymer precipitates out of solution as a consequence of equal chemical potentials between two phases, one richer in polymer, of solute and solvent, respectively.[32] Thus CP provides a simple and powerful tool for qualitative characterization of the polymer thermodynamics in systems with LCST behavior and their interactions with low molecular amphiphiles. A more hydrophobic cellulose ether will have a lower CP than a more hydrophilic one. The EHEC fraction CST-103 in this study is more hydrophobic than the HPMC fraction as can be seen in Figure 1, where CP is plotted as a function of the ibuprofen concentration. The CP values for the binary 0.1% EHEC/water and 0.1% HPMC/water systems are 29 and 45 °C, respectively. When ibuprofen is added, the systems diverge even more. The CP of HPMC increases with increasing ibuprofen concentration, slowly at first, and with an increasing positive derivative in the ibuprofen concentration range 150−200 mM. The EHEC fraction on the other hand has an unaffected CP up to 80 mM ibuprofen and then passes through a minimum at 150 mM whereafter CP increases steeply. Both polymers thus interact with ibuprofen which at higher drug concentrations markedly increases the solubility of the polymers. The reason for this is the formation of a micellar ibuprofen phase into which the polymers solubilize their hydrophobic parts. Similar CP curves have been reported for these cellulose ethers in the presence of sodium dodecyl sulfate, SDS.[20,33] From these CP data a rough estimate of cmc of ibuprofen in the presence of the polymer fractions can be made; its value is found to be about 150−200 mM for both EHEC and HPMC. The minimum in CP observed for the EHEC/ibuprofen system is most likely a salting-out effect due to a combination of a quite hydrophobic polymer and the considerable ionic strength from >100 mM of the sodium salt of ibuprofen, resulting in conformational changes of the polymer. The salting-out effect is further illustrated by the addition of NaCl (not shown in figure) which lowers CP over the whole drug concentration span for both polymers. An interesting effect is the difference in derivatives of the CP curves between the polymer concentrations, at higher drug concentrations. For both polymers, the derivative is higher at 0.1% polymer than at 0.5% polymer. This is a composition-dependent effect as it takes more ibuprofen to increase CP by one degree by solubilization, if more polymer is present in the solution.

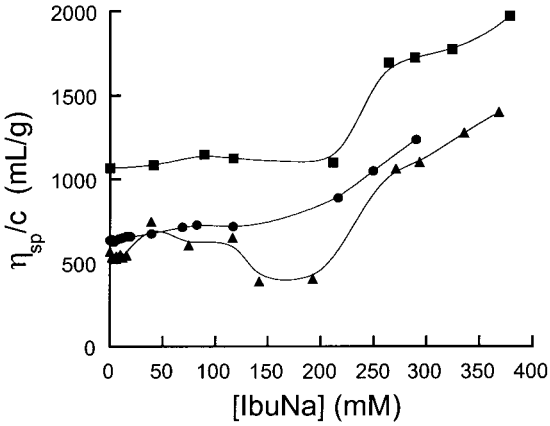

Figure 2—The reduced viscosity, η_{sp}/c, for the EHEC/ibuprofen-system as a function of the ibuprofen concentration, [IbuNa], for ▲ 0.1%, ● 0.2% and ■ 0.5% EHEC at 20 °C.

Capillary viscometry is another experimentally simple but very powerful method to explore semidilute polymer systems since aggregation phenomena most often affect the hydrodynamic flow properties, especially in polymer−amphiphile systems.[5] The EHEC/SDS/water system, for example, shows a maximum in the reduced viscosity close to the onset of polymer−surfactant interaction with respect to the surfactant concentration, for certain compositions, due to network formation.[6] The reduced viscosity for the EHEC/ibuprofen/water system is shown in Figure 2. The system HPMC/ibuprofen/water follows the same trends although the effects with this more hydrophilic polymer are smaller. Not shown in the figure but important to note is that the relative viscosity of the binary ibuprofen/water system is close to 1 for the whole concentration range investigated. The formation of pure ibuprofen micelles, as expected, was thus not measurable by capillary viscometry. No data are shown between approximately 100 and 200 mM ibuprofen because of the phase separation, cf. Figure 1. For the polymer concentrations shown in Figure 2, the reduced viscosity increases at higher drug concentrations above cmc. This evidence for EHEC−ibuprofen interaction is most likely an effect of the extension in space of the polymer chains, i.e., an increase in hydrodynamic volume, as these solubilize into ibuprofen micelles. For the lowest EHEC concentration, 0.1%, there is a decrease in the reduced viscosity prior to the cmc, which is coupled to the salting-out effect as discussed above. The polymer shrinks in this region of composition, with a notable effect on the reduced viscosity since the polymer concentration is here below the critical overlap concentration, c^*. c^* is the onset of polymer coil−coil entanglement with respect to the polymer concentration. A similar effect, also due to in-

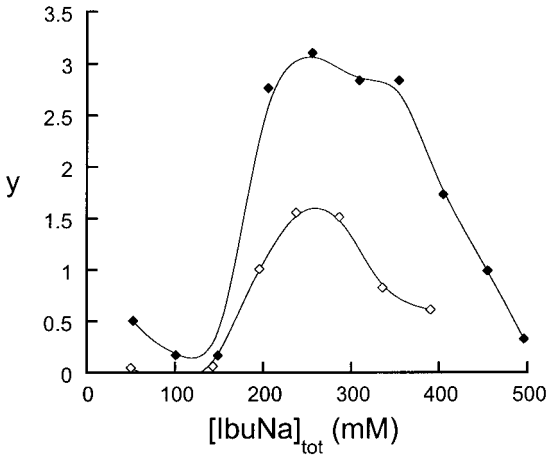

Figure 3—Equilibrium dialysis data for ◆ 1.0% EHEC, and 1.0% ◇ HPMC at 20 °C. y, mmoles of iboprofen bound per gram polymer as a function of the total concentration of ibuprofen, $[IbuNa]_{tot}$.

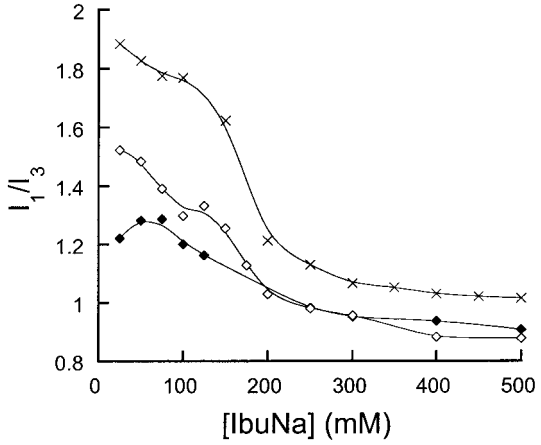

Figure 4—The micropolarity index, I_1/I_3, of pyrene in: × water solutions of ibuprofen, ◆ the ibuprofen/1.0% EHEC/water system, and ◇ the ibuprofen/1.0% HPMC/water system, as functions of the ibuprofen concentration, [IbuNa], at 20 °C.

tramolecular aggregation with respect to EHEC, but most likely not by salting-out, has been reported for the 0.1% EHEC/SDS/water system.[6] The absolute values in reduced viscosity, ≤2000 mL/g for 0.5% EHEC, are low compared to that of the maximum detected for the EHEC/SDS/water system, about 3800 mL/g for 0.3% EHEC,[6] indicating a more flexible network with weaker intermolecular tie points for the present system under study. Only 5 mM of SDS is present at the maximum in reduced viscosity in the EHEC/SDS system, which suggest that the surfactant act as "connector" between hydrophobic sites on the polymer chains. In the case of ibuprofen, more than 200 mM is present at the higher values in reduced viscosity. Furthermore, the values of reduced viscosity for the EHEC/SDS system drop well below 1000 mL/g at higher SDS concentrations, whereas there is an increase in the reduced viscosity for the EHEC/ibuprofen system instead, above 1000 mL/g. One interpretation is that SDS molecules at higher amphiphile concentrations more effectively "dress" the hydrophobic parts of EHEC and hereby the intermolecular ties between the EHEC chains diminish, as compared to ibuprofen which has a lower surface activity and also is a sterically more hindered molecule with its aromatic ring.

The adsorption of ibuprofen to the two polymer fractions was determined by equilibrium dialysis according to the principle employed for the SDS/cellulose ether/water systems previously studied.[6,18−20,22,33] The adsorption isotherm expressed as the number of millimoles of ibuprofen bound per gram of EHEC, *y*, as a function of the ibuprofen concentration, is shown in Figure 3. Significant amounts of ibuprofen bind to EHEC at [IbuNa] ≥ 150 mM. There is a positive second derivative in the adsorption isotherm up to about 180 mM ibuprofen, and then there follows a steep cooperative binding to $y = 3$ at an ibuprofen concentration of just above 200 mM. After this, *y* levels off on a plateau and then decreases again after 350 mM ibuprofen. The adsorption isotherm of HPMC is similar to that of EHEC up to $y = 1.5$ and then decreases. At the maximum in *y*, about 15% at most of the total amount of ibuprofen is EHEC-bound ($c_p y = 30$, cf., eq 1). This is to be compared with the adsorption of SDS onto 1% EHEC which reaches a maximum of $y = 3$ when about 75% of the total amount of SDS present in the solution is adsorbed (unpublished results). There is a major difference between a polymer−surfactant system such as EHEC/SDS and the EHEC/ibuprofen system. The former usually shows an onset of surfactant−polymer aggregation with respect to the surfactant concentration (usually denoted cac, critical aggregation concentration) well below the cmc for the corresponding binary surfactant/water system.[5] The maximum in adsorption is here typically reached before any ordinary micelles are formed in the solution. The EHEC/ibuprofen system, on the other hand, reaches the maximum in *y* at concentrations exceeding the ordinary cmc. This suggests a weaker mechanism of binding in the latter system, in accordance with the argument that the value of cac is a measure of the thermodynamic strength of polymer−amphiphile adsorption, cac being lower for a stronger binding.[5] In short terms, SDS forms micelles onto EHEC polymer chains below the cmc of SDS, whereas ibuprofen first forms micelles into which EHEC distributes. There is, however, significant adsorption of ibuprofen onto EHEC from about 150 mM before free "ordinary" micelles of ibuprofen start to form in the solution, with a cooperative binding as a result. A small significant binding of ibuprofen onto EHEC is also observed below 100 mM ibuprofen. This suggests that premicellar ibuprofen clusters form on the EHEC chains, and the result is consistent with the fluorescence data discussed below. After the maximum, dialysis adsorption isotherms generally show a decrease in *y*, as is the case also for the EHEC/SDS/water system.[20] The reason for this cannot be fully explained, but the membrane dialysis system tends to equilibrate by increasing the concentration of amphiphile on the side of the dialysis membrane having no polymer, as soon as free micelles are present in the solution. Thus, although it is unclear whether the entire decrease in *y* is a true redistribution from bound to free micelles, the dialysis experiments in this higher concentration region monitor a change in interaction between ibuprofen and the cellulose ethers—stronger for EHEC than for HPMC in accord with the higher hydrophobicity of the former.

Fluorescence probe techniques have been utilized in this study to give information on micellar sizes and characteristics. The fine vibrational emission spectrum of pyrene is sensitive to the polarity of the immediate surroundings of the probe,[23] see the Experimental Section. The micropolarity index I_1/I_3 is presented as a function of the ibuprofen concentration in Figure 4. The binary ibuprofen/water system gives values of $I_1/I_3 \approx 1.8$ for low drug concentrations, indicating a polar probe environment close to that of water. At intermediate ibuprofen concentrations there is a steep drop in I_1/I_3 down to ≈1.0 to 1.1 which indicates formation of micelles. These values are comparable to those of pyrene dissolved in most common surfactant micelles.[23] The cmc, as taken at the inflection point of the sigmoidal drop of the curve, is about 180 mM. In the presence of 1%

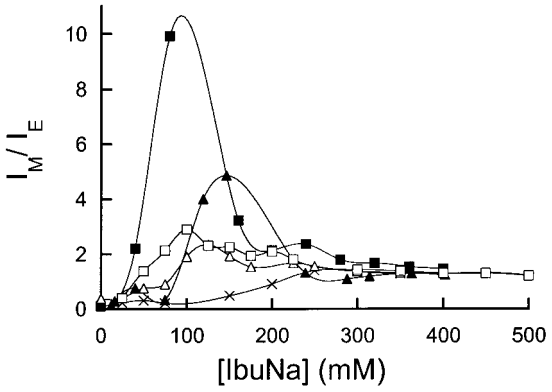

Figure 5—The microviscosity inex I_M/I_E of P3P as a function of the ibuprofen concentration, [IbuNa], at 20 °C. × no polymer present; ▲ 0.1% EHEC; ■ 0.5% EHEC; △ 0.1% HPMC, □ 0.5% HPMC.

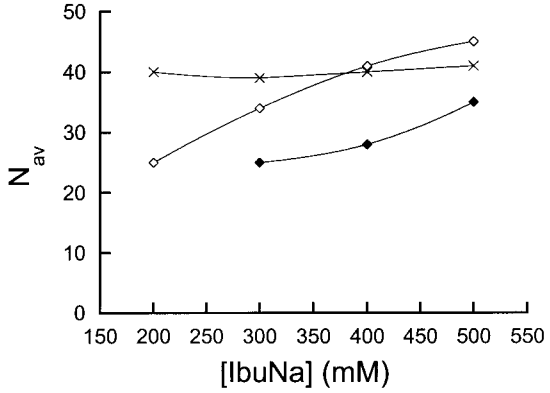

Figure 6—Average aggregation numbers of the total ensemble of ibuprofen micelles formed in solution, N_{av}, as a function of the ibuprofen concentration, [IbuNa], at 20 °C. × no polymer present; ◆ 1.0% EHEC; ◇ 1.0% HPMC.

polymer, the general trend with a drop in I_1/I_3 at cmc remains, but the absolute values are now lower. The HPMC sample gives $I_1/I_3 \approx 1.5$ at 25 mM ibuprofen and levels off at 0.9 at the higher drug concentrations. Hence, 1% HPMC mediates a more hydrophobic environment for the ensemble of pyrene molecules throughout the composition interval (25−500 mM ibuprofen). There is, for this curve, a significant decrease in I_1/I_3 in the ibuprofen concentration range 25−100 mM which can be interpreted as adsorption of ibuprofen onto HPMC in this composition interval. The more hydrophobic sample EHEC, fraction CST-103, gives even lower values of I_1/I_3 at ibuprofen concentrations below cmc than that of HPMC, suggesting that EHEC forms more polymer-dense mixed clusters with less water penetration. Pyrene thus monitors a complex interaction pattern of ibuprofen with both polymer samples starting at low ibuprofen concentrations in the range 25−50 mM.

The onset of polymer−ibuprofen interaction can also be investigated by the fluorescent microviscosity probe P3P. As further outlined in the Experimental Section, the intramolecular monomer-to-excimer emission intensity ratio, I_M/I_E, is a qualitative index of the microviscosity at the site of solubilization of the ensemble of probe molecules.[25] For a set of cellulose ethers of varying hydrophobicity, it was found that the onset of SDS−polymer interaction with respect to the surfactant concentration, here denoted c_1, as monitored by an abrupt increase in I_M/I_E, correlated with a similar abrupt decrease in I_1/I_3 for each polymer sample, as monitored by pyrene.[26] I_M/I_E is presented in Figure 5 as a function of the ibuprofen concentration in the absence as well as presence of polymer. The binary system ibuprofen/water displays an increase in I_M/I_E at cmc from about 0.2 to 1.5, an increase comparable in magnitude to that of SDS (up to about $I_M/I_E = 1$).[8] The reason for ibuprofen micelles being slightly more rigid than SDS micelles as monitored by P3P, might have its origin in the stiff aromatic ibuprofen molecule as compared to the more flexible hydrocarbon tail of SDS. Furthermore, the flat aromatic pyrene entities of P3P might associate to the aromatic ring of ibuprofen, with a decrease in the degrees of freedom for P3P. The ternary EHEC/ibuprofen/water and HPMC/ibuprofen/water systems display qualities similar to the corresponding polymer/SDS/water systems,[26] including a well-developed maximum in I_M/I_E right after c_1 and a lower plateau in I_M/I_E at higher amphiphile concentrations. The maximum in microviscosity corresponds to, as argued earlier,[8] mixed micelles or clusters with a high molar ratio polymer/ibuprofen which effectively hinders the molecular motion and excimer formation of P3P. At higher ibuprofen concentrations, the mixed micelles have a lower molar ratio polymer/ibuprofen—the mixed micelles now resemble free not polymer bound micelles—which increases the molecular mobility of P3P. Also, the fraction of micelles not bound to the polymer at higher ibuprofen concentrations is large, and much larger than in the EHEC/SDS case,[8] which tends to shift the value of I_M/I_E toward that of ordinary free micelles. The numerical value of the maximum of I_M/I_E for the 0.5% EHEC sample is about 10. This is more than three times the maximum value in I_M/I_E observed for the 0.5% HPMC sample, which is about 3. Consequently, as monitored by P3P, EHEC forms more rigid and dense mixed polymer−ibuprofen micelles than HPMC, in the lower ibuprofen concentration regime. This finding is in accord with the higher hydrophobicity of EHEC, and correlates with the values of I_M/I_E for the corresponding polymer/SDS/water systems.[26] P3P, like pyrene, monitors the onset of polymer−drug interaction to be in the range 25−50 mM ibuprofen for both polymer samples. Figure 5 also illustrates that a maximum in microviscosity does not need to be coupled to a maximum in bulk viscosity, cf., Figure 2. The former will definitely affect the transport properties of drug molecules in solution, but might pass undetected by only using conventional rheological methods.

The average aggregation numbers of ibuprofen micelles—the average number of ibuprofen molecules per micelle—were determined by a combination of static and time-resolved fluorescence quenching as described in the Experimental Section. In the model calculation of the aggregation numbers the cmc of ibuprofen is taken to be 180 mM throughout the calculation in accord with the data shown above. This assumption is probably not totally correct as there might be a redistribution of free ibuprofen monomers into micelles above the cmc, but the calculation still gives a good estimate of the micelle sizes and shows the effect of the presence of polymer in the system. As can be seen in Figure 6 where the average aggregation numbers of all micelles present in the system, N_{av}, are plotted as a function of the ibuprofen concentration, N_{av} for the binary system ibuprofen/water remains about 40 in the concentration range investigated. This is in accord with the start−stop process signifying micellization including a certain micelle size distribution for a certain solute, solvent, temperature, and ionic strength.[5] The ibuprofen micelles are comparable in size with many surfactant micelles, e.g., SDS, which have aggregation numbers in the range 60−70 as monitored by the same technique.[5] Turning next to the ternary 1% cellulose ether/ibuprofen/water systems, no aggregation numbers could be determined at 100 mM ibuprofen since not enough quencher could be solubilized in the clusters for accurate determinations. At 200 mM and 300 mM ibuprofen, the total micelle concentrations are significantly higher if 1% HPMC is present in the solutions as compared to the polymer-free case, cf., Table 1. This is

Table 1—Total Micelle Concentrations [micelle] (mM)

[IbuNa] (mM)	no polymer present	1% EHEC	1% HPMC
200	0.49	-	0.79
300	3.11	4.70	3.58
400	5.48	7.82	5.36
500	7.87	9.21	7.11

an indication of polymer-bound micelles which alter the micellar concentrations. The effect is smaller average aggregation numbers including both polymer-bound and free micelles, N_{av}, as presented in Figure 6. At 400 mM and 500 mM ibuprofen, the effect of HPMC on N_{av} diminish, suggesting the total ensemble of micelles at these high drug concentrations to be similar to the binary ibuprofen/water system, in accord with the P3P data of Figure 5. The more hydrophobic polymer sample EHEC CST-103 affects the micellar concentrations and hence N_{av} to an even larger degree, which seems correct as EHEC binds more ibuprofen ($y_{max} = 3$) than HPMC does ($y_{max} = 1.5$) as shown by the dialysis experiments. At higher ibuprofen concentrations, N_{av} for the EHEC/ibuprofen system also strives toward that of the binary system. The aggregation numbers of polymer-bound micelles are hence smaller than free micelles, an observation in line with the corresponding cellulose ether/SDS systems.[7,22] An illustrative example of this is the 300 mM ibuprofen/1% EHEC solution. The EHEC-bound ibuprofen concentration is, with $y = 3$ from Figure 3, 30 mM. This gives, with the cmc = 180 mM, 90 mM of ibuprofen incorporated into free micelles. With a total micelle concentration from Table 1 of 4.70 mM and $N_{av} = 40$ for free micelles, the average aggregation number of polymer-bound micelles becomes 12.

Conclusion

The aggregation behavior of ibuprofen in aqueous solution, with and without addition of interacting polymer, can be well-characterized by a combination of phase equilibrium data, adsorption isotherms, rheology measurements, and fluorescence probe investigations. It is shown that cmc of ibuprofen in pure water is 180 mM, and that above cmc, micelles are formed which resemble ordinary surfactant micelles, as monitored by fluorescence quenching and microviscosity measurements. In the presence of a cellulose ether, adsorption to the polymer occurs below cmc, but the strong cooperative part of the adsorption coincides with the normal cmc, in contrary to the normally accepted model for polymer−surfactant interaction.[5] The more complex interaction pattern of the ibuprofen−cellulose ether system might be mediated by the ionic strength which varies considerably in the investigated ibuprofen concentration interval (0−500 mM) and thus changes the system with changed drug concentration. The present study was undertaken to provide a background for transport studies in drug−polymer systems. Obviously the results obtained indicate that since, for instance, aggregation numbers and microfluidity of the mixed polymer−drug micelles can vary considerably as a function of composition these facts must be taken into account in order to correctly describe the irreversible process of mass transport in drug release from such systems.

References and Notes

1. Attwood, D.; Florence, A. T. *Surfactant Systems*; Chapman & Hall: Bristol, 1983.
2. Florence, A. T.; Attwood, D. *Physicochemical Principles of Pharmacy*, 3rd ed.; Macmillan: London, 1998.
3. Greminger, G. K. J.; Krumel, K. L. Alkyl and Hydroxyalkylcellulose. In *Handbook of Water-Soluble Gums and Resins*; Davidson, R. L., Ed.; McGraw-Hill: New York, 1980; p 3.
4. Persson, B.; Nilsson, S.; Sundelöf, L.-O. On the Characterization Principles of Some Technically Important Water Soluble Nonionic Cellulose Derivatives. Part II: Surface Tension and Interaction With a Surfactant. *Carbohydr. Polym.* **1996**, *29*, 119.
5. *Interactions of Surfactants with Polymers and Proteins*; Goddard, E. D., Ananthapadmanabhan, K. P., Eds.; CRC Press: Boca Raton, 1993.
6. Holmberg, C.; Nilsson, S.; Singh, S. K.; Sundelöf, L.-O. Hydrodynamic and Thermodynamic Aspects of the SDS-EHEC−Water System. *J. Phys. Chem.* **1992**, *96*, 871.
7. Nilsson, S.; Holmberg, C.; Sundelöf, L.-O. Aggregation numbers of SDS micelles formed on EHEC. A steady-state fluorescence quenching study. *Colloid Polym. Sci.* **1995**, *273*, 83.
8. Evertsson, H.; Nilsson, S. Microviscosity in Clusters of Ethyl Hydroxyethyl Cellulose and Sodium Dodecyl Sulfate Formed in Dilute Aqueous Solutions as Determined with Fluorescence Probe Techniques. *Macromolecules* **1997**, *30*, 2377.
9. Gaikar, V. G.; Latha, V. Hydrotropic Properties of Sodium Salt of Ibuprofen. *Drug Dev. Industr. Pharm.* **1997**, *23*, 309.
10. Fini, A.; Zecchi, V.; Rodriguez, L.; Tartarini, A. Solubility-Dissolution Relationship for Ibuprofen, Fenbufen and their Sodium Salts in Acid Medium. *Pharm. Acta Helv.* **1984**, *59*, 106.
11. Fini, A.; Zecchi, V.; Tartarini, A. Dissolution Profiles of NSAID Carboxylic Acids and their Salts of Different Counterions. *Pharm. Acta Helv.* **1985**, *60*, 58.
12. Fini, A.; Laus, M.; Orienti, I.; Zecchi, V. Dissolution and Partition Thermodynamic Functions of Some Nonsteroidal Antiinflammatory Drugs. *J. Pharm. Sci.* **1986**, *75*, 23.
13. Fini, A.; Fazio, G.; Feroci, G. Solubility and solubilization properties of nonsteroidal antiinflammatory drugs. *Int. J. Pharm.* **1995**, *126*, 95.
14. Paavola, A.; Yliruusi, J.; Rosenberg, P. Controlled release and dura mater permeability of lidocaine and ibuprofen from injectable poloxamer-based gels. *J. Controlled Release* **1998**, *52*, 169.
15. Reinwald, G.; Zimmermann, I. A Combined Calorimetric and Semiempirical Quantum Chemical Approach To Describe the Solution Thermodynamics of Drugs. *J. Pharm. Sci.* **1998**, *87*, 745.
16. Nilsson, S.; Sundelöf, L.-O.; Porsch, B. On the Characterization Principles of Some Technically Important Water Soluble Nonionic Cellulose Derivatives. *Carbohydr. Polym.* **1995**, *28*, 265.
17. Fischman, M. L.; Eirich, F. R. Interactions of Aqueous Poly(N-vinylpyrrolidone) with Sodium Dodecyl Sulphate I. Equilibrium Dialysis Measurements. *J. Phys. Chem.* **1971**, *75*, 3135.
18. Holmberg, C.; Sundelöf, L.-O. Temperature Dependence of Hydrodynamic Properties and Surfactant-Polymer Interaction in Solution. The EHEC/SDS/Water System. *Langmuir* **1996**, *12*, 883.
19. Holmberg, C. Phase conditions, hydrodynamic features and salt influence in the polymer-amphiphile interaction for the EHEC/SDS/water system. *Colloid Polym. Sci.* **1996**, *274*, 836.
20. Holmberg, C.; Nilsson, S.; Sundelöf, L.-O. Thermodynamic properties of surfactant/polymer/water systems with respect to clustering adsorption and intermolecular interaction as a function of temperature and polymer concentration. *Langmuir* **1997**, *13*, 1392.
21. Nilsson, S.; Holmberg, C.; Sundelöf, L.-O. Approach to hydrodynamic equilibrium and its time dependence in the system EHEC/SDS/Water. *Colloid Polym. Sci.* **1994**, *272*, 338.
22. Evertsson, H.; Nilsson, S.; Holmberg, C.; Sundelöf, L.-O. Temperature effects on the interactions between EHEC and SDS in dilute aqueous solutions. Steady-state fluorescence quenching and equilibrium dialysis investigations. *Langmuir* **1996**, *12*, 5781.
23. Kalyanasundaram, K.; Thomas, J. K. Environmental Effects on Vibronic Band Intensities in Pyrene Monomer Fluorescence and Their Application in Studies of Micellar Systems. *J. Am. Chem. Soc.* **1977**, *99*, 2039.
24. Evertsson, H.; Holmberg, C. Salt influence in the polymer-surfactant interaction in solution. A fluorescence probe investigation of the EHEC/SDS/water system. *Colloid Polym. Sci.* **1997**, *275*, 830.
25. Zachariasse, K. A. Intramolecular Excimer Formation With Diarylalkanes as a Microfluidity Probe for Sodium Dodecyl Sulphate Micelles. *Chem. Phys. Lett.* **1978**, *57*, 429.
26. Evertsson, H.; Nilsson, S. Microviscosity in Dilute Aqueous Solutions of SDS and Nonionic Cellulose Derivatives of

Different Hydrophobicity: Fluorescence Probe Investigations. *Carbohydr. Polym.* **1998**, *35*, 135.
27. Evertsson, H.; Nilsson, S.; Welch, C. J.; Sundelöf, L.-O. Molecular Dynamics in Dilute Aqueous Solutions of Ethyl-(hydroxyethyl)cellulose and Sodium Dodecyl Sulfate as Investigated by Proton NMR−Relaxation. *Langmuir* **1998**, *14*, 6403.
28. Infelta, P. P.; Grätzel, M.; Thomas, J. K. Luminescence Decay of Hydrophobic Molecules Solubilized in Aqueous Micellar Systems. A Kinetic Model. *J. Phys. Chem.* **1974**, *78*, 190.
29. Tachiya, M. Application of a Generating Function to Reaction Kinetics in Micelles. Kinetics of Quenching of Luminescent Probes in Micelles. *Chem. Phys. Lett.* **1975**, *33*, 289.
30. Turro, N. J.; Yekta, A. Luminescent Probes for Detergent Solutions. A Simple Procedure for Determination of the Mean Aggregation Number of Micelles. *J. Am. Chem. Soc.* **1978**, *100*, 5951.
31. Almgren, M.; Löfroth, J.-E. Determination of Micelle Aggregation Numbers and Micelle Fluidities from Time-Resolved Fluorescence Quenching Studies. *J. Colloid Interface Sci.* **1981**, *81*, 486.
32. Flory, P. J. *Principles of Polymer Chemistry*; Cornell University Press: Ithaca, 1953.
33. Nilsson, S. Interactions between water soluble cellulose derivatives and surfactants. Part 1: The HPMC−SDS-water system. *Macromolecules* **1995**, *28*, 7837.

Acknowledgments

This work has been financially supported by the Swedish Natural Science Research Council and the Swedish Council for the Engineering Sciences.

JS990092U

Solubility Parameters as Predictors of Miscibility in Solid Dispersions

DAVID J. GREENHALGH,[†] ADRIAN C. WILLIAMS,*[,†] PETER TIMMINS,[‡] AND PETER YORK[†]

Contribution from *Drug Delivery Group, Postgraduate Studies in Pharmaceutical Technology, the School of Pharmacy, University of Bradford, BD7 1DP, U.K., and Bristol-Myers Squibb, Pharmaceutical Research Institute, Moreton, Merseyside, L46 1QW, U.K..*

Received March 18, 1999. Accepted for publication July 30, 1999.

Abstract □ This paper reports interactions and possible incompatibilities in solid dispersions of hydrophobic drugs with hydrophilic carriers, with solubility parameters employed as a means of interpreting results. Systems containing ibuprofen (IB) and xylitol (XYL) in varying proportions and systems of IB with other sugars and a sugar polymer were produced using solvent evaporation and fusion methods. Additionally, bridging agents were employed with IB/XYL systems to facilitate the production of a solid dispersion. Results show that IB formed no interactions with any of the sugar carriers but interacted with all the bridging agents studied. The bridging agents were immiscible with XYL in the liquid state. Results of other reported drug/carrier systems and those from the systems studied in this paper were interpreted using Hildebrand solubility parameters. A trend between differences in drug/carrier solubility parameters and immiscibility was identified with incompatibilities evidence when large solubility parameter differences exist between drug and carrier. It was concluded that Hildebrand parameters give an indication of possible incompatibilities between drugs and carriers in solid dispersions, but that the use of partial solubility parameters may provide a more accurate prediction of interactions in and between materials and could provide more accurate indications of potential incompatibilities.

Introduction

Solid dispersions have been employed to enhance the dissolution rates of poorly water-soluble drugs, including ethenzamide,[1] nifedipine,[2,3] furosemide,[4] griseofulvin,[5,6] and tolbutamide.[6,7] However, although some amorphous dispersions are currently marketed, few solid dispersions have been developed into commercial products, due to various limitations of these systems, including physical instabilities on storage[8,9] and problems of drug/carrier immiscibility.[10,11] If the drug and the carrier are incompatible, dispersion of the drug into the carrier can be problematic, with irregular crystallization, uniformity problems, and possibly little improvement in drug dissolution rate. With a hydrophobic drug the carrier must be hydrophilic to facilitate fast dissolution of the therapeutic agent into the aqueous medium of the gastrointestinal tract. In this paper solid dispersions of ibuprofen (IB) with various sugars and polymer carriers were investigated. Results were interpreted in terms of solubility parameters, an approach which was extended to literature reports of similar systems in order to probe the applicability of this method for predicting drug/carrier compatibility.

Cohesive energy represents the total attractive forces within a condensed state material and can be defined as the quantity of energy needed to separate the atoms/molecules of a solid or liquid to a distance where the atoms or molecules possess no potential energy, i.e., no interactions occur between atoms or molecules. Further, cohesive energy density (CED) is the cohesive energy per unit volume. The CED for a material can be used to predict its solubility in other materials; if two components have similar values, they are likely to be soluble in each other, since interactions in one component will be similar to those in the other component. Thus, the overall energy needed to facilitate mixing of the constituents will be small, as the energy required to break the interactions within the components will be equally compensated for by the energy released due to interactions between unlike molecules. In addition, CED values can be transformed into Hildebrand solubility parameters (δ), defined as the square root of the CED,

$$\delta = (\mathrm{CED})^{0.5} = (\Delta E_v/V_m)^{0.5} \quad (1)$$

where ΔE_v is the energy of vaporization and V_m the molar volume.

Solubility parameters are widely used to describe the cohesive forces within materials and have been used to describe many physical properties of a material and predict interactions between materials.[12−14] The use of solubility parameters to predict solubility/miscibility is attractive and can be applied to low molecular weight materials and polymers. Solubility parameters can be evaluated by solubility studies of test materials in solvents of known solubility parameter, from refractive index values by using inverse gas chromatography, from heat of vaporization data (not suitable for many polymers), or by calculation using group contribution methods. The group contribution method was used in this paper to calculate Hildebrand solubility parameters, since these data compare well with values obtained by other methods. For example, sulfisomidine has a solubility parameter of 25.7 $MPa^{1/2}$ calculated using Fedors group contribution method and a value of 25.9 $MPa^{1/2}$ by the peak solubility method.[15] Caffeine (anhydrous) gives a solubility parameter of 28.0 $MPa^{1/2}$ using the group contribution method,[16] 28.3 $MPa^{1/2}$ by the peak solubility method,[17] and 29.9 $MPa^{1/2}$ by dissolution calorimetric measurements.[18]

Calculation of the molar vaporization energy of a material (and ultimately its Hildebrand parameter) using the group contribution method involves the summation of molar vaporization enthalpies of structural fragments in the material. The molecular volume of the material is derived from its density and molecular weight (molecular weight/density) or it can be calculated using the volume of the molecular fragment present in the material in an additive fashion similar to the calculation of vaporization energy. This enables the solubility parameter to be calculated using eq 1. An example of the calculation of solubility

* Corresponding author. Tel: +44 (0)1274 234756. Fax: +44 (0)1274 234769. E-mail: A. C.Williams@bradford.ac.uk.
[†] University of Bradford.
[‡] Bristol-Myers Squibb.

10.1021/js9900856 CCC: $18.00
Published on Web 10/01/1999

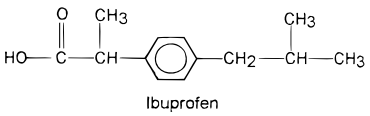

Ibuprofen

GROUP, z	^zU/kJ mol^{-1}	Σ^zU/kJ mol^{-1}	^zV/cm^3 mol^{-1}	Σ^zV/cm^3 mol^{-1}
1(COOH)	27.61	27.61	28.5	28.5
1 Phenylene	31.9	31.9	52.4	52.4
2(CH)	3.43	6.86	-1.0	-2.0
3(CH_3)	4.71	14.13	33.5	100.5
1(CH_2)	4.94	4.94	16.1	16.1
	Total	85.44	Total	195.5

$$\delta = (85440/195.5)^{1/2} = 20.9\ \text{MPa}^{1/2}$$

Figure 1—Calculation of the Hildebrand solubility parameter for ibuprofen. ^zU = molar cohesive energy. ^zV = molar volume. All group contributions to the molar vaporization energy and molar volume were obtained from Fedors.[19] Values apply at 25 °C.

parameters using the group contribution method is shown in Figure 1.

A short review of solid dispersion systems reported in the literature has been included in this paper and the Hildebrand solubility parameter has been calculated for the materials used. The aim was to report any incompatibilities between components in the solid dispersions and to use solubility parameters of the drug and carrier as a possible explanation, and subsequently as a predictor, for the incompatibilities. Hildebrand solubility parameters were also calculated for the materials used in this paper.

Experimental Section

Materials—The following materials were used as supplied: Ibuprofen (IB) (APS−Berk Pharmaceuticals, Eastbourne, U.K.), xylitol (XYL), sucrose, xylose, maltose, mannose, sorbitol, dextran 6, 40, 110 (Sigma-Aldrich Co. Ltd., Poole, U.K.), methanol HPLC grade (BDH Laboratory Supplies, Poole, U.K.), poloxamer 188 (Lutrol F68) (BASF plc, Cheadle Hume, U.K.), polysorbate 20, 40, 60, 80, and polyoxyethylene 40 stearate (Croda Oleochemicals, Hull, U.K.).

Preparation of Ibuprofen−Xylitol Dispersions—*Fusion Method*—IB (mp 75 °C) and XYL (mp 93 °C) were mixed at 1:1, 1:3, and 3:1 w/w to give batches of 5 g before heating to 130 °C for 1 h followed by immersion in liquid nitrogen (−196 °C) for 5 min. After solidification, samples were stored at room temperature in desiccators over P_2O_5 for 24 h before grinding and analysis by differential scanning calorimetry (DSC) and X-ray powder diffraction (XRPD).

Solvent Evaporation—Five gram batches of IB:XYL (1:1, 1:3, 3:1, and 1:9 w/w) were dissolved in the minimum volume of methanol at 40 °C. The solvent was removed under vacuum (850 mbar) using a rotary evaporator at 50 °C and 100 rpm. Samples were dried for 24 h under vacuum in a desiccator containing P_2O_5. The coevaporates formed were powders which were used without processing.

Ibuprofen−Xylitol Solubility/Miscibility Studies—Various compositions of finely ground IB and XYL (0.1−16% w/w) to give batches of 5 g were mixed in glass beakers. The mixtures were heated to 90 °C for 30 min and were stirred every 2−3 min. Visual inspections of the mixtures were made before the samples were heated to 120 °C for 30 min, again being stirred every 2−3 min. Further observations of the number of phases were made.

Miscibility Studies of Ibuprofen with other Sugars—Five gram samples of IB were heated in glass beakers to 130 °C. Sucrose (mp 190 °C), xylose (mp 158 °C), maltose (mp 128 °C), mannose (mp 135 °C), and sorbitol (mp 99 °C) were individually mixed with molten IB samples at a level of 1% w/w. The mixtures were stirred every 5 min and were maintained at 130 °C for 1 h. Five gram samples of maltose, sorbitol, and mannose were heated to 140 °C, whereupon 1% w/w IB was added to each sugar melt; the three mixtures were stirred every 5 min and were maintained at 140 °C for 1 h. This was not carried out with sucrose (mp 190 °C) and xylose (mp 158 °C) due to their high melting point and the rapid vaporization of IB above 150 °C, as confirmed by thermogravimetric analysis where a 12.1% weight loss in a sample of IB was noted between 150 °C and 200 °C (heating rate 10 °C/min). Samples were inspected for the presence of phase separation.

Preparation of Ibuprofen-Sugar Coevaporates—A 0.4 g sample of each individual sugar (sucrose, maltose, sorbitol) was dissolved in methanol at 65 °C, whereupon IB (1.6 g) was added and dissolved into the sugar solutions (1:4 w/w, sugar:drug). Solvent was removed on a rotary evaporator at 40 °C under vacuum. The coevaporates formed were transferred to a vacuum oven and evacuated to 850 mbar at room temperature overnight. The dried powders were used as produced. Coevaporates were stored in sealed vials at −18 °C for 24 h before characterization by DSC and XRPD.

Preparation of Ibuprofen−Dextran 40 Dispersion—IB (4.5 g, 90% w/w) and dextran 40 (0.5 g, 10% w/w) were dissolved in the minimum amount of a cosolvent mixture of ethanol:water (1:1 w/w) at 60 °C. The cosolvents were removed by rotary evaporation under vacuum at 50 °C. Samples were dried overnight in a vacuum oven evacuated to 850 mbar at room temperature. Samples were ground to a powder before characterization by DSC and XRPD.

Miscibility Study of Ibuprofen and Dextran 40—IB (5 g) was heated to 120 °C and 1% w/w dextran 40 was added; the melt was maintained at 120 °C for 1 h and was stirred every 5 min. Visual inspection of the melt was made to note if the dextran particles dissolved in the molten IB.

Preparation of Ibuprofen−Xylitol Dispersions incorporating Lutrol F68—Samples of IB:XYL:Lutrol F68 (1:8:1, 1:8.9:0.1, 0.5:9.4:0.1, and 0.5:9.45:0.05) were prepared to give batches of 5 g. The mixtures were heated to 110 °C for 30 min with stirring every 2−3 min before being allowed to cool to room temperature. All three components were molten at 110 °C (Lutrol F68, mp 55 °C). Samples of the melts were withdrawn using a heated Pasteur pipet (110 °C) and placed on a heated glass slide (110 °C) to be viewed under a microscope during cooling.

Miscibility Studies of Lutrol F68 with Ibuprofen and Xylitol—IB (2 g) was heated to 80 °C and XYL (2 g) to 110 °C in glass beakers, whereupon 25% w/w Lutrol F68 was mixed into the melts. Samples were stirred every 10 min and were maintained at their respective temperatures for 2 h before being allowed to cool to room temperature. The experiments were repeated using 10%, 5%, 2%, and 1% w/w Lutrol F68. Visual inspection of all the mixtures was undertaken when the samples were molten.

Miscibility Studies of Other Potential Bridging Agents with Ibuprofen and Xylitol—IB at 80 °C and XYL at 110 °C were individually mixed with other potential bridging agents, i.e., polysorbate 20, 40, 60, 80 and polyoxyethylene 40 stearate at 2% and 98% w/w to give batches of 4 g. Each mixture was heated in glass beakers to make visual assessment of the melts easier. Mixtures were maintained at their respective temperatures for 1 h with stirring every 5 min before being allowed to cool to room temperature. Visual inspection of all the mixtures was undertaken when samples were molten.

Preliminary Studies of the Interaction between Lutrol F68 and Ibuprofen—Various proportions of Lutrol F68 and IB (0−100% w/w) were mixed to give samples which had a total weight of 5 g. Each composition was heated to 90 °C for 30 min with vigorous stirring every 2−3 min before crash-cooling in liquid nitrogen. After cooling, samples were immediately transferred to a desiccator and stored over P_2O_5 for 24 h before characterization. The samples were left intact until analysis but were then ground with a mortar and pestle. All samples were characterized by DSC and XRPD. A 1:3 w/w IB:Lutrol F68 physical mix was also prepared and characterized by DSC and XRPD.

Characterization of Materials and Dispersions—*Visual Inspection*—Molten samples were viewed to assess phase separation. If components are immiscible, distinct boundaries between the constituents are expected, i.e., two liquid layers or possibly globules of one component in the continuous phase of the second component.

Thermal Analysis—Samples and starting materials were analyzed using a Perkin-Elmer Series 7 differential scanning calorimeter. Aluminum pierced and crimped pans were used in all analyses. Melting points, heat of fusion, and glass transition temperatures (T_g) quoted are the mean of three determinations,

unless otherwise stated. Temperature ranges and scan rates for each experiment are given with the results.

X-ray Powder Analysis—Samples were powdered in a mortar and pestle before X-ray analysis. X-ray patterns were obtained using a Siemens D5000 diffractometer (Stuttgart, Germany). Samples were scanned from 2° to 72° 2θ (sampling interval of 0.05°) at 1°/min using Ni-filtered Cu Kα radiation. Operating voltage and current were 40 kV and 30 mA, respectively. Diffractograms of the individual starting materials and solid dispersions were recorded.

Uniformity Study—A Philips PU 8740 UV/VIS Scanning spectrophotometer was used to analyze IB distribution within the 1:9 IB:XYL coevaporate. A calibration curve was constructed using six standard solutions of ibuprofen in methanol (range 2.0−30 μg/mL) analyzed at the λ_{max} of 221 nm. A rectilinear relationship between absorbance and ibuprofen concentration was obtained between 0.08 and 1.0 absorbance (correlation coefficient of 0.9983). XYL and methanol show no interference over the range 90−300 nm. Ten random samples (50 mg) of the unprocessed coevaporate were dissolved, filtered (0.2 μm membrane filter), and diluted with methanol to give a theoretical IB concentration in the range 0−30 μg/mL. Absorbance values for each sample at λ_{max} were converted to IB concentration and to IB concentration per gram of coevaporate using the respective weights of each random sample. The standard deviation and coefficient of variation of the IB content of the samples were used as a measure of homogeneity in the coevaporate.

Solubility Parameters and Review of Literature—Hildebrand parameters were calculated using the molar vaporization energies and molar volume values obtained by Fedors,[19] unless otherwise stated. These values are regarded as being less accurate estimations of cohesive energy[20] but are useful due to the great number of groups considered compared with other data sets. This is important as many drug molecules have complex structures.

The criterion for inclusion of solid dispersion systems in the review was the presentation of phase diagrams in the report of the systems. It was also important that the analysis of the phase diagram was by more than DSC alone, such as thermomicroscopy or capillary tube melting, so that immiscibility in the liquid state could be reported; this would not be detected by DSC analysis. Three systems were reported which did not include a phase diagram, but they were included primarily due to the evidence of liquid/liquid immiscibility by visual inspection. In these cases it was not the degree of immiscibility in the liquid state which was important but the fact that immiscibility had been identified. All the solid dispersion systems reviewed were classified into arbitrary compatibility categories based on their phase diagrams. The categories were from A (highest compatibility) to E (lowest compatibility).

Results and Discussion

Ibuprofen−Xylitol Systems—*Visual Analysis*—Visual inspection of all compositions of the IB:XYL fusion samples and samples from the solubility/miscibility study showed two distinct phases in the molten state. In the solubility/miscibility study, the mixtures at 90 °C showed particles of XYL undissolved in the IB melts at all compositions. Results indicate that the solubility of XYL in molten IB is below 0.1% w/w up to 120 °C.

DSC Studies—DSC scans (25−120 °C at 20 °C/min) of the resolidified IB:XYL fusion samples and coevaporates in Figure 2 show melting endotherms of IB (mp 75−78 °C) and XYL (mp 96−97 °C), in all compositions studied (1:1, 3:1, and 3:1 w/w). No evidence for interactions between drug and carrier is given by the DSC data, supporting the visual inspection of the melts that the drug and carrier are immiscible. The heat of fusion, corrected for dilution within the sample ($\Delta H_{f\,corr}$) and melting onset temperature of IB used in the study and those of IB in the fusion and coevaporate samples are in Table 1.

The onset of melting temperatures (Table 1) is essentially unchanged for IB in the fusion and coevaporate samples with xylitol, as compared with the starting material, again indicating little or no interaction between the drug and carrier. The melting endotherm of XYL in all dispersions with IB remained unchanged in terms of onset and peak melting temperatures compared with XYL alone. The similarity in melting points of the two components after fusion and coevaporation with the data for the starting materials indicates that no major degradation of the components occurred during the preparation procedure. This is also the case with all other systems examined in this work. The variability in $\Delta H_{f\,corr}$ (large standard deviation) shown in both coevaporate and fusion samples for IB is attributed to heterogeneity in the samples arising from the immiscibility.

X-ray Powder Analysis—XRPD diffractograms of fusion and coevaporate samples show both drug and carrier to be present in crystalline form. Peaks characteristic of IB and XYL are shown in all compositions and dispersion types. No shifts in peak positions for IB and XYL were noted, and no new peaks were observed. XRPD analysis of the resolidified fusion and coevaporate samples indicates two separate phases with no change in the crystal structures of IB and XYL. X-ray analysis gave no evidence of any interaction between the two components. Figure 3 shows diffractograms of IB, XYL, and two samples taken from the 1:3 IB:XYL coevaporate; one coevaporate sample shows peaks characteristic of XYL but none of IB, while the second sample from the same coevaporate shows the reverse. The results illustrate that IB and XYL do not

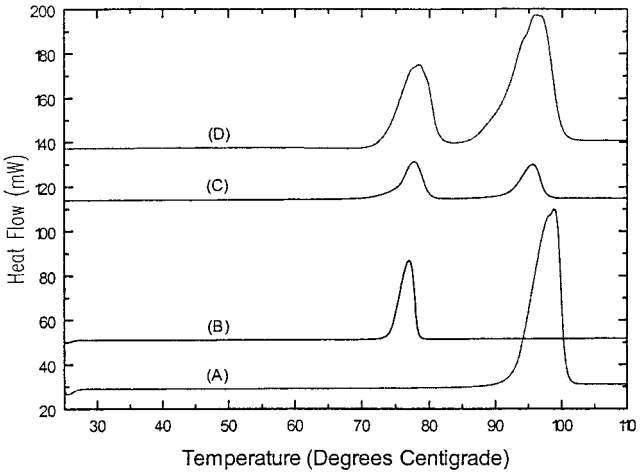

Figure 2—DSC data for xylitol alone (A), ibuprofen alone (B), 1:1 w/w IB:XYL fused sample (C), and 1:1 w/w IB:XYL coevaporate (D).

Table 1—Melting Point and Heat of Fusion of Ibuprofen in Various Solid Dispersions[a]

sample	onset of melting (°C)	melting peak (°C)	$\Delta H_{f\,corr}$ (kJ/mol)
ibuprofen	73.7 ± 0.1	75.4 ± 0.1	25.8 ± 0.2
1:1 w/w IB:XYL fusion sample	73.7 ± 0.7	78.3 ± 0.2	17.0 ± 10.0
1:3 w/w IB:XYL fusion sample	73.4 ± 0.3	76.3 ± 0.6	13.0 ± 8.0
3:1 w/w IB:XYL fusion sample	73.6 ± 0.4	79.0 ± 2.0	14.0 ± 8.0
1:1 w/w IB:XYL coevaporate	73.9 ± 0.9	77.2 ±0.5	27.0 ± 21
1:3 w/w IB:XYL coevaporate	76.0 ± 2.0	78.0 ± 2.0	33.0 ± 49
3:1 w/w IB:XYL coevaporate	74.0 ± 2.0	77.6 ± 0.8	29.5 ± 0.8
4:1 w/w IB:sucrose coevaporate	75.0 ± 2.0	80.0 ± 1.0	25.0 ± 1.0
4:1 w/w IB:maltose coevaporate	74.4 ± 0.7	78.0 ± 1.0	24.7 ± 0.1
4:1 w/w IB:sorbitol coevaporate	74.1 ± 0.4	79.6 ± 0.3	29.1 ± 0.8
9:1 w/w IB:dextran 40 coevaporate	69.7 ± 0.1	74.9 ± 0.2	19.5 ± 0.3

[a] $\Delta H_{f\,corr} = \Delta H_{obs}$ (heat of fusion of ibuprofen in sample)/theoretical % IB in sample × 100. Note: The $\Delta H_{f\,corr}$ for ibuprofen in each sample should be equivalent to the heat of fusion of the ibuprofen starting material, if ibuprofen is unaffected by the presence of excipients and the drug is uniform within the sample.

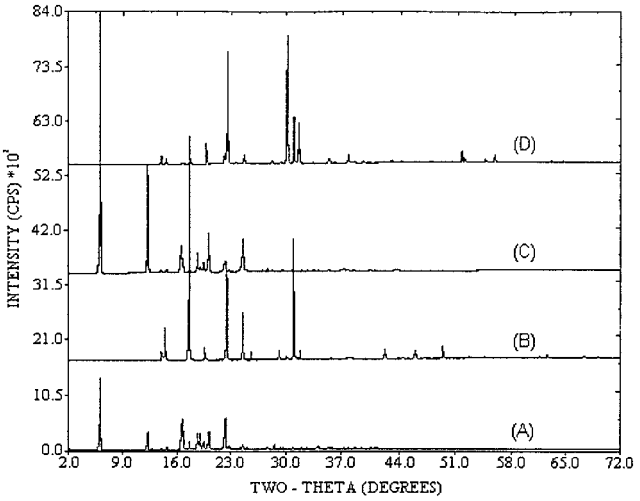

Figure 3—X-ray powder diffractograms: ibuprofen (A), xylitol (B), and IB:XYL 1:3 w/w coevaporate (C and D).

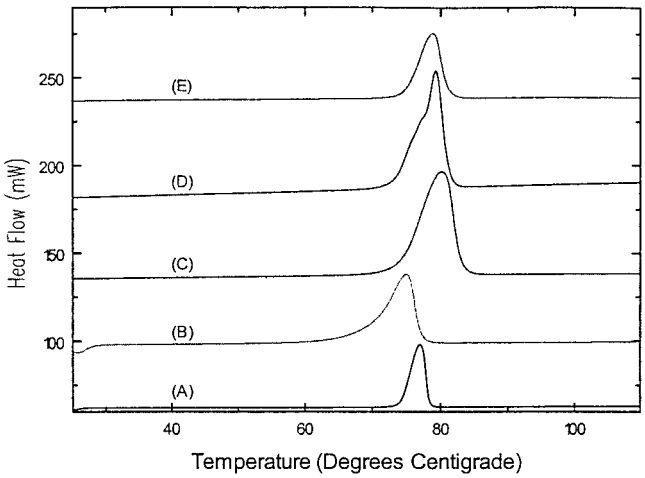

Figure 4—DSC data for ibuprofen alone (A), 1:9 w/w IB:dextran 40 coevaporate (B), 4:1 w/w IB:sorbitol (C), 4:1 w/w IB:sucrose (D), and 4:1 w/w IB:maltose (E).

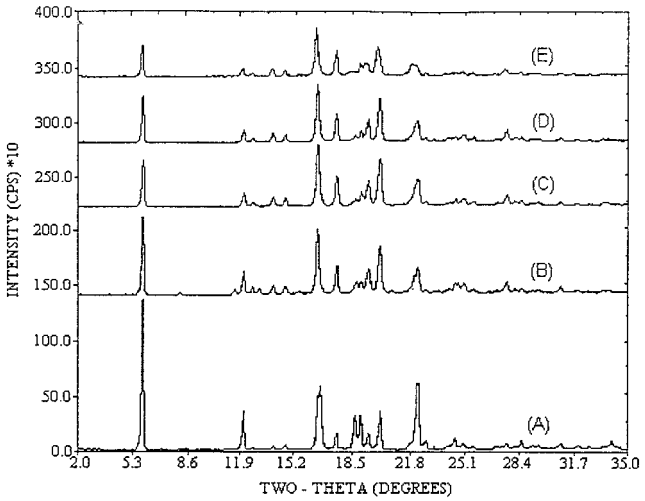

Figure 5—X-ray powder diffractograms: ibuprofen (A), IB:sucrose 4:1 w/w coevaporate (B), IB:sorbitol 1:4 w/w coevaporate (C), IB:maltose 4:1 w/w coevaporate (D), and IB:dextran 40 9:1 w/w coevaporate (E).

cocrystallize in the solvent evaporation samples, suggesting that neither drug nor carrier maintains the supersaturation of the other in solution. This would lead to the two components crystallizing out at different rates, creating isolated domains of drug and sugar.

Uniformity Study of the 1:9 IB:XYL Coevaporate—The ibuprofen content, as determined by UV spectrophotometric analysis of 10 random samples taken from the coevaporate, gave a standard deviation of ±41.9 mg/g, leading to a coefficient of variation of 64%. This shows very poor uniformity in the coevaporate at a scale of scrutiny of 50 mg (sample size). This provides further evidence of the incompatibility between IB and XYL.

Miscibility Studies of Ibuprofen with Other Sugars—*Visual Analysis*— Inspection of molten IB individually mixed with 1% w/w sucrose, xylose, and mannose showed the presence of undissolved sugar particles in all cases. Mixtures of maltose (1% w/w) with ibuprofen and sorbitol (1% w/w) with IB showed globules of sugar in the IB melts. Results show all sugars to have a solubility/miscibility below 1% w/w with ibuprofen at 130 °C. Melts of maltose, sorbitol, and mannose at 140 °C containing 1% w/w IB again show two phases with globules of IB being clearly visible.

Ibuprofen–Sugar Coevaporates—*DSC Analysis*— Coevaporates of IB:sucrose, IB:maltose, IB:sorbitol (all 4:1 w/w) were scanned from −30 to 130°C at 20 °C/min. The melting endotherm of IB was present in all three coevaporates, and the peak temperature of IB in the coevaporate remained unchanged in comparison to the starting material (Table 1). This invariance suggests that there is no disruption of the IB crystal lattice or interaction between the drug and carrier. Table 1 shows the $\Delta H_{f\,corr}$ of IB in the coevaporates to be very different from that of IB starting material. This was attributed to poor distribution of the drug in the coevaporates and correlates with the visual evidence that the sugars studied were immiscible with ibuprofen. Figure 4 shows DSC data for the IB:sugar coevaporates.

Many sugars are reported to form glasses.[21–24] No glass transition was noted over the temperature range from −30 to 130 °C for any of the sugar carriers in the coevaporates. A sample of sorbitol (5 mg) was heated in the DSC to 130 °C and maintained at this temperature for 10 min, whereupon it was cooled at 50 °C/min to −30 °C. The sample was immediately reheated in the DSC to 130 °C at 20 °C/min. A glass transition was observed at −2 °C with an associated endotherm representing the enthalpy of relaxation. Timko and Lordi[25] reported the T_g for sorbitol to be −2 °C. Maltose has been reported to have a T_g at 95 °C[24] and sucrose to have a T_g at 74 °C.[26] It must be borne in mind that glass transition temperatures can vary depending on the heating rate and with the water content of the sample.

The melting endotherms of sorbitol and maltose were not detected in the coevaporates by DSC analysis. The IB:sucrose coevaporate was not heated past the melting point of sucrose due to rapid vaporization of IB above 150 °C. The lack of melting endotherm for the sugar carriers could indicate that the sugars exist as amorphous glasses within the coevaporates. Additionally, no glass transitions were detected, probably due to the relatively low level of sugars present in the coevaporates and resulting from sampling heterogeneity due to segregation of the drug and carriers in the solid dispersions. The absence of melting endotherms for the sugar carriers is probably due to both poor homogeneity in the samples (carrier domains not sampled) and amorphous deposition of the sugars.

X-ray Powder Diffraction Studies—The X-ray diffractograms shown in Figure 5 were taken 24 h after coevaporate production. All three coevaporates produced diffraction patterns which are almost identical to each other and almost identical to that of ibuprofen starting material. The individual hydrophilic carriers cannot be easily detected

in any of the traces. Three samples of each coevaporate were analyzed by XRPD, but only one run is shown, as all the spectra produced for each coevaporate were identical. No increase in the noise level which might indicate the presence of an amorphous sugar can be seen, although the X-ray powder diffractometer may not be able to detect glassy material at a theoretical level of 20%. The XRPD data suggest that sampling and analysis of IB rich regions of the coevaporate has occurred. Segregation of the coevaporate may have occurred due to the separate crystallization of the drug and carrier.

Ibuprofen−Dextran 40 Coevaporates—*DSC Results of the Coevaporate*—Table 1 shows the melting peak temperature of IB in the dextran 40 coevaporate to be similar to the IB starting material, but the corrected heat of fusion ($\Delta H_{f\,corr}$) value is very low. The onset of melting for ibuprofen in the coevaporate is significantly lower (4 °C) compared to that of the IB starting material. The low value of $\Delta H_{f\,corr}$ is likely to be due to poor uniformity of the drug in the coevaporate; miscibility studies of IB and dextran 40 show that the two components form separate phases when mixed. The melting endotherm of IB shown in Figure 4 has a shallow onset slope which starts to rise at approximately 55 °C, this could indicate the presence of residual solvent in the coevaporate. Ibuprofen has a relatively high solubility in ethanol (1−1.5 parts ethanol[27]) and possibly forms a strong association with the solvent.

X-ray Powder Diffraction Studies—All diffractograms of the coevaporate show the crystalline structure of IB (Figure 5). One sample does show a small diffuse pattern in a diffractogram which could indicate the presence of dextran 40. X-ray analysis of dextran 40 shows it to be amorphous with no sharp diffraction peaks. Other samples do not show a significant diffuse pattern characteristic of dextran 40, indicating the absence of the carrier in the samples studied with the possibility of regions of different drug/carrier concentration being present in the coevaporate. The X-ray diffractograms show no interaction between ibuprofen and dextran 40, as no shifts in position of peaks characteristic of ibuprofen occur. No new peaks appear in any of the spectra. The intensity of peaks characteristic of IB in the dextran coevaporate are lower than the peaks in the IB starting material, even after taking into account the dilution factor of dextran 40. This could possibly be due to a decrease in IB particle size in the coevaporate or particle orientation on analysis. Several changes in relative intensities of peaks characteristic of IB are shown between the starting material and the IB−Dextran 40 coevaporate in Figure 5. Changes in crystal habit and preferred orientation of IB may have occurred in the coevaporate. If indeed this has occurred, it is debatable as to whether the presence of dextran 40 is responsible for this change. It is possible that the strong affinity of the solvent ethanol for IB has somehow modified the growth kinetics of different crystal faces on the growing IB crystals. The effect of solvent of crystallization on the morphology of IB has been shown, with needlelike crystals being produced when IB is recrystallized from hexane and more equidimensional crystals being produced when recrystallized from ethanol.[28]

Miscibility Study of Ibuprofen and Dextran 40—Inspection of the IB melt at 120 °C containing 1% w/w dextran 40 showed particles of the carbohydrate dispersed in the melt; dextran 40 is not soluble in IB under these conditions.

Ibuprofen−Xylitol Dispersions Incorporating Lutrol F68—*Microscopy*—In all cases the ternary dispersions showed two phases when molten with a dispersion of the lipophilic IB globules in the XYL continuous phase. It was noted that with the binary system of IB and XYL in the molten state, phase separation was quite distinct with two completely separate regions. Vigorous stirring of the melts created globules of one phase dispersed in the continuous phase of the second component. The dispersion was not stable and reverted to separate phases within a matter of seconds on discontinuation of stirring. The incorporation of Lutrol F68 caused visible "macroglobules" of IB in the XYL continuous phase. The dispersion of globules was relatively stable in comparison to the binary system of IB: XYL, as discontinuation of stirring did not result in complete phase separation of IB and XYL. Results suggest that the addition of Lutrol F68 has lowered the interfacial tension between IB and XYL. Microscopy highlighted the two phases and showed separate crystallization of the phases, with xylitol crystallizing first in all sample compositions. The IB phase crystallized 2−3 h after the crystallization of XYL.

DSC Analysis—Many of the samples taken from the resolidified mixtures of various ratios of drug:carrier: bridging agent only showed the melting endotherm of XYL (onset, 92 ± 1 °C, $n = 5$) when analyzed by DSC (10−110 °C at 5 °C/min). The possibility that IB and Lutrol F68 were amorphous in the dispersion was disproved with subsequent XRPD experiments and by preliminary interaction studies. The absence of melting endotherms for Lutrol F68 and especially for IB was attributed to the phase separation and heterogeneity observed by microscopy. A sample of the 1:1:8 IB:Lutrol F68:XYL dispersion showed a melting endotherm of 44 °C (onset, 39 °C), which did not correspond to the melting points of any of the components; melting onset of Lutrol F68 is 52.0 ± 0.5 °C (Figure 5). This suggested an interaction between components in the sample. This was further investigated by studying dispersions of Lutrol F68 with IB produced by the fusion method.

X-ray Powder Analysis—Diffractograms of all resolidified ternary mixtures showed heterogeneity in the samples with two phases present. Peaks characteristic of IB and XYL were identified. The absence of any shifts in peak positions or the presence of new peaks indicated no change in the crystal structures of IB or XYL in any of the dispersions. XRPD did not detect any peaks characteristic of Lutrol F68 in any of the samples.

Miscibility Studies—*Lutrol F68 with IB and XYL*—Inspection indicated that at least 25% w/w Lutrol F68 dissolved in IB at 80 °C, whereas a 1% w/w Lutrol F68 in xylitol mix showed a fine dispersion of Lutrol F68 at 110 °C.

Polysorbate 20, 40, 60, 80 and Polyoxyethylene 40 Stearate with IB and XYL—Inspection of the melts (80 °C) showed IB to be miscible with all of the bridging agents at 2% and 98% w/w, while XYL showed two phases with every bridging agent at the 2% and 98% w/w levels (110 °C).

Preliminary Interaction Studies of Ibuprofen and Lutrol F68—The resolidified IB:Lutrol F68 samples were analyzed by DSC from 0 to 120 °C at 5 °C/min. A binary phase diagram produced from the DSC curves of the dispersions showed the system to be a simple eutectic with a eutectic composition between 65 and 70% w/w Lutrol F68 (approximate mole ratio 20:1, IB:Lutrol F68) and a eutectic melting point of 37 ± 2 °C (onset temperature). This eutectic behavior between IB and Lutrol F68 has been documented previously.[29] Figure 6 shows DSC data on the physical mix and fusion samples of the IB:Lutrol F68 system. It can be seen that both the physical mix and fusion sample have a melting endotherm at approximately 37 °C. It appears that eutectic formation can occur by simply mixing. Three samples of the 1:3 w/w (slight excess of Lutrol F68) physical mix were analyzed by DSC and all show the same single melting endotherm at 39.6 ± 0.3 °C (onset temperature).

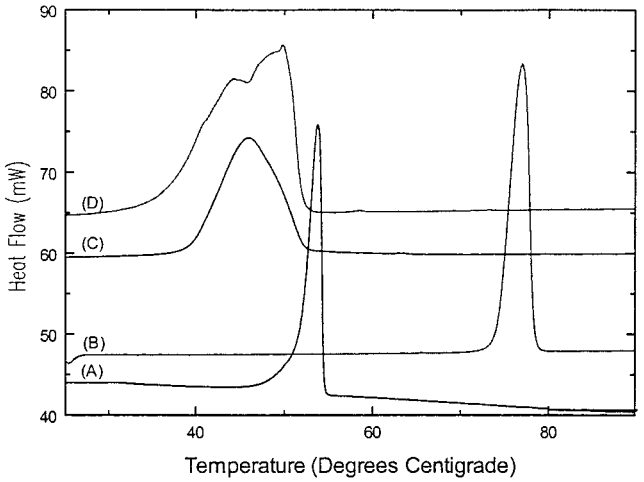

Figure 6—DSC analysis of Lutrol F68 alone (A), ibuprofen alone (B), 1:3 w/w IB:Lutrol F68 physical mixture (C), and 1:3 w/w IB:Lutrol F68 fused sample (D).

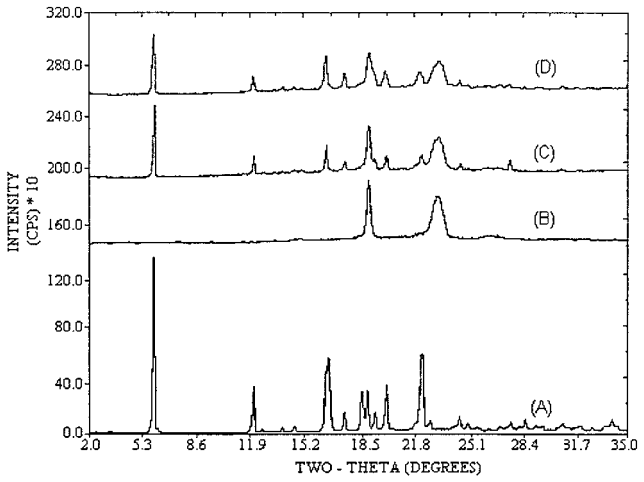

Figure 7—X-ray powder diffractograms: ibuprofen (A), Lutrol F68 (B), IB: Lutrol F68 1:3 w/w ground mixture (C), and IB:Lutrol F68 1:3 w/w fusion sample (D).

XRPD Analysis—Diffractograms of the IB:Lutrol F68 solid dispersions indicate IB to be crystalline and Lutrol F68 to be semicrystalline. Figure 7 shows traces of IB, Lutrol F68, a 1:3 w/w IB–Lutrol F68 physical mix, and fusion sample at 25 °C. Peaks characteristic of IB and Lutrol F68 can be seen in both the physical mix and fusion sample. The diffractograms of the physical mix and fusion samples in Figure 7 show that fusion of the components does not cause interactions between the drug and carrier on a bulk scale at 25 °C; crystal surface interactions may occur undetected by XRPD. Little change in crystallinity occurs on fusing the drug and carrier, as illustrated by the similar peak intensities in the traces of the physical mix and fusion sample (Figure 7). Further analysis of XRPD data from the binary system shows no shifts in peak position for IB or Lutrol F68, suggesting no changes in their bulk crystal structures. No evidence for solid solution formation between 10 and 90% w/w Lutrol F68 was found.

Solubility Parameters—Table 3 gives a list of drug/carrier systems which have been used in this and other selected studies in an attempt to produce solid dispersions of poorly water-soluble drugs. A brief description of each system, the solubility parameters of the components, and the difference in solubility parameters of the two materials are given in an attempt to identify a link between immiscibility problems and differences in the solubility parameter. The systems have been categorized in terms of miscibility, using the classification system in Table 2.

Several of the drug/carrier systems in Table 3 show a strong link between differences in solubility parameter and incompatibility. IB, tolbutamide, and nifedipine show interactions with carriers that possess similar solubility parameters (differences ranging from 1.6 to 7.0 $MPa^{1/2}$) and immiscibility problems with carriers where the difference in solubility parameter is above 10 $MPa^{1/2}$ (differences ranging from 10.8 to 18.0 $MPa^{1/2}$). The systems in Table 3 have been classified into arbitrary groups. Category B contains several different types of phase diagram, but these cannot be differentiated further by studying $\Delta\delta$. For example, 70% w/w of phenobarbital dissolves in citric acid at its melting point and $\Delta\delta$ is 4.3 $MPa^{1/2}$. Within the same category naproxen shows negligible solubility in PEG 4000 at its melting point but $\Delta\delta$ is only 3.5 $MPa^{1/2}$. From the data in Table 3 it is difficult to predict what type of phase diagram will result with drug/carrier systems where the $\Delta\delta$ is below 7.5 $MPa^{1/2}$. However, Table 3 does show a general trend in that systems with a $\Delta\delta$ ranging from 1.6 to 7.5 $MPa^{1/2}$ show complete miscibility when molten; systems with a $\Delta\delta$ from 7.4 to 15.0 $MPa^{1/2}$ show some sign of immiscibility in the liquid state, and systems with a $\Delta\delta$ above 15.9 exhibit total immiscibility over the entire composition range. The lack of a clear link between the type of phase diagram and $\Delta\delta$ where $\Delta\delta$ is relatively small (i.e. systems in category B) may relate to the accuracy of the solubility parameters quoted, especially with polymer carriers. It is also considered that Fedors' values of group contributions are less accurate than other data sets.[20] Further, Hildebrand parameters do not detail types of interactions in materials, unlike Hansen partial solubility parameters, which give the relative strengths of the dispersion forces, polar forces, and hydrogen bonding forces present in the material. If Hansen parameters were compared between drug and carrier, clearer links between partial solubility parameters and degree of miscibility may be established. The lack of a clear relationship between phase diagrams and $\Delta\delta$ may also relate to the fact that materials may exhibit two or more solubility parameters in an effort to adapt to their environment,[39] which is not accounted for with Hildebrand parameters. This can occur with materials that possess functional groups capable of hydrogen bonding; this "chameleonic effect" has been reported with sulfamethyoxypyridazine in solvents of vary-

Table 2—Classification of Miscibility

category	type of phase diagram
A	Both components completely miscible at all compositions in the liquid state. Large degree of solid/solid solubility (above 5% w/w). Complex formation.
B	Both components completely miscible at all compositions in the liquid state. Eutectic systems (immeasurable solid solution formation), where there is substantial solubility of one component in the second component at its melting point. Systems where there is a melting point depression of only the highest melting point component but negligible solubility of this material in the second component at its melting point.
C	Both components completely miscible at all compositions in the liquid state. Limited or no solubility of component A in B or B in A below melting point of either component.
D	Some degree of immiscibility when both components are in the liquid state.
E	Complete immiscibility at all proportions when both components are molten.

Table 3—Solubility Parameters and Classification of Solid Dispersions in Terms of Miscibility

drug/carrier system (category)	description	δ (MPa)$^{1/2}$	$\Delta\delta$[a]	ref
ibuprofen/PVP (A)	IB forms a 1:1 drug:polymer complex in the solid state (XRPD and DSC studies).	20.9/22.5[b]	1.6	Najib et al.[30]
chlorthalidone/urea (B)	Forms a eutectic system. Eutectic composition contained 35% w/w chlorthalidone.	32.6/38.5	5.9	Bloch et al.[31]
diazepam/PEG 4000 (B)	Forms a eutectic system. Eutectic composition contained 17% w/w diazepam.	27.4/19.9[c]	7.5	Anastasiadou et al.[32]
famotidine/xylitol (B)	Forms a eutectic system. Eutectic composition contained ca. 2.4% w/w famotidine.	29.6/37.1	7.5	Mummaneni and Vasavada[33]
flurbiprofen/PEG 400 and 6000 (B)	Forms a eutectic system by physical mixing, coevaporation, and comelting. Eutectic composition contained 35% w/w flurbiprofen with PEG 4000 and 33% w/w with PEG 6000.	23.7/19.9,[c] 23.7/19.8[c]	3.8, 3.9	Lacoulonche et al.[34]
griseofulvin/PEG 2000 (B)	Melting point depression of drug (liquidus curve), but not of PEG (solidus curve). Negligible solubility of drug in PEG at its mp. Liquidus curve meets solidus curve at 0% drug and mp of PEG. The rising liquidus curve with increasing amount of drug analogous to the solubility of the drug in molten PEG at various temperatures.	23.9/20.1[c]	3.8	Kaur et al.[35]
griseofulvin/polyoxyethylene 40 stearate (POES) (B)	Melting point depression of drug (liquidus curve), but not of POES (solidus curve). Negligible solubility of drug in POES at its mp. Liquidus curve meets solidus curve at 0% drug and mp of POES. The rising liquidus curve with increasing amount of drug analogous to the solubility of the drug in molten POES at various temperatures.	23.9/19.8[c]	4.1	Kaur et al.[35]
ibuprofen/Lutrol F68 (B)	Forms a eutectic system. Eutectic composition contained 30–35% w/w ibuprofen.	20.9/19.0[d]	1.9	Reported in this paper. Hawley et al.[29]
naproxen/PEG 4000 and 6000 (B)	Melting point depression of drug (liquidus curve), but not of PEG (solidus curve). Negligible solubility of drug in PEG at its mp. Liquidus curve meets solidus curve at 0% drug and mp of PEG. The rising liquidus curve with increasing amount of drug analogous to the solubility of the drug in molten PEG at various temperatures.	23.4/19.9, 23.4/19.8	3.5, 3.6	Mura et al.[36]
nifedipine/ethylurea ETU (B)	Melting point depression of drug (liquidus curve), but not of ETU (solidus curve). Negligible solubility of drug in ETU at its mp. Liquidus curve meets solidus curve at 0% drug and mp of ETU. The rising liquidus curve with increasing amount of drug analogous to the solubility of the drug in molten ETU at various temperatures	24.8/28.9	4.1	Suzuki and Sunada[3]
nifedipine/nicotinamide (B)	Forms a eutectic system. Eutectic composition contained 25% w/w nifedipine.	24.8/31.8	7.0	Suzuki and Sunada[3]
nifedipine/PEG 6000 (B)	Melting point depression of drug (liquidus curve) but not of PEG (solidus curve). Negligible solubility of drug in PEG at its mp. Liquidus curve meets solidus curve at 0% drug and mp of PEG. The rising liquidus curve with increasing amount of drug analogous to the solubility of the drug in molten PEG at various temperatures.	24.8/19.8[c]	5.0	Suzuki and Sunada[3]
phenobarbital/citric acid (B)	60–70% w/w phenobarbital is soluble in citric acid at its melting point. All mixtures show a single homogeneous phase when molten.	29.5/33.8	4.3	Timko and Lordi[37]
tolbutamide/PEG 2000 (B)	Melting point depression of drug (liquidus curve) but not of PEG (solidus curve). Negligible solubility of drug in PEG at its mp. Liquidus curve meets solidus curve at 0% drug and mp of PEG. The rising liquidus curve with increasing amount of drug analogous to the solubility of the drug in molten PEG.	23.2[e]/20.1[c]	3.1	Kaur et al.[35]
tolbutamide/polyoxyethylene 40 stearate (B)	10% w/w tolbutamide dissolves in POES at its melting point; liquidus curve (drug melting) meets solidus curve (POES melting) at 10% w/w tolbutamide and mp of POES. The rising liquidus curve with increasing amount of drug analogous to the solubility of the drug in molten POES at various temperatures. No mp depression of POES at any composition.	23.2[e]/19.8[c]	3.4	Kaur et al.[35]
acetaminophen/dextrose (D)	Liquid immiscibility over large composition range in phase diagram. Visual inspection of melts shows two phases. Two T_gs representing glass solution of carrier in drug in midrange of phase diagram, corresponds to two phases when both components are molten. Single T_g at low and high % drug; single phase when drug and carrier are molten.	30.8/43.1	12.3	Timko and Lordi[25]
acetaminophen/sorbitol (D)	Liquid immiscibility over large composition range in phase diagram. Visual inspection of melts shows two phases. Two T_gs representing glass solution of drug in carrier and glass solution of drug in carrier and glass solution of carrier in drug in midrange of phase diagram; corresponds to two phases when both components are molten. Single T_g at low and high % drug, single phase when drug and carrier are molten.	30.8/38.2	7.4	Timko and Lordi[25]
nifedipine/erythritol[f] (D)	At 25% w/w nifedipine, two liquid phases identified when components are molten.	24.8/35.6	10.8	Suzuki and Sunada[3]
nifedipine/urea[f] (D)	At 25% w/w nifedipine, two liquid phases identified when components are molten.	24.8/38.5	13.7	Suzuki and Sunada[3]
nifedipine/xylitol[f] (D)	At 25% w/w nifedipine, two liquid phases identified when components are molten.	24.8/37.1	12.3	Suzuki and Sunada[3]
phenobarbital/sorbitol (D)	Liquid immiscibility over large composition range in phase diagram. Visual inspection of melts shows two phases. Two T_gs representing glass solution of drug in carrier and glass solution of carrier in drug in midrange of phase diagram; corresponds to two phases when both components are molten. Single T_g at low and high % drug; single phase when drug and carrier are molten.	29.5/38.2	8.7	Timko and Lordi[25]
tolbutamide/mannitol (D)	Eutectic formation. Eutectic composition contained 94% w/w tolbutamide. Formation of two liquid phases at 40 and 80% w/w mannitol above melting point of mannitol.	23.2[e]/38.2	15.0	El-Banna et al.[11]
hexobarbital/dextrose (F)	Liquid/liquid immiscibility over complete composition range. Visual inspection of melts. Two T_gs representing pure drug and pure carrier were present over entire composition range.	27.2/43.1	15.9	Timko and Lordi[25]
ibuprofen/maltose (F)	Immiscible when both components are molten at 1% and 99% w/w; visual inspection of melts.	20.9/38.9	18.0	reported in this paper

Table 3 (Continued)

drug/carrier system (category)	description	δ (MPa)$^{1/2}$	$\Delta\delta^a$	ref
ibuprofen/sorbitol (F)	Immiscible when both components are molten at 1% and 99% w/w, visual inspection of melts.	20.9/38.2	17.3	reported in this paper
ibuprofen/xylitol (F)	Immiscible when both components are molten at 25% w/w, 50% w/w, 75% w/w and 99.9% w/w, ibuprofen	20.9/37.1	16.2	reported in this paper

[a] $\Delta\delta$ is difference in solubility parameters between drug and carrier. [b] The molar group contributions to polymer cohesive energies compiled by Van Krevelen and Hoftyzer[38] were used. These tables contain no value for the amide group in the molecule, so Fedors' value[19] for the group was used. [c] The Hildebrand solubility parameter was calculated using entire molecule. Group molar attraction constants of Van Krevelen and Hoftyzer[38] were used. [d] The Hildebrand solubility parameter for Lutrol (polyoxyethylene–polyoxypropylene–polyoxyethylene block copolymer) was calculated using molar group contributions to polymer cohesive energies compiled by Van Krevelen and Hoftyzer.[38] [e] A value for the contribution of the $-SO_2-$ group to the molar vaporization energy of the molecule was obtained from Martin et al.[15] Values for the other groups within the molecule were obtained from tables compiled by Fedors.[19] [f] Drug/carrier systems could belong to category E as the degree of immiscibility in the liquid state is not known.

ing polarity, with the drug showing solubility maxima in solvents with Hildebrand solubility parameters of 30.9 MPa$^{1/2}$ (lower solubility peak) and 20.9 MPa$^{1/2}$ (higher solubility peak). The Hildebrand solubility parameter of sulfamethoxypyridazine was calculated at 25.0 MPa$^{1/2}$ using Fedors' group contribution method.[39] Benzoic acid also shows a solubility parameter of 26.9 MPa$^{1/2}$ in highly polar solvents and 23.1 MPa$^{1/2}$ in less polar mixtures;[39] the calculated value was 24.4 MPa$^{1/2}$. Many of the drugs in Table 3 possess several polar and hydrogen bonding groups within the molecule and are probably capable of interacting with different materials in a number of different ways. The donor−acceptor capacity of hydrogen-bonding groups in drug and carrier must be considered to maximize interaction between the two materials. One further consideration when using solubility parameters is that δ may modify with temperature. It is possible that different materials will have solubility parameters which change to varying degrees with a change in temperature; these differences may become significant at high temperatures and may play a role in high melting point drug/carrier systems, for example, phenobarbital (mp 174−178 °C) and citric acid (mp 152−156 °C). Crystallinity can also have an effect on solubility parameters, as was shown by Egawa et al.,[40] where amorphous cefalexin was shown to have higher partial solubility parameters compared to a crystalline sample.

However, despite the limitations of the approach, solubility parameters may provide a simple and generic capability for rational selection of carriers in the preparation of solid dispersions. From the data generated in the present study, miscibility was shown between ibuprofen and Lutrol F68, where solubility parameters differed only by 1.9 and where a eutectic system was formed. Similarly, from the literature, ibuprofen/PVP systems where $\Delta\delta$ is only 1.6 were also completely miscible.[30] In contrast, our data have also demonstrated immiscibility where solubility parameters are markedly different; ibuprofen with maltose, sorbitol, and xylitol did not form solid dispersions and $\Delta\delta$ values were 18.0, 17.3, and 16.2, respectively. These data thus appear to support the validity of using solubility parameter differences as a tool for judicial selection of carrier components. Subsequent analysis and further refinement of this approach would need to address other factors such as crystallization inhibition by the excipient.

Conclusion

Ibuprofen has been shown to be incompatible with many sugar carriers when attempting to form solid dispersions. The coevaporate and fusion samples of ibuprofen with xylitol and the other sugar carriers show a decreased uniformity of the drug in the carrier compared to simple mixing. Both coevaporates and fusion samples must be powdered and blended to get a homogeneous dispersion. The mixing of ibuprofen with noninteracting sugar carriers may increase the drug's dissolution rate to a small extent, but overall it is probable that a drug and carrier combination where interactions between components occur will show a faster dissolution rate of the hydrophobic drug in aqueous medium. The use of bridging agents to facilitate dispersion of ibuprofen into xylitol did not prove successful, since none of the bridging agents mixed with xylitol. All bridging agents were miscible with ibuprofen.

This paper has highlighted a trend in terms of increasing degrees of immiscibility with increasing difference in solubility parameter between drug and carrier. The use of Hildebrand solubility parameters to predict compatibility has been reported by Suzuki and Sunada[41] and was found useful for selecting a suitable polymer as a component of combined carriers in solid dispersions of nifedipine. The Hildebrand solubility parameters used in this paper are relatively quick to calculate using group contribution methods and have the advantage that data for different structural groups are readily available, enabling calculation of solubility parameters for many complex drug molecules. However, it has been highlighted that the use of Hildebrand parameters in predicting accurately the phase diagram and specific level of interaction between drugs and carriers is limited. Several reasons for the observed anomalies have been discussed, including the fact that Hildebrand parameters give the overall cohesive energy in the materials but less information on the relative strengths of the various types of forces present (dispersion, polar, and hydrogen bonding). On this basis improved predictive qualities can be obtained using the Hansen partial solubility parameters (δ_d, δ_p, and δ_h). One practical problem of calculating Hansen parameters using group contribution methods is the limited data available on structural groups, thus causing difficulties for complex drug molecules. A database of partial solubility parameters for carriers and the determination of the contribution to partial solubility parameters of more structural groups found in drug molecules may enable prediction of compatible carriers which form strong associations with the drug, resulting in anticipating solid dispersion systems with fast drug dissolution rates.

References and Notes

1. Danjo, K.; Nakata, T.; Otsuka, A. Preparation and Dissolution of Ethenzamide Solid Dispersions using Various Sugars as Dispersion Carriers. *Chem. Pharm. Bull.* **1997**, *45*, 5 (11), 1840−1844.
2. Save, T.; Venkitachalam, P. Studies on Solid Dispersions of Nifedipine. *Drug Dev. Ind. Pharm.* **1992**, *18* (15), 1663−1679.
3. Suzuki, H.; Sunada, H. Comparison of Nicotinamide, Ethylurea and Polyethylene Glycol as Carriers for Nifedipine Solid Dispersion Systems. *Chem. Pharm. Bull.* **1997**, *45*, 5 (10), 1688−1693.

4. Akbuga, J.; Gursoy, A.; Kendi, E. The Preparation and Stability of Fast Release Furosemide-PVP Solid Dispersion. *Drug Dev. Ind. Pharm.* **1988**, *14* (10), 1439−1464.
5. Chiou, W. L.; Reigelman, S. Preparation and Dissolution Characteristics of Several Fast-Release Solid Dispersions of Griseofulvin. *J. Pharm. Sci.* **1969**, *58*, 1505−1509.
6. Kaur, R.; Grant, D. J. W.; Eaves, T. Comparison of Polyethylene Glycol and Polyoxyethylene Stearate as Excipients for Solid Dispersion Systems of Griseofulvin and Tolbutamide II: Dissolution and Solubility Studies. *J. Pharm. Sci.* **1980**, *69*, 1321−1326.
7. McGinity, J. W.; Maincent, P.; Steinfink, H. Crystallinity and Dissolution Rate of Tolbutamide Solid Dispersions prepared by the Melt Method. *J. Pharm. Sci.* **1984**, *73*, 1441−1444.
8. Ford, J. L.; Rubinstein, M. H. Preparation, Properties and Aging of Tablets prepared from the Chlorpropamide-Urea Solid Dispersion. *Int. J. Pharm.* **1981**, *8*, 311−322.
9. Sugimoto, I.; Kuchiki, A.; Nakagawa, H. Stability of Nifedipine-Poly(vinylpyrrolidone) Coprecipitate. *Chem. Pharm. Bull.* **1981**, *29* (6), 1715−1723.
10. Kanig, J. L. Properties of Fused Mannitol in Compressed Tablets. *J. Pharm. Sci.* **1964**, *53*, 188−192.
11. El-Banna, H. M.; Daabis, N. A.; Mortada, L. M.; Abd-Elfattah, S. Physicochemical Study of Drug Binary Systems Part 3: Tolbutamide-Urea and Tolbutamide−Mannitol Systems. *Pharmazie* **1975**, *30*, 788−792.
12. Rowe, R. C. Adhesion of Film Coatings to Tablet Surfaces − a Theoretical Approach based on Solubility Parameters. *Int. J. Pharm.* **1988**, *41*, 219−222.
13. Rowe, R. C. Interactions in Coloured Powders and Tablet Formulations: a Theoretical Approached based on Solubility Parameters. *Int. J. Pharm.* **1989**, *53*, 47−51.
14. Rowe, R. C. Polar/Nonpolar Interactions in the Granulation of Organic Substrates with Polymer Binding Agents. *Int. J. Pharm.* **1989**, *56*, 117−124.
15. Martin, A.; Wu, P. L.; Valesquez, T. Extended Hildebrand Solubility Approach: Sulfonamides in Binary and Ternary Solvents. *J. Pharm. Sci.* **1985**, *74* (3), 277−282.
16. Ticehurst, M. D. Characterisation of the Surface Energetics of Pharmaceutical Powders by Inverse Gas Chromatography. Ph.D. Thesis 1994, University of Bradford, U.K.
17. Adjei, A.; Newburger, J.; Martin, A. Extended Hildebrand Approach: Solubility of Caffeine in Dioxane-Water Mixtures. *J. Pharm. Sci.* **1980**, *69* (6), 659−661.
18. Rey-Mermet, C.; Ruelle, P.; Nam-Tran, H.; Buchmann, M.; Kesselring, U. W. Significance of Partial and Total Cohesion Parameters of Pharmaceutical Solids determined from Dissolution Calorimetric Measurements. *Pharm. Res.* **1991**, *8* (5), 636−642.
19. Fedors, R. A Method for Estimating both the Solubility Parameters and Molar Volumes of Liquids. *Polym. Eng. Sci.* **1974**, *14* (2), 147−154.
20. Barton, A. F. M. *Handbook of Solubility Parameters and other Cohesion Parameters*, 4th ed.; CRC Press Inc.: Boca Raton, FL, 1988; p 62.
21. Roos, R.; Karel, M. Water and Molecular Weight Effects on Glass Transitions in Amorphous Carbohydrates and Carbohydrate Solutions. *J. Food Sci.* **1991**, *56* (6), 1676−1681.
22. Roos, R. Melting and Glass Transitions of Low Molecular Weight Carbohydrates. *Carbohydr. Res.* **1993**, *238*, 39−48.
23. Finegold, L.; Franks, F.; Hatley, R. H. M. Glass/Rubber Transitions and Heat Capacities of Binary Sugar Blends. *J. Chem. Soc., Faraday Trans. 1* **1989**, *85* (9), 2945−2951.
24. Orford, P. D.; Parker, R.; Ring, S. G. Aspects of the Glass Transition Behaviour of Mixtures of Carbohydrates of Low Molecular Weight. *Carbohydr. Res.* **1990**, *196*, 11−18.
25. Timko, R. J.; Lordi, N. G. Thermal Analysis Studies of Glass Dispersion Systems. *Drug Dev. Ind. Pharm.* **1984**, *10* (3), 425−451.
26. Saleki-Gerhardt, A.; Zografi, G. Non-Isothermal Crystallization of Sucrose from the Amorphous State. *Pharm. Res.* **1994**, *11* (8), 1166−1173.
27. *Clark's Isolation and Identification of Drugs*, 2nd ed.; Moffat, A. C., Jackson, J. V., Moss, M. S., Widdop, B., Eds.; The Pharmaceutical Press: London, 1986; p 677.
28. Bunyan, J. M. E.; Shankland, N.; Sheen, D. B. Solvent Effects on the Morphology of Ibuprofen. *Particle Design via Crystallisation* AIChE Symp. Series, **1991**, *87* (284), 44−57.
29. Hawley, A. R.; Rowley, G.; Lough, W. J.; Chatham, S. Physical and Chemical Characterisation of Thermosoftened Bases for Molten Filled Hard Gelatin Capsule Formulations. *Drug Dev. Ind. Pharm.* **1992**, *18* (16), 1719−1739.
30. Najib, N. M.; El-Hinnawi, M. A.; Suleiman, M. S. Physicochemical Characterisation of Ibuprofen-Poly(vinylpyrrolidone) Dispersions. *Int. J. Pharm.* **1988**, *45*, 139−144.
31. Bloch, D. W.; Elegakey, M. A.; Speiser, P. P. Solid Dispersion of Chlorthalidone in Urea Phase Diagram and Dissolution Characteristics. *Pharm. Acta Helv.* **1982**, *57*, 231−235.
32. Anastasiadou, C.; Henry, S.; Legendre, B.; Souleau, C.; Duchene, D. Solid Dispersions: Comparison of Prepared Melts and Coprecipitates of Diazepam and Polyoxyethylene Glycol 4000. *Drug Dev. Ind. Pharm.* **1983**, *9*, 103−115.
33. Mummaneni, V,; Vasavada, R. C. Solubilization and Dissolution of Famotidine from Solid Glass Dispersions of Xylitol. *Int. J. Pharm.* **1990**, *66*, 71−77.
34. Lacoulonche, F.; Chauvet, A.; Masse, J.; Egea, M. A.; Garcia, M. L. An Investigation of FB Interactions with Poly(ethylene glycol) 6000, Poly(ethylene glycol) 4000 and Poly-ϵ-caprolactone by Thermoanalytical and Spectroscopic Methods and Modeling. *J. Pharm. Sci.* **1998**, *87* (5), 543−551.
35. Kaur, R.; Grant, D. J. W.: Eaves, T. Comparison of Polyethylene Glycol and Polyoxyethylene Stearate as Excipients for Solid Dispersion Systems of Griseofulvin and Tolbutamide I: Phase Equilibra. *J. Pharm. Sci.* **1980**, *69* (11), 1317−1320.
36. Mura, P.; Manderioli, A.; Bramanti, G.; Ceccarelli, L. Properties of Solid Dispersions of Naproxen in Various Polyethylene Glycols. *Drug Dev. Ind. Pharm.* **1996**, *22*, 909−916.
37. Timko, R. J.; Lordi, N. G. Thermal Analysis Studies of Glass Dispersion Systems. *Drug Dev. Ind. Pharm.* **1984**, *10* (3), 425−451.
38. Van Krevelen, D. W.; Hoftyzer, P. J. Properties of Polymers: Their Estimation and Correlation with Chemical Structure, 2nd ed.; Elsevier: Amsterdam, 1976; pp 129−159.
39. Escalera, J. B.; Bustamante, P.; Martin, A. Predicting the Solubility of Drugs in Solvent Mixtures: Multiple Solubility Maxima and the Chameleonic Effect. *J. Pharm. Pharmacol.* **1994**, *46*, 172−176.
40. Egawa, H.; Maeda, S.; Yonemochi, E.; Oguchi, T.; Yamamoto, K.; Nakai, Y. Solubility Parameter and Dissolution Behavior of Cefalexin Powders with Different Crystallinity. *Chem. Pharm. Bull.* **1992**, *40*, 819−820.
41. Suzuki, H.; Sunada, H. Influence of Water-Soluble Polymers on the Dissolution of Nifedipine Solid Dispersions with Combined Carriers. *Chem. Pharm. Bull.* **1998**, *46*, 6 (3), 482−487.

Acknowledgments

D.J.G. thanks the BBSRC and Bristol-Myers Squibb Pharmaceutical Research Institute for Financial Support. The authors also thank APS−Berk Pharmaceuticals (Eastbourne, England) for donating ibuprofen, BASF plc (Cheadle Hulme, U.K.) for the polysorbates and polyoxyethylene 40 Stearate, and Croda Oleochemicals (Hull, U.K.) for the Lutrol F68.

JS9900856

Solid-State Behavior of Cromolyn Sodium Hydrates

LINNA R. CHEN,[†,‡] VICTOR G. YOUNG JR.,[§] DAVID LECHUGA-BALLESTEROS,[||] AND DAVID J. W. GRANT*,[†]

Contribution from *Department of Pharmaceutics, College of Pharmacy, and Department of Chemistry, University of Minnesota, Minneapolis, Minnesota 55455; and Inhale Therapeutics Systems, 150 Industrial Road, San Carlos, California 94070.*

Received March 4, 1999. Final revised manuscript received July 7, 1999.
Accepted for publication August 30, 1999.

Abstract □ Cromolyn sodium (CS, disodium cromoglycate) is an antiasthmatic and antiallergenic drug. The solid-state behavior of CS is still not completely understood. CS forms nonstoichiometric hydrates and sorbs and liberates water in a continuous manner, although with hysteresis. The reported continuous changes in crystal lattice parameters of CS, which are associated with the changes in water stoichiometry, renders CS physically variable, which may complicate formulation and processing. In addition, controversies still remain as to whether CS exists as different stoichiometric hydrates, mainly because of its variable powder X-ray diffraction (PXRD) patterns (Cox, J. S. G. et al. *J. Pharm. Sci.* **1971**, *60*, 1458–65), which indicates a variable crystal structure. The objectives of this study are (a) to understand this unusual water uptake in the light of the molecular and crystal structures of CS, (b) to understand the relationship between the crystal structure and the PXRD patterns using Rietveld analysis, and (c) to investigate whether CS exists as different stoichiometric hydrates. The crystal structure of CS containing 6.44 molecules of water per molecule of CS was determined at 295 and 173 K. The packing arrangements in these structures (space group *P*1) are similar to those in a previous report, in which the water stoichiometry is 5 to 6, but the bond lengths, bond angles, and lattice parameters are different, reflecting the different water stoichiometries. In the crystal structure solved at 295 K, the position of only one of the two sodium ions could be determined. In the crystal structure solved at 173 K, the previously undetermined sodium ion is disordered over three sites, while four of eight water positions are partially occupied. The 2-hydroxypropane chain that links the two cyclic moieties of CS was found to be flexible, perhaps allowing the CS crystal to accommodate variable amounts of water. The lack of a fixed coordination site for the second sodium ion may contribute to the disorder of the water molecules. The nonstoichiometric water content of CS is mainly attributed to the water molecules that are associated with the two unoccupied sodium sites. From the PXRD patterns of CS powder, equilibrated at various relative humidities, the various lattice parameters, including previously unreported α, β, and γ values, were calculated using Rietveld analysis. The peak shifts in these PXRD patterns are quantitatively explained by slight changes in the unit cell parameters. The recently described solid forms of CS were prepared and were found to correspond to the original crystalline CS, described by Cox et al. (1971), but with contamination by the known M mesophase in various proportions. The present results support a variable crystal structure and not the existence of different stoichiometric hydrates of CS.

Introduction

Background—Cromolyn sodium (CS, the disodium salt of 1,3-bis(2-carboxychromon-5-yloxy)-2-hydroxypropane, also known as disodium cromoglycate, Figure 1), was introduced as an antiasthmatic and antiallergenic drug in 1967.[1] Despite a history of more than 30 years, the solid-state behavior of CS is still not completely understood.

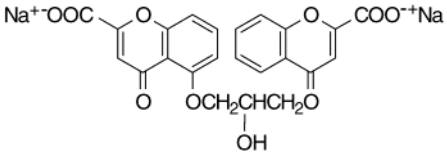

Figure 1—Molecular structure of cromolyn sodium.

In 1971, Cox et al.[2] reported that CS exists as two liquid crystalline phases (M and N) and a crystalline hydrate phase that sorbs and liberates water continuously and reversibly (although with a hysteresis loop) to give an infinite series of nonstoichiometric hydrates with a limiting composition of about 9 molecules of water per molecule of CS. The nonstoichiometric hydrate is physically unstable, in the sense that its composition changes readily as a function of the environmental relative humidity (RH). This potential for change may complicate formulation and processing. Understanding the reasons why cromolyn sodium forms nonstoichiometric hydrates, from the perspective of molecular and crystal structures, may help future preformulation and formulation of nonstoichiometric hydrates.

No polymorph of the crystalline hydrate phase was found by Cox et al.[2] The PXRD pattern of this phase was observed to change considerably with the surrounding RH, which the authors attributed to lattice expansion upon water sorption. In the same work, the lattice parameters, *a*, *b*, and *c*, of CS, were successfully calculated for RH values from 0 to 88%. However, only the changes in these lattice parameters *a*, *b*, and *c* were used to account for the shift in the PXRD peak positions. These changes alone could neither account for the peaks at small 2θ angle that correspond to *d*-spacings much larger than *a*, *b*, or *c*, nor for the observed appearance and disappearance of some PXRD peaks, because all six parameters, *a*, *b*, *c*, α, β, and γ, are actually influential. Further study is therefore needed to understand how the properties of the crystalline hydrate phase of CS change in response to the surrounding RH and to explain fully the changes in the PXRD patterns in the light of the molecular and crystal structures.

The crystal structure of cromolyn sodium with 5 or 6 water molecules per CS molecule was partially solved at room temperature by Hamodrakas et al. in 1973.[3] Unfortunately, the three-dimensional coordinates of the crystal structure were not reported or registered in any structural database. Hamodrakas et al.[3] located the positions of only one sodium ion and two water molecules and found that the other sodium ion and water molecules were disordered. Therefore, to further understand the crystal structure and to correlate it with the physical properties, redetermination of the crystal structure is necessary.

The detailed analysis of the two liquid crystalline phases, M and N, of CS, was provided by Hartshorne and Woo-

* Corresponding author. Telephone: (612) 624−3956. Facsimile: (612) 626−2125. E-mail: grant001@tc.umn.edu.
[†] Department of Pharmaceutics, University of Minnesota.
[‡] Present address: Parke-Davis Pharmaceutical Research, 2800 Plymouth Road, Ann Arbor, MI 48105.
[§] Department of Chemistry, University of Minnesota.
[||] Inhale Therapeutics Systems.

10.1021/js9900710 CCC: $18.00
Published on Web 10/06/1999

Table 1—Unit Cell Parameters[a] (space group *P*1) of Cromolyn Sodium Hydrate Equilibrated at Various Relative Humidities (RH)[8]

RH (%)	moles of water[b]	aqueous solution[8]	*a* (Å)	*b* (Å)	*c* (Å)	α (deg)	β (deg)	γ (deg)	*V* (Å^3)	R_p[c] (%)	R_{wp}[d] (%)
0	0	pure P_2O_5		~11.08	~14.6	~92.4					
6.4	2–3	LiBr	3.79	11.07	15.21	90.11	97.41	94.21	631	13.32	19.25
11.3	3–4	LiCl	3.84	11.10	15.31	90.30	97.25	94.31	646	14.67	21.89
21.6	4–5	CH_3COOK	3.91	11.17	15.41	90.05	97.60	94.37	665	10.00	12.14
32.8	4.5–6	$MgCl_2$	3.92	11.18	15.42	90.11	97.60	94.55	668	14.35	18.43
57.5	5.5–6.5	NaBr	3.93	11.19	15.55	90.07	97.22	94.63	676	7.12	9.02
75.3	6.5–7.5	NaCl	3.96	11.19	15.69	92.53	97.33	94.53	686	7.83	9.74
80.9	7–8	KBr	3.96	11.21	15.94	92.41	97.21	94.40	699	7.12	10.54

[a] The setting of the unit cell follows Hamodrakas et al.,[3] who interchanged *b* and *c* of Cox et al.[2] [b] Number of moles of water associated with 1 mol of cromolyn sodium in sorption (lower number) and desorption (higher number) from Cox et al.[2] [c] Profile residual: $R_p = \sum|y_i(o) - y_i(c)|/\sum y_i(o) \times 100\%$, where $y_i(o)$ is the observed signal and $y_i(c)$ is the calculated signal. [d] The weighted profile residual. $R_{wp} = [\sum w_i[y_i(o) - y_i(c)]^2/\sum w_i[y_i(o)]^2]^{0.5} \times 100\%$, where $y_i(o)$ is the observed signal and $y_i(c)$ is the calculated signal.

dard.[4] Their X-ray diffraction study showed that the M phase has one intense sharp peak and two faint but sharp peaks at 2.4° to 6.0° 2θ, and a broad peak at 25.5° to 26.0° 2θ. The positions of the sharp peaks were reported to vary with the water composition, while the position of the broad peak remained invariant. This X-ray diffraction study also showed that the N phase, which exists at high water compositions, gives only the broad line at 25.5 to 26.0° 2θ. The CS crystalline hydrate phase readily converts to the M liquid crystalline phase and does so reversibly under certain circumstances.[4] The conversion from the M to the N liquid crystalline phase is also rapid and reversible.[4] Mesophase N is a nematic liquid crystal, whereas M is a "middle" phase in which the molecules are arranged as rods of indefinite length, parallel to the optic axis, and with the molecular planes oriented at 90°, on average, to the axes of the rods.[4]

In 1996 and 1997, Oguchi et al.[5,6] reported two new crystalline forms of CS, termed forms B and C, and applied designation form A to the original crystalline form of CS reported by Cox et al.[2] Oguchi et al.[5,6] reported differences between these forms of CS in their powder X-ray diffraction (PXRD) patterns, moisture sorption diagrams, and differential scanning calorimetric (DSC) traces. However, doubts remain as to whether B and C are truly new crystalline forms of CS. First of all, the hysteresis in water sorption and desorption of B and C is still not well explained. Second, the sharp diffraction peaks at small 2θ angles correspond to the sharp diffraction peaks of large *d*-spacings for the M liquid crystalline phase.[4] Other differences in the PXRD patterns may be attributed to the lattice expansion caused by the uptake of nonstoichiometric water, as reported by Cox et al.[2] On the other hand, the moisture sorption diagrams of B and C show stepwise water uptake, which is a characteristic of stoichiometric hydrates. Therefore, further investigations are needed to prove or to disprove the existence of the new crystalline forms of CS. In view of these conflicting interpretations, this report seeks to clarify the solid-state behavior of CS hydrates. Because the exact nature of the reported new forms A, B, and C is not clear, they are termed materials A, B, and C in this report.

Hypotheses To Be Tested—(1) Contamination of solid cromolyn sodium hydrate phases by liquid crystalline phases can occur under certain conditions, which will complicate the PXRD patterns, the moisture sorption isotherms, and the thermal analytical data. (2) The unusual nonstoichiometric water uptake of CS can be explained in light of its particular molecular and solid-state structures.

Specific Aims of the Work—(1) To redetermine the crystal structure of CS and to locate the second sodium ion and all the water molecules, and hence (2) to explain why cromolyn sodium forms nonstoichiometric hydrates and sorbs and liberates water continuously, (3) to understand the influence of relative humidity on the PXRD patterns of CS crystalline hydrate, and (4) to investigate whether CS exists as different stoichiometric crystalline hydrates.

Experimental Section

Materials—Cromolyn sodium, in the form of hydrated white crystalline powder, was a gift from Fisons, plc, Pharmaceutical Division (now Astra Charnwood and Rhône-Poulenc Rorer, Loughborough, UK). The glass capillaries, 0.5 and 1.0 mm in diameter and 0.01 mm in thickness, used to house single crystals for structure determination and small crystallites for obtaining PXRD patterns of CS at various defined RH values, were purchased from the Charles Supper Company (Natick, MA). The silicon powder, 60 mesh, used as a peak position reference for the PXRD experiments, was obtained from Aldrich Chemical Co. (Milwaukee, WI). Methanol was obtained from Fisher Scientific (Fair Lawn, NJ). Water was deionized and glass distilled in-house.

The single crystal used for the structural determination was crystallized from a slightly supersaturated solution of CS in water + methanol mixtures (v:v = 10:9, water activity = 0.76).[7] The elemental analysis of the crystals was carried out to ascertain their sodium stoichiometry.

Elemental Analysis—The prepared single crystals were dried at 170 °C for 30 min prior to elemental analysis by Quantitative Technology (Whitehouse, NJ). The carbon and hydrogen weight percentages were calculated from the evolved carbon dioxide and water vapor upon combustion. The sodium weight percentage was determined from atomic absorption.

Preparation of the Reported Crystalline Materials of Cromolyn Sodium—The three reported[5] materials of CS were prepared here by the methods outlined[5,6] for further characterization. Material A, the original CS crystal form reported by Cox et al.,[2] was crystallized from ethanol + water mixture (v:v = 4:7, water activity = 0.88).[7] Material B was crystallized by slow diffusion of *n*-hexane + 2-propanol (v:v = 1:1) into a 10% w/v aqueous solution of CS. Material C was crystallized from ethanol + water mixture (v:v = 6:9, water activity = 0.87).[7]

Optical Microscopy—Crystals of materials A, B, and C were observed under a video-enhanced microscope (Nikon Optiphot-Pol, Tokyo, Japan) equipped with the Metamorph Imaging System software (Universal Imaging Co., West Chester, PA).

Powder X-ray Diffraction (PXRD)—The PXRD patterns of materials A, B, and C were determined under ambient condition using a powder X-ray diffractometer (D-5005, Siemens, Munich, Germany) with Cu Kα radiation at 40 mA and 45 kV. The sample was packed in a quartz holder and scanned at room temperature (23 °C) at a step size of 0.05° with a counting time of 1 s per step.

The PXRD patterns of the original CS powder[2] were determined after equilibration at defined RH values. For this purpose the CS powder was sealed in glass capillaries together with saturated salt solutions (Table 1) of known relative humidity values[8,9] and allowed to equilibrate at 23 °C for more than one week. After equilibration, the PXRD patterns were obtained using a microdiffractometer (Bruker AXS, Siemens, Munich, Germany), equipped with an area detector (HI−STAR, Siemens, Munich, Germany) and a data analysis software (General Area Detector Diffraction System, GADDS, Siemens, Munich, Germany). Cu Kα radiation at 40 mA and 45 kV was used. The diffraction data were collected

Table 2—Isotropic Temperature Factors and Occupancies of the Sodium Ions and Oxygen Atoms in the Water Molecules in the Cromolyn Sodium Structure Solved at 173 K

atom	isotropic temperature factor	occupancy[a]
Na(1)	0.0384	1
Na(2)	0.0316	0.316
Na(3)	0.0419	0.319
Na(4)	0.0518	0.365
O(12)	0.1049	1
O(13)	0.0325	1
O(14)	0.0922	0.684
O(15)	0.0940	0.681
O(16)	0.1239	0.635
O(17)	0.0623	0.439
O(18)	0.7954	1
O(19)	0.1773	1

[a] The occupancies of Na(2), Na(3), and Na(4) add up to 1. The occupancies of O(12)–O(19) add up to 6.44.

for 3000 s in a frame of 30° 2θ and a resolution of 0.02° 2θ. The sample was spun at 1 cycle per 5 s to minimize the effect of preferred orientation. At a given RH value, the same PXRD pattern was obtained when the original CS crystals were recrystallized from methanol + water mixtures (v:v = 2:1, water activity = 0.60)[7] and gently ground in an agate mortar.

Crystal Structure Determination and Refinement—An elongated crystal of CS, 0.40 × 0.20 × 0.05 mm, was covered with a thin layer of heavy oil to prevent moisture exchange with the environment, was attached to a glass fiber with epoxy resin, and was mounted on a goniometer (SMART system, Siemens, Munich, Germany) for data collection at 173 and 295 K. A cryogenic nitrogen stream was used to obtain the low temperature, 173 K. To determine the crystal structure of CS with low water content, a crystal was equilibrated at 23 °C and at 0, 11.6, or 21.6% RH for more than one month in a sealed glass capillary 0.5 mm in diameter,[10] which was then mounted on the diffractometer. An initial set of cell constants and an orientation matrix were calculated from reflections collected from three sets of 20 frames which were oriented such that the orthogonal wedges of reciprocal space were surveyed. This procedure produced orientation matrixes determined from 54 reflections. Final cell constants were calculated from a set of 3593 strong reflections of the actual data collection.

The data collection technique used was hemisphere collection. A randomly oriented reciprocal space was surveyed to the extent of 1.3 hemispheres to a resolution of 0.84 Å. Three major swaths of frames were collected with 0.30° steps in ω. Because the lattice is triclinic, some additional sets of frames were collected to provide a more accurate absorption correction.

A successful direct-methods solution (SHELX-V5.0, Siemens Industrial Automation, Inc., Madison, WI) was calculated and revealed most non-hydrogen atoms from the E-map. Several full-matrix least squares/difference Fourier cycles were performed which located the remainder of the non-hydrogen atoms. All non-hydrogen atoms were refined with anisotropic displacement parameters. All hydrogen atoms were placed in ideal positions and refined as riding atoms with individual (or group, if appropriate) isotropic displacement parameters.

Lattice Parameter Determination—The unit cell parameters of the original CS crystal form equilibrated at various RH values were refined using a Rietveld module (DBWS, Cerius 2, San Diego, CA), which interfaces with the DBWS[11] program for Rietveld refinement. Because CS gives complex diffraction patterns with severe peak overlap, it is difficult to index and to measure accurately the positions of each diffraction peak, as required for conventional unit cell parameter least squares refinements. The Rietveld method, which obtains a global least-squares fit between the calculated and the observed powder patterns, is a well-accepted method for refining accurate unit cell parameters.[12] The crystal structure of the original CS crystal form, solved at 295 K, was used as the starting trial structure. The diffraction intensities, peak shape (modeled by pseudo-Voigt profile shape function), systematic instrumental error in powder pattern measurement, and the unit cell parameters were refined.

Calculation of Theoretical Powder X-ray Patterns—The theoretical PXRD pattern of a given structure was calculated from the crystal structure using suitable software (Diffraction Simulation Module, Cerius2, San Diego, CA).

Table 3—Crystallographic Data, Data Collection, Solution and Refinement Parameters for the Crystal Structure of Cromolyn Sodium Prepared from Methanol + Water Mixtures (v:v = 9:10, water activity = 0.76) and Solved at 173 K

Crystallographic Data	
empirical formula	$C_{23}H_{26.88}Na_2O_{17.44}$
crystal habit, color	plate, colorless
crystal size	0.40 × 0.20 × 0.05 mm
crystal system	triclinic
space group	*P*1
	a = 3.8715 (3) Å, α = 92.868 (1)°
	b = 11.0771 (8) Å, β = 95.864 (2)°
	c = 15.6930 (12) Å, γ = 94.400 (2)°
volume	666.36 (9) Å^3
Z	1
formula weight	628.34
density (calcd)	1.566 Mg/m^3
absorption coefficient	0.162 mm^{-1}
F(000)	326
Data Collection	
diffractometer	Siemens SMART Platform CCD
wavelength	0.71073 Å
temperature	173 (2) K
θ range for data collection	1.31 to 25.05°
index ranges	$-4 \le h \le 4$, $-13 \le k \le 13$, $0 \le l \le 18$
reflections collected	5034
independent reflections	2329 (R_{int} = 0.0382)
Solution and Refinement	
system used	SHELXTL-V5.0
solution	direct methods
refinement method	full-matrix least-squares on F^2
weighting scheme	$w = [\sigma^2(F_o^2) + (AP)^2 + (BP)]^{-1}$, where $P = (F_o^2 + 2F_c^2))/3$, A = 0.1658, and B = 0.3236
absorption correction	SADABS (Blessing, 1995)[14]
max. and min transmission	1.000 and 0.581
absolute structure parameter	0.5 (12)
data/restraints/parameters	2327/4/419
R indices ($I > 2\sigma(I)$ = 1976)	*R*1 = 0.0825, *wR*2 = 0.2133
R indices (all data)	*R*1 = 0.0934, *wR*2 = 0.2280
goodness-of-fit on F^2	1.036
largest diff peak and hole	0.991 and –0.425 eÅ^{-3}

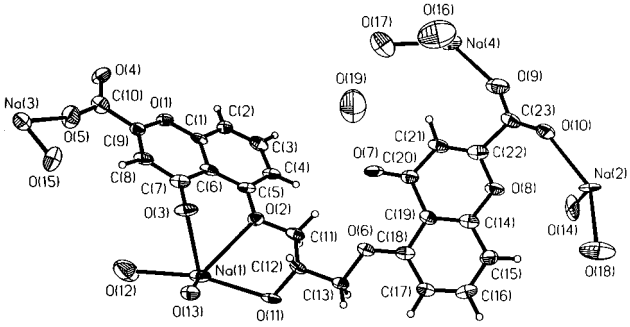

Figure 2—Thermal ellipsoid diagram, showing the atomic labeling scheme, of cromolyn sodium crystallized from methanol + water mixtures (v:v = 9:10, water activity = 0.76) and solved at 173 K.

Results and Discussion

Crystal Structure of the Original Crystalline Phase of Cromolyn Sodium—The CS structure was initially determined at 295 K and is similar to the structure previously reported.[3] The space group was determined as *P*1, a chiral space group, even though the molecule itself

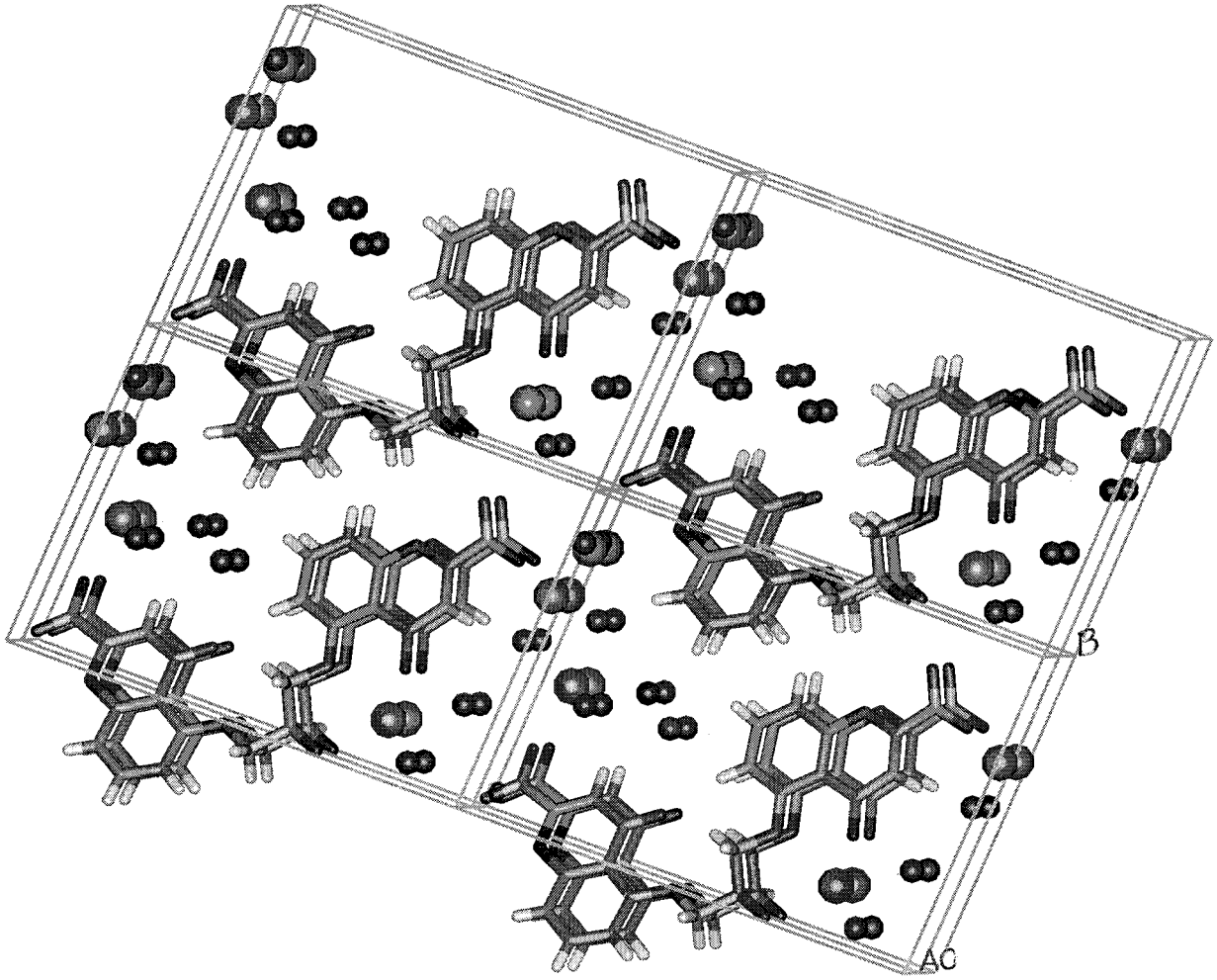

Figure 3—Crystal packing diagram, looking down the *a*-axis and showing 2*2*2 unit cells, for cromolyn sodium crystallized from methanol + water mixtures (v:v = 9:10, water activity = 0.76) and solved at 173 K. The smaller balls represent the oxygen atoms of the water molecules that have been located crystallographically, while the larger balls represent the located sodium ions.

is achiral. Examination of the molecular structure shows that the carbon atom bonded to the hydroxyl group can act as a chiral center in the crystal because the two cyclic moieties attached to this carbon are inequivalent in three-dimensional space. The CS crystallized as a racemic conglomerate of the two packing enantiomers. The structure solved at 173 K was a mirror image of the structure solved at 295 K and of that reported in the literature. Inversion was necessary for direct visual comparison of the three structures. The structures solved at 295 and 173 K were essentially identical. The intramolecular bond lengths and bond angles differed by less than 0.04 Å or 2°.

The structure was determined at 173 K in an attempt to locate all the water molecules and sodium ions. The smaller thermal motions at the lower temperature allowed better refinements of the water and sodium positions. The sodium positions are differentiated from the water positions by their coordination environment and smaller displacements (Table 2). Table 3 shows the crystallographic data and refinement parameters. Figure 2 is the thermal ellipsoid diagram with the atomic labeling scheme, while Figure 3 displays the crystal packing of 2*2*2 unit cells. Both Figures 2 and 3 show the ordered sodium ions, Na(1), and the disordered sodium ions, Na(2), Na(3), and Na(4), at 173 K, discussed in the next paragraph. Table 4 compares the intramolecular bond lengths and angles of the structure solved at 173 K with those of the structures solved at 295 K. Table 5 gives the sodium coordination distances in the structure solved at 173 K.

For the structure solved at 173 K, one sodium cation, Na(1), is tightly held in coordination with five neutral oxygen atoms of one ketone, one alcohol, and one ether group and two water molecules (Figure 4a). The second sodium ion is disordered over three partially occupied sites, Na(2), Na(3), and Na(4), in a maze of Na−O contacts (Figure 4b, c, and d, respectively). Four out of eight water positions are partially occupied. The occupancies of the sodium ions and water molecules are provided in Table 2. The three disordered sodium positions, Na(2), Na(3), and Na(4), all appear to have inferior coordination when compared to Na(1). All three disordered sodium positions have at least one water oxygen that must be displaced, due to unrealistically short contacts, if they are to occupy these sites. These contacts are Na(2)/O(14), Na(3)/O(15), and Na(4)/O(16). A restraint was used to force the sum occupancy of the three partially occupied sodium positions to unity. The occupancies of the unrealistic oxygen contacts were forced to have residual occupancy with respect to the sodium sites. Finally, O(17) appears to be partially occupied and not paired with a specific sodium ion. The total count of water molecules was 6.44 per cromoglycate anion.

Elemental analysis was deemed necessary because only one sodium ion could be located. Elemental analysis, in duplicate, afforded as follows: C 53.11, 52.97; H 2.91, 3.02; Na 8.32, 8.39%. These results agree well with those calculated from the molecular formula of cromolyn sodium: C 53.92; H 2.75; Na 8.97%. The observed differences between the experimental and the calculated weight per-

Table 4—Comparison of the Intramolecular Bond Angles and Bond Lengths of the Cromolyn Sodium Structures Reported by Hamodrakas et al.[3] at 298 K with Those Solved at 295 K and at 173 K in the Present Work

angle[a]	ref 3	295 K	173 K	bond[a]	ref 3	295 K	173 K
C6–C1–01	119.5 (1.6)	122.1	122.3 (6)	O1–C1	1.42 (2)	1.359	1.355 (10)
C6–C1–C2	122.6 (1.8)	122.1	120.5 (7)	C1C2	1.41 (3)	1.389	1.406 (11)
O1–C1–C2	117.9 (1.4)	115.8	117.2 (6)	C2–C3	1.37 (3)	1.350	1.335 (12)
C1–C2–C3	119.6 (1.7)	118.9	120.0 (7)	C3–C4	1.35 (3)	1.395	1.416 (12)
C2–C3–C4	118.8 (1.8)	121.5	122.5 (7)	C4–C5	1.42 (3)	1.369	1.404 (11)
C3–C4–C5	124.4 (1.8)	120.0	118.4 (8)	C5–C6	1.42 (3)	1.422	1.420 (12)
C4–C5–C6	118.5 (1.6)	120.6	120.3 (70	C6–C7	1.53 (3)	1.443	1.474 (11)
C4–C5–O2	128.0 (1.6)	124.0	122.8 (7)	C6–C1	1.44 (2)	1.406	1.418 (10)
C6–C5–O2	113.5 (1.5)	115.4	116.8 (2)	C7–O3	1.26 (2)	1.224	1.249 (10)
C5–C6–C1	115.8 (1.8)	116.7	118.2 (6)	C7–C8	1.44 (3)	1.438	1.432 (13)
C5–C6–C7	125.8 (1.5)	124.0	124.2 (7)	C8–C9	1.33 (3)	1.332	1.339 (11)
C1–C6–C7	118.3 (1.7)	119.2	117.6 (7)	C9–O1	1.37 (2)	1.345	1.345 (2)
C6–C7–C8	116.2 (1.5)	114.3	114.6 (7)	C9–C10	1.55 (4)	1.506	1.506 (13)
C6–C7–O3	124.5 (1.6)	124.9	122.7 (8)	C10–O4	1.25 (3)	1.226	1.229 (11)
C8–C7–O3	119.2 (1.7)	120.8	122.6 (7)	C10–O5	1.28 (3)	1.233	1.257 (11)
C7–C8–C9	120.5 (1.9)	122.7	123.6 (7)	C5–O2	1.34 (2)	1.335	1.345 (9)
C8–C9–O1	125.4 (1.8)	122.7	121.3 (7)	O2–C11	1.44 (2)	1.427	1.432 (10)
C8–C9–C10	121.0 (1.9	123.5	123.4 (7)	C11–C12	1.56 93)	1.503	1.500 (10
C10–C9–O1	113.7 (1.6)	113.8	115.3 (7)	C12–O11	1.40 (2)	1.420	1.440 (8)
C9–C10–O4	115.7 (1.9)	117.7	117.4 (7)	C12–C13	1.59 (3)	1.477	1.515 (12)
C9–C10–O5	117.9 (1.8)	115.3	115.2 (8)	C13–O6	1.40 (2)	1.432	1.443 (9)
O4–C10–O5	126.3 (2.0)	127.0	127.4 (9)	O6–C18	1.38 (3)	1.332	1.316 (10)
O2–C11–C12	102.1 (1.5)	106.7	105.7 (6)	C18–C17	1.31 (3)	1.367	1.405 (12)
C11–C12–O11	108.6 (1.5)	108.6	109.4 (6)	C17–C16	1.40 (3)	1.371	1.365 (13)
C11–C12–C13	108.6 (1.5)	111.3	111.6 (6)	C16–C15	1.34 (3)	1.371	1.363 (13)
O11–C12–C13	105.9 (1.4)	110.4	109.7 (6)	C15–C14	1.36 (3)	1.357	1.389 (13)
C12–C13–O6	99.9 (2.4)	106.9	106.0 (6)	C14–C19	1.36 (3)	1.380	1.372 (12)
C15–C14–C19	126.8 (1.7)	123.7	123.8 (8)	C14–O8	1.37 (2)	1.380	1.389 (10)
C15–C14–C8	112.7 (1.6)	115.2	113.6 (8)	O8–C22	1.31 (3)	1.326	1.367 (11)
O8–C14–C19	120.3 (1.7)	121.1	122.6 (7)	C22–C23	1.49 (3)	1.542	1.543 (11)
C14–C15–C16	117.6 (1.8)	119.0	118.3 (8)	C23–O9	1.24 (3)	1.224	1.231 (12)
C15–C16–C17	121.1 (1.8)	120.5	120.7 (8)	C23–O10	1.25 (3)	1.217	1.228 (12)
C16–C17–C18	118.7 (1.7)	120.7	121.8 (7)	C22–C21	1.28 (3)	1.320	1.326 (13)
C17–C18–O6	124.4 (1.6)	124.5	124.5 (7)	C21–C20	1.43 (3)	1.442	1.436 (11)
C17–C18–C19	124.0 (1.8)	120.1	118.1 (7)	C20–O7	1.25 (3)	1.216	1.215 (11)
O6–C18–C19	111.6 (1.7)	115.4	117.4 (7)	C20–C19	1.43 (3)	1.461	1.493 (12)
C14–C19–C18	111.5 (1.8)	115.9	117.3 (7)	C19–C18	1.45 (3)	1.435	1.430 (11)
C14–C19–C20	121.7 (1.7)	120.3	119.5 (7)				
C18–C19–C20	126.7 (1.8)	123.7	123.2 (7)				
C19–C20–O7	125.2 (1.7)	125.9	123.5 (7)				
C19–C20–C21	113.3 (1.8)	113.3	113.8 (7)				
O7–C20–C21	121.3 (1.7)	120.8	122.7 (8)				
C20–C21–C22	122.3 (1.9)	122.4	122.7 (8)				
C21–C22–O8	124.9 (1.7)	123.7	123.6 (7)				
C21–C22–C23	122.5 (1.8)	124.7	125.8 (8)				
O8–C22–C23	112.1 (1.6)	111.5	110.6 (7)				
C22–C23–O9	117.1 (1.8)	115.7	114.5 (8)				
C22–C23–O10	114.8 (1.7)	116.8	117.4 (8)				
O9–C23–O10	127.8 (1.8)	127.5	128.0 (8)				
C1–O1–C9	120.0 (1.3)	119.0	120.5 (6)				

[a] The atom parentheses are omitted for clarity.

centages were ascribed to residual moisture, which the samples may have sorbed from the ambient environment during transfer from the drying oven to the analyzer. Nevertheless, these results indicate that the sodium stoichiometry of the prepared single crystals is indeed two (not one) sodium cation per cromoglycate anion, in accordance with the requirement of charge balance. Thus, one of the sodium ions, and some of the associated water molecules, are disordered in the CS crystal structure, explaining why the location of the sodium ion cannot be refined.

In the packing diagram (Figure 3), large sodium and water channels, which occupy approximately 50% of the cell volume, can be observed parallel to the *a*-axis and perpendicular to the plane of cromoglycate anions. The presence of relatively large sodium and water channels allows easy passage of water molecules with minimum energy expenditure and minimum disruption to the packing arrangements.

The entire structure of CS, equilibrated at 295 K and at RH values of 0, 11.4, and 21.6%, could not be solved by single crystal X-ray diffraction, suggesting significant reductions in crystallinity and emphasizing that the water molecules are structural elements necessary for holding together the crystal structure. On reducing the RH, both the water content and the crystallinity decreased gradually, suggesting that the transition between the crystalline form A and the amorphous form cannot be precisely defined.

Comparison of the Unit Cell Parameters of Cromolyn Sodium Structures with Different Water Contents—The lattice parameters, expressed as a function of RH and water content (Table 1), were derived from the PXRD patterns (Figure 5) using the Rietveld method. Figure 6 compares the observed PXRD pattern with that calculated after Rietveld refinement.

As the RH in the environment decreased, the unit cell parameters, *a*, *b*, *c*, α, and the volume, *V*, also decreased

Table 5—Sodium Coordination Distances of the Cromolyn Sodium Structure Solved at 173 K. The Structure Corresponds to 6.44 Water Molecules per Cromoglycate Anion

sodium ion			
position	occupancy	sodium ion–oxygen[a] notation[b]	distance (Å)
Na1	1	Na1 (0,0,0)–O2 (0,0,0)	2.699
		Na1 (0,0,0)–O3 (–1,0,0)	2.592
		Na1 (0,0,0)–O3 (0,0,0)	2.495
		Na1 (0,0,0)–O11 (0,0,0)	2.488
		Na1 (0,0,0)–O12 (0,0,0)	2.508
		Na1 (0,0,0)–O13 (0,0,0)	2.430
		Na1 (0,0,0)–O13 (0,0,0)	2.380
Na2	0.316	Na2 (0,0,0)–O5 (0,1,–1)	2.358
		Na2 (0,0,0)–O10 (0,0,0)	2.446
		Na2 (0,0,0)–O14 (0,0,0)	2.316
		Na2 (0,0,0)–O14 (1,0,0)	1.937[c]
		Na2 (0,0,0)–O18 (0,0,0)	2.316
Na3	0.319	Na3 (0,0,0)–O5 (0,0,0)	2.506
		Na3 (0,0,0)–O5 (1,0,0)	2.696
		Na3 (0,0,0)–O14 (0,0,0)	1.990[c]
		Na3 (0,0,0)–O18 (0,0,0)	2.316
		Na3 (0,0,0)–O15 (0,0,0)	1.694[c]
		Na3 (0,0,0)–O18 (0,0,0)	2.409
Na4	0.365	Na4 (0,0,0)–O9 (0,0,0)	2.388
		Na4 (0,0,0)–O15 (–1,0,–1)	2.484
		Na4 (0,0,0)–O16 (0,0,0)	1.762[c]
		Na4 (0,0,0)–O16 (–1,0,0)	2.589
		Na4 (0,0,0)–O17 (0,0,0)	2.464
		Na4 (0,0,0)–O18 (0,–1,0)	2.271

[a] These atoms are shown in Figure 4a–d. The atom parentheses are omitted for clarity. [b] (0,0,0) refers to the original unit cell. The digit 1 indicates forward transition by one unit cell. The digit –1 indicates backward transition by one unit cell. [c] This sodium ion–oxygen distance is unreasonably small, so the water molecule will be displaced when the sodium ion occupies this position.

(Table 1). The general trend of the unit cell dimensions as a function of RH is consistent with Cox et al.,[2] but the cell lengths differed slightly (<1%). The α angle was approximately 90° at RH ≤ 58.5%, but was approximately 92.5° at RH ≥ 75.4%. The β and γ angles were found to be relatively constant, at approximately 97.5° and 94.5°, respectively, over the entire RH values examined. At 0% RH, CS is mainly amorphous, as indicated by the broad amorphous halo, with only four distinguishable PXRD peaks for the (001), (010), (01−1), and (011) planes (Figure 5). From the 2θ values of these four peaks and with the assumption that the values of the lattice parameters, a, β and γ, at 6.5% RH are approximately equal to those at 0% RH, the lattice parameters b, c, and α of the CS structure at 0% RH were estimated (Table 1).

Molecular Conformation of the Cromolyn Anion—The structure of cromolyn sodium reported by Hamodrakas et al.[3] contains 5 to 6 (~5.5) water molecules per cromoglycate anion, while that solved here contains 6.44 water molecules per cromoglycate anion. Comparison between two structures can provide insight into the influence of water content on the molecular conformation of the cromolyn anion.

The two structures show similarities in packing arrangements and in most intramolecular bond lengths and bond angles. The major differences occur in the torsional angles of the two carboxylate groups and in the torsional and bond angles of the 2-hydroxypropane linking chain. The part of the 2-hydroxypropane chain that is coordinated to Na(1) is more rigid than the part that is not (Figure 7a). The largest changes in bond angle occur in C(12)−C(13)−O(6) and C(13)−O(6)−C(18), and are approximately 6° and 5°, respectively. As the water content increases from ~5.5 to 6.44, the two carboxylate groups rotate away from each other (Figure 7a), while the angle formed by the planes of

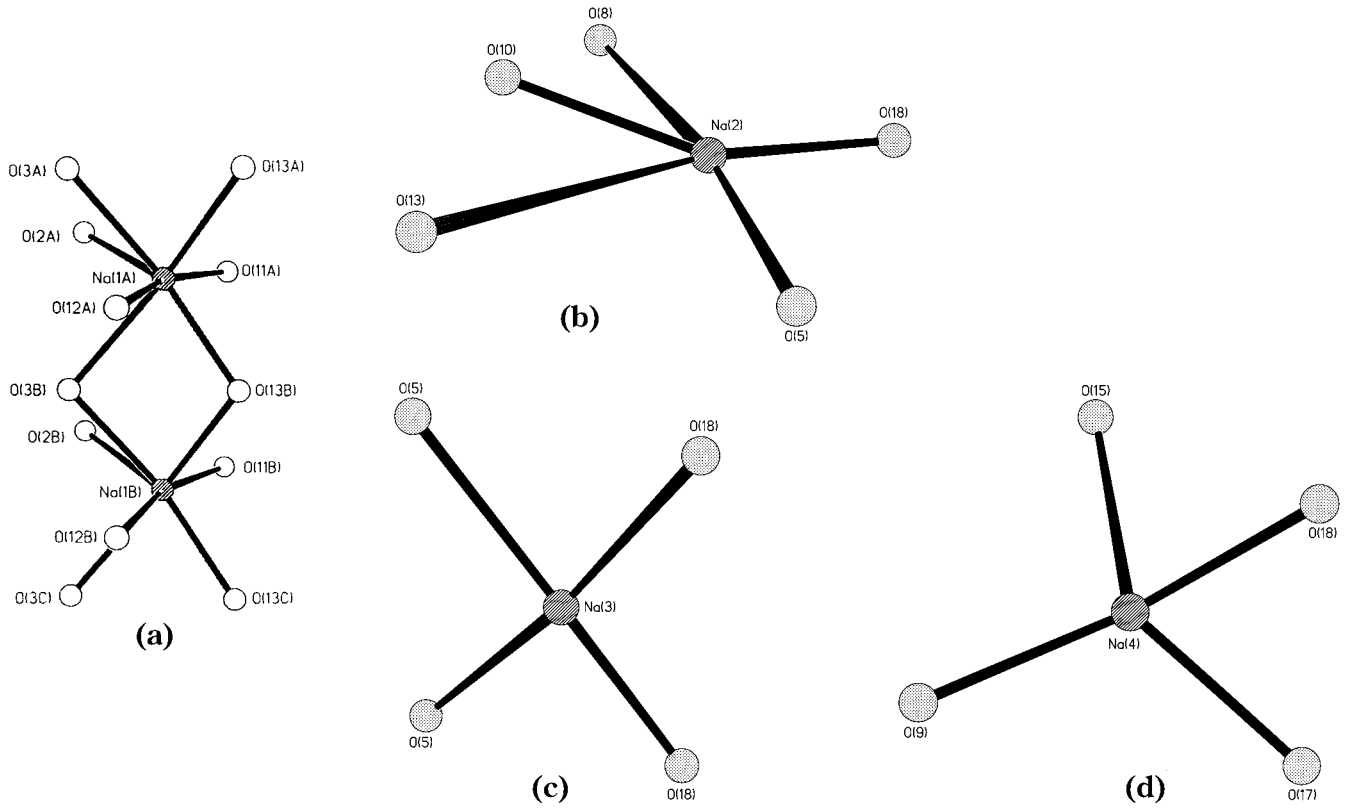

Figure 4—Coordination environment of: (a) the first (ordered) sodium ion, Na(1), shown in two neighboring unit cells (A and B); and the second (disordered) sodium ion at the three partially occupied sites, (b) Na(2), (c) Na(3), and (d) Na(4). The striped circles represent the sodium sites. The open circles represent the oxygen atoms coordinated to Na(1). The dotted (gray) circles represent the oxygen atoms coordinated to Na(2), Na(3), or Na(4).

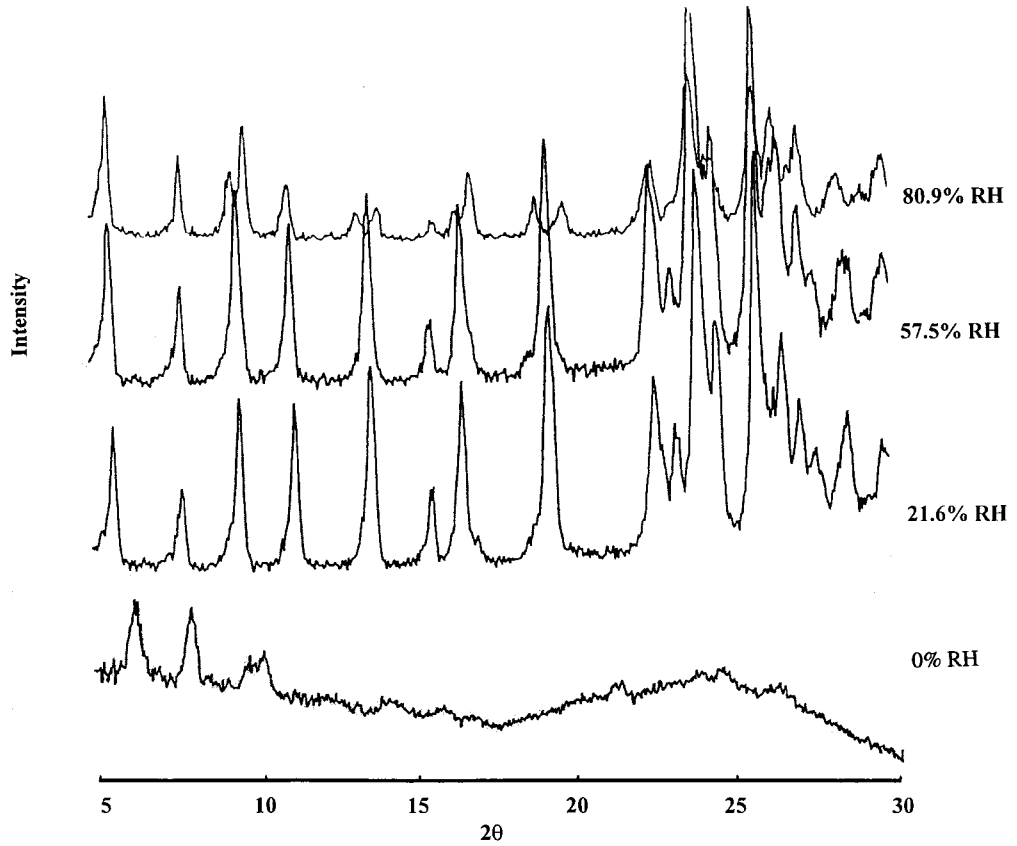

Figure 5—Powder X-ray diffraction patterns of cromolyn sodium crystallites equilibrated at four relative humidities: 80.9, 57.5, 21.6, and 0% at 23 °C.

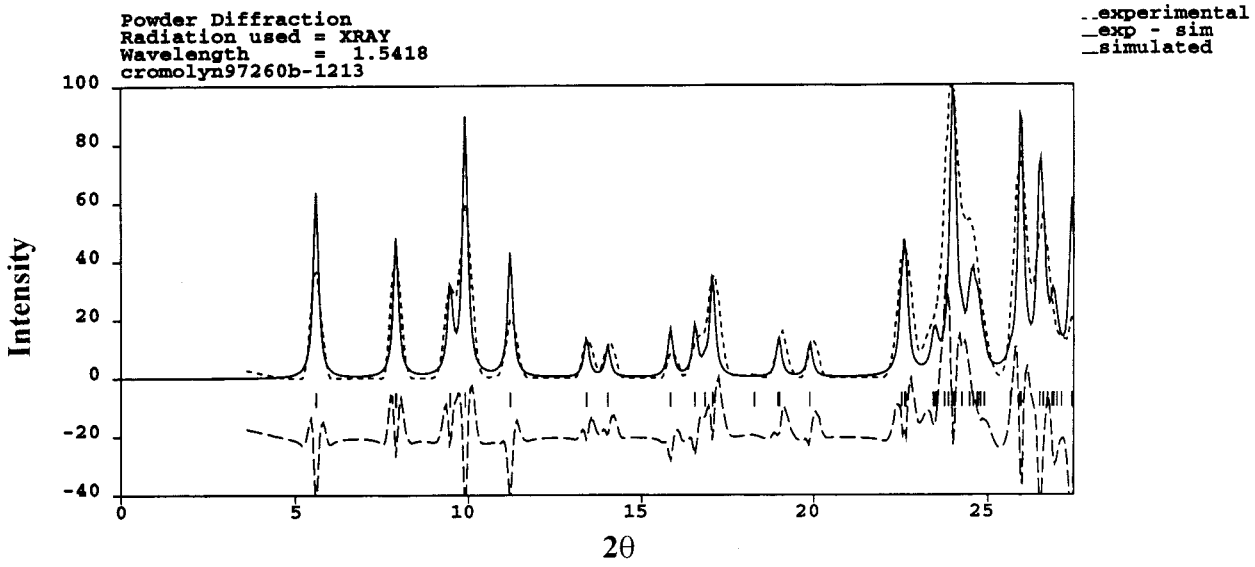

Figure 6—Powder X-ray diffraction patterns of cromolyn sodium: observed after equilibration at 80.9% relative humidity at 23 °C (top dashed line); calculated from the Rietveld-refined crystal structure at 173 K (top full line); difference between the calculated and the observed patterns (bottom dashed line). The vertical sticks mark the positions of the calculated diffraction peaks.

the two cyclic moieties decreases (Figure 7b) to form a larger water channel and stronger hydrophobic interactions between the cromoglycate anions in the *a* and *b* crystallographic directions. Because the carboxylate groups are coordinated to the second sodium ion, Na(2), Na(3), and Na(4), the change in torsional angles, C(8)−C(9)−C(10)−O(5) and C(21)−C(22)−C(23)−O(9), most likely reflect the change in its relative position.

In symmetrical molecules containing two planar moieties, such as CS or biphenyl,[13] the question arises whether the planar groups are in the same plane. For biphenyl in the crystalline state, Bushing[13] found that, above the transition temperature, the molecules have an average coplanar conformation, whereas below the transition temperature one phenyl ring is twisted relative to the other by as much as 10° at 22 K. While the two phenyl rings in biphenyl are linked by a covalent bond, the two cyclic moieties in CS are linked by a flexible 2-hydroxypropane chain, as discussed above. In the solution state, the cyclic moieties of CS are coplanar and the molecule (divalent anion) is symmetric. However, CS crystallizes in the space group, *P*1, corresponding to a complete lack of symmetry.

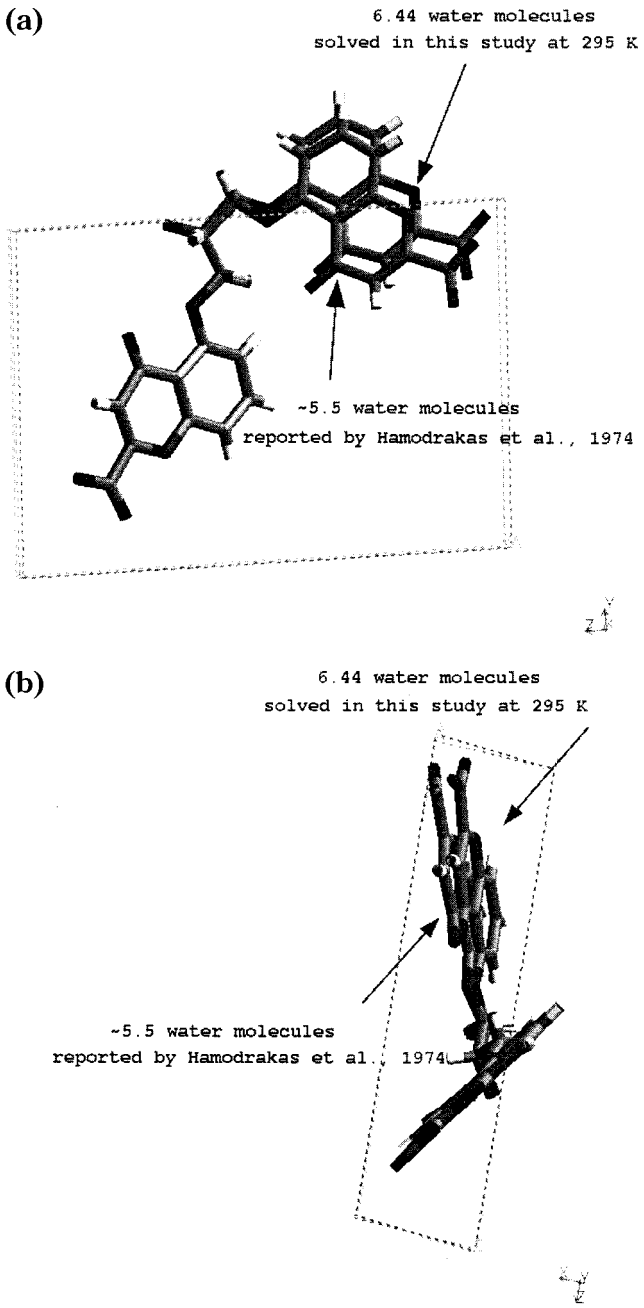

Figure 7—Overlay of the unit cells of the following two cromolyn sodium structures solved at 295 K: the structure with ~5.5 molecules of water per molecule of cromolyn sodium (reported by Hamodrakas et al., 1974);[3] the structure with 6.44 molecules of water per molecule of cromolyn sodium (solved in the present study); looking down (a) the *a*-axis and (b) the *b*-axis. The sodium ions and water molecules are omitted.

Moreover, the crystal contains a channel parallel to the short *a*-axis in which the disordered array of sodium ions and water molecules is found. It is possible that the crystal might achieve an ordered state with a certain water content at a certain temperature. However, this behavior has not been observed and would require further study.

Water Uptake of Cromolyn Sodium and Its Relationship to Structural Features—The high affinity for water and the reversible water sorption–desorption behavior of CS (Cox et al.,[2] also summarized in Table 1) can be understood from its molecular and crystal structures.

The hygroscopicity of CS is due to its ionic nature and the various polar functional groups: carboxylate, carbonyl, ether, and hydroxyl. The large sodium and water channels

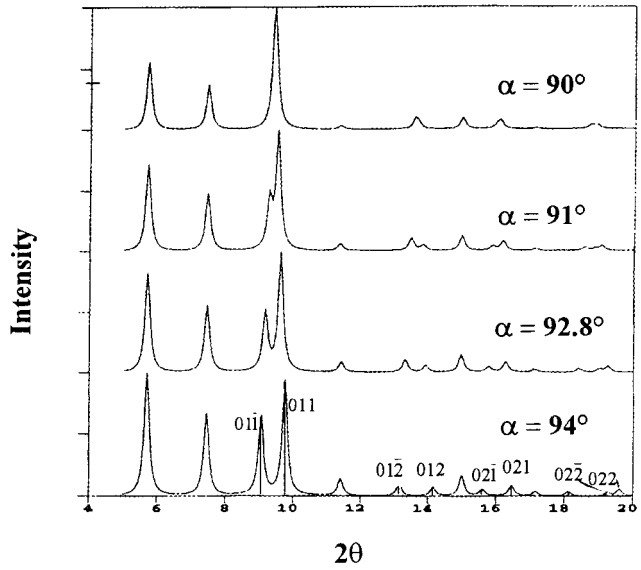

Figure 8—Theoretical powder X-ray diffraction patterns calculated by varying the α angle of the crystal structure of cromolyn sodium crystallized from methanol + water mixtures (v:v = 9:10, water activity = 0.76) and solved at 295 K.

along the *a*-axis, seen from the crystal packing diagram (Figure 3), allow easy passage of water molecules with little energy expenditure and minimal disruption to the crystal packing. This feature may explain the reversible water uptake of CS. Several factors contribute to the continuous and nonstoichiometric uptake of water by CS. First and foremost, the flexible 2-hydroxypropane chain linking the two cyclic moieties can relax readily to accommodate continuous lattice expansion caused by the continuous uptake of water. Second, the disordered sodium ion and the variable size of the large water channel cause the water to be disordered and allow for variable nonstoichiometric water contents that depend on the occupancies of the second sodium ion and the size of the water channel.

Powder X-ray Diffraction Pattern of Cromolyn Sodium as a Function of Relative Humidity—As stated above, the crystal structure of CS equilibrated at RH < 22% could not be solved by single-crystal X-ray diffraction, suggesting significant reductions in crystallinity. As the immediate environmental RH decreases, the PXRD pattern of CS (Figure 5) shows peak shifts toward smaller *d*-spacing (larger 2θ). Some PXRD peaks disappear and some appear as the RH changes. These appearances and disappearances can be explained by the change in the α angle of the crystal structure. The α angle is approximately 92.5° at RH ≥ 75.4% and is approximately 90° at RH ≤ 58.5%. As the α angle changed from 92.5° to 90°, the (100) and (004) peaks separated and the following pairs of peaks merged: (01−1) and (011); (01−2) and (012); (02−1) and (021); (02−2) and (022) (Figure 8).

Studies of the Different Crystalline Forms of Cromolyn Sodium Previously Reported[5,6]—The crystalline materials A, B, and C, prepared here following the procedures outlined by Oguchi et al.,[5,6] are all elongated transparent slabs (Figure 9); their PXRD patterns (Figure 10) correspond to those of the original crystal form of CS reported by Cox et al.,[2] with the exception of a diffraction peak below 5° 2θ, attributed to the formation of M liquid crystalline phase.[4] Close examination of the PXRD patterns of materials A, B, and C reported by Oguchi et al.,[5,6] reveals peaks corresponding to the M liquid crystalline phase.[4] Excluding the peaks corresponding to the liquid crystalline phase, the PXRD pattern of material A is identical to that of the original crystal form of CS equilibrated at RH ≤ 58%.

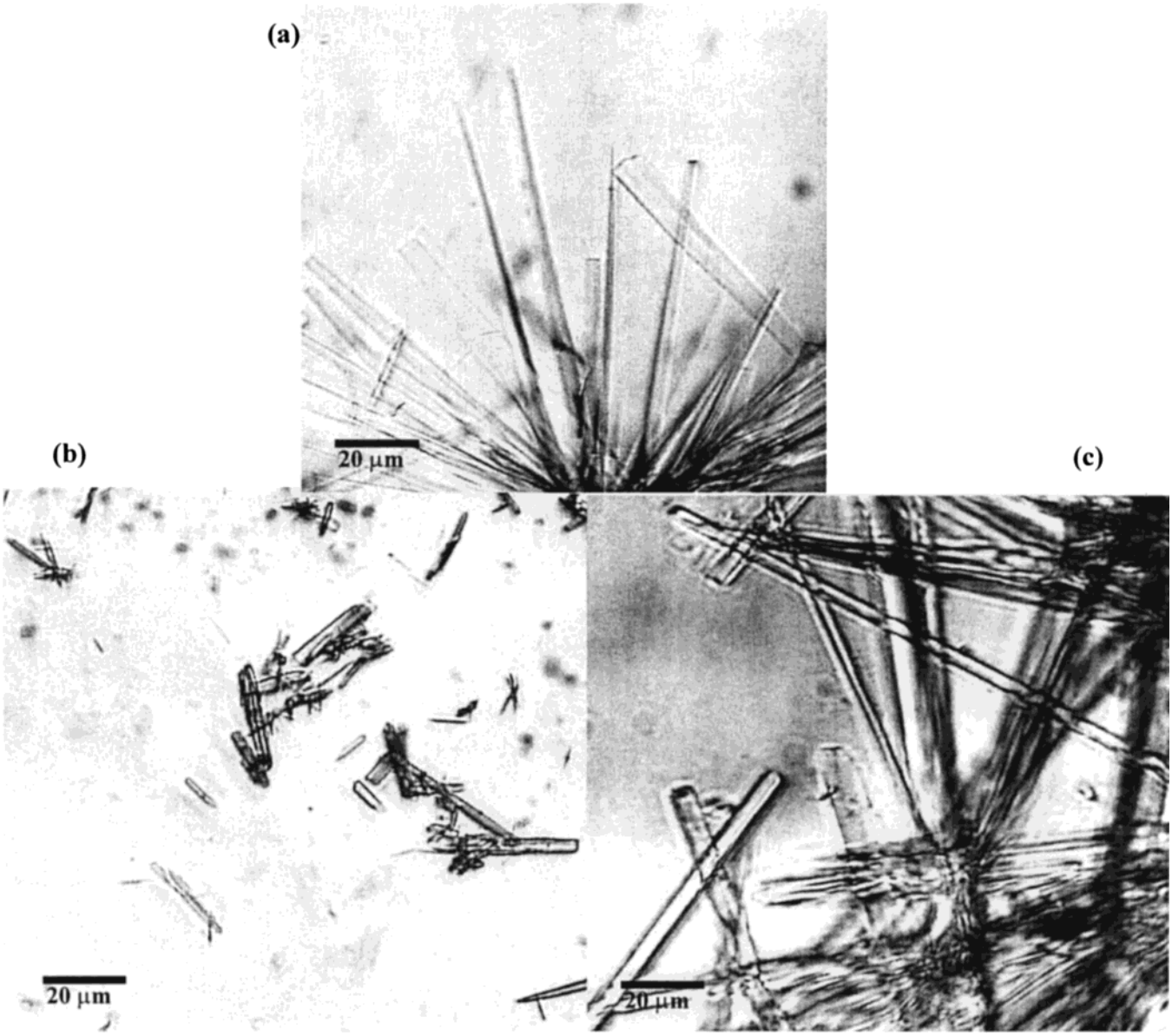

Figure 9—Photomicrographs of (a) material A, (b) material B, and (c) material C, prepared in our laboratory, according to procedures described by Oguchi et al.,[5–6] and submerged in silicone oil.

Similarly, the PXRD pattern of material B can be superimposed on the PXRD pattern of the original crystal form of CS equilibrated at RH ≥ 75.4%, with the exception of some small shoulder peaks, which can be attributed to fluctuations in the lattice parameters.[2] The sharp diffraction peaks in the PXRD pattern of material C can also be superimposed on the PXRD pattern of the original crystal form of CS equilibrated at RH ≥ 75.4%. When damp freshly harvested materials A, B, and C were observed under the polarized microscope, the crystals changed to a birefringent gel within 5 min. PXRD analysis showed that this gel is the M mesophase of CS.[4] The preferential evaporation of the alkanol used to prepare materials A, B, and C increased the water concentration and caused the observed formation of the M mesophase. These results indicate that materials A, B, and C are the original crystalline hydrate form[2,3] of CS contaminated by varying proportions of M, and hence explain the moisture sorption diagrams and the DSC curves of Oguchi et al.[5,6] The reported[6] DSC curve of material C appears identical to that of the M mesophase in the present work. The steps observed in the reported[5,6] moisture sorption diagrams are probably a reflection of the

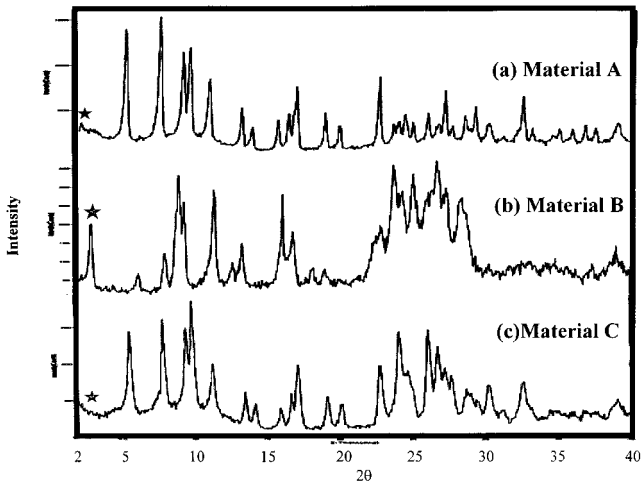

Figure 10—Powder X-ray diffraction patterns of (a) material A, (b) material B, and (c) material C prepared in our laboratory, according to the procedures described by Oguchi et al.[5,6]

reduction in the number of degrees of freedom caused by contamination with the liquid crystalline phase, M, in accordance with Gibbs phase rule and are not evidence for the formation of stoichiometric hydrates.

Conclusions

1. The "new forms" of CS reported by Oguchi et al.[5,6] have been prepared, characterized, and shown to be contaminated by the liquid crystalline phase, M, which complicated the PXRD pattern, moisture sorption, and the thermal analytical data.

2. Only one crystalline hydrate form of CS is observed, is nonstoichiometric, and corresponds to that reported by Cox et al.[2]

3. The crystal structure of CS with 6.44 water molecules per cromoglycate anion has been solved at 295 and 173 K. At 0% RH, loss of crystallinity accompanies loss of water, suggesting that the water molecules are necessary for holding together the crystalline structure. The second sodium ion of the CS occupies three partial crystallographic sites.

4. The solved crystal structure of CS is compared with that of Hamodrakas et al.,[3] which contains 5 to 6 water molecules per cromoglycate anion. The CS crystal structure is found to be flexible. The bond and torsional angles in the 2-hydroxypropane linking chain can change the relative orientations of the two cyclic moieties to accommodate lattice expansion or contraction resulting from water adsorption and desorption. The torsional angles of the two carboxylate groups can also change with changing water content.

5. The high water affinity and reversible water sorption−desorption of CS can be explained in terms of its molecular and crystal structure. The ionic nature and the polar groups of CS explain its hygroscopicity. The reversible and nonstoichiometric water sorption and desorption can be explained by the presence of large water channels, the flexible 2-hydroxypropane linking chain, and the disordered second sodium ion and the surrounding water molecules.

References and Notes

1. Cox, J. S. G. Disodium cromoglycate (FPL 670) ('Intal'): a specific inhibitor of reaginic antibody−antigen mechanisms. *Nature* **1967**, *216*, 1328−9.
2. Cox, J. S. G.; Woodard, G. D.; McCrone, W. C. Solid-state chemistry of cromolyn sodium (disodium cromoglycate). *J. Pharm. Sci.* **1971**, *60*, 1458−65.
3. Hamodrakas, S.; Geddes, A. J.; Sheldrick, B. X-ray analysis of disodium cromoglycate. *J. Pharm. Pharmacol.* **1974**, *26*, 54−6.
4. Hartshorne, N. H.; Woodard, G. D. Mesomorphism in the system disodium cromoglycate-water. *Mol. Cryst. Liq. Cryst.* **1973**, *23*, 343−68.
5. Oguchi, T.; Hindle, M.; Forbes, R. T.; York, P. Cromolyn sodium: characterization of a new polymorph. *Pharm. Res.* **1996**, *13*, S-173, PT 6067.
6. Oguchi, T.; Satoh, A.; Fujita, K.; Yonemochi, E.; Yamamoto, K. Characterization of the solid-state properties of cromolyn sodium. *Pharm. Res.* **1997**, *14*, S-202, 1607.
7. Gölles, F. The examination and calculation of thermodynamic data from experimental measurements. I. The numerical integration of the vapor-pressure curves of the system methanol−water. *Monatsh. Chem.* **1961**, *92*, 981−91. II. The numerical integration of the vapor-pressure curves of the system ethanol-water. *Monatsh. Chem.* **1962**, *93*, 191−220.
8. Nyqvist, H. Saturated salt solutions for maintaining specified relative humidities. *Int. J. Pharm. Technol. Prod. Mfr.* **1983**, *4*, 47−8.
9. Weast, R. C., Ed. *Handbook of Chemistry and Physics*, 55th ed.; CRC Press: Cleveland, OH, 1974; D159.
10. Steiner, T.; Koellner, G. Crystalline β-cyclodextrin hydrate at various humidities: fast, continuous, and reversible dehydration studied by X-ray diffraction. *J. Am. Chem. Soc.* **1993**, *116*, 5122−28.
11. Sakthivel, A.; Wiles, D. B.; Young, R. A. DBWS-9411 (a program for Rietveld analysis). Georgia Institute of Technology: Atlanta, GA, 1995.
12. Post, J. E.; Bish, D. L. Rietveld refinement of crystal structures using powder X-ray diffraction data. In *Modern Powder Diffraction* (Reviews in Mineralogy, Vol. 20); Bish, D. L., Post, J. E., Eds.; Mineralogical Society of America: Washington, DC, 1989; pp 277−306.
13. Bushing, W. R. Modeling the phase change in crystalline biphenyl by using a temperature-dependent potential. *Acta Crystallogr.* **1983**, *A39*, 340−347.
14. Blessing, R. An empirical correction for absorption anisotropy. *Acta Crystallogr.* **1995**, *A51*, 33−8.

Acknowledgments

We thank Dr. Raj Suryanarayanan, Department of Pharmaceutics, College of Pharmacy, University of Minnesota, for helpful discussions. We also thank the following: Inhale Therapeutic Systems, San Carlos, CA, for financial support; Fisons, plc, Pharmaceutical Division (now Astra Charnwood and Rhône-Poulenc Rorer), Loughborough, UK, for a gift of cromolyn sodium; and the Supercomputing Institute of the University of Minnesota for financially supporting our use of the Medicinal Chemistry/Supercomputing Institute Visualization − Workstation Laboratory.

JS9900710

Diffusion Modeling of Percutaneous Absorption Kinetics. 1. Effects of Flow Rate, Receptor Sampling Rate, and Viable Epidermal Resistance for a Constant Donor Concentration

YURI G. ANISSIMOV AND MICHAEL S. ROBERTS*

Contribution from *Department of Medicine, University of Queensland, Princess Alexandra Hospital, Woolloongabba, Queensland, 4102, Australia.*

Received February 18, 1999. Accepted for publication July 19, 1999.

Abstract □ A diffusion model for the percutaneous absorption of a solute through the skin is developed for the specific case of a constant donor concentration with a finite removal rate from the receptor due to either perfusion rate or sampling. The model has been developed to include a viable epidermal resistance and a donor–stratum corneum interfacial resistance. Numerical inversion of the Laplace domain solutions were used for simulations of solute flux and cumulative amount absorbed and to model specific examples of percutaneous absorption. Limits of the Laplace domain solutions were used to define the steady-state flux, lag time, and receptor concentration. Steady-state approximations obtained from the solutions were used to relate the steady-state flux and the effective permeability coefficient to the viable epidermis resistance, a donor–stratum corneum interfacial resistance, receptor removal rate, and partitioning between the receptor and donor phases. The lag time was shown to be dependent on these parameters and on the volume of the receptor phase. It is concluded that curvilinear cumulative amount and flux–time profiles are dependent on the processes affecting percutaneous absorption, the shapes of the profiles reflecting the processes most determining transport.

Introduction

The interpretation of percutaneous absorption kinetics is highly dependent on the assumed mathematical model representation of transport across the epidermis. This information is then commonly applied to (1) optimize topical formulations, (2) develop transdermal delivery systems, (3) provide risk assessment for skin contaminants, and (4) predict the effect of physiological processes (such as changes in dermal blood flow) on the rate of percutaneous penetration.[1] A number of mathematical models have been used to describe percutaneous absorption kinetics.[2] Most percutaneous absorption kinetic models describe the time dependency of the cumulative amount of solute penetrating the epidermis into a sink receptor phase.[2] The models derived recognize constant and depleting donor concentrations and the resistance of the viable epidermis. When a constant donor concentration exists, the cumulative amount of solute penetrating the epidermis under steady-state conditions ($Q_{ss}(t)$) is linearly related to the exposure time t:

$$Q_{ss}(t) = J_{ss}A(t - \text{lag}) \quad (1)$$

where J_{ss} is the steady-state flux, lag is the lag time, and A is the area of application. The steady-state flux of solutes through the epidermis can be expressed in terms of an apparent permeability coefficient k'_p, and the difference in vehicle (C_{d0}) and receptor compartment ($C_{r\,ss}$) concentrations:[1−4]

$$J_{ss} = k'_p(C_{d0} - C_{r\,ss}) \quad (2)$$

A number of studies have shown that k'_p is defined by the resistances of both the stratum corneum and viable epidermis.[4−7] $C_{r\,ss}$ is defined by k'_p, A, C_{d0}, and the rate of removal of solute from the receptor compartment, designated as a clearance Cl_r:[8]

$$C_{r\,ss} = \frac{k'_pAC_{d0}}{Cl_r + k'_pA} \quad (3)$$

It is apparent that an increased Cl_r will reduce $C_{r\,ss}$ (eq 3) and, accordingly, increase J_{ss} (eq 2). A number of studies have shown that an increase in perfusion flow rate can increase percutaneous absorption.[9−11] In addition, a number of studies have shown that percutaneous absorption of lipophilic solutes is highly dependent on the nature of the receptor fluid and that certain receptor fluids underestimate *in vivo* absorption.[12−19]

We are not aware of mathematical expressions describing the curvilinear $Q(t)$ versus time profiles associated with nonsink conditions using a diffusion model for epidermal transport. Guy and Hadgraft[20] have given a theoretical expression for the diffusion-controlled release of a solute from a slab into a nonsink receptor. Curvilinear $Q(t)$ versus time profiles also occur when there is depletion in the donor phase associated with the application of a finite donor.[2] Parry et al.[21] presented an expression for the accumulation of solute in the receptor compartment with time when there was no clearance of solute from the receptor. Guy and Hadgraft[22] reported a pharmacokinetic model in which the influx into the membrane was assumed to be an exponential decline in vehicle concentration and the efflux from the membrane was defined by a first-order rate constant.

In this paper, we derive diffusion equations for the cumulative amount of solute penetrating through the epidermis from a constant donor concentration into a finite receptor volume with a finite removal clearance. Given the potential contribution of the viable epidermis and unstirred water layers as a resistance to transport into the dermis or receptor,[1−7] we have included this effect in our derivations. We have also included the complementary contribution of the vehicle−stratum corneum resistance, as this is relevant to transdermal patch delivery with delivery being controlled in part by a membrane or adhesive patch component. The Laplace expressions for cumulative amount−time and flux−time relationships are then used to define steady-state flux and lag times. These expressions were also used to characterize the effects of changing various determinants on the profiles described by the relationships and to explain experimental data. Given that

* Corresponding author. Fax: 61-7-3240 5806. E-mail: M.Roberts@mailbox.uq.edu.au.

10.1021/js990053i CCC: $18.00
Published on Web 10/08/1999

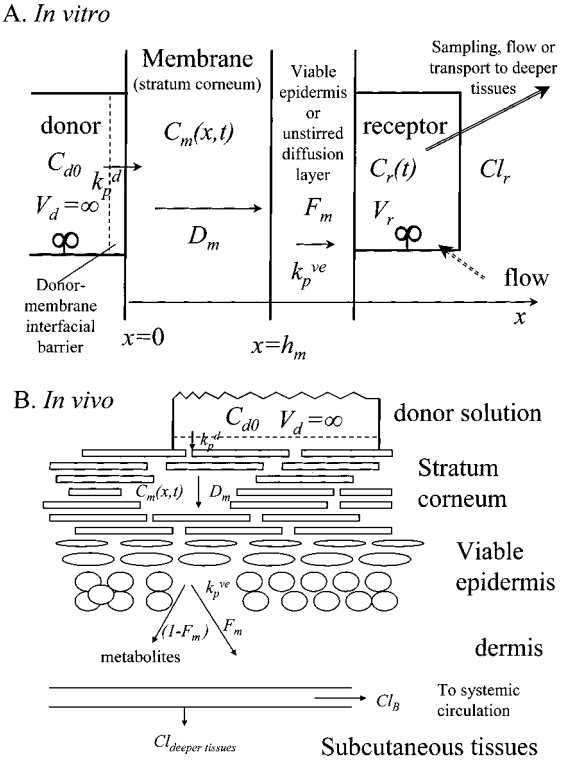

Figure 1—Schematic diagram of the model. (A) *In vitro* and (B) *in vivo* (see text for explanations of symbols).

many receptor fluids yield percutaneous absorption fluxes *in vitro* considerably lower than for *in vivo* with highly lipophilic compounds,[23] we have also considered the estimation of the apparent permeability coefficient from the apparent solubility of the solutes in a given receptor fluid.

Theory

Figure 1 shows a schematic diagram of the model used in this work. Both donor and receptor phases are represented as a well stirred compartments. The transport of solute through the stratum corneum, referred to in this section as the membrane, is described by the diffusion equation:

$$\frac{\partial C_m}{\partial t} = D_m \frac{\partial^2 C_m}{\partial x^2} \tag{4}$$

where $C_m(x,t)$ is the concentration of solute in the membrane at distance x at time t, and D_m is the diffusion coefficient. We assume there is no solute initially present in the membrane. The initial condition is therefore:

$$C_m(x,0) = 0 \tag{5}$$

The boundary conditions at the donor surface ($x = 0$) are defined by the partitioning of the solute between donor phase and membrane:

$$C_m(0,t) = K_m C_{d0} \tag{6}$$

where C_{d0} is the concentration in the donor phase, K_m is the partition coefficient between the membrane and donor ($K_m = C_m^{ss}/C_d^{ss}$ at the equilibrium between the membrane and donor).

Donor Surface Boundary Conditions—When an interfacial barrier exists adjacent to the membrane in the donor phase, boundary condition 6 becomes:

$$-D_m \frac{\partial C_m}{\partial x}|_{x=0} = k_p^d \left(C_{d0} - \frac{C_m}{K_m} \right) \tag{7}$$

where k_p^d is permeability coefficient through this barrier. In the specific case when this barrier is an unstirred diffusion layer in the donor phase, $k_p^d = D_{dl}/h_{dl}$, where D_{dl} and h_{dl} are diffusion coefficient and thickness of the layer.

Receptor Surface Boundary Conditions—The boundary conditions at the receptor surface ($x = h_m$, h_m is effective thickness of the membrane) are:

$$-D_m \frac{\partial C_m}{\partial x}|_{x=h_m} = k_p^{ve} \left(\frac{C_m}{K_m} - \frac{C_r}{K_r} \right) \tag{8}$$

$$V_r \frac{dC_r}{dt} = -AD_m \frac{\partial C_m}{\partial x}|_{x=h_m} - Cl_r C_r \tag{9}$$

where Cl_r is the removal rate (mL/min) of solution containing solute from the receptor phase, V_r is the volume of the receptor, K_r is the partition coefficient between the receptor and donor ($K_r = C_r^{ss}/C_d^{ss}$ at the equilibrium between the receptor and donor), A is the area of application, and C_r is the concentration in the receptor. In eq 8, k_p^{ve} is the permeability coefficient of solute due to a barrier between the membrane and receptor. In the specific case of the viable epidermis or an unstirred aqueous diffusion layer being the barrier, $k_p^{ve} = K_{ve}D_{ve}/h_{ve}$ where h_{ve} is the thickness of the viable epidermis/layer, D_{ve} is the diffusion coefficient in the viable epidermis/layer, and K_{ve} is the partition coefficient between the viable epidermis/layer and donor ($K_{ve} = C_{ve}^{ss}/C_d^{ss}$ at the equilibrium between the viable epidermis/layer and the donor). It is also noted that k_p' (eq 2) can be expressed in terms of k_p^{sc} and k_p^{ve} by[3–8] $1/k_p' = 1/k_p^{sc} + 1/k_p^{ve}$, where k_p^{sc} is the stratum corneum permeability coefficient. We have limited this analysis to pseudo-steady-state permeability coefficients k_p^{ve} and k_p^d for transport in the viable epidermis and unstirred receptor/donor diffusion layers, as representation of transport by the diffusion equation unnecessarily increases the complexity of the solutions, given that the lag time in the viable epidermis and unstirred diffusion layers is normally very small. While Cl_r *in vitro* is defined by either sampling rate or flow rate, Cl_r *in vivo* is defined by the sum of removal by blood flow and clearance by transport into deeper tissues below the application site.[3]

Laplace Domain Solution—We now consider the Laplace domain solution of eq 4 with boundary conditions 6–9. The Laplace transform of eq 4 with initial condition 5 is:

$$s\hat{C}_m = D_m \frac{d^2\hat{C}_m}{dx^2} \tag{10}$$

where hat over function (ˆ) denotes the Laplace transform.

The Laplace transforms of boundary condition expressions 6–9 are:

$$-D_m \frac{d\hat{C}_m}{dx}|_{x=0} = k_p^d \left(\frac{C_{d0}}{s} - \frac{\hat{C}_m}{K_m} \right) \tag{11}$$

$$-D_m \frac{d\hat{C}_m}{dx}|_{x=h_m} = k_p^{ve} \left(\frac{\hat{C}_r}{K_r} \right) \tag{12}$$

$$V_r s\hat{C}_r = -AD_m \frac{d\hat{C}_m}{dx}|_{x=h_m} - Cl_r \hat{C}_r \tag{13}$$

The general solution to eq 10 is

$$\hat{C}_m(x,s) = A_1 \sinh\left(\sqrt{st_d}\frac{x}{h_m}\right) + B_1 \cosh\left(\sqrt{st_d}\frac{x}{h_m}\right) \quad (14)$$

where A_1 and B_1 are constants independent of x to be determined by the boundary conditions, and t_d is the parameter with the dimension of time:

$$t_d = \frac{h_m^2}{D_m} \quad (15)$$

Substitution of $\hat{C}_m(x,s)$ in the form of eq 14 to boundary condition 11 yields for B_1:

$$B_1 = \frac{C_{d0}K_m}{s} + \frac{\sqrt{st_d}}{\kappa_d}A_1, \quad (16)$$

where dimensionless parameter κ_d is the relative permeability of the diffusion layer in the donor:

$$\kappa_d = \frac{k_p^d}{k_p^{sc}} \quad (17)$$

and k_p^{sc} is the permeability coefficient of membrane:

$$k_p^{sc} = \frac{K_m D_m}{h_m} \quad (18)$$

Solving boundary conditions 12 and 13 for A_1 with $\hat{C}_m(x,s)$ in the form of eq 14 and with B_1 determined in eq 16 yields expression for A_1:

$$A_1 = -\frac{C_{d0}K_m}{s}\frac{g_2(s)}{g_1(s) + \frac{\sqrt{st_d}}{\kappa_d}g_2(s)} \quad (19)$$

where functions $g_1(s)$ and $g_2(s)$ are:

$$g_1(s) = 1 + \frac{\kappa_{ve}}{Cl_{rN} + V_{rN}st_d} + \frac{\kappa_{ve}}{\sqrt{st_d}}\tanh\sqrt{st_d} \quad (20)$$

$$g_2(s) = \left(1 + \frac{\kappa_{ve}}{Cl_{rN} + V_{rN}st_d}\right)\tanh\sqrt{st_d} + \frac{\kappa_{ve}}{\sqrt{st_d}} \quad (21)$$

and dimensionless parameters κ_{ve}, Cl_{rN}, and V_{rN} are defined as:

$$\kappa_{ve} = \frac{k_p^{ve}}{k_p^{sc}} \quad (22)$$

$$Cl_{rN} = \frac{Cl_r K_r}{k_p^{sc}A} \quad (23)$$

$$V_{rN} = \frac{V_r K_r}{V_m K_m} \quad (24)$$

We note that the kinetic interpretations of parameters introduced here are as follows: t_d is of the order of magnitude of the diffusion time through membrane; κ_{ve} is a measure of the relative resistance of membrane ($1/k_p^{sc}$) to the resistance of the viable epidermis/aqueous layer ($1/k_p^{ve}$); Cl_{rN} is a measure of the magnitude of the removal rate from the receptor phase (Cl_r) relative to transport through the membrane ($k_p^{sc}A$); V_{rN} is the ratio of the amount of drug in the receptor phase and membrane ($C_rV_r/[C_mV_m]$) assuming equilibrium exists between phases.

Substitution of A_1 from 19 and B_1 from 16 to eq 14 yields the equation for the concentration in the membrane:

$$\hat{C}_m(x,s) = \frac{C_{d0}K_m}{s}\frac{g_1(s)\cosh\left(\sqrt{st_d}\frac{x}{h_m}\right) - g_2(s)\sinh\left(\sqrt{st_d}\frac{x}{h_m}\right)}{g_1(s) + \frac{\sqrt{st_d}}{\kappa_d}g_2(s)} \quad (25)$$

Flux of Solute—The flux of solute into the receptor phase is given by:

$$\hat{J}(s) = -D_m\frac{d\hat{C}_m}{dx}|_{x=h_m}. \quad (26)$$

Hence, from eqs 25 and 26:

$$\hat{J}(s) = \frac{k_p^{sc}C_{d0}}{s}\left[\left(\frac{1}{Cl_{rN} + V_{rN}st_d} + \frac{1}{\kappa_{ve}} + \frac{1}{\kappa_d}\right)\cosh\sqrt{st_d} + \left(\frac{1}{\sqrt{st_d}} + \frac{\sqrt{st_d}}{\kappa_d}\left[\frac{1}{\kappa_{ve}} + \frac{1}{Cl_{rN} + V_{rN}st_d}\right]\right)\sinh\sqrt{st_d}\right]^{-1} \quad (27)$$

Amount of Solute Absorbed—The cumulative amount of solute absorbed $Q(t)$ over time t into the receptor can be derived from the flux–time relationship for a solute:

$$Q(t) = \int_0^t AJ(t')dt' \quad (28)$$

Or in the Laplace domain:

$$\hat{Q}(s) = \frac{A\hat{J}(s)}{s} \quad (29)$$

Hence, from eqs 27 and 29:

$$\hat{Q}(s) = \frac{k_p^{sc}AC_{d0}}{s^2}\left[\left(\frac{1}{Cl_{rN} + V_{rN}st_d} + \frac{1}{\kappa_{ve}} + \frac{1}{\kappa_d}\right)\cosh\sqrt{st_d} + \left(\frac{1}{\sqrt{st_d}} + \frac{\sqrt{st_d}}{\kappa_d}\left[\frac{1}{\kappa_{ve}} + \frac{1}{Cl_{rN} + V_{rN}st_d}\right]\right)\sinh\sqrt{st_d}\right]^{-1} \quad (30)$$

Receptor Phase Concentration—Combining eqs 26 and 13 yields

$$V_r s\hat{C}_r = A\hat{J}(s) - Cl_r\hat{C}_r \quad (31)$$

Rearrangement yields the receptor concentration $\hat{C}_r(s)$:

$$\hat{C}_r(s) = \frac{A\hat{J}(s)}{V_r s + Cl_r} \quad (32)$$

Simulations and Data Analysis

Simulations in this section have been performed by numerical inversion of functions from the Laplace domain to the time domain using the program SCIENTIST (Micro-Math Scientific software). Numerical inversion of the Laplace domain solutions were used in these simulations for simplicity. The inversion of $\hat{Q}(s)$ to the time domain for arbitrary t is only possible in a form of an infinite sum of residues of function $e^{st}\hat{Q}(s)$ at its singularities and involves solving bulky transcendental equations. A solution in this form

was felt to be of limited value as reliable numerical inversion techniques are now available.[24]

Experimental data illustrating the effect of receptor composition (aqueous solutions containing Volpo N 20 or bovine serum albumin) and sampling times on the penetration of octyl salicylate as a 10% solution in liquid paraffin through 20 μm high density polyethylene membrane were produced by our group.[18,25] In addition, solubilities of octyl salicylate determined in Volpo N 20 6% (9.73 ± 0.21 mg/mL) and 4% bovine serum albumin (0.24 ± 0.01 mg/mL)[18,25] were used for data interpretation.

Results

The present model shows that, under conditions of constant donor concentration, the cumulative amount absorbed $Q(t)$, the flux $J(t)$ and the receptor phase concentration $C_r(t)$ can be expressed in Laplace domain by eqs 30, 27, and 32, respectively. These values have been expressed in terms of six parameters reflecting both intrinsic and extrinsic determinants of the resulting time profiles. The two usual intrinsic variables are the stratum corneum permeability coefficient (k_p^{sc}) and the diffusion time through the stratum corneum (t_d). The extrinsic variables are κ_d, κ_{ve}, Cl_{rN}, and V_{rN}. These variables are determined by receptor (dermal) clearance, receptor (dermal) volume (assuming it is effectively well-mixed), receptor phase composition (affinity for solute), viable epidermal (aqueous diffusion layer) resistance, and the vehicle–membrane interfacial resistance. We now consider the effects of each of these determinants on $Q(t)$, $J(t)$ and $C_r(t)$ versus t profiles. Later we express equations 30, 27 and 32 as steady state approximations and consider the explicit effects of each determinant.

Receptor (Dermal) Clearance—The effect of receptor (dermal) clearance on $Q(t)$ versus t profiles is defined by Cl_{rN}, which expresses Cl_rK_r relative to $k_p^{sc}A$ (eq 23). Figure 2a shows normalized plots of $Q/(k_p^{sc}AC_{d0}t_d)$ versus t/t_d for a specific case where both the relative viable epidermis resistance (κ_{ve}) and relative receptor volume (V_{rN}) equal 0.5, and there is no donor–stratum corneum interfacial resistance ($\kappa_d \rightarrow \infty$). It is apparent that as Cl_{rN} decreases, corresponding to a reduction in sampling rate, the cumulative amount absorbed decreases in a curvilinear manner. However, at long times, an apparent steady-state flux is reached. Figure 2b shows that decreasing the receptor clearance results in a lower steady-state flux (slope of relationship), a longer time to reach steady state, and, in this case, a negative lag time (lag_2). Figure 2c and Figure 2b show that the flux is reduced and receptor phase concentration increased by decreasing the receptor clearance.

Receptor (Dermal) Volume—Figure 3a shows that the volume of the receptor phase, as represented by $V_{rN}(= V_rK_r/[V_mK_m])$, eq 24 also affects the cumulative amount–time profiles. This analysis assumes that this volume is effectively well-mixed. The curvilinear profiles are less pronounced as V_{rN} increases. When $V_{rN} \rightarrow \infty$, the profile is equivalent to that for infinite sampling. It is apparent from Figure 3a that reducing the receptor volume results in the same steady-state flux when a finite receptor volume exists, as distinct from the much higher steady-state flux with sink conditions as defined by $V_{rN} \rightarrow \infty$. Figure 3a also shows that decreasing V_{rN} decreases the time to reach steady state. Consistent with this observations, V_{rN} affects the time for $C_r(t)$ to reach steady state, but not the actual $C_{r\,ss}$, when a finite volume exists.

Receptor Solution Composition—The receptor solution composition will determine the partition coefficient of the solute between the stratum corneum and receptor solution K_r and, in turn, $Cl_{rN}(= Cl_rK_r/(k_p^{sc}A)$, eq 23) and

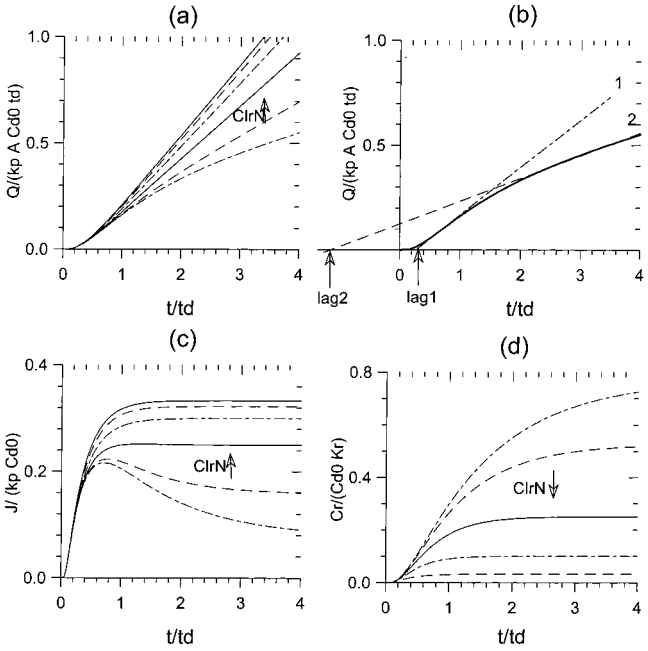

Figure 2—(a) Normalized cumulative amount absorbed versus normalized time profiles for $\kappa_{ve} = V_{rN} = 0.5$ and $\kappa_d = \infty$ based on eq 30 (κ_{ve} represents ratio of resistance of membrane, $1/k_p^{sc}$, to the resistance of the viable epidermis/aqueous layer, $1/k_p^{ve}$, κ_d represents ratio of resistance of membrane, $1/k_p^{sc}$, to the resistance of the vehicle–stratum corneum interface, $1/k_p^d$, whereas V_{rN} defines ratio of receptor–membrane effective distribution volumes). The curves on each graph represent Cl_{rN} values of 0.1, 0.3, 1, 3, 10, and ∞, with arrows indicating the increase of Cl_{rN} (Cl_{rN} defines relative rate of receptor clearance to permeability through membrane). (b) The curve corresponding to $Cl_{rN} = 0.1$ from part a (solid line) is presented together with its steady-state (dashed line) and quasi-steady-state (dash-dotted line) extrapolations. Intercepts of extrapolations with x axis define negative (lag2) and positive (lag1) lag times for the steady and quasi steady states. (c) Normalized flux versus normalized time (t/t_d). (d) Normalized receptor concentration versus normalized time.

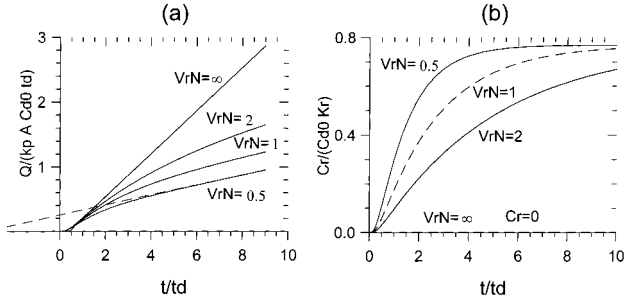

Figure 3—(a) Normalized cumulative amount absorbed versus normalized time profiles for different receptor phase volumes (varying V_{rN}) with $\kappa_{ve} = 0.5$, $Cl_{rN} = 0.1$, and $\kappa_d = \infty$. On each graph, curves represent V_{rN} values of 0.5, 1.0, 2.0, and ∞, respectively, starting from lower curve (see Figure 2 for simplistic description of κ_{ve}, V_{rN}, and Cl_{rN}). (b) Corresponding receptor concentrations C_r normalized for donor concentration C_{d0}.

$V_{rN}(= V_rK_r/(V_mK_m)$, eq 24). Figure 4a shows that as K_r decreases, the cumulative amount absorbed also decreases. It is apparent that reduced K_r is associated with a lower steady-state flux. Given that K_r is also defined by the solubility in the receptor divided by that in the donor when Henry's law applies, similar profiles can be shown for a given vehicle or donor phase when the receptor composition is characterized by the solubility of the solute in the receptor phase.

Figure 4b shows that a decreased K_r (and receptor phase solubility for solute) leads to a decreased C_r but does not greatly affect the time to reach $C_{r\,ss}$. It is evident in Figure 4c that experimental data, in which the Volpo N20 con-

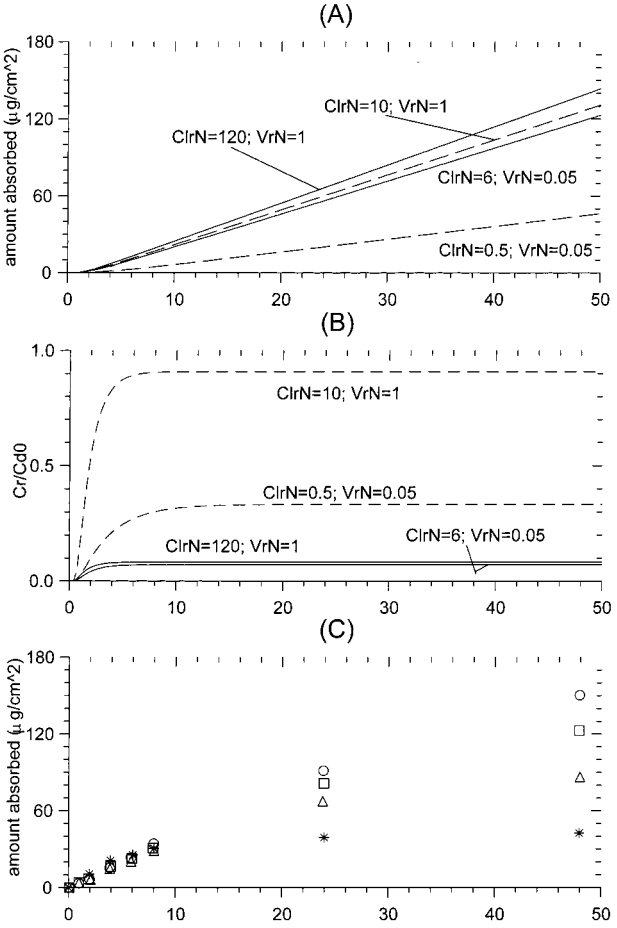

Figure 4—Effect of sampling times, sampling rate, and receptor composition on the amount absorbed versus time plots. A: Simulations with eq 48 of a rapid sampling rate (solid lines, $Cl_{rN} = 12K_r$, and $V_{rN} = 0.1K_r$) and slower sampling rate (dashed lines, $Cl_{rN} = K_r$, and $V_{rN} = 0.1K_r$) for two different partition coefficients K_r (0.5, 10) and $t_d = 10$h; B: corresponding receptor concentration C_r normalized for donor concentration C_{d0}; C: experimental data for 10% octyl salicylate in liquid paraffin (v-v) applied to 20 μm high density polyethylene membranes[18,25] with different receptor fluids and a high sampling rate for the first eight hours. (○), (□), (△), and (*) represent 10% of Volpo-N 20, 6% of Volpo-N 20, 3% of Volpo-N 20, and 4% of bovine serum albumin (BSA) in the receptor phase, respectively.

centration in the receptor phase was reduced, is consistent with lower penetration for receptor phase in which the solute is less soluble. An even lower penetration is observed for the BSA receptor phase in which octyl salicylate is 1/40 the solubility in 6% Volpo N20. Figure 4c also shows that the effects of receptor phase variability on penetration is diminished as the receptor sampling rate is increased.

Contribution of Viable Epidermis (aqueous diffusion layer)—Figures 5a and 5b show plots of normalized cumulative amount penetrating versus time when the resistance of the viable epidermis is 1/10th and 10×, respectively, that of the stratum corneum. It is apparent that as the relative resistance of the viable epidermis or aqueous diffusion layer increases, the steady-state flux is reduced and the lag time increased. Further, the significant effect of receptor clearance observed when there is a relatively low viable epidermal resistance effectively disappears when the relative resistance is high.

Contribution of Vehicle–Stratum Corneum Interfacial Resistance—An effect, similar to that when viable epidermis is significant, applies when the relative resistance of the vehicle–stratum corneum interface is high. Figure 5c and Figure 5d show that when this resistance becomes high, the steady-state flux is reduced, lag time is

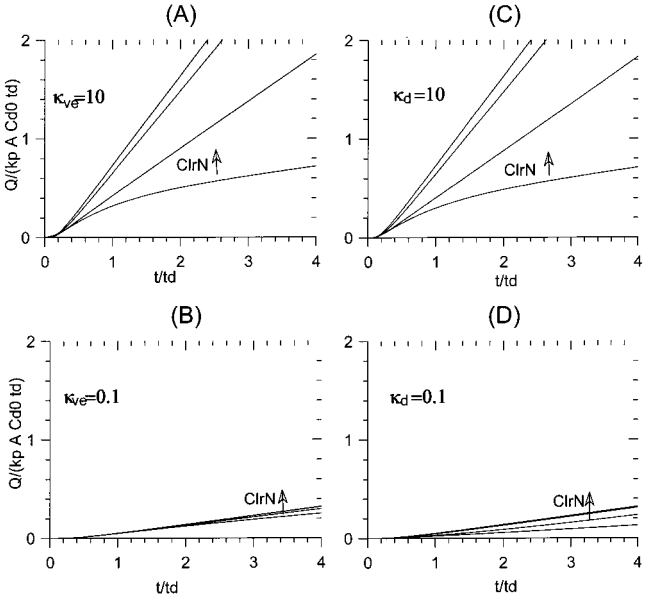

Figure 5—(a,b) Effect of epidermal resistance as described by κ_{ve} (k_p^{ve}/k_p^{sc}) on normalized amount absorbed versus normalized time profiles for $V_{rN} = 0.5$ and $\kappa_d = \infty$; (c,d) Effect of vehicle–stratum corneum resistance as described by κ_d (k_p^{d}/k_p^{sc}) on normalized amount absorbed versus normalized time profiles for $V_{rN} = 0.5$ and $\kappa_{ve} = \infty$. The curves on each graph represent Cl_{rN} values of 0.1, 1, 10, and ∞ starting from the lower curve, respectively.

increased, and removal clearance effects are less pronounced. The receptor (dermal) concentration (not shown) is also decreased.

Steady-State Approximations—It is apparent in Figures 2–5 that a steady-state regime is approached at long times ($t \gg t_d$) by $Q(t)$, $J(t)$, and $C_r(t)$. For ($t \gg t_d$), the resulting $Q_{ss}(t)$, J_{ss}, and $C_{r\,ss}$ are defined by the singularity at $s = 0$. Hence, for $Q_{ss}(t)$:

$$Q_{ss}(t) \approx k_p^{sc} A C_{d0} \left(t \lim_{s \to 0} q(s) + \lim_{s \to 0} \frac{dq(s)}{ds} \right) \qquad (33)$$

where

$$q(s) = \left[\left(\frac{1}{Cl_{rN} + V_{rN} s t_d} + \frac{1}{\kappa_{ve}} + \frac{1}{\kappa_d} \right) \cosh \sqrt{s t_d} + \left(\frac{1}{\sqrt{s t_d}} + \frac{\sqrt{s t_d}}{\kappa_d} \left[\frac{1}{\kappa_{ve}} + \frac{1}{Cl_{rN} + V_{rN} s t_d} \right] \right) \sinh \sqrt{s t_d} \right]^{-1} \qquad (34)$$

Writing eq 33 in an identical form to that described in equation 1 yields expressions for the steady-state flux, J_{ss}, and lag time, lag, given by:

$$J_{ss} = C_{d0} k_p^{sc} \left[1 + \frac{1}{\kappa_{ve}} + \frac{1}{\kappa_d} + \frac{1}{Cl_{rN}} \right]^{-1} \qquad (35)$$

$$\text{lag} = \frac{t_d}{6} \left(1 + \frac{2(Cl_{rN}^2 \kappa_d + \kappa_{ve} Cl_{rN} \kappa_d + \kappa_{ve} Cl_{rN}^2) + 6(Cl_{rN}^2 + \kappa_{ve} Cl_{rN} - \kappa_{ve} V_{rN} \kappa_d)}{Cl_{rN}(Cl_{rN} \kappa_d + \kappa_{ve} \kappa_d + Cl_{rN} \kappa_{ve} + Cl_{rN} \kappa_{ve} \kappa_d)} \right) \qquad (36)$$

The corresponding expression for $C_{r\,ss}$ is

$$C_{r\,ss} = \frac{A C_{d0} k_p^{sc}}{Cl_r} \left[1 + \frac{1}{\kappa_{ve}} + \frac{1}{\kappa_d} + \frac{1}{Cl_{rN}} \right]^{-1} \qquad (37)$$

In the absence of a significant viable epidermis and donor diffusion layer resistance and when sink conditions apply, the steady-state flux due to transport across the stratum corneum J_{ss}^{sc} is given by $C_{d0}k_p^{sc}$. Hence, if the steady-state flux J_{ss} is defined for given values of κ_d, Cl_{rN}, and κ_{ve}, J_{ss}^{sc} can be estimated from J_{ss}, Cl_{rN}, κ_d, and κ_{ve} using eq 35. It is to be noted, that when infinite sink conditions apply, $Cl_r \rightarrow \infty$ so that $Cl_{rN} \rightarrow \infty$, noting $\kappa_{ve} = k_p^{ve}/k_p^{sc}$, $\kappa_d = k_p^d/k_p^{sc}$ (eqs 22, 17) and $J_{ss}^{sc} = C_{d0}k_p^{sc}$, the steady-state flux can be rearranged into the form:

$$J_{ss} = C_{d0}\left(\frac{1}{k_p^{sc}} + \frac{1}{k_p^{ve}} + \frac{1}{k_p^d}\right)^{-1} = C_{d0}k_p' \qquad (38)$$

where k_p' is the apparent permeability coefficient defined in eq 2 and C_{d0} is the donor concentration.

The determinants of J_{ss} under nonsink conditions can be better understood by equating the definition for J_{ss} defined in eqs 2 and 35:

$$J_{ss} = k_p'(C_{d0} - C_{r\,ss}) = C_{d0}k_p^{sc}\left[1 + \frac{1}{\kappa_{ve}} + \frac{1}{\kappa_d} + \frac{1}{Cl_{rN}}\right]^{-1} \qquad (39)$$

Hence, after some rearrangement

$$k_p'\left(1 - \frac{C_{r\,ss}}{C_{d0}}\right) = \left(\frac{1}{k_p^{sc}} + \frac{1}{k_p^{ve}} + \frac{1}{k_p^d} + \frac{1}{k_p^r}\right)^{-1} \qquad (40)$$

where $k_p^r(=Cl_rK_r/A)$ is an "effective" removal permeability coefficient for the receptor. Equation 39 could therefore be expressed as:

$$J_{ss} = C_{d0}\left(\frac{1}{k_p^{sc}} + \frac{1}{k_p^{ve}} + \frac{1}{k_p^d} + \frac{1}{k_p^r}\right)^{-1} = k_p''C_{d0} \qquad (41)$$

Hence, the "effective" permeability coefficient recognizing nonsink condition k_p'' reflects not only the stratum corneum and viable epidermis permeability coefficients, but also the "effective" removal permeability coefficient and donor interface resistance.

Using eq 32 with $s = 0$ and $\hat{J}(0) = J_{ss}$ the steady state concentration in the receptor phase can be defined as:

$$C_{r\,ss} = \frac{C_{d0}A}{Cl_r}\left(\frac{1}{k_p^{sc}} + \frac{1}{k_p^{ve}} + \frac{1}{k_p^d} + \frac{1}{k_p^r}\right)^{-1} \qquad (42)$$

The removal clearance is of particular importance in determining the steady state concentration in the receptor phase $C_{r\,ss}$. Noting eq 41, eq 42 can be expressed as

$$C_{r\,ss} = \frac{C_{d0}Ak_p''}{Cl_r} \qquad (43)$$

Thus, even if the removal permeability coefficient $k_p^r(=Cl_rK_r/A)$ is not rate limiting in epidermal transport, it may be a significant determinant of local tissue concentrations.

The removal permeability coefficient k_p^r or Cl_{rN} is also a major determinant of whether lag time is positive or negative. Rearranging eq 36 yields:

$$\text{lag} = \frac{t_d}{6}\left[1 + \frac{2\left(\frac{1}{\kappa_{ve}} + \frac{1}{Cl_{rN}} + \frac{1}{\kappa_d}\right) + 6\left(\frac{1}{\kappa_{ve}\kappa_d} + \frac{1}{\kappa_d Cl_{rN}} - \frac{V_{rN}}{Cl_{rN}^2}\right)}{\frac{1}{\kappa_{ve}} + \frac{1}{Cl_{rN}} + \frac{1}{\kappa_d} + 1}\right] \qquad (44)$$

It is apparent that lag time will approach $t_d/6$ when κ_{ve}, Cl_{rN}, and κ_d are infinitely large. Further, the potential to have a negative lag time, as shown in Figures 2b and 3a will only occur when Cl_{rN} is small and the receptor volume is relatively large, so that the term in square brackets in eq 44 becomes negative.

In summary the data shown in Figures 2−5 arise from the explicit effects of the vehicle−stratum corneum, stratum corneum, viable epidermal, and "effective" removal permeability constants on k_p'' and, hence, J_{ss}. J_{ss} will be largely defined by whichever permeability constant is smallest. The lag time will be determined not only by these variables but also by receptor volume. Finally, $C_{r\,ss}$ is dependent on the relative magnitudes of $C_{d0}Ak_p''$ and Cl_r (eq 43).

Discussion

The present work has evolved from our overview of mathematical models in percutaneous absorption[2] and the realization that receptor clearance effects had been only examined to a limited extent. A major impetus for the present study was the apparent inconsistency in the results obtained for the penetration of sunscreens through excised human skin and polyethylene membranes *in vitro*.[18,25,26] It was not until we experimented with different receptor compartments as shown in Figure 4c and confirmed that no receptor depletion had occurred that we become aware of the dominant role of composition and sampling or flow rate on the absorption of the lipophilic solutes. Interestingly, the most commonly used receptor fluid remains pH 7.4 phosphate-buffered saline.[27] It has been suggested that $C_r(t)$ should not exceed 10% of its saturation solubility,[28] as a consequence a greater variety of receptor phases ranging from 25% (v/v) aqueous ethanol, 50% aqueous methanol, various albumin solutions, and various surfactant solutions[27] may be necessary when the water solubility is less than 10 μg/mL.[29] However, this principle is compromised by effects of solubilizers, particularly on the stratum corneum.[27]

The choice of a suitable receptor solution can also be compromised by a need to maintain skin viability.[19] Macpherson et al.[30] have reported that the pesticide aldrin is absorbed through skin into ethanol−water but not aqueous receptor fluids. However, skin viability was not supported by an ethanol−water system. It may therefore be difficult to find a suitable receptor solution providing both *in vivo* equivalent "sink" conditions and viability. In this instance, it may be preferable to estimate k_p^r from Cl_r and K_r and substitute into eq 41 to find k_p', i.e., $1/k_p' = 1/k_p'' - 1/k_p^r$. It should be noted that a flow through *in vitro* system will facilitate both skin viability[31] and consistency in Cl_r over time.

Numerical inversion of Laplace transforms defined by eqs 27 to 32 have been used in this work. The validity of such an approach has been studied by many authors including Purves[32] who showed that numerical inversion of the Laplace transform for the two compartment dispersion model described by Roberts et al.[33] was identical to

the analytical solution given by them. A better understanding of the behavior of a system is often achieved by an examination of the limits of the Laplace solution and the resulting analytical solutions. Such an approach has been described by Guy and Hadgraft[20,22] for other models in percutaneous absorption.

In this work we have reported the steady-state flux and lag time which can be defined from Laplace expressions as $s \rightarrow 0$. The resulting expressions show the interrelationship between receptor phase solubility, receptor phase volume, and sampling rate on *in vitro* absorption kinetics, thus allowing an estimation of k_p' when $C_{r\,ss}$ becomes significant. These relationships are also important in quantitatively interpreting the effects of perfusate flow rate on percutaneous absorption[9−11] and the reported underestimated *in vivo* absorption provided by a number of *in vitro* studies on lipophilic solutes.[12−19]

This model is also directly applicable to *in vivo* studies in both humans and animals. The expression given allows the combined affects of epidermal transport kinetics and changing blood flow on *in vivo* absorption to be understood as codeterminants of plasma concentration−time profiles after topical application. This effect is most explicitly apparent in the expressions for the steady-state flux and lag times. Cooper[34] considered some pharmacokinetics of solutes into a single compartmental model after topical application. Similar, but more complex expressions, can be developed when the present model is combined with the disposition of drugs in the body. The *in vivo* pharmacokinetics are probably best described in terms of the Laplace transform of plasma concentration $\hat{C}_p(s)$, or another biological concentration effect being expressed as a potentially complex function of parameters describing both the absorption through skin and disposition kinetics in the systemic circulation. As discussed by Roberts *et al*.[2] for a case when plasma concentration does not affect the absorption kinetics (infinite sink condition), $\hat{C}_p(s)$ can be expressed as a product of the input into the systemic circulation $\hat{J}(s)$ and disposition in the body Cl(*s*) ie $\hat{C}_p(s) = \hat{J}(s)\mathrm{Cl}(s)$. The solution for $C_p(t)$ is then most readily obtained by numerical inversion of the resulting Laplace transform $\hat{C}_p(s)$. The steady-state plasma concentration in this case is simply J_{ss}/CL, where CL is the clearance of solute from the body.

Equation 41 is an extension of expressions given by Scheuplein and Blank[35] and Robinson.[36] Scheuplein and Blank[35] expressed k_p^r in terms of the skin blood flow in the upper 200 μm of the dermis. They suggested that the removal permeability coefficient was large in comparison to the stratum corneum permeability coefficient, except possibly for small lipid-soluble molecules like octanol and permeant gases. In reality, the removal permeability coefficient *in vivo* is defined by both clearance into perfusing blood and transport into deeper tissues.[37] The latter process, however, normally contributes only 10−30% to the overall removal clearance ($k_p^r A/K_r$). Benowitz et al.[38] suggested vasoconstriction of dermal blood vessels by intravenously administered nicotine as a cause for a slowing of nicotine transdermal absorption.

Importantly, eq 43 shows that even if the removal permeability coefficient $k_p^r (= \mathrm{Cl}_r K_r/A)$ is not rate limiting in epidermal transport, it may be a significant determinant of local tissue concentrations. Increased local tissue concentrations have been observed when the local blood flow has been decreased in perfused skin preparations.[39,40] A reduction of effective blood flow by vasoconstriction[41] also leads to higher local tissue concentrations. A reduced form of eq 43 corresponding to the case of $K_r = 1$, k_p^{ve}, and k_p^d not being rate limiting has been used to explain structure−permeability absorption relationships:[1]

$$C_{r\,ss} = \frac{C_{d0} A k_p^{sc}}{\mathrm{Cl}_r(1 + 1/\mathrm{Cl}_{rN})} = \frac{C_{d0} A k_p^{sc}}{\mathrm{Cl}_r + k_p^{sc} A/K_r} \tag{45}$$

Roberts[1] has suggested that $\mathrm{Cl}_r \ll k_p^{sc} A/K_r$ for phenols so that their viable epidermal concentrations reflect those applied as aqueous solutions. In contrast, for steroids $\mathrm{Cl}_r \gg k_p^{sc} A/K_r$, and low concentrations will be found in the viable epidermis. The resulting expression for $\mathrm{Cl}_r \gg k_p^{sc} A/K_r$ is:

$$C_{r\,ss} = \frac{C_{d0} A k_p^{sc}}{\mathrm{Cl}_r} \tag{46}$$

Equation 46 is now in the same form as the classical steady-state plasma concentration expression associated with a constant input rate ($C_{d0} A k_p^{sc}$) and clearance from the body.[3]

Removal rate *in vitro* and *in vivo* is a major determinant of the apparent lag time. When k_p^{ve} and k_p^d are very large, lag reduces to:

$$\mathrm{lag} = \frac{t_d}{6}\left(1 + \frac{2\mathrm{Cl}_{rN} - 6V_{rN}}{\mathrm{Cl}_{rN}(1 + \mathrm{Cl}_{rN})}\right) \tag{47}$$

Thus a negative lag is predicted when $V_{rN} > (\mathrm{Cl}_{rN} + 3)\,\mathrm{Cl}_{rN}/6$. The remaining complexity of this expression and the difficulty in estimating lag times accurately from experimental data provides some justification in recommending that lag time values be interpreted with caution. In particular, it should be noted that short or negative lag times may be associated with a long time to reach steady state. We therefore consider an approximate estimate of this time when only Cl_{rN} is rate limiting. When κ_{ve}, $\kappa_d \rightarrow \infty$, the expression for $\hat{Q}(s)$ reduces to:[2]

$$\hat{Q}(s) = \frac{k_p^{sc} A C_{d0}}{s^2} \frac{\sqrt{st_d}}{\dfrac{\sqrt{st_d}}{\mathrm{Cl}_{rN} + V_{rN} st_d}\cosh\sqrt{st_d} + \sinh\sqrt{st_d}} \tag{48}$$

Inverting this equation to time domain yields:

$$Q(t) = Q_{ss}(t) + k_p^{sc} A C_{d0} t_d \sum_{n=1}^{n=\infty} \frac{\exp(-\gamma_n^2/t_d)}{\gamma^4{}_n \dfrac{d}{dx} f(x)|_{x=-\gamma_n{}^2}} \tag{49}$$

where $Q_{ss}(t)$ is defined in eq 1,

$$f(x) = \frac{1}{\mathrm{Cl}_{rN} + V_{rN} x}\cosh\sqrt{x} + \frac{\sinh\sqrt{x}}{\sqrt{x}} \tag{50}$$

and γ_n are roots of equation:

$$\tan\gamma = \frac{\gamma}{V_{rN}\gamma^2 - \mathrm{Cl}_{rN}} \tag{51}$$

If time to steady state t_{ss} is defined as the time for $Q(t) - Q_{ss}(t)$ to become less than $[Q(0) - Q_{ss}(0)]/e$, then t_{ss} can be written as:

$$t_{ss} \approx \frac{t_d}{\gamma_1^2} \tag{52}$$

where *e* is the base of the natural logarithm and γ_1 is the smallest root of eq 51. When $(\mathrm{Cl}_{rN}/V_{rN})^{1/2} < \pi/2$, it can be

shown that $(Cl_{rN}/V_{rN})^{1/2} < \gamma_1 < \pi/2$, and the upper bound on t_{ss} is therefore $t_d V_{rN}/Cl_{rN}$. Numerical inversion of eq 48 for $Q(t)$ was used to confirm that $t_d V_{rN}/Cl_{rN}$ is a reasonable approximation for t_{ss} for $Cl_{rN} < 3$ and when lag is negative. Hence, whereas lag is short or negative for large V_{rN} and small Cl_{rN}, t_{ss} is normally long.

A number of authors have suggested that the viable epidermis or aqueous diffusion layer may be a transport limitation between the stratum corneum and the receptor phase. This limitation could be due to a desorption process[22,42] or a viable epidermis/aqueous diffusion layer resistance.[4,6,7] In each case, an infinitely rapid sampling rate is implicitly assumed. Figure 5 showed that a dominant viable epidermal resistance will reduce the steady-state flux, increase the lag time, and reduce the effect of sampling clearance. A comparison of Figures 5a and 5b shows that the presence of ether viable epidermis or equivalent transport limitation or a sampling limitation may be discerned by examining the shapes of the profiles. A viable epidermis transport limitation will be defined by a profile which is similar in shape to the traditional profile in the absence of such a limitation but characterized by a lower steady-state flux. In contrast, a sampling limitation is defined by a curvilinear profile with a negative intercept.

The skin first-pass effect may be important in interpreting some percutaneous absorption studies. Hotchkiss[43] has reviewed the vide range of solutes metabolized by skin. As well as metabolism by skin, there may be an incomplete availability of solutes from vehicles. Skin microflora has been shown to metabolize benzoyl peroxide, glyceryl trinitrate, betamethasone-17-valerate, and estradiol.[43] However, the half-lives for metabolism are often long, limiting the affect on absorption kinetics. In contrast, irreversible adsorption (sometimes with chemical reaction) have been observed with solutes such as hair dyes. Indeed, the competing adsorption provided by hair for hair dyes and other solutes[44] would reduce availability further. In the specific case when there is no epidermal resistance and there is a "perfect" receptor sink, the values for J_{ss}, Q_{ss}, and $C_{r\,ss}$ may be reduced to $F_m J_{ss}$, $F_m Q_{ss}$, and $F_m C_{r\,ss}$[3] where $F_m < 1$ is the availability of unmetabolized solute due to metabolism in the epidermis. When the epidermal resistance is finite or there is not a "perfect" receptor sink as well as when metabolism or irreversible binding takes place in the stratum corneum, metabolism will affect both the flux profiles and time lags due to the diffusive processes involved. The appropriate model for this situation is developed in a later paper.

The present analysis has also included a vehicle−stratum corneum interfacial permeability constant. Such a term is particularly relevant to transdermal patch systems where a rate-limiting membrane or adhesive may affect or control the rate of delivery from the patch material. The term is also applicable to solutions in which there is an unstirred layer in the vehicle at the interface or when there is a partitioning limitation in the transfer of solute from the vehicle to the stratum corneum. There has been an assumed flux from a constant donor concentration of solute in the vehicle into the stratum corneum in certain of the percutaneous absorption kinetics models.[22] This assumed flux can also be represented by the vehicle−stratum corneum interfacial permeability constant defined in the present model.

The present model has been limited to a constant well-mixed donor vehicle with various permeability "barriers" determining transport. In practice, diffusion in the vehicle may also determine percutaneous absorption. Guy and Hadgraft[45] have recognized such an effect in their evaluation of the effect of applied vehicle thickness on the percutaneous absorption of solutes. When diffusivity in the vehicle is rate limiting, with permeability "barriers" present, the profiles for $Q(t)$ versus t are described by a burst effect.[46] The shapes of the profiles do not differ greatly from those obtained in this work, assuming a constant donor concentration but with accumulation to steady state in the receptor (dermis). Analysis of donor concentrations on the vehicle−stratum corneum interface before or on completion of a percutaneous absorption study or varying the removal rate from the receptor is therefore required to distinguish these two effects.

Conclusion

This work has shown that the experimental protocol and *in vivo* perfusion conditions can markedly affect percutaneous absorption kinetics. These need to be recognized in undertaking percutaneous absorption studies and their perturbations on the resulting kinetics realized from the shape of the profiles obtained, as discussed in this work. Knowledge of the exact conditions can enable actual permeability coefficients to be estimated from apparent steady-state fluxes. Such calculations are particularly pertinent that nonsink receptor conditions be used to maintain viable skin. A major limitation in assessing the current literature for structure−skin permeability relationships[47,48] is the lack of available experimental information to make the appropriate corrections to reported steady-state permeability constants.

A second outcome of this work is the description of the effects of perfusate flow rate, finite receptor volume, and viable epidermis/aqueous diffusion layer resistance on percutaneous absorption kinetics and dermal concentrations. A necessary limitation in the present work to derive simple Laplace expressions has been the assumption of well-stirred vehicle and receptor phases. A subsequent paper will consider the effects of finite donor volume and epidermal metabolism on percutaneous absorption kinetics.

References and Notes

1. Roberts, M. S. Structure-permeability considerations in percutaneous absorption. In *Prediction of Percutaneous Penetration*; Scott, R. C., Guy, R. H., Hadgraft, J., Eds., IBC Technical Services: London, 1991; Vol. 2, pp 210−228.
2. Roberts, M. S.; Anissimov, Y. G.; Gonsalvez, R. A. Mathematical models in percutaneous absorption. In *Percutaneous Absorption*, 3rd ed.; Bronaugh, R., Maibach, H. I., Eds., Marcel Dekker: New York, 1998; pp 1−55.
3. Roberts, M. S.; Walters, K. A. The relationship between structure and barrier function of skin. In *Dermal Absorption and Toxicity Assessment*; Roberts, M. S., Walters, K. A., Eds., Marcel Dekker: New York, 1998; pp 1−42.
4. Scheuplein, R. J.; Blank, I. H. Mechanism of percutaneous absorption iv. penetration of non electrolytes (alcohols) from aqueous solutions and from pure liquids. *J. Invest. Dermatol.* **1973**, *60*, 286−296.
5. Roberts, M. S.; Anderson, R. A.; Swarbrick, J. Permeability of human epidermis to phenolic compounds. *J. Pharm. Pharmacol.* **1977**, *29*, 677−683.
6. Roberts, M. S.; Anderson, R. A.; Swarbrick, J.; Moore, D. E. The percutaneous absorption of phenolic compounds: The mechanism of diffusion across the stratum corneum. *J. Pharm. Pharmacol.* **1978**, *30*, 486−490.
7. Cleek, R. L.; Bunge, A. L. A new method for estimating dermal absorption from chemical exposure. 1. General approach. *Pharm. Res.* **1993**, *10*, 497−506.
8. Siddiqui, O.; Roberts, M. S.; Polack, A. E. Percutaneous absorption of steroids relative contributions of epidermal penetration and dermal clearance. *J. Pharmacokinet. Biopharm.* **1989**, *17*, 405−424.
9. Crutcher, W.; Maibach, H. I. The effect of perfusion rate on *in vitro* percutaneous penetration. *J. Invest. Dermatol.* **1969**, *53*, 264−269.
10. Anjo, D. M.; Feldman, R. J.; Maibach, H. I. Methods for predicting percutaneous absorption in man. In *Percutaneous*

absorption of steroids; Mauvais-Jarvis, P., Vickers, C. F. H., Wepierre, J., Eds., Academic Press: New York, 1980; Chapt. 3.
11. Bronaugh, R. L.; Stewart, R. F. Methods for *in vitro* percutaneous absorption studies IV: The flow-through diffusion cell. *J. Pharm. Sci.* **1985**, *74*, 64−67.
12. de Lange, J.; van Eck, P.; Bruijnzeel, P. L.; Elliot, G. R. The rate of percutaneous permeation of xylene, measured using the perfused pig ear model, is dependent on the effective protein concentration in the perfusing medium. *Toxicol. Appl. Pharmacol.* **1994**, *127*, 298−305.
13. Moloney, S. J. The *in vitro* percutaneous absorption of glycerol trioleate through hairless mouse skin. *J. Pharm. Pharmacol.* **1988**, *40*, 819−821.
14. Roper, C. S.; Howes, D.; Blain, P. G.; Williams, F. M. Prediction of the percutaneous penetration and metabolism of dodecyl decaethoxylate in rats using *in vitro* models. *Arch. Toxicol.* **1995**, *69*, 649−654.
15. Wester, R. C.; Maibach, H. I.; Bucks, D. A.; McMaster, J.; Mobayen, M.; Sarason, R.; Moore, A. Percutaneous absorption and skin decontamination of PCBs: *in vitro* studies with human skin and *in vivo* studies in the rhesus monkey. *J. Toxicol. Environ. Health.* **1990**, *31*, 235−246.
16. Roper, C. S.; Howes, D.; Blain, P. G.; Williams, F. M. Percutaneous penetration of 2-phenoxyethanol through rat and human skin. *Food Chem. Toxicol.* **1997**, *35*, 1009−1016.
17. Kasting, G. B.; Francis, W. R.; Bowman, L. A.; Kinnett, G. O. Percutaneous absorption of vanilloids: *in vivo* and *in vitro* studies. *J. Pharm. Sci.* **1997**, *86*, 142−146.
18. Jiang, R.; Roberts, M. S.; Prankerd, R. J.; Benson, H. A. E. Percutaneous absorption of sunscreen agents from formulations: self association of octylsalicylate and effects on skin flux. *J. Pharm. Sci.* **1997**, *86*, 791−796.
19. Bronaugh, R. L. A flow-through diffusion cell. In *In vitro Percutaneous Absorption: Principles, Fundamentals and Applications*; Bronaugh, R. L., Maibach, H. I., Eds., CRC Press: Boca Raton, 1991; pp 17−23.
20. Guy, R. H.; Hadgraft, J. Theoretical comparison of release rates of drugs into sink and nonsink conditions. *J. Pharm. Sci.* **1981**, *70*, 1243−1245.
21. Parry, G. E.; Bunge, A. L.; Silcox, G. D.; Pershing, L. K.; Pershing, D. W. Percutaneous absorption of benzoic acid across human skin. *in vitro* experiments and mathematical modelling. *Pharm. Res.* **1990**, *7*, 230−236.
22. Guy, R. H.; Hadgraft, J. Physicochemical interpretation of the pharmacokinetics of percutaneous absorption. *J. Pharmacokinet. Biopharm.* **1983**, *11*, 189−203.
23. Bronaugh, R. L.; Stewart, R. F. Methods for *in vitro* percutaneous absorption studies III: Hydrophobic compounds. *J. Pharm. Sci.* **1984**, *73*, 1255−1258.
24. Yano, Y.; Yamaoka, K.; Tanaka, H. A non-linear least squares program, MULTI(FILT), based on fast inverse laplace transform (FILT) for microcomputers. *Chem. Pharm. Bull.* **1989**, *37*, 1535−1538.
25. Jiang, R. *Effect of Vehicle Formulation on Skin Permeation of Sunscreen Agents*. Ph.D. dissertation, University of Queensland, 1998.
26. Jiang, R.; Benson, H. A.; Cross, S. E.; Roberts, M. S. In vitro human epidermal and polyethylene membrane penetration and retention of the sunscreen benzophenone-3 from a range of solvents. *Pharm. Res* **1998**, *15*, 1863−1868.
27. Brain, K. R.; Walters, K. A.; Watkinson, A. C. Investigation of skin permeation *in vitro*. In *Dermal Absorption and Toxicity Assessment*; Roberts, M. S., Walters, K. A., Eds., Marcel Dekker: New York, 1998; pp 161−187.
28. Skelly, J. P.; Shah, V. P.; Maibach, H. I.; et al. FDA and AAPS report of the workshop on principles and practices of *in vitro* percutaneous penetration studies: relevance to bioavailability and bioequivalence. *Pharm. Res.* **1987**, *4*, 265−267.
29. Bronaugh, R. L. *In vitro* methods for the percutaneous absorption of pesticides. In *Dermal Exposure to Pesticide Use*; Honeycutt, R., Zweig, G., Ragsdale, N. N., Eds.; American Chemical Society: Washington, DC, 1985; pp 33−41.
30. Macpherson, S. E.; Scott, R. C.; Williams, F. M. Percutaneous absorption and metabolism of aldrin by rat skin in diffusion cells. *Arch. Toxicol.* **1991**, *65*, 599−602.
31. Bronaugh, R. L. Current issues in the *in vitro* measurements of percutaneous absorption. In *Dermal Absorption and Toxicity Assessment*; Roberts, M. S., Walters, K. A., Eds., Marcel Dekker: New York, 1998; pp 155−159.
32. Purves, R. D. Accuracy of numerical inversion of laplace transforms for pharmacokinetic parameter estimation. *J. Pharm. Sci.* **1995**, *84*, 71−74.
33. Roberts, M. S.; Donaldson, J. D.; Rowland, M. Models of hepatic elimination: comparison of stochastic models to describe residence time distributions and to predict the influence of drug distribution, enzyme heterogeneity and systemic recycling on hepatic elimination. *J. Pharmacokinet. Biopharm.* **1988**, *16*, 41−83.
34. Cooper, E. R. Pharmacokinetics of skin penetration. *J. Pharm. Sci.* **1976**, *65*, 1396−1397.
35. Scheuplein, R. J.; Blank, I. H. Permeability of the skin. *Physiol. Rev.* **1971**, *51*, 702−747.
36. Robinson, P. J. Prediction-simple risk models and overview of dermal risk. In *Dermal Absorption and Toxicity Assessment*; Roberts, M. S., Walters, K. A., Eds.; Marcel Dekker: New York, 1998; pp 203−229.
37. Singh, P.; Roberts, M. S. Dermal and underlying tissue pharmacokinetics of salicylic acid after topical application. *J. Pharmacokinet. Biopharm.* **1993**, *21*, 337−373.
38. Benowitz, N. L.; Jacob, P.; Olsson, P.; Johansson, C. J. Intravenous nicotine retards transdermal absorption of nicotine: evidence of blood flow−limited percutaneous absorption. *Clin. Pharmacol. Ther.* **1992**, *52*, 223−230.
39. Riviere, J. E.; Sage, B.; Williams, P. L. Y. Effects of vasoactive drugs on transdermal lidocaine iontophoresis. *J. Pharm. Sci.* **1991**, *80*, 615−620.
40. Cross, S. E.; Roberts, M. S. Importance of dermal blood supply and epidermis on the transdermal iontophoretic delivery of monovalent cations. *J. Pharm. Sci.* **1995**, *84*, 584−592.
41. Singh, P.; Roberts, M. S. Effects of vasoconstriction on dermal pharmacokinetics and local tissue distribution of compounds. *J. Pharm. Sci.* **1994**, *83*, 783−791.
42. Kubota, K.; Ishizaki, T. A. Theoretical consideration of percutaneous drug absorption. *J. Pharmacokinet. Biopharm.* **1985**, *13*, 55−72.
43. Hotchkiss, S. A. M. Dermal metabolism. In *Dermal Absorption and Toxicity Assessment*; Roberts, M. S., Walters, K. A., Eds.; Marcel Dekker: New York, 1998; pp 43−101.
44. Dressler, W. E. Percutaneous absorption of hair dyes. In *Dermal Absorption and Toxicity Assessment*; Roberts, M. S., Walters, K. A., Eds.; Marcel Dekker: New York, 1998; pp 489−536.
45. Guy, R. H.; Hadgraft, J. A theoretical description relating skin penetration to the thickness of the applied medicament. *Int. J. Pharm.* **1980**, *6*, 321−332.
46. Hadgraft, J. Calculations of drug release rates from controlled release devices. The slab. *Int. J. Pharm.* **1979**, *2*, 177−194.
47. Potts, R. O.; Guy, R. H. Predicting skin permeability. *Pharm. Res.* **1992**, *9*, 663−669.
48. Roberts, M. S.; Pugh, W. J.; Hadgraft, J.; Watkinson, A. C. Epidermal permeability-penetrant structure relationships: 1. An analysis of methods of predicting penetration of monofunctional solutes from aqueous solutions. *Int. J. Pharm.* **1995**, *126*, 219−233.

Acknowledgments

We are grateful to the financial support of the National Health & Medical Research Council of Australia and the Queensland and New South Wales Lions Medical Research Foundation.

JS990053I

Physical Properties of Parabens and Their Mixtures: Solubility in Water, Thermal Behavior, and Crystal Structures

FERDINANDO GIORDANO,*,† RUGGERO BETTINI,† CRISTINA DONINI,† ANDREA GAZZANIGA,‡ MINO R. CAIRA,§ GEOFFREY G. Z. ZHANG,||,⊥ AND DAVID J. W. GRANT||

Contribution from *Dipartimento Farmaceutico, University of Parma, Viale delle Scienze, 43100 Parma, Italy, Istituto Chimico Farmaceutico, University of Milan, Viale Abruzzi 43, 20131 Milan, Italy, Department of Chemistry, University of Cape Town, Rondebosch 7701, South Africa, and Department of Pharmaceutics, College of Pharmacy, University of Minnesota, Weaver-Densford Hall, 308 Harvard Street, S. E., Minneapolis, Minnesota 55455-0343.*

Received February 9, 1999. Final revised manuscript received June 28, 1999.
Accepted for publication August 30, 1999.

Abstract □ The peculiar solubility behavior of propylparaben (propyl ester of 4-hydroxybenzoic acid) in aqueous solution, when tested separately and together with methyl-, ethyl-, and butyl-parabens, has been investigated in detail. The results clearly indicate that the decrease in solubility (≈50% compared to the solubility value of propylparaben alone) is typical of those mixtures containing also ethylparaben, as demonstrated by solubility experiments on binary, ternary, and quaternary mixtures of the parabens. Phase diagrams of all the six binaries show that propylparaben and ethylparaben are the only pair that form almost ideal solid solutions near the melting temperatures. Moreover, phase-solubility analysis shows that propylparaben and ethylparaben, at room temperature, can also form solid solutions whose solubility is related to the composition of the solid phase at equilibrium. To achieve an independent confirmation of the possible solid solution formation that supports the above interpretation of the solubility behavior, the crystal structures of the four parabens have been examined and isostructurality has been found to exist only between ethylparaben and propylparaben. Powder X-ray diffraction has also been performed on ethylparaben, propylparaben, and their solid solutions obtained by recrystallization from water. The progressive shift of distinctive diffraction peaks with phase composition clearly indicates that propylparaben and ethylparaben form substitutional solid solutions. The small value (<1) of the disruption index provides thermodynamic support for substitutional solid solutions based on isostructural crystals.

Introduction

Parabens (esters of 4-hydroxybenzoic acid) are preservatives widely used in cosmetics, food products, and pharmaceutical formulations. Parabens are generally used in combination to take advantage of synergistic effects, are active over a wide pH range, have a broad spectrum of antimicrobial activity, and are most effective against yeasts and molds.[1] The antimicrobial activity of the parabens increases as the chain length of the alkyl moiety is increased; their aqueous solubility, however, decreases, so the sodium salts of the parabens are also frequently used in formulations. An alternative approach to increasing solubility is the use of cyclodextrin complexation. Many reports[2−4] deal with the formation of inclusion compounds with natural and semisynthetic cyclodextrins to increase the aqueous solubility of selected parabens.

Recently[5] the solubilities of four parabens (methyl, ethyl, propyl, and butyl esters) have been measured singly and together in water and in aqueous solutions of 2-hydroxypropyl-β-cyclodextrin. Aqueous solubilities (without 2-hydroxypropyl-β-cyclodextrin) of all parabens were found to agree well with literature values[6,7] when determined separately. Rather surprisingly, however, when the solubilities in water at 25 °C of the four parabens were measured together, the solubility of propylparaben was found to be reduced by approximately 50%, with relatively small increases or decreases (within 10%) for methyl-, ethyl-, and butyl-paraben.

Changes of solubility generally can be attributed to the formation of hydrates, recrystallization of more stable polymorphs, or interaction phenomena in solution as well as in the solid state.[8−11] In the system under investigation, it is intriguing and stimulating that the solubility of only one component (propylparaben) seemed to be significantly affected when tested in the combination of four homologues. The massive decline of propylparaben solubility has hitherto remained unexplained: furthermore no evaluation of the physical nature or chemical composition of the solid phases present at equilibrium has been reported.

Aiming to find a plausible explanation for the unpredictable behavior described above for propylparaben[5] we report here the results of investigations with the same four homologues (methyl- (M), ethyl- (E), propyl- (P), and butyl- (B) paraben). In particular, the solubilities in water of each paraben from the binary, ternary, and quaternary mixtures are measured. The solid phases recovered at equilibrium from solubility experiments are characterized by their thermal behavior, using differential scanning calorimetry (DSC), thermogravimetry (TGA), and hot stage microscopy (HSM), by their composition using high performance liquid chromatography (HPLC), and by their structural properties, using powder X-ray diffractometry (PXRD). The solubility profiles at ambient temperature are also investigated by means of phase solubility analysis as suggested by Higuchi and Connors.[12] Moreover, the phase diagrams of all possible binaries are drawn from DSC measurements and compared with the corresponding calculated ones.

Finally, to complete the physicochemical characterization and to accomplish a comprehensive understanding of the solid state properties of these compounds by relating molecular scale properties and bulk properties, the crystal structures of propylparaben and butylparaben are also determined and critically evaluated together with those of

* Corresponding author: Tel: +39-0521-905079, fax: +39-0521-905006, e-mail: giordano@unipr.it.
† University of Parma.
‡ University of Milan.
§ University of Cape Town.
|| University of Minnesota.
⊥ Present address: Abbott Laboratories, Department 04P3, Building AP9, 100 Abbott Park Road, Abbott Park, IL 60064-6120.

10.1021/js9900452 CCC: $18.00
Published on Web 10/07/1999

methyl paraben and ethyl paraben whose crystallographic data have been reported previously.[13,14]

Experimental Section

Materials—Methyl-, ethyl-, propyl-, and butyl-paraben were obtained from Sigma Chemical Company (St. Louis, MO) and were used as received. Organic solvents were of chromatographic grade purity. Double-distilled water was used for solubility experiments and buffer preparation.

Aqueous Solubility—The solubility in water for each paraben, singly or from the binary, ternary, and quaternary mixtures, was determined by equilibrating the liquid phase with a known weight of each component in powdered form at 25.0 ± 0.5 °C with agitation. In all cases, a 5-day period had previously been shown to afford equilibrium. Three independent sets of experiments were performed on single components or their combinations.

Recrystallization from Water—Mixtures containing E and P in molar ratios of 1:1 and 1:2 were recrystallized from water by dissolving 200 mg of the mixture in 200 mL of water at 75 °C and allowing, after filtration, the spontaneous cooling to ambient temperature. The crystalline solid phase which separated at equilibrium was recovered by vacuum filtration: both the filtrate and the solid phase were analyzed for E and P contents by HPLC.

HPLC Analysis—Samples of the solution under examination, appropriately diluted with the mobile phase (methanol/0.04 M ammonium acetate, 55:45, v:v), were analyzed with an HPLC system (LC-10 AS Shimadzu, Japan); detector (UV−vis, SPD-10A Shimadzu) at λ = 256 nm; column (C-18 BondapaK, Waters, Milford, MA) 10 μm, 3.9 × 300 mm; flow rate 0.8 mL min^{-1}. Peak integration was performed with a C-R6A Cromatopac (Shimadzu, Japan). Linearity of response in the 0−20 mg mL^{-1} concentration range was assessed for each compound from plots of peak area against concentration.

Thermal Analyses—Differential scanning calorimetry (DSC) and thermogravimetry (TGA) were performed by means of a Mettler 821e STARe system and a TG50 cell (Mettler Toledo, Switzerland): hot stage microscopy (HSM) was carried out with a HFS 91 Linkam hot stage (Linkam, UK) and a Nikon Labophot microscope (Nikon, Japan).

Experimental phase diagrams of binary systems were constructed by plotting melting temperatures taken from DSC curves versus composition. Solid mixtures of each binary system were prepared by combining appropriate volumes of methanolic solutions with known concentrations of each paraben and slowly evaporating the solvent under reduced pressure. Four to six samples for each mixture were scanned at 10 K min^{-1} from 40 °C to a temperature 10 K above the melting point of the higher melting component under a flux of dry nitrogen (100 mL min^{-1}).

Calculation of the liquidus curves was performed using the Schröder−Van Laar equation[15] in its simplified form:

$$\ln x = \frac{\Delta H_A^f}{R}\left(\frac{1}{T_A^f} - \frac{1}{T^f}\right)$$

where x is the mole fraction of the more abundant component of a mixture whose melting terminates at T^f (in Kelvin), ΔH_A^f (cal mol^{-1}), and T_A^f (also in Kelvin) are the enthalpy of fusion and the melting point of the pure component, respectively, and R is the gas constant, 1.9869 cal mol^{-1} K^{-1}.

Phase Solubility Analyses on Binary Systems—Fixed amounts (approximately twice the quantity necessary for a saturated solution) of the accurately weighed paraben with increasing amounts (up to an excess with respect to its solubility) of the second paraben under investigation were placed in 100 mL flasks, which were then filled to volume with water. After equilibration at constant temperature (25.0 ± 0.5 °C), the suspension was filtered through a 0.22 μm Millipore filter. The filtrate, after appropriate dilution with the mobile phase (described under HPLC analysis), was assayed for each paraben concentration, while the solid residue was examined by thermal analyses (DSC and TGA). The concentrations of both parabens in solution were then plotted against the total amount of the second paraben in the system. The compositions of both the solid and liquid phases at equilibrium for each preparation were thereby precisely determined.

X-ray Crystal Structure Determination—Large transparent prismatic crystals of propylparaben and butylparaben were grown from solution in methanol and cyclohexane, respectively, by slow evaporation of the solvent at ambient temperature and pressure. Crystal densities were measured at 20 °C by flotation in aqueous KI solution. Preliminary unit cell and space group data for each species were obtained from precession photographs taken with Cu Kα-radiation (λ = 1.5418 Å). For the propylparaben crystal, the space group $P2_1/c$ was uniquely determined from the systematic absences, whereas for butylparaben, extinction conditions indicated the space groups Cc or $C2/c$. The latter, chosen on the basis of intensity statistics which indicated a centric distribution, was vindicated by successful structural solution and refinement.

Reflection intensity data were measured at 293(2) K on a Nonius Kappa CCD diffractometer using Mo Kα radiation (λ = 0.71069 Å) and a crystal to detector distance of 35 mm. Both data collections involved 1.0° ϕ-rotations followed by 1.0° ω-rotations and exposure times per frame of 34 s (propylparaben) and 20 s (butylparaben), yielding 21849 and 11601 measured reflection intensities, respectively. Cell refinement and data reduction were performed with programs DENZO16 and maXus17. Both structures were solved by direct methods (program SHELXS8618) which revealed the non-hydrogen atoms of the two independent molecules in the asymmetric unit of the propylparaben crystal and the single molecule in that of the butylparaben crystal. The hydrogen atoms were located in difference electron-density maps; those attached to C were included in idealized positions in a riding model (C−H 0.93−0.97 Å) and the hydroxyl H atoms refined freely. All H atoms were treated isotropically and non-H atoms anisotropically. Full-matrix least-squares refinement on F^2 was performed with program SHELXL9319. The C atoms of the alkyl chain of the butylparaben molecule were found to be disordered, all four occupying two alternative sites each. Final refinement yielded site-occupancy factors of 0.61 and 0.39 for the two arrangements.

Powder X-ray Diffraction (PXRD)—PXRD traces were recorded on a Philips PW1050/25 goniometer with Cu Kα-radiation (λ = 1.5418 Å) produced at 50 kV and 40 mA. The system was calibrated with a silicon standard which yielded peak positions of 28.45 ± 0.01° 2θ before and after each scan. All samples were manually ground, sieved (through a 200 μm screen), and packed successively in the same aluminum sample holder for reproducibility of conditions, taking care also to minimize preferred orientation effects. Full PXRD traces (scan speed 1.0° 2θ min^{-1}, step size 0.1° 2θ, 2θ-range 8−32°) were recorded for pure ethylparaben (E), pure propylparaben (P), and the two solid phases obtained by recrystallization from water of mixtures of E and P of molar compositions 1:1 and 1:2, respectively.

PXRD traces in the narrow 2θ-range 23.0−26.5° were recorded for the same four samples. To optimize the resolution of these traces, each sample was scanned in three passes, accumulating the counts at a scan speed of 0.50° 2θ min^{-1} with a step size of 0.02° 2θ.

Indexing of reflections was achieved using program Lazy Pulverix,[20] with single-crystal X-ray data (unit cell, space group, atomic coordinates, thermal parameters) for E and P as input.

Results and Discussion

Solubility—The solubility data from binary, ternary, and quaternary mixtures are collected in Table 1. It is evident that a decrease of P solubility in water (approximately 50%) can be detected only for mixtures containing also E (bold figures), as shown previously by McDonald et al.[5] for the combination of the four parabens. Furthermore, a decrease (approximately 10%) of E solubility from all mixtures containing P is also seen.

Crystal Structures of Parabens—Table 2 summarizes the available single crystal X-ray data and selected physical properties of the four parabens under discussion. It should be noted that for compounds M, E, and P, the number of molecules per unit cell (Z) exceeds the site multiplicity of the general equivalent positions of the respective space groups, namely 4 for both Cc and $P2_1/c$. Thus, M contains three crystallographically independent molecules in the

Table 1—Solubilities of Parabens in Water (25.0 ± 0.5 °C, M × 10²) as Single Components (italics), Binaries, Ternaries (M + E + P, P + E + B, P + M + B, M + E + B), and quaternary (M + E + P + B) Mixtures[a]

	M	E	P	B	M+E+P	P+E+B	P+M+B	M+E+B	M+E+P+B
M	*1.610*	1.681	1.681	1.680	1.640	–	1.630	1.580	1.680
E	0.598	*0.578*	**0.514**	0.563	**0.521**	**0.496**	–	0.555	**0.527**
P	0.220	**0.111**	*0.218*	0.209	**0.111**	**0.109**	0.211	–	**0.110**
B	0.113	0.109	0.104	*0.105*	–	0.110	0.111	0.108	0.110

[a] Solubility values for E and P from mixtures containing both compounds are printed in boldface; $n \geq 4$; cv $\leq$ 3%.

Table 2—Selected Physical and Crystallographic Data of 4-Hydroxybenzoate Esters

	methyl (M)[13]	ethyl (E)[14]	propyl (P)	butyl (B)
system	monoclinic	monoclinic	monoclinic	monoclinic
space group	*Cc*	$P2_1/c$	$P2_1/c$	*C2/c*
a, Å	13.568(5)	11.765(4)	12.0435(2)	20.0870(7)
b, Å	16.959(7)	13.182(1)	13.8292(3)	8.2182(2)
c, Å	12.458(6)	11.579(4)	11.7847(3)	14.7136(5)
β, deg	130.10(3)	107.76(3)	108.63(1)	121.39(1)
V, Å^3	2192.9	1710.2	1860.0	2073.4
d, (calcd) g cm^{-3}	1.382	1.291	1.287	1.244
d, (measd) g cm^{-3}	1.361	1.25(1)	1.28(1)	1.23(1)
Z	12	8	8	8
R (on F)	0.054	0.056	0.090	0.062
obsd reflections	1098	2189	2922	1379
all reflections	–	–	3728	2121
wR_2 (on F^2)	–	–	0.222	0.186
MW	152.15	166.18	180.2	194.23
formula	$C_8H_8O_3$	$C_9H_{10}O_3$	$C_{10}H_{12}O_3$	$C_{11}H_{14}O_3$
CAS reg. no[a]	99-76-3	120-47-8	94-13-3	94-26-8

[a] Provided by author.

asymmetric unit while both E and P contain two. While the occurrence of more than one molecule in the asymmetric unit may suggest an incorrect choice of unit cell and/or space group, we have in these instances confirmed the data listed in Table 2 by preliminary X-ray photography of all three compounds and by successful structural refinements of not only compound P, but also M and E in recent structure redeterminations.[21] Compound B, crystallizing in the space group *C*2/*c*, has Z equal to the number of general equivalent positions and therefore contains only one molecule in the asymmetric unit.

Full details of the crystal and molecular structures of P and B will be published elsewhere.[21] For the purposes of the present study, however, the salient feature evident from a comparison of the space group and unit cell data is that compounds E and P are isostructural and different in crystal structure from either M or B. The term "isostructural" is used here in the sense defined by Kálmán and Párkányi[22] to denote the fact that E and P crystallize in the same space group with very similar unit cell dimensions and with atomic coordinates which are in close correspondence for common atoms.

Details of the common crystal packing mode in the isostructural species E and P, as exemplified by compound P, are illustrated in Figure 1. This figure shows that the two crystallographically independent molecules (A, B) form separate, but structurally analogous, infinite chains by head-to-tail hydrogen bonding involving the OH group as donor and the carbonyl O atom as acceptor. Within a given chain, successive molecules are related by a 2-fold screw axis (2_1) parallel to b, array A being generated by the 2_1 located at x = $^1/_2$, z = $^1/_4$ and array B by the 2_1 at $x = 0$, z = $^1/_4$. The symmetry-independent molecules A and B are nearly coplanar, and the resulting crystal structure, shown in projection in Figure 2, consequently has a distinctive layered nature. The layers lie midway between the (202)

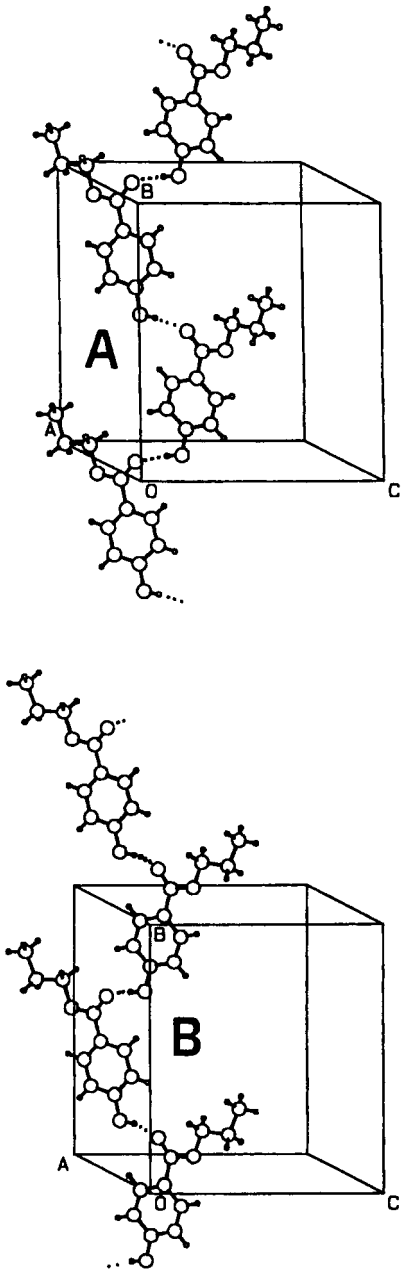

Figure 1—Head-to-tail hydrogen bonding arrays for the two crystallographically independent molecules A and B in propylparaben. Analogous arrays occur in the isostructural species ethylparaben.

crystal planes, thus accounting for the fact that the (202) reflection is predominant in the PXRD patterns of E and P.

A detailed exposition of the variations in molecular structures and packing modes for crystals of M, E, P, and B will be discussed elsewhere.[21] Here, it is relevant to emphasize the isostructurality of E and P (both crystallizing in space group $P2_1/c$) and to contrast their common crystal packing arrangement with the different packing

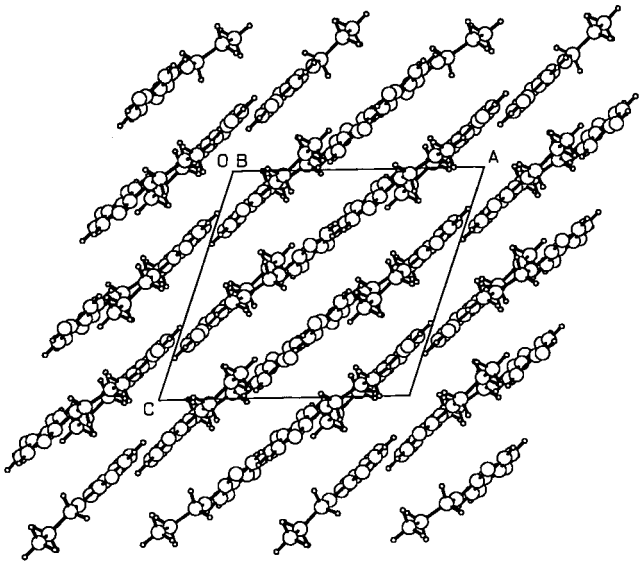

Figure 2—The [010] projection of the propylparaben crystal structure showing the characteristic molecular layers situated midway between the (202) planes.

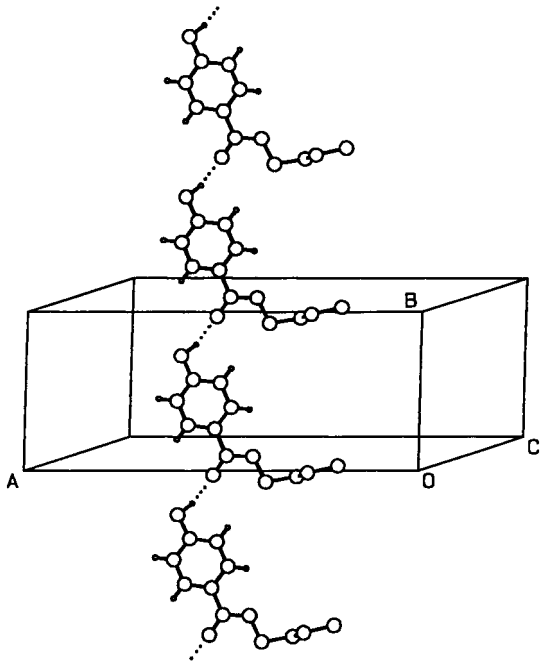

Figure 3—Head-to-tail hydrogen bonding array in the crystal of butylparaben. For clarity only the dominant conformer of the butyl chain is shown and the H atoms are omitted.

modes observed in M (*Cc*) and B (*C*2/*c*). The molecules in all four paraben crystals associate by head-to-tail (O−H···O) hydrogen bonding, leading to infinite chains, as discussed above for E and P. However, successive molecules of the chains in E and P are generated by 2_1-axes, whereas those in B are related by translation only, as shown in Figure 3. The resulting layered structure of B superficially resembles those of E and P, but the layers are distorted due to noncoplanarity of the butyl substituent and the aromatic ring as well as to the observed disorder of the butyl chain. The crystal packing mode in M is unique and complicated, owing to the presence of three symmetry-independent methyl paraben molecules. Alternate molecules in the hydrogen bonded chains have their aromatic ring planes nearly orthogonal to one another, giving rise to a complex packing arrangement[13] devoid of the layers which are characteristic of the crystal structures of E, P, or B.

Table 3—Thermal Data[a] of the Four Parabens

	methyl (M)	ethyl (E)	propyl (P)	butyl (B)
ΔH^f, J g^{-1}	166.5 (4.9)	158.6 (5.0)	150.7 (4.7)	137.2 (4.2)
T^f, °C	126.0 (0.4)	115.8 (0.7)	96.1 (0.5)	68.6 (0.6)

[a] $n \geq 4$; sd in parentheses.

Table 4—Observed and Calculated Eutectics for the Binary Systems

	M + E	M + P	M + B	E + P	E + B	P + B
X_{eut}, calcd[a]	0.46	0.35	0.78	0.40	0.24	0.33
T_{eut}, obsd, °C	86.5	76.5	57.0	–	59.0	55.0
T_{eut}, calcd, °C	88.5	77.8	59.8	76.0	58.3	54.6

[a] Mole fraction of the first component of the binary system; values calculated by the intersection point of the liquidus curves obtained through the Schröder–Van Laar equation.

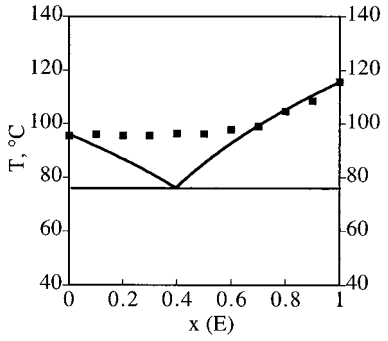

Figure 4—Phase-diagram of the ethylparaben–propylparaben binary system. ■ = experimental points (onset temperatures from DSC measurements).

Cocrystallization, or solid solution formation, is a well-known consequence of isostructurality.[22] For the four parabens involved, the increments in the volume of the asymmetric unit of the crystal through the series M → E → P → B are 31.1, 18.7, and 26.7 Å^3, the smallest of these being a consequence of the isostructurality of E and P. This fact indicates that the molecules of E and P, in these crystal packing arrangements, have a high degree of molecular complementarity; substitution of one molecule for the other during crystallization of physical mixtures should therefore be favored. This conjecture was explored by means of thermal methods of analysis and its validity subsequently confirmed by PXRD measurements.

Thermal Analytical Studies—Thermal data of the pure compounds and their binaries are collected in Tables 3 and 4. There was no evidence of any solvate formation (TGA measurements) for samples recrystallized from water or methanol.

While experimental data for binaries fit the calculated phase diagrams reasonably well for the combinations, M + E, M + P, M + B, E + B, and P + B, the plot of melting point against the mole fraction for the E + P system (Figure 4) shows a large plateau region up to a mole fraction for x(E) value of about 0.6. No eutectic melting was observed at any composition, either in DSC runs or by HSM. It should be noticed that all melted samples readily recrystallized upon cooling; in all cases melting temperatures and heats measured during the second runs were not significantly different from those determined during the first runs.

These results suggest a solid solution behavior that is not far from ideal and that is probably substitutional, indicating a minimal disturbance of the crystal lattice when P molecules are progressively substituted by E, in the x(E) range, 0 to 0.6. The smooth dependence of the melting point of E and P combinations on the mole fraction of either E or P, shown in Figure 4, has a barely perceptible minimum

at x(E) near 0.4, which is close to the unrealized eutectic composition predicted by the Schröder−Van Laar equation in its simplified form (Table 4). This trend in melting point is paralleled by the enthalpies of fusion (ΔH^f, kJ mol^{-1} = 26.4 for pure E, minimum value of 20.5 at 0.436 x(E), 27.5 for pure P) and consequently by the entropies of fusion (ΔS^f, J K^{-1} mol^{-1} = 67.8 for pure E, minimum value of 55.1 at 0.436 x(E), 74.1 for pure P). This behavior corresponds to a continuous series of solid solutions that show minor deviations from ideal behavior toward molecular segregation with weaker interactions between unlike molecules (E + P) than between like molecules (E + E or P + P). (Extreme deviations from ideality toward complete segregation would, of course, correspond to a eutectic system, often with limited miscibility in the solid state at compositions near the pure components).

A measure of the extent of lattice disorder created in the "host" crystal lattice by "guest" molecules in solid solution is provided by a dimensionless "disruption index" (di).[23] The di is evaluated as the negative slope of the plot of the molar entropy of fusion, ΔS^f, of the host (+ guest) against the ideal molar entropy of mixing, ΔS^m, of the host + guest at low mole fractions of the guest (additive or impurity molecules).[23] If the guest simply "dilutes" the host without causing any lattice disruption, both the solid solution and its liquid melt will behave as ideal solutions, so ΔS^f will not be changed by the presence of the guest and therefore the di will be zero. If the guest disrupts the crystal lattice of the host by forming lattice defects or imperfections, additional disorder will be created in the host crystal lattice but not in the liquid melt which is randomly disordered and probably behaves almost ideally, so ΔS^f will decrease significantly and the di will be appreciable. Thus, di measures the extent of disruption of the crystal lattice of the "host" by molecules of the "guest". For solid solution in which P is the host and E is the guest, the di is 0.6, suggesting very little lattice disruption. A similar, but less accurate, value is given by a solid solution in which E is the host and P is the guest. Small values of di less than 1.0 are also given by metallic systems, e.g., for Cd or In as the guest in $InCd_3$ as the host or for $InCd_3$ as the guest in Cd as the host. Evidently, the substitution of Cd atoms for In atoms and vice versa in these metallic systems gives little lattice disruption, presumably because the Cd and In atoms occupy similar volume;[23] they are also neighbors in the periodic table. The isostructurality of E and P (Table 2) readily explains the small value of di. On the other hand, the additional methylene group in the P molecule as compared with E explains the slight tendency toward molecular segregation deduced above from the plots of melting point, enthalpy of fusion, and entropy of fusion against mole fraction of E or P in the solid solution of E + P. By contrast, if the host and guest are different small organic molecules and therefore possess different crystal lattices, the di is appreciable and of the order 5 to 10.[23] If the host and guest are opposite enantiomers, or other closely related isomers, the di is significantly larger, of the order 20, because of the greater disorder (disruption) created by chiral discrimination in ordered structures.[24] If the host is a molecular crystal and the guest is a polymeric surfactant, di can be much larger, of the order 200.[25]

Powder X-ray Diffraction Patterns—The PXRD traces for the pure phases E and P are shown superimposed in Figure 5. Each individual experimental pattern matches the computed pattern calculated from the corresponding single crystal X-ray data, confirming that the forms present are those listed in Table 2. The close similarity of the traces in Figure 5 confirms the isostructurality of E and P that is established above from the single crystal X-ray diffraction data. Furthermore, the peaks in the trace for P occur at slightly lower 2θ-values than the corresponding peaks for E, in accordance with the larger unit cell parameters of P (Table 2).

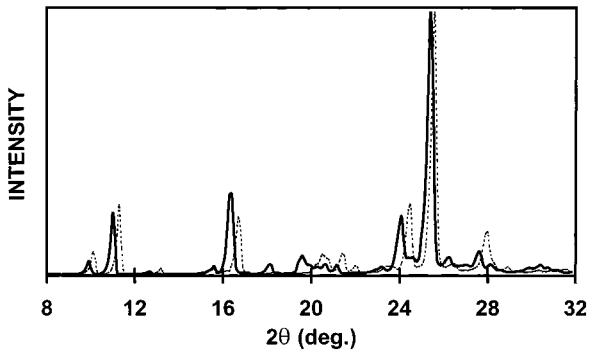

Figure 5—Powder X-ray diffraction patterns of pure propylparaben (solid trace) and pure ethylparaben (dotted trace).

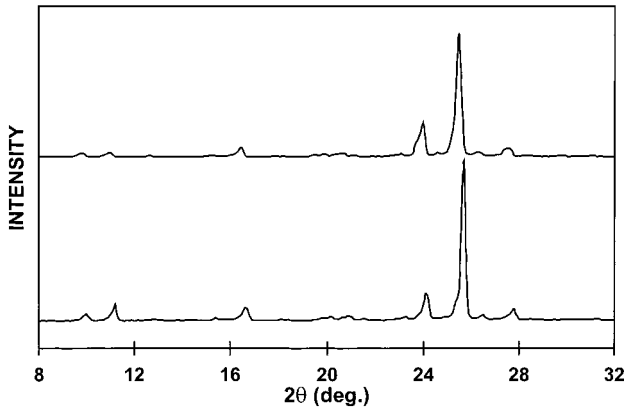

Figure 6—Powder X-ray diffraction patterns of two solid phases obtained by recrystallization of E/P mixtures with P:E molar ratios 2:1 (upper trace) and 1:1 (lower trace).

To validate the partial conclusions suggested by thermal analyses and phase diagrams, the two samples obtained by recrystallization of P + E mixtures from water were subjected to a detailed study. While the original mixtures contained P:E molar ratios of 1:1 and 2:1, HPLC analyses yielded P:E molar ratios of 0.97:1 and 3:1 for the two recrystallized phases, respectively. Figure 6 shows the PXRD traces for these species. The close similarity of these traces to each other, and to those shown for the pure phases (Figure 5), leads to the conclusion that all four phases are isostructural, which strongly supports the notion that the phases obtained by recrystallization of physical mixtures are solid solutions of E and P.

For quantitative confirmation, the narrow 2θ-range 23.0−26.5° was selected, within which two prominent, representative diffraction peaks appeared for all four phases. From simulated patterns of E and P, these peaks were identified as the (310) and (202) reflections, with calculated 2θ-shifts, $\Delta(2\theta)$, of 0.52° and 0.26°, respectively, for the pure components E and P. Figure 7 shows the PXRD traces for E, P, and the two samples indicated as being solid solutions. It is evident from these traces that, as the percentage of P in the sample increases, there is a general shift of corresponding peaks to lower 2θ-values and hence to larger d spacings. This finding is consistent with the expected increase in unit cell volume, which should accompany progressive substitution of ethyl paraben molecules by propyl paraben molecules in the solid state. In support of this conclusion, which is based on the measurement of small angular differences, it is pertinent to note that, for the extreme members of the series of solid solutions, E and P, the experimental $\Delta(2\theta)$ values for the

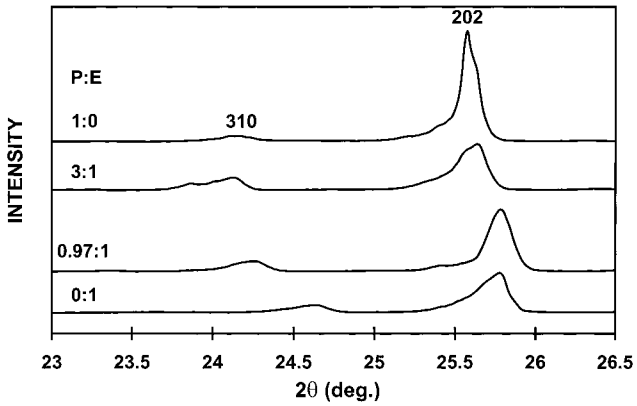

Figure 7—High-resolution powder X-ray diffraction patterns showing shifts of the (310) and (202) peaks as a function of P:E molar ratio in the solid phase.

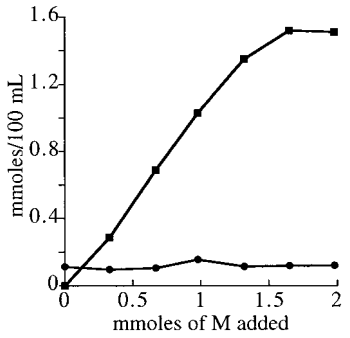

Figure 8—Phase-solubility diagram for the M + B system: ■ methylparaben, ● butylparaben ($n \geq 4$; cv $\leq$ 3%).

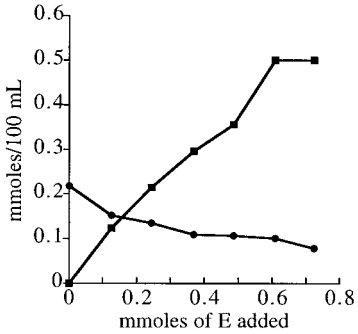

Figure 9—Phase-solubility diagram for the E + P system: ■ ethylparaben, ● propylparaben ($n \geq 4$; cv $\leq$ 3%).

(310) and (202) reflections are ~0.5° and ~0.2°, in close agreement with the calculated values stated above. Because the unit cell involved is monoclinic, with the packing arrangement shown in Figures 1 and 2, progressive substitution of E molecules by P molecules is expected to lead to anisotropic unit cell expansion. From the data in Table 2, we note that the percentage increase in unit cell lengths on proceeding from E to P are 2.4, 4.9, and 1.8% for a, b, and c, respectively. In summary, the combined evidence from single-crystal X-ray diffraction and powder XRD studies confirms that E and P form substitutional solid solutions.

Phase-Solubility Investigations—The phase-solubility diagrams of the M + B and E + P systems are shown in Figures 8 and 9. When methylparaben is progressively added to a saturated solution of butylparaben, the saturation concentration of the latter (i.e., the solubility of B, circles in Figure 8) is not affected. The system becomes invariant (three phases and three components, at constant temperature and pressure) for both M and B, only when two solid phases are in equilibrium with a liquid phase

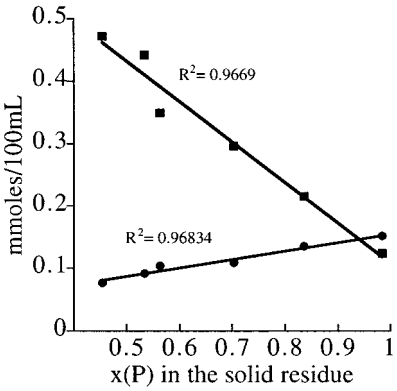

Figure 10—Relationship between composition of the solid phase at equilibrium and composition of the solution for each component: ■ ethylparaben, ● propylparaben. Data derived from phase-solubility analyses.

which is independently saturated by both compounds. Analogous patterns (not reported here) were found for other binaries.

For the E + P system, shown in Figure 9, the addition of increasing amounts of E to suspensions of P in water gives rise to a phase-solubility pattern that is different not only from the example reported above, involving no significant interaction between components, but also from the phase diagram for the formation of a solid stoichiometric complex.[12] In the E + P system, in fact, the concentration of the more abundant compound (P in this example) should remain constant until solid P is completely transformed into the solid solution P + E of lower solubility.

By plotting the data of Figure 9 as concentration of each paraben in the aqueous solution against the mole fraction of P in the solid residue, Figure 10 is obtained. It is evident that the solubilities of each paraben are affected by the presence of the second component. E can therefore be found in the solid-phase just after the first addition to a suspension of P in water, although its solubility is far below that of pure E.

Within the composition range explored and represented (x(P) in the solid residue from 0.985 to 0.45), the solubilities of E and P are clearly linear functions of the solid composition at equilibrium.

Conclusions

The solubility behavior for propylparaben in the mixture of four components has been investigated in detail. As a necessary preliminary step, we simplified the quaternary system by examining all possible binary systems. The results clearly show that this peculiar behavior can be ascribed to the simultaneous presence of ethylparaben and propylparaben, as demonstrated by the individual solubility values for binary, ternary, and quaternary mixtures. Phase diagrams of all binaries show that, among all the systems investigated, P and E are the only pair that form almost ideal solid solutions.

Furthermore, phase-solubility analyses have shown that P and E at room temperature form solid solutions whose solubility is strictly related to the composition of the solid phase at equilibrium.

To obtain independent structural confirmation that solid solution formation explains the solubility behavior, the crystal structures of propylparaben and butylparaben have been solved, and the structural analogies between E and P have been demonstrated. PXRD of E, P, and their putative solid solutions each recrystallized from water show peaks whose 2θ-positions progressively shift as the composition proceeds from that of one pure compound to the other.

While not forgetting that crystallization is an irreversible, nonequilibrium process, the solid with the lowest chemical potential of E or P tends to crystallize out of the solution that contains both E and P. This solid solution contains a lower mole fraction of E and P than does pure E or P, respectively, because it has a lower chemical potential of E or P, respectively, and therefore has a lower solubility with respect to E or P. Therefore, if E is the solid in excess, E will tend to dissolve, whereas if P is the solid in excess, P will tend to dissolve, and the solid solution will crystallize out. The concentration of E or P in equilibrium with this solid solution (the measured apparent solubility) is less than that in equilibrium with pure E or P (the true solubility).

References and Notes

1. Wade, A., Weller, P. J., Eds. *Handbook of Pharmaceutical Excipients*, 2nd ed.; American Pharmaceutical Association: Washington, DC, 1994; pp 49−51, 191−193, 310−313, 411−414.
2. Cohen, J.; Lach, J. L. Interaction of Pharmaceuticals with Schardinger Dextrins I. *J. Pharm. Sci.* **1963**, *52*, 132−136.
3. Lach, J. L.; Cohen, J. Interaction of Pharmaceuticals with Schardinger Dextrins II. *J. Pharm. Sci.* **1963**, *52*, 137−142.
4. Matsuda, H.; Ito, K.; Sato, Y.; Yoshizawa, D.; Tanaka, M.; Taki, A.; Sumiyoshi, H.; Utsuki, T.; Hirayama, F.; Uekama, K. Inclusion Complexation of p-Hydroxybenzoic Acid Esters with 2-Hydroxypropyl-beta-cyclodextrins. On Changes in Solubility and Antimicrobial Activity. *Chem. Pharm. Bull.* **1993**, *41*, (8), 1448−52.
5. McDonald, C.; Palmer, L.; Boddy, M. The Solubility of Esters of 4-Hydroxybenzoic Acid, Determined Separately and Together, in Aqueous Solutions of 2-Hydroxypropyl-β-cyclodextrin. *Drug Dev. Ind. Pharm.* **1996**, *22*, 1025−1029.
6. Grant, D. J. W.; Mehdizadeh, M.; Chow, A. H.-L.; Fairbrother, J. E. Nonlinear van't Hoff Solubility−temperature Plots and their Pharmaceutical Interpretation. *Int. J. Pharm.* **1984**, *18*, 25−38.
7. Forster, S.; Buckton, G.; Beezer, A. E. The Importance of Chain Length on the Wettability and Solubility of Organic Homologs. *Int. J. Pharm.* **1991**, *72*, 29−34.
8. Brittain, H. G.; Grant, D. J. W. Solubility of Pharmaceutical Solids. In *Physical Characterization of Pharmaceutical Solids*; Brittain, H. G. Ed.; Marcel Dekker: New York, 1995; pp 321−386.
9. Khankari, R. K.; Grant, D. J. W. Pharmaceutical Hydrates. *Thermochim. Acta* **1995**, *248*, 61−79.
10. Giron, D. Thermal Analysis and Calorimetric Methods in the Characterisation of Polymorphs and Solvates. *Thermochim. Acta* **1995**, *248*, 1−59.
11. Giordano, F.; Bettinetti, G.; Cursano, R.; Rillosi, M.; Gazzaniga, A. A Physicochemical Approach to the Investigation of the Stability of Trimethoprim-Sulfamethoxazole (Co-Trimoxazole) Mixtures for Injectables. *J. Pharm. Sci.* **1995**, *84*, 1254−1258.
12. Higuchi, T.; Connors, A. Phase-solubility Techniques. *Adv. Anal. Chem. Instr.* **1965**, *4*, 117−212.
13. Lin, X., Studies on the crystal structure of p-substituted benzoates. I. The crystal structure of methyl p-hydroxybenzoate. *J. Struct. Chem.* **1983**, *2*, 213−217.
14. Lin, X., Studies on the crystal structure of p-substituted benzoates. III. The crystal structure of ethyl p-hydroxybenzoate. *J. Struct. Chem.* **1986**, *5*, 281−285.
15. Jacques, J.; Collet, A.; Wilen, S. H. *Enantiomers, Racemates, and Resolutions*; John Wiley & Sons: Interscience Publ.: New York, 1981; pp 46, 47.
16. Otwinowski, Z.; Minor, W. Processing of X-ray diffraction data collected in oscillation mode. In *Methods in Enzymology*; Carter, C. W., Sweet, R. M., Eds.; Academic Press: New York, 1997; pp 307−326.
17. Mackay, S.; Gilmore, C. J.; Edwards, C.; Tremayne, M.; Stewart, N,; Shankland, K. maXus: A Computer Program for the Solution and Refinement of Crystal Structures from Diffraction Data. University of Glasgow, Scotland, UK, Nonius BV, Delft, The Netherlands and MacScience Co. Ltd.: Yokohama, Japan, 1998.
18. Sheldrick, G. M. SHELXS86. In Crystallographic Computing 3; Sheldrick G. M., Kruger, C., Goddard, R., Eds.; Oxford University Press: Oxford, UK, 1985; pp 175−178.
19. Sheldrick, G. M. SHELXL93. Program for the Refinement of Crystal Structures, University of Göttingen, Germany, 1993.
20. Yvon, K.; Jeitschko, W.; Parthe, E. J. LAZY PULVERIX, A Computer Program for Calculating X-ray and Neutron Diffraction Powder Patterns. *J. Appl. Crystallogr.* **1977**, *10*, 73−74.
21. Caira, M. R.; Giordano, F.; Grant, D. J. W.; et al. Unpublished results.
22. Kálmán, A.; Párkányi, L. Isostructurality of Organic Crystals: a Tool to Estimate the Complementarity of Homo- and Heteromolecular Associates. In *Advances in Molecular Structure Research*; Hargittai, M., Hargittai, I., Eds.; JAI Press: Greenwich, CT, 1997; Vol. 3, p 206.
23. York, P.; Grant, D. J. W. A Disruption Index for Quantifying the Solid State Disorder Induced by Additives or Impurities. I. Definition and Evaluation from Heat of Fusion. *Int. J. Pharm.* **1985**, *25*, 57−72.
24. Duddu, S. P.; Grant, D. J. W. The Use of Thermal Analysis in the Assessment of Crystal Disruption. *Thermochim. Acta* **1995**, *248*, 131−145.
25. Al-Meshal, M.; York, P.; Grant, D. J. W. Disruptive Effects of Surfactant Molecules Incorporated into Phenylbutazone Crystals. *J. Pharm. Pharmacol.* **1985**, *37* (Suppl), 58.

Acknowledgments

F.G. and A.G. gratefully acknowledge financial support of Italian MURST (Ministero dell'Università e della Ricerca Scientifica e Tecnologica) and CNR (Consiglio Nazionale delle Ricerche). M.R.C. thanks the FRD (Pretoria) and the University of Cape Town for financial support. Part of this work was carried out in fulfilment of a Fulbright Scholarship of F.G. as Visiting Professor at the College of Pharmacy, University of Minnesota, Minneapolis.

JS9900452

Structural Characterization of Substrates for the Anion Exchange Transporter in Caco-2 Cells‖

TAKUO OGIHARA,[†,‡] IKUMI TAMAI,[†,§] AND AKIRA TSUJI*[,†,§]

Contribution from *Department of Pharmacobiodynamics, Faculty of Pharmaceutical Sciences, Kanazawa University, 13-1 Takara-machi, Kanazawa 920-0934, Japan, and CREST, Japan Science and Technology Corporation, 4-1-8 Moto-machi, Kawaguchi 332-0012, Japan.*

Received January 12, 1999. Final revised manuscript received May 27, 1999.
Accepted for publication August 10, 1999.

Abstract □ The present study was conducted to characterize the structural specificity of an anion exchange transporter in intestinal epithelial cells. The transport of carboxylic acids with hydroxyl group(s) at the 2, 3, 4, and/or 5 positions with respect to carboxylate was examined by using Caco-2 cells in the presence of bicarbonate ions on the basolateral side to enhance the activity of the anion-exchange transporter. In the presence of the bicarbonate ion gradient, transport of L-lactic acid consisted of a saturable process and a nonsaturable process as judged from the Eadie–Hofstee plot. The transport of L-lactic acid at 1 μM was reduced by sodium azide, dinitrophenol, and 4,4′-diisothiocyanostilbene-2,2′-disulfonic acid (DIDS). It was also reduced by 2-, 4-, and 5-hydroxycarboxylic acids such as hydroxyacetic acid, 4-hydroxybutyric acid, and 5-hydroxydecanoic acid, but not by 3-hydroxycarboxylic acids such as 3-hydroxypropionic acid and 3-hydroxybutyric acid. Transport of both 2- and 4-hydroxybutyric acids involved saturable and nonsaturable processes, whereas that of 3-hydroxybutyric acid was nonsaturable and was not inhibited by DIDS. These results indicate that 3-hydroxycarboxylic acids might not be substrates for this anion exchange transporter in intestinal epithelial cells, suggesting that the position of hydroxylation is significant for molecular recognition by the transporter.

Introduction

We have demonstrated that at least two types of carrier-mediated transport mechanisms, energized by an inward-directed proton gradient (proton cotransport) and/or an outward-directed bicarbonate gradient (anion-exchange transport), are involved in the intestinal absorption of monocarboxylic acids such as acetic acid, L- and D-lactic acids, nicotinic acid, benzoic acid, and salicylic acid, by means of studies using rabbit and rat jejunal brush-border membrane vesicles (BBMVs), a human carcinoma cell line, Caco-2, and gene products expressed in *Xenopus laevis* oocytes and in mammalian cells.[1−13] These carrier-mediated transport processes are likely to predominate over passive diffusion according to the pH-partition hypothesis[14] in the absorption of various monocarboxylic acids across the intestinal membrane.

Previously, we have demonstrated that pravastatin, a 3-hydroxy-3-methylglutaryl coenzyme A (HMG-CoA) reductase inhibitor, and (*R*)-mevalonic acid, an intermediate in terpenoid and cholesterol biosynthesis, are transported across intestinal epithelial cells via a proton-cotransport mechanism. However, these compounds are not transported by an anion-exchange transport mechanism in intestinal BBMVs or in isolated intestinal tissues mounted in Ussing-type chambers.[11] Pravastatin and (*R*)-mevalonic acid have a structural similarity in terms of the hydroxyl groups at the 3 and 5 positions with respect to the carboxylate, so such structural characteristics might determine their transport across the intestinal epithelial cells via the anion-exchange transport mechanism. The present study was intended to characterize the common structure of monocarboxylic acids which is required for transport via the anion-exchange transporter in intestinal epithelial cells, by examining the transcellular transport of substituted monocarboxylic acids, especially those with a hydroxyl group at the 2, 3, 4, or 5 position of the carboxylates.

Materials and Methods

Materials and Cell Culture—Caco-2 cells were obtained from American Type Culture Collection (Rockville, MD) and cultivated as described previously.[9] All cells used in this study were between passages 53 and 108. The cells were grown for 21 to 23 days on a polycarbonate membrane (Transwell: 11.2 mm in diameter and 3.0 μm pore size, effective area of 1 cm^2, Costar, Bedford, MA). L-[^{14}C]Lactic acid (5.55 GBq/mmol), [^{14}C]-2-hydroxybutyric acid (2.04 GBq/mmol), [^{14}C]-3-hydroxybutyric acid (2.05 GBq/mmol), [^{14}C]-4-hydroxybutyric acid (2.04 GBq/mmol), and (*R*)-[^{3}H]mevalonolactone (555 GBq/mmol) were purchased from American Radiolabeled Chemicals Inc. (St. Louis, MO). Mevalonic acid was prepared by hydrolysis of the mevalonolactone according to the method reported previously.[11,15] [^{14}C]Salicylic acid (2.04 GBq/mmol) was obtained from Moravek Biochemicals (Brea, CA). [^{14}C]-Benzoic acid (0.70 GBq/mmol) and [^{3}H]mannitol (1110 GBq/mmol) were purchased from New England Nuclear (Boston, MA). 5-Hydroxydecanoic acid was kindly supplied by Mochida Pharmaceutical Co., Ltd. (Tokyo). All other chemicals were of reagent grade or the highest purity commercially available.

Transcellular Transport Experiments—The conditions of each experiment are described in figure legends or table footnotes. A typical experiment on L-lactic acid transport was performed as follows. For the study of the transcellular transport across Caco-2, the cells grown on a polycarbonate membrane were washed twice with Hank's balanced salt solution (HBSS; 0.952 mM $CaCl_2$, 5.36 mM KCl, 0.441 mM KH_2PO_4, 0.812 mM $MgSO_4$, 136.7 mM NaCl, 0.385 mM Na_2HPO_4, 30 mM D-glucose, and 10 mM HEPES for pH 7.4 or 10 mM MES for pH 6.0), and the osmolarity was adjusted to 315 mOsm/kg.[9] To initiate transport, 1.5 mL of HBSS (pH 7.4, 37 °C) was put on the basolateral side (receiver side), and 0.5 mL of the test solution (pH 6.0 or pH 7.4, 37 °C) containing a radio-labeled compound was loaded on the apical side (donor side) of a cell insert. At 15, 30, 45, and 60 min after that, 0.5-mL

* To whom correspondence should be addressed. Tel +81-76-234-4478, fax +81-76-234-4477, e-mail: tsuji@kenroku.kanazawa-u.ac.jp.
† Kanazawa University.
‡ Present affiliation: Research Center, Mochida Pharmaceutical Co., Ltd., 722 Jimba-aza-uenohara, Gotemba, Shizuoka 412-8524, Japan.
§ CREST.

‖ Abbreviations: BBMVs, brush-border membrane vesicles; HBSS, Hank's balanced salt solution; HEPES, 2-[4-(2-hydroxyethyl)-1-piperazinyl]ethanesulfonic acid; MES, 2-(*N*-morpholino)ethanesulfonic acid; DNP, 2,4-dinitrophenol; DIDS, 4,4′-diisothiocyanostilbene-2,2′-disulfonic acid; ^{1}H NMR, proton nuclear magnetic resonance.

10.1021/js9900093 CCC: $18.00
Published on Web 09/24/1999

aliquots of the solution were removed from the receiver side and replaced with an equal volume of fresh HBSS. In the case of the bicarbonate-gradient condition, modified HBSS (0.952 mM $CaCl_2$, 5.36 mM KCl, 0.441 mM KH_2PO_4, 0.812 mM $MgSO_4$, 111.7 mM NaCl, 0.385 mM Na_2HPO_4, 25 mM $NaHCO_3$, 30 mM D-glucose, and 10 mM HEPES, pH 7.4 with the osmolarity of 315 mOsm/kg, 37 °C), which contained a suitable amount of bicarbonate ion to maintain the bicarbonate gradient during the experiments, was used on the basolateral side. The amount of the radio-labeled compound transported by cells was estimated by radioactivity measurement and expressed as permeability (μL/mg protein), obtained by dividing the transported amount by the initial concentration in the donor compartment and correcting for the cellular protein amount. Each result represents the mean ±SEM of three experiments using the same cultivation of Caco-2 cells. Radioactivity was determined with a liquid scintillation counter (LS6000TA, Beckman, Fullerton, CA). Cellular protein was measured by the method of Lowry et al.[16] with bovine serum albumin as a standard.

Measurement of Physicochemical Properties—The partition coefficient of each compound between *n*-octanol and HBSS (pH 7.4), log $D_{7.4}$, was determined by means of the flask shaking method.[17] The proton nuclear magnetic resonance (^{1}H NMR; 300 MHz) spectra were obtained in dimethyl sulfoxide-d_6 using tetramethylsilane as an internal standard at room temperature.

Data Analysis—The permeability coefficient (μL/min/mg protein) was determined from the slope of the initial linear portion of the permeability (μL/mg protein) versus time (min) curves by linear regression analysis. A permeability coefficient of 1 μL/min/mg protein corresponded to 15.4×10^{-6} cm/s, since cellular protein averaged 0.922 mg/cm^2. To estimate the kinetic parameters for the saturable transport across Caco-2 monolayers, the transport rate (J) was fitted to one of the following equations, consisting of both saturable and nonsaturable-linear terms, by using a nonlinear least-squares regression analysis program (WinNonlin, SCI, Apex, NC),

$$J = J_{max} \times S/(K_t + S) + k_d \times S \quad (1)$$

or

$$J = J_{max,1} \times S/(K_{t,1} + S) + J_{max,2} \times S/(K_{t,2} + S) + k_d \times S \quad (2)$$

where J_{max} is the maximum transport rate for the carrier-mediated process, S is the concentration of substrate, K_t is the half-saturation concentration (Michaelis constant), subscript integers 1 and 2 indicate saturable processes of high and low affinity, respectively, and k_d is the first-order rate constant. Statistical analysis was performed by using Student's two-tailed t test. A difference between means was considered to be significant when the P-value was less than 0.05.

Results

pH and Bicarbonate Ion Dependence of L-Lactic Acid Transport—Figure 1 shows the time-courses of the permeability of L-[^{14}C]lactic acid and [^{3}H]mannitol from the apical to the basolateral side across a Caco-2 cell monolayer in the presence or absence of a proton or bicarbonate gradient, or both. The permeability of L-[^{14}C]lactic acid increased linearly with time after an initial lag period of a few minutes, as reported previously.[9] In the bicarbonate-free condition, the permeability coefficient of L-[^{14}C]lactic acid at the apical pH of 6.0 was 0.365 ± 0.020 μL/min/mg protein, being significantly higher than that (0.176 ± 0.010 μL/min/mg protein) observed at the apical pH of 7.4. In the presence of 25 mM bicarbonate ions on the basolateral side, the permeation rates of L-[^{14}C]lactic acid at the apical pH values of 6.0 and 7.4 were 1.32 and 1.33 times faster (0.482 ± 0.031 and 0.233 ± 0.010 μL/min/mg protein, respectively) than those observed in the absence of a bicarbonate ion gradient, respectively. Since the permeability coefficients of L-[^{14}C]lactic acid under all conditions examined were significantly higher than that (0.087 ± 0.001 μL/min/mg protein) of [^{3}H]mannitol, which reflects the paracellular permeability, L-lactic acid transport occurred mainly by transcellular permeation rather than through the paracellular pathway.

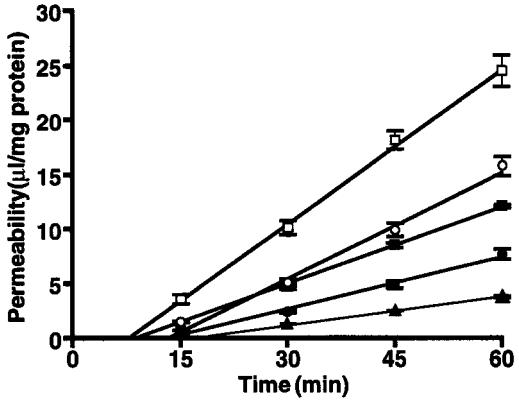

Figure 1—Time-courses of the transport of L-[^{14}C]lactic acid and [^{3}H]mannitol from the apical side to the basolateral side across Caco-2 cell monolayers. Permeability of L-[^{14}C]lactic acid (1 μM) was measured at 37 °C by incubating Caco-2 monolayers in HBSS buffer at an apical pH of 6.0 (□, ○), or 7.4 (●, ■) with a constant basolateral pH of 7.4, in the presence of 0.952 mM $CaCl_2$, 5.36 mM KCl, 0.441 mM KH_2PO_4, 0.812 mM $MgSO_4$, 136.7 mM NaCl, 0.385 mM K_2HPO_4, 25 mM D-glucose and 10 mM HEPES for pH 7.4 or 10 mM MES for pH 6.0 (circles). When bicarbonate-containing HBSS buffer at a basolateral pH of 7.4 was used (squares), 111.7 mM NaCl and 25 mM $NaHCO_3$ were contained instead of 136.7 mM NaCl. [^{3}H]Mannitol (33 nM; ▲) transport was measured at 37 °C in Caco-2 monolayers in HBSS buffer at an apical pH of 7.4 and bicarbonate-containing HBSS buffer at a basolateral pH of 7.4. An aliquot was withdrawn from the basolateral side at each time indicated. Each point represents the mean ± SEM of three experiments using the same culture of Caco-2 cells.

Concentration Dependence of L-Lactic Acid Transport—Figure 2 illustrates the relationship between the initial transport rate of L-[^{14}C]lactic acid and the concentration in the medium (from 1 μM to 20 mM) under the two different conditions, namely at the apical pH values of 6.0 (panel A) and 7.4 (panel B), while the pH on the basolateral side was kept at 7.4 with 25 mM bicarbonate ions. The results indicate that the permeation rate of L-[^{14}C]lactic acid under both conditions involves both saturable and nonsaturable processes, as shown in the inset of Figure 2. When the data at the apical pH of 6.0 were analyzed by means of an Eadie–Hofstee plot, two different types of transport processes were observed, as illustrated in panel A. Kinetic analysis of the concentration-dependent permeation according to eq 2, gave $J_{max,1}$ and $K_{t,1}$ values of 0.098 ± 0.021 nmol/min/mg protein and 0.28 ± 0.10 mM, and $J_{max,2}$ and $K_{t,2}$ values of 1.46 ± 0.20 nmol/min/mg protein and 10.9 ± 2.0 mM, respectively. The k_d value was 0.056 ± 0.043 μL /min/mg protein (mean ± SD). At the apical pH of 7.4, the Eadie–Hofstee plot apparently shows a single saturable process. Kinetic analysis of L-lactic acid transport according to eq 1 gave J_{max}, K_t, and k_d values of 1.03 ± 0.36 nmol/min/mg protein, 8.26 ± 2.80 mM, and 0.056 ± 0.010 μL/min/mg protein, respectively. Accordingly, the transport of L-[^{14}C]lactic acid across Caco-2 cell monolayers seems to be bicarbonate-ion dependent. So, in subsequent experiments, transport studies were performed at apical and basolateral pH values of 7.4 in the presence of 25 mM bicarbonate ions on the basolateral side to magnify the relative activity of anion-exchange transport.

Inhibitory Effect on Monocarboxylate Transport—Table 1 shows the effects of the bicarbonate ion gradient, metabolic inhibitors, and monocarboxylates on the transport of L-[^{14}C]lactic acid, [^{3}H]mevalonic acid, [^{14}C]benzoic acid, [^{14}C]salicylic acid, and [^{3}H]mannitol. DNP (1 mM), an uncoupler of oxidative phosphorylation, sodium azide

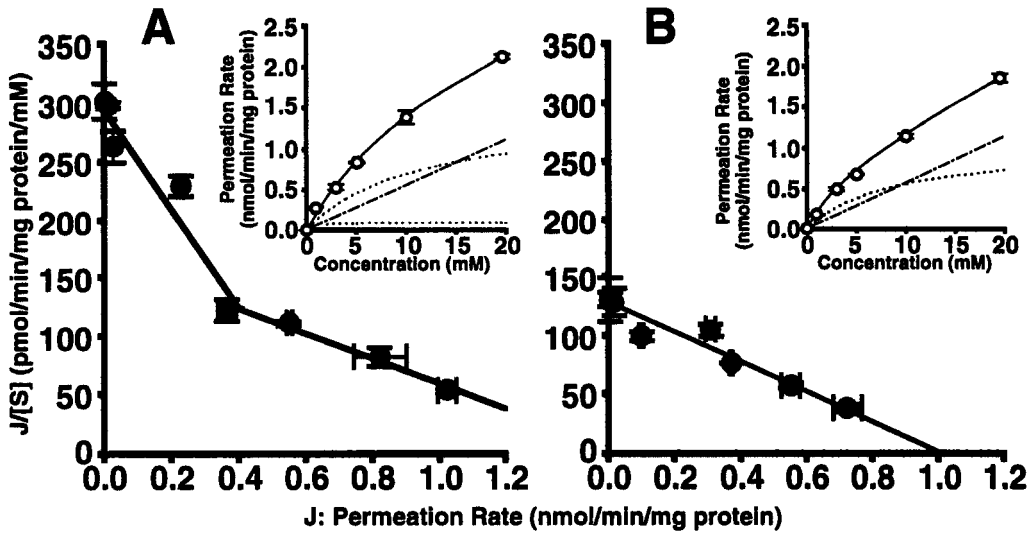

Figure 2—Concentration dependence of L-[^{14}C]lactic acid transport across Caco-2 cell monolayers at an apical pH of 6.0 (panel A) or 7.4 (panel B), at a constant basolateral pH of 7.4 with 25 mM bicarbonate. The concentrations of L-lactic acid used were 1, 10, and 100 μM and 1, 3, 5, 10, and 20 mM, which were adjusted by addition of the nonlabeled compound to L-[^{14}C]lactic acid (1 μM). The incubation conditions were identical to those described in the legend to Figure 1. The broken lines represent the contribution of the saturable (••••) and nonsaturable (–•–) components to the permeation, calculated from the kinetic parameters obtained as described in the results. Each point represents the mean ± SEM of three experiments using the same culture of Caco-2 cells.

Table 1—**Effect of Various Compounds and Condition on Monocarboxylic Acid and Mannitol Transports**[a]

condition	relative permeability (% of control)[b]				
	L-[^{14}C]lactic acid	(*R*)-[^{3}H]mevalonic acid	[^{14}C]benzoic acid	[^{14}C]salicylic acid	[^{3}H]mannitol
control	100.0 ± 3.8	100.0 ± 12.2	100.0 ± 0.7	100.0 ± 5.7	100.0 ± 1.8
bicarbonate free	75.4 ± 4.1*	88.2 ± 1.8	52.9 ± 1.3*	40.4 ± 1.6*	99.8 ± 3.4
+1 mM DNP	43.9 ± 2.2*				106.2 ± 2.9
+10 mM NaN_3	54.5 ± 6.0*				101.2 ± 3.9
+2 mM DIDS	32.4 ± 1.1*	97.4 ± 0.9	45.4 ± 0.5*	41.4 ± 1.9*	98.0 ± 6.4
+10 mM L-lactic acid	45.8 ± 3.2*				
+10 mM (*R*)-mevalonic acid	88.4 ± 5.8	86.8 ± 6.4			
+10 mM (*S*/*R*)-mevalonic acid	104.8 ± 6.0				
+10 mM benzoic acid	42.0 ± 6.1*		59.8 ± 1.3*		
+10 mM salicylic acid	47.6 ± 1.3*			57.9 ± 3.6*	

[a] Note: Transport of L-[^{14}C]lactic acid (1 μM), (*R*)-[^{3}H]mevalonic acid (50 nM), [^{14}C]benzoic acid (10 μM), [^{14}C]salicylic acid (10 μM), and [^{3}H]mannitol (33 nM) were measured at 37 °C for 60 min by incubating Caco-2 cells in HBSS buffer (apical pH 7.4, basolateral pH 7.4 with bicarbonate) in the presence of each inhibitor. The other incubation conditions were the same as described in the legend to Figure 1. [b] Each value represents the mean ± SEM of three experiments using the same cultivation process of Caco-2 cells and is expressed as percentage of the control. *Significantly different from the control value by Student's *t* test ($p < 0.05$).

(10 mM), a respiratory chain inhibitor, and DIDS (2 mM), an anion exchange inhibitor, significantly diminished the transport of L-[^{14}C]lactic acid. Salicylic acid and benzoic acid (10 mM) were inhibitory, whereas neither (*R*)- nor racemic mevalonic acid (10 mM) had any effect on the transport of L-[^{14}C]lactic acid. Moreover, the permeability of [^{3}H]mevalonic acid was not affected by the bicarbonate ion gradient or the addition of DIDS to the transport buffer. Further, mevalonic acid transport was not saturable as shown by the apparent lack of inhibition by unlabeled mevalonic acid. In contrast, the permeability of [^{14}C]salicylic acid and [^{14}C]-benzoic acid was significantly reduced in the absence of the bicarbonate gradient and was inhibited by DIDS and 10 mM of each of these unlabeled compounds in the transport buffer. The transport of [^{3}H]mannitol did not change in the presence of DNP, sodium azide, or DIDS.

Structural Specificity of the Anion-Exchange Transporter—As shown in Table 2, to examine the properties of the anion-exchange transporter responsible for L-lactic acid transfer across Caco-2 cells, the effects of various monocarboxylic acids bearing a hydroxyl group and their derivatives were examined in the presence of a bicarbonate gradient. The permeability of L-[^{14}C]lactic acid was reduced by 2- and 4-hydroxycarboxylic acids (10 mM) such as hydroxyacetic acid, 2-hydroxybutyric acid, and 4-hydroxybutyric acid. It was also reduced by a 5-hydroxycarboxylic acid (10 mM), 5-hydroxydecanoic acid. In contrast, 3-hydroxycarboxylic acids (10 mM), such as 3-hydroxypropionic acid, 3-hydroxybutyric acid, and 3-hydroxy-3-phenylpropionic acid, did not show any significant inhibitory effect on

Table 2—**Inhibitory Effect of Monocarboxylic Acids on L-[^{14}C]Lactic Acid Transport**[a]

inhibitor	relative permeability (% of control)[b]
hydroxyacetic acid	80.3 ± 3.2*
3-hydroxypropionic acid	95.6 ± 2.0
4-hydroxybutyric acid	72.8 ± 3.5*
2-hydroxybutyric acid	59.9 ± 1.6*
3-hydroxybutyric acid	93.8 ± 12.7
3-hydroxy-3-phenylpropionic acid	89.5 ± 3.9
3-methoxypropionic acid	64.7 ± 1.2*
5-hydroxydecanoic acid	58.0 ± 0.6*

[a] Note: Transport of L-[^{14}C]lactic acid (1 μM) was measured at 37 °C for 60 min by incubating Caco-2 cells in HBSS buffer (apical pH 7.4, basolateral pH 7.4 with bicarbonate) in the presence of each inhibitor. The other incubation conditions were the same as described in the legend to Figure 1. [b] Each value represents the mean ± SEM of three experiments using the same cultivation process of Caco-2 cells and is expressed as percentage of the control. *Significantly different from the control value by Student's *t* test ($p < 0.05$).

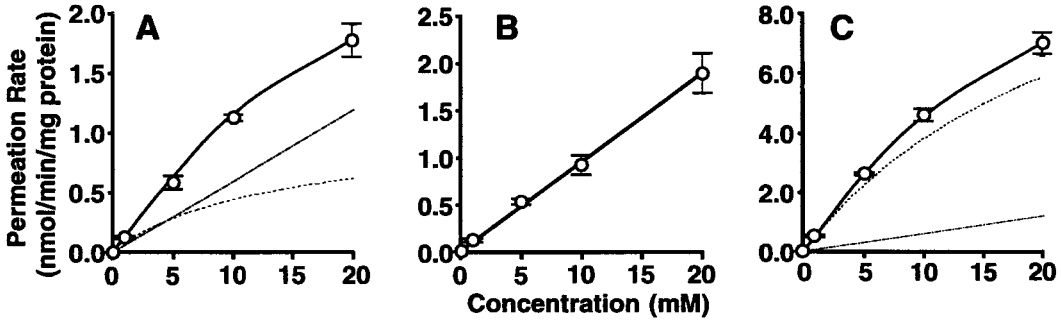

Figure 3—Concentration dependence of the transport of hydroxybutyric acids across Caco-2 cell monolayers. 2-Hydroxybutyric acid (panel A), 3- hydroxybutyric acid (panel B), and 4-hydroxybutyric acid (panel C) were examined. The concentrations of each hydroxybutyric acid (2.5 μM, and 1, 5, 10, and 20 mM) were adjusted by addition of the nonlabeled compound to [^{14}C]hydroxybutyric acid (2.5 μM). The incubation conditions were identical to those described in the legend to Figure 1. The broken lines represent the contribution of the saturable (••••) and nonsaturable (–•–) components to the permeation, calculated from the kinetic parameters obtained as mentioned in the results. Each point represents the mean ± SEM of three experiments using the same culture of Caco-2 cells.

Table 3—Inhibitory Effect of DIDS on [^{14}C]Hydroxybutyric Acids Transport[a]

substrate	permeability coefficient (μL/min/mg protein)[b]	
	control	+2 mM DIDS
[^{14}C]2-hydroxybutyric acid	0.125 ± 0.009	0.084 ± 0.005*
[^{14}C]3-hydroxybutyric acid	0.111 ± 0.008	0.108 ± 0.014
[^{14}C]4-hydroxybutyric acid	0.555 ± 0.032	0.459 ± 0.011*

[a] Note: Transport of [^{14}C]hydroxybutyric acid (2.5 μM) was measured at 37 °C for 60 min by incubating Caco-2 cells in HBSS buffer (apical pH 7.4, basolateral pH 7.4 with bicarbonate) in the presence of each inhibitor. The other incubation conditions were the same as described in the legend to Figure 1. [b] Each value represents the mean ± SEM of three experiments using the same cultivation process of Caco-2 cells. *Significantly different from the control value by Student's *t* test ($p < 0.05$).

the transport of L-[^{14}C]lactic acid, though 10 mM 3-methoxypropionic acid was inhibitory.

Transport Properties of 2-, 3-, and 4-Hydroxybutyric Acids—Figure 3 illustrates the relationship between the initial transport rate of [^{14}C]2-, 3-, and 4-hydroxybutyric acids and the concentration in the medium from 1 μM to 20 mM at the apical pH of 7.4, while the pH on the basolateral side was kept at 7.4 with a 25 mM bicarbonate ion gradient. The results indicate that the permeation of 2- and 4-hydroxybutyric acids involve saturable and nonsaturable processes. Kinetic analysis of the concentration-dependent permeation gave J_{max}, K_t, and k_d values of 2.21 ± 0.22 nmol/min/mg protein, 3.75 ± 0.40 mM, and 0.09 ± 0.01 μL/min/mg protein for 2-hydroxybutyric acid, and 8.44 ± 2.67 nmol/min/mg protein, 23.9 ± 6.41 mM, and 0.12 ± 0.03 μL/min/mg protein for 4-hydroxybutyric acid, respectively. In contrast, the saturable process was not observed for 3-hydroxybutyric acid within the tested concentration range. The first-order rate constant, k_d, was 0.09 ± 0.01 μL/min/mg protein.

Table 3 shows the effects of DIDS on the transport of [^{14}C]-2-, 3-, and 4-hydroxybutyric acids. Permeability of [^{14}C]-2- and 4-hydroxybutyric acids (2.5 μM) in the presence of 2 mM DIDS amounted to 67.1% and 82.6% of the respective control values. The permeability of [^{14}C]-3-hydroxybutyric acid was not affected by DIDS.

Discussion

In the present study, we set out to establish conditions that would maximize the relative activity of anion-exchange transport and to clarify the structural features of substrates required for intestinal transport by examining the transcellular transport of several hydroxy-monocarboxylic acids and their derivatives across monolayers of Caco-2 cells. In the presence of a bicarbonate ion gradient, but not a proton gradient, the concentration dependence of L-lactic acid transport was explained by the participation of a single saturable component, which might be ascribed to the anion-exchange transport mechanism. Under the same conditions, the transport of L-[^{14}C]lactic acid was inhibited by DIDS, which is a typical inhibitor of the anion-exchange transporter. Similar anion antiport activity with bicarbonate was found in the transport of propionic acid and acetic acid.[18,19,3] Previously, we observed enhanced uptake of nicotinic acid when an outward-directed bicarbonate gradient was imposed in isolated jejunal BBMVs.[11] It appears that similar anion-exchange transport mechanisms are involved in the permeation and absorption of monocarboxylic acids in the human intestine.

Mevalonic acid, a 3-hydroxycarboxylic acid, had no effect on the transport of L-[^{14}C]lactic acid in the presence of a bicarbonate ion gradient. In addition, as our previous study using rabbit intestinal BBMVs[11] indicated, the permeation of [^{3}H]mevalonic acid was not affected by the bicarbonate gradient or DIDS. The transport of L-[^{14}C]lactic acid was also inhibited by 2-, 4-, and 5-hydroxycarboxylic acids but not by 3-hydroxycarboxylic acid. These observations suggested that the position of hydroxylation might be an important determinant of monocarboxylate transport by the anion antiport system. Accordingly, we compared the transport of several hydroxycarboxylic acids. The concentration dependence of the 2- and 4-hydroxybutyric acid transport indicated that the permeation involves saturable and nonsaturable processes, whereas that of 3-hydroxybutyric acid was nonsaturable. Since the partition coefficients (as hydrophobic/hydrophilic parameters) of these compounds are almost the same (log $D_{7.4}$ 2-hydroxybutyric acid: −2.35, 3-hydroxybutyric acid: −2.72, 4-hydroxybutyric acid: −2.40), differences in hydrophobicity do not account for the result. It is suggested that 3-hydroxycarboxylic acids might not be substrates for the anion-exchange transporter in intestinal epithelial cells. Interestingly, 3-methoxypropionic acid was shown to have affinity for the anion-exchange transporter, because the transport of L-[^{14}C]lactic acid was inhibited by 3-methoxypropionic acid. This result suggests that a hydrogen bond between the 3-hydroxyl group of carboxylate and the transporter protein might block appropriate interaction with the anion-exchange transporter. It was expected that salicylic acid would not be a substrate for the anion-exchange transporter because it could be regarded as a 3-hydroxycarboxylic acids. However, contrary to expectation, the permeability of [^{14}C]salicylic acid was significantly reduced by the bicarbonate ion-free condition, DIDS, and unlabeled salicylic acid. Within the salicylic acid molecule, there is a relatively stable hydrogen bond conjugated with

the aromatic benzene ring, namely between the 3-hydroxyl group and oxygen of the carboxylic group. This is demonstrated by the ^{1}H NMR signals of the 3-hydroxyl group in salicylic acid and in 3-hydroxybutyric acid (salicylic acid: 11.3 ppm, 3-hydroxybutyric acid: 7.02 ppm). This internal hydrogen bond in salicylic acid might be too strong to allow the blocking interaction with transporter proteins, whereas the relatively "flexible" 3-hydroxyl group in other carboxylic acids can interfere with the proper binding of the substrate to the anion-exchange transporters.

Recently, we demonstrated that the anion exchanger AE2, which is present in several tissues,[20−25] transported organic monocarboxylic acids, when the AE2 gene was transiently overexpressed in HEK 293 cells.[12] So, AE2 might be partially responsible for monocarboxylic acid/anion exchange in the intestine, although more studies are needed on this point.

In conclusion, we have established some of the required structural characteristics for substrates of the anion-exchange transporter using Caco-2 cell monolayers. The observations suggest that an anion antiport system is involved in the intestinal absorption of monocarboxylic acids in parallel with a proton gradient-dependent monocarboxylic acid transporter. Therefore, intestinal absorption of many acidic drugs may proceed, at least in part, via the anion-exchange transporter, rather than by passive diffusion according to the pH-partition hypothesis.

References and Notes

1. Tsuji, A.; Simanjuntak, M. T.; Tamai, I.; Terasaki, T. pH-dependent intestinal transport of monocarboxylic acids: Carrier-mediated and H^+-cotransport mechanism versus pH-partition hypothesis. *J. Pharm. Sci.* **1990**, *79*, 1123−1124.
2. Simanjuntak, M. T.; Tamai, I.; Terasaki, T.; Tsuji, A. Carrier-mediated uptake of nicotinic acid by rat intestinal brush-border membrane vesicles and relation to monocarboxylic acid transport. *J. Pharmacobio-Dyn.* **1990**, *13*, 301−309.
3. Simanjuntak, M. T.; Terasaki, T.; Tamai, I.; Tsuji, A. Participation of monocarboxylic anion and bicarbonate exchange system for the transport of acetic acid and monocarboxylic acid drugs in the small intestinal brush-border membrane vesicles. *J. Pharmacobio-Dyn.* **1991**, *14*, 501−508.
4. Tsuji, A.; Takanaga, H.; Tamai, I.; Terasaki, T. Transcellular transport of benzoic acid across Caco-2 cells by a pH-dependent and carrier-mediated transport mechanism. *Pharm. Res.* **1994**, *11*, 30−37.
5. Takanaga, H.; Tamai, I.; Tsuji, A. pH-Dependent and carrier-mediated transport of salicylic acid across Caco-2 cells. *J. Pharm. Pharmacol.* **1994**, *46*, 567−570.
6. Tamai, I.; Takanaga, H.; Ogihara, T.; Yoneda M.; Tsuji, A. Proton-cotransport of pravastatin across intestinal brush-border membrane. *Pharm. Res.* **1995**, *12*, 1727−1732.
7. Tamai, I.; Takanaga, H.; Maeda, H.; Sai, Y.; Ogihara, T.; Higashida H.; Tsuji, A. Participation of a proton-cotransporter, MCT1, in the intestinal transport of monocarboxylic acids, *Biochem. Biophys. Res. Commun.* **1995**, *214*, 482−489.
8. Takanaga, H.; Tamai, I.; Inaba, S.; Sai, Y.; Higashida, H.; Yamamoto, H.; Tsuji, A. cDNA cloning and functional characterization of rat intestinal monocarboxylate transporter. *Biochem. Biophys. Res. Commun.* **1995**, *217*, 370−377.
9. Ogihara, T.; Tamai, I.; Takanaga, H.; Sai, Y.; Tsuji, A. Stereoselective and carrier-mediated transport of monocarboxylic acids across Caco-2 cells. *Pharm. Res.* **1996**, *13*, 1828−1832.
10. Takanaga, H.; Maeda, H.; Yabuuchi, H.; Tamai, I.; Higashida, H.; Tsuji, A. Nicotinic acid transport mediated by pH-dependent anion antiporter and proton cotransporter in rabbit intestinal brush-border membrane. *J. Pharm. Pharmacol.* **1996**, *48*, 1073−1077.
11. Tamai, I.; Takanaga, H.; Maeda, H.; Yabuuchi, H.; Sai, Y.; Suzuki, Y.; Tsuji, A. Intestinal brush-border membrane transport of monocarboxylic acids mediated by proton-coupled transport and anion antiport mechanisms. *J. Pharm. Pharmacol.* **1997**, *49*, 108−112.
12. Yabuuchi, H.; Tamai, I.; Sai, Y.; Tsuji, A. Possible role of anion exchanger AE2 as the intestinal monocarboxylic acid/anion antiporter. *Pharm. Res.* **1998**, *15*, 411−416.
13. Ogihara, T.; Tamai, I.; Tsuji, A.Application of fractal kinetics for carrier-mediated transport of drug across intestinal epithelial membrane. *Pharm. Res.* **1998**, *15*, 620−625.
14. Brodie, B. B.; Hogben, C. A. M.; Some physicochemical factors in drug action. *J. Pharm. Pharmacol.* **1957**, *9*, 345−380.
15. Kim, C. M.; Goldstein, J. L.; Brown, M. S.; cDNA cloning of MEV, a mutant protein that facilitates cellular uptake of mevalonate, and identification of the point mutation responsible for its gain of function. *J. Biol. Chem.* **1992**, *267*, 23113−23121.
16. Lowry, O. H.; Rosebrough, N. J.; Farr, A. L.; Randall, R. J. Protein measurement with the Folin phenol reagent. *J. Biol. Chem.* **1951**, *193*, 265−275.
17. Leo, A.; Hansch, C.; Elkins, D. Partition coefficients and their uses. *Chem. Rev.* **1971**, *71*, 525−616.
18. Titus, E.; Ahearn, G. A. Short chain fatty acid transport in the intestine of a herbivorous teleost. *J. Exp. Biol.* **1988**, *135*, 77−94.
19. Harig, J. M.; Soergel, K. H.; Barry, J. A.; Ramaswamy, K. Transport of propionate by human ileal brush-border membrane vesicles. *Am. J. Physiol.* **1991**, *260*, G776−782.
20. Demuth, D. R.; Showe, L. C.; Ballantine, M.; Palumbo, A.; Fraser, P. J.; Cioe, L.; Rovera, G.; Curtis, P. J. Cloning and structural characterization of human nonerythroid band 3-like protein. *EMBO J.* **1986**, *5*, 1205−1214.
21. Alper, S. L.; Kopito, R. R.; Libresco, S. M.; Lodish, H. F. Cloning and characterization of a murine band 3-related cDNA from kidney and from a lymphoid cell line. *J. Biol. Chem.* **1988**, *263*, 17092−17099.
22. Gehrig, H.; Muler, W.; Appelhans, H. Complete nucleotide sequence of band 3 related anion transport protein AE2 from human kidney. *Biochim. Biophys. Acta* **1992**, *1130*, 326−328.
23. Kudrycki, K. E.; Newman, P. R.; Shull, G. E.; cDNA cloning and tissue distribution of mRNAs for two proteins that are related to the band 3 Cl^-/HCO_3^- exchanger. *J. Biol. Chem.* **1990**, *265*, 462−471.
24. Lindsey, A. E.; Schneider, K.; Simmons, D.; Baron, M. R.; Lee, B. S.; Kopito, R. R. Functional expression and subcellular localization of an anion exchanger cloned from choroid plexus. *Proc. Natl. Acad. Sci. U.S.A.* **1990**, *87*, 5278−5282.
25. Chow, A.; Dobbins, J. W.; Aronson, P. S.; Igarashi, P. cDNA cloning and localization of band 3-related protein from ileum. *Am. J. Physiol.* **1992**, *263*, G345−352.

Acknowledgments

The authors are indebted to Prof. Oyo Mitsunobu, College of Sciences and Engineering, Aoyama Gakuin University, and to Dr. Kazuo Kato and Mr. Kazuyuki Matsuura, Research Center, Mochida Pharmaceutical Co., Ltd., for discussions and valuable advice during preparation of the manuscript.

JS9900093

Role of an Isomorphic Desolvate in Dissolution Failures of an Erythromycin Tablet Formulation

JOHN F. BAUER,* WALTER DZIKI, AND JOHN E. QUICK

Contribution from *PPD Analytical Development Center, Abbott Laboratories, 1401 Sheridan Road, D.4P2, North Chicago, Illinois 60064-6293.*

Received January 12, 1999. Accepted for publication July 29, 1999.

Abstract □ The investigation of dissolution failures for erythromycin dihydrate tablet formulation over a 12-month period using a near-infrared spectroscopy technique revealed the role of a desolvated dihydrate in the retardation of dissolution. Near infrared spectroscopy (NIR) indicated a dehydrated dihydrate of erythromycin is produced during formulation and gradually binds with $Mg(OH)_2$. The binding delays the process of dissolution. NIR was used to successfully predict that humidifying the tablets would reverse the binding and increase the dissolution rate.

Introduction

The occurrence of a variety of crystal forms for many pharmaceuticals has been well established and investigated.[1−11] The first recognition of this phenomenon of polymorphism may have been as early as the 18th century.[12] The fact that pharmaceuticals can exist as various polymorphs and/or solvates can be problematic in terms of stability, processing, and solubility since the different crystal forms and solvates of a drug can differ in these physical properties. In fact, the different polymorphs of a compound can be as different in these properties as are individual compounds from each other.

The established analytical techniques used to demonstrate that a compound exists in various crystal forms include X-ray powder diffraction (XRD), differential scanning calorimetry (DSC), solid-state C-13 nuclear magnetic resonance (SS NMR), polarized light microscopy (PLM), and near- and mid-infrared (NIR and IR) spectroscopy.

For several years the pharmaceutical literature reported various crystal forms and hydrates of erythromycin including an anhydrate, a monohydrate, and a dihydrate. In an earlier work[13] we proposed that the crystal form of erythromycin dihydrate as determined by X-ray powder diffraction was unchanged when the water was removed, indicating minimal if any difference in the crystal structure in the presence or absence of water. As a result of readily available channels or tunnels within the crystal lattice,[14] water is readily transported into and out of the crystal lattice depending on the environmental conditions. Pfeiffer et al.[15] has referred to molecules of this kind as pseudopolymorphs, and Stephenson et al.[16] note that the desolvated state or isomorphic desolvate is of higher energy than the solvated form and that there is a driving force to fill the void created when the solvent is removed. In this paper we will present an example of this tendency to fill the void created when the water is removed from erythromycin dihydrate, its resultant effect on tablet behavior, and the use of NIR spectroscopy to investigate the problem.

* Corresponding author. Tel: 847-937-8549. Fax: 847-938-5703. e-mail: John.Bauer@Abbott.com@internet.

Experimental Section

Materials—Several formulations of erythromycin dihydrate containing no magnesium hydroxide as well as the primary formulation which contained magnesium hydroxide were investigated. All formulations were manufactured at Abbott Laboratories and used erythromycin dihydrate USP grade. The USP grade erythromycin dihydrate was also manufactured at Abbott Laboratories through a fermentation process followed by a series of aqueous and organic extractions. This material was dried at less than 95 °C. All bulk lots met Abbott specifications.

Microscopy was performed using a Nikon Microphot-FXA polarized light microscope and a Leica Stereo Microscope Model MZAPO. X-ray powder diffraction was performed with a Nicolet I2 X-ray powder diffractometer fitted with a diffracted beam monochromator tuned for copper radiation at 1.54180 Å. All samples were ground to similar particle size immediately prior to X-ray analysis. Thermal gravimetric analysis (TGA) was performed using a TA Instruments Model 2950 TGA module with a Model 3100 Thermal Analyst, at a heating rate of 5 °C/min, and a sample weight of about 15−20 mg. A Nicolet Magna-IR Spectrometer Model 750 bench with a Nicolet SabIR near-infrared (NIR) diffuse reflectance fiber optic probe accessory were used to obtain NIR spectra at a resolution of 8 cm^{-1} with 16 scans. Intact tablets were place directly on the probe tip whereas bulk material was put into a clear glass one dram vial and then placed on the probe tip. The NIR spectrum of a bulk material was an average spectrum of four spectra acquired after manually mixing the sample for about 15 s followed by manual tapping to remove air gaps. Dynamic moisture sorption gravimetry (DMSG) was performed on a VTI Corp. Model MB300G sorption microbalance using vacuum to control the relative humidity (RH). The Automated system controlled the RH and temperature to which the sample was exposed, while continually recording sample weight changes. Sample weights were typically about 5−10 mg. Sorption and desorption isotherms were performed at 25 ± 0.1 °C with 5 ± 1% RH step intervals from 0 to 95% RH. Samples were dried under vacuum for up to 240 min (approximate RH = 0−1% RH) before each experiment. The weight loss observed during the drying period was used to estimate how tightly each sample held water. After the drying period, sorption isotherms started at 5% RH. A weight equilibrium criteria of less than 3 μg weight change over three 7 min periods was used to move to the next RH step. When the equilibrium conditions were achieved for the 95% RH step, the desorption step started. Typical sample run times were between about 24 and 48 h. Dissolution testing of tablets was performed using a single tablet in a dissolution medium of 0.05 M phosphate buffer pH 6.8 ± 0.05 at 60 °C. Quantitation was performed by UV absorbance at 236 nm versus a reference standard of erythromycin dihydrate. Intrinsic dissolution of bulk drug samples was performed at 37 °C with the same dissolution media. Quantitation was accomplished by HPLC versus a reference standard at 205 nm using an octadecylsilyl column at 50 °C and an eluent of 35% acetonitrile/65% 0.06 M phosphate buffer (pH 6.6).

Background

Twelve-month stability samples for a lot (lot 15, Table 1) of Erythromycin dihydrate, 250 mg tablets, were found

10.1021/js9900102 CCC: $18.00
Published on Web 09/16/1999

Table 1—Correlation of Moisture Content (TGA) with XRD and NIR Spectroscopy for Various Erythromycin Tablet Lots

lot number	relative (crystallinity)	TGA	NIR (OH)
1	high	4.69	high
2	moderate	3.63	moderate
3	moderate	3.43	moderate
4	moderate	3.91	moderate
5	low	3.28	low
6	low	2.76	low
7	low	2.54	low
8	moderate	3.85	moderate
9	low	2.25	low
10	low	2.88	low
11	moderate	2.86	low
12	low	3.11	low
13	low	2.68	low
14	moderate	3.02	low
15	low	2.73	low
16	low	1.70	low
17	low	2.50	low
18	high	4.33	high

to fail the dissolution specification at the 60 min interval but pass at the 90 min interval. Historically, sporadic tablets of this formulation (lots 3, 6, 13 Table 1) had failed dissolution; however, this lot, which had very good initial dissolution of greater than 99%, released at 60 min failed uniformly at the 12-month time point with an average of 71% released at 60 min. Other lots of this same formulation (lots 1, 18, Table 1) had maintained very high dissolution for periods greater than 12 months. Material which had acceptable dissolution over the 12-month period will be referred to as passing while those with decreased dissolution will be designated as failing. One of these former lots (lot 1, Table 1) was used as a reference for passing tablets. The manufacturing process for erythromycin tablets involves milling and drying, and these factors have historically been shown to affect crystallinity and, as would be expected, water content. Initial work concentrated on these properties as well as examination of the tablet coating.

Results and Discussion

X-ray powder diffraction was performed on the erythromycin dihydrate tablets using computer subtraction of a placebo diffraction pattern to examine the consistency of the crystal form of erythromycin in the tablet. Figure 1 shows two representative diffraction patterns. Pattern A is that of the passing tablet, and pattern B represents a failing tablet. Both tablets give the characteristic spectrum of erythromycin dihydrate; however, resolution differences were observed, which most likely reflect a difference in crystallinity. In addition, significant changes in the relative intensities of the X-ray peaks can be observed between passing and failing lots. As previously reported,[13] crystalline erythromycin can vary in water content over a large range (50−200%) of dihydrate theory without affecting the X-ray pattern. TGA of these samples showed two weight losses, indicating the presence of a small amount of surface water as well as interstitial water. The most highly crystalline lot shows a continuous weight loss approximately equal to the dihydrate stoichiometry of 4.7%. In addition, NIR spectroscopy[17] was used to further evaluate their water content by examining the hydroxyl peak (water combination band) at approximately 1.95 μm, which reflects hydroxyl contributions from erythromycin as well as from water. Table 1 shows a compilation of XRD patterns in terms of resolution, amount of water from TGA weight loss,

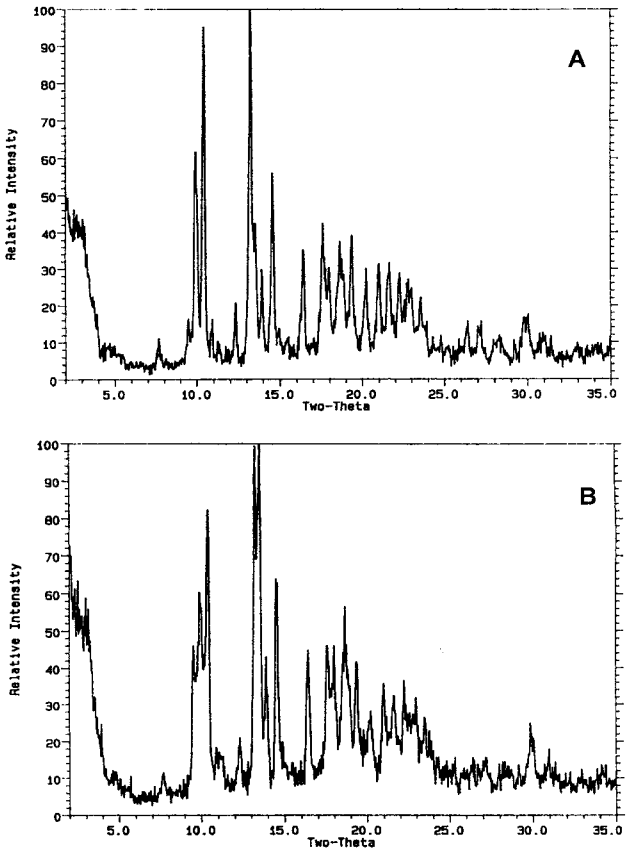

Figure 1—XRD of passing and failing Erythromycin tablet lots. (A) Passing tablets. (B) Failing tablets.

and the relative amount of hydroxyl content by NIR. The data indicate that the samples with low water content relative to the theoretical dihydrate stoichiometry also show broader, less-resolved peaks in the X-ray pattern. The NIR hydroxyl content also follows the same trend, i.e., lower hydroxyl content corresponds to broader X-ray peaks. Samples with less than 3.3% weight loss up to 136 °C show the lowest crystallinity and hydroxyl content compared to lot 1 which is the stoichiometric dihydrate. NIR spectroscopy was used in the remainder of the study to evaluate the water content of the tablets nondestructively on individual tablets, thereby allowing further testing on the same tablet by dissolution to investigate the correlation shown in Table 1.

While selecting a sample of amorphous erythromycin to characterize by NIR and XRD, a mesomorphic form or mesophase of erythromycin was identified which has not been previously reported. This material has a well-defined crystal habit and shows birefringence when examined by PLM but as shown in Figure 3 appears mostly amorphous by XRD showing only either a strong broad single line or multiple lines near 2 θ values of 9.4−9.6. The XRD and PLM data are consistent with a solid phase having 2-D order but lacking 3-D order. Amorphous erythromycin was produced separately by freeze-drying an aqueous solution of erythromycin. Examination of the XRD data described above suggests a possible transformation of the pattern for crystalline erythromycin dihydrate over time in the 250 mg formulation to a pattern representing a mixture of erythromycin dihydrate and the mesophase. However, since erythromycin dihydrate can produce an isomorphic dehydrated dihydrate, these XRD patterns could also represent a conversion to mesophase plus dehydrated dihydrate. This latter explanation is consistent with the parallel decrease in water content.

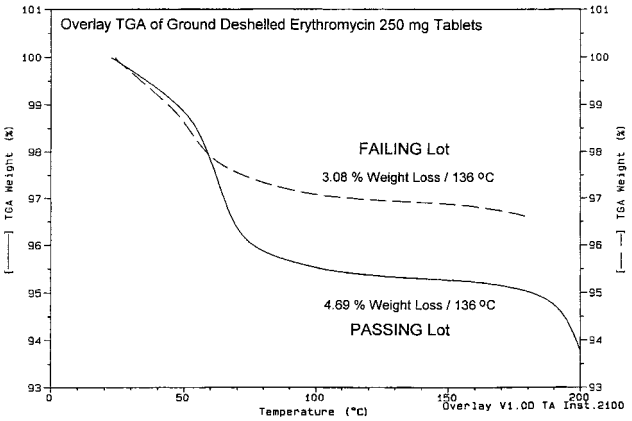

Figure 2—Overlay TGA of passing and failing lots of deshelled 250 mg erythromycin tablets.

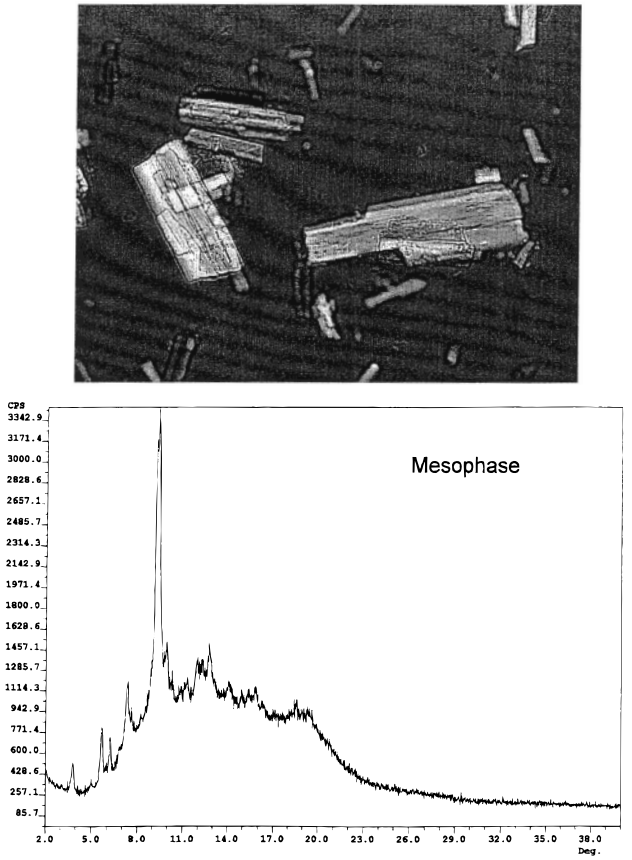

Figure 3—Characterization of erythromycin mesophase by PLM and XRD.

Table 2—Intrinsic Dissolution Data for Erythromycin Crystal Forms in Aqueous Solution (pH = 5.96)

form	amount dissolved in 60 min, mg
dihydrate	0.8
amorphous	2.8
mesophase	5.0

A basic tenet of solubility states that higher energy level crystal forms as well as amorphous material should have high intrinsic solubility compared to the more stable forms. The data presented in Table 2 show the intrinsic solubility relationship of mesophase, amorphous, and dihydrate forms of erythromycin. These data indicate that conversion to mesophase alone should not result in dissolution failure.

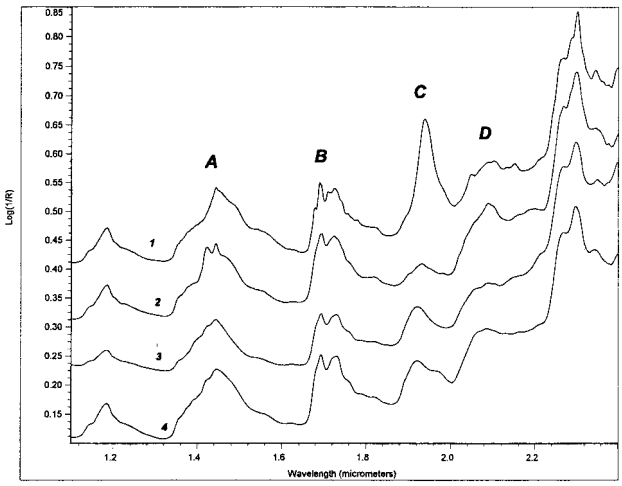

Figure 4—NIR spectra of (1) erythromycin dihydrate, (2) dehydrated erythromycin dihydrate, (3) erythromycin amorphous, and (4) erythromycin mesophase.

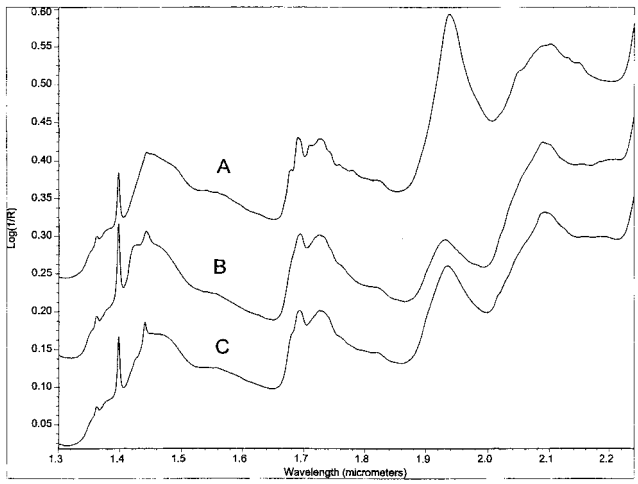

Figure 5—NIR spectra of (A) passing tablets, (B) dehydrated dihydrate, and (C) failing tablets.

Although erythromycin maintains its crystallographic order when dried, the local chemical environment is significantly influenced by the loss of water. When the dehydrated dihydrate is formed, this higher energy crystal form of erythromycin is more reactive and hygroscopic. Close examination of the NIR data (Figure 4) of bulk erythromycin dihydrate, isomorphic dehydrate, mesophase, and amorphous erythromycin indicates that each of the forms have distinguishing characteristics in the NIR spectral areas 1.45, 1.7, 1.95, and 2.1 μm (regions A, B, C, and D in Figure 4). Comparison of the NIR spectra of the passing lot, failing lot, and a dried passing lot (Figure 5) shows that the spectra of the samples are different particularly in the 1.4−1.5 μm region. These comparisons indicate that the majority of the erythromycin form in the failing lot is not dihydrate, isomorphic dehydrate, mesophase, or amorphous material.

Erythromycin tablets with greater drug load (333 and 500 mg) are prepared with corn starch and drug as the two predominant ingredients. The 250 mg tablets contain mainly drug, corn starch, and magnesium hydroxide. All other components are common to all formulations and are present in the same small quantities in all formulations. These include colorants and coatings. Samples of the higher dosage formulation were found to contain the same low (i.e., 3.3% or less) levels of water; however, no dissolution failures were observed after storage. If the reduced dis-

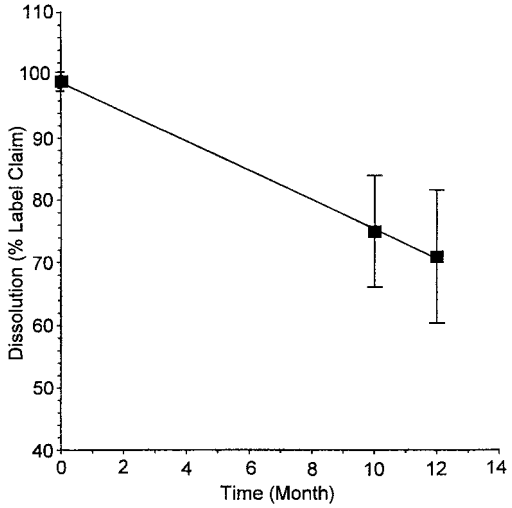

Figure 6—Comparison of failing lot 15 dissolution (% label claim) versus time.

solution rate were a result of changes in the excipients over time, for example, dehydration, the same dissolution failures would be expected with the higher dosage formulation. TGA and DMSG studies on the bulk drug and excipients indicate that the water in the formulation is preferentially lost from erythromycin upon heating rather than from the excipients.

Since the performance of the 250 mg tablet is different than that of the 333 and 500 mg tablets, an interaction with an excipient unique to the 250 mg tablet formulation was suspected. The only excipient unique to the 250 mg formulation is magnesium hydroxide, and the lack of dissolution failures in the higher dosage formulation even with low water content indicates that in the absence of this ingredient, changes in the other excipients over time do not result in dissolution failures. This could only explain part of the phenomenon, however, since only random tablets and one individual lot exhibited dissolution failures.

Dissolution of failing lot 15 was monitored over a 12-month period and analyzed at the initial and 10- and 12-month time points (Figure 6). Although only three points were obtained, there was very good linear correlation between the decrease in dissolution (% label claim) and time, with a correlation coefficient of greater than 0.99. Over the same period of time, moisture content by LOD of the coated tablets was 2.6, 2.1, and 2.4% (initial and 10- and 12-month, respectively). However, by comparison the typical passing lot 1 gave LOD values of 3.8, 3.7, and 3.8% (initial and 10- and 12-month, respectively). The decrease in dissolution can be associated with the constant low level of water in the coated tablets over time. This constant low level of water in the coated tablets prevents rehydration of the dehydrated erythromycin dihydrate and maintains erythromycin in the activated state.

When erythromycin dihydrate dehydrates to form a desolvated dihydrate, it reduces the number of hydrogen bonds in the structure dramatically from three to zero. This results in a void in the lattice which has a high hydrogen bonding potential. As noted by Stephenson et al.[16] over time the tunnels slowly relax unless either water is reabsorbed or an alternate ligand is obtained. The 250 mg tablet formulation contains $Mg(OH)_2$, a hydroxyl-rich material, as one of the excipients. Interaction of the activated dehydrated dihydrate of erythromycin with $Mg(OH)_2$ is a possible mechanism for filling the void created in the crystal lattice as a result of overdrying. This interaction in the solid state requires a finite period of time and would correlate well with the slow onset of dissolution failures in the 250 mg formulation over time.

Figure 7 shows schematically a process whereby overdrying could create dehydrated dihydrate in the tablet fill. As a result of the granulation and compaction of the tablet, the $Mg(OH)_2$ could then become associated with the same sites in the dehydrated dihydrate which tend to interact or bind with water in the dihydrate. Over time the association of $Mg(OH)_2$ with dehydrated erythromycin dihydrate could strengthen to a degree where the reversing of the binding interaction necessary for the dissolution of erythromycin becomes a progressively slower process. The extent of this binding would depend on time and the amount of overdrying. Therefore, it would account for both whole lot failure as well as isolated individual tablet failures. Close examination of the NIR spectra in the region of the $Mg(OH)_2$ peak shows discernible differences between passing lots and failing lots of the 250 mg tablets (Figure 8) and supports the model of $Mg(OH)_2$ interacting with the dehydrated dihydrate.

The extent of erythromycin/magnesium hydroxide binding in the tablets was estimated from dissolution data. Figure 6 displays the relationship between the dissolution of the tablet and time. A good linear relationship was observed. Hence, the rate of dissolution retardation in the coated tablet, lot 15, can be estimated at 2.4% per month.

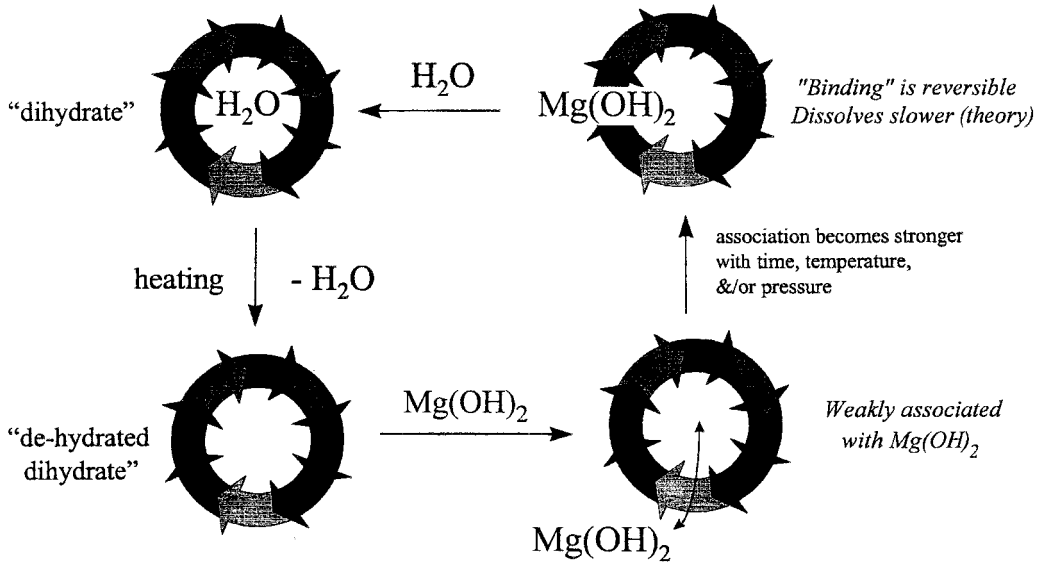

Figure 7—Schematic representation of reversible binding in erythromycin tablets.

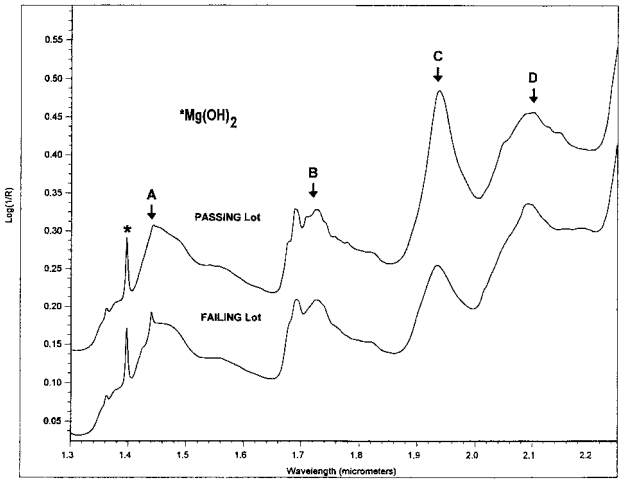

Figure 8—Four spectral regions of difference in the NIR spectra of passing and failing lots of deshelled erythromycin tablets.

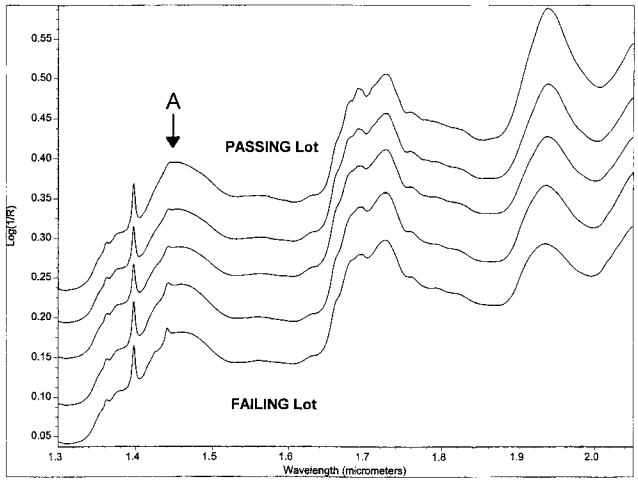

Figure 9—Series of NIR spectra of erythromycin tablets showing progression from passing to failing lot.

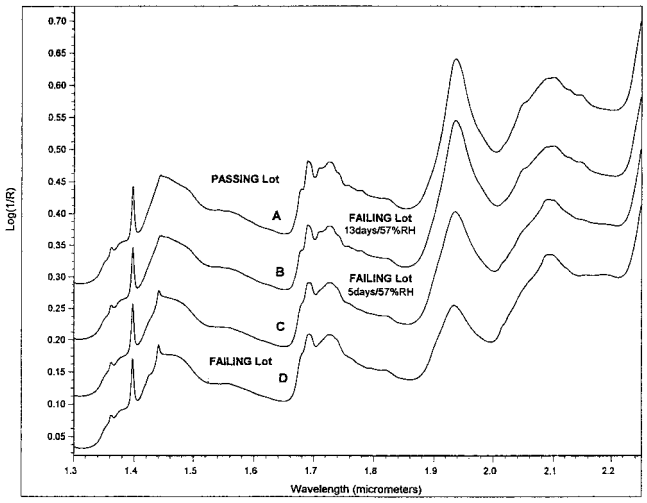

Figure 10—NIR spectra of (A) deshelled passing lot, (B) failing lot after exposure to high humidity for 5 days, (C) failing lot after exposure to high humidity for 13 days, and (D) failing lot.

Four spectral regions were examined at about 1.45, 1.7, 1.95, and 2.1 μm. The region of 1.45 μm represents overtones of hydroxyl and alkyl groups, the region at about 1.7 μm represents overtones of alkyl groups, the region near 1.95 μm represents combination bands of hydroxyl groups (and water content) of the sample, and the region near 2.1

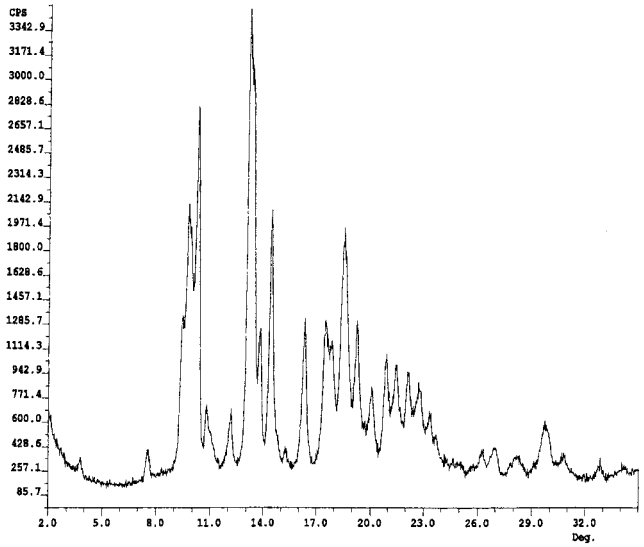

Figure 11—XRD of admixture of dehydrated dihydrate of erythromycin and magnesium hydroxide stored in a closed container for 12 months.

μm represents the first overtones of C−H stretching, and combination bands of alcohol hydroxy groups. As can be seen in Figure 8, the passing lot shows a significantly larger water peak (region C) and a broad multiplet at about 2.1 μm (region D), but not much definition in the area of 1.45 m (region A). The failing lot shows a distinct shoulder and a sharp peak in the region of 1.45 μm, a smaller peak in the water region, and a sharper and smoother peak in the 2.1 μm region. These changes indicate conformational and perhaps structural differences similar to those observed upon drying erythromycin dihydrate but more defined and sharper particularly in the 1.45 μm region. Figure 9 shows spectra of the 250 mg whole tablets for a series of lots displaying the progression (region A) from passing to failing lots.

The NIR data suggest that in the absence of water, dehydrated erythromycin dihydrate interacts with $Mg(OH)_2$ in the 250 mg tablets. This association occurs slowly over time (12 months), suggesting that it is a relatively unselective reaction. Thus, the binding process should be reversible in the presence of a more selective (or reactive) ligand. Since water forms a stable complex with erythromycin (dihydrate), it should be able to displace $Mg(OH)_2$ and reverse the complex formation.

To investigate the proposed reversibility of this phenomenon, tablets from the failing lot were exposed to high humidity (57% RH). Figure 10 shows the NIR spectra for a failing lot, the failing lot exposed to 57% RH for 5 and 13 days, and a passing lot of deshelled tablets. The NIR spectrum of the failing lot exposed to 57% RH/13 days converted to that of the passing lot after exposure to water vapor in the solid state.

Dissolution testing on these moisture-exposed tablets gave results >98% within 60 min, confirming that the binding phenomenon can be reversed.

Dried erythromycin, i.e., the dehydrated dihydrate, compressed with $Mg(OH)_2$ and stored in closed containers for a period of 12 months indicated spectral changes in the NIR spectrum similar to those detected in erythromycin tablets after 12 months. X-ray powder diffraction on the mixture showed a pattern matching that of the failing tablets (Figure 11).

Conclusion

Erythromycin dihydrate when dried is converted to an isomorphic dehydrated dihydrate which exists as an acti-

vated high energy form with a tendency to fill the void created by the loss of water. In erythromycin tablet formulations where water cannot be easily reabsorbed, this has been shown to result in binding to other hydroxyl-rich excipients such as $Mg(OH)_2$ which then adversely effects the properties of the formulation. This phenomenon can be reversed by exposing the tablets to water vapor for a relatively short period of time.

NIR spectroscopy has been shown to be a useful technique in the study of such crystal form transformation and binding. It allows a determination of such properties as drug and moisture content on individual tablets nondestructively thereby allowing further testing on the same tablet to establish a direct correlation with other properties. In addition, it has proven to be predictive of dissolution failures in erythromycin tablet formulations.

References and Notes

1. Haleblian, J.; McCrone, W. Pharmaceutical Applications of Polymorphism. *J. Pharm. Sci.* **1969**, *58* (8), 911−929.
2. Berger, A.; Ramberger, R. On the Polymorphism of Pharmaceuticals and Other Molecular Crystals I. *Mikrochim. Acta* **1979**, *11*, 259−271.
3. Berger, A.; Ramberger, R. On the Polymorphism of Pharmaceuticals and Other Molecular Crystals II. *Mikrochim. Acta* **1979**, *11*, 273−316.
4. Kimura, K.; Hirayama, F.; Uekama, K. Characterization of Tolbutamide Polymorphs (Berger's Forms II and IV) and Polymorphic Transition Behavior. *J. Pharm. Sci.* **1999**, *88* (4), 385−391.
5. Suryanarayananx, R. Polymorphism in Anhydrous Theophylline-Implications on the Dissolution Rate of Theophylline Tablets. *J. Pharm Sci.* **1997**, *86* (11), 1256−1263.
6. Martinez-Oharriz, M. C. Polymorphism of Sulindac: Isolation and Characterization of a New Polymorph and Three New Solvates. *J. Pharm. Sci.* **1997**, *86* (2), 248−251.
7. Fort, J. J. Polymorphism and Crystallization Behavior of Abbott-79175, a Second-Generation 5-Lipoxygenase Inhibitor. *J. Pharm. Sci.* **1996**, *85* (7), 773−780.
8. Kuhnert-Brandstatter, M. The Future of Microscopy. *Pure Appl. Chem.* **1965**, *10*, 133.
9. Mesley, R. J.; Clements, R. L. Infrared Identification of Barbiturates with Particular Reference to the Occurrence of Polymorphism. *J. Pharm. Pharmacol.* **1968**, *20*, 341.
10. Mesley, R. J.; Clements, R. L.; Flaherty, B.; Goodhead, K. The Polymorphism of Phenobarbitone. *J. Pharm. Pharmacol.* **1968**, *20*, 341.
11. Byrn, S. R. *Solid State Chemistry of Drugs*; Academic Press: New York, 1982.
12. Dunitz, J.; Bernstein, J. Disappearing Polymorphs. *Acc. Chem. Res.* **1995**, *28* (4), 193−200.
13. Bauer, J.; Quick, J.; Oheim, R. Alternate Interpretation of the Role of Water in the Erythromycin Structure. *J. Pharm. Sci.* **1985**, *74* (8), 899−900.
14. Stephens, G.; Stowell, J.; Toma, P.; Pfeiffer, R.; Byrn, S. Solid State Investigations of Erythromycin A Dihydrate: Structure, NMR Spectroscopy, and Hygroscopicity. *J. Pharm. Sci.* **1997**, *86* (11), 1239−1244.
15. Pfeiffer, R. R.; Yang, K. S.; Tucker, M. A. Crystal Pseudopolymorphism of Cephaloglycin and Cephalexin. *J. Pharm. Sci.* **1970**, *59*(12), 1809−1812.
16. Stephenson, G.; Groleau, E.; Kleemann, R.; Xu, W.; Rigsbee, D. Formation of Isomorphic Desolvates: Creating a Molecular Vacuum. *J. Pharm. Sci.* **1985**, *87* (5), 899−900.
17. MacDonald, B. F.; Prebble, K. A. Some Applications of Near-Infrared Reflectance Analysis in the Pharmaceutical Industry. *J. Pharm. Biomed. Anal.* **1993**, *11*, 1077−1085.

Acknowledgments

James Fort, Yang Sun, Dale Brinker, Elizabeth Easterbrook, and Edward Wodziak for suppling and analyzing materials used in these studies and Diane Horgen for the typing of this manuscript.

JS9900102

Interaction between Water and Poly(vinylpyrrolidone) Containing Polyethylene Glycol

TAKESHI HAMAURA* AND J. MICHAEL NEWTON

Contribution from *Department of Pharmaceutics, The School of Pharmacy, University of London, 29/39 Brunswick Square, London, WC1N 1AX, UK.*

Received August 31, 1998. Accepted for publication August 17, 1999.

Abstract □ Information on the interaction between water and polymers is indispensable for manufacturing solid dispersion of a drug by hot-melt extrusion because this interaction affects various properties of the water–polymer mixtures, such as their viscoelastic properties. In this study, poly(vinylpyrrolidone) K30 (PVP) containing 0%, 10%, and 20% poly(ethylene glycol) 400 (PEG) was used as model amorphous polymers. The interaction of water with these polymers was assessed by the evaluation of the glass transition temperature (T_g), the point on the isotherm corresponding to the weight of sorbed water required to form a complete monolayer on the solid surface (apparent W_m), and the maximal amount of nonfreezing water, which were measured by differential scanning calorimetry and water sorption isotherms. In all of the systems with a water content below a certain water fraction (0.1 for PVP, 0.12 for PVP–PEG 10%, and 0.16 for PVP–PEG 20%), the T_g values were successfully predicted using theoretical equations, whereas the experimental T_g values were higher than predicted for those with a water content above these water fraction levels. In addition, these values of water fraction are similar to the apparent W_m values determined using the Guggenheim–Anderson–DeBoer (GAB) equation (0.110, 0.117, and 0.147 weight fraction of water for PVP, PVP–PEG 10%, and PVP–PEG 20%, respectively). Nonfreezing water is detected above 0.47, 0.49, and 0.51 weight fraction of water for PVP, PVP–PEG 10%, and PVP–PEG 20%, respectively. Miscibility between water and PVP or PVP–PEG seems to change according to the water content in the system. All parameters increase with the concentration of PEG in the sample. This may be explained by the fact that PEG has a larger number of polymer repeating units, which may therefore interact with water more than PVP.

Introduction

Recently, a hot-melt extrusion technique has been applied to produce a polymer-based solid dispersion of a drug as a drug delivery system.[1,2] Amorphous hydrophilic polymers are often used as a component of such solid dispersions for the modification of drug dissolution. During the hot-melt extrusion process, the drug is incorporated into a rubbery state of amorphous polymer mass.[2] Therefore, the glass transition temperature (T_g) of the amorphous polymer is one of the most important factors in the hot-melt extrusion process because the viscoelastic properties of the polymer, namely whether the polymer is rubbery or glassy at the manufacturing temperature, are affected by the T_g value.[3] The T_g value of the polymer can be reduced to an appropriate temperature for the manufacturing process by adding a plasticizer such as poly(ethylene glycol) to the polymer. Moreover, it has been demonstrated that the water in the polymer acts as a plasticizer to lower the T_g value of the polymer–water systems by increasing the molecular mobility and free volume.[4–6] Amorphous polymer and plasticized polymer generally contain some amount of water, and water is sometimes added during the hot-melt extrusion process. As the water content affects the T_g value of the system, it is necessary to determine the interaction between water and polymers, in particular the effect of water content on the T_g value of the systems as basic information for the hot-melt extrusion process. However, although there have been some reports describing the relationship between the water content and the T_g value of polymer–water binary systems,[7,8] there have been few reports on plasticized polymer–water ternary systems.[6]

In this study, three components, poly(vinylpyrrolidone) K30 (PVP) as a model amorphous polymer, poly(ethylene glycol) 400 (PEG) as a model plasticizer, and water, were chosen and the interaction of water with PVP containing 0%, 10% and 20% PEG was studied. The experimental T_g values of the systems containing various amounts of water were determined using differential scanning calorimetry (DSC) and were compared with those predicted by theoretical equations. The apparent W_m (the point on the isotherm corresponding to the weight of adsorbed water required to form a complete monolayer on the solid surface) was estimated by analyzing the water sorption isotherm of PVP and PVP–PEG. Furthermore, a maximal amount of nonfreezing water was calculated by DSC studies on aqueous PVP and PVP–PEG solutions.

Experimental Section

Materials—Poly(vinylpyrrolidone) K30 (viscosity average of molecular weight, 42 500), PVP (BASF) and poly(ethylene glycol) 400 (nominal molecular weight, 400), PEG (Colorcon) were used without further treatment. Aqueous solutions of PVP–PEG 0–40% were spray dried using a Mini Büchi 190 spray dryer (Büchi) to obtain homogeneous samples. The spray-dried samples were vacuum-dried at 70 °C for 48 h in an oven. After vacuum-drying, the samples were stored in closed glass bottles. The PEG concentrations are expressed as a percentage (w/w PVP). All other reagents employed were of analytical reagent grade.

Water Sorption Isotherm—Approximately 400 mg of spray dried PVP, PVP–PEG 10%, and PVP–PEG 20% mixtures were accurately weighed into glass bottles and stored at 20 °C in desiccators containing saturated inorganic salt solutions giving various equilibrium relative humidities (RH) (7–75% RH) until a constant weight was obtained (at least 5 weeks). The salts used (with their corresponding relative humidities at 20 °C) were lithium bromide (7% RH), lithium chloride (11% RH), potassium acetate (23% RH), magnesium chloride (33% RH), potassium carbonate (43% RH), magnesium nitrate (54% RH), sodium bromide (59% RH), and sodium chloride (75% RH). The water content of the samples was calculated using the initial water content and the change in weight induced by storing the samples under each relative humidity condition. The initial water content of the samples was determined by drying at 120 °C for 5 h.

* Present address of corresponding author: Product Development Laboratories, Sankyo Co. Ltd. 1-2-58 Hiromachi, Shinagawa, Tokyo, Japan. Tel.: +81(3)3492-3131. Fax: +81(3)5436-8568. E-mail: khamau@shina.sankyo.co.jp.

10.1021/js980354c CCC: $18.00
Published on Web 10/07/1999

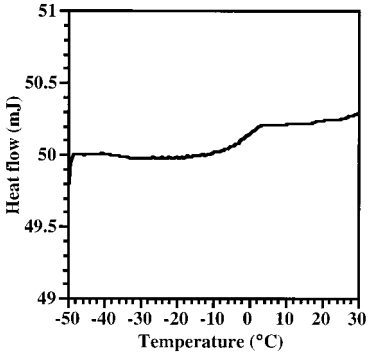

Figure 1—Typical DSC curve of a PVP–water system (glass transition).

Determination of T_g by DSC—Differential scanning calorimetry (DSC) measurements were performed using a Perkin-Elmer DSC 7 with a refrigerating system (Perkin-Elmer, Beaconsfield, UK). Samples (3−8 mg) stored under various RH were carefully transferred into aluminum pans in the desiccator, and the pans were hermetically sealed to prevent water loss during the DSC experiments. The samples were placed into the DSC under a nitrogen atmosphere and heated to 10−25 K above their T_g. The samples were subsequently cooled at 20 K/min to 273 or 223 K and then reheated. The first heating run exhibited an enthalpy relaxation endotherm at around the T_g value. Therefore, the T_g value of the samples was determined from the second heating cycle. Figure 1 illustrates a typical DSC curve of the second run for a sample of the PVP−water system (PVP stored under 75% RH). The T_g value was calculated by the half-extrapolated capacity method.[9] No endothermic peak relating to the melting of PEG was found even in the DSC curves of the PVP−PEG 10% and PVP−PEG 20% mixtures.

For determination of the T_g value of samples containing no water, samples (4−7 mg) were stored over P_2O_5 in a sealed desiccator for more than 5 weeks and DSC studies were carried out in open aluminum pans. The samples were repeatedly heated to 10−25 K above their T_g and subsequently cooled to 273 K at 20 K/min under a dry nitrogen purge. As the samples exhibited negligible differences between the T_g value determined from the second heating cycle and that from the third heating cycle, the T_g value determined from the second heating cycle was considered as the T_g value of the sample containing no water. All experiments were performed at least twice.

Determination of Freezing Water by DSC—To determine the amount of freezing water in the systems, a Perkin-Elmer DSC 7 with a cooling accessory (Perkin-Elmer, Beaconsfield, UK) was also used. Samples (5−15 mg) of various concentrations of aqueous PVP solution containing 0%, 10%, and 20% PEG were transferred into hermetically sealed aluminum pans to prevent water loss during the experiments. Samples were placed into the DSC and cooled to 223 K to promote freezing of any unbound water. Then, they were heated at 10 K/min to 303 K under a nitrogen atmosphere. Figure 2 depicts some typical melting endotherms of PVP−water systems. In the DSC curves, a small baseline change (occasionally small peak) is found at around 243 K (−30 °C). It seems that the baseline changes are caused by heterogeneity in the system, and the changes may be attributed to the glass transition or recrystallization. However, as the changes are considerably small and are not sometimes reproducible, it is difficult to determine what causes them only from the conventional DSC studies. Therefore, in this study, only the enthalpy of fusion of ice corresponding to the amount of freezing water was determined. Determination by other methods such as a modulated temperature DSC is necessary to elucidate what causes the baseline changes. The experiments were performed at least three times.

Equation To Predict the Value of the T_g^{mix} of the Systems—An equation for the prediction of the value of the T_g of a ternary system was employed. This equation is an extension of the Gordon−Taylor equation,[8,10] the equation for the prediction of the T_g value of a binary system. By assuming perfect volume additivity at the T_g and no specific interaction among the three systems, we can write

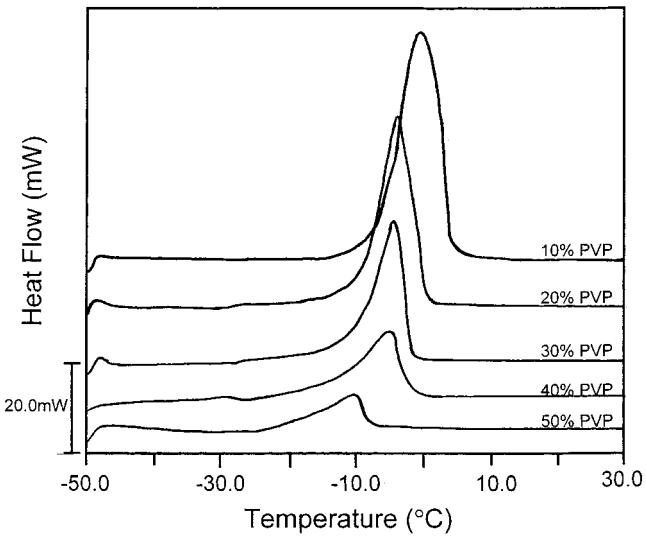

Figure 2—Typical DSC curves of PVP–water systems (melting peak).

$$T_g^{mix} = \Phi_1 T_{g1} + \Phi_2 T_{g2} + \Phi_3 T_{g3} \quad (1)$$

where F is the volume fraction of each component. As $\Phi = [(\Delta\alpha w)/\rho]$, where $\Delta\alpha$ is the change in thermal expansivity of T_g and $\Delta\alpha T_g \approx$ constant,[11] it is possible to rewrite the equation as

$$T_g^{mix} = \frac{w_1 T_{g1} + K_2 w_2 T_{g2} + K_3 w_3 T_{g3}}{w_1 + K_2 w_2 + K_3 w_3} \quad (2)$$

where w_1, w_2, and w_3 are the weight fractions, and T_{g1}, T_{g2}, T_{g3}, and T_g^{mix} are the glass transition temperatures in Kelvin of components 1, 2, 3, and the mixture.[12] The constants K_2 and K_3 can be approximated as $K_2 = (\rho_1 T_{g1})/(\rho_2 T_{g2})$ and $K_3 = (\rho_1 T_{g1})/(\rho_3 T_{g3})$, where ρ is the density of the materials. This equation is the Gordon−Taylor equation when we consider $w_3 = 0$. The constants K_2 and K_3 were calculated from the value of the T_g of 135,[13] 450, and 198 K[13] (−138, 177, and −75 °C, respectively) for water, PVP, and PEG and the densities of 1.00, 1.25, and 1.12 g/cm^3, respectively. The densities were measured using an air pycnometer (Air comparison pycnometer model 930, Beckman).

A similar equation, eq 3, can be readily derived for mixtures containing i components

$$T_g^{mix} = \frac{\sum K_i w_i T_{gi}}{\sum K_i w_i} \quad (3)$$

where $K_i = (\rho_1 T_{g1})/(\rho_i T_{gi})$.

X-ray Powder Diffraction—X-ray powder diffraction patterns were monitored by a diffractometer with Cu Kα radiation and a nickel filter at 40 kV and 40 mA (RINT 2200V, RIGAKU). The samples of spray-dried PVP, PVP−PEG 10%, and PVP−PEG 20% stored over P_2O_5 in a sealed desiccator were transferred into a sample holder and scanned at 4°/min over a range of 2°−40°. All samples exhibited halo X-ray powder diffraction patterns and were considered to be amorphous.

Multiple Regression Analysis—A nonlinear multiple regression program, MULTI, developed by Yamaoka et al.,[14] was used to carry out multiple regression analysis. The correlation coefficient (r) was calculated using the following equation

$$r = \left(1 - \frac{\mathrm{ESS}}{\mathrm{EMS}}\right)^{1/2} \quad (4)$$

where ESS is the sums of squares of the deviation of the theoretical values from the experimental values and EMS is the sum of squares of the deviation of the experimental values from their mean.

Statistical Analysis—The calculated maximal amount of nonfreezing water in PVP and PVP−PEG mixtures was statistically

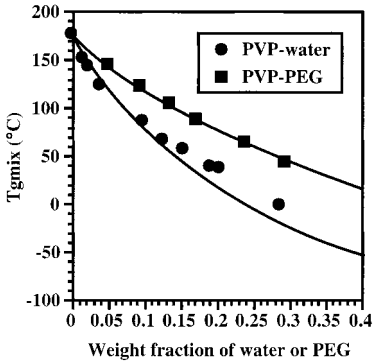

Figure 3—Effect of the weight fraction of water or PEG on the T_g^{mix} of PVP–water or PVP–PEG systems. The symbols represent experimental data points and the solid line represents the fit to the Gordon–Taylor equation (eq 2 in the text).

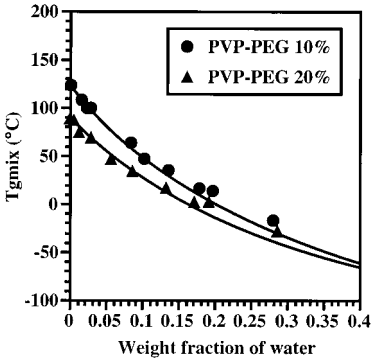

Figure 4—Effect of the weight fraction of water on the T_g^{mix} in PVP–PEG–water systems. The symbols represent experimental data points and the solid line represents the fit to the extended Gordon–Taylor equation (eq 2 in the text).

compared among each other using the Student's *t* test. Differences with $p < 0.05$ were considered significant.

Results and Discussion

Glass Transition Temperature of PVP−PEG and PVP−Water Binary Systems—Figure 3 shows the T_g value of PVP−water and PVP−PEG binary systems as a function of the weight fraction of water or PEG. The solid lines on the plots represent T_g values predicted by the Gordon−Taylor equation (eq 2). The T_g value decreases significantly with increasing weight fraction of water or PEG, showing that water as well as PEG acts as a good plasticizer. In the case of the PVP− PEG systems, the experimental T_g data fitted the predicted values well over the entire range studied. Therefore, it is considered that PVP and PEG mix ideally over the entire range studied (0−0.29 weight fraction of PEG). In the case of the PVP−water system, above a water fraction of around 0.1, the experimental T_g values for the PVP−water system were higher than predicted, whereas below this water fraction there was no difference between the experimental and theoretical T_g values. The results obtained for the PVP−water system are in excellent agreement with previous findings.[8] It is considered that PVP and water are miscible ideally up to a water fraction of around 0.1, but they mix nonideally above this water fraction. In other words, it seems that the Gordon−Taylor equation is not suitable to predict the T_g values of the PVP−water system above a water fraction of around 0.1. There could be other factors affecting the systems, which are not taken into consideration in the Gordon−Taylor equation.

Glass Transition Temperature of PVP−PEG−Water Ternary Systems—Two amorphous PVP−PEG systems containing 10% and 20% PEG (0.09 and 0.17 weight fraction of PEG in the PVP−PEG systems, respectively) were chosen to determine the effect of water on the T_g values in the PVP−PEG−water systems. At these PEG fractions, PVP and PEG mix ideally, as stated above. Figure 4 depicts the T_g value of these two ternary systems of PVP−PEG−water as a function of the weight fraction of water. The solid lines on the plots represent values of T_g^{mix} predicted by the extended Gordon−Taylor equation (eq 2). As can be seen, the T_g data fitted the predicted T_g values well up to a water fraction of around 0.12 for the PVP−PEG 10%−water system and up to a water fraction of around 0.16 for the PVP−PEG 20%−water system. Therefore, it is suggested that these three components are miscible ideally with each other at a low water content. However, above a certain water content, deviations between the experimental and theoretical T_g values of the PVP−PEG−water system were observed, as in the PVP−water system. It should be noted that the water fraction at which the deviations begin increases with the concentration of PEG (0%, 10%, 20%) in the sample.

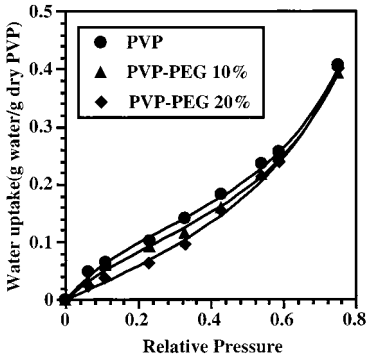

Figure 5—Water vapor absorption isotherms for PVP and PVP–PEG at 20 °C. The symbols represent experimental data points and the solid lines on the plot represent curve-fitted values using the GAB equation (eq 5 in the text).

Water Vapor Sorption Isotherms for PVP and PVP−PEG Mixtures—It is suggested that the miscibility between water and PVP or PVP−PEG systems changes at a certain water content based on the T_g studies. The interaction of water with other components has also been estimated by studies of water vapor sorption isotherms. W_m, the weight of adsorbed water required to form a complete monolayer on the solid surface, is one of the critical factors needed to characterize quantitatively the water sorption isotherms. W_m is calculated by fitting the sorption isotherm to the Brunauer−Emmett−Teller (BET) equation[15] or the Guggenheim−Anderson−DeBoer (GAB) equation,[16−18] which is an extension of the BET equation. The BET and GAB equations are generally applied to physical adsorption. The mechanism of water sorption to an amorphous solid like PVP is different from that of physical adsorption. However, even in an amorphous solid, it has been suggested that there is evidence indicating that at the point on the isotherm corresponding to the water content of W_m (apparent W_m), certain effects of water on solids change significantly and the apparent W_m value can be an important parameter relating to the interaction of polymer with water.[19−21]

Figure 5 shows the water vapor sorption isotherms for PVP containing 0%, 10%, and 20% PEG at 20 °C. The water content at each RH decreases with increasing concentration of PEG in the samples and the water uptake is significantly inhibited by the addition of PEG at 20−50% RH. All the water sorption isotherms of PVP and PVP−PEG are sigmoidal in shape (type II[22]). Therefore, the GAB equation,

given by eq 5, (where k is the GAB constant, W is the mass of gas sorbed per mass of dry solid at a relative pressure of p/p_o, and C_B is a constant which reflects the overall free energy of sorption)

$$W = \frac{kW_m\frac{p}{p_o}C_B}{\left(1 - k\frac{p}{p_o}\right)\left(1 - k\frac{p}{p_o} + kC_B\frac{p}{p_o}\right)} \quad (5)$$

was fitted to the data and the apparent W_m values were obtained by multiple regression analysis, though mixtures such as the PVP–PEG system are different from the systems for which the GAB equation was originally intended. As shown in Figure 5, the calculated W values, which are represented as a solid line, fitted the experimental W values very well for PVP containing 0%, 10%, and 20% PEG systems with a correlation coefficient greater than 0.995. The values of apparent W_m calculated are 0.124, 0.133, and 0.173 g of water/g of solid (0.110, 0.117, and 0.147 weight fraction of water, respectively) for PVP containing 0%, 10%, and 20% PEG, respectively. The relative humidities at which the W value is equal to the calculated apparent W_m value, (the RH(W_m)) was 28%, 36%, and 48% RH for PVP containing 0%, 10%, and 20% PEG, respectively. The apparent W_m value increases with the concentration of PEG in the sample. This suggests that in the sample containing a higher concentration of PEG, the interaction with water changes significantly when a larger amount of water is sorbed (the apparent W_m).

As mentioned above, the deviation of the experimental T_g values from those predicted seems to begin at a higher weight fraction of water in the sample containing a higher content of PEG. Also, the apparent W_m values increase with increasing PEG concentration in the sample. It should be remembered that the experimental T_g values were measured using a nonisothermal method (DSC), whereas the W_m values were estimated from isothermal measurements (the sorption isotherms). However, both values, the apparent W_m values and the weight fraction at which the deviation of the experimental T_g values seems to begin, are similar, which suggests that water interacts ideally with the polymer up to the higher water content in the sample containing the higher amount of PEG.

The Maximal Amount of Nonfreezing Water in PVP and PVP–PEG Mixtures—When samples contain immiscible water, the system shows a melting peak of water at 0 °C or less during heating after prior cooling. This component of water in the system can be regarded as freezing water, which is classified into two types,[23,24] type I, free, freezing water melting at 0 °C; and type II, loosely bound, freezing water with a melting point below that of pure water. Nonfreezing water is classified as type III. The PVP and PVP–PEG samples stored under conditions of RH up to 75% showed no melting peak of water in the DSC experiments. Consequently, no detectable freezing water exists in these systems, though some of them have the appearance of a transparent gel. Thus, to determine the interaction of water with PVP and PVP–PEG over a wide range, the melting peak of water in various concentrations of aqueous PVP and PVP–PEG solutions was detected using DSC, and the maximal amount of nonfreezing water which can be contained in the PVP–water and PVP–PEG–water systems was calculated.

Two methods have been applied to obtain the maximal amount of nonfreezing water in a polymer–water system.[25] Sung[26] reported that when there is a linear relationship between the enthalpies of water (J/g of dry polymer) and the ratio of water to polymer, the extrapolation to zero enthalpy gives the maximal amount of nonfreezing water in the system. Ford and Mitchell[27] also reported that when a linear relationship exists between the enthalpies of water (J/g of sample) and the percentage of water in the system, the maximal amount of nonfreezing water in the system is calculated from the extrapolation to zero enthalpy. Figure 6a,b shows Sung's plot and Ford and Mitchell's plot for the PVP–water system. In both cases, there is a linear relationship between the enthalpies of water and the ratio of water to polymer or the percentage of water. From both Sung's plot and Ford and Mitchell's plot, the maximal amounts of nonfreezing water are calculated to be around 0.47 of the weight fraction of water, corresponding to around 5.4 mol of water per polymer repeating unit (PRU) of PVP. Although the experimental T_g values could not be measured due to the limitations of the cooling system (minimum temperature 223 K), it is expected that more than one T_g value would be detected in the sample containing freezing water due to its heterogeneity.[12,28]

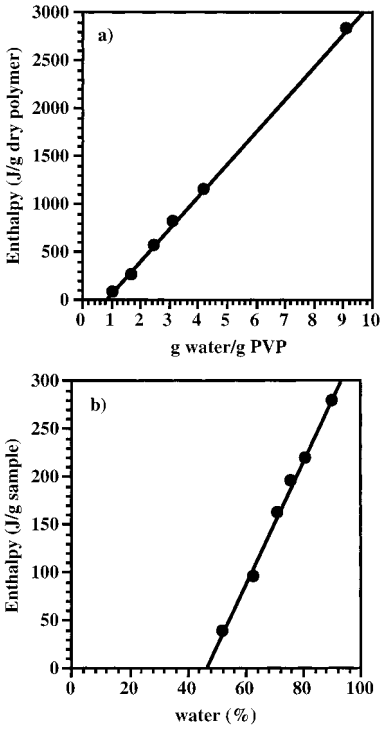

Figure 6—Relationship between (a) enthalpies of fusion and water/PVP ratio for PVP solutions (Sung's plot) and (b) enthalpies of fusion and water percentage for PVP solutions (Ford and Mitchell's plot).

In the case of the ternary systems, Sung's method does not seem to be suitable for obtaining the maximal amount of nonfreezing water, because it is impossible to calculate the enthalpies of water based on J/g of dry polymer. Therefore, only the Ford and Mitchell method was applied to obtain the maximal amount of nonfreezing water. As shown in Figure 7, there is a linear relationship between the enthalpies of water (J/g of sample) and the percentage of water in both PVP–PEG 10% and 20% systems. The maximal amount of nonfreezing water is calculated to be 0.49 and 0.51 for PVP–PEG 10% and 20% systems. These results indicate that freezing water is detected above 0.47, 0.49, and 0.51 weight fraction of water for PVP containing 0%, 10%, and 20% PEG, respectively. These values were analyzed to be significantly different. It is suggested that as PEG interacts with larger amounts of water compared to PVP, larger amounts of water can exist as nonfreezing water by adding PEG to PVP.

The Miscibility between Water and PVP or PVP–PEG Systems—From the results obtained above, the

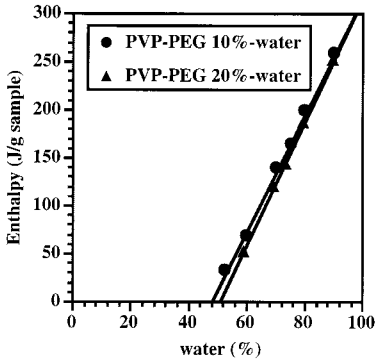

Figure 7—Relationship between enthalpies of fusion and water percentage for PVP–PEG solutions (Ford and Mitchell's plot).

miscibility between water and PVP can be expressed with certain assumptions as follows: up to the apparent W_m value (around 0.1 weight fraction of water), PVP and water mix ideally and the experimental T_g values of the PVP−water system can be estimated using the Gordon−Taylor equation. It has been reported that the interaction between the hydrophilic polymer and water may change according to the water content.[6] For example, in the case of amylose−water systems, it was assumed that the polymer−water system formed by hydrogen bonds is more compact than the polymer−polymer system with less than 10% water content and that a looser network is formed due to the occurrence of water−water interactions at a higher water content. As the miscibility of PVP and water also relates to the hydrogen bonds between them, it is speculated that the interaction between PVP and water changes at the weight fraction of around 0.1. This water fraction corresponds to the ratio of two water molecules (M_w = 18) to three PRU of PVP (PRU of PVP = 111).

On the other hand, above a 0.47 water weight fraction of water, corresponding to around 5.4 mol of water per PRU of PVP, freezing water is detected in the PVP−water system. It is expected that more than one T_g value may be detected due to the heterogeneity in the system. At a weight fraction of water of 0.1−0.47, though water still exists as nonfreezing water in the system, the miscibility of water and PVP must have decreased as the experimental T_g value did not decrease as much as predicted. In the case of maize starch and hydroxypropylmethyl cellulose, it has been reported that three states of sorbed water, internally absorbed water, monolayer-adsorbed water, and externally adsorbed water, could be estimated by analyzing the water sorption and desorption patterns using the Young−Nelson equations.[25,29] The interaction between water and solid is considered to be significantly influenced by these states of water. In the case of the PVP−water system, as the hypotheses based on the Young−Nelson equations are inadequate, the three states of water cannot be calculated using the Young−Nelson equations.

In the PVP−PEG−water systems, though the interaction among the three components are more complicated, it is speculated that the miscibility between water and the PVP−PEG system can be expressed, as in the case of PVP, except that both the apparent W_m values (or water fraction at which the deviations of the T_g values begin) and the maximal amount of nonfreezing water increase with increasing concentration of PEG in the sample. In the PVP−PEG−water systems, it may fairly be presumed that the three components interact with each other by hydrogen bonds. The PRU of PEG (CH_2OCH_2, PRU of PEG = 44) is smaller than the PRU of PVP (111) and PEG has more groups that may interact with water from the hydrogen bonds than PVP. Therefore, this may explain why PVP containing the higher concentration of PEG interacts with water up to the higher water fraction (the apparent W_m and the maximal amount of nonfreezing water).

Conclusion

The interaction between water and PVP containing 0%, 10%, and 20% PEG was studied using DSC and water sorption isotherms. The miscibility between water and PVP seems to change according to the water content in the system. Up to the apparent W_m value (around 0.1 weight fraction of water), PVP and water mix ideally and the experimental T_g values of the PVP−water system can be estimated using the Gordon−Taylor equation. From a 0.1 weight fraction of water to 0.47, which is calculated as the maximal amount of nonfreezing water, although water still exists as nonfreezing water in the system, the miscibility of water and PVP must have decreased as the experimental T_g value did not decrease as much as predicted. On the other hand, at a water weight fraction above 0.47, freezing water was present in the system and it is expected that there may be more than one T_g value due to the heterogeneity in the system. All parameters, the water fraction at which the deviation of the T_g values begins, the apparent W_m value, and the maximal amount of nonfreezing water, increase with the concentration of PEG in the sample. This may be explained by the fact that PEG has more polymer repeating units, which may interact with water more than PVP.

References and Notes

1. Grunhagen, H. H. Extrusion set to revolutionize tablet making. *Manufacturing Chemist* **1994**, *Dec*, 12−13.
2. Nakamichi, K.; Yasuura, H.; Fukui, H.; Oka, M.; Izumi, S.; Andou, T.; Simizu, N.; Ushimaru. K. New preparation method of solid dispersion by twinscrew extruder. *Pharm. Technol. Jpn.* **1996**, *12*, 715−729.
3. Hancock, B. C.; Zografi, G. Characterization and Significance of the Amorphous State in Pharmaceutical Systems. *J. Pharm. Sci.* **1997**, *86*, 1−12.
4. Levine, H.; Slade, L. Water as a plasticizer: Physicochemical aspects of low-moisture polymeric systems. In *Water Science Reviews*; Franks, F., Ed.; Cambridge University: Cambridge, 1987; pp 79−185.
5. Shalaev, E. Y.; Zografi, G. How does Residual Water Affect the Solid-State Degradation of Drugs in the Amorphous State? *J. Pharm. Sci.* **1996**, *85*, 1137−1141.
6. Lourdin, D.; Coignard, L.; Bizot, H.; Colonna, P. Influence of Equilibrium Relative Humidity and Plasticizer Concentration on the Water Content and Glass Transition of Starch Materials. *Polymer* **1997**, *38*, 5401−5406.
7. Oksanen, C. A.; Zografi, G. The relationship between the glass transition temperature and water vapor absorption by poly(vinylpyrrolidone). *Pharm. Res.* **1990**, *7*, 654−657.
8. Hancock, B. C.; Zografi, G. The relationship between the glass transition temperature and the water content of amorphous pharmaceutical solids. *Pharm. Res.* **1994**, *11*, 471−477.
9. Wendlandt, W. *Thermal Analysis*, 3rd ed.; Wiley and Sons: New York, 1986; pp 436−440.
10. Gordon, M.; Taylor, J. S. Ideal Copolymers and the Second-Order Transitions of Synthetic Rubbers. 1. Noncrystalline Copolymers. *J. Appl. Chem.* **1952**, *2*, 493−500.
11. Simha, R.; Boyer, R. F. General Relation Involving the Glass Transition Temperature and Coefficient of Expansion of Polymers. *J. Chem. Phys.* **1950**, *21*, 581−591.
12. Lu, Q.; Zografi, G. Phase behavior of binary and ternary amorphous mixtures containing indomethacin, citric acid, and PVP. *Pharm. Res.* **1998**, *15*, 1202−1206.
13. Velhoeven, J.; Schaeffer, R.; Bouwstra, J. A.; Junginger, H. E. The physicochemical characterization of poly(2-hydroxyethyl methacrylate-*co*-methacrylic acid: 2. Effect of water, PEG400 and PEG6000 on the glass transition temperature. *Polymer* **1989**, *30*, 1946−1950.
14. Yamaoka, K.; Tanigawara, Y.; Nakagawa, T.; Uno, T. A Pharmacokinetic Analysis Program (MULTI) for Microcomputer. *J. Pharmacobio-Dyn.* **1981**, *4*, 879−885.
15. Brunauer, S.; Emmett, P. H.; Teller, E. Adsorption of gases in multimolecular layers. *J. Am. Chem. Soc.* **1938**, *60*, 309−319.

16. Guggenheim, E. A. *Applications of statistical Mechanics*; Clarendon Press: Oxford, 1966; pp 186−206.
17. Anderson, R. B., Modifications of the Brunauer, Emmett and Teller equation. *J. Am. Chem. Soc.* **1946**, *68*, 686−691.
18. DeBoer, J. H. *The Dynamic Character of Adsorption*, 2nd ed.; Clarendon Press: Oxford, 1968; pp 200−219.
19. Zografi, G. States of water associated with solids. *Drug. Dev. Ind. Pharm.* **1988**, *14*, 1905−1926.
20. Zografi. G.; Kontny, M. J.; Yang, A. Y. S.; Brenner, G. S. Surface area and water vapor sorption of microcrystalline cellulose. *Int. J. Pharm.* **1984**, *18*, 99−116.
21. Faroongsarng, D.; Peck, G. E. The swelling & water uptake of tablets III: Moisture sorption behavior of tablet disintegrants. *Drug Dev. Ind. Pharm.* **1994**, *20*, 779−798.
22. Martin, A.; Swarbrick, J.; Cammarata, A. Physical Chemistry, Physical Chemical Principles in the Pharmaceutical Sciences, 3rd ed.; Lea & Febiger: Philadelphia, 1983; pp 445−468.
23. Hatakeyama, H.; Hatakeyama, T., Interaction between water and hydrophilic polymers. *Thermochim. Acta* **1998**, *308*, 3−22.
24. Joshi, H. N.; Wilson, T. D. Calorimetric studies of dissolution hydroxypropyl methylcellulose E5 (HPMC E5) in water. *J. Pharm. Sci.* **1993**, *82*, 1033−1038.
25. Nokhodchi, A.; Ford, J. L.; Rubinstein, M. H. Studies on the interaction between water and (Hydroxypropyl) methylcellulose. *J. Pharm. Sci.* **1997**, *86*, 608−615.
26. Sung Y. K. Interaction of water with hydrophilic methacrylate polymers., Ph.D. Thesis, University of Utah, 1978.
27. Ford, J. L.; Mitchell, K. Thermal analysis of gels and matrix tablets containing cellulose ethers. *Thermochim. Acta* **1995**, *248*, 329−345.
28. Turi, E. A. (Ed.) *Thermal Characterization of Polymeric Materials*, 2nd ed.; Academic Press: New York, 1997; pp 2384−2400.
29. York, P. Analysis of moisture sorption hysteresis in hard gelatin capsules, maize starch, and maize starch:drug powder mixtures. *J. Pharm. Pharm.* **1980**, *18*, 269−273.

Acknowledgments

Takeshi Hamaura acknowledges Sankyo Company Ltd. for financial support.

JS980354C

Disorder, Molecular Mobility, and Solid-State Kinetics: The Two-Environment Model

RAYMOND D. SKWIERCZYNSKI†

3M Pharmaceuticals 3M Center, Bldg 260-4A-04, St. Paul, Minnesota 55144-1000

Received July 28, 1998.
Accepted for publication June 9, 1999.

Solid-state reactions that yield sigmoid-shaped kinetic profiles have been described by either chemical models[1,2] that assume that the reaction occurs in a liquid layer on the surface of the solid, or by physical models[3,4] that are based on nucleation and growth or on diffusion. The objective of this communication is to introduce and apply the Two-Environment Model to describe the reaction kinetics of a crystalline solid, aspartame. The Two-Environment Model is based on the postulate that the chemical reaction can occur in two environments within the solid material and that the process in each environment is described with a simple zero-order rate constant. The second environment (E2), which is more disordered than the first environment (E1), is created by the formation of product. The Two-Environment Model, which is derived from first principles, builds on the basis of the nucleation-and-growth models by linking the chemistry of the reaction with the physical changes that occur in the solid matrix as the reaction proceeds.

In the solid-state, aspartame (A) undergoes a thermally induced cyclization to form two products, a diketopiperazine and methanol. Postulate that this reaction proceeds by parallel processes that occur in two different environments within the material. The first process is described by the following zero-order reaction, where Z represents the products.

$$A \xrightarrow{k^{(1)}} Z$$

The second process, also zero-order in A, is promoted by a physical change in the solid material that is directly proportional to the extent of the reaction at time t, $\alpha(t)$:

$$A \xrightarrow{\alpha(t)k^{(2)}} Z$$

The rate equation for the disappearance of A is

$$-\frac{dx_A}{dt} = k^{(1)} + \alpha(t)k^{(2)} \quad (1)$$

where x_A is the mole fraction of A remaining at time t, and $k^{(1)}$ and $k^{(2)}$ are the zero-order rate constants for the processes that occur in environments 1 and 2, respectively. The units on $k^{(1)}$ and $k^{(2)}$ are mole fraction/time, or simply time^{-1}. The process in E1 is predominant at the beginning of the reaction because $\alpha(t)$ is zero or small. The process in E2 becomes more important as the reaction proceeds, that is, as $\alpha(t)$ approaches unity.

The variables $\alpha(t)$ and x_A are related by eq 2.Dif-

$$x_A = 1 - \alpha(t) \quad (2)$$

ferentiating eq 2 with respect to time yields

$$\frac{dx_A}{dt} = -\frac{d\alpha(t)}{dt} \quad (3)$$

Substituting eq 3 into eq 1 gives

$$\frac{d\alpha(t)}{dt} = k^{(1)} + \alpha(t)k^{(2)} \quad (4)$$

The general solution of eq 4 is

$$\alpha(t) = \frac{k^{(1)}}{k^{(2)}}[e^{k^{(2)}t} - 1] + \alpha_o e^{k^{(2)}t} \quad (5)$$

where α_o is the extent of the reaction at $t = 0$. In practice, however, A usually does not decompose while the sample is equilibrated to the reaction temperature. For this special case in which $\alpha_o = 0$, eq 5 simplifies to eq 6.

$$\alpha(t) = \frac{k^{(1)}}{k^{(2)}}[e^{k^{(2)}t} - 1] \quad (6)$$

The rate constants are obtained by fitting the kinetic data to the integrated rate equations.

Aspartame[5,6] was chosen as the test system because its decomposition reaction is a simple unimolecular thermally induced aminolysis (Scheme 1). This reaction proceeds under anhydrous conditions. Thus water is not a reactant, does not form a liquid layer on the surface of the solid, and cannot plasticize the material. The aminolysis is quantitative, not autocatalytic, and yields equimolar ratios of diketopiperazine solid and gaseous methanol.[5]

The reaction was monitored by measuring the mass of the material under isothermal conditions by TGA (Model 2950, TA Instruments, New Castle, DE). About 14−30 mg of aspartame hemihydrate Form II (Sigma Chemical, St. Louis, MO) was placed into a (10-mm diameter × 1-mm depth) platinum TGA pan, dehydrated to produce anhydrous aspartame in situ by heating to 135 °C for 1 min,[7−9] and equilibrated at the reaction temperature. Five reaction temperatures were examined: 130.00, 140.00, 150.00, 160.00, and 170.00 °C. Isothermal conditions (±0.05 °C) were maintained until the reaction was completed. α_o was determined experimentally.

Representative kinetic curves are shown in Figures 1 and 2. The solid lines were obtained by fitting the data to eq 5 or 6 using nonlinear regression techniques**.** The fitted curves are in excellent agreement with the data. The results are reproducible and summarized in Table 1.

Note that $k^{(2)}$ is greater than $k^{(1)}$ for each temperature examined. If the chemistry were the rate-determining step, $k^{(1)}$ would equal $k^{(2)}$ because the same chemical reaction occurs in both environments. If one were to examine the reaction at the molecular level, three important steps must happen for aminolysis to occur: (1) The molecule must have mobility for the primary amine at the *N*-terminus to make contact with the carbonyl carbon at the *C*-terminus; (2) the reacting moieties must collide in the correct orientation; and (3) the moieties must have enough energy for the chemistry to occur. In this light, aminolysis of aspartame in the solid state is similar to aminolysis in solution. The difference, however, is that in solution the rate-determining

† Corresponding author. Tel (651) 733-6881. Fax (651) 575-1729. E-mail rdskwierczynski@mmm.com.

10.1021/js980303f CCC: $18.00
Published on Web 09/18/1999

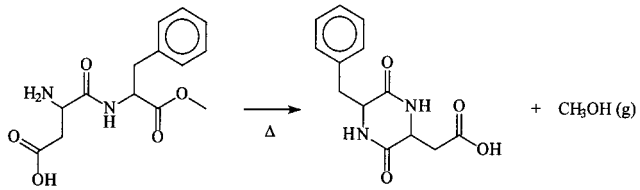

Scheme 1. Aminolysis of aspartame.

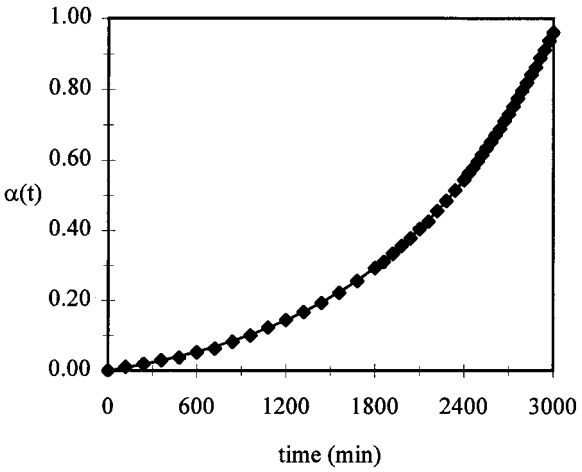

Figure 1—Data are from trial 1 at 130 °C. The line was obtained by fitting the data to eq 6: $k^{(1)} = 6.88 \times 10^{-5}$ min^{-1} and $k^{(2)} = 8.55 \times 10^{-4}$ min^{-1}.

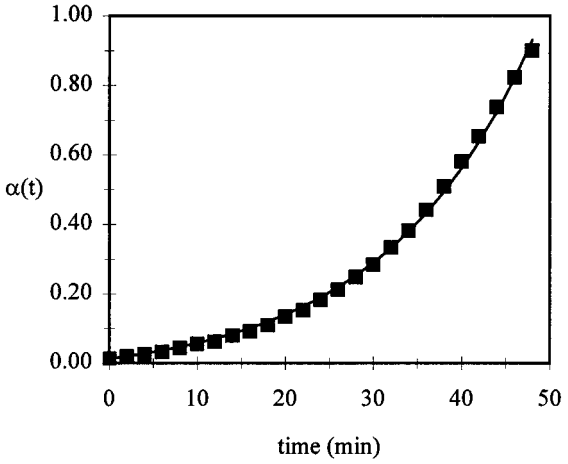

Figure 2—Data are from trial 1 at 160 °C. The line was obtained by fitting the data to eq 5: $k^{(1)} = 1.96 \times 10^{-3}$ min^{-1}, $k^{(2)} = 6.72 \times 10^{-2}$ min^{-1}, and $\alpha_o = 0.0127$.

Table 1—Summary of Results

T (°C)	α_o	$10^4 k^{(1)}$ (min^{-1})	$10^3 k^{(2)}$ (min^{-1})	t_{50} (min)	N
130	0	0.67 (0.02)[a]	0.90 (0.05)	2281	2
140	0	0.26 (0.01)	3.65 (0.08)	569	3
150	0	8.2 (0.1)	15.6 (2)	150	3
160	0.009 (0.003)	22 (2)	64 (3)	39.3	3
170	0.036 (0.002)	90 (6)	242 (4)	8.25	3
180	0.080 (0.004)	*b*	*b*	1.84	3

[a] The numbers in parentheses are standard deviations. [b] The reaction was too fast to analyze.

step is controlled by *chemistry*. The rate-determining step in the solid state is controlled by *physics*: the easier it is for reactants to collide, the faster the reaction will proceed.

This conclusion is consistent with Transition-State Theory.[10,11] The activation parameters listed in Table 2 were determined from an Eyring plot[11] (Figure 3). Even though the enthalpy of activation for the process in E2 is

Table 2—Activation Parameters for the Rate Processes that Occur in Each Environment

environment	$\Delta H^{\ddagger}$, kJ mol^{-1}	$\Delta S^{\ddagger}$, J K^{-1} mol^{-1}	$\Delta G^{\ddagger}$, kJ mol^{-1}
1	174	19	166[a]
2	205	119	155

[a] $\Delta G^{\ddagger}$ was calculated at 150 °C.

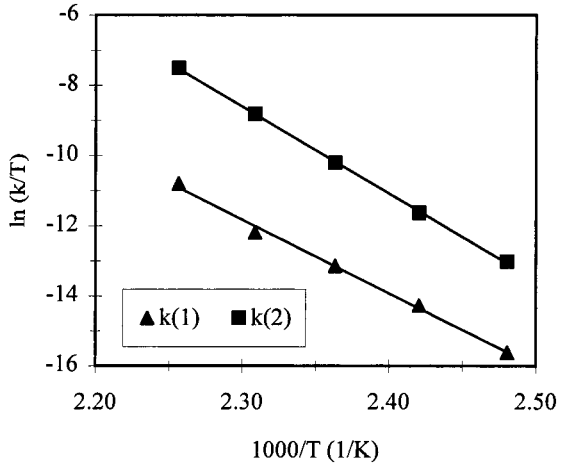

Figure 3—Eyring plot of the kinetic data.

31 kJ mol^{-1} *greater* than $\Delta H^{\ddagger}$ for the E1 process, the rate of aminolysis in E2 is faster than that in E1. This faster reaction rate can be explained by the lower Gibbs free energy of activation in E2. The rate-detemining-step for the process in E2 is entropically favored. In essence, the increased disorder in E2 serves as a "physical catalyst" for the solid-state aminolysis reaction by facilitating the mobility of the aspartame molecules.

Leung and Grant[12] also examined the solid-state demethylation of aspartame hemihydrate (form II) under isothermal conditions between 166 and 181 °C. Their data, in the range $0.1 < \alpha(t) < 0.9$, were fitted to the Prout–Tompkins equation, which models nucleation-and-growth kinetics. They reported an activation energy of 268 kJ mol^{-1}, which corresponds to a $\Delta H^{\ddagger}$ of 272 kJ mol^{-1}. In the Two-Environment Model, the process in E2 is dominant when $\alpha(t) > 0.1$. Here, as in Prout–Tompkins kinetics, new nuclei are generated by the strain that is introduced in the crystal lattice as the reaction proceeds. The large discrepancy between $\Delta H^{\ddagger}$ for E2 (205 kJ mol^{-1}) and the $\Delta H^{\ddagger}$ obtained by Leung and Grant clearly illustrates that solid-state kinetics is complex and that activation parameters are model dependent.

One advantage that the Two-Environment Model has over existing nucleation-and-growth models is that the Two-Environment Model can be used to estimate shelf-life (t_{90}) from kinetic data gathered at elevated temperatures. This advantage exists because the Two-Environment Model uses data in the region where $\alpha(t) < 0.1$, the portion of the kinetic curve that is most relevant to the pharmaceutical scientist. For example, the shelf life of aspartame at 120 °C can be estimated by first determining $k^{(1)}$ and $k^{(2)}$ from extrapolation of the fitted lines in the Eyring plot: $k^{(1)} = 1.76 \times 10^{-5}$ min^{-1} and $k^{(2)} = 1.75 \times 10^{-4}$ min^{-1}. Substituting these $k^{(1)}$ and $k^{(2)}$ values into eq 6, letting $\alpha(t) = 0.1$, and solving for t, gives an estimated t_{90} of 3900 min. The experimentally determined t_{90} was 3400 min.

In conclusion, the Two-Environment Model marries the chemistry of a solid-state reaction with the molecular mobility of the reactant. The model is consistent with transition-state theory and suggests that disorder that is induced in the solid material as the reaction proceeds acts

as a physical catalyst. The Two-Environment Model describes the solid-state aminolysis of aspartame.[13,14] The model can also serve as a practical tool for shelf life estimation.

References and Notes

1. Leeson, L. J.; Mattocks, A. M. Decomposition of Aspirin in the Solid State. *J. Am. Pharm. Assoc. Sci. Ed*. **1958**, *47*, 329−333.
2. Bawn, C. E. H. In *Chemistry of the Solid State*; Garner, W. E., Ed.; Butterworth Scientific: London, 1955; pp 254−267.
3. Carstensen, J. T. *Solid Pharmaceutics Mechanical Properties and Rate Phenomena*; Academic: New York, 1980, Chapter 6.
4. Byrn, S. R. *Solid-state Chemistry of Drugs*; Academic: New York, 1980.
5. Skwierczynski, R. D.; Connors, K. A. Demethylation Kinetics of Aspartame and L-Phenylalanine Methyl Ester in Aqueous Solution. *Pharm. Res.* **1993**, *10*, 1174−1180.
6. Skwierczynski, R. D. Molecular Mobility, Disorder, and Solid-State Kinetics: The Two-Environment Model. presented at the 12th Annual Meeting of the American Association of Pharmaceutical Scientists, Boston, MA, November 1997; paper 1541.
7. S. S. Leung and co-workers have characterized hydrated and anhydrous aspartame crystals. The dehydration performed in this study was consistent with their results. S. S. Leung, personal communication.
8. Leung, S. S.; Padden, B. E.; Munson, E. J.; Grant, D. J. W. Solid-State Characterization of Two Polymorphs of Aspartame Hemihydrate *J. Pharm. Sci*. **1998**, *87*, 501−507.
9. Leung, S. S.; Padden, B. E.; Munson, E. J.; Grant, D. J. W. Hydration and Dehydration Behavior of Aspartame Hemihydrate. *J. Pharm. Sci*. **1998**, *87*, 508−513.
10. Laidler, K. J. *Chemical Kinetics*, 3rd ed.; Harper and Row: New York, 1987, Chapter 4.
11. Connors, K. A. *Chemical Kinetics*; VCH: New York, 1990, Chapter 5.
12. Leung, S. S.; Padden, B. E.; Munson, E. J.; Grant, D. J. W. Solid State Stability Studies of Model Dipeptides: Aspartame and Aspartylphenylalanine *J. Pharm. Sci*. **1997**, *86*, 64−71.
13. The Two-Environment Model has also been used to describe the solid-state kinetics of thermally induced methyl transfer in tetraglycine methyl ester. This reaction is bimolecular. Skwierczynski, R. D.; Shalaev, E. Y.; Byrn, S. R.; Zografi, G. Unpublished results.
14. Skwierczynski, R. D. Application of the Two-Environment Model to Describe the Solid-State Kinetics of Materials in which a Liquid Layer Does Not Exist. Presented at the 8th Annual Symposium on the Molecular Properties of Crystalline and Amorphous Solids in Pharmaceutical Systems, Madison, WI, October 1998.

JS980303F

A publication of the **American Pharmaceutical Association** and the **American Chemical Society**

JOURNAL OF
Pharmaceutical Sciences

December 1999
Volume 88, Number 12

MINIREVIEW

Analytical Ultracentrifugation in the Pharmaceutical Industry

J. LIU AND S. J. SHIRE*

Contribution from *Department of Pharmaceutical Research and Development, Genentech, Inc., South San Francisco, California 94080*

Received May 7, 1999. Final revised manuscript received October 4, 1999.
Accepted for publication October 5, 1999.

Introduction

Hydrodynamic and thermodynamic techniques have been used extensively to characterize and determine the size, shape, molecular weight, and interaction of macromolecules. One of the most widely used techniques is that of analytical ultracentrifugation whereby the concentration gradients of sedimenting molecules are measured during the application of a centrifugal force. The design of instrumentation to accomplish this was a significant challenge and through the classic work of Thé Svedberg[1,2] resulted in a centrifuge that laid the foundations for modern protein chemistry and molecular biology. In particular, the early experiments on hemoglobin demonstrated conclusively that proteins were actually homogeneous macromolecular entities.[3] Since those classic experiments, great strides have been made in instrumentation as well as in analysis of sedimentation data. The purpose of this review is not to recount the huge amount of work in sedimentation in biochemistry but rather to review and discuss how analytical centrifugation has been used in the pharmaceutical industry. For those interested in a historical perspective as well as some of the latest advances in the field, several excellent recent books are available.[4−6]

Instrumentation

An analytical ultracentrifuge is a centrifuge that maintains good temperature and rotational speed control and is equipped with optical systems that allow for the determination of concentration gradients during the sedimentation experiment. The original analytical ultracentrifuge designed by Svedberg was driven by an oil turbine,[1] and despite the improvements made in the design, Svedberg wished to design a centrifuge that could attain higher rotor speeds in order to obtain greater separation of macromolecules in a high sedimentation field. Considerable effort went into redesigning the centrifuge as well as designing new rotors that could be accelerated up to 400000*g*.[7] By the mid-1930s oil turbine centrifuges were used routinely in Svedberg's and a few other laboratories. The proliferation of this technology occurred when the electrically driven ultracentrifuge was developed by Pickels and colleagues, leading to the availability of a commercial instrument, the Spinco model E in 1947, which proved to be the workhorse for analytical centrifugation technology. This centrifuge was equipped with UV absorption, Rayleigh interference, and Schlieren optical detection systems. Although the basic design of the commercial instrument did not change over the next 40 years, a few major improvements were made. Notably the old gear-driven mechanical speed control was replaced with a superior electronic control unit.

The Schlieren and interference optical systems used photographic film or glass plates for acquisition of data. This necessitated the upkeep of good darkroom facilities, as well as the use of expensive optical comparators for magnification and analysis of the images. The UV optical system also used photographic technology and subsequent densitometric scanning to convert the images into concentration gradients. Arguably, one of the key improvements was the replacement of the UV absorption system with a split beam photoelectric UV absorption optical scanning detector. The invention of the UV photoelectric scanning system[8] eliminated the need for development and processing of film and made the investigation of UV-absorbing macromolecules a less time-consuming endeavor. Moreover, the development of the photoelectric scanner enabled many researchers to acquire the data via A/D converters for input

10.1021/js9901458 CCC: $18.00
Published on Web 11/09/1999

into the newly emerging desktop computer, further decreasing the time for analysis. Additional improvements of the model E were also made by various laboratories in developing real-time Rayleigh interference optical systems that used video camera technology to acquire the data for input into computers. However, the majority of the biochemistry labs using the commercial instrument did not have the benefits of these additional improvements.

The difficulty in acquisition and analysis of centrifuge data from the model E may have resulted in a decrease in the use of analytical ultracentrifugation as more rapid, but less quantitative, techniques were developed and refined. In particular, a major use of the analytical ultracentrifuge was the determination of macromolecular mass. Techniques such as SDS polyacrylamide gel electrophoresis and gel sieving chromatography enabled researchers to obtain rough estimates of molecular weight more rapidly than with the model E.

The field of protein biotechnology that evolved, allowing researchers to express proteins in bacterial and mammalian cell culture systems, focused on many qualitative issues, such as expression and activity levels. As recombinant DNA technology evolved and became more commercialized, techniques were developed to express and purify large quantities of human proteins from mammalian cell lines. As more of the expressed proteins have entered the stage for development into human pharmaceuticals, there has been a greater need to use more sophisticated and rigorous physicochemical techniques to determine the best conditions for purification and ultimately formulation of the protein drug. In addition, the development of "rational drug design" required the use of more quantitative techniques to understand in detail the interactions of macromolecules with their biological targets. As will be discussed later, analytical ultracentrifugation remains one of the best techniques for investigation of molecular interactions. Thus, there was a need for a modern commercial ultracentrifuge that was "user" friendly and relatively maintenance free.

A new analytical ultracentrifuge, the XLA/I, has been designed that includes complete computer interface, and novel precision absorption scanning and integrated Rayleigh interference optical systems. The instrument is equipped with a highly precise and stable temperature control system and has a maximum speed of 60 000 rpm. The absorption optics uses a highly stable, UV-enhanced xenon flashlamp as the light source and a toroidal diffraction grating monochromator to provide the wavelength range from 190 to 800 nm.[9] The Rayleigh optical system uses a 30 mW, 675 nm laser as the light source.[10] It is extremely useful for analyzing the sedimentation of nonabsorbing macromolecules in solution.

Theory

The purpose of this section is to acquaint the reader with the essential and general facets of analytical ultracentrifugation theory. There are several excellent references that should be consulted for a greater in-depth treatment of the theoretical background of this field.[11–16]

The optical systems of an analytical ultracentrifuge can be used independently or in conjunction with each other to provide complementary information about the hydrodynamic and thermodynamic properties of macromolecules in solution. The analytical ultracentrifuge can be operated in two basic modes: sedimentation velocity and sedimentation equilibrium, and the type of information that can be obtained is dependent on which of the two basic modes is used.

Sedimentation Velocity—Sedimentation velocity is often conducted at relatively high rotor speeds for, at most, a few hours. The larger sedimenting species under a strong centrifugal field forms a unique sedimenting boundary in solution. The velocity and shape of the moving boundary can be used to estimate the sedimentation coefficient (s), diffusion coefficient (D) of macromolecular species, and in some case the stoichiometries and equilibrium constants of interacting systems.[17]

During a sedimentation velocity experiment, macromolecules are separated on the basis of not only the size but also the shape. The sedimentation rate of macromolecular species is directly related to the molecular mass M and translational diffusion coefficient D by the Svedberg equation,

$$s = \frac{v}{\omega^2 r} = \frac{M(1 - \bar{v}\rho)}{Rf} = \frac{M(1 - \bar{v}\rho)D}{RT} \qquad (1)$$

where v is the rate of sedimentation, ω the angular velocity, r the radial distance from the center of rotation, M the molecular weight, $\bar{v}$ the partial specific volume of solute, ρ the density of solvent, f the frictional coefficient, R the gas constant, and D the diffusion coefficient. In theory, the sedimentation coefficient of each species can be determined by analyzing the rate of movement of a midpoint in the boundaries, or more rigorously the migration of the second moment of the boundary. However, such analysis only yields an average s value for a complicated system composed of multiple sedimenting species. The diffusional spreading of the boundaries can obscure the presence of other species. These problems can be addressed at least in part by several more sophisticated sedimentation velocity methods, including the Van Holde and Weischet method,[18,19] the time derivative method,[17,20] and the whole boundary curve fitting method.[21] The sedimentation coefficient and diffusion coefficient determined from these methods can be used to study more about the shape and size of the sedimenting species.[22,23]

Sedimentation Equilibrium—Sedimentation equilibrium is performed at lower rotor speeds. Under these conditions the rate of sedimentation under the centrifugal field is opposed by the rate of diffusion, and eventually when they reach the equilibrium, a time invariant exponential concentration gradient of solute is established throughout the centrifuge cell. The concentration distribution at equilibrium can be rigorously described with thermodynamic theory and has been widely used to determine the molecular weight, stoichiometry, binding affinity, and virial coefficient. For an ideal, non-interacting multiple-component system, the concentration distribution at equilibrium can be described as

$$C(r) = \delta + \sum_{i=1}^{n} c_i(r_0) e^{M_i(1-\bar{v}\rho)\omega^2(r^2 - r_0^2)/(2RT)} \qquad (2)$$

where $C(r)$ is the concentration at radial position, r, $c_i(r_0)$ the concentration of the ith species at an arbitrary radial reference position, r_0, δ the baseline offset, M_i the molecular weight of ith species, T the temperature in kelvin, ω the angular velocity, $\bar{v}$ the partial specific volume of solute, ρ the density of solvent, and R the gas constant. For a system containing only a single sedimenting ideal species, the molecular weight measurement can be made by simply fitting the data of concentration as a function of radius position. For more complicated systems, in principle eq 2 can be further modified to allow the sedimentation equilibrium data to be fit to models that incorporate self-association or heteroassociation systems as well as correc-

tions for thermodynamic nonideality by including virial coefficients as fitting parameters.[24]

Applications

Structure-Based Drug Research and Design—Often the interactions and biological activities of proteins are regulated and impacted by their quaternary structure. Analytical ultracentrifugation has proven to be one of the most important and widely used methods for the characterization of self-association and heteroassociation of macromolecules in solution. Investigation of these interactions enables researchers to design molecules that can modulate these important functional interactions.

Examples of this approach have been discussed by Holzman and Snyder.[25] In one of the examples discussed, sedimentation equilibrium analysis was used to characterize the interaction of the ligand CTP with an enzyme, CKS (CTP:CMP-3-deoxy-D-mannooctulosonate cytidylyl transferase), responsible for growth in Gram-negative bacteria. This enzyme activates an eight-carbon sugar, KDO, for incorporation into the outer bacterial cell-wall lipopolysaccharide. These studies conclusively demonstrated that CTP modulates enzyme oligomerization and that an analogue of KDO that inhibits the enzyme activity modulates the oligomerization in a similar fashion as does CTP. In particular, the analytical ultracentrifuge studies strongly suggested that the active enzyme is a homodimer. This was further supported by the determination of the X-ray crystal structure of CKS that shows that the enzyme crystallizes as an asymmetric unit comprising two monomers.[25]

Another recent example shows how both sedimentation velocity and equilibrium techniques can be used to investigate in detail the self-association of insulin analogues under formulation conditions.[26] The implications for the pharmacokinetic and dynamic responses of these insulin analogues were discussed, and it was suggested that sedimentation analysis can help in developing improved rapid-acting insulin therapies. In addition, as already pointed out by Varley et al.,[27] the analytical ultracentrifuge is one of the few techniques whereby analysis can be performed directly on the formulation and result in quantification of the protein interactions under those conditions.

Molecular biology has provided a clearer understanding of the structure and function of target molecules on cell surfaces that are often involved in regulating biological responses. This knowledge has allowed pharmaceutical scientists involved with the research and discovery of new pharmaceutical entities to undertake a rational drug design approach. By studying the detailed interactions of receptors or cell surface molecules with their target molecules, researchers can design pharmaceuticals that can modulate these interactions. An excellent example of the application of sedimentation equilibrium analysis to characterize protein ligand and receptor interactions is the recent work by Philo and his colleagues. The heteroassociation of erythropoietin (EPO) and the extracellular domain of the EPO receptor, sEPOR (soluble form of erythropoietin receptor), was analyzed by sedimentation equilibrium[28] at several rotor speeds. Global analysis of several data sets clearly demonstrated that two sEPOR can bind to a single EPO monomer with very different binding affinity. These data suggest that dimerization of receptors by erythropoietin may be important for signal transduction and activity. Thus, it may be possible to increase the potency of the molecule be engineering a second binding site with greater affinity. Other examples of the characterization of receptor protein ligand interactions are the studies on TNF-α and -β (tumor necrosis factor) with the soluble forms of their target receptors.[29,30] Those studies demonstrated that the TNF oligomer unit is capable of binding more than one receptor.

There have been reported a wide range of applications of the use of sedimentation equilibrium to characterize protein oligomerization including the dimerization of human growth hormone by zinc,[31] the trimeric structure of TNF-α,[32] self-association of biglycan,[33] dimerization of human relaxin,[34] and self-association of human interferon alpha.[35] However, for more complicated self-assembly systems, sedimentation velocity analysis has been found to be very useful due to its sensitivity to both size and shape. This approach has been extensively applied to characterize many complicated systems, including the assembly and disassembly of cpn60,[36] salt-dependence of folding of chromatin,[37] amyloid protein aggregation,[25] and assembly of viruses.[38–40] In addition, sedimentation velocity can be used to characterize complex size distributions because of the separation power of the technique coupled with recent advances in analysis of heterogeneity by determination of the differential sedimentation coefficient distribution function.[20] Recently, this method was used to characterize a number of immune complex distributions formed by several monoclonal antibodies.[41] Not only was the size of the complexes determined, but also the potential structure of the complex was investigated by hydrodynamic modeling. This detailed structural information about protein interactions has provided an important basis for the further effort to develop and improve this drug therapy.

Stability and Homogeneity—For biopharmaceutical products, it is important to know whether they are stable and homogeneous under certain process and storage conditions. The degradation products of biopharmaceuticals often include aggregates and fragments. One possible way to identify these degradation products is to determine their average molecular weights by using sedimentation equilibrium analysis.[27,42] For highly purified and homogeneous molecules, the average molecular weights for the pure and non-self-associated macromolecules under ideal conditions should be very similar to the monomer molecular weights. On the other hand, for macromolecules that have undergone aggregation or fragmentation, the apparent average molecular weights under ideal conditions will diverge from the monomer molecular weights.

The purity of biopharmaceuticals can also be determined by sedimentation velocity analysis. Several sedimentation velocity methods have been developed to determine the distribution of protein species. Among these methods, the van Holde and Weischet analysis[18,19] has been well documented to provide a rigorous test of sample homogeneity.[43] This method has been extensively utilized by several groups to study the homogeneity of macromolecules. These include the characterization of oligonucleosomes,[44] transcription factors, sigma 70,[45] and NusA and transcription termination factor rho.[46] A different extrapolation method based on the time derivative of concentration distribution has also been found very useful to identify impurities from macromolecules.[17,20] This method has been used in combination with other techniques, such as SDS polyacrylamide gel electrophoresis and gel sieving chromatography, to help us to determine the purity and homogeneity of macromolecules in solution.[47]

Activity of Biopharmaceuticals—The binding affinity of protein interaction is an important thermodynamic parameter that will affect the activity of many biological molecules. The sedimentation equilibrium experiment is one of the most rigorous thermodynamic methods to measure binding affinity.[43] This technique generates large quantities of high-quality data with broad concentration ranges from a single experiment. Therefore, it can greatly increase the confidence of model determination with non-

linear least-squares fitting. The sedimentation equilibrium method has been successfully and extensively used by a number of investigators to determine the association constants of an interacting system.[28,48,49]

For more complicated and high-affinity bivalent antibody and antigen interactions, the sedimentation equilibrium methods are often limited, due to the sensitivity of the current analytical ultracentrifuge detectors and complication of complex distribution. Conventional methods, such as ELISA and biosensor, have often been used to determine such interactions. Analysis by ELISA is highly dependent on having the appropriate antibody for detection that does not interfere with the binding reaction that is being studied. Apparent affinity constants are often determined by using an ELISA to measure the amount of free ligand in solution. This requires extensive control experiments to ensure that the dilutions and process used in the ELISA do not perturb the interaction equilibrium.[50] In addition the immobilization of complexes onto the plate surfaces may also perturb the association equilibrium. Biosensor measurements also require immobilization of one of the reactants, and the manner in which the macromolecule is immobilized may alter the thermodynamics of interaction because of complications from molecule orientation on the surface and interference with the polymer matrix used for immobilization. The latter may alter the kinetic measurements because of mass transport through the matrix support. These complications have been discussed along with criteria needed to assess the reliability of biosensor data.[51] An alternative approach based on the sedimentation velocity method has recently been suggested by us to study the interaction of human IgE with an anti-IgE antibody.[52] In this method, a soluble form of the IgE high-affinity receptor (sFcϵRI) is used as a binding competitor to probe the IgE and anti-IgE monoclonal antibody (rhuMAb E25) interaction. Since the sFcϵRI is much smaller in size than rhuMAbE25 ($\sim$42 vs 150 kDa) and binds at or near the same site on IgE as rhuMAb E25, it is possible to distinguish the complexes formed by IgE$-$sFcϵRI and IgE$-$rhuMAb E25 by using sedimentation velocity experiments. By studying the shift of the complex distribution, we are able to distinguish the binding activity of rhuMAb E25 from that of other similar monoclonal antibodies.

Molecular Crowding Effect on Protein Drug Interaction and Formulation—Physiological media, such as human serum or cytoplasm, are very crowded environments that contain many large macromolecules. The volume exclusion arising from these high concentrations of macromolecules can have a large qualitative effect upon the equilibria and kinetics of protein drug interaction.[53] Sedimentation equilibrium is an ideal method to study protein drug interaction in a crowded environment. Although the current design of analytical ultracentrifuge optical detection systems lacks the sensitivity and specificity to distinguish a specific protein from the crowded background molecules, an alternative method that combines the sensitivity and specificity of radioisotope labeling and ELISA with preparative centrifugation techniques has been suggested.[54,55] This technology can increase the concentration range of traditional sedimentation equilibrium experiments. It has been used successfully to characterize a number of macromolecules, including ovalbumin, albumin, and γ globulin.[55,56]

The excluded volume effect resulting from small inert crowding molecules can also play an important role in protein drug formulation. Many protein drugs such as monoclonal antibodies requiring high dosing and sc administration will need to be formulated at a very high protein concentration. In addition, sugars have often been used to increase protein stability in solution[57] due to their exclusion from the surface of protein molecules. This has been attributed to a lowering of the protein free energy by minimization of exposed surface area.[58] Stabilization of the more compact folded form of the protein will obviously result in a surface area reduction. However, the surface area can also be reduced by intermolecular association, and thus, the excluded volume effect of sugars in liquid formulations can increase the propensity of proteins to self-associate. Recently it was shown, by sedimentation equilibrium analysis together with scale particle theory, that the high concentration of sugar and protein can dramatically increase the weak self-association of protein that may not be detectable at low and ideal conditions.[59] Such weak association can potentially decrease protein stability and affect other physical chemical properties.

Summary

The analytical ultracentrifuge has been cited as "still the tool of choice" to characterize associating systems.[60] The original development of the analytical ultracentrifuge helped provide the key data for the cornerstone of modern molecular biology and protein chemistry. At the height of its popularity few major labs in the country were without an analytical model E. Unfortunately, despite some of the improvements in the model E, the technology rapidly became a specialized area for researchers interested in improving the instrumentation for rapid data access and analysis. As cheaper and easier techniques were developed to measure rough molecular weights and obtain qualitative information on macromolecular association, the use of the centrifuge rapidly declined. Recently, with the advent of newer instrumentation, proliferation of user groups, workshops, and establishment of the National Analytical Ultracentrifugation Center at Storrs Connecticut, the technology has reemerged and is being used to a greater extent in academia as well as the pharmaceutical industry. This minireview, hopefully, has captured many of the recent advances and problems being investigated in the pharmaceutical and biotechnology arena.

References and Notes

1. Svedberg, T.; Heyroth, F. F. *J. Am. Chem. Soc.* **1929**, *51*, 550.
2. Svedberg, T.; Rinde, H. *J. Am. Chem. Soc.* **1924**, *46*, 2677.
3. Svedberg, T.; Fahraeus, R. A new method for determining the molecular weight of the proteins. *J. Am. Chem. Soc.* **1926**, *48*, 430.
4. Schuster, T. M., Laue, T. M., Eds. *Modern analytical ultracentrifugation: acquisition and interpretation of data for biological and synthetic polymer systems*; Emerging biochemical and biophysical techniques; Birkhauser: Boston, MA, 1994; 351 pp.
5. Harding, S. E., Rowe, A. J., Horton, J. C., Eds. *Analytical Ultracentrifugation in Biochemistry and Polymer Science*; Royal Society of Chemistry: Cambridge, 1992; 629 pp.
6. Lewis, M. S., Weiss, G. H., Eds. *Fifty Years of the Ultracentrifuge*; North-Holland Publishing Company: Amsterdam, 1976; 286 pp.
7. Svedberg, T. *Chem. Rev.* **1934**, *14*, 1.
8. Schachman, H. K.; Edelstein, S. J. Ultracentrifugal studies with absorption optics and a split-beam photoelectric scanner. *Methods Enzymol.* **1973**, *27*, 3–59.
9. Giebeler, R. The Optima XL-A: A New Analytical Ultracentrifuge with a Novel Precision Absorption Optical System. In *Analytical Ultracentrifugation in Biochemistry and Polymer Science*; Harding, S. E., Rowe, A. J., Horton, J. C., Eds.; Royal Society of Chemistry: Cambridge, 1992; pp 16–25.
10. Furst, A. The XL-I analytical ultracentrifuge with Rayleigh interference optics. *Eur. Biophys. J.* **1997**, *35*, 307–310.
11. Bowen, T. J. *An Introduction to Analytical Ultracentrifugation*; Wiley-Interscience: London, 1970.
12. Cantor, C. R.; Schimmel, P. R. *Biophysical Chemistry. Part II: Techniques for the Study of Biological Structure and Function*; W. H. Freeman and Company: San Francisco, 1980.

13. Tanford, C. *Physical Chemistry of Macromolecules*; John Wiley & Sons: New York, 1961.
14. Williams, J. W., Ed. *Ultracentrifugal Analysis in Theory and Experiment*; Academic Press: New York, 1963; 282 pp.
15. Schachman, H. K. *Ultracentrifugation in Biochemistry*; Academic Press: New York, 1959.
16. Van Holde, K. E. Sedimentation Analysis of Proteins. In *The Proteins*; Neurath, H., Hill, R. L., Eds.; Academic Press: New York, 1975; pp 226−287.
17. Stafford, W. F. I. Sedimentation velocity spins a new weave for an old fabric. *Curr. Opin. Biotechnol.* **1997**, *8*, 14−24.
18. Van Holde, K. E.; Weischet, W. Boundary analysis of sedimentation-velocity experiments with monodisperse and paucidisperse solutes. *Biopolymers* **1978**, *17*, 1387−1403.
19. Demeler, B.; Saber, H.; Hansen, J. C. Identification and interpretation of complexity in sedimentation velocity boundaries. *Biophys. J.* **1997**, *72*, 397−407.
20. Stafford, W. F. Boundary analysis in sedimentation transport experiments: a procedure for obtaining sedimentation coefficient distributions using the time derivative of the concentration profile. *Anal. Biochem.* **1992**, *203*, 295−301.
21. Philo, J. Measuring sedimentation, diffusion, and molecular weights of small molecules by direct fitting of sedimentation velocity concentration profiles. *Modern analytical ultracentrifugation*; Schuster, T. M., Laue, T. M., Eds.; Birkhauser: Boston, 1994; pp 156−170.
22. Laue, T. M. Advances in sedimentation velocity analysis. *Biophys. J.* **1997**, *72*, 395−396.
23. Byron, O. Construction of hydrodynamic bead models from high-resolution X-ray crystallographic or nuclear magnetic resonance data. *Biophys. J.*, **1997**, *72*, 408−415.
24. Mcrorie, D. K.; Voelker, P. J. *Self-associating systems in the analytical ultracentrifuge*; Beckman Instruments, Inc.: Fullerton, CA, 1993.
25. Holzman, T. F.; Snyder, S. W. Applications of Analytical Ultracentrifugation to Drug Design. In *Modern analytical ultracentrifugation: acquisition and interpretation of data for biological and synthetic polymer systems*; Schuster, T. M., Laue, T. M., Eds.; Birkhauser: Boston, MA, 1994; pp 298−314.
26. Richards, J. P.; Stickelmeyer, M. P.; Flora, D. B.; Chance, R. E.; Frank, B. H.; DeFelippis, M. R. Self-association properties of monomeric insulin analogs under formulation conditions. *Pharm. Res.* **1998**, *15*, 1434−1441.
27. Varley, P. G.; Brown, A. J.; Dawkes, H. C.; Burns, N. R. A case study and use of sedimentation equilibrium analytical ultracentrifugation as a tool for biopharmaceutical development. *Eur. Biophys. J.* **1997**, *25*, 437−443.
28. Philo, J. S.; Aoki, K. H.; Arakawa, T.; Narhi, L. O.; Wen, J. Dimerization of the extracellular domain of the erythropoietin (EPO) receptor by EPO: one high-affinity and one low-affinity interaction. *Biochemistry* **1996**, *35*, 1681−1691.
29. Pennica, D.; Kohr, W. J.; Fendly, B. M.; Shire, S. J.; Raab, H. E.; Borchardt, P. E.; Lewis, M.; Goeddel, D. V. Characterization of a recombinant extracellular domain of the type 1 tumor necrosis factor receptor: evidence for tumor necrosis factor-alpha induced receptor aggregation. *Biochemistry* **1992**, *31*, 1134−1141.
30. Pennica, D.; Lam, V. T.; Weber, R. F.; Kohr, W. J.; Basa, L. J.; Spellman, M. W.; Ashkenazi, A.; Shire, S. J.; Goeddel, D. V. Biochemical characterization of the extracellular domain of the 75-kilodalton tumor necrosis factor receptor. *Biochemistry* **1993**, *32*, 3131−3138.
31. Cunningham, B. C., Mulkerrin, M. G.; Wells, J. A. Dimerization of human growth hormone by zinc. *Science*, **1991**, *253*, 545−548.
32. Arakawa, T.; Yphantis, D. A. Molecular weight of recombinant human tumor necrosis factor-alpha. *J. Biol. Chem.* **1987**, *262*, 7484−7485.
33. Liu, J.; Laue, T. M.; Choi, H. U.; Tang, L. H.; Rosenberg, L. The self-association of biglycan from bovine articular cartilage. *J. Biol. Chem.* **1994**, *269*, 28366−28373.
34. Shire, S. J.; Holladay, L. A.; Rinderknecht, E. Self-association of human and porcine relaxin as assessed by analytical ultracentrifugation and circular dichroism. *Biochemistry* **1991**, *30*, 7703−7711.
35. Shire, S. J. pH-dependent polymerization of a human leukocyte interferon produced by recombinant deoxyribonucleic acid technology. *Biochemistry* **1983**, *22*, 2664−2671.
36. Mendoza, J. A.; Demeler, B.; Horowitz, P. M. Alteration of the quaternary structure of cpn60 modulates chaperonin-assisted folding. Implications for the mechanism of chaperonin action. *J. Biol. Chem.* **1994**, *269*, 2447−2451.
37. Hansen, J. C.; Wolffe, A. P. A role for histones H2A/H2B in chromatin folding and transcriptional repression. *Proc.Nat. Acad. Sci. U.S.* **1994**, *91*, 2339−2343.
38. Schuster, T. M.; Scheele, R. B.; Adams, M. L.; Shire, S. J.; Steckert, J. J.; Potschka, M. Studies on the mechanism of assembly of tobacco mosaic virus. *Biophys. J.* **1980**, *32*, 313−329.
39. Shire, S. J.; Steckert, J. J.; Adams, M. L.; Schuster, T. M. Kinetics and mechanism of tobacco mosaic virus assembly: direct measurement of relative rates of incorporation of 4S and 20S protein. *Proc. Nat. Acad. Sci. U.S.* **1979**, *76*, 2745−2749.
40. Shire, S. J.; McKay, P.; Leung, D. W.; Cachianes, G. J.; Jackson, E.; Wood, W. I.; Raghavendra, K.; Khairallah, L.; Schuster, T. M. Preparation and properties of recombinant DNA derived tobacco mosaic virus coat protein. *Biochemistry* **1990**, *29*, 5119−5126.
41. Liu, J.; Lester, P.; Builder, S.; Shire, S. J. Characterization of complex formation by humanized anti-IgE monoclonal antibody and monoclonal human IgE. *Biochemistry* **1995**, *34*, 10474−10482.
42. Wingfield, P.; Graber, P.; Moonen, P.; Craig, S.; Pain, R. H. The conformation and stability of recombinant-derived granulocyte-macrophage colony stimulating factors. *Eur. J. Biochem.* **1988**, *173*, 65−72.
43. Hansen, J. C.; Lebowitz, J.; Demeler, B. Analytical ultracentrifugation of complex macromolecular systems. *Biochemistry* **1994**, *33*, 13155−13163.
44. Hansen, J. C.; Ausio, J.; Stanik, V. H.; van Holde, K. E. Homogeneous reconstituted oligonucleosomes, evidence for salt-dependent folding in the absence of histone H1. *Biochemistry* **1989**, *28*, 9129−9136.
45. Gill, S. C.; Yager, T. D.; von Hippel, P. H. Escherichia coli sigma 70 and NusA proteins. II. Physical properties and self-association states. *J. Mol. Biol.* **1991**, *220*, 325−333.
46. Geiselmann, J.; Yager, T. D.; Gill, S. C.; Calmettes, P.; von Hippel, P. H. Physical properties of the *Escherichia coli* transcription termination factor rho. 1. Association states and geometry of the rho hexamer. *Biochemistry* **1992**, *31*, 111−121.
47. Liu, J.; Ruppel, J.; Shire, S. J. Interaction of human IgE with soluble forms of IgE high affinity receptors. *Pharm.Res.* **1997**, *14*, 1388−1393.
48. Laue, T. M.; Johnson, A. E.; Esmon, C. T.; Yphantis, D. A. Structure of bovine blood coagulation factor Va. Determination of the subunit associations, molecular weights, and asymmetries by analytical ultracentrifugation. *Biochemistry* **1984**, *23*, 1339−1348.
49. Kim, S. J.; Tsukiyama, T.; Lewis, M. S.; Wu, C. Interaction of the DNA-binding domain of Drosophila heat shock factor with its cognate DNA site: a thermodynamic analysis using analytical ultracentrifugation. *Protein Sci.* **1994**, *3*, 1040−1051.
50. Friguet, B.; Chaffotte, A. F.; Djavadi-Ohaniance, L.; Goldberg, M. E. Measurements of the true affinity constant in solution of antigen−antibody complexes by enzyme-linked immunosorbent assay. *J. Immunol. Methods* **1985**, *77*, 305−319.
51. Schuck, P.; Minton, A. P. Analysis of mass transport-limited binding kinetics in evanescent wave biosensors. *Anal. Biochem.* **1996**, *240*, 262−272.
52. Liu, J.; Shire, S. J. A Novel Solution Based Receptor Inhibition Assay to Evaluate the Interaction of Anti IgE Monoclonal Antibody and its Fab Mutant. *Pharm. Res.* **1995**, *12*, S-97.
53. Minton, A. P. Influence of excluded volume upon macromolecular structure and associations in 'crowded' media. *Curr. Opin. Biotechnol.* **1997**, *8*, 65−69.
54. Minton, A. P. Analytical centrifugation with preparative ultracentrifuges. *Anal. Biochem.* **1989**, *176*, 209−216.
55. Darawshe, S.; Rivas, G.; Minton, A. P. Rapid and accurate microfractionation of the contents of small centrifuge tubes: application in the measurement of molecular weight of proteins via sedimentation equilibrium. *Anal. Biochem.* **1993**, *209*, 130−135.
56. Pollet, R. J.; Haase, B. A.; Standaert, M. L. Macromolecular characterization by sedimentation equilibrium in the preparative ultracentrifuge. *J. Biol. Chem.* **1979**, *254*, 30−33.
57. Arakawa, T.; Kita, Y.; Carpenter, J. F. Protein−solvent interactions in pharmaceutical formulations. *Pharm. Res.* **1991**, *8*, 285−291.
58. Arakawa, T.; Timasheff, S. N. Stabilization of protein structure by sugars. *Biochemistry* **1982**, *21*, 6536−6544.
59. Liu, J.; Shire, S. Weak self-association of proteins at accelerated concentration. *Pharm. Res.* **1998**, *1*, S537.
60. Schachman, H. K. Is there a future for the ultracentrifuge? In *Analytical ultracentrifugation in biochemistry and polymer science*; Harding, S. E., Rowe, A. J., Horton, J. C., Eds.; The Royal Society of Chemistry: Cambridge, England, 1992.

JS9901458

A Convenient Assay Method for the Quality Control of Peptides and Proteins

NEIL PURDIE,* DENNIS W. PROVINCE, AND ERIN A. JOHNSON

Contribution from *Chemistry Department, Oklahoma State University, Stillwater, Oklahoma 74078-0447.*

Received June 25, 1999. Accepted for publication September 23, 1999.

Abstract □ The development of a convenient and very accurate procedure with which to discriminate among subsets of structurally similar peptides and proteins, and measure enantiomeric purities with very good accuracy, has been described in a series of recent articles. A factor preventing its general application to all peptide forms is that comparisons were originally limited to closed subsets of structurally similar types, e.g., dipeptides, tripeptides, and insulin drug forms. In the most recent of these articles, a modification to the method was described which did enable the comparisons to be extended between sets, in particular the di-and tripeptides. That same modification is extended even further in this article to include additional di- and tripeptides, glycylglycine oligomers, insulin drug forms, and neuropeptides. The same principal component analysis treatment used for data reduction and statistical comparisons in prior work enables the discrimination among 49 of the total of 51 analytes investigated.

Introduction

It was originally demonstrated that members of a series of structurally analogous dipeptides[1] and a separate series of tripeptides[2] could be differentiated one from the other by (i) complexing pure forms of the analytes to Cu(II) in aqueous pH 13 solutions and (ii) measuring the visible range circular dichroism (CD) spectra. Complete differentiation within each series was not entirely possible on the basis of just the CD spectral data. It was only achieved when two novel data reduction algorithms were applied to the experimental data. The algorithms are peculiar only to CD data and are applicable in every circumstance where multiwavelength CD detection is used.

Differentiations within groups were based upon comparisons made among the individual members and how they differed from an arbitrarily chosen reference. For the di-and tripeptides these were glycylalanine (GA) and glycylglycylalanine (GGA), respectively. Differentiation between groups was not possible because there was no ligand common to both series. This was resolved by complexing the Cu(II) ion with the auxiliary ligand D-histidine which was made to undergo ligand exchange with the same peptide analytes under the same solution conditions.[2,3] The Cu(II)-D-histidine host complex in effect acts as a chiral derivatizing agent which produces a diastereoisomer, or mixed chiral complex, on partial ligand exchange with each peptide.

Reasons for choosing D-histidine are that it forms a very stable Cu(II) complex, it undergoes rapid ligand exchange, and the Cu(II)−D-histidine host complex has a fairly intense biphasic (i.e., positive and negative bands) visible CD spectrum which affords good analytical sensitivity and an extra element of selectivity to the analyses. Although less expensive, the L-histidine enantiomer has a CD spectrum for the Cu(II)-complex that bears a closer resemblance to the spectra for Cu(II)-L-peptide forms and therefore diminishes the discrimination capability.

A second reason for choosing an auxiliary ligand is that it, rather than the analytes, takes on the thermodynamic responsibility for solubilizing the Cu(II) in strongly basic (pH 13) solutions. For the same reason racemic tartrate is used in the classical biuret test[4] which, until recently, was a method of choice to measure total blood proteins.[5] Apart from the introduction of the CD detector, the only change between this test and the biuret procedure is replacing DL-tartrate with D-histidine. All of the accepted experimental procedures that pertain to the biuret test apply to this modification. The first metal to ligand attachment is made through the N-atom of the terminal amine, with subsequent chelation through binding of the amide nitrogens of the next two peptide bonds.[6] Protein aggregation in the presence of high pH or Cu(II) ion is not a problem.[4] Auxiliary ligand concentrations are always kept in large excess over the metal ion concentration.

An added analytical advantage to using a chiral auxiliary ligand is that the CD spectrum for the host is not baseline. As a result, analytical sensitivities are increased significantly allowing for the use of much smaller quantities of the analyte for each assay. With D-histidine as the auxiliary ligand, the quantity of the analyte material can be decreased by a factor of 10−100 relative to the amounts used earlier.[2,3] This is a significant savings factor if amounts of the analytes are very small to begin with as they invariably are in the production of trial quantities of new drug forms.

The strategy of using Cu−D-histidine as a chiral derivatizing agent as a way to enhance analytical selectivity was successfully demonstrated by the total discrimination among manufactured forms of human, porcine, human Lyspro, and bovine insulins and between the A- and B-chains of bovine insulin.[7] These constitute a unique set of compounds for evaluating the analytical selectivity (even specificity) of the method since the polypeptide sequence changes are minimal and as it turns out remote from the active site, which is the coordinating to the Cu(II) ion. Human and porcine insulins differ only in the identity of the B30, acid terminus, residues which are L-threonine and L-alanine, respectively. The sequence variation is as remote as it can possibly be from the B-amine terminus, the known binding site.[6] Human insulin and the human LysPro variant forms differ only by reversal of the B28−B29 lysine-proline sequence one place removed from the acid terminus

10.1021/js990209e CCC: $18.00
Published on Web 10/28/1999

of the B-chain. Bovine and human analogues differ by two residue substitutions at points A8 (alanine for threonine) and A10 (valine for isoleucine), positions that are part of one of the cyclical sequences in the molecules. Differentiation among these structural variants is routine.

From the obvious analytical specificity of the method toward the insulins,[7] it is evident that interactions other than just the primary coordination and chelation of the residues at the amine terminus are factors to be considered in donor−receptor interactions. A possible major influence might be long-range chiral−chiral interactions between host and analyte ligands. From an analytical perspective, the evidence suggests that the general selectivity among proteins will be very broad. The simplicity of the experimental procedure and the specificity of the data reduction and data handling algorithms make the method an attractive alternative to chromatography for QC applications by manufacturers and regulatory agencies.

The modified biuret reagent and detection procedure might ultimately qualify as an Analyte Specific Reagent (ASR) as it is defined by the Food and Drug Administration in the ASR Rule[8,9] and be applicable to peptides and protein forms.

A major, new frontier in the pharmaceutical industry is the focus on the therapeutic properties of peptide and protein drug forms.[10] Because the number of chiral centers has virtually no limit,[11] the magnitude of the chirality regulatory control problem is increased almost exponentially. Since chiral derivatizations will not produce a single diastereoisomer, even the very best chiral chromatographic methods face what are probably insurmountable challenges.[12] In these circumstances a bulk spectroscopic method has many advantages. The intent of this work was to get a better sense for how general the analytical selectivity is with a special focus on QC of peptides and proteins.

Experimental Section

Chemicals—The full complement of peptide and proteins analytes used for the study is (**1**) glycyl-L-alanine (GA), (**2**) glycyl-(D)-alanine (Ga), (**3**) glycyl-(L)-phenylalanine (GF) (**4**) glycylglycine (GG), (**5**) glycyl-(L)-histidine (GH), (**6**) glycyl-(L)-isoleucine (GI), (**7**) glycyl-(L)-lysine (GK), (**8**) glycyl-(L)-methionine (GM), (**9**) glycyl-(L)-proline (GP), (**10**) glycyl-(L)-tyrosine (GY), (**11**) (L)-alanyl glycine (AG), (**12**) (L)-alanyl-(L)-alanine (AA), (**13**) (L)-alanyl-(L)-tyrosine (AY), (**14**) (L)-tyrosylglycine (YG), (**15**) (L)-tyrosyl-(L)-alanine (YA), (**16**) (L)-tyrosyl-(L)-tyrosine (YY), (**17**) glycylglycyl-(L)-alanine (GGA), (**18**) glycylglycylglycine (GGG) (**19**) glycylglycyl-(L)-histidine (GGH), (**20**) glycylglycyl-(L)-isoleucine (GGI), (**21**) glycylglycyl-(L)-leucine (GGL), (**22**) glycylglycyl-(L)-phenylalanine (GGF), (**23**) glycyl-(L)-histidylglycine (GHG), (**24**) (L)-leucylglycylglycine (LGG), (**25**) (L)-tyrosylglycylglycine (YGG), (**26**) (GGGG), (**27**) (GGGGG), (**28**) (GGGGGG), (**29**) DSLET, (**30**) DTLET, (**31**) DADLE, (**32**) DAGO), (**33**) DALDA amide, (**34**) DPDPE amide, (**35**) CTAP amide, (**36**) DynorphinA (1−9), (**37**) DynorphinA (1−11), (**38**) DynorphinA (1−13), (**39**) DynorphinA (1−13) amide, (**40**) DynorphinB (1−13), (**41**) Met^5-enkephalin amide, (**42**) Leu^5-enkephalin, (**43**) Leu^5-enkephalin amide, (**44**) (D)-Ala^2-Leu^5-enkephalin amide, (**45**) β-endorphin, (**46**) ICI 174,864, (**47**) PLO 17 amide, (**48**) human insulin, (**49**) porcine insulin, (**50**) Lyspro human insulin, (**51**) bovine insulin.

The glycine oligomers and di- and tripeptides were Sigma Chemical Co. products. Peptides were reported to have an enantiomeric purity (EP) in excess of 99.8%. Neuropeptides **29**−**41** and **45**−**47** were provided by CHIRON. Leu^5-enkephalins were obtained from Sigma. Insulins were taken from manufactured lots from Lilly, Novo Nordisk, and Sigma. Reagent grade D-histidine was from Sigma Chemical Co. and reported to have an EP better than 99.8%. Reagent grade $CuSO_4 \cdot 5H_2O$ was obtained from Fisher Scientific.

Solution Preparations—Stock solutions of the reference Cu(II)−D-histidine complex in 0.10 M NaOH were prepared in which the Cu(II) and D-histidine concentrations were 20 mM and 80 mM, respectively. KI (30 mM) was added as a stabilizer.[4] Working solutions of copper-D-histidine were prepared by diluting aliquots from the stock by a factor of 10 with 0.10 M NaOH. To simplify any future quality control QC application by making it even more amenable to automation, we chose to use equal masses of the analytes rather than equal concentrations. Normalizing the concentration of the analyte to a single value is not a critical factor when the equilibrium constants for the ligand exchange processes differ as much as they might be expected to differ for the range of materials used in this study. Aliquots of 10.0 mg were added to the copper−D-histidine stock prior to its dilution with 0.10 M NaOH. From the range of molar masses the actual analyte concentrations in the working solutions varied from 0.2 to 1.20 mM. All are intentionally lower than the total copper ion concentration and not enough to exchange completely with the D-histidine. Throughout this range the signal to analyte concentration correlation is linear.[1−3] A mass as large as 10.0 mg is prohibitively high especially when the method is to be applied to trial drugs where quantities are very limited. The problem can be alleviated to a large degree by reducing the volume of the working solution. CD signals are relatively intense. With access to more modern CD instrumentation than the Model series used here, the cell volume could be reduced by at least 10−100 fold with no loss of signal quality.

CD spectra measured after ligand exchange are simple aggregates of weighted spectra for the host and mixed ligand complexes. Any unbound ligand does not absorb in the visible range. Formation constants and complexation stoichiometries are incidental to QC quantitative interpretations. The purpose of QC methods is to ensure that the presumed chemical and enantiomeric purities of commercial drug products meet the reference standard. Provided the specified procedure for the assay is accurately defined and followed in every detail, the purity will be determined by comparing the CD spectral data for a product lot with the spectrum for reference standard material.

Measurements—CD spectra were measured using a Jasco 500-A automatic recording spectropolarimeter coupled to an IBM-compatible PC through a Jasco IF-500 II serial interface and data-processing software. Experimental parameters: wavelength range 400−700 nm; sensitivity 100 mdeg/cm; time constant 0.25 s; scan rate 200 nm/min; path length 5.0 cm; temperature ambient.

Calibrating the day to day reproduciblity of the system was done by measuring the CD spectrum for the Cu(II)−D-histidine reference working solution. Statistical data used to determine spectral reproducibilities were based on the standard deviations (SD) for the maximum ellipticities measured at the wavelengths 487 nm and 682 nm. The SD values were 7.42 ± 0.07 mdeg and −214 ± 0.60 mdeg, respectively, within and between stocks.[2,7]

Results and Discussion

CD activity in the visible range for chiral Cu(II) complexes is a result of disymmetric perturbations of the ground and excited-state ligand field orbitals by the chiral ligands.[6] Three CD-active electronic transitions are reported to occur over the wavelength range of the visible absorbance band.[6] Bands in the UV range, attributable to only the chirality in the ligands, both bound and unbound, are typically broad, very intense, and quite insensitive to changes in the environment of the coordinating metal ion. The lack of selectivity is the major reason for not exploiting the obvious analytical sensitivity advantage that is inherent in the intense UV bands.

Cu(II)−D-Histidine and Peptide Complexes—The microsymmetry of the Cu(II) ion first coordination sphere is tetragonal, or more accurately, an axially distorted octahedron, distortion being a consequence of Jahn−Teller effects.[13] In strong base D-histidine is anionic and binds to Cu(II) via the terminal amine-N, the carboxylate functional group, and a pyrimidine N-atom, to form a tridentate 1:1 complex.[6] Other coordinate positions might be occupied by hydroxide ions. The stability of the complex and the favorable mass action maintained by keeping the ligand in large excess over the metal means that virtually all of

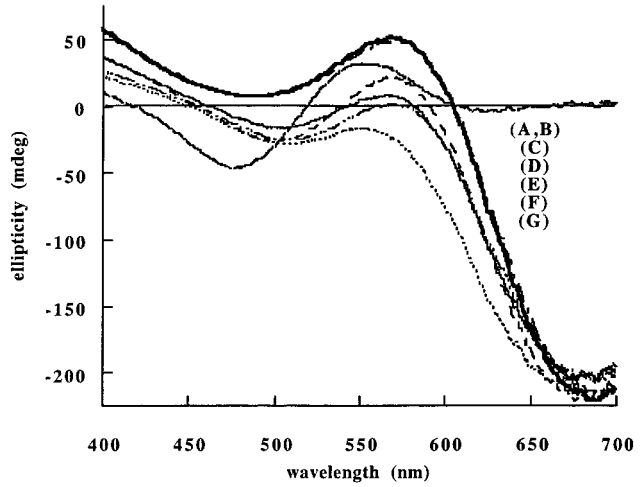

Figure 1—Visible range CD spectra for Cu(II) complexes with D-histidine and mixed D-histidine/dipeptides. (A) D-Histidine host, (B) GP, (C) GH, (D) GI, (E) GK, (F) GM, and (G) GF, arranged in order of the decreasing signal size at 570 nm. Curves A and B are superimposed and therefore indistinguishable.

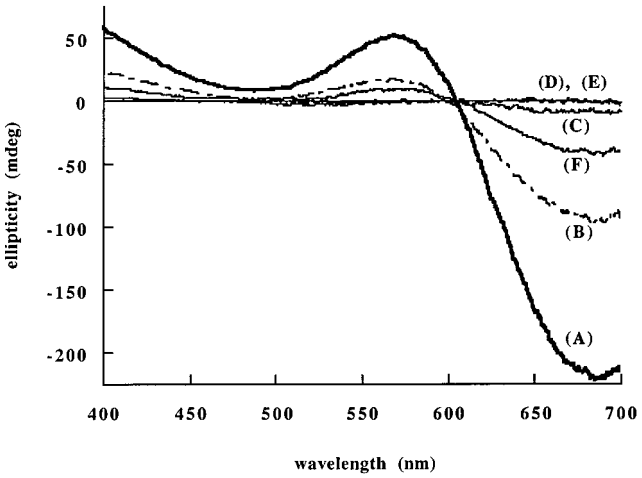

Figure 2—Visible range CD spectra for Cu(II) complexes with D-histidine and mixed D-histidine/oligoglycylglycines. (A) D-Histidine host, (B) GG, (C) GGG, (D) GGGG, (E) GGGGG, and (F) GGGGGG, arranged in order of the decreasing signal size at 700 nm.

the Cu^{2+} ion is in the form of the complex. The CD spectrum for the Cu(II)−D-histidine host chiral derivatizing agent is included for reference in Figures 1−5.

Complexing peptides to Cu(II) at high pH involves first attachment via the N-atom of the terminal amine group followed by ring closure(s) through bonding with the N-atoms of successive amide bonds until maximum thermodynamic stability is achieved.[6] Side-chain substituents on the amino acid residues lie out of the coordinate plane and are factors only in inter- and intramolecular interactions within the coordination sphere, unless a potential Lewis base is present, e.g., in L-histidine-containing peptides. Side-chain histidines are legitimate competitors for ligation positions, competing favorably with the terminal amine for the Cu(II) ion. The issue is moot if the test is restricted to QC where the binding mechanism would be the same for the reference standard and the sample. Metal to ligand stoichiometries for metal di- and tripeptide equilibria are 1:1 under pH > 12 conditions.[14] Coordinations with hydroxide ion and/or additional amide N-atoms in longer oligopeptides are variations that could affect the stoichiometry but not the analytical selectivity of the method.

Visible CD spectra for the Cu(II)−di and tripeptides in the absence of D-histidine were the objects of earlier work.[1,2]

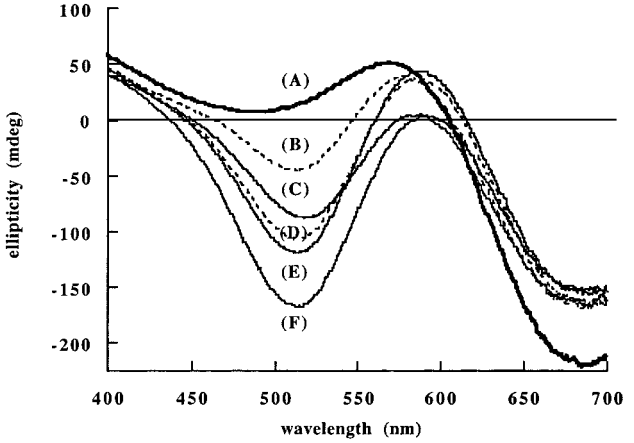

Figure 3—Visible range CD spectra for Cu(II) complexes with D-histidine and mixed D-histidine/Dynorphin neuropeptides. (A) D-Histidine, (B) Dynorphin B (1–13), (C) Dynorphin A (1–9), (D) Dynoprhin A (1–13), (E) Dynorphin A (1–11), and (F) Dynorphin A (1–13)-amide.

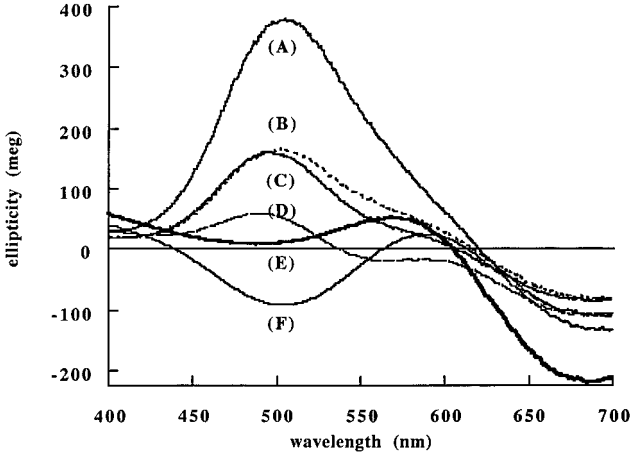

Figure 4—Visible range CD spectra for Cu(II) complexes with D-histidine and mixed D-histidine/enkephalin analogues. (A) a^2-Leu^5-enkephalin amide, (B) Leu^5-enkephalin amide, (C) Leu^5-enkephalin, (D) Met^5-enkephalin amide, (E) D-histidine, and (F) β-endorphin.

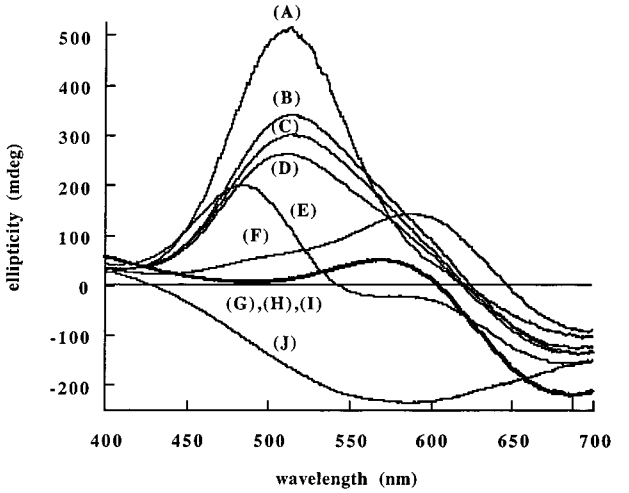

Figure 5—Visible range CD spectra for Cu(II) complexes with D-histidine and mixed D-histidine/modified neuropeptides. (A) DPDPE, (B) DTLET, (C) DADLE, (D) DSLET; (E) DALDA; (F) DAGO; (G) D-histidine, (H) ICI 174,864, (I) PLO 17, and (J) CTAP.

Spectra for Cu(II)−D-histidine and Cu(II)−(D-histidine-peptide) mixed complexes were the focus for di- and tripeptide ligands.[3,7] Evidence was provided that confirmed that the stoichiometries and the complex formation con-

stants were similar in magnitude within each series.[1,2] One would expect that for peptides to coordinate to the metal ion there has to be ligand exchange, or in some instances ligand addition with an expansion in the number of coordinating sites. Spectral variations that are the bases for the first level of analytical selectivity therefore are attributable to the individual stereochemical and conformational nature of the structures of the coordinated chiral ligands and to the relative rotational strengths of the three CD-active bands. That the CD-active electronic transitions are also sensitive to other factors besides the coordination geometry is reported for the insulins[7] in the Introduction section, where it is clear that minimal changes in peptide sequences that are remote from the binding site significantly alter the CD spectrum for the Cu(II)−D-histidine host complex.

Cu(II)−D-Histidine Ligand Exchange with Peptides:—Ligand exchange, as it is used in this context, is intended to cover all the mechanistic processes by which a peptide can become part of the Cu(II) complex entity. Total ligand exchange is not a possibility since mass action heavily favors the D-histidine ligand. Since D-histidine is bonded at three coordination sites, three other positions of the distorted octahedron are open to peptide addition reactions. Between these extremes are combinations of exchange/addition mechanisms, in which D-histidine is partially substituted, e.g., by loss of coordination to the carboxylate, and peptide is fractionally added. Nor should the possibility of outer-sphere ligand−ligand coordination be overlooked, e.g., in the insulin series.[7] The product of this ensemble of events is a compound mixture of "unreacted" histidine complex (always in excess) and a concentration distribution of peptide-containing complexes that clearly will vary with the structural properties and solution concentration of the analyte. It is the variability in the last in particular that enhances the analytical selectivity of the procedure. The method is not intended to determine the identity of any potential impurity, only to indicate that purity standards set by regulatory agencies have or have not been met.

Spectra for the mixed complexes are simple sums of the CD spectra for the components. Those that incorporate dipeptides that were not reported before[1] are shown in Figure 1. Spectra for the glycyloligomers, dynorphins, enkephalins, and structurally modified enkephalins are shown in Figures 2−5, respectively. Insulin spectra were previously published.[7] Selectivity distinctions are manifest by shifts in wavelength, sign, and signal intensity in the D-histidine band that maximizes at 550 nm. Besides the first-order chirality changes that occur within the first coordination sphere, there are others that are associated with reorganization of the tertiary structure in solution. Its disruption on ligand exchange could cause specific amino acid residues to impinge upon the 3-D architectural structure of the coordination sphere (outer-sphere complexation), adding more complexity to a mechanistic interpretation, but more diversity to the discriminations.

The broad absorbance band of Cu(II) complexes in aqueous media is known to consist of three subbands.[6] All are CD-active. Signs vary depending upon the nature of the ligands which, when taken altogether, form the basis for a broad analytical selectivity. The one obstacle to achieving total selectivity in Figure 1, for example, is separating the spectrum for GP from the spectrum for the D-histidine host complex. Whether ligands have exchanged is not known but is unlikely. For the other dipeptides in Figure 1 the general tendency is toward more negative spectra.

The only addition to the original mixed-tripeptide series[2] is the spectrum for GGG, Figure 2. As the length of the glycine-oligopeptides is increased, the characteristic shape of the host CD spectrum is retained as its intensity is diminished from GG through GGG, reaching what is essentially zero for the tetramer and the pentamer, after which the signal increases in intensity for the hexamer to reach a value that is about one-fourth of the original host complex. The hexamer result was reproducible and is not an experimental artifact. A possible explanation might be derived from an analogous result observed in a study of a series of dye-derivatized oligosaccharides where the visible range CD induction was attributed to incipient helicity (a single turn) when the oligomer length exceeded the dimension of the tetramer.[15] Whatever the mechanism, it is clear that the length of a peptide is a factor that is significant in the overall binding mechanism.

An expansion on the conclusions from the insulin study is manifested by the five Dynorphins all of which have the identical amino acid sequence through the first seven residues (YGGFLRR), far beyond what is believed to be the minimum for saturating the coordination positions on the Cu(II) ion. For the Dynorphin A analogues, the first *nine* residues in the sequence are identical, yet the spectra are easily distinguishable, Figure 3. The spectral response to an increase in length for the Dynorphin A neuropeptides is also nonmonotonic and most easily seen at 510 nm, the 1−11 analogue producing the greatest spectral change. There can be no question that ligand tertiary structures and their mutual molecular interactions with the primary architecture of the D-histidine complex are major factors in binding and therefore in broadening the analytical selectivity.

This last observation is an interesting concept to consider in the context of understanding factors that contribute to quantitative structure−activity relationships (QSAR). Interpretations of spectral changes should perhaps be revised to include, even emphasize, ligand−ligand interactions that do not involve their exchange. In other words, the *intact* Cu(II)−D-histidine complex might function as a model for a "receptor site" for peptides. If there is any validity to this concept, the possibility exists that the panorama of CD spectral changes observed in Figures 3−5 might eventually be capable of establishing in vitro correlations of molecular structure with therapeutic function. In that case visible range CD would have an important potential role as an insinuative ASR probe to better learn of the subtleties of chiral−chiral interactions in QSAR.

Data for the enkephalin analogues and β-endorphin are plotted in Figure 4. With the exception of a^2-Leu^5-enkephalin, all begin with the same YGG sequence, as do the Dynorphins. The primary coordination mechanism, therefore, will involve the same three Lewis bases, yet the spectra are unique, including an easy distinction between the acid and amide analogues of Leu^5-enkephalin. Spectra for the pentamers are dominated by positive bands over the short wavelength range. Sign inversion by these pentamers, relative to the 30-peptide protein, β-endorphin, and all of the Dynorphins, might be related to a restriction of outer sphere ligand ligand interactions. Signal enhancement is observed when D-alanine is injected into the sequence in a^2-Leu^5-enkephalin. It is surprising, but significant, that an enantiomeric switch did not cause the spectrum to be inverted in the D-histidine complex environment. This speaks to the relative importance of the retention of the chirality of the receptor in the binding mechanism.

The structurally engineered enkephalins and a few miscellaneous neuropeptides are the subjects of Figure 5. There is no evidence that ICI 174,864 and PLO 17 had sufficient influence on the D-histidine host complex to alter its spectrum. The terminal amine of ICI 174,864 is diallyl-

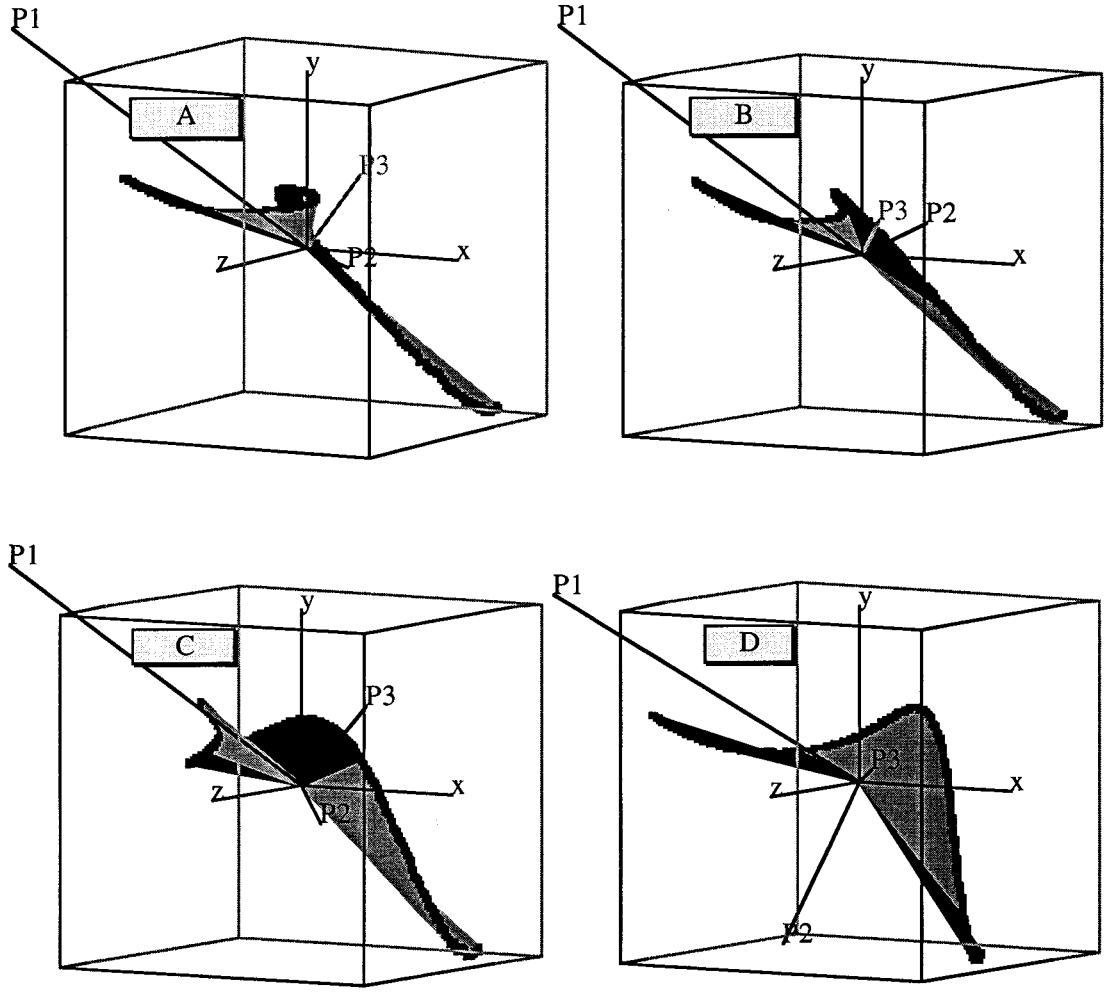

Figure 6—Representative plots resulting from the 3-D data reduction Spinning Plot algorithm for (A) Dynorphin A (1–13), (B) Dynorphin B (1–13), (C) a^2-Leu^5-enkephalin amide, and (D) CTAP. All four diagrams have the same *x*, *y*, *z* orientations. Dark lines that mark the perimeters of the curves mirror the CD spectra although the appearance is disguised by the orientation of the axes especially in A and B. P1, P2, and P3 are the eigenvectors for the principal components that are listed in Table 2. The distance from the origin to the extremity of each vector is the eigenvalue for that PC. Points to note are the different orientations in space for P2 ad P3 which are the most sensitive to the identity of the analyte.

substituted, and P^2 of PLO 17 is *N*-methylated. Both of these modifications adversely affect the primary coordination to the metal ion.

CTAP and DPDPE have disulfide rings and two D-enantiomers in their molecular structures. Between them they produce the greatest changes of any observed to date: strongly negative for CTAP and strongly positive for DPDPE. A positive signal for DPDPE is consistent with the effect of there being a D-enantiomer in the second position; see a^2-Leu^5-enkephalin. The N-terminal residue of CTAP is (D)F. There is insufficient information at this time to make a decision on whether the positional change from second to first is a major contributing factor in determining the sign of the CD spectrum.

The DSLET, DTLET, DADLE, DAGO, DALDA, and DPDPE modified enkephalins all have a D-amino acid residue in the second position. Similarities with the spectra for the natural enkephalins, Figure 4, exist, particularly the tendency toward strong positive bands at shorter wavelengths. Spectra for the DSLET, DTLET, and DADLE trio bear a strong resemblance to one another, but in what follows, they will be shown to be unique. For DALDA, a tetramer, and DAGO, which has an N-Me substituent on G3, structural differences are a bigger factor in determining spectral selectivity.

Data Reduction Algorithm—All the conclusions on analytical selectivity that have been reached so far in this paper are largely intuitive. For QC applications, a quantitative procedure is needed that will identify and/or verify a drug substance and measure its chemical and enantiomeric purities.

Two- and three-dimensional data reduction algorithms were introduced in prior work.[1,2,7] They are described as data reduction models because the objective was to reduce the 1500 data points, that make up the experimentally measured CD spectra, to a few definitive numbers which are characteristic of each analyte. Each procedure serves a special purpose. The 2-D model is effective in determining EP's with an accuracy unsurpassed by any other procedure.[1] The 3-D model, in contrast, is better suited for enantiomeric identification, and chemical purity determinations.[2,3] Only the former is considered in the context of this article.

The mathematical algorithm[16] used for the visual presentation of the 3-D data reduction is a three parameter Spinning Plot, available in a number of commercially available statistical software packages. The variables are wavelength (*x*-axis), CD data for the host complex (*y*-axis), and CD data for the mixed complexes (*z*-axis). Since CD signals are positive, negative, and zero, when two CD spectra are plotted, one against the other, four sign combinations are possible at any wavelength. Repeats of (*y*-, *z*-) coordinate points can occur at wavelength values, x_1 and x_2, that are not adjacent to each other in the spectra.

Table 1—Data Reduction by PCA of the Spinning Plot Data for the Histidine and (Histidine-a^2-Leu^5-enkephalin Amide) Mixed Complexes)

principal components	PC1	PC2	PC3
Eigenvalues	2.6942	0.2222	0.0836
Eigenvectors	–0.57655	0.59226	0.56287
	0.56405	0.78691	–0.25025
	0.59114	–0.17321	0.78776

When that occurs, plots are observed to "wrap-around" and become three-dimensional, Figure 6. To enhance the 3-D perspective, front and back quadrants are distinguished by dark and light shading. Distinctions are very evident.

With a total of 1500 data points for each variable, the system is overdetermined. In the data reduction procedure, data are subjected to a Principal Component Analysis (PCA) iterative process by which vectors of information are plotted against one another to derive principal components (PC's) which have length and directional properties that best describe the least-squares fit in the orthogonal directions of maximum variance. The number of PC's is equal to the number of variables, in this case three. PCA

Table 2—Eigenvalues from the PCA of Spinning Plots Data[a]

ligand	PC21	PC22	PC23	PC31	PC32	PC33
D-histidine	0.83992	0.38375	0.38375	0.00000	–0.70711	0.70711
AA	0.77506	0.61813	0.13116	0.29450	–0.53700	0.79051
AG	0.76020	0.64224	0.09811	0.32854	–0.51030	0.79477
AY	0.71550	0.69846	0.01430	0.40965	–0.42606	0.80127
YA	0.82951	0.25849	0.49507	0.14781	0.75322	–0.64094
YG	0.83631	0.29769	0.46060	0.10154	0.74112	–0.66365
YY	0.82003	0.51030	0.25913	0.15363	–0.63241	0.75925
Ga	0.80167	0.16171	0.57548	0.25970	0.77290	–0.57895
GA	0.83012	0.46494	0.30777	0.09642	–0.66336	0.74206
GG	0.83619	0.42950	0.34106	0.05456	–0.68392	0.72752
GY	0.80165	0.56357	0.19935	0.22146	–0.58973	0.77664
GH	0.00877	0.43018	0.90270	0.70517	0.63739	–0.31060
GK	0.81801	0.51753	0.25105	0.16291	–0.62704	0.76176
GI	0.83394	0.44463	0.32689	0.07247	–0.67544	0.73384
GP	0.84001	0.38129	0.38601	0.00293	0.70825	–0.70596
GM	0.82126	0.50619	0.26326	0.14870	–0.63535	0.75777
GF	0.75011	0.65664	0.07851	0.34779	–0.49267	0.79770
GGH	0.10485	–0.53847	0.83609	0.74200	0.60213	0.29475
GGI	0.02622	–0.63506	0.77202	0.73000	0.53978	0.41922
GGL	0.01357	–0.68830	0.72530	0.75108	0.48586	0.44702
GGF	–0.44698	–0.11093	0.88764	0.62046	0.67635	0.39696
GGA	–0.38508	–0.18286	0.90459	0.63138	0.66270	0.40274
LGG	0.31024	–0.02795	0.95025	0.67492	0.71043	–0.19945
YGG	0.41007	0.17842	0.89443	0.62412	0.66022	–0.41783
GHG	0.28915	0.26294	0.92046	0.64903	0.65295	–0.39040
GGG	0.79242	0.58094	0.18596	0.23681	–0.57395	0.78390
GGGG	–0.21947	0.18640	0.95765	0.70420	0.70962	0.02326
GGGGG	0.31758	–0.11740	0.94094	0.68218	0.71751	–0.14072
GGGGGG	0.83965	0.38788	0.38018	0.00477	–0.70522	0.70897
ICI 174,864	0.84001	0.38117	0.38613	0.00308	0.70831	–0.70590
PLO 17	0.83996	0.38273	0.38469	0.00121	0.70758	–0.70663
DynA (1–9)	0.82174	0.31009	0.47811	0.10080	0.74666	–0.65752
DynA (1–11)	0.64991	–0.07015	0.75677	0.50870	0.77995	–0.36457
DynA (1–13)	0.71161	0.00665	0.70254	0.42627	0.79079	–0.43926
DynA (1–13) amide	0.46401	–0.24232	0.85204	0.65364	0.74285	–0.14469
DynB (1–13)	0.83467	0.31635	0.45082	0.08315	0.73681	–0.67097
Met^5-enkephalinamide	0.59226	0.78691	–0.17321	0.56287	–0.25025	0.78776
Leu^5-enkephalin	0.58906	–0.18064	0.78764	0.56592	0.78798	–0.24253
Leu^5-enkephalinamide	0.68754	–0.03088	0.72549	0.45375	0.79829	–0.39603
a^2-Leu^5-enkephalinamide	0.60088	–0.13899	0.78716	0.55588	0.78031	–0.28656
β-endorphin	0.64855	–0.06949	0.75799	0.51106	0.77775	–0.36596
DSLET	0.72467	0.02654	0.68858	0.40629	0.79064	–0.45806
DTLET	0.68731	–0.02556	0.72591	0.46507	0.78316	–0.41276
DADLE	0.69716	–0.01355	0.71678	0.45019	0.78638	–0.42301
DAGO	0.70559	–0.00098	0.70862	0.47225	0.74621	–0.42301
DALDA	0.19164	0.79400	–0.57692	0.78289	0.23084	0.57776
DPDPE	0.51998	–0.20656	0.82883	0.62089	0.75778	–0.20067
CTAP	0.00507	–0.69886	0.71524	0.74454	0.48012	0.46384
human insulin	0.44975	0.83226	–0.32415	0.67287	–0.07705	0.73574
porcine insulin	0.42652	0.83526	–0.34701	–0.68620	–0.04888	0.72577
human Lyspro	0.31055	0.83468	–0.45483	0.73854	0.08936	0.66826
bovine insulin	0.55210	0.80567	–0.21466	0.59970	–0.20485	0.77356

[a] Key to structures reading from amine end. Lower case letters are D-enantiomer forms, (asterisks indicate ring structures): DSLET (YsGFLT); DTLET (YtGFLT); DADLE (YaGFL); DAGO (Y.a. G(N-Me)FG); DALDA (YrFK amide); DPDPE (Ype*GFpe*); CTAP (fC*YwRTP*eT amide); DynorphinA (1–9) (YGGFLRRIR); DynorphinA (1–11) (YGGFLRRIRPK); DynorphinA (1–13) (YGGFLRRIRPKLK); Dynorphin B (1–13) (YGGFLRRQFKVVT); b-endorphin (YGGFMTSEKSQTPLVTLFKNAIKNAYKKGE); Met5-enkephalin (YGGF(N-Me)M); Leu5-enkephalin (YGGFL); (D)-alanine-Leu5-enkephalin (YaGFL); ICI 174,864 (N,N-diallyl YAiAiFL); PLO 17 (YP(N-Me)Fp) amide.

solutions are expressed as three eigenvalues, over which the total variance is proportionated, and nine eigenvectors, that describe the 3-D spatial orientations of the eigenvalues. In the end, the original 1500 data points are reduced to three vectors of proportionately different lengths, the eigenvalues. The *x*- and *y*-variables are numerically the same for all analytes. Only the *z*-axis variable is analyte dependent. Taken as sets of three variables, however, the resultant PC's are all analyte dependent and as a result are the derived characteristic properties for standard reference materials against which all other preparations will be compared.

Eigenvalues and eigenvectors for PC1, PC2, and PC3, calculated for a^2-Leu^5-enkephalin amide, are given in Table 1. Their spatial projections are superimposed on the coordinate axes of Figure 6C. Eigenvectors give the most sensitive response to the identity of the analytes. Standard deviations in eigenvector values, calculated from repeated experimental measurements, are on the order of ±0.009, so considerable precision is attainable when making analytical differentiations or purity determinations.

Eigenvectors for all of the analytes are presented in Table 2. First on the list is the special case where spectral data for the host complex are plotted on both the *y*- and *z*-axes. This provides a common reference set against which values for all of the analytes can be compared. A cursory examination shows that the selectivity is least for PC11, PC12, and PC13, so the initial focus should be on the remaining six. Comparing only P22, P23, P31, and P32, the ambiguities are so few in number that it is claimed that 49 of the original 51 analytes are statistically and individually identifiable.

Nonlinearities observed in the spectral data for the glycyloligomer and Dynorphin A series are quantified in the results of the PCA.

The two exceptions to achieving total specificity among this group of polypeptides that range from 2 to 51 amino acid residues are ICI 174,846, and PLO 17. Differences between the factors for these analytes and the D-histidine reference are not statistically significant, implying that the host complex remains impervious to substitution. Sign inversions do occur for P32 and P33, but these are associated with the shortest eigenvalue PC3 and are open to uncertainty in interpretation. The same argument might be true for GP.

Quantitative applications of the 3-D Spinning Plot data reduction algorithm are discussed in prior work.[1−3] Results from these articles show that correlations between PC23 values and concentration are linear, making the analytical selectivity not only qualitative but also quantitative.

Summary

By introducing an auxiliary chiral ligand as a substitute for the achiral tartrate ion in the biuret test, a chirality-sensitive test has been created for a series of polypeptides whose sequences range from 2 to 51 residues. Sequence variations exist at both termini and internally (for the insulins[7]). In all but two instances the CD spectrum for the host is significantly altered.

D-histidine is but one of many potential auxiliary ligands. All but two of the current analytes could function in the role of host ligand. How close the already exceptional selectivity achieved by the current method can approach analyte specific reagent (ASR) status might ultimately depend on the identity of the auxiliary ligand. As the significance of the subtleties of the interligand chiral−chiral interactions become better understood, there is reason to expect that CD detection and multivariate modeling used together could contribute to a better understanding of QSAR models and predictions, receptor binding mechanisms, and drug design.

References and Notes

1. Purdie, N; Province, D. W. Algorithms for the quantitative validation of chiral properties of peptides *Chirality* **1999**, *11*, 546−53.
2. Purdie, N.; Province, D. W.; Johnson, E. A. Tripeptide Discriminations Using Circular Dichroism Detection. *J. Pharm. Sci.* **1999**, *88*, 715−21.
3. Purdie, N; Province, D. W. Peptide quality control test using ligand exchange on Cu(II) ion and circular dichroism detection *J. Pharm. Biomed. Anal.*, submitted.
4. Kingley, G. R. The direct biuret method for the determination of serum proteins as applied to photoelectric and visual colorimetry *J. Lab. Clin. Med.* **1942**, *27*, 840−6.
5. Tietz, N. W. *Fundamentals of Clinical Chemistry*, 3rd ed.; Saunders: Philadelphia, 1987.
6. Sigel, H.; Martin, R. B. Coordinating properties of the amide bond. Stability and structure of metal ion complexes of peptides and related ligands. *Chem. Rev.* **1982**, *82*, 384−426.
7. Purdie, N.; Province, D. W.; Layloff, T. P.; Nasr, M. M. Algorithms for validating chiral properties of insulins. *Anal. Chem.* **1999**, *71*, 3341−46.
8. *Federal Register 62243*; Food and Drug Administration: Washington, DC, November 1998.
9. Weiss, S. M. Clinical new Update. Mol. Diagn. **1998**, *3* (1), 63−5.
10. Collins, A. N.; Sheldrake, G. N.; Crosby, J., Eds. *Chirality in Industry, The Commercial Manufacture and Applications of Optically Active Compounds*; Wiley: New York, 1994.
11. Ostresh, J. M.; Dorner, B.; Blondelle, S. E.; Houghton, R. A. Soluble combinatorial libraries of peptide, peptidomimetics, and organics: fundamental tool for basic research and drug discovery. *Combinatorial Chemistry, Synthesis and Application*, Wiley: New York, 1997; Chapter 11.
12. Ward, T. J.; Armstrong, D. W. In *Chromatographic Chiral Separations*; Zief, M., Crane, J., Eds.; Chromatographic Science Series, Vol.40; Marcel Dekker: New York, 1988.
13. Cotton, F. A.; Wilkinson, G. *Advanced Inorganic Chemistry. A Comprehensive Text*, 4th ed.; Wiley-Interscience, New York, 1980.
14. Martell, A. E.; Sillen, L. G. *Stability Constants*; Special Publication No. 17; The Chemical Society: London, 1964.
15. Engle, A. E.; Hyatt, J. A.; Purdie, N. Induced Circular Dichroism Study of the Aqueous Solution Complexation of Cello-Oligosaccharides and Related Polysaccharides with Aromatic Dyes. *Carbohydr. Res.* **1994**, *181*, 265.
16. Kaiser, H. F. The varimax criterion for analytic rotation in analysis. *Psychometrika* **1985**, *23*, 187−200.

JS990209E

Clustering of CD Spectral Data as a Prototype QSAR Model for Neuropeptides

NEIL PURDIE* AND DENNIS W. PROVINCE

Contribution from *Department of Chemistry, Oklahoma State University, Stillwater, Oklahoma 74078-0447*

Received June 25, 1999. Accepted for publication September 23, 1999.

Abstract □ An analytical method that might eventually qualify as a general quality control assay procedure for polypeptide drug forms was described in the companion article to this paper. The detector is visible range circular dichroism spectroscopy. Multivariate data analysis reduced the spectral data to essentially four principal components (or factors) that are characteristic of each analyte. The level of analytical selectivity achieved among 51 analytes is very high. Using an alternative factor analysis algorithm, the selectivity is even more conveniently accomplished in the form of a 2-D cluster diagram presentation that has the potential of being a prototypical predictive in vitro model for correlating experimental data with structure–activity or structure–function relationships. Clustering of the analytes is a consequence not only of the chiral interactions associated with ligand exchange in the immediate primary coordination sphere of the host derivatizing reagent, but also of long-range intermolecular interactions between the coordination architecture of the host and the chiral polypeptides.

Introduction

Chirality is a common molecular property among natural products and an important factor in determining the efficacy of drug substances.[1] For an enantiomeric pair the isomer with proven clinical therapeutic value is called the eutomer, the other the distomer. Possibilities exist that a distomer can be toxic or mutagenic, making the assay of both enantiomers an essential part of regulatory tests. Measuring the chemical purity of an enantiomeric form is done by conventional standardized methods. Accurate measurement of the enantiomeric purity (EP) is a much more difficult problem. How to measure EP's quantitatively and routinely has recently become a major concern for manufacturing and regulatory agencies. The measurement of EP, or the related quantity enantiomeric excess (EE), expressed as a ratio of the two isomers, has now reached the status of being a requirement imposed by the Food and Drug Administration in new drug submissions.

Manufacturers have the option of choosing between either the enantiomeric resolution of readily synthesized racemic mixtures, or stereospecific syntheses.[1] Resolutions are typically long, demanding, and costly processes which in the end invariably fail to achieve 100% EP. Chiral chromatographic procedures significantly reduce the work load and costs for enantiomeric resolutions,[2,3] but separations that are complete are still not generally accomplished. More and more often, stereospecific synthesis has become the favored option. Since 100% EP is seldom achieved, both procedures are perhaps better thought of as enantiomeric enrichment processes. Monitoring the possible reduction of EP during the shelf life of a drug substance through racemization, especially if it is in solution or in suspension, is an analytical add-on to protocols that are submitted for approvals.

As a result, regulatory agencies are facing a rapidly increasing work load with respect to certifying and approving analytical methods to measure not only chemical purities but also EE (impurities) of chiral drug forms.[4,5] There is also the issue of defining what are the acceptably safe EE threshold levels below which a product is to be rejected from either manufacture or distribution. To ease the load, there is an urgent need for accurate and convenient routine experimental procedures that will give chemical and chiral impurity data, and preferably in an automated way if at all possible.

The problem is immense and still expanding. Pharmaceutical and biotechnology industries are investing more and more R&D resources into the production of chiral substances. With the advent and continued momentum of combinatorial chemistry,[6–9] the number of potential new chiral drug substances is increasing exponentially. Nowhere, perhaps, are these numbers increasing faster than in the area of peptide, peptidomimetic, and protein drug forms. Identifying which real or virtual compounds are worthy of further development is an exceptionally difficult problem. Culling out the few new potential drug substances by performing individual in vivo assays was not really an option and led quickly to the development of mixture assays.[7–9]

Viable alternatives, with the potential for automation, are quantitative structure−activity relationship (QSAR) screening algorithms that are based upon in vitro chromatographic or spectroscopic data of one kind or another. Exploitation of QSAR models is done in two parts, calibration and prediction. In the first step, measured experimental data and therapeutic properties of known drug forms are mathematically correlated to derive a calibration model. The calibration model is in turn exploited to predict the therapeutic potential of a new drug form. The prediction is based entirely on the measured experimental data, e.g., retention times or absorbance, for each new substance. The broader the therapeutic range represented in the calibration, the better the prediction model. These particular experimental methods, however, do not always address the question of how important molecular chirality is, in the therapeutic function of a drug.

The motivation for this study and previous related studies on peptides and proteins[10–13] was to address the lack of emphasis that is given to causal relationships between chirality and function, especially since molecular chirality is so commonplace among natural and synthetic drug substances. Protein receptor sites are chiral. How the chirality of a receptor kinetically reconfigures itself to accommodate the chirality of the drug molecule, and vice versa, is a factor in the discrimination between eutomers and distomers. That steric selectivity has been exploited, almost without recognition, in the development of a myriad of clinical assays that are based upon analytical specificities attributed to monoclonal and polyclonal antibodies and their interactions with antigens. Despite the importance

10.1021/js990210d CCC: $18.00
Published on Web 10/28/1999

of the chirality recognition, at no time has a test been based upon chirality detection. Antibodies have been elevated to the exalted rank of Analyte Specific Reagents (ASR). That same high selectivity, however, is a natural deterrent to the derivation of broad based or generally predictive QSAR models.

Direct spectroscopic methods are a more attractive option over chromatography because of their comparative simplicity of operation and consistent reproducibility in the recalibration of standards, etc. Mass spectrometry is selective but not with respect to chirality differentiation. Detectors that measure absorbance and fluorescence in the visible-UV range are notorious for their lack of analytical selectivity, but can be improved upon by using derivatization reactions, multivariate analyses methods, such as principal component analysis (PCA), factor analysis, and artificial neural networking in data handling,[14] or experimentally by introducing time as an added analytical variable.

Spectroscopic methods with the power to detect molecular chiralities are circular dichroism (CD) and optical rotatory dispersion (ORD). In the specialized area of screening peptides and proteins, however, the vast majority of CD investigative work is done on data from the UV range.[15] The purposes there are to obtain predictive information that can be used to resolve the question of 3-D structural properties of proteins in solution, apportion solution structures between helix and sheet forms, and investigate the kinetics and thermodynamics of folding–unfolding mechanisms, etc. CD bands in the UV are broad and without discrete features. Like absorbance, their potential for establishing QSAR models is limited.

In a series of recent articles, visible range CD spectral data were used to selectively differentiate among di- and tripeptides,[10,11] insulins,[12] and neuropeptides.[13] Mathematical algorithms were derived with which to determine their chemical and enantiomeric purities.[12,13] The absorbance property required for CD to occur in the visible range, was provided by first binding the peptides to Cu(II) ion in pH 13 aqueous solution. Visible absorbance spectra of Cu(II) complexes are comprised of three electronic transitions[16] all of which are CD-active. For the completed studies, peptides were either bound directly to the copper ion[10,11] or displaced an auxiliary ligand,[12,13] e.g., D-histidine. Major accomplishments from these articles that are of relevance to the goals of this one are the ability to discriminate between human and porcine insulins[12] (two 51 amino acid residue proteins whose sequences differ in the identity of one acid at the B30 terminal amino acid only) and between human insulin and the human LysPro variant form in which the order of the B29 L-lysine and B30 L-proline are reversed, and to achieve a level of *quantitative* analytical selectivity that approaches specificity among 51 peptides.[13]

The specific objective of this article was to derive a cluster correlation diagram between visible range CD data on one hand and molecular stuctures, and their corresponding clinical therapeutic functions, on the other. Success would mean we will have a prototypical in vivo predictive QSAR model of some general applicability. CD spectral data are taken from the previous companion article.[13] Only tripeptides and longer oligopeptides are included to test the general practicality of a clustering algorithm. Special mention is given to the subgroup of 19 neuropeptides, classified by their particular clinical functional actions.

Experimental Section

Chemicals—Thirty-five oligo-and polypeptides used for the study were the tripeptides GGA, GGG, GGH, GGI, GGL, GGF, GHG, LGG, and YGG; the higher oligoglycines GGGG, GGGGG, and GGG-GGG; the enkephalins DSLET, DTLET, DADLE, DAGO, DALDA amide, DPDPE amide, Met^5-enkephalin, Leu^5-enkephalin, Leu^5-enkephalin amide, (D)-Ala^2-Leu^5-enkephalin amide, and β-endorphin; the Dynorphins A (1–9), A (1–11), A (1–13), A (1–13) amide and B (1–13); and the miscellaneous CTAP amide, ICI 174,-864, PLO 17 amide, and human, porcine, Lyspro, and bovine insulins. Amino acid sequences are included in the footnote to Table 1.

Commercial sources for the oligopeptides and insulins were listed previously.[13] Reagent grade D-histidine, reported to have an EP better than 99.8%, was obtained from Sigma Chemical Co. Reagent grade $CuSO_4 \cdot 5H_2O$ was obtained from Fisher Scientific.

Solution Preparations—These are described in greater detail in the prior companion article on the 51 peptide and protein forms.[12,13] Working solutions for the assays were prepared by diluting aliquots of Cu(II)–D-histidine stock solutions by a factor of 10 with 0.10 M NaOH such that the final composition was 2.0 mM in Cu(II) ion, 8.0 mM in D-histidine, and 3.0 mM in KI added as stabilizer, in 0.1 M base. To make future quality control (QC) procedures more amenable to automation, we chose to add equal masses of the analytes (10 mg) to the aliquot of stock prior to its dilution rather than use equal concentrations. From the range of molar masses of the neuropeptides, the actual analyte concentrations in the working solutions varied from 0.2 to 1.20 mM. All are intentionally lower than the total copper ion concentration and not enough to exchange completely with the D-histidine ligand. With modern CD instrumentation, the mass of analyte can be reduced 10–100 fold.

Measurements—CD spectra were measured using a Jasco 500-A automatic recording spectropolarimeter coupled to an IBM-compatible PC through a Jasco IF-500 II serial interface and data processing software. Experimental parameters were wavelength range 400–700 nm, sensitivity 100 mdeg/cm, time constant 0.25 s, scan rate 200 nm/min, path length 5.0 cm, temperature ambient. With 2 nm spectral resolution, the full measured spectrum consists of 1500 data points.

Calibrating the day to day reproduciblity of the system was done by measuring the CD spectrum for the Cu(II)–D-histidine reference working solution. Statistical data used to determine spectral reproducibilities were based on the standard deviations (SD) for the maximum ellipticities measured at the wavelengths 487 and 682 nm. The SD values were 7.42 ± 0.07 mdeg and -214 ± 0.60 mdeg, respectively, within and between stocks.[10,11]

Results and Discussion

The assay works on the premise that chiral ligand exchange of the polypeptides for D-histidine, complexed to Cu(II) ion in strong aqueous base solution, will induce a change from the CD spectrum for the host that is characteristic of the peptide analyte. The host metal complex serves as a CD-inducing and color-derivatizing agent for the neuropeptides which otherwise would be CD transparent in the visible range. Spectra for the products,[13] uncorrected for the host spectrum, are the bases for subsequent mathematical correlations.

If there is any truth to the concept that the CD spectra for the mixed complexes correlate with molecular, and therefore therapeutic, function, there should be strong spectral similarities within specific groups and obvious dissimilarities among groups. In other words the focus is on proving a pattern recognition of polypeptides by type. With this thought in mind, we can dispense with the conventional practice of measuring metal–ligand stoichiometries which should be similar within each subset, and dispense with the need to measure formation constants, expecting the variations in these values within a group to vary very little. Therefore, provided the specified procedure for the assay is defined and followed in every detail, analyte recognition and the measured accuracy in their determinations will be considerably improved over univariate (one wavelength) determinations.

The mathematical basis for achieving the analytical selectivity claimed in the previous article[13] was data

Table 1—Principal Component (PC) Values and Cluster Assignments Derived from the PCA Calculation Made from the Correlation of *Y*-Matrix for Tripeptides, Oligopeptides, and Insulins[a]

peptide	PC1	PC2	PC3	PC4	PC5	PC6	cluster
GGH	1.90754	1.07084	–5.80304	0.56910	0.76218	0.21884	1
GGI	–3.33190	0.93815	–1.31367	0.58205	0.24248	–0.20411	2
GGL	–2.48178	1.54899	–0.83902	0.41809	0.19503	0.00979	2
GGF	–7.02666	2.48361	–3.42084	1.26270	0.26464	–0.10426	2
GGA	–3.30146	3.77231	–1.58899	0.32102	0.18140	–0.05297	2
LGG	–1.08595	4.62576	0.36281	–0.11674	–0.31355	–0.04903	3
YGG	2.21496	5.92887	2.47355	0.39291	0.07784	–0.13505	3
GHG	0.71513	5.73447	2.83448	–1.50678	0.67706	0.58728	3
GGG	–1.00748	4.63183	–0.13142	–0.38407	–0.38924	0.05335	3
GGGG	–0.98249	5.10671	–0.20555	–0.41400	–0.41839	0.05011	3
GGGGG	–0.99244	5.08708	–0.19114	–0.44882	–0.43975	0.02403	3
G6	–0.77889	3.13769	0.20912	–0.37229	–0.29460	0.05897	3
DSLET	5.61386	–1.78747	0.05173	–0.40400	–0.03030	–0.07857	5
DTLET	7.31482	–1.43674	0.18100	–0.71373	0.16854	–0.28908	5
DADLE	6.56303	–1.40095	–0.08242	–0.55754	0.03430	0.08077	5
DAGO	3.42481	2.26752	3.32135	1.53333	0.39364	–0.18805	3
DynA9	–2.14370	–2.52980	1.56920	0.06199	–0.31105	–0.06093	4
DynA11	–1.76459	–1.76269	2.87524	0.67279	–0.10279	0.16660	4
DynA13	–1.68912	–2.25739	2.67589	0.60244	–0.03417	0.16794	4
DynAA13	–3.56666	–1.56817	2.52575	0.30886	–0.11321	0.02043	4
Met-enk	–0.23515	–0.57906	–0.51375	0.22497	0.00360	–0.01722	1
DynB13	–0.85486	–2.64485	1.81267	–0.06927	–0.33628	0.04186	4
β-endorph	–1.99505	–0.50226	2.52819	0.28876	0.38610	–0.01400	4
DALDA	2.65449	–4.29649	–2.52405	2.10245	–0.56252	0.57465	1
CTAP	–8.64881	–4.24805	–3.13553	–2.15925	–0.19259	0.10251	6
DPDPE	8.93870	–0.60145	–2.26189	–0.70663	0.34742	–0.03321	5
ICI174	0.05242	–5.16070	1.98254	–0.22740	0.19753	–0.04955	4
PLO17	0.09633	–5.23027	1.97495	–0.21865	0.22239	–0.00471	4
α-Leu-enk	7.96527	–1.32821	–1.88627	0.03077	–0.34296	0.02164	5
L-enkeph	2.32657	0.48518	–1.23225	0.05665	–0.48166	–0.18311	1
Lenkamid	2.83518	0.95343	–0.72967	–0.17806	–0.45585	–0.21976	1
human ins	–2.64882	–2.89625	–0.41242	–0.34787	0.11478	–0.12309	4
porcine	–2.72926	–2.93333	–0.46651	–0.35625	0.14004	–0.10869	4
lyspro ins	–2.87639	–2.22205	–0.51801	–0.00418	0.23594	–0.04509	4
bovine ins	–2.48166	–2.38724	–0.02859	–0.23897	0.17400	–0.1182	4

[a] Key to Structures reading from amine end. Lower case letters are D-enantiomer forms, (asterisks indicate ring structures): DSLET (YsGFLT); DTLET (YtGFLT); DADLE (YaGFL); DAGO (YaG(N-Me)FG); DALDA (YrFK amide); DPDPE (Ype*GFpe*); CTAP (fC*Y-wRTP*eT amide); DynorphinA (1–9) (YGGFLRRIR); DynorphinA (1–11) (YGGFLRRIRPK); DynorphinA (1–13) (YGGFLRRIRPKLK); Dynorphin B (1–13) (YGGFLRRQFKVVT); b-endorphin (YGGFMTSEKSQTPLVTLFKNAIKNAYKKGE); Met5-enkephalin (YGGF(N-Me)M); Leu5-enkephalin (YGGFL); (D)-alanine-Leu5-enkephalin (YaGFL); ICI 174,864 (N,N-diallyl YAiAiFL);

reduction of the 1500 data points in the CD spectra for each analyte, taken separately, to twelve factors (3 eigenvalues and 9 eigenvectors) using PCA done on Spinning Plot data.[17] Spinning Plots are created by plotting wavelength, CD spectral data for the Cu(II)–D-histidine host complex, and the Cu(II)–(D-histidine-peptide) mixed complexes on the *x*, *y*, and *z* coordinate axes, respectively. Calculations are described in detail in the prior article.[13] Factors showing the most sensitivity to the identities of the analytes are the eigenvectors. The real analytical value of the tabulated data is the quantitative nature of the chemical and EP assays that can be accomplished using PCA data vs concentration correlations. Potential correlations of principal components with molecular structures are difficult to find when data are in tabular form.

PCA and Clustering Model—The model was developed using only the spectral data for the tripeptides and higher oligomers. Dipeptides were excluded because they lack the 3-D rotational conformational structures that are common to longer peptides.

In clustering, the strategy is to base correlations upon how well spectral patterns align with molecular "types" in a graphical manner. The major departure from Spinning Plot data reduction algorithm is that the spectral data for all 35 analytes are treated collectively. What follows is a description of the genesis of a possible calibration model. Spectral data for new analytes are required before the relative success of the model in making predictions can be tested.

To make modeling calculations more managable for a desktop computer, the original 1500 data points were reduced in number to 31 by choosing values at 10 nm intervals. The first step was to group the (35 × 31) CD data sets through a (correlation-of-*Y* variables) calculation, that expresses the relative strengths of successive pairwise correlations of CD signals in the form of a square matrix. PCA was then used to reduce the dimensionality of the correlation-of-*Y*'s matrix to just six factors or principal components (PC's), Table 1. These six factors account for 99.93% of the total variations among all of the *Y* variables in all 35 individual spectra. The first factor, PC1, has the maximum variation. The second factor, PC2, is orthogonal to the first and has the next greatest variation, and so on through all six factors.

Clustering is a technique of grouping together rows of PC's that share similar values across a number of variables. The hierarchical clustering option was used here. In this option, clustering starts with each point being its own "cluster". Through a series of iterative steps the two closest clusters are successively combined, by Ward's method, until ultimately all points are grouped as a single cluster. Between the extremes of 1 and 35 clusters there is an optimum number on which to base the model. As a rule of thumb the number of clusters would not exceed the number of "types" of analytes, assuming that that prior knowledge is available. Selection of the optimum cluster condition is linked to the relative magnitudes of the proportional changes between successive PC values. For this data set,

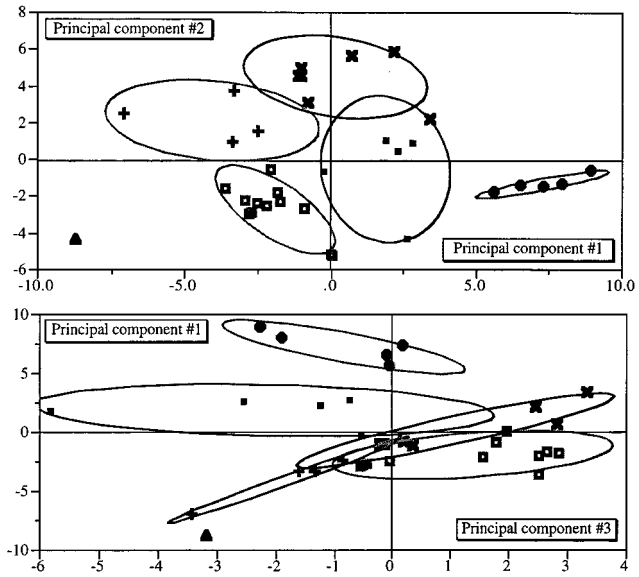

Figure 1—(a) Correlation of PC1 vs PC2 (Table 1) derived from the PCA of the correlation of *Y* matrix for the 35 peptides used for the model. Individual clusters are associated with (+) GGX tripeptides; (x) oligoglycinates and non-GGX tripeptides; (●) enkephalins; (◘) Dynorphins; (■) insulins (black); and (+) D^2-modified enkephalins. (b) Correlation of PC3 vs PC2 from the same source. The perspective is from a direction that is at right angles to the projection in part a. The same markers are used to designate the peptides by type. The special reason for part b is to demonstrate that the Dynorphins and the insulins are separable in the third dimension.

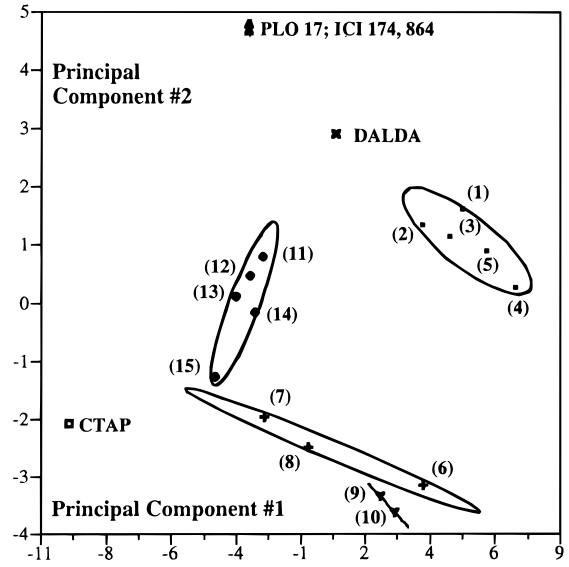

Figure 2—Repeat of the correlation of Figure 1a drawn exclusively for the 19 neuropeptides only. Cluster outliers are identified by name. Coordinates for the host D-histidine complex would correspond with the coordinates for PLO 17 and ICI 174,864. The δ-receptor cluster consists of (**1**) DTLET; (**2**) DSLET; (**3**) DADLE; (**4**) a^2-Leu^5-enkephalin; and (**5**) DPDPE. The μ-receptor cluster consists of (**6**) DAGO; (**7**) Met^5-enkephalin; and β-endorphin. The alternate δ-receptor cluster is comprised of (**9**) Leu^5-enkephalin and (**10**) Leu^5-enkephalin amide. The κ-cluster of the Dynorphins consists of (**11**) B (1–13); (**12**) A (1–13); (**13**) A (1–9); (**14**) A (1–11); and (**15**) A (1–13) amide.

the optimum number of clusters, or types, is 6; the tripeptides, oligoglycinates, dynorphins, enkephalins, insulins, and a miscellaneous group composed of the structurally unrelated CTAP, ICI 174,864, and PLO 17.

Figure 1 is a presentation of two 2-D cluster diagrams prepared by plotting different pairs of PC values, PC1 vs PC2 in Figure 1a, and PC3 vs PC1 in Figure 1b. The relationship between the two figures is that the projection of the lower diagram is from a direction that is orthogonal to the projection for the upper diagram. Together they represent two 2-D perspectives of a 3-D figure. Figure 1a shows the excellent segregation of the data points over five distinct cluster areas that encompass multiple points, and one "area" that is but a single point, i.e., CTAP. The four insulins and the Dynorphins appear to occupy a single cluster in the 2-D space of Figure 1a, but on viewing the same diagram from an orthogonal direction, Figure 1b, the types are clearly separated in the third dimension. Future studies should be able to exploit 3-D clustering option in a more direct manner for even greater discriminations.

The range in values for all PC's is very wide which enables good spatial separation of the clusters. Limits on the range of PC1 values are set by the Cys-Pen and Pen-Pen disulfide linked ring peptides, CTAP and DPDPE, which produce the greatest changes in the CD spectral data from that of the host complex.[13] Two other structural features of CTAP make it unique. It is the only peptide in the pool with an aromatic substituent on the amine terminus, and that residue is also in a D-enantiomeric form.

Neuropeptides Subgroup—Clustering of the 19 neuropeptides subgroup is shown separately from the tripeptides and insulins data in Figure 2. All except CTAP and ICI 174,864 have a Y-residue at the amine terminus. Data points on the PC1 vs PC2 plot are segregated over three distinct areas, plus a few individually distinct locations. The next question is whether these areas correlate with different protein receptor selectivities and affinities.

Three known peptide neuroreceptors, μ, δ, and κ, have been identified in the literature.[18,19] It has been proposed, but not generally agreed upon, that there is duality in the structures of potential μ and δ receptors. Neuropeptide drug forms have special affinity for one or another of the receptors. Dynorphins, for example, are structurally disposed to bind to κ receptors. Some drugs are reported to show multiplicity by binding to more than one receptor.

Beginning with the cluster outliers, CTAP is a confirmed μ-selective antagonist. DALDA on the other hand is considered to be the most selective μ-agonist known. Their relative locations are consistent with the diversity in their affinities. Distinction between PLO 17 and ICI 174,864 (a μ-agonist and a δ-selective antagonist, respectively), however, cannot be made since the spectral evidence is that they do not participate in ligand exchange. The host Cu(II)—D-histidine complex, therefore, would occupy the same coordinate position and be a natural reference point against which to "measure" relative receptor selectivities and affinities.

Compounds **1**—**5** in Figure 1 are the designer D^2-enantiomer-enkephalin analogues, DTLET, DSLET, DADLE, a^2-Leu^5-enkephalin, and DPDPE, respectively. These are recognized δ-receptor drugs. Structurally DADLE is the enantiomer of a^2-Leu^5-enkephalin because of the inversion of the chirality at the acid terminus. The chirality change appears to have little effect on their proximity in the cluster which might have been expected since it is located so far from the amine terminus which is the primary point contact between the ligand and the host metal complex. DALDA fits the description of a D^2-enantiomerically substituted enkephalin, yet it lies outside the "δ-receptor cluster". The result is consistent with the fact that DALDA favors binding to a μ-neuroreceptor (vide supra). Its absence from the "δ-receptor cluster" might be related to its being the only tetramer in the class.

The two natural Leu^5-enkephalins **9** and **10**, in which all residues are L-enantiomer forms, also show a preference for δ-receptors.[18,19] Their coordinates, however, are quite remote from the designer D^2-enkephalins "δ-receptor cluster". Effects of enantiomeric substitutions at amino acid

terminus residues may be a factor in proposing that there is structure multiplicity among neuroreceptors and among agonists.

DAGO (**6**) is yet another designer D^2-substituted enkephalin whose location is remote from the "δ-receptor cluster". Its spectral properties and PC coordinates place it in an entirely different cluster with Met^5-enkephalin (**8**) and β-endorphin (**7**) which are μ-receptors. DAGO is also classified as a μ-receptor agonist.[18,19] The locations of the Met^5 analogue, β-endorphin, and DAGO together define the "μ-receptor cluster" space. Structurally what DAGO and Met^5-enkephalin have in common is an N-Me substituent on the third and fourth residues, respectively. The substituent lies outside the plane of the primary tetragonal coordination sphere of the Cu(II) ion complex and as such adds a new chirality dimension to the ligand−ligand interactions. The observation that DAGO is a confirmed μ-receptor agonist and associates itself in space with two other μ-receptors, while its structure would suggest otherwise, is perhaps the most compelling reason for believing that a calibration model has been identified that could be the genesis of a QSAR model for predicting the receptor selectivities of new peptide drug forms.

As a general rule, Dynorphins bind to the κ-receptor.[18,19] All five included here form a tight single "κ-receptor cluster" which we suspect is related to their having identical initial sequences and a diminished outer-sphere involvement with the first coordination sphere of the metal complex. In close juxtaposition to the Dynorphins is the 30-residue β-endorphin which has the same sequence as the Dynorphins over the first four residues. Areas where the clusters impinge or intersect are conceivably indicators of possible duality in receptor binding functions.

The preliminary calibration model has provided some encouraging results. As more neuropeptides are added to the data pool, the boundaries and the compositions of the clusters will necessarily change. A much larger data pool is required before the predictive capabilities of the model can be critically and confidently tested.

Summary

An idea for a potential QSAR model for peptide drug substances is described. The model is based upon visible range CD data measured for a series of mixed Cu(II)−(D-histidine-peptide) complexes. Spectral responses to the ligand substitution reactions are a function of the identities of the coordinating bases in the analyte ligands and of the extended 3-D solution structure of the peptides. The model differs from other QSAR models in that longer range intermolecular forces that contribute to receptor−agonist interactions are a tangible part of the model. The value of the model as a predictive tool is still uncertain because the number of objects is still very small. It is quickly and easily expandable as other neuropeptides become available. The focus here was on neuropeptides. Drugs whose pharmacological functions are different will, in all likelihood, be treated as separate entities in cluster diagrams that are specific to each category or type.

References and Notes

1. Collins, A. N.; Sheldrake, G. N.; Crosby, J., Eds. *Chirality in Industry, The Commercial Manufacture and Applications of Optically Active Compounds*; Wiley: New York, 1994.
2. Fell, A. F., Ed. Special Issue on Chiral Discrimination. *Trends Anal. Chem*. **1993**, *12*, 125−189.
3. Ward, T. J.; Armstrong, D. W. In *Chromatographic Chiral Separations*, Zief, M., Crane, L. J., Eds.; Chromatographic Science Series, Vol. 40; Marcel Dekker: New York, 1988.
4. Rapaka, R. S.; Dhawan, B. N.; Renugopalakrishnan, V. An update of selected topics in the biology and chemistry of opiod peptides. *Opiod Peptides: An Update; NIDA Research Monograph 87*; National Institute on Drug Abuse: Washington, DC, 1988; pp 217−232.
5. Gueriguian, J. L.; Chiu, Y. Y. H. A few thoughts on the development and regulation of neuropeptides *Opiod Peptides: An Update; NIDA Research Monograph 87*; National Institute on Drug Abuse: Washington, DC, 1988; pp 405−413.
6. Houghten, R. A.; Dooley, C. T. Synthetic peptide combinatorial libraries may be used to determine peptide ligands for opioid receptors. *NIDA Research Monograph 134*; National Institute on Drug Abuse: Washington, DC, 1993; pp 66−73.
7. Hruby, V. J.; Lam, K. S.; Lebl, M.; Kazmierski, W.; Hersh, E. M.; Salmon, S. E. Preparation of large peptide libraries with one peptide per bead and their use for the discovery of peptides that bind to acceptors. *NIDA Research Monograph 134*; National Institute on Drug Abuse: Washington, DC, 1993; pp 75−83.
8. Wilson, S. R.; Czarnik A. W., Eds. *Combinatorial Chemistry, Synthesis and Application*; Wiley: New York, 1997.
9. Ostresh, J. M.; Dorner, B.; Blondelle, S. E.; Houghton, R. A. Soluble combinatorial libraries of peptide, peptidomimetics, and organics: fundamental tool for basic research and drug discovery. *Combinatorial Chemistry, Synthesis and Application*; Wiley: New York, 1997; Chapter 11.
10. Purdie, N.; Province, D. W. Algorithms for the quantitative validation of chiral properties of peptides. *Chirality* **1999**, *11*, 546−53.
11. Purdie, N.; Province, D. W.; Johnson, E. A. Tripeptide discriminations using circular dichroism detection. *J. Pharm. Sci.* **1999**, *88*, 715−21.
12. Purdie, N.; Province, D. W.; Layloff, T. P.; Nasr, M. M. Algorithms for validating chiral properties of insulins. *Anal. Chem*. **1999**, *71*, 3341−46.
13. Purdie, N.; Province, D. W.; Johnson, E. A. A convenient assay method for the quality control of peptides and proteins. *J. Pharm. Sci.* **1999**, *88*, 1242−1248.
14. Wold, S.; Sjostrom, M. Chemometrics, present and future success, *Chemom. Intell. Lab. Syst.* **1998**, *44*, 3−14.
15. Towell, J. F., III; Manning, M. C. In *Analytical Applications of Circular Dichroism, Techniques and Instrumentation in Analytical Chemistry*; Purdie, N., Brittain, H. G., Eds.; Elsevier Scientific: Amsterdam, 1994; Vol. 14, pp 175−205.
16. Sigel, H.; Martin, R. B. Coordinating properties of the amide bond. Stability and structure of metal ion complexes of peptides and related ligands. *Chem. Rev*. **1982**, *82*, 384−426.
17. Kaiser, H. F. The varimax criterion for analytic rotation in factor analysis. *Psychometrika* **1985**, *23*, 187−200.
18. Casy, A. F.; Parfitt, R. T. Enkephalins, endorphins, and other opiod peptides. In *Opiod Analgesics, Chemistry and Receptors*; Plenum: New York, 1986; Chapter 10, pp 333−384.
19. Schiller, P. W. Development of receptor-specific opioid analogues. *Progress in Medicinal Chemistry*; Ellis G. P., West, G. B., Eds.; Elsevier Science: Amsterdam, 1991; Vol. 28.

JS990210D

Effect of Cyclodextrins and Polymers on Triclosan Availability and Substantivity in Toothpastes in Vivo

THORSTEINN LOFTSSON,*,† NIGEL LEEVES,‡ BIRNA BJORNSDOTTIR,† LISA DUFFY,‡ AND MAR MASSON†

Contribution from *Department of Pharmacy, University of Iceland, P.O. Box 7210, IS-127 Reykjavik, Iceland, and Procter and Gamble Technical Centres Ltd., Oral Care Department, Rusham Park, Whitehall Lane, Egham, Surrey TW20 9NW, UK.*

Received July 19, 1999. Final revised manuscript received September 23, 1999.
Accepted for publication September 27, 1999.

Abstract □ The aqueous solubility of triclosan is only about 10 μg/mL. This very low solubility can hamper its biological activity in the oral cavity, which could explain the mixed clinical results obtained from triclosan toothpaste trials. Triclosan availability in a silica-based toothpaste was improved through cyclodextrin solubilization. The triclosan in vivo availability was optimized through a series of phase-solubility studies and triclosan release studies. It was found that in toothpastes, natural β-cyclodextrin (βCD) was just as good a solubilizer as the more water-soluble βCD derivatives. Furthermore, the amount of cyclodextrin could be reduced by as much as 60% through the addition of a small amount of carboxymethylcellulose (CMC), without affecting triclosan release from the toothpaste. Optimally, cyclodextrins resulted in an almost 3-fold enhancement of triclosan availability compared to an identical toothpaste containing no cyclodextrin. In vivo studies in humans showed that replacing triclosan with triclosan/βCD in the toothpaste resulted in only moderate improvement in triclosan substantivity. However, replacing triclosan with triclosan/βCD/CMC complex resulted in significant improvement in triclosan substantivity. Furthermore, the in vivo studies showed that replacing free triclosan with triclosan/βCD/CMC complex resulted in an almost 3-fold increase in initial triclosan concentration in saliva after brushing and about 2-fold increase in duration of activity.

Introduction

Addition of antibacterial agents to oral care products is an effective way for preventing bacterial plaque formation on tooth surfaces and consequent formation of gingivitis.[1−3] However, the antiplaque activity of an antibacterial agent is not solely related to in vitro antimicrobial activity. Other factors, such as the availability of the antibacterial agent in the oral product and its substantivity in the mouth (i.e., the magnitude and duration of antibacterial effect in saliva) appear to be important parameters.[3,4] The release rate of the antibacterial agent from the oral care product into the aqueous salvia and consequent partition of the agent into the lipophilic intraoral sites can be a crucial factor for effective plaque inhibitation. Furthermore, the concentration of the antimicrobial agent in saliva must be above the minimal inhibitory concentration to exert a bacteriostatic effect. Thus, to ensure a bacteriostatic concentration, the antibacterial agent must be soluble in the aqueous saliva and, at the same time, the agent must be lipophilic to be able to partition from salvia into the lipophilic intraoral sites. Cationic antibacterial agents which exhibit prolonged substantivity in the mouth, such as chlorhexidine, are among the most effective antiplaque agents available. However, their incompatibility with anionic surfactants, staining of teeth and disturbances of taste have limited their usage in oral care products.

Triclosan (Figure 1) is a lipophilic, water-insoluble antibacterial agent which is commonly added to toothpastes, and other oral care products, as a dental antiplaque agent. In general, the availability and substantivity of triclosan is significantly less than those of chlorhexidine and, thus, triclosan is a less effective antiplaque agent than chlorhexidine.[5] However, formulations which improve the availability and/or substantivity, such as triclosan containing liposomes[6] and triclosan/copolymer dentifrice,[7] can significantly improve the antiplaque effect. It has been shown that good delivery of an antiplaque agent, such as triclosan, requires a highly optimized formulation.[8]

Cyclodextrins are cyclic oligosaccharides with a lipophilic central cavity and hydrophilic outer surface. Cyclodextrins are able to form complexes with lipophilic water-insoluble compounds by taking up the compound, or more frequently some lipophilic moiety of the compound, into the cavity. No covalent bonds are formed or broken during the complex formation, and free (i.e., unbound) molecules are in equilibrium with molecules bound in the complex.[9,10] Cyclodextrins increase the delivery of lipophilic, water-insoluble drugs into biological membranes by increasing the drug availability at the hydrated surface of the membrane.[11] The most common natural cyclodextrins are α-cyclodextrin (αCD), β-cyclodextrin (βCD), and γ-cyclodextrin (γCD), which consist of six, seven, and eight glucopyranose units, respectively. These natural cyclodextrins, in particular βCD, and their complexes have limited aqueous solubility. Therefore, numerous water-soluble cyclodextrin derivatives have been synthesized. The complexation efficacy of cyclodextrins is rather low and, thus, relatively large amounts of cyclodextrins are frequently needed to solubilize small amounts of a lipophilic, water-insoluble compound. It is possible to enhance both the aqueous solubility of the complexes and the complexation efficacy by adding small amounts of a water-soluble polymer to the aqueous complexation media.[12] The bioavailability of lipophilic drugs in aqueous cyclodextrin solutions is, in general, improved by addition of the polymers. The purpose of this study was to enhance the availability and substantivity of triclosan through cyclodextrin complexation.

Materials and Methods

Materials—Triclosan was purchased from Ciba-Geigy (Greensboro, NC). β-Cyclodextrin (βCD), γ-cyclodextrin (γCD), and randomly methylated β-cyclodextrin (RMβCD), with a degree of substitution of 1.8, were purchased from Wacker-Chemie (Munich, Germany). α-Cyclodextrin (αCD) was obtained from Nihon Shokuhin Kato Co. (Tokyo, Japan) and 2-hydroxypropyl-β-cyclodextrin

* Corresponding author. Phone: +354 525 4464, fax: +354 525 4071, e-mail: thorstlo@hi.is.
† University of Iceland.
‡ Procter&Gamble (H&BC) Ltd.

10.1021/js9902466 CCC: $18.00
Published on Web 11/03/1999

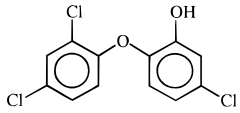

Figure 1—The structure of triclosan, mol wt 289.54, pK_a 7.9.

(HPβCD), with a degree of substitution 2.9, from Janssen Biotech N.V. (Olen, Belgium). Maltosyl β-cyclodextrin (MβCD) was kindly donated by Ensuiko Sugar Refining Co. (Yokohama, Japan) and sulfobutyl ether β-cyclodextrin sodium salt (SBEβCD) by CyDex Inc. (Overland Park, KS). Hydroxypropyl methylcellulose Ph.Eur.'97 (HPMC) was purchased from Mecobenzon (Copenhagen, Denmark), and poly(vinylpyrrolidone) (PVP) of molecular weight 40 000 and carboxymethylcellulose sodium salt (CMC), low viscosity, from Sigma Chemical Co. (St. Louis, MO). All other chemicals used in this study were of reagent or analytical grade and obtained from commercial sources.

The silica-based dentifrice used throughout this study consisted of hydrated silica, sorbitol, glycerine, water, sodium lauryl sulfate, tetrapotassium and tetrasodium pyrophosphate, carbomer, poly(ethylene glycol), sodium phosphate, sodium saccharine, sodium fluoride, and xanthan gum.

Solubility Determinations—An excess amount of triclosan was added to each of the aqueous unbuffered cyclodextrin solutions. The pH of the solutions was between 5 and 6. The solutions were then heated in an autoclave in sealed vials to 121 °C for 20 min. After cooling to room temperature (22−23 °C), a small amount of solid triclosan was added to each vial to promote triclosan precipitation. Then the suspensions were allowed to equilibrate for 5 days at room temperature. After equilibration was attained, an aliquot of each suspension was filtered through a 0.45 μm membrane filter, diluted with the mobile phase, and analyzed by HPLC. Each experiment was performed three times, and the results are presented as the mean ± standard deviation (SD).

Preparation of the Dry Triclosan/βCD Complex Powder—The dry complex was prepared by heating a suspension of triclosan and βCD in an aqueous 0.5% (w/v) CMC solution, or an aqueous solution containing from 0.0 to 1.0% CMC, in an autoclave for 40 min. This was followed by equilibration, at room temperature (22−23 °C) for at least 3 days, and lyophilization.

Preparation of Triclosan/Cyclodextrin-Containing Toothpaste—Cyclodextrin solutions were made by dissolving suitable amount of cyclodextrin (the amount was calculated from the phase-solubility studies) in water or the aqueous polymer solutions. Solutions containing lower and higher cyclodextrin concentrations were also made, altogether 10 different solutions/suspensions for each cyclodextrin derivative. An appropriate amount of triclosan was then added to each solution, and these were heated (120−140 °C) in an autoclave for 40 min. The solutions were allowed to equilibrate for 2 days. A triclosan/cyclodextrin solution/suspension (7.255 g) was then mixed thoroughly with 42.745 g of the silica-based dentifrice resulting in 50 g of toothpaste containing 0.28% (w/w) triclosan. Alternatively, an appropriate amount of lyophilized triclosan/βCD was mixed with 42.705 g of the silica-based dentifrice and water added ad 50 g. After mixing, the samples were allowed to equilibrate for at least 1 day before the triclosan availability was evaluated.

Triclosan Availability Evaluations—The effect of the triclosan/cyclodextrin complex on the permeability of triclosan through a semipermeable cellophane membrane molecular weight cutoff 6 000−8 000 (Spectra/Pore, Fisher Scientific, Pittsburgh, PA) was investigated. The membrane was placed in a Franz diffusion cell (Vangard International Inc., Neptune, NJ) containing 12 mL of an aqueous isotonic pH 7.4 phosphate buffer solution containing 5% (w/v) HPβCD (to solubilize triclosan) and additional 2% (w/v) sodium chloride (to obtain isotonicity with the toothpaste) as a receptor phase. The donor phase consisted of 3 mL of the toothpaste which was applied to the membrane surface (area 3.14 cm^2). The triclosan concentration in the toothpaste was 0.28% (w/w). The assembled diffusion cells were kept at room temperature (about 23 °C), and samples (30 μL) were removed from the donor phase and analyzed by HPLC. The triclosan flux was obtained by plotting the amount of triclosan which went through the membrane against time. The results presented are the means of two experiments.

Table 1—Triclosan Solubility in Aqueous 5.0% (w/v) Cyclodextrin Solution (mean ± SD, $n = 3$) with or without 0.20% (w/v) Polymer[a]

cyclodextrin and polymer	solubility of triclosan (mg/mL)
αCD in water (no polymer)	0.32 ± 0.00
αCD in aqueous PVP solution	0.29 ± 0.00
αCD in aqueous CMC solution	0.43 ± 0.00
αCD in aqueous HPMC solution	0.44 ± 0.00
βCD* in water (no polymer)	0.09 ± 0.00
βCD* in aqueous PVP solution	0.07 ± 0.01
βCD* in aqueous CMC solution	0.09 ± 0.00
βCD* in aqueous HPMC solution	0.21 ± 0.01**
HPβCD in water (no polymer)	1.75 ± 0.03
HPβCD in aqueous PVP solution	1.60 ± 0.02
HPβCD in aqueous CMC solution	1.78 ± 0.01
HPβCD in aqueous HPMC solution	1.42 ± 0.02
MβCD in water (no polymer)	0.65 ± 0.01
MβCD in aqueous HPMC solution	0.98 ± 0.00
RMβCD in water (no polymer)	1.39 ± 0.02
RMβCD in aqueous PVP solution	1.37 ± 0.02
RMβCD in aqueous CMC solution	1.52 ± 0.02
RMβCD in aqueous HPMC solution	3.70 ± 0.08
SBEβCD in water (no polymer)	2.14 ± 0.03
SBEβCD in aqueous PVP solution	2.07 ± 0.06
SBEβCD in aqueous CMC solution	2.15 ± 0.01
SBEβCD in aqueous HPMC solution	2.22 ± 0.06

[a] *The solubility of βCD in water is 1.85% (w/v). βCD formed a 5% (w/v) suspension before addition of triclosan. **The water-soluble polymers can increase the aqueous solubility of βCD and its complexes.

Triclosan Substantivity Evaluations—Six healthy volunteers (5 males and 1 female), who were not either pregnant, receiving antimicrobial therapy, or had dental disease, were recruited for this part of the study. Sampling was separated by at least 2 days, and all the volunteers used a nontriclosan toothpaste throughout the study, with at least a two-day wash-out period prior to commencing the study. Participants were not allowed to brush their teeth for at least 2 h prior to the test occasion.

For each product evaluation, each participant gave an initial saliva sample prior to brushing with the sample toothpaste, to confirm the absence of triclosan. Each brushed for 1 min with 1.5 g of the test toothpaste and then rinsed the mouth with 20 mL of deionized water. Unstimulated saliva samples were then taken at 10, 20, and 60 min postbrushing. The saliva was weighed into 10 mL volumetric flasks, 4 mL of methanol and 2 mL of the HPLC mobile phase were added, and the sample was mixed and made to volume with methanol. Finally, the sample was filtered through a 0.45 μm membrane filter and analyzed by HPLC.

HPLC Analysis of Triclosan—The quantitative determination of triclosan was performed on a high performance liquid chromatographic (HPLC) component system from Merck Hitachi (Dramstadt, Germany), consisting of a pump (model no. L-6200A) operated at 1.5 mL/min, autosampler (model no. L-7200) with injection volume adjusted to 20 μL, LiChrosorb RP-18 (125/4 mm, 5 μm) column, UV/vis detector (model no. L-4200) operated at 283 nm, and an integrator (model no. D-2500). The mobile phase consisted of acetonitrile and 40 mM aqueous pH 3.0 disodium hydrogen phosphate (50:50). A standard curve was determined for each run.

Results

Cyclodextrin Solubilization of Triclosan—In the preliminary studies all the cyclodextrins tested, except the natural γCD, formed water-soluble complexes with triclosan. However, αCD had much less solubilizing effect than the βCDs and, thus, only the natural βCD and its derivatives were studied further (Table 1). The natural βCD and its triclosan complex have very limited solubility in water. The βCD derivatives, i.e., RMβCD, SBEβCD, HPβCD, and MβCD, formed water-soluble complexes with triclosan, and, frequently, addition of a water-soluble polymer increased the solubilizing effect of the cyclodextrin. All the βCD derivatives formed linear phase−solubility

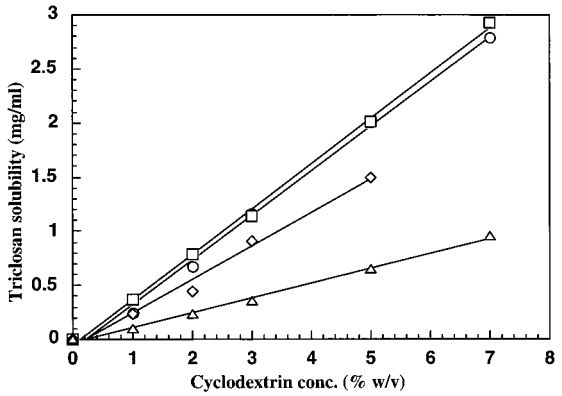

Figure 2—The phase-solubility diagrams of triclosan in aqueous cyclodextrin solutions at 22 °C. HPβCD (○), SBEβCD sodium salt (□), RMβCD (◇), and MβCD (Δ).

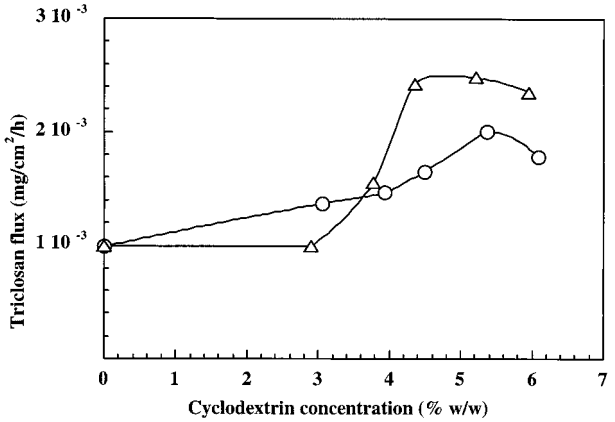

Figure 3—The triclosan flux from a toothpaste as a function of cyclodextrin concentration, RMβCD without polymer (○), RMβCD containing 0.2% HPMC (Δ). The initial triclosan concentration in the toothpaste was 0.28% (w/w).

diagrams, indicating that one cyclodextrin molecule forms a complex with one triclosan molecule (i.e., 1:1 complexes)[13] (Figure 2). The amount of cyclodextrin needed to solubilize triclosan in the toothpaste formulations was estimated from these and comparable phase−solubility diagrams.

Evaluation of Triclosan Availability in Toothpaste Formulations—On the basis of previous investigations, it can be assumed that the triclosan availability in the toothpaste formulations will be at its maximum when just enough cyclodextrin is used to solubilize triclosan in the toothpaste. Addition of too much or too little cyclodextrin will result in less than optimum triclosan availability.[11,12] The approximate amounts of the various cyclodextrins needed to dissolve 0.28% (w/w) triclosan in the toothpaste formulations was estimated from phase−solubility diagrams of triclosan in aqueous cyclodextrin solutions. Since the various constituents of the toothpaste formulation will interfere with the complexation, final adjustments of the cyclodextrin concentrations had to be based on the rate of triclosan release from the triclosan/cyclodextrin-containing toothpastes. Figure 3 shows a representative release profile observed as the flux of triclosan from the toothpaste through a semipermeable cellophane membrane. The maximum triclosan flux and the optimum cyclodextrin concentration from toothpastes containing 0.28% (w/w) triclosan and the various cyclodextrins is shown in Table 2. Optimally, the cyclodextrins resulted in 2- to 3-fold flux enhancement compared to toothpaste containing no cyclodextrin, i.e., addition of triclosan/cyclodextrin complexes to the toothpaste formulations resulted in 2- to 3-fold enhancement of the triclosan availability. Surprisingly, although βCD and its triclosan complex have limited

Table 2—The Flux of Triclosan from the Toothpastes at Optimum Cyclodextrin Concentration[a]

cyclodextrin	cyclodextrin concn (% w/w)	flux (mg/cm²/h)	flux ratio[b]
αCD	7.30	1.91×10^{-3}	1.9
αCD with PVP	7.30	1.50×10^{-3}	1.5
βCD	7.30	2.10×10^{-3}	2.1
βCD with CMC	3.00	2.20×10^{-3}	2.2
HPβCD	4.64	2.27×10^{-3}	2.3
HPβCD with PVP	6.09	2.26×10^{-3}	2.3
SBEβCD	6.09	0.57×10^{-3}	0.6
SBEβCD with PVP	4.64	1.31×10^{-3}	1.3
RMβCD	5.37	2.01×10^{-3}	2.0
RMβCD with CMC	5.22	2.48×10^{-3}	2.5

[a] The triclosan concentration in the toothpastes was in all cases 0.28% (w/v). In some cases 0.20% (w/v) polymer was added during the triclosan/cyclodextrin complex formation. The flux was determined at 22 to 23 °C. [b] The flux divided by the triclosan flux obtained from a toothpaste containing no cyclodextrin (0.99×10^{-3} mg/cm²/h).

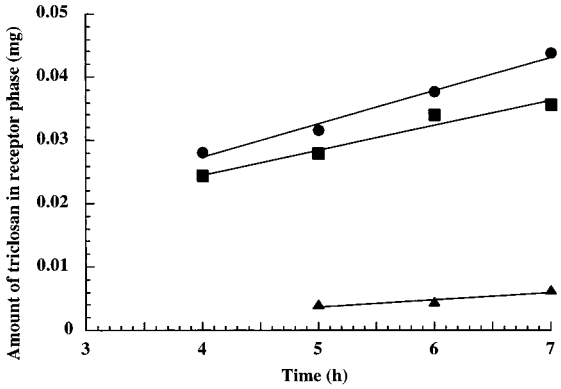

Figure 4—Representative figure which shows the release of triclosan from toothpastes containing no βCD or CMC (▲), triclosan/βCD complex (■), or triclosan/βCD/CMC complex (●) through a semipermeable cellophane membrane at 22 to 23 °C. The triclosan concentration toothpaste was kept constant at 0.28% (w/w). The βCD concentration in the toothpaste was 3.0% (w/w) when it was present in the toothpaste. When CMC was present, the CMC concentration was kept at 0.50% (w/v) during the preparation of the triclosan/βCD/CMC complex.

solubility in pure water, addition of triclosan/βCD complexes to the toothpaste resulted in significant enhancement of the triclosan availability. Furthermore, addition of CMC reduced significantly the amount of βCD needed to enhance the triclosan availability.

The effect of βCD concentration on the flux of triclosan from toothpaste formulations was investigated. During preparation of the dry triclosan/βCD complex powder, the CMC concentration was kept constant at 0.50% (w/v), but the βCD concentration was varied. The dry complex powder was then mixed into the toothpaste resulting in 0.28% (w/w) triclosan concentration in the final toothpaste formulation. The triclosan availability in the toothpaste was evaluated by determining the triclosan flux from the toothpaste through a semipermeable cellophane membrane (Figure 4). As can be seen in Figure 5 the optimum βCD concentration was 3% (w/v). Then the optimum polymer concentration was determined. Triclosan/βCD complexes were prepared in aqueous solutions containing from 0.00 to 1.00% (w/v) CMC. The βCD concentration and the triclosan concentration were kept constant in the final toothpaste formulation, at 3.0% (w/w) and 0.28% (w/w), respectively (Figure 6). Maximum triclosan flux (i.e., maximum triclosan availability) was obtained when the CMC concentration during preparation of the triclosan/βCD complex was between 0.10 and 0.20% (w/v). No further

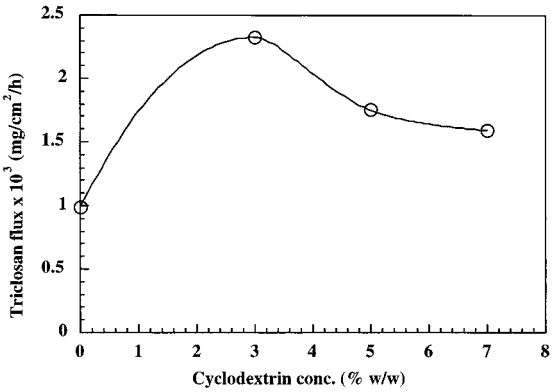

Figure 5—The effect of βCD concentration in the toothpaste formulation of the flux of triclosan through a semipermeable cellophane membrane at 22 to 23 °C. The triclosan concentration was kept constant at 0.28% (w/w), and CMC concentration was kept at 0.50% (w/v) during the preparation of the triclosan/βCD complex.

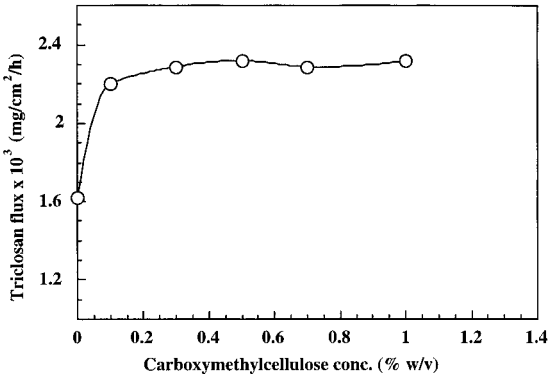

Figure 6—The effect of CMC concentration during preparation of the complex on the flux of triclosan from the toothpaste through a semipermeable cellophane membrane at 22 to 23 °C. The triclosan concentration was kept constant at 0.28% (w/v), and the βCD concentration was kept constant at 3.0% (w/v) in the toothpaste.

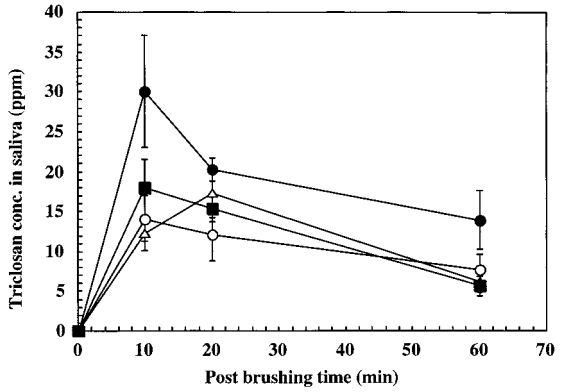

Figure 7—The triclosan concentration in saliva (mean ± SEM, $n = 6$) at various times after brushing with toothpaste containing free triclosan (no cyclodextrin or polymer complex) (○), triclosan/βCD complex without polymer (■), triclosan/HPβCD complex without polymer (Δ), and triclosan/βCD/CMC complex (●).

increase in the triclosan flux was observed from complexes prepared at higher CMC concentrations.

Triclosan Substantivity Evaluations—Figure 7 shows the effect of cyclodextrin complexation of the triclosan saliva concentration time profile after brushing with toothpastes containing four different triclosan formulations. The area under the curves (AUC) from 0 to 60 min gives a rough estimate of how much triclosan is initially retained in the mouth after brushing. Replacing triclosan by triclosan/βCD complex or triclosan/HPβCD complex results in about 10% increase in AUC, indicating only minor improvement of the triclosan retention in the mouth. This was partly due to somewhat shorter duration, i.e., faster triclosan clearance, after brushing with the triclosan/cyclodextrin-containing toothpastes. However, replacing triclosan by triclosan/βCD/CMC complex resulted in about 80% increase in the AUC. Furthermore, the duration of the antibacterial effect was improved significantly upon replacing triclosan with the triclosan/βCD/CMC complex. Thus, formulation of triclosan in the toothpaste as a triclosan/βCD/CMC complex improves significantly the substantivity of triclosan in the mouth. The minimum inhibitory concentration (MIC) of triclosan versus a variety of oral bacteria is $\leq$10 ppm.[8,14]

Discussion

Through cyclodextrin complexation it is possible to increase the aqueous solubility of lipophilic, water-insoluble drugs, and other lipophilic compounds, without changing their molecular structure. That is, the cyclodextrins do not affect their intrinsic abilities to permeate into lipophilic biological membranes or interact with pharmacological receptors. The cyclodextrin molecules are relatively large (molecular weight ranging from almost 1000 to over 1500), with a hydrated outer surface, and under normal conditions, cyclodextrin molecules will only permeate biological membranes with considerable difficulty.[15,16] It is thought that cyclodextrins act as true carriers by keeping hydrophobic molecules in solution and delivering them to the surface of a lipophilic biological membrane, e.g., the oral mucosa, where they partition into the membrane.[11,16,17] The relatively lipophilic membrane has low affinity for the hydrophilic cyclodextrin molecules, and therefore they remain in the aqueous membrane exterior, e.g., the aqueous mucus layer or saliva. However, simply adding cyclodextrins to aqueous dentifrice formulations will not automatically result in enhanced triclosan penetration through the aqueous mucus layer into the lipophilic mucosa. Frequently, formation of cyclodextrin complexes results in decreased availability of an antibacterial agent.[16] Addition of small amounts of water-soluble polymers to aqueous cyclodextrin solution and heating increase the cyclodextrin complexation of lipophilic, water-insoluble compounds. The polymers do not only increase the complexation but also increase the availability of the compound in the cyclodextrin-containing formulation.[12,18] Furthermore, in the present formulation, addition of the ionized CMC prevented the formation of association colloids, resulting in clear triclosan cyclodextrin solutions. It is well-known that the polymers, such as carbohydrates, form complexes with mono- and oligosaccharides as well as with numerous other compounds.[19] Such interactions will influence the physicochemical properties of both the polymers and the saccharides. For example, carbohydrates are known to enhance the solubilizing abilities of surfactants.[12] In this present study the polymers enhanced the triclosan release rate from cyclodextrins (Figure 4) and the triclosan retention in the buccal area (Figure 7). Macromolecules, such as CMC, and their complexes are washed more slowly from biological surfaces than comparable smaller molecules. This could explain, at least partly, the enhanced triclosan retention observed when the simple triclosan/βCD complex in the toothpaste is replaced by the triclosan/βCD/CMC complex.

The availability of triclosan in the silica-based toothpaste formulation was optimized through a series of solubility studies in aqueous cyclodextrin solutions as well as through a series of triclosan release studies from the toothpaste through a cellophane membrane. Cyclodextrin formed 1:1

complexes with βCD and its derivatives. The availability of triclosan (i.e., the triclosan release rate) was improved significantly in the toothpaste formulation although the triclosan/βCD complex has limited solubility in pure aqueous solutions. This enhanced availability could be due to the solubilizing effects of the surfactants used in the formulation. Through addition of the water-soluble polymer CMC, it was possible to reduce the amount of βCD in the formulation by as much as 60% without affecting the triclosan availability (i.e., the release rate from the toothpaste). The result was a silica-based toothpaste containing 0.28% (w/w) triclosan and only 3.0% (w/w) βCD, or only 30−50 mg of βCD per brushing.

It has been suggested that the salivary concentration decline of an agent, such as triclosan, after using a dentifrice containing the agent follows first-order kinetics which can be described by the following equation:[20−22]

$$C_t = C_0 e^{-(Ft/V)} \qquad \text{(eq 1)}$$

where C_t is the concentration of the agent at time t, C_0 is the initial concentration of the agent (i.e., the concentration at t equal to zero), F is the saliva flow rate, and V is the volume of saliva in the mouth. Other investigators have fitted triclosan salivary elimination to a two-phase model (i.e., a two-compartment open model):[2,8]

$$C_t = Ae^{-\alpha t} + Be^{-\beta t} \qquad \text{(eq 2)}$$

where the initial concentration of dissolved triclosan is the sum of A and B (i.e., $C_0 = A + B$), and α and β are hybrid first-order rate constants for the distribution phase and elimination phase, respectively. The distribution phase represents the rapid initial decline in the salivary triclosan concentration due to simultaneous (a) adsorption and absorption of the lipophilic triclosan to and into the oral mucosa, plaque, and other intraoral sites, and (b) triclosan elimination with saliva as described by eq 1. The elimination phase represents the somewhat slower decline in the salivary triclosan concentration after equilibrium has been reached between triclosan in saliva and triclosan in the various intraoral sites. According to both models, high initial concentration of triclosan dissolved in saliva should result in high oral substantivity. However, it has been shown that the concentration of triclosan at the site of biological action (i.e., in the oral mucosa or plaque) is more relevant to clinical activity than the salivary concentration profiles.[4] Triclosan must be in a hydrophilic, water-soluble form to be able to penetrate the aqueous mucous layer to the surface of the mucosa (and other intraoral sites), but at the same time triclosan must be in a lipophilic form to be able to partition into mucosa and its sites of action. High initial salivary concentration of available (i.e., dissolved) triclosan (or more precisely, high triclosan activity) will enhance triclosan delivery to the various oral triclosan reservoirs and its sites of action.

Formulating triclosan as a water-soluble triclosan/βCD/CMC complex resulted in high initial triclosan concentration and a high oral triclosan substantivity. At 10 min the triclosan salivary concentration was determined to be 13 ppm when the toothpaste contained free triclosan (i.e., without cyclodextrin), which is comparable to reported triclosan salivary levels after brushing with other triclosan-containing dentifrices[8] but at the same time point the triclosan concentration was 30.0 ppm when the toothpaste contained the triclosan/βCD/CMC complex. The profile could be fitted to a two-phase model with a short distribution phase ($t_{1/2} \approx 0.3$ h) and extended elimination phase ($t_{1/2}$ between 1 and 2 h). The duration of activity, based on MIC of 10 ppm, was extended from about 0.7 h (free triclosan) to about 1.5 h (triclosan/βCD/CMC complex). Thus, replacing free triclosan with the triclosan/βCD/CMC complex resulted in almost 3-fold increase in C_0 and about 2-fold increase in the duration of activity.

References and Notes

1. Hull, P. Chemical inhibitation of plaque. *J. Clin. Periodontol.* **1980**, *7*, 431−442.
2. Gilbert, R. J.; Williams, P. E. O. The oral retention of antiplaque efficacy of triclosan in human volunteers. *Br. J. Clin. Pharmacol.* **1987**, *23*, 579−583.
3. Addy, M.; Jenkins, S.; Newcombe, R. Toothpastes containing 0.3% and 0.5% triclosan. II. Effects of single brushings on salivary bacterial counts. *Am. J. Dent.* **1989**, *2*, 215−219.
4. Cummins, D.; Creeth, J. E. Delivery of antiplaque agents from dentifrices, gels, and mouthwashes. *J. Dent. Res.* **1992**, *71*, 1439−1449.
5. Jenkins, S.; Addy, M.; Newcombe, R. G. Dose response of chlorhexidine against plaque and comparison with triclosan. *J. Clin. Periodontol.* **1994**, *21*, 250−255.
6. Jones, M. N.; Song, Y. H.; Kaszuba, M.; Reboiras, M. D. The interaction of phospholipid liposomes with bacteria and their use in the delivery of bactericides. *J. Drug Targeting* **1997**, *5*, 25−34.
7. Renvert, S.; Birkhed, D. Comparison between 3 triclosan dentifrices on plaque, gingivitis and salivary microflora. *J. Clin. Periodontol.* **1995**, *22*, 63−70.
8. Creeth, J. E.; Abraham, P. J.; Barlow, J. A.; Cummins, D. Oral delivery and clearance of antiplaque agents from triclosan-containing dentrifrices. *Int. Dent. J.* **1993**, *43*, 387−397.
9. Loftsson, T.; Brewster, M. E. Pharmaceutical applications of cyclodextrins. 1. Drug solubilization and stabilization. *J. Pharm. Sci.* **1996**, *85*, 1017−1025.
10. Stella, V. J.; Rajewski, R. A. Cyclodextrins: their future in drug formulation and delivery. *Pharm. Res.* **1997**, *14*, 556−567.
11. Masson, M.; Loftsson, T.; Masson, G.; Stefansson, E. Cyclodextrins as permeation enhancers: some theoretical evaluations and in vitro testing. *J. Controlled Release* **1999**, *59*, 107−118.
12. Loftsson, T. Increasing the cyclodextrin complexation of drugs and drug biovailability through addition of water-soluble polymers. *Pharmazie* **1998**, *53*, 733−740.
13. Higuchi, T.; Connors, K. A. Phase-solubility techniques. *Adv. Anal. Chem. Instrum.* **1965**, *4*, 117−212.
14. Gilbert, R. J.; Fraser, S. B.; van der Ouderaa, F. J. G. Oral disposition of triclosan (2,4,4′-trichloro-2′-hydroxydiphenyl ether) delivered from dentifrice. *Caries Res.* **1987**, *21*, 29−36.
15. Rajewski, R. A.; Stella, V. J. Pharmaceutical applications of cyclodextrins. 2. In vivo drug delivery. *J. Pharm. Sci.* **1996**, *85*, 1142−1168.
16. Loftsson, T.; Stefánsson, E. Effect of cyclodextrins on topical drug delivery to the eye. *Drug Devel. Ind. Pharm.* **1997**, *23*, 473−481.
17. Loftsson, T.; Bodor, N. The effect of cyclodextrins on percutaneous transport of drugs. In *Percutaneous penetration enhancers*; Smith, E. W., Maibach, H. I., Eds.; CRC Press: Boca Raton, FL, 1995; pp 335−342.
18. Loftsson, T.; Järvinen, T. Cyclodextrins in ophthalmic drug delivery. *Adv. Drug Deliv. Rev.* **1999**, *36*, 59−79.
19. Tomaski, P.; Schilling, C. H. Complexes of starch with organic guests. In *Advances in carbohydrate chemistry and biochemistry, Vol. 53*; Horton, D., Ed.; Academic Press: San Diego, CA, 1998; pp 345−426.
20. Afflitto, J.; Fakhry-Smith, S.; Gaffar, A. Salivary and plaque triclosan levels after brushing with a 0.3% triclosan/copolymer/NaF dentifrice. *Am. J. Dent.* **1989**, *2*, 207−210.
21. Simon, W. *Mathematical techniques for physiology and medicine*; Academic Press: New York, 1972.
22. Dawes, C. A mathematical model of salivary clearance of sugar from the oral cavity. *Caries Res.* **1983**, *17*, 321−334.

JS9902466

Diphenhydramine Disposition in the Sheep Maternal–Placental–Fetal Unit: Determinants of Plasma Drug Concentrations in the Mother and the Fetus†

SANJEEV KUMAR,‡ GEORGE R. TONN,‡ K. WAYNE RIGGS,‡ AND DAN W. RURAK*,§

Contribution from *Division of Pharmaceutics and Biopharmaceutics, Faculty of Pharmaceutical Sciences, and B.C. Research Institute of Children's and Women's Health, Department of Obstetrics and Gynecology, Faculty of Medicine, The University of British Columbia, Vancouver, B.C., Canada*

Received July 16, 1999. Final revised manuscript received September 28, 1999. Accepted for publication October 5, 1999.

Abstract □ The objective of this study was to identify the important factors that determine plasma concentrations of diphenhydramine (DPHM) in the mother and the fetus after maternal as well as fetal steady-state drug administration. Inter-relationships were evaluated between maternal and fetal placental and nonplacental clearances, plasma protein binding, and steady-state plasma concentrations of DPHM among data obtained from 18 pregnant sheep during late gestation. The major determinant of plasma DPHM concentrations in the mother after maternal as well as fetal administration appears to be maternal plasma protein binding and maternal nonplacental clearance. In contrast, the major determinant of fetal plasma DPHM concentrations after maternal drug administration was the extent of fetal first-pass hepatic drug uptake from the umbilical vein. However, after fetal drug administration, the fetal plasma concentrations were related to the extent of fetal plasma protein binding and fetal placental and nonplacental clearances. The index of fetal-to-maternal placental drug transfer after fetal drug administration (steady-state maternal-to-fetal plasma concentration ratio) was related to steady-state fetal plasma unbound fraction and fetal placental and nonplacental clearance. However, this index was not related to the magnitude of the factors operating on the maternal side of the placenta such as maternal plasma protein binding and maternal nonplacental clearance. This might indicate a lack of complete equilibration of the unbound drug concentrations on the two sides of the placenta at the exchange site.

Introduction

Although the kinetics of placental transfer of most drugs appear to follow the principles of simple diffusion across biological membranes, the extent and time course of fetal drug exposure are not related solely to the ease of placental drug transfer. Instead these are the result of a complex interplay between the kinetics of placental drug transfer as well as many other factors related to maternal and fetal components of the pregnant unit. These include the relative extent of maternal and fetal plasma protein binding of the drug, the efficiency of maternal and fetal drug elimination via metabolism or renal excretion, and recirculation of the drug between amniotic and allantoic fluid compartments and the fetal circulation.[1,2] The measurement of area under the fetal plasma concentration vs time curve (AUC) or steady-state concentration after maternal drug administration, although a clinically useful index of the extent of fetal drug exposure, does not provide any information about the different factors determining its magnitude. The computation of maternal and fetal placental and nonplacental clearances according to a two-compartment pharmacokinetic model after separate maternal and fetal steady-state drug administration provides a more detailed insight into various factors determining fetal drug exposure (Figure 1).[3] This pharmacokinetic modeling essentially partitions the complex array of these pharmacokinetic factors into three main categories, i.e., factors related to the placenta (maternal and fetal placental clearance), the mother (maternal nonplacental clearance), and the fetus (fetal nonplacental clearance). Thus, it is possible to separately examine the effect of various physicochemical (e.g., drug lipophilicity and pK_a, etc.), and maternal and fetal biological variables (e.g., plasma protein binding, placental blood flows, drug metabolism capacity) on these three categories of pharmacokinetic factors and the resultant effects on fetal drug exposure. This makes it feasible to determine the relative importance of each pharmacokinetic variable in determining fetal exposure to a particular drug, and to make comparisons among different drugs in terms of the most important factor(s). However, a detailed analysis of the importance of various placental, maternal, and fetal pharmacokinetic factors in determining fetal drug exposure has rarely been performed for any drug.

Diphenhydramine or 2-(diphenylmethoxy)-*N*,*N*-dimethylamine (DPHM) is a potent histamine H1-receptor antagonist. It has been widely used during human pregnancy for the treatment of nausea and vomiting, insomnia, allergic rhinitis, and common coughs and colds. Previous studies in our laboratory, using chronically instrumented pregnant sheep, demonstrated that DPHM readily crosses the ovine placenta and is eliminated from the fetus via both placental and nonplacental routes.[4] In continuation of these studies, we have utilized DPHM as a model high-clearance drug that undergoes rapid and extensive placental transfer, to examine the factors affecting different aspects of maternal–fetal drug disposition of this class of compounds. This includes the study of comparative maternal–fetal drug

* Corresponding author. Phone: 604-875-2430. Fax: 604-875-2496. E-mail: drurak@cw.bc.ca.

† Abbreviations: DPHM, diphenhydramine; [$^2H_{10}$]DPHM, deuterium-labeled diphenhydramine; CL_{mm}, maternal total body clearance; CL_{ff}, fetal total body clearance; CL_{mf}, maternal to fetal placental clearance; CL_{fm}, fetal to maternal placental clearance; CL_{mo}, maternal nonplacental clearance; CL_{fo}, fetal nonplacental clearance; C_m, maternal plasma steady-state DPHM concentration after maternal administration; C_f, fetal plasma steady-state DPHM concentration after maternal administration; C_m', maternal plasma steady-state DPHM (or [$^2H_{10}$]-DPHM) concentration after fetal administration; C_f', fetal plasma steady-state DPHM (or [$^2H_{10}$]DPHM) concentration after fetal administration; k_o, maternal drug infusion rate; k_o', fetal drug infusion rate; M-UF, maternal steady-state plasma unbound fraction of the drug; F-UF, fetal steady-state plasma unbound fraction of the drug; r, Pearson correlation coefficient.

‡ Division of Pharmaceutics and Biopharmaceutics.

§ B.C. Research Institute of Children's and Women's Health.

10.1021/js990244l CCC: $18.00 Published on Web 10/26/1999

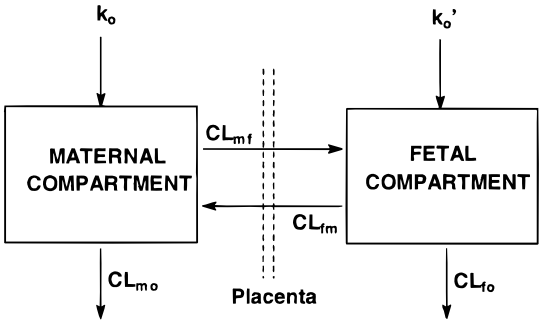

Figure 1—A representation of various placental and nonplacental drug clearances in the two-compartment pharmacokinetic model of the maternal-fetal unit. CL_{mo}: maternal nonplacental clearance; CL_{fo}: fetal nonplacental clearance; CL_{mf}: placental clearance from the mother to the fetus; CL_{fm}: placental clearance from the fetus to the mother.

clearance,[4] *in utero* fetal hepatic drug uptake and its relation to fetal drug clearance,[5] and *in utero* functional capacity of fetal drug metabolism pathways compared to the mother.[6] As part of these studies, we have determined DPHM placental and nonplacental clearances in 18 pregnant sheep during the final two weeks of their gestation. In the current study, we have retrospectively examined the inter-relationships between maternal and fetal clearances (placental and nonplacental) and plasma concentrations of DPHM among the data obtained from the above three studies in order to identify the most important factor(s) determining these concentrations after maternal as well as fetal drug administration.

Experimental Section

Animals and Surgical Preparation—A total of 18 pregnant sheep were employed in these studies. All studies were approved by the University of British Columbia Animal Care Committee, and the procedures performed on sheep conformed to the guidelines of the Canadian Council on Animal Care. The detailed surgical procedures employed have already been described in previous publications.[4–6] Briefly, 18 pregnant Dorset Suffolk crossbred ewes, with a maternal body weight of 76.9 ± 12.6 kg (mean ± SD), were surgically prepared between 115 and 129 days gestation (term ~145 days). Surgery was performed aseptically under halothane (1–2%) and nitrous oxide (60%) anesthesia (balance O_2), following induction with intravenous (iv) sodium pentothal (1 g) and intubation of the ewe. Polivinyl or silicone rubber catheters (Dow Corning, Midland, MI) were implanted in both fetal femoral arteries and lateral tarsal veins and a maternal femoral artery and vein. Catheters were also implanted in the fetal carotid artery ($n = 4$), common umbilical vein ($n = 2$), fetal trachea ($n = 18$), fetal urinary bladder (via a suprapubic incision, $n = 5$), and the amniotic cavity ($n = 18$) for purposes unrelated to this manuscript. In some animals, electrodes (Cooper Corporation, Chatsworth, CA) were implanted biparietally on the dura to record the fetal electrocorticogram (ECoG). In four of the animals, a transit-time 4SB blood flow transducer (Transonic Systems, Inc., Ithaca, NY) was placed around the common umbilical artery to measure umbilical blood flow. The catheters, electrodes, and flow transducer cables were tunneled subcutaneously and exteriorized via a small incision on the flank of the ewe and were stored in a denim pouch when not in use. All catheters were flushed daily with approximately 2 mL of sterile 0.9% sodium chloride containing 12 units of heparin/mL to maintain catheter patency. Intramuscular injections of ampicillin 500 mg were given to the ewe on the day of surgery and for 3 days postoperatively. Ampicillin (500 mg) was also given via the amniotic cavity immediately following surgery and daily thereafter. Following surgery, animals were kept in holding pens with other sheep and were given free access to food and water. The sheep were allowed to recover for 4–8 days prior to experimentation.

Protocol—All experiments were conducted between 124 and 140 days gestation. A total of 31 experiments were conducted in 18 pregnant sheep. Each animal received one of the following:

(1) A 90 min separate maternal and fetal steady-state DPHM (DPHM hydrochloride, Sigma Chemical Co., St. Louis, MO) infusion with an appropriate washout period between ($n = 8$, experiments from ref 4).

(2) A 6 h separate maternal and fetal steady-state DPHM infusion with an appropriate washout period between ($n = 3$, experiments from ref 6).

(3) A 6 h separate maternal and fetal steady-state [$^2H_{10}$]DPHM (a deuterium labeled analogue of DPHM synthesized in our laboratory; Tonn et al., 1993) infusion with an appropriate washout period between ($n = 2$, experiments from ref 6).

(4) A 6 h simultaneous steady-state infusion of DPHM to the mother and [$^2H_{10}$]DPHM to the fetus ($n = 5$, experiments from ref 5).

The doses were prepared in sterile water for injection and were sterilized by filtering through a 0.22 μm nylon syringe filter (MSI, Westboro, MA) into a capped empty sterile injection vial.

Drug (DPHM or [$^2H_{10}$]DPHM) was administered to the mother in each experiment as a 20 mg iv loading dose over 1.0 min, followed immediately by an infusion at 670 μg/min via the maternal femoral vein. In fetal experiments, a 5.0 mg iv loading dose of DPHM or [$^2H_{10}$]DPHM was given via the fetal lateral tarsal vein over 1.0 min, followed by an infusion of the same compound at 170 μg/min. Simultaneous serial blood samples were collected from the fetal (1.5 mL) and maternal (3.0 mL) femoral arterial catheters. Fetal femoral arterial samples (0.5 mL) were also collected at the same time intervals for blood gas analysis and measurement of glucose and lactate concentrations. All fetal blood removed for sampling was replaced at intervals during the experiment by an equal volume of maternal blood obtained prior to the start of the experiment. Amniotic and tracheal fluid (2.0 mL) and fetal (5.0 mL) and maternal urine (10.0 mL) samples were also collected in some animals to examine the excretion of DPHM into these fluids; these data have been reported previously.[4–6]

Maternal and fetal blood samples collected for drug analysis were placed into heparinized Vacutainer tubes (Becton-Dickinson, Rutherford, NJ), gently mixed, and then centrifuged at 2000*g* for 10 min. The plasma supernatant was removed and placed into clean borosilicate test tubes with poly(tetrafluoroethylene) (PTFE)-lined caps. Amniotic fluid and urine samples were also placed into clean borosilicate test tubes. All samples were stored frozen at −20 °C until the time of analysis.

Physiological Recording and Monitoring Procedures—From at least 24 h prior to and at least 24 h after each infusion period, amniotic pressure, fetal tracheal and femoral arterial pressures, and fetal heart rate were continuously monitored. In some animals with implanted cortical electrodes and fetal bladder catheters, fetal electrocortical activity and urine flow rate were also measured. Some of these data have been reported separately.[7]

Fetal blood pH, P_{O_2}, and P_{CO_2} were measured using an IL 1306 pH/blood gas analyzer (Allied Instrumentation Laboratory, Milan, Italy). Blood O_2 saturation and hemoglobin concentration were determined using a Hemoximeter (Radiometer, Copenhagen, Denmark). Blood glucose and lactate concentrations were determined with a 2300 STAT plus glucose/lactate analyzer (Y.S.I. Inc. Yellow Springs, OH). All of these fetal blood gases and metabolite concentrations have been reported in our earlier publications and were within the normal range observed in our and other laboratories at this stage of gestation in fetal sheep.[4–6]

Protein Binding of DPHM and [$^2H_{10}$]DPHM in Fetal and Maternal Plasma—The plasma protein binding/unbound fraction of DPHM (or [$^2H_{10}$]DPHM) was measured ex vivo in pooled fetal and maternal steady-state plasma samples using an equilibrium dialysis procedure as described by Yoo et al. (1993).[4] Maternal plasma protein binding was measured in plasma samples obtained during maternal drug infusion, whereas fetal plasma protein binding was measured in plasma samples obtained during fetal drug infusion.

Drug Analysis—The concentrations of DPHM in all biological fluids collected were measured using either a gas chromatographic nitrogen phosphorus detection method[8] (studies in ref 4) or by a GC-MS assay capable of measuring both DPHM and [$^2H_{10}$]DPHM simultaneously[9] (studies in refs 5 and 6). Both these assays have been shown to be comparable to each other with a similar limit of quantitation (2.0 ng/mL).[9]

Pharmacokinetic Analysis—The maternal and fetal steady-state arterial plasma DPHM and [$^2H_{10}$]DPHM concentration data were treated according to a two-compartment open model in order

Table 1—Steady-State Maternal and Fetal Plasma Unbound Fractions and Total Plasma Concentrations of DPHM in 18 Pregnant Sheep

	steady-state unbound fraction		total steady-state DPHM plasma concentration (ng/mL)[a]			
			maternal infusion		fetal infusion	
ewe	maternal plasma	fetal plasma	C_m	C_f	C_m'	C_f'
121	0.048	0.165	360.3	35.5	53.9	658.0
125	0.110	0.173	215.8	29.6	26.5	697.9
130	0.072	0.301	185.4	20.8	25.3	274.9
133	0.087	0.222	207.8	56.0	26.4	367.0
138	0.168	0.326	197.8	49.6	39.5	509.8
202	0.157	0.364	152.9	18.3	22.4	323.4
204	0.193	0.402	236.1	29.1	36.5	192.1
480	0.293	0.263	140.3	51.2	17.9	557.9
2101	0.066	0.296	225.4	18.2	31.9	227.6
122z	0.082	0.428	266.0	27.8	41.5	137.2
2177	0.069	0.255	236.7	32.6	43.9	187.8
2181	0.091	0.191	244.1	114.2	39.6	383.6
2241	0.050	0.299	331.6	35.5	66.3	283.7
4230	0.145	0.326	224.6	124.1	37.4	250.7
4227	0.180	0.242	251.5	60.7	40.2	374.7
2174	0.032	0.262	268.1	30.5	27.8	176.1
1225A	0.106	0.527	179.1	3.5	33.9	132.5
303Y	0.211	0.377	181.1	38.9	24.5	225.6
mean	0.120	0.301	228.0	43.1	35.3	331.1
SD	0.069	0.094	56.1	31.2	11.9	172.4

[a] C_m and C_f: steady-state maternal and fetal total femoral arterial plasma DPHM concentrations, respectively, after maternal administration; C_m' and C_f', steady-state maternal and fetal total femoral arterial plasma DPHM concentrations, respectively, after fetal administration.

to estimate the placental and nonplacental clearance parameters of DPHM (or [$^2H_{10}$]DPHM when present) in the ewe and fetus (Figure 1). This model assumes steady-state plasma concentrations and drug elimination from both the maternal and fetal compartments. The equations to estimate placental and nonplacental clearance parameters have been previously described.[3] Pharmacokinetic modeling of the data, wherever necessary, was carried out using the nonlinear least-squares fitting program ADAPT II.[10]

Statistical Analysis—All values are reported as mean ± SD. All linear correlational analyses were performed by computing Pearson correlation coefficient (r). The significance level was $p < 0.05$ in all cases. Fetal weight *in utero* at the time of experimentation was estimated from the weight at birth and the time interval between the experiment and birth.[11]

Results

The average maternal body weight was 76.9 ± 12.6 kg, and the estimated fetal body weights on the day of maternal and fetal DPHM (or [$^2H_{10}$]DPHM) infusion were 2.61 ± 0.61 and 2.56 ± 0.54 kg, respectively.

The mean gestational age on the day of maternal and fetal steady-state DPHM infusion experiments was 130.9 ± 4.1 (range 124−140) and 130.4 ± 3.7 (range 125−136) days, respectively, and these were not statistically different (paired t-test, $p > 0.05$). Average washout period between maternal and fetal DPHM infusion experiments was 2.4 ± 2.2 d. Table 1 presents maternal and fetal steady-state plasma unbound fractions and steady-state total plasma concentrations of DPHM in 18 pregnant sheep. Maternal and fetal clearances (total body, placental and nonplacental clearances) of the drug in these 18 sheep calculated using the two-compartment pharmacokinetic model are presented in Table 2. The average maternal plasma unbound fraction (M-UF) was significantly lower compared to the average fetal plasma unbound fraction (F-UF, unpaired t-test, $p < 0.0001$). Maternal and fetal steady-state unbound plasma drug concentrations were calculated by multiplying the appropriate total plasma concentration

Table 2—Steady-State Maternal and Fetal DPHM Clearances in 18 Pregnant Sheep during Late Gestation

	clearance[a] (mL/min/kg)					
ewe	CL_{mm}[b]	CL_{mo}[c]	CL_{mf}[c]	CL_{ff}[c]	CL_{fo}[c]	CL_{fm}[c]
121	28.2	27.8	7.4	71.7	29.4	42.3
125	43.7	43.2	18.2	126.2	65.1	61.1
130	37.9	37.2	24.8	235.4	108.8	126.6
133	37.3	35.8	53.6	203.9	101.8	102.1
138	56.3	54.9	31.8	120.2	25.6	94.6
202	49.6	48.9	40.4	356.9	150.8	206.1
204	46.3	44.6	43.0	328.6	128.4	200.2
480	56.8	55.5	78.3	201.8	100.3	101.5
2101	36.8	36.1	25.2	312.6	138.2	174.3
122z	41.5	39.4	48.1	459.9	177.1	282.8
2177	39.0	37.3	54.6	396.3	106.6	289.7
2181	43.8	40.5	97.8	209.0	75.4	133.6
2241	30.7	29.7	26.1	243.4	51.6	191.8
4230	43.7	38.2	125.1	267.4	92.1	175.3
4227	31.9	30.6	31.2	145.5	53.9	91.5
2174	24.6	23.5	44.9	317.2	187.5	129.7
1225A	45.5	45.2	7.6	452.6	115.1	337.5
303Y	57.6	55.1	52.6	285.4	133.0	152.4
mean	41.7	40.2	45.0	263.0	102.3	160.7
SD	9.6	9.4	30.3	111.8	46.4	80.7

[a] CL_{mm}, Maternal total clearance; CL_{mf}, maternal placental clearance; CL_{mo}, maternal nonplacental clearance; CL_{ff}, fetal total clearance; CL_{fm}, fetal placental clearance; CL_{fo}, fetal nonplacental clearance. [b] Per kg maternal weight. [c] Per kg estimated fetal weight at the time of fetal experiment.

with the corresponding plasma unbound fraction. The average maternal and fetal steady-state unbound plasma drug concentrations after maternal administration (C^u_m and C^u_f, respectively) were 25.1 ± 11.4 (range 8.6−45.6) and 12.0 ± 8.6 (range 1.9−40.4) ng/mL, respectively; these same unbound concentrations after fetal drug infusion (C^u_m' and C^u_f', respectively) were 3.9 ± 1.8 (range 0.9−7.2) and 89.3 ± 32.0 (range 46.1−166.2) ng/mL, respectively.

All clearances, except CL_{mm} and CL_{mo}, are normalized to the estimated fetal body weight on the day of experiment; CL_{mm} and CL_{mo} are normalized to maternal body weight. Since CL_{mo} and CL_{mf} are normalized differently, their sum does not equal CL_{mm} in Table 2. All fetal clearances were significantly higher compared to the corresponding maternal clearance parameters (unpaired t-test, $p < 0.0001$ in all cases), as reported previously.[4−6] However, the contribution of CL_{fo} to CL_{ff} (39.5 ± 10.7%) was significantly lower compared to that of CL_{mo} to CL_{mm} (96.3 ± 2.8%) (unpaired t-test, $p < 0.0001$).

Inter-Relationships between Maternal and Fetal Plasma DPHM Concentrations, Unbound Fractions and the Two-Compartment Model Clearance Estimates—DPHM concentration in maternal plasma after maternal drug infusion (C_m) exhibited a highly significant negative linear relationship with M-UF of the drug (Figure 2A). In contrast, fetal plasma concentration after maternal infusion (C_f) was not related significantly to either maternal ($r = 0.1751$, $p = 0.5$) or fetal ($r = -0.3676$, $p > 0.1$) plasma unbound fraction (data not shown). Analogous to the maternal situation, DPHM concentration in the fetal plasma after fetal drug infusion (C_f') was inversely related to F-UF (Figure 2B). Also, maternal plasma DPHM concentration after fetal drug infusion (C_m') was not related to F-UF ($r = -0.0966$, $p > 0.5$; data not shown), whereas its negative relationship with M-UF was near statistical significance ($r = 0.4612$, $p = 0.05$, data not shown). The data in Figure 3 demonstrate the relationships between maternal and fetal total body clearances (CL_{mm} and CL_{ff}, respectively) and respective steady-state plasma unbound fractions of DPHM. CL_{ff} appears to be linearly related to F-UF whereas the relationship of CL_{mm} with M-UF is closer

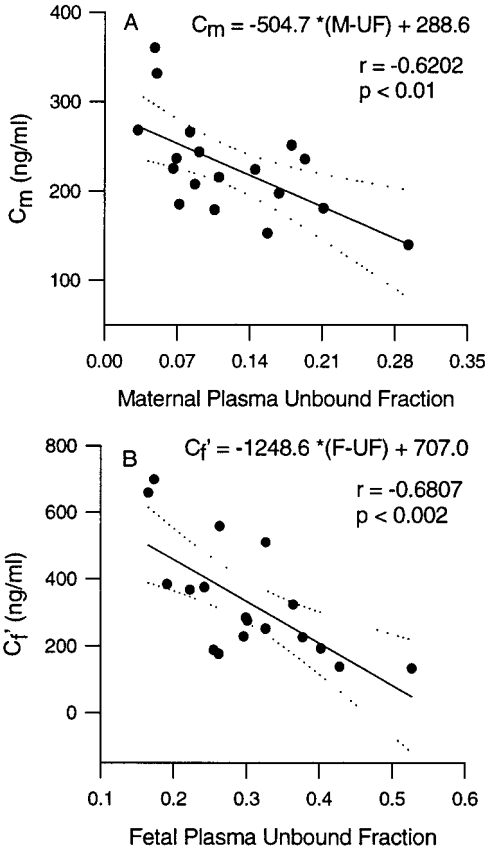

Figure 2—Relationships between (A) maternal unbound fraction and steady-state plasma concentration of the drug after maternal drug administration, and (B) fetal unbound fraction and steady-state plasma concentration of the drug after fetal drug administration. Scatter points are the experimental data in different sheep. The regression line (solid) and the 95% confidence interval (dotted) are also shown.

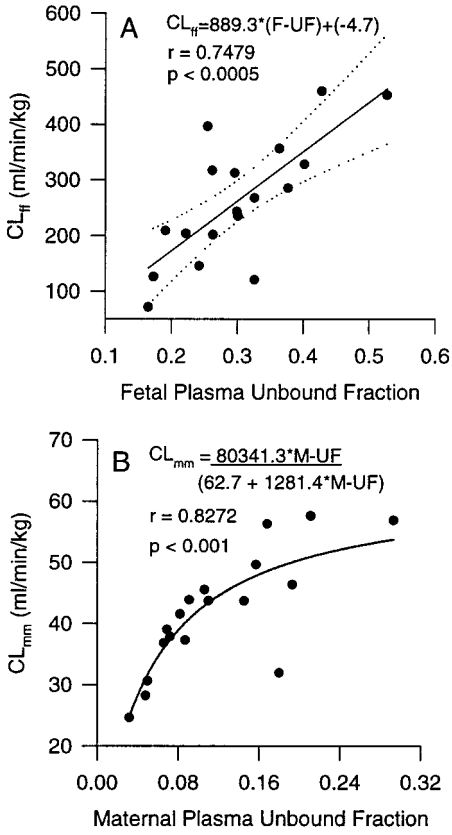

Figure 3—Relationships between fetal and maternal DPHM clearances and the corresponding plasma unbound fractions of the drug. (A) CL_{ff} vs F-UF; (B) CL_{mm} vs M-UF. The CL_{mm} vs M-UF relationship was analyzed according to the well-stirred model of organ clearance. M-UF: steady-state maternal plasma unbound fraction; F-UF: steady-state fetal plasma unbound fraction; CL_{mm}: maternal total body clearance; CL_{ff}: fetal total body clearance.

to a hyperbola. Hence, the data in Figure 3B were fitted with a well-stirred model of organ drug elimination.[12]

To determine the influence of various two-compartment clearance terms on maternal and fetal plasma DPHM concentrations after maternal or fetal drug administration, different concentration vs clearance relationships were analyzed according to the simple steady-state clearance model of the form: $CL = I_o/C_{ss}$. The majority of the interanimal variability in C_m was reflected in the estimated value of total CL_{mo} (not weight-normalized, because the total clearance is the actual determinant of plasma concentrations) as demonstrated by an excellent fit of the concentration vs clearance data to this model (Figure 4A). However, C_m was not significantly related to the other three clearance parameters of the two-compartment model (CL_{mf}, CL_{fo}, and CL_{fm}). Similarly, the majority of interanimal variability in C_f was reflected in the final estimates of CL_{mf} (Figure 4B). In contrast, when the drug was administered to the fetus, the interanimal variability in C_f' was due to relatively equal contributions from the magnitude of CL_{fo} and CL_{fm} (Figures 4C,D). Also, in contrast to the situation with C_f above (Figure 4B), the C_m' concentration was not related to the magnitude of CL_{fm} (Figure 4E). Instead the variation in C_m' among different animals was best explained by the differences in their maternal nonplacental clearance (Figure 4F).

Relationships between the Indices of Fetal Drug Exposure/Placental Transfer and Plasma Protein Binding—The average C_f/C_m ratio based on total plasma drug concentrations was 0.20 ± 0.14. The same ratio calculated using unbound drug concentrations was significantly higher (0.50 ± 0.30, paired *t*-test, $p < 0.0001$). Plasma total drug C_f/C_m ratio was not significantly correlated with maternal or fetal nonplacental clearance or F-UF; its positive relationship with M-UF was only near statistical significance ($r = 0.4029$, $p < 0.1$, data not shown). The mean C_m'/C_f' ratios during fetal drug administration based on total and unbound plasma drug concentrations were 0.14 ± 0.08 and 0.05 ± 0.02, respectively, the latter being significantly lower (paired *t*-test, $p < 0.0001$). In contrast to the C_f/C_m ratio above, the C_m'/C_f' ratio was positively correlated with total (not weight-normalized) CL_{fo} and CL_{fm} (Figures 5A,B), whereas its inverse relationship with total CL_{mo} was only near statistical significance ($r = -0.4138$, $p < 0.1$, data not shown). The C_m'/C_f' ratio also exhibited a highly significant positive relationship with F-UF (Figure 5C) but not with M-UF (data not shown).

Discussion

A number of variables such as the lipophilicity and plasma protein binding of the drug, placental blood flows (uterine and umbilical), the efficiency of maternal and fetal drug elimination/metabolism, and the gestational age of the fetus have been postulated to affect the degree of placental drug transfer and fetal drug exposure.[1,2,13] The influence of many of these variables on the kinetics of placental drug transfer and fetal drug exposure has not been extensively studied under controlled experimental conditions either in vitro or in vivo. Our objective in this study was to examine the role of different factors that determine plasma concentrations of DPHM in the mother and the fetus after maternal as well as fetal drug admin-

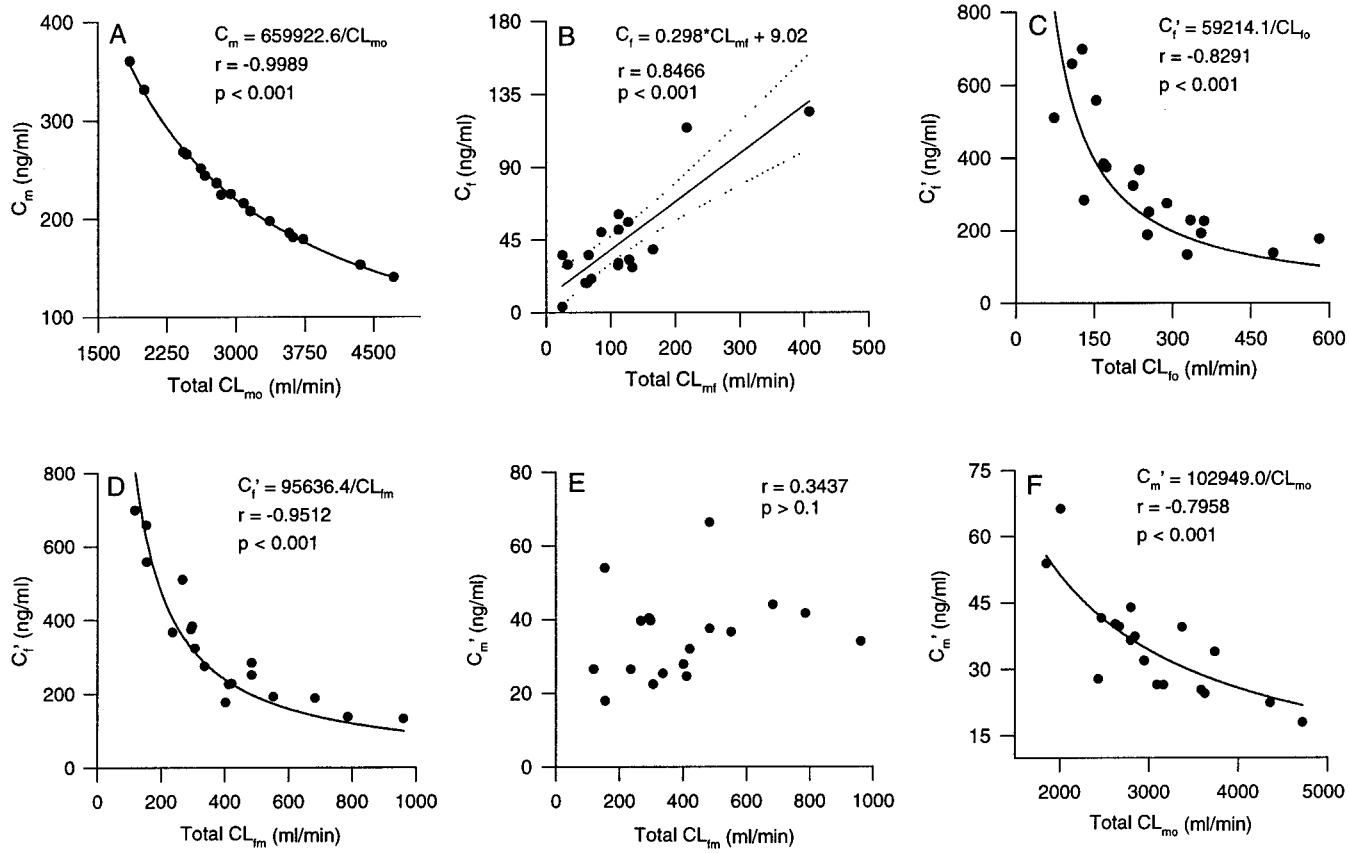

Figure 4—Influence of various clearance parameters of the two-compartment model on different maternal–fetal plasma concentrations. (A) CL_{mo} vs C_m; (B) CL_{mf} vs C_f; (C) CL_{fo} vs C_f'; (D) CL_{fm} vs C_f'; (E) CL_{fm} vs C_m'; and (F) CL_{mo} vs C_m'. All relationships except B and E were analyzed according to the steady-state clearance model, $CL = I_0/C_{ss}$; the solid lines represent the best-fit lines determined by this model. CL_{mo}: maternal nonplacental clearance; CL_{mf}: placental clearance from the mother to the fetus; CL_{fo}: fetal nonplacental clearance; CL_{fm}: placental clearance from the fetus to the mother; C_m': steady-state maternal plasma DPHM concentration after fetal infusion; C_f': steady-state fetal plasma DPHM concentration after fetal infusion.

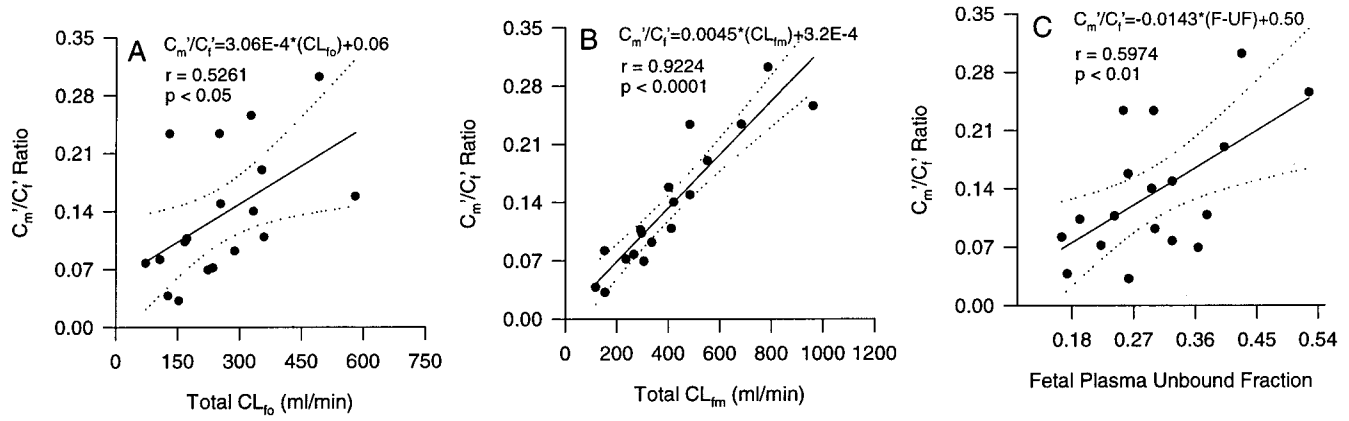

Figure 5—Relationships between the index of steady-state placental drug transfer after fetal administration (C_m'/C_f' ratio) and its determining factors. (A) C_f'/C_m' vs CL_{fo}; (B) C_f'/C_m' vs CL_{fm}; and (C) C_f'/C_m' vs F-UF. Scatter points are the experimental data in different sheep. The regression line (solid) and the 95% confidence interval (dotted) are also shown. CL_{fo}: fetal nonplacental clearance; CL_{fm}: placental clearance from the fetus to the mother; F-UF: steady-state fetal plasma unbound fraction; C_m': steady-state maternal plasma DPHM concentration after fetal infusion; C_f': steady-state fetal plasma DPHM concentration after fetal infusion.

istration in chronically instrumented pregnant sheep during late gestation. We have utilized DPHM as a model high-clearance drug that undergoes rapid and extensive placental transfer in pregnant sheep for assessing the importance of different variables The average CL_{mo} and CL_{fo} (40.2 and 102.3 mL/min/kg, respectively, Table 2) of DPHM are ~70% and 75% of the reported hepatic blood flow in pregnant sheep and late gestation fetal lambs, respectively (60 and 137 mL/min/kg, respectively).[19,20] Similarly, the average CL_{fm} of DPHM (160.7 mL/min/kg, Table 2) is ~80% of the umbilical blood flow estimates in sheep at this stage of gestation (200 mL/min/kg[21]), suggesting a high rate of DPHM placental transfer.

Inter-Relationships between Maternal and Fetal Plasma DPHM Concentrations, Unbound Fractions and the Two-Compartment Model Clearance Estimates—Although the two-compartment model is the simplest pharmacokinetic representation of the maternal–fetal unit, the exact relationships between the four clearance parameters of this model (CL_{mo}, CL_{mf}, CL_{fo}, and CL_{fm}) and various maternal–fetal plasma drug concentrations (C_m, C_f, C_f', C_m') are not directly obvious. Also, the influence of

maternal and fetal plasma drug protein binding in determining these concentrations is generally speculative and has rarely been determined experimentally. The data in Figure 2 indicate that maternal and fetal plasma protein binding is an important determinant of C_m and C_f', respectively, possibly because of its profound effects on respective clearance values (Figure 3). In contrast, C_f was not related to either M-UF or F-UF. When the drug is administered to the mother, it transfers across the placenta and enters the fetal circulation via the umbilical vein. A portion of the umbilical venous blood flow (~30−70%) passes through the fetal liver before reaching the fetal circulation. We have demonstrated earlier that after maternal dosing, a significant fraction of DPHM (~45%) transferred across the placenta and into the umbilical vein is metabolized by the fetal liver and does not reach the fetal circulation.[5] This phenomenon leads to a variable reduction in the "true" C_f and may underlie the lack of any relationship observed above.[5] Thus, for many drugs the major determinant of C_f after maternal drug administration may, in fact, be the extent of this fetal hepatic first-pass uptake/metabolism of the drug rather than maternal or fetal plasma protein binding or systemic clearance. This phenomenon also results in only a limited fetal exposure to DPHM after maternal administration (~20% compared to the mother) despite its high "near flow-limited" placental permeability. Analogous to C_f, the C_m' concentration bore no relationship with F-UF on the other side of the placenta. Instead its negative correlation with M-UF was near statistical significance, indicating that the latter could be a determinant of this concentration via its effects on maternal clearance of the drug (see below).

The estimated value of I_o from the fitting of plasma concentration vs clearance data to the $CL = I_o/C_{ss}$ relationship represents the rate of drug elimination via that clearance route. The data in Figure 4A indicate that CL_{mo} is the major determinant of C_m. This should generally be true for most high clearance drugs because the absolute magnitude of CL_{mo} will be much higher compared to any other clearance parameter (for DPHM, $CL_{mo} = 3058.5 \pm 745.5$ mL/min; $CL_{mf} = 114.5 \pm 88.6$ mL/min; $CL_{fo} = 257.5 \pm 135.0$ mL/min; $CL_{fm} = 408.5 \pm 225.1$ mL/min). The estimated value of the I_o coefficient (659.9 μg/min) relative to the total maternal drug infusion rate (670 μg/min) indicates that ~98% of the drug infused to the mother is eliminated via maternal nonplacental routes. Despite a variable underestimation of C_f, a large amount of variability in the measured C_f was carried over to the CL_{mf} parameter, indicating that this clearance parameter is also almost equally underestimated (Figure 4B). After fetal drug infusion, both CL_{fo} and CL_{fm} appear to be important determinants of C_f' (in contrast to the mother where only CL_{mo} is important, see above). The I_o coefficients of C_f' vs CL_{fo} and C_f' vs CL_{fm} relationships were 59.2 and 95.6 μg/min, respectively, which when added together approach the total fetal drug infusion rate of 170 μg/min. In contrast to the C_f vs CL_{mf} relationship (Figure 4B), the variability in C_m' was not related to the magnitude of estimated CL_{fm} (Figure 4E). This is understandable because, as discussed above, the major determinant of maternal plasma concentrations is expected to be CL_{mo}. Based on this, CL_{mo} does in fact appear to explain the variation in C_m' among different animals (Figure 4F).

Relationships between the Indices of Fetal Drug Exposure/Placental Transfer and Plasma Protein Binding—After maternal drug administration, the steady-state fetal-to-maternal arterial plasma concentration ratio (C_f/C_m) is commonly used as an index of the efficiency of placental drug transfer and fetal exposure to the drug.[1] Different total vs unbound C_f/C_m ratios indicate that the magnitude of total drug C_f/C_m ratio is partly determined by the differences in maternal and fetal plasma protein binding. It has been postulated that fetal plasma protein binding and total fetal clearance are important factors determining the steady-state C_f/C_m ratio and $C_f/C_m = CL_{mf}/[CL_{fm} + CL_{fo}]$.[1−3] However, in our experiments, the total drug C_f/C_m ratio neither exhibited any significant relationship with CL_{fm}, CL_{fo} or CL_{ff} ($CL_{fm} + CL_{fo}$), nor with F-UF. The positive relationship of C_f/C_m with M-UF approached statistical significance despite the errors in C_f, and this was mainly because of a highly significant negative correlation between C_m and M-UF (Figure 2A). The lack of expected relationships among the above variables may also be related to the errors in the measurement of "true C_f" due to fetal first-pass hepatic uptake of the drug present in the umbilical venous blood.[5]

To overcome this problem, we evaluated the factors affecting the analogous index of placental transfer after fetal drug administration, i.e., the C_m'/C_f' ratio. On similar lines to the C_f/C_m ratio above, it can be hypothesized that CL_{fm}, CL_{mo}, and CL_{mf} will be the important factors determining the C_m'/C_f' ratio, i.e., $C_m'/C_f' = CL_{fm}/(CL_{mo} + CL_{mf})$. However, the C_m'/C_f' ratio did not show any relationship with CL_{mf} (again this could be due to errors in CL_{mf} estimates), and its inverse relationship with CL_{mo} (as well as CL_{mm}) was only near statistical significance. Thus, CL_{mo} (and CL_{mm}) does not appear to be an important determinant of the C_m'/C_f' ratio. Total CL_{fo}, total CL_{fm} and F-UF are the important variables determining C_f' (Figures 4C,D and 2B). An increase in any of these variables leads to a fall in C_f' (Figures 4C,D and 2B) and hence to a significant increase in the C_m'/C_f' ratio (Figures 5A−C), C_m' being unaffected by any of these factors. In contrast, the C_m'/C_f' ratio was not significantly related to M-UF. Thus, in this situation, CL_{fo}, CL_{fm}, and F-UF appear to be the most important factors determining the C_m'/C_f' ratio, mainly via their effects on C_f'.

The two-compartment model of the maternal−fetal unit involves both maternal and fetal drug elimination (Figure 1). This system never reaches a state of "true" equilibrium (no net transfer of drug across the placenta) after maternal or fetal drug administration. It, however, does reach a steady-state where the rate of placental drug transfer becomes equal to the rate of drug elimination from the other side. For example, after maternal dosing, fetal drug elimination creates and maintains a maternal-to-fetal gradient of (unbound) drug concentrations, thus leading to a continuous passage of the drug from the mother to the fetus at steady-state. Similarly, during fetal dosing, maternal drug elimination creates a fetal-to-maternal (unbound) drug concentration gradient and leads to continuous passage of the drug from the fetus to the mother. The driving force for placental transfer is this difference in unbound drug concentrations across the placenta. For compounds such as DPHM that are rapidly diffusible across the placenta and whose placental transfer is not limited by low placental permeability, the maternal and fetal unbound concentrations at the site of placental exchange should fully equilibrate with each other and the rate of placental drug transfer should be directly related to the magnitude of unbound concentration gradient and variables affecting this gradient. However, from a number of observations, it appears that at least for fetal-to-maternal placental drug transfer, the factors operating on the opposite side of the placenta have minimal, if any, effect on the kinetics of DPHM placental transport. These observations include (i) the C_m'/C_f' ratio is not affected by CL_{mo} and M-UF, and (ii) the C_m' concentration is not at all influenced by F-UF or CL_{fm}. This is in contrast to the above "unbound drug equilibrium" hypothesis of placental trans-

port where these variables are considered the predominant factors affecting passage of the drug across the placenta. Because of errors in the measurement of C_f, it is not entirely clear if the same phenomenon occurs in the maternal-to-fetal direction of DPHM placental transfer. The presence of this phenomenon in at least the fetal-to-maternal direction may indicate that the unbound concentrations of the drug on both sides of the placenta may not be in complete equilibrium with each other at the site of placental exchange, as is generally assumed. The steady-state concentrations of a number of highly diffusible markers, which are not plasma protein bound and have blood flow limited clearance (e.g., antipyrine, ethanol, D_2O), do not equilibrate completely between the maternal and fetal placental outflow vessels (uterine and umbilical veins, respectively) in the sheep and cow.[14−16] This has generally been attributed to the inefficiencies that exist within the placental vasculature such as partial shunting of the uterine and umbilical blood flows to nonexchange areas of the placenta and to nonplacental tissues, and unequal maternal−fetal perfusion in different regions of the placenta.[15−17] However, the fact that DPHM placental transport is tightly coupled to many variables operating only on one side of the placenta and to none on the other strongly suggests that the assumption of a complete equilibrium between the unbound drug concentrations on the two sides of placenta may not be entirely accurate. The possibility of this phenomenon can be realized by considering the anatomical structure of the epitheliochorial sheep placenta, which has a number of tissue layers separating maternal and fetal blood flows. Also, the available evidence on the geometrical arrangement of maternal and fetal placental blood flows at the placental exchange site suggests a relatively less efficient concurrent (sheep and cow) and pool flow (human) arrangement in many species.[15−17] These factors along with a rapid transit time of the blood through the placental circulation may lead to incomplete equilibration of the unbound drug concentrations in maternal and fetal blood at the placental exchange site even for compounds with very high placental permeability.[18] It remains to be determined if a similar phenomenon exists during drug passage through the hemochorial human placenta which has fewer anatomical tissue layers compared to sheep.

In summary, the major determinant of plasma DPHM concentrations in the mother after maternal as well as fetal administration is maternal plasma protein binding and maternal nonplacental clearance. In contrast, the major determinant of fetal plasma DPHM concentrations after maternal drug administration appears to be the extent of fetal first-pass hepatic drug uptake from the umbilical vein. After fetal drug administration, the fetal plasma concentrations are related to the extent of fetal plasma protein binding and fetal placental and nonplacental clearances. The index of fetal-to-maternal placental drug transfer after fetal administration (steady-state C_m'/C_f' ratio) is related to steady-state fetal plasma unbound fraction and fetal placental and nonplacental clearance. However, this index was not related to the magnitude of the factors operating on the maternal side of the placenta such as maternal plasma protein binding and maternal nonplacental clearance. This might indicate a lack of complete equilibration of the unbound drug concentrations on the two sides of the placenta at the exchange site.

References and Notes

1. Reynolds, F.; Knott, C. Pharmacokinetics in pregnancy and placental drug transfer. In *Oxford Reviews of Reproductive Biology*; Milligan, S. R., Ed.; Oxford University Press: New York, 1989; pp 389−449.
2. Rurak, D. W.; Wright, M. R.; Axelson, J. E. Drug disposition and effects in the fetus. *J. Dev. Physiol.* **1991**, *15*, 33−44.
3. Szeto, H. H.; Umans, J. G.; Rubinow, S. I. The contribution of trans-placental clearances and fetal clearance to drug disposition in the ovine maternal-fetal unit. *Drug. Metab. Disp.* **1982**, *10*, 382−386.
4. Yoo, S. D.; Rurak, D. W.; Taylor, S. M.; Axelson, J. E. Transplacental and nonplacental clearances of diphenhydramine in the chronically instrumented pregnant sheep. *J. Pharm. Sci.* **1993**, *82*, 145−149.
5. Kumar, S.; Tonn, G. R.; Kwan, E.; Hall, C.; Riggs, K. W.; Axelson, J. E.; Rurak, D. W. Estimation of transplacental and nonplacental diphenhydramine clearances in the fetal lamb: the impact of fetal first-pass hepatic drug uptake. *J. Phamacol. Exp. Ther.* **1997**, *282*, 617−632.
6. Kumar, S.; Riggs, K. W.; Rurak, D. W. Comparative formation, distribution and elimination kinetics of diphenylmethoxyacetic acid (a diphenhydramine metabolite) in maternal and fetal sheep. *Drug Metab. Disp.* **1999**, *27*, 463−470.
7. Rurak, D. W.; Yoo, S. D.; Kwan, E.; Taylor, S. M.; Riggs, K. W.; Axelson, J. E. Effects of diphenhydramine in the fetal lamb after maternal or fetal administration. *J. Pharmacol. Exp. Ther.* **1988**, *247*, 271−278.
8. Yoo, S. D.; Axelson, J. E.; Rurak, D. W. Determination of diphenhydramine in biological fluids by capillary gas chromatography using nitrogen−phosphorus detection. *J. Chromatogr.* (*Biomed. Appl.*). **1986**, *378*, 385−393.
9. Tonn, G. R.; Mutlib, A.; Abbott, F. S.; Rurak, D. W.; Axelson, J. E. Simultaneous Analysis of diphenhydramine and a stable isotope analogue ($^2H_{10}$) diphenhydramine using capillary gas chromatography with mass selective detection in biological fluids from chronically instrumented pregnant ewes. *Biol. Mass Spectrom.* **1993**, *22*, 633−642.
10. D′Argenio, D. Z.; Schumitzky, A. ADAPT II User's Guide: Pharmacokinetic/Pharmacodynamic Systems Analysis Software. Biomedical Simulations Resource, Los Angeles, CA, 1997.
11. Koong, L. J.; Garrett, W. N.; Rattray, P. V. A description of the dynamics of fetal growth in sheep. *J. Anim. Sci.* **1975**, *41*, 1065−1068.
12. Wilkinson, G. R.; Shand, D. G. A physiologic approach to hepatic drug clearance. *Clin. Pharmacol. Ther.* **1975**, *18*, 377−390.
13. Hill, M. D.; Abramson, F. P. The significance of plasma protein binding on the fetal/maternal distribution of drugs at steady-state. *Clin. Pharmacokin.* **1988**, *14*, 156−170.
14. Meschia, G.; Battaglia, F. C.; Bruns, P. D. Theoretical and experimental study of transplacental diffusion. *J. Appl. Physiol.* **1967**, *22*, 1171−1178.
15. Wilkening, R. B.; Anderson, S.; Martensson, L.; Meschia, G. Placental transfer as a function of uterine blood flow. *Am. J. Physiol.* **1982**, *242*, H429−H436.
16. Reynolds, L. P.; Ferrel, C. L.; Ford, S. P. Transplacental diffusion and blood flow of gravid bovine uterus. *Am. J. Physiol.* **1985**, *249*, R539−R543.
17. Bassily, M.; Ghabrial, H.; Smallwood, R. A.; Morgan, D. J. Determinants of placental drug transfer: studies in isolated perfused human placenta. *J. Pharm. Sci.* **1995**, *84*, 1054−1060.
18. Power, G. G.; Longo, L. D. Fetal circulation times and their implications for tissue oxygenation. *Gynecol. Invest.* **1975**, *6*, 342−355.
19. Katz, M. L.; Bergman, E. N. Simultaneous measurements of hepatic and portal venous blood flow in the sheep and dog. *Am. J. Physiol.* **1969**, *216*, 946−952.
20. Edelstone, D. I.; Rudolph, A. M.; Heymann, M. A. Liver and ductus venosus blood flows in the fetal lamb in utero. *Circ. Res.* **1978**, *42*, 426−433.
21. Hedriana, H. L.; Brace, R. A.; Gilbert, W. M. Changes in blood flow to the ovine chorion and amnion across gestation. *J. Soc. Gynecol. Invest.* **1995**, *2*, 727−734.

Acknowledgments

These studies were supported by funding from the Medical Research Council of Canada. S.K. was the supported by a University of British Columbia Graduate Fellowship. D.W.R. is the recipient of an investigatorship award from the British Columbia Children's Hospital Foundation.

JS990244L

Cocaine and Alcohol Interactions in the Rat: Effect of Cocaine and Alcohol Pretreatments on Cocaine Pharmacokinetics and Pharmacodynamics

WEI-JIAN PAN*,† AND MOHSEN A. HEDAYA‡

Contribution from *Pharmacology/Toxicology Graduate Program, Department of Pharmaceutical Sciences, College of Pharmacy, Washington State University, Pullman, Washington 99164-6510.*

Received June 9, 1999. Final revised manuscript received August 23, 1999.
Accepted for publication September 16, 1999.

Abstract □ This experiment was designed to investigate the effect of pretreatment with cocaine and alcohol on cocaine pharmacokinetics and pharmacodynamics. Four groups of rats ($n = 8$ per group) received one of the following pretreatments for two weeks: none, alcohol (10% v/v in drinking water), cocaine (15 mg/kg/day ip), and alcohol+cocaine (10% v/v in drinking water+15 mg/kg/day ip). On the day of the experiment, cocaine was administered (30 mg/kg, ip) to each rat, either alone or in combination with alcohol (5 g/kg, po), in a balanced crossover experimental design. Plasma and brain ECF concentrations of cocaine and its three metabolites: benzoylecgonine, norcocaine, and cocaethylene were assayed by HPLC–UV. The percent change in brain dopamine concentration, mean arterial blood pressure, and heart rate were determined simultaneously. A sigmoid-E_{max} model was used to describe the brain cocaine concentration–neurochemical effect (dopamine) relationship, and an indirect pharmacodynamic response model was used to describe the plasma cocaine concentration–cardiovascular effect relationships. Alcohol pretreatment led to significant increase in cocaine AUC_p, $\alpha_{t1/2}$, and $\beta_{t1/2}$. Cocaine pretreatment significantly increased cocaine bioavailability, absorption rate constant, TBC, and the formation clearance of cocaethylene. Acute alcohol coadministration with cocaine increased cocaine AUC_p and bioavailability, reduced the fraction of cocaine dose converted to benzoylecgonine, and increased the formation of norcocaine. These results indicate that the pharmacokinetics of cocaine, either administered alone or in combination with alcohol, is significantly altered due to prior cocaine and/or alcohol use. Both cocaine and alcohol pretreatments increased the E_{max} for dopamine, with no effect on the EC_{50}. Acute alcohol coadministration with cocaine significantly increased the E_{max} for dopamine and reduced the EC_{50}. Cocaine pretreatment significantly decreased the I_{max} for blood pressure, IC_{50}, and R_{max}. For the heart rate response, both alcohol and cocaine pretreatments significantly increased the IC_{50}, with no effect on I_{max}. These results indicate that both cocaine and alcohol pretreatments as well as acute alcohol coadministration lead to significant alterations in cocaine pharmacodynamics that are due, at least in part, to the changes in cocaine pharmacokinetics. If similar effects occur in humans, chronic cocaine and alcohol abusers may respond differently to cocaine administration compared to naïve users and may be at higher risks of cocaine central nervous system toxicity.

Introduction

Concomitant cocaine and alcohol abuse has been associated with increased incidence of cocaine-related morbidity and mortality.[1] Studies in humans showed that alcohol consumption with cocaine led to significantly higher plasma cocaine and norcocaine concentrations and the formation of the pharmacologically active metabolite cocaethylene, whereas the concentrations of benzoylecgonine and ecgonine methyl ester were reduced.[2] In animal experiments, alcohol coadministration increased the plasma and brain cocaine concentrations and modified cocaine metabolic profile similar to what was observed in humans.[3,4] Results obtained from awake rats demonstrated that the changes in the neurochemical and cardiovascular responses to cocaine when administered with alcohol can be explained, at least partially, by the changes in cocaine pharmacokinetics and the contribution of cocaine metabolites to the pharmacological effects of cocaine.[5,6] These findings clearly indicate that factors that can alter cocaine pharmacokinetics and metabolic profile can lead to changes in the neurochemical and cardiovascular responses to cocaine administration.

Prior exposure to cocaine and alcohol has also been shown to alter cocaine pharmacokinetics, pharmacodynamics, and toxicities. We have reported previously that pretreating Wistar rats with 10% alcohol in drinking water for two weeks significantly slows the elimination rate of both cocaine and cocaethylene.[3] Several studies have demonstrated that 2−3 weeks of alcohol consumption enhances striatal [^{3}H]dopamine release and D_2 receptor binding in both the nucleus accumbens (N ACC) and striatum.[7−9] A human study has shown that alcohol pretreatment increases the preference for cocaine over monetary reinforcement, and that combined cocaine and alcohol abuse increases the risk of cardiac toxicity compared to cocaine alone.[10] In male mice, alcohol pretreatment in liquid diet for 5 days potentiates cocaine-induced hepatotoxicity, an effect dependent on the induction of the hepatic cytochrome P-450 mixed function oxidases.[11] Similar effects have also been observed in humans.[12] Cocaine absorption from the abdominal cavity to the systemic circulation after ip administration to rats is significantly faster after repeated cocaine administration.[13] Intermittent cocaine pretreatment for 1−9 days to laboratory animals augments brain extracellular fluid (ECF) dopamine, including that of the N ACC, which leads to enhancement of locomotor activity and stereotypy (i.e., sensitization).[14−16] In vitro studies in rodents have shown that cocaine pretreatment markedly induces cytochrome P-450 enzymes that are responsible for norcocaine formation.[17,18] Results from these investigations indicate that cocaine pharmacokinetics in individuals who have used cocaine and/or alcohol previously may be different from that in naïve users. This implies that alcoholics and cocaine addicts may respond differently to cocaine administration, and this may have significant clinical implications.

* Corresponding author. Phone: (847)-935-5335. Fax: (847)-938-5193. E-mail: weijian.pan@abbott.com.
† Current address: Department of Clinical Pharmacokinetics and Toxicokinetics, Abbott Laboratories, Abbott Park, IL 60064-6104.
‡ Current address: College of Pharmacy, Tanta University, Tanta, Egypt.

10.1021/js990184j CCC: $18.00
Published on Web 10/21/1999

The primary objective of this study was to investigate the effect of alcohol, cocaine, and combined alcohol and cocaine pretreatments on the pharmacokinetic and pharmacodynamic interactions between cocaine and alcohol. This was achieved by studying cocaine absorption, brain distribution, elimination, and metabolism when cocaine was given alone and in combination with alcohol to rats that were pretreated with alcohol, cocaine, or cocaine+ alcohol. The neurochemical and cardiovascular responses to cocaine administration were monitored simultaneously during the pharmacokinetic studies. The neurochemical response was assessed by determining the changes in brain N ACC dopamine level, while the cardiovascular responses were monitored by measuring the changes in the mean arterial blood pressure and heart rate. The information obtained from this study can help to identify and predict pharmacokinetic factors that may lead to increased risks of toxicity with combined cocaine and alcohol abuse. This is the first report to investigate the effect of pretreatment with cocaine and alcohol on cocaine pharmacokinetics and pharmacodynamics. The possible interactions among these pretreatments and acute alcohol coadministration were also examined.

Materials and Methods

Chemicals and Reagents—Cocaine hydrochloride and cocaethylene hydrochloride were purchased from Research Biochemicals International (Natick, MA). Bupivacaine and sodium fluoride were obtained from Sigma Chemical (St. Louis, MO). Chloroform was supplied by Burdick and Jackson Laboratory (Muskegon, MI). The dehydrated 200 proof ethyl alcohol (USP) was purchased from McCormick Distilling (Weston, MO). All solvents were of high performance liquid chromatographic (HPLC) grade, and all chemicals were of analytical reagent (AR) grade.

Cocaine and Alcohol Pretreatments—Male Wistar rats (250−350 g, Simonsen Laboratories, Gilroy, CA) were maintained one per cage on a 12-h light/dark cycle with Purina chow pellets and water ad libitum for 7 days before use in the experiments. Water and food consumption and body weight were recorded daily. Thirty-two rats were assigned randomly to one of the following four pretreatment groups (n = 8 rats per group): control (no pretreatment), alcohol pretreatment, cocaine pretreatment, and combined cocaine and alcohol pretreatment. For the alcohol pretreatment group, the rats were allowed free access to 10% alcohol in water (v/v) as their sole source of drinking water. Cocaine pretreatment was accomplished by injecting the rats with 15 mg/kg cocaine ip once daily for 14 days, and the rats were allowed free access to drinking water. In the combined cocaine and alcohol pretreatment group, the rats were allowed free access to 10% alcohol in water (v/v) as their sole source of drinking water and were injected with 15 mg/kg cocaine ip once daily for 14 days. During the entire two weeks of pretreatments, the rats in all groups were maintained one per cage on a 12-h light/dark cycle with Purina chow pellets ad libitum. Water and food consumption and rat body weight were recorded daily. The pretreatment duration (14-day) and the daily doses of cocaine (15 mg/kg/day, ip) and alcohol (~3 g/kg/day, po) for the pretreatments were chosen based on the results of previous studies.[3,9,13−15,19]

Animal Care and Preparation—All animal preparation procedures were in accordance with the *Guide for the Care and Use of Laboratory Animals* (National Institutes of Health Publication No. 85-23, revised 1985) and were approved by the institutional animal care and use committee at Washington State University. Details of the animal preparation procedures were described previously.[20] Briefly, after 7 days of pretreatment, the brain microdialysis guide cannula was implanted in the rat brain followed, 7 days later, by femoral vein and artery cannulation, and abdominal and gastric catheter implantation. The brain microdialysis probe was inserted into the guide cannula to replace the dummy probe, and the targeted area was the N ACC. The rats from each of the four pretreatment groups were given 30 mg/kg ip cocaine alone and in combination with 5 g/kg alcohol in a crossover experimental design with 48-h washout period between treatments.

Pharmacokinetic and Pharmacodynamic Studies—On the day of the experiment, one of the femoral artery cannulae was connected to a pressure transducer linked to a blood pressure analyzer (Digi-Med Model 190, Micro-Med, Louisville, KY) for monitoring the mean arterial blood pressure and heart rate. The signals from the analyzer were collected, updated, and averaged every one minute by a system integrator (Digi-Med Model 200, Micro-Med, Louisville, KY) and were stored in a computer for subsequent analysis. Meanwhile, the brain microdialysis effluent was collected every 20 min (at 1 μL/min) into HPLC autosampler vials containing 20 μL of dopamine mobile phase and vortex-mixed. Five microliters of this mixture was injected immediately into an HPLC equipped with an electrochemical (EC) detector for dopamine analysis. Once a stable dopamine baseline was achieved, the rats were treated with either 10 g/kg normal saline or 5 g/kg alcohol (50% v/v in normal saline) through the gastric catheter. Twenty minutes later, 30 mg/kg of cocaine was administered through the abdominal catheter. After drug administration, 10 blood samples, each of 0.2 mL were collected through the femoral artery cannula at 2, 5, 10, 15, 30, 60, 90, 120, 180, 240 min in heparin and sodium fluoride pretreated vacutainers to avoid cocaine and cocaethylene hydrolysis by plasma carboxylesterases. Plasma samples were obtained by centrifugation and were stored at −20 °C until analyzed for cocaine and its metabolites by HPLC with ultraviolet (UV) detection. The effluent of the microdialysis probe was continuously collected every 20 min throughout the experiment into HPLC autosampler vials containing 20 μL of dopamine mobile phase (pH 4). The purpose of this treatment was to maintain dopamine, cocaine, and its metabolites under acidic condition to reduce their spontaneous oxidation and hydrolysis. After mixing the vial content, 5 μL was injected immediately into the HPLC-EC system for dopamine analysis, and the rest was analyzed for cocaine and its metabolites by HPLC−UV. The mean arterial blood pressure and the heart rate were continuously monitored during the entire experiment.

After the above two treatments, the rats from each of the four pretreatment groups received cocaine iv (6.8 mg/kg) and cocaethylene iv (3.9 mg/kg) through the femoral vein cannula with a 24-h washout period between the treatments. The purpose of the iv cocaine administration was to determine the systemic bioavailability for ip cocaine. The pharmacokinetic parameters for cocaethylene obtained after iv administration in this study and those for benzoylecgonine and norcocaine obtained from one of our previous studies were used to determine the effect of alcohol on cocaine metabolic profile.[6] This was accomplished by comparing the fraction of cocaine dose converted to each of the metabolites when ip cocaine was administered either alone or in combination with alcohol, in each of the pretreatment groups.

Analytical Methods—*Cocaine and Its Metabolites*—Plasma and microdialysis probe effluent were analyzed for cocaine and its metabolites using the method developed in our laboratory.[21] The actual concentrations of cocaine and its metabolites in the brain ECF were determined from the probe effluent concentration after correcting for the probe recovery which was determined from an in vitro calibration experiment.[22]

Dopamine—The microdialysis probe effluent was injected directly into an HPLC system equipped with EC detector for dopamine analysis immediately after collection. Details of the analytical procedures used for dopamine determination in the microdialysis probe effluent were described previously.[20]

Pharmacokinetic Analysis—A two-compartment pharmacokinetic model with elimination from the central compartment was used to investigate the effect of acute alcohol coadministration, and alcohol or cocaine pretreatment on cocaine absorption, distribution, and elimination after ip cocaine administration. Cocaine pharmacokinetic parameters were estimated by fitting cocaine plasma and brain ECF concentrations to the two equations that describe cocaine concentration−time profile in plasma and in the brain ECF simultaneously utilizing PCNONLIN 4.0 (SCI Software, Lexington, KY).[5,6] The bioavailability of cocaine after ip administration was calculated from the corresponding areas under the plasma concentration−time curves (AUC_p) after ip and iv cocaine administrations to each rat. The fraction of the ip cocaine dose converted to each of the metabolites was calculated as described previously.[6]

Pharmacodynamic Analysis—The sigmoid-E_{max} pharmacodynamic model was used to describe the brain ECF cocaine concentration−neurochemical response relationship. The phar-

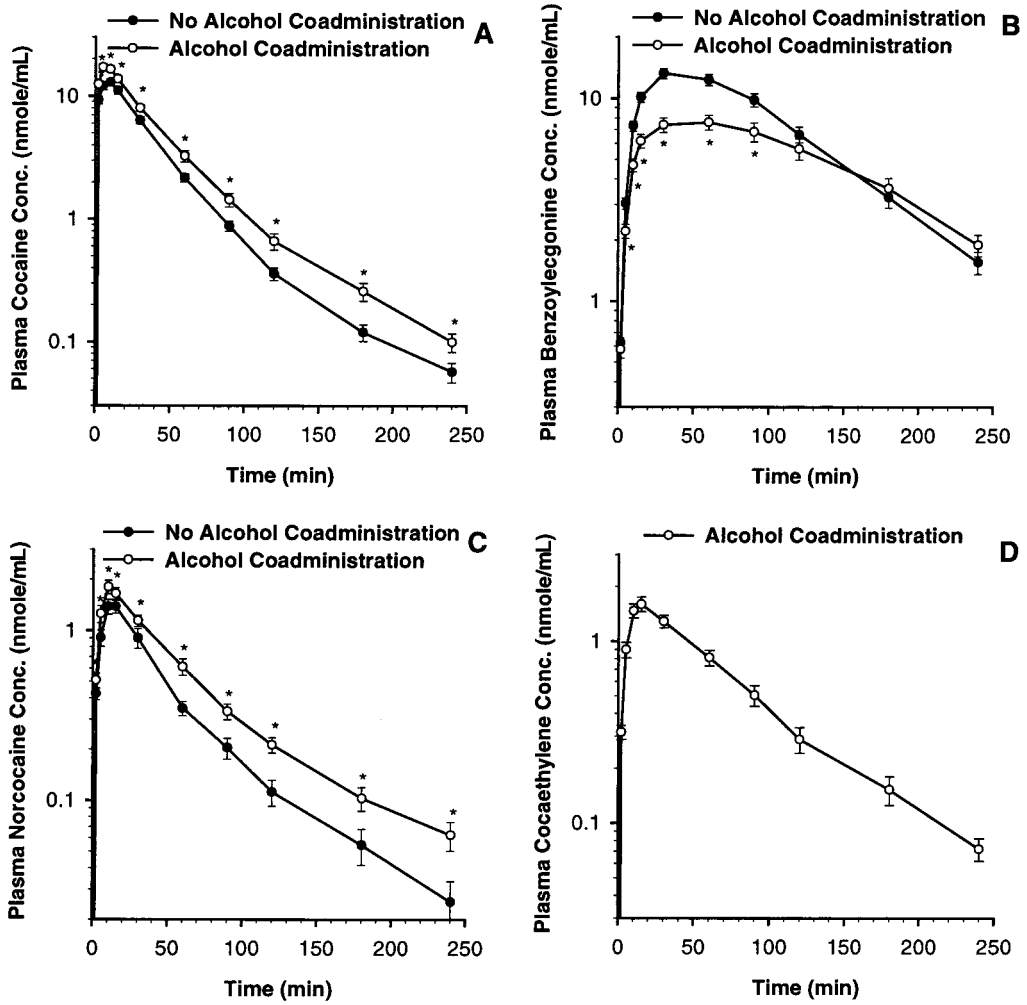

Figure 1—Plasma concentration–time profiles of cocaine (A), benzoylecgonine (B), norcocaine (C), and cocaethylene (D) after 30 mg/kg ip cocaine challenge to rats that were not (●) and were (○) coadministered with 5 g/kg acute alcohol. Each data point is presented as mean ± SE ($n = 32$). *Significantly different from that of no alcohol coadministration ($p < 0.05$).

macodynamic model parameters were estimated by fitting the percent change in dopamine brain ECF concentration and the cocaine brain ECF concentration to the model equation utilizing PCNONLIN. The relationship between plasma cocaine concentration and the change in mean arterial blood pressure and heart rate after ip cocaine administration was characterized by an indirect mechanism-based pharmacodynamic response model.[5,23] The mathematical expression that describes the relationship between the change in the pharmacological response and the drug concentration is:

$$\frac{dR}{dt} = k_{in} - k_{out}\left(1 - \frac{I_{max}C_p^n}{IC_{50}^n + C_p^n}\right)R \qquad (1)$$

where R is the observed response (percent change in mean arterial blood pressure or heart rate), k_{in} is the apparent zero-order rate constant for response production, k_{out} is the first-order rate constant for response dissipation, I_{max} is the maximum inhibition of the factor that produces the effect, IC_{50} is the plasma cocaine concentration that leads to 50% inhibition of the factor that produces the effect, C_p is the plasma cocaine concentration at the time of the observed response, and n is the sigmoidicity factor.[5,6] The maximum response that will be achieved as the ip dose is very high or IC_{50} approaches zero is:

$$R_{max} = \frac{R_0}{1 - I_{max}} \qquad (2)$$

where R_{max} is the maximum response and R_0 is the basal response (100%).

The indirect pharmacodynamic model parameters were estimated by fitting the percent change in mean arterial blood pressure or heart rate and the plasma cocaine concentration at different time points to eq 1. Nonlinear regression analysis was performed using PCNONLIN as detailed previously.[5,6]

Statistical Analysis—In this study, the control, alcohol, cocaine, and cocaine+alcohol pretreatments, together with ip cocaine administration (with and without acute alcohol coadministration), represented a four-way factorial experiment ($2 \times 2 \times 2 \times 2$) with repeated measures on the acute alcohol treatment factor. This experimental design allowed studying the effect of pretreatment with alcohol and cocaine and the effect of acute alcohol coadministration on the pharmacokinetics and pharmacodynamics of cocaine. The subgroup differences were partitioned within the analysis of variance (ANOVA) structure when examining the effect of one of the three main factors. The significance of the interaction between the two pretreatment factors (cocaine+alcohol pretreatment) and their interaction with acute alcohol coadministration factor could also be determined with the analysis of variance. Note that testing interaction effects is equivalent to testing whether there is synergism between the two treatments. Because no measurement for heart rate was made for the control (i.e., naïve) group, the analysis of variance for this response was conducted assuming no interactions between treatment factors. The statistical analyses of the estimated pharmacokinetic and pharmacodynamic parameters of cocaine and its metabolites were performed using the Statistical Analysis System Release 6.12 (SAS Institute Inc., Cary, NC). Multiple comparisons with Bonferroni correction were conducted to examine the selected statistical differences between treatments. A difference of $p < 0.05$ was considered statistically significant.

Table 1—Pharmacokinetic Parameters of Cocaine and Its Metabolites in the Rat Either with or without Alcohol or Cocaine Pretreatments or Acute Alcohol Coadministration (mean ± SE, $n = 32$)

pharmacokinetic parameter	alcohol pretreatment		cocaine pretreatment		alcohol coadministration	
	no	yes	no	yes	no	yes
			Cocaine			
AUC_p (nmol·min/mL)	528 ± 36	639 ± 39[a]	594 ± 46	573 ± 30	490 ± 29	677 ± 40[c]
AUC_b (nmol·min/mL)	605 ± 67	768 ± 62	751 ± 79	622 ± 47	634 ± 63	736 ± 68
AUC_b/AUC_p	1.152 ± 0.087	1.31 ± 0.11	1.36 ± 0.13	1.102 ± 0.060	1.325 ± 0.099	1.13 ± 0.10[c]
TBC (mL/min/kg)	125.0 ± 5.4	112.6 ± 5.0	107.7 ± 3.7	129.9 ± 6.0[b]	121.9 ± 5.4	115.6 ± 5.3
F	0.719 ± 0.043	0.762 ± 0.037	0.669 ± 0.035	0.812 ± 0.041[b]	0.65 ± 0.04	0.832 ± 0.033[c]
k_a (min^{-1})	0.361 ± 0.035	0.419 ± 0.039	0.306 ± 0.031	0.474 ± 0.037[b]	0.401 ± 0.042	0.378 ± 0.032
$\alpha_{t1/2}$ (min)	11.45 ± 0.88	16.45 ± 0.89[a]	13.5 ± 1.1	14.39 ± 0.92	15.07 ± 0.91	12.8 ± 1.0
$\beta_{t1/2}$ (min)	39.7 ± 3.2	66.5 ± 4.6[a]	49.9 ± 5.2	56.4 ± 4.0	52.0 ± 4.6	54.3 ± 4.7
V_c (L/kg)	2.84 ± 0.18	3.34 ± 0.17[a]	2.69 ± 0.18	3.49 ± 0.15[b]	3.13 ± 0.19	3.05 ± 0.17
$V_{d\beta}$ (L/kg)	7.21 ± 0.74	10.62 ± 0.83[a]	7.39 ± 0.71	10.43 ± 0.88[b]	9.2 ± 1.0	8.63 ± 0.64
			Benzoylecgonine			
AUC_p (nmol·min/mL)	1620 ± 170	1560 ± 120	1710 ± 170	1460 ± 120	1740 ± 120	1440 ± 160[c]
AUC_b (nmol·min/mL)	196 ± 25	200 ± 29	245 ± 33	151 ± 16[b]	226 ± 31	170 ± 21[c]
AUC_b/AUC_p	0.125 ± 0.012	0.128 ± 0.015	0.149 ± 0.016	0.1034 ± 0.0083[b]	0.128 ± 0.015	0.125 ± 0.011
f_m	0.270 ± 0.028	0.259 ± 0.020	0.285 ± 0.028	0.244 ± 0.020	0.289 ± 0.020	0.240 ± 0.027[c]
f_m·TBC (mL/min/kg)	32.3 ± 2.7	30.4 ± 2.5	30.0 ± 2.3	32.7 ± 2.9	34.7 ± 2.7	28.0 ± 2.4[c]
			Norcocaine			
AUC_p (nmol·min/mL)	83.0 ± 9.6	99.4 ± 8.7	89 ± 10	93.9 ± 7.9	74.3 ± 8.2	108.1 ± 9.3[c]
AUC_b (nmol·min/mL)	57 ± 12	52.7 ± 4.9	60 ± 12	50.1 ± 4.6	52 ± 10	58.0 ± 7.6
AUC_b/AUC_p	0.631 ± 0.067	0.642 ± 0.076	0.687 ± 0.089	0.585 ± 0.048	0.713 ± 0.083	0.559 ± 0.055
f_m	0.122 ± 0.014	0.146 ± 0.013	0.131 ± 0.015	0.137 ± 0.012	0.110 ± 0.012	0.159 ± 0.014[c]
f_m·TBC (mL/min/kg)	15.1 ± 1.5	16.4 ± 1.5	13.4 ± 1.4	18.1 ± 1.5[b]	12.7 ± 1.3	18.8 ± 1.5[c]
			Cocaethylene			
AUC_p (nmol·min/mL)	114 ± 11	137 ± 10	129 ± 13	121.7 ± 8.3		126 ± 11
AUC_b (nmol·min/mL)	86 ± 16	102 ± 11	98 ± 17	90.3 ± 9.7		94 ± 13
AUC_b/AUC_p	0.730 ± 0.091	0.807 ± 0.098	0.78 ± 0.12	0.759 ± 0.064		0.768 ± 0.094
f_m	0.280 ± 0.040	0.210 ± 0.022	0.186 ± 0.034	0.303 ± 0.052[b]		0.245 ± 0.033
f_m·TBC (mL/min/kg)	38.4 ± 6.7	25.8 ± 3.4	20.3 ± 4.3	43.9 ± 9.0[b]		32.1 ± 5.3

[a] Significantly different from no alcohol pretreatment ($p < 0.05$, $F_{1,24}$). [b] Significantly different from no cocaine pretreatment ($p < 0.05$, $F_{1,24}$). [c] Significantly different from no acute alcohol coadministration ($p < 0.05$, $F_{1,24}$).

Results

During the pretreatment period, the rats in alcohol and cocaine+alcohol groups consumed 7.14 ± 0.58 mL/kg/day and 7.83 ± 0.43 mL/kg/day of alcohol, respectively. The surgical procedures for microdialysis guide cannula implantation caused slight reduction in water and food intakes; however, these values soon returned to their preoperative levels. Meanwhile, the rats in all groups gained weight steadily, and the rate of increase was 2.1 ± 1.8 g/day for the alcohol group, 3.2 ± 1.2 g/day for the cocaine group, and 2.49 ± 0.97 g/day for the cocaine+alcohol group. There were not any significant signs of malnutrition or changes in the general health of the rats during the pretreatment period as indicated by their steady body weight gain.

The plasma concentration−time profiles for cocaine and its metabolites after ip administration of cocaine alone and in combination with alcohol are presented in Figure 1. A summary of the pharmacokinetic parameters for cocaine and its metabolites after different pretreatments is listed in Table 1. Alcohol pretreatment caused significant increase in cocaine AUC_p ($p = 0.044$), without affecting area under the brain ECF concentration−time curve (AUC_b) and brain to plasma distribution ratio (AUC_b/AUC_p). Cocaine distribution half-life ($\alpha_{t1/2}$) was increased ($p = 0.0019$), elimination half-life ($\beta_{t1/2}$) was prolonged ($p = 0.0003$), and the volume of distribution of cocaine during the elimination phase ($V_{d\beta}$) was larger ($p = 0.011$) due to alcohol pretreatment. The systemic bioavailability of cocaine (F) significantly increased ($p = 0.026$) due to cocaine pretreatment. However, the increase in cocaine bioavailability was offset by the increase in cocaine total body clearance (TBC, $p = 0.037$), causing no significant changes in cocaine AUC_p, AUC_b, or AUC_b/AUC_p after cocaine pretreatment. Cocaine pretreatment also increased k_a ($p = 0.0043$), volume of distribution of the central compartment (V_c, $p = 0.0046$), and $V_{d\beta}$ ($p = 0.022$). Alcohol coadministration with cocaine caused significant increases in cocaine AUC_p ($p = 0.0005$) and F ($p = 0.0001$), and significant decrease in AUC_b/AUC_p, which was similar to what has been reported previously.[5] Alcohol coadministration significantly decreased cocaine TBC ($p = 0.041$) and acted synergistically with alcohol pretreatment to prolong $\beta_{t1/2}$ ($p = 0.0067$) and increase $V_{d\beta}$ ($p = 0.0047$).

Pretreatment with alcohol or cocaine did not have any significant effect on benzoylecgonine formation. However, these two pretreatments acted synergistically to significantly reduce the formation of benzoylecgonine ($p = 0.048$). Meanwhile, acute alcohol coadministration with cocaine significantly reduced benzoylecgonine AUC_p ($p = 0.021$), AUC_b ($p = 0.023$), f_m ($p = 0.021$), and formation clearance (f_m·TBC, $p = 0.0029$). Norcocaine formation clearance after cocaine administration was significantly increased due to cocaine pretreatment ($p = 0.042$), and the combined pretreatment with cocaine and alcohol significantly increased norcocaine formation ($p = 0.038$). Meanwhile, acute alcohol coadministration with cocaine led to significant increase in norcocaine AUC_p ($p = 0.0002$), f_m ($p = 0.0002$), and f_m·TBC ($p = 0.0001$). Cocaine pretreatment significantly increased cocaethylene f_m·TBC ($p = 0.020$). Even though alcohol pretreatment did not have any effect on cocaine metabolic conversion to cocaethylene, it acted synergistically with cocaine pretreatment to significantly increase the formation of cocaethylene ($p = 0.033$) and f_m·TBC ($p = 0.026$).

The brain ECF dopamine concentration−time profiles after cocaine administration with and without alcohol in

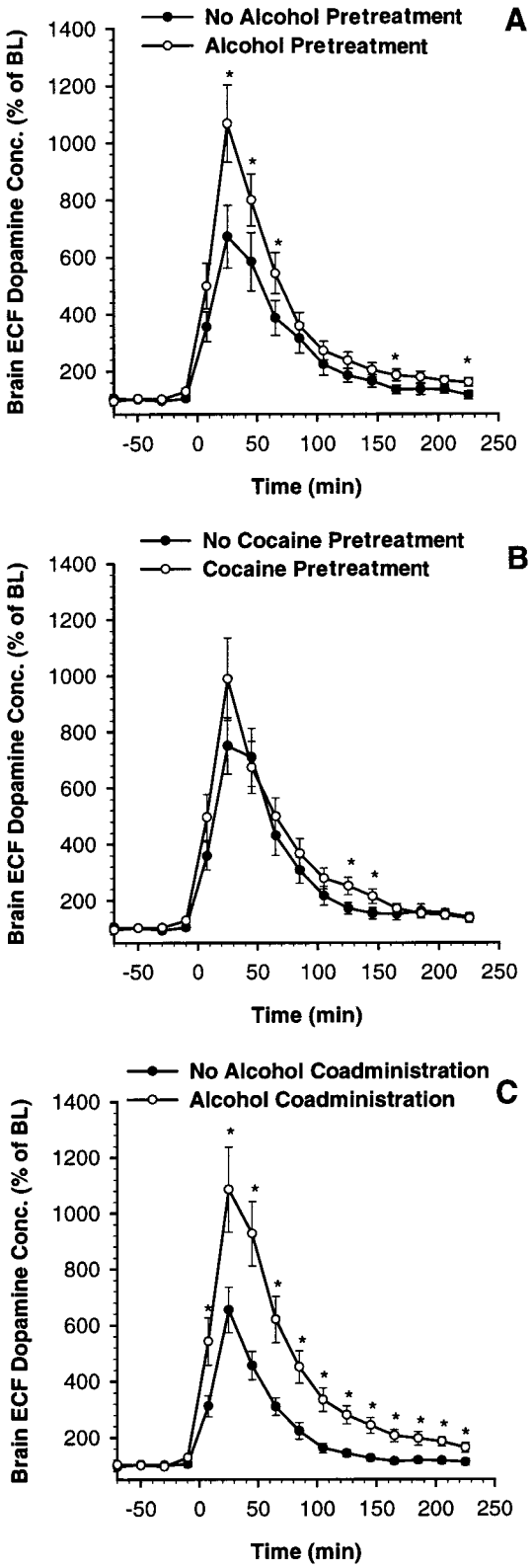

Figure 2—Brain ECF dopamine concentration–time profiles after 30 mg/kg ip cocaine challenge to (A) alcohol naive (●) and alcohol pretreated (○) rats. *Significantly different from that of alcohol naive rats ($p < 0.05$); (B) cocaine naive (●) and cocaine pretreated (○) rats. *Significantly different from that of cocaine naive rats ($p < 0.05$); (C) rats that were not (●) and were (○) coadministered with 5 g/kg acute alcohol. *Significantly different from that of no alcohol coadministration ($p < 0.05$). Each data point is presented as mean ± SE ($n = 32$). BL = Baseline.

the different pretreatment groups are shown in Figure 2. The brain ECF dopamine concentration increased rapidly after 30 mg/kg ip cocaine administration, and it gradually declined to its baseline value at the end of the 4-hour experiment period. Alcohol pretreated rats had significantly higher brain ECF dopamine concentrations in response to cocaine administration when compared to alcohol naïve rats. Cocaine pretreatment did not have any significant effects on dopamine levels after a cocaine challenge dose when compared with cocaine naïve rats. Alcohol coadministration with cocaine significantly increased the magnitude and duration of the brain ECF dopamine level augmentation when compared with cocaine administration alone. The estimated pharmacodynamic parameters of neurochemical response to cocaine are summarized in Table 2. Estimates of the sigmoid-E_{max} pharmacodynamic model parameters showed that alcohol and cocaine pretreatments increased the E_{max} for the neurochemical response to cocaine administration but these changes were not statistically significant. On the other hand, alcohol coadministration with cocaine caused significant increase in E_{max} ($p = 0.018$) and significant reduction in EC_{50} ($p = 0.014$).

The mean arterial blood pressure increased rapidly after ip cocaine challenge. It then declined slowly and did not return to its baseline value at the end of the 4-h experiment (Figure 3). Alcohol and cocaine pretreatments, as well as acute alcohol coadministration with cocaine, caused significant reduction in the mean arterial blood pressure elevation in response to cocaine administration. Since alcohol alone caused, on average, 5−10% decrease in blood pressure, we partitioned this effect from the combined effect of cocaine+alcohol and used the corrected values in the pharmacodynamic modeling.[5] The estimated pharmacodynamic parameters for the mean arterial blood pressure response to cocaine are summarized in Table 3. Analysis with the indirect pharmacodynamic inhibitory model showed that alcohol pretreatment caused reduction in IC_{50} ($p = 0.058$). Cocaine pretreatment significantly decreased the I_{max} ($p = 0.0012$), IC_{50} ($p = 0.0052$), and R_{max}, which is the maximum response to cocaine administration ($p = 0.0041$). Alcohol and cocaine pretreatments did not have any effect on the onset and dissipation rate constants of the blood pressure response. However, alcohol and cocaine pretreatments acted synergistically to reduce the IC_{50} for the pressor response ($p = 0.029$). On the other hand, acute alcohol coadministration increased the rate constant for blood pressure response production (k_{in}) ($p = 0.0093$) and its dissipation (k_{out}) ($p = 0.0085$).

The heart rate decreased rapidly after cocaine ip administration and neither alcohol nor cocaine pretreatments had any significant effect on the change in heart rate in response to cocaine administration (Figure 4A,B). Meanwhile, cocaine caused more reduction in heart rate when it was administered with alcohol (Figure 4C), even though alcohol administration alone led to increase in heart rate (data not shown). Because alcohol alone caused, on average, 10−20% increase in heart rate, we partitioned this effect from the combined effect of cocaine+alcohol, and the corrected values were used in the pharmacodynamic modeling. The estimated pharmacodynamic parameters for the heart rate response to cocaine administration are also summarized in Table 3. Alcohol and cocaine pretreatments caused significant increase in IC_{50} ($p = 0.0001$ and 0.0017, respectively). On the other hand, acute alcohol coadministration increased the rate constant for the heart rate response production (k_{in}) ($p = 0.032$) and its dissipation (k_{out}) ($p = 0.065$).

Discussion

Illicit drugs are mostly consumed by addicts who often abuse multiple drugs simultaneously. This observation

Table 2—Pharmacodynamic Parameters for the Neurochemical Response to Cocaine in the Rat Either with or without Alcohol or Cocaine Pretreatments or Acute Alcohol Coadministration (mean ± SE, $n = 32$)

pharmacodynamic parameter	alcohol pretreatment		cocaine pretreatment		alcohol coadministration	
	no	yes	no	yes	no	yes
E_{max} (% of baseline)	1100 ± 200	1530 ± 240	1160 ± 190	1480 ± 250	980 ± 140	1650 ± 270[a]
EC_{50} (nmol/mL)	9.0 ± 1.1	8.57 ± 0.85	8.38 ± 0.86	9.2 ± 1.1	10.35 ± 0.94	7.26 ± 0.96[a]
n	1.86 ± 0.31	1.69 ± 0.30	1.96 ± 0.30	1.60 ± 0.31	1.94 ± 0.40	1.62 ± 0.16

[a] Significantly different from no acute alcohol coadministration ($p < 0.05$, $F_{1,24}$).

Table 3—Pharmacodynamic Parameters for the Mean Arterial Blood Pressure and Heart Rate Response to Cocaine in the Rat Either with or without Alcohol or Cocaine Pretreatments or Acute Alcohol Coadministration (mean ± SE, $n = 32$)

pharmacodynamic parameter	alcohol pretreatment		cocaine pretreatment		alcohol coadministration	
	no	yes	no	yes	no	yes
			Mean Arterial Blood Pressure			
k_{in} (% of baseline/min)	30.9 ± 5.3	31.0 ± 5.0	27.7 ± 4.5	34.2 ± 5.6	20.6 ± 2.3	41.2 ± 6.3[c]
k_{out} (min^{-1})	0.283 ± 0.050	0.310 ± 0.054	0.257 ± 0.043	0.336 ± 0.059	0.191 ± 0.022	0.402 ± 0.065[c]
I_{max}	0.253 ± 0.018	0.239 ± 0.015	0.287 ± 0.014	0.205 ± 0.014[b]	0.232 ± 0.015	0.260 ± 0.017
IC_{50} (nmol/mL)	13.0 ± 2.0	9.2 ± 1.2	14.0 ± 1.9	8.1 ± 1.1[b]	11.5 ± 1.9	10.7 ± 1.3
R_{max} (% of baseline)	136.5 ± 3.7	133.1 ± 2.9	142.3 ± 3.2	127.3 ± 2.9[b]	132.0 ± 2.9	137.6 ± 3.6
			Heart Rate			
k_{in} (% of baseline/min)	41.7 ± 5.6	47.5 ± 5.6	43.5 ± 8.7	46.6 ± 4.6	35.2 ± 6.3	56.0 ± 4.7[c]
k_{out} (min^{-1})	0.442 ± 0.056	0.472 ± 0.055	0.436 ± 0.086	0.475 ± 0.045	0.374 ± 0.066	0.550 ± 0.043
I_{max}	0.270 ± 0.021	0.273 ± 0.015	0.291 ± 0.017	0.263 ± 0.015	0.260 ± 0.024	0.284 ± 0.011
IC_{50} (nmol/mL)	1.48 ± 0.30	7.3 ± 1.2[a]	4.8 ± 1.1	5.7 ± 1.2[b]	6.4 ± 1.5	4.3 ± 1.0
R_{max} (% of baseline)	138.7 ± 4.2	139.6 ± 3.2	142.3 ± 3.6	137.8 ± 3.4	137.8 ± 5.3	140.7 ± 2.3

[a] Significantly different from no alcohol pretreatment ($p < 0.05$, $F_{1,24}$). [b] Significantly different from no cocaine pretreatment ($p < 0.05$, $F_{1,24}$). [c] Significantly different from no acute alcohol coadministration ($p < 0.05$, $F_{1,24}$).

clearly illustrates the importance of studying possible interactions between illicit drugs and changes in the disposition and pharmacological effects of these substances of abuse when two or more of them are consumed simultaneously. Most of the studies conducted thus far involve administration of a single drug in naïve animals or in subjects that had been abstinent for several months from drugs. Our investigation was designed to study how prior cocaine and alcohol use, acute alcohol coadministration, and interactions among these factors can affect the pharmacokinetics and pharmacodynamics of cocaine.

Alcohol pretreatment for two weeks significantly prolonged cocaine distribution and elimination half-lives and significantly increased cocaine volume of distribution. Similar effect on cocaine elimination half-life has been reported previously in anesthetized rats.[3] Cocaine AUC_p increased significantly after alcohol pretreatment, which may have resulted from the inhibition of cocaine metabolism because its bioavailability did not change significantly. Alcohol metabolism in mammals is mediated by cytosolic alcohol dehydrogenase, microsomal CYP2E1, and peroxisomal catalase.[24] CYP2E1 catalyzes the biotransformation of a variety of endogenous and exogenous compounds and is inducible by alcohol. It is possible that CYP2E1 induction by alcohol pretreatment may be involved in the changes in cocaine metabolism and pharmacokinetics. Studies have shown that both acute and chronic alcohol administration decrease hepatic glutathione content and shift its reduction vs oxidation ratio to an unfavorable condition for the cell.[25] Another effect related to alcohol pretreatment is the promotion of lipid peroxidation in the liver.[26] These two CYP2E1-dependent events can lead to intracellular oxidative stress and slow the liver biotransformation activity. These results imply that prior use of alcohol can lead to higher and prolonged cocaine plasma concentrations after administration of the same cocaine dose which may, in turn, increase cocaine-related toxicities.

We pretreated the rats with ip cocaine administration because it is easier than iv and more drug will reach the systemic circulation compared to oral and subcutaneous administration. Cocaine pretreatment significantly increased the rate and extent of cocaine absorption after an ip challenge dose of cocaine. However, the increase in cocaine bioavailability was not accompanied by an increased in AUC_p and AUC_b. This may be due to the significant increase in cocaine TBC. Cocaine pretreatment also increased cocaine volume of distribution which may explain why its elimination half-life was not affected by cocaine pretreatment.

Acute alcohol coadministration with cocaine significantly increased cocaine AUC_p and systemic bioavailability. Meanwhile, cocaine $\beta_{t1/2}$ and TBC were not significantly different, indicating that the increase in cocaine AUC_p was primarily due to the increase in cocaine bioavailability. The enhanced cocaine systemic bioavailability may be caused by the inhibitory effect of alcohol on cocaine presystemic metabolism which resulted in a larger fraction of the cocaine dose escaping the first-pass metabolism and reaching the systemic circulation. Examination of the significant interactions between different factors showed that acute alcohol and alcohol pretreatment acted synergistically to prolong cocaine elimination half-life and volume of distribution. The increase in the plasma cocaine concentration after alcohol coadministration with cocaine was accompanied by less than proportional increase in cocaine AUC_b and thus caused decrease in AUC_b/AUC_p. We have previously demonstrated that in the presence of much higher plasma alcohol concentration, brain ECF cocaine concentration was significantly increased in rats.[4] These results showed that combined alcohol and cocaine use can lead to higher cocaine concentrations, which may augment cocaine pharmacological effects and toxicities.

Alcohol pretreatment did not have any significant effect on cocaine metabolic profile. However, cocaine pretreatment significantly reduced benzoylecgonine formation and significantly increased the formation of the active metabolite cocaethylene. The increased formation of cocaethylene may have significant pharmacological and toxicological

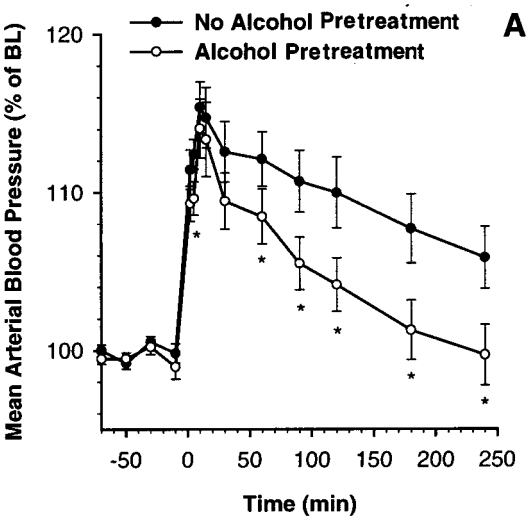

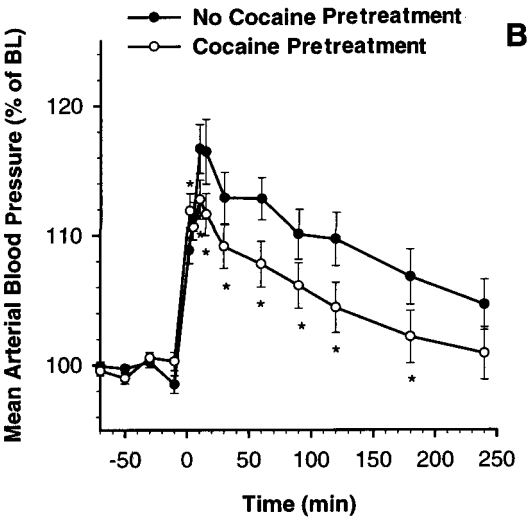

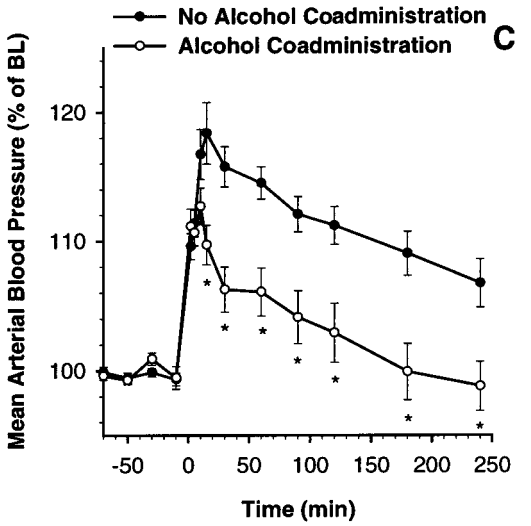

Figure 3—Mean arterial blood pressure–time profiles after 30 mg/kg ip cocaine challenge to (A) alcohol naive (●) and alcohol pretreated (○) rats. *Significantly different from that of alcohol naive rats ($p < 0.05$); (B) cocaine naive (●) and cocaine pretreated (○) rats. *Significantly different from that of cocaine naive rats ($p < 0.05$); (C) rats that were not (●) and were (○) coadministered with 5 g/kg acute alcohol. *Significantly different from that of no alcohol coadministration ($p < 0.05$). Each data point is presented as mean ± SE ($n = 32$). BL = Baseline.

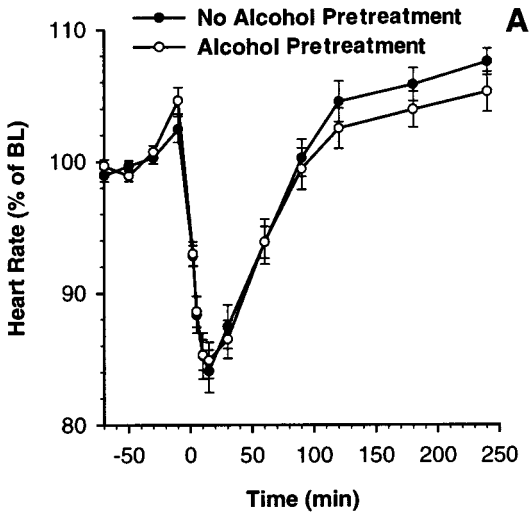

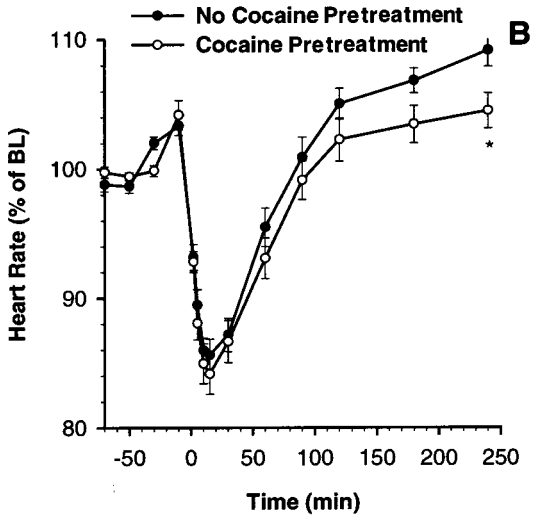

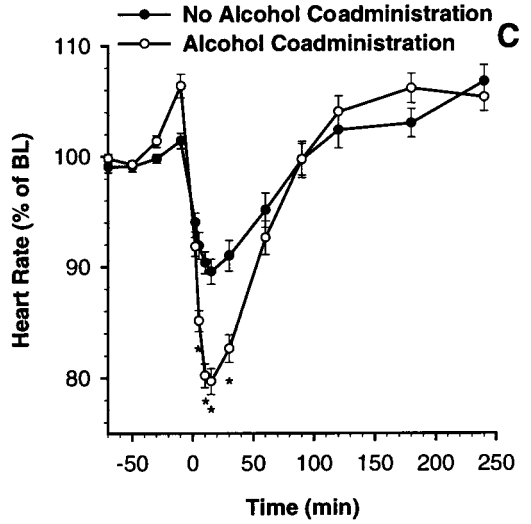

Figure 4—Heart rate–time profiles after 30 mg/kg ip cocaine challenge to (A) alcohol naive (●) and alcohol pretreated (○) rats; (B) cocaine naive (●) and cocaine pretreated (○) rats. *Significantly different from that of cocaine naive rats ($p < 0.05$); (C) rats that were not (●) and were (○) coadministered with 5 g/kg acute alcohol. *Significantly different from that of no alcohol coadministration ($p < 0.05$). Each data point is presented as mean ± SE ($n = 32$). BL = Baseline.

consequences. This is because, compared to cocaine, cocaethylene has been shown to be more potent with respect to the neurochemical, heart rate, and QRS interval responses and is equipotent in causing mean arterial blood

pressure increase.[6] Cocaine and alcohol coadministration significantly reduced benzoylecgonine formation, with approximately 25% of cocaine dose converted to the active metabolite cocaethylene. The fact that alcohol coadministration caused only 5% reduction in the precent of the cocaine dose converted to benzoylecgonine, but approximately 25% of cocaine dose was converted to cocaethylene indicates that cocaethylene formation is not solely on the expense of benzoylecgonine formation. These results imply that alcohol may also affect the metabolism of cocaine to ecgonine methyl ester. Another significant effect of acute alcohol coadministration on cocaine metabolism was the significant increase in the formation of norcocaine. On the other hand, cocaine+alcohol pretreatment led to more than additive effect on the reduction of benzoylecgonine and increase of norcocaine formation. The changes in cocaine metabolic profile due to alcohol coadministration, specifically the formation of cocaethylene and the increased formation of norcocaine, can significantly alter cocaine pharmacological and toxicological effects because of the contribution of these two metabolites to the neurochemical and cardiovascular effects of cocaine.[6]

The N ACC dopamine concentration enhancement in response to cocaine administration was significantly higher in the rats pretreated with alcohol for two weeks. This difference was more significant in the first hour after cocaine administration. Pharmacodynamic analysis showed an approximately 40% increase in the E_{max} for the neurochemical response to cocaine administration. This can be explained by the higher and prolonged cocaine concentrations as a result of alcohol pretreatment. Neurochemical and behavioral sensitization after repeated cocaine treatment has been well documented.[14–16] In our study, however, cocaine pretreatment continued until the day before the challenge dose of cocaine, and it did not have any significant effect on the neurochemical response to an ip cocaine challenge. This lack of neurochemical sensitization may be due to the apparent short term tolerance to the brain ECF dopamine augmentation during the early withdrawal period after repeated cocaine administration.[27]

Dopamine concentration−time profile in response to cocaine administration was significantly higher throughout the experiment period when alcohol was coadministered. The enhanced magnitude and potency of cocaine neurochemical effect was also reflected in the significant changes in the pharmacodynamic model estimates for E_{max} and EC_{50}. This may be explained by the higher cocaine concentrations achieved after combined cocaine and alcohol administration. Because both cocaethylene and norcocaine contribute significantly to the neurochemical response of cocaine,[6,28] the formation of cocaethylene and the increased formation of norcocaine due to alcohol coadministration may further enhance this pharmacological response. These findings imply that, in humans, simultaneous cocaine and alcohol abuse may increase the risk of cocaine-related toxicity in the central nervous system.

Cocaine pretreatment significantly reduced the maximum inhibitory effect of cocaine on the monoamine reuptake, significantly increased the potency of this action, and reduced the maximum mean arterial blood pressure response. These findings indicate that although the maximum increase in mean arterial blood pressure may be lower after repeated exposure to cocaine, the increase in mean blood pressure will be higher for a given cocaine dose after this pretreatment. Alcohol pretreatment increased the potency of the effect of cocaine on the blood pressure. Cocaine and alcohol pretreatments acted together to cause more than an additive effect on increasing the potency of cocaine effect on the mean arterial blood pressure. This may imply that prior use of both cocaine and alcohol can increase the risk of cardiovascular complications in response to cocaine use. Acute alcohol administration with cocaine increased the onset and the dissipation rate constants for the effect of cocaine on the mean arterial blood pressure. This means that alcohol coadministration caused faster increase in the mean arterial blood pressure and faster return to baseline after ip cocaine challenge. The clinical significance of these findings should not be underestimated. Simultaneous administration of cocaine and alcohol may cause higher risks of developing stroke and seizure due to sudden and faster increase in vascular resistance during the first few minutes. Meanwhile, the faster decrease in blood pressure is accompanied by lower vascular tone of the cerebral and epicardial coronary arteries. This may explain the reduced dysphoria such as migraine and chest pain that are often described by abusers of this drug combination as compared to cocaine alone.

The effect of cocaine on heart rate is dependent on its dose. In rats, intra-arterial cocaine doses of up to 0.5 mg/kg increased heart rate, whereas doses above 1.0 mg/kg decreased heart rate.[29] Due to the high cocaine challenge dose used in our study, the heart rate was reduced in all the three groups of rats under investigation. High concentrations of cocaine can block the sodium channel in sensory neurons as well as affect the cardiac action potential leading to slower heart rate and slower cardiac conduction.[30,31] Decreased heart rate may also be caused by activation of vagal baroreceptor reflex.[29] In this study, the time course of the decrease in heart rate in reponse to cocaine administration was not affected by alcohol or cocaine pretreatment. However, pharmacodynamic model parameters showed decreased potency of cocaine effect on the heart rate. On the other hand, alcohol coadministration caused significantly lower heart rate compared to cocaine administration alone, with the most outstanding difference shown in the first hour. Changes in cocaine pharmacokinetics, especially the increase in cocaine AUC_p, the formation of cocaethylene and the increased formation of norcocaine may be responsible for the changes in cocaine pharmacodynamics when alcohol was given with cocaine. Cocaethylene is believed to be implicated in the increased cocaine-related mortality when alcohol is coabused. Cocaethylene has been proven to be more potent than cocaine in mediating lethality in mice.[32] In anaesthetized dogs, cocaethylene causes significant myocardial depression and slight heart rate increase.[33] The reduction in myocardial contractility may lead to a remarkable decrease in hepatic blood flow and, consequently, reduce metabolism of both cocaine, cocaethylene, and norcocaine in the liver. Therefore, changes in the pharmacodynamics with cocaine+alcohol coadministration may in return affect the pharmacokinetics and metabolism of cocaine. However, caution should be exercised when extrapolating these observations in animals to humans. Studies in humans have shown that the appearance of cocaethylene in plasma does not alter subjective and cardiovascular effects of cocaine,[34] and that cocaethylene alone produces milder subjective effects and comparable cardiovascular effects to those of cocaine alone.[35,36]

In conclusion, alcohol pretreatment increases the plasma and brain cocaine concentrations due to inhibition of cocaine elimination. Cocaine pretreatment enhances the systemic bioavailability and clearance of cocaine and increases the formation of norcocaine and cocaethylene. Alcohol coadministration with cocaine increases the plasma and brain cocaine concentrations due to the increase in cocaine systemic bioavailability and reduction of its clearance. Meanwhile, benzoylecgonine formation is significantly reduced, and norcocaine formation is significantly increased. Cocaine and alcohol pretreatments and acute

alcohol coadministration lead to alterations in cocaine pharmacodynamics that are due, at least in part, to the changes in cocaine pharmacokinetics. Alcohol coadministration with cocaine caused significant changes in cocaine neurochemical and cardiovascular responses, and repeated cocaine and alcohol users may respond differently to cocaine administration compared to naïve users. If prior use of alcohol and/or cocaine has similar effects on cocaine pharmacokinetics and pharmacodynamics in humans, the findings of this investigation would indicate that alcoholics and cocaine addicts are at higher risks of cocaine toxicity. The risks may be even higher in these abusers when they consume cocaine and alcohol simultaneously.

References and Notes

1. Vanek, V. W.; Dickey White, H. I.; Signs, S. A.; Schechter, M. D.; Buss, T.; Kulics, A. T. Concurrent Use of Cocaine and Alcohol by Patients Treated in the Emergency Department. *Ann. Emerg. Med.* **1996**, *28*, 508−514.
2. Farre, M.; Torre, R.; Llorente, M.; Lamas, X.; Ugena, B.; Segura, J.; Cami, J. Alcohol and Cocaine Interactions in Humans. *J. Pharmacol. Exp. Ther.* **1993**, *266*, 1364−1373.
3. Hedaya, M. A.; Pan, W. J. Cocaine and Alcohol Interactions in Naive and Alcohol-Pretreated Rats. *Drug. Metab. Dispos.* **1996**, *24*, 807−812.
4. Hedaya, M. A.; Pan, W. J. Effect of Alcohol Coadministration on the Plasma and Brain Concentrations of Cocaine in Rats. *Drug. Metab. Dispos.* **1997**, *25*, 647−650.
5. Pan, W. J.; Hedaya, M. A. Cocaine and Alcohol Interactions in the Rat: Effect on Cocaine Pharmacokinetics and Pharmacodynamics. *J. Pharm. Sci.* **1999**, *88*, 459−467.
6. Pan, W. J.; Hedaya, M. A. Cocaine and Alcohol Interactions in the Rat: Contribution of Cocaine Metabolites to the Pharmacological Effects. *J. Pharm. Sci.* **1999**, *88*, 468−476.
7. Lai, H.; Carino, M. A.; Horita, A. Effects of Ethanol on Central Dopamine Functions. *Life Sci.* **1980**, *27*, 299−304.
8. Barbaccia, M. L.; Bosio, A.; Lucchi, L.; Spano, P. F.; Trabucchi, M. Neuronal Mechanisms Regulating Ethanol Effects on the Dopaminergic System. *Life Sci.* **1982**, *30*, 2163−2170.
9. Pecins-Thompson, M.; Peris, J. Behavioral and Neurochemical Changes Caused by Repeated Ethanol and Cocaine Administration. *Psychopharmacology* **1993**, *110*, 443−450.
10. Higgins, S. T.; Roll, J. M.; Bickel, W. K. Alcohol Pretreatment Increases Preference for Cocaine over Monetary Reinforcement. *Psychopharmacology* **1996**, *123*, 1−8.
11. Smith, A. C.; Freeman, R. W.; Harbison, R. D. Ethanol Enhancement of Cocaine-Induced Hepatotoxicity. *Biochem. Pharmacol.* **1981**, *30*, 453−458.
12. Hoyumpa, A. M., Jr. Alcohol Interactions with Benzodiazepines and Cocaine. *Adv. Alcohol. Subst. Abuse* **1984**, *3*, 21−34.
13. Pan, H. T.; Menacherry, S.; Justice, J. B., Jr. Differences in the Pharmacokinetics of Cocaine in Naive and Cocaine-Experienced Rats. *J. Neurochem.* **1991**, *56*, 1299−1306.
14. Kalivas, P. W.; Duffy, P.; DuMars, L. A.; Skinner, C. Behavioral and Neurochemical Effects of Acute and Daily Cocaine Administration in Rats. *J. Pharmacol. Exp. Ther.* **1988**, *245*, 485−492.
15. Kalivas, P. W.; Duffy, P. Effect of Acute and Daily Cocaine Treatment on Extracellular Dopamine in the Nucleus Accumbens. *Synapse* **1990**, *5*, 48−58.
16. Heidbreder, C. A.; Thompson, A. C.; Shippenberg, T. S. Role of Extracellular Dopamine in the Initiation and Long-Term Expression of Behavioral Sensitization to Cocaine. *J. Pharmacol. Exp. Ther.* **1996**, *278*, 490−502.
17. Boelsterli, U. A.; Lanzotti, A. C.; Oertle, M. Identification of Cytochrome P-450IIB1 as a Cocaine-Bioactivating Isoform in Rat Hepatic Microsomes and in Cultured Rat Hepatocytes. *Drug. Metab. Dispos.* **1992**, *20*, 96−101.
18. Pellinen, P.; Stenbäck, F.; Kojo, A.; Honkakoski, P.; Gelboin, H. V.; Pasanen, M. Regenerative Changes in Hepatic Morphology and Enhanced Expression of CYP2B10 and CYP3A During Daily Administration of Cocaine. *Hepatology* **1996**, *23*, 515−523.
19. Pettit, H. O.; Pan, H. T.; Parsons, L. H.; Justice, J. B., Jr. Extracellular Concentrations of Cocaine and Dopamine are Enhanced During Chronic Cocaine Administration. *J. Neurochem.* **1990**, *55*, 798−804.
20. Pan, W. J.; Hedaya, M. A. An Animal Model for Simultaneous Pharmacokinetic/Pharmacodynamic Investigations: Application to Cocaine. *J. Pharmacol. Toxicol. Methods* **1998**, *39*, 1−8.
21. Pan, W. J.; Hedaya, M. A. Sensitive and Specific High-Performance Liquid Chromatographic Assay with Ultraviolet Detection for the Determination of Cocaine and its Metabolites in Rat Plasma. *J. Chromatogr. B Biomed. Sci. Appl.* **1997**, *703*, 129−138.
22. Menacherry, S.; Hubert, W.; Justice, J. B., Jr. In Vivo Calibration of Microdialysis Probes for Exogenous Compounds. *Anal. Chem.* **1992**, *64*, 577−583.
23. Sharma, A.; Jusko, W. J. Characterization of Four Basic Models of Indirect Pharmacodynamic Responses. *J. Pharmacokin. Biopharm.* **1996**, *24*, 611−635.
24. Parkinson, A. Biotransformation of Xenobiotics. In *Casarett & Doull's Toxicology: The basic science of poisons*, 5th ed.; Klaassen, C. D., Ed.; McGraw-Hill: New York, 1996; pp 113−186.
25. Fernandez-Checa, J. C.; Ookhtens, M.; Kaplowitz, N. Effect of Chronic Ethanol Feeding on Rat Hepatocytic Glutathione. Compartmentation, Efflux, and Response to Incubation with Ethanol. *J. Clin. Invest.* **1987**, *80*, 57−62.
26. Ekström, G.; Ingelman-Sundberg, M. Rat Liver Microsomal NADPH−Supported Oxidase Activity and Lipid Peroxidation Dependent on Ethanol-Inducible Cytochrome P-450 (P-450IIE1). *Biochem. Pharmacol.* **1989**, *38*, 1313−1319.
27. Kalivas, P. W.; Duffy, P. Time Course of Extracellular Dopamine and Behavioral Sensitization to Cocaine. I. Dopamine Axon Terminals. *J. Neurosci.* **1993**, *13*, 266−275.
28. Hearn, W. L.; Flynn, D. D.; Hime, G. W.; Rose, S.; Cofino, J. C.; Mantero-Atienza, E.; Wetli, C. V.; Mash, D. C. Cocaethylene: a unique cocaine metabolite displays high affinity for the dopamine transporter. *J. Neurochem.* **1991**, *56* (2), 698−701.
29. Kiritsy-Roy, J. A.; Halter, J. B.; Gordon, S. M.; Smith, M. J.; Terry, L. C. Role of the Central Nervous System in Hemodynamic and Sympathoadrenal Responses to Cocaine in Rats. *J. Pharmacol. Exp. Ther.* **1990**, *255*, 154−160.
30. Przywara, D. A.; Dambach, G. E. Direct Actions of Cocaine on Cardiac Cellular Electrical Activity. *Circ. Res.* **1989**, *65*, 185−192.
31. Beckman, K. J.; Parker, R. B.; Hariman, R. J.; Gallastegui, J. L.; Javaid, J. I.; Bauman, J. L. Hemodynamic and Electrophysiological Actions of Cocaine: Effects of Sodium Bicarbonate as an Antidote in Dogs. *Circulation* **1991**, *83*, 1799−1807.
32. Hearn, W. L.; Rose, S.; Wagner, J.; Ciarleglio, A.; Mash, D. C. Cocaethylene is more potent than cocaine in mediating lethality. *Pharmacol. Biochem. Behav.* **1991**, *39* (2), 531−533.
33. Wilson, L. D.; Henning, R. J.; Suttheimer, C.; Lavins, E.; Balraj, E.; Earl, S. Cocaethylene causes dose-dependent reductions in cardiac function in anesthetized dogs. *J. Cardiovasc. Pharmacol.* **1995**, *26* (6), 965−973.
34. Perez-Reyes, M.; Jeffcoat. A. R. Ethanol/cocaine interaction: cocaine and cocaethylene plasma concentrations and their relationship to subjective and cardiovascular effects. *Life Sci.* **1992**, *51* (8), 553−563.
35. Perez-Reyes, M. Subjective and cardiovascular effects of cocaethylene in humans. *Psychopharmacology (Berlin)* **1993**, *113* (1), 144−147.
36. Perez-Reyes, M.; Jeffcoat, A. R.; Myers, M.; Sihler, K.; Cook, C. E. Comparison in humans of the potency and pharmacokinetics of intravenously injected cocaethylene and cocaine. *Psychopharmacology (Berlin)* **1994**, *116* (4), 428−432.

Acknowledgments

This work was supported by a grant from the National Institute of Neurological Disorder and Stroke (NS/OD36399-01).

JS990184J

Sulfathiazole Polymorphism Studied by Magic-Angle Spinning NMR

DAVID C. APPERLEY,[†] RICHARD A. FLETTON,[‡] ROBIN K. HARRIS,*[,†] ROBERT W. LANCASTER,[‡] STEWART TAVENER,[§] AND TERRY L. THRELFALL[§]

Contribution from *Industrial Research Laboratories, University of Durham, South Road, Durham, DH1 3LE, U.K., Glaxo Wellcome R & D, Medicines Research Centre, Gunnels Wood Road, Stevenage, Hertfordshire, SG1 2NY, U.K., and Department of Chemistry, University of York, Heslington, York, YO10 5DD, U.K.*

Received June 4, 1999. Accepted for publication August 30, 1999.

Abstract □ The literature on sulfathiazole polymorphs has many confusions and inconsistencies. These are largely resolved by the distinctive appearance of ^{13}C magic-angle spinning NMR spectra, which immediately show the number of molecules in the crystallographic asymmetric unit. The spectra presented include those of a newly-recognized form. The assignments of the spectra are established and discussed in relation to such factors as electronic structure of the aromatic ring, second-order quadrupolar effects originating from the nitrogen nuclei, and hydrogen bonding. The results are compared to literature information on the crystal structures. When the amino group acts as a hydrogen bond acceptor, there is a shielding effect on C-4 to the extent of ca. 8 ppm (which should be compared to a further shielding by ca. 10 ppm for sulfathiazole sulfate). The fact that the spectrum of form III is similar to the sum of those of forms IV and V is rationalized in relation to the crystal structures. Some surprising variability of spectra with temperature and with specific sample is reported.

Introduction

The polymorphism of sulfathiazole has been the subject of investigation for almost 60 years.[1−7] It has been described as the classic polymorphic system.[3] We have recently demonstrated that there are at least five polymorphs of sulfathiazole, and we have carried out a single-crystal structure determination of the fifth polymorph,[7,8] although it now appears that this polymorph was the one first synthesized,[9] first described in a patent,[10] and first published in the literature by two independent groups,[11,12] but subsequently overlooked for more than 40 years.[13] It would seem that all five polymorphs had been seen and described by 1947, but not clearly differentiated.[1,2,11,12,14] Furthermore, we have shown that the common material of commerce does not have the polymorphic structure described by Kruger and Gafner,[15] as has been assumed for a quarter of a century, but has the structure first determined by Babilev et al.[16] The sources of confusion which have led to this unusual situation are 5-fold, namely the irreproducibility of the crystallization, the tendency to crystallize as mixtures, the close similarity in structure and properties of three of the polymorphs, the sample-to-sample variability in stability, and the differences between the pharmaceutical and crystallographic enumeration of the polymorphs. In order for the present discussion to be clear, Table 1 sets out the nomenclature of the polymorphs. Only minimal information for differentiating between them is incorporated in the table, since it is intended to publish further details of the physical characteristics elsewhere. The crystal structures of all five have now been published,[7,8,15,16] so confusion should now be minimal. Samples of all sulfathiazole polymorphs (particularly of I and IV) show huge variation in stability. During this investigation we have also prepared and characterized over 100 solvates of sulfathiazole, as well as numerous salts, and have determined the crystal structures of many of these.[17] It has therefore appeared highly desirable to determine definitively, to collate, to record, and to correlate the physical properties of the multiple solid forms of sulfathiazole. In this article the solid-state NMR spectra of the five polymorphs of known structure, purity, and provenance are presented and interpreted: previously only the spectra of four polymorphs, determined by one of us (D.C.A.), have been briefly mentioned[4] but not seriously discussed. For the purposes of discussing the NMR spectra, the carbon-atom numbering is shown below (note that some authors[5] invert the numbering of C-8 and C-9).

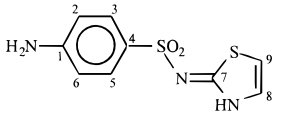

However, this figure is not intended to convey conformational information. Note that in all cases the sulfonimido tautomer is present, rather than the sulfonamido structure.

Polymorphs I−III each have two molecules in the asymmetric unit. The supramolecular structure of polymorph I may be described in broad terms as consisting of two orthogonal planes of crystallographically distinct but rather similar sulfathiazole molecules, and that of polymorph II as two parallel interleaved planes of somewhat differently bonded molecules. Polymorph IV has only one molecule in the asymmetric unit in a distinctive supramolecular pattern based on a layered hydrogen-bonded ring system. Polymorph V is of a similar structure but with a different ring system. Polymorph III in effect combines[5] the ring systems of IV and V. Consequently, the three polymorphs are very similar in all their spectral and physicochemical

Table 1—Nomenclature for Sulfathiazole Polymorphs

melting point/°C	crystallography[a]	pharmacy[b]	proposed[c]
202	I	I	I
197		II	II
175	III	III	III
<175	II	IV	IV
175	IV	III	V[d]

[a] From the Cambridge Crystallographic Database. [b] For example, as used by Burger and Dialer[3] and by Anwar, Tarling, and Barnes.[4] [c] For use in this article. [d] Structure determined by Babilev et al.[16] Now known to be the common commercial material.

* To whom correspondence should be addressed. Phone +44-(0)191-374-3121. Fax +44-(0)191-386-1127. e-mail r.k.harris@durham.ac.uk.
[†] University of Durham.
[‡] Glaxo Wellcome R & D.
[§] University of York.

10.1021/js990175a CCC: $18.00
Published on Web 10/14/1999

behavior, and the properties of polymorph III are to a large extent either the average or the superposition of those of polymorphs IV and V. Great care is therefore needed to distinguish between them as they almost invariably occur as mixtures.

Recently, Blagden et al.[5] have discussed the hydrogen-bonding networks and other packing arrangements of four of the forms using a graph-set approach. Anwar, Tarling, and Barnes[4] have collated powder XRD and Raman spectra of four sulfathiazole polymorphs, though the relationships to those of Blagden et al. are not totally clear.

Experimental Section

Origin of Samples—*Polymorph I*—For almost 60 years, the single reliable preparation of a pure sulfathiazole polymorph by crystallization has been of form I from a solution in 1-propanol. The characteristics of commercial material have changed recently, as noted below, and useful samples can no longer be made this way, as has been independently encountered by Blagden et al.[5] The sample used here was made by heating commercial material at 180 °C for 15 min. This procedure is reliable. The product is often pink, but this does not interfere with the NMR spectral characteristics. An earlier sample made by crystallization from 1-propanol proved to be sensitive to spinning and partly converted to form IV during NMR examination. Polymorph I is not the themodynamically stable form at room temperature. Its kinetic stability varies enormously between samples, from hours to years. Transformation on spinning is rare but for that very reason is all the more noteworthy.

Polymorph II—A supersaturated aqueous solution was evaporated to dryness in a beaker.[4] It is desirable not to let the temperature drop below 100 °C at any time until the sample is totally dry. The supersaturated solution is best prepared by boiling down an undersaturated (<2 g per 100 cm^{-3}) solution, itself made in the presence of trace surfactant, otherwise only a mixture of III/IV/V may result. The nature of the material from this experiment is dependent on the history of the solution. Solutions made initially by dissolution in an organic solvent followed by displacement of the solvent by water have not yielded polymorph II in our hands. It has been suggested that cocrystals of urea with sulfathiazole produce form I on dissolution,[18] but in our experience addition of urea encourages the formation of form II. Polymorph II has and continues to be mistaken for form I, despite its distinctive melting point and infrared spectrum.

Polymorph III—Recent commercial sulfathiazole from Aldrich has been of form III of a polymorphic purity (ca. 99%) which cannot be achieved in small-scale laboratory preparations. The size of vessel is a significant factor in the preparation of sulfathizole polymorphs. A sample made by the replacement of acetone by dichloromethane in boiling solution as well as one from Aldrich batch HN 3506 were used here: the crystallization history of the latter is unknown.

Polymorph IV—The stability of sulfathiazole polymorphs is a characteristic not of the form in question, but of the specific sample, related to the stability of the individual crystals, as can be deduced from the observations of Anwar,[19] presumably because the transitions are defect-mediated. Of over 50 samples of polymorph IV in our hands few were better than 90% polymorphically pure and none better than 98% when originally prepared, as determined by powder XRD. The usual impurities are polymorphs III and V. Furthermore, many have altered on storage. The sample used here was crystallized from acetonitrile.

Polymorph V—For many decades, bulk sulfathiazole was purified by dissolution in alkali followed by neutralization. The product on a laboratory scale is of variable polymorphic composition, but on a commercial scale this procedure gives form V in better than 90% polymorphic purity. Batch 61376 from Aldrich, of 98% polymorphic purity, was used here.

The polymorphic status of our samples was checked first by NIR/IR DRIFT spectra of the solids.[20] Infrared and near-infrared spectroscopy can distinguish between the polymorphs but are poor at assessing the polymorphic purity, particularly of polymorphs III–V, because of the close similarity of the spectra and many near coincidences. The polymorphic purity of the samples was determined by XRD powder diffraction on unground samples using the intense peaks at 21.9, 21.7, and 22.1° 2θ characteristic of polymorphs III, IV, and V, respectively. Grinding causes polymorphic transition,[21,22] and it obscures the distinctions between polymorphs in the 22° 2θ region. Polymorph I also has its strongest band at 21.9° 2θ but can readily be distinguished elsewhere in the pattern.

Nuclear Magnetic Resonance—Solid-state ^{13}C NMR spectra were recorded with cross polarization, magic-angle spinning, and high-power proton decoupling using a Varian Unity Plus 300 spectrometer operating at 75.43 MHz and ambient probe temperature (ca. 26 °C). A probe using 7 mm o.d. rotors made of zirconia was employed. Typical operating conditions: contact time 3 ms; recycle delay 30 s for some spectra but 300 or 400 s for those obtained later; number of transients 100–1000; spin rate 4.5–5.5 kHz. The total accumulation times were optimized by the use of a flip-back pulse after each acquisition.[23] For assignment purposes, spectra of nonprotonated and protonated carbons were separately obtained using a dipolar dephasing pulse sequence.[24] Carbon chemical shifts were referenced to the signal for tetramethylsilane via a replacement sample of solid adamantane (methylene carbon, $\delta_C = 38.4$ ppm).

Values of T_1 for the protons were measured by the inversion–recovery method on static samples and were found to be between 200 and 500 s at ambient probe temperature. Proton relaxation times in the rotating frame were estimated to be <20 ms for form I but >100 ms for the other polymorphs.

Solution-state ^{13}C NMR spectra were obtained at 100.58 MHz using a Bruker DPX 400 spectrometer at ambient probe temperature (ca. 25 °C). Solutions in both DMSO-d_6 and CD_3OD were examined, with chemical shifts referenced to the signal for tetramethylsilane. Approximately 20 000 transients were accumulated in each case, with a pulse angle of 90° and a recycle delay of 1s (though this resulted in reduced intensity for the quaternary carbons).

Powder X-ray Diffraction—The XRD traces were obtained using a Philips X′pert MPD diffractometer with a θ–2θ goniometer fitted with an Anton Paar TTK variable temperature camera. Cu Kα radiation of wavelength 1.54056 Å was used, with a diffracted beam monochromator. A sealed xenon detector was employed. Diffractograms were collected over the range 5–35° for 2θ, using a step size of 0.02° and a count time of 1 s.

Results and Discussion

The 75 MHz ^{13}C-{^1H} CPMAS spectra of the five polymorphic forms of sulfathiazole are shown in Figure 1. The relevant data are listed in Table 2. The resonances cover a relatively narrow range of chemical shifts ($\delta_C = 106$–172 ppm) because only sp^2-hybridized carbon atoms are involved. The spectra are all noticeably different, so that solid-state NMR is an excellent technique for monitoring the polymorphic form of sulfathiazole. Indeed, we propose that the solid-state NMR spectra, as presented here, be used in future alongside X-ray powder diffraction to define the polymorphic form of sulfathiazole samples. It is feasible to analyze mixtures of forms semiquantitatively (Figure 2) though the usual precautions regarding cross-polarization conditions need to be borne in mind. Assignment of the spectra (Table 1) may be readily made using three criteria:

(a) Comparison with solution-state shifts (see Table 2).

(b) The spectra obtained using the dipolar dephasing ("nonquaternary suppression") pulse sequence,[24] which show peaks arising from C-1, C-4, and C-7 only. Such edited spectra give even clearer distinction between the forms than the complete spectra, since then the resonances of C-4 are clear of all other peaks and are readily distinguishable in chemical shifts and/or splittings between the various polymorphs (Figure 2). The only difficulty that might occur is differentiating between form III on one hand and a combination of forms IV and V on the other.

(c) The broadening induced for the resonances of C-1, C-7, and C-8 by the second-order effects arising from dipolar coupling to quadrupolar ^{14}N nuclei ("residual dipolar splitting").[25] Although in principle such effects give

Table 2—Solid-State ^{13}C NMR Assignments for Five Polymorphs of Sulfathiazole

carbon atom	form I	form II	form III	form IV	form V	solution (DMSO-d_6)	solution (CD_3OD)
1[a]	153.2, 152.2, 151.2	155.5, 154.3, 153.2	151.1	151.0, 150.6	150.5	152.65	154.64
2,6	115.7,[b] 114.2[b]	115.2,[b] 114.0, 112.8	120.3,[b] 118.6[b]	120.2, 118.6	120.5, 118.3	112.90	115.24
3,5	132.1,[b] 130.2[b]	129.6,[b] 128.6[b]	130.7, 129.8, 127.3[b]	130.6, 127.3	129.8, 127.5	128.15	130.22
4	127.0, 125.9	127.9[b]	134.6, 133.8	133.8	134.5	128.32	130.24
7[a]	171.0, 170.2, 168.8	169.8, 168.5	169.5	169.4	169.3	168.37	171.49
8[a]	123.4	123.6	125.4	126.2	125.1	124.67	126.28
9	109.2, 107.7	108.1, 107.5	108.4, 106.8	106.5	108.5	107.90	109.86

[a] Bonded to ^{14}N, so second-order splittings occur. Some peak maxima are listed. [b] Double intensity peak.

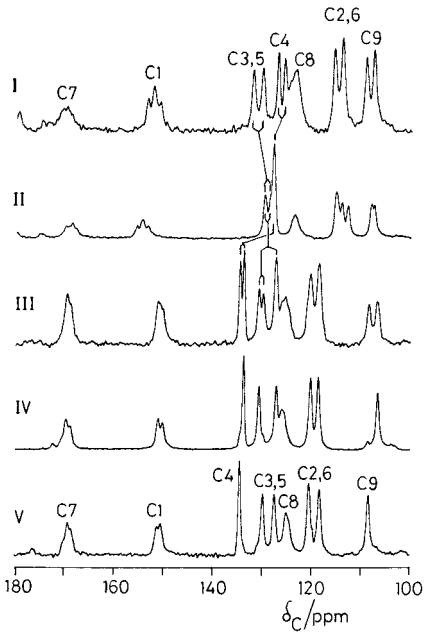

Figure 1—Carbon-13 CPMAS spectra, recorded at 75.43 MHz and ambient probe temperature with high-power proton decoupling, for the five polymorphs of sulfathiazole. The recycle delays were 30 s. Assignments are indicated for forms I and V. For the others, see Table 2.

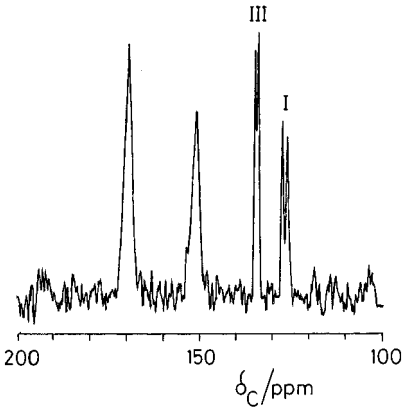

Figure 2—Carbon-13 CPMAS spectrum at ambient probe temperature for a mixture of sulfathiazole polymorphs I and III. The recycle delay was 30 s. The dipolar dephasing pulse sequence was used. Integration of the peaks assigned to C-4 suggests that the mixture contains ca. 46% of form I (assuming the CP and dipolar dephasing characteristics of the two polymorphs are similar).

rise to 1:2 or 2:1 doublets in ^{13}C spectra (for coupling to one ^{14}N), at our magnetic field for most of the sulfathiazole samples the relevant signals are merely broadened, with some ill-defined fine structure. It may be noted that C-7 is dipolar-coupled to two ^{14}N spins.

These considerations result in unambiguous assignments for nearly every peak in all polymorphs, though there are some accidental near-equivalences which result in overlapping signals.

A cursory glance at the spectra already conveys substantial information. Thus, for C-9 the resonance is clearly split into two for forms I−III but not for forms IV and V, showing that the asymmetric crystallographic unit consists of two molecules in the former cases, but only one in the latter. These conclusions are supported by the detailed X-ray structures. Other signals are also split for forms I−III, which generally have a more complex appearance than those for forms IV and V, but complications affect the situation except for C-4, which gives a clear doublet for forms I and III. However, the signal for this carbon is only a singlet for form II (as for forms IV and V), presumably because of accidental near-equivalence of the two expected peaks for II. The spectrum of form IV shown in Figure 1 indicates that the sample contains a small amount (ca. 5%) of form V (or ca. 10% of form III) as an "impurity".

Another factor potentially influencing the spectra and worthy of note at this point is internal rotation of the phenylene ring about the S−C bond. If this is slow on the NMR time scale, C-2 and C-6 will be nonequivalent (given the unsymmetrical nature of the molecule as a whole), thus giving rise to two lines for forms IV and V, but four lines for the other three forms. A similar situation exists for C-3 and C-5. At ambient probe temperature, the spectra for forms IV and V do indeed show the four lines for the phenylene CH carbons which are expected on the basis of slow internal rotation. However, there are obviously accidental degeneracies for forms II and III, since **three** lines are observed for C-2,6 for the former and for C-3,5 for the latter, while for the remaining phenylene C−H carbons in these two forms only **two** lines are resolved. At all events, these observations show that at ambient probe temperature, internal rotation is slow on the NMR time scale. The situation is somewhat different for form I. The spectrum displayed in Figure 1 shows only two lines for each of the carbon pairs C-2,6 and C-3,5, but on lowering the temperature to −40° and below, three lines are observed for C-2,6 (Figure 3a), which at first sight suggests that fast phenylene-group internal rotation is occurring for form I at room temperature. However, a more-detailed study shows that the spectrum of form I has a complex temperature variation which cannot be simply attributed to the slowing of internal rotation. In fact, we link these changes to those observed[19] in the powder XRD pattern at elevated temperatures, which indicate strong anisotropic lattice expansion. We have extended such measurements to low temperatures, confirming the significant changes. Thus, Figure 4 shows powder XRD traces of sulfathiazole polymorph I at 150, 25, and −85 °C. However, on carrying out MAS NMR experiments at elevated temperature (+80 °C, nominal), the spectrum changed considerably (Figure 3b), indicating that internal rotation probably is becoming rapid on the NMR time scale. Thus the resonance for C-2,6 has

Table 3—Summary of Dihedral Angles for the Sulfathiazole Polymorphs

form	C3–C4–S1–N2	C3–C4–S1–O1	C3–C4–S1–O2	C5–C4–S1–N2	C5–C4–S1–O1	C5–C4–S1–O2	C7–N2–S1–O1	C7–N2–S1–O2	C7–N2–S1–C4
1	–100	20.2	148.2	81.5	–158.2	–30.2	–36.9	–164.7	81.5
1	–118.0	3.4	131.6	66.8	–171.7	–43.5	–35.0	–163.0	83.9
2	–134.7	–12.8	112.0	46.3	168.2	–67.0	–37.0	–163.0	82.0
2	–139.0	–18.0	108.6	41.6	162.6	–70.9	–20.0	–147.2	97.7
3	–127.8	–6.1	119.9	51.0	172.7	–61.4	–39.5	–168.3	77.9
3	–127.5	–6.1	120.7	54.4	175.7	–57.4	–36.6	–166.2	81.1
4	–128.2	–6.4	120.1	52.9	174.7	–58.8	–38.1	–167.3	79.6
5	–127.5	–6.8	120.3	53.3	174.1	–58.8	–36.6	–166.2	80.3

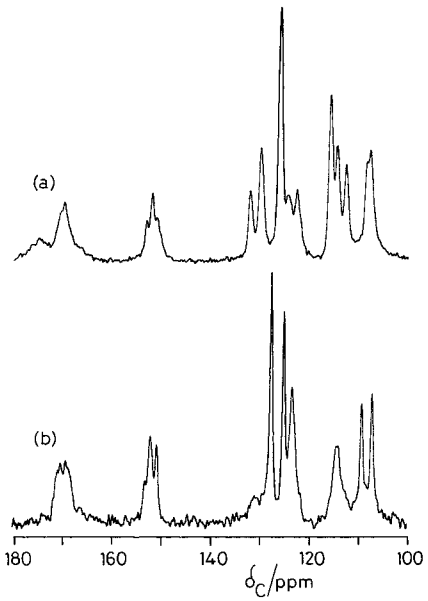

Figure 3—Carbon-13 CPMAS spectrum for polymorph I of sulfathiazole at nominal temperatures of (a) –45 °C and (b) +80 °C. The recycle delays were 300 s for a and 400 s for b.

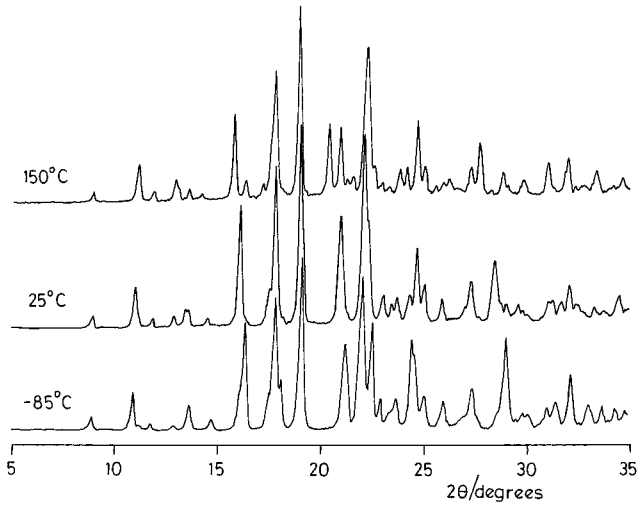

Figure 4—Powder XRD traces for sulfathiazole form I at 150 °C, 25 °C, and –85 °C.

become broad, while that arising from C-3,5 is so broadened as to be scarcely visible. The other signals show only small shift changes but no broadening. The phenomenon is reversible. The crystallographic changes indicated by the variable-temperature powder XRD patterns presumably facilitate the internal rotation.

As stated above, the spectra of the five forms all differ significantly. Clearly this must be caused by a combination of intramolecular and intermolecular (packing) considerations. Since the two rings are essentially planar in all

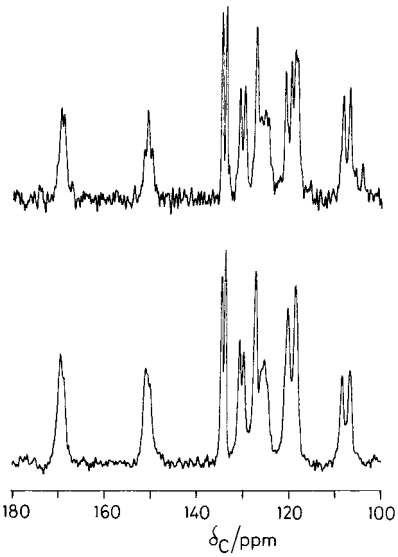

Figure 5—Carbon-13 CPMAS spectra at ambient probe temperature, showing a small variability between different samples of polymorph III.

cases, variations in intramolecular effects arise mainly from differences in (a) conformation expressed by dihedral angles about the S−C and S−N bonds, or (b) electronic structure of the phenylene ring. The S−N bond itself is approximately in the plane of the thiazole ring (maximum deviation just under 20°). The important intermolecular effects arise from the nature of the hydrogen bonding network and from the relationship of the rings in one molecule to the carbon atoms in a neighboring molecule. During the course of this work, we have found a small variability in spectra between different samples of form III (Figure 5). This particularly relates to the peaks assigned to C-2,6. Powder XRD patterns and near-infrared spectra also showed some distinctive characteristics in different samples. We have no current explanation for this variability, which is being further investigated. It is conceivable that two different "type-III" polymorphs with similar structures are involved. The unusual relationship between the structures of III−V suggest ways in which other variations are possible.

The largest difference between the spectra concerns the signals of C-4, which are at significantly lower frequencies for forms I and II than for the others. Indeed there is a crossover with the C-3,5 peaks for forms I and II compared to the other polymorphs. Such a difference between I and II on one hand and the other forms can also be observed for the C-2,6 signals. However the high-frequency shifts for C-3,5 in form I distinguishes it from all other forms. The position of the C-9 signal clearly differs between forms IV and V. The chemical shifts of C-1, C-7, and C-8 are harder to characterize because of the complicating effects of residual dipolar splittings arising from coupling to ^{14}N.

Table 3 lists the two sets of dihedral angles of relevance, which we have derived and collated from the published

crystal structures for forms I and III−V, as given in the Cambridge Crystallography Database and from detailed work on form II, as yet unpublished.[7,8] The major variations between the polymorphs seem to be for C3−C4−S1−N2 in both molecules of form I and for the three angles related to the N2−S1 bond for one of the inequivalent molecules of form II. It is difficult to see how these differences could account for the observed chemical shift variations.

A close look at the C−C bond lengths around the phenylene ring[8] shows that they distinctly alternate for form II, being 1.427, 1.354, and 1.416 Å for the averages of the C-1 to C-2/C-1 to C-6, C-2 to C-3/C-6 to C-5 and C-3 to C-4/C-5 to C-4 bonds, respectively. Such alternation does not appear to occur for polymorphs III and IV, though this conclusion is hampered by the relative inaccuracy of the structure determinations (that for III contains a scarcely believable distortion, with 1.386 Å quoted for C-1 to C-2 and 1.430 Å for C-6 to C-1 in the case of one of the inequivalent molecules, with estimated errors of 0.007 Å). Unfortunately the quoted errors for the relevant bonds in form I are even higher (ca. 0.013 Å), so the bonding situation is rather uncertain.

A more likely origin for the difference in the chemical shifts for forms I and II on one hand and the remaining polymorphs on the other lies in the hydrogen-bonding variations involving the NH_2 group. In forms III−V, the amino nitrogen acts as a hydrogen bond acceptor (the donor atom being the ring NH nitrogen of another molecule), leading to a partial positive charge on the amino nitrogen. This H-bonding occurs as part of a dimeric ring structure referred to by Davey and co-workers[5] as a β dimer (see below). Hydrogen bonding of this type also causes a low-frequency shift in the infrared spectrum for these three polymorphs, giving bands at ca. 3280 cm^{-1}. The NMR effect of charge on the amino nitrogen can be attested from ^{13}C CPMAS measurements on solid sulfathiazole monosulfate hemihydrate. The chemical shift of C-4 in this case is δ_C = 144.8 ppm, a full 17 ppm to higher frequency of those found for forms I and II, but only ca. 10 ppm higher than those for forms III−V. A similar effect is seen on the signal for C-1, which, for the sulfate, is at δ_C =135.7 ppm.

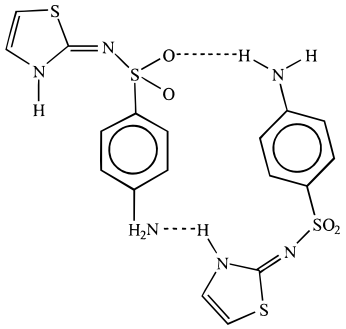

A β-ring dimer

Figure 1 shows that the spectrum of form III is remarkably similar to the sum of those for polymorphs IV and V, suggesting that the conformations and environments of the two molecules in the asymmetric unit of form III are similar to those of the unique molecules of the other two forms. Davey and co-workers[5] showed that III, IV, and V (which are referred to as III, II, and IV, respectively in their, crystallographic, notation) contain chains of β-ring dimers. These chains are linked into two-dimensional sheets, by additional amine nitrogen to imide nitrogen hydrogen bonds between each chain in form V, and between alternate chains in form III. However, there are no such H-bonds between chains in form IV. This difference between the forms will have associated structural changes, which appear to provide a satisfactory explanation for our comment that the form III spectrum closely resembles the sum of those of forms IV and V. The structural differences give rise to a chemical shift of ca. 0.8 ppm for C-4, 1.6 ppm for C-9, and 0.9 ppm for either C-3 or C-5 (these being the splitting magnitudes for form III).

Conclusion

We have shown that the five known polymorphs of sulfathiazole are clearly distinguished by their ^{13}C MAS NMR spectra. However, there are substantial changes in the spectrum of form I with temperature and of that of form III with sample. The spectra have been fully assigned and their appearance rationalized in terms of their crystal structures. The differences in hydrogen bonding explain why spectra of forms III−V are similar but differ substantially from those of forms I and II. Moreover, the fact that the spectrum of form III (which shows clearly the existence of two molecules in the asymmetric unit) is closely similar to the superposition of the spectra of forms IV and V may also be attributed to the hydrogen bonding network variations.

References and Notes

1. Grove, D. C.; Keenan, G. L. The dimorphism of sulfathiazole. *J. Am. Chem. Soc.* **1941**, *63*, 97−99.
2. Miyazaki, H. Polymorphism and melting points of sulfathiazoles. *Jpn. J. Pharm. Chem.* **1947**, *19*, 133−134; *Chem. Abstr.* **1951**, *45*, 3559h.
3. Burger, A.; Dialer, R. D. New investigational results of sulfathiazole polymorphism. *Pharm. Acta Helv.* **1983**, *58*, 72−78.
4. Anwar, J.; Tarling, S. E.; Barnes, P. Polymorphism of sulfathiazole. *J. Pharm. Sci.* **1989**, *78*, 337−342.
5. Blagden, N.; Davey, R. J.; Liebermann, H. F.; Williams, L.; Payne, R.; Roberts, R.; Rowe, R.; Docherty, R. Crystal structure and solvent effects in polymorphic systems: sulfathiazole. *J. Chem. Soc. Faraday* **1998**, *94*, 1035−1045; with Corrigendum, *Ibid*., *Idem*., **1998**, *94*, 1919.
6. Blagden, N.; Davey, R. J.; Rowe, R.; Roberts, R. Disappearing polymorphs and the role of reaction byproducts: the case of sulphathiazole. *Int. J. Pharm*. **1998**, *172*, 169−177.
7. Hughes, D.; Hursthouse, M. B.; Lancaster, R. W.; Tavener, S., Threlfall, T. L.; Turner, P. How many polymorphs has sulphathiazole? *J. Pharm. Pharmacol.* **1997**, *49*, S4, 20.
8. Hughes, D.; Hursthouse, M. B.; Lancaster, R. W.; Malik, A.; Tavener, S.; Threlfall, T. L. A new polymorph of sulfathiazole. *Acta Crystallogr. C*, in press.
9. Newbery, G. May and Baker laboratory notebook, February 18, 1938.
10. May and Baker, *Brit. Patent*. 517,272.
11. Fosbinder, R. J.; Walter, L. A. Sulfanilamido derivatives of heterocyclic amines. *J. Am. Chem. Soc.* **1939**, *61*, 2032−2033.
12. Lott, W. A.; Bergheim, F. H. 2-(p-Aminobenzenesulfonamido)-thiazole: a new chemotherapeutic agent. *J. Am. Chem. Soc.* **1939**, *61*, 3593−3594.
13. Lagas, M.; Lerk, C. F. Polymorphism of sulfathiazole. *Int. J. Pharm*. **1981**, *8*, 11−24.
14. Roblin, R. O.; Williams, J. H.; Winnek, P. S.; English, J. P. Chemotheraphy II. Some sulfanilamido heterocycles. *J. Am. Chem. Soc.* **1940**, *62*, 2002−2005.
15. Kruger, G. J.; Gafner, G. The crystal structure of sulfathiazole II. *Acta Crystallogr. B* **1971**, *27*, 326−333. The crystal structures of polymorphs I and II of sulphathiazole. *Acta Crystallogr. B.* **1972**, *28*, 272−283.
16. Babilev, F. V.; Belskii, V. K.; Simonov, Y. A.; Arzamastev, A. P. Polymorphism of Norsulphazol. *Khim-Farm. Zh*. **1987**, *21*, 1275−1280.
17. Egan, A. L.; Hughes, D. S.; Hursthouse, M. B.; Lancaster, R. W.; Tavener, S.; Threlfall, T. L. Over 100 solvates of sulfathiazole. Manuscript in preparation.
18. Chiou, W. L.; Niazi, S. Phase diagram and dissolution rate studies on sulfathiazole-urea solid dispersions. *J. Pharm. Sci.* **1971**, *60*, 1333−1338.
19. Anwar, J. Analysis of time-resolved powder diffraction data using a powder decomposition method with restraints. *J. Appl. Crystallogr*. **1993**, *26*, 413−421.

20. Elliott, P.; Threlfall, T. L. Mid-infrared diffuse reflectance spectra from neat polymorph samples. Manuscript in preparation.
21. Shaktshneider, T. P.; Boldyrev, V. V., Phase transformations in sulfathiazole during mechanical activation. *Drug Dev. Int. Pharm*. **1993**, *19*, 2055−2067.
22. Sekiguchi, K.; Shirotani, K. I.; Yuasa, H.; Suzuki, F.; Nakagura, F. Size reducibility of sulfathiazole by heat transition and subsequent ball-milling. *Chem. Pharm. Bull. Jpn*. **1980**, *28*, 3203−3209.
23. Tegenfeldt, J.; Haeberlen, U. Cross polarization in solids with flip-back of I-spin magnetization. *J. Magn. Reson*. **1979**, *36*, 453−457.
24. Opella, S. J.; Frey, M. H. Selection of nonprotonated carbon resonances in solid-state NMR. *J. Am. Chem. Soc.* **1979**, *101*, 5854−5856.
25. Harris, R. K.; Olivieri, A. C. Quadrupolar effects transferred to spin-$^1/_2$ magic-angle spinning spectra of solids. *Prog. NMR Spectrosc.* **1992**, *24*, 435−456.

JS990175A

Physiologically Based Pharmacokinetics of Digoxin in *mdr*1a Knockout Mice

MASAMI KAWAHARA,[†,‡] ATSUSHI SAKATA,[†] TOSHIAKI MIYASHITA,[†] IKUMI TAMAI,[†,§] AND AKIRA TSUJI*[,†,§]

Contribution from *Faculty of Pharmaceutical Sciences, Kanazawa University, 13-1 Takara-machi, Kanazawa 920-0934, Japan, and CREST, Japan Science and Technology Corporation, 4-1-8 Hon-machi, Kawaguchi 332-0012, Japan.*

Received June 4, 1999. Final revised manuscript received September 28, 1999.
Accepted for publication October 5, 1999.

Abstract □ To determine the contribution of the *mdr*1a gene product to digoxin pharmacokinetics, we constructed a physiologically based pharmacokinetic model for digoxin in *mdr*1a (–/–) and *mdr*1a (+/+) mice. After intravenous administration, total body clearance and tissue-to-plasma concentration ratios for muscle and heart were decreased in *mdr*1a (–/–) mice as compared with *mdr*1a (+/+) mice, and in particular, the digoxin concentration in the brain was 68-fold higher than that in *mdr*1a (+/+) mice at 12 h. On the other hand, *mdr*1a gene disruption did not change the contributions of renal and bile clearances to total clearance, the plasma protein binding, or the blood-to-plasma partition coefficient. Brain concentration–time profiles in *mdr*1a (+/+) and *mdr*1a (–/–) mice showed a different pattern from those in plasma and other tissues, indicating digoxin accumulation in the brain tissue. Because there was no difference in the uptake or release of digoxin by brain tissue slices from the two types of mice, we assumed the brain tissue compartment to consist of two parts (a well-stirred part with influx and efflux clearance and an accumulative part). Simulation with this model gave excellent agreement with observation when active efflux clearance across the blood–brain barrier was assumed to be zero in *mdr*1a (–/–) mice. The observations in other tissues in both types of mice were also well simulated.

Introduction

The *MDR*1 gene encodes human P-glycoprotein. In mice, two P-glycoproteins (encoded by the *mdr*1a and *mdr*1b genes) appear to perform the function of the single human protein.[1−5] The tissue distribution of these two isoforms in the mouse is different but partly overlapping. The mouse *mdr*1a gene is predominantly expressed in the intestine, liver, and capillary endothelial cells of brain and testis, whereas the *mdr*1b gene is predominantly expressed in the adrenal, placenta, ovary, and pregnant uterus.[3,6] Similar levels of *mdr*1a and *mdr*1b expression are found in the kidney. Schinkel et al. reported that the absence of the *mdr*1a P-glycoprotein has a pervasive influence on the tissue distribution and pharmacokinetics of drugs such as ivermectin, vinblastine, cyclosporin A, digoxin, etc.[7,8] The most striking effects were observed in the brain, owing to the high level of *mdr*1a P-glycoprotein at the blood−brain barrier. The use of *mdr*1a (−/−) mice allowed us to investigate pharmacokinetically the in vivo function of P-glycoprotein.

Digoxin is widely used in the treatment of congestive heart failure and is a substrate of P-glycoprotein.[9] Schinkel et al. reported a 35-fold higher concentration of digoxin in *mdr*1a (−/−) mouse brain than in *mdr*1a (+/+) mouse brain 4 h after intravenous administration.[8] They also suggested that the pharmacokinetics of digoxin in *mdr*1a (−/−) mice was quite different from that in *mdr*1a (+/+) mice. Mayer et al. also found that the brain level of [^{3}H]digoxin in *mdr*1a (−/−) mice continuously increased over a period of 3 days, resulting in a 200-fold higher concentration than in *mdr*1a (+/+) mice.[10] Clinically, digoxin may be coadministrated with other drugs which potentially inhibit P-glycoprotein in the treatment of cancer in elderly patients, and this may lead to dangerous side effects of digoxin, including nausea, tremor, or heart failure.

In this study, we investigated the pharmacokinetics of digoxin in *mdr*1a (−/−) mice by modifying the physiologically based pharmacokinetic model in rats reported by Harrison and Gibaldi,[11] in order to reveal the role of the *mdr*1a gene product in relation to tissue distribution and renal or biliary clearance. In particular, we tried to simulate the change of brain digoxin concentration due to loss of active efflux across the blood−brain barrier in *mdr*1a (−/−) mice.

Materials and Methods

Chemicals—[^{3}H]Digoxin (555 GBq/mmol) and SOLVABLE were obtained from New England Nuclear (Boston, MA), digoxin from Sigma Chemical Co. Ltd. (St. Louis, MO), and Clear-sol I, a liquid scintillation fluid, from Nacarai-Tesque Inc. (Kyoto, Japan). Other drugs and chemicals were commercial products.

Animals—Male *mdr*1a (−/−) mice (body weight 25−30 g) were obtained from Taconic Farms Inc. (Germantown, NY). Male C57BL/6 mice (body weight 25−30 g) obtained from Sankyo Laboratory Co. Ltd. (Hamamatsu, Shizuoka, Japan) were used as the control mice because genetically compatible wild-type *mdr*1a (+/+) mice, F2 and F3 generations of 129/Ola and FVB mice, were not available in Japan at the time when we started this study. We confirmed in a preliminary study that male C57BL/6 mice showed similar disposition kinetics of several drugs, P-glycoprotein substrates including tacrolimus, digoxin, and cyclosporin A, to the wild-type (+/+) mice (data not shown). Animals were maintained with free access to water and food in an air-conditioned room in the Institute for Experimental Animals, Faculty of Medicine, Kanazawa University.

Digoxin Pharmacokinetic Study—[^{3}H]Digoxin at 1 mg/kg (2.96 MBq/kg, 0.5 mg/mL in 40% ethanol solution) was administered to each mouse via a 29 G syringe into a jugular vein. At each sampling time, a midline incision was made under ether anesthesia, and whole blood was taken into a heparin-coated syringe from the inferior vena cava. Blood samples were centrifuged at 12 000 rpm for 3 min to obtain plasma. Brain, heart, liver, kidney, and muscle were isolated, washed in ice-cold saline, and then weighed. The contents of the intestine were removed and washed in ice-cold saline. About 0.1 g of each tissue was weighed and then dissolved by vibration (100 strokes/min) in SOLVABLE

* Author to whom correspondence should be addressed. Tel: +81-76-234-4479. Fax: +81-76-234-4477. E-mail: tsuji@kenroku.kanazawa-u.ac.jp.
† Faculty of Pharmaceutical Sciences, Kanazawa University.
‡ Present address: Hospital Pharmacy, School of Medicine, Kanazawa University, 13-1 Takara-machi, Kanazawa 920-8641.
§ CREST, Japan Science and Technology Corporation.

10.1021/js9901763 CCC: $18.00
Published on Web 11/06/1999

at below 60 °C for 2 h. After decolorization with H_2O_2, Clear-sol I and 5 N HCl were added, and the radioactivity was measured with a liquid scintillation counter (LSC-3500, ALOKA, Tokyo, Japan).

Tissue Slice Uptake Study—Preparation of tissue slices for uptake or release experiments was performed according to Gutierrez and Delgadoo-Coello.[12] Brain or skeletal muscle was collected from the completely bled mouse and was sliced with a razor blade 5−8 mm in diameter and 0.2−0.5 mm in thickness, in ice-cold Krebs-Ringer's Tris buffer (pH 7.4). Tissue slices weighing 5−20 mg were preincubated at 37 °C for 10 min in the presence or absence of 500 μM ouabain with continuous bubbling with 95% O_2/5% CO_2. Uptake experiments were started by replacing the buffer with [^{3}H]digoxin (7 nM)-containing buffer in the presence or absence of ouabain (500 μM). To terminate the uptake, tissue slices were washed three times with ice-cold buffer and solubilized with 5% sodium dodecyl sulfate in the counting vial, then Clear-sol I was added, and the radioactivity was measured with a liquid scintillation counter. Release experiments were carried out in a similar way, preincubation was done at 37 °C for 90 min in the buffer solution containing [^{3}H]digoxin, and then the buffer solution was exchanged for digoxin-free buffer at the starting time for the release study.

Plasma Protein Binding and Blood-to-Plasma Partition Coefficient—Plasma-free fraction of digoxin was measured by ultrafiltration. Two and one-half microliters of 40% ethanol solution containing [^{3}H]digoxin was added to 100 μL of plasma obtained from mice to produce a final concentration of 0.1−1000 ng/mL. After incubation at 37 °C for 30 min, samples were filtered with a Centrifree (Amicon Inc., Beverly, MA) at 1000 g, 37 °C for 10 min. Digoxin-free fraction was calculated according to the equation

$$f_p = C_f/C_p$$

where f_p, C_f, and C_p are digoxin-free fraction in the plasma, concentration of free digoxin in plasma calculated from the radioactivity in the filtrate, and total digoxin concentration in plasma, respectively.

Blood-to-plasma partition coefficient (R_B) was measured in vivo. One milliliter of blood samples was collected at 4 and 12 h after administration of [^{3}H]digoxin at 1 mg/kg (2.96 MBq/kg, 0.5 mg/mL in 40% ethanol solution). The blood sample was divided into two parts. One part was solubilized with SOLVABLE. The other part was centrifuged at 12 000 rpm for 3 min, and the radioactivity in solubilized whole blood and plasma was measured. The value of R_B was calculated as follows:

$$R_B = C_{blood}/C_p$$

where C_{blood} and C_p are digoxin concentrations in whole blood and in plasma, respectively.

Measurement of Renal and Bile Clearances—To determine the renal and bile clearances, mice were midline-incised and the renal artery or bile duct was ligated under ether anesthesia according to Harrison and Gibaldi.[11] [^{3}H]Digoxin was injected at a dose of 1 mg/kg (2.96 MBq/kg, 0.5 mg/mL in 40% ethanol solution), and the blood was sampled at 0.25, 0.5, 1, 2, and 4 h after the administration. Plasma samples were obtained by centrifugation at 12 000 rpm for 3 min, and then the radioactivity was measured with a liquid scintillation counter. Bile clearance was calculated from the difference between total clearance and the clearance obtained in bile-duct-ligated mice. Renal clearance was calculated from the difference between total clearance and the clearance obtained in renal-artery-ligated mice.

Physiologically Based Pharmacokinetic Model—A physiologically based pharmacokinetic model was constructed according to Harrison and Gibaldi,[11] including enterohepatic recirculation. As shown in Figure 1, the brain compartment was additionally modified in this study for investigation of the influence of *mdr*1a gene disruption. Since the digoxin plasma concentration−time profile was assumed to be biexponential up to 4 h (see Figure 2), we predetermined the pharmacokinetic parameters between plasma and brain with a hybrid model shown in Figure 3. In this hybrid model analysis, it was assumed that the drug penetrates by passive diffusion bidirectionally in both types of mice and is actively excluded by P-glycoprotein from the brain only in *mdr*1a (+/+) mice. The passive diffusion was defined as uptake clearance, and the efflux by P-glycoprotein was defined as efflux clearance

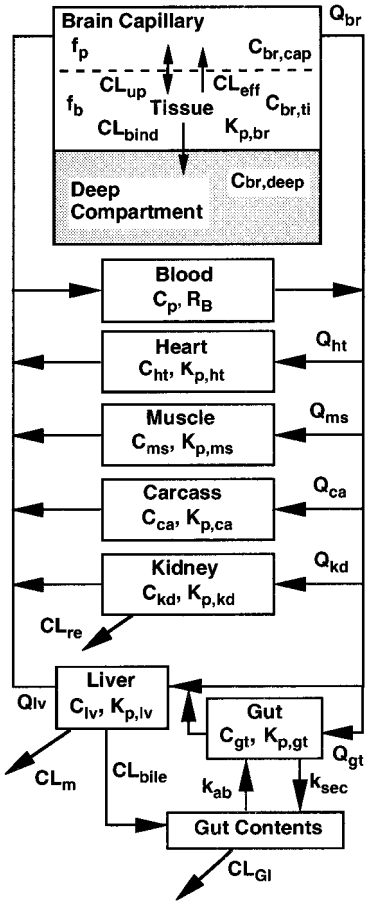

Figure 1—Physiologically based pharmacokinetic model for digoxin in mice: Q_i, CL_i, C_i and $K_{p,i}$ represent plasma flow rate, clearance, tissue drug concentration, and tissue-to-plasma concentration ratio for tissue i, respectively. The brain compartment was divided into three parts; CL_{up}, CL_{eff}, and CL_{bind} are the uptake clearance by passive diffusion, the efflux clearance by P-glycoprotein, and the binding clearance by accumulation, respectively.

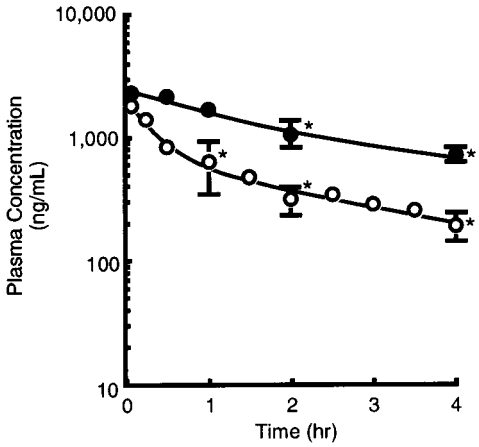

Figure 2—Plasma concentration–time profiles of [^{3}H]digoxin after 1 mg/kg intravenous administration in *mdr*1a (+/+) and *mdr*1a (–/–) mice. Drug solutions were administered to the lightly anesthetized *mdr*1a (+/+) and *mdr*1a (–/–) male mice via a jugular vein. Plasma concentrations were determined from the radioactivity. Open (○) and closed (●) symbols represent the results obtained in *mdr*1a (+/+) mice and *mdr*1a (–/–) mice, respectively (n = 3–5 for points marked with an asterisk (*); n = 1 for other points).

in this study. Two steps were taken in this determination. (1) The brain concentration−time profile in *mdr*1a (−/−) mice was simulated by means of the Runge−Kutta−Gill integration method using the hybrid model which employed a least-squares biexponential fitting to the plasma concentration−time profile. (2) The efflux clearance was estimated from the brain concentration−time

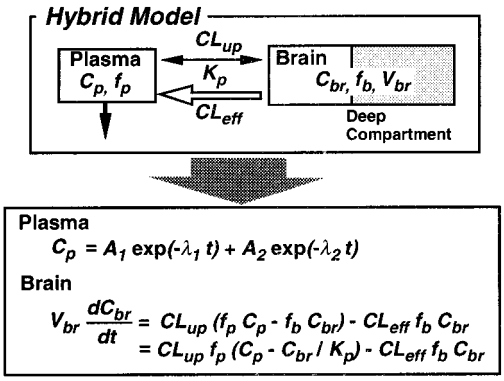

Figure 3—Hybrid pharmacokinetic model for brain distribution of drugs excluded by an active efflux system in mice. This model was employed for estimation of the values of CL_{up} and CL_{eff} in the brain under the condition that the distribution volume of brain was too small to affect significantly the systemic disposition of a test drug. In this model, it was assumed that the drug penetrates by passive diffusion with an uptake clearance (CL_{up}) bidirectionally in both types of mice and is actively excluded with an efflux clearance (CL_{eff}) by P-glycoprotein from the brain tissue only in *mdr*1a (+/+).

Table 1—Pharmacokinetic Parameters for Digoxin after 1 mg/kg Intravenous Administration in *mdr*1a (+/+) and *mdr*1a (–/–) Mice

	*mdr*1a (+/+)	*mdr*1a (–/–)
AUC (μg·min/mL)	155.4	439.8
MRT (min)	169.2	214.8
CL_{tot} (mL/min/kg)	6.44	2.27
V_d (L/kg)	1.09	0.488

profile in *mdr*1a (+/+) mice. Recently, Chen and Pollack have reported the simulation study of pharmacokinetics–pharmacodynamics of [D-penicillamine[2,5]]enkephalin[13] by a similar manner in *mdr*1a (–/–) mice.

As reported by Schinkel et al. the brain digoxin concentration in *mdr*1a (–/–) mice was very much higher than those in other tissues at 4 h after the administration.[8] Digoxin seems to be accumulated in brain tissue in *mdr*1a (–/–) mice. Then, the brain compartment was divided into three parts. The first compartment is brain capillary, the second is well-stirred brain tissue (interstitial fluid and intracellular space), and the third is a digoxin strongly binding deep compartment. The accumulation clearance to the deep compartment was determined by trial-and-error simulation.

Differential equations (see Appendix) were solved simultaneously by a FACOM-M776/20 in Kanazawa University Information Processing Center.

Results

Plasma Concentration–Time Profiles of Digoxin in *mdr*1a (+/+) and *mdr*1a (–/–) Mice—Figure 2 shows the plasma concentration–time profiles of digoxin after 1 mg/kg intravenous administration in *mdr*1a (+/+) and *mdr*1a (–/–) mice. Pharmacokinetic parameters were determined by moment analysis and are listed in Table 1. In *mdr*1a (–/–) mice, total clearance of digoxin was decreased to 30% of that in *mdr*1a (+/+) mice, and the distribution volume was also decreased to 50%. We also studied antipyrine plasma concentration–time profiles, which is considered as a marker of passive diffusion; there was no difference in these parameters between *mdr*1a (+/+) and *mdr*1a (–/–) mice (data not shown).

Tissue Distribution Study—Plasma and tissue digoxin concentration–time profiles were measured after 1 mg/kg administration in *mdr*1a (+/+) and *mdr*1a (–/–) mice. Tissue-to-plasma concentration ratios (K_p) were determined from the elimination phase according to Chen and Gross.[14] As shown in Table 2, K_p values of heart, muscle, intestine, and carcass were decreased largely in *mdr*1a (–/–) mice, being about half of those in *mdr*1a (+/+) mice. On the other hand, the K_p values of kidney and liver were slightly changed.

Table 2—Tissue-to-Plasma Concentration Ratios of Digoxin in *mdr*1a (+/+) and *mdr*1a (–/–) Mice

	*mdr*1a (+/+)	*mdr*1a (–/–)
brain	9.4	*a*
heart	1.13	0.626
muscle	0.804	0.424
kidney	1.07	0.797
liver	1.87	2.09
intestine	2.59	0.535
carcass	1.12	0.309

[a] K_p value of *mdr*1a (–/–) mice could not be determined by the method of Chen and Gross,[14] because it failed to reach the terminal phase.

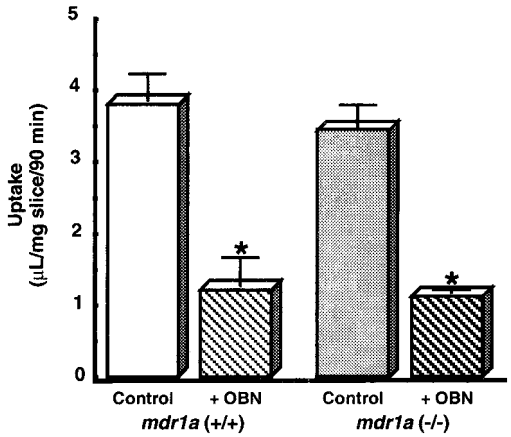

Figure 4—Effect of ouabain on the uptake of digoxin by brain slices from *mdr*1a (+/+) and (–/–) mice. Both types of mice were decapitated, and the brains were isolated and sliced with a razor blade in ice-cold buffer. The slices were preincubated at 37 °C for 10 min in the absence or presence of ouabain (500 μM), and then the uptake of [^{3}H]digoxin (7 nM) was measured for 90 min. Each column represents the mean ± SEM ($n = 4$). (*) Significantly different from control *mdr*1a (+/+) mice by Student's *t*-test ($p < 0.05$).

Brain and Muscle Slice Uptake Study—To clarify whether the changes in K_p values are related to the participation of P-glycoprotein, tissue binding, or other factors, an uptake study with brain and muscle slices was carried out.

As shown in Figure 4, there was no significant difference between digoxin uptake by brain slices of the two types of mice. In the presence of 500 μM ouabain, which completely inhibits digoxin binding to Na^+/K^+-ATPase, digoxin uptake was decreased to 30% of the control. It is likely that uptake clearance and binding of digoxin in the brain are not affected by the *mdr*1a gene product. The release of digoxin from brain slices was also at the same level in both types of mice. Although approximately 90% of digoxin still remained after 60 min, the amounts were decreased to 50% in the presence of 500 μM ouabain (data not shown). The brain digoxin concentration in *mdr*1a (+/+) mice was little changed at 12 h after administration in vivo, while the plasma digoxin concentration was decreased. These results strongly suggest that digoxin accumulation in the brain tissue results from binding of the drug with Na^+/K^+-ATPase, the contribution of which was estimated from the in vitro uptake study to account for approximately 70% of total brain digoxin concentration.

As shown in Figure 5, digoxin uptake by muscle slices was significantly decreased in *mdr*1a (–/–) mice, being about half of that in *mdr*1a (+/+) mice. This is the same as the in vivo distribution, indicating that the distribution

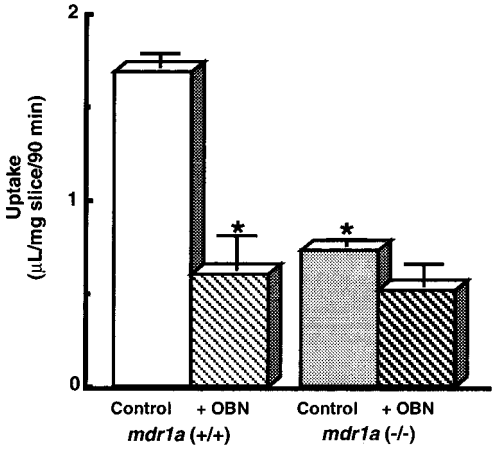

Figure 5—Effect of ouabain on the uptake of digoxin by muscle slices from *mdr*1a (+/+) and (–/–) mice. Muscle slices from both types of mice were preincubated at 37 °C for 10 min in the absence or presence of ouabain (500 μM), and then the uptake of [^{3}H]digoxin (7 nM) was measured for 90 min. Each column represents the mean ± SEM ($n = 4$). (*) Significantly different from control *mdr*1a (+/+) mice by Student's *t*-test ($p < 0.05$).

Table 3—Renal and Bile Clearances in *mdr*1a (+/+) and *mdr*1a (–/–) Mice[a]

clearance	*mdr*1a (+/+) (mL/min/kg)	*mdr*1a (–/–) (mL/min/kg)
CL_{tot}	5.64 (100)	1.91 (100)
CL_{re}	3.15 (55.9)	0.99 (51.8)
CL_{bile}	2.30 (40.8)	0.84 (44.0)
CL_m	0.19 (3.4)	0.08 (4.2)

[a] Renal and bile clearances of both types of mice were determined from the decrease in apparent total clearance in renal-artery-ligated and bile-duct-ligated mice, respectively. Percentage contributions to total clearance are shown in parentheses. Metabolic clearance was assumed to be residual clearance.

volume has decreased in *mdr*1a (−/−) mice. Digoxin uptake by muscle slices of both types of mice was decreased to the same level in the presence of 500 μM ouabain. Approximately 80% of digoxin was released after 60 min (data not shown).

Plasma-Free Fraction and Blood-to-Plasma Partition Coefficient of Digoxin—Plasma-free fraction (f_p) of digoxin was estimated to be about 0.78 in both types of mice, and there was no significant change with digoxin concentration from 0.1 to 1000 ng/mL. The R_B values of *mdr*1a (+/+) and *mdr*1a (−/−) mice were 0.898 ± 0.040 and 0.883 ± 0.033 ($n = 5-6$, mean ± SEM), respectively. These results suggest that plasma protein binding and binding to blood cells were not affected by the *mdr*1a gene product.

Estimation of Renal and Bile Clearances—To determine the contributions of renal and bile clearances, 1 mg/kg digoxin was administered intravenously to renal artery- or bile-duct-ligated mice. Renal or bile clearance was estimated from the difference from total clearance, and the results are listed in Table 3. Renal and bile clearances were 55.9% and 40.8% of total clearance in *mdr*1a (+/+) mice, and 51.8% and 44.0% in *mdr*1a (−/−) mice, respectively. In *mdr*1a (−/−) mice, total clearance was decreased to 30% of the control, while there was little change in the contribution of renal and bile clearances to total clearance.

Plasma, urine, and bile samples were analyzed by high-performance liquid chromatography. No metabolite was detected by HPLC in urine, bile, or plasma. Metabolic clearance in both types of mice seems to be very small. Furthermore, as shown in Table 3, the sum of renal and biliary clearances was nearly equal to the total clearance in both types of mice, supporting the above findings.

Physiologically Based Pharmacokinetic Model for Digoxin in Mice—After the determination of renal and bile clearances, enterohepatic clearances were estimated. GI tract clearance was estimated by scaling down from the data reported by Harrison and Gibaldi for rats.[11] The absorption and secretion rate constants were assumed to be the same as those in rats. In *mdr*1a (−/−) mice, the secretion clearance was assumed to be zero, because there was no P-glycoprotein expression in the small intestine of *mdr*1a (−/−) mice.

The brain digoxin concentration−time profile showed a quite different pattern from that of plasma. In *mdr*1a (+/+) mice, the brain digoxin concentration increased rapidly after administration and then decreased slowly after 4 h. In *mdr*1a (−/−) mice, the brain digoxin concentration increased slowly to a plateau. Therefore, the brain digoxin pharmacokinetics was considered to be complex. Because this phenomenon could not be described by a uniform compartment, the brain compartment was divided into three parts. The first is the capillary blood space compartment, the second is the well-stirred interstitial and intracellular compartment, and the third is the digoxin strongly binding compartment (deep compartment). The volumes of the capillary blood space and interstitial fluid or brain tissue were taken from the literature. Since the amount of digoxin uptake by brain slices decreased to 30% of the control in the presence of ouabain, the Na^+/K^+-ATPase-related binding space was estimated to be about 70% of brain tissue volume. Estimated uptake and efflux clearances (see Figure 3) were 2.5 μL/min and 0.4 mL/min, the accumulation clearance to the deep compartment was 0.1 μL/min determined by trial-and-error simulation. All parameters used in this pharmacokinetic model are listed in Table 4.

Finally, plasma and tissue digoxin concentration−time profiles in both types of mice were simulated according to the physiologically based model illustrated in Figure 1 and in the Appendix, and the results are shown in Figure 6a,b. All tissues and plasma concentration−time profiles up to 12 h after administration were well predicted.

Discussion

We have shown here that the conspicuous difference of brain digoxin concentration between *mdr*1a (−/−) and (+/+) mice can be simulated with this physiologically based model. It is noteworthy that the efflux clearance determines the distinctive pharmacokinetics of digoxin in *mdr*1a (−/−) mice. P-Glycoprotein in the kidney and liver acts as a secretion pump, while it acts as an absorption barrier or efflux pump in the small intestine for a variety of structurally unrelated hydrophobic and neutral or cationic compounds, including many cytotoxic drugs, and also as a transporter of steroid hormones in the adrenals and placenta.[9,15−23] Furthermore, P-glycoprotein in brain capillary endothelial cells acts as a blood−brain barrier to lipophilic drugs.[1,24−30] As P-glycoprotein is expressed in almost all tissues of the body, the absence of P-glycoprotein may cause remarkable changes in drug pharmacokinetics. In fact, Schinkel et al. reported that the pharmacokinetics of substrates of P-glycoprotein was changed in several tissues and dramatically in the brain of *mdr*1a (−/−) mice.[7,8]

Schinkel et al. reported that there are no physiological abnormalities in *mdr*1a (−/−) mice.[7] We also confirmed that the plasma protein binding, blood-to-plasma partition ratio, and metabolic feature of digoxin were the same in both types of mice. However, the digoxin concentration in the brain of *mdr*1a (−/−) mice was markedly increased, owing to the absence of efflux clearance via P-glycoprotein at the blood−brain barrier. Moreover, the digoxin concen-

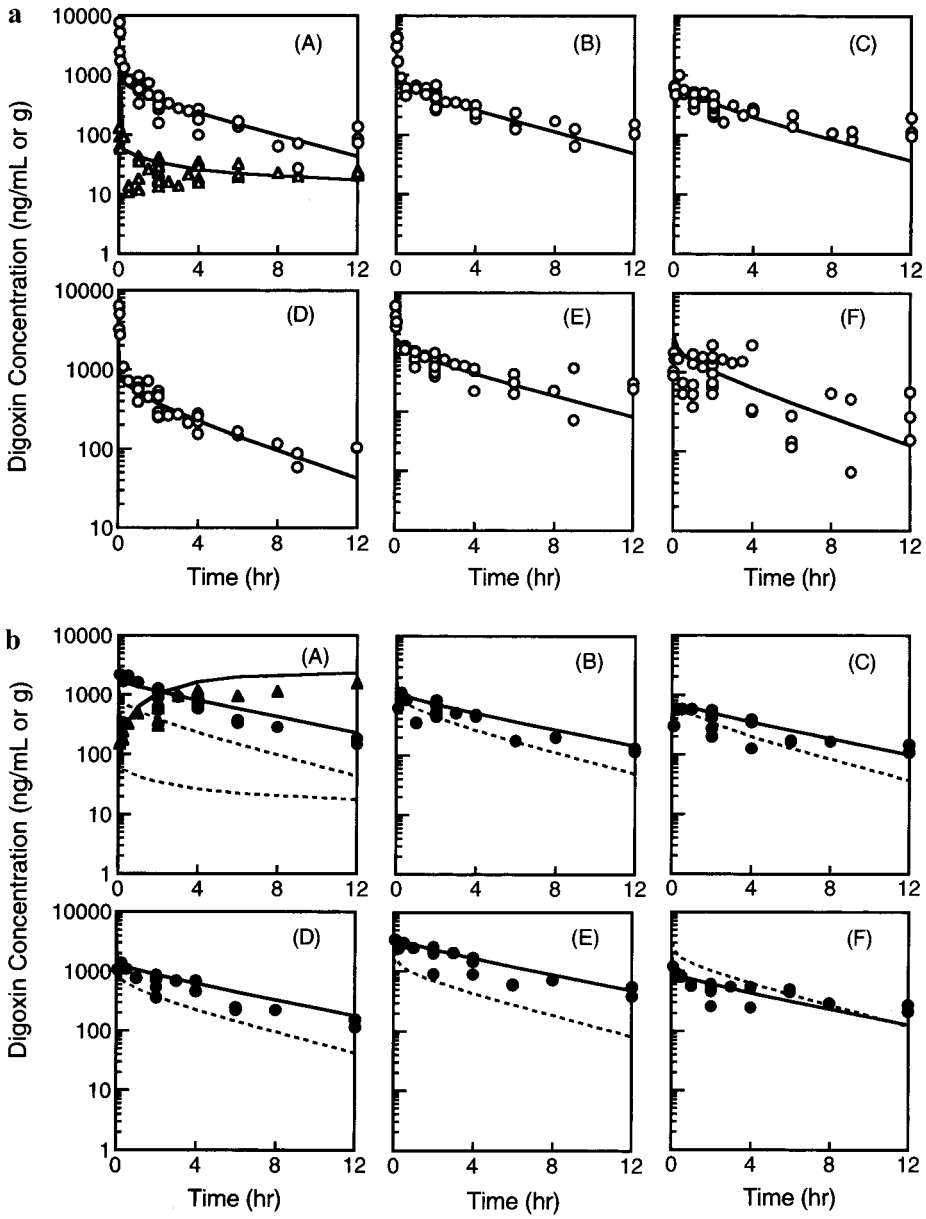

Figure 6—(a) Predicted and observed plasma and tissue concentrations of digoxin in *mdr*1a (+/+) mice after 1 mg/kg intravenous administration: (A) plasma (○), brain (△), (B) heart, (C) muscle, (D) kidney, (E) liver, and (F) gut. Solid lines represent the simulation curves from the physiologically based pharmacokinetic model. (b) Predicted and observed plasma and tissue concentrations of digoxin in *mdr*1a (–/–) mice after 1 mg/kg intravenous administration. (A) plasma (●), brain (▲), (B) heart, (C) muscle, (D) kidney, (E) liver, and (F) gut. Solid and dashed lines represent the simulation curves for *mdr*1a (–/–) mice and for *mdr*1a (+/+) mice, respectively.

tration in the brain of both types of mice remained high after 4 h. This phenomenon suggests that there is a deep compartment concerned with digoxin accumulation, and this is consistent with the conclusion from the brain slice study that digoxin binds to Na^+/K^+-ATPase.

Mayer et al. reported that urinary excretion of digoxin in *mdr*1a (−/−) mice was increased twice that of *mdr*1a (+/+) mice, and fecal excretion was decreased.[10] More than 16% of the administered digoxin was directly excreted in the intestinal lumen of *mdr*1a (+/+) mice within 90 min and at least 20% of metabolite was excreted in urine in their study. We also reported active secretion from the small intestine in rats.[22] However the contribution of renal clearance to total clearance was little changed in this study. Furthermore, we could not detect any metabolite in urine, bile, or plasma in either type of mouse. The reasons for these differences are unclear, but total radioactivity recovered was almost 100% of initial radioactivity. Although we used literature values for the active secretion and absorption rate constant of the intestine,[11] we could successfully simulate the digoxin pharmacokinetics in *mdr*1a (−/−) mice by neglecting the efflux clearance in the brain and intestine.

Plasma and tissue digoxin concentrations were increased and total body clearance was decreased in *mdr*1a (−/−) mice. However, the K_p values of kidney and liver were little changed. As Schinkel et al. reported that the *mdr*1b gene is up-regulated in liver and kidney of *mdr*1a (−/−) mice,[7] we also observed an increase of *mdr*1b gene expression in those organs (data not shown). This result suggests that digoxin clearance in *mdr*1a (−/−) mice may be supported by the up-regulated *mdr*1b gene in these organs.

In conclusion, we constructed a physiologically based pharmacokinetic model of digoxin in mice by adding a subdivided brain compartment based on the model of Harrison and Gibaldi in rats.[11] Our model could simulate the pharmacokinetics of digoxin in all tissues of *mdr*1a (+/+) and *mdr*1a (−/−) mice. The difference of the brain

Table 4—Pharmacokinetic Parameters for Digoxin in *mdr*1a (+/+) and *mdr*1a (–/–) mice[a]

clearance (mL/hr)	*mdr*1a (+/+)	*mdr*1a (–/–)
CL_{tot}[b]	7.44	2.52
CL_{re}[b]	4.16	1.31
CL_{bile}[b]	3.04	1.11
CL_m[b]	0.25	0.11
CL_{GI}[c]	0.019	0.019
k_{ab}[c,d]	0.036	0.036
k_{sec}[c,d]	0.72	

	Volume[e] (mL)	Blood Flow[e] (mL/min)
blood	1.0	4.38
heart	0.10	0.28
liver	1.30	1.10
kidney	0.34	0.80
intestine	1.50	0.90
muscle	10.0	0.50
gut contents	0.8	
carcass	6.9	1.61
brain capillary	0.025	0.089
brain tissue	0.068	
deep compartment	0.158	

[a] All parameters were estimated for mice with 22.0 g body weight. [b] Measured. [c] Estimated from ref 11. [d] Rate (h^{-1}). [e] Cited from Mordenti, J., et al. *J. Pharm. Sci.* **1986**, *75*, 1028–1040.

digoxin concentration between *mdr*1a (+/+) and *mdr*1a (−/−) mice could be explained completely in terms of the existence or absence of efflux clearance at the brain capillaries. Since P-glycoprotein regulates the distribution of digoxin into the brain by active efflux transport, co-administration with P-glycoprotein reversal drugs may cause serious side effects of digoxin.

Appendix

Mass balance equations are listed below.

blood pool:

$$V_p R_B(dC_p/dt) = R_B[(Q_{ht}C_{ht}/K_{p,ht}) + (Q_{ms}C_{ms}/K_{p,ms}) + (Q_{kd}C_{kd}/K_{p,kd}) + (Q_{li}C_{li}/K_{p,li}) + (Q_{ca}C_{ca}/K_{p,ca}) + Q_{br}C_{br,cap}] - R_B Q_{blood}C_p$$

brain capillaries:

$$V_{br,cap}R_B(dC_{br,cap}/dt) = R_B[Q_{br}(C_p - C_{br,cap}) - CL_{up}f_p(C_{br,cap} - C_{br,ti}/K_{p,br}) + CL_{eff}f_bC_{br,ti}]$$

brain tissue:

$$V_{br,ti}(dC_{br,ti}/dt) = CL_{up}f_p(C_{br,cap} - C_{br,ti}/K_{p,br}) - CL_{eff}f_bC_{br,ti} - CL_{bind}C_{br,ti}$$

brain deep compartment:

$$V_{br,deep}(dC_{br,deep}/dt) = CL_{bind}C_{br,ti}$$

heart, muscle, carcass:

$$V_i(dC_i/dt) = R_B Q_i(C_p - C_i/K_{p,i})$$

kidney:

$$V_{kd}(dC_{kd}/dt) = R_B Q_{kd}(C_p - C_{kd}/K_{p,kd}) - CL_{re,int}f_pC_{kd}/K_{p,kd}$$

liver:

$$V_{li}(dC_{li}/dt) = R_B(Q_{li} - Q_{gt})C_p + R_B Q_{gt}C_{gt}/K_{p,gt} - R_B Q_{li}C_{li}/K_{p,li} - (CL_m + CL_{bile,int})f_pC_{li}/K_{p,li}$$

gut wall:

$$V_{gt}(dC_{gt}/dt) = R_B Q_{gt}(C_p - C_{gt}/K_{p,gt}) + k_{ab}C_{gc}V_{gc} - k_{sec}C_{gt}V_{gt}$$

gut contents:

$$V_{gc}(dC_{gc}/dt) = k_{sec}C_{gt}V_{gt} + CL_{bile,int}f_pC_{li}/K_{p,li} - k_{ab}C_{gc}V_{gc} - CL_{GI}C_{gc}$$

where R_B = blood to plasma partition coefficient for digoxin, V_i = volume for tissue i, C_i = concentration for tissue i, Q_i = blood flow rate for tissue i, $K_{p,i}$ = tissue to plasma concentration ratio for tissue i, f_p (f_b) = plasma (tissue) free fraction, k_{ab} (k_{sec}) = absorption (secretion) rate constant, CL_{re} = renal clearance, CL_m = metabolic clearance, CL_{bile} = biliary clearance, CL_{up} = brain tissue uptake clearance, CL_{eff} = brain tissue efflux clearance, CL_{bind} = brain deep compartment binding clearance, and CL_{GI} = GI clearance (fecal clearance).

References and Notes

1. Tsuji, A.; Terasaki, T.; Takabatake, Y.; Tenda, Y.; Tamai, I.; Yamashima, T.; Moritani, S.; Tsuruo, T.; Yamashita, J. P-glycoprotein as the drug efflux pump in primary cultured bovine brain capillary endothelial cells. *Life Sci.* **1992**, *51*, 1427−1437.
2. Thiebaut, F.; Tsuruo, T.; Hamada, H.; Gottesman, M. M.; Pastan, I.; Wilingham, M. C. Cellular localization of the multidrug resistance gene product in normal human tissues. *Proc. Natl. Acad. Sci. U.S.A.* **1987**, *84*, 7735−7738.
3. Croop, J. M.; Raymond, M.; Haver, D.; Devault, A.; Arceci, R. J.; Gros, P.; Housman, D. E. The three mouse multidrug resistance (*mdr*) genes are expressed in a tissue-specific manner in normal mouse tissues. *Mol. Cell. Biol.* **1989**, *9*, 1346−1350.
4. Sugawara, I.; Kataoka, I.; Morishita, Y.; Hamada, H.; Tsuruo, T.; Itoyama, S.; Mori, S. Tissue distribution of P-glycoprotein encoded by a multidrug-resistant gene as revealed by a monoclonal antibody, MRK16. *Cancer Res.* **1988**, *48*, 1926−1929.
5. Cordon-Cardo, C.; O'Brien, J. P.; Casals, D.; Rittman-Grauer, L.; Biedler, J. L.; Melamed, M. R.; Bertino, J. R. Multidrug-resistance gene (P-glycoprotein) is expressed by endothelial cells at blood-brain barrier sites. *Proc. Natl. Acad. Sci. U.S.A.* **1989**, *86*, 695−698.
6. Schinkel, A. H.; Mol, C. A. A. M.; Wagenaar, E.; van Deemter, L.; Smit, J. J. M.; Borst, P. Multidrug resistance and the role of P-glycoprotein knockout mice. *Eur. J. Cancer* **1995**, *31*, 1295−1298.
7. Schinkel, A. H.; Smit, J. J. M.; van Tellingen, O.; Beijnen, J. H.; Wagenaar, E.; van Deemter, L.; Mol, C. A. A. M.; van der Valk, M. A.; Robanus-Maandag, E. C.; te Riele, H. P. J.; Berns, A. J. M.; Borst, P. Disruption of the mouse *mdr*1a P-glycoprotein gene leads to a deficiency in the blood-brain barrier and to increased sensitivity to drugs. *Cell* **1994**, *77*, 491−502.
8. Schinkel, A. H.; Wagenaar, E.; van Deemter, L.; Mol, C. A. A. M.; Borst, P. Absence of the mdr1a P-glycoprotein in mice affects tissue distribution and pharmacokinetics of dexa-

methasone, digoxin, and cyclosporin A. *J. Clin. Invest*. **1995**, *96*, 1698−1705.
9. Tanigawara, Y.; Okumura, N.; Hirai, M.; Yasuhara, M.; Ueda, K.; Kioka, N.; Komano, T.; Hori, R. Transport of digoxin by human P-glycoprotein expressed in a porcine kidney epithelial cell line (LLC-PK1). *J. Pharmacol. Exp. Ther*. **1992**, *263*, 840−845.
10. Mayer, U.; Wagenaar, E.; Beijnen, J.; Smit, J. W.; Mijer, D. K. F.; Asperen, J.; Bornst, P.; Schinkel, A. H.; Substantial excretion of digoxin via the intestinal mucosa and prevention of long-term digoxin accumulation in the brain by the mdr1a P-glycoprotein. *Br. J. Pharmacol*. **1996**, *119*, 1038−1044.
11. Harrison, L. I.; Gibaldi, M.; Physiologically based pharmacokinetic model for digoxin distribution and elimination in the rat. *J. Pharm. Sci*. **1977**, *66*, 1138−1142.
12. Gutierrez, M. C.; Delgado-Coello, B. A.; Influence of pipecolic acid on the release and uptake of [^{3}H]GABA from brain slices of mouse cerebral cortex. *Neurochem. Res*. **1989**, *14*, 405−408.
13. Chen, C.; Pollack, G. M.; Altered disposition and antinociception of [D-Penicillamine^{2,5}]Enkephalin in *mdr*1a-gene-deficient mice. *J. Pharmacol. Exp. Ther*. **1998**, *287*, 545−552.
14. Chen, H.-S. G.; Gross, J. F. Estimation of tissue-to-plasma partition coefficients used in physiological pharmacokinetic models. *J. Pharmacokinet. Biopharm*. **1979**, *7*, 117−125.
15. Borst, P.; Schinkel, A. H.; Smit, J. J. M.; Wagenaar, E.; van Deemter, L.; Smith, A. J.; Eijdems, E. W. H. M.; Bass, F.; Zaman, G. J. R. Classical and novel forms of multidrug resistance and the physiological functions of P-glycoproteins in mammals. *Pharmacol. Ther*. **1993**, *60*, 289−299.
16. Kamimoto, Y.; Gatmaitan, Z.; Hsu, J.; Arias, I. M. The function of Gp170, the multidrug resistant gene product, in rat liver canalicular membrane vesicle. *J. Biol. Chem*. **1989**, *264*, 11693−11698.
17. Speeg, K. V.; Maldonado, A. L.; Liaci, J.; Muirhead, D. Effect of cyclosporine secretion by the kidney multidrug transporter studied in vivo. *J. Pharmacol. Exp. Ther*. **1992**, *261*, 50−55.
18. Hori, R.; Okumura, N.; Aiba, T.; Tanigawara, Y. Role of P-glycoprotein in renal tubular secretion of digoxin in the isolated perfused rat kidney. *J. Pharmacol. Exp. Ther*. **1993**, *266*, 1620−1625.
19. Hsing, S.; Gatmaitan, Z. C.; Arias, I. M. The function of Gp170, the multidrug resistance gene product, in the brush border of rat intestinal mucosa. *Gastroenterology* **1992**, *102*, 879−885.
20. Leu, B. L.; Huang, J. D. Inhibition of intestinal P-glycoprotein and effect on etoposide absorption. *Cancer Chemother. Pharmacol*. **1995**, *35*, 432−436.
21. Hunter, J.; Hirst, B. H.; Simmons, N. L. Drug absorption limited by P-glycoprotein-mediated secretory drug transport in human intestinal epithelial Caco-2 cell layers. *Pharm. Res*. **1993**, *10*, 743−749.
22. Terao, T.; Hisanaga, E.; Sai, Y.; Tamai, I.; Tsuji, A. Active secretion of drugs from the small intestinal epithelium in rats by P-glycoprotein functioning as an absorption barrier. *J. Pharm. Pharmacol*. **1996**, *48*, 1083−1089.
23. Ueda, K.; Okamura, N.; Hirai, M.; Tanigawara, Y.; Saeki, T.; Kioka, N.; Komano, T.; Hori, R. Human P-glycoprotein transports cortisol, aldosterone, and dexamethasone, but not progesterone. *J. Biol. Chem*. **1992**, *267*, 24248−24252.
24. Tsuji, A.; Tamai, I.; Sakata, A.; Tenda, Y.; Terasaki, T. Restricted transport of cyclosporin A across the blood-brain barrier by a multidrug transporter, P-glycoprotein. *Biochem. Pharmacol*. **1993**, *46*, 1096−1099.
25. Tatsuta, T.; Naito, M.; Oh-hara, T.; Sugawara, I.; Tsuruo, T. Functional involvement of P-glycoprotein in blood-brain barrier. *J. Biol. Chem*. **1992**, *267*, 20383−20391.
26. Ohnishi, T.; Tamai, I.; Sakanaka, K.; Sakata, A.; Yamashima, T.; Yamashita, J.; Tsuji, A. In vivo and in vitro evidence for ATP-dependency of P-glycoprotein-mediated efflux of doxorubicin at the blood-brain barrier. *Biochem. Pharmacol*. **1995**, *49*, 1541−1544.
27. Gilman, A. G.; Rall, T. W.; Nies, A. S.; Taylor, P. *The pharmacological basis of therapeutics*; McGraw-Hill Book Co.: Singapore, 1991; pp 1811.
28. Sakata, A.; Tamai, I.; Kawazu, K.; Deguchi, Y.; Ohnishi, T.; Saheki, A.; Tsuji, A. *In vivo* evidence for ATP-dependent and P-glycoprotein-mediated transport of cyclosporin A at the blood-brain barrier. *Biochem. Pharmacol*. **1994**, *48*, 1989−1902.
29. Tamai, I.: Tsuji, A. Drug delivery through the blood-brain barrier. *Adv. Drug Deliv. Rev*. **1996**, *19*, 401−424.
30. Tsuji, A.; Tamai, I. Blood-brain barrier function of P-glycoprotein. *Adv. Drug Deliv. Rev*. **1997**, *19*, 287−298.

JS9901763

Carrier-Mediated Transport of Monocarboxylic Acids in BeWo Cell Monolayers as a Model of the Human Trophoblast

NAOKI UTOGUCHI,† MALIN MAGNUSSON, AND KENNETH L. AUDUS*

Contribution from *Department of Pharmaceutical Chemistry, The University of Kansas, Lawrence, Kansas 66047.*

Received May 31, 1999. Final revised manuscript received September 20, 1999.
Accepted for publication September 29, 1999.

Abstract □ The monolayer-forming, human choriocarcinoma cell line, BeWo, was used to study the mechanisms of monocarboxylic acid transport across the human trophoblast. Benzoic acid, acetic acid, and lactic acid were used as markers for monocarboxylic acid carrier-mediated transport. The uptake of benzoic acid by BeWo cells was saturable ($K_t = 0.6 \pm 0.3$ mM) at higher concentrations and significantly inhibited by typical metabolic inhibitors, sodium azide and 2,4-dinitrophenol. A selection of different monocarboxylic acids, including a natural substrate lactic acid, also substantially inhibited the uptake of benzoic acid and acetic acid by BeWo cells, whereas dicarboxylic acids did not affect the uptake of either marker. Monocarboxylic acid uptake was pH-dependent and inhibited by carbonyl cyanide *p*-trifluoromethoxyphenylhydrazone (FCCP), a protonophore. Kinetic analysis using Lineweaver–Burk plots revealed that monocarboxylic acids competitively inhibited the uptake of benzoic, lactic, and acetic acid by BeWo cells. In transport experiments, the permeation of benzoic acid from apical-to-basolateral side was greater than the permeation from the basolateral-to-apical side, and the transport of benzoic acid from apical-to-basolateral side was inhibited by monocarboxylic acids. The findings obtained in the present study confirm the existence of an asymmetric, carrier-mediated transport system for monocarboxylic acids across the BeWo cell, a representative of the human trophoblast.

Introduction

The placenta, in part, serves as a semipermeable barrier separating the maternal and fetal circulations. The placental barrier is comprised of a single layer of trophoblasts that have an important role in controlling the passage of molecules from mother to fetus. In general, the absorption of drugs across the single layer of trophoblasts can be explained in terms of the pH-partition hypothesis which is well illustrated by passive diffusion mechanisms.[1,2] However, with the use of brush-border-membrane vesicle techniques or cultured cells,[3] it has become increasingly clear that there are a number of carrier-mediated transport mechanisms present at the placental barrier including systems for amino acids,[3,4] transferrin,[5] and dopamine.[6] These carriers take on pharmaceutical relevance due to the fact that nutrients and hormones, as well as drugs and drugs of abuse, can be transported across the placental barrier by these mechanisms.[7]

Carrier-mediated transport mechanisms for monocarboxylic acids exist in many cell types.[8−10] In fact, there are known to be at least seven putative monocarboxylic acid transporter (MCT) isoforms. The mRNA representing five of the seven MCTs has been shown in human placenta.[11] Using brush border membrane preparations, a functional, proton-dependent MCT has been observed in tissues from rat[12,13] and human[14] placenta. A functional, bidirectional, and carrier-mediated mechanism for lactic acid, presumably a MCT, has also been demonstrated in the perfused human placental lobe model.[15] In addition to the transport of lactic acid,[11,14,15] a MCT at the placental barrier presents a potential mechanism by which monocarboxylic acid drugs and drugs of abuse may readily distribute between maternal and fetal compartments. Therefore, the characterization of a placental MCT system can contribute to an understanding of the trophoblast transport mechanisms controlling fetal exposure to substances possessing a monocarboxylic acid constituent.

The objective of this study was to investigate the presence of a functional MCT in BeWo cell monolayers, a representative human trophoblast culture system.[16] BeWo cell monolayers have been applied to studies of the polarized trans-trophoblast transport of serotonin and transferrin, monoamine uptake processes, and relevant nutrient uptake and transport systems.[16−18] The existence of MCT systems in the BeWo cells would provide an in vitro tool representative of the human trophoblast to characterize trans-placental transport mechanisms that influence drug distribution in pregnancy. The BeWo cell line is particularly attractive for the studies of drug distribution at the placenta barrier because it is stable, relatively easy to maintain by passage, and grows to a confluent monolayer in a relatively short period of time. Indeed, in contrast to primary cultures, the cell line is one of the few existing trophoblast cell culture systems to form a confluent monolayer that allows trans-trophoblast transport studies. More importantly, the BeWo cell displays morphological properties and biochemical marker enzymes and hormone secretion common to normal trophoblasts.[16]

Materials and Methods

Materials—[^{14}C]Benzoic acid (55 Ci/mol), [^{14}C]-L-lactic acid (150 Ci/mmol), and [^{14}C]acetic acid (55 Ci/mol) were obtained from American Radiolabeled Chemicals (St. Louis, MO). Fetal bovine serum (FBS) was from JRH Bioscience (Lenexa, KS). Penicillin–streptomycin as a mixture was from Gibco (Gaithersburg, MD). Translucent polycarbonate filters (13 mm diameter, 0.4 μm pore size) were purchased from Fisher Scientific. All other chemicals were of the purest available analytical grade and purchased from Fisher or Sigma (St. Louis, MO).

Cell Culture—The BeWo cell line was originally derived from a human choriocarcinoma. The BeWo clone (b30) was obtained from Dr. Alan Schwartz (Washington University, St. Louis, MO). The cells were cultured by the methods previously described, and the cells used in these experiments were from passages 28 to 40.[16] Briefly, the cells were cultured in Dulbecco's modified Eagle's medium (DMEM) with 10% heat-inactivated FBS containing 0.37% sodium bicarbonate and 1% antibiotics (10 000 U/mL penicillin and 10 mg/mL streptomycin). The cells were maintained

* Corresponding author. Tel: 785-864-4138, fax: 785-864-5736. e-mail: audus@ukans.edu.
† Present address: Showa College of Pharmaceutical Sciences, Machida, Tokyo 194-8543, Japan.

10.1021/js990173q CCC: $18.00
Published on Web 10/27/1999

in 175-cm^2 flasks at pH 7.4 under 5% CO_2 and 95% humidity at 37 °C. The cells were harvested by exposure to a trypsin−EDTA solution (0.25% trypsin and 0.02% EDTA in HBSS) and passed onto 12-well tissue culture plates or polycarbonate membranes coated with rat tail collagen in 100-mm culture dishes. With the seeding density of 10 000 cells/cm^2, the cells formed confluent monolayers between 2 and 3 days and were used for experiments at that time.

Uptake Experiments—The BeWo cells at confluence were washed twice with Hank's balanced salt solution (HBSS; 136.7 mM NaCl, 0.385 mM Na_2HPO_4, 0.441 mM KH_2PO_4, 0.952 mM $CaCl_2$, 5.36 mM KCl, 0.812 mM $MgSO_4$, 25 mM D-glucose, and 10 mM HEPES (2-[4-(2-hydroxyethyl)-1-piperazinyl]ethanesulfonic acid) for adjustment to pH 7.0 or 7.5 or 10 mM MES (2-morpholinoethanesulfonic acid, monohydrate) for adjustment to pHs < 6.5 and then the test solution containing [^{14}C]benzoic acid or [^{14}C]acetic acid or [^{14}C]-L-lactic acid was added at 0.25 μCi/mL as a marker for monocarboxylic acid carrier-mediated transport. The pH of the test solution was 6.0 except in the pH-dependent uptake experiments. After 30 s, the test solution was aspirated away, and the cells were washed with ice-cold HBSS three times. For quantitation of drug uptake, the cells were suspended in 1.0 N NaOH, and the suspension was incubated at 37 °C overnight at which point a half volume of 2.0 N HCl was added. Radioactivity was quantitated using a liquid scintillation counter. Cellular protein was quantified using a protein assay kit (Pierce) with bovine serum albumin as a standard. Details of the conditions for each experiment are given in the figure legends or table footnotes.

In one series of experiments, an equivalent amount of choline chloride replaced sodium chloride in the HBSS and was used as a sodium-depleted buffer.

Transport Experiment—A horizontal Side-Bi-Side diffusion apparatus (Crown Glass) was used to measure the transmonolayer permeability of cells grown on the surface of 0.4 μm pored polycarbonate filters, as previous described.[16] The cells faced the donor chamber as the apical side, and the polycarbonate membrane faced the receiver chamber as the basolateral side. The water jacket surrounding the donor and the receiver chambers was thermostated at 37 °C. The contents of each chamber were continuously stirred at 600 rpm with magnetic stir bars. When the apical-to-basolateral transport studies were performed, the pH of the donor (apical) side was 6.0 and that of receptor (basolateral) side was 7.4. When the basolateral-to-apical transport studies were performed, the pH of the donor (basolateral) side was 6.0 and that of the receptor (apical) side was 7.4. The concentration of added [^{14}C]benzoic acid was 0.25 μCi/mL. A 0.2-mL aliquot from the receiver chamber was taken at several time points up to 60 min.

Calculation of Apparent Permeability Coefficients—Apparent permeability coefficients for the monolayers of cells, P_e, were calculated from the following relationship

$$1/P_t = 1/P_e + 1/P_m \quad (1)$$

where P_t is apparent permeability coefficient for the collage-coated membrane in the presence of monolayers, and P_m is the apparent permeability coefficient for collagen-coated polycarbonate membrane alone.[19]

Michaelis−Menten Parameters—To estimate the values of the kinetic parameters of saturable uptake by BeWo cells, the uptake rate (J) was fitted to the following equation, which consists of both saturable and nonsaturable linear terms, using a nonlinear least-squares regression analysis program MULTI:[20]

$$J = J_{max} \times C/(K_t + C) + k \times C \quad (2)$$

where J_{max} is the maximum uptake rate for a carrier-mediated process, C is the benzoic acid concentration, K_t is the half-saturation concentration (Michaelis constant), and k is a first-order rate constant.

Statistical Analysis—All results were expressed as means ± standard deviation (SD). Statistical analysis between two groups was performed using Student's t-test, and one-way analysis of variance (ANOVA) was used for single and multiple comparisons. P values of 0.05 or less were considered to indicate a statistically significant difference.

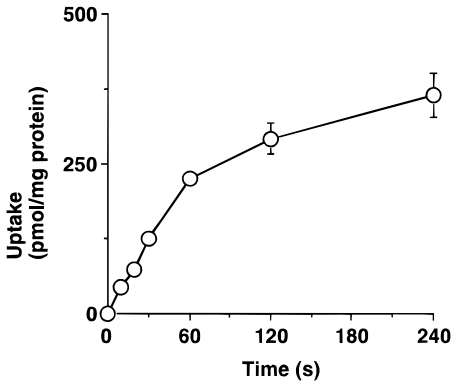

Figure 1—Time course of [^{14}C]benzoic acid uptake by BeWo cells. The vertical bar through each point represents the SD for four replicate experiments.

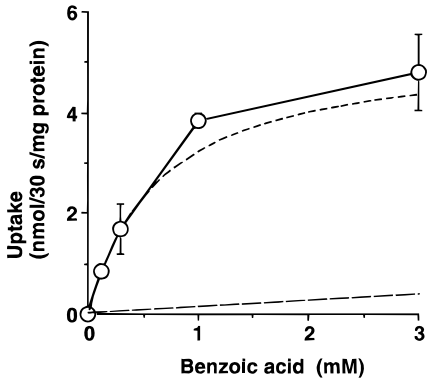

Figure 2—Concentration dependency of [^{14}C]benzoic acid uptake by BeWo cells. The uptake of [^{14}C]benzoic acid by BeWo cells was measured at 37 °C for 30 s. The upper dotted line represents the uptake for the saturable component calculated from the kinetic parameters obtained as described in the text. The lower dotted line represents the uptake for the nonsaturable component calculated from the kinetic parameters. The vertical bar through each point represents the SD of four replicate experiments.

Results

[^{14}C]Benzoic acid was rapidly accumulated in BeWo cells with time (Figure 1). The uptake was linear initially and reached equilibrium at about 2 min. Therefore, all subsequent uptake studies and kinetic analysis were performed from data collected through 30 s.

Figure 2 shows the relationship between the initial rate of uptake of [^{14}C]benzoic acid and its concentration in the incubation buffer. The results indicated that the uptake of benzoic acid consisted of two processes, a saturable process evident at low concentrations and an apparently nonsaturable process evident at high concentrations. The uptake processes were analyzed according to eq 2. The kinetic parameters calculated for benzoic acid uptake were a J_{max} of 0.52 ± 0.22 nmol/30 s/mg of protein, a K_t of 0.64 ± 0.26 mM, and a k of 0.11 ± 0.06 μL/30 s/mg of protein. The upper dotted line represents the uptake for the saturable component calculated from the kinetic parameters. The lower dotted line represents the uptake for the nonsaturable component calculated from the kinetic parameters. At any given concentration, the uptake by saturable component was higher than that by nonsaturable one.

The effects of metabolic inhibitors on the uptake of [^{14}C]-benzoic acid were studied to determine whether this uptake required cell-dependent energy expenditure (Table 1). Sodium azide (10 mM), a respiratory chain inhibitor, or 2,4-dinitrophenol (1 mM), an uncoupler of oxidative phosphorylation, significantly inhibited the uptake of [^{14}C]-benzoic acid by the BeWo cells. Moreover, carbonyl cyanide

Table 1—Effects of Metabolic Inhibitors, Ionophore (carbonyl cyanide *p*-(trifluoromethoxy)phenylhydrazone; FCCP), anion-exchange (4,4′-diisothiocyanostilbene-2,2′-disulfonic acid; DIDS) Inhibitors, and Sodium-Depleted Buffer on [^{14}C] Benzoic Acid Uptake by BeWo Cell Monolayers at 37 °C[a]

inhibitor	concn	relative uptake (percent of control)[b]
sodium azide	10 mM	20.1 ± 5.2[c]
2,4-dinitrophenol	1 mM	13.3 ± 7.4[c]
FCCP	50 μM	9.3 ± 1.4[c]
DIDS	100 μM	117.5 ± 8.1
sodium-depleted buffer	no treatment	101.7 ± 11.7

[a] BeWo cells were pretreated with these agents for 15 min prior to performing an uptake experiment. [b] Each value represents the mean ± standard deviation of four experiments. [c] $P < 0.001$ versus untreated control (100%).

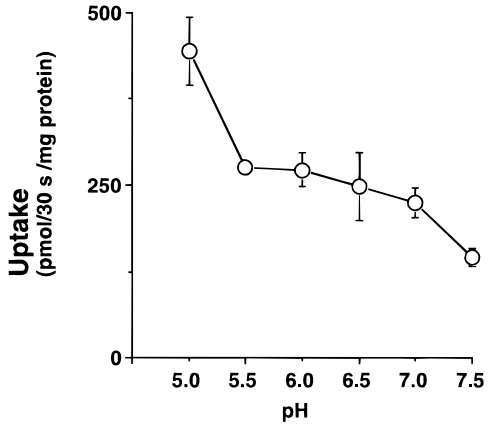

Figure 3—pH dependence of [^{14}C]benzoic acid uptake by BeWo cells. The uptake of [^{14}C]benzoic acid by BeWo cells was determined at the indicated pH at 37 °C. The vertical bar through each point represents the SD of four replicate experiments.

p-(trifluoromethoxy)phenylhydrazone (FCCP; 50 μM), a protonophore, significantly inhibited the uptake (Table 1), whereas 4,4′-diisothiocyanostilbene-2,2′-disulfonic acid (DIDS; 0.1 mM), an anion-exchange inhibitor, had no inhibitory effect on benzoic acid uptake. Finally, the uptake of benzoic acid in a sodium-depleted buffer was not different from the control, suggesting the mechanism was not sodium-dependent (Table 1). Figure 3 illustrates the effect of incubation buffer pH in the range from 5.0 to 7.5 on [^{14}C]-benzoic acid uptake by BeWo cells. The rate of [^{14}C]benzoic acid uptake decreased with increasing pH from an acidic to a neutral pH. These findings, together with the concentration dependence and sensitivity to metabolic inhibitors, strongly suggested that [^{14}C]benzoic acid uptake by BeWo cells was dependent on a proton gradient and was carrier-mediated.

To investigate the properties of the carrier involved in [^{14}C]benzoic acid uptake by BeWo cells, we studied the effects of various mono- and dicarboxylic acids on this uptake (Table 2). Each monocarboxylic acid, including lactic acid, significantly inhibited the uptake of [^{14}C]benzoic acid, whereas none of the dicarboxylic acids had a significant inhibitory effect on the uptake of the marker. We also found that the BeWo cells take up [^{14}C]acetic acid and that this uptake was significantly inhibited by monocarboxylic acids, including lactic acid (Table 2). In contrast, dicarboxylic acids had no marked effect on the uptake of [^{14}C]acetic acid by BeWo cells. These results implied that the carrier that mediates monocarboxylic acid uptake by BeWo cells was a nonspecific monocarboxylic acid carrier. Additionally, the carrier is relatively stereoselective as distinguished by the variable inhibition by the two lactic acid isomers.

Table 2—Effects of Selected Carboxylic Acids on [^{14}C]Benzoic Acid or [^{14}C]Acetic Acid Uptake by BeWo Cell Monolayers at 37 °C[a]

		relative uptake (percent of control)[b]	
		[^{14}C]benzoic acid	[^{14}C]acetic acid
monocarboxylic acids	benzoic acid	10.8 ± 0.2[c]	19.5 ± 2.7[c]
	D-lactic acid	20.4 ± 1.8[c]	26.5 ± 4.2[c]
	L-lactic acid	6.1 ± 1.3[c]	13.4 ± 1.5[c]
	propionic acid	12.7 ± 0.9[c]	18.9 ± 2.6[c]
	acetic acid	10.1 ± 2.0[c]	36.9 ± 2.9[c]
	p-aminobenzoic acid	5.5 ± 0.1*	20.7 ± 3.4*
	acetylsalicylic acid	12.3 ± 1.3*	11.1 ± 1.0*
	salicylic acid	3.5 ± 0.1*	9.3 ± 0.7*
dicarboxylic acids	glutaric acid	91.0 ± 8.5	107.2 ±12.8
	fumaric acid	113.8 ± 5.5	98.4 ±10.4
	maleic acid	92.1 ± 7.3	102.4 ±28.4

[a] [^{14}C]Benzoic acid or [^{14}C]acetic acid uptake by BeWo cells were performed in the presence of 10 mM (2000-fold excess) of the indicated carboxylic acid. [b] Each value represents the mean ± standard deviation of four experiments. [c] $P < 0.001$ versus untreated control (100%).

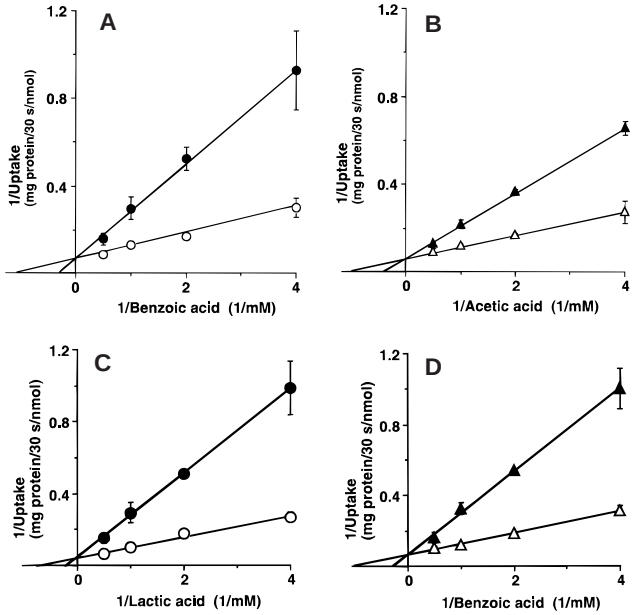

Figure 4—Lineweaver–Burk plots. (A) The concentration-dependent uptake of [^{14}C]benzoic acid by BeWo cells. Uptake was measured in the absence (open circles) or presence of 2 mM acetic acid (closed circles). (B) The concentration-dependent uptake of [^{14}C]acetic acid by BeWo cells. Uptake was measured in the absence (open triangles) or presence of 2 mM benzoic acid (closed triangles). (C) The concentration-dependent uptake of [^{14}C]-L-lactic acid by BeWo cells. Uptake was measured in the absence (open circles) or presence of 2 mM benzoic acid (closed circles). (D) The concentration-dependent uptake of [^{14}C]benzoic acid by BeWo cells. Uptake was measured in the absence (open circles) or presence of 2 mM L-lactic acid (closed circles). The vertical bar through each data point in the figures represents the SD of four replicate experiments.

To study the mechanism of the benzoic acid or acetic acid or lactic acid uptake inhibition by the monocarboxylic acids, we analyzed the inhibitory effect kinetically. Figure 4A shows a Lineweaver–Burk plot for the uptake of [^{14}C]-benzoic acid by BeWo cells in the absence or presence of 2 mM acetic acid. Acetic acid competitively inhibited the uptake of benzoic acid by the BeWo cells. Figure 4B shows a Lineweaver–Burk plot for the uptake of [^{14}C]acetic acid by BeWo cells in the absence or presence of 2 mM benzoic acid. Similarly, Figures 4C and 4D confirm that lactic acid and benzoic acid interact with the BeWo uptake mechanism by a competitive process. Table 3 summarizes the kinetic data and indicates that the K_m's and K_i's for benzoic,

Table 3—Lineweaver–Burke Uptake and Inhibition Constants for Monocarboxylic Acid Uptake by BeWo Cell Monolayers at 37 °C

	k_m (mm)[b]	benzoic acid k_i (mm)[b]	acetic acid k_i (mm)[b]	lactic acid k_i (mm)[b]
[^{14}C]benzoic acid[a]	1.0 ± 0.1	–	1.1 ± 0.2	0.7 ± 0.3
[^{14}C]acetic acid[a]	0.8 ± 0.2	0.8 ± 0.3	–	–
[^{14}C]lactic acid[a]	1.4 ± 0.2	0.7 ± 0.2	–	–

[a] [^{14}C]Benzoic acid or [^{14}C]acetic acid or [^{14}C]lactic acid uptake by BeWo cells were performed alone and in the presence of 2 mM (1- to 8-fold excess) of the indicated monocarboxylic acid. [b] Each value represents the mean ± standard deviation of four experiments.

Table 4—Apparent Permeability Coefficients for the Passage of [^{14}C]Benzoic Acid across BeWo Cell Monolayers at 37 °C

direction of benzoic acid permeation across monolayer	treatment	permeability coefficient ($\times 10^3$ cm/s)
apical to basolateral	none	4.90 ± 1.01
	+ benzoic acid[a]	0.45 ± 0.04[b]
	+ valproic acid[a]	0.64 ± 0.21[b]
basolateral to apical	none	1.06 ± 0.70[b]

[a] [^{14}C]Benzoic acid permeation across BeWo cell monolayers was performed in the presence of 10 mM (2000-fold excess) of the indicated carboxylic acid in the apical chamber. [b] $P < 0.001$ versus untreated benzoic acid permeation apical to basolateral.

acetic, and lactic acid for the apparent moncarboxylic acid uptake mechanism were similar.

The trans-trophoblast passage of [^{14}C]benzoic acid across the BeWo monolayer was found to be asymmetric, with the permeability coefficient greater in the apical-to-basolateral direction than that in the basolateral-to-apical direction, as shown in Table 4. The passage of [^{14}C]benzoic acid across the BeWo monolayers was inhibited by an excess amount of unlabeled benzoic acid or other monocarboxylic acid (valproic acid) as shown in Table 4, affirming that the transcellular passage of the monocarboxylic acid appeared similar to the uptake process.

Discussion

Passive diffusion is the primary mechanism by which xenobiotics cross the placental barrier.[1] However, some carrier-mediated transport systems in the trophoblast have been described using brush-border membrane vesicles or cultured cells,[3,5,6] including functional MCTs.[12−14] These carrier systems are notable for mediating the distribution of both endogenous and exogenous substances across the placental barrier.[7] Recent studies in knockout mice have effectively illustrated the relevance of placental transport mechanisms, e.g., P-glycoprotein, in protecting the fetus from exposure to chemicals.[21] Consequently, the recognition of transport mechanisms is important for developing an understanding of the molecular mechanisms and role of the trophoblast in regulating drug passage across the placental barrier. There is also a critical need for in vitro systems of human origin that allow characterization of mechanisms regulating drug distribution between mother and fetus to aid in the future design and development of drugs that can be safely administered in pregnancy.[22,23]

In the present study, we used benzoic acid uptake and transport, as a marker for the monocarboxlic acid transport[8] in BeWo cell monolayers. The establishment of functional MCT mechanisms in the BeWo cells offers the opportunity to characterize mechanisms of monocarboxylic acid transport at the molecular and biochemical level, extending limited studies performed with brush border preparations[12−14] and the perfused human placental lobe.[15]

The processing of benzoic acid by the BeWo monolayers was characterized by saturable uptake and transport. The processes were significantly inhibited by metabolic inhibitors and indicated that benzoic acid uptake is energy dependent. Benzoic acid transport and uptake were also significantly inhibited by in a competitive manner by unlabeled benzoic acid, acetic acid, and lactic acid. Further, benzoic acid uptake and transport were significantly inhibited by monocarboxylic acids but not selected dicarboxylic acids. The competitive nature of the transport, evidenced by the kinetic parameters, was consistent with observations reported for the transport of monocarboxylic acids in placental brush border vesicles.[12−14]

The advantage of the BeWo monolayer system is that trans-trophoblast transport properties can be characterized in a polarized cell.[16] We were able to show the passage of benzoic acid across the BeWo monolayers was bidirectional and of a faster rate going in the apical-to-basolateral side direction across the monolayers in the presence of a pH gradient. These observations are in good agreement with the lactate transport studies performed in the perfused human placental lobe model.[15] Further, our studies suggested a functional asymmetry in the carrier mechanism.

Caco-2 cells, which are a well-characterized model of the intestinal epithelium, possess a monocarboxylic acid transport system which is pH dependent.[8] The activation of benzoic acid uptake by acidic pH can be explained by H^+ cotransport, OH^- exchange system, or a possible change in affinity to the carrier protein depending on the extracellular pH. The uptake of benzoic acid by BeWo monolayers increased with a decreased pH. The lack of an inhibitory effect of DIDS, an inhibitor of anion exchange, suggests that an OH^- exchange system with benzoic acid was not involved in uptake or transport by BeWo cells. Many types of transporters are Na^+ dependent. However, benzoic acid uptake by BeWo cells was also not inhibited in the Na^+-depleted buffer in this study. Benzoic acid is an acidic compound; therefore, a decrease in pH increases the fraction of nonionized benzoic acid. According to the pH-partition hypothesis, this increase in the fraction of nonionized form increases the passive accumulation of benzoic acid across the BeWo cell membrane. Data presented here (e.g., Figure 3), and other studies conducted in absence of pH gradients, where the rate of transfer and asymmetry of transport for representative monocarboxylic acid drugs (e.g, acetylsalicylic acid and ibuprofen) is substantially diminished (data not shown), are alone insufficient to conclude that the uptake of benzoic acid is proton-gradient-dependent. However, the need for a proton gradient was affirmed with our results that showed FCCP, a protonophore, strongly inhibited the uptake of benzoic acid. Collectively then, our results indicated that monocarboxylic acid uptake was proton-gradient-dependent and were entirely consistent with similar studies conducted with human trophoblast brush border membrane preparations.[14] From a pharmacological and physiological perspective, this is significant since a pH gradient does develop across the placenta with advancing pregnancy. The developing pH gradient does influence drug distribution across the placenta[24] and may possibly influence the MCT carrier's role in regulating the distribution of monocarboxylic acids between the mother and fetus. The physiological role of a MCT in the trophoblast is likely related to the regulation of the distribution of L-lactic acid and related substrates across the placental barrier.[14,15]

Monocarboxylic acids are transported out of muscle and into liver (i.e., the so-called Cori cycle) by proton-coupled transporters, MCTs, that exhibited distinct substrate specificities and could be differentially inhibited by α-cyanocinnamates. MCT1 isolated from a Chinese hamster ovary cell cDNA library, is found in cardiac muscle, erythrocytes, basolateral intestinal epithelium, and skeletal

muscle. MCT2, cloned from hamster liver, is functionally similar to MCT1 in terms of transport capabilities, but its tissue distribution is significantly different.[25] A third transporter isoform, MCT3, was identified in chick retinal pigment epithelium. More recently, four new MCT homologues have been cloned and sequenced in human tissue (MCT3-MCT7).[11] There is currently no direct information of the type of functional MCTs associated with BeWo cells or human trophoblasts. Thus, further studies with molecular probes and selective substrates, when available, will be required to precisely identify which of the seven monocarboxylic acid transporter isoforms may be present in the human placental barrier. Elucidating the precise forms of functional MCTs in the trophoblast remains an ongoing objective of our laboratory.

In summary, our present results support limited evidence in the literature[12−15] that monocarboxylic acids and nutrients, drugs, drugs of abuse, and other xenobiotics that have a monocarboxylic acid constituent have the potential to be substrates for proton-gradient-dependent transport across the human trophoblast. This work further demonstrates the possible utility of a human, monolayer-forming cell line, BeWo, to characterize putative trans-trophoblast transport mechanisms and their potential roles in controlling nutrients, drugs, and drugs of abuse distribution across the placental barrier.

References and Notes

1. Stulc, J. Extracellular transport pathways in the haemochrorial placenta. *Placenta* **1989**, *15*, 113−119.
2. Hay, W. W., Jr. Placental transport of nutrients to the fetus. *Horm. Res.* **1994**, *42*, 215−222.
3. Kubo, Y.; Yamada, K.; Fujiwara, A.; Kawasaki, T. Characterization of amino acid transport systems in human placental brush-border membrane vesicles. *Biochem. Biophy. Acta* **1987**, *904*, 309−318.
4. Yudilevich, D. L.; Sweiry, J. H. Transport of amino acids in the placenta. *Biochem. Biophys. Acta* **1985**, *822*, 169−201.
5. Cerneus, D. P.; Van der Ende, A. Apical to basolateral transferrin receptors in polarized BeWo cells recycle through separate endosomes. *J. Cell Biol.* **1991**, *114*, 1149−1158.
6. Ramamoorthy, S.; Leibach, F. H.; Mahesh, V. B.; Ganapathy, V. Active transport of dopamine in human placental brush border membrane vesicles. *Am. J. Physiol.* **1992**, *262*, C1189−C1196
7. Ganapathy, V.; Prasad, P. D.; Ganapathy, M. E.; Leibach, F. H. Drugs of abuse and placental transport. *Adv. Drug Del. Rev.* **1999**, in press.
8. Tsuji, A.; Takanaga, H.; Tamai, I.; Terasaki, T. Transcellular transport of benzoic acid across Caco-2 cells by a pH-dependent and carrier-mediated transport mechanism. *Pharm. Res.* **1994**, *11*, 30−37.
9. Poole, R. C.; Halestrap, A. P. Transport of lactate and other monocarboxylates across mammalian plasma membranes. *Am. J. Physiol.* **1993**, *264*, C761−C782.
10. Roth, D. A.; Brooks, G. A. Lactate transport is mediated by a membrane-bound carrier in rat skeletal muscle sarcolemmal vesicles. *Arch. Biochem. Biophys.* **1990**, *279*, 377−385.
11. Price, N. T.; Jackson, V. N.; Halestrap, A. P. Cloning and sequencing of four new mammalian monocarboxylate transport (MCT) homologues confirms the existence of a transporter family with an ancient past. *Biochem. J.* **1998**, *329*, 321−328.
12. de la Torre, A. SR; Serrano, M. A.; Alvarado, F.; Medina, J. M. Carrier-mediated L-lactate transport in brush border membrane vesicles from rat placenta during late gestation. *Biochem. J.* **1991**, *278* (Pt 2), 535−541.
13. de la Torre, A. SR; Serrano, M. A.; Medina, J. M. Carrier-mediated beta-D-hydroxybutyrate transport in brush-border membrane vesicles from rat placenta. *Pediatr. Res.* **1992**, *32*, 317−323.
14. Balkovetz, D. F.; Leibach, F. H.; Mahesh, V. B.; Ganapathy, V. A proton gradient is the driving force for uphill transport of lactate in human placental brush-border membrane vesicles. *J. Biol. Chem.* **1988**, *263*, 13823−13830.
15. Carstensen, M. H.; Leichtweiss, H. P.; Schroder, H. Lactate carriers in the artificially perfused human term placenta. *Placenta* **1983**, *4*, 165−174.
16. Liu, F.; Soares, M. J.; Audus K. L. Permeability properties of monolayers of the human trophoblast cell line BeWo. *Am. J. Physiol.* **1997**, *273*, C1596−C1604.
17. A. Van der Ende, A du Maine, A. L. Schwartz, and G. J. Strous. Modulation of transferrin-receptor activity and recycling after induced differentiation of BeWo choriocarcinoma cells. *Biochem. J.* **1990**, *270*, 451−457.
18. Prasad, P. D.; Hoffmans, B. J.; Moe, A. J.; Smith, C. H.; Leibach, F. H.; Ganapathy, V. Functional expression of the plasma membrane serotonin transporter but not the vesicular monoamine transporter in human placental trophoblasts and choriocarcinoma cells. *Placenta* **1996**, *17*, 201−207.
19. Adson, A.; Raub, T. J.; Burton, P. S.; Barsuhn, C. L.; Hilgers, A. R.; Audus, K. L.; Ho, N. F. H. Quantitative Approaches to Delineate Paracellular Diffusion in Epithelial Cell Culture Monolayers. *J. Pharm. Sci.* **1994**, *83*, 1529−1536.
20. Yamaoka, K.; Tanigwara, Y.; Nakagawa, T.; Uno, T. A pharmacokinetic analysis program (MULTI) for microcomputer. *J. Pharmacobio-Dyn.* **1981**, *4*, 879−885.
21. Lankas, G. R.; Wise, L. D.; Cartwright, M. E.; Pippert, T.; Umbenhauer, D. R. Placental P-glycoprotein deficiency enhances susceptibility to chemically induced birth defects in mice. *Reprod. Toxicol.* **1988**, *12*, 457−463.
22. Dancis, J.; Liebes, L. Drug delivery during pregnancy: Evaluation in vitro of new drugs. *Reprod. Fertil. Dev.* **1995**, *7*, 1485−1489.
23. Audus, K. L. Controlling drug delivery across the placenta. *Eur. J. Pharm. Sci.* **1999**, *8*, in press.
24. Johnson, R. F.; Herman, N. L.; Johnson, H. H.; Arney, T. L.; Paschall, R. L.; Downing, J. W. Effects of fetal pH on local anesthetic transfer across the human placenta. *Anesthesiology* **1996**, *85*, 608−615.
25. Garcia, C. K.; Brown, M. S.; Pathak, R. K.; Goldstein, J. L. cDNA cloning of MCT2, a second monocarboxylate transporter expresed in different cells than MCT1. *J. Biol. Chem.* **1995**, *270*, 1843−1849.

Acknowledgments

This work was supported by a grant from National Institute of Drug Abuse (NIDA N01DA-4-7405). The authors also acknowledge the support of Corning Costar Corporation for support of the Cellular and Molecular Biopharmaceutics Handling Laboratory.

JS990173Q

Study of Binding of 12(*S*)-Hydroxy-5(*Z*),8(*Z*),10(*E*),14(*Z*)-eicosatetraenoic Acid to Bovine Serum Albumin Using Dynamic Surface Tension Measurements

P. CHEN,[†] Z. POLICOVA,[‡] C. R. PACE-ASCIAK,[§] AND A. W. NEUMANN*[,‡]

Contribution from *Department of Chemical Engineering, University of Waterloo, Waterloo, Ontario, Canada N2L 3G1, Department of Mechanical and Industrial Engineering, University of Toronto, Toronto, Ontario, Canada M5S 3G8, Division of Neurosciences, Research Institute, The Hospital for Sick Children, 555 University Avenue, Toronto, Ontario, Canada M5G 1X8, and Departments of Pharmacology and Pediatrics, Faculty of Medicine, University of Toronto, Toronto, Ontario, Canada M5S 1A8.*

Received April 19, 1999. Accepted for publication September 3, 1999.

Abstract □ In a recent paper,[1] we demonstrated that molecular interactions between biopolymers and other smaller molecules can be detected by means of dynamic surface tension measurements. In the present paper, we demonstrate that the same methodology can be employed for investigating dose effects and specificity of molecular interactions. Three similar lipids were chosen for this study: 12(*S*)-hydroxy-5(*Z*),8(*Z*),10(*E*),14(*Z*)-eicosatetraenoic acid (12(*S*)-HETE-free acid), methyl 12(*S*)-hydroxy-5(*Z*),8(*Z*),10(*E*),14(*Z*)-eicosatetraenoate (12(*S*)-HETE-methyl ester), and 5(*Z*),8(*Z*),11(*Z*),14(*Z*)-eicosatetraenoic acid (arachidonic acid-free acid). These substances were added to a fatty acid free bovine serum albumin (BSA) aqueous solution at different lipid concentrations. The characteristic tension response indicates that molecular interactions between 12(*S*)-HETE-free acid and BSA exist. The detected interactions are concentration dependent: at a molecular ratio of lipid to protein of 1:1, the binding of 12(*S*)-HETE-free acid to BSA is hydrophobic in nature; at the molecular ratio of lipid to protein of 10:1, a secondary binding occurs and is hydrophilic in nature. Similar molecular interactions were not detected between 12(*S*)-HETE-methyl ester or arachidonic acid-free acid and BSA, indicating that the interactions between 12(*S*)-HETE-free acid and BSA are specific. As an independent means, surface elasticity is used to probe the molecular interactions at the interface. In the case of 12(*S*)-HETE-free acid but not its methyl ester or arachidonic acid, distinct higher surface elasticities were observed at lipid concentrations in excess of a molecular ratio of lipid to protein of 1:1. This finding reinforces the above stipulations.

1. Introduction

Intermolecular interactions between macromolecules and smaller organic molecules at different surfaces are of fundamental importance to various industrial and biological processes. Mixtures of polymers and surfactants and their surface adsorption kinetics often play a vital role in emulsions or dispersions of a large number of chemical engineering products.[2−5] The interplay between proteins and lipids or lipidlike biomolecules is central to one of the most important functions of proteins, namely the adsorption at biological interfaces, and the structure of biomembranes.[6−8] Although a large amount of work has been done in this area,[5,9−12] the fundamental understanding of the mechanisms is limited. This is partially because most studies have focused on the isotherm, i.e., the equilibrium behavior of polymers or proteins and smaller molecules at interfaces. The dynamic processes, which are far more important in many biological and engineering systems, have been largely ignored.

Recently, we have developed a dynamic surface tension method for studying the dynamics of protein−lipid interactions at interfaces.[1] This method depends on the measurement of dynamic surface tension response to a saw-tooth change in surface area, where both protein and lipid are competing to adsorb. By analyzing the tension response, one can obtain information about both surface competitive adsorption and molecular interactions between the two molecules. Using this method, we studied the binding of Hepoxilin, a newly developed lipidic biomolecule derived from arachidonic acid, to bovine serum albumin.[1]

The dynamic surface tension has been measured by axisymmetric drop shape analysis (ADSA).[13−16] This approach to obtaining surface tension is based on the shape of a sessile or pendant drop. In essence, the shape of a drop is determined by a combination of surface tension and gravity effects. Surface forces tend to make drops spherical whereas gravity tends to elongate a pendant drop or flatten a sessile drop. When gravitational and surface tensional effects are comparable, then, in principle, one can determine the surface tension from an analysis of the shape of the drop. ADSA is devised specifically for drops with axial symmetry. Over the last 15 years, this technique has been developed to allow for measurement of a wide range of surface tensions under both static and dynamic conditions.[13−16]

The advantages of ADSA are numerous as compared with conventional surface tension techniques such as the Wilhelmy plate, the du Noüy ring tensiometer, and those based on the volume or weight of a pendant drop.[8,16] For example, in comparison with the Wilhelmy plate technique, ADSA requires only small amounts of the sample liquid; this becomes significantly advantageous when the sample is rare and expensive to obtain, such as in the case of many biological studies. ADSA also easily facilitates the study of both liquid−vapor and liquid−liquid interfacial tensions; it has been applied to materials ranging from organic liquids to molten metals, and from pure solvents to concentrated solutions. Measurements with ADSA have been satisfactorily made over a wide range of temperature and pressure.[13−16] In addition, since the profile of liquid drops may be recorded by photographs or digital image representation, it is possible to study surface tension in dynamic systems where the properties are time-dependent.

* To whom correspondence should be addressed.
[†] Department of Chemical Engineering, University of Waterloo.
[‡] Department of Mechanical and Industrial Engineering, University of Toronto.
[§] The Hospital for Sick Children and Departments of Pharmacology and Pediatrics, University of Toronto.

10.1021/js9901256 CCC: $18.00
Published on Web 10/30/1999

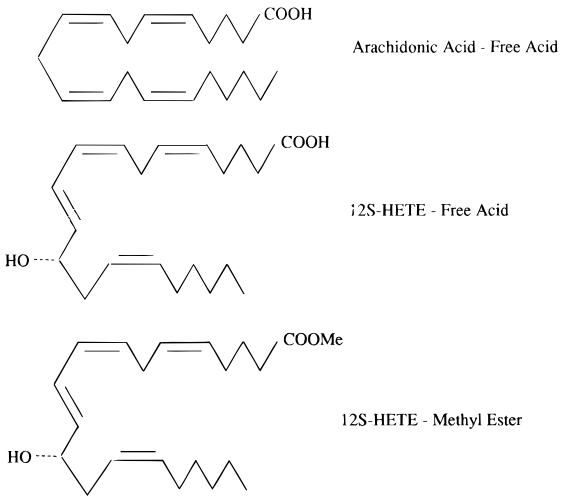

Figure 1—Schematic of molecular structures for (a) 12(*S*)-hydroxy-5(*Z*),-8(*Z*),10(*E*),14(*Z*)-eicosatetraenoic acid (12(*S*)-HETE-free acid), (b) methyl 12(*S*)-hydroxy-5(*Z*),8(*Z*),10(*E*),14(*Z*)-eicosatetraenoate (12(*S*)-HETE-methyl ester form), and (c) 5(*Z*),8(*Z*),11(*Z*),14(*Z*)-eicosatetraenoic acid (arachidonic acid-free acid). It is seen that 12(*S*)-HETE-free acid differs from arachidonic acid-free acid by having an additional hydroxyl group and a cis–trans conjugated diene system, while the difference between 12(*S*)-HETE-free acid and 12(*S*)-HETE-methyl ester is at the carboxyl end.

A number of studies have been carried out on biological interfaces using ADSA.[17−20] For example, the interfacial tension, and hence the surface energetics, of human serum albumin at the water−decane interface was studied as a function of temperature and protein concentration.[17,18] The results allow one to infer protein affinity for such an interface as well as a surface charge distribution of the protein molecules. Incorporating a captive bubble method and ADSA, one can also study low surface tension phenomena in lung surfactant systems and hence draw physiological significance of these substances.[21,22] The study of intermolecular interactions between proteins and lipids has been a recent application of ADSA dynamic surface tension measurements.[1]

In most biological systems, two questions are usually asked in connection with molecular interactions such as binding: one, is there a dose effect, i.e., is there a concentration dependence of the binding; the other is the specificity, i.e., is such binding specific to the molecules under study. In this paper, we demonstrate that the dynamic surface tension method[1] can be employed for the study of dose effects and specificity of molecular interactions. We investigate the molecular interactions between delipidated bovine serum albumin (BSA) and three slightly different lipids: 12(*S*)-HETE-free acid, 12(*S*)-HETE-methyl ester form, and arachidonic acid-free acid. Figure 1 shows their molecular structures; it can be seen that 12(*S*)-HETE-free acid differs from arachidonic acid by having an additional hydroxyl group and a cis−trans conjugated diene system, while the difference between 12(*S*)-HETE-free acid and 12(*S*)-HETE-methyl ester is at the carboxyl end. It was interesting to investigate whether these subtle structural differences would distinguish one molecule from another in terms of their interactions with bovine serum albumin at the surface.

Biologically, the study of the molecular interactions between lipids and protein also has important practical implications. The binding of lipid to a membrane protein would significantly alter the surface properties of the membrane, such as hydrophobicity, and hence affect membrane-assisted enzymatic reactions involving, for example, phospholipases,[23,24] i.e., possibly ion channel behavior and adhesion of cells. Indeed 12(*S*)-HETE has been shown to affect phospholipases[23,24] and potently causes tumor cells to adhere to the vascular endothelium.[25]

The objectives of this paper are (1) to measure dynamic surface tension response to a saw-tooth change in the surface area of solution drops using axisymmetric drop shape analysis (ADSA); (2) to probe the molecular interactions or binding between BSA, as a model protein, and three lipids; (3) to investigate the concentration dependence and specificity of the molecular binding; (4) to present a new means to characterize surface molecular interactions by calculating surface elasticity. The last objective is not only an additional means to detect molecular interactions but also provides a further physical/mechanical property of the lipid−protein monolayer.

2. Materials and Methods

A. Materials—The sample of bovine serum albumin (Sigma Chemical Co., St. Louis, MO) was essentially fatty acid and globulin free, with an average molecular weight of 67 000. It was used without further purification. Deionized and glass-distilled water was used. 12(*S*)-HETE-free acid and arachidonic acid were purchased from Cayman Chemicals (Ann Arbor, MI). The methyl ester derivative was prepared with an ether solution of diazomethane.[26] The reaction for methyl ester synthesis was complete as judged by the layer chromatography. The material was purchased from Cayman Chemicals as the free acid and converted into the methyl ester by methods used routinely in our laboratory, i.e., ethereal diazomethane. The molecular weights of these compounds are 320, 304, and 334, respectively. Since these lipids are not soluble in water, they have been initially dissolved in 1 μL of dimethyl sulfoxide (DMSO) before addition to 1 mL BSA aqueous solutions. Three types of mixed solutions were prepared: (1) 0.02 mg/mL BSA aqueous solution containing 12(*S*)-HETE-free acid at a concentration ranging from 0.001 to 1.0 μg/mL. Note that, within this range, a concentration of 0.1 μg/mL corresponded to a molecular ratio between 12-HETE-free acid and BSA of approximately 1:1; (2) 0.02 mg/mL BSA aqueous solution containing 12(*S*)-HETE-methyl ester at a concentration ranging from 0.01 to 1.0 μg/mL; (3) 0.02 mg/mL BSA aqueous solution containing arachidonic acid at a concentration ranging from 0.001 to 1.0 μg/mL. Two control experiments were performed using the following two solutions: (1) a pure BSA aqueous solution at a concentration of 0.02 mg/mL and 1 μL of DMSO; (2) a BSA-free solution of 1 μg of 12(*S*)-HETE-free acid in a mixture of 1 μL of DMSO in 1 mL of water (instead of a BSA solution).

B. Axisymmetric Drop Shape Analysis-Profile (ADSA-P)—The dynamic surface tension response to a saw-tooth variation in surface area was measured by ADSA-P. Detailed descriptions of ADSA-P are given elsewhere.[13−20] Briefly, ADSA-P fits the theoretical drop profile dictated by the Laplace equation of capillarity to the experimentally determined drop profile. An objective function is constructed which describes the deviation of the theoretical profile from the experimental one. This function is minimized by a nonlinear least-squares regression procedure, yielding the interfacial tension. The program also provides the drop volume, surface area, and the radius of curvature at the apex. The program requires several randomly chosen coordinate points along the drop profile, the value of the density difference across the interface, and the magnitude of the local gravitational constant as input. Each single image of a drop is analyzed 10 times with 20 different, arbitrary profile coordinate points each time.

During the experiment, the sample solution formed a pendant drop at the tip of a Teflon capillary, enclosed in a quartz cuvette which was mounted in an environmental chamber. The surface area of the drop was varied in a saw-tooth pattern through the volume change produced by a motorized syringe connected to the other end of the Teflon capillary.[1] In each run, drop images were captured at 0.3 to 1 s intervals for 6 min. Within this time period, repeated tension response cycles were established, based on which the analyses for molecular interactions were conducted. All the experiments were performed at 37 °C.

3. Results and Discussion

A. Molecular Interactions and Dose−Effects—Figure 2 shows the dynamic surface tension response to

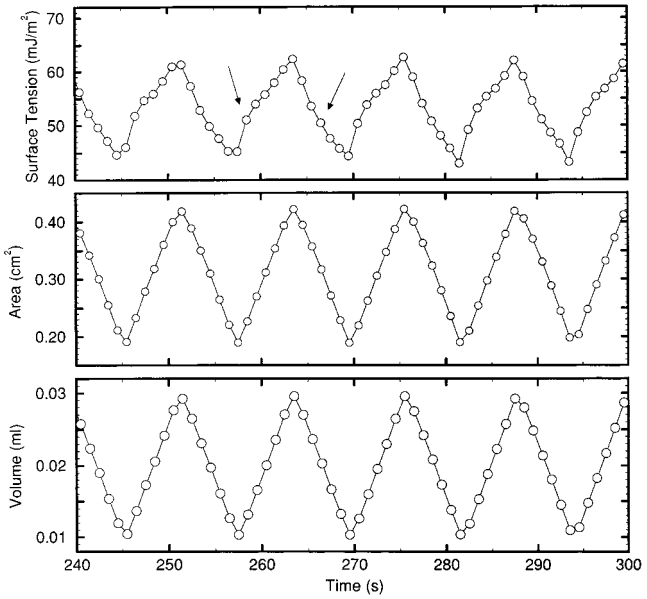

Figure 2—Dynamic surface tension response to a saw-tooth change in surface area, within the time range of 240 to 300 s from the beginning of the experiment with the BSA aqueous solution at a concentration of 0.02 mg/mL and 1 μL DMSO. Each cycle shows a characteristic, skewed shape in the tension response, with two kinks in the two branches corresponding to surface expansion and compression, respectively.

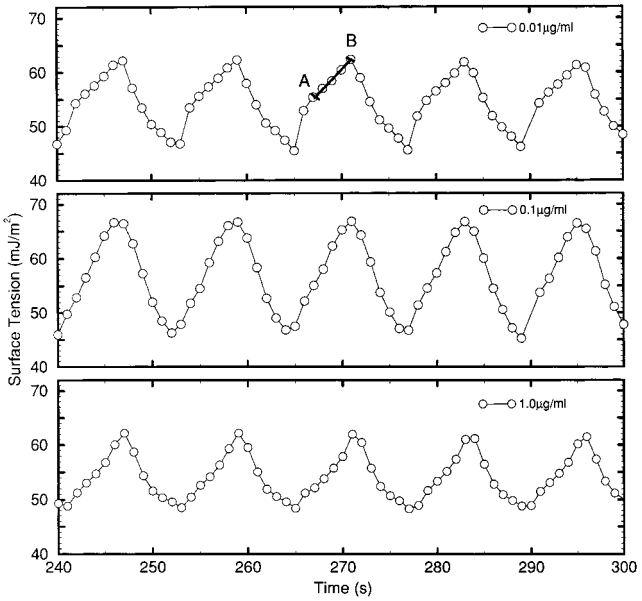

Figure 3—Dynamic surface tension response to the same saw-tooth variation in surface area as that in Figure 2 for the BSA solution to which 12(*S*)-HETE-free acid had been added. A series of 12(*S*)-HETE-free acid concentrations were measured: 0.001, 0.005, 0.01, 0.02, 0.05, 0.1, and 1.0 μg/mL of BSA aqueous solution; however, only three concentrations are shown here since for concentrations below 0.1 μg/mL the tension response is similar to that of 0.01 μg/mL. It is seen that at low 12(*S*)-HETE-free acid concentrations the tension response to the area variation is similar to that observed in Figure 2. However, at the concentration of 0.1 μg/mL, a distinct pattern change is observed in the dynamic surface tension response: the skewed pattern in the tension response of the BSA solution is replaced by a rather symmetric one. As the concentration of 12(*S*)-HETE-free acid increases to 1.0 μg/mL, yet another different, symmetric pattern is observed in the tension response, indicating a dose effect on the surface tension behavior and hence on the surface physicochemical properties.

the saw-tooth change in surface area within the time range from 240 to 300 s from the beginning of the experiment with the aqueous BSA solution at a concentration of 0.02 mg/mL. It has been shown[1] that at early times (less than 60 s) the tension response reflects the initial adsorption process of BSA to the surface and does not repeat itself from cycle to cycle. Only after 120 s does the tension response start showing constant cycles, as shown in Figure 2. Each cycle shows a characteristic, skewed shape, with two kinks occurring in the two branches corresponding to surface expansion and compression.

As demonstrated in a previous paper,[1] the error associated with each individual surface tension value is generally small, less than 0.2 mJ/m^2 at the 95% confidence level; hence, the tension response to the saw-tooth variation in surface area (Figure 2) reliably represents the true physicochemical properties of the surface of a protein and/or lipid adsorption film.

Figure 3 shows the dynamic surface tension response to the same saw-tooth variation in surface area as that in Figure 2 for the BSA solution to which 12(*S*)-HETE-free acid had been added. A series of 12(*S*)-HETE-free acid concentrations were used in the experiment: 0.001, 0.005, 0.01, 0.02, 0.05, 0.1, and 1.0 μg/mL BSA aqueous solution; however, only three concentrations are shown in Figure 3 since for concentrations below 0.1 μg/mL the tension response was found to be similar to that of the concentration of 0.01 μg/mL. It can be seen that at low 12(*S*)-HETE-free acid concentrations ($\leq$0.05 μg/mL) the tension response to the area variation is similar to that observed in Figure 2 for the pure BSA solution: the characteristic, skewed shape indicates that the surface is covered mainly with BSA molecules. However, at the concentration of 0.1 μg/mL, a distinct pattern change is observed in the dynamic surface tension response: the skewed pattern of the BSA solution is replaced by a rather symmetric one. This indicates that the surface properties are not determined solely by BSA, i.e., the added 12(*S*)-HETE-free acid plays a role. It is noted that the 0.1 μg/mL concentration corresponds to a molecular ratio between 12(*S*)-HETE-free acid and BSA of approximately 1:1. As the concentration of 12(*S*)-HETE-free acid increases to 1.0 μg/mL, yet another asymmetric pattern emerges in the tension response. Clearly, there is a dose–effect on the surface tension behavior and hence on the physicochemical properties. At concentrations above 0.1 μg/mL, the tension response to the area change provides a useful tool to probe possible molecular interactions between 12(*S*)-HETE-free acid and BSA.

To investigate further the effects of 12(*S*)-HETE-free acid, a control experiment was performed, in which 1 μg of 12(*S*)-HETE-free acid dissolved in 1 μL of DMSO was added to 1.0 mL water, i.e., in the absence of BSA. The results are shown in Figure 4, where minimal changes in dynamic surface tension pattern are observed in response to the same saw-tooth variation in surface area as that in Figures 2 and 3. If there were no interaction between 12-(*S*)-HETE-free acid and BSA in the mixed solution, the resulting surface tension would have to be a superposition of the surface tensions of the individual lipid and protein solution. However, from Figures 2–4, the tension response of the mixture at a concentration of 12(*S*)-HETE-free acid of 0.1 μg/mL does not reflect the pattern of the pure BSA solution at all. Therefore, molecular interactions must exist between 12(*S*)-HETE-free acid and BSA, likely forming lipid–protein complexes due to 12(*S*)-HETE-free acid interacting with BSA. These complexes, being species different from albumin alone, no longer show the skewed shape of BSA, presumably caused by conformational changes.

In general, the appearance of kinks in the tension response to surface area variations (e.g., Figure 2) reflects a phase or structural transition of the surface molecules.[8] Disappearance of the kinks, at the lipid concentration of

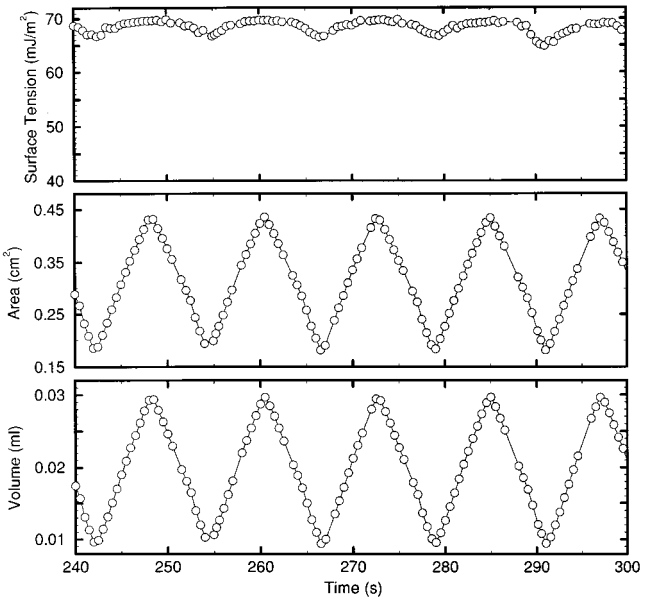

Figure 4—Dynamic surface tension response to the same area variation as that in Figure 2 for a control experiment in which 1 μg of 12(*S*)-HETE-free acid dissolved in 1 μL of DMSO was added to 1.0 mL of water, in the absence of BSA. Rather symmetric cycles with small amplitudes are observed for the tension response.

0.1 μg/mL (Figure 3), indicates that the binding of lipid to protein stablizes the surface phase at one molecular configuration. Furthermore, since the distinct change in the tension response pattern of BSA occurs at the concentration of 0.1 μg/mL of 12(*S*)-HETE-free acid, corresponding to a molecular ratio of 1:1, such interactions between 12-(*S*)-HETE-free acid and BSA are presumably connected with a single binding site (see also below).

Another observation in Figure 3 is that the tension value reached at the peaks for the concentration 0.1 μg/mL is significantly higher than that for the other concentrations including the pure BSA solution (Figure 2). This indicates that the mixture, at the 1:1 molecular ratio, is more hydrophilic than BSA itself; therefore, the molecular interactions between 12(*S*)-HETE-free acid and BSA may be hydrophobic in nature, such that the hydrophobic end of the lipid attaches to a similar part of the protein, leaving the hydrophilic end of the lipid exposed to the surrounding water environment.

At the 12(*S*)-HETE-free acid concentration of 1.0 μg/mL (Figure 3), the molecular ratio between lipid and protein is roughly 10:1. One might think that the resulting dynamic surface tension should predominantly be due to the presence of 12(*S*)-HETE-free acid at the surface. However, the tension response of the lipid alone (Figure 4) shows a very different response, with a much smaller amplitude. If we were to assume that BSA has only one binding site for 12(*S*)-HETE-free acid, then 9 out of 10 lipid molecules would exist in water freely, and the resulting surface properties of the mixture would have to be dominated by the surface properties of the free lipid. However, from Figure 4, the free lipid solution has high surface tension values, above 65 mJ/m^2; from Figure 3, the maximum tension value is also above 65 mJ/m^2 for the mixture of the lipid and the protein at the concentration of 0.1 μg/mL. If there were no interaction between lipid and protein−lipid complex, the tension response of the combination would be expected to be at the same high level. This, however, is not the case; the maxima for 1.0 μg/mL in Figure 3 are clearly below 65 mJ/m^2. Therefore, one needs to conclude that not all additional lipid molecules remain free, but rather bind to BSA, at least to such a degree that the surface tension is significantly lowered. Since the maximum tension value at the 1.0 μg/mL concentration is smaller than that at the 0.1 μg/mL concentration, the new complex, as a result of the new binding of the lipid to the protein, is more hydrophobic, compared with the protein−lipid complex of 1:1 ratio, i.e., 0.1 μg/mL of 12(*S*)-HETE. Hence, the additional binding of the lipid to the protein is presumably hydrophilic in nature.

It should be noted that, even at 12(*S*)-HETE-free acid concentrations lower than 0.1 μg/mL, one may not rule out the possibility of the aforementioned new binding of lipid to protein, or secondary binding of lipid to protein. Such binding is presumably associated with some low affinity sites, and hence it does not amount to any sizable extent and contributes little to the tension response. At 1:1 molar ratio (corresponding to 0.1 μg/mL) or less, 12(*S*)-HETE-free acid mainly interacts with BSA at the single binding site of high affinity; this will predominantly dictate the properties of the surface molecules and affect the pattern of the tension response. Only at higher molar ratios, e.g., 10:1, as the high affinity binding site has already been occupied, this secondary binding becomes important in changing the tension response (Figure 3).

In the above analysis leading to the conclusion of 12(*S*)-HETE-free acid binding to BSA and the dose-dependence of such molecular binding, we tacitly assumed that the DMSO, used as dissolving agent for the lipid, does not interact with BSA, nor does the DMSO play a role in the surface tension response after the initial few cycles. It has been established that, for a mixture of DMSO and BSA, the surface molecular population is dominated by small DMSO molecules only at early stages of the cycling experiment below 60 s, due to DMSO's much higher diffusion coefficient.[1] With the passage of time, BSA gradually adsorbs at the surface, and BSA molecules stay at the surface once they adsorb. This leads to a squeeze-out of the DMSO molecules from the surface. After repeated cycles, the surface properties are essentially determined by the BSA molecules adsorbed at the surface, and no DMSO contribution to the surface tension response can be detected. This indicates that DMSO is merely a vehicle for carrying lipids, and it does not contribute to the tension response at late stages of the cycling experiment, as shown in Figures 2−6.

B. Specificity—To study the possible specificity of the molecular binding of 12(*S*)-HETE-free acid to BSA, two similar lipids, 12(*S*)-HETE-methyl ester and arachidonic acid-free acid, were used to perform the same tension response experiment as that for 12(*S*)-HETE-free acid. The results for 12(*S*)-HETE-methyl ester are shown in Figure 5 for three concentrations at 0.01, 0.1, and 1.0 μg/mL. Again, 0.1 μg/mL corresponds to a molecular ratio of lipid to protein of approximately 1:1. All three concentrations show a skewed pattern, similar to that of the pure BSA solution (Figure 2). This suggests the dominance of protein adsorption at the surface, while 12(*S*)-HETE-methyl ester molecules play little role in producing the surface tension response. When comparing Figure 5 with Figure 3 at the same concentrations, the disappearance of kinks in the tension response differentiates the two lipids in their interations with BSA.

It has been established that there are generally one to two high affinity fatty acid-binding sites on albumin and a number of low affinity sites.[27−29] The distinct difference between Figure 5 and Figure 3 indicates that the lipid−protein interactions depend on the type of lipid, and a slight variation in molecular structure can significantly alter the lipid binding to albumin and hence the surface physical chemical properties, as reflected in surface tension. Con-

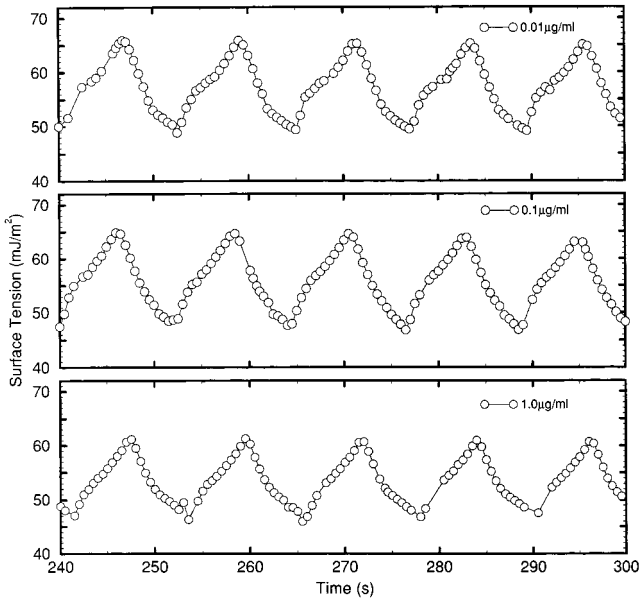

Figure 5—Dynamic surface tension response to the same area variation as that in Figure 2 for the BSA solution to which 12(*S*)-HETE-methyl ester had been added at three concentrations of 0.01, 0.1, and 1.0 μg/mL. At all three concentrations a skewed pattern is seen, similar to that of the pure BSA solution.

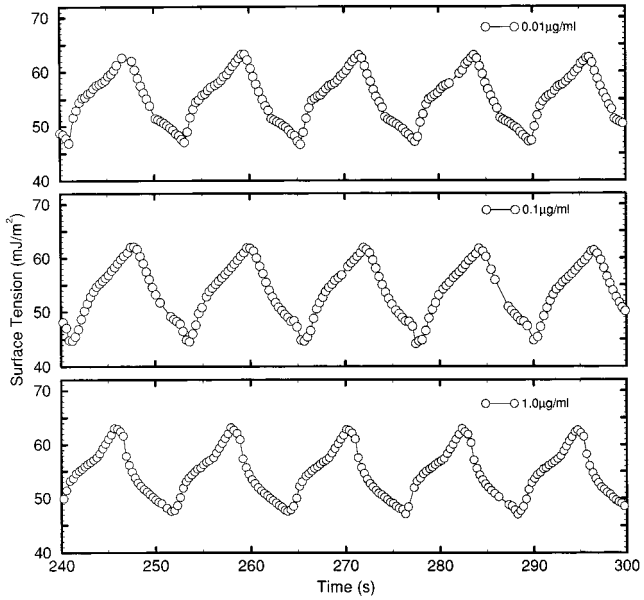

Figure 6—Dynamic surface tension response to the same area variation as that in Figure 2 for the BSA solution to which arachidonic acid-free acid had been added. Three lipid concentrations are shown: 0.01, 0.1, and 1.0 μg/mL. It was found in the experiment that at concentrations of 0.001, 0.005, and 0.05 μg/mL, the tension response is similar to that of 0.01 μg/mL. For all these concentrations, a skewed shape is always observed in the cycling tension response.

versely, surface tension measurement would provide a useful tool to differentiate lipid interactions with albumin, particularly to detect possible conformational changes as a result of the lipid binding to albumin.

Figure 6 shows the dynamic surface tension response to the same saw-tooth area variation that was used above, with arachidonic acid-free acid added to the BSA solution. A series of arachidonic acid concentrations were used: 0.001, 0.005, 0.01, 0.05, 0.1, and 1.0 μg/mL; however, only three concentrations are shown since for concentrations below 0.1 μg/mL the tension response is very similar to that of 0.01 μg/mL. Throughout these concentrations, a skewed

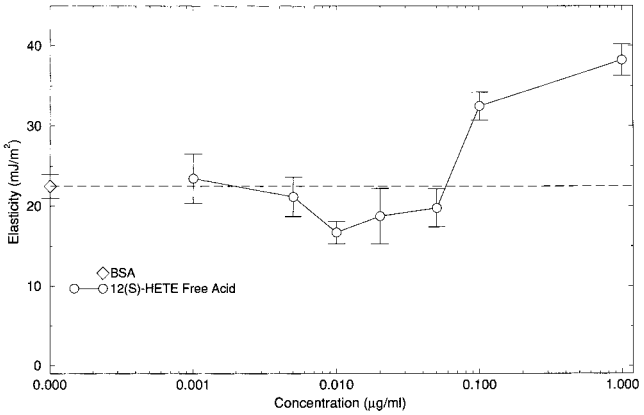

Figure 7—Surface elasticity as a function of the 12(*S*)-HETE-free acid concentration. The error bars in elasticity result from a statistical analysis, based on the Student's *t*-distribution, of a series of linear curve fits to the expansion branches of different cycles, at the 95% confidence level. There is a distinct increase in elasticity at the 12(*S*)-HETE-free acid concentration of 0.1 μg/mL, corresponding to the dose effect as observed in the dynamic surface tension response to the saw-tooth area change (Figure 3).

shape is always observed in the cycling tension response. In contrast to the observation in Figure 3 for 12(*S*)-HETE-free acid, there is no distinct change in the tension response as the arachidonic acid concentration passes 0.1 μg/mL, corresponding to a molecular ratio between lipid and protein of approximately 1:1. As previously shown with 12-(*S*)-HETE-methyl ester, Figure 6 indicates that molecular interactions between these concentrations of arachidonic acid and BSA is significantly different from those between 12(*S*)-HETE-free acid and BSA. This implies that the detected molecular binding of 12(*S*)-HETE-free acid to BSA is rather specific, and that a subtle variation in the lipid molecular structure leads to significantly different interaction properties between the lipid and the protein.

It should be noted that, in the above comparison or analysis, several less significant features are neglected, and the emphasis is placed on the high affinity binding between BSA and 12(*S*)-HETE-free acid. For example, the magnitude of changes seems slightly greater for 12(*S*)-HETE-methyl ester than for 12(*S*)-HETE-free acid at the concentration of 0.01 μg/mL (Figure 5, top panel vs Figure 3, top panel). This indicates that the interactions between the methyl ester and BSA might be slightly different from those between the free acid and BSA. Further, for the free acid, the disappearance of kinkiness at 0.1 μg/mL and higher does not seem to be complete, and a slight trace of kink remains at these concentrations. This might indicate that the high affinity interaction between the lipid and the protein does not completely block the BSA properties, although a significant change has been induced and resulted in the tension response variations. To explain all these detailed features in the tension response, more work will be conducted with respect to the mechanisms of surface molecular interactions and dynamic surface tension response to surface area changes.

C. Elasticity—As stated in the Introduction, surface elasticity is an important surface physicochemical property; it can be used as a measure of interfacial molecular interactions. The definition of the Gibbs surface elasticity, E, is

$$E = A\frac{\mathrm{d}\gamma}{\mathrm{d}A}$$

where γ is the surface tension, and A is the surface area. Figure 7 shows the surface elasticity as a function of the 12(*S*)-HETE-free acid concentration. The slope in the

surface elasticity definition was obtained through a linear curve fit to the relatively straight portion of the expansion branch, after the kink appears (Figure 3, from point A to B). The error bars in the elasticity result from a statistical analysis, based on the Student's *t*-distribution, of a series of expansion branches of different cycles, at the 95% confidence level. It can be seen that there is a distinct increase in elasticity at the 12(*S*)-HETE-free acid concentration of 0.1 μg/mL, corresponding well to the dose−effect observed in the dynamic surface tension (Figure 3). At lipid concentrations above 0.1 μg/mL, the formation of lipid−protein complexes not only changes the dynamic surface tension response to the area variation but also increases the elasticity of the adsorbed layer.

4. Conclusions

1. From the dynamic surface tension response to a patterned variation in surface area, molecular interactions between 12(*S*)-HETE-free acid and BSA have been observed.

2. The molecular interactions between 12(*S*)-HETE-free acid and BSA are concentration dependent. At the concentration corresponding to a molecular ratio of lipid to protein of 1:1, a distinct surface tension response was detected, indicating that such molecular interactions are based on one binding site for 12(*S*)-HETE on BSA. The binding appears hydrophobic in nature, i.e., the hydrophobic end of the lipid attached to a similar part of the protein.

3. At the concentration corresponding to a molecular ratio of lipid to protein of 10:1, secondary binding of 12(*S*)-HETE-free acid to BSA was detected from the dynamic surface tension response. This secondary binding appears to be hydrophilic in nature.

4. Comparison with two similar lipid molecules, 12(*S*)-HETE-methyl ester and arachidonic acid-free acid, indicates that the molecular interactions between 12(*S*)-HETE-free acid and BSA are specific.

5. Surface elasticity can be independently used for detecting molecular interactions and dose effects. In the case of 12(*S*)-HETE-free acid in BSA solution, distinctly higher surface elasticities were found at lipid concentrations in excess of the molecular ratio of lipid to protein of 1:1.

References and Notes

1. Chen, P.; Policova, Z.; Susnar, S. S.; Pace-Asciak, C. R.; Demin, P. M.; Neumann, A. W. Dynamic Surface Tension Responses to Surface Area Change of Protein/Small-Medium Organic Molecule Solutions. *Colloids Surf., A* **1996**, *114*, 99−111.
2. de Gennes, P. G. Interactions Between Polymers and Surfactants. *J. Phys. Chem*. **1990**, *94*, 8407−8413.
3. Cabane, B.; Duplessix, R. Organization of Surfactant Micelles Adsorbed on a Polymer Molecule in Water: A Neutron Scattering Study. *J. Phys*. **1982**, *43*, 1529−1542. Decoration of Semidilute Polymer Solutions with Surfactant Micelles. *J. Phys*. **1987**, *48*, 651−662.
4. Kekicheff, P.; Cabane, B.; Rawiso, M. Macromolecules Dissolved in a Lamellar Lyotropic Mesophase. *J. Colloid Interface Sci*. **1984**, *102*, 51−70.
5. Rosen, M. J. *Surfactants and Interfacial Phenomena*, 2nd. ed.; Wiley: New York, 1989.
6. Robb, I. D. Polymer/Surfactant Interactions. In *Anionic Surfactants;* Surfactant Science Series, Vol. 11; Lucassen-Reynders, E. H., Ed.; Dekker: New York, 1981; pp 109−142.
7. Gaines, G. L., Jr. *Insoluble Monolayers at Liquid−Gas Interfaces*; Interscience: New York, 1966.
8. Adamson, A. W. *Physical Chemistry of Surfaces*, 5th ed.; Wiley: New York, 1990.
9. Eijt, S. W. H.; Wittebrood, M. M.; Devillers, M. A. C. Rasing, Th. Dynamics of Protein-Surfactant Exchange at the Air−Water Interface Studied by Optical Second Harmonic Generation and Ellipsometry. *Langmuir* **1994**, *10*, 4498−4502.
10. Wahlgren, M.; Welin-Klintstroem, S.; Arnebrant, T.; Askendal, A.; Elwing, H. Competition Between Fibrinogen and a Non-Ionic Surfactant in Adsorption to a Wettability Gradient Surface. *Colloids Surf., B* **1995**, *4*, 23−31.
11. Hlady, V.; Andrade, J. D. Fluorescence Emission from Adsorbed Bovine Serum Albumin and Albumin-bound 1-Anilinonaphthalene-8-sulfonate Studied by TIRF. *Colloids Surf*. **1988**, *32*, 359−369.
12. Norde, W. Adsorption of Proteins from Solution at the Solid−Liquid Interface. *Adv. Colloid Interface Sci*. **1986**, *25*, 267−340.
13. Rotenberg, Y.; Boruvka, L.; Neumann, A. W. Determination of Surface Tension and Contact Angle from the Shapes of Axisymmetric Fluid Interfaces. *J. Colloid Interface Sci*. **1983**, *93*, 169−183.
14. Cheng, P.; Li, D.; Boruvka, L.; Rotenberg, Y.; Neumann, A. W. Automation of Axisymmetric Drop Shape Analysis for Measurements of Interfacial Tensions and Contact Angles. *Colloids Surf*. **1990**, *43*, 151−167.
15. Cheng, P. ; Neumann, A. W. Computational Evaluation of Axisymmetric Drop Shape Analysis-Profile (ADSA-P). *Colloids Surf*. **1992**, *62*, 297−306.
16. Lahooti, S.; del Rio, O. I.; Cheng, P.; Neumann, A. W. Axisymmetric Drop Shape Analysis (ADSA). In *Applied Surface Thermodynamics;* Neumann, A. W., Spelt, J. K., Eds.; Marcel Dekker Inc.: New York, N. Y., 1996; Chapter 10, pp 441−507.
17. Cabrerizo-Vílchez, M. A.; Policova, Z.; Kwok, D. Y.; Chen, P.; Neumann, A. W. The Temperature Dependence of the Interfacial Tension of Aqueous Human Albumin Solution/Decane. *Colloids Surf., B* **1995**, *5*, 1−9.
18. Chen, P.; Lahooti, S.; Policova, Z.; Cabrerizo-Vílchez, M. A.; Neumann, A. W. Concentration Dependence of the Film Pressure of Human Serum Albumin at a Water/Decane Interface. *Colloids Surf., B* **1996**, *6*, 279−289.
19. Miller, R.; Treppo, S.; Voigt, A.; Zingg, W.; Neumann, A. W. Contact Angle Kinetics of Human Albumin Solutions at Solid Surfaces. *Colloids Surf*. **1993**, *69*, 203−208.
20. Chen, P.; Kwok, D. Y.; Prokop, R. M.; del Rio, O. I.; Susnar, S. S.; Neumann, A. W. Axisymmetric Drop Shape Analysis (ADSA) and its Applications. In *Studies in Interface Science, vol. 6: Drops and Bubbles in Interfacial Research;* Möbius, D., Miller, R., Eds.; Elsevier: Amsterdam, The Netherlands 1998; pp 61−168.
21. Jyoti, A.; Prokop, R. M.; Neumann, A. W. Manifestation of the Liquid-Expanded/Liquid-Condensed Phase Transition of a Dipalmitoyl Phosphatidylcholine Monolayer at the Air−Water Interface. *Colloids Surf., B* **1997**, *8*, 115−124.
22. Prokop, R. M.; Jyoti, A.; Eslamian, M.; Garg, A.; Mihaila, M.; del Rio, O. I.; Susnar, S. S.; Policova, Z.; Neumann, A. W. A Study of Captive Bubbles with Axisymmetric Drop Shape Analysis. *Colloids Surf., A* **1998**, *131*, 231−247.
23. Zakaroff, A.; Meskini, N.; Joulain, C.; Nemoz, G.; Lagarde, M.; Prigent, A. F. 12(S)HETE Primes a Phospholipase D Pathway in Activated Human Blood Mononuclear Cells. In *Frontiers in Bioactive Lipids;* Vanderhoek, J. Y., Ed.; Plenum Press: New York, 1996; pp 291−297.
24. Meskini, N.; Zakaroff, A.; Joulain, C.; Nemoz, G.; Lagarde, M.; Pregent, A. F. Triggering of a Phospholipase D Pathway Upon Mitogenic Stimulation of Human Peripheral Blood Mononuclear Cells Enriched with 12(S)-Hydroxyicosatetraenoic Acid. *Eur. J. Biochem*. **1995**, *233*, 907−915.
25. Honn, K. V.; Tang, D. G.; Gao, X.; Butovich, I. A.; Liu, B.; Timar, J.; Hagmann, H. 12-Lipoxygenases and 12(S)-HETE: Role in Cancer Metastasis. *Cancer and Metastasis Rev*. **1994**, *13*, 365−396.
26. Pace-Asciak, C. R.; Granström, E.; Samuelsson, B. Arachidonic Acid Epoxides. *J. Biol. Chem*. **1983**, *258*, 6835−6840.
27. Peters, Th., Jr., Serum Albumin. *Adv. Protein Chem*. **1985**, *37*, 161−236.
28. Carter, D. C.; Ho, J. X. Structure of Serum Albumin. *Adv. Protein Chem*. **1994**, *45*, 153−196.
29. Huntley, T. E.; Neitzel, J. K.; Elson, M. K. Binding Properties of Purified Adult and Fetal Bovine Serum Albumin. *Biochim. Biophys. Acta* **1977**, *490*, 112−119.

Acknowledgments

This research was supported financially by the Medical Research Council of Canada to A.W.N. (MT 5462) and to CPR-A (MT 4181).

JS9901256

Measurement and Prediction of Hydrophobicity Parameters for Highly Lipophilic Compounds: Application of the HPLC Column-Switching Technique to Measurement of log *P* of Diarylpyrazines

CHISAKO YAMAGAMI,*,† KOZUE ARAKI,† KYOKO OHNISHI,† KAORU HANASATO,† HARUKO INABA,‡ MASAHIRO AONO,‡ AND AKIHIRO OHTA‡

Contribution from *Kobe Pharmaceutical University, Motoyamakita-machi, Higashinada, Kobe, 658-8558, Japan, and Tokyo University of Pharmacy and Life Science, Horinouchi, Hachioji, Tokyo,192-0392, Japan.*

Received April 12, 1999. Accepted for publication September 20, 1999.

Abstract □ In the preparatory stage of structure–activity relationship (QSAR) studies of anti-platelet aggregant pyrazine derivatives, log *P* values (*P*: 1-octanol/water partition coefficient) of diarylpyrazines were measured by a newly developed HPLC column-switching technique. The system consists of two processes: (1) adsorption of the sample at the top end of a short precolumn, and then (2) quantifying the enriched analyte by a conventional analytical column. By using the log *P* values thus obtained, the correction factor for the steric hindrance caused by the vicinal diphenyl groups was estimated. The log *k* values (*k*; retention factor) were also measured with methanol-buffer (pH 7.4) eluents and related to log *P*. The eluent of 50% methanol content (M50) gave a good linear relationship over a wide range of log *P* ($-0.3 < \log P < 5.2$), indicating that log k_{M50} parameter is useful for predicting the log *P* value.

Introduction

The logarithm of 1-octanol/water partition coefficient, log *P*, has been used as a measure of hydrophobicity of organic compounds and has played an important role in structure–activity relationship studies.[1,2] A conventional procedure for measurement of log *P* is the shake-flask method which consists of determining the equilibrium concentration of a substance in the aqueous or in both the aqueous and the octanol phases. This method, however, is not usually applicable to highly lipophilic compounds (log $P > 3$) because of extremely low concentrations of test compounds in the aqueous phase. To solve this problem, some procedures, such as re-extraction of the aqueous phase before the measurement of concentrations and the use of radiolabeled solutes, have been used to get a satisfactory response with the detector used.[3]

In addition to direct measurements, the log *P* value is often estimated by calculations or by retention parameters derived from reversed-phase HPLC, hereafter referred to as the HPLC method. The most widely used methodology for calculating log *P* was first proposed by Fujita et al., being based on an additive-constitutive, free energy related property of log *P*.[4] Thus, by using π defined as the difference in log *P* between a derivative with a given X substituent (RX) and the parent compound (RH),

$$\pi_X = \log P_{(RX)} - \log P_{(RH)} \quad (1)$$

log *P* values for multisubstituted compounds might be expressed as:

$$\log P_{(YRX)} = \log P_{(HRH)} + \pi_X + \pi_Y \quad (2)$$

Although many other empirical ways for log *P* calculations have been proposed subsequently,[5–8] most of them essentially assume such additivity. In accord with expectation, eq 2 fails in solute systems which involve electronic and/or steric interactions between the substituents, and various correction methods are proposed so that the predicted log *P* values may approach the experimental results.[6,7]

In HPLC approaches, the logarithm of the retention factor, *k*, is used as a hydrophobicity parameter. Usually C-18 bonded silica is used as a stationary phase with methanol–water mixtures as the mobile phase, and a Collander type relationship as shown by eq 3 is assumed.[9]

$$\log P = a \log k + b \quad (3)$$

Since the log *k* value depends on the mobile phase composition, extensive studies have been made to find optimal mobile phase conditions producing a good linear relationship.[10–15] Many investigators have used the log k_W parameter, (log *k* extrapolated to 0% methanol) to eliminate organic solvent effects.[10,11,16,17] On the other hand, other reports use isocratic log *k* values at an appropriate methanol concentration.[13–15,18,19] It is very often observed that hydrogen bonding effects of solutes with the surrounding molecules break a linearity, making the HPLC approach less effective for the estimate of log *P*. In an attempt to establish a standard HPLC procedure for predicting reliable log *P* values, we have studied the relationship between log *P* and log *k* for various series of fundamental heteroaromatic compounds, such as monosubstituted pyridines, diazines, and thiophenes, under various HPLC conditions.[13–15,20] Our results have demonstrated that hydrogen donating solutes (amphiprotics) usually behave differently from nonamphiprotics and should be treated separately.[13–15] Moreover, the log k_W method tends to overestimate log *P* for strong hydrogen acceptors. For this reason, most of pyridines and diazines which have *N*-atom(s), a strong hydrogen acceptor, in the parent rings have been found to yield values for log k_W much higher than that corresponding to the true value for log *P*. Instead, we have found that isocratic log *k* obtained with an eluent containing around 50% methanol usually results in a good linear relationship with log *P*, permitting us to reliably predict values for log *P* over the range, $-1 < \log P < 3$.[13–15,20]

Even when such empirical predictive methods are known to be reliable, accurate experimental values of log *P* for several compounds are required.

* Corresponding author. Telephone: +81-78-441-7547. Fax: +81-78-435-2080. E-mail: yamagami@kobepharma-u.ac.jp.
† Kobe Pharmaceutical University.
‡ Tokyo University of Pharmacy and Life Science.

10.1021/js990112s CCC: $18.00
Published on Web 10/22/1999

In the course of our QSAR studies of bioactive compounds, we were interested in analyzing the structure–activity relationship of a series of diaryl pyrazines which has recently been found, by one of the authors, to have potent anti-platelet aggregation activity.[21] Knowing reliable log *P* values of these compounds was a prerequisite for this purpose. We, therefore, undertook measurement and evaluation of log *P* values for these compounds. The conventional shake-flask method failed not only because of their high lipophilicity but also of very low solubility of some compounds even in octanol. Although we were well experienced in predicting the log *P* value of pyrazines with log $P < 3$ by the HPLC method, it seemed dangerous to apply our relationship to a wider lipophilicity range (log $P > 4$). Accordingly, we attempted to develop a method to determine experimentally log *P* values for highly lipophilic compounds by using the HPLC column-switching system. The column-switching technique is widely used for on-line sample enrichment and cleanup, and has been increasingly applied to environmental analyses and the isolation of clinical samples.[22,23] We expected that this method would be applicable to our measurements of log *P* by loading large volumes of the sample solutions onto a precolumn and succeeded in obtaining log *P* values ranging from 3.5 to 5.2.

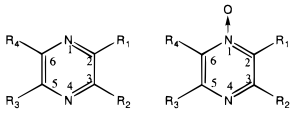

This report describes a novel procedure to measure log *P* values above 3 by using HPLC with a column-switching system. The log *P* values thus obtained were evaluated in terms of the additivity of π values and also related to log *k* values to examine how the log *P* values might be predicted by the HPLC approach. For comparison, some pyrazine *N*-oxides (PR→O) were also studied.

Materials and Methods

Materials—Compounds used in this study are given in Tables 1 and 2. Most of the diaryl pyrazines in Table 1 (**1**, **3**, **4**, **8**, **10**, **12**, **13**, **15**–**17**, **20**-**22**, and **24**) and monosubstituted pyrazines (**28**–**35**) in Table 2 were prepared as previously described.[21,24] Compounds **5**, **6**, **18**, and **19** were prepared by treatment of the 5-Cl derivatives with an appropriate sodium alkoxide according to the method for preparing the corresponding monosubstituted pyrazines.[24] Alkylpyrazines (**36**–**45**) were purchased from Tokyo Kasei Organic Chemicals (Tokyo, Japan). The references for preparation of the other compounds are given in the footnotes to Tables 1 and 2. HPLC-grade methanol and water, 1-octanol of the grade for log *P* measurements, and a phosphate buffer solution (pH 7.4) were purchased from Nacalai Tesque.

Measurement of log *P*: Conventional Shake-Flask Method—The log *P* for compounds with medium or low hydrophobicity (log $P < 3$) was measured by a conventional shake-flask method. The concentration of samples in both of the water and octanol phases was determined by HPLC.

Column-Switching Method—Samples (0.5–30 mg) were dissolved in 1 mL of octanol and then shaken with 100 mL of distilled water. The phases were allowed to separate overnight at 25 °C. Persistent emulsions were not observed to occur with our compounds. After pipetting off the octanol phase, the aqueous phase was collected into centrifuge tubes, preventing contamination by octanol, and then centrifuged twice for 5–10 min. As the solute concentration of lipophilic compounds in the aqueous phase was too low to detect by HPLC, sample enrichment on a precolumn was performed before conventional quantitative analysis by using a column-switching technique as follows.

HPLC System—The column-switching system (Figure 1) consisted of two isocratic HPLC pumps (LC 9A, Shimadzu, Kyoto), an autoinjector (IS-25, Kyoto Chromato, Kyoto,

Table 1—Log *P* Values of (Di)arylpyrazines

	R_1	R_2	R_3	R_4	log *P*[a]	log P_{add}[b]
1	Ph	H	H	H	2.07	
2[c]	4-OMe-Ph[d]	H	H	H	2.24	
3	Ph	Ph	H	H	3.19	4.4
4	Ph	Ph	Me	H	3.52	4.9
5	Ph	Ph	OMe	H	4.21	5.4
6	Ph	Ph	OEt	H	4.73	5.9
7[e]	Ph	Ph	Cl	H	4.05	5.4
8	Ph	Ph	*i*-Pr	H	4.71	
9[e]	4-Me-Ph	4-Me-Ph	H	H	4.10	
10	4-F–Ph	4-F–Ph	Me	H	3.75	
11[e]	4-CN–Ph	4-CN–Ph	Me	H	2.52	
12	Ph	Ph	2-OMe-Bn[f]	H	5.18	
13	Ph	Ph	3-OMe-Bn[f]	H	5.20	
14[e]	4-OMe-Ph	4-OMe-Ph	H	H	3.42	4.7
15	4-OMe-Ph	4-OMe-Ph	Me	H	3.66	5.2
16	4-OMe-Ph	4-OMe-Ph	Et	H	4.22	5.7
17	4-OMe-Ph	4-OMe-Ph	Cl	H	4.30	5.7
18	4-OMe-Ph	4-OMe-Ph	OMe	H	4.47	5.7
19	4-OMe-Ph	4-OMe-Ph	OEt	H	5.00	6.3
20	4-OMe-Ph	4-OMe-Ph	CN	H	3.70	5.0
21	4-OMe-Ph	4-OMe-Ph	COOMe	H	3.41	4.8
22	4-OMe-Ph	4-OMe-Ph	Me	Me	4.10	5.2
23[g]	Ph	Me	Ph	H	4.28	4.9
24	Ph	Me	H	Ph	4.29	4.9
25[h]	Ph	Et	Ph	Et	4.94	6.3
26[i]	Ph	Et	H	Ph	4.66	5.4
27[j]	Ph	Et	Et	Ph	4.83	6.3

[a] Measured by the column-switching method except for **1** and **2**. [b] Sum of log *P* of pyrazine (–0.26) and $\sum$ pyrazine-π (R_1, R_2, R_3, R_4). [c] Superscript of the compound number identifies the reference for the preparation: Ohta, A. et al. *J. Heterocycl. Chem*. **1982**, *19*, 1061–1067. [d] 4-X-Ph refers to 4-X-substituted phenyl. [e] Ohta, A. et al. *J. Heterocycl. Chem*. **1982**, *19*, 465–473. [f] 2-OMe-Bn and 3-OMe-Bn refer to 2-OMe-benzyl and 3-OMe-benzyl, respectively. [g] Ohta, A. et al. *Heterocycles* **1984**, *22*, 2317–2321. [h] Ohta, A. et al. *Heterocycles* **1986**, *24*, 785–792. [i] Ohta, A. et al. *Heterocycles* **1987**, *26*, 2449–2454. [j] Ohta, A. et al. *J. Heterocycl. Chem*. **1983**, *20*, 311–320.

Table 2—Log *P* Values of Variously Substituted Pyrazines (PR) and Pyrazine *N*-Oxides (PR→O)

	substituents	log *P*[a]		substituents	log *P*[a]
	PR		**40**	2-Me,3-Bu	2.10
28	H	–0.26	**41**	2-Me,3-*i*Bu	1.96
29	Me	0.21	**42**	2,3-diEt	1.51
30	Et	0.69	**43**	triMe	0.95
31	OMe	0.73	**44**	2,3-diEt,5-Me	1.95
32	OEt	1.28	**45**	tetraMe	1.28
33	OPr	1.84	**46**[b]	2,5-diMe-3,6-diCl	2.40
34	COOMe	–0.23		**PR→O**	
35	COOEt	0.28	**47**[c]	2,5-diMe-3Cl	0.44
36	2,3-diMe	0.54	**48**[d]	2,5-diMe-6Cl	0.19
37	2,6-diMe	0.54	**49**[e]	2,5-diMe-3,6-diCl	1.08
38	2-Me,3-Et	1.07	**50**[f]	2,3-bis(4-Cl–Ph),5-Cl	3.66
39	2-Me,3-Pr	1.57	**51**[f]	2,3-bis(4-Br–Ph)	3.41

[a] The data for compounds **28**–**35** and **36**–**45** were taken from refs 24 and 29, respectively. Those for the others were measured in this work. [b] Superscript of the compound number identifies the reference for the preparation: Baxter, R. A. et al. *J. Chem. Soc*. **1948**, 1859–1862. [c] Ohta, A. et al. *Chem. Pharm. Bull*. **1979**, *27*, 2027–2041. [d] Ohta, A. et al. *J. Heterocycl. Chem*. **1981**, *18*, 555–558. [e] Ohta, A. et al. *J. Heterocycl. Chem*. **1982**, *19*, 781–784. [f] Ohta, A. et al. *J. Heterocycl. Chem*. **1982**, *19*, 465–473.

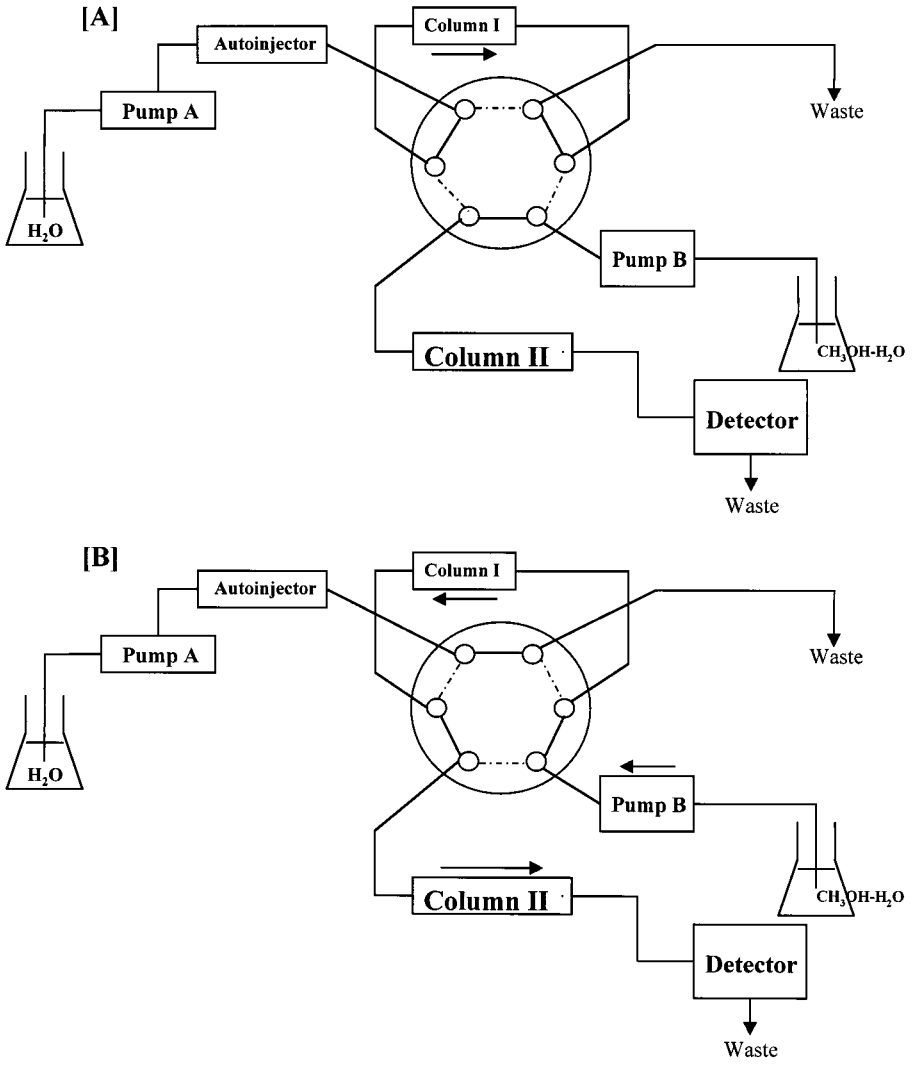

Figure 1—Schematic representation of the HPLC column-switching system. (A) Sample enrichment process. (B) Analytical process.

Japan) fitted with a 10 mL sample loop, a 10 mL syringe and a Rheodyne 7125 injection valve, and a universal valve-switching module ACP 1010 with a Rheodyne 7000 six-port, two-position valve (Anachem, Luton, England). The following columns were connected to the six-port valve. Column I (precolumn for concentration): Capcell Pak C18, UG 80 (Shiseido, Tokyo, Japan), 35 × 4.6 mm i.d. Column II (analytical column): Cosmosil 5C18-AR−II (Nacalai Tesque, Kyoto, Japan). 150 × 4.6 mm i.d.

Column-Switching HPLC Analysis—A 5−9 mL aliquot of the centrifuged aqueous phase, giving an appropriate peak area on the final chromatogram, was automatically injected onto column I by pump A using pure water as the mobile phase at a flow rate of 5.0 mL/min (at position A, Figure 1). This process allowed the solute to be adsorbed at the top end of the column I. After 4 min, the valve was switched to the position B (Figure 1), and the preconcentrated (adsorbed) analyte was eluted to the analytical column II (back flush mode) with an aqueous solution containing 70−90% methanol delivered by pump B. The signals were analyzed by a photodiode array detector SPD-MV10A (Shimadzu, Kyoto, Japan). Eluent compositions were chosen so that the analytical time would be less than 10 min for each sample. The average peak area of a given sample for the aqueous phase, A_W, was obtained from repeated 5−7 cycles. To analyze the corresponding octanol phase under comparable conditions to those for the aqueous phase, the following two-step dilution was performed. First, a 200 μL aliquot of the octanol phase was diluted with methanol to 1.00 mL. The methanolic solution thus obtained was then diluted with pure water by an appropriate factor as described below. The resulting homogeneous solution was analyzed quantitatively in the same manner as in the analysis of the aqueous phase. Injection volume was the same as that for the aqueous phase. The second dilution with water was done at two dilution factors so that the resulting peak areas, A_o (1) and A_o (2), obtained as described above would be $A_o(1) < A_W < A_o(2)$ and also the ratio of $A_o(2)/A_o(1)$ would be 2−5. With these data, the P value was calculated as $P = fA_o/A_W$, where f represents the overall dilution factor. Agreement of log P from two A_o values, A_o (1) and A_o (2), was usually obtained to within 0.05 log unit. The mean value was taken as the P value. For each compound, measurements were carried out at least in duplicate, and the P values thereby obtained were reproducible to within ±0.1 log unit for most cases.

Measurement of log *k*—The log k value was determined as previously described with a Capcell Pak C18 column (50 × 4.6 mm i.d., Shiseido, Tokyo, Japan) at 25 °C.[13] Methanol−0.01 M phosphate buffer (pH 7.4) mixtures containing 50, 60, and 70% MeOH (hereafter designated as M50, M60, and M70, respectively) prepared by volume were used as the eluent. Log k parameters were determined by $k = (t_R - t_0)/t_0$, where, t_0 and t_R are retention times of methanol and a given analyte, respectively.

Table 3—Pyrazine-π (π_{PR}) and Benzene-π(π_{PhX})

X	π_{PR}[a]	π_{PhX}[b]
F	0.55	0.14
Cl	0.96	0.71
Br	1.19	0.86
Me	0.47	0.56
Et	0.95	1.02
OMe	0.99	–0.02
OEt	1.54	0.38
CN	0.25	–0.57
COOMe	0.03	–0.01
COOEt	0.54	0.51
Ph	2.33[c]	1.96
4-MeO-Ph	2.50[c]	–

[a] Taken from ref 24. [b] Taken from ref 2. [c] This work.

Results and Discussion

log *P* of Diarylpyrazines—Before measuring log *P* values for our compounds, we attempted to determine the log *P* value of curcumin with our column-switching system. Curcumin has attracted our interest in the previous structure−activity relationship study,[25] and its experimental log *P* value is reported to be 4.26.[26] We obtained a value of 4.28, very close to 4.26, indicating that this newly developed procedure works satisfactorily. Therefore, we applied this method to determining log *P* values of diaryl pyrazines (Table 1). Inspection of Table 1 shows that introduction of two hydrophobic aryl substituents increases extensively the hydrophobicity of molecules. We have previously shown[24] that the π value in the pyrazine system (Table 3), derived from the log *P* values of monosubstituted pyrazines and pyrazine itself, often differs from the widely used benzene-π values and, therefore, that pyrazine-π values should be used in the analysis of log *P* values of pyrazines. By using pyrazine-π values, where available, estimated log *P* values, log P_{add}, were calculated on assumption of the additivity, that is, the sum of log *P* of pyrazine (−0.26) and pyrazine-π values of the substituents (Table 1).

It is noteworthy that experimental log *P* values of all compounds in Table 1 were much lower than log P_{add} values. In particular, in 2,3-diarylpyrazines, **3**−**7** and **14**−**22**, the difference was over one log unit. Steric hindrance between the two benzene rings may contribute to reducing the hydrophobicity of molecules (*ortho*-diaryl effect). This argument would also be supported by comparing the log *P* values of the three isomeric diphenyl-methylpyrazines (**4**, **23**, and **24**). Among them, only the isomer **4** having two adjacent phenyl groups gave a log *P* value (3.52) much smaller than those for **23** (4.28) and **24** (4.29), which have two phenyl substituents at 2,5- and 2,6-positions, respectively. An X-ray analysis of 2,3-diphenylpyrazine **3** has demonstrated that the dihedral angles between the two phenyl substituents and the pyrazine ring are approximately 50° and 40°.[27] Our semiempirical MO calculations of 2,3-diphenylpyrazine by the AM1 method[28] (the MOPAC 93 program package incorporated in an ANCHOR II modeling system, Fujitsu, Japan) gave a similar result. Such nonplanar conformation would cause resonance inhibition, decreasing the degree of conjugation and consequently reducing hydrophobicity below expectations for a molecule with full delocalization of π-electrons. The use of the additivity rule overestimated log *P* for **3** by 1.2 and that for **14** by 1.3, suggesting that the steric hindrance between the two vicinal benzene rings makes a negative contribution of about −1.2 to log *P*. This finding conforms to a well-known phenomenon that an extension of the resonating system requires a positive correction factor.[2]

Table 4—Substituent Effects of R_3

compound	R_3	R_1,R_2	log P_{obsd}	log P_{pred}[a]	compound	R_3	R_1,R_2	log P_{obsd}	log P_{pred}[b]
4	Me	Ph	3.52	3.66	**15**	Me	4-OMe-Ph	3.66	3.89
5	OMe	Ph	4.21	4.18	**16**	Et	4-OMe-Ph	4.22	4.37
6	OEt	Ph	4.73	4.73	**17**	Cl	4-OMe-Ph	4.30	4.38
7	Cl	Ph	4.05	4.15	**18**	OMe	4-OMe-Ph	4.47	4.41
					19	OEt	4-OMe-Ph	5.00	4.96
					20	CN	4-OMe-Ph	3.70	3.67
					21	COOMe	4-OMe-Ph	3.41	3.45

[a] Sum of log *P*(**3**) and pyrazine-π(R_3). [b] Sum of log *P*(**14**) and pyrazine-π(R_3).

We also examined the substituent effect of R_3 on log *P* when R_3 is introduced to 2,3-diarylpyrazines, **3** and **14**, in terms of the *ortho*-diaryl effect discussed above and pyrazine-π values. As the R_3 substituent hardly suffers from steric effects, we may expect normal substituent effects in these pyrazines. The sum of log *P* of **3** or **14**, and pyrazine-π of R_3 was calculated (log $P_{pred.}$) and compared with the experimental log *P*. As shown in Table 4, they were in fairly good agreement. It is not unexpected that the deviation from the experimental value is somewhat larger than the expected experimental error in some compounds because some additional minor corrections for the electronic interactions between the substituents and the ring *N*-atoms as well as for the steric effect between R_2 and R_3 should be taken into account for detailed analysis.[24] These results revealed that the pyrazine-π is very helpful in making a rough estimate of log *P* of even highly lipophilic pyrazines, provided severe steric effects are not involved. It should be emphasized that the use of benzene-π instead of pyrazine-π for the substituent on the pyrazine ring would lead to erroneous estimated values.

Comparisons of log *P* for a series of variously substituted alky-diphenylpyrazines (**4** and **23**−**27**) indicates that steric repulsion by the vicinal alkyl and phenyl substituents also requires a correction of −0.6 to −0.7 in log *P*. As the corresponding reduction in log *P* in the vicinal dialkyl substituents is very small (∼−0.15),[29] large correction factor suggests twisting of the benzene ring even in this case. Nonplanar conformations were also indicated by the MO calculations. Measurements and more quantitative analyses of log *P* for a larger size data set including more lipophilic compounds are now in progress.

Log *k*: Prediction of log *P* by the HPLC Approach—Our previous studies on several series of monosubstituted heteroaromatic compounds have revealed that the relationship between log *P* (−1 < log *P* < 3) and log *k* obtained with various compositions of methanol−water eluents usually require some correction terms for hydrogen-bonding effects and can be expressed by the following general equation for nonamphiprotics:[30]

$$\log k = a \log P + \rho\sigma_I + sS_{HA} + \text{const} \qquad (4)$$

In this equation, the σ_I parameter represents Charton's electronic substituent constant,[31] and the S_{HA} parameter is that we have recently proposed as the hydrogen-accepting indicator for the substituent.[30] In general, contributions of the two correction terms are of minor importance when the eluent contains 50% MeOH (M50), so that we could assume the log *k*−log *P* linearity. However, these contributions are found to increase with decreasing methanol content. Strong hydrogen-accepting substituents, such as COOR and $CONMe_2$, deviate substantially from the line formed by non-hydrogen bonders and weak hydrogen acceptors in the plot of log *k* against log *P*. If such a predictive capability of M50 eluent holds for compounds

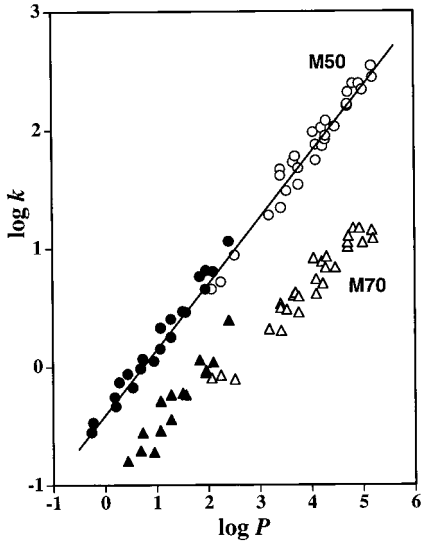

Figure 2—Relationship between log *k* and log *P* for variously substituted pyrazines. Open symbols represent (di)arylpyrazines, and closed symbols represent the other pyrazines.

with much higher log *P* values, the log k_{M50} approach would be of practical value in prediction of log *P*. Accordingly, we measured log *k* values for the present compounds under the same conditions and studied the relationship between log *P* and log *k*. To make the results comparable with those previously studied, we selected from many of the related compounds studied earlier, typical compounds including esters and *N*-oxides which were previously classified as deviants in water rich eluents.[13] Some *N*-oxides of diarylpyrazines were also added to the data set. Compounds used for log *k* measurements in addition to the (di)arylpyrazines in Table 1 are listed in Table 2 with their log *P* values. It should be noted that the compounds studied in this work are non-hydrogen bonding or hydrogen accepting. Log *k* values of all the compounds in Tables 1 and 2 obtained with the M50 and M70 eluents are plotted against log *P* in Figure 2. The M50 eluent again produced a satisfactory linear relationship of the form shown in eq 5:

$$\log k_{M50} = 0.554 \log P - 0.384 \quad (5)$$
$$n = 51,\ r = 0.996,\ s = 0.085$$

The relationship for the M60 eluent was somewhat inferior to eq 5 (the data not shown). As the data set contains molecules having strongly hydrogen-accepting substituents and/or a sterically hindered conjugated system, finding a simple linear equation covering a range of hydrophobicity of 6 log units seems to be rather surprising. It is of interest to notice that our earlier work on a series of monosubstituted pyrazines found the value of 0.58 as the slope of the log *P* term, being very close to the value of 0.55 shown by eq 5, in the corresponding equation. Although measuring log *k* values of monosubstituted pyrazines in more methanol-rich eluents such as M60 and M70 has been technically difficult, it has now become very clear, by combination of all the results obtained so far, that an optimum eluent composition yielding almost linear relationships would be at 50% MeOH or at methanol concentrations near 50%. Since the measurement of log *k* is easier and quicker than log *P*, particularly in very hydrophobic compounds, the log k_{M50} parameter can be expected to be a powerful tool for predicting the log *P* value. Care should be taken, however, in treating amphiprotic compounds by the HPLC method. When alkyl-bonded stationary phases are used, amphiprotics often give separate lines parallel to that for nonamphiprotics in the log *k*−log *P* plot.[13,15] This phenomenon is unavoidable because octanol is more hydrogen accepting than the stationery phase. Finding an effective procedure for treating these is still to be investigated.

Conclusion

In this study, we developed a novel procedure for measuring the log *P* value of highly lipophilic diaryl pyrazines by the HPLC column-switching technique. This method enabled us to measure the extremely low concentration of solutes by direct injection of a large volume (5−9 mL) of aqueous phase onto a precolumn. The log *P* values thus obtained ranged from about 3 to 5.2. By using these data, a large correction factor of about −1.2 was estimated as the *o*-diphenyl effect, which was thought to be attributable to the loss of coplanarity. The effects of sterically unhindered substituents attached to the pyrazine ring on log *P* could be well estimated by using the pyrazine-π value obtained in our earlier work.[24] The log *k* values were also measured with different compositions of methanol−buffer (pH 7.4) eluents, and a good linear relationship between log *P* and log *k* was found to hold at 50% MeOH, in conformity with our previous finding,[13,14] over the log *P* range from −0.3 to 5.2. To our knowledge, there have been no previous studies where log *k* values for a set of compounds determined under exactly the same HPLC conditions have been related to experimentally measured log *P* values over such a wide range. The present result seems to afford a nice example demonstrating that the use of the k_{M50} parameter provides reliable and practical method to predict quickly the log *P* value.

Development of procedures for obtaining reliable log *P* values for lipophilic compounds has become increasingly important not only in QSAR studies of bioactive compounds but also in environmental chemistry and toxicology where the log *P* is used as a parameter for evaluating the fish bioconcentration and toxicity.[32−34] Our present study would be also expected to be helpful for research in such fields.

References and Notes

1. Hansch, C.; Fujita, T. ρ-σ-π Analysis. A method for the correlation of biological activity and chemical structure. *J. Am. Chem. Soc.* **1964**, *86*, 1616−1626.
2. Hansch, C.; Leo, A. *Exploring QSAR−Fundamentals and Applications in Chemistry and Biology*; American Chemical Society: Washington, DC, 1995; pp 125−168.
3. Camilleri, P.; Watts, S. A.; Boraston, J. A. A surface area approach to determination of partition coefficients. *J. Chem. Soc., Perkin Trans. 2* **1988**, 1699−1707.
4. Fujita, T.; Iwasa, J.; Hansch, C. A new substituent constant, π, derived from partition coefficients. *J. Am. Chem. Soc.* **1964**, *86*, 5175−5180.
5. Rekker, R. *The Hydrophobic Fragmental Constant*; Elsevier: New York, 1977.
6. CLOGP program, Pomona College Medchem Project.
7. Fujita, T. Substituent effects in the partition coefficient of disubstituted benzenes: bidirectional Hammett-type relationships. *Prog. Phys. Org. Chem.* **1983**, *14*, 75−113.
8. Bodor, N.; Huang, M.-J. An extended version of a novel method for the estimation of partition coefficients. *J. Pharm. Sci.* **1992**, *81*, 272−281.
9. Collander, R. The partition of organic compounds between higher alcohols and water. *Acta Chem. Scand.* **1951**, *5*, 774−780.
10. Braumann, T. Determination of hydrophobic parameters by reversed-phase liquid chromatography: Theory, experimental techniques, and application in studies on quantitative structure−activity relationships. *J. Chromatogr.* **1986**, *373*, 191−225.
11. Minick, D. J.; Frenz, J. H.; Patrick, M. A.; Brent, D. A. A comprehensive method for determining hydrophobicity constants by reversed-phase high-performance liquid chromatography. *J. Med. Chem.* **1988**, *31*, 1923−1933.

12. Lambert, W. J. Modeling oil-water partitioning and membrane permeation using reversed-phase chromatography. *J. Chromatogr. A.* **1993**, *514*, 469−484.
13. Yamagami, C.; Ogura, T.; Takao, N. Relationship between capacity factors and octanol−water partition coefficients for monosubstituted pyrazines and the related pyridines. *J. Chromatogr.* **1990**, *514*, 123−136.
14. Yamagami, C.; Fujita, T. Hydrophobicity parameter of heteroaromatic compounds derived from various partitioning systems. In *Classical and Three-dimensional QSAR in Agrochemistry*; Hansch, C., Fujita, T., Eds.; ACS Symposium Series 606, American Chemical Society: Washington, DC, 1995; pp 36−47.
15. Yamagami, C.; Yokota, M.; Takao, N. Hydrogen-bond effects of ester and amide groups in heteroaromatic compounds on the relationship between the capacity factor and the octanol−water partition coefficient. *J. Chromatogr. A* **1994**, *662*, 49−60.
16. Garst, J. E.; Accurate, wide-range, automated, high-performance liquid chromatographic method for the estimation of octanol/water partition coefficients II: Equilibrium in partition coefficient measurements, additivity of substituent constants, and correlation of biological data. *J. Pharm. Sci.* **1984**, *73*, 1623−1629.
17. Dross, K. P.; Mannhold, R.; Rekker, R. F. Drug Lipophilicity in QSAR Practice: II. Aspects of R_M-determinations; Critics of R_M-corrections; Interrelations with partition coefficients. *Quant. Struct.-Act. Relat.* **1992**, *11* , 36−44.
18. Bechalany, A.; Tsantili-Kakoulidou, A.; Tayar, N. El.; Testa, B. Measurement of lipophilicity indices by reversed-phase high-performance liquid chromatography: comparison of two stationary phases and various eluents. *J. Chromatogr.* **1991**, *541*, 221−229.
19. Kuchař, M.; Rejholec, V.; Kraus, E.; Miller, V.; Rábek, V. Influence of intramolecular interactions on chromatographic behaviour of arylaliphatic acids. I. Comparison of reversed-phase thin-layer and high-performance liquid chromatography. *J. Chromatogr.* **1983**, *280*, 279−288.
20. Yamagami, C.; Masaki, Y. Relationship between capacity factor and octanol−water partition coefficients of monosubstituted thiophenes. *Chem. Pharm. Bull.* **1995**, *43*, 2238−2242
21. Ohta, A.; Takahashi, H; Miyata, N.; Hirono, H.; Nishio, T.; Uchino, E.; Yamada, K.; Aoyagi, Y.; Suwabe, Y.; Fujitake, M.; Suzuki, T.; Okamoto, K. Anti-platelet aggregation activity of some pyrazines. *Biol. Pharm. Bull.* **1997**, *20*, 1076−1081.
22. Dorsey, J. G.; Cooper, W. T.; Siles, B. A.; Foley, J. P.; Barth, H. G. Liquid chromatography: Theory and methodology. *Anal. Chem.* **1996**, *68*, 515R-568R.
23. LaCourse, W. R.; Dasenbrock, C. O. Column liquid chromatography: Equipment and instrumentation. *Anal. Chem.* **1998**, *70*, 37R−52R.
24. Yamagami, C.; Takao, N.; Fujita, T. Analysis and prediction of partition coefficients of monosubstituted diazines. *Quant. Struct.-Act. Relat.* **1990**, *9*, 313−320.
25. Motohashi, N.; Ashihara, Y; Yamagami, C.; Saito, Y. Antimutagenic effects of dehydrozingerone and its analogs on UV-induced mutagenesis in *Escherichia coli*. *Mutat. Res.* **1997**, *377*, 17−25.
26. Freese, E.; Levin, B. C.; Pearce, R.; Sreevalsan, T.; Kaufman, J. J.; Koski, W. S.; Semo, N. M. Correlation between the growth inhibitory effects, partition coefficients and teratogenic effects of lipophilic acids. *Teratology* **1979**, *20*, 413−439.
27. Kitano, Y.; Ashida, T.; Ohta, A.; Watanabe, T.; Akita, Y. Structure of 2,3-diphenylpyrazine, $C_{16}H_{12}N_2$. *Acta Crystallogr.* **1983**, *C39*, 136−139.
28. Dewar, M. J. S.; Zoebisch, E. G.; Healy, E. F.; Stewart, J. J. P. AM1: A new general purpose quantum mechanical molecular model. *J. Am. Chem. Soc.* **1985**, *107*, 3902−3909.
29. Yamagami, C.; Takao, N.; Fujita, T. Analysis and prediction of partition coefficients of disubstituted pyrazines. *J. Pharm. Sci.* **1991**, *80*, 772−777.
30. Yamagami, C.; Kawase, K.; Fujita, T. A new hydrogen-accepting scale of monosubstituted (di)azines for the relationship between retention factor and octanol−water partition coefficient. *Quant. Struct.-Act. Relat.* **1999**, *18*, 26−34.
31. Charton, M. Electrical effect substituent constants for correlation analysis. *Prog. Phys. Org. Chem.* **1981**, *13*, 119−252.
32. Fox, K.; Zauke, G.-P.; Butte, W. Kinetics of bioconcentration and clearance of 28 polychlorinated biphenyl congeners in zebrafish (*Brachydanio rerio*). *Ecotoxicol. Environ. Saf.* **1994**, *28*, 99−109.
33. Leblanc, G. A. Tropic-level differences in the bioconcentration of chemicals: implications in assessing environmental biomagnification. *Environ. Sci. Technol.* **1995**, *29*, 154−160.
34. Devillers, J.; Domine, D.; Bintein, S. Fish bioconcentration modeling with log *P*. *Toxicol. Methods* **1998**, *8*, 1−10.

Acknowledgments

We thank Professor Toshio Fujita of EMILE project for useful discussion. This work was partly supported by Kobe Pharmaceutical University Collaboration Fund.

JS990112S

Characterization of Lipophilicity Scales Using Vectors from Solvation Energy Descriptors

YASUSHI ISHIHAMA* AND NAOKI ASAKAWA

Contribution from *Analytical Research Laboratories, Eisai Co., Ltd., 5-1-3 Tokodai, Tsukuba, Ibaraki 300-2635, Japan.*

Received April 12, 1999. Final revised manuscript received September 29, 1999. Accepted for publication October 5, 1999.

Abstract □ Lipophilicity scales were characterized by an approach using vectors provided from solvation energy descriptors (SED) of solutes such as an excess molar refraction, the dipolarity/polarizability, the hydrogen-bond acidity, the basicity, and the McGowan characteristic volume. The five components of the SED vector were obtained from the coefficients of the five SED terms of the linear solvation energy relationship (LSER) equation for the lipophilicity scales. The analogy between two lipophilicity scales was expressed as the angle between the two SED vectors, while the difference in the contribution of the five independent SEDs to these two lipophilicity scales was quantified by the difference of the unit vectors of the SED vectors. These approaches were applied to several lipophilicity scales measured using microemulsions, micelles, an immobilized artificial membrane column, and an octanol–water system. As a result, the quantitative classification of these scales was successfully carried out, and the difference in the scales was well characterized. In addition, this vector approach was extended to the estimation of the contribution of each constituent of the microemulsions to the lipophilicity scale. Furthermore, some biological parameters such as skin permeability and the distribution between blood and brain could be predicted by the summation of the SED vectors obtained from the chromatographic systems. These results suggest that complex biological systems can be expressed quantitatively by simple chemical models with their SED vectors.

Introduction

In the passage of drugs throughout the body, the permeability of cell membranes is quite important for the prediction of their in vivo activities from their in vitro results. Therefore, the lipophilicity of drugs such as the logarithm of the partition coefficients between 1-octanol and water (log P_{ow}) has been used as a parameter for the structure optimization of the drug candidates. Because recent developments in combinatorial chemistry allowed the synthesis of a large number of compounds as drug candidates, the demand for high-throughput measurement of biologically appropriate lipophilicity is steadily increasing.

In our previous study, the lipophilicity scale by electrokinetic chromatography (EKC) with the microemulsion of sodium dodecyl sulfate (SDS), 1-butanol, *n*-heptane, and a buffer provided the excellent correlation with log P_{ow} for neutral compounds with various hydrogen-bonding abilities.[1] In quantitative structure−activity relationship studies (QSAR) for some bioactivities of the drugs, their lipophilicity from the microemulsion provided a better correlation with their bioactivities than other lipophilicity scales.[2,3] In addition, it was suggested that the lipophilicity scales from the microemulsions could be designed by selecting the constituents and their concentration.[4]

On the other hand, other lipophilicity scales such as the logarithm of the capacity factors (log k') in various chromatographic systems including HPLC[5−7] and micellar EKC (MEKC)[8−15] have been developed, and they provided diverse and unique properties as lipophilicity scales. In optimizing the structure of drug candidates, these lipophilicity scales often provided different results, although they have viability for high-throughput analysis. Therefore, selecting the lipophilicity scales suitable for predicting the bioactivities of drug candidates is quite important for optimizing their structures. For this purpose, the characterization and classification of these scales were required.

The correlation coefficients of the linear relationship between two scales have been often used for the comparison between these two scales. It is, however, well-known that the correlation coefficient strongly depends on the test set of solutes. Alternatively, the linear solvation energy relationship (LSER) analysis has been used for the characterization of the retention behaviors of solutes in many chromatographic media, and the quantitative prediction of the retention times of the solutes from their structure was performed.[16−18] Recently, this approach was applied to MEKC to classify the separation selectivity of the micelles[19−22] and was also used for evaluating the correlation between log P_{ow} and migration index (MI) measured by microemulsion EKC (MEEKC).[4]

The general equation of LSER based on the solvation energy descriptors (SED) of solutes is as follows:

$$\log \mathrm{SP} = c + rR_2 + s\pi_2^{\mathrm{H}} + a\sum\alpha_2^{\mathrm{H}} + b\sum\beta_2 + vV_x \quad (1)$$

where log SP is the dependent variable, i.e., the lipophilicity scales (LS) such as log k' and MI in this case, and the independent variables are solute descriptors as follows: R_2 is an excess molar refraction, π_2^{H} is the solute dipolarity/polarizability, $\sum\alpha_2^{\mathrm{H}}$ and $\sum\beta_2$ are the solute hydrogen-bond acidity and basicity, and Vx is the McGowan characteristic volume in units of cm^3 mol^{-1}/100.[17] The obtained coefficients of eq 1 were used for characterization of the lipophilicity scales as well as the prediction of the separation selectivity in the chromatographic media. To classify these scales, the ratios of the coefficients such as *r*/*v*, *a*/*v*, *b*/*v*, and *s*/*v* were calculated and compared with those from another scale. This approach was quite useful to judge the analogy between two scales. Unfortunately, however, it was difficult to simultaneously compare the set of the coefficients or coefficient ratios between the plural scales. For example, Abraham et al. reported on the following scales:[4]

(*r*/*v*, *s*/*v*, *a*/*v*, *b*/*v*) =
(0.12, −0.23, 0.01, −0.94) for log P_{ow}

(*r*/*v*, *s*/*v*, *a*/*v*, *b*/*v*) =
(0.18, −0.24, 0.00, −0.87) for log *P* (pentanol−water)

(*r*/*v*, *s*/*v*, *a*/*v*, *b*/*v*) =
(0.09, −0.23, −0.02, −0.92) for log k' (microemulsion)

It was impossible to judge which was similar to octanol−water, pentanol−water, or the microemulsion. Therefore, an approach for analyzing these scales simultaneously was required.

* Corresponding author. Tel: (+81-298) 47-5763, fax: (+81-298) 47-5771, e-mail: y-ishihama@hhc.eisai.co.jp.

10.1021/js990119+ CCC: $18.00
Published on Web 11/04/1999

Table 1—System for Measurement of Lipophilicity Scales

system	scale	constituents
ME(SDS)	MI_{SDS}	SDS (1.44%)/1-butanol (6.49%)/ heptane (0.82%)/buffer[a]
ME(CTAC)	MI_{CTAC}	CTAC (1.44%)/1-butanol (6.49%)/ heptane (0.82%)/buffer[a]
ME(DTAC)	MI_{DTAC}	DTAC (1.44%)/1-butanol (6.49%)/ heptane (0.82%)/buffer[a]
MC(SDS)	$\log k'_{SDS}$	50 mM SDS in buffer[a]
MC(DTAC)	$\log k'_{DTAC}$	50 mM DTAC in buffer[a]
MC(S/B)	$\log k'_{S/B}$	25 mM SDS and 25 mM Brij 35 in buffer[a]
OW	$\log P_{OW}$	1-octanol and water
IAM	$\log k'_{IAM}$	IAM column with buffer[a] as the mobile phase

[a] buffer: 50 mM sodium phosphate and 100 mM sodium borate (pH 7.0).

Recently, Valko et al. reported on the characterization of the various HPLC columns using the gradient retention parameter named chromatographic hydrophobicity indices (CHI) and their SED coefficients.[23] They described that the principal component analysis and the nonlinear mapping technique provide an appropriate tool for comparison of various HPLC partition systems.

In this paper, we demonstrate that the lipophilicity scales could be characterized using the coefficients of the five SED terms of the LSER equation as vector components. The analogy of the lipophilicity scales was evaluated using the scalar product of the vectors, and the difference in the five independent factors which affect the lipophilicity scales was quantified by these unit vectors. This vector approach was also employed to obtain the actual structural information of the microemulsions from the vectors of their individual constituent system. Furthermore, it was applied to predict some biological systems according to the summation of plural vectors from simple chemical systems.

Experimental Section

Capillary electrophoresis was performed using P/ACE 2100 (Beckman, Fullerton, CA). For three microemulsions (ME) and three micelles (MC), EKC was used for the determination of the lipophilicity scales from these systems. The experimental details were described in previous papers.[1−3,8] In all cases, 50 mM phosphate−100 mM borate solution (pH 7.0) was used as the buffer. The ME and MC solutions employed are listed in Table 1. Uncoated fused silica capillary with 50-μm i.d. and 27-cm length (GL Sciences, Tokyo, Japan) was employed. The capillary was thermostated at 25 °C. The applied voltage was 7.5 kV, and the detection wavelength was 214 nm. The injection was performed by pressure (0.5 psi, 2 s). In the cases of the micellar systems, the values of log k' were used as lipophilicity scales, while in the cases of the microemulsions, the migration indexes (MI) were calculated from the log k' of test solutes and references.[1−3]

A Shimadzu LC-10A system (Kyoto, Japan) equipped with an SPD-10A UV detector (Shimadzu) was used for the measurement of the lipophilicity scale from immobilized artificial membrane (IAM) column (4.6-mm i.d., 100-mm length, Resis, Morten Grove, IL). In this case, log k' was used as a lipophilicity scale using a phosphate buffer at pH 7.0 (ionic strength: 0.05) as a mobile phase and UV 220 nm as a detection wavelength. All tested samples listed in Table 2 were purchased from Aldrich (Milwaukee, WI), Sigma (St. Louis, MO), Wako (Osaka, Japan), and Tokyo Kasei Kogyo (Tokyo, Japan).

The measured log P_{ow} values were obtained from the database of Mac-logP ver. 1.0.3 (BioByte Corp., Claremont, CA).

Methodology

To obtain the set of the five coefficients (r, s, a, b, v) of eq 1, a regression analysis is performed using the measured lipophilicity values and the SED values of solutes listed in Table 2. The SED coefficient vector of lipophilicity scale i (LS_i), $\vec{\omega}$, is defined as follows:

$$\vec{\omega}_i = (r_i, s_i, a_i, b_i, v_i) \tag{2}$$

The analogy between LS_i and LS_j is expressed as cos θ_{ij} between $\vec{\omega}_i$ and $\vec{\omega}_j$ as follows:

$$\cos\theta_{ij} = \frac{\vec{\omega}_i.\vec{\omega}_j}{|\vec{\omega}_i||\vec{\omega}_j|} = \frac{r_i r_j + s_i s_j + a_i a_j + b_i b_j + v_i v_j}{\sqrt{r_i^2 + s_i^2 + a_i^2 + b_i^2 + v_i^2}\sqrt{r_j^2 + s_j^2 + a_j^2 + b_j^2 + v_j^2}} \tag{3}$$

Table 2—Solutes Employed

sample name	solvation energy descriptor				
	R_2	π_2^H	$\Sigma\alpha_2^H$	$\Sigma\beta_2$	V_x
pyrimidine	0.606	1.00	0	0.65	0.634
pyrazine	0.629	0.95	0	0.61	0.634
4-methylpyrimidine	0.595	1.00	0	0.63	0.775
methylpyrazine	0.629	0.90	0	0.65	0.775
4,6-dimethylpyrimidine	0.580	1.00	0	0.65	0.916
ethylpyrazine	0.616	0.90	0	0.66	0.916
pyrrole	0.613	0.73	0.41	0.29	0.577
resorcinol	0.980	1.00	1.10	0.58	0.834
n-methylbenzamide	0.950	1.49	0.40	0.71	1.114
methyl 2-furoate	0.560	1.00	0	0.50	0.893
benzyl alcohol	0.803	0.87	0.39	0.56	0.916
1-methylpyrrole	0.559	0.79	0	0.31	0.718
acetanilide	0.870	1.40	0.50	0.67	1.113
p-methoxyphenol	0.900	1.17	0.57	0.48	0.975
furan	0.369	0.53	0	0.13	0.536
p-nitroaniline	1.220	1.91	0.42	0.38	0.990
phenol	0.805	0.89	0.60	0.30	0.775
2,5-dimethylpyrrole	0.639	0.70	0.35	0.44	0.859
benzaldehyde	0.820	1.00	0	0.39	0.873
quinoxaline	1.300	1.22	0	0.59	1.003
ethyl 2-furoate	0.560	1.00	0	0.50	1.033
benzonitrile	0.742	1.11	0	0.33	0.871
acetophenone	0.818	1.01	0	0.48	1.014
thiophene	0.687	0.57	0	0.15	0.641
2-methylfuran	0.372	0.50	0	0.14	0.677
nitrobenzene	0.871	1.11	0	0.28	0.891
p-cresol	0.820	0.87	0.57	0.31	0.916
o-cresol	0.840	0.86	0.52	0.30	0.916
m-cresol	0.822	0.88	0.57	0.34	0.916
p-nitroanisole	0.970	1.29	0	0.40	1.090
anisole	0.708	0.75	0	0.29	0.916
methyl benzoate	0.733	0.85	0	0.46	1.073
benzene	0.610	0.52	0	0.14	0.716
indole	1.200	1.12	0.44	0.31	0.946
propiophenone	0.804	0.95	0	0.51	1.155
p-nitrotoluene	0.870	1.11	0	0.28	1.032
p-chlorophenol	0.915	1.08	0.67	0.20	0.898
2-ethylfuran	0.361	0.50	0	0.14	0.818
p-ethylphenol	0.800	0.90	0.55	0.36	1.057
2-methylindole	1.200	1.05	0.44	0.37	1.087
3-methylindole	1.200	1.06	0.44	0.35	1.087
1-methylindole	1.206	1.03	0	0.37	1.087
butyrophenone	0.797	0.95	0	0.51	1.296
benzofuran	0.888	0.83	0	0.15	0.905
toluene	0.601	0.52	0	0.14	0.857
2-naphthol	1.520	1.08	0.61	0.40	1.144
chlorobenzene	0.718	0.65	0	0.07	0.839
p-propylphenol	0.793	0.88	0.55	0.37	1.198
ethylbenzene	0.613	0.51	0	0.15	0.998
naphthalene	1.340	0.92	0	0.20	1.085
propylbenzene	0.604	0.50	0	0.15	1.139
butylbenzene	0.600	0.51	0	0.15	1.280
anthrathene	2.290	1.34	0	0.28	1.454

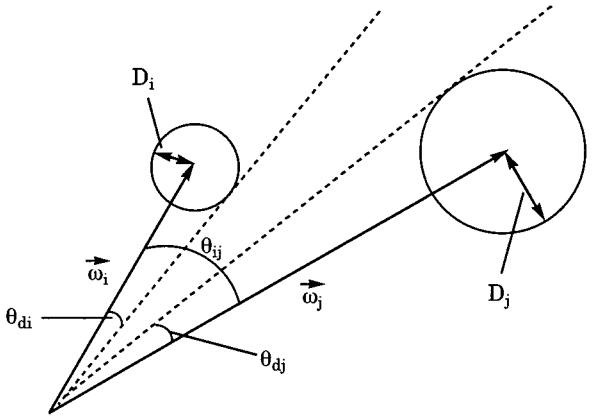

Figure 1—Two-dimensional model space of SED vectors.

Thus, as the correlation is higher, the value of cos θ_{ij} becomes closer to 1. When the analogy of LS_j ($j = 1, 2, ...$) to LS_i is examined, the analogy ranking of LS_j ($j = 1, 2,...$) to LS_i is established according to cos θ_{ij}. However, to judge the analogy between LS_i and LS_j, cos θ_{ij} is insufficient and the deviation of the vector should be also considered. In this study, D, which is a 95% confidence level of the coefficients of SED, is used as the deviation of each vector as follows:

$$D = TINV(0.05, N) \times \mathrm{SE} \quad (4)$$

where TINV is the inverse of the Student's t-distribution for the specified degrees of freedom, N, and SE is the average of the standard errors of the coefficients of SED.

Therefore, the analogy between two systems can be evaluated by the following equation:

$$J = \cos\theta_{ij} - \cos(\theta_{di} + \theta_{dj}) \quad (5)$$

where θ_{di} and θ_{dj} are the angles of the deviations of $\vec{\omega}_i$ and $\vec{\omega}_j$, respectively, as shown in Figure 1. The value of $\cos(\theta_{di} + \theta_{dj})$ can be calculated as follows:

$$\cos(\theta_{di} + \theta_{dj}) = \sqrt{\left(1 - \frac{D_i^2}{|\vec{\omega}_i|^2}\right)\left(1 - \frac{D_j^2}{|\vec{\omega}_j|^2}\right)} - \frac{D_i D_j}{|\vec{\omega}_i||\vec{\omega}_j|} \quad (6)$$

In eq 5, when J is greater than zero, these two systems are found to be analogue systems, and in the opposite case, these systems should be distinguished. This vector algorithm is based on the commercial UV spectra database searching program in Shimadzu CLASS−VP Chromatography Data System (Kyoto, Japan).

Concerning the difference in each SED factor of the lipophilicity, the unit vector, $\vec{\omega}_u$, is employed:

$$\vec{\omega}_u = \frac{\vec{\omega}_u}{|\vec{\omega}_u|} = (r_u, s_u, a_u, b_u, v_u) \quad (7)$$

To quantify the difference in each SED factor, the difference in the components of the unit vectors between LS_i and LS_j is evaluated as follows:

$$\Delta\vec{\omega}_u = (\Delta r_u, \Delta s_u, \Delta a_u, \Delta b_u, \Delta v_u) = (r_{ui} - r_{uj}, s_{ui} - s_{uj}, a_{ui} - a_{uj}, b_{ui} - b_{uj}, v_{ui} - v_{uj}) \quad (8)$$

Using the vector, the contribution of each SED factor to the lipophilicity from one system can be compared with that from other systems.

Results and Discussion

Characterization of Lipophilicity Scales by Vector Approaches—lipophilicity scales measured in this study are summarized in Table 1. As for the microemulsion (ME) systems, an anionic ME using SDS as a surfactant and two cationic MEs using CTAC and DTAC, which have different hydrocarbon chain length with the same hydrophilic group, were employed to measure the lipophilicity of 53 compounds listed in Table 2. For micelles (MCs), three different surfactants, anionic SDS, cationic DTAC, and neutral Brij 35, were used. In these MC systems, the capacity factors of several hydrophobic compounds could not be measured because they coeluted with the MC tracers (AO-10-dodecyl bromide).[1,24] Therefore, only 49 compounds were used in this study. Concerning the IAM column, which has the zwitterionic phosphatidyl choline moiety as the stationary phase, 53 compounds were used although analysis was quite time-consuming because no organic modifier was used. The results of LSER regression analyses are listed in Table 3. The correlation coefficients of the analysis were quite high, except for IAM and MC(S/B). The results of MC(SDS) and IAM by others[18] are also listed in Table 3 to compare with our results. For these two MC(SDS)s, little difference was observed, whereas obvious difference was observed between two IAM systems. This might be caused by the difference in the mobile phase, i.e., 10% acetonitrile was employed in ref 18, whereas no organic modifier was used in this study. This was supported by another LSER result from the fast-gradient IAM system recently reported.[23] In this study, considering the reasonability, the results from the IAM system without organic modifier were used in further study.

Table 3—Results of LSER Analyses

systems	SED coefficients					
	r	*s*	*a*	*b*	*v*	R^2
ME(SDS)	0.699	–1.721	–0.129	–6.932	7.474	0.988
S.E.	0.153	0.183	0.119	0.230	0.214	
ME(CTAC)	0.909	–1.533	0.688	–7.509	7.301	0.994
S.E.	0.295	0.194	0.202	0.250	0.273	
ME(DTAC)	1.262	–1.507	0.700	–7.858	7.572	0.995
S.E.	0.276	0.182	0.189	0.234	0.256	
OW	0.537	–0.926	0.019	–3.537	3.794	0.996
S.E.	0.049	0.058	0.038	0.073	0.068	
IAM	0.280	–0.225	0.517	–2.306	2.657	0.939
S.E.	0.123	0.148	0.096	0.186	0.173	
MC(SDS)	0.497	–0.399	–0.254	–1.669	2.765	0.994
S.E.	0.075	0.057	0.073	0.160	0.167	
MC(DTAC)	0.749	–0.430	0.871	–2.667	2.823	0.976
S.E.	0.100	0.098	0.066	0.127	0.121	
MC(S/B)	–0.094	–0.032	0.615	–2.695	2.519	0.947
S.E.	0.162	0.093	0.123	0.257	0.266	
IAM from ref 18	0.81	–0.42	0.69	–2.00	1.87	
S.E.						
MC(SDS) from ref 22[a]	0.46	–0.48	–0.16	–1.71	2.81	0.982
S.E.	0.06	0.07	0.04	0.08	0.09	
MC(SC) from ref 22[a]	0.56	–0.74	0.15	–2.49	2.65	0.970
S.E.	0.08	0.1	0.06	0.11	0.12	

[a] The original data were cited from ref 19.

Regarding cos θ values between SED vectors, it would be necessary to indicate what value of cos θ could be regarded as "good" analogy because this parameter was not familiar. Therefore, for the eight scales described in Table 1, cos θ values were compared with the corresponding correlation coefficients (r). As shown in Figure 2, $r = 0.90$ corresponds to about cos $\theta = 0.96$, while this relationship was only a yardstick and some deviation was observed for this linear relationship.

Using the LSER coefficients and their D values, analyses of the SED vectors were performed. In Table 4, analogy ranking between one system and the other systems are performed using cos θ. The values of cos θ between three ME systems were quite close to 1, while the values of cos

Table 4—Analogy Ranking between Lipophilicity Scales *i* and *j*

	analogy ranking	LS_i								
		ME (SDS)	ME (CTAC)	ME (DTAC)	OW	IAM	MC (SDS)	MC (DTAC)	MC (S/B)	MC (SC)[a]
LS_j ($\cos\theta_{ij}$)	1	OW	ME (DTAC)	ME (CTAC)	ME (SDS)	ME (CTAC)	OW	IAM	IAM	OW
		0.9992	0.9996	0.9996	0.9992	0.9900	0.9736	0.9898	0.9877	0.9979
	2	ME (CTAC)	OW	OW	MC (SC)	MC (DTAC)	ME (SDS)	ME (DTAC)	ME (CTAC)	ME (DTAC)
		0.9953	0.9964	0.9960	0.9979	0.9898	0.9734	0.9842	0.9796	0.9960
	3	MC (SC)	ME (SDS)	MC (SC)	ME (CTAC)	ME (DTAC)	MC (SC)	ME (CTAC)	ME (DTAC)	ME (CTAC)
		0.9947	0.9953	0.9960	0.9964	0.9896	0.9692	0.9820	0.9770	0.9952
	4	ME (DTAC)	MC (SC)	ME (SDS)	ME (DTAC)	MC (S/B)	IAM	MC (SC)	MC (DTAC)	ME (SDS)
		0.9941	0.9952	0.9941	0.9960	0.9877	0.9570	0.9800	0.9699	0.9947
	5	IAM	IAM	IAM	IAM	OW	ME (DTAC)	OW	ME (SDS)	IAM
		0.9818	0.9900	0.9896	0.9829	0.9829	0.9569	0.9718	0.9652	0.9822
	6	MC (SDS)	MC (DTAC)	MC (DTAC)	MC (SDS)	MC (SC)	ME (CTAC)	MC (S/B)	OW	MC (DTAC)
		0.9734	0.9820	0.9842	0.9736	0.9822	0.9561	0.9699	0.9630	0.9800
	7	MC (DTAC)	MC (S/B)	MC (S/B)	MC (DTAC)	ME (SDS)	MC (DTAC)	ME (SDS)	MC (SC)	MC (SDS)
		0.9653	0.9796	0.9770	0.9718	0.9818	0.9355	0.9653	0.9572	0.9692
	8	MC (S/B)	MC (SDS)	MC (SDS)	MC (S/B)	MC (SDS)	MC (S/B)	MC (SDS)	MC (SDS)	MC (S/B)
		0.9652	0.9561	0.9569	0.9630	0.9570	0.9126	0.9355	0.9126	0.9572

[a] Data were cited from ref 22; original data were reported by ref 19.

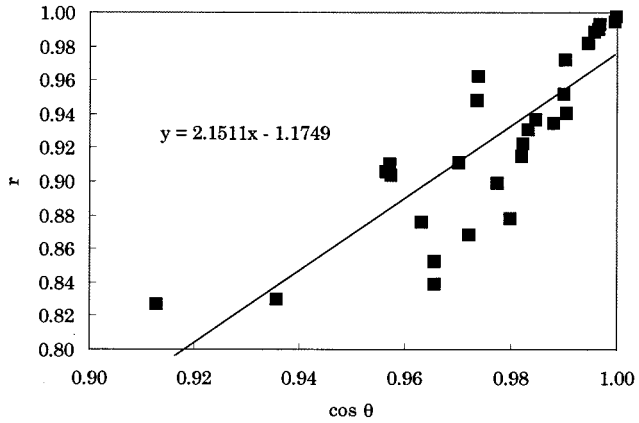

Figure 2—Relationship between cos θ and r for eight lipophilicity scales described in Table 1.

Table 5—Analogy Judgment by *J* Values[a]

system	ME (SDS)	ME (CTAC)	ME (DTAC)	OW	IAM	MC (SDS)	MC (DTAC)	MC (S/B)	MC (SC)[b]
ME(SDS)	○								
ME(CTAC)	×	○							
ME(DTAC)	×	○	○						
OW	○	×	×	○					
IAM	×	×	×	×	○				
MC(SDS)	×	×	×	×	×	○			
MC(DTAC)	×	×	×	×	×	×	○		
MC(S/B)	×	×	×	×	△	×	×	○	
MC(SC)[a]	×	△	△	○	×	×	×	×	○

[a] $J \geq 0$: ○, $J < 0$: ×, Out of Judgment: △. When either the analogy of LS_i to LS_j or the analogy of LS_j to LS_i was out of judgment, △ was indicated. [b] Data were cited from ref 22; original data were reported by ref 19.

θ between four different MC systems were not more than 0.98. As for IAM system, higher analogy to systems using cationic surfactants such as ME(CTAC), MC(DTAC), and ME(DTAC) was observed. This would be caused by the cationic choline moiety of the packing material of the IAM column. In Table 5, the results of analogy judgment using the J values are indicated. Note that varied D values may provide the ranking/judgment reversal, which is the phenomenon that the high-ranked vector with larger cos θ and smaller D value provides $J < 0$ and low-ranked vector with smaller cos θ and larger D value provides $J > 0$ when the deviations of the LSER regression analyses for these LSs are varied. Therefore, the accuracy of the analogy judgment

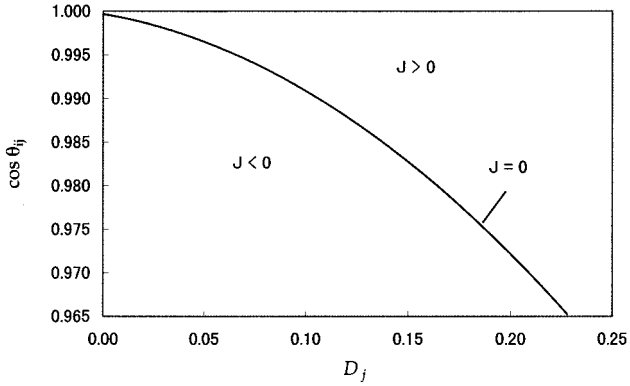

Figure 3—Relationship between cos θ_{ij}, D_j, and J values using the SED unit vectors of ME(SDS) ($\vec{\omega}_i$) and simulated unit vectors ($\vec{\omega}_j$). $\vec{\omega}_i$ = (0.015, 0.018, 0.012, 0.022, 0.021), D_i = 0.035.

depended on D values of SED vectors employed. The relationship between cos θ, D, and J values was simulated using the unit vector of ME(SDS)(LS_i) and the unit vectors of the other scales(LS_j). As shown in Figure 3, the ranking/judgment reversal would occur when D_j of lower-ranked LS_j is large enough. Therefore, the restriction to judge the analogy between two LSs was required, considering the purpose of the study. In this case, to prevent the ranking/judgment reversal, the analogy judgment was restricted by the rule that if the J value of one of the ranked vectors is less than zero, the judgment of the lower-ranked vectors with $J > 0$ should not be performed, i.e., "Out of Judgment" should be indicated for the lower-ranked vectors with $J > 0$. In Table 5, this rule was applied and the ranking/judgment reversal between some SED vectors was prevented.

Concerning the analogy to OW, so far as we know, the ME(SDS)[1,4] and sodium cholate micelle (MC(SC))[12,25] systems provided the best correlation. In this study, the LSER data from MC(SC) was cited from the report by Poole et al.[22] Using the data, the vector analyses were performed. As a result, both ME(SDS) and MC(SC) were each correlated with OW, whereas the J value between ME(SDS) and MC(SC) indicated that the analogy between them was not found despite a large cos θ value (0.9947). From the J values, two cationic ME systems were different from the anionic ME(SDS) although the cos θ values between these three systems were quite close to 1. The relationship between three MEs, OW, and MC(SC) on the basis of their J values is roughly illustrated in Figure 4. ME(SDS) should

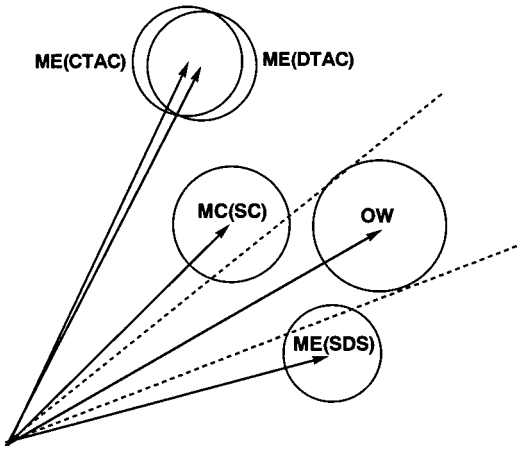

Figure 4—Relationship between ME(SDS), OW, MC(SC), ME(DTAC), and ME(CTAC) in two-dimensional model space of SED vectors. The angles and the length of these vectors are not accurate, because the actual space of these vectors are five-dimensional.

be, in the strict sense, distinguished from MC(SC) and cationic ME systems, while Poole et al. classified ME(SDS) and MC(SC) as the same group.[22]

Next, the unit vectors of the SED vectors were calculated to evaluate the difference in each independent descriptor of these LSs. Using the vector approach, it was quite easy to analyze plural scales simultaneously, and the contribution of each SED between all scales could be compared. The results of the unit vector analysis are shown in Figure 5. Note that this approach was based on the assumption that these five descriptors were almost equivalent to each other. This assumption would be valid because LSER descriptors of solutes had been originally adjusted to be almost the same order, and no artifact caused by the LSER descriptors has been reported so far.[16,17,26,27] Additionally, because the results were used only for the comparison in the same descriptor between the different scales, the assumption would not cause inappropriate evaluation. As shown in Figure 5a, among the components of the unit vector, the a_u component, i.e., the contribution of the hydrogen-bond basicity of the systems or hydrogen-bond acidity of the solutes to their lipophilicity scale was the most diverse between the employed scales. The scale with the most positive contribution of the a_u component was MC(CTAC), and the most negative one was MC(SDS). On the other hand, the b_u component was almost independent of the scales. These three MEs, OW, and MC(SC) systems provided almost the same values in all components, whereas IAM, MC(SDS, DTAC, and S/B) provided different values. The difference in each component of the unit vectors between OW and other scales is shown in Figure 5b. As expected from Figure 4, the a_u and r_u components of MC(SC) were larger than those of OW, while the a_u and r_u components of ME(SDS) were smaller than those of OW. The b_u, v_u and s_u components of MC(SC) were smaller than those of OW, while the b_u, v_u and s_u components of ME(SDS) were larger than those of OW.

As a consequence, the analogy between these employed scales and the difference in the contribution of each descriptor to the lipophilicity scales were well quantified by the SED vectors and their unit vectors, respectively.

Application of These Vector Approaches—The approach using the SED vectors and their unit vectors from various chemical two-phases partition models would be useful to express other scales using plural and diverse vectors because the independent vectors are suitable to describe another vector by addition or subtraction of these vectors with a certain ratio. Two typical examples are shown below:

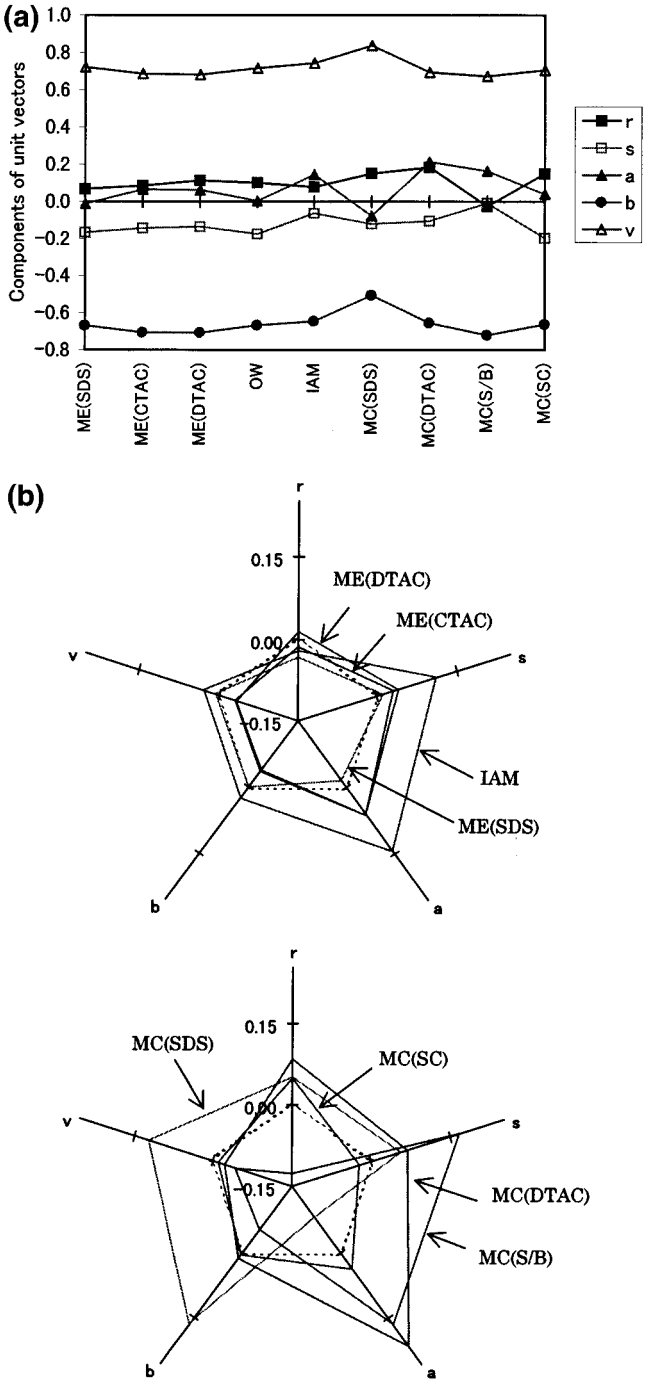

Figure 5—(a) Component of unit vectors. (b) Difference in the unit vector of OW from those of other systems. The dot lines indicate OW.

(1) Structural Information of Microemulsion from Each Constituent Vector—It was previously reported that the partition behaviors of solutes in ME(SDS) could be expressed by the behavior in each constituent system such as water−surfactant, water−alcohol, and water−alkane systems.[4] In this study, the same results were obtained using this vector approach for not only ME(SDS) but also ME(DTAC) as shown in Tables 6 and 7. In this approach, reproducible MI could be directly used as the lipophilicity scale, while MI had to convert to irreproducible log k' in a previous study because the lipophilicity scales such as MI and log P were not equivalent (e.g., log P = 0.518MI − 0.854 for ME(SDS)).[1] As a result, ME(DTAC) as well as ME(SDS) could be expressed by the summation of the SED vectors of the constituents with actual mixing molar ratio. In addition, the vector approach allowed the

Table 6—Estimation of Lipophilicity Scales from ME(SDS) by Its Constituents

system	SED coefficients					ME constituent ratio[a]	
	r	*s*	*a*	*b*	*v*	actual	regressed
MC(SDS)	0.497	–0.399	–0.254	–1.669	2.765	0.050	0.000
water–alkane	0.65	–1.66	–3.52	–4.82	4.28	0.081	0.030
water–pentanol	0.58	–0.79	0.02	–2.84	3.25	0.869	0.970
ME (observed)	0.699	–1.721	–0.129	–6.932	7.474		
ME (calcd with actual ratio)	0.582	–0.842	–0.283	–2.941	3.310		
ME (calcd with regressed ratio)	0.582	–0.816	–0.088	–2.900	3.281		

analogy	cos θ
ME (obs) and ME (calcd with actual ratio)	0.9965
ME (obs) and ME (calcd with regressed ratio)	0.9976

[a] These ratios were expressed as molar ratio. The regressed ratio was calculated from the regression analysis described in the text.

Table 7—Estimation of Lipophilicity Scales from ME(DTAC) by Its Constituents

system	SED coefficients					ME constituent ratio[a]	
	r	*s*	*a*	*b*	*v*	actual	regressed
MC(DTAC)	0.749	–0.430	0.871	–2.667	2.823	0.050	0.671
water–alkane	0.65	–1.66	–3.52	–4.82	4.28	0.081	0.103
water–pentanol	0.58	–0.79	0.02	–2.84	3.25	0.869	0.226
ME (observed)	0.909	–1.533	0.688	–7.509	7.301		
ME (calcd with actual ratio)	0.594	–0.842	–0.224	–2.992	3.312		
ME (calcd with regressed ratio)	0.701	–0.638	0.227	–2.928	3.069		

analogy	cos θ
ME (obs) and ME (calcd with actual ratio)	0.9897
ME (obs) and ME (calcd with regressed ratio)	0.9963

[a] These ratios were expressed as molar ratio. The regressed ratio was calculated from the regression analysis described in the text.

regression analyses using the mixing ratio of the constituents as a variable parameter to obtain the minimum values of $(1 - \cos\theta)$. The comparison of the obtained regressed mixing ratio with the actual ones would provide the structural information of the microemulsion. As shown in Table 6, the contribution of SDS was more suppressed than that expected by the actual mixing ratio. Interestingly, however, in the case of ME(DTAC), the contribution of DTAC in the mixing ratio was more increased than the actual one. This would be caused by the influence of the bulkiness of the hydrophilic portion of the surfactants on the surface-shielding effect of 1-butanol.[1,2] A similar phenomenon was observed in the case of micelles.[8] Although ME(SDS) and ME(DTAC) provided the large cos θ value, the analogy was not found according to the *J* value, as previously shown. The results of the regressed mixing ratio in ME(SDS) and ME(DTAC) supported the reasonability of the *J* value analysis, and this approach would be useful to investigate complex partition systems such as microemulsions.

(2) Prediction of Biological Systems from Chemical Systems—it is important to predict the scales from complex biological systems whose lipophilicity scales are difficult or time-consuming to measure with high reproducibility. Using the vector approach, the SED vectors from the biological systems would be promptly expressed by the vectors from some chemical systems, although the partition behavior of the minimum test set of solutes in the biological systems had to be measured to obtain the SED coefficients. In this study, two biological systems, skin and blood–brain barrier (BBB), were investigated.

(2.1) Skin—Water/skin partition coefficients (K_m) of some alcohols and steroids (22 compounds) were measured using excised human skin, and the LSER equation was calculated by Abraham et al.[26] as follows:

$$\log K_m = -(0.03 \pm 0.14) - (0.37 \pm 0.11)\pi_2^H + (0.33 \pm 0.15)\sum\alpha_2^H - (1.67 \pm 0.16)\sum\beta_2 + (1.87 \pm 0.17)V_x \quad (9)$$

$$n = 22,\ r^2 = 0.943,\ \mathrm{sd} = 0.166,\ F = 70$$

In this case, *R* was removed because each descriptor of the compounds employed was not independent. Using the four SED coefficients, the analogy ranking of various chemical systems to the skin system was evaluated (Table 8). Interestingly, the skin system showed the high-ranked analogy to cationic IAM, cationic ME(CTAC), and ME(DTAC). In this case, the analogy judgment was not performed because the *D* value of the skin SED unit vector was quite large (0.06). Next, the analysis of their unit vectors was performed (Figure 6). As a result, the a_u, b_u, and v_u components of the skin system were between IAM and others (cationic MEs). Thus, the skin system was examined to be expressed by IAM and ME(CTAC). To obtain the ratio of IAM and ME(CTAC), a regression analysis for the unit vector of the skin system using the ratio as a variable parameter was performed, and the results are shown as follows:

$$\vec{\omega}_u(\mathrm{skin}) = 0.746\vec{\omega}_u(\mathrm{ME(CTAC)}) + 0.252\vec{\omega}_u(\mathrm{IAM}) \quad (10)$$

$$\cos\theta = 0.9960$$

The value of cos θ was improved in comparison with that by each single vector. Thus, the skin permeation of the drug candidates would be efficiently predicted by the two chromatographic systems such as ME(CTAC) and IAM with higher reproducibility, although the preliminary LSER regression analysis was not accurate enough to judge the analogy between the observed skin vector and the regressed skin vector.

Table 8—Analogy Ranking to Skin Permeability

	ME(SDS)	ME(CTAC)	ME(DTAC)	OW	IAM	MC(SDS)	MC(DTAC)	MC(S/B)
analogy ranking	4	1	2	5	3	8	7	6
cos θ	0.9904	0.9954	0.9941	0.9903	0.9920	0.9795	0.9841	0.9872

Table 9—Analogy Ranking to BBB

	ME(SDS)	ME(CTAC)	ME(DTAC)	OW	IAM	MC(SDS)	MC(DTAC)	MC(S/B)	MC[a] (LiPFOS)	AW[b]
analogy ranking	3	5	6	4	7	2	9	10	8	1
cos θ	0.8372	0.7890	0.7879	0.8345	0.7268	0.8580	0.7002	0.6701	0.7145	0.9544
analogy ranking (reg)[c]	6	4	2	8	2	1	5	8	6	–
cos θ (reg)[c]	0.9545	0.9551	0.9552	0.9544	0.9552	0.9558	0.9547	0.9544	0.9545	–

[a] The data were cited from ref 22. LiPFOS: lithium perfluorooctanesulfonate. [b] The data were cited from ref 27. AW: alkane–water. [c] cos θ (reg): the angle between BBB vector and regressed BBB vector which was calculated by the summation of alkane–water and the indicated system with the regressed ratio.

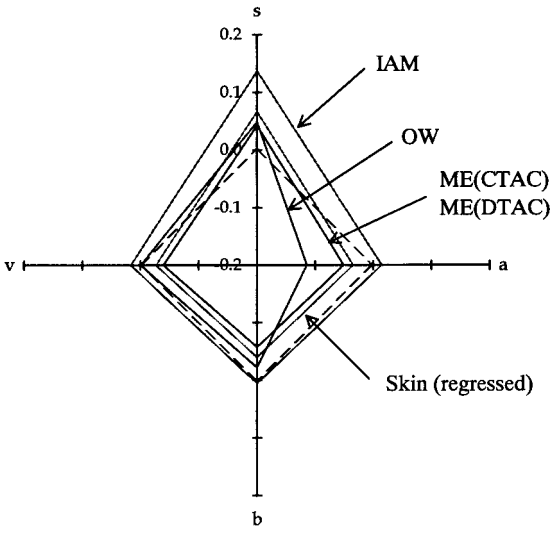

Figure 6—Difference in the unit vector of skin from those of other chemical systems including the regressed skin system.

(2.2) Blood−Brain Barrier—Young et al.[28] and Abraham et al.[27] determined the distribution coefficients between blood and brain (K_{BB}) for 57 compounds, and the following LSER equation was found:

$$\log K_{BB} = -(0.04 \pm 0.06) + (0.20 \pm 0.10)R_2 - (0.69 \pm 0.12)\pi_2^H - (0.71 \pm 0.33)\sum\alpha_2^H - (0.70 \pm 0.11)\sum\beta_2 + (1.00 \pm 0.10)V_x \quad (11)$$

$$n = 57,\ r^2 = 0.907,\ \mathrm{sd} = 0.197,\ \mathrm{F} = 99$$

Using these SED coefficients, the analogy ranking of various chemical systems was investigated (Table 9). In this case, the values of cos θ was not so close to 1 except the case of AW. In addition, the analogy judgment was not also performed because the D value of the BBB SED unit vector was 0.10. Next, the combination of AW with another system was employed to express the BBB system. The ratio of the two vectors was calculated by regression analysis using the ratio as a variable parameter to obtain the minimum value of (1 − cos θ) between the regressed and actual vectors from the BBB. The obtained values of cos θ are also listed in Table 9. As a result, the best combination for the BBB system was MC(SDS) and AW, and the cos θ was slightly improved as follows:

$$\vec{\omega}_u(\mathrm{BBB}) = 0.107\vec{\omega}_u(\mathrm{MC(SDS)}) + 0.861\vec{\omega}_u(\mathrm{AW}) \quad (12)$$

$$\cos\theta = 0.9558$$

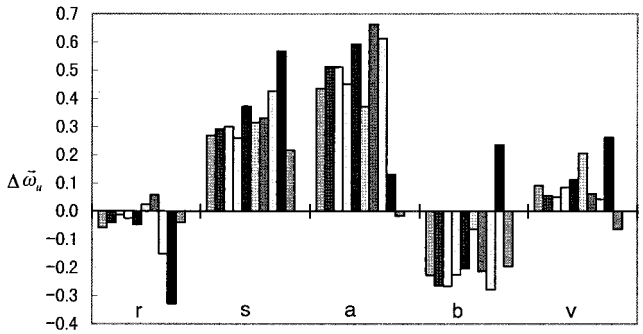

Figure 7—Difference in the unit vector of BBB from those of other chemical systems. Columns: (left) ME(SDS), ME(CTAC), ME(DTAC), OW, IAM, MC(SDS), MC(DTAC), MC(S/B), MC(LiPFOS), and AW.

This equation was not sufficient to express the complex BBB system by the simple chemical systems because the s_u and a_u components of the unit vector of BBB were smaller than those of other 10 unit vectors employed in this study (Figure 7). It would be necessary to search other simple chemical scales with smaller s_u, a_u, and v_u and larger r_u and b_u components as well as to improve the accuracy of the LSER regression analysis for log k_{BB}.

Conclusions

We developed the vector approaches to treat LSER analysis data more efficiently and quantitatively. This allows us to characterize various lipophilicity scales simultaneously. Using the vector approach, not only a complex chemical system such as a microemulsion, but also biological systems such as the skin and BBB, could be expressed by some simple chemical systems, although some improvement on the accuracy of the biological SED vectors would be required. These approaches would facilitate the selection of the chemical systems suitable for the prediction of the hydrophobic interaction of drugs in the body.

References and Notes

1. Ishihama, Y.; Oda, Y.; Uchikawa, K.; Asakawa, N. Evaluation of Solute Hydrophobicity by Microemulsion Electrokinetic Chromatography. *Anal. Chem.* **1995**, *67*, 1588−1595.
2. Ishihama, Y.; Oda, Y.; Asakawa, N. A Hydrophobicity Scale Based on the Migration Index from Microemulsion Electrokinitic Chromatography of Anionic Solutes. *Anal. Chem.* **1996**, *68*, 1028−1032.
3. Ishihama, Y.; Oda, Y.; Asakawa, N. Hydrophobicity of Cationic Solutes Measured by Electrokinetic Chromatography with Cationic Microemulsions. *Anal. Chem.* **1996**, *68*, 4281−4284.

4. Abraham, M. H.; Treiner, C.; Roses, M.; Rafols, Y.; Ishihama, Y. Linear Free Energy Relationship Analysis of Microemulsion Electrokinetic Chromatographic Determination of Lipophilicity. *J. Chromatogr. A* **1996**, *752*, 243−249.
5. Kaliszan, R. Quantitative Structure-Retention Relationships. *Anal. Chem*. **1992**, *64*, 619A−631A.
6. Ong, S.; Liu, H.; Pidgeon, C. Immobilized-Artificial-Membrane Chromatography: Measurements of Membrane Partition Coefficient and Prediction Drug Membrane Permeability. *J. Chromatogr. A* **1996**, *728*, 113−128.
7. Valko, K.; Bevan, C.; Reynolds, D. Chromatographic Hydrophobicity Index by Fast-Gradient RP-HPLC: A High-Throughput Alternative to log P/log D. *Anal. Chem*. **1997**, *69*, 2022−2029.
8. Ishihama, Y.; Oda, Y.; Uchikawa, K.; Asakawa, N. Correlation of Octanol−Water Partition Coefficients with Capacity Factors Measured by Micellar Electrokinetic Chromatography. *Chem. Pharm. Bull*. **1994**, *42*, 1525−1527.
9. Chen, N.; Zhang, Y.; Terabe, S.; Nakagawa, T. Effect of Physicochemical Properties and Molecular Structure on the Micelle-Water Partition Coefficient in Micellar Electrokinetic Chromatography. *J. Chromatogr. A* **1994**, *678*, 327−332.
10. Smith, J.T.; Vinjamoori, D. V. Rapid Determination of Logarithmic Partition Coefficients between *n*-Octanol and Water Using Micellar Electrokinetic Capillary Chromatography. *J. Chromatogr. B* **1995**, *669*, 59−66.
11. Herbert, B. J.; Dorsey, J. G. *n*-Octanol−Water Partition Coefficient Estimation by Micellar Electrokinetic Capillary Chromatography. *Anal. Chem*. **1995**, *67*, 744−749.
12. Yang, S.; Bumgarner, J. G.; Kruk, L. F. R.; Khaledi, M. G. Quantitative Structure−Activity Relationships Studies with Micellar Electrokinetic Chromatography Influence of Surfactant Type and Mixed Micelles on Estimation of Hydrophobicity and Bioavailability. *J. Chromatogr. A* **1996**, *721*, 323−335.
13. Garcia, M. A.; Diez-Masa, J. C.; Marina, M. L. Correlation between the Logarithm of Capacity Factors for Aromatic Compounds in Micellar Electrokinetic Chromatography and their Octanol−Water Partition Coefficients. *J. Chromatogr. A* **1996**, *742*, 251−256.
14. Hanna, M.; Biasi, V.; Bond, B.; Salter, C.; Hutt, A. J.; Camilleri, P. Estimation of the Partition Characteristics of Drugs: A Comparison of a Large and Diverse Drug Series Utilizing Chromatographic and Electrophoretic Methodology. *Anal. Chem*. **1998**, *70*, 2092−2099.
15. Masucci, J. A.; Caldwell, G. W.; Foley, J. P. Comparison of the Retention Behavior of β-blockers Using Immobilized Artificial Membrane Chromatography and Lysophospholipid Micellar Electrokinetic Chromatography. *J. Chromatogr. A* **1998**, *810*, 95−103.
16. Kamlet, M. J.; Doherty, R. M.; Abraham, M. H.; Taft, R. W. Solubility Properties in Biological Media. 12. Regarding the Mechanism of Nonspecific Toxicity or Narcosis by Organic Nonelectrolytes. *Quant. Struct.-Act. Relat*. **1988**, *7*, 71−78.
17. Abraham, M. H. Scales of Solute Hydrogen-bonding: Their Construction and Application to Physicochemical and Biochemical Processes. *Chem. Soc. Rev*. **1993**, *22*, 73−83.
18. Abraham, M. H.; Chadha, H. S.; Leitao, R. A. E.; Mitchell, R. C.; Lambert, W. J.; Kaliszan, R.; Nasal, A.; Haber, P. Determination of Solute Lipophilicity, as log P(Octanol) and log P(alkane) Using Poly(Stylene-Divinylbenzene) and Immobilised Artificial Membrane Stationary Phases in Reversed-phase High-Performance Liquid Chromatography. *J. Chromatogr. A* **1997,** *766*, 35−47.
19. Yang, S.; Khaledi, M. G. Chemical Selectivity in Micellar Electrokinetic Chromatography: Characterization of Solute-Micelle Interactions for Classification of Surfactants. *Anal. Chem*. **1995**, *67*, 499−510.
20. Yang, S.; Bumgarner, J. G.; Khaledi, M. G. Chemical Selectivity in Micellar Electrokinetic Chromatography II: Rationalization of Elution Patterns in Different Surfactant Systems. *J. Chromatogr. A* **1996**, *738*, 265−274.
21. Muijselaar, P. G.; Claessens, H. A.; Cramers, C. A. Characterization of Pseudostationary Phases in Micellar Electrokinetic Chromatography by Applying Linear Solvation Energy Relationships and Retention Indexes. *Anal. Chem*. **1997**, *69*, 1184−1191.
22. Poole, C. F.; Poole, S. K.; Abraham, M. H. Recommendations for the Determination of Selectivity in Micellar Electrokinetic Chromatography. *J. Chromatogr. A* **1998**, *798*, 207−222.
23. Valko, K.; Plass, M.; Bevan C.; Reynolds, D.; Abraham, M. H. Relationships between the Chromatographic Hydrophobicity Indices and Solute Descriptors Obtained by Using Several Reversed-phase, Diol, Nitrile, Cyclodextrin and Immobilised Artificial Membrane-bonded High-Performance Liquid Chromatography Columns. *J. Chromatogr. A* **1998**, *797*, 41−55.
24. Seals, T. H., Davis, J. M., Murphy, M. R., Smith, K. W., Stevens, W. C. *Anal. Chem*. **1998**, *70*, 4549−4562.
25. Wu, Y. S.; Lee, H. K.; Li, S. F. Y. Rapid Estimation of Octanol−Water Partition Coefficients of Pesticides by Micellar Electrokinetic Chromatography. *Electrophoresis* **1998**, *19*, 1719−1727.
26. Abraham, M. H.; Chadha, H. S. Applications of a Solvation Equation to Drug Transport Properties. In *Lipophilicity in Drug Action and Toxicology*; Mannhold, R., Kubinyi, H., Timmerman, H., Eds.; VCH: Weinheim (Germany), 1996; Chapt. 18, pp 311−337.
27. Abraham, M. H.; Chadha, H. S., Mitchell, R. C., Hydrogen Bonding. 33. Factors That Influence The Distribution of Solutes between Blood and Brain. *J. Pharm. Sci*. **1994**, *83*, 1257−1268.
28. Young, R. C.; Mitchell, R. C.; Brown, T. H.; Ganellin, C. R.; Griffiths, R.; Jones, M.; Rana, K. K.; Saunders: D.; Smith, I. R.; Sore, N. E.; Wilks, T. J. *J. Med. Chem*. **1988**, *31*, 656−671.

JS990119+

Evaluation of a Novel, Natural Oligosaccharide Gum as a Sustained-Release and Mucoadhesive Component of Calcitonin Buccal Tablets

HEMANT H. ALUR, JASON D. BEAL, S. INDIRAN PATHER,† ASHIM K. MITRA, AND THOMAS P. JOHNSTON*

Contribution from *Division of Pharmaceutical Sciences, School of Pharmacy, University of Missouri, Kansas City, Missouri 64110.*

Received March 5, 1999. Final revised manuscript received September 20, 1999.
Accepted for publication September 24, 1999.

Abstract □ The objective of this study was to evaluate the gum from *Hakea gibbosa* (hakea) as a sustained-release and mucoadhesive component in buccal tablets for a model peptide, namely, salmon calcitonin. Flat-faced core tablets containing either 12 or 32 mg of hakea and 40 μg (200 IU) of salmon calcitonin (sCT) per tablet were formulated using a direct compression technique and were coated with Cutina on all but one face. The in vitro release profiles were sigmoidal in nature and according to a mathematical model indicated super Case II transport as the primary mechanism of release. The resulting plasma sCT and calcium concentrations were determined following both intravenous administration and buccal application of mucoadhesive tablets in rabbits. Following intravenous administration, the mean values determined for $t_{1/2}$ (α), $t_{1/2}$ (β), V_d, and CL for sCT were 0.76 ± 0.06 min, 67 ± 18 min, 1484 ± 454 mL/kg, and 19 ± 2 mL/min·kg, respectively. Following the application of the mucoadhesive buccal tablets which contained 40 μg of sCT and either 12 or 32 mg of hakea, the calculated apparent bioavailability (F) and clearance (CL) were 37 ± 6% and 19 ± 3.3 mL/min·kg and 16 ± 8% and 18 ± 0.4 mL/min·kg, respectively. Serum calcium concentrations indicated that biologically active sCT was delivered across the rabbit buccal mucosa. The strength of mucoadhesion of the tablets was also quantitated in terms of the force of detachment as a function of time. The force of detachment for the mucoadhesive buccal tablets containing either 12 or 32 mg of hakea and 40 μg of sCT increased from 4.47 ± 0.68 to 8.41 ± 1.0 N and 8.23 ± 1.62 to 14.98 ± 1.63 N, respectively, from 5 to 90 min following application to excised rabbit intestinal mucosa. These results demonstrate that the novel, natural gum from *Hakea gibbosa* may be used to sustain the release of sCT from a unidirectional-release buccal tablet. The mechanism of in vitro release is likely to involve peptide diffusion/polymer dissolution. The mucoadhesive strength, as measured by the force of detachment, can be modulated by altering the amount of hakea in the tablet. The mucoadhesive buccal tablets described in this paper represent an improved transbuccal delivery system for therapeutic polypeptides.

Introduction

Proteins and peptides are currently emerging as a major class of future therapeutic drugs. With the advent of and improvement in techniques like solid-phase synthesis, combinatorial chemistry, and protein biotechnology, more and more proteins and peptides are being made available in large quantities. Pharmaceutical scientists are facing increasing challenges with respect to the formulation of new and novel delivery systems and exploring new routes to successfully deliver these bioactive agents. Noninvasive delivery of proteins and peptides has been met with limited success for a variety of reasons[1,2] including (a) low permeability due to hydrophilicity, globular structure, and size, (b) inactivation by enzymes at the site of delivery or absorption prior to reaching the systemic circulation, and (c) short residence time of the drug as well as the delivery system at the site of absorption, all leading to subtherapeutic levels in the systemic circulation.

Calcitonin (CT) is a single-chain 32 amino acid polypeptide with a disulfide bridge between cysteine residues at positions 1 and 7 and has a molecular weight of 3432 Da. The hormone is secreted by the parafollicular cells of the thyroid glands in mammals and by the ultimobronchial glands in birds and fishes. CT functions as a hypocalcemic agent by inhibiting bone resorption and reducing the renal tubular reabsorption of calcium, and it is used in the treatment of Paget's disease, hypercalcemia, and osteoporosis.[3,4] Treatment calls for daily or alternate day subcutaneous or intramuscular injections for an extended period. This is bothersome and inconvenient for patients. Salmon calcitonin (sCT) is one of the calcitonins and is currently available in a sterile solution for injection and nasal spray form. Lee et al.[5] reported to have developed biodegradable porous PGA microspheres of sCT which provide sustained levels of sCT for over 5 days following a single subcutaneous (sc) injection. The buccal mucosa has been investigated recently for the delivery of this bioactive peptide.[6] Buccal mucosa is an easily accessible tissue, which is less sensitive to irritation or irreversible damage.[7] It also provides drug delivery by avoiding the harsh environment of the gastrointestinal tract and first-pass metabolism.[7]

The risk of accidental swallowing and salivary washout limits the use of solutions or conventional buccal tablets, and it has led to the development of self-adhesive buccal tablets as the preferred dosage form.[8] Mucoadhesive dosage forms retain the dosage form in intimate contact with the mucosa (absorbing membrane) thereby increasing the total amount of drug which penetrates the mucosa.[9]

Previous studies[10,11] have shown the efficacy of a novel, natural gum from *Hakea gibbosa* as a sustained-release and mucoadhesive component in mucoadhesive buccal tablets for the delivery of a low molecular weight organic compound. Thus, the present study was undertaken to investigate the possibility of using this novel excipient as a sustained-release and mucoadhesive component of buccal tablets for peptide and protein delivery. Hakea gum is a polysaccharide exudate from the tree *Hakea gibbosa* (Family: Proteaceae). The trees are indigenous to New South

* To whom correspondence should be addressed at the Division of Pharmaceutical Sciences, University of Missouri—Kansas City, Katz Pharmacy Building, Room 211A, 5100 Rockhill Road, Kansas City, MO 64110-2499. Phone: (816) 235-1624. Fax: (816) 235-5190. E-mail: johnstont@umkc.edu.

† Present address: Cima Labs Inc., 7325 Aspen Lane, Brooklyn Park, MN 55428.

10.1021/js9900755 CCC: $18.00
Published on Web 11/04/1999

Wales, Australia. The gum has a molecular weight of greater than 2×10^6 and is totally water soluble at a concentration of 2% w/v. The gum is composed of sugars such as galactose, mannose, xylose, arabinose, and glucuronic acid. The chemical structure of the gum has been previously reported.[10,12]

Materials and Methods

Materials—Salmon calcitonin sCT (5001 IU/mg) was a generous gift from Rhone-Poulenc-Rorer (Vitry Sur Seine Cedex, France). All solutions were prepared in deionized distilled water. The hakea gum was a gift from Dr. Peter Eagles of the University of the Western Cape, Cape Town, South Africa. The gum was obtained from the Kirstenbosch Botanical Gardens. All other materials, except for the gum, were used as received. The gum was purified by first dissolving it in water and then filtering the 2% solution through muslin cloth. The filtered solution was freeze-dried using a model 10-MR SAVirtis tabletop freeze drier (Gardiner, NY).

Cutina (castor oil, hydrogenated) was obtained from Henkel Corporation, NJ. Xylazine (100 mg/mL), ketamine (100 mg/mL), and pentobarbital sodium (50 mg/mL) solutions were provided by the Laboratory Animal Center at the University of Missouri—Kansas City (Kansas City, MO). Heparin sodium injection (10000 units/mL) was purchased from Elkins-Sinn, Inc. (Cherry Hill, NJ). I-Cath intravenous placement units with stylet attachment (catheter, 22G × 12 in.; needle 19G × 21 in.) was purchased from Charter Med, Inc. (Lakewood, NJ), and tuberculin syringes (1 cc) were obtained from Becton and Dickinson (Sandy, UT).

Blood samples were collected into 1.5 mL Eppendorf tubes containing heparin sodium (100 units/mL) and centrifuged using a Beckman GS-15R centrifuge (Palo Alto, CA).

Male New Zealand albino rabbits, weighing between 2.0 and 2.5 kg, were purchased from Myrtle's rabbitry (Thompson, TN). The animals were housed individually for at least 1 week prior to experimentation and allowed food and water ad libitum. The average weight of the rabbits at the time of the study was 2.8 ± 0.3 kg ($n = 9$).

The bioadhesion experiments were carried out on a model LTC universal tension-compression stand (John Chatillon and Sons, Inc., Greensboro, NC) equipped with a model DFM-10 digital force gauge (John Chatillon and Sons, Inc., Greensboro, NC).

Methods—*Tablet Preparation*—Flat-faced core tablets were prepared by direct compression, and the tablets were coated with Cutina on all but one face using a compression coating technique. Release of sCT was unidirectional, occurring from only the uncoated tablet face.

(a) Direct Compression—The tablets were prepared by initially mixing the sCT and hakea for 10 min. Subsequently, spray-dried lactose (hydrous N.F. grade, Fast-Flow 316) and Cab-o-sil (M-5 grade, amorphous fumed silica) were incorporated and the powder was mixed for an additional 10 min. Finally, magnesium stearate was added and the mixing continued for an additional 5 min. Mixing was performed by mechanical rotation at 225 rpm.

(b) Tablet Compression—Both core and coated tablets were prepared on a model B, No. 0-24R carver press (Summit, NJ). The core tablets (weight: 101.5 mg) had a diameter of 1 cm and a thickness of 0.1 cm and were compressed at a force of 5000 psi. The coated tablets (final weight: 202.5 mg) were compressed at 2000 psi force to generate a final diameter of 1.2 cm and a thickness of 0.2 cm.

(c) Release Study—The in vitro release studies were performed using jacketed glass vessels (250 mL) obtained from Fisher Scientific (Pittsburgh, PA). The dissolution medium consisted of 200 mL of deionized water (pH 7.0) at 37 °C. The dissolution medium was stirred with a magnetic stir bar at a speed of 50 rpm. Sink conditions were maintained throughout the duration of release study. The in vitro release samples (1 mL) were analyzed for sCT using an enzyme immunoassay kit (EIAH-6003) obtained from Peninsula Laboratories (Belmont, CA) after appropriate dilutions were made with deionized water. The release studies were carried out for 90, 420, and 600 min for buccal tablets containing 40 μg of sCT and 0, 12, and 32 mg of hakea, respectively.

Animal Preparation—The animals were prepared for both intravenous and buccal sCT studies by anesthetizing with an im injection of a 1:5 mixture of xylazine (1.9 mg/kg) and ketamine (9.3 mg/kg). Following induction of anesthesia, a catheter was placed in the marginal ear vein for blood sample collection. After the collection of each sample, the cannula was flushed with 0.2 mL of a 10% (v/v) heparin/normal saline solution to keep the cannula patent. A light plane of anesthesia was maintained by an im injection of one-third of the initial dose of xylazine and ketamine mixture as needed. All the blood samples were centrifuged at 3000 rpm for 10 min to separate the plasma and the retrieved plasma, was stored at −20° C until the time of analysis. At the end of the experiments the rabbits were euthanized by injecting an overdose of pentobarbital solution (3−5 mL) into the catheter.

The research adhered to the principles of Laboratory Care (NIH publication no. 85-23, revised 1985), and the animal protocol was approved by the animal care and use committee of the University of Missouri—Kansas City.

Intravenous sCT Study—Following the induction of anesthesia, sCT (40 μg) was administered as a bolus through the cannulated ear vein of the rabbit. A blood sample (2 mL) was obtained 5 min before and then at 5, 10, 20, 45, 60, 90, and 120 min following the injection.

Buccal sCT Study—Upon the induction of anesthesia, a tablet was applied to the buccal mucosa of the rabbit by pressing it firmly against the mucosa for 1.5 min. A drop of water was placed on the releasing face of the tablet before it was applied to the buccal mucosa. A blood sample (2 mL) was obtained 5 min before and then at 5, 10, 20, 45, 60, 90, 120, and 180 min following the application of the mucoadhesive buccal tablets containing 40 μg of sCT and 12 mg of hakea. The tablet was removed at 180 min, and additional blood samples were obtained at 210, 240, 270, and 300 min following the removal of the buccal tablet. For tablets containing 40 μg of sCT and 32 mg of hakea, a similar blood sampling protocol was followed until 180 min as with 12 mg hakea.

Quantitation of Plasma sCT—Plasma samples were analyzed for sCT using an enzyme immunoassay kit (EIAH-6003) obtained from Peninsula Laboratories (Belmont, CA). The sensitivity of the assay ranged from 0 to 25 ng/mL. The assay was linear over the range 0.04−2.0 ng/mL. The sCT contained in the samples was extracted using C18 Sep columns (Peninsula Laboratories Belmont, CA) before being analyzed by enzyme immunoassay. The reason for the inclusion of an extraction step was to avoid a precipitation reaction between rabbit IgG present in the samples and goat anti-rabbit IgG coated on the EIAH plates. The extraction procedure was obtained from Peninsula Laboratories (Belmont, CA) and was followed without any modification. The samples were appropriately diluted with the EIA buffer prior to analysis.

Quantitation Of Plasma Calcium—Plasma calcium was quantitated by the *o*-cresolphthalein complexone method using a Sigma diagnostics kit for calcium (Sigma, St. Louis, MO). The method involves colorimetric determination of calcium at 575 nm (Procedure No. 587, Sigma Diagnostics).

Bioadhesion Study—Rabbit small intestine was selected as a model membrane since the intestine provided a flat and uniform surface and the surface area of the buccal mucosa in a rabbit is only slightly larger than the buccal tablets evaluated in these studies. A 2 cm long piece of intestinal mucosa was mounted on the platform of the tension-compression stand. The tablet was applied using super glue to the bottom face of a stainless steel disk attached to the force gauge. The mucosal surface was hydrated by placing 20 μL of distilled water on the tissue surface. The tablet and the mucosal surfaces were brought into contact, and a constant force of 20 N was applied. The tablet was pulled off the tissue surface at 5, 10, 20, 30, 45, 60, and 90 min following application of force. The value for the force of detachment was measured in newtons by lowering the platform of the tension-compression stand at a constant rate of 1 mm min^{-1}.

Data And Statistical Analysis—The in vitro release from the unidirectional buccal tablets was modeled using the basic equation $F = kt^n$,[13] and from the values of n, the mechanism of in vitro release was determined.

The plasma sCT concentrations obtained after both intravenous and buccal administration were not corrected for baseline levels of sCT (~0.41 ± 0.21 ng/mL, $n = 6$) for the ease of comparison with previous published findings. The plasma sCT concentration versus time data obtained following intravenous administration

were fit to a polyexponential equation using the R STRIP program. The data were fit to a two-compartment model with elimination from the central compartment. The model-dependent phamacokinetic parameters AUC, *A*, *B*, $t_{1/2}$ (α), and $t_{1/2}$ (β) were obtained from the fit, whereas the volume of the central compartment (V_c) and the volume of distribution in the β-phase (V_d (β)) were obtained using standard equations.[14]

The area under the plasma sCT concentration versus time curve was calculated using the trapezoidal rule within the time periods of 0−2 h following buccal administration although the experiments were carried out beyond 2 h. In an attempt to estimate the apparent bioavailability, the data was truncated at 2 h following buccal administration because the total duration of the intravenous experiments was 2 h. Equations 1 and 2 were used to estimate the apparent bioavailability and clearance of sCT following buccal administration.[15,16] The C_{max}, C_{min}, and t_{max} were estimated directly from the plasma sCT versus time profiles following buccal administration. In eqs 1 and 2, *F* denotes the

$$F = \frac{(\text{dose}_{IV})\,(\text{AUC}_{0-t_{buccal}})}{(\text{dose}_{buccal})\,(\text{AUC}_{0-t_{IV}})} \quad (1)$$

$$\text{CL} = \frac{FD}{\text{AUC}_{0-t_{buccal}}} \quad (2)$$

apparent bioavailability, *D* is the dose of sCT contained in the buccal tablets, and $\text{AUC}_{0-t_{buccal}}$ represents the area under the plasma sCT concentration vs time curve following buccal administration from 0 to 2 h. A dose of 40 μg of sCT was used to calculate the apparent bioavailability as the amount of sCT remaining in the tablet after buccal administration was not estimated.

The area above the calcium reduction curve from 0 to 2 h (AAC) was obtained as described previously.[17,18] The plasma calcium concentration at each time point after the administration of sCT was subtracted from the baseline calcium concentration, which was obtained prior to administration of sCT. Next, the AAC was calculated using the trapezoidal method. The data was again truncated at 2 h following buccal administration for ease of comparison with the intravenous data.

All experiments were conducted in triplicate, and the results were expressed as the mean value ± the standard deviation. Mean values were compared for statistical significance at the 5% level using Student's one-tail *t*-test.

Results

In Vitro Release Study—In vitro release profiles from buccal tablets containing 0, 12, and 32 mg of hakea with 40 μg of sCT are shown in Figure 1. The release profiles are sigmoidal in nature for buccal tablets with 40 μg of sCT and either 12 or 32 mg of hakea. The mechanism of in vitro release was determined from the values of *n* obtained by modeling the first 60% of the release to the equation $F = kt^n$.[13] The values of *k* (kinetic constant) and *n* (diffusional exponent) are listed in Table 1. The values of *n* are greater than 1, indicating super Case II transport as the mechanism of sCT release.

Intravenous sCT Study—The plasma sCT concentration versus time profile following intravenous administration was best explained using a biexponential equation and is shown in Figure 2. The values of the model-dependent phamacokinetic parameters are listed in Table 2. The change in the plasma calcium concentration is also depicted in Figure 2, and the relative AAC_{0-2h} is listed in Table 2. It can be noted from the pharmacokinetic parameters that the extravascular distribution of sCT was very rapid.

Buccal sCT Study—The plasma sCT concentration vs time profiles following administration of the 40 μg sCT buccal tablets with either 12 or 32 mg of hakea are shown in Figures 3 and 4, respectively. The relevant pharmacokinetic parameters are listed in Table 3. From Figures 3 and 4, it is apparent that hakea effectively sustained the release of sCT from the buccal tablets and also maintained an elevated plasma sCT concentration during the entire application period. The apparent bioavailability (*F*) of sCT from the tablets with 12 mg of hakea was significantly ($p < 0.05$) greater than that from the tablets with 32 mg of hakea. The C_{max} and C_{min} decreased while the t_{max} increased with an increase in the amount of hakea contained in the tablet (Table 3). The change in the plasma calcium concentration has also been illustrated in Figures 3 and 4, and the mean values of AAC_{0-2h} are listed in Table 3. AAC_{0-2h} for sCT tablets with 12 mg of hakea was not significantly different ($p > 0.05$) from AAC_{0-2h} for tablets with 32 mg of hakea.

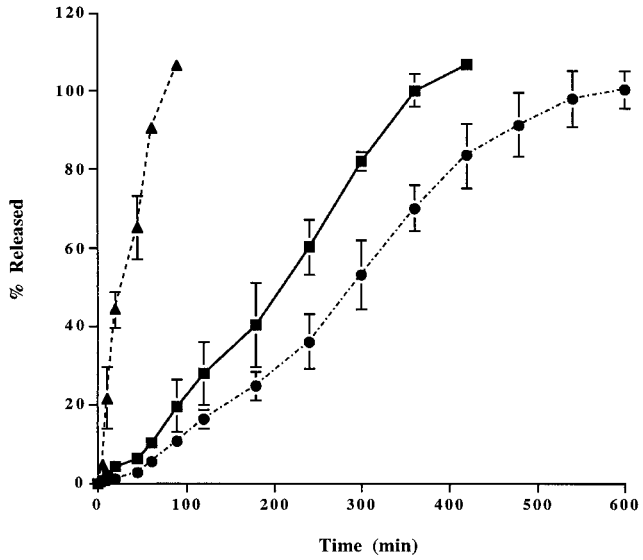

Figure 1—In vitro release profiles of sCT from directly compressed tablets which contained 40 μg of sCT and 0 mg of hakea (▲), 12 mg of hakea (■), or 32 mg of hakea (●). All data points represent the mean value ± standard deviation of three experiments. Lines through mean values are included to illustrate the trend and do not represent a mathematical fit of the data.

Table 1—Diffusional Exponent (*n*) and Kinetic Constant (*k*) Values[a]

parameters	40 μg of sCT and 12 mg of hakea	40 μg of sCT and 32 mg of hakea
n	1.24 ± 0.07	1.37 ± 0.05*
$k \times 10^{-7}$	2.0 ± 1.8	3.4 ± 1.3

[a] Mean ± SD, $n = 3$. The * symbol indicates a statistically significant increase in the mean value of the diffusional exponent when a 40 μg sCT tablet containing 12 mg of hakea was compared with a tablet containing 32 mg of hakea at $p < 0.05$ using Student's one-tail *t*-test.

Bioadhesion Study—A profile showing the mean values of the force of detachment of the sCT buccal tablets following their application to excised rabbit intestinal mucosa is shown in Figure 5. It can be noted that the mean values of the force of detachment increased with time and reached a plateau at later time points. The mean values of the force of detachment were significantly ($p < 0.05$) greater at each time point for tablets containing 32 mg of hakea when compared to the tablets which contained 12 mg of hakea and were significantly greater for tablets containing 12 mg of hakea when compared to the tablets which contained no hakea.

Discussion

In the present study, controlled release of sCT both in vitro and in vivo was successfully demonstrated using the natural gum, hakea as an excipient. The in vitro release profiles were sigmoidal in nature and consisted of an initial slow-releasing phase followed by a linear phase, where the

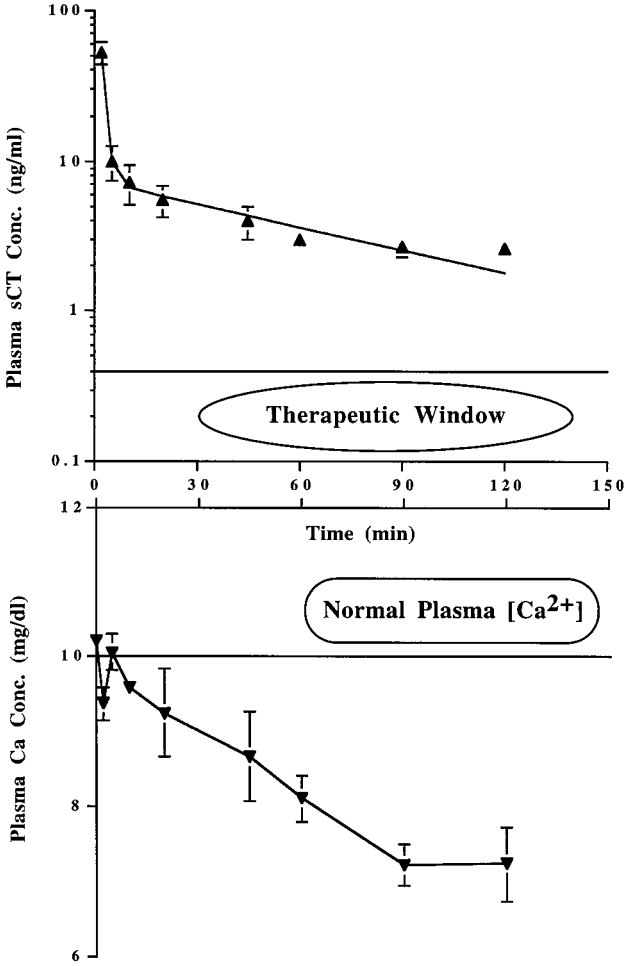

Figure 2—Plasma profiles of sCT (▲) and calcium (▼) in rabbits following intravenous administration of 40 μg (200 IU) of sCT. All data points represent the mean value ± standard deviation of three experiments. The line (—) represents the mathematical fit of the intravenous data. Therapeutic window of sCT = 0.1–0.4 ng/mL (from ref 6).

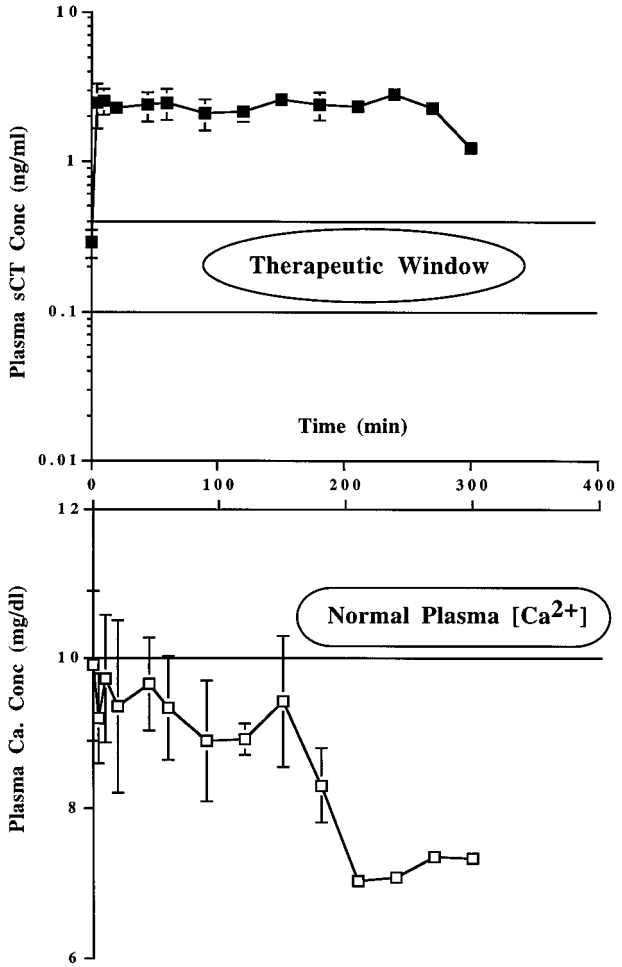

Figure 3—Plasma profiles of sCT (■) and calcium (□) in rabbits following the application of buccal tablets containing 40 μg (200 IU) of sCT and 12 mg of hakea. Buccal tablets were removed at 180 min. All data points represent the mean value ± standard deviation of three experiments. Lines through mean values are included to illustrate the trend and do not represent a mathematical fit of the data. Therapeutic window of sCT = 0.1–0.4 ng/mL (from ref 6).

Table 2—Pharmacokinetic Parameters[a] of sCT after Intravenous Bolus Administration of 40 mg of sCT in New Zealand Albino Rabbits for a Two-Compartment Open Model

pharmacokinetic parameters	
AUC_{0-2h} (ng·min/mL)	807 ± 119
$AUC_{0-\infty}$ (ng·min/mL)	1002 ± 171
CL (mL/min·kg)	19 ± 2
A (ng/mL)	290 ± 89
B (ng/mL)	7.6 ± 2.5
$t_{1/2}$ (α) (min)	0.76 ± 0.06
$t_{1/2}$ (β) (min)	67 ± 18
V_c (mL)	143 ± 43
$V_d(\beta)$ (mL/kg)	1484 ± 454
AAC_{0-2h} (mg·min/dL)[b]	208 ± 27

[a] Mean ± SD, $n = 3$. [b] Area above the calcium reduction curve.

release appeared to follow zero-order kinetics (Figure 1). The values for the diffusional exponent (n) were greater than 1 (Table 1), indicating that the mechanism of sCT release was super Case II transport.[19] That is, the release of sCT from the buccal tablets is likely due to the combination of polypeptide diffusion and polymer relaxation/dissolution. This mechanism also explains the initial slow-releasing phase, where the polymer was not completely hydrated, resulting in an incomplete relaxation of the side chains. Insufficient hydration would lead to the creation of an aqueous pore through which the free diffusion of sCT would be hindered. Upon complete hydration, the polymer presumably began to dissolve with subsequent relaxation of the side chains. Relaxation of hakea's numerous side chains would then allow free diffusion of sCT from the tablet matrix. This mechanism would tend to support zero-order release kinetics during the linear portion of Figure 1. Banga et al.[20] reported that the diffusion of three polypeptides, vasopressin, calcitonin, and insulin, from hydrogel formulations was dependent on their molecular size.

The intravenous profile in this study was best described by a two-compartment model which is consistent with the work of Heiber et al. using dogs[6] and Sinko et al. using rats.[18] Sinko et al.[18] using a noncompartmental pharmacokinetic analysis reported the values (mean value of three different doses) for CL, $t_{1/2}$, k_e, and V_{ss} of 2.58 ± 0.34 mL/min, 40 ± 7.8 min, 0.02 ± 0.002 min^{-1}, and 0.14 ± 0.001 L, respectively, in rats. Beveridge et al.[21] reported terminal elimination half-lives ranging between 60 and 90 min following iv, im, and sc administration of 35 μg of sCT to humans.

The tablets which contained 32 mg of hakea demonstrated a significantly ($p < 0.05$) lower mean value of the apparent bioavailability (F) compared to tablets which contained 12 mg of hakea. The C_{max} and C_{min} decreased while the t_{max} increased when the amount of hakea in the tablet was increased from 12 to 32 mg (Figures 2 and 3;

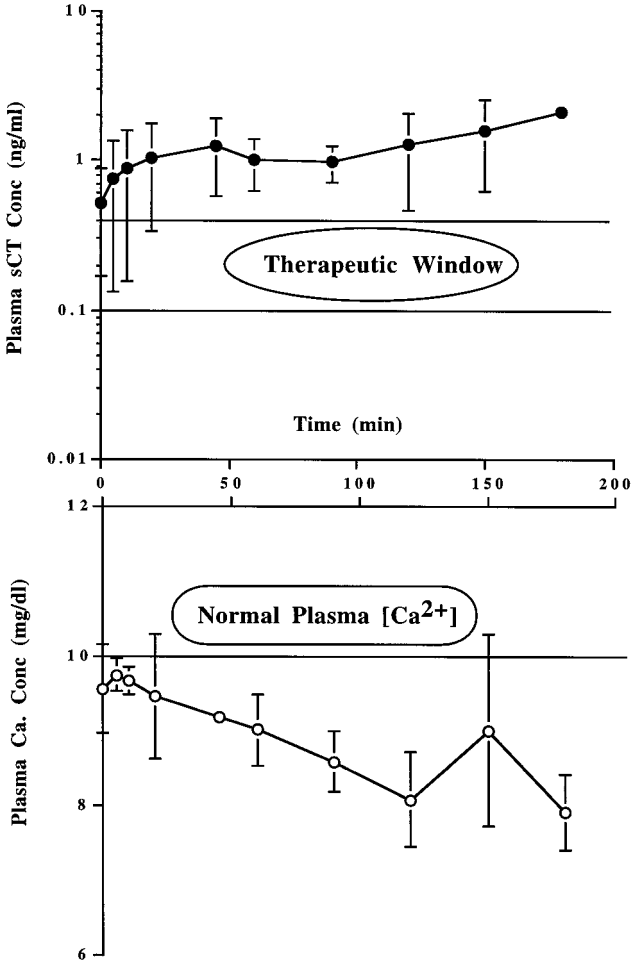

Figure 4—Plasma profiles of sCT (●) and calcium (○) in rabbits following the application of buccal tablets containing 40 μg (200 IU) of sCT and 32 mg of hakea. All data points represent the mean value ± standard deviation of three experiments. Lines through mean values are included to illustrate the trend and do not represent a mathematical fit of the data. Therapeutic window of sCT = 0.1–0.4 ng/mL (from ref 6).

Table 3—Pharmacokinetic Parameters[a] of sCT after Buccal Administration in New Zealand Albino Rabbits for a Two-Compartment Open Model

pharmacokinetic parameters	40 μg of sCT and 12 mg of hakea	40 μg of sCT and 32 mg of hakea
AUC_{0-2h} (ng·min/mL)	273 ± 49*	125 ± 63
CL (mL/min·kg)	19 ± 3.3	18 ± 0.4
F (%)	37 ± 6†	16 ± 8
C_{max} (ng/mL)	2.50 ± 0.5	1.33 ± 0.65
C_{min} (ng/mL)	2.00 ± 0.2	0.68 ± 0.41
t_{max} (min)	70 ± 17	140 ± 17
AAC_{0-2h} (mg·min/dL)[b]	74 ± 35	71 ± 59

[a] Mean ± SD, n = 3. The * symbol indicates a statistically significant increase in the mean value of the area under the curve from 0 to 120 min when a 40 μg sCT tablet containing 12 mg of hakea was compared with a tablet containing 32 mg of hakea at $p < 0.05$ using Student's one-tail t-test. The † symbol indicates a statistically significant increase in the mean value of the apparent bioavailability (F) when a 40 μg sCT tablet containing 12 mg of hakea was compared with a tablet containing 32 mg of hakea at $p < 0.05$ using Student's one-tail t-test. [b] Area above the calcium reduction curve.

Table 3). The results tend to suggest that hakea effectively retarded the rate of release of sCT from the dosage form. The values of F (%) calculated in the present study were 37 ± 6 and 16 ± 8 for buccal tablets with 12 and 32 mg of hakea, respectively. Dua et al.[22] reported percent bioavailability values of 0.16, 0.80, and 0.71 for low viscosity (1

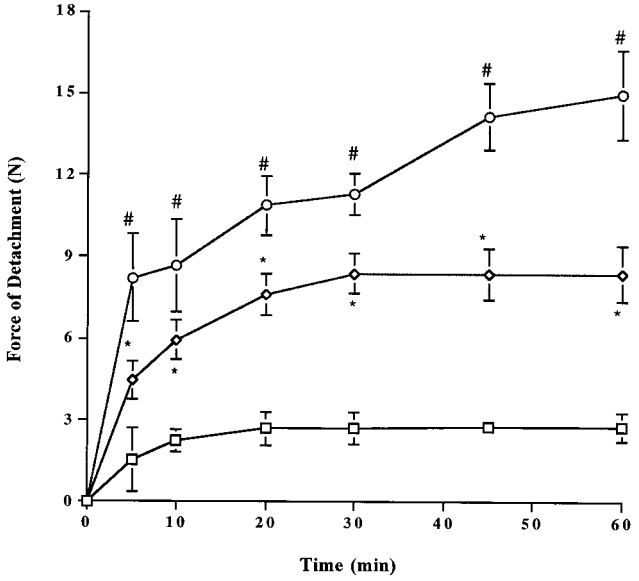

Figure 5—The force of detachment from excised rabbit intestinal mucosa for directly compressed buccal tablets which contained 40 μg of sCT and 0 mg of hakea (□), 12 mg of hakea (◇), or 32 mg of Hakea (○). All data points represent the mean value ± standard deviation of five experiments. Lines through mean values are included to illustrate the trend and do not represent a mathematical fit of the data. The * symbol indicates a statistically significant increase in the mean value of the force of detachment of a tablet containing 12 mg of hakea from that of a tablet containing 0 mg of hakea at $p < 0.05$ using Student's one-tail t-test. The # symbol indicates a statistically significant increase in the mean value of the force of detachment of a tablet containing 32 mg of hakea from that of a tablet containing 12 mg of hakea at $p < 0.05$ using Student's one-tail t-test.

cps) isotonic, hypertonic, and hypotonic formulations, respectively, after intranasal administration of salmon calcitonin at a dose of 2000 IU in rabbits. The percent bioavailability values were 0.14, 0.62, and 0.81 following intranasal administration of high-viscosity (76 cps) formulations prepared with 1% methylcellulose containing 2000 IU of salmon calcitonin in rabbits.[22] Heiber et al.[6] reported the delivery of 550 IU of sCT across canine buccal mucosa but did not report a value for bioavailability. Sinko et al.[18] reported a bioavailability of 16.2 ± 5.1% following subcutaneous (mean value of four different doses) and 0.022 ± 0.018% following intraduodenal administration (mean value of two different doses) in rats. An absolute bioavailability of 1.6% was reported without any permeation enhancer at a dose of 200 IU (40 μg) and 10.3% with 0.5% sodium tauro-24, 25-dihydrofusidate as a permeation enhancer at a dose of 405 IU (90 μg) following intranasal administration of sCT in humans.[23] Estimates of the absolute bioavailability of several other therapeutic polypeptides following buccal administration are 1−5%, 0.1%, and 1% for thyrotropin releasing hormone (TRH) in humans,[24] oxytocin in rabbits,[16] and buserelin in pigs,[17] respectively.

The plasma sCT levels obtained in this investigation using sCT buccal tablets which contained hakea were greater than therapeutic plasma levels (0.1−0.4 ng/mL). These levels were achieved without the use of a permeation enhancer. Heiber et al. also reported sCT plasma levels in excess of the therapeutic range when buccal tablets were evaluated in dogs.[6] The present study demonstrated that the buccal route provided a greater systemic bioavailability than the other routes of sCT administration discussed previously and that the buccal tablets which contained hakea not only achieved therapeutic plasma levels but also sustained the plasma concentration of sCT for 2−3 h. However, in the present study, the authors did observe a departure of plasma sCT concentrations following buccal

administration which would have been anticipated on the basis of our in vitro release studies. More recent findings in our laboratory (unpublished observations) suggest that the increased bioavailability of sCT in the present study may potentially result from hakea inhibiting proteolytic enzymes located in the oral cavity which are responsible for chemical degradation of sCT and/or inhibition of the polypeptide's biological activity. The mechanism of enhanced bioavailability will be the subject of future experimentation.

In the present study, the drug-releasing, uncoated surface adhered to the buccal mucosa during the entire application period. This mucosal binding possibly minimized the loss of drug into the surrounding oral cavity and the gastrointestinal tract in the event that sCT dissolved in saliva were potentially swallowed. Upon the removal of buccal tablets with 40 μg of sCT and 12 mg of hakea, the plasma sCT concentration did not decrease as observed following an intravenous dose suggesting that the sCT may accumulate in the buccal mucosa resulting in a reservoir effect. This has also been observed by Heiber et al.[6]

The pharmacodynamic response to biologically active sCT represents a reduction in plasma calcium concentrations. Figures 3 and 4 illustrate the absorption of biologically active sCT across the buccal mucosa of rabbits. The results demonstrated that the dual compaction process during the manufacturing of the tablet did not affect its biological activity adversely. The values of AAC_{0-2h} for the 40 μg sCT buccal tablets with 12 and 32 mg of hakea were not significantly different ($p > 0.05$), which may be due to the potency of sCT, i.e., the dose required to elicit the maximum pharmacological response is very small. As such, this pharmacological response reaches a maximum beyond which further lowering of plasma calcium concentrations does not occur as the dose is increased (negative feedback control of plasma calcium).[25] Sinko et al.[16] estimated that the maximal lowering of plasma calcium occurs at a plasma sCT concentration of 10 pg/mL in rats. Dua et al.[22] obtained a similar maximal percent decrease in plasma calcium concentrations (% max_d) following intranasal administration of different formulations in rabbits, although the (%) values reported for the bioavailability were quite different. This may have resulted from homeostasis and negative feedback control. Many investigators rely on the pharmacodynamic response to assess the absolute bioavailability[26–29] which may result in an overestimation for the reasons cited above.

Sustained-release, mucoadhesive dosage forms have the advantage of not only adhering to the mucus membrane for the required length of time but also sustaining the release of drug substances. In the present study, the amount of hakea incorporated into the buccal tablet was observed to be a critical factor in defining the resulting bioadhesive strength. A potential reason for an increase in the mucoadhesive bond strength with increasing hakea content (Figure 5) may be due to enhanced water uptake by the gum resulting in tablet swelling and mobilization of flexible polysaccharide chains for interpenetration and physical entanglement with the mucus.

Hakea possesses both hydroxyl and carboxyl terminal groups which can contribute to bioadhesion. Both these functional groups have to be in the un-ionized form in order for it to optimally interact with the negatively charged mucin molecule (under neutral or slightly acidic conditions). The bioadhesive strength increased with time and reached a plateau (Figure 5), suggesting that the process of bioadhesion is saturable and that the mechanism of bioadhesion is likely due to chain interpenetration and physical entanglement[30] of hakea with mucus rather than secondary bond formation (e.g., hydrogen bonding). The fact that the bioadhesive strength reaches a plateau at later time points could be due to the limited surface area of the tablet and exhaustion of the sialic acid residues of the mucin molecule with which the gum can interact in the circular surface area covered by the tablet.

In conclusion, the ability of the novel gum to sustain the release of sCT has been demonstrated both in vitro and in vivo. Moreover, in vitro bioadhesive strength versus time measurements demonstrated that the gum possessed excellent mucoadhesive properties. The tablets were convenient to apply and remove from the buccal mucosa and did not appear to damage the underlying tissue. The mechanism of bioadhesion may potentially result from chain interpenetration and physical entanglement of hakea with the mucus layer. The rate of release of the drug substance as well as the bioadhesive bond strength of the formulation can be modulated by varying the amount of hakea included in the tablet. Thus, the polysaccharide bioadhesive gum hakea may be utilized for not only the sustained delivery of a variety of water-soluble, low molecular weight drug substances but also therapeutic polypeptides.

References and Notes

1. Lang, S.; Rothen-Rutishauser, B.; Perriard, J.; Schmidt, M. C.; Merkle, H. P. Permeation and pathways of human calcitonin (hCT) across excised bovine nasal mucosa. *Peptides* **1998**, *19*, 599−607.
2. Harris, D.; Robinson, J. R. Bioadhesive polymers in peptide drug delivery. *Biomaterials* **1990**, *11*, 652−658.
3. Patel, S.; Lyons, A. R.; Hosking, D. J. *Drugs* **1993**, *46*, 594−617.
4. Hosking, D. J.; Bijvoet, O. L. M. Therapeutic Uses of calcitonin. In *Endocrinology of Calcium Metabolism*; Parsons, J. A., Ed.; Raven Press: New York, 1982; pp 485−535.
5. Lee, K. C.; Soltis, E. E.; Newman, P. S.; Burton, K. W.; Mehta, R. C.; DeLuca, P. P. In vivo assessment of salmon calcitonin sustained release from biodegradable microsphere. *J. Controlled Release* **1991**, *17*, 199−206.
6. Heiber, S. J.; Ebert, C. D.; Dave, S. C.; Smith, K.; Kim, S. W.; Mix, D. In-vivo buccal delivery of calcitonin. *J. Controlled Release* **1994**, *28*, 269−271.
7. Rathbone, M. J.; Drummond, B. K.: Tucker, I. G. The oral cavity as a site for systemic drug delivery. *Adv. Drug Delivery Rev.* **1994**, *13*, 1−22.
8. Merkle, H. P.; Anders, R.; Sandow, J.; Schurr, W. In *Delivery systems for peptide drugs*; Davis, S. S., Lllum, L., Tomlinson, E., Eds.; Plenum Press: New York, 1986; pp 159−175.
9. Ahuja, A.; Khar, R. K.; Ali, J. Mucoadhesive delivery systems. *Drug Dev. Ind. Pharm.* **1997**, *23*, 489−515.
10. Alur, H. H.; Pather, S. I.; Mitra, A. K.; Johnston, T. P. Evaluation of Hakea gibbosa as a sustained-release and mucoadhesive component in buccal tablets. *Pharm. Dev. Technol.* **1999**, *4*, 347−358.
11. Alur, H. H.; Pather, S. I.; Mitra, A. K.; Johnston, T. P. Transmucosal delivery of chlorpheniramine maleate using a novel natural mucoadhesive gum as an excipient of buccal tablets. *Int. J. Pharm.* **1999**, *188* (1), 1−10.
12. Eagles, P. F. K. Structures of complex plant polysaccharides, Exudates from Hakea sericea and Hakea gibbosa. Ph.D. Thesis, Department of Chemistry, University of Capetown, South Africa, March 1992.
13. Peppas, N. A.; Sahalin, J. J. A simple equation for the description of solute release III. Coupling of diffusion and relaxation. *Int. J. Pharm.* **1989**, *57*, 169−172.
14. Gibaldi, M.; Perrier, D. *Pharmacokinetics*, 2nd ed.; Marcel Dekker: New York, 1982; pp 445−449.
15. Hoogstraate, A. J.; Verhoef, J. C.; Pijpers, A.; van Leengoed, L. A. M. G.; Verheijden, J. H. M.; Junginger, H. E.; Bodde, H. E. In vivo buccal delivery of the peptide drug buserelin with glycodeoxycholate as an absorption enhcncer in pigs. *Pharm. Res.* **1996**, *13*, 1233−1237.
16. Li, C.; Bhatt, P. P.; Johnston, T. P. Transmucosal delivery of oxytocin to rabbits using a mucoadhesive buccal patch. *Pharm. Dev. Technol.* **1997**, *2*, 265−274.
17. Kobayashi, S.; Kondo, S.; Juni, K. Study on pulmonary delivery of salmon calcitonin in rats: Effects of protease inhibitors and absorption enhancers. *Pharm. Res.* **1994**, *11*, 1239−1243.
18. Sinko, P. J.; Smith, C. L.; Mcwhorter, L. T. M.; Stern, W.; Wagner, E.; Gilligen, J. P. Utility of pharmacodynamic

measures for assessing the oral bioavailability of peptides. I. Administration of recombinant salmon calcitonin in rats. *J. Pharm. Sci.* **1995**, *84*, 1374−1378.
19. Batra, V.; Bhowmick, A.; Behera, B. K.; Ray, A. R. Sustained-release of ferrous sulfate from polymer-coated gum arabica pellets. *J. Pharm. Sci.* **1994**, *83*, 632−635.
20. Banga, A. K.; Chien, Y. W. Hydrogel-based iontotherapeutic delivery devices for transdermal delivery of peptide/protein drugs. *Pharm. Res.* **1993**, *10*, 697−702.
21. Beveridge, T.; Niederer, W.; Nuesch, E.; Petrin, A. Z. *Z. Gastroenterol.* **1979**, *236*, E15−E19.
22. Dua, R.; Zia, H.; Needham, T. The influence of tonicity and viscosity on the intranasal absorption of salmon calcitonin in rabbits. *Int. J. Pharm.* **1997**, *147*, 233−242.
23. Lee, W. A.; Ennis, R. D.; Longenecker, J. P.; Bengtsson, P. The bioavailability of intranasal salmon calcitonin in healthy volunteers with and without a permeation enhancer. *Pharm. Res.* **1994**, *11*, 747−750.
24. Schurr, W.; Knoll, B.; Ziegler, R.; Anders, R.; Merkle, H. P. Comparative study of intravenous, nasal, oral and buccal TRH administration among healthy subjects. *J. Endocrinol. Invest.* **1985**, *8*, 41−45.
25. Mohamadi, M.; Becker, K. L.; Bivins, L. E. Paradoxical effects of salmon calcitonin on serum calcium: Studies on intact and thyroparathroidectomized men and dogs. *Acta Endocrinol.* **1975**, *79*, 351−355.
26. Kobayashi, S.; Kondo, S.; Juni, K. Pulmonary delivery of salmon calcitonin dry powders containing absorption enhancers in rats. *Pharm. Res.* **1996**, *13*, 80−83.
27. Santi, P.; Volpato, N. M.; Bettini, R.; Catellani, P. L.; Massimo, G.; Colombo, P. Transdermal iontophoresis of salmon calcitonin can reproduce the hypocalcemic effects of intravenous administration. *Farmaco* **1997**, *52*, 445−448.
28. Schipper, N. G.; Verhoef, J. C.; Romeijn, S. G.; Merkus, F. W. Methylated beta-cyclodextrins are able to improve the nasal absorption of salmon calcitonin. *Calcif. Tissue Int.* **1995**, *56*, 280−282.
29. Golomb, G.; Avramoff, A.; Hoffman, A. A new route of drug administration: intrauterine delivery of insulin and calcitonin. *Pharm. Res.* **1993**, *10*, 828−833.
30. Park, H.; Robinson, J. R. Physico-chemical properties of water insoluble polymers important to mucin/epithelial adhesion. *J. Controlled Release* **1985**, *2*, 47−57.

Acknowledgments

This work was supported by grants from the University of Missouri Research Board (T.P.J.) and Hoechst-Marrion-Russel (A.K.M.). The authors are grateful to Dr. Peter Eagles and Mr. Yusuf Alexander of the University of the Western Cape, South Africa, for the generous supply of the hakea gum. The authors would also like to acknowledge Rhone-Poulenc-Rorer for their generous donation of sCT.

JS9900755

Protein Behavior at the Water/Methylene Chloride Interface

HONGKEE SAH*

Contribution from *Department of Pharmaceutical Sciences, The University of Tennessee, College of Pharmacy, Room 214, 26 South Dunlap Street, Memphis, Tennessee 38163.*

Received February 25, 1999. Accepted for publication September 3, 1999.

Abstract □ The objective of this study was to investigate the behaviors of proteins at the water/methylene chloride interface to better understand denaturing effects of emulsification upon proteins. Ribonuclease A (RNase) and human serum albumin (HSA) were used as model proteins throughout this study. Their behaviors at the interface were studied in terms of protein recovery after emulsification, interfacial protein aggregation, and dynamic interfacial tension. This study demonstrated that protein instability during emulsification was traced to consequences of the adsorption and conformational rearrangements of proteins at the water/methylene chloride interface. Compared to HSA, RNase was much more vulnerable to the interface-induced aggregation reactions that led to formation of water-insoluble aggregates upon emulsification. Even though HSA was almost completely recovered from the emulsified aqueous phase, the protein underwent dimerization and oligomerization reactions to some extent. The results also demonstrated that the extent of interfacial RNase aggregation was affected by its aqueous concentration and the presence of HSA. Interestingly, RNase stability during emulsification was almost achieved by dissolving an adequate quantity of HSA in the RNase solution. HSA seemed to compete for the interface site and to effectively keep RNase out the interface, minimizing the likelihood of the interface-induced RNase aggregation. These results indicated that competitive adsorption modes of proteins could be used to stabilize a protein of interest against the denaturing effects of emulsification.

Introduction

The field of protein and vaccine delivery systems based on emulsions and biodegradable poly-*d*,*l*-lactide-*co*-glycolide (PLGA) microspheres has grown exponentially. However, increasing concerns about the issues of protein instability during manufacturing processes exist. Maintaining protein stability is of paramount importance, because destabilized proteins lose biological efficacy and aggregate to increase the possibility of an unwanted immune response. Among a variety of manufacturing processes, emulsification of an aqueous protein solution in an organic solvent is considered a major risk factor that presents an obstacle to the successful development of emulsion- and microsphere-based protein delivery systems.[1−4] It is generally agreed that the observed instability stems from exposure of proteins to cavitation, heat, or shear produced during emulsification.[5,6] Protein inactivation is also speculated to arise from protein denaturation at the aqueous solution−organic solvent interface and protein interaction with polymer residuals dissolved in the organic solvent.[7−9] Another possible mechanism suggested elsewhere is that an organic solvent diffuses to an aqueous protein solution and interacts with hydrophobic domains of the protein, eventually disrupting its structural integrity.[10−12]

* Corresponding author. Tel: (901) 448−5505. Fax: (901) 448−6092. E-mail: hsah@utmem1.utmem.edu.

The current study suggests that protein instability during emulsification is traced to consequences of protein contact with the water/organic solvent interface around emulsion droplets. Because of amphipathicity and flexible conformation, proteins are surface active so that they tend to adsorb at water/organic solvent interfaces.[13] This event seems not only to disturb the delicate conformation of proteins but also to trigger various physicochemical transformations, leading to protein destabilization reactions. Currently, however, many questions remain unanswered with regard to the origins of protein instability against the interfaces, mechanisms that govern protein destabilization at water/organic solvent interfaces, and competitive protein behavior at the interfaces. As a starting point to tackle these important issues, this study sought to investigate the behavior of model proteins ribonuclease A (RNase) and human serum albumin (HSA) at the water/methylene chloride (W/MC) interface.

Materials and Methods

Materials—Ribonuclease A (RNase; type III-A from bovine pancreas; R5125) and human serum albumin (HSA; A3782) were obtained from Sigma Chemical Company (St. Louis, MO). Major physicochemical properties of the two proteins are compared in Table 1. A precast, 1.5-mm thick Tris-glycine gel (8−16%) was purchased from Novex (San Diego, CA). Methylene chloride of HPLC grade was used throughout this study.

Emulsification to Generate the Water/Methylene Chloride (W/MC) Interface—A protein sample was dissolved in distilled water to make 0.2−1.5 mg/mL concentrations. Aliquots (3 mL) of the solution were placed inside a 20-mL vial containing methylene chloride (12 mL). The mixture was emulsified for 1 min at room temperature by a rotor/stator-type VirtiShear Tempest IQ2 homogenizer (The VirTis Co., Gardiner, NY) equipped with a 10-mm shaft. During emulsification, the rotational speed of the homogenizer rotor was set at 16 000 rpm.

Quantitation of Protein Distribution between Water and the W/MC Interface—Emulsification led to the formation of water-insoluble RNase aggregates that resided in the interface. To determine the aqueous protein concentration and the amount of the aggregates, the aqueous phase was separated from the methylene chloride phase by centrifugation at 3500 rpm for 10 min (IEC Centrifuge/International Centrifuge Company, Needham Heights, MA). A protein sample collected from the aqueous phase was subjected to a native size exclusion chromatography (SEC)-HPLC experiment which was described later. Equation 1 was used to determine the percentage of a protein recovered in the aqueous phase after emulsification. The amount of interfacially aggregated protein was equal to that of protein disappearing from the aqueous phase after emulsification.

$$\text{protein recovered (\%)} = \frac{\text{measured aqueous protein concn after emulsification}}{\text{known aqueous protein concn before emulsification}} \times 100 \quad (1)$$

Assay for Water-Insoluble RNase Aggregates Obtained from the W/MC Interface—Ultraviolet spectral and dynamic light scattering experiments were performed to assess whether

10.1021/js9900654 CCC: $18.00 *Published on Web 10/21/1999*

Table 1—Major Properties of Ribonuclease A (RNase) and Human Serum Albumin (HSA)

protein	RNase[a]	HSA[b]
amino acids	124	585
mass (D)	13 680	69 000
dimensions (nm^3)	$3.8 \times 2.8 \times 2.2$	$12 \times 2.7 \times 2.7$
diffusion coefficient ($m^2\ s^{-1}$)	1.26×10^{-10}	0.70×10^{-10}
number of disulfide bonds	4	17
number of free thiol group	0	1
isoelectric point	9.4–9.6	4.6–4.9

[a] Data from Scheraga and Rupley[14] and Haynes et al.[15] [b] Data from Haynes et al.[15] and Peters, Jr.[16]

the aggregates differed from native RNase. Before the experiments, the water-insoluble aggregates were dissolved in a 0.5% SDS aqueous solution or 6 M urea. For the UV spectral experiment, a HP 8453 UV−visible spectrophotometer (Hewlett-Packard Company, Palo Alto, CA) was used to monitor the spectra of native and aggregated RNase molecules over the wavelength of 200 to 320 nm. In addition, their first derivative spectra were also obtained using a Savitsky−Golay algorithm offered by the spectrophotometer software.

For the dynamic light-scattering experiment, RNase sample solutions in 0.5% SDS or 6 M urea were filtered through a Whatman Anotop Plus filter with 0.1 μm porosity. The sample solutions were placed inside the microsample chamber of a DynaPro-801TC (Protein Solutions, Inc., Charlottesville, VA) and were illuminated by the laser. The instrument determined the hydrodynamic radius by analyzing the scattered light (the angle of detection was 90°).

Homogenization Effects on Protein Recovery—A 0.5 mg/mL RNase or HSA solution (15 mL) was put into a 20-mL size vial and was homogenized in the absence of methylene chloride under the same experimental conditions described earlier. Later, protein concentration was determined by SEC−HPLC analysis. The protein sample was also subjected to SDS−PAGE experiments.

Dissolved Methylene Chloride Effect on Protein Recovery—To prepare an aqueous solution saturated with methylene chloride, 4 mL of methylene chloride was added to 16 mL of water. The mixture was then vigorously shaken for 1 h at room temperature with an Eberbach shaker (Eberbach Co., Ann Arbor, MI) and was centrifuged to obtain the methylene chloride−saturated aqueous phase. RNase was then dissolved in the solution phase at a 0.5 mg/mL concentration. After the methylene chloride−saturated aqueous RNase solution (15 mL) was homogenized as described earlier, its concentration was determined by SEC−HPLC analysis and was compared with that of unhomogenized RNase solution.

SEC−HPLC—This experiment was performed to measure the total protein content and to assess the composition of water-soluble protein species before and after emulsification. When water-insoluble protein aggregates were analyzed, they were dissolved in a 0.5% SDS aqueous solution before the SEC−HPLC experiment. Protein samples were eluted from a TSK Gel G3000 SW analytical column (7.5-mm inner diameter × 60-cm length) by a mobile phase consisting of 50 mM phosphate buffer solution containing 0.1 M NaCl (pH 7.0). The flow rate was maintained at 0.8 mL/min, and the elution of protein samples was monitored by a UV detector set at 280 nm. The concentration of each protein species was determined by a calibration curve constructed by peak area integration of protein standards with known concentrations. Throughout this study, the average of at least three experimental determinations was reported with a standard deviation.

SDS−PAGE—A gradient 8−16% Tris-Glycine gel was placed inside Novex Xcell II Mini-Cell. RNase samples were mixed well with a Laemmli Tris-Glycine loading buffer and were housed inside the gel wells. The running buffer consisted of 25 mM Tris, 192 mM glycine, and 0.1% SDS at pH 8.3. After being run at a 125 V constant voltage (Power PAC300/Bio-Rad Laboratories, Hercules, CA) for 125 min, the gel was stained for 30 min with a 0.1% Coomassie Blue solution containing 10% glacial acetic acid and 50% methanol. Protein bands were visualized after the gel was destained overnight with an aqueous solution containing 20% methanol and 10% glacial acetic acid.

Inhibition of RNase Interfacial Aggregation—To investigate the effect of HSA upon the degree of RNase recovery, 0.2−5.0 mg/mL HSA was dissolved in a 0.35 mg/mL RNase solution before emulsification. After the aqueous protein mixture solution was emulsified in methylene chloride, the degree of RNase recovery was determined following the SEC−HPLC analysis mentioned earlier.

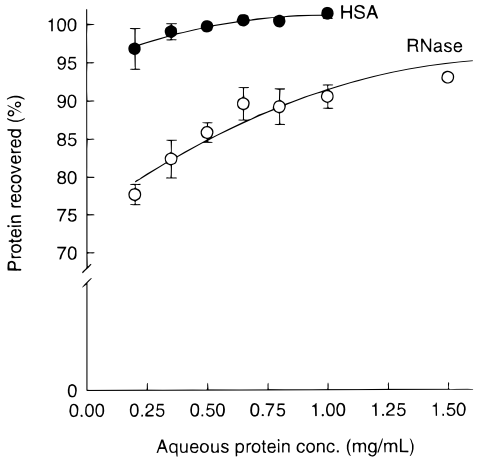

Figure 1—The percentage of protein recovery after emulsification. After an aqueous protein solution was emulsified in methylene chloride, the degree of protein recovery was determined by eq 1.

Measurement of Dynamic Interfacial Tension—Protein adsorption at the W/MC interfaces was investigated by a drop volume tensiometer (Model DVT-10/Krüss USA, Charlotte, NC). The tensiometer was considered suitable for studying the adsorption of surface active materials at interfaces, when they slowly attained equilibrium interfacial tension.[17,18] In this experiment, an aqueous 0.5 mg/mL RNase or HSA solution was placed in a 100-μL size gastight Hamilton syringe. A pump (Model 44/Harvard Apparatus, South Natick, MA) was used to deliver the protein solution at a constant rate to methylene chloride phase via a bore capillary (0.254-mm inner diameter) with a specially tapered tip. The flow rate ranged from 15 to 0.5 mL/h. As the protein solution was pumped into the methylene chloride phase, a drop grew and detached off the tip of the bore capillary. The time required for detachment of each droplet was defined as interface development time. Combined knowledge on the interface development time and the flow rate allowed us to calculate the volume of each droplet. Interfacial tension was then determined by eq 2.[19]

$$\sigma = \frac{V_{\text{drop}}\,(\rho_{\text{m}} - \rho_{\text{w}})g}{\pi d} \tag{2}$$

where σ was interfacial tension; V_{drop}, the volume of an aqueous droplet; g, the acceleration due to gravity; d, diameter of the bore capillary; ρ_{m}, methylene chloride density; and ρ_{w}, the density of water phase. The interfacial tension measurement was repeated five times, and their mean ± standard deviation was reported.

Results

Under our SEC−HPLC experimental conditions, only one peak representing monomeric RNase species was observed when the protein solution was not subject to emulsification. The same monomeric peak was detected with RNase solutions emulsified in methylene chloride, but there was a substantial reduction in the content of RNase monomer. A loss in its aqueous content was found to be caused by the formation of water-insoluble aggregates residing in the W/MC interface. Besides, the extent of RNase recovery was affected by changes in its aqueous concentration prior to emulsification (Figure 1). For instance, 77.7 ± 1.4% (mean ± standard deviation) of RNase was recovered after a 0.2 mg/mL RNase solution was emulsified in methylene chloride. An increase in its concentration to 1.5 mg/mL before emulsification enhanced its

Table 2—Changes in the Composition of Water-Soluble HSA Species Triggered by Emulsification. After Emulsifying 0.2–1.0 mg/mL HSA Solutions in Methylene Chloride, the Compositions of HSA in the Aqueous Phase Were Determined by HPLC Analysis[a]

protein concn (mg/mL)	monomer %	dimer %	oligomer % (total μg)[b]
0.20	71.2 ± 0.3	24.3 ± 0.2	4.6 ± 0.1 (27.3 ± 0.4)
0.35	75.8 ± 0.2	21.2 ± 0.1	3.1 ± 0.2 (32.0 ± 2.2)
0.50	78.5 ± 0.4	19.2 ± 0.4	2.4 ± 0.1 (36.0 ± 0.1)
0.65	79.8 ± 0.2	18.1 ± 0.1	2.2 ± 0.1 (42.0 ± 1.4)
0.80	80.8 ± 0.2	17.3 ± 0.3	1.9 ± 0.1 (45.6 ± 0.1)
1.00	80.8 ± 0.2	17.2 ± 0.4	2.1 ± 0.1 (63.0 ± 4.2)

[a] All determinations are performed at least three times, and mean ± standard deviation is reported. Before emulsification, HSA consisted of 86.7 ± 0.5% monomer and 13.3 ± 0.5% dimer. [b] The actual amount of a new water-soluble HSA oligomer is in parentheses.

degree of recovery up to 92.9 ± 0.2%. The data in Figure 1 were likely to give a false impression that fewer RNase molecules became aggregated at high concentrations. The amount of RNase aggregates in fact increased at high concentrations: emulsifying 0.2 and 1.5 mg/mL RNase solutions resulted in the formation of 133.9 ± 8.2 and 317.4 ± 10.8 μg of water-insoluble RNase aggregates, respectively.

Similar experiments were repeated to investigate the behavior of HSA at the W/MC interface developed during emulsification. From the viewpoint of percentage of protein recovery, HSA exhibited stronger resistance toward emulsification-induced aggregation reactions than RNase did (Figure 1). HSA was almost completely recovered in the aqueous phase. For instance, when a 0.2 mg/mL HSA solution was emulsified, protein recovery was 96.8 ± 2.7%. Moreover, at ≥0.35 mg/mL concentrations, at least 99.1% of HSA was recovered from the aqueous phase emulsified. However, it was found that some proportion of HSA molecules underwent dimerization and oligomerization reactions on emulsification (Table 2). Unemulsified HSA contained 86.7 ± 0.5% monomer and 13.3 ± 0.5% dimer, and homogenization of an aqueous HSA solution alone did not cause any change in the protein composition. On the contrary, after a 0.2 mg/mL HSA solution was emulsified in methylene chloride, the protein consisted of 71.2 ± 0.3% monomer, 24.3 ± 0.2% dimer, and 4.6 ± 0.1% oligomer. It should also be mentioned that the extent of HSA oligomerization also was concentration-dependent, such that the actual amount of the new water-soluble HSA oligomer species increased at high concentrations (Table 2).

Before carrying out the SEC−HPLC experiment, water-insoluble RNase aggregates obtained from the W/MC interface were dissolved using SDS which is known to disrupt the quaternary structures of most proteins and dissociate them into monomeric species. Figure 2 illustrates the SEC−HPLC chromatograms. The appearance of new RNase aggregates, despite the SDS treatment, indicated that the emulsification-associated RNase aggregation was an irreversible process, and the aggregates were not easily dissociable. To further back up this supposition, the hydrodynamic radius of monomeric RNase was compared with that of the water-insoluble RNase aggregates (Table 3). RNase monomer in 0.5% SDS solution was estimated to have the hydrodynamic radius of 2.0 nm. In contrast, the mean hydrodynamic radius of the water-insoluble RNase aggregates was determined to be 12.7 nm. In addition, an increase in the polydispersity observed with water-insoluble RNase aggregates represented that the aggregates were polydisperse in size and consisted of species with different hydrodynamic radii (the polydispersity in Table 3 indicates the standard deviation of the spread of sample sizes about the reported mean hydrodynamic radius). In particular, the DynaPro-801TC seemed to overestimate the hydrodynamic radius of RNase samples in 6 M urea. This result may have arisen from the fact that RNase species in 6 M urea exist in unfolded states.

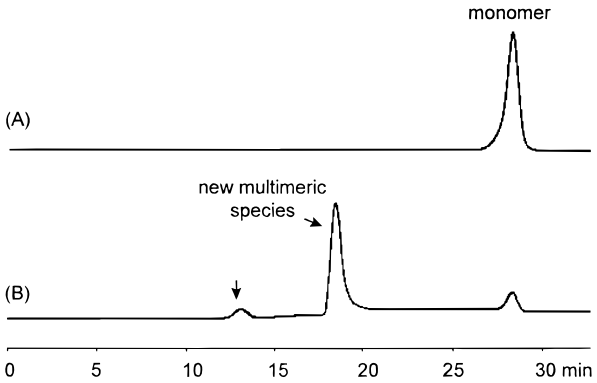

Figure 2—SEC–HPLC chromatograms of (A) standard RNase before emulsification and (B) water-insoluble RNase aggregates collected from the W/MC interface after emulsification. RNase aggregates were dissolved in a 0.5% SDS aqueous solution before injection to the SEC–HPLC.

Figure 3 illustrates the UV spectra of monomeric RNase and water-insoluble RNase aggregates. The spectrum and its first derivative for RNase aggregates were different from those of monomeric RNase (these differences were confirmed by a linear regression-based spectral match function provided by the HP 8453 UV−Visible spectrophotometer). Especially, the broadening of bands and shifts in wavelength were observed with RNase aggregates in comparison to RNase monomer. It can be inferred from the result that RNase aggregation might have changed the local environment of the chromophores, e.g., peptide groups, aromatic amino acids, and disulfide bonds, in RNase molecules.

To test whether the observed RNase aggregation might be caused by mechanical shear stress and/or the continual creation of a new air/water interface, a 0.5 mg/mL RNase solution (15 mL) was homogenized in the absence of methylene chloride. Slight foaming was observed after the treatment, but the foam dissipated rapidly. No considerable change in the content of RNase monomer was observed after homogenization (the aqueous solution homogenized was found to contain 99.67 ± 0.72% of the initially used amount of RNase). In addition, the SDS−PAGE results shown in Figure 4 demonstrated that RNase samples before and after homogenization exhibited the same gel patterns. A similar trend was observed when homogenization was performed on the methylene chloride−saturated aqueous RNase solution. Foaming also occurred during homogenization, but the foam disappeared when the solution was kept still. In this case, 99.0 ± 0.1% of the initial RNase amount was found in the solution.

So far, it has been suggested in this study that exposure of proteins at the W/MC interface initiated protein destabilization reactions. To prove this supposition, protein adsorption and conformational changes at the interface were demonstrated by analyzing the W/MC interfacial tension. In our study, the Krüss DVT-10 tensiometer determined the interfacial tension to be 27.84 ± 0.38 mN/m when the aqueous phase did not contain any protein molecules. At the same time, the volume of a single water droplet was found to be 7.17 ± 0.10 μL. The presence of either RNase or HSA at a 0.5 mg/mL concentration in water led to a considerable reduction in the interfacial tension, as well as the volume of an aqueous droplet (Table 4). Besides, changes in the interfacial tension were affected by interface development time that was manipulated by the flow rate of pumping a protein solution into methylene chloride. A lower flow rate, which provided a longer

Table 3—Comparison of the Properties of Monomeric RNase and Water-Insoluble RNase Aggregates. Prior to Analysis, the Water-Insoluble Aggregates Obtained from the W/MC Interface Were Dissolved in 0.5% SDS Aqueous Solution or 6 M Urea[a]

	RNase monomer dissolved in		RNase aggregates dissolved in	
	0.5% SDS solution	6 M urea	0.5% SDS solution	6 M urea
diffusion coefficient (10^{-13} m^2 s^{-1})	1229 ± 40	985 ± 44	197.4 ± 9.9	149.1 ± 4.7
hydrodynamic radius (nm)	2.0 ± 0.1	2.3 ± 0.2	12.7 ± 0.7	16.9 ± 0.6
polydispersity (nm)	0.9 ± 0.1	1.3 ± 0.1	7.1 ± 0.4	16.3 ± 0.6

[a] Data were reported as mean ± standard deviation ($n = 8$).

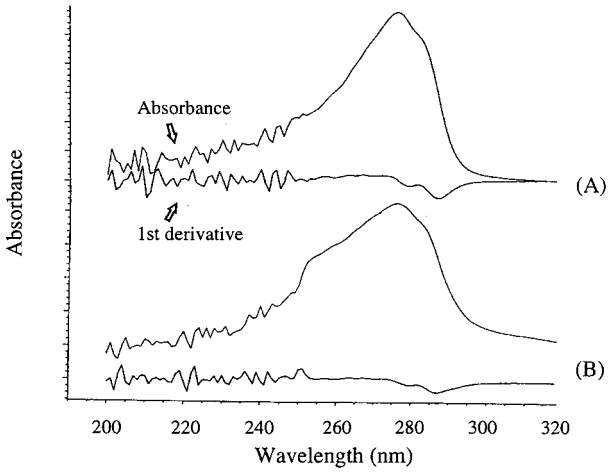

Figure 3—Absorption and first derivative spectra of (A) RNase monomer and (B) water-insoluble RNase aggregates. The protein samples were in 0.5% SDS aqueous solution.

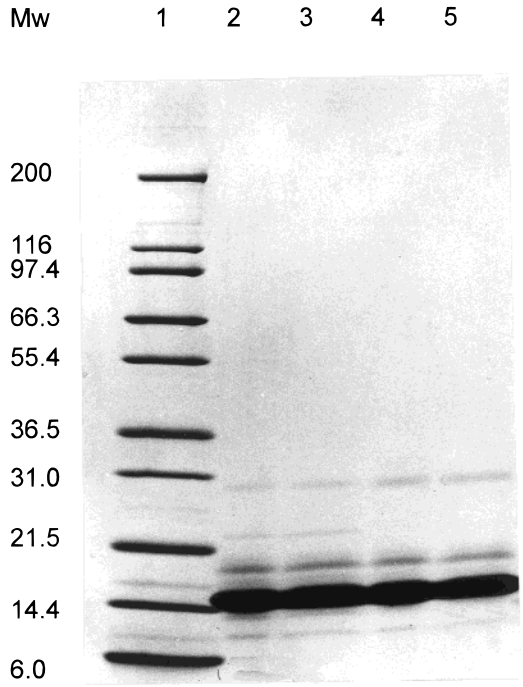

Figure 4—SDS–PAGE gel patterns of RNase samples before (lanes 2, 3) and after (lanes 4, 5) homogenization. Molecular markers (kDa) are shown in lane 1.

interface development time, led to a greater reduction in the aqueous droplet volume and the interfacial tension (a linear relationship between the volume of an aqueous droplet and the W/MC interfacial tension is well depicted by eq 2). A longer interface development time—more prolonged exposure of proteins to the interface—seemed to permit more protein molecules to adsorb and undergo conformational rearrangements at the interface. An additional interesting point observed in Table 4 was that, at relatively higher flow rates, the surface activity of RNase was greater than that of HSA. By contrast, the same conclusion did not remain valid when the flow rate was decreased below 1 mL/h. HSA was found to be more surface active when exposed to the interface for longer periods of time.

In terms of the degree of protein recovery, HSA exhibited superior stability over RNase against the W/MC interface-induced aggregation reactions (Figure 1). It was also speculated that owing to their surface activity, proteins would compete for adsorption sites at the W/MC interface. On the basis of these considerations, different levels of HSA (0.2 ~ 5.0 mg/mL) were codissolved in a 0.35 mg/mL RNase solution before emulsification to minimize RNase instability toward the W/MC interface. When RNase was the only protein species present in the aqueous phase, 82.4 ± 2.5% of RNase was recovered from the emulsified aqueous phase. When a sufficient quantity of HSA was added into the aqueous phase, the degree of RNase recovery was increased considerably (Figure 5). At ≥0.8 mg/mL HSA concentrations, more than 96.6 ± 1.2% of RNase was recovered from the emulsified aqueous phase. These data indicated that the use of HSA contributed to stabilizing RNase against the interface-triggered destabilizing reactions.

Discussion

Water/oil interface is ascribed to be highly mobile in comparison to water/air and water/solid interfaces so that proteins are less likely to adsorb irreversibly and destabilize at the water/oil interface.[20] However, our experimental results demonstrate that the W/MC interface developed during emulsification is detrimental to the stability of RNase molecules. Our control experiments also demonstrated that homogenization-associated effects (e.g., cavitation, shear, and continual creation of a new air/water interface) and methylene chloride molecules dissolved in water are not the main causes of RNase instability observed with emulsification. Exposure of RNase molecules to the W/MC interface is held accountable for inducing considerable conformational changes leading to aggregation reactions and a subsequent reduction in its monomer content. In addition, a series of experiments provides evidence that the interface-triggered aggregation reactions are essentially irreversible (Figure 2 and Table 3). It remains to be investigated whether the formation of these RNase aggregates is induced by noncovalent, physical associations or by intermolecular covalent linkages.

It was previously reported that, although some proteins and vaccines were stable in organic solvents, they became inactivated either upon exposure to water—organic solvent mixture or during the emulsion-based microencapsulation process.[21,22] Most reports ascribed that organic solvent molecules dissolved in an aqueous phase could interact with hydrophobic domains of proteins, thereby triggering structural rearrangements detrimental to protein integrity. On the basis of this consideration, a rapid microsphere hardening process is recommended to maintain protein

Table 4—Effects of the Flow Rate on Dynamic Changes in the W/MC Interfacial Tension (mN/m) and the Volume (μL) of an Aqueous Droplet. To Manipulate Interface Development Time (IDT in seconds), the Flow Rate of Pumping a 0.5 mg/mL Protein Solution into the Methylene Chloride Phase Was Changed from 15 mL/h to 0.5 mL/h

	when the aqueous phase contained RNase			when the aqueous phase contained HSA		
flow rate (mg/mL)	IDT	droplet volume	interfacial tension	IDT	droplet volume	interfacial tension
15	1.45	6.03 ± 0.08	23.42 ± 0.31	1.70	7.07 ± 0.16	27.43 ± 0.06
10	2.12	5.89 ± 0.09	22.87 ± 0.34	2.50	6.95 ± 0.11	26.95 ± 0.43
7.0	2.99	5.80 ± 0.09	22.52 ± 0.34	3.51	6.83 ± 0.08	26.49 ± 0.33
5.0	4.00	5.55 ± 0.06	21.54 ± 0.24	4.81	6.68 ± 0.13	25.92 ± 0.52
3.0	6.56	5.47 ± 0.08	21.23 ± 0.31	7.40	6.16 ± 0.11	23.92 ± 0.30
1.0	18.06	5.02 ± 0.05	19.46 ± 0.19	17.24	4.79 ± 0.07	18.59 ± 0.27
0.5	33.52	4.65 ± 0.01	18.07 ± 0.04	30.88	4.29 ± 0.01	16.64 ± 0.05

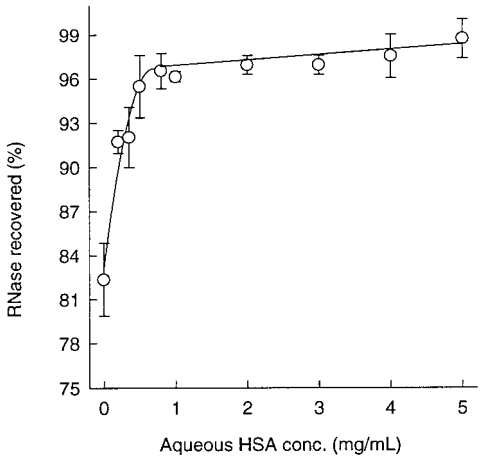

Figure 5—The effect of HSA on RNase recovery. Prior to emulsification, HSA (0.2 to 5.0 mg/mL) was codissolved in a 0.35 mg/mL RNase solution. The solution was emulsified in methylene chloride, and the percentage of RNase recovery was determined.

stability by minimizing exposure time of a protein to methylene chloride.[23] However, our results clearly substantiate that protein destabilization reactions occur primarily over a very short emulsification time scale that lasted for only 1 min in our experiment. This conclusion is in line with other reports suggesting that emulsification of preparing a primary w/o emulsion is the main risk factor responsible for protein inactivation when microspheres are prepared by the w/o/w microencapsulation process.[1–3,7]

In the current study, it has also been shown that the degree of the interfacial RNase aggregation is influenced by aqueous protein concentrations and the presence of another protein, HSA. With regard to the effect of protein concentration upon its stability, two hypotheses have been proposed to explain that a smaller fraction of proteins becomes inactivated at high concentrations. The first one takes into consideration that only a limited amount of a protein could interact at water/oil interfaces.[3] Under this condition, the protein is suggested to act as a self-protectant at high concentrations, thereby inhibiting its interaction with the interface. The other hypothesis elaborates on the role of energy barrier on protein adsorption.[24] At low protein concentrations, there is no barrier to adsorption and subsequent interfacial reactions. By contrast, at high protein concentrations, an energy barrier comes into play to prohibit further protein adsorption. At 0.2 to 1.5 mg/mL RNase concentrations used in our study, the protein aggregation increased with its aqueous concentration increasing. This result suggests that, in dilute concentrations, protein adsorption at the interface is enhanced by an increase in its aqueous concentration, because a great concentration gradient facilitates the mass transfer of RNase to the interface. As a consequence, collision frequencies and reactions among RNase molecules are increased. This contention agrees well with a widespread assertion that the extent of protein aggregation is kinetically controlled and the rate of aggregation is proportional to protein concentration.[25]

Serum albumins, particularly bovine serum albumin, have been popularly coencapsulated with therapeutic proteins into PLGA microspheres via the w/o/w emulsion and the spray-drying processes.[1,7,26–28] In these studies, it was reported that serum albumins improved the encapsulation efficiency of proteins and vaccines and contributed to preserving their activities. Currently, little information is available with regard to stabilization mechanisms of serum albumins for therapeutic proteins and their behaviors at the W/MC interface. From the data on the effect of HSA concentration upon the degree of RNase recovery (Figure 5), it can be inferred that the mass transfer phenomenon influences the kinetics of protein adsorption. According to this theory, a protein present in excess should occupy an interface first, because a steeper concentration gradient provides a greater diffusion rate to the protein. As a result of this, HSA at higher concentrations seems to effectively keep RNase molecules out of the W/MC interface, minimizing the likelihood of the interface-induced RNase aggregation. The other possible stabilizing function of HSA is that the protein molecules may adsorb preferentially at the interface and strip the adsorbed RNase molecules off the interface. In studies of protein behavior at solid/water interfaces, it has been demonstrated that HSA displaces IgG and fibrinogen adsorbed at solid surfaces.[29–31] The so-called "Vroman effect" describes this phenomenon that proteins can replace one another at biomaterial surfaces.[32,33]

Another important discussion should be made with regard to the quantity of serum albumins to be used for protecting therapeutic proteins. In most studies, a large quantity of serum albumins—their aqueous concentrations range from 50 to 400 mg/mL—has been used to enhance the stability of therapeutic proteins and vaccines during the emulsion-based microencapsulation procedure.[1,7,26–28] The data in Figure 5 indicate that the denaturing effects of the W/MC interface upon RNase can almost be avoided at HSA concentrations as low as 0.5 mg/mL. One should caution that the use of an excess amount of HSA leads to the generation of more HSA oligomer, as evidenced in Table 2. Therefore, a minimal quantity of HSA should be used to rule out the possibility of an untoward immune response toward the new HSA oligomer.

Finally, the tensiometer data in Table 4 provide direct evidence on the adsorption of proteins at the W/MC interface. Dynamic changes in the interfacial tension as a function of the interface development time also indicate that adsorbed protein molecules undergo conformational rearrangements in a way to minimize the free energy of the system. During the initial development of the W/MC interface, RNase seems to diffuse more rapidly to the

interface than HSA does, as indicated by their respective diffusion coefficients (Table 1). This is the reason that a lower W/MC interfacial tension is seen with an aqueous RNase solution over relatively short interface development times. Once adsorbed in the interface, HSA displays a much faster rate of the interfacial tension decrease. These results indicate that HSA possesses quite a flexible conformation and undergoes a fast conformational rearrangement at the interface, whereas rigid RNase undergoes a slow conformational rearrangement process. As a result, with the aging of the interface, an aqueous HSA solution provides a lower W/MC interfacial tension than an aqueous RNase solution does. This conclusion is consistent with a previous assertion that RNase has a relatively greater conformational stability than HSA.[34] On the basis of the results of the recovery of these two proteins after emulsification (Figure 1), however, it can be suggested that the conformational flexibility and the W/MC interface-induced aggregation are not closely related. Further investigations need to be performed to unravel their different behaviors at the interface.

In summary, protein adsorption at the W/MC interface and its effect upon protein integrity have been corroborated to explain protein instabilization observed with emulsification. Competitive protein adsorption modes have been used to stabilize a protein of interest—RNase in this study—against the denaturing effects of the W/MC interface. Information reported in this study might aid in the successful development of protein delivery systems such as emulsions and PLGA microspheres.

References and Notes

1. Morlock, M.; Knoll, H.; Winter, G.; Kissel, T. Microencapsulation of rh-Erythropoietin Using Biodegradable Poly(D,L-lactide-*co*-glycolide): Protein Stability and the Effects of Stabilizingt Excipients. *Eur. J. Pharm.* Biopharm. **1997**, *43*, 29−36.
2. Raghuvanshi, R. S.; Goyal, S.; Singh, O.; Panda, A. K. Stabilization of Dichloromethane-Induced Protein Denaturation During Microencapsulation. *Pharm. Dev. Technol.* **1998**, *3*, 269−276.
3. Cleland, J. L.; Jones, A. J. S. Stable Formulations of Recombinant Human Growth Hormone and Interferon-γ for Microencapsulation in Biodegradable Microspheres. *Pharm. Res.* **1996**, *13*, 1464−1474.
4. Sah, H. Stabilization of Proteins Against Methylene Chloride/Water Interface-Induced Denaturation and Aggregation. *J. Controlled Release* **1999**, *58*, 143−151.
5. Gombotz, W. R.; Pettit, D. K. Biodegradable Polymers for Protein and Peptide Drug Delivery. *Bioconjugate Chem.* **1995**, *6*, 332−351.
6. Lu, W.; Park, T. G. Protein Release from Poly(lactic-*co*-glycolic acid) Microspheres: Protein Stability Problems. *PDA J. Pharm. Sci. Technol.* **1995**, *49*, 13−19.
7. Chen, L.; Apte, R. N.; Cohen, S. Characterization of PLGA Microspheres for the Controlled Delivery of IL-1α for Tumor Immunotherapy. *J. Controlled Release* **1997**, *43*, 261−272.
8. Putney, S. D.; Burke, P. A. Improving Protein Therapeutics with Sustained-Release Formulations. *Nature Biotechnol.* **1998**, *16*, 153−157.
9. Crotts, G.; Park, T. G. Stability and Release of Bovine Serum Albumin Encapsulated within Poly(D,L-lactide-*co*-glycolide) Microparticles. *J. Controlled Release* **1997**, *44*, 123−134.
10. Volkin, D. B.; Klibanov, A. M. Minimizing Protein Inactivation. In *Protein Function: A Practical Approach*; Creighton, T. E., Ed.; Oxford University Press: Oxford, 1985; pp 1-24.
11. Verrechia, T.; Huve, P.; Basile, D.; Veillard, M.; Spenlehauer, G.; Couvreur, P. Adsorption/Desorption of Human Serum Albumin at the Surface of Poly(lactic acid) Nanoparticles Prepared by a Solvent Evaporation Process. *J. Biomed. Mater. Res.* **1993**, *27*, 1019−1028.
12. Schwendeman, S. P.; Cardamone, M.; Klibanov, A.; Langer, R.; Brandon, M. R. Stability of Proteins and Their Delivery from Biodegradable Polymer Microspheres. In *Microparticulate Systems for the Delivery of Proteins and Vaccines*; Cohen, S., Bernstein, H., Eds.; Marcel Dekker: New York, 1996; pp 1-46.
13. Horbett, T. A. Adsorption of Proteins and Peptides at Interfaces. In *Stability of Protein Pharmaceuticals*; Ahern, T. J.,Manning, M. C., Eds.; Plenum Press: New York, 1992; Vol. 2, pp 195−214.
14. Scheraga, H. A.; Rupley, J. A. Structure and Function of Ribonuclease. In *Advances in Enzymology*; Nord, F. F., Ed.; Interscience Publishers/John Wiley & Sons: New York, 1962; pp 161−261.
15. Haynes, C.; Sliwinsky, E.; Norde, W. Structural and Electrostatic Properties of Globular Proteins at Polystyrene-Water Interface. *J. Colloid Interface Sci.* **1994**, *164*, 394−409.
16. Peters, T., Jr. Serum Albumin. *Adv. Protein Chem.* **1985**, *37*, 161−245.
17. Joos, P.; Rillaerts, E. Theory on the Determination of the Dynamic Surface Tension with the Drop Volume and Maximum Bubble Pressure Methods. *J. Colloid Interface Sci.* **1981**, *79*, 96−100.
18. Tornberg, E.; Lundh, G. A Study of the Surface Enlargement in the Drop Volume Method and Its Relation to Protein Adsorption at A/W and O/W Interfaces. *J. Colloid Interface Sci.* **1981**, *79*, 76−84.
19. Rulison, C. J.; Lochhead, R. J. Kinetic Study of the Adsorption of Nonionic and Anionic Surfactants and Hydrophobically Modified Water-Soluble Polymers to Oil−Water Interfaces. *Am. Chem. Soc. Symp. Ser.* **1995**, *615*, 280−313.
20. Walstra, P.; De Roos, A. L. Proteins at Air−Water and Oil−Water Interfaces: Static and Dynamic Aspects. *Food Rev. Int.* **1993**, *9*, 503−525.
21. Griebenow, K.; Klibanov, A. M. Protein Denaturation on Aqueous-Organic Mixtures but Not in Pure Organic Solvents. *J. Am. Chem. Soc.* **1996**, *118*, 11695−11700.
22. Dunca, J. D.; Wang, P. X.; Harrington, C.; Schafer, D. P.; Matsuoka, Y.; Mestecky, J. F.; Compans, R. W.; Novak, M. J. Comparative Analysis of Oral Delivery Systems for Live Rotavirus Vaccines. *J. Controlled Release* **1996**, *41*, 237−247.
23. Ghaderi, R.; Carlfors, J. Biological Activity of Lysozyme After Entrapment in Poly(d, l-lactide-*co*-glycolide) Microspheres. *Pharm. Res.* **1997**, *14*, 1556−1562.
24. Magdassi, S.; Garti, N. Surface Activity of Proteins. In *Interfacial Phenomena in Biological Systems*; Bender, M., Ed.; Marcel Dekker: New York, 1991; pp 289−299.
25. Speed, M. A.; King, J.; Wang, D. I. C. Polymerization Mechanism of Polypeptide Chain Aggregation. *Biotech. Bioeng.* **1997**, *54*, 333−343.
26. Chang, A. C.; Gupta, R. K. Stabilization of Tetanus Toxoid in Poly(DL-lactic-*co*-glycolic acid) Microspheres for the Controlled Release of Antigen. *J. Pharm. Sci.* **1996**, *85*, 129−132.
27. Johansen, P.; Men, Y.; Audran, R.; Corradin, G.; Merkle, H. P.; Gander, B. Improving Stability and Release Kinetics of Microencapsulated Tetanus Toxoid by Co-Encapsulation of Additives. *Pharm. Res.* **1998**, *15*, 1103−1110.
28. Audran, R.; Men, Y.; Johansen, P.; Gander, B.; Corradin, G. Enhanced Immunogenicity of Microencapsulated Tetanus Toxoid with Stabilizing Agents. *Pharm. Res.* **1998**, *15*, 1111−1116.
29. Sevastianov, V. I.; Tremsina, Y. S.; Eberhart, R. C.; Kim, S. W. Effect of Protein Competition on Surface Adsorption-Density Parameters of Polymer-Protein Interfaces. *Am. Chem. Soc. Symp. Ser.* **1995**, *602*, 195−208.
30. Vroman, L.; Adams, A. L. Adsorption of Proteins out of Plasma and Solutions in Narrow Spaces. *J. Colloid Interface Sci.* **1986**, *111*, 391−402.
31. Brash, J. L. The Fate of Fibrinogen Following Adsorption at the Blood-Biomaterial Interface. *Ann. N.Y. Acad. Sci.* **1987**, *516*, 206−222.
32. Vroman, L.; Adams, A. L.; Fischer, G. C.; Munoz, P. Interaction of High Molecular Weight Kininogen, Factor XII and Fibrinogen in Plasma at Interfaces. *Blood* **1980**, *55*, 156−159.
33. Wojciechowski, P.; Ten Hove, P.; Brash, J. L. Phenomenology and Mechanism of the Transient Adsorption of Fibrinogen from Plasma (Vroman Effect). *J. Colloid Interface Sci.* **1986**, *111*, 455−465.
34. Norde, W.; Lyklema, J. The Adsorption of Human Plasma Albumin and Bovine Pancreas Ribonuclease at Negatively Charged Polystyrene Surfaces. *J. Colloid Interface Sci.* **1978**, *66*, 257−265.

Acknowledgments

The author thanks Dr. Jie Zheng at St. Jude Children's Research Hospital for his kind help in using the DynaPro 801-TC analyzer.

JS9900654

Skin Penetration of Nonsteroidal Antiinflammatory Drugs out of a Lipophilic Vehicle: Influence of the Viable Epidermis

BERNHARD P. WENKERS AND BERNHARD C. LIPPOLD*

Contribution from *Institut für Pharmazeutische Technologie, Heinrich-Heine-Universität, Universitätsstrasse 1, 40225 Düsseldorf, Germany.*

Received January 30, 1999. Accepted for publication September 20, 1999.

Abstract □ The skin penetration of 10 nonsteroidal antiinflammatory drugs (NSAIDs) was investigated after application in the lipophilic vehicle light mineral oil. The skin permeabilities and maximum fluxes, which were calculated from the concentration decreases of the applied solutions in the steady state phases, were correlated with physicochemical parameters, mainly the vehicle solubilities and the partition coefficients of the model drugs according to the Fickian diffusion laws. The objective of the study was to characterize the barrier function of the stratum corneum and the viable epidermis and to predict their influences on the skin permeabilities and the maximum fluxes of the NSAIDs by model equations. The permeability of the human skin for NSAIDs applied in a lipophilic vehicle is a function of their hydrophilicity, while the maximum flux is primarily dependent on their vehicle solubilities. The viable epidermis was found to represent the decisive resistance to the drug transport.

Introduction

The percutaneous treatment of rheumatic diseases with nonsteroidal antiinflammatory drugs (NSAIDs) causes less side effects than the peroral application. It has been controversially discussed whether NSAIDs applied to the skin will directly penetrate into tissues and joints deeper than 1 cm.[1−4] Based on this background, the question shall be investigated of whether skin penetration of the NSAIDs as model drugs out of the lipophilic vehicle light mineral oil can be described by the same physicochemical parameters according to the Fickian diffusion laws as out of a hydrophilic vehicle. The stratum corneum is considered as the main barrier for the percutaneous drug transport.[5−7] Thus, for the prediction of skin permeability, the partition coefficient between the stratum corneum and the vehicle $PC_{SC/V}$ is of particular importance. It is often related to the in vitro partition coefficient between octanol and the vehicle $PC_{Oct/V}$.[8−10] Consequently, drugs of similar size and high lipophilicity show high permeabilities out of aqueous solutions, as it has been repeatedly shown in the literature.[8−12] In contrast, the permeabilities of lipophilic drugs out of lipophilic vehicles should be low,[11,12] which was demonstrated for the first time by Blank.[13] The additional resistance of the viable epidermis has not yet been investigated. In this case, it must be considered that the permeant has to partition not only out of the vehicle into the stratum corneum but subsequently from the stratum corneum into the barrier of the viable epidermis, not behaving like a sink. Accordingly, the partition coefficient between the stratum corneum and the viable epidermis $PC_{SC/E}$ or the partition coefficient between the viable epidermis and the vehicle $PC_{E/V}$ must be taken into account.[14]

For the prediction of the maximum flux of a drug, its solubility in the rate-limiting barrier(s) is decisive, being independent of the applied vehicle.[6,15] Because the solubility in the barrier(s) is unknown, the maximum flux of the drug is expressed as the product of its barrier permeability and its vehicle solubility and thus can be correlated with physicochemical parameters.[6,11,12,14,15]

Theory

Permeability—The permeability of a membrane for a diffusing substance is defined by its resistance. To characterize the influences of the resistances of the stratum corneum SC and the viable epidermis E, respectively, on the drug transport out of a lipophilic vehicle V in the steady state or the pseudo-steady-state,[15] respectively, three model equations can be derived.[14,16]

Model 1—The stratum corneum alone is decisive

$$R_{skin} = \frac{1}{P_{skin}} = \frac{d_{SC}}{D_{SC} PC_{SC/V}} \leftrightarrow P_{skin} = \frac{D_{SC} PC_{SC/V}}{d_{SC}} \leftrightarrow \lg P_{skin} = \lg\left(\frac{D_{SC}}{d_{SC}}\right) + \lg PC_{SC/V} \quad (1)$$

where R_{skin} is the skin resistance, P_{skin} is the skin permeability, d_{SC} is the thickness of the stratum corneum, D_{SC} is the diffusion coefficient in the stratum corneum, and $PC_{SC/V}$ is the partition coefficient between the stratum corneum and the vehicle.

Model 2—The viable epidermis alone is decisive

$$R_{skin} = \frac{1}{P_{skin}} = \frac{d_E}{D_E PC_{E/V}} \leftrightarrow P_{skin} = \frac{D_E PC_{E/V}}{d_E} \leftrightarrow \lg P_{skin} = \lg\left(\frac{D_E}{d_E}\right) + \lg PC_{E/V} \quad (2)$$

where d_E is the thickness of the rate-limiting layer in the viable epidermis, D_E is the diffusion coefficient in the viable epidermis, and $PC_{E/V}$ is the partition coefficient between the viable epidermis and the vehicle.

Model 3—Both the stratum corneum and the viable epidermis contribute to the skin resistance

* Corresponding author. Tel: ++49/211/81-14220. Fax: ++49/211/81-14251. E-mail: lippold@uni-duesseldorf.de.

10.1021/js990032o CCC: $18.00 *Published on Web 10/26/1999*

$$R_{skin} = \frac{1}{P_{skin}} = \frac{d_{SC}}{D_{SC} PC_{SC/V}} + \frac{d_E}{D_E PC_{E/V}} \Leftrightarrow$$

$$P_{skin} = \frac{D_{SC} D_E PC_{SC/V}}{d_{SC} D_E + d_E D_{SC} PC_{SC/E}} \quad (3)$$

$$\Leftrightarrow \lg P_{skin} = \lg(D_{SC} D_E) + \lg PC_{SC/V} - \lg(d_{SC} D_E + d_E D_{SC} PC_{SC/E}) \quad (4)$$

where $PC_{SC/E}$ is the partition coefficient between the stratum corneum and the viable epidermis, equal to $PC_{SC/V}/PC_{E/V}$.

The in vivo partition coefficients $PC_{SC/V}$, $PC_{E/V}$, and $PC_{SC/E}$ can be approached in vitro by partition coefficients with octanol (for the stratum corneum) and phosphate buffer (pH 7.4) (for the viable epidermis), respectively, in a linear regression equation according to Collander[17] (eqs 5−7)

$$\lg PC_{SC/V} = a \lg PC_{Oct/MO} + b \quad (5)$$

$$\lg PC_{E/V} = a' \lg PC_{PBS/MO} + b' \quad (6)$$

$$\lg PC_{SC/E} = a'' \lg PC_{Oct/PBS} + b'' \quad (7)$$

where $PC_{Oct/MO}$ is the partition coefficient between octanol and the vehicle light mineral oil, (for its determination see the Experimental Section), $PC_{PBS/MO}$ is the partition coefficient between phosphate buffer (pH 7.4) and light mineral oil, $PC_{Oct/PBS}$ is the partition coefficient between octanol and phosphate buffer (pH 7.4), a, a', a'' are regression coefficients according to Collander, and b, b', b'' are intercepts according to Collander.

From the substitution of the in vivo partition coefficients in the model eqs 1, 2, and 4 by the Collander terms in eqs 5−7, eqs 8−10 result.

$$\text{model 1: } \lg P_{skin} = \lg\left(\frac{D_{SC}}{d_{SC}}\right) + a \lg PC_{Oct/MO} + b \quad (8)$$

$$\text{model 2: } \lg P_{skin} = \lg\left(\frac{D_E}{d_E}\right) + a' \lg PC_{PBS/MO} + b' \quad (9)$$

$$\text{model 3: } \lg P_{skin} = \lg(D_{SC} D_E) + a \lg PC_{OCT/MO} + b - \lg(d_{SC} D_E + d_E D_{SC} PC_{Oct/PBS}{}^{a''} 10^{b''}) \quad (10)$$

Correlations of the experimentally determined skin permeabilities with the partition coefficients of eqs 8−10 give information about the importance of the resistances of the stratum corneum and the viable epidermis, respectively, for the transport of the NSAIDs through the skin. The diffusion coefficients of the NSAIDs in eqs 8−10, which are mainly dependent on the molecular size, represented by the molecular volume, are assumed to be equal. On the basis of the theory of the required volume for free diffusion, Cohen and Turnbull[18] derived an exponential relationship between the diffusion coefficient D and the molecular volume MV (eq 11)

$$D = D^0 e^{-\beta MV} \quad (11)$$

where D is the diffusion coefficient, D^0 is the diffusion coefficient of a hypothetical molecule with a molecular volume 0, β is the regression coefficient of the molecular volume, and MV is the molecular volume.

With the help of eq 11 the model equations for the models 1 and 2 (eqs 8 and 9) can be rewritten as eqs 12 and 13

$$\text{model 1: } \lg P_{skin} = \lg\left(\frac{D^0_{SC}}{d_{SC}}\right) - \frac{\beta_{SC}}{2.303} MV + a \lg PC_{Oct/MO} + b \quad (12)$$

$$\text{model 2: } \lg P_{skin} = \lg\left(\frac{D^0_E}{d_E}\right) - \frac{\beta_E}{2.303} MV + a' \lg PC_{PBS/MO} + b' \quad (13)$$

where β_{SC} and β_E are regression coefficients of the molecular volumes concerning the stratum corneum and the viable epidermis, respectively.

The contributions of the molecular volumes in eqs 12 and 13 can be determined by a multiple linear regression analysis.

Maximum Flux—The maximum flux J_{max} results from the multiplication of the skin permeability with the vehicle solubility (eq 14)

$$J_{max} = P_{skin} c_{sMO} \quad (14)$$

where J_{max} is the maximum flux, and c_{sMO} is the solubility in the vehicle light mineral oil.

After finding the logarithms for eq 14, $\lg J_{max}$ is the sum of the skin permeability term and the vehicle solubility term, which can again be evaluated by a multiple linear regression analysis with $\lg P_{skin}$ being expressed by the model eqs 8−10.

$$\lg J_{max} = \lg P_{skin} + \lg c_{sMO} \quad (15)$$

Experimental Section

Materials—The following NSAIDs were used: aspirin (Merck, Darmstadt, Germany), diclofenac free acid (Novartis, Basel, Switzerland), diflunisal (MSD, Rahway, NJ), flufenamic acid, ibuprofen (Sankyo, Pfaffenhofen, Germany), ketoprofen (Bayer, Leverkusen and Rhône Poulenc Rorer, Cologne, Germany), naproxen (PharmActiv, Feldkirchen-Westerham, Germany), nabumeton (SmithKline Beecham, Worthing, Great Britain), piroxicam (Pfizer, Karlsruhe, Germany), tenoxicam (Hoffmann-La Roche, Basel, Switzerland). Light mineral oil was a gift of Parafluid Mineralölgesellschaft, Hamburg, Germany.

Solubilities—For the determination of the solubilities of the NSAIDs in the vehicle light mineral oil an excess amount of substance was suspended in 25 mL of light mineral oil, and the suspension was moved in a water bath of 32 °C in rotating bottles (30 min^{-1}) for 24 h. The suspension was filtered through warmed cellulose acetate filters with 0.45 μm pore diameter (Sartorius, Göttingen, Germany) in a warmed flask. After the appropriate dilution, the concentrations of the saturated solutions were measured spectrophotometrically (DMR 10, Carl Zeiss, Oberkochen, Germany). The solubilities were calculated as the mean of three determinations with a standard deviation less than 10%.

Partition Coefficients—The partition coefficients between octanol (Oct) and the aqueous phase (W*) $PC_{Oct/W*}$, between light mineral oil (*MO*) and the aqueous phase W* $PC_{MO/W*}$, and between octanol and phosphate buffer (pH 7.4) $PC_{Oct/PBS}$ were determined after shaking at 32 °C and spectrophotometric measurement of the separated, clearly centrifuged phases (Varifuge, Heraeus, Osterode, Germany). W* stands for the aqueous phase containing the NSAIDs in the undissociated form, i.e., 0.1 M hydrochloric acid and citrate buffer (pH 3.6 for piroxicam and 3.2 for tenoxicam), ionic strength 0.1, containing citric acid and sodium hydroxide, respectively. *PBS* stands for phosphate buffer (pH 7.4), ionic strength 0.17, containing monobasic potassium phosphate and dibasic sodium phosphate. The experiments were performed as triplicate, and the standard deviations were generally less than 10%. The partition coefficients between octanol and the vehicle light mineral oil $PC_{Oct/MO}$ were calculated by dividing $PC_{Oct/W*}$ by $PC_{MO/W*}$.[19] The partition coefficients between phosphate buffer (pH 7.4) and light mineral oil $PC_{PBS/MO}$ were obtained from the quotients of $PC_{Oct/MO}$ and $PC_{Oct/PBS}$. The $PC_{Oct/W*}$ could be confirmed by R_{MW}-values obtained with TLC[4,20,21] and by calculation with

Table 1. —Molecular Volumes MV, Vehicle Solubilities c_{sMO}, Skin Permeabilities P_{skin} with Geometrical Standard Deviations s_g, and Maximum Fluxes J_{max} with s_g of the Investigated NSAIDs

NSAIDs	MV ($cm^3 \cdot mol^{-1}$)	c_{sMO} (mg·100 mL^{-1})	P_{skin} ($cm \cdot h^{-1}$)	s_g	J_{max} ($\mu g \cdot cm^{-2} \cdot h^{-1}$)	s_g
diclofenac	210.5	2.83	0.0135	+0.0075 –0.0048	0.38	+0.27 –0.16
flufenamic acid	196.4	95.1	0.0041	+0.0028 –0.0017	3.94	+2.68 –1.59
ibuprofen	184.1	2522.6	0.0046	+0.0028 –0.0018	116.65	+80.54 –47.64
ketoprofen	203.1	12.8	0.0164	+0.0181 –0.0086	2.10	+2.40
naproxen	181.4	7.87	0.0297	+0.0297 –0.0146	2.34	+2.64 –1.24
nabumeton	189.5	351.2	0.0051	+0.0020 –0.0014	17.81	+8.35 –5.68
piroxicam	243.9	5.98	0.0221	+0.0088 –0.0063	1.32	+0.55 –0.39
tenoxicam	236.3	0.60	0.0720	+0.0343 –0.0232	0.43	+0.24
aspirin	117.5	3.12	0.1093	+0.0640 –0.0404	3.41	+2.13 –1.31
diflunisal	174.2	1.69	0.0532	+0.0361 –0.0213	0.88	+0.66 –0.38

the fragmental constant system according to Rekker and Mannhold.[4,22,23] All partition coefficients mentioned above could be described by the corresponding solubility ratios[24,25] with a good correlation.[4]

Molecular Volumes—The molecular volumes of the NSAIDs were calculated from the incremental van der Waals volumes according to Bondi.[26,27]

In Vivo Studies—Twenty-four healthy volunteers, their ages ranging from 20 to 40, took part in the study, which was approved by the ethics committee of the University of Düsseldorf. Every volunteer gave written consent after detailed information. The skin penetration of the NSAIDs was investigated according to the statistical plan of a 4 × 4 × 2 Latin rectangle in three series with eight volunteers and diclofenac as reference drug in every series. Every volunteer could take four substances on his upper arms whose positions were varied systematically. Special glass chambers for the reception of the test solutions were fixed on every volunteer's upper arms with wire frames and elastic bandages, preventing leakage.[9,28] After conditioning with the vehicle light mineral oil for 2 h (renewed hourly) to elute most of the extractable material, the drug solutions with concentrations[4] between 0.45 and 126 mg·100 mL^{-1} were filled in the glass chambers over a time period of 7 or 8 h and exchanged by the original solutions every 1 to 2 h, respectively. The concentration depletion in the glass chambers varies between 2 and 33% per hour in the steady state, depending on the respective drug.[4] The solutions of the NSAIDs taken out of the glass chambers were diluted and their concentration decreases measured spectrophotometrically. The skin permeabilities were calculated as geometrical means from the last three or four data points of the steady-state phases,[9,28] which became apparent after 3 or 4 h, respectively (Figure 1).[4] Changes of the chamber volumes and UV-active material extracted from the skin were taken into account by correction factors.[4,28] The maximum fluxes were calculated from eq 14.

Statistical Calculations—A linear regression analysis was performed for the models 1 and 2 using Excel 8.0 (Microsoft Corporation, Redmond, WA) and PlotIt 3.0 (Scientific Programming Enterprises, Haslet, MI). The nonlinear regression analysis for model 3 and the multiple linear regression analyses of eqs 12, 13, and 15 were calculated with the statistical program SPSS 6.1.3 (SPSS, Inc., Chicago, IL).

Results

The molecular volumes MV, vehicle solubilities c_{sMO}, skin permeabilities P_{skin}, and maximum fluxes J_{max} of the investigated NSAIDs are shown in Table 1. The geometrical standard deviations s_g are also listed for the skin penetration data. Most of them amount up to ±60%, as already documented by Southwell et al.,[29] and partially exceed this range (ketoprofen, naproxen). The skin permeabilities were found to be log-normally distributed.[4,30–32] The logarithms of the skin permeabilities, maximum fluxes, $PC_{Oct/MO}$, $PC_{PBS/MO}$, $PC_{Oct/W*}$, and $PC_{Oct/PBS}$, all necessary for the correlations according to eqs 8–10, are arranged in Table 2.

Table 2. —Logarithms of the Partition Coefficients between Octanol and the Vehicle Light Mineral Oil $PC_{Oct/MO}$, between Phosphate Buffer (pH 7.4) and Light Mineral Oil $PC_{PBS/MO}$, between Octanol and Phosphate Buffer (pH 7.4) $PC_{Oct/PBS}$ and between Octanol and Water with the Drug in Its Undissociated Form $PC_{Oct/W*}$, Skin Permeabilities P_{skin} (in $cm \cdot h^{-1}$), and Maximum Fluxes J_{max} (in $\mu g \cdot cm^{-2} \cdot h^{-1}$) of the Investigated NSAIDs

NSAID	lg $PC_{Oct/MO}$	lg $PC_{PBS/MO}$	lg $PC_{Oct/PBS}$	lg $PC_{Oct/W*}$	lg P_{skin}	lg J_{max}
diclofenac	2.91	0.93	1.98	4.32	–1.87	–0.42
flufenamic acid	1.93	–0.22	2.15	4.67	–2.38	0.60
ibuprofen	1.15	–0.07	1.22	4.21	–2.34	2.07
ketoprofen	3.54	3.57	–0.03	3.35	–1.79	0.32
naproxen	2.84	2.49	0.35	3.22	–1.53	0.37
nabumeton	0.57	–2.31	2.88	3.29	–2.30	1.25
piroxicam	1.49	1.69	–0.20	1.69	–1.66	0.12
tenoxicam	1.67	2.51	–0.84	0.78	–1.14	–0.36
aspirin	3.96	5.94	–2.04	1.26	–0.96	0.53
diflunisal	3.36	2.78	0.58	4.24	–1.28	–0.05

Permeabilities—The results of the correlations according to the models 1–3 (eqs 8–10) are presented in eqs 16–18 and graphically shown in Figures 2–4:

model 1 (Figure 2, eq 8):

$$\lg P_{skin} = 0.28 \lg PC_{Oct/MO} - 2.37 \quad (16)$$
$$r = 0.615,\ s = 0.42,\ p_{slope} = 0.058,\ n = 10$$

model 2 (Figure 3, eq 9):

$$\lg P_{skin} = 0.19 \lg PC_{PBS/MO} - 2.05 \quad (17)$$
$$r = 0.856,\ s = 0.28,\ p_{slope} = 0.0016,\ n = 10$$

model 3 (Figure 4, eq 10):

$$\lg P_{skin} = 4.50 + 0.10 \lg PC_{Oct/MO} - \lg(5.40 \times 10^{-7} + 2.03 \times 10^{-3}(PC_{Oct/PBS})^{0.25}) \quad (18)$$
$$r = 0.876,\ s = 0.26,\ n = 10$$

(assumptions:

$$D_{SC} = 10^{-10}\ cm^2 \cdot s^{-1} \text{ and } D_E = 10^{-7}\ cm^2 \cdot s^{-1})^{4,9}$$

The insignificant influence of the molecular volumes on the diffusion coefficients is described by the results of the multiple linear regression analyses according to eqs 12 and 13, which are presented in eqs 19 and 20.

model 1 (eq 12):

$$\lg P_{skin} = -2.72 - 0.00154MV + 0.30 \lg PC_{Oct/MO} \quad (19)$$
$$r = 0.622,\ s = 0.45,\ n = 10$$

model 2 (eq 13):

$$\lg P_{skin} = -2.41 - 0.00177MV + 0.20 \lg PC_{PBS/MO} \quad (20)$$
$$r = 0.863,\ s = 0.29,\ n = 10$$

The contributions of the different molecular volumes (Table 1) to the skin permeabilities and the improvement of the correlation coefficients compared with eqs 16 and 17 are not statistically significant ($F = 0.0989$ and $F =$

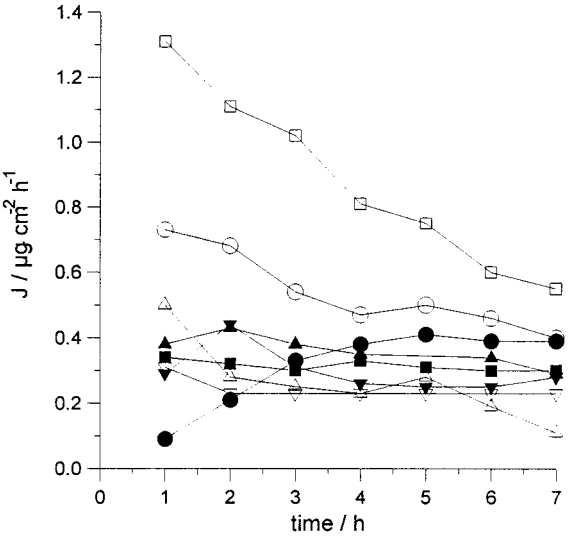

Figure 1—Penetration profiles of tenoxicam, vehicle light mineral oil, c = 0.45 mg·100 mL^{-1}, n = 8 volunteers.

0.330).[33] Thus, the diffusion coefficients of the investigated NSAIDs can be considered as constant.

Maximum Fluxes—According to eqs 15 and 16−18, the regression eqs 21−23 result for the maximum fluxes J_{max} (Table 2). In the equations of model 1 and 2 (eqs 21 and 22) the logarithms of the skin permeabilities have been substituted by eqs 16 and 17, respectively.

model 1 (eq 16, eq 15):

$$\lg J_{max} = 0.08 \lg PC_{Oct/MO} + 0.67 \lg c_{sMO} - 1.18 \quad (21)$$
$$r = 0.939,\ s = 0.29,\ n = 10$$

model 2 (eq 17, eq 15):

$$\lg J_{max} = 0.11 \lg PC_{PBS/MO} + 0.78 \lg c_{sMO} - 1.44 \quad (22)$$
$$r = 0.970,\ s = 0.21,\ n = 10$$

model 3 (eq 18, eq 15):

$$\lg J_{max} = 0.64 \lg P_{skin\ calcd} + 0.78 \lg c_{sMO} - 0.15 \quad (23)$$
$$r = 0.978,\ s = 0.18,\ n = 10$$

The regression coefficients of the vehicle solubilities c_{sMO} in all three models contribute most significantly ($p \ll 0.001$) to the regressions, while the significance of the regression coefficients of the partition coefficients and the calculated skin permeabilities $P_{skin\ calcd}$, respectively, increases from an insignificant ($p = 0.4849$, model 1) to a significant ($p = 0.0270$, model 2) and finally to a highly significant level ($p = 0.0085$, model 3).

Discussion

Permeabilities—As expected, the experimentally determined permeabilities P_{skin} generally decrease with increasing lipophilicity of the NSAIDs expressed as $PC_{Oct/W*}$ (Table 2). For example, aspirin and tenoxicam, the two drugs with the highest permeabilities (Table 1), show the lowest $PC_{Oct/W*}$ (Table 2). Vice versa, flufenamic acid and ibuprofen, the two drugs with the lowest permeabilities (Table 1), exhibit rather high $PC_{Oct/W*}$ values. However, assuming the stratum corneum as the decisive barrier, the respective regression equation relating the permeabilities to $PC_{Oct/MO}$ according to model 1 (Figure 2, eq 16) leads to an unsatisfactory correlation ($r = 0.615$). In contrast, Hagedorn-Leweke and Lippold[9] found a good correlation ($r = 0.949$) for the skin permeabilities of sunscreens and

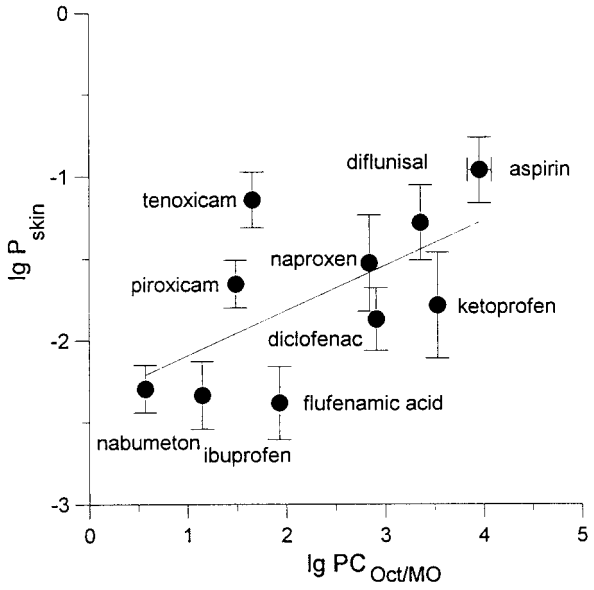

Figure 2—Correlation of the skin permeabilities P_{skin} (in cm·h^{-1}) with the partition coefficients between octanol and the vehicle light mineral oil $PC_{Oct/MO}$ according to model 1 (eq 16).

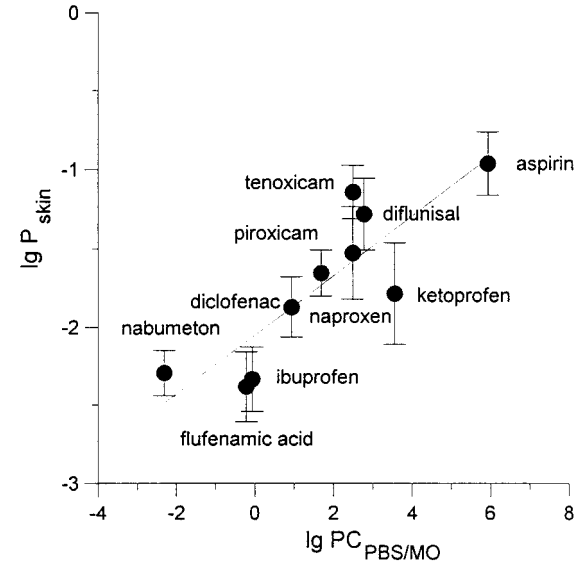

Figure 3—Correlation of the skin permeabilities P_{skin} (in cm·h^{-1}) with the partition coefficients between phosphate buffer (pH 7.4) and the vehicle light mineral oil $PC_{PBS/MO}$ according to model 2 (eq 17).

other compounds out of a propylene glycol−water mixture 30:70 (v/v) with the same study design using the partition coefficients between octanol and the hydrophilic vehicle $PC_{Oct/V}$ for the calculations in analogy to model 1 (eq 1). When using the lipophilic vehicle light mineral oil, the stratum corneum does not seem to represent the decisive resistance to the skin penetration of the NSAIDs. Considering the viable epidermis as the rate-limiting barrier to the drug transport (model 2), the correlation of the skin permeabilities with the respective partition coefficient between phosphate buffer (pH 7.4) and the vehicle light mineral oil $PC_{PBS/MO}$ clearly improves ($r = 0.856$, eq 17, Figure 3). A nonlinear regression analysis with $PC_{Oct/MO}$ and $PC_{Oct/PBS}$ (model 3) also leads to a very good correlation concerning the permeability data ($r = 0.876$, eq 18, Figure 4). The proportion between the resistances of the stratum corneum and the viable epidermis can be calculated from eqs 3 (overall resistance R_{skin} of stratum corneum and viable epidermis), 17 (estimate of the permeability of the

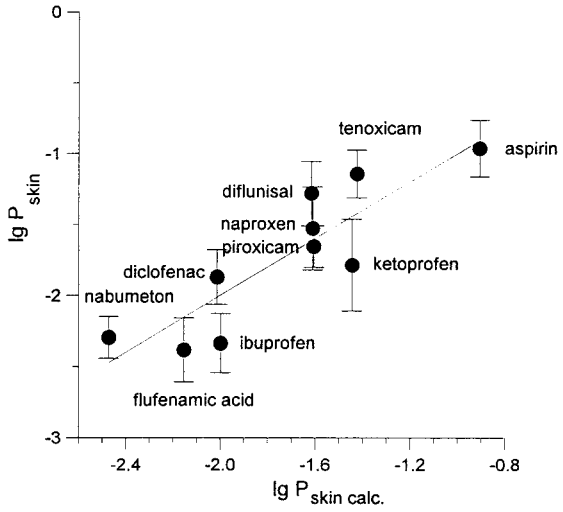

Figure 4—Correlation of the skin permeabilities P_{skin} (in cm·h^{-1}) with the skin permeabilities calculated from eq 18 $P_{skin\ calcd}$ (in cm·h^{-1}) according to model 3.

viable epidermis alone, equal to the reciprocal of its resistance), and 18 (overall permeability P_{skin} of stratum corneum and viable epidermis) and amounts to about 1:5. Thus, the viable epidermis seems to be the decisive barrier to the skin penetration of the NSAIDs out of the lipophilic vehicle light mineral oil.

Altogether, the skin permeabilities of the NSAIDs out of light mineral oil are determined by their hydrophilicity, which is under the assumption of the viable epidermis as the main barrier a function of the $PC_{PBS/MO}$. However, when using a hydrophilic vehicle, the permeabilities will primarily depend on the lipophilicity of the penetrating substances according to model 1.[8,9] This is in accordance with the observations documented by Blank[11−13] that the skin permeabilities of homologous alkanols decrease with their chain length out of lipophilic vehicles (isopropyl palmitate, mineral oil, olive oil) but increase out of hydrophilic vehicles (buffer solution, poly(ethylene glycol) 600).

Maximum Fluxes—The correlation coefficients of the maximum fluxes in eqs 21−23 are higher than those of the skin permeabilities in eqs 16−18, but they do not differentiate as clearly as those of the skin permeabilities between the three assumed models. Obviously, the maximum fluxes are more influenced by the vehicle solubilities c_{sMO}, which enclose about 4 orders of magnitude (Table 1), than by the partition coefficients. The regression coefficients of the vehicle solubilities in eqs 21−23 are highest significant, while the regression coefficients of the partition coefficients and the respective calculated skin permeabilities increase from insignificant to significant and finally to highly significant. Additionally, the latter are numerically lower than the regression coefficients of the vehicle solubilities. Thus, the maximum fluxes of the NSAIDs out of the lipophilic light mineral oil are primarily dependent on the vehicle solubilities. The increase of the significance levels of the regression coefficients of the skin permeabilities calculated from eqs 16−18 additionally confirms the importance of the viable epidermis as a barrier for the drug transport. Hagedorn-Leweke and Lippold[9] also found the decisive influence of the solubility of their investigated sunscreens in the hydrophilic vehicle on the measured maximum fluxes. Therefore, for the investigated cases, it can be concluded that the maximum flux is primarily dependent on the vehicle solubility and after that a function of the hydrophilicity or lipophilicity, expressed as octanol−vehicle partition coefficient, of the penetrating substances. For the development of cutaneous preparations, drugs with high vehicle solubilities can be recommended. In the case of a lipophilic vehicle, they should have a high partition coefficient between octanol and the vehicle and not a too high partition coefficient between octanol and phosphate buffer (pH 7.4) according to model 3.

The apparent diffusion distance of the NSAIDs out of the vehicle light mineral oil in the viable epidermis and dermis, that is, the thickness of the respective barrier d_E (eq 10) can be calculated from eq 18 (model 3) to about 2.6 mm. Obviously, real sink conditions in the skin can only be achieved beyond this distance. Singh and Roberts[1] found a direct penetration depth of about 3−4 mm from dermopharmacokinetic measurements with NSAIDs in vivo in rats. Therefore, a direct penetration of NSAIDs into deeper tissues and joints at high concentrations, as intended with the percutaneous treatment of relevant rheumatic diseases (see Introduction), does not seem to be realistic.

Conclusions

The viable epidermis, not the stratum corneum, is the rate-limiting barrier for the transport of NSAIDs out of a lipophilic vehicle. The skin permeability of NSAIDs is a function of the hydrophilicity of the drugs, i.e., of their partition coefficients between phosphate buffer (pH 7.4) and the lipophilic vehicle. However, the maximum flux of NSAIDs is primarily dependent on their vehicle solubility. For the development of cutaneous preparations, drugs with high vehicle solubilities and skin permeabilities as high as possible should be preferred.

Abbreviations

a, a', a''	regression coefficients according to Collander
b, b′, b″	intercepts according to Collander
β	regression coefficient of the molecular volume (eqs 11−13)
c_{sMO}	solubility in the vehicle light mineral oil
D	diffusion coefficient
d	thickness of the layer
E	living epidermis
F	statistical F-value
J_{max}	maximum flux
MO	light mineral oil
MV	molecular volume
n	number of experiments
NSAID	nonsteroidal antiinflammatory drug
Oct	octanol
p	statistical error probability
P_{skin}	skin permeability
$P_{skin\ calcd}$	skin permeability calculated from eq 18
PBS	phosphate buffer (pH 7.4)
$PC_{E/V}$	partition coefficient between the viable epidermis and the vehicle
$PC_{MO/W*}$	partition coefficient between the vehicle light mineral oil and the aqueous phase W*
$PC_{Oct/MO}$	partition coefficient between octanol and the vehicle light mineral oil
$PC_{Oct/PBS}$	partition coefficient between octanol and phosphate buffer (pH 7.4)
$PC_{Oct/V}$	partition coefficient between octanol and the vehicle
$PC_{Oct/W*}$	partition coefficient between octanol and the aqueous phase W*

$PC_{PBS/MO}$	partition coefficient between phosphate buffer (pH 7.4) and the vehicle light mineral oil
$PC_{SC/V}$	partition coefficient between the stratum corneum and the vehicle
r	correlation coefficient
R_{skin}	skin resistance
s	standard deviation
s_g	geometrical standard deviation
SC	stratum corneum
TLC	thin layer chromatography
V	vehicle
W*	aqueous phase containing the model drugs in the undissociated form

References and Notes

1. Singh, P.; Roberts, M. S. Skin Permeability and Local Tissue Concentrations of Nonsteroidal Antiinflammatory Drugs after Topical Application. *J. Pharmacol. Exp. Ther.* **1994**, *268*, 144−151.
2. Lippold, B. C. Lokal − und Regionaltherapie: Vorteile, neue Entwicklungen, Beispiele (Erster Teil). *Pharm. Unserer Zeit* **1997**, *26*, 187−191.
3. Lippold, B. C. Lokal − und Regionaltherapie: Vorteile, neue Entwicklungen, Beispiele (Zweiter Teil). *Pharm. Unserer Zeit* **1997**, *26*, 232−237.
4. Wenkers, B. P. Penetration von nichtsteroidalen Antirheumatika aus einem lipophilen Vehikel durch die menschliche Haut in vivo. Thesis, Heinrich-Heine-Universität Düsseldorf, 1998.
5. Barry, B. W. *Dermatological Formulations*; Marcel Dekker: New York, 1983; pp 14−21.
6. Lippold, B. C. *Biopharmazie*; Wissenschaftliche Verlagsgesellschaft mbH: Stuttgart, 1984; pp 99−131.
7. Flynn, G. L. Cutaneous and Transdermal Delivery: Processes and Systems of Delivery. In *Modern Pharmaceutics*; Banker, G. S., Rhodes, C. T., Eds.; Marcel Dekker: New York, 1996; pp 239−298.
8. Potts, R. O.; Guy, R. H. Predicting Skin Permeability. *Pharm. Res.* **1992**, *9*, 663−669.
9. Hagedorn-Leweke, U.; Lippold, B. C. Absorption of Sunscreens and Other Compounds through Human Skin In Vivo: Derivation of a Method to Predict Maximum Fluxes. *Pharm. Res.* **1995**, *12*, 1354−1360.
10. Anderson, B. D.; Raykar, P. V. Solute Structure − Permeability Relationships in Human Stratum Corneum. *J. Invest. Dermatol.* **1989**, *93*, 280−286.
11. Roberts, M. S.; Walters, K. A. The Relationship between Structure and Barrier Function of Skin. In *Dermal Absorption and Toxicity Assessment*; Roberts, M. S., Walters, K. A., Eds.; Marcel Dekker: New York, 1998; pp 1−42.
12. Roberts, M. S. Structure − permeability Considerations in Percutaneous Absorption. In *Prediction of Percutaneous Penetration*; Scott, R. C., Guy, R. H., Hadgraft, J., Boddé, H. E., Eds.; IBC Technical Services: London, 1991; pp 210−228.
13. Blank, I. H. Penetration of Low-Molecular-Weight Alcohols into Skin. *J. Invest. Dermatol.* **1964**, *43*, 415−420.
14. Flynn, G. L.; Yalkowsky, S. H.; Roseman, T. J. Mass Transport Phenomena and Models: Theoretical Concepts. *J. Pharm. Sci.* **1974**, *63*, 479−509.
15. Lippold, B. C. Biopharmazeutische Gesichtspunkte zur Entwicklung und Anwendung von Salben. *Pharm. Ind.* **1976**, *38*, 201−207.
16. Martin, A. N. M.; Swarbrick, J.; Cammarata, A. *Physikalische Pharmazie*; Stricker, H., Ed.; Wissenschaftliche Verlagsgesellschaft mbH: Stuttgart, 1987; pp 283−290.
17. Collander, R. On "Lipid Solubility". *Acta Physiol. Scand.* **1947**, *13*, 363−381.
18. Cohen, M. H.; Turnbull, D. Molecular Transport in Liquids and Gases. *J. Chem. Phys.* **1959**, *31*, 1164−1169.
19. Lippold, B. C.; Reimann, H. Wirkungsbeeinflussung bei Lösungssalben durch Vehikel am Beispiel von Methylnicotinat Teil I: Relative thermodynamische Aktivität des Arzneistoffes in verschiedenen Vehikeln und Freisetzungsverhalten. *Acta Pharm. Technol.* **1989**, *35*, 128−135.
20. Dross, K.; Sonntag, C.; Mannhold, H. On the Precise Estimation of R_M Values in Reversed-Phase Thin-Layer Chromatography Including Aspects of pH Dependence. *J. Chromatogr.* **1993**, *639*, 287−294.
21. Dross, K.; Sonntag, C.; Mannhold, R. Determination of the Hydrophobicity Parameter R_{MW} by Reversed-Phase Thin-Layer Chromatography. *J. Chromatogr. A* **1994**, *673*, 113−124.
22. Rekker, R. F.; Mannhold, R. *Calculation of Drug Lipophilicity*; VCH Verlagsgesellschaft mbH: Weinheim, 1992; pp 14−33.
23. Mannhold, R.; Rekker, R. F.; Sonntag, C.; ter Laak, A. M.; Dross, K.; Polymeropoulos, E. E. Comparative Evaluation of the Predictive Power of Calculation Procedures for Molecular Lipophilicity. *J. Pharm. Sci.* **1995**, *84*, 1410−1419.
24. Yalkowsky, S. H.; Sinkula, A. A.; Valvani, S. C. *Physical Chemical Properties of Drugs*; Marcel Dekker: New York, 1980; pp 202−266.
25. Yalkowsky, S. H.; Valvani, S. C.; Roseman, T. J. Solubility and Partitioning VI: Octanol Solubility and Octanol−Water Partition Coefficients. *J. Pharm. Sci.* **1983**, *72*, 866−870.
26. Bondi, A. van der Waals Volumes and Radii. *J. Phys. Chem.* **1964**, *68*, 441−451.
27. van Krevelen, D. W.; Hoftyzer, P. J. *Properties of Polymers*, 2nd ed.; Elsevier: Amsterdam, 1976; pp 51−65.
28. Leopold, C. S.; Lippold, B. C. A New Application Chamber for Skin Penetration Studies In Vivo with Liquid Preparations. *Pharm. Res.* **1992**, *9*, 1215−1218.
29. Southwell, D.; Barry, B. W.; Woodford, R. Variations in Permeability of Human Skin within and between Specimens. *Int. J. Pharm.* **1984**, *18*, 299−310.
30. Williams, A. C.; Cornwell, P. A.; Barry, B. W. On the Non-Gaussian Distribution of Human Skin Permeabilities. *Int. J. Pharm.* **1992**, *86*, 69−77.
31. Cornwell, P. A.; Barry, B. W. Effects of Penetration Enhancer Treatment on the Statistical Distribution of Human Skin Permeabilities. *Int. J. Pharm.* **1995**, *117*, 101−112.
32. Schlittgen, R. *Einführung in die Statistik*, 4th ed.; R. Oldenbourg Verlag: München, 1993; pp 358−442.
33. Sachs, L. *Angewandte Statistik*, 8th ed.; Springer-Verlag: Berlin, 1997; pp 560−579.

JS990032O

Oil-in-Water Liposomal Emulsions: Characterization and Potential Use in Vaccine Delivery

JEAN M. MUDERHWA,*,†,‡ GARY R. MATYAS,† LYNN E. SPITLER,‡ AND CARL R. ALVING†

Contribution from *Department of Membrane Biochemistry, Walter Reed Army Institute of Research, Washington, D.C. 20307-5100, and Jenner Biotherapies, Inc., 1895 Mountain View Drive, Tiburon, California 94920-1809*

Received January 12, 1999. Final revised manuscript received June 25, 1999.
Accepted for publication September 7, 1999.

Abstract □ Emulsification of mineral oil by phospholipids donated by liposomes composed of dimyristoyl phosphatidylcholine, dimyristoyl phosphatidylglycerol, cholesterol, and lipid A by extrusion resulted in the formation of oil-in-water liposomal emulsions containing a substantial number of intact liposomes. Increasing the proportion of liposomes from 25 mM to 150 mM phospholipid and increasing the oil content from 2.5% (v/v) to 42.5% (v/v) changed the flow characteristics of the emulsions from fluid liquidlike to viscous. Likewise, the degree of stability of the emulsions was liposomal phospholipid concentration-dependent, ranging from partial emulsification in the range 25–100 mM to complete stabilization in the range 125–150 mM. Despite some loss of liposome integrity, as evidenced by the release of liposomal trapped glucose, emulsification of liposomes containing encapsulated prostate-specific antigen (PSA) exhibited antigen-specific immunostimulation in mice. These results suggest that liposomes containing encapsulated antigen can serve as constituents for the formulation of oil-in-water vaccines.

Introduction

For many years, liposomes have been utilized as carriers of vaccines for inducing high titers of antibodies and for induction of cytotoxic T-lymphocytes.[1−4] The purpose of the present study was to examine the emulsifying characteristics of liposomes as constituents of oil-in-water emulsion adjuvants for vaccines. We and others have also previously reported that liposomes could be emulsified directly within incomplete Freund's adjuvant and other water-in-oil emulsions and that depending on the proportion of liposomes, such emulsification resulted in the formation of stable emulsions containing a large fraction of intact liposomes.[5,6] The liposomes that were destroyed by the emulsification process donated phospholipid molecules to assist the stabilizing properties of Span 80 and Arlacel A, respectively.[5,6] Thus, if liposomes containing encapsulated antigen were emulsified within Freund's adjuvant or any other water-in oil emulsion, at least some of the antigen would be released free into the emulsion and might thereby lose the beneficial immunostimulatory effects derived from encapsulation in liposomes. These observations raised the question whether the emulsification of oil by nondegraded liposomes in oil-in-water emulsions for vaccine design could be more difficult to achieve than with water-in-oil emulsions such as Freund's adjuvant because of more efficient donation of phospholipid molecules to effect droplet dispersion.

* Corresponding author. Telephone: (301) 319−9477; fax: (301) 319−9035, e-mail: gary.matyas@na.amedd.army.mil.
† Walter Reed Army Institute of Research.
‡ Jenner Biotherapies.

The fact that liposomes can be emulsified directly by an oil emulsion such as incomplete Freund's adjuvant or any oil without being either completely degraded themselves or without degrading the emulsion itself is very appealing in adjuvant technology. The immunogenic power of emulsions is well-known, as they are extremely powerful for inducing antibodies to emulsified antigens.[7−10] However, although emulsions are not noted for inducing cytotoxic T-lymphocyte (CTL) responses,[7−10] liposomes are among the most potent carriers for inducing CTLs.[3,4] Therefore, if the properties of each were additive, formulations of liposomes with water-in-oil or oil-in-water emulsions could have potential for being versatile adjuvants.

The data reported herein demonstrate that emulsification of mineral oil by phospholipids donated by liposomes results in the formation of oil-in-water emulsions that still contain substantial amounts of intact liposomes. Furthermore, it is also shown that formulations of liposome-encapsulated antigen in the oil-in-water emulsions exhibited strong immunostimulating activity for induction of antibodies and an antigen-specific lymphoproliferative response in mice.

Materials and Methods

Lipids—Dimyristoyl phosphatidylcholine (DMPC), dimyristoyl phosphatidylglycerol (DMPG), cholesterol (CHOL), and lipid A (LA) were purchased from Avanti Polar Lipids (Alabaster, AL). The fluorescent phospholipid *N*-(7-nitrobenz-2-oxa-1,3-diazol-4-yl)-1,2-dihexadecanoyl-*sn*-glycero-3-phosphoethanolamine, triethylammonium salt (N-NBD-PE) was purchased from Molecular Probes (Eugene, OR). LA was stored at −20 °C and dissolved in chloroform containing 10% methanol (v/v) before use. Solutions of phospholipids and CHOL were prepared in chloroform containing 0.75% ethanol (v/v) and stored at −20 °C until use. The phospholipid concentration in stock solutions, liposomes, and liposomal emulsions was determined by assaying aliquots for organic phosphorus by using the procedure of Bartlett[11] as modified by Gerlach and Deuticke.[12] Cholesterol content of stock solutions, liposomes, and liposomal emulsions was determined as described elsewhere.[13]

Emulsion Constituents—Materials used in emulsion preparations included light mineral oil (Sigma Chemical Co., St. Louis, MO) and liposomes containing or lacking PSA. Occasionally, trace amounts of N-NBD-PE-labeled liposomes were used in the formulation of emulsions to determine the presence of liposomal spherules.

Other Reagents—Chloroform was redistilled before use. After distillation, ethanol was added to chloroform as a preservative at 0.75% (v/v). Sodium deoxycholate from Sigma was purified by crystallization from hot acetone−water. All other reagents were reagent grade and were used without further purification.

Antigen—Protein-specific antigen (PSA) from donor human seminal fluid (M_r 30 000), which had been purified to a single gel band by extensive precipitation and column chromatography steps, including inhibition of protease activity, was purchased from Cortex Biochem, Inc. (San Leandro, CA). The antigen was exten-

10.1021/js990011u CCC: $18.00
Published on Web 10/21/1999

sively dialyzed against isotonic Tris-glycine (20 mM)/NaCl (150 mM) buffer, pH 7.4, and stored at 4 °C until use. Its purity was checked by sodium dodecyl sulfate−polyacrylamide gel electrophoresis (SDS−PAGE) using 15% acrylamide gels and silver stain.[14] The results showed that the sample had one predominant band corresponding to the enzyme and two to three minor bands indicating degradation products.

The relative concentration of PSA was determined by the method of Lowry et al.[15] using bovine serum albumin as a standard. The amount of antigen encapsulated in liposomes was determined by using a modification of the Lowry protein assay.[16]

Animals—BALB/c mice were from Jackson Laboratory (Bar Harbor, ME). The animals were handled and housed according to a protocol approved by the Laboratory Animal Care and Use Committee of the Walter Reed Army Institute of Research. They were given standard laboratory food and water ad libitum.

Preparation of Liposomes—Liposomes (multilamellar vesicles) and liposome-encapsulated glucose or PSA were prepared essentially as described elsewhere.[6,16,17] Multilamellar liposomes were made from a mixture of DMPC/DMPG/CHOL in molar ratio of 9:1:7.5. LA was incorporated at a dose of 2.5 μg/μol of phospholipid. Fluorescent liposomes contained a phospholipid, N-NBD-PE, at 2 mol % with respect to the phospholipid concentration.

Preparation of Oil-in-water Liposomal Emulsions— Oil-in-water (o/w) liposomal emulsions were prepared by the stepwise addition method, as described elsewhere,[18] using two 3- or 5-mL B−D syringes connected by a three-way stopcock with rotating male Luer-lock adapter and a switch-key. The Luer-lock adapter (bore diameter = 0.10 cm) supported the 18 gauge needle for sample drawing. Liposomes containing or lacking PSA were added in a stepwise fashion and extruded backward and forward (2 passes/s) with light mineral oil under shear forces for 5 min. Liposomal emulsions (1−3 mL total volume) were also occasionally prepared by vortex-mixing at 2500 rpm for 5 min in 1.5 cm × 10 cm glass tubes. The amounts of liposomes and oil used were such that the final liposomal phospholipid concentration in the emulsions was in the range 25−150 mM and the oil concentration was varied from 2.5 to 42.5% (v/v). The quality of the emulsion was tested by placing a few drops of the sample on the surface of cold (iced) distilled water, as described by Freund.[19] A satisfactory o/w emulsion was produced if the drops lost their integrity by spreading on the surface of the water.

Measurement of Emulsion Viscosity—The viscosity of the emulsions was measured immediately after manufacture using the Cannon model LV 2000 rotational viscometer. The measurement temperature was controlled at 25 °C with a circulating water bath. The Cannon rotational viscometer operates on the principle of a spindle rotating while immersed in the material being tested and measuring the torque necessary to overcome the viscous resistance to rotation. From the spindle speed, torque measurements, and spindle characteristics, the viscometer calculates and displays the viscosity in centipoise (cP) or milliPascal sec (mPa·s). Using TL5 and TL7 spindles for less and more viscous emulsions, respectively, the shear rates were varied in the range 0.084−79.2 s^{-1}.

Emulsion Stability—Emulsion (1−3 mL) was poured from the syringe into 1.0 cm × 10 cm screw-cap glass tubes and incubated at 37 °C. This temperature was chosen for its physiological relevance to antigen stability in immunization studies. The stability of the emulsion was assessed by detection of phase separation with time. The height of the oil phase above the emulsion was measured using a ruler, and the results were expressed in % oil separated using the following formula:

$$\frac{\text{height of oil (upper phase)}}{\text{total height of emulsion sample} \times F}$$

where the factor F stands for the initial fraction of oil in the emulsion. The value of F was in the range 0.025−0.425. The smallest amount of separated oil that could be measured was ≤5%.

The rates of separation of the emulsions were expressed in % oil per minute as reported previously.[20,21] These rates were calculated from the slopes of the time of the percent of oil separated using the initial velocity data.

Liposome Stability—Liposome stability in the o/w emulsions was assayed spectrophotometrically by enzymatic assay of trapped glucose released, as previously described,[16] with the following modification. Normal saline (2 mL) was added to the emulsion (1 mL), and the mixture was vortexed for 2 min at 2000 rpm. Following centrifugation at 27 000 × g for 15 min at 25 °C, the oil phase was removed and the pellet was resuspended in the aqueous supernatant and glucose. As this procedure completely separated the oil from the water and lipids, all of the released glucose was detected in the liposomes resulting from resuspension of the pellet in the aqueous phase. This was confirmed in control experiments by demonstrating that the total amount of trapped glucose detected in emulsified liposomes was identical to the amount detected in the absence of an emulsion after disruption of the liposomes with chloroform and 10% Triton X-100.[16] Glucose release values of emulsified liposomes above 5% compared to baseline were judged to be positive.

The presence of liposomal spherules in the emulsion was determined by fluorescence microscopy using trace amounts of N-NBD-PE-labeled liposomes in the emulsion. A few drops of the sample were spread on a microscope slide immediately after manufacture and visualized by fluorescence with an Olympus (VANOX-S) microscope using an oil immersion 100× objective, or with an Olympus IX70 inverted microscope with a 40× objective. Images were collected with an Olympus camera and digitized from the 35-mm slides. The particle diameter of the emulsions was determined by measuring 50 emulsion droplets from photomicrographs prepared by fluorescence microscopy using oil immersion 100× objective.

Immunization Studies—BALB/c mice (five mice per group) were immunized intramuscularly (posterior thigh) with 100 μL of either liposome-encapsulated PSA (PSA-liposomes) or PSA-liposomes formulated in o/w emulsions. Each of these formulations contained 25 μg of antigen and 25 μg of LA per dose. Mice were bled by tail vein at 0, 2, and 5 weeks and the serum samples were analyzed for antibody titers by ELISA as described in detail elsewhere.[22]

For splenic T-lymphocyte proliferation studies, mice were euthanized by CO_2 followed by cervical dislocation and bleeding by cardiac puncture. The freshly removed spleens were placed in Hank's balanced salt solution [HBSS (Gibco Laboratories, Grand Island, NY)], and a single cell suspension was prepared. Following centrifugation, the cells were resuspended at 5 × 10^6 cells/mL in RPMI-1640 (Gibco Laboratories, Grand Island, NY):EHAA (Whittaker Bioproducts, Walkersville, MD) (1:1, v/v) supplemented with 8 mM L-glutamine, 100 units/mL pencillin, 100 μg/mL of streptomycin, 1 mM sodium pyruvate, 1X MEM nonessential amino acids, 100 μM 2-mercaptoethanol, and 0.5% BALB/c normal mouse serum. Subsequently, the cells were seeded at a density of 5 × 10^5 cells/well in 96-well fat-bottom tissue culture plates (Costar, Cambridge, MA) containing several dilutions of PSA in triplicate, in a total volume of 0.2 mL. Following 4 days of incubation at 37 °C in 5% CO_2 and 95% relative humidity, the cells were labeled with 1 μCi/well of [^{3}H]Thymidine [TdR, specific activity 6.7 Ci/mM (NEN, Boston, MA)]. The plates were then incubated overnight at 37 °C and the cell cultures harvested onto glass fiber filters with the Skatron cell harvester and processed for scintillation spectrometry. Radioactivity was quantified using the Pharmacia LKB liquid scintillation counter. Data were expressed in stimulation index, i.e., the ratio of counts from cells incubated with PSA over counts from the control.

Results

Rheological Properties of Liposomal Emulsions—The flow characteristics of liposomal emulsions were established using samples formulated with 42.5% (v/v) of mineral oil and liposomes containing different concentrations of phospholipid. Figure 1 shows that values of the viscosity increased slowly, but gradually with the lipid composition from 0.03 × 10^3 cP to 1.53 × 10^3 cP in the range 25−100 mM. Further increase of liposomal phospholipid concentration to from 125 mM to 150 mM resulted in an abrupt change of viscosity from the value of 7.80 × 10^3 cP to the value of 98.10 × 10^3 cP.

Figure 2 shows that with samples containing 50 mM and 100 mM liposomal phospholipid, values of the viscosity were very low and their increase with the oil concentration was negligible, with the change being from the mean of

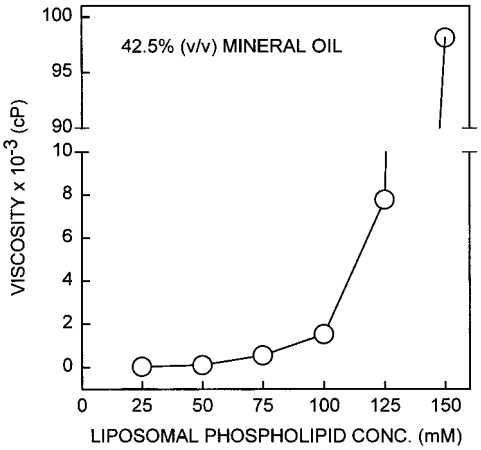

Figure 1—Viscosity characteristics of emulsions versus liposomal phospholipid concentration. The emulsions were formulated by extrusion with 42.5% (v/v) of mineral oil and liposomes containing different concentrations of phospholipid. The final liposomal phospholipid concentration used in the emulsions varied from 25 to 150 mM. Viscosity values were measured at 25 °C immediately after manufacture of the emulsions. The data were the mean of two to four determinations with a variability of ≤5%.

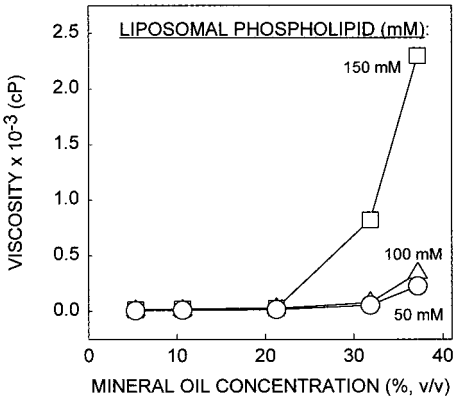

Figure 2—Viscosity characteristics of emulsions versus mineral oil concentration. The emulsions were formulated by extrusion with increasing amounts of oil in the range 5.3–37.5% (v/v) and liposomes containing different concentrations of phospholipid. The final liposomal phospholipid concentrations in the emulsions were 50 mM, 100 mM, and 150 mM as indicated in the figure. Viscosity values were measured at 25 °C immediately after manufacture of the emulsions. The data were the mean of two to four determinations with a variability of ≤5%.

0.01×10^3 cP to the mean of 0.23×10^3 cP in the range 5.3−37.5% (v/v). However, for samples formulated with 150 mM phospholipid, the viscosity which was also low at 0.02×10^3 cP did increase significantly with the oil concentration only beyond 21.3% (v/v) until it reached the value of 2.30×10^3 cP at 37.5% (v/v).

Stability Characteristics of Liposomal Emulsions—Emulsions containing 42.5% (v/v) of mineral oil and 25 mM to 150 mM of liposomal phospholipid were prepared by vortex-mixing at 2500 rpm and incubated at 37 °C. Figure 3 shows the time course of oil separated in percent of the total added, and Table 1 summarizes the rates of separation of the samples versus phospholipid concentration. Samples containing 25 mM and 50 mM liposomal phospholipid were rapidly destabilized with the percent oil separated increasing with time at rates of 1.434% and 1.184% separation per minute to complete separation after 1 and 5 h, respectively. Emulsions formulated with 100 mM and 125 mM phospholipid were slowly destabilized up to 48 h at rates of 0.003% and 0.002% separation per minute; they were thereafter destabilized rapidly to complete separation after 96 h. Interestingly, sample emulsion

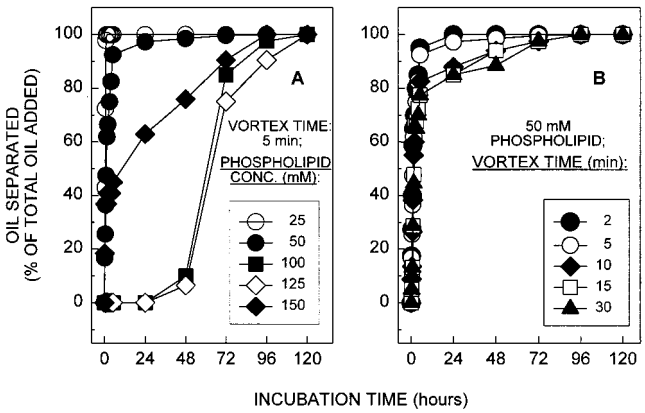

Figure 3—Time course of the degree of stability of emulsions formulated by vortex-mixing with 42.5% (v/v) of mineral oil and liposomes containing different concentrations of phospholipid. The final liposomal phospholipid concentration in the emulsions was varied from 25 mM to 150 mM as indicated. Emulsion samples were incubated at 37 °C, and their stability was assessed by detection of phase separation with time. The data were the means of two determinations with variability of ≤5%.

Table 1—Rates of Separation in % Oil Per Minute versus Phospholipid Concentration for o/w Liposomal Emulsions Prepared by Vortex-Mixing [a]

liposomal phospholipid concentrationin in o/w emulsions (mM)	rate of separation (in % oil per min)
25	1.434
50	1.184
100	0.003
125	0.002
150	1.227

[a] Liposomal emulsions were prepared with 42.5% (v/v) of mineral oil and liposomes containing different concentrations of phospholipid. The resulting samples were incubated at 37 °C, and their stability was assessed by the appearance of phase separation with time. The rates of separation were calculated from the slopes of the time of the % of oil separated using initial velocity data.

containing 150 mM liposomal phospholipid was destabilized at a rate of 1.227% per minute to complete separation after 96 h, suggesting that at the higher phospholipid concentration used where the viscosity of the sample was substantially increased, vortex of the sample was inefficient to adequately promote mixing of the components. Thus, none of the emulsions formulated by vortex-mixing was stable.

Emulsions prepared by syringe extrusion containing 42.5% (v/v) of mineral oil and 25 mM to 150 mM liposomal phospholipid were incubated at 37 °C and examined for the appearance of phase separation. Figure 4 illustrates the gross physical appearance of these emulsions following a 72-h incubation period, while Figure 5 depicts the phospholipid dose dependence of their degree of stability for the same time period. The degree of stability of the dispersions ranged from complete separation at lower phospholipid concentrations, i.e., 25 mM and 50 mM (Figure 4A,B and Figure 5), to complete stabilization at higher phospholipid content, i.e., 125 mM and 150 mM (Figure 4E,F and Figure 5). However, while the sample formulated with 75 mM liposomal phospholipid was near complete separation with 87.5% of the oil becoming separated (Figure 4C and Figure 5), the dispersions containing 100 mM phospholipid were relatively stable with only 5% of the oil being separated (Figure 4D and Figure 5).

Figure 6 shows the time course of oil separated in percent of the total added following incubation at 37 °C of emulsion samples formulated with liposomes lacking (Figure 6A) or containing PSA (Figure 6B), and Table 2 summarizes the

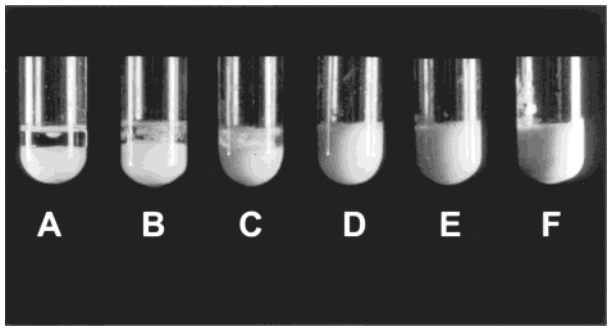

Figure 4—Gross physical appearance of emulsions formulated by extrusion with 42.5% (v/v) of mineral oil and liposomes containing different concentrations of phospholipid, following 72 h of incubation at 37 °C. The final liposomal phospholipid concentrations in the emulsions were (A) 25, (B) 50, (C) 75, (D) 100, (E) 125, and (F) 150 mM. Phase separation was evidenced by the development of two phases: a clear oil phase at the top and a milky aqueous phase containing liposomes at the bottom.

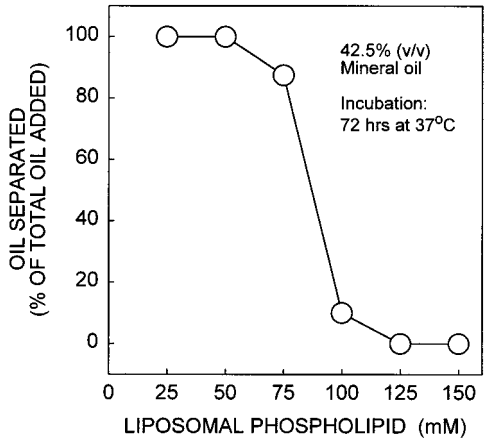

Figure 5—Phospholipid concentration dependence of the degree of stability of liposomal emulsions following 72 h of incubation at 37 °C. The emulsions were formulated by extrusion with 42.5% (v/v) of mineral oil and liposomes containing different concentrations of phospholipid. The final liposomal phospholipid concentration used in the emulsions varied from 25 to 150 mM. Stability of the emulsions was assessed by detection of phase separation.

rates of separation of the samples versus lipid composition. These rates were calculated from the slopes of the time of the percent of oil separated using the initial velocity data plotted in Figure 6A,B. Samples containing 25 mM and 50 mM liposomal phospholipid were rapidly destabilized with the percent of oil separated increasing with time (Figure 6A,B). For emulsions formulated with liposomes lacking PSA (Figure 5A), phase separation occurred at rates of 1.322% and 0.381% per minute (Table 2) to complete separation after 12 and 48 h, respectively (Figure 6A). Emulsions formulated with PSA-liposomes (Figure 6B) were destabilized more rapidly at rates of 1.895% and 0.919% per minute (Table 2) to complete separation after 2 and 24 h, respectively (Figure 6B). For the emulsions formulated with liposomes lacking (Figure 6A) or containing PSA (Figure 6B) at 75 mM phospholipid, the percent of oil separated increased gradually and almost linearly with time (Figure 6A,B), at rates of 0.012% and 0.045% per minute, respectively (Table 2), to complete separation after 96 h (Figure 6A,B). Furthermore, the samples prepared with liposomes lacking (Figure 5A) or containing PSA (Figure 6B) at 100 mM phospholipid were stable up to 72 and 24 h of incubation, respectively, after which they became destabilized toward 5% and 39% of oil separated at 120 h at rates of 0.001% and 0.003% per minute,

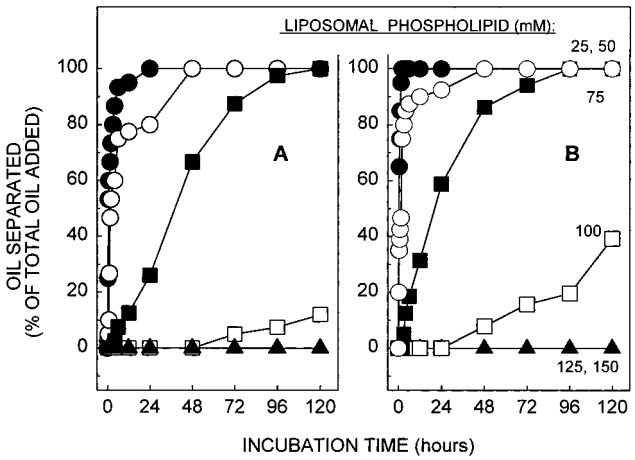

Figure 6—Time course of the degree of stability of emulsions formulated by extrusion with 42.5% (v/v) of mineral oil and empty liposomes (Figure 6A) or PSA-liposomes (Figure 6B), containing different concentrations of phospholipid. The final liposomal phospholipid concentration used in the emulsions varied from 25 to 150 mM as indicated in the figure. Emulsion samples formulated with PSA-liposomes contained 6.5 μg PSA per 100 μL. The samples were incubated at 37 °C, and their degree of stability was assessed by detection of phase separation with time. The data were the mean of two to three determinations with a variability of $\leq$8%.

Table 2—Rates of Separation in % Oil Per Minute versus Phospholipid Concentration for o/w Liposomal Emulsions[a]

liposomal phospholipid concentration in o/w emulsions (mM)	rate of separation (in % oil per min) of emulsions formualted with	
	empty liposomes	PSA-liposomes
25	1.322	1.895
50	0.381	0.919
75	0.012	0.045
100	0.001	0.003
125	0.000	0.000
150	0.000	0.000

[a] Liposomal emulsions were formulated with 42.5% (v/v) of mineral oil and empty liposomes or PSA-liposomes containing different concentrations of phospholipid. Emulsion samples formulated with PSA-liposomes contained 6.5 μg PSA/100 μL. The samples were incubated at 37 °C, and their stability was assessed by the appearance of phase separation with time. The rates of separation were calculated from the slopes of the time of the % of oil separated using initial velocity data.

respectively. However, emulsions formulated with 125 mM and 150 mM liposomal phospholipid were stable over the 120-h incubation period regardless of the lack or addition of PSA.

Effect of Mineral Oil Concentration on the Stability of the Emulsions—The oil concentration dependence of the degree of stability of the dispersions was established using emulsion samples containing various amounts of mineral oil and 25−150 mM liposomal phospholipid. Figure 7 shows that samples containing 25 mM and 50 mM liposomal phospholipid were unstable regardless of the oil concentration and the incubation time, with 91−100% of the oil becoming separated following 6 to 72 h of incubation at 37 °C. For emulsions formulated with 75 mM liposomal phospholipid, the percent oil separated increased with time and was inversely proportional to mineral oil concentration, until it reached the plateau of 88% after 72 h over the range 10−42.5% (v/v) of oil. The 100 mM-liposomal phospholipid sample was stable at all mineral oil concentrations following 6 and 24 h of incubation, but was relatively stable after 72 h, with only 5−15% of the oil being separated over the range 5−42.5% (v/v) of oil. However, samples containing 125 mM and 150 mM liposomal phospholipid were stable up to 72 h regardless of the oil content.

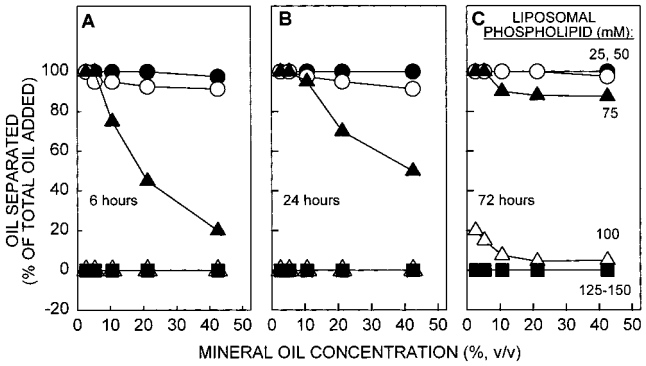

Figure 7—Mineral oil concentration dependence of the stability of liposomal emulsions. The emulsions were formulated by extrusion with increasing amounts of mineral oil in the range 2.5–42.5% (v/v) and liposomes containing different concentrations of phospholipid. The final liposomal phospholipid concentration in the emulsions was varied from 25 to 150 mM as indicated in the figure. The samples were incubated at 37 °C, and their stability was assessed by detection of phase separation following 6, 24, and 72 h of incubation. The data were the mean of two determinations with a variability of ≤5%.

Appearance of Fluorescent Liposomes in Emulsions—Fluorescent liposomes that were nearly spherical in shape were easily observed surrounding the surface of oil droplets in the emulsions (Figure 8B–D). Figure 8A shows, as a control experiment, the photomicrograph of fluorescent, nonemulsified liposomes.

Stability of Liposomes As Determined by Release of Trapped Glucose—In the previous experiment with N-NBD-PE, liposome-like structures appeared to be present in the emulsions (Figure 8B–D), but the experiment could not determine whether intact liposomes remained that retained their permeability properties. Figure 9A shows that release of liposomal trapped glucose, measured immediately after manufacture of the emulsions, increased gradually with the liposomal phospholipid concentration from 16% to 43% in the range 25–125 mM. Furthermore, Figure 9B depicts the shelf life characteristics of the liposomes formulated in the emulsions at selected lipid compositions following incubation at 37 °C. The increase of release of trapped glucose with time was not substantial irrespective of the phospholipid composition, with the average increase being in the range 5.5–7% over the 20-day incubation period.

Antibody Response to PSA Encapsulated in Emulsified and Nonemulsified Liposomes—PSA-liposomes formulated in emulsions were tested for their ability to induce antibodies to PSA. Figure 10 shows that immunization of mice with the unencapsulated PSA formulation did not induce antibodies to PSA over a period of 5 weeks. In contrast, the use of liposome-encapsulated PSA resulted in a level of serum IgG that increased gradually over 5 weeks to reach a final concentration of approximately 120 μg/mL. When mice were immunized with the liposomal emulsion formulations, the serum IgG titers were in the range 35–137 μg/mL depending on the phospholipid composition at 5 weeks (Figure 10). It is clear that the liposomes in the emulsion retained their potent activities as carriers of antigen.

Proliferative Response of Splenic T-Lymphocytes—The ability of PSA to induce splenic T-lymphocyte proliferation in vitro was investigated by immunizing mice with unencapsulated PSA, liposome-encapsulated PSA, and PSA-liposomes formulated in the emulsion containing 150 mM phospholipid. Figure 11 shows the PSA concentration dependence of stimulation index in vitro. There was no

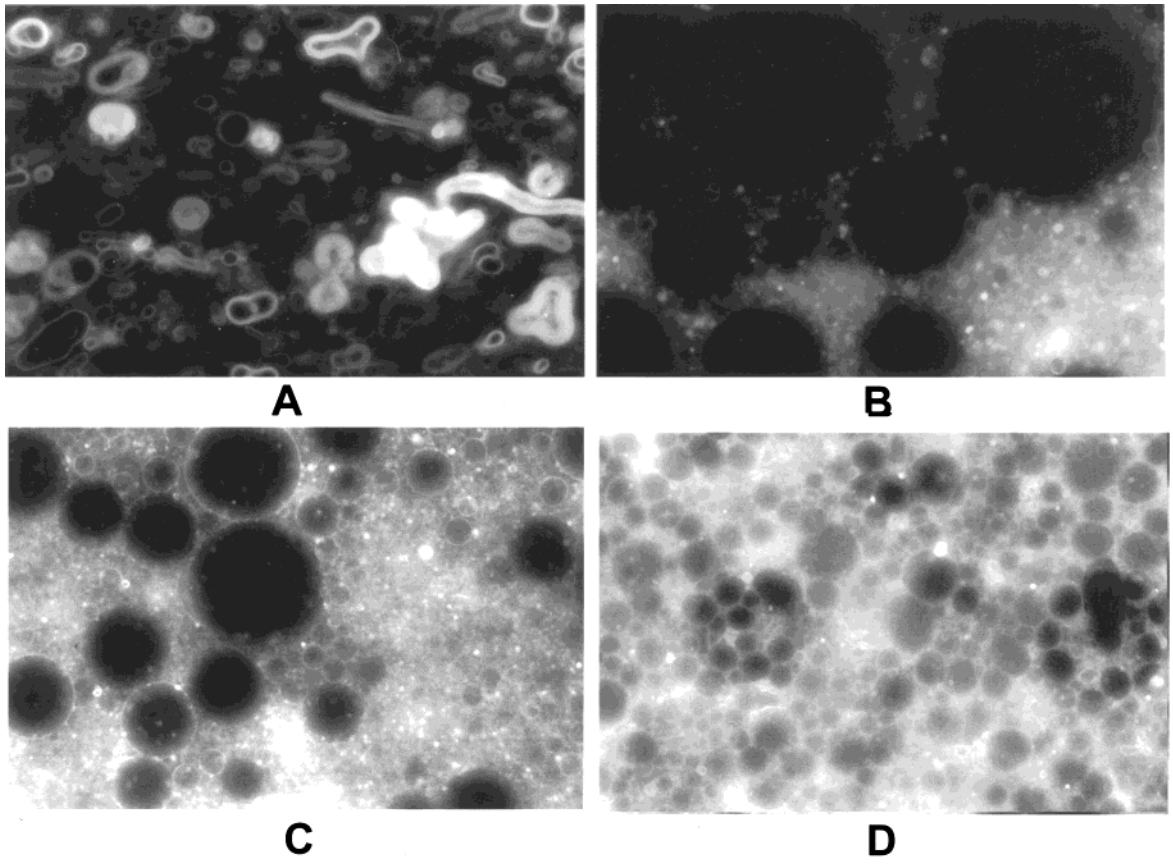

Figure 8—Photomicrographs of nonemulsified fluorescent liposomes (Figure 8A), and emulsions (Figure 8B–D) formulated with 42.5% (v/v) of mineral oil and liposomes containing trace amounts of N–NBD-PE. The final liposomal phospholipid concentrations in the emulsions were 25 (Figure 8B), 50 (Figure 8C), and 125 mM (Figure 8D). Fluorescent microscopy was performed immediately after manufacture of the samples.

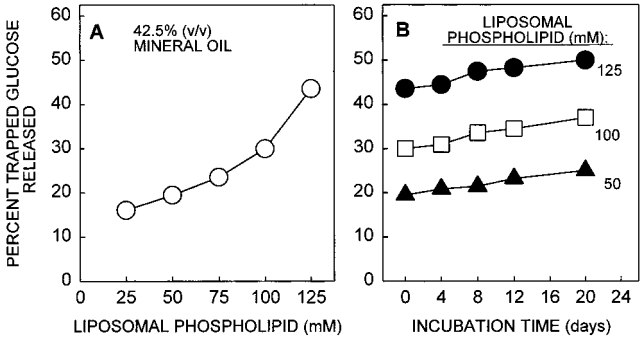

Figure 9—Phospholipid concentration (Figure 9A) and time (Figure 9B) dependencies of the stability of liposomes within the emulsions as determined by measurement of release of liposomal trapped glucose. The emulsions were formulated with 42.5% of mineral oil and liposomes containing different amounts of phospholipid. The final liposomal phospholipid concentration in the emulsions was varied from 25 to 125 mM. Liposomal trapped glucose released was determined immediately after manufacture (Figure 8A) and following incubation of the samples at 37 °C up to 20 days (Figure 8B). The data were the mean of 2 determinations with a variability of ≤5%.

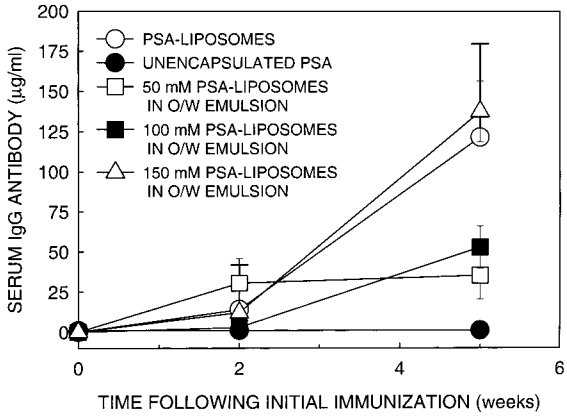

Figure 10—Antibody response to PSA; PSA was encapsulated in emulsified and nonemulsified liposomes. BALB/c mice (n = 5) were immunized intramuscularly with the indicated formulations each of which contained 25 μg of antigen and 25 μg of LA per dose. The final liposomal phospholipid concentrations in the emulsions were 50 mM, 100 mM, and 150 mM as indicated in the figure. Sera were collected at weeks 0, 2, and 5, and analyzed for antigen-specific antibodies by ELISA.

splenic T-cell proliferation when mice were immunized with the unencapsulated PSA formulation. Stimulation index values were low and remained close to 1.0 with increasing PSA concentration (Figure 11). However, when mice were immunized with liposome-encapsulated PSA and emulsified PSA-liposomes, stimulation index values increased gradually for both formulations in a PSA concentration-dependent manner toward 4.1 and 5.7, respectively. Stimulation index data obtained with the liposomal emulsion were slightly higher than those obtained with liposomes themselves (Figure 11), but the relative differences observed were not statistically significant. No proliferation occurred in a set of in vitro control experiments using ovalbumin instead of PSA (data not shown).

Discussion

This work is part of a larger effort to develop a variety of liposome-based adjuvant and carrier combinations for vaccines. It describes an approach for the creation of practical emulsified oil-in-water liposomal vaccines. The important factors for formulation were the degree of stability of the emulsions, the integrity of the liposomes

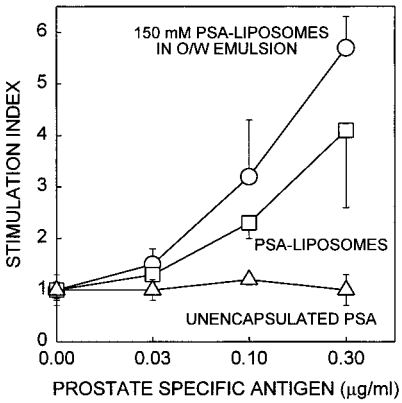

Figure 11—Lymphocyte proliferation response to PSA; PSA was encapsulated in emulsified and nonemulsified liposomes. BALB/c mice (n = 5) were immunized intramuscularly with the indicated formulations which each contained 25 μg of antigen and 25 μg of LA per dose. The final liposomal phospholipid concentration in the emulsion was 150 mM as indicated in the figure. Spleens were removed from mice at week 5 and processed for T-lymphocyte proliferation as described in the material and methods section. Data were expressed in stimulation index, i.e., the ratio of counts from cells incubated with PSA over counts from nonstimulated cells. Nonstimulated cells had about 190 to 250 counts per minute.

within the emulsion, and the ability of emulsified liposome-encapsulated antigen to exhibit immunostimulating activity.

The results show that the physicochemical properties, including viscosity and stability, of the emulsions changed with the liposomal phospholipid concentrations. At lower concentrations, over the range 25−100 mM, the emulsions were less viscous or fluid-liquidlike (Figure 1) and had different degrees of stability, ranging from complete to partial destabilization (Figures 4, 5, and 6A). Conversely, at higher concentrations, over the range 125−150 mM, they were viscous (Figure 1) and stable (Figures 4, 5, and 6A). Because rheological properties can affect the flow of emulsions through a needle or a catheter, the stable and viscous emulsions were so thickened that they could not be easily handled. This simply calls for formulation of emulsions of low viscosity for ease of injection. Our data showed that stable emulsions of low viscosity could be formulated over the range 125−150 mM liposomal phospholipid by lowering the oil concentration up to 2.5% (v/v) (Figures 2 and 7).

The rates of separation of the unstable emulsions which were inversely proportional to phospholipid concentration, were much higher with emulsified PSA-liposomes (Figure 6 and Table 2), probably due to perturbation of the bulk phase as well as the interfacial region brought about by released PSA from liposomes. Proteins are well-known to induce long-range electrostatic forces as well as variations in several physicochemical parameters, including surface potential and surface viscosity.[23] Thus, PSA could behave like a detergent displacing phospholipid molecules from the surface of oil droplets, thereby increasing the van der Waals attractive forces in the medium.

Fluorescence studies showed that the emulsions retained liposomal structures (Figure 8), but the integrity of liposomes within the emulsion was not maintained completely intact, as shown by the release of as much as 16% to 43% of the trapped marker with increasing lipid composition (Figure 9A). As suggested by the shelf life characteristics of liposomes within the emulsions (Figure 9B), no substantial leakage of intact liposomes occurred during incubation. Thus, the partial degradation of liposomes in the emulsions was not due directly to interaction or collision of liposomes with the oil droplets, but solely due to shear forces of the extrusion process involved in the manufacture of the dispersions. This conclusion is also supported by the

observation that no substantial degradation of liposomes occurred when, in control experiments, the emulsion samples were prepared by vortex-mixing. As expected, none of the latter emulsions was stable regardless of the liposomal phospholipid concentration (Figure 3). However, its possible that the slight increase in the release of glucose with time (Figure 9B) could be due to diffusion from the remaining intact liposomes. Alternatively, the glucose could be released by Brownian motion induced collision of oil droplets with intact liposomes resulting in the destruction of the liposomes.

The partial degradation of liposomes in the emulsions (Figure 9A) donated phospholipid molecules that provided partial or complete emulsification of the oil. Phospholipids, which form the bulk phase of liposomes, have been classically viewed as being particularly effective as emulsifiers for oil-in-water emulsions.[24] The photomicrographs shown in Figure 8 support the view that emulsification of liposomes with the oil was more effective with increasing the proportion of liposomes, with subsequent reduction of the size of the oil drops. The mean values of the particle diameters of the emulsion containing 25, 50, and 125 mM phospholipid were 12.5, 2.5, and 0.625 μm, respectively. These values were obtained by measurement of the oil droplets. The tiny continuous dots coating the oil droplets could be part of the phospholipid monomolecular layers at the interface which have been reported to impart a significant steric stabilization to the emulsion droplets.[25,26] The protective effect of phospholipid monolayers against coalescence and coagulation would be quite analogous to the reported repulsive forces arising from purely osmotic and finite-volume restricting effects of compressed coils of polymer-covered surfaces.[27,28]

The integrity of liposomes is a critical aspect of the vaccine formulation because, as demonstrated by some reports,[29−31] ingested liposomes provide intracellular targeting in phagocytic cells, with distribution of the liposomal antigen both to the cytoplasm and Golgi apparatus via the major histocompatibility (MHC) class I antigen presentation pathway and to low pH compartments. Despite the partial degradation of liposomes in the emulsions, the data showed that both PSA-liposomes formulated in emulsions and nonemulsified PSA-liposomes exhibited a comparable immunostimulating activity with regard to induction of not only antibody titers (Figure 10), but also antigen-specific lymphoproliferative responses (Figure 11) in mice. The relative differences observed in both responses were not statistically significant. Although the three liposomal emulsion formulations tested, which were administered to mice immediately after manufacture, had different degrees of stability in vitro, they exhibited comparable immunogenic properties in vivo (Figure 11). Similar results were reported on the adjuvant activity of o/w emulsions stabilized by a combination of Tween 80/Span 80 surfactants and for which the degree of stability did not affect antibody response as long as an emulsion was formed; stable emulsions were as effective as unstable ones.[32] Moreover, experiments are currently underway to examine the influence, if any, of the degree of stability of o/w liposomal emulsions on their immunogenic properties.

Overall, the data presented in this work show that emulsification of liposomes with mineral oil resulted in the formation of o/w liposomal emulsions containing a substantial number of intact liposomes that could still exhibit some immunostimulating activity in mice. These results are very encouraging for examining further biochemical and immunogenic properties of the emulsified o/w liposomal formulation and its extension to other vaccines. Further experiments will address the effect of oil concentration, the nature of the antigen, and the integrity of the liposomes as well as the degree of stability of the emulsion on the quality of the immune response generated by these formulations. Because oil emulsions induce predominantly humoral immunity[7−10] through their capacity to concentrate and orient antigens on oil droplets for effective delivery to cells of the immune system,[33,34] and liposomes are known as the best carriers for cell-mediated immune responses[3,4] through the MHC class I pathway,[29−31] combination of both mechanisms in a single vaccine could lead to a synergistic adjuvant effect.[35,36] The PSA-liposomal vaccine formulated in the emulsion has exhibited the highest immunostimmulating activity for induction of antibody titers and antigen-specific lymphoproliferative response in current clinical trials of prostate cancer patients (unpublished data).

References and Notes

1. Gregoriadis, G. Immunological adjuvants: a role for liposomes. *Immunol. Today* **1990**, *11*, 89−97.
2. Phillips, N. C. Liposomal carriers for the treatment of acquired immune deficiency syndromes. *Bull. Inst. Pasteur* **1992**, *90*, 205−230.
3. Alving, C. R.; Koulchin, V.; Glenn, G. M.; Rao, M. Liposomes as carriers of peptide antigens: induction of antibodies and cytotoxic T-lymphocytes to conjugated and unconjugated peptides. *Immunol. Rev.* **1995**, *145*, 5−31.
4. Alving, C. R. and Wassef, N. M. Cytotoxic T-lymphocytes induced by liposomal antigens: mechanisms of immunologic presentation. *AIDS Res. Hum. Retrovirol.* **1994**, *10*, S91−S94.
5. Yoshioka, T.; Skalko, N.; Gursel, M.; Gregoriadis, G.; Florence, A. T. A nonionic surfactant vesicle-in-water-in-oil (v/w/o) system: potential uses in drug and vaccine delivery. *J. Drug Targ.* **1995**, *2*, 533−539.
6. Muderhwa, J. M.; Rothwell, S. W.; Alving, C. R. Emulsification of liposomes with incomplete Freund's adjuvant: stability of the liposomes and the emulsion. *J. Liposome Res.* **1998**, *8*, 183−194.
7. Hilleman, M. R. Critical appraisal of emulsified oil adjuvants applied to viral vaccines. *Prog. Med. Virol.* **1966**, *8*, 131−182.
8. Edelman, R. Vaccine adjuvants. *Rev. Infect. Dis.* **1980**, *2*, 370−383.
9. Woodard, L. H. Surface chemistry and classification of vaccine adjuvants and vehicles. In *Bacterial Vaccines*; Mizrahi, A., Ed.; Advances in Biotechnology Processes; Alan R. Liss, Inc.: New York, 1990; Vol. 13, pp 281−306.
10. Gupta, R. K.; Siber, G. R. Adjuvants for human vaccines: current status, problems and future prospects. *Vaccine* **1995**, *13*, 1263−1276.
11. Bartlett, G. R. Phosphorus assay in column chromatography. *J. Biol. Chem.* **1959**, *234*, 466−469.
12. Gerlach, E.; Deuticke, B. Eine einfache method zur mikrobestimmung von phosphat in der papierchromatographie. *Biochem. Z.* **1963**, *337*, 477−479.
13. Zlatkis, A.; Zak, B.; Boyle, A. J. A new method for the direct determination of serum cholesterol. *Lab. Clin. Med.* **1953**, *41*, 486-492.
14. Laemmli, U.K. Cleavage of structural proteins during the assembly of the head of bacteriophage T4. *Nature (London)* **1970**, *227*, 680−685.
15. Lowry, O. H.; Rosebrough, N. J.; Farr, A. L.; Randall, R. J. Protein measurement with the Folin phenol reagent. *J. Biol. Chem.* **1951**, *193*, 265−285.
16. Alving, C. R.; Shichijo, S.; Mattsby-Baltzer, I.; Richards, R. L.; Wassef, N. M. Preparation and use of liposomes in immunological studies. In *Liposome Technology*, 2nd ed., Gregoriadis, G., Ed.; CRC Press: Boca Raton, FL, 1993; Vol. III, pp 317−343.
17. Muderhwa, J. M.; Wassef, N. M.; Spitler, L. E.; Alving, C. R. Effects of aluminum adjuvant compounds, Tweens, and Spans on the stability of liposomes permeability. *Vaccine Res.* **1996**, *5*, 1−13.
18. Moncada, C.; Torres, V.; Israel, Y. Simple method for the preparation of antigen emulsions for immunization. *J. Immunol. Methods* **1993**, *162*, 133−140.
19. Freund, J. The mode of action of immunologic adjuvants. *Adv. Tuberc. Res.* **1956**, *1*, 130−148.
20. Vold, R. D.; Mittal, K. L. Effect of age on ultracentrifugal stability of liquid petrolatum-water emulsions. *J. Pharm. Sci.* **1972**, *61*, 769−772.

21. Vold, R. D.; Acevedo, M. C. Comparison of ultracentrifugal stability parameters with long-term shelf stability of emulsions. *J. Am. Oil Chem. Soc.* **1977**, *54*, 84−90.
22. Richards, R. L.; Hayre, M. D.; Hockmeyer, W. T.; Alving, C. R. Liposomes, lipid A, and aluminum hydroxide enhance the immune response to a synthetic malaria sporozoite antigen. *Infect. Immunol.* **1988**, *56*, 682−686.
23. Bonté, F.; Juliano, R. L. Interactions of liposomes with serum proteins. *Chem. Phys. Lipids* **1986**, *40*, 359−372.
24. Becher, P. *Emulsions: Theory and Practice*, American Chemical Society Monograph Series, Reinhold Publishing Co.: New York, 1965.
25. Férézou, J.; Lai, N.-T.; Leray, C.; Hajri, T.; Frey, A.; Cabaret, Y.; Courtieu, J.; Lutton, C.; Bach, A. C. Lipid composition and structure of commercial parenteral emulsions. *Biochim. Biophys. Acta* **1994**, *1213*, 149−158.
26. Handa, T.; Nakagaki, M. Monolayer-bilayer equilibrium of phospholipid: stabilization of neutral lipid droplets in aqueous medium and catabolism of plasma lipoproteins. *Adv. Colloid Interface Sci.* **1992**, *38*, 45−67.
27. Israelachvili, J. N. *Intermolecular and surface forces with applications to colloidal and biological systems*; Academic Press: New York, 1985.
28. Ross, S.; Morrison, I. D. *Colloidal systems and interfaces*; John Wiley & Sons: New York, 1988.
29. Verma, J. N.; Wassef, N. M.; Wirtz, R. A.; Atkinson, C. T.; Aikawa, M.; Loomis, L. D.; Alving, C. R. Phagocytosis of liposomes by macrophages: intracellular fate of liposomal malaria antigen. *Biochim. Biophys. Acta* **1991**, *1066*, 229−238.
30. Rao, M.; Rothwell, S. W.; Wassef, N. M.;, Pagano, R. E.; Alving, C. R. Visualization of peptides derived from liposome-encapsulated proteins in the *trans*-Golgi area of macrophages. *Immunol. Lett.* **1997**, *59*, 99−105.
31. Richards, R. L.; Rao, M.; Wassef, N. M.; Glenn, G. M.; Rothwell, S. W.; Alving, C. R. Liposomes containing lipid A serve as an adjuvant for induction of antibody and cytotoxic T-cell responses against RTS,S malaria antigen. *Infect. Immunol.* **1998**, *66*, 2859−2865.
32. Woodard, L. F.; Jasman, R. L. Stable oil-in-water emulsions: preparation and use as vaccine vehicles for lipophilic adjuvants. *Vaccine* **1985**, *3*, 137−144.
33. Hunter, R.; Strickland, F.; Kezdy, F. The adjuvant activity of nonionic block polymer surfactants I. The role of hydrophile-lipophile balance. *J. Immunol.* **1981**, *127*, 1244−1250.
34. Retzinger, G. S.; Meredith, S. C.; Takayama, K.; Hunter, R. L.; Kezdy The role of surface in the biological activities of trehalose 6,6′-dimycolate. *J. Biol. Chem.*, **1981**, *256*, 8208−8216.
35. Edelman, R.; Tacket, C. O. Adjuvants. *Int. Rev. Immunol.* **1990**, *7*, 51−66.
36. Alving, C. R.; Wassef, N. M.; Richards, R. L. Use of adjuvants for enhancement of antibody responses. In *Handbook of Experimental Immunology*; Weir, D., Blackwell, C., Herzenberg, L., Eds.; Vol.2A: The Lymphoid System; Sect. 3: Antibody Responses and Affinity Maturation (Nossal, G., section Ed.); Blackwell Scientific Publications: Oxford, 1996, pp 87.1−87.10.

Acknowledgments

This work was performed under a cooperative research and development agreement between the Walter Reed Army Institute of Research, Washington, DC, and Jenner Biotherapies, Inc., San Ramon, CA, and was partially supported by both institutions. The authors gratefully acknowledge the outstanding technical assistance of Ms. Elaine Morrison.

JS990011U

In Vitro Transepithelial Drug Transport by On-Line Measurement: Cellular Control of Paracellular and Transcellular Transport

PETER R. WIELINGA,[†] ESTHER DE WAAL,[†] HANS V. WESTERHOFF,[‡] AND *JAN LANKELMA*[*,†,‡]

Contribution from *Academisch Ziekenhuis Vrije Universiteit, Department of Medical Oncology, P.O. Box 7057, Room BR232, 1007 MB Amsterdam, The Netherlands; and BioCentrum Amsterdam, Vrije Universtiteit, Department of Molecular Cell Physiology, De Boelelaan 1087, 1081 HV Amsterdam, The Netherlands.*

Received December 28, 1998. Final revised manuscript received August 19, 1999.
Accepted for publication September 21, 1999.

Abstract □ Studies on transcellular transport across epithelial cell layers are performed mostly by discontinuous sampling of the transported compound. This has several drawbacks, e.g., it gives disturbances in volume, it limits the time-resolution, and is often laborious. In this report we introduce a method to measure transepithelial transport of fluorescent compounds continuously. The time-resolution is at the (sub)minute scale, allowing the measurement of the change in transport rate before and after transport modulation. We will describe how we used the method to measure transcellular and paracellular transport. For highly membrane-impermeable compounds, the paracellular transport and the regulation of the tight junctions was studied in wild-type and MDR1 cDNA transfected epithelial canine kidney cells (MDCKII). The effect of the multidrug transporter P-glycoprotein (Pgp) on the transepithelial transport was studied. Addition of the Pgp inhibitor SDZ PSC 833 showed a modulation of the idarubicin (IDA) and daunorubicin (DNR) transport, which was larger during transport from the basolateral to the apical side than in the reverse direction. By modeling the transepithelial transport, we found that in these cells Pgp had more effect on the basolateral to apical transport than vice versa, which can be attributed to a relatively large passive permeation coefficient for the cellular basolateral plasma membrane.

Introduction

Compartmentalization is important for multicellular organisms' functioning, so that the different biochemical tasks necessary for life are performed in the proper place under the proper conditions. The barriers between such compartments are often such that only regulated biochemical transport and communication can take place between the different compartments. Examples of such barriers are the epithelial cells in the gut and the endothelial cells of the blood−brain barrier.[1−4] Characteristic for these cell layers is that a-specific transport can hardly take place, due to the architecture of these layers. Tight junctions connect neighboring cells firmly to each other and hardly leave any (paracellular) space between the cells. Thereby a barrier is created with high transepithelial electrical resistance (TER) that is highly impermeable for most hydrophilic compounds.[5−8] Specific transporters and carriers regulate the transport of this class of compounds across these barriers.[6,8] For lipophilic compounds, which are able to passively diffuse across the cellular plasma membrane, epithelia and endothelia are often equipped with specialized proteins that regulate the transcellular transport (through the cells) of this class of compounds. An important example of such a transporter is P-glycoprotein (Pgp)[9−11] which functions as an ATP-dependent multispecific cellular drug efflux pump. Pgp was discovered as a transmembrane protein that induced cellular multidrug resistance (MDR),[11] i.e., resistance against several different anticancer drugs, e.g., daunorubicin (DNR), vincristine, taxol. However, not only are some anticancer drugs substrates, but many other types of compounds also interact with Pgp, e.g., cardiac drugs (verapamil, diltiazem), immunosuppressors (cyclosporins) and anti-AIDS drugs.[12,13] Epithelia and endothelia, with MDR1 Pgp localized in their apical plasma membrane, are found at several strategic sites in the body. Examples of such sites are the endothelial cells of the blood−brain and the blood−testes barrier and the epithelial cells lining the gut, where Pgp mediates drug transport out of the brain, the testes, and the body, respectively.[13−16]

Much knowledge on transepithelial transport has come from in vivo studies. However, ethical constraints limit the type of experiments that can be conducted in vivo. Also, because of the complexity of the multicellular organisms, it is often difficult to pinpoint which phenomena are related to specific molecular processes. In vitro models simulate the in vivo situation and do not have these drawbacks. Until now transepithelial transport has been measured discontinuously in time, mainly by measuring either the amount of substrate (mostly radioactively labeled, or fluorescent) transported from the apical to the basolateral (A to B) side of the cells (or vice versa) or by measuring the TER.[17−20] By combining knowledge of the study of MDR,[21,22] the use of fluorescence for detection, and the experience in developing in vitro techniques,[23,24] we developed a technique that can be used to study transepithelial transport continuously. The method makes use of commercially available plasticware and a fluorometer, equipment present in most biochemical laboratories. The method detects the transport of fluorescent substrates on-line, it has a high time-resolution, and effects of transport modulators can be studied within one experiment, thereby reducing the number of parameters that may give rise to errors.

With the method we successfully studied transepithelial transport in several different cell lines (Caco-2, LLC-PK1, and MDCKII). Here we describe how the technique is performed, and we report results obtained with the epithelial Madin−Darby canine kidney cell line MDCKII. We applied the method to carry out two types of experiments: (1) experiments in which the regulation of the tight junction is studied and (2) experiments in which the control of Pgp on the transepithelial transport is studied. Using a 70 kDa plasma membrane-impermeable fluorescein isothiocyanate-

* Corresponding author. Phone: +31-20-444 2603; fax: +31-20-444 3844; e-mail: J.Lankelma@azvu.nl.
[†] Academisch Ziekenhuis Vrije Universiteit.
[‡] BioCentrum Amsterdam.

10.1021/js980497z CCC: $18.00
Published on Web 11/11/1999

labeled dextran (FITC-dextran) or the highly negatively charged organic anion calcein (Cal), the paracellular transport (through the space between the cells) was studied, both in the wild-type MDCKII cells and the MDR1 cDNA transfected MDCKII-MDR1 cells. The influence of Pgp on the transcellular transport (involving the plasma membrane) was studied in the MDCKII-MDR1 using the membrane-permeable, fluorescent anticancer drugs daunorubicin (DNR) and idarubicin (IDA). While highly similar in chemical structure, these anthracyclines differ in their lipophilicity and membrane permeability, with IDA being more lipophilic than DNR. For both DNR and IDA, the transport from the basolateral to the apical (B to A) compartment and vice versa (A to B) and the effect of Pgp inhibition were studied. A drug transport model was developed to explain the differences in kinetics that were observed.

Experimental Section

Chemicals—Verapamil (Vp), diltiazem (Dil), calcein (Cal), fluorescein isothiocyanate labeled dextran (FITC-dextran) (MW = 70 kDa), 2-deoxy-D-glucose (deoxyglucose), and digitonin were obtained from Sigma (St. Louis, MO). DNR and IDA were from Farmitalia Carlo Erba (Brussels, Belgium). SDZ PSC 833 was obtained from Novartis (Basel, Switzerland). Cell culture media and supplements were obtained from Flow (Irvine, UK), and culture plastics from Nunc (Roskilde, Denmark). Fetal calf serum (FCS) was from Gibco (Paisley, UK), 4-(2-hydroxyethyl)-1-piperazine ethanesulfonic acid (HEPES) was from Serva (Heidelberg, Germany), and sodium azide (NaN_3) and ethylenediaminetetraacetic acid (EDTA) were from Baker Chemicals (Deventer, The Netherlands). Sodium penicillin G was from Yamanouchi (Leiderdorp, The Netherlands), and streptomycin sulfate was from Radiumfarma-Fisiopharma (Italy). Microporous polycarbonate membrane inserts (transwell No. 3413) with a pore size of 0.4 μm and a diameter of 6.5 mm were from Corning Costar (Badhoevedorp, The Netherlands). Plastic fluorescence cuvettes were from Falcon (Leiden, The Netherlands).

Cell Culture and Media—MDCKII cells, wild-type and MDR1 cDNA transfected (MDCKII-MDR1),[25] were obtained from Drs. Evers and Borst (NKI, The Netherlands) and cultured as previously described.[18] Cells were cultured in a cell incubator in humidified air (supplemented with 5% CO_2) at 37 °C, in DMEM with 20 mM HEPES (pH 7.4), supplemented with 7.5% heat-inactivated FCS, and penicillin (0.05 mg/mL) and streptomycin (0.1 mg/mL). For the transepithelial transport experiments, the cells were seeded on transwell membrane inserts (transwell vial) at 2500 cells/mm,^{2} and the medium was refreshed every day. Confluency of the cell monolayer on the microporous membrane was monitored by measuring the transepithelial electrical resistance (TER) using a Millicell electrical resistance meter (Millipore). On the basis of this measurement, the cells could be used for transport assays between day 3 to 6, when TER values were between 600 and 300 $\Omega \cdot mm^2$ and approximately $80-90 \times 10^3$ cells were present on the microporous membrane.

Experimental Setup—A transwell vial with cells grown to confluency was placed in a fluorescence cuvette. To fit a transwell vial (Costar), the cuvette was composed of a well of a 24-well polystyrene plate (Costar) placed on top of a polystyrene fluorescence cuvette (Falcon). A square, with the inner measurement of the cuvette, was taken out of the bottom of the 24-well plate well, creating a free opening between the cuvette and the well (see Figure 1). The cuvette was placed in a thermostated cuvette holder equipped with a magnetic stirrer, the latter situated under the cuvette holder. After each experiment the cuvette was cleaned and sterilized with ethanol for reuse. The medium in the lower compartment (cuvette) was stirred with a Teflon-coated magnetic stirrer bar. The medium in the upper compartment (transwell vial) was stirred with a small Teflon stirrer, attached to a small 24 V electric motor. The motor was attached to a metal plate with a free space fitting the top of the cuvette (see Figure 1). This ensured that the motor was placed properly. The Teflon stirrer speed was controlled at 100–150 rpm. During the experiments 3100 μL medium was present in the cuvette and 250 μL in the transwell

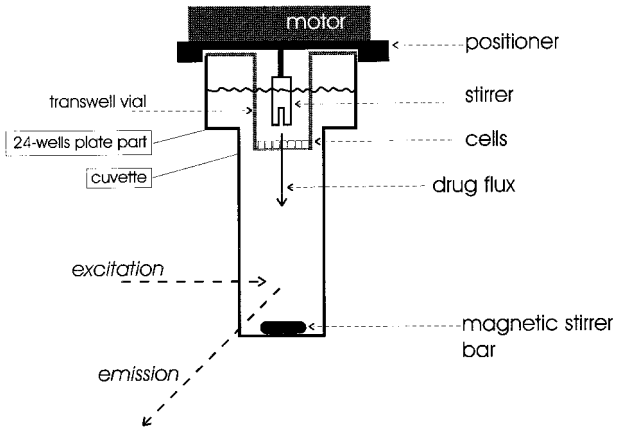

Figure 1—Schematic drawing of the experimental measurement setup. The cuvette used for the transepithelial experiments was composed of two parts: (1) a 24-well plate well on top of (2) a plastic fluorescence cuvette. The medium in the cuvette had a volume of 3100 μL and that in the transwell vial 250 μL. A Teflon stirrer driven by a 24 V electric motor stirred the medium in the transwell vial and a magnetic stirrer bar that in the cuvette. Transepithelial transport was monitored by measuring the fluorescent substrate (added to the transwell vial) that appeared in the cuvette.

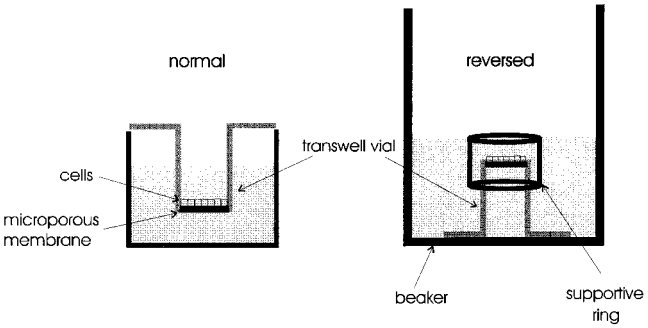

Figure 2—Normal and "reversed" growth of cells on a microporous membrane is illustrated. The left panel shows how cells are normally grown. The transwell vial is hanging in a 24-well plate well, and the cells are grown at the inside of the transwell vial. The right panel shows the "reversed" growth. Now the transwell vial is turned upside down and is completely immersed in growth medium. A polyethylene ring is placed over the transwell vial creating a compartment in which cells can be seeded.

vial. Transport experiments were performed in medium A with 1% FCS. Medium A is a phosphate-buffered saline (PBS) based medium supplemented with essential amino acids for MEM (Flow) with 5.5 mM glucose, 4 mM L-glutamine, and 20 mM HEPES, without bicarbonate (pH 7.4). To remove dust particles, which gave extra background noise during the transport measurements, the medium was filtered (0.22 μm, Millipore).

The detection was most sensitive when fluorescent compounds were added to the transwell vial (upper compartment), and the appearance of the substrate was monitored in the cuvette (the lower compartment). To measure transport from the apical to the basolateral side of the cells (A to B), cells were seeded in the transwell insert. After attachment and growth of the cells, with the basolateral side facing the microporous membrane, the transwell vial was suited to measure transport from A to B. To measure the reversed process, transport from B to A, cells were grown "reversed", at the opposing side of the microporous membrane. In Figure 2 the difference between both ways of growing the cells is illustrated. Before seeding, the transwell was placed in a beaker filled with ±15 mL of growth medium. The transwell was placed upside down, in such a way that there was no air present under the membrane. Then a plastic (polyethylene) supportive ring, which loosely fitted the transwell, was placed around the transwell and approximately 5000 cell/mm^2 were brought within the supportive ring. After 1 day the supportive ring was removed, and confluency was checked by measuring the TER.

Transepithelial Efflux Experiments and Calculations—Just before the start of the transepithelial transport experiment the cells were washed with medium A (at 37 °C), and the growth

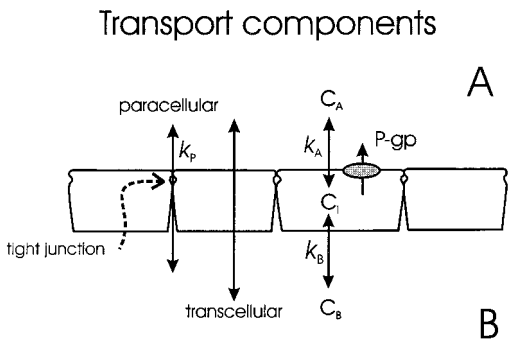

Figure 3—Schematic presentation of an epithelial cell monolayer and the different transport components. Tight junctions are indicated. Pgp is localized in the apical plasma membrane and is modeled using Michaelis–Menten kinetics. The free substrate concentrations in the different compartments are defined as C_A, the apical compartment concentration; C_i, the intracellular concentration; and C_B, the basolateral compartment concentration. Passive plasma membrane transport across the apical membrane is dependent on C_A and C_i and proceeds with a first-order rate constant k_A. Similarly, passive transport across the basolateral membrane takes place, depending on C_B and C_i, and proceeds with a first-order rate constant k_B.

medium was replaced by medium A supplemented with 5% FCS and antibiotics. Then the transwell vial was placed in the cuvette, and the fluorescent substrate was added to the transwell vial. The fluorescence in the cuvette was measured on a computer-controlled fluorometer (FluoroMax, SPEX Industries, Edison, NJ) at excitation and emission wavelengths of 480 and 590 nm for DNR and IDA and 480 and 525 nm for Cal and FITC-dextran. At the end of the experiment both the cells (with 25 μM digitonin) and the microporous membrane (mechanically) were disrupted, and then the equilibrating fluorescence (F_{eq}) was measured, which was used for calibration. The normalized fluorescence (F_n) was calculated according to $F_n = (F - F_b)/(F_{eq} - F_b)$, with F = measured fluorescence and F_b = background fluorescence. From this normalized trace, representing the normalized increase in fluorescence in time ($\Delta F_n/\Delta t$), the flux (J) in pmol/min·cm^2 was calculated using $J = (\Delta F_n/\Delta t)C_T V_T V_C(V_T + V_C)^{-1}A^{-1}$, in which C_T = the applied concentration at the start of the experiment; V_T = volume of the medium in the transwell vial; V_C = volume of the medium in the cuvette; A = surface (0.33 cm^2). (Note: the substrate is diluted in V_C ($V_C \gg V_T$), and therefore backflux from the cuvette compartment is neglected.) Dividing J by C_T gives the permeability (k) (length·time^{-1}).[17] Alternatively, the permeation coefficient (volume·time^{-1}·number of cells^{-1}) may be calculated when reference is made to the amount of cells instead of surface.[23,24]

Octanol/Water Partition Coefficient—The octanol/water partition coefficient is the ratio of the anthracycline concentration in the octanol phase divided by that in the water (= phosphate-buffered saline (PBS)) phase at equilibrium. The ratio was determined at ambient temperature (20–25 °C), by adding 750 μL octanol to 750 μL of a 10 μM anthracycline solution prepared in PBS (pH 7.3). The two phases, which do not mix, were then vigorously shaken for 1 min and centrifuged to separate both phases again. Aliquots of 25 μL of both phases were separately dissolved in 150 μL ethanol (70% solution in water) in a 96-well plate. To obtain an equal medium composition in all the wells, 25 μL PBS was added to the wells containing the 25 μL octanol anthracycline solution, and 25 μL octanol was added to the wells containing the PBS anthracycline solution. The fluorescence of the plate was determined on a Spectrafluor plate reader (Tecan, Austria), using an excitation filter of 492 nm and an emission filter of 595 nm. After background correction, the octanol/water partition coefficient was calculated by the fluorescence of the octanol phase divided by the fluorescence of the water phase.

A Model for Transepithelial Drug Transport—A biomathematical transport model was developed to describe transepithelial transport and the effect of Pgp inhibition by SDZ PSC 833 for transepithelial drug transport from A to B and vice versa. Figure 3 shows a schematic presentation of epithelial cells, with C_A = the apical compartment concentration; C_i = the intracellular concentration; and C_B = the basolateral compartment concentration. The paracellular flux is the concentration in the transwell vial times the paracellular permeation coefficient k_p (per unit surface). The passive plasma membrane flux over the apical membrane is the difference between C_A and C_i times the passive permeation coefficient of the apical membrane k_A (per unit surface). Similarly, the passive flux across the basolateral membrane is the difference between C_B and C_i times the passive permeation coefficient of the basolateral membrane k_B (per unit surface). Pgp is expressed at the apical side of the cell. The Pgp-mediated transport rate (v_{Pgp}) is supposed to follow Michaelis–Menten kinetics:

$$v_{Pgp} = \frac{V_{max} C_i}{K_M + C_i} \tag{1}$$

with K_M = the Michaelis constant and V_{max} = the maximum transport rate. When $C_i \ll K_M$, eq 1 can be simplified to

$$v_{Pgp} = \frac{V_{max}}{K_m} C_i \tag{2}$$

For the transport from A to B, $R_{A\rightarrow B}$ is defined as the transepithelial flux after inhibition (J_{-Pgp}) divided by the transepithelial flux before inhibition (J_{+Pgp}):

$$R_{A\rightarrow B} = \left(\frac{J_{-Pgp}}{J_{+Pgp}}\right)_{A\rightarrow B} \tag{3}$$

At quasi-steady-state (either with or without Pgp transport), the flux across the apical membrane (= $C_o k_A - C_i k_A$) equals the flux across the basolateral membrane (= $C_i k_B$) and $R_{A\rightarrow B}$ can be described in terms of the fluxes across the basolateral membrane plus the paracellular flux. Then eq 3 becomes

$$R_{A\rightarrow B} = \frac{C_i k_B + C_A k_p}{C_i' k_B + C_A k_p} \tag{4}$$

with C_i = the free intracellular concentration in the presence of SDZ PSC 833 and C_i' = the free intracellular concentration in the absence of SDZ PSC 833. (Note that since DNR is strongly diluted in the cuvette compartment the backflux into the cells is neglected.)

In the quasi-steady-state ($dC_i/dt = 0$) the intracellular concentration is constant and is determined by the influx from the apical compartment and the efflux out from the cellular compartment, which gives

$$0 = C_A k_A - C_i' k_A - C_i'\left(\frac{V_{max}}{K_M}\right) - C_i' k_B \tag{5}$$

The possibility that the "unstirred" cytosol acted as an additional barrier was neglected. Based on Fick's first law of diffusion, a diffusion coefficient at 37 °C of 4×10^{-6} cm^2/s, and an average diffusion path length of 5×10^{-6} m, it can be calculated that for the examples mentioned the cytosol forms less than 5% of the total resistance (= the reciprocal permeability) of the cell monolayer. When eq 5 is rewritten, the equation for the intracellular concentration evolves to:

$$C_i' = \frac{C_A}{1 + \frac{k_B}{k_A} + \left(\frac{V_{max}}{K_M k_A}\right)} \tag{6}$$

Equation 6 gives the equation for the intracellular concentration when Pgp is active. When Pgp is inactive ($V_{max} = 0$), the last term in the denominator is zero. Substitution into eq 4 and dividing by ($C_A k_B$) gives the equation for the SDZ PSC 833 induced slope change in terms of k_A, k_B, k_p, and V_{max}/K_M:

$$R_{A\rightarrow B} = \frac{\left[1 + \frac{k_B}{k_A}\right]^{-1} + \frac{k_p}{k_B}}{\left[1 + \frac{k_B}{k_A} + \left(\frac{V_{max}}{K_M k_A}\right)\right]^{-1} + \frac{k_p}{k_B}} \tag{7}$$

An equation for $R_{B\rightarrow A}$, defined as the flux without SDZ PSC 833

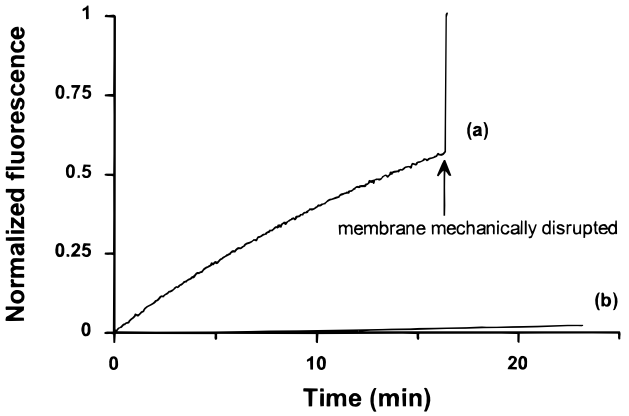

Figure 4—DNR (2 μM) transport from the upper to the lower (cuvette) compartment (a) without cells and (b) with MDCKII cells grown on the microporous membrane.

divided by the flux with SDZ PSC 833, can be derived in a similar way as was done for $R_{A\rightarrow B}$. $R_{B\rightarrow A}$ is given by

$$R_{B\rightarrow A} = \frac{k_B(C_B - C_i') + C_B k_p}{k_B(C_B - C_i) + C_B k_p} \quad (8)$$

C_i and C_i' are now given by

$$C_i' = \frac{C_B}{1 + \frac{k_A}{k_B} + \left(\frac{V_{max}}{K_M k_B}\right)} \quad (9)$$

Substitution of eq 9 into eq 8 gives the equation for $R_{B\rightarrow A}$:

$$R_{B\rightarrow A} = \frac{\left[1 + \left(\frac{V_{max}}{K_M k_A}\right)\right]\left[1 + \frac{k_A}{k_B} + \left(\frac{V_{max}}{K_M k_B}\right)\right]^{-1} + \frac{k_p}{k_A}}{\left[1 + \frac{k_A}{k_B}\right]^{-1} + \frac{k_p}{k_A}} \quad (10)$$

Results and Discussion

Transport with and without Cells on the Microporous Membrane—Figure 4 shows the transport of daunorubicin (DNR) with and without cells present in the transwell vial. Without cells the DNR transport is much faster than with cells on the microporous membrane. Without cells on the membrane, the influence of stirring or not stirring of the upper compartment was clearly reflected in the transport rate after turning the stirrer on and off (data not shown). With cells on the membrane this effect was hardly visible for DNR transport, indicating that diffusion in the transwell compartment was not limiting for the transepithelial transport of DNR. To ensure good mixing of a broad range of compounds, the medium was always gently stirred.

After adding DNR to the transwell compartment with cells on the membrane, a lag time of approximately 30 min was first observed. Thereafter the transport rate became virtually constant. During the lag time, the intracellular free DNR concentration increases until the cellular influx of DNR equals the cellular efflux from the cells. When this is the case, both the transepithelial transport and intracellular free drug concentration stay constant and are at quasi-steady-state. For the DNR transport in wild-type and MDR1 cDNA transfected MDCKII-MDR1 cells, this quasi-steady-state continued for at least 2 h. From $\Delta F_n/\Delta t$ (see Figure 4) at quasi-steady-state the permeation coefficient in cm/min was determined (see Experimental Section). For the DNR transport from A to B the transepithelial permeation coefficients were 0.67 ± 0.05 ($\times 10^{-3}$) cm/min for the wild-type MDCKII cells and 0.44 ± 0.3 ($\times 10^{-3}$) cm/min for the MDCKII-MDR1 cells (Table 1). The increased expression of Pgp in the apical[25] membranes of the MDCKII-MDR1 cells, after transfection of wild-type cells with the MDR1 cDNA, led to a lower A to B transepithelial transport rate compared to the untransfected MDCKII cells (due to backward pumping to A).

Table 1—Transepithelial Transport for MDCKII-MDR1 Cells

	Direction	MDCKII-MDR1 ($\times 10^{-3}$) cm/min	MDCKII ($\times 10^{-3}$) cm/min
DNR	A to B	0.44 ± 0.3[a]	0.67 ± 0.05
Cal	A to B	0.17 ± 0.01	0.04, 0.07
FITC-dextran	A to B	0.04 ± 0.02	0.02, 0.01

[a] Data are given as the mean ± SD of at least three experiments or stated otherwise.

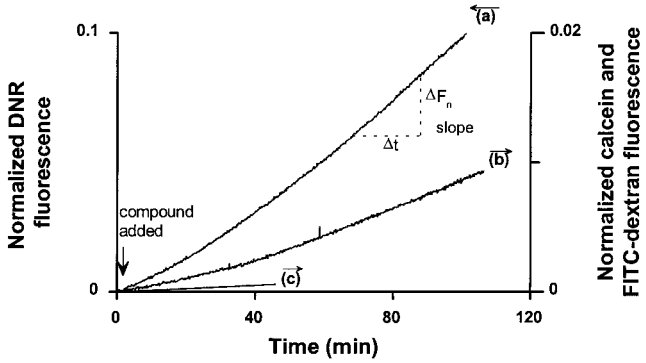

Figure 5—Comparison of (a) DNR (2 μM), (b) Cal (0.4 μM) and (c) FITC-dextran (8 μM) transport across MDCKII wild-type cells grown on microporous membranes. Fluorescent compounds were added to the upper compartment, and transport from the apical to the basolateral side of the cells was measured by monitoring the fluorescence in the cuvette. Representative traces are shown.

Paracellular Transport—To investigate the tightness of the monolayers, the transport of the plasma membrane permeable DNR was compared with that of highly plasma-membrane-impermeable compounds. Figure 5 shows the A to B transport of the organic anion calcein (Cal), the bulky compound FITC-dextran (70 kDa), and DNR for the MDCKII cells. Table 1 presents the transepithelial permeation coefficients for the wild-type and the MDCKII-MDR1 cells for the transport from A to B. The transepithelial transport of Cal for the MDCKII-MDR1 cells is approximately 4 times faster than for the wild-type cells. For FITC-dextran the transepithelial permeation for the wild-type cells was approximately 2 times slower. Why there are these differences between the two lines is not clear. It cannot be explained by differences in TER values of the batches of cells that were used since these were comparable. Possibly components cotransfected or the MDR1 gene itself causes this difference in the epithelial permeability. More certainty about this may be obtained by a detailed mechanistic study, but this does not lie within the scope of this study.

To show the tightness of the cell monolayer, the effect of opening the tight junctions by the calcium chelator EDTA[8,27] was studied. Figure 6 shows the effect of EDTA on the transepithelial transport of FITC-dextran. After a constant flux was observed, EDTA was added as indicated in the figure. A lag time of ~15 min after the EDTA addition was observed, and then the increased transport rate became constant. The inset shows transepithelial transport during the transition from closed to opening of the tight junctions in more detail.

From the constant fluxes before and after addition of EDTA, transepithelial permeation coefficients were calculated. Table 2 gives the transepithelial permeation coef-

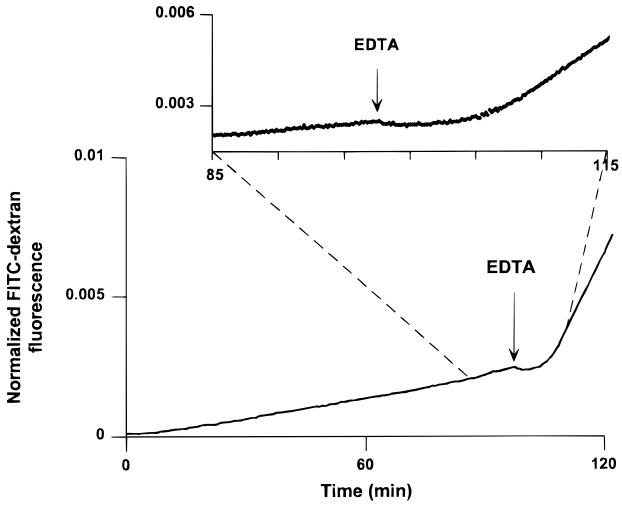

Figure 6—The effect of binding the extracellular calcium with EDTA (2 mM) on the transport FITC-dextran (8 μM) across MDCKII-MDR1 cells. FITC-dextran was added to the upper compartment, and the transport from the apical to the basolateral side of the cells was measured by monitoring the fluorescence in the cuvette. The inset shows the transition from closed to open tight junctions in more detail (85 to 115 min). The traces are representative for at least three experiments.

Table 2—Permeation Coefficients: The Effect of Opening of the Tight Junctions (TJ) for MDCKII-MDR1 Cells

	direction	control[b] ($\times 10^{-3}$) cm/min	TJ open with EDTA[b] ($\times 10^{-3}$) cm/min	R_{TJ}[c]
DNR	B to A	0.8 ± 0.4[a]	2.9 ± 1.0	5.3 ± 2.6
IDA	B to A	1.6 ± 0.2	2.1, 2.9	1.3, 1.7
DNR	A to B	0.7 ± 0.3	4.0 ± 1.1	5.3 ± 1.7
IDA	A to B	2.2 ± 0.9	2.4, 2.9	0.9, 1.1
FITC-dextran	both	0.04 ± 0.02	0.5 ± 0.2	13.1 ± 4.7

[a] Data are given as the mean ± SD of at least three experiments or stated otherwise. [b] SDZ PSC 833 (5–20 μM) was present to inhibit Pgp. [c] Please note that R_{TJ} cannot be derived from the first two columns, because R_{TJ} was calculated from individual (paired) data.

ficients for FITC-dextran, DNR, and IDA for the transport from A to B and vice versa, both in the presence and absence of EDTA. DNR and IDA were used because they are highly similar in chemical structure, but differ in lipophilicity. The difference in lipophilicity was measured by their octanol/water partition coefficient. The partition coefficients were 16.6 ± 0.2 for IDA (mean ± SEM; n =3) and 4.9 ± 0.1 for DNR. The IDA transepithelial transport in the presence of SDZ PSC 833 was a factor 2−3 larger than that of DNR, reflecting the difference in lipophilicity. In all tested cases the permeability increased after addition of EDTA. This increase of the paracellular transport component is expected to be independent of the lipophilicity. It therefore reduces the relative difference between total transport of DNR and IDA through the cellular layer. Measurement of transport from A to B showed a slightly larger permeability for DNR than for IDA. We attribute this to biological variations between cellular layers. To partially avoid effects of these biological variations, the ratio (R_{TJ}) of the fluxes before and after addition of EDTA was calculated within the same experiment. R_{TJ} is presented in Table 2 and decreased in the order FITC-dextran > DNR > IDA. For the hydrophilic compound FITC-dextran the transepithelial flux was strongly dependent on the paracellular route, while for the highly lipophilic IDA, opening of the tight junction hardly influenced the flux, which is in accordance with what can be expected from an increase in lipophilicity (comparing DNR and IDA). This illustrates that the dependence of total transport on the

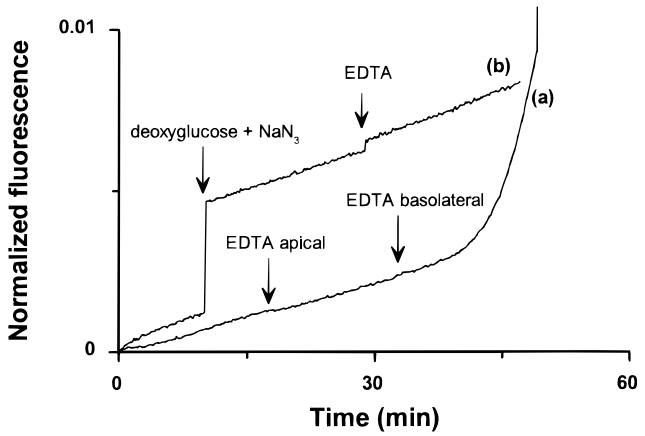

Figure 7—Specificity of the EDTA effect on transepithelial transport of FITC-dextran (8 μM) of MDCKII cells. (a) Effect of adding EDTA apically or basolaterally. As indicated, EDTA (2 mM) was first added to the apical side and then to the basolateral side. (b) Effect of ATP-depletion by the addition of deoxyglucose (6 mM final concentration) and NaN_3 (10 mM final concentration) on the EDTA effect. Deoxyglucose and NaN_3 were added to both the apical and basolateral compartments. Thereafter, EDTA (2 mM) was added (apically and basolaterally). The traces are representative for at least three experiments.

paracellular transport decreases as the lipophilicity/passive membrane permeability increases. From the effects of the tight junctions on the transport, we may conclude that the cell layers stayed intact under the applied conditions. Note that the data presented here were obtained with the MDCKII-MDR1 cells in the presence of SDZ PSC 833 to inhibit Pgp. Similar results were also found for the wild-type MDCKII cells and LLC-PK1[20] cells (data not shown).

Cellular Control of the Tight Junction—The tightness of epithelia and endothelia may be regulated by the cells in order to control the flux of certain molecules (or cells).[8,9] The mechanism by which EDTA triggers the cells to open the paracellular transport route is still under investigation.[6,7,26,28] Extracellular calcium and calcium-dependent protein kinases (PKC) have shown to be directly or indirectly involved in the tight junction tightness.[27,29–31] To show the usefulness of the current method in such regulations studies, we examined (1) the effect of adding EDTA to either side of the monolayer and (2) the influence of ATP-depletion-induced metabolic inhibitors.

Figure 7 (line a) shows the transport of FITC-dextran and the effect of EDTA added to the apical or to the basolateral side. Addition of EDTA to the apical side had no effect. Only when EDTA was present at the basolateral side, then the tight junction opened and an increased FITC-dextran transport was observed. These results are similar to recent observations on the basolateral side specificity of Ca^{2+}.[32,33] Figure 7 (line b) shows the effect of adding an excess of both the nonmetabolizable deoxyglucose (6 mM) and the respiratory inhibitor NaN_3 (10 mM), added to both compartments, on the FITC-dextran transport. It can be seen that addition of NaN_3/deoxyglucose caused an instant increase in the background fluorescence, which may be related to the yellowish color. Looking at the fluxes, it can be seen that the ATP-depletion itself did not affect the FITC-dextran transport rate. However, under these conditions EDTA did not open the tight junctions anymore. Similar results were also obtained for LLC-PK1 cells both measuring the transepithelial transport and measuring the TER (data not shown). This strongly suggests that the effect of EDTA on the tight junctions is ATP-dependent and most probably involving ATP dependent phosphorylation mechanisms.[31,34–36] However, at this point we cannot exclude direct interactions between deoxyglucose or NaN_3

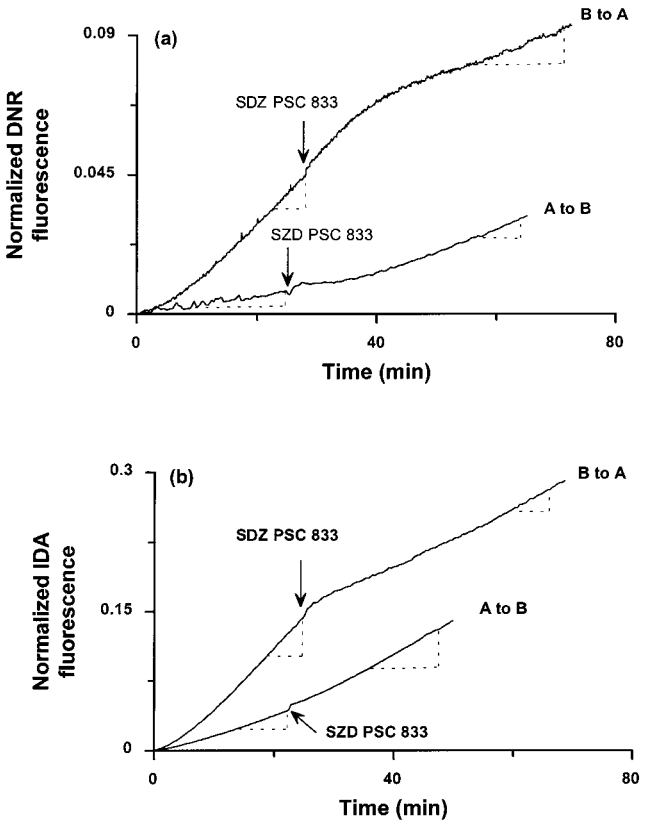

Figure 8—SDZ PSC 833 modulation of (a) the DNR (2 μM) and (b) the IDA (2 μM) transepithelial transport across MDCKII-MDR1 cells. The effect of SDZ PSC 833 was measured for the transport from A to B and from B to A, as indicated. After reaching the quasi-steady-state, SDZ PSC 833 (5–20 μM) was added to the cells to inhibit Pgp. The traces are representative for at least three experiments.

and EDTA. These experiments show that our system can be useful for further elucidating mechanisms of paracellular transport. This application shows that the method can be useful to study (1) compounds that diffuse rapidly (e.g., when the tight junctions are open) and (2) modulators that induce rapid changes (in the minute time range) in the transepithelial transport.

Effect of Pgp on Transepithelial DNR and IDA Transport—The apical localization of Pgp results in a decreased flux from A to B and an increased flux from B to A. Consequently, inhibition of Pgp will lead to an increase in transepithelial flux from A to B and to a decrease from B to A. To be able to perform experiments in which Pgp can be modulated, three Pgp inhibitors, verapamil (Vp), diltiazem (Dil), and SDZ PSC 833, were tested for their effect on the paracellular transport of FITC-dextran across MDCKII-MDR1 cells. At concentrations needed to rapidly inhibit Pgp, Dil (>0.5 mM) and Vp (>200 μM) increased the FITC-dextran transport (not shown). Pgp inhibitor SDZ PSC 833 (1−25 μM) did not influence the FITC-dextran (and Cal) transport and was used for further study of the effect of Pgp inhibition on the transepithelial transport of DNR and IDA. Figure 8 shows the transepithelial transport using the MDCKII-MDR1 cells for DNR (Figure 8a) and IDA (Figure 8b) for transport from A to B and vice versa. After the quasi-steady-state was reached, the effect of Pgp inhibition was measured by adding SDZ PSC 833 (5 μM) to both compartments, as is indicated in Figures 8a and 8b. The addition of SDZ PSC 833 to the cuvette gave rise to an increase of the background fluorescence, due to the weak fluorescence of SDZ PSC 833. In later experiments it was found that addition of 5−20 μM SDZ PSC 833 only to the transwell compartment was sufficient to inhibit Pgp with a lower disturbance of the background signal. After the addition of SDZ PSC 833, the transepithelial flux changed slowly and stabilized after approximately 30 min. In the case of A to B transport, the flux increased, and in the case of B to A transport, the flux decreased (Figure 8; Table 3). From the fluxes at quasi-steady-state, the transepithelial permeation coefficients were calculated, which are presented in Table 3. To be able to compare the effect of Pgp inhibition for the different compounds, the effect of SDZ PSC 833 was quantified by the ratio of the fluxes before and after Pgp inhibition. This ratio was called the SDZ PSC 833-induced slope change (R). To be able to compare R for the transport from A to B and vice versa, the R was defined as the larger slope divided by the smaller slope. Table 3 shows the obtained SDZ PSC 833-induced slope changes. For FITC-dextran, addition of SDZ PSC 833 did not lead to change in the flux. For IDA and DNR, addition of SDZ PSC 833 led to changes in the transepithelial fluxes. Moreover, it was found that for both IDA and DNR the effect of Pgp inhibition was largest for the transport from B to A.

Table 3.—Permeation Coefficients: the Effect of SDZ PSC 833-Induced Pgp Inhibition for MDCKII-MDR1 Cells

	direction	control ($\times 10^{-3}$) cm/min	with SDZ PSC 833 ($\times 10^{-3}$) cm/min	R[b]
DNR	B to A	2.6 ± 1.0[a]	0.8 ± 0.4	3.7 ± 1.4
IDA	B to A	3.8 ± 1.3	1.6 ± 0.2	2.4 ± 0.6
DNR	A to B	0.44 ± 0.3	0.7 ± 0.3	1.6 ± 0.5
IDA	A to B	1.4 ± 0.5	2.2 ± 0.9	1.5 ± 0.2
FITC-dextran	both	0.04 ± 0.02	0.04 ± 0.02	1.1 ± 0.3

[a] Data are given as the mean ± SD of at least three experiments. [b] Please note that R cannot be derived from the first two columns, because R was calculated from individual (paired) data.

Comparison of Experimental Data with the Model—To seek an explanation for the difference in effects of SDZ PSC 833 on the transport from A to B and vice versa, a biomathematical transport model was developed (see Experimental Section). Figure 3 shows a schematic presentation of an epithelial monolayer. Using eqs 7 and 10, which describe R for transport from A to B ($R_{A\rightarrow B}$) and from B to A ($R_{B\rightarrow A}$), respectively, the theoretical differences between the transport from the A to B and transport vice versa were studied for nonsaturating conditions. Figure 9a shows a simulation of the relationship between R and the Pgp concentration ($\sim V_{max}/(K_M k_A)$). In this simulation the passive permeation coefficients were kept constant and equal. The figure shows a linear relationship between the Pgp concentration and $R_{A\rightarrow B}$. A nonlinear relationship was found for $R_{B\rightarrow A}$. In the lower range ($V_{max}/(K_M k_A) \ll 1$) $R_{B\rightarrow A}$ increases almost linearly with increasing Pgp concentration. At values of $V_{max}/(K_M k_A) > 1$, $R_{B\rightarrow A}$ goes to a plateau and Pgp loses control over the transepithelial flux. The latter can be explained by the high Pgp activity, resulting in C_i values approaching zero and the basolateral membrane getting more and more in control of the transcellular flux. In the extreme case Pgp completely clears the cell of almost all drug, while the transcellular flux becomes equal to the flux across the basolateral membrane ($= C_B k_B$). When also paracellular transport is taking place, R decreases (dashed lines Figure 9a) and $R_{A\rightarrow B}$ seems to be more affected by the paracellular flux than $R_{B\rightarrow A}$. The simulations in Figure 9a show that in general one may expect that Pgp has a higher control over the transport from A to B than vice versa, which seems in contradiction with our experiments. However, k_B and k_A may not be equal for these cells. Figure 9b shows the relationship between k_B/k_A and both $R_{B\rightarrow A}$ and $R_{A\rightarrow B}$. At low ratios of k_B/k_A, $R_{A\rightarrow B}$ is larger than $R_{B\rightarrow A}$; however, at higher ratios of k_B/k_A (>2)

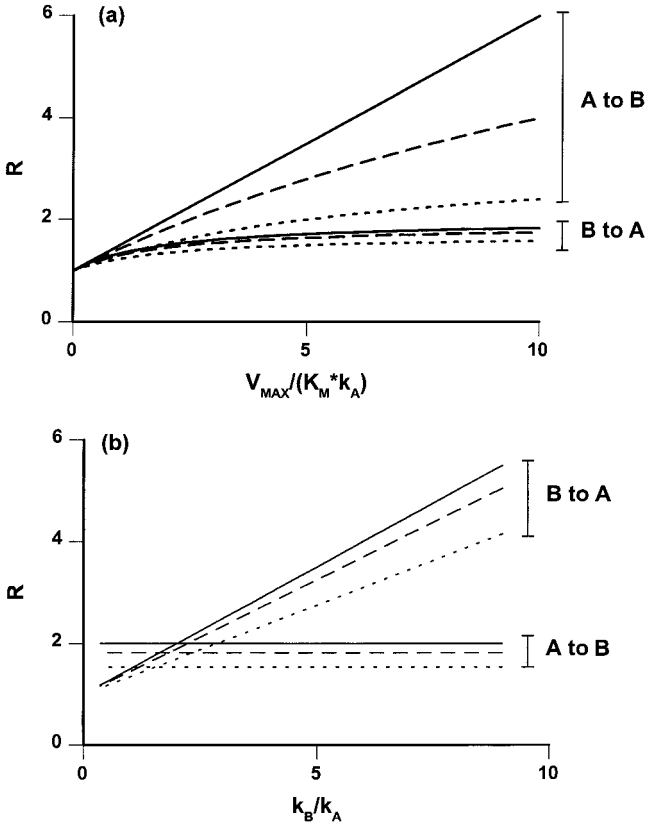

Figure 9—Simulations of the SDZ PSC 833-induced slope change for the transport from A to B and from B to A. In (a) Pgp was varied by changing the dimensionless factor $V_{max}/(K_M k_A)$, while k_A and k_B were both kept constant at 6.25×10^{-3} cm/min. These relative estimates correspond to those of moderately multidrug resistant cells.[21] (b) Simulation of the dependence R on the ratio of the basolateral over the apical membrane permeation coefficient (k_B/k_A). V_{max}/K_M was kept constant at 12.5×10^{-3} cm/min; ($k_B + k_A$) was set at 12.5×10^{-3} cm/min, and the ratio k_B/k_A was varied. In both a and b three conditions are shown: (1) when there is no paracellular transport (solid lines); (2) when the paracellular permeability is 10% (long dashes); (3) 30% (short dashes) of the total transepithelial permeability.

the situation is reversed and $R_{B\to A}$ becomes larger than $R_{A\to B}$. When the paracellular transport of DNR and IDA are approximately equal to the transepithelial transport of Cal, then the paracellular transport will make up 10−30% of the total transepithelial transport of DNR and IDA. Introducing a paracellular flux in the model leads to an overall decrease of the ratios (dashed lines Figure 9b). However, the crossing of the lines for $R_{A\to B}$ and $R_{B\to A}$ occurs at approximately the same k_B/k_A (range 1.6−2). At $k_B > 2k_A$ the model predicts similar results as found in the experiments. Although the relations plotted in Figure 9b still are dependent on the V_{max}/K_M, the passive membrane permeabilities, and the paracellular permeability, these results show that for both DNR and IDA, $k_B > k_A$. On the basis of our transport data for DNR and IDA, k_B will be approximately 3−7 times larger than k_A, and this estimate tends to be larger for DNR than for IDA. This difference could be due to the differences in passive membrane permeation coefficients (Figure 9a).

An explanation for the larger k_B may be a larger basolateral membrane than apical membrane surface. The simplest model of a cell is a cube, with the tight junction localized to the top rim of the cells, with 1/6 of the membrane localized apically and 5/6 localized basolaterally. However, most epithelial cells contain microvilli at their apical side and basolateral clefts at their basolateral side, making it more complicated to compare both surface areas. A low number of microvilli when compared to basolateral clefts may also explain our observation. However, different compositions in lipids or proteins of the apical and basolateral membranes may also explain such differences in membrane permeabilities. For instance basolaterally located transport proteins, like the organic cation transporter (Oct1),[37] may increase the basolateral transport for neutral as well as for the protonated[38] form of DNR and IDA. Recent studies have shown that such transport proteins may be involved in the basolateral uptake of organic cations and are present in renal cell lines.[39]

In summary, we present here a new method to measure the transepithelial transport of fluorescent compounds online and at (sub)minute time resolution. It makes use of commercially available plasticware and a fluorometer, equipment present in most biochemical laboratories. It is simple to perform and relatively inexpensive. To reduce the influence of stagnant layers[17] on the transport, the media in both the apical and basolateral compartments can be continuously stirred and thermostated. We have shown that both paracellular and transcellular transport and modulation of both types of transport can be studied. Moreover, the paracellular transport studies showed that the monolayer stayed intact during the experiments (up to 4 h) and was not disrupted by the stirring of the medium, which was confirmed by microscopy (not shown). Related to this point we like to bring up that when the cell monolayer was already leaky at the beginning of the experiment (less than 5% of the cases) this became directly evident from the transport that was observed. Thus the method allowed us to terminate and discard such experiments. Comparing the fluorescent compounds DNR, IDA, Cal, and FITC-dextran, we found the highest transepithelial transport rate for the highly membrane-permeable IDA and the lowest for bulky and membrane-impermeable FITC-dextran. Site specificity for the EDTA-induced opening of the tight junctions was bound to basolateral side of the cells, which has also been reported by other groups.[32,33] Moreover, we found that adding an excess of metabolic inhibitors could inhibit the effect EDTA on the tight junctions. These experiments show that the method can be useful to study paracellular transport. For the transepithelial transport of DNR and IDA with the MDCKII-MDR1 cells, we found that Pgp inhibition was most effective for transport form B to A. Modeling showed that this was possible at $k_B > 2k_A$. We estimated that k_B was approximately 3−7 larger than k_A. The biomathematical transport model showed that the effect of Pgp on the transepithelial transport is dependent on the Pgp concentration and on the ratio of k_B/k_A. At higher Pgp concentrations and at lower ratios of k_B/k_A, Pgp gets more control over the A to B transepithelial transport, but loses control over the B to A transport. Extrapolation of these results to the in vivo situation of patients receiving anticancer drugs such as DNR or other Pgp-interacting drugs suggests that decreased efflux from the blood or increased influx from the lumen of the gut by treatment with Pgp modulators can differ quantitatively, depending on the contribution of transport components for uptake and efflux across the apical or basolateral membrane. Where there is a basolaterally localized uptake system involved in the transport, it may be worthwhile to inhibit this transport, thereby indirectly reducing the Pgp-mediated excretion. Moreover, inhibition of Pgp after an intravenous bolus injection of Pgp substrate drugs may lead to unexpected differences in clearance from the blood and uptake into the brain, depending on the (passive) permeation properties of the drug that is used. Using the method described here, one may study these properties in greater detail and so may understand and predict the in vivo situation better.

References and Notes

1. Topp E. M. Barriers to delivery of macromolecules. *Med. Chem. Res.* **1997**, *7*, 493−508.
2. Hayashi M.; Tomita M.; Awazu S. Transcellular and paracellular contribution to transport processes in the colorectal route. *Adv. Drug Deliv. Rev.* **1997**, *28*, 191−204.
3. Lennernas H. Human intestinal permeability. *J. Pharm. Sci.* **1998**, *87*, 403−410.
4. Staddon J. M.; Rubin L. L. Cell adhesion, cell junctions and the blood-brain barrier. *Curr. Opin. Neurobiol.* **1996**, *6*, 622−627.
5. Cereijido M.; Valdes J.; Shoshani L.; Contreras R. G. Role of tight junctions in establishing and maintaining cell polarity. *Annu. Rev. Physiol.* **1998**, *60*, 161−177.
6. Mitic L. L.; Anderson J. M. Molecular architecture of tight junctions. *Annu. Rev. Physiol.* **1998**, *60*, 121−142.
7. Spring K. R. Routes and mechanism of fluid transport by epithelia. *Annu. Rev. Physiol.* **1998**, *60*, 105−119.
8. Koepsell H. Organic cation transporters in intestine, kidney, liver, and brain. *Annu. Rev. Physiol.* **1998**, *60*, 243−266.
9. Gottesman M. M.; Hrycyna C. A.; Schoenlein P. V.; Germann U. A.; Pastan I. Genetic analysis of the multidrug transporter. *Annu. Rev. Genet.* **1995**, *29*, 607−649.
10. Germann U. A. P-glycoprotein − A mediator of multidrug resistance in tumour cells. *Eur. J. Cancer* **1996**, *32A*, 927−944.
11. Juliano R. L.; Ling V. A surface glycoprotein modulating drug permeability in Chinese hamster ovary cell mutants. *Biochim. Biophys. Acta* **1976**, *455*, 152−162.
12. Ford J. M. Experimental reversal of P-glycoprotein-mediated multidrug resistance by pharmacological chemosensitisers. *Eur. J. Cancer* **1996**, *32A*, 991−1001.
13. Lee C. G. L.; Gottesman M. M.; Cardarelli C. O.; Ramachandra M.; Jeang K. T.; Ambudkar S. V.; Pastan I.; Dey S. HIV-1 protease inhibitors are substrates for the MDR1 multidrug transporter. *Biochemistry* **1998**, *37*, 3594−3601.
14. Borst P.; Schinkel A. H. Genetic dissection of the function of mammalian P-glycoproteins. *Trends Genet.* **1997**, *13*, 217−222.
15. Schinkel A. H. The physiological function of drug-transporting P-glycoproteins. *Semin. Cancer. Biol.* **1997**, *8*, 161−170.
16. van Asperen J.; Mayer U.; van Tellingen O.; Beijnen J. H. The functional role of P-glycoprotein in the blood-brain barrier. *J. Pharm. Sci.* **1997**, *86*, 881−884.
17. Adson A.; Burton P. S.; Raub T. J.; Barsuhn C. L.; Audus K. L.; Ho N. F. H. Passive diffusion of weak organic electrolytes across Caco-2 cell monolayers: Uncoupling the contributions of hydrodynamic, transcellular, and paracellular barriers. *J. Pharm. Sci.* **1995**, *84*, 1197−1204.
18. Evers R.; Kool M.; van Deemter L.; Janssen H.; Calafat J.; Oomen L. C. J. M.; Paulusma C. C.; Elferink R. P. J. O.; Baas F.; Schinkel A. H.; Borst P. Drug export activity of the human canalicular multispecific organic anion transporter in polarized kidney MDCK cells expressing cMOAT (MRP2) cDNA. *J. Clin. Invest.* **1998**, *101*, 1310−1319.
19. Madara J. L. Regulation of the movement of solutes across tight junctions. *Annu. Rev. Physiol.* **1998**, *60*, 143−159.
20. Mullin J. M.; Soler A. P.; Laughlin K. V.; Kampherstein J. A.; Russo L. M.; Saladik D. T.; George K.; Shurina R. D.; O'Brien T. G. Chronic exposure of LLC−PK1 epithelia to the phorbol ester TPA produces polyp-like foci with leaky tight junctions and altered protein kinase C-alpha expression and localization. *Exp. Cell Res.* **1996**, *227*, 12−22.
21. Wielinga P. R.; Heijn M.; Broxterman H. J.; Lankelma J. P-glycoprotein-independent decrease in drug accumulation by phorbol ester treatment of tumor cells. *Biochem. Pharmacol.* **1997**, *54*, 791−799.
22. Lankelma J.; Spoelstra E. C.; Dekker H.; Broxterman H. J. Evidence for daunomycin efflux from multidrug-resistant 2780AD human ovarian carcinoma cells against a concentration gradient. *Biochim. Biophys. Acta* **1990**, *1055*, 217−222.
23. Wielinga, P. R.; Heijn, M.; Westerhoff, H. V.; Lankelma, J. A method for studying plasma membrane transport with intact cells using computerized fluorometry. *Anal. Biochem.* **1998**, *263*, 221−231.
24. Lankelma J.; Laurensse E.; Pinedo H. M. A flow-through tissue culture system with fast dynamic response. *Anal. Biochem.* **1982**, *127*, 340−345.
25. Bakos, E.; Evers, R.; Szakacs, G.; Tusnady, G. E.; Welker, E.; Szabo, K.; de Haas, M.; van Deemter, L.; Borst, P.; Varadi, A.; Sarkadi, B. Functional Multidrug Resistance Protein (MRP1) Lacking the N-terminal Transmembrane Domain. *J. Biol. Chem.* **1998,** *273*, 32167−32175.
26. Adson A.; Raub T. J.; Burton P. S.; Barsuhn C. L.; Hilgers A. R.; Audus K. L.; Ho N. F. H. Quantitative approaches to delineate paracellular diffusion in cultured epithelial cell monolayers. *J. Pharm. Sci.* **1994**, *83*, 1529−1536.
27. Stuart R. O.; Nigam S. K. Regulated assembly of tight junctions by protein kinase C. *Proc. Natl. Acad. Sci. U.S.A.* **1995**, *92*, 6072−6076.
28. Kovbasnjuk O. N.; Szmulowicz U.; Spring K. R. Regulation of the MDCK cell tight junction. *J. Membr. Biol.* **1998**, *161*, 93−104.
29. Stuart R. O.; Sun A.; Panichas M.; Hebert S. C.; Brenner B. M.; Nigam S. K. Critical role for intracellular calcium in tight junction biogenesis. *J. Cell. Physiol.* **1994**, *159*, 423−433.
30. Tomita M.; Hayashi M.; Awazu S. Absorption-enhancing mechanism of EDTA, caprate, and decanoylcarnitine in Caco-2 cells. *J. Pharm. Sci.* **1996**, *85*, 608−611.
31. Mullin J. M.; Kampherstein J. A.; Laughlin K. V.; Clarkin C. E. K.; Miller R. D.; Szallasi Z.; Kachar B.; Soler A. P.; Rosson D. Overexpression of protein kinase C-delta increases tight junction permeability in LLC−PK1 epithelia. *Am. J. Physiol. Cell. Physiol.* **1998**, *44*, C544−C554.
32. Collaresbuzato C. B.; Mcewan G. T. A.; Jepson M. A.; Simmons N. L.; Hirst B. H. Paracellular barrier and junctional protein distribution depend on basolateral extracellular Ca2+ in cultured epithelia. *Biochim. Biophys. Acta* **1994**, *1222*, 147−158.
33. Lynch R. D.; Tkachukross L. J.; Mccormack J. M.; Mccarthy K. M.; Rogers R. A.; Schneeberger E. E. Basolateral but not apical application of protease results in a rapid rise of transepithelial electrical resistance and formation of aberrant tight junction strands in MDCK cells. *Eur. J. Cell. Biol.* **1995**, *66*, 257−267.
34. Citi S.; Denisenko N. Phosphorylation of the tight junction protein cingulin and the effects of protein kinase inhibitors and activators in MDCK epithelial cells. *J. Cell. Sci.* **1995**, *108*, 2917−2926.
35. Collaresbuzato C. B.; Jepson M. A.; Simmons N. L.; Hirst B. H. Increased tyrosine phosphorylation causes redistribution of adherens junction and tight junction proteins and perturbs paracellular barrier function in MDCK epithelia. *Eur. J. Cell. Biol.* **1998**, *76*, 85−92.
36. Sakakibara A.; Furuse M.; Saitou M.; AndoAkatsuka Y.; Tsukita S. Possible involvement of phosphorylation of occludin in tight junction formation. *J. Cell. Biol.* **1997**, *137*, 1393−1401.
37. Grundemann D.; Gorboulev V.; Gambaryan S.; Veyhl M.; Koepsell H. Drug excretion mediated by a new prototype of polyspecific transporter. *Nature* **1994**, *372*, 549−552.
38. Skovsgaard T.; Nissen N. I. Membrane transport of anthracyclines. *Pharm. Ther.* **1982**, 18, 293−311.
39. Smit J. W.; Weert B.; Schinkel A. H.; Meijer D. K. F. Heterologous expression of various P-glycoproteins in polarized epithelial cells induces directional transport of small (type 1) and bulky (type 2) cationic drugs. *J. Pharmacol. Exp. Ther.* **1998**, *286*, 321−327.

Acknowledgments

We like to thank Drs. Evers and Borst for the gift of the MDCKII-MDR1 cells. This study was supported by the Dutch Cancer Society (KWF grant VU 94-773 to J.L.).

JS980497Z

Diffuse Reflectance Near-Infrared Spectroscopy as a Nondestructive Analytical Technique for Polymer Implants

RONALD L. BRASHEAR,[†] DOUGLAS R. FLANAGAN,[*,†] PAUL E. LUNER,[†] JEFFERY J. SEYER,[†] AND MARK S. KEMPER[‡,§]

Contribution from *College of Pharmacy, Division of Pharmaceutics, The University of Iowa, Iowa City, Iowa 52242, and Foss NIRSystems, Silver Spring, Maryland 20904.*

Received December 17, 1998. Final revised manuscript received June 28, 1999.
Accepted for publication September 20, 1999.

Abstract □ A near-infrared spectroscopic method to quantify drugs or excipients within polymeric matrixes is proposed. Cylindrical implants were fabricated by a melt-mold technique containing various ratios of poly(ϵ-caprolactone) (PCL) and poly(ethylene glycol) (PEG) and various loadings of lomefloxacin HCl with a constant ratio (70:30 w/w) of PCL/PEG. Near-infrared (NIR) spectra were obtained on intact sections of larger implants using a Foss NIRSystems Model 5000 monochrometer equipped with a Rapid Content Analyzer. Spectral data were treated with second derivative transformation followed by linear regression and PLS to obtain correlation with lomefloxacin or PEG content. Lomefloxacin content was separately determined by UV analysis (287 nm) using a validated extraction procedure. The NIR method was tested by comparing predicted loadings of test implants with either theoretical values based on weight (PEG) or with UV analysis results (lomefloxacin). Second derivative spectral values at particular wavelength ratios (PEG, 2064 nm/1698 nm; lomefloxacin, 2172 nm/2226 nm and 1824 nm/1862 nm) yielded linear results for PEG or lomefloxacin content. PEG content determined by NIR spectroscopy was in excellent agreement with theoretical content. Lomefloxacin content determined by NIR spectroscopy was also in excellent agreement with UV analysis. NIR analysis is interpreted through the use of corresponding mid-infrared spectral data.

Introduction

Polymeric drug delivery systems such as implants and microspheres are finding widespread use in drug delivery. Quantitative analysis of excipients or active ingredients within these dosage forms usually involves destructive extraction procedures followed by an assay, typically HPLC or UV spectroscopy. In cases where only small amounts of drug are available, as in early formulation development, or in cases where dose uniformity is an issue, a nondestructive analytical technique would be useful, allowing subsequent use of the dosage form.

Near-infrared (NIR) spectroscopy is a rapid and nondestructive analytical tool which is gaining acceptance in the pharmaceutical industry as a technique for qualitative and quantitative analysis. NIR applications in the pharmaceutical industry include qualitative identification of raw materials,[1,2] quantitative analysis of drug content in tablets and powder blends,[3−10] determination of moisture content,[11−16] detection of degradation products within solid formulations,[17] and determination of crystallinity.[18] Although quantitative analysis of drugs and excipients has been demonstrated for intact tablets, NIR spectroscopy has not been utilized in quantitative analysis of polymeric dosage forms.

Polymeric dosage forms are often used to provide sustained release of various pharmaceutical entities. When the polymer acts as a solid matrix, the rate of release may be controlled by addition of inert, water-soluble excipients such as poly(ethylene glycol) or sodium chloride. These excipients rapidly dissolve and release upon exposure to water, increasing the effective diffusion coefficient and the release rate of the drug. Because the rate of release is related to the quantity of these pore-forming excipients as well as the quantity of drug in the system, it is important to be able to assess both the quantity and uniformity of these excipients within a polymeric dosage form. The application of NIR spectroscopy for quantitation of excipients and actives within polymeric drug delivery systems would provide a rapid and nondestructive alternative to other analytical techniques. This work investigates the use of diffuse reflectance near-infrared spectroscopy as a nondestructive analytical tool for quantifying poly(ethylene glycol) and lomefloxacin hydrochloride within intact polymer implants.

Experimental Section

Materials—Poly(ϵ-caprolactone) flakes (Scientific Polymer Products Inc., Ontario, NY), poly(ethylene glycol) 600 NF (Union Carbide, Danbury, CT, Lot 578269), and lomefloxacin HCl (G. D. Searle, Skokie, IL., Lot NA007) were used as received. Methylene chloride (Fisher Scientific, Lot #963694), 0.1 N hydrochloric acid (Fisher Scientific, Lot #924316-24), and distilled water were used in the extraction procedure as received. Borosilicate glass disposable culture tubes were used as received for fabrication of implants.

Poly(ϵ-caprolactone)/Poly(ethylene glycol) Implant Preparation—Poly(ϵ-caprolactone) (PCL) and poly(ethylene glycol) (PEG) (0, 5, 10, 15, 20, 25, and 30% w/w) were placed in a 20 mL glass scintillation vial. The materials were melted by placing the vial in a water bath at 75 °C. Upon melting, the two phases were thoroughly mixed with an overhead mixer to ensure uniform dispersion of PEG within the polymer melt. The resulting dispersion was transferred to a 10 mL Becton-Dickenson syringe and injected into precut 5 mm diameter borosilicate tubes. After cooling to room temperature, the implants were removed from the tubes and stored in a vacuum desiccator until use. Implants containing 12.5% and 22.5% w/w PEG were formed using the procedure described for use in validating the near-infrared standard curve.

Poly(ϵ-caprolactone)/Poly(ethylene glycol)/Lomefloxacin Hydrochloride Implant Preparation—Implants containing lomefloxacin HCl were prepared using PCL and PEG 600 at a constant weight ratio of 70:30. After complete dispersion of PEG within the polymer melt, powdered lomefloxacin HCl (5, 10, 15, 20, and 25% w/w) was slowly added with continuous agitation from an overhead mixer to ensure uniform dispersion of drug. The resulting dispersion was injected into the precut borosilicate tubes,

* To whom correspondence should be addressed.
[†] The University of Iowa.
[‡] Foss NIRSystems.
[§] Current address: Nicolet Instrument Corporation, Madison, WI 53711.

10.1021/js9804821 CCC: $18.00
Published on Web 11/06/1999

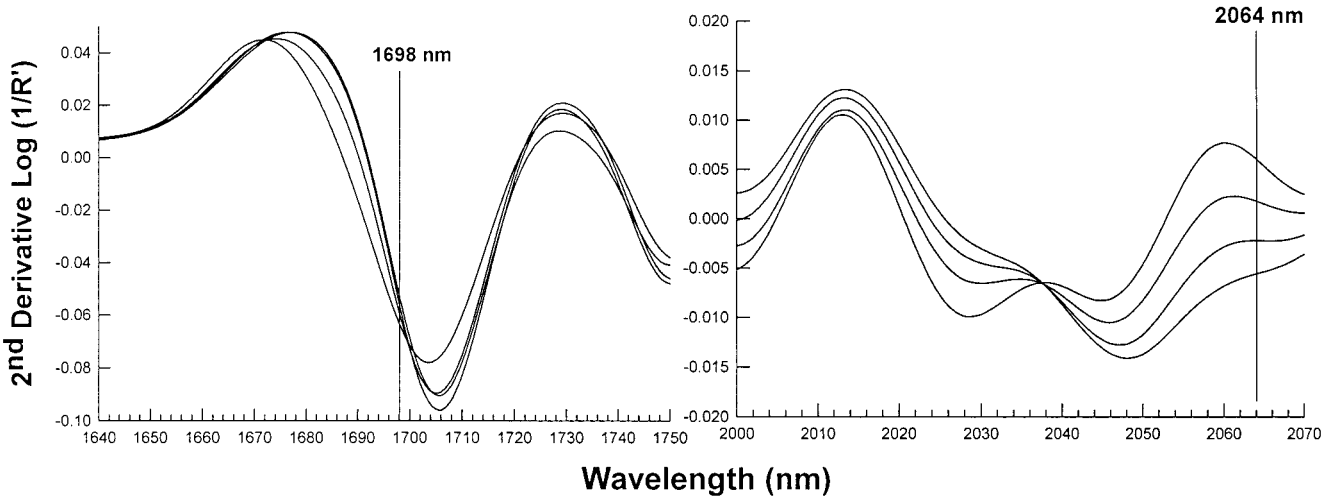

Figure 1—Expanded second derivative NIR spectra for implants containing various poly(ethylene glycol) (PEG) contents. PEG contents from top to bottom at 2064 nm are 0, 10, 20, and 30% w/w PEG 600; the normalizing wavelength (1698 nm) is indicated.

cooled to room temperature, removed from the tubes, and stored in a vacuum desiccator.

Near-Infrared Analysis—Two implants from each batch were selected at random. A surgical scalpel was used to cut two 5 mm slices from each implant. Each slice was placed on a glass cover slip and placed in the center of the sample holder using the iris centering device. Both radial surfaces from each slice were scanned in reflectance mode from 1100 to 2500 nm using a Foss NIRSystems Model 5000 monochrometer equipped with a Rapid Content sampler. Reflectance values obtained were relative to that from a nominally 80% reflective Coors standard ceramic disk. Relative reflectance values (R') were transformed by $\log(1/R')$.

Extraction and Chemical Assay for Lomefloxacin Hydrochloride Implants—After acquiring NIR spectra, each polymer slice was weighed and dissolved in methylene chloride (10 mL) in a 125 mL separatory flask. Hydrochloric acid (1 mM, 50 mL) was added to the separatory flask, forming two phases. The flask was shaken thoroughly, and the two phases were allowed to separate. Upon separation, the aqueous phase (top) was removed and placed into a 250 mL volumetric flask. This extraction procedure was repeated four times, and the resulting pooled extracts were diluted to volume with 1 mM HCL. An appropriate dilution was made and lomefloxacin quantified by measuring its absorbance at 287 nm using a Hewlett-Packard UV/Vis Spectrophotometer (Model 8450). An extraction efficiency of 99.6%, with a standard deviation of 0.85% ($n = 3$), was determined by separately adding known amounts of each component of the implant to a separatory flask and performing the extraction procedure.

NIR Spectral Analysis and Standard Curve Generation—A second derivative transformation of each NIR spectrum was performed using the NIRSystems Spectral Analysis Software (NSAS Version 3.50). The software was also utilized to scan the resulting second derivative spectra to determine a ratio of wavelengths which provided high correlation between the second derivative response and the theoretical PEG content or lomefloxacin content from extraction and UV analysis. A ratio of responses at two wavelengths was chosen rather than the response at a single wavelength to correct for baseline shifts. Baseline shifts are attributable to subtle changes in path length resulting from sample variations such as surface roughness, changes in sample positioning, or changes in sample density. The use of wavelength ratios has been shown to normalize spectra and yield more reproducible results.[19,20] A standard curve was generated by plotting the second derivative ratio versus PEG or lomefloxacin HCl content.

Partial least squares (PLS) analysis on second derivative spectra[21] was also performed for comparative purposes. Derivatized spectra have been shown to produce calibration models with more accurate and reproducible results.[22] A PLS calibration equation was generated using NSAS Version 3.50 and then utilized to predict lomefloxacin loadings in the validation data set.

Validation Set Generation—A separate batch of implants (20% w/w lomefloxacin HCl) was produced using the procedure described above in order to validate the standard curve generated. These implants were not used in the generation of the standard curve. Four implants from this batch were selected at random, and NIR spectra were obtained on two slices from each implant, as described previously. Lomefloxacin content was determined using the extraction and UV assay described above. The lomefloxacin content determined from the UV assay was then compared to the calculated lomefloxacin content using the NIR methods.

Statistical Analysis—A paired *t*-test was employed for comparison of lomefloxacin HCl content predicted by the NIR method and the results from extraction/UV assay. Using the paired *t*-test, 95% confidence intervals were constructed for the difference in the lomefloxacin hydrochloride content predicted by the NIR method and the results from the extraction/UV assay (i.e., NIR results − UV results). The null hypothesis (H_o) for this test was that of no significant difference while the alternative hypothesis (H_a) was that of significant difference. The results of a paired t-test give an indication of the accuracy of the NIR method compared with the extraction/UV assay. To perform a more robust statistical analysis on a small sample set, a nonparametric statistical analysis (Wilcoxon signed rank test at 95% confidence) was also employed.[23] The results of this statistical test provided a 95% confidence interval and a *p*-value which may be used in a manner similar to that obtained from the parametric paired *t*-test. An *F*-test for sample variance was employed at a 95% significance level to compare the precision of various NIR methods with the extraction/UV assay. In addition to the tests described above, standard error of calibration (SEC) and standard error of prediction (SEP) values were calculated for single wavelength and PLS models. Statistical analyses were performed on a microcomputer using MINITAB for Windows (Release 12.1), SAS, Version 6.12 (SAS Institute, Cary, NC), and Microsoft Excel 97.

Results and Discussion

NIR for Determination of PEG Content in PCL/PEG Implants—NIR spectra for PCL implants containing various PEG contents were obtained. To correct for the baseline shifts apparent in the samples and to amplify small spectral differences attributable to PEG content, a second derivative transformation of the NIR spectra was performed. Using the NSAS software, the spectra were analyzed to determine a wavelength ratio which best correlated with the known PEG content. A ratio of the responses at 2064 nm/1698 nm provided the highest correlation with PEG content. This region of the second derivative NIR spectrum is shown in Figure 1. The second derivative values at 2064 nm correspond well with changes in PEG content. A standard curve was constructed from the second derivative ratio of responses at 2064 nm/1698 nm versus the theoretical PEG content (% w/w) of each implant. The resulting standard curve is shown in Figure 2. The calibration data was analyzed by linear regression

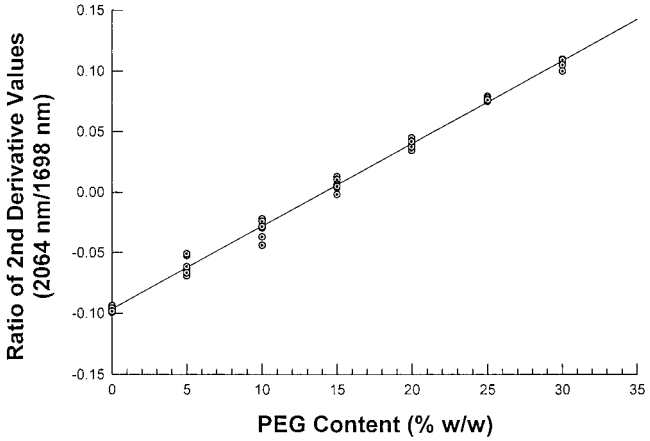

Figure 2—NIR standard curve for poly(ethylene glycol) (PEG) content in poly(ϵ-caprolactone) implants using a ratio of second derivative values (2064 nm/1698 nm) (R^2 = 0.998, S. E. = 0.0045).

Table 1—Comparison of NIR Predicted and Theoretical PEG 600 Content in Poly(ϵ-caprolactone) Implants

theoretical content (% w/w)	predicted content (% w/w) (n = 16)	standard deviation (% w/w) (n = 16)	relative error (%)
12.50	12.68	0.31	1.44
22.49	22.76	0.56	1.20

and excellent linearity throughout the entire range of PEG loadings (0−30% w/w) was obtained (R^2 = 0.998, SE = 0.0045).

Predicting PEG Content in PCL/PEG Implants from NIR Spectra—To test the robustness and accuracy of the NIR technique for the prediction of PEG content within a PCL implant, two batches of implants with theoretical PEG loadings of 12.5% and 22.5% w/w were prepared. NIR spectra were obtained and a second derivative transformation was performed. Using the second derivative of the response at 2064 and 1698 nm and the standard curve in Figure 2, PEG content was calculated and compared to theoretical PEG content. Table 1 shows the PEG content determined by the NIR method is in excellent agreement with the theoretical content. This method provides a rapid analytical technique for measuring PEG content with low relative error (1.2−1.4%) which is significant for two reasons. First, the technique is nondestructive, allowing subsequent use of the implant in other studies such as stability studies, in vitro/in vivo release studies, or polymer/excipient interaction studies, etc. Second, this technique provides an analytical method for quantitation of an excipient lacking a UV chromophore. Typical approaches to quantification of PEG or other excipients lacking a chromophore rely on methods such as refractive index detection with HPLC[24] or chemical reaction methods, which are more time-consuming and destroy the dosage form.

NIR for Determination of Lomefloxacin HCl Content in PCL/PEG Implants—NIR spectra for PCL/PEG implants containing various contents of lomefloxacin HCl are shown in Figure 3. A second derivative transformation of the NIR spectra of implants containing lomefloxacin was performed. The extraction procedure, previously described, was used to determine lomefloxacin content, and the results are summarized in Table 2. To determine a wavelength ratio which provided the best correlation between the second derivative NIR values and lomefloxacin content (Table 2), second derivative spectra were analyzed using the NSAS software. A ratio of the responses at 2172 nm/2226 nm provided the highest correlation with lomefloxacin content. This region of the second derivative NIR spectrum has been expanded in Figure 4A. A standard curve was constructed from the second derivative ratio of responses at 2172 nm/2226 nm versus lomefloxacin content determined from the extraction/UV assay results. The resulting standard curve, shown in Figure 4B, demonstrates excellent linearity (R^2 = 0.992, S. E. = 0.036).

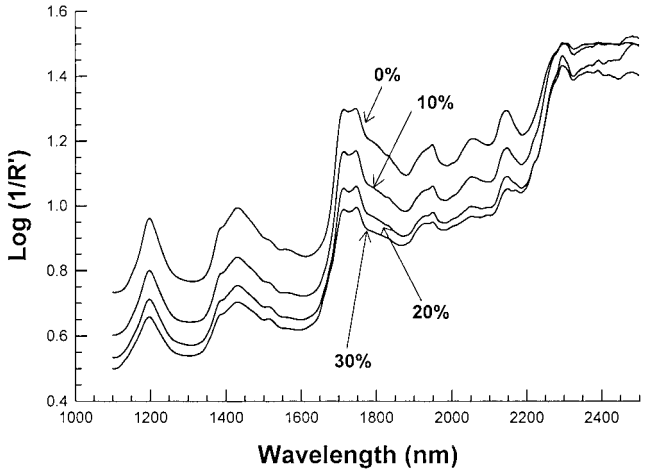

Figure 3—NIR spectra for poly(ϵ-caprolactone) implants containing various lomefloxacin HCl contents (% w/w) as indicated on each spectrum.

Table 2—Lomefloxacin HCl Content of Calibration Samples As Determined by the Extraction Procedure with UV Analysis

implant no.	lomefloxacin HCl content (% w/w)	implant no.	lomefloxacin HCl content (% w/w)
5-1	5.75	15-3	15.04
5-2	5.55	15-4	15.08
5-3	4.62	20-1	19.13
5-4	4.84	20-2	18.92
10-1	10.05	20-3	17.75
10-2	10.25	25-1	25.11
10-3	9.82	25-2	23.83
10-4	9.87	25-3	24.82
15-1	14.80	25-4	24.66
15-2	14.70		

In addition to using single wavelength analysis, partial least squares analysis was performed on second derivative spectra for comparison. A three-factor calibration equation was developed with an R^2 of 0.998 and a standard error of 0.66.

Predicting Lomefloxacin HCl Loading in PCL/PEG Implants—Implants containing approximately 20% w/w lomefloxacin HCl were produced to test the predictive ability of the NIR method. NIR spectra and second derivative spectra were obtained on 5 mm slices of four implants, as described previously, and subjected to extraction and subsequent UV assay. The second derivative response at 2172 nm/2226 nm was then used with the standard curve (Figure 4B) to predict lomefloxacin HCl content. The three-factor PLS calibration equation was also used to determine lomefloxacin content using the "Predict Percent" feature of the NSAS software. Lomefloxacin contents determined from both NIR methods and the extraction/UV method are shown in Table 3. These results were statistically analyzed for significant differences in the accuracy and precision of the two methods. Results of the statistical analysis are summarized in Table 4. The paired t-test and Wilcoxon signed rank test gave 95% confidence intervals containing zero and p-values greater than 0.05, indicating that results for lomefloxacin content predicted by NIR were not statisti-

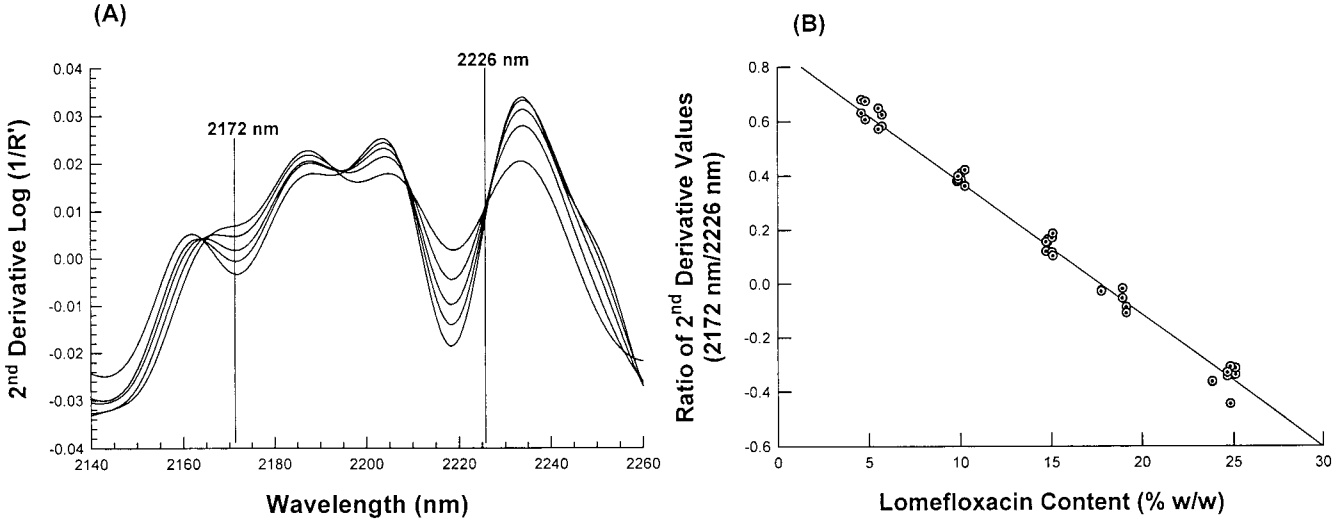

Figure 4—(A) Expanded second derivative NIR spectra for PCL:PEG implants containing lomefloxacin HCl. Content from top to bottom at 2172 nm: 25, 20, 15, 10, and 5% w/w; the normalizing wavelength (2226 nm) is indicated. (B) NIR standard curve for lomefloxacin HCl content in PCL:PEG implants using a ratio of second derivative values (2172 nm/2226 nm) (R^2 = 0.992, S. E. = 0.0364).

Table 3—Lomefloxacin Content of Validation Samples as Determined by Extraction/UV Procedure and NIR Methods

	extraction/UV procedure (% w/w)	NIR 2172 nm/ 2226 nm (% w/w)	NIR 1824 nm/ 1862 nm (% w/w)	NIR PLS analysis 3 factors (% w/w)
	18.84	18.33	19.11	19.91
	18.98	18.73	19.95	20.33
	18.57	18.49	17.52	18.84
	18.61	18.03	17.14	19.11
	18.93	18.59	21.89	18.85
	19.01	20.29	16.40	19.15
	19.36	21.59	19.54	19.58
	19.26	19.88	20.28	19.01
average	18.95	19.24	18.98	19.35
std dev	0.28	1.23	1.84	0.54
% RSD	1.48	6.38	9.69	2.79

Table 4—Statistical Analysis of NIR and Extraction/UV Techniques for Determination of Lomefloxacin Content within PCL Implants

statistical test	2172 nm/ 2226 nm versus extraction/UV	1824 nm/ 1862 nm versus extraction/UV	PLS (three factors) versus extraction/UV
SEC	0.77	1.76	0.66
SEP	1.05	1.73	0.70
paired *t*-test			
•95% interval	(–0.545, 1.137)	(–1.412, 1.480)	(–0.059, 0.864)
•*p*-value	$p > 0.05$	$p > 0.05$	$p > 0.05$
Wilcoxon signed rank test			
•95% interval	(–0.42, 1.07)	(–1.26, 1.57)	(–0.015, 0.810)
•*p*-value	$p > 0.05$	$p > 0.05$	$p > 0.05$
F-test	$p < 0.05$	$p < 0.05$	$p > 0.05$

cally different than results from UV analysis in terms of accuracy. SEC and SEP values (Table 4) for each calibration model were similar to one another and low in value (i.e. < 2%), further validating the calibration models. The NIR calibration models may be compared by means of the *F*-test shown in Table 4. While both single wavelength and PLS methods give results comparable in accuracy to the extraction/UV method, the PLS method yields more precise results (*p*-value > 0.05) than the single wavelength method. The smaller SEC and SEP values for the PLS model further verify this result. This finding suggests that PLS models may be more useful when accurate and precise mean content is required.

NIR Spectral Interpretation—The results above demonstrate the utility of NIR spectroscopy for determination of lomefloxacin HCl within polymer implants. To structurally interpret NIR results, it is advantageous to utilize a portion of the NIR spectrum unique to the compound of interest and that is predictable from mid-infrared data. With this approach, a nondestructive analytical technique directly related to structural features of the analyte could be developed. Interpretation is often accomplished with the use of wavelength tables which relate common functionalities to corresponding NIR absorption bands.[20,25–28] One disadvantage of using these tables is that absorption bands for a given functionality are often broad, resulting in several functionalities which may be expected to have overtone transitions within the same region. This ambiguity may be alleviated through the use of the corresponding mid-infrared data. NIR absorption bands are the result of overtones or combinations of overtones originating in the fundamental midrange (4000−600 cm^{-1}) infrared region of the spectrum.[29] When frequencies of fundamental transitions in the mid-infrared region of the spectrum are known, the position of expected near-infrared absorption bands may be calculated. The overtone transitions (λ) will occur at integer multiples (n) of fundamental vibrational frequencies (ν_{IR}), which may be estimated from known mid-infrared absorption bands using:

$$\lambda = \frac{10\,000\,000}{n\nu_{IR}(cm^{-1})} \quad (1)$$

Sanzgiri et al. obtained the mid-infrared spectrum for lomefloxacin HCl and assigned mid-infrared absorption bands to various functionalities (Table 5).[30] Overtone transitions from the mid-infrared absorption bands were calculated using eq 1.

As shown previously, the NIR response at a wavelength ratio of 2172 nm/2226 nm correlated well with lomefloxacin content, and these results were comparable to UV analysis. These wavelengths do not correspond to the predicted overtone transitions of the assigned bands (Table 5). Because the use of infrared data did not provide a useful interpretation of the 2172 nm region, various NIR tables

Table 5—Mid-Infrared Transitions and Calculated Overtone Transitions for Lomefloxacin HCl[a]

infrared fundamental[a]	assignment	theoretical 1st overtone (nm)	theoretical 2nd overtone (nm)
3703 nm (2700 cm^{-1})	NH_2^+ stretch	1852	1235
6172 nm (1620 cm^{-1})	carbonyl stretch (pyridinone ring)	3086	2058
8278 nm (1208 cm^{-1})	aryl fluorides	4139	2759

[a] Mid-infrared absorption peaks and assignments are from Sanzgiri et al.[30]

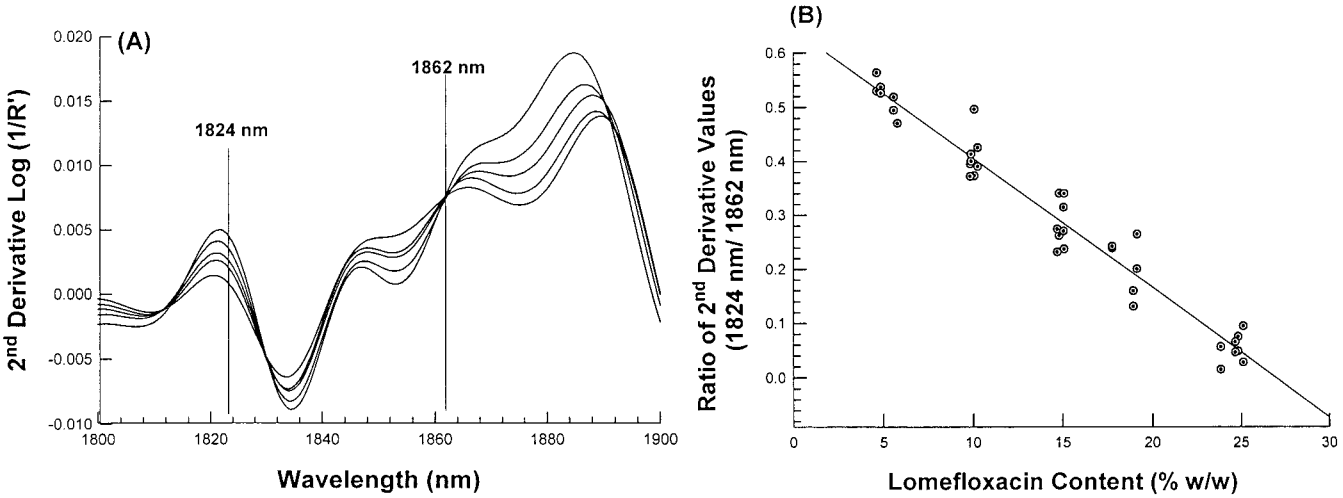

Figure 5—(A) Expanded second derivative NIR spectra for PCL:PEG implants containinglomefloxacin HCl contents. Content from top to bottom at 1824 nm: 25, 20, 15, 10, and 5% w/w; the normalizing wavelength (1862 nm) is indicated. (B) NIR standard curve for lomefloxacin HCl content in PCL:PEG implants using a ratio of second derivative values (1824 nm/1862 nm) (R^2 = 0.955, S. E. = 0.0364).

were utilized to provide an interpretation of why this provided good correlation. Amines are reported to have an combination N−H stretch in the region of 2100−2200 nm.[14] Lomefloxacin HCl is the only amine-containing species within these implants, and thus we may interpret our correlation at 2172 nm as being due to N−H combination frequencies within the NIR. It should be noted that increasing relative reflectance values within the NIR spectra will lead to decreasing second derivative values. The 2172 nm wavelength could not be predicted from mid-IR data since the mid-IR data will only provide information about overtone transitions occurring from specific functional groups, not from combination frequencies.

Since a reasonable correlation attributable to an amine combination was found at 2172 nm, we may also expect to find good correlation in the region where a first overtone may be expected from the mid-IR data. From Table 5, a protonated amine vibrational stretch would be expected to have a theoretical first overtone transition at 1852 nm. The second derivative spectra of lomefloxacin-containing implants were investigated for correlation with lomefloxacin content in the range of 1800 to 1900 nm corresponding with the theoretical first overtone transition as predicted from the known IR spectrum. Another wavelength ratio (1824 nm/1862 nm) also provided good correlation with lomefloxacin content. This region of the NIR spectra has been expanded and is shown in Figure 5A. A standard curve was constructed from the second derivative ratio of responses at 1824 nm/1862 nm versus lomefloxacin content determined from the extraction/UV assay results. The resulting standard curve (R^2 = 0.955, S. E. = 0.036) is given in Figure 5B. The increased scatter in the data may be attributable to the weaker absorbance found in the 1800−1900 nm range. Various other transitions such as carbon−hydrogen first overtone transitions also occur in this region and may also contribute to the increase in scatter of the data at 1824 nm.[14] To test the predictive ability of the NIR at this new wavelength ratio, second derivative responses at 1824 and 1862 nm were obtained from the test set of implants and used with the standard curve in Figure 5B to predict lomefloxacin content as shown in Table 3. A statistical analysis was performed to compare these results with previous NIR and extraction/UV results. Results from this statistical analysis are shown in Table 4. As can be seen from Table 4, the paired *t*-test and Wilcoxon signed rank test give 95% confidence intervals containing zero and *p*-values greater than 0.05. Furthermore, the SEC and SEP values for the NIR calibration at this new wavelength are similar to one another and small in value. These results indicate that there is no statistical difference in the accuracy of mean lomefloxacin content predicted by NIR (1824 nm/1862 nm) or UV analysis. The significance of this is that the wavelengths correlated well with first overtone expectations for a protonated amine as calculated from mid-infrared data. This ratio also provided reasonable correlation with results from extraction/UV analysis. The high correlation in the 1800−1900 nm region where an expected N−H first overtone transition would occur supports the proposed N−H combination interpretation for the 2172 nm/2226 nm ratio. These results demonstrate that mid-infrared data may be useful in structural interpretation of NIR spectra and can help to verify interpretation of NIR combination transitions not predictable from mid-IR spectra alone.

Although the 1824 nm/1862 nm wavelength ratio provides results with comparable accuracy as the extraction/UV technique, the *F*-test demonstrates the single wavelength NIR method (1824 nm/1862 nm) does not give results with the same precision (i.e. p-value < 0.05). The PLS method appears to be the most robust method in terms of accuracy and precision; however, it should be noted that the PLS method does not allow for a similar direct interpretation of the NIR data.

Conclusions

NIR spectroscopy is an accurate and nondestructive method for quantifying components within polymeric implants and provides a useful alternative to traditional destructive techniques. This nondestructive technique may be particularly useful in the early stages of product development when drug supply is limited or when dose uniformity is an issue within test formulations. In the case of polymer matrix systems, excipients such as poly(ethylene glycol) are not normally assayed. Given the importance these excipients have in controlling the release rate of active components, it is critical to assess both the quantity and uniformity of these excipients within the polymeric dosage form. NIR seems to provide an excellent and rapid nondestructive method for quantitation of poly(ethylene glycol), an excipient which is tedious and time-consuming to quantify by other analytical methods.[24] Preliminary work suggests that similar results may be obtained for quantifying actives within other polymeric dosage forms such as microspheres or films.[31] Selection of analytical wavelengths in the near-infrared region corresponding to structural features of the analyte may be accomplished with the use of corresponding mid-infrared spectral data and NIR frequency (wavelength) tables.

References and Notes

1. Morisseau, K. M.; Rhodes, C. T. Pharmaceutical uses of near-infrared spectroscopy. *Drug Devel. Ind. Pharm.* **1995**, *21*, 1071−1090.
2. Plugge, W.; Vlies, C. Near-infrared spectroscopy as a tool to improve quality. *J. Pharm. Biomed. Anal.* **1996**, *14*, 891−898.
3. Kirsch, J. D.; Drennen, J. K. Near-infrared spectroscopy: Applications in the analysis of tablets and solid pharmaceutical dosage forms. *Appl. Spectrosc. Rev.* **1995**, *30*, 139−174.
4. Dreassi, E.; Ceramelli, G.; Savini, L.; Corti, P.; Perruccio, P. L.; Lonardi, S. Application of near-infrared reflectance analysis to the integrated control of antibiotic tablet production. *Analyst* **1995**, *120*, 319−323.
5. Wargo, D. J.; Drennen, J. K. Near-infrared spectroscopic characterization of pharmaceutical powder blends. *J. Pharm. Biomed. Anal.* **1996**, *14*, 1415−1423.
6. Han, S. M.; Faulkner, P. G. Determination of SB 216469-S during tablet production using near-infrared reflectance spectroscopy. *J. Pharm. Biomed. Anal.* **1996**, *14*, 1681−1689.
7. Buchanan, B. R.; Baxter, M. A.; Chen, T.-S.; Qin, X.-Z.; Robinson, P. A. Use of near-infrared spectroscopy to evaluate an active in a film-coated tablet. *Pharm. Res.* **1996**, *13*, 616−621.
8. Blanco, M.; Coello, J.; Iturriaga, H.; Maspoch, S.; Pezuela, C. Quantitation of the active compound and major excipients in a pharmaceutical formulation by near-infrared diffuse reflectance spectroscopy with fibre optical probe. *Anal. Chem. Acta* **1996**, *333*, 147−156.
9. Khan, P. R.; Jee, R. D.; Watt, R. A.; Moffat, A. C. The identification of active drugs in tablets using near-infrared spectroscopy. *J. Pharm. Sci.* **1997**, *3*, 447−453.
10. Lodder, R. A.; Hieftje, G. M. Analysis of intact tablets by near-infrared reflectance spectrometry. *Appl. Spectrosc.* **1988**, *42*, 556−558.
11. Jones, J. A.; Last, I. R.; MacDonald, B. F.; Prebble, K. A. Development and transferability of near-infrared methods for determination of moisture in a freeze-dried injection product. *J. Pharm. Biomed. Anal.* **1993**, *11*, 1227−1231.
12. Last, I. R.; Prebble, K. A. Suitability of near-infrared methods for the determination of moisture in a freeze-dried injection product containing different amounts of the active ingredient. *J. Pharm. Biomed. Anal.* **1993**, *11*, 1071−1076.
13. Ciurczak, E. Uses of near-infrared spectroscopy in pharmaceutical analysis. *Appl. Spectrosc. Rev.* **1987**, *23*, 147−163.
14. MacDonald, B. F.; Prebble, K. A. Some applications of near-infrared reflectance analysis in the pharmaceutical industry. *J. Pharm. Biomed. Anal.* **1993**, *11*, 1077−1085.
15. Buice, R. G.; Gold, T. B.; Lodder, R. A.; Digenis, G. A. Determination of moisture in intact gelatin capsules by near-infrared spectrophotometry. *Pharm. Res.* **1995**, *12*, 161−163.
16. Lonardi, S.; Viviani, R.; Mosconi, L.; Bernuzzi, M.; Corti, P.; Dreassi, E.; Murratzu, C.;Corbin, G. Drug analysis by near-infrared reflectance spectroscopy. Determination of the active ingredient and water content in antibiotic powders. *J. Pharm. Biomed. Anal.* **1989**, *7*, 303−308.
17. Drennen, J. K.; Lodder, R. A. Nondestructive near-infrared analysis of intact tablets for determination of degradation products. *J. Pharm. Sci.* **1990**, *79*, 622−627.
18. Seyer, J. J.; Luner, P. E.; Kemper, M.; Majuru, S. Amorphous content determination in semicrystalline mixtures using diffuse reflectance near-infrared spectroscopy. *Pharm.* Res. **1997**, *14*, S445.
19. Norris, K. H.; Williams, P. C. Optimization of mathematical treatments of raw near-infrared signal in the measurement of protein in hard red spring wheat. I. Influence of particle size. *Cereal Chem.* **1984**, *61*, 158−165.
20. Murray, I.; Williams, P. C. In *Near-Infrared Technology in the Agricultural and Food Industries*; Williams, P., Norris, K., Eds.; American Association of Cereal Chemists, Inc.: St. Paul, MN, 1990; pp 17−34.
21. Geladi, P.; Kowalski, B. Partial least-squares regression: a tutorial. *Anal. Chim. Acta* **1986**,*185*, 1−17.
22. Blanco, M.; Coello, J.; Eustaquio, A.; Iturriaga, H.; Maspoch, S. Development and validation of a method for the analysis of a pharmaceutical preparation by near-infrared diffuse reflectance spectroscopy. *J. Pharm. Sci.* **1999**, *88*, 551−556.
23. Dougherty, E. R. *Probability and Statistics for the Engineering, Computing, and Physical Sciences*; 1st ed.; Prentice Hall: Englewood Cliffs, NJ, 1990.
24. Donovan, M. D.; Flynn, G. L.; Amidon, G. L. Absorption of poly(ethylene glycol)s 600 through 2000: The molecular weight dependence of gastrointestinal and nasal absorption. *Pharm. Res.* **1990**, *7*, 863−868.
25. Whetsel, K. B. Near-infrared spectrophotometry. *Appl. Spectrosc. Rev.* **1968**, *2*, 1−67.
26. Weyer, L. G. Near-infrared spectroscopy of organic substances. *Appl. Spectrosc. Rev.* **1985**, *21*, 1−43.
27. Workman, J. J. Interpretive spectroscopy for near-infrared. *Appl. Spectrosc. Rev.* **1996**, *31*, 251−320.
28. Miller, C. E. Near-infrared spectroscopy of synthetic polymers. *Appl. Spectrosc. Rev.* **1991**, *26*, 277−339.
29. Ciurczak, E. W. Handbook of Near-Infrared Analysis. 1st ed.; Burns, D. A., Ciurczak, E. W., Eds.; Vol. 13; Marcel Dekker, Inc.: New York, 1992; pp 7−11.
30. Sanzgiri, Y. D.; Knaub, S. R.; Riley, C. M. Lomefloxacin. In *Analytical Profiles of Drug Substances*; Brittain, H. G., Ed.; Vol. 23; Academic Press: San Diego, CA, 1994; pp 321−369.
31. Brashear, R. L.; Flanagan, D. R.; Luner, P. E.; Seyer, J. J.; Kemper, M. Diffuse reflectance near-infrared spectroscopy as a nondestructive analytical technique for polymer implants and microspheres. *PharmSci* **1998**, *1*, 20.

Acknowledgments

Financial support for this research was provided by Glaxo Wellcome and through an AFPE NACDS Association Fellowship in Pharmaceutics. Lomefloxacin HCl was generously donated by G.D. Searle. The authors thank Jeff Isaacson of the University of Iowa Statistical Consulting Center and S. Sunny Hong for their statistical consultation. The authors also thank Dr. J. K. Guillory, Dr. D. E. Wurster, and A. Al Maaieh for their helpful discussions and suggestions.

JS9804821

Effects of Buffer Composition and Processing Conditions on Aggregation of Bovine IgG during Freeze-Drying

JEANNE-MARIE SARCIAUX,[†] SAID MANSOUR,[‡] MICHAEL J. HAGEMAN,[§] AND STEVEN L. NAIL*,[†]

Contribution from *Department of Industrial and Physical Pharmacy, Purdue University, West Lafayette, Indiana 47907, Department of Material Sciences, Purdue University, West Lafayette, Indiana 47907, and Pharmaceutical Development, Pharmacia&Upjohn Inc, Kalamazoo, Michigan 49001.*

Received September 21, 1998. Accepted for publication September 15, 1999.

Abstract □ The objective of this study was to identify critical formulation and processing variables affecting aggregation of bovine IgG during freeze-drying when no lyoprotective solute is used. Parameters examined were phosphate buffer concentration and counterion (Na versus K phosphate), added salts, cooling rate, IgG concentration, residual moisture level, and presence of a surfactant. No soluble aggregates were detected in any formulation after either freezing/thawing or freeze-drying. No insoluble aggregates were detected in any formulation after freezing, but insoluble aggregate levels were always detectable after freeze-drying. The data are consistent with a mechanism of aggregate formation involving denaturation of IgG at the ice/freeze–concentrate interface which is reversible upon freeze–thawing, but becomes irreversible after freeze-drying and reconstitution. Rapid cooling (by quenching in liquid nitrogen) results in more and larger aggregates than slow cooling on the shelf of the freeze-dryer. This observation is consistent with surface area measurements and environmental electron microscopic data showing a higher surface area of freeze-dried solids after fast cooling. Annealing of rapidly cooled solutions results in significantly less aggregation in reconstituted freeze-dried solids than in nonannealed controls, with a corresponding decrease in specific surface area of the freeze-dried, annealed system. Increasing the concentration of IgG significantly improves the stability of IgG against freeze-drying-induced aggregation, which may be explained by a smaller percentage of the protein residing at the ice/freeze–concentrate interface as IgG concentration is increased. A sodium phosphate buffer system consistently results in more turbid reconstituted solids than a potassium phosphate buffer system at the same concentration, but this effect is not attributable to a pH shift during freezing. Added salts such as NaCl or KCl contribute markedly to insoluble aggregate formation. Both sodium and potassium chloride contribute more to turbidity of the reconstituted solid than either sodium or potassium phosphate buffers at similar ionic strength, with sodium chloride resulting in a substantially higher level of aggregates than potassium chloride. At a given cooling rate, the specific surface area of dried solids is approximately a factor of 2 higher for the formulation containing sodium chloride than the formulation containing potassium chloride. Turbidity is also influenced by the extent of secondary drying, which underscores the importance of minimizing secondary drying of this system. Including a surfactant such as polysorbate 80, either in the formulation or in the water used for reconstitution, decreased, but did not eliminate, insoluble aggregates. There was no correlation between pharmaceutically acceptability of the freeze-dried cake and insoluble aggregate levels in the reconstituted product.

Introduction

Freeze-drying is usually the method of choice for manufacture of protein pharmaceutical and diagnostic agents which are physically or chemically unstable in aqueous solution and may be used in protein purification for concentration of proteins and to store the process intermediate in a relatively nongrowth promotive state. However, a major challenge in development and manufacture of such products is minimization of damage to proteins due to stresses arising from the freeze-drying process itself. Much of the published literature on freeze-drying of proteins deals with the use of protective solutes, particularly disaccharides, to minimize freeze-drying-induced damage.[1−4] There is only a small body of literature on the effects of processing conditions on protein integrity in the absence of protective solutes.[5−7]

Immunoglobulins represent a class of proteins which are important both as pharmaceuticals and as diagnostic agents. Immunoglobulins are also prone to formation of aggregates during freezing[8] and freeze-drying.[3,9] While protective solutes have been shown to be effective in minimizing aggregation, the use of sucrose, for example, as an excipient should be approached with caution for IgG formulations intended to be administered in large doses due to reported acute renal toxicity.[10] In addition, some immunoglobulins for which the final formulation is a sterile solution are freeze-dried as a process intermediate, where it may be desireable to minimize added solutes.

Within the limited body of published literature on aggregation of immunoglobulins in response to freeze-drying, variation in the immunoglobulin used as well as experimental conditions (protein concentration, buffer composition, added salts, and specific freezing and freeze-drying conditions) makes the formulation of general conclusions regarding the relative impact of these variables on aggregate formation uncertain. For example, Hansson[8] reported that high levels of insoluble aggregates (42%) were formed after multiple freeze−thaw cycles at −20 °C as measured by ultracentrifugation. In this study, IgG was dissolved in 0.05 M phosphate buffer and 0.5 N NaCl at pH 7. The buffer salt used (sodium or potassium) was not specified, and the buffer contained an unusually high level of added salts. Paborji et al.,[9] using 0.05 M sodium phosphate buffer and 0.5 N NaCl, investigated the impact of multiple freeze/thaw cycles on aggregation of a chimeric

* Corresponding author. Phone (765) 494-1401. Fax (765) 494-6545 email: slnail@pharmacy.purdue.edu.
[†] Department of Industrial and Physical Pharmacy, Purdue University.
[‡] Department of Material Sciences, Purdue University.
[§] Pharmacia&Upjohn Inc.

10.1021/js980383n CCC: $18.00
Published on Web 10/22/1999

L6 mouse−human monoclonal IgG_1 antibody by size exclusion HPLC (HPSEC). Loss of monomer and the formation of soluble dimers (2.5−16%) were observed under these conditions. Higher buffer concentration favored dimer formation, but the effect of pH change during freezing on dimer formation was uncertain. IgG concentration in the range of 1−10 mg/mL was reported not to have a significant effect on aggregation.

Identification of critical solution attributes and processing factors is essential in order to minimize empiricism in the development of formulation and processing conditions for protein pharmaceuticals. The broad objective of this project was to develop a better understanding of the role of formulation and process parameters in development of aggregates during freezing and freeze-drying of bovine IgG when no lyoprotectant is present. The specific objectives were to determine the relative importance of the following factors in aggregate formation after freeze/thaw and freeze-drying of bovine IgG formulations: IgG concentration, phosphate buffer composition, added salt, cooling rate, residual moisture, and the presence of surfactants typically used to minimize surface denaturation.

Experimental Section

Materials—Bovine IgG was obtained from Calbiochem-Novabiochem Corporation (La Jolla, CA) as a solution of concentrated bovine IgG in 0.01 M sodium phosphate buffer (pH 7.2) containing 0.15 N NaCl. The IgG solution was dialyzed against various buffer compositions using a dialysis cassette (Slide-A-Lyzer, Pierce Chemical Company, Rockford, IL) for at least 12 h at 4 °C with gentle stirring. IgG concentration was determined at 280 nm using a molar absorption coefficient of 1.3 mg^{-1} mL cm^{-1} (obtained from Calbiochem-Novabiochem Corporation). Disodium, monosodium, dipotassium, monopotassium phosphate, potassium chloride, and sodium chloride salts were obtained from Mallinckrodt Chemical (Paris, KY). Urea and sodium n-dodecyl sulfate (SDS) were obtained from Sigma Chemical Company (St. Louis, MO) and Calbiochem-Novabiochem Corporation (La Jolla, CA), respectively. Polysorbate 80 was obtained from Sigma Chemical Co (St Louis, MO). All materials were reagent grade or better.

Methods—The pH was adjusted at 25 °C with 0.1 N KOH, NaOH, or HCl to 7.1 for solutions of IgG in the presence of 0.22 N KCl and 0.22 N NaCl. The concentration of IgG was 1 mg/mL except where noted.

Freezing and Freeze-Drying—IgG solutions (1.5 mL fill volume) were placed in 5 mL serum vials (Baxter Scientific, McGaw Park, IL). Two freezing methods were investigated. Fast cooling was carried out by dipping vials in liquid nitrogen before transferring to a freeze-dryer shelf precooled to −45 °C. Slow cooling was accomplished by placing vials directly on the shelf of the lyophilizer at room temperature and decreasing the shelf temperature at a rate of 2 °C/min. For freeze−thaw experiments, thawing was carried out by allowing frozen solutions to thaw at room temperature.

Frozen solutions were held at −45 °C for at least 6 h before beginning freeze-drying (Lyoflex 08, BOC Edwards Calumatic, Tonawanda, NY or Dura-Stop, FTS Systems, Inc., Stone Ridge, NY). The system was evacuated to a pressure of 100 mTorr at −40 °C and held for 26 h (primary drying). The shelf temperature was then increased to 25 °C at a heating rate of 0.1 °C/min and held for a period of 24 h. Type T thermocouples were placed in the bottom center of two different vials to monitor product temperature. A sample thief was used to withdraw vials at different times during drying without disturbing the cycle. At the end of secondary drying, the samples were stoppered under vacuum and analyzed within 24 h.

Annealing experiments were carried out by rapidly cooling vials containing solutions of IgG in 0.01 M potassium phosphate buffer with 0.22 N NaCl (pH 7.1) by dipping in liquid nitrogen, followed by placing on the freeze-dryer shelves at −45 °C. Vials were then warmed to −15 °C at a rate of 2 °C/min for 3 h, followed by decreasing the shelf temperature to −45 °C. Rapidly cooled vials that were not annealed were used as a control. Freeze-drying was carried out as described above.

Measurement of pH Changes during Freezing—A method similar to that described by Gomez[11] was used to measure pH in frozen solutions. A special combination pH electrode (Ingold, Mettler-Toledo, Wilmington, MA) using a reference solution consisting of a mixture of glycerol and potassium chloride permits measurement of pH at temperatures as low as −30 °C. Calibration was done at room temperature with buffers of pH 4, 7, and 10 (Baxter Diagnostics, Inc., Deerfield, IL). A universal pH indicator solution (Fisher Scientific, NJ) was also used to visually verify the results, particularly for quench-cooling in liquid nitrogen. A 5 mL serum vial containing 4 mL of the appropriate formulation, two type T thermocouples (32 gauge), and the pH electrode was placed on the lyophilizer shelf at room temperature. The shelf temperature was decreased from 25 °C to −30 °C at a rate of 2 °C/min and held at −30 °C for at least 4 h. The results of pH changes obtained under these conditions were reproducible (standard deviation of ±0.17 at −30 °C).

Determination of Insoluble Aggregates—Absorbance was measured at 350 nm by a UV/visible spectrophotometer (Shimadzu Model 160U, Kyoto, Japan). All measurements were carried out in triplicate, and the appropriate buffer solution without IgG was used as a blank. To study the effect of bovine IgG concentration on aggregation, concentrations ranging from 0.5 to 8 mg/mL in the same buffer system were freeze-dried as described above and reconstituted with distilled water. A limited number of studies were also carried out where reconstituted freeze-dried solids were filtered and the absorbance measured at 280 nm in order to compare the two methods.

Size Exclusion Chromatography—High performance size exclusion chromatography (HPSEC) was used to measure soluble aggregates. The system consisted of a solvent pump, injector, UV detector and integrator (Waters Inc, Milford, MA). A Bio-Sil TSK-400 column (300 × 7.8 mm) from Biorad (Hercules, CA) was used with detection at 280 nm. The mobile phase consisted of 0.1 M Na phosphate buffer containing 0.01 M sodium azide and 150 mM NaCl at a final pH of 6.8. The flow rate was 1 mL/min and analysis time was approximately 20 min. The column was calibrated with molecular weight standards (Biorad Inc, Hercules, CA), including thyroglobulin (670 000), bovine γ globulin (158 000), chicken ovalbumin (44 000), horse myoglobulin (17 000), and vitamin B-12 (1350). Before injection, samples were filtered through a 0.22 mm filter (Acrodisc LC, Waters Corporation, Ann Arbor, MI). The injection volume was 100 μL.

Other Methods—Water content was determined by Karl Fischer (KF) analysis with coulometric end point detection (Model 150, Denver Instruments, Arvada, CO). All measurements were carried out in triplicate. Dynamic light scattering studies on reconstituted IgG solutions were done by Protein Solutions, Inc. (Model SEM F60, Charlottesville, VA) using a He Ne laser at 633 nm. Scattering was measured at 60° from the incident beam.

The specific surface area of freeze-dried powders was measured by nitrogen adsorption (Model ASAP 2010 Micromeritics, Norcross, GA). Five data points were used to determine the adsorption isotherm. Lyophilized samples were outgassed at 30 °C for at least 48 h to remove moisture. Four replicates were determined for each sample. Environmental scanning electron microscopy was used to examine lyophilized powders (Model 2020, Philips, Inc., Wilmington, MA). Ten milligrams of the appropriate lyophilized powder was spread on a conductive carbon tape and placed on an aluminum mount. The accelerating voltage was 15 kV at a chamber pressure of 5 Torr.

Results and Discussion

Characterization and Quantitation of Aggregates—Absorbance at wavelengths ranging from 350 to 650 nm[7,12−14] is commonly used as a convenient measure of relative levels of insoluble aggregates in protein formulations, particularly at low levels of aggregation.[15] Absorbance vs wavelength data are presented in Figure 1 for IgG at 1 mg/mL in 0.01 M potassium phosphate buffer containing 0.22 N NaCl after freeze−thawing and after freeze-drying and rehydration following both slow and fast cooling. Note that absorbance is negligible for freeze/thawed samples in the range of 325−500 nm. A sharp increase in optical density due to scattering from insoluble

Table 1—Summary of Absorbance at 350 nm, Percent Aggregate after Filtration, and Surface Area of Freeze-Dried Solids

buffer formulations with 1 mg/ml IgG	freezing conditions	absorbance (350 nm)	% aggregate	surface area (m^2/g)
0.01 M KPB + 0.22 N NaCl	slow	0.71 ± 0.04	20.0 ± 1.9	6.6 ± 1.4
0.01 M KPB + 0.22 N NaCl	quench cooled	0.81 ± 0.06	29.9 ± 0.7	10.9 ± 1.3
0.01 M KPB + 0.22 N KCl	slow	0.36 ± 0.02	10.0 ± 2.0	3.6 ± 0.2
0.01 M KPB + 0.22 N KCl	quench cooled	0.5 ± 0.03	14.0 ± 2.0	5.3 ± 0.1
0.01 M KPB + 0.22 N NaCl	quench cooled and then annealed 3 h at –15 °C	0.55 ± 0.02	12.2 ± 1.0	7.7 ± 1.3
0.01 M KPB + 0.22 N NaCl	quench cooled	1.0 ± 0.01	32.7 ± 1.7	17.6 ± 0.5

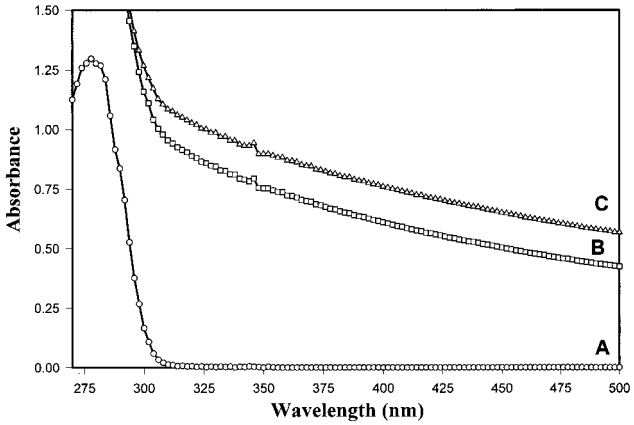

Figure 1—Absorbance vs wavelength of samples containing IgG (1 mg/ml) in a 0.01 M potassium phosphate buffer containing 0.22 N NaCl: (A) after freezing/thawing, (B) after freeze-drying following cooling at 2 °C/min, (C) after freeze-drying following quench-cooling in liquid nitrogen.

aggregates is observed after freeze-drying and, as expected, the extent of scattering increases with decreasing wavelength. Freeze-drying following rapid cooling consistently results in higher absorbance compared with slow cooling. On the basis of these data, 350 nm provides the best sensitivity for measuring turbidity while avoiding absorption due to the protein itself. This wavelength was used in all subsequent studies. A good rank order correlation was observed between absorbance at 350 nm and the quantity of protein remaining after filtration of reconstituted freeze-dried solids (Table 1).

HPSEC chromatograms of the formulation represented in Figure 1 are shown in Figure 2, where the peak at 9.8 min represents the IgG monomer. No soluble aggregates are observed after either freeze–thawing or freeze-drying. The monomer peak area is the same after freeze–thawing as that for the unfrozen solution, but decreases after freeze-drying because of formation of insoluble aggregates which are filtered out during sample preparation. Again, rapid cooling results in higher levels of insoluble aggregates than slow freezing, as reflected by the smaller peak area of the rapidly cooled, freeze-dried material. A peak arising (12.5 min retention time) from an IgG fragment with an apparent molecular weight less than about 6000 was always observed in chromatograms of freeze-dried IgG, but was not characterized further in this study.

The insoluble aggregates were completely dissolved by either 6 M urea or by 0.4% (w/v) sodium dodecyl sulfate (SDS). Only one peak, corresponding to the IgG monomer, was observed in the HPSEC chromatogram of solubilized aggregated material (data not shown). These observations support the conclusion that only noncovalent aggregates are observable under the experimental conditions reported here.

Dynamic light scattering data for insoluble aggregates formed by both fast and slow cooling are shown in Figure 3. Rapid freezing consistently results in larger aggregates, with an average particle size of about 1 μm, as compared

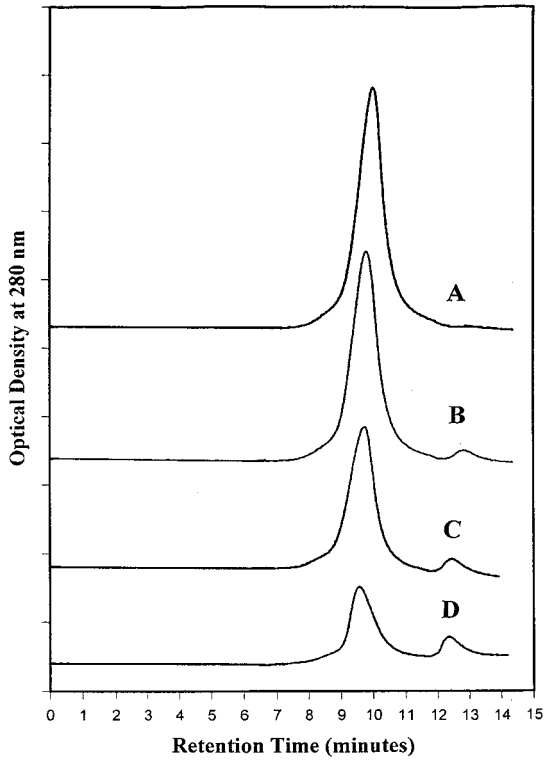

Figure 2—HPSEC chromatograms of bovine IgG in 0.01 M potassium phosphate buffer containing 0.22 N NaCl: (A) solution before any treatment, (B) after freezing/thawing, (C) after freeze-drying (slow cooling at 2 °C/min), (D) after freeze-drying (quench-cooling in liquid nitrogen).

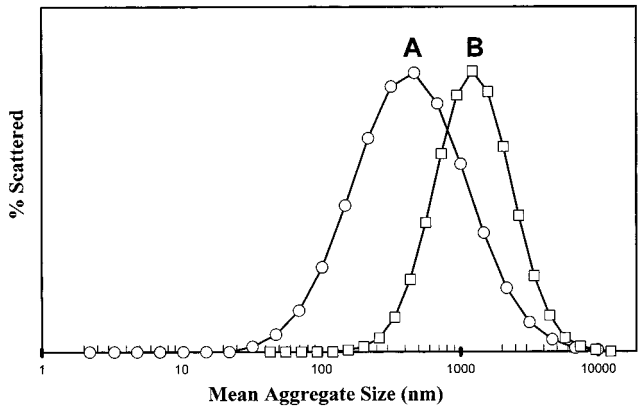

Figure 3—Effect of freezing rate on mean aggregate size of IgG, determined by dynamic light scattering: (A) slow cooling, (B) quench-cooling in liquid nitrogen.

with an average particle size of about 400 nm for slow cooling. The reason for the difference in average particle size is not known at present.

The data in Figures 1–3 demonstrate that fast cooling consistently results in higher levels of aggregated protein in a buffer containing 0.01 M potassium phosphate (pH 7.1)

with 0.22 N NaCl as compared with slow cooling. Similar results were obtained with 0.01 M potassium phosphate buffer (pH 7.1) and 0.22 N KCl (absorbance values of 0.36 vs 0.50 for slow and rapid cooling, respectively). These data add to the growing body of published data supporting the conclusion that rapid freezing can be detrimental to protein integrity. Eckhardt et al.,[14] using several formulations of human growth hormone and an apparatus for controlling cooling rate, demonstrated that the level of insoluble aggregate after freeze/thawing is directly related to the freezing rate over the range of 0.5 °C to 50 °C/min. Hsu et al.,[12] using formulations of tissue plasminogen activator (tPA), reported a direct relationship between freezing rate and development of turbidity in reconstituted samples during storage. These investigators postulated that denaturation takes place at the solid/void interface, which results in aggregate formation upon reconstitution. Chang and co-workers,[7] using multiple freeze−thaw cycles of phosphofructokinase, lactate dehydrogenase, glutamate dehydrogenase, interleukin-1 receptor antagonist, tumor necrosis factor, and ciliary neurotropic factor demonstrated that slow freezing resulted in less turbidity in thawed samples than freezing in liquid nitrogen. Jiang and Nail,[6] using lactate dehydrogenase and β-galactosidase, also reported that rapid freezing in liquid nitrogen resulted in lower recovery of enzyme activity after freeze−thawing compared with freezing in a freeze-dryer.

Strambini and Gabellieri[16] have proposed a mechanism for freezing-induced damage to proteins involving partial unfolding of proteins after adsorption to the ice surface. If this mechanism is operative, then more rapid freezing would be expected to result in a higher ice/freeze-concentrate interfacial area, a greater extent of protein adsorption, and more damage to the protein. While no aggregation is detected in bovine IgG after freeze/thawing under the conditions reported here, our data are consistent with this mechanism, where partial denaturation following adsorption to the ice surface is reversible after freeze/thawing. However, subsequent drying would result in a partially denatured protein in the solid state, which forms aggregates upon reconstitution.

To test the hypothesis that rapid freezing inhibits sodium phosphate precipitation, a pH universal indicator was used. No difference was observed after slow vs fast cooling (both showing an acidic pH shift) despite a significant difference in the amount of aggregates after freeze-drying and reconstitution.

Environmental SEM photomicrographs (Figure 4) show distinctly different morphologies for the freeze-dried powders following cooling at different rates. The slowly cooled specimen appears as relatively large filaments, whereas the rapidly cooled material appears to be more finely divided.

Table 1 summarizes specific surface area data for freeze-dried solids from 1 mg/mL bovine IgG in potassium phosphate buffer containing both NaCl and KCl. The specific surface area of freeze-dried solids is significantly higher for quench-cooled relative to slowly cooled solutions. An unexpected result is that the specific surface area of freeze-dried solids from solutions containing NaCl is significantly higher than those containing KCl. The reason for this is not known at present, but the reduced specific surface area of solids containing KCl correlates with a lower degree of aggregation in the KCl system. This is further support for an aggregation mechanism involving partial denaturation at the ice/freeze−concentrate interface.

Effect of Annealing—If protein denaturation, and subsequent aggregation upon reconstitution, is promoted by a high ice/freeze−concentrate interfacial area following freezing, then annealing the system after fast freezing should decrease aggregation by decreasing the interfacial area. Results of an experiment to test this hypothesis are shown in Table 1. Note that the decrease in specific surface area of the annealed material relative to the quench-cooled control (17.6 vs 7.7 m^2/g) is accompanied by a decrease in percent aggregates in the reconstituted solids from 32% to about 12%. These data lend further support to an aggregation mechansim involving denaturation at the ice/freeze-concentrate interface that becomes irreversible upon drying.

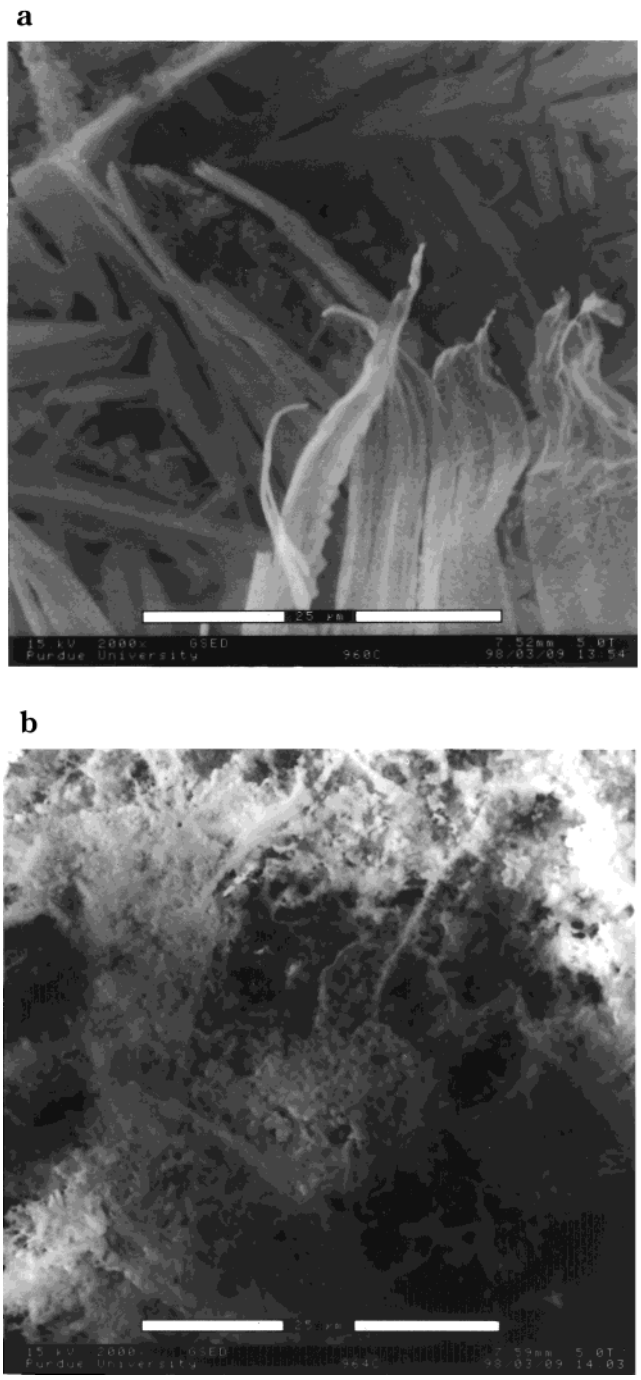

Figure 4—ESEM photomicrographs of freeze-dried IgG following (A) slow cooling, and (B) quench-cooling in liquid nitrogen. Magnification 2000×.

Effect of IgG Concentration—The effect of IgG concentration on both absorbance at 350 nm and on percent aggregate as determined by measuring the absorbance after filtration of the reconstituted solution after freeze-drying is shown in Figure 5 for solutions in 0.01 M

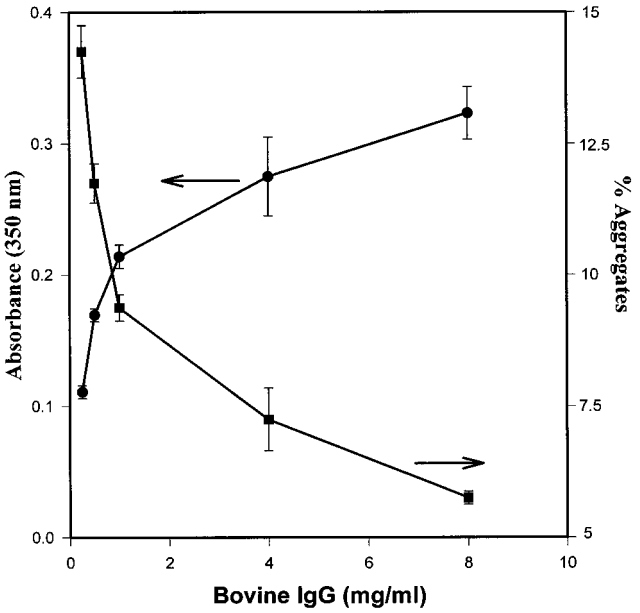

Figure 5—Effect of IgG concentration on absorbance at 350 nm and percent aggregated IgG after lyophilization. Buffer system was 0.01 M potassium phosphate with 0.22 N NaCl, frozen at a cooling rate of 2 °C/min. Error bars represent standard deviation of triplicate measurements from three separate vials.

Table 2—Residual Moisture vs IgG Concentration

bovine IgG concentration (mg/mL) before lyophilization	residual moisture
0.5	1.25 ± 0.13
1	1.32 ± 0.14
2	1.4 ± 0.2
4	2.5 ± 0.02
8	2.5 ± 0.2

potassium phosphate buffer containing 0.22 N NaCl at pH 7.1. Even though absorbance at 350 nm increases as protein concentration increases from 0.5 to 8 mg/mL, the level of insoluble aggregates decreases by more than half. This direct effect of protein concentration on stabilization against damage caused by freeze-drying has been reported by other investigators. Hansson[17] reported that the quantity of aggregate formed in human IgG after multiple freeze−thaw cycles decreased with increasing IgG concentration until, at 50 mg/mL IgG, no aggregation was observed after multiple freeze−thaw cycles. Chang et al.[7] reported that increasing the concentration of interleukin-1 receptor antagonist (from 1 to 100 mg/mL) diminished the level of aggregates from 50% to 0.01%. This effect has also been reported for β-galactosidase[6,18] and lactate dehydrogenase.[6,19] However, to our knowledge, this concentration effect has not been explained.

Residual moisture level at each concentration was measured in order to test the hypothesis that higher concentrations of protein, under the same process conditions, will result in higher residual moisture levels and prevent damage caused by "overdrying". Data are summarized in Table 2. The data do indicate that residual moisture increases with increasing concentration. However, the range of residual moisture levels is only from 1.25% to 2.5%. In the range of 4 to 8 mg/mL IgG, the residual moisture level is approximately constant, but the amount of insoluble aggregate decreases significantly. It appears that residual moisture is, at most, only a partial explanation for the concentration effect.

Anchordoquy and Carpenter[20] reported that dissociation of lactate dehydrogenase subunits, and subsequent loss of activity, was due to the large pH decrease associated with the phosphate buffer during freezing. This effect was inhibited by protective levels of polymers such as bovine serum albumin and poly(vinylpyrrolidone). To test the hypothesis that higher protein concentration inhibits crystallization of buffer salts, pH shift during freezing was measured for the lowest and highest protein concentrations used in this study. Minimal difference in pH shift was observed between the lowest and highest concentrations (4.0 vs 4.2 for 0.5 mg/mL and 8 mg/mL, respectively). Therefore, pH change during freezing does not appear to be a likely explanation for the concentration effect. The data need to be interpreted with some caution, however, since the freezing conditions were different for the experiments in which the apparent pH during freezing was measured (freezing to −30 °C) versus the freezing conditions prior to freeze-drying (freezing to −45 °C).

Increasing IgG concentration was associated with an increase in specific surface area of the freeze-dried solids (from 6.6 m^2/g at 1 mg/mL to 9.0 m^2/g at 8 mg/mL) over the concentration range studied. Combined with the absorbance data in Figure 5, these data suggest that the concentration effect may be another manifestation of aggregation as an interfacial phenomenon. The increased specific surface area of freeze-dried solids with increased concentration is accompanied by increased absorbance at 350 nm of the reconstituted solution, suggesting that the increased turbidity arises from a larger amount of protein at the ice/freeze−concentrate interface during freezing. However, the fractional amount of protein at the interface must decrease with increasing concentration, given that the specific surface area increases by a factor of about 1.5 while the concentration increases by a factor of 8. The lower percentage of protein at the interface would explain the decrease in percent aggregated protein with increased concentration.

Another explanation for the protein concentration effect that was considered is the influence of protein concentration on T_g' (the glass transition of the maximally freeze-concentrated solute), where increased protein concentration would be expected to increase T_g'. However, as with many protein formulations not containing a lyoprotectant, thermal analysis of the frozen systems did not reveal a glass transition (data not shown). The freeze-drying conditions used for the study (primary drying at −40 °C) represent the approximate lower temperature limit for production scale freeze-drying. While the low primary drying temperature should minimize collapse during freeze-drying, the potassium phosphate buffer system without added salt did exhibit collapse. As discussed below, we observed no effect of collapse during freeze-drying on level of aggregation upon reconstitution. We conclude that any protein concentration effect on T_g' would not explain the observations reported here.

Effect of Buffer Composition on Aggregation—The effect of systematic variation in solution composition at a constant IgG concentration and nearly constant ionic strength on turbidity of the reconstituted solid is shown in Figure 6. The effect of the phosphate buffer (Na vs K salt) at two concentrations (0.1 M vs 0.01 M) is examined where ionic strength is adjusted with either NaCl or KCl. At a constant buffer concentration, the potassium salt consistently results in a significantly lower level of aggregate relative to sodium phosphate ($P < 0.001$). Adding either NaCl or KCl results in increased aggregation relative to buffer alone, and sodium chloride always results in more aggregation than the same concentration of potassium chloride.

pH was measured during the freezing process in order

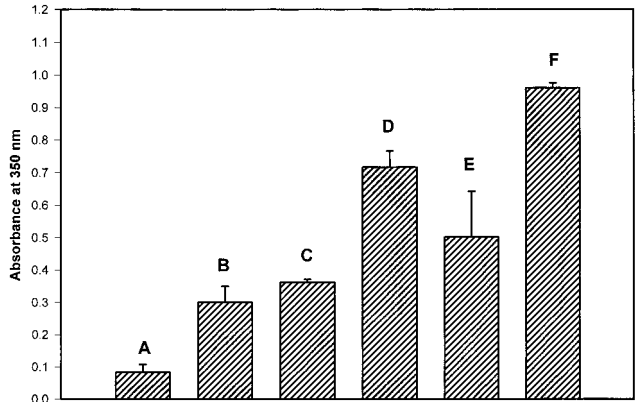

Figure 6—Effect of solution composition at similar ionic strength ($I = 0.24$ M) on IgG aggregation after freeze-drying in (A) 0.1 M potassium phosphate, (B) 0.1 M sodium phosphate, (C) 0.01 M potassium phosphate containing 0.22 N KCl, (D) 0.01 M potassium phosphate containing 0.22 N NaCl, (E) 0.22 N KCl, and (F) 0.22 N NaCl. Error bars represent standard deviation based on measurements from three separate vials.

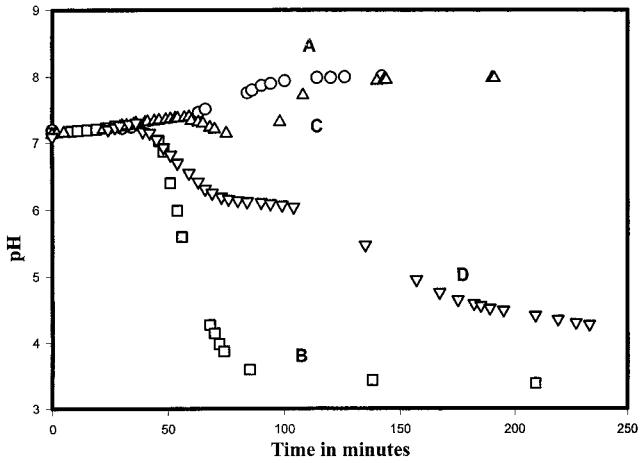

Figure 7—Apparent pH during freezing for (A) 0.1 M potassium phosphate buffer, (B) 0.1 M sodium phosphate buffer, (C) 0.01 M potassium phosphate buffer containing 0.22 N KCl, and (D) 0.01 M potassium phosphate buffer containing 0.22 N NaCl.

to examine the relationship between aggregation and pH shift during freezing. The data are summarized in Figure 7. As expected, pH increases somewhat (from 7.2 to about 8) during freezing for the potassium phosphate buffer, whereas pH decreases for the sodium phosphate buffer system (from 7.2 to about 3.5). The effect of added salt is to delay crystallization of both monobasic potassium phosphate and dibasic sodium phosphate. For potassium phosphate containing KCl, the pH of the frozen system reaches a similar pH to that of potassium phosphate buffer alone after about 100 min. For sodium phosphate buffer alone, the apparent pH reaches its equilibrium value after 100 min, but the sodium phosphate buffer containing NaCl is still slowly decreasing after 4 h. These data are in agreement with data reported by Gomez,[11] where an inhibition of disodium phosphate dodecahydrate precipitation was observed in the presence of 8 mM Na phosphate buffer containing 0.15 N NaCl.

As mentioned above, comparison of the data in Figures 6 and 7 should be made with some caution, because the pH measurements were made at −30 °C, whereas freezing of the IgG solutions was carried out at −45 °C. However, the data in Figure 7 support the conclusion that pH shift during freezing does not affect aggregation. Comparing curves B and D in Figure 7 with corresponding data in Figure 6, the level of aggregate is considerably greater for the solution containing NaCl relative to that containing sodium phosphate alone. Even if it is assumed that the solution containing sodium chloride eventually reaches the same pH during freezing as that containing buffer alone, the aggregate levels would be expected to be the same for the two systems if the pH shift during freezing were driving the aggregation process. Curves A and C in Figure 7 show that the two potassium phosphate buffer solutions reach the same apparent pH after about 2 h, but, again, the solution containing added salt results in a significantly higher level of aggregated protein. The absence of an effect of pH shift upon freezing on IgG aggregation is further illustrated in Figure 6, where 0.22 N KCl or NaCl alone (pH adjusted to 7.1) is compared to the corresponding solutions containing 0.01M potassium phosphate. Aggregate levels are significantly greater for solutions containing salt alone, where the apparent pH at −30 °C after 4 h is 6.4 and 7.0 for 0.22 N NaCl and KCl, respectively.

In studying the effect of formulation variables on the stability of freeze-dried human growth hormone, Pikal and co-workers[21] noted that the destabilizing effect of added NaCl could be attributed to either ionic strength or a specific ion effect of Na^+ or Cl^- and concluded that Cl^- is the most likely cause of the adverse effect. Our data support the conclusion that the effect of buffer solution composition on IgG aggregation is neither a pH shift effect nor an ionic strength effect, but rather a specific ion effect. Further work is in progress to test the hypothesis that the effects of added salts on IgG aggregation resulting from freeze-drying is predicted by the Hofmeister series, where destabilizing ions promote aggregation.

The freeze-dried cakes resulting from 0.1 M potassium phosphate buffer were collapsed, whereas freeze-dried solids resulting from 0.1 M sodium phosphate buffer retained their macroscopic structure. For potassium buffer systems containing NaCl or KCl, no collapse was observed. Besides illustrating that collapse during freeze-drying does not necessarily correlate with decreased integrity of a freeze-dried protein, this observation suggests that an alternative explanation for the data in Figure 6 is that residual moisture levels are different for the formulations, and that this difference in residual moisture level influences aggregation. Residual moisture levels were significantly different (2.8 ± 0.3% for 0.1 M potassium phosphate vs 1.5 ± 0.4% for 0.1 M sodium phosphate alone). To study this effect further, two formulations containing 0.01 M potassium phosphate (pH 7.1) and either 0.22 N KCl or NaCl, were compared with respect to both residual moisture level and insoluble aggregate levels by using a sample thief to remove samples during secondary drying. All samples retained their macroscopic structure. Data are summarized in Figure 8. The top panel shows that the difference in absorbance at 350 nm between the two buffer solutions is not distinguishable until the 49 h sample, at which time the absorbance of the sodium chloride system is significantly higher and remains so throughout the drying cycle. Although the residual moisture level in the potassium chloride formulation is higher than the sodium chloride formulation early in secondary drying, the residual moisture levels in the two formulations are not significantly different by the end of the cycle. The data in Figure 8 support the conclusion that the salt effect becomes evident only as the residual moisture level is decreased to 2−5%. Below this level, there is a significant effect of the added salt which is not explained by differences in residual moisture. No difference in cake appearance was observed between time 1, time 2, and samples taken at the end of the cycle (Figure 9). These data are consistent those of Hsu et al.[22] for tPA, where protein integrity is lost by overdrying.

Effect of a Surfactant on Aggregation—Nonionic

Table 3—Effect of Polysorbate 80 on IgG Aggregation

sample information	medium of reconstitution	absorbance (350 nm)
0.01 M KPB + 0.22 N NaCl, pH 7.1 containing 1 mg/mL bovine IgG	distilled water	0.54 ± 0.06
0.01 M KPB + 0.22 N NaCl, pH 7.1 containing 1 mg/mL bovine IgG and 0.02% w/w Tween 80	distilled water	0.18 ± 0.02
0.01 M KPB + 0.22 N NaCl, pH 7.1 (25 °C) containing 1 mg/mL bovine IgG and 0.1% w/w Tween 80	distilled water	0.18 ± 0.05
0.01 M KPB + 0.22 N NaCl, pH 7.1 containing 1 mg/mL bovine IgG	0.02% w/w Tween 80	0.15 ± 0.01

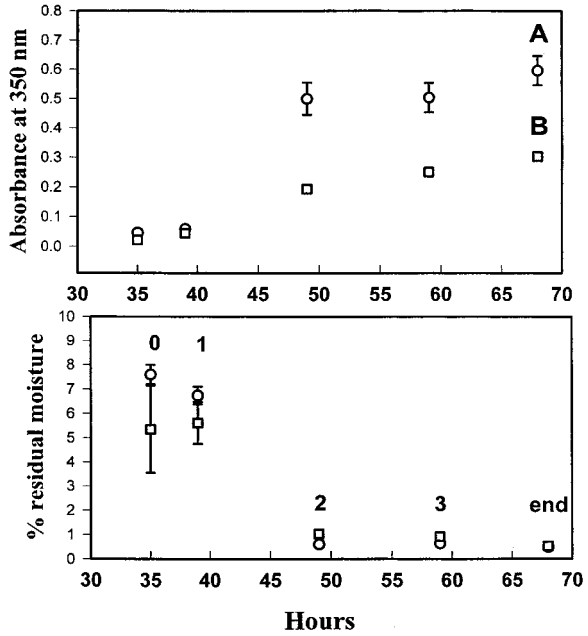

Figure 8—Effect of secondary drying time on absorbance at 350 nm and residual moisture: (A) 0.01 M potassium phosphate containing 0.22 N NaCl, (B) 0.01 M potassium phosphate containing 0.22 N KCl. Error bars represent the standard deviation of triplicate measurements from three separate vials.

Figure 9—Reconstituted vials of lyophilized bovine IgG in 0.01 M potassium phosphate with 0.22 N NaCl removed during secondary drying, showing development of turbidity in the reconstituted product.

surfactants are commonly used in formulations to prevent protein adsorption to surfaces and to minimize interfacial denaturation by preferentially adsorbing to hydrophobic surfaces and to hydrophobic regions of proteins. Table 3 summarizes absorbance data at 350 nm obtained for reconstituted solids with and without polysorbate 80 in the medium of reconstitution or in the formulation before freeze-drying. Use of a surfactant—either in the reconstitution medium or in the formulation—significantly decreases, but does not eliminate, aggregation. No difference is observed in aggregation between a formulation containing 0.02% or 0.1% w/w polysorbate 80. No significant difference was observed between incorporation of the surfactant in the formulation and incorporation in the medium of reconstitution. These data contrast with those of Chang and co-workers,[7] who reported essentially complete protection of six different proteins by incorporation of 0.01% polysorbate 80 into the formulation prior to freezing. Incorporation of surfactant into the reconstitution medium instead of the formulation was less effective in the case of interleukin-1 receptor antagonist, but still reduced the quantity of aggregate relative to reconstitution with water alone (23% vs 50% aggregate, respectively).

Practical Considerations—The data reported here are consistent with the body of literature pointing to protein aggregation resulting from freezing and freeze-drying as an interfacial phenomenon. While further investigation is warranted, particularly in the area of specific ion effects, several broad conclusions may serve as guidelines for development of protein formulations and processing conditions. First, keep the protein concentration as high as practical. Second, minimize the buffer concentration and do not use additional salts unless necessary. From the standpoint of aggregation, potassium phosphate buffer appears to be preferable to sodium phosphate buffer, and potassium chloride is preferable to sodium chloride. Identification of critical process parameters should include thermal history of freezing, since a number of reports suggest that rapid freezing should be avoided. Particular attention should be given to establishment of residual moisture specifications, particularly since the conventional wisdom that "the dryer, the better," is not always true.

References and Notes

1. Wang, Y. J.; Hanson, M. A. Parenteral formulations of Proteins and Peptides: Stability and Stabilizers. *J. Parenter. Sci. Technol.* **1988**, *42*, S2−S26.
2. Carpenter, J. F.; Pretrelski, T. J.; Anchodorquy, T. J.; Arakawa, T. Interactions of Proteins with Stabilizers During Freezing and Drying. In *Formulations and Delivery of Proteins and Peptides*; Cleland, J. L., Langer, R., Eds.; American Chemical Society: Washington, DC, 1994; pp 134−147.
3. Duddu, S. P.; Zhang, G.; Dalmonte, P. R. The Relationship Between Protein Aggregation and Molecular Mobility Below the Glass Transition Temperature of Lyophilized Formulations Containing a Monoclonal Antibody. *Pharm. Res.* **1997**, *14*, 596−600.
4. Ressing, M. E.; Jiskoot, W.; Talsma, H.; Van Ingen, C. W.; Coen Beuvery, E.; Crommelin, D. J. A. The Influence of Sucrose, Dextran and Hydroxypropyl-B-cyclodextrin as Lyoprotectants for a Freeze-Dried Mouse IgG2a Monoclonal Antibody (MN12). *Pharm. Res.* **1992**, *9*, 266−270.
5. Nema, S.; Avis, K. E. Freeze−Thaw Studies of a Model Protein, Lactate Dehydrogenase, in the Presence of Cryoprotectants. *J. Parenter. Sci. Technol.* **1993**, *47*, 76−83.
6. Jiang, S.; and Nail, S. L. Effect of Process Conditions on Recovery of Protein Activity After Freezing and Freeze-Drying. *Eur. J. Pharm. Biopharm.* **1998**, *45*, 249−257.
7. Chang, B. S.; Kendrick, B. S.; and Carpenter, J. F. Surface-Induced Denaturation of Proteins during Freezing and its Inhibition by Surfactants. *J. Pharm. Sci.* **1996**, *85*, 1325−1330.
8. Hansson, U. Aggregation of Human Immunoglobulin G Upon Freezing. *Acta Chem. Scand.* **1968**, *22*, 483−489.
9. Paborji, M.; Pochopin, N. L.; Coppola, W. P.; Bogardus, J. B.; Chemical and Physical Stability of Chimeric L6, a Mouse Human Monoclonal Antibody. *Pharm. Res.* **1994**, *11*, 764−771.

10. Winward, D. B.; Brophy, M. T. Acute Renal Failure After Administration of Intravenous Immunoglobulin: Review of the literature and case report. *Pharmacotherapy* **1995**, *15*, 765−772.
11. Gomez, G. Crystallization-Related pH Changes During Freezing of Sodium Phosphate Buffer Solutions. Ph.D. Dissertation, University Microfilms, Inc., Ann Arbor, MI, 1995.
12. Hsu, C. C.; Nguyen, H. M.; Yeung, D. A.; Brooks, D. A.; Koe, G. S.; Bewley, T. A.; Pearlman, R. Surface Denaturation at Solid-Void Interface. A Possible Pathway by Which Opalescent Particulates Form During the Storage of Lyophilized Tissue-Type Plasminogen Activator at High Temperatures. *Pharm. Res.* **1995**, *12*, 69−77.
13. Tomono, T.; Ikeda, K.; Suzuki, T. A New Intact Immunoglobulin for Intravenous Use Stabilized by Chemically Modified Gelatin Derivatives. *Vox. Sang.* **1986**, *51*, 81−86.
14. Eckhardt, B. M.; Oeswein, J. Q.; Bewley, T. A. Effect of Freezing on Aggregation of Human Growth Hormone. *Pharm. Res.* **1991**, *8*, 1360−1364.
15. Shahrokh, Z.; Stratton, P. R.; Eberlein, G. A.,; Wang, Y. J. Approaches to Analysis of Aggregates and Demonstrating Mass Balance in Pharmaceutical Protein (Basic Fibroblast Growth Factor) Formulations. *J. Pharm. Sci.* **1994**, *83*, 1645−50.
16. Strambini, G. B.; Gabellieri, E. Proteins in Frozen Solutions: Evidence of Ice-Induced Partial Unfolding. *Biophys. J.* **1996**, *70*, 971−976.
17. Hansson, U. Correlation Between Amount of Aggregates Formed on Freezing of Immunoglobulin G and Protein Concentration. *Acta Chem. Scand.* **1969**, *23*, 1828−1829.
18. Izutsu, K.; Yoshioka, Y.; Terao, Y. Stabilization of β-galactosidase by Amphiphilic Additives During Freeze-Drying. *Int. J. Pharm.* **1993**, *90*, 187−194.
19. Izutsu, K.; Yoshioka, Y.; Kojima, S. Physical Stability and Protein Stability of Freeze-Dried Cakes During Storage at Elevated Temperatures. *Pharm. Res.* **1994**, *11*, 994−999.
20. Anchordoquy, T. J., and Carpenter, J. F. Polymers Protect Lactate Dehydrogenase during Freeze-Drying by Inhibiting Dissociation in the Frozen State. *Arch. Biochem. Biophys.* **1996**, *332*, 231−238.
21. Pikal, M. J.; Dellerman, K. M.; Roy, M. L.; Riggin, R. M. The Effects of Formulation Variables on the Stability of Freeze-dried Human Growth Hormone. *Pharm. Res.* **1991**, *8*, 427−436.
22. Hsu, C. C.; Ward, C. A.; Pearlman, R.; Nguyen, H. M.; Yeung, D. A.; Curley, J. G. Determining the Optimum Residual Moisture in Lyophilized Protein Pharmaceuticals. *Dev. Biol. Standard.* **1991**, *74*, 255−271.

Acknowledgments

The authors acknowledge Dr. John Carpenter for helpful criticism of the manuscript, and Robert Verberig for photographic assistance. The analytical support of Protein Solutions, Inc. for particle size determination is gratefully acknowledged. Financial support (fellowships for J.M. Sarciaux) provided by Astra, Pfizer, and Pharmacia&Upjohn, Inc., is also greatly appreciated.

JS980383N

Notes on the Inverse Gaussian Distribution and Choice of Boundary Conditions for the Dispersion Model in the Analysis of Local Pharmacokinetics

AKIHIRO HISAKA*,† AND YUICHI SUGIYAMA‡

Contribution from *Development Research Laboratory, Banyu Pharmaceutical Co. Ltd., 810, Nishijo, Menuma-Machi, Osato-Gun, Saitama, 360-0214, Japan, and Faculty of Pharmaceutical Sciences, University of Tokyo, 7-3-1, Hongo, Bunkyo-ku, Tokyo 113-0033, Japan.*

Received September 25, 1998. Final revised manuscript received September 8, 1999.
Accepted for publication September 24, 1999.

Abstract □ The dispersion model has been widely used to analyze local pharmacokinetics in the organs and the tissues since the 1980's. However, an ambiguity still remains in selecting the boundary conditions which are necessary to solve the basic equation of the model. In this note, theoretical considerations are given to this problem and we present here some deficiencies of the mixed boundary conditions. It seems that theoretical confusion exists in the literature for the mixed boundary conditions. It is well-known that the solution of the dispersion model with a bolus input is the inverse Gaussian distribution for the mixed boundary conditions. However, it is rarely recognized that the inverse Gaussian distribution requires an open boundary at either the inlet or the outlet. For the analysis of local pharmacokinetics, the use of the classical Danckwerts (or closed) boundary conditions is recommended.

Introduction

To predict in vivo organ clearances from in vitro findings, a mathematical model that assumes certain structured blood flow is indispensable. It has been reported that the convection dispersion model[1,2] and distributed tube model[3,4] are sound models which give appropriate predictions of organ clearance in various situations. These two models afford similar predictions in linear kinetics,[5] but not in nonlinear kinetics.[4−6] This is because the distributed tube model does not assume any micromixing of the blood stream in the bed. In contrast, micromixing is incorporated naturally into the dispersion model.

The dispersion model was proposed by Roberts et al. in the 1980s[1,2] and has been used to analyze local pharmacokinetics in various situations.[7−11] The dispersion model is expressed by a partial differential equation, and to obtain its solution, the entrance and the exit boundary conditions are necessary. A drawback of the dispersion model is an ambiguity in selecting the boundary conditions.[4] Roberts et al. initially chose the Danckwerts (or closed) boundary conditions (DBC) because it satisfies the extremes of the well-stirred and tube model predictions,[1] but later favored the mixed boundary conditions (MBC).[5] MBC have also been preferred by several other investigators.[4,7−9]

The solution for MBC is apparently equivalent to a probabilistic distribution of the rate of first passage of particles moving randomly (as a random walk) that is referred to as the inverse Gaussian distribution.[2] A random walk is a discrete process but is superimposed on a convection flow by limiting the size of the steps and by expanding the basic equation in a Taylor series.[12] Accordingly, MBC has been related to the first passage time.[5] However, there is a pitfall, as will be discussed later.

In this correspondence, theoretical considerations are given to the ambiguity of the boundary conditions of the dispersion model. Some deficiencies of MBC will be discussed. We recommend the use of DBC.

Deficiencies of the Mixed Boundary Condition

The dispersion model is described by a partial differential equation as follows:[1,2]

$$\frac{\partial C}{\partial T} = D_N \frac{\partial^2 C}{\partial Z^2} - \frac{\partial C}{\partial Z} - R_N C \qquad (1)$$

where C is the normalized concentration of a substance at the normalized cross-section Z and at the normalized time T, D_N is the dispersion number, and R_N is the efficiency number. DBC is defined as follows:[2,5,13]

$$C - D_N\, \partial C/\partial Z = C_{in} \text{ at } Z = 0 \text{ for } T \geq 0 \qquad (2)$$

$$\partial C/\partial Z = 0 \qquad \text{at } Z = 1 \text{ for } T \geq 0 \qquad (3)$$

where C_{in} is the concentration in the entering stream. MBC is expressed as follows:[2,5,14]

$$C = C_{in} \qquad \text{at } Z = 0 \text{ for } T \geq 0 \qquad (4)$$

$$C \rightarrow 0 \text{ or } \partial C/\partial Z \rightarrow 0 \text{ as } Z \rightarrow \infty \text{ for } T \geq 0 \qquad (5)$$

The analytical solution of the dispersion model after bolus input with MBC is given by:[2]

$$C(T,Z) = \frac{Z}{2}\left(\frac{1}{\pi D_N T^3}\right)^{1/2} \exp\left(-\frac{(Z-T)^2}{4D_N T}\right) \qquad (6)$$

where the elimination is not considered. As described above, eq 6 also represents the inverse Gaussian distribution.[15]

† Banyu Pharmaceutical Co.
‡ University of Tokyo.

10.1021/js9803860 CCC: $18.00
Published on Web 10/30/1999

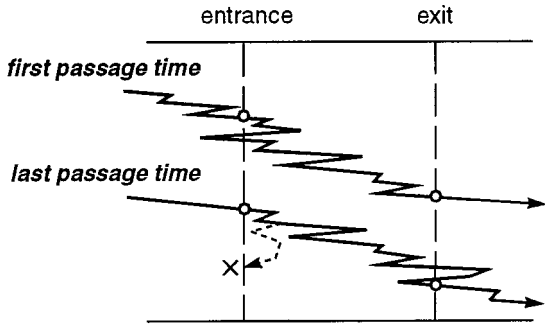

Figure 1—Schematic representation of a first passage time and a last passage time of a particle moving randomly in the bed. The first passage time starts when the particle first enters the bed and continues until it first reaches the exit. The last passage time starts when the particle last leaves the entrance and continues until it exits from the bed, never to return. Note that these sojourn times may include some time spent outside the bed. The dotted line indicates the trajectory of a lost particle in the case of MBC.

It should be noted, however, that the probabilistic distribution of first passage times of a random walk becomes the inverse Gaussian distribution where the inlet boundary is open.[12] The situation of MBC is distinct from the first passage time because its inlet is not open as indicated by eq 4. In reality, MBC is equated to the last passage times.[12] As shown in Figure 1, these two sojourn times are different but apparently equivalent because the time for roaming on the inlet in the first passage times corresponds to that for the outlet in the last passage times.

The dispersion assumed in the dispersion model represents mixing of the blood streams flowing through the microcapillaries in the tissue.[5] Accordingly, dispersion occurs within the tissue but must end at the boundaries. In this instance, both the first and the last passage times are inappropriate because an open boundary is postulated. As MBC is the last passage time, the dispersion is assumed across the exit,[10] which is physiologically irrelevant because the blood never returns from the distal vessels.

Another deficiency of MBC is that it cannot properly control the transfer of mass across the inlet. The peculiarity is obvious for a bolus case. The total mass of the drug is given by integration of eq 6:

$$\int_0^\infty C(T,Z)\,dZ = \{1 + \mathrm{erf}(\alpha^{1/2}/2)\}/2 + (\pi\alpha)^{-1/2}e^{-\alpha/4} \quad (7)$$

where $\alpha = T/D_N$. Equation 7 takes a minimum value of 1 when $\alpha \to +\infty$, namely $T \to +\infty$ and/or $D_N = 0$, but scatters to $+\infty$ as α or T approaches 0. It implies that the mass retained in the bed becomes infinity at the time of injection (Figure 2).

It is generally agreed in the field of chemical engineering that the correct boundary conditions are those that show the flux

$$\phi = C - D_N \partial C/\partial Z \quad (8)$$

to be continuous at the boundary.[12] Since the differential term in eq 8 is ignored for the inlet of MBC (eq 4), the implicit flux occurs when $\partial C/\partial Z \neq 0$ at $Z = 0$. This is the reason for the excessive mass in eq 7. The mass is increased explosively at the time of injection when $\partial C/\partial Z$ becomes $-\infty$ at the inlet and then evaporates gradually after the injection when $\partial C/\partial Z > 0$.

Availability predictions of the dispersion model at steady-state for any boundary conditions in linear kinetics have been reported (eqs 6 and 7 in reference 16). However, they are irrelevant for MBC. If $\partial C/\partial Z$ is less than zero at the inlet of MBC, which occurs when $R_N > 0$, the mass needs to be pored into the bed more than the flow rate allows to satisfy eq 4. This is impossible. In other words, MBC does not have a reasonable solution for steady-state conditions when $R_N > 0$ because of the improper inlet definition.

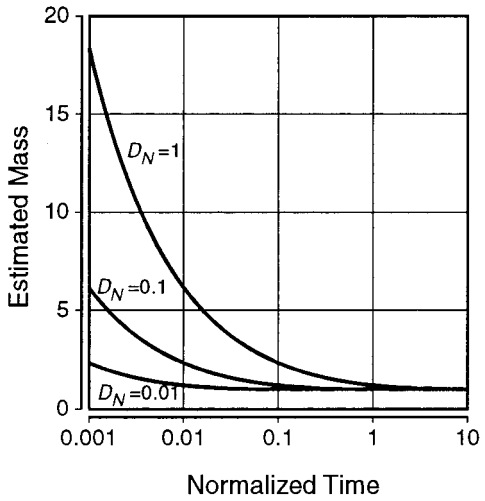

Figure 2—Overestimation of mass retained in the bed by the dispersion model with the mixed boundary condition after bolus input. Note that the mass must be 1.0 independently of time or dispersion number (D_N). The mass is calculated by eq 7.

Danckwerts Boundary Condition

DBC is a necessary consequence of the restrictions for mass conservation and discontinuity of mixing at the boundary.[17] This is currently the most physiological assumption for the solutes that are carried by the bloodstream in the organ, because micromixing of the blood never occurs across the boundaries. In the future, however, DBC might be reexamined for unnatural discontinuities at the boundaries. Continuous or stepwise change of dispersion has been considered theoretically.[18,19] These conditions are advantageous to simulate the real dynamics in the organ, although they are inapplicable to the current analyses because the change of the dispersion in the organ is unknown.

A major shortcoming of DBC is that its analytical solution is mathematically complex.[2] Yet a solution is possible for linear kinetics with inverse Laplace transformation techniques that are used frequently to solve the two-compartment dispersion model.[7,20,21] In addition, several numerical methods have been introduced to calculate the dispersion model for nonlinear kinetics.[14,22–24] It is now possible to obtain non-steady-state solutions of nonlinear multicompartment dispersion models with any input function.[23]

Practical Considerations

Despite the evident theoretical defects, it must be emphasized that most of the analyses done with MBC in the literature are still relevant because its solution is very similar to that of DBC where the dispersion number is small[5] (especially for $D_N \leq 0.2$). However, the results of some studies need to be interpreted cautiously.

First of all, it must be recognized that MBC offers unrealistically spreading outflow curves at higher D_N. After a bolus dose, the dimensionless variance of the outflow curves for MBC is calculated by:[2]

$$CV^2 = 2D_N \quad (9)$$

Equation 9 implies CV^2 exceeds that for even the well-

stirred situation ($CV^2 = 1$) when $D_N > 0.5$. This overspreading occurs primarily because the excessive mass is transferred to the outlet very rapidly in the early period. Another reason is the long-lasting nature of the curve generated with the open outlet condition. Therefore, it is an error caused by the improper definitions. CV^2 of the dispersion model for DBC is calculated by:[2]

$$CV^2 = 2D_N - 2D_N2(1 - e^{-1/D_N}) \quad (10)$$

in which CV^2 never exceeds 1, increases monotonically as D_N grows, and reaches the well-stirred situation at infinity (refer to Figure 3 in ref 10). All theoretical considerations that relate to the shape of the outflow curves of MBC may have potential problems.

Several investigators simulated availabilities with MBC and DBC for various situations and discussed the difference between the two conditions.[5,25] However, the physiological meaning of the difference is obscure. In linear pharmacokinetics, availability is determined by the residence time distribution of the solute (namely, the shape of the outflow curves),[5] and as Nauman concluded, both open and closed systems afford the same residence time distribution when time spent outside the system boundaries is excluded from the total,[12] which is a reasonable assumption for clearance of drugs. Consequently, availability is independent of boundary conditions for linear kinetics if the conditions are realistic. Unfortunately, MBC is not. The difference between MBC and DBC simply represents the extent of errors raised by MBC. Analogous consideration needs to be paid to interpretation of the dispersion numbers calculated with MBC and DBC.[10]

It is advocated that the extent of intrahepatic mixing is very close to the well-stirred situation because the "mixedness" of solutes is maximized at usual dispersion numbers and then decreases as the dispersion number increases, and this suggestion of maximum mixedness in the liver may explain the discrepancy between the apparent validity of the well-stirred model.[26] In this report, "mixedness" was evaluated based on the relative entropy of the outflow curves predicted by the dispersion model of MBC. However, the curves predicted by MBC may become unrealistic as discussed above. For this reason, the evaluation of "mixedness" seems to be erroneous. The conclusion of this report needs some modification.

In the extended use of the dispersion model, MBC would be more troublesome. In nonlinear kinetics, availability predictions by MBC could be inaccurate because clearance depends on the mass retained in the bed. Moreover, it is difficult to calculate nonlinear differential equations with boundary conditions that do not conserve mass. The assumption of MBC is incompatible with physiologically based pharmacokinetics because organs cannot be connected in a tandem manner due to the requirement of the open outlet.

The inverse Gaussian distribution is frequently adopted as a distribution function for parallel tube models.[4,5,9,10,14,25] From an empirical viewpoint, it is relevant if the model explains real data properly. However, for greatly spreading curves, the appropriateness of the shape needs to be verified because the influence of the improper boundary definitions of its generating function becomes apparent.

The dispersion model has been criticized for its inability to explain the tail part of the dilution curves after bolus input.[8–10] In this instance, the characteristic does not differ between DBC and MBC. However, it seems more reasonable to consider the temporal adsorption of substances to the surface of the vasculature as a possible reason for deviation from the model.[11] If such adsorption occurs, the dilution curve needs to be analyzed with the multicompartment dispersion model[7,23] even for vascular references.

Conclusion

MBC has theoretical deficiencies both at the entrance and the exit. Although analyses performed thus far with MBC are still relevant as approximations in most cases, the use of DBC is recommended to avoid theoretical confusion. Considering the recent progress in the development of numerical methods, the calculation of DBC is not a major problem. When the inverse Gaussian distribution is applied in pharmacokinetic considerations, it should be recognized that an open boundary is assumed at the inlet or the outlet.

References and Notes

1. Roberts, M. S.; Rowland, M. Hepatic Elimination – Dispersion Model. *J. Pharm. Sci.* **1985**, *74*, 585–587.
2. Roberts, M. S.; Rowland, M. A Dispersion Model of Hepatic Elimination. 1. Formulation of the Model and Bolus Considerations. *J. Pharmcokin. Biopharm.* **1986**, *14*, 227–260.
3. Forker, E. L.; Luxon, B. Hepatic Transport Kinetic and Plasma Disappearance Curves: Distributed Modeling Versus Conventional Approach. *Am. J. Physiol.* **1978**, *235*, E648–E660.
4. Bass, L.; Roberts, M. S.; Roginson, P. J. On the Relation between Extended Forms of the Sinusoidal Perfusion and of the Convection-Dispersion Models of Hepatic Elimination. *J. Theor. Biol.* **1987**, *126*, 457–482.
5. Roberts, M. S.; Rowland, M. Models of Hepatic Elimination: Comparison of Stochastic Models to Describe Residence Time Distributions and to Predict the Influence of Drug Distribution, Enzyme Heterogeneity, and Systemic Recycling on Hepatic Elimination. *J. Pharmacokin. Biopharm.* **1988**, *16*, 41–83.
6. Weiss, M. A Note on the Interpretation of Tracer Dispersion in the Liver. *J. Theor. Biol.* **1997**, *184*, 1–6.
7. Yano, Y.; Yamaoka, K.; Aoyama, Y.; Tanaka, H. Two-Compartment Dispersion Model for Analysis of Organ Perfusion System of Drugs by Fast Inverse Laplace Transform (FILT). *J. Pharmacokin. Biopharm.* **1989**, *17*, 179–202.
8. Weiss, M.; Stedtler, C.; Roberts, M. S. On the Validity of the Dispersion Model of Hepatic Drug Elimination when Intravascular Transit Time Densities are Long-tailed. *Bull. Math. Biol.* **1997**, *59*, 911–929.
9. Tirona, R. G.; Schwab, A. J.; Geng, W.; Pang, K. S. Hepatic Clearance Models, Comparison of the Dispersion and Goresky Models in Outflow Profiles from Multiple Indicator Dilution Rat Liver Studies. *Drug Metab. Dispos.* **1998**, *26*, 465–475.
10. Scwab, A. J.; Geng, W.; Pang, K. S. Application of the Dispersion Model for Description of the Outflow Dilution Profiles of Noneliminated Reference Indicators in Rat Liver Perfusion Studies. *J. Pharmacokin. Biopharm.* **1998**, *26*, 163–181.
11. Hisaka, A.; Nakamura, T.; Sugiyama, Y. Analysis of Nonlinear Hepatic Clearance of a Cyclopentapeptide, BQ-123, with the Multiple Indicator Dilution Method Using the Dispersion Model. *Pharm. Res.* **1999**, *16*, 103–109.
12. Nauman, E. B. Residence Time Distributions in Systems Governed by the Dispersion Equation. *Chem. Eng. Sci.* **1981**, *36*, 957–966.
13. Danckwerts, P. V. Continuous Flow Systems: Distribution of Residence Times. *Chem. Eng. Sci.* **1953**, *2*, 1–13.
14. Roberts, M. S.; Donaldson, J. D.; Jackett, D. Availability Predictions by Hepatic Elimination Models for Michaelis-Menten Kinetics. *J. Pharmacokin. Biopharm.* **1989**, *17*, 687–719.
15. Sheppard, C. W.; Savage, L. J. The Random Walk Problem in Relation to the Physiology of Circulatory Mixing. *Phys. Rev.* **1951**, *83*, 489–490.
16. Roberts, M. S.; Rowland, M. A Dispersion Model of Hepatic Elimination. 2. Steady-state Considerations – Influence of Hepatic Blood Flow, Binding within Blood, and Hepatocellular Enzyme Activity. *J. Pharmacokin. Biopharm.* **1993**, *14*, 261–288.

17. Perl, W.; Chinard, F. P. A Convection-Diffusion Model of Indicator Transport through an Organ. *Circ. Res*. **1968**, *22*, 273−298.
18. Pearson, J. R. A. A Note on the "Danckwerts" Boundary Conditions for Continuous Flow Reactors. *Chem. Eng. Sci.* **1959**, *10*, 281−284.
19. Novy, R. A.; Davis, H. T.; Scriven, L. E. Upstream and Downstream Boundary Conditions for Continuous-Flow Systems. *Chem. Eng. Sci.* **1990**, *45*, 1515−1524.
20. Piessens, R.; Huysmans, R. Algorithm 619: Automatic Numerical Inversion of the Laplace Transform, *ACM Trans. Math. Software* **1984**, *10*, 348−353.
21. Schalla, M.; Weiss, M. Pharmacokinetic curve fitting using numerical inverse laplace transformation. *Eur. J. Pharm. Sci*. **1999**, *7*, 305−309.
22. Poulain, C. A.; Finlayson, B. A.; Bassingthwaighte, J. B. Efficient Numerical Methods for Nonlinear-Facilitated Transport and Exchange in a Blood-Tissue Exchange Unit. *Ann. Biomed. Eng.* **1997**, *25*, 547−564.
23. Hisaka, A.; Sugiyama, Y. Analysis of Nonlinear and Nonsteady State Hepatic Extraction with the Dispersion Model Using the Finite Difference Method. *J. Pharmacokin. Biopharm*. **1998**, *26*, 495−519.
24. Fukumura, K.; Yamaoka, K.; Higashimori, M.; Nakagawa, T. Analysis program based on finite element method, MULTI(FEM), for evaluation of dose-dependent local disposition of drug in liver. *J. Pharm. Sci.* **1999**, *88*, 538−43.
25. Mellick, G. D.; Anissimov, Y. G.: Bracken, A. J.; Roberts, M. S. Metabolite Mean Transit Times in the Liver as Predicted by Various Models of Hepatic Elimination. *J. Pharmacokin. Biopharm*. **1997**, *25*, 477−505.
26. Weiss, M. On the Degree of Solute Mixing in Liver Models of Drug Elimination. *J. Pharmacokin. Biopharm*. **1997**, *25*, 363−375.

JS9803860